Proceedings of the 12th European Review Meeting on Severe Accidents Research (ERMSAR2026)

Universidad Carlos III de Madrid, Madrid, Spain

May 18-22, 2026

ERMSAR 2026 was organized under the frame of the SEAKNOT project. This project has received funding from the Euratom Research and Training Programme 2021-2023 under grant agreement No 101060327.

The content of the papers reflects only the authors' views and do not necessarily reflect those of the European Union or EURATOM. Neither the European Union nor EURATOM can be held responsible for them.

DOI: 10.5445/IR/1000196279

FOREWORD

The 12th edition of the ERMSAR (European Review Meeting on Severe Accident Research) Conference was held from 18 to 22 May 2026 in Madrid, hosted and locally organized by CIEMAT, two years after the 11th edition in Stockholm. ERMSAR 2026 was organized within the framework of the EURATOM SEAKNOT project and NUGENIA Technical Area 2 of the SNETP Association, in cooperation with the International Atomic Energy Agency and the OECD Nuclear Energy Agency.

The conference brought together 223 participants, including 35 students, from 27 countries. Scientific contributions originated from 84 institutions located in 26 countries, while 23% of the participants represented non-European Union institutions. The programme comprised 112 oral papers and 43 posters, making ERMSAR 2026 the largest edition in the historical series and confirming its role as a reference international forum fully devoted to severe accident research.

The technical programme was organized into eight thematic tracks:

No.	Technical topic	Papers	Posters
1	Analysis, management, and consequences of severe accidents for Gen I-III reactors	16	12
2	Containment behaviour, including hydrogen explosion risk	15	5
3	Ex-vessel corium interactions and coolability	17	6
4	In-vessel corium and debris coolability	15	5
5	Source-term issues	20	4
6	Severe accidents in Small Modular Reactors (SMRs)	16	4
7	Severe accidents in Generation IV concepts	7	5
8	Other applications, including fusion reactors, interim spent nuclear fuel storage and Accident Tolerant Fuels (ATFs)	6	4
ERMSAR 2026 total		**112**	**43**

The meeting combined parallel technical sessions with plenary lectures, expert panels and round-table discussions. It addressed severe accident phenomenology, hydrogen behaviour, corium management, source-term assessment, risk and uncertainty methodologies, simulation tools, and the safety of operating reactors, SMRs, Generation IV systems, advanced fuels, fusion applications and other nuclear installations.

As major conclusions from ERMSAR 2026, it is possible to highlight:

- Fundamental severe accident phenomenology and mitigation remain major research priorities, particularly for corium coolability, containment and hydrogen behaviour, and source-term assessment.
- SMRs and Generation IV systems require credible safety demonstrations, extensions of current code capabilities, and new experimental evidence for verification and validation.
- Severe accident assessments are becoming more integrated, linking accident progression and management with uncertainty analysis, radiological consequences and emergency response.
- International cooperation and the preservation and transfer of expertise remain essential; the participation of 35 students supported direct interaction between young researchers and senior experts.

These open-access proceedings, published by the KIT Library with an international Digital Object Identifier, provide a durable record of the scientific work presented at ERMSAR 2026. They complement the selected extended papers prepared for the Annals of Nuclear Energy Virtual Special Issue.

ERMSAR 2028 will take place in Bled, Slovenia, continuing more than two decades of scientific exchange and cooperation within the international severe accident community.

Editors: Fabrizio Gabrielli, Luis E. Herranz, and Sandro Paci

Celebrating Excellence in European Severe Accident Research Communication & Dissemination

The Opening Session of ERMSAR 2026 included the first recognition ever given to the contribution done over decades to Communication and Dissemination of European Severe Accident research, as one of the activities with visible and specific achievements. Among them it is worth highlighting:

- The Severe Accident Phenomenology course (SAP), which has become the international reference in severe accident education.
- The ERMSAR conference series, once born as a European Review Meeting and now turned into the worldwide topical conference on severe accident research.
- The distinctive Textbook on severe accident phenomenology and nuclear safety, a must-reading for all newcomers and professionals.
- The Severe Accident Summer Camp, for the first time came to light in 2025 with an excellent reception in the Community.

On behalf of the entire European Severe Accident Community, upon the approval of the NUGENIA/TA2 Coordination Team, Prof. Luis E. Herranz, NUGENIA/TA2 Leader at the time, delivered such a recognition to:

***Professor Sandro Paci of the University of Pisa**, for the continuous and relentless role played in these outstanding achievements through his relevant participation in EC projects and distinctive leadership of the Education and Training activities within the SNETP/NUGENIA Technical Area 2 (Severe Accidents).*

An outstanding ovation became the soundtrack of the event in the Auditorium of the Campus Puerta de Toledo of the Carlos III University.

Prof. Luis E. Herranz (left) awards Prof. Sandro Paci (right) on behalf of the SNETP/NUGENIA Technical Area 2

ORGANIZATION

Technical Program Committee

Luis E. Herranz	Centro de Investigaciones Energéticas, Medioambientales y Tecnológicas, CIEMAT, Spain
Fabrizio Gabrielli	Karlsruhe Institute of Technology, KIT, Germany
Sandro Paci	University of Pisa, Italy
Martina Adorni	Nuclear Energy Agency, France
Ahmed Bentaib	Autorité de sûreté nucléaire et de radioprotection, ASNR, France
Sevostian Bechta	Royal Institute of Technology, KTH, Sweden
Matthias Braun	Framatome GmbH, Germany
Stephan Brumm	European Commission's Joint Research Centre, Netherlands
Laure Carenini	Autorité de sûreté nucléaire et de radioprotection, ASNR, France
Martin Freitag	Becker Technologies, Germany
Pavlin Groudev	Institute for Nuclear Research and Nuclear Energy, Bulgaria
Sanjeev Gupta	Framatome GmbH, Germany
Thorsten Hollands	Gesellschaft für Anlagen- und Reaktorsicherheit, GRS, Germany
Guillermo Urzua Torres	Framatome GmbH, Germany
Didier Jacquemain	Nuclear Energy Agency, France
Christophe Journeau	Commissariat à l'énergie atomique et aux énergies alternatives, CEA, France
Teemu Kärkela	VTT, Finland
Stephan Kelm	Forschungszentrum Jülich, FZJ, Germany
Ivo Kljenak	Jozef Stefan Institute, IJS, Slovenia
Alexei Miassoedov	IAEA, Austria
Terttaliisa Lind	Paul Scherrer Institute, PSI, Switzerland
Pascal Piluso	Commissariat à l'énergie atomique et aux énergies alternatives, CEA, France
Federico Rocchi	Agenzia nazionale per le nuove tecnologie, l'energia e lo sviluppo economico sostenibile, ENEA. Italy
V. H. Sanchez Espinoza	Karlsruhe Institute of Technology, KIT, Germany
Walter Tromm	Karlsruhe Institute of Technology, KIT, Germany

Organizing committee

Luis E. Herranz	Centro de Investigaciones Energéticas, Medioambientales y Tecnológicas, CIEMAT, Spain
Mónica García	Centro de Investigaciones Energéticas, Medioambientales y Tecnológicas, CIEMAT, Spain
Joan Fontanet	Centro de Investigaciones Energéticas, Medioambientales y Tecnológicas, CIEMAT, Spain
Carlos Aguado	Centro de Investigaciones Energéticas, Medioambientales y Tecnológicas, CIEMAT, Spain

LIST OF THE PARTICIPANTS

Name	Institution	Country
Acharya, G.	KTH	Sweden
Adorni, M.	OECD-NEA	France
Aguado, C.	CIEMAT	Spain
Ahn, Kwang-Il	KAERI	Republic of Korea
Aleza Enciso, S.	CSN	Spain
Alsalman, S.	KFUPM	Saudi Arabia
Angelucci, M.	University of Pisa	Italy
Asatsuma, H.	University of Tokyo	Japan
Aubets, H.	KTH	Sweden
Bang, Kwang-Hyun	Tetras Co	Republic of Korea
Barrio, F.	CIEMAT	Spain
Basnet, S.	UEF	Finland
Batek, D.	UJV Rez, a.s.	Czech Republic
Bechta, S.	KTH	Sweden
Beck, S.	GRS	Germany
Bentaib, A.	OECD-NEA	France
Bocanegra Melian, R.	ENSO	Spain
Borondo, L.	IBERDROLA	Spain
Braun, M.	Framatome GmbH	Germany
Brumm, S.	EC, JRC	Netherlands
Busbach, R. A.	MVM Paks NPP LTD.	Hungary
Butterworth, M. J.	Gexcon	United Kingdom
Camy, R.	EDF	France
Capeková, S.	UJD SR	Slovakia
Cardon, C.	Framatome	France
Carenini, L.	ASNR	France
Cazado, M. E.	KIT	Germany
Chantereau, P.	NUVIA	France
Chen, E.	CNPE Co., Ltd	China
Cilia, E.	ENEA	Italy

Clark, G.	Amentum	United Kingdom
Collado Arévalo, A.	CSN	Spain
Darnowski, P.	WUT	Poland
Dastvareh, B.	CNL	Canada
De Malmazet, E.	EDF	France
Dibon, G.	TechnicAtome	France
Dieter, K.	Becker Techn.	Germany
Dittmer, S:	Ringhals AB, Vattenfall	Sweden
Dougall, A.	EDF	United Kingdom
Du, Y.	KTH	Sweden
Durouchoux, P.	TechnicAtome	France
Mathe, E.	TechnicAtome	France
Endo, Y.	NFD	Japan
Engström, B.	KTH	Sweden
Farkas, R.	HUN-REN	Hungary
Farmer, M.	ANL	United States
Fernandez-Cosials, K.	UPM	Spain
Fichot, F.	ASNR	France
Fontanet, J.	CIEMAT	Spain
Fowles, J.	Rolls-Royce	United Kingdom
Bouillon, F	Framatome	France
Fuketa, T.	NFD	Japan
Gabicagogeascoa, C.	UPM	Spain
García Martin, M.	CIEMAT	Spain
García-Herranz, A.	UPM	Spain
Gardner, L.	CNL	Canada
Giannetti, F.	University of Rome 'La Sapienza'	Italy
Giner Gonzalez, A.	Westinghouse	Spain
Glover, J.	ONR	United Kingdom
Gold, C.	Gexcon UK Ltd	United Kingdom
Gong, Y.	CNPE Co., Ltd	China
Gregoire, A.-C.	ASNR	France
Grippo, G.	University of Bologna	Italy

Guo, Z.	National University of Singapore	China
Guo, P.	CNPE Co., Ltd	Singapore
Gupta, S.	Framatome	Germany
Gyuricza, E.	Paks II. Ltd.	Hungary
Hage, M.	GRS	Germany
Hagiwara, R.	TEPCO	Japan
Ham, J.	KAERI	Republic of Korea
Han, Kum-Ho	FNC Technology	Republic of Korea
Hansson Concilio, R.	Forsmark	Sweden
Harta, T	MHI NSEngineearing	Japan
Hermann, J.	Becker Techn.	Germany
Hernández Avellaneda, A.	Empresarios	Spain
HERRANZ, L.E.	CIEMAT	Spain
Hollands, T.	GRS	Germany
Hudson, R.	EDF	United Kingdom
Hudson, D.	Rolls-Royce	United Kingdom
Ilunga Wa Ilunga, A.	BCIDE	Democratic Republic of Congo
Ilvonen, M.	VTT	Finland
Iorizzo, A.	EC, RTD	Belgium
Bittan, J.	EDF	France
Jimenez, G.	UPM	Spain
Jiménez Balbuena, Z. I.	KIT	Germany
Joâo, B.	ASNR	France
Eskhult, J.	Swedish Radiation Safety Authority	Sweden
Jonsson, M.	KTH	Sweden
Journeau, C.	CEA	France
Jubin, K.	SNU	Republic of Korea
Jung, J.	KAERI	Republic of Korea
Kaliatka, A.	LEI	Lithuania
Kang, J.	KAERI	Republic of Korea
Kärkelä, T.	VTT	Finland
Kikuchi, W.	NRA	Japan
Kim, B.	KEPCO E&C	Republic of Korea

Kim, H.	Sejong University	Republic of Korea
Kim, T.	Seoul National University	Republic of Korea
Kim, D.	Chosun University	Republic of Korea
Klauck, M.	FZJ	Germany
Klein-Heßling, W.	GRS	Germany
Kljenak, I.	JSI	Slovenia
Kobayashi, Y.	Waseda University	Japan
Kokalj, J.	JSI	Slovenia
Kolesnik, M.	KIT	Germany
Komrska, J.	CTU	Czech Republic
At Khen, K.	EDF	France
Krist, F.	Ruhr-Universität Bochum	Germany
Kwon, M.	Seoul National University	Republic of Korea
LEE, Y.	KENTECH	Republic of Korea
Lee, Y.	Sejong university	Republic of Korea
Lee, B.	KAERI	Republic of Korea
Li, N.	CNPE Co., Ltd	China
Li, X.	JAEA	Japan
li, x.	KTH	Sweden
Lin, T.	Studsvik Nuclear AB	Sweden
Lind, T.	PSI	Switzerland
Bernadou, L.	TechnicAtome	France
Lovasz, L.	GRS	Germany
Lu, C.	GRS	Germany
Luxat, D.	SNL	United States
M.-Tiborcz, L.	GRS	Germany
Malicki, M.	PSI	Switzerland
Mann, S.	EDF	United Kingdom
Principato, M.	University of Rome 'La Sapienza'	Italy
Mariraju, A.	Aalen University of Applied Sciences	Germany
Mariraju, P.	Friotherm	Germany
Marshall, C.	FNC Technology	United Kingdom
Marta, G.	University of Rome 'La Sapienza'	Italy

Martin Garcia, M.	Westinghouse	Spain
Martinez-Delcayrou, A.	EDF	France
Mascari, F.	ENEA	Italy
Mashiko, T.	University of Tokyo	Japan
Matějů, I.	Typ Agency s.r.o.	Czech Republic
Mathé, G.	TechnicAtome	France
Mazurok, O.	ES Group LLC	Czech Republic
McGill, G.	UK National Nuclear Laboratory	United Kingdom
McMinn, P.	Fauske and Associates	United States
Mehdi Zadeh, F.	Canadian Nuclear Safety Comission	Canada
Meredith, A.	Rolls-Royce	United Kingdom
Mészáros, B.	CVREZ	Czech Republic
Miassoedov, A.	IAEA	Austria
Michel, B.	ASNR	France
Mizokami, S.	TEPCO	Japan
Monod, R.	ASNR	France
Morreale, A.	CNL	Canada
Mourier, T.	CEA	France
Murat, O.	KIT	Germany
Mykhailenko, O.	ES Group LLC	Ukraine
Na, H.	Sejong University	Republic of Korea
Na, Y.	KAERI	Republic of Korea
Bakouta, N.	EDF	France
Nikolaiev, B.	Research Center REZ	Czech Republic
Nishimura, Y.	University of Tokyo	Japan
Paci, S.	University of Pisa	Italy
Pandazis, P.	GRS	Germany
Park, Hyun Sun	Seoul National University	Republic of Korea
Park, K.	KAERI	Republic of Korea
Parrado Rodriguez, I.	Westinghouse	Spain
Pashynskyi, V.	Westinghouse	Finland
Pérez Ferragut, M.	Energy Software SL	Spain
Petrosillo, G.	CEA	France

Piluso, P.	CEA	France
Prószyński, K.	CBRN	Poland
Quan, F.	CNPE Co., Ltd	China
Ramos Perez, A.	PSI	Switzerland
Reinecke, E.-A.	FZJ	Germany
Rémi, C.	CEA	France
Richter, N.	Ruhr-Universität Bochum	Germany
Ricketts, M.	Rolls-Royce	United Kingdom
Robledo Sanz, F.	CSN	Spain
Rocchi, F.	ENEA	Italy
Le Tellier, R.	CEA	France
Rydl, A.	INSET s.r.o.	Czech Republic
Salmaoui, M.	Bel V	Belgium
Sanchez, F.	CEA	France
Sánchez, M.	CSN	Spain
Sarr, J.P.A.	EDF	France
Schaefer, D.A.	KIT	Germany
Buhlmann, S.	Framatome	Germany
Renaudière, S.	CEA	France
Seiler, N.	CEA	France
Masashi, S.	NRA	Japan
Serrano, C.	IBERDROLA	Spain
Sevón, T.	VTT	Finland
Shimomura, K.	JAEA	Japan
Son, D.	KAERI	Republic of Korea
Song, H.	KHNP	Republic of Korea
Souvi, S. M. O.	ASNR	France
Špaček, J.	CEZ	Czech Republic
Stakhanova, A.	KIT	Germany
Steinbrück, M.	KIT	Germany
Stephan, S.	FZJ	Germany
Suzuki, Y.	The Institute ofApplied Energy	Japan
Tanarro Onrubia, A.	Westinghouse	Spain

Tarczal, L.	MVM Paks NPP LTD.	Hungary
Thorn, J.	Vattenfall AB	Sweden
Tichý, Š.	ÚJV Řež, a. s.	Czech Republic
Tinfena, G.	University of Rome 'La Sapienza'	Italy
Tóthné Laki, É.	MVM Paks NPP LTD.	Hungary
Turner, M.	CMS	United Kingdom
Vácha, P.	UJV Rez, a.s.	Czech Republic
Valinčius, M.	LEI	Lithuania
Vázquez-Rodríguez, C.	FZJ	Germany
Venzhego, G.	SSM	Sweden
Villarreal-Larrauri, A.	EDF	France
Vorobyov, Y.	ES Group LLC	Spain
Wang, W.	CNPE Co., Ltd	China
Wannop, G.	EDF	United Kingdom
Wawrzyńczak-Szaban, A.	NCBJ	Poland
White, T.	Rolls-Royce	United Kingdom
Wu, Y.	FZJ	Germany
Xiaoyang, G.-L.	KIT	Germany
Xu, R.	The University of Tokyo	Japan
Yamashita, T.	JAEA	Japan
Yip, L.	Rolls-Royce	United Kingdom
Yokoyama, R.	The University of Tokyo	Japan
Yoo, H.	Sejong university	Republic of Korea
Yu, Y.		China
Zambaux, J.-A.	ASNR	France
Zhao, D	National University of Singapore	Singapore
Zhao, L.	KTH	Sweden

12th CONFERENCE ON
SEVERE ACCIDENTS RESEARCH
May 18-22, 2026 - Madrid, Spain
ERMSAR 2026
12th CONFERENCE ON
SEVERE ACCIDENTS RESEA
May 18-22, 2026 - Madrid, Spain
ERMSAR 2026
Organized by
NETP
In cooperation with
IAEA
Sponsored by
enusa
KIT
NETP

The 12th European Review Meeting on Severe Accidents Research

May 18-22, 2026, Universidad Carlos III de Madrid, Madrid, Spain

Conference Program

MONDAY, MAY 18th, 2026

PLENARY SESSION: WELCOME AND OPENING

Chairs: S. Paci (University of Pisa), F. Gabrielli (KIT)

Welcoming Addresses

Félix Barrio, Head of the International Relations Division at CIEMAT

Santiago Aleza, Deputy Director for Engineering Nuclear Safety Directorate, CSN

Opening of the ERMSAR2026 Conference

L. E. Herranz (CIEMAT); Coordinator of the SEAKNOT Project

PLENARY SESSION: SINGULAR CAREERS IN THE SEVERE ACCIDENT RESEARCH

Chair: T. Lind (PSI)

30 years of materials science for nuclear safety. From unexpected findings to improved severe accident codes
M. Steinbruck (KIT)

Research, Insights, and Lessons Learned During a Career Focused on Ex-Vessel Severe Accident Behavior
M. Farmer (ANL)

Technical Session 3.1: Severe Accident Scenarios - Small Modular Reactors

Chairs: M. Garcia Martin (CIEMAT), F. Mascari (ENEA)

ID062	**Analysis of Postulated Severe Accidents in Generic Integral PWR Small Modular Reactors: Outcomes on Integral Codes' Modelling Capabilities from the Horizon Euratom SASPAM-SA Project** M. E. Cazado (KIT)	**Paper** **Presentation**
ID157	**Rolls-Royce SMR 3D Hydrogen Combustion Assessment Approach**	**Paper** **Presentation**

J. Fowles (Rolls-Royce SMR Limited), A. Meredith (Rolls-Royce SMR Limited), J Butterworth (Gexcon)

ID065 **Severe accident analysis of SASPAM-SA Design II LW-SMR dry containment using containmentFOAM** — Paper, Presentation
S. C. Vázquez-Rodríguez (FZJ)

ID131 **Analysis of LDR Lite Reactor's Resistance to Design Extension Conditions** — Paper, Presentation
A. Kaliatka (LEI)

Technical Session 2.1: In-vessel Corium and debris coolability

Chairs: L. Carénini (ASNR), M. Braun (Framatome)

ID143 **Reflooding of a damaged core in case of severe accident: synthesis of experimental results, modelling and consequences for the reactor scale** — Paper, Presentation
F. Fichot (ASNR)

ID013 **Simulation of the low Prandtl metallic layer of a corium pool** — Paper, Presentation
N. Seiler (CEA)

ID053 **Analysis of In-Vessel Retention in a VVER-1000 Reactor Design using AC2** — Paper, Presentation
P. Pandazis (GRS)

ID105 **Towards a High fidelity numerical simulation of In-vessel corium pool under severe accident scenarios** — Paper
A. Alasif (King Fahd University of Petroleum and Minerals)

Technical Session 1.1: Severe Accident Scenarios

Chairs: M. Angelucci (University of Pisa), D. Luxat (Sandia National Lab)

ID021 **Analysis of dose rates in the containment during the Fukushima accident** — Paper, Presentation
T. Sevón (VTT)

ID054 **Preliminary Analytical Justification of Long-Term Containment Cooling System with Steam Condensing Heat Exchanger for NPPs with VVER-1000 Reactors** — Paper, Presentation
Y. Vorobyov (Energy Safety Group LLC)

ID091 **ASTEC Modelling of the AP1000 and Cold-Leg Small-Break LOCA Simulations with Long-Term Cooling Cut-off** — Paper, Presentation
D. Zhao (National University of Singapore)

ID080 **Instrumentation survivability Assessment during a Severe Accident; Incorporating radiation monitoring in MELCOR to evaluate the impact on SAMGs** — Paper, Presentation
K. Fernandez-Cosials (Universidad Politécnica de Madrid)

Technical Session 6.1: Source term

Chairs: A.-C. Grégoire (ASNR), T. Kärkelä (VTT)

ID198 **Extension of Fission Product Transport Modeling in MELCOR** — Presentation
D. Luxat (SNL)

ID187 **Severe Accident Source Term Analyses for VVER-1000 Focused on Iodine Speciation: Sensitivity Studies with Derived Best-Practices Using ASTEC/SOPHAEROS** — Paper, Presentation
Štěpán Tichý (UJV)

ID184 **Evaluation of the effect of different transport path modelling on FP behaviour in AC2/ATHLET-CD** — Paper, Presentation
L. Tiborcz (GRS)

ID058 **Development of Evaluation Technology for Radiological Source Term in the Containment Using CINEMA Code During Severe Accidents** — Paper, Presentation
D. Son (KAERI)

Technical Session 5.1: Hydrogen risk and Containment behavior

Chairs: M. Malicki (PSI), K. Dieter (Becker Technologies GmbH)

ID096 **AMHYCO Project Outcomes and Lessons Learned** — Paper, Presentation
G. Jiménez (Universidad Politécnica de Madrid)

ID097 **CFD Analysis of the Containment Behavior during a TLAP Sequence in a Generic KWU PWR with containmentFOAM** — Paper, Presentation
S. Kelm (FZJ)

ID126 **ETSON-AMHYCO Benchmark Exercise on Flame Propagation in Representative Reactor Containment Atmosphere in Case Severe Accident Late Phases** — Paper, Presentation
A. Bentaib (NEA)

ID038 **Suppression Pool Modelling with the CESAR Thermal-Hydraulic Module of ASTEC** — Paper, Presentation
J.-A. Zambaux (ASNR)

Technical Session 4.1: Ex-vessel Corium and debris coolability

Chairs: S. Bechta (KTH), P. Piluso (CEA)

ID134 **Development of the SAFARI Code for Comprehensive Severe Accident Analysis in Nuclear Reactors: Steam Explosion Analysis Module** — Paper
K. Ju Bin (Seoul National University)

ID018 **Effect of Corium Properties Uncertainties on a PWR SBO Severe Accident** — Paper, Presentation
L. E. Herranz (CIEMAT)

ID011 **Consideration on Floating Crusts During Molten Core Concrete Interaction** — Paper, Presentation
C. Journeau (CEA)

Technical Session 3.2: Severe Accident Scenarios: Small Modular Reactors

Chairs: M.E. Cazado (KIT), S. Brumm (JRC)

ID180 **SASPAM-SA WP5: Source Term Estimation of Generic SMR Designs** — Paper, Presentation
T. Hollands (GRS)

ID048 **Gas phase iodine release from iPWR pool based on MELCOR and IMPAIR calculation** — Paper, Presentation
M. Malicki (PSI)

ID185 **MELCOR DEC-B Transient analysis in a generic integral Pressurized Water Reactor** — Paper, Presentation
F. Giannetti (University of Rome ‘La Sapianza’)

Technical Session 7.1: Spent Fuel Pools

Chairs: A. Stakhanova (KIT), S. Paci (University of Pisa)

ID111 **Recent Activities at Canadian Nuclear Laboratories on LOCA Progression in CANDU Spent Fuel Pools** — Paper, Presentation
B. Dastvareh (CNL)

ID073 **Validation of the Theoretical Approach for Modelling of the Hydride Morphology with Experimental Data for Zircaloy-4 obtained from SPIZWURZ bundle Test** — Paper, Presentation
M. Kolesnik (KIT)

TUESDAY, MAY 19th, 2026

Technical Session 1.2: Severe Accident Scenarios - Uncertainty and Sensitivity Analyses

Chairs: L. Tiborcz (GRS), F. Giannetti (University of Rome 'La Sapienza')

ID006	**Employment of relative time scale in the U&S analysis of the MBLOCA scenario in a generic KONVOI NPP** A. Stakhanova (KIT)	Paper Presentation
ID009	**Calibration of the Postulated Scenario of Fukushima-Daiichi Unit 1 through the Application of Uncertainty Quantification** L. E. Herranz (CIEMAT)	Paper Presentation
ID026	**Integrated Severe Accident Analysis for a VVER-1000: Accident Progression, Uncertainty Quantification, and Radiological Consequences Assessment** M. Angelucci (University of Pisa)	Paper Presentation

Technical Session 2.2: In-vessel Corium and debris coolability

Chairs: X. Gaus-Liu (KIT), F. Fichot (ASNR)

ID066	**Direct numerical evaluation of core equivalent conductivity: a comparative analysis of open rod and flat plate assemblies** R. Le Tellier (CEA)	Paper Presentation
ID151	**Experimental Investigation of Debris-Bed Formation for Optimizing Core-Catcher Design** T. Mashiko (University of Tokyo)	Paper Presentation
ID115	**A comparison of EATF and Zircalloy-4 cladding behaviour under severe accident conditions from 1600°C till 1970°C in steam/argon atmosphere** P. Piluso (CEA)	Paper Presentation

Technical Session 3.3: Severe Accident Scenarios - Small Modular Reactors

Chairs: F. Mascari (ENEA), M. Malicki (PSI)

ID117	**Investigation of Severe Accident Progression in Integral PWR SMRs** G. Acharya (KTH)	Paper Presentation
ID107	**Evaluation of Hypothetical Severe Accident Progression with ATF Cladding in Generic Integral PWR Designs in the Frame of the SASPAM-SA Project** M. E. Cazado (KIT)	Paper Presentation
ID164	**Comparative Analysis of Containment Behavior in a Generic iPWR Design under Postulated BDBA Conditions Using ASTEC v3.1.2 and MELCOR v2.2 codes** E. Cilia (ENEA)	Presentation
ID046	**SASPAM-SA: Assessment of existing experimental data in WP3** T. Lind (PSI)	Paper Presentation

Technical Session 3.4: Severe Accident Scenarios - Small Modular Reactors

Chairs: S. Brumm (JRC), F. Rocchi (ENEA)

ID148	**Assessment of Emergency Planning Zone for iPWRs within the Horizon Euratom SASPAM-SA Project**	Paper Presentation

M. Ilvonen (VTT)

ID191	**Performance Assessment of Passive Safety Systems and Identification of Conditions Leading to Design Extension Scenarios** E. Cilia (University of Bologna)	Paper Presentation
ID119	**Effect of Delayed Recovery of ECCS during Severe Accidents in Integral PWR SMRs** G. Acharya (KTH)	Paper Presentation
ID181	**Investigation of In Vessel Melt Retention by a stand-alone Lower Plenum ASTEC model of integral-PWR design#1 in the SASPAM-SA project** S. Brumm (JRC)	Paper Presentation

Technical Session 5.2: Hydrogen risk and Containment behavior

Chairs: S. Kelm (FZJ), G. Jiménez (Universidad Politécnica de Madrid)

ID092	**PARs for Hydrogen Measurement in Nuclear Containments in Severe Accidents** L. Gardner (CNL)	Paper Presentation
ID093	**Development of a database for PAR model validation based on THAI experiments and its application in the framework of the AMHYCO project** E.-A. Reinecke (FZJ)	Paper Presentation
ID069	**Fission product behavior and Source Term Impacts in Ex-Vessel Phase using THAI Test Data: the OECD/NEA THEMIS Project** K. Dieter (Becker Technologies GmbH)	Paper Presentation
ID078	**Development status of the flammability risk monitoring system in severe accidents** Y. Na (KAERI)	Paper Presentation

Technical Session 6.2: Source term

Chairs: T. Lind (PSI), T. Kärkelä (VTT)

ID195	**Developing a Concept for the Prediction of Long-Term Radionuclide Leaching from Corium in Post-Accident Scenarios** T. Jankowski (RUB)	Paper Presentation
ID031	**FissiOn pRoducts bEhavior under SeverE accident with New fuel concepts The OECD/NEA FORESEEN Project** A.-C. Grégoire (ASNR)	Paper Presentation
ID201	**Scaling Effects in Iodine Retention for Filtered Containment Venting: Experimental Findings and Safety Implications** S. Gupta (Framatome GmbH)	Paper Presentation
ID182	**A Deep Learning Surrogate Model for Rapid Prediction of Atmospheric Radioisotope Dispersion** O. Murat (KIT)	Paper Presentation

PLENARY SESSION: EXPECTATIONS FROM SA R&D (ROUND TABLE)

Chair: A. Bentaib (NEA)

Expectations from SA R&D. A Regulator Point of View — Presentation

M. Sánchez (CSN)

Notes to the Severe Accident Research Community Based on the Experience of the Fukushima Daiichi Accident — Presentation

T. Fuketa (NDF; NRA)

L. Borondo Arribas (Iberdrola) — Presentation

Severe Accident in NPP Research and Application — Presentation

A. Giner (Westinghouse)

Poster Session

ID015	**MAAP5 Analysis of High-Pressure Severe Accidents in a Small Modular Reactors** Byung Jo Kim (KEPCO E&C)	Abstract Poster
ID019	**Development and Evaluation of an Ablation-Resistant Basemat Concrete for Severe Accident Mitigation in LWRs** E. Chen (CNPE)	Abstract Poster
ID023	**Aerosol Removal Behavior by Containment Spray** B. Lee (KAERI)	Abstract
ID025	**Development of performance verification test methodology for passive radioactive material filtration system** K.H. Park (KAERI)	Abstract Poster
ID027	**Experimental analysis of molten salt aerosol in tank of confined volume: evaporation, airborne and deposition.** Jun-young Kang (KAERI)	Abstract
ID029	**Additional primary depressurized line (APDL) for NPP Units with VVER-440/V-213** O. Mykhailenko (ES Group LLC)	Abstract Poster
ID030	**SOCRATES EU project on liquid source term during a severe nuclear accident – WP 3: Boundary evolution conditions in the bulk liquid phase** A.-C. Grégoire (ASNR)	Abstract Poster
ID032	**Preliminary Experimental Study on the Elemental Iodine Adsorption Filter for a Passive Radioactive Material Filtration System** J. Jung (KAERI)	Abstract Poster
ID035	**Re-examination of the VULCANO VE-U9 Corium Spreading Test Using a Novel Pressure-Substitution Implicit Solver and Crust Fracture Model** R. Yokoyama (University of Tokyo)	Abstract
ID047	**SOCRATES: Leaching behaviour of radionuclides in severe accidents** T. Lind (PSI)	Abstract Poster
ID055	**Containment of Radioactive Water Large Volumes and Concept of a Long-Term Containment Cooling System with Steam Condensing Heat Exchanger for NPPs with VVER-1000 Reactors** O. Mazurok (ES Group LLC)	Abstract Poster

ID056	**Implementation and Analytical Justification of Long-Term Containment Cooling System with Additional Spray Circuit, Heat Exchangers, and Turbine-Driven Pumps for NPPs with VVER-440 Reactors** V. Ivanov (ES Group Europe s.r.o.)	Abstract Poster
ID063	**Analysis of Postulated Design Basis Accidents in General Integral PWR Small Modular Reactors: Outcomes on Integral Codes' Modelling Capabilities from the Horizon Euratom SASPAM-SA Project** F. Gabrielli (KIT)	Poster
ID070	**Three-Dimensional Numerical Prediction of Natural Convection in Corium Pools Using Advanced RANS Turbulence Models** Alsalman Shahad (KFPUM)	Abstract
ID077	**Recalescence Behavior of Molten Refractory Oxides during Fast Cooling by Aerodynamic Levitation** Y. Gong (CNPE)	Abstract Poster
ID085	**High-Temperature Interactions of Corium, Steel, and Boron Carbide: Experimental Simulation of Fukushima Daiichi Unit 3** B. Mészáros (Centrum Výzkumu Řež)	Abstract Poster
ID089	**Detection, Segmentation, and Reconstruction of Overlapping Bubbles in Pool Scrubbing Experiments at the SAAB Facility** Y. Wu (FZJ)	Abstract Poster
ID090	**Experimental Study of Molten Corium–Serpentinite Concrete Interaction Using Cold Crucible Induction Melting** B. Nikolaiev (Centrum Výzkumu Řež)	Abstract
ID094	**Effect of Pt Coating Methods on Hydrogen Recombination Activation for Passive Autocatalytic Recombiners** Dae-Hyun Kim (Chosun University)	Abstract Poster
ID095	**Study of prototypical corium at solid state containing fission products: crystallographic and microstructural analysis, impact on weathering and leaching mechanisms** T. Mourier (CEA)	Abstract Poster
ID098	**Computational Thermodynamic Study of the Ex-Vessel Molten Corium** Y. Du (KTH)	Abstract Poster
ID101	**Evaluation of accident tolerant fuel using MELCOR2.2 on representative accident sequences in typical Japanese PWR** M. Sekine (NRA)	Abstract Poster
ID106	**QUENCH-19: Bundle Experiment on ATF FeCrAl Claddings under Severe Accident Conditions** D. Schaefer (KIT)	Abstract Poster
ID116	**Experimental investigation of top-flooding of corium in the MERELAVA facility** S. Renaudière de Vaux (CEA)	Abstract Poster
ID118	**MELCOR Analysis of the Nordic BWR Pressure Suppression Pool During SBO Accident** G. Acharya (KTH)	Abstract Poster
ID122	**Assessing the Capabilities of MELCOR V2.2 against the QUENCH-19 Bundle Test with FeCrAl Cladding** M. E. Cazado (KIT)	Abstract Poster
ID124	**The PIANOFORTE CATAPULT Project: Comprehensive Assessment and Preparedness for Emerging Nuclear Technologies**	Abstract Poster

F. Gabrielli (KIT)

ID127	**ASSAS project: Creating Infrastructure and Training Database for Surrogate Models for a Severe Accident Simulator** A. Stakhanova (KIT)	Poster
ID141	**3D Estimation Diagrams of Units 1–3 at the Fukushima Daiichi Nuclear Power Station Updated in 2025** T. Yamashita (JAEA)	Abstract Poster
ID142	**SOCRATES Horizon Euratom project on liquid source term** T. Kärkelä (VTT)	Abstract Poster
ID158	**Comparison of Monte Carlo and Wilks' Methods for Uncertainty Quantification of a Severe Accident in a PWR** P. Darnowski (Warsaw University of Technology)	Abstract Poster
ID162	**Development of the SAFARI Code for Comprehensive Severe Accident Analysis in Nuclear Reactors: Framework and Methodology.** Hyun Sun Park (Seoul National University)	Abstract
ID166	**Impact of FeCrAl Cladding Material on the Progression of a Severe Accident in a Generic BWR Mark-I NPP: analysis of a SBO Scenario with the ASTEC Code** O. Murat (KIT)	Abstract Poster
ID167	**Study of the Impact of Polydisperse Droplet Distribution in the Spray System Using GOTHIC-3D** C. Gabicagogeascoa (Universidad Politécnica de Madrid)	Abstract Poster
ID169	**Investigating Severe Accident Scenarios for NNRs: Developing the GIROSCOPE Methodological Framework for EP&R** A. Wawrzyńczak-Szaban (NCBJ)	Abstract Poster
ID193	**3D Simulation of Debris Bed Quenching with Top-Flooding for FLOAT Experiments** J. Kokalj (JSI)	Abstract Poster
ID202	**MELCOR Severe Accident Analysis in LDR-lite: a District Heating Reactor** M. Principato (PSI)	Abstract Poster
ID204	**Analysis of IVMR through ERVC for i-SMR using CINEMA Computer Code** Rae-Joon Park (KEARI)	Abstract Poster
ID205	**Analysis of Spreading Distance in Spill Out Accident of Molten Salt Reactor** Rae-Joon Park (KAERI)	Abstract Poster
ID208	**Development of a Fission Product Mitigation System for Severe Accident Conditions in Small Modular Reactors** Jaehoon Jung (KAERI)	Abstract Poster

Technical Session 1.3: Severe Accident Scenarios - Uncertainty and Sensitivity Analyses

Chairs: M. Angelucci (University of Pisa), L. E. Herranz (CIEMAT)

ID156	**Uncertainty quantification and sensitivity analysis of phenomenological uncertainty in the MAAP model for a severe accident loss of secondary heat sink** C. Marshall (Frazer-Nash Consultancy)	Paper Presentation
ID188	**Severe Accident analysis in a generic iPWR and uncertainty quantification of the results** F. Mascari (ENEA)	Paper Presentation
ID155	**Stepwise Uncertainty Analysis Methodology: First insights** R. Bocanegra Melian (ENSO)	Paper Presentation

Technical Session 2.3: In-vessel Corium and debris coolability

Chairs: M. E. Cazado (KIT), M. Malicki (PSI)

ID147	**W-STORM sensitivity and uncertainty analysis for In Vessel Retention in integral Pressurized Water Reactors** M. Principato (PSI)	Paper Presentation
ID114	**Experimental Study on the Naturally Stratified Melt Pool Based on High-Temperature Chloride Salts and Mg–Al Alloys** F. Quan (China Nuclear Power Engineering Co., Ltd)	Paper Presentation
ID159	**Stand-alone analysis and evaluation of uncertainties of IVMR in SMR using AC2 code** M. Valincius (LEI)	Paper Presentation

Technical Session 4.2: Ex-vessel Corium and debris coolability

Chairs: F. Giannetti (University of Rome 'La Sapienza'), C. Journeau (CEA)

ID022	**Geometrical prerequisites for ex-vessel recriticality in flooded cavity containments** B. Engström (KTH)	Paper Presentation
ID153	**Performance of innovative sacrificial materials for PWR retrofitting - a reactor case study** P. Vacha (UJV)	Paper Presentation
ID136	**Development of the SAFARI Code for Comprehensive Severe Accident Analysis in Nuclear Reactors: Molten Corium-Concrete Interaction Analysis Module** J. Sung Choi (Seoul National University)	Paper Presentation

WEDNESDAY, MAY 20th, 2026

PLENARY SESSION: R&D INTERNATIONAL FRAMEWORKS: NEW PROJECT PLATFORMS AND DATABASES FOR SA (ROUND TABLE)

Chair: F. Rocchi (ENEA)

Euratom Research activities on Severe Accidents

A. Iorizzo (European Commission)

Recent IAEA Activities Related to Severe Accidents

A. Miassoedov (International Atomic Energy Agency)

Enabling Nuclear Safety Research: NEA Frameworks and Databases

M. Adorni (OECD Nuclear Energy Agency)

Technical Session 2.4: In-vessel Corium and debris coolability

Chairs: N. Seiler (CEA), A. Miassoedov (IAEA)

ID067	**A path forward to improve corium thermodynamic assessment by using surface tension data: results for the U-O binary system** R. Le Tellier (CEA)	Paper Presentation
ID109	**Estimation of the cooling rate of U-Zr-Fe-Cr-O sample which underwent melting** Y. Endo (Nippon Nuclear Fuel Development co., Ltd.)	Paper Presentation
ID059	**Critical Heat Flux in Pool boiling configuration for In-Vessel Melt Retention: literature review and recents experiments in THS-15 facility** K. At Khen (EDF)	Paper Presentation
ID145	**BWR RPV Lower Head Penetration Failure Caused by Eutectic Reactions with Zr-Rich Simulated Metal: ELSA-3 Test** K. Shimomura (JAEA)	Paper Presentation
ID102	**Investigation on In-Vessel Phase of BDB-LOCA of Supercritical Water-cooled Fast Reactor** Y. Kobayashi (Waseda University)	Paper Presentation

Technical Session 1.4: Severe Accident Scenarios

Chairs: L. Carénini (ASNR), M. Braun (Framatome)

ID037	**Integral Phenomena Identification and Ranking Table on Severe Accidents: Methodology and Major Outcomes** L. E. Herranz (CIEMAT)	Paper Presentation
ID138	**More than two decades of activities on Severe Accident Management Guidelines (SAMG) in Tecnatom and Westinghouse** A. Tanarro Onrubia (Westinghouse)	Paper Presentation
ID150	**Simulating the asymmetrical behavior of TMI-2 accident with AC2/ATHLET-CD** L. Lovasz (GRS)	Paper Presentation
ID007	**ASSAS Simulator for Severe Accident analysis for educational purposes** M. Martin Garcia (Westinghouse)	Paper Presentation

Technical Session 4.3: Ex-vessel Corium and debris coolability

Chairs: S. Bechta (KTH), C. Journeau (CEA)

ID108	**Merging NUCLEA and Mephista databases: Over three decades of building a European Nuclear Thermodynamic Database for severe accident phenomenology.** B. Michel (ASNR)	Paper Presentation
ID057	**Simulation of Melt Debris Spreading Behavior in a Core Catcher Using THERMOS** W. Kikuchi (NRA)	Paper Presentation
ID076	**Experimental Study on the Interaction Between Molten Corium Simulant and Sacrificial Materials** N. Li (China Nuclear Power Engineering Co., Ltd)	Paper Presentation
ID083	**Advancing the Jet Breakup Length Model for Fuel-Coolant Interaction in Light Water Reactors** Kwang-Hyun Bang (Tetras Co.)	Paper Presentation
ID087	**Numerical Simulation of Melt Dry Spreading in CoSMUS Experiments** L. Zhao (KTH)	Paper Presentation

Technical Session 5.3: Hydrogen risk and Containment behavior

Chairs: G. Jiménez (Universidad Politécnica de Madrid), E.-A. Reinecke (FZJ)

ID002	**Influence of Containment Pressurization Rates on the Assessment of Severe Accident Risk** Kwang-Il Ahn (KAERI)	Paper Presentation
ID045	**Benchmark on Counter Current Flow in Multi-Compartment Containment using THAI Test Data** J. Hermann (Becker Technologies GmbH)	Paper Presentation
ID068	**Systematic analysis of the influence of the spray actuation on the hydrogen risk using a 3D GOTHIC PWR-W model** C. Vázquez-Rodríguez (FZJ)	Paper Presentation
ID003	**Assessment and Applicability of a Stand-Alone Containment Methodology for Hydrogen and CO Risk Evaluation in Severe Accidents** J. Fontanet (CIEMAT)	Paper Presentation

Technical Session 6.3: Source term

Chairs: A.-C. Grégoire (ASNR)

ID129	**Investigation on Effect of Aerosol Generation Rates on Deposition on Obstacle Structure Surface under Venting Decontamination in the Decommissioning of Fukushima Daiichi Nuclear Power Plant after Severe Accident** R. Xu (University of Tokyo)	Paper Presentation
ID039	**Chemistry of Chromium in the Reactor Coolant System in severe accident conditions from an ATF type core** J. Bouchain (ASNR)	Paper Presentation

ID043	**Interfacial gas transfer in gas-liquid flows: a comparative study of advanced experimental and computational techniques** A. Ramos-Perez (PSI)	Paper Presentation
ID207	**Impact of ASTEC's Advanced Modeling in Gas and Adsorbed Phases Chemistry on the Source Term** S. M. O. Souvi (ASNR)	Paper Presentation

Technical Session 4.4: Ex-vessel Corium and debris coolability

Chairs: P. Piluso (CEA), X. Gaus-Liu (KIT)

ID049	**Further development of a machine learning model for predicting the long-term coolability of debris beds** N. Richter (RUB)	Paper Presentation
ID121	**AI-Driven Estimation of Corium Thermophysical Properties for Ex-Vessel Corium Stabilization Simulations** R. Monod (ASNR)	Paper Presentation
ID130	**Investigation on the Melt Transport Behavior in the Drywell of Fukushima Daiichi Nuclear Power Plant Unit-1 with MPS Method** X. Li (JAEA)	Paper Presentation
ID139	**An advanced graph neural network application to highly viscous newtonian fluid flow towards the rapid corium spreading simulation** H. Asatsuma (University of Tokyo)	Paper Presentation

Technical Session 1.5: Severe Accident Scenarios - Integral Codes and Research Frameworks

Chairs: J. Fontanet (CIEMAT), L. Lovasz (GRS)

ID196	**A Modernized Architecture for MELCOR** D. Luxat (SNL)	Presentation
ID189	**CNL Severe Accident Analysis Research to Support Safe Deployment of Small modular and Advanced Reactors** A. Morreale (CNL)	Paper Presentation
ID192	**Development of the SAFARI Code for Comprehensive Severe Accident Analysis in Nuclear Reactors: Containment Thermal-Hydraulics Analysis Module** K.H. Han (FNC Technology)	Presentation

Technical Session 6.4: Source term

Chairs: A. Bentaib (NEA), I. Kljenak (JSI)

ID001	**Assessment of pool scrubbing predictive capabilities: benchmarking SPARC90 against an ad-hoc database** G. Tinfena (University of Pisa)	Paper Presentation
ID005	**Pool Scrubbing in Water Cooled SMRs: Scenarios, Peculiarities and Challenges** L.E. Herranz (CIEMAT)	Paper Presentation
ID075	**MAAP6 Mechanistic Pool Scrubbing Model** P. McMinn (Westinghouse)	Paper Presentation

ID125	**COCOSYS simulation of CsI decomposition under irradiation and the formation of organic iodide in the containment** C. Lu (GRS)	**Paper** **Presentation**

Technical Session 5.4: Hydrogen risk and Containment behavior

Chairs: S. Gupta (Framatome), K. Dieter (Becker Technologies GmbH)

ID128	**Ex-Vessel Severe Accident 3D Simulation with GOTHIC 8.3(QA): Methodology and Application to a PWR-KWU Containment** G. Jiménez (Universidad Politécnica de Madrid)	**Paper** **Presentation**
ID146	**Implementation of a Safety-Related Air-Cooling System in a PWR-W Dry Containment using GOTHIC 3D** A. García-Herranz (Universidad Politécnica de Madrid)	**Paper** **Presentation**
ID173	**Passive Autocatalytic Recombination of Hydrogen – An Application in the ITER Fusion Reactor** M. Braun (Framatome GmbH)	**Paper** **Presentation**

THURSDAY, MAY 21st, 2026

Technical Session 6.5: Source term

Chairs: S. Kelm (FZJ), I. Kljenak (JSI)

ID008	**Factors influencing radiation-induced Corium matrix dissolution** H. Aubets (KTH)	Paper Presentation
ID170	**Optimising Electrostatic Precipitators for Severe Accident Scenarios: Impact of Key Operational Parameters** S. Basnet (University of Eastern Finland)	Paper Presentation
ID100	**Overview of Fission Product Behavior Modeling in the SIRIUS Code** J. Ham (KAERI)	Paper Presentation
ID079	**Advanced Modeling of Fission Product Release from Irradiated Fuel during Severe Accident Scenarios** G. Petrosillo (CEA)	Paper Presentation

Technical Session 7.2: Generation IV Systems - Sodium Fast Reactors

Chairs: N. Seiler (CEA), A. Miassoedov (IAEA)

ID197	**Validation of Species Transport Modeling in Liquid Sodium Systems: Extension of SPARC-90/University of Wisconsin-Madison Benchmarks to Modernized MELCOR** D. Luxat (SNL)	Presentation
ID140	**Experimental validation of the core catcher safety measures in Gen IV ESFR conceptual design against long-term ablation** Gaus-Liu Xiaoyang (KIT)	Paper Presentation
ID010	**Investigation of film boiling in liquid sodium: qualification of the SERUA experimental program** R. Clavier (CEA)	Paper Presentation
ID034	**Benchmarking of Advanced GPU-Accelerated Discrete Element Method and Elastoplastic Constitutive Granular Flow Models for Large-Scale Debris Bed Formation in Severe Accidents of Sodium Fast Reactors** R. Yokoyama (University of Tokyo)	Paper Presentation

Technical Session 7.3: Advanced Technological Fuels and Materials

Chairs: M. E. Cazado (KIT), L. Tiborcz (GRS)

ID040	**Cr-coated claddings modelling in the severe accident code ASTEC** L. Carénini (ASNR)	Paper Presentation
ID064	**Development and Validation of the FeCrAl oxidation model of the ASTEC integral code based on the QUENCH Experimental Results** Z. I. Jiménez Balbuena (KIT)	Paper Presentation
ID052	**The integral air ingress CODEX-ATF-AIT experiment** R. Farkas (HUN-REN Centre for Energy Research)	Paper
ID071	**Comparative Analyses of Creep Models for Predicting Behavior of RPV Steel under Extreme High Temperatures** X. Li (KTH)	Paper Presentation

Technical Session 4.5: Ex-vessel Corium and debris coolability

Chairs: P. Piluso (CEA), T. Hollands (GRS)

ID161 **Development of the SAFARI Code for Comprehensive Severe Accident Analysis in Nuclear Reactors: Corium–Coolant Interaction Analysis Module** — Paper, Presentation
M. Kwon (Seoul National University)

ID200 **Evaluation of concrete ablation by a hot heat-generating solid** — Paper, Presentation
A. Villarreal-Larrauri (EDF)

Technical Session 7.4: Generation IV Systems

Chairs: A. Stakhanova (KIT), S. Gupta (Framatome)

ID154 **High temperature oxidation behavior of silicon carbide fuel matrix during Beyond Design Basis Accident in Gen IV reactors** — Paper, Presentation
Y. Nishimura (University of Tokyo)

ID199 **MSR Modeling Capabilities and Development with the MELCOR Reactor Simulation** — Presentation
D. Luxat (SNL)

ID149 **Computational verification of the functionality of the cooling system of the ALLEGRO reactor core catcher** — Paper, Presentation
J. Komrska (UJV)

CLOSING PLENARY SESSION

Chairs: S. Paci (University of Pisa), F. Gabrielli (KIT)

ERMSAR2026 An Overview in Numbers

F. Gabrielli (KIT)

Closing and Final Remarks

L.E. Herranz (CIEMAT), Coordinator of the SEAKNOT project

Introduction to ERMSAR2028

I. Kljenak (JSI)

The 12th European Review Meeting on Severe Accidents Research

May 18-22, 2026, Universidad Carlos III de Madrid, Madrid, Spain

PLENARY SESSION: SINGULAR CAREERS IN THE SEVERE ACCIDENT RESEARCH

Chair: T. Lind (PSI)

30 years of materials science for nuclear safety. From unexpected findings to improved severe accident codes

M. Steinbrück (KIT)

Research, Insights, and Lessons Learned During a Career Focused on Ex-Vessel Severe Accident Behavior

M. Farmer (ANL)

30 years materials science for nuclear safety

From unexpected findings to improved severe accident codes

Martin Steinbrück, Mirco Große, Juri Stuckert

12th Confenece on Severe Accident Research (ERMSAR 2026)

May 18-22, 2026 – Madrid, Spain

IAM-AWP

Background

- Intensive research into severe accidents worldwide and at Karlsruhe following the TMI-2 accident (1979)
- At KfK/FZK, large-scale experiments on many in-vessel and ex-vessel phenomena
- QUENCH program initiated by Peter Hofmann after completion of the CORA program
  - Determination of the hydrogen source term during reflood of an overheated reactor core
- Intensive research on ATF worldwide and at Karlsruhe after Fukushima Daiichi (2011)
  - KIT presentation at ERMSAR 2024
- My carrier at Karlsruhe started with the commissioning of the QUENCH facility

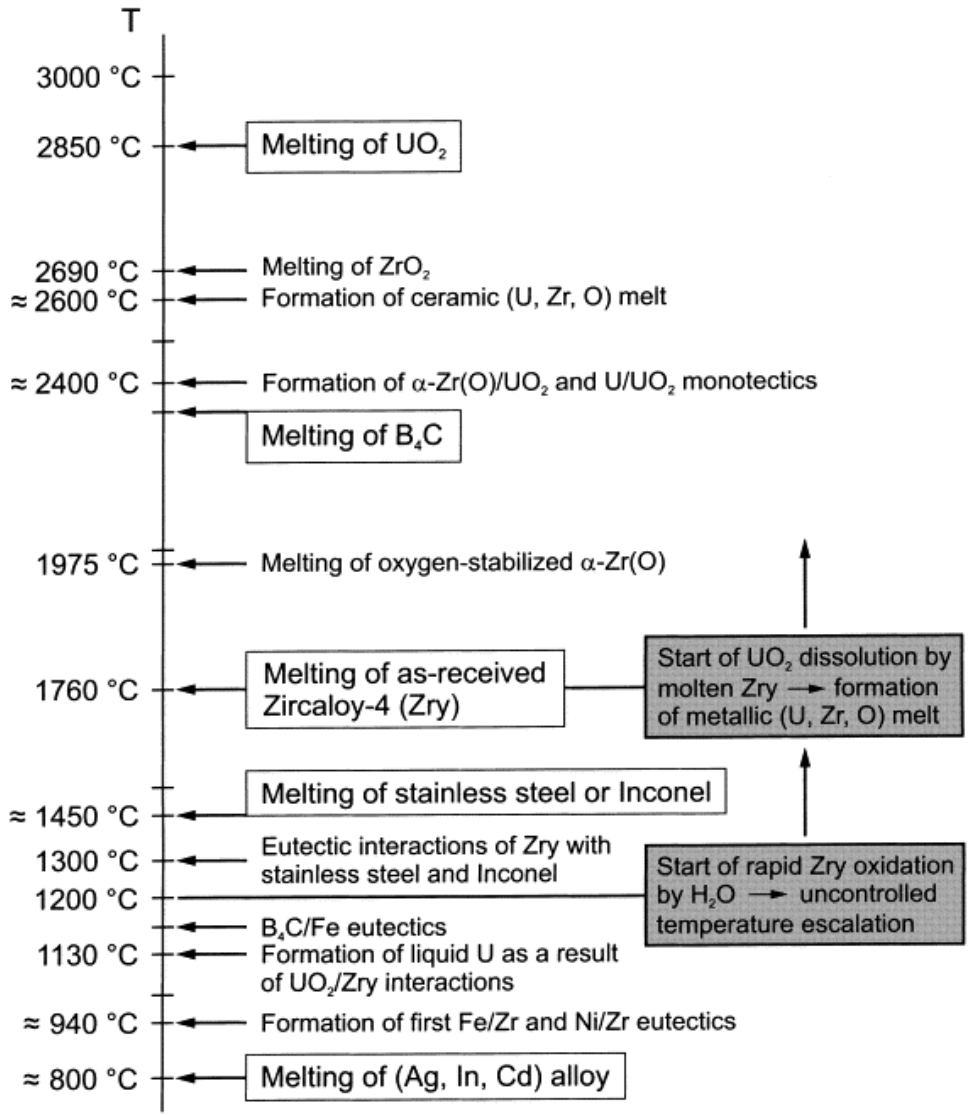

P. Hofmann, JNM 270 (1999) 194

Content

1. Background
2. The “quench effect” on hydrogen source term
3. The effect of nitrogen on cladding oxidation and degradation
4. The effect of B_4C-SS eutectic interactions on accident progression
5. Takeaways

The “quench effect” on hydrogen source term

In search of the "quench effect"

- Water injection is the primary AMM for cooling an uncovered core during a severe accident scenario
- Analysis of the TMI-2 accident as well as subsequent integral in-pile and out-of-pile experiments (PBF, LOFT, PHEBUS, CORA) has shown that water injection can result in temperature runaway, which is connected with intense hydrogen release
- The QUENCH program was designed to understand this phenomenon and to provide quantitative data on the hydrogen source term
- Initially we looked for a single “quench effect”

Sepold et al., NED204 (2001) 205–220:

However, before the water succeeds in cooling the fuel elements, water injection can trigger a renewed enhanced oxidation of the Zircaloy cladding and, at the same time, cause a rapid increase in temperature and hydrogen generation.
This phenomenon was demonstrated by analyses of the TMI-2 accident and in results of out-of-pile (CORA) and in-pile LWR bundle experiments (LOFT, Phebus). It was explained as being due to the generation of new metal surfaces by cracking and fragmentation of the oxygen-embrittled cladding tubes during flooding, and to enhanced exothermal oxidation of the newly formed metal surfaces *(Hofmann et al., Report FZKA 5846, 1997)*.

Single-rod QUENCH tests – Main results

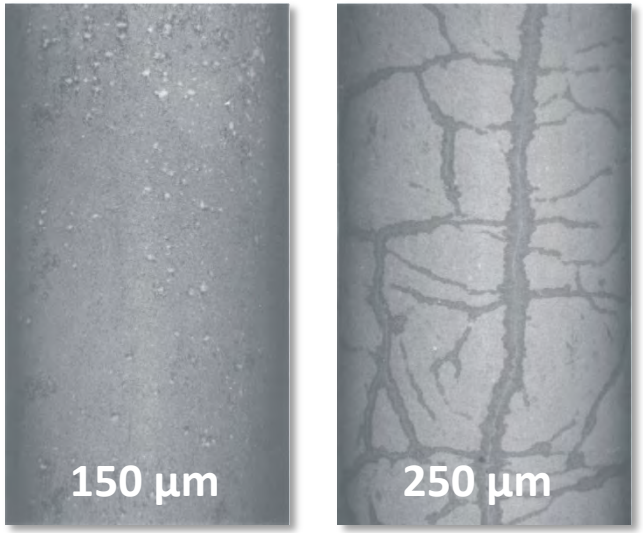

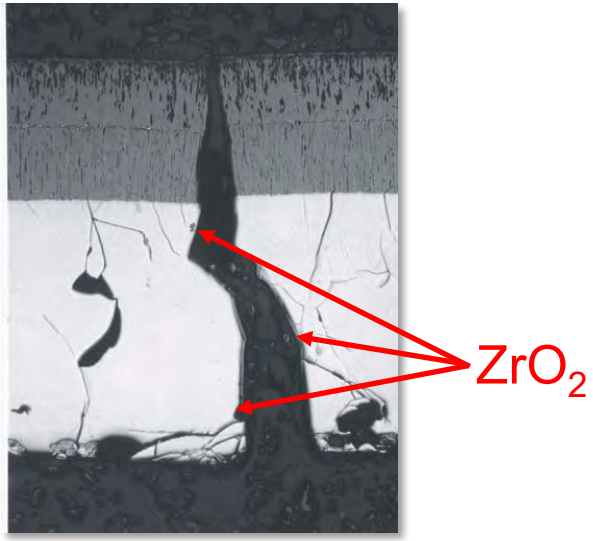

- Through-wall crack for pre-oxidation >200 µm with a density of 0.5 mm/mm^2
- Oxidation of crack surfaces connected with hydrogen generation and partly absorption by the metal

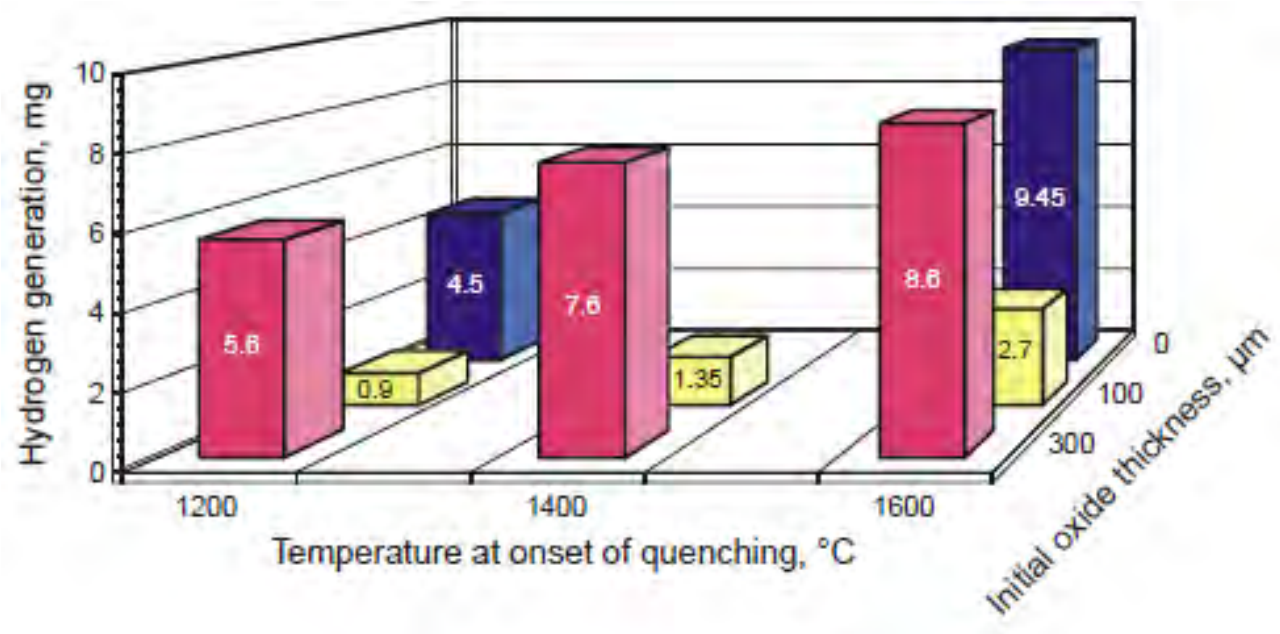

Hydrogen generation vs. oxide thickness

Crack formation in QUENCH-01 bundle test

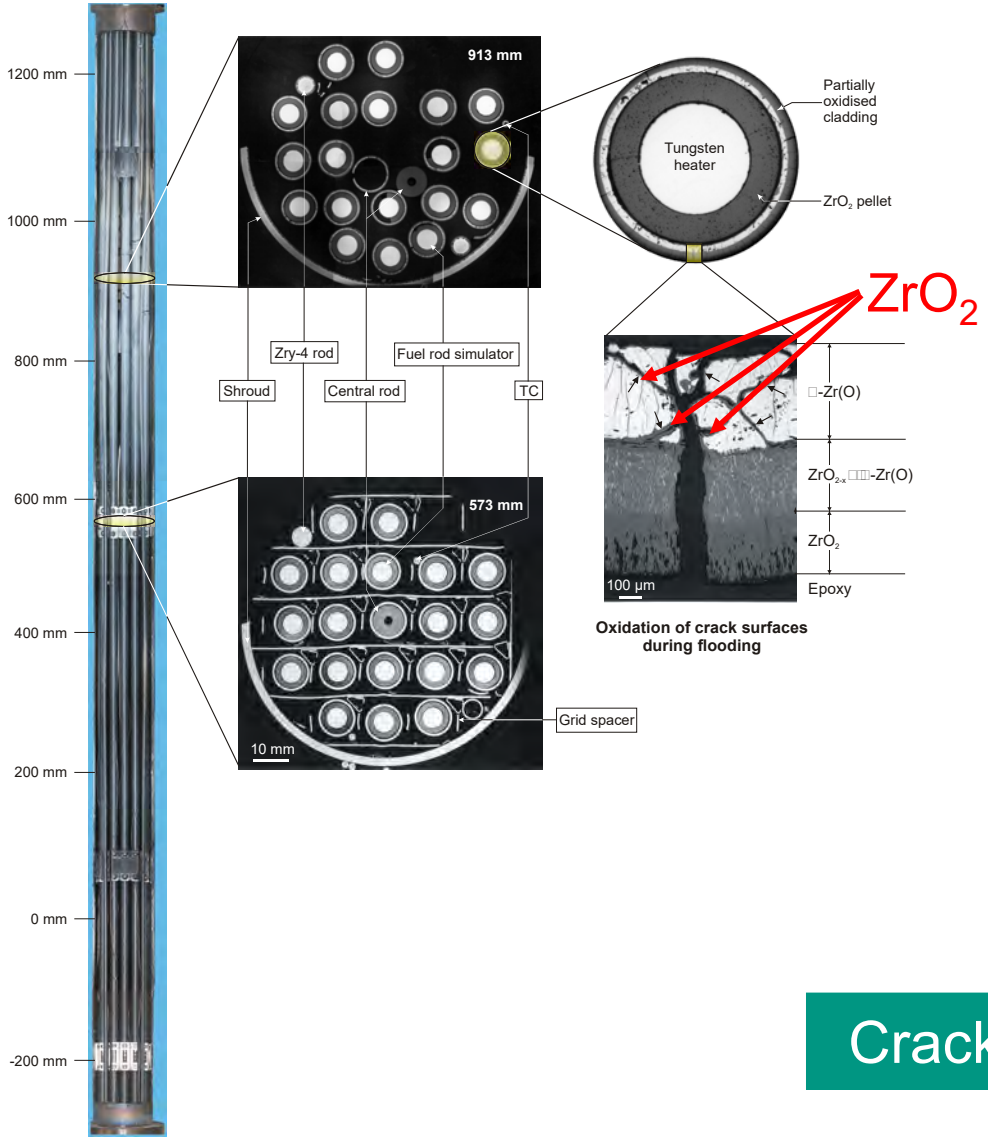

- Estimation of hydrogen production by crack oxidation gives only ca. 1-2 g for the whole bundle
- This could not explain temperature runaway during reflood

However:

- *Solution enthalpy of 1 g H_2 in 1 kg Zr increases temperature by 200 K*

Crack formation and oxidation are only minor effects

Successful reflood depends on many parameters

Reflood
Water injection → steam production

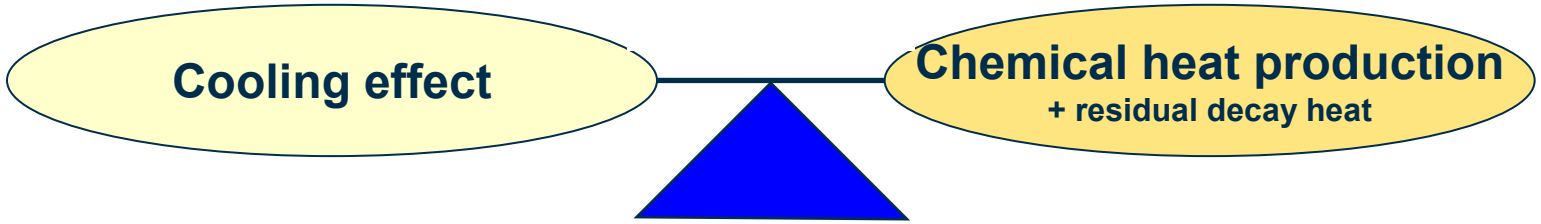

$Q_c \sim h\,(T_{Zr} - T_c)$

$Q_R \sim \Delta_R H\,(K(T)/t)^{0.5}$

$Zr + 2\,H_2O \rightarrow ZrO_2 + 2\,H_2 + 580\ kJ$

Influenced by

- **ΔT**
- Flooding rate
- Cooling medium
- Pressure
- Hydraulic diameter
- …

- **Oxidation kinetics**
- Temperature (Arrhenius type)
- Degree of pre-oxidation
- Surface available for oxidation
- Material composition
- **Steam availability**

Summary of QUENCH bundle tests

- Depending on the energy balance after reflood initiation, there will be a cooldown or temperature escalation
- Successful reflood if
  - Less chemical (and residual decay) energy is produced than can be eliminated by cooling
  - Cooling water rate is > 1 g/s rod
  - No oxidizable melt in contact with steam
- Ultimately, we discovered that a variety of factors must be considered
- QUENCH experiments are used for validation of many SA codes

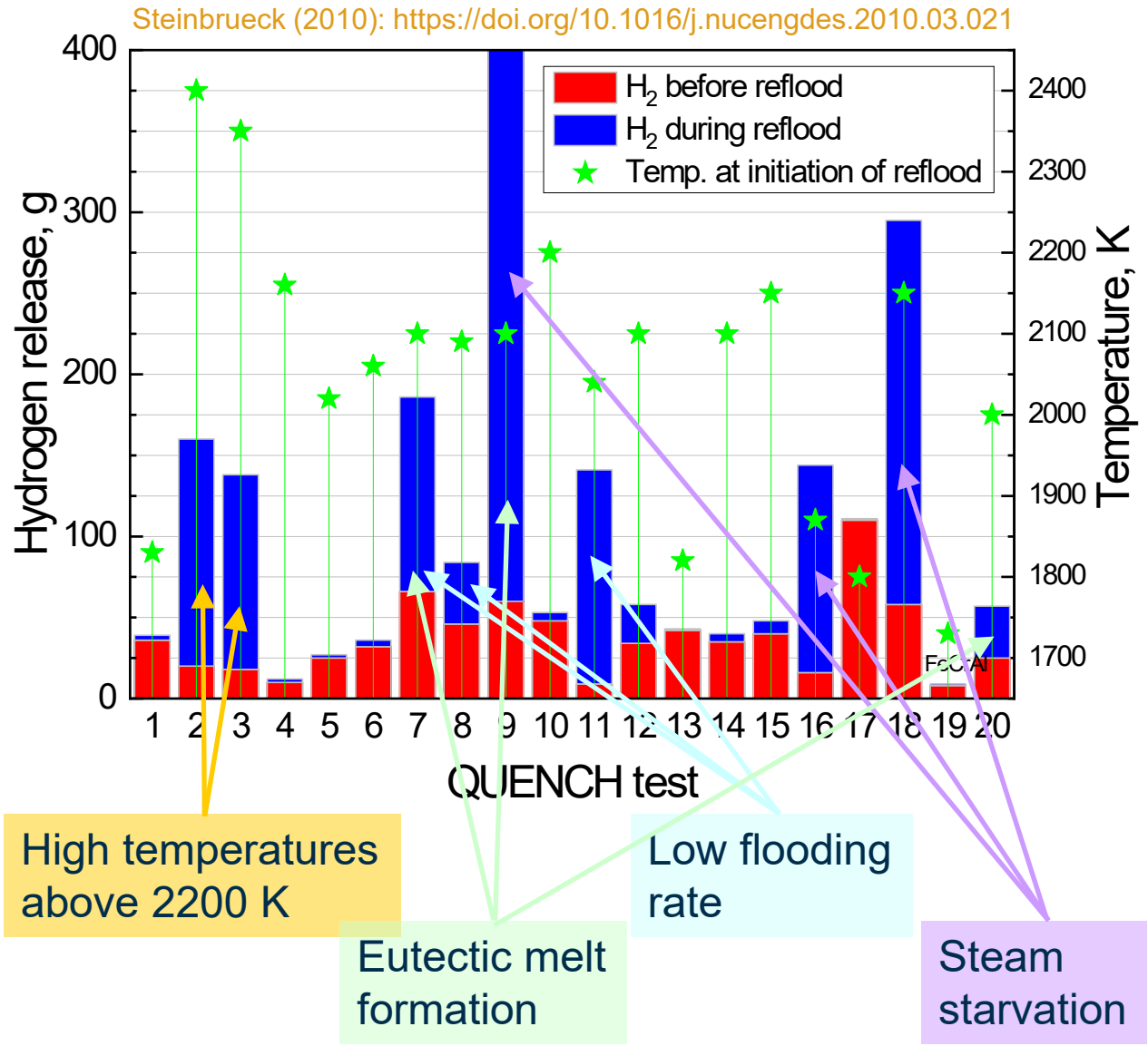

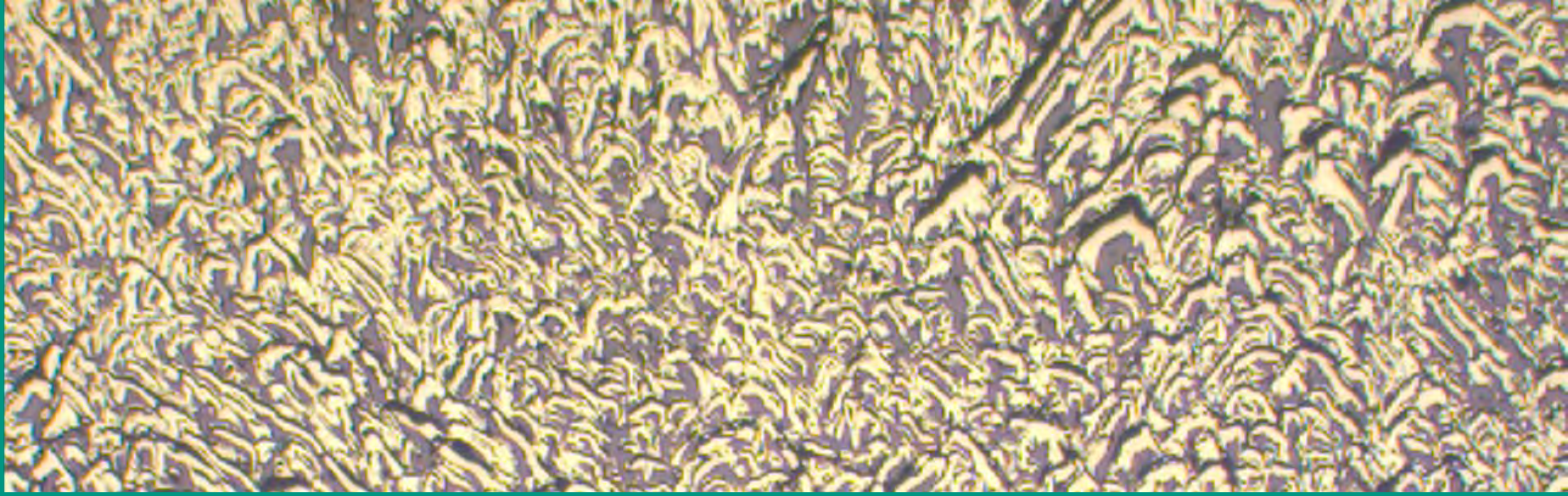

The effect of nitrogen on cladding oxidation and degradation

Nitrogen in LWRs

- The “inert” gas nitrogen is used to inertize BWR containments and in ECCS pressurizers
- Air contains nitrogen and ingress may occur into reactor core, spent fuel pond, or transportation cask
- Typically, nitrogen comes into contact with the cladding after steam oxidation, mixing with the steam

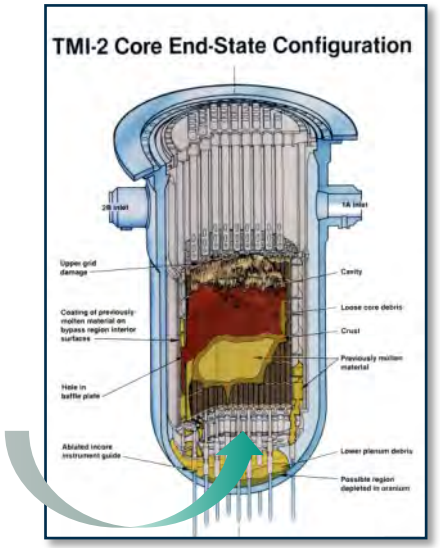

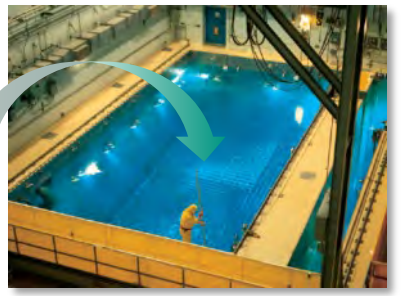

What are the consequences on hydrogen source term and cladding degradation?

The effect of nitrogen on the oxidation and degradation of Zr alloys

6 hours at 800°C

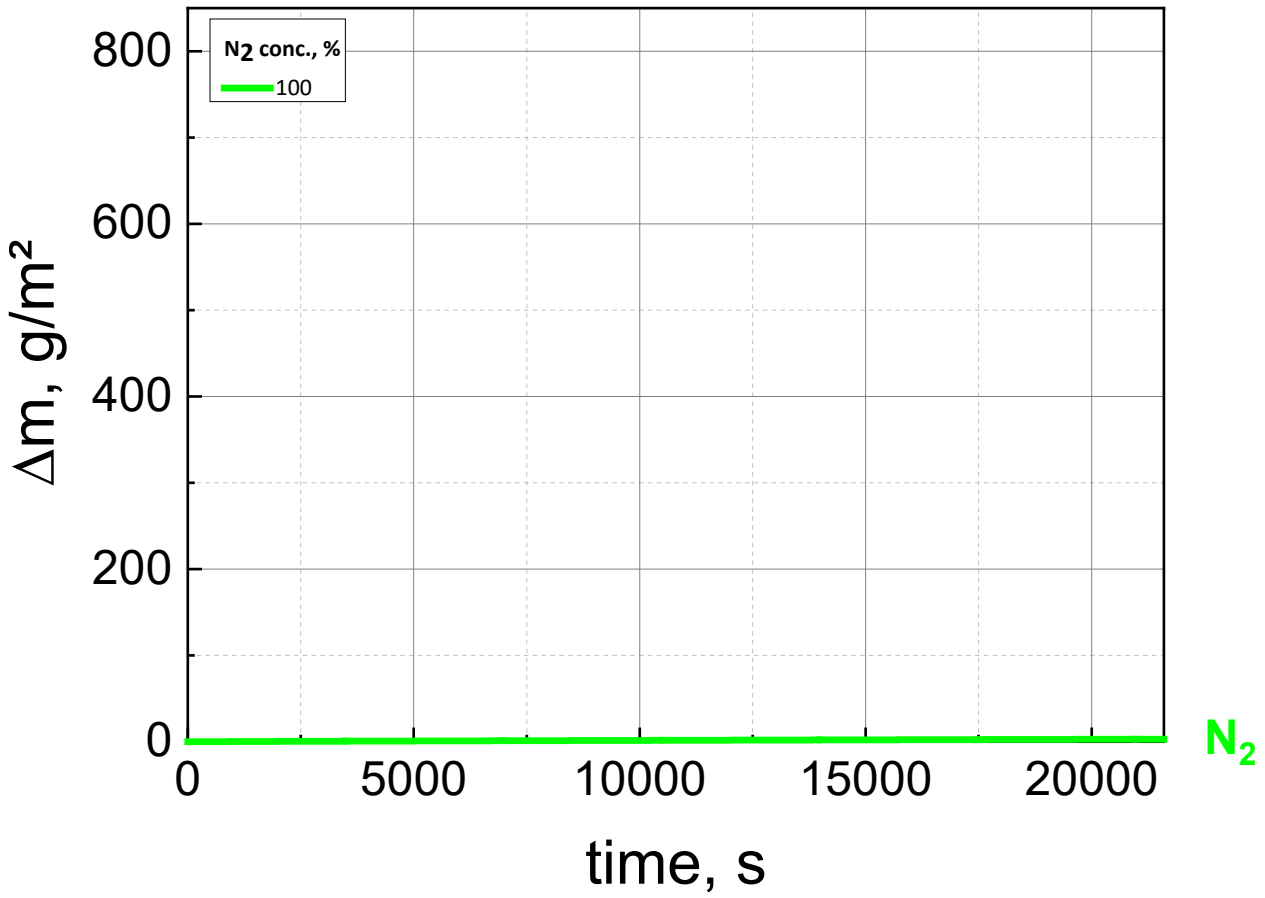

The effect of nitrogen on the oxidation and degradation of Zr alloys

6 hours at 800°C

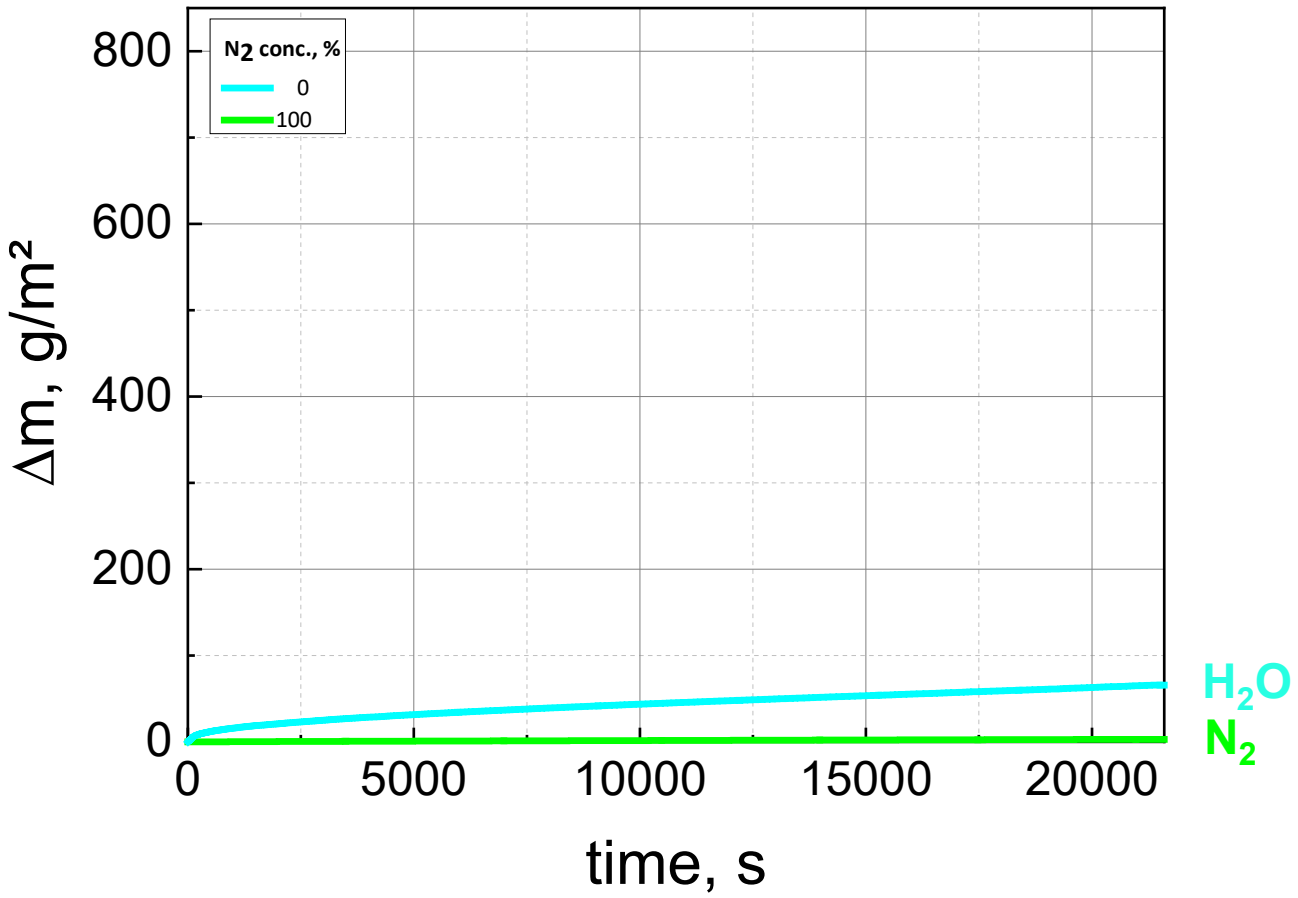

The effect of nitrogen on the oxidation and degradation of Zr alloys

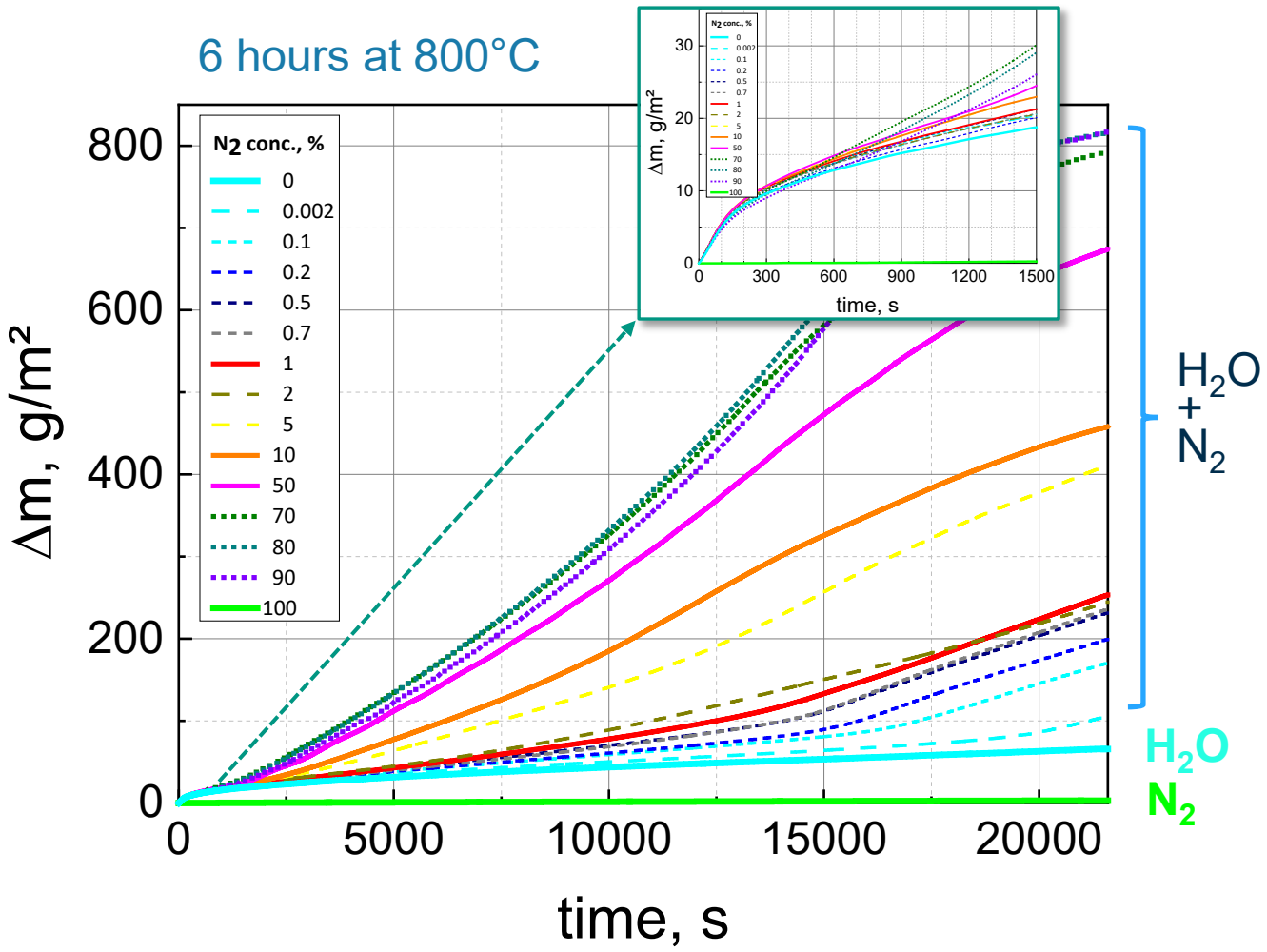

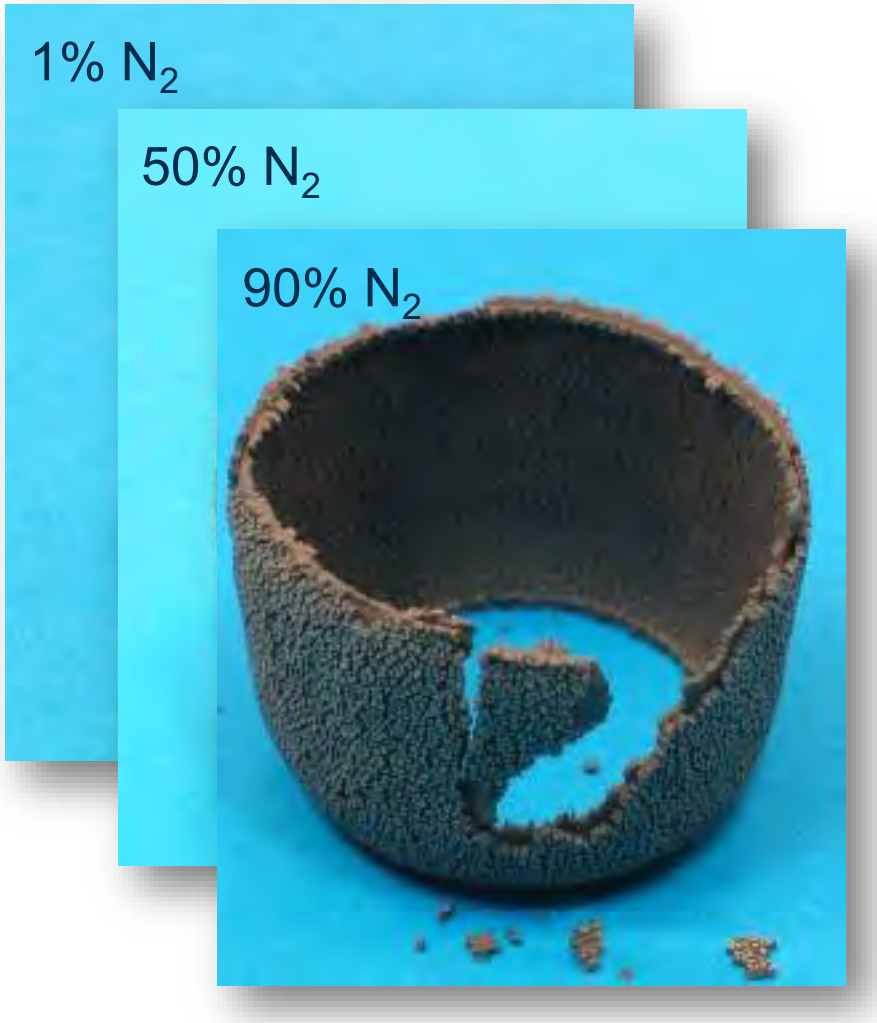

In-situ Neutron imaging

Example: 2h oxidation of Zry-4 at 900 °C in steam and steam/N_2

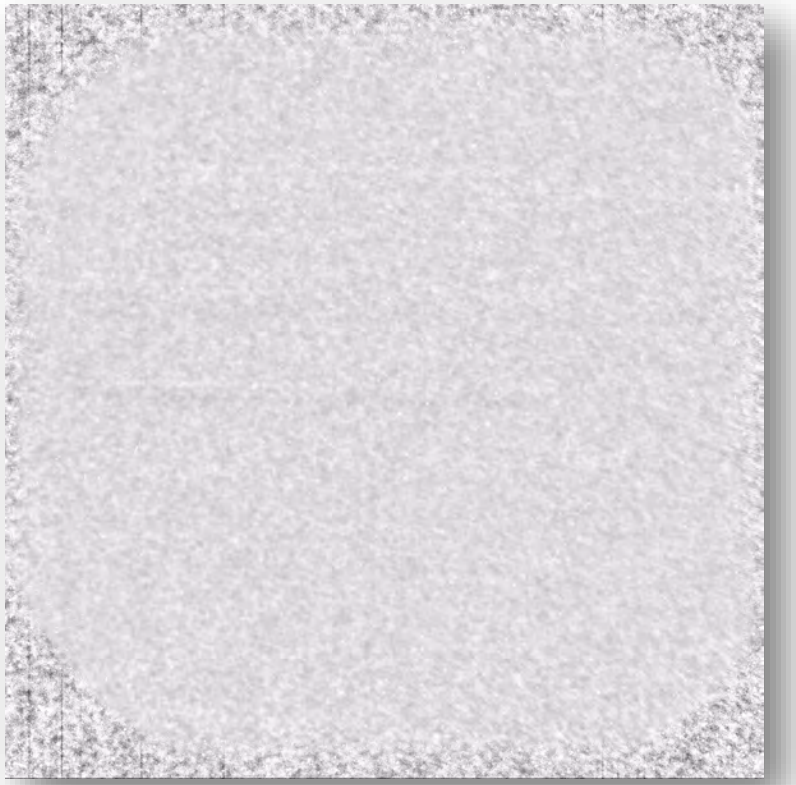

Steam

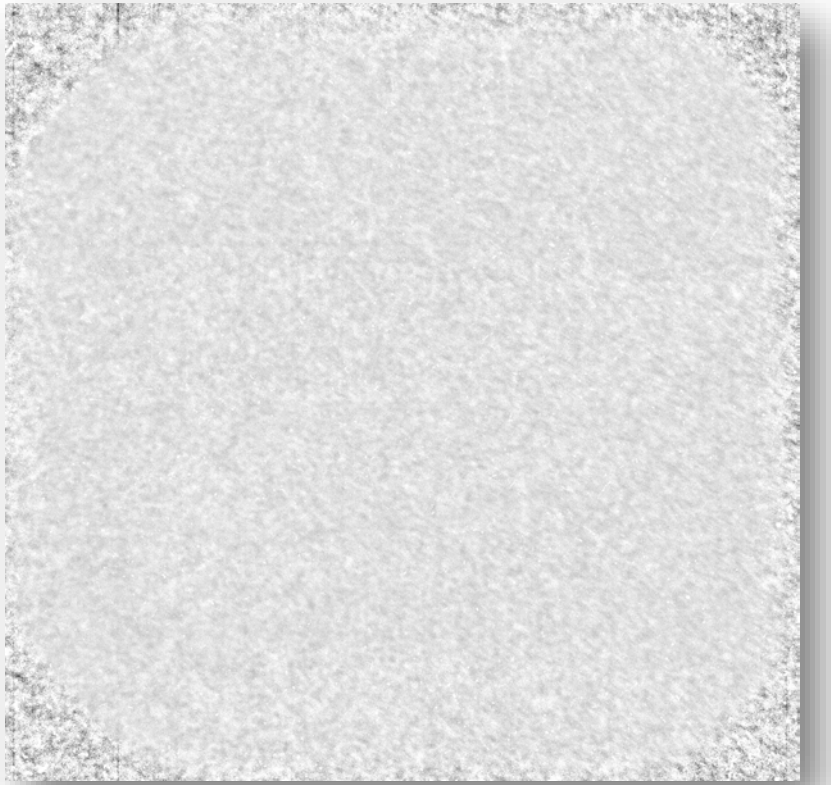

Steam + nitrogen

Grosse (2018): https://doi.org/10.1016/j.physb.2018.03.030

Mechanism of air oxidation

- Diffusion of the gas mixture through imperfections in the oxide scale to the metal/oxide interface
- Consumption of oxygen/steam
- Remaining nitrogen reacts with zirconium and forms ZrN
- ZrN is re-oxidized by fresh air with continuing reaction, associated with a volume increase by 48%

➢ Formation of porous and non-protective oxide scales

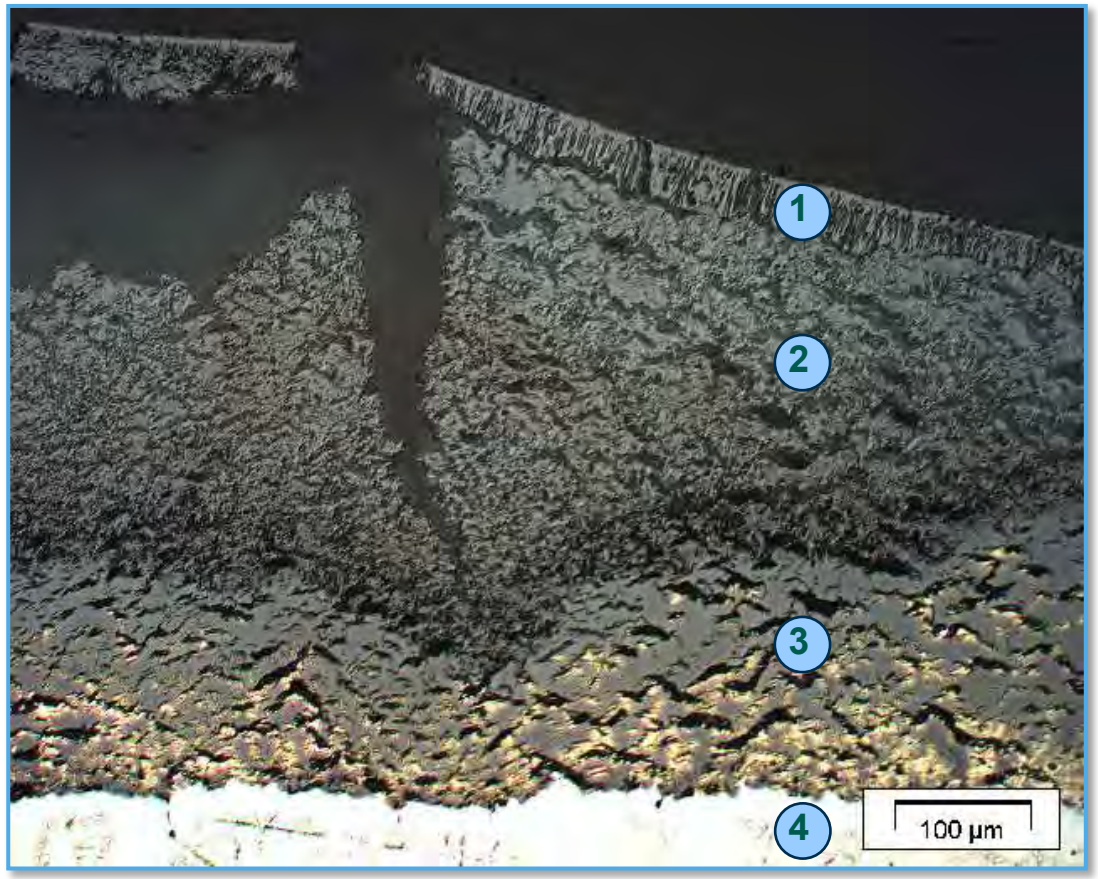

1 – initially formed dense oxide ZrO_2

2 – porous oxide after oxidation of ZrN

3 – ZrO_2 / ZrN mixture

4 – α-Zr(O)

Mechanism of air oxidation

Thermodynamic view

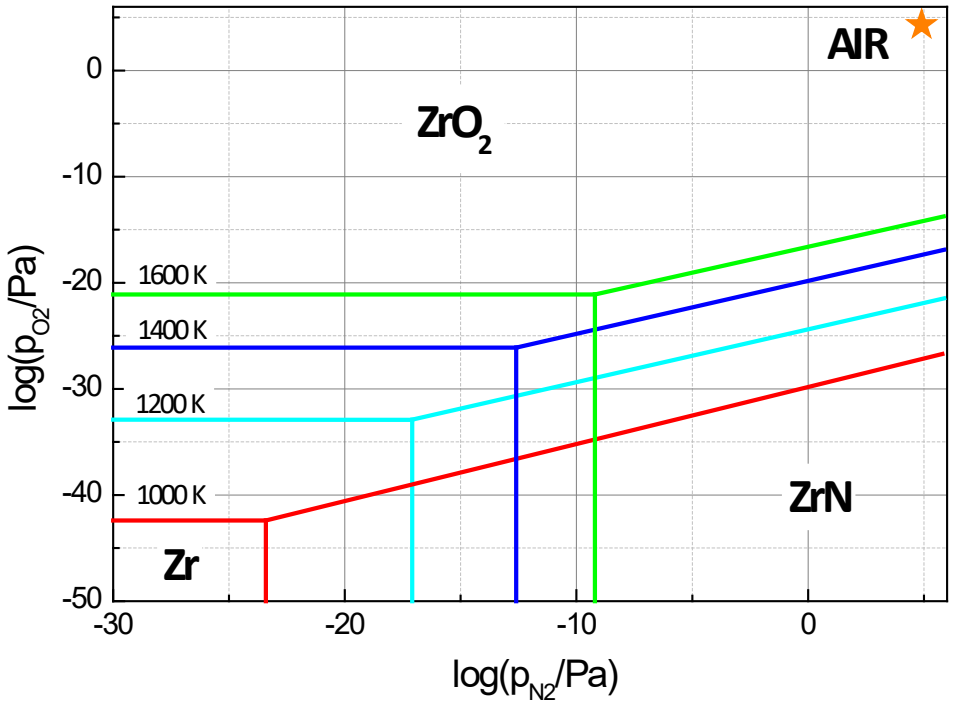

Stability diagram Zr-O-N

- ZrN only stable at very low oxygen partial pressure

Kinetic view

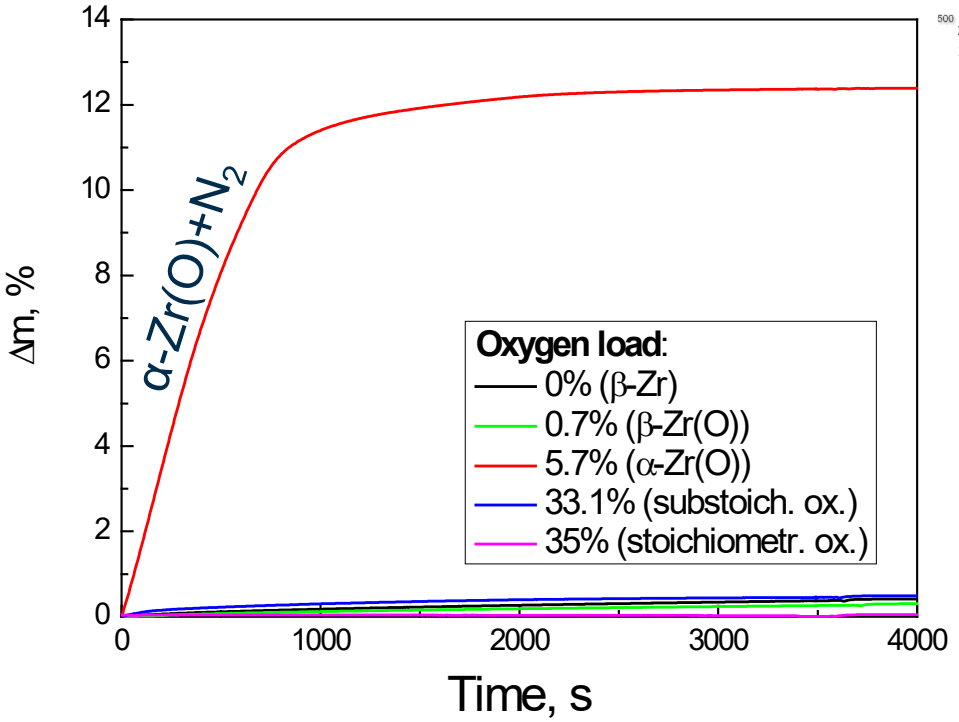

Reaction of ZrO_x with nitrogen (1200°C)

- Fast reaction of oxygen-stabilized Zr with nitrogen

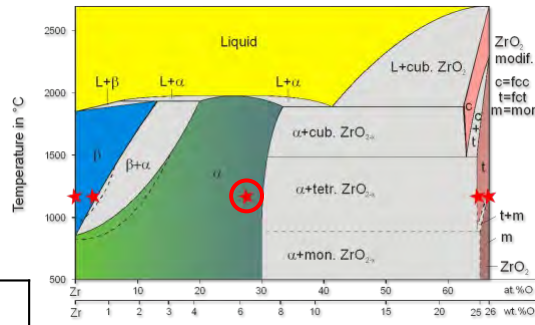

Both conditions are present locally at the metal-oxide interface

More information, see paper from Steinbrück
https://doi.org/10.1016/j.jnucmat.2009.04.018
http://dx.doi.org/10.1016/j.jnucmat.2013.12.024

Summary of oxidation in N_2 containing atmosphere

- Oxidation of zirconium alloys in atmospheres containing air or nitrogen is a very complex process, strongly dependent on experimental boundary conditions
- Local conditions (i.e. at M/O interface) may be different from ambient conditions
- Nitrogen causes early loss of barrier effect against FP release and contributes to enhanced hydrogen source term
- The effect of nitrogen (“air ingress”) has been considered in the severe accident codes, using experimental data from KIT and other laboratories

Nitrogen is not an inert gas under the conditions of a nuclear accident!

The effect of B_4C-Fe eutectic interaction on accident progression

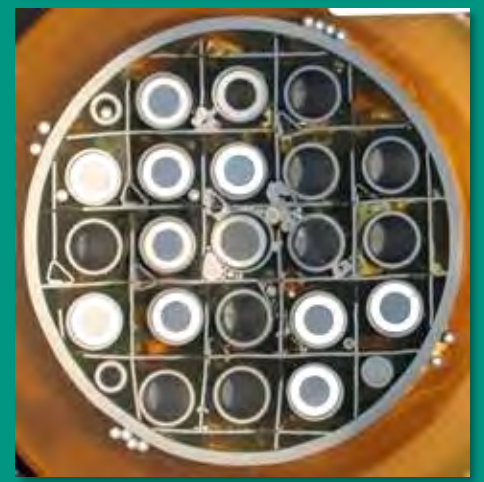

B_4C control rods in LWRs

- Boron carbide is used in boiling water reactors (BWR), VVERs, some pressurized water reactors (PWR)
- Oxidation of B_4C (containing melts) in steam produces large amounts of hydrogen, C+B containing gases, and heat
- Surrounded by stainless steel (cladding, blades) and Zry (guide tubes, canisters)

T_{eut} < 1200°C

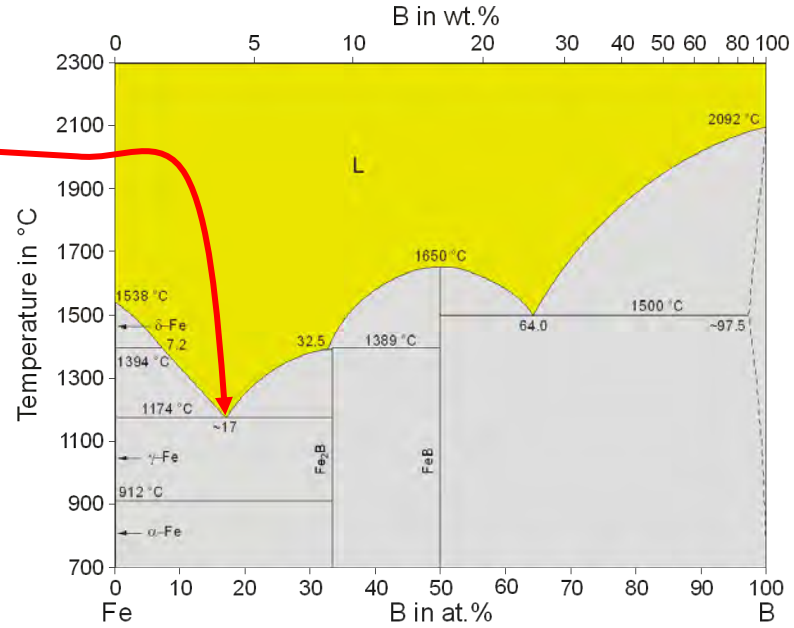

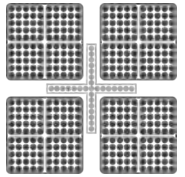

BWR control blade

B_4C pellet

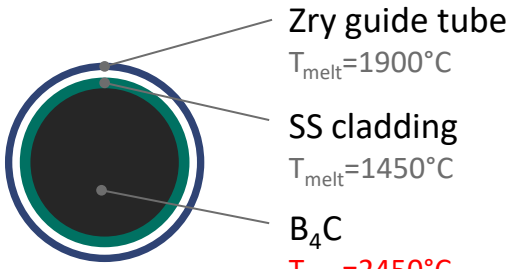

BWR control rod

Eutectic interaction of stainless steel with B_4C

1 h at approx. 1250 °C

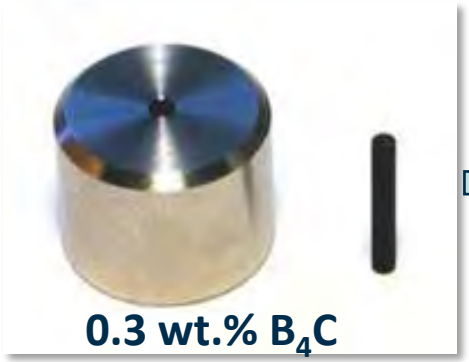

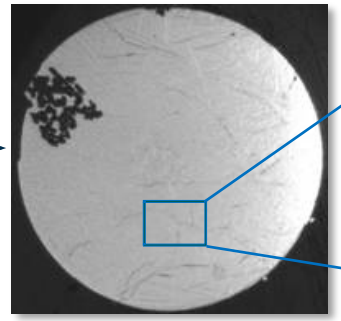

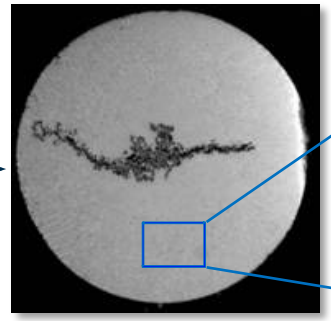

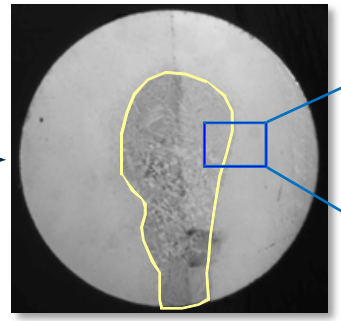

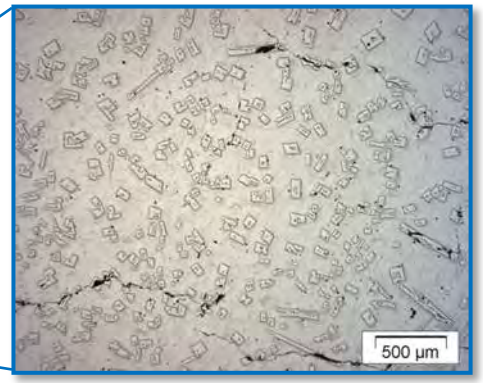

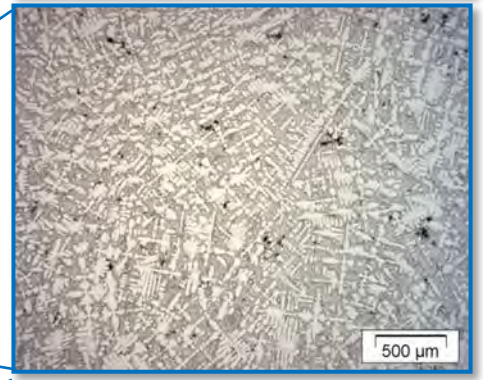

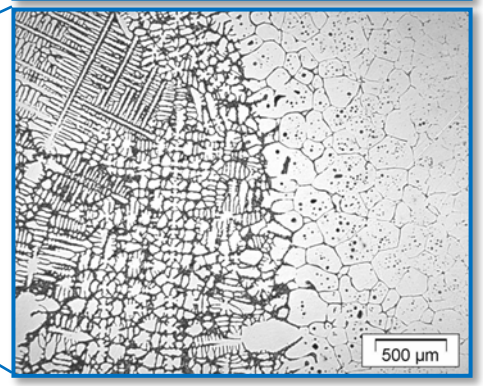

Complete liquefaction of stainless steel

1/3 of SS liquefied

Eutectic interaction of stainless steel with B_4C (kinetics)

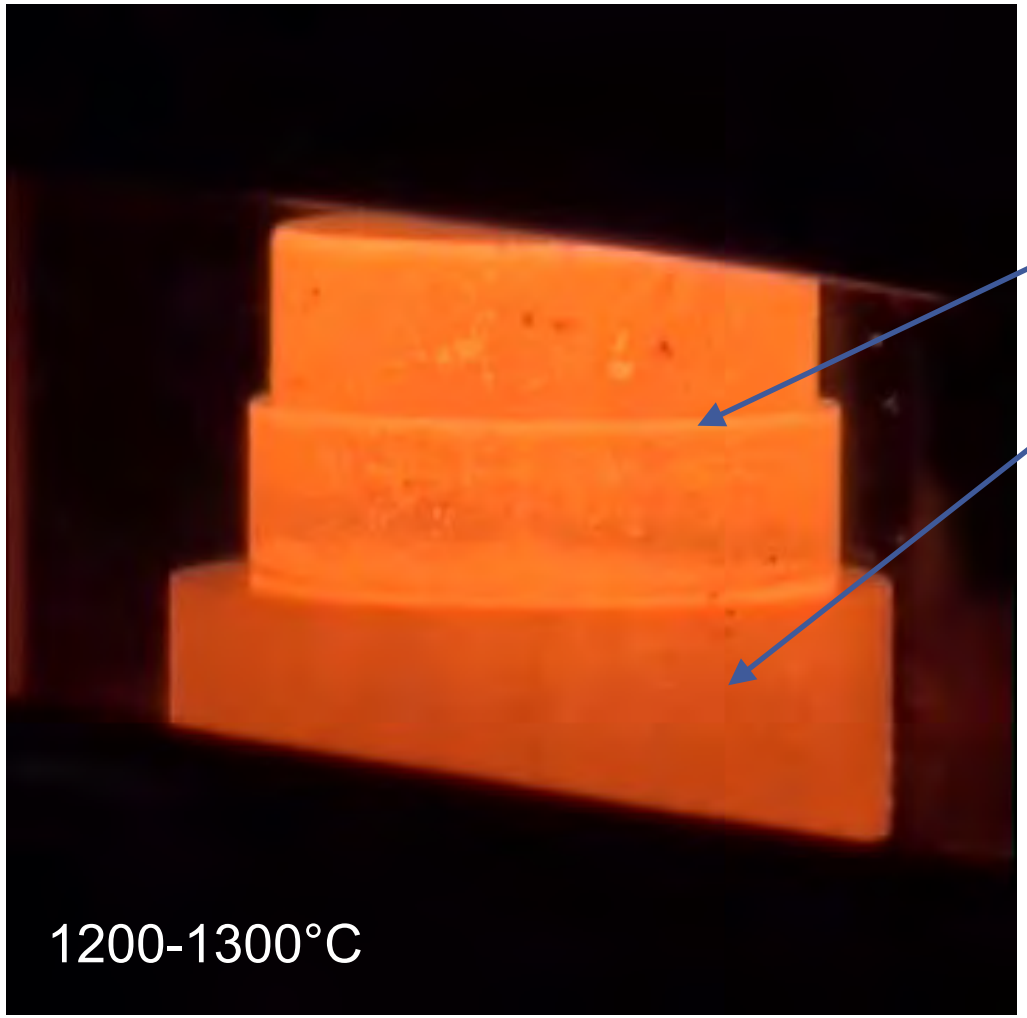

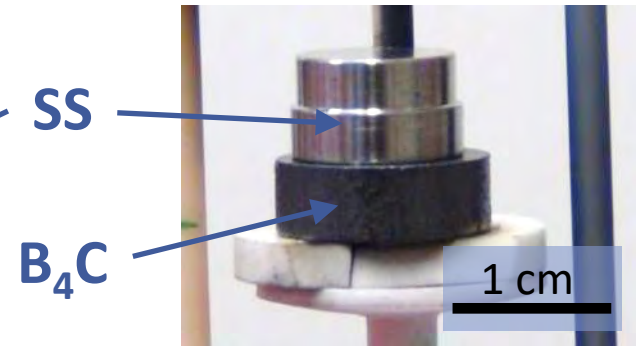

Rapid and complete melting of SS at 1250°C starting at B_4C/SS interface

Degradation of boron carbide control rods (pellet size)

- Apparently intact samples up to 1400°C, but…

T ≤ 1200 °C:

- Intact specimen with B_4C/SS/Zry-4

T ≤ 1400 °C:

- Intact specimen due to “crucible effect” (melt kept by the external ZrO_2 scale)

T ≥ 1500 °C:

- Failure of the oxide shell and rapid oxidation of absorber melt and B_4C pellet

Degradation of B_4C control rods (single rod)

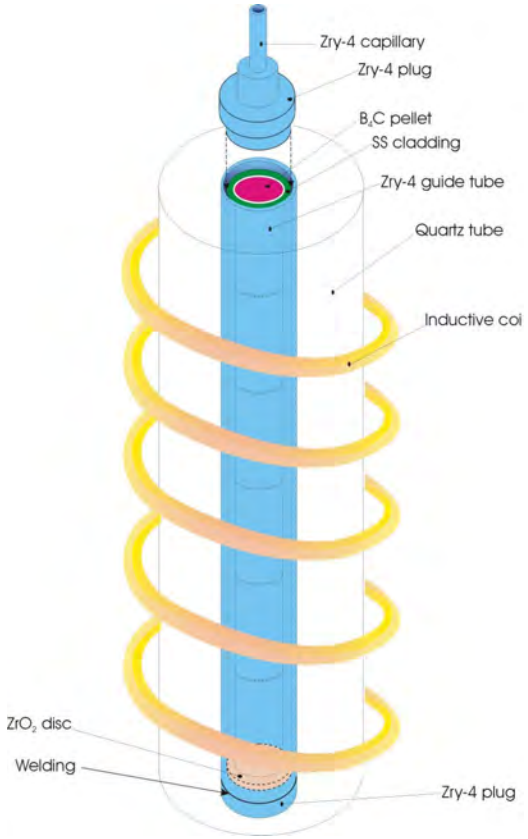

Inductive heating of the specimen in the QUENCH rig

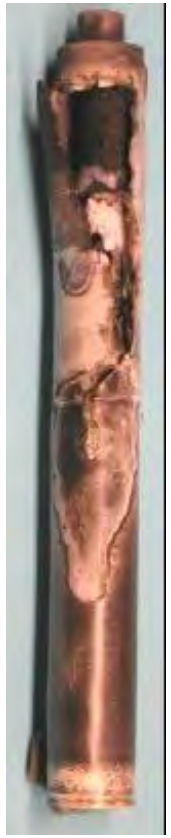

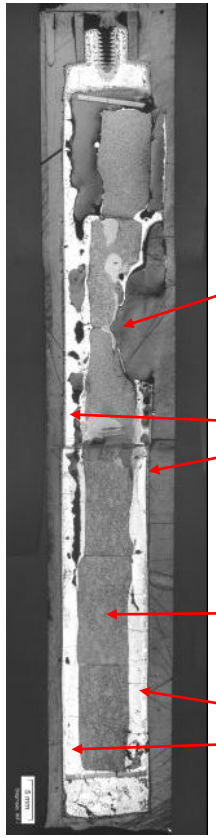

Local oxidation of B_4C

ZrO_2 scale enclosing the absorber melt

Partly dissolved B_4C pellet

Relocated absorber melt

Post-test appearance and axial cross-section of a specimen after 30 min isothermal test at 1470 °C

Steinbrueck (2010): https://doi.org/10.1016/j.jnucmat.2010.02.022

Degradation of B_4C control blade (BWR bundle test CORA-16)

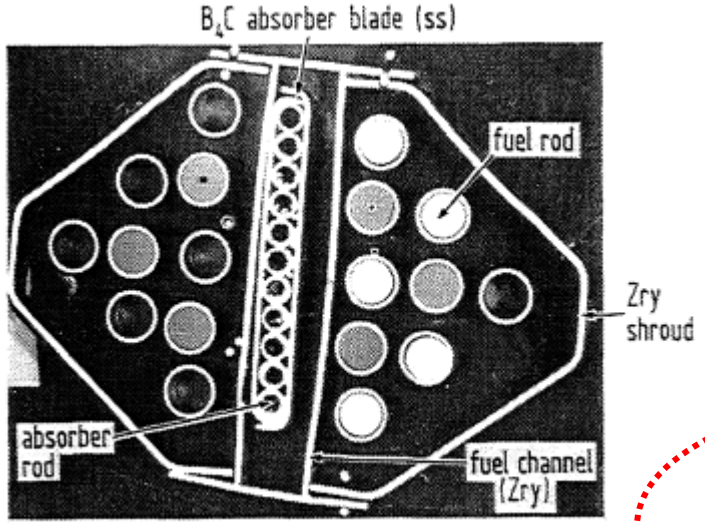

16-08 (1145mm), bottom view

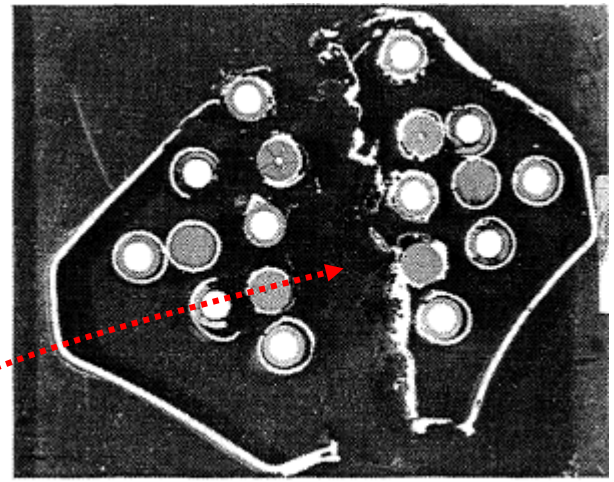
16-07 (963mm), top view

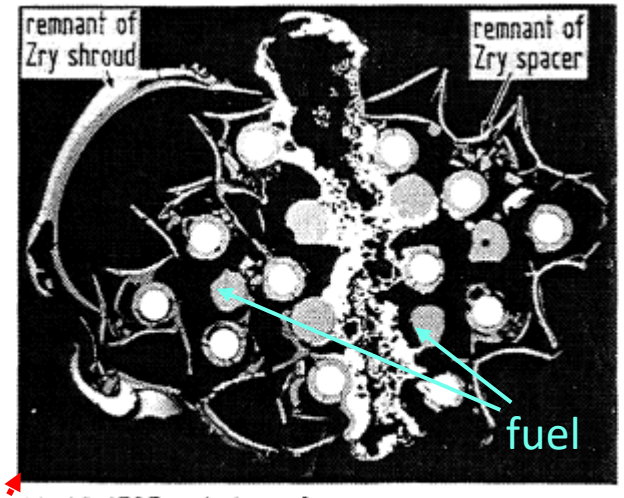

16-09 (525mm), top view
center grid spacer elevation

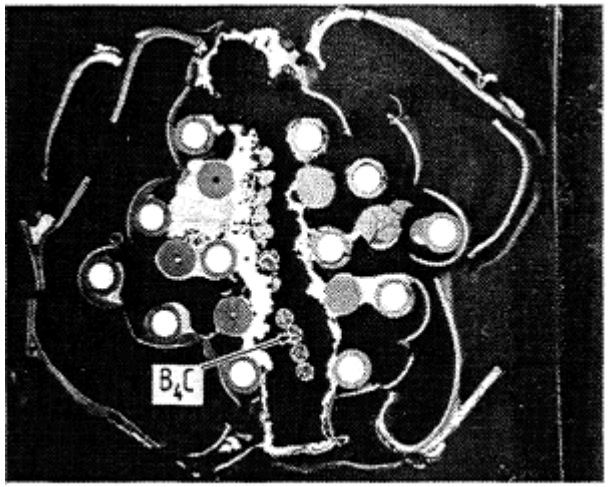

16-03 (310mm), top view

- Complete loss of absorber blade
- Dissolution of cladding and fuel
- Massive melt relocation (SS, Zry, UO_2)

16-01 (110mm), top view

Oxidation of eutectic melts

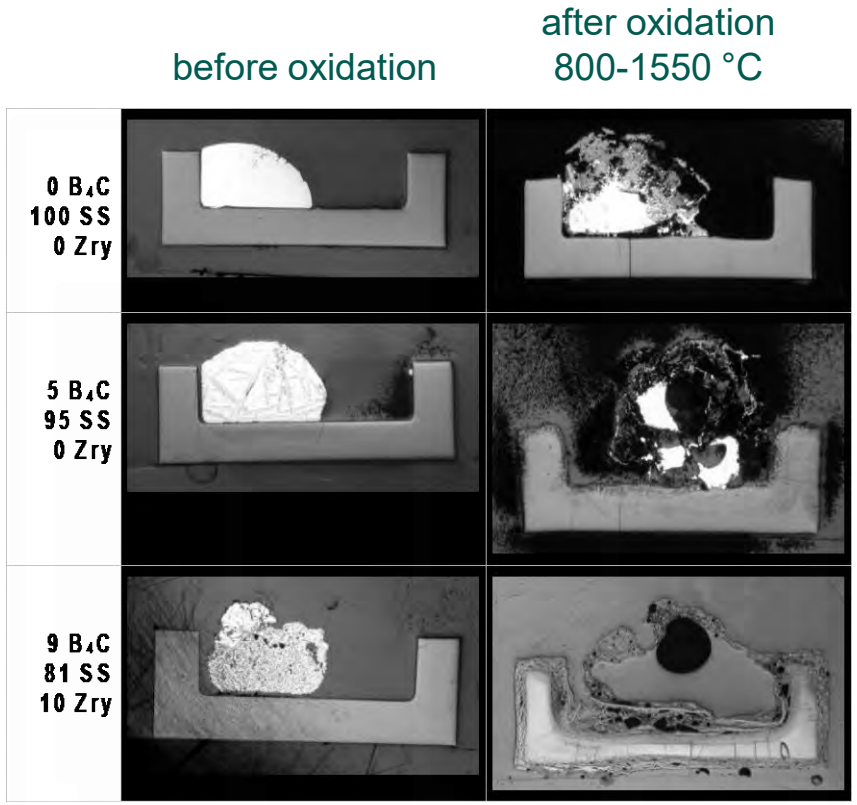

Strong interaction of oxidized melt with ZrO_2 crucible

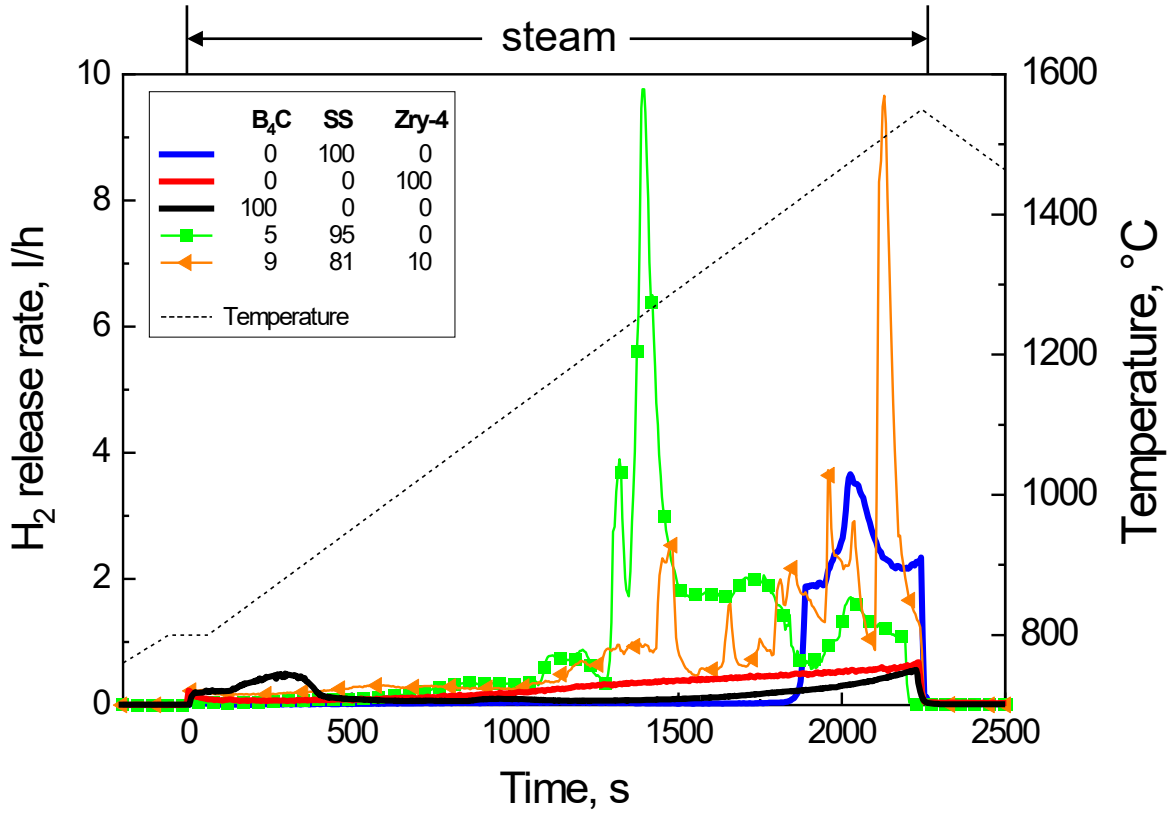

High oxidation rates beyond melting temperature

Summary of B_4C effects in severe accidents

- Low-temperature eutectic melts form at temperatures several hundred Kelvin below the melting temperatures of the materials involved
- These chemically aggressive melts may attack surrounding core structures including fuel, thus influencing corium behavior and the FP source term
- Oxidation of B_4C and B_4C-containing melts results in the release of large amounts of hydrogen and heat
- Further reaction products (CO, CO_2, boric acids) have to be taken into account for accident analyses as well
- No methane (relevant for FP chemistry) is produced during high-temperature oxidation of B_4C

Takeaways

- Not everything is as it seems at first glance
- Experiments must be designed to be as prototypical as possible
- Equilibrium thermodynamics (also locally!) and kinetics must be considered
- The key to the success of the QUENCH program lies in the interlocking of large-scale bundle experiments, separate-effects tests, modelling, and code validation and application

Acknowledgement

- ERMSAR Organizing Committee
- Helmholtz Association for funding program NUSAFE at KIT
- Program NUSAFE and IAM institute's management for broad support of our activities
- Funding and supporting organizations as German ministries, EURATOM program, OECD-NEA, etc.

- And last but not least the QUENCH team

RESEARCH, INSIGHTS, AND LESSONS LEARNED DURING A CAREER FOCUSED ON LWR EX-VESSEL SEVERE ACCIDENT BEHAVIOR

MITCH FARMER
Manager, LWR Programs
Nuclear Science & Engineering Division
Argonne National Laboratory

Presentation at 12th European Review Meeting in Severe Accidents Research (ERMSAR) Conference
Madrid, Spain, May 18, 2026

PRESENTATION BACKGROUND & OBJECTIVES

Background:

- Over the last 30+ years, Argonne has conducted various test programs focused on improving the understanding ex-vessel severe accident behavior (ACE/MCCI, COMET, MACE, OECD/MCCI, ROSAU…)
- To successfully execute these programs, there was a need to evolve the technology for producing core-melts to meet test objectives.
  - Due to the complexity of this work (principally related to core melt production techniques) a few ‘bumps in the road’ were encountered along the way.

Objectives:

- Provide a high-level overview of the evolution of core melt production technology.
- Present a few case studies illustrating difficulties encountered along the way, the resultant lessons-learned, and steps taken to address them in subsequent tests.

APPROACH

1. Summarize the overall evolution of core melt production technology and its application in tests (2 viewgraphs).
2. Provide video examples of ‘good day’ and ‘bad day’ test outcomes.
3. Discuss three tests where difficulties were encountered and what was done to address lessons learned in subsequent experiments.

EVOLUTION OF CORE MELT PRODUCTION TECHNOLOGY

A long road….

- Early ACE/MCCI tests focused on studying fission product release during MCCI under dry cavity conditions.
  - Used ‘Direct Electrical Heating (DEH)’ to produce core melt.
  - Tungsten starter coils were embedded in crushed UO_2 pellets near the top of the powder bed.
  - Pellets heated until onset of melting; subsequent growth of melt zone to encompass the entire melt mass.
  - Process took several hours to melt a few hundred kg *in-situ* before ‘the test’ could start.
- During the follow-on MACE program, focused on debris coolability, decision made to switch from DEH to exothermic chemical reactions to produce melt.
  - Several motivating factors, but primary reason was that testing & analysis indicated a need for very large melt mass ($\geq$ 2000 kg) to achieve ‘prototypic’ conditions for coolability testing.
  - DEH approach impractical for producing this amount of melt.

MELT PRODUCTION VIA EXOTHERMIC CHEMICAL REACTIONS

- Methodology:
  1. Heat of reaction calculations performed to define candidate mixtures to produce a target melt composition (UO_2, ZrO_2, steel, concrete oxides).
  2. Samples ignited to verify melt pool formation & reaction temperature
  3. Mixture adjusted as needed & test is repeated.
- Results for 1 kg test producing a 70 % oxidized PWR melt at 2400˚C is shown.
- This technology used in large scale tests up to 2 metric ton scale.

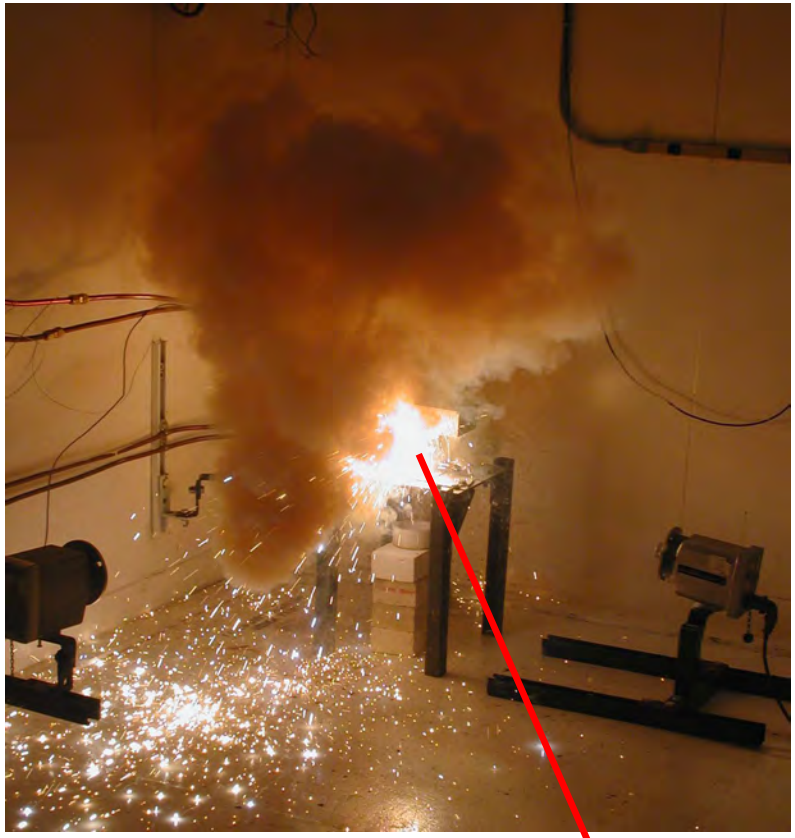

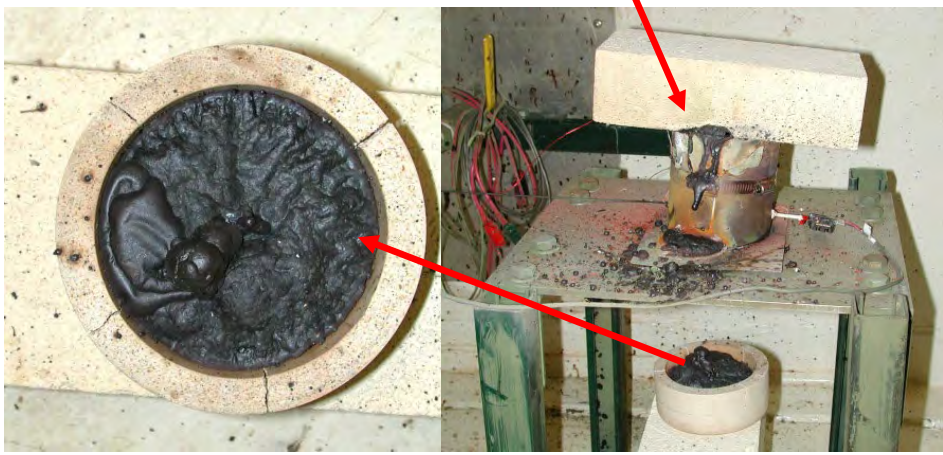

REACTOR CONTAINMENTS AS TEST FACILITIES AT ARGONNE (CELLS 4 & 5, BLDG. 315)

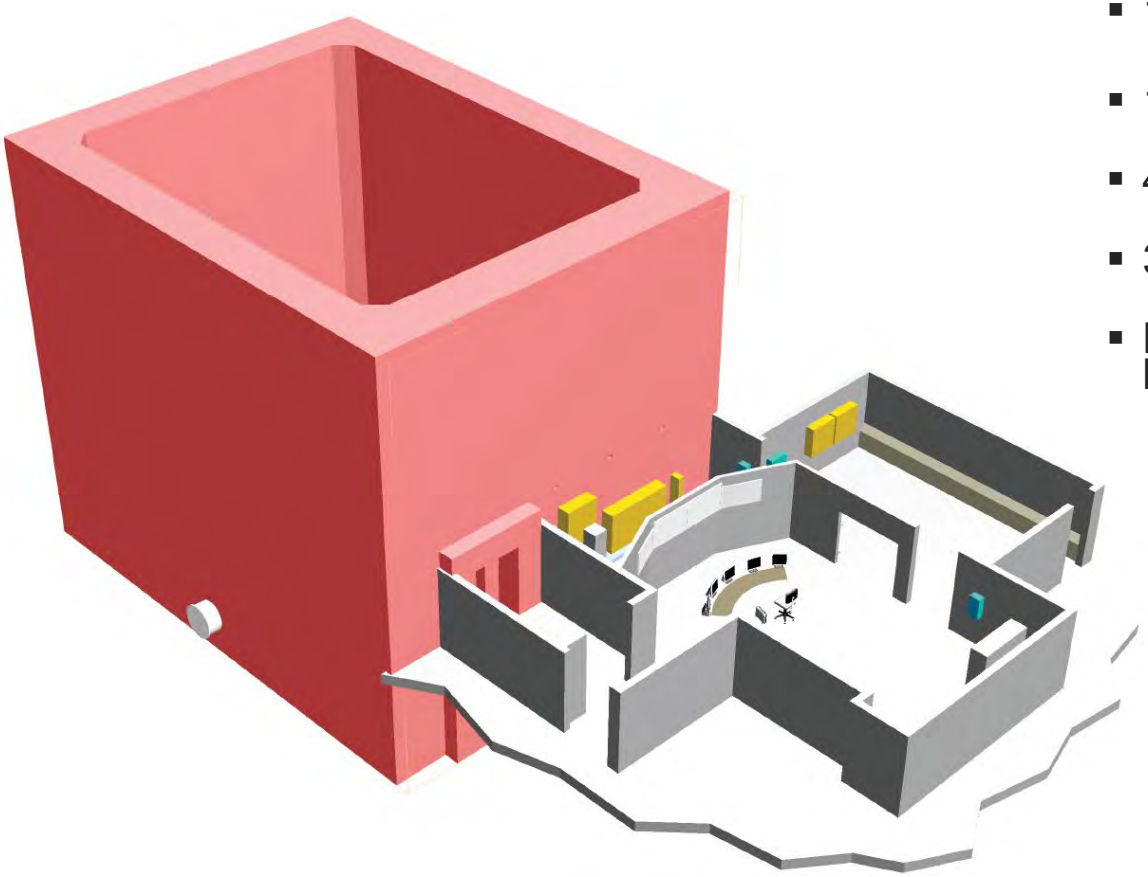

- Formerly housed ZPPR 6 & 9 reactors
- 1.2 m thick walls
- 12 x 9 x 9 m high (1000 m^3)
- 45 kg TNT explosion rating
- 3.4 bar pressure rating
- Potential test hazards include fires, hydrogen and steam explosions

GOOD DAY VIDEO CLIPS…

Video obtained from cameras mounted in lid of test section

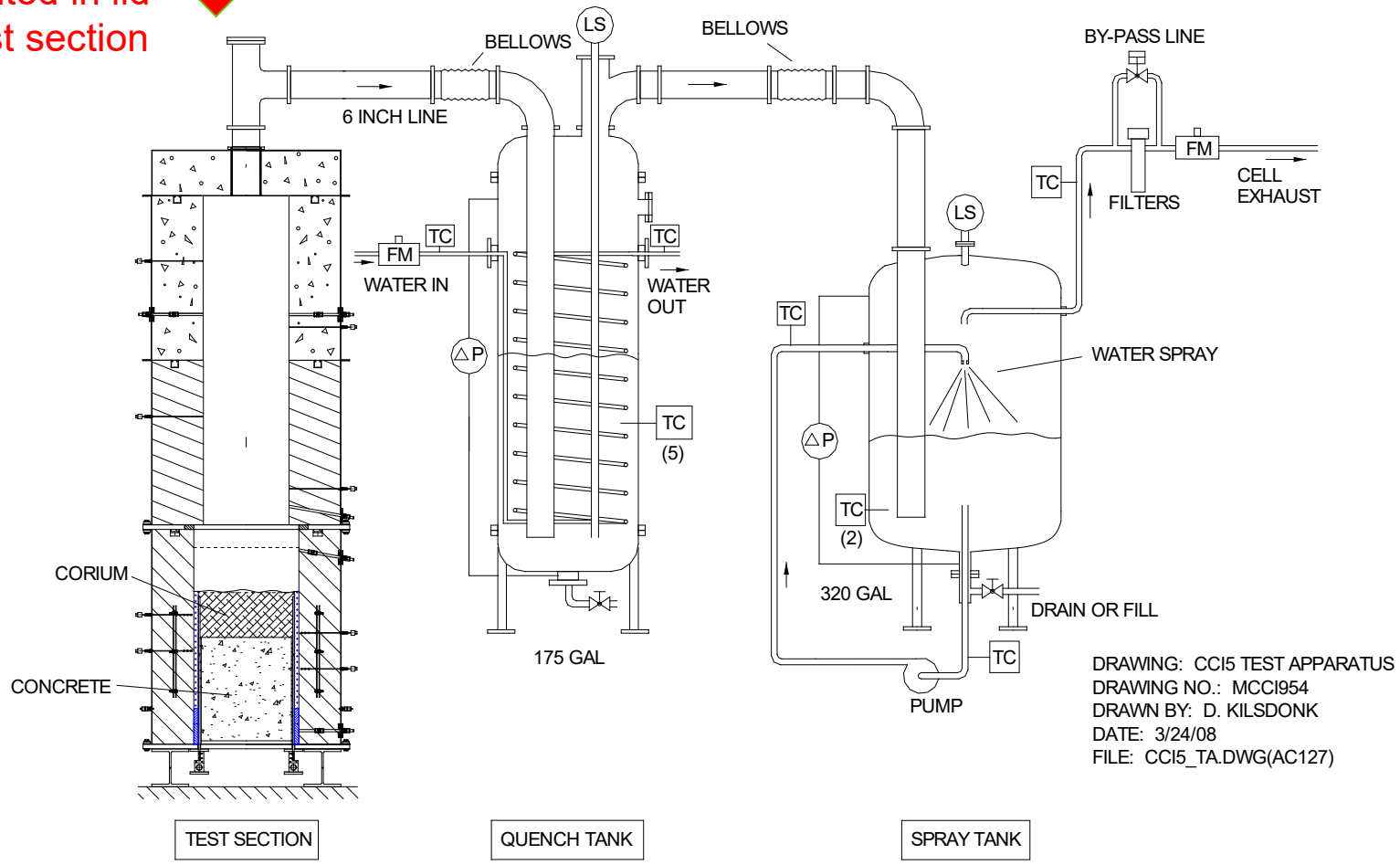

Argonne NATIONAL LABORATORY

BAD DAY VIDEO CLIPS…

- Recorded by surveillance cameras mounted at various locations within the test cell.

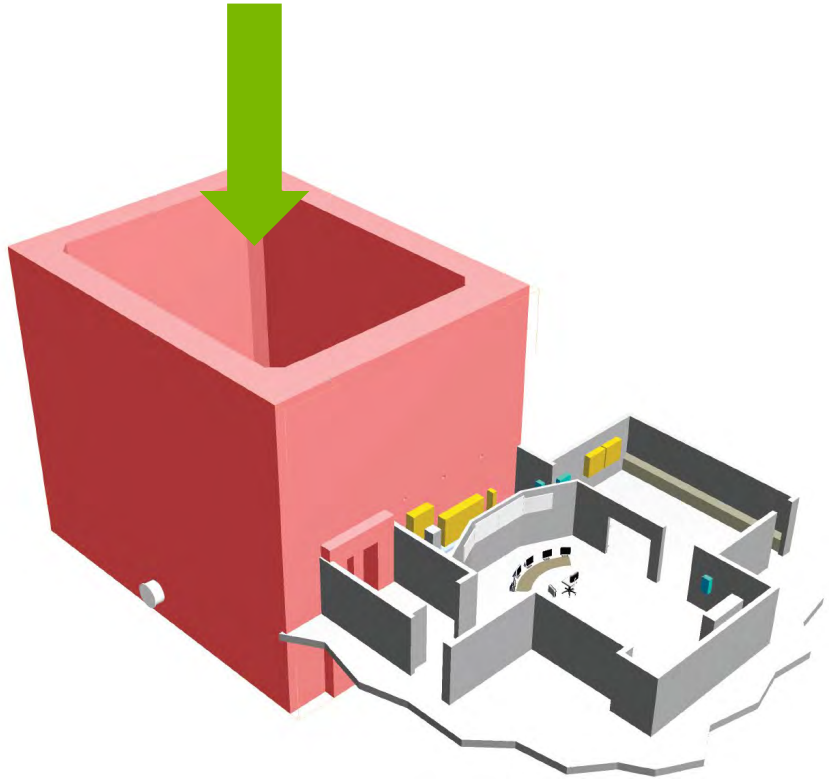

CASE STUDIES ON LESSONS LEARNED

Experiments discussed herein:

1. MACE M1b/M2: Experiments investigating debris coolability using limestone/common sand and siliceous concrete basemats, respectively.
2. MACE M3: Large scale experiment intended to investigate coolability for the case of a limestone/common sand concrete basemat.
3. COMET-U: Tests investigating debris coolability via water injection at the melt-substrate interface.

- Much of the information shared in this presentation is unpublished as it describes non-successful test outcomes and the associated corrective actions, as opposed to successful test outcomes that are routinely published.

1. MACE M1B/M2

- These tests used DEH to produce the melt.
  - M1b: LCS concrete basemat
  - M2: SIL basemat
- Featured a 'new' monolithic test section design made from castable refractory MgO.
  - Castable MgO used as a liner in steel industry furnaces/ladles.
  - No additional protective layer applied over MgO surfaces in contact with melt.
  - Tungsten electrodes sat immediately adjacent to opposing MgO sidewalls.
- M1b: operationally successful.
- M2: *not* successful. East electrode sidewall (~ 30 cm thick) failed by melt-through after 2.5 hours of powder melting via DEH.
- Subsequent posttest examination of M1b indicated that sidewall melt-through nearly occurred in that test also.

MgO sidewalls

Typical tungsten electrode installation

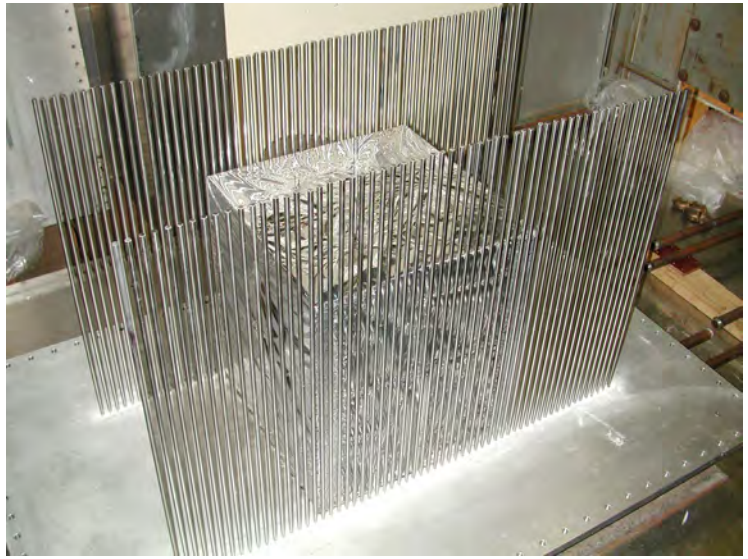

M2: WHAT HAPPENED?

- Investigation carried out by internal committee (featuring chemists) to identify failure mechanism and to recommend corrective actions.
- Culprit: rapid SiO_2 reaction with MgO forming silicates [forsterite (Mg_2SiO_4) and enstatite ($MgSiO_3$)] at temperatures > 800°C.
  - Observed in steel industry for high silica slag; not widely reported in literature.
  - M2 powder charge contained ~ 6 wt% SiO_2; M1b ~ 2 wt%
- Result: test section re-designed to prevent reoccurrence (see next page).
- **Lesson learned**: chemistry plays a key role in high temperature testing, so get to know your local chemist well!!

M1b posttest debris configuration

Little erosion of non-electrode sidewalls

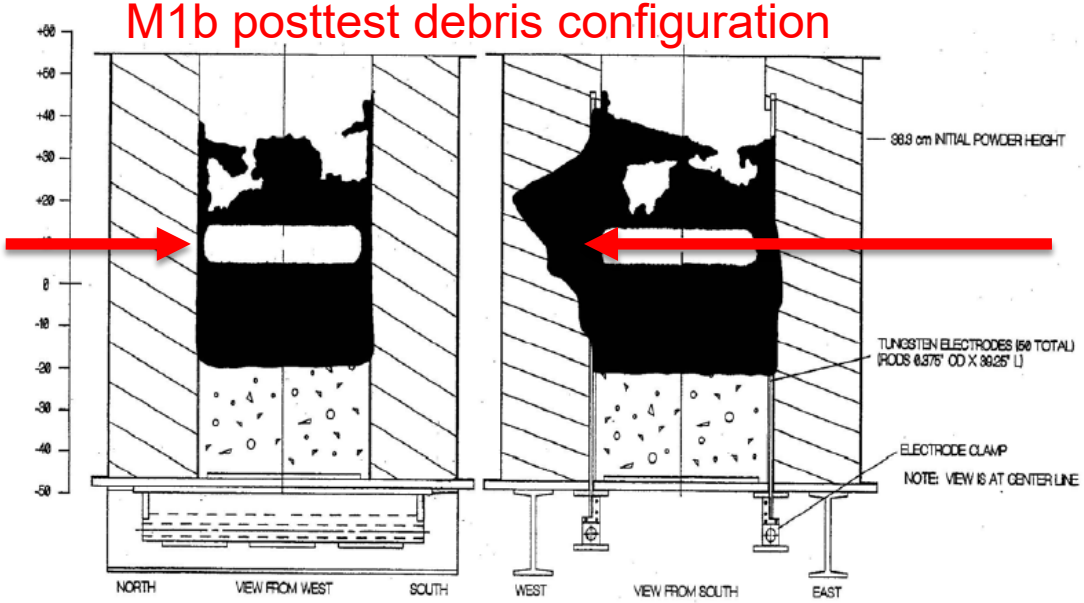

Heavy erosion of west electrode sidewall

Argonne NATIONAL LABORATORY

CORRECTIVE ACTIONS BASED ON M1B/M2

- Test section redesigned to accommodate protective layer of UO_2 or U_3O_8 powder/pellets covering sidewall inner surfaces to chemically protect MgO.
  - Required adding metal forms for electrodes to keep UO_2/U_3O_8 from covering (electrically insulating) powder-facing surfaces during loading.
- Instrumented W backup plates added to detect melt contact; monitored during test.
- Additional thermocouples added to monitor exterior test section exterior temperatures.
- Lower section redesigned to be modular so that walls could be removed and examined posttest. Benefit: enabled better PTE plus parts could be reused.
- **Once these changes were implemented, no MgO sidewall attack occurred in the balance of tests conducted**.

M3 lower section design

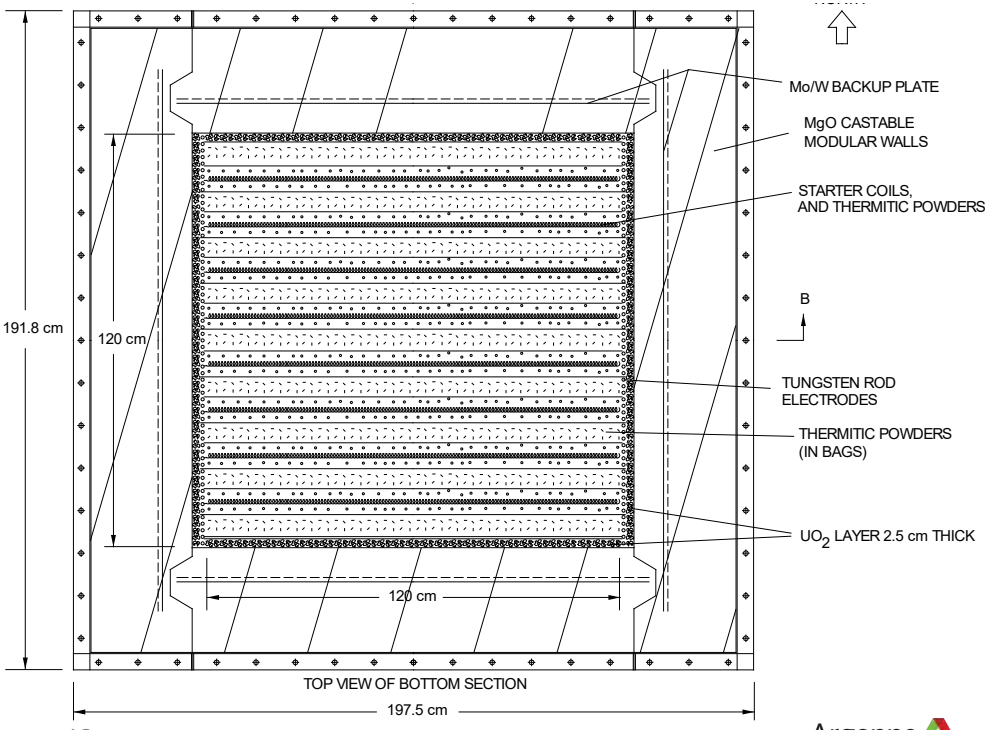

Argonne NATIONAL LABORATORY

2. MACE M3

- After M2, project review group (PRG) requested test scale increase to as large as possible to approach ‘prototypic’ test conditions. Result: 120 cm x 120 cm test section cross-sectional area; 2000 kg melt mass.
- Involved extensive R&D to develop an exothermic chemical mixture (‘thermite’) for large scale melt production.
- Mixing & loading of 2000 kg powder charge performed, and final facility preps were underway.
- PRG member raised concern that thermowells for melt temp measurements would act as ‘table legs’ supporting crust and undermining scale-up basis.
- → test section disassembled, thermite unloaded, thermowells cut down *in situ*, loading/assembly repeated, and test executed after 8-month delay following thermite mixing.

M3 test section design

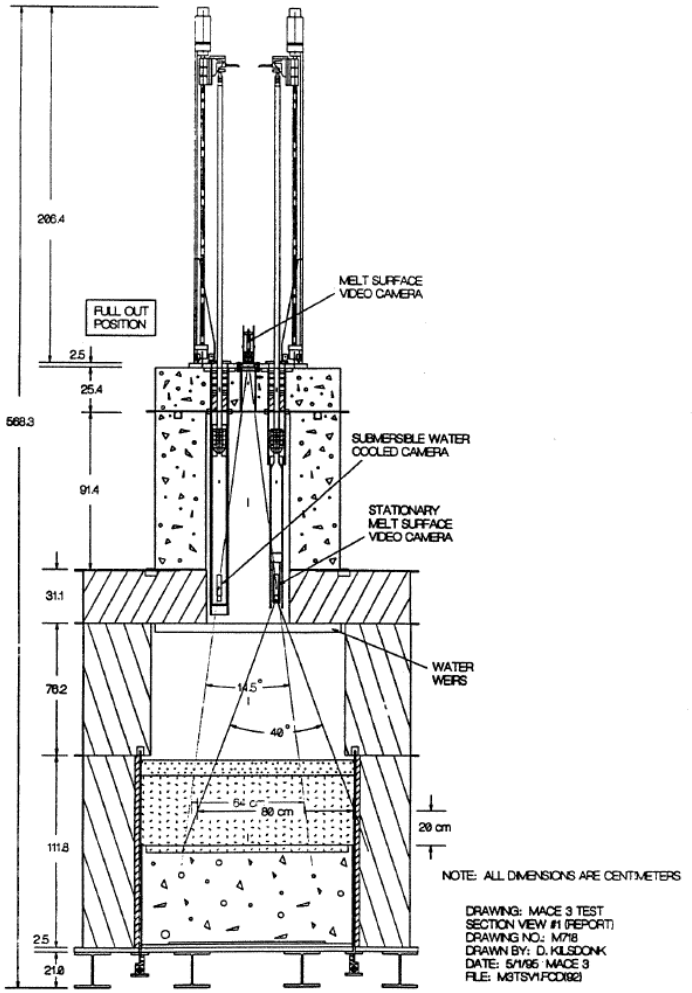

- Result: test aborted at startup due to failures at flange locations leading to discharge of gases (including H_2) into the test cell (video)

M3: WHAT HAPPENED?

- Investigation committee formed (included chemical and structural specialists, others) to identify cause(s) and recommend corrective actions.
- Failure mechanism: excessive non-condensable gas release during thermite burn led to test section over-pressurization.

Root causes:

- Moisture uptake by the thermite during 8 month time interval between mixing and test initiating.
  - Led to excessive gas release during the burn.
- Bagging material inadequate for long-term storage of hygroscopic material to prevent moisture uptake.
  - Simple plastic bags were used to store/load the thermite.

Top view of M3 powder bed after loading

CORRECTIVE ACTIONS BASED ON M3

- To minimize moisture absorption, candidate bagging materials tested (with thermite) based on weight gain method.
  - Aluminized Saran bags selected.
- Gas sample test (GST) procedure developed to characterize impurity content of thermite (based on ideal gas law).
- Based on system ΔP calcs, established a criterion for maximum allowable 'moisture' content to start test (0.3 wt%).
- Procedure developed to monitor thermite moisture uptake internal to the test section.
- Test section continuously purged with Argon during pretest preparations.
- Safety plan updated and revised.
- **Repeat test M3b successful!!**
- **Lesson re-learned**: chemistry plays a key role in high temperature testing, so get to know your local chemists well!!

Top view of M3b powder bed after loading

M3b posttest debris distribution

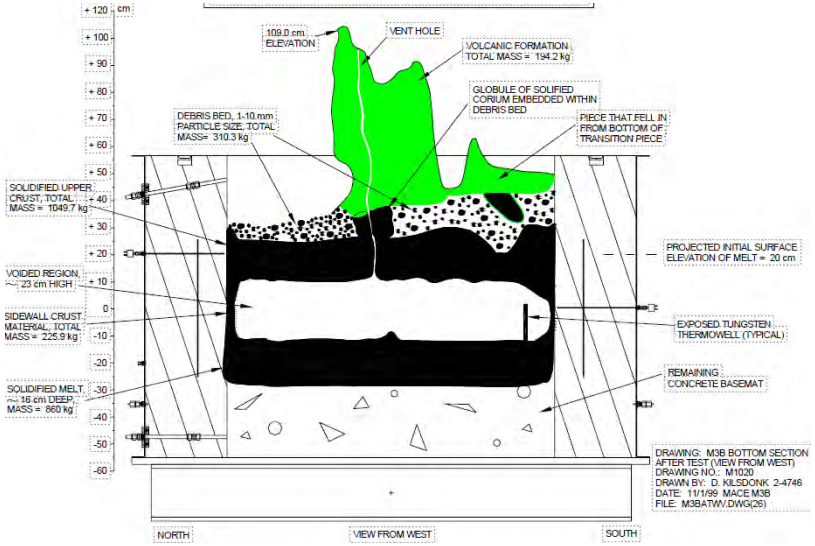

Argonne NATIONAL LABORATORY

3. COMET-U

- KIT (FZK) developed a novel coolability concept based on bottom water injection through an array of tubes cast in the basemat.
- Reactor material tests (-U series) carried out to supplement simulant material tests at KIT.
- Target melt composition to be produced by thermite reaction (specified by KIT) included core and concrete oxides, plus B_2O_3.
  - Boria a concrete additive for criticality control in case of an ex-vessel accident.
  - Present at a level of 1.3 wt% in the thermite.
- Test operationally successful, showing positive coolability attributes for this concept.
- *However,* thermite reaction was extremely vigorous, leading to melt through of main steam-line during burn phase.

COMET-U test section

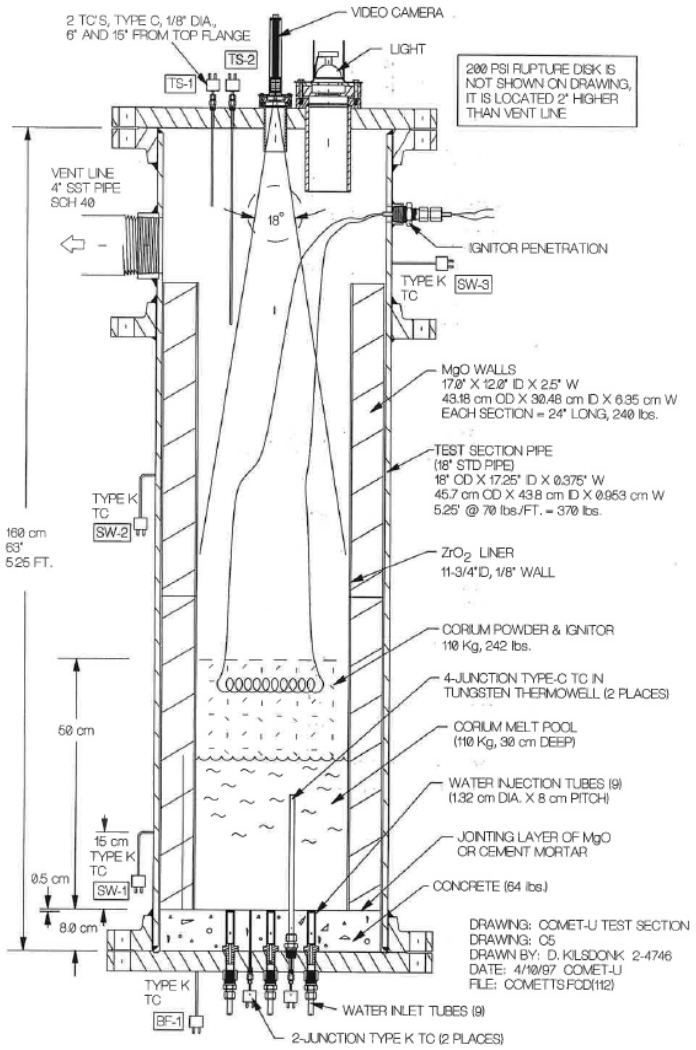

Argonne NATIONAL LABORATORY

COMET-U: WHAT HAPPENED?

- Tests carried out to develop a thermite to produced target melt composition.
  - Principally based on GST's to check reaction temperature and to verify an acceptable level of *noncondensable* gas production.
- Subsequent analysis of thermite constituents revealed that B_2O_3 has a relatively low boiling point range of 1500-1860 °C, significantly less than thermite reaction temperature of ~ 2000 °C.
- Thus, B_2O_3 likely boiled during the thermite burn, leading to excessive voiding in the melt located over the downward-progressing burn front.
- Entrained core debris led to rapid thermal attack in the vent/steamline adjacent to the test section top flange and subsequent meltthrough.
- B_2O_3 present in the thermite at a level of 1.3 wt% can be compared to the test initiation criterion of $\leq$ 0.3 wt% H_2O based on M3 corrective actions.
- Note that B_2O_3 is a *condensable* burn gas byproduct, vs. *non-condensable* gas products identified as part of GST's.

CORRECTIVE ACTIONS BASED ON COMET-U

- Thermite development procedures modified to include a screening based on normal boiling point temperature vs. expected thermite reaction temperature.
- Aside from GST's, additional developmental test(s) at larger scale (typically 1-2 kg) are carried out to verify acceptable burn behavior.
- **Over-arching lesson-learned**: testing with high temperature reactor materials featuring exothermic chemical reactions to produce core melt are difficult and complex. Consult your local chemist on a regular basis as part of the development process!!

SUMMARY

- Severe accident experiments are a complex and difficult undertaking and are not always successful.
- When tests don’t go right, it is critically important to investigate the process to determine contributing factors so that corrective actions can be taken.
- IMO, the evolution of melt production technology from DEH to exothermic chemical reaction technology was a critical step required to enable large scale severe accident experiments.
- Although there were several bumps in the road, this technology has enabled many successful and high-value experiments to be conducted, both in the US and abroad.
- The tests have led to improved understanding of severe accident phenomenology and have informed the development of industry accident management guidelines.

ACKNOWLEDGEMENTS

- Thanks to the ERMSAR organizing committee for the opportunity to attend and present at this conference!
- The work performed in this area at Argonne was and continues to be a team effort, and special thanks go to Jeremy Licht, Steve Lomperski, Nathan Bremer (active), and Bob Aeschlimann, Dennis Kilsdonk, and Lou McUmber (retired). All are highly skilled laboratory specialists, and this work would not be possible without their efforts!

The 12th European Review Meeting on Severe Accidents Research

May 18-22, 2026, Universidad Carlos III de Madrid, Madrid, Spain

TECHNICAL SESSION 3.1: SEVERE ACCIDENT SCENARIOS - SMALL MODULAR REACTORS

Chairs: M. Garcia Martin (CIEMAT), F. Mascari (ENEA)

ID062	**Analysis of Postulated Severe Accidents in Generic Integral PWR Small Modular Reactors: Outcomes on Integral Codes' Modelling Capabilities from the Horizon Euratom SASPAM-SA Project** M. E. Cazado (KIT)	Paper Presentation
ID157	**Rolls-Royce SMR 3D Hydrogen Combustion Assessment Approach** J. Fowles (Rolls-Royce SMR Limited), A. Meredith (Rolls-Royce SMR Limited), J Butterworth (Gexcon)	Paper Presentation
ID065	**Severe accident analysis of SASPAM-SA Design II LW-SMR dry containment using containmentFOAM** S. C. Vázquez-Rodríguez (FZJ)	Paper Presentation
ID131	**Analysis of LDR Lite Reactor's Resistance to Design Extension Conditions** A. Kaliatka (LEI)	Paper Presentation

ANALYSIS OF POSTULATED SEVERE ACCIDENTS IN GENERIC INTEGRAL PWR SMALL MODULAR REACTORS: OUTCOMES ON INTEGRAL CODES' MODELLING CAPABILITIES FROM THE HORIZON EURATOM SASPAM-SA PROJECT

F. Gabrielli*, M. E. Cazado, V.H. Sanchez-Espinoza
Karlsruhe Institute of Technology
Hermann-von-Helmholtz-Platz, 1,76344 Eggenstein-Leopoldshafen, Germany
fabrizio.gabrielli@kit.edu, mauricio.cazado@kit.edu, victor.sanchez@kit.edu

F. Mascari[1], P. Maccari[1], G. Grippo[1,2], G. Agnello[1,3]
[1] ENEA, [2] UNIBO, [3]UNIPA, Italy
fulvio.mascari@enea.it, pietro.maccari@enea.it, gianmarco.grippo2@unibo.it, giuseppe.agnello04@unipa.it

M. Di Giuli
Tractebel Engineering
Boulevard S. Bolivar 36,1000, Bruxelles, Belgium
mirco.digiuli@tractebel.engie.com

J. Bittan, N. Bakouta
Electricité de France
7 boulevard Gaspard Monge, 91120 Palaiseau, France
jeremy.bittan@edf.fr, nikolai.bakouta@edf.fr

M. Malicki, T. Lind, M. Principato
Paul Scherrer Institut
Forschungsstrasse 111, CH-5232 Villigen PSI, Switzerland
mateusz.malicki@psi.ch, terttaliisa.lind@psi.ch, marcello.principato@psi.ch

M. Makarenko, Yu. Yesipenko, O. Zhabin, D. Gumenyuk
State Scientific and Technical Center for Nuclear and Radiation Safety
35-37 V. Stusa Street, Kyiv, 03142, Ukraine
mv_frankova@sstc.ua, jv_yesipenko@sstc.ua, oi_zhabin@sstc.ua, dv_gumenyuk@sstc.ua

C. Vázquez-Rodríguez, S. Kelm, M. Klauck, E.-A. Reinecke
Forschungszentrum Jülich GmbH
Wilhelm-Johnen-Straße, Jülich, 52428, Germany
s.kelm@fz-juelich.de, e.-a.reinecke@fz-juelich.de, c.vazquez-rodriguez@fz-juelich.de

M. K. Koch, J. Krieger, G. Stahlberg, T. Jankowski
Ruhr-Universität Bochum, PSS
Universitätsstrasse 150, 44801 Bochum, Germany
marco.koch@pss.rub.de, julia.krieger@pss.rub.de, gregor.stahlberg@pss.rub.de, tobias.jankowski@pss.rub.de

M. Garcia Martin, L. E. Herranz
Centre for Research on Energy, Environment and Technology (CIEMAT)
Avda. Complutense 40, Madrid 28040 Spain
monica.gmartin@ciemat.es, luisen.herranz@ciemat.es

N. Reinke
Gesellschaft für Anlagen- und Reaktorsicherheit (GRS) GmbH
Schwertnergasse 1, 50677 Köln, Germany
nils.Reinke@grs.de

A. Bentaib
Nuclear Safety and Radiation Protection Authority (ASNR)
Avenue de la division Leclerc 31, 92262 Fontenay-aux Roses, France
ahmed.bentaib@asnr.fr

L. Carenini
Nuclear Safety and Radiation Protection Authority (ASNR)
Cadarache BP3, 13115 Saint-Paul-lez-Durance, France
laure.carenini@asnr.fr

J.-C. de la Rosa Blul
European Commission Joint Research Centre
Westerduinweg 3, 1755 LE Petten, The Netherlands
Juan-Carlos.DE-LA-ROSA-BLUL@ec.europa.eu

A. Kaliatka, M. Valincius
Lithuanian Energy Institute
Breslaujos str. 3, 44403 Kaunas, Lithuania
algirdas.kaliatka@lei.lt, mindaugas.valincius@lei.lt

M. Constantin
Regia Autonoma Tehnologii Pentru Energia Nucleara
Street Campului 1, 115400, Mioveni, Romania
marin.constantin@nuclear.ro

F. Giannetti
Sapienza University of Rome
Corso Vittorio Emanuele II 244, 000186 Rome, Italy
fabio.giannetti@uniroma1.it

T. Sevon
VTT Technical Research Centre of Finland
Kivimiehentie 3, Espoo, Finland
tuomo.sevon@vtt.fi

P. Groudev
Institute for Nuclear Research and Nuclear Energy, Bulgarian Academy of Sciences
Tzarigradsko Chaussee 72, 1784 Sofia, Bulgaria
pavlinpg@inrne.bas.bg

G. Acharya, K. Mahmoud, P. Kudinov, D. Grishchenko
Royal Institute of Technology
SE-100 44 Stockholm, Sweden
govatsa@kth.se, kmmhma@kth.se, pkudinov@kth.se, dmitrygr@kth.se

ABSTRACT

The HORIZON-EURATOM SAPSAM-SA project, coordinated by ENEA (Italy), was launched in 2022 aiming at investigating applicability and transfer of knowledge and expertise gained from operating large-LWR reactors to innovative iPWRs, in view of the European licensing needs with respect to severe accident (SA) and EPZ. Two generic iPWR concepts are considered in SASPAM-SA: the iPWR Design 1 (submerged containment, ~60 MWe) and the iPWR Design 2 (~300 MWe), which employs several passive systems and a dry containment. In the framework of the WP2 (coordinated by KIT, Germany) of the project, three hypothetical SA scenarios have been postulated for each design and analyzed by means of the AC2, ASTEC, EdF-MAAP, MAAP, and MELCOR codes. Additionally, CFD models have been developed to evaluate containment thermal hydraulics using ANSYS CFX and containmentFOAM. The primary objective was

assessing the ability of state-of-art SA codes to predict the key physical phenomena occurring during such postulated scenarios in the selected generic iPWRs. The paper presents the results of such large calculation campaigns. The results show a general consistency among the different codes in predicting the key physical phenomena and events characterizing the progression of the postulated SA scenarios, e.g., H_2-onset, beginning of the core degradation and the absence of RPV failure in all the scenarios. Furthermore, the SASPAM-SA WP2 user's feedback are provided aiming at assessing preliminary best practice and lessons learned regarding the modelling capabilities of the codes employed.

KEYWORDS
SMR, iPWR, Severe Accident, EU project

1. INTRODUCTION

Small Modular Reactors (SMRs) are innovative nuclear power plants expected to be deployed worldwide in the near term. In Europe, particular interest has been focused on Integral Pressurized Water Reactors (iPWRs), owing to their enhanced safety features largely based on passive systems. While these features significantly strengthen the first three levels of the Defence-in-Depth (DiD) concept, a systematic demonstration of iPWR capabilities for preventing and managing Severe Accidents (SAs), corresponding to DiD levels 4 and 5, is still required [1].

To address this need, the HORIZON-EURATOM project 'Safety Analysis of SMR with Passive Mitigation Strategies – Severe Accidents' (SASPAM-SA), coordinated by ENEA, was launched in 2022 and involves 23 partners from 13 European countries [2–6]. The project aims to assess the applicability of knowledge gained from large Light Water Reactors (LWRs) to iPWRs, supporting licensing and siting activities and contributing to a European, independent perspective on iPWR safety for DiD levels 4 and 5 [1]. A key focus is the evaluation of Reactor Pressure Vessel (RPV) and containment behavior under postulated SA scenarios.

Two generic iPWR concepts are considered: a ~60 MWe design with submerged containment (Design-1) and a ~300 MWe design with dry containment and multiple passive safety systems (Design-2). Without assessing the designs themselves, SASPAM-SA evaluates the capability of integral SA codes and Computational Fluid Dynamics (CFD) tools to simulate the key phenomena occurring in iPWRs. These reactors are characterized by integral configuration and strong thermal-hydraulic coupling between the primary system, containment, and safety systems, posing challenges to current modelling approaches. Relevant phenomena include natural circulation in the integral RPV, thermal stratification in large pools, primary–containment interactions, and in-vessel melt retention [7].

Within this framework, an extensive calculation campaign was conducted in WP2 of the project, involving 16 institutions and employing state-of-the-art European and non-European integral codes (AC2, ASTEC, EdF-MAAP, MAAP, and MELCOR), together with CFD tools (ANSYS CFX and containmentFOAM). The activity included the development and assessment of generic but representative datasets for both iPWR designs, as well as the postulation and analysis of hypothetical Design Basis Accidents (DBAs) and SAs. Since the study is based on generic designs and no Probabilistic Safety Analysis (PSA) was performed, SA scenarios were selected according to severity rather than probability of occurrence.

This paper presents the main results of the calculation campaign, together with preliminary best practices and recommendations for the application of integral codes to iPWRs, derived from the lessons learned by the SASPAM-SA WP2 participants. The ultimate objective is to provide a preliminary assessment of the capability of the considered codes to simulate the dominant phenomena driving accident progression, with particular emphasis on the behavior and interaction of passive safety systems in an SMR configuration.

Specifically, the analysis addresses passive decay heat removal, primary automatic depressurization, passive high- and low-pressure safety injection, containment pressure suppression, and passive flooding of the reactor cavity. It is emphasized that this activity was not intended as a classical benchmark. Instead, starting from common specifications for the two generic designs—based on open literature and engineering judgment—each participant was allowed to explore different modelling approaches (e.g., decay heat assumptions, nodalization strategies, and physical models). This approach enabled both a quantitative

evaluation of the impact of modelling choices on selected figures of merit and a qualitative assessment of the codes' ability to reproduce the key physical phenomena occurring during the postulated scenarios.

2. THE GENERIC iPWR DESIGN-1 AND DESIGN-2

The generic iPWR Design-1 and Design-2 considered in the SASPAM-SA project are shown in Figure 1. Their specifications were defined in WP2 based on open literature [8] and reflect the main features of the most promising European iPWR concepts. These generic designs are used to broadly assess the capability of SA and Computational Fluid Dynamics (CFD) codes to simulate phenomena and processes typical of iPWRs.

The investigated Design-1 (Figure 1, left) is a natural-circulation iPWR with an integral RPV housing a shrouded core and riser, an integrated pressurizer (PRZ), and a helical-coil steam generator. The RPV is enclosed in a steel containment largely submerged in a water pool acting as the ultimate heat sink. The Emergency Core Cooling System (ECCS) relies on passive coolant circulation between the RPV and containment through Reactor Vent Valves (RVVs) and Reactor Recirculation Valves (RRVs), while the Chemical and Volume Control System (CVCS) is connected to the downcomer above the core.

The investigated Design-2 (Figure 1, right) features a dry containment and several passive safety systems. The reactor operates in forced circulation under normal conditions and switches to passive mitigation during accidents. Its integral RPV contains the core, eight helical-coil steam generators, eight primary pumps, the control rod drive mechanisms, and the pressurizer, with hot coolant flowing upward through a circular riser to the pump suctions located above the steam generators.

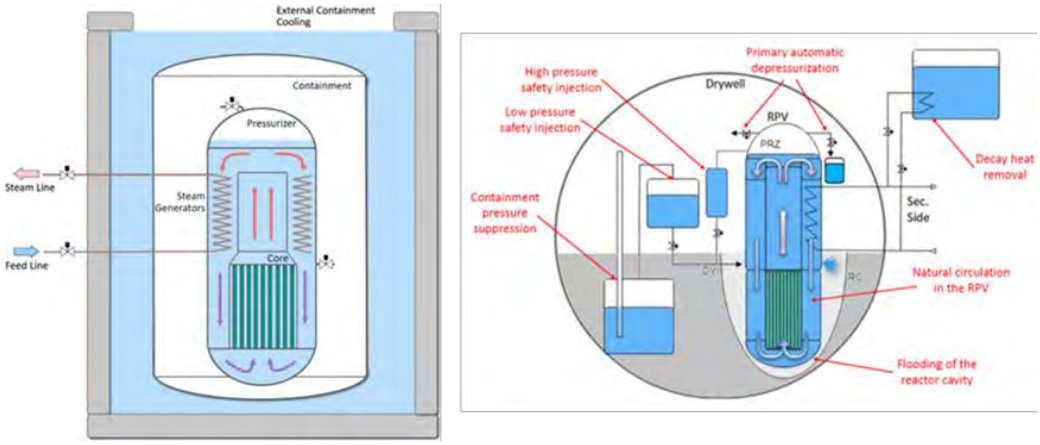

Figure 1. Layout of the generic iPWR Design-1 (left) and Design-2 (right) [9].

In addition to the design specifications, a database of decay heat and isotopic inventories covering burnups from 20 to 60 MWd/kgU, with a 2.5 MWd/kgU step, was generated using the CASMO code, developed by Studsvik, and is hereafter referred to as WP2data. To assess the impact of different decay heat assumptions, two additional datasets were considered: the 1973 ANS standard data (ANS73) and the same data increased by 20% (ANS73+20%). The results indicate that, following scram, the decay power predicted by WP2data is approximately 30% lower than that of the 1973 ANS standard [9]. Note that the WP2data have been computed by employing generic core model for both iPWR designs characterized by a lower power density than in the 1973 ANS standard, usually based on large reactors.

3. DEVELOPMENT OF THE DATASETS OF INTEGRAL AND CFD CODES

The full list of the partners and of the integral and CFD codes employed are given in Table I for the iPWR Design-1 and Design-2, respectively. In order to increase the efficiency of the activities, some partners joined the project by sharing their own datasets, upon request. Such sharing allowed a sensible acceleration of the activity. As shown in Table I, Tractebel and PSI made available the ASTECv2.2 and MELCORv2.2

datasets, respectively, of the iPWR Design-1. Similarly, ENEA and ENEA/UNIROMA1 made available the ASTECv3.1 and MELCORv2.2 datasets, respectively, of the iPWR Design-2. Furthermore, ASNR and GRS, as ASTEC and AC2 developers, respectively, supported the users. New datasets of the EdF-MAAP and AC2 codes have been developed for the iPWR Design-1 by EdF and RUB, respectively. Similarly, for the iPWR Design-2, new datasets of the MAAPv5.06 and AC2 codes have been assessed by JRC and LEI, respectively. Concerning CFD codes, new datasets using ANSYS CFX and containmentFOAM were developed by SSTC NRS and FZJ for the iPWR Design-1 and Design-2, to be mainly employed in the SASPAM-SA WP devoted to the CNMT analyses.

Table I. iPWR designs: codes, partners, and contributions

Code	Partners Design-1/Design-2	Contribution/Role	Design
ASTECv3.1	KIT / ENEA	Contribution to a new dataset /sharing	1–2
ASTECv2.2/v3.1	Tractebel / ENEA	Dataset sharing	1–2
MELCORv2.2	KTH, PSI / CIEMAT, KTH, UNIROMA1	Dataset use/sharing	1–2
MAAPv5.06	— / JRC	New dataset	2
EdF-MAAP5.04	EdF / —	New dataset	1
AC2	RUB / LEI	New dataset	1–2
ANSYS CFX	SSTC NRS / —	New dataset (CFD)	1
CAD/containmentFOAM	— / FZJ	New dataset (CFD)	2
AC2	GRS / GRS	AC2 user support	1–2
ASTEC	ASNR / ASNR	ASTEC user support	1–2
—	RATEN / RATEN	Support in the definition of the scenarios	1–2

4. ANALYSIS OF THE POSTULATED SEVERE ACCIDENTS IN THE GENERIC DESIGN-1

Three SA scenarios are postulated for the generic iPWR Design-1. In all scenarios, the ECCS is assumed to actuate when both of the following conditions are met: the containment (CNMT) water level exceeds ~5.8 m and the pressure difference between the reactor pressure vessel (RPV) and the CNMT falls below ~6.2 MPa or ~6.9 MPa, depending on the modelling choices of the code user.

SA-1 is initiated by a break in the CVCS make-up line combined with a loss of AC power. The RVVs are assumed to be operational, while the RRVs are assumed to be stuck closed. The break discharges directly into the CNMT. To investigate the effect of coolant reverse flow following ECCS activation, the break height was varied in the datasets, and reverse flow was either allowed or suppressed depending on the modelling approach.

SA-2 is initiated by the inadvertent opening of one RVV (~12.7 cm) at the top of the pressurizer, also combined with a loss of AC power. The remaining two RVVs are assumed to be available and actuated as in SA-1, while both RRVs are unavailable. This configuration prevents water recirculation from the CNMT to the RPV, leading to progressive core degradation.

SA-3 is initiated by a smaller break (~4.3) in the pressurizer vent line, again combined with a loss of AC power. As in SA-2, the remaining RVVs are available and actuated as in SA-1, while the RRVs are unavailable. Owing to the smaller break size compared to SA-2, a slower accident progression is expected.

4.1. Results: accident progression

The results by the different integral codes using the decay heat power ANS73+20% are presented. The behavior of the water level in the RPV and in the CNMT predicted by the AC2, ASTECv3.1, EdF-MAAP, and MELCOR codes is shown in Figure 2 (left) during the postulated SA-1.

Following the accident initiator, the RPV depressurizes while the pressure in the CNTM increases and does reach ~0.1 MPa at the end of the scenario. Because RRVs are stack, the core is isolated and the water level decreases below the top of active fuel (TAF) quite early and it is completely uncovered at ~25,000 s. The results concerning the water level in the containment at the end of the transient show a deviation of ~1 m, the final value being 9 m ± 0.5 m. The results show a quite good agreement among the codes. Furthermore, the ASTECv3.1 and EdF-MAAP results for all the postulated SAs are shown in Figure 2 (right). One may observe a good agreement between the two codes and, as expected, a slower accident progression going from the SA-1 to the SA-3.

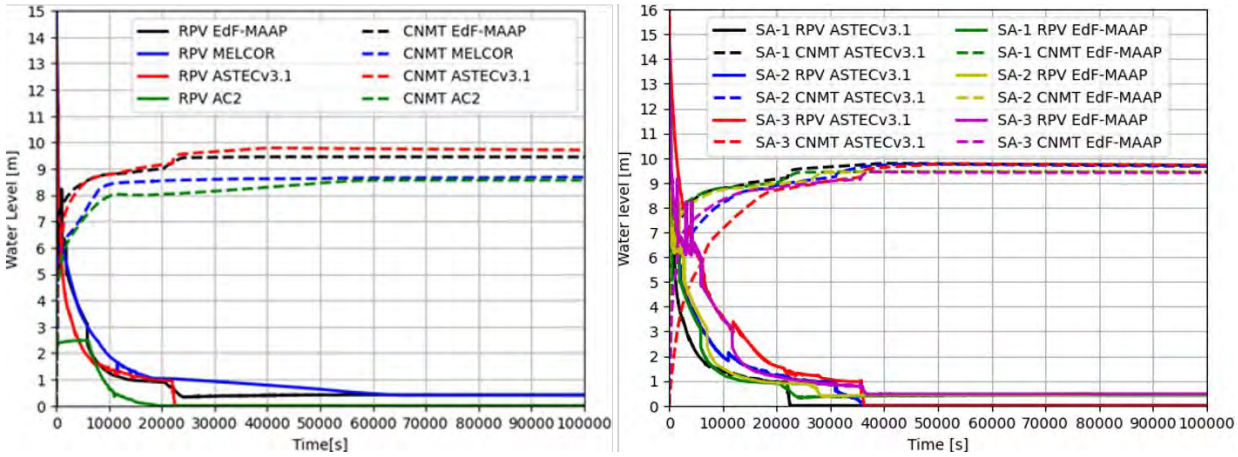

Figure 2. Water level in the RPV and in the CNMT in the SA-1 (left) and in all the SAs (right).

The results for selected key events during the progression of the postulated SA-1 (black), SA-2 (blue), and SA-3 (green) are summarized in Table II. As previously mentioned, starting from the common design specifications, each participant explored the code capabilities using different modelling options, leading to a spread of results.

In particular, deviations in the timing of ECCS activation are observed due to differences in the break height and in the set point of the RPV–CNMT pressure difference adopted by the partners. Earlier ECCS activation is predicted in simulations employing a lower break height (7.3 m instead of 9 m) and a lower pressure difference set point (6.2 MPa instead of 6.9 MPa), resulting in a shorter time to reach the CNMT water level of 5.8 m. For instance, MELCOR predicts ECCS activation at 339 s when the break is set at 7.3 m and no reverse flow is imposed, in agreement with ASTECv3.1 and EdF-MAAP using the same assumptions. Conversely, when higher values are adopted for both parameters, ECCS activation is delayed, as observed in AC2 and ASTECv3.1 (CPA), where it occurs at ~950 s. Two different CNMT modelling approaches and code versions for ASTEC have been adopted: ASTECv2.2 (CESAR) and ASTECv3.1 (CPA). Further details on the modelling options and results are provided in [10, 11] for ASTECv2.2 and ASTECv3.1, [10] for EdF-MAAP, [12–15] for MELCOR v2.2, and [16, 17] for AC2.

For SA-1, the deviation in hydrogen onset among ASTEC, EdF-MAAP, and AC2 is approximately 2,000 s, increasing to ~5,000 s in MELCORv2.2, likely due to the earlier ECCS activation. Nevertheless, the sequence of major phenomenological events related to core degradation shows reasonable agreement among the codes, considering modelling uncertainties. Core damage is predicted to start at ~10,000 s by all codes, with ASTECv3.1 and EdF-MAAP showing good agreement on the timing of the first corium slump with Fission Products (FP) to the Lower Plenum (LP), while in MELCOR simulations core damage begins later, at ~15,000 s. For SA-2 and SA-3, ASTECv3.1 (CPA) and EdF-MAAP show reasonable qualitative agreement on hydrogen onset and on the timing of the first corium slump to the lower plenum, whereas ASTECv2.2 (CESAR) predicts a delayed response in SA-2.

Despite the observed deviations arising from both modelling choices and uncertainties in core degradation and relocation models, no RPV failure is predicted by any of the codes in any scenario up to 70 h after the initiating event, owing to the effectiveness of External Reactor Vessel Cooling (ERVC).

Table II. Progression of the postulated SA scenarios (ANS73+20% decay heat data)

Event	ASTECv3.1 (CPA)	ASTECv2.2 (CESAR)	EdF-MAAP	MELCORv2.2	AC2
ECCS signal [s]	318-950 1,432-1,782 6,000-6,285	259 1992 4,600	349 91 1,162	339-495	4,537
H_2 on-set [s]	4,050-5,530 8,974-10,100 17,377-17,500	6,400 20,000 23444	7,800 11,757 16,348	8,910-10,320	7,482
Start of FPs release from fuel pellets [s]	4,234-6,665 10,294-16,789 18,763-24,259	6,780 18,851 23,580	11,888 13,822 17,508	13,105-14,865	9,171
1st corium slump with FPs in LP [s]	17,789-19,350 26,794-33,989 33,153-42,699	21,118 42,501 45,481	20,366 26,586 35,581	14,100	11,050
Core Bottom of Active Fuel (BAF) Uncovery [s]	22,435-30,801 35,954-54,709 33,153-42,669	29,713 49,108 49,108	20,370 23,680 39,555	18,072	15,254
In-vessel H_2 [kg]	54-61 60-67 54-59	77 93 100	80 77 81	50-64	72
Max. CNMT pressure [MPa]	2.8-4.3 3.9-4.1 1.3-1.6	5.3 4.2 2.1	2.3 2.8 1.6	5.5-6.1	
RPV failure	No	No	No	No	No

4.2. Results: core degradation

The time-dependent evolution of the corium mass in the core and relocated to the LP for the postulated SA-1, as predicted by AC2, EdF-MAAP, MELCORv2.2, ASTECv2.2 (CESAR), and ASTECv3.1 (CPA), is shown in Figure 3 (left and right, respectively). In the SA-1, the codes show a reasonable agreement on the timing of material relocation in the LP, the max deviation being of ~6,000 s when AC2 is compared with the other codes.

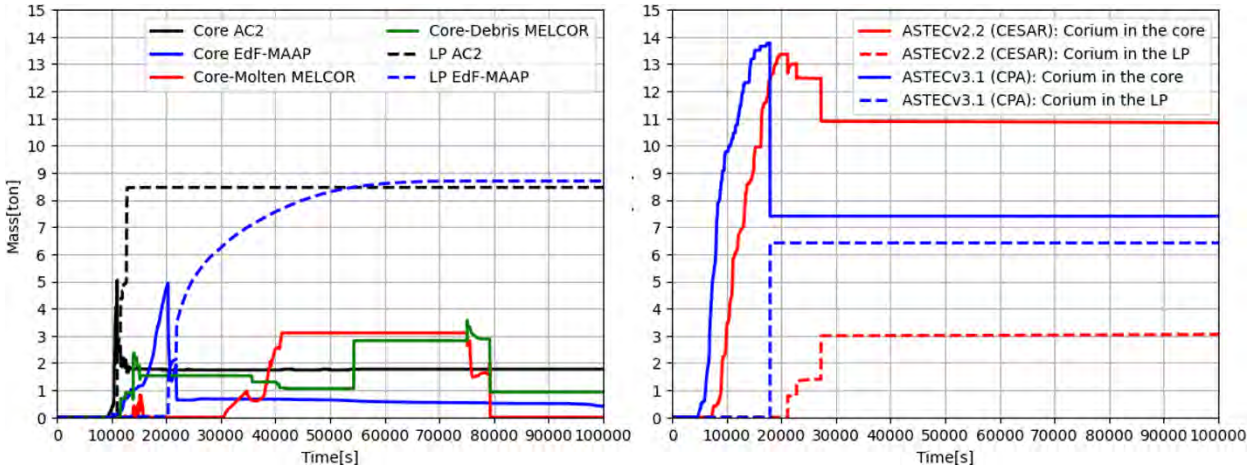

Figure 3. SA-1: Mass of molten material and debris in the core and relocated in the LP (SA-1).

For the molten material remaining in the core, ASTECv3.1 predict a range of ~7.5-10 t depending on the module employed for the CNMT behavior (Figure 3, right). With respect to LP relocation, AC2, EdF-MAAP, and ASTECv3.1 (CPA) show reasonable agreement (~9 t, with ASTEC slightly lower), whereas ASTECv2.2 (CESAR) predicts a significantly smaller relocated mass (~3 t). ASTECv3.1 (CPA) generally predicts a larger amount of molten material remaining in the core than EdF-MAAP, reflecting differences in core relocation modelling, as EdF-MAAP tends to relocate most of the corium to the LP. Similarly, for AC2. MELCORv2.2 predicts ~6 t relocated to the LP (drops in (Figure 3, left), with debris accounting for approximately 50% of the total mass. Nevertheless, it must be noted that the parametric analyses performed at PSI indicate a wide range of core damage (~17–100%), of corium remaining in the core, and amount of material relocated in the LP, depending on the modelling assumptions [13].

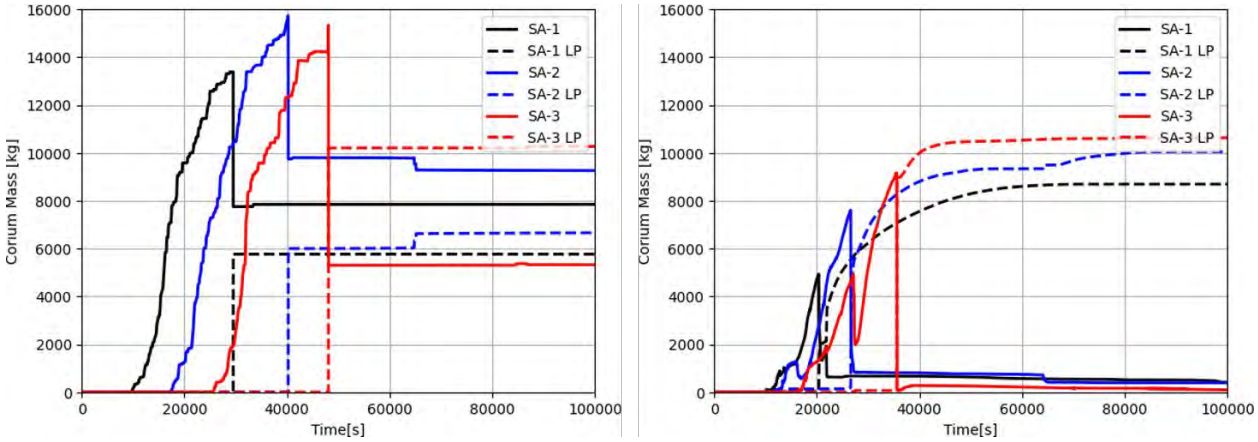

Figure 4. Core degradation: ASTECv3.1 (WP2data) left and EdF-MAAP (ANS73+20%) right.

To assess the impact of different decay heat data, ASTECv3.1 (CPA) simulations were performed for all postulated scenarios using WP2data, with results shown in Figure 4 (left). Comparison with the ASTEC v3.1 (CPA) SA-1 results in Figure 3 (right) confirms that the lower decay heat leads, as expected, to a delayed progression of core degradation. EdF-MAAP results for all postulated scenarios obtained using the ANS73+20% decay heat are shown in Figure 4 (right). Despite the different decay heat assumptions, ASTECv3.1 (CPA) and EdF-MAAP show qualitative agreement on the corium mass relocated to the LP in SA-3, while deviations of ~3-4 t are observed for SA-1 and SA-2. The results in Figure 4 also reveal the slowing of the progression from the SA-1 to the SA-3, the latest being also characterized by a large amount of corium relocated in the LP.

4.3. Hydrogen generation

The time-dependent behaviour of the in-vessel H_2 production computed by the codes by employing the ANS73+20% decay heat data is shown in Figure 5 (left).

The results show that the final total amount of hydrogen produced by the codes lies in the band of ~70 ± 10 kg. Furthermore, the results relevant to the total amount of the in-vessel H_2 produced from the parametric analyses performed by considering the effects of different modelling options (see, e.g. [10-17]) is shown in Figure 5 (right).

It may be observed that the maximum deviation among the results is ~25-35 kg in the SA-1. In the SA-2, ASTECv3.1 (CPA) and EdF-MAAP show a reasonable agreement, while a larger deviation is observed in the SA-3. Note that the steel oxidation conservative approach in EdF-MAAP, lead to higher values than ASTEC (CPA), as discussed in [18]. Finally, ASTECv2.2 (CESAR) provides significantly larger values.

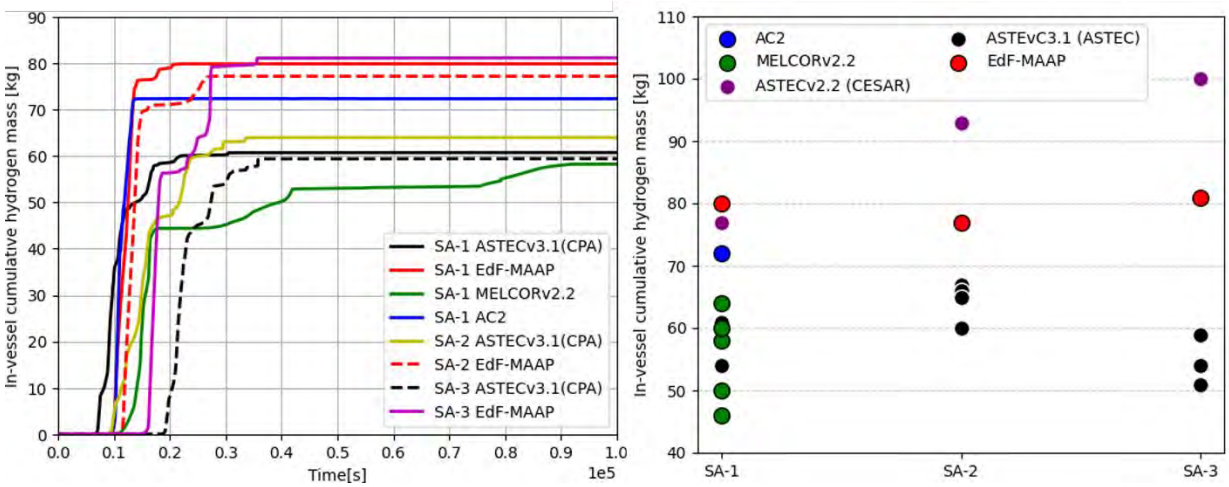

Figure 5. In-vessel H_2 production.

5. ANALYSIS OF THE POSTULATED SEVERE ACCIDENTS IN THE GENERIC DESIGN-2

Three SA scenarios are postulated for the generic iPWR Design-2, assuming a progressive increase in the failure of safety systems from SA-1 to SA-3.

In SA-1, a guillotine break of one Direct Vessel Injection (DVI) line (Figure 1) is assumed, together with the unavailability of the EHRS due to failure of the corresponding valves to open. SA-2 assumes the same guillotine DVI break, combined with the unavailability of both the EHRS and the Automatic Depressurization System (ADS-1), again due to valve failure. In SA-3, the same DVI break is assumed, together with the unavailability of all safety systems as a result of the failure of the associated valves to open.

Regarding modelling options, the WP2data set was adopted for all analyses. The CNMT design pressure was set to ~1.4 MPa in the ASTEC v3.1 and AC2 models, ~1.2 MPa in the MELCOR v2.2 datasets, and to ~2.4 MPa in the MAAP v5.06 model. These non-homogeneous hypotheses for containment response to high pressures induced large difference in the pressure evolution, determinately affecting the SA progression. To investigate the accident progression without containment failure, a drywell-to-environment leak was modelled in one of the two MELCOR v2.2 datasets used for the SA-1 and SA-3 analyses, with the leak area increasing as a function of the pressure difference between the two volumes. This modelling option, hereafter referred to as MELCOR v2.2-leak, is currently under further investigation within the work package dedicated to CNMT behavior. More details on the modelling options and results are in [19] (ASTECv3.1) and [20] (MELCORv2.2). Even if CFD analyses are not discussed here, details of the analysis of the SA-1 in Design-2 by means of containmentFOAM can be found in [21].

5.1. Results: accident progression

The behavior of the pressure in the RPV and in the CNMT (dots) as well as the water level in the cavity predicted by the ASTECv3.1 and MELCORv2.2 codes in all the postulated scenarios is shown in left and right sides of Figure 6, respectively. The DVI break leads to a fast depressurization of the RPV, and a slower pressurization trend occurs in the CNMT, while the SCRAM is performed after a short delay. The failure of the EHRS triggers a fast pressurization of the CNMT, which reaches the design value (1.4 MPa) rather soon.

Regarding the SA-1, the comparison of the ASTECv3.1 and MELCORv2.2-leak results show a different behavior of the CNMT pressure. The MELCORv2.2-leak results show that the CNMT pressure remains constant at ~1.2 MPa. A massive reverse flow from the Pressure Suppression System (PSS) tanks is predicted by ASTECv3.1 after CNMT failure, while not by MELCOR v2.2-leak and MAAP v5.06 leading to a fast increase of the water level above the DVI line in the ASTECv3.1 and not in MELCORv2.2 and MAAPv5.06 (not shown) analyses.

Due to the failure of the ADS-1 in the SA-2, the results show, as expected, slower depressurization of the RPV and of the CNMT. At the same time, the rapid decrease in CNMT pressure forces water from PSS tanks to the reactor cavity. As a result, the water level in the cavity rapidly increases (Figure 6), the ASTECv3.1 and MELCORv2.2 results showing a reasonable agreement (~2 m difference).

The failure of all the safety systems in the SA-3 leads to a much slower RPV and CNMT depressurization than in the SA-1 and SA-2 scenarios as shown in Figure 6 by the ASTECv3.1 and MELCORv2.2 results, as well as in AC2 and MAAPv5.06 (not shown). As expected, the MELCORv2.2 dataset with the drywell/environment leak modelled predicts constant CNMT pressure of ~1.2 MPa. As observed in the SA-1 and SA-2, water rapidly fills the reactor cavity. Because of both the CNMT depressurization and the postulated failure of the Long term Gravity Make-up System (LGMS), the water level in the cavity predicted by ASTECv3.1, the MELCORv2.2 dataset w/o the leak modelled in Figure 6 (right) and MAAPv5.06 (not shown) decreases, while it remains constant in the MELCOR v2.2-leak simulations.

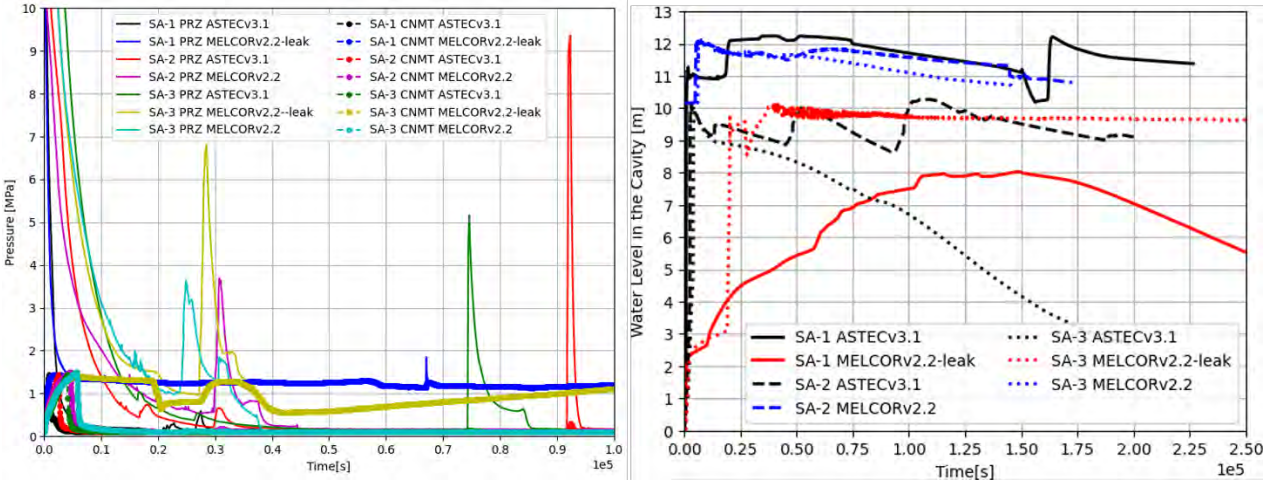

Figure 6. Pressure in the RPV and in the CNMT (left) and water level in the cavity (right).

The results for selected key events during the progression of the postulated SA-1 (black), SA-2 (blue), and SA-3 (green) are shown in Table III, where 'NA' indicates 'Not Activated', while '–' denotes unavailable results. Overall, all codes predict, as expected, a faster accident progression from the SA-1 to the SA-3.

For SA-1, ASTECv3.1 and MELCOR v2.2-leak show reasonable agreement up to the time at which the TAF level is reached. Beyond this point, H_2 onset and the start of core degradation occur earlier in ASTEC v3.1 than in MELCORv2.2-leak. MAAPv5.06 predicts earlier for most events compared to ASTEC v3.1 and MELCOR v2.2-leak, mainly due to the higher containment design pressure adopted (2.4 MPa versus 1.4 MPa), which avoids containment failure. Such discrepancies due to the different modelling of the CNMT further prove the larger impact of the tight coupling between RPV and CNMT on the SA progression in iPWRs than in large PWRs, which will be more extensively studied in another WP focused on the CNMT behavior in the SASPAM-SA project. A major discrepancy among the codes concerns corium relocation to the lower plenum: while ASTEC v3.1 predicts no corium slump due to water injection in the vessel, both MELCORv2.2-leak and MAAP v5.06 predict corium relocation, as discussed in the following section. Note that the degraded core is stabilized up to 70 h from the accident initiator.

For SA-2, ASTECv3.1 and MELCORv2.2 show reasonable agreement in the timing of the main accident phases, although ASTECv3.1 predicts a significantly slower decrease of the core water level. The main differences concern the H_2 onset, predicted by MELCORv2.2 ~4,000 s later than by ASTECv3.1, and the first corium slump, which occurs ~60,000 s earlier in MELCORv2.2. MAAPv5.06 again shows deviations for several events, largely attributable to the higher containment design pressure. Nevertheless, reasonable agreement with MELCORv2.2 is observed for the time to reach the BAF level (~4,000 s) and for the onset of upper core failure. In contrast, H_2 onset is predicted by MAAPv5.06 ~4,000 s earlier than ASTECv3.1.

For SA-3, ASTECv3.1, MELCOR v2.2, and AC2 show overall qualitative agreement up to CNMT failure, with maximum differences of ~2,000 s. Large discrepancies are observed for the timing of the low pressure difference (DP) RPV–containment signal, which is predicted by AC2 ~27,000 s and 40,000 s earlier than by MELCOR v2.2 and ASTEC v3.1, respectively. As in SA-1 and SA-2, the MAAP v5.06 results exhibit a slight faster progression due to the higher containment design pressure. In ASTECv3.1, both the attainment of the BAF level and the first corium slump to the LP occur later than in the other codes.

As for Design-1, no RPV failure is predicted by any of the codes in any scenario up to 70 h after the initiating event, owing to the effectiveness of the ERVC.

Table III. Progression of the postulated SA scenarios

Event	ASTECv3.1	MELCORv2.2	MAAPv5.06	AC2
Actuation of emergency boration tank [s]	311/311/NA	172/153/NA	177/177/NA	NA
Low DP RPV-CNMT signal [s]	18,581/45,303/ 53,532	-/44,718/ 38,200	1,488/11,099/ 8,818	11,700
Actuation of LGMS [s]	18,586/45,308/ NA	10230/44,720/N A	1,493/11,104/N A	NA
Low LGMS mass signal [s]	150,174/133,087/-	131,340/-/-	37,080/64,847/-	-
Actuation of ADS-2 [s]	150,174/133,087/ NA	103,440/-/NA	37080/-/NA	NA
CNMT failure [s]	800/2,500/ 4,020	680/4,630/ 3,090-5,730	32,700/62,192/ 13,327	2,504
Swell level TAF reached []	5,830/2,000/ 5,280	3,136/610/ 1,690-4,250	2,804/2,804/ 2,675	3,600
H_2 on-set [s]	11,500/8,000/ 7,294	18,138/12,290/ 9,070-12,290	4,762/4,762/ 3,980	7,000
Start of FPs release from fuel [s]	12,528/9,651/ 10,386	-/12,610/-	-	7,000
Swell level BAF reached [s]	-/76,860/ 72,960	58,059/23,970/ 18,680-23,800	19,800/19,800/ 12,411	11,000
Core rings start to fail [s]	12,528/9,700/ 10,386	31,664/13,450/ 10,270-14,630	10,231/10,231/ 9,955	13,500
First corium slump [s]	-/92,900/74,610	67,060/29,850/ 24,300-27,300	10,231/10,231/ 9,955	-
RPV failure	No	No	No	No

5.2. Results: core degradation

Figure 7 shows the time-dependent evolution of the corium mass in the core and relocated to the LP for the postulated SAs as predicted by ASTEC v3.1 and MELCOR v2.2. The results indicate an increasing severity of accident progression from SA-1 to SA-3.

For SA-1 (Table III), corium relocation to the LP is predicted by MELCORv2.2-leak but not by ASTECv3.1. In ASTECv3.1, a quasi-steady state is reached between 50,000 s and 150,000 s. At~19,000 s, the RPV pressure approaches the CNMT pressure, water then flows in the RPV through the break, and a fast steam generation occurs (peak pressure in Figure 6). ~60 t of molten material form in the core is stabilized by the water injected in the vessel and no relocation to the LP occurs.

In contrast, MELCORv2.2-leak predicts an initial corium slump to the LP at 67,060 s, followed by partial reflooding until LGMS depletion and two additional slumps at later times (at ~145,700 s and ~159,000 s, Figure 7), resulting in ~95 t of mostly debris relocated to the LP by the end of the simulation. MAAPv5.06 predicts limited relocation (~13 t, not shown) and a stable LP configuration w/o ablation [18].

For SA-2, ASTECv3.1 predicts relocation of ~100 t of molten material to the LP starting at 92,900 s, while MELCORv2.2 predicts relocation of mostly debris (~70 t) beginning at approximately 29,800 s. MAAPv5.06 predicts relocation of ~50 t starting at 10,200 s.

In SA-3, ASTECv3.1, MELCORv2.2, and MAAPv5.06 (not shown in Figure 7) show reasonable agreement on the onset of core degradation and on the total relocated mass in the LP (~91 t, ~70 t, and ~74 t, respectively), although significant discrepancies remain in the predicted timing of relocation.

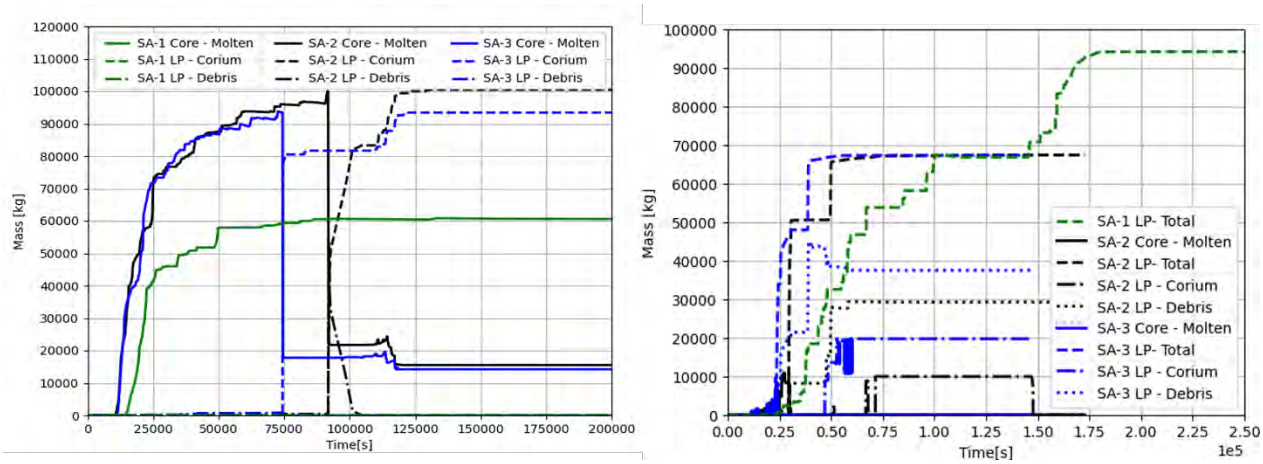

Figure 7. Core melting and material relocation in the LP: ASTECv3.1 (left), MELCORv2.2 (right).

5.3. Hydrogen generation

The time-dependent behaviour of the in-vessel H_2 production computed by the ASTECv3.1, MELCORv2.2, and MAAPv5.06 codes in the postulated SAs are show in Figure 8.

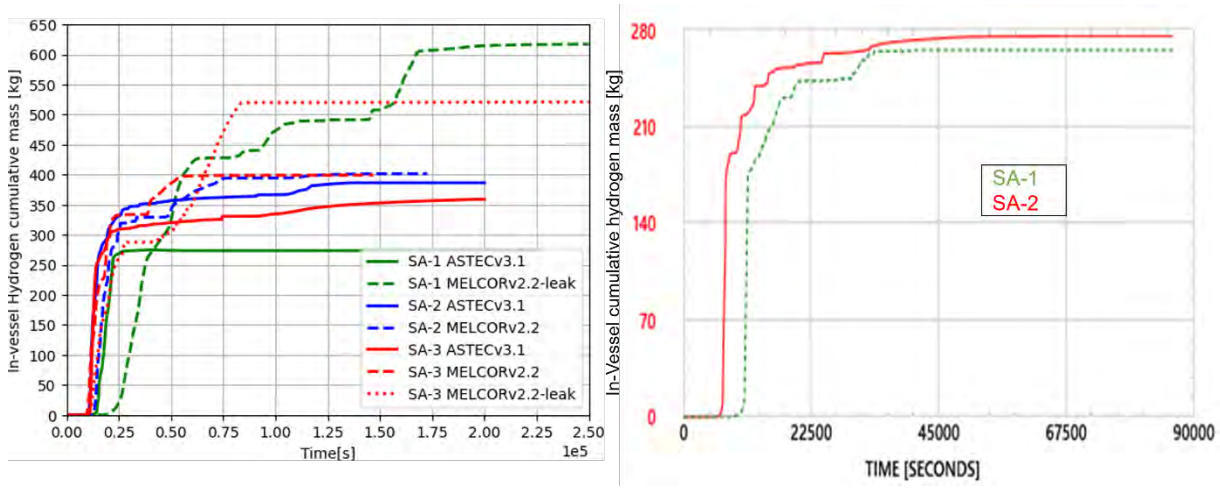

Figure 8. In-vessel H_2 production: ASTECv3.1 and MELCORv2.2 (left) and MAAPv5.06 (right).

In the SA-1, the ASTECv3.1 and MAAPv5.06 results show a good agreement on the maximum amount of H_2 (~280 kg), while the value predicted by the MELCOR v2.2-leak is almost the double (~600 kg) due to the occurrence of three slumps in the LP, which are responsible of the increase of the H_2 production, a significant contribution coming from the steel oxidation. The results relevant to the SA-2 show a quite good agreement between ASTECv3.1 and MELCORv2.2, a deviation of ~20 kg being observed. Furthermore, the MAAPv5.06 simulation predicts a value of ~280 kg, namely ~100 kg lower than ASTECv3.1 and MELCORv2.2. Regarding the SA-3, the ASTECv3.1 and MELCOR v2.2 results show a reasonable agreement, the deviation on simulated H_2 production being ~50 kg, while MAAP v5.06 (not shown in Figure

8) predicts a lower amount (~280 kg). Finally, the MELCOR v2.2-leak simulation shows a much larger value (~525 kg), the increase at ~50,000 s mainly due to the stainless-steel oxidation.

6. PRELIMINARY TAKEAWAYS

The capabilities of the state-of-art integral codes to predict key thermal-hydraulics and core degradation phenomena in the two generic iPWR designs selected in the SASPAM-SA project have been analyzed. Furthermore, an additional goal of the WP2 was providing the necessary data for more detailed investigations in the other WPs of the project regarding in-vessel melt retention, CNMT behavior, and source term.

With respect to the performance of the integral codes, the strong thermal–hydraulic coupling between the different components and passive systems characterizing the iPWR designs (compared with large water-cooled reactors), represents a major challenge for such tools.

The results reveal that the integral codes are capable to predict the key phenomena occurring in the postulated SAs. Despite modelling differences, the codes generally show qualitative agreement on accident progression trends, while quantitative discrepancies are observed in timing and mass inventories.

The following preliminary lessons learned summarize the main findings and best practices applicable across codes, designs, and accident classes:

- As in LWR accident simulations, nodalization of the RPV, core, containment, reactor pool, and safety systems play a key role. Particular sensitivity has been found to axial and radial core nodalization, as expected. Same thing might apply to passive safety systems. Hence, sensitivity studies on nodalization are highly recommended before adopting a final model;
- ERVC modelling is recommended for both DBA and SA analyses, while simplified correlations may underestimate cooling effectiveness. For example, the AIDA module in AC2 is recommended;
- Uncertainty and sensitivity analyses are indispensable to grasp a better assessment of safety margins, to identify dominant parameters, to quantify modelling uncertainty, to support the interpretation of results, and to assess code capabilities;
- In water-cooled SMRs, heavily based on natural circulation, core coolability parameters, e.g., heat-transfer coefficients, and steam flow patterns have a significant impact on core degradation (at least for MELCOR code, for which the study was performed) and must be explicitly considered during input-deck development and may play a stronger role than in large PWRs. In particular, MELCOR analyses looks showing a possible cooling of the core due to natural convection with steam for iPWR Design-1, which does represent a significant difference with large power PWR and seems to be an interesting point for the further analyses in the future;
- Long accident timelines increase computational demands: reduced decay heat and corium mass in SMRs lead to slow SA progression, requiring long simulation times and careful resource management.

There are not reference calculations that allow concluding that the deviations found are larger than in LWR scenarios. Besides, rooting the source of discrepancies might require cross-comparison of input decks, which was beyond this WP scope. Even so, there are some efforts ongoing to identify potential sources in the differences of code modeling approaches.

ACKNOWLEDGMENTS

Funded by the European Union. Views and opinions expressed are, however, those of the author(s) only and do not necessarily reflect those of the European Union or European Commission - Euratom. Neither the European Union nor the granting authority can be held responsible for them.

REFERENCES

1. IAEA, *SMR Regulators' Forum Pilot Project Report: Considering the Application of a Graded Approach, Defence-in-Depth and Emergency Planning Zone Size for Small Modular Reactors*, Vienna, Austria (2018).
2. European Commission, *Safety Analysis of SMR with PAssive Mitigation strategies - Severe Accident - SASPAM-SA Project*, https://cordis.europa.eu/project/id/101059853/de, (2023).
3. https://www.saspam-sa.eu
4. https://zenodo.org/communities/saspam-sa/about
5. F. Mascari et al., "Horizon Euratom SASPAM-SA project: main ideas and first outcomes", *Proc. of the International Conference on Small Modular Reactors and their Applications*, Vienna, Austria October 21–25 (2024).
6. L.E. Herranz, B. Poubeau, L. Chailan; F. Mascari, "Looking ahead to severe accident research" (2025) *EPJ Nuclear Sciences and Technologies*, **11**, 28 (2025) https://doi.org/10.1051/epjn/2025025.
7. OECD/NEA, *A state-of-the-art report on scaling in system thermal-hydraulics applications to nuclear reactor safety and design*, NEA/CSNI/R(2016)14, Paris, France (2017).
8. SASPAM-SA, *Milestone 2.1: Generic Data on Design 1 and Design 2*, (2023).
9. F. Gabrielli, et al., "Analysis of Postulated Severe Accidents in Generic Integral PWR Small Modular Reactors in the Frame of the Horizon SASPAM-SA Project", *Proc. of ERMSAR2024*, Stockholm, Sweden, May 13-16 (2024), https://doi.org/10.5445/IR/1000174165/v2.
10. M. Di Giuli, J. Bittan, N. Bakouta, A.M. Swaidan, "Comparison between EDF MAAP5.04 and ASTECv3 codes on hypothetical severe accidents in an integral PWR", *Nuclear Engineering and Design*, **444** (2025), https://doi.org/10.1016/j.nucengdes.2025.114407.
11. M. E. Cazado, F. Gabrielli, V. H. Sanchez Espinoza, "Analysis of Accident Scenarios in a Generic Natural Circulation Small Modular Reactor with the ASTEC Code in the Framework of the SASPAM-SA Project", *Mecánica Computacional*, **41** (2024) https://doi.org/10.70567/mc.v41i18.91.
12. M. Malicki, T. Lind, "MELCOR 2.2 iPWR LOCA type accident analysis, PART I: Thermal-hydraulics", *Nuclear Engineering and Design*, **428** (2024) https://doi.org/10.1016/j.nucengdes.2024.113433.
13. M. Malicki, T. Lind, "MELCOR 2.2 iPWR LOCA type accident analysis, PART II: BDBA". *Nuclear Engineering and Design*, **430** (2024) https://doi.org/10.1016/j.nucengdes.2024.113667.
14. M. Malicki, P. Darnowski, T. Lind, "An iPWR MELCOR 2.2 Study on the Impact of the Modeling Parameters on Code Performance and Accident Progression", *Energies*, **17** (2024) https://doi.org/10.3390/en17133279.
15. G. Acharya, D. Grishchenko, P. Kudinov, "Investigation of Severe Accident Progression in Integral PWR SMRs", *Proc. of ICONE32*, Weihai, Shandong, China, June 22-26 (2025).
16. J. Krieger, M. Koch, G. Stahlberg, "Analyses of a postulated severe accident in a generic Small Modular Reactor using AC2", *Proc. of Kerntechnik*, Leipzig, Germany, June 11-13 (2024).
17. G. Stahlberg, J. Krieger, M. Koch, "Analyses of an integral Pressurized Water Reactor during postulated Accident Conditions using the System Code Package AC²", *Proc. of NUTHOS-14*, Vancouver, BC, Canada, August 25-28 (2024).
18. J. Bittan, N. Bakouta, J.-A. Zambaux, L. Carénini, "Comparison between EDF MAAP5.04 and ASTECV3 codes on a hypothetical severe accident on the ELSMOR project E-SMR design", *Annals of Nuclear Energy*, **215** (2025) https://doi.org/10.1016/j.anucene.2025.111258.
19. P. Maccari, et al., "Analysis of BDBA sequences in a generic IRIS reactor using ASTEC code", *Annals of Nuclear Energy*, **182** (2023) https://doi.org/10.1016/j.anucene.2022.109611
20. M. Principato, F. Giannetti, M. Imperatori, et al., "Analyses of the MELCOR capability to simulate integral PWR using passive systems in a DBA scenario", *Nuclear Engineering and Design*, **437** (2025) https://doi.org/10.1016/j.nucengdes.2025.114004
21. C. Vázquez-Rodríguez, S. Kelm, "Severe accident analysis of SASPAM-SA Design II LW-SMR dry containment using containmentFOAM", *Proc. of ERMSAR2026*, Madrid, Spain, May 18-22 (2026).

SAFETY ANALYSIS OF SMR WITH PASSIVE MITIGATION STRATEGIES - SEVERE ACCIDENT

Analysis of Postulated Severe Accidents in Generic Integral PWR Small Modular Reactors: Outcomes on Integral Codes' Modelling Capabilities from the Horizon Euratom SASPAM-SA Project

M. E. Cazado
on behalf of the SASPAM-SA WP2 Community

Karlsruhe Institute of Technology

SASPAM-SA Consortium reserves all rights in this document and in the information contained therein.
Reproduction, use or disclosure to third party without express authorization is strictly prohibited.

SASPAM-SA Project: Motivation and Goals

SAFETY ANALYSIS OF SMR WITH PASSIVE MITIGATION STRATEGIES - SEVERE ACCIDENT

- 'Safety Analysis of SMR with PAssive Mitigation strategies - Severe Accidents' (SASPAM-SA) project (2022-2026), coordinated by ENEA (F. Mascari) - 23 partners from 13 European countries

- **Systematic demonstration of Integral Pressurised Water Reactors (iPWRs) ability to prevent and to manage Severe Accidents (SA) (DiD levels 4-5) for licensing**

- Project goals:
  - transfer LWR safety knowledge to iPWRs
  - investigating the key elements to create a European independent point of view on the safety of iPWRs with respect to DiD levels 4-5

SASPAM-SA Consortium reserves all rights in this document and in the information contained therein. Reproduction, use or disclosure to third party without express authorization is strictly prohibited.

Generic iPWR Designs

SAFETY ANALYSIS OF SMR WITH PASSIVE MITIGATION STRATEGIES - SEVERE ACCIDENT

iPWR Design-1

Submerged containment, P~60 MWe

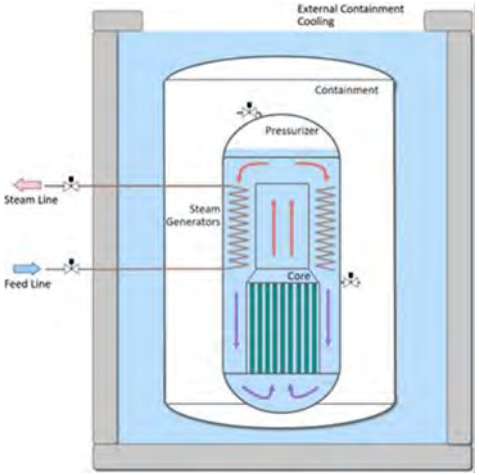

iPWR Design-2

Dry containment, several passive systems, P~300 MWe

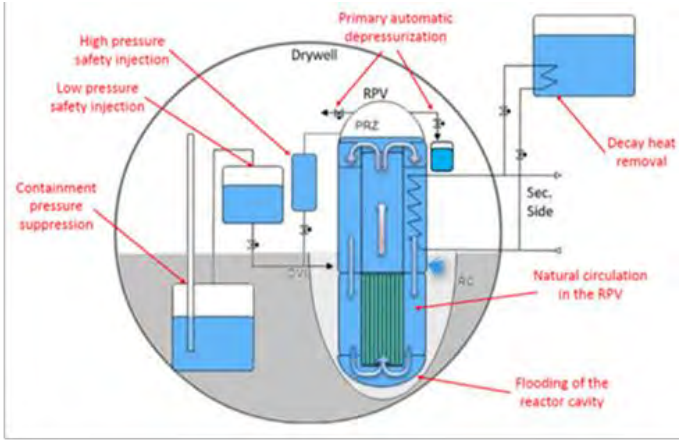

- The designs incorporate the main safety features of the most promising concepts ready for deployment in the European market
- It is not the project's objective to assess the design of such concepts

SASPAM-SA Consortium reserves all rights in this document and in the information contained therein. Reproduction, use or disclosure to third party without express authorization is strictly prohibited.

Objectives of the WP2 (SCENARIOS)

SAFETY ANALYSIS OF SMR WITH PASSIVE MITIGATION STRATEGIES - SEVERE ACCIDENT

- **Evaluating the capabilities of state-of-art European and non-European integral SA codes and Computational Fluid Dynamics (CFD) tools to simulate the key phenomena occurring in generic iPWR designs**

- Methodology:
  - Development of the iPWR Design-1 and Design-2 database (generic designs, decay heat) based on open-literature
  - Assessment of generic, but representative, SA and CFD codes' datasets
  - Postulating DBA and SA sequences
  - Analysis the postulated DBA and SA scenarios
  - Feedback/recommendations from the codes' users

- Input data/Boundary conditions for the activities foreseen in the other WPs

SASPAM-SA Consortium reserves all rights in this document and in the information contained therein. Reproduction, use or disclosure to third party without express authorization is strictly prohibited.

iPWR Design-1 and -2: Codes and Datasets

SAFETY ANALYSIS OF SMR WITH PASSIVE MITIGATION STRATEGIES - SEVERE ACCIDENT

iPWR Design-1

Partner	Code
EDF	EDF-MAAP5.04
GRS	Support to the AC^2 users
IRSN	Support to the ASTEC users
KIT	ASTECv3.1
KTH	MELCORv2.2
PSI	MELCORv2.2
RATEN	Scenarios
RUB	AC^2
SSTC NRS	ANSYS CFX (CFD)
TRACTEBEL	ASTECv2.2/v3.1

iPWR Design-2

Partner	Code
CIEMAT	MELCORv2.2
ENEA	ASTECv3.1/MELCORv2.2
FZJ	CAD and containmentFOAM
GRS	Support to the AC^2 users
JRC	MAAP 5.06
IRSN	Support to the ASTEC users
LEI	AC^2
RATEN	Scenarios
UNIROMA1	MELCORv2.2

SASPAM-SA Consortium reserves all rights in this document and in the information contained therein. Reproduction, use or disclosure to third party without express authorization is strictly prohibited.

Methodology

- Keyword: Sharing
  - The datasets are shared among the partners upon request

- **No PSA assessments employed** (generic designs) → SA scenarios selected in terms of severity and not of probability to occur

- Having in mind the goal ('*Evaluating the SA codes capabilities in iPWR applications..*') → **No 'classical' code-to-code benchmarks**
  - Each partner free to perform sensitivity analyses (e.g., height of the break, inverse flow modelling, decay heat, …)
  - Three sets of decay heat and fuel inventories available: WP2 (computed by CASMO), ANS73, and ANS73+20%

SASPAM-SA Consortium reserves all rights in this document and in the information contained therein. Reproduction, use or disclosure to third party without express authorization is strictly prohibited.

iPWR Design-1: Postulated SA Scenarios

- **Initiators**
  - **SA-1**: 100% **break** on the CVCS **makeup line**
  - **SA-2**: Inadvertent opening of **1 RVV valve**
  - **SA-3:** 100% **break** on the **Venting line**

- **Accident progression:**
  - Loss of AC @t = 0 s
  - Loss of FDW and Reactor SCRAM
  - Isolation of the MSL
  - Activation of the ECCS

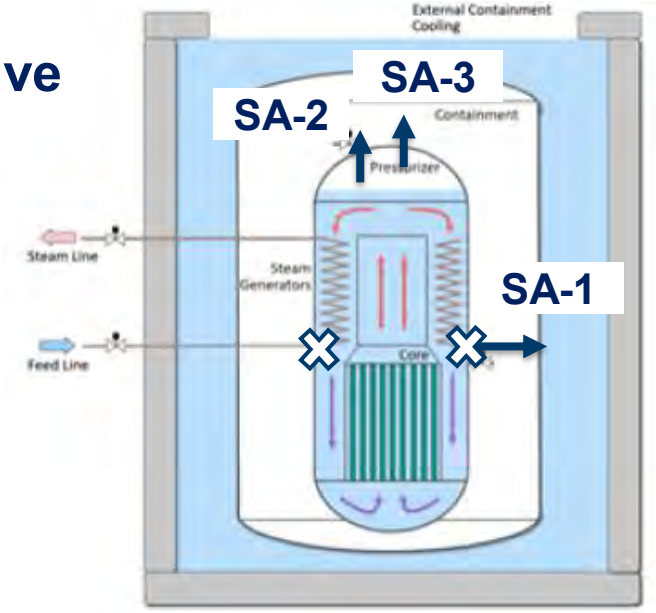

SASPAM-SA Consortium reserves all rights in this document and in the information contained therein. Reproduction, use or disclosure to third party without express authorisation is strictly prohibited.

iPWR Design-1 SA Scenarios: Modelling Parameters

- ECCS activation
  - CNMT water level ≈ 5.8 m
  - RPV-CNMT pressure difference ≈ 6.2–6.9 MPa
  - Opening of 3 RVVs and failure of 2 RRVs
- Break-height (7.3 m vs 9 m) influences ECCS timing
- Reverse-flow allowed/suppressed in some datasets
- ASTEC: CNMT modelled by using CPA (v3.1) or CESAR (v2.2)

SASPAM-SA Consortium reserves all rights in this document and in the information contained therein. Reproduction, use or disclosure to third party without express authorisation is strictly prohibited.

iPWR Design-1: SA-1 Accident Progression

Event	ASTECv3.1 (CPA)	ASTECv2.2 (CESAR)	EdF-MAAP	MELCORv2.2	AC2
ECCS signal [s]	318-950	259	349	339-495	4,537

- Deviations due to differences on the break height and on the set point of the RPV–CNMT pressure difference assumed, e.g.:
- Earlier ECCS activation in MELCOR (break is set at 7.3 m, no reverse flow, RPV-CNMT pressure 6.2 MPa) in agreement with ASTECv3.1 and EdF-MAAP using the same assumptions
- Conversely, when higher values adopted (break is set at 9 m, RPV-CNMT pressure 6.9 MPa), ECCS activation is delayed, as observed in AC2 and ASTECv3.1 (CPA), where it occurs at ~950 s

SASPAM-SA Consortium reserves all rights in this document and in the information contained therein. Reproduction, use or disclosure to third party without express authorization is strictly prohibited.

iPWR Design-1: SA-1 Accident Progression

Event	ASTECv3.1 (CPA)	ASTECv2.2 (CESAR)	EdF-MAAP	MELCORv2.2	AC2
H_2 on-set [s]	4,050-5,530	6,400	7,800	8,910-10,320	7,482
Start of FPs release from fuel pellets [s]	4,234-6,665	6,780	11,888	13,105-14,865	9,171
1st slump in LP [s]	17,789-19,350	21,118	20,366	14,100	11,050
In-vessel H_2 [kg]	54-61	77	80	50-64	72
RPV failure	**No**	**No**	**No**	**No**	**No**

- **H2 on-set**: deviation among ASTEC, EdF-MAAP, and AC2 of ~2,000 s, increasing to ~5,000 s in MELCORv2.2
- Reasonable agreement among the codes, considering modelling differences and uncertainties
- **No RPV failure** predicted by any of the codes in any scenario up to 70 h due to the External Reactor Vessel Cooling (ERVC)

SASPAM-SA Consortium reserves all rights in this document and in the information contained therein. Reproduction, use or disclosure to third party without express authorization is strictly prohibited.

iPWR Design-1: RPV and CNMT Water levels

SAFETY ANALYSIS OF SMR WITH PASSIVE MITIGATION STRATEGIES - SEVERE ACCIDENT

- Decay heat data: ANS73+20%

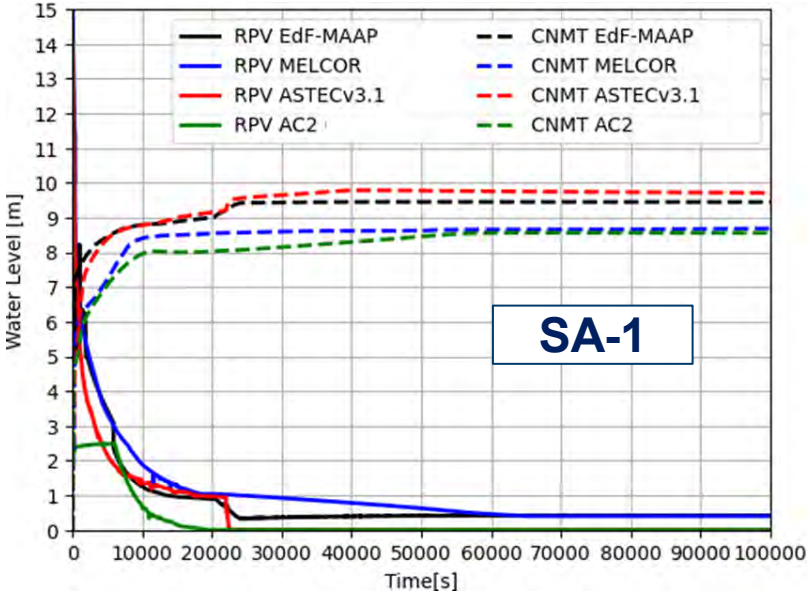

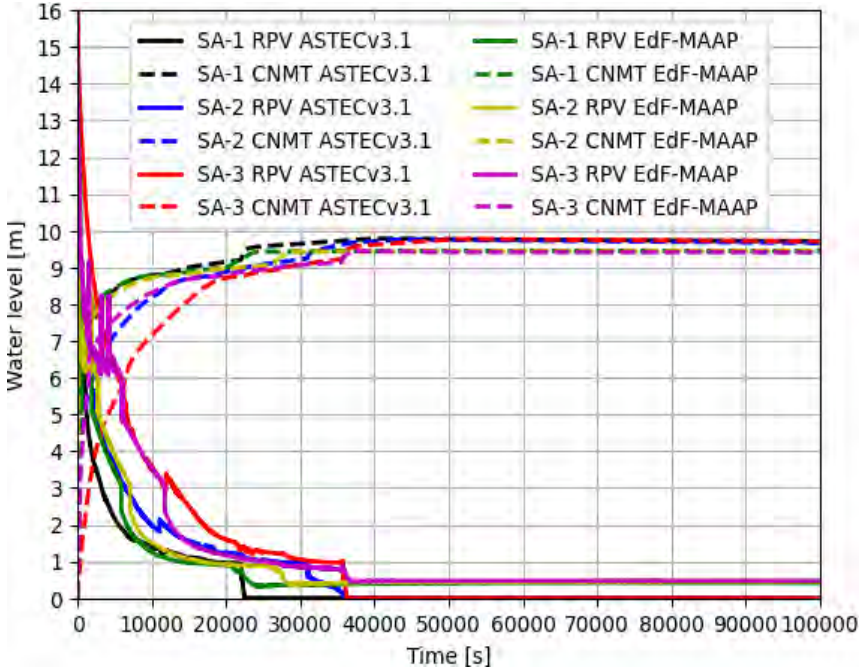

- RRVs stack → core isolated → completely uncovered at ~25,000 s
- Quite good agreement among the codes

SASPAM-SA Consortium reserves all rights in this document and in the information contained therein. Reproduction, use or disclosure to third party without express authorization is strictly prohibited.

iPWR Design-1: SA-1 Core Degradation

(courtesy of M. Di Giuli, Tractebel)

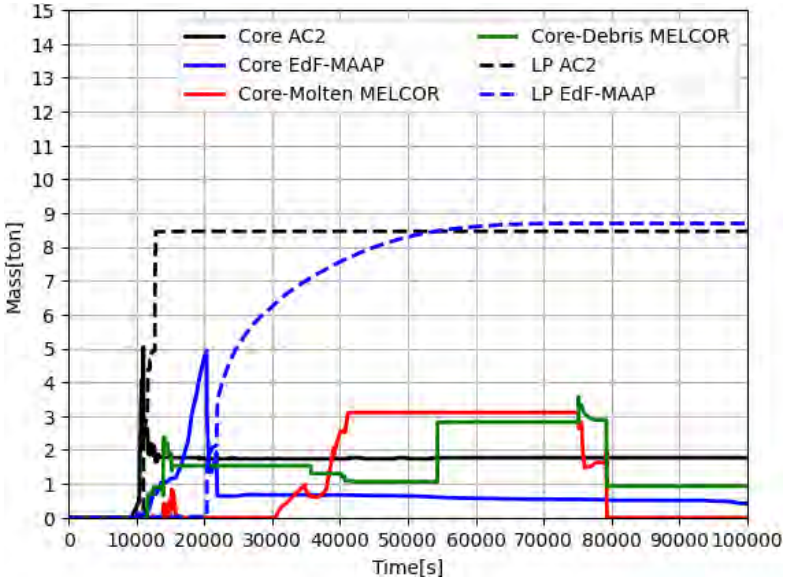

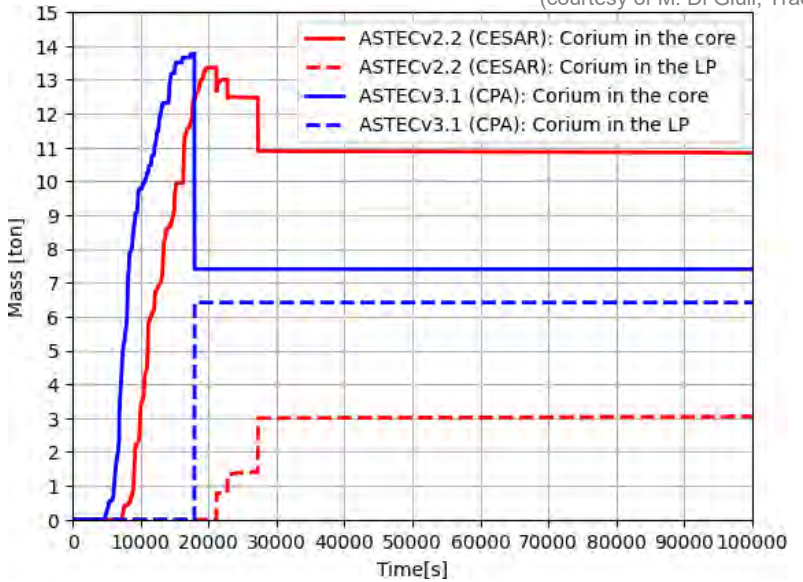

- Reasonable agreement on the timing of material relocation in the LP
- Mass of material relocated in the LP: good agreement among AC2, EdF-MAAP, MELCOR, and ASTECv3.1 (CPA) (~7-9 t), ASTECv2.2 (CESAR) smaller amount (~3 t)
- MELCOR: parametric analysis (PSI) indicated a wide range of core damage (17-100%)

SASPAM-SA Consortium reserves all rights in this document and in the information contained therein. Reproduction, use or disclosure to third party without express authorization is strictly prohibited.

iPWR Design-1: SA results and Decay Heat

ASTECv3.1
(Decay heat SASPAM-SA)

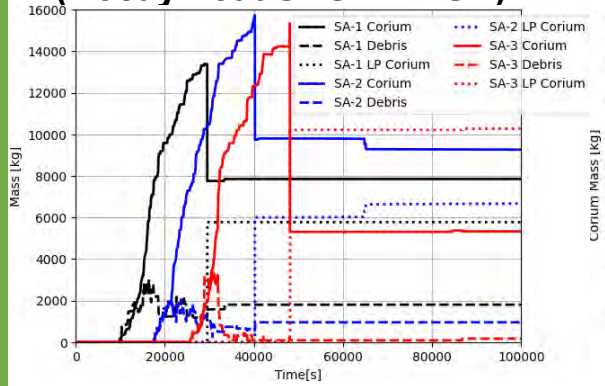

EdF-MAAP
(Decay heat ANS73)

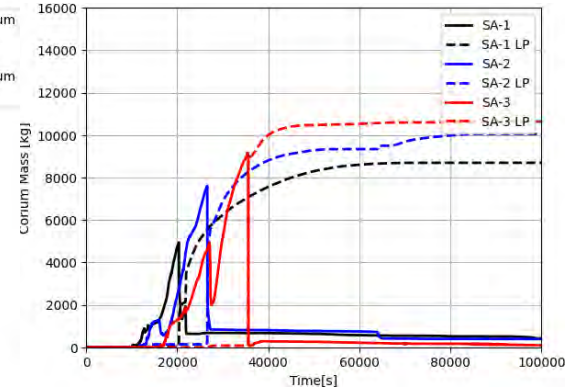

MELCOR
(Decay heat ANS73 and ANS73+20%)

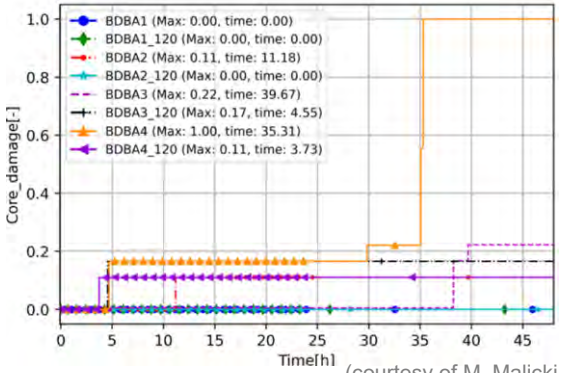

(courtesy of M. Malicki, PSI)

- **No RPV failure is predicted by the codes for any of the postulated SA scenarios**
- Deviation on the timing of material relocation to the LP is ~3,000 s, when using the same decay heat data
- ASTECv3.1 (CPA) vs. EdF-MAAP: deviations of ~3-4 t for SA-1 and SA-2, good agreement in SA-3

SASPAM-SA Consortium reserves all rights in this document and in the information contained therein. Reproduction, use or disclosure to third party without express authorization is strictly prohibited.

iPWR Design-1: Hydrogen Production

SAFETY ANALYSIS OF SMR WITH PASSIVE MITIGATION STRATEGIES - SEVERE ACCIDENT

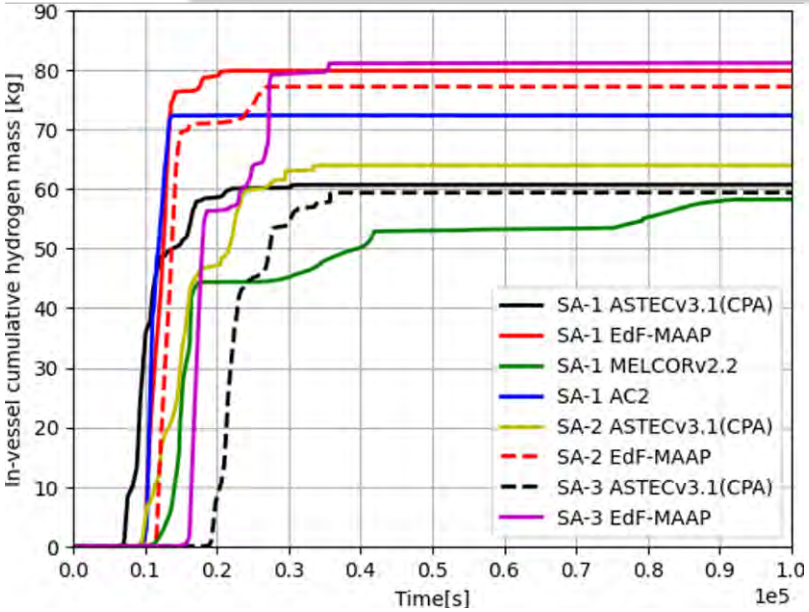

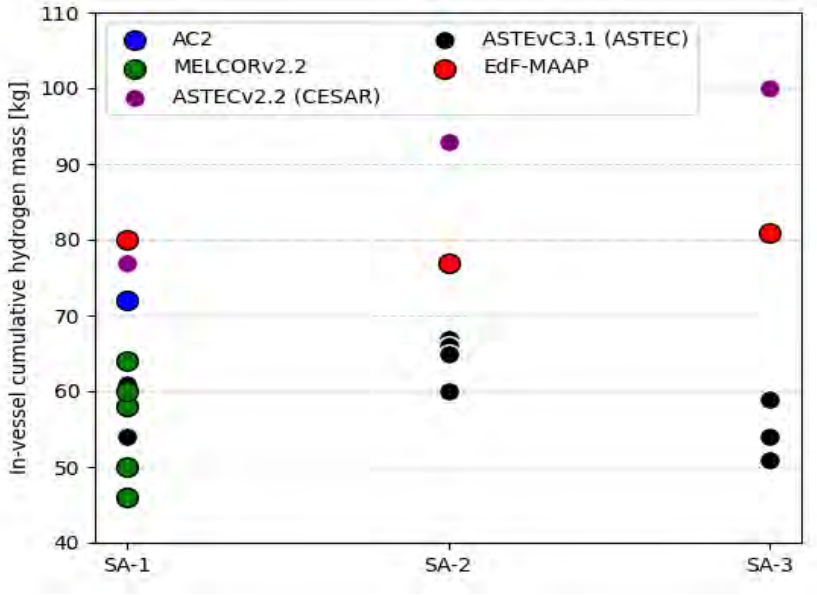

- Same decay heat data (ANS73+20%) → Results in the band of ~70 ± 10 kg
- All the modelling options, max. deviation of ~25-35 kg in the SA-1
- Steel oxidation conservative approach in EdF-MAAP leads to higher values than ASTEC (CPA)
- ASTECv2.2 (CESAR) provides significantly larger values

SASPAM-SA Consortium reserves all rights in this document and in the information contained therein. Reproduction, use or disclosure to third party without express authorization is strictly prohibited.

iPWR Design-2: Postulated SA Scenarios

- **Guillotine break of one Direct Vessel Injection (DVI) line +**

(courtesy of ENEA)

SA-1: Unavailability of EHRS systems

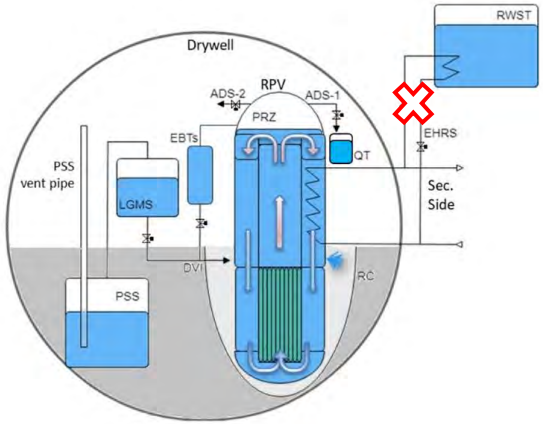

SA-2: Unavailability of EHRS and ADS-1 systems

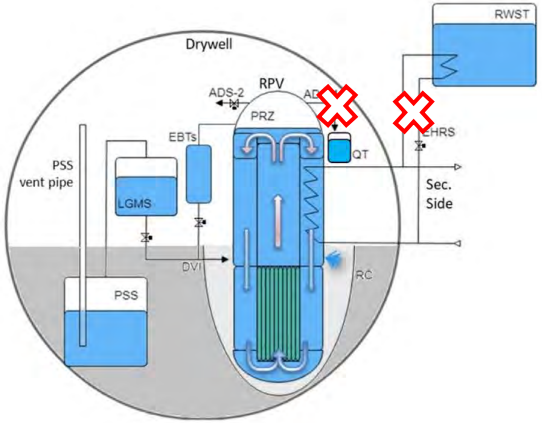

SA-3: Unavailability of all the safety systems

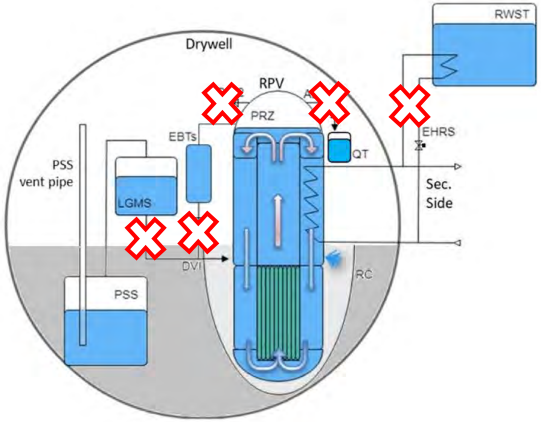

- CNMT design pressure: 1.4 MPa (ASTEC v3.1, AC2 models), 1.2 MPa (MELCORv2.2), 2.4 MPa (MAAP v5.06), drywell-ENV leak vs. local Pressure (MELCORv2.2)

EHRS: Emergency Heat Removal System ADS: Automatic Depressurization System

SASPAM-SA Consortium reserves all rights in this document and in the information contained therein. Reproduction, use or disclosure to third party without express authorization is strictly prohibited.

iPWR Design-2: Accidents' Progression

SAFETY ANALYSIS OF SMR WITH PASSIVE MITIGATION STRATEGIES - SEVERE ACCIDENT

	Event	ASTEC v3.1	MELCOR v2.2	MELCOR v2.2	MAAP v5.06	AC²
SA-3 unavailability of all safety systems	**Containment failure***	**4,020**	**3,090**	**5,730**	**13,327**	**2,504**
	Core uncover (TAF)	5,280	4,250	1,690	2,675	3,600
	H2 onset	**7,294**	**12,290**	**9,070**	**3,980**	**7,000**
	Start of FPs release	10,386	-	-	-	7,000
	Core uncover (BAF)	72,960	23,800	18,680	12,411	11,000
	First core failure	10,386	14,630	10,270	9,955	13,500
	First corium slump	**74,610**	**27,300**	**24,300**	**9,955**	**-**

- **No lower head vessel failure up to 70 h due to the ERCV**
- The codes are able to predict key thermal-hydraulics and core degradation phenomena
- General good agreement on the timing of the main events
- Large deviation on the timing of the relocation to the LP

SASPAM-SA Consortium reserves all rights in this document and in the information contained therein. Reproduction, use or disclosure to third party without express authorization is strictly prohibited.

iPWR Design-2: Accidents' Progression

SAFETY ANALYSIS OF SMR WITH PASSIVE MITIGATION STRATEGIES - SEVERE ACCIDENT

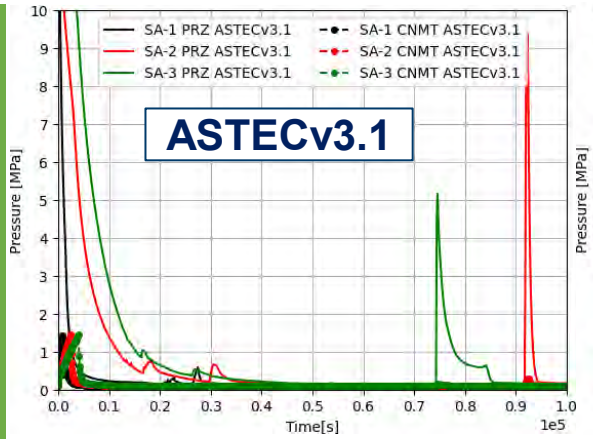

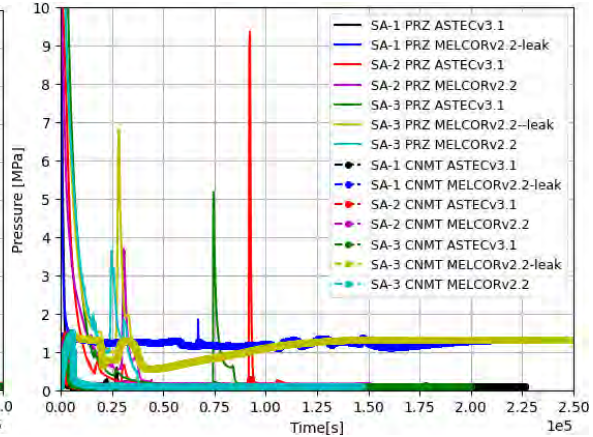

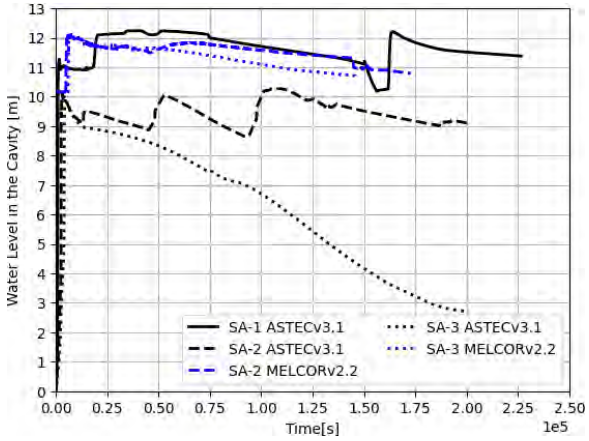

- DVI break → fast depressurization of the RPV and slower CNMT pressurization
- SA-1 (EHRS failure) → fast CNMT pressurization (different CNMT behaviour depending on the design pressure modelling) → after CNMT failure (ASTEC), water level increase in the cavity
- SA-2 (+ADS-1 failure) and SA-3 all systems fail) → slower progression → rapid increase on the cavity water level
- All the codes able to identify the progression of the key TH phenomena

SASPAM-SA Consortium reserves all rights in this document and in the information contained therein. Reproduction, use or disclosure to third party without express authorization is strictly prohibited.

iPWR Design-2: Core Degradation Results

SAFETY ANALYSIS OF SMR WITH PASSIVE MITIGATION STRATEGIES - SEVERE ACCIDENT

ASTECv3.1

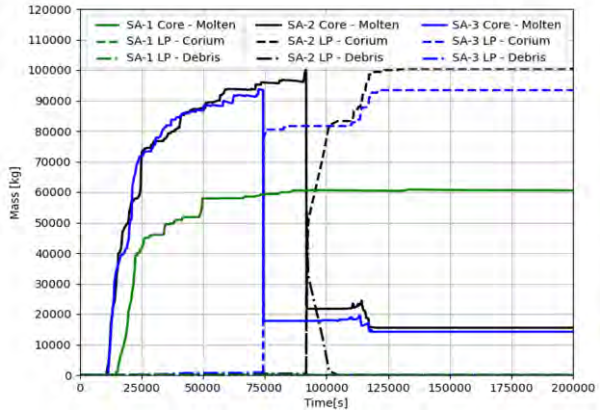

MAAP v5.06

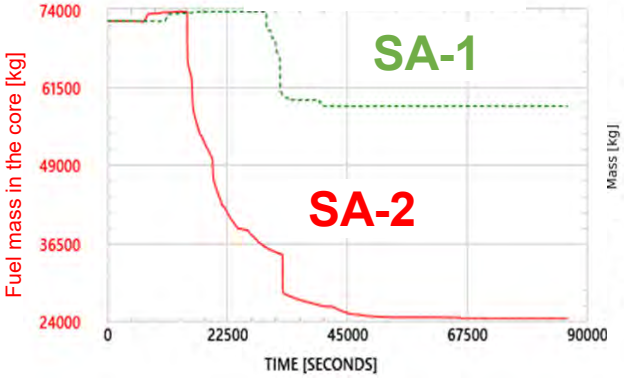

(courtesy of J. C. de la Rosa Blul, JRC)

MELCORv2.2

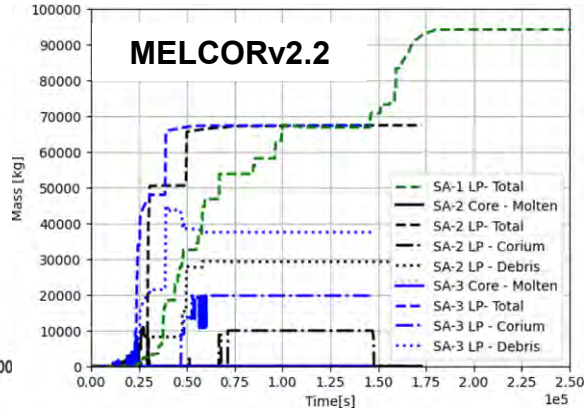

- Increase of the systems unavailability (SA-1 to SA-3) → Increase of the severity of the core degradation conditions
- **No RPV failure in any scenario**
- Deviation on mass relocated in the LP (SA-2 and SA-3) ~20-50 ton
- SA-1: different prediction on the relocation in the LP

SASPAM-SA Consortium reserves all rights in this document and in the information contained therein. Reproduction, use or disclosure to third party without express authorization is strictly prohibited.

iPWR Design-2: Hydrogen Production

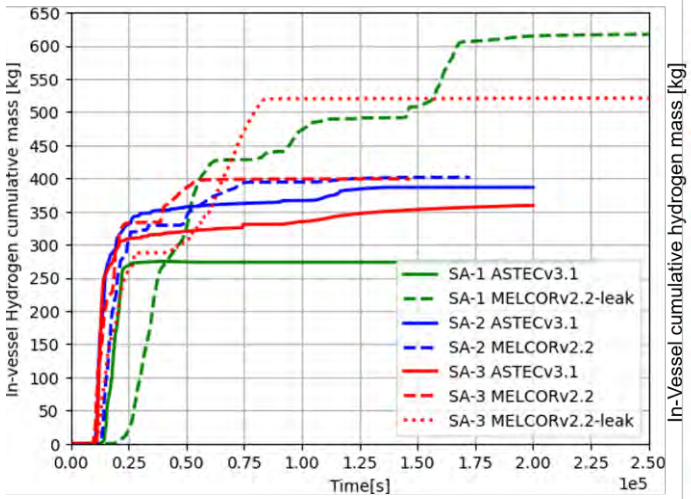

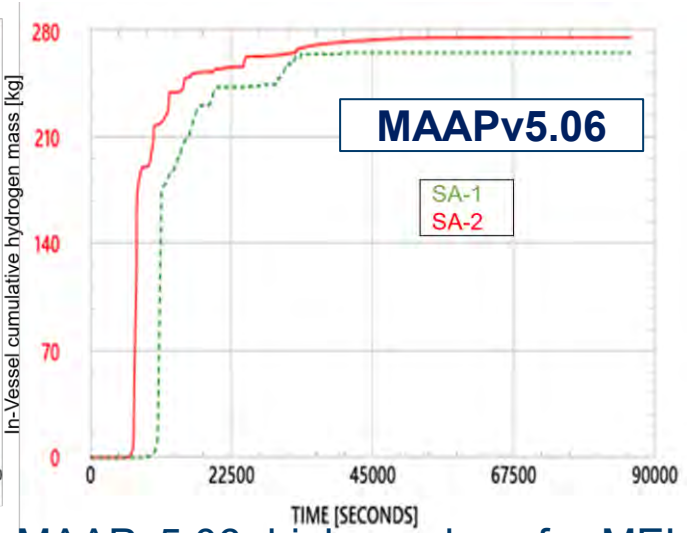

- SA-1: good agreement ASTECv3.1 and MAAPv5.06, higher values for MELCORv2.2 due to the occurrence of three slumps in the LP
- SA-2: good agreement ASTECv3.1 and MELCORv2.2 (deviation of ~20 kg); larger deviation against MAAPv5.06 (~100 kg)
- SA-3: similar deviations as in SA-2

SASPAM-SA Consortium reserves all rights in this document and in the information contained therein. Reproduction, use or disclosure to third party without express authorization is strictly prohibited.

Preliminary Lessons Learned

- **Sensitivity studies on nodalization** are highly recommended before adopting a final model
- **ERVC modelling** is recommended
- **Uncertainty and sensitivity analyses** are indispensable
- **Core coolability parameters and steam flow patterns may play a stronger role than in large PWRs**, e.g. MELCOR analyses show a possible core cooling due to natural convection with steam for iPWR Design-1 → significant difference with large power PWR
- Reduced decay heat and corium mass in SMRs lead to slow SA progression → **large wall-clock time and careful resource management necessary**

SASPAM-SA Consortium reserves all rights in this document and in the information contained therein. Reproduction, use or disclosure to third party without express authorization is strictly prohibited.

Preliminary Takeaways and Outlook

- Integral codes are able to predict the key TH phenomena occurring in iPWRs in the postulated SA scenarios
- Despite modelling differences, the codes generally show qualitative agreement on accident progression trends
- There are not reference calculations that allow concluding that the deviations found are larger than in LWR scenarios
- Efforts ongoing:
  - identifying potential sources in the differences of code modelling approaches
  - Generic small BWR (from CNL): SAs‘ postulation and MELCOR analyses

SASPAM-SA Consortium reserves all rights in this document and in the information contained therein. Reproduction, use or disclosure to third party without express authorization is strictly prohibited.

..finally

- The SASPAM-SA WP2's Community

  F. Mascari, A. Bersano, P. Maccari, G. Grippo, G. Agnello, S. Ederli, F. Gabrielli, V.H. Sanchez-Espinoza, M. Di Giuli, J. Bittan, N. Bakouta, M. Malicki, T. Lind, M. Makarenko, Yu. Yesipenko, O. Zhabin, D. Gumenyuk, S. Kelm, E.-A. Reinecke, C. Vázquez-Rodríguez, M. Klauck, M. K. Koch, J. Krieger, G. Stahlberg, T. Jankowski, M. Garcia Martin, L. E. Herranz, N. Reinke, A. Bentaib, L. Carenini, J.-C. de la Rosa Blul, A. Kaliatka, M. Valincius, M. Constantin, F. Giannetti, T. Sevon, P. Groudev, G. Acharya, K. Mahmoud, P. Kudinov, D. Grishchenko, A. Morreale, G. Patterson

- Special mention to EDF (J. Bittan), ENEA (A. Bersano), and Tractebel (M. Di Giuli) for their efforts in leading the activities in the working groups

SASPAM-SA Consortium reserves all rights in this document and in the information contained therein. Reproduction, use or disclosure to third party without express authorization is strictly prohibited.

Acknowledgement/Disclaimer

Funded by the European Union

Funded by the European Union. Views and opinions expressed are however those of the author(s) only and do not necessarily reflect those of the European Union or European Commission-Euratom.
Neither the European Union nor the granting authority can be held responsible for them.

SASPAM-SA Consortium reserves all rights in this document and in the information contained therein. Reproduction, use or disclosure to third party without express authorization is strictly prohibited.

Rolls-Royce SMR 3D Hydrogen Combustion Assessment Approach

Jonathan Fowles, Alex Meredith, Joe Butterworth
Rolls-Royce SMR Limited
7th Floor, 11 York Street, Manchester, M2 3GR, United Kingdom
jonathan.fowles@rolls-royce-smr.com; alex.meredith@rolls-royce-smr.com;
joe.butterworth@gexcon.com

ABSTRACT

Rolls-Royce SMR has developed a three step analysis process for assessing the risk arising from hydrogen build-up in the containment building of a pressurised water reactor. The process uses MAAP5 to predict the severe accident evolution, fuel clad oxidation rate, and hydrogen and steam release rates into the containment atmosphere. 3D GOTHIC predictions are used to assess the localised gas composition in regions of the containment, and estimate the risk of energetic hydrogen combustion using the sigma (σ) and lambda (λ) correlations for flame acceleration and deflagration to detonation transition. Boundary conditions are then transferred to the FLACS-CFD code to perform combustion assessments, including predictions of overpressures if the conditions for flame acceleration or deflagration to detonation transition are met.

KEYWORDS
Containment Gas Mixing, Hydrogen, DDT, Combustion

1. INTRODUCTION

During the extremely unlikely event of a Severe Accident (SA) occurring on a Pressurised Water Reactor (PWR) such as the Rolls-Royce SMR, the interaction of high temperature steam and zirconium fuel cladding leads to oxidation and the rapid production of large quantities of hydrogen. Hydrogen is also generated from other sources such as hydrolysis, steel and boron carbide oxidation and molten core concrete interaction. This hydrogen is released into the containment atmosphere with the potential formation of combustible gas mixtures.

The integrity of the containment vessel and essential safety equipment could be challenged by the onset of energetic combustion modes, such as flame acceleration and deflagration to detonation transition (DDT) that can result in significant increases in containment pressure and temperature. The possibility of these combustion modes is highly dependent on the relative gas concentrations of hydrogen, oxygen and any dilutants (e.g. steam), on both a global and local scale.

Mitigative safety measures such as Passive Autocatalytic Recombiners (PARs) and ignitors are therefore deployed to remove hydrogen from the containment atmosphere and prevent the occurrence of energetic combustion that could challenge the integrity of the containment vessel or any Systems, Structures or Components (SSCs) delivering essential safety functions.

Analysis of the accident evolution, and local containment conditions, is used to determine the risk arising from hydrogen combustion in containment, support the design substantiation of safety systems and provide evidence to support safety case claims. The three-step assessment approach deployed by Rolls-Royce SMR to support these key objectives is described here.

Public – Not Listed – Not Subject to Export Controls

2. Hydrogen Assessment Approach

A three step assessment approach has been developed by Roll-Royce SMR. The intention is to identify limiting credible SA scenarios that may pose a risk to containment integrity from slow deflagration, and assess the possibility of localised accumulation of hydrogen that could lead to flame acceleration and DDT. The steps are summarised as follows, and described in detail in the following sub-sections:

1. Global Risk Evaluation: scenarios of interest are identified from analysis of a range of SAs with an integral SA code (e.g. MAAP, MELCOR, ASTEC, etc). A survey of credible conditions is performed to identify the most limiting scenarios for subsequent assessment. Figures of merit such as total hydrogen production, hydrogen release rate, and average hydrogen concentration in containment are used to quantify and compare the relative severity of accident sequences.
2. Flame Acceleration/Detonation Risk Evaluation: 3D containment gas mixing analysis is performed on a local scale to evaluate the potential for conditions favourable for flame acceleration and DDT using the sigma (σ) and lambda (λ) indices respectively. Source term boundary conditions are provided from assessments performed in Step 1, and a detailed representation of containment geometry and key phenomena impacting gas mixing, steam generation and condensation are included. Predictions of localised gas mixture concentration, temperature, pressure are used as inputs to the σ and λ assessments. If the occurrence of flame acceleration or DDT cannot be excluded, then subsequent combustion analysis is recommended.
3. Localised Combustion Assessment: Gas mixture and turbulence predictions from Step 2 are supplied as boundary conditions to a combustion code to perform detailed analysis of turbulent flame propagation, possibility of DDT, and resultant localised pressure loadings throughout containment.

The resultant temperature and pressure loadings from Step 3 can be compared against safety acceptance criteria to determine the possibility of failure of the containment vessel or SSCs within containment. Alternatively, transient pressure loadings can be used as boundary conditions to subsequent dynamic structural integrity assessments to assess the containment vessel response to a specific accident sequence.

3. Global Risk Evaluation

The first step of the assessment process is to identify the scenarios of interest for hydrogen management. Initially knowledge of the SA physical phenomena and engineering judgement is used to postulate scenarios that could lead to more onerous conditions for hydrogen generation and release to containment.

Typically the severity of scenarios will depend upon the following three aspects:

1. The overall hydrogen generation in the core and the rate of release into the containment. A sustained period of high fuel temperature and fuel clad/steam oxidation will lead to rapid oxidation and hydrogen generation, and high hydrogen concentrations in containment.
2. The overall steam generation in core and the rate of release into the containment. Steam generated in the core (e.g. due to safety water injection), will be available for fuel clad oxidation and hydrogen generation. Steam release into the containment reduces the relative hydrogen concentration, and further acts as a dilutant to hydrogen combustion. Typically LOCA scenarios that balance the coolant circuit depressurisation rate with injection of safety water lead to the greatest sustained steaming of the core and hydrogen generation.
3. The location of hydrogen release into the containment. Releases into the confined regions of containment (e.g. through a reactor coolant system breach) are expected to be more onerous for localised flame acceleration.

Public – Not Listed – Not Subject to Export Controls

It is difficult to ascertain the exact combination of these aspects that could lead to the most onerous hydrogen conditions through engineering judgement alone. Furthermore, the prediction of hydrogen generation in SA codes is known to be highly sensitive to relatively small changes to the in-core transient progression and conditions, which can be impacted by the relative balance of competing thermal hydraulic phenomena.

Therefore, it is recommended that a large survey of calculations is used to determine the general trends in hydrogen generation and dependency on system functionality/timing. For LOCA scenarios this includes a survey of all credible coolant circuit break sizes to identify the limiting break size that maximises hydrogen generation. For scenarios where high levels of hydrogen generation are predicted, a larger number of calculations with a refined parameter space should be performed to reduce the overall uncertainty. However, it is acknowledged that within the large domain of calculation parameters it is unlikely to be able to fully resolve all dependencies and identify the most limiting conditions.

To identify scenarios of interest the following figures of merit are recommended:

- Total hydrogen production during the in-core accident phase. During this phase, rapid oxidation of fuel cladding, and therefore hydrogen production is expected. Scenarios with greater hydrogen production during this phase would be expected to present a more significant risk of hydrogen combustion. However, this metric does not consider other important factors, such as the rate of release and the balance against hydrogen removal rates, as well as local dependencies relating to release location.
- Peak hydrogen concentration in containment. High hydrogen concentration typically indicates a higher risk of energetic combustion. Hydrogen concentration above 10% typically indicates a possible risk of conditions that could lead to flame acceleration/DDT but does not resolve local dependencies. A volume average hydrogen concentration below 10% could also lead to a localised risk of flame acceleration.
- Steam concentration at the time of peak hydrogen concentration. Peak hydrogen concentration is a good indicator of risk, but if coincident with a high steam concentration, then the overall risk of combustion may be low. For steam concentrations greater than ~50-60%, the mixture will become inert and combustion will not be possible.

It is acknowledged that no single parameter can be used to fully determine hydrogen risk, particularly on a local scale that the coarse containment nodalisation typically adopted by integral codes cannot resolve. Therefore, the identified figures of merit alongside engineering judgement are used to rank scenarios of interest.

When performing the global assessment to identify the most limiting scenarios, the inclusion of the mitigative safety measures, and modelling approach, should be justified based the capability of the code/model to adequately predict hydrogen removal so as not to impair scenario identification. For example, the performance of an individual PAR unit is subject to the localised gas conditions that cannot be resolved by coarse nodalisation. However, reduced hydrogen removal of a unit in one location is expected to be balanced by a unit located elsewhere with more favourable conditions and the overall impact on global average conditions will not be significantly impacted. Therefore, it is considered appropriate to include the effects of PARs within this assessment step. Whereas ignitors are expected to remove hydrogen at a much faster rate, and therefore the potential impact on containment conditions during the phase of hydrogen release is more significant. Furthermore, the coarse nodalisation typically adopted in integral codes may be expected to overpredict the hydrogen burn, which can impair the scenario identification process. Therefore, ignitors are typically not represented in this analysis step unless their inclusion can be appropriately justified.

Public – Not Listed – Not Subject to Export Controls

Scenarios will be considered for detailed analysis if the following are met:

- Global hydrogen concentration exceeds 10%,
- Rapid release of hydrogen would be expected into a confined region of containment,
- PARs as the sole mitigation are not expected to be effective in mitigating the release rate of hydrogen.

The outcome of this step is the identification of a subset of limiting accident scenarios for both local hydrogen conditions and global hydrogen conditions. A global slow deflagration assessment can be conservatively performed by evaluating the Adiabatic Isochoric Complete Combustion pressure attained.

For Roll-Royce SMR this step is performed using the MAAP 5.06 SA code [2], and typically several hundred LOCA analyses are used to identify those that are most limiting for containment conditions.

4. Flame Acceleration/Detonation Risk Evaluation

Scenarios of interest identified from the previous step are evaluated with a detailed 3D representation of containment to assess the possibility of flame acceleration or detonation. Therefore, localised gas mixing analyses are performed to predict the localised gas concentrations and conditions throughout the containment. This enables the assessment of the σ and λ criteria to predict the likelihood of flame acceleration and detonation respectively [1].

To provide confidence in gas mixing predictions, a structured approach using a Phenomena Identification and Ranking Table (PIRT) and Test and Assessment Matrix (TAM) is used to determine the phenomena and features that need to be included, such as:

- Accurate representation of the containment layout, including potential coolant circuit depressurisation safety systems and coolant circuit break locations (if relevant) and their release orientation, on a length scale/nodalisation sufficient to resolve relevant phenomena for hydrogen combustion.
- Inclusion of source term information (steam/hydrogen release) from MAAP analysis.
- Representation of heat removal mechanisms from containment.
- Representation of heat sources that could influence containment conditions (e.g. PARs exhaust).
- Adequate representation of thermal hydraulic phenomena within containment to accurately predict gas mixing and mixture concentration.
- Representation of mitigative measures such as PARs.

The localised mixing assessments are performed for the duration of interest where there is judged to be a risk, and this will be used to identify local regions of risk if the σ and λ criteria are for flame acceleration and DDT are met.

It is noted that σ and λ are empirically derived correlations that largely rely on experimental data derived from tests of combustion of homogeneous clouds in simple geometries. The application in the analysis approach to potentially inhomogeneous gas mixtures and complex geometries introduces uncertainty. An appropriate break-down of the regions over which they are assessed must be used. For example, the calculation of the σ and λ-indices based on the global average conditions and gas concentrations, would not be appropriate for assessing the localised risk within potentially confined regions around the coolant circuit pipework and steam generators. Whilst both criteria are necessary conditions for the onset of flame acceleration and detonation respectively, they do not guarantee occurrence.

As illustrated in the previous section, there is considerable uncertainty in SA sequence evolution that could lead to differences in hydrogen generation. Furthermore, there are uncertainties associated with

Public – Not Listed – Not Subject to Export Controls

predictions of gas mixing and therefore localised conditions and gas concentrations. A common approach to bound the uncertainties associated with hydrogen generation is to scale the hydrogen generation of the most limiting cases to the equivalent generation of 100% fuel clad oxidation. Additional sources of hydrogen generation in the period of interest (e.g. oxidation of B_4C control rods) may also be added to this scaled value. Nonetheless, a balanced approach must be used to ensure excessive conservatism is not represented, for example scaling of scenarios where it is physically impossible to reach 100% fuel clad oxidation would be inappropriate.

Sensitivity analysis should be used to understand the impact of uncertainties in the mixing analysis or features that cannot be adequately captured in the precursor global analysis. In particular, this may relate to the specific location and orientation or gas release from the coolant circuit which could impact mixing and local hydrogen concentration.

The following figures of merit are used to aid judgement in identifying the most limiting accident sequences and periods of risk:

- Volume of gas clouds within combustion limits can be used to estimate the possibility of flame propagation and burn completeness.
- Timing within the accident sequence that σ and λ criteria are met.
- Duration that σ and λ criteria are met. The period of risk of flame acceleration/detonation may be significant in combination with consideration of ignition sources.
- Volume of containment where σ and λ criteria are met. A larger volume meeting the criteria means that more potential ignition sources could lead to flame propagation across containment.
- Concentration of hydrogen when σ and λ criteria are met. The possibility of highly energetic combustion occurring is believed to be low when hydrogen concentration is close to the flammability limit [1].

The outcome of this analysis step allows the down-selection of scenarios, and proposal for limiting scenarios, times, and approximate containment locations for subsequent combustion analysis.
For Roll-Royce SMR this step is performed using the 3D GOTHIC containment code [3]. GOTHIC is a thermal-hydraulic software package that solves the conservation equations for mass, momentum and energy for multicomponent, multi-phase compressible flow in lumped parameter and/or multi-dimensional geometries. GOTHIC is well-established within the nuclear industry for performing containment thermal hydraulic analysis, including for hydrogen distribution during SAs.

5. Localised Combustion Assessment

For the scenario(s) of interest assessed by the previous step that indicate a possibility of flame acceleration based on the σ-criterion, detailed combustion analysis can be performed. The aim of the combustion analysis is to calculate the consequences of deflagration in terms of the resultant temperature and pressure loading, including the effects of flame acceleration due to turbulence generation. The σ and λ criteria, as assessed in Step 2, are necessary conditions for flame acceleration and detonation, and detailed combustion analysis can be used to further resolve the risk posed.

The combustion assessment incorporates the following features:

- Accurate representation of the containment layout on a length scale/nodalisation sufficient to resolve relevant phenomena for hydrogen combustion, including turbulence generation.
- Inclusion of relevant boundary conditions such as gas mixture, temperature, pressure and turbulence prior to deflagration.
- Representation of an ignition source at a selected location.

Public – Not Listed – Not Subject to Export Controls

The output of analysis includes:

- Magnitude and duration of temperature and pressure loadings due to deflagration at selected monitor points (e.g. equipment and/or the containment vessel).
- Global pressure response during and following deflagration.
- The likelihood of DDT.

For the assessments of relevant scenarios of interest, combustion is initiated at a time and location within containment considered to be the most onerous. The identification of appropriate times relies upon the figures of merit (σ- and λ-criteria) assessed in analysis Step 2, and engineering judgement. The outcome of initial combustion assessments, and sensitivity studies considering alternative ignition locations or model parameter settings can improve understanding of the relative severity and output uncertainty associated with the accident scenario. Alternative ignition locations may also be more onerous for different target SSCs requiring assessment.

The overall objective of the Roll-Royce SMR SA containment safety measure (including hydrogen reduction measures) is to prevent combustion leading to flame acceleration that could challenge containment vessel or SSC integrity. When considering uncertainty in the end to end approach, it may be unfeasible to demonstrate deterministically that flame acceleration can be prevented in totality for every plausible SA sequence. Therefore, if flame acceleration cannot be excluded by design provision, it may be necessary to demonstrate that the design of the containment vessel and relevant SSCs can withstand the predicted dynamic loadings. The outputs of detailed combustion analysis can be supplied to finite element code analysis to predict the structural response of the containment vessel and associated structures. The analysis steps are iterative, with refined analyses performed to ensure the lowest risk position is reached where practicable through optimisation of the mitigative safety measure design.

For Roll-Royce SMR localised combustion analysis is performed by the combustion code FLACS-CFD. FLACS-CFD is an advanced tool for performing engineering calculations for safety applications related to combustion of flammable gases. The software includes a 3-dimensional CFD code that solves Favre-averaged transport equations for mass, momentum, enthalpy, turbulent kinetic energy, rate of dissipation of turbulent kinetic energy, mass-fraction of fuel and mixture-fraction on a structured Cartesian grid using a finite volume method. One of the key features that distinguishes FLACS-CFD from most commercial CFD codes is the use of the distributed porosity concept for representing complex geometries on relatively coarse computational meshes [4]. This improves calculation time for assessments of large problem domains, such as a nuclear power plant containment building.

6. Verification, Validation and Uncertainty Quantification

Rolls-Royce SMR deploy the PIRT and TAM approach to ensure that all relevant phenomena in the problem domain are identified and that analysis code capability in representing the phenomena is reviewed and demonstrated to be adequate in the domain of interest. The approach allows the identification of the most significant phenomena for assessments and prioritisation of verification, validation and uncertainty quantification (VVUQ) activities.

The objectives of the analysis should always be used to guide the prioritisation of VVUQ activities. Often validation for hydrogen relates to peak pressure attained following combustion (slow deflagration, flame acceleration and detonation), however if the safety case objective is to prevent the occurrence of energetic combustion then the focus of validation should be to enable accurate prediction of the onset of flame acceleration and DDT rather than the resultant peak pressure.

The three-step assessment approach outlined herein intends to utilise the advantages of fast solving analysis codes where possible, acknowledging that there are inherent shortfalls and utilising successive

Public – Not Listed – Not Subject to Export Controls

steps with more detailed analysis as required. The following fundamental limitations guide the assessment approach, and also elicit areas where additional validation would be advantageous to improve confidence in predictions:

- Integral codes (e.g. MAAP) with coarse containment nodalisation are unlikely to be sufficient to resolve localised gas concentrations and the risk of flame acceleration and DDT on a local scale. To address this, the Roll-Royce SMR approach incorporates GOTHIC to perform 3d localised gas mixing assessments with appropriate application of the σ and λ criteria.
- The σ and λ criteria are necessary conditions for the occurrence of flame acceleration and detonation respectively, however are derived from experimental data predominantly representing uniform gas clouds in simple geometries. The application to complex containment geometries and inhomogeneous gas clouds introduces uncertainty to the approach for identifying scenarios that could lead to flame acceleration/DDT. To address this, the Roll-Royce SMR approach incorporates FLACS-CFD to perform detailed combustion load assessments and is used to support substantiation of the chosen application of the σ and λ criteria.
- The prediction of peak pressure resulting from flame acceleration/DDT is subject to high uncertainty. There is limited validation evidence for atmospheres with high hydrogen concentration and steam dilutant, particularly for complex geometries with increased potential for turbulence-induced flame acceleration, applicable to PWR containments. This limitation becomes more significant when considering containment scale geometry. Ultimately, the objective of the Roll-Royce SMR hydrogen reduction system is to prevent the occurrence of flame acceleration. Therefore, the aim of the analysis is to adequately predict the occurrence of flame acceleration through application of the σ criterion, minimising the reliance on peak pressure predictions, and the associated uncertainties.

Rolls-Royce SMR is supportive of the THEMIS-2 test programme, as a key source of further validation data in this area.

7. Summary

A three step assessment approach has been developed by Roll-Royce SMR. The intention is to identify limiting credible SA scenarios that may pose a risk to containment and SSC integrity from slow deflagration, and assess the possibility of localised accumulation of hydrogen that could lead to flame acceleration and DDT. The assessment approach utilises fast solving codes for coarse evaluation of a large number of scenarios, and optimised utilisation of detailed analysis methods to evaluate the possibility of occurrence of flame acceleration/DDT for limiting scenarios and the potential consequences. The advantages of each analysis step/code are utilised whilst acknowledging limitations and uncertainties in each step. The overall aim is to provide demonstration that containment safety measures and hydrogen reduction systems are able to reduce the risk associated with hydrogen deflagration during a SA as far as possible.

REFERENCES

1. OECD Nuclear Energy Agency, Flame Acceleration and Deflagration to Detonation Transition in Nuclear Safety, NEA/CSNI/R(2000)7, (2000).
2. ELECTRIC POWER RESEARCH INSTITUTE, Modular Accident Analysis Program Version 5.06 (MAAPv5.06) — PWR/BWR, EPRI, Palo Alto, (2021).
3. ELECTRIC POWER RESEARCH INSTITUTE, GOTHIC Thermal Hydraulic Analysis Package - User Manual - Version 8.4(QA), EPRI, Palo Alto, (2022).
4. Gexcon AS, FLACS-CFD v24.1 User Manual, (2024).

Public – Not Listed – Not Subject to Export Controls

Rolls-Royce SMR 3D Hydrogen Combustion Assessment Approach

Jonathan Fowles, Alex Meredith, Joe Butterworth (Gexcon)

 © 2026 Rolls-Royce SMR Ltd

Public – Not Listed – Not Subject to Export Controls

Introduction

- Hydrogen release during a Severe Accident poses a risk to containment integrity in the event of combustion.
- Assessments should effectively identify and analyse limiting accident scenarios.
- This presentation describes the process developed by Roll-Royce SMR and Gexcon to identify limiting credible scenarios that may pose a risk to containment.
- The assessments utilise fast solving codes for coarse evaluation of a large number of scenarios, and optimised use of detailed analysis methods for energetic combustion modes.

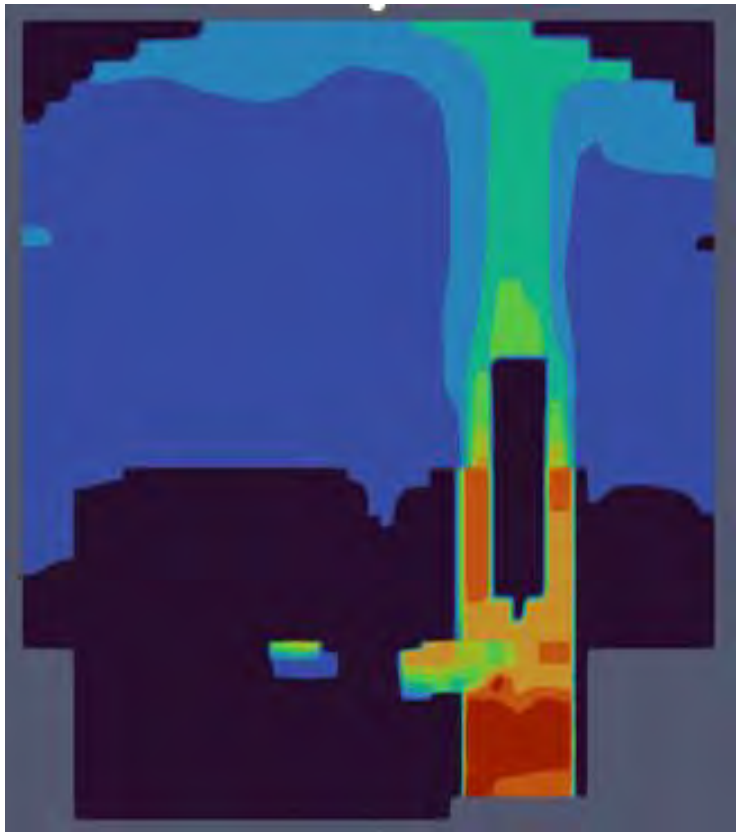

Public – Not Listed – Not Subject to Export Controls

Assessment Process

Public – Not Listed – Not Subject to Export Controls

Risk Assessment Process

- Identification of limiting credible SA scenarios that may pose a risk to containment integrity from slow deflagration,
- Assess the possibility of localised accumulation of hydrogen that could lead to flame acceleration/DDT.
- Evaluate consequences of energetic hydrogen combustion
- Provide boundary conditions for structural integrity assessments

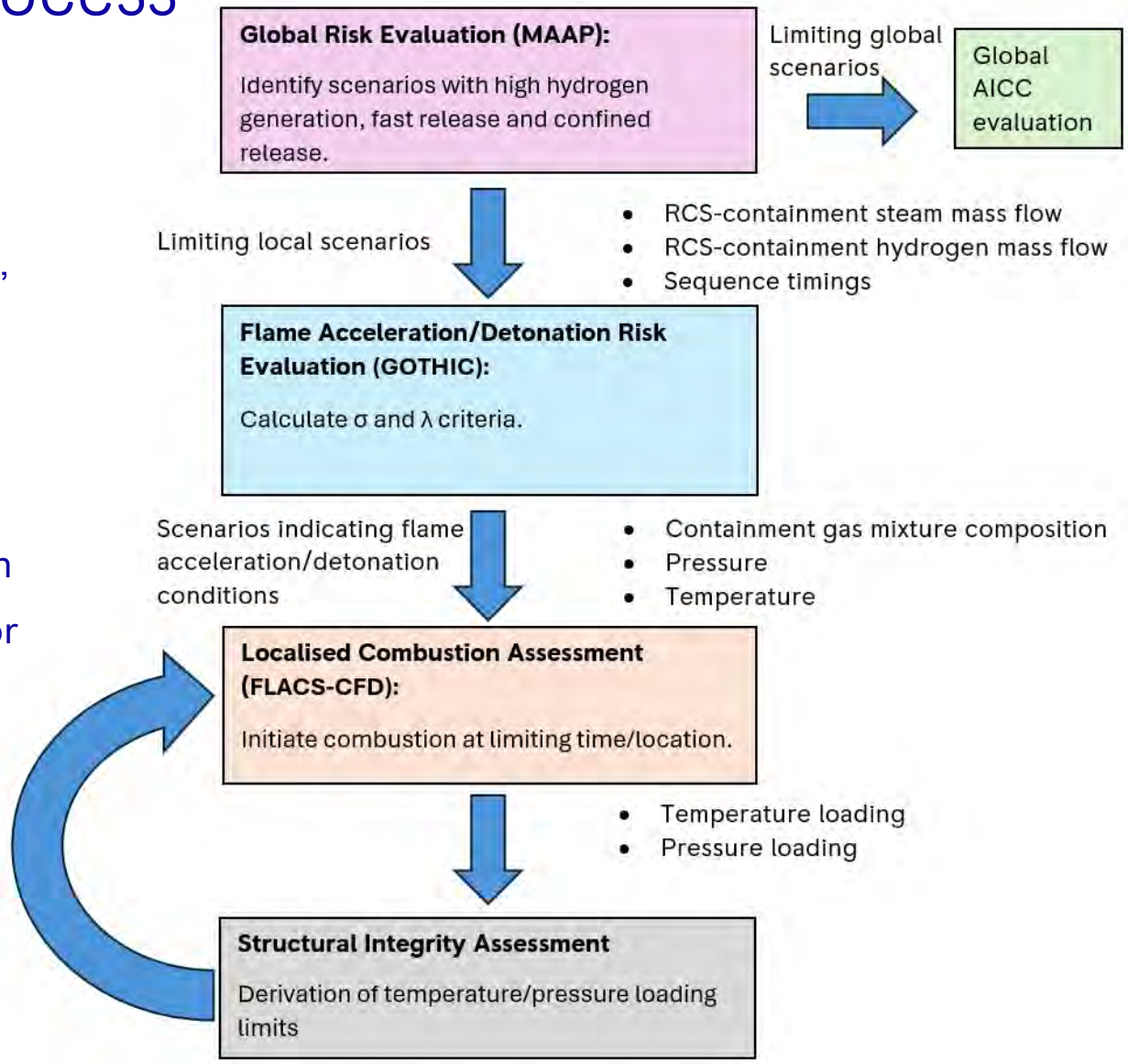

Public – Not Listed – Not Subject to Export Controls

Global Risk Evaluation

Public – Not Listed – Not Subject to Export Controls

Global Risk Evaluation - MAAP

- Integral SA code (e.g. MAAP) is used to identify the most limiting SA scenarios on a global basis.
- Representation of core and RCS allows predictions of hydrogen generation and release into containment
- Coarse containment nodalisation provides good representation of global gas concentrations.
- Adiabatic Isochoric Complete Combustion (AICC) pressure, conservatively represents the pressure rise due to slow deflagration.
- Due to the coarse containment nodalisation, it is not considered suitable for the assessment of localised combustion risk.

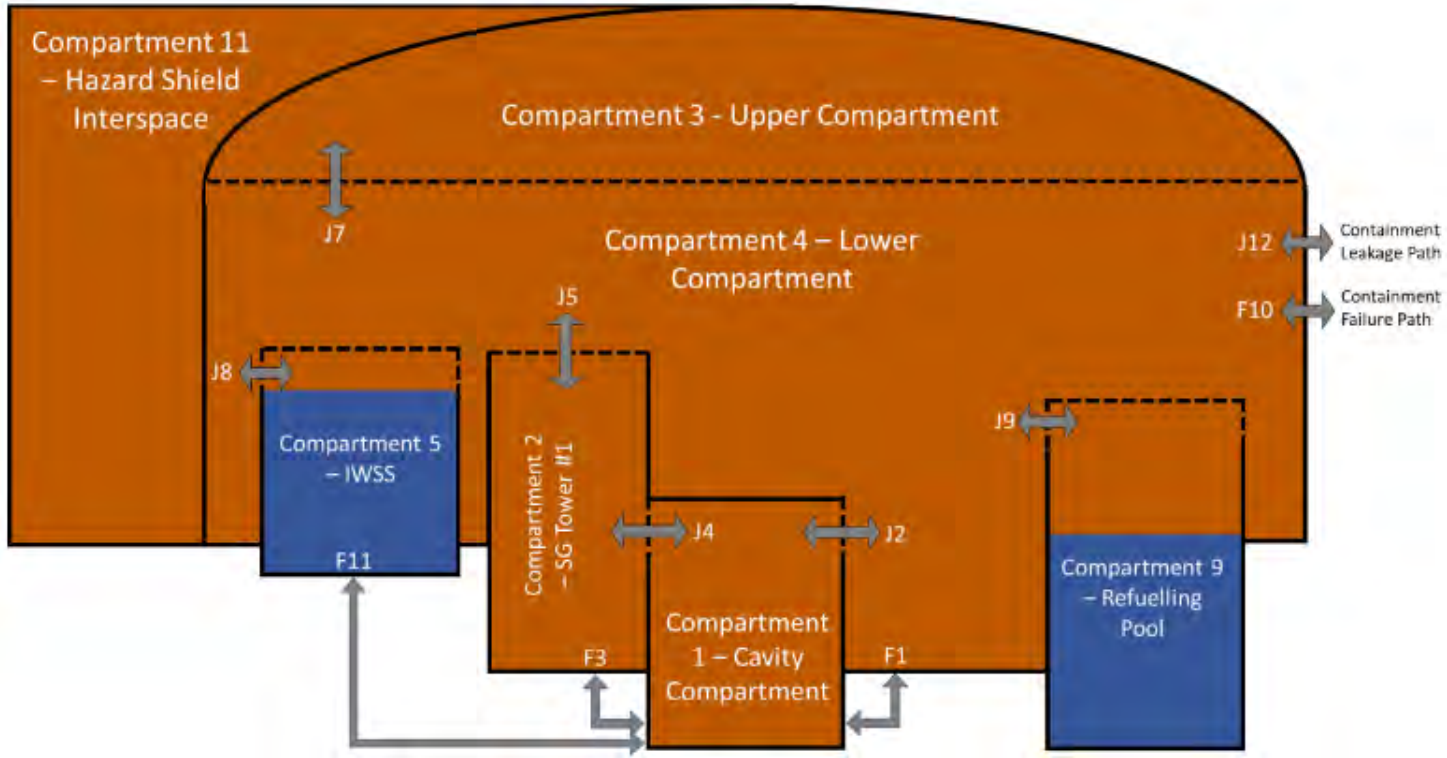

Public – Not Listed – Not Subject to Export Controls

Global Risk Evaluation - MAAP

- Fast solving integral codes allow the evaluation of a large number of SA scenarios.
- E.g. LOCA scenarios typically maximise the duration of fuel clad/steam interaction by varying:
  - Break size.
  - Safety injection water sources.
  - RCS depressurisation timing.
- Figures of merit (FoM) used to estimate localised conditions, including:
  - Total hydrogen generation.
  - Peak hydrogen concentration in containment/compartments.
  - Steam concentration during hydrogen release.
- Source terms for the most onerous scenarios are transferred to the next step for localised assessment.

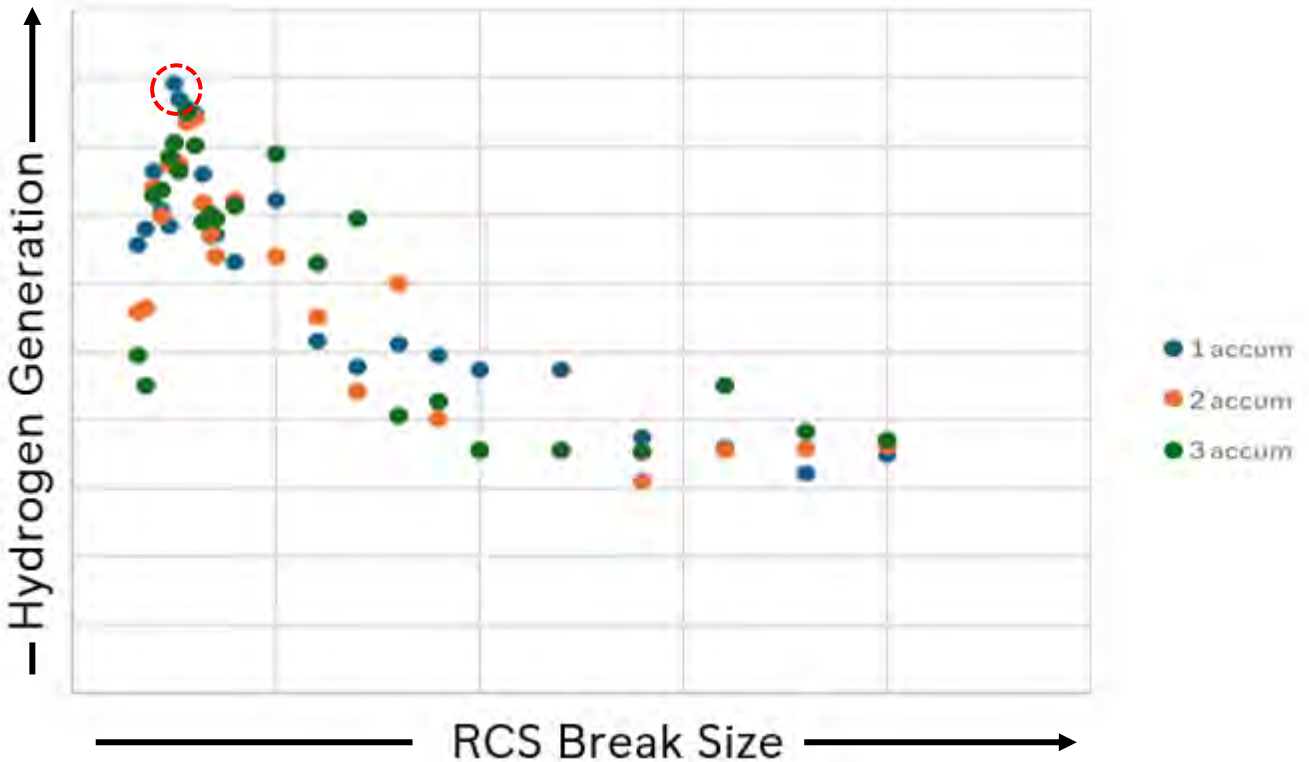

Public – Not Listed – Not Subject to Export Controls

Flame Acceleration & Detonation Risk Evaluation

Public – Not Listed – Not Subject to Export Controls

Flame Acceleration & Detonation Risk Evaluation - GOTHIC

- Detailed assessments of “scenarios of interest” are performed using code capable of modelling 3D gas mixing and heat transfer (e.g. GOTHIC).
- Detailed containment geometry model is used, with a target cell size of ~1m^3.
- Heat sinks represented by thermal conductors spanned across blockage surfaces/cells.
- MER/hydrogen source terms are injected at the cell faces representative of release location/direction.
- To bound uncertainty in hydrogen generation, the hydrogen mass flow rate is scaled to achieve the equivalent of 100% fuel clad oxidation.
- Mitigative safety measures, such as PARs, can be included in assessment.

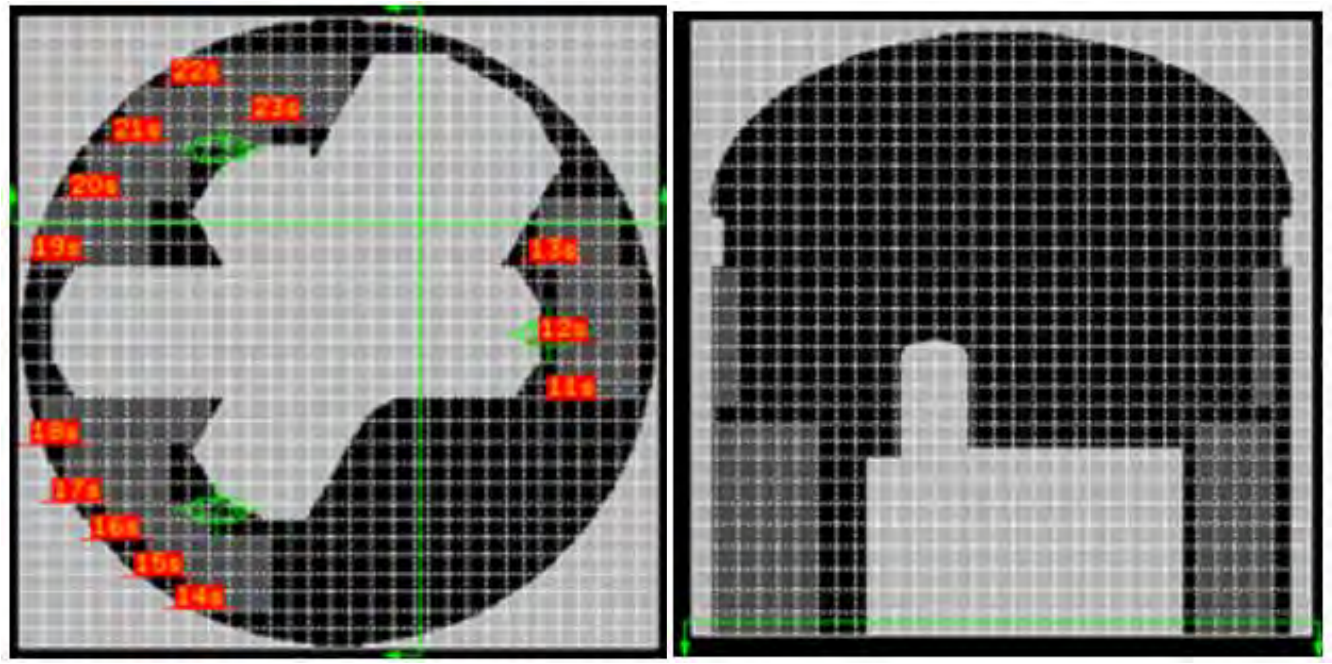

Public – Not Listed – Not Subject to Export Controls

Flame Acceleration & Detonation Risk Evaluation - GOTHIC

- The 3D mixing results are used to assess the likelihood of FA and DDT through the Sigma (σ) and Lambda (λ) criteria:
  - Regional/room assessments performed based on cell average conditions.
  - Cell-by-cell assessment can be used to inform on “cloud size”.
- If the σ and λ criteria are met, the following FoM are reviewed:
  - Volume of gas clouds exceeding combustion limits/criteria.
  - Timing within accident that criteria are satisfied.
  - Time duration criteria are satisfied or “time at risk”.
  - Relative concentration of hydrogen and steam.
  - Location of clouds, considering potential for turbulence.

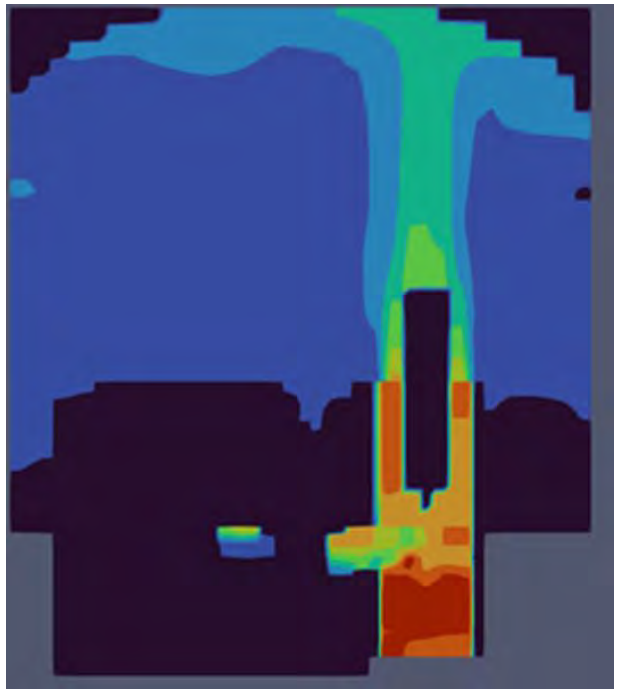

Localised Hydrogen Concentration

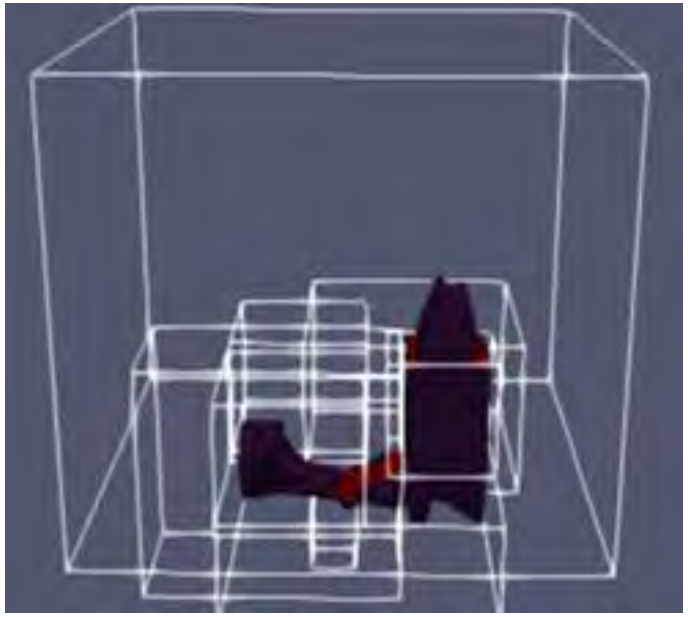

Gas Volume Satisfying σ Criterion

Public – Not Listed – Not Subject to Export Controls

Flame Acceleration & Detonation Risk Evaluation - GOTHIC

- The outcome of this analysis step allows identification of scenarios with the greatest potential for flame acceleration.
- The limiting scenarios, time within scenario, and approximate containment locations are taken forward for subsequent combustion analysis.
- Cell-by-cell conditions at the selected time are extracted, processed and used as the initial conditions for the combustion assessment (FLACS-CFD):
  - Gas Concentrations (e.g. H2, O2, Steam)
  - Temperature
  - Pressure
  - Turbulent Kinetic Energy

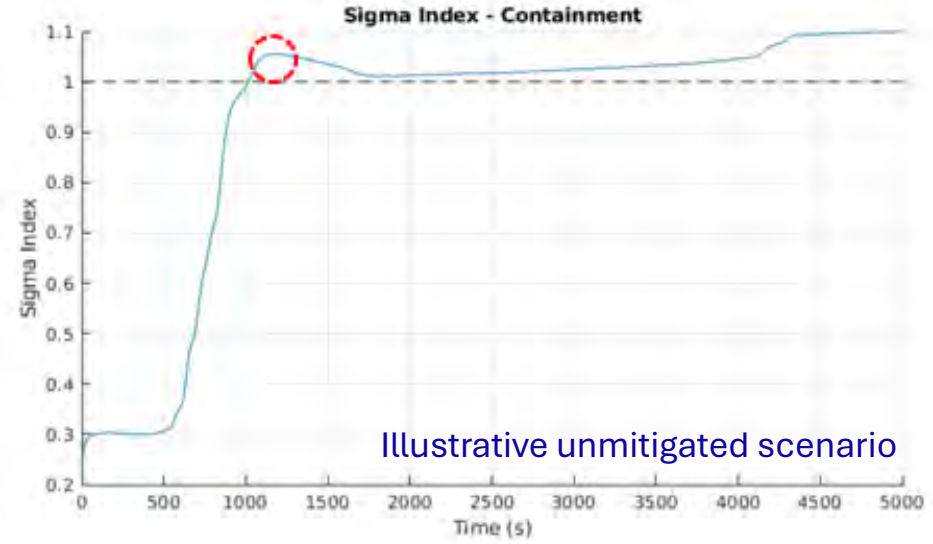

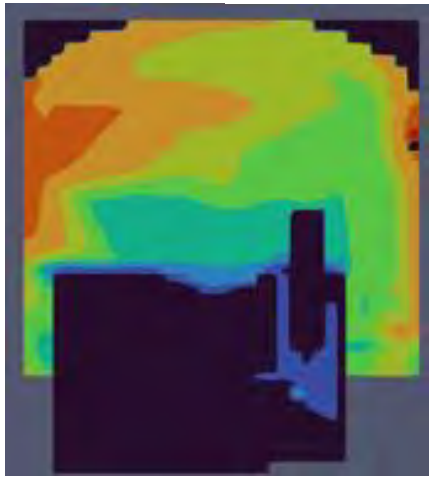

GOTHIC

Pre-processor

Localised Hydrogen Concentration

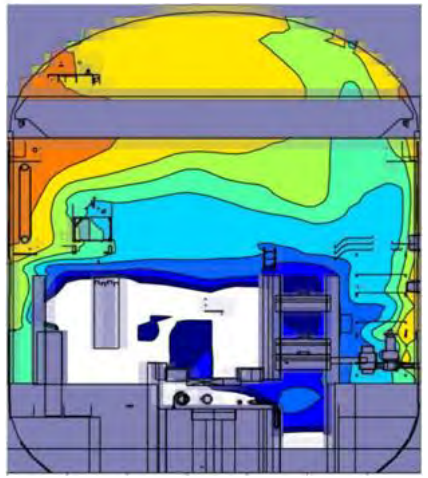

FLACS-CFD

Public – Not Listed – Not Subject to Export Controls

Localised Combustion Assessment

Public – Not Listed – Not Subject to Export Controls

Localised Combustion Assessment – FLACS-CFD

FLACS-CFD simulates vapour cloud explosions for 60+ fuels including hydrogen, accounting for the effect of contributing and mitigating effects (such as confinement and congestion due to realistic geometry).

Relevant models:

- Flame propagation and pressure build-up
- Propagation of blast waves
- Porosity Distributed Resistance model

Extensive validation:

- Many cases relevant for hydrogen
- Hydrogen Balloon, Sandia FLAME, etc.
- Confined and congested cases are relevant for both hydrocarbon industry and containment
- Generally good performance, some spread

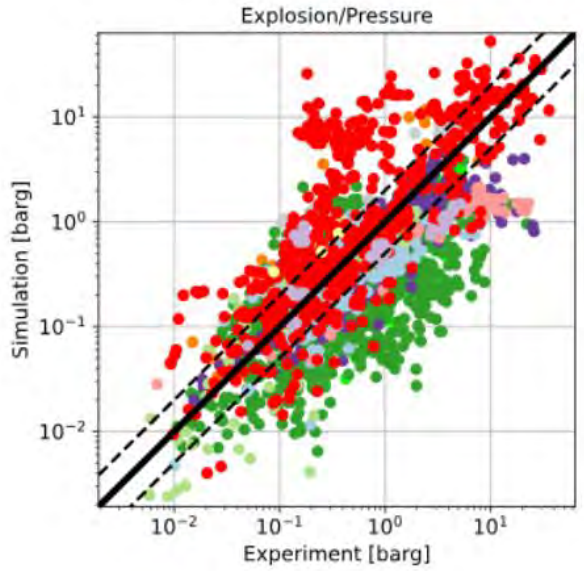

Public – Not Listed – Not Subject to Export Controls

Localised Combustion Assessment – FLACS-CFD

FLACS-CFD uses input data from GOTHIC analysis to predict the consequences of containment combustion and predict flame acceleration and detonation based on local conditions.

Overview of method:

- Set up FLACS-CFD grid
- Interpolate data from GOTHIC to FLACS-CFD
- Select ignition locations
- Simulate
- Check velocities for flame acceleration
- Automatic detection of detonation based on spatial pressure gradient
- Output overpressures and pressure-time curves at monitor points to determine loading on containment shell

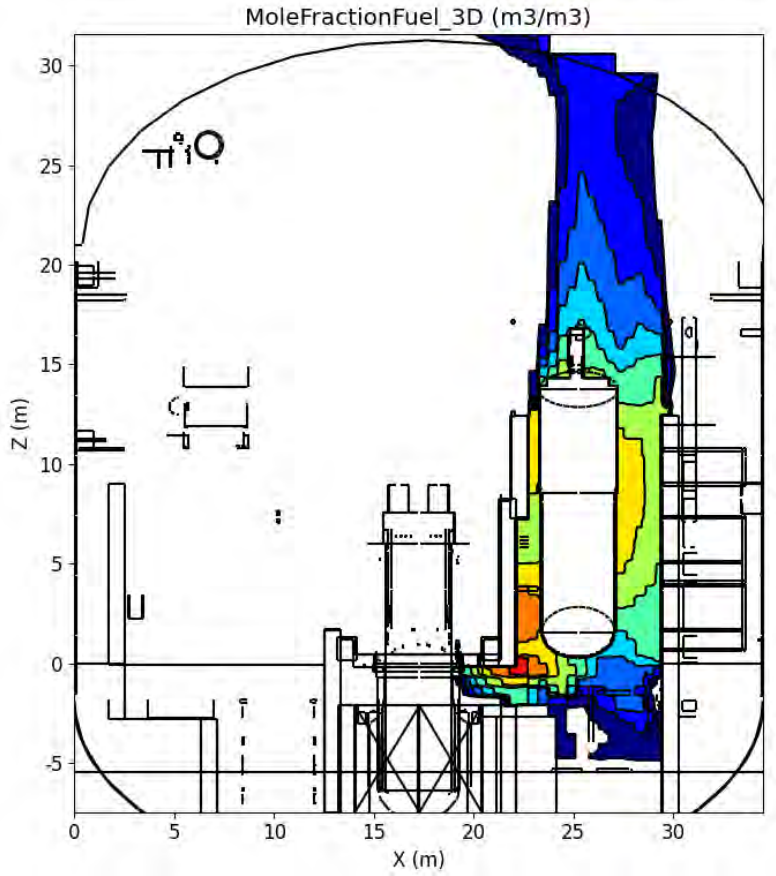

Slice through containment showing initial hydrogen concentrations above a threshold for hydrogen released in a steam generator compartment

Public – Not Listed – Not Subject to Export Controls

Localised Combustion Assessment – FLACS-CFD

FLACS-CFD can predict local flame acceleration where sigma criteria are not met according to a global analysis, especially where higher hydrogen concentrations intersect with small-bore pipework and other blockages.

The solver accounts for:

- Inerting
- Spatial distribution of hydrogen
- Confinement and congestion
- Laminar, wrinkled, and turbulent burning regimes

Example explosion simulation:

- Sigma criteria not met globally
- Localized flame acceleration around crane structure
- Local loading on containment

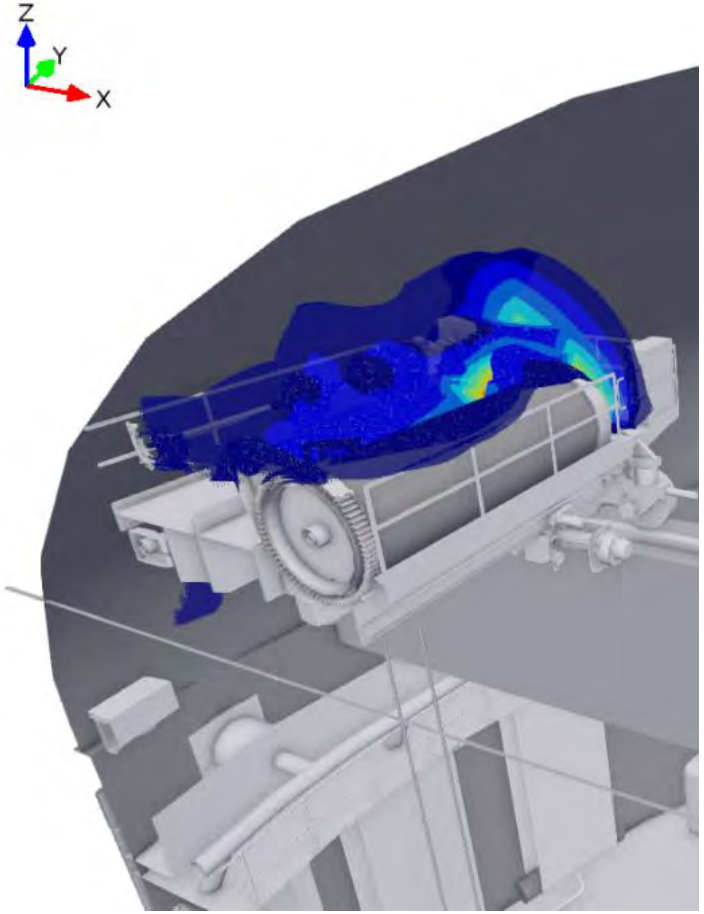

Slice through containment showing velocity magnitude as flame accelerates around crane structure

Public – Not Listed – Not Subject to Export Controls

Localised Combustion Assessment – FLACS-CFD

FLACS-CFD calculates the spatial pressure gradient and automatically triggers the Deflagration-to-Detonation Transition (DDT) when this exceeds a specified value.

Comparing to lambda criteria:

- Spatial pressure gradient criterion set to give slightly conservative prediction of DDT compared to validation cases
- When lambda criterion met, simulations show high likelihood of DDT
- Simulations will be targeted at times where the lambda criterion is close to being met, to show whether DDT is predicted for borderline cases

Following DDT prediction:

- Dedicated burning model for detonation
- Can be disabled to investigate development of spatial pressure gradient over time

Slice through containment showing pressure development

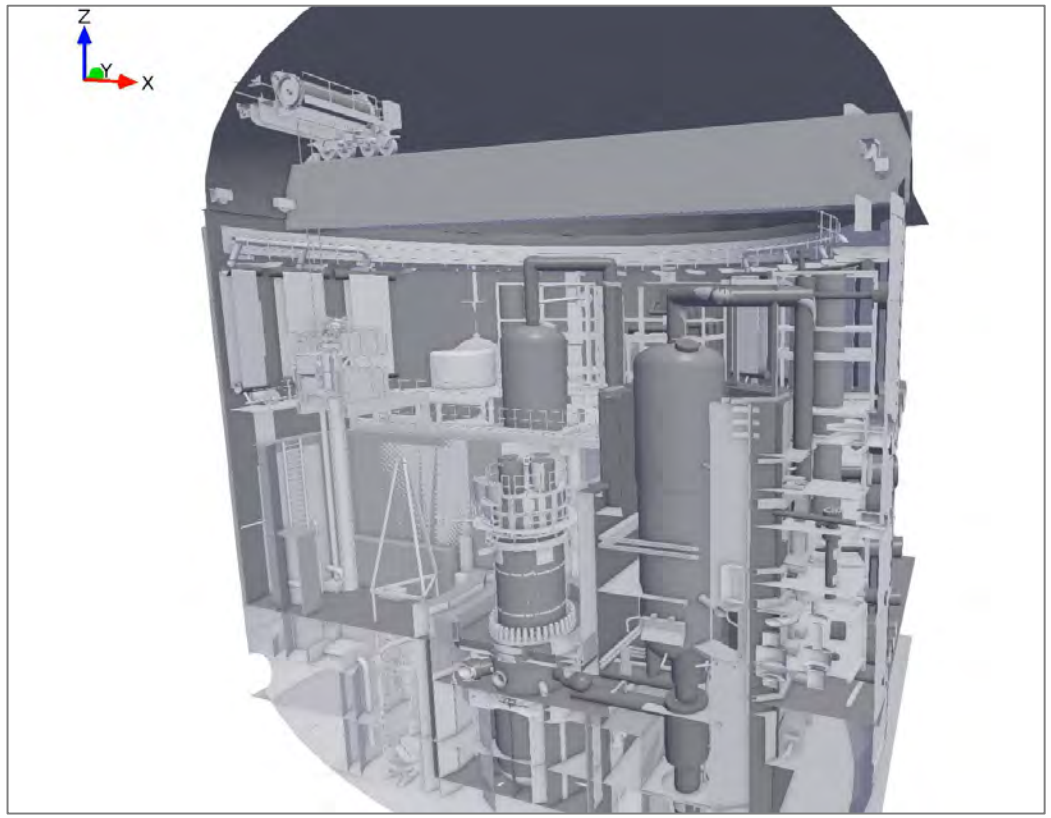

Public – Not Listed – Not Subject to Export Controls

Verification, Validation and Uncertainty Quantification

Public – Not Listed – Not Subject to Export Controls

Verification, Validation and Uncertainty Quantification (VVUQ)

- Rolls-Royce SMR deploy the PIRT and TAM approach:
  - Identify all relevant phenomena in the problem domain.
  - Assess analysis code capability in representing phenomena according to importance.
- Allows identification of the most significant phenomena/modelling limitations and prioritisation of VVUQ.
- The objectives of the analysis should always be used to prioritise VVUQ activities.

For example:
Validation for hydrogen combustion often prioritises accurate peak pressure prediction, whereas if the safety case objective is to prevent the occurrence of energetic combustion then the priority is to adequately predict the onset of FA/DDT.

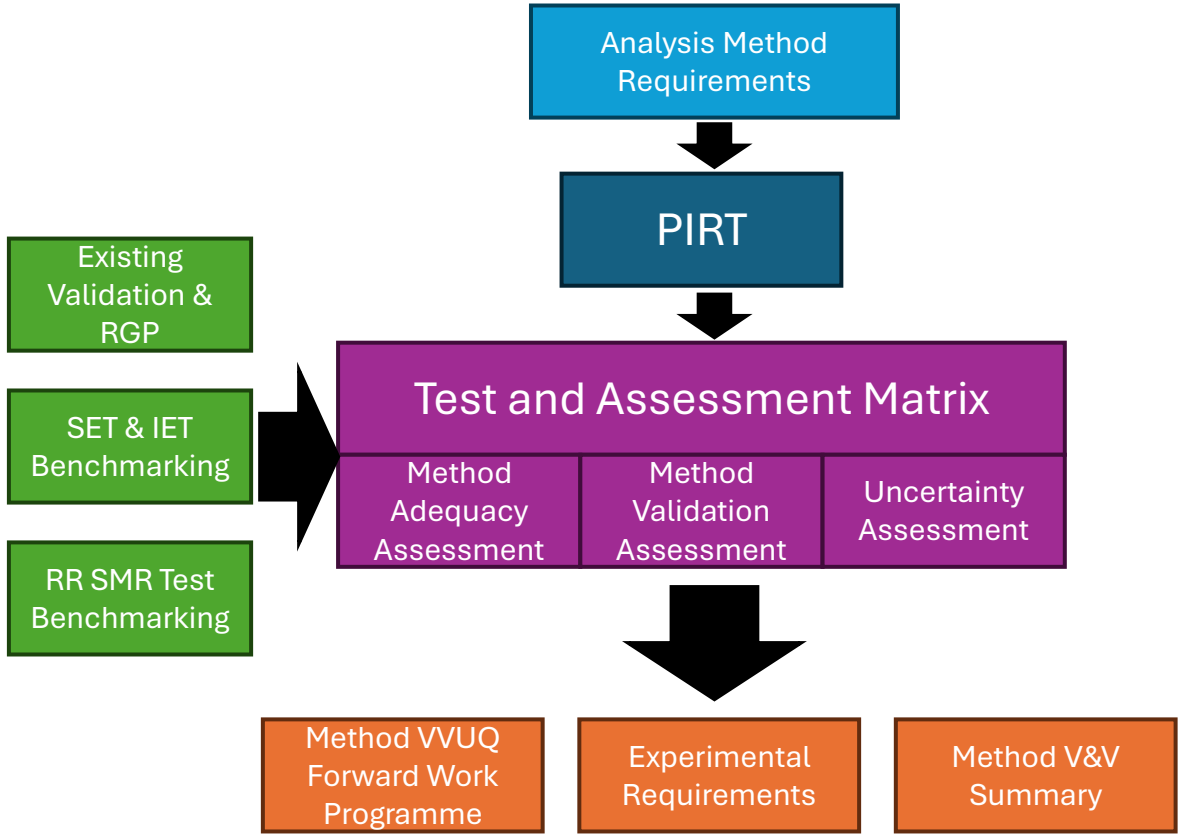

Public – Not Listed – Not Subject to Export Controls

Summary

Public – Not Listed – Not Subject to Export Controls

Summary

- A three-step process has been developed for the assessment of SA hydrogen risk.
    1. Global Assessment in MAAP.
    2. Localised gas mixing assessment in GOTHIC.
    3. Localised combustion assessment in FLACS-CFD.
- The approach allows identification and assessment of limiting credible scenarios for the Rolls Royce SMR and provides conditions for detailed finite element assessments of the containment vessel.
- Iterative approach allows optimisation of safety systems to manage hydrogen release and development of a robust safety case for severe accidents.

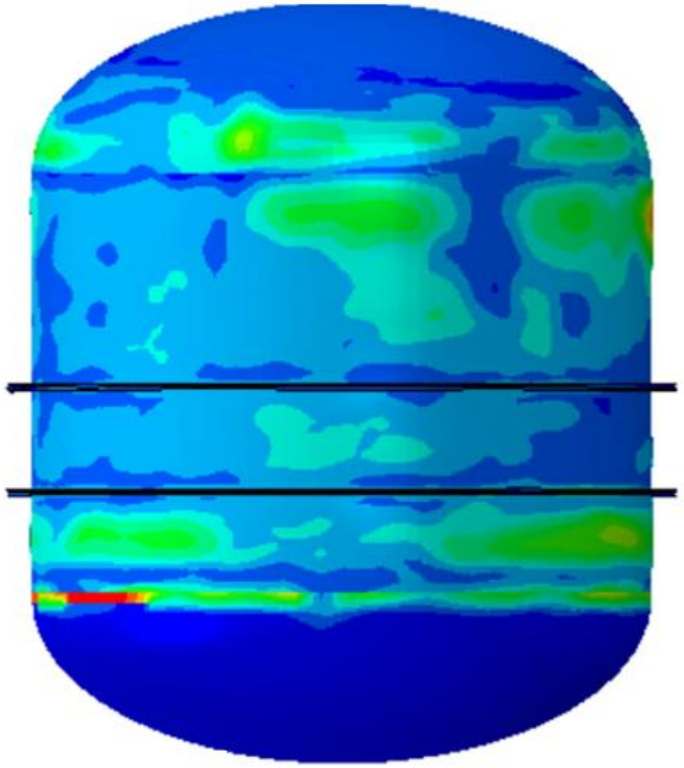

Public – Not Listed – Not Subject to Export Controls

ROLLS ROYCE SMR

BE SAFE. BE BOLD. BE INCLUSIVE. BE IMPACTFUL. BE CREATIVE. BE ENGAGED

Public – Not Listed – Not Subject to Export Controls

SEVERE ACCIDENT ANALYSIS OF SASPAM-SA DESIGN II LW-SMR DRY CONTAINMENT USING CONTAINMENTFOAM

Carlos Vázquez-Rodríguez, Stephan Kelm
Forschungszentrum Jülich (FZJ)
Wilhelm-Johnen-Straße, 52428 Jülich, Germany
c.vazquez-rodriguez@fz-juelich.de; s.kelm@fz-juelich.de

ABSTRACT

The Horizon Euratom SASPAM-SA Project investigates the transferability of severe-accident knowledge and methods developed for large LWRs to Light-Water SMRs. While most SASPAM-SA partners rely on lumped-parameter tools (MELCOR, ASTEC, AC2), this work uses *containmentFOAM*, an open-source CFD add-on to OpenFOAM®-11, to complement those calculations with 3D, high-fidelity insight into the containment response of SASPAM-SA Design II, which features a containment with several passive safety systems. With that purpose, and using MELCOR data as boundary conditions, two different time windows of one of the SA sequences postulated in SASPAM-SA are analysed with *containmentFOAM*.

The first window covers the blowdown phase, where the large mass and energy release drives a rapid displacement and redistribution of the initial gases, with nitrogen transport to the Passive Suppression System (PSS) as the central aspect. The second window targets a later stage of the transient including the first significant hydrogen release, during which the hydrogen molar fraction rises from zero to about 0.1 and the flow field is governed by weak buoyancy-driven motions. In both windows, the local transport of non-condensables to the PSS end up determining the pressurization of the containment, that ultimately affect the severe accident progression. *containmentFOAM's* simulations indicate that the blowdown phase quickly approaches a well-mixed atmosphere, suggesting that the added value of resolving 3D details is limited. In contrast, during the later time window, the weak buoyancy-driven flows sustain gas stratification, affecting the hydrogen distribution and its transport to the PSS.

KEYWORDS
SMR, CFD, *containmentFOAM*, OpenModelica

1. INTRODUCTION

The most recent energy outlooks published by the International Atomic Energy Agency (IAEA) postulates the deployment of up to 162 GW of Small Modular Reactors (SMRs) by 2050 [1]. Among the concepts under consideration, Light Water SMRs (LW-SMRs) are the most likely ones to be deployed in the near term. They generally share key characteristics with currently operating large LWRs, while incorporating evolutionary design features that provide safety benefits and reinforce the first three levels of the Defence-in-Depth (DiD) principles [2,3]. Nevertheless, the path from conceptualization [4] to the licensed concept [5] of an reactor is complex, effort-intensive, and time-consuming, always involving numerous interactions between designers and regulators. Moreover, even for plants with advanced features strengthening DiD levels 1–3, regulators require independent provisions for Severe Accident (SA) prevention and mitigation to be incorporated in the design (DiD level 4). Consequently, scenarios that could lead to a SA must be postulated and studied deterministically (see [2] for details). In this context, the Horizon Euratom SASPAM-SA project [6], coordinated by ENEA (Italy), addresses the identification of potential postulated SA

sequences for two generic concepts representative of a range of LW-SMRs. The SASPAM-SA Design-I features a generic integral Pressurised Water Reactors (i-PWR) of about 60 MWe embedded in a containment submerged in a pool, whereas Design-II consists of a generic 300 MWe i-PWR with a containment and several passive systems. The postulated SA sequences for each design are summarised in [6] for completeness.

Aligned with SASPAM-SA evaluation of the applicability of large PWR know how to LW-SMR, the postulated sequences calculated with Lumped Parameter (LP) codes were used in previous work [7] as a screening exercise to identify how LW-SMR specific phenomena required targeted upgrades of the *containmentFOAM* model library. *ContainmentFOAM* is a CFD toolbox —developed at Forschungszentrum Jülich as an add-on for OpenFOAM (currently v11)— with a modelling basis originally consolidated for the phenomenology prevailing in dry large-PWR containments. It is focused on multi-species transport and condensation-driven heat transfer and aiming at technical-scale safety analyses. Among the different upgrading needs, the stronger coupling between the containment atmosphere and the Pressure Suppression System (PSS) motivated the main development effort, since the transport and accumulation of non-condensables at the PSS is the driving phenomenon for the containment pressurisation. A fully high-fidelity, two-phase CFD representation of containment and PSS was discarded, as it would be computationally prohibitive. The proposed solution was a multi-fidelity coupling framework where *containmentFOAM* resolves the containment space while the PSS is treated at system level, with data exchanged through an Functional Mock-up Interface (FMI) based coupling to OpenModelica [7]. This coupling was validated against experiments with comparable coupled phenomena and tested with a preliminary application at the technical scale [7,8].

Within SASPAM-SA, most partners rely on LP SA codes (MELCOR, ASTEC, AC2) with empirical models to replicate the severe accident phenomenology at an affordable computational cost for simulating transients of several days. Within SASPAM-SA, *containmentFOAM*'s role was to complement those calculations with high-fidelity, 3D insights into the containment response of Design II for selected time windows. The objective of the present work is not to replace the LP analyses, but to identify and simulate phases of the SASPAM-SA sequences where local heterogeneities, not resolved in 0D/1D models, can become safety-relevant. In particular, the 3D transport and accumulation of non-condensable gases (N_2 and H_2) to the PSS. Following this scope, Section 2 introduces the selected SASPAM-SA transient and defines the two analysed time windows, Section 3 presents the Design II *containmentFOAM* model, and Section 4 discusses the results for the blowdown phase (Section 4.1) and for the later phase dominated by hydrogen transport (Section 4.2).

2. SEVERE ACCIDENT TIME WINDOWS FROM SASPAM-SA SEQUENCES

SASPAM-SA Design-II is a generic ~300 MWe integral PWR concept with a dry, inertised containment integrating several passive safety systems, including a PSS coupled to the drywell. This section is intended to describe the main characteristics of the SASPAM-SA Design-II SA postulated sequences simulated with SA codes, which will be necessary to better understand the containment analyses that will be presented in Section 4. A more comprehensive description of the Design Basis Accident (DBA) and all the SA postulated in SASPAM are available in [9] and [6,10], respectively.

For the response the DBA (Direct Vessel Injection (DVI) break) the different systems —Reactor Pressure Vessel (RPV-P_1), Containment/Drywell (P_2) and PSS (P_3)— are expected to behave as a closely coupled thermal-hydraulic system driven by natural circulation. In the initial pressure-suppression stage (see Figure 1, containing all the needed acronyms), ADS actuation rapidly couples the RPV and containment pressures, limiting the coolant inventory discharged thanks to the faster pressure equalization ($P_1 = P_2$). The resulting pressure rise in the drywell promotes venting to the PSS, where steam is efficiently condensed in the subcooled pool and the pressure increase becomes dominated by the progressive accumulation of non-

condensables in the PSS gas space. After the drywell peak, P_1 and P_2 decrease due to primary-side cooling and wall condensation, and since P_3 decreases more slowly the pressure gradient then reverses ($P_3 > P_2$), pushing water from the PSS into the drywell and flooding the reactor cavity. When the cavity water level rises above the break elevation, the long-term cooling loop is closed and stable cooling is established (right sketch in Figure 1), with the coupled system approaching $P_1 \approx P_2 \approx P_3$ while decay heat is removed by the passive Emergency Heat Removal System (EHRS).

As already concluded at [10], SASPAM-SA confirmed that the pivotal safety system was the EHRS (the combined failure of all the other safety systems still resulted in a successful long-term cooling of the core). Therefore, SASPAM-SA sequences combined the failure of the EHRS with additional safety systems (ADS-Automatic Depressurization System, LGMS-Long Term Gravity Make-up System, EBT-Emergency Borated Tank) [6]. From the containment-analysis perspective, one evident time window to investigate is the blowdown phase, since the SA codes predict a pressure increase above 11 bar during the first 1000 s. In this early transient, containment phenomenology is dominant: wall condensation rates and the transport of non-condensable gases to the PSS are expected to be at their maximum. And evaluation of the 3D flows should also confirm the nearly homogeneous containment conditions usually assumed for blowdown, or whether the coupling with the PSS can still generate safety-relevant local heterogeneities. In addition, the rapid evolution of the containment conditions is reinforced by ADS actuation, which motivated the selection of the SA sequence including ADS-1 actuation (SA3). Figure 2 summarizes the corresponding pressure evolution (P_1, P_2 and P_3), the main system actuations, and the associated phenomenological windows.

A second time window of interest was selected between 30,000 s and 50,000 s, at the beginning of the core-degradation phase (between PhW2 and PhW3 in Figure 2). In this period, after the first Filtered Containment Venting System (FCVS) actuation, core oxidation starts and hydrogen is released to the containment. With the ADS-1 valve open, the more elevated release favours the hydrogen stratification. The potential 3D heterogeneities can affect hydrogen transport to the PSS and the non-condensable distribution, which in turn influence steam condensation and containment pressure evolution. A proper prediction of the pressure response in this phase is particularly relevant because it is linked to the observed FCVS cycling in Figure 2, and therefore to the timing of venting actions and the associated source-term evolution.

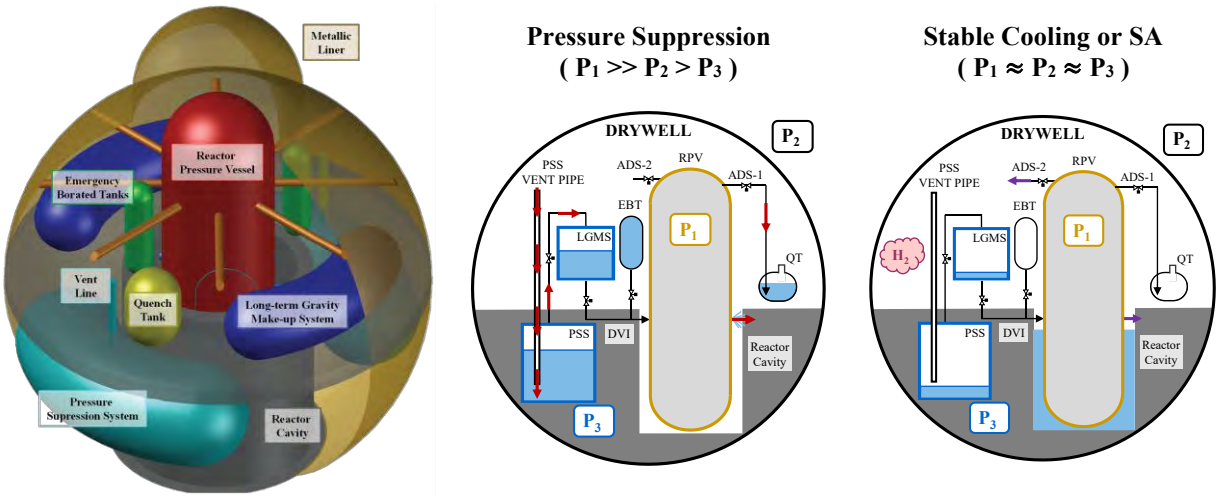

Figure 1. On the left, 3D CAD representation of Design-II containment. The additional 2D sketches represent the status of passive safety tanks in different stages of DBA and SA

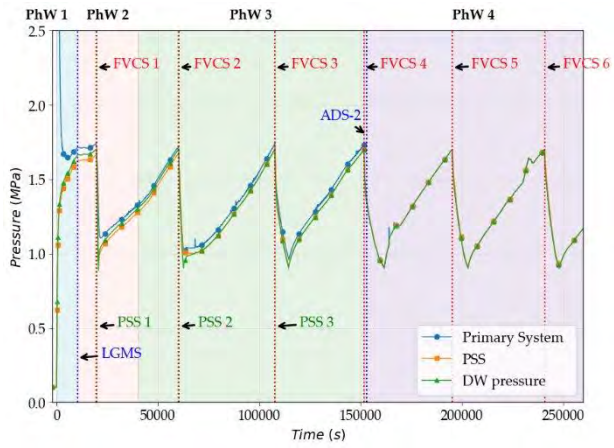

Phenomena Windows	Phenomena	Duration
PhW1 - Thermal-hydraulic phase	Blowdown, ADS-1, EBT ,LGMS, PSS reverse flow, onset of oxidation	10300 s
PhW2 - Core degradation phase	Onset of oxidation, FCVS, PSS Reverse flow, Onset of core damage	30000 s
PhW3 - Containment phenomena	FCVS, PSS reverse flow	110000 s
PhW4 - Reflood	ADS-2, Reflood, FCVS	11000 s

Figure 2. P_1, P_2 and P_3 pressure evolution for the selected SA with colour codes for phenomena windows. The figure is produced and table is adapted from the work of Sapienza University of Rome [11]

3. SASPAM-SA DESIGN-II containmentFOAM MODEL

The CFD model is based on the geometry shown on the left of Figure 1. The containment consists of a steel shell with an inner diameter of about 25 m and an upper removable head for outage requirements. Compared with conventional large-PWR containments, the internal layout is simpler and less compartmentalised. According to the available design information, the containment should be evaluated as two main halves with different pressure evolutions, separated by a concrete floor: an upper half containing the RPV, QT, LGMS and EBT, and a lower half containing the PSS tanks, connected to the upper region through the vent lines.

The geometric information was taken from the common SASPAM-SA database developed as reference input for the LP analyses [12]. Since the level of detail required for a 3D CFD model is significantly higher than for a 0D control-volume representation, missing geometric data had to be completed by engineering judgement. This process led to a detailed CAD model of Design-II, which was then used as the basis for the *containmentFOAM* model, and also helped identify and correct inconsistencies in the initial geometry database used by the LP modellers. To preserve consistency with the SA-code models, the final 3D geometry was checked against the common database, yielding relative deviations below 1.2% for free volume and 2.8% for wall surface. Minor adaptations were then introduced to facilitate meshing, the main ones being a local modification of vent-line thickness, and the non-inclusion of the feed and main steam lines.

The containment model was subdivided into three regions: the containment gas space (FLUID), the concrete cavity (CONCRETE), and the containment shell (STEEL). As shown in Figure 3, a hybrid meshing strategy was adopted: automatic unstructured meshes were used for the FLUID and CONCRETE domains, while the STEEL was kept as a block-structured hexahedral mesh. The FLUID domain was discretised with 2.3 million predominantly hexahedral cells using cfMesh (cut-cell approach with cubic base cells), with a base cell size of 0.4 m and up to two local refinement levels (0.2 and 0.1 m) around relevant geometric features (e.g., vent lines, QT and LGMS), as illustrated in Figure 3. The CONCRETE region was meshed with about 0.37 million unstructured cells (cfMesh), whereas the STEEL was represented by a block-structured mesh of about 0.36 million hexahedral cells generated with ICEM. Wall condensation was only modelled on the concrete surfaces and on the STEEL shell, with all other internal structures treated as adiabatic. Boundary-layer resolution was applied on condensing walls (Figure 3), with average y^+ below 2, while thicker near-wall layers were accepted on non-condensing adiabatic structures due to less restrictive wall functions without condensation. For the FLUID mesh, the main quality indicators were satisfactory for the present calculations (maximum skewness 1.18, maximum non-orthogonality 55 with average ≈5, average cell volume ratio 0.85). A formal mesh sensitivity analysis was, however, not yet performed.

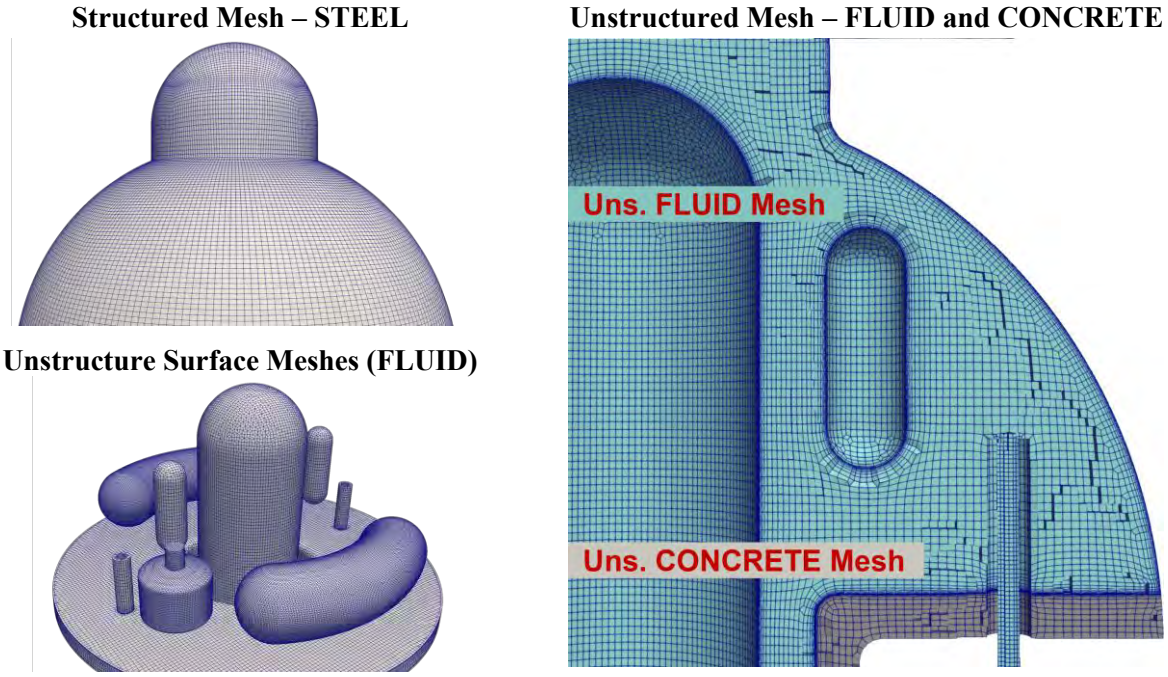

Figure 3. Hybrid meshing: structured steel-shell mesh and unstructured fluid/concrete meshes

The 'baseline model set' for *containmentFOAM* technical scale analysis, which was intensively validated before (e.g., [8,13–15]), was employed. Its main characteristics are summarized and described in Table I. Essentially, it founds on a single-phase simplification of the containment atmosphere, where wall condensation is modeled using a diffusion layer approach [16] and bulk condensation a homogeneous equilibrium model [17]. Solids use a simpler approach only solving for the energy equation to represent heat diffusion. All structures allowing condensation are represented by a conjugate heat transfer (CHT) approach.

A key enabling element of the present model is the *containmentFOAM*-OpenModelica multi-fidelity coupling implemented through the FMI-2 standard, where the containment is resolved in 3D CFD and the PSS is represented by a system-level model exchanged as an Functional Mock-up Unit (FMU). The main rationale for using OpenModelica was its flexibility and the availability of reusable components and modelling libraries that can be readily adapted to the needs of the coupling. FMI then provides a code-agnostic framework for information exchange and coupled simulation. This approach was introduced and validated in previous work [7], so only the main hypotheses of the PSS-FMU are recalled here: the PSS is represented by a lumped 0D two-phase single-node model with complete steam condensation into a subcooled pool, non-condensable bypass of the pool, user-defined heat transfer coefficients, and no pool-surface evaporation. PPOOLEX was selected as validation benchmark because it also involves a containment and a pressure-suppression pool with two closely coupled gas spaces, where the pressure evolution is strongly driven by non-condensable transport. For the evaluated PPOOLEX tests, the validation demonstrated both qualitative and quantitative accuracy of the coupling framework. The impact of the PSS-FMU simplifications, mostly the neglected evaporation, on the present Design-II calculations is discussed in the Results section.

The boundary conditions were taken from the MELCOR calculations for SASPAM-SA Design-II provided by Sapienza University of Rome (UniRoma) and detailed in [6]. Three injection sources were considered in the CFD model (the two sides of the DVI break and the ADS-1 discharge above the QT). For each source, the release rate, composition and temperature were directly imposed from the MELCOR injection tables. Steam, hydrogen and enthalpy releases were applied as volumetric sources (order of 1 m^3), with a simplified averaged representation of directional momentum.

Table I. Physical Models (adapted from [18])

Physics	Model
governing equations	Unsteady Reynolds-averaged Navier-Stokes equations, total energy equation, transport equation for species mass fraction
turbulent transport	k-ω based Shear Stress Transport (SST) model, including production and dissipation terms for buoyancy based on SGDH; Turbulent heat and mass transport: SGDH, Pr_t=Sc_t=0.85
multi-species transport	Ideal mixture approach. Each individual set of gas transport, properties (heat capacity, viscosity, conductivity) is implemented by tables, being temperature dependent for H_2 and N_2, and pressure and temperature dependant for H_2O. Effective binary diffusion model with pressure and temperature diffusion coefficients (Fuller model)
wall treatment and condensation	Wall condensation: single phase 'diffusion-layer' approach, continuous wall functions
thermal radiation	P_1 model, gray participating mixture, (κ_{H2O}=10 $bar^{-1}m^{-1}$, NCG transparent), ε_{wall} = 0.6
system models	PSS: Single node lumped two phase model built with OpenModelica. Complete condensation of steam into subcooled water, and no surface evaporation

4. SIMULATION RESULTS

4.1. SASPAM-SA3: Blowdown phase

For the blowdown case, the set-up illustrated in Figure 4 preserves the same modelling basis introduced in Section 3. The PSS coupling is treated implicitly through the FMI interface located at the end of the vent lines. There, *containmentFOAM* provides the local pressure, temperature and gas composition at the outlet patch, and the OpenModelica PSS FMU returns the mass flow rate imposed at the CFD boundary as a function of the counter-pressure (water column plus non-condensables in the PSS gas space). In addition, Figure 4 shows the three release locations (DVI-1, DVI-2 and ADS-1) and flow rates used for the blowdown. For the DVI break sources, MELCOR's liquid discharge (initially at 155 bar) cannot be injected directly into the single-phase CFD containment model, which is at near-atmospheric conditions. Therefore, an isenthalpic expansion correction was applied to estimate the available energy for flashing liquid into a steam flow for *containmentFOAM* (from the LP-code break conditions to the CFD saturation conditions).

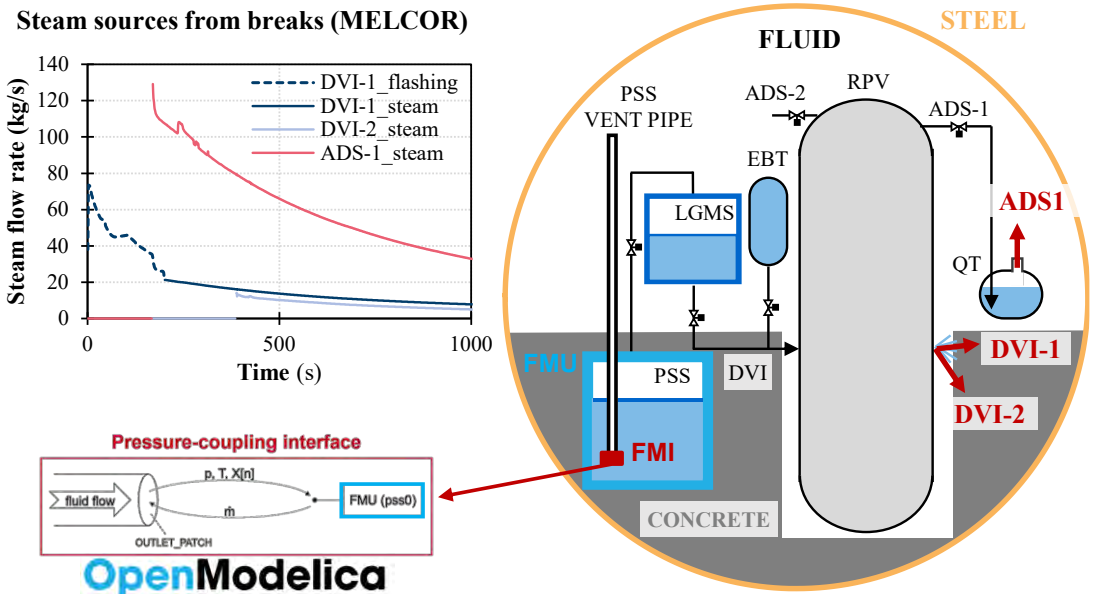

Figure 4. Sketch of case set-up: FMI coupling, location and flow rate of volume sources, and mesh regions

A constant time-step strategy was adopted to improve the stability of the FMI coupling in this first time window, starting from Δt=0.001 s and increasing up to 0.003 s toward the end of the transient. The calculations were run on 96 cores, with a wall-clock time of about 140 h (13 440 core-h), which corresponds to roughly 170 s of simulated transient per day. The time step control kept the maximum CFL number below 2, with a maximum of 5 outer PIMPLE iterations and all residuals below 10^{-4} (generally below 10^{-5}). It should also be noted that the highest local velocities of the blowdown are not fully represented because the releases are imposed as volumetric sources (not surface/patch injections). However, these very fast transients remains a challenge for high fidelity codes, and the authors are not aware of comparable CFD simulations of the containment blowdown phase in the open literature.

Figure 5 compares the blowdown results from MELCOR, the *containmentFOAM* base case, and a parametric *containmentFOAM* case with modified energy transfer from the PSS liquid to the PSS gas ("colder PSS"), just included to complement the interpretation of the results. The four graphs are shown together to support a consistent reading of the blowdown response. In fact, although the global containment-pressure evolution remains comparable between cases, other quantities that are usually considered relevant in containment analyses (e.g., wall condensation and transport to the PSS) can differ significantly.

Before ADS-1 actuation (≈ 200 s), the *containmentFOAM* base case reproduces the MELCOR pressure increase with good qualitative and quantitative agreement. After ADS-1 opens, both curves keep a similar trend but progressively diverge, reaching at 1000 s about 1.2 MPa in MELCOR and about 1.4 MPa in the *containmentFOAM* base case. This difference is not straightforward to interpret from the other graphs, since the CFD/FMU calculation predicts both higher steel-liner condensation and higher transport to the PSS,

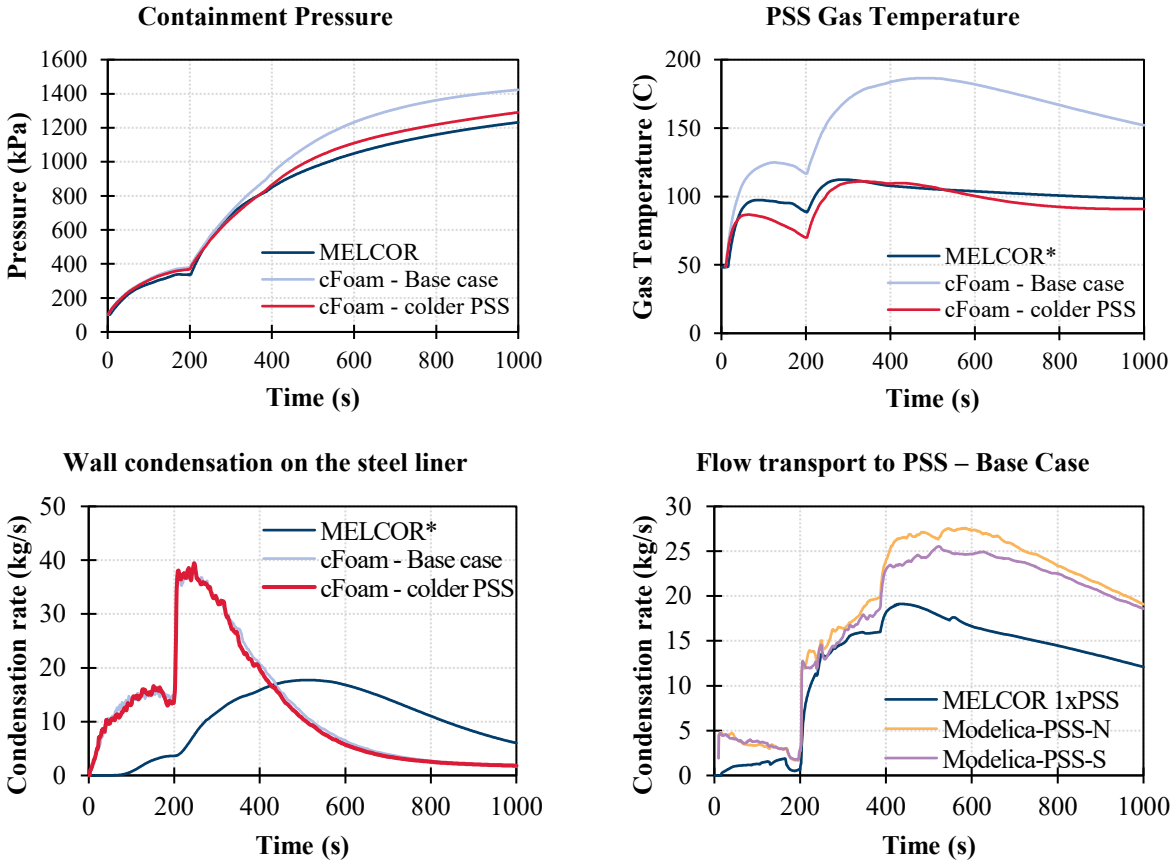

Figure 5. MELCOR (UniRoma) vs *containmentFOAM* blowdown calculations comparison

which would a priori suggest a lower containment pressure. The key point is that the additional transport to the PSS is largely associated with steam (which condenses in the pool), while the transported nitrogen inventory (not shown here) is comparatively similar. Therefore, the understanding of the pressure evolution should be mainly based on the higher gas temperature in the PSS gas space predicted by the OpenModelica PSS model, which increases the PSS counter-pressure and, consequently, the containment pressure.

This interpretation motivated the parametric "colder PSS" case, where the effective heat-transfer coefficient (including natural convection and evaporation effects) used in the PSS FMU in all PPOOLEX validation experiments was increased from 30 to 130 W/m^2 K. The latter value was estimated just to replicate the MELCOR PSS gas temperature evolution, and not as a realistic figure. As shown in Figure 5, this adjustment strongly reduces the difference in PSS gas temperature after ADS-1 actuation (peak values of about 185 °C in the base case, versus about 110 °C in MELCOR and in the colder-PSS case), and the containment pressure correspondingly moves much closer to MELCOR (at 1000 s, from about 1.4 MPa in the base case to about 1.28 MPa, compared with about 1.2 MPa in MELCOR). Having closer backpressures from the PSS, allowed to investigate how the pressure equalization affected the containment phenomena. Interestingly, the wall-condensation curve and the transport-to-PSS flow rates remain of the same order as in the base case, which reinforces that the improved pressure comparability is mainly linked to the PSS gas-space conditions, rather than to changes in the main containment-side mechanisms. The remaining code-to-code differences are still under investigation and cannot be resolved further with the currently available comparison data.

Regarding 3D effects, no additional plots are included at this sub section because the containment atmosphere is mostly homogeneous after ADS-1 actuation. The present minor heterogeneities —see the asymmetry seen in Figure 5 for the flow rates to PSS-N (North) and PSS-S (South) in the base case— indicate some 3D influence on the transport processes, but no safety-relevant impact on the global blowdown response. Overall, for the blowdown time window, the results indicate that the pressure build-up is mainly controlled by the state of the non-condensables accumulated in the PSS gas space (especially N_2 inventory and gas temperature). So, as an insight for LP codes, the detailed representation of PSS physics seems to be more influential than a more detailed 3D resolution (or complex nodalization) of the containment atmosphere.

4.2. SASPAM-SA3: Late phase with hydrogen transport

Similarly to Section 4.1, the evaluation of the second time window of interest is introduced by presenting a sketch of the case set-up (Figure 6). Apart from the evident variation of the mass source flow rates, now also including the hydrogen mass flow rate in a secondary axis, one clear visual difference is that now the cavity is mostly occupied by water, which has been included in the model to actuate as an additional condensing surface. To keep the single-phase approach, the water pool is represented by a thin solid region that allows the water surface to reach the containment steam saturation temperature while the bulk is maintained at the liquid temperature estimated by MELCOR. However, the main difference with the previous case set-up is the replacement of the FMU-FMI coupling by a pressure boundary condition representing the containment pressure predicted by MELCOR. This replacement was motivated by preliminary tests showing that, in this late window, the simplified PSS-FMU (without pool-surface evaporation) lead to unphysically high flow rates from the containment to the PSS. Due to this limitation —combined with 100% steam in the containment: conditions beyond the current validation basis of the FMU— the PSS pressure can only increase by the heat transferred by a hotter water pool, and not by the increasing steam partial pressure. Consequently, the missing steam build-up in the PSS gas space was artificially compensated by excessive steam/enthalpy transport to heat up the pool and pressurise the PSS gas. Therefore, a MELCOR pressure boundary was imposed to evaluate the effect of 3D transport vs the MELCOR reference data under equivalent pressures.

The time step control followed the same criteria described in Section 4.1, but with significantly larger time steps due to the lower velocities of this time window. The time step was automatically adjusted to keep the maximum CFL below 1, typically reaching ≈ 0.008-0.01 s. The calculation was run on 256 cores of FZJ's

high performance computing facility JURECA, and advanced about 1550 s of transient per day. This corresponds to about 12.9 days of wall-clock time (≈310 h), i.e., approximately 80 000 core-h.

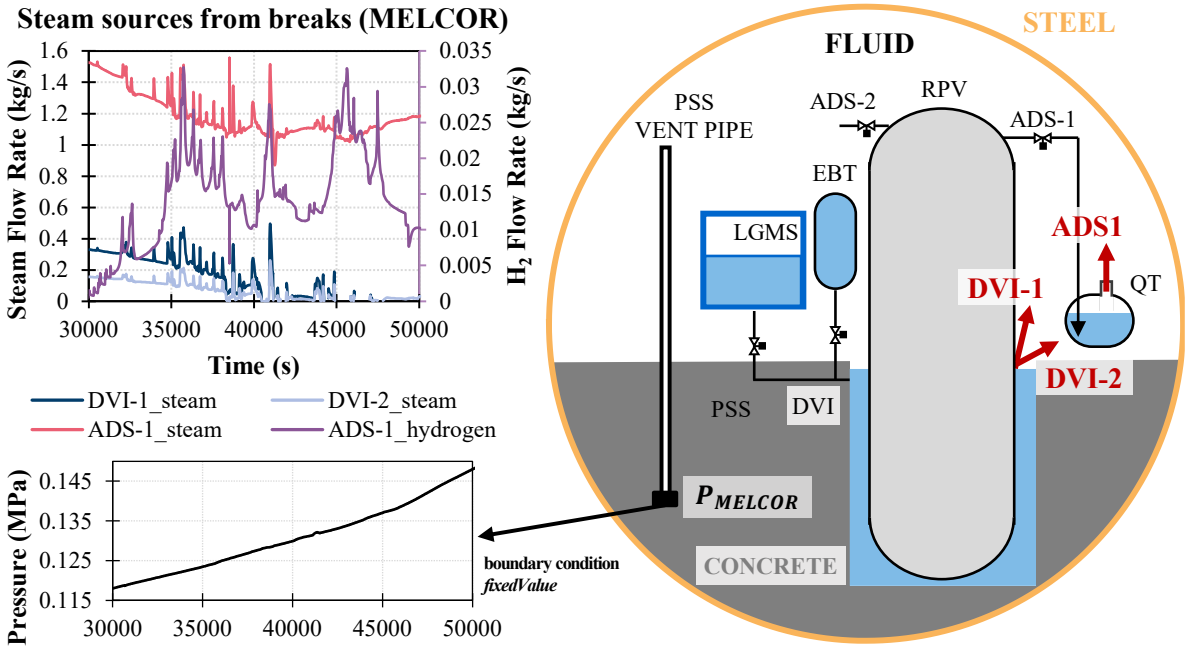

Figure 6. Sketch of case set-up: Outlet pressure, location and flow rate of volume sources, and mesh regions

To assess the hydrogen distribution and its transport from the containment to the PSS during PhW2-3, two complementary types of results are presented. First, Figure 7 compares *containmentFOAM* and MELCOR by means of two global variables: (i) the containment averaged hydrogen volume fraction; and (ii) the integral mass transported from the containment to the PSS, shown separately for steam and hydrogen. Then, to interpret the origin of the differences in these global trends, Figure 8 provides selected 3D CFD visualizations of the identified heterogeneities, focusing on the temperature field and on the hydrogen distribution in the upper containment and at the vent line connecting containment and PSS. The plotting times of Figure 8 are chosen to highlight the heterogeneities.

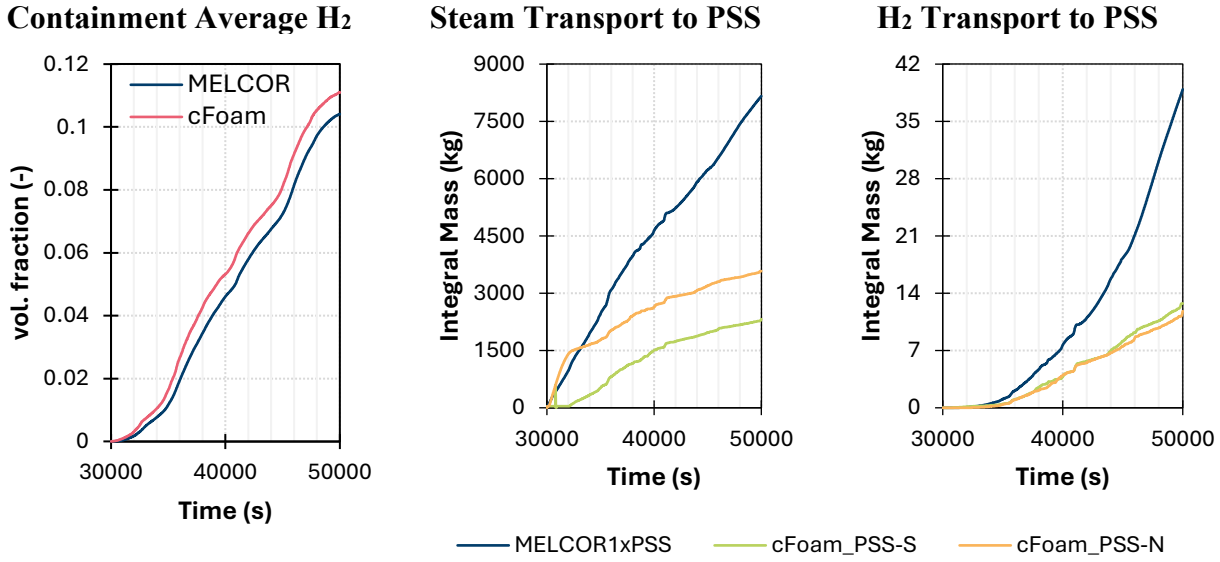

Figure 7. MELCOR (UniRoma) vs *containmentFOAM* hydrogen distribution comparison

Figure 7 shows that both calculations predict a similar global build-up of hydrogen, with *containmentFOAM* consistently higher and reaching 11.1% at the end of the transient, compared with 10.1% in MELCOR. At the same time, the integral steam and hydrogen mass transported to the PSS is lower in *containmentFOAM*. A more complete interpretation of this LP-CFD comparison (including wall condensation rates and gas temperature) is currently being performed. However, even with that information, a consolidated quantitative explanation of the code-to-code differences has not yet been reached yet. In principle, since both codes use the same mass sources and *containmentFOAM* reproduces the MELCOR pressure evolution, the lower transport to the PSS should imply higher wall-condensation rates in *containmentFOAM*, but this point cannot yet be demonstrated rigorously with the currently available MELCOR output and will require further exchanges with UniRoma.

Even if any interpretation should remain qualitative, Figure 7 and Figure 8 show that the containment conditions are no longer homogeneous, unlike the blowdown phase of Section 4.1. Figure 7 indicates a clear asymmetry in the transport to PSS-N and PSS-S, especially for steam during the first part of the window. The non-integrated mass-flow data (not shown here) confirmed that the dominant vent line changes during the transient. Figure 8 represents the heterogeneities behind these differences. The temperature field exhibits a vertical stratification, with the upper region hotter than the lower one and top-to-bottom differences reaching up to about 40 °C, with the stratification growing as the transient progresses. The hydrogen field shows a similar behaviour, with higher volume fractions in the upper containment and different hydrogen concentrations at the two vent-line entrances. These heterogeneities are sufficient to create different conditions in the flow transported to PSS-N and/or PSS-S.

It is important to underline that this analysis remains limited by the simple outlets based on MELCOR's pressure used at the CFD side. The lack of a PSS model able to store and track the effects of the different mass and composition histories coming from each side does not allot to evaluate the feedback of these heterogeneities on the thermodynamic state of each PSS gas space. Improving the current analysis will require a more advanced PSS model, with a modelling basis able to represent the relevant PSS physics and evaluating the impact of the identified 3D differences into a quantitative system response.

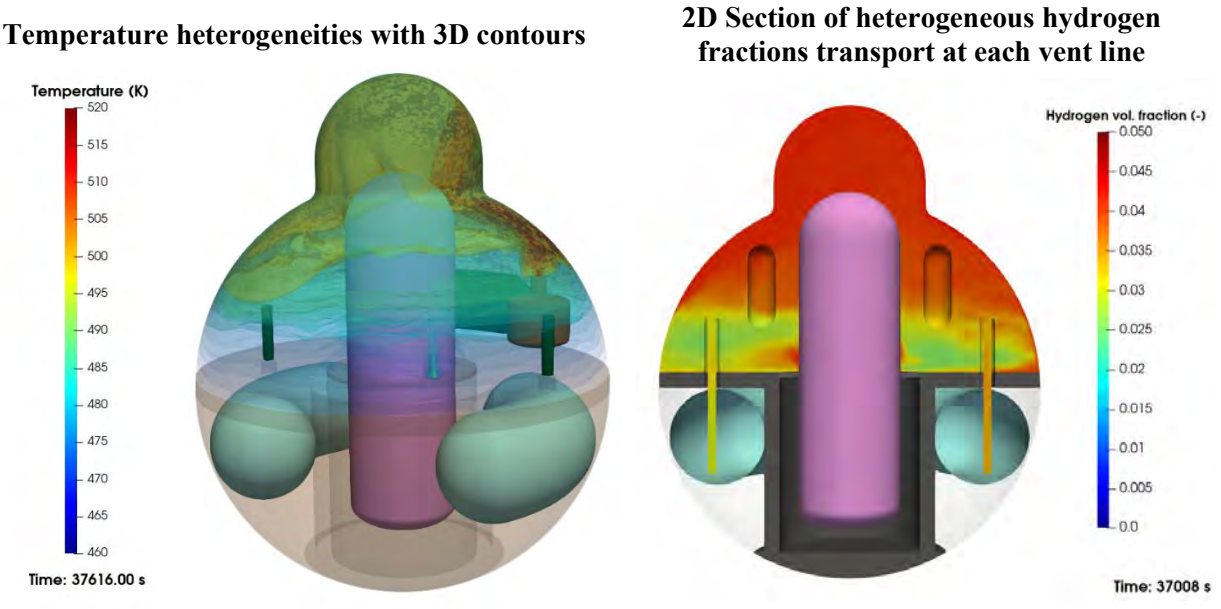

Figure 8. Insights on the identified 3D heterogeneities for the simulations of PhW2 time window

5. CONCLUSIONS

This work, developed in the framework of SASPAM-SA, moved from the conceptual exploration of *containmentFOAM* application to LW-SMR severe-accident analysis —identifying on the way a list of model development needs— to the technical scale safety evaluation presented in this work. The main enabling step was the implementation of the *containmentFOAM*-OpenModelica multi-fidelity coupling, which allowed the containment response and the PSS feedback to be simulated in a coupled manner at an affordable computational cost. Within this framework, two complementary time windows (PhW1 and PhW3) were analysed for SASPAM-SA Design-II: the fast-changing blowdown case, which is particularly demanding for CFD in terms of stability and computational cost, and a later hydrogen-transport window, closer to the original modelling basis of *containmentFOAM*. Despite the known limitations of the current set-up (discussed below), the blowdown calculation with flashing correction and coupled PSS feedback constitutes a relevant step forward with respect to the current open literature on CFD containment analyses.

The role of CFD analysis in SASPAM-SA is to complement the integral calculations of LP codes, with the objective of identifying when 3D effects add safety-relevant information and when simpler representations are sufficient. In this sense, the two analysed windows provide different messages:

- Blowdown window (PhW1): the CFD results confirm that the containment atmosphere rapidly evolves towards nearly homogeneous conditions after ADS-1 actuation. The observed 3D heterogeneities are limited and do not appear to produce a significant safety-relevant impact on the global blowdown response. For this phase, the results indicate that the dominant modelling challenge is not the 3D containment resolution itself, but the adequate representation of the PSS response, since the pressure evolution is mainly controlled by the species partial pressures in the PSS gas space (inventory, composition, and temperature).
- Late hydrogen-transport window (PhW3): *containmentFOAM* predicted a non-homogeneous distribution of temperature and gas composition at different points of this 20.000 second window characterised by low momentum sources and buoyancy driven flows. The heterogeneities induced differences in the mass and composition of each containment-PSS vent lines. However, the quantitative impact of the heterogeneities could not be quantified since the CFD domain is closed by a MELCOR-based pressure outlet and not by a PSS model able to store and evolve the different mass and composition histories reaching each PSS. Whether these heterogeneities accumulate or compensate each other in the actual PSS response remains to be evaluated.

Therefore, the current limiting factor of the multi-fidelity framework is the simplified physics of the PSS FMU. The PSS model was initially conceived mainly as a computationally efficient system-level closure providing counter-pressure feedback to the *containmentFOAM* high-fidelity model. However, in the present Design-II applications, its simplification of the physics, particularly the too simple modelling of the pool surface heat and mass transfer, proved to be a limiting factor for the global accuracy of the analyses. Therefore, the priority to advance these first application of *containmentFOAM* to LW-SMR safety analysis —where our CFD toolbox even proved its ability to simulate a blowdown— is to extend the current PSS FMU modelling basis and, in parallel, to investigate similar couplings with validated established codes.

ACKNOWLEDGMENTS

This work has been partially funded by the European Union through the SASPAM-SA project, HORIZON-EURATOM-2021-NRT-01 under grant agreement No. 101059853. Views and opinions expressed are, however, those of the author(s) only and do not necessarily reflect those of the European Union or the European Commission-Euratom. Neither the European Union nor the granting authority can be held responsible for them. We acknowledge the valuable technical discussions within the SASPAM-SA consortium. In particular, we thank Sapienza University of Rome (UniRoma), led by Fabio Giannetti, for the MELCOR simulations used in this work, and especially Marcello Principiato for his continuous support and prompt feedback during the iterative exchanges and model adaptations required for a consistent comparison with the *containmentFOAM* calculations.

We gratefully acknowledge the support of the German Federal Ministry for the Environment, Climate Action, Nature Conservation and Nuclear Safety (BMUKN) for funding code maintenance and integration of *containmentFOAM* within the national CFD reference package CF2REF (Fkz 150 1633B). Preparatory work for adapting *containmentFOAM* to LW-SMR applications was supported by the Innovation Pool of the Helmholtz Research Field Energy within the project "Safety assessment of generic SMR" (2021–2024). We thank the John von Neumann Institute for Computing (NIC) for computing time on the supercomputer JURECA at Jülich Supercomputing Centre (JSC) under project 'va4cf'.

REFERENCES

1. IAEA, *Energy, Electricity and Nuclear Power Estimates for the Period up to 2050*, Reference Data Series, INTERNATIONAL ATOMIC ENERGY AGENCY (2025).
2. Morreale, A. C., "Severe Accident Analyis Of A Generic Integral Pressurized Water Reactor with MELCOR", *Fourth International Conference on Generation IV & Small Reactors (G4SR-4)*, Toronto, ON (2022).
3. IAEA, *SMR Regulators' Forum Pilot Project Report: Considering the Application of a Graded Approach, Defence-in-Depth and Emergency Planning Zone Size for Small Modular Reactors* (2018).
4. Reyes, J. N., "NuScale Plant Safety in Response to Extreme Events", *Nuclear Technology*, **178**(2), pp. 153–163 (2012).
5. NuScale Power, LLC, personal communication (July 13, 2020).
6. Gabrielli, F., et al., "Analysis of postulated severe accidents in generic integral PWR Small Modular Reactors: Outcomes on integral codes' modelling capabillities from the Horizon Euratom SASPAM-SA Project", *12th European Review Meeting on Severe Accident Research* (2026).
7. Vázquez-Rodríguez, C., Sturm, K. J. X., George, A., and Kelm, S., "Development of a LW-SMR dry containment model with containmentFOAM", *11th European Review Meeting on Severe Accident Research* (2024).
8. Vázquez-Rodríguez, C. and Kelm, S., "Development of containmentFOAM towards LW-SMR analyses", *5th Generation IV and Small Reactors (G4SR) Conference*, The Westin Ottawa, ON, Canada, October 1-4 (2024).
9. Principato, M., Giannetti, F., Imperatori, M., D'Onorio, M., Garcia, M., Herranz, L. E., Bersano, A., and Mascari, F., "Analyses of the MELCOR capability to simulate integral PWR using passive systems in a DBA scenario", *Nuclear Engineering and Design*, **437**, p. 114004 (2025).
10. Maccari, P., Agnello, G., Mascari, F., and Ederli, S., "Analysis of BDBA sequences in a generic IRIS reactor using ASTEC code", *Annals of Nuclear Energy*, **182**, p. 109611 (2023).
11. Principato, M., Marta, G., and Gianetti, F., "UNIROMA1 WP5 Annual Meeting", presented at SASPAM-SA 4th Consortium Meeting, Roma, Italy (2026).
12. Gabrielli, F., di Giuli, M., Malicki, M., Bersano, A., Maccari, P., and Gianetti, F., *SASPAM-SA M21: Generic Data on Design 1 and Design 2* (2024).
13. Kelm, S., Kampili, M., Liu, X., George, A., Schumacher, D., Druska, C., Struth, S., Kuhr, A., Ramacher, L., Allelein, H.-J., Prakash, K. A., Kumar, G. V., Cammiade, L. M. F., and Ji, R., "The Tailored CFD Package 'containmentFOAM' for Analysis of Containment Atmosphere Mixing, H2/CO Mitigation and Aerosol Transport", *Fluids*, **6**(3), p. 100 (2021).
14. Kelm, S., Vijaya Kumar, G., Kampili, M., George, A., Ji, R., Cammiade, L. M. F., Prakash, K. A., and Allelein, H.-J., "Technical Scale CFD Analysis of the Pressurization and Transport Processes in the Battelle Model Containment during the ISP 37 VANAM M3 Test", Hsinchu, Taiwan (2022).
15. Kelm, S., et al., "Progress in the Development of the containmentFOAM CFD Package for Analysis of Current and future LWRs", Busan, Korea (2025).
16. Kumar, G. V., Cammiade, L. M., Kelm, S., Prakash, K. A., Groß, E. M., Allelein, H.-J., Kneer, R., and Rohlfs, W., "Implementation of a CFD model for wall condensation in the presence of non-condensable gas mixtures", *Applied Thermal Engineering*, **187**, p. 116546 (2021).
17. George, A., Kelm, S., Cheng, X., and Allelein, H.-J., "Efficient CFD modelling of bulk condensation, fog transport and re-evaporation for application to containment scale", *Nuclear Engineering and Design*, **401**, p. 112067 (2023).
18. Kelm, S., Vázquez-Rodríguez, C., and Klauck, M., "CFD Analysis of the containment behavior during a TLAP sequence in a generic KWU PWR with containmentFOAM", *12th European Review Meeting on Severe Accident Research* (2026).

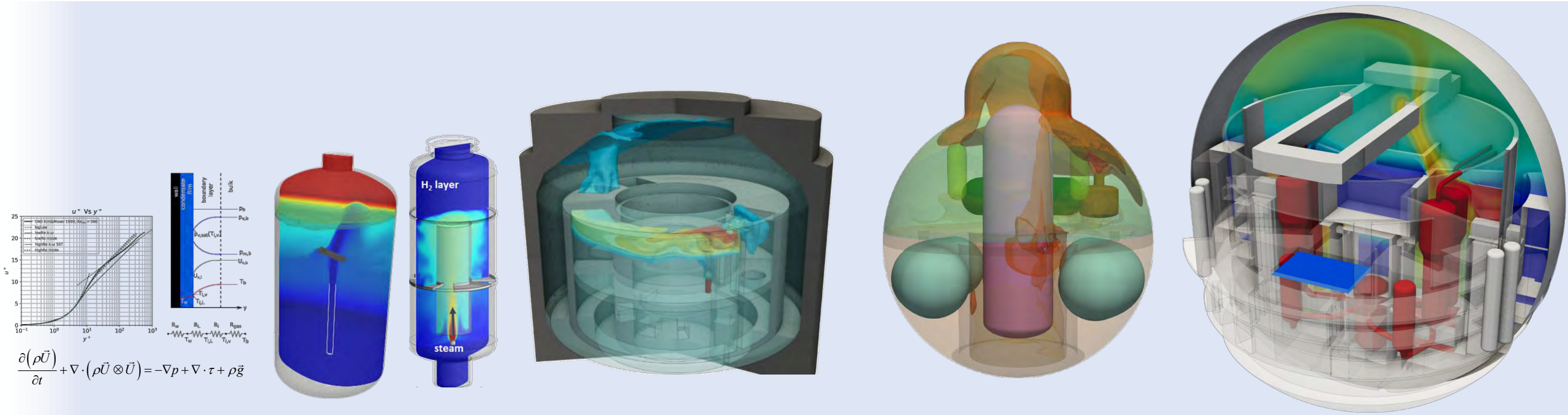

Severe accident analysis of SASPAM-SA Design-II LWR SMR containment using containmentFOAM

Carlos Vázquez-Rodríguez, Stephan Kelm - Forschungszentrum Jülich (FZJ)

12h European Review Meeting on Severe Accident Research (ERMSAR2026) - Madrid, Spain, May 18-22, 2026

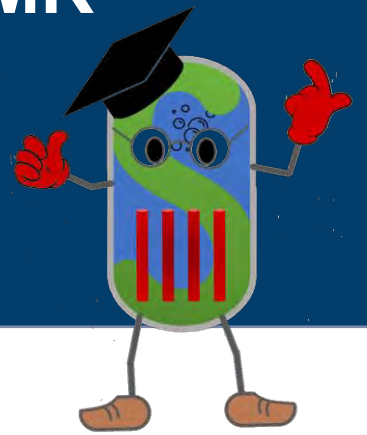

containment FOAM

Supported by:

Federal Ministry
for the Environment, Nature Conservation,
Nuclear Safety and Consumer Protection

based on a decision of
the German Bundestag
Project No. 150 1633B

JÜLICH Forschungszentrum
Mitglied der Helmholtz-Gemeinschaft

Background

Open-Source software for large dry PWR developed at FZJ

- Developments built on 10 years' ANSYS CFX experience
  - Kelm, S. et al. 2016. A comparative assessment of different experiments on buoyancy driven mixing processes by means of CFD. Annals of Nuclear Energy. 93, (Jul. 2016), 50–57.
  - Kelm, S. et al. 2019. Development of a multi-dimensional wall-function approach for wall condensation. Nuclear Engineering and Design. 353, (Nov. 2019), 110239
  - Lehmkuhl, J. et al. 2016. Improvement of wall condensation modeling with suction wall functions for containment application. Nuclear Engineering and Design. 299, (Apr. 2016), 105–111.
  - Kelm, S. et al. 2019. A Review of the CFD Modeling Progress Triggered by ISP-47 on Containment Thermal Hydraulics, Nuclear Science and Engineering. 193, (Sept. 2018).
- Solutions to model safety systems and technical components
  - Kelm, S. et al. 2021. The **Tailored CFD Package 'containmentFOAM' for Analysis of Containment Atmosphere** Mixing, H2/CO Mitigation and Aerosol Transport. Fluids. 6, 3 (Mar. 2021), 100.
- **OpenFOAM tailored** for large dry containment flows
  - George, A. et al. 2023. Efficient CFD modelling of **bulk condensation, fog transport** and re-evaporation for application to containment scale. Nuclear Engineering and Design. 401, (Jan. 2023), 112067.
  - Liu, X. et al. 2022. Monte Carlo method with SNBCK nongray gas model **for thermal radiation** in containment flows. Nuclear Engineering and Design. 390, (Apr. 2022), 111689.
  - Vijaya Kumar, G. et al. 2021. Implementation of a CFD model for **wall condensation** in the presence of non-condensable gas mixtures. Applied Thermal Engineering. 187, (Mar. 2021), 116546.

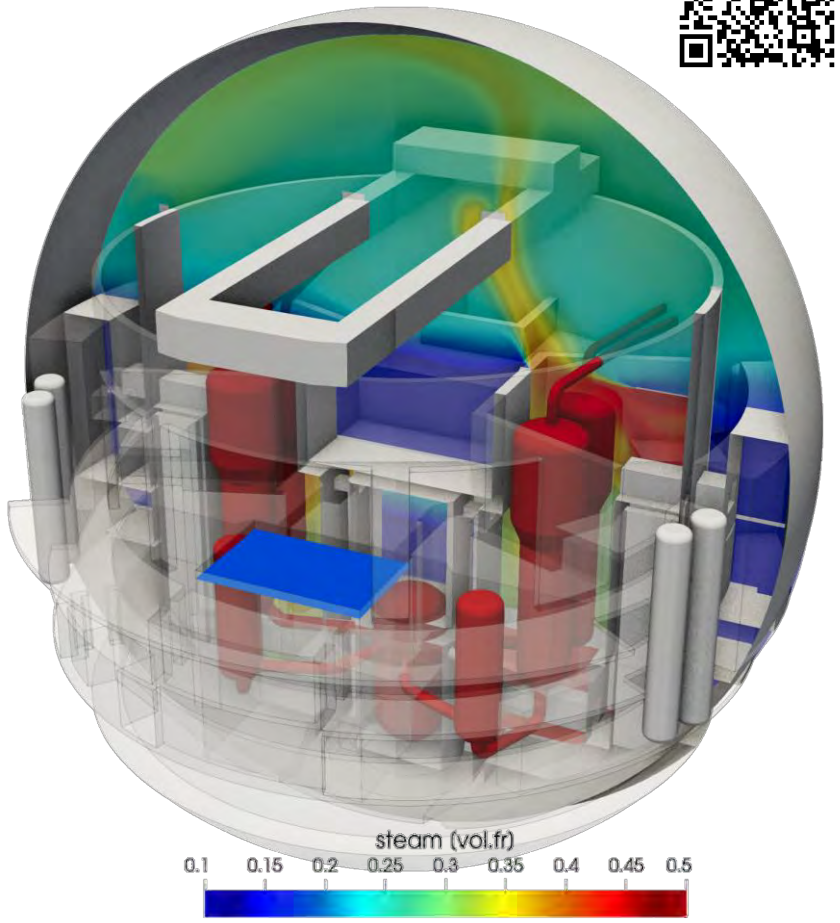

Steam distribution inside a dry PWR containment, 3D CAD Geometry by L. Serra-Lopez (UPM)

Background

EU Euratom SASPAM-SA Project:

- Applicability of SA know-how to LW-SMR
- Generic designs based on Open Literature
- Most of partner using Lumped Parameter codes (ASTEC, MELCOR, AC-2, MAAP)
- **CFD to complement LP codes**

Phenomenological differences:

- Higher pressures (film-condensation)
- Closer coupling RCS and containment
- Central role of containment response for SA progression in the primary

Code upgrades towards LW-SMR analysis:

- Based on SASPAM-SA sequences
- All ongoing. Preliminary experimental-scale testing performed, and known future improvements
- Coupling framework main priority for SASPAM-SA

Coupling validated with available data:

- Code agnostic: FMI Standard
- Multi-Fidelity approach (Modelica FMU)
- Validated with PPOOLEX MIX Series

OUTLINE

1. SA Sequences from SASPAM-SA
2. containmentFOAM Model Development
3. SASPAM-SA: Blowdown Sequence
4. SASPAM-SA: Late phase H_2 Transport
5. Conclusions

1. SA Sequences from SASPAM-SA

The role of the containment on the SA progression

- SASPAM-SA Design-II: A 300 MWe **LW-SMR concept fully relying on passive safety cooling**, including **two Pressure Suppression Systems** (PSS) in a 3000 m^3 **N_2-inertised** containment.

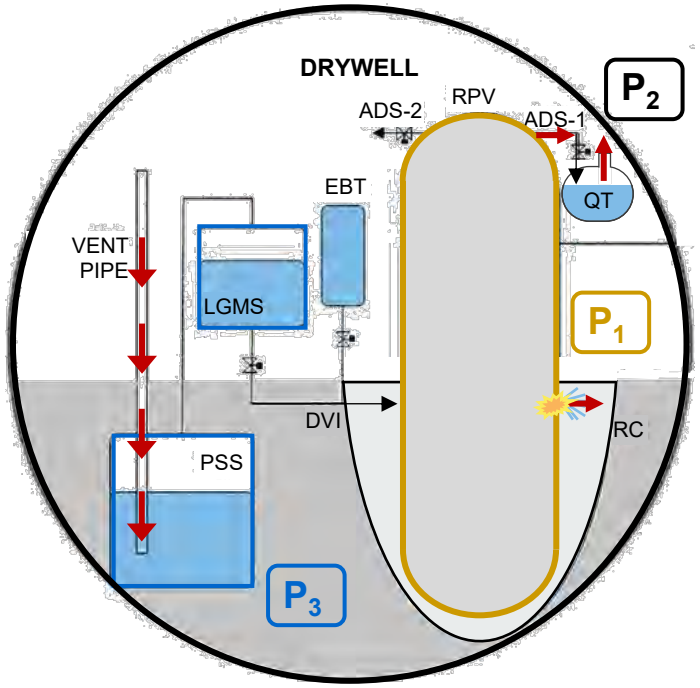

Design II – Blowdown

$P_3 \ll P_2 \leq P_1$

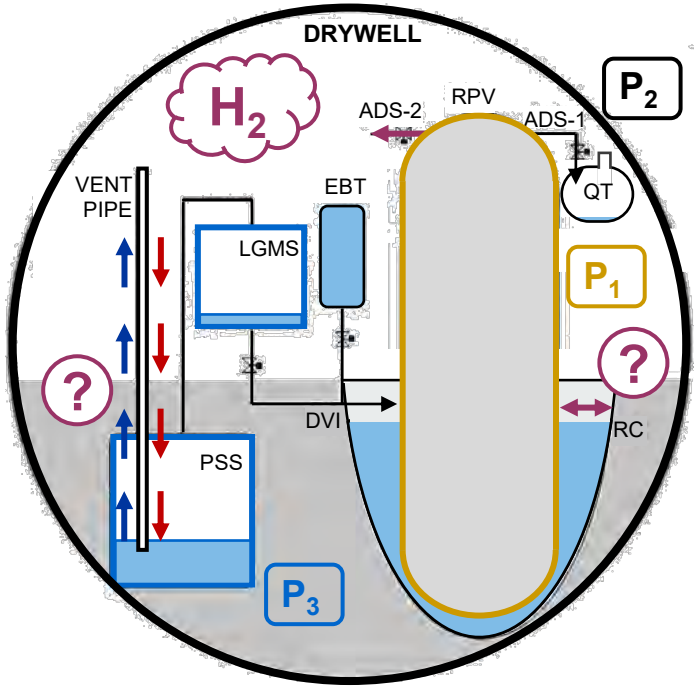

Design II – Severe accident?

$P_3 \approx P_2 \approx P_1$

MELCOR 3-days P_1, P_2, P_3 prediction

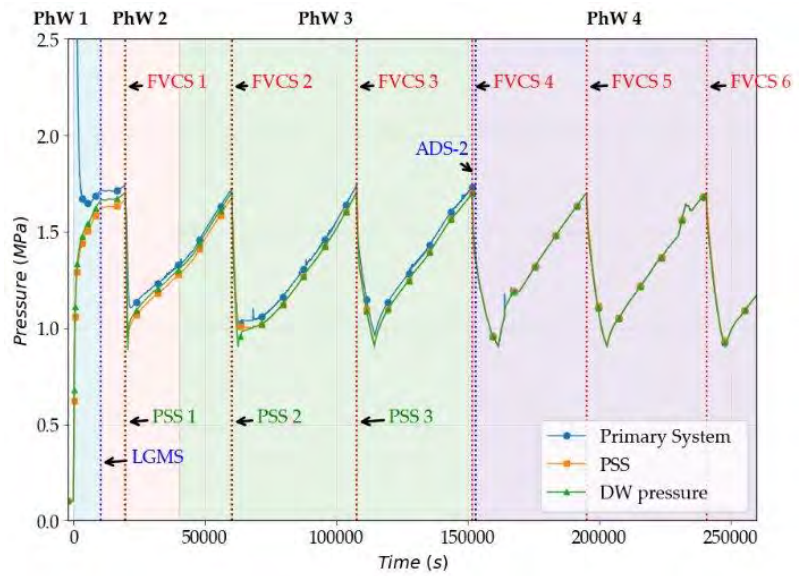

Containment thermal-hydraulics as a key issue for the SA unfolding

1. SA Sequences from SASPAM-SA

The role of the containment on the SA progression

- Where is the added value of CFD for SASPAM-SA? → **High-fidelity simulation of the containment needed to discard undesired impact of simplifications in SA progression**

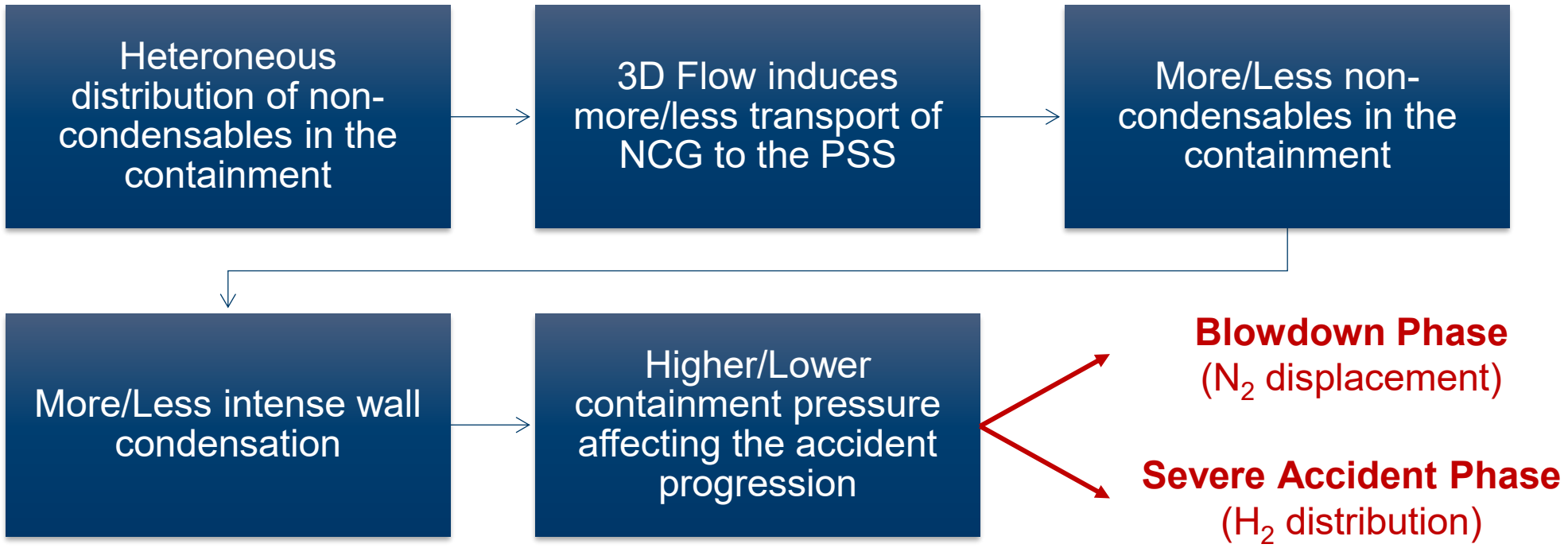

OUTLINE

1. SA Sequences from SASPAM-SA
2. containmentFOAM Model Development
3. SASPAM-SA: Blowdown Sequence
4. SASPAM-SA: Late phase H_2 Transport
5. Conclusions

2. containFOAM Model Development

Careful replication of the geometry used by SA codes

- 3D CAD based on the **SASPAM-SA common geometry database** (free volume difference ≈ 1%).
- Final numbers in our CFD Model
  - Free Volume
    - Database: 3677 m^3
    - CFD: 3654 m^3
  - Steel Containment total area
    - Database: 1005 m^2
    - CFD: 1031 m^2

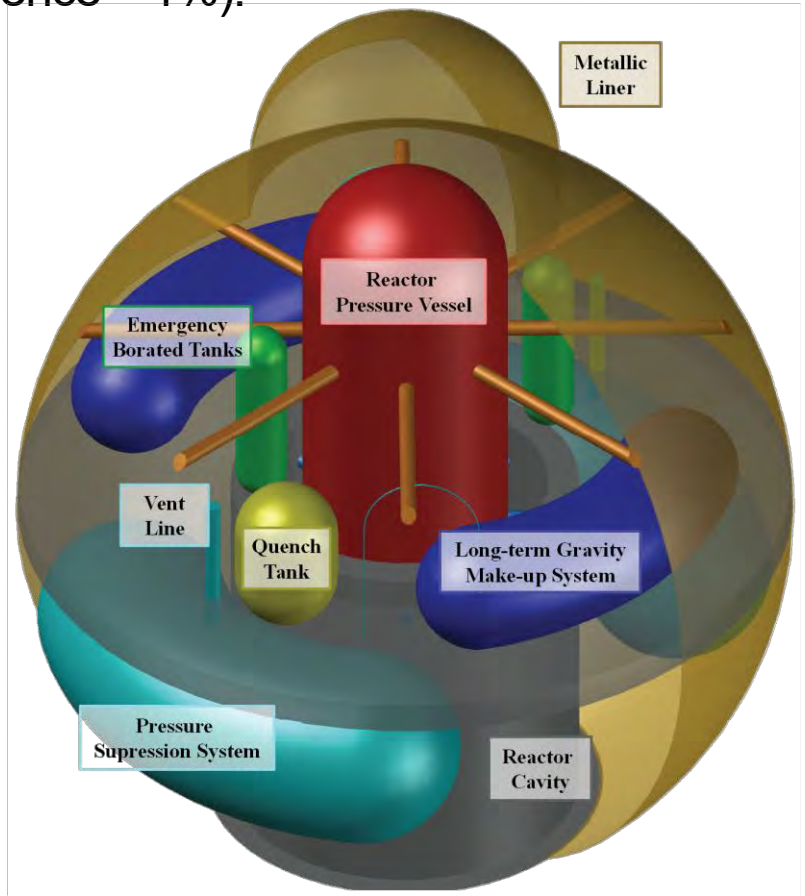

FLUID and **CONCRETE** regions obtained by subtracting the space occupied by the tanks using **SpaceClaim**

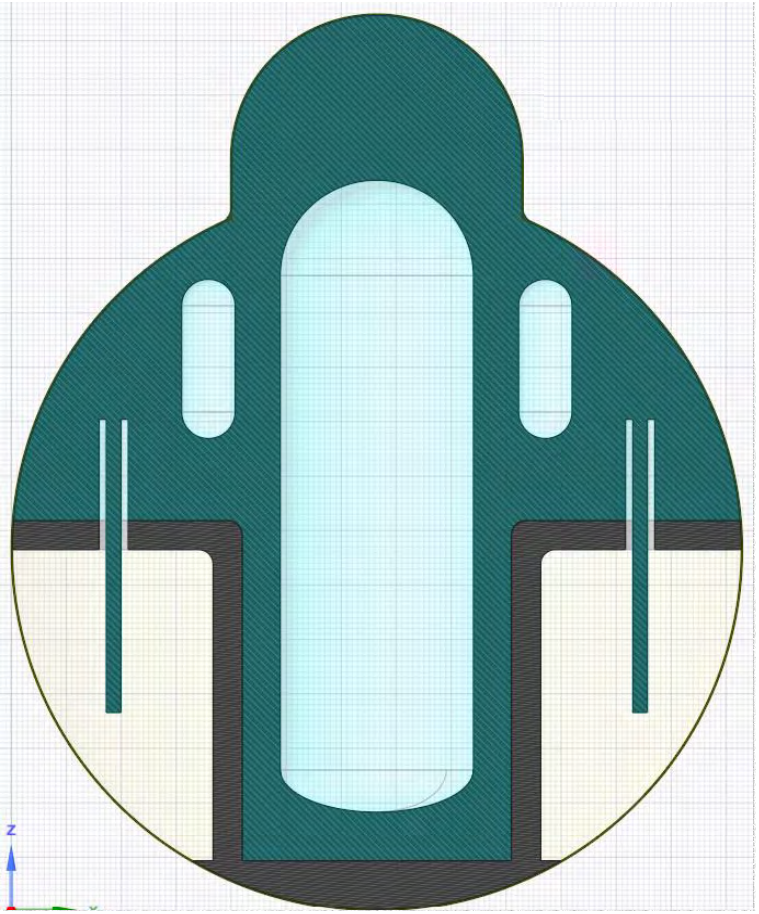

2. containmentFOAM Model Development

JÜLICH Forschungszentrum

Surface Mesh

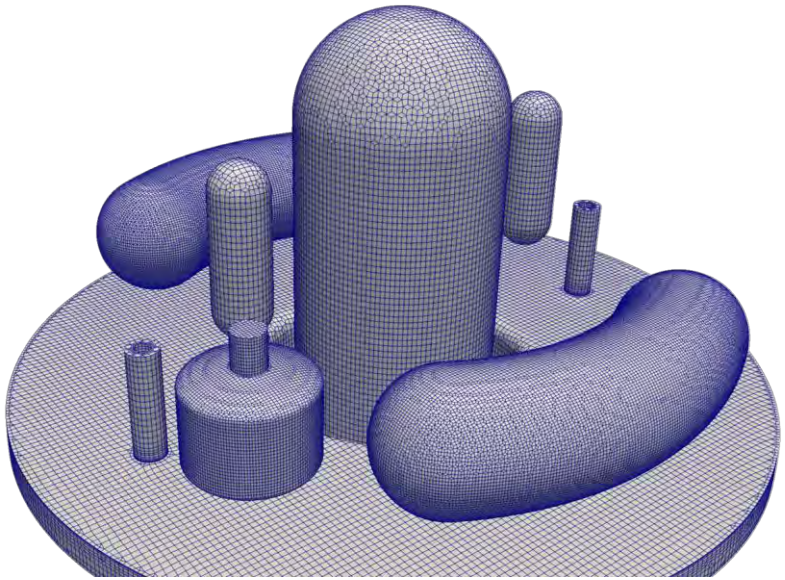

Zoom to
Fluid and Concrete Meshes

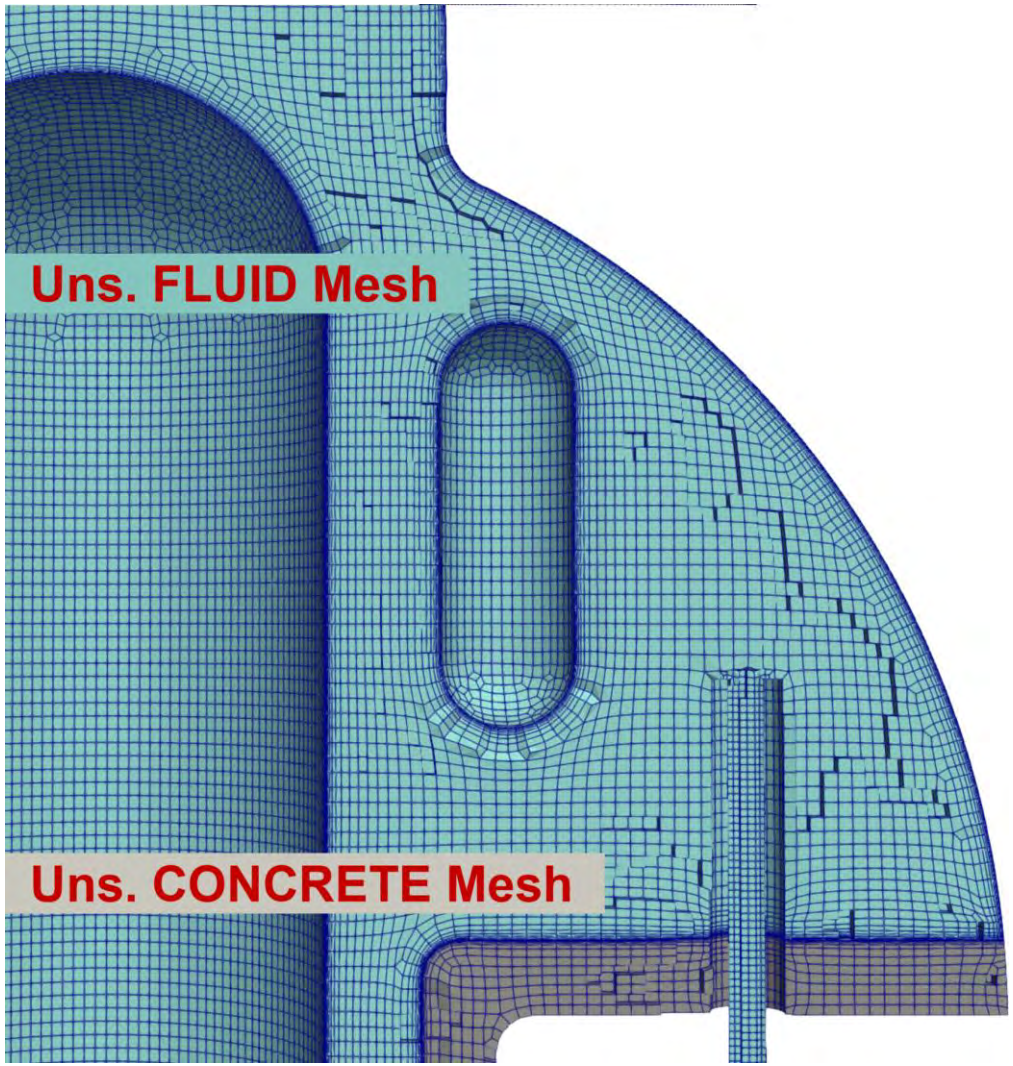

- Full 3D complete geometry
  - Ref. size: 0.2 m
  - Up to 2 refinements: QT, Vent Pipes, and LGMS
  - Concrete floor and steel containment included as solids (CHT simulation)
- **Boundary layer** for concrete and steel containment
  - Condensing walls: **y^+<4**
  - All other: Adiabatic
  - Simplified sharp edges
- Approximately **3 million cells**
  - FLUID: 2.3 million cells
  - Solids: 750 000 cells

2. containmentFOAM Model Development

Careful replication of the geometry used by SA codes

- 'Baseline model set' for *containmentFOAM* technical scale analysis, with volume sources implementing release rate, composition and temperature calculated from MELCOR (inc. **flashing**)
- Modelling strategy: Use the validated OpenModelica FMU to represent the PSS

cFoam Physical Models
Multi-species single phase solver
Conjugate heat transfer
Wall condensation: Single Phase Diffusion Layer Model
Homogeneous condensation: Fog as passive scalar
Turbulence: k-ω SST including SGDH buoyancy terms
Radiation: P1 Model

OpenModelica PSS FMU features

- Complete steam condensation
- 0D Two-Phase non-equilibrium
- **No free surface evaporation**
- User-defined HTCs

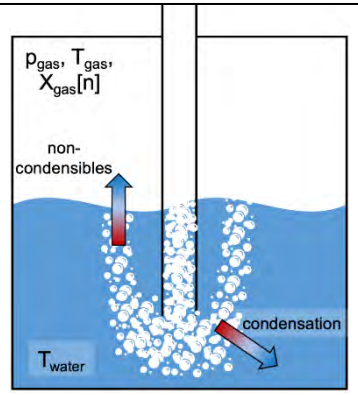

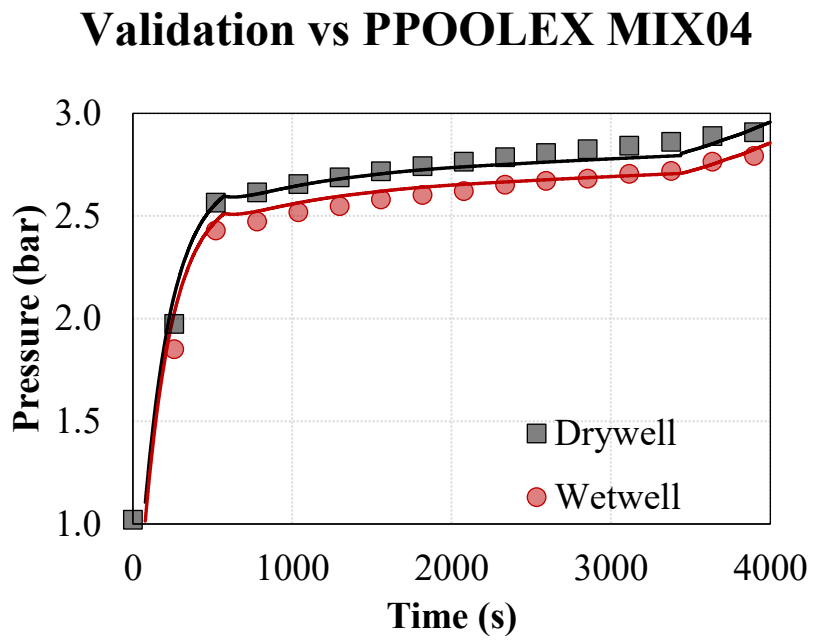

Kelm, S. et al. 2021. The Tailored CFD Package 'containmentFOAM' for Analysis of Containment Atmosphere Mixing, H2/CO Mitigation and Aerosol Transport. Fluids. 6, 3 (Mar. 2021), 100.

Vázquez-Rodríguez et al. "Development of a LW-SMR dry containment model with containmentFOAM," ERMSAR 2024

OUTLINE

1. SA Sequences from SASPAM-SA
2. containmentFOAM Model Development
3. SASPAM-SA: Blowdown Sequence
4. SASPAM-SA: Late phase H_2 Transport
5. Conclusions

3. SASPAM-SA Design II: Blowdown Sequence

Model set-up: CFD containment, PSS in Modelica, and MELCOR boundary conditions

Steam sources from breaks (MELCOR)

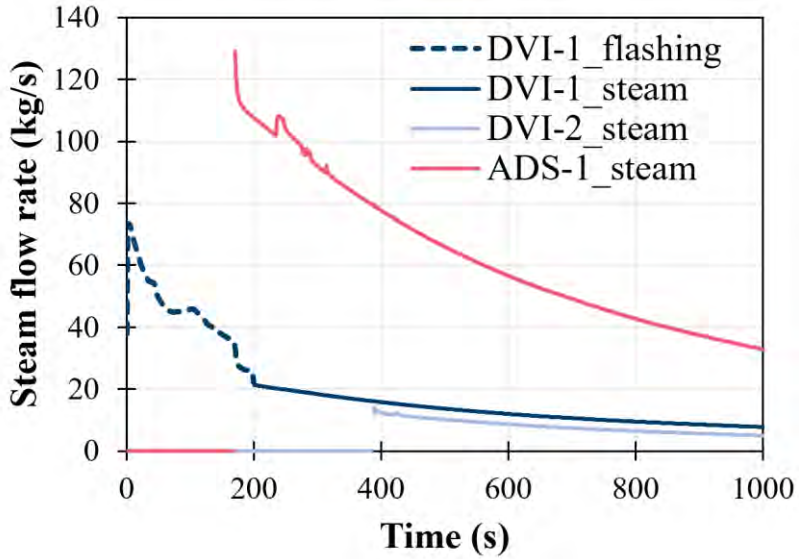

Pressure-coupling interface

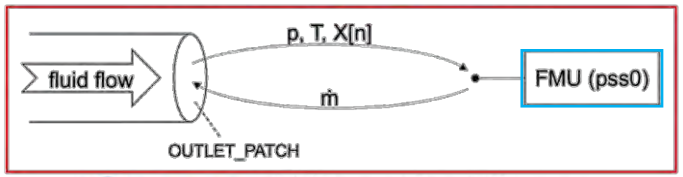

OpenModelica

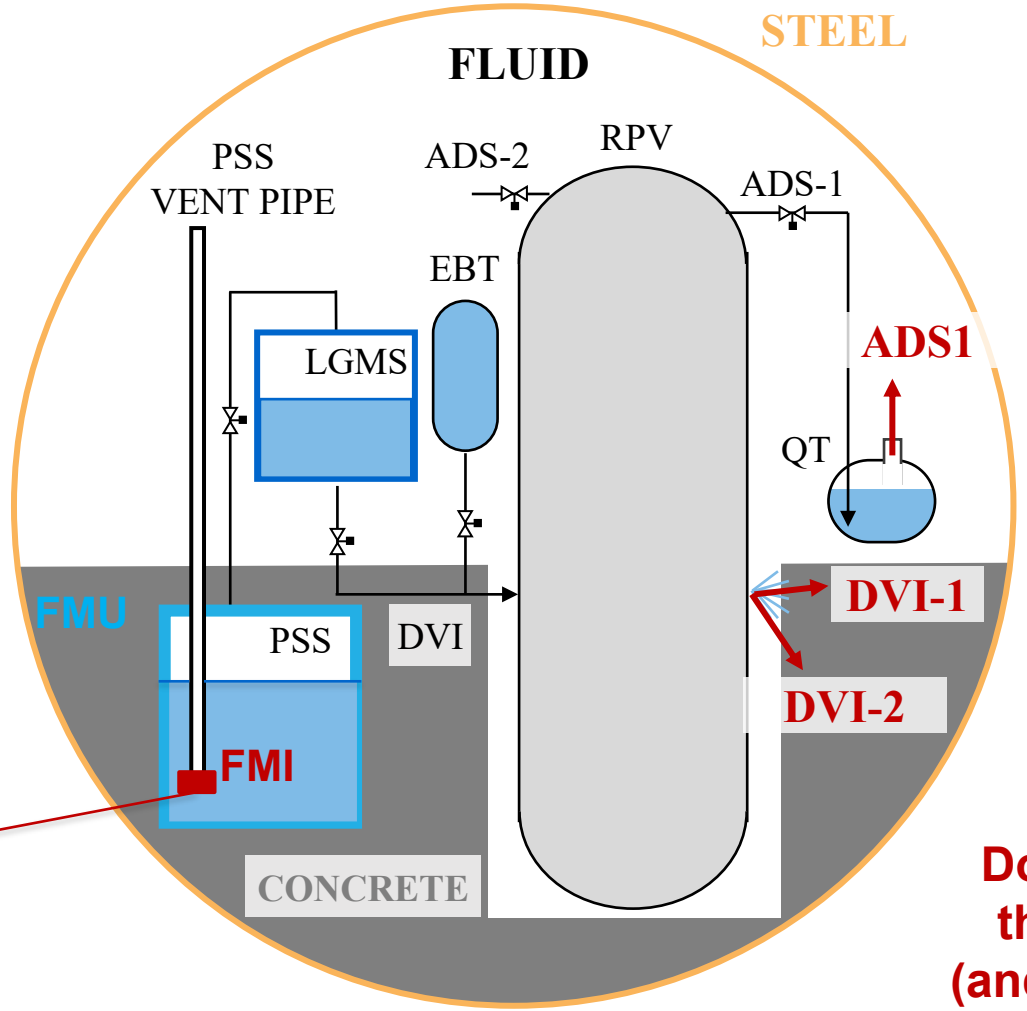

- **CFD Blowdown**: Stability and computational cost
- Flashing for DVI-I (isenthalpic expansion of liquid)
- **Parametric case** to better understand the containment designs dynamics
- Constant time step, CFL <2 (0.001 s to 0.003 s)
- **13 440 core-h** (96 processors and 140 h clock-time)

Do 3D heterogeneities affect the N_2 transport to the PSS (and therefore pressurization?)

3. SASPAM-SA Design II: Blowdown Sequence

Some insights from the flow fields

Temperature field

Mostly homogeneous. Progressive heating-up

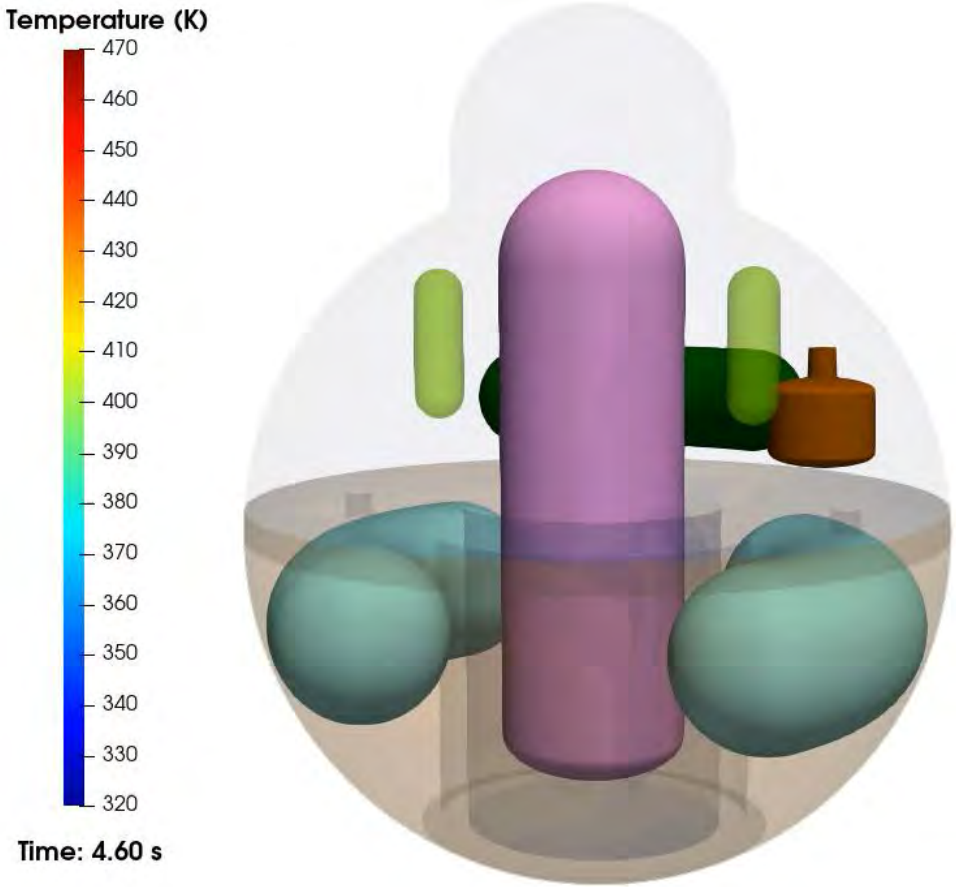

Steam distribution

Blowdown jet impingement fills the cavity with steam. Complete mixing after ADS-1 operation

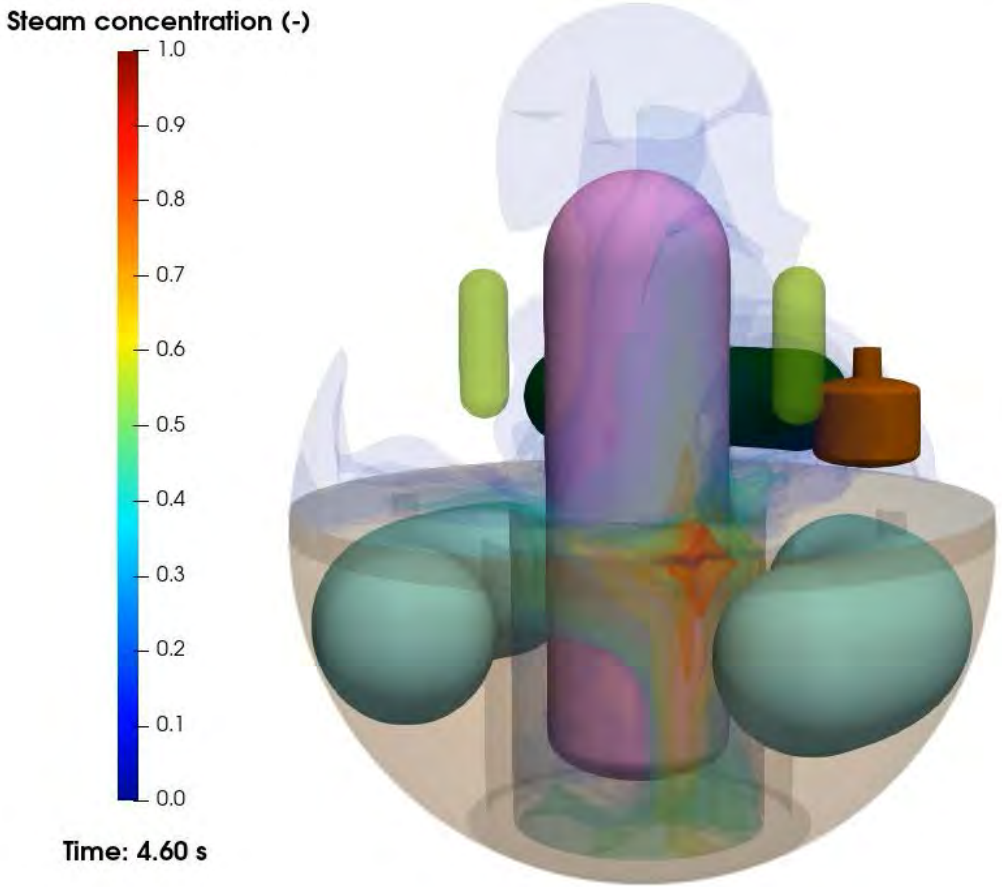

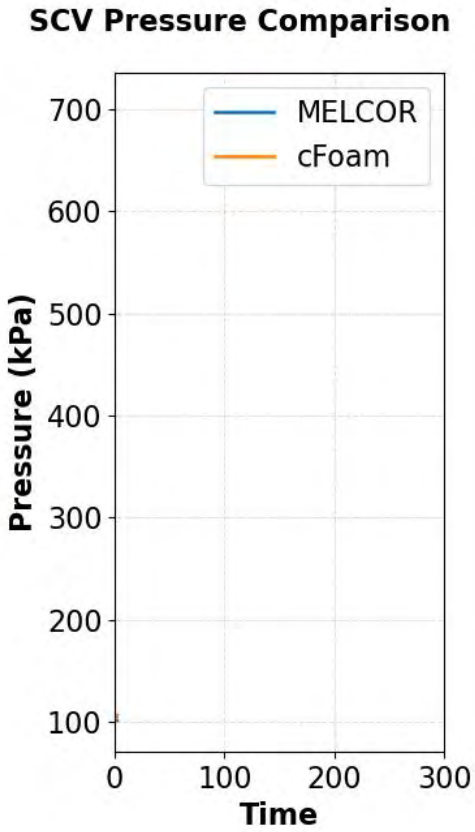

3. SASPAM-SA Design II: Blowdown Sequence

Some insights from the flow fields

Steam Distribution – Screenshot 1
Stratification: Cavity filled with steam

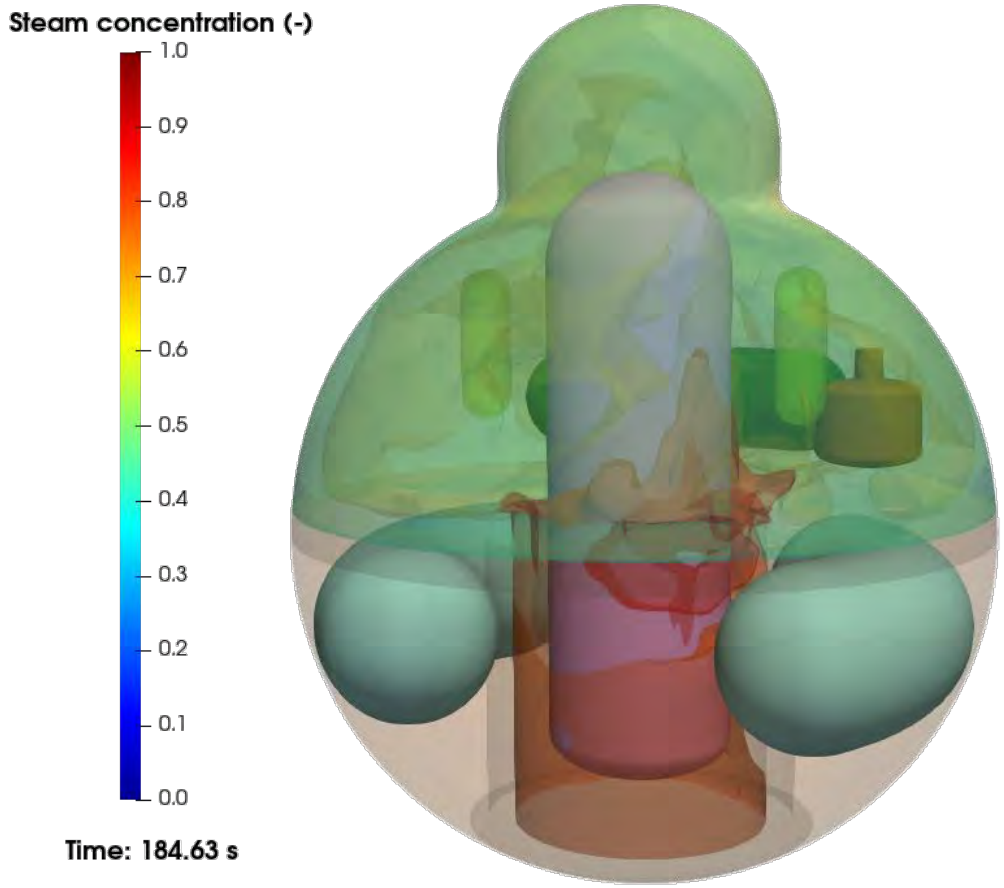

Steam Distribution – Screenshot 2
Injection from the ADS-1 tank, before full mixing

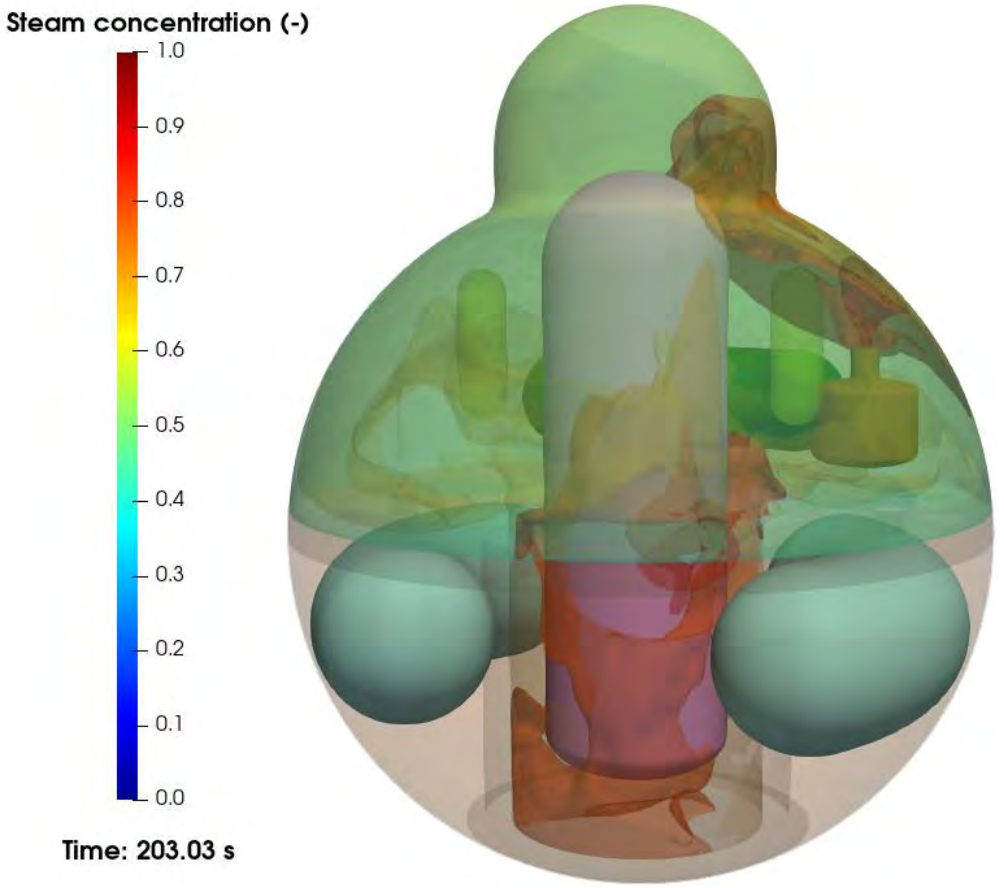

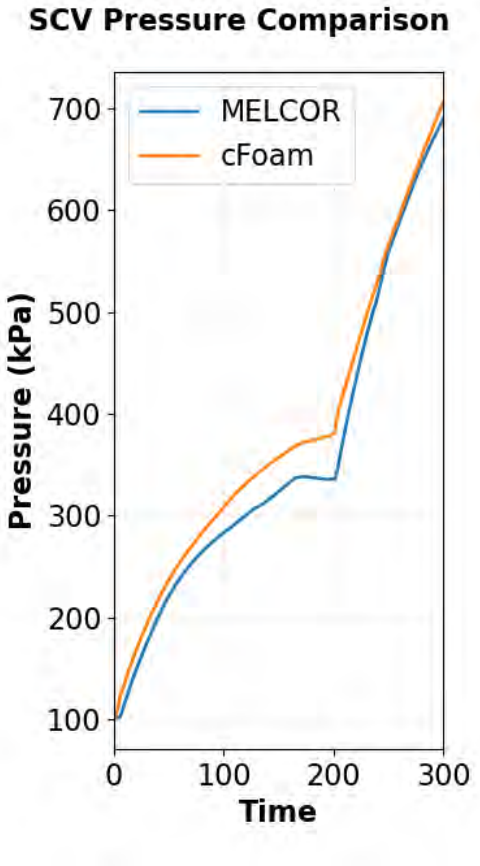

3. SASPAM-SA Design II: Blowdown Sequence

Quantitative insights in different zones of the containment

- This second graph compares the average steam volume fraction in different regions

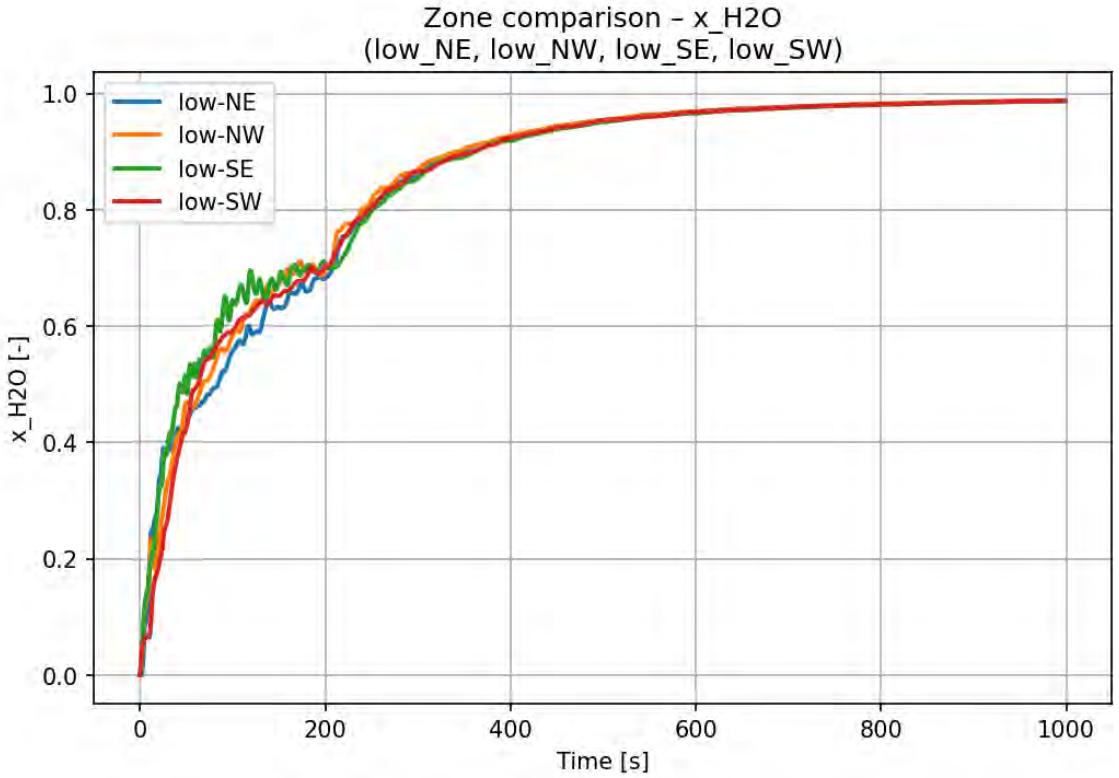

Large homogeneity, especially after the activation of the ADS-1 (≈ 200 s)

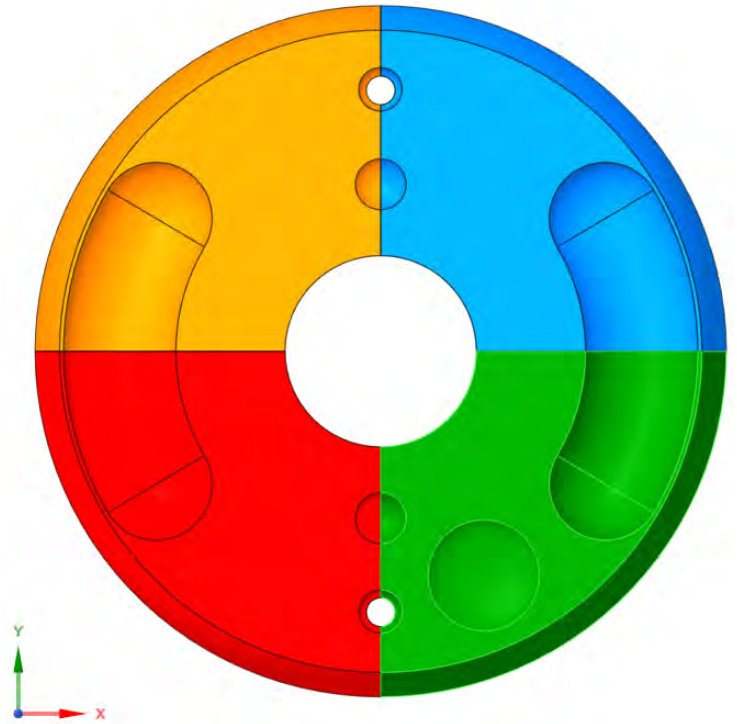

Cell zones delimiting the regions. Zones colour corresponding to lines on the left

3. SASPAM-SA Design II: Blowdown Sequence

Understanding the pressure build-up with the parametric case

- How did we get higher pressures with higher wall condensation and PSS transport?

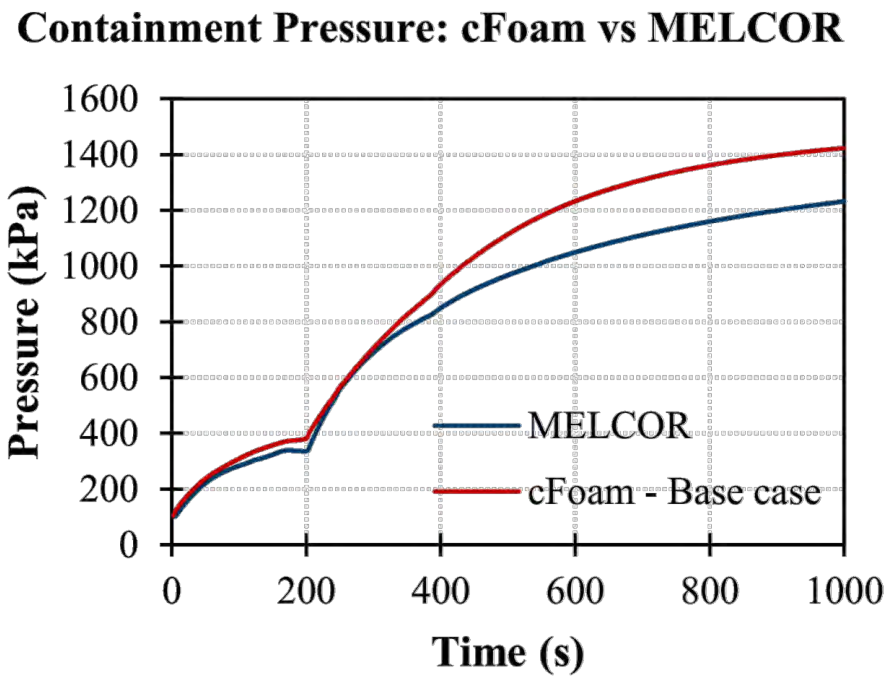

3. SASPAM-SA Design II: Blowdown Sequence

Quantitative insights: Main containment phenomena

- Evaluations of the main phenomena affecting the containment pressure evolution
  - The mass **flow towards the PSS was significantly larger in containmentFOAM** coupled simulations
  - The **wall condensation was also larger** in containmentFOAM
  - Deeper understanding of comparison with MELCOR requires additional data exchange with UniRoma

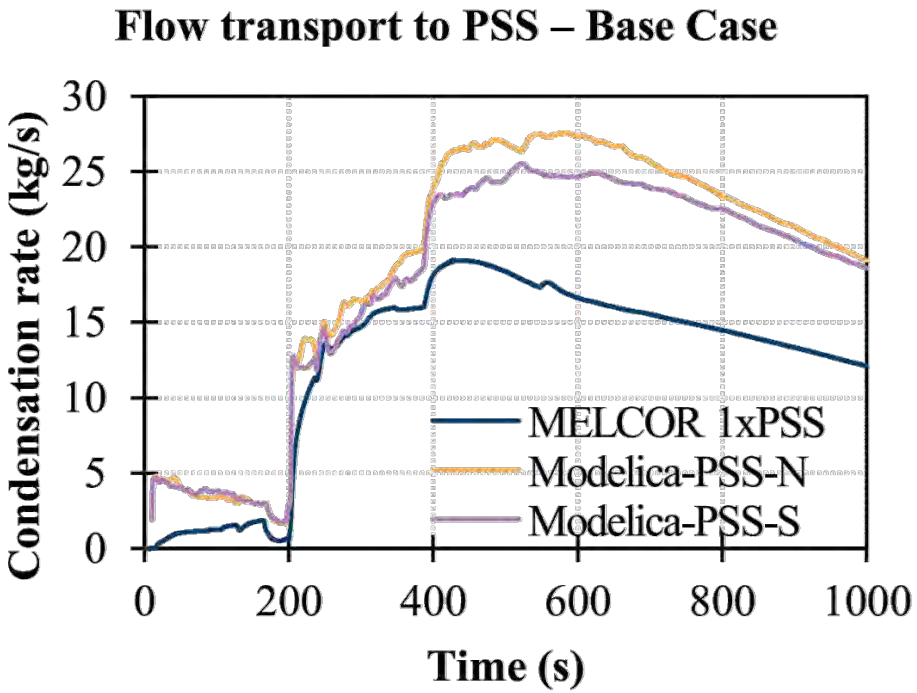

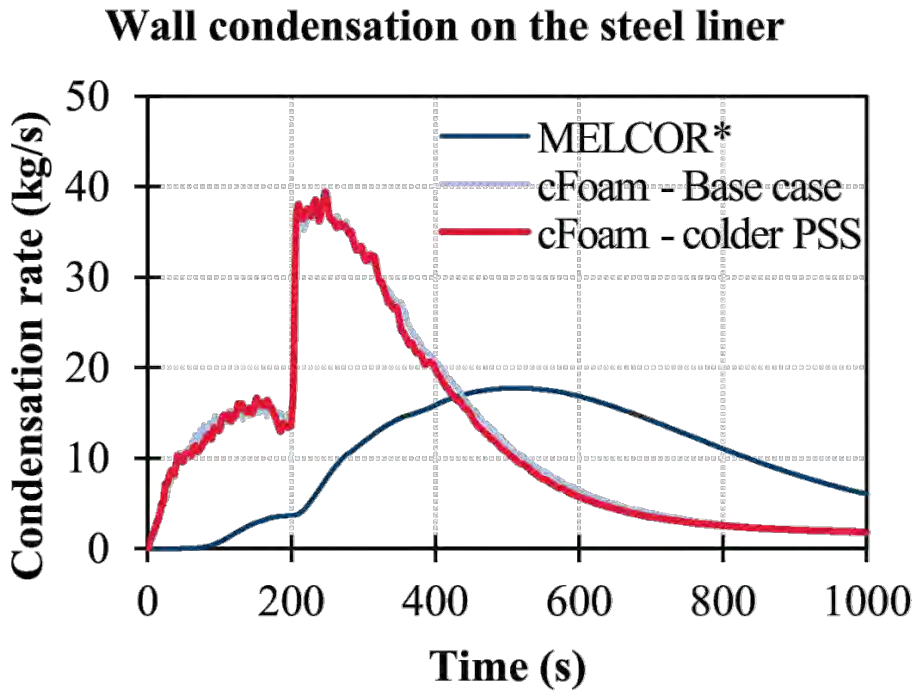

3. SASPAM-SA Design II: Blowdown Sequence

Understanding the pressure build-up with the parametric case

- How did we get higher pressures with higher wall condensation and PSS transport? → *'colderPSS'*
  - Closer pressure prediction even if **no effect to condensation and mass flow rates to the PSS**
  - Eventually, the **pressure increase is closely linked to what happens in the PSS** → $(T \ \& \ x_{N_2})$
  - Insight for LP: Detailed representation of **PSS physics more relevant than containment nodalization**

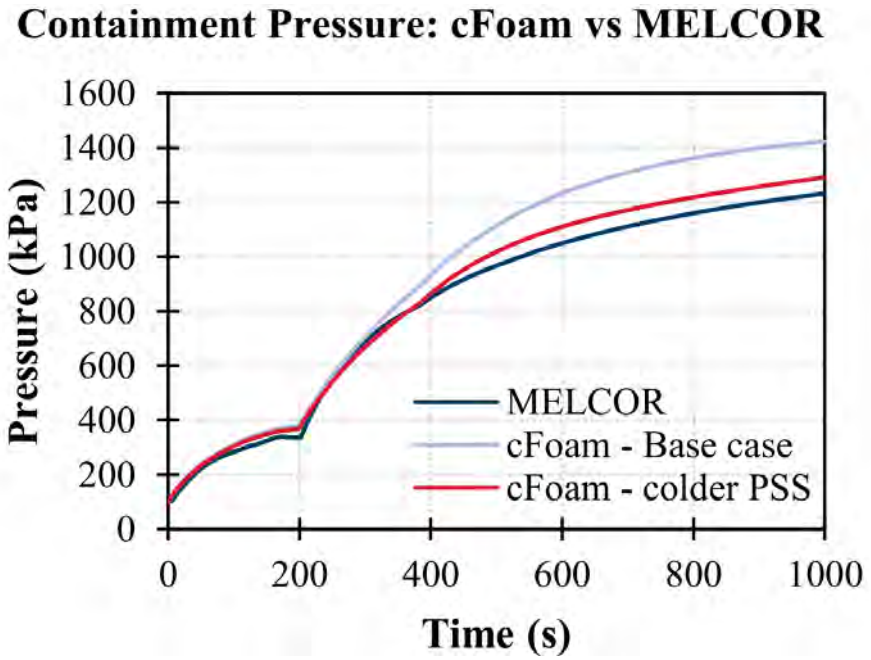

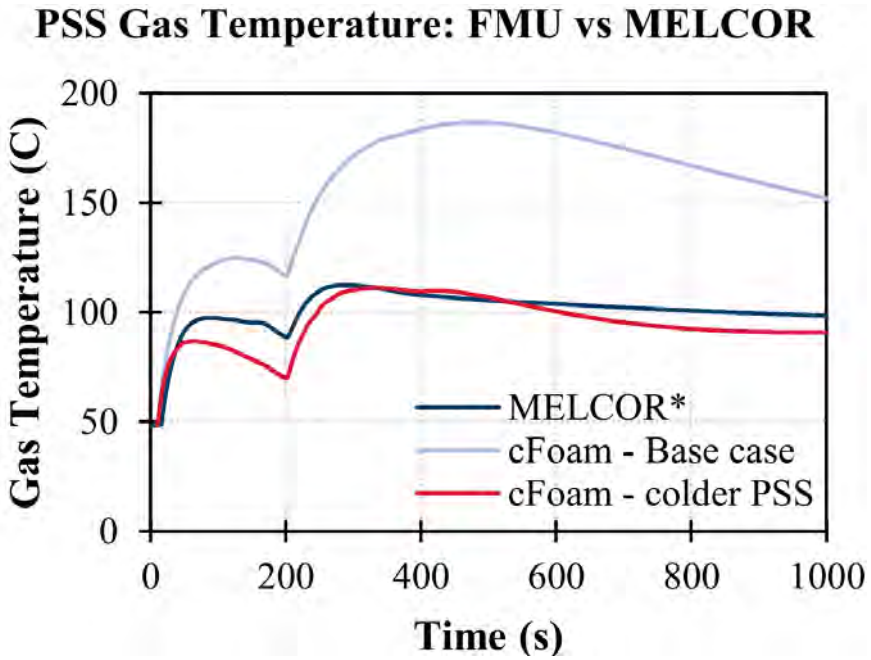

PSS Model Limitations

- Homogeneous pool temperature
- 100% steam latent heat to pool
- No heat losses at PSS walls
- No evaporation/condensation

OUTLINE

1. SA Sequences from SASPAM-SA
2. containmentFOAM Model Development
3. SASPAM-SA: Blowdown Sequence
4. SASPAM-SA: Late phase H_2 Transport
5. Conclusions

4. SASPAM-SA Design-II: Late phase H_2 Transport

Model set-up: CFD containment and MELCOR boundary conditions

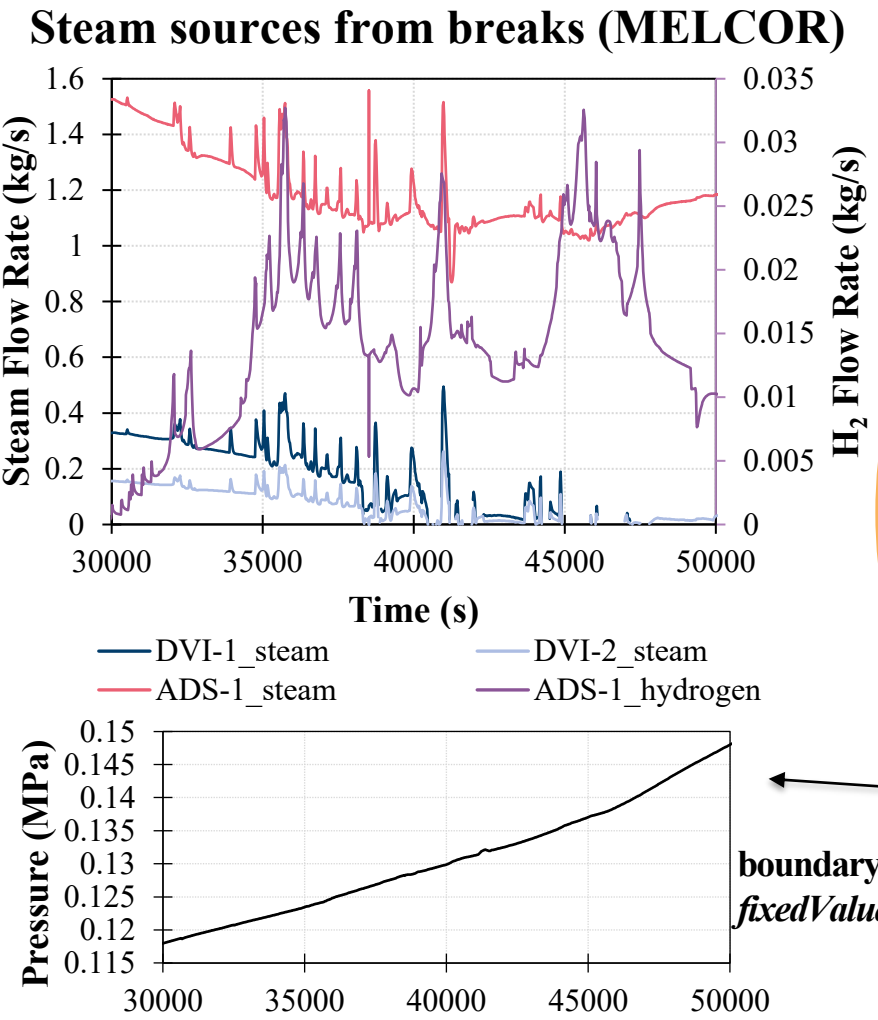

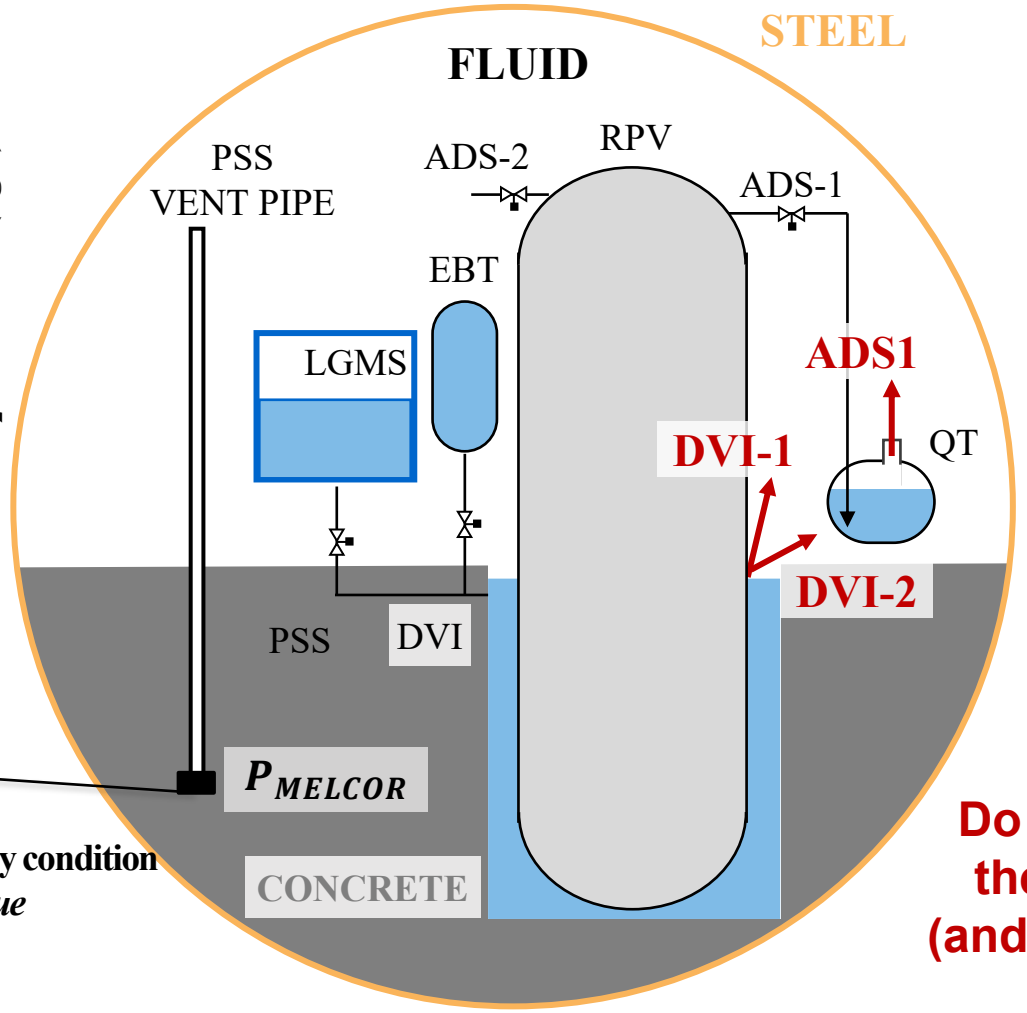

- Cavity occupied by water and 100% steam in containment with H_2 injection
- **Unsuccessful coupling** due to FMU limitations
- Solid temperature initialise based on MELCOR T_{sat}
- Larger time steps (0.008 s to 0.01 s)
- 80000 core-h (256 processors and 12.9 days clock time)

Do 3D heterogeneities affect the H_2 transport to the PSS (and therefore pressurization?)

4. SASPAM-SA Design-II: Late phase H_2 Transport

Some insights from the flow fields

Temperature field

Clear vertical stratification with differences building up to 45°C

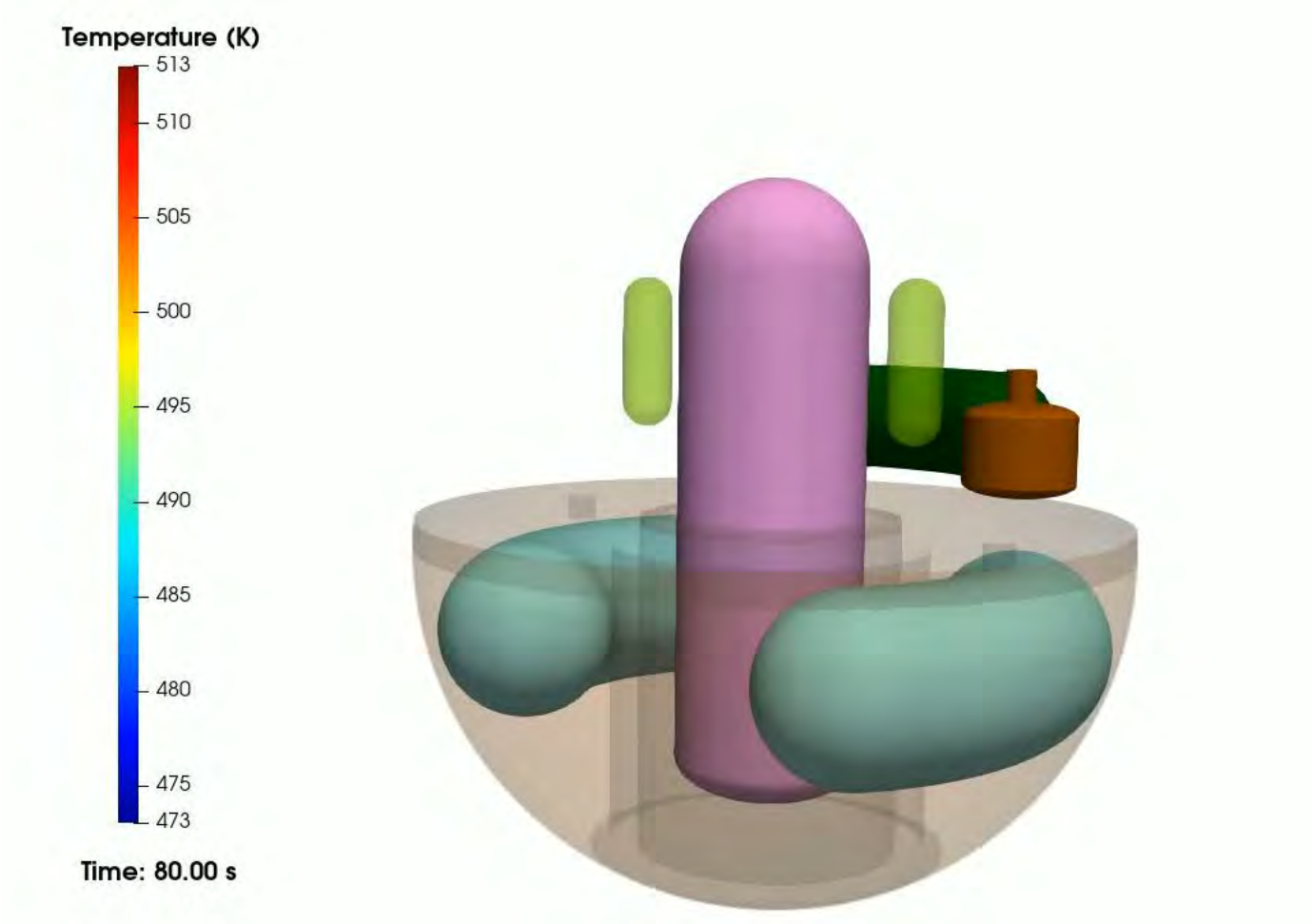

4. SASPAM-SA Design-II: Late phase H_2 Transport

JÜLICH Forschungszentrum

Some insights from the flow fields

Temperature – Screenshot 1

Heterogeneities beyond the vertical stratification

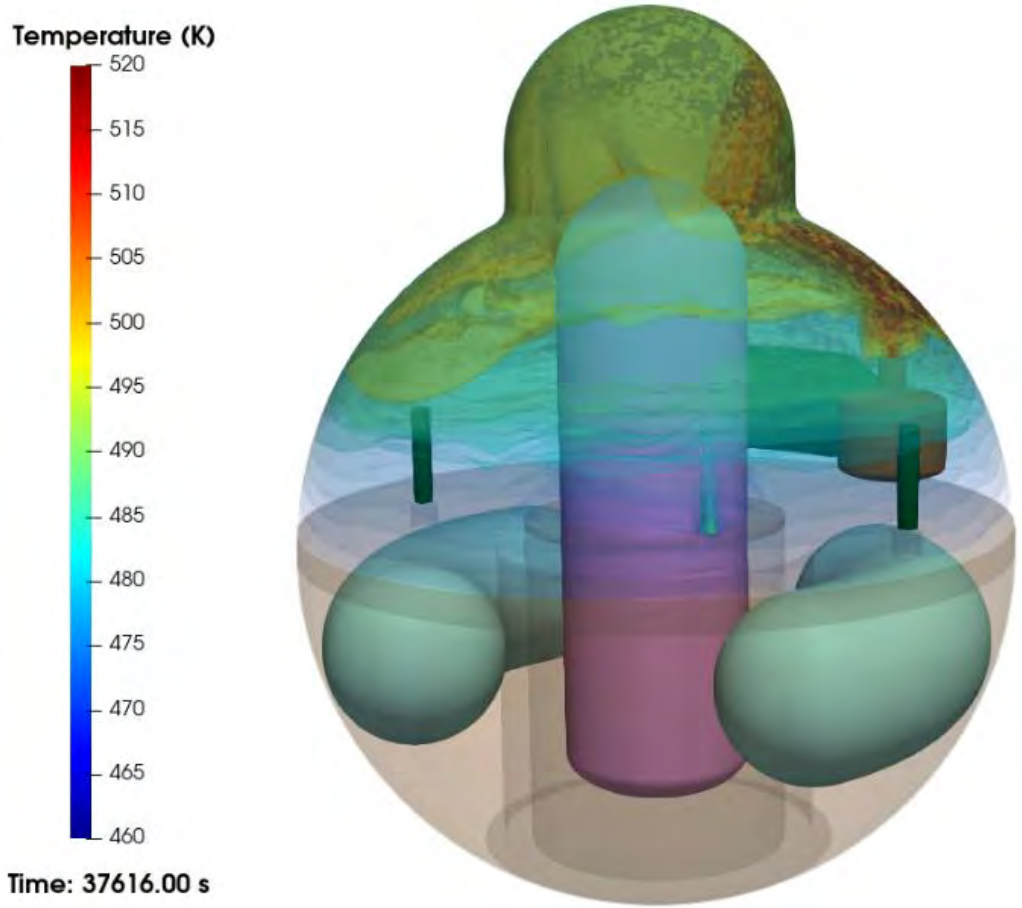

Hydrogen Distribution – Screenshot 2

The smaller hydrogen heterogeneities affect the H_2 transport

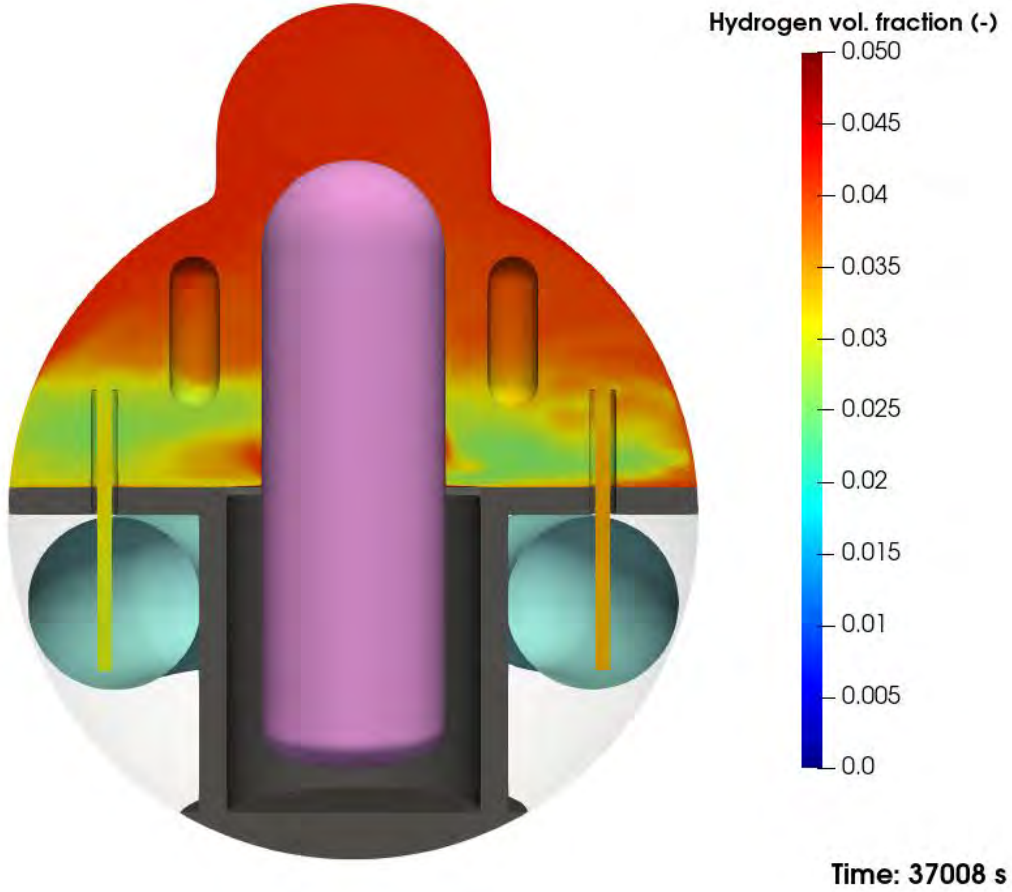

4. SASPAM-SA Design-II: Late phase H_2 Transport

JÜLICH Forschungszentrum

Comparison with MELCOR predictions

- Again, visible differences vs MELCOR. Yet, these **should remain qualitative without PSS coupling**
  - 3D heterogeneities could produce different pressure evolutions in the PSS (not quantifiable without FMU)

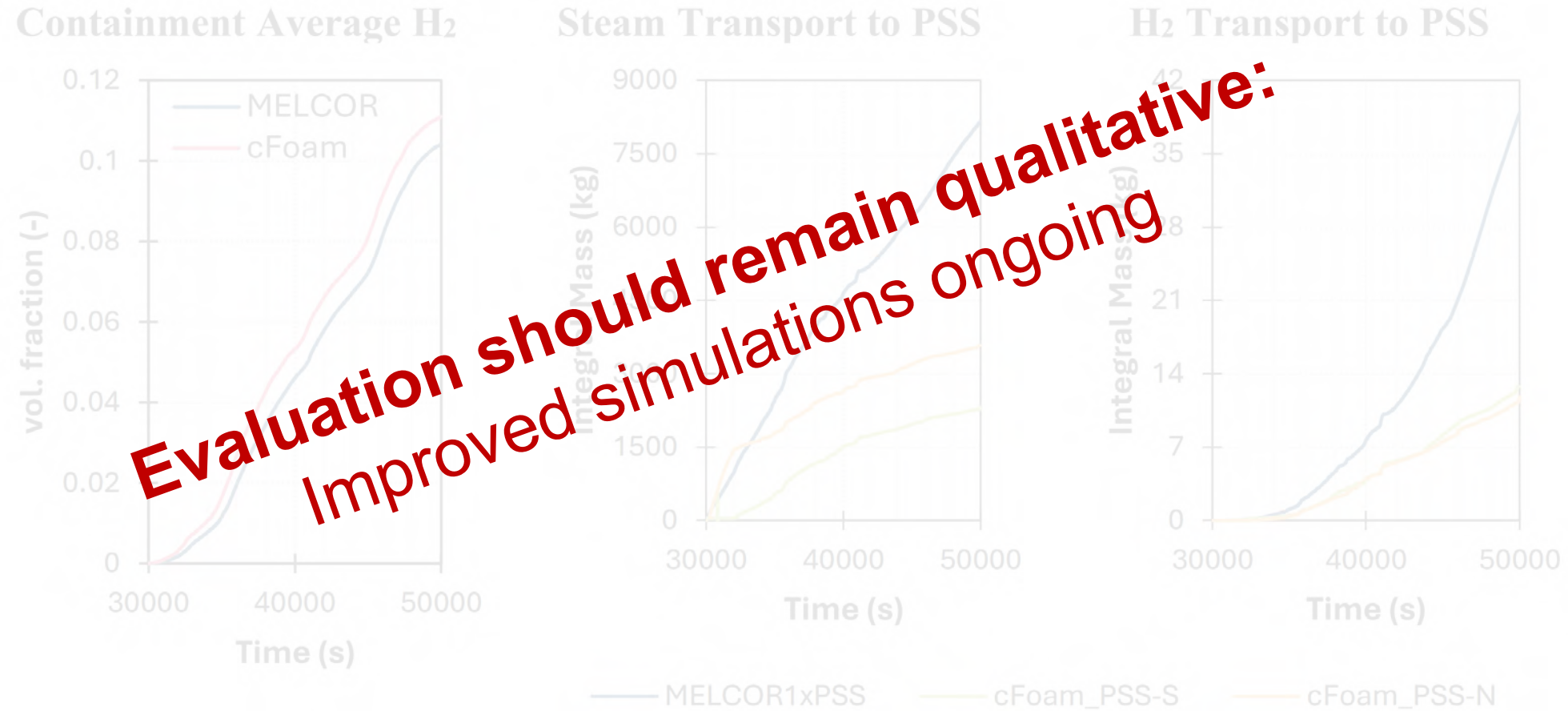

Evaluation should remain qualitative:
Improved simulations ongoing

OUTLINE

1. SA Sequences from SASPAM-SA
2. containmentFOAM Model Development
3. SASPAM-SA: Blowdown Sequence
4. SASPAM-SA: Late phase H_2 Transport
5. Conclusions

5. Conclusions

Takeaway messages

- **CFD** insights for the blowdown phase:
  - It is confirmed that the **blowdown produced homogeneous conditions** in the containment (good for LP)
  - The small **heterogeneities appear to have no significant safety impact**
  - Message for LP: **PSS modelling is crucial to model the blowdown** and currently need to be improved
- **CFD** insights for the late SA time windows:
  - Buoyancy-driven flows cause **stratification and local heterogeneities**
  - Heterogeneities may affect containment wall condensation and PSS pressure build-up
  - The safety relevance of the observations **cannot be evaluated without improving the PSS** modelling
- SASPAM-SA revealed modelling challenges to simulate LW-SMRs with containmentFOAM
  - The code upgrades implemented in parallel to the project make it **ready to support SMR safety analysis**
  - **See #97 S. Kelm (Today 14:25, A.01)** for the most advanced technical scale application of the code
- Many upgrades (film condensation, two-phase flows, PCCSs, etc.) towards LW SMR safety analysis currently under validation. If interested, **let's discuss over the week!**

Severe accident analysis of SASPAM-SA Design-II LWR SMR containment using containmentFOAM

Carlos Vázquez-Rodríguez, Stephan Kelm - Forschungszentrum Jülich (FZJ)

12h European Review Meeting on Severe Accident Research (ERMSAR2026) - Madrid, Spain, May 18-22, 2026

containmentFOAM

Supported by:

Federal Ministry
for the Environment, Nature Conservation,
Nuclear Safety and Consumer Protection

based on a decision of
the German Bundestag
Project No. 150 1633B

JÜLICH
Forschungszentrum
Mitglied der Helmholtz-Gemeinschaft

ANALYSIS OF LDR LITE REACTOR'S RESILIENCE TO DESIGN EXTENSION CONDITIONS

A. Kaliatka*, T. Kaliatka
LEI Lithuanian Energy Institute
Breslaujos str. 3, 44403 Kaunas, Lithuania
algirdas.kaliatka@lei.lt, tadas.kaliatka@lei.lt

C. Lombardo
ENEA Italian National Agency for New Technologies, Energy and Sustainable Economic Development, Via dei Mille 21, Bologna, Italy
calogera.lombardo@enea.it

ABSTRACT

Passive safety features without requiring an active power source have been in use in nuclear power plants to accomplish safety functions for many decades. However traditionally, the use of such passive features was of limited extent. The situation is different with the LDR-50 reactor, designed at VTT since 2020 for low temperature heat production applications, which exclusively leverage the physical laws to initiate safety functions.

Within the frame of HORIZON EUROPE EURATOM project "Ensuring Assessment of Safety Innovation for SMR" (EASI-SMR) the safety justification of LDR Lite reactor is performed. LDR Lite is an "academic", simplified and publicly available version of LDR-50. In this paper the analysis of typical initiated events, leading to design extension conditions (loss of offsite power supply, loss of coolant and imbalance between heat generated in the reactor and heat demand) are presented. The system thermal-hydraulic computer code RELAP5 was used for the analysis. The developed RELAP5 model is tested comparing the calculation results with VTT (Centre for Nuclear Safety in Finland) calculation results. The analysis results, presented in this paper, demonstrated the resilience of LDR Lite reactor concept to design extension conditions. It is shown that in LDR Lite case the natural circulation of coolant and self-pressurizing of primary circuit allows us to avoid overheating of reactor core.

KEYWORDS
LDR Lite, natural circulation, self-pressurizing

1. INTRODUCTION

LDR-50 design was developed at VTT since 2020 and is now being commercialized by Steady Energy. The LDR Lite is a public version of the LDR-50 reactor design for low temperature heat production applications. The main specifics of this 50 MW_{th} integrated pressure water reactor are boron less operation, natural circulation driven primary circuit, self-pressurization and passive decay heat removal through a dual vessel design [1, 2]. Reactor operates at 150 °C temperature and 0.8 MPa pressure and must be connected to district heating network via intermediate (secondary) water loop and heat exchangers. In normal operation, heat is extracted through the main heat exchangers. The reactor module is comprised of two nested pressure vessels:

* Footnote, if necessary, in Times New Roman font and font size 10

(1) inner reactor vessel, and (2) outer containment vessel (Figure 1). The reactor with containment is submerged into big water pool. The intermediate space between the reactor and containment vessels is partially filled with water, which assures the decay heat transfer from the rector into water pool. This pool can receive decay heat for several weeks without any cooling or operator action.

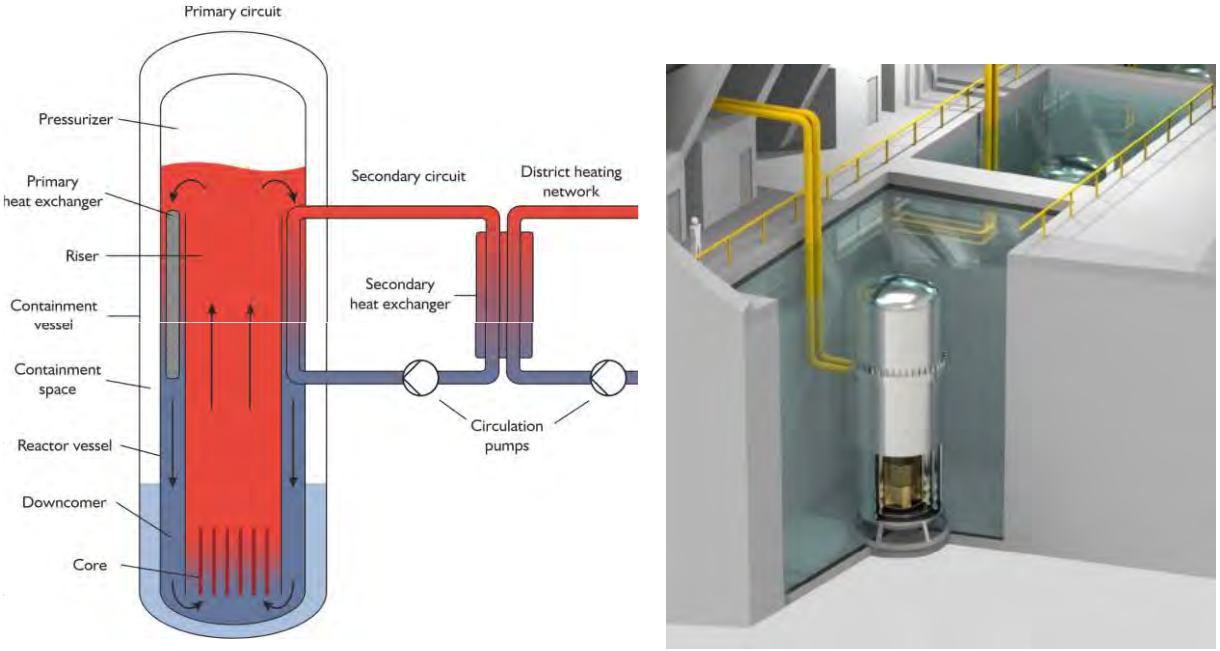

Figure 1. The LDR-50 reactor design [1, 2].

Within the frame of HORIZON EUROPE EURATOM project "Ensuring Assessment of Safety Innovation for SMR" (EASI-SMR) the safety justification of LDR Lite reactor is performed. This paper deals about the work performed in parallel to this EASI- SMR project. To analyse the resilience of LDR Lite reactor three initiating events, which can cause design extension conditions, were modelled:

1. Station Blackout (SBO);
2. Loss of coolant (LOCA);
3. Reduction of coolant flow in secondary circuit.

2. LDR LITE MODEL DEVELOPED USING RELAP5 CODE

The LDR Lite thermal-hydraulic model was developed using RELAP5 code. The RELAP5 code has been developed by Idaho National Engineering Laboratory [3] for best estimate transient simulation of light water reactor during design basis accidents. The code models coupled behaviour of the reactor coolant system and the core for loss-of-coolant accidents, and operational transients. RELAP5 code in Lithuanian Energy Institute (LEI) is used since 1995. For the analysis of thermal-hydraulic processes in LDR Lite reactor, the simplified model for RELAP5 code is developed (Figure 2):

- The reactor core was simplified and only thermal-hydraulic (no reactor neutronics) was modelled. The reactor core is modelled by four flow paths (max, min, average power and core bypass).
- The secondary circuit is modelled only with boundary conditions.
- Heat transfer from bottom and top in axial direction from the reactor vessel into containment are not modelled.
- Containment and water pool are modelled as two pipe elements with crossflows each. This allows to model the heat transfer in containment and water pall using convection of coolant.
- The containment and water pool are modelled as a group of concentric cylindrical rings.

- In the RELAP5 model the outside walls of water pool are not modelled (adiabatic condition is assumed).

The impact of modelling simplifications is following:

a) Impact of secondary circuit as boundary conditions. The detailed modelling of heat exchanger in secondary circuit and secondary thermal inertia will add additional heat removal. Thus, the approach without detailed modelling of secondary circuit leads to conservative results, which is fully justified when evaluating the safety of reactor.

b) No axial heat transfer at top/bottom of reactor vessel and containment. The additional heat transfer area will provide greater heat dissipation from reactor core into water pool. The very significant influence of heat loses into the water pool was presented in sensitivity analysis (answer to the comment No. 1). Thus, the approach without axial heat transfer at top/bottom of vessel and containment slightly decreases heat loses to final heat sink and gives more conservative results.

c) Adiabatic pool outer walls. The approaches with adiabatic pool outer wall enable the heat removal from water pool, which leads to a conservative result.

In conclusion, we can say that all simplifications allow us to obtain conservative results.

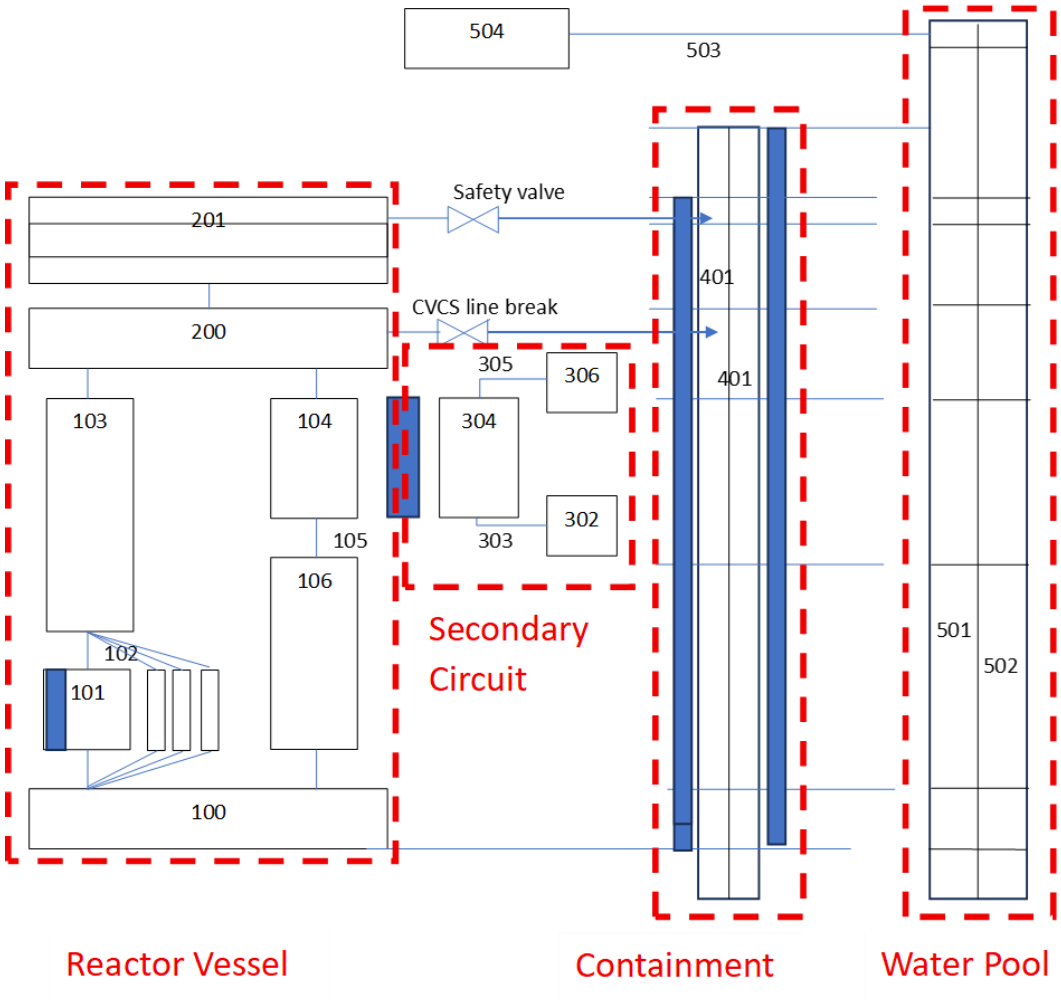

Figure 2. LDR Lite reactor model nodalization scheme, developed for RELAP5 code

The volume of primary circuit in the reactor vessel is ~ 41 m^3. The volume of containment is ~ 27.5 m^3, while the water mass is ~ 5000 kg. The water pool volume is 1000 m^3 (mass is 10E+05 kg) [1]. Initially, at cold state (at zero reactor power) the pressure in pressurizer and containment is atmospheric, water temperature in reactor and containment is 20°C. The water level in pressurizer is 7.02 m, and containment water level – 1.7 m, when the bottom of reactor lower plenum is at elevation 0.0 m.

At the hot full power steady state conditions, the reactor power is 50 MW, the pressurizer pressure is 0.65 MPa, core inlet and outlet temperatures are 109 and 157 °C respectively. The total primary mass flow is 244 kg/s. Secondary circuit inlet and outlet temperatures are 77 and 125 °C respectively. Secondary circuit mass flow is 245 kg/s at 1.5 MPa pressure. The water temperature in containment increases from 20 up to 67 °C, pressure – increases from 0.1 up to 0.132 MPa. The heat loss to water pool is about 190 kW. Because it is assumed adiabatic condition on the water pool outer walls, the water temperature in pool is continuously increasing (it is assumed, that at beginning of accident the water temperature is 24°C.

3. STATION BLACKOUT. COMPARISON OF LEI AND VTT CALCULATION RESULTS

In this section the LEI calculation results are compared to the VTT calculation [4], performed using APROS code (developed by VTT and Fortum). In case of station blackout, the pump in secondary circuit is stopped, what stops the heat removal from the reactor. At the same time, the reactor shutdown system is activated and heat release from fuel assemblies decreases from nominal power 50 MW down to decay power (Figure 3). After reactor shutdown, the fuel temperature decreases (Figure 4). This leads to the decrease of coolant flow rate in primary circuit from 244 kg/s don to ~ 10 kg/s (Figure 5). Pressure in pressurizer decreases also from 0.70 MPa down to ~ 0.30 MPa (Figure 6). The decay heat in reactor core is utilised transferring the heat to the water pool through containment; thus, the containment water temperature is slightly increasing (Figure 7) as well as temperature of water in pool (Figure 8). In summary, it can be noted that LDR Lite reactor is equipped with water pool, which plays a role of huge heat sink and decay heat from reactor core is transferred into water pool (Figure 9). This ensures safety of this reactor.

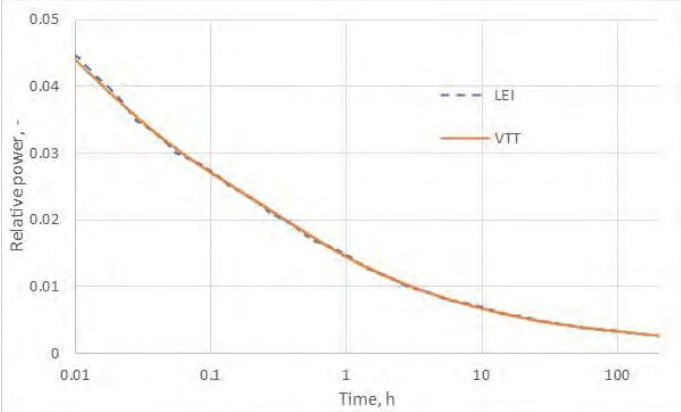

Figure 3. SBO. Reactor power.

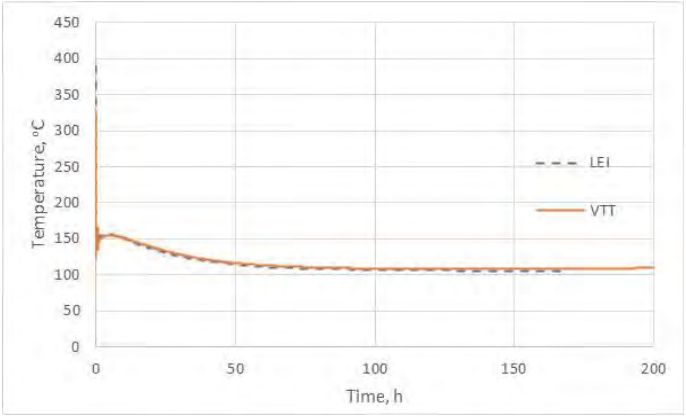

Figure 4. SBO. Maximum fuel temperature.

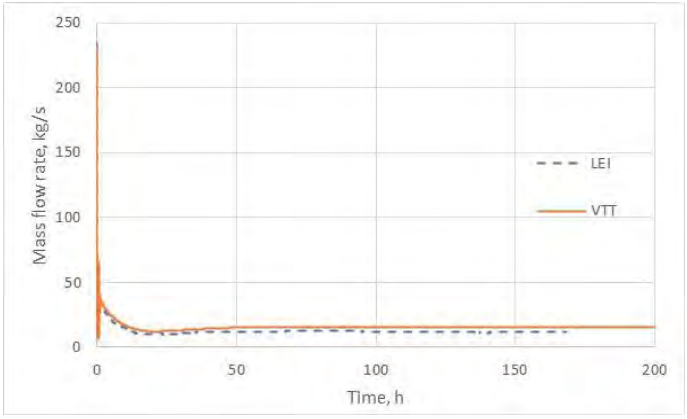

Figure 5. SBO. Core mass flow rate.

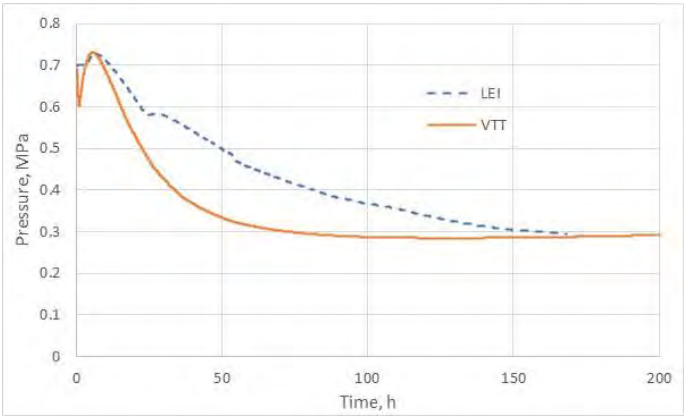

Figure 6. SBO. Pressurizer pressure.

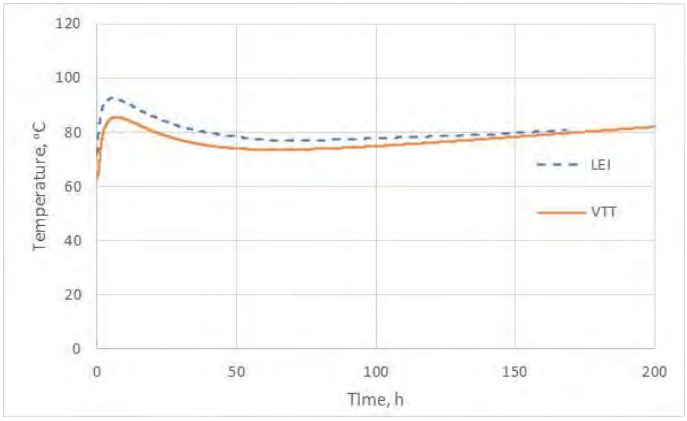

Figure 7. SBO. Containment water temperature.

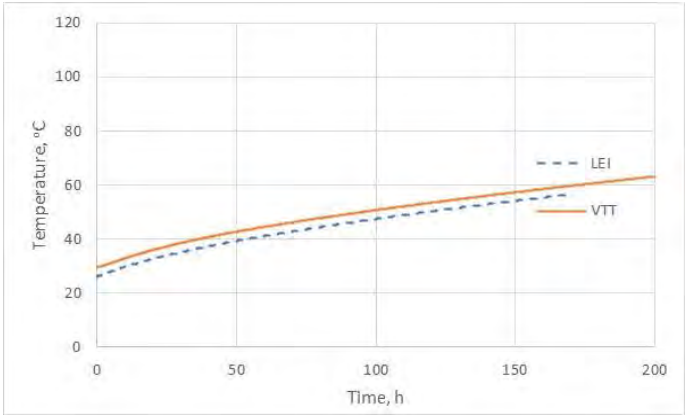

Figure 8. SBO. Pool water temperature.

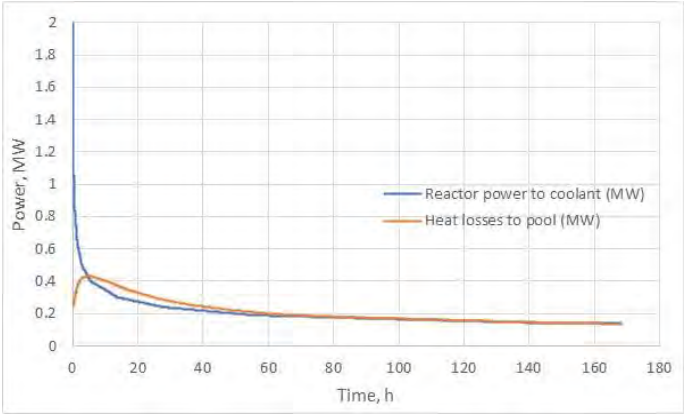

Figure 9. SBO. Comparison of decay heat released in reactor core and heat absorbed by the water pool.

Figure 9 demonstrated that the heat losses to water pool are very important. To analyse the influence of heat transfer from containment into water pool, two cases were compared. In first case, the coolant convection in the gap between the reactor vessel and containment vessel was without limitation. This increases the heat transfer coefficient from containment into water pool. In second case it was evaluated that the mentioned gap is narrow, thus could be some limitations for the coolant convection – this could lead to the decreased heat transfer coefficient from containment into water pool (see Figure 10). The differences in to heat transfer

leads to the significant difference in pressure behaviour in the pressurizer (Figure 11), while remaining parameters are not changing.

The comparison of VTT and LEI results for SBO scenario calculation demonstrated qualitative and quantitative compliance of parameters. Small discrepancies of some parameters are caused by slightly different nodalization.

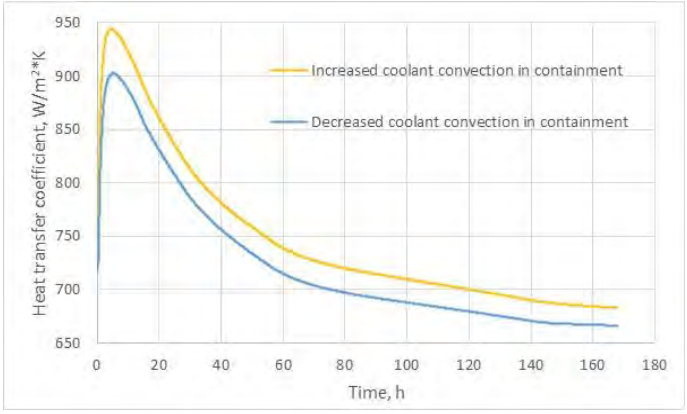

Figure 10. SBO. Two cases of heat transfer coefficient from containment into water pool.

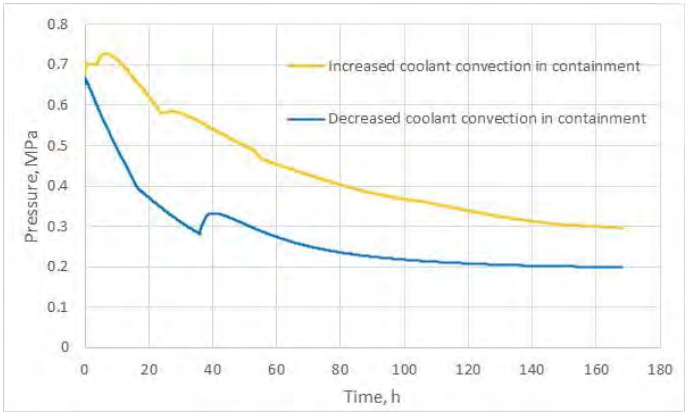

Figure 11. SBO. Two cases of heat transfer coefficient from containment into water pool. Pressurizer pressure.

4. LOSS OFF COOLANT ACCIDENT

The Chemical and Volume Control System (CVCS) pipes are only pipes connecting primary reactor circuit with the system outside reactor containment. Thus, break of CVCS line (0.025 m diameter) with discharge into containment was selected as LOCA scenario. This line is connected to the upper reactor plenum at elevation 7.045 m, when initial water level in pressurizer at nominal reactor power is at elevation 8.21 m. There is a check valve installed in the CVCS system; thus, the discharge is possible only from the reactor primary circuit side. In RELAP5 model the Henry Fauske choked flow model is applied for break discharge and two-phase critical flow treatment modelling.

The water and steam mixture through the break is discharged into the containment (Figure 12). The reactor shutdown system is activated immediately due to pressure increase in the containment (Figure 13). The reactor power decreased from nominal power 50 MW down to decay power, the pump in secondary circuit is stopped and the heat is not removed through the reactor heat exchangers. The pressure in reactor vessel after the break is decreased and equalizes with the pressure in containment (Figure 13). Due to significant

pressure decrease and start of water boiling, the coolant flow rate through reactor core starts to fluctuate around zero (Figure 14). The coolant temperatures in reactor vessel decreases (Figure 15). As it is seen from this figure, the water temperature in upper plenum (which is connected to the break) is equal to saturated temperature, what indicates that the water is starting to boil in upper part of the reactor. Fuel and cladding temperatures decrease down to coolant temperature (Figure 16). This is because the water level in reactor vessel remains much higher than location of fuel assemblies (Figure 17). The water level in containment increases, however, within 25 hours after the accident, the water level in the containment did not reach the water level in the reactor vessel. Figure 18 demonstrated that after the reactor shutdown the reactor decay heat is transferred into water pool, which ensures complete safety of the reactor.

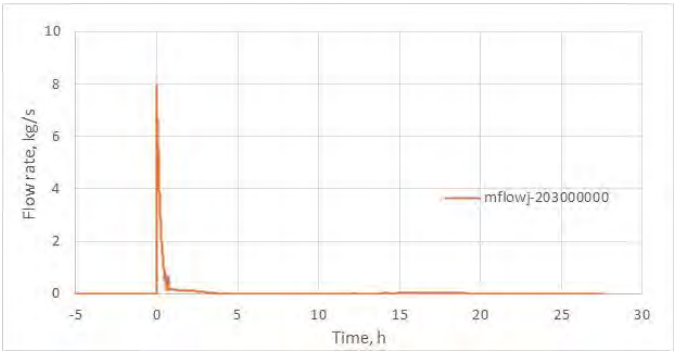

Figure 12. LOCA. Release of coolant from the break.

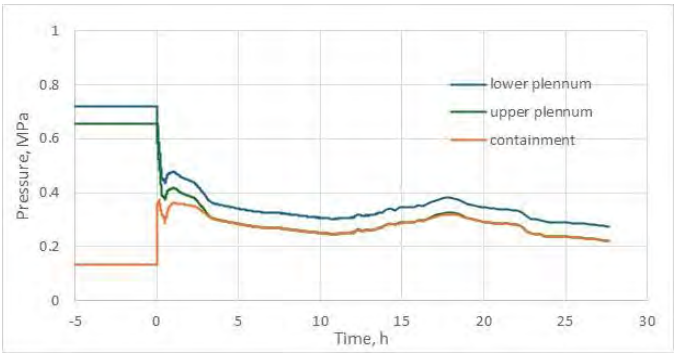

Figure 13. LOCA. Pressure behaviour in reactor primary circuit and containment.

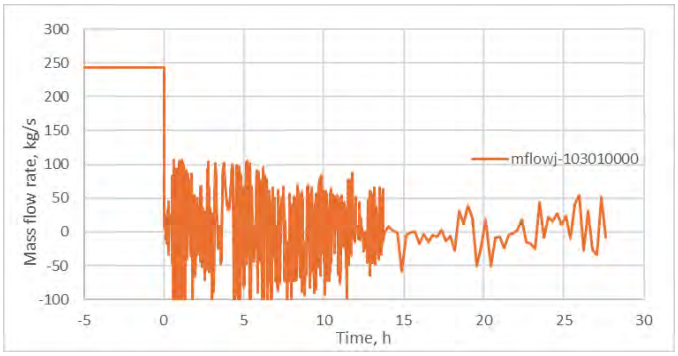

Figure 14. LOCA. Coolant flow rate through reactor riser.

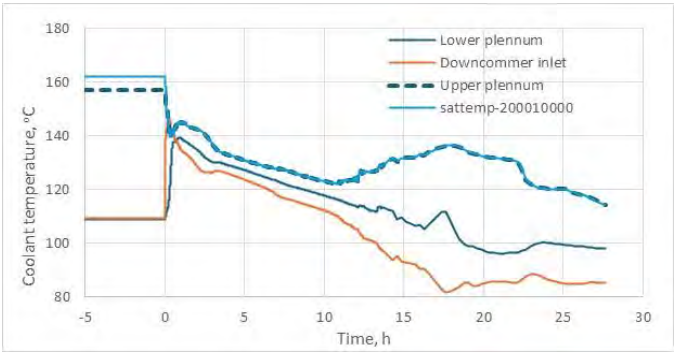

Figure 15. LOCA. Coolant temperature in reactor primary circuit.

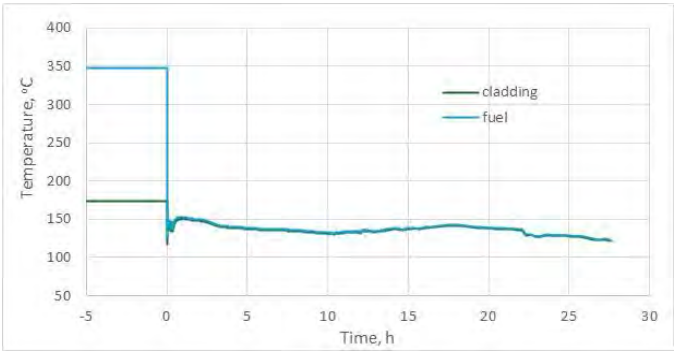

Figure 16. LOCA. Reactor fuel and cladding temperature behaviour.

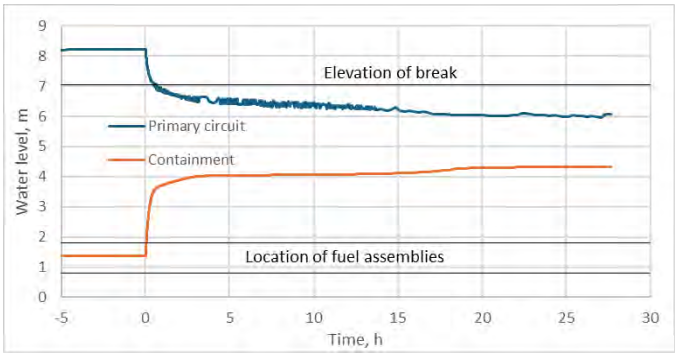

Figure 17. LOCA. Behaviour of water level in primary circuit and containment.

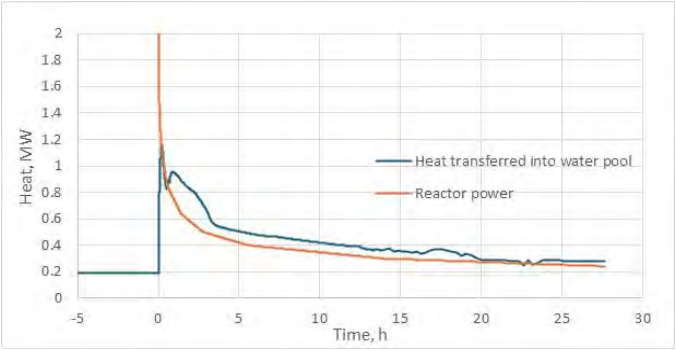

Figure 18. LOCA. Comparison of decay heat from reactor with heat removal through heat exchanger of secondary circuit.

The investigation of nodalization influence on calculation results was carried out by changing the pressurizer simulation. The pressurizer is 1.5 m height and 7.3 m^3 volume element, placed in the reactor vessel top. In the simplified model case this pressurizer is modelled as single volume, while in the modified model – this element was divided into 3 identical volumes. The performed analysis showed, that in case of simplified model the initial (steady state) pressure in pressurizer is slightly higher than in in three volumes case (see Figure 19). This slightly higher pressure leads to slightly higher release of steam through the break within first seconds after break initiation. However, this practically does not lead to differences in containment pressure and further behaviour of pressure in pressurizer and containment remains practically identical.

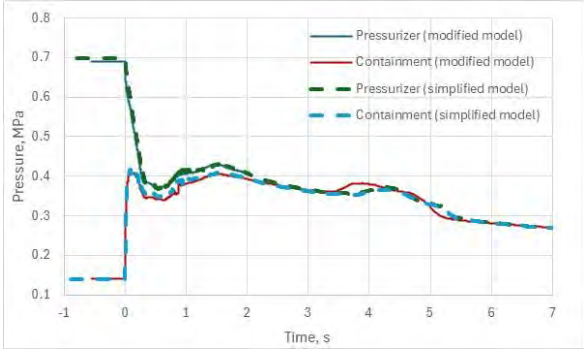

Figure 19. LOCA. The pressure behaviour in pressurizer and containment using different pressurizer models.

5. DECREASE OF SECONDARY WATER FLOW

The LDR Lite reactor is designed specifically for low-temperature district heating, not electricity, aiming for safe, simple, featuring passive safety, self-pressurization, and boron-free operation. The previously sections demonstrate that in case of SBO and LOCA, after the reactor shutdown, the reactor decay heat is transferred into huge water pool, which ensures cooling of fuel assemblies and safe cooldown of the reactor. In the following section it is shown that the passive safety and self-pressurization systems ensure reactor resilience to design extension conditions even when the heat removal from the reactor to become unbalanced.

It is assumed that for unknown reasons (for example due to a pump failure) the flow rate through secondary circuit decreases from 245 down to 150 kg/s (Figure 20). At the same time, it is assumed that none of the safety systems are activated and reactor power remains constant (50 MW). The decreased flow rate causes an increase of water temperature at the heat exchanger outlet from 125 up to 155 ºC (Figure 21). Hoverer, the pressure in secondary circuit is 1.5 MPa, the water remains subcooled. Such change in secondary water temperature leads to short term disbalance in heat removal through reactor heat exchangers (Figure 22). As is seen from presented figure, a few minutes after the accident the heat transfer returns to the initial value. At the same time the coolant temperatures in primary circuit are increasing also (Figure 23). The temperatures of fuel and cladding increases by 15 – 20 ºC as well. This leads the increase of coolant flow rate through reactor core (Figure 24). The increase of coolant temperature leads to increase of pressure in reactor vessel – the pressure in pressurizer reaches the safety valve actuation set-point (Figure 25). The overpressure protection system is actuated at 1 MPa pressure and steam from the pressurizer is released into containment (Figure 26). This leads to the increase of pressure in containment from 0.132 up to 0.22 MPa (Figure 27). Water temperature in containment increases by ~ 15 ºC, but the saturation temperature is not reached. Due to steam release from the pressurizer, the water level in primary circuit is decreased, while in containment – increases (Figure 28). The water level in reactor vessel remains much higher than location of fuel assemblies. At the same time, the loss of coolant leads to slight decrease in pressure and within approximately 10 hours the new steady state is reached. As the water temperatures in the primary circuit and in containment increased, heat transfer into water pool increased also (Figure 29). As is seen from this

figure, after reaching a new steady state, heat transfer to the water pool begins to gradually decrease, which proves that automatic self-pressure maintenance and mode regulation are achieved, and the reactor is operating safely.

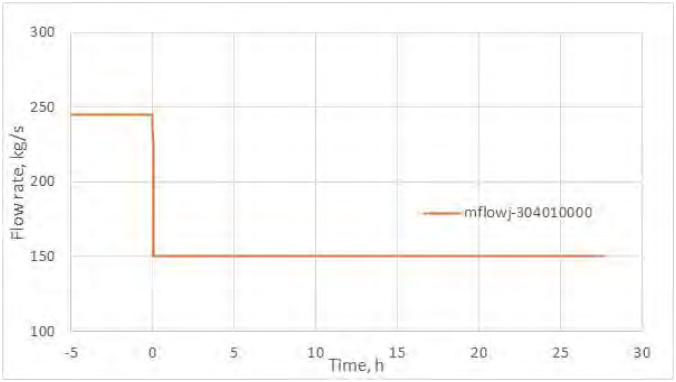

Figure 20. Decrease of secondary water flow. Water flowrate in secondary circuit.

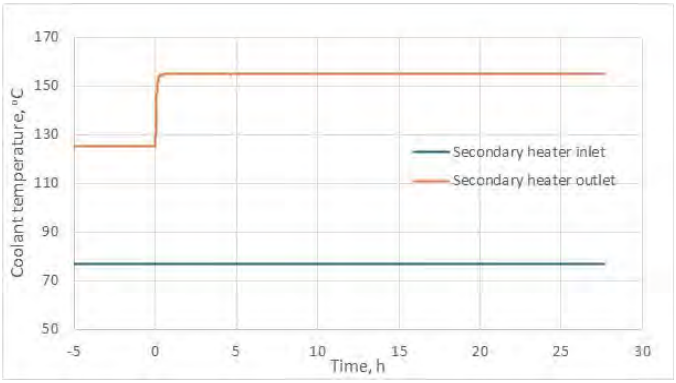

Figure 21. Decrease of secondary water flow. Water temperature in secondary circuit.

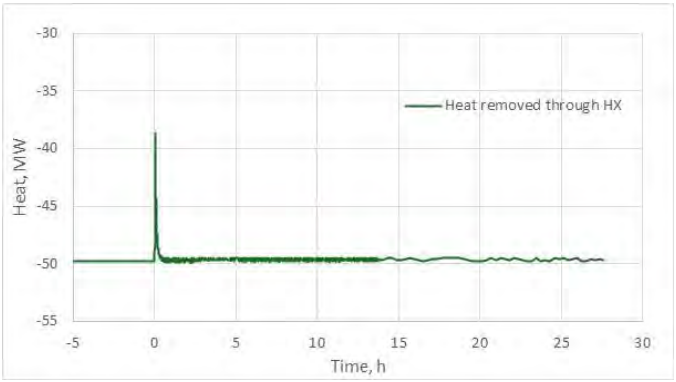

Figure 22. Decrease of secondary water flow. Heat removal through heat exchanger in secondary circuit.

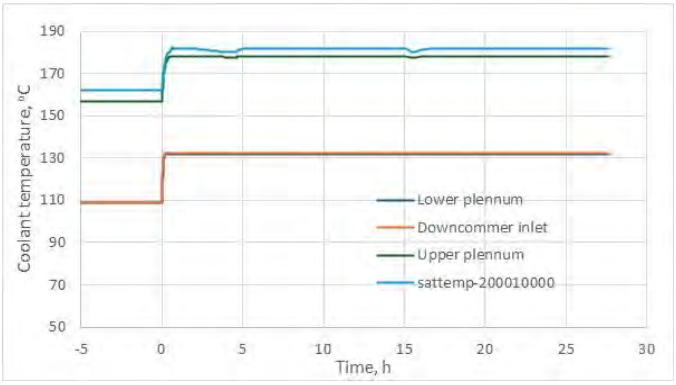

Figure 23. Decrease of secondary water flow. Increase of coolant temperature in primary circuit.

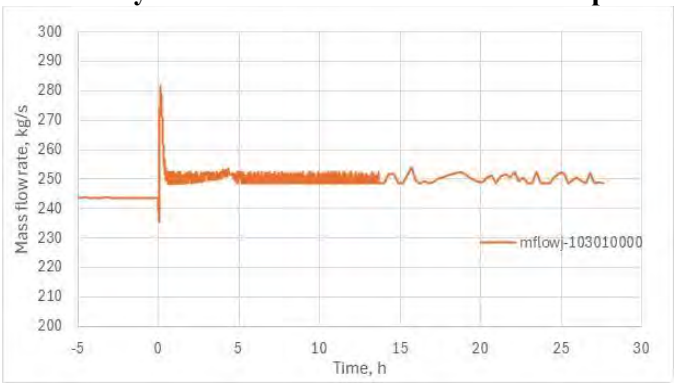

Figure 24. Decrease of secondary water flow. Coolant flow rate through reactor riser.

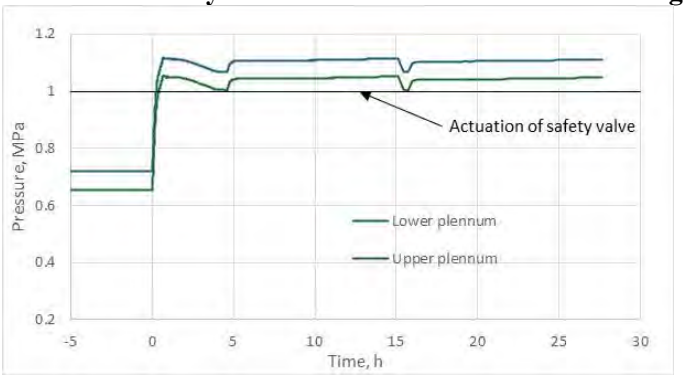

Figure 25. Decrease of secondary water flow. Increase of pressure in primary circuit.

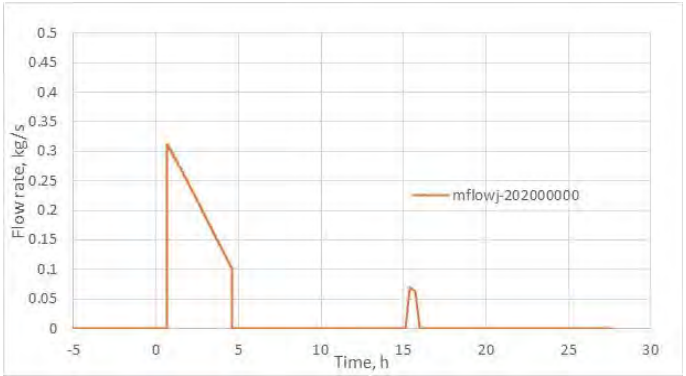

Figure 26. Decrease of secondary water flow. Release of coolant from pressurizer through safety valve.

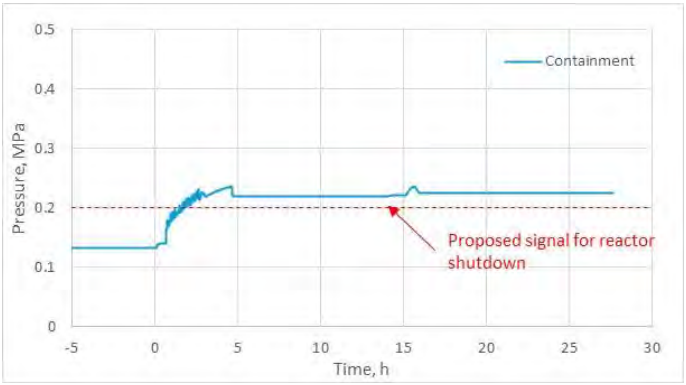

Figure 27. Decrease of secondary water flow. Increase of pressure in containment.

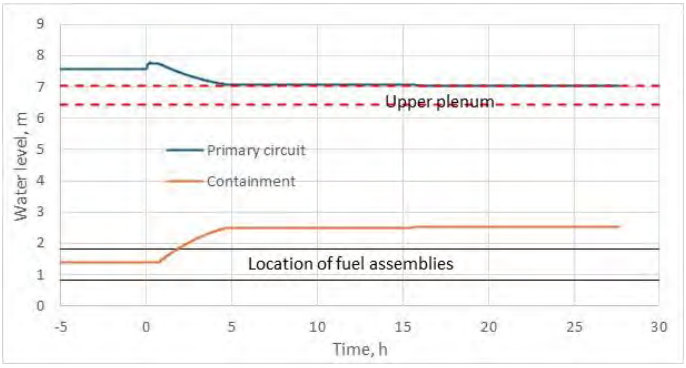

Figure 28. Decrease of secondary water flow. Behaviour of water level in primary circuit and in containment.

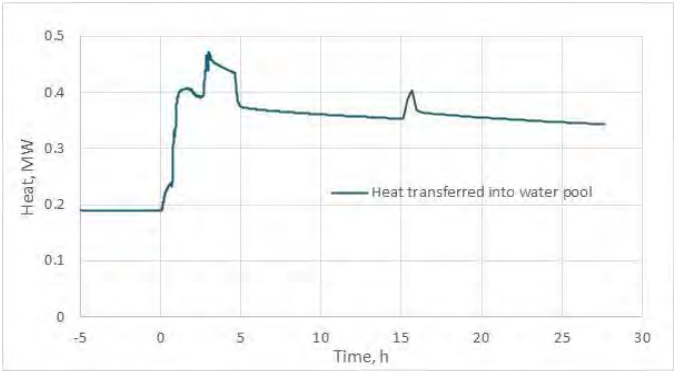

Figure 29. Decrease of secondary water flow. Heat transfer into water pool.

The investigation of nodalization influence on calculation results was carried out by changing the pressurizer simulation (in the same case as for LOCA case). In the simplified model case this pressurizer is modelled as single volume, while in the modified model – this element was divided into 3 identical volumes. The changes in nodalization only insignificantly change the behaviour of pressure in pressurizer and containment (see Figure 30), while remaining parameters are not changing.

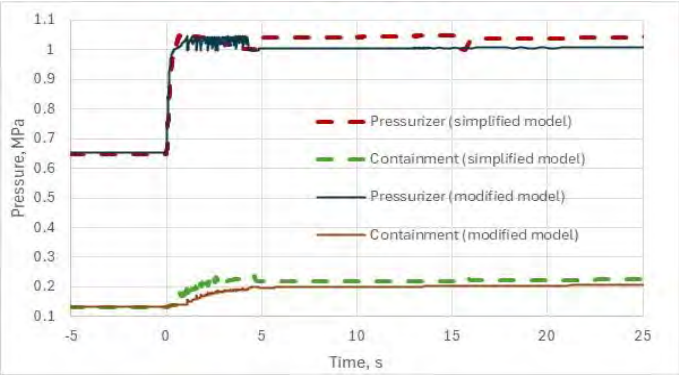

Figure 30. Decrease of secondary water flow. The pressure behaviour in pressurizer and containment using different pressurizer models.

The LDR Lite reactor is under development, thus we did not meet the acceptance criteria used in open literature. On the other hand, the performed safety justifications allowed us to propose acceptance criteria:
Peak cladding temperature. The performed analysis of selected accidents shows that fuel and cladding temperatures are decreasing after reactor shutdown. In the case of coolant flow in secondary circuit reduction the reactor power remains constant, and the fuel and cladding temperatures increased up to 5%. The recommended acceptance criteria for fuel could be the same as for PWR plants with analogical fuel assemblies. However, it is necessary to evaluate, that LDR Lite reactor will be located in the city are, therefore the acceptance criteria may be stricter – for example peak cladding temperature should be below 900 ºC (related to steam – zirconium oxidation reaction risk).
Minimum liquid level above core. In LDR Lite reactor this criterion is related to the maintenance of natural circulation in primary circuit. In the coolant flow in secondary circuit reduction case, it was shown that water level should be not below elevation 7.00 m (see Figure 28) – the upper plenum should be filled by water.
Maximum containment pressure. In LDR Lite reactor the containment is protected by containment overpressure protection valve, which actuation pressure is 1.00 MPa. Thus, acceptance criterion related containment pressure is 1.10 MPa (plus 10% from overpressure protection valve). It is recommended to shutdown reactor if pressure in containment is higher as 0.2 MPa (see Figure 27).
Long-term pool temperature margin to boiling. Recommended value - 90 ºC.

6. CONCLUSIONS

To analyse the resilience of LDR Lite reactor three initiating events, which can cause design extension conditions, were modelled:

- SBO
- LOCA
- Reduction of coolant flow in secondary circuit

The comparison of VTT and LEI results for SBO scenario demonstrated qualitative compliance of parameters and confirms the suitability of the created model. The performed analyses of SBO and LOCA demonstrated that after the reactor shutdown the reactor decay heat is transferred into water pool, which ensures safe cooldown of the reactor. The analysis of decrease of secondary water flow demonstrated that selected LDR design ensures resilience to interference. Even without activation of safety systems, the automatic self-pressurization and mode adjustment is achieved, new steady state is reached, and the reactor is safely operating. Thus, the design of reactor, low core power and availability of water pool as an ultimate heat sink, assures the resilience of LDR Lite reactor concept to design extension conditions.

ACKNOWLEDGMENTS

Funded by the European Union. Views and opinions expressed are, however, those of the author(s) only and do not necessarily reflect those of the European Union or European Commission - Euratom. Neither the European Union nor the granting authority can be held responsible for them.

The authors thank Rebekka Komu (VTT) for assistance in developing the reactor model.

REFERENCES

1. R. Komu, R. Tuominen, "LDR Design Document Public Material. LDR lite benchmark specifications", LDR-PUB-VTT-10002-R4, VTT Technical Research Centre of Finland (2024).
2. J. Leppänen, “LDR-50 District heating reactor & LDR lite benchmark”, Presentation on PHYSOR-2024, https://serpent.vtt.fi/kraken/images/1/1d/Introduction_to_LDR_50.pdf (2024).
3. NRC, 2001. U. S. Nuclear regulatory commission. SCDAP/RELAP5/MOD3 code manual. User’s guide and input manual. NUREG/CR-6150 3. Rev. 2 (2001).
4. B. Verdonschot, P. Breijder, F. Roelofs, R. Komu, “Analysis of Station Blackout for the LDR-50 SMR in SPECTRA and APROS”. *Proceedings of the 2024 ANS Winter Conference “Advances in Thermal Hydraulics (ATH 2024)”*, Orlando, FL, November 17-21, 2024 pp. 182-191 (2024).

ANALYSIS OF LDR LITE REACTOR'S RESILIENCE TO DESIGN EXTENSION CONDITIONS

A. Kaliatka (LEI), T. Kaliatka (LEI)
C. Lombardo (ENEA)

The 12h European Review Meeting on Severe Accident Research (ERMSAR2026)
Madrid, Spain, May 18-22, 2026

Content

Introduction

LDR LITE Model Development

1. Station Blackout (SBO)
2. Loss of coolant (LOCA)
3. Reduction of coolant flow in secondary circuit

Conclusions

Introduction

- LDR-50 design was developed at VTT since 2020 and is now being commercialized by Steady Energy.
- The LDR Lite is a public version of the LDR-50 reactor design for low temperature heat production applications.
- The main specifics:
  - 50 MW_{th} integrated pressure water reactor,
  - boronless operation,
  - self-pressurization,
  - natural circulation driven primary circuit,
  - passive decay heat removal through a dual vessel design.

To analyse the resilience of LDR Lite reactor three initiating events, which can cause design extension conditions, were modelled:

1. Station Blackout (SBO);
2. Loss of coolant (LOCA);
3. Reduction of coolant flow in secondary circuit.

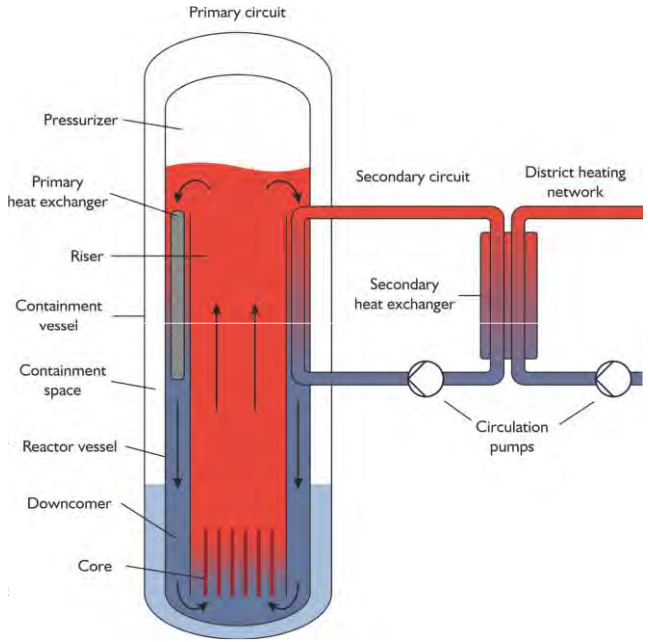

LDR LITE Model Development

RELAP5 Mod 3.2

- The reactor core was simplified and only thermal-hydraulic (no reactor neutronics) was modelled. The reactor core is modelled by four flow paths (max, min, average power and core bypass).
- The secondary circuit is modelled only with boundary conditions.
- Heat transfer from bottom and top in axial direction from the reactor vessel into containment are not modelled.
- Containment is modelled as two pipe element.
- Water pool is modelled as two pipe element.
- The containment and water pool are modelled as a group of concentric cylindrical rings.
- In the RELAP5 model the outside walls of water pool are not modelled (adiabatic condition is assumed).

LDR LITE Model Development

RELAP5 Mod 3.2

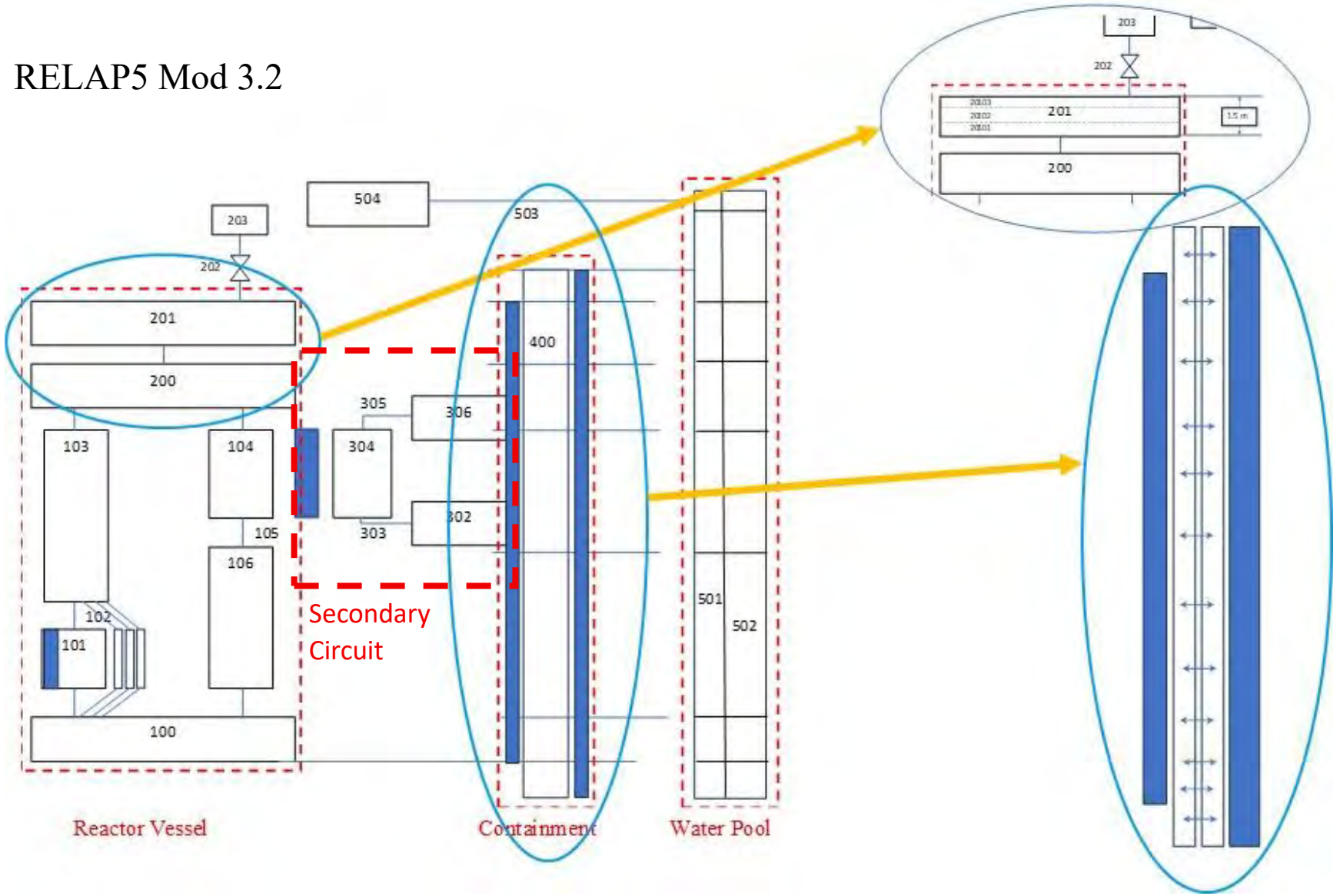

- Changes in pressurizer modelling.

- Changes in containment modelling.
- The heat transfer in the gap between reactor vessel and containment vessel
- Convection & conduction

Station Blackout Analysis. Comparison of LEI and VTT Calculation Results (1)

Relative reactor power to coolant

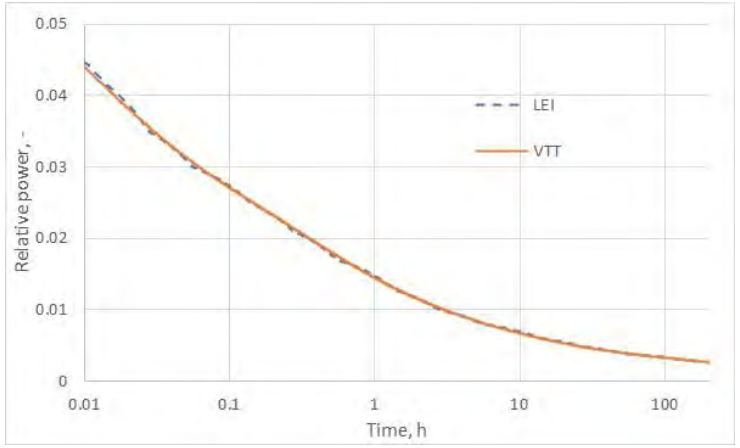

Maximum fuel temperature

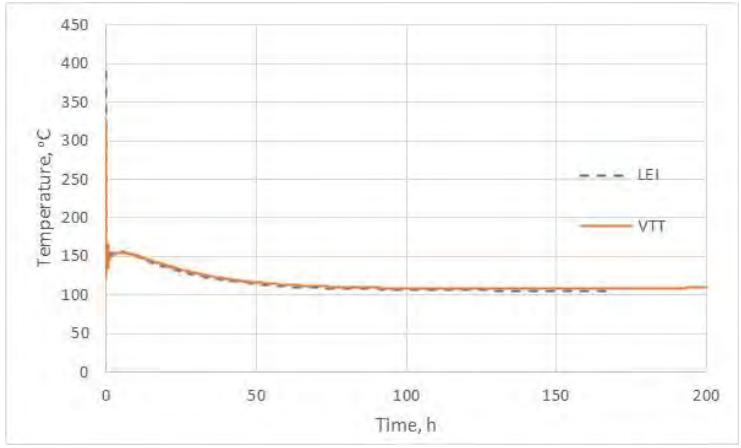

Pressurizer pressure

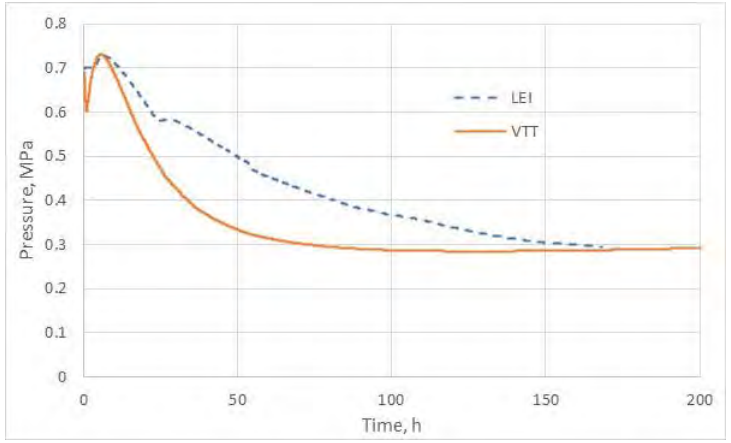

Core mass flow rate

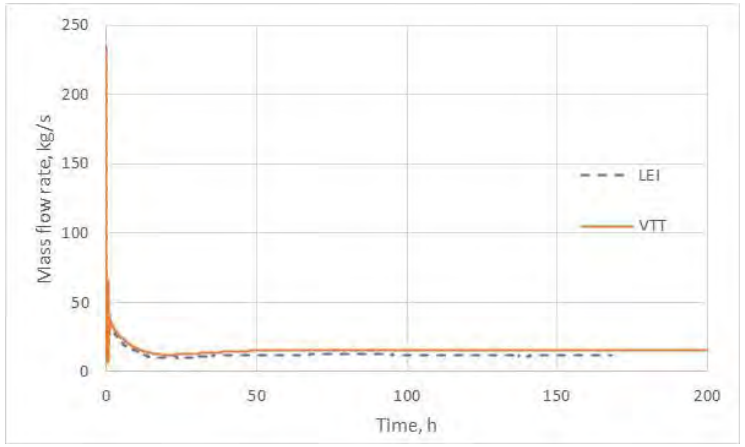

Containment liquid temperature

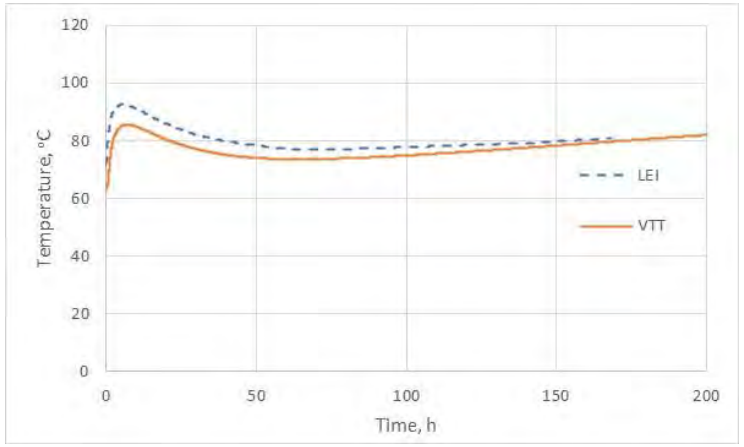

Pool temperature

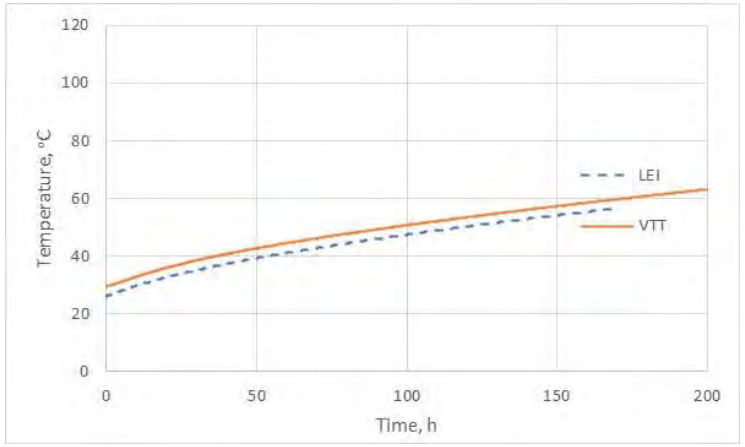

Station Blackout Analysis. Comparison of LEI and VTT Calculation Results (2)

Pressurizer pressure

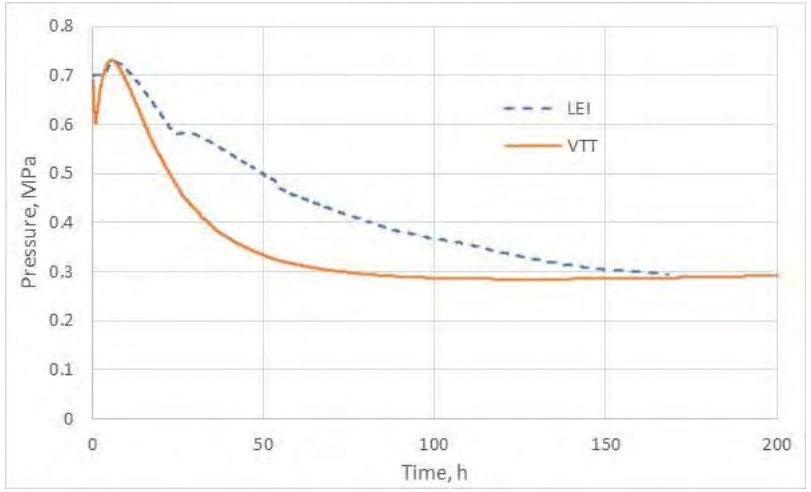

Heat losses to pool

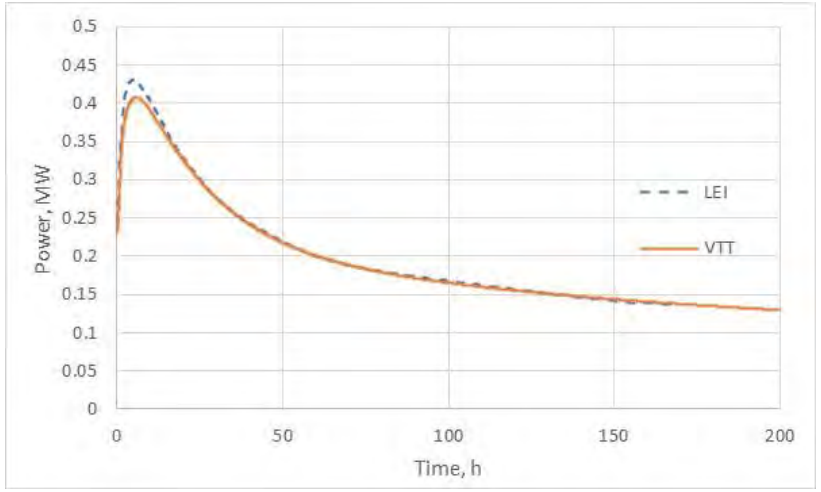

Energy balance

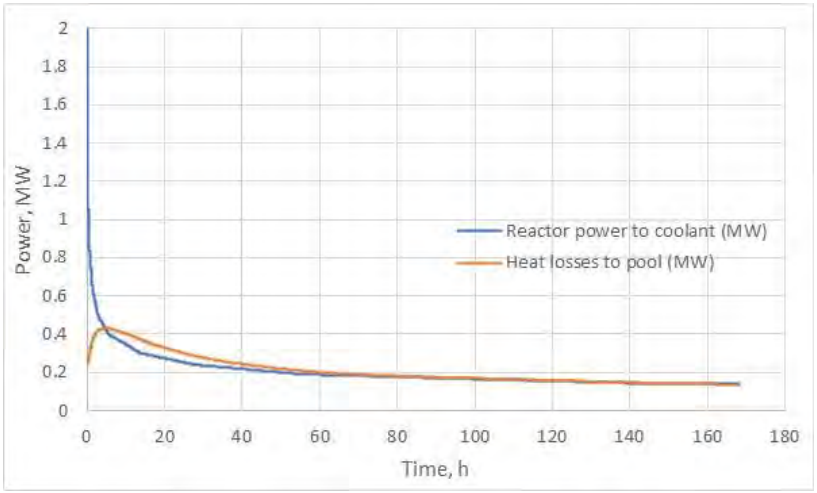

Assuming that mass of water in pool is about 1000 tones – it takes about three weeks to reach boiling of water in pool!

Loss off Coolant Accident Analysis (1)

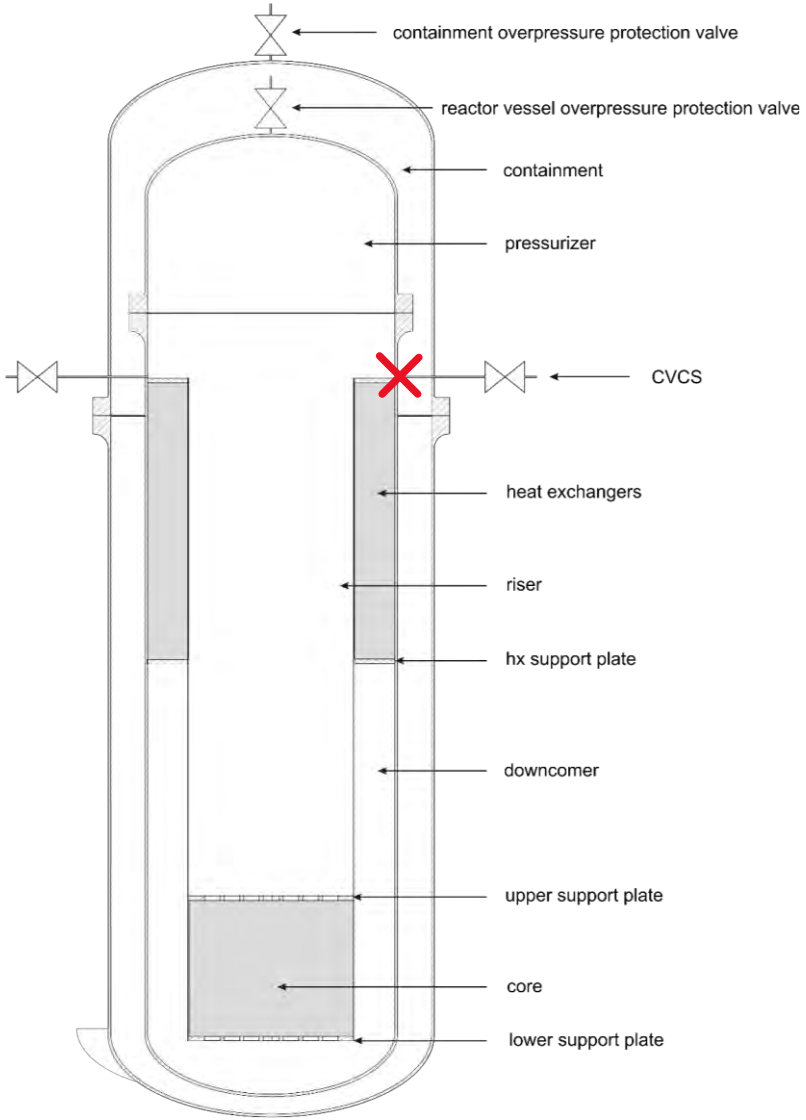

LDR lite module with the break location marked with red cross

Chemical and volume control system (CVCS)

Loss off Coolant Accident Analysis (2)

Release of coolant from the break

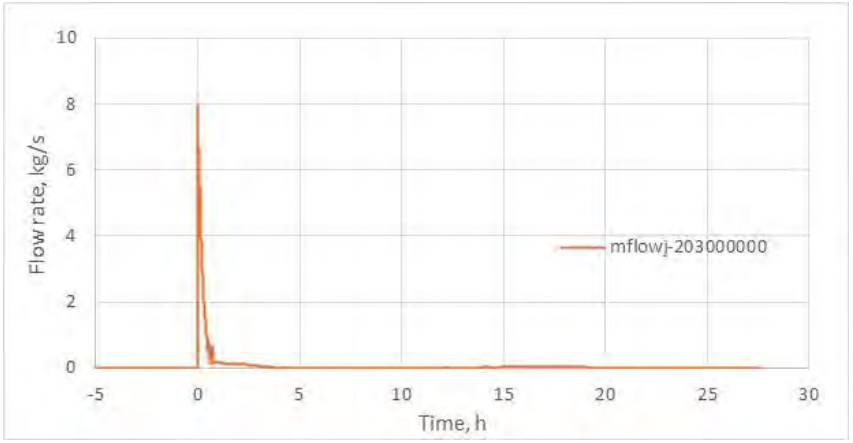

Pressure behaviour in reactor primary circuit and containment

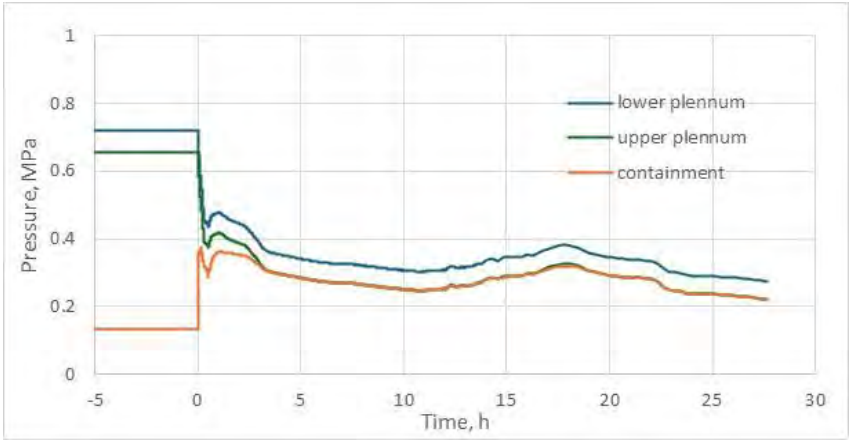

Coolant flow rate through reactor core

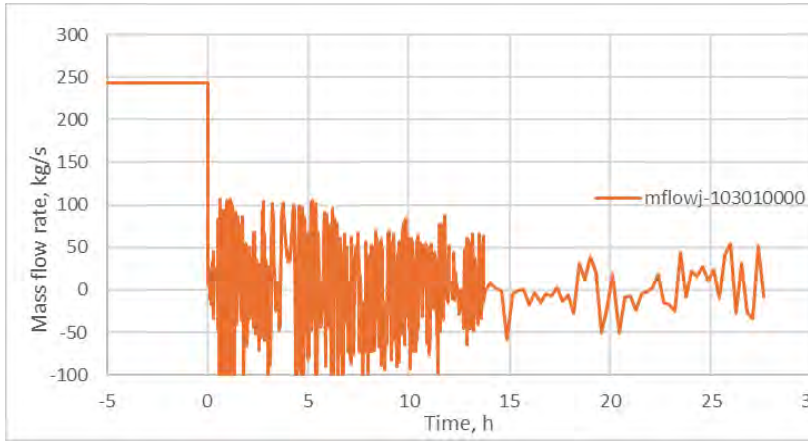

Coolant temperature in reactor primary circuit

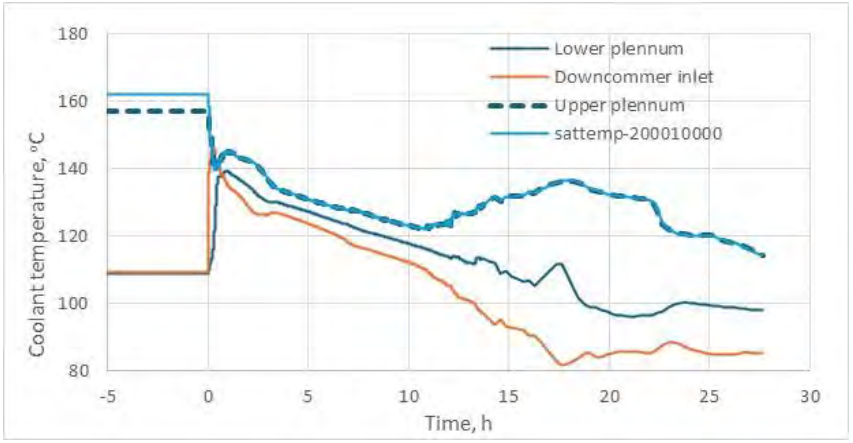

Reactor fuel and cladding temperature behaviour

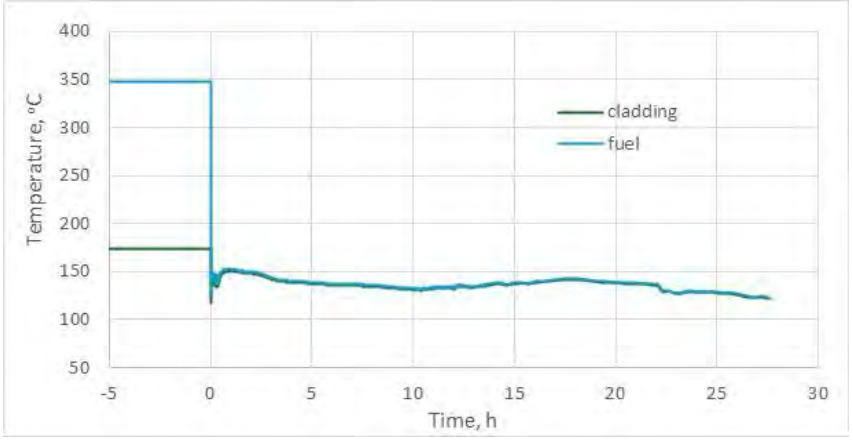

Behaviour of water level in primary circuit and containment

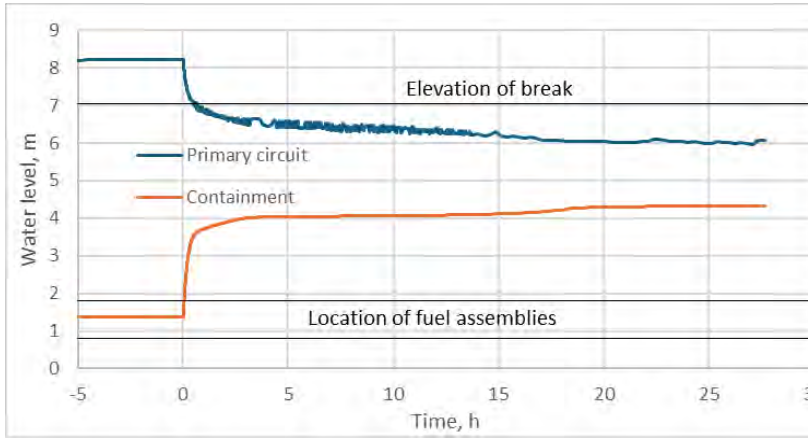

Decrease of Secondary Water Flow Analysis (1)

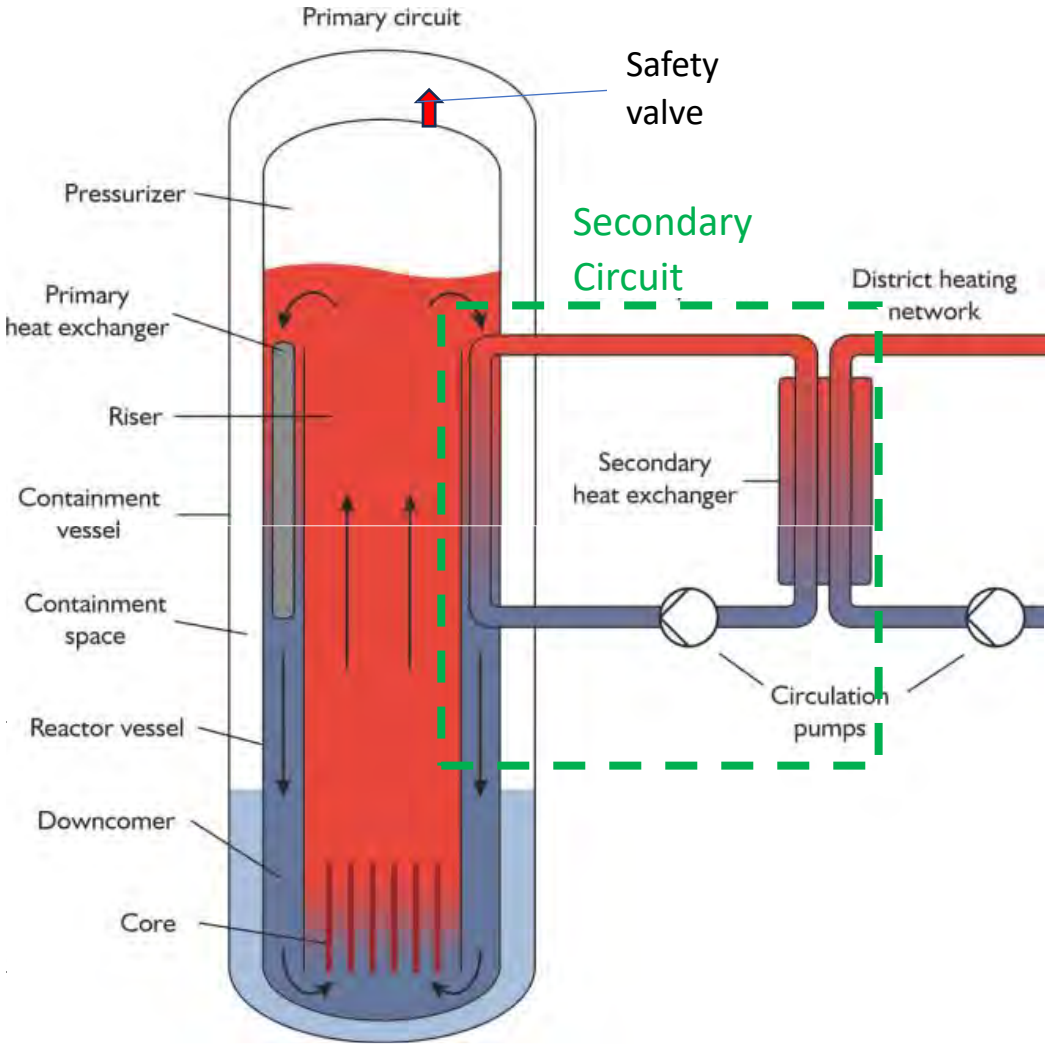

The initiating event (hypothetical assumption) could be clogging of pipes or failure of pump in secondary circuit

Decrease of Secondary Water Flow Analysis (2)

Water flowrate in secondary circuit

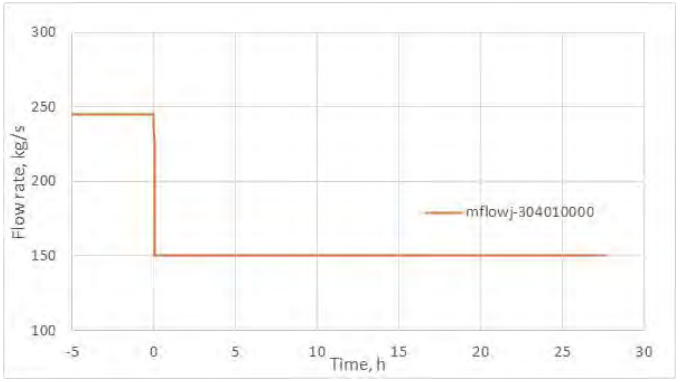

Water temperature in secondary circuit

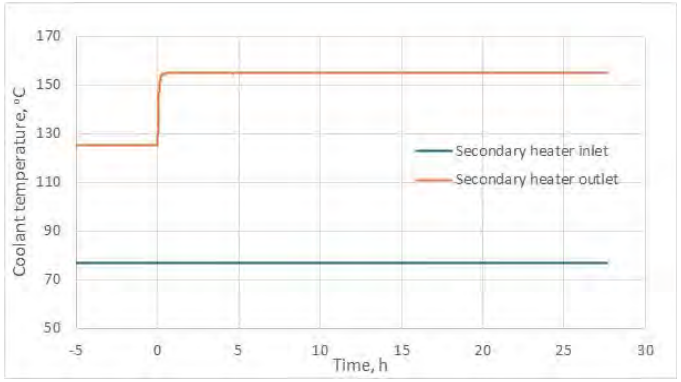

Heat removal through heat exchanger in secondary circuit

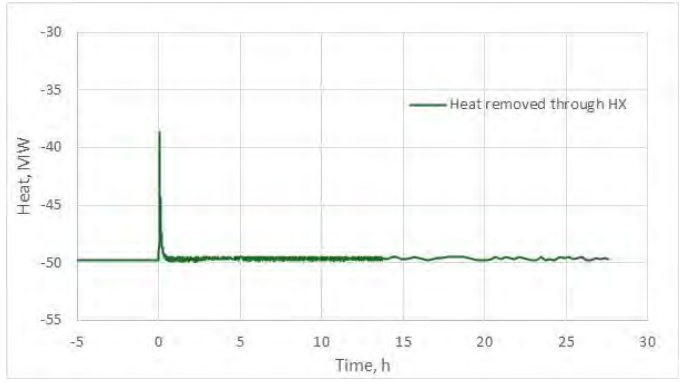

Increase of coolant temperature in primary circuit

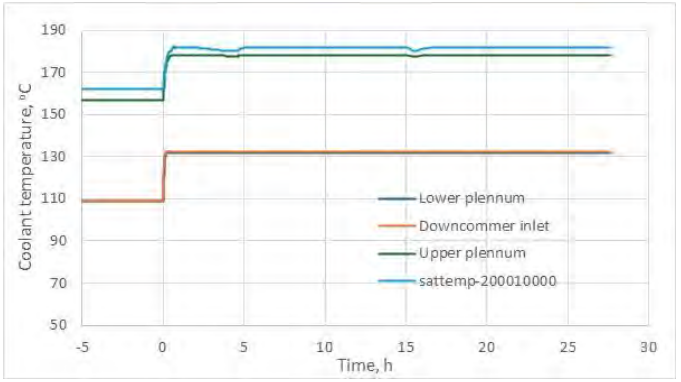

Coolant flow rate through reactor core

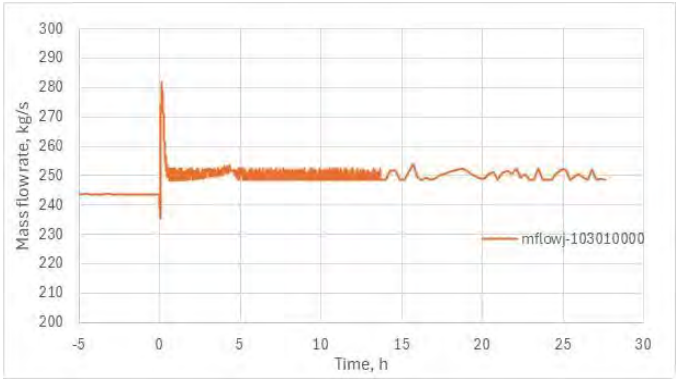

Increase of pressure in primary circuit

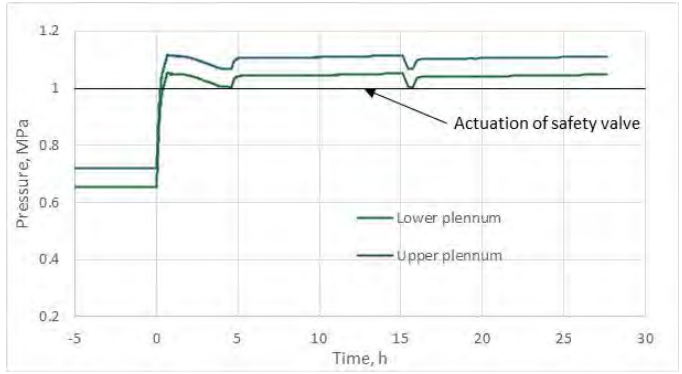

Decrease of Secondary Water Flow Analysis (3)

Release of coolant from pressuriser through safety valve

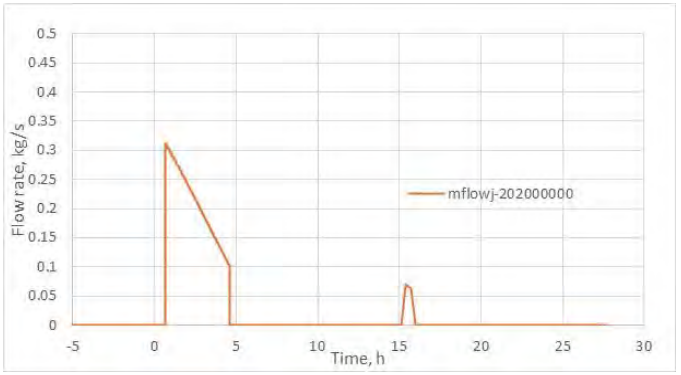

Increase of pressure in containment

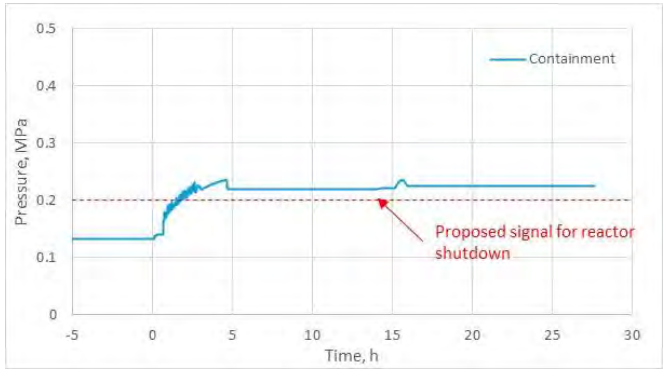

Behaviour of water level in primary circuit and in containment

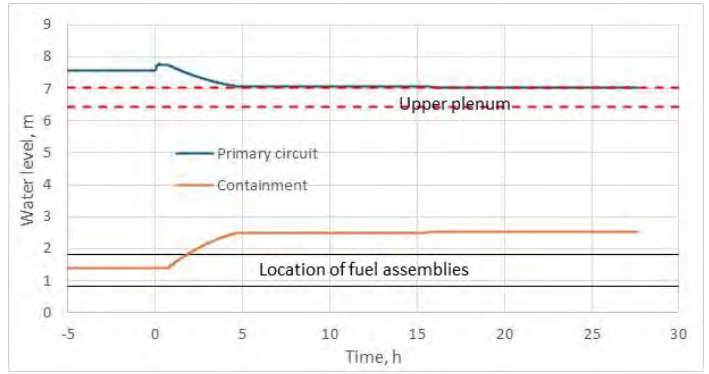

Heat transfer into water pool

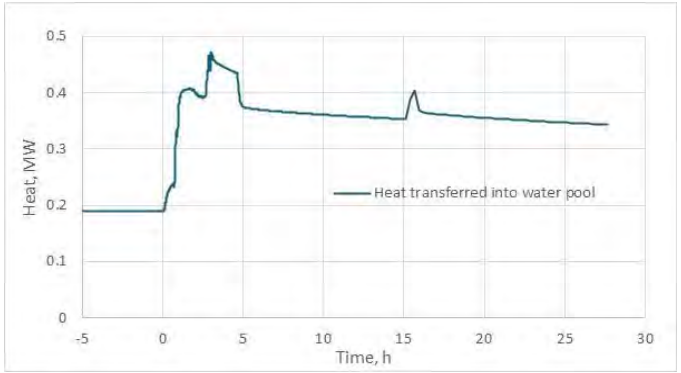

It is shown that the passive safety and self-pressurization systems ensure reactor resilience to design extension conditions even when the heat removal from the reactor to become unbalanced.

Conclusions

To analyse the resilience of LDR Lite reactor three initiating events, which can cause design extension conditions, were modelled:

- SBO
- LOCA
- Reduction of coolant flow in secondary circuit

- The comparison of VTT and LEI results for SBO scenario demonstrated qualitative compliance of parameters and confirms the suitability of the created model.
- The performed analyses of SBO and LOCA demonstrated that after the reactor shutdown the reactor decay heat is transferred into water pool, which ensures safe cooldown of the reactor.
- The analysis of decrease of secondary water flow demonstrated that selected LDR design ensures resilience to interference.
- Even without activation of safety systems, the automatic self-pressurization and mode adjustment is achieved, new steady state is reached, and the reactor is safely operating.

- **The design of reactor, low core power and availability of water pool as an ultimate heat sink, assures the resilience of LDR Lite reactor concept to design extension conditions.**

Acknowledgments

Funded by the European Union under grant agreement No 101164810. Views and opinions expressed are however those of the author(s) only and do not necessarily reflect th ose of the European Union. Neither the European Union no r the granting authority can be held responsible for them.

The authors thank Rebekka Komu (VTT) for assistance in developing the reactor model.

LITHUANIAN ENERGY INSTITUTE

Algirdas Kaliatka

2026-05-18

LITHUANIAN
ENERGY
INSTITUTE

https://www.lei.lt/en

Breslaujos g. 3, Kaunas

monika.inceryte@lei.lt

+37064156542

The 12th European Review Meeting on Severe Accidents Research

May 18-22, 2026, Universidad Carlos III de Madrid, Madrid, Spain

TECHNICAL SESSION: 2.1 IN-VESSEL CORIUM AND DEBRIS COOLABILITY

Chairs: L. Carénini (ASNR), M. Braun (Framatome)

ID143	**Reflooding of a damaged core in case of severe accident: synthesis of experimental results, modelling and consequences for the reactor scale** F. Fichot (ASNR)	Paper Presentation
ID013	**Simulation of the low Prandtl metallic layer of a corium pool** N. Seiler (CEA)	Paper Presentation
ID053	**Analysis of In-Vessel Retention in a VVER-1000 Reactor Design using AC2** P. Pandazis (GRS)	Paper Presentation
ID105	**Towards a High fidelity numerical simulation of In-vessel corium pool under severe accident scenarios** A. Alasif (King Fahd University of Petroleum and Minerals)	Paper

REFLOODING OF A DAMAGED CORE IN CASE OF SEVERE ACCIDENT: SYNTHESIS OF EXPERIMENTAL RESULTS AND MODELLING - CONSEQUENCES FOR THE REACTOR SCALE

Florian Fichot
Autorité de Sûreté Nucléaire et de Radioprotection (ASNR)
PSN-RES/SAM/LEPC, F13115 Saint Paul lès Durance, France
florian.fichot@asnr.fr

ABSTRACT

This paper presents the conclusions of experimental and analytical investigations of the bottom reflooding of debris (particle) beds at high temperature. Particle beds are assumed to be representative of the configuration of a PWR core in the late stages of a severe accident in PWR reactors, as observed after TMI-2 accident. Large scale experiments were performed in the PEARL facility of IRSN (now ASNR), to investigate the effects of water injection flow rate, pressure, particle size and presence of a possible bypass at the periphery. As a complement to experimental measurements, numerical simulations were performed to interpret measured data and experimental observations. One of the important results is the evidence that the coolant flow is not uniform across the debris bed and that the quench front does not propagate uniformly: regions with smaller particles or higher temperature are quenched at a lower rate than other parts of the debris bed and a part of the injected water flows around those critical regions. This may lead to significant delay to quench such zones which may eventually melt before being quenched. In such situations, the coolability of the whole core would be questionable and it may be followed by a progression of the molten pool, even under water. Some criteria leading to unsuccessful reflooding are identified in the paper.

KEYWORDS
Reflooding; damaged core; severe accident; molten pool; debris bed

1. INTRODUCTION

Reflooding of a nuclear reactor core after a Loss of Coolant Accident (LOCA) may occur at different stages of the accident. In case of temporary failure of the safety injection systems, the fuel elements may be strongly damaged or even molten (severe accident) when reflooding occurs. The impact of reflooding on a severely damaged core is quite different from the impact in LOCA situations: temperatures are much higher (above 1500 K and up to 2800 K) and the geometry of fuel elements is lost (the cylindrical rod geometry may have disappeared completely). Both aspects play a significant role during reflooding. First we discuss the geometry of the severely damaged core.

1.1 Geometry of an in-vessel debris bed

When the reactor core is extremely damaged, fuel rods are transformed into debris beds after their collapse. This may result from the quenching of very hot rods during the reflooding of the core, as it was assumed in TMI-2 reactor, above the core molten pool, with debris size of the order of several millimeters (Tolman et al., 1988, Broughton et al., 1989). In those studies, the uncertainties about the thermal hydraulic behavior in the debris bed and the time that was necessary to cool it down were underlined. However, the accurate knowledge of the geometry of the debris bed could never be determined from later experiments, although

debris formation was observed in tests such as LOFT-LP-FP2 (Coryell et al., 1994) and PBF-1.4. The range of variation of the size of the TMI-2 in-core debris and their porosity could be estimated by (Akers et al, 1989). Recently, an analytical approach was used by (Nguyen et al. 2017) who were able to simulate the collapse of a fuel rod assembly which was pre-cracked into fragments. The number of fragments was varied in a range that may be expected for fuel rods with a standard average burn-up. They found that, for loose debris beds, the porosity was near 0.41. It corresponds to the upper parts of 'in-core' debris beds such as the ones observed in TMI-2 or in LOFT-LP-FP2 experiment. When additional damaged structures accumulate above an existing bed, the contact force network changes, the fragments rearrange and the porosity decreases. The calculated cases where compression was applied demonstrated that it is possible to reach a "dense" porosity value of 0.32. Similar values for porosity could be found in lower parts of debris beds (Akers et al., 1986). Together with the decrease of the porosity, the rearrangement of fuel fragments also implies a decrease of the surface in contact with the coolant flow, due to a greater proportion of face-face contacts. It was found that the specific surface area can be reduced by about 5% by compression, which is not much. In addition, the work of (Nguyen et al. 2017) made a link between the variations in geometry which were calculated here and the coolability of the debris bed. A model was used to correlate directly the parameters such as porosity and mean Sauter diameter to the fluid behavior in the porous medium. The model gave average values for permeability of 7.10^{-9} m^2, with an uncertainty range of 30% and values for the passability of 14.10^{-5} m, with an uncertainty range of 15%. If the debris bed is compressed, both values are divided by 2, approximately. Considering that, in a damaged core, assemblies with different burn-up and lineic power would be present, those results indicate that a large debris bed will be non-homogeneous in permeability and passability and that it is reasonable to consider that the uncertainties on those parameters correspond to the range estimated above. But the most significant non-homogeneity is the possible presence of intact rods, as observed at the periphery of the TMI-2 core (Tolman et al., 198, Broughton et al., 1989). This corresponds to regions where the permeability/passability would be approximately 100 times larger than in the particle bed: this is a very large contrast which has a direct impact on the flow, as it will be shown in the next sections of this paper.

1.2 Objectives of the paper

The objective of this paper is to make a synthesis of experimental and analytical results obtained in situations of reflooding of a debris bed and, from that understanding, to analyze some trends that can be expected at the reactor scale. This brings conclusions about the efficiency or success of reflooding, depending on the stage of degradation (porosity, homogeneity, timing) and on the available water sources to inject water (flow rate). It is important to mention that the details of derivation of models and their validation are not presented in this paper but are extensively provided in the papers and reports indicated in references. This paper just recalls them in order to address the extrapolation to reactor scale with credibility.

In the first part, we examine the simplest configuration of a homogeneous debris bed (porosity, particle diameter), from analytical and experimental points of view. This brings first conclusions about the efficiency of reflooding and about the existence of spatial instabilities which appear spontaneously and lead to reduce the efficiency of cooling. In the second part, we investigate a more realistic configuration of a debris bed divided in two zones with different porosities and particle diameters. This shows that a significant part of the inlet water flow may be diverted to the most porous debris bed, reducing significantly the efficiency of cooling in the less porous debris bed. This is observed both experimentally and in models/calculations. Finally, using the validated modelling approach, we examine the situation of a debris bed surrounded by intact rods, over a significant height of the reactor core. Series of calculations provide some trends for the time to completely quench the debris bed before it reaches the melting temperature: this gives the range of conditions for which an in-vessel reflooding could be considered as successful. A short discussion about the generalization of those results is added as a conclusion.

2 HOMOGENEOUS DEBRIS BED: ANALYSIS OF 1D REFLOODING AND

EXPERIMENTAL RESULTS

Reflooding tests with homogeneous debris beds were carried out in the PRELUDE facility of IRSN at atmospheric pressure. Published experimental results and analyses with the ICARE/CATHARE code can be found in (Fichot et al. 2012, Repetto at al. 2013 and Bachrata et al. 2013). The phenomenology of PRELUDE tests with water injection from below a homogeneous debris bed (no bypass or more compact zone) was analyzed in (Fichot et al. 2012) and more details can be found in (Bachrata 2012, Ph.D. thesis). The main learnings and conclusions of those studies are provided in this section. There are two important characteristics of the quench front progression:

- The quench front is flat (1D) in several cases, within the range of experimental parameters tested, but several cases also show a curved front (2D). When the front is curved, it moves faster at the periphery than at the center.
- Despite the spatial non-uniformity of the front, the progression seems to remain quasi-steady overall, and an average speed of progression can be determined. A relatively short unsteady phase is observed at the beginning. This is particularly visible in steam production.

This rather simple behaviour when the front is 1D allows the derivation of a simple model which is presented in the next subsection.

2.1 Mass and energy balances for a simplified 1D model

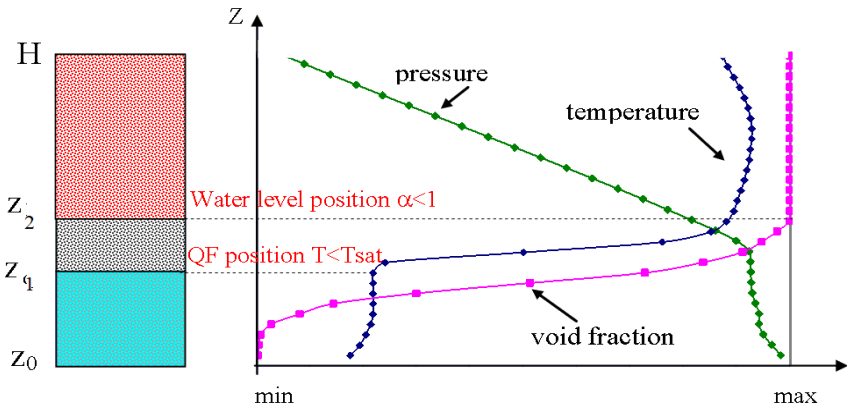

Integrating the mass and energy equations between the bottom (z_1) and the top (z_2) of the two-phase zone, that is to say, by taking a balance over the height, and assuming that this zone propagates in a quasi-steady manner (velocity U_q and height (z_2- z_1) constant), we arrive at the following two relations:

$$\rho_g\left(j_g(z_2) - U_q\right) = \rho_l\left(j_l(z_1) - U_q\right)$$

$$\rho_g\left(j_g(z_2) - U_q\right)\left(h_g^{\{sat\}} + Cp_g\Delta T_g\right) + (1-\varepsilon)U_q\rho_s Cp_s\Delta T_s = \varepsilon\rho_l\left(j_l(z_1) - U_q\right)\left(h_l^{\{sat\}} + Cp_l\Delta T_l\right)$$

This amounts to verifying the conservation of water mass in the frame of reference moving at velocity U_q and stating that all the energy lost by the particles is used to evaporate the liquid and raise the gas temperature to T_{max} (we could also have assumed that the gas exits at T_{sat}, which slightly alters the balance). In what follows, we will neglect the effect of water subcooling (the term $Cp_l\Delta T_l$ is negligible compared to Δh_{sat}).

Combining these two equations gives a relationship between the velocity of the front U_q and the injection velocity $j_l(z_1)$:

$$U_q = j_{inj} \frac{\varepsilon\rho_l\left(\Delta h_{sat} + Cp_g\Delta T_g\right)}{(1-\varepsilon)\rho_s Cp_s\Delta T_s + \varepsilon\rho_l\left(\Delta h_{\{sat\}} + Cp_g\Delta T_g\right)}$$

We thus see the emergence of an essential parameter of reflooding, which we denote γ_E, the ratio between the energy initially stored in the solid and the maximum energy that the surrounding fluid can remove (if it does not move).

$$\gamma_E = \frac{(1-\varepsilon)\rho_s Cp_s\Delta T_s}{\varepsilon\rho_l\left(\Delta h_{sat} + Cp_g\Delta T_s\right)}$$

We can then simply express the equation which relates the front velocity to the injection velocity:

$$\gamma_u = \frac{U_q}{u_{inj}} = \frac{1}{1+\gamma_E}$$

In the preceding expression, we assumed that $j_{inj} = u_{inj}$, that is, that the void fraction $\alpha \approx 0$ upstream of the front, which is not necessarily the case when the residual power is not negligible (especially when the quench front is slow).
Combining this with the mass conservation equation, we find the proportionality relationship between the inlet water flow rate and the outlet steam flow rate:

$$\rho_g\, j_{g(z_2)} = \frac{\rho_l u_{inj}\,\gamma_E}{1+\gamma_E}\left(1-\frac{\rho_g}{\rho_l}\right)$$

Thus we get an expression for the ratio γ_Q between the produced steam and injected water flow rates:

$$\gamma_Q = \frac{\gamma_E}{1+\gamma_E}\left(1-\frac{\rho_g}{\rho_l}\right)$$

Figure 1 shows the values given by the equation for γ_Q by varying the initial temperature difference of the particles relative to the saturation temperature. Two assumptions are made: either $T_g = T_{max}$ at the two-phase zone exit, or $T_g = T_{sat}$. The latter assumption is less realistic because the vapor reaches thermal equilibrium with the particles quite quickly. With the first assumption, it is clear that the conversion rate tends towards an asymptotic value and that the results obtained from tests at 2500 °C would give a conversion rate only slightly higher than that obtained for tests at 900 °C. Therefore, PRELUDE tests are representative of much higher temperature cases (from a thermal hydraulic point of view).

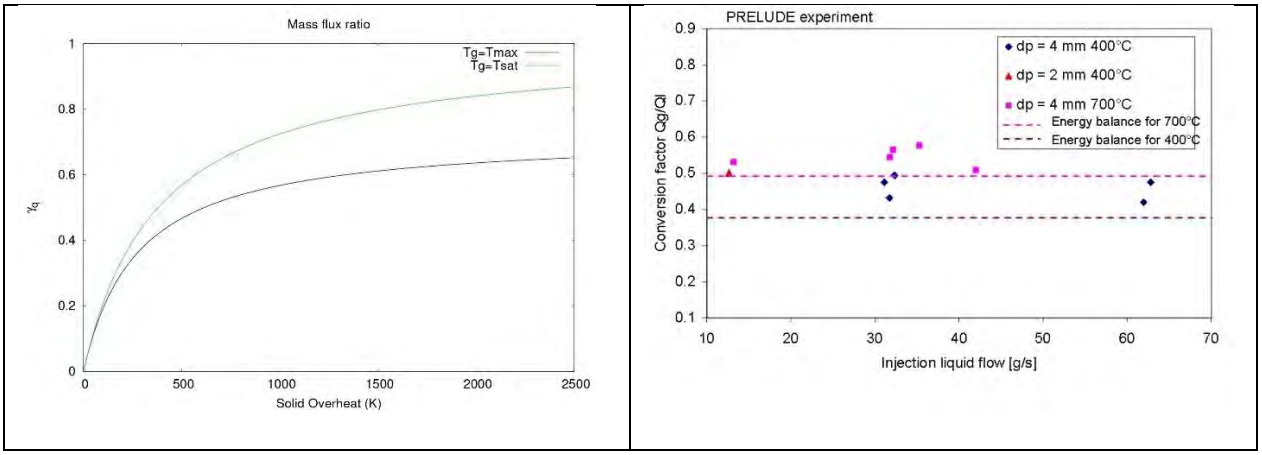

Figure 1: Ratio of steam produced to water injected, as a function of initial overheat of particles	*Figure 2: Conversion rate as a function of inlet flow rate (experimental data and model prediction)*

2.2 Steam production

The equation for γ_Q shows that, to a first approximation, the water-to-steam conversion rate does not depend on the debris diameter, nor, more generally, on the permeability or passability of the debris bed. This result appears to be partially confirmed by experimental measurements of the steam flow rate for particles of different diameters, as shown in (Bachrata et al., 2012), when comparing to the maximum value reached. However, for small particles (2mm and 1mm), there was no plateau observed after reaching the maximum value, which therefore limits the interpretation made with a steady-state model. The absence of a plateau may be due to the presence of water above the bed shortly after the start of reflooding.
The conversion rate given by the simplified approach is also independent of the water injection rate. This is confirmed by the experimental results in Figure 2. However, it can also be seen that the measured conversion rate is higher than the theoretical conversion rate. A similar discrepancy had already been observed in experiments conducted at Brookhaven National Laboratory (BNL) by (Tutu et al., 1984). This means that some of the assumptions made are not verified. In particular, it cannot be verified that the thickness of the two-phase zone is constant or that the gas exits this two-phase zone at T_{max}.
Calculations with a more detailed model implemented in ICARE/CATHARE (and presented in (Fichot et al. 2012) show that the proportionality to the injection rate and the quasi-steady-state behavior with a plateau are indeed observed for some tests. However, not all tests exhibit a well-defined plateau. As the speed increases, the peak produced during the initial phase has a predominant effect, especially as the duration of the plateau phase decreases.

2.3 Velocity of progression of the quench front

The relation for γ_u is shown in Figure 3. Two assumptions were again made regarding the steam temperature at the outlet of the two-phase zone. As with the flow rate ratio γ_q, the velocity ratio does not tend towards zero but towards an asymptotic value and varies very little beyond $T_{max} = 1000$°C. Therefore, the figure is limited to the temperature range corresponding to the tests performed.

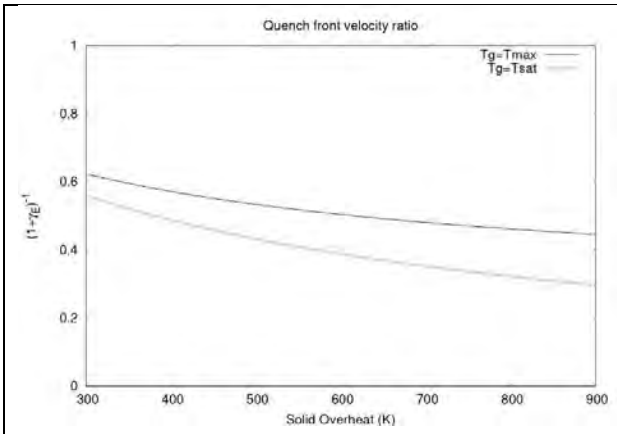

Figure 3: Ratio of quench front to inlet velocities as a function of initial overheat of particles

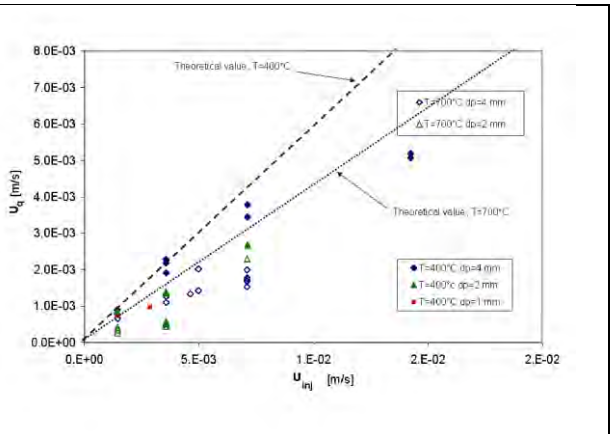

Figure 4: Quench front velocity as a function of inlet velocity (experimental data and 1D model predictions

From experimental measurements, the propagation speed of the quenching front can also be estimated. This is done by measuring the time interval between the arrival of water at the bottom of the bed and the moment

a thermocouple measures the value T_{sat} plus a few degrees. The results presented in Figure 4 show the degree of uncertainty in the evaluation of this speed. The ratio between the two speeds differs quite significantly from the theoretical value given above. This can be explained firstly by the uncertainty of the evaluation based on the thermocouple measurements. It may also indicate that the boundaries z_1 and z_2 of the two-phase zone do not progress at the same speed (which was assumed to be identical to the quench front speed U_q)

The quasi-steady progression is a remarkable result. However, it provides little information for modeling, since we have seen that it leads to finding the solution to the problem simply from the fluid mass balance and the energy balance of the debris bed. To go further in the analysis and in the validation of the models, it is necessary to study transient phases or more complex geometries such as non-homogeneous particle beds, which is done in the next section.

To conclude, **the 1D approximation of the front moving at constant speed is a valid representation when seeking a rapid assessment of the front progression and its consequences on steam production and on the pressure gradient in the debris bed**. In particular, it allows assessing the potential for fluidization of the debris bed.

The 1D approximation of the front moving at constant speed has its limitations. Among these limitations, we have already mentioned the curvature of the front (which increases with the pressure gradient generated by the steam flow). Some of those limitations disappear when using the two-phase flow model, as in (Bachrata et al., 2012).

3 NON-HOMOGENEOUS DEBRIS BED: ANALYSIS OF 2D REFLOODING AND EXPERIMENTAL RESULTS

2D reflooding was investigated in the PEARL facility (Chikhi & Fichot, 2017, Chikhi et al., 2017) at IRSN. The damaged part of the core is represented by a bed of spheres which are heated in order to simulate residual power. This debris bed is surrounded by an area representing a less damaged zone, such as remaining fuel assemblies. The scale of the experiment was approximately 1/8 of the reactor scale. The main results obtained from those experiments are presented below.

One of the main results is the effect of water entrainment in the bypass channel, which occurs under some conditions and affects the timing of quenching as well as the temperature of steam at the outlet. Indeed, the direct application of the 1D model for the conversion rate shows that it provides a good prediction only when the injection flow rate is low or when the temperature of the bed is low. If the temperature is higher or the injection velocity is higher, the conversion ratio is over predicted. This, together with temperature measurements indicated that the increase in steam production leads to a deviation of a part of the injected liquid into the bypass, where it is not converted into steam and flows up to the top of the particle bed, as observed in the temperature measurements in the bypass (which remains at saturation temperature).

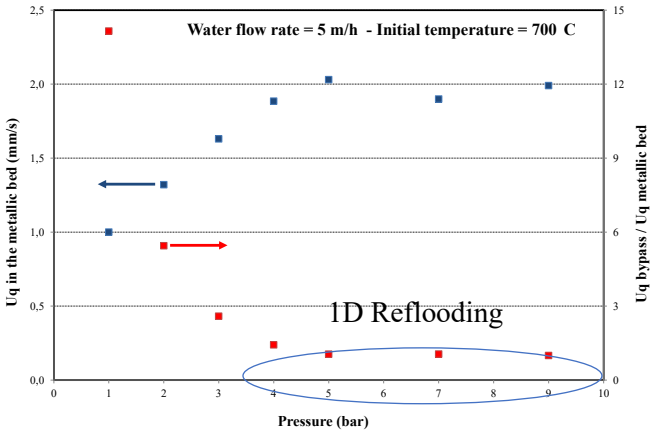

Figure 5: Effect of pressure on the quench front velocity (experimental data, Mutelle et al. 2017)

The quench front velocity in the heated bed and the ratio of QF velocities in the bypass and in the metallic bed are plotted as a function of pressure in Figure 5. It shows that the reflooding time tends first to decrease with increasing pressure then is rather constant when the pressure is above 4-5 bar. At high pressure, the QF velocities in the bypass and in the central bed are identical, indicating that the upward flow of water is one-dimensional. Conversely, when the pressure decreases below 4-5 bar, the ratio between the QF velocities increases. Thus, the reflooding switches from one-dimensional to two-dimensional. In 2D cases, the water outflow from the bypass, before the end of complete quenching is confirmed by the video recordings.
Despite the presence of water above the bed, it is worth noticing that the flow rate of steam is large enough to maintain a counter-current flow limitation and thus to preclude water ingression from the top of the bed. From the experimental data and the calculations, it appears that the entrainment of water probably depends on a threshold value of the axial pressure gradient generated in the debris bed by the intense flow of steam. Below this threshold, the progression of the quench front is uniform across the section and the phenomenon is 1D. Above this threshold, water submitted to a large pressure gradient is able to move at a faster velocity than the injection velocity, in the bypass region. This leads to an accumulation of water above the debris bed before its complete quenching. It is interesting to notice that the bypass actually emphasizes the instability of the quench front velocity already observed in the 1D tests (PRELUDE).

According to these results, the exact values of the thresholds could not be yet exactly identified (neither from the experimental data nor from the calculations) because it depends on several coupled parameters: the injection velocity, the maximum temperature in the debris bed, the pressure, and the aspect ratio of the bed and bypass. But the existence of two different reflooding situations, the 1D and the 2D, is clear from the experiment and is confirmed by the calculations.

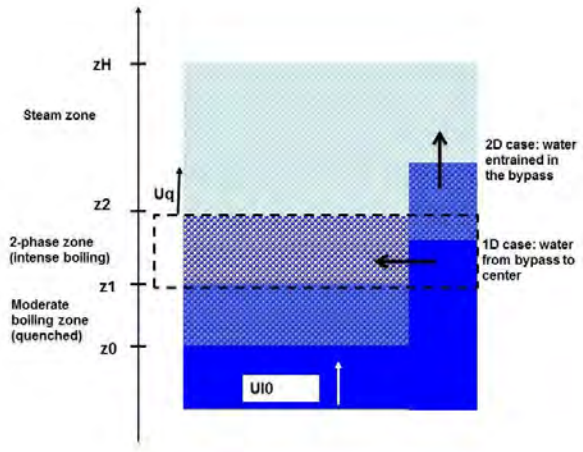

Figure 6: scheme of the liquid flow distribution with a lateral bypass

In order to adapt the simplified 1D approach to the 2D cases, we consider the schematical flow represented in Figure 6: the central bed and the bypass are considered as parallel 1D channels. Mass transfers of steam or water are possible between the channels and are calculated from radial pressure differences. We introduce a parameter characterizing the relative cross section of the center bed, weighted by the permeabilities:

$$R_{lb} = \frac{S_c + S_b}{S_c \frac{K_c}{K_b} + S_b}$$

At this point, we introduce also an empirical parameter k_{ent} representing the fraction of water flow entrained in the bypass. In 1D cases, this parameter is set to 0 and for 2D cases, it is assumed to increase linearly when the pressure decreases or when the velocity increases. The threshold for 1D/2D transition is

taken from experimental data. Obviously, this parameter has more complex variations than the proposed empirical variations, but the purpose of the approach presented in this paper is to remain simple and address only the main effects of the presence of the bypass.
In a similar way as for the 1D case, the quench front velocity ratio γ_u is derived:

$$\gamma_u = \frac{U_q}{u_{inj}} = \frac{1}{1+\gamma_u} + \frac{(1 - R_{lb}k_{ent})}{1+\gamma_u}\frac{S_b}{S_c}$$

From that equation, it appears that **the quench front is faster than without bypass when the entrained fraction of water in the bypass is low (high pressure cases)** because some water flows from the bypass into the central bed. But **it may become slower if the entrained fraction is high**. This evaluation was compared favorably with experimental data in (Mutelle et al, 2017), where the linear decrease of QF velocity was also found in the experiment. The maximum QF velocity ratio predicted by the model is 0.52 which corresponds to a velocity of 1.8mm/s, close to the experimental measurement (2mm/s).
For the conversion ratio, we get:

$$\gamma_q = \frac{\rho_g u_{gc}(z_2)S_c + \rho_g u_{gb}(z_2)S_b}{\rho_l u_{inj}(S_c + S_b)} = \frac{\gamma_u}{1+\gamma_u}\left(1 - k_{ent}R_{lb}\frac{S_b}{S_c + S_b}\right)$$

From that equation, it appears that **the conversion ratio is always lower than or equal to the value without bypass** because of the entrained fraction of water in the bypass. If we apply this formula over the range of parameters corresponding to PEARL experiments, the maximum conversion ratio starts at 0.64 (at highest pressure and lowest temperature) and it decreases down to 0.38 (at 1bar and highest temperature). This is close to the experimental results obtained in the PEARL tests, as presented in (Mutelle et al., 2017).
In parallel with those simple evaluations, intensive validation of the 2D two-phase model were made, by comparison with PEARL data. Validation was made for ICARE/CATHARE model (Chikhi et al. 2017) and for MC3D model (Mutelle et al. 2017, Raverdy et al. 2017). Both models are rather similar. Validation of a comparable 2D model in ASTEC code was made by (Gómez et al., 2021)

Those observations and conclusions are important to evaluate the consequences of accident management by injection of water in the core. **The 1D reflood is more efficient** because all the water entering the central bed is used to cool down the debris whereas, **in case of 2D reflood**, a part of that water is diverted into the bypass and accumulated at the top of the bed. However, **the presence of water on top of the debris bed before complete quenching leads to decrease the temperature of steam above the bed which is a good point** for the integrity of the top part of the vessel and of the hot leg of the primary circuit.
At this point, it is possible to also draw some conclusions about the analytical approaches that can be used to evaluate the impact of reflooding at the reactor scale. From the analyses of the reflooding experiments with homogeneous debris beds (PRELUDE) and non-homogeneous debris beds (PEARL), two main outcomes were obtained on the analytical side: (i) a simple model to predict the quench front velocity and conversion ratio (water to steam) and (ii) the validation of a general multi-dimensional model for two-phase flow in a debris bed (implemented in ICARE/CATHARE code). The simple model catches the effect of inlet flow redistribution into higher permeability bypass and helps explain this process, which is driven partly by the imbalance of pressure between the central debris bed and the bypass and partly by the interfacial friction between water and steam flowing at high velocity. Nevertheless, the simple approach has a limited accuracy and requires an empirical parameter: it cannot be used in all configurations. **Therefore, the recommended approach for reactor scale evaluations is to use a 2D two-phase model**.

4 APPLICATION TO REACTOR SCALE

The flowrates considered in PEARL cover a range of water velocity from 2 to 20m/h. In a reactor where the vessel diameter is typically 4m, this corresponds to a volumetric flowrate of 24m3/h to 240m3/h or a mass

flowrate of 6kg/s to 60kg/s. Those are rather low flowrates compared to a low-pressure safety injection but are comparable to injection flow rates of mobile devices that are currently considered for "ultimate" SAM actions, for which the maximum flow rate is higher than 100kg/s. The pressures considered in PEARL cover a range from 1 to 9bar which is typical of the ranges of pressure reached in severe accident sequences when the pressure release valves are open. The temperature of the bed in PEARL is lower than in the reactor where debris would be in the range 1500K-2500K. The melting of debris occurs between 2500 and 2900K. A debris bed formed in the core could have a height between 1m (TMI2 case) and up to 2m if we consider that the top half of the core is severely damaged before reflooding.
In order to define a realistic reactor case, it is considered that fuel rods have collapsed into a debris bed at the upper part of the assemblies (1m high), over a cross section representing 85% of the total area of the core. Therefore, there is a bypass at the periphery, covering 15% of the total area (compared to 30% in PEARL). The permeability of that bypass is more than 10 times higher than the permeability of the central bed. We assume a rather high residual power of 200 W/kg, and a porosity of 0.39. The rest of the reactor conditions are specified in Table 1.

To investigate the coolability limits of a debris bed formed inside the core region, the ICARE/CATHARE code was used, describing the debris bed and the bypass as 2D, axisymmetric zones. Sensitivity studies are made for 4 parameters. For each calculation, we compare the time to reach total quenching with the "virtual" time to reach melting in the debris bed (in the calculations, debris can reach temperatures above their melting point)
The impact of debris temperature on the coolability limit is shown in Figure 7. The dependency is almost linear: a higher temperature decreases the velocity of the quench front (almost linearly, as in the 1D model) and strongly decreases the time to reach melting. In the present case, the threshold temperature is 2500K. Even if the debris are initially at a rather low temperature (around 1500K), the margin for cooling is only 1 hour. Therefore, it appears that **the main issue with the quenching of debris beds is not necessarily their low permeability but, first of all, their high temperature which lets very little time margin to reflood the core**.

The impact of injection velocity on the coolability limit is shown in Figure 8. It shows that there is a critical value below which the flow rate is insufficient to quench the debris bed before melting: this is quite obvious. But it also shows that **there is not much benefit increasing the flow rate up to high values** because it does not reduce significantly the quenching time: this result was confirmed experimentally in (Chikhi et al. 2017). The critical value, in the present case, is around 5mm/s which corresponds approximately to a mass flow rate of 200 t/h for a high power PWR. **Such flow rate can be delivered easily** by a low-pressure safety injection pump or by the Chemical and Volume Control System (CVCS) or a by fire pump.

The impact of porosity on the coolability limit is shown in Figure 9. In the present case, the threshold porosity is around 25-30%: this is close to the value that can be reached if the debris bed is strongly compressed (i.e. 28% in the study of (Nguyen et al., 2017)), Such low porosity could exist at the bottom of the debris bed, and it might even be lower if relocated metal melt is present. The dependency with porosity is very non linear and we see that it is almost impossible to quench a region where the porosity is lower than 15% (2h would be necessary). **As a conclusion, we may expect that some regions of the debris bed, in particular the bottom part, may melt before quenching (even if the top part iss quenched).**

The impact of the relative cross-section of the central bed on the coolability limit is shown in Figure 10. It shows that if the central bed occupies less than 50% of the total area, it cannot be quenched before melting. This is amplified as the relative cross section decreases. This result may seem unphysical at first sight but it is explained by the decrease of the pressure gradient in the bypass when the central bed cross-section decreases: for a central bed with a small radius, the vertical pressure gradient becomes close to hydrostatic (0.1 bar/m) which is small compared to the pressure gradient generated by a direct injection with a pump (in case of homogeneous debris bed covering the whole cross section of the core). This shows that, **in case**

of a debris bed occupying only a limited part of the total cross section, the permeability becomes the limiting parameter for the quenching time. It is the effect of the parameter that we defined as R_{lb}.

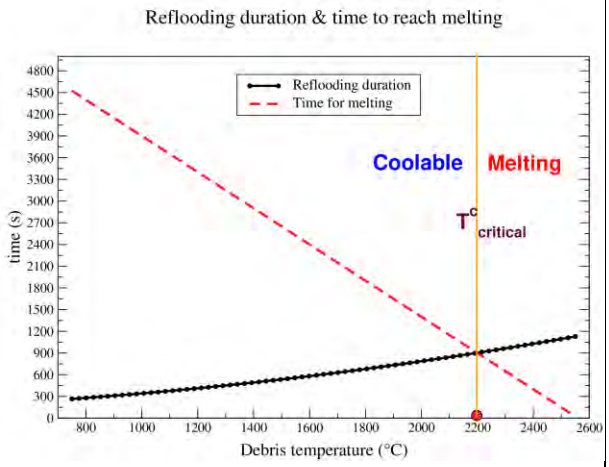

Figure 7: Comparison of reflooding and melting times as a function of initial temperature

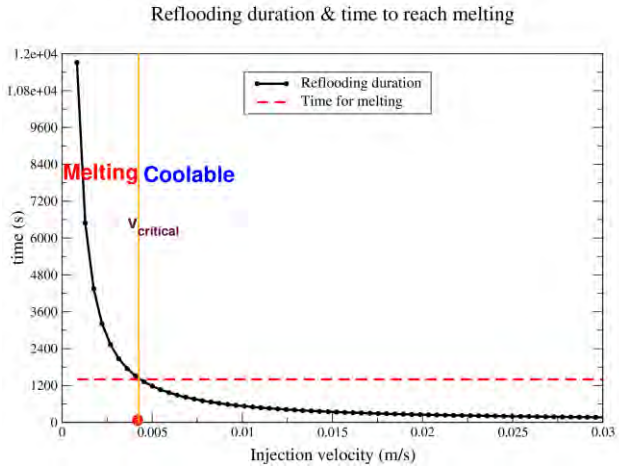

Figure 8: Comparison of reflooding and melting times as a function of injection velocity

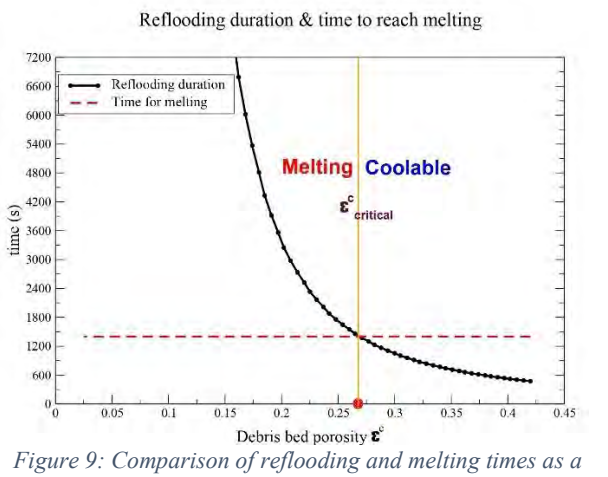

Figure 9: Comparison of reflooding and melting times as a function of debris bed porosity

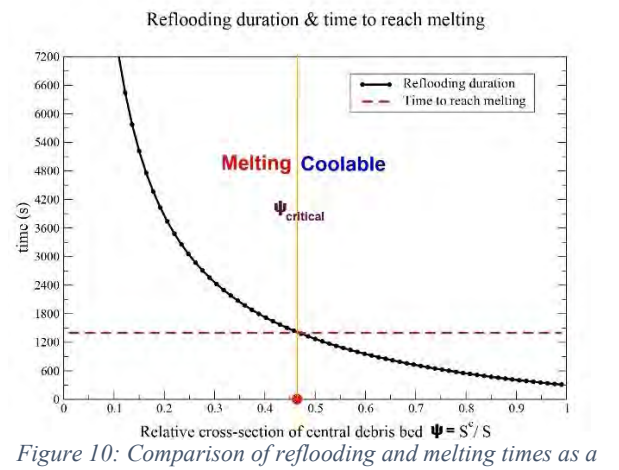

Figure 10: Comparison of reflooding and melting times as a function of relative cross-section of central debris bed

5 CONCLUSIONS

The large series of experiments performed at IRSN, for homogeneous debris bed in the PRELUDE facility and for non-homogeneous debris bed in the PEARL facility, have provided data to validate two-phase flow models able to simulate the reflooding of 2D debris bed.
In parallel, the analysis of results with simple approaches and with 2D simulations have provided an understanding of the behavior of water and steam during reflooding, in particular the phenomena of water entrainment between regions with different porosities/permeabilities.
Extrapolations at the reactor scale and for severe accident conditions lead to the following conclusions:

- The time to successfully quench the whole damaged core, at a late stage where debris have formed, is quite short: approximately 20 to 60 minutes in the realistic case studied in this paper, which

means that the probability of recovering a safety injection during this time frame is very low (considering that a severe core damage occurs only when all water sources are lost for some time)

- A minimum injection flow rate is necessary but increasing this flow rate does not lead to a significant reduction in total quenching time: low porosity/permeability regions are not sensitive to the flow rate. This means that it is very likely that some parts of the core would be quenched while other parts would melt, in spite of the core reflooding.
- It is likely that the core region would be covered by water quickly after reflooding starts (even if some parts remain unquenched): the benefit of this situation is that steam entering the hot leg would be rather cold. This means that reflooding would not induce heating and mechanical failure in the circuit or steam generator tubes.

As a conclusion, if water is injected in the core at a late stage, when the core is already severely damaged, it is expected that only a part of the core can be quenched while other parts will melt. Nevertheless, this will have several benefits and very few drawbacks. The drawbacks are: a hydrogen production peak (likely to be comparable to the early degradation phase) and a containment pressure peak, comparable to what is expected in a LOCA sequence. The benefits are: a decrease of temperatures in the hot leg (preventing mechanical failure) and the stabilization of some part of the fuel within the core region. This last point makes it easier to stabilize the molten corium, either in the lower plenum of the vessel, or ex-vessel.

6 NOMENCLATURE and REFERENCE VALUES

Table 1: List of variables and their values in experiments and reactor case

description	variable	Exp. range	Reactor case
water velocity at inlet	u_{inj}	2-20 mm/s	11 mm/s
quench front velocity	U_q	m/s	m/s
volumetric flow rate	j	2-20 mm/s	mm/s
initial temperature of particles	T_s	400-900 °C	2000 °C
Residual power per unit of mass	Q_{res}	100-300 W/kg	200 W/kg
porosity of the bed	ε	0.39	0.39
permeability of the bed	K	10^{-9} -10^{-8} m^2	10^{-8} m^2
outlet pressure	P_{ext}	1-9 bar	3 bar
height of debris bed	H	0.2-0.5m	1m
diameter of particles	d_p	1-2-4 mm	3 mm
Density of particles	ρ	7800 kg/m3	8000 kg/m3
heat capacity of particles	Cp	J/kg/K	J/kg/K
latent heat of vaporization of water	Δh_{sat}	J/kg	J/kg

7 ACKNOWLEDGMENTS

ICARE/CATHARE calculations and some parts of the analysis of experimental data were done during the Ph.D. theses of (Andrea Bachrata, 2012) and (Ali Swaidan, 2018).

8 REFERENCES

1. E.L. Tolman, P. Kuan, J.M. Broughton, TMI-2 accident scenario update, Nuclear Engineering and Design, Volume 108, Issues 1–2, 1988, https://doi.org/10.1016/0029-5493(88)90055-6
2. Broughton, J. M., Kuan, P., Petti, D. A., & Tolman, E. L. (1989). A Scenario of the Three Mile Island Unit 2 Accident. *Nuclear Technology*, *87*(1), 34–53. https://doi.org/10.13182/NT89-A27637

3. Coryell, E.W., Akers, D.W., Allison, C.M., Carboneau, M.L., Hobbins, R.R., Hohorst, J.K., Jensen, S.M., Modro, S.M., 1994. Summary of Important Results and SCDAP/ RELAP5 Analysis for OECD LOFT Experiment LP-FP-2, U.S. Nuclear Regulatory Commission, NUREG/CR-6160, EGG-2721
4. Petti, D.A., Martinson, Z.R., Hobbins, R.R., Allison, C.M., Carlson, E.R., Hagrman, D.L., Cheng, T.C., Hartwell, J.K., Vinjamuri, K., Seifken, L.J., 1989. Power Burst Facility (PBF) Severe Fuel Damage Test 1–4 Test Results Report, U.S. Nuclear Regulatory Commission, NUREG/CR-5163.
5. Akers, D.W., Carlson, E.R., Cook, B.A., Ploger, S.A., Carlson, J.O., 1986. TMI-2 core debris grab samples- Examination and analysis, Sandia National Laboratory, GEND-INF-075
6. Nguyen, D. H., Fichot, F., & Topin, V. (2017). Investigation of the structure of debris beds formed from fuel rods fragmentation. Nuclear Engineering and Design, 313, 96–107. https://doi.org/10.1016/j.nucengdes.2016.11.019
7. Fichot, F., Bachrata, A., Repetto, G., Fleurot, J., & Quintard, M. (2012). Quenching of a highly superheated porous medium by injection of water. *Journal of Physics: Conference Series*, *395*. https://doi.org/10.1088/1742-6596/395/1/012144
8. Repetto, G., Garcin, T., Eymery, S., & Fichot, F. (2013). Experimental program on debris reflooding (PEARL) - Results on PRELUDE facility. Nuclear Engineering and Design, 264, 176–186. https://doi.org/10.1016/j.nucengdes.2012.11.024
9. Bachrata, A., Fichot, F., Repetto, G., Quintard, M., & Fleurot, J. (2013). Quench Front Progression in a Superheated Porous Medium: Experimental Analysis and Model Development. Journal of Energy and Power Engineering, 7, 514–523
10. Bachrata, A. (2012). *Modélisation du renoyage d'un cœur dans le cas d'un réacteur fortement dégradé* [Université de Toulouse]. https://theses.hal.science/tel-04274113
11. Fichot, F., Duval, F., Trégourès, N., Béchaud, C., & Quintard, M. (2006). The impact of thermal non-equilibrium and large-scale 2D/3D effects on debris bed reflooding and coolability. Nuclear Engineering and Design, 236(19–21), 2144–2163. https://doi.org/10.1016/j.nucengdes.2006.03.059
12. N.K. Tutu, T. Ginsberg, J. Klein, J. Klages, and C.E. Schwarz. "Debris bed quenching under bottom flood conditions", Technical Report NUREG/CR-3850, Brookhaven National Labs., 1984.
13. Tung, V. X., & Dhir, V. K. (1987). Quenching of debris beds having variable permeability in the axial and radial directions. Nuclear Engineering and Design, 99(C), 275–284. https://doi.org/10.1016/0029-5493(87)90127-0
14. Chikhi, N., & Fichot, F. (2017). Experimental and theoretical study of large scale debris bed reflood in the PEARL facility. Nuclear Engineering and Design, 312, 48–58. https://doi.org/10.1016/j.nucengdes.2016.05.009
15. Chikhi, N., Fichot, F., & Swaidan, A. (2017). Effect of water entrainment on the coolability of a debris bed surrounded by a by-pass: Integral reflood experiments and modelling. Annals of Nuclear Energy, 110, 418–437. https://doi.org/10.1016/j.anucene.2017.06.033
16. Mutelle, H., Fichot, F., & Piar, L., Reflooding of Large Scale Debris Bed with Bypass: Effect of Pressure and Water Flowrate. *Proceedings of Nureth-17* conference, (2017).
17. Raverdy, B., Meignen, R., Piar, L., Picchi, S., & Janin, T. (2017). Capabilities of MC3D to investigate the coolability of corium debris beds. Nuclear Engineering and Design, 319, 48–60. https://doi.org/10.1016/j.nucengdes.2017.04.005
18. Gómez-García-Toraño, I., Laborde, L., Fichot, F., & Mutelle, H. (2022). *Reflooding of degraded cores in ASTEC V2 . 1 : Modelling and validation on PEARL experiments*. *393* (2021). https://doi.org/10.1016/j.nucengdes.2022.111768
19. Swaidan, A. (2018). *Study of water injection with evaporation in a heterogeneous highly degraded nuclear reactor core*. [Université de Toulouse]. https://theses.fr/2018INPT0002

REFLOODING OF A DAMAGED CORE IN CASE OF SEVERE ACCIDENT:

SYNTHESIS OF EXPERIMENTAL RESULTS AND MODELLING & CONSEQUENCES FOR THE REACTOR SCALE

Florian Fichot - ASNR

ERMSAR Conference - May 18-21, 2026 - Madrid

REFLOODING OF A DEGRADED CORE AT IRSN/ASNR

SEVERAL COMPLEMENTARY EXPERIMENTS:

- PRELUDE (1D), PEARL (2D), CALIDE, Compact Mass
- T. Garcin, G. Repetto, N. Chikhi, R. Clavier, H. Mutelle, C. Sartoris, …

MODELLING & NUMERICAL SIMULATION:

- ICARE/CATHARE, MC3D, ASTEC
- F. Fichot, M. Quintard, A. Bachrata, N. Chikhi, A. Swaidan, V. Topin, D.H Nguyen, L. Laborde, L. Piar, I. Gomez-Garcia-Toraño, R. Meignen, S. Picchi, B. Raverdy, …

DEBRIS BED FORMATION IN A DAMAGED CORE (1)

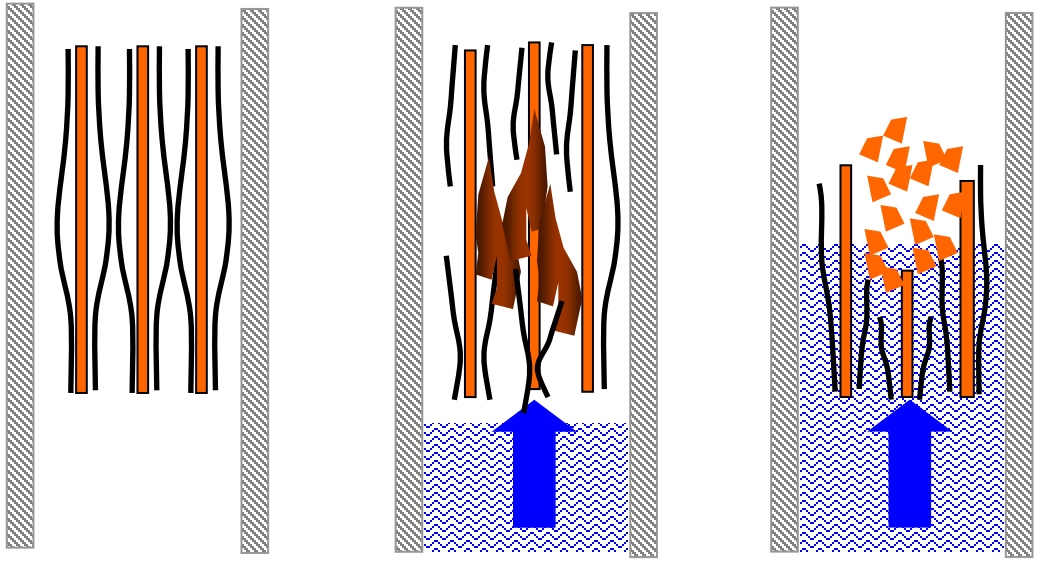

Large fragments (≈ 3 mm) resulting from fuel fragmentation under operating conditions

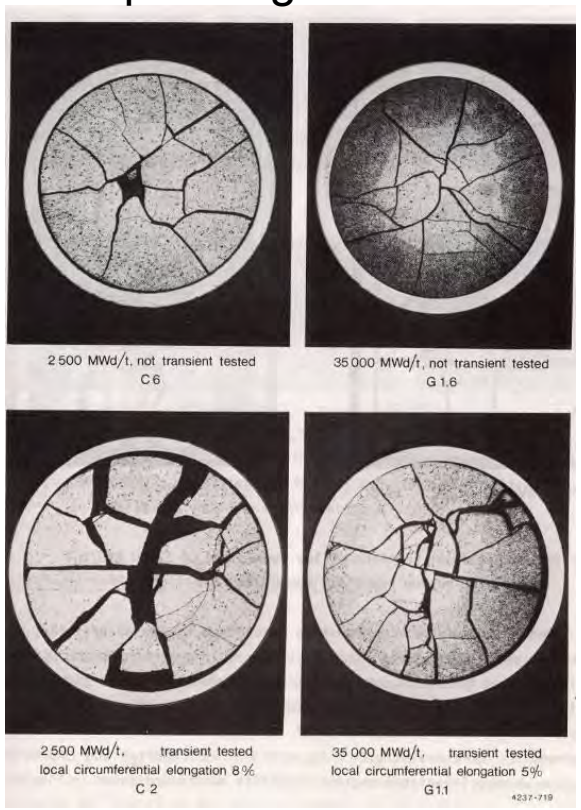

E.H. Karb et al. 1983, LWR fuel rod behavior in the FR2 in-pile tests simulating the heatup phase of a LOCA

DEBRIS BED FORMATION IN A DAMAGED CORE (2)

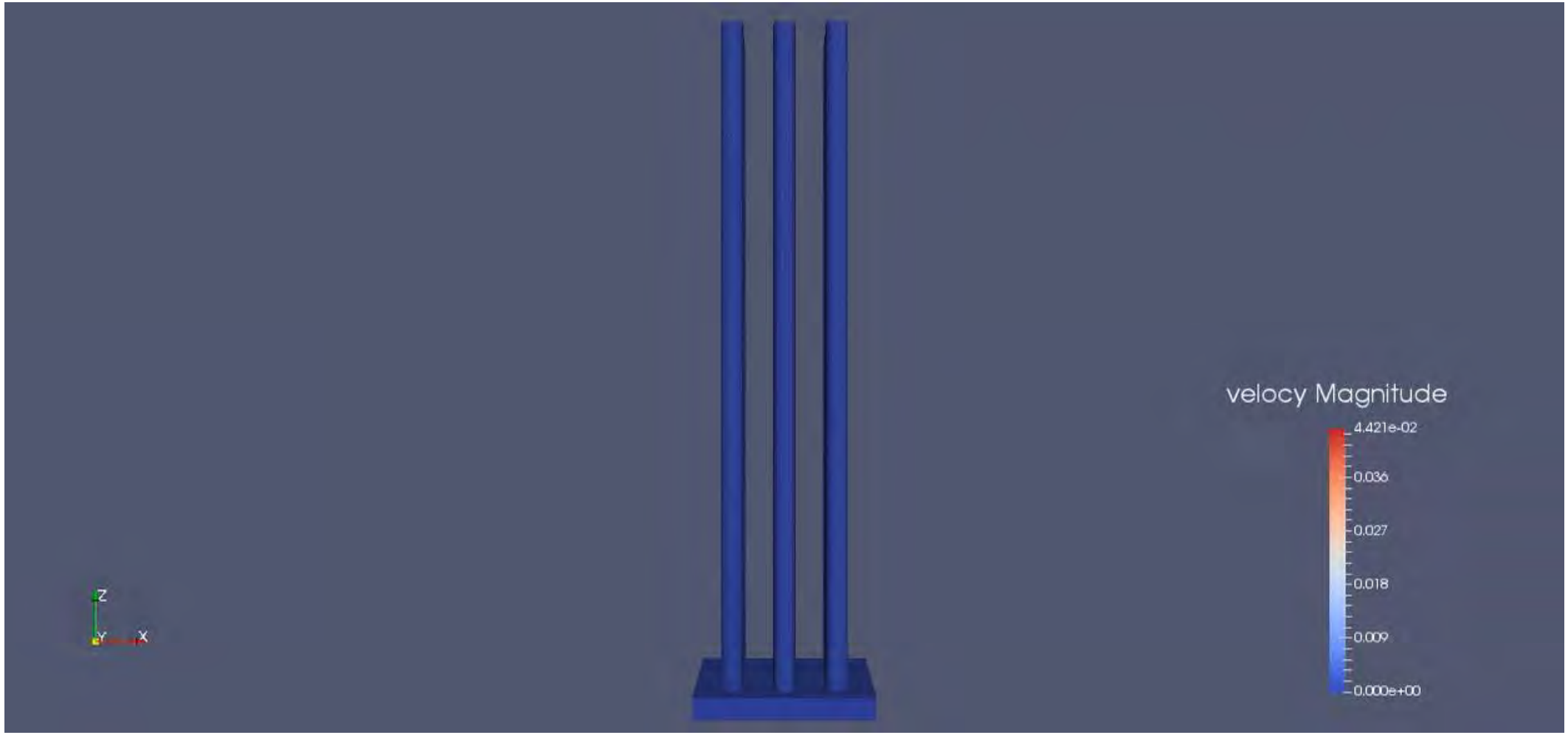

Calculations of debris collapse from fragmented fuel columns (with Contact Dynamics granular approach)

DEBRIS BED FORMATION IN A DAMAGED CORE (3)

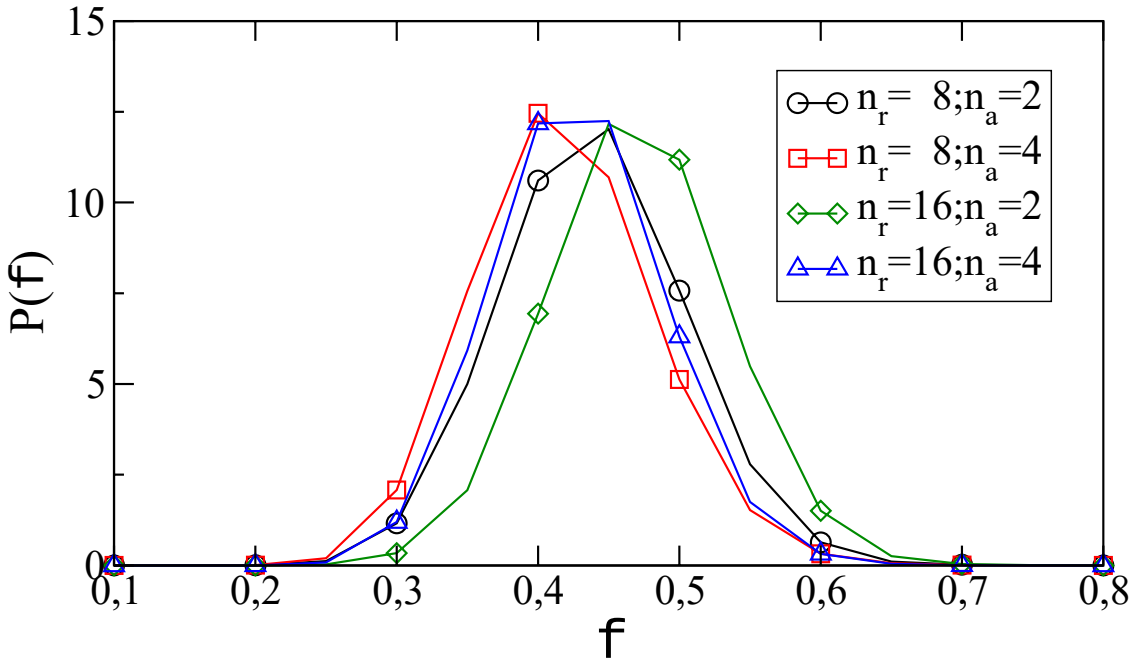

Distributions of porosity for various fragmentations of fuel pellets → rather large average porosity and significant statistical variations

1D REFLOODING (PRELUDE FACILITY)

- Quasi-steady progression of quench front
- High velocity of steam flow → steep pressure gradient
- Results are consistent with earlier tests performed at Brookhaven NL (Tutu et al. 1984)
- If pressure gradient is too high: quench front becomes 2D (instability)

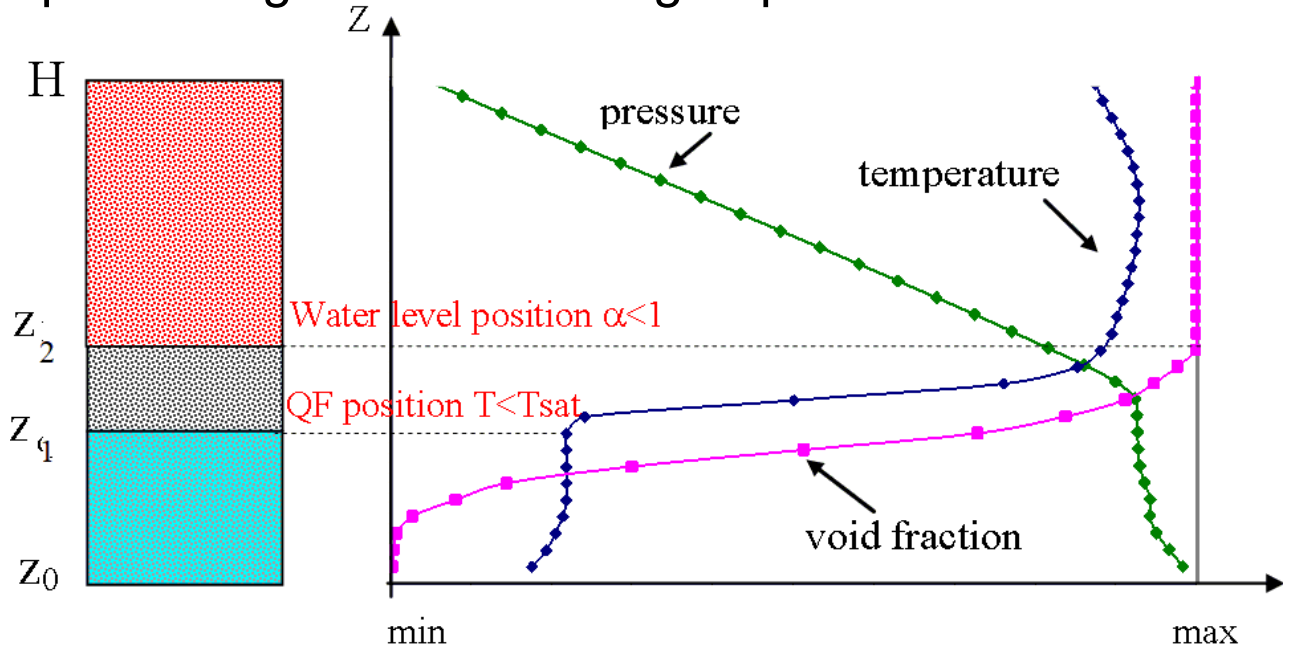

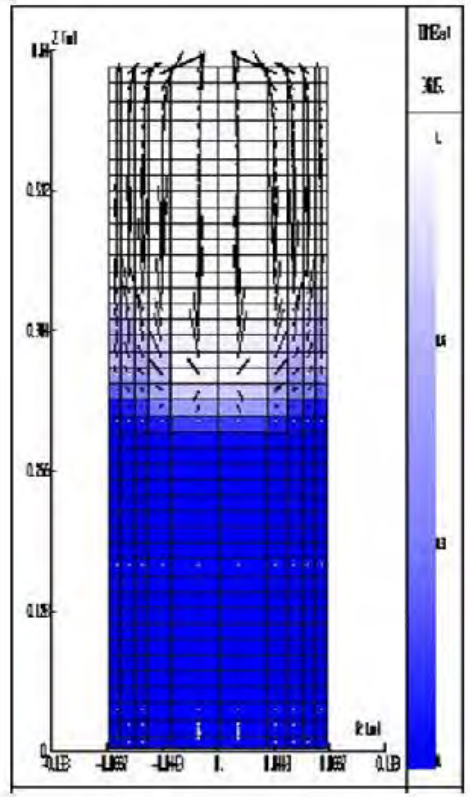

Calculated void fraction → 2D deformation of quench front, as observed experimentally

N.K. Tutu, T. Ginsberg, J. Klein, J. Klages, and C.E. Schwarz. “Debris bed quenching under bottom flood conditions”, technical report NUREG/CR-3850, Brookhaven National Labs., 1984.

1D REFLOODING

A SIMPLIFIED 1D STEADY-STATE APPROACH PROVIDES

- Constant quench front velocity
- Conversion ratio water → steam

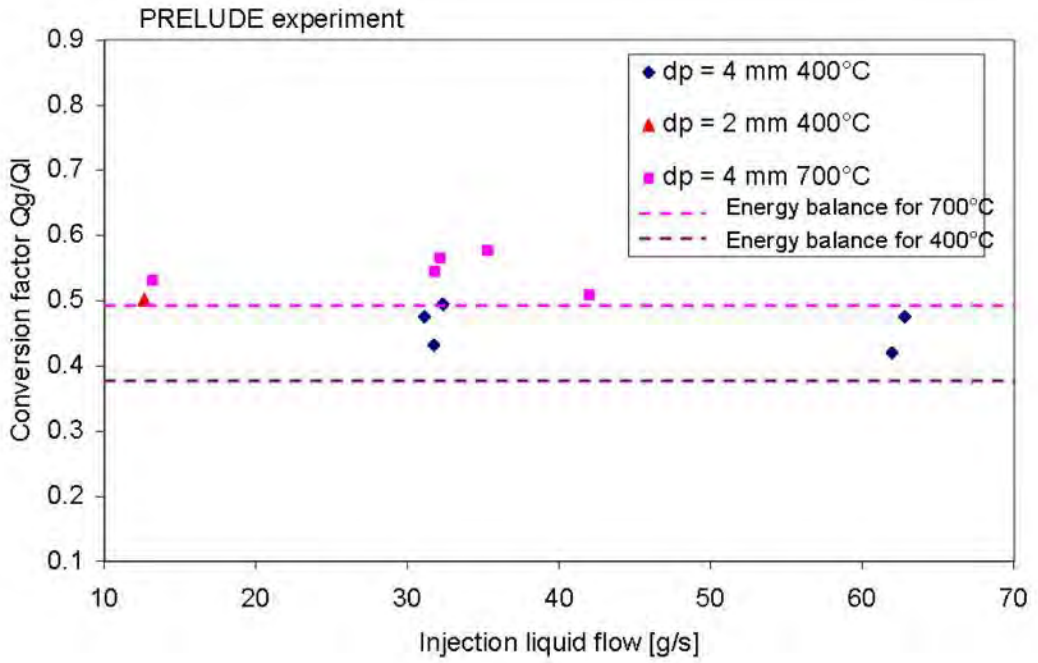

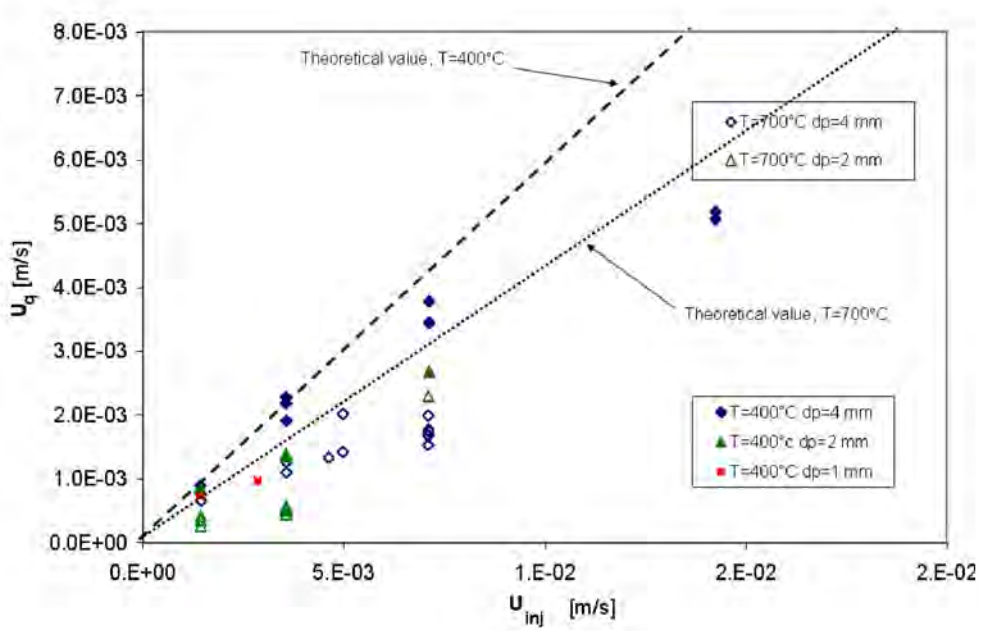

Accuracy of 1D steady-state model = +/-15%

CONCLUSIONS ON 1D REFLOODING

Quasi-steady progression of QF is observed in all cases

QF may be 2D with entrainment of water at the periphery

The overall behaviour can be predicted with a 2D 2-phase numerical model

1D approximation of the front moving at constant speed is a valid representation when seeking a rapid assessment of the front progression and its consequences on steam production and on the pressure gradient in the debris bed

- It gives a relatively good approximation at steady-state, within +/- 15% uncertainty range
- It is inaccurate in the transient phases (quench front entering or leaving the core)

2D REFLOODING (PEARL FACILITY)

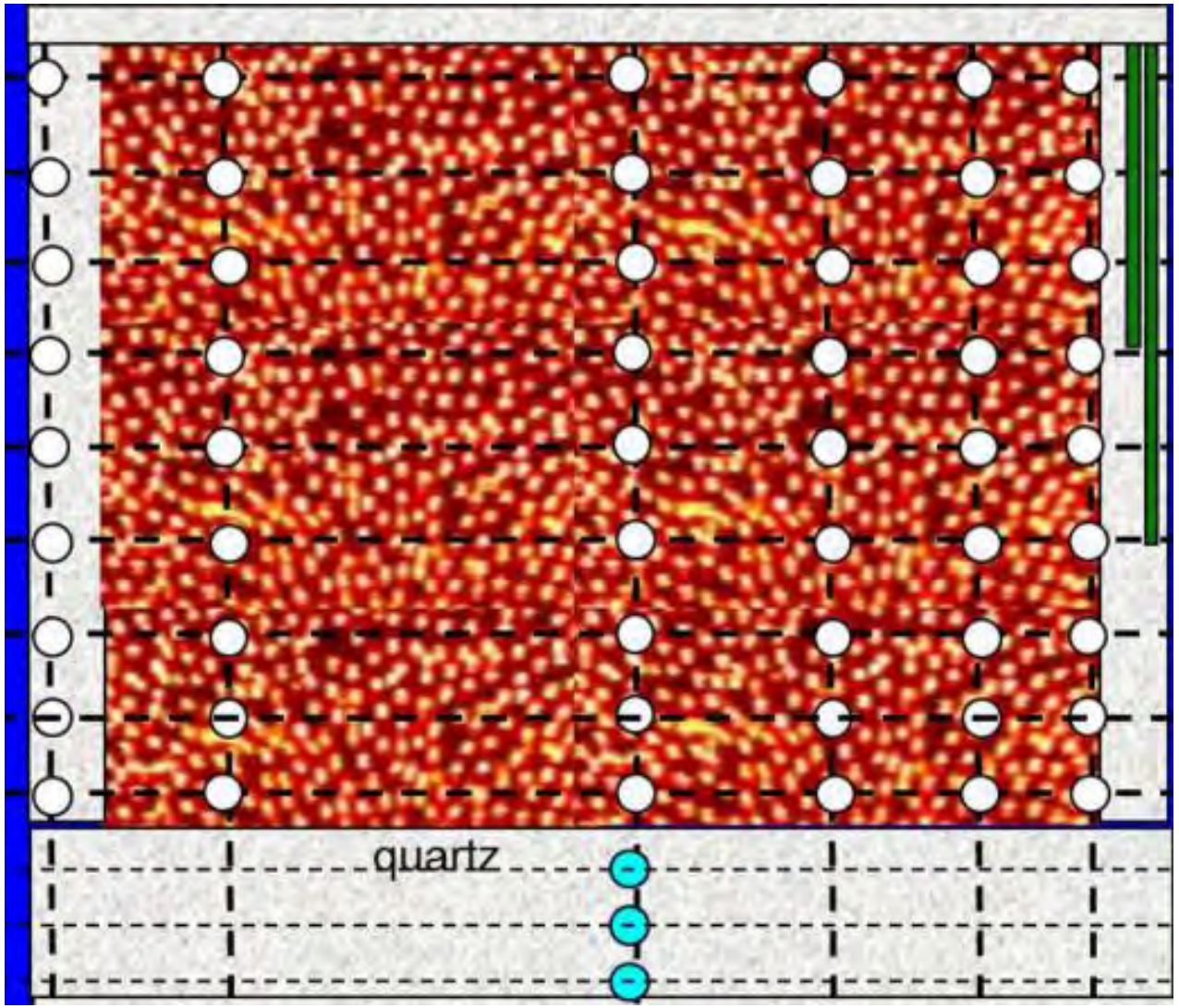

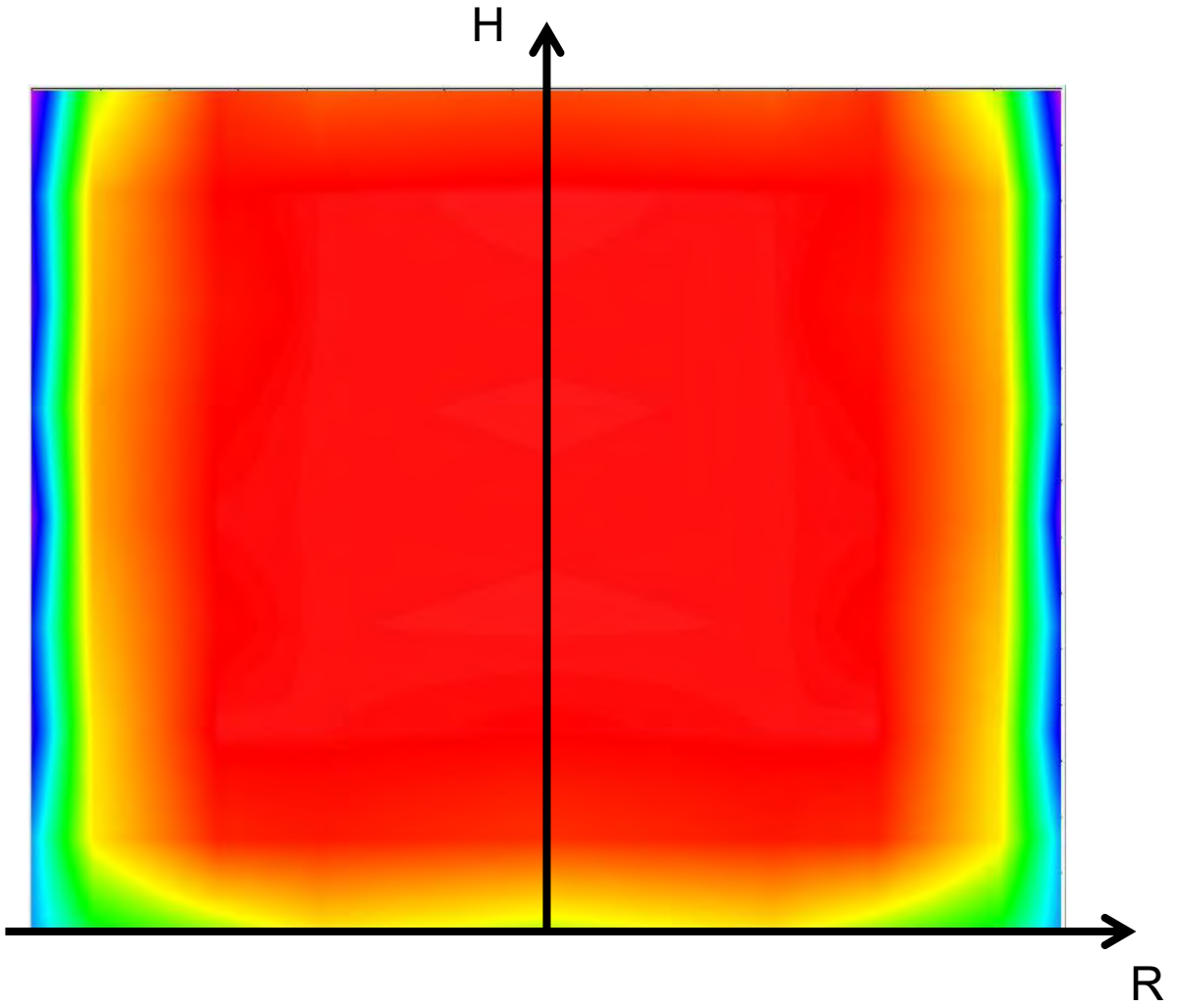

ANALYTICAL MODEL FOR 2D STEADY-STATE PROGRESSION

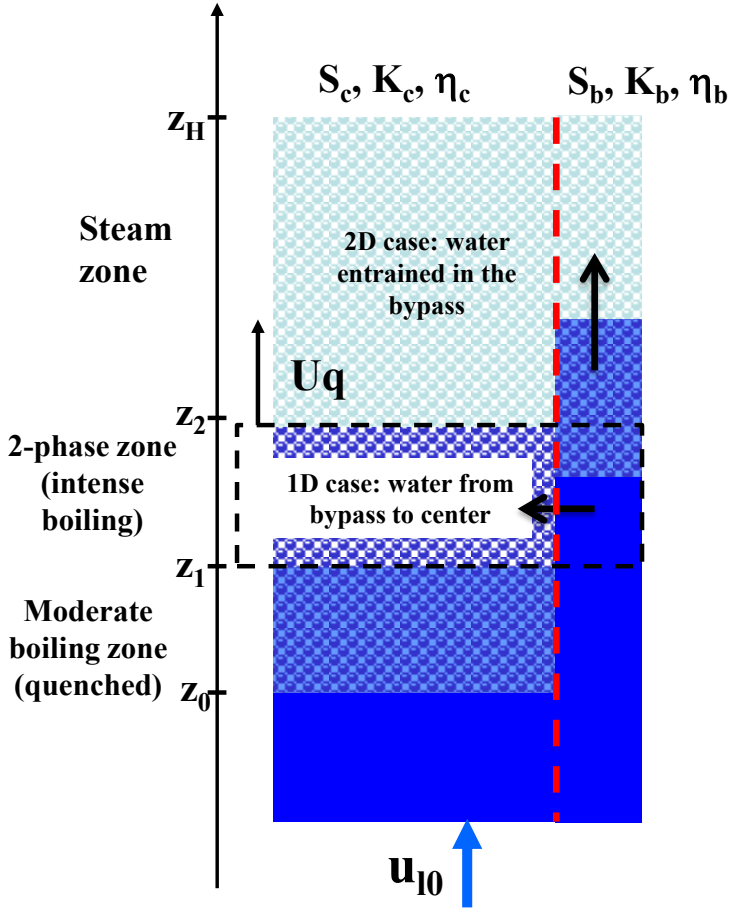

- Assumptions :
  - 3 different zones with steady velocity (= Uq)
  - No heat losses and no heat exchange in the bypass
  - A fraction of water is entrained from the central bed to the bypass: parameter k_{ent}

- Mass balance in each zone and energy balance for the whole system give :

Quench front velocity ratio

$$\frac{U_q}{u_{l0}} = \frac{1}{1+\gamma}\left[1+\frac{S_b}{S_c}(1-R_{lb}k_{ent})\right]$$

with :

$$R_{lb} = \frac{u_{lb}(z_1)}{u_{lo}} = \frac{(S_c+S_b)}{(S_c\frac{K_c}{K_b}+S_b)} = 2.1$$

$$\gamma = \frac{(1-\varepsilon)\rho_s Cp_s \Delta T_s}{\varepsilon \rho_l (\Delta h^{sat} + Cp_g \Delta T_g)}$$

- The QF is faster in the presence of bypass than without bypass when k_{ent} is low (1D mode) because some water flows from the bypass to the central bed. It may become lower if the entrained fraction is high.

- Maximun QF velocity ratio = 0.52 corresponding to 1.8 mm/s close to the experimental value (= 2 mm/s)

2D 2-PHASE MODEL

A TWO-PHASE FLOW MODEL WAS DEVELOPED AND FITTED TO EXPERIMENTAL DATA:

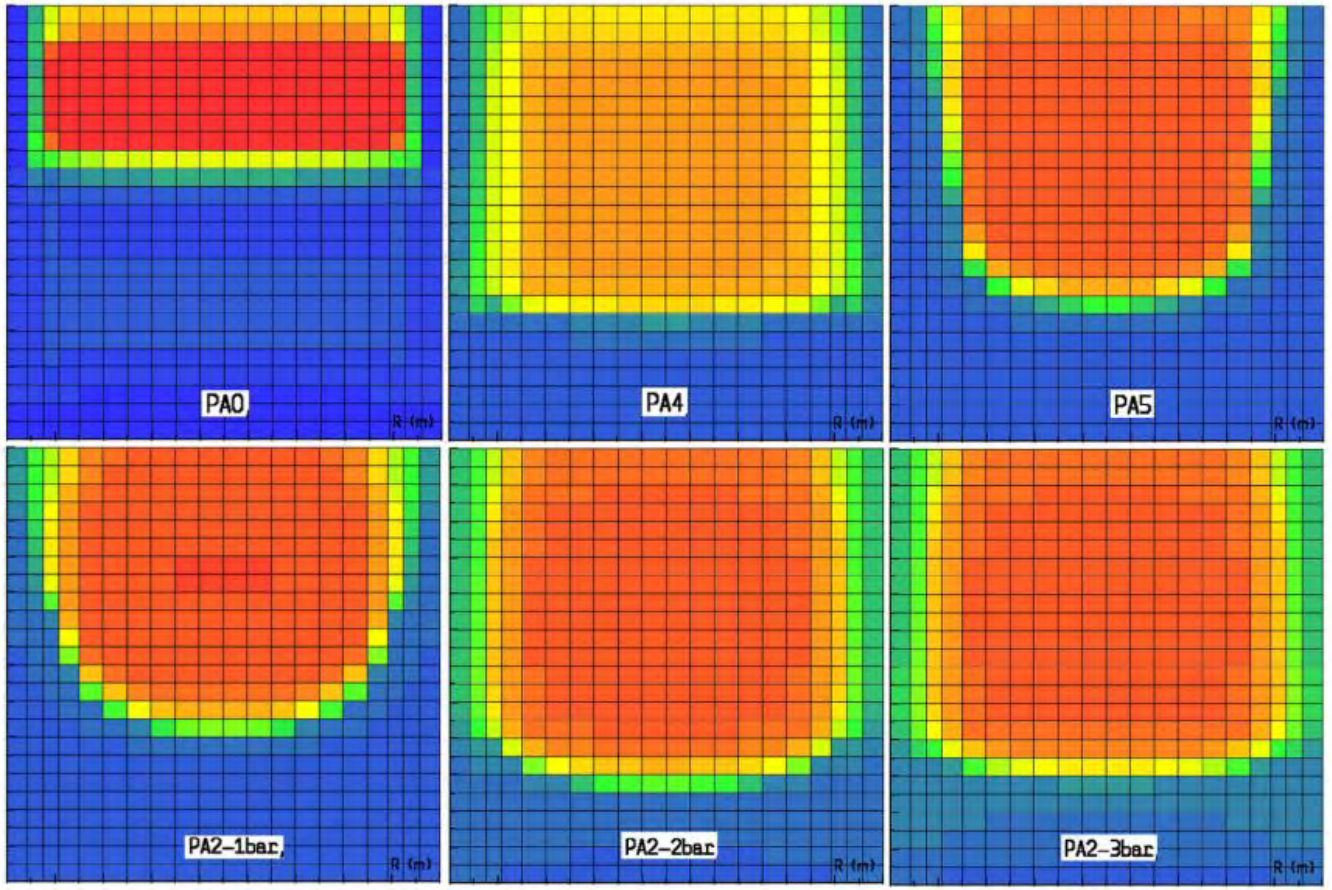

- It is able to reproduce experimental data, including the 2D behaviour of quench front
- It uses only local closures (friction terms, HF) → it can be extrapolated to reactor scale

APPLICATION TO REACTOR CASES

- A 1m high debris bed is generated near the top of the core
- It is surrounded by non damaged rods (bypass)

description	variable	Exp. range	Reactor case
water velocity at inlet	u_{inj}	2-20 mm/s	11 mm/s
volumetric flow rate	j	2-20 mm/s	2-30 mm/s
initial temperature of particles	T_s	400-900 °C	**2000 °C**
Residual power per unit of mass	Q_{res}	100-300 W/kg	200 W/kg
porosity of the bed	ε	0.39	0.39
permeability of the bed	K	10^{-9} -10^{-8} m^2	10^{-8} m^2
outlet pressure	P_{ext}	1-9 bar	3 bar
height of debris bed	H	0.2-0.5m	**1m**
diameter of particles	d_p	1-2-4 mm	3 mm
Density of particles	ρ	7800 kg/m3	8000 kg/m3

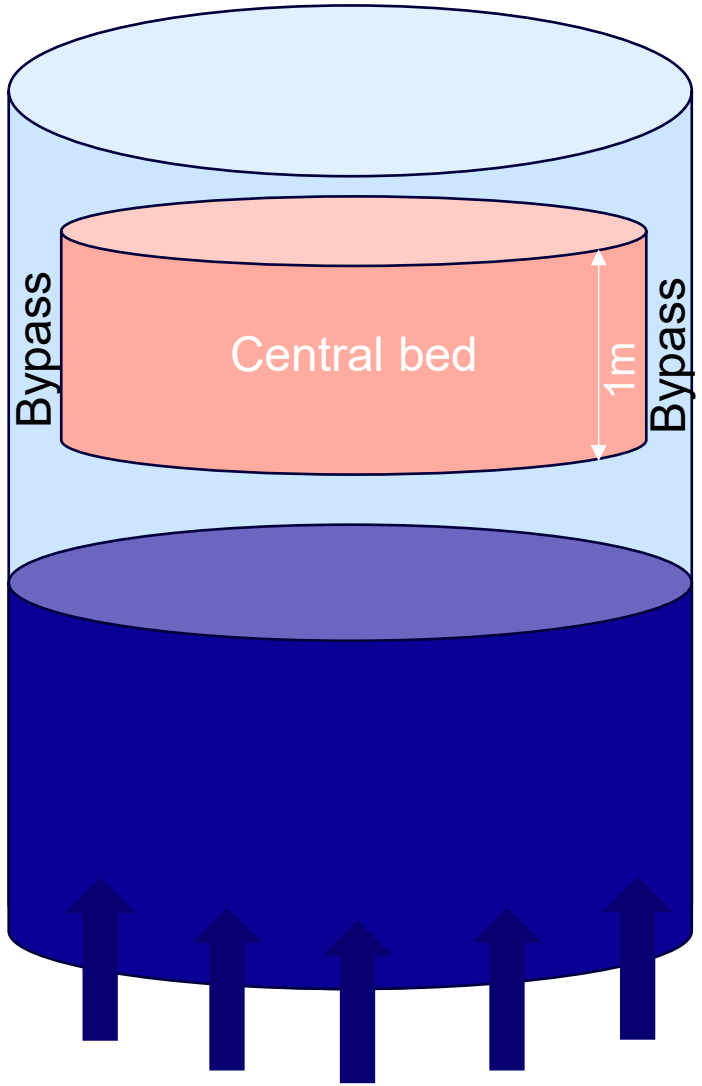

COOLABILITY LIMITS IN A REACTOR CORE (1)

EFFECT OF CORE TEMPERATURE:

- A higher temperature decreases the velocity of the quench front and strongly decreases the time to reach melting
- Even if the debris are initially at a rather low temperature (around 1500K), the margin for cooling is only 1 hour
- If BDBA conditions are reached, the main SAM issue is to recover a water source in a short time

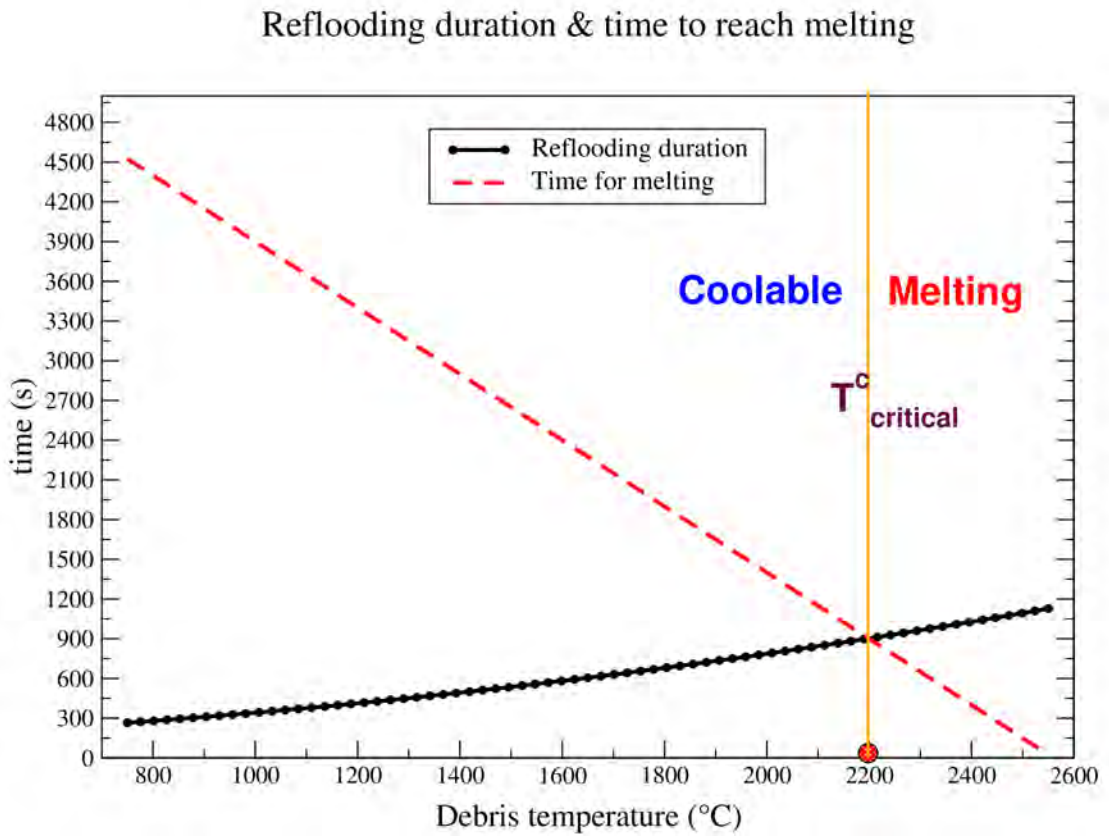

COOLABILITY LIMITS IN A REACTOR CORE (2)

EFFECT OF INJECTION VELOCITY:

- The critical value is around 5mm/s which corresponds approximately to a mass flow rate of 200 t/h for a high power PWR

- A high flow rate may reduce significantly the total quenching time but … would it be available?

- Low flow rates lead to debris melting

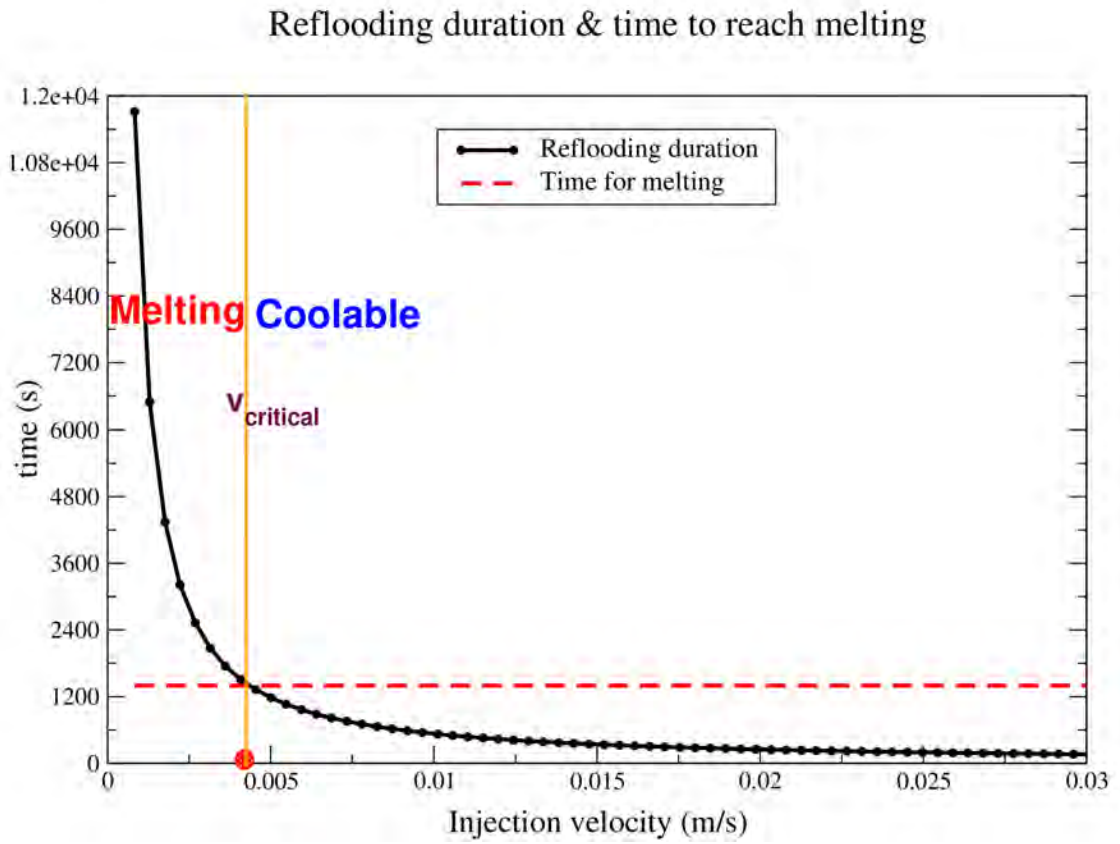

COOLABILITY LIMITS IN A REACTOR CORE (3)

EFFECTS OF POROSITY AND BYPASS CROSS SECTION:

- threshold porosity is around 25-30% (strongly compressed bed)
- if central bed occupies less than 50% of total area, it cannot be quenched before melting (= gravitational flooding)

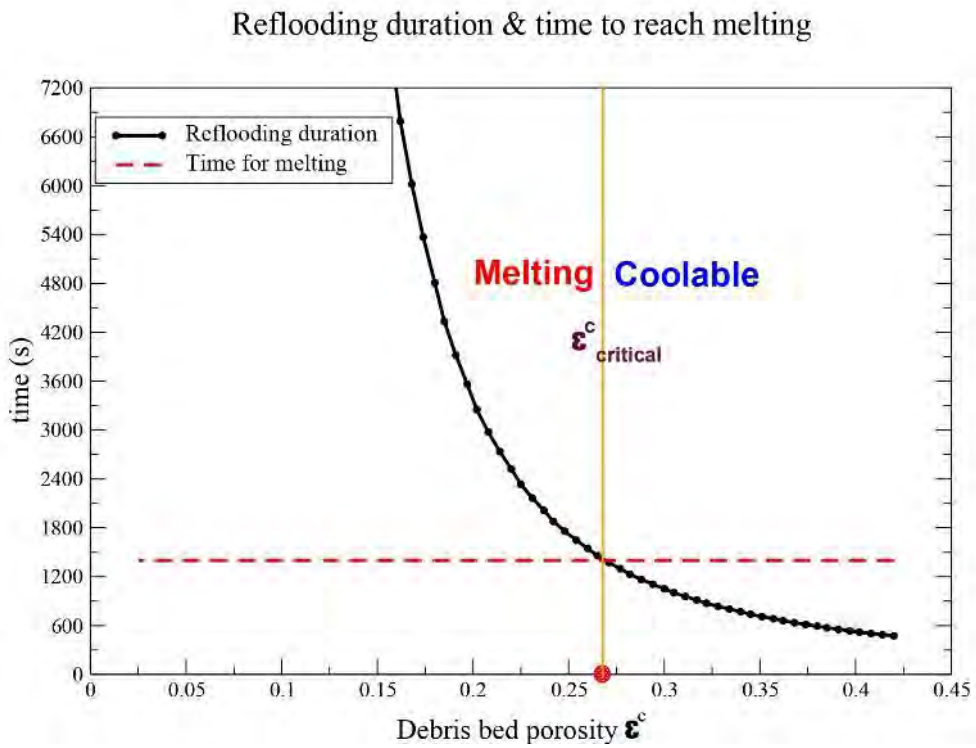

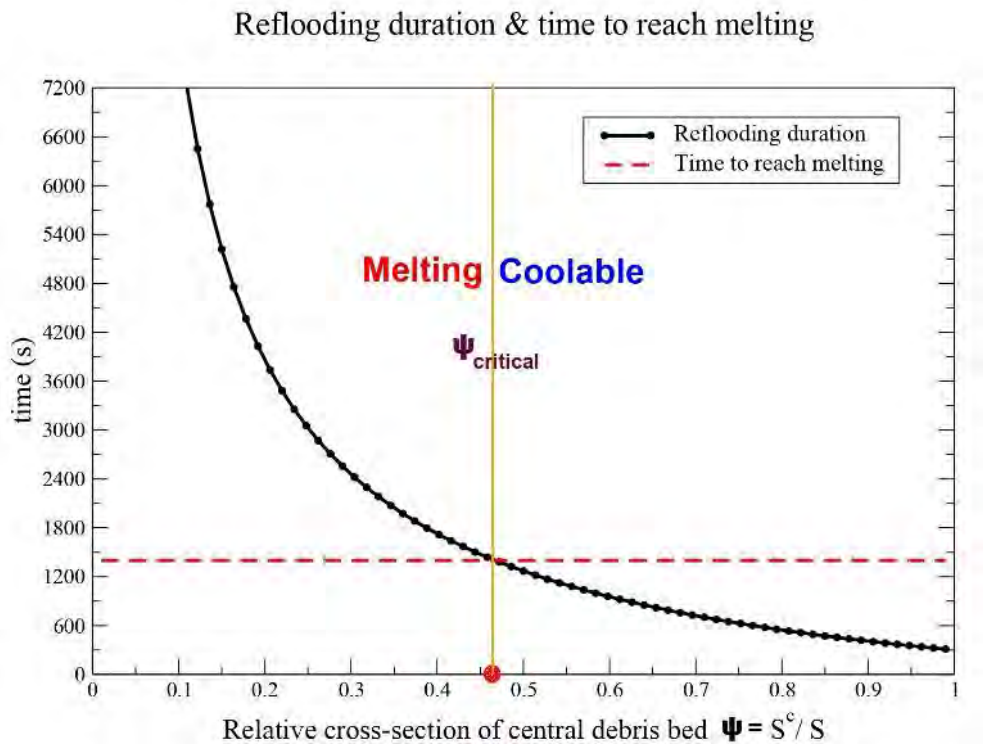

CONCLUSIONS FOR ACCIDENT MANAGEMENT

Extrapolations at the reactor scale and for severe accident conditions lead to the following conclusions:

- The time to successfully quench the whole damaged core, at a late stage where debris have formed, is quite short: approximately 20 to 60 minutes in the realistic cases studied in this paper, which means that the **probability of recovering a safety injection during this time frame is very low** (reflooding may be successful for longer sequences, with lower residual power)

- A minimum injection flow rate is necessary but increasing the flow rate does not lead to significant reduction of quenching time → **Low porosity/permeability regions are not sensitive to the flow rate**. This means that it is very likely that **some parts of the core would be quenched while other parts would melt**, in spite of the core reflooding.

- **It is likely that the core region would be covered by water quickly after reflooding starts** (even if some parts remain unquenched): the benefit of this situation is that steam entering the hot leg would be rather cold. This means that reflooding would not induce heating and mechanical failure in the circuit or steam generator tubes.

- → **it is necessary to implement a strategy for corium stabilization**, either in the lower head or in the containment (core catcher or backfitting for corium spreading and flooding)

REFERENCES

Nguyen, D. H., Fichot, F., & Topin, V. (2017). Investigation of the structure of debris beds formed from fuel rods fragmentation. Nuclear engineering and design, 313, 96–107. Https://doi.Org/10.1016/j.Nucengdes.2016.11.019

Fichot, F., Bachrata, A., Repetto, G., Fleurot, J., & Quintard, M. (2012). Quenching of a highly superheated porous medium by injection of water. Journal of physics: conference series, 395. Https://doi.Org/10.1088/1742-6596/395/1/012144

Repetto, G., Garcin, T., Eymery, S., & Fichot, F. (2013). Experimental program on debris reflooding (PEARL) - results on PRELUDE facility. Nuclear engineering and design, 264, 176–186. Https://doi.Org/10.1016/j.Nucengdes.2012.11.024

Bachrata, A., Fichot, F., Repetto, G., Quintard, M., & Fleurot, J. (2013). Quench front progression in a superheated porous medium: experimental analysis and model development. Journal of energy and power engineering, 7, 514–523

Bachrata, A. (2012). Modélisation du renoyage d'un cœur dans le cas d'un réacteur fortement dégradé [université de toulouse]. Https://theses.Hal.Science/tel-04274113

Fichot, F., Duval, F., Trégourès, N., Béchaud, C., & Quintard, M. (2006). The impact of thermal non-equilibrium and large-scale 2D/3D effects on debris bed reflooding and coolability. Nuclear engineering and design, 236(19–21), 2144–2163. Https://doi.Org/10.1016/j.Nucengdes.2006.03.059

Chikhi, N., & Fichot, F. (2017). Experimental and theoretical study of large scale debris bed reflood in the PEARL facility. Nuclear engineering and design, 312, 48–58. Https://doi.Org/10.1016/j.Nucengdes.2016.05.009

Chikhi, N., Fichot, F., & Swaidan, A. (2017). Effect of water entrainment on the coolability of a debris bed surrounded by a by-pass: integral reflood experiments and modelling. Annals of nuclear energy, 110, 418–437. Https://doi.Org/10.1016/j.Anucene.2017.06.033

Mutelle, H., Fichot, F., & Piar, L., Reflooding of large scale debris bed with bypass: effect of pressure and water flowrate. Proceedings of NURETH-17 conference, (2017).

Raverdy, B., Meignen, R., Piar, L., Picchi, S., & Janin, T. (2017). Capabilities of MC3D to investigate the coolability of corium debris beds. Nuclear engineering and design, 319, 48–60. Https://doi.Org/10.1016/j.Nucengdes.2017.04.005

Gómez-garcía-toraño, I., Laborde, L., Fichot, F., & Mutelle, H. (2022). Reflooding of degraded cores in ASTEC V2 . 1 : modelling and validation on PEARL experiments. 393 (2021). Https://doi.Org/10.1016/j.Nucengdes.2022.111768

Swaidan, A. (2018). Study of water injection with evaporation in a heterogeneous highly degraded nuclear reactor core. [Université de toulouse]. Https://theses.Fr/2018INPT0002

DEBRIS BED FORMATION IN A DAMAGED CORE (2)

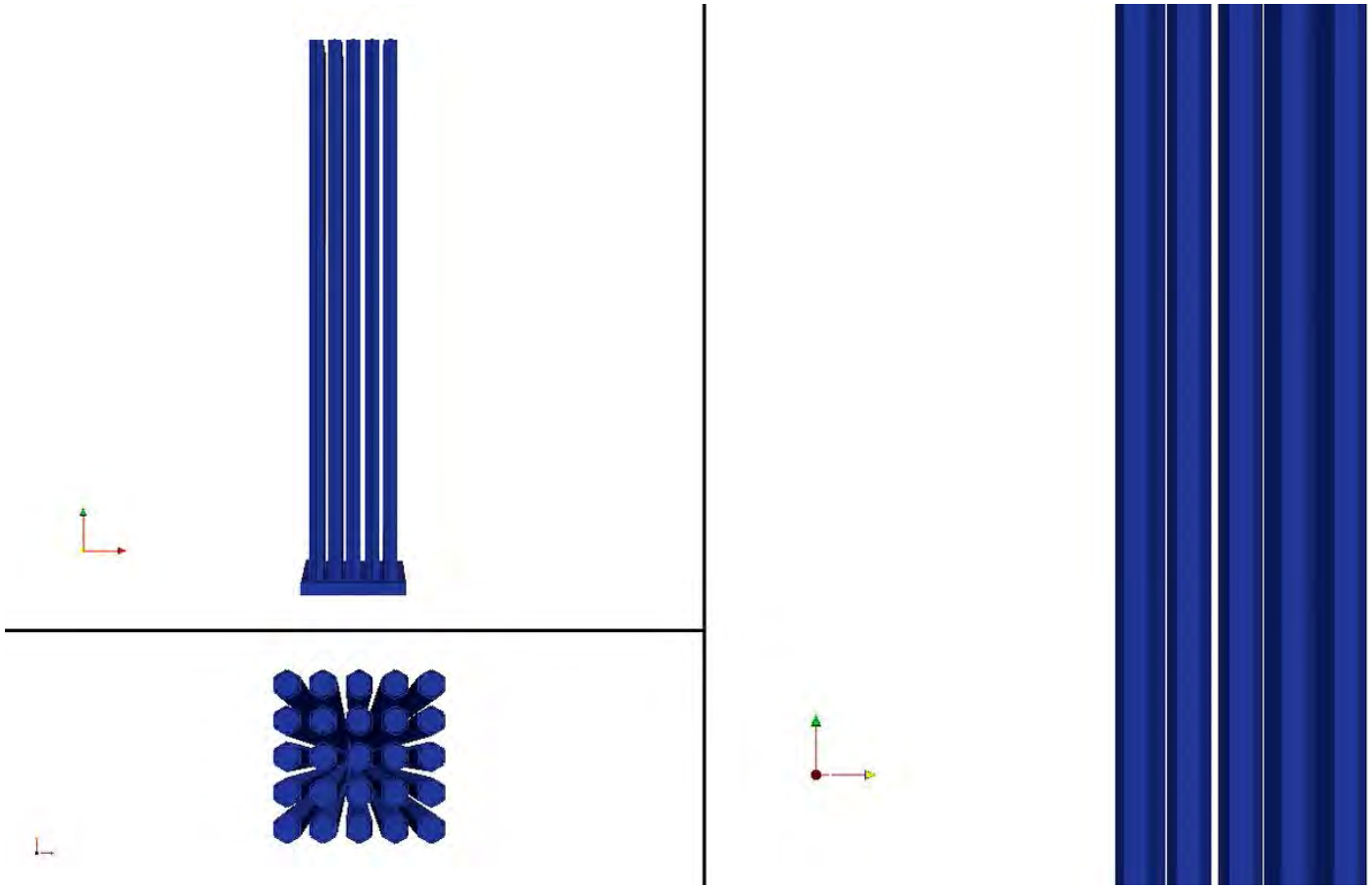

The presence of large fragments of claddings and confined space limits the compaction of debris → rather large porosity and non-isotropic porous medium, with larger axial permeability

OXIDATION: MELTING OF ZR IN DEBRIS

- If Zr is present in the debris bed: strong oxidation will lead to melting of Zr and relocation → reduction of porosity

- If porosity below 25/30% → probable melting UO_2 eventually

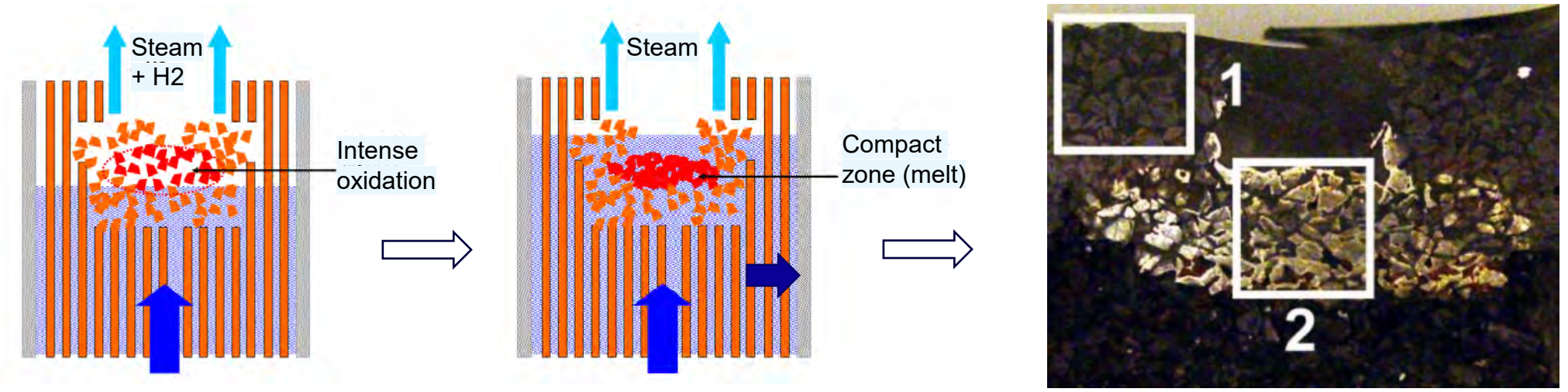

STABILIZATION OF A MOLTEN POOL SURROUNDED BY DEBRIS

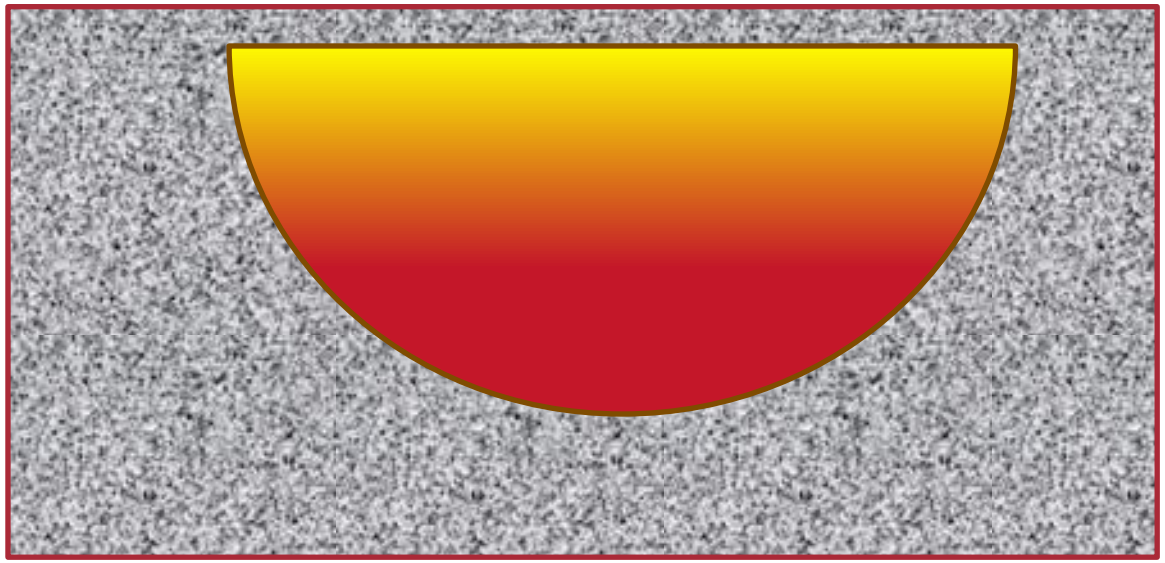

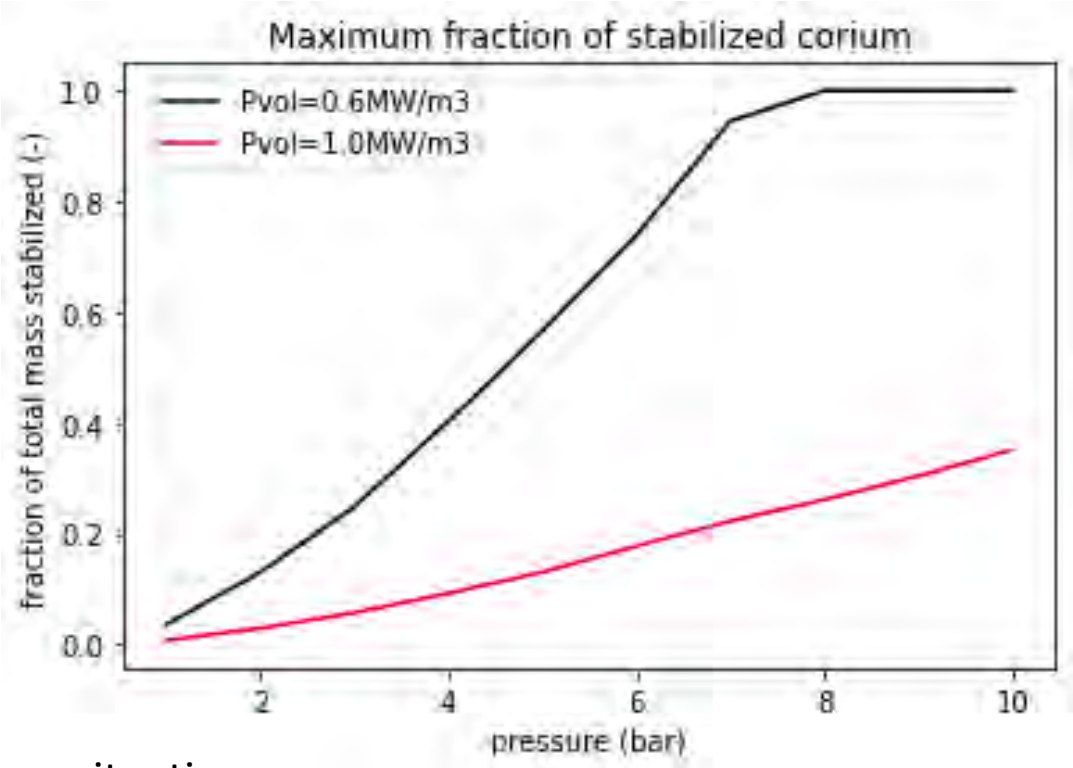

- Mass of stabilized corium increases with pressure

- Stabilization of a large fraction of the core may be reached in some situations:
  - Late melting of core (more than 12h after scram)
  - High primary pressure (as in TMI-2: near 100bar)

- Otherwise, only a limited fraction of the core may be stabilized → relocation to lower plenum

SIMULATION OF THE LOW PRANDTL LAYER OF A CORIUM POOL

M. Johnson
Scalian, R&D Lab, France
michael.johnson@asnr.fr

N. Seiler
CEA, DES, IRESNE, DTN, SMTA
F-13108 Saint-Paul-Lez-Durance, France
nathalie.seiler@cea.fr

ABSTRACT

As part of the In-Vessel Retention strategy, it is necessary to maintain the local heat flux from the corium pool onto the reactor wall below the critical heat flux. In the stratified configuration of the corium pool, the maximum flux is observed at the level of a highly conductive steel-rich shallow light metal layer, referred to as the focusing effect. Two LES WALE simulations are presented of natural convection in a low Prandtl number fluid (Pr≈0.11) heated from below ($Ra_\Phi = 10^8$) where 10 % and 90 % of thermal losses occur at the upper boundary respectively, mimicking different modes of heat dissipation from the free surface. Strong cooling at the upper boundary produced fluid dynamics broadly consistent with Rayleigh-Bénard convection. Weak cooling of the upper surface revealed an important localized focusing effect, with a local lateral heat flux of around three times the magnitude of heat injection from below, close to the free surface. The dominant lateral heat dissipation produced four large convection cells, demarcated by branches of elevated radial velocity, which rotated in the $r - \theta$ plane. A mild increase in lateral heat dissipation is observed in the proximity of the high velocity branches. The simulations demonstrate very good agreement with corresponding spectral-DNS simulations indicating that the LES WALE approach may offer a computationally feasible solution to extending existing correlations for natural convection in the light metal layer into a higher Rayleigh number regime ($Ra_\Phi > 10^8$), which may be observed in the early stages of a severe accident.

KEYWORDS
focusing effect, In-Vessel Retention, natural convection, LES

1. INTRODUCTION

In the event of a severe accident within a Pressurised Water Reactor (PWR), and the transfer of very high-temperature molten core materials (corium) to the lower part of the reactor pressure vessel (RPV), the In-Vessel Retention (IVR) mitigation strategy aims to safely dissipate the decay heat generated within the corium in order to prevent the loss of RPV integrity [1]. Safety studies often focus on a stratified corium pool configuration [2], whereby a dense oxide-rich pool containing most of the fuel and fission products dissipates heat to an overlying shallow 'light-metallic' layer, rich in molten stainless steel, uranium and zirconium. An assumption of a stable oxidic crust at the interface between the stratified layers enables each molten layer to be investigated independently [3]. The shallow cylindrical light metal layer is thereby subject to an imposed heat flux from the underlying oxidic corium pool, dissipating heat from its free surface and laterally towards the reactor wall.
The fluid dynamics in the light metal layer are the subject of significant research interest due to the implications of a potential 'focusing effect' [4] [5]. The focusing effect relates to an intensification of the lateral

heat flux imparted from the shallow, highly conductive light metal layer toward the reactor wall. A significant focusing effect could pose a high risk of RPV failure if the lateral heat flux at the reactor wall exceeds the critical heat flux [6]. For severe accident integral codes, such as ASTEC [7], the 0D representation of the light metallic layer requires robust empirical models [8] to accurately describe the heat dissipation within a computationally efficient framework necessary to simulate the transient in close to real time.
To this end, a recent international benchmark exercise on the prediction of the lateral heat flux profile observed during the BALI-Metal experiment [9] was undertaken within the IAEA CRP J46002 framework [5]. Experimental observations of the fluid dynamics were generally well predicted by various CFD approaches. The test case in a thin cuboidal geometry (Figure 1), in which ~42-47 % of the heat injected from below is released at the upper boundary, exhibits significant concurrent heat dissipation from both the upper and lateral boundaries. This results in relatively complex fluid dynamics from the superposition of two convection regimes, Rayleigh-Bénard convection driven by heat transfer in the vertical direction, and larger convection cells produced by buoyancy in the fluid subject to rapid cooling adjacent to the lateral wall and heating along the lower boundary. Depending on the ratio of heat dissipation at the upper and lateral surfaces, either of these competing convection regimes may become dominant. The hybrid fluid dynamics of the light metal layer under different cooling conditions at the upper boundary have been thoroughly characterized by both spectral-DNS simulations [8] and experimentally [10].
Simulations of a prototypic light metal layer with a Rayleigh number of $Ra_{\Phi} = 8.5 \times 10^{11}$ and radiative heat loss at the upper boundary [5] revealed fluid dynamics consistent with the dominant lateral thermal losses, resulting in downward acceleration of cool fluid along the reactor wall, expulsion of a cold jet from the base of the lateral wall along the lower boundary, and detachment of warm fluid from the lower boundary close to the center of the reactor, as illustrated in Figure 1.

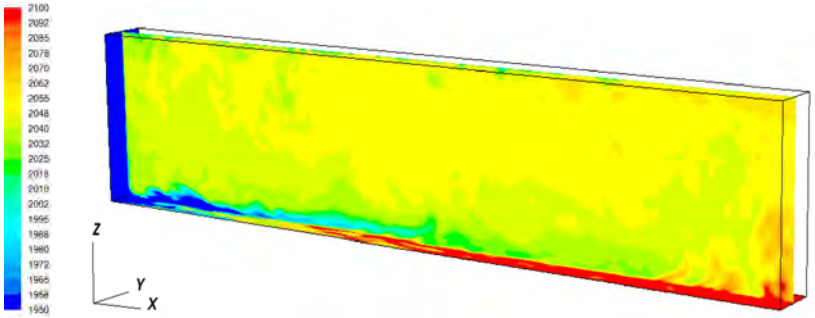

Figure 1: An instantaneous temperature field at steady state from an LES WALE simulation of a prototypical light metal layer with radiative heat loss from the upper boundary [5].

The IAEA CRP J46002 benchmark enabled assessment of different numerical approaches to simulating the fluid dynamics of the light metal layer, including different sub-grid turbulence models, near-wall treatments and different resolutions of spatial discretization. The benchmark also highlighted a number of issues requiring further research:

- The BALI-Metal experiments were performed using water (Pr ≈ 7) as a simulant. Additional experimental data in more representative low-Prandtl number fluids closer to metallic corium (Pr ≈10^{-2}), would be valuable.
- Simulations performed using a representative shallow cylindrical geometry, in order to observe the global 3D fluid dynamics, are required to in addition to those in a quasi-2D, or thin cuboidal, geometry representing a thin slice through the metal layer in the $r - z$ plane, as employed for the BALI-Metal experiments.
- Severe gradients in the lateral heat flux profile are observed both at the base of the lateral wall, below the cold jet, and close to the free surface where the maximum focusing effect is observed

(see Figure 2, [5]). The heterogeneity in the localized focusing effect at the lateral wall, particularly close to the free surface, should be considered during safety studies, rather than simply the surface-averaged lateral heat dissipation from the metal layer onto the reactor wall.

- Simulations should take particular care to ensure sufficient mesh refinement within the critical zones at the lower and upper extremes of the lateral boundary. The benchmark revealed some departure between numerical approaches within the corner between the heated lower boundary and the base of the cold lateral wall (Figure 2). Some approaches identified a significant spike in lateral heat flux below the cold jet, which was not clear from simulations with less near-wall mesh refinement. Further validation was deemed to be required regarding the local heat flux observed at the top and bottom of the lateral wall.

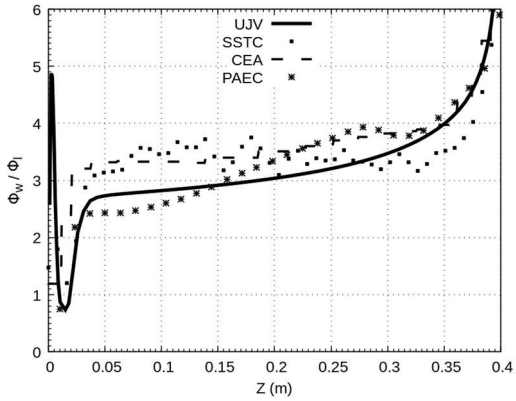

Figure 2: Distribution of the predicted dimensionless lateral heat flux profiles (the ratio of lateral heat flux to the heat flux injected from below) for a prototypic test case [5].

Following the IAEA CRP J46002 benchmark, the CEA is expanding its investigation into the fluid dynamics of the light-metallic layer by validating its CFD code TrioCFD with simulations of a low-Prandtl number fluid in a representative cylindrical geometry. The selected test cases are taken from a study by [8], which presents an extensive investigation of the fluid dynamics for conditions of $10^2 \leq Ra_\Phi \leq 10^9$; with Ra_Φ, the Rayleigh number based heat flux, $4 \leq \Gamma = \mathrm{R}/H \leq 16$; R and H being the radius and height, respectively, $0.1 \leq \widehat{\Phi}_u = -\frac{\Phi_u}{\Phi_l} \leq 0.9$ (the ratio of upper and lower heat flux) and $Pr = 0.1$ using a spectral-DNS code [11]. This investigation has enabled significant progress in the understanding of the complex convection behaviour resulting from the superposition of flow fields characteristic of Rayleigh-Bénard convection ($\widehat{\Phi}_u \to 1$) and convection induced by lateral cooling ($\widehat{\Phi}_u \to 0$). Spectral-DNS simulations were validated using experimental data acquired using air and air-SF_6 mixtures as low-Prandtl number fluids [12] with particle image velocimetry (PIV) characterisation of the velocity field. The current study presents a numerical investigation of two test cases, pertaining to a prototypic corium test fluid with a Prandtl number of $Pr = 0.11$, an external Rayleigh number of $Ra_\Phi = 10^8$, an apect ratio of $\Gamma = 4$, and upward heat flux ratios of $\widehat{\Phi}_u = \{0.1, 0.9\}$. Simulations are performed using a finite volume discretisation and an LES WALE [13] sub-grid turbulence closure model. Results are compared with corresponding simulations undertaken using spectral-DNS [8].

2. NUMERICAL METHODS

The dimensions of the cylindrical light metal layer are reduced by a factor of around 5 in comparison with the radius of a typical PWR. The simulation scale was chosen for consistency with the dimensions of an

experimental rig used to investigate the natural convection fluid dynamics in low Prandtl number fluids [12][14].

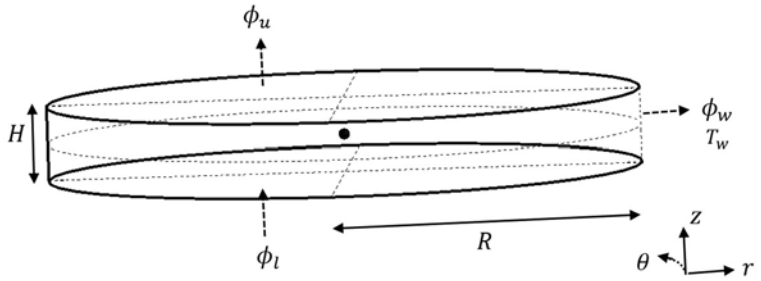

Figure 3: Schematic of the cylindrical fluid layer of depth H and radius R with heat flux of ϕ_l, ϕ_u and ϕ_w and the lower, upper and lateral walls respectively.

The light metal later is represented as a shallow cylinder 0.11 m in depth and 0.44 m in radius, corresponding to an aspect ratio of $\Gamma = R/H = 4$. The fluid layer is heated from below by a uniform flux of $\Phi_l = 2.1\ 10^5$ W m^{-2}, corresponding to an external Rayleigh number of $Ra_\Phi = 10^8$. Heat is dissipated from the upper boundary, with a uniform heat flux of Φ_u, and from the lateral wall with a heterogeneous heat flux, $\Phi_w(\theta, z)$. Hereafter, heat flux data at surface $i \in u, w, l$, for the upper, lateral and lower boundaries respectively, will be presented in dimensionless form, $\widehat{\Phi}_i = -\Phi_i/\Phi_l$. Thus, heat dissipation from the upper and lateral boundaries will present with a positive dimensionless heat flux. In the present investigation, two test cases are simulated with $\widehat{\Phi}_u$ = 0.1 and 0.9 respectively. The vertical lateral boundary is considered to be isothermal, with a wall temperature fixed at the melting point of the fluid, thereby mimicking a crust of the same composition at the lateral wall of the reactor vessel. The velocity boundary conditions at all three boundaries are modelled as no-slip.

The prototypic light metallic corium to be simulated is assumed to be composed largely of stainless steel with non-negligible concentrations of uranium and zirconium. The fluid is assumed to be incompressible, using a Boussinesq approximation to account for the density variation with temperature. The assumed physical properties the light metal layer are detailed in Table I. The Prandtl number of the fluid is 0.11, enabling comparison with corresponding spectral-DNS simulations using a fluid with a Prandtl number of 0.10 [8].

Table I. Estimated physical properties of the prototypic light metallic corium, assumed to be independent of temperature.

Density (kg m^{-3})	Dynamic viscosity (Pa s)	Thermal conductivity (W m^{-1} K^{-1})	Specific heat capacity (W kg^{-1} K^{-1})	Linear expansion coefficient (m^{-1})	Thermal diffusivity (m^2 s^{-2})	Melting point (K)
7000	5×10^{-3}	20	450	3×10^{-5}	6.3×10^{-6}	1700

The natural convection fluid dynamics in the light metal layer are resolved numerically by large eddy simulation (LES), using the TrioCFD code [15]. LES can offer a significant reduction in computational cost in comparison with direct numerical simulations (DNS) by low-pass filtering the Navier-Stokes equations. Larger scales are directly resolved, as with DNS, while the smallest length scales of the energy cascade, which are computationally intensive to resolve, are modelled. Here, the low-pass filter is applied at the mesh resolution and thus the mesh was constructed at a resolution sufficient to directly resolve at least 80 % of the turbulence energy spectrum. The discretisation of the fluid was informed by results of the spectral-DNS simulations of Rein [12]. The domain-averaged turbulence kinetic energy and dissipation rate indicated

Taylor scales of 9.4 mm and 10.1 mm at $\widehat{\Phi}_u = 0.1$ and 0.9 respectively. An unstructured mesh of tetrahedral elements was constructed with a 9 mm resolution in the bulk, refined through the boundary layer to a resolution of 900 μm at the walls, comparable to the Kolmogorov length scale. The resulting mesh consisted of around 9 million tetrahedral elements.

In the filtered Navier-Stokes equations, LES uses a turbulent eddy viscosity, ν_t, to model the sub-grid stress tensor. The Wall-Adapting Local Eddy-viscosity (WALE) implementation [13] uses a spatiotemporal operator to model the eddy viscosity derived from both the strain and rotation of the flow, rather than simply the former as in the case of classical Smagorinky approaches [16]. Furthermore, the operator reproduces realistic asymptotic decay in the eddy viscosity towards the wall without implementation of a near-wall filter [13]. LES WALE simulations have previously shown promise [5] in accurately simulating natural convection driven by an imposed heat flux at the lower boundary within the quasi-2D geometry employed for the BALI-Metal experiments [9]. Closure of the energy conservation equation is treated similarly as in [5], using a turbulent thermal diffusivity to resolve the sub-grid turbulent heat flux. The Simple Gradient Diffusion Hypothesis (SGDH) assumes proportionality between the turbulent shear stress and turbulent heat flux, which enables the turbulent thermal diffusivity to be approximated as $\alpha_t = \nu_t/\mathrm{Pr}_t$, where the coefficient of proportionality, Pr_t, is the turbulent Prandtl number. The turbulent Prandtl number is estimated in the 0.85-0.9 range for many engineering fluids with molecular Prandtl numbers close to unity [17] and close to 2 in liquid metals [18]. The two test cases presented are simulated using a turbulent Prandtl number of 2.

The two simulations were tracked until the thermal losses reached an apparent equilibrium with the heat injection from below and the mean and maximum fluid temperatures converged to a steady state. They achieved a pseudo-steady state after around 500 s of simulation time. Statistical analysis of the turbulent fluctuations in the resolved variables was then performed.

2.1. Non-dimensionalisation and nomenclature

In order to facilitate comparison with corresponding spectral-DNS calculations [8], results will be presented using the same non-dimensionalisation scheme, where the dimensionless temperature, $\hat{T}$, time, $\hat{t}$, length, $\hat{l}$, and heat flux, $\widehat{\Phi}_i$, are expressed as follows:

$$\hat{T} = \left(T - T_{mp}\right)\frac{\lambda}{\Phi_l H},\ \hat{t} = \frac{H^2}{\alpha},\ \hat{l} = \frac{l}{H},\ \widehat{\Phi}_i = -\frac{\Phi_i}{\Phi_l} \quad (1)$$

where T_{mp} is the melting point. Temporal-averages of variable 'x' are presented as $\bar{x}$ and fluctuations are $x' = x - \bar{x}$ respectively. Domain-averages over all spatial dimensions are denoted $\langle x \rangle$, while spatial-averages over dimensions i and j are expressed $\langle x \rangle_{i,j}$.

3. RESULTS AND DISCUSSION

The following sections discuss the structure of the convective flow observed during the two test cases, through the distribution of the mean temperature and velocity fields, the turbulence kinetic energy and its dissipation rate, as well as the distribution of the thermal losses from the lateral wall. An initial transient period was simulated. The calculation was deemed to have achieved a pseudo-steady state when the heat dissipation from the upper and lateral walls reached equilibrium with the heat injection from below. The rate of energy accumulation in the fluid normalized by the rate of energy input at the lower boundary is expressed as $\Delta W = 1 - \widehat{\Phi}_l - \frac{1}{\pi R^2}\int_0^H \int_0^{2\pi} \widehat{\Phi}_l \, d\theta \, dz$.

From $\hat{t} = 0.265$ (or 505 s), both test cases converged to $|\Delta W| < 0.023$ (Figure 4a), indicating that the energy accumulation/dissipation rate, including temporal fluctuations, was less than 2.3 % of the energy injection rate. At pseudo steady-state, statistical analysis of the stationary and transient components of the resolved fields was performed. The turbulence kinetic energy ($\hat{k}$) and dissipation rate ($\hat{\varepsilon}$) are estimated from half the

sum of the variance in the velocity components and the gradients of the fluctuating components of the velocity as follows:

$$\hat{k} = \left(\frac{H^2}{\alpha^2}\right)\frac{\overline{(u_i')^2}+\overline{(u_j')^2}+\overline{(u_k')^2}}{2}\ ;\quad \overline{(u_i')^2} = \frac{1}{t_2-t_1}\int_{t_1}^{t_2}(u_i(t)-\bar{u}_i)^2\,\mathrm{d}t\ ;\qquad \hat{\varepsilon} = \left(\frac{H^4}{\alpha^3}\right)\frac{\nu}{2}\overline{\left(\frac{\partial u'_\iota}{\partial x_J}+\frac{\partial u'_J}{\partial x_\iota}\right)^2} \quad (2)$$

With H the height of the domain, α and ν the thermal and dynamic viscosity, respectively
The evolution of the domain average turbulence kinetic energy and dissipation rate during the post-processing period shows that both metrics had converged to constant values from $\hat{t} > 0.34$ ($t > 650$ s) for the two test cases (see Figure 4b).

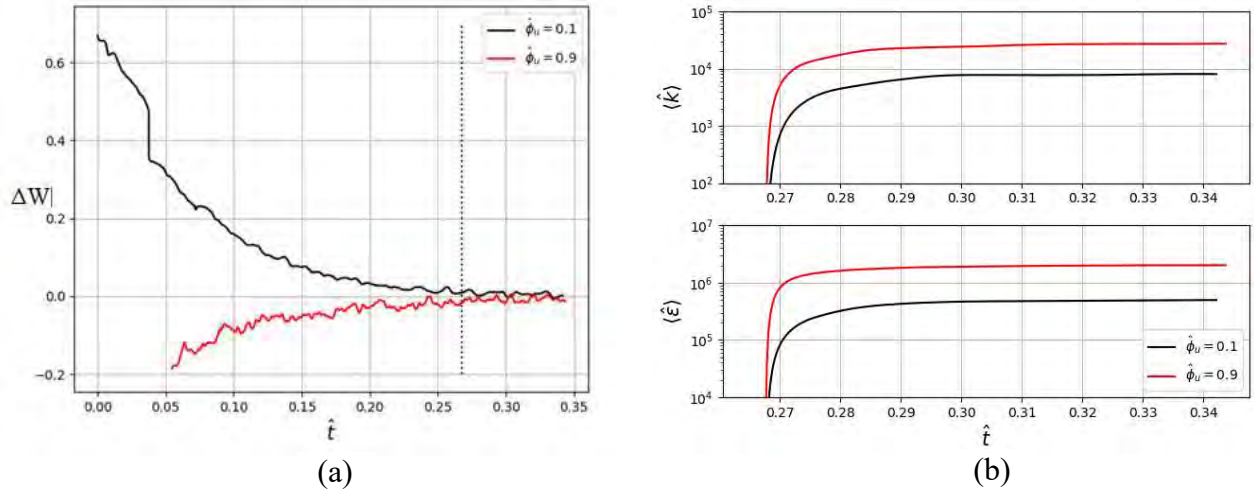

(a) (b)

Figure 4: (a) Normalised heat accumulation rate in the fluid and (b) convergence of the estimated domain average turbulent kinetic energy (top) and dissipation rate (bottom) during statistical post-processing at steady state.

3.1 Convective flow behaviour where lateral thermal losses are dominant ($\hat{\Phi}_u = 0.1$)

Two planar views of the instantaneous temperature field, superposed with the instantaneous velocity vectors, are presented at $\theta = 0°$ and $\hat{z} = 0.9$ in Figure 5a and b respectively for the test case with dominant lateral heat loss.
The fluid accelerates downwards along the cold lateral wall and a high velocity cold jet is expelled from the base of the lateral wall towards the centre of the fluid layer. As fluid increases in temperature along the heated lower boundary, warm metal eventually detaches, close to the centre of the fluid layer, and rises towards the free surface in a high temperature 'chimney'. This recirculation is observed as a convection cell in the $r - z$ plane occupying the full radius and height of the metal layer. From the $r - \theta$ plane at $\hat{z} = 0.9$, four high velocity 'branches' are observed demarcating four roughly equivalent convection cells. The rotational pattern and number of branches are consistent with observations from spectral-DNS simulations [8] and experiments using air ($Pr = 0.7$) as a low-Prandtl number simulant [14] above a threshold Rayleigh number, required to establish the rotating flow, in the order of $Ra_\Phi \sim 10^5$.
Animation of the temperature and velocity fields indicated that the high-temperature, high-velocity branches rotated in an anticlockwise direction through an angle of around 65° during a period of $\hat{t} = 0.022$, corresponding to a dimensionless rotation time of $\hat{t}_{360°} = 0.122$, or just under 4 minutes. Given the relatively

slow rotation, simulating several rotational cycles at steady state entails significant computational expense, and thus it remains unclear whether a constant rotational velocity has been established.

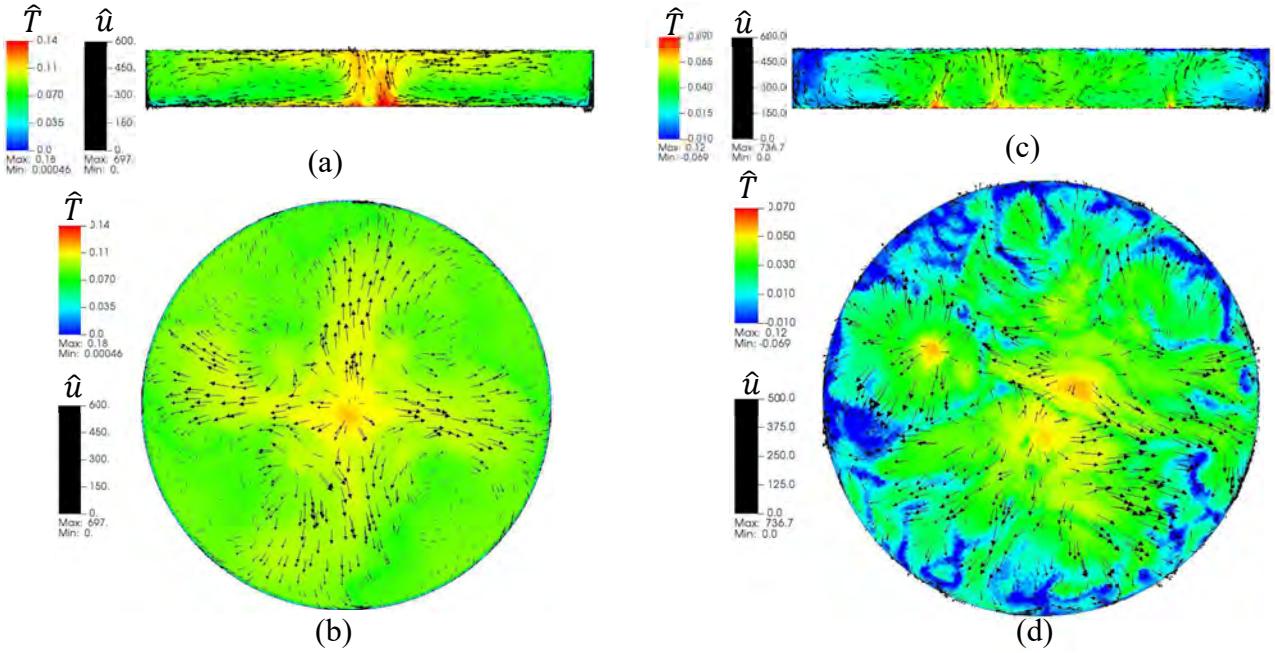

Figure 5: Visualisation of the dimensionless instantaneous temperature field superposed with the dimensionless instantaneous velocity vectors for the $\widehat{\Phi}_u = 0.1$ (a,b) and $\widehat{\Phi}_u = 0.9$ (c,d) test cases in (a,c) the $r - z$ plane at $\theta = 0°$ and (b,d) the $r - \theta$ plane at $\hat{z} = 0.9$

3.2 Convective flow behaviour where thermal losses at the upper boundary are dominant ($\widehat{\Phi}_u = 0.9$)

Two equivalent planar views of the instantaneous temperature field, superposed with the instantaneous velocity vectors, are presented for the $\widehat{\Phi}_u = 0.9$ test case at $\theta = 0°$ and $\hat{z} = 0.9$ in Figure 5c and d respectively. Downward acceleration of fluid is observed at the outer boundary; however, given the reduced lateral heat dissipation, this acceleration is less significant than the $\widehat{\Phi}_u = 0.1$ test case. Rather than generating very large permanent convection cells occupying the full radius of the fluid later, the weaker acceleration drives smaller outer convection cells. These outer convection cells remain larger in radial dimension than the axial direction, but are significantly less large in radial dimension than those observed during the $\widehat{\Phi}_u = 0.1$ test case.

Towards the centre of the fluid layer, multiple convection cells comparable in dimension to the depth of the fluid layer are observed. Hot plumes of fluid detach from the lower boundary at various locations rather than in a single chimney close to the centre of the fluid layer. The hot plumes detach, rise towards the free surface. These fluid dynamics at the centre of the fluid layer appear consistent with Rayleigh-Bénard convection. Relatively mild lateral heat dissipation from the fluid layer appears sufficient to drive larger, less axisymmetric convection cells adjacent to the outer boundary and a departure from conventional Rayleigh-Bénard convection in the outer radial zone. In the case of especially poor cooling at the upper boundary, or below a threshold dimensionless upward heat flux, $\widehat{\Phi}_u$, the non-axisymmetric outer convection cells occupy

the full radius of the fluid layer and the rotating permanent convection cell configuration is established. The fluid dynamics appear consistent with those observed by [8].

3.3 The mean temperature and turbulence fields

A two-dimensional representation of the stationary component of the temperature field was obtained from a temporal average of the temperature field in the $0.26 < \hat{t} < 0.34$ period, averaged in the theta axis ($0 \leq \theta \leq 360°$). This 2D mean temperature field, $\langle \hat{\tilde{T}} \rangle_\theta$, was then interpolated at regular intervals in the $\hat{z}$ axis and averaged to obtain a depth averaged radial temperature profile, $\langle \hat{\tilde{T}} \rangle_{\theta,z}$, for comparison with spectral-DNS results from [8] (see Figure 6). The LES and spectral-DNS predictions superpose very closely for the $\widehat{\Phi}_u = 0.1$ test case, with only a marginally elevated temperature in the hot chimney at the centre of the metal layer ($\hat{r} < 0.3$) predicted by the LES WALE simulation. The LES WALE simulation predicts a marginally lower bulk temperature for the $\widehat{\Phi}_u = 0.9$ case, but the two numerical approaches appear to exhibit excellent agreement in their predictions of the temperature field.

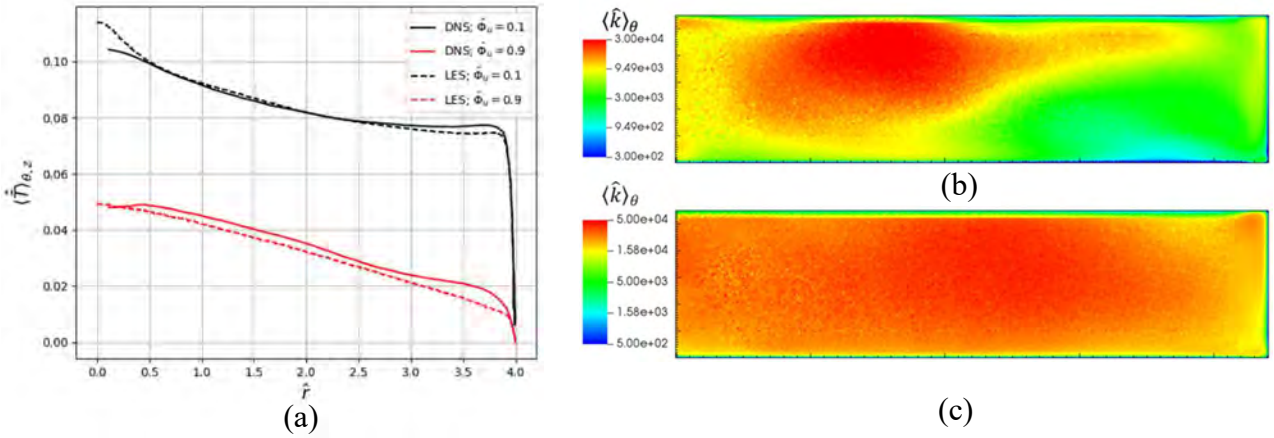

Figure 6: (a) Comparison of the radial profiles of the depth averaged mean temperature between the LES WALE and spectral-DNS [8] simulations, and the theta-averaged turbulence kinetic energy fields, $\langle \hat{k} \rangle_\theta$, for the (b) $\widehat{\Phi}_u = 0.1$ and (c) $\widehat{\Phi}_u = 0.9$ test cases (increasing in $\hat{r}$ from left to right).

The theta-averaged turbulence kinetic energy fields are presented (using a logarithmic scale) for the two test cases in Figure 6b-c. For the $\widehat{\Phi}_u = 0.1$ test case, elevated turbulence kinetic energies are observed at the centre of the large rotating convection cells previously observed in Figure 5 with a concentration of turbulence kinetic energy closer to the centre of the fluid layer, $\hat{r} < \Gamma/2$. The turbulence kinetic energy dissipates rapidly within the upper and lower boundary layers. For the $\widehat{\Phi}_u = 0.9$ test case, the multiple, more axisymmetric convection cells of shorter duration, more consistent with Rayleigh-Bénard convection, produce a more homogeneous distribution of turbulence kinetic energy in the $r - z$ plane through the bulk, while also dissipating rapidly through the boundary layers.

3.4 Distribution of the thermal losses from the lateral wall

The spatial distribution of the dimensionless instantaneous heat flux at the lateral wall, $\widehat{\Phi}_w$, is presented for the two test cases in Figure 7. For the $\widehat{\Phi}_u = 0.1$ test case, a relatively uniform band of elevated heat dissipation is observed at the top of the lateral wall, revealing the focusing effect. The heat flux is around 3-times

the magnitude of the rate of heat injection from below. Diminished thermal losses are observed at the base of the lateral wall, in the region from which the cold jet is propelled along heated lower boundary. At intermediate depths ($0.2 < \hat{z} < 0.9$) focusing effects in the order of $1.4 < \hat{\phi}_w < 2.4$ are observed, with elevated heat dissipation in the proximity of the high velocity 'branches' previously observed in Figure 5.
For the $\widehat{\Phi}_u = 0.9$ test case, negligible heat losses are observed over much of the lateral boundary, $\hat{\phi}_w < 0.3$, punctuated by zones of elevated heat dissipation in the vicinity of the outer convection cells. Maximum local heat flux values comparable in magnitude to the rate of heat injection from below are observed. Unlike the significant, permanent lateral heat dissipation at the top of the fluid layer in the $\widehat{\Phi}_u = 0.1$ test case, the zones of elevated local heat dissipation ($\hat{\phi}_w > 0.7$) are transient in nature, presenting over the timescale of near-wall convection cells. By contrast, a very thin permanent layer adjacent to the lower boundary exhibits heat dissipation in excess of the rate of heat injection, $\hat{\phi}_w < 1.4$.

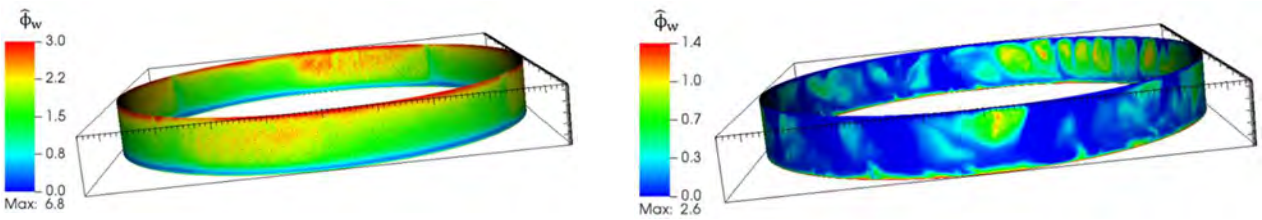

(a) (b)

Figure 7: Instantaneous dimensionless heat flux from the lateral wall, $\widehat{\Phi}_w$, for the (a) $\widehat{\Phi}_u = 0.1$ and (b) $\widehat{\Phi}_u = 0.9$ test cases.

The steady-state component of the lateral heat flux is approximated by the non-dimensional heat flux field, averaged over time and the theta-axis, $\left\langle \widehat{\Phi}_w \right\rangle_\theta$, which is presented for the two test cases as a function of axial position in Figure 8. Corresponding results of spectral-DNS simulations [8] are presented for comparison. The LES demonstrates particularly good agreement with the spectral-DNS for depths of $\hat{z} < 0.8$. The elevated heat dissipation immediately adjacent to the heated lower boundary and the reduction in heat dissipation at the base of the cold jet are in particularly good agreement between LES and spectral-DNS.
For the $\widehat{\Phi}_u = 0.9$ test case with dominant heat dissipation from the free-surface, the LES prediction of the lateral heat flux in the vicinity of the free surface ($\hat{z} > 0.9$) exhibits some departure from the spectral-DNS. For both simulations, the dimensionless lateral heat flux becomes negative in this region, implying local fluid temperatures below the corium melting point. This is an artefact of approximating the corium-crust interface at a fixed location in order to avoid the computational expense of modelling the transient displacement of the solidification front. The negative dimensionless lateral heat flux predicted by both LES and spectral-DNS approaches indicates a likelihood of some crust development at the confluence of the lateral wall and the free surface. The mild departure between the LES and spectral-DNS in the region where the metal is anticipated to solidify is not of significant concern.
The LES simulation of the test case with dominant lateral heat dissipation, $\widehat{\Phi}_u = 0.1$, exhibits a more significant departure from the spectral-DNS close to the free surface ($\hat{z} > 0.9$). This region is of particular interest since the maximum focusing effect is observed very close to the free surface. While the spectral-DNS indicates a continuous increase in lateral heat dissipation up to a maximum of $\langle \hat{\phi}_w \rangle_\theta \approx 3.5$ very close to the free surface, the LES peaks at $\langle \hat{\phi}_w \rangle_\theta \approx 2.8$ marginally below the free surface with a very mild reduction in the immediate proximity of the free surface. The disparity is considered to be a numerical artefact of the spatial discretisation employed for the LES simulation close to the free surface. The significant refinement of the unstructured mesh over a narrow upper boundary layer results in a relatively large ratio in characteristic mesh dimension between neighbouring cells, which poses a challenge for the finite volume element (VEF) discretisation scheme [15].

The axial profile of the lateral heat dissipation for the $\widehat{\Phi}_u = 0.1$ test case qualitatively resembles the thin cuboidal simulation results of a prototypic test case [5], where $\widehat{\Phi}_u = 0.34$, $\Gamma = 5$ and $Ra_\Phi = 8.5 \times 10^{11}$, presented in Figure 2. The reduction in lateral heat dissipation in the vicinity of the base of the cold jet, the progressive increase in heat dissipation towards the free surface at intermediate depths, and the rapid escalation of the focussing effect close to the free surface are common features of the two simulations and can be considered characteristic of test cases with poor cooling at the upper boundary. However, for the thin cuboidal simulation at an elevated Rayleigh number, the weak lateral dissipation zone at the base of the cold jet is shallower, the magnitude of the lateral heat dissipation from intermediate depths and the severity of the focussing effect are greater in the thin cuboidal simulation. Care should be taken when comparing the magnitude of heat losses from the lateral wall between the thin cuboidal and cylindrical geometries as the cylindrical geometry offers a much greater surface for lateral heat dissipation. Consequently, $\langle \widehat{\Phi}_w \rangle = \Gamma(1 - \widehat{\Phi}_u)$ for the thin cuboidal geometry, while $\langle \widehat{\Phi}_w \rangle = \frac{\Gamma}{2}(1 - \widehat{\Phi}_u)$ for cylindrical geometries. It is reassuring that simulations in both the cylindrical and thin cuboidal geometry produce consistent trends in the lateral heat flux profiles for cases which poorly dissipate heat at the upper boundary. However, the heterogeneity in lateral heat flux as a function of angular coordinates identified in Figure 7, driven by the rotation of large persistent convection cells, demonstrates a clear advantage of simulating the full cylindrical domain and averaging heat flux for cases where the required computational resources are not prohibitive.

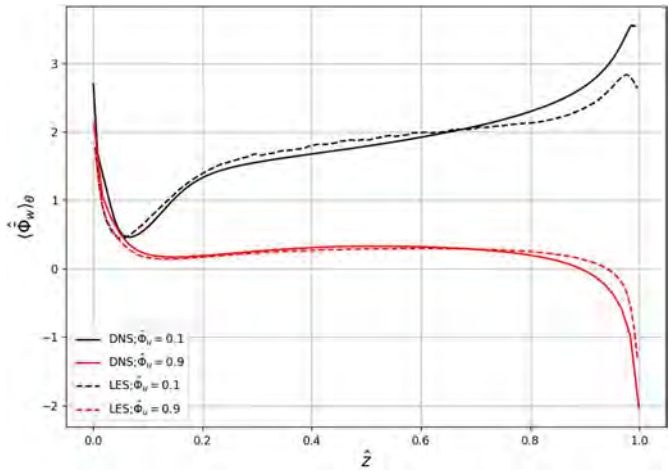

Figure 8: Comparison of the theta-averaged dimensionless heat flux at the lateral wall between LES (present study) and spectral-DNS [8].

4. CONCLUSIONS

Maintaining a local lateral heat flux from a stratified corium pool below the critical heat flux is an essential component of the In-Vessel Retention strategy. A maximum flux is observed at the level of a highly-conductive steel-rich shallow light metal layer, referred to as the focusing effect. Two LES WALE simulations were performed to assess the lateral heat flux distribution from a cylindrical pool of low Prandtl number fluid ($Pr = 0.11$), heated from below with an external Rayleigh number of $Ra_\Phi = 10^8$, with strong and weak cooling at the upper surface (90% and 10% of the rate of heat injection from below respectively, or $\widehat{\Phi}_u = 0.9$ and 0.1). Simulations demonstrated very good agreement with corresponding spectral-DNS simulations [8] in terms of the steady state temperature and lateral heat flux distributions. The LES WALE approach to modelling the smallest length scales of the turbulent energy cascade may therefore offer a computationally feasible solution to extending existing correlations for natural convection in the light metal layer into a higher Rayleigh number regime ($Ra_\Phi > 10^8$), taking into account lateral profile.

In the case of dominant heat dissipation at the upper surface was characterized by more axisymetric and shorter-lived convection cells away from lateral boundary comparable in dimension with the depth of the fluid layer, consistent with Rayleigh-Bénard convection. Slightly larger, les axisymmetric convection cells were observed adjacent to the lateral boundary. The simulations indicate that additional metallic crust is likely to develop at lateral wall in the vicinity of the upper surface. The case of weak heat dissipation at the upper surface was characterized by significant downward acceleration of fluid at the lateral boundary, ex-pulsion of a cold jet from the base of the lateral wall and recirculation of warm fluid in a chimney at the center of the fluid layer. These phenomena resulted in the formation of four[1] large permanent convection cells, demarcated by branches of elevated radial velocity, occupying the radius and depth of the fluid layer, which were observed to rotate in an anticlockwise direction. The maximum local heat dissipation from the lateral boundary was in the order of three times the magnitude of heat injection from below.
The lateral heat flux profile and convective flow behaviour in the $r-z$ plane observed for the case of limited heat dissipation at the upper boundary appear consistent with simulations of a prototypic test case, with a significantly elevated Rayleigh number of $Ra_{\Phi} = 8.5 \times 10^{11}$ and radiative heat dissipation at the upper surface, performed within the IAEA CRP J46002 framework [5]. The prototypic test case was simu-lated using a quasi-2D geometry, representing a thin slice through the $r-z$ plane. While the quasi-2D geometry appears sufficient to predict the mean heat dissipation behaviour at the lateral boundary, the tran-sient peaks in local heat flux in the vicinity of the rotating branches is only captured by simulating the full cylindrical geometry. Work is ongoing to smooth the near-wall mesh refinement to determine whether better agreement with the spectral-DNS can be achieved in a small zone of elevated heat dissipation adjacent to the lateral and upper boundaries. Future work includes plans to couple LES WALE simulations with an enthalpy-porosity model to account for steel solidification.

ACKNOWLEDGMENTS

This numerical work was granted access to the HPC resources of the CEA's Very Large Computing Centre (TGCC) under the GENCI allocations 2024-2025 A0162A15096. The authors wish to thank Laure Carénini and Florian Rein of ASNR for sharing data from spectral-DNS simulations presented in [8] and [12].

REFERENCES

[1]. Carénini, L., Fichot, F. & Seignour, N., Modelling issues related to molten pool behaviour in case of In-Vessel Retention strategy, Annals of Nuclear Energy, 118, 363-374 (2018)
[2]. Le Tellier, R., Saas, L., & Bajard S. Transient stratification modelling of a corium pool in a LWR vessel lower head, Nuclear Engineering and Design, 287, 68-77 (2015)
[3]. Salay, M., Fichot, F., 2004. Modelling of corium stratification in the lower plenum of a reactor vessel. In: Proceedings of MASCA Seminar 2004, Aix-en-Provence, France, June 10–11, 2004.
[4]. Le Guennic C. et al, Synthesis of the WP2.3 results on the metallic layer and new correlations, Inter-national Seminar In-vessel retention: outcomes of IVMR project, Palais des Congrès, Juan-les-Pins, France, January 21-22, 2020
[5]. Seiler, N., Johnson, M., Drouillet, A., Bian, B., Villanueva, W., Zhabin, O., Vorobyov, Y., Kratochvil, M., Vyskocil, L., Abu Bakar. M. Natural convection in a shallow pool heated from below and impli-cations for the thermal focusing effect at the lateral wall, Nuclear Engineering and Design 431 113703 (2025)
[6]. Noh, W. N., & Suh, K. Y., Critical heat flux for APR1400 lower head vessel during a severe accident, Nuclear Engineering and Design, 258, 116-129 (2013).

[1] For this given Rayleigh number

[7]. Chatelard, P., & Laborde, L., ASTEC V2. 2 code validation: Illustrative results and main outcomes. Nuclear Engineering and Design, *413*, 112547 (2023).
[8]. Rein, F., Carénini, L., Fichot, F., Favier, B., & le Bars, M. Interaction between forced and natural convection in a thin cylindrical fluid layer at low Prandtl number. Journal of Fluid Mechanics, 977 (2023).
[9]. Bonnet J.M., Villermaux C., Assessment of Reactor Vessel Integrity (ARVI) BALI-metal test reports: focusing effect investigation, Report of the 5th Framework progamme on nuclear fission, European Commission, SAM-ARVI-D.2.1.2 (2001).
[10]. Rein, F., Carénini, L., Fichot, F., Favier, B., & le Bars, M. New correlations for focusing effect evaluation of the light metal layer in the lower head of a nuclear reactor in case of severe accident, Nuclear Engineering and Design, 428, 113540 (2024).
[11]. Fischer, P. F. An Overlapping Schwarz Method for Spectral Element Solution of the Incompressible Navier-Stokes Equations. Journal of Computational Physics, 133, 84–101, 1997
[12]. Rein, F, Étude des Régimes de Convection Mixte dans une Couche de Fluide Mince : Application aux situations de rétention des matériaux fondus dans la cuve d'un réacteur nucléaire en situation d'accident grave, PhD thesis, Aix-Marseille University, France, 2024.
[13]. Nicoud F., Ducros F., Subgrid-scale stress modelling based on the square of the velocity gradient tensor, Flow, Turbulence and Combustion 62, 183–200 (1999).
[14]. Rein, F., Carénini, L., Fichot, F., Favier, B., Le Bars, M. Experimental study of the convection in a thin cylindrical gas layer with imposed bottom and top fluxes and imposed side temperature. Journal of Fluid Mechanics, 1006, A22, 2025.
[15]. Angeli, P.-E., Bieder, U., Fauchet, G., 2015. Overview of the TrioCFD code: main features, V&V procedures and typical applications to nuclear engineering. NURETH 16–16th International Topical Meeting on Nuclear Reactor Thermal-hydraulics, 30 August–4 September 2015, Chicago, Illinois, USA.
[16]. Smagorinsky J., General circulation experiments with the primitive equations I. The basic experiment, Monthly Weather Review 91 99–164, 1963.
[17]. Huang, X., Pang, B., Chai, X., & Yin, Y. Proposal of a turbulent Prandtl number model for Reynolds-averaged Navier–Stokes approach on the modeling of turbulent heat transfer of low-Prandtl number liquid metal. Frontiers in Energy Research, 10, 1-17, 2022
[18]. Mathur, A., Roelofs, F., Fiore, M., & Koloszar, L., State-of-the-art turbulent heat flux modelling for low-Prandtl flows. Nuclear Engineering and Design. 406. 112241, 2023.

SIMULATION OF THE LOW PRANDTL LAYER OF A CORIUM POOL

Johnson M, **Seiler N**

The 12th European Review Meeting on Severe Accident Research (ERMSAR2026), CIEMAT, Madrid, Spain, May 18-22, 2026

Contents

1. **Introduction and context**
2. **Numerical methods**
3. **Results and discussion**
4. **Conclusions and perspectives**

Introduction and context (1/2)

Context: In-Vessel Retention Strategy.
Importance of properly simulating the focusing effect on the metallic layer (stratified corium pool configuration) → Pressure vessel integrity

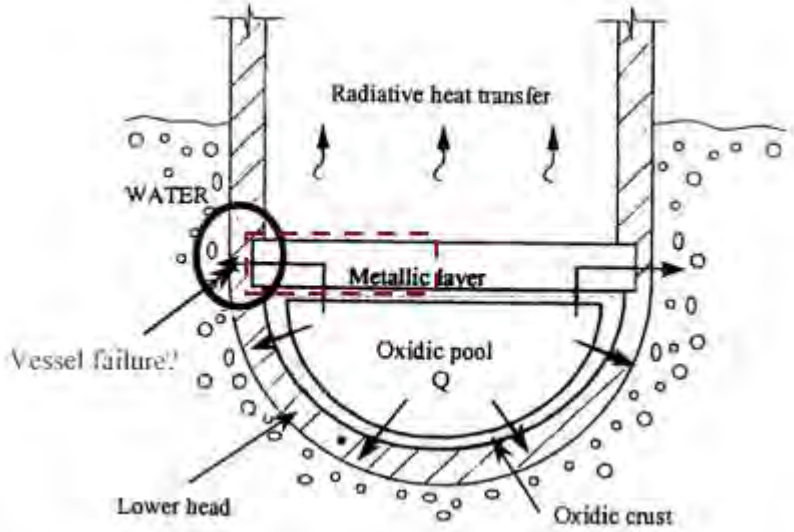

⇒ **IAEA CRP J466002**: CFD benchmark on the thermo-hydraulics in this layer → local insights

Seiler et al. 2023 Nuclear Engineering and Design, 431, 2025, 113703

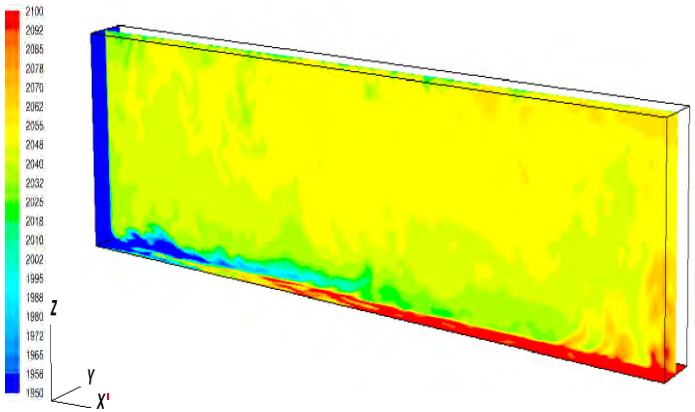

Thin cuboidal geometry, prototypical case : $\frac{P_{up}}{P_{down}}$~45 %, of $Ra_{\Phi} = 8.5 \times 10^{11}$

→ complex fluid dynamics - superposition of two convection regimes :

- Rayleigh-Bénard convection driven by heat transfer in the vertical
- direction large convection cell produced by buoyancy in the fluid

→ Local axial heat flux profile → local focusing effect

Introduction and context (2/2)

→ **issues requiring further research**

Simulations	Reality
Validation of CFD tools on BALI-Metal experiments (Pr ≈ 7)	metallic liquid (Pr ≈10^{-2})
Quasi-2D, thin cuboidal geometry	3D fluid dynamics in a shallow cylindrical geometry
• CFD simulation : severe gradients in the lateral heat flux profile (local maximum focusing effect) • Macroscopic simulation : surface-averaged lateral heat dissipation	local maximum focusing effect
Critical zones for the CFD simulation at the lower and upper extremes of the lateral boundary (low velocity)	

Objective : extension to
- low-Prandtl number fluid
- a representative cylindrical geometry

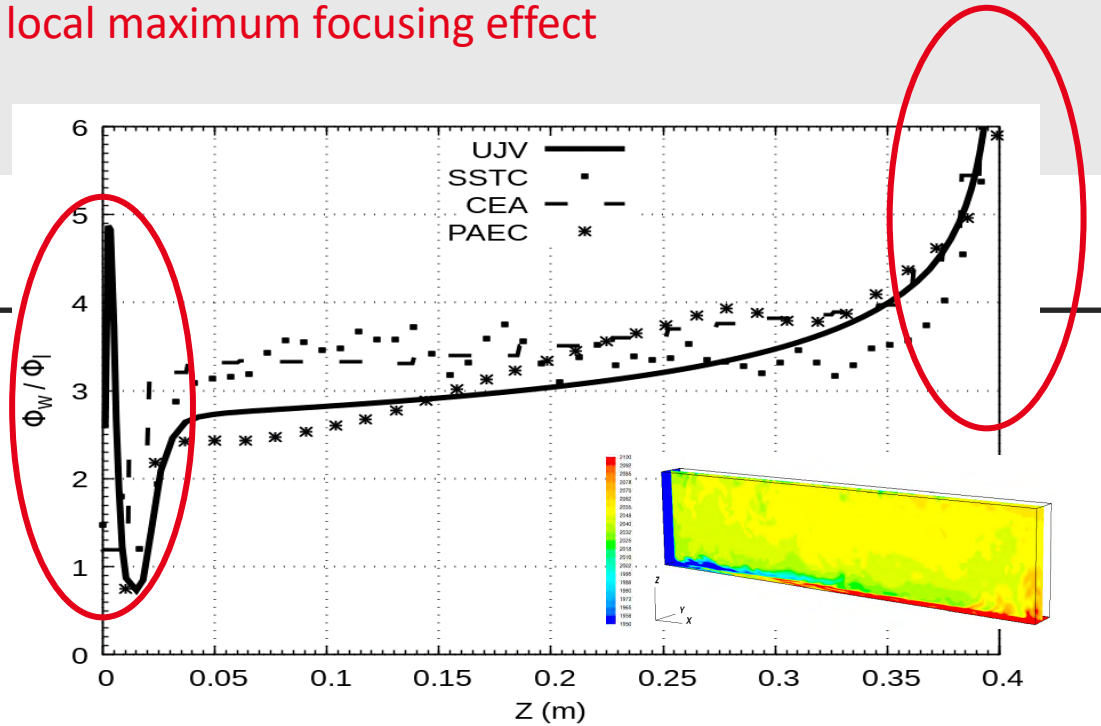

Evolution of lateral heat flux over lower one along the height (vessel surface)

Test case & Numerical method (1/2)

Representative test case : Rein et al. 2025, 10.1017/jfm.2025.2. hal-05177850

FOCUS experiment *(data not available)*
- Cylindrical ($\Gamma = R/H = 4$) ; R=0.44 m
- Seeded SF6 – low Prandtl

Prior to experiment : **DNS NEK 5000 simulations**
- Pr=0.11 - $Ra_\Phi = 10^8$
- $\Phi_l = 2.1\ 10^5$ W m^{-2} - uniform
- 2 cases : $\widehat{\Phi}_u = \frac{\phi_u}{\phi_l} = 0.1$ and 0.9 - ϕ_u uniform, $\phi_w(\theta, z)$
- Vertical boundary, $T_w = cst$ - melting point (mimicking a crust)
- Velocity boundary conditions at all three boundaries as no-slip

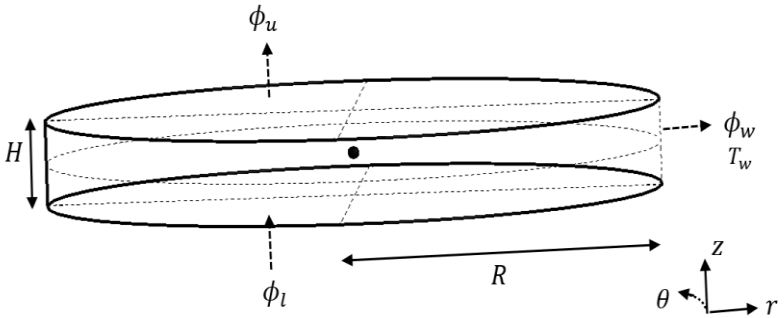

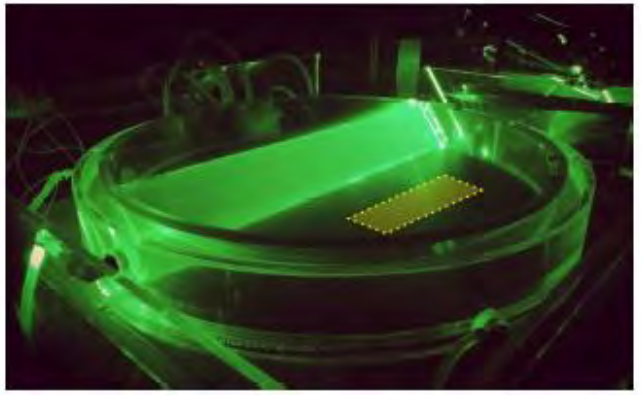

Our simulation (same methodology than in **CRP J466002**):
- Geometry $\Gamma = R/H = 4$) ; R=0.44 m
- Pr=0.11
- Same boundary conditions as DNS NEK 5000 simulations
- Incompressible TrioCFD code - Boussinesq approximation
- LES simulations :
  - Wall-Adapting Local Eddy-viscosity (WALE) – near wall turbulence
  - Simple Gradient Diffusion Hypothesis (SGDH) Pr_t=2 (liquid metal)
- Meshing respecting turbulent length scale : 900 μm near walls- 9mm in bulk
  → ~ 36 million tetrahedral elements

Density (kg m^{-3})	Dynamic viscosity (Pa s)	Thermal conductivity (W m^{-1} K^{-1})	Specific heat capacity (W kg^{-1} K^{-1})	Linear expansion coefficient (m^{-1})	Thermal diffusivity (m^2 s^{-2})	Melting point (K)
7000	5×10^{-3}	20	450	3×10^{-5}	6.3×10^{-6}	1700

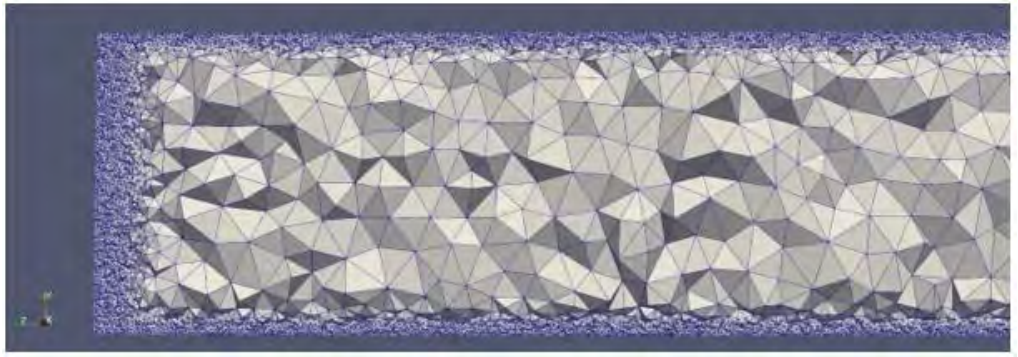

Test case & Numerical method (2/2)

Establishment of **pseudo-steady state**, following :

- Energy balance $\Delta W = 1 - \hat{\Phi}_u - \frac{1}{\pi R^2}\int_0^H \int_0^{2\pi} \hat{\Phi}_w \, d\theta \, dz$
- Different metrics

Steady-state $\hat{t} = t\frac{\alpha}{H^2} > 0.34$ i.e. 650 s

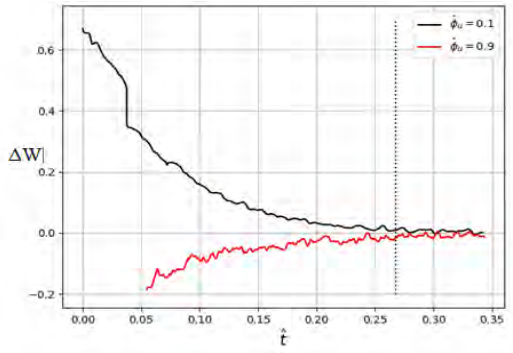

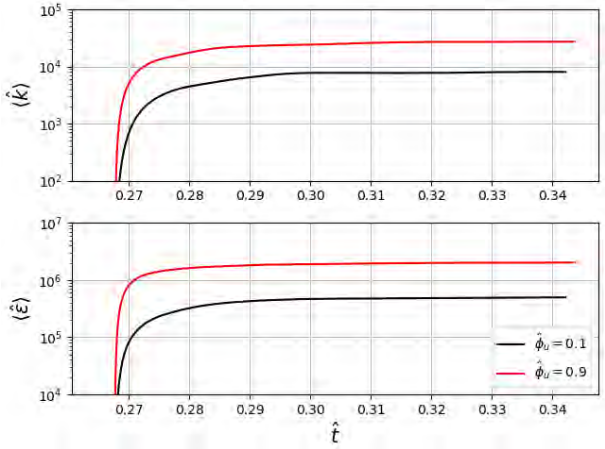

Some results

Temporal and azimuthal and then axial averages

Good agreement with DNS results

- $\hat{\Phi}_u$ =0.1 – LES overestimation in the hot chimney (pool centre- $\hat{r} < 0.3$)
- $\hat{\Phi}_u$ =0.9 – LES marginally lower bulk temperature prediction

$$\hat{T} = \frac{T}{T_{ad}}$$

$$T_{ad} = (T - T_{mp})\frac{\lambda}{\Phi_l H}$$

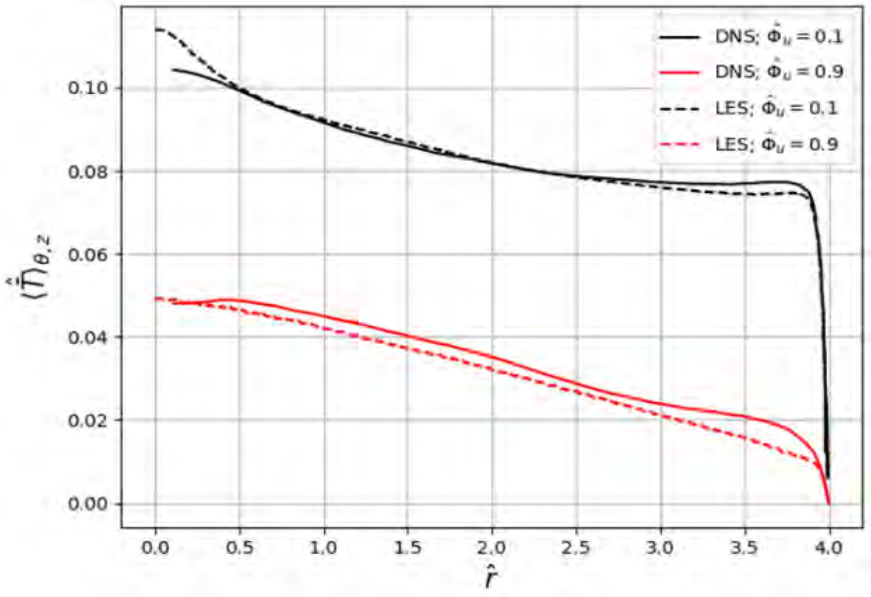

Results

$\hat{\Phi}_u = 0.1$

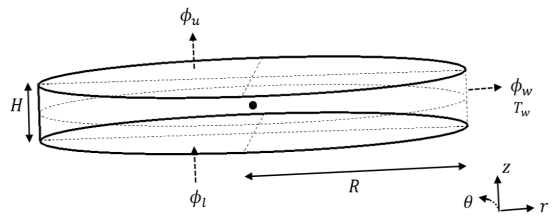

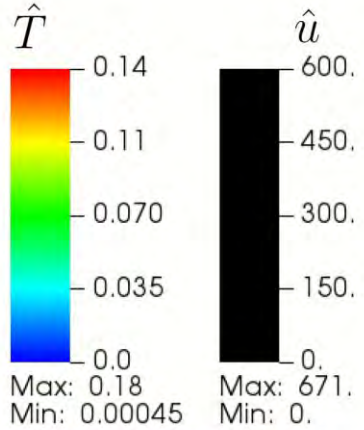

$\hat{t} \times 10^3 = 0$

r-z plane, θ=0°

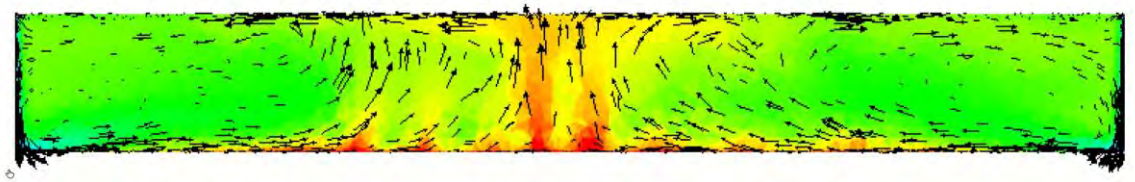

$t = 42\,\mathrm{s}$

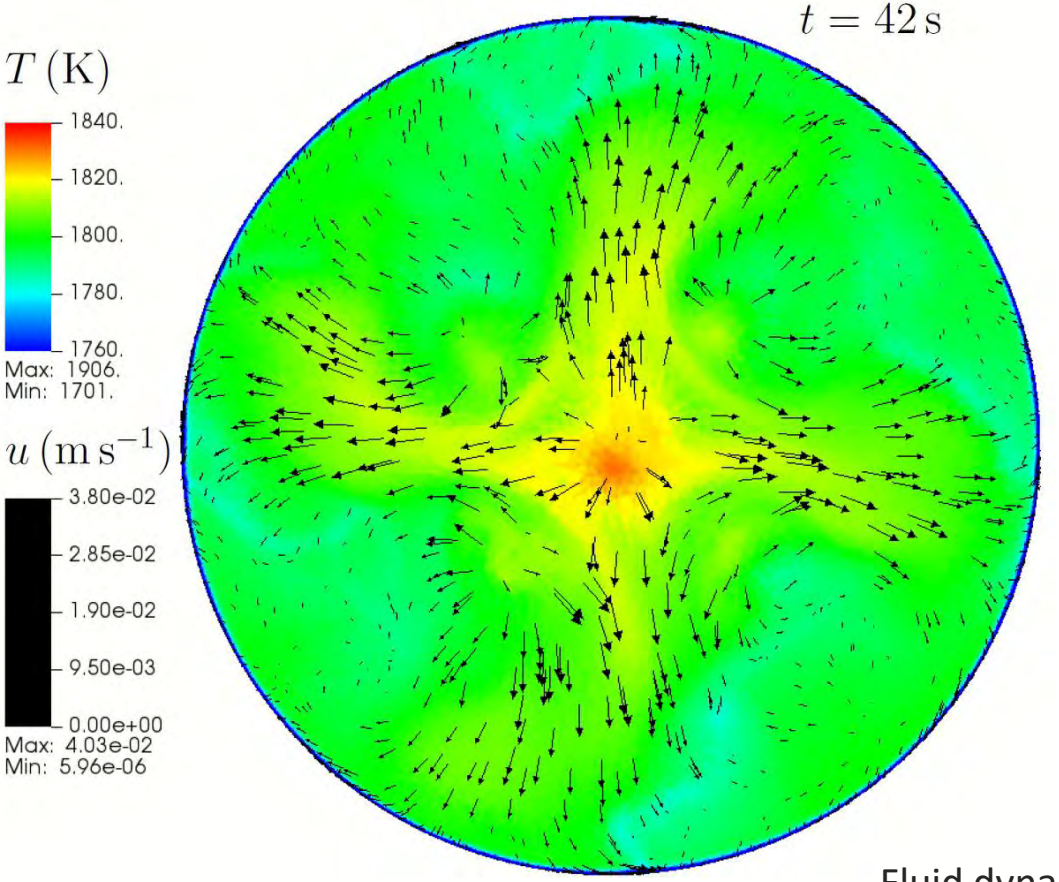

- Large convection cell in the $r - z$ plane
- Four high velocity ‘branches’
- Rotation pattern (anticlockwise and period ~4 min) and number of branches consistent with DNS simulations

Fluid dynamics constistent with DNS results of Rein et al.

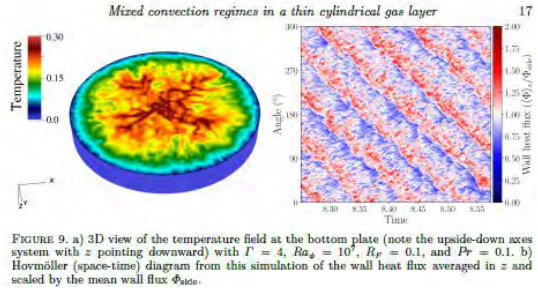

FIGURE 9. a) 3D view of the temperature field at the bottom plate (note the upside-down axes system with z pointing downward) with $\Gamma = 4$, $Ra_\Delta = 10^7$, $R_P = 0.1$, and $Pr = 0.1$. b) Hovmöller (space-time) diagram from this simulation of the wall heat flux averaged in z and scaled by the mean wall flux Φ_{wide}.

Results

$\hat{\Phi}_u = 0.9$

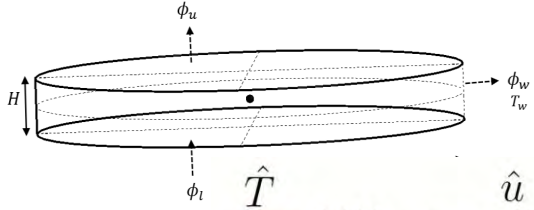

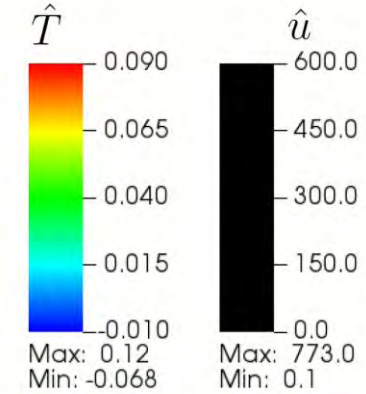

$\hat{t} \times 10^3 = 0$

r-z plane, θ=0°

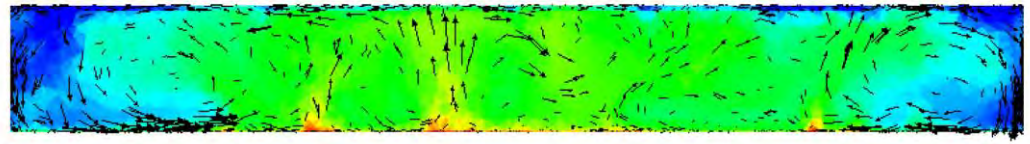

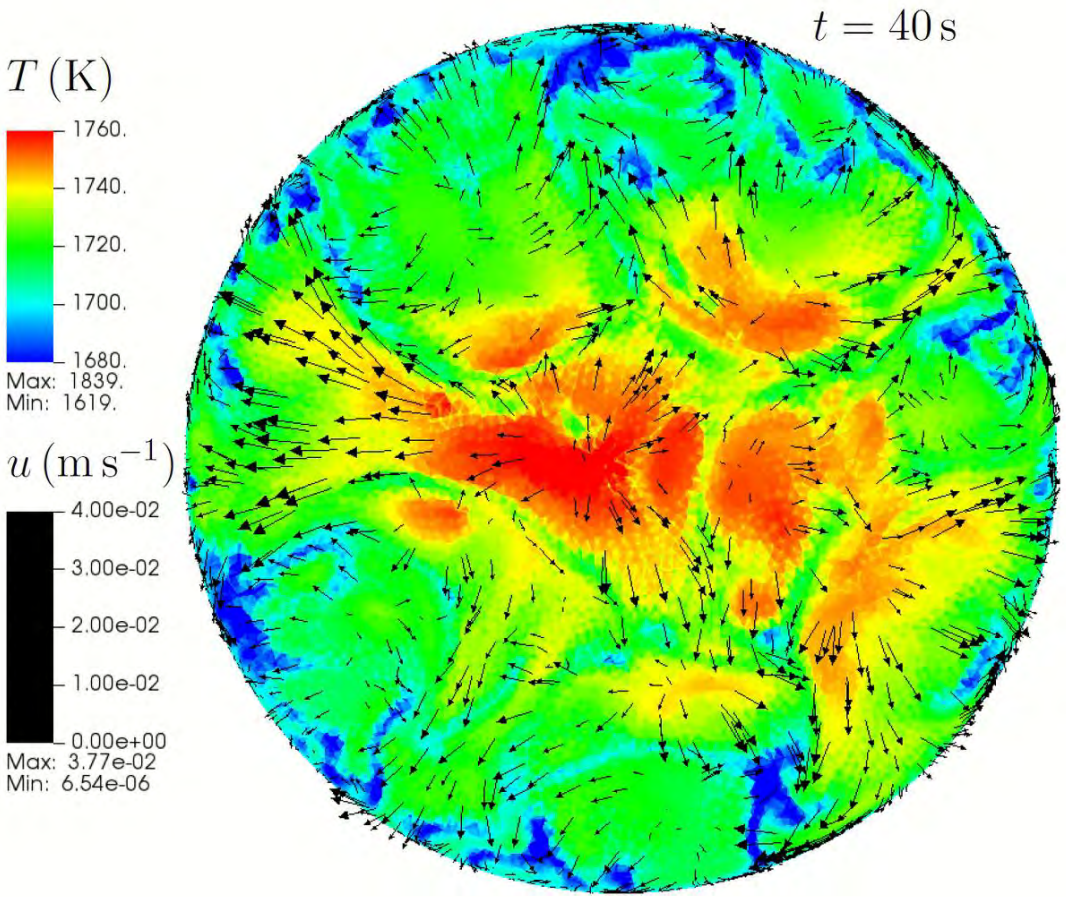

- Weaker acceleration → smaller outer convection cells (larger radially than axially)
- Fluid dynamics at the center ~ Rayleigh-Bénard cells.

Fluid dynamics constistent with DNS results of Rein et al.

Results – lateral heat flux

Spatial distribution of dimensionless instantaneous heat flux

$\hat{\Phi}_u$ =0.1

- Uniform band of elevated heat dissipation at the top of the lateral wall → the focusing effect (× 3 Φ_l).
- Elevated heat dissipation in the proximity of the high velocity 'branches'

$\hat{\Phi}_u$ = 0.1

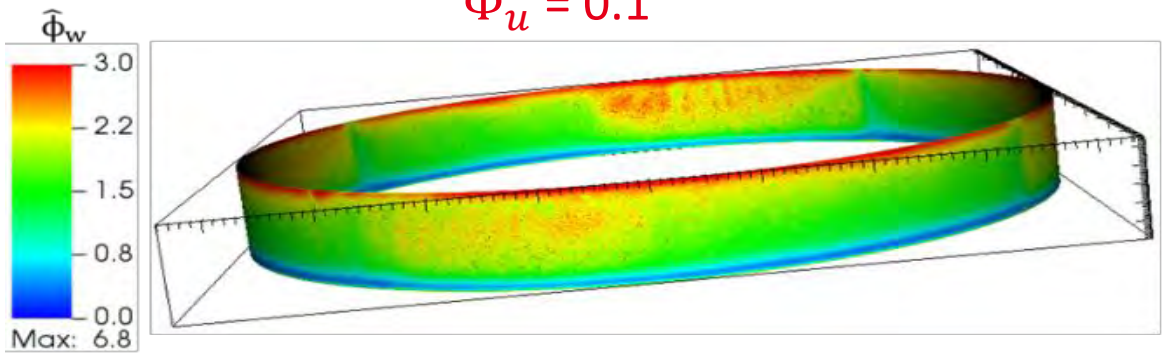

$\hat{\Phi}_u$ =0.9

- Negligible heat losses (~Φ_l) , punctuated by transient zones of elevated heat dissipation in the vicinity of the outer convection cells,
- More dissipation in a thin permanent layer adjacent to the lower boundary

$\hat{\Phi}_u$ = 0.9

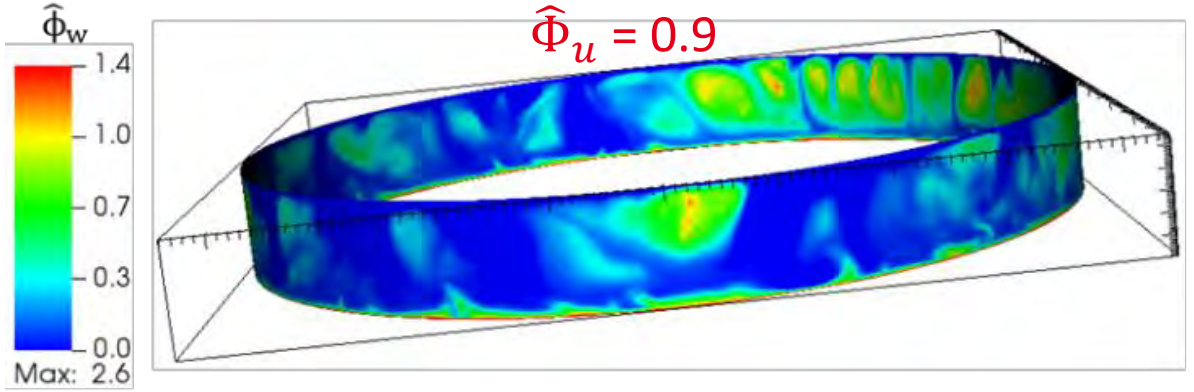

Results – lateral heat flux

θ-averaged dimensionless heat flux

Good agreement with DNS for $\hat{z} < 0.8$ (pool top)

$\hat{\Phi}_u$ =0.1

- lower heat flux at the bottom and at the top with the LES model than with the DNS model,
- At the top, very low speeds are very difficult to simulate accurately in both DNS and LES.

$\hat{\Phi}_u$ =0.9

- Higher heat flux at the bottom
- Negative in the top region, implying local fluid temperatures below the corium melting point (curst solidification should be considered)

Such areas with right angles not representative of the reactor geometry ; ablation or formation of crusts

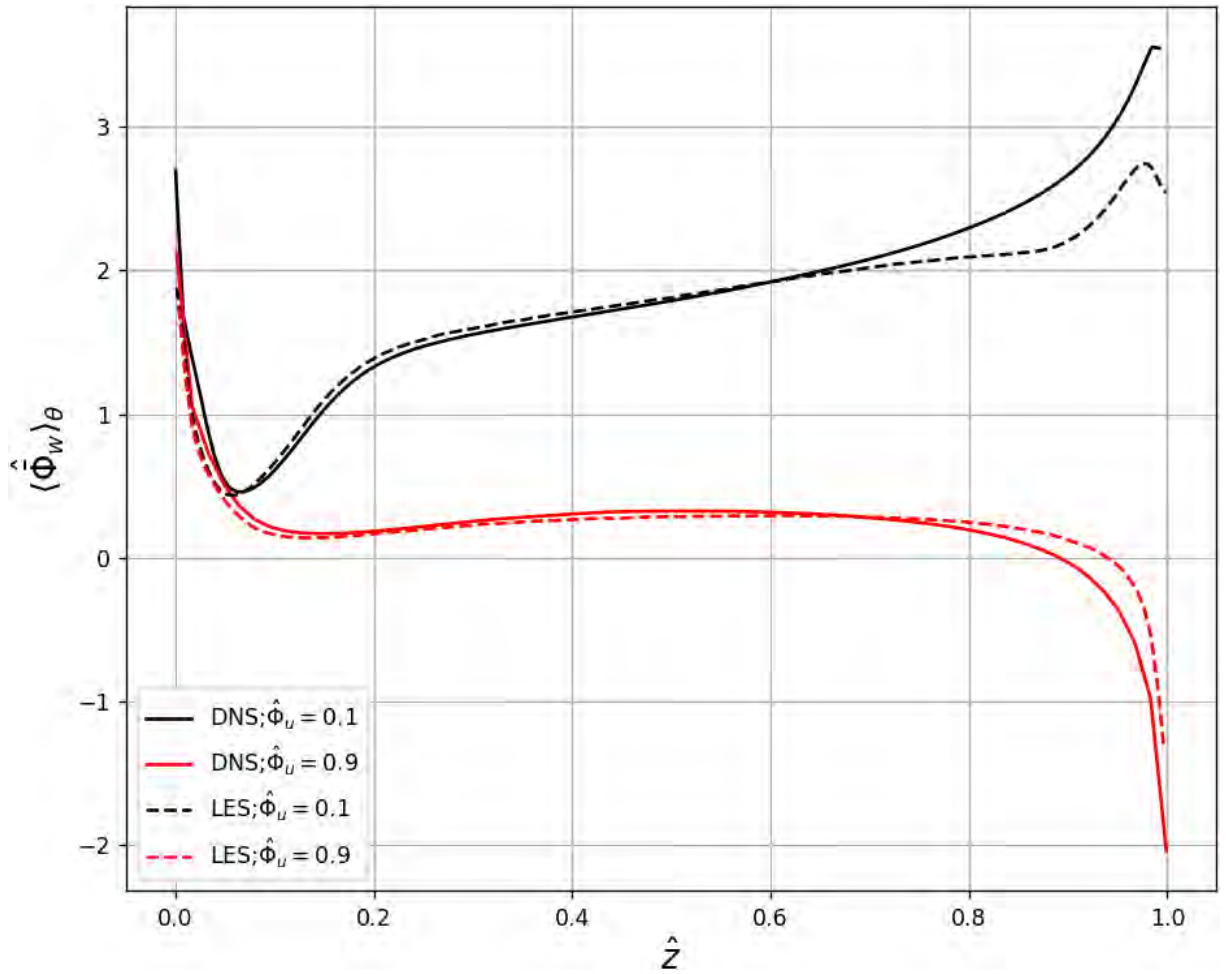

Conclusions and perspectives

- CFD simulations help to derive reliable lateral axial profile of heat flux on the reactor vessel.
- Validation of the LES simulation against DNS results for a low-Prandtl-number cylindrical case showed :
  - The adapted turbulence model is valid for Prandtl numbers <<1
  - 3D geometry affects flow dynamics, leading to the formation of rotating convection cells

- The thermal-hydraulics of a metal pool under IVR conditions are complex and can vary significantly depending on the ratio of the heat flux released from the top.
  - If this ratio is high, the flow exhibits small Rayleigh–Bénard convection loops and weak lateral flows, which can even lead to crust formation at the top of the pool;
  - In the case of a weak ratio, a large convection loop, spanning the width of the pool, dominates the flow. Azimuthally, these loops are separated, leading to warm branches that exhibit a rotational motion. This situation can lead to significant local heat fluxes at the top of the pool.

- **Perspectives** :
  - It would be interesting to take the axial flow profile into account in macroscopic codes – instead of an average value.
  - couple LES WALE simulations with an enthalpy-porosity model to account for steel solidification.

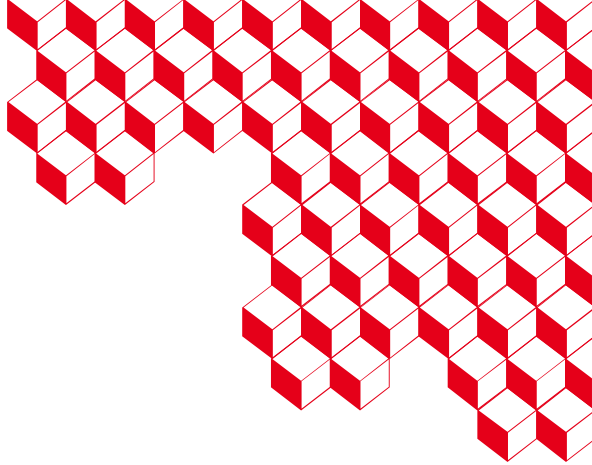

Thank you for your attention

Analysis of In-Vessel Retention in a VVER-1000 Reactor Design using AC²

P. Pandazis*, L. Lovász, A. Wielenberg
Gesellschaft für Anlagen- und Reaktorsicherheit (GRS) gGmbH
Boltzmannstraße 14, 85748, Garching, Germany
peter.pandazis@grs.de, liviusz.lovasz@grs.de, andreas.wielenberg@grs.de

ABSTRACT

Use of In-Vessel Retention (IVR) through External Reactor Vessel Cooling (ERVC) is a widely considered severe accident management strategy for light water reactors. Its objective is to prevent reactor pressure vessel (RPV) failure during severe accidents with core melt and relocation into the lower plenum. Once design specific criteria are met, the reactor cavity is flooded, enabling external vessel cooling to transfer the decay heat of the relocated corium to the containment. While IVR is not implemented as a standard accident management strategy in VVER-1000 reactors, extensive research and benchmarking over the past decade have investigated its feasibility.
Due to the complexity of the underlying phenomena, the effectiveness of this strategy should be assessed using integral calculations with lumped parameter codes. In this study, the latest version of the German code system package AC² is applied to analyse a hypothetical IVR scenario in a VVER-1000 reactor. The thermal-hydraulics is modelled with ATHLET, the severe accident phenomena in the reactor coolant system (such as core degradation, and late-phase processes) are simulated with ATHLET-CD, while the containment response is modeled in a simplified manner using COCOSYS. In recent years, several new models and methods have been implemented in the lower plenum module of ATHLET-CD to improve its capability for simulating IVR scenarios as well as modelling the lower plenum of VVER reactor designs.
This paper presents the current modeling capabilities of AC², highlighting the newly implemented features, and demonstrates their applicability through the simulation of a station blackout combined with a large-break LOCA in a VVER-1000/320 reactor equipped for hypothetical IVR. The analysis covers the full progression of the accident, from the initiating event to the stabilization of corium within the RPV lower plenum with a focus on the heat transfer during ERVC.

KEYWORDS
In-vessel melt retention, external cooling, AC², ATHLET-CD, severe accident, VVER-1000

1. INTRODUCTION

In case of a severe accident in a light water reactor, the core dries out, heats up, and starts to melt. In a later phase, the molten core material (corium) relocates into the lower plenum (LP) of the reactor pressure vessel (RPV). The hot corium starts to heat-up and ablate the vessel wall and, without any countermeasure, the thermal load could lead to RPV failure, releasing corium into the containment. Severe accident management (SAM) strategies for mitigating the radiological consequences of severe accidents have received increased attention since the Fukushima Daiichi accident. One common SAM strategy for new plant designs as well as for retrofitting existing nuclear power plants is the in-vessel retention (IVR) of corium by external reactor vessel cooling (ERVC) [1].

The IVR concept aims to maintain RPV integrity by ensuring successful removal of decay heat from the relocated corium through external RPV cooling, thus limiting damage to the RPV wall. For this purpose, the outer surface of the RPV needs to be flooded—if possible before corium relocation—by dedicated safety provisions once a specific criterion is met during accident progression. The coolant evaporates at the RPV surface, and the resulting steam–water mixture returns to the containment, where it condenses, enabling long-term operation. The key points of the IVR strategy are the cooling efficiency (often limited by the critical heat flux, CHF) and the thermal load. The thermal load largely depends on the relocated corium mass and composition as well as on the decay heat. These, in turn, depend on the course of the accident and on the reactor size and design [2].

The IVR strategy was originally developed in the mid-1990s for mid-size reactors such as the AP-600 and the VVER-440 design [1]. Since then, the concept has been extended and adopted for new large Generation III/III+ reactor designs with electrical outputs exceeding 1000 MWe. Since high-power new designs such as the AP-1000, APR-1400, and HPR-1000 are already in operation with the IVR concept, IVR has also been intensively investigated over the past decades for retrofitting the VVER-1000/320 design [3], [4].

Severe accident system codes are commonly used to investigate IVR scenarios and to support the safety demonstration of the concept. In this work, the latest version of the German severe-accident code system AC^2 is applied. In recent years, several code improvements relevant to IVR and VVER reactor applications have been introduced, supported by international research projects and benchmark exercises. The present paper describes VVER design-specific model improvements relevant to IVR simulations. Furthermore, the applicability of the approach is demonstrated by simulating a large-break LOCA scenario with a concurrent station blackout (SBO) in a generic VVER-1000/320 reactor equipped with a hypothetical IVR concept.

2. APPLIED CODE SYSTEM AND MODEL IMPROVEMENTS

The code system AC^2, developed by GRS, is dedicated for the analysis of the whole spectrum of operational transients, design-basis accidents and beyond design-basis accidents [5], [6]. It includes the code ATHLET to model thermal-hydraulics in the primary circuit, ATHLET-CD to model severe accident phenomena and COCOSYS to model containment phenomena. The investigation of an IVR scenario requires a complete AC^2 simulation involving all three code parts. ATHLET-CD has a modular architecture including ATHLET for simulation of the complete thermal-hydraulic part [7]. The central core degradation module is ECORE, which defines the core section with fuel assemblies and structures and models the oxidation and the core degradation processes. The fission product inventory of the core and the total decay heat after SCRAM is calculated with the modules OREST/FIPISO. The module FIPREM calculates the fission product release of dedicated elements as a function of the partial pressures and the module SAFT simulates the fission product transport. The late phase phenomena in the LP are simulated with the module AIDA.

The key ATHLET-CD module for IVR simulation is AIDA. Fig 1. shows an overview of the current modelling scheme of this module. AIDA simulates the corium thermal behaviour, the heat conduction and damage to the LP wall and the external cooling. In the current version of AIDA, the relocated corium instantaneously forms a contiguous molten pool at the bottom of the LP. The MASCA experiments have revealed the existence of two immiscible liquid phases at equilibrium in the corium pool, one metal and another consisting of oxides [8]. The current code version provides the conventional representation of the stratified pool with two corium layers, a heavier oxide in the bottom and a lighter metal layer above of it, without considering the complex thermochemical stratification processes. The corium pools are each modelled as one-dimensional. The crust formation, dependent on the boundary conditions, is modelled around and in between the corium layers.

The heat transfer between melt and the external cooling is calculated in two dimensions. This includes the calculation of crust formation at the wall, the heat transfer between melt and crust as well as crust and wall,

heat conduction in the wall and also the heat transfer between wall and reactor pit volumes. Heat conduction in the vessel wall is solved with an explicit finite-difference scheme that accounts for progressive wall ablation. When a wall nodes melt, it is filled immediately by corium, while the effect of crust insertion is considered. Assuming molten metal pushed up by the crust into the metal layer, the node mass is added directly to the metallic layer. Crust formation at the layer interfaces depends on the layer temperatures and strongly influences the interlayer heat transfer.

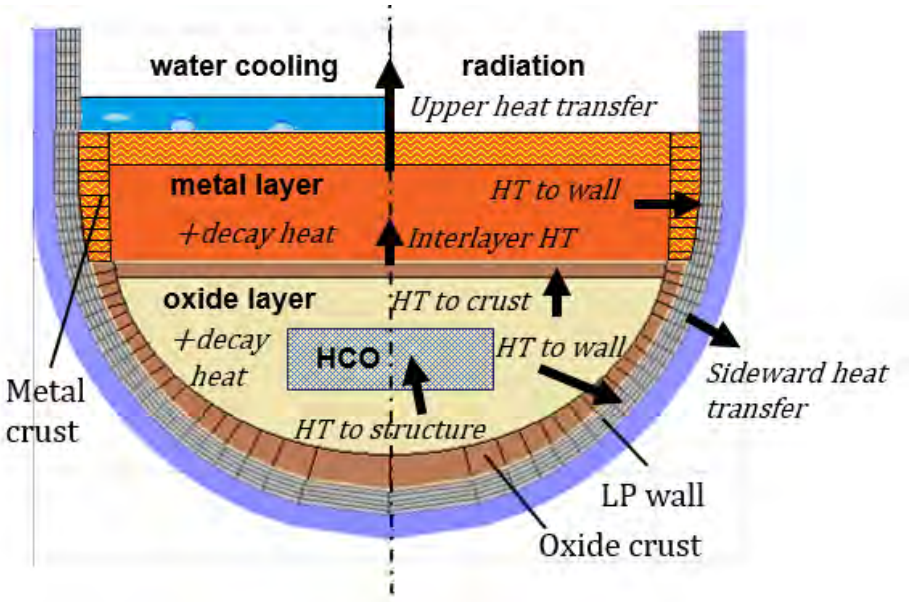

Figure 1. Modelling scheme of AIDA adapted from [9]

In recent years, several modelling improvements have been implemented in AIDA to enhance its capability to simulate IVR in VVER-1000 reactors. The following section briefly describes these.

2.1 Model improvements in AIDA

2.1.1 Metal layer modelling

The VVER-1000 geometry leads to significant amount of metal in the corium pool, which results in a thick metal layer above the oxide. The material properties of the metal layer can differ significantly from those of the vessel wall due to differences in material type, composition, and thermal history, which limits the heat transfer between them. The temperature difference between the molten metal layer and the wall (which can exceed 1500 degree) promotes solidification at the interface, forming a solidified metal crust. These crusts introduce additional thermal resistance. Accurate modelling of this crust is therefore particularly important in the case of a thick metal layer with a large heat-transfer area, as it strongly influences the heat transfer from the metal layer to the vessel wall.

Therefore, a new metal layer crust model has been introduced in AIDA. The thickness and the temperature of the sideward crust is calculated for every wetted wall node in every timestep. The heat transfer between metallic melt and crust is calculated using a Nusselt number based on the Chawla–Chan correlation [10]:

$$\mathrm{Nu}_{\text{metal layer}} = 0.508\ \mathrm{Pr}^{0.25}\ \mathrm{Ra}^{0.25}\ \left(\frac{20}{21}+\mathrm{Pr}\right)^{-0.25} \quad (1)$$

The heat transfer between crust and wall is calculated as conduction. With this, the heat balance is solved for the crust elements in every timestep, taking phase changes into account, calculating crust thickness

(evolution, melting) and from that crust temperature. Upper metal crust forms when the surface temperature drops below the solidification point due to significant heat loss through radiation or flooding of the LP. The upper crust is modeled as a single node with constant thickness above the metal layer's upper surface, using volume-averaged material properties. The heat flux from the metal layer to the crust is calculated assuming a thermal boundary layer, due to the comparatively large upper surface area and weaker convection. The thickness and the temperature is solved in the same way as for the sideward crust [9].

2.1.2 Consideration of internal structures

The LP of the VVER-1000 contains a considerable number of internal structures within the lower head (see Fig. 2). These include the lower core barrel (~14 t) and the fuel assembly (FA) supports (~ 7 t). After corium relocation, the corium gets in contact with the internals and starts to heat them up and melt them. In the new AIDA model, the internal structures are defined as standard ATHLET heat conduction objects (HCO). AIDA reads the volume and surface area of the coupled HCO and derives an equivalent cylindrical structure. Depending on the position of the structure, the wetted area and the heat transfer for both layers will be calculated separately. The heat transfer between oxide layer and the HCO is calculated similarly to the heat transfer between oxide layer and LP wall, using a Nusselt correlation selected by user. The heat transfer between metal layer and the HCO is calculated using the Bonnet-Seiler correlation [15]. Crust formation is taken into account in a simplified manner as a heat resistance. The transferred heat is considered in the corium layer balance equations as well as in the ATHLET model. After the HCO is completely molten, its mass will be automatically added to the metal layer [9]. Progressive ablation of the HCO is not considered in the current code version.

2.1.3 Improvements in geometry modelling

A large part of the decay heat is contained in the oxide layer. This heat is transported through the upper surface (via interlayer crust and metal layer) to the inner RPV area and through the sideward crust and wall to the cavity (possibly filled with water). This causes a geometry-dependent natural circulation in the molten pool, except in the bottom region, which is characterized by stratification. Also, the external cooling represents a complex, geometry-dependent three-dimensional multiphase flow process [1]. This implies that the heat transfer is strongly dependent on the LP shape.

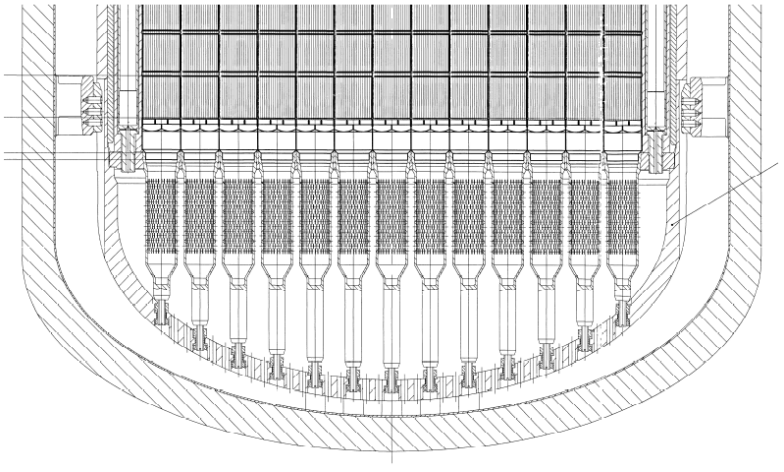

Figure 2. Lower plenum geometry of VVER-1000 [3]

The improved AIDA model simulates the VVER-1000 (see Fig. 1) LP wall with an ellipsoid shape and a non-constant wall thickness. The transition between the bottom and the cylindrical cross-section is modelled continuously. The shape of the LP wall is also considered in the heat transfer distribution along the inner wall. The heat transfer is calculated with a Nusselt correlation using the averaged parameters of the corium

layer. In AIDA, a simplified geometrical factor is introduced to transform this into more realistic two-dimensional heat transfer distribution at the inner wall surface considering the fluid flow patterns in the molten pool [9]. This factor has been optimized based on new benchmark simulations and experimental calculations.

3. POSTULATED SCENARIO

To demonstrate the new code capabilities, a large-break LOCA scenario with a simultaneous station blackout was chosen to obtain an early core meltdown with a large decay-heat level. A DN 850 mm break opens on the cold leg of loop 1. The break is located close to the RPV. At break initiation, the reactor is in normal operation at an up-rated thermal power of 3120 MW (104%) at end-of-cycle. The primary coolant mass flow is 84,800 m³/h, and the core outlet temperature is 320 °C. The coastdown of the main coolant pumps starts immediately after break opening. No active safety systems are available; therefore, only the passive hydro accumulators and the pressurizer inject water into the primary circuit during the transient.

The containment is equipped with a hypothetical system that starts injecting water into the reactor cavity once the core outlet temperature reaches 650 °C. This system is assumed to have enough water inventory to provide coolant for more than 24 hours. The initial water temperature is 60 °C. External cooling of the RPV is assumed to occur via natural circulation. Please note that to date no IVR system has been developed and approved for VVER-1000 reactors. The investigated scenario is intended for demonstration purposes only.

The calculation has been done from the transient initialization until corium stabilization (more heat transfer from corium than decay heat in the corium and no more wall ablation happens).

4. SIMULATION MODEL

The code system AC^2 version 2025.0 has been used for investigations with the improved AIDA module. The VVER-1000 input deck for these calculations has been developed over many years at GRS [11], [12] and has been adapted for a recent IAEA benchmark on IVMR [4], [13].

4.1 Thermal-hydraulic model

The primary and the secondary circuit are modelled with ATHLET, based on a two-fluid model with fully separated balance equations for liquid and vapor. The model represents the primary circuit and, partially, the secondary circuit of a VVER-1000 reactor. The primary circuit includes the RPV, the pressurizer, four hydro accumulators, and four loops modelled separately with their steam generators (see Fig. 2). The hydro accumulators, each containing 50 m³ of boron water, inject into the reactor when the pressure drops below 5.9 MPa: two inject into the upper plenum and two into the downcomer. The RPV model consists of the core region divided into five channels and a bypass (cross connected), the downcomer, the upper plenum, and the LP. The downcomer is divided into four parallel segments to accurately simulate asymmetric flow.

The LP structures, the bottom part of the barrel and the fuel assembly supports are modelled together as one horizontal cylindrical plate, representing their average dimension and mass. The structure is connected to the two representative lower-plenum thermo-fluid objects. The structure failure is modelled using a simple melting criterion.

The secondary circuit is modelled with the horizontal steam generators and the main steam lines up to the turbines. The pressure relief system of the secondary side, the so called BRU-A is modelled with VVER BOP model.

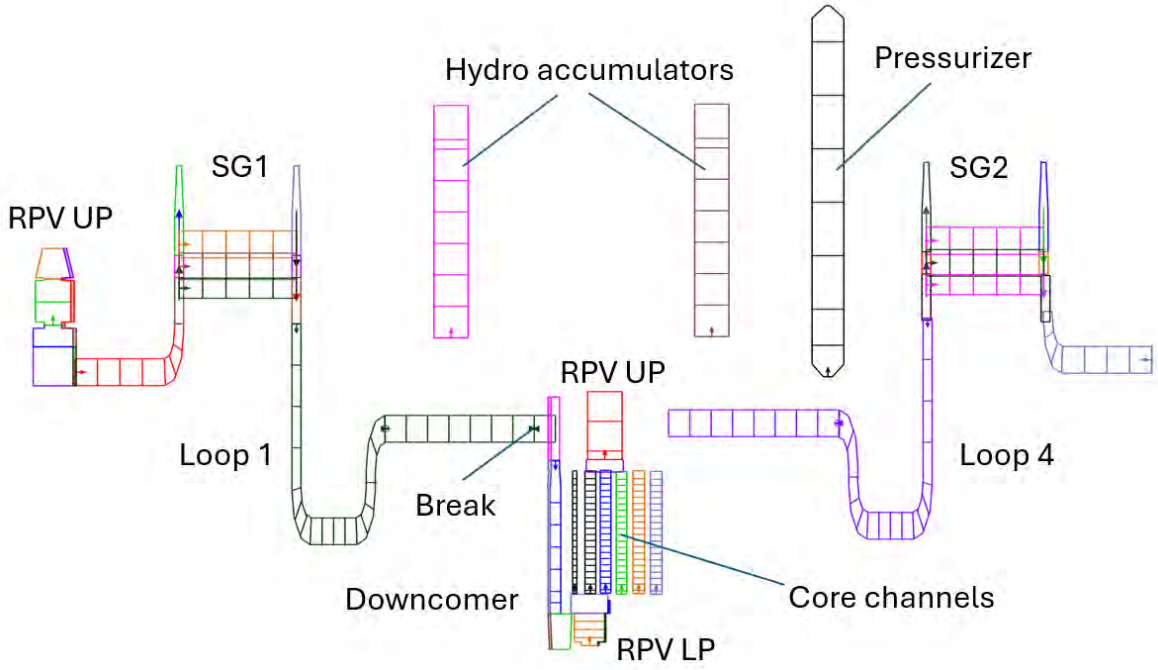

Figure 3. Schematic view of the PC thermal hydraulic model (RPV and loop 1 & 2) with nodalisation

The containment processes are modelled with COCOSYS. The present investigation focuses on the effectiveness of IVR; therefore, a simplified VVER-1000 containment model has been applied. The containment model provides the backpressure for the break discharge flow and the coolant properties in the reactor cavity for external cooling modelling. The heat transfer from the LP to the cavity is calculated by AIDA and is introduced into the containment cavity. Accordingly, the containment model consists of only three compartments, the cavity, the upper dome and the rest of the containment.

4.2 Severe accident model

To model severe accident phenomena, the ATHLET model has been extended with the ATHLET-CD modules, ECORE, OREST/FIPISO, FIPREM and AIDA. The present investigation is not focused on the source term, therefore the fission product transport module SAFT was not activated. The module ECORE simulates the core oxidation and core degradation processes such as ballooning and melting of the fuel and control rods. In the present model, hexagonal VVER-type fuel has been applied. The 163 fuel assemblies and the 18x163 B_4C control rods are divided into five groups which are assigned to five concentric core sections. The core channels are divided into 18 vertical nodes [12], [13].

The initial thermal reactor power is 3120 MW. The decay heat after SCRAM is calculated from fission product inventor with the modules OREST/FIPISO and the fission product release with the module FIPREM. The oxidation of the cladding is calculated with the Cathcart correlation under consideration of possible steam starving phenomena [9].

In the early phase of the accident, molten corium relocates and accumulates on the core support (grid) plate. Further relocation into the LP can only occur after failure of the grid plate or failure of the core barrel. In the present simulation, grid plate failure is assumed. Failure is assumed to occur when the grid plate reaches its melting temperature and when at least 45 t of molten oxide has already accumulated on it. This criterion is based on achieving reasonable relocation time [14].

AIDA starts after grid plate failure. The LP geometry has a horizontal inner radius of 2.046 m and a vertical inner radius of 0.958 m. The wall has a thickness of 0.241 m at the bottom and 0.194 m at the cylindrical region. The wall thickness between these two points is calculated using a continuous transition. The cylindrical part of the LP is modelled with a height of 1.6 m to ensure that all molten material fits within the AIDA simulation domain. The RPV wall has been nodalized with 20 nodes in radial and with 124 nodes in axial direction. As mentioned in Section 2.1.2, about 20 t of LP internal structures is considered via ATHLET HCO with a distance of 0.3 m from the LP bottom. For the temperature dependent LP wall properties (density, heat capacity and heat conduction) the built-in VVER steel (15X2HMFA) model was used.

The relocated melt instantaneously forms a stratified molten pool with a light metal layer on the top and with an oxide layer at the bottom. In the model 15 % of the decay heat is assumed to be generated in the metal layer. Heat transfer between the oxide layer and the crust is modelled using the Bonnet–Seiler correlations [15]. The heat transfer in the metal layer has been modelled as described in Section 2.1.1.

The external cooling is modelled with a simplified, AIDA built-in ERVC model [9]. The inlet and the outlet of the ERVC channel is coupled to the COCOSYS domain for the rest of the containment. Therefore, the inlet parameters; temperature and mass flow are provided by COCOSYS since AIDA calculates the heat transfer into the cavity cooling channel and thus cooling effectiveness. In the present simulation a constant heat transfer coefficient of 20,000 W/(m^{2}K) has been applied along the external wall, based on relevant, previous benchmark calculations [3].

5. SIMULATION RESULTS

The postulated large break causes a rapid pressure decrease in the primary circuit and triggers an immediate SCRAM. The pressurizer empties after approximately 20 s, and the passive injection from the hydro accumulators stops at about 55 s. After that, no further water is injected into the primary circuit. The time points of the key events of the transient are shown in Table I.

Table I. Key accident events

Event	Time [s]
Initial event of the accident	0.1
End of water supply from HA-1	55
Fuel rod burst	466
Core dry out	480
Intense hydrogen generation	1,200
Start of fuel melting	1,529
Corium relocation to the lower head	1,859
LP structure failure	4,496
Corium stabilization	~12,000

The core degradation phase starts shortly before total core dry-out, with fuel rod bursting at 466 s. Runaway oxidation, accompanied by intense hydrogen generation, starts about 1,200 s after the initiating event. The core begins to melt and corium relocates onto the grid plate. After 1,859 s, a total of 70 t of corium has

already accumulated on the grid plate, leading to its collapse and subsequent corium relocation into the LP. Fig. 4 shows the oxide melt and crust volume and the metal layer volume in the LP. The evolution of the oxide volume shows that corium continues to relocate into the LP thereafter, up to approximately 7,000 s. During this period, about 70 t of oxide corium is present in the LP. Interaction of the corium with the cold vessel wall initially leads to intense crust formation. Later, as the lower-plenum wall heats up, the crust begins to remelt and thin. After corium stabilization (around 12,000 s), the crust starts to grow slowly again. The LP wall starts to ablate at ca. 3,000 s. Wall ablation lasts until approximately 10,000 s and stabilizes at a minimum wall thickness of 50 mm. The 29.5 t of ablated wall material is added to the metal layer, which has a mass of about 120 t at the end of the calculation.

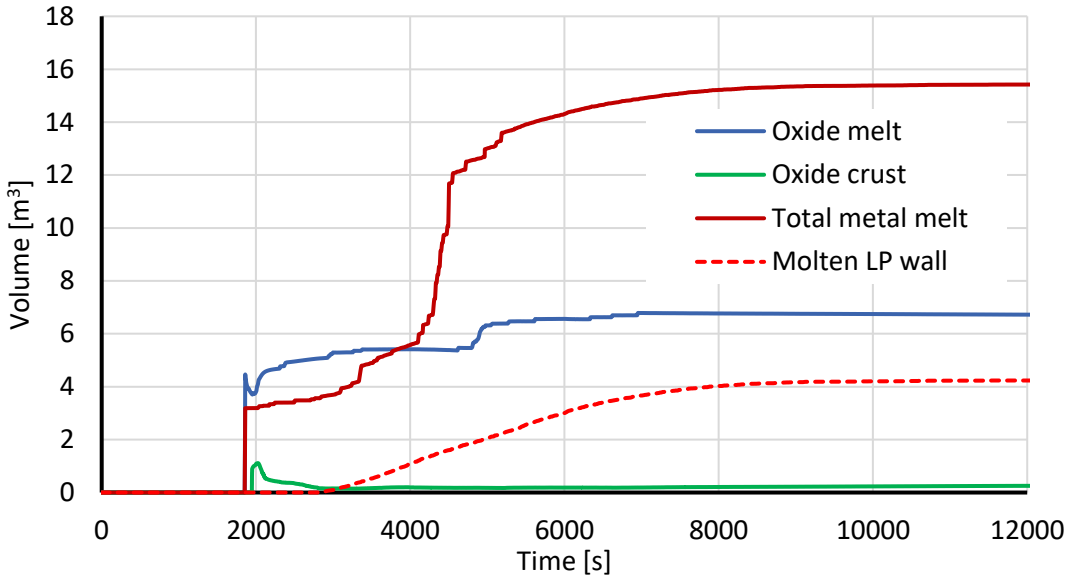

Figure 4. Volumes of relocated corium component

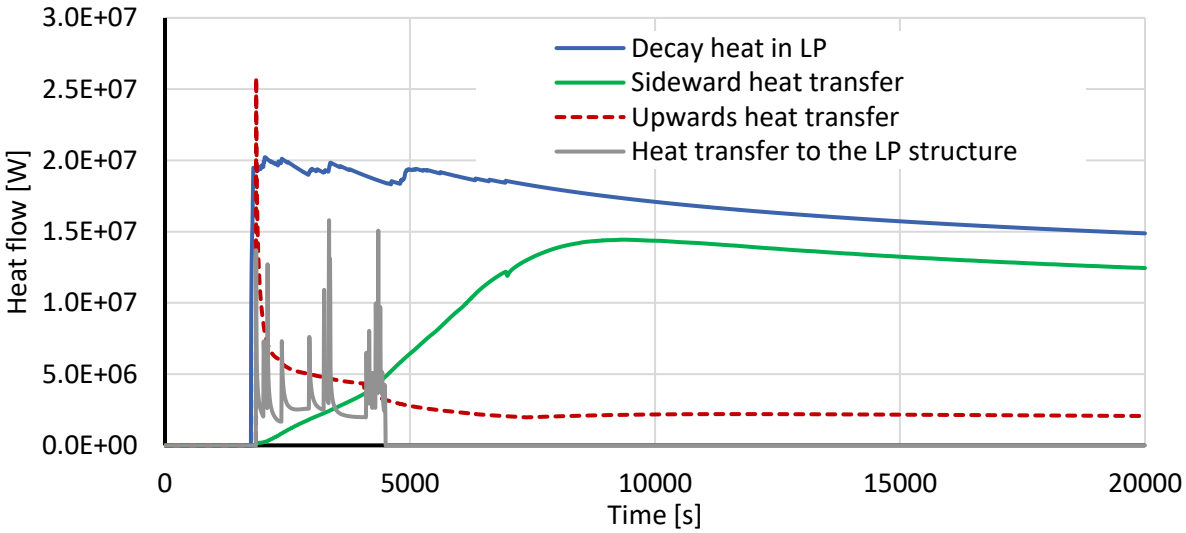

Figure 5. Heat balance of the corium pool

The heat balance of the corium pool shows Fig. 5. The corium mixture has a temperature of 2,500 K at relocation. Since the separation of corium phases is modelled as immediate, the still hot metal layer faces the remaining water in the LP, which leads to a large upper heat transfer immediately after relocation. At the same time, the upper metal layer crust starts to develop, which leads to a significant decrease of the

upper heat flux. At about 4,100 s the LP dries out and the upper heat transfer changes to radiation causing a strong decrease of the heat flux. The stepwise increase in decay heat also indicates further corium relocation (blue curve in Fig. 5). The grey curve shows the heat transfer from the corium pool to the coupled lower-plenum internal structure. The evolution of the layer heights influences the heat-transfer area to the structure. For example, when further oxide relocation occurs, the oxide layer height increases suddenly, leading to a larger heat-transfer area and larger temperature differences. This can cause transient peaks in the heat transfer. The approximately 20 t of lower-plenum structure melts completely up within ca. 2630 s, at about 4496 s after the initiating event. Without modelling the lower-plenum structures, the corresponding enthalpy of fusion would be redirected and could lead to non-negligibly higher lateral and upward heat transfer during this phase. The heat-balance figure shows that, at approximately 12,000 s, the decay heat becomes equal to the transferred heat, and since no further wall ablation occurs, the corium begins to stabilize.

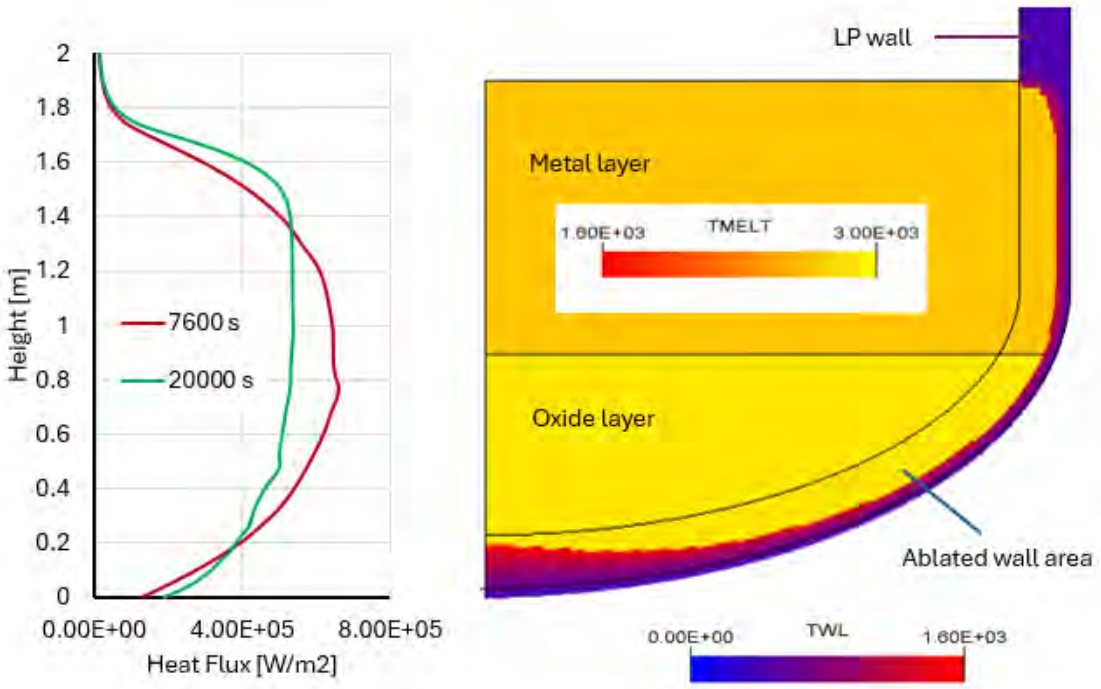

Figure 6. Left: Heat flux from corium to ERVC at maximum (7600 s) and at the calculation end (20000 s). Right: Wall ablation and corium composition at the end of the calculation.

During the simulations a maximal sideward heat flux of 0.66 MW/m^2 has been calculated at 7,600 s after accident initiation. At this time, a metal layer crust thickness of approximately 66 mm upward and an average of 28 mm sidewards has been calculated. At the end of the simulation, the upper crust thickness slowly decreased to 48 mm, while the average sideward thickness increased to 43 mm, forming together a nearly homogeneous crust around the metal layer. The heat flux evolution along the wall is shown in Fig. 6 left at 7,600 s and at the end of the simulation. As expected for a thick metal layer, the maximum heat flux is reached at the upper edge of the oxide layer. This result is consistent with the literature and indicates that the improved metal-layer model achieves improved physical predictions without overrepresenting the focusing effect [3].

The right side of Fig. 6 shows the wall ablation and the corium pool configuration at the end of the simulation. In the simulation, the corium layers fill the ablated wall nodes. The wall ablation profile shows that significant ablation occurs in the region of the metal layer and in the upper part of the oxide layer, while

the wall at the bottom remains nearly intact. These results are consistent with corium pool physics and with findings reported in the literature [3].

6. CONCLUSIONS

The lower plenum module AIDA of ATHLET-CD has been equipped with new models which improve its applicability to safety demonstration of IVR in case of VVER-1000 reactor designs. The new modelling approach considers the LP wall geometry of a VVER-type reactor more realistically. Furthermore, AIDA has also been equipped with a model to simulate the LP internal structures, which are also considered in the heat-balance calculations of the corium layers. In addition, the metal-layer modelling has been extended to calculate crust formation at the sideward and upper interfaces of the metal layer.

The model improvements have been successfully demonstrated with the investigation of a hypothetical IVR scenario in a generic VVER-1000 reactor. The consideration of the LP structures implies a larger heat-transfer area for the layers and simultaneously consumes decay heat from the corium. In addition, crust formation around the metal layer has an insulating effect, which avoids overpredicting the focusing effect for thick metal layers. These improvements lead to lower lateral and upper heat fluxes and, consequently, to a larger remaining wall thickness. Overall, the results are more realistic for IVR scenario behaviour.

The development, verification, and validation of AC^2 codes are ongoing. Further improvements of the lower plenum model are planned, including an improved representation of LP structures and relocation paths, as well as the consideration of thermochemical processes, to provide a more realistic representation of the corium pool. In addition, in the framework of international cooperation, the new modelling approach will be further verified through code-to-code benchmark exercises.

ACKNOWLEDGMENTS

The development and the validation of AC^2 is sponsored by the German Federal Ministry for the Environment, Climate Action, Nature Conservation and Nuclear Safety (BMUKN) on the basis of decisions by the German Bundestag within several projects.

REFERENCES

1. T.G. Theofanus, C. Liu, S. Additon, S. Angelini, O. Kymäläinen, T. Salmassi, In-vessel coolability and retention of a core melt, Volume I & II, 1996.
2. F. Fichot, L. Carénini, N. Bakouta, H. Esmaili, L. Humphries, T. Laato, R. Le Tellier, L. Saas, I. Melnikov, P. Pandazis, S. Weber, R.J. Park, A. Filippov, V. Strizhov, Elaboration of a Phenomena Identification Ranking Table (PIRT) for the modelling of In-Vessel Retention, *Ann. Nucl. Energy 146 (2020)* 107617. https://doi.org/10.1016/j.anucene.2020.107617.
3. M. Sangiorgi, A. Grah, G. Pascal, In-Vessel Melt Retention (IVMR) analysis of a VVER-1000 NPP, 2016.
4. L. Carénini, W. Ma, P. Matejovic, P. Pandazis, S. Massara, A. Miassoedov, The IAEA Coordinated Research Project on developing a phenomena identification and ranking table and a validation matrix, and performing a benchmark for In-Vessel Melt Retention, in: F. Gabrielli, L.E. Herranz, S. Paci (Eds.), *Proceedings of the 10th European Review Meeting on Severe Accidents Research (ERMSAR2022): Severe Accident Research Eleven Years after the Fukushima Accident*, Karlsruher Institut für Technologie (KIT), 2022.
5. A. Wielenberg, L. Lovasz, P. Pandazis, A. Papukchiev, L. Tiborcz, P.J. Schöffel, C. Spengler, M. Sonnenkalb, A. Schaffrath, Recent improvements in the system code package AC2 2019 for the

safety analysis of nuclear reactors, *Nuclear Engineering and Design.* https://doi.org/10.1016/j.nucengdes.2019.110211.

6. F.C. Weyermann, D. Eschricht, A. Wielenberg, T. Steinhoff, P.J. Schöffel, C. Spengler, L. Lovasz, AC² 2025.0 User Manual, 2025.
7. L. Lovasz, H. Austregesilo, C. Bals, C. D'Alessandro, T. Hollands, C. Lu, P. Pandazis, L. Tiborcz, Weber, ATHLET-CD 3.5 User's Manual, 2025.
8. V.G. Asmolov, S.V. Bechta, V.B. Khabensky, V.V. Gusarov, V.Y. Vishnevskii, Y.G. Degaltsev, S.S. Abalin, E.V. Krushinov, S.A. Vitol, V.I. Amljashev, S.Y. Kotova, V.N. Zagryazkin, E.K. Dyakov, V.F. Strizhov, N.P. Kiselev, Partitioning of U, Zr and FP between molten oxidic and metallic corium, in: *OECD Nuclear Energy Agency (NEA) (Ed.), MASCA Seminar 2004: MASCA Project (2000-2003)/Vol.1*, 2004.
9. L. Lovasz, C. Bals, C. D'Alessandro, T. Hollands, C. Lu, C. Köllein, H. Austregesilo, P. Pandazis, L. Tiborcz, S. Weber, ATHLET-CD 3.5 Models and Methods, 2025.
10. C.T. Tran, P. Kudinov, T.N. Dinh, An approach to numerical simulation and analysis of molten corium coolability in a BWR lower head, Nuclear Engineering and Design 240, 2010.
11. H. Wolff, Wissenschaftlich-technische Zusammenarbeit mit den atomrechtlichen Behörden und deren Sachverständigenorganisationen zur nuklearen Sicherheit in Betrieb befindlicher Kernkraftwerke und zur Konzeptbewertung von Anlagen mit Reaktoren der Generation 3+ (INT KoNuS): Abschlussbericht, Gesellschaft für Anlagen- und Reaktorsicherheit (GRS) gGmbH, Köln, Garching b. München, Berlin, Braunschweig, 2023.
12. S. Arndt, A. Aures, I. Bakalov, S. Beck, J. Bousquet, F. Dierschow, R. Henry, T. Hollands, A. Kerner, R. Kilger, C. Köllein, T. Lötsch, T.-K. Rollar, J. Sievers, H. Wolff, J. Zert, Wissenschaftlich-technische Untersuchungen zur nuklearen Sicherheit im Ausland: Modelle und Analysen für Anlagen russischen Designs und Wissensnetze, 2023.
13. L. Carenini, M.A. Bakar, A. Filippov, R. Le Tellier, I. Melnikov, P. Pandazis, M. Valincius, Z. Wu, Y. Zhang, IVMR modelling with tranisent effects during molten pool formation and stabilization - outcomes from model's comparison performed in the IAEA CRP J46002, in: F. Gabrielli, L.E. Herranz, S. Paci (Eds.), *Proceedings of the 11th European Review Meeting on Severe Accidents Research (ERMSAR2024)*: KTH Royal Institute of Technology, Stockholm, Sweden, 2024.
14. P. Tusheva, Modelling and analysis of severe accidents for VVER-1000 Reactors. Dissertation, Dresden, Germany, 2012.
15. J. Bonnet, J.M. Seiler, Thermal hydraulic phenomena in corium pools: the BALI experiment, *ICONE-7: 7. international conference on nuclear engineering*, Tokyo (Japan), 19-23 Apr 1999, 1999.

The 12h European Review Meeting on Severe Accident Research
ERMSAR 2026

Analysis of In-Vessel Retention in a VVER-1000 Reactor Design using AC²

P. Pandazis, L. Lovasz, A. Wielenberg

Gesellschaft für Anlagen- und Reaktorsicherheit (GRS) gGmbH

Madrid, Spain, May 18-22, 2026

Outline

- Background
- Applied code and model improvements
- AC^2 model of the VVER-1000 reactor
- Simulation of IVR in VVER-1000 reactor
- Summary

Background – In-Vessel Retention

Severe Accident Management Strategy with the aim:

Stabilizing corium in lower plenum via external RPV cooling to prevent vessel failure

- Developed for AP600/1000 and VVER-440
- Licensed in several countries
- Considered for different reactor types

Key points are:

- Thermal load to wall (reactor size and design)
- Cooling efficiency

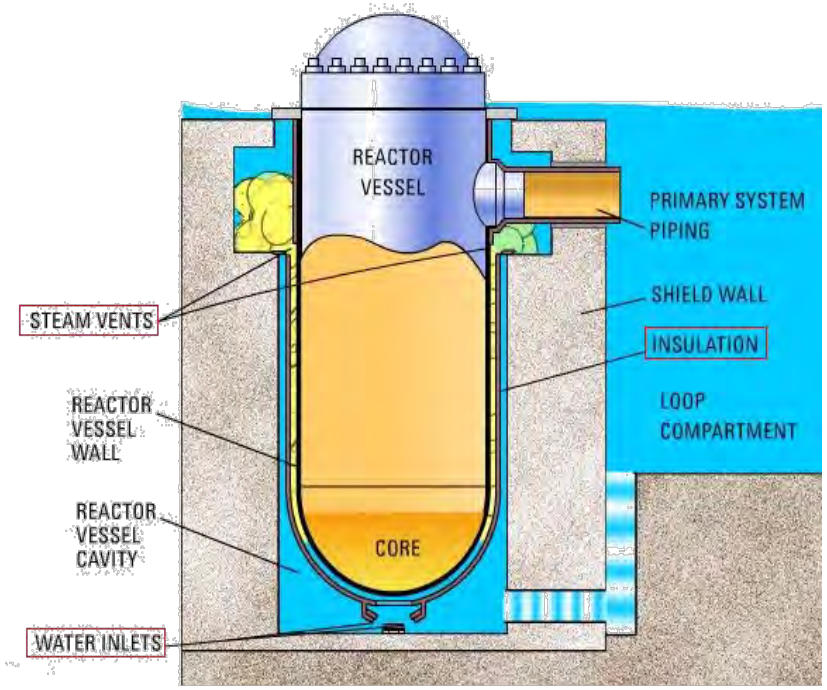

Scheme of IVR by AP1000

Source: AP1000 Brochure, Westinghouse

Several investigations in the last years for retro-fitting the **VVER-1000/320** design ⟹ using AC² to investigate the IVR concept

Applied code system – AC²

- Using the German code package **AC² 2025.0** (developed by GRS)
- Modular architecture, ATHLET: thermal hydraulics, ATHLET-CD: severe accident phenomena, COCOSYS: containment phenomena

ATHLET-CD modules:

- Core degradation
- Fission product inventory
- Fission product release
- Fission product transport
- Lower plenum behaviour

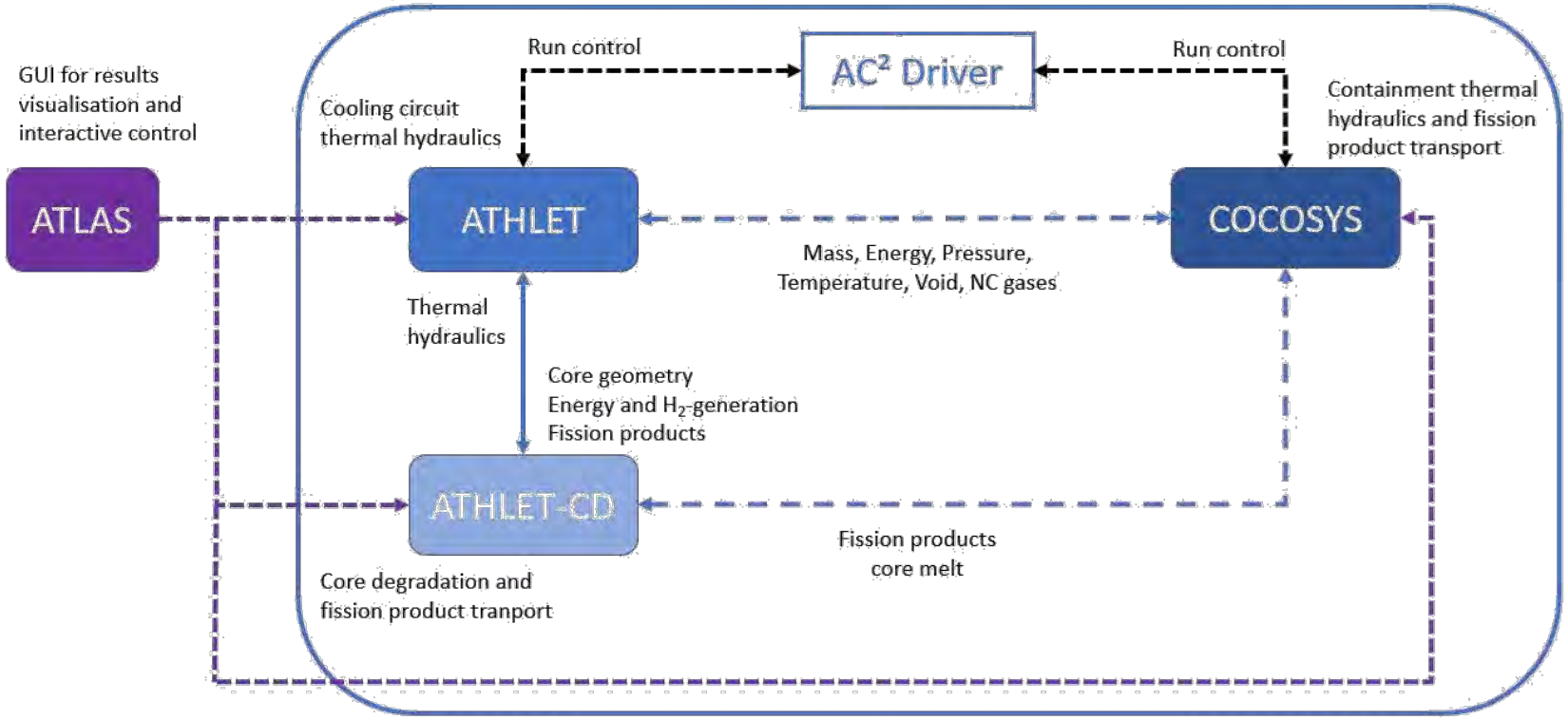

Applied code system – lower plenum module AIDA

Lower plenum module:

- Stand Alone
- Instantaneous melt segregation
- Two-layer model
- Molten pools (1D)
- Crust formation (2D)
- Wall model with ablation (2D)
- Top and lateral cooling
- ERVC model

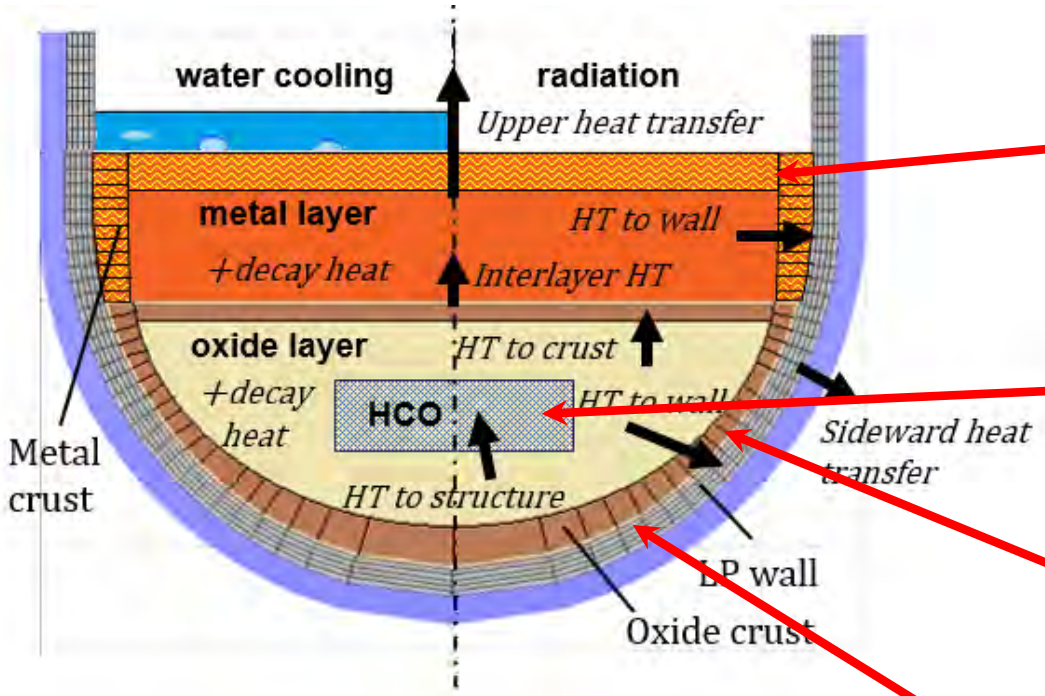

Modelling scheme of AIDA

Recent AIDA improvements relevant to VVER-1000:

- Modelling of upper and sideward metal layer crust formation
- Internal structure modelling
- New heat flux distribution factor to model shallow lower plenum geometries
- Update of 15Kh2NMFA RPV (VVER) steel properties

AIDA modelling improvements

LP geometry has a significant effect on the effectiveness of ERVC. VVER-1000 LP has:

- Shallow, ellipsoid shape
- Transition in thickness from bottom to cylindrical part
- Significant amount of lower plenum internal structures (core barrel, FA supports, over 20 t)

1. Improvement in geometry modelling:

- Pool characteristics for external and upper cooling: stratification (lower part) + convection (upper part)
- Improved transition of 1D to 2D heat flux distribution
- LP wall shape modelling with different wall thickness

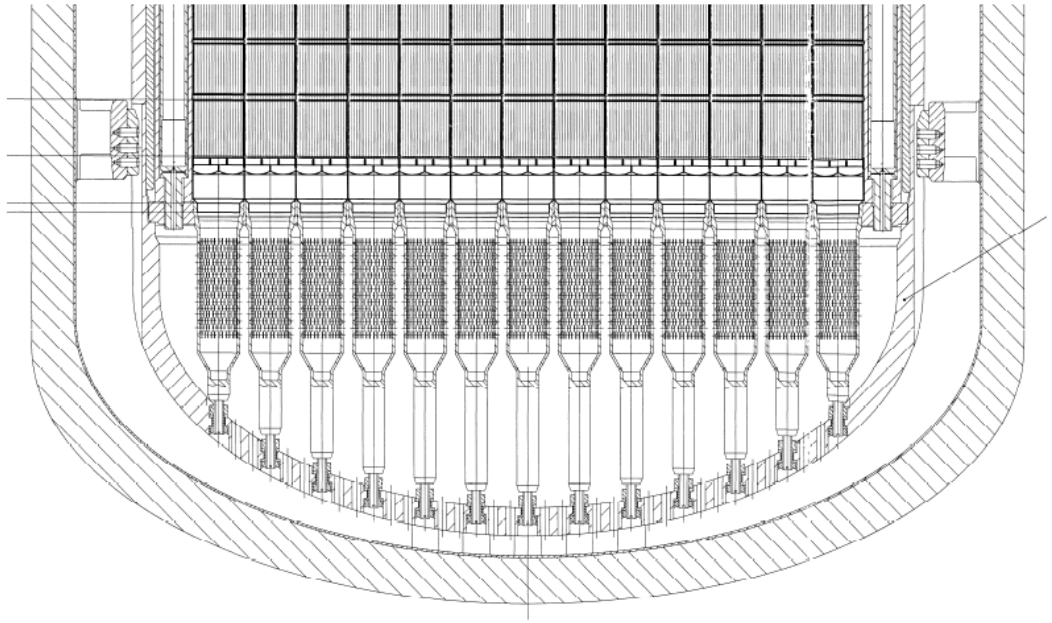

Lower plenum of VVER-1000/320*

*M. Sangiorgi, A. Grah, G. Pascal, In-Vessel Melt Retention (IVMR) Analysis of a VVER-1000 NPP, 2016.

AIDA modelling improvements

2. Improvement in metal layer modelling

- Thick metal layer in VVER-1000
- Solidification at interface (temperature gradient)
- Crust acts as a thermal resistance
- Heat balance is solved for every crust elements incl. phase change

3. Consideration of internal structures

- Modeling with standard ATHLET HCOs
  - Currently one horizontal plate
- Consideration in pool heat balances and volume
- ATHLET failure modelling
- After failure, the melt is added to the metal layer

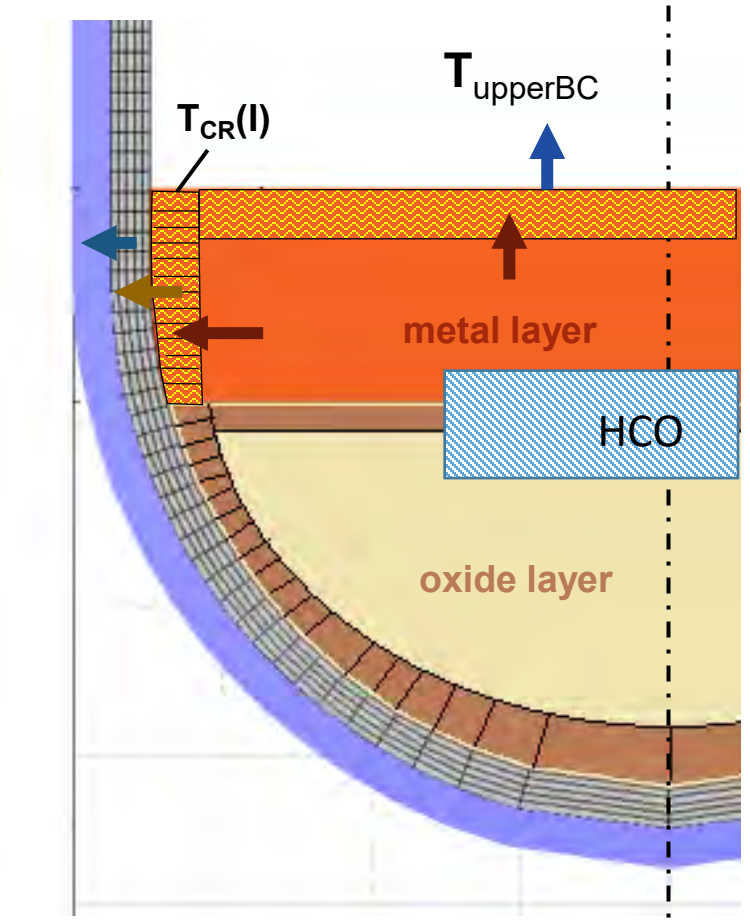

AIDA model

Simulation of IVR in VVER-1000

Postulated scenario:

- LOCA by normal reactor operation at 3120 MW
- Core mass flow: 84,800 m^3/h
- Core outlet temperature: 320 °C
- DN850 mm break in the cold leg of loop 1 + simultaneous SBO
  → only passive hydro-accumulator and pressurizer injection
- Simulation until corium stabilization

The hypothetical IVR system:

- Water injection into the cavity starts once the core outlet temp. reaches 650 °C
- Initial ERVC water temperature is 60 °C
- Enough water is assumed for more than 24 h
- External cooling via natural circulation

Simulation done with AC^2 2025.0

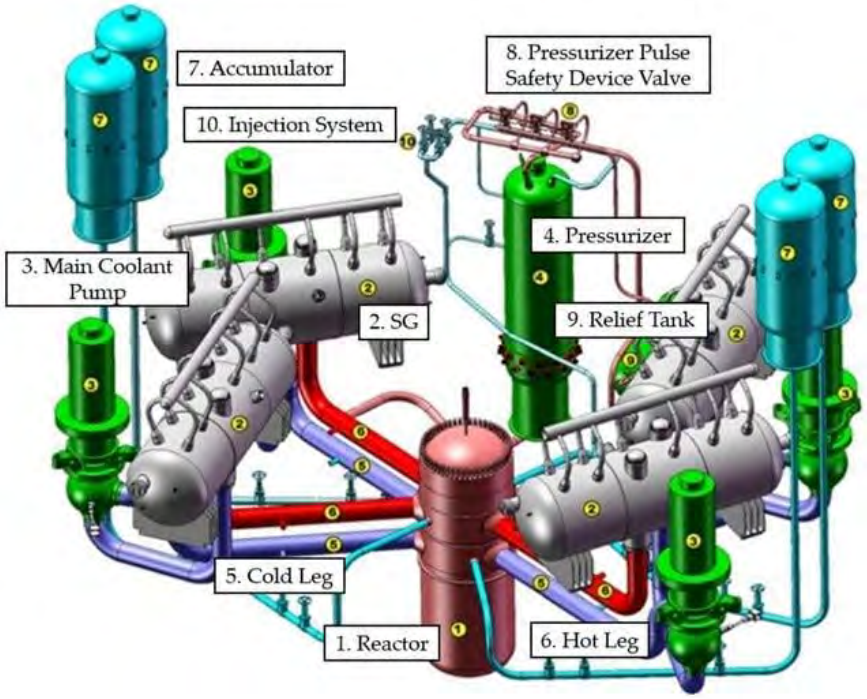

Primary circuit of VVER-1000*

*G. Nesti, G. Mazzini, A. Dambrosio, M. D'Onorio, Advancements in PARCS/TRACE Coupling and Simulation of Rod Ejection Accident in VVER-1000 Nuclear Reactor, Energies 2025.

Simulation of IVR in VVER-1000 – thermohydraulic model

- **Primary circuit** (ATHLET): RPV, loops, HAs, SGs, Pressurizer
- Two-fluid model with fully separated balance equations (6 eq. model)
- All 4 loops are modelled separately
- The 4 HA inject after p_{pc} < 5.9 MPa
- RPV is divided in 5 channel + bypass
- LP structures are modelled in lower plenum with a horizontal plate
- **Secondary circuit** (ATHLET): horizontal SG, main steam lines up to the turbines
- Pressure relief system BRU-A is modelled with realistic BOP model
- Equipped with a simple COCOSYS **containment** model (only three compartment)

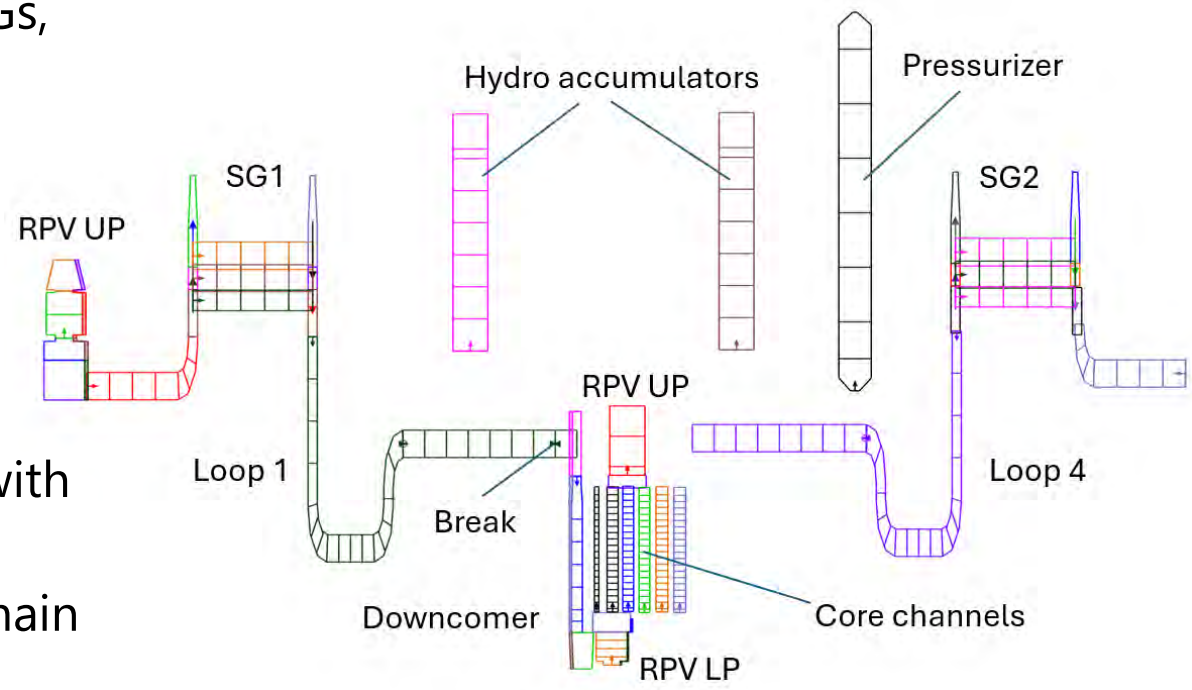

Schematic view of the primary circuit ATHLET model (RPV and Loop 1 & 2)

Simulation of IVR in VVER-1000 – ATHLET-CD model

- Calculated fission product inventory, release and decay heat after SCRAM
- Oxidation modelled with Cathcart correlation, incl. steam starvation
- Without modelling of fission product transport
- Five concentric core channels (defined in TH model)
- 163 fuel assemblies divided in 5 groups
- 18x163 B_4C control rod
- VVER fuel type (hexagonal)
- Molten corium accumulates on the grid plate → start of relocation: grid plate failure (mass & temp. criterion)

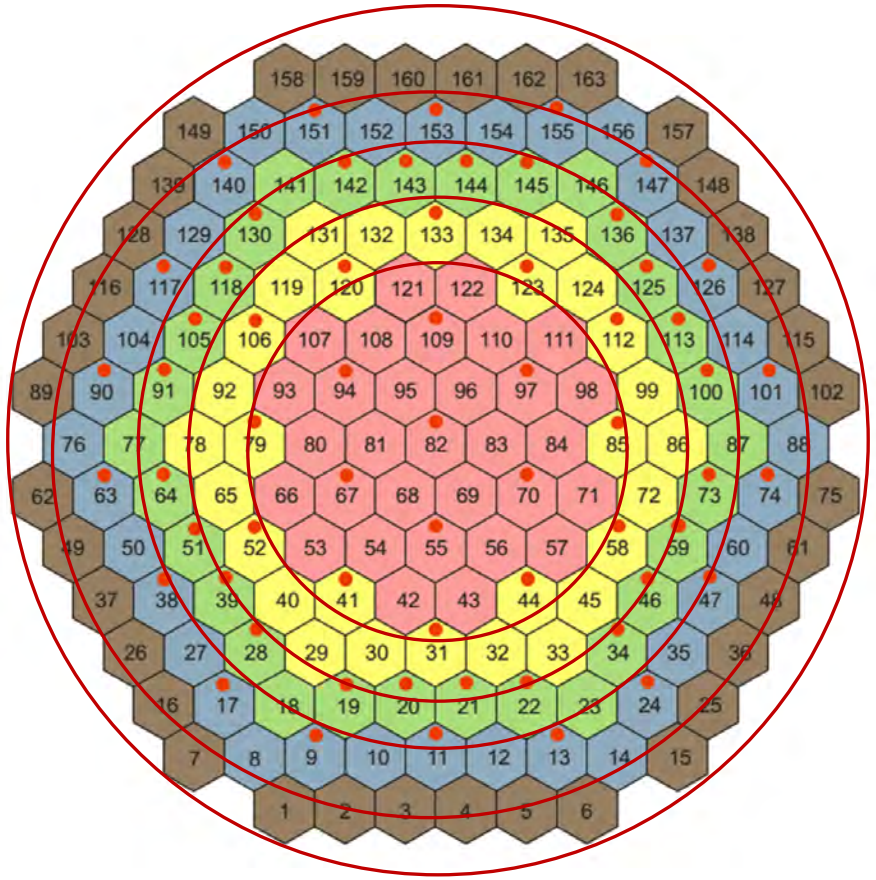

FA groups in the 5 core section

Simulation of IVR in VVER-1000 – ATHLET-CD AIDA model

- Start after grid plate failure
- Wall nodalisation: 124 axial x 20 radial nodes
- Two-layer model
- 15% of the decay heat is assumed in metal layer
- Bonnet-Seiler correlation for heat transfer between melt-pool and crust
- VVER steel model
- Constant outer wall HTC of 20,000 (W/m^2K)
- Heat transfer is calculated by AIDA
- ERVC parameters are coupled to COCOSYS

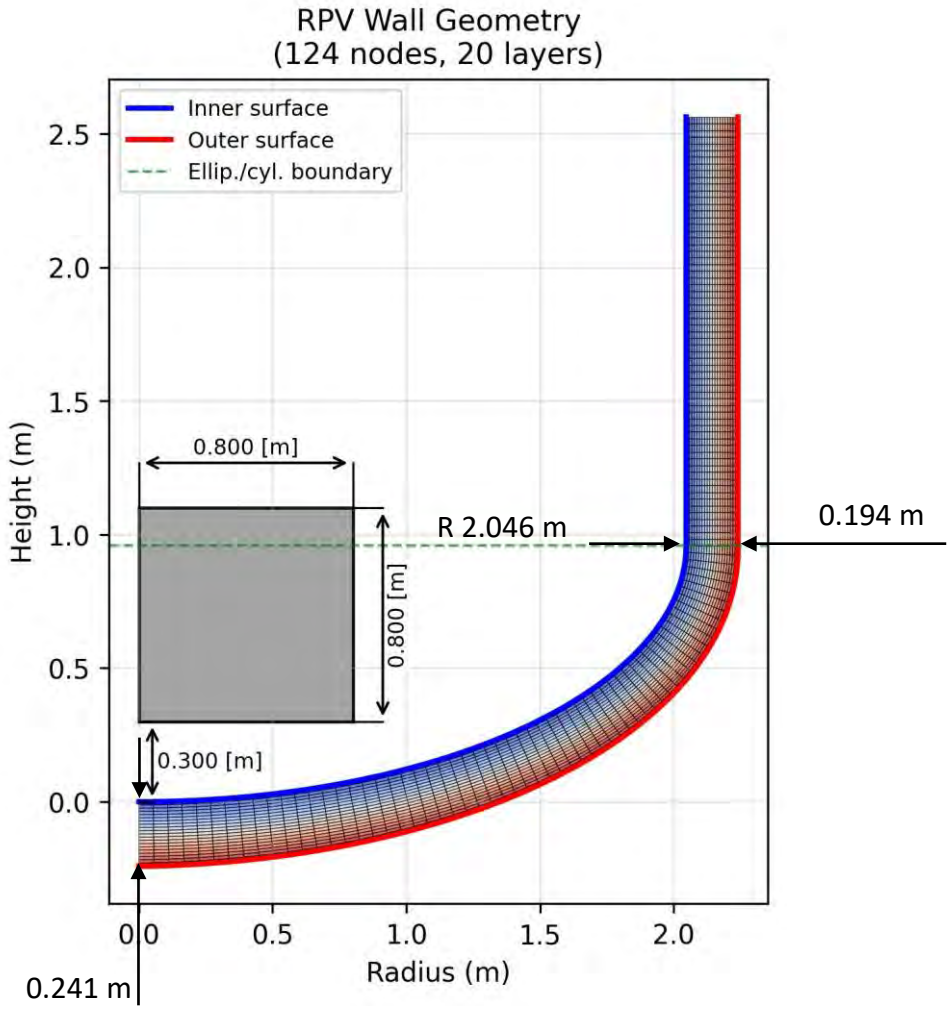

AIDA geometry model

Simulation of IVR in VVER-1000 - Results

- Immediate SCRAM because of rapid pressure decrease
- Pressurizer is empty after 20 s
- HA stops at 55 s
- After that no more water injection
- Underestimation of hydrogen generation, about 150 t at the simulation end, steam starvation

Event	Time [s]
Initial event of the accident	0.1
End of water supply from HA-1	55
Fuel rod burst	466
Core dry out	480
Intense hydrogen generation	1,200
Start of fuel melting	1,529
Corium relocation to the lower head	1,859
LP structure failure	4,496
Corium stabilization	~12,000

Key accident events

Simulation of IVR in VVER-1000 - Results

- LP dry out at ~4100 s
  → switch to radiation
- Peaks in heat transfer to LP structure → layer evolution affects the heat transfer area
- At the calculation end:
  - ~70 t of oxide
  - ~120 t of metal
- Wall ablation from 3000 – 10000 s (ca 29.5 t in total)
- Corium stabilization at ~ 12000 s
  - no further wall ablation
  - decay heat < transferred heat

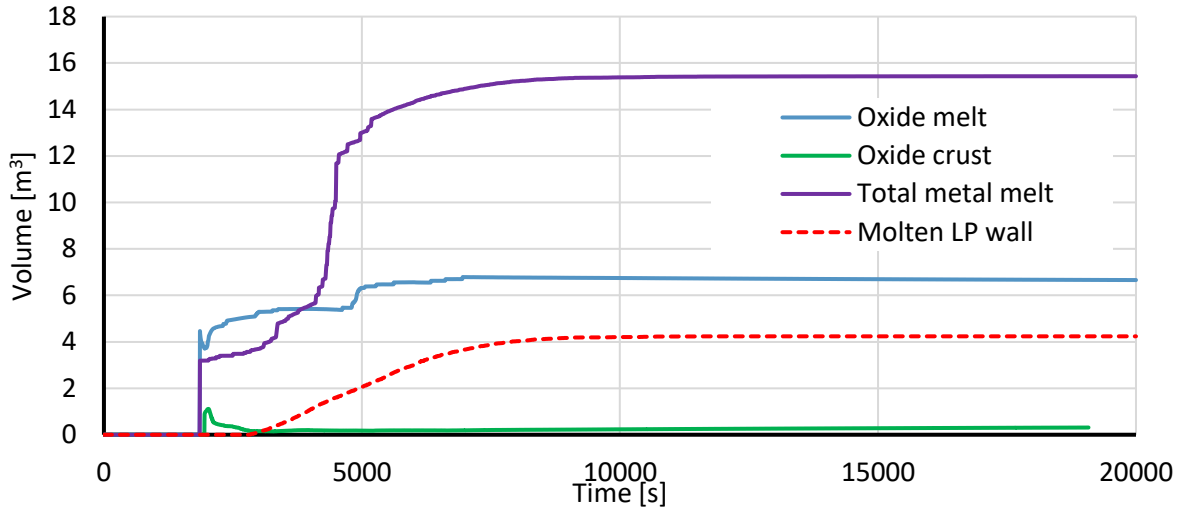

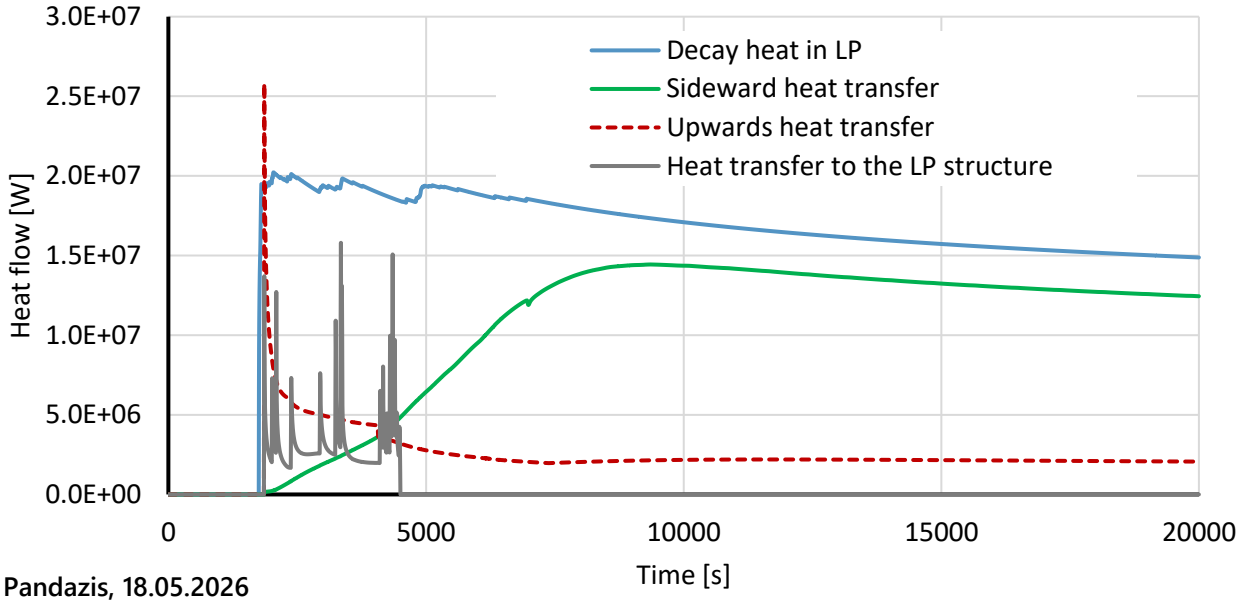

Simulation of IVR in VVER-1000 – lower plenum

Corium pool evolution

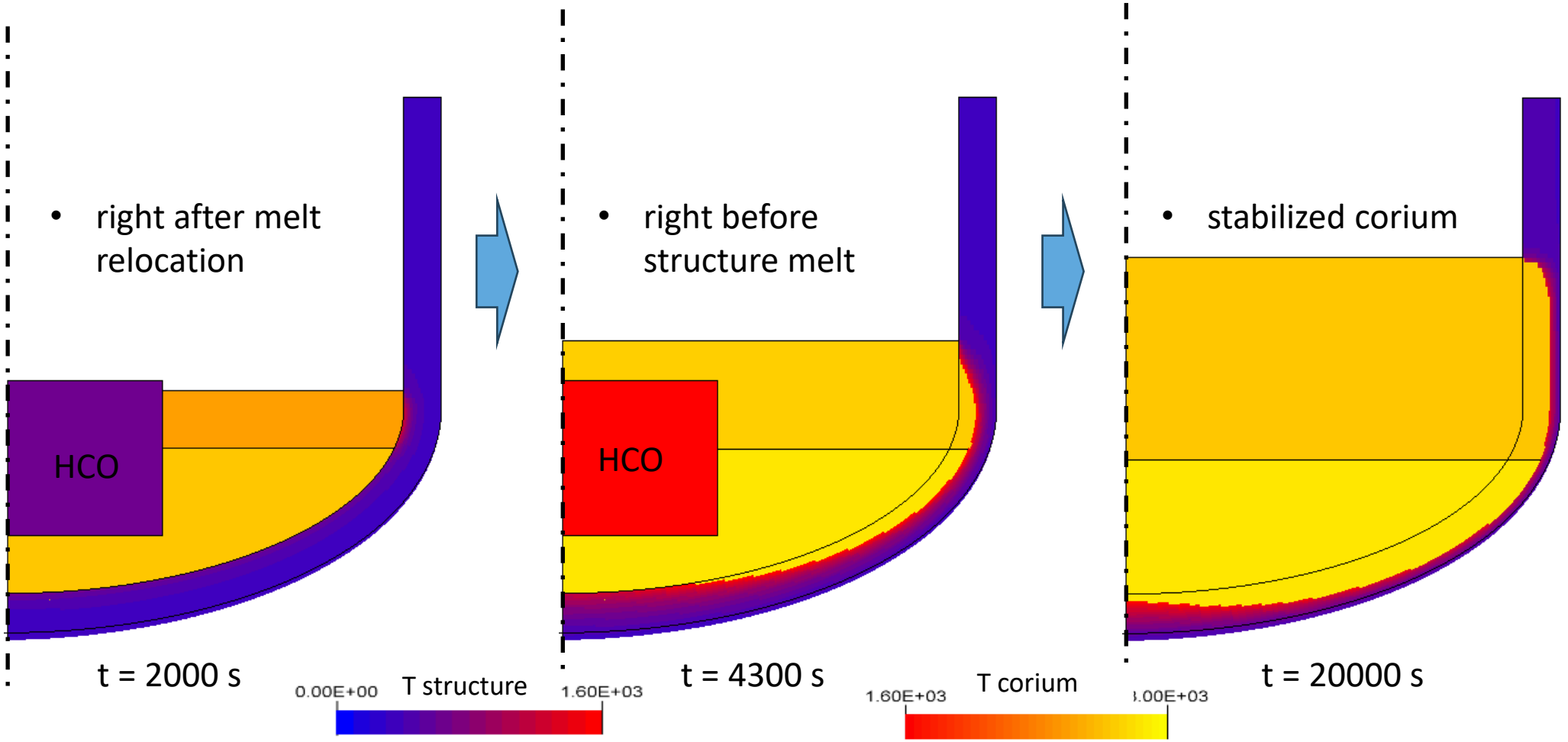

Simulation of IVR in VVER-1000 - Results

- Maximum sideward heat flux: 0.66 MW/m^2
- Max. ablation at the upper edge of the oxide layer
- Bottom wall remains intact
- Min. wall thickness: ~50 mm

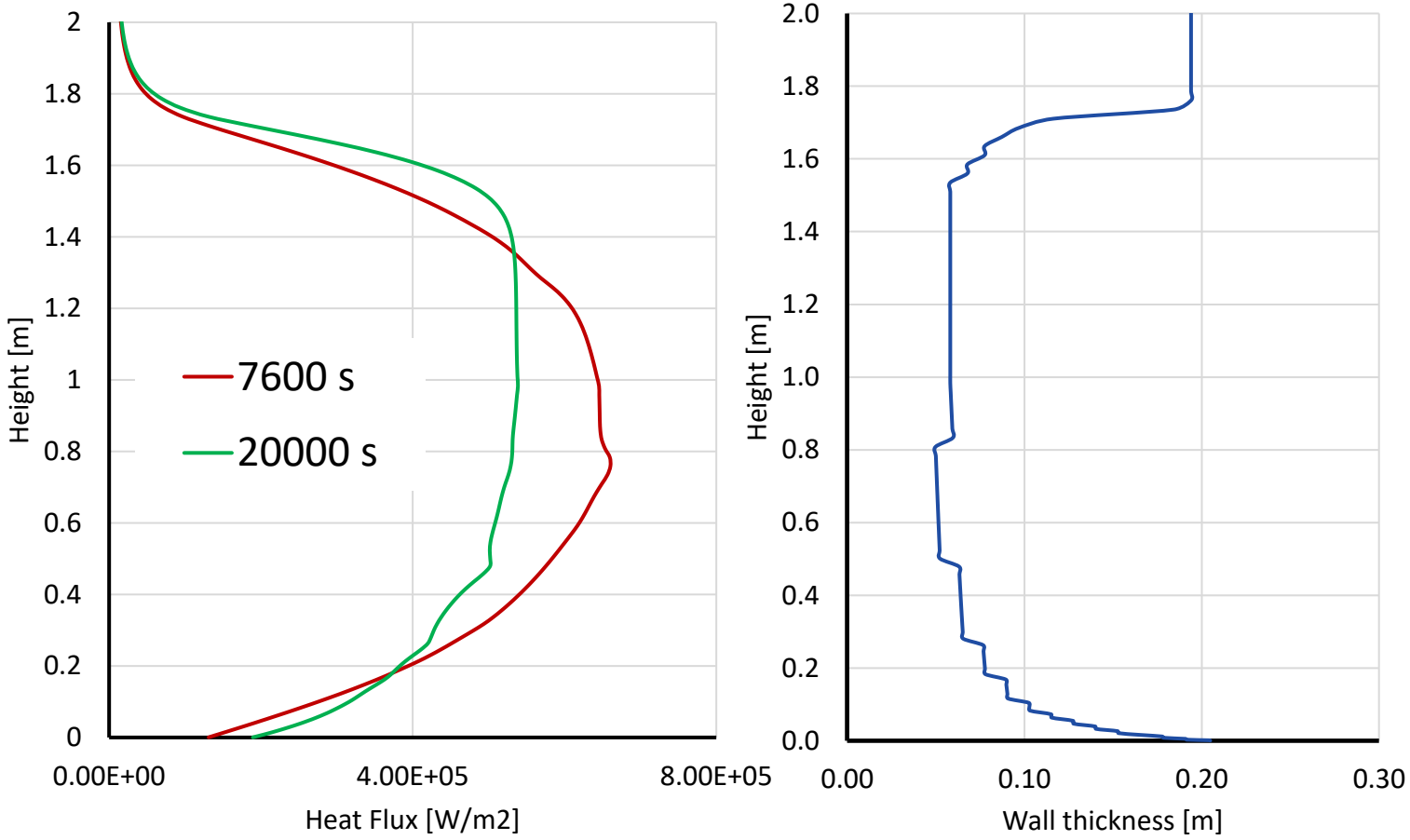

Heat flux along the wall

Residual wall thickness

Conclusion

- AC^2, ATHLET-CD lower plenum module improved for IVR safety assessment in VVER-1000 reactors
  - More realistic lower plenum wall geometry and shallow pool heat transfer modelling
  - Extension of the metal layer modelling with crust formation
  - More realistic modelling of lower plenum internal structures
- Demonstration by simulation of a hypothetical IVR scenario in generic VVER-1000
  - LP structures increase heat transfer area and absorb part of the corium decay heat
  - Metal layer crust reduces the focusing effect and avoids upper heat transfer overprediction
  - Results show lower heat fluxes and more realistic heat flux distribution at the LP wall
- Ongoing development, verification and validation of the modelling approach
- Improved representation of the lower plenum structures are planned

Peter.Pandazis@grs.de

Gesellschaft für Anlagen- und Reaktorsicherheit (GRS) gGmbH

Schwertnergasse 1

50667 Köln

Federal Ministry
for the Environment, Climate Action,
Nature Conservation and Nuclear Safety

Thank you for your attention!

The work was carried out as part of a research project commissioned by the Federal Ministry for the Environment, Climate Action, Nature Conservation and Nuclear Safety (BMUKN)

www.grs.de

FOLLOW US

TOWARDS A HIGH-FIDELITY NUMERICAL SIMULATION OF IN-VESSEL CORIUM POOL UNDER SEVERE ACCIDENT SCENARIOS

Abdullah Alasif [1], Zainab Al Tarouti [1], Tomasz Kwiatkowski [1,2], and Afaque Shams [1,2]
[1]Mechanical Engineering Department, King Fahd University of Petroleum & Minerals (KFUPM)
[2]Interdisciplinary Research Center for Industrial Nuclear Energy (IRC-INE), (KFUPM)
Dhahran, Saudi Arabia
Abdullah.asif@kfupm.edu.sa; s202176570@kfupm.edu.sa; tomasz.kwiatkowski@kfupm.edu.sa; Afaque.shams@kfupm.edu.sa

ABSTRACT

Predicting the flow and heat transfer of in-vessel corium pools poses a significant challenge. Internally heated natural convection induced by the decay heat of fission products is extremely difficult to predict with standard numerical models. This difficulty can hinder the development of accurate severe-accident integral codes and limit the advancement of In-Vessel Retention (IVR) safety systems designed to protect reactor pressure vessel (RPV) integrity in the event of severe accidents. Computational Fluid Dynamics (CFD) is commonly categorized into three approaches: Direct Numerical Simulation (DNS), Large Eddy Simulation (LES), and Reynolds-Averaged Navier-Stokes Simulation (RANS). While DNS provides the highest accuracy at a substantial computational cost, RANS offers the most efficient but least precise results. LES strikes a well-balanced tradeoff between accuracy and computational cost. This work investigates corium pool flow and heat transfer using RANS, validating the results against a new DNS benchmark at a high Rayleigh number (Ra = 1.6 x 10^6). Various turbulence closure models, including SST k-ω, Low-Re k-ε, Two-Layer Cubic k-ε, AHFM-CC, and GEKO, are evaluated. The results indicated that while all models capture the generic flow structure, the k-ω based models provide superior flow predictions but inaccurate thermal fields. Conversely, the Cubic k-ε model improves flow profile accuracy over linear models, and the AHFM-based model yields precise temperature prediction in the stratification region, despite overpredicting velocity.

KEYWORDS
Computational Fluid Dynamics (CFD); Corium Pools; In-vessel Retention Safety Systems; Internally heated natural convection; RANS turbulence models

1. INTRODUCTION

In a severe accident scenario (e.g., Loss of Coolant Accident - LOCA), the reactor core may overheat and melt due to decay heat, forming a molten mixture known as corium. Containing this corium pool within the Rector Pressure Vessle (RPV) is essential to prevent the corium pool from penetrating the vessel, and subsequent contamination of soil and groundwater with radioactive material [1], [2]. To prevent such a scenario, a safety system has been proposed: External Reactor Vessel Cooling (ERVC). A schematic view of the system is shown in Figure 1 [3]. Advancing the design of such systems requires a comprehensive understanding of the flow and heat transfer in corium pools. In the event of a meltdown, the corium pool will be heated internally by the decay heat generated by radioactive material in the core. This heat will drive the molten corium to circulate through the pool because of the density difference created by the fluid's temperature difference, a phenomenon called Internally Heated Natural Circulation (IHNC).

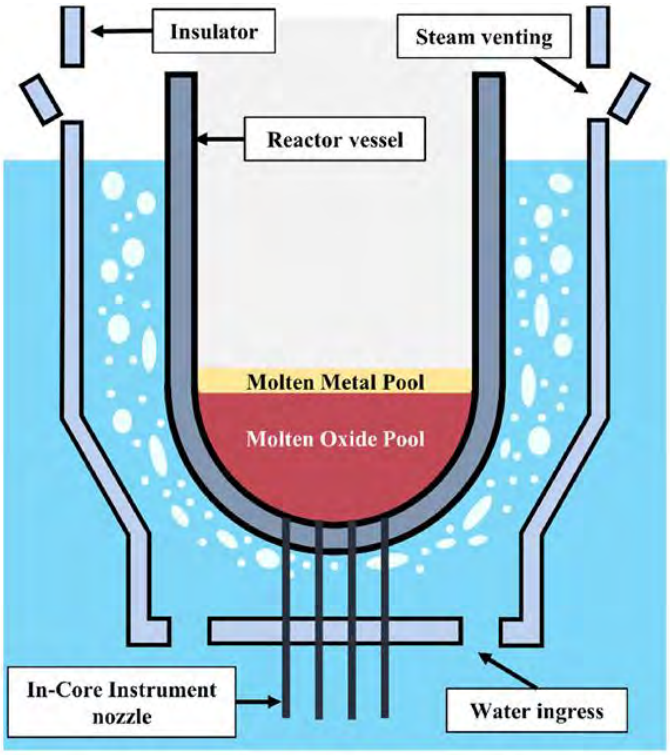

Figure 1. Schematic of the External Reactor Vessel Cooling System [3]

As shown in Figure 1, a corium pool generally consists of two layers: a low-density molten metal pool and a heavier pool of molten oxides, where heat is generated by radioactive decay. The flow behavior of corium pools during cooling has been extensively investigated. Numerous experiments using surrogate materials under various conditions have been conducted, with the resulting data sets available in the literature. A comprehensive list of such experiments was reported by Bian et al. [4]. However, these experiments were typically conducted at low temperatures using materials with relatively high Prandtl numbers (Pr), whereas corium exhibits a significantly lower Pr number of approximately 1 as per Smirnov et al. [5].

A remedy for the difficulties of experimental setups is the utilization of Computational Fluid Dynamics (CFD). Unlike physical experiments, CFD and other numerical methods offer the flexibility to investigate phenomena under extreme conditions. However, since CFD approximates real-life physics by numerically solving the governing equations, numerical error remains a constant concern. CFD is primarily categorized into three approaches: Reynolds-Averaged Navier-Stokes (RANS), Large Eddy Simulation (LES), and Direct Numerical Simulation (DNS). While RANS models all turbulent scales, making it computationally efficient but less accurate, DNS and LES resolve varying degrees of theses scales [6]. Specifically, DNS resolves all turbulence scales, providing the highest accuracy and offering insights into turbulence-related quantities that are often inaccessible through experiments. Consequently, DNS data is extremely valuable for validating lower order methods such as RANS.

Numerous studies available in the literature have investigated and validated numerical models of internally heated corium pools under cooling conditions. In 2018, Shams [7] evaluated the thermal fields of the corium pool using RANS models. Specifically, the Reynold Stress Model with Elliptic Blending (RSM-EB), the Low Reynolds k-ε, and the Low Reynolds k-ε coupled with an Algebraic Heat Flux Model (AHFM) were validated against BALI experimental data. The AHFM-based model (hereafter referred to as AHFM-CC (Calibrated Coefficients) yielded the most accurate results and was specifically calibrated for highly buoyant flows.

Sharma et al. [8] followed a similar approach to Shams [7], utilizing Unsteady RANS (URANS) to test various AHFM formulations with the low-Reynolds k-ε framework. Their findings showed good agreement with the BALI experimental data for the AHFM-based models. In addition, the complex geometries of the lower plenum of Pressurized Water Reactors (PWR) and Boiling Water Reactors (BWR) were investigated. However, the researchers lacked proper validation for these geometries, as the BALI experimental setup - a quarter of a circular slice – does not fully represent the three-dimensional (3D) hemispherical geometry characteristic of a reactor vessel's lower plenum.

In 2025, Guo et al. [9] investigated Detached Eddy Simulation (DES), Wall-Modified Large Eddy Simulation (WMLES), and URANS methods using ANSYS Fluent. The results were validated against the LIVE-3D experimental thermal fields data. The study concluded that WMLES provided the most accurate results, followed by the Realizable k-ε and Generalized Energy k-ω (GEKO) models.

Recently, Bian et al. [4] performed a DNS study of a hemispherical, internally heated corium pool. This study is highly valuable for validating lower-order methods, such as RANS, as it provides detailed data on heat transfer quantities, including: temperature, temperature variance, turbulent heat flux, and heat fluxes. In addition, flow parameters, such as velocity, turbulent kinetic energy, and the buoyancy production term, were reported. Dovizio et al. [1] utilized these DNS results to validate several RANS turbulence models, including the Low-Reynolds k-ε with Yap correction, the Shear Stress Transport (SST) k-ω, the Realizable k-ε, and RSM-EB. While the iteration-averaged temperature profiles showed acceptable agreement with the DNS data; the flow-field predictions were notably less accurate across all models. This discrepancy is likely related to the assumption that an inherently unsteady phenomenon is treated with a steady-state approach and averaging across iterations.

From a qualitative perspective, nearly all models reported in the literature successfully captured the fundamental flow behavior of internally heated corium pools. The characteristic behavior, established through both experimental and DNS studies, is illustrated in Figure 2.

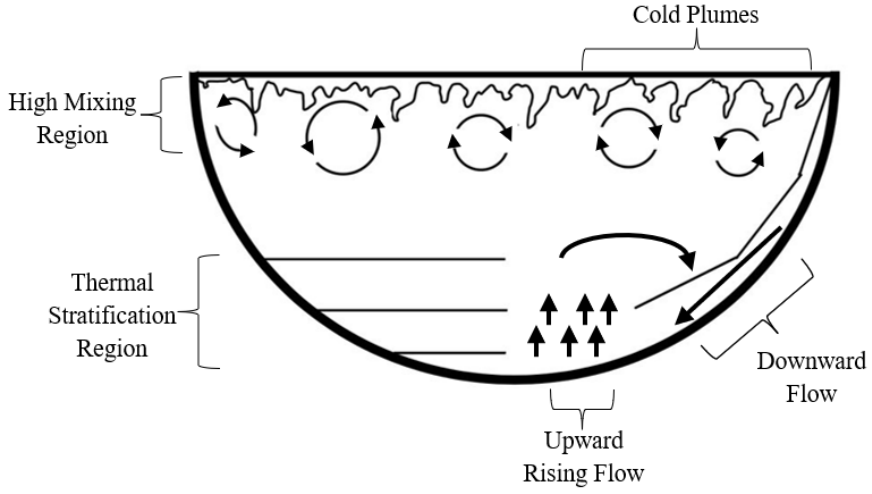

Figure 2. Flow regions inside an internally heated corium pool.

This study aims to investigate the performance of different turbulence models by adopting a URANS approach. Specifically, the Low-Reynolds k-ε with Yap correction, SST k-ω, k-ε cubic, AHFM-CC, and GEKO models are evaluated. All numerical results are validated against the DNS data reported by Bian et al. [4].

2. METHODOLOGY

This section describes the numerical methods and modelling techniques used to simulate the internally heated corium pool.

2.1. Geometry

The adopted geometry is a direct replica of the hemispherical geometry simulated by Bian et al. [3] in their DNS study, featuring a 2 m radius representing the lower plenum of a Light Water Reactor (LWR). A schematic of the geometry and locations chosen for data extraction are shown in Figure 3 below. To analyze the results, a vertical midline was established to capture flow and thermal profiles. Furthermore, 50 horizontal planes were utilized to extract flow and thermal field data, with each plane's data being spatially averaged to ensure a robust comparison with the benchmark.

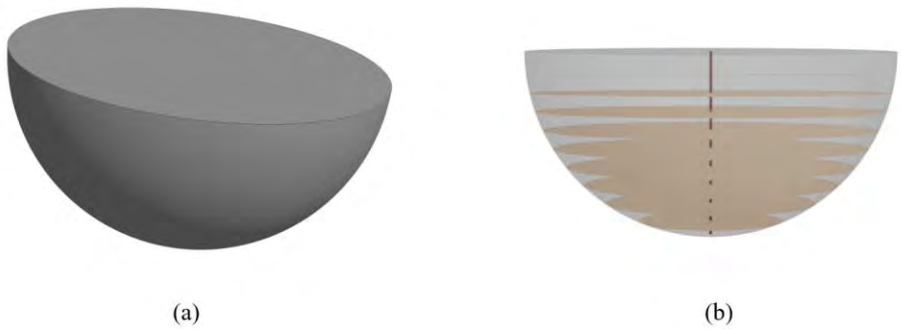

Figure 3. Geometry considered (a) and measurement locations (b).

2.2. Numerical Setup

Two finite-volume codes were employed in this study, namely STAR-CCM+ (Version 19.04.009-R8) and Ansys Fluent 2025 R2. Both codes were used with the SIMPLE algorithm for velocity-pressure coupling. In addition, the second-order upwind scheme was used for spatial discretization. Since the case considered is inherently an unsteady physical phenomenon, an unsteady approach was adopted. Unlike the previously mentioned studies, the authors found that considering a steady-state solution for this case produces results with high uncertainty, especially for the flow fields. Consequently, an implicit unsteady numerical scheme with second-order temporal discretization was utilized. The simulation used a time step (Δt) of 5 seconds with 10 inner iterations per step, ensuring that the average Courant-Friedrichs-Lewy number (CFL) remained below 1. A total flow time of 55 150 seconds was simulated, with parameters being temporally averaged over the final 8 000 seconds.

2.3. Turbulence Modeling

The numerical codes employed in this study utilize the finite volume method (FVM) to solve the Navier-Stokes equations. A RANS-based approach is used, where instantaneous variables, such as velocity, pressure, and temperature, are decomposed into mean and fluctuating components via Reynolds decomposition. This approach simplifies the governing equations, utilizing the eddy viscosity hypothesis to account for the Reynolds stresses. These stresses are resolved by introducing two additional transport equations: one for turbulent kinetic energy (k) and another for the dissipation rate (ϵ) or specific dissipation rate (ω). For the sake of brevity, only the most essential equations are highlighted here. The reader may refer to the Ansys Fluent or STAR-CCM+ theory guides for more detailed information about the models [10], [11]. A summary of the governing equations for incompressible fluids is provided below [12]:

The continuity equation:

$$\frac{\partial \overline{u_i}}{\partial x_i} = 0 \tag{1}$$

The momentum equation:

$$\frac{\partial(\rho\overline{u_i})}{\partial t} + \frac{\partial}{\partial x_j}\left(\rho\,\overline{u_i}\,\overline{u_j}\right) = -\frac{\partial \overline{P}}{\partial x_i} + \frac{\partial}{\partial x_j}\left[\mu\left(\frac{\partial \overline{u_i}}{\partial x_j} + \frac{\partial \overline{u_j}}{\partial x_i}\right) - \rho\,\overline{u_i' u_j'}\right] + F_i \tag{2}$$

The Reynolds stress is defined as:

$$\tau_{ij} = -\rho\,\overline{u_i' u_j'} \tag{3}$$

The energy equation:

$$\rho c_p\left(\frac{\partial \overline{T}}{\partial t} + \overline{u_j}\frac{\partial \overline{T}}{\partial x_j}\right) = k\frac{\partial^2 \overline{T}}{\partial x_j^2} - \frac{\partial}{\partial x_j}\left(\rho c_p\,\overline{T' u_j'}\right) \tag{4}$$

To solve Reynolds Stresses, the eddy viscosity approach is considered:

$$\tau_{ij} = 2\mu_t S_{ij} + \frac{2}{3}\rho k \delta_{ij} \tag{5}$$

$$\mu_t = \rho C_\mu \frac{k^2}{\varepsilon} \tag{6}$$

Four baseline turbulence models are considered: the Low Reynolds linear k-ε model, the two-layer standard cubic k-ε model, the SST k-ω model, and the GEKO model. The transport equations for turbulent kinetic energy (k) and the turbulent dissipation rate (ε) in the standard k-ε framework are given by [13]:

$$\frac{\partial(\rho k)}{\partial t} + \frac{\partial(\rho \overline{U_j} k)}{\partial x_j} = \frac{\partial}{\partial x_j}\left[\left(\mu + \frac{\mu_t}{\sigma_k}\right)\frac{\partial k}{\partial x_j}\right] + P_k - \rho\varepsilon \tag{7}$$

$$\frac{\partial(\rho\varepsilon)}{\partial t} + \frac{\partial(\rho \overline{U_j}\varepsilon)}{\partial x_j} = \frac{\partial}{\partial x_j}\left[\left(\mu + \frac{\mu_t}{\sigma_\varepsilon}\right)\frac{\partial \varepsilon}{\partial x_j}\right] + C_{1\varepsilon}\frac{\varepsilon}{k}P_k - C_{2\varepsilon}\rho\frac{\varepsilon^2}{k} \tag{8}$$

In the cubic formulation, the Reynolds stresses are calculated as [14]:

$$\rho\overline{u_i' u_j'} = 2k\rho\left(C_1 S_{ij} + C_2(S^2)_{ij} + C_3(S\Omega - \Omega S)_{ij} + C_4(\Omega^2)_{ij}\right) + \frac{2}{3}\rho k\delta_{ij} \tag{9}$$

The Low Reynolds formulation of the k-ε equations are given in [15].
The basic equations of the SST k-ω model from STAR-CCM+ are [11]:

$$\frac{\partial(\rho k)}{\partial t} + \frac{\partial(\rho k u_i)}{\partial x_i} = \frac{\partial}{\partial x_j}\left(\Gamma_k \frac{\partial k}{\partial x_j}\right) + G_k - \rho f_{\beta^*}\beta^*(k\omega - k_0\omega_0) + G_b \tag{12}$$

$$\frac{\partial(\rho\omega)}{\partial t} + \frac{\partial(\rho\omega u_i)}{\partial x_i} = \frac{\partial}{\partial x_j}\left(\Gamma_\omega \frac{\partial \omega}{\partial x_j}\right) + G_\omega - \rho f_\beta \beta(\omega^2 - \omega_0^2) + D_\omega \tag{13}$$

The GEKO model is a k-ω-based model with coefficients that can be tuned for specific applications. The full description of the model is not published yet. The default settings of the GEKO model are considered with the full buoyancy effect option enabled.
All aforementioned models account for the turbulent heat flux using the Simple Gradient Diffusion Hypothesis (SGDH). An alternative approach is the Algebraic Heat Flux Model (AHFM) to account for the turbulent heat flux. As previously demonstrated by Shams [7], a calibrated AHFM model can yield high accurate results for internally heated corium pools. In this approach, the turbulent heat flux is calculated as follows:

$$\overline{T' u_i}' = -C_{t0}\frac{k}{\varepsilon}\left(C_{t1}\overline{u_i' u_j}'\frac{\partial \overline{T}}{\partial x_j} + C_{t2}\overline{T' u_j}'\frac{\partial \overline{u_i}}{\partial x_j} + C_{t3}\beta g_i \overline{T'^2}\right) + C_{t4}a_{ij}\overline{T' u_j}' \tag{15}$$

Table I. Coefficients for the AHFM-CC

C_{t0}	C_{t1}	C_{t2}	C_{t3}	C_{t4}
0.2	0.25	0.6	$-4.5 * 10^{-9}(\log(RaPr))^7 + 2.5$	0

2.4. Mesh

Three different meshes were generated using the Automated Mesher of STAR-CCM+, utilizing a three-dimensional polyhedral mesh with prism layers applied at the walls. A grid convergence study was conducted in accordance with the method proposed by Eca and Hoekstra [16] for Grid Convergence. The characteristics of the considered meshes are summarized in Table II.

Table II. Details of Different Types of Mesh

Mesh	Number of cells (In Million)	Base Size (mm)	Number of Prism Layers	Average CFL	Maximum y+	Φ (maximum velocity in m/s)
Mesh C	0.62	37.8	16	0.08	0.180	0.000758
Mesh B	1.2	30	20	0.09	0.04	0.000760
Mesh A	2.4	23.8	25	0.1	0.007	0.000759

The grid convergence study was conducted using the SST k-ω in STAR-CCM+. From the measured variable values, an oscillatory convergence behavior was observed. Figure 4 illustrates the velocity profile across 50 horizontal planes for various mesh densities. The Grid Convergence Index (GCI) between Mesh A and B was 0.184%. To minimize numerical error in the subsequent validation study, Mesh A (shown in Figure 5) was selected.

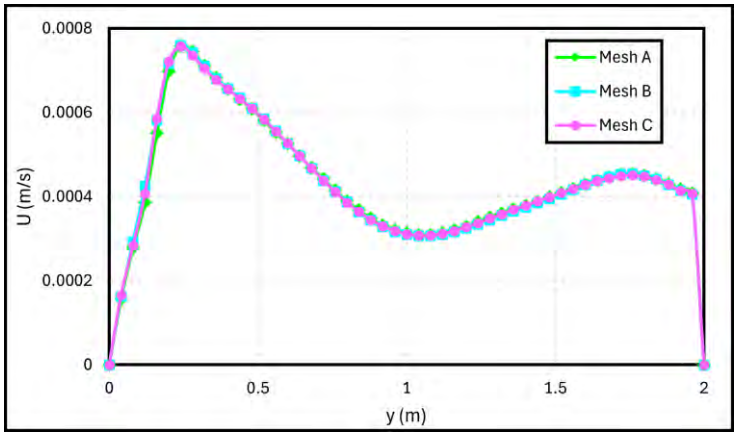

Figure 4. Mean velocity across the 50 horizontal planes for different types of mesh

Figure 5. Final adopted mesh (Mesh A)

2.5. Boundary Conditions

For boundary conditions, no-slip isothermal walls are assumed for all walls of the hemisphere. The wall temperature is 2623.15 K. An internal volumetric heat source of 6.11 W/m^3 is applied. The thermophysical properties of the material are given in Table III [17].

Table III. Material Properties [17].

Density (kg/m^3)	Thermal Conductivity (W/m.K)	Viscosity (Pa.s)	Specific heat (J/kg.K)	Thermal Expansion coefficient (1/K)
7588.4	3	0.0027	540	6.71x10^{-5}

3. RESULTS

This section presents the results obtained from the six different turbulence models. A detailed analysis of the flow physics is provided, followed by a comparative discussion of the predictive accuracy of each model.

3.1. Physics of the Flow

As mentioned in the previous section, the turbulence models with the adopted methodology were applied to the selected test case. Due to the low heat generation rate, the observed changes in temperature and velocity remain relatively small, hence two normalized values are used for comparison with the DNS data [17]. The normalization for velocity and temperature are defined in equations (16) and (17), respectively:

$$U^* = \frac{UH}{\alpha} \tag{16}$$

$$T^* = \frac{(T-T_0)\,\alpha}{H^2\, Q_{\mathrm{vol}}\, \rho c_p} \tag{17}$$

Where U is the velocity magnitude, H is the radius of the hemisphere, α is the thermal diffusivity, Q_{vol} is the volumetric heat source, T is the temperature, T_0 is the temperature of the wall, ρ is the density c_p is the specific heat.

Figure 6 shows the mean velocity contours for the different models on a vertical mid-plane section. All tested models reproduced the main flow behavior of internally heated corium pools, consistent with the reference as shown in Figure 2. Specifically, each model predicted an accelerated downward flow near the side wall, albeit with varying intensities. It is also worth noting that the laminar and the low-Re k-ε models

exhibited nearly identical flow patterns. This observation is particularly interesting as the laminar approach neglects Reynold stresses entirely. Furthermore, it was observed that k-ω-based models predict lower turbulence in the upper high-mixing region than the other models.
Figures 7 and 8 present the instantaneous and mean normalized temperature distribution, respectively. The k-ω based models predicted fewer cold plumes, while all models captured some degree of thermal stratification in the lower region of the pool. This stratification was more pronounced in the laminar and k-ε-based models than in the k-ω-based ones.

3.2. Quantitative Assessment

Quantitative comparison across the different models are presented in Figures 9 and 10. As previously mentioned, data were sampled along the vertical midline and across 50 horizontal planes, with a spatial average computed for each plane. Figure 9 reports the normalized mean velocity; it is evident that none of the tested RANS models fully captured the flow field of this specific case with high accuracy. In addition, it was found from Figure 9(b) that the velocity profiles of the laminar, low-Re k-ε, and the low-Re k-ε with AHFM-CC yield almost identical velocity profiles. This is an interesting finding, as it is quite uncommon for the low-Re k-ε model to laminarize the flow across the whole domain. A similar finding was reported by Dovizio et al. [17]where the turbulent kinetic energy (k) was almost zero for the low-Re k-ε model results tested on the same case. This behavior may be attributed to the damping function of the low-Re k-ε model. One possible explanation is the activation of the damping function across the whole domain, which enforces low values of the turbulent viscosity and treats the case as a laminar one. A further investigation is required to verify the main underlying reason of the exact mechanism. Results also indicate that the k-ω-based models can produce more accurate flow results than linear low-Re k-ε models. In addition, the cubic formulation of the k-ε model yields more accurate results than the linear low-Re k-ε models.

As illustrated in Figure 10, the laminar, low-Re k-ε model and the AHFM-CC models accurately predicted the temperature profile within the stratification region. However, all investigated models overpredicted the temperature in the high-mixing region near the top wall. This discrepancy suggests that the models underpredict the turbulence intensity in this zone, resulting in insufficient mixing and reduced heat transfer, which ultimately leads to higher predicted temperatures. Consequently, a model with good prediction capabilities for turbulence should be considered.

A classical approach to improving accuracy is the use of LES, however, this entails a significant increase in computational cost. An alternative remedy for such complex flows is the use of non-linear eddy-viscosity models, which account for turbulence anisotropy and typically offer better predictions in high-mixing zones. In this study, however, the cubic k-ε model failed to accurately capture the physics in the stratification region. This suggests that a non-linear approach, coupled with a robust closure for turbulent heat flux such as AHFM, may be necessary to achieve higher accuracy. Such a combination could facilitate the development of a tailored turbulence model for specifically optimized for internally heated flows.

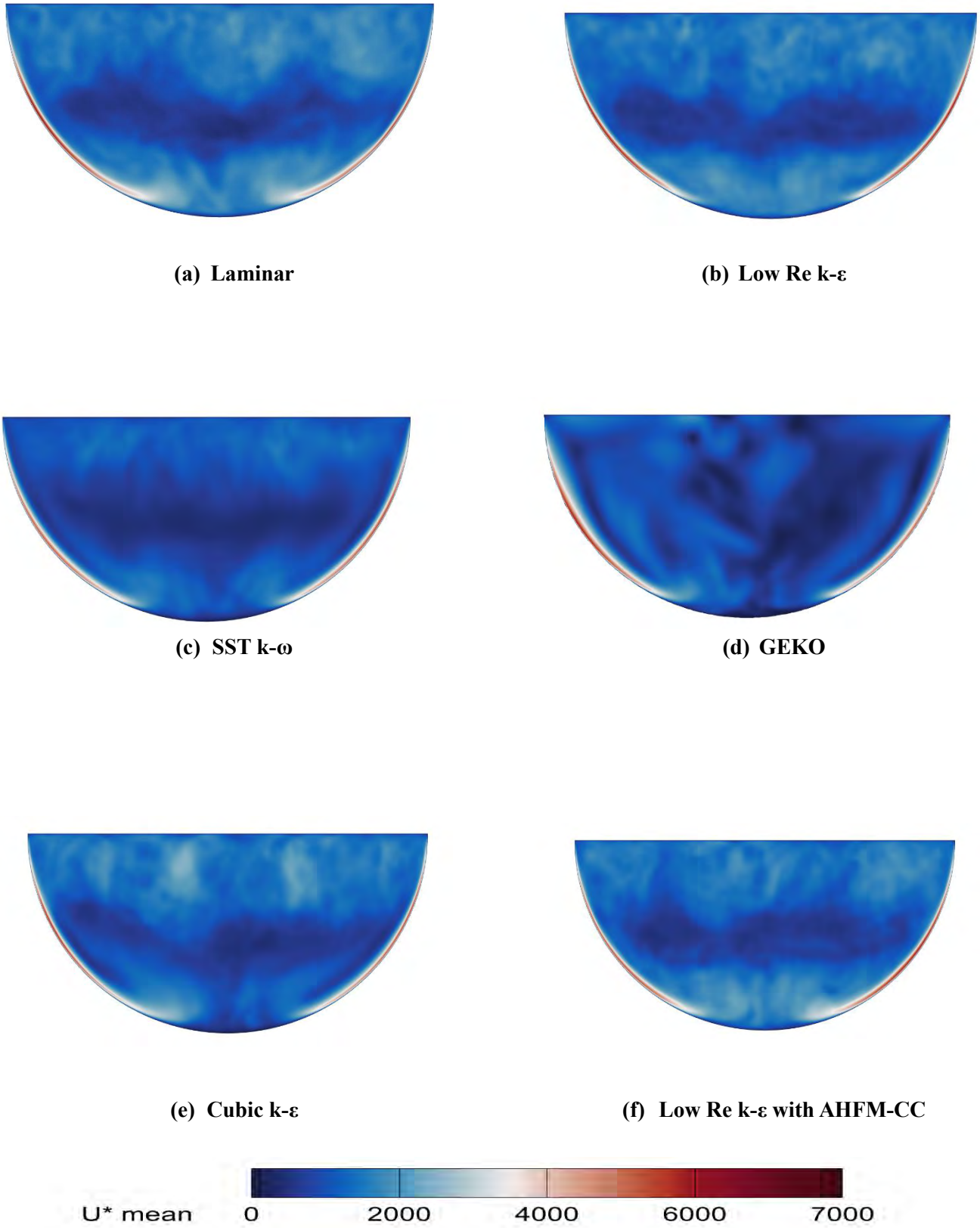

(a) Laminar

(b) Low Re k-ε

(c) SST k-ω

(d) GEKO

(e) Cubic k-ε

(f) Low Re k-ε with AHFM-CC

Figure 6. The mean normalized velocity (U*) contours.

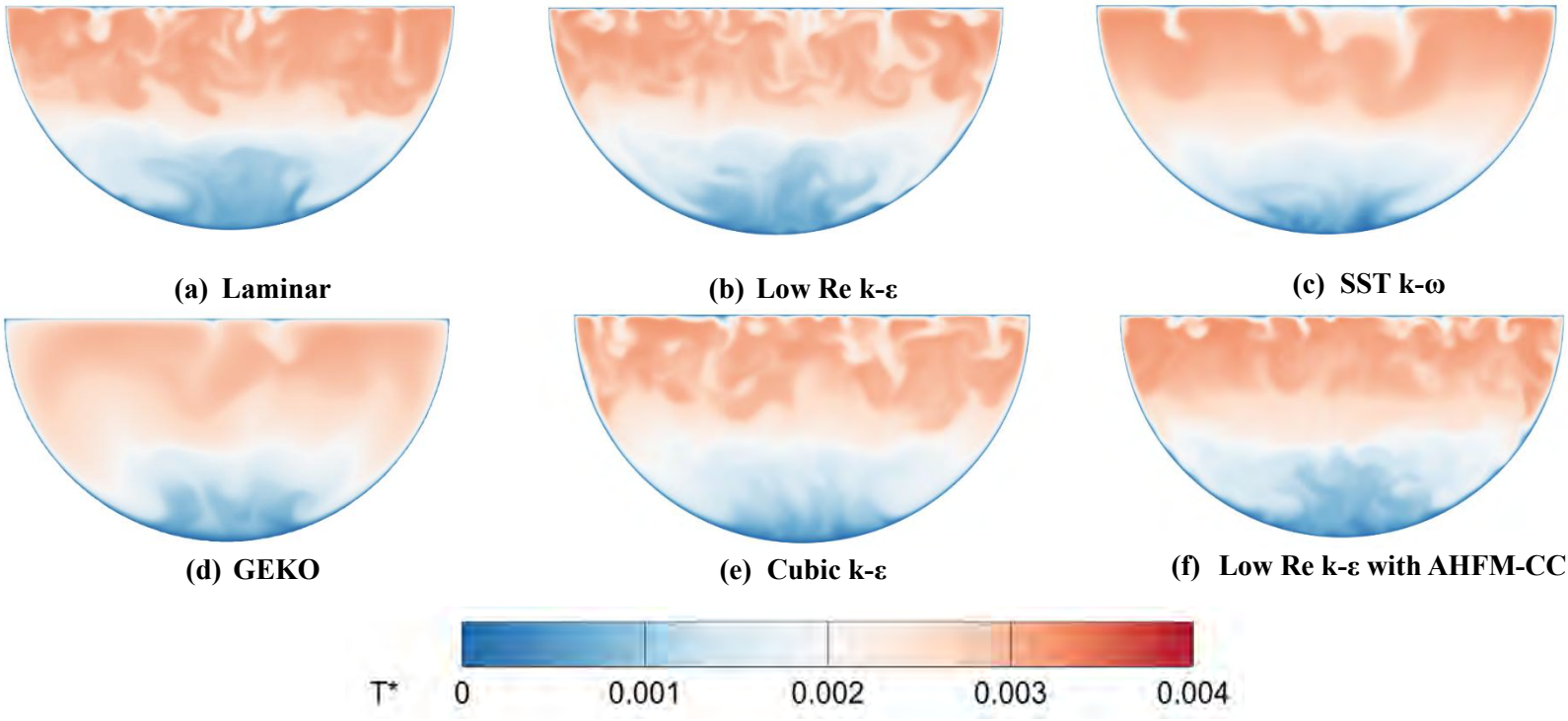

Figure 7. The normalized instantons temperature (T*) contours.

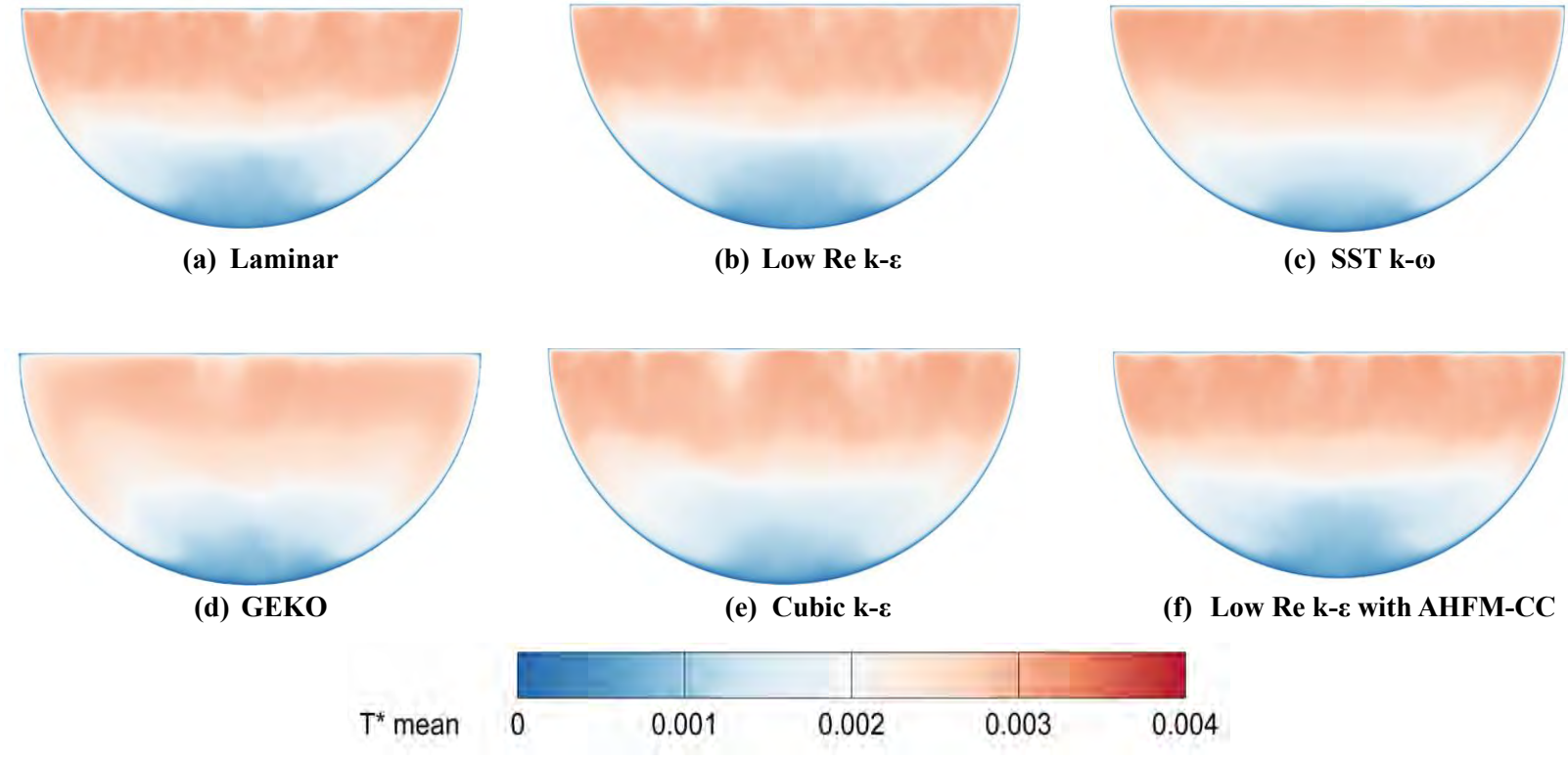

Figure 8. The normalized mean temperature (T*) contours.

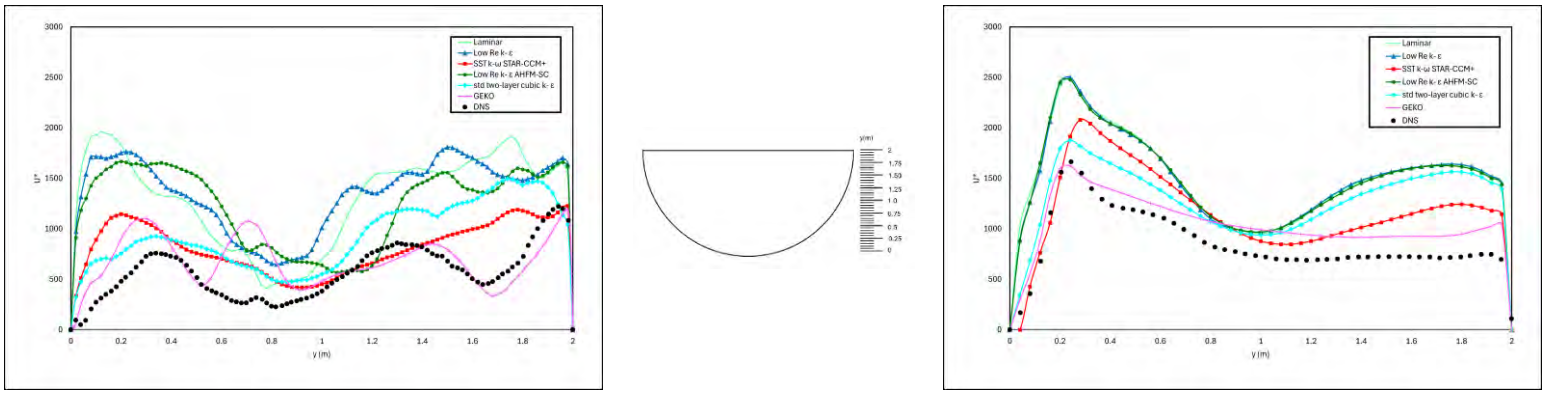

(a) (b)

Figure 9. The normalized mean velocity (U*) at the middle line (a) and across the 50 horizontal planes (b).

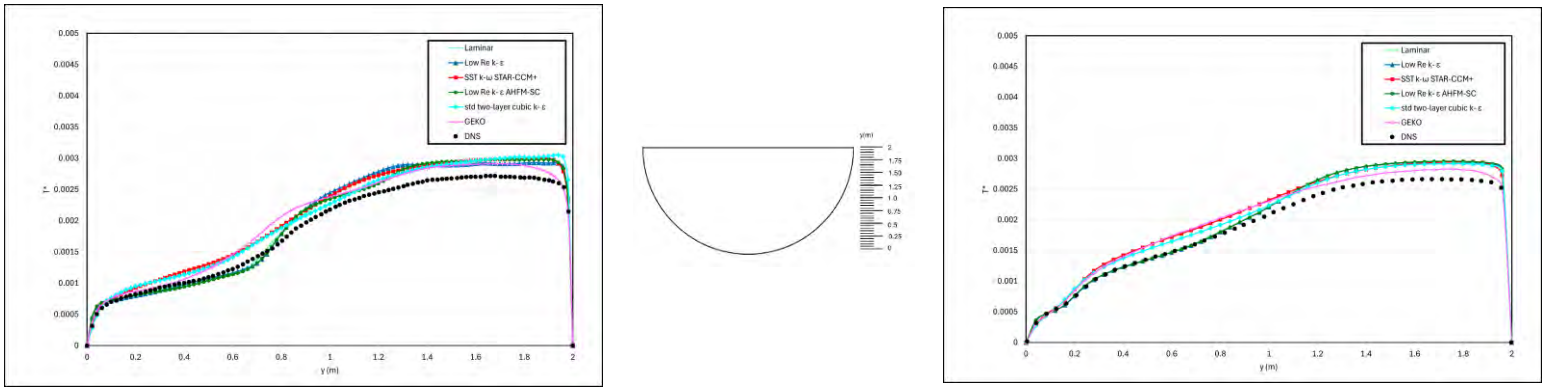

(a) (b)

Figure 10. The normalized mean temperature (T*) at the middle line (a) and across the 50 horizontal planes (b).

4. CONCLUSIONS

In this study, the flow and heat transfer of internally heated corium pools have been investigated. A URANS approach with different turbulence models has been evaluated and validated against high-fidelity DNS data. The results indicated that all tested models successfully reproduce the fundamental flow patterns expected in such systems. Specifically, k-ω-based models provided superior flow field predictions but exhibited inaccuracies in thermal distribution. Conversely, the non-linear cubic k-ε model demonstrated improved velocity profile accuracy compared to linear formulations. While the AHFM-based model yielded precise temperature prediction in the stratified region, it tended to overpredict the velocities. As a final recommendation for future work, combining AHFM closures for turbulent heat flux with higher-order eddy-viscosity models is suggested to achieve better predicted thermal and flow-field results for internally heated corium pools.

ACKNOWLEDGMENTS

The authors acknowledge the support provided by King Fahd University of Petroleum and Minerals (KFUPM) for this research. This template was adapted from the template for ERMSAR 2019 posted on the Internet.

NOMENCLATURE

C_p	Specific heat at constant pressure, J/kg K	Ω	Vorticity, 1/s
H	Height, m	α	Thermal diffusivity, m^2/s
k	Turbulent kinetic energy, m^2/s^2	δ_{ij}	Kronecker delta
P	Pressure, Pa	ε	Turbulent dissipation rate, m^2/s^3
Q_{vol}	Volumetric heat source, W/m^3	μ	Dynamic viscosity, Pa s
S	Strain tensor, 1/s		
T	Temperature, K	μ_t	Turbulent viscosity, Pa s
u	velocity, m/s	ρ	Density, kg/m^3

Non-Dimensional Numbers

Pr	Prandtl number; $(\frac{\mu C_p}{k})$
Ra	Rayleigh number; $(\frac{g\Delta T l^3}{\alpha v})$
y^+	Dimensionless wall distance; $(\frac{\rho y u_\tau}{\mu})$

REFERENCES

1. O. Kymäläinen, H. Tuomisto, and T. G. Theofanous, “In-vessel retention of corium at the Loviisa plant,” Nuclear Engineering and Design, vol. **169**, no. 1–3, pp. 109–130, Jun. 1997, doi: 10.1016/S0029-5493(96)01280-0.
2. R. Henry and H. Fauske, “External Cooling of a Reactor Vessel Under Severe Accident Conditions,” Nuclear Engineering and Design, vol. **139**, pp. 31–43, Jun. 1993.
3. T. H. Lee, Y. G. Lee, K. Lim, Y. J. Kim, S. H. Park, and E. S. Kim, “Numerical simulation on in-vessel molten corium behavior with external vessel cooling using smoothed particle hydrodynamics,” Nuclear Engineering and Technology, vol. **56**, no. 10, pp. 4018–4030, Oct. 2024, doi: 10.1016/j.net.2024.05.003.
4. B. Bian, D. Dovizio, and W. Villanueva, “Direct numerical simulation of internally heated natural convection in a hemispherical geometry,” Int. J. Heat Mass Transf., vol. **220**, Mar. 2024, doi: 10.1016/j.ijheatmasstransfer.2023.124997.
5. S. Alexandrovich Smirnov, S. Bechta, V. Khabensky, A. Sulatsky, and D. Efremov, “DNS of Molten Corium Pool Inductively Heated in a Cold Crucible Direct numerical simulation of molten corium pool inductively heated in the cold crucible,” 2007. [Online]. Available: https://www.researchgate.net/publication/269113416
6. M. Pizzarelli, “The status of the research on the heat transfer deterioration in supercritical fluids: A review,” International Communications in Heat and Mass Transfer, vol. **95**, pp. 132–138, Jul. 2018, doi: 10.1016/j.icheatmasstransfer.2018.04.006.
7. A. Shams, “Towards the accurate numerical prediction of thermal hydraulic phenomena in corium pools,” Ann. Nucl. Energy, vol. **117**, pp. 234–246, Jul. 2018, doi: 10.1016/j.anucene.2018.03.031.
8. A. K. Sharma, M. Pellegrini, K. Okamoto, M. Furuya, and S. Mizokami, “Validation and application of numerical modeling for in-vessel melt retention in corium pools,” Int. J. Heat Mass Transf., vol. **196**, Nov. 2022, doi: 10.1016/j.ijheatmasstransfer.2022.123313.
9. P. Guo, P. Yu, F. Quan, Y. Yuan, J. Yu, and W. Ma, “Assessment of Different Turbulence Models on Melt Pool Natural Convection Simulations With Internal Heat Source,” Int. J. Energy Res., vol. **2025**, no. 1, 2025, doi: 10.1155/er/5995562.
10. Ansys®, “Ansys Fluent Theory Guide,” 2025. [Online]. Available: http://www.ansys.com
11. Siemens Digital Industries Software, “Simcenter STAR-CCM+, version 2406.0001,” 2023, Siemens.
12. S. B. Pope, “Turbulent Flows,” 2000.

13. B. E. Launder and D. B. Spalding, “The numerical computation of turbulent flows,” Comput. Methods Appl. Mech. Eng., vol. **3**, no. 2, pp. 269–289, Mar. 1974, doi: 10.1016/0045-7825(74)90029-2.
14. F. S. Lien, W. L. Chen, and M. A. Leschziner, “Low-Reynolds-Number Eddy-Viscosity Modelling Based on Non-Linear Stress-Strain/Vorticity Relations,” in Engineering Turbulence Modelling and Experiments, Elsevier, 1996, pp. 91–100. doi: 10.1016/B978-0-444-82463-9.50015-0.
15. A. Shams, F. Roelofs, E. Baglietto, S. Lardeau, and S. Kenjeres, “Assessment and calibration of an algebraic turbulent heat flux model for low-Prandtl fluids,” Int. J. Heat Mass Transf., vol. **79**, pp. 589–601, 2014, doi: 10.1016/j.ijheatmasstransfer.2014.08.018.
16. L. Eça and M. Hoekstra, “A procedure for the estimation of the numerical uncertainty of CFD calculations based on grid refinement studies,” J. Comput. Phys., vol. **262**, pp. 104–130, Apr. 2014, doi: 10.1016/j.jcp.2014.01.006.
17. D. Dovizio, B. Bian, W. Villanueva, and E. Komen, “Validation of CFD RANS of an internally heated natural convection in a hemispherical geometry,” Nuclear Engineering and Design, vol. **428**, Nov. 2024, doi: 10.1016/j.nucengdes.2024.113471.

The 12th European Review Meeting on Severe Accidents Research

May 18-22, 2026, Universidad Carlos III de Madrid, Madrid, Spain

TECHNICAL SESSION 1.1: SEVERE ACCIDENT SCENARIOS

Chairs: M. Angelucci (University of Pisa), D. Luxat (Sandia National Lab)

ID021	**Analysis of dose rates in the containment during the Fukushima accident** T. Sevón (VTT)	Paper Presentation
ID054	**Preliminary Analytical Justification of Long-Term Containment Cooling System with Steam Condensing Heat Exchanger for NPPs with VVER-1000 Reactors** Y. Vorobyov (Energy Safety Group LLC)	Paper Presentation
ID091	**ASTEC Modelling of the AP1000 and Cold-Leg Small-Break LOCA Simulations with Long-Term Cooling Cut-off** D. Zhao (National University of Singapore)	Paper Presentation
ID080	**Instrumentation survivability Assessment during a Severe Accident; Incorporating radiation monitoring in MELCOR to evaluate the impact on SAMGs** K. Fernandez-Cosials (Universidad Politécnica de Madrid)	Paper Presentation

ANALYSIS OF DOSE RATES IN THE CONTAINMENT DURING THE FUKUSHIMA ACCIDENT

Tuomo Sevón
VTT Technical Research Centre of Finland
Kivimiehentie 3, Espoo, Finland
tuomo.sevon@vtt.fi

ABSTRACT

Dose rates that were measured during the Fukushima accident using the CAMS (Containment Atmosphere Monitoring System) were analyzed. Distributions of Kr, Xe, I and Cs in the containment drywell and wetwell, calculated with the MELCOR code, were converted to dose rates using conversion factors published by Uchida et al. The calculated dose rates were then compared with the measurements. While the wetwell dose rates were reproduced reasonably well, significant discrepancies were observed in the drywell dose rates, particularly for units 2 and 3. The calculated peak drywell dose rates occurred much too early, and the long-term dose rates were significantly underestimated. Several possible reasons for these discrepancies were identified, including missing models of iodine chemistry, wash-off of deposited aerosols by condensed water, desorption of chemisorbed CsOH, complex structures and piping in the drywell, three-dimensional effects, debris spreading from the pedestal to the drywell, and absence of conversion factors for certain nuclides.

KEYWORDS
Fukushima, MELCOR, dose rate, CAMS

1. INTRODUCTION

Simulation results of the Fukushima accident are typically compared with the measured pressures and water levels, as they are directly available as outputs of accident analysis codes. In addition to these parameters, dose rates in the drywell and wetwell were measured during the accident using the CAMS (Containment Atmosphere Monitoring System). However, accident analysis codes do not directly calculate dose rates. Recently, Uchida et al. [1] published conversion factors that enable the conversion of becquerels of Cs, I, Xe and Kr in the drywell and wetwell to dose rates, accounting for the detector geometry.

This paper analyses results of VTT's MELCOR calculations of the Fukushima accident at units 1, 2 and 3. The calculated fission product distributions are converted to dose rates and compared with the measured dose rates during the accident. The analysis considers magnitudes of the dose rates, their trends, and the timing of sudden changes.

A similar analysis was previously conducted in the OECD Nuclear Energy Agency BSAF project (Benchmark Study of the Accident at the Fukushima Daiichi Nuclear Power Station); see figures 2.7, 3.6 and 4.6 of reference [2]. Very large differences among the benchmark participants were found, but their reasons were not analyzed in detail.

2. METHODS

2.1. MELCOR Models

The dose rate analysis is based on the MELCOR simulations published in references [3], [4] and [5]. The models were developed with the objective of reproducing the measured pressures and water levels as accurately as possible. The drywell was modeled with three control volumes: pedestal, drywell, and a small "drywell hot" volume that receives the assumed leaks from the steam line before mixing the gases with the entire drywell volume. The gas space of the wetwell was modeled with a single control volume. Both the drywell and wetwell were modeled with cylindrical symmetry, so possible azimuthal asymmetry of the fission product distributions was not represented.

One of the main uncertainties in the accident modeling is the timing and flow rate of water injections with the fire engines. At unit 1, there is consensus that a significant amount of water did not reach the reactor before 270 h [6]. At unit 2, attempts to pump seawater to the reactor began 77 h 11 min after the earthquake (March 14, 19:57) [7]. When the accident was modeled with the injection starting at that time, the Reactor Pressure Vessel (RPV) did not fail. However, camera inspections of the drywell have shown that the RPV has failed and debris has been discharged to the pedestal. The RPV failure could be reproduced by assuming that water could be injected only when the pressure was below 0.3 MPa. In this scenario, the injection started at 91 h 11 min. The debris ejection to the pedestal was calculated to begin at 94 h 6 min. In the unit 3 simulation, the first water injection took place at 42 h 39 min (March 13, 9:25), but the injection was stopped several times [8].

Three pressure peaks were measured at the unit 2 reactor between 77 and 83 h. The first and the third peaks were assumed to be caused by Safety Relief Valve (SRV) closing and reopening. At the time of the second peak, the model calculated core plate failure, dropping hot debris into the water in the lower plenum and increasing the pressure. The pressure decrease after 89 h was assumed to have been caused by a leak from the drywell to the reactor building. A 40 cm^2 leak area provided the best match to the measurements.

The water level measurement systems at all three units were distorted by boiling of water in the measurement system, causing the indicated water level to be much higher than the actual level. This boiling was caused by leaks of superheated steam from a steam line to the drywell, heating the measurement system pipes. The measurement systems were added to the MELCOR models, and the leak area and timing that best matched the measurement data were determined. At unit 1, a small 1.7 cm^2 leak was opened at 6.5 h [3]. At unit 2, the best agreement with the measurements was obtained by assuming an 8 cm^2 leak at 78.5 h [4]. And at unit 3, a 20 cm^2 leak was opened at 42.2 h, coinciding with the actuation of the Automatic Depressurization System [5].

2.2. Converting MELCOR Results to Dose Rates

The locations of the CAMS detectors are shown in Fig. 1. Uchida et al. [1] provide conversion factors χ_{ik} from activity to dose rate for nuclide i at location k, taking into account the geometry of the containment and the detector locations. The unit of the conversion factors is (Sv/h) / PBq. Conversion factors are provided for 8 nuclides: Cs-134, Cs-136, Cs-137, I-131, I-132, I-133, Xe-133 and Kr-88. For the wetwell CAMS, conversion factors are available for three locations: water, gas, and deposited on the wall. For the drywell CAMS, conversion factors are available for five locations: gas in the spherical part, wall of the spherical part, drywell floor, and the outer surface of the biological shield (separating the pedestal from the drywell), separately for lower and upper parts of the shield. The conversion factors for the drywell floor were not available in tables, but were estimated from Fig. 11 of [1]. Uchida et al. estimate that the uncertainty of the conversion factors is a factor of two.

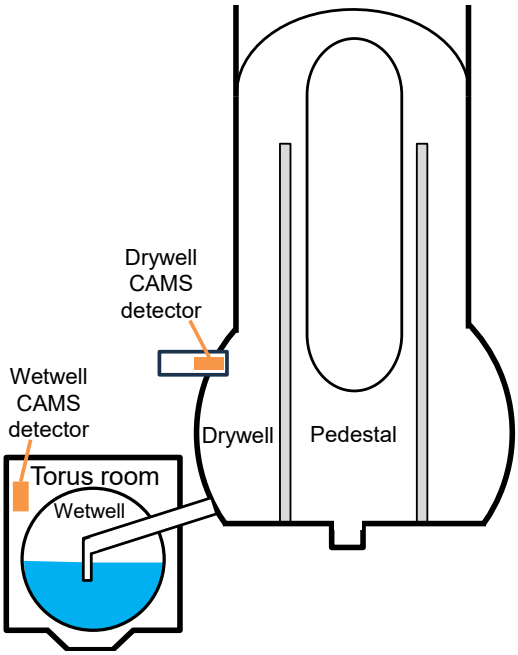

Figure 1. Locations of the CAMS detectors.

For the wetwell, Uchida et al. [1] provide three correction factors that account for the changing water level of the suppression pool. A rising water level increases the conversion factors for the gas phase and wall deposition because the gas volume and wall area decrease, so the same total activity in the gas or on the wall corresponds to a higher concentration. Conversely, a rising water level decreases the conversion factor for the water phase because the concentration of fission products in the water decreases. Private communication with S. Uchida indicated that reference [1] contains typos in the correction factor equations (4-9) and (4-10). The correct forms of the wall and gas correction factors are

$$w_{wall} = 0.24 \cdot [1 - exp\{-4 \cdot (h_s/R_s + 1)\}] + 0.76 \quad (1)$$
$$w_{gas} = 0.4 \cdot [1 - exp\{-4 \cdot (h_s/R_s + 1)\}] + 0.6 \quad (2)$$

Here h_s is the water level measured from the center of the wetwell, and R_s is the smaller radius of the wetwell torus. The effects of the water level correction factors on the dose rates were small, less than 30 %. Another error in reference [1] is that in table A1b, the gas and wall columns have been swapped.

The MELCOR simulations provide the amount of fission product i at location k as a function of time t: $\Phi_{ik}(t)$. The unit of $\Phi_{ik}(t)$ is fraction of core inventory. The dose rate (Sv/h) is then calculated as

$$\Gamma(t) = \sum_k \sum_i \chi_{ik} exp(-\lambda_i t) S_i \Phi_{ik}(t) \quad (3)$$

Here λ_i is the decay constant of nuclide i, and S_i is the core inventory (PBq) of nuclide i at the time of the reactor shutdown [9]. In addition, the water level correction factors were applied for the wetwell dose rates.

The drywell control volume in the MELCOR model includes both the spherical and cylindrical parts. Because the conversion factor was provided only for the spherical part, and the detector does not see the cylindrical part, $\Phi_{ik}(t)$ for $k = gas$ was multiplied by the volume of the spherical part divided by the total volume. Effectively, it was assumed that the fission product concentration is uniform in the drywell gas space. When water was present on the drywell floor, fission products in the water were taken into account using the drywell floor conversion factor.

3. RESULTS

3.1. Unit 1

The wetwell and drywell dose rates at unit 1 are plotted in Figs 2 and 3, respectively. For reference, the measured reactor pressure is also shown. The measurement data was taken from [10]. The MELCOR calculation ends at 168 h because, at that time, the model predicts melt-through of the concrete biological shield between the pedestal and the drywell. Camera inspections have confirmed that this did not occur, so it was not reasonable to continue the calculation further. Overestimation of the long-term concrete ablation is a known issue with severe accident codes [11]. The −50 % and +100 % curves of the calculation results are shown because the estimated uncertainty of the conversion factors is factor of two [1]. The peak value of the wetwell MELCOR CAMS curve (277 Sv/h at 5.2 h) is not visible because the scale was adjusted to better display the measured dose rates. The measured dose rates become available at 63 h, while the core degradation and RPV failure occurred much earlier.

The wetwell dose rates are reproduced reasonably well from 63 to 144 h, considering the factor-of-two uncertainty in the conversion factors. However, the measured wetwell dose rate increases steeply at 144 h, without any apparent reason. The measured pressure does not show any changes at this time, and no significant events were recorded at the plant.

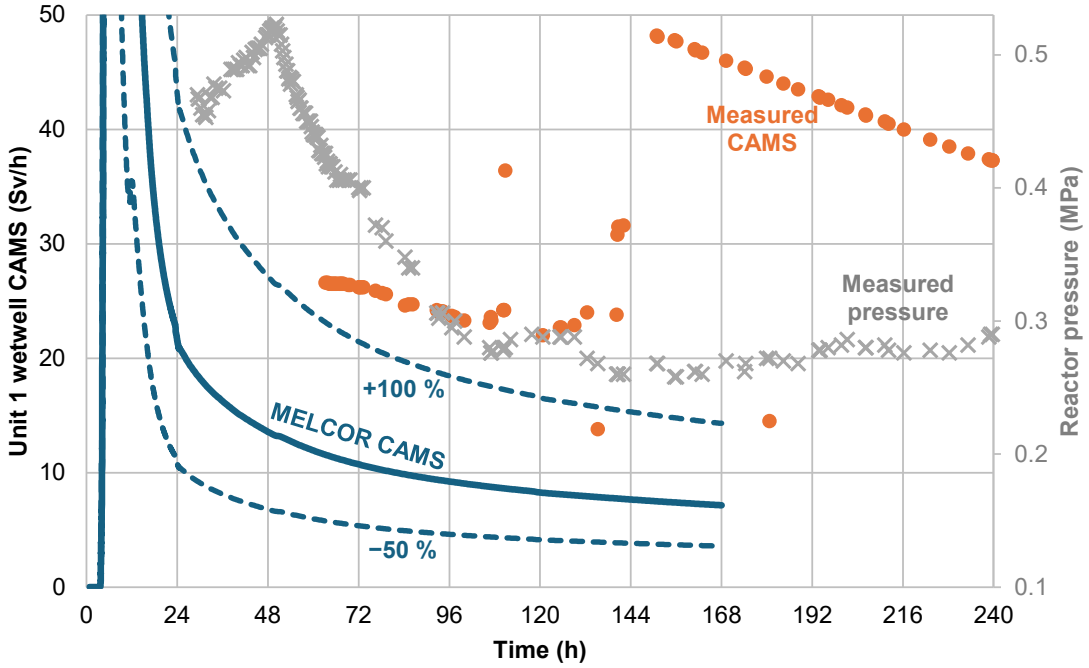

Figure 2. Wetwell dose rate at unit 1.

The decreasing trend of the drywell dose rate of unit 1 from 63 to 84 h is captured quite well by the calculation (Fig. 3). However, the measured dose rate starts increasing at 84 h, again for no apparent reason. After 125 h, the measured dose rate drops to a few millisieverts per hour. Although the figure appears to show a good match, the calculated dose rate is actually around 500 mSv/h during that period. The very low measured dose rates are suspected to be erroneous [6]. Then, at 194 h, the measured dose rates suddenly increase, again with no apparent reason.

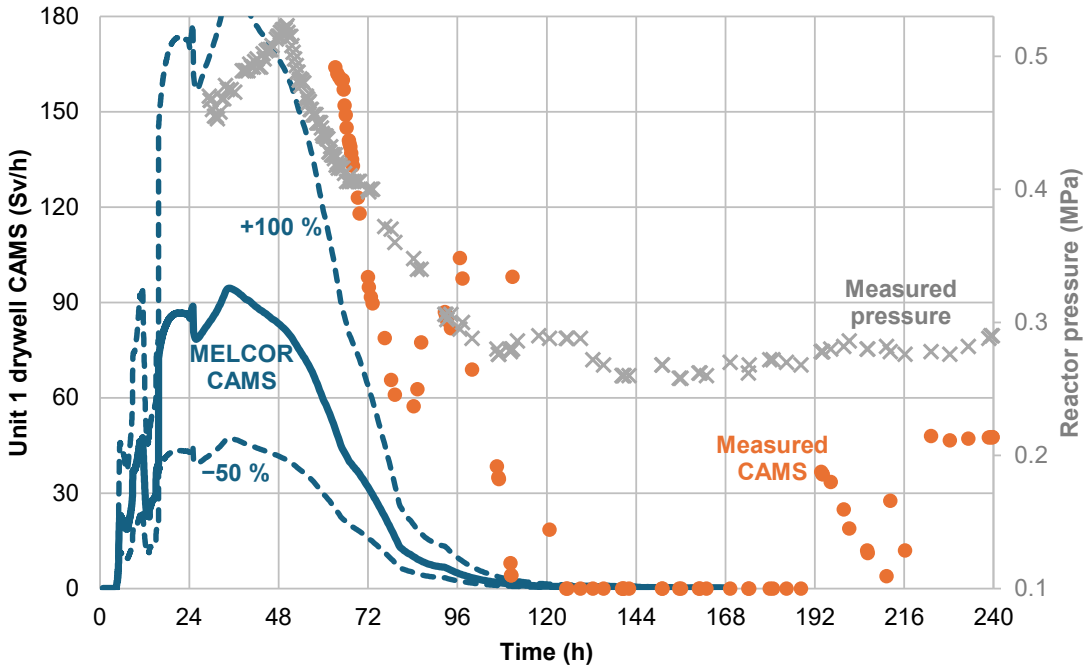

Figure 3. Drywell dose rate at unit 1.

3.2. Unit 2

Unit 2 is the most interesting case because dose rate measurements are available during the time when the core degradation was taking place. The wetwell dose rate at unit 2 is plotted in Fig. 4. For reference, the measured drywell pressure is also shown. The dose rate is calculated quite well, again taking into account the factor of two uncertainty in the conversion factors. Both the measured and the calculated dose rates jump at 78.5 h, when a SRV was opened and a gasket leak from a steam line to the drywell assumed. This event is visible also as a rapid increase of the drywell pressure.

At the peak, 73.5 % of the calculated dose in the wetwell is caused by fission products in the gas phase, 26 % in the water, and only 0.5 % deposited on the wall. The situation changes over time, as aerosols deposit and gases leak out of the containment. At 163 h, only 0.4 % of the calculated wetwell dose is caused by fission products in the gas phase, 80.5 % in the water, and 19.1 % deposited on the wetwell wall.

The drywell dose rate at unit 2 is plotted in Fig. 5. Both the measured and the calculated dose rates start increasing at 78.5 h, but the calculated peak dose rate occurs 18 h too early. Also in the BSAF-2 benchmark, almost all participants calculated the peak dose rate at an earlier time than measured (Figure 3.6 of [2]). (Note that the VTT results shown in [2] were calculated with an earlier version of the model, which did not predict RPV failure at unit 2.) The long-term drywell dose rate is underestimated by a factor of about 24.

At the peak, 96.1 % of the calculated dose in the drywell is caused by fission products in the gas phase, 3.2 % on the floor, and only 0.7 % deposited on the walls. The situation changes over time, as aerosols deposit and gases leak out of the containment. At 163 h, only 0.2 % of the calculated drywell dose is caused by fission products in the gas phase, 1.1 % on the floor, and 98.7 % deposited on the walls.

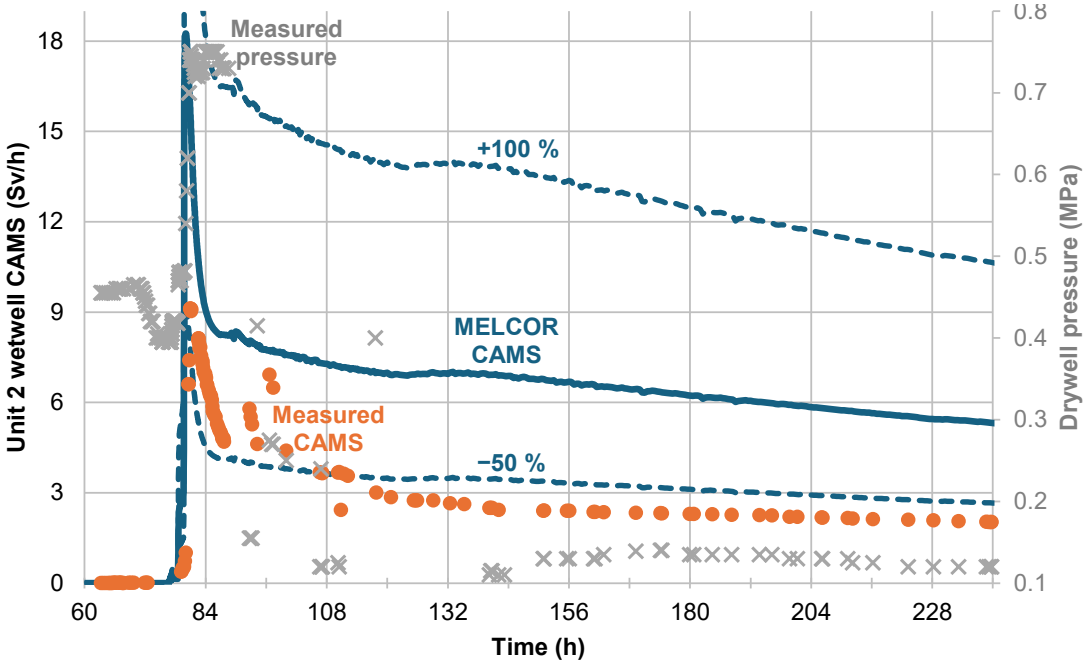

Figure 4. Wetwell dose rate at unit 2.

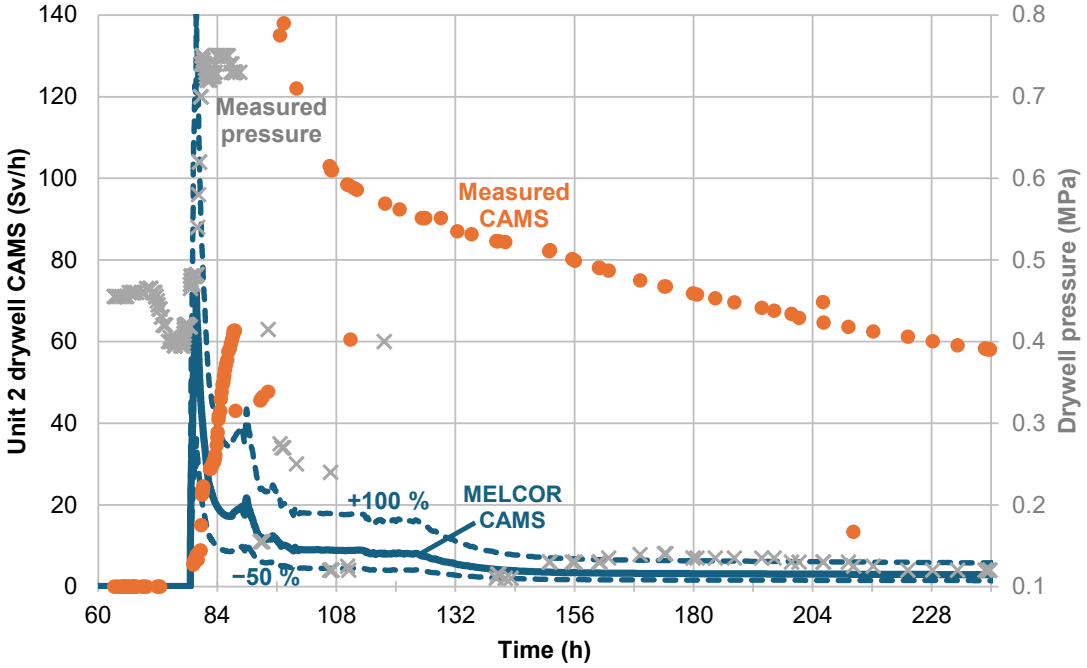

Figure 5. Drywell dose rate at unit 2.

3.3. Unit 3

At unit 3, the dose rates measurements are available from 61 to 68 h, and again starting at 161 h. Similarly to unit 1, the core degradation period was already over when the CAMS became available. The calculation reproduces the wetwell dose rates well, as shown in Fig. 6. The MELCOR calculation ends at 141 h, but simple extrapolation shows that the dose rate is at the same level as the measurements beyond 161 h. There

were two CAMS detectors, A and B, and the B detector showed about 30 % lower readings than the A detector. The detectors may be located at different angular positions, but the exact locations are unknown.

The unit 3 drywell dose rates are presented in Fig. 7. The measured dose rate peaks at 64 h, but the measurement was not available during the time when the calculation predicts the highest dose rate (45 h, soon after the ADS actuation and assumed steam line leak). The results look similar to unit 2 (Fig. 5): the peak value is calculated much too early, and the long-term dose rate is significantly underestimated.

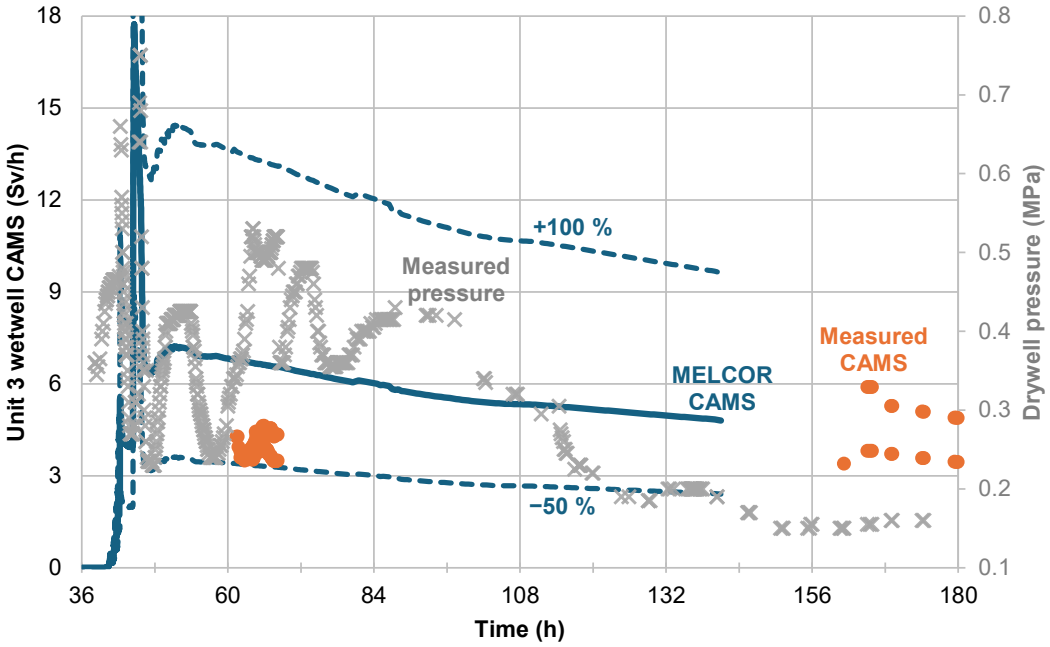

Figure 6. Wetwell dose rate at unit 3.

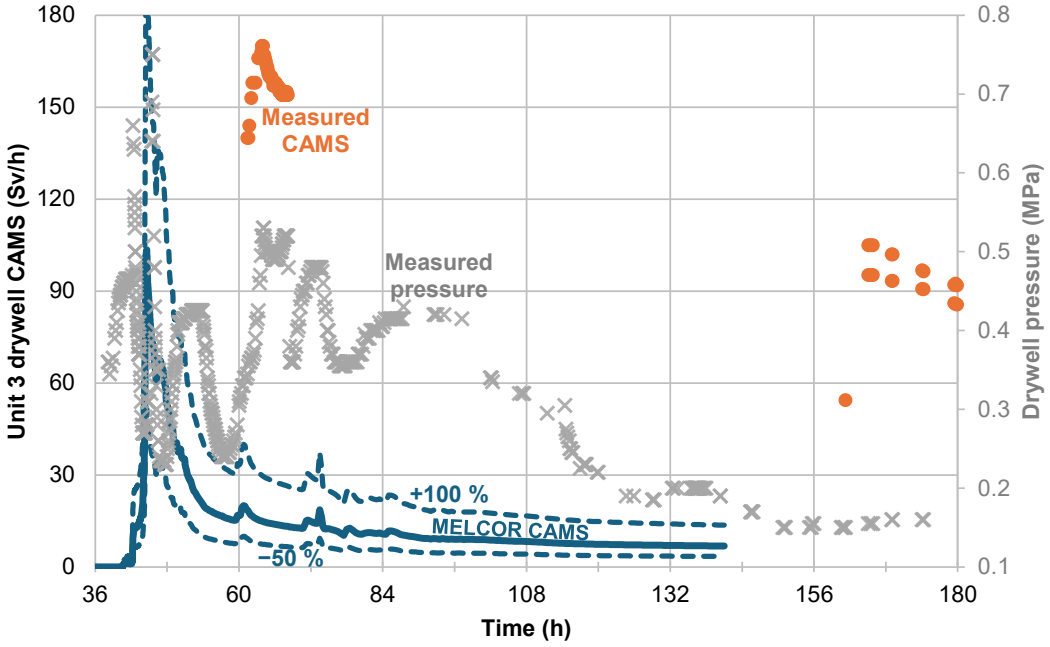

Figure 7. Drywell dose rate at unit 3.

4. DISCUSSION

The measured dose rates seem to follow exponential decay curves at late phases of the accident. Fig. 8 shows decay curves fitted to the unit 2 dose rates after 100 h. The drywell dose rate decreases with an effective half-life of 8.2 d, while the wetwell dose rate follows the effective half-life of 7.9 d. Similar curves can be fitted to the other units' dose rates, yielding effective half-lives between 7.7 and 11.6 d.

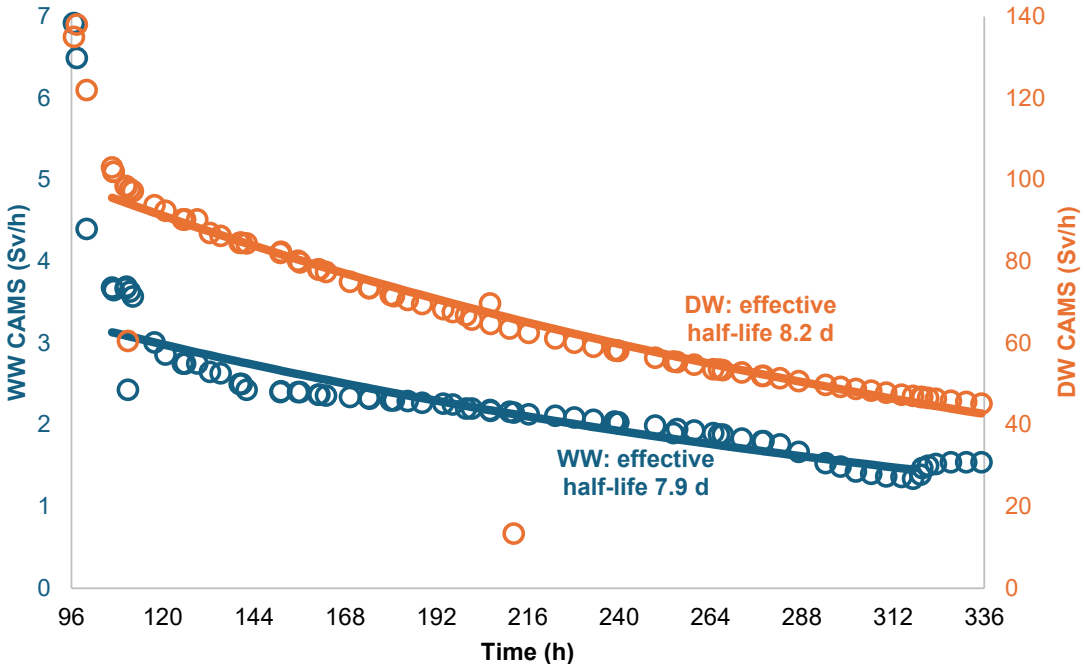

Figure 8. Exponential decay curves fitted to unit 2 dose rates after 100 h.

Half-lives of all the nuclides considered in the analysis are presented in Table I. The effective half-lives of the measured dose rates (7.7–11.6 d) are very close to I-131. This suggests that iodine was the main source of the containment dose rate during the first few days of the accident. The half-life of Xe-133 is also close to the measured values, but the conversion factors from becquerels to dose rates are so small for Xe-133 that its contribution to the dose rate was very small, despite its large inventory. If cesium was a significant contributor to the dose rates, the measured effective half-life should be much longer.

Table I. Half-lives of the considered nuclides.

Nuclide	Half-life
Kr-88	2.8 h
Xe-133	5.3 d
I-131	8 d
I-132	2.3 h
I-133	21 h
Cs-134	2.1 a
Cs-136	13 d
Cs-137	30 a

A source or uncertainty is that conversion factors for tellurium are not available. Te-132 has the half-life of 3.2 d, so it may reduce the effective half-life. Another uncertainty is that radioactive decay is not the only phenomenon that reduces the dose rate. The release of fission products from the containment to the environment also plays a role, as well as wash-off of deposited fission products from the walls by condensed water.

Cesium has a significant effect on the calculated dose rates. For example at unit 2 at 163 h, Cs causes 55.5 % of the calculated wetwell dose rate and 59.1 % of the calculated drywell dose rate. The corresponding numbers for iodine are only 44.2 % and 40.9 %.

Using unit 2 drywell at 163 h as an example, the measured dose rate was 77.4 Sv/h, while the calculated dose rate was only 3.3 Sv/h. For the calculated dose rate to reach the measured value, additional 9 % of the Cs inventory, or alternatively 14 % of the I inventory, would have to move to the lower part of the biological shield outer surface (which has the highest conversion factors). The distribution of the Cs and I at the selected instant is presented in Table II. More than half of the Cs and I is in the wetwell water. Possible overestimation of the retention in the water could explain the significantly underestimated drywell dose rate and the somewhat overestimated wetwell dose rate (Fig. 4). Alternatively, desorption of the CsOH that is calculated to be chemisorbed in the RPV could rise the calculated dose rate to the measured level. Possible underestimation of the release of Cs and I from the fuel could also explain the underestimated dose rate. However, if more fission products were released from the fuel or desorbed from the reactor, all of them would not be deposited in the drywell.

Table II. Distribution of Cs and I at unit 2 at 163 h.

	% of inventory	
	Cs	I
Fuel	12.5	18.8
RPV	19.4	0.3
Steam lines	0.8	0.7
Pedestal	4.8	4.7
Drywell outside pedestal	3.0	3.3
Wetwell	57.0	67.5
Reactor building	0.4	0.8
Environment	2.1	3.9

Nine possible causes were identified for the underestimated drywell dose rates at late phases of the accident:

1. The model may underestimate aerosol deposition in the drywell, possibly due to missing deposition surfaces, such as small piping of auxiliary systems, supporting structures, and maintenance platforms and walkways.
2. The detector may measure radiation coming from inside of pipes that contain highly radioactive materials. This effect could not be modeled.
3. There may be 3-dimensional effects. The drywell is modeled with a cylindrical symmetry, but the fission product deposition may be asymmetric, with more fission products deposited close to the detector. [12] Asymmetry could also explain why the calculated peak occurs earlier than the measured peak, if the leak from the steam line to the drywell was located at another side of the drywell than the detector.

4. MELCOR assumes that condensed water washes off all deposited fission products from heat structure surfaces, but this may not be a correct assumption, especially for species that are not water soluble.
5. Possible overestimation of the fission product retention in the wetwell water can explain the discrepancy.
6. MELCOR assumes that a significant amount of CsOH vapor is chemisorbed on steel structures in the reactor. For example at unit 2 at 163 h, 19.4 % of the Cs inventory is retained in the reactor. MELCOR assumes that the chemisorbed CsOH is never desorbed. If this assumption is incorrect, desorption of the chemisorbed CsOH from the reactor could explain the high dose rates in the drywell during the late phases.
7. If fuel debris has spread from the pedestal to the drywell, the detector may directly "see" the debris. This effect was not taken into account in the analysis.
8. The effective half-lives of the measured dose rates suggest that I-131 was the main source of the containment dose rate. Iodine has a very complicated chemistry that is not modeled by MELCOR. For example, adsorption of gaseous iodine on the drywell wall could explain the high dose rates.
9. The analysis considered the eight nuclides listed in Table I because the conversion factors have been published only for them. Other nuclides, such as tellurium, may have caused significant dose rates in the drywell.

One of the objectives of the analysis was to find opportunities for improving the MELCOR models. This objective was not reached. Discrepancies between the calculated and measured dose rates were found, and possible reasons for the discrepancies were identified. But the identified reasons remain speculative because fixing any of them is beyond reach. It would require changing the MELCOR source code (e.g. iodine chemistry, or desorption of chemisorbed CsOH), or modeling phenomena for which sufficient information is not available (e.g. radiation from inside of pipes or directly from debris, or nuclides for which conversion factors have not been published).

5. CONCLUSIONS

Results of MELCOR calculations of the Fukushima accident at units 1, 2 and 3 were analyzed. The calculated distributions of Kr, Xe, I and Cs in the wetwell and drywell were converted to dose rates using conversion factors published by Uchida et al. [1] and compared with the measured dose rates during the accident.

The results of the unit 2 and 3 analyses are similar. For both units, the dose rates in the wetwell are reproduced reasonably well, taking into account uncertainties in converting becquerels to dose rates. However, the drywell results are not so good. The calculated peak dose rates in the drywell occur much too early (even though the timing of the measured peak at unit 3 is uncertain, as it may have occurred at a time when measurement data was not recorded). And the calculated drywell dose rates in the late phases of the accident are significantly underestimated.

The unit 1 results are somewhat different. The wetwell dose rates are reproduced reasonably well from 63 to 144 h. But the measured dose rate increased steeply at 144 h, without any apparent reason. The decreasing trend of the drywell dose rate from 63 to 84 h is captured quite well by the calculation. However, the measured dose rate started increasing at 84 h, again for no apparent reason.

During late phases of the accident, the measured dose rates decreased with effective half-lives between 7.7 and 11.6 d. This suggests that I-131 (half-life 8 d) may have been the main source of the containment dose rate during the first few days after the accident. Uncertainties in iodine chemistry and adsorption may have caused the discrepancies in the calculated drywell dose rates.

Several other possible causes for the underestimated drywell dose rates in the late phases of the accident were identified. These include complex structures and piping in the drywell, 3-dimensional effects, models for wash-off of deposited fission products due to condensed water, desorption of chemisorbed CsOH from the reactor, debris spreading from the pedestal to the drywell, and other nuclides besides Kr, Xe, I and Cs. Testing the possible causes was beyond reach of this work.

ACKNOWLEDGMENTS

This work was funded by SAFER2028, the Finnish national nuclear safety and waste management research programme. The work benefited from discussions at meetings of the OECD NEA FACE project.

REFERENCES

1. S. Uchida, M. Pellegrini and M. Naitoh, "Conversion factors bridging radiocative fission product distributions in the primary containment vessel of Fukushima daiichi npp and dose rates measured by the containment atmosphere monitoring system," *Nuclear Engineering and Design*, **380**, 111303 (2021).
2. OECD NEA, *Benchmark Study of the Accident at the Fukushima Daiichi Nuclear Power Plant, Summary Report*. https://www.oecd-nea.org/upload/docs/application/pdf/2021-09/7525_bsaf.pdf (2021).
3. T. Sevón, "Analyzing reactor water level measurements in the Fukushima Daiichi 1 accident," *Progress in Nuclear Energy*, **160**, 104707 (2023).
4. T. Sevón, "Analysis of reactor water level measurements during the Fukushima unit 2 accident," *Nuclear Engineering and Design*, **366**, 110760 (2020).
5. T. Sevón, "Analysis of reactor water level measurements during the Fukushima unit 3 accident," *Proceedings of the 19th International Topical Meeting on Nuclear Reactor Thermal Hydraulics (NURETH-19)*, virtual meeting, March 6–11, 2022.
6. L.E. Herranz et al., "Overview and outcomes of the OECD/NEA benchmark study of the accident at the Fukushima Daiichi NPS (BSAF) Phase 2 – Results of severe accident analyses for Unit 1," *Nuclear Engineering and Design*, **369**, 110849 (2020).
7. TEPCO, "Estimation of reactor water levels at the time when core damage and core melt progressed at Unit-2," https://www.tepco.co.jp/en/press/corp-com/release/betu17_e/images/171225e0232.pdf (2017).
8. OECD NEA, *Benchmark Study of the Accident at the Fukushima Daiichi Nuclear Power Plant (BSAF Project), Phase I Summary Report*. https://www.oecd-nea.org/upload/docs/application/pdf/2021-02/csni-r2015-18.pdf (2015).
9. K. Nishihara, H. Iwamoto and K. Suyama, "Estimation of Fuel Compositions in Fukushima-Daiichi Nuclear Power Plant," JAEA-Data/Code 2012-018, https://jopss.jaea.go.jp/pdfdata/JAEA-Data-Code-2012-018.pdf (2012).
10. "Information Portal for the Fukushima Daiichi Accident Analysis and Decommissioning Activities," https://fdada.info/en/home2/accident2/measured2/am_download2/
11. M. Pellegrini, et al., "Analysis of the long-term interaction between molten core and dry concrete at Fukushima Daiichi Unit 1," *Nuclear Technology*, **211**(10), pp. 2595–2608 (2025).
12. S. Uchida, et al., "An approach toward evaluation of long-term fission product distributions in the Fukushima Daiichi nuclear power plant after the severe accident," *Nuclear Engineering and Design*, **380**, 111256 (2021).

Analysis of dose rates in the containment during the Fukushima accident

Tuomo Sevón

ERMSAR, Madrid, Spain, 18–22 May 2026

Introduction

- Measurement data available from the Fukushima accident:
  - Pressures in reactor and containment
  - Water level in reactor
  - Dose rates in containment ("CAMS data")
- Simulation results usually compared with pressures and water level because direct outputs of severe accident codes
- Dose rates not directly calculated by codes
  - ➢ Conversion factors (Bq → Sv/h) published:

  Uchida, S., Pellegrini, M. & Naitoh, M., Nuclear Engineering and Design 380 (2021)
- This presentation: Convert MELCOR results of unit 1, 2 and 3 accidents to dose rates, compare with measured dose rates

MELCOR models of units 1, 2 and 3

- Developed by VTT, results published in 2020–2023
- Tuned to reproduce measured pressures and water levels as well a possible
- Assumptions of water injection with fire engines:
  - Unit 1: injection unsuccessful until 270 h
  - Unit 2: injection rate restricted so that RPV failure calculated
  - Unit 3: injection as reported by TEPCO
- Assumed leaks of superheated steam from steam line to drywell at all units:
  - Timing: when the water level measurement system "went crazy"
  - Leak sizes: tuned to match the measurement data as well as possible

Nuclides and locations

- Conversion factors available for 8 nuclides: Cs-134, Cs-136, Cs-137, I-131, I-132, I-133, Xe-133, Kr-88
- Source locations:
  - Wetwell: water, gas, deposited on wall
  - Drywell: spherical part gas; deposited on wall, floor, and biological shield surface
- Correction factor depending on wetwell water level
- Uchida et al. estimate uncertainty of the conversion factors: factor of two

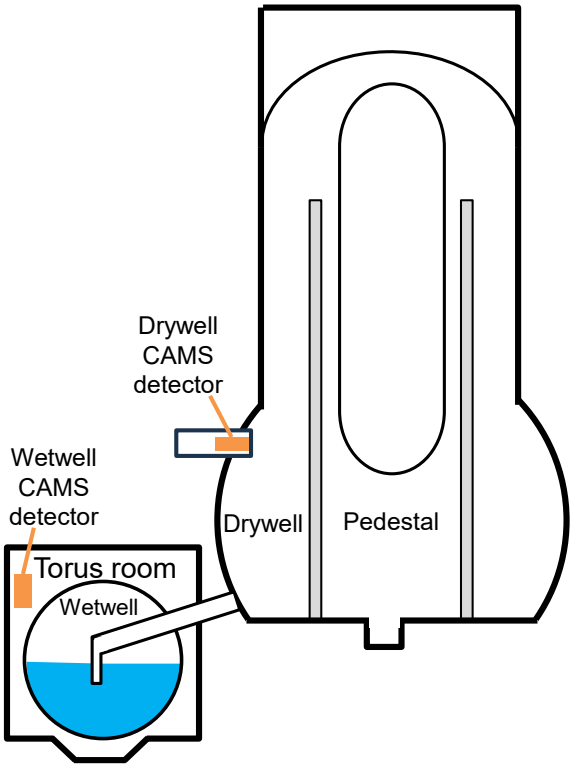

Converting MELCOR results to dose rates

$$\Gamma(t) = \sum_k \sum_i \chi_{ik}\, e^{-\lambda_i t}\, S_i\, \Phi_{ik}(t)$$

- Γ = dose rate (Sv/h)
- χ_{ik} = conversion factor (Sv/h / PBq) for nuclide *i*, location *k*, from Uchida et al.
- λ_i = decay constant for nuclide *i* (1/s)
- S_i = inventory of nuclide *i* at reactor shutdown (PBq), from JAEA-Data/Code 2012-018
- $\Phi_{ik}(t)$ = amount of nuclide *i* at location *k* at time *t* (fraction of inventory), from MELCOR

Results

Unit 2 wetwell dose reproduced quite well

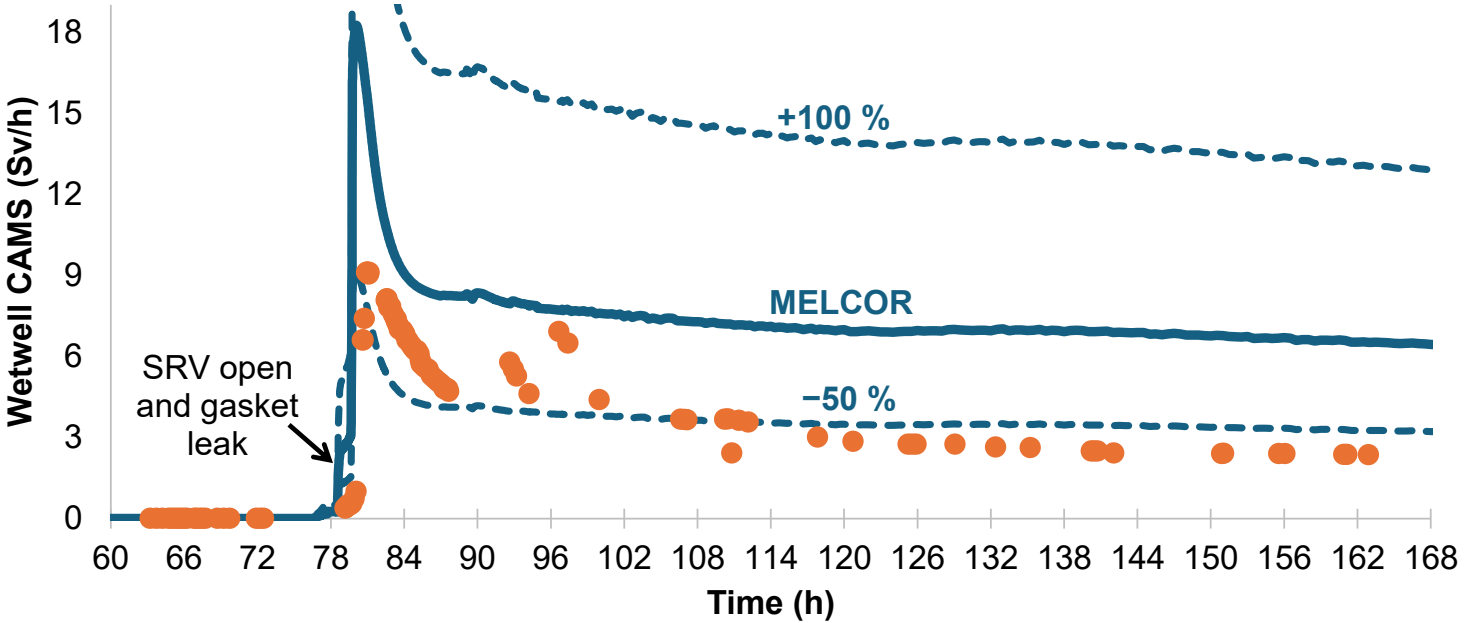

Unit 2 drywell CAMS: Peak 18 h too early, long-term dose rate grossly underestimated

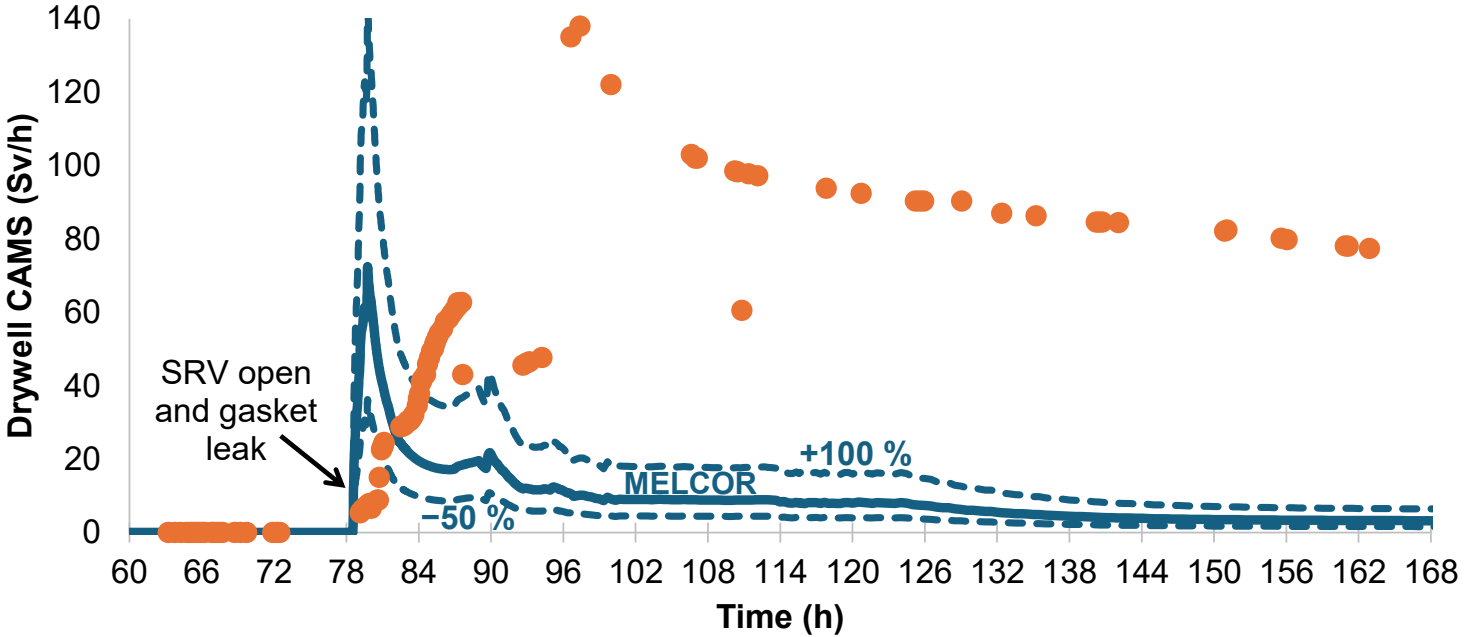

Measured dose rates suggest the main source was I-131 (half-life 8 days)

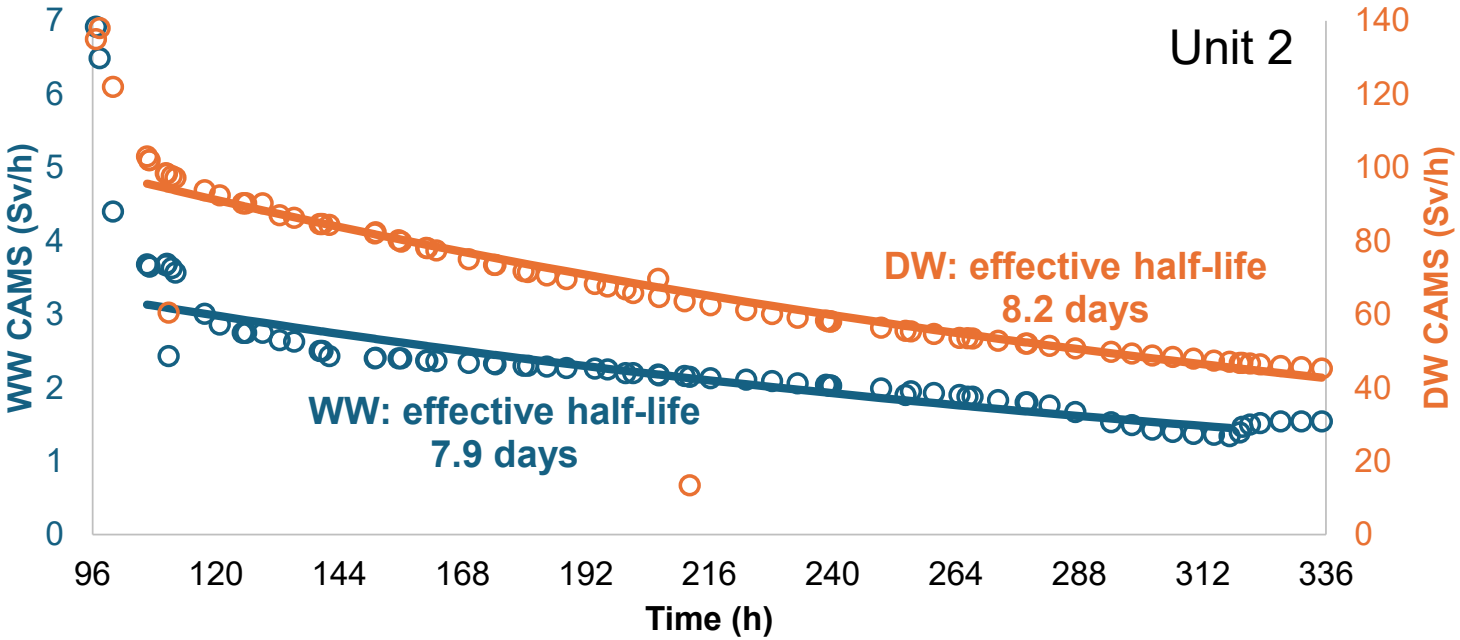

Unit 1 wetwell CAMS: OK until 144 h, then reason for increase unknown

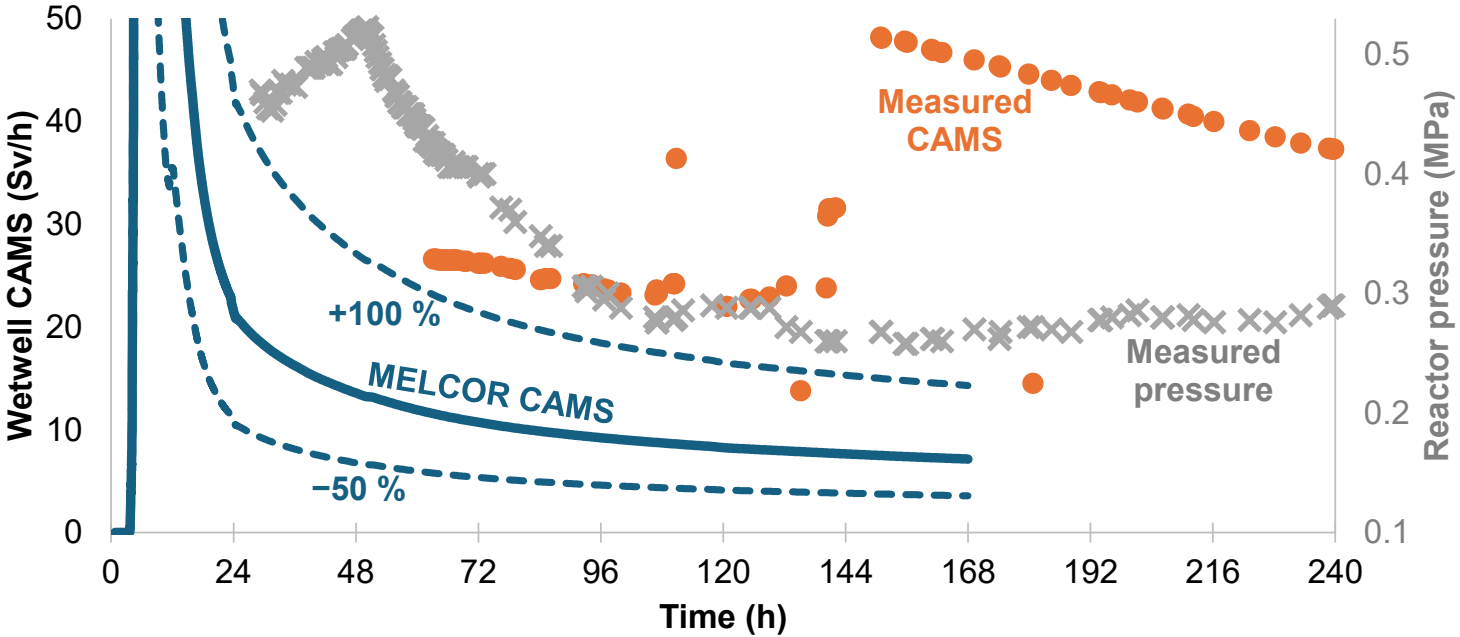

Unit 1 drywell CAMS: OK until 84 h, then reason for increase unknown

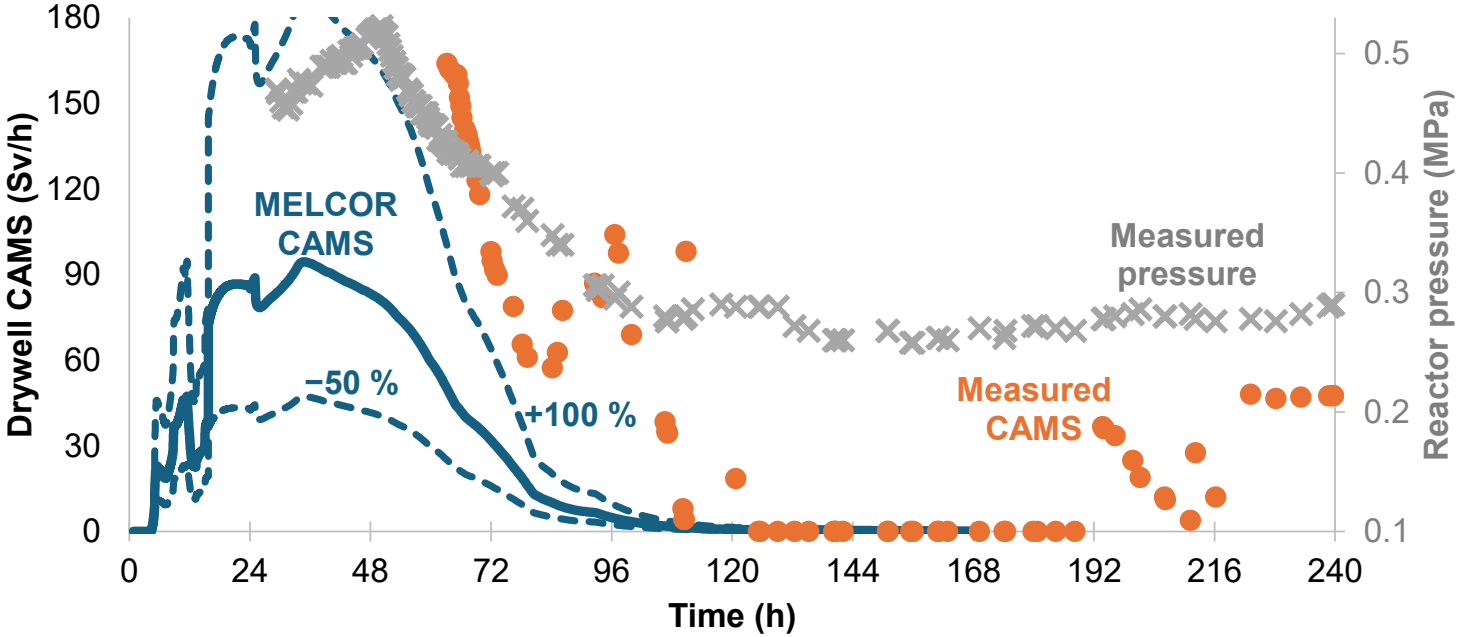

Unit 3 wetwell CAMS reproduced quite well

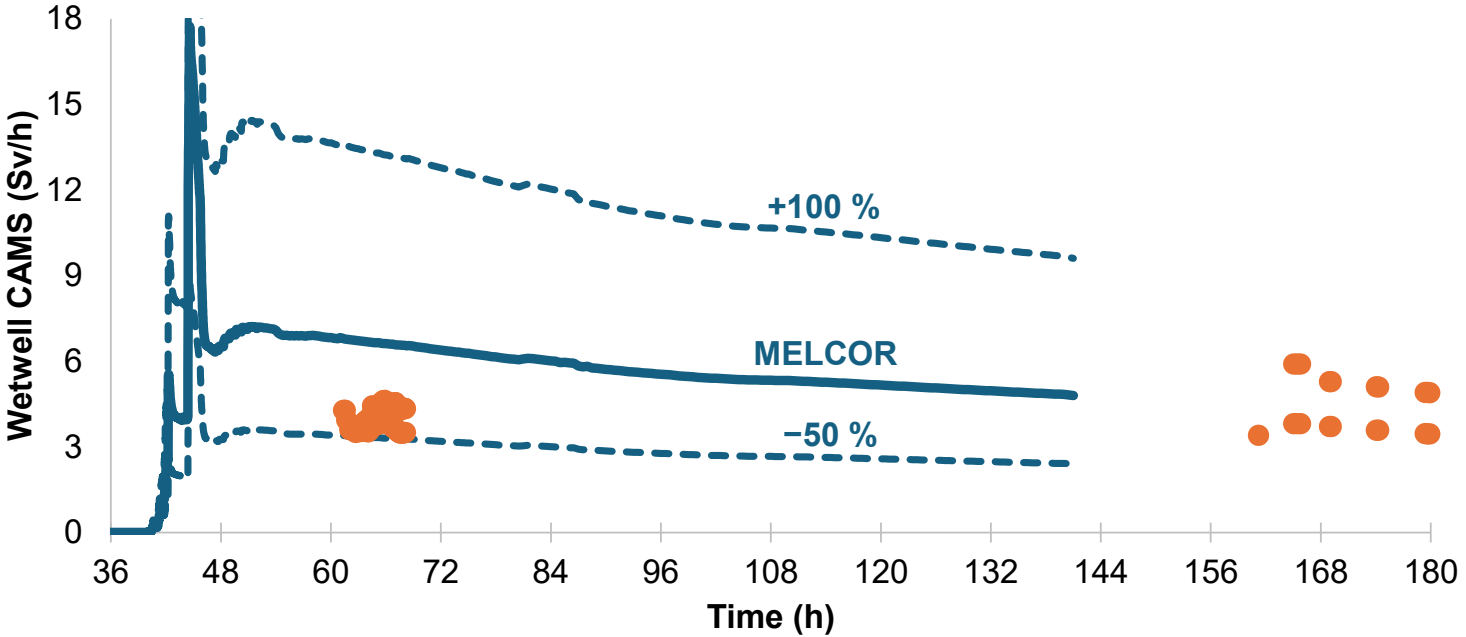

Unit 3 drywell CAMS: grossly underestimated

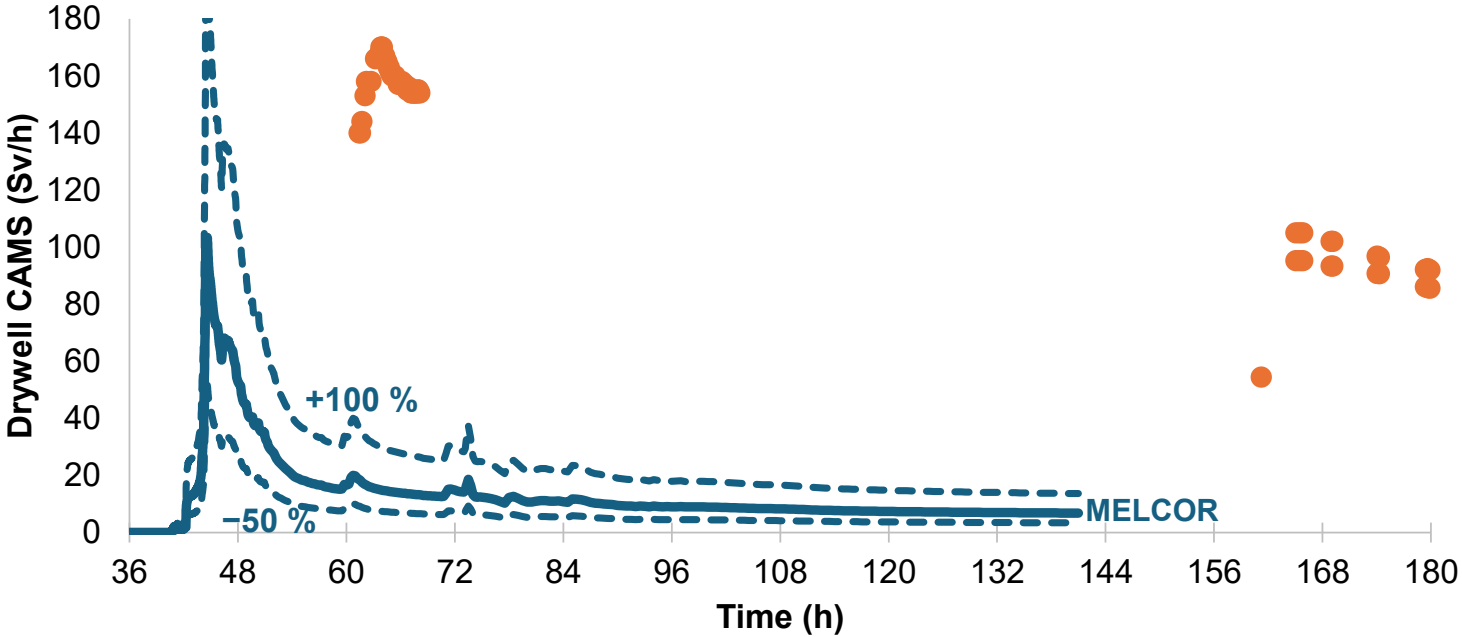

Discussion

Summary of results

- Units 2 and 3:
  - Wetwell dose rates reproduced quite well
  - Drywell dose rates: calculated peaks much too early, dose rates in late phases significantly underestimated
- Unit 1:
  - Wetwell dose rate reproduced quite well from 63 to 144 h
  - Drywell dose rate reproduced quite well from 63 to 84 h
  - Measured dose rates increased steeply at 144 h (wetwell) and 84 h (drywell), without any apparent reason

Possible causes for underestimated drywell dose rates at late phases

- Deposition surfaces missing from model
- Detector may measure radiation coming from inside of pipes
- Detector may "see" debris that has spread from pedestal to drywell
- MELCOR assumes condensed water washes off deposited aerosols
- Missing model of CsOH desorption from steel structures in RPV
- Iodine chemistry
- Nuclides for which conversion factors unavailable, e.g. tellurium

Photo: TEPCO

Conclusions

- MELCOR-calculated distributions of Kr, Xe, I, Cs in Fukushima wetwell and drywell converted to dose rates
- Wetwell dose rates reproduced quite well
- Drywell peak dose rates calculated much too early
- Drywell dose rates in late phases significantly underestimated
- Several possible reasons for discrepancies identified, but difficult to test their contributions
- One of the objectives was to find opportunities for improving the MELCOR models, but that was found difficult

PRELIMINARY ANALYTICAL JUSTIFICATION OF LONG-TERM CONTAINMENT COOLING SYSTEM WITH STEAM CONDENSING HEAT EXCHANGER FOR NPPS WITH VVER-1000 REACTORS

Yu. Vorobyov, O. Mazurok (Ph.D.), V. Ivanov, O. Mykhailenko, A. Tiurin, A. Hanenko
Energy Safety Group LLC
Laboratornyi Lane, 1, office 244, 01133, Kyiv, Ukraine
info@e-s-group.com.ua

E. Kostov (Ph.D.), Á. Pérez-Salado Kamps (Ph.D.), V. Pashynskyi, C. Hartmann (Ph.D.), H. Troselius
Westinghouse Electric Germany GmbH
Dudenstrasse 6, 68167, Mannheim, Germany
kostovee@westinghouse.com, perez3a@westinghouse.com,
valerii.pashynskyi@westinghouse.com, hartma1c@westinghouse.com,
troselht@westinghouse.com

ABSTRACT

Severe accidents in VVER-1000 reactors involve a high probability of molten core material leaving the reactor and spreading in the containment. Achieving a stable safe state during such accidents requires effective containment heat removal to minimize the release of fission products and liquid radioactive waste into the environment.

To preserve containment integrity, a Long-Term Containment Cooling System (LTCCS) with steam-condensing and water-water heat exchangers is proposed for VVER-1000 plants. The concept was developed and patented by Westinghouse in cooperation with its subcontractor, ES Group. This paper presents preliminary analytical results and expected phenomena associated with this concept. Modeling of reactor system and LTCCS was performed using MELCOR code.

The LTCCS design guarantees containment pressure/temperature reduction and stabilization below design limits. LTCCS with total heat removal capacity of ~10-18 MW is sufficient to reduce containment pressure to near-atmospheric levels and water temperature below saturation. The steam generated by boiling of water covering the molten core materials is condensed, while the containment water is circulated by turbine-driven pump (RTS Pump™ by KSB)[1] and cooled in water-water heat exchanger. The condensate returns to the containment by gravity drainage.

LTCCS operation also enables continuous long-term venting of non-condensable gases, including hydrogen, through the Containment Filtered Venting System (CFVS). This gradually decreases the fraction of non-condensables (NC) in the containment atmosphere while increasing the steam fraction, that improves condenser efficiency and eliminates the late hydrogen hazard. In addition, the LTCCS eliminates multiple CFVS venting cycles. Preliminary calculations confirm the effectiveness of the proposed LTCCS concept.

KEYWORDS
Severe Accident, Long Term Cooling, Severe Accident Management, Ex-vessel Phase, Steam Condenser

[1] RTS Pump is a trademark of KSB.

1. INTRODUCTION

The analysis of severe accidents (SA) for VVER-1000 reactors indicates a high probability of core melt/fragments leaving the reactor pressure vessel (RPV) with spreading in the containment. The issue of long-term slow containment pressure buildup and floor melt-through for ex-vessel phase should be addressed by special cooling actions as one of the back-fitting measures for Gen. II reactors [9]. The ex-vessel corium cooling measures are continuously analyzed for VVER-1000 reactors [10-14]. Safe end-state requires reliable heat removal from debris to minimize releases. To ensure the containment integrity under such conditions implementation of the long-term containment cooling system (LTCCS) is proposed.

The objective of the present study is to justify that the proposed LTCCS can maintain containment pressure below 5 kgf/cm² (abs) and average temperature below 150 °C under representative SA scenarios. The work forms part of the Analytical Justification Report prepared by ES Group LLC in cooperation with Westinghouse Electric Germany GmbH and ES Group Europe s.r.o. within Energoatom's safety-improvement program for operating VVER-1000 units in Ukraine. Previous analytical and experimental studies confirmed the technical feasibility of the LTCCS concept for VVER-1000. However, plant-specific justification was required to quantify its performance margins. This paper summarizes study of LTCCS with steam condenser [1], focusing on expected phenomena, consequences and system performance.

2. METHODOLOGY

2.1. VVER-1000 LTCCS layout and system concept description

The LTCCS layout for VVER-1000 V-320 and V-302 (338) designs is similar (Fig. 1). The system consists of two containment circuits (steam and water) and cooling water loop. During ex-vessel phase of SA the corium spread on the containment floor is flooded with cooling water. Boiling of this water produces steam that rises to the upper containment part. In the steam circuit the gas mixture is directed through LTCCS ducts to condenser, where it is cooled and condensed into a tank. This condensate is returned to the containment via condensate turbine-driven pump or by gravity depending on the system layout. This keeps the containment water balance, ensures the corium remains covered and creates a closed-loop circulation of the water-steam inventory.

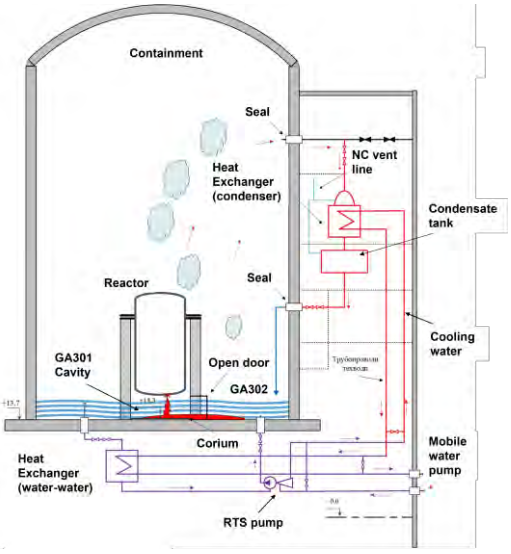

Figure 1. VVER 1000 V-320 LTCCS concept layout.

The water circuit circulates containment water through water-water heat exchanger by turbine-driven RTS pump. Both circuits can operate separately from each other, or in the base version they operate together. External cooling water pump (e.g. mobile diesel pump) first supplies water to the condenser. Cooling water also drives the RTS pump turbine. Then heated cooling water passes to water-water heat exchanger and exits outside the Reactor Building. Cooling water loop pressure is designed to be higher than containment, thereby preventing any transfer of contaminated water outside. LTCCS is designed to avoid containment vacuum conditions and requires no containment entry during SA. The system can operate in conjunction with other SAM systems, such as CFVS and Passive Autocatalytic Recombiners (PAR). LTCCS operation prevents containment pressure buildup, thereby avoiding additional filtered venting cycles. System does not require external power supply and needs external mobile water source (regular pumping unit).

Advantages of LTCCS for VVER-1000:

- Closed-loop water recirculation: Steam is condensed, returned to the containment, and water is cooled in recirculation mode preventing accumulation of contaminated water.
- Containment pressure management: External flexible cooling (FLEX) system ensures stable containment pressure control.
- Corium stabilization: Returned condensate ensures water coverage over molten materials.
- Functional independence: Separation from Defense-in-Depth (DiD) Levels 1,2,3 systems.
- Diverse heat removal path: Independent from Design Basis Accident (DBA) systems.
- Safe condensation: No risk of clogging or direct contact with corium cooling water (steam circuit).

Condenser capacity is preliminarily sized to match decay heat at 72 hours after the Initiating Event (IE). The operation of the system is expected to begin no later than 72 hours after the IE. Once the accident progresses to the ex-vessel phase, the containment is flooded with borated water to create a corium cooling pool.

The LTCC system concept accounts for:

- The removal of NC gases (to support condensation).
- Integration with the CFVS.
- Ensuring dry reactor cavity prior RPV failure to prevent steam explosions.
- Capability to remove heat both from the corium and the spent fuel pool (SFP).
- Long-term containment floor water cooling

2.2. General approach to computational analysis

The computational analysis consisted of sequential steps:

- LTCCS modeling.
- Determination of LTCCS flow rates and condensation capacity.
- Assessment of impact on SA progression.
- Assessment of release to the environment.

Thermal-hydraulic analysis of the LTCCS, RCS and containment is performed using the MELCOR code. After model preparation, representative SA sequences were analyzed to assess LTCCS performance and interaction with CFVS. Acceptance criteria from the CFVS justification [3] and LTCCS-specific criteria were applied.

2.3. Calculation model of VVER-1000/V-320 for MELCOR

MELCOR code version 1.8.5 RL [2] is used to perform the analyses. The South-Ukraine NPP (SUNPP) Unit 3 MELCOR model (VVER-1000/V-320) from analytical justification for the CFVS [3] is taken as start one. This model is modified from Zaporizhzhya NPP model [4] and consists of primary and secondary circuits, reactor core, containment, CFVS, LTCCS and associated systems, other systems and control functions.

RPV is modeled by 7 control volumes (CV001 - CV007) including downcomer (DC), core and upper plenum (UP) (see Fig.2). Four circulation loops are modeled with hot legs, cold legs, reactor coolant pumps (RCPs) and steam generators (SGs). The pressurizer and piping are represented by 5 control volumes. Pressurizer (PRZR) safety valves are modeled as flow paths FL440,441,442 connecting the PRZR dome with pressure relief tank (PRT). The rupture membrane is modeled by flow path (FL443) connecting PRT with containment (CV629). Emergency core cooling systems (ECCS) of low pressure (LP) and high pressure (HP) injection are modeled as water-energy sources. The model is equipped with control systems and controllers.

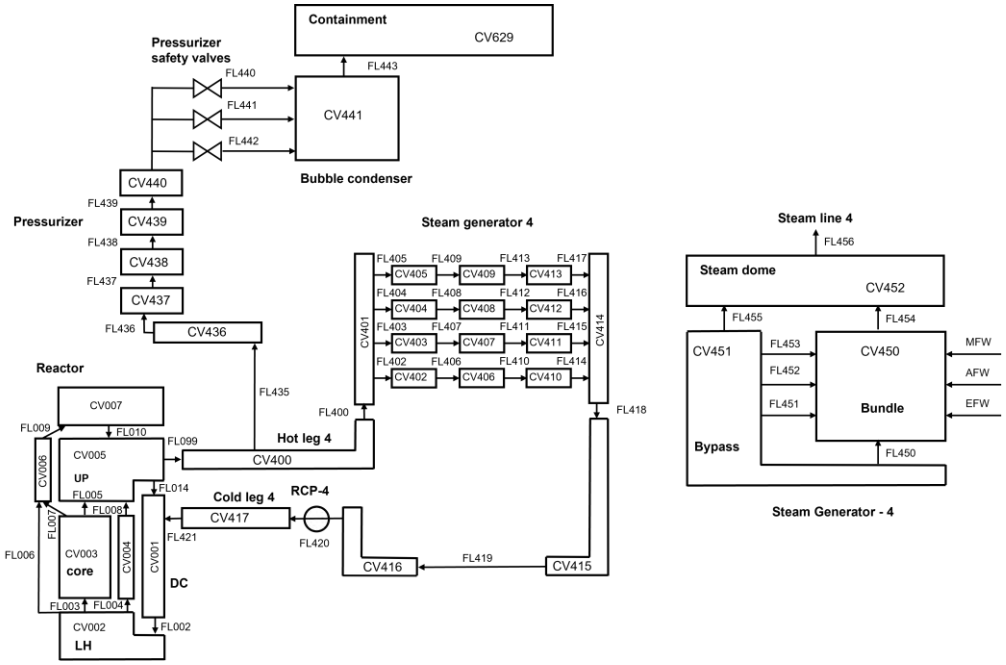

Figure 2. Nodalization scheme of the reactor, primary circuit and SG of Loop 4.

Secondary circuit comprises 32 control volumes and 66 flow paths. Each SG contains three control volumes for the secondary side (see Fig.2) with steam lines and steam dump valves to condenser (BRU-K) and atmosphere (BRU-A). Each SG has two safety valves (SVs). Feedwater systems (normal/auxiliary/emergency) are represented as water sources. The containment model consists of 23 control volumes connected by 46 flow paths. To represent natural convection and hydrostatic pressure gradient, the reactor hall is divided into four control volumes: dome (CV620) and cylindrical part (CV617, 618 and 619). CV617 and 618 represent the wall area, and CV619 models the central part (see Fig.3a).

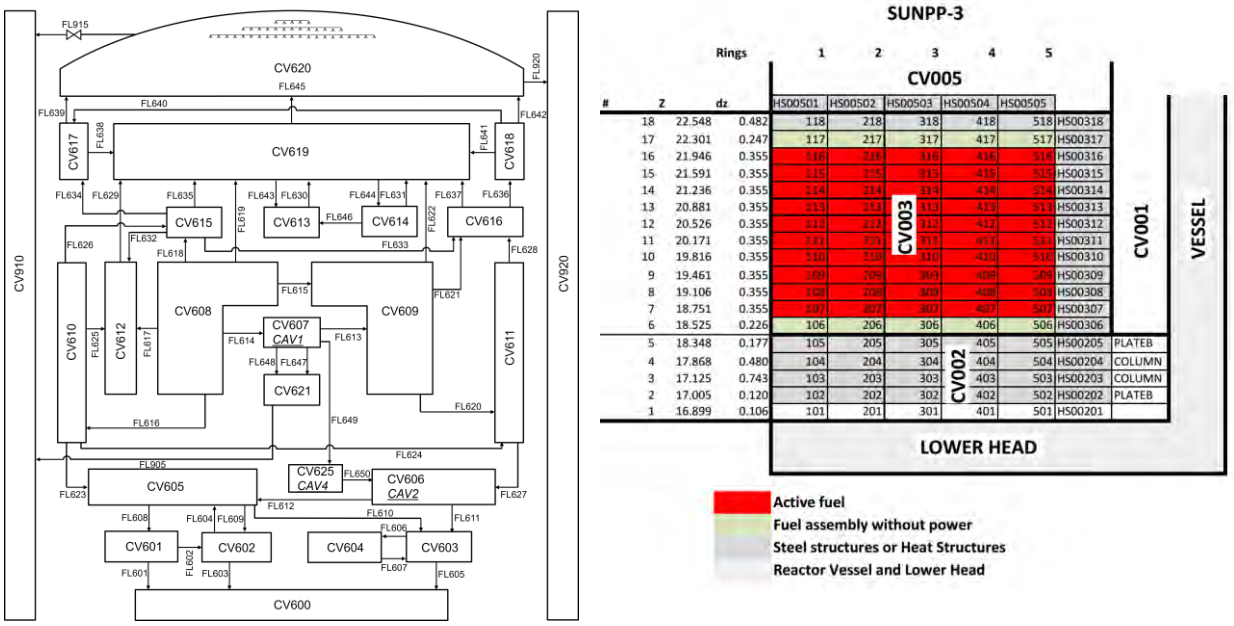

a) b)

Figure 3. Nodalization of the containment (a) and core model (b).

The core model includes 5 radial rings and 18 axial segments. Core is bounded by heat structures in the radial direction. In the axial direction, the core is bounded by the lower plate of guide tubes unit. The first axial section includes reactor lower plenum (segments 1-6). Second section models the reactor core itself, which is divided into 10 axial segments of equal height. Third section models the upper part of unheated core and guide tubes unit lower plate (Fig.3b).

The reactor cavity model includes rooms GA301 (beneath the reactor), room GA302 and part of room GA308 beyond the reactor cavity door [5] (Fig.4). The main cavity door is assumed to open after melt discharge enabling corium spreading on containment floor. Document [6] recommends overflow height 0.15m for a melt with liquidus temperature, and 0.5m with solidus. The analysis assumes 0.15m overflow thickness and uses Control Functions (CF) to model melt overflow, considering relative melt thickness and concrete erosion (see Fig.4). It is assumed that the presence of water does not interfere with corium spreading.

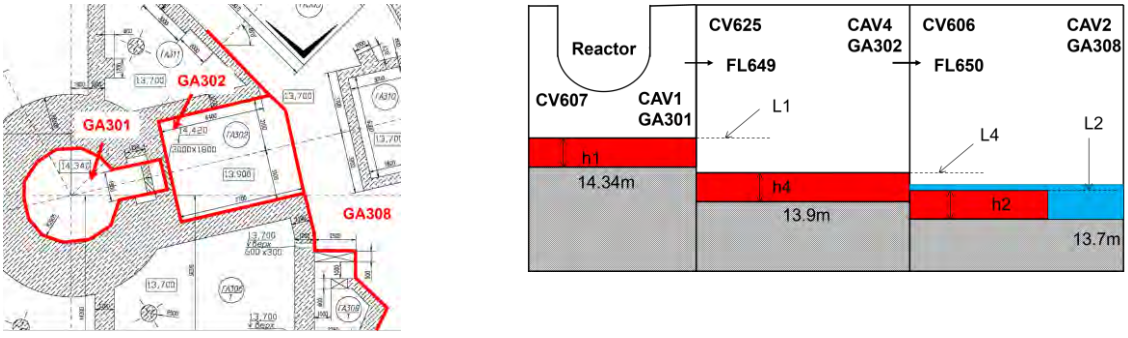

a) b)

Figure 4. Reactor cavity compartments (a) and approach to cavity modeling in MELCOR (b).

The model is equipped with 90 units (RVK-1000) of passive autocatalytic hydrogen recombiners (PARs). CFVS model includes pipes, scrubber, nitrogen system and discharge orifice (Fig. 5). SFP energy source 2.587 MW is added to CV614 corresponding nominal state [7]. SFP is supposed to be leak tight during SA.

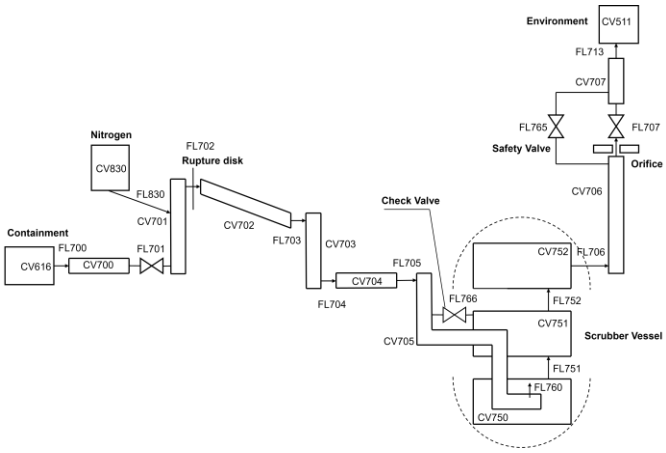

Figure 5. Nodalization of CFVS model.

2.4. LTCCS model

Preliminary parameters of LTCCS are taken from [8]. Based on the preliminary conceptual design (Fig.1) the MELCOR model is developed (Fig. 6). LTCCS steam part pipeline is modeled by a series of volumes CV800-801, 811, 813, 814 with 0.5m inlet diameter and 0.25m at the outlet of the condenser. The condenser is represented by vertical volumes CV805-808 with total height of 2m, and 4000 heat exchange tubes with internal cross-section of 1.018m^2 and heat exchange area 503m^2. Such condenser has margin to adjust condensing power in analysis. CV812 models a 10m^3 volume condensate collection tank. Flow paths connect the system to the scrubber model (CV705) and to environment (CV820). Venting path to the scrubber FL821 (diameter 0.050m) removes NC gases behind the condenser. FL813 with 0.030m diameter ensures passive condensate drain to containment.

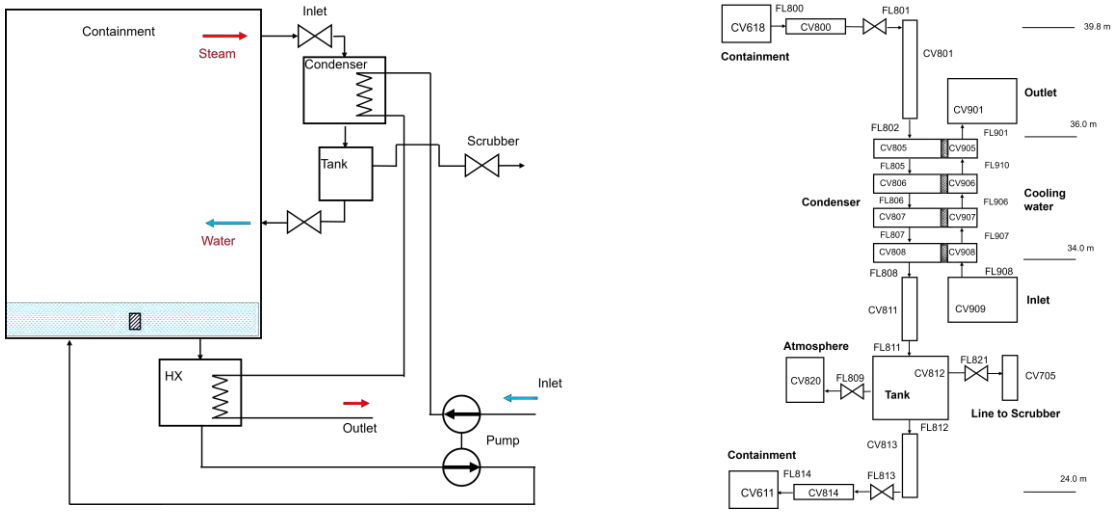

a) b)

Figure 6. LTCCS simplified scheme (a) and its MELCOR model nodalization (b).

The LTCCS water circuit is modeled by control variables with countercurrent heat exchange scheme. The power of water-water heat exchanger is chosen equal to 10 MW at 320 m^3/h cooling water flow rate (high pressure) and a water flow rate of 320 m^3/h for low pressure side (containment). The cooling water pipeline is modeled by volumes CV901, 909 and condenser volumes CV905-908. The condenser model is tested to obtain condensing power for 320 m^3/h cooling water flow rate with temperature of 20°C (Table I). The scrubber NC venting line is fully open, scrubber level is nominal. The model reproduces condensation power 10.5 MW at 3 kgf/cm^2 (abs.) with 98% steam mole fraction meeting 10 MW requirement from [8]. This power corresponds approximately to core decay heat at 5-7 days after the IE (without SFP). The maximum condenser capacity 28.7 MW is chosen with a margin.

Table I. Condensation capacity of the LTCCS condenser model

№	Pressure, kgf/cm^2 (abs.)	Mole fraction of steam, %	Capacity, MW
1	3	95	5.3
2	3	98	10.5
3	3	99	18.0
4	3	99.9	28.7
5	2	99.9	10.9

2.5. Identification of scenarios, initial and boundary conditions

Station blackout (SBO) is selected as a representative initiating event. Primary breaks sequences exhibit generally similar containment conditions at later SA phases. Three scenarios are analyzed:

- Scenario 1. SBO with SAM actions (without LTCCS)
- Scenario 2. SBO with SAM actions and LTCCS start (steam circuit, condenser capacity limited to 15 MW)
- Scenario 3. SBO with SA management actions and LTCCS start (steam and water circuit, condenser capacity limited to 10 MW)
- Scenario D1. SBO with SAM actions and LTCCS start (steam circuit, condenser capacity limited to 10 MW).

After core exit (CE) temperature rises above 450°C personnel open 3 pressurizer SVs according to SAM. CFVS operates by the containment pressure (open-close) setpoints 5 kgf/cm^2 - 3 kgf/cm^2 (abs.). After the 1st CFVS cycle, containment flooding to 0.9m level is started. LTCCS cooling water flow rate 320 m^3/h with 20° C temperature is assumed.

LTCCS start is assumed after active in-vessel and ex-vessel phase main events and aerosols settling. Start requires water level in the containment; therefore, it is assumed after containment filling to +0.3m above the floor after 1st CFVS venting cycle. The start conditions need future refinement. The condensing capacity is controlled by changing NC gas venting behind the condenser. Condensing power might be monitored via cooling water flow and exit temperature. The analysis covers time intervals of 72 hours (3 days), 7 days (600000s) or 10 days (900000s) and assumes initial nominal power state.

2.6. Acceptance criteria

Acceptance criteria from CFVS justification [3]:

- Containment pressure is limited by 5 kgf/cm^2 (abs.) (short peak < 6 kgf/cm^2 (abs) permitted).
- Scrubber level stays in the range 0.75 - 2.1 m.
- Steam-gas mixture is outside of detonation region on Shapiro-Moffetti diagram.

LTCCS operation criteria:

- Containment pressure approaches to atmospheric and stabilizes.
- Containment water/steam temperature is stabilized or steadily decreases.
- Containment water temperature is stabilized at less than 100ºC for compartments without debris.
- LTCCS thermal total capacity is equal to or consistently greater than decay heat.

3. RESULTS OF ANALYSIS

3.1. Scenario timelines

The main Scenario 3 events are presented in Table II.

Table II. Sequence of main events for Scenario 3

Time, s	Event	Description
0	Station blackout	Postulated IE and failures
2020	Pressurizer SVs periodic opening	RCS pressure above 192 kgf/cm^2
7220	Containment pressure above 1.3 kgf/cm^2 (abs.)	Spray setpoint reached, no spray available
10000	Opening of 3 Pressurizer SVs	SAM action, CE temperature > 450ºC
10530	Hydroaccumulators (HA) injection	RCS pressure below 60 kgf/cm^2
20000	Fuel elements collapse	Core damage starts
25300	Complete damage of all fuel assemblies	
34940	RPV lower head failure	MCCI and melt spreading begins
35900	Opening of CFVS venting	Containment pressure > 5 kgf/cm^2 (abs.)
73000	Closure of CFVS venting	Containment pressure < 3 kgf/cm^2 (abs.)
75500	Containment flood from the external source	SAM action, flow rate 15 kg/s
86500	Start of the LTCCS (steam and water circuit)	SAM action, containment level 0.3 m
86500	Containment pressure 3.97 kgf/cm^2 (abs.)	Maximum value after LTCCS start
120000	Termination of containment flood	SAM action, containment level 0.9 m
300000	Containment water temperature <100ºC	For compartments without debris
650000	Containment pressure 1.04 kgf/cm^2 (abs.)	Containment pressure close to atmospheric
750000	Water level in CFVS scrubber 0.75 m	Less than criterion, make-up needed
900000	End of calculation	Containment pressure 1.03 kgf/cm^2 (abs), water temperature 85-92ºC (without debris) and 100ºC (with debris), steam temperature 93-127ºC

3.2. Pressure and temperature in the containment

Timely LTCCS activation reduces and stabilizes containment pressure below the design limit of 5 kgf/cm^2 (abs.). LTCCS operation with only steam circuit allows stabilizing containment pressure above atmospheric at the level of 1.7-1.8 kgf/cm^2 (abs.). Stabilization occurs once LTCCS condensation power matches decay heat, typically within 3–5 days depending on system condenser capacity. The duration of stabilization phase is unlimited. In contrast, combined operation with water circuit allows reduce containment pressure nearly to atmospheric value 1.03 kgf/cm^2 (abs.). Figure 7a compares containment pressure with and without LTCCS operation. Containment pressure stabilization corresponds to the balance of LTCCS power and total heat released in the containment (melt, aerosols, SFP) without CFVS venting cycles.

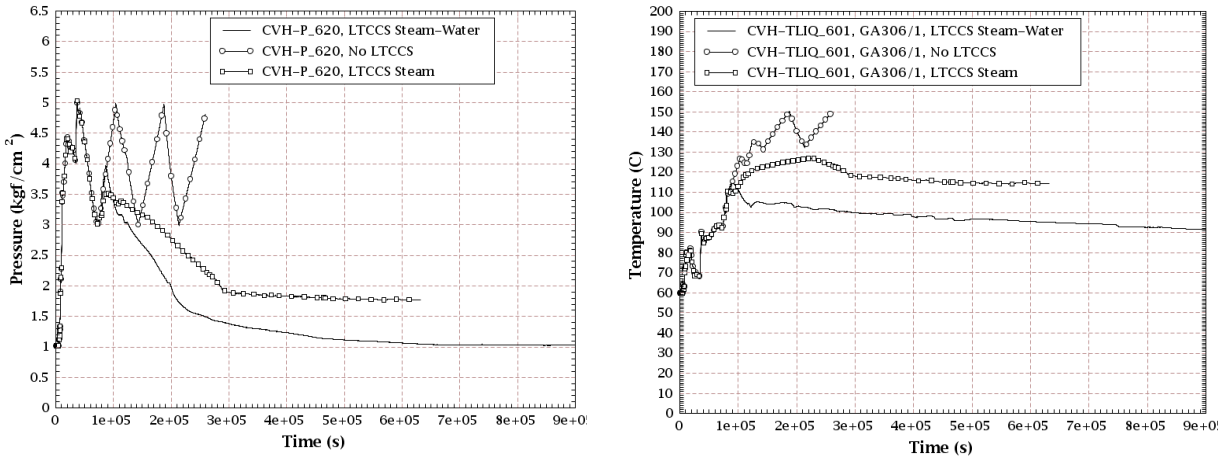

a) b)

Figure 7. Pressure (a) and water temperature (b) in the containment with LTCCS operation (steam and water circuit, Scenario 3), with LTCCS operation (steam circuit, Scenario 2) and without LTCCS operation (Scenario 1).

Containment water and steam temperature follow similar trends (Fig. 7b). Some temporary gas temperature stratification persists because LTCCS does not mix containment atmosphere. Water covering the corium remains saturated while sump water may be cooler.

3.3. LTCCS thermal heat removal capacity

Condensing capacity depends on condenser design (heat transfer area, geometry) and inlet conditions. A condenser with margin is selected to allow condensing capacity adjustment by NC venting control. This effectively decreases condensing surface area while NC present in the mixture. Figure 8a compares condensing capacity and heat removed from the water with decay power. NC venting valve open ratio for Scenario 3 is provided at Figure 8b. Total LTCCS power constantly exceeds core decay heat by 10-15% at any containment pressure. When NC gases are present, the system condensing capacity can be effectively controlled. For the analyzed range (10-15 MW), LTCCS ensures successful stabilization while lower condensing capacity may result in additional CFVS cycles.

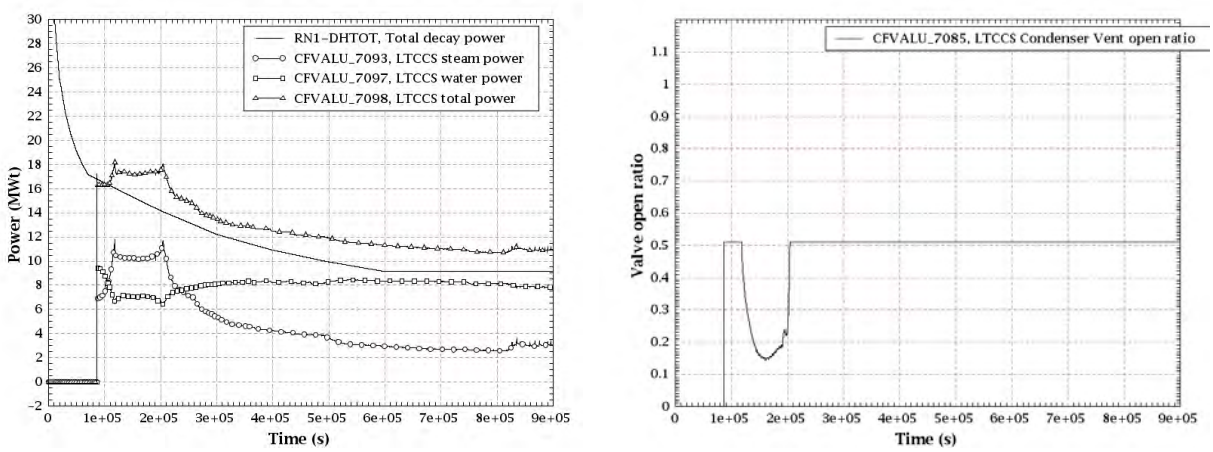

a) b)

Figure 8. Condensing, water circuit and total LTCCS power (a) and NC venting valve open ratio (b) (steam and water circuit, Scenario 3).

3.4. Containment floor flooding and level

Successful LTCCS performance relies on the water covering corium on containment floor. Containment is flooded by personnel actions to a level of 0.9m providing ~0.3m coverage above the melt locations. Flooding requires ~600-650 tons of additional water, yielding a total containment floor pool inventory of ~750-780 tons. This inventory remains inside the containment to maintain the closed cooling loop (Fig. 9) while sump water resides below the floor elevation. Containment level increases with time due to return of boiled off water from SFP to the floor. Technical solutions will be proposed during LTCCS implementation that will allow stabilizing and redistributing such a water flow in a long term.

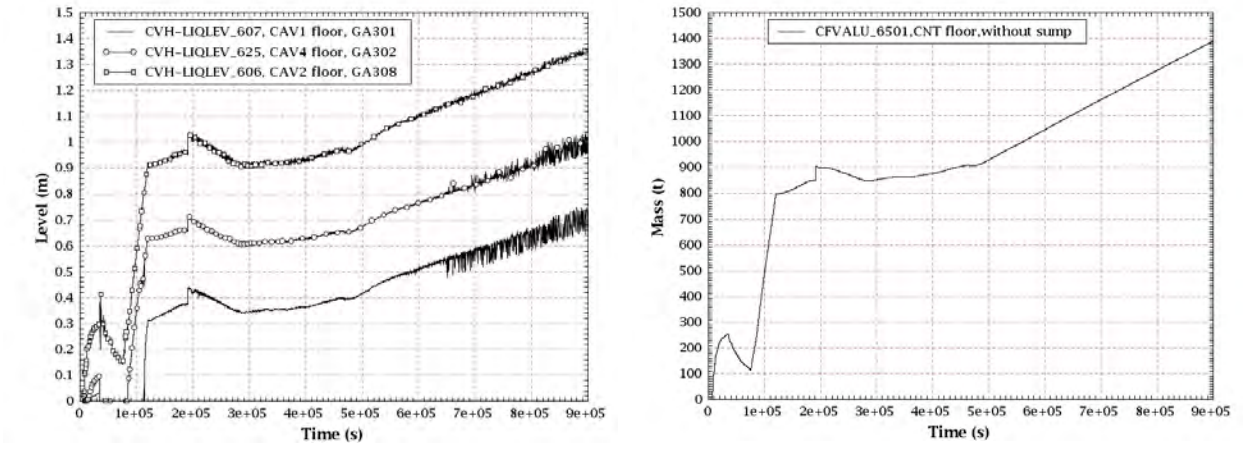

a) b)

Figure 9. Water level (a) and water mass (b) on containment floor for Scenario 3.

3.5. Containment atmosphere and condensate flow

Venting of NC gases downstream of condenser reduces mole fraction and progressively replaces containment atmosphere with steam. This solves the late phase hydrogen problem by discharging it to the

environment (Fig. 10a). This containment atmosphere state requires additional SAM guidance if safety systems (e.g., spray system) become available later. The pressure drop driving steam-gas mixture flow into the LTCCS is created by condensation ("suction" effect). Condensation occurs at approximately containment pressure, vacuum formation is prevented by low inlet resistance. Iterative analysis of various system layouts showed that the condensate gravity drainage is feasible through 30 mm diameter pipe (Fig. 10b). Final drain line routing to containment will depend on available penetrations and LTCCS layout.

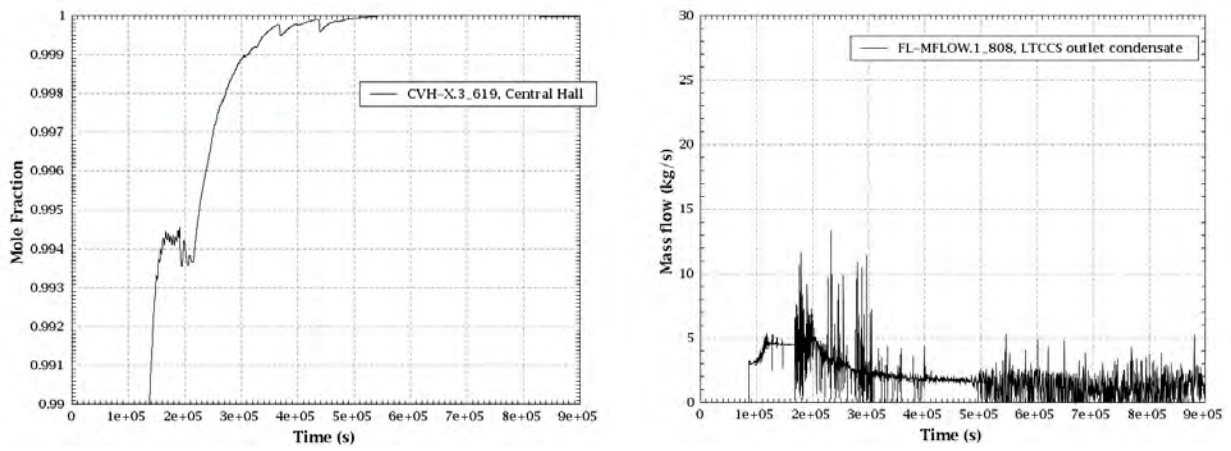

a) b)

Figure 10. Mole fraction of steam in the containment (a) and condensate flow rate (b) for Scenario №3.

3.6. Impact on SFP

The presence of fuel in the SFP results in gradual heating and boiling of SFP water during SA. LTCCS operation delays SFP boil-off by reducing the number of CFVS cycles giving time gain before SFP make-up. With LTCCS operating, the SFP level decreases with water remaining near saturation temperature (Fig. 11). Long-term containment water balance needs further evaluation. Possible partial return of the water from containment floor back to SFP by RTS pump is under analysis.

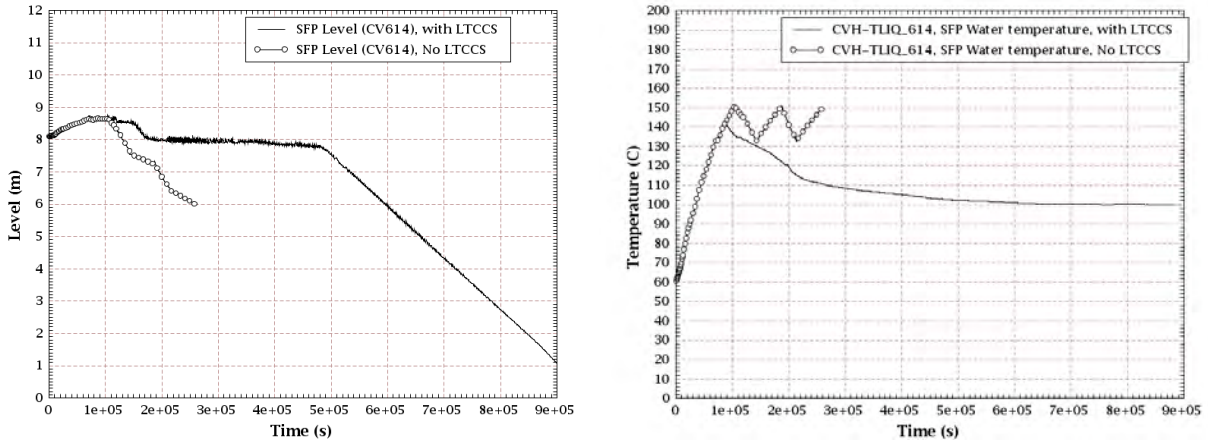

a) b)

Figure 11. Water level (a) and temperature (b) in the SFP for Scenario 3.

3.7. LTCCS cooling water flow rate and temperature

Selected LTCCS cooling water flow rate of 320 m^3/h is adequate for both of 10MW and 15MW condensation capacity. The water heating on the condenser is equal to 40° C for 15MW and 30° C for 10MW (Fig. 12). Therefore, flow rates in the range of 300-400 m^3/h are acceptable for the system.

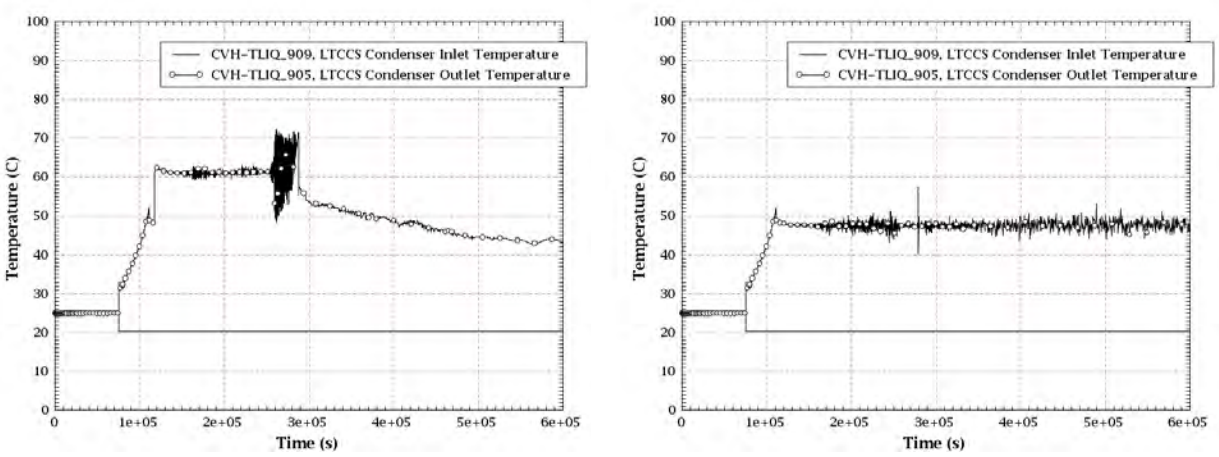

a) b)

Figure 12. Cooling water temperature at the inlet/outlet of the LTCCS condenser for 15MW power (a) and 10MW power (b)

3.8. Radioactivity release and hydrogen safety

Activity release to the environment is reduced with LTCCS operation. Main reasons for the reduction are the absence of CFVS subsequent venting and decreased containment pressure. The 3 days cumulative aerosols mass of Cs class that entered CFVS is changed from 6% (% of core content) to 4% and for containment leaks from 0.0039% to 0.0032% for the sequence without LTCCS operation (Scenario 1) and with LTCCS (Scenario 3). The deflagration conditions in the containment volumes are not reached due to the high steam concentration. The maximum hydrogen concentration in and behind LTCCS condenser is calculated to be 5%. However, there are no ignition initiators in these locations and the temperatures are low. Therefore, hydrogen safety is not critical for LTCCS path. In the later phase due to the almost complete removal of NC gases from containment, the hydrogen safety problem is completely resolved.

3.9. Melt/debris spreading and criticality of fission materials

To maintain containment integrity, corium must spread effectively after RPV failure. The analysis indicates a dry state of subreactor cavity for V-320 and V-302/V-338 reactor designs (VVER-1000) at melt ejection. Melt overflow through the cavity door and further spreading takes place under low water level (0.1-0.2 m) or without water. Ensuring rapid melt overflow and spreading in coolable geometry requires further spreading analysis, including MCCI and water flooding. The criticality of core materials is more dangerous in the state of debris, when the moderator can penetrate between fuel parts in the reactor. However, given the presence of control rod absorbers and boron in HA water, this is unlikely. Outside the reactor, the concrete oxides are mixed and the melt configuration does not allow water penetrating deeply inside. The criticality in such states seems practically impossible.

4. CONCLUSIONS

Implementation of LTCCS for VVER-1000 reactors significantly enhances plant's capability to achieve and maintain safe stable state during SA. The analysis demonstrates that LTCCS concept reliably reduces and stabilizes containment pressure and temperature below the design limits of 5 kgf/cm^2 (abs.) and 150ºC. Stabilization pressure remains nearly atmospheric with steam condensation supported by continuous boiling over core materials and containment water is cooled to temperatures less than saturation in LTCCS water circuit. Total LTCCS power (steam and water circuits) exceeds decay heat power for all containment pressures. Analysis assumes coolable state of core materials after spreading over the containment floor.

Hydrogen safety is not adversely affected by delayed LTCCS activation. By the time of LTCCS operation, a significant amount of hydrogen and oxygen has been recombined by PARs. As LTCCS progressively removes non-condensable gases, the containment atmosphere becomes increasingly steam-dominated, eliminating late-phase hydrogen risks. Lower stabilized containment pressure reduces radiological release by decreasing leak-path flows and minimizing CFVS actuation. Joint LTCCS–CFVS operation is feasible and may be advantageous in certain accident-management scenarios.

Extended post-accident operation of LTCCS is required to reduce containment parameters towards near-normal operating conditions. Final containment water level management will require additional technical provisions. Sizing of the water circuit flow, heat exchangers and piping might be changed. Recommendations for optimized accident management will be further developed.

NOMENCLATURE

RCS	Reactor coolant system
MCCI	Molten core-concrete interaction
SAMG	Severe accident management guidelines
SAM	Severe accident management

REFERENCES

1. "Conceptual technical solution for the management of large volumes of radioactive water that may be generated in severe accidents". KTP-M.0.41.378-23, Energoatom, (2025).
2. "MELCOR Computer Code Manuals. Reference Manuals Version 1.8.5". Sandia National Laboratories. NUREG/CR-6119, Vol.2 Rev.2 SAND2000-2417/1 (2000).
3. "Report on the calculation and analytical justification of the containment filtered venting system for South Ukraine NPP Unit 3", Ae 17838/Dok (2018).
4. "Description of the computer model of the core and containment for the MELCOR code", Zaporizhzhya NPP, Unit 1, 01-461.01.ЛИП.ЗП.ОТ.279 (2011).
5. "Safety Analysis Report (Adaptation). Additional materials. Chapter 6: Probabilistic safety analysis. Level 2 PSA. Database. Part 1: Data on containment", South Ukraine NPP, Unit 3, 57-803.203.017.DB00 Version A (2009).
6. "MELCOR Best Practices as Applied in the State-of-the-Art Reactor Consequence Analyses. (SOARCA) Project", NUREG/CR-7008, August 2014.
7. "Analysis of severe accidents in SFP, development of the analytical justification of SFP SAMGs strategies for the plant operating at the rated power for non-pilot power units 2 and 3 of SUNPP", SUNPP (2015).
8. "VVER-1000 Long Term Containment Cooling Conceptual Technical Solution", Attachment to Letter EMEA-SAS-VVER-25-015, Westinghouse (2025).

9. "State-of-the-Art Report on Molten Corium Concrete Interaction and Ex-Vessel Molten Core Coolability", Nuclear Safety and Regulation, NEA/CSNI/R(2016)15, NEA No. 7392, (2017).
10. "Reactor Core and Containment Cooling Systems: Long-Term Management and Reliability (RCCS-2021)", *NEA Specialist Workshop Proceedings*, 18-20 October 2021, Virtual Meeting NEA/CSNI/R(2022)11 (2025).
11. M. Kotouč, et al.: "Assessment of Ex-Vessel Corium Coolability in the Containment of the VVER-1000 Reactor as a Measure of Severe Accident Mitigation," *Proceedings of the 2022 10th European Review Meeting on Severe Accident Research*, Karlsruhe, Germany, May 16-19, (2022).
12. Jan Komrska, Tomas Janda and Petr Vokac, "Overview of Ex-Vessel Severe Accident Scenarios Simulations at UJV Rez", *Proceedings of the 11th European Review Meeting on Severe Accidents Research (ERMSAR2024)*, KTH, Stockholm, Sweden, May 13-16, 2024, pp. 1766-1791 (2024).
13. J. Duspiva, "Comparison of In-Vessel and Ex-Vessel Retention", *Proceedings of ASME 2014 VVER Workshop in Prague*, Prague, Czech Republic, 2014, pp. 1–25 (2014).
14. J. Duspiva, "Corium Localization for Existing VVER-1000 Units", *Mitigation of Severe Accident Challenges in Nuclear Power Plants, Vol. 2*, International Atomic Energy Agency, Vienna, Austria, pp. 45–60 (2019).

ENERGY SAFETY GROUP

Westinghouse

HIGH STANDARD ENGINEERING

Preliminary Analytical Justification of Long-Term Containment Cooling System with Steam Condensing Heat Exchanger for NPPS with VVER-1000 Reactors

Yu. Vorobyov, O. Mazurok (Ph.D.), V. Ivanov, O. Mykhailenko, A. Tiurin, A. Hanenko, Energy Safety Group LLC
E. Kostov (Ph.D.), Á. Pérez-Salado Kamps (Ph.D.), V. Pashynskyi, C. Hartmann (Ph.D.), H. Troselius, Westinghouse Electric Germany GmbH

The 12h European Review Meeting on Severe Accident Research (ERMSAR2026)
Madrid, Spain, May 18-22, 2026

CONTENT

1. VVER-1000 LTCCS layout and system concept
2. General approach to TH analysis
3. MELCOR model
4. LTCCS model
5. Scenarios, initial and boundary conditions
6. Acceptance criteria
7. Analysis results
8. Issues and problems
9. Design changes
10. Conclusions

Heat removal basis

- Ex-vessel corium spreading in **C**onta**i**N**m**en**T** (**CNT**)
- Corium cooling by water pool (boiling)
- Steam condensation in condenser
- Water pool is cooled in heat exchanger

System layout

- Main steam circuit (contaminated)
- Auxiliary water circuit (contaminated)
- Cooling water external circuit (clean)
- Common cooling circuit for condenser and heat exchanger

System layout feature

- Turbine-driven water pump (RTS pump)
- Sequential cooling for condenser and heat exchanger
- First condenser cooling
- Second heat exchanger cooling

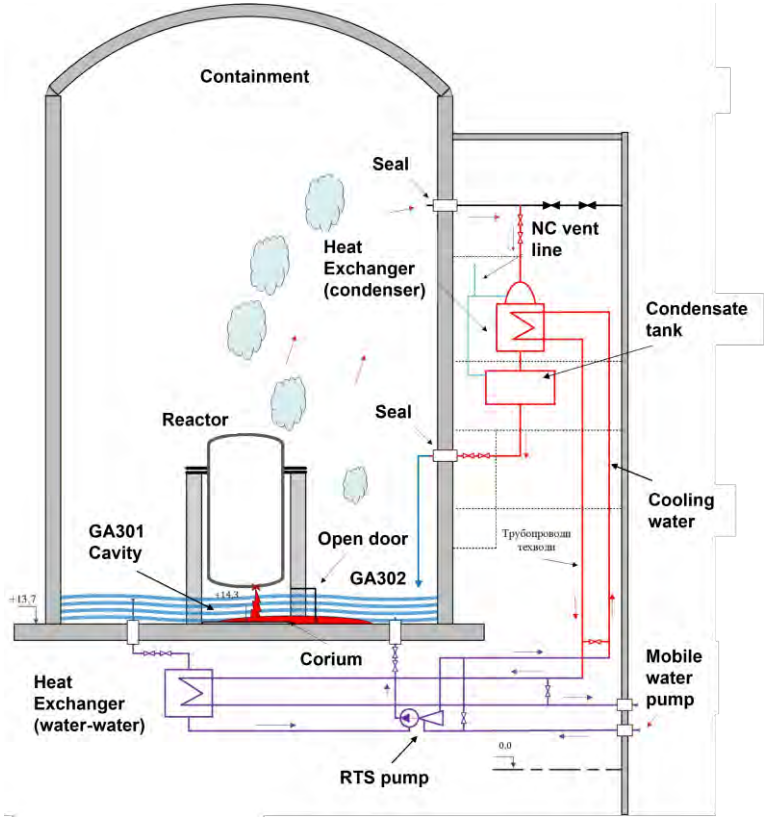

LTCCS VVER-1000 general layout

Advantages

- efficiency due to boiling-condensation
- corium stabilization
- pressure decrease to atmospheric
- water temperature decrease less than 100 ºC
- functional independence from DBA equipment
- long-term water retention within containment
- no need of water evacuation from containment
- no need of external electric supply

Concept covers:

- removal of non-condensable (NC) gases with H_2
- integration with filtered venting (CFVS)
- dry reactor cavity prior RPV failure
- heat removal from spent fuel pool (SFP)
- long-term containment floor water cooling
- reducing effects of corium on the base slab

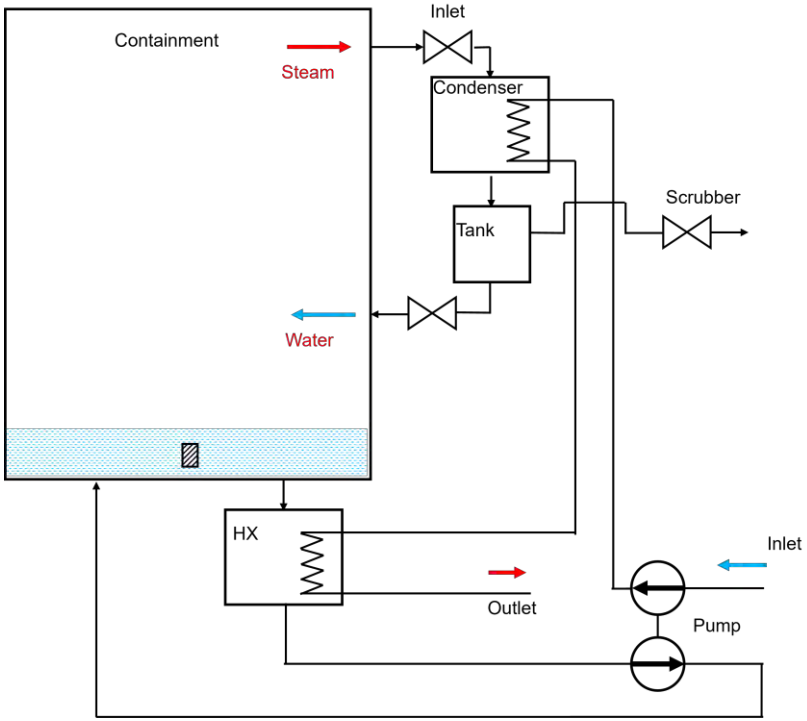

LTCCS VVER-1000 general layout workflow

Approach

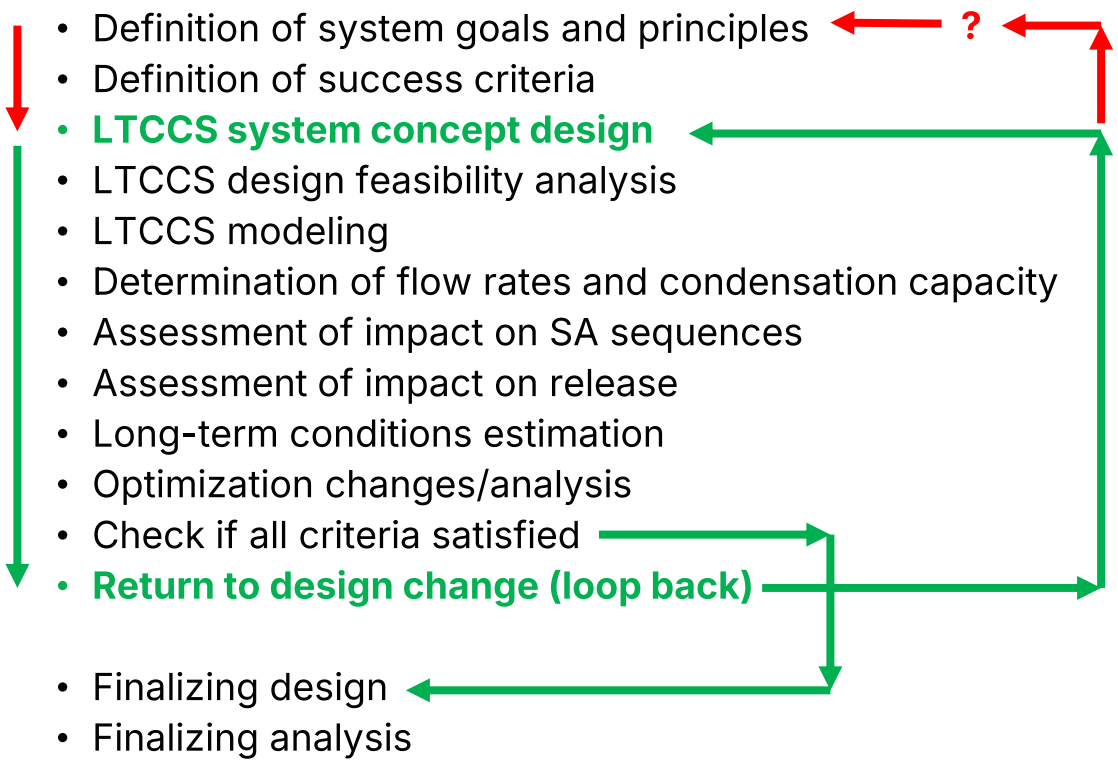

!!! Even small problem CAN loop back the Process !!!

RCS Model

- 4 loop MELCOR model
- Simple reactor TH modeling
- SG primary detailed
- SG secondary with bypass
- Core 18 axial levels

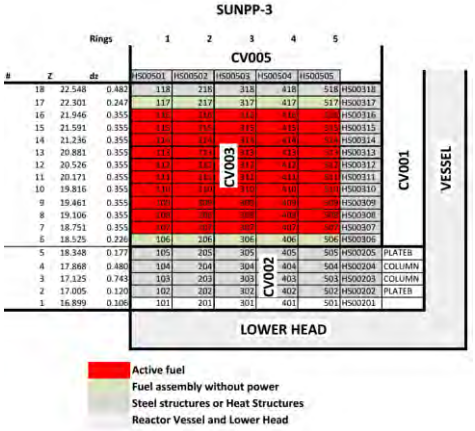

MELCOR core nodalization

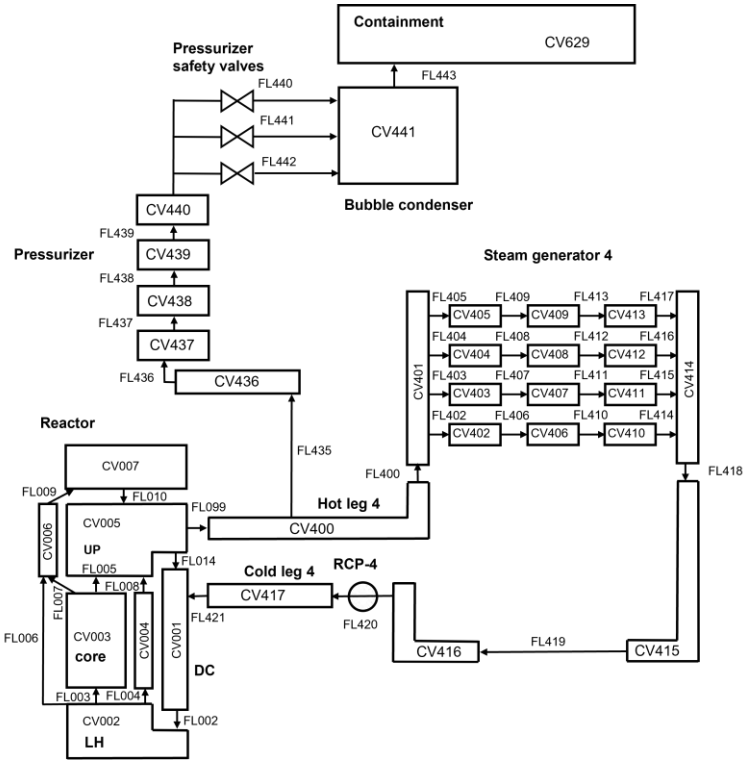

VVER-1000 primary MELCOR nodalization (loop #4)

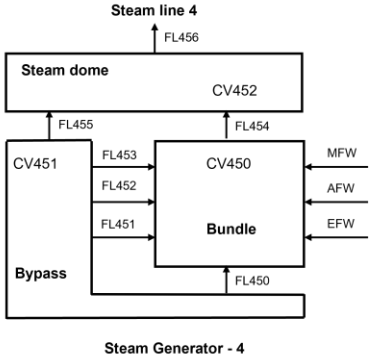

Steam Generator - 4

Containment and Cavity Model

- Detailed containment model
- Axial compartments levels
- Cavity detailed model (3 cavities)
- Melt overflow and height dynamic approach (radius(t))
- CAV1 overflow height 0.2m
- CAV2, CAV4 overflow height 0.15m
- SFP (CV614) heat power 2.6 MW

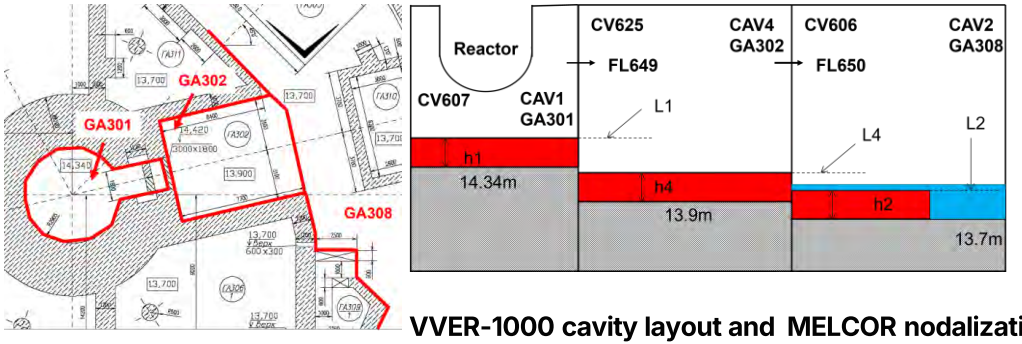

VVER-1000 cavity layout and MELCOR nodalization

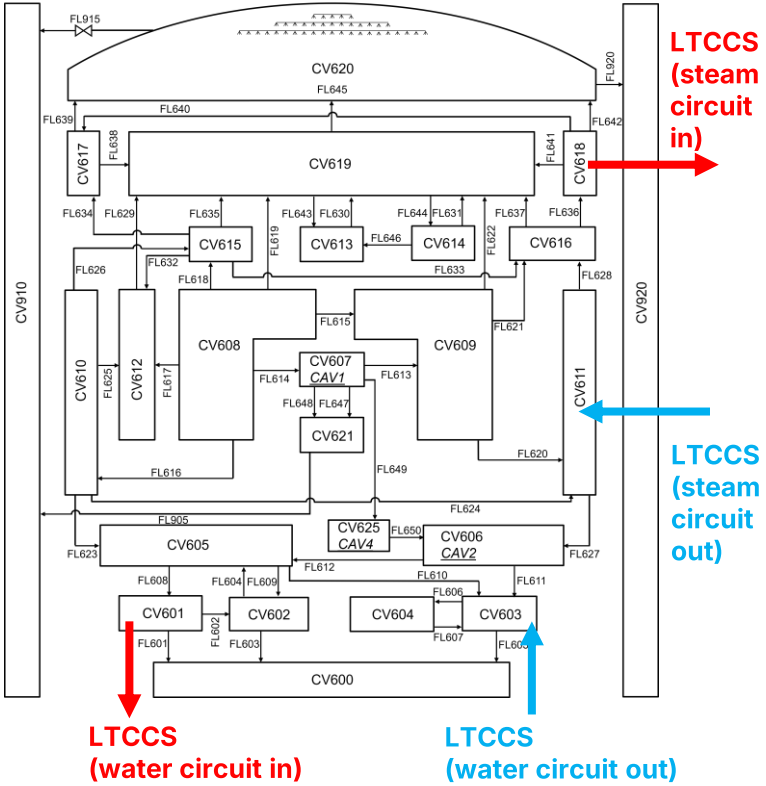

MELCOR containment nodalization

CFVS model

- Detailed model with scrubber
- Open – close setpoints 5 – 3kgf/cm^2
- Passive rupture disk opening
- Initial scrubber water level
- Filled with nitrogen
- Flow is based on real tests (at plant)

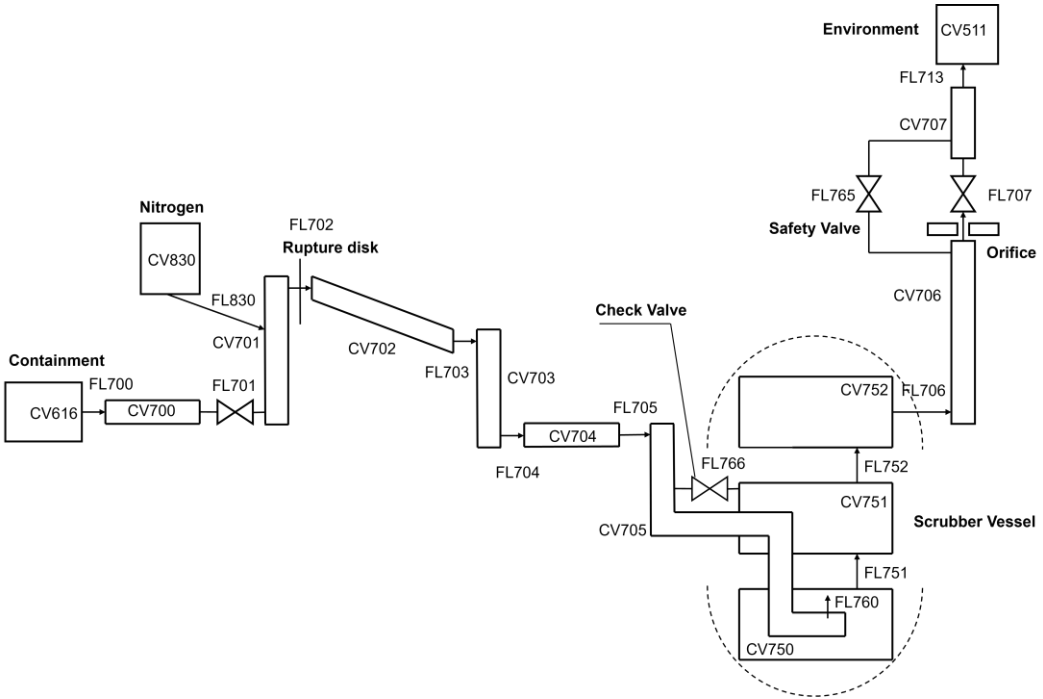

CFVS MELCOR nodalization

LTCCS model (steam circuit)

- Detailed model with condenser
- Condensate drain to containment
- NC venting after condenser to scrubber (FL821)

Condenser model

• Inlet diameter	0.5m	
• Heat transfer area	503m^2	
• Cooling water flow (external)	320t/h	
• Temperature of cooling water	20°C	
• Condenser power (3bar, 98% steam)	10.5 MW	
• Condensate flow		4.9kg/s
• NC venting flow (50mm diam.)	0.23kg/s	

LTCCS model (water circuit, control functions)

• Heat exchanger power	~10.0 MW
• RTS (turbine-driven) pump flow	320t/h

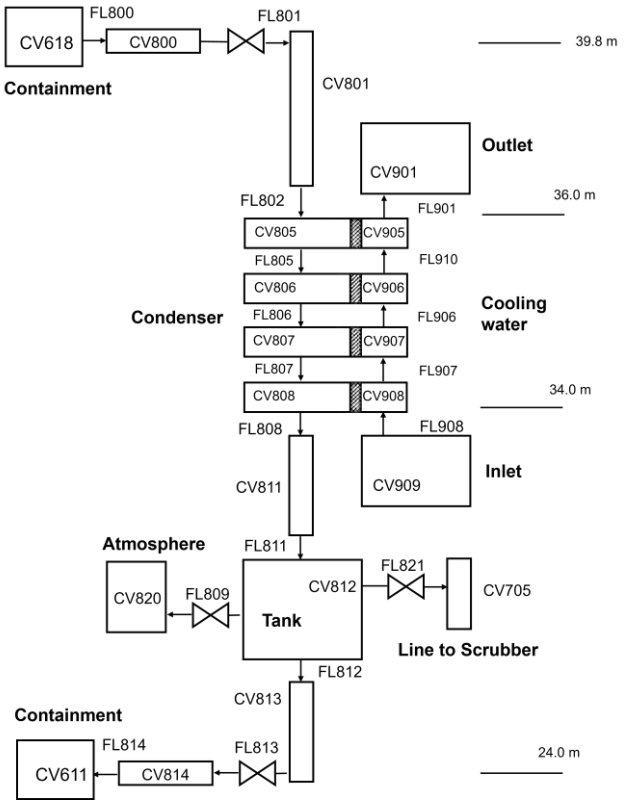

LTCCS MELCOR nodalization

Condenser model power

- Pressure 3bar (abs.), 95% steam — 5.3 MWt
- Pressure 3bar (abs.), 98% steam — 10.5 MWt (**Base**)
- Pressure 3bar (abs.), 99% steam — 18.0 MWt
- Pressure 3bar (abs.), 99.9% steam — 28.7 MWt (**Max**)
- Pressure 2bar (abs.), 99.9% steam — 10.9 MWt

Condenser power control (initial phase)

- Need of NC venting
- NCs can be used for condensing power control
- NC venting valve open control to scrubber (FL821)
- Possible for initial phase with NCs in containment

Scenarios

- **Scenario 1**. SBO with SAM actions (without LTCCS)
- **Scenario 2**. SBO with SAM actions and LTCCS start (steam circuit, condenser capacity limited to 15 MW)
- **Scenario 3. (Base analysis)** SBO with SA management actions and LTCCS start (steam and water circuit, condenser capacity limited to 10 MW)

SAM actions

- SAMG enter on core exit > 450°C
- Open of 3 PORVs

LTCCS related actions

- Start of containment flood to +0.9m level
- LTCCS start at +0.3m containment level

LTCCS activation basis

- After CFVS 1st cycle
- After active core damage and melt spreading (aerosols settling)
- Not later than 72h

SFP related actions

- No SFP external make-up (action is possible)

Acceptance criteria

- Containment pressure is limited by 5 kgf/cm^2 (abs.) (short peak < 6 kgf/cm^2 (abs) permitted)
- Scrubber level stays in the range 0.75 - 2.1 m
- Steam-gas mixture is outside of detonation region on Shapiro-Moffetti diagram
- **Corium is in coolable state***
- **SFP fuel is in coolable condition***
- **Containment water balance is constant***

*** - needs adaptation or special measures**

LTCCS acceptance criteria

- Containment pressure approaches to atmospheric and stabilizes
- Containment water/steam temperature is stabilized or steadily decreases
- Containment water temperature is stabilized at less than 100ºC for compartments without debris
- LTCCS thermal total capacity is equal to or consistently greater than decay heat

Events and actions (Scenario 3)

• Loss of power, DGs failure	0s
• PRZ SVs open (CE temp > 450ºC)	10000s
• RV failure, debris/melt spreading	34940s
• CFVS open, pressure > 5 kgf/cm^2	35900s
• CFVS closed, pressure < 3 kgf/cm^2	73000s
• CNT flood external source start (15kg/s)	75500s
• LTCCS start (steam and water circ.)	**86500s**
• CNT flood external source stop	120000s
• CNT water temperature **< 100ºC**	**300000s**
• CNT pressure **1.04 kgf/cm^2** (abs.)	**650000s**
• End of calculation (10.4days)	900000s

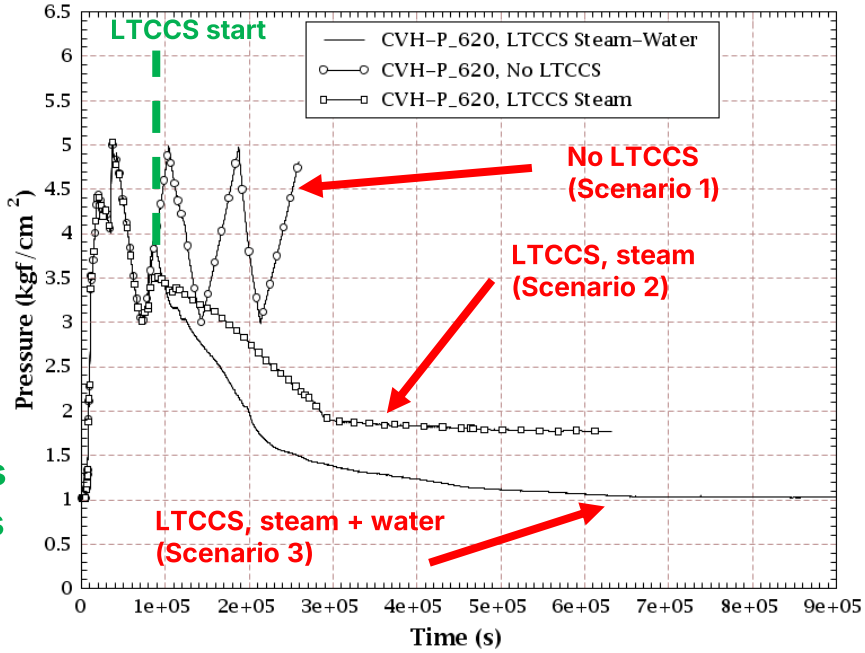

Containment pressure (comparison)

CNT pressure

- Stabilizes at **1.7-1.8** kgf/cm^2 (abs.) if only **steam** circuit in operation
- Stabilizes at **1.03-1.04** kgf/cm^2 (abs.) if **steam + water** circuits in operation

End state (Scenario 3)

- CNT pressure (abs.) 1.03 kgf/cm^2
- CNT water temp. (no debris) 85-92ºC
- CNT water temp. (debris) 100ºC
- CNT steam/atm. temp. 93-127ºC
- CNT steam fraction 99.999% vol.
- H2 fraction 0 - 0.1% vol.
- Steam circuit power ~3.2MW
- Water circuit power ~7.9MW
- Core decay heat ~9.2MW
- SFP decay heat ~2.6MW

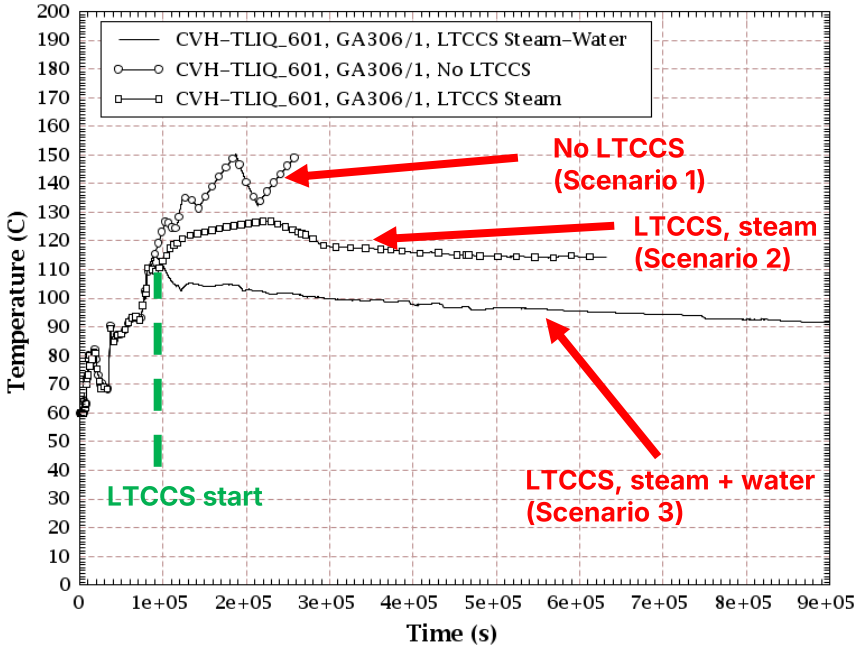

Containment water temperature (comparison, no debris compartment)

CNT water/steam temperature

- Stabilizes at 114-115ºC >100ºC if only **steam** circuit in operation
- Decreases Twater < **100ºC** if **steam + water** circuits in operation
- Steam dome temperature 127ºC and decreasing

LTCCS thermal power (Scenario 3)

- Steam circuit power is controlled max ~10MW
- Steam power controlled by venting (initial phase
- Steam power is defined by HE area (late phase)

- Water circuit power ~6 - 10MW
- Water circuit power increases (late phase)
- Total LTCCS power > decay heat
- Decay + SFP ~ Total LTCCS

Condenser power control

- NC venting after condenser
- Valve position operation

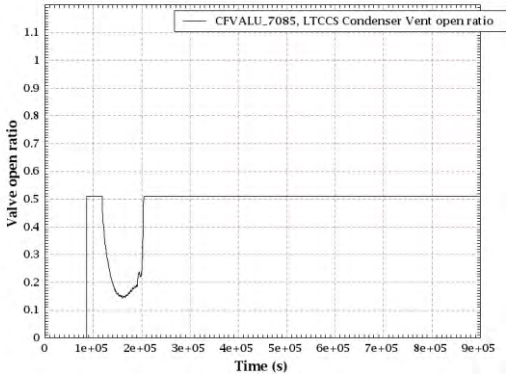

LTCCS NC venting valve position after condenser

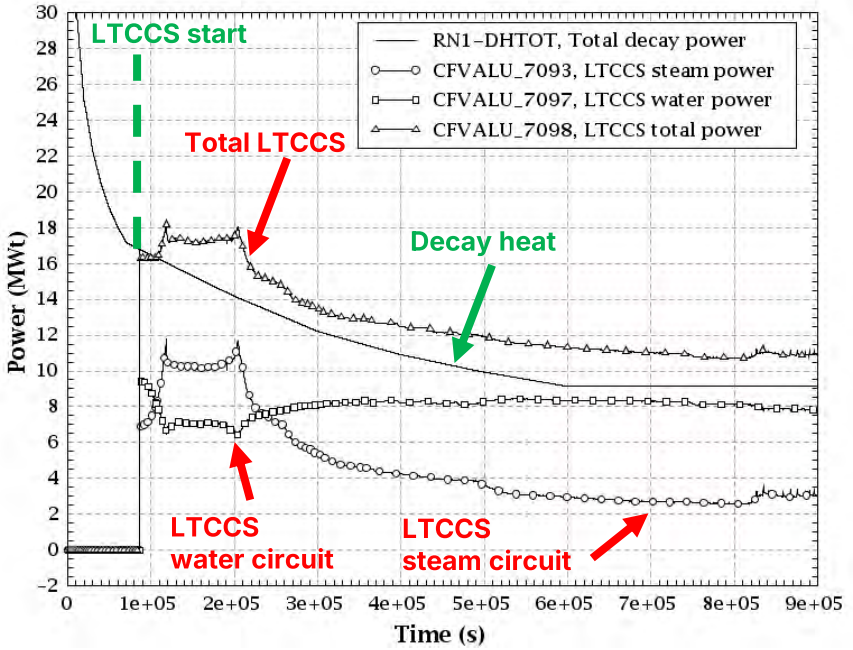

Core total decay heat and LTCCS thermal power (extracted)

Containment water level (Scenario 3)

- Flooded to cover all debris ~0.9m
- Added ~500-600t to flood containment (CNT)
- Start of increase after SFP intense boiling
- Needs stabilization

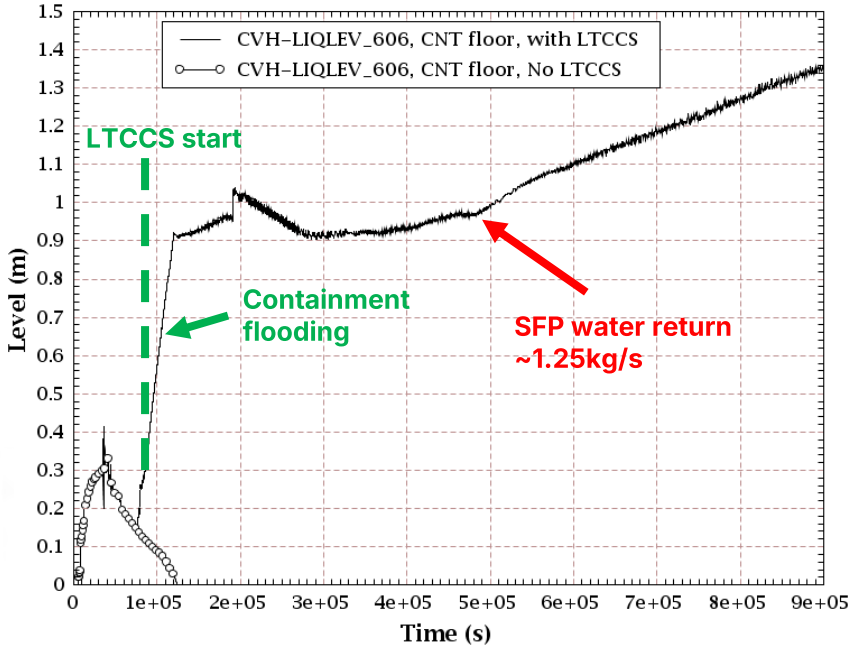

Containment floor water level

Containment floor water mass

- Needs stabilization

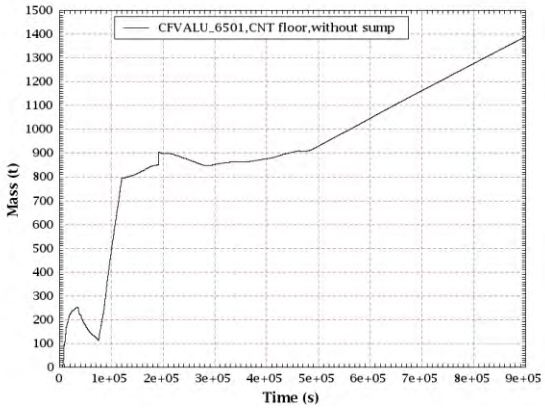

Containment floor water mass (without sump)

SFP water level (Scenario 3)

- After CNT pressure decrease SFP -> boil
- Evaporated SFP water returns to CNT floor
- SFP balance needed
- No fuel damage in SFP is accounted for

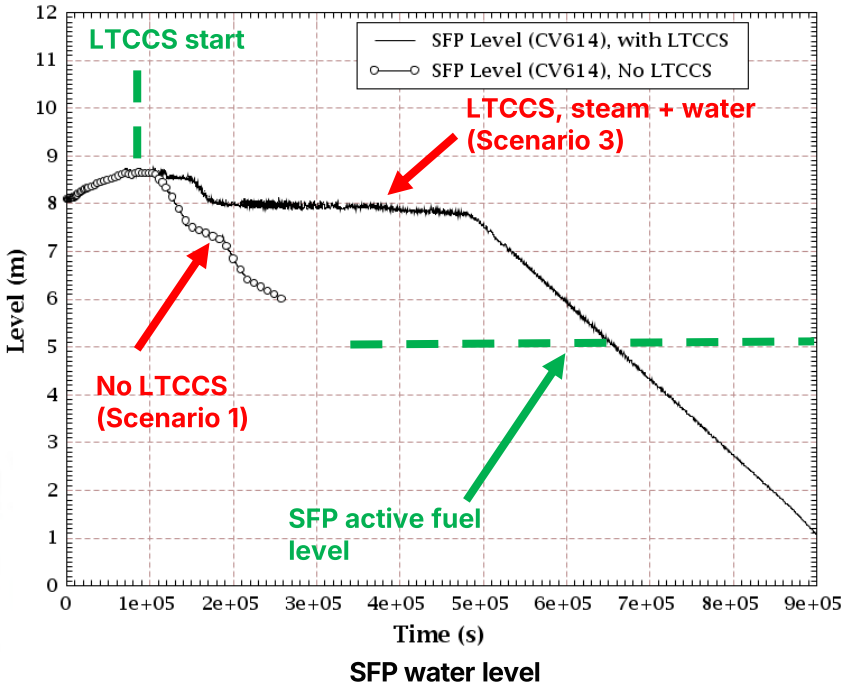

SFP water level

SFP water temperature

- Needs cooldown

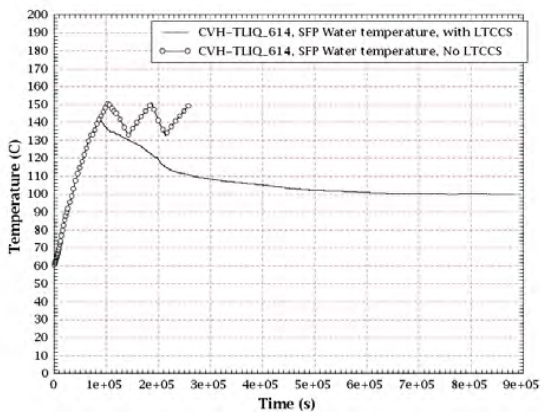

SFP water temperature

LTCCS water temperatures (Scenario 3)

- Max cooling “clean” circuit temperature <70ºC
- Inlet cooling “clean” circuit temperature 20ºC
- No outlet water boiling

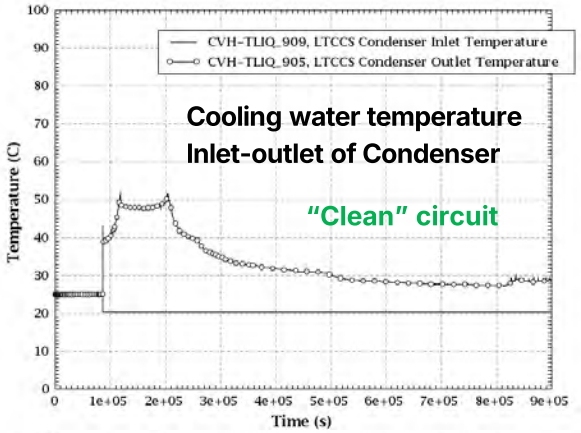

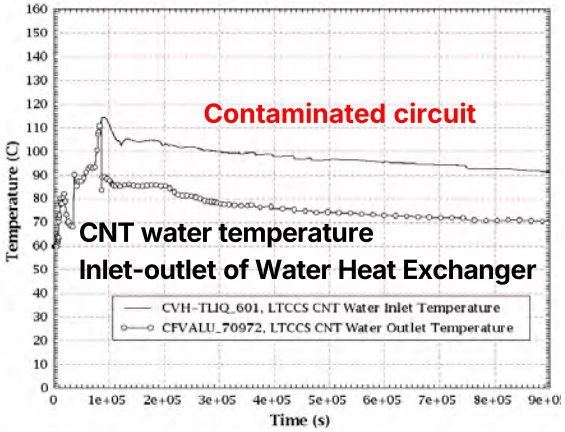

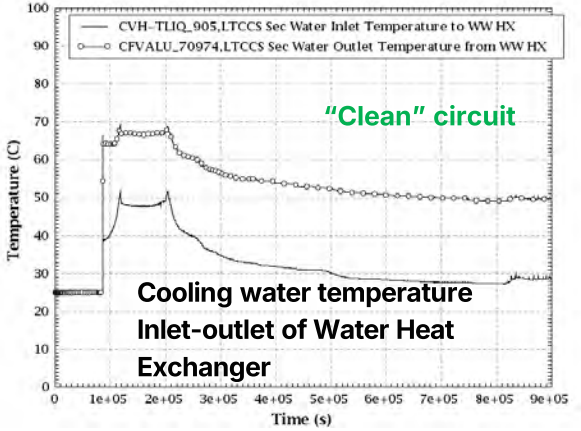

Cavity MELCOR analysis

- CAV1 ablation depth 0.33m, level 0.2m
- CAV4 ablation depth 0.11m, level 0.15m
- CAV2 ablation depth 0.04m, level 0.19m
- Corium is in coolable geometry

Corium mass distribution (CAV1, CAV4, CAV2):

- After RPV failure: 18%, 44%, 38%
- End of analysis: 18%, 32%, 50%

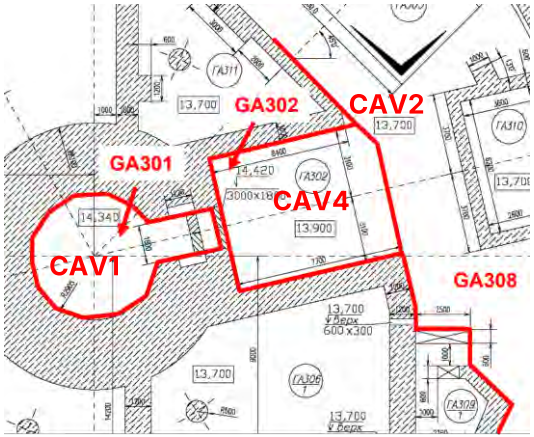

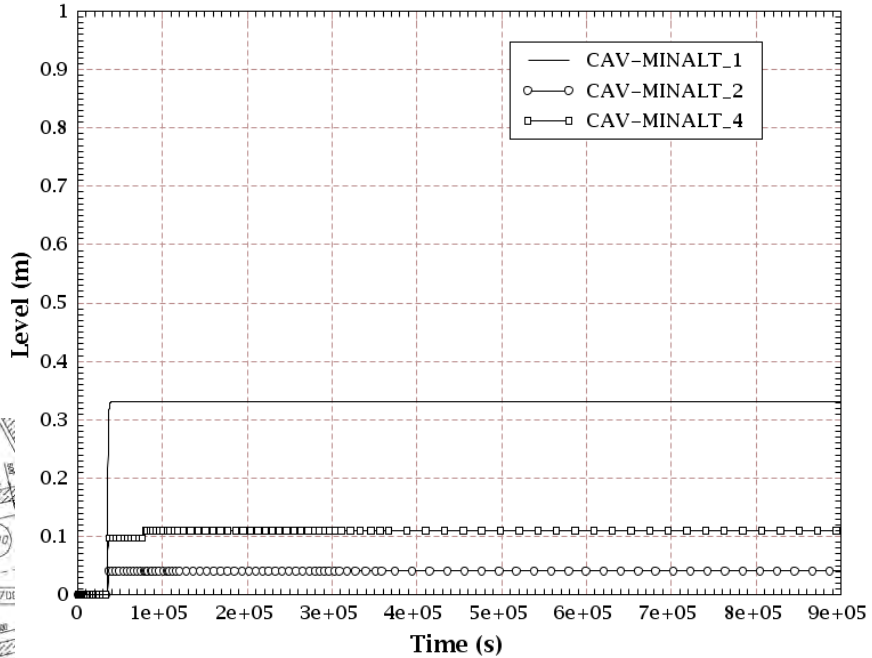

Cavities ablation depth

Hydrogen safety

Containment

- H_2 generated in-vessel 402kg
- H_2 generated ex-vessel 240kg
- Dome max H_2 fraction 2.1-2.9% (vol.)
- End of analysis H_2 fraction 0%
- Not globally flammable

LTCCS

- Inside LTCCS H_2 fraction <5%
- No detonation in LTCCS

Activity release to environment

- Aerosol CFVS activity release decrease 33%
- Containment leak release decrease 18%

Containment long-term

- Containment openable conditions
- Needs NC inlet procedure (very late)

Issues to consider (in process)

- Detailed melt spreading analysis
- Detailed melt impact analysis in cavities
- Estimation of MCCI/spreading success probability (from ejection to coolability)
- Long-term TH analysis (half year)
- Long-term water balance analysis
- LTCCS interruptions analysis
- LTCCS failures analysis
- LTCCS condenser aerosols load
- Sump boiling possibility analysis
- Detailed criticality analysis
- Analysis of refuel and shutdown states
- Cavity door thermal/accident analysis
- Cavity isolation thermal radiation analysis
- Etc...

Optimization issues (in process)

- Common or separate cooling circuits
- System detailed specifications
- System start conditions
- SFP cooling line
- Number of RTS pumps and heat exchangers
- Improve cavity melt spreading from CAV1
- Shielding measures to containment (melt attack)
- Bound or not the melt spreading area?
- Optimize containment flooding
- Optimize water circuit flow
- Increase cavity door open probability
- Etc ...

Melt spreading analysis (Example)

Oxide only, 0-3600s, T(ini)=2700 ºC, Vol(ini)=12m^3 , water elev. 14m, impact opposite door, special developed calculation program (MSP)

Preliminary estimations

- Melt final thickness is not uniform
- Melt final thickness depends on flow time
- Central sump, ducts and isolation are in analysis

Fast (flow time 200s)

Vol(end)=24.6m^3, Area(end)=100.3m^2

Melt thickness

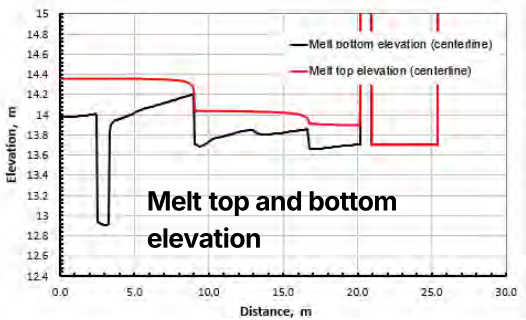

Middle (flow time 600s)

Vol(end)=25.1m^3, Area(end)=97.2m^2

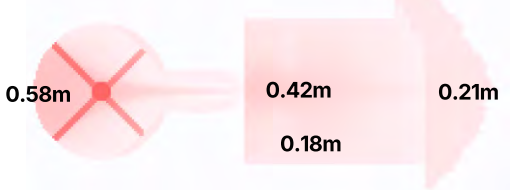

Melt thickness

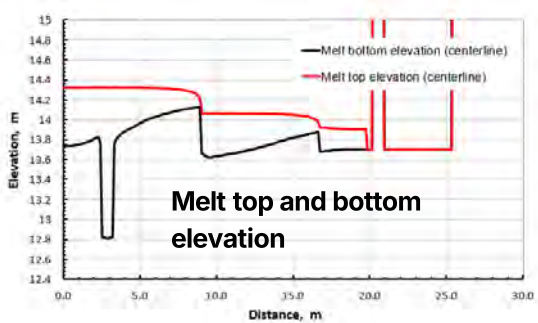

Slow (flow time 1200s)

Vol(end)=25.1m^3, Area(end)=79.4m^2

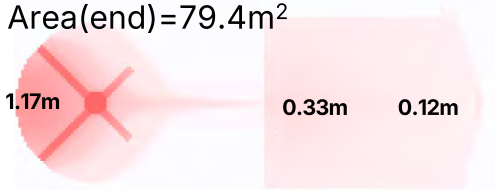

Melt thickness

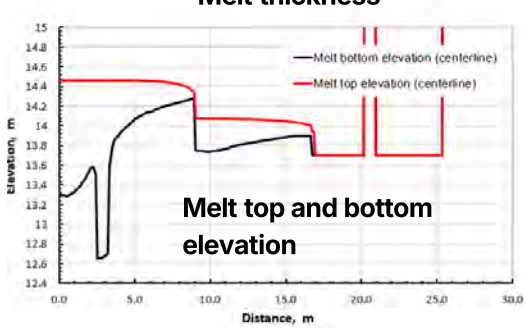

Melt spreading analysis (Example)

Oxide-metal mixture, 0-3600s, T(ini)=2700ºC, Vol(ini)=21m^3 , water elev. 14m, impact opposite door

Preliminary estimations

- CAV4 tends to low level and “rivers”
- CAV2 tends to agglomerate
- Slower flow -> more nonuniformity

Fast (flow time 200s)

Vol(end)=39.7m^3, Area(end)=295.3m^2

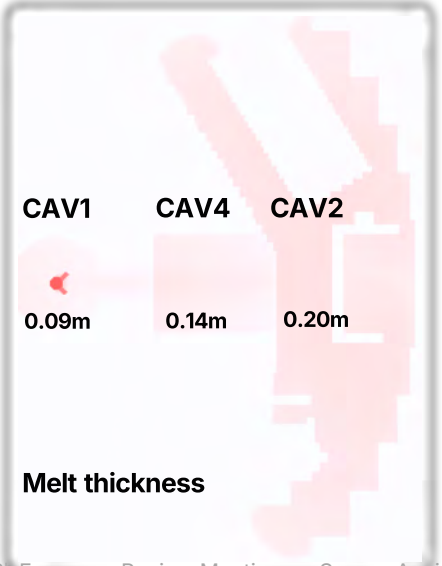

Middle (flow time 600s)

Vol(end)=40.3m^3, Area(end)=203.4m^2

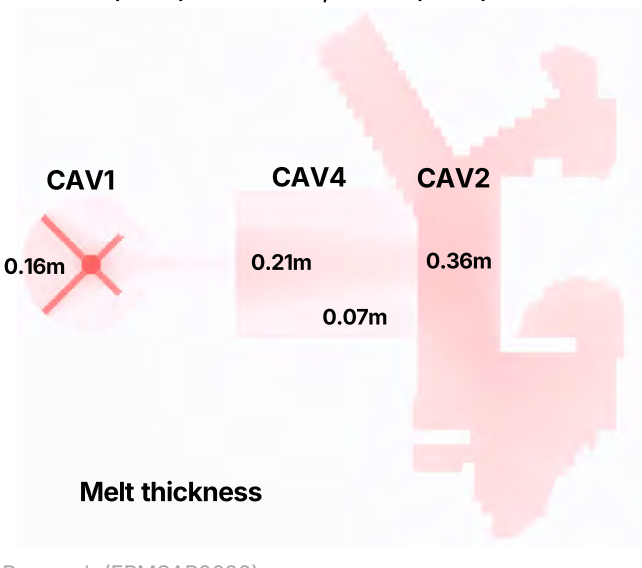

Slow (flow time 1200s)

Vol(end)=40.2m^3, Area(end)=216.7m^2

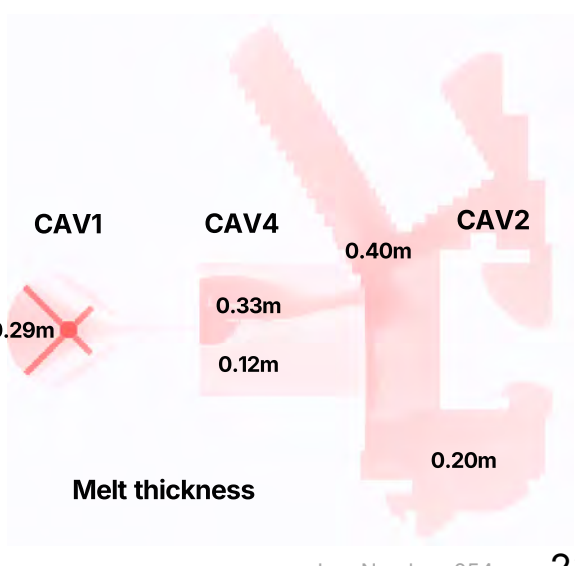

LTCCS with common cooling circuit

- Longer piping
- SFP line added

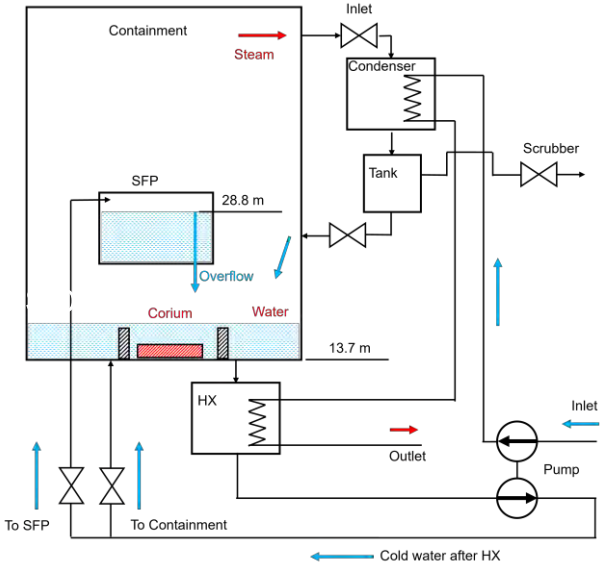

LTCCS layout with common cooling circuit

Combine?

LTCCS with separate cooling circuits

- Two or one external source?
- Simpler?

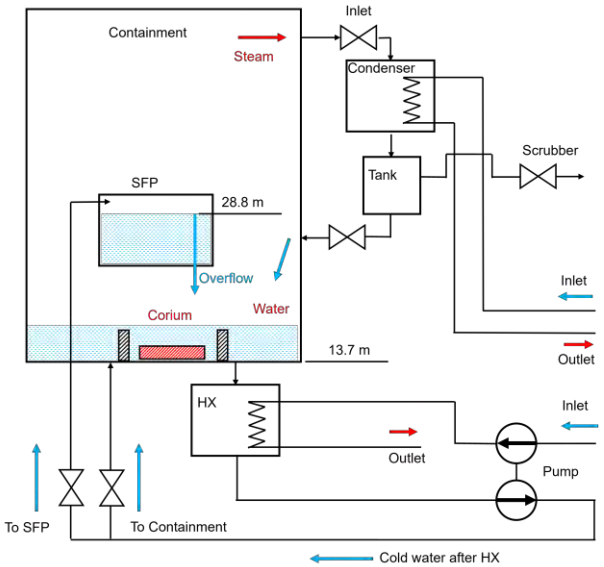

LTCCS layout with separate cooling circuits

LTCCS function

- LTCCS is successful in achieving safe stable end state for SA with ex-vessel phase
- Containment pressure and temperatures are decreased
- Late hydrogen problem in containment is resolved
- Contaminated water is circled inside containment

Analysis scope

- Basis to increase containment survivability
- Justification analysis
- Optimization analysis
- System specifications as a result of analysis
- Iterative process

Design

- Compromising between success probability, simplicity and feasibility
- Sizing, number of pumps and scheme is under development

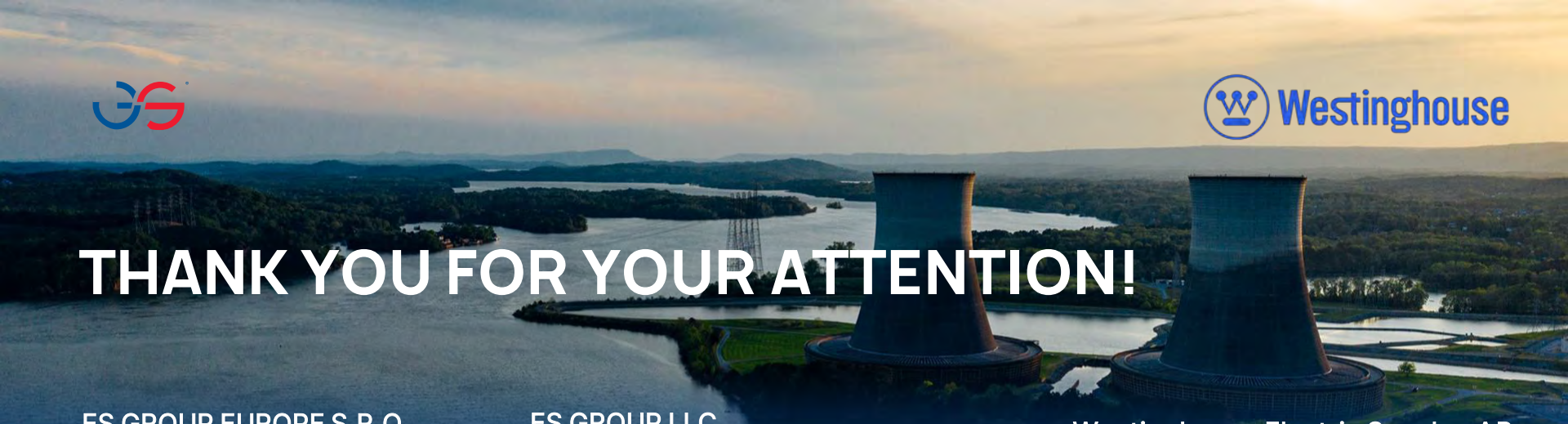

THANK YOU FOR YOUR ATTENTION!

ES GROUP EUROPE S.R.O.
Tel.: +420 777 630 595
E-mail: info@e-s-group.eu
Address
Republikanská 1102/45, 312 00
Plzeň, Czech Republic

ES GROUP LLC
Tel.: +38 044 299 94 80
E-mail: info@e-s-group.com.ua
Address
Laboratorniy Lane,1, office 244
01133 Kyiv, Ukraine

Official website
https://e-s-group.eu/

Connect with us on LinkedIn
linkedin.com/company/energy-safety-group/

Westinghouse Electric Sweden AB
Address
Mladost-4, Business Park Sofia,
Building 4 and Building 8A, floor 7,
Sofia, 1766, Bulgaria
Westinghouse Electric Sweden AB
Address
SE-721 36 Västerås, Sweden
Westinghouse Electric Germany GmbH
Address
Dudenstrasse 6, 68167, Mannheim,
Germany

ASTEC MODELLING OF THE AP1000 AND COLD-LEG SMALL-BREAK LOCA SIMULATIONS WITH LONG-TERM COOLING CUT-OFF

ZHAO Dawei, GUO Zhexi, XIAO Sicong
Singapore Nuclear Research and Safety Institute, National University of Singapore
16 Prince George's Park, S(118415), Singapore
dw.zhao@nus.edu.sg; guo.zhexi@nus.edu.sg; snrxs@nus.edu.sg

ABSTRACT

In this study, the AP1000 reactor pressure vessel (RPV) and reactor coolant system (RCS), including their passive safety systems, are modelled using the ICARE and CESAR modules in ASTEC, respectively. A 10-inch small-break loss-of-coolant accident (SB-LOCA) is simulated to evaluate the thermohydraulic performance of the passive residual heat removal (PRHR) system and three passive water injection systems: the core makeup tank (CMT), the accumulators (ACC), and the in-containment refuelling water storage tank (IRWST). Heat removal by the PRHR and the emergency water injections from the CMT, ACC, and IRWST show reasonable agreement with NOTRUMP results reported in the AP1000 Design Control Document [1] and another CESAR/ASTEC work by Di Giuli et al. [2]. These passive safety systems, in combination with the ADS, guarantee continuous emergency core cooling from less than 15 seconds after pipe-break initiation to approximately 25,000 seconds (~7 hours). Under the hypothetical condition that condensation on the containment vessel inner surface for long-term core cooling and lower head external cooling are unavailable, the in-vessel core degradation process is simulated and the potential radiological source term is estimated using the ICARE module.

KEYWORDS
AP1000, ASTEC, Small-Break LOCA, Passive safety, In-vessel degradation

1. INTRODUCTION

Despite increasing popularity and interest in novel nuclear reactor technologies and small modular reactors, large pressurised water reactors (PWRs) remain the most widely deployed around the world with a long history of operation. This means there is a wealth of operational experience and data, on which past analyses and computer codes were based, and efforts by the global scientific community to improve safety and performance of large PWRs are still ongoing. One such example is the AP1000 by Westinghouse [1], which is the subject of this study. Like many new designs, the AP1000 tries to incorporate passive safety systems designed to keep the plant within safe physical margins without external electricity and human intervention for extended periods of time, a concept strongly highlighted after the Fukushima accident. Even in the event of severe accidents (SAs) where the reactor core is damaged or melted, these systems are supposed to keep the release of radioactive material at low levels to minimise impact on human health and the environment.

To aid in the siting and overall planning of reactor deployment, prediction of the quantity and extent of these releases is of importance. To this end, SA simulations enable quantitative assessment of the radiological source term based on a chain of complex and diverse physical processes. A couple of widely recognised SA codes have been in use across the world, one of which is MELCOR [3] developed in the U.S. This work is performed with the other SA code—ASTEC (Accident Source Term Evaluation Code)—developed by the Autorité de sûreté nucléaire et de radioprotection (ASNR) in France [4].

The transient progression of a 10-inch small-break loss-of-coolant accident (SB-LOCA) had been simulated and analysed in the AP1000 Design Control Document [1] using NOTRUMP, which is a specific SB-LOCA system thermal-hydraulic (TH) code that incorporates passive safety features developed for AP600 safety analysis, and it had been verified against applicable plant test data [5]. Another work [2] also simulated the 10-inch SB-LOCA using the CESAR module in ASTEC instead. These two sets of results form the basis for comparison in this work, where the ICARE module is used in addition to CESAR in ASTEC to model TH and post-degradation phenomena in the reactor pressure vessel (RPV). A hypothetical scenario without long-term cooling is simulated to give preliminary insights into the roles of various structural components and safety systems in the management of source term release.

2. AP1000 RPV AND RCS MODEL

The reactor core models for fuel and vessel structures in the RPV beneath the upper core plate are built with the ICARE module of ASTEC. The reactor core simulation covers TH performance, reactor core degradation progression including cladding and steel structure oxidations, fuel rod embrittlement or melting, corium mixing and relocation, and corium behaviour in the lower plenum etc. In Fig.1, the reactor core area is split into 3 concentric core flow channels from reactor core centre to baffle inner surface, which contains 25, 68 and 64 fuel assembles, respectively. In the fuel area, each core flow channel is split into 15 meshes in the axial direction. Each fuel assembly includes 264 UO_2 fuel rods with Zr cladding, 24 AgInCd (AIC) control rods and 1 instrument guide tube. 15 spacer grids are set along the axial direction of the fuel assembly. The reactor core power is set at 3400 MW. The core axial power profile from Figure 4.3-16 in [1] is used. The reactor core decay heat is calculated from the inventory of fuel and fission products by the FP_HEAT Structure in ASTEC. From baffle outer surface to barrel inner surface is the reactor core bypass flow channel. The downcomer flow channel is set between barrel outer surface and reactor vessel inner wall. The bottoms of the downcomer, bypass and the 3 core flow channels are connected to the top of the lower plenum.

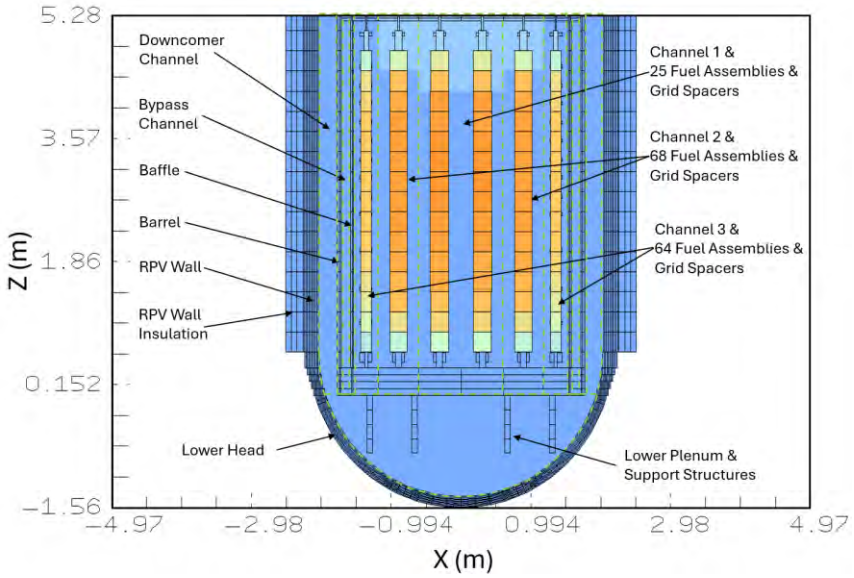

Figure 1. Reactor Core Nodalisation Scheme in ICARE.

In Fig. 2, the models for the reactor coolant system (RCS), including the primary and secondary loops, are built via the CESAR modules in ASTEC. The RCS primary loop is composed of RPV upper plenum structures, two coolant loops and one pressuriser (PZR). In each RCS primary loop, one hot leg (HL) links

the RPV upper plenum and the hot box of a steam generator (SG). Two reactor coolant pumps (RCPs) are set at the bottom of the SG cold box driving the coolant to RPV downcomer via two cold legs (CLs). The pump coast-down curve in [6] is adopted when the RCP shuts down.

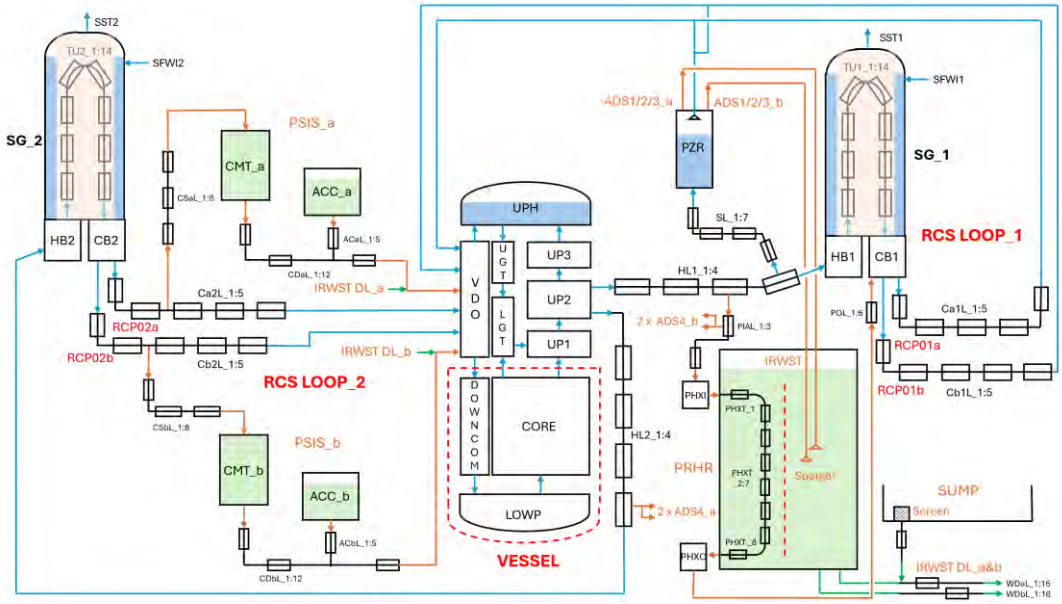

Figure 2. RCS Nodalisation Scheme in CESAR.

The primary loop and secondary loop in the RCS are coupled at the U-tube heat exchange area in the SGs. The RCS secondary loop is composed of SG feedwater pump, downcomer, riser, separator, steam dome and main steam line. The SG feedwater pump provides feedwater at defined pressure and temperature that serve as boundary conditions. The SG riser in the secondary loop shares the U-tube wall in the primary loop for heat transfer. A 'CONNECTI' structure of type 'BREAK' with constant back-pressure is set at the end of the SG main steam line to attain the correct main steam outlet pressure without modelling the unknown piping configuration to the steam turbine.

3. AP1000 PASSIVE SAFETY SYSTEM MODELS

In the AP1000 design, PZR, passive residual heat removal system (PRHR) and automatic depressurisation systems (ADSs) are located on RCS LOOP_1. The core makeup tank (CMT) and accumulator (ACC) are set in each cold leg of RCS LOOP_2.

The PZR is modelled by a 'swollen' type volume with sprays and heaters for maintaining RCS pressure. At the top of the PZR, there are 2 parallel groups of ADS_1/2/3 valves with discharge lines connected to the In-containment Refuelling Water Storage Tank (IRWST). The IRWST is modelled as 3 axial layers with one volume at the bottom and one volume at the top, while the middle layer is split into 2 parallel pipes connecting the bottom and top volumes, forming a loop within the IRWST. The heat exchange tube of the PRHR is coupled with one of the IRWST parallel pipes. When the PRHR is actuated, natural circulation could be generated in the IRWST.

The CMT is modelled by a 'swollen' type volume with a suction line connecting its top to the RCP downstream of the SG cold leg. Downstream of the CMT, a discharge line from the CMT bottom is extended to the direct vessel injection (DVI) nozzle on the RPV downcomer. Even under high pressure conditions,

borated water in the CMT could be driven by gravity and natural circulation for emergency water injection. The ACC is modelled by an 'Accumulator' type 'SYSTEM' component connected to the CMT discharge line. The gas pressure of compressed nitrogen at the ACC top is 4.8 MPa. Gas expansion coefficient is set at 1.3 with isotherm expansion at 1.0 and adiabatic expansion at 1.4. From the bottom of the IRWST, 2 discharge lines with check valves are connected to 2 CMT discharge lines, separately, for water injection under low pressure conditions. On each cold leg of RCS LOOP_2, the CMT, ACC and IRWST discharge lines share one common DVI on the RPV downcomer.

The reactor trip and safety systems actuation signals have been modelled according to Table 15.0-4a&b and Table 15.6.5-10 of the AP1000 Design Control Document [1].

4. STEADY STATE CALCULATION

Before transient calculation of the accident scenario, the initial steady-state NPP operation condition is calculated. The 'REGU' structures in ASTEC are used to adjust initial settings like local flow resistances, initial water loading, PZR heater power or spray flow etc., for aligning the steady state simulation to some representative parameters during normal operation, like PZR pressure and water level, reactor core water flow and bypass flow, reactor core inlet and outlet temperatures, steam produced, and pressure drops. This runs for 20,000 s to achieve the required steady-state initial conditions. Steady-state calculations and nominal AP1000 operation parameters are listed in Table I.

Table I. Comparison of ASTEC Steady State Simulations with reference nominal values [1]

NPP representative operating parameter	ASTEC simulations	Design values[1]
Pressuriser pressure (MPa)	15.5997	15.6
Vessel flow (kg/s)	15169.95	15170.14
Reactor core bypass flow (kg/s)	378.82	378.82
Bypass flow to reactor core upper head (kg/s)	227.25	227.25
Average core inlet temperature (°C)	282.17	280.67
Average core outlet temperature (°C)	323.88	323.3
Steam flow from SG (kg/s)	938.85	943.1
Steam pressure from SG (MPa)	5.753	5.760
Reactor core pressure drop (kPa)	294.97	275.1±27.58
RPV pressure drop (kPa)	441.43	429.5±42.75
SG pressure drop (kPa)	340.71	~343.0

5. 10-INCH SB-LOCA SIMULATION

A 10-inch SB-LOCA is assumed to occur at the bottom of a cold leg connected to CMT_a. The simulation results are compared with NOTRUMP simulations in the AP1000 design control document [1] and CESAR results [2]. In addition, the reactor core degradation progression is analysed when post-LOCA long-term cooling is unavailable due to exclusion of the containment and its cooling system models in this simulation.

5.1. Emergency reactor core cooling

The AP1000 passive safety systems actuations in this 10-inch SB-LOCA simulation follows 3 variables in emergency reactor core cooling progression: RZR pressure, CMT water level and IRWST water storage

with pre-set setpoint and time delays listed in Table II. The event times for the emergency reactor core cooling progressions of the 10-inch SB-LOCA are shown in Table II.

Table II. Safety Systems Sequence in AP1000 10-inch SB-LOCA Transient

Event	Setpoints and Delays	CESAR [2]	NOTRUMP [1]	CESAR + ICARE (this work)
Break initiation		0.0	0.0	0.0
Reactor trip signal	PZR pressure < 12.41 MPa + 0.2 s	4.3	5.2	5.2
Safeguards signal ('S' signal)	PZR pressure < 11.72 MPa + 2 s	5.4	6.4	8.8
PRHR & CMT actuation	'S' signal + 5 s			13.8
Steam turbine isolation	'S' signal + 6 s	12.5	11.2	14.8
Reactor coolant pumps trip	'S' signal + 6 s	10.5	12.4	14.8
Accumulator injection starts		102.2	85.0	94.6
ACC_a empties		477.8	418.2	806.7
ACC_b empties		478.3	425.5	806.8
ADS_1 actuation	67.5% CMT level + 32 s	817.0	750.0	580.2
ADS_2 actuation	ADS_1 actuation + 48 s	877.0	820.0	630.2
ADS_3 actuation	ADS_2 actuation + 120 s	997.0	940.0	750.2
ADS_4a actuation	20% CMT level & ADS_3 actuation + 128 s	1535.0	1491.0	1215.2
IRWST injection starts		1650	~1800	1245.2
ADS_4b actuation	ADS_4a actuation + 120 s			1275.2
CMT_b empties		1830	1800	1510.2
CMT_a empties		~2000	1900	1510.2

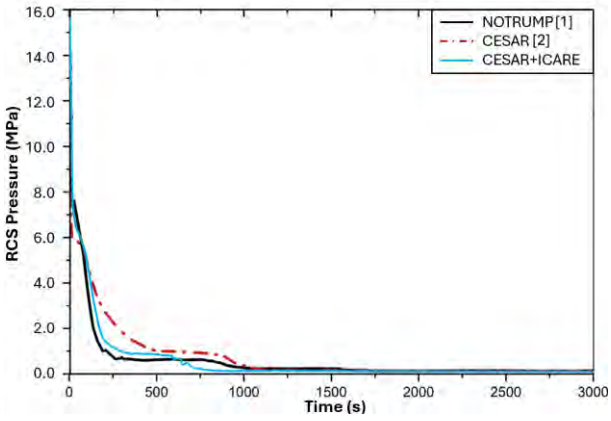

Figure 3. RCS pressure drop curve.

The event times for reactor trip, 'S' signal and ACC injection in the present study show a reasonable agreement with NOTRUMP results in the blowdown phase and in the early stage of the natural circulation phase. The pressure drop speed is dominated by discharge flow rates from the pipe-break. In the first 100 s after the pipe is broken, the discharge liquid flow rates in Fig. 4a agree quite well in all 3 simulations. Even

though there are slight deviations in discharge gas flow rates in Fig. 4b, the RCS pressure drop shows nearly the same decline rate till the ACC injection actuation pressure of 4.8 MPa.

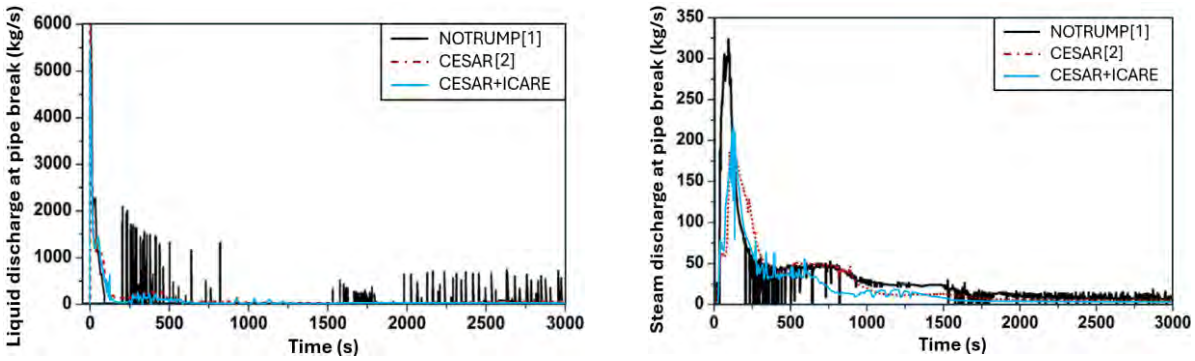

(a) **(b)**

Figure 4. (a) Liquid and (b) Steam Discharge Flows at Pipe-Break.

In the natural circulation phase, the emergency water injection flow to the RPV from the DVI is dominated by natural circulation in the CMT loop and pressure difference between ACC compressed gas and RCS system. In Fig. 5a&b, natural circulation is quickly set up in the CMT loop within 6 s after 'S' alarm. When ACC is triggered as RCS pressure drops below 4.8 MPa, CMT natural circulation flow is suppressed by ACC discharge flow. After ACC is emptied, CMT natural circulation flow rate firstly recovers to a higher level and then slips down till CMT water is depleted. The natural circulation flows in CMT_a and CMT_b loops are almost the same as in the other 2 simulations.

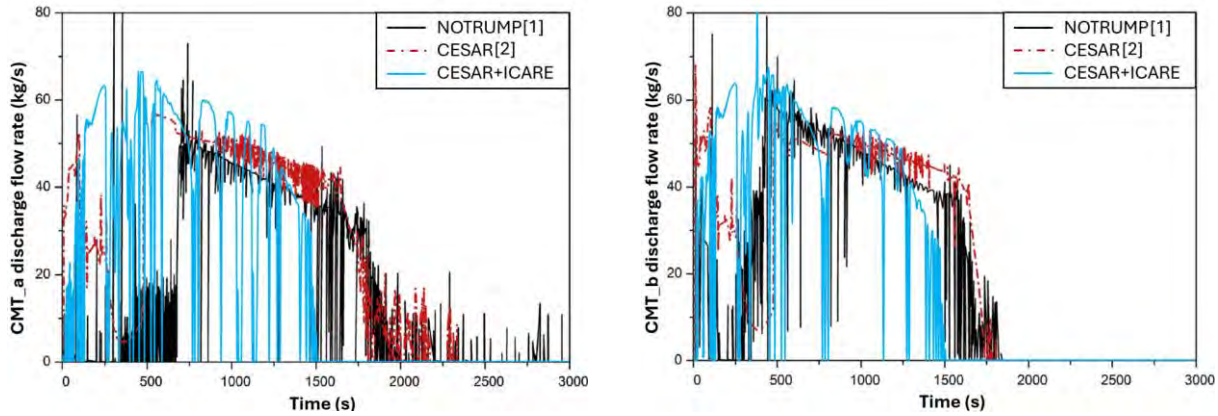

(a) **(b)**

Figure 5. (a) CMT_a and (b) CMT_b Discharge Flows.

In Fig. 6a, the ACC discharge flow in the present study shows a different trend. The ACC discharge flows are generally suppressed, which leads to a longer ACC discharge period. From Fig. 3, RCS pressure decline rate is significantly reduced after ~250 s. The decrease of pressure difference between ACC and RCS system induces suppression of ACC discharge flows. However, the CMT discharge flow rate is shortly recovered during this ACC discharge flow suppression period. As water level in CMT decreases to 67.5 %, ADS_1 is triggered much earlier at ~580.2 s than in the other 2 simulations. The series of ADS_1/2/3 actuations re-accelerates RCS pressure drop and ACC discharge flow rate starts to increase. When the water level in the

CMT reaches 20 %, additional RCS depressurisations by ADS_4 a&b start from 1215.2 s in Table II, which guarantee the long-term cooling water injection from IRWST is triggered at ~1245.2 s in Fig. 6b before CMT water is depleted at ~1510.2 s in Fig. 5 a&b.

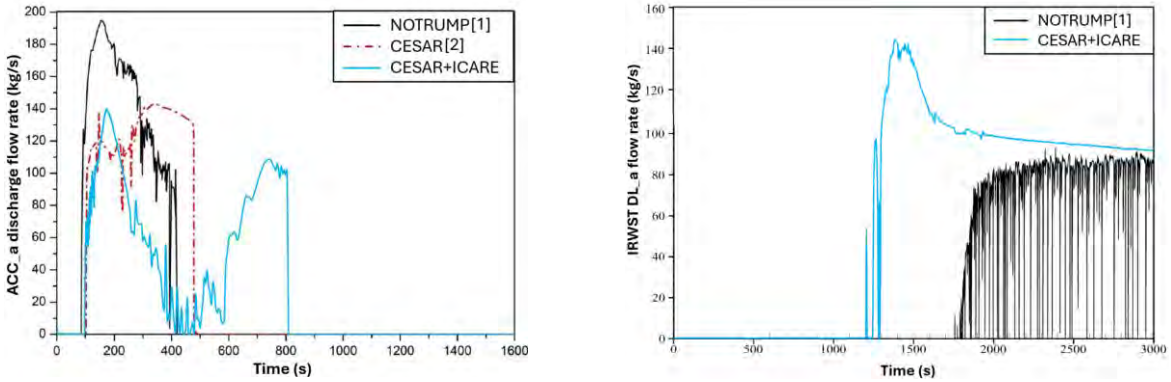

(a) **(b)**

Figure 6. Discharge Flows from (a) ACC_a and (b) IRWST_a.

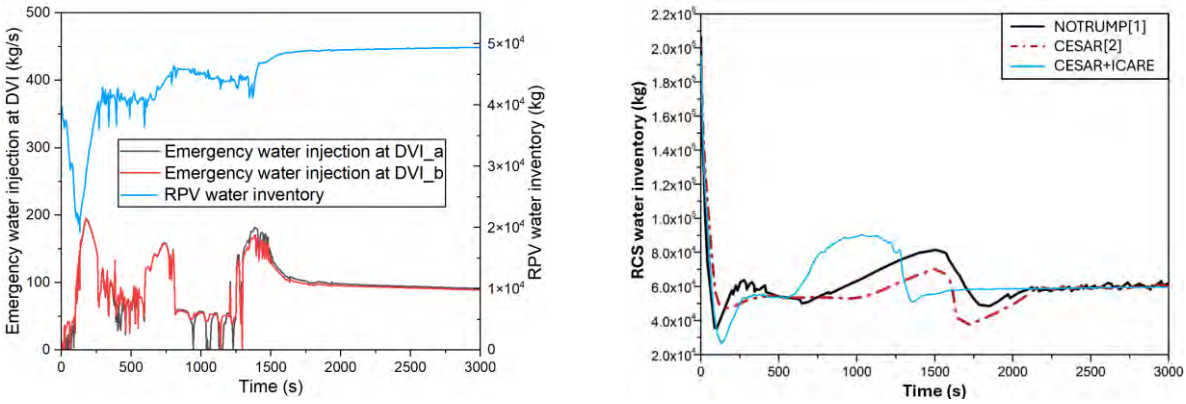

(a) **(b)**

Figure 7. (a) DVI Injection Flows & RPV Water Inventory and (b) Water Inventories in RCS.

In Fig. 7a, the CMT, ACC and IRWST work together with ADS_1/2/3/4 to guarantee continuous emergency water injection from the DVI after pipe-break. The first DVI flow peak brought about by ACC actuation successfully reverses the RCS and RPV water inventory decrease as shown in Fig. 7a & b. The second DVI flow peak following ACC injection after ADS_1 is triggered at ~580.2 s contributes to the RCS and RPV water inventory step. The third DVI flow peak at the beginning of IRWST discharge compensates for the massive water loss due to ADS_4a/b ruptures.

Besides continuous emergency water injection, heat transfer in the PRHR system also contributes to preventing reactor core overheating, especially in the early stages of the LOCA as shown in Fig. 8. In Fig. 9, fuel cladding temperature is well controlled with maximum temperature remaining below 650 K. However, the temperature peaks on the declining fuel cladding temperature curve in the present simulation indicate that the fuel claddings are shortly exposed to steam. The first two fuel cladding temperature peaks are triggered in the early blowdown phase of the LOCA. The prompt ACC discharge actuation effectively increases RPV water inventory and re-wets the fuel cladding surface. The DVI flow peak brought about by ACC discharge guarantees the reactor core safely transits to the long-term cooling stage.

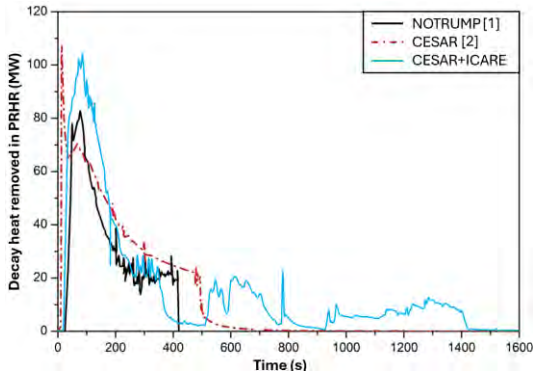

Figure 8. Heat Discharge in PRHR.

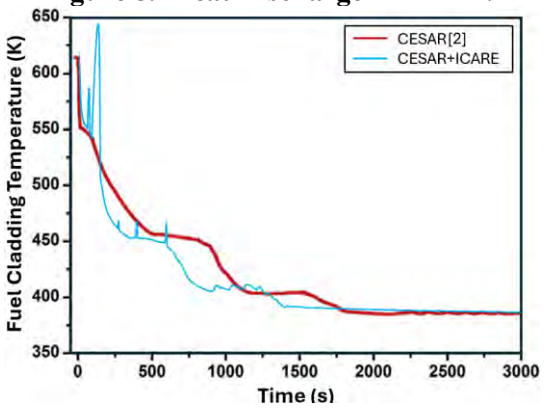

Figure 9. Max. Cladding Temperature Curve.

5.2. In-vessel core degradation with long-term cooling cut-off

In the long-term cooling stage, water discharged from the IRWST compensates for water loss in the reactor core. In the AP1000 design, steam leaking through ADS_1/2/3/4 and the piping break will be cooled and condenses on the steel containment vessel inner surface by the passive containment cooling system for at least 72 hours. Driven by gravity, the condensate collected in the sump flows back to the RPV via the IRWST discharge line. The steel containment vessel works as the third barrier—both in retaining radioactive materials and in serving as the ultimate heat sink, which could provide long-term cooling water for a submerged reactor core as shown in Fig. 10.

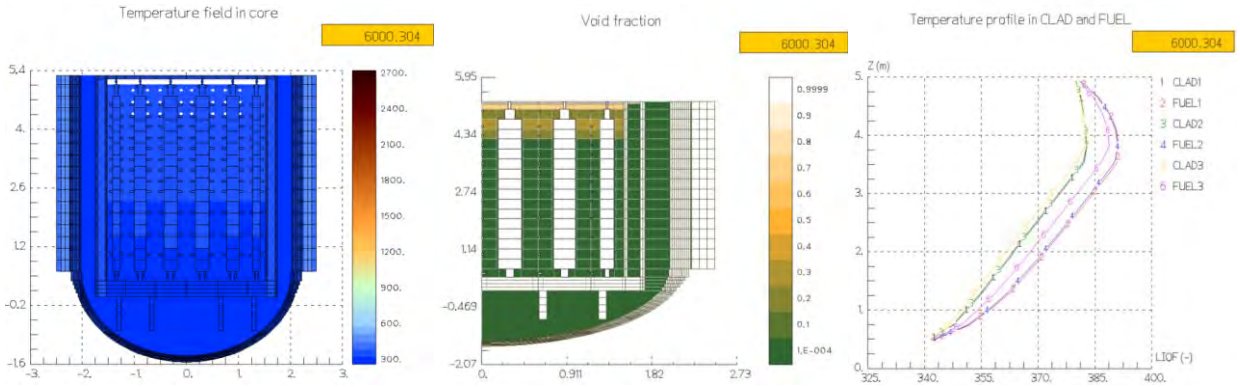

Figure 10. Temperature & Void Fraction Fields in Core, and T_{Clad} and T_{Fuel} Profiles at 6000.3 s.

In the present study, we removed the containment and its passive containment cooling system. After IRWST water is depleted, the water source for long-term cooling is cut off to simulate the reactor core degradation process using ICARE module. In Fig. 11, IRWST discharge flow drops abruptly at ~22000 s as IRWST water inventory approaches zero without supply from containment condensation. Without sufficient cooling water supply, water temperature in the reactor core gradually increases. As shown in Fig. 11 and Fig. 12, the fuel and cladding temperatures at reactor core bottom increase from ~340 K to 374 K due to the surrounding water temperature increase. The significant void fraction increase in reactor core upper section in Fig. 12 indicates there is violent boiling on cladding surfaces. The nucleate boiling on cladding wall in reactor core upper section suppresses the fuel and cladding temperatures on the top of fuel and cladding temperatures profile in Fig. 12. However, when the IRWST discharge flows cannot compensate for the water loss via evaporation, the increasing void fraction will trigger boiling crisis on cladding surfaces.

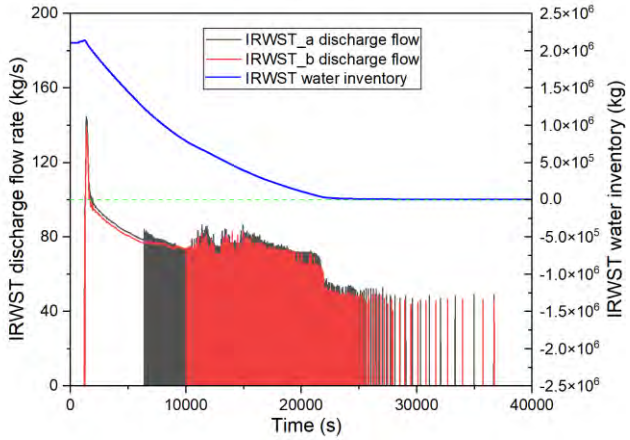

Figure 11. IRWST Inventory and Discharge Flows in Long-term Cooling Period.

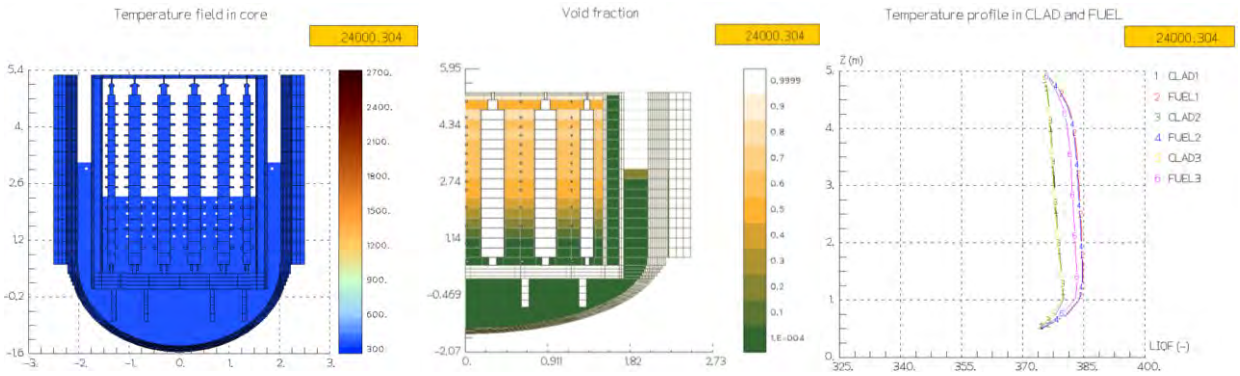

Figure 12. Temperature & Void Fraction Field in Core and T_{Clad} & T_{Fuel} Profiles at 24000.3 s.

In Fig. 11, the water inventory in IRWST is almost depleted at ~25000 s, around 7 hours after the pipe is broken. After wetting by steam flow and entrained water droplets are lost, cladding temperatures in the reactor core upper section increase to ~850 K at 26630.3 s as shown in Fig. 13 and Fig. 14. Oxidation starts on high-temperature Zr cladding surfaces and steel vessel structure surfaces with hydrogen generation as shown in Fig. 15a. The exothermic reaction between Zr and steam aggravates fuel cladding failure.

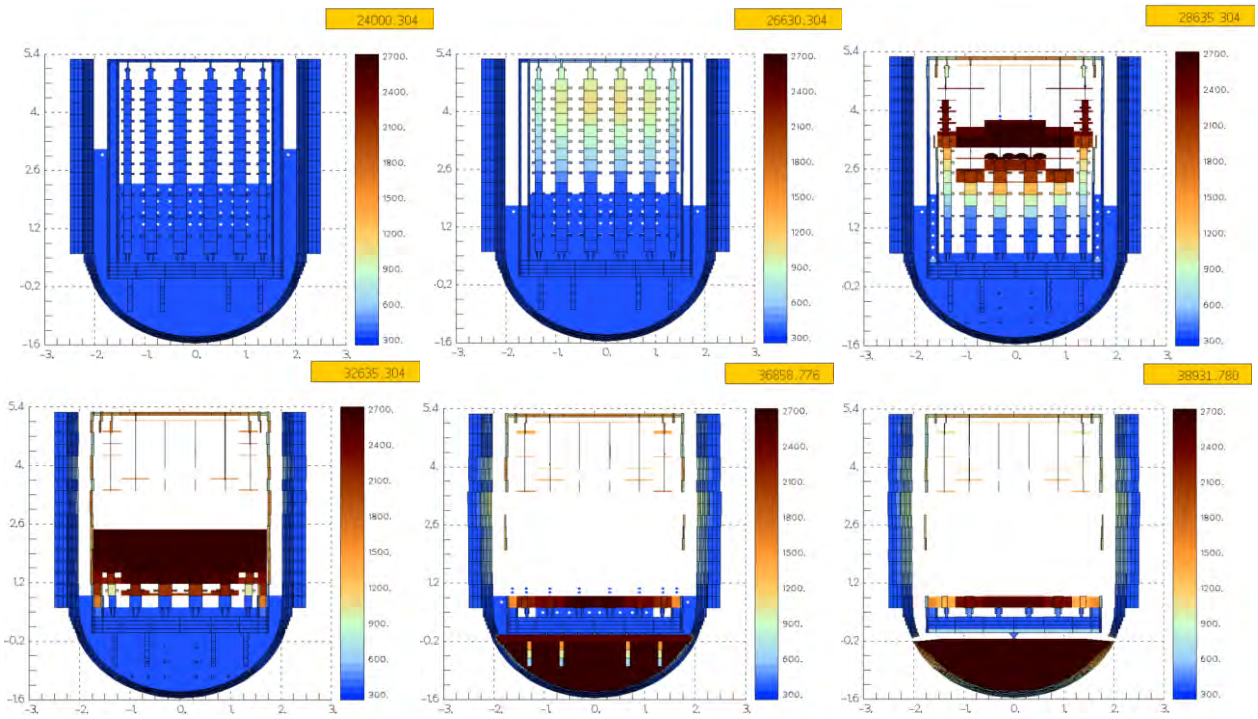

Figure 13. Reactor Core Temperature Field.

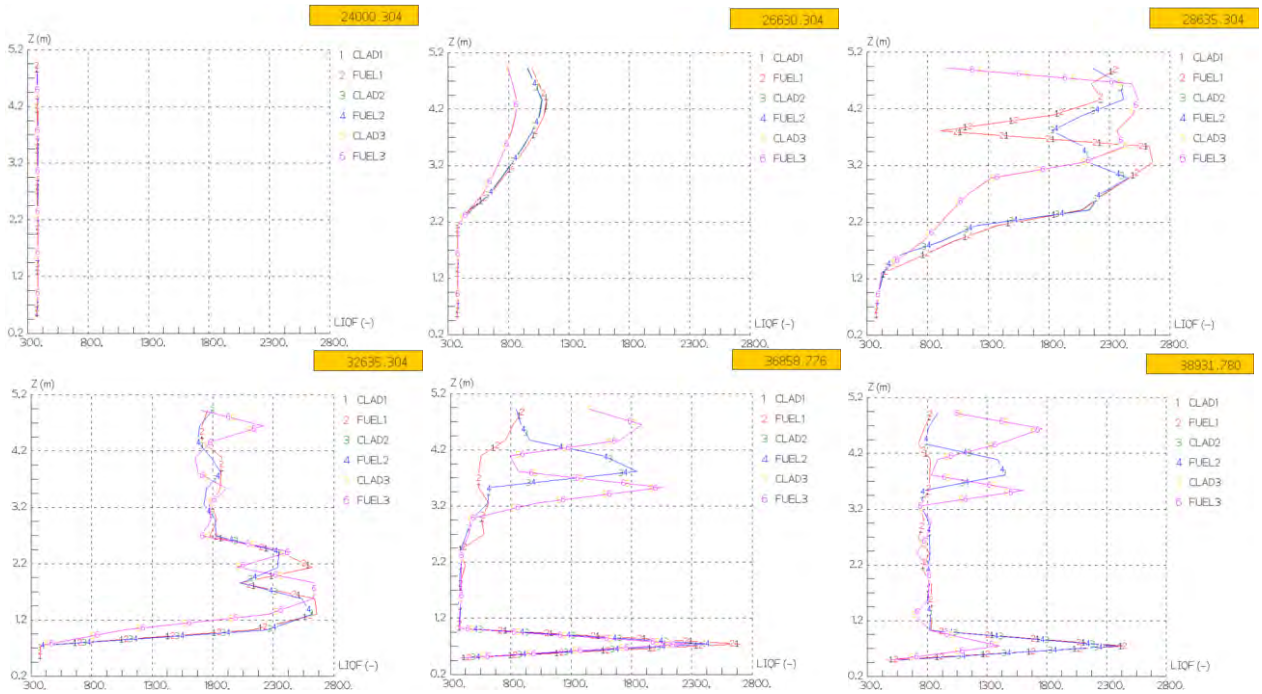

Figure 14. Fuel and Cladding Temperature Profiles.

At 28635.3 s in Fig. 13, most of the fuel, cladding and vessel structures in the reactor core upper section are liquefied and relocated to the lower section, which leads to massive radioactive material release as shown

in Fig. 15b. With molten corium gradually slumping to the lower plenum, a molten corium pool is formed at ~36635.3 s with a light metal layer on the top in Fig. 13.

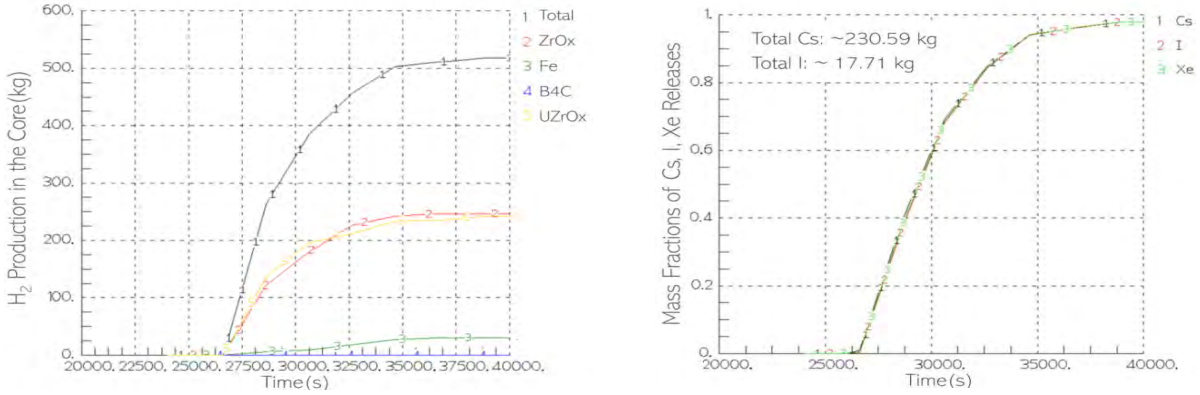

(a) **(b)**

Figure 15. Hydrogen Production and Radioactive Material Release.

As lower head external cooling is excluded in the present study, the lower head wall suffers from high heat flux from light metal layer and its deadweight, which induces vessel rupture near the molten corium pool surface level referring to ductile failure based on Oeuf model, a mechanical model to describe the behavior of a reactor vessel lower head loaded by thermal, pressure and weight loads under severe conditions in ICARE [7]. Partial corium above lower heat rupture elevation (-0.147 m) flows out of the lower head. Lower head (LH) collapses at 38931.8 s, around 4 hours after IRWST water depleted, marks the final stage of the in-vessel accident progression in ICARE calculation. The in-vessel core degradation progression and estimated source term releases are listed in Table III.

Table III. Safety Systems Sequence in AP1000 10-inch SB-LOCA Transient

Time (s)	Event
26630.3	First cladding creep rupture
26630.3	Start of FPs release from fuel pellets
26915.3	Start of structural material release
27990.3	First material slump in lower plenum
36858.8	Lower head vessel failure • Ductile failure based on Oeuf model [7] • H_2 mass produced during in-vessel phase = 510.926 kg • Aerosol mass produced during in-vessel phase = 9086.69 kg Corium flows out of the lower head • Corium mass transferred from the lower head = 14431.6 kg • Remaining corium mass in the lower plenum = 97678.6 kg
38931.8	Lower head collapse

6. CONCLUSIONS

The AP1000 RCS and its safety systems, including the PRHR system, ADS and 3 passive water injection systems—CMT, ACC and IRWST, are modelled by the CESAR module in ASTEC. The thermohydraulic

performance of those passive safety systems in the 10-inch SB-LOCA are simulated. Heat removal driven by natural circulation in the IRWST pool, and emergency water injections from CMT, ACC and IRWST, driven respectively by natural circulation, compressed gas and gravity, show reasonable agreement with NOTRUMP results in the AP1000 design control document [1] and another CESAR/ASTEC work by [2]. The ADS depressurisation design plays an important role in maintaining ACC discharge flow rate and actuating IRWST injection before CMT water is depleted. The 3 passive water injection systems, in combination with the ADS, guarantee continuous emergency core cooling from less than 15 seconds after the pipe-break until approximately 25,000 seconds (~7 hours), effectively slowing down reactor core water level decline rate and preventing fuel and cladding from overheating.

The containment and passive containment cooling system in the AP1000 design are intentionally removed for demonstrating the in-vessel core degradation process by the ICARE module in ASTEC. Without containment providing condensation water for reactor core long-term cooling and lower head external cooling, reactor core melt-down along with massive hydrogen and radioactive material release is inevitable. The in-vessel core degradation simulation underscores the critical role of the containment as the third barrier in the AP1000 design, both in retaining radioactive materials and in serving as the ultimate heat sink for long-term cooling.

ACKNOWLEDGMENTS

The authors acknowledge the support by the National Research Foundation Singapore (A-8002968-00-00).

REFERENCES

1. Westinghouse Electric Company LLC, “Westinghouse AP1000 Design Control Document Rev. 19” (2011).
2. M. Di Giuli, M. Sumini, F. De Rosa, “Modeling of AP1000 and simulation of 10-inch cold leg small break LOCA using the CESAR thermal-hydraulic module of ASTEC,” *Progress in Nuclear Energy*, **83**, 387-397 (2015).
3. L.L. Humphries, B.A. Beeny, F. Gelbard, D.L. Louie, J. Phillips, R.C. Schmidt, N.E. Bixler, “MELCOR Computer Code Manuals, SAND2021-0726 O” (2021).
4. P. Chatelard, L. Laborde, “ASTEC V2.2 code validation: Illustrative results and main outcomes,” *Nuclear Engineering and Design*, **413**, 112547 (2023).
5. Westinghouse Electric Company LLC, “NOTRUMP Final Validation Report for AP600, WCAP-14807 Rev. 5” (1998).
6. Y. Zhong, D. Xia, W.X. Zhou, “Extended Study of Reactor Coolant Pump Coastdown Phenomenon with RELAP/Mod3,” *ICONE25-66311*, Shanghai, China, July 2-6 (2017).
7. The French Authority for Nuclear Safety and Radiation Protection, “ASTEC: Physical modelling of the ICARE module V3.1.1” (2011).

12th CONFERENCE ON
SEVERE ACCIDENTS RESEARCH
May 18-22, 2026 - Madrid, Spain
ERMSAR 2026

ASTEC MODELLING OF THE AP1000 AND COLD-LEG SMALL-BREAK LOCA SIMULATIONS WITH LONG-TERM COOLING CUT-OFF

Zhao Dawei, Guo Zhexi, Xiao Sicong

18 May, 2026

NUS National University of Singapore | Singapore Nuclear Research and Safety Institute

AP1000 & Typical Passive Safety Systems

The AP1000 reactor is the first operating Gen III+ reactor with fully passive safety systems, modular construction design and one of the most compact footprints among Gen-III+ NPPs. Those advanced design philosophy have been adopted in many innovative LW-SMR designs.

- Passive Core Cooling System (PXS)
- High Pressure Safety Injection with Core Makeup Tanks (CMTs)
- Medium Pressure Safety Injection with Accumulators
- Low Pressure Reactor Coolant Make from the IRWST
- Automatic Depressurization System
- Passive Residual Heat Removal

- Containment Isolation
- Passive Containment Cooling System (PCS)
- Main Control Room Emergency Habitability System

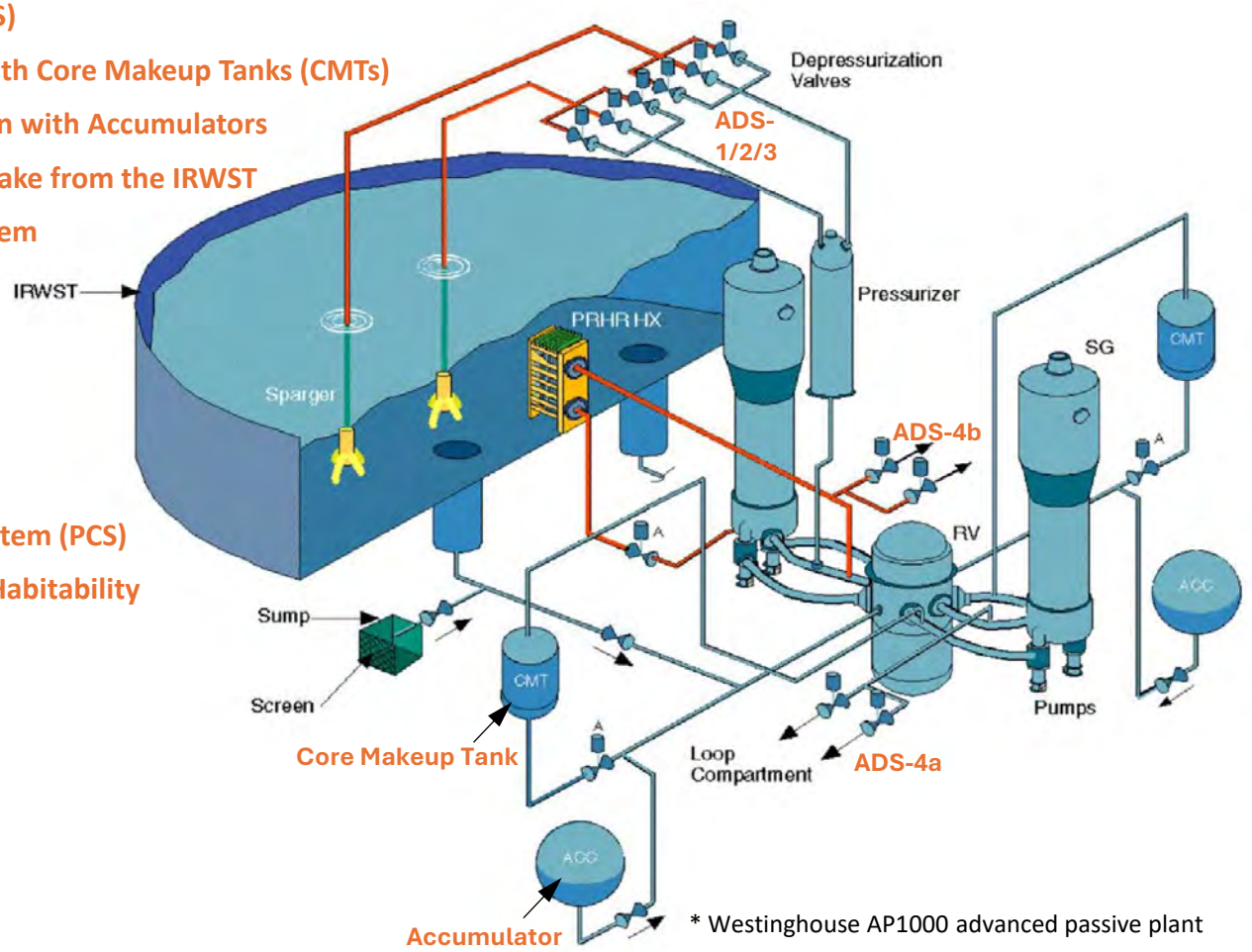

* Westinghouse AP1000 advanced passive plant

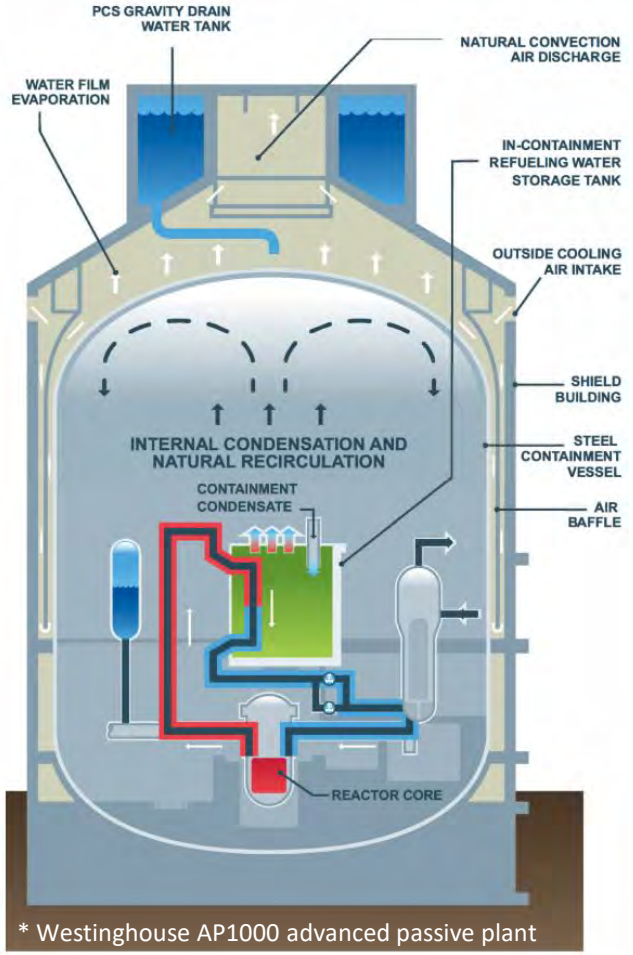

* Westinghouse AP1000 advanced passive plant

AP1000 Nodalization Scheme in CESAR & ICARE

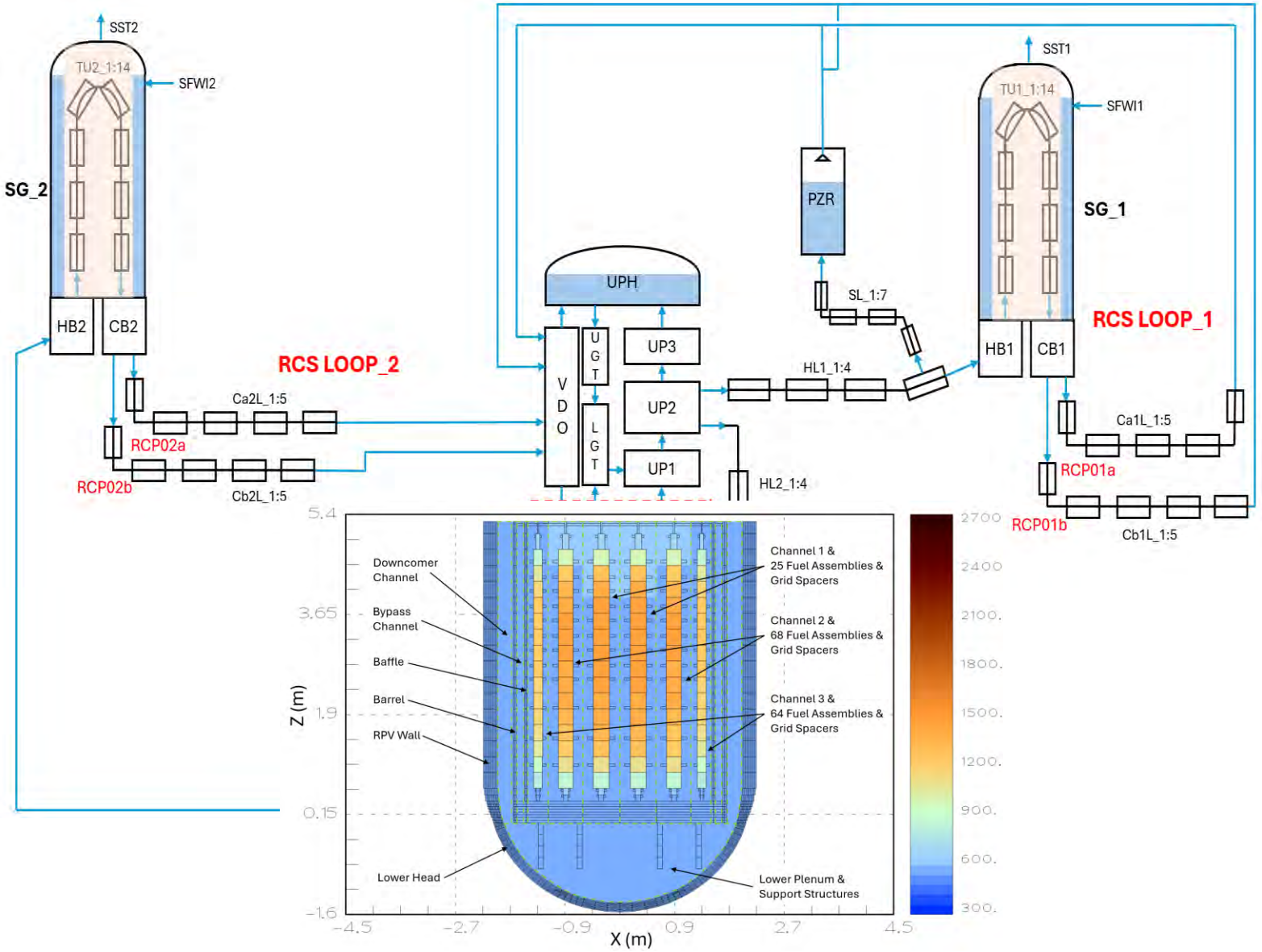

Steady State Calc. Results Comparisons

Plant parameters	Design value in AP1000 DCD *	ASTEC Calc.
Vessel flow (kg/s)	15169.90	15170.05
Head cooling flow (kg/s)	227.25	227.25
Bypass flow (kg/s)	378.82	378.82
Core out temp (℃)	323.30	323.88
Vessel out temp (℃)	321.10	322.19
SG out temp (℃)	272.80	272.97
Core in temp (℃)	280.67	282.17
SG steam flow (kg/s)	943.10	939.32
PRZ pressure (Pa)	15.60	15.5998
Steam pressure (MPa)	5.760	5.76092
Core DP (kPa)	275.1±27.58	277.79
Vessel DP (kPa)	429.5±42.75	441.42
SG DP (kPa)	~ 343.00	340.71

* Westinghouse AP1000 Design Control Document Rev. 19

NC in IRWST & Passive SS Pressure Drop Calibrations

63.41kg/s

PIAL_1:3

IRWST

PHXI

PHXT_1

PRHRHX

PHXT _2:7

PHXT _8

PHXO

POL_1:6

IRWST Discharge Line a&b

WDaL_1:16

WDbL_1:16

63.41kg/s

50 kg/s

50 kg/s

PRHR DP: ~ 9.3 kPa

DP for IRWST

DL_a: ~ 13.93 kPa

DL_b: ~ 15.58 kPa

Natural Circulation in IRWST

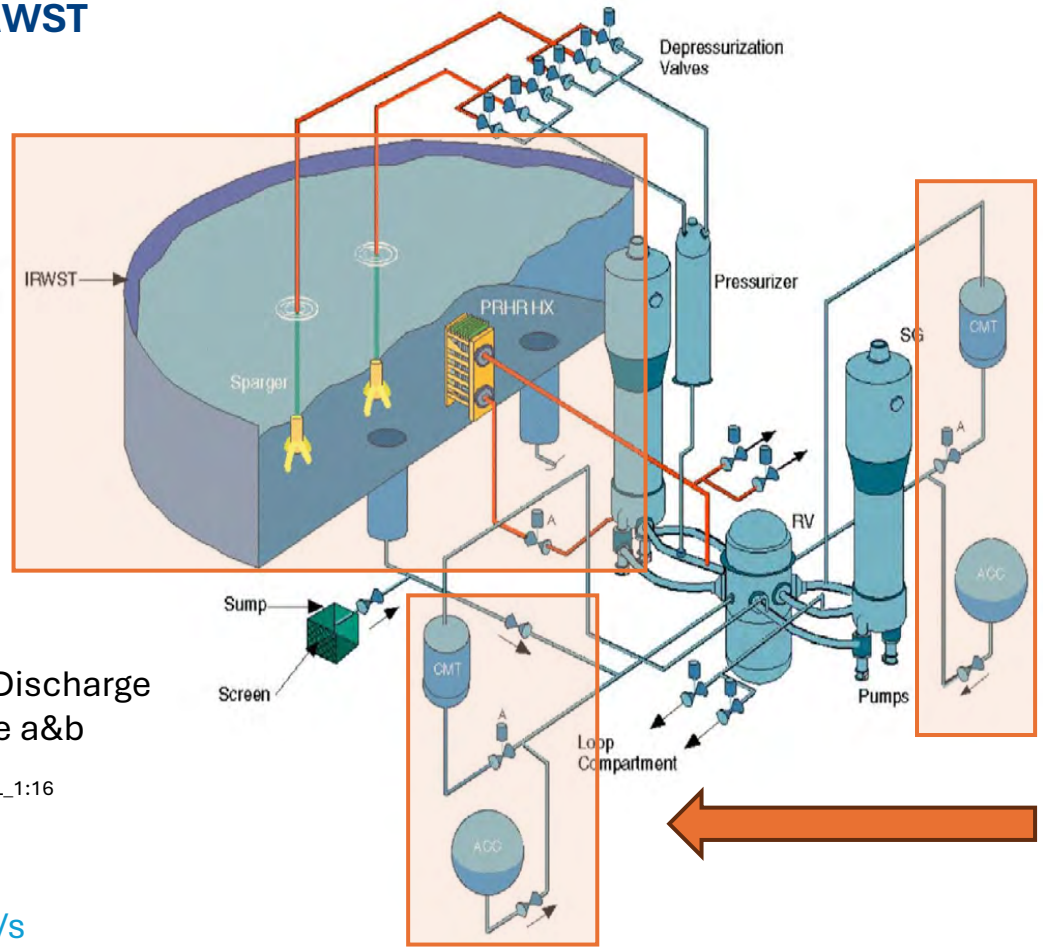

* Westinghouse AP1000 advanced passive plant

Pressure Drop Calibration in Passive SS

CMT_a

ACC_a

CSaL_1:8

ACC DP: ~ 31.16 kPa

ACaL_1:5

IRWST

CDaL_1:11

IRWST DL_a

30 kg/s

CMT DP: ~ 43.82 kPa

50 kg/s

NUS National University of Singapore | Singapore Nuclear Research and Safety Institute

AP1000 with Safety Systems Nodalization Scheme

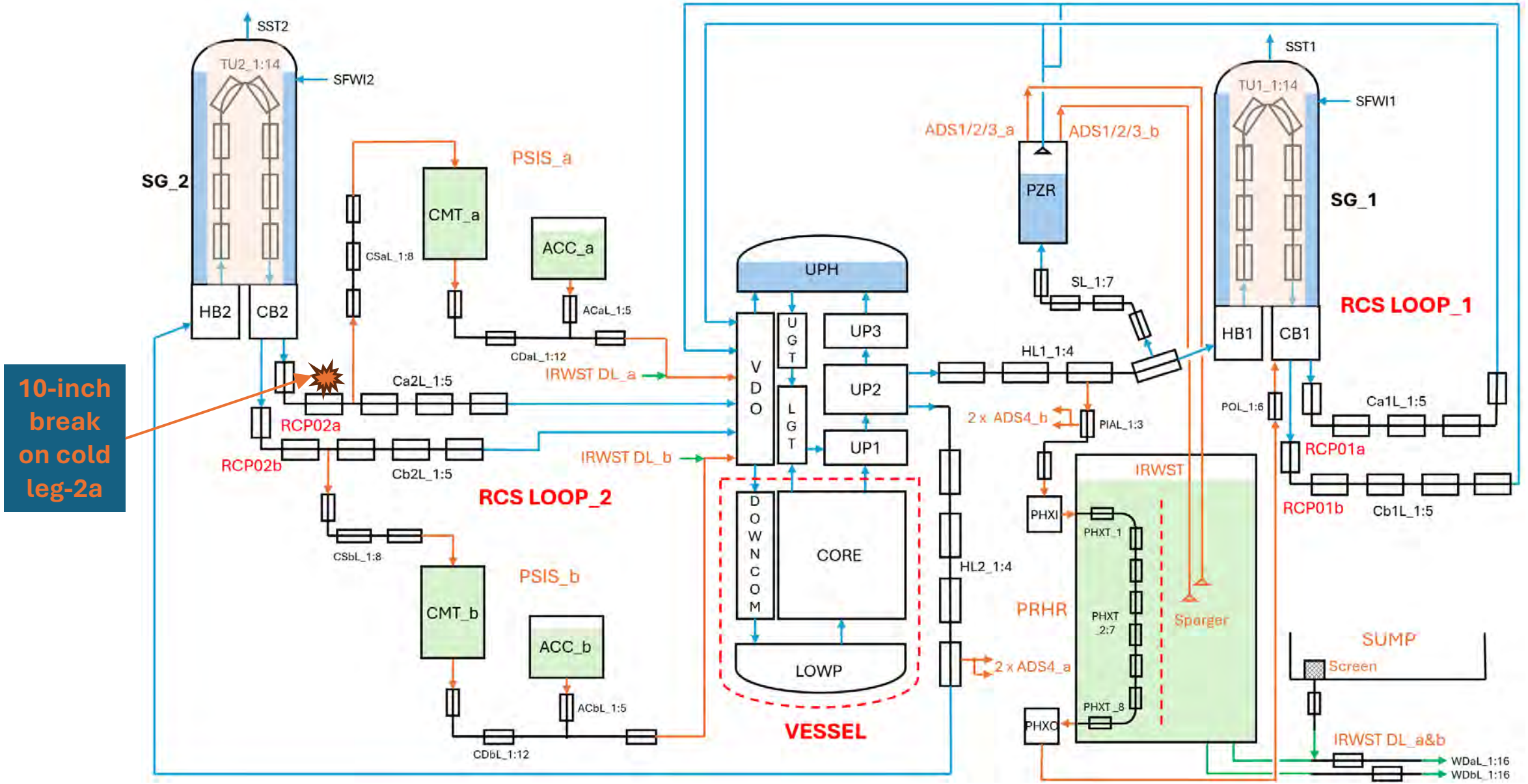

AP1000 SS Setpoints & Initial Conditions in Accident Analysis

Safety system setpoints and time delay assumed in accident analysis*

Function	Setpoint safety system*	Time delay (s)*
Reactor SCRAM on low pressurizer pressure	PZR pressure lower than 124.1 bar(1800 psia)	0.2
Safeguards signal('S' signal)	PZR pressure lower than 117.2 bar(1700 psia)	2
PRHR signal	'S' signal	5
CMTs signal	'S' signal	5
RCPs trip	'S' signal	6
Main feedwater isolation	'S' signal	ramped closed between 2 and 7s
SGs secondary isolation (turbine stop valves closure)	'S' signal	6
Main steam safety valves actuation	Main steam lines pressure higher than 851.5 bar(1235 psia)	
ADS stage 1(4-inch) actuation on CMT L level	67.5% CMT water level	32 + 40 s for valve open
ADS stage 2(8-inch)	ADS 1 stage signal	48 + 100 s for valve open
ADS stage 3(8-inch)	ADS 2 stage signal	120 + 100 s for valve open
ADS stage 4A actuation on CMT LL level	20% CMT water level and 128 s after ADS 3 stage signal	4s for valve open
ADS stage 4B actuation on CMT LL level	60 s after ADS 4A stage signal	4s for valve open
IRWST signal	P(RCS) < (P(IRWST) + Head-losses)	0

Initial Conditions*

Systems	Initial Parameters*
Core power	102 percent of the nominal core power
Decay heat	modeled according to the ANS-1971 (Reference 2) standard, with 20-percent uncertainty added.
IRWST	Temperature: 48.89℃(120F), nominal full-power operation level of 8.778m(28.8 feet).
Containment	Pressure: 0.1013529 MPa(14.7 psia) for small-break LOCA, 0.137895 MPa(20.0 psia) for DEDVI.
Active single failures of the passive safeguards systems	The limiting failure is judged to be one out of four ADS Stage 4 valves failing to open on demand, the failure that most severely impacts depressurization capability.

* Westinghouse AP1000 Design Control Document Rev. 19, Section15.6

AP1000 SB-LOCA Simulation: Event Times

The AP1000 passive safety systems actuation sequence is following **3 variables** in emergency reactor core cooling progression:
1) RCS pressure; 2) CMT water level; 3) IRWST water storage

Event	NOTRUMP *	CESAR **	CESAR + ICARE (this work)
Break initiation	0.0	0.0	0.0
Reactor trip signal	5.2	4.3	5.2
'S' signal	6.4	5.4	8.8
PRHR & CMT actuation			13.8
Steam turbine isolation	11.2	12.5	14.8
Reactor coolant pumps trip	12.4	10.5	14.8
Accumulator injection starts	85.0	102.2	94.6
ACC_a empties	418.2	477.8	806.7
ACC_b empties	425.5	478.3	806.8
ADS_1 actuation	750.0	817.0	580.2
ADS_2 actuation	820.0	877.0	630.2
ADS_3 actuation	940.0	997.0	750.2
ADS 4_a actuation	1491.0	1535.0	1215.2
IRWST injection starts	~1800	1650	1245.2
ADS 4_b actuation			1275.2
CMT_b empties	1800	1830	1510.2
CMT_a empties	1900	~2000	1510.2

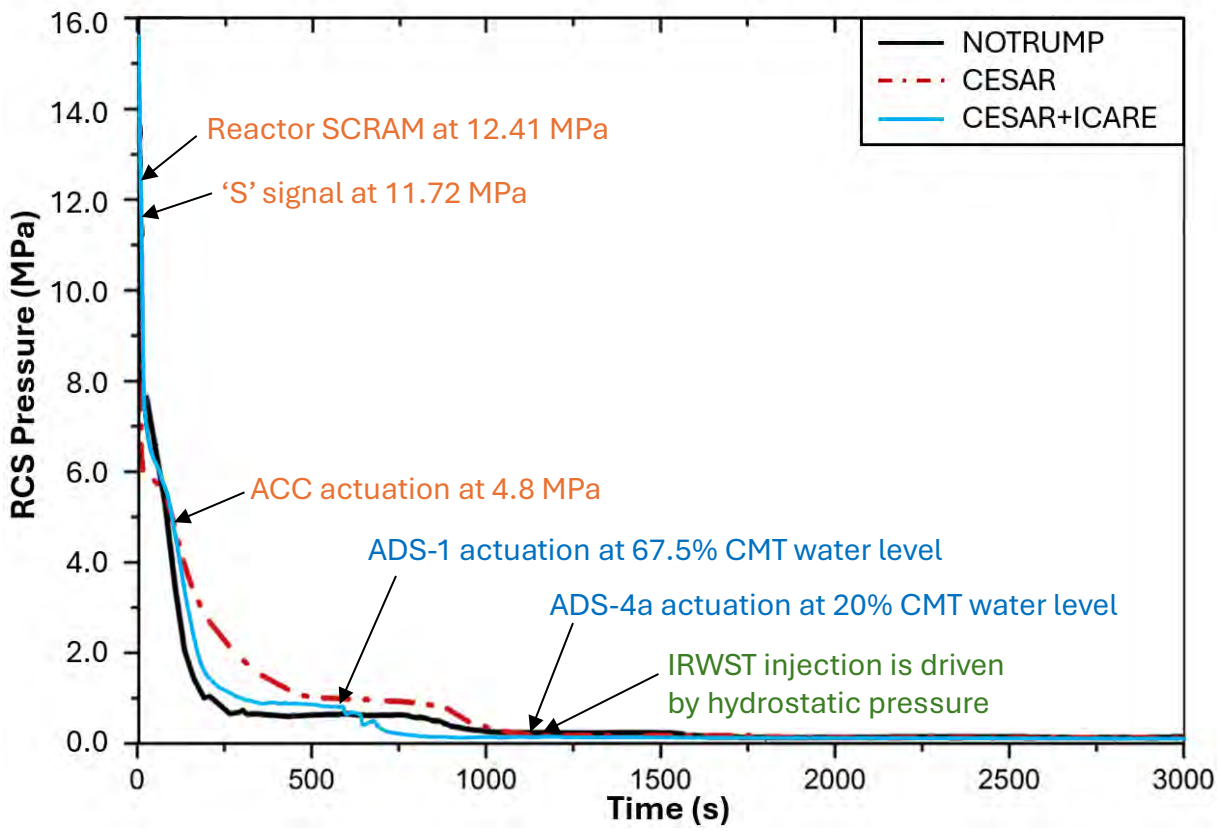

* Westinghouse AP1000 Design Control Document Rev. 19
** Modeling of AP1000 and simulation of 10-inch cold leg small break LOCA using the CESAR thermal-hydraulic module of ASTEC

AP1000 SB-LOCA Simulation: RCS Depressurization

Liquid Discharge Flows at Pipe-Break

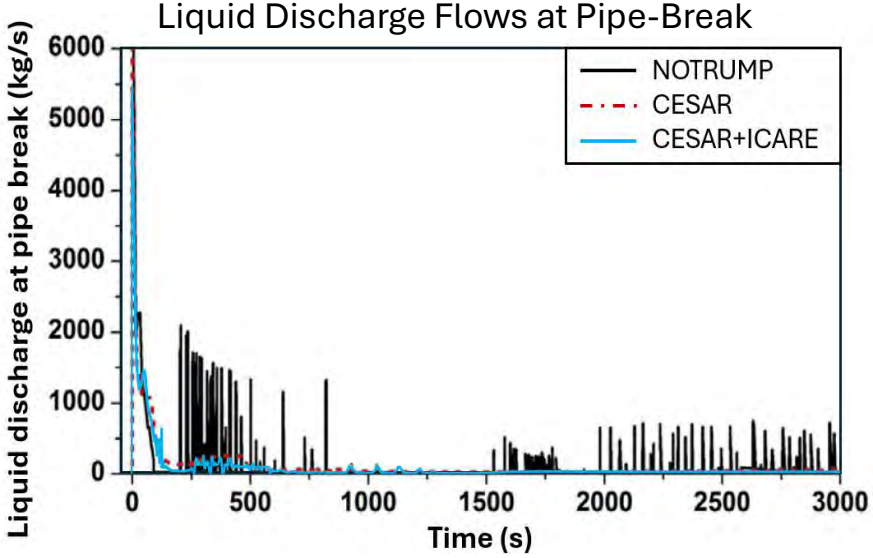

Steam Discharge Flows at Pipe-Break

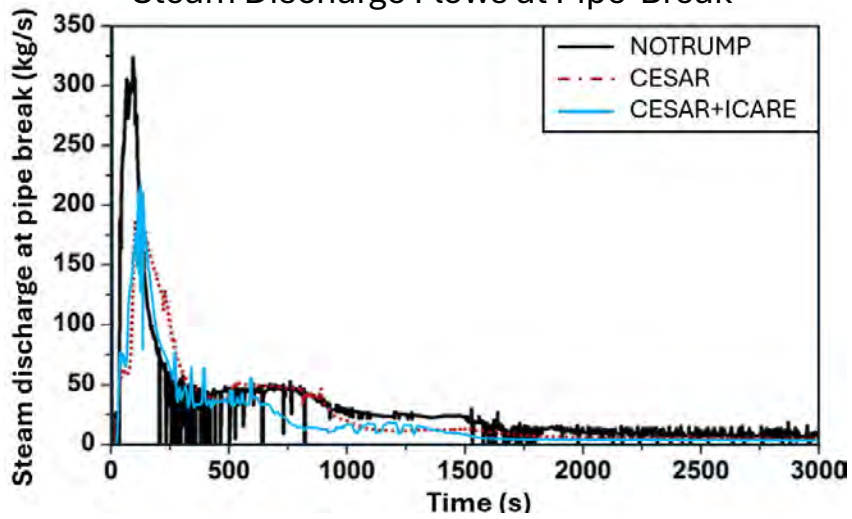

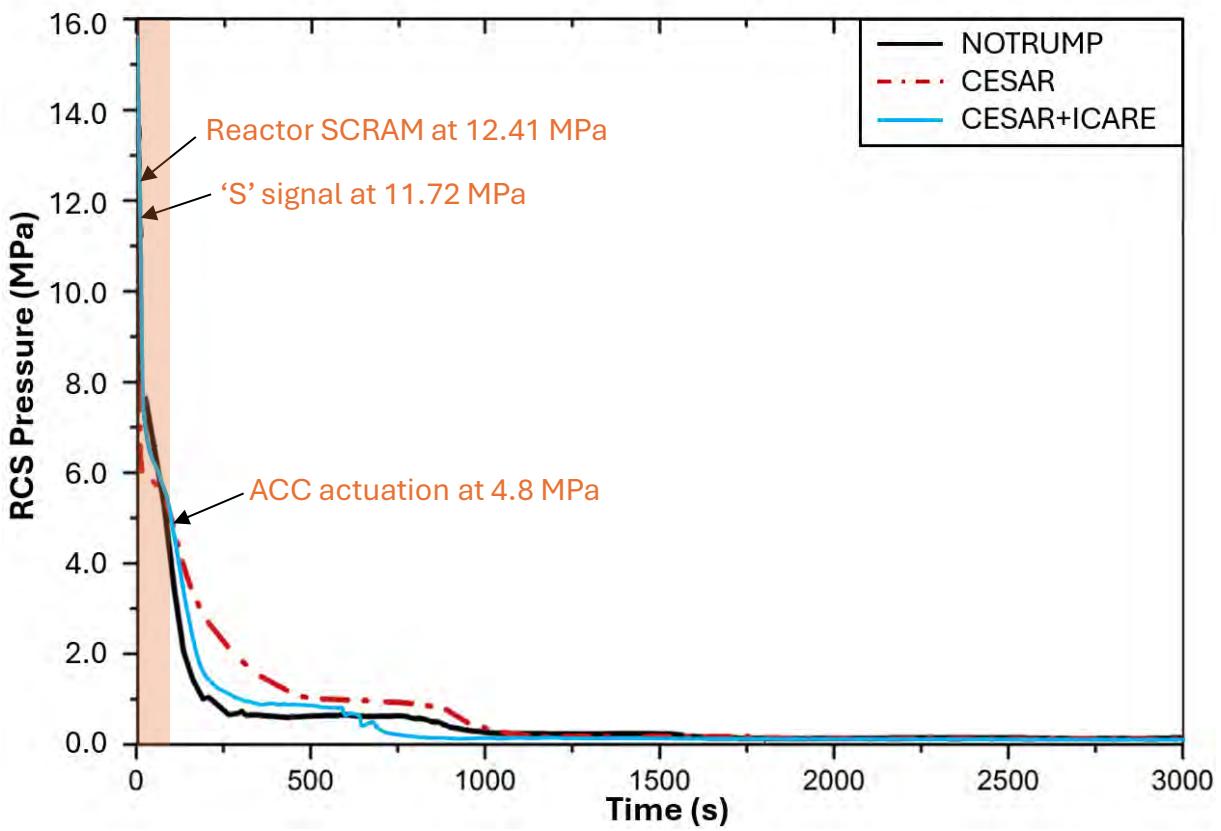

In the first 100 s after the pipe is broken, the discharge liquid flow rates agree quite well in all 3 simulations. Even though there are slight deviations in discharge steam flow rates, the RCS pressure drop shows nearly the same decline rate till the ACC injection actuation pressure(4.8 MPa).

AP1000 SB-LOCA Simulation: Flow Circulations in PRHR & CMT Loops

The isolation valves on CMT & PRHR are opened at 5s after 'S' signal. As RCPs trip 1s later, the residual pump head during RCP coast-down drives the flow circulations in the PRHR loop and CMT loops in the following few seconds.

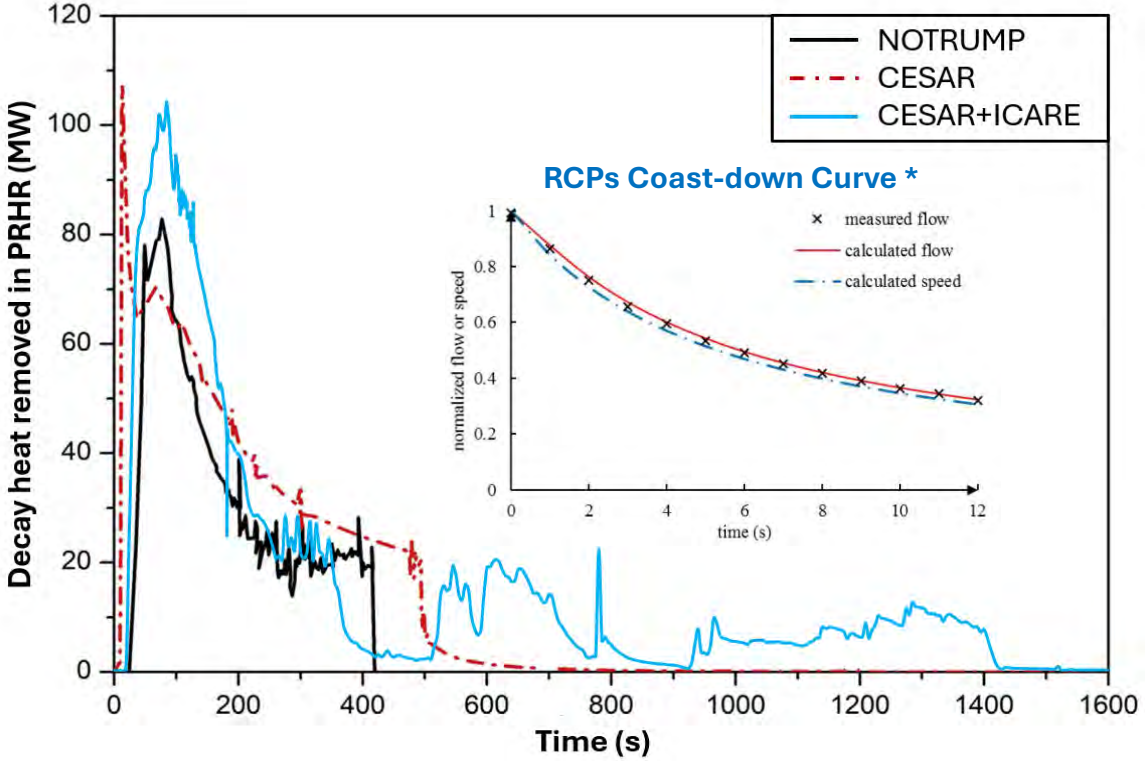

The partial reactor core decay heat is transferred through PRHR loop and dispersed to refueling water via the C-type heat exchanger submerging in IRWST water pool.

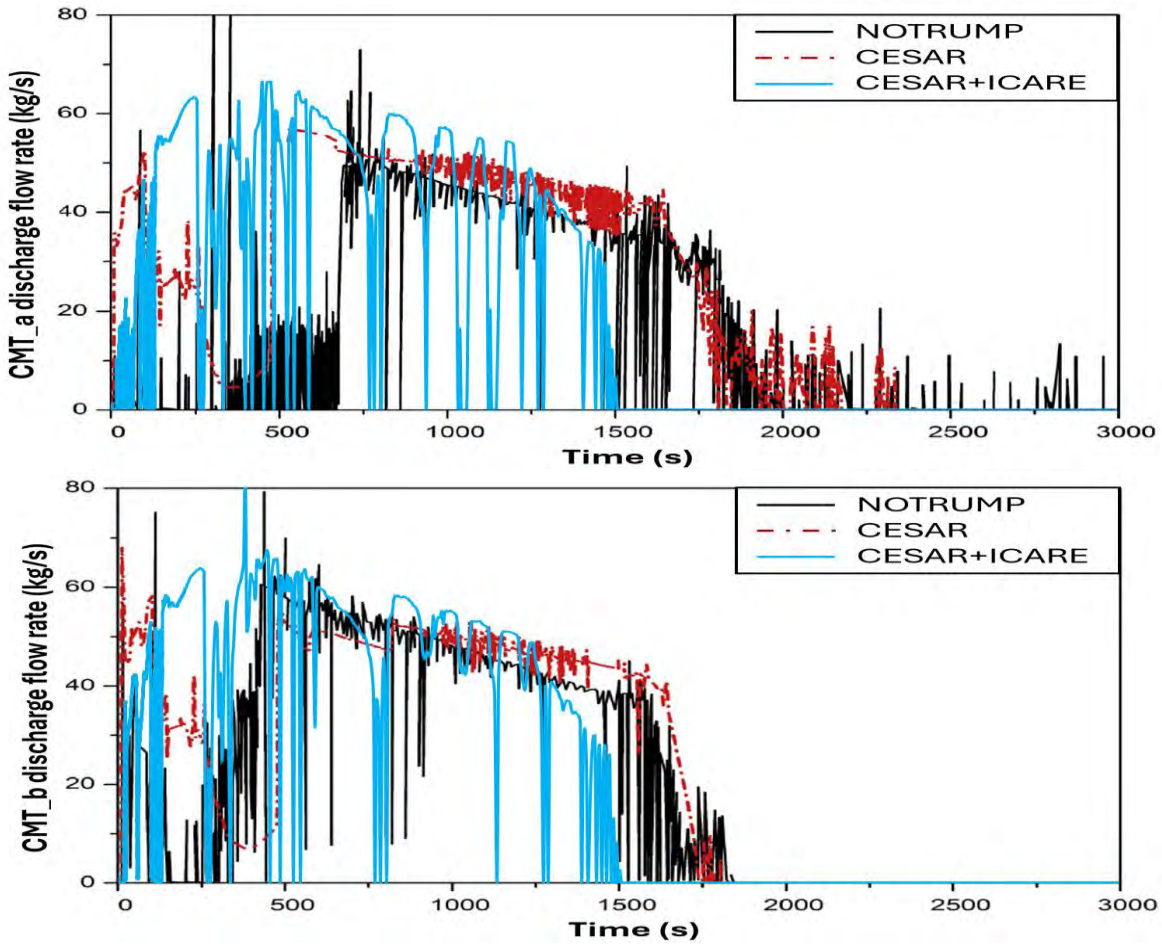

The flow circulations in CMT_a & b loops start the emergency water injection in the first few mins before RCS pressure drop to ACC actuation pressure.

* Extended Study of Reactor Coolant Pump Coastdown Phenomenon with RELAP/Mod3

AP1000 SB-LOCA Simulation: ACC & IRWST Injections and ADS

- The series of ADS_1/2/3 actuations at 67.5% CMT water level re-accelerates RCS pressure drop and ACC discharge flow rate starts to increase.
- When the water level in the CMT reaches 20 %, additional RCS depressurizations by ADS_4, which guarantee the long-term cooling water injection from IRWST is triggered before CMT water is depleted.

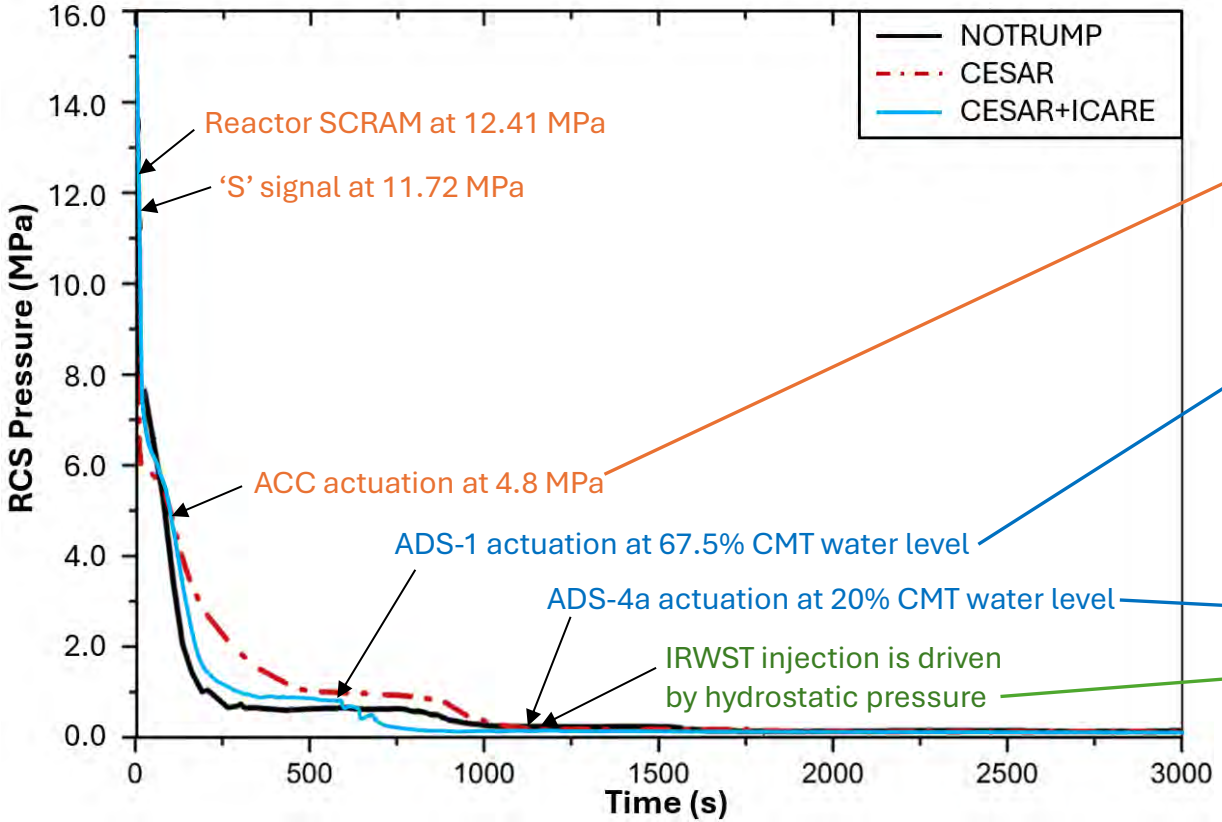

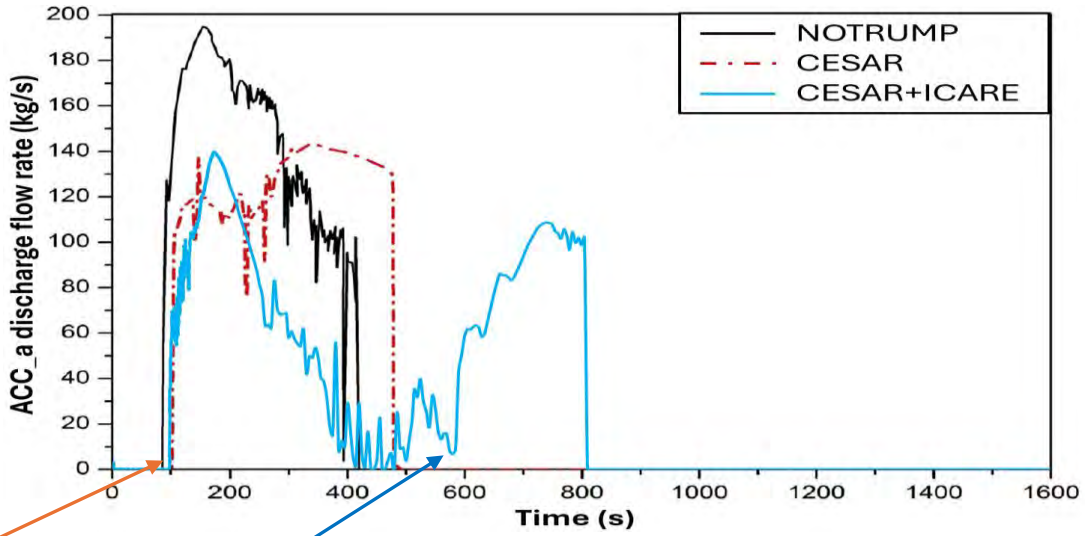

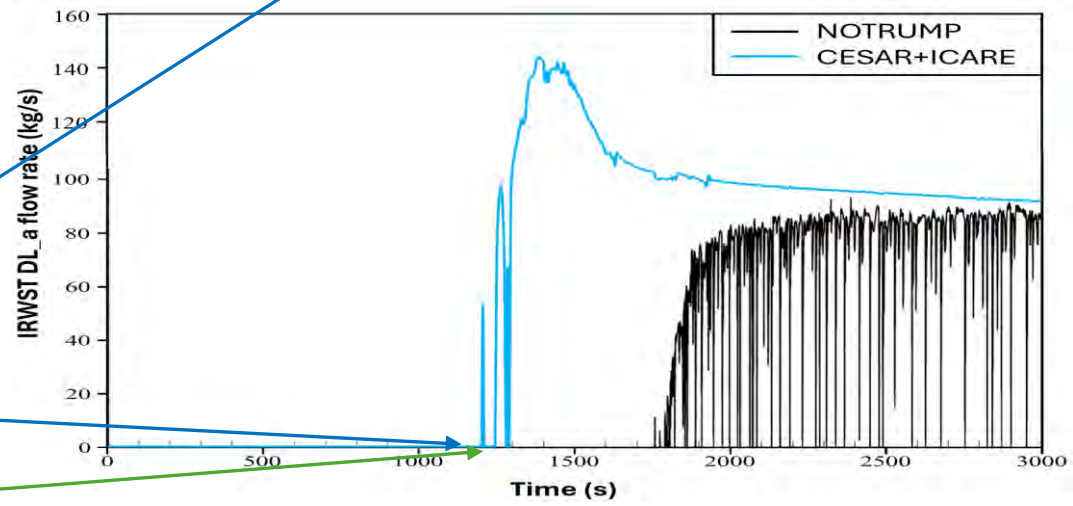

AP1000 SB-LOCA Simulation: DVI Injection

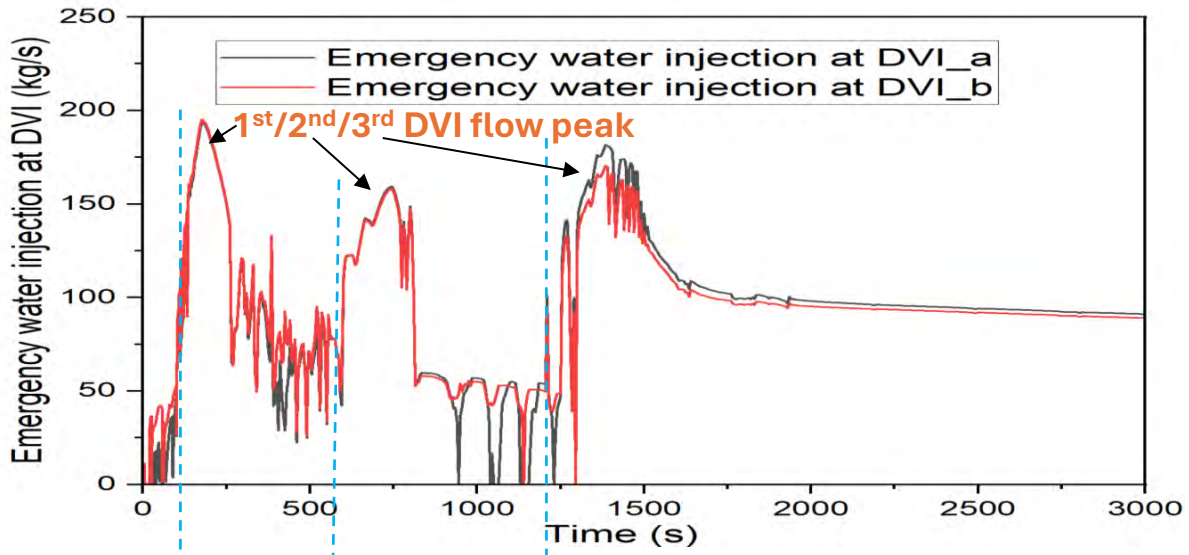

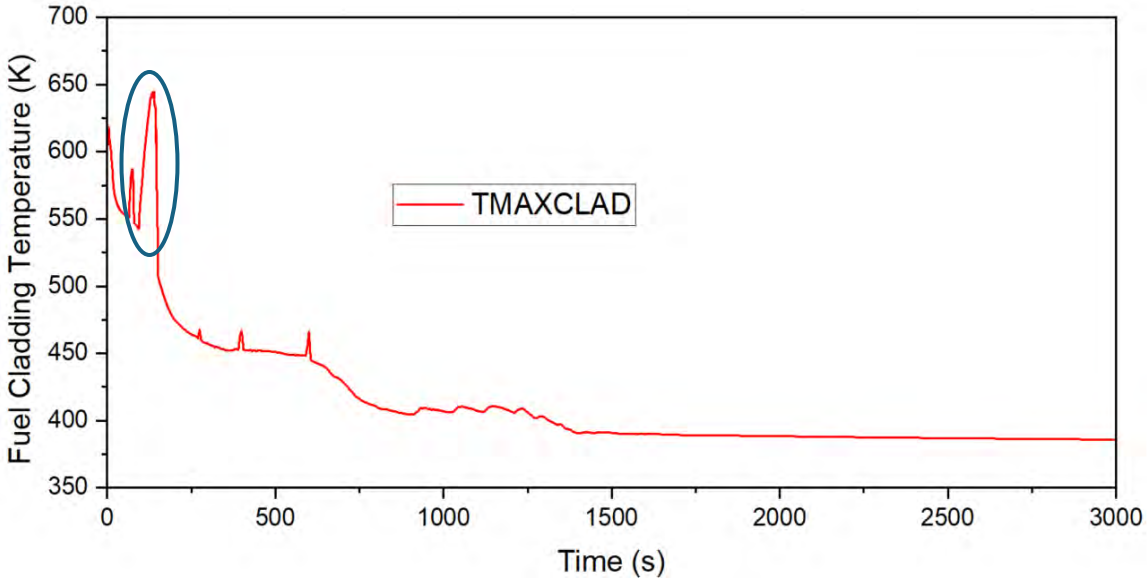

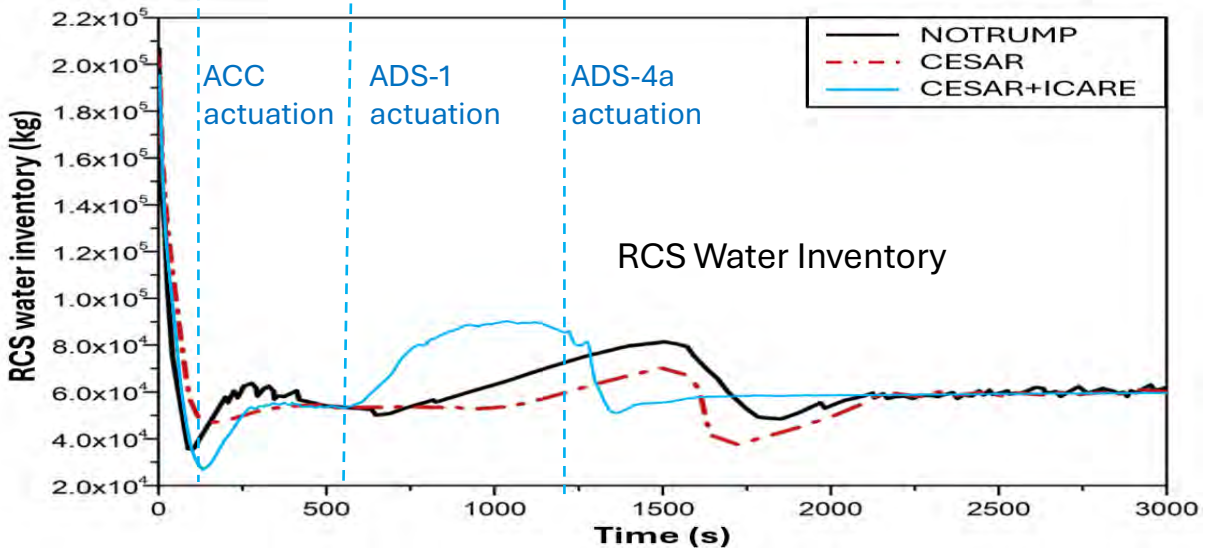

The CMT, ACC and IRWST work together with ADS_1/2/3/4 to guarantee **continuous water injection** from the DVI after pipe-break. The fuel cladding temperature is well controlled with maximum temperature remaining **below 650 K**.

- The **1st DVI flow peak** brought about by ACC actuation successfully reverses the RCS water inventory decrease and re-wets the fuel cladding surface.
- The **2nd DVI flow peak** following ACC injection after ADS_1 is triggered at ~580.2 s contributes to the RCS water inventory step.
- The **3rd DVI flow peak** at the beginning of IRWST discharge compensates for the massive water loss due to ADS_4a/b ruptures.

NUS National University of Singapore | Singapore Nuclear Research and Safety Institute

AP1000 PCS and Long-term Cooling Cut-off

* Status of dynamic water film model development in 3-D CFD code GASFLOW-MPI for analysis of passive containment cooling system

- In the AP1000 design, steam leaking through ADS_1/2/3/4 and the piping break will be cooled and condenses on the steel containment vessel inner surface by the passive containment cooling system(PCS) for at least 72 hours. Driven by gravity, the condensate collected in the sump flows back to the RPV via the IRWST discharge line.
- The steel containment vessel(Thk: 41.2~44.5mm) works as the 3rd barrier—both in retaining radioactive materials and in serving as the ultimate heat sink, which could provide long-term cooling water for a submerged reactor core.
- A shield building with reinforced concrete structure is designed surrounding the steel containment vessel to provide structural protection against severe weather or aircraft impacts(withstand a large commercial aircraft crash), and passive cooling functionality.
- Some security conditions, such as **drone attacking**, should be given more attention as it may bypass the shield building and directly attack at the weak points from inside, such as the water distribution system and air baffle of PCS.

NUS National University of Singapore | Singapore Nuclear Research and Safety Institute

AP1000 SB-LOCA Simulation: Long Term Core Cooling Cut-off

Assuming PCS malfunctioning and IRWST water supply from containment condensation is completely cut-off, the IRWST water storage could maintains 6~7 h injection. As IRWST water injection flow decline, water temperature in the reactor core gradually increases. The boiling region spreads towards reactor core bottom and void fractions in reactor core upper section approaches to 1.

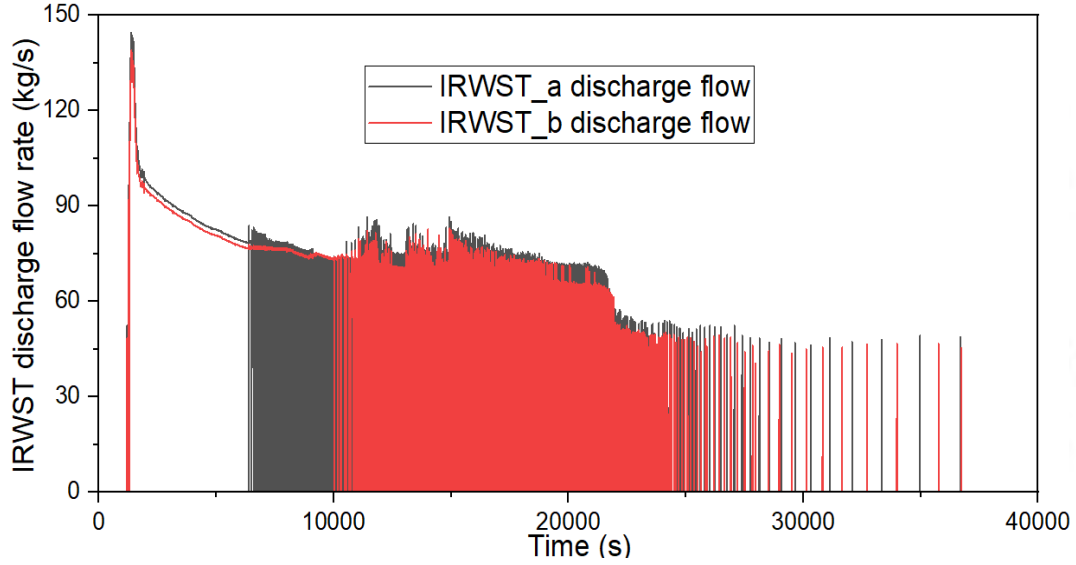

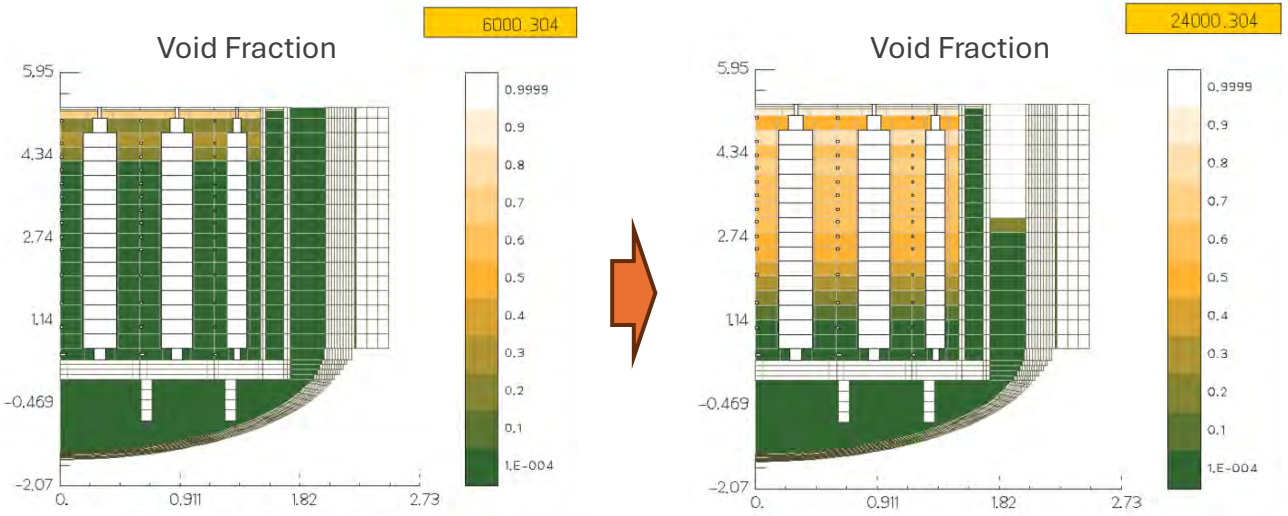

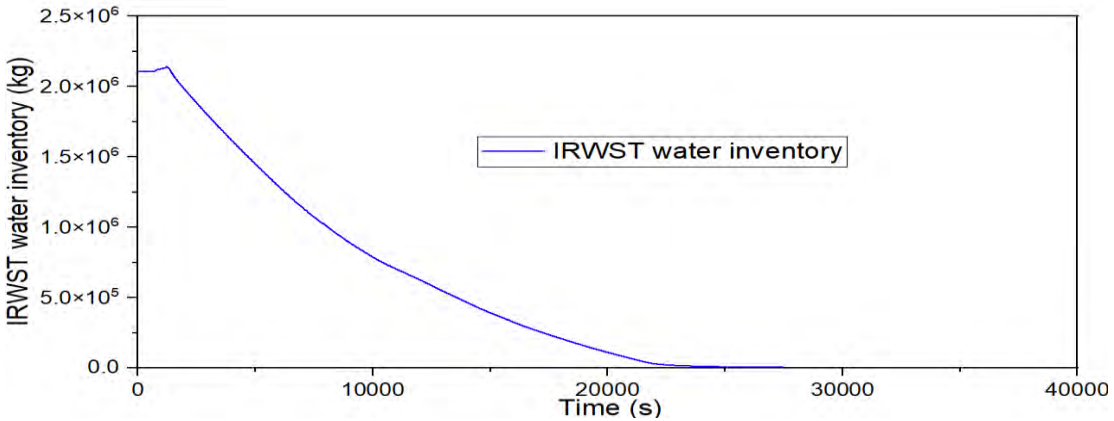

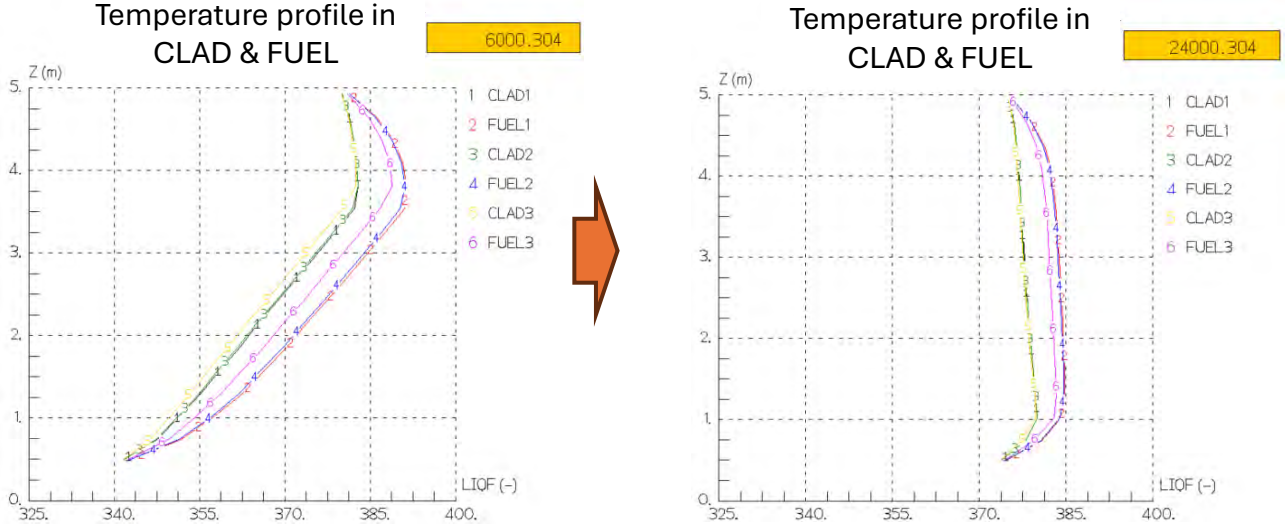

AP1000 SB-LOCA Simulation: In-vessel core degradation

Temperature Field in Core

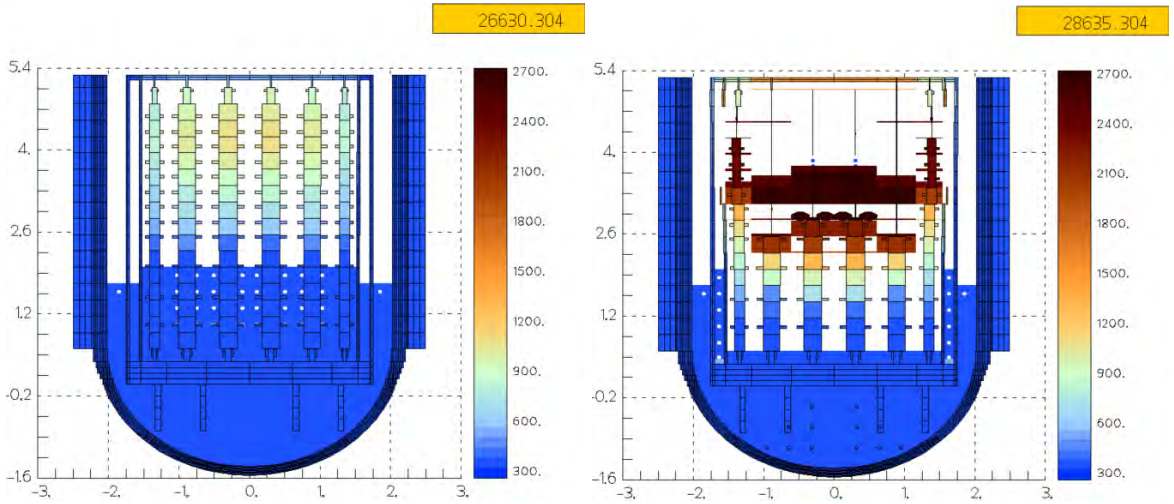

Temperature Profile in CLAD and FUEL

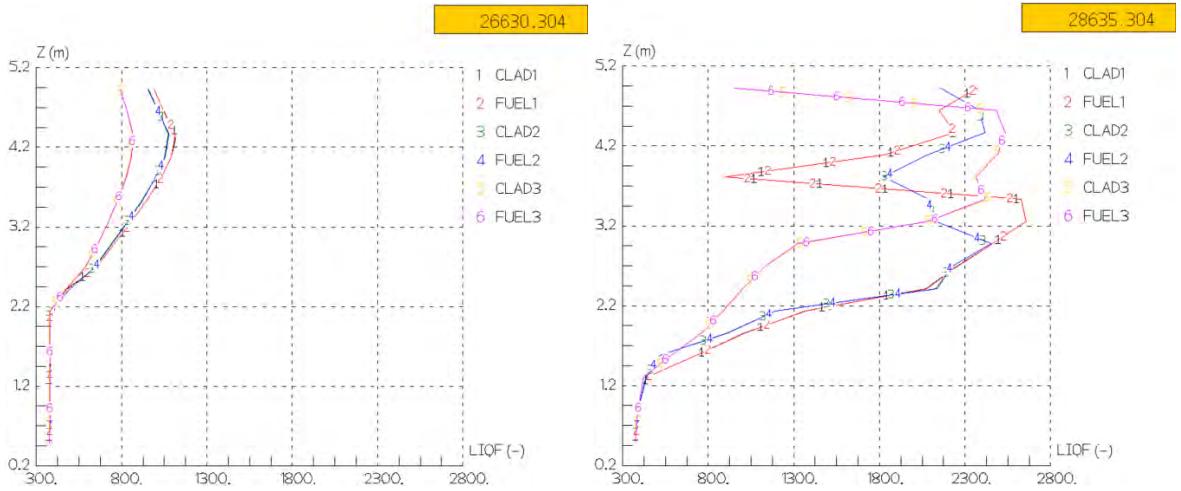

Time (s)	Event
26630.3	First cladding creep rupture Start of FPs release from fuel pellets
26915.3	Start of structural material release
27990.3	First material slump in lower plenum

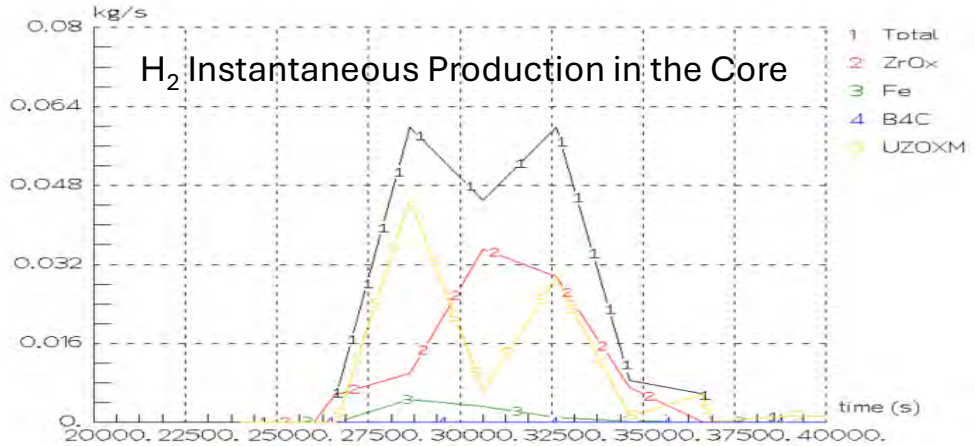

Sump water injection is not considered in current Calc. The reactor core water level decreasing is irreversible after IRWST water depleted. The upper section of the core begins to overheat due to reduced heat transfer with diminishing steam flow and fewer entrained water droplets. Oxidation reaction speeds up on high-temperature Zr cladding and steel vessel structure surfaces when fuel cladding and vessel structure temperatures exceed ~1200 K. The exothermic reaction between Zr and steam aggravates fuel cladding failure and generates massive hydrogen.

AP1000 SB-LOCA Simulation: In-vessel core degradation

In this study, lower head external cooling by water in cavity is excluded. With molten corium gradually slumping to the lower plenum, a molten corium pool is formed with light metal layer on the top. The lower head wall suffers from high heat flux from light metal layer and its deadweight, which induces vessel rupture at the molten corium pool surface level, ~4h after IRWST water depleted.

Time (s)	Event
32635.3	First slump of corium with FPs in lower plenum
36858.8	Lower head vessel failure Corium flows out of the lower head
38931.8	Lower head vessel collapse

Temperature Field in Core

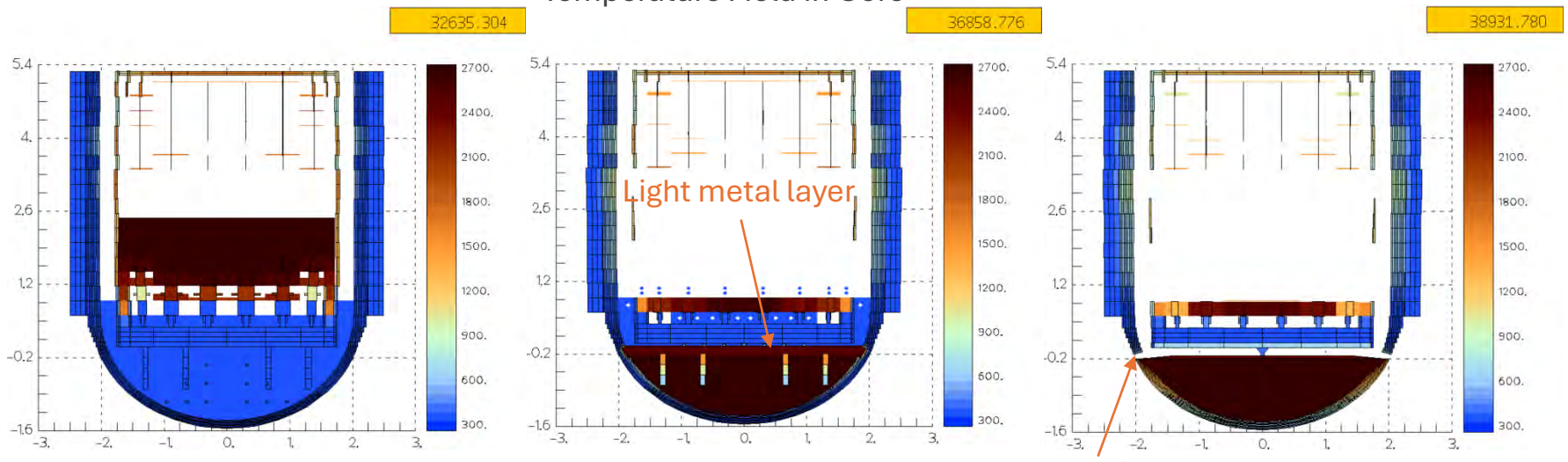

Temperature Profile in CLAD and FUEL

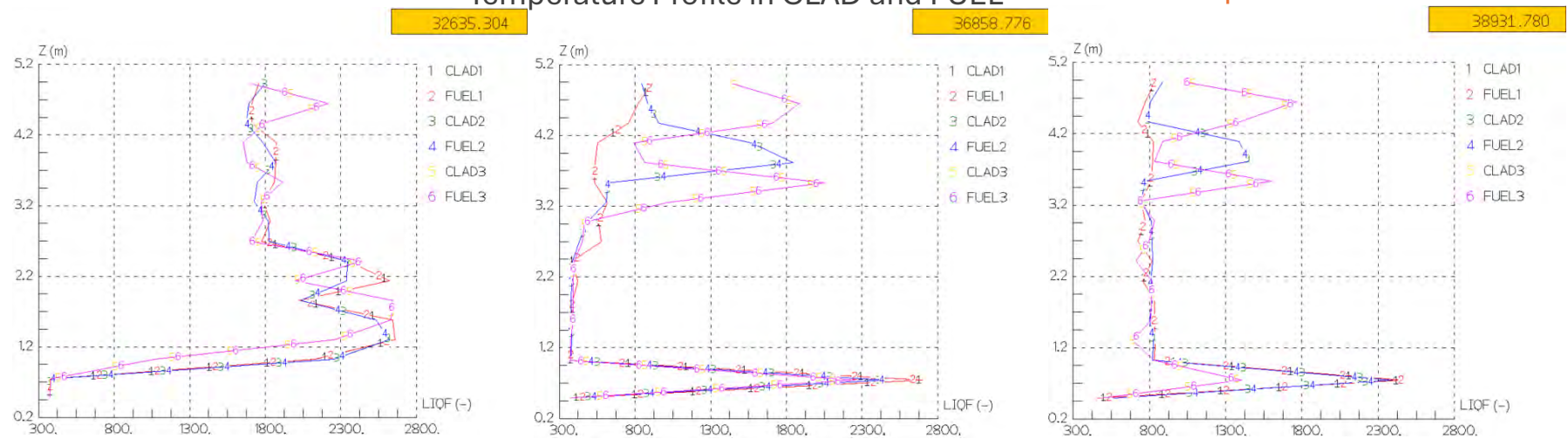

AP1000 SB-LOCA Simulation: Source Term

Source Term Analysis
Lower head vessel failure • **Ductile failure based on Oeuf model** • **H_2 mass produced during in-vessel phase = 510.926 kg** • **Aerosol mass produced during in-vessel phase = 9086.69 kg**

- If the drone attack disrupted the integrity of steel containment vessel, massive radioactive material released from the reactor core would easily bypass the steel containment vessel and disperse into environment.

H_2 Production in the Core

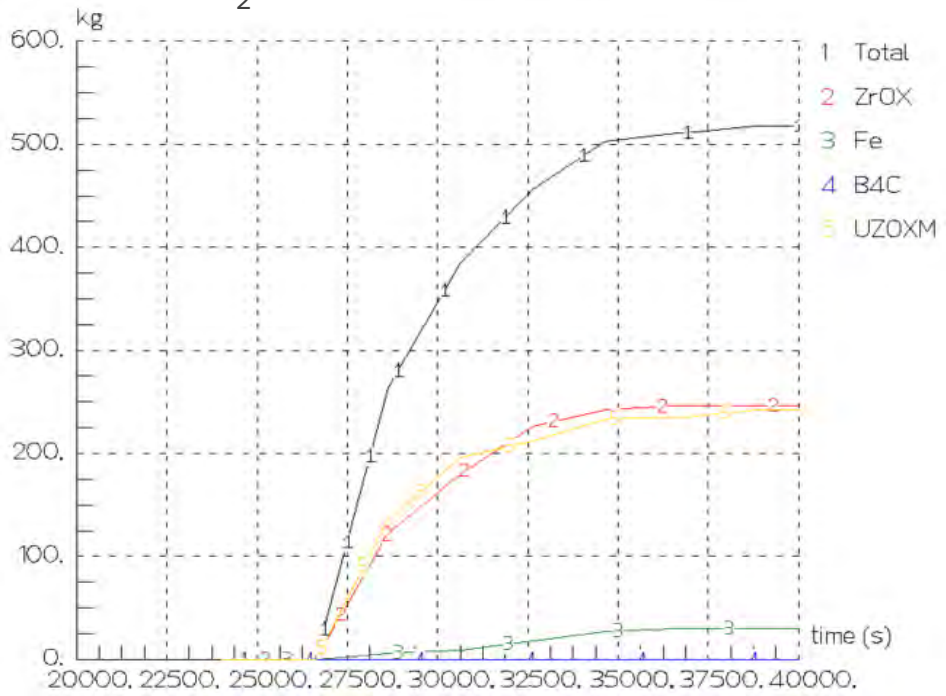

Cs, I, Xe Releases

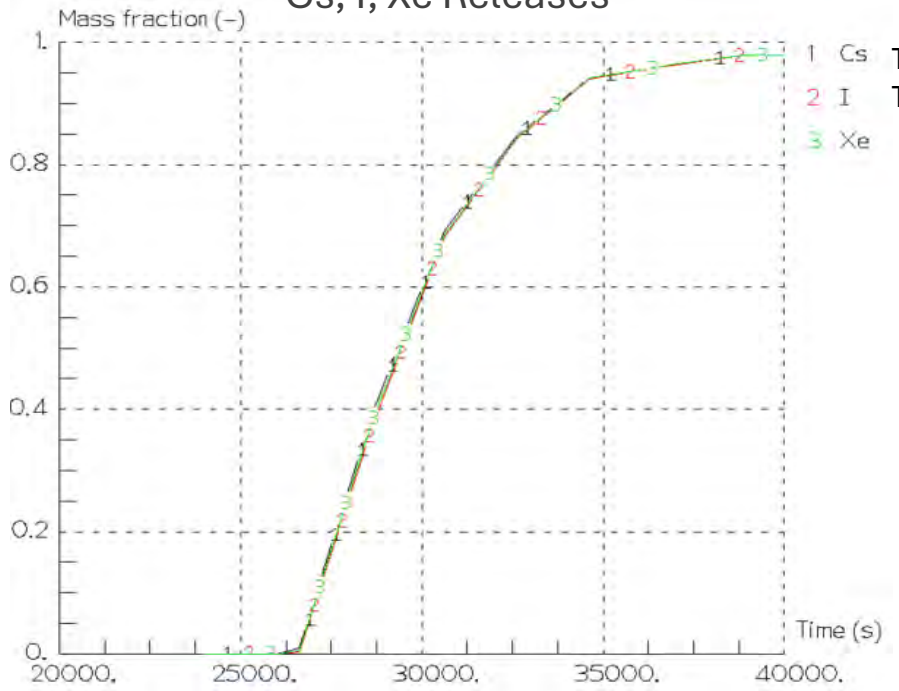

Total Cs: ~230.59 kg
Total I: ~ 17.71 kg

Conclusions

- The AP1000 and its safety systems are modelled in ASTEC. The thermohydraulic performance of passive safety systems in the 10-inch SB-LOCA are simulated, which shows reasonable agreement with NOTRUMP results in the AP1000 DCD Rev. 19 and CESAR/ASTEC work by M. Di Giuli.
- The ADS depressurization design plays an important role in maintaining ACC discharge flow rate and actuating IRWST injection before CMT water is depleted. The PXS in combination with the ADS guarantee continuous emergency injection from less than 15 s after the pipe-break until ~7 h, effectively slowing down reactor core water level decline rate and preventing fuel and cladding from overheating.
- In case the passive cooling functionality of shield building was seriously destroyed, the IRWST long-term cooling water supply from containment condensation would be cut-off and the reactor core meltdown progress would not be terminated w/o SAMP. The possibility and risk of drone attacking on AP1000 PCS from shield building inside should be given more attention.

NUS National University of Singapore | Singapore Nuclear Research and Safety Institute

Any Questions or Conclusion?

AP1000 SB-LOCA Simulation: Lower Head Failure w Ex-Vessel Cooling

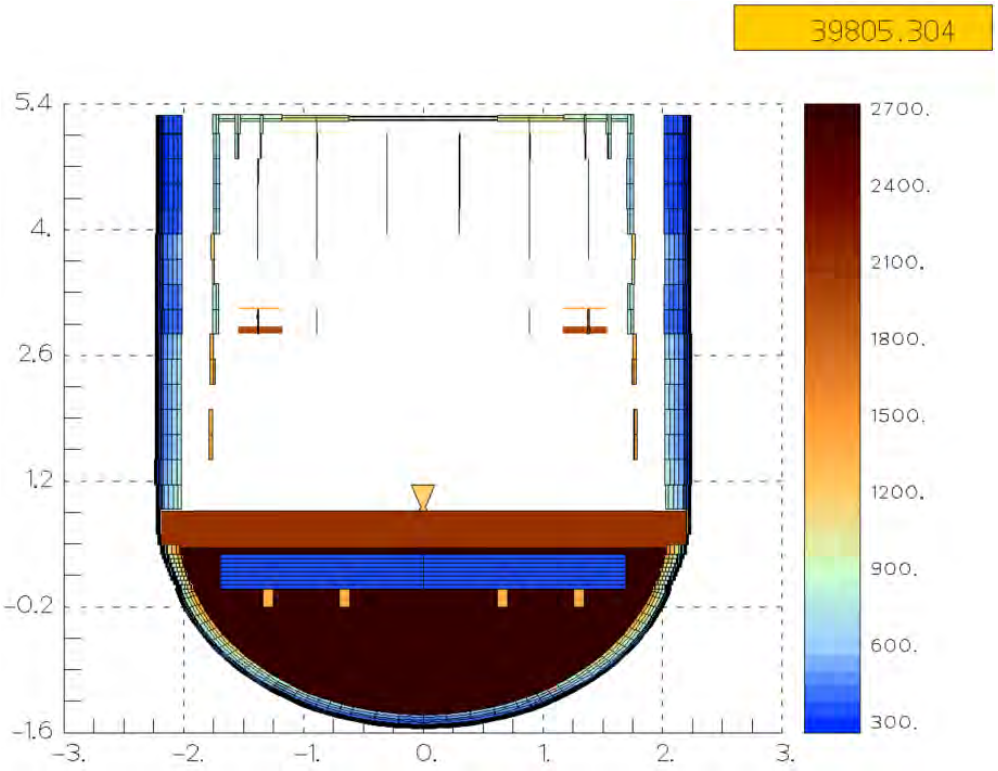

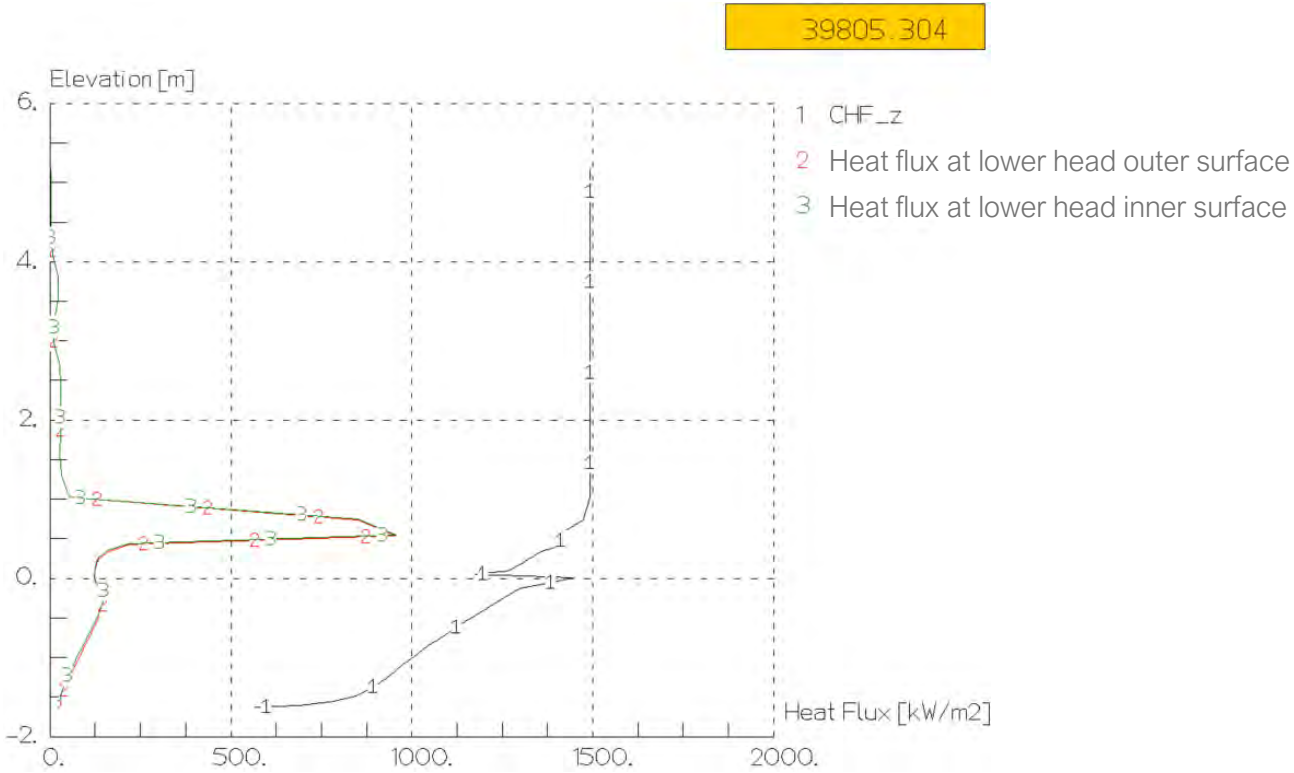

With Ex-Vessel cooling water flow rate setting at 200 kg/s in the ERVC channel, the lower head failure is postponed for ~ 1 h.

INSTRUMENTATION SURVIVABILITY ASSESSMENT DURING A SEVERE ACCIDENT; INCORPORATING RADIATION MONITORING IN MELCOR TO EVALUATE THE IMPACT ON SAMGs

Fernández-Cosials K.*, Rivilla R. and Queral C.
Department of Energy and Fuels
Universidad Politécnica de Madrid
*: Kevin.fcosials@upm.es

Robledo F.
Consejo de Seguridad Nuclear (CSN)

ABSTRACT

The instrumentation of a nuclear power plant is a vital element in the management of any accidental sequence, as its wrong behavior can lead control and protection systems or plant operators to take non-optimal or even incorrect actions. This makes the analysis of the instrumentation performance under severe accident (SA) conditions, as well as other SSC (Structures, Systems and Components), currently one of the most relevant aspects of nuclear safety. In Generation-II plants, the instrumentation is licensed using a pressure and temperature profile as expected during design basis accidents. After core degradation, the SA phenomena are not considered on its design limits. During a SA, it is likely that the pressure, temperature or dose rate range and physical limits of the instrumentation is exceeded, and therefore, their measurements may not be reliable throughout the remaining accident development. As those measurements may be used to mitigate the consequences of the SA, its correct use or interpretation can make a difference in the accident management.
For this reason, a methodology for instrumentation survival and assessment is proposed. It consists of the identification of the mitigation actions to perform together with the parameters that trigger its initiation and the instrumentation required for its development. The damage condition of the instruments is assessed in a continuous manner during the accident, rather than a binary state (function/not function). As a continuation of a previous study the monitoring of radiation is included in a continuous manner, besides thermal-hydraulic parameters extracted from the MELCOR output. The radiation monitoring program used will be released as an open source for other MELCOR users. The impact of the instrumentation degradation is then applied to a Station Black-Out simulation, identifying sources of measurement errors and its effect on the performance of Severe Accident Guidelines actions.

KEYWORDS
Instrumentation Survivability; Dose damage; SAMGs.

1. INTRODUCTION

During a Severe Accident (SA), the correct functioning and interpretation of the instrumentation plays a vital role in the evolution of such [1]. It can be argued that in both, TMI-II and Fukushima Unit-1, the correct interpretation of faulty instrumentation would have modified the accident pace, [2]. During an accident progression, while initially applying Emergency Response Guidelines (ERG), the harsh containment conditions are taken into account in the instrumentation values and additional uncertainties due to accident-induced factors such as elevated temperature, pressure, and radiation are incorporated. These adverse-condition uncertainties are conservatively combined to represent limiting instrument deviations. The use of separate normal and adverse setpoint minimizes unnecessary uncertainty during normal operation while ensuring conservatism under post-accident conditions. In particular, a recalibration procedure normally

occurs after an accumulated certain dose in the instruments to account for a higher uncertainty. The transition between these regimes is plant-specific and is determined by the environmental sensitivity of qualified equipment.

Nevertheless, if the accident progresses to core damage and into the Severe Accident Management Guidelines (SAMGs) the instrumentation is assessed in a survivability approach as the environmental conditions exceed those of the design basis. The most common manner to approach instrumentation survivability is to divide the severe accident in different phases and assume a binary status for the instrumentation, failed-not failed. Assessment of temperature, pressure, humidity limits and other casuistic are taken into account. Previous survivability analysis applied to different technologies of such can be found in [3], [4], [5], [6], [7].

Other more complex approaches, evaluate the status of the instrumentation in a continuous manner along the transient, as well as including a range of failures by the instruments, instead of a binary approach, [8]. Nonetheless, this last methodology lacked the dose rate as important parameter affecting the instrumentation performance [9].

The dose received by the instrumentation during a SA could reach very large values. The environmental qualification of instrumentation already takes the dose into account as a limiting value for Design Basis Events, [10], [11]. Typical values for these doses rates can range between 10 to 10^6 Rads/h (0.1 to 10^4 Gy/h), [12]. As mentioned, radiation generates degradation of electronics which is attributed to mainly total ionizing dose, and ionizing dose-rate due to gamma rays. The displacement damage and total ionizing dose effect are both accumulated effects on the electronics, whereas dose-rate effects are typically of a transient nature but can cause permanent damage to devices.

The assessment of the in-containment dose during a SA is not commonly shown in SA research studies. Many conventional SA codes do not directly calculate this dose and post-processing of data must be done. In the study of [13], the gamma dose is calculated using MELCOR, reaching 1-100 MRads (10^4 to 10^6 Gy); but the procedure for such calculation is not entirely provided. Other studies using ASTEC code which has a specific module for dose calculation do show the activity but they do not the in-containment dose, [14], [15].

In this study, a comprehensive methodology to assess the instrumentation survivability during a severe accident that incorporates radiation damage will be presented. The detailed calculation of the instrumentation dose rate will be described, and the code used will be made available for the general public to use. The methodology will be applied to a Station Black-Out (SBO) scenario in a Boiling Water Reactor (BWR) using the MELCOR code.

The paper proceeds as follows: first, a short introduction to the state of the art is made (Section 1). Second, a description of the MELCOR BWR model and Dose calculation tool is provided in Section 2. Third, a summary of the SAMGs applied to a BWR is reported (Section 3). Then, the results of the methodology applied to a SBO are described in Section 4. Finally, conclusions are drawn (Section 5).

2. MELCOR Model and Dose Calculation

2.1. MELCOR BWR modelling

The MELCOR code is a fully integrated, engineering level computer code, capable of modeling accident phenomena in Light Water Reactors (LWRs). Sandia National Laboratories (SNL) developed it for the U.S. Nuclear Regulatory Commission for SA analysis, initially for Probabilistic Safety Assessment level 2. The MELCOR capabilities include the simulation of thermal-hydraulic behaviors of Reactor Coolant System

(RCS) and containment, core damage process, relocation, molten core concrete interaction, behavior of fission products or hydrogen generation, among others, [16]. Currently, MELCOR and other SA codes, are subject of research such as SOARCA, MUSA, SASPAM-SA [17] and IAEA CRP "Advancing the State-of-Practice in Uncertainty and Sensitivity Methodologies for Severe Accident Analysis in Water-Cooled Reactors" projects which are focused on identifying and quantifying uncertainty sources in SA analyses, [18], [19].

The model reproduced in MELCOR is a BWR/6 Mark III generic reactor. The model has been used in previous research, [20]. It includes control volumes for RCS as the recirculation pumps and loops (RCL), core bypass, channel, separators, upper head (UH), lower head (LH), annulus (AN) and core active region among others, the nodalization can be seen in Figure 1. The RCS coolant is initially at 562 K and the initial RPV level is 14.1 m. The containment model is separated into 8 control volumes including the reactor cavity (CA), drywell (DW), wetwell (WW), Weir Annulus, Compartment A of containment (CTA, which corresponds to the Containment Rooms) and Compartment B of containment (CTB, including Upper Pool and near Dome), Upper Dome (UD) [21], and an external volume for the environment, Figure 1. The Auxiliary Building (AB) is not included in the model, and the instrumentation located there is not expected to suffer any damage in this analysis. The main instrumentation of the plant is located in its correspondent control volume and are modelled with a small thermal conductor to account for thermal inertia.

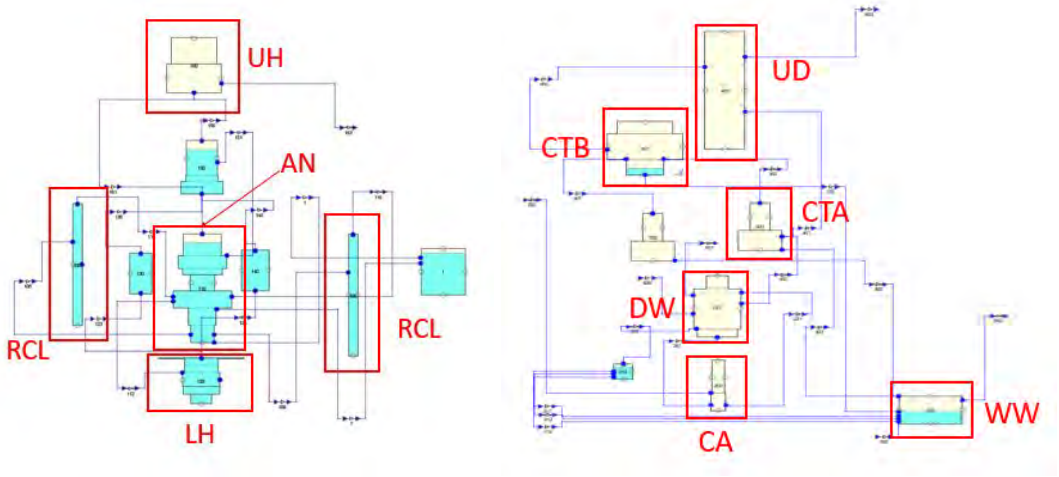

Figure 1. MELCOR Nodalization of the BWR/6 RCS (left) and Mark-III containment (right)

2.2. In-containment Dose Calculation with MELCOR: RadSim development

In order to calculate amount of each radioisotope in containment, the MELCOR code can be supposedly standalone used to provide a result. Based on an initial fission products inventory (provided by the user), the BONUS module can provide with the activities [22]. Nonetheless, utilization of such features is absent in the open literature and therefore, the authors tried to develop a user-friendly post-processing tool that uses open materials for radioactive chains, radiation energy and fission products inventory; this program has been named "RadSim" and is set as an open-source python code. The length limit of this paper prevents for a very detailed description of the code.

The objective of RadSim is to use the amount of a RN class provided by the MELCOR output file, and then directly calculate the dose found in the different control volumes, either in the RCS or containment, as seen in Figure 1. The flowchart of the working procedure of RadSim is shown in Figure 2. Initially, the initial proportion of isotopes the JEFF 3.3 nuclear data library, available through the JANIS platform, has been used as a reference [23]. From this database, only those isotopes whose thermal uranium-235 fission yield

is greater than 0.008 were selected. Based on this criterion, a total of 180 isotopes were identified and included in the analysis. The new proportions for each class are calculated by dividing the yield of each isotope by the sum of the yields of all isotopes belonging to the same class. In this way, it is ensured that the sum of proportions within each class equals 1, and that the initial distribution realistically reflects the relative contribution of each isotope according to experimental fission data. Once these proportions are determined, the mass of each class, which is directly imported from MELCOR, is distributed according to these coefficients.

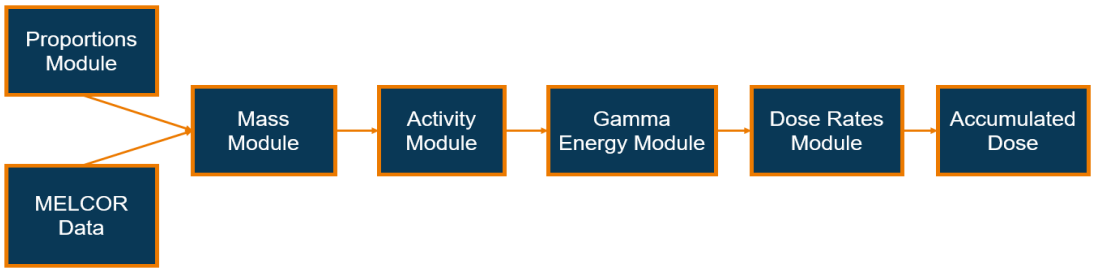

Figure 2. RadSim working scheme

The decay calculation starts from the moment when the chain reaction is terminated. If the reactor shutdown is successful, the neutron flux is interrupted, and the proportions at that instant evolve only through radioactive decay processes until the end of the simulation. For this process, the Python open source library "*radioactivedecay*" is used, which makes it possible to calculate with precision the evolution of masses and isotopic composition over time [24]. The isotopes that appear due to decay but also belong to another class in the list remain in the class where their precursors appeared, in order to avoid overlaps between classes and simplify the processing. This is an assumption that is done by MELCOR in different calculations, and it is maintained in RadSim. A dictionary is created assigning a gamma energy to each isotope. The gamma energy is the value in MeV that corresponds to the gamma emission of each radionuclide. This energy is the characteristic value of the gamma rays emitted by that nucleus. The values have been taken directly from the JEFF 3.3 library available in JANIS. Similar procedure is made for beta emissions.

For the dose calculation, the beta emissions due to their low penetration capability, their contributions are associated with the bremsstrahlung rays created during its scattering. The photonic dose rate will be defined as in [22]:

$$D^{\gamma}{}_{i} = (5.77 \cdot 10^{-5})\emptyset_i E_i \left(\frac{\mu_{a,i}}{\rho}\right)_{air}$$

Where $D^{\gamma}{}_{i}$ is the absorbed gamma dose rate of isotope i (Rads/h), $\emptyset_i$ is the gamma flux of isotope i (1/ (cm^2 s)), E_i is the gamma ray energy of the isotope i (MeV) and μ is the mass absorption coefficient for air to energy E_i, it is defined as follows, as in [22]:

$$\left(\frac{\mu_{a,i}}{\rho}\right)_{air} = a + bE + c[\ln(E)]^2 + d\sqrt{E} + e[\ln(E)]$$

For the mass attenuation coefficient, the coefficient will be defined as:

$$\left(\frac{\mu_{s,i}}{\rho}\right)_{air} = f + gE^h$$

To calculate the gamma flux on the different control volumes, four different geometrical approaches are provided: homogeneous sphere, circular source, shielding and point source. In the homogeneous sphere hypothesis, the volume where the isotopes are distributed uniformly is equivalent to the control volume from MELCOR. Different distances can be defined in the script for the different hypothesis. The intent of the shielding approach is to simulate a cable so thick polymer layer has been used to simulate it, and the mass attenuation coefficients for that material have been taken from [25].

The code will be available in an open-source repository in GitHub and it is expected that MELCOR user's community engage with the tool for further enhancements or improvements.

3. SAMGs feasibilities and Instrumentation in a BWR

The Severe Accident Management Guidelines (SAMGs) are a structured set of guidelines developed to support decision-making during severe accidents, when the plant is no longer within the scope of normal or emergency operating procedures. In conventional Boiling Water Reactors (BWRs), the SAMGs are organized around the control of specific variables in defined plant areas.

In general, two main Severe Accident Guidance (SAG) are defined [26], [27], [28]: SAG-1 (RPV and Primary Containment Flooding), dedicated to vessel and containment flooding strategies, and SAG-2 (Containment and Radioactivity Release control), focused on containment control and fission product release management. Each includes several sub-guides addressing specific conditions or parameters to be monitored. The SAMGs are supported by the Technical Support Guidelines (TSGs), which provide detailed data, limit values, and technical references to justify and document the decisions taken during accident management.

When a BWR accident enters SA, control is formally transferred from the main control room to the Technical Support Center (TSC). This transition marks the activation of the SAMGs. TSC becomes responsible for assessing plant conditions and determining the most appropriate recovery strategies. Within this framework, Candidate High-Level Actions (CHLAs) are evaluated as potential measures to mitigate the consequences such as vessel flooding, containment venting, or boron injection, depending on the plant state [29]. To implement SAMGs effectively, it is essential to have an accurate understanding of the plant condition at every stage of the accident. This requires the continuous availability and reliability of the instrumentation, which provides the critical data needed to support decision-making within the SAMGs. As seen during the Fukushima accident, not having access to plant variables, or being that information corrupted, can lead to worst outcomes [30].

In this work, a detailed analysis of all SAMGs was carried out to identify the variables required for the correct CHLA implementation. In some cases, the need for certain variables is explicit within the guide itself, while in others it becomes evident through the TSGs that appear at specific steps of the procedure. These supporting documents introduce additional information or criteria that depend on variables not directly mentioned in the main guide but still necessary for decision-making.

By considering both levels of information, it was possible to determine the complete set of parameters that must be known simultaneously to assess the evolution of the plant and the capability to follow each guide. In total, sixteen key variables were identified as necessary for the proper application of the SAMGs, namely: DW temperature, DW pressure, containment radiation, containment hydrogen concentration, boron tank level, injected flow to the RPV, RPV level, RPV pressure, RPV temperature, containment pressure, containment (suppression pool) level, suppression pool pressure, suppression pool temperature, SRV position, reactor power, and containment temperature.

In SAG-1, these variables are used in the generic sub-guides (RC/F-1, RC/F-2, RC/F-3, RC/F-4, RC/F-5, RC/P and RC/Q), while in SAG-2 they support the decision-making process in other sub-guides (CN/T, DW/T, PC/H, PC/P, PC/R, SP/L and SP/T).

For this study, a review of SAG sources [31], [32], [33], [34] was carried out to identify the instrumentation typically available in a BWR Mark III. Based on this information, the location of each instrument was established in a reference plant and then linked to the corresponding control volumes of the BWR model implemented in MELCOR, which was used for the analysis. From this mapping, the instruments considered relevant for severe accident conditions were selected, identifying those capable of providing the measurements required to follow the SAMGs.

The following table presents the variables to be monitored, the corresponding instruments that could measure them, and the control volume of the model where each would be located. These control volumes represent real plant locations. Instrumentation assigned to the auxiliary building correspond to devices that, according to the reviewed sources, are located outside the containment. It should be noted that some instruments identified as potentially useful do not measure the variable directly but can provide indirect indications or allow their estimation, which under SA conditions can still offer valuable information for decision-making.

VARIABLES	INSTRUMENTATION	VARIABLES	INSTRUMENTATION
DW TEMPERATURE	DW Thermocouples (DW) CTA Thermocouples (CTA) SP Thermocouples (WW)	RPV TEMPERATURE	UH Vessel Thermocouples (UH) LH Vessel Thermocouples (LH) FW Thermocouples (LH) Suction Pipes Thermocouples (RCL)
DW PRESSURE	DW Pressure Transmitters (DW/CTA) CTA Pressure Transmitters (CTA)	CONTAINMENT PRESSURE	CTA Pressure Transmitters (CTA) DW Pressure Transmitters (DW/CTA)
CONTAINMENT RADIATION	CTA Radiation Detectors (CTA) DW Radiation Detectors (DW)	CONTAINMENT LEVEL	SP Level Transmitters (AB) SP Thermocouples (WW)
CONTAINMENT HYDROGEN	Containment Hydrogen Concentration Analyzer (AB) DW Hydrogen Concentration Analyzer (AB)	SP PRESSURE	SP Thermocouples (WW) CTA Pressure Transmitters (CTA) DW Pressure Transmitters (DW/CTA)
BORON TANK LEVEL	Boron Tank Level Transmitter (CTA) Boron Injection Pressure Transmitters (CTA)	SP TEMPERATURE	SP Thermocouples (WW) DW Thermocouples (DW) CTA Thermocouples (CTA)
INJECTED FLOW RPV	Feedwater Flow Transmitters (DW) HPCS Flow Transmitter (AB) Boron Injection Pressure Transmitters (CTA) Vessel Level - Wide Range (DW/CTA) Vessel Level - Fuel Range (DW/CTA) Feedwater Pressure Transmitters (AB)	SRV POSITION	SRV Position Indicators (DW)
REACTOR POWER	Average Power Range Monitors (AN) Control Rods Position (DW)	CONTAINMENT TEMPERATURE	CTA Thermocouples (CTA) DW Thermocouples (DW) SP Thermocouples (WW)
RPV LEVEL	Vessel Level (Wide Range) (DW/CTA) Vessel Level (Fuel Range) (DW/CTA)	RPV PRESSURE	Vessel Pressure Transmitters (DW/CTA) RCP Pressure Transmitters (RCL)

Table 1. Necessary or useful variables identified in SAMGs with the instrumentation and its location assignation

The assessment of instrumentation damage in a BWR during a severe accident requires a clear framework for characterizing the degradation of measurement capabilities as environmental conditions worsen. For this purpose, the present work adopts as reference the methodology established in the study presented in [8], where instrumentation performance in a PWR was evaluated under a SA. Five Damage Conditions (DC) were defined to classify the ability of each instrument to provide meaningful information as the accident progresses. These categories are fundamentally based on the concept of Environmental Qualification (EQ), and other relevant phenomena. EQ values, based on IEEE standards, define the boundary between normal

operating capability and progressive degradation, and constitute the basis upon which the DC classification is constructed.

The five Damage Conditions adopted in this study are presented in Table 2, which summarizes the meaning of each category and the corresponding degree of degradation in the instrumentation.

Instrument Damage Condition	Description
DC-1 (Normal Operating Conditions)	Normal operating conditions, suitable for measurement. They are within the EQ (Environmental Qualification) range and the readings are fully reliable.
DC-2 (Anomalous Operating Conditions I)	Challenging conditions or slightly above the EQ design, but the measurements are still useful both in trend and in value.
DC-3 (Anomalous Operating Conditions II)	The design limit has been significantly exceeded; the measurements are no longer valid in absolute value, although the information on trends and orders of magnitude is still useful.
DC-4 (Damaged Operating Conditions)	The measurements are only reliable in terms of trend, not quantitative or order magnitude information. In this state, the instrument cannot be recalibrated, and therefore, once level DC-4 is reached, it cannot decrease.
DC-5 (Destruction Conditions)	The measurements of such instrument have no value at all. Instrument is completely unusable, and it cannot and should not be employed for any measurement.

Table 2. Damage Conditions defined for the instrumentation

For pressure and temperature instrumentation, the DC used in this work were defined using the same environmental limits as in the reference study mentioned before [8]. The present analysis applies those same limits and thresholds to the instrumentation in the BWR, so that the Damage Conditions for these two variables are defined in a consistent and coherent way with the methodology presented in [8]. Other issues for instrumentation failure have also been considered, like the possibility of the evaporation of the reference column of water for the RPV level transmitters [30], or the failure of the hydrogen monitors due to the condensation that could led to a blockage on its sample line. This series of hypotheses has been established based on the methodology followed in [8].

In addition to those variables, this study includes radiation as an additional factor affecting instrumentation performance. To define the radiation-related damage levels, the environmental qualification values specified by IEEE standards 1974 for this variable have been used as the reference [10], [11]. Based on these values, five categories are established: DC-1, for doses below the IEEE qualification value; DC-2, for exposures between 1 and 4 times that value; DC-3, for doses between 4 and 7 times the IEEE limit; DC-4, for 7 to 10 times that value; and DC-5, for conditions exceeding 10 times the IEEE qualification value. This criterion is consistent with previous studies [35], [36], [37], which indicate that instrumentation operability is significantly degraded when the Total Integrated Dose (TID) reaches values on the order of several MGy (i.e., several hundreds of Mrads).

Table 3 shows the EQ values stablished by IEEE for radiation mentioned before [10], [11]. It represents the cumulative dose that instrumentation is design or qualified to support during a Design Basis Event (DBE) in the containment of a nuclear power plant. This values are expected to appeared in a DBE in a PWR. For BWR, the cumulated dose expected in the accident is 26 MRads according to IEEE but as the instrumentation available in both technologies is similar, and should resist both DBE, the most descriptive limits (the ones for PWR) have been selected to define EQ values and stablish DC.

Time	1h	12h	1 day	10 days	1 month	6 month	1 year
Cumulative Dose (Mrads)	4	20	24	40	55	110	150

Table 3. Environmental Qualification generic values for radiation stablished by the IEEE [ref]

4. Application to a Station Black-Out scenario

In this study, a severe accident scenario corresponding to a SBO has been simulated using the MELCOR code applied to a BWR Mark III. The Radionuclide (RN) MELCOR package, which performs the tracking of radionuclei classes throughout the control volumes of the model, has been used as input for RadSim. In this way, the rate and accumulated dose received by the different instrumentation in the different can be determined, see for example Figure 3. Using dose values together with the pressure, temperature and other conditions of the same volumes, the damage level of the instrumentation can be assessed. This allows the evaluation of SAMG decision paths according to the ability to monitor the parameters required in each guideline.

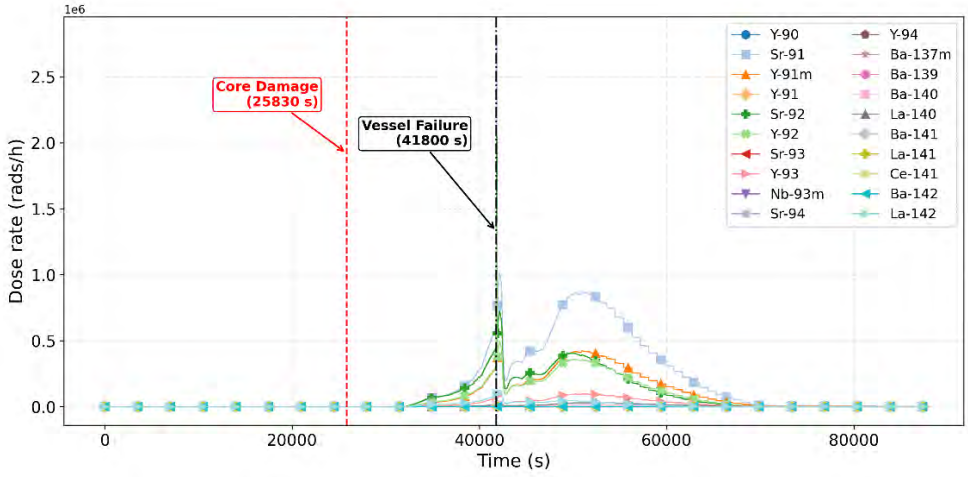

Figure 3. Dose Rate evolution of Class 3 isotopes at CTA considering the Point Source Hypothesis

The simulated sequence corresponds to a SBO case, in which the reactor loses all onsite and offsite power and relies initially on the Reactor Core Isolation Cooling (RCIC) system to control vessel inventory. Following reactor shutdown with residual decay heat, the RCIC system operates from the beginning of the event and maintains water injection until its failure is supposed at 15,000 s (e.g. due to battery discharge and loss of control of the RCIC). From that moment, with no further vessel makeup flow, the vessel water level begins to decrease and the core becomes progressively exposed, with initial uncovery occurring at approximately 22,000 s, marking the start of a rapid temperature escalation. As heat removal is no longer available, core temperatures rise sharply, and cladding temperature exceed 1477 K at around 27,000 s, indicating the onset of core damage. The degradation intensifies until 28,500 s, when conditions reach those associated with core melting. Due to restrictions in the article length, no detailed description of the accident is possible.

4.1 Instrumentation damage levels during the SBO sequence

The instrumentation will suffer degradation during the accident provoke by the extremely harsh condition that can be reached in different locations of the plant. The thresholds usually stablished are the EQ values defined for instrumentation [10], [11] in containment for these variables (422K and 0.41MPa), and it is assumed that if they are exceeded, those instruments will enter DC-2. Most instruments will fail once the vessel failure occurs, as the temperatures and pressures that will be reached in the environment will be so high that its failure is unavoidable. Although those conditions are temporary, caused by temporary peaks in those variables, they caused the instrumentation to reach DC-5 and no recovery of its operability is considered, as mentioned before.

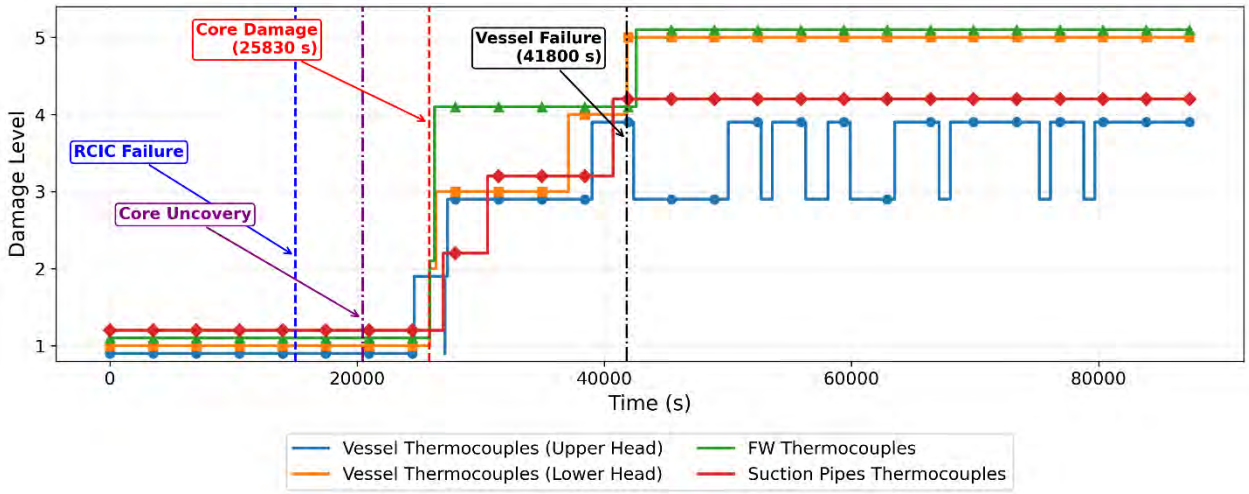

Figure 4. DC evolution of the instrumentation used to measure RPV Temperature considering temperature and pressure as the limiting variables

The main new feature of this analysis consists on the consideration of radiation as a new variable for evaluating the survivability of instrumentation. With the thresholds mentioned previously for defining instrumentation damage conditions in this study, radiation has resulted to be the most limiting variable during this sequence for many instruments, see Figure 4. Once the core melts and later on, vessel failure occurs, the accumulated doses reached in the different locations of the containment provoke the rapidly failure of all the instrumentation located in there (Figure 5).

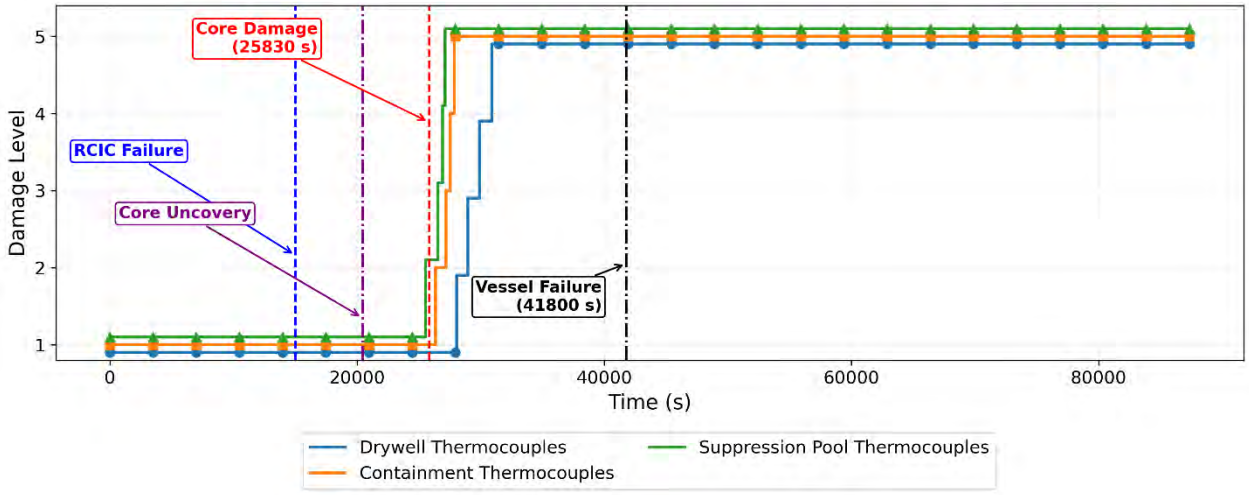

Figure 5. DC evolution of the instrumentation used to measure DW Temperature considering radiation as the limiting variable

4.2 Severe Accident Management Guidelines Availability assessment

In order to mitigate the consequences, the guides established to control in-vessel phenomenology during SA are located first in the priority scale. Actions in this guide (SAG-1) are developed for avoiding or controlling aspects like cladding oxidation and deformation, or core melting and relocation. If vessel failure is identified (RPV depressurization), the next group of guidelines (SAG-2) must be applied, which are responsible to mitigate the consequences of the containment phenomenology. The actions applied in these guides are designed to control the effects of phenomena like molten core relocation, molten core-concrete interaction, and, ultimately, containment integrity and fission products release. Their primary objective is to halt fuel degradation if it has already begun. If this cannot be achieved, the next goal is to preserve containment integrity for as long as possible, thereby increasing the available time to implement additional actions and strategies aimed at preventing the release of fission products. If these objectives also cannot be achieved, the SAMGs then focus on minimizing radioactive releases to the environment and reducing the overall impact of the accident.

For evaluating the availability to obtain the different measurements identified for the correct execution of the mitigating strategies, a classification method on the availability state of the instrumentation is defined. The availability states are established according to the Damage Condition (DC) reached by the instruments associated with each variable. A measurement is considered “Good” when all related instruments remain at DC-1, meaning they operate under normal conditions and provide reliable information. The state “Careful” is assigned when at least one instrument has reached DC-2, indicating initial degradation, although the measurement is still usable. The state “Warning” corresponds to situations in which one or more instruments have reached DC-3 or DC-4; in this case, the information may be affected, but it can still provide useful indications. Finally, the measurement is classified as “Blind” when all associated instruments reach DC-5, implying complete failure and total loss of information for that variable. See the availability state in Figures 6 and 7 for Pressure in the RPV and SP as examples. The intervals of time for which the availability state is identified as Careful or Warning are also shown in the figures.

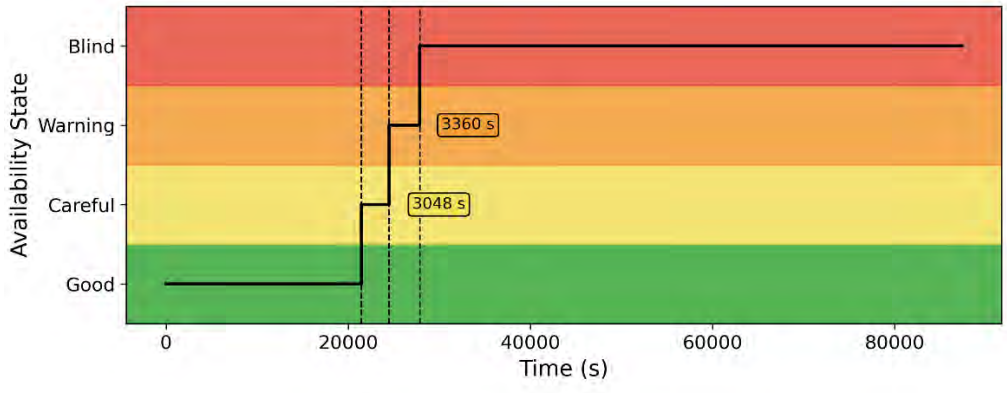

Figure 6. Availability to measure RPV Pressure considering all limiting variables

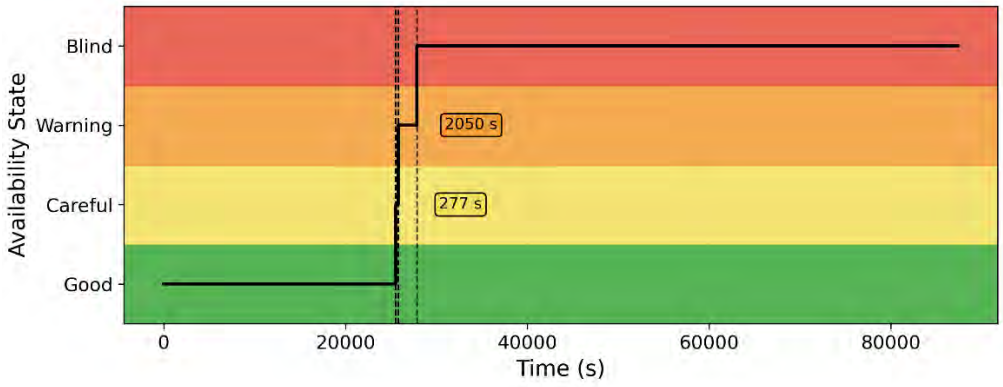

Figure 7. Availability to measure Suppression Pool Pressure considering all limiting variables

5. Conclusions

The main objective of this study was to develop a complete evaluation of the instrumentation survivability during severe accidents in BWR, adding full radiation assessment as the novelty, and the impact that its failure can provoke for the correct execution of the mitigation strategies that are stablished to overcome this accidental scenario.

For pursuing this analysis, the RadSim program was developed. This open-source python code has multiple capabilities that lead to the SAMGs availability evaluation during the severe accident. Furthermore, RadSim has other features like dose rates calculation for different geometrical hypotheses or evaluating the decay of the multiple isotopes present in the nuclear power plant, making it a state-of-the-art tool.

The output of this analysis is a code which is capable of developing an assessment of the applicability of the SAMGs. This assessment can help to identify the state of the instrumentation and the possibility to perform the different measurements needed. Precisely, radiation dose has been identified as the most limiting variable in the analysis, highlighting the importance of considering this variable as crucial when performing this kind of evaluations.

Future work includes dose assessment of the instrumentation in other containment and reactor designs, as well as the evaluation of the SAMGs based on that input.

ACKNOWLEDGMENTS

The work has been performed in the framework of the CSARP agreement between UPM and CSN. Additionally, the authors would like to thank the comments from an anonymous reviewer which have enhanced the quality of the work.

REFERENCES

[1] A. Bari and J. Jiang, “Environmental considerations in the qualification of monitoring instruments for severe accidents,” in *Instrumentation and Control Systems for Nuclear Power Plants*, Elsevier., 2023, pp. 957–984. doi: 10.1016/B978-0-08-102836-0.00017-5.

[2] K. Nozaki *et al.*, “Discussion of Accident Progression of Fukushima Daiichi Unit 1 based on Behavior of Fuel Range Water Level Indicator Readings (NUTHOS10-1130),” in *The 10th International Topical Meeting on Nuclear Thermal-Hydraulics, Operation and Safety (NUTHOS-10)*, Okinawa, Japan, 2014.

[3] J. H. Scobel and N. A. Powell, “Severe Accident Equipment Survivability Assessment for the Westinghouse AP1000® Nuclear Power Plant,” presented at the 17th International Topical Meeting on Nuclear Reactor Thermal Hydraulics, NURETH-17, Xi’an, China, 2017.

[4] L. Li and G. Lin, “Instrument Survivability Assessment During Severe Accident in HPR1000,” in *Nuclear Power Plants: Innovative Technologies for Instrumentation and Control Systems. SICPNPP 2018. Lecture Notes in Electrical Engineering*, vol. 507, Y. Xu, H. Xia, F. Gao, W. Chen, Z. Liu, and P. Gu, Eds., Singapore: Springer Singapore, 2019, pp. 233–240. doi: 10.1007/978-981-13-3113-8_27.

[5] G. Huang *et al.*, "Research on equipment survivability assessment in severe accidents for CANDU6," *Progress in Nuclear Energy*, vol. 149, p. 104250, Jul. 2022, doi: 10.1016/j.pnucene.2022.104250.
[6] W. C. Arcieri and D. J. Hanson, "Instrumentation Availability During Severe Accidents for a Boiling Water Reactor with a Mark I Containment (NUREG/CR-5444)," 1992. [Online]. Available: https://www.osti.gov/servlets/purl/5856947
[7] A. Murata, K. Isoda, T. Ikeuchi, T. Matsui, F. Shiraishi, and M. Oba, "Classification method of severe accident condition for the development of severe accident instrumentation and monitoring system in nuclear power plant," *Journal of Nuclear Science and Technology*, vol. 53, no. 6, pp. 870–877, Jun. 2016, doi: 10.1080/00223131.2015.1076746.
[8] K. Fernández-Cosials, C. Queral, M. Sánchez-Perea, and F. Robledo, "Time assessment of instrumentation survivability and severe accident guidelines application," *Nuclear Engineering and Design*, vol. 386, p. 111559, Jan. 2022, doi: 10.1016/j.nucengdes.2021.111559.
[9] L. E. Herranz, "«Personal Communication»," 2021.
[10] "IEEE Standard for Qualifying Class 1E Equipment for Nuclear Power Generating Stations," vol. Std 323-2003, 2003.
[11] *IEEE Standard for Qualifying Class IE Equipment for Nuclear Power Generating Stations*, 1974. doi: 10.1109/IEEESTD.1974.6568022.
[12] N. D. Ezell, F. Reed, and M. Ericson, "Radiation-Hard Electronics for Nuclear Instrumentation in Terrestrial Reactors," presented at the 12th Nuclear Plant Instrumentation, Control and Human-Machine Interface Technologies (NPIC&HMIT 2021), Illinois: American Nuclear Society, pp. 556–563. doi: 10.13182/T124-34243.
[13] J. L. Rempe, D. L. Knudson, and R. J. Lutz, "Scoping Study Investigating PWR Instrumentation during a Severe Accident Scenario, INL/EXT-15-35940," Idaho National Laboratory, INL/EXT-15-35940, 2015. [Online]. Available: https://lwrs.inl.gov/Reactor Safety Technologies/Final INL-EXT-15-35940 9-17-15.pdf
[14] E. Pauli and P. G. Straße, "PREDICTION OF THE RADIOLOGICAL CONSEQUENCES OF A SEVERE ACCIDENT SCENARIO IN A GENERIC KONVOI NUCLEAR," presented at the 10th International Conference on Severe Accident Research (ERMSAR 2022), Karlsruhe, 2022, pp. 1–13.
[15] A. Mercan, F. Gabrielli, V. Sanchez Espinoza, and W. Raskob, "Analysis of the consequences of a LBLOCA with SBO severe accident in a generic VVER-1000 by means of ASTEC and JRODOS codes," *Nuclear Engineering and Design*, vol. 400, p. 112078, Dec. 2022, doi: 10.1016/j.nucengdes.2022.112078.
[16] L. L. Humphries *et al.*, "MELCOR Computer Code Manuals Vol. 2: Reference Manual Version 2024.0."
[17] F. Gabrielli *et al.*, "ANALYSIS OF POSTULATED SEVERE ACCIDENTS IN GENERIC INTEGRAL PWR SMALL MODULAR REACTORS IN THE FRAME OF THE HORIZON EURATOM SASPAM-SA PROJECT," presented at the 11th International Conference on Severe Accident Research (ERMSAR 2024), 2024.
[18] K. Fernandez-Cosials, C. Queral, M. Sánchez-Perea, and F. Robledo, "Study of the User Effect Impact in Forward Uncertainty Propagation Approaches Applied to Severe Accident," *Nuclear Technology*, pp. 1–16, Jul. 2025, doi: 10.1080/00295450.2025.2508953.
[19] L. E. Herranz *et al.*, "The EC MUSA Project on Management and Uncertainty of Severe Accidents: Main Pillars and Status," *Energies*, vol. 14, no. 15, p. 4473, Jul. 2021, doi: 10.3390/en14154473.
[20] A. García-Morillo, "Response Analysis to a SBO scenario for BWR reactors with containment Mark-II and Mark-III type," Masther´s Thesis, 2022.
[21] G. Jimenez *et al.*, "BWR Mark III containment analyses using a GOTHIC 8.0 3D model," *Annals of Nuclear Energy*, vol. 85, pp. 687–703, Nov. 2015, doi: 10.1016/j.anucene.2015.06.025.
[22] L. L. Humphries, "MELCOR Dose Rate Calculations," presented at the Workshop on Operational Experience and Advances in MELCOR Modeling, Shenzhen, China, Nov. 19, 2012.
[23] "JANIS." Accessed: Jan. 09, 2026. [Online]. Available: https://www.oecd-nea.org/janisweb/
[24] "Welcome to radioactivedecay's documentation! — radioactivedecay 0.6.1 documentation." Accessed: Dec. 09, 2025. [Online]. Available: https://radioactivedecay.github.io/
[25] R. Mirji and B. Lobo, "Computation of the mass attenuation coefficient of polymeric materials at specific gamma photon energies," *Radiation Physics and Chemistry*, vol. 135, pp. 32–44, Jun. 2017, doi: 10.1016/j.radphyschem.2017.03.001.
[26] R. Harter, "Accident Progression and Critical Issues During Reactor Accidents - an End User Perspective," presented at the International Experts Meeting on Assessment and Prognosis in Response to a Nuclear or Radiological Emergency, International Atomic Energy Agency Vienna, Austria, Apr. 20, 2015.
[27] NEA, "BWR Severe Accident Mitigation Guidelines (SAMG) Information Compilation and Reactor Water Level Measurement," vol. NEA/CNRA/R(2022), Apr. 2025.
[28] *Topical issues in nuclear installation safety: proceedings of an International Conference on Topical Issues in Nuclear Installation Safety: Safety Demonstration of Advanced Water Cooled Nuclear Power Plants organized by the International Atomic Energy Agency and held in Vienna, Austria, 6-9 June 2017*. Vienna: IAEA, 2018.
[29] EPRI, "Severe Accident Management Guidance Technical Basis Report—Volume 1: Candidate High-Level Actions and Their Effects," vol. 1025295, Palo Alto, CA 2012.
[30] T. Sevón, "Analyzing reactor water level measurements in the Fukushima Daiichi 1 accident," *Progress in Nuclear Energy*, vol. 160, p. 104707, Jun. 2023, doi: 10.1016/j.pnucene.2023.104707.
[31] D. Chien and D. Hanson, "Accident Management Information Needs for a BWR with a MARK I Containment," ON: TI91012401, NUREG/CR--5702, EGG--2639, May 1991. doi: 10.2172/5785313.
[32] D. A. Clayton and W. P. Poore, III, "Fukushima Daiichi – A Case Study for BWR Instrumentation and Control Systems Performance during a Severe Accident," Oak Ridge National Laboratory (ORNL), ORNL/TM-2013/154, 2013.
[33] D. A. Clayton and W. P. Poore, III, "Key Parameters for Operating Diagnosis of BWR Plant Condition during a Severe Accident," Oak Ridge National Laboratory (ORNL), ORNL/LTR-2014/320, 2014.
[34] D. Clayton and W. P. Poore, "Post-Severe Accident Environmental Conditions for Essential Instrumentation for Boiling Water Reactors," Oak Ridge National Laboratory (ORNL), ORNL/TM-2015/278, Jun. 2015.
[35] "Review Of The Containment Equipment Qualification Criteria And Instrumentation Surveillance Under Severe Accident ConditionS," AMHYCO Project, Internal Deliverable. WP1-Task 1.4, May 2021.
[36] "Rosemount 3155N Nuclear Qualified Pressure Transmitter." EMERSON, Sep. 2025.
[37] M. Menouni *et al.*, "1-Grad total dose evaluation of 65 nm CMOS technology for the HL-LHC upgrades," *J. Inst.*, vol. 10, no. 05, pp. C05009–C05009, May 2015, doi: 10.1088/1748-0221/10/05/C05009.

Instrumentation survivability assessment during a severe accident; incorporating radiation monitoring in MELCOR to evaluate the impact on SAMGs

Kevin Fernández-Cosials[1], Rodrigo Rivilla[1], Cesar Queral[1], Robledo F.[2]

Kevin.fcosials@upm.es

1: Universidad Politécnica de Madrid (Spain)

2: Consejo de Seguridad Nuclear (Spain)

Index

1. Motivation and Objective

2. Development and Capabilities

3. Application to a SBO in a BWR/6 Mark III

1. Motivation

- **Motivation**: Instrumentation Survivability during a Severe Accident
  - Requirements of Environmental Qualification rely on Pressure, Temperature, Humidity and … **Radiation Dose.**
  - **MELCOR** does not provide *an easy method* to obtain Doses in-containment during the SA.
  - In order to obtain instrumentation damage in a continuous manner during a Severe Accident and help TSC crew with EOPs/SAMGs, **rad-doses should be taken into account**.
- **Objectives**:
  - Develop a script that takes as Input MELCOR RN Data, and Outputs Doses for instrumentation located in each CV.
  - Apply a **complete Instrumentation survivability** assessment to a SBO in a BWR Mark III.

2. Capabilties and Development

- **Input**:
  - MELCOR outputs RN classes mass in each containment Control Volume.
  - MELCOR outputs Pressure, Temperature and Humidity of each Containment Control Volume.
  - MELCOR outputs temperature of HS and volumes of CV.

RN Classes	Representative	Isotopes
1. Noble Gases	Xe	He, Ne, Ar, Kr, Xe, Rn, H, N
2. Alkali Metals	Cs	Li, Na, K, Rb, Cs, Fr, Cu
3. Alkaline Earths	Ba	Be, Mg, Ca, Sr, Ba, Ra, Es, Fm
4. Halogens	I	F, Cl, Br, I, At
5. Chalcogens	Te	O, S, Se, Te, Po
6. Platinoids	Ru	Ru, Rh, Pd, Re, Os, Ir, Pt, Au, Ni
7. Early Transition Elements	Mo	V, Cr, Fe, Co, Mn, Nb, Mo, Tc, Ta, W
8. Tetravalent	Ce	Ti, Zr, Hf, Ce, Th, Pa, Np, Pu, C
9. Trivalents	La	Al, Sc, Y, La, Ac, Pr, Nd, Pm, Sm, Eu, Gd, Tb, Dy, Ho, Er, Tm, Yb, Lu, Am, Cm, Bk, Cf

2. Capabilties and Development

- **Transformation**:
  - RN masses → Isotope Masses → Isotope decay chains evolution → In-containment dose evolution.

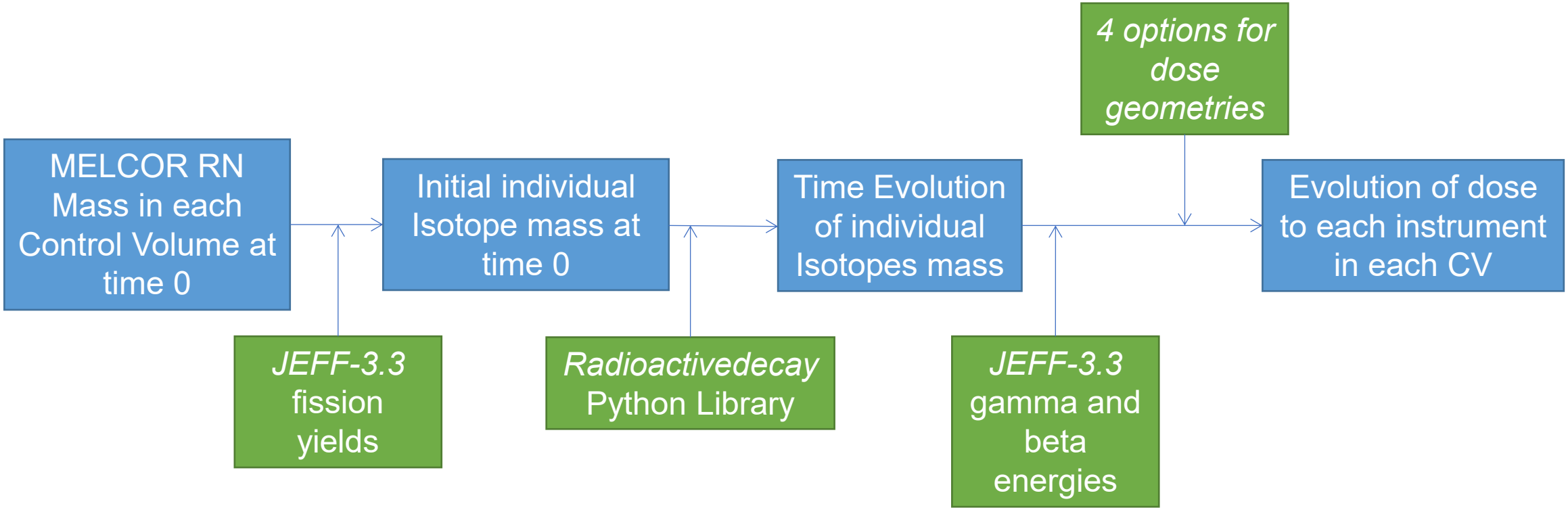

2. Capabilties and Development

- **Transformation**:
  - RN masses → Isotope Masses → Isotope decay chains evolution → In-containment dose evolution.

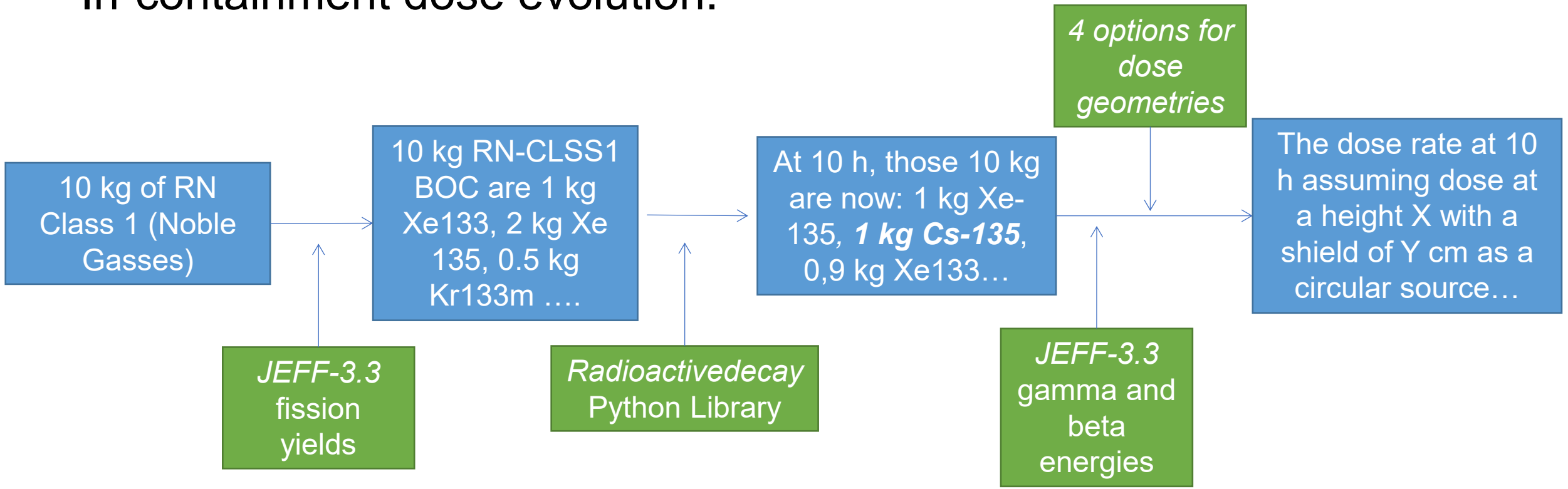

2. Capabilties and Development

- **Module-based approach of RADSIM**:

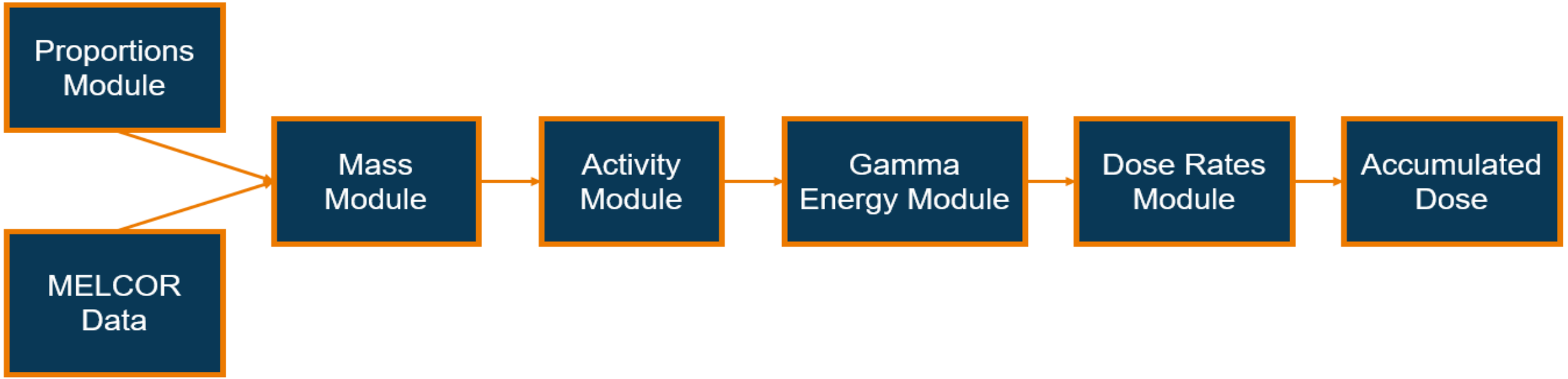

- **Open-Source code. Can be found in Github.**

2. Capabilties and Development

- **Geometry Calculation Options**:

$$D^{\gamma}{}_i = (5.77 \cdot 10^{-5}) \emptyset_i E_i \left(\frac{\mu_{a,i}}{\rho}\right)_{air}$$

$$\left(\frac{\mu_{a,i}}{\rho}\right)_{air} = a + bE + c[\ln(E)]^2 + d\sqrt{E} + e[\ln(E)]$$

$$\left(\frac{\mu_{s,i}}{\rho}\right)_{air} = f + gE^h$$

Methodology based on L. L. Humphries, “MELCOR Dose Rate Calculations,” presented at the Workshop on Operational Experience and Advances in MELCOR Modeling, Shenzhen, China, Nov. 19, 2012.

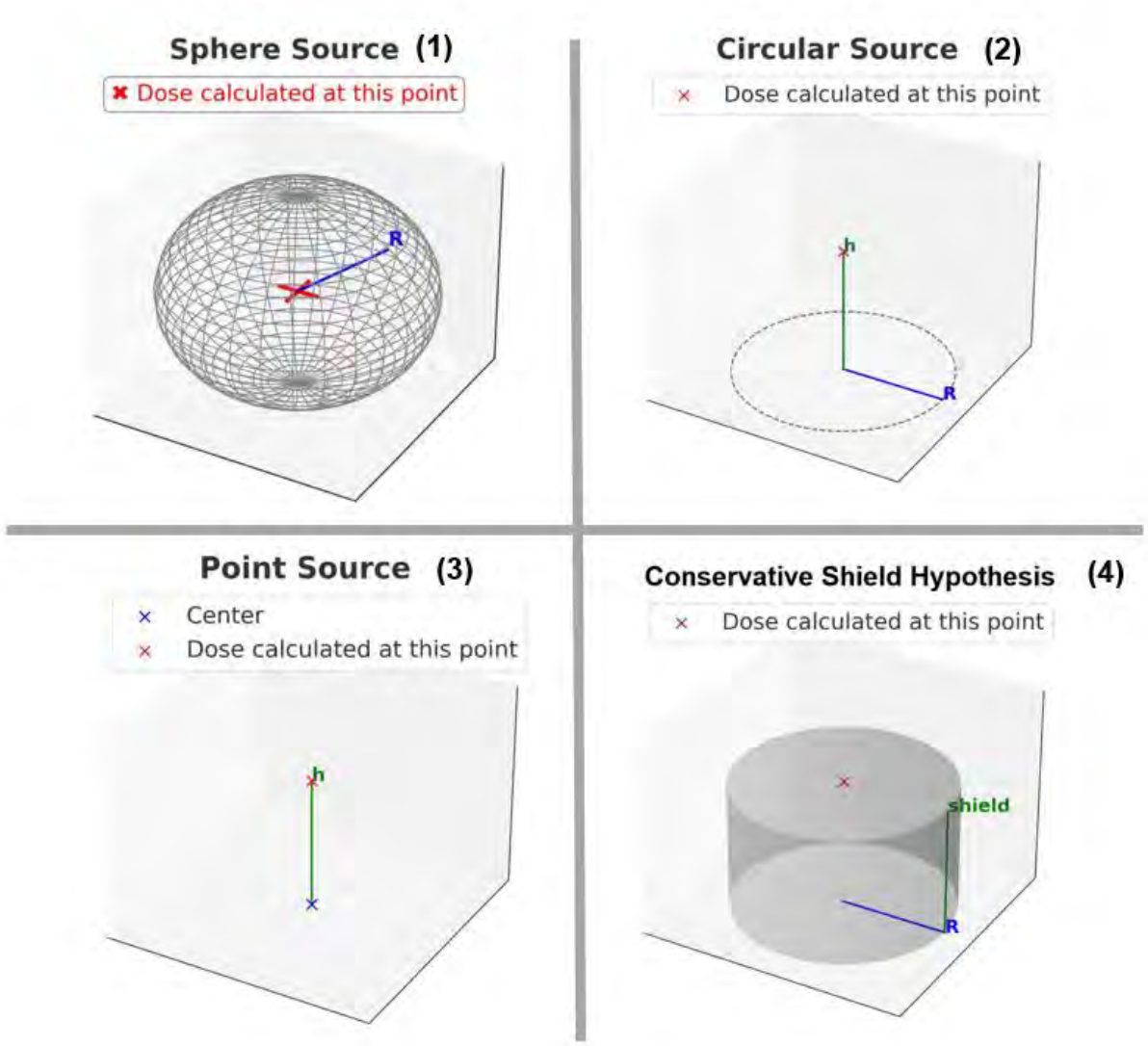

3. Example of Application SBO on BWR. Steps

- 1. Identification of all containment instrumentation.
- 2. Identification of physical Variables required in Specific SAMGs.
- 3. Define Degradation Level
- 4. Evaluation of Instrumentation & SAMG blindness along the SA.

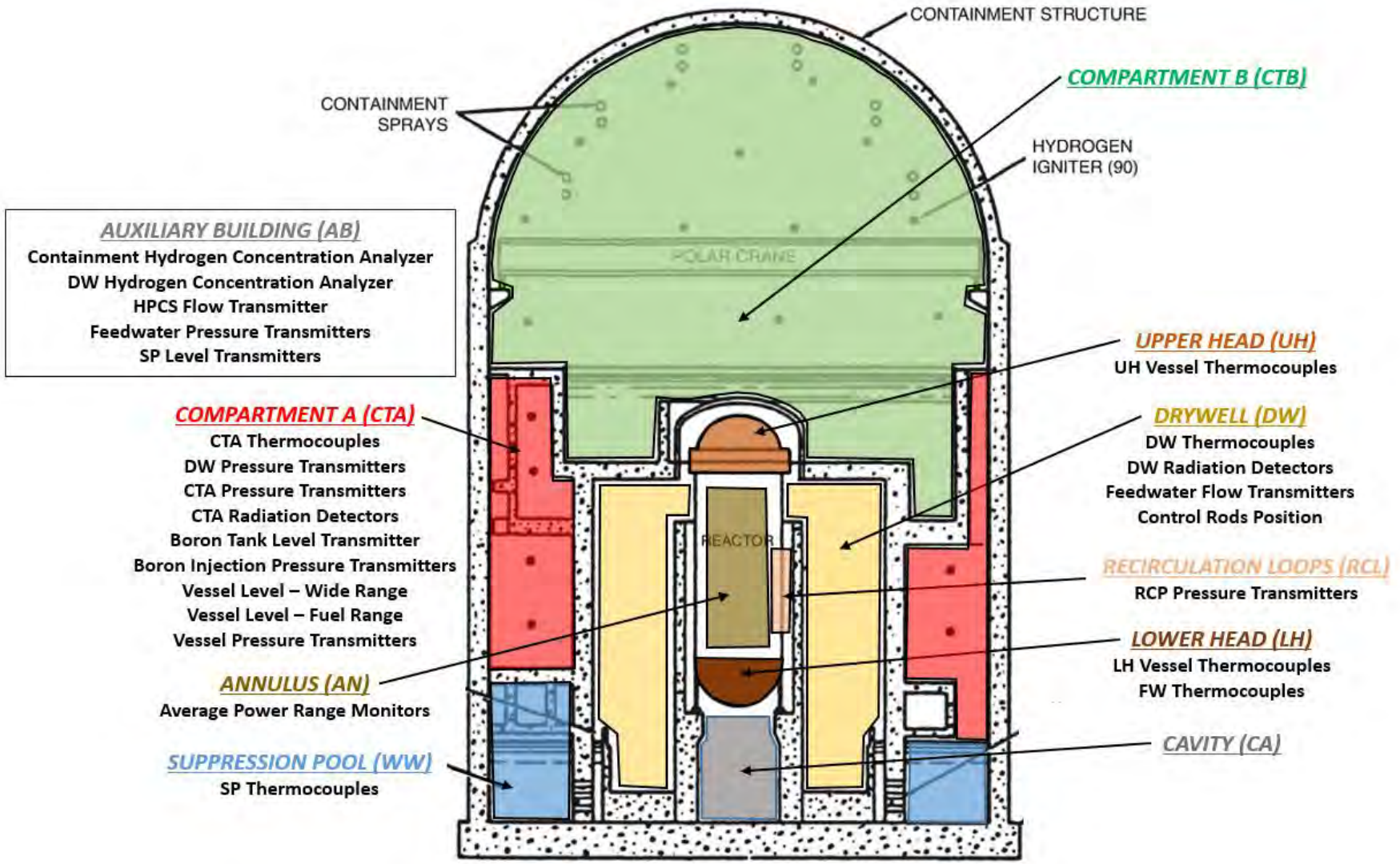

3. Example of Application SBO on BWR. Existing Methodology

VARIABLES	INSTRUMENTATION	VARIABLES	INSTRUMENTATION
DW TEMPERATURE	DW Thermocouples (DW) CTA Thermocouples (CTA) SP Thermocouples (WW)	RPV TEMPERATURE	UH Vessel Thermocouples (UH) LH Vessel Thermocouples (LH) FW Thermocouples (LH) Suction Pipes Thermocouples (RCL)
DW PRESSURE	DW Pressure Transmitters (DW/CTA) CTA Pressure Transmitters (CTA)	CONTAINMENT PRESSURE	CTA Pressure Transmitters (CTA) DW Pressure Transmitters (DW/CTA)
CONTAINMENT RADIATION	CTA Radiation Detectors (CTA) DW Radiation Detectors (DW)	CONTAINMENT LEVEL	SP Level Transmitters (AB) SP Thermocouples (WW)
CONTAINMENT HYDROGEN	Containment Hydrogen Concentration Analyzer (AB) DW Hydrogen Concentration Analyzer (AB)	SP PRESSURE	SP Thermocouples (WW) CTA Pressure Transmitters (CTA) DW Pressure Transmitters (DW/CTA)
BORON TANK LEVEL	Boron Tank Level Transmitter (CTA) Boron Injection Pressure Transmitters (CTA)	SP TEMPERATURE	SP Thermocouples (WW) DW Thermocouples (DW) CTA Thermocouples (CTA)
INJECTED FLOW RPV	Feedwater Flow Transmitters (DW) HPCS Flow Transmitter (AB) Boron Injection Pressure Transmitters (CTA) Vessel Level - Wide Range (DW/CTA) Vessel Level - Fuel Range (DW/CTA) Feedwater Pressure Transmitters (AB)	SRV POSITION	SRV Position Indicators (DW)
REACTOR POWER	Average Power Range Monitors (AN) Control Rods Position (DW)	CONTAINMENT TEMPERATURE	CTA Thermocouples (CTA) DW Thermocouples (DW) SP Thermocouples (WW)
RPV LEVEL	Vessel Level (Wide Range) (DW/CTA) Vessel Level (Fuel Range) (DW/CTA)	RPV PRESSURE	Vessel Pressure Transmitters (DW/CTA) RCP Pressure Transmitters (RCL)

3. Example of Application SBO on BWR. Existing Methodology

Instrument Damage Condition	Description
DC-1 (Normal Operating Conditions)	Normal operating conditions, suitable for measurement. They are wit hin the EQ (Environmental Qualification) range and the readings are f ully reliable.
DC-2 (Anomalous Operating Conditions I)	Challenging conditions or slightly above the EQ design, but the measurements are still useful both in trend and in value.
DC-3 (Anomalous Operating Conditions II)	The design limit has been significantly exceeded; the measurements are no longer valid in absolute value, although the information on trends and orders of magnitude is still useful.
DC-4 (Damaged Operating Conditions)	The measurements are only reliable in terms of trend, not quantitative or order magnitude information. In this state, the instrument cannot be recalibrated, and therefore, once level DC-4 is reached, it cannot decrease.
DC-5 (Destruction Conditions)	The measurements of such instrument have no value at all. Instrument is completely unusable, and it cannot and should not be employed for any measurement.

3. Example of Application SBO on BWR. Damage Conditions

	SP TC	DW TC	UH Vessel TC	LH Vessel TC	CTA TC	FW TC	Suction Pipes TC
DC-1	273-422K	273-422K	273-645K	273-645K	273-422K	273-645K	273-645K
DC-2	CEC>EQ	CEC>EQ	645K < T_{UH} < 923K	645K < T_{LH} < 923K	CEC>EQ	645K < T_{LH} < 923K	645K < T_{RCL} < 923K
DC-3	T_{SP} >673K	T_{DW} >673K	923K < T_{UH} < 1173K	923K < T_{LH} < 1173K	T_{CTA} >673K	-	923K < T_{RCL} < 1173K
DC-4	-	-	1173K < T_{UH} < 1570K	1173K < T_{LH} < 1570K	-	923K < T_{LH} < 1570K	1173K < T_{RCL} < 1570K
DC-5	T_{SP} >1530K	T_{DW} >1530K	T_{UH} >1570K	Vessel Failure	T_{CTA} >1530K	T_{UH} >1570K	T_{RCL} >1570K

Damage Condition (DC)	DC-1	DC-2	DC-3	DC-4	DC-5
Value	< IEEE values	From 1 to 4 times IEEE values	From 4 to 7 times I EEE values	From 7 to 10 times IEEE values	> 10 times IEEE values

3. Example of Application SBO on BWR. SAG-1

Variables	RC/F-1	RC/F-2	RC/F3	RC/F-4	RC/F-5	RC/P	RC/Q
DW TEMPERATURE	▲						▲
DW PRESSURE	▲						▲
CONTAINMENT RADIATION	●	●	●	●	●	●	▲
CONTAINMENT HYDROGEN	▲	▲	▲	▲	▲		▲
BORON TANK LEVEL							●
INJECTED FLOW RPV	▲	▲	▲	▲	▲		▲
RPV LEVEL	●	▲	●	▲	▲	●	●
RPV PRESSURE	▲	▲	▲	▲	▲		▲
RPV TEMPERATURE				▲	▲		
CONTAINMENT PRESSURE	●	●	●	●	●	●	
CONTAINMENT LEVEL	●	●	●	●	●	●	
SP PRESSURE	▲	▲			▲		
SP TEMPERATURE							
REACTOR POWER							●
CONTAINMENT TEMPERATURE	▲	▲	▲	▲	▲		

●: Variable directly used in guide

▲: Variable only used in TSG inside the guide

3. Example of Application SBO on BWR. MELCOR Model

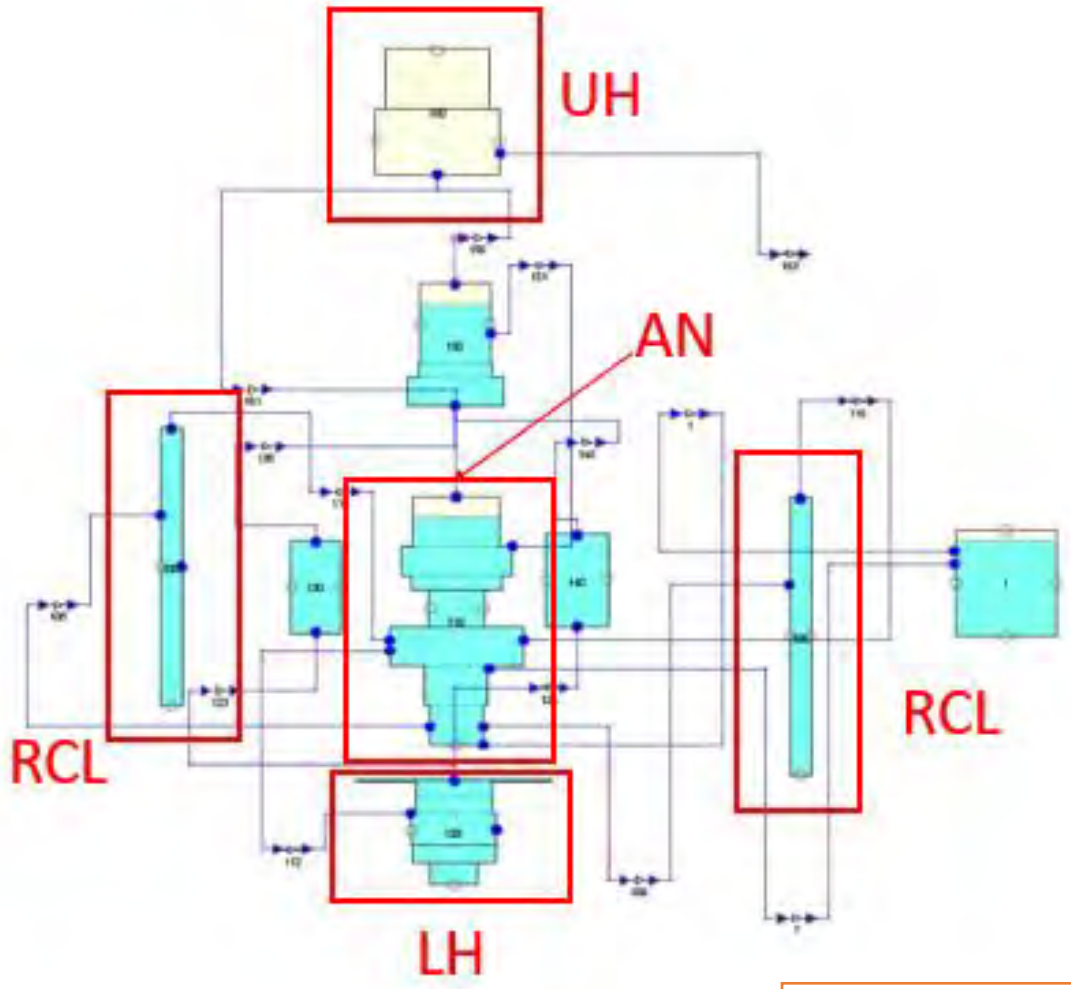

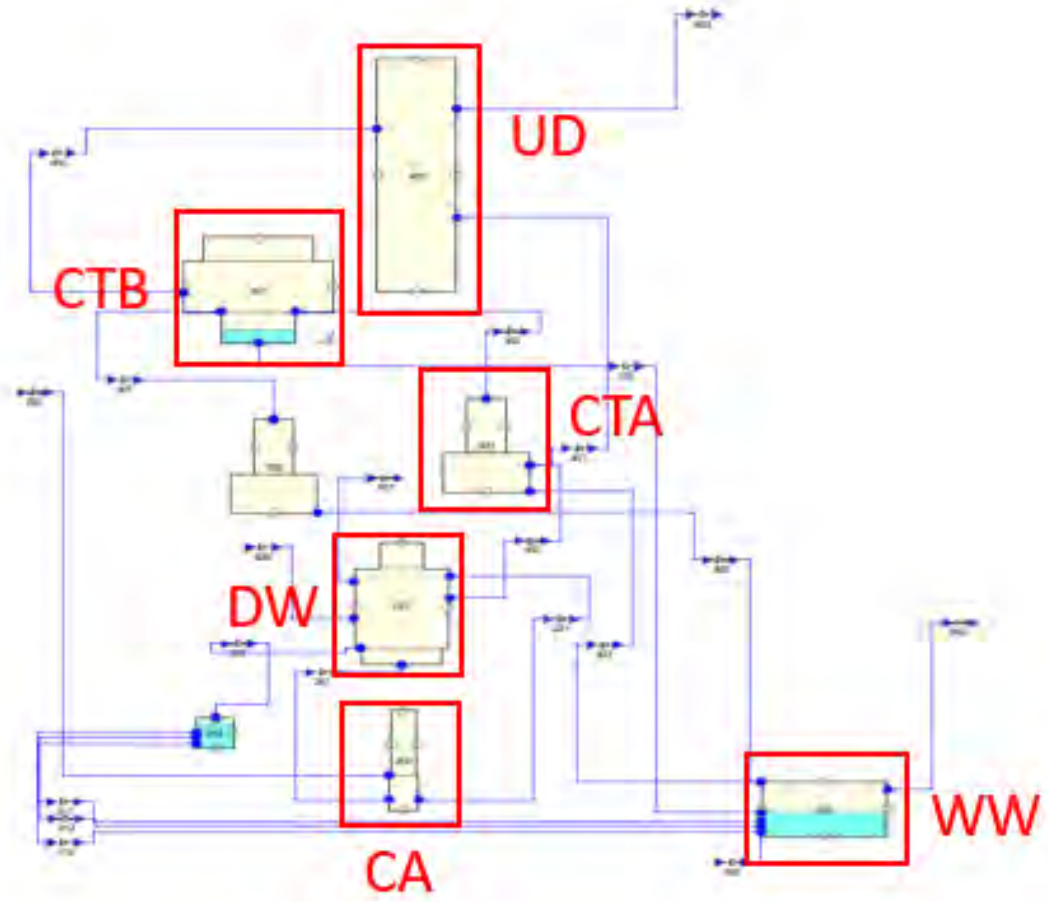

MELCOR 2.2 used for the analysis.

3. Example of Application SBO on BWR. Transient Evolution

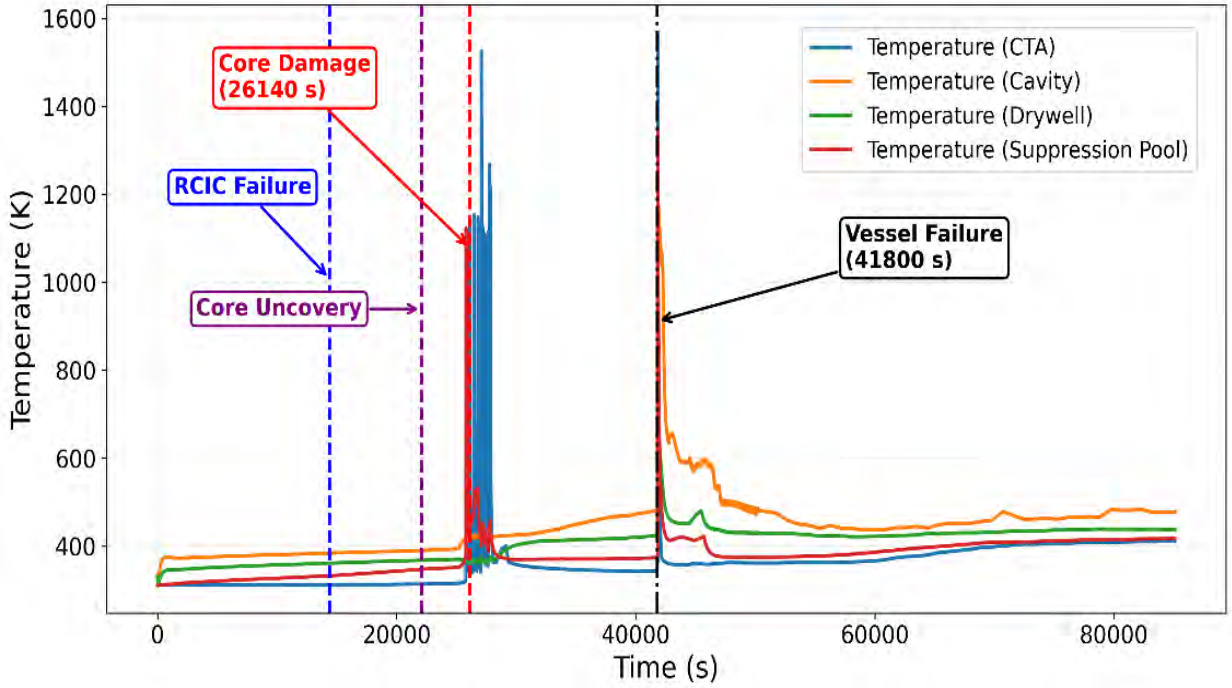

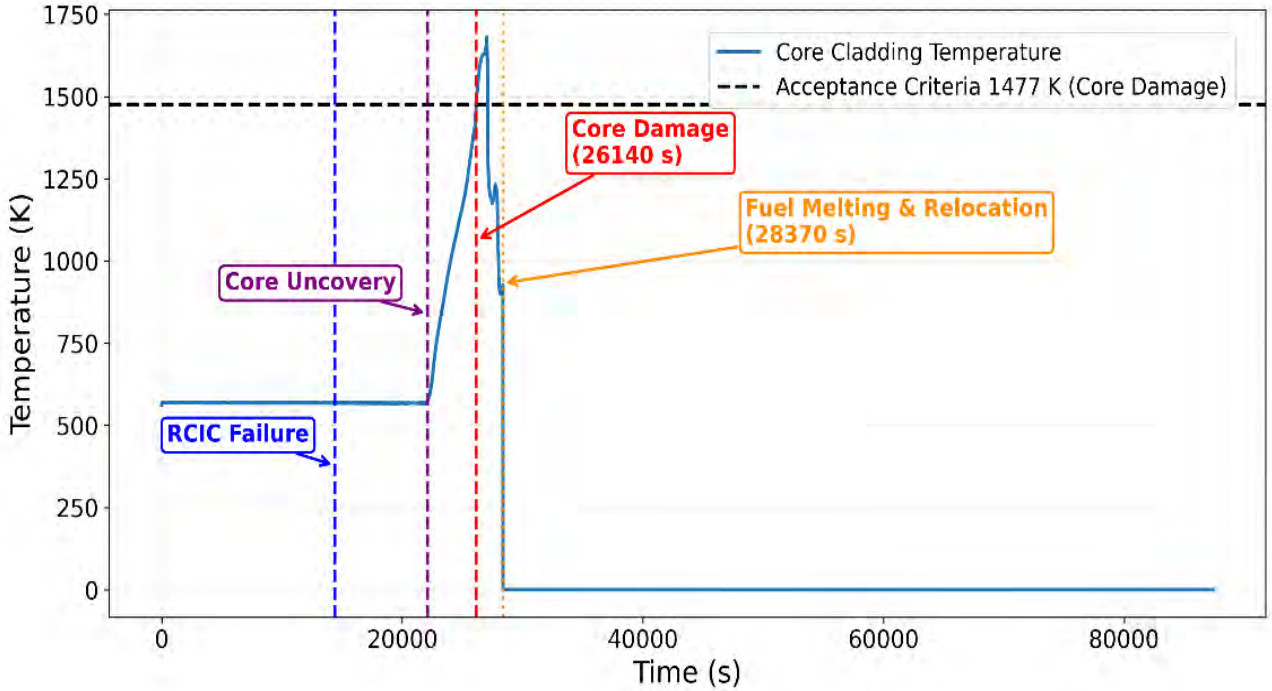

3. Example of Application SBO on BWR. Isotope mass contribution

Class 3 (Alkali Earths) in CTA

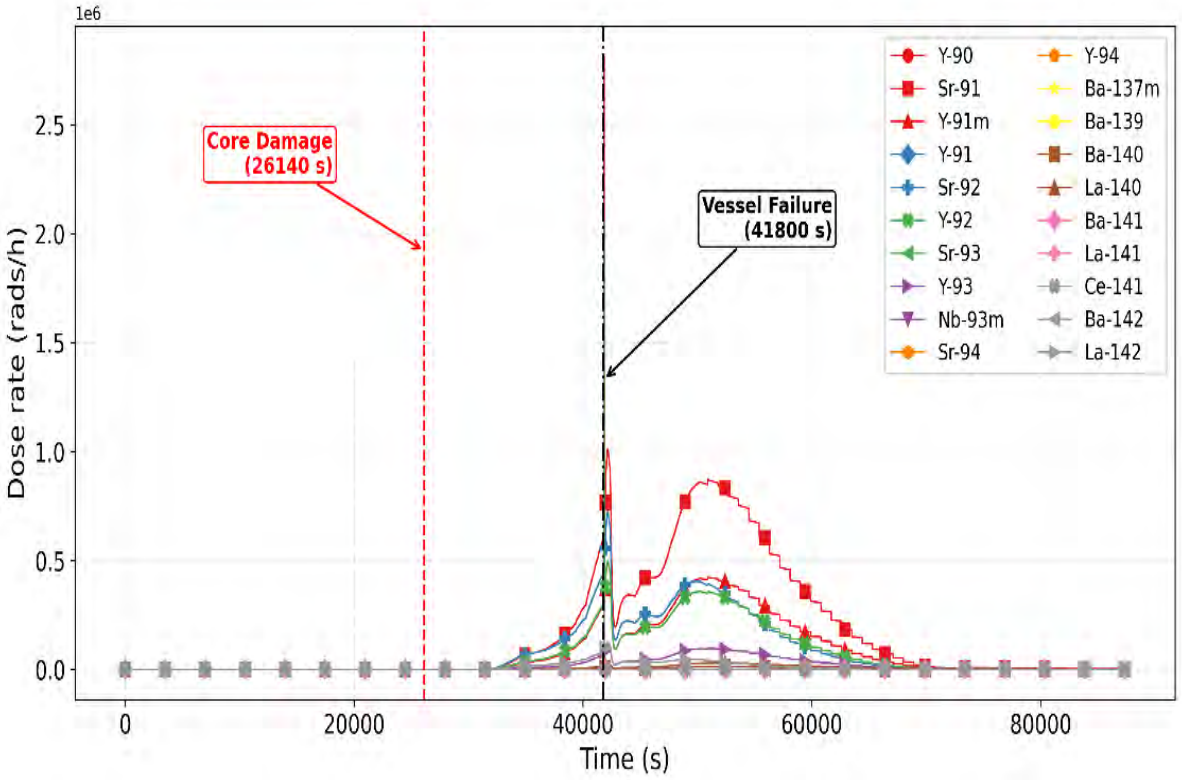

Class 1 (Noble Gases) in CTA

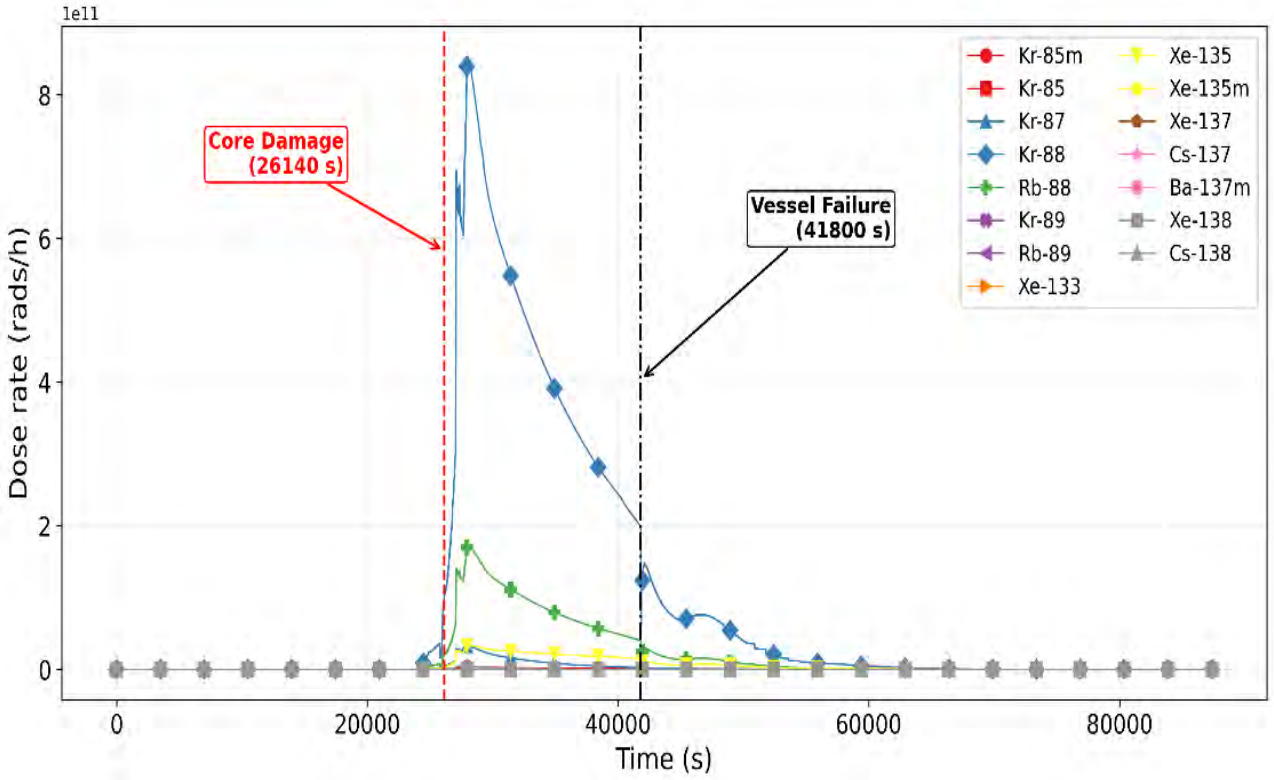

Results using **point-source** hypothesis

3. Example of Application SBO on BWR. Accumulated dose

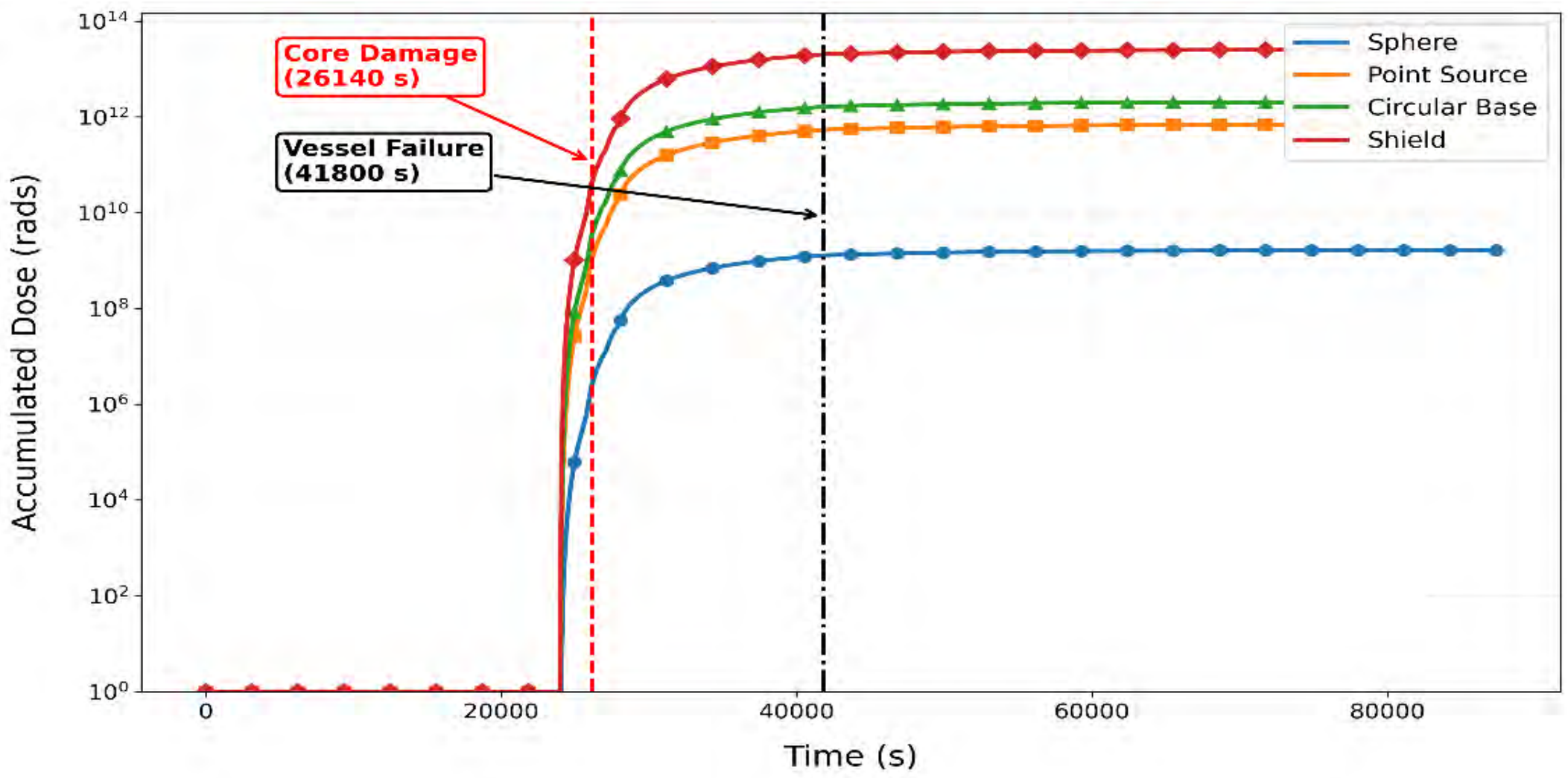

3. Example of Application, SBO on BWR. Doses on different volumes

Sphere Source Hypothesis at CTA

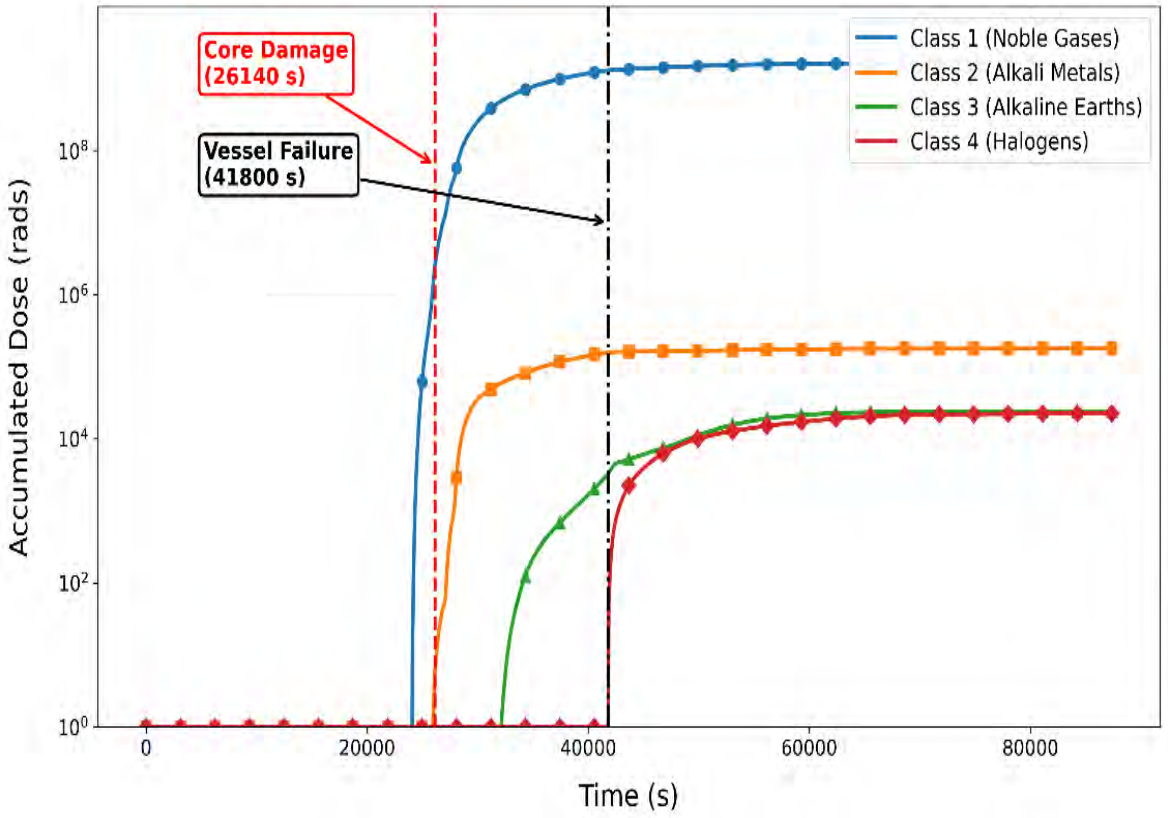

Sphere Source Hypothesis at DryWell

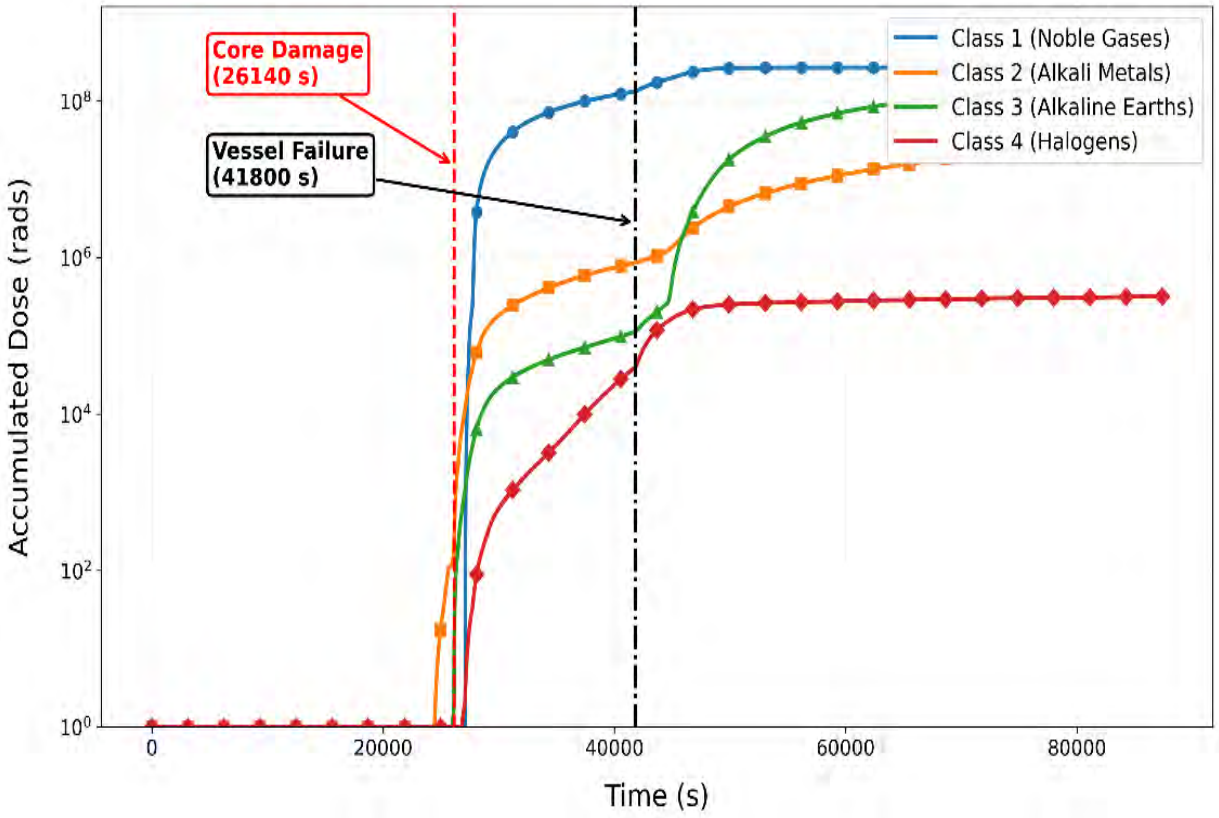

3. Example of Application SBO on BWR. Code-to-code comparison.

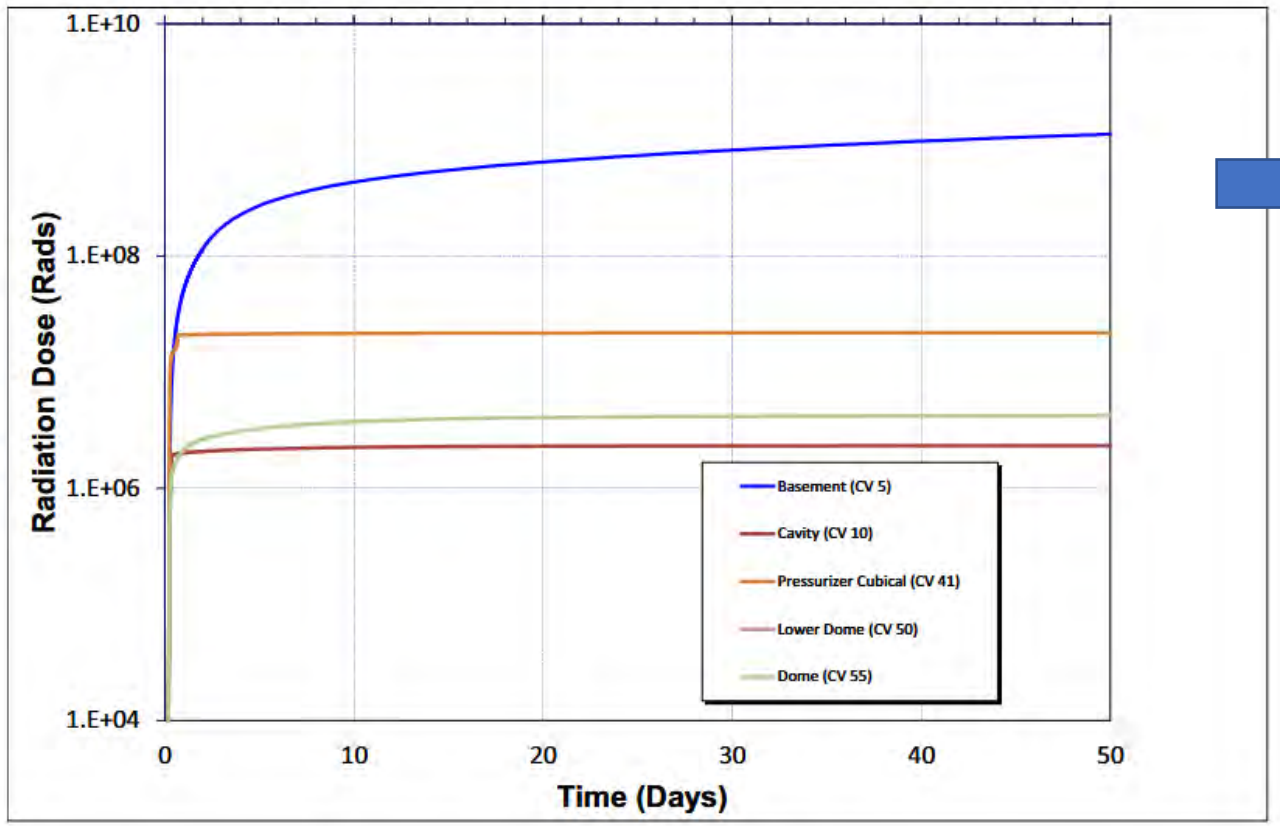

Scoping Study Investigating PWR Instrumentation during a Severe Accident Scenario

Joy L. Rempe, Rempe and Associates, LLC

Darrell L. Knudson, Idaho National Laboratory

Robert J. Lutz, Lutz Nuclear Safety Consultant, LLC

September 2015

Results obtained are in the same order of magnitude that Rempe et al.'s SBO 2015 study.

3. Example of Application SBO on BWR. Full Instrumentation damage survivability.

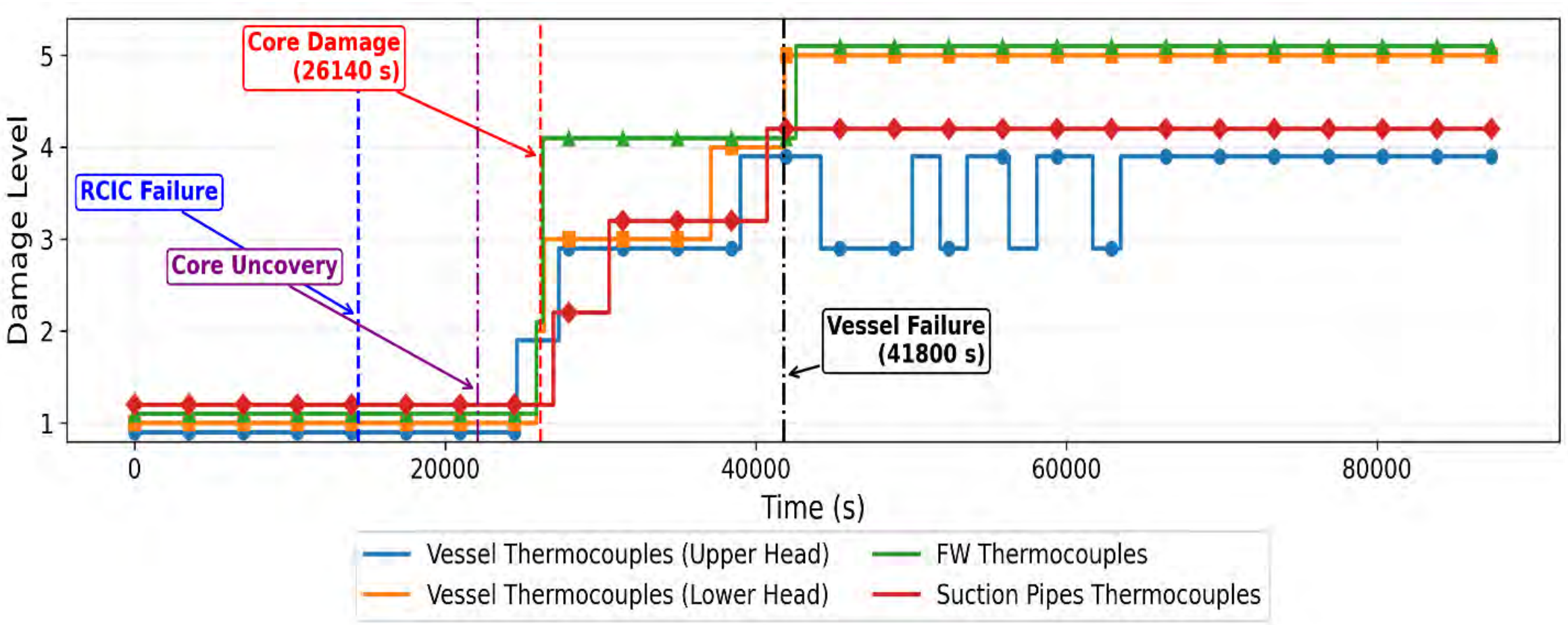

A Survivability Analysis that takes into account Temperature, Pressure and Dose in a continuous manner

3. Example of Application SBO on BWR. Full Instrumentation damage survivability.

Without Taking into account radiation

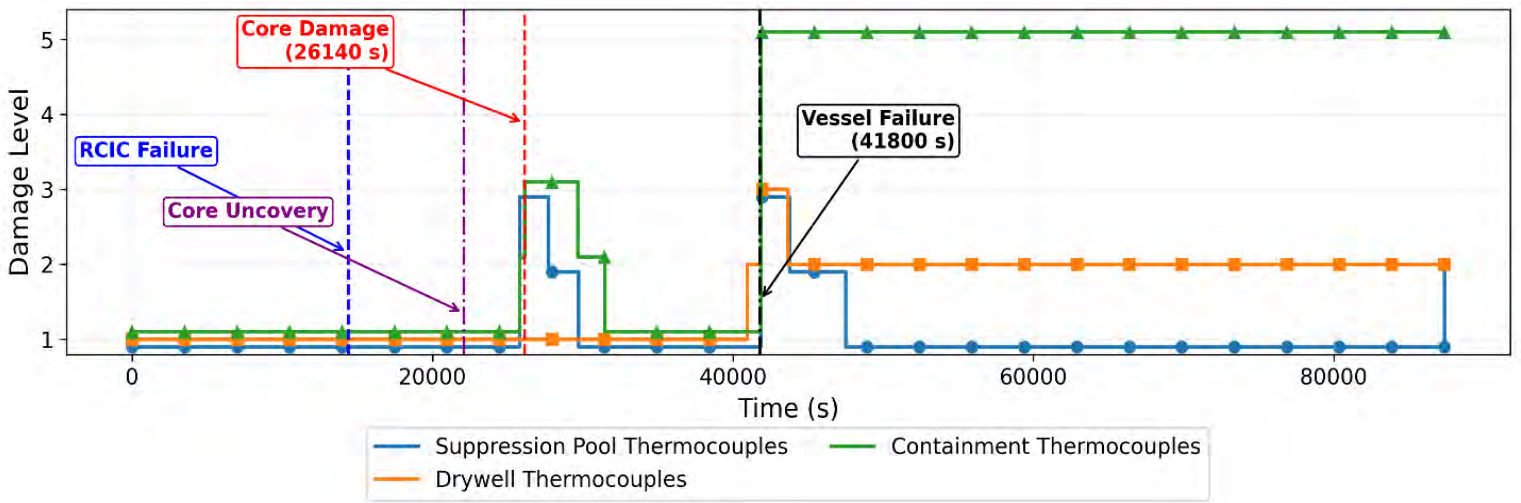

Taking into account radiation

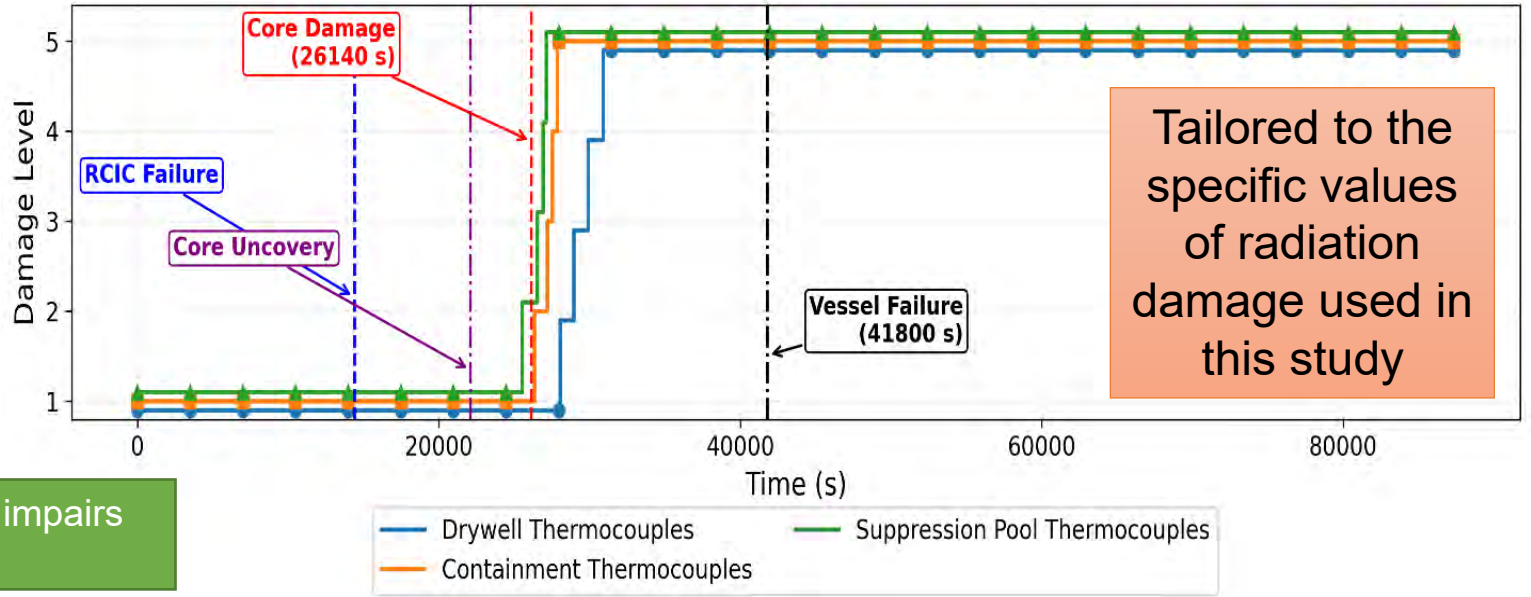

Tailored to the specific values of radiation damage used in this study

Radiation Damage (set at ~ 100 Mrads) impairs more instruments than expected

3. Example of Application SBO on BWR. Full Instrumentation damage survivability.

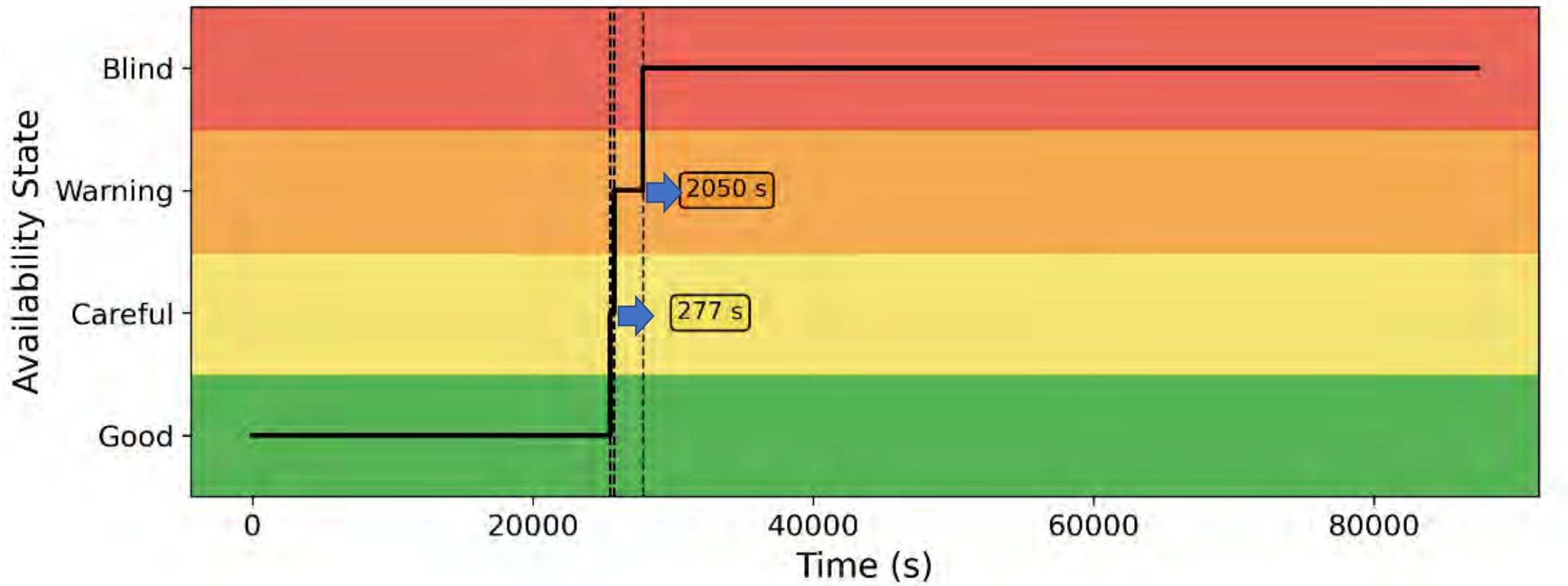

Availability to measure Suppression Pool Pressure

Radiation Damage (set at ~ 100 Mrads) impairs more instruments than expected

3. Example of Application SBO on BWR. Full Instrumentation damage survivability.

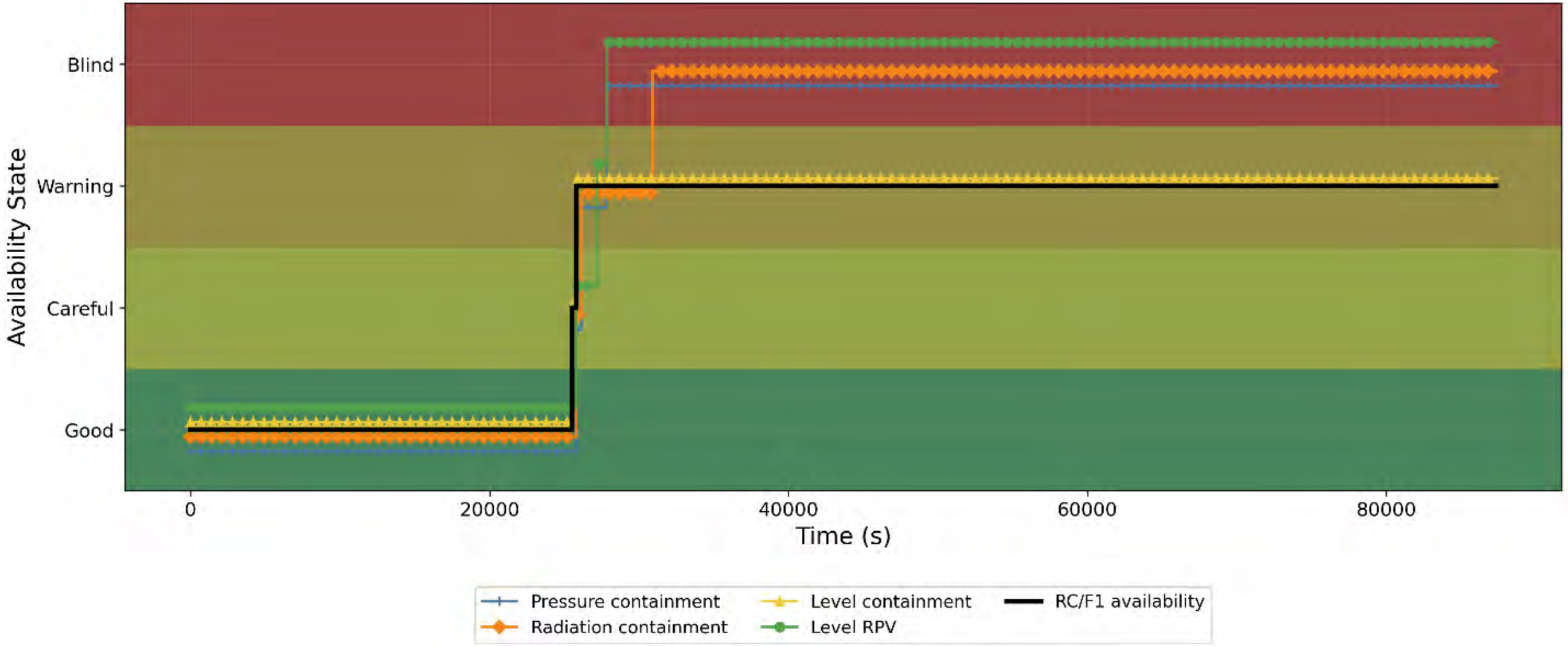

Conclusions

- A post-processing application to calculate dose rates in-containment during a Severe accident has been developed. RADSIM. Uses JEFF 3.3 Data and a full radioactive chain calculation, and provides more flexibility to dose calculation than other counterparts.
- Code-to-code comparison of results appear to be adequate.
- A full assessment of BWR Mark III instrumentation and SAMGs dependence has been developed.
- Core Damage and Vessel Failure dominate instrumentation survivability in consonance with other instrumentation survivability methodoloties.
- Radiation Damage can dominate Instrumentation damage under certain hypothesis.

Want to test?

- If you want to test the RADSIM tool or contribute, feel free to scan the code.

https://github.com/el-tarro/UPM-Nuclear-Repository-Public/tree/e4eeab80ce5138daef61e02beccc7fe5122979f9/Codes/MELCOR_2X/DOSE%20RATE%20CALCULATION

Thank you for your attention

Instrumentation survivability assessment during a severe accident; incorporating radiation monitoring in MELCOR to evaluate the impact on SAMGs

Kevin Fernández-Cosials[1], Rodrigo Rivilla[1], Cesar Queral[1], Robledo F.[2]

Kevin.fcosials@upm.es

1: Universidad Politécnica de Madrid (Spain)

2: Consejo de Seguridad Nuclear (Spain)

The 12th European Review Meeting on Severe Accidents Research

May 18-22, 2026, Universidad Carlos III de Madrid, Madrid, Spain

TECHNICAL SESSION 6.1: SOURCE TERM

Chairs: A.-C. Grégoire (ASNR), T. Kärkelä (VTT)

ID198	**Extension of Fission Product Transport Modeling in MELCOR** D. Luxat (SNL)	Presentation
ID187	**Severe Accident Source Term Analyses for VVER-1000 Focused on Iodine Speciation: Sensitivity Studies with Derived Best-Practices Using ASTEC/SOPHAEROS** Š. Tichý (UJV)	Paper Presentation
ID184	**Evaluation of the effect of different transport path modelling on FP behaviour in AC2/ATHLET-CD** L. Tiborcz (GRS)	Paper Presentation
ID058	**Development of Evaluation Technology for Radiological Source Term in the Containment Using CINEMA Code During Severe Accidents** D. Son (KAERI)	Paper Presentation

ADVANCING NUCLEAR SAFETY TECHNOLOGY

Extension of Fission Product Transport Modeling in MELCOR

David L. Luxat · Lucas Albright · Brad Beeny · Troy Haskin · Dallin Keesling
Dept. 8852 · Nuclear Energy Safety Technologies · Sandia National Laboratories

SAND2026-XXXXP

Sandia National Laboratories is a multimission laboratory managed and operated by National Technology & Engineering Solutions of Sandia, LLC, a wholly owned subsidiary of Honeywell International Inc., for the U.S. Department of Energy's National Nuclear Security Administration under contract DE-NA0003525.

Bottom line up front

Where the work stands

- Modernized architecture running alongside the established baseline — one simulation manager, one time loop
- Original MELCOR unchanged — packages, input decks, source
- Three generic engines for FP transport: species transport, particle balance, chemistry
- Each engine is configuration-driven — reads species, reactions, materials from the input deck
- New physics enters at any granularity: correlation, fluid or material, submodel, integrator, external code

What this opens up

- A common platform for continued FP-modeling evolution — baseline preserved underneath
- Contributions from the community without forking: national labs, regulators, vendors, universities
- Open-ended validation campaigns — new models in the same harness as the built-ins
- Every addition named, versioned, and recorded in the run log
- Auditability MELCOR is trusted for, preserved end to end

The architecture extends MELCOR's fission-product modeling without modifying the original packages. The existing validation basis for those packages is unaffected.

Original MELCOR and new physics in one time loop

Not a replacement — an enabler. Every validated package from the original MELCOR runs underneath in the same time loop as the new native packages.

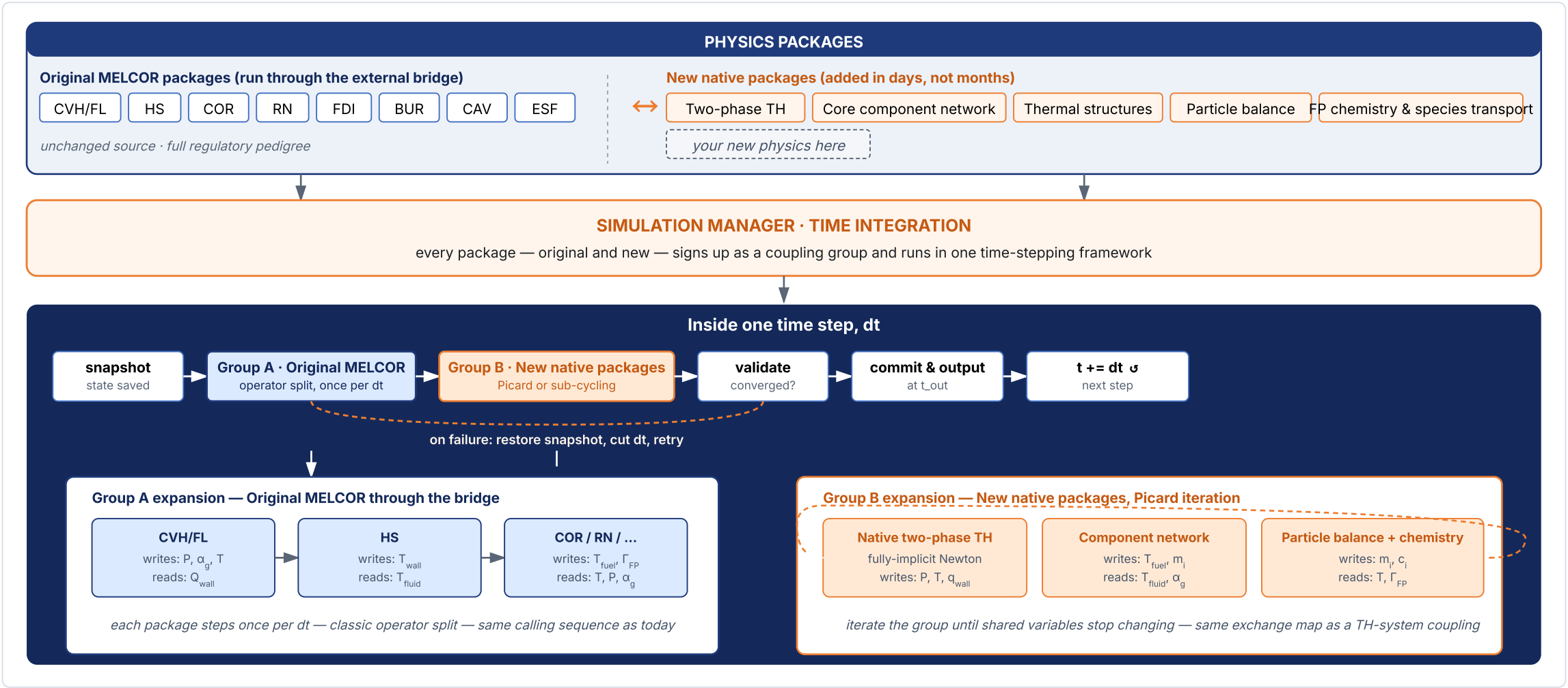

Five places extensions plug in

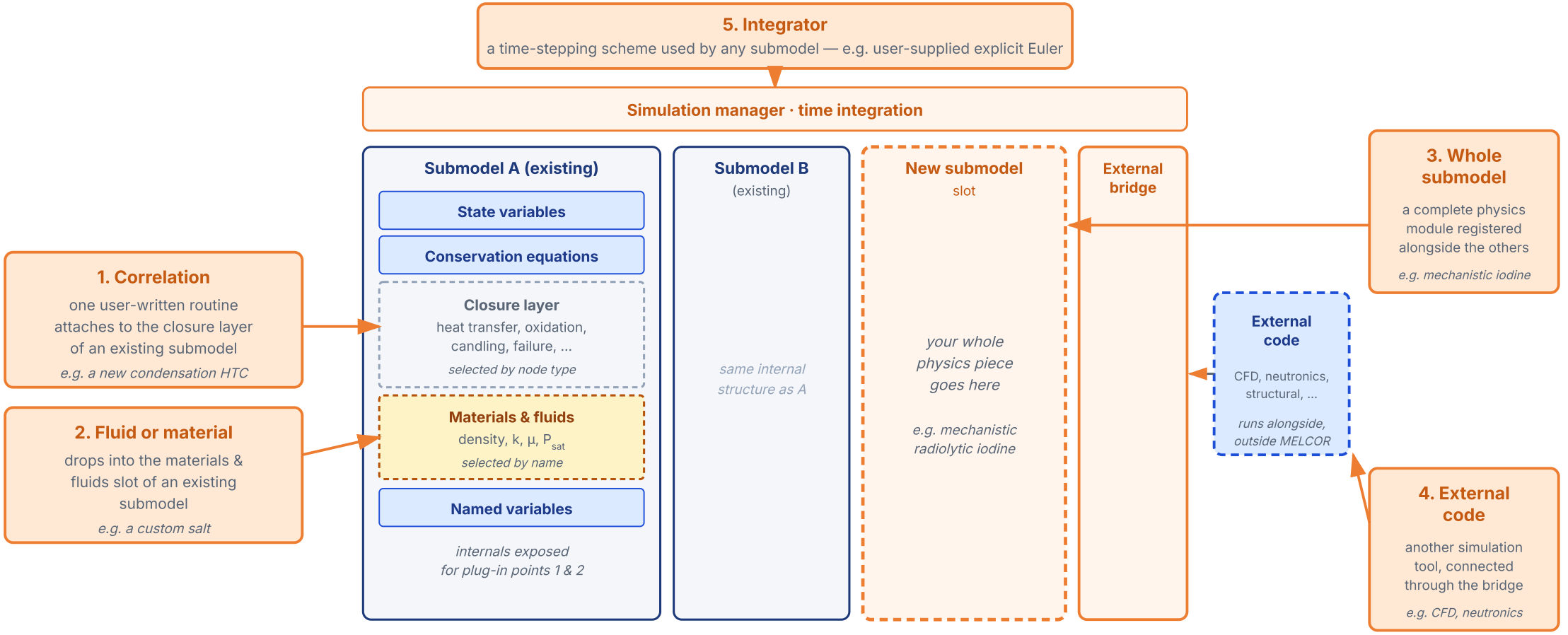

the rest of the deck walks through points 1 and 3, with two worked examples

Writing a plugin — what the engineer has to define

The same three steps for every kind of plugin: name the new piece, declare what it reads and writes, and supply the physics. What changes by plugin type is the kind of physics being written.

1. Name the new piece
the input deck will reference it by name

→

2. Declare its inputs & outputs
the named quantities it reads and writes

→

3. Supply the physics
the equations or property functions

→

Compile
to a shared module

What "the physics" means — depending on which kind of plugin you are writing:

1. Correlation

A single closure relation: heat-transfer coefficient, friction factor, oxidation rate.

Inputs to declare
the dimensionless groups or local conditions it consumes — Re, Pr, void fraction, wall temperature

Output to declare
the value returned at each call — e.g. h, f, k(T)

The physics
the formula or tabulated form — pure point-wise evaluation, no time stepping

2. Fluid or material

A new working fluid for the thermal-hydraulics, or a new structural material for the walls.

Inputs to declare
temperature, pressure, and composition where the properties depend on them

Outputs to declare
fluid: density, specific heat, conductivity, viscosity, vapor pressure. Solid: k(T), ρ(T), creep law

The physics
the property correlations — from a reference compilation or your own data fits

3. Whole submodel

A complete piece of physics with its own state and its own time evolution.

State to declare
the variables this submodel owns — masses per species, temperature, phase fraction

Coupling to declare
which named quantities it consumes from the rest of MELCOR and which it exposes back

The physics
the conservation equations and the closure relations that feed them

4. External code

Another simulation tool (CFD, neutronics, structural) coupled in alongside MELCOR.

Boundary conditions to declare
what the external code reads from MELCOR — T, P, void fraction, source rates

Source terms to declare
what it returns — wall heat flux, species generation, deformation

The physics
already exists — you supply the wrapper that exchanges data each timestep

5. Integrator

An alternative time-stepping scheme for submodels that need one.

Inputs to declare
the named state vector to advance and the time interval

Outputs to declare
the advanced state plus convergence and step-control diagnostics

The algorithm
the time-stepping logic itself — explicit, implicit, predictor-corrector, sub-cycling

PART 1

Fission-Product Transport Capabilities

Three pillars — species, particles, chemistry

Source-term calculations need three capabilities running together. The modernized path treats each one as a generic engine that accepts user-supplied configuration — from the input deck or from a plugin.

Activation today is through integration with the modernized thermal-hydraulic submodule: it provides the volumes, the flow fields, and the boundary conditions that all three engines consume.

Species transport

How dissolved and gas-phase species move through the system — convection, diffusion, deposition, and trap kinetics.

- Fick + Soret diffusion in fluids; advection from the thermal-hydraulics
- Mass transfer across interfaces (Sherwood correlations: laminar/turbulent plate, Dittus–Boelter, packed bed)
- Diffusion + Oriani / McNabb–Foster trap kinetics in metal walls
- Permeation barriers (Al_2O_3, Er_2O_3, Cr_2O_3)

tritium permeation, deposited FP plateout, structural permeation

Particle balance (sectional PBE)

How particles are born, grow, agglomerate, and deposit — in **any** carrier phase: vapor plenum, liquid pool, or frozen layer.

- Sectional bins (1 nm to 1 µm, log-spaced), multi-species, multi-component
- Classical-nucleation theory; agglomeration; breakup; deposition
- Heterogeneous nucleation on solid seeds; crust-face plateout; melt-back resuspension
- Coupling to species transport for wall deposition flux

aerosol source term, noble-metal precipitation, debris-bed plateout

Chemistry

How species transform into one another — radiolytic, kinetic, equilibrium — expressed as a reaction network read from the input deck.

- Generic chemistry engine: species list + reaction list
- Rate-law types: unimolecular, bimolecular, radiolysis source
- Phase-transfer via Henry's law / two-film mass transfer
- Same engine hosts a 3-species fast option or a ~35-species mechanistic model

iodine speciation, organic iodide, FP–radical interactions

Particle balance — one engine, three carrier phases

The sectional particle-balance engine is carrier-agnostic. The same machinery counts and advances particles in a gas plenum, a salt pool, or a freezing crust — only the carrier-specific closures change.

Common machinery, registered once and dispatched by carrier type:
nucleation · agglomeration · breakup · condensation/evaporation · deposition · resuspension

Vapor carrier

Classical aerosol PBE in the gas plenum or cover-gas system.

- **Nucleation** — classical-nucleation theory driven by supersaturation
- **Agglomeration** — Brownian + turbulent shear
- **Deposition** — gravitational settling, thermophoresis, diffusiophoresis, wall plateout
- **Data** — CsI, CsOH, NaI from JANAF tables; surface tension and saturation pressure built in

e.g. containment aerosol source term; off-gas to charcoal bed

Liquid carrier

Particulates suspended in a coolant, salt pool, or sump.

- **Nucleation** — same classical form, driving force now dissolved-species supersaturation
- **Agglomeration** — DLVO-modulated: Hamaker constant, zeta potential, ionic strength
- **Deposition** — Sherwood-based wall mass transfer; settling under gravity
- **Application** — noble-metal precipitation in molten salt (Mo, Ru, Pd); pool-scrubbing capture

e.g. molten-salt-reactor noble-metal source; liquid-phase iodide carryover

Solid (frozen) carrier

Particles entrained in a freezing layer or debris bed.

- **Heterogeneous nucleation** — on existing solid seeds in the bulk: $J_{het} = J_{hom}(1 + \gamma\, \alpha_{sp})$
- **Crust deposition** — particulate flux onto the growing freezing front
- **Resuspension** — on melt-back, frozen-trapped inventory returns to the liquid carrier
- **Coupling** — reads α_{sp} and freeze/melt rates from the solidification submodel

e.g. freeze-plug trapped inventory; crust-face plateout in molten salt

Generalized chemistry — the species mole balance

Each control volume integrates a species mole balance for every tracked species. The same equation shape applies whether the network has three species or three hundred — only the stoichiometry tables and the rate-constant functions change.

Per-volume species mole balance

$$\mathrm{d}n_i/\mathrm{d}t = V \cdot \Sigma_r \nu_{i,r} \cdot R_r + J_i^{\mathrm{phase}} - \lambda_i n_i$$

Terms

- $\mathrm{d}n_i/\mathrm{d}t$ — moles of species i in the control volume
- $V \cdot \Sigma_r \nu_{i,r} \cdot R_r$ — net production/consumption from all reactions: the stoichiometric coefficient $\nu_{i,r}$ picks up species i in each reaction r, weighted by the volumetric rate density R_r [$\mathrm{mol \cdot m^{-3} \cdot s^{-1}}$]
- J_i^{phase} — aqueous↔gas exchange (covered next slide)
- $-\lambda_i n_i$ — radioactive decay of species i

The integrator sees N coupled ODEs per control volume

- N species ⇒ N coupled ODEs per volume; reactions are the off-diagonal coupling terms
- Jacobian assembled automatically from the stoichiometry table and the rate-constant derivatives
- Fast scoping networks: N ≈ 3 (iodine baseline). Mechanistic networks: N ≈ 35–50 (radiolytic chemistry)
- Stiff in radiolysis regimes — same fully-implicit integrator path used elsewhere in the modernized layer

The user does not write the ODE solver, the Jacobian assembly, or the time integration. Only the stoichiometry and rate-constant functions are user-supplied — through the species and reaction lists.

Generalized chemistry — rate-law forms and phase transfer

Three rate-law forms cover essentially every reaction class in containment chemistry. Phase transfer between aqueous and gas-phase species uses Henry's-law two-film relaxation.

Three rate-law forms — one per reaction entry

Unimolecular — first-order in one reactant

$$R_r = k_r(T, \mathrm{pH}, \dot{D}) \cdot c_A$$

radiolytic oxidation/reduction, hydrolysis, dissociation

Bimolecular — second-order, two reactants

$$R_r = k_r(T) \cdot c_A \cdot c_B$$

radical–radical recombination, radical–iodine reactions, scavenging

Radiolysis source — zero-order in species

$$R_r = G_r \cdot \dot{D} \cdot \rho_{\mathrm{liquid}}$$

water radiolysis from gamma/beta dose; G-values per Elliot & Bartels compilation

Phase transfer — Henry's-law two-film

$$J_i^{\mathrm{phase}} = -(1/\tau_{\mathrm{relax}}) \cdot (c_i^{\mathrm{aq}} - c_i^{\mathrm{aq,eq}})$$

$$c_i^{\mathrm{aq,eq}} = p_i^{\mathrm{gas}} / H_i(T)$$

The aqueous concentration relaxes toward Henry's-law equilibrium with the gas-phase partial pressure on a timescale τ_{relax}. The user names the aqueous/gas pair, supplies the partition coefficient $H_i(T)$, and supplies a numerical value of τ_{relax} for each pair — the code does not derive it. Typical choice: a film-theory estimate $\tau \sim V_{\mathrm{liq}}/(k_L A)$, or an empirical fit.

Generalized chemistry — couplings into the modernized code

All chemistry inputs and outputs are named exchange variables. The chemistry engine reads boundary conditions and drivers from other modernized modules each timestep, and writes back the quantities those modules consume.

Reads (boundary conditions, drivers)

- **T, P, control-volume V** — from the modernized thermal-hydraulics
- **pH** — from a pH-tracking model or as a user-supplied field
- **dose rate $\dot{D}$** — from the decay-heat / dose-source module
- **solid particle volume fraction α_{sp}** — from the particle balance, when heterogeneous nucleation applies

Writes (back into the coupled state)

- **dissolved-species inventories c_i** — to species transport for advection, deposition, wall plateout
- **gas-phase partial pressures p_i** — to thermal-hydraulics for the cover-gas mass balance
- **supersaturation drivers $S_i = c_i/c_i^{sat}$** — to particle balance for nucleation and condensation
- **radioactive decay source** — to the decay-heat module

Every exchange variable is named in the input deck and recorded in the run log. The chemistry engine has no implicit dependencies on the rest of the code.

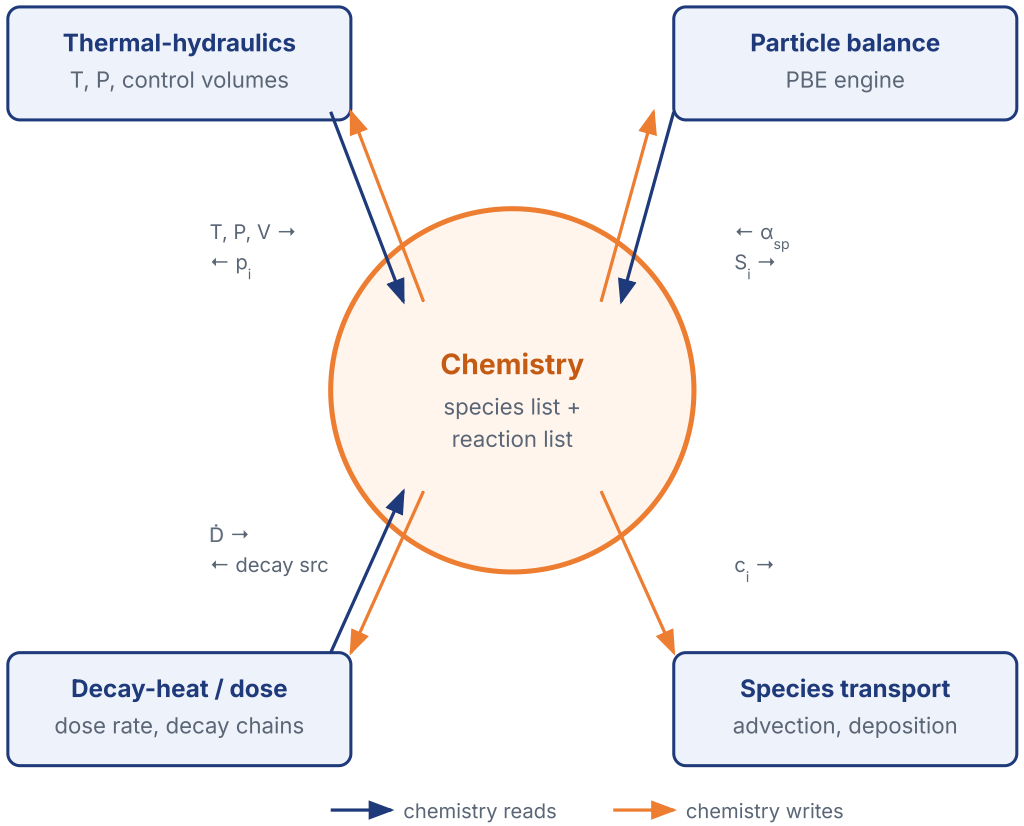

PART 2

Replacing Rate Correlations

Pool release — the rate-correlation library

Four mass-transfer kernels for pool → cover-gas release. Each species in the input deck declares which kernel applies; the plugin evaluates it each timestep and writes the per-species release rate.

Henry's-law mass transfer — aqueous pools

$$dm_i/dt = -k_l \cdot A_{pool} \cdot (c_{aq} - p_i/H_i(T))$$

Supplied per species: liquid-side mass-transfer coefficient k_l, Henry constant $H_i(T)$.

I_2, CsI, CsOH, TeO_2 in water.

Raoult's-law mass transfer — multi-component liquids

$$dm_i/dt = -h_m \cdot A_{pool} \cdot (P_i^{liq} - P_i^{gas}) \cdot M_i/RT$$

$P_i^{liq} = \gamma_i\, x_i\, P_{sat,i}(T)$; Antoine form. Supplied per species: A, B, γ_i.

CsF, LiI, Li_2Te, TF in salt; Cs in sodium.

Bubble degassing — dissolved gases

$$dm_i/dt = -k_b \cdot A_{pool} \cdot m_i$$

First-order depletion. Supplied per species: k_b.

Xe, Kr in every coolant; T_2 in salt.

Aerosol entrainment — non-volatile species

$$dm_i/dt = -e_{ent} \cdot A_{pool} \cdot (m_i/m_{pool})$$

Mechanical droplet entrainment from the pool surface; rate scales with surface mass-fraction.

NaI, Na_2Te in sodium.

Worked example — FLiBe pool with thermal transient, 7 days

A molten-salt drain-tank pool driven through a temperature ramp from nominal 950 K up to 1050 K and back. The plugin's Antoine vapor-pressure response is exercised by the transient; the bubble path is set by inventory rather than T, and the two behaviours appear side by side in one plugin.

Scenario

- FLiBe (66 mol% LiF / 34 mol% BeF_2); pool volume 10 m^3, surface 5 m^2, off-gas plenum 100 m^3
- T_{pool} transient: 950 K (1 day) → ramp to 1050 K → 2 days at 1050 K → ramp back to 950 K → final 2 days nominal
- 7-day total, 10-minute output cadence
- Seven species: CsF, LiI, Li_2Te, TF (vapor-Raoult); T_2, Xe, Kr (bubble)

What the temperature transient brings out

- Raoult release rates climb roughly one order of magnitude through the 1050 K plateau, then relax back when T_{pool} returns to 950 K
- Cumulative Cs, I, Te release inflects upward during the hot phase — the integrated fraction depends strongly on the high-temperature dwell
- Each Raoult species responds differently — CsF, LiI, Li_2Te, TF have different Antoine slopes
- T_2 bubble rate is set by remaining inventory, not by T_{pool}; TF Raoult tracks the temperature transient instead

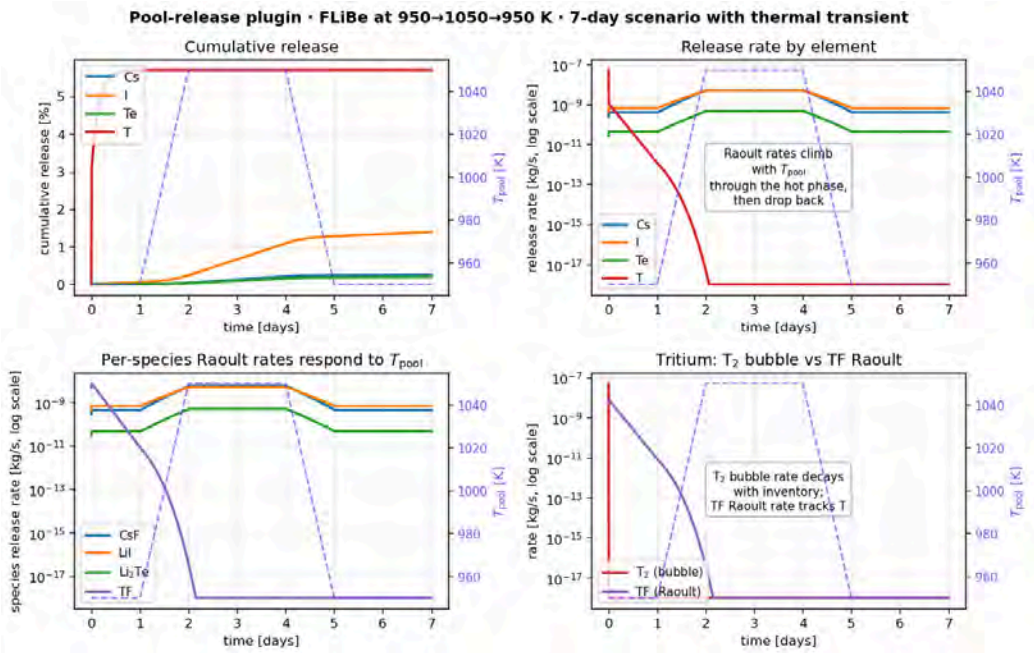

Worked example — sodium pool with thermal transient, 30 days

A liquid-sodium primary pool driven through a 30-day temperature transient: 700 K → 900 K (hot phase) → 750 K (intermediate) → 700 K. The plugin's vapor-Raoult and aerosol-entrainment modes respond to T_{pool} in qualitatively different ways — one tracks the transient closely, the other does not.

Scenario

- Liquid sodium; pool volume 50 m^3, surface 25 m^2, cover-gas plenum 500 m^3
- T_{pool} transient: 700 K (3 days) → ramp to 900 K → 7 days at 900 K → ramp to 750 K → 6 days at 750 K → ramp back to 700 K
- 30-day total, 30-minute output cadence; 4321 adaptive timesteps
- Five species: Cs (vapor-Raoult); NaI, Na_2Te (aerosol entrainment); Xe, Kr (bubble)

What the temperature transient brings out

- Cs Raoult rate swings two orders of magnitude as T_{pool} rises to 900 K and returns — the Antoine vapor pressure is the dominant sensitivity
- Cumulative Cs release shows distinct slopes per temperature plateau: steep through the 900 K phase, shallower in the 750 K phase, baseline at 700 K
- NaI and Na_2Te aerosol entrainment is set by the inventory and pool-surface model — effectively T-independent on this scale, so the I and Te dynamics is decoupled from the transient
- Two physically distinct release modes, one set of inputs — the deck visibly separates the responses

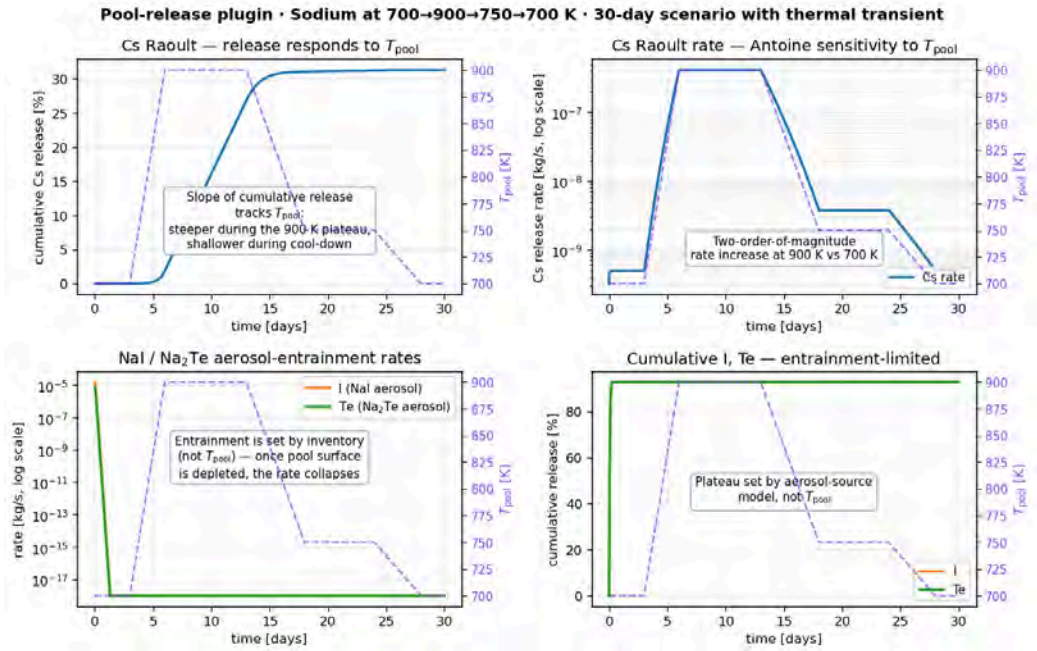

PART 3

Replacing a Whole Submodel

A LIRIC-style mechanistic iodine model — implemented in the modernized submodule

A mechanistic radiolytic iodine model is currently implemented in the modernized submodule. It tracks roughly 35 species and 180 reactions, including water radiolysis, the full iodine speciation chain, organic-iodide formation, radical scavenging, and aqueous↔gas phase partition.

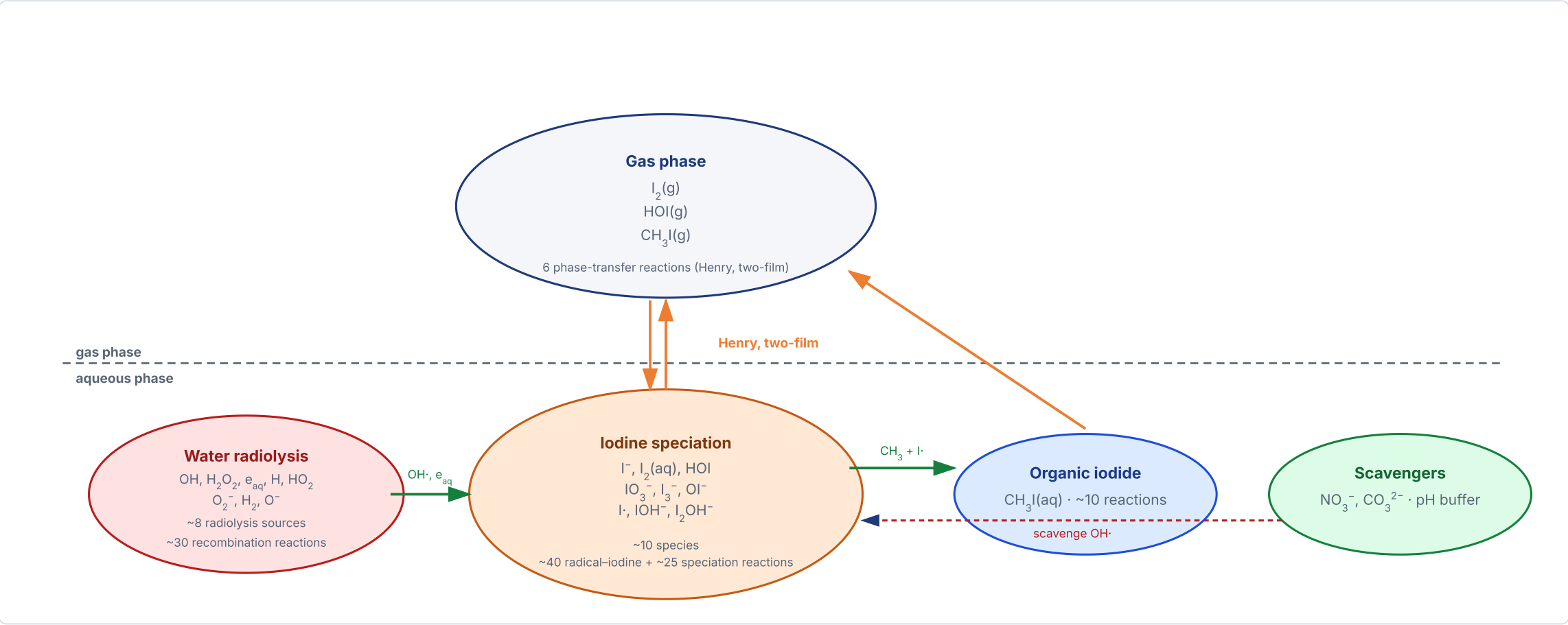

Simplified iodine modeling plugin

A 3-species, 3-reaction network of the IMOD class. The forward radiolytic oxidation drives iodide toward I_2; the reverse radiolytic reduction returns I_2 to iodide. Together they set a pH-dependent kinetic steady state rather than monotonically exhausting iodide.

- **Species.** I^-(aq), I_2(aq), I_2(g)
- **Radiolytic oxidation.** $I^- \rightarrow \frac{1}{2} I_2$, first-order in iodide. Native form $k_1 = \alpha \cdot$ dose rate.
- **Radiolytic reduction.** $I_2 \rightarrow 2\ I^-$, first-order in I_2, **pH-dependent**. Captures the O_2^- / H_2O_2-mediated reduction pathway from Wren et al., **Nucl. Tech.** 129(3), 2000 (§II.B.2, §II.C.2).
- **Henry's-law transfer.** I_2(aq) ↔ I_2(g) at a relaxation timescale τ against a partition coefficient.

Not modelled in this network: organic-iodide formation (I_2 + RH → RI), AgI precipitation, I_2 hydrolysis.

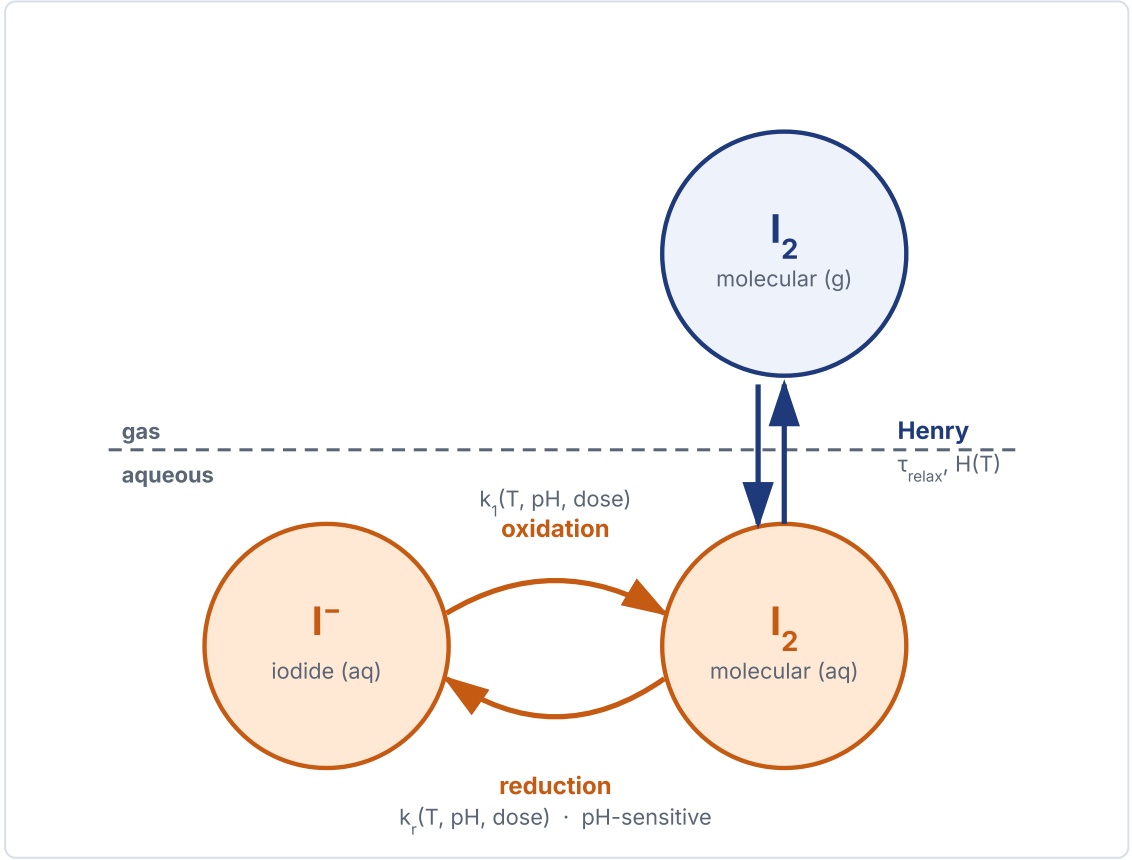

Result — iodine chemistry tracks a buffered pH ramp

12-hour transient. The pool buffer ramps pH between 4.5 and 9.0 (and back). Chemistry equilibrates fast; the question is whether the source term **follows** the pool when conditions move — or stays stuck.

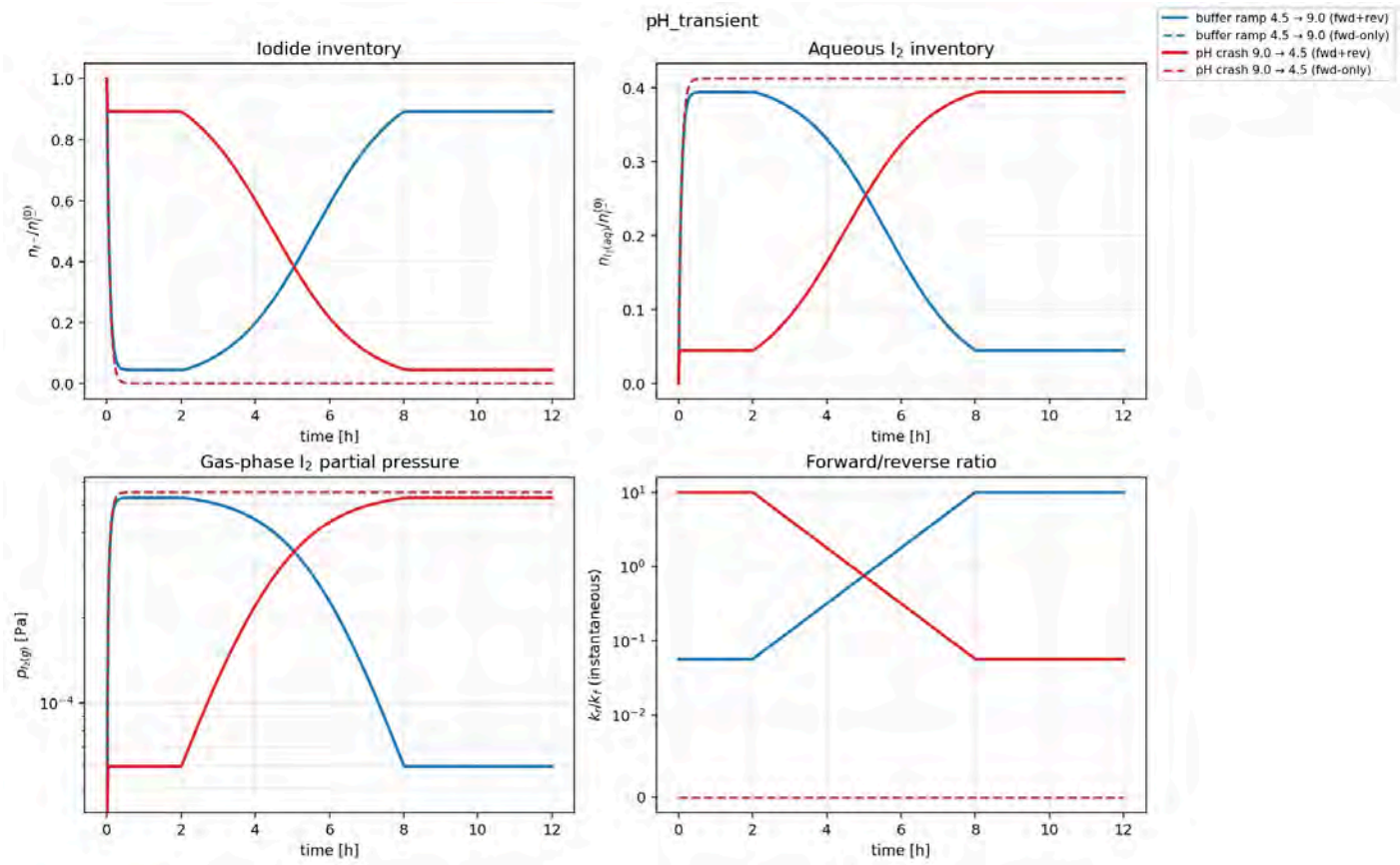

Ramp ↑ pH 4.5 → 9.0 (red)

Iodide regenerates as the pool becomes alkaline; gas-phase I_2 falls **three orders of magnitude** over the 6-hour ramp; forward/reverse ratio swings from ~0.1 to ~10.

Ramp ↓ pH 9.0 → 4.5 (blue)

Mirror image — iodide is re-oxidized; gas-phase I_2 climbs three orders of magnitude. Reversibility is in the kinetics, not just thermodynamics.

Forward-only twins (dashed)

No response to pH at all. Once iodide is exhausted there is no path back — the dashed gas-phase I_2 sits at the ceiling for the entire transient.

ADVANCING NUCLEAR SAFETY TECHNOLOGY

Thank you

David L. Luxat · Lucas Albright · Brad Beeny · Troy Haskin · Dallin Keesling
dlluxat@sandia.gov
Dept. 8852 · Nuclear Energy Safety Technologies · Sandia National Laboratories

SAND2026-XXXXP

Sandia National Laboratories is a multimission laboratory managed and operated by National Technology & Engineering Solutions of Sandia, LLC, a wholly owned subsidiary of Honeywell International Inc., for the U.S. Department of Energy's National Nuclear Security Administration under contract DE-NA0003525.

Severe Accident Source Term Analyses for VVER-1000 Focused on Iodine Speciation: Sensitivity Studies with Derived Best-Practices Using ASTEC/SOPHAEROS

Štěpán Tichý[1,2]
[1]ÚJV Řež, a. s.
Hlavní 130, 250 68 Husinec - Řež, Czech Republic
[2]Department of Nuclear Reactors
Faculty of Nuclear Sciences and Physical Engineering, Czech Technical University in Prague,
V Holešovičkách 2, 180 00 Prague 8, Czech Republic
stepan.tichy@ujv.cz

ABSTRACT

Severe accident management and source term evaluation are essential for nuclear safety, especially in large light-water reactors such as the VVER-1000. This paper presents best-practice methodologies and sensitivity analyses using the ASTEC code, focusing on iodine chemistry and transport processes in the containment. Iodine is of particular concern because of its volatile forms, complex speciation, and sensitivity to containment thermohydraulic conditions. The analyses use the SOPHAEROS module to model fission product deposition, re-volatilization, and chemical transformations across multi-compartment containment geometries. Special attention is given to iodine speciation among gaseous molecular iodine (I_2), organic iodides, and aerosols, and to the effects of temperature, humidity, and radiation on interconversion mechanisms.

Sensitivity studies emphasize the importance of boundary conditions, especially thermodynamic parameters that control iodine volatility and long-term retention within the containment. In total, over 80 reactions with iodine in the containment are considered in the ASTEC code, among which those happening in the sump are of major importance. Those reactions are radiation, temperature, pH and I^- concentration dependent and govern thus iodine retention and re-volatilization.

Results of the sensitivity analyses indicate that containment thermodynamic conditions, together with sump acidity and iodine mass transfer – reflected by changes in iodide (I^-) concentration due to entrainment by droplets from an operating containment spray system – are decisive factors in predicting the iodine source term to the environment. These findings underscore the need for harmonized best-practice approaches in ASTEC applications and offer valuable guidance for developing improved accident management strategies not only for VVER-1000 type reactors.

KEYWORDS
Iodine Speciation, Severe Accident, VVER-1000, ASTEC/SOPHAEROS, Containment

1. INTRODUCTION

Iodine is a key contributor to radiological risk during severe accidents (SA) because it appears in several volatile forms and can be transported efficiently to the environment, especially in its gaseous forms, if not retained by in-vessel or containment processes. European R&D programs such as PHEBUS FP [1] and the

associated state-of-the-art report on iodine chemistry [2] have established that iodine behavior in containment (CTMT) is governed by a complex interplay between aqueous chemistry, gas-phase reactions, radiolytic effects, and interactions with CTMT surfaces.

In parallel, the ASTEC [3] integral severe-accident code has been developed and validated as the European reference for source-term evaluation, including the SOPHAEROS module for fission-product (FP) transport and iodine chemistry.

In this work, the ASTEC code, with the simulations centered around the SOPHAEROS module is applied to an integral model of a VVER-1000 nuclear power plant subjected to a cold-leg guillotine break leading to loss of coolant accident (G-LOCA) scenario. The study focuses on the sensitivity of iodine speciation to the pH variation in the CTMT sump with sump pH values spanning from 5 to 9. For each analyzed variant, the evolution of iodine amount retained in the CTMT sump and the total amount of gaseous forms of iodine in the CTMT atmosphere was evaluated, with particular attention to molecular iodine (I_2). In addition to pH variation, selected calculations also included the activation of the CTMT spray system, which significantly alters the thermodynamic conditions in the CTMT atmosphere – namely the atmosphere pressure, temperature, and relative humidity. These changes influence both the production of I_2 in the sump and the mass-transfer processes controlling the release of volatile iodine species into the gas phase.

The objective of this sensitivity study is to study the influence of sump pH and CTMT thermodynamic conditions on iodine speciation, with emphasis on the resulting quantity of total mass of gaseous iodine in CTMT atmosphere. The results provide insights relevant for SA management, modelling best practices, and the interpretation of iodine-related uncertainties in source-term assessments.

2. COMPUTATIONAL FRAMEWORK AND MODELLING APPROACH

The analyses presented in this study were performed using ASTEC V3.1.2 applied to an integral model of a VVER-1000 plant. The simulations cover the full sequence from in-vessel degradation accompanied with FPs release and their transport within the primary circuit. Focus is then placed on physical processes, mass transfer, and the subsequent chemical and radiolytic transformations of fission products within the CTMT.

2.1. ASTEC Code and SOPHAEROS Module

The integral code ASTEC covers all relevant phenomena occurring during a SA progression and namely couples primary/secondary circuit thermal-hydraulics (module CESAR [4]), core degradation phenomena (module ICARE [5]), FP release, transport and chemical reactions in the circuits and in the CTMT, the state of which is evaluated using the CPA module [6]. Radiological dose rates are automatically calculated by the DOSE module [7], based on FP decay heat and activity inventories provided by the ISODOP module [8].

For the present study, emphasis is placed on the SOPHAEROS module [9] within the ASTEC code, which models FP transport and iodine chemistry in multi-volume circuits and CTMT. The model accounts for a wide range of transport and interaction processes, including deposition, condensation, agglomeration, physical and chemical sorption, resuspension, evaporation, aerosol dynamics, and mass-transfer reactions across several domains (liquid, atmosphere, walls). FPs are treated in both aerosol and gaseous forms, encompassing condensable vapors and non-condensable gases, and are tracked through six distinct physicochemical states: airborne gases, condensed vapors, suspended aerosols, deposited aerosols, gases sorbed on structures, and FPs dissolved in sump water. These states apply to all FPs. In addition, six iodine-specific states are considered, describing iodine compounds sorbed on painted, concrete, and steel surfaces under dry, submerged, or wetted (water-film) conditions.

These reactions, along with liquid-gas, wall-gas and wall-liquid mass-transfer pathways, are summarized in Fig 1, which illustrates the large number of potential reactions (more than 80) that may occur within the CTMT. The module thus enables direct assessment of how sump conditions (pH, radiation field), CTMT thermodynamic states and mass-transfers influence the partitioning of iodine between the aqueous and gaseous phases.

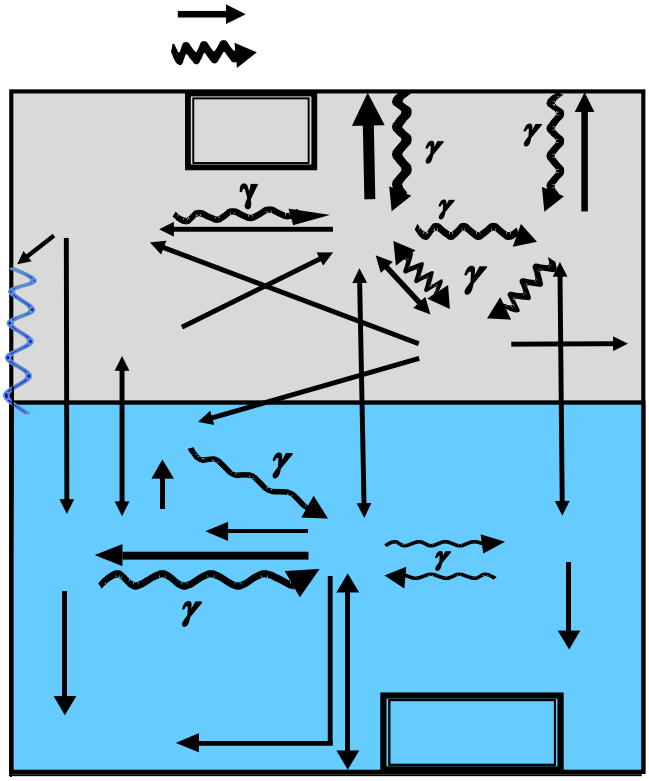

Figure 1. Thermal, radiolytic and mass transfer reactions of iodine considered in SOPHAEROS [10]

2.2. VVER-1000 Plant and Containment Model

The integral model represents a NPP with reactor VVER-1000 including core, primary circuit and a CTMT that includes a water sump, located at the very bottom of the CTMT, which collects liquid from the CTMT compartments. In addition, coolant leakage from the primary circuit into the CTMT leads to the formation of smaller local water pools within the steam generator compartments. Model of CTMT includes distinct surface families (painted, concrete, steel). As the focus of this article is on the forms and speciation of iodine in CTMT, the input model description limits to the nodalization scheme of the core/reactor pressure vessel (RPV) on Fig. 2. The primary circuit is represented by a 1+2+1 loop configuration, providing pathways for FP transport from the reactor to the CTMT.

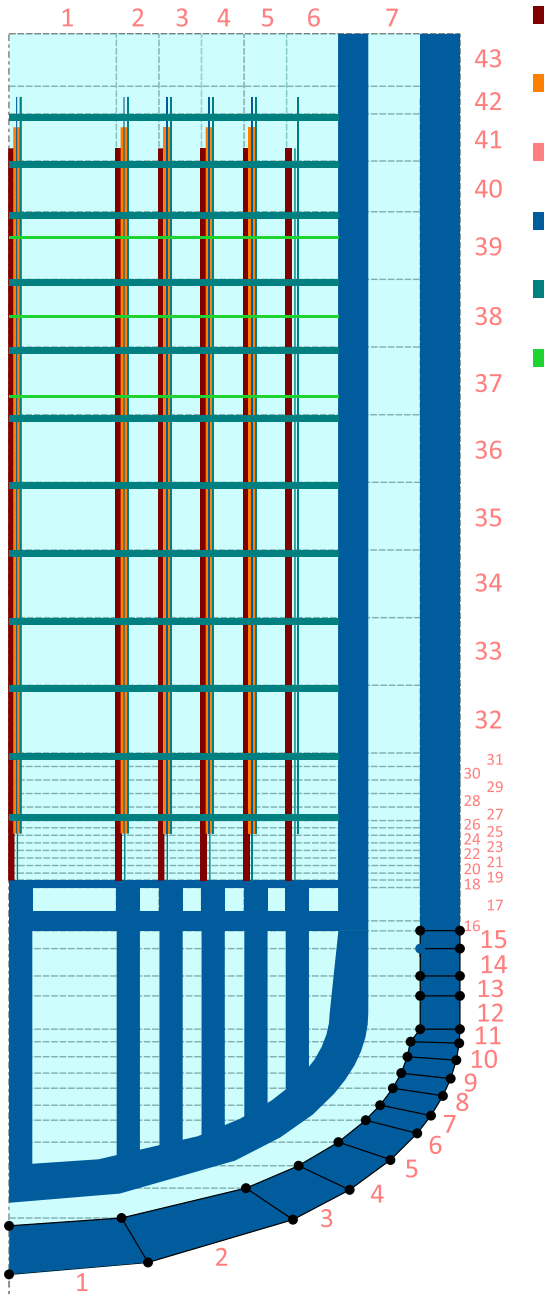

Figure 2. Nodalization scheme of the RPV

The CTMT is modelled using a 36-zone nodalization that represents individual compartments, CTMT water sump and characteristic surface groups. Its layout is shown in Fig. 3. This level of discretization enables the model to capture spatial variations in gas concentrations, temperature and relative humidity that influence iodine partitioning between aqueous, gaseous and other possible phases. During the G-LOCA sequence, the model enables proper tracking of materials and FPs and thermal-hydraulic loads into the CTMT, allowing the assessment of how evolving conditions affect iodine behavior. In selected simulations, the CTMT spray system is activated to assess how spray-induced cooling and substantial decrease of pressure and humidity modify the CTMT atmosphere and the resulting distribution of iodine between the sump and atmosphere.

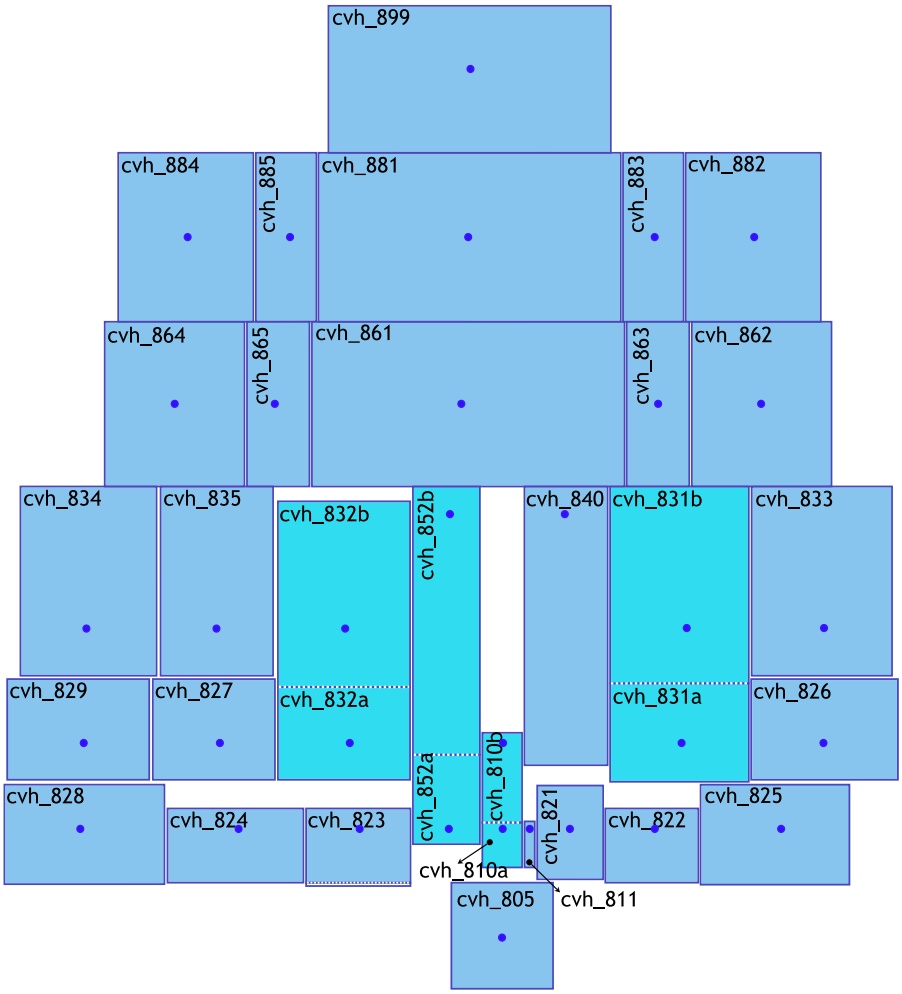

Figure 3. CTMT nodalization for the iodine speciation ASTEC/SOPHAEROS analysis. Reactor shaft is in volume cvh_810. Primary break is modeled in cvh_831b and CTMT sump is in cvh_805.

3. SENSITIVITY ANALYSIS METHODOLOGY

The sensitivity analysis was designed to quantify how selected chemical and thermodynamic conditions in the CTMT influence iodine behavior during a cold-leg G-LOCA sequence. The only parameter varied in the study was the pH of the CTMT sump. Since the default chemistry of the sump reflects the presence of boric acid originating from primary coolant leakage, the pH was adjusted over the range of 5 to 9, representing conditions achievable through the natural buffering capacity of the system as well as through potential operator-initiated additives such as KOH or hydrazine (N_2H_4). This range ensures that both slightly acidic and slightly alkaline environments are represented, allowing evaluation of chemical pathways that are strongly pH dependent. For each pH variant, ASTEC tracked the evolution of dissolved iodine species, with particular focus on iodide (I^-) and molecular iodine (I_2) in the sump, as well as the total amount of gaseous iodine present in the CTMT atmosphere.

Lower pH enhances radiolytic oxidation of I^- through the governing equation (1) and increases the formation of volatile iodine species. It is therefore expected that lower pH would lead to a higher I_2 concentration in the sump (but not necessarily in the CTMT atmosphere; that would depend on mass-transfer from sump) whereas more alkaline conditions favor retention of iodine in non-volatile aqueous forms such as I^-.

$$2I^- + 1/2\ O_2 + 2H^+ \rightarrow I_2 + H_2O \quad (1)$$

To assess the additional influence of CTMT thermodynamic conditions, two additional cases included activation of the CTMT spray system, namely the simulations with pH 5 and pH 9. These spray-assisted variants were chosen to represent the two extreme chemical conditions in the study and to allow a clear comparison of how pH, together with spray-induced changes in pressure, temperature, and relative humidity, modulates mass-transfer from the sump and thus the formation of gaseous iodine in the CTMT atmosphere.

The radiation level, influencing mainly the creation of OH radicals and thus contributing to I^- oxidation, was left to be calculated by the DOSE module, working in close coupling with the ISODOP module. Additionally constant organic concentration was set on the walls as boundary condition.

4. RESULTS OF SENSITIVITY ANALYSIS

A total of seven integral ASTEC simulations were performed to evaluate the influence of CTMT sump chemistry and thermodynamic conditions on iodine behavior during a cold-leg G-LOCA (2x850 mm) sequence. Five calculations covered the pH variation study, with fixed sump pH values of 5, 6, 7, 8 and 9. Two additional simulations were conducted with activation of the CTMT spray system, applied only to the boundary cases at pH 5 and pH 9 to provide a clear contrast between the chemical extremes. This set of simulations forms the basis for the following evaluation of both the in-vessel progression and the subsequent iodine behavior in the CTMT.

4.1 Results of the in-vessel phase of the integral ASTEC calculation

Illustration of the G-LOCA progression through the SA phase up to RPV failure is provided in Fig. 4 to Fig. 6; those 3 graphs summarize the in-vessel progression for all seven simulations, while the timing of main events and selected values at the instant of lowerhead failure are summarized in Table I. Up to the onset of core degradation, all seven simulations evolve indistinguishably; the cold-leg break depressurization and early heat-up proceed in the same manner across the pH-only variants and the two spray-assisted cases, in which the spray systems were activated within the first seconds of the simulation after the CTMT absolute pressure reached 120 kPa, with no activation delay assumed, and remained activated until the end of the simulation.

The initial FPs release from fuel occurs at a comparable instant for all simulations, with a slight advance in the non-spray runs relative to the spray-activated cases. Once rapid degradation of the core begins, small divergences appear that are attributable to numerical noise associated with solving and updating a large, coupled matrix in the integral calculation. The scatter of results indicates rather the inherent sensitivity of integral SA codes to the input parameters. A consistent, scenario-relevant deviation is the earlier timing of vessel failure in the spray-activated variants, where the RPV fails tens of minutes sooner than in the corresponding non-spray cases. Integrated releases from the primary to CTMT differ only marginally – at the level of a few percent.

The pressure evolution in the CTMT shows that the activation of the spray systems results in a noticeable pressure reduction and a subsequently more moderate pressurization rate, as seen in Fig. 6. First small pressure peaks correspond to first relocation of corium to lower plenum. The change in the pressurization trend observed between the third and fourth hour is attributable to the failure of the hermetic doors separating the reactor cavity – into which the corium relocated following RPV failure – from the CTMT.

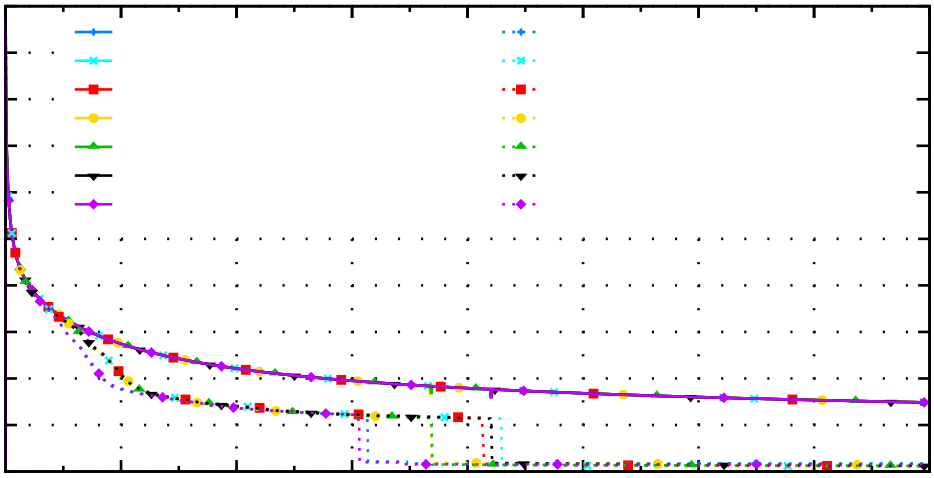

Figure 4. Decay power indication cladding rupture and FPs release, as well as RPV failure.

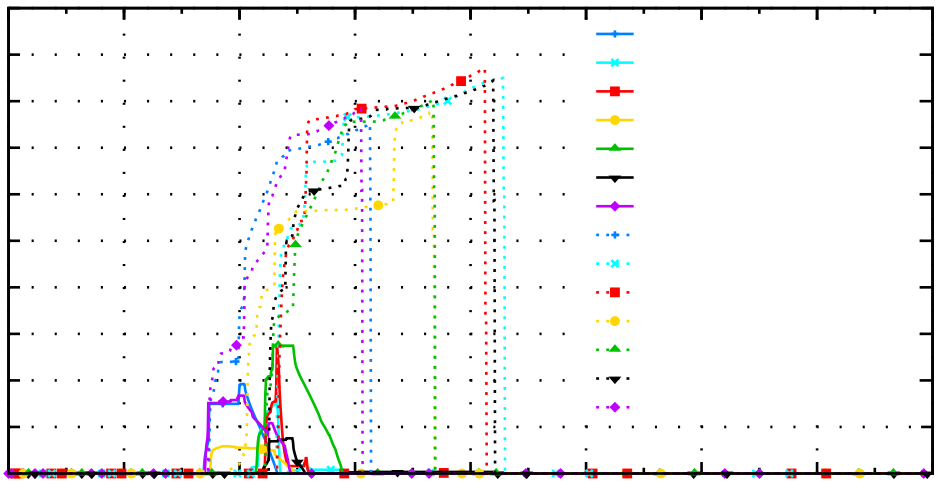

Figure 5. Mass of solid debris (PD) and molten corium (MAG) in the lower plenum.

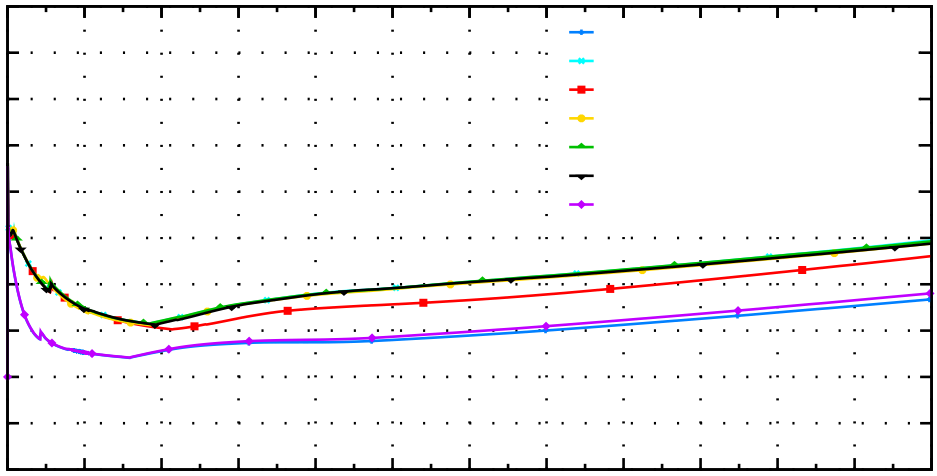

Figure 6. CTMT pressure (absolute).

Table I. Timing of main events and evaluation of iodine release at time of RPV lower head failure

Event	pH 5	pH 6	pH 7	pH 8	pH 9	pH 5 SPRAY	pH 9 SPRAY
Initial event (G-LOCA)	0 s						
Start of FP release	48 s					53 s	
1st material slump in lower plenum	3556 s	3617 s	2869 s	3473 s	3584 s	3037 s	3055 s
Lower head failure	7706 s	7432 s	6605 s	6631 s	7558 s	5634 s	5498 s
Total mass of iodine leaked into CTMT	3381 g	3380 g	3385 g	3588 g	3401 g	3799 g	3522 g

4.2 Results of the CTMT-phase of the integral ASTEC calculation

The CTMT-phase iodine behavior is shown in Fig. 7 to Fig. 10 , covering I^- and I_2 in the CTMT sump and the total gaseous iodine in the atmosphere for all seven simulations. Across the pH-only variants (no spray), the total mass of gaseous iodine (Fig. 10) remains relatively similar despite the chemically driven increase of dissolved I_2 in the sump at lower pH, with only minor run-to-run scatter attributable to numerical noise. Fig. 7 confirms the expected decrease of I^- with decreasing pH for the spray-variation cases. For the no-spray variations, the differences are not discernible due to the selected scale. The slight deviation observed for the pH 8 case results from the higher iodine release compared with the other no-spray simulations. Fig. 8 shows the corresponding increase of dissolved I_2, consistent with enhanced radiolytic oxidation in more acidic conditions. However, this shift in sump speciation does not translate into higher total gaseous iodine mass in the CTMT atmosphere when sprays are not active. The prevailing thermodynamic conditions during G-LOCA – elevated pressure and high relative humidity – limit the liquid-to-gas mass transfer of I_2.

Toward the end of the transient, cyclic rises and drops of gaseous iodine are observed, driven by alternating heating and cooling of small sump that developed within the steam-generator compartments as a consequence of primary coolant depletion. These temperature oscillations periodically enhance or suppress I_2 transfer across the water–atmosphere interface, producing the small late-time fluctuations.

When the CTMT spray system is activated, the thermodynamic state of the CTMT is markedly altered and the iodine response changes accordingly. The spray-induced wash-down of airborne aerosols provides a continuous pathway for transferring iodine species from the containment atmosphere to the sump, resulting in substantially higher I^- inventories (Fig. 7) in the CTMT sump in the spray-assisted scenarios than in the corresponding non-spray variants. This leads to a higher dissolved I^2 inventory in the sump (Fig. 9). In parallel, spray operation leads to a decrease of pressure and increase of mass transfer from the sump to the gas phase resulting in higher amount of total gaseous iodine compared to the non-spray cases, with the effect most prominent at pH 5 (Fig. 10).

The spray cools the atmosphere, decreases pressure, and lowers relative humidity, thereby increasing the driving force for I_2 volatilization and enhancing mass transfer from the sump to the gas phase; at the same time, spray wash-down redistributes aerosol-borne iodine to the sump, reinforcing the coupling between chemistry and transport. In the paired spray simulations at pH 5 and pH 9, the pH-dependent chemistry remains evident – greater radiolytic oxidation at pH 5 yields more dissolved I_2 and, under spray-modified conditions, a higher gaseous-iodine level – highlighting the combined influence of sump chemistry, CTMT thermodynamics and resulting FP mass transfers on the iodine source term.

Overall, the CTMT-phase results confirm the expected pH-dependent shift in sump chemistry, characterized by decreasing I^- and increasing dissolved I_2 at lower pH, while also demonstrating that these chemical changes do not, under non-spray conditions, lead to a higher total gaseous iodine mass in CTMT atmosphere. The higher CTMT pressure without spraying limits liquid–gas transfer. When sprays are activated, the modified conditions enhance I_2 volatilization due to decreased pressure in the CTMT, and the concurrent wash-down redistributes aerosol-borne FPs increasing the sump iodine inventory, resulting in a clearer rise in gaseous iodine, particularly at low pH.

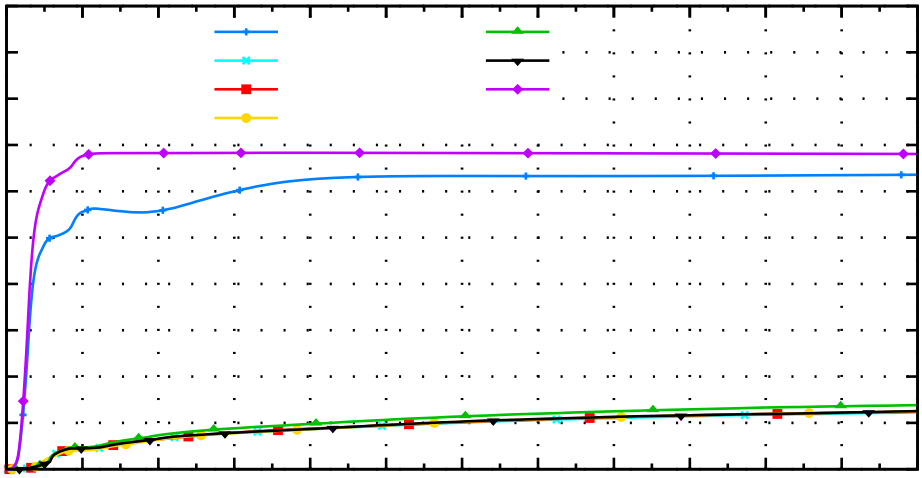

Figure 7. Mass of I^- in the sump of CTMT (liquid phase)

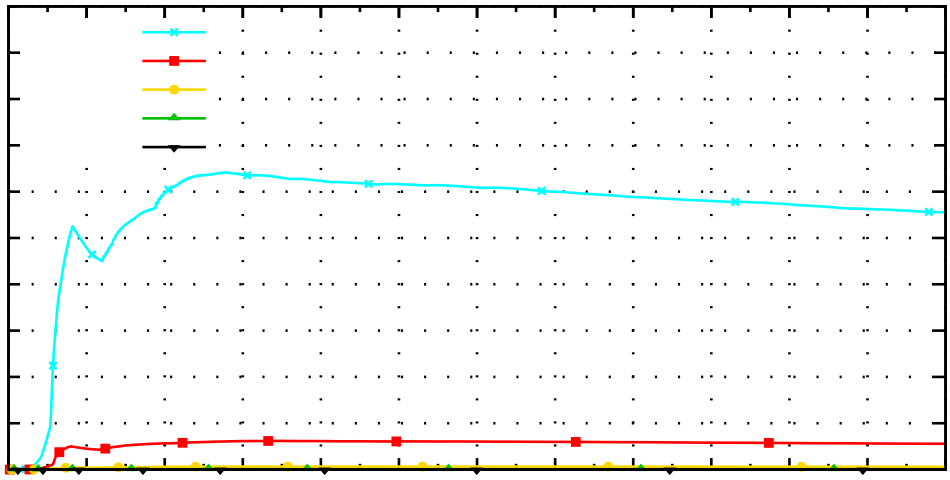

Figure 8. Mass of I_2 in the sump of CTMT (liquid phase) excluding simulations with CTMT spray system activated

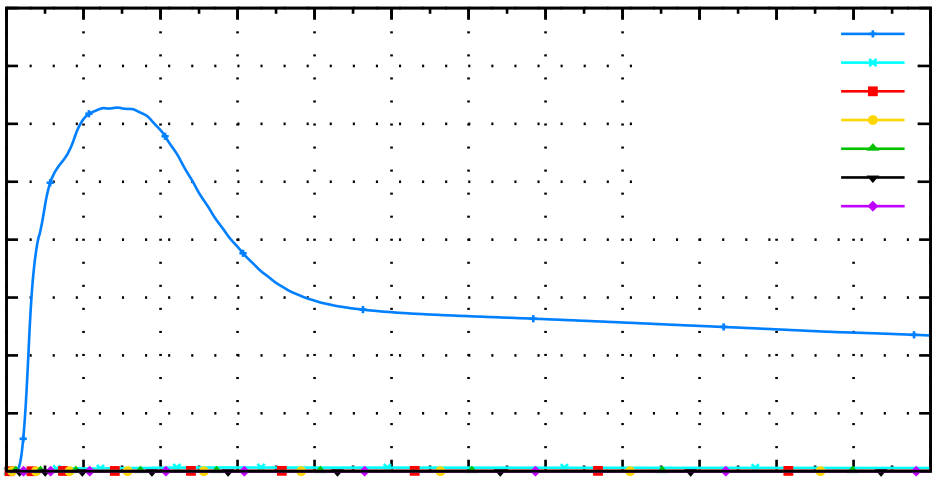

Figure 9. Mass of I_2 in the sump of CTMT (liquid phase) including simulations with CTMT spray system activated

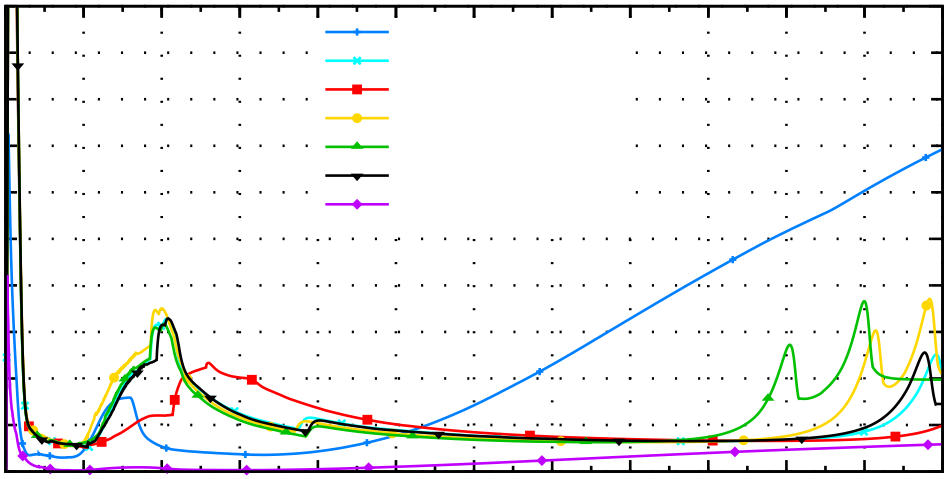

Figure 10. Total mass of gaseous iodine (mainly I_2 and CH_3I) in CTMT

5. CONCLUSIONS

This work employed the integral code ASTEC V3.1.2 to assess iodine behavior in a VVER-1000 CTMT during a cold-leg G-LOCA (2x850 mm) scenario, with a focus on sump chemistry and on the thermodynamic evolution of the CTMT during spray operation, together with the associated FP mass transfer mediated by the spray droplets. Seven integral simulations were performed: five with fixed sump pH values (5–9) and two spray-assisted with fixed values pH 5 and pH 9. The analysis targeted I^- and I^2 in the CTMT sump and the total gaseous iodine inventory in the CTMT atmosphere.

The results confirm the expected pH dependence of sump speciation: as pH decreases, radiolytic oxidation shifts iodine from I^- toward dissolved I^2. However, in non-spray configurations this chemical shift does not translate into a larger total iodine gaseous mass in the CTMT atmosphere. Under G-LOCA conditions, elevated pressure and high relative humidity constrain liquid–gas mass transfer of I_2, thereby stabilizing the gaseous iodine level across pH-only variants.

Activation of the CTMT spray system markedly changes the iodine response. Spray-modified pressure – temperature–humidity conditions enhance I_2 volatilization and interfacial mass-transfer, while spray wash-down increase the sump-borne iodine inventory (notably I^-). The combined effect is a clear rise in gaseous iodine present in the CTMT atmosphere (relative to the non-spray cases), most pronounced at pH 5, consistent with stronger radiolytic production of I_2 at lower pH. These findings highlight that the gaseous iodine source term is co-controlled by sump chemistry, together with CTMT thermodynamics and iodine mass transfer – reflected by changes in iodide (I^-) concentration due to entrainment by droplets from an operating containment spray system rather than by chemistry alone.

The author is aware of the uncertainties present in the study of ASTEC integral simulations. Variations between runs are limited to differences in timing of RPV failure in the order of tens of minutes and leak magnitudes at the percent level. These differences in timing and leak magnitudes reflect numerical scatter inherent to large coupled integral calculations but do not alter the qualitative accident course. In line with

previous observations, the scatter of results indicates rather the inherent sensitivity of integral SA codes to the input parameters, underlining the value of complementary uncertainty and sensitivity analyses when interpreting source-term outcomes.

To further reduce the influence of numerical scatter and to better isolate CTMT-phase phenomena, it is therefore advisable to perform stand-alone CTMT (module CPA) calculations with SOPHAEROS module, using as boundary conditions the coolant, hydrogen, and fission-product releases to the CTMT, together with the thermodynamic evolution, obtained from the in-vessel phase computed by the integral model.

From a modelling and severe-accident-management perspective, the study supports three practical best-practice messages. First, representing sump chemistry alone is insufficient to project gaseous iodine; accurate prediction requires concurrent, time-consistent treatment of CTMT thermodynamic states that govern liquid-gas mass-transfer and possible FPs mass transfers, linked e.g. spray operation. Second, when sprays are credited, their dual role – thermodynamic modification of the CTMT atmosphere and relocation of aerosol-borne FPs to the sump – should be modelled explicitly, as it can both increase gaseous iodine via enhanced I_2 volatility and simultaneously increase sump inventories via wash-down. These conclusions provide a consistent basis for refining ASTEC applications not only to VVER-type plants and for prioritizing measurements and operator guidance related to CTMT thermodynamics and sump chemistry in late-phase accident management.

Third, even though Fig. 7 shows a pronounced increase in I^- concentration in the sump when sprays are operating under alkaline conditions (which should be the high-priority mitigation measure), Fig. 10 demonstrates that the gaseous iodine level in the CTMT atmosphere remains low regardless of spray operation, owing to the basic additives present in the sump. This finding clearly indicates that spray operation does not adversely affect the iodine source term as long as the sump is maintained sufficiently alkaline.

NOMENCLATURE

CTMT	Containment
FP	Fission Product
LOCA	Loss of Coolant Accident
RPV	Reactor Pressure Vessel
SA	Severe Accident

REFERENCES

1. B. Clément and R. Zeyen, “The objectives of the Phébus FP experimental programme and main findings,” *Annals of Nuclear Energy,* **61**, pp. 4-10 (2010)
2. NEA, *State of the art report on iodine chemistry*, pp. 16-40, OECD Publishing, Paris, France (2007)
3. L. Chailan and L. Laborde, *Overview of the ASTEC V3.1 integral code*, IRSN, Paris, France (2022)
4. V. Topin and L. Carénin, *ASTEC: CESAR physical and numerical modelling*, IRSN, Paris, France (2021)
5. V. Topin and L. Carénin, *ASTEC ICARE module : User Manual*, IRSN, Paris, France (2021)
6. N. Reinke, *ASTEC V2.1 CPA reference manual Rev. 1*, IRSN, Paris, France (2016)
7. L. Cantrel, *Description of the DOSE module of ASTEC V2,* IRSN, Paris, France (2009)
8. F. Cousin and F. Jacq, *ISODOP module : theoretical manual,* IRSN, Paris, France (2015)
9. O. Coindreau and F. Kremer, *ASTEC SOPHAEROS module: User manual,* IRSN, Paris, France (2021)
10. L. Bosland, “Presentation of Iodine chemistry in containment with SOPHAEROS module in ASTEC V3.1.1”, *Proceedings of the ASTEC Training Course*, Aix-en-Provence, France, January 15-19 (2024).

NUCLEAR RESEARCH INSTITUTE

Severe Accident Source Term Analyses for VVER-1000 Focused on Iodine Speciation: Sensitivity Studies with Derived Best-Practices Using ASTEC/SOPHAEROS

Štěpán Tichý

18.05.2026

UJV Group
PEOPLE | INNOVATION | TECHNOLOGY

CEZ GROUP

UJV Group, a member of CEZ GROUP

NUCLEAR RESEARCH INSTITUTE

COMPUTATIONAL FRAMEWORK

Code

- ASTEC Code V3.1.2
- Used modules includes: ICARE, CESAR, CPA, DOSE, ISODOP, MEDICIS and SOPHAEROS

UJV model

- Integral model of NPP with VVER-1000 reactor including core, primary circuit and a CTMT that includes a water sump, located at the very bottom of the CTMT
- Simulations cover the full G-LOCA on cold leg sequence from in-vessel degradation with fission product (FP) release and transport within primary circuit
- Focus is placed on physical processes, mass transfer, and the subsequent chemical and radiolytic transformations of FPs within the containment (CTMT)

SOPHAEROS MODULE

- The model accounts for a wide range of transport and interaction processes that may occur within CTMT including:
  - Deposition
  - Condensation
  - Agglomeration
  - Physical and chemical sorption,
  - Resuspension
  - Evaporation
  - Aerosol dynamics
  - Mass-transfer reactions across several domains (liquid, atmosphere, walls).

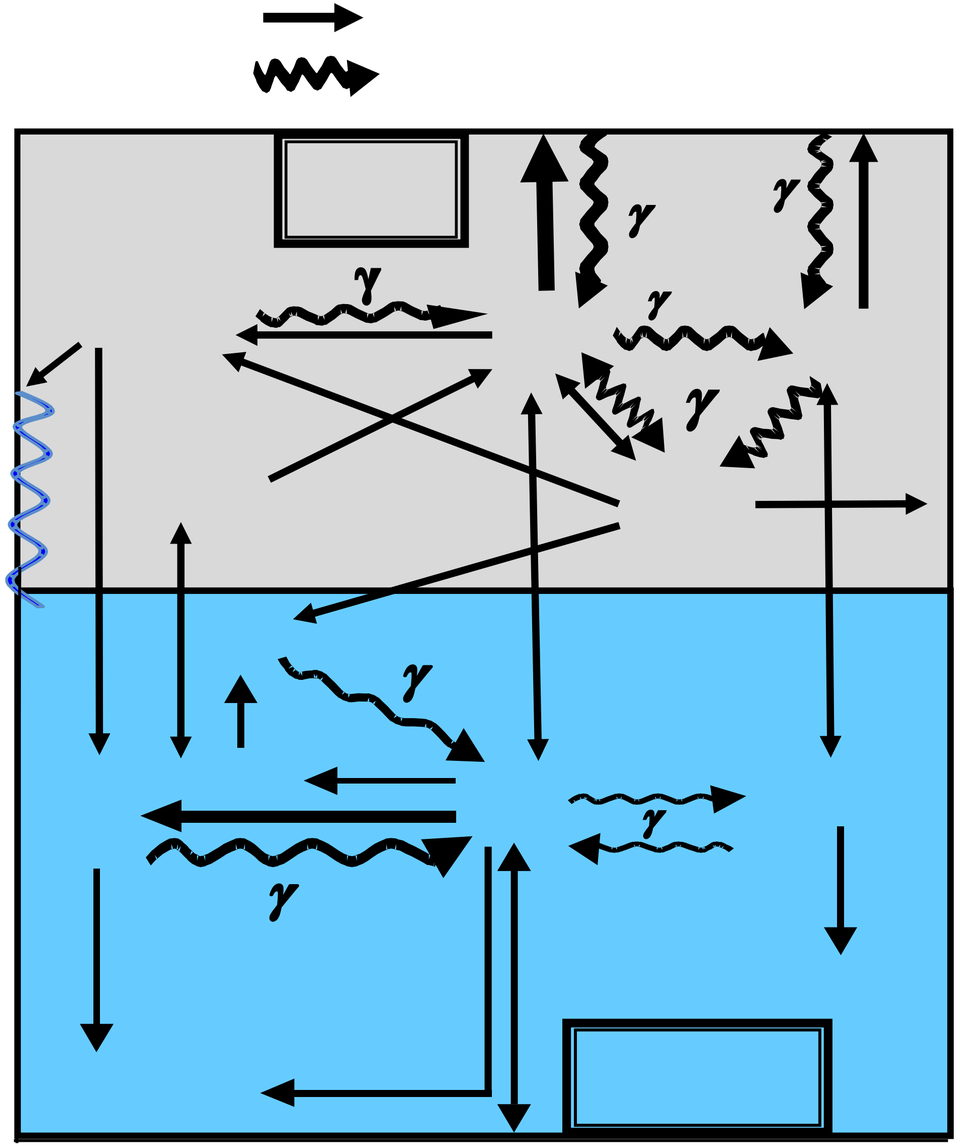

Thermal, radiolytic and mass transfer reactions of iodine considered in SOPHAEROS: O. Coindreau and F. Kremer, *ASTEC SOPHAEROS module: User manual,* IRSN, Paris, France (2021)

REACTOR VESSEL MODEL

- Core is divided in 6+1 radial channels and 32 axial levels
- Primary circuit is represented by a 1+2+1 loop configuration, providing pathways for FP transport from the reactor to the CTMT

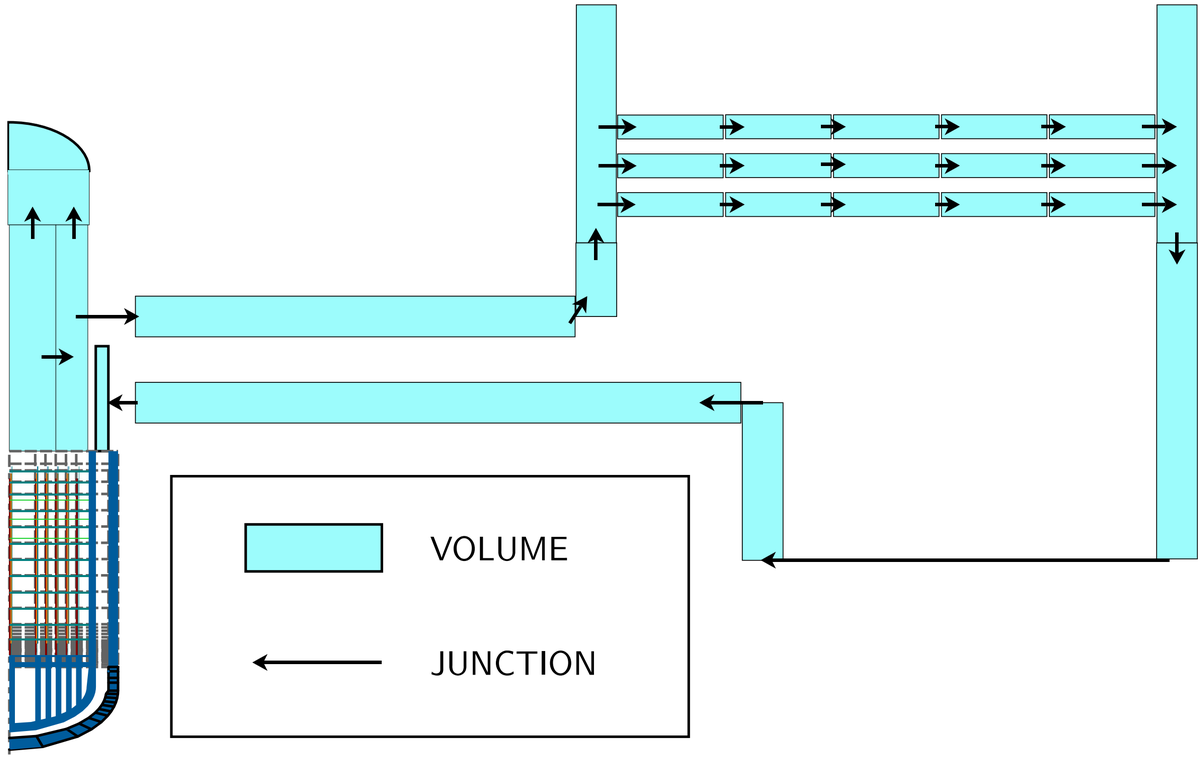

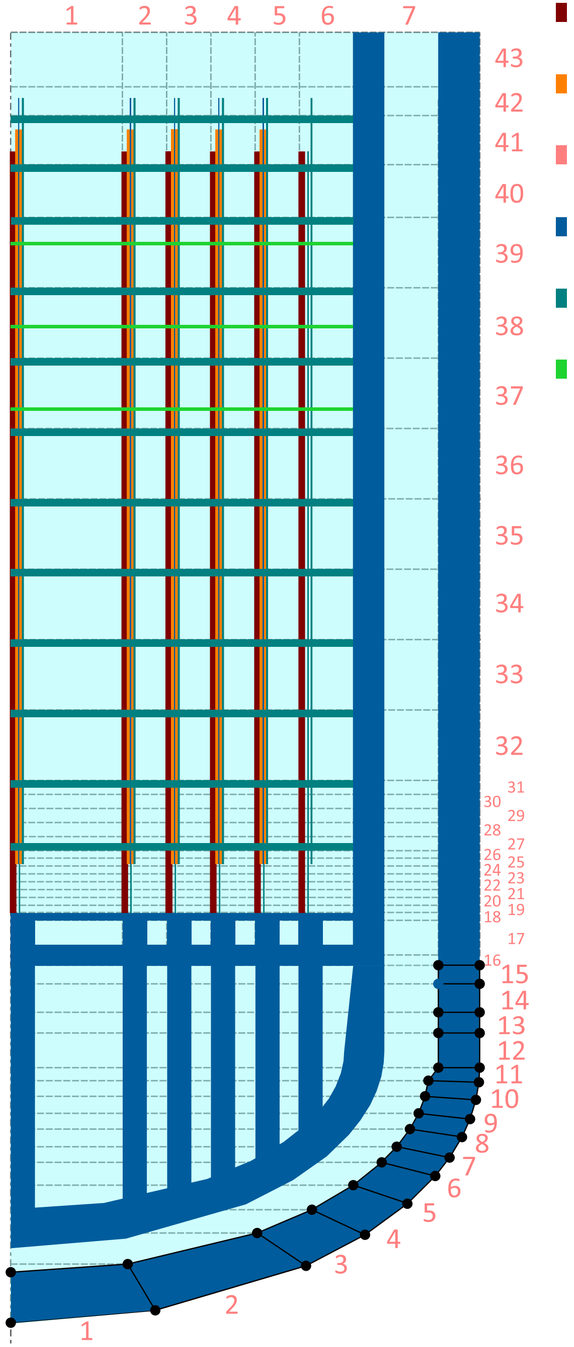

CONTAINMENT MODEL

- CTMT model is made of 36 zones
- Model includes CTMT spray system and water sump, located at the very bottom of the CTMT (cvh_805), which collects liquid from the CTMT compartments
- In addition, coolant leakage from the primary circuit into the CTMT leads to the formation of smaller local water pools within the steam generator compartments.
- Model of CTMT includes distinct surface families (painted, concrete, steel)

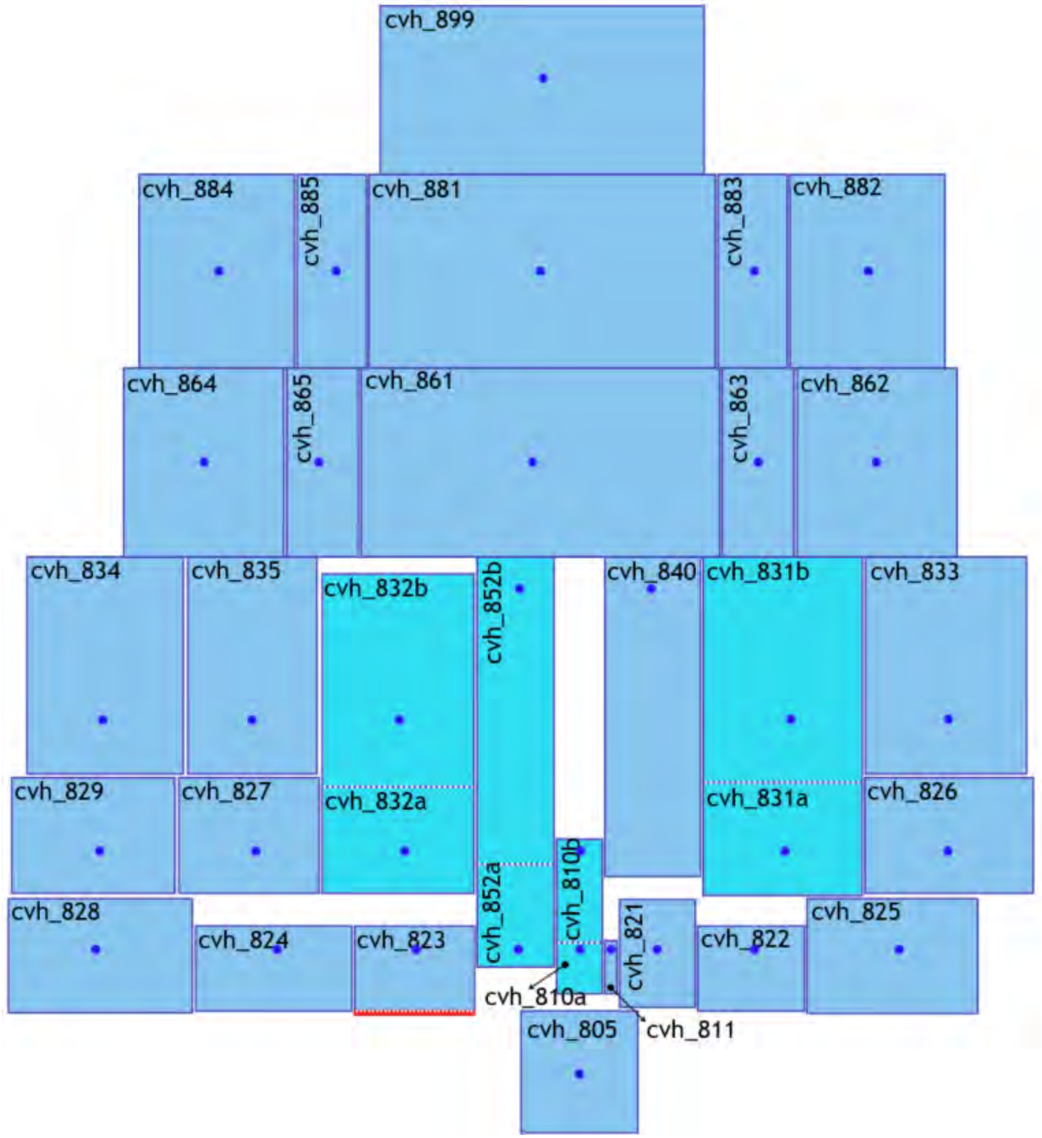

SENSITIVITY ANALYSIS METHODOLOGY

NUCLEAR RESEARCH INSTITUTE

- **Speciation**: distribution of an element among defined chemical species (oxidation states, compounds, complexes) in a system
- Assesment of chemical forms is importat for Source Term prediction
- Chemical speciation of FP (especially iodine) is highly sensitive to containment conditions

Key influencing parameters:

- **Temperature, Pressure and Relative humidity**– affect condensation, volatility, and mass transfers.
- **pH and Redox Potential** – influence solubility and chemical transformation (e.g. I- to I_2).
- **FP Concentrations** – determine reaction pathways and product stability.
- Due to system complexity, predictions are uncertain; experimental data (e.g., from the Phebus program) provide essential validation

SENSITIVITY ANALYSIS FOCUSED ON IODINE SPECIATION

NUCLEAR RESEARCH INSTITUTE

- UJV model of VVER-1000 in ASTEC integral code was used for the analysis
- The only varied parameter was **pH of the CTMT sump**

- Total of **7** ASTEC simulations were performed to evaluate the influence of CTMT sump chemistry and thermodynamic conditions on iodine speciation during G-LOCA scenerio
  - **5** calculations covered the pH variation in CTMT Sump in Range 5–9
  - pH varied within range of achievable conditions through presence of boric acid (H_3BO_3) and potential operator-initiated additives such as KOH or hydrazine (N_2H_4).
  - **2** additional simulations were conducted with activation of the CTMT spray system, applied only to the boundary cases at pH 5 and pH 9 to provide a clear contrast

- Expected increase in gaseous iodine with decreasing pH
- Expected increase in I_2 and CH_3I and decrease in I^- in sump water due to radiolytic oxidation ($I_2 \leftrightarrow I^-$) in more acidic environment (lower pH)
- Expected decrease in pressure and temperature in CTMT with spray system activated

CTMT PRESSURE (ABSOLUTE)

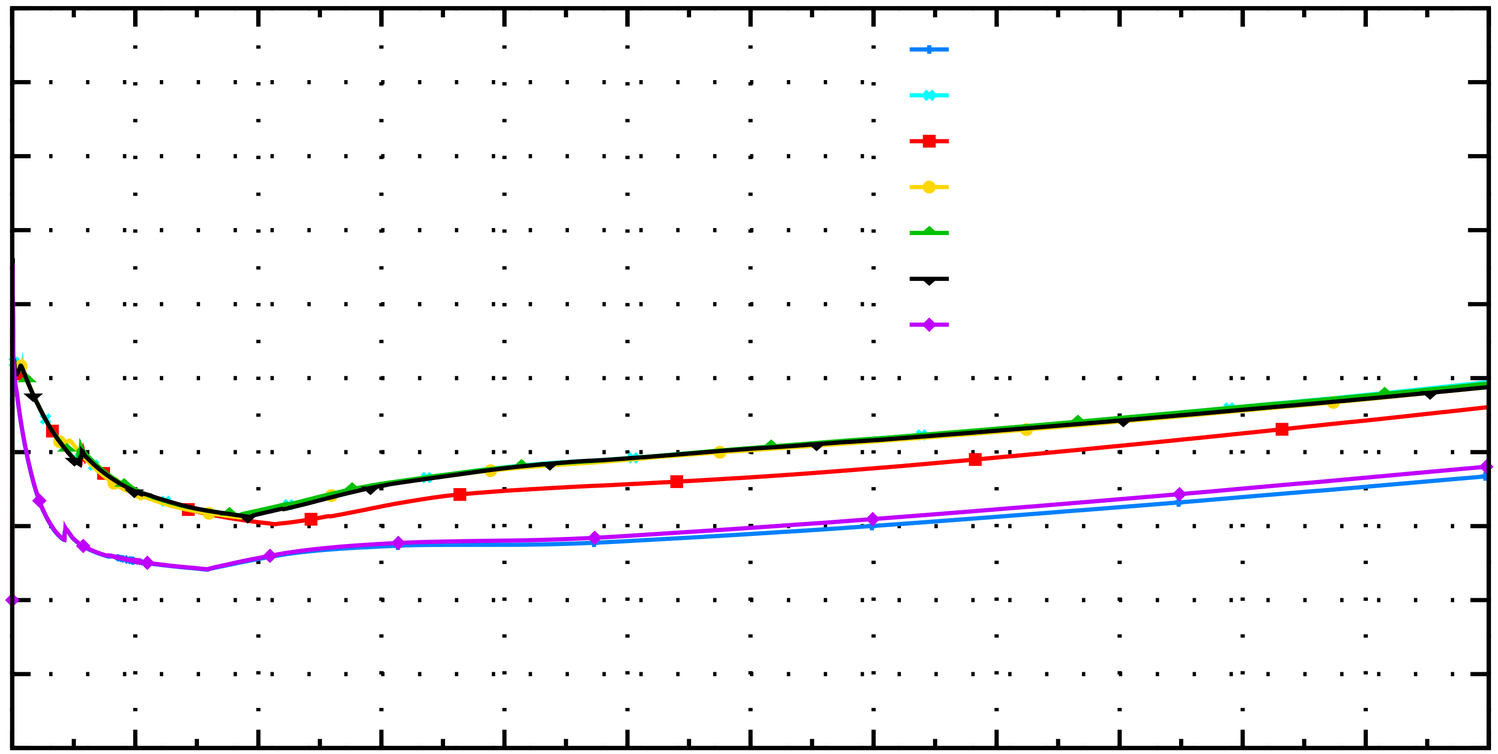

TIMING OF MAIN EVENTS AND EVALUATION OF IODINE RELEASE AT TIME OF LOWER HEAD FAILURE

Event	pH 5	pH 6	pH 7	pH 8	pH 9	pH 5 SPRAY	pH 9 SPRAY
Initial event (G-LOCA)	0 s						
Start of FP release	48 s					53 s	
1st material slump in lower plenum	3556 s	3617 s	2869 s	3473 s	3584 s	3037 s	3055 s
Lower head failure	7706 s	7432 s	6605 s	6631 s	7558 s	5634 s	5498 s
Total mass of iodine leaked into CTMT	3381 g	3380 g	3385 g	3588 g	3401 g	3799 g	3522 g

MASS OF I- IN THE SUMP OF CTMT (LIQUID PHASE)

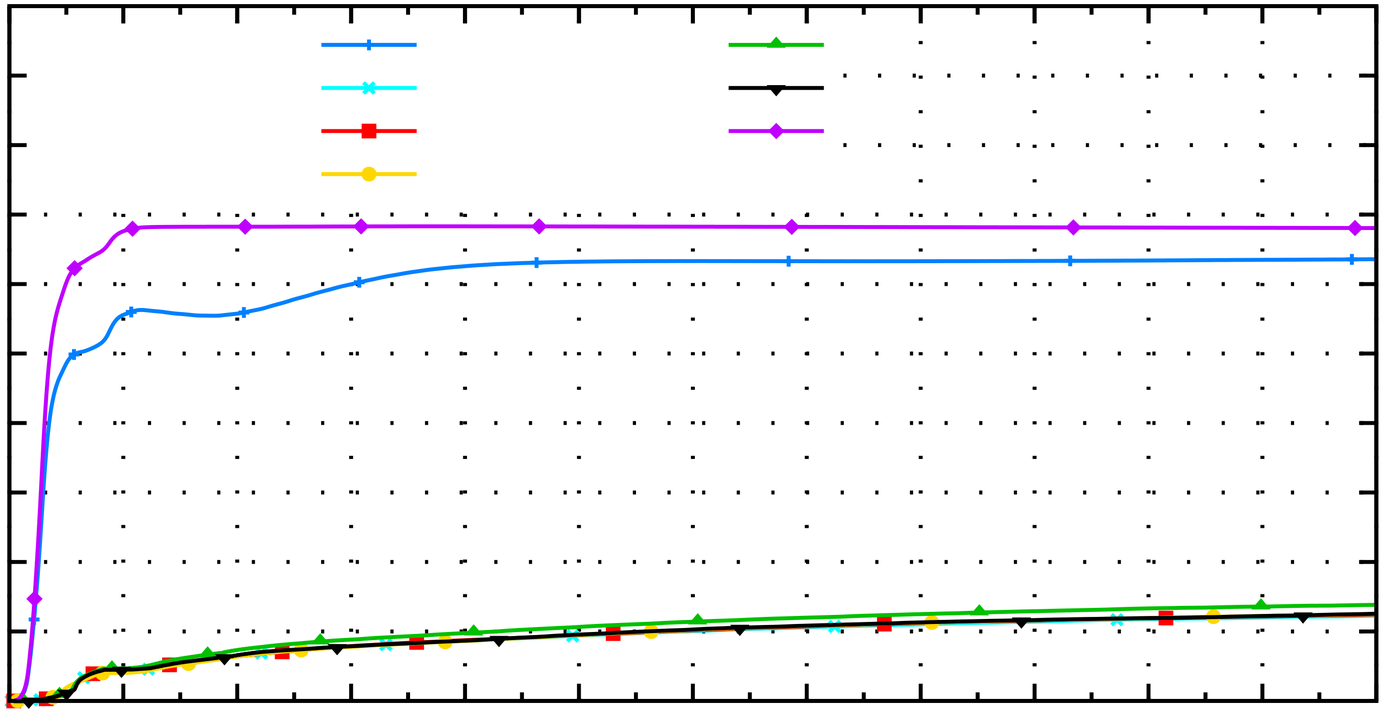

MASS OF I_2 IN THE SUMP OF CTMT EXCLUDING SIMULATIONS WITH SPRAY SYSTEM ACTIVATED

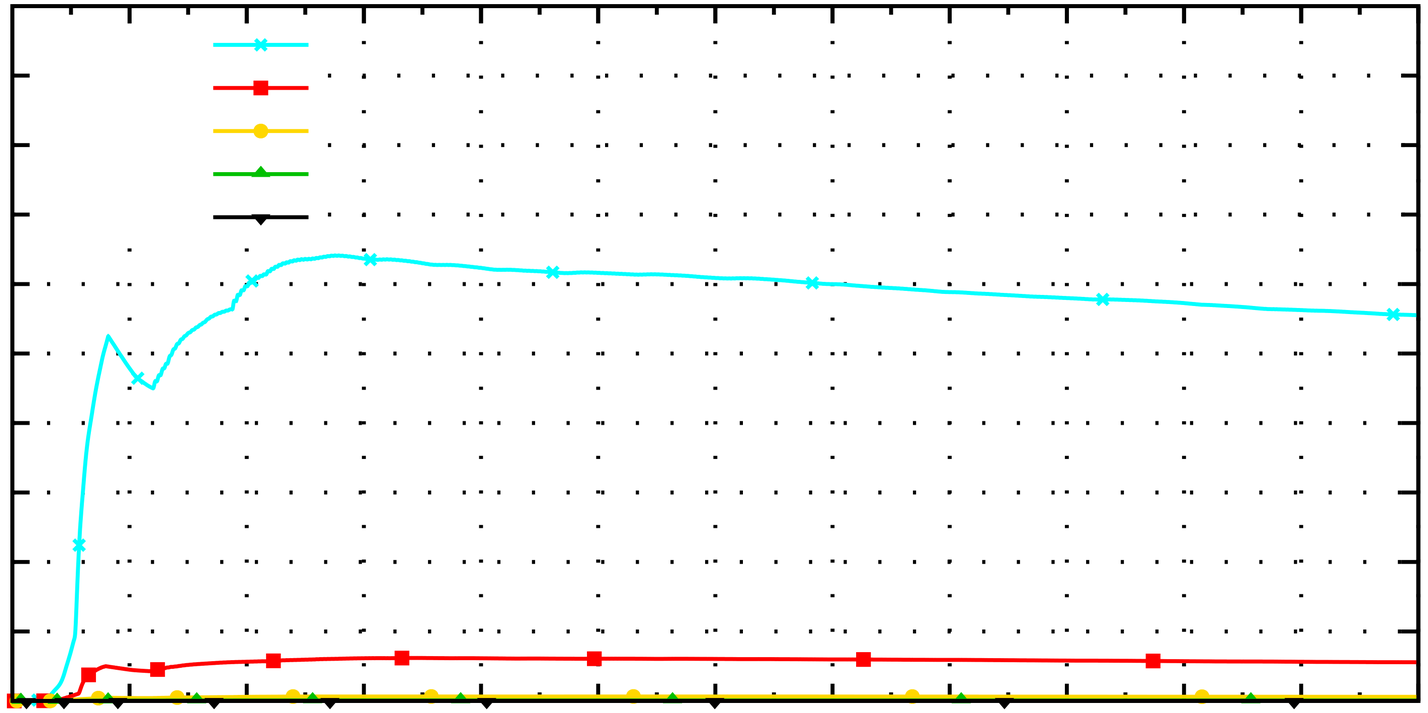

NUCLEAR RESEARCH INSTITUTE

MASS OF I_2 IN THE SUMP OF CTMT INCLUDING SIMULATIONS WITH SPRAY SYSTEM ACTIVATED

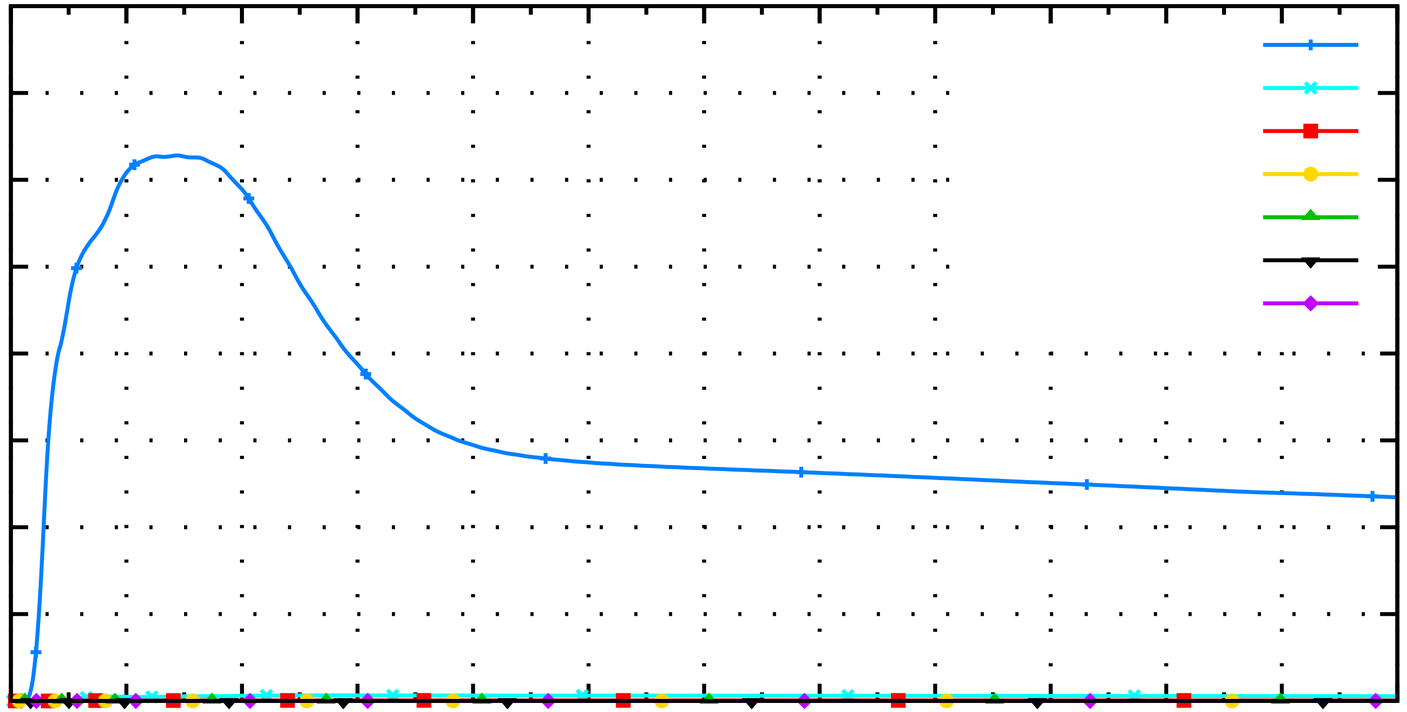

NUCLEAR RESEARCH INSTITUTE

TOTAL MASS OF GASEOUS IODINE (MAINLY I_2 AND CH_3I) IN CTMT

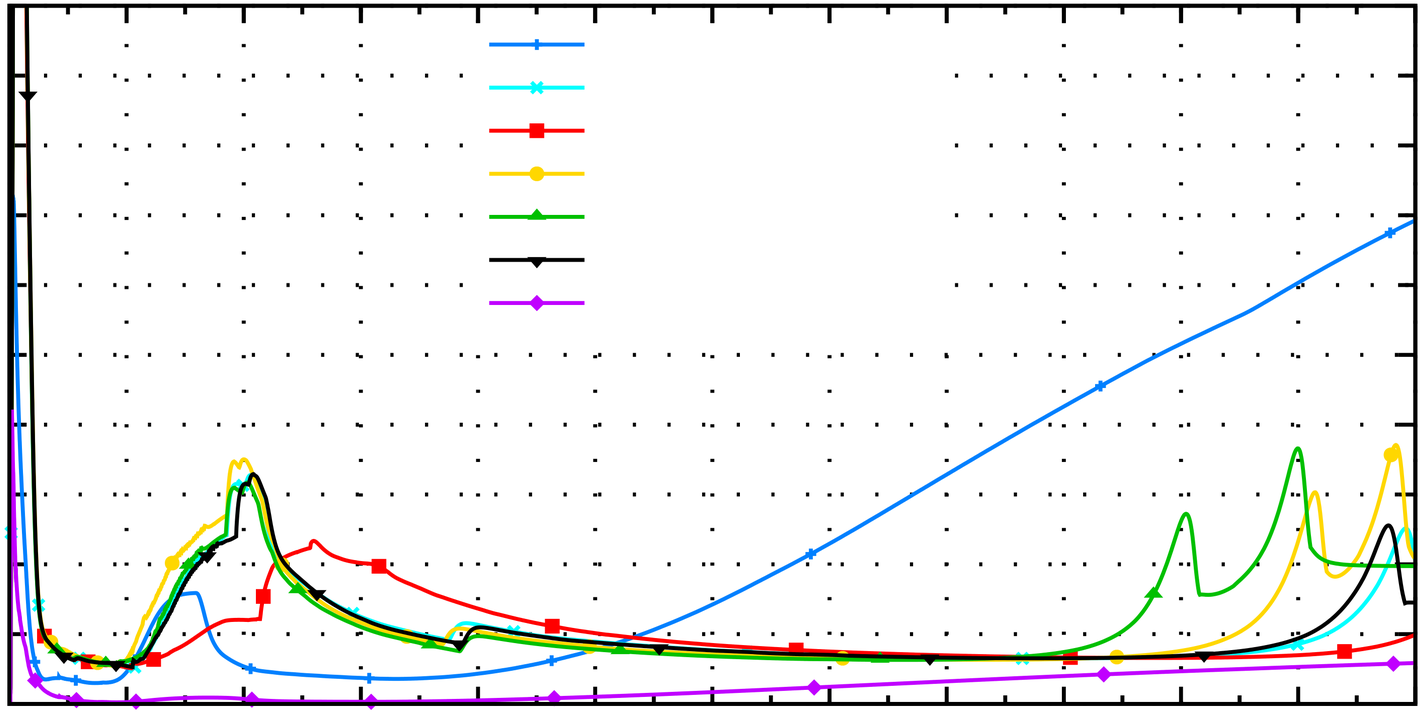

SENSITIVITY ANALYSIS CONCLUSION (1/2)

NUCLEAR RESEARCH INSTITUTE

Sump chemistry effect confirmed

- With pH decrease, radiolytic oxidation shifts iodine from I^- toward dissolved I_2

Non-spray configurations

- In non-spray configurations this chemical shift does not translate into a larger total iodine gaseous mass in the CTMT atmosphere
- Under G-LOCA conditions, elevated pressure and high relative humidity constrain liquid–gas mass transfer of I_2, thereby stabilizing the gaseous iodine

Spray configurations

- Activation of the CTMT spray system alters thermodynamic conditions and enhance I_2 volatilization and interfacial mass-transfer
- Spray wash-down increase the sump-borne iodine inventory (notably I^-)
- Combined effect is a clear rise in gaseous iodine present in the CTMT atmosphere (relative to the non-spray cases), most pronounced at pH 5

SENSITIVITY ANALYSIS CONCLUSION (2/2)

NUCLEAR RESEARCH INSTITUTE

Uncertainties

- Analysis showed variations between simulation runs
- Differences are mainly observed in RPV failure timing (tens of minutes) and leak magnitudes (percent level).
- These differences reflect numerical scatter inherent to large coupled integral calculations but do not alter the qualitative accident course

→ Uncertainty and sensitivity analyses are essential for reliable interpretation of source-term predictions

→ To further reduce the influence of numerical scatter and to better isolate CTMT-phase phenomena, it is therefore advisable to perform stand-alone CTMT calculations using boundary conditions obtained from the in-vessel phase computed by the integral model

CLOSING REMARKS

- Accurate prediction of gaseous iodine requires coupled modelling of sump chemistry and CTMT thermodynamic conditions.
- Spray systems have a dual effect: they modify CTMT atmospheric conditions and relocate aerosol-borne fission products to the sump.
- Under alkaline conditions, spray operation does not significantly increase the iodine source term in the CTMT atmosphere.
- Maintaining sufficiently alkaline sump conditions is a key mitigation measure for limiting gaseous iodine release.
- To reduce the influence of numerical scatter it is advisable to perform stand-alone CTMT calculations using boundary conditions obtained from the in-vessel phase.

Thank you for your attention

Štěpán Tichý
E-mail: stepan.tichy@ujv.cz

UJV Group
PEOPLE | INNOVATION | TECHNOLOGY

CEZ GROUP

UJV Group, a member of CEZ GROUP

EVALUATION OF THE EFFECT OF DIFFERENT TRANSPORT PATH MODELLING ON FP BEHAVIOUR IN AC²/ATHLET-CD

L. Tiborcz, T. Hollands
Gesellschaft für Anlagen- und Reaktorsicherheit (GRS) gGmbH
Boltzmannstr 14, Garching, Germany
livia.tiborcz@grs.de; thorsten.hollands@grs.de;

ABSTRACT

One of the main foci of a severe accident analysis is the fission product (FP) and aerosol behaviour needed for the evaluation of a possible source term. The models implemented in system codes are highly complex, derived from limited available data and must rely on several other modules (like thermal-hydraulic) for their BC/IC. Therefore, it is of high importance to assess their capabilities, to identify possible limitations and to ensure their reliability. Within AC²/ATHLET-CD, a new modelling approach is under development and verification in order to be able to include the full core and consequently to close the transport path modelling within the RCS. This is expected to have an effect on the FP behaviour simulation particularly in cold leg break scenarios, during which transport through the reverse flow direction with lower expected retention rates can impact the amount of FP predicted to reach the containment.
In this paper a postulated cold leg LOCA concurrent with an SBO in a generic German PWR is investigated. Next to the traditional modelling the new developments are tested and compared to the standard modelling approach. The focus is on the FP behaviour in the RCS and subsequently the release into the containment.

KEYWORDS
FP behaviour, V&V, AC²/ATHLET-CD

1. INTRODUCTION

One of the main questions during a potential severe accident concerns the radiological impact on the environment. Even before the accident at the TMI-2 nuclear power plant, probabilistic safety assessments were carried out to evaluate the radiological consequences of a possible release of radioactive material into the environment [1,2]. At the time, however, a lot of experts considered studies of severe accidents to be largely theoretical. After the accident advanced research programs were started to investigate and better understand the phenomena during a severe accident scenario. Ever since the accident in the Fukushima Daichii NPP a special focus is put on severe accident analysis and source term evaluation.

Severe accident system codes such as AC², MELCOR, or ASTEC model highly complex phenomena using empirical and semi-empirical approaches. Their objective is to deliver dependable results within a reasonable computational time for the analysis of accident evolution, covering both in-vessel and ex-vessel processes up to the determination of the source term [3]. These code use simplifications both in their physical models as well as in their geometrical representation of the facility in order to keep computational time manageable.

In the present paper, an advanced modelling approach under development within SAFT (module responsible for simulating fission product (FP) and aerosol behaviour in the reactor cooling system AC²/ATHLET-CD) is presented. The approach extends the representation of transport paths to be able to include the core region, thereby enabling the closed representation of the reactor cooling system (RCS) loop including the possibility of reverse flow. This is expected to increase the consistency of the modeling (e.g. mass balance of FPs) also to better represent scenarios during which there is a reverse flow or where transport and deposition processes within the core region could significantly impact the predicted source term. This modelling approach, though with a slightly older AC² version, has been investigated in a coupled scenario (with explicit modelling of the containment), focusing on source-term uncertainty analysis [4]. In this paper, we provide a detailed comparison between the simple and advanced modelling approaches while applying only ATHLET-CD.

2. MODELLING APPROACH

2.1. ATHLET-CD and SAFT

The AC² code system [5,6], developed by GRS, integrates the system codes ATHLET, ATHLET-CD, and COCOSYS together with the numerical toolkit NUT. It provides a best-estimate analysis framework for the comprehensive simulation of nuclear power plant behaviour across the full range of operating transients, design-basis accidents, and design extension conditions up to severe accidents, including the evaluation of the source term.

SAFT is the module responsible for the simulation of transport and deposition of fission products within the RCS. The module is simulating the main vapour-phase (e.g. homogenous/heterogenous nucleation, condensation/evaporation, sorption, etc.) and aerosol phenomena (e.g. different agglomeration processes, Brownian diffusion, settlings, thermophoresis, diffusiophoresis, remobilisation processes, etc.) with the help of mechanistic and semi-empirical models. The basis of the chemical modelling is the calculation of thermodynamic chemical equilibrium utilizing a transient approach based on the deviation from the equilibrium. Changes in carrier gas mass due to chemical reactions or decay as well as the energy involved in chemical reactions are neglected. The chemical speciation is influenced by temperature, carrier gas composition, and concentration of the different gaseous species. The required boundary conditions, such as thermohydraulic parameters, surface temperatures, and release data, are supplied by various ATHLET and ATHLET-CD modules.

In the currently accepted modelling approach for SAFT [7], modelling within the core region is not recommended and is provided only for test purposes. In the thermal-hydraulic (TH) module, the core region is modelled using a multi-channel approach, usually interconnected via so-called cross-connection objects (CCOs), yielding a quasi-3D representation of the core [8]. This is highly important and beneficial for thermal-hydraulic calculations, but it requires careful consideration from the SAFT network point of view. This issue is addressed by taking cross-connection objects (CCO) into account. These objects are essentially a series of junctions without any physical volume that connect the control volumes (CVs) of different thermal-fluid objects (TFOs). At the same time, if cross-connection objects are present at other locations in the SAFT network, they are also automatically taken into account. This can lead to “dead-ends” within the SAFT network: a thermal-hydraulic connection exists, but no fission product (FP) transport modelling is considered (as shown in Figure 1). This situation is similar to an open-ended SAFT loop, where the SAFT network is not closed and, consequently, at least one thermal-hydraulic connection is not accounted for in the FP transport modelling. This might cause issues such as FP accumulation in the last CV or mass-balance errors due to mass losses. These cases are handled in the same way as previous dead-ends: an artificial outlet is created for information purposes. This information can then be used by the user to decide whether the representation of the transport paths should be modified to include the neglected parts of the network (note

that this strongly depends on the thermal-hydraulic conditions). These considerations underline the need for correct and comprehensive modelling of the transport network and a solid thermal-hydraulic representation.

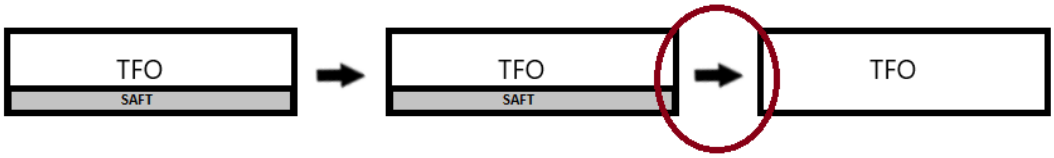

Figure 1 Dead-End in SAFT transport path [9]

Another important aspect when considering the core region is the location of the fission product (FP) source. In the recommended modelling approach (without the core region) FPs are assumed to appear in the upper plenum and are subsequently transported further through the system. This approach may overestimate the amount of FP entering the upper plenum/hot leg, however, it is considered conservative. In the proposed advanced approach, an algorithm is implemented in SAFT to extract the exact location of cladding and fuel failure(s) within the core region (based on dedicated clad and fuel failure models in ATHLET-CD), accounting for both axial and radial positions. Moreover, the approach is not limited to the initial cladding burst; subsequent failures are also identified and included as additional FP source locations. At the moment, however, the melting of structures within the core region is not yet taken into account. The melting and relocation of structures affect both the available surface area and its position, on which deposition could occur. It is planned to address these effects in the future, not only using the concentric core region approach (traditional TH modeling approach of the core), but also the more advanced one subdividing the core rings into radial slices for better representation of local effects [10].

2.1. Postulated Accident Scenario

As the proposed modelling approach is expected to affect the predicted source term under cold-leg LOCA conditions, a cold-leg medium-break LOCA has been selected as the reference scenario. The analysis is performed for a generic German PWR (Konvoi) concurrent to a station blackout (SBO). The plant has a four-loop configuration, as illustrated in Figure 2, with nominal parameters summarized in Table I. No active severe accident management measures are assumed. Due to the SBO, all active heat removal systems are unavailable, and only the hydro-accumulators are assumed to operate as designed. The break is assumed to occur at the lowest point of the loop seal in Loop 1, which also contains the pressurizer, with a break area of 200 cm^2.

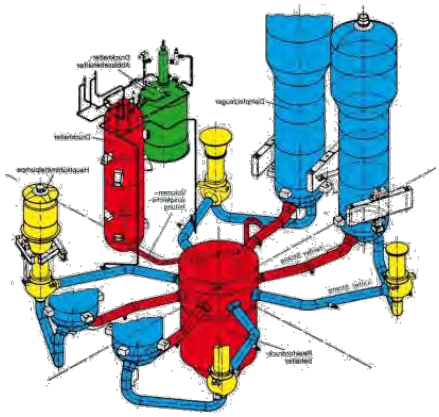

Figure 2 Schematic representation of generic German PWR [11]

Table I Nominal operational conditions [11]

Parameter	Nominal value
Reactor Power	3750 MW_{th}
Operational pressure	157 bar/65 bar
Core inlet/outlet temperature	292°C/325°C
# of fuel assemblies	193
Coolant mass flow rate	19.8 t/s

The ATHLET-CD model of the reactor contains a detailed representation of all loops, including the steam generators (SG) and their secondary sides (Figure 3). The core region is represented by four parallel channels, to each a concentric core ring with a rod object is assigned. The rings have outer diameters of 0.8 m, 1.15 m, 1.49 m, and 1.72 m, representing 14,700 rods in the innermost ring and 14,400 rods in each of the three outer rings. The number of control rods per ring, from innermost to outermost, is 312, 768, and 384, with no control rods placed in the outermost ring. Axially, the active core is divided into 20 nodes. Critical discharge is calculated using ATHLET's built-in CDR1D model. The fission product release is described by Arrhenius-type correlations, which for certain elements account for the partial pressure as well. Transport and deposition of the fission products are modelled within the SAFT module. Previous versions of the input deck have been used successfully in other investigations with earlier AC^2 versions, see e.g. [4,12].

In case of the basis calculation ("simple") the transport path is modelled starting from the upper plenum. From here Loop1 (loop with the break location) is only represented up to the break position in the SAFT network: upper plenum → hot leg →SG → cold leg → break location. In this case five SAFT-Loops are defined due to the representation of the SG (different length U-tubes are grouped into three sets to better represent the heat exchange between the primary and secondary sides) and the upper plenum. The model comprises 19 TFO-objects, 81 control volumes and 87 junctions.

In case of the advanced approach, the core region, lower plenum and downcomer are also taken into account in the SAFT network, allowing the transport paths to be fully closed. The resulting transport network include a forward direction—upper plenum → hot leg → steam generator (SG) → cold leg → break location—and a reverse direction—core → lower plenum → downcomer → cold leg → break location. Within the core region, the bypass channel is also included in order to preserve mass balance. In total, ten SAFT loops are defined, accounting for multiple core channels, the aforementioned SG modelling, and a detailed representation of the upper plenum. The model comprises 27 TFO-objects, 191 control volumes and 270 junctions. In this configuration, there is no thermal-hydraulic dead-end from SAFT point of view, unlike in the simple approach, where at the break position the fluid might flow in the direction of the core (or from it), which is not considered in the FP transport, thus resulting in a sink/neglected source. (Note: A handling mechanism is implemented in SAFT to address such dead-end situations in the simplified approach by providing an estimate of the associated losses.)

Figure 4 shows the schematic representation of the two modelling approaches. In the simple version only the path indicated in orange is included, whereas in the advanced approach the path shown in purple is additionally taken into account, together with the explicit representation of the core region.

Simulations have been carried out with a developer version based on the current release AC^2-2025 [6]. Altogether 30,000 s have been simulated including a 5,000 s steady-state normal operation at the beginning to ensure stable initial conditions prior to the initiation of the transient.

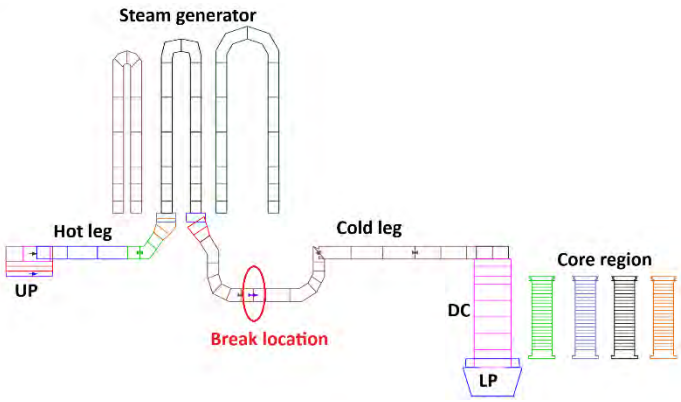

Figure 3 ATHLET-CD nodalisation of Loop1 (adapted from [4])

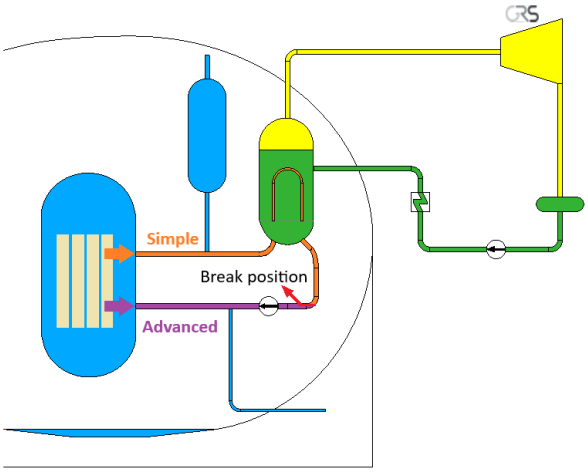

Figure 4 Schematic view of the FP transport modelling

3. RESULTS

As the FP and aerosol transport module heavily relies on the thermal-hydraulic conditions provided by several other ATHLET modules, establishing a robust base-case simulation is essential. It is worth mentioning that, thanks to the modular nature of AC^2, the models describing the severe accident phenomena can be introduced in a stepwise manner. Consequently, both the development of the input deck and the required preparation time can be significantly reduced by avoiding the simultaneous inclusion of all models. This approach facilitates input verification, shortens the time required to identify input errors, and helps prevent compensating modelling errors.

The timing of the main events predicted by ATHLET-CD is summarized in Table II. Following the initiation of the break, the SCRAM signal leads to an almost immediate shutdown of nuclear power generation. The resulting loss of coolant causes a quick primary side depressurization (Figure 5.), while the secondary side depressurization is much slower. This is due to the limited heat transfer caused by the nearly stagnant vapor filling the primary-side U-tubes. The initially single-phase liquid discharge under critical flow conditions is followed by two-phase flow; at later stages of the accident, single-phase vapor flow becomes dominant. Given the assumption of a station blackout (SBO), active emergency core cooling systems, such as high- and low-pressure injection systems, are unavailable, leaving only the hydro-accumulators operational. At the same time, due to the severity of the initiating event, the accumulators are rapidly depleted without having a noticeable effect on the system pressure. The results are consistent with those reported in [4].

Table II Accident sequence

Event	Time [s]
Break opening	5,000
Start of ACC	5,884
1st clad failure	8,859
1st CR failure	9,207
1st fuel rod failure	9,842/10,068*
Start of relocation to LP	10,106/10,181*
LP failure	13,613/13,557*

*simple/advanced

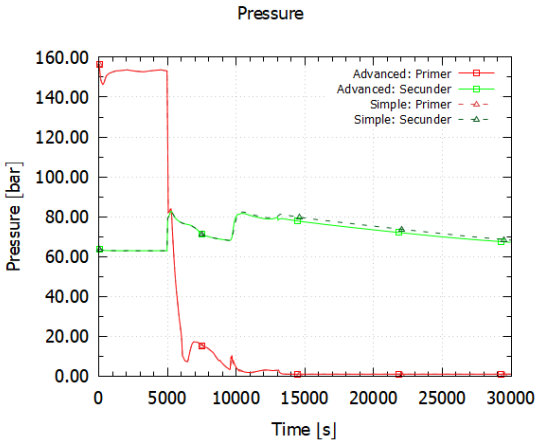

Figure 5 Pressure in RCS

The temperature within the core region initially decreases (no heat generation, but sufficient coolant) but gradually increases as the accident progresses due to the decreasing core liquid levels. The cladding oxidation excursion occurs at approximately ~9,200 s, quickly producing almost all the predicted hydrogen of about ~600 kg, corresponding to about 11.5% of the cladding being oxidised. As shown in Figure 6 slight differences are observed between the predictions obtained with the two modelling approaches. These differences arise because SAFT not only receives information from other thermal-hydraulic modules but also feeds back calculated quantities (e.g. deposition), into the system. These quantities form the basis, for example, for determining the location and distribution of the decay heat source within the RCS. This, in turn, affects the thermal-hydraulic response, which then influences fission product behaviour, and so on.

As the core progressively melts, the molten material is eventually relocated to the lower plenum (LP). This relocation first occurs at about ~10,100 s, based on a corium mass criterion as shown in Figure 7. The lower plenum is predicted to fail at around ~13,600 s, releasing the accumulated molten material into the containment. Continued core melting results in additional relocation of material to the lower plenum, which is then instantaneously relocated into the containment. The containment is not modelled in detail in this study (i.e. no COCOSYS model); it is only represented as a pressure-enthalpy boundary condition at the break location.

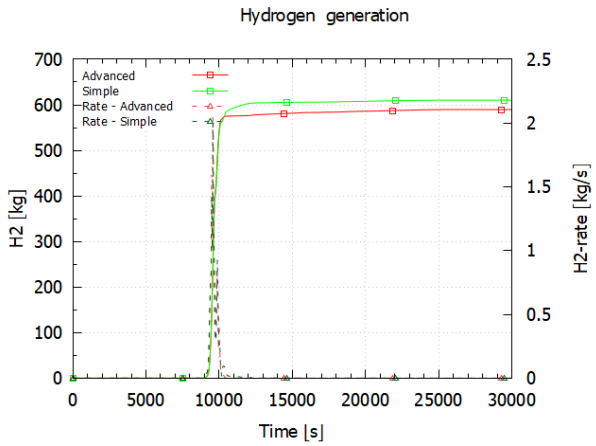

Figure 6 Hydrogen production

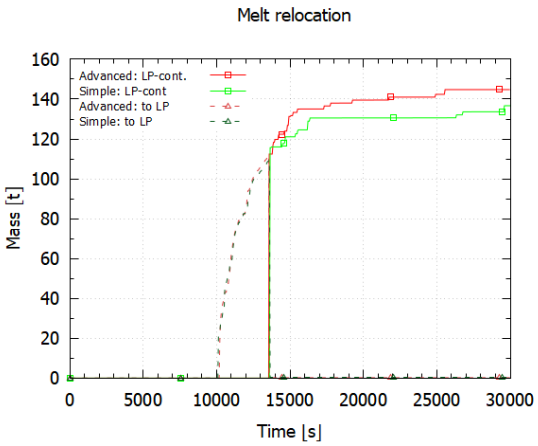

Figure 7 Melt relocation to LP/containment

The FP release starts with the first cladding failure, which occurs in both modelling approaches at the same time at 8,859 s. As shown in the thermal-hydraulic results, the simulation results are identical for both modelling approaches up until the 1st cladding burst occur, after which the FP and aerosol module is activated. At this stage, the release is dominated by the gap release (fill gas and highly volatile fission product in gaseous form).
The release from the core is calculated by the module FIPREM based on Arrhenius type correlations. In case of the simple modelling approach all FP and aerosol released from the core are assumed to enter the upper plenum and are then transported through the hot leg, SG, and cold leg to the break location. Depending on the thermal-hydraulic conditions, this assumption may lead to an overestimation of the actual amount of FPs and aerosols reaching the upper plenum.

In the advanced modelling approach, the release occurs at the exact position of the cladding failure within the core region, as determined by the mechanical models predicting cladding rupture. In this scenario, the first failure occurs in the innermost core ring (hottest) at the 18th axial position, which corresponds to ~3.2 m within the active core. This approach allows an exact localization of each FP source within the core region and enables the consideration of local thermal-hydraulic conditions for potential retention or reverse flow. Furthermore, by closing the FP and aerosol transport loop possible circulation within the RCS can be accounted for. In the simulation results, we see that there was intermittent flow reversal in core channels. In addition, we also observe retention of fission products in core regions, at least temporarily, and even for volatile FPs such as caesium and iodine.

From a radiological point of view the two most important FPs are iodine and cesium, therefore in the following we will focus on these two. Figure 8 shows the iodine and cesium mass balances within the RCS. Both being highly volatile, the release amounts to almost the entire initial inventory (i.i.) in case of iodine, and about ~90 i.i.% for cesium. As can be seen, the release from the core shows no difference in case of iodine, whereas in case of cesium a slightly smaller amount is released when applying the advanced modelling approach. This is not the case when considering the overall behavior within the RCS. A much higher retention is predicted with the simple modelling approach compared to the advanced one. Consequently, higher release rates into the containment are predicted using the advanced modelling approach. For iodine 60 i.i% is predicted to reach the containment with the advanced modelling approach, compared to about 45 i.i% with the simple approach. In case of cesium this difference is even more pronounced: 52 i.i% reaches the containment as opposed to 22 i.i%. These differences have a significant impact on the potential radiological consequences to the environment.

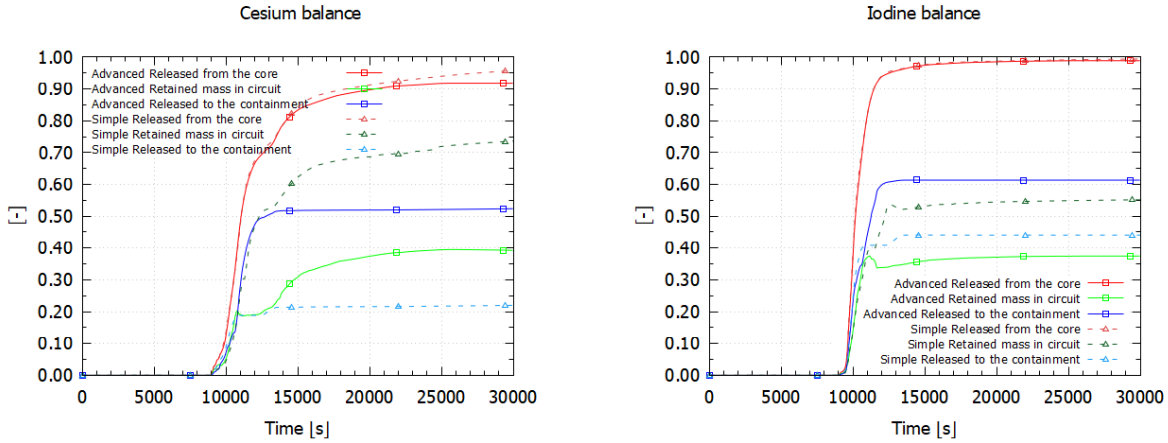

Figure 8 Cs and I balance

Figure 9 depicts the mass flow rates and retained caesium masses within the RCS for both the simple as well as for the advanced modelling approaches (qualitative predictions for iodine are similar, therefore only caesium is shown here). The scale for the retention on the figures is the same in both cases for easier comparison. In Figure 9 the highest deposition can be observed within the SG and at the beginning of the hot leg in both cases. This is due to the geometrical features (bends) and the temperature distribution (high ΔT). In the advanced approach, however, the absolute retention values are lower, while additional retention is observed within the core region, including the lower plenum and downcomer. This underlines the complex nature of FP transport phenomena and their modelling. On the one hand the advanced modelling approach leads to lower predicted deposition in the hot leg/SG area (partially due to the fact, that less FPs reach the hot leg, as some are directly transported in the other direction through the downcomer into the cold leg), on the other hand deposition is predicted to also occur in regions previously neglected (core region). Which aspect is more dominant is determined by the thermal-hydraulic conditions, underlining once again the importance of TH-modelling.

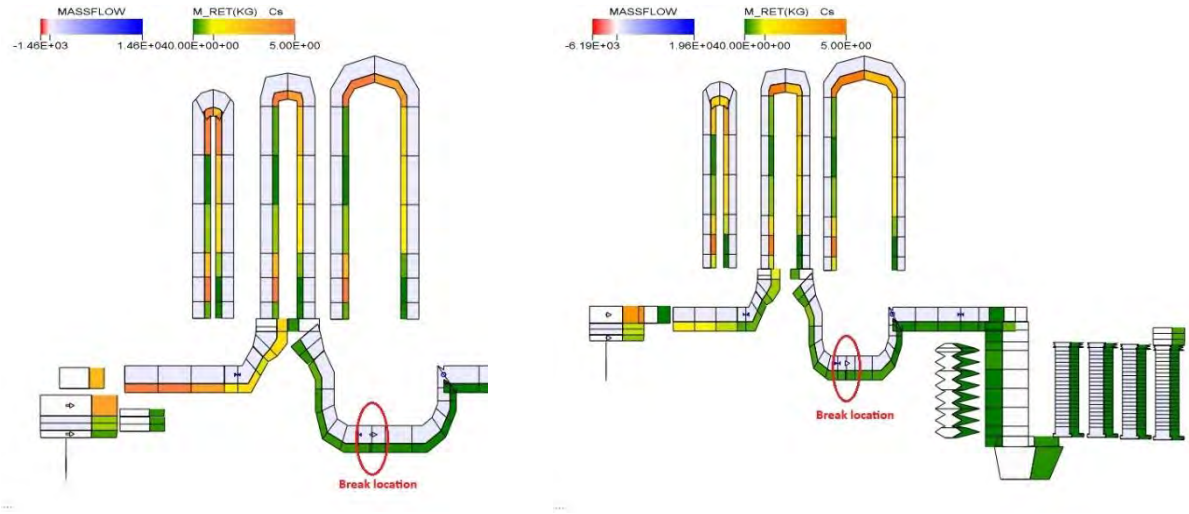

simple advanced

Figure 9 Mass flow rate and retained Cs mass at 30,000s - simple vs advanced modelling

Figure 10 depicts the global retention mechanism for all FPs within the SAFT-network. In both cases thermophoresis and settling are predicted to be responsible for the majority of FP retention. However, their relative importances differ between the two approaches. Applying the simple approach thermophoresis initially dominates, particularly during the oxidation excursion, but its importance rapidly decreases and settling accounts for approximately 80% of retention After the LP failure, the significance of settling gradually decreases but remains the dominant mechanism, contributing roughly 55% of the total retention by the end of the simulation time.

Applying the advanced modelling approach, no such dominance of settling can be observed. Thermophoresis remains the dominant mechanism throughout the oxidation period and continues to govern FP retention until the LP failure, although its absolute contribution is lower than in the simplified approach. Even after this time point, settling, though predicted to be the more dominant mechanism, never reaches the same relative significance it showed in case of the simple modelling approach. This is mainly due to the relevance of temperature gradients in the core region and in the downcomer facilitating thermophoretic processes. It's interesting to note that by the end of the simulation the relative dominances are the same, but as seen in Figure 9, the actual predicted retention values are significantly different.

Bend and eddy impaction also contribute, particularly in the advanced modelling approach due to the presence of geometrical bends when taking into account the core region/down-comer. Nevertheless, their overall significance is much lower, even negligible on the long run.

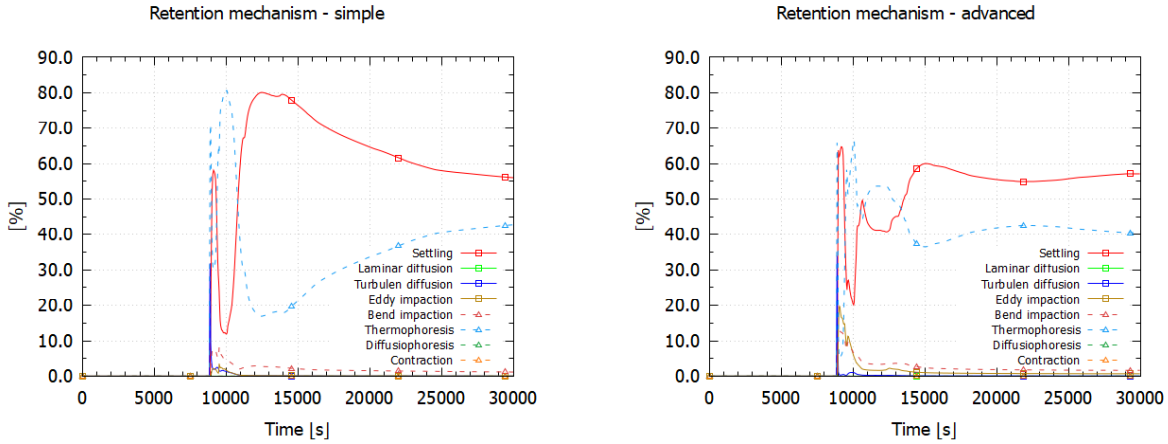

Figure 10 Retention mechanism - simple vs advanced modelling

Figure 11 shows the void fraction and the retained cesium within the core region and downcomer at 14,000 s using the advanced modelling approach. This illustrates the previously discussed retention within the lower plenum and downcomer. At certain times, retention can also be observed within the core region, however, due to remobilization processes, these are later transported further. Nevertheless, this retention within the core region affects both the timing and the composition of the source term. Additionally, depending on the thermal-hydraulic conditions, FPs can reach the break location via the downcomer, a pathway neglected in the simplified modelling approach.

The ratio of fission products (FPs) reaching the break location in each direction (forward through the hot leg and reverse through the downcomer) is another important question. Unfortunately, at the moment, no standard SAFT module output provides this information directly. However, when looking at the normalized carrier fluid rates (1/s) derived based on thermal-hydraulic conditions and directly used in the transport calculation to determine the FP mass transport (kg/s) between consecutive control volumes and through the outlet(s) we can get an idea. Figure 12 shows the normalized carrier gas flow rates in SAFT-Volume #37, where the break is located. The red line indicates the junction on the left side (SG side), the green line the junction on the right side (downcomer side), while the blue line represents the outlet. The positive flow rate in each junction corresponds to the direction indicated by the arrows (left → right, outlet). The negative value of the green line indicates a significant reverse flow rate from the direction of the downcomer, which contributes substantially to the break flow rate up to approximately the LP failure time. It should be noted that this only demonstrates the source term contribution from this reverse flow direction but does not provide a direct measure of the actual FP mass transported through this direction. Nevertheless, when combined with the retention information shown in Figure 9, it can be concluded that the reverse flow contributes significantly to the source term entering the containment

At later times, no reverse flow is predicted. However, in the simplified modelling approach, FPs transported from the normal flow direction through the cold leg back into the core region would be neglected (and lost), whereas this is accounted for in the advanced modelling approach.

The LP failure introduces a new challenge, as it creates an additional opening from the RCS into the containment. It should be noted that by the time LP fails most volatile and semi-volatile FPs have already been released, leaving predominantly low-volatile FPs in the RCS and the core melt. This dynamic change in the transport path is currently not modelled and should be addressed in future work. This would also be useful e.g. when coupling AC^2 with structure-mechanic codes determining the failure position and area within the RCS. Additionally, at present, no release from the molten material is calculated, which further contributes to the uncertainty of the results. These modelling limitations should be addressed in future developments work.

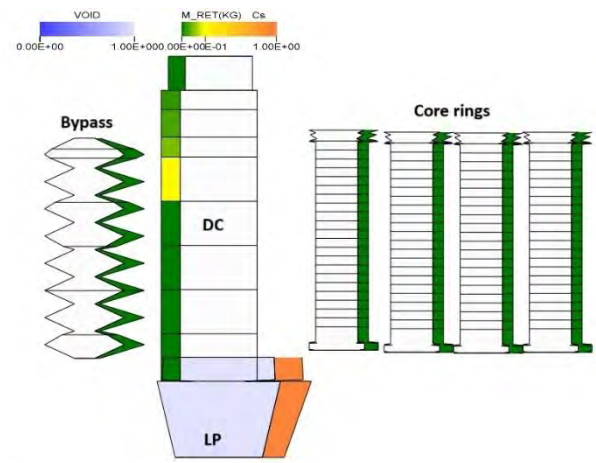

Figure 11 Advanced modelling - void and retained Cs mass in the core region at 14,000s

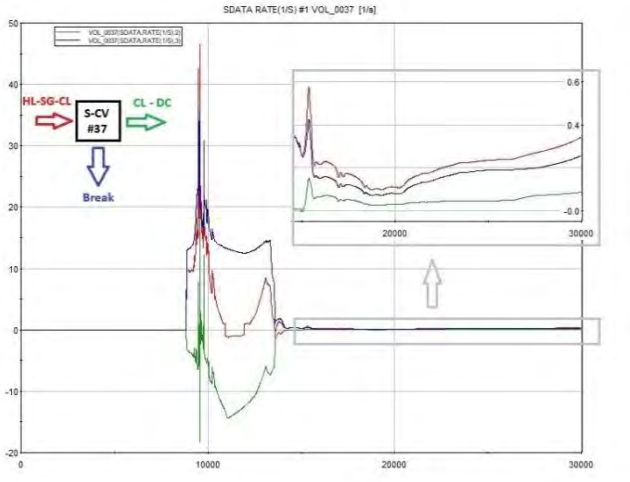

Figure 12 Rate (1/s) values in Saft CV#37 (break location)

Another limitation of the current modelling is the inability to simulate remobilization and transport in fully water-filled CVs. At the moment, only soluble compounds are transported in water. Future developments should address remobilization and entrainment processes in fully water-filled CVs. This limitation is only relevant when the void fraction is zero, as occurs at certain time points in the lower plenum (LP) in our study. Nevertheless, in other scenarios involving reflooding, severe accident management (SAM) measures, or similar conditions, this will be a significant factor in determining the release to the containment and thus the possible source term to the environment.

4. SUMMARY AND OUTLOOK

In the present study, the application of a new advanced modelling approach for FP and aerosol transport within the RCS has been shown. The advanced approach enables explicit modelling of the core region, allowing the SAFT loop to be fully closed. This is expected to have a non-negligible impact on source term evaluation in specific accident scenarios. As a demonstration, a medium-size cold-leg LOCA concurrent with a SBO has been selected and successfully simulated using both the simplified and advanced modelling approaches for a SAFT network.

The results showed a significant influence on the FP and aerosol behaviour between the two approaches. Not only did the dominant retention mechanism change, but the quantitative prediction of the source term is also affected. Applying the advanced approach in the given scenario, a substantially higher release into the containment has been simulated compared to previous calculations [13,14], while thermophoresis played a more significant role in retaining FPs.

At the same time, some shortcomings in code capabilities have also been identified, which should be addressed in the future. The first is the availability of output information: currently, no direct data are provided to determine the exact value of the source term from each flow direction. Another important area for future development is the modelling of remobilization and transport of non-soluble FPs in fully water-filled CVs.

Finally, it should be noted that including the core region significantly increases the number of SAFT loops and CVs, leading to higher computational demand. In our case, applying the advanced modelling approach (with all other modelling assumptions unchanged) resulted in a 70% increase in required computational resources. Therefore, the use of such an approach should always be weighed against the potential gain in the accuracy of predicted results. However, GRS is currently integrating core degradation models, including SAFT, into ATHLET, which enables the use of parallelization for these models as well and will impact the feasibility of such detailed analyses.

ACKNOWLEDGMENTS

The development and the validation of AC^2 is sponsored by the German Federal Ministry for the Environment, Climate Action, Nature Conservation and Nuclear Safety (BMUKN) on the basis of decisions by the German Bundestag within several projects.

References

1. "Reactor safety study. An assessment of accident risks in U. S. commercial nuclear power plants. Executive summary: main report.," Nuclear Regulatory Commission, Washington, D.C. (USA) (1975).
2. *Deutsche Risikostudie Kernkraftwerke*: *Eine Untersuchung zu dem durch Störfälle in Kernkraftwerken verursachten Risiko; eine Studie der Gesellschaft für Reaktorsicherheit im Auftrage des Bundesministeriums für Forschung und Technologie*, Verl. TÜV Rheinland, Köln (1979).
3. International Atomic Energy Agency (Ed.), *Status and Evaluation of Severe Accident Simulation Codes for Water Cooled Reactors*, Vol. 1872, IAEA, Vienna (2019).
4. L. TIBORCZ and T. HOLLANDS. "Uncertainty Quantification of a Postulated Severe Accident Scenario in a Generic German PWR," *21st International Topical Meeting on Nuclear Reactor Thermal Hydraulics (NURETH-21),* Busan, Korea, 2025-08-31/2025-09-05 (2025).
5. A. WIELENBERG et al. "Recent improvements in the system code package AC2 2019 for the safety analysis of nuclear reactors," *Nuclear Engineering and Design, 354* (2019).
6. F. C. WEYERMANN et al. "AC² 2025.0 User Manual," GRS-P-15 / Vol. 1 Rev. 5, Gesellschaft für Anlagen- und Reaktorsicherheit (GRS) gGmbH (Dec. 2025).
7. L. LOVASZ et al. "Creating an ATHLET-CD input deck - detailed sample tutorial," Gesellschaft für Anlagen- und Reaktorsicherheit (GRS) gGmbH (Dec. 2025).
8. P. J. SCHÖFFEL et al. "ATHLET 3.5 User Manual," GRS-P-1/Vol 1 Rev. 14 (2025).
9. L. TIBORCZ et al. "Validation of the Fission Product Transport Module in the Code System AC² 2021," *NUTHOS-13 2022 Proceeding Book: 13th International Topical Meeting on Nuclear Reactor Thermal-Hydraulics, Operation and Safety,* Hsinchu, Taiwan, 2022-09-05/2022-09-10, N13P148 (2022).
10. L. LOVASZ et al. "Comparison of a Hypothetical Strongly Asymmetrical Severe Accident Using the Standard and the New Nodalization Method with the Code System AC2,"

27th International Conference Nuclear Energy for New Europe (NENE2018): Book of Abstracts, Portoroz, Slovenia, 2018-09-10/2018-09-13 (2018).
11. T. STEINRÖTTER. “Systemtechnikschulung Sicherheitskonzept: Sicherheitsprinzipien (Teil 1),” (2018).
12. L. TIBORCZ and S. BECK. “Uncertainty and sensitivity analysis of a postulated severe accident in a generic German PWR with the system code AC2,” *Nucl. Eng. Design*, **431**, 113670 (2025).
13. L. TIBORCZ et al. “Source Term assessment for a severe accident scenario in a generic German PWR with AC2,” *27th International Conference Nuclear Energy for New Europe (NENE2018): Book of Abstracts,* Portoroz, Slovenia, 2018-09-10/2018-09-13 (2018).
14. L. TIBORCZ et al. “Simulation of a Severe Accident in a German Generic PWR with the Code System AC²,” *26th International Conference Nuclear Energy for New Europe (NENE2017): Book of Abstracts,* Bled, Slovenia, 2017-09-11/2017-09-14 (2017).

Evaluation of the effect of different transport path modelling of FP behavior in AC^2/ATHLET-CD

L. M.-Tiborcz, T. Hollands

ERMSAR 2026 - The 12th European Review Meeting on Severe Accidents Research, Madrid, Spain, 18-22.05.2026

AC² – Severe Accident System Code

General Features:

- complex systems and phenomenology
- empirical, semi-empirical models
- reliable data vs reasonable time frame

AC² - in- and ex-vessel phenomena
- normal operation → severe accidents

Importance of code evaluation and V&V

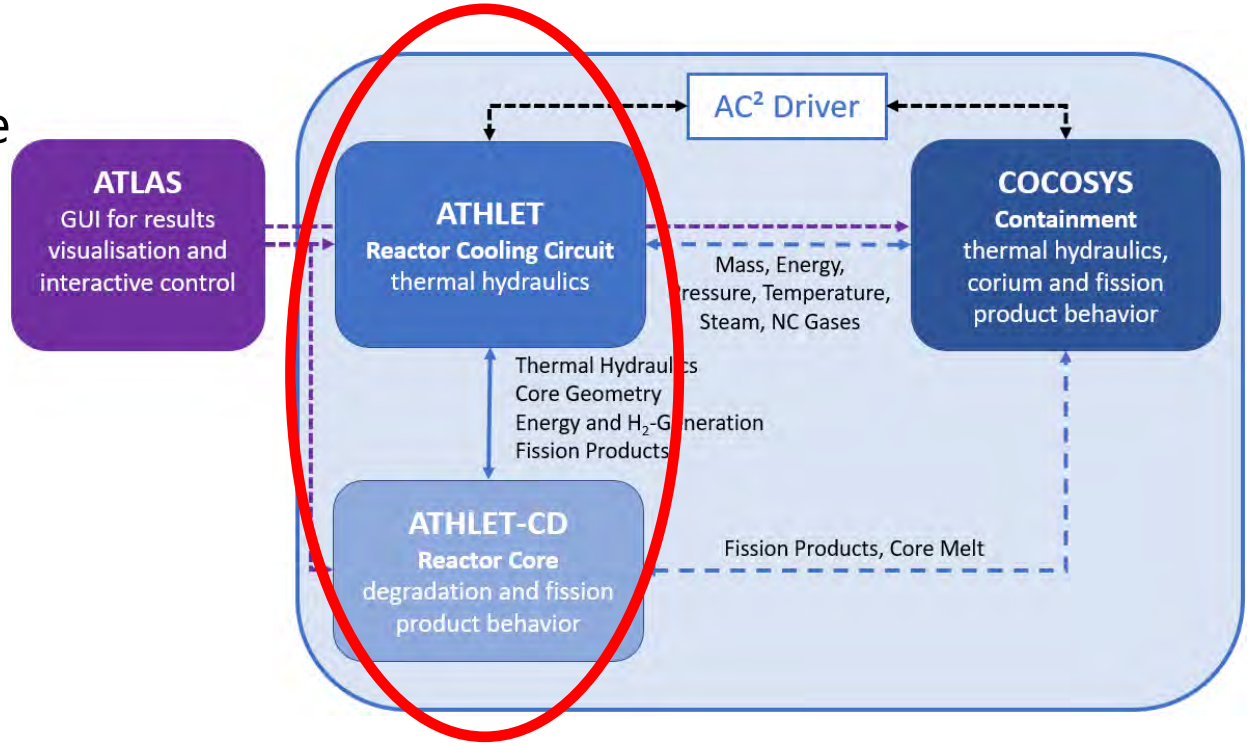

The transport module SAFT (Simulation of Aerosol and Fission Product Transport)

- FP and Aerosol behaviour within the RCS
- Vapour phase and aerosol phenomena
- Mechanistic; semi-empirical modelling
- Simplified chemical modelling
- Boundary conditions (TH params, surface T/material, etc.) ← ATHLET, ATHLET-CD

Aerosol	Vapour
• Agglomeration: gravitational, Brownian diffusion, turbulent diffusion • Deposition mechanism: Brownian diffusion, turbulent diffusion, eddy impaction, sedimentation, thermophoresis, diffusiophoresis, impaction in bends, deposits in flow contractions • Remobilization: revaporisation, mechanical resuspension • Dedicated pool scrubbing model for SG flooded secondary side	• homogeneous nucleation • heterogeneous nucleation • condensation/revaporisation • wall sorption • vapour phase chemistry • preliminary model for kinetics of gas chemistry

Modelling the core region in SAFT

- AC2 2025.0 – recommendation is to start from the UP
- Development and verification work: to include the Core region

→ possibility to close the FP transport loop

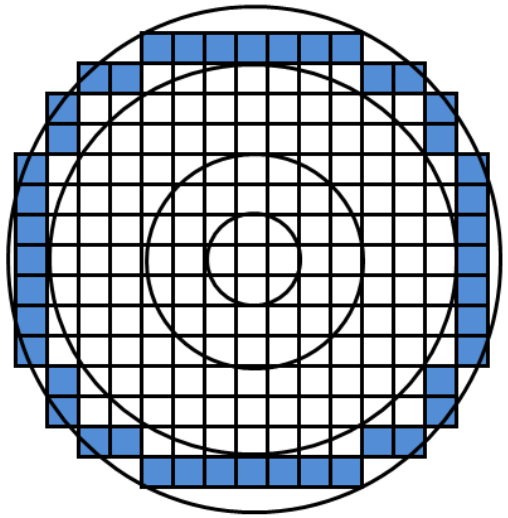

Subdivision into concentric rings

Source: Lovasz, L. 2026. *Further development of ATHLET-CD for simulations of accidents with asymmetrical characteristics. Dissertation - submitted*. PSS.

- TH: concentric core rings + Cross Connection Objects
- SAFT: modelling based on TH (ATHLET) modelling

- CCO can be included all/nothing approach
  - All/None Core rings
  - CCO outside the core region

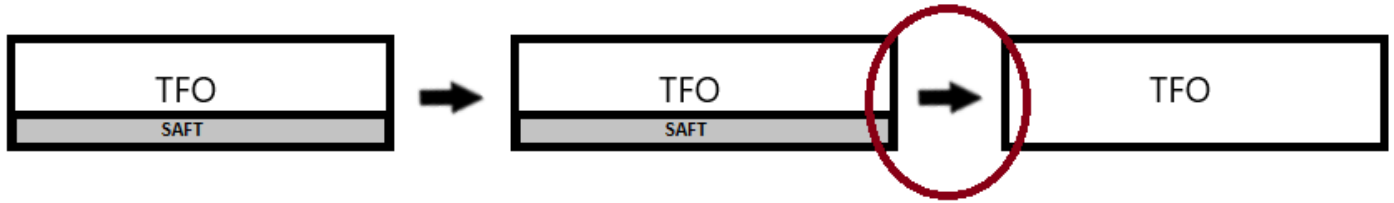

SAFT “Dead End”

Source term positioning

- Traditional modelling approach:
  - All FP appears in the 1st SAFT CV (based on TH modelling)
  - Some overestimation may be present, but generally “conservative”
- New modelling approach:
  - Separate routine to find exact position of FP release
  - Exact axial/radial position
  - Based on cladding failure (dedicated model within ATHLET-CD)
  - Not only initial, but subsequent failures are also identified
- Missing:
  - Consideration of the melting of structures
    - Planned to be addressed in the future
    - Not only for concentric rings, but also for more flexible nodalisations

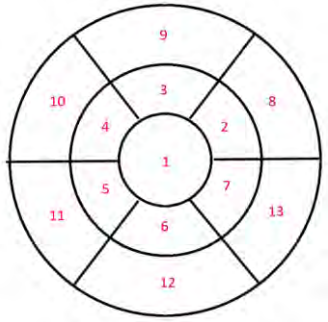

Source term positioning

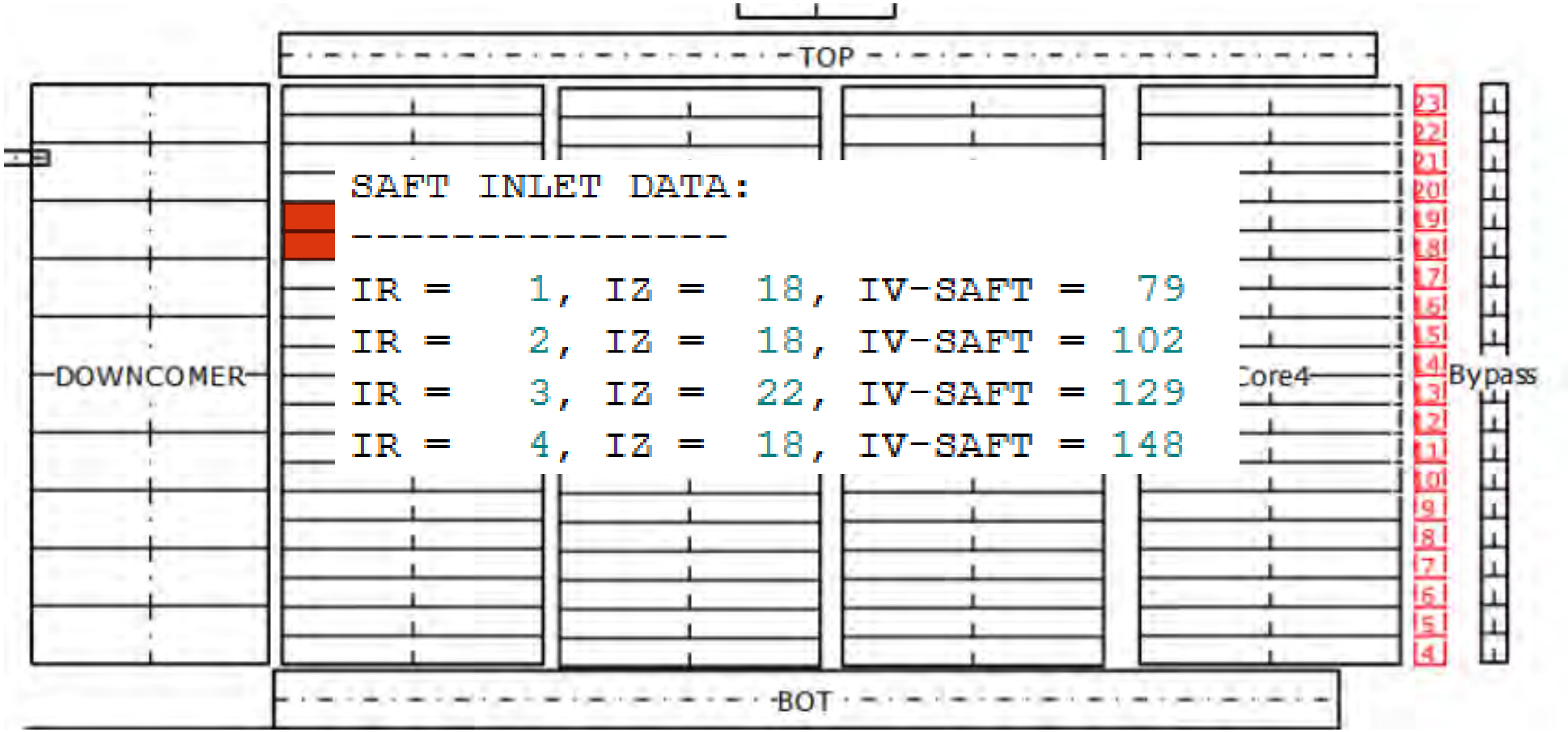

Postulated Accident Scenario

- Cold leg medium break LOCA with SBO (200 cm^2)
- Generic German PWR (Konvoi)
- No SAM actions

Parameter	Nominal value
Reactor Power	3 750 MW_{th}
Operational pressure	157 bar/65 bar
Core inlet/outlet temperature	292 °C/325 °C
# of fuel assemblies	193
Coolant mass flow rate	19.8 t/s

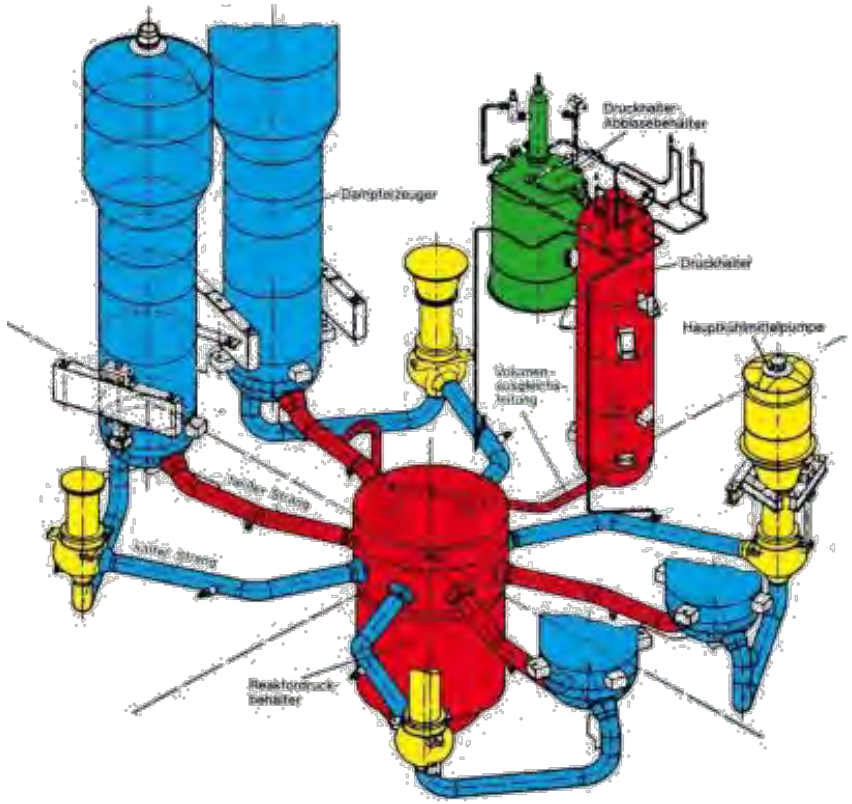

Source: T. STEINRÖTTER. “Systemtechnikschulung Sicherheitskonzept: Sicherheitsprinzipien (Teil 1),” (2018).

Modelling approach in AC²/ATHLET-CD

- Model based on previous simulations
- Full, 4 loop TH reactor model
- 4 core rings/rods with realistic radionuclide inventory
- FP release: Arrhenius type correlation f(T, p_p*)
- SAFT – 2 options
  - Simple
  - including core region with
    fully closed SAFT-Loop
- 217 TFOs, over 600 junctions

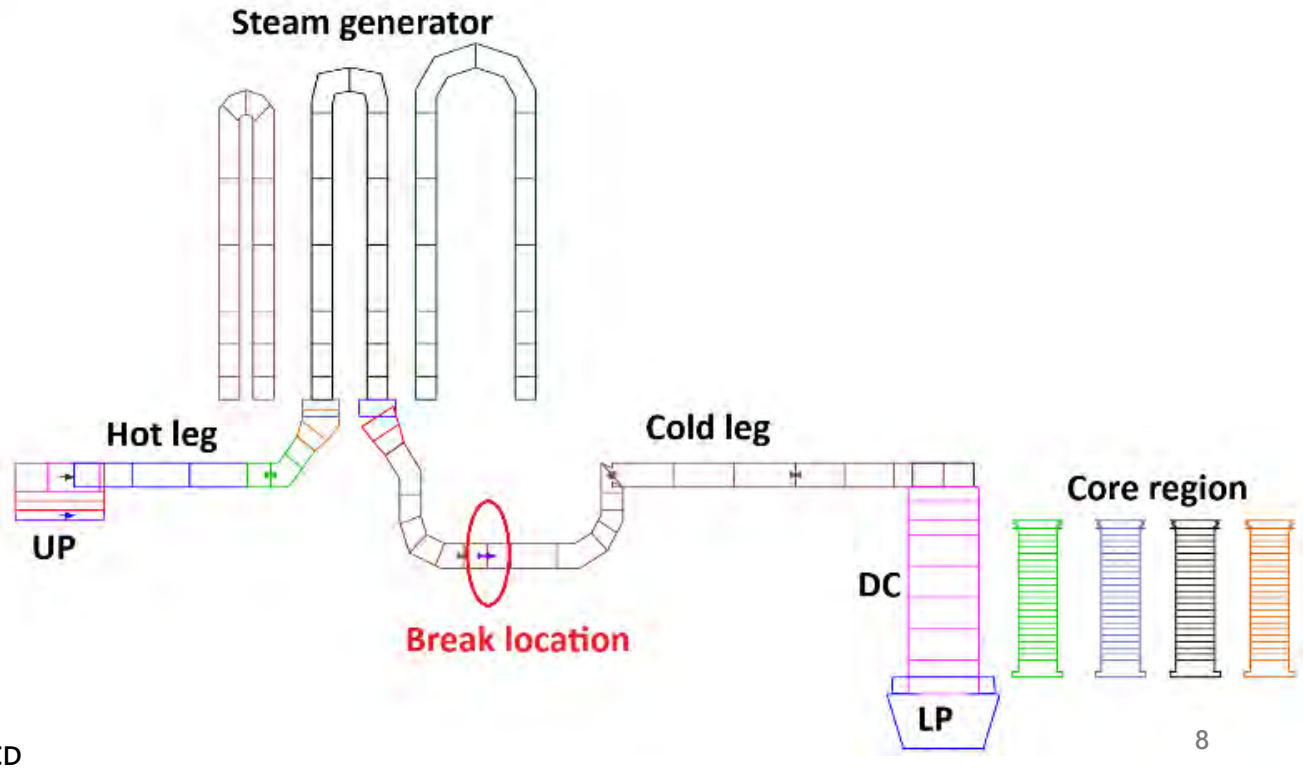

Different transport path modelling approaches

Old modelling approach (simple):

UP → HL → SG → CL → Break

New modelling approach (advanced)

includes also the core region

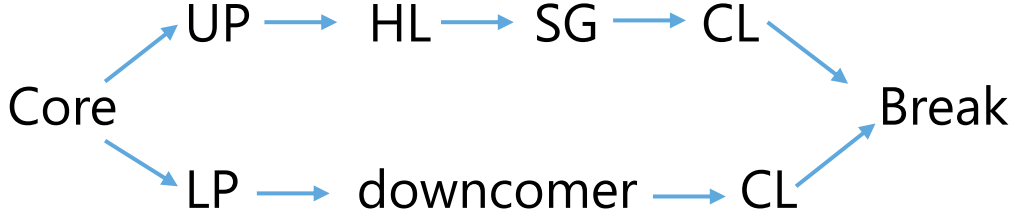

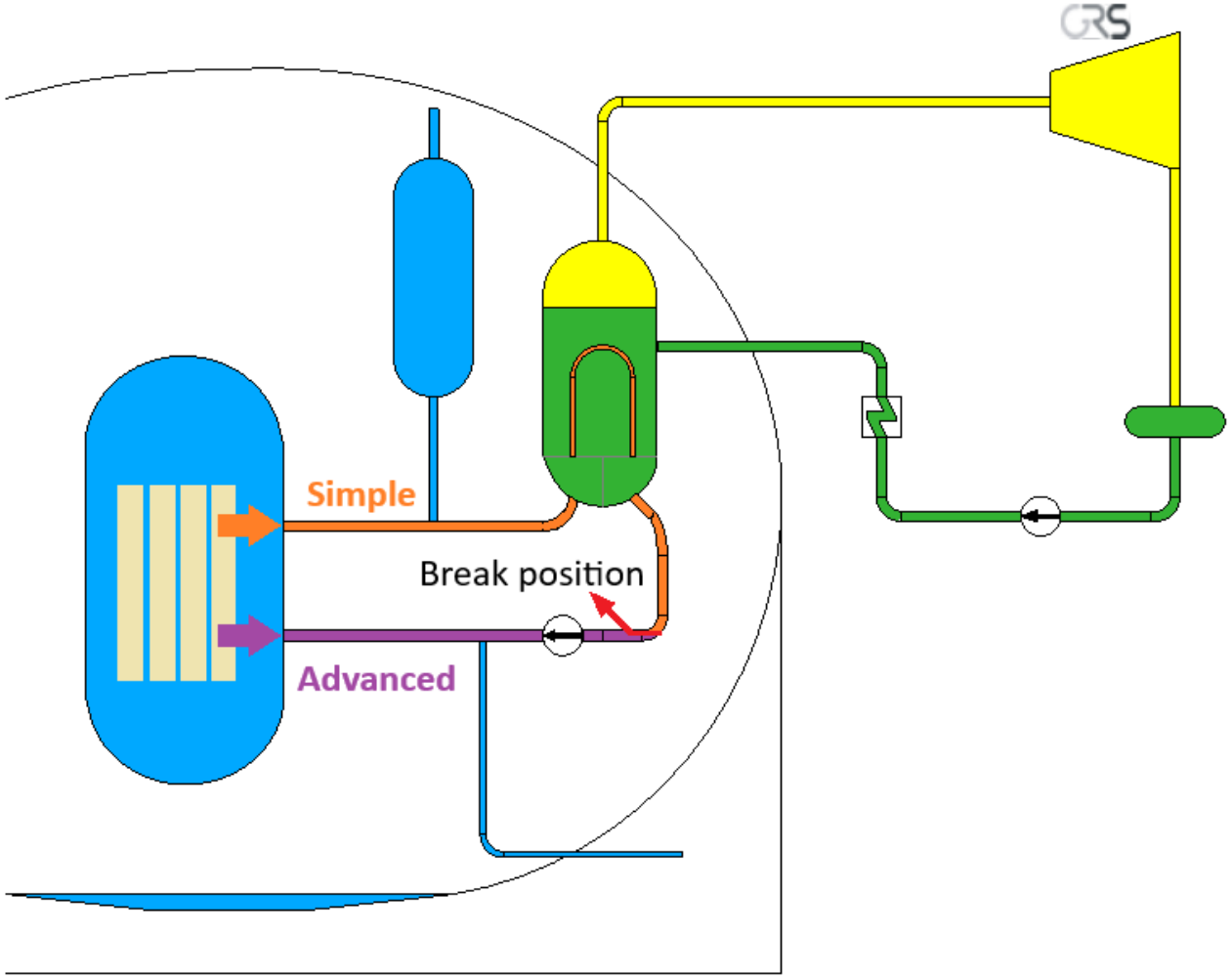

Simulation results

Event	Time [s]
Break opening	5,000
Start of ACC	5,884
1st clad failure	8,859
1st CR failure	9,207
1st fuel rod failure	9,842/10,068*
Start of relocation to LP	10,106/10,181*
LP failure	13,613/13,557*

*simple/advanced

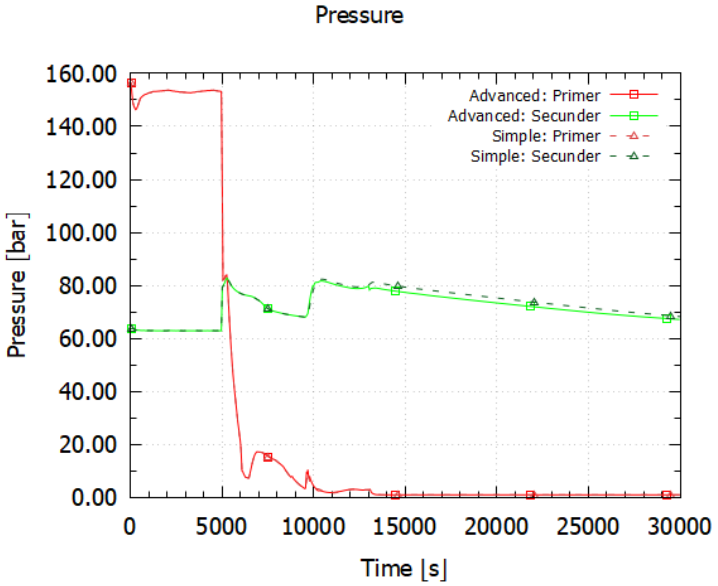

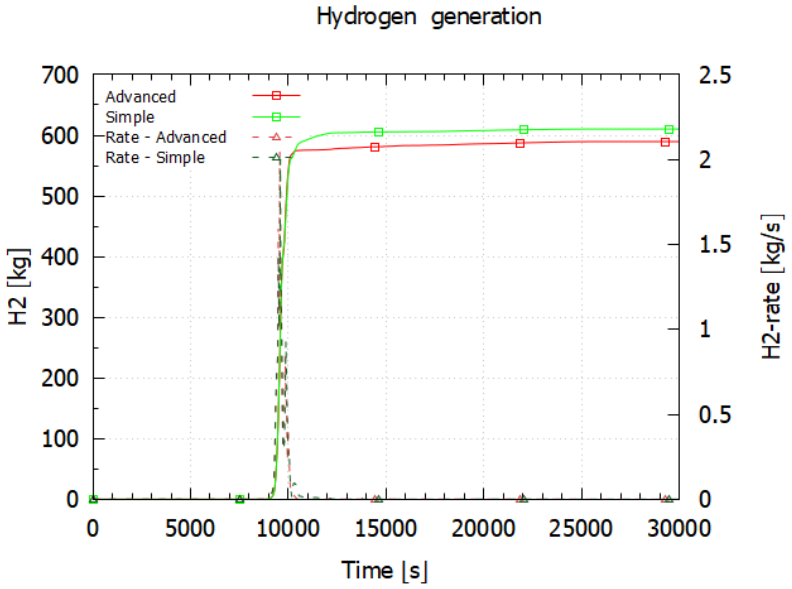

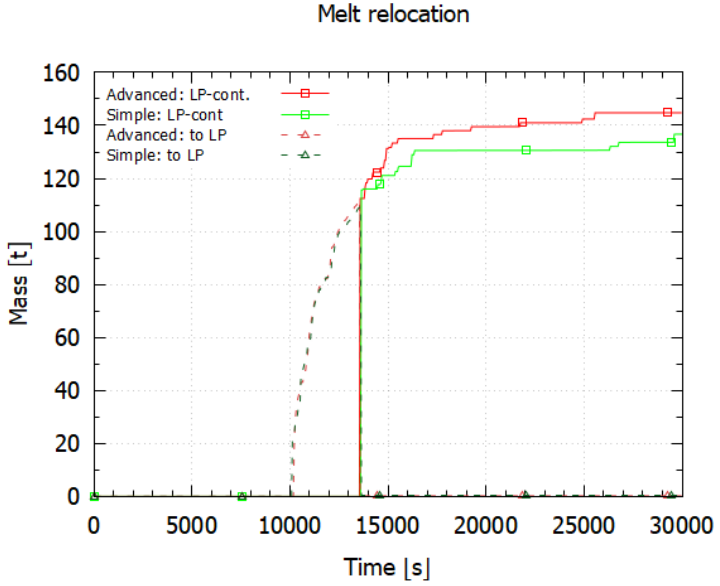

FP behavior

1st FP release ~8,859s in both cases

Traditional modelling approach:

higher retention in RCS

FP → starts in UP

Advanced modelling approach

higher release

1st burst: Rod 1., node 18

~3.2m within the active core

Cesium release into containment

22 i.i.% vs 52 i.i%

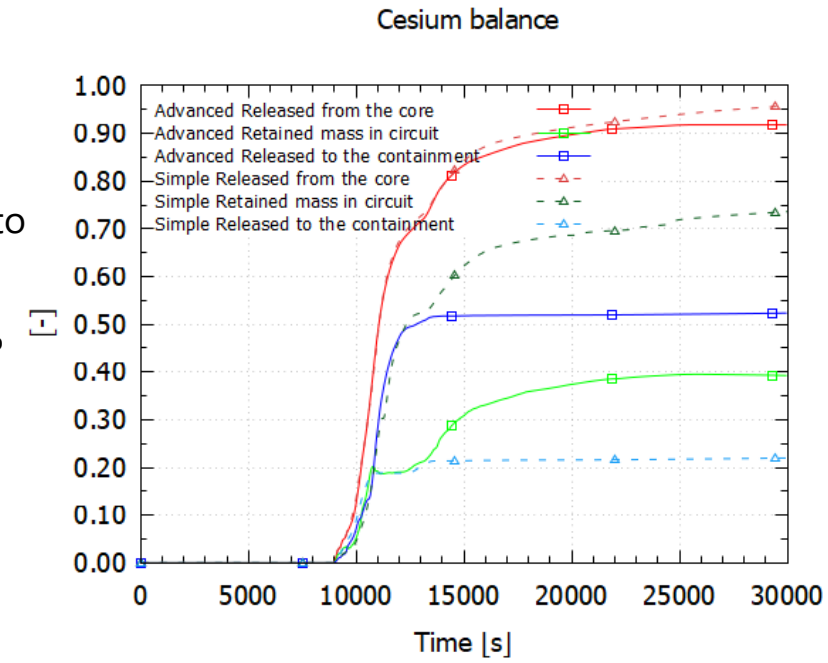

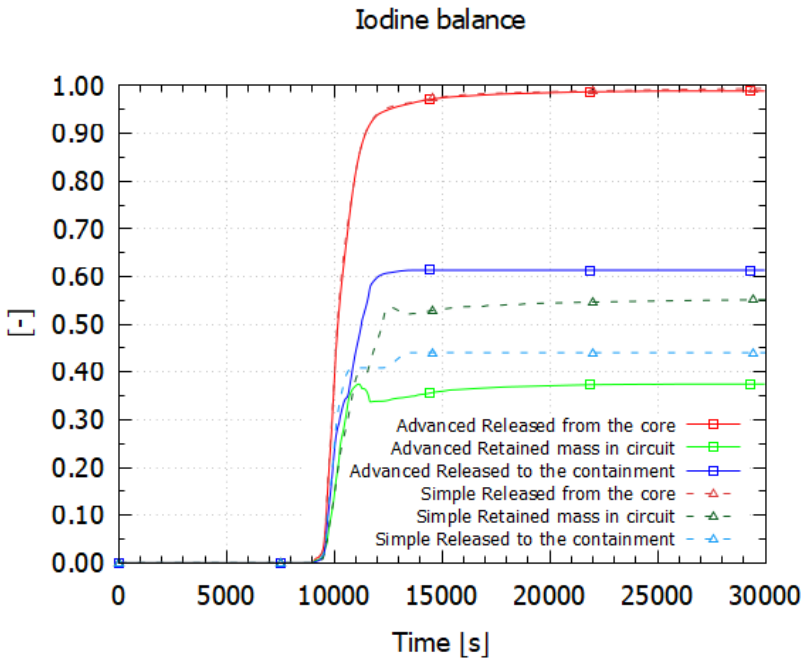

Iodine release into containment

45 i.i.% vs 60 i.i%

FP behavior – retention: Cesium @ 30,000s

Retention: mainly within SG, beginning of hot leg

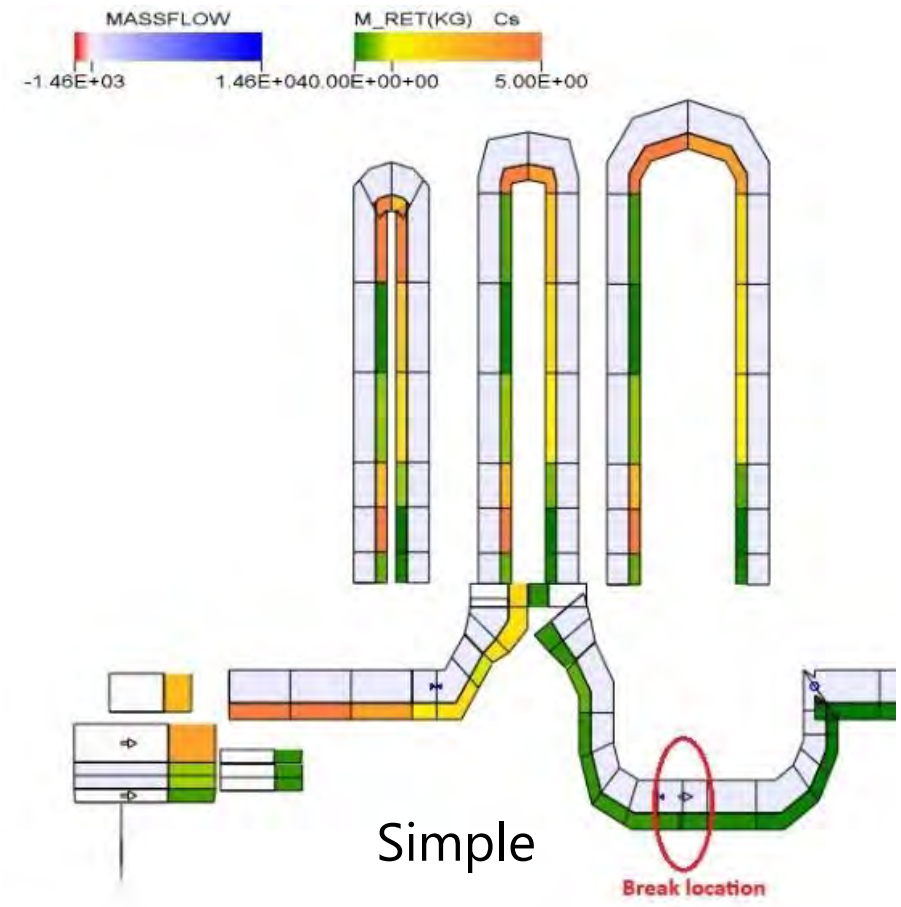

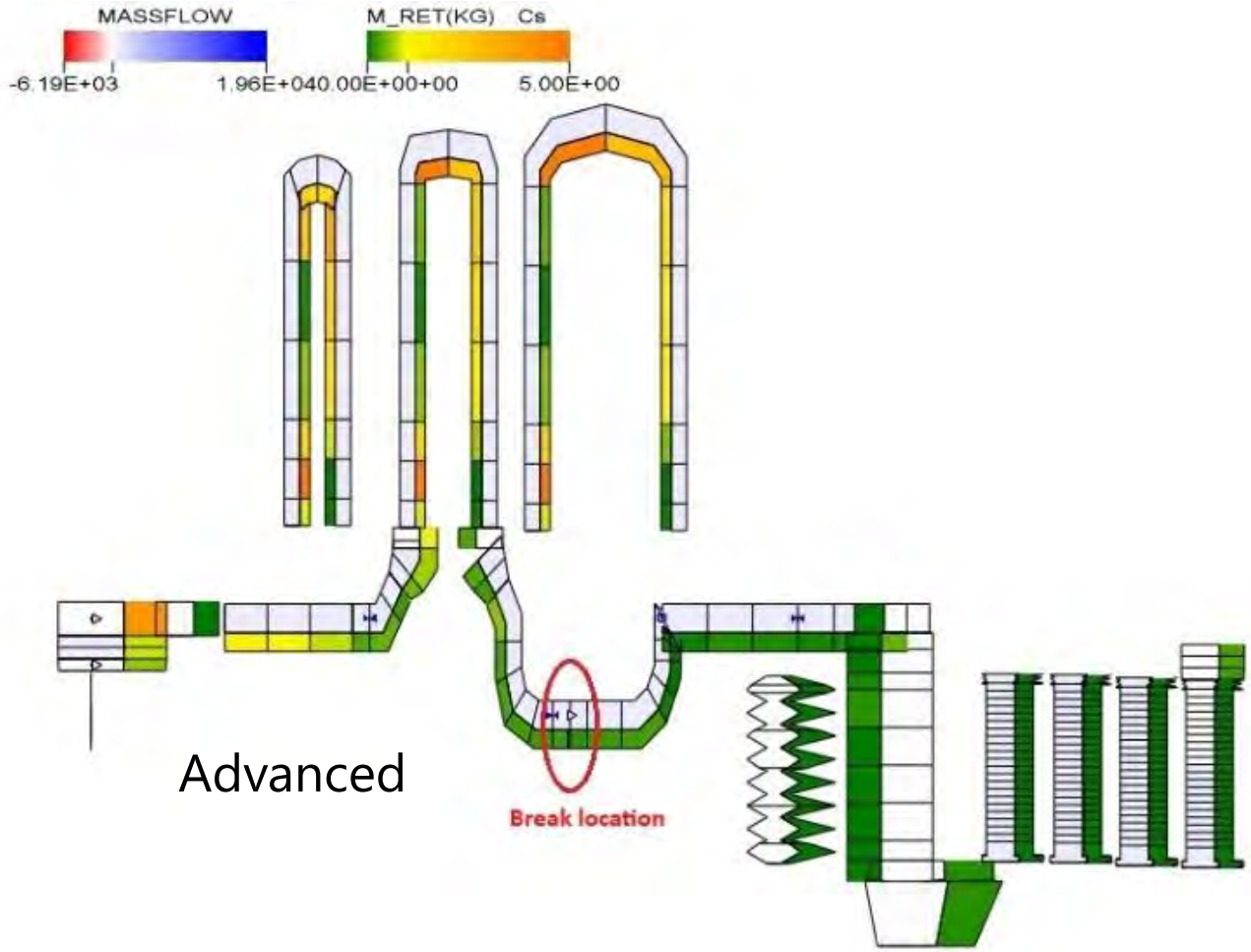

FP behavior – Cs retention @ 14,000 s in the advanced modelling approach

- additionally: core region/LP/CL
- neglected in the simple modelling
- reverse flow
- remobilization is strong in the core/LP regions

affects timing/composition of the source term into the containment

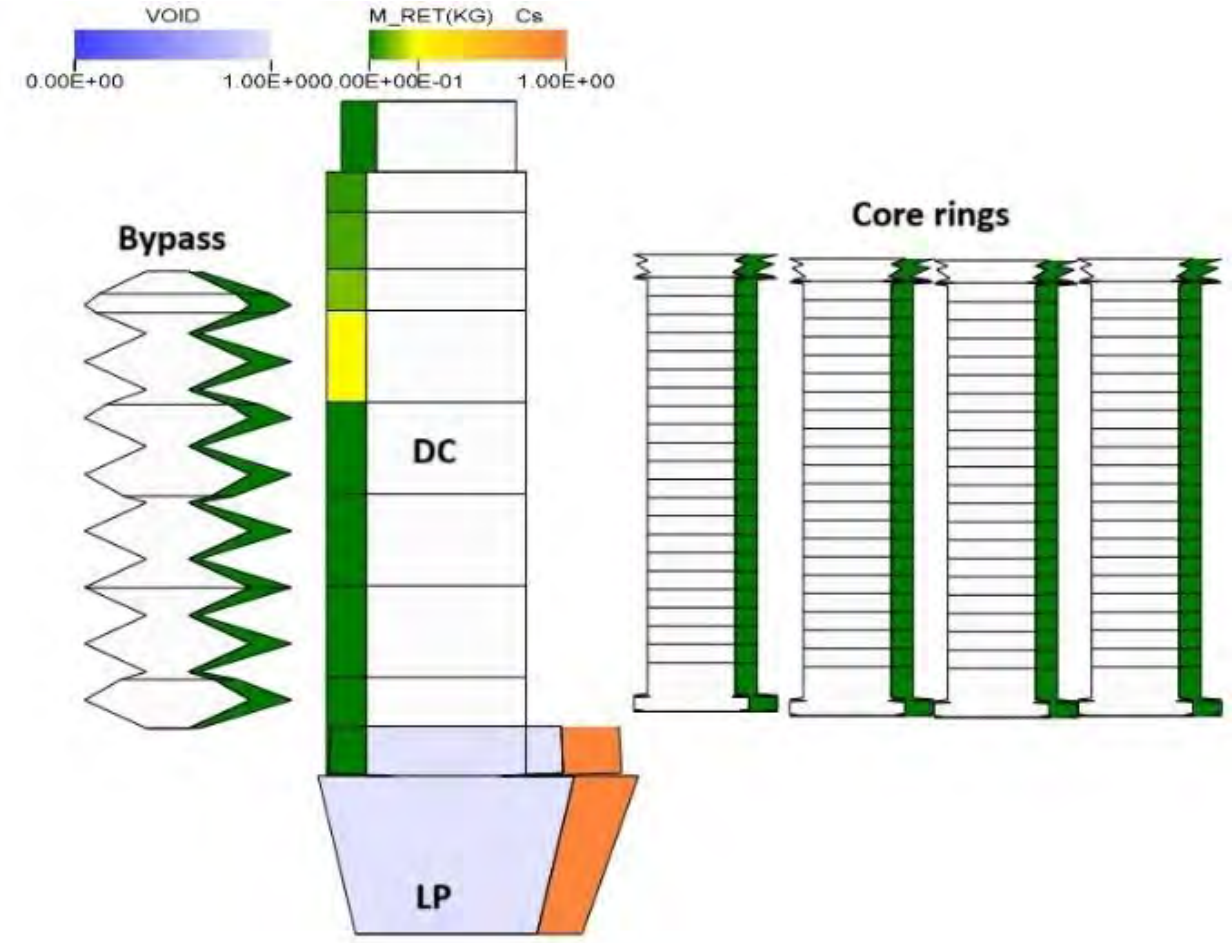

FP behavior - retention

Dominant retention mechanism

- thermophoresis and settling
- relative importance differs

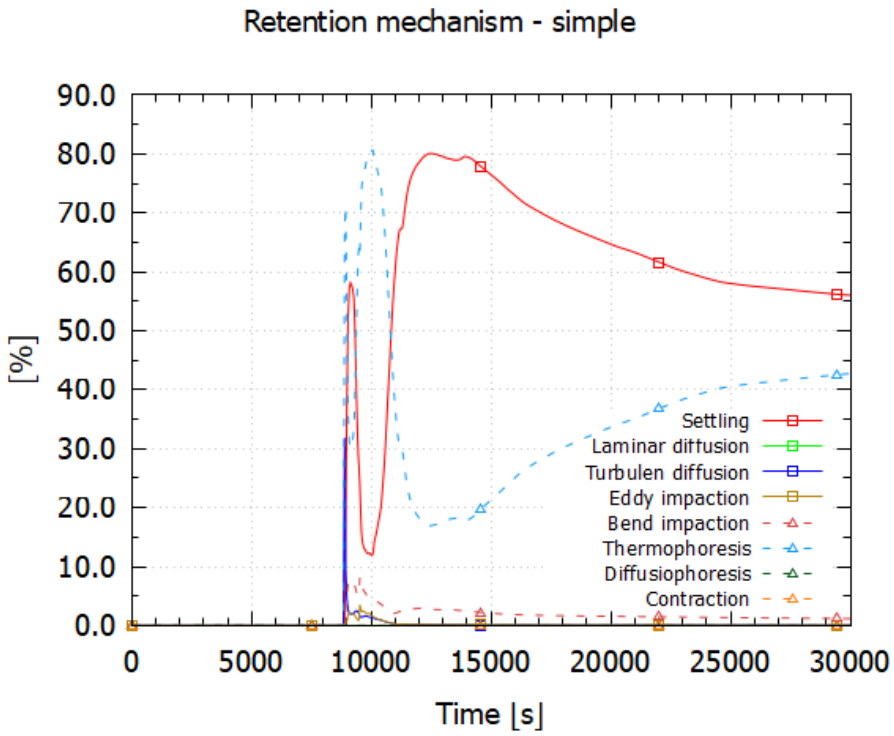

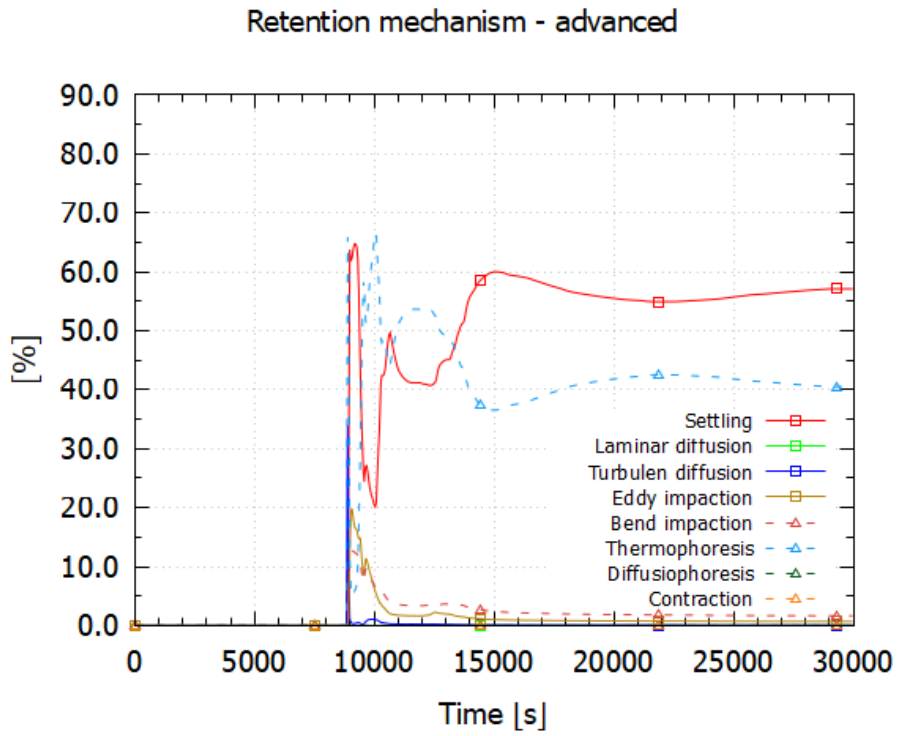

FP behavior – release

- ST release from both direction
- At the moment no separate value
- Normalized rate values give some orientation, combined with retention values
- Significant contribution from reverse direction

Future development work: save explicit values from each direction

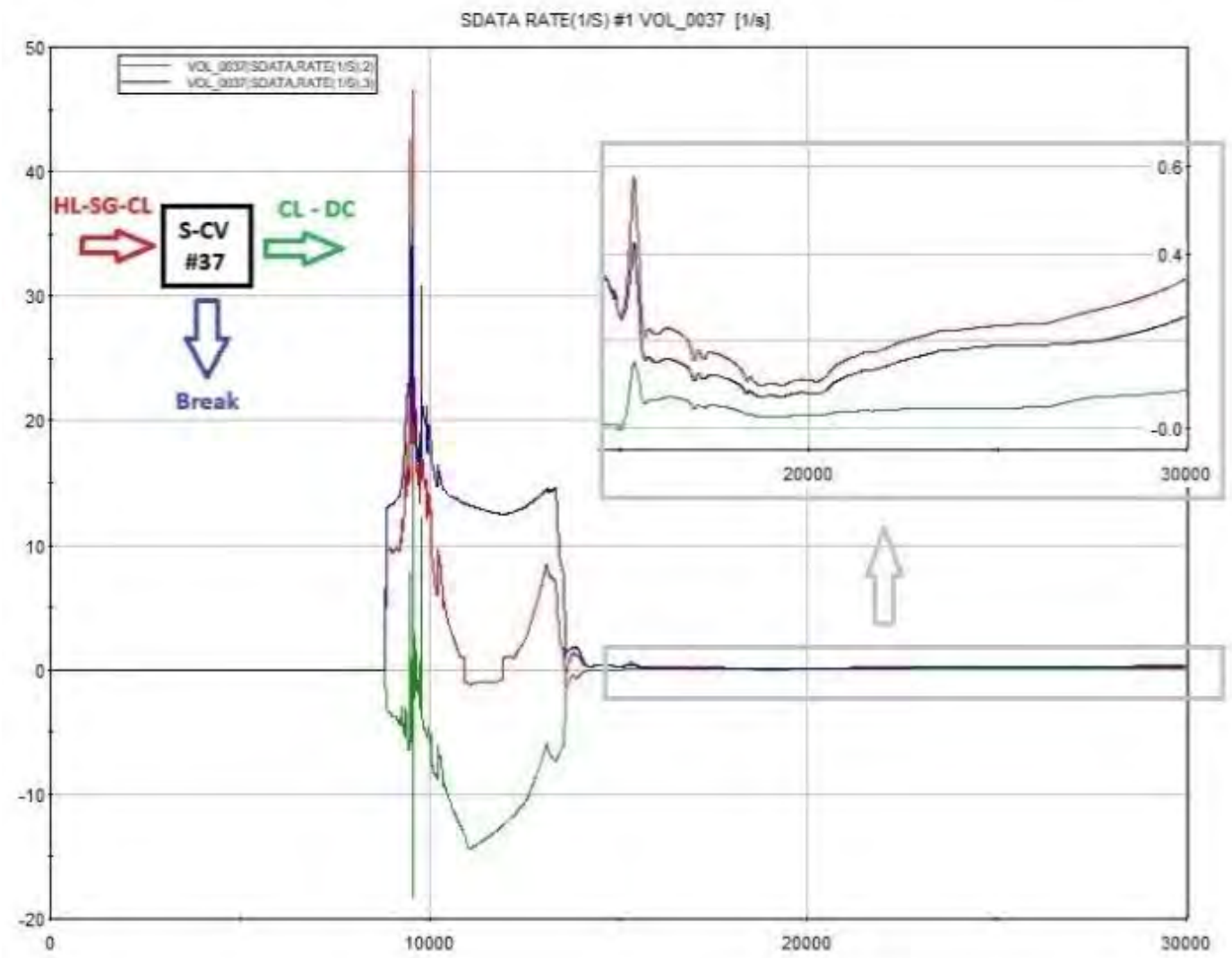

Challenges, future work

- Explicit outlet values from each direction
- Dynamic handling of SAFT-outlets (e.g. LP failure)
- Fully water filled CVs → no aerosol/vapor transport
  - void=0, can be relevant in e.g. LP
  - Reflooding, SAM measures
- Extension of V&V

Summary

- Introduction of new, advanced modelling approach
  - explicit modeling of the core region
  - limitations/recommendations
- Demonstration of simulation capabilities on postulated reactor severe accident
- Results show significant influence of modelling approach (importance of underlying TH)
- Identification of future development and V&V needs
- Need for numerical overview for possible computational time reduction
  - advanced modelling approach needed in this case +70%
  - Note: integration of ATHLET-CD modules into ATHLET → parallelization possibilities

Thank You for your attention!

The development and the validation of AC^2 is sponsored by the German Federal Ministry for the Environment, Climate Action, Nature Conservation and Nuclear Safety (BMUKN) on the basis of decisions by the German Bundestag within several projects.

DEVELOPMENT OF EVALUATION TECHNOLOGY FOR RADIOLOGICAL SOURCE TERM IN THE CONTAINMENT USING CINEMA CODE DURING SEVERE ACCIDENT

Donggun Son[1*], Jun-young Kang[1], Jaehyun Ham[1]
[1]Korea Atomic Energy Research Institute (KAERI), Daejeon, Republic of Korea
989-111 Daedeok-daero, Yuseong-gu, Daejeon, 34057, Korea
donggunson@kaeri.re.kr; kkang0620@kaeri.re.kr; jhham@kaeri.re.kr

Byung Jo Kim
[2]KEPCO Engineering & Construction (KEPCO E&C)
269, Hyeoksin-ro, Gimcheon-si, Gyeongsangbuk-do, 39660, Korea
bjokim@kepco-enc.com

Yeon-Gun Lee
[3]Sejong University
209, Neungdong-ro, Gwangjin-gu, Seoul, 05006, Korea
yglee@sejong.ac.kr

ABSTRACT

Quantitative evaluation of the radiological source term (ST) inside the containment during a severe accident is essential for plant-specific severe accident management guidance (SAMG), emergency response planning, and the design of mitigation systems. However, widely used deterministic Alternative Source Term approaches (e.g., U.S. reactor-based methodologies) may not fully represent the design characteristics and severe accident phenomenology of Korean pressurized water reactors, including OPR1000 and APR1400. This paper presents recent advances to the domestically developed integrated severe accident analysis code CINEMA (Code for INtegrated severe accident Evaluation and MAnagement) to enable plant-specific assessment of containment source term for OPR1000. The fission product (FP) behavior module SIRIUS (SImulation of Radioactive nuclide Interaction Under Severe accident) was improved and applied to nine representative severe accident scenarios selected from Level 2 PSA insights and deterministic considerations, including SBO, TLOCCW, LOCA classes, and SGTR. CINEMA predictions were compared against MAAP5 results under consistent boundary and initial conditions to assess credibility of thermal-hydraulic trends, major event timing, and the containment inventory of key radionuclide groups, with particular emphasis on iodine and cesium. In addition, uncertainty and sensitivity analyses were performed using MELCOR to identify dominant contributors to ST variability; the aerosol shape factor (CHI) was found to be the most influential parameter affecting iodine and cesium release through its impact on aerosol transport and deposition. Code performance was also benchmarked against the PHEBUS FPT-1 international experiment, demonstrating prediction capability within the experimental error band for key quantities. Finally, this work introduces the Fission Product Evaluation Module (FPeval) v2.0 as a post-processing tool to quantify mass distribution by containment nodes, release mechanisms, and radionuclide decay from CINEMA outputs. The resulting severe accident “big data” is expected to support improved SAMG strategies and future AI-assisted real-time accident response and mitigation facilities for Korean reactors.

* Corresponding Author, donggunson@kaeri.re.kr

KEYWORDS
Severe Accident; Source Term; CINEMA; OPR1000

1. INTRODUCTION

A severe accident (SA) in a nuclear power plant involves complex, coupled phenomena such as core heat-up and degradation, fission product release, transport and deposition in the reactor coolant system, and multi-compartment containment thermal-hydraulics with aerosol behavior. A central objective of SA analysis is the evaluation of the radiological source term (ST) [1], i.e., the time-dependent quantity and chemical/aerosol form of radionuclides that are released into the containment and potentially to the environment, which directly supports emergency planning, habitability assessment, and mitigation strategy development.

Historically, licensing and safety evaluations have relied on conservative Alternative Source Term (AST) [2] methodologies originally developed for U.S. reactor designs. While such approaches provide standardized assumptions, limitations have been recognized when applying them to reactors with different design and operational characteristics. In the Korean context, OPR1000 and APR1400 include plant-specific features that can influence severe accident progression and containment retention (e.g., large containment volume and wet cavity-related phenomena). Therefore, a plant-specific, mechanistic evaluation capability is required to support domestic SAMG and to provide credible source-term data for engineered mitigation concepts.

To address this need, the integrated severe accident analysis code CINEMA [3] has been developed and continuously advanced. CINEMA integrates modules for in-vessel progression, system thermal-hydraulics, ex-vessel and containment behavior, and fission product/aerosol behavior. This paper focuses on the development and application of CINEMA for quantitative containment ST evaluation for OPR1000 severe accident scenarios.

The objectives of this paper are as follows:

1. Present the CINEMA code architecture and key modeling features for source term evaluation, with emphasis on the SIRIUS [4] fission product module and the post-processing tool FPeval v2.0 [5].
2. Describe the selection and modeling of nine representative OPR1000 severe accident scenarios [5].
3. Demonstrate credibility via comparative assessment against MAAP5 results for thermal-hydraulics and radionuclide inventories [5].
4. Identify dominant uncertainty contributors to iodine and cesium release using MELCOR-based uncertainty and sensitivity analysis, and discuss implications [5].
5. Summarize key findings and expected applications to SAMG enhancement and future real-time/AI-assisted decision support.

2. METHODOLOGY

2.1. Overview of CINEMA Code Architecture

CINEMA (Code for INtegrated severe accident Evaluation and MAnagement) is a domestically developed, integrated severe accident analysis framework designed to simulate coupled in-vessel, ex-vessel, and containment phenomena while enabling mechanistic evaluation of fission product release and aerosol behavior.

CINEMA consists of the following main components:

- CSPACE [6]: In-vessel and primary/secondary system severe accident thermal-hydraulics and core damage progression (coupling of COMPASS [7] and SPACE-SAM [6]).
- SACAP [3]: Containment thermal-hydraulics and ex-vessel severe accident phenomena (e.g., MCCI, hydrogen combustion, DCH), including mitigation features.
- SIRIUS: Fission product release, transport, chemistry, aerosol generation and deposition within the RCS and containment.

- MASTER [3]: An integration/coupling framework to exchange boundary conditions and state variables among modules. Figure 1 shows the conceptual architecture and information flow.

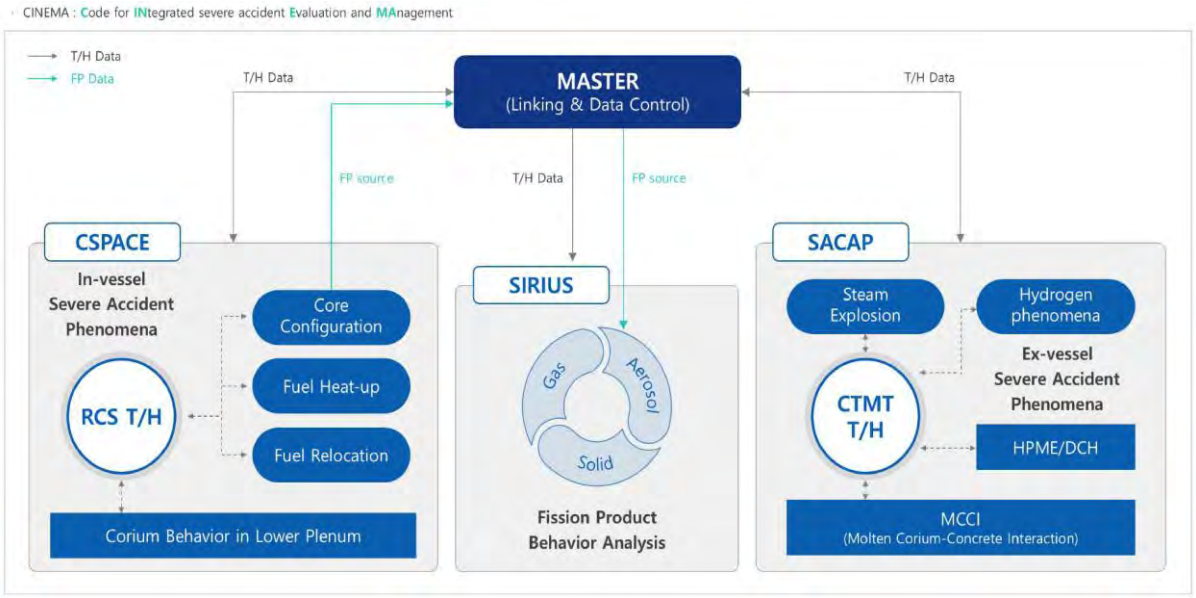

Figure 1. CINEMA architecture and coupling among CSPACE, SIRIUS, SACAP, and MASTER.

2.2. In-vessel and System Thermal-Hydraulics: CSPACE (COMPASS + SPACE-SAM) Module

CSPACE is a coupled code system combining:
- SPACE-SAM: An enhanced system thermal-hydraulic code to simulate severe accident conditions, including improvements such as time-step control for rapid hydrogen generation, refined metastable property models, improved non-condensable gas treatment, critical flow model enhancement, and internal energy equation refinements.
- COMPASS: A core degradation and melt progression module representing initial core configuration, heat-up under uncover, fuel relocation, debris bed and molten pool formation, and lower head integrity evaluation.

CSPACE provides time-dependent thermal-hydraulic boundary conditions (temperatures, pressures, flows, steam/non-condensable compositions) required by SIRIUS for fission product and aerosol transport calculations.

2.3. Containment and Ex-vessel Phenomena: SACAP Module

SACAP evaluates thermal-hydraulic behavior in containment compartments and models major severe accident phenomena such as steam explosion, molten corium–concrete interaction (MCCI), hydrogen combustion, and direct containment heating (DCH), as well as mitigation systems (e.g., igniters, PARs) if applicable. Conservation equation fidelity is designed to be comparable to, or higher than, integral severe accident codes commonly used for containment analyses. SACAP provides containment conditions (pressure, temperature, compartment flows, aerosol removal conditions) to SIRIUS and receives radionuclide/aerosol source terms for multi-compartment tracking.

2.4. Fission Product and Aerosol Behavior: SIRIUS Module

SIRIUS (SImulation of Radioactive nuclide Interaction Under Severe accident) predicts:
- In-core fission product release into the RCS (gas phase),

- Transport through the RCS and associated retention mechanisms,
- Aerosol formation and evolution, and
- Release and behavior inside containment compartments.

Key aerosol processes include condensation, evaporation, adsorption, impaction, gravitational settling, diffusion, and thermophoretic deposition. Since SIRIUS does not directly simulate core melt thermal-hydraulics, it relies on boundary conditions from CSPACE and SACAP. This structure enables consistent coupling between severe accident progression and radionuclide behavior.

2.5. Scenario Selection for OPR1000 Severe Accident Evaluation

Nine representative severe accident scenarios were selected based on:
- Review of Level 2 PSA results to identify dominant accident sequences contributing to risk, and
- Deterministic considerations to cover a spectrum of initiating events and system availability conditions.

The scenario set includes: SBO (Station Blackout), TLOCCW (Total Loss of Component Cooling Water), LOCA classes (SLOCA/LLOCA/MLOCA), and SGTR (Steam Generator Tube Rupture). Table 1 provides the scenario list and main characteristics used for analysis.

Table 1. Representative OPR1000 severe accident scenarios considered in this study (nine cases). [8]

Index	Sequence name	Remarks
1	SBOR _S38	(SBO)(TDAFW for 8 hours)(Late Recovery of AC Power)(Recirculation Spray)
2	TLOCCW_S 10	(TLOCCW) (TDAFW failed) (Bleed Operation failed)
3	MLOCA _S3	(MLOCA)(HPSI) (Recirculation failed)
4	LLOCA_BE _BASE	(LLOCA)(SIT)(SI failed)(CS failed)
5	LLOCA_BE _MACST	(LLOCA)(SIT)(SI failed)(CS failed)(IVI)(Late Recovery of CS) (Recirculation Spray)
6	SLOCA_BE _BASE	(SLOCA)(SIT)(SI failed)(Bleed Operation failed)(CS failed)
7	SLOCA_BE _MACST	(SLOCA)(SIT)(SI failed)(Bleed Operation failed)(CS failed) (IVI)(Late Recovery of CS) (Recirculation Spray)
8	SGTR_BE_ BASE	(SGTR)(Broken SG Isolation)(SIT)(Bleed)(Feed failed)(CS failed)
9	SGTR_BE_ MACST	(SGTR)(Broken SG Isolation)(SIT)(Bleed)(Feed failed)(CS failed) (IVI)(Late Recovery of CS) (Recirculation Spray)

2.6. Post-processing and Quantification of Source Term: FPeval v2.0 Module

To support systematic and reproducible ST quantification from CINEMA runs, the Fission Product Evaluation Code (FPeval) v2.0 was developed as a post-processing tool operating on CINEMA output files (e.g., log/output/rsplt).

FPeval v2.0 performs:
- Quantification of radionuclide mass distribution by containment node/compartment,
- Evaluation of release amounts by release mechanism categories (e.g., gap release, in-vessel release, ex-vessel release, late in-vessel release),
- Nuclide-specific radioactive decay tracking, and
- Automatic recording of key accident progression times (e.g., core uncovery, relocation, vessel failure).

This framework enables consistent comparison among scenarios and between codes, and it supports generation of structured datasets suitable for further analysis and visualization.

2.7. Code Credibility Assessment and Benchmarking Strategy

Two complementary approaches were used to assess credibility:

1. Code-to-code comparison: CINEMA results were compared to MAAP5 simulations under equivalent conditions to verify trends in key thermal-hydraulic variables, major event timings, and containment inventories of major radionuclide groups (with emphasis on iodine and cesium).
2. Experimental benchmark: CINEMA was benchmarked against the PHEBUS FPT-1 [9] international experiment to evaluate the capability to reproduce representative severe accident source-term behavior within experimental uncertainty.

2.8. Uncertainty and Sensitivity Analysis Using MELCOR [9]

Uncertainty and sensitivity analyses were conducted using MELCOR to:
- Identify key uncertain parameters affecting containment ST,
- Quantify the variability range of iodine and cesium releases, and
- Provide insight for prioritizing model improvements and instrumentation/mitigation strategies.
Uncertain variables were selected following criteria widely used in severe accident uncertainty studies, covering in-vessel progression (e.g., fuel failure criteria), ex-vessel/containment parameters (e.g., leakage, failure pressure), aerosol parameters, and FP chemistry-related variables. Particular attention was given to the aerosol shape factor (CHI) due to its influence on aerodynamic behavior and deposition.

3. RESULTS AND DISCUSSION [5]

3.1. Severe Accident Progression Characteristics for the Nine Scenarios of OPR1000 [8]

CINEMA simulations were executed for the nine OPR1000 scenarios to quantify severe accident progression, including:
- Timing of core uncovery and heat-up,
- Onset of significant fission product release,
- Core relocation to the lower plenum,
- Lower head failure timing (if predicted), and
- Transition to ex-vessel phase and containment pressurization behavior.

The scenario set produced differentiated progression patterns consistent with expected initiating event characteristics. For example, LOCA-driven sequences generally exhibit rapid depressurization and different retention/removal behaviors compared to SBO-driven sequences where prolonged heat-up and hydrogen generation can dominate.

SOE	MAAP5 (s)	CINEMA (s)	Description for CINEMA
SGTR(SG#1) start	0	0	
MSSV first open (SG#2)	1927	850/860	
SG dryout	5606	5790/3670	CtrlVar @101/102 = 0.0
PSV first open	8619	8730	Mflowj@ C527 〉 0.0
Core uncover	9245	9700	Voidg @ C185/C190/C195 = 1.0
SAMG entry	10232	11210	Tempg @ C201 〉 923K
Gap release		11443	Flag_gap = 1.0
SDS stuck open	12032	13010	Mflowj@ C526/C528 〉 0.0
SIT injection start	12616	13640	Mflowj@ C835/C840/C845/C850 〉 0.0
SIT dryout		61350	Mflowj@ C835/C840/C845/C850 = 0.0
Core relocation in lower head vessel	43512	71390	Corium_t @ C199 〉 0.0
Failure of reactor pressure vessel	53151	76650	Mflowj@ C970 〉 0.0
Containment spray on	77069	96350	Lp @ SACAP 〉 618667 kpa(abs)
IVI/SGI on	77074	96350	Mflowj@ C844 〉 0.0
Containment recirculation on	85765	104185	Spray + 7835s time delay

Figure 2. Example timeline of key severe accident events for representative scenarios (core uncovery, relocation, vessel failure).

3.2. Comparison of Thermal-Hydraulic Trends: CINEMA vs. MAAP5

To confirm that CINEMA properly reproduces the RCS and containment thermal-hydraulic response, key metrics were compared with MAAP5, including:
- Primary system pressure evolution,
- Core heat-up indicators and major event timings,
- Containment pressure rise and stabilization behavior.

Across the nine scenarios, CINEMA predicted the timing of major events (e.g., core uncovery and vessel failure indicators) and containment pressurization trends consistent with MAAP5 when equivalent inputs were applied. Agreement in thermal-hydraulic behavior is a prerequisite for meaningful source term comparison because fission product release, transport, and deposition strongly depend on temperature, steam flow, and non-condensable gas conditions.

3.3. Comparison of Containment Radionuclide Inventories (I and Cs Groups)

The principal target of this study is the quantitative evaluation of radiological ST within containment, focusing on major contributors to early and intermediate dose and contamination concerns: iodine (I) and cesium (Cs) groups. For the nine scenarios, CINEMA predicted the distribution of iodine and cesium within containment compartments in strong agreement with MAAP5, typically within approximately 10–20% difference under the study's comparison basis. This level of agreement supports the conclusion that SIRIUS improvements allow CINEMA to achieve prediction performance comparable to established severe accident codes for the considered metrics.

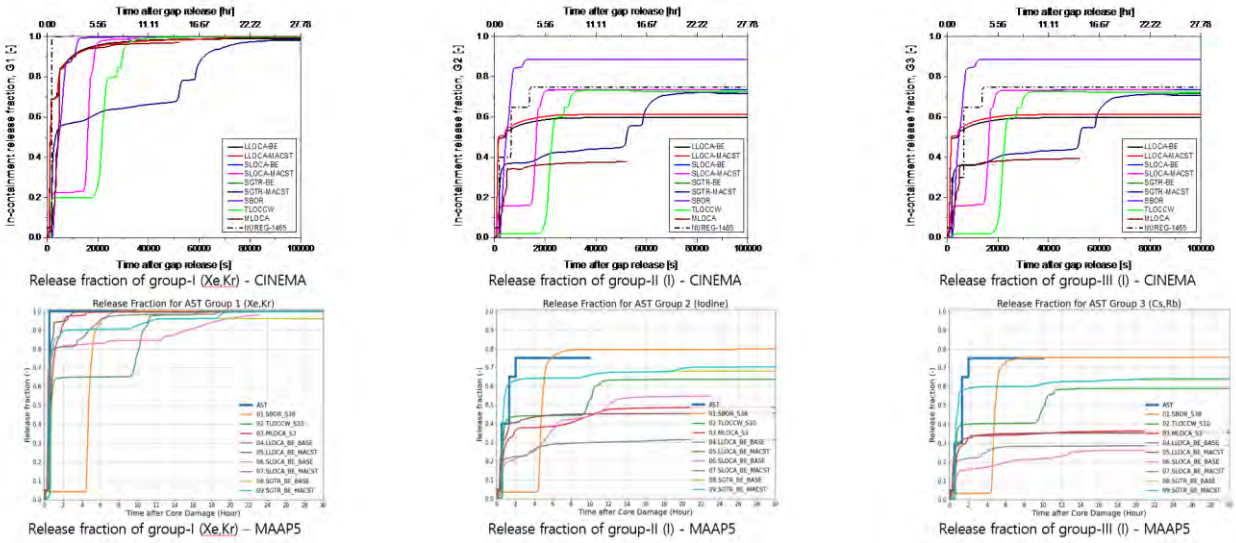

Figure 3. Comparison of key release fraction of FP groups between CINEMA and MAAP5.

3.4. Plant-Specific Effects Reflected in CINEMA Results

A key motivation for CINEMA-based ST evaluation is to reflect Korean reactor design characteristics. Two notable impacts were observed:
1. Large containment volume effect: Larger volume tends to reduce concentration peaks, influence aerosol dynamics, and alter deposition/removal behavior.
2. Wet cavity-related scrubbing/retention effect: The presence of water pools and relevant flow paths can enhance aerosol and soluble radionuclide removal depending on accident sequence and transport route.

CINEMA produced differentiated results consistent with these plant-specific features and showed enhanced mitigation capabilities compared with simplified standardized methodologies.

3.5. Source Term Trends by Accident Type

Clear qualitative differences were observed among accident categories:
- LOCA-series accidents generally produced relatively higher containment release fractions or release rates for iodine and cesium, driven by rapid changes in thermal-hydraulics, direct transport paths, and aerosol behavior under high steam flow.
- SGTR cases exhibited more limited containment release in the evaluated metrics, attributed to scrubbing/retention effects associated with secondary-side transport pathways.
These differentiated trends are important for SAMG because they influence prioritization of containment spray strategies, hydrogen control considerations, and monitoring needs.

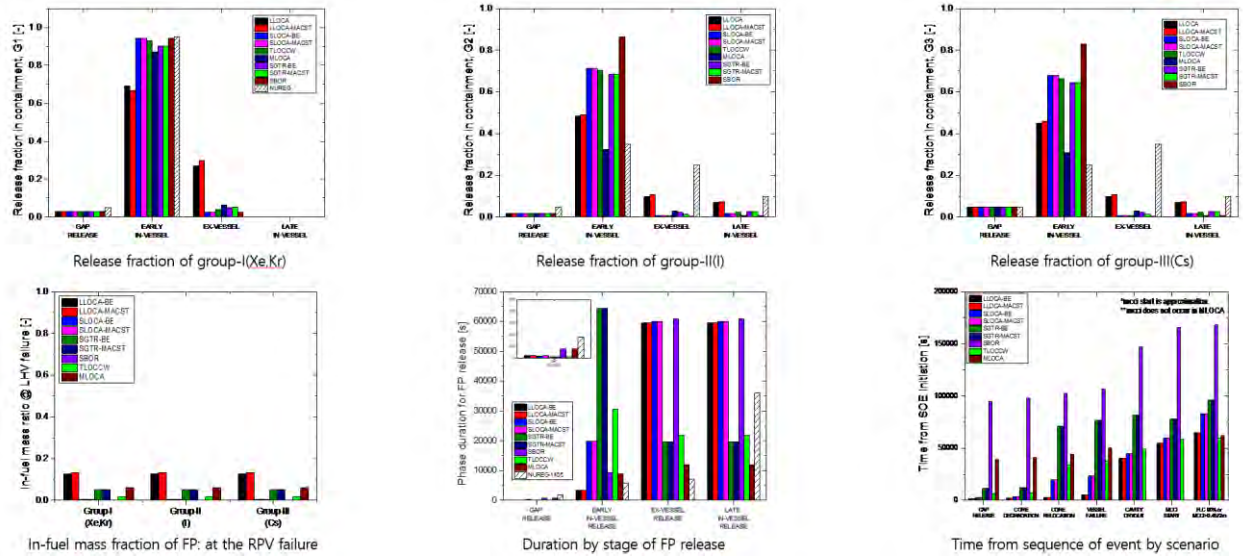

Figure 4. Release fraction of FP groups: by phases of FP release

3.6. Spatial Distribution of Radionuclides in Containment Compartments

Using CINEMA outputs and FPeval v2.0, radionuclide mass distribution across containment nodes (e.g., upper compartments, wet cavity region) was quantified. This provides:
- A basis for evaluating compartment-specific dose and contamination drivers,
- Guidance for instrumentation placement (e.g., where aerosol loading or iodine concentration may be highest), and
- Input for targeted mitigation concepts such as filtered venting or localized aerosol removal.

3.7. Uncertainty and Sensitivity Analysis: Dominant Role of Aerosol Shape Factor (CHI) [9]

The MELCOR-based uncertainty and sensitivity analyses indicated that the aerosol shape factor (CHI) is the most influential parameter affecting iodine and cesium release in the evaluated set. CHI governs the aerodynamic behavior of aerosols, impacting deposition rates and removal from the containment atmosphere; therefore, it significantly affects the airborne fraction and time-dependent availability for leakage or venting pathways.

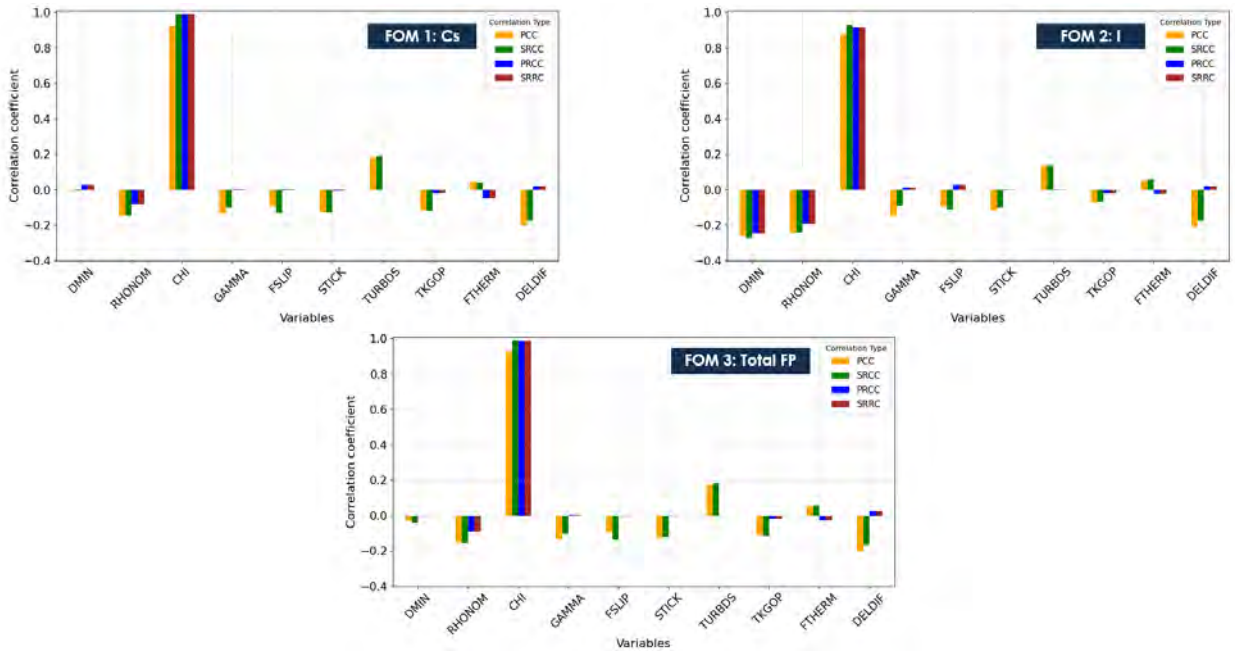

Figure 5. Sensitivity ranking of uncertainty parameters for iodine and cesium release.

3.8. Benchmark Against PHEBUS FPT-1 Experiment The MELCOR [9]

Benchmarking against the PHEBUS FPT-1 international experiment was conducted to assess the ability of CINEMA to represent key behaviors relevant to source-term analysis. The results showed that CINEMA predictions for important variables such as fuel temperature and source term release were within the experimental error band (approximately 30% for the considered comparison basis). This provides additional support for the reliability of CINEMA/SIRIUS modeling for severe accident ST applications.

3.9. Implications for SAMG and Future Applications

The developed CINEMA-based ST evaluation framework and the generated severe accident dataset can contribute to:
- Strengthening plant-specific SAMG strategies for OPR1000 and APR1400,
- Supporting the design and performance assessment of radioactive material mitigation facilities,
- Enabling development of AI-assisted real-time severe accident response systems by providing high-volume, structured analysis data.

4. CONCLUSIONS

This study advanced the domestically developed integrated severe accident analysis code CINEMA to enable quantitative evaluation of radiological source term within the OPR1000 containment during severe accidents, with an emphasis on iodine and cesium behavior.
The main conclusions are:
1. Nine representative OPR1000 severe accident scenarios (including SBO, TLOCCW, LOCA classes, and SGTR) were selected based on Level 2 PSA insights and deterministic coverage considerations, and were analyzed using CINEMA.
2. CINEMA thermal-hydraulic behavior and fission product release predictions showed strong agreement with MAAP5 under equivalent conditions, with iodine and cesium containment inventory metrics typically within a 10–20% difference.

3. The post-processing tool FPeval v2.0 was developed to quantify radionuclide mass distribution by containment node, categorize release mechanisms, track nuclide decay, and automatically record key severe accident event times from CINEMA output files.
4. Uncertainty and sensitivity analyses using MELCOR identified the aerosol shape factor (CHI) as the dominant contributor influencing iodine and cesium release behavior via aerosol deposition and removal processes.
5. Benchmarking against the PHEBUS FPT-1 experiment indicated CINEMA prediction performance within the experimental uncertainty range for key comparison quantities, supporting its applicability to mechanistic source term evaluation [10, 11, 12, 13, 14, 15].
Overall, the proposed CINEMA-based evaluation technology provides a foundation for plant-specific SAMG enhancement and for future development of AI-assisted real-time severe accident response and mitigation applications for Korean reactors.

ACKNOWLEDGMENTS

This work was supported by the Korea Institute of Energy Technology Evaluation and Planning (KETEP) and the Ministry of Climate, Energy & Environment (MCEE) of the Republic of Korea (No. KETEP-20224B10300050) with supported by a National Research Foundation of Korea (NRF) grant funded by the Korean government (Ministry of Science and ICT; Grant No. RS-2022-00144357). In addition, this work was supported by Korea Hydro & Nuclear Power Co., Ltd. through the CINEMA code development project (No. L25S048000).

REFERENCES

1. J. J. DiNunno et al. Calculation of distance factors for power and test reactor sites. No. TID-14844. Division of Licensing and Regulation, AEC (1961).
2. L. Soffer et al. Accident source terms for light-water nuclear power plants. final report. No. NUREG--1465. Nuclear Regulatory Commission, Washington, DC (United States). Div. of Systems Technology (1995).
3. D. H. Kim et al. "Development of an Integrated severe accident analysis computer program packages in Korea." Proceedings of the 8th European review meeting on severe accident research (ERMSAR-2017) (2017).
4. K. S. Ha et al. "SIRIUS: a code on fission product behavior under severe accident." Transactions of the Korean Nuclear Society Spring Meeting, Jeju, Korea. (2017).
5. D. Son et al. (3-1-1-3-S) Development of reference radioactive source term analysis technology in containment building under severe accident, Final report of RS-2022-00144357 (2025)
6. J. H. Song et al. "CSPACE for a simulation of core damage progression during severe accidents." Nuclear Engineering and Technology 53.12 (2021): 3990-4002.
7. M. Z. Podowski et al. "COMPASS-New modeling and simulation approach to PWR in-vessel accident progression." Nuclear Engineering and Technology 51.8 (2019): 1916-1938.
8. Kim, Byung Jo, and Sun Hong Yoon. "Estimation of In-Containment Source Terms under Severe Accident for OPR1000 Plant with MAAP5 Code." Transactions of the Korean Nuclear Society Spring Meeting, Jeju, Korea, May 9-10, (2024).
9. H. S. Park, et al. "Uncertainty Analysis of Radionuclide Release into Containment During Severe Accidents: Application of MELCOR 2.2 to the PHEBUS FPT-1 Test." Nuclear Engineering and Technology (2025): 104045.
10. J. H. Bae et al. "Core degradation simulation of the PHEBUS FPT3 experiment using COMPASS code." Nuclear Engineering and Design 320 (2017): 258-268.
11. R. -J. Park et al. "Development of IVR-ERVC evaluation method and its application to the SMART." Annals of Nuclear Energy 161 (2021): 108463.

12. R. -J. Park et al. "Simulations of Core Damage Progression for TMI-2 Severe Accident Using CINEMA Computer Code." Science and Technology of Nuclear Installations 2023.1 (2023): 8322393.
13. R. -J. Park et al. "CINEMA-SMART development and its application to SBLOCA analysis for Korean small integral reactor." Annals of Nuclear Energy 181 (2023): 109529.
14. W. Jeong et al. "Simulation of high temperature fuel rod bundle behavior during the QUENCH-06 experiment using CINEMA code." Annals of Nuclear Energy 182 (2023): 109598.
15. J. H. Song et al. "A comparative simulation of severe accident progressions by CINEMA and MAAP5." Nuclear Engineering and Design 404 (2023): 112181.

Development of Evaluation Technology for Radiological Source Term in the Containment Using CINEMA Code During Severe Accident

Donggun Son[1]*

Presenter / Corresponding Author

Korea Atomic Energy Research Institute

Jun-young Kang[1], Jaehyun Ham[1]

Korea Atomic Energy Research Institute

Byung Jo Kim[2]

KEPCO E&C

Yeon-Gun Lee[3]

Sejong University

SEJONG UNIVERSITY
Science & Technology Research Institute

[1] KAERI, Daejeon, Korea · [2] KEPCO E&C, Gimcheon, Korea · [3] Sejong University, Seoul, Korea

* donggunson@kaeri.re.kr

Table of Contents

- 20-min presentation overview

01 **Background & Motivation**
Plant-specific SA source term challenges for Korean PWRs

02 **CINEMA Code Architecture**
CSPACE · SIRIUS · SACAP · MASTER · FPeval v2.0

03 **Scenario Selection**
9 representative OPR1000 severe accident scenarios

04 **Results — Thermal-Hydraulics**
CINEMA vs. MAAP5 comparison

05 **Results — Radionuclide Inventories**
I and Cs group containment release fractions

06 **PHEBUS FPT-1 Benchmark**
MELCOR analysis

07 **Uncertainty & Sensitivity**

08 **Conclusions & Applications**
SAMG · AI-assisted accident response

Keywords: Severe Accident · Source Term · CINEMA · OPR1000 · SIRIUS · PHEBUS FPT-1 · MELCOR

Why Plant-Specific Source Term Evaluation?

- Limitations of Alternative Source Term (AST) methods for Korean PWR designs

Current Practice & Limitations

U.S. PWR based AST (NUREG-1465)

Conservative, standardized assumptions — not tailored to Korean OPR1000 / APR1400 design features

Large containment volume

Korean PWRs have larger free volumes → different aerosol dynamics, concentration peaks

Wet cavity configuration

Enhanced scrubbing / retention effects via water pool pathways — not in generic models

Fission product transport paths in containment

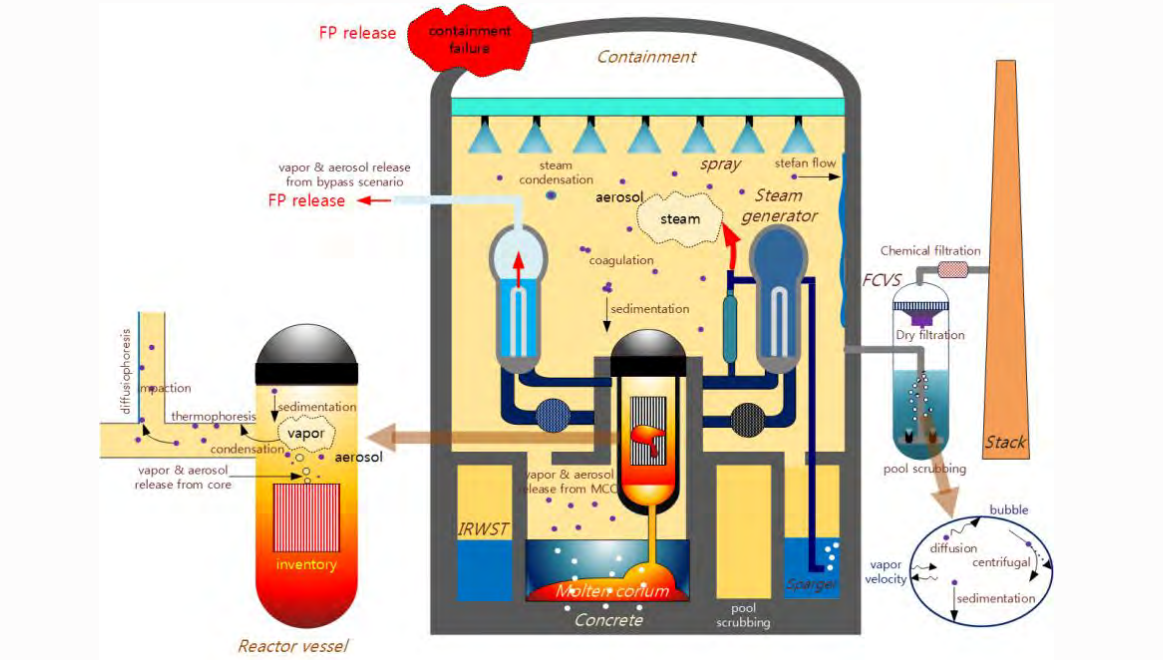

Fig. 1 Schematic of fission product release, transport and deposition in containment

Objectives of This Study

01	02	03	04	05
CINEMA Advancement	**9 Scenarios OPR1000**	**Code-to-Code Comparison**	**PHEBUS Benchmark**	**Uncertainty Analysis**
Improve SIRIUS FP module	SBO · TLOCCW · LOCA · SGTR	CINEMA vs. MAAP5	FPT-1 validation MELCOR	MELCOR FP model

Intelligent Accident Mitigation System Development

Measurement system

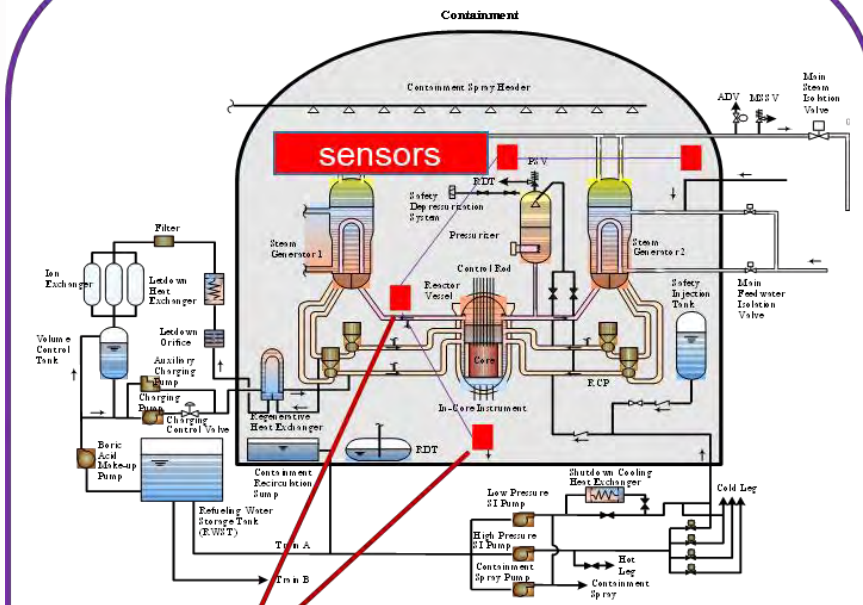

Signal processor

MCR

Emergency response center

Source term reduction system

Optimal accident mitigation strategy

Real-time measurement data

Integrated severe accident analysis code

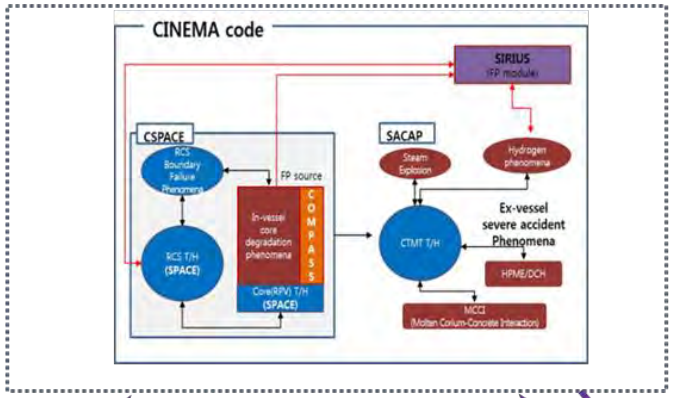

Measurement

Accident mitigation plan

Accident prediction

In-containment condition measurement system

Measurement

Optimized model based on AI

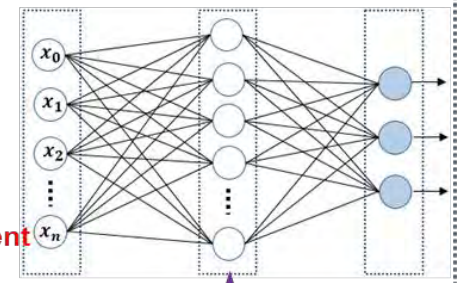

Source term evaluation criteria

CINEMA — Integrated Severe Accident Analysis Code

- Coupled in-vessel · ex-vessel · containment · fission product behavior

CSPACE

COMPASS + SPACE-SAM

In-vessel core degradation & primary system thermal-hydraulics. Boundary conditions (T, P, flow, gas) → SIRIUS.

SACAP

Containment & Ex-vessel

Multi-compartment containment T/H, MCCI, H_2 combustion, DCH, mitigation systems (igniters, PARs).

SIRIUS

FP & Aerosol Behavior

Gap/in-vessel FP release, RCS transport, aerosol generation, condensation/settling/deposition in containment.

Focus of this study

FPeval v2.0

Post-processing Tool

Mass distribution by node/mechanism, nuclide decay, key event timings — structured dataset for SA big data.

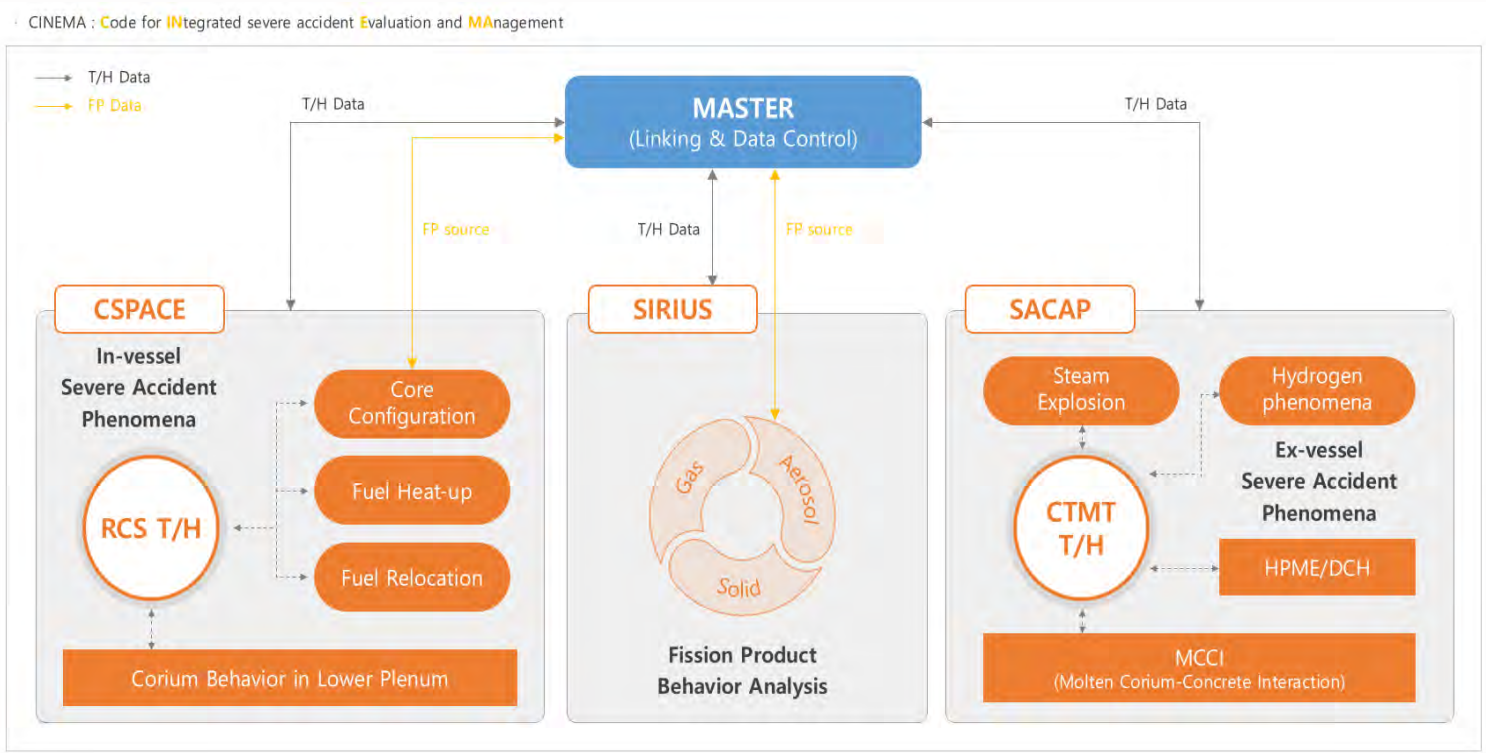

Fig. 2 CINEMA architecture: CSPACE, SIRIUS, SACAP, MASTER coupling

21 May (Thursday), Auditorio, J. Ham, Overview of Fission Product Behavior Modeling in the SIRIUS Code

CINEMA stands for **C**ode for **IN**tegrated severe accident **E**valuation and **MA**nagement

Requirement Traceability Matrix (ex. CSPACE)

- Phenomena coverage — test cases mapped to requirements and reference experiments

Requirement	Test Case ID	Phenomena	Reference
Steady state of NPP	REQ-3-1_SDD-4-1-1-IT-1	Steady state of OPR1000	Safety analysis
Thermal-hydraulic phenomena of SA	REQ-3-1_SDD-4-2-1-IT-1 REQ-3-1_SDD-4-2-2-IT-1 REQ-3-1_SDD-4-2-3-IT-1 REQ-3-1_SDD-4-2-4-IT-1	Rapid depressurization Hydrogen expansion Hydrogen mixing Critical flow	MELCOR assessment Analytic solution
Core heatup and oxidation	REQ-3-1_SDD-4-3-1-IT-1 REQ-3-1_SDD-4-3-1-IT-2 REQ-3-1_SDD-4-3-1-IT-3	Core heatup, oxidation	CORA-13 QUENCH-06 Phebus FPT-0, 1, 3
Core slumping and relocation	REQ-3-1_SDD-4-4-1-IT-1 REQ-3-1_SDD-4-4-1-IT-2 REQ-3-1_SDD-4-4-1-IT-3	Material relocation	QUENCH-06 Phebus FPT-0, 1, 3 LOFT-FP-LP2
Core degradation and corium pool	REQ-3-1_SDD-4-5-1-IT-1 REQ-3-1_SDD-4-5-1-IT-2	Corium relocation, core blockage	Phebus FPT-0, 1, 3 LOFT-FP-LP2
Corium pool in lower plenum	REQ-3-1_SDD-4-6-1-IT-1 REQ-3-1_SDD-4-6-2-IT-1 REQ-3-1_SDD-4-6-3-IT-1	Corium pool formation RPV wall heat transfer RPV failure	LIVE-L3A, L6 OLHF
SAMG action	REQ-3-1_SDD-4-7-1-IT-1 REQ-3-1_SDD-4-7-1-IT-2	Natural convection, etc. Safety injection, etc.	MAAP5 calculation
Integrated severe accident	REQ-3-1_AC-TEST-1	TMI-2 accident	TMI-2 accident data

List of Published Papers

- CINEMA · CSPACE · COMPASS — peer-reviewed journal articles

Year	Authors	Title	Journal / Volume
2017	Bae et al.	Core degradation simulation of the PHEBUS FPT3 experiment using **COMPASS** code	*Nuclear Engineering and Design, 320, 258–268*
2021	Song et al.	**CSPACE** for a simulation of core damage progression during severe accidents	*Nuclear Engineering and Technology, 53, 3990–4002*
2021	Park et al.	Development of **IVR-ERVC** evaluation method and its application to the **SMART**	*Annals of Nuclear Energy, 161, 108463*
2023	Jeong et al.	Simulation of high temperature fuel rod bundle behavior during the QUENCH-06 experiment using **CINEMA**	*Annals of Nuclear Energy, 182, 109598*
2023	Park et al.	Simulations of Core Damage Progression for TMI-2 Severe Accident Using **CINEMA**	*Science and Technology of Nuclear Installations, 8322393*
2023	Song et al.	A comparative simulation of severe accident progressions by **CINEMA** and MAAP5	*Nuclear Engineering and Design, 404, 112181*
2023	Park et al.	**CINEMA**-SMART development and its application to SBLOCA analysis for Korean small integral reactor	*Annals of Nuclear Energy, 181, 109529*
2025	Park et al.	Uncertainty Analysis of Radionuclide Release into Containment During Severe Accidents: MELCOR 2.2 to PHEBUS FPT-1	*Nuclear Engineering and Technology, 104045*
2026	Shin et al.	Assessment of thermal safety margins for the IVR-ERVC strategy of the i-SMR using **CINEMA**	*Nuclear Engineering and Design, 58, 104307*
2026	Shin et al.	Analysis of thermal-hydraulic and aerosol behavior in the VANAM-M3 experiment using **CINEMA**	*Annals of Nuclear Energy, 236, 112454*

10	**6**	**3**	**2**
Total peer-reviewed papers	CINEMA / CINEMA-based	CSPACE / COMPASS	2026 (in press)

9 Representative OPR1000 Severe Accident Scenarios

- Selected from PSA insights + deterministic coverage considerations

#	Sequence Name	Initiating Event	Key Conditions	Explanation
1	**SBOR_S38**	**SBO**	TDAFW 8h · Late AC recovery · Recirc. spray	PSA representative
2	**TLOCCW_S10**	**TLOCCW**	TDAFW failed · Bleed op. failed	PSA representative, Total Loss of Component Cooling Water
3	**MLOCA_S3**	**MLOCA**	HPSI · Recirculation failed	PSA representative, Medium Loss of Coolant Accident
4	**LLOCA_BE_BASE**	**LLOCA**	SIT · SI failed · CS failed	Deterministic coverage considerations, Large LOCA by Best Estimates
5	**LLOCA_BE_MACST**	**LLOCA**	SIT · SI failed · CS failed · IVI · Late CS recov.	Deterministic coverage considerations, Large LOCA with In-Vessel Injection
6	**SLOCA_BE_BASE**	**SLOCA**	SIT · SI failed · Bleed failed · CS failed	Deterministic coverage considerations, Small LOCA by Best Estimates
7	**SLOCA_BE_MACST**	**SLOCA**	SIT · SI failed · Bleed failed · CS failed · IVI	Deterministic coverage considerations, Small LOCA with In-Vessel Injection
8	**SGTR_BE_BASE**	**SGTR**	Broken SG isolation · SIT · Bleed · CS failed	Deterministic coverage considerations, Steam Generator Tube Rupture
9	**SGTR_BE_MACST**	**SGTR**	Broken SG isolation · SIT · Bleed · CS failed · IVI	Deterministic coverage considerations, SGTR with In-Vessel Injection

SBO 1 case | **TLOCCW** 1 case | **LOCA (M/L/S)** 5 cases | **SGTR** 2 cases

CINEMA for Korean PWR Analysis

- OPR1000: CINEMA / MAAP5 nodalization comparison

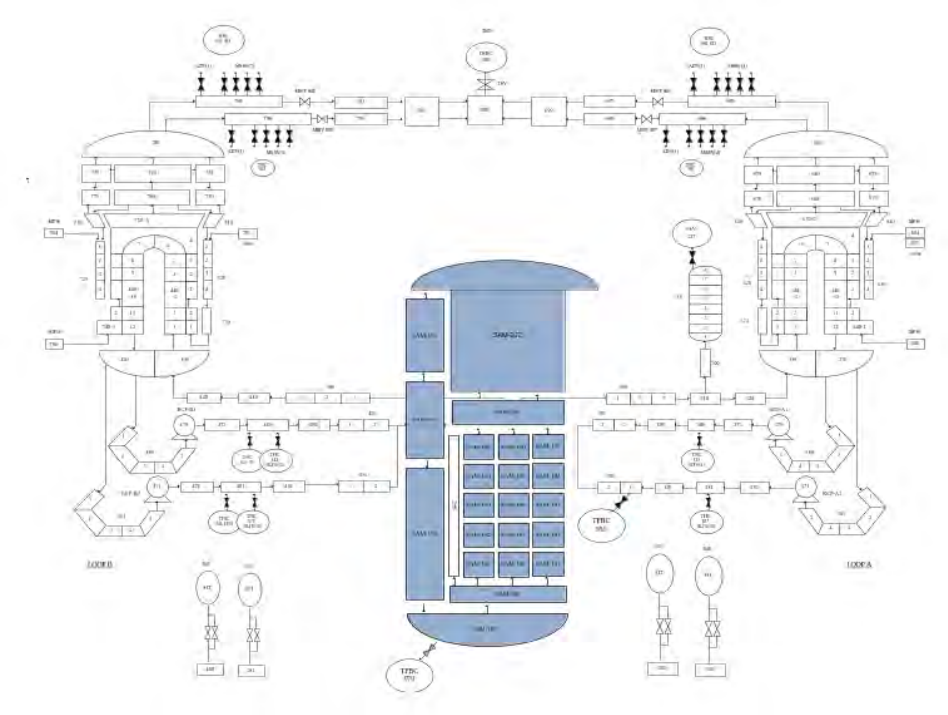

Fig. A CINEMA nodalization — OPR1000 primary system

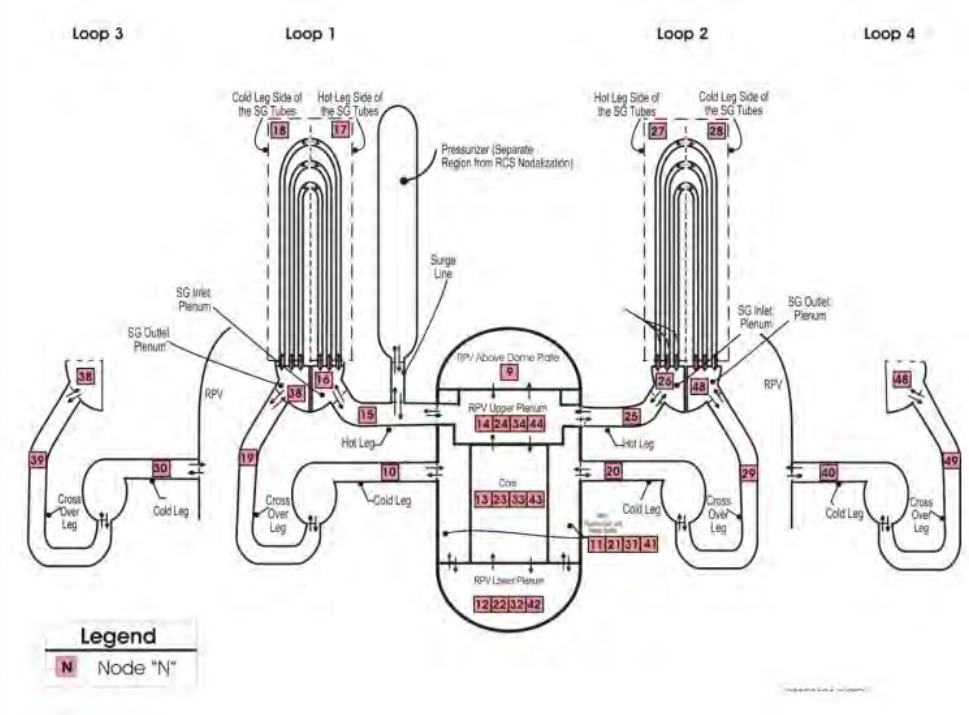

Fig. B MAAP5 nodalization — OPR1000 primary system

OPR1000	CINEMA	MAAP5	Purpose
Korean standard PWR — 2-loop / 4-loop nodalization	Mechanistic SA code — detailed core degradation model	Industry SA code — fast-running lumped parameter	Cross-validation of SA progression predictions

CINEMA vs. MAAP5: Thermal-Hydraulic, FP release fraction comparison

- Consistent boundary & initial conditions — 9 scenarios · Major event timings & Severe accident phenomena & FP release to containment

Objects of comparison

Primary system pressure

Evolution under accident progression — depressurization, injection, steam behavior

Core heat-up indicators

Onset of fuel damage, core relocation timing

Major event timings

Core uncovery · Vessel failure → prerequisite for ST comparison

In-vessel, in containment physics

RPV failure by corium attack
Pressure rise and stabilization under FP/steam/H_2 release

In-containment release fraction: CINEMA vs. MAAP5

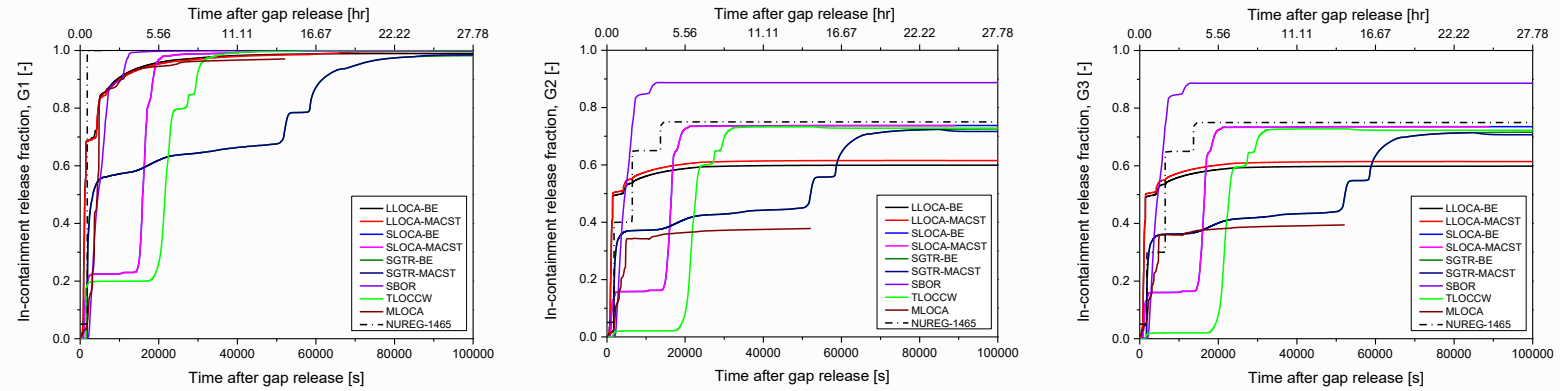

Fig. 3a Group-I (Xe, Kr), II (I), III (Cs) in-containment release fraction — CINEMA (9 scenarios)

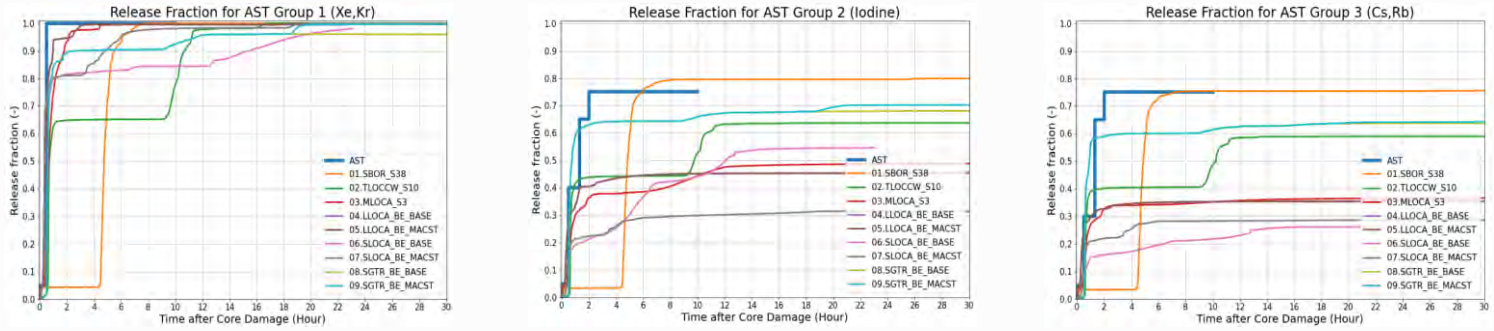

Fig. 3b Group-I (Xe, Kr), II (I), III (Cs) in-containment release fraction — MAAP5 (9 scenarios)

Key finding: CINEMA reproduces MAAP5 major event timings and containment pressurization trends under equivalent inputs across all **9** scenarios — prerequisite confirmed for meaningful ST comparison. CINEMA–MAAP5 iodine & cesium inventory agreement typically within 10–20% under consistent inputs.

Radiological Source Term Evaluation for OPR1000

- Source term evaluation results by CINEMA, as compared to that by alternative source term.

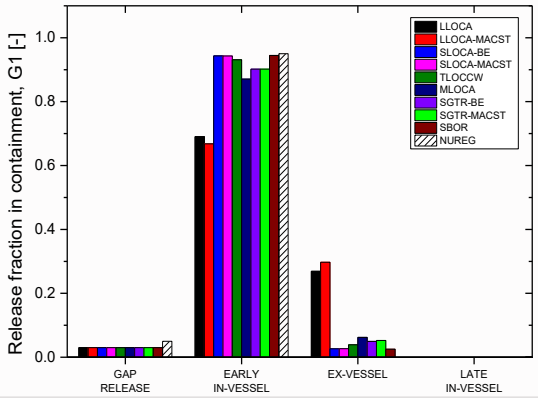

Release fraction of group-I(Xe,Kr)

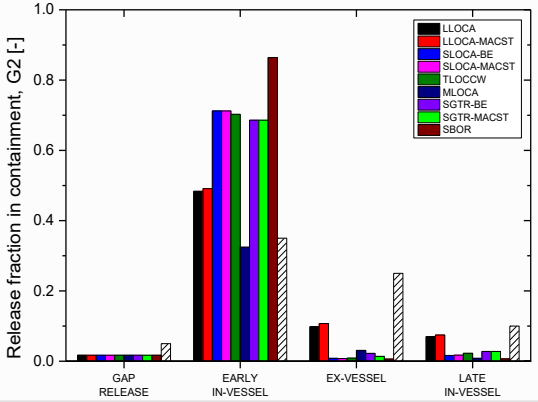

Release fraction of group-II(I)

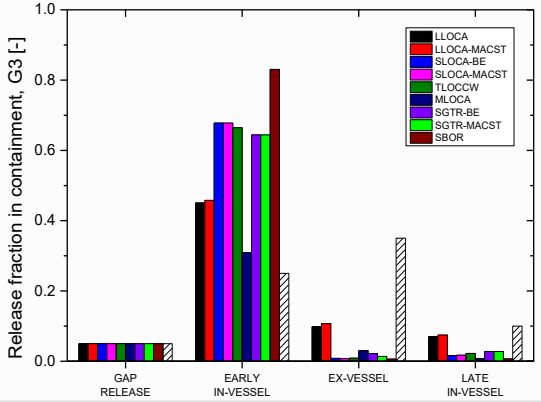

Release fraction of group-III(Cs)

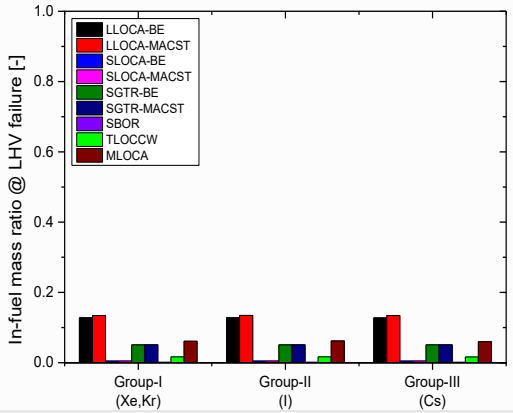

In-fuel mass fraction of FP: at the RPV failure

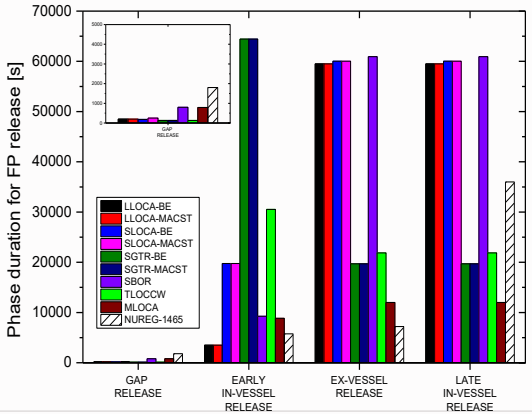

Duration by stage of FP release

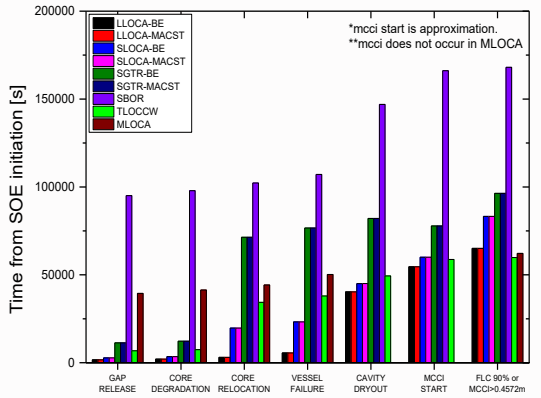

Time from sequence of event by scenario

Key finding: In general, for the severe accident scenarios of the OPR1000, source term release to the containment mainly occurred at Early in-vessel phase.
In our results, duration of FP release stages show big difference by accident scenarios. That leads to necessity of mechanical source term (MST) evaluation.

Experimental Benchmark: PHEBUS FPT-1

- CINEMA / MELCOR predictions vs. international experimental data — within ±30% uncertainty band

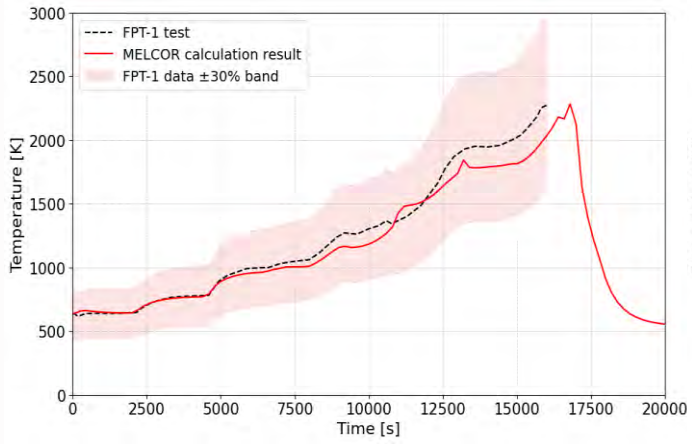

<Fuel temperature at 300 mm>

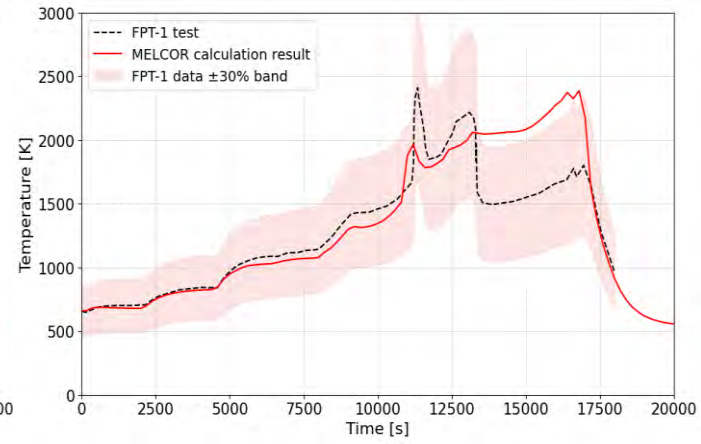

<Fuel temperature at 400 mm>

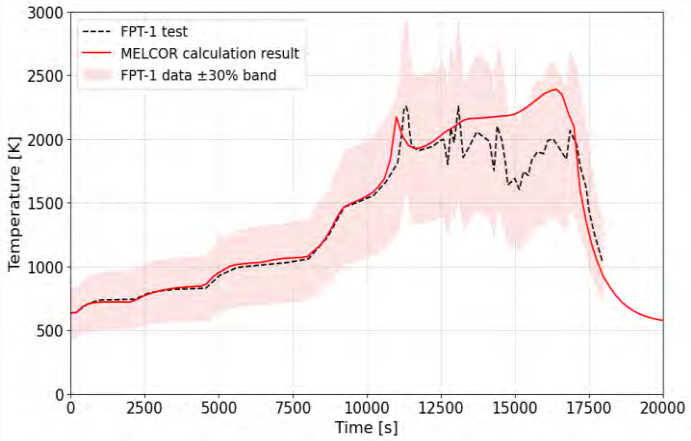

<Cladding temperature at 600 mm>

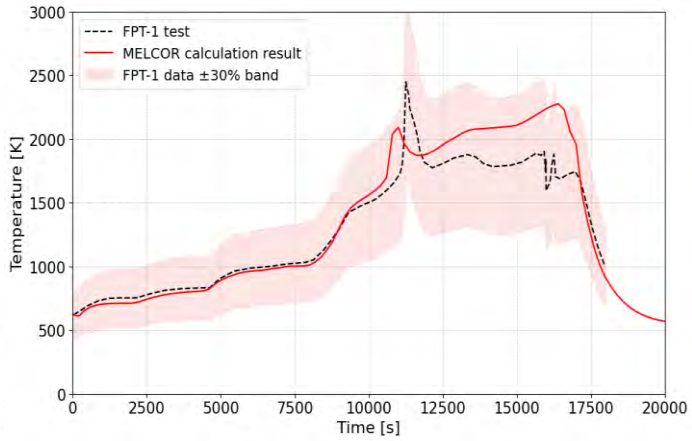

<Cladding temperature at 700 mm>

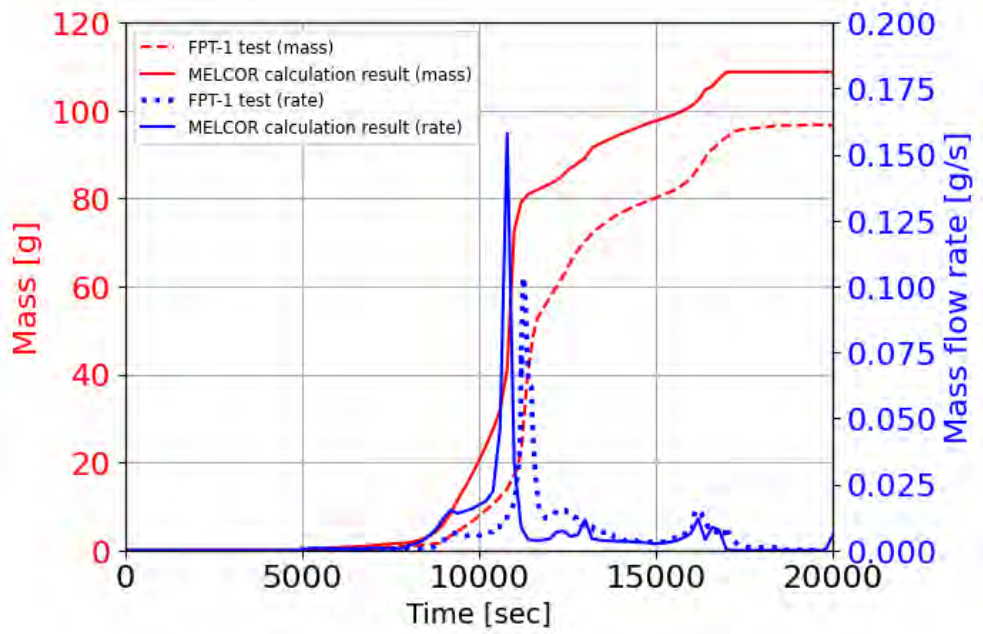

<Accumulated hydrogen mass and generation rate>

Dominant Role of Aerosol Shape Factor (CHI)

- MELCOR uncertainty & sensitivity analysis — iodine and cesium release variability

UA variables

RHONOM	*Nominal density of aerosol*
CHI	*Dynamic shape factor of aerosol*

① Brownian diffusion velocity $v_{diff} = \frac{\sigma T C_m}{3\pi\mu\chi d_p \Delta}$

② Gravitational settling velocity $v_{grav} = \frac{d_p^2 \rho_p g C_m}{18\mu\chi}$

③ Thermophoretic deposition velocity

$$v_{therm} = \frac{3\mu C_m (c_t Kn + k_{gas}/k_p)}{2\chi\rho_{gas} T (1 + 3F_{slip} Kn)(1 + 2c_t Kn + k_{gas}/k_p)} \nabla T$$

As CHI increases, the deposition rate decreases, leading to an increase in the transport fraction to the containment vessel.

CHI dominates iodine and cesium release variability via aerosol deposition rate → prioritize **aerosol measurement instrumentation**

Cs/I release fraction uncertainty band (MELCOR)

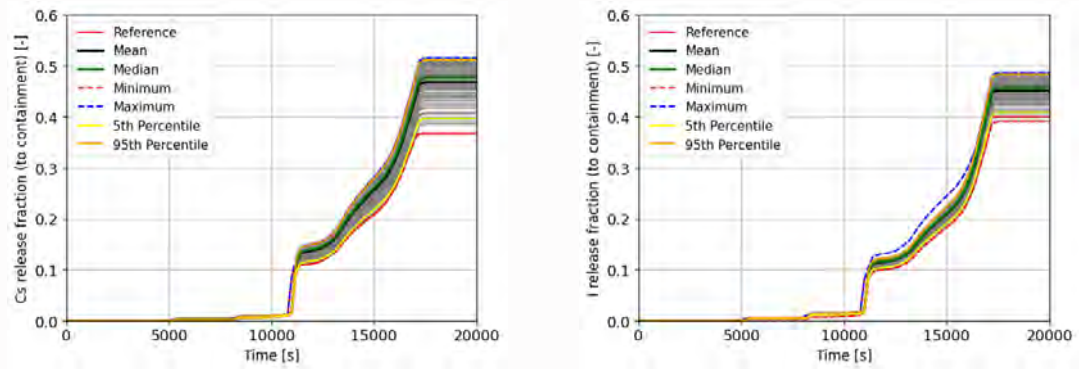

Fig. 5a Cs/I release fraction — uncertainty band (5th/50th/95th percentile)

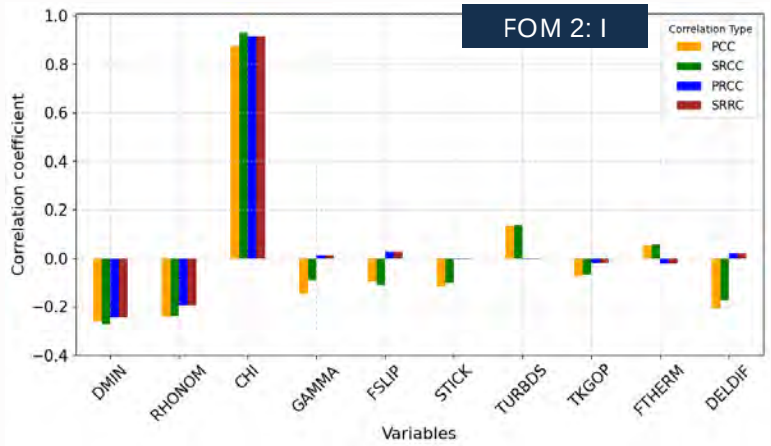

Fig. 5b Sensitivity ranking — CHI (aerosol shape factor) dominant contributor for I

Applications: SAMG Enhancement & AI-Assisted Response

- CINEMA-based ST evaluation as foundation for next-generation accident management

01

Plant-Specific SAMG Enhancement

· OPR1000 / APR1400 — differentiated ST data per accident type

· Containment spray strategy prioritization by accident category

· Quantified influence of wet cavity and large containment volume

· Source for updating severe accident event trees in L2 PSA

02

Mitigation System Design Support

· Compartment-specific radionuclide loading → optimal sensor placement

· Filtered venting strategy — spatial ST distribution input

· Localized aerosol removal design guidance

· Performance assessment of mitigation systems under diverse SAs

03

AI-Assisted Real-Time Accident Response

· SA big data from 9+ scenarios → training dataset for ML models

· Real-time state estimation and source term prediction

· Neural network–based optimal accident response recommendation

· Integration with plant monitoring (measurement data input)

CINEMA (SA analysis) → FPeval v2.0 (big data) → ML / AI model → Real-time optimal accident response recommendation

© KAERI 2026

Treatment Effect Analysis & AI Learning Methodology

- Causal inference for SA mitigation — model architecture, training data, and prediction pipeline

WHAT IS TREATMENT EFFECT ANALYSIS?

Origin	Causal inference in medicine — "Does this drug improve patient outcome?"
Core idea	Estimate the effect of an action by comparing outcomes with vs. without it
This work	Mitigation action = treatment variable → compare predicted radioactive release under each action in a single forward pass

GRPO-TS predicts SA progression for a fixed scenario — TEA adds the missing capability: "Which mitigation action minimizes release?"

TEA MODEL ARCHITECTURE

Decoder: per-action prediction in one batch pass

Pre-SA Time-Series → Time-Series Encoder → Latent Vector Z → Mitigation Encoder → **Predicted Mass Fraction**

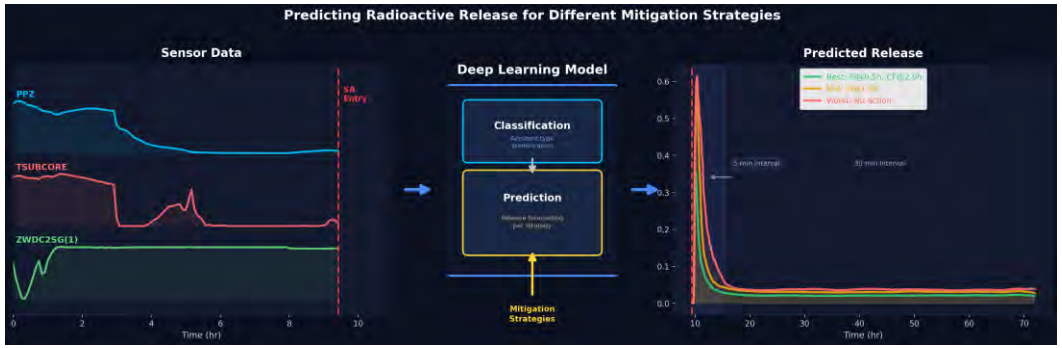

Fig. 1 TEA-based time-series prediction model — Sensor Data → Classification → Prediction → Predicted Release

TRAINING DATASET & PREDICTION PIPELINE

208 cases	526 cases	4 types	70:15:15
LLOCA (break size × SIT)	SBO (11 accident states)	Mitigation actions (SADP, SASI, SACF, SACS)	Train : Valid : Test split ratio

1	2	3	4	5
Pre-SA Encoding	Time-Interval Prediction	Per-Strategy Mass Fraction	Integration-Based Ranking	Accident-Type Filtering

Model Validation & Data Sufficiency Study

- LLOCA (37 test cases) and SBO (67 test cases) — classification accuracy, Mean Absolute Error, R², and learning curve

VALIDATION METRICS — TEST SET PERFORMANCE

LLOCA 37 test cases

73.0 %	0.0067	0.981
Classification Accuracy	Mean Absolute Error	R² Score

Note: Classification performed on only 1–3 pre-SA time steps → source of classification error. Improvement planned.

SBO 67 test cases

95.5 %	0.0068	0.937
Classification Accuracy	Mean Absolute Error	R² Score

SBO: Higher pre-SA sequence length → stronger classification signal.

DATA SUFFICIENCY STUDY — LEARNING CURVE ANALYSIS

Test Loss	Not yet converged — continues decreasing with more data. Plateau not reached.
Test R²	Still increasing — further gains anticipated with larger dataset.
Est. convergence	~5,000 samples with identical initiating event / mitigation action combinations.
Regulatory basis	NRC · CNSC · ONR (2024): no fixed data threshold — learning curve convergence is the recommended sufficiency criterion (PNAS, 2024).

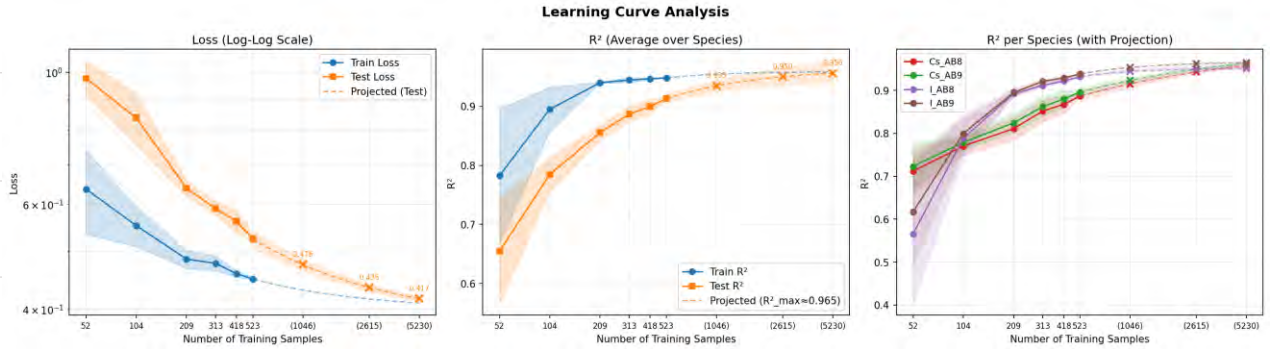

Fig. 5 Learning Curve — Test Loss (left) and R² (right) vs. number of training samples

Augmentation plan: (1) Vary mitigation injection timing (0.5–6 h) (2) Diversify mitigation intensity (3) Large-scale generation via timing combination methodology

React-Based Web UI — Real-Time Strategy Recommendation

- CSV upload → accident classification → strategy ranking → user-controlled parameter exploration

WORKFLOW

1	2	3	4	5
Upload CSV	Auto-Classify	Batch Predict	Rank Strategies	Explore & Compare

DIAGNOSIS TAB

CSV Upload Upload pre-SA plant time-series → accident type automatically classified

Auto-Ranking All strategy combinations evaluated in one batch → Best 4 / Worst 4 extracted

Mass Fraction Cs & I release in compartments 8 & 9 predicted · time-integral used as ranking criterion

Comparison View Side-by-side overlay of predicted release curves · Full ranking table of all 20 strategies

STRATEGY EXPLORER

Real-Time Prediction User adjusts mitigation parameter sliders → predicted release curve updates instantly

Untrained Values Accepts parameter values outside the training range — interpolation / extrapolation applied

No-Action Comparison Reference curve with no mitigation overlaid automatically — quantifies benefit of each action

Use Case Compare SI injection start time → quantify early vs. delayed injection effect on Cs / I release

Tech stack: React · TypeScript · Node.js · WebSocket real-time comm · AI inference server integration

© KAERI 2026 · Intelligent Accident Mitigation Research Division

React-Based Web UI — Accident Diagnosis & Strategy Recommendation

- CSV upload → accident classification → Best 4 / Worst 4 optimal mitigation strategies auto-generated

Accident Classification

Upload CSV of pre-SA plant time-series data → model classifies accident type automatically

Strategy Auto-Ranking

All mitigation strategy combinations evaluated → Best 4 (lowest release) and Worst 4 (highest release) extracted

Mass Fraction Prediction

Cs and I mass fraction in compartments 8 & 9 predicted → time integral used as ranking criterion

Strategy Comparison

Side-by-side overlay of predicted release curves for selected strategies · Full ranking table provided

Fig. 6. Diagnosis Tab — SBO Cond11: Best 4 / Worst 4 strategy auto-extraction

Fig. 6 Diagnosis Tab — classification result (SBO Cond11) and Best 4 / Worst 4 mitigation strategy comparison

Tech stack: React · TypeScript · Node.js · WebSocket real-time communication · AI inference server integration

Web UI — Full Ranking & Strategy Explorer

- Side-by-side strategy comparison · full ranking table · user-controlled parameter tuning with real-time prediction

Fig. 7. Full Ranking — strategy comparison and ranked table

Fig. 7 Strategy Comparison and Full Ranking — overlay of predicted release + full ranking table (20 strategies)

Use case Compare SI injection start time → quantify early vs. delayed injection on Cs/I release

Fig. 8. Strategy Explorer — user-controlled mitigation parameter tuning

Fig. 8 Strategy Explorer — sliders for mitigation action parameters → real-time predicted release curve

Key feature Untrained parameter values also accepted — interpolation / extrapolation applied

Conclusions

- CINEMA-based ST evaluation technology for OPR1000 containment during severe accidents

1

9 Representative Scenarios

SBO · TLOCCW · LOCA classes · SGTR selected from Level 2 PSA insights and deterministic coverage — analyzed with CINEMA for quantitative ST evaluation.

2

CINEMA–MAAP5 Agreement

T/H trends, major event timings, and I/Cs containment inventories within ~10–20% under equivalent conditions — confirming SIRIUS module credibility.

3

FPeval v2.0 Tool

Post-processing framework: mass distribution by containment node, release mechanism categorization, nuclide decay tracking, automatic event time recording.

4

UA about PHEBUS FPT-1 Benchmark: Aerosol Shape Factor CHI

MELCOR uncertainty & sensitivity analysis identified CHI as the dominant contributor to I and Cs release variability via aerosol transport and deposition.

5

Application to the AI model database

CSV upload → accident classification → Best 4 / Worst 4 optimal mitigation strategies auto-generated,

Acknowledgment: Supported by KETEP–MCEE (No. KETEP-20224B10300050) & NRF–MSIT (Grant No. RS-2022-00144357), Republic of Korea.

Thank You

Questions & Discussion

Corresponding Author
Donggun Son
Korea Atomic Energy Research Institute (KAERI)
donggunson@kaeri.re.kr

Paper
Development of Evaluation Technology for Radiological Source Term in the Containment Using CINEMA Code
ERMSAR 2026 · Madrid, Spain · May 18–22, 2026

The 12th European Review Meeting on Severe Accidents Research

May 18-22, 2026, Universidad Carlos III de Madrid, Madrid, Spain

TECHNICAL SESSION 5.1: HYDROGEN RISK AND CONTAINMENT BEHAVIOR

Chairs: M. Malicki (PSI), K. Dieter (Becker Technologies GmbH)

ID096	**AMHYCO Project Outcomes and Lessons Learned** G. Jiménez (Universidad Politécnica de Madrid)	Paper Presentation
ID097	**CFD Analysis of the Containment Behavior during a TLAP Sequence in a Generic KWU PWR with containmentFOAM** S. Kelm (FZJ)	Paper Presentation
ID126	**ETSON-AMHYCO Benchmark Exercise on Flame Propagation in Representative Reactor Containment Atmosphere in Case Severe Accident Late Phases** A. Bentaib (NEA)	Paper Presentation
ID038	**Suppression Pool Modelling with the CESAR Thermal-Hydraulic Module of ASTEC** J.-A. Zambaux (ASNR)	Paper Presentation

AMHYCO PROJECT OUTCOMES AND LESSONS LEARNED

Gonzalo Jiménez*
Universidad Politécnica de Madrid, 28040 Madrid, Spain
gonzalo.jimenez@upm.es

Ahmed Bentaib
Authorité de Sûreté Nucléaire et de Radioprotection (ASNR), 92260 Fontenay Aux Roses, France
ahmed.bentaib@asnr.fr

Luis Enrique Herranz
CIEMAT, 28040 Madrid, Spain
luisen.herranz@ciemat.es

Nabiha Chaumeix
CNRS-Ingénierie, I.C.A.R.E., 45071 Orléans, France
nabiha.chaumeix@cnrs-orleans.fr

Stephan Kelm, Ernst-Arndt Reinecke
Forschungszentrum Juelich, 42425 Juelich, Germany
s.kelm@fz-juelich.de; e.-a.reinecke@fz-juelich.de

Matthias Braun
Framatome GmbH, Paul-Gossen-Strasse 100, D-91052 Erlangen, Germany
matthias.braun@framatome.com

Marco K. Koch
Ruhr-Universitaet Bochum, 44801 Bochum, Germany
marco.koch@pss.rub.de

Ivo Kljenak
Institut Jozef Stefan, 1000 Ljubljana, Slovenia
ivo.kljenak@ijs.si

Oleksandr Sevbo
Limited Liability Company Energorisk, 03148 Kyiv, Ukraine
sevbo@energorisk.com.ua

D.C. (Dirk) Visser
Nuclear Research and Consultancy Group, 1755 ZG Petten, The Netherlands
visser@nrg.eu

Zhe (Rita) Liang
Canadian Nuclear Laboratories, Chalk River, ON K0J 1J0, Canada
zhe.liang@cnl.ca

Mina Lazarevic
LGI Consulting, 75011 Paris, France

mina.lazarevic@lgi.earth

*corresponding author

ABSTRACT

During a severe accident, one of the potential threats to the containment is the release of flammable gases leading to combustion risk. Severe Accident Management Guidelines (SAMGs) as well as dedicated hardware are in place to mitigate this combustion risk and protect the containment integrity. Advancements in SAMGs are the focus of AMHYCO, an EU-funded Horizon2020 project (Euratom 2019/2020, GA No 945057) conducted between October 2020 and March 2025. In this paper, the main outcomes and lessons learned from the AMHYCO project are presented. A comprehensive bibliographic review was conducted, providing a common foundation to build the knowledge gained during the project. An extensive set of accident transients was simulated, covering in-vessel as well as ex-vessel phenomena. Based on these simulations, a set of challenging accident sequences was selected for further assessment from the combustion risk perspective across the different power plant types (PWR-KWU, PWR-W, PWR-VVER). At the same time, three generic containment models for the three considered reactor designs were created to enable full containment analysis using lumped parameter (LP) models, 3-dimensional (3D) containment codes, and CFD simulations. To further consolidate the modelling base, combustion experiments and performance tests on passive auto-catalytic recombiners (PARS) in H_2/CO atmospheres were performed at CNRS, France, and FZJ, Germany, respectively. Based on these experiments, a new PAR correlation, referred to as AMHYCO PAR correlation, was proposed. Additionally, several accident sequences were simulated using LP, 3D, and CFD approaches for the three PWR containment types, assessing the impact of the installment of PAR, the effects of filtered containment venting, and (re-)activation of containment cooling systems on the global and local combustion risk. Finally, a set of recommendations to the SAMGs developers and NPP operators was developed, outlining the importance of mitigation systems and especially proper management of the containment cooling systems.

KEYWORDS
AMHYCO, combustion risk, in-vessel phase, ex-vessel phase, passive auto-catalytic recombiners, containment response, SAMGs

1. INTRODUCTION

The risk associated to combustible gases generated during a severe accident are among the most relevant threats to containment integrity. An appropriate management of the associated risk is paramount to protect the containment and, thus, prevent the uncontrolled release of radioactive material into the environment. This management of combustible gases includes, on one side, suitable hardware like, e.g., Passive Autocatalytic Recombiners (PARs), and, on the other side, elaborated guidance to operate the plants in case of a core damage accident. These procedures are referred to as Severe Accident Management Guidelines (SAMG).

2. MAIN OUTCOMES OF THE PROJECT

The main objective of the AMHYCO project is to extend the knowledge about the presence and the mitigation of combustible gases, especially in the late stage of a severe accident where not only hydrogen from the core oxidation is present but also possible carbon monoxide, generated by a molten corium-concrete interaction (MCCI). Based on the examinations, the AMHYCO project makes recommendations concerning hardware backfitting as well as updates to SAMG. The project utilized a methodology that is organized in five different technical work packages (WPs). These WPs are at the same time successive and

interlinked. In the next sections, the AMHYCO technical WPs and the tasks therein will be briefly described, and the main outcomes and lessons learned are summarized.

2.1. WP1: Critical review

The WP1 aims at reviewing the status of existing methodologies and practices related to gas combustion risk management in the late phase of severe accidents. Most of the combustible gas mitigation strategies adopted in European countries are based on the use of PARs. Therefore, a critical assessment of the PAR behaviour, especially in the up-to-now lesser explored late phases of a severe accident, is performed. Similarly, a survey of the available experimental data and engineering combustion models is provided. In addition, a review of the safety equipment qualification criteria and gas monitoring systems, as well as the existing SAMGs is established with the aim to pave the way towards the SAMGs enhancement. The main outcomes of the WP1 are gathered in the AMHYCO (public) deliverable D1.1 "Critical assessment of key elements of combustible gases management in containment." (Bentaib, 2022) and can be summarized as follows:

- The literature review showed that despite the extensive research performed in the last decades, additional experimental and theoretical investigations are needed to fill the knowledge gaps regarding the PARs behaviour in representative conditions of late phase of the severe accidents.
- The literature review showed that the H_2/CO combustion in representative conditions of severe accident late phases is rarely investigated. Additional experimental and theoretical investigations are needed to fill the observed knowledge gaps.
- Regarding the existing PWR SAMGs concerning containment risk management, the literature review showed that the adopted requirements address in-vessel conditions; therefore, their extension to ex-vessel conditions needs to be established for the containment and the auxiliary buildings connected to the containment. It was also identified that all the adopted requirements aim to preserve the containment integrity; the availability of the safety systems, such as sprays or venting line, needed for severe accident late phases, needs to be addressed in extended requirements. It should be pointed out that only a few countries adopt quantitative criteria for the requirement, and only a few existing SAMGs contain instructions about the usage of safety systems (containment sprays and air coolers) in the late phase of a severe accident.
- It was also identified that the existing monitoring systems do not measure carbon monoxide content separately (hydrogen gas detectors using gas heat conductance measurements are insensitive to CO while hydrogen detectors using catalytic recombination measure CO as hydrogen).

2.2. WP2: Characterization of sequences with relevant combustion risk

Given the current European nuclear reactor fleet, three PWR reactor designs are modelled (PWR-W: Western: French and Westinghouse; PWR-KWU; PWR-VVER) and the most relevant sequences are chosen according to a set of agreed criteria: high molar fractions of combustible gases (H_2 + CO) in control volumes whose conditions are within flammability limits; a large total mass of combustible gas (H_2 + CO) within the containment; and high combustible gas (H_2 + CO) release rates. Besides, a qualitative assessment was needed.

This WP has been structured consistently with the reactor types addressed, and it includes a specific task (2.1) to produce a "Generic Containment (GC)" of each PWR type. The individual databases were built based on open information on each containment design, which was then used to build three CAD (Computer Aided Design) models. From each containment CAD model, different proposals were made for both Lumped Parameter (LP) codes and 3D codes nodalization. Additional information about the process as well as the generic containments data for the three PWR types can be found in the AMHYCO (public) deliverable D2.1 "Data for the generic containment analysis (PWR-W, PWRVVER, PWR-KWU)" (Serra et al., 2024) and in open publications (Vázquez-Rodríguez et al., 2025; Serra et al., 2025).

The second objective of the AMHYCO work package 2 (WP2) was to identify bounding accident sequences in which the combustible gases (H_2 and CO) could jeopardize containment integrity (tasks 2.2 to 2.4). The simulations of different accident sequences with integral codes provided relevant estimations of the behaviour of the combustible gases in the containment. Therefore, one of the main tasks of this work package was the identification of the most challenging accident sequence regarding the gas combustion risk based on selection criteria previously set. Different sequences of the three PWR reactor types were simulated with different codes and hypotheses, starting with the nodalization used by each organization before the start of AMHYCO (therefore, not coming from the generic containment nodalization), as a difference of what was done in WP4, as it will be seen later.

Partner	Reactor type	Code	Number of plant nodes	Number of cont. nodes
IRSN/ASNR	PWR-900 (Framatome)	ASTEC v2.1	~160	14
IRSN/ASNR	PWR-1300 (Framatome)	ASTEC v2.1	~160	18
JSI	PWR-700 (Westinghouse)	MELCOR 2.2	158	13
CIEMAT	PWR-1000 (Westinghouse)	MELCOR 2.2	157	19
Framatome	KWU-1300	MELCOR 2.2	69	30
RUB	KWU-1300	AC^2 2019.1	283	23
Energorisk	VVER	MELCOR v1.8.5	126	21

Table 1. WP2 reactor type, code, and nodalizations

The detailed analyses of the results obtained for each design, as well as the hypotheses and approximations made in the simulations, were reported in the AMHYCO (public) deliverable D2.2 “Identification and analysis of accident sequences posing high H_2/CO combustion risk (PWR-W, PWR-VVER, PWR-KWU)” (Herranz et al., 2023) and synthesized in open publications (Herranz et al., 2022; 2025). The analysis was mostly focused on the gas composition in different compartments (particularly those taking a high share of the total containment building, i.e., upper compartment and dome) and its corresponding Shapiro diagram. The main outcomes of these tasks 2.2 to 2.4 can be summarized as follows:

- The severe accident sequences that posed a higher risk of gas combustion (H_2 and CO) were SBLOCA (20 cm^2) and LBLOCA, for PWR-W, LOCA (80 cm^2) for PWR-KWU, and SBO with sprays for PWR-VVER.
- A key factor heavily conditioning sequence selection is the availability of containment cooling systems. Their capability of condensing steam during the ex-vessel phase results in a boost of combustible gas molar fraction. In this respect, the partial restoration of sprays after an SBO can pose a threat to the containment integrity.
- As expected, the largest gas accumulation (as long as PARs are not modelled) is found in the ex-vessel phase. The composition of the concrete greatly influences the amount of released gas and the CO fraction.
- Whenever PARs are modelled, O_2 starvation in the ex-vessel phase (low oxygen situation due to the consumption of oxygen by the PARs in the in-vessel phase) makes gas composition exit the flammable region of the Shapiro diagram, even if the combustible gas fraction well exceeds 9 vol%. Even though a lack of oxygen prevents an in-containment combustion in the late phase of an accident, the hydrogen and carbon monoxide stored within the containment still represents a combustion risk in case a containment leakage occurs.

- The presence of a PAR system can significantly reduce the size and magnitude of possible combustible gas clouds within the containment.
- Cavity flooding partially quenches the core melt and thus reduces the release rate of combustion gases resulting from MCCI. Additionally, the strong release of steam during the quenching leads to a fast dilution of the combustible gases.
- Sequences evolving with high in-containment pressure normally do not imply a high risk for hydrogen and CO combustion because of the high steam concentration of these sequences, (e.g., SBO).

The characterization of the highest risk scenarios found (initial and boundary conditions) was reported in detail and passed onto WPs 3 and 4, as a basis for experimental matrices and benchmarking containment analysis approaches, respectively.

2.3. WP3: Experimental investigations

The objective of WP3 was to experimentally investigate phenomena related to hydrogen and carbon monoxide combustion and mitigation, which were still not covered by existing numerical models. The focus was set on the combustion of hydrogen/carbon monoxide/steam mixtures, as well as on the operational behaviour of PARs under boundary conditions representative of the late phase of a severe accident. Hence, following the conclusions of the review performed in WP1 and the scenarios selected in WP2, WP3 provided specific experimental data to assess and enhance the numerical tools used in WP4. WP3 was organized in two major tasks: Task 3.1 (combustion) and Task 3.2 (PARs). The experimental program was conducted in two laboratories: investigations on the H_2/H_2O and $H_2/CO/CO_2/H_2O$ combustion under different conditions were performed at CNRS/ICARE in Orléans/France (see Section 2.3.1), while the operational behaviour of PARs under conditions of the ex-vessel phase of a severe accident was investigated at FZJ in Juelich/Germany (see Section 2.3.2).

2.3.1 Task 3.1: Combustion

The major outputs of this task were related to (i) flammability domain, (ii) laminar and turbulent flame speed, (iii) fundamental flame parameters, and (iv) combustion regimes of H_2/CO mixtures in air or in oxygen starvation conditions and with or without diluents, mainly water vapor and carbon dioxide.

The flammability limits were determined using two different criteria: (a) a visual criterion using a high-speed imaging system, (b) a pressure criterion using a high-frequency piezo-electric pressure transducer. For each condition in terms of initial temperature and initial pressure, ignition energy (Ciccarelli and Dorofeev, 2008; Grosseuvres et al., 2019), the upper and lower flammability limits were determined by performing hundreds of runs to establish a probability of ignition from which the upper and lower flammability were deduced. The combustible gas composition was, on a molar basis: 50% CO + 50% H_2. The major results, Figure 1, showed that:

- the initial pressure had nearly no effect on the LFL and induced a decrease of UFL from 72.4±0.6% at 1 bar and 23°C to 69.3±0.4% at 3.5 bar.
- Raising the initial temperature from 23 to 90°C induced a decrease of the flammability limits from 6.9±0.4% to 5.8±0.3%.
- For oxygen starvation, the LFL was not affected, but a strong drop of the UFL was found from 72.4±0.6% for normal air conditions to 45.7±0.9%.
- Finally, the inerting point of a stoichiometric {50% H_2 + 50% CO}/ air by carbon dioxide was determined to be 52±1 % at 1 bar and 22°C.

The ternary diagram of $H_2/CO/Air/CO_2$ was determined, as a supplementary work for WP4, at an initial pressure of 1 bar and 25°C (Figure 2). The major result was that with this additional diagram, the

flammability limits were known over different ratios of CO_2 (from 0 to 60%). And it has also shown that the inerting point was not obtained for the stoichiometric mixture but on the rich side.

The dynamics of laminar flames have been investigated, from which the laminar flame speed, the Markstein length, and the combustion overpressures have been determined. These detailed experiments showed that reducing the O_2 content in the air had no significant effect both on S_b^0 (unstretched burning flame speed) and L_b (Markstein length of the burnt gases), this is not surprising since the studied mixtures remained on the lean side. The negative L_b indicates that the flame is enhanced by stretch and curvature of the flame. This is an important feature when considering the effect of the turbulence on the increase of the burning rate. The increase of the initial temperature to 60°C led to an increase of the laminar flame speed. The predominance of the thermo-diffusive instabilities, for the range of the studied conditions, illustrates that they must be considered by the 3D and CFD codes as the laminar flame speed is increased by a factor close to 2 depending on the size of the flame and on the exact composition without any turbulence. The measured combustion overpressure showed that for mixtures containing less than 13% of {50%H_2 + 50% CO}, the combustion is incomplete as the flames are dominated by buoyancy. This limit is not modified by the depletion of oxygen.

The detailed experimental and numerical results of Task 3.1 can be found in the AMHYCO (public) deliverable D3.1 “Synthesis and outcomes of performed experiments and numerical results related to H_2/CO/H_2O combustion” (Chaumeix et al., 2024).

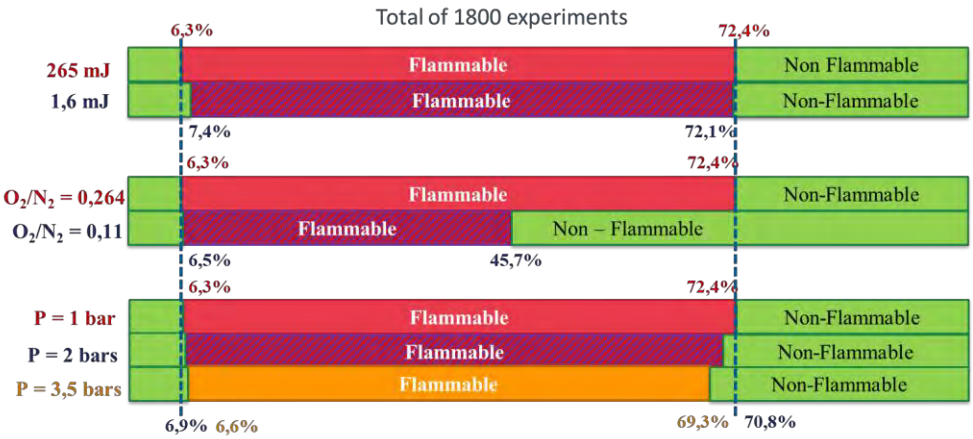

Figure 1. Summary of the experimental flammability limits determined in task 3

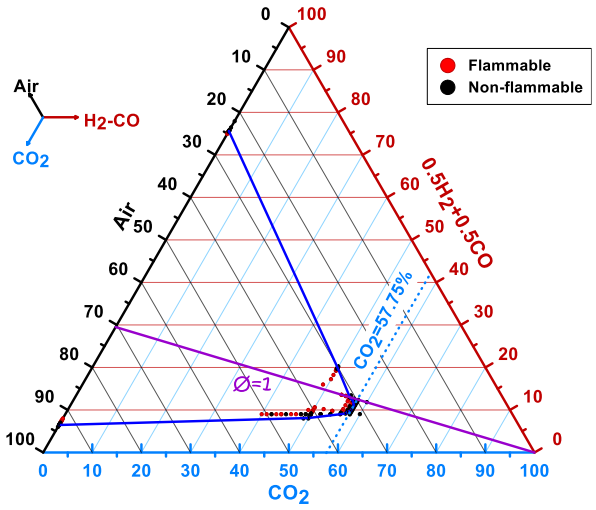

Figure 2. Ternary diagram of H_2-CO-CO_2-Air at 1 bar and 25°C determined in task 3.1

2.3.1 Task 3.2: Passive Auto-catalytic Recombiners

The main objective of AMHYCO Task 3.2 was to ensure that the impact of the challenging boundary conditions of a severe accident on the PAR performance is properly addressed in numerical PAR models, which are to be used in full containment accident simulations in the work program of WP4. For this purpose, experimental studies and model development activities have been performed to improve the predictive capabilities of the following four numerical models used to assess the efficiency of PARs as hydrogen mitigation measures: Framatome correlation (correlation-based model for the specific Framatome-PAR type); REKO-DIREKT (mechanistic PAR model involving diffusion-controlled reaction kinetics), developed by FZJ (Reinecke et al., 2016); SPARK (mechanistic PAR model involving full surface and gas-phase chemistry), developed by IRSN (Meyet et al., 2014) and PARUPM (mechanistic PAR model involving surface chemistry), developed by UPM (Jiménez et al., 2007).

The experimental program was addressing knowledge gaps on PAR operation in the presence of hydrogen and carbon monoxide, which could be divided into three different regimes: Regime I: Undisturbed parallel reaction of hydrogen and carbon monoxide with oxygen (oxygen-rich atmosphere); Regime II: Constrained parallel reaction of hydrogen and carbon monoxide with oxygen (oxygen-lean atmosphere) and Regime III: Interruption of reaction due to catalyst deactivation (poisoning).

The experimental program was conducted in the REKO facilities at FZJ, enabling well-defined boundary conditions for single catalyst sheets (REKO-1 flow channel), catalyst sections (REKO-3 flow channel) and down-scaled PARs (REKO-4 pressure vessel). The test program was complemented by results from national and international THAI programs provided by Becker Technologies through the SAMHYCO-NET project, the precursor to the AMHYCO project. For the first time, the experimental program has investigated the effect of carbon monoxide on both platinum- and palladium-based catalysts, to obtain information on the differences in behaviour.

The results of the AMHYCO experimental program have elucidated the behaviour of recombiners in all three operating states mentioned previously. The processes in regime I are well understood and mechanistic approaches for the different PAR models exist. For the transition from regime I to regime II the approach of diffusion-controlled reaction kinetics has been successfully applied to provide a criterion that is applicable for both correlation models as well as detailed codes. This approach is independent of the type of catalyst (Pt or Pd). The experimental data obtained for Regime III from the catalyst poisoning tests suggest that gas temperature and oxygen concentration are the most relevant parameters to describe PAR

poisoning for both catalyst types. The results allowed for the derivation of empirical criteria for catalyst poisoning with sufficient (if necessary, conservative) precision, which are based on easy-to-obtain parameters (gas temperature and oxygen concentration) even for those PAR models that don't involve surface chemistry.

The Framatome correlation is used by most of the AMHYCO partners participating in WP4. Improvements of the correlation based on the laws of diffusion-controlled reaction kinetics have been implemented and validated, which allow for a more consistent transition from oxygen-rich to oxygen-lean PAR operation. The improved model, called the "AMHYCO correlation" (Braun and Reinecke, 2025) has been transferred for testing and implementation in the corresponding thermo-hydraulic codes within the WP4 framework.

Within the AMHYCO project, the PARUPM code has been proposed as an appropriate tool for assessing the performance of PARs in full containment simulations. In the framework of Task 3.2, the PARUPM code has been further developed and validated (Domínguez-Bugarín et al., 2022; 2025). Most relevant enhancements include the implementation of a chimney model as well as a diffusion-based reaction model. The results obtained demonstrate that the physico-chemical strategy used in the PARUPM model can simulate the behaviour of the recombiner under various conditions, from typical concentrations and settings to more extreme ones such as oxygen starvation, catalyst poisoning, or elevated inlet temperatures. Furthermore, the code can reproduce the behaviour of a PAR in transient conditions, where pressure, temperature, and gas concentrations are constantly changing at the recombiner inlet. The PARUPM code has been implemented in the 3D thermo-hydraulic analysis code GOTHIC in WP4.

The further development of the SPARK code includes an update of the surface reaction mechanisms for platinum-based catalysts as well as an approach to implement a surface mechanism for palladium-based catalysts. The new Pt mechanism allows PAR simulation during deactivation conditions in the presence of carbon monoxide. The enhanced SPARK code has been used for post-calculations of both REKO-1 and REKO-3 data to verify that the SPARK code can reproduce the experimental results. The numerical results are consistent with the experimental results for all the cases, confirming that the SPARK code can predict the catalyst temperature for rich-oxygen conditions, oxygen starvation conditions, and in the presence of steam.

Advancements of the REKO-DIREKT code concern the implementation of different poisoning criteria for both catalyst types (Pt and Pd) based on the findings from REKO-3 poisoning experiments. The status of the PAR model has been validated against the new THAI database developed in Task 3.2. General good agreement was obtained, specifically regarding the catalyst temperature, which is one of the specific features of the code.

The detailed experimental and numerical results of Task 3.2 can be found in the AMHYCO (public) deliverable D3.2 "Synthesis and outcomes of performed experiments and numerical results related to PAR behaviour" (Reinecke et al., 2023).

2.4. WP4: Full containment analysis

The main objective of WP4 was to employ the results obtained in WPs 1-3 to define and conduct a comprehensive analytical assessment and finally provide the insights for a review and potential extension of the SAMGs and EOPs within WP4. Following the approach of WP2, an analysis was conducted for the European PWR concepts, W(estern), KWU and VVER. However, while WP2 used the available plant specific models and nodalization schemes, in WP4 generic containments and partly scaled input tables (from WP2) were employed to prepare a common open basis of the analysis, enable a better comparability of the simulation results.

Full containment analyses were conducted in a consecutive analysis chain, consisting of three levels of increasing detail: As a basis, the identified sequences were simulated completely with lumped parameter containment models e.g., built in ASTEC or MELCOR. On this basis, the most penalizing cases were

additionally investigated by 3D models developed in GOTHIC to address potential asymmetric / 3D conditions that may lead to higher combustion risk. As a last step, relevant compartments and/or time frames identified in the 3D analysis were simulated in detailed CFD-grade local containment studies (e.g., using containmentFOAM or ANSYS Fluent) to substantiate GOTHIC analysis and answer remaining open issues. The increasing level of spatial details achieved with the different codes was also utilized to assess the view on the accident from the control room (available sensors) against the full insights provided by the simulations to propose an upgrade of the SA instrumentation.

To ensure comparability of the simulation results, a common generic containment database (D2.1) was utilized (Serra et al., 2024) to develop the containment models within the different codes. The demonstrated agreement of the different codes and models paved the way for a detailed and systematic assessment of the effectiveness or impact of mitigative measures like PARs, fan coolers, sprays, and filtered containment venting systems regarding the in-containment combustion risk. The latter was evaluated in terms of the evolution of the flammable gas cloud as well as its potential of developing flame acceleration conditions, rather than by conducting combustion analyses to exclude the definition of ignition source and timing from the parameter space.

The simulations of the unmitigated reference simulations consistently show that without any hydrogen mitigation measures (no PARs), the containment atmosphere always has pockets where ignition and flame acceleration could occur. In some scenarios, the containment atmosphere even became globally flammable, with the potential of having fast dynamic combustion processes. Furthermore, the mass of combustible gas increases with time due to the ongoing MCCI. This emphasizes the need for combustible gas control hardware to protect the containment integrity and prevent potential loads resulting from a flame acceleration during both the in- and ex-vessel phases for all containment designs.

The experimental work as well as the comparison of the improved ‘AMHYCO PAR correlation’ (Braun and Reinecke, 2025) against the established manufacturer’s correlation (in this case, the Framatome correlation) confirm that PAR operation in the late phase is impaired more strongly by oxygen starvation and parallel recombination of CO. The ‘AMHYCO PAR correlation’ revealed to be conservative compared to the existing manufacturers’ correlation, i.e., resulting in a slower depletion of H_2, CO and O_2 in the late phase.

Besides limiting the H_2 mass in containment, the main effect of PARs was the consumption of O_2 and thus the inertisation of the containment atmosphere in the late phase. The capacity and efficiency of the PAR system primarily affected the peak concentration of H_2 and CO and the time until this inertisation was reached, but PAR systems could deplete the combustible mixtures effectively even with reduced capacities (cf. Figure 3). In all studied scenarios and for all the containment designs, the implementation of PARs prevented the global formation of a gas mixture, which could lead to flame acceleration conditions, while local flame acceleration conditions partially remained possible.

Furthermore, thanks to the O_2 removal, PWR-W and PWR-VVER cooling actions (i.e., spray and containment coolers) to decrease the containment pressure in the late phase of the accident can be taken without increasing the risk of combustion. Considering the steam concentration in the containment, it is clear that for all options, the steam concentration is far below the steam inertisation limit, and thus, the effects of different cooling means on the flammability are small.

The reactivation of the PWR-KWU’s Emergency Core Cooling System did not further increase the combustion risk, since it was primarily cooling the melt pool and not globally the containment atmosphere. In the specific case of containment venting in the PWR-KWU, the combustion risk was further reduced by the removal of combustible gases by the PARs. The later the FCVS is operated, the more the inertisation of the containment atmosphere due to PAR operation also reduces the risk of a combustion event in the first or subsequent operations of the FCVS system.

Equipment survivability (here according to IEEE 323-1974: $T_{gas} > 149.8$ °C, $P < 4.82$ bar) can be challenged in scenarios without containment cooling and with high pressures, i.e. SBO sequences. 3D simulations

revealed a strong heterogeneity of the gas temperature, in particular when PARs are considered. They should be used in future to substantiate LP code analysis and allow quantifying thermal stratifications.

While the 3D and CFD analysis generally showed well-comparable trends for the CV-averaged quantities to the system code analysis, local stratifications and stagnation zones (e.g., dead-end compartments) were identified. Those can result in locally flammable conditions, or e.g., standing flames, which cannot be identified by using the coarse system code nodalization. Furthermore, pointwise evaluation of possible sensor locations showed stronger oscillations with high peak values compared to the rather smooth monotonous evolution of the CV mean values. Consequently, for decision making, it should be accounted for that sensor readings might be affected by local heterogeneities and/or cannot capture local accumulations (e.g., dead-end compartments). While a global combustion event is most likely prevented by PARs, a local combustion (e.g., in dead-end compartments) is possible and should be evaluated or conservatively treated, e.g., by checking the availability of the equipment in these areas under a combustion event.

To conclude, it is important to note that the established approach to combustion risk and flame acceleration assessment, that is considering CO as additional H_2, is quite conservative and should be re-evaluated when improved experimental data and correlations becomes available. In particular, the assessment of flammability and potential flame acceleration of arbitrary mixtures of H_2-CO-O_2 mixtures, including large amounts of diluting gases, obtained in WP3, became available too late to be employed on the evaluation. Nevertheless, these correlations substantiate the findings achieved so far based on a conservative treatment of CO as additional H_2.

Future investigations should substantiate the conclusions taken so far by addressing further scenarios, operator actions and further exploiting 3D / CFD analysis tools to get insight into localized phenomena. The generic containment database (D2.1) and input decks created in WP4 proved to be a well-suited basis for this work and can be refined based on 3D simulation results. Also, sensitivities and propagation of uncertainties should be considered to identify crucial input parameters and modeling choices.

The detailed lessons learned from WP4 can be found in the AMHYCO (public) deliverable D4.3 “Lessons Learned during the Full Containment Analysis of KWU, Western and VVER PWRs and Quality Assurance Measures” (Kelm et al., 2025) and in open publications (Serra et al., 2025; Kelm et al., 2026).

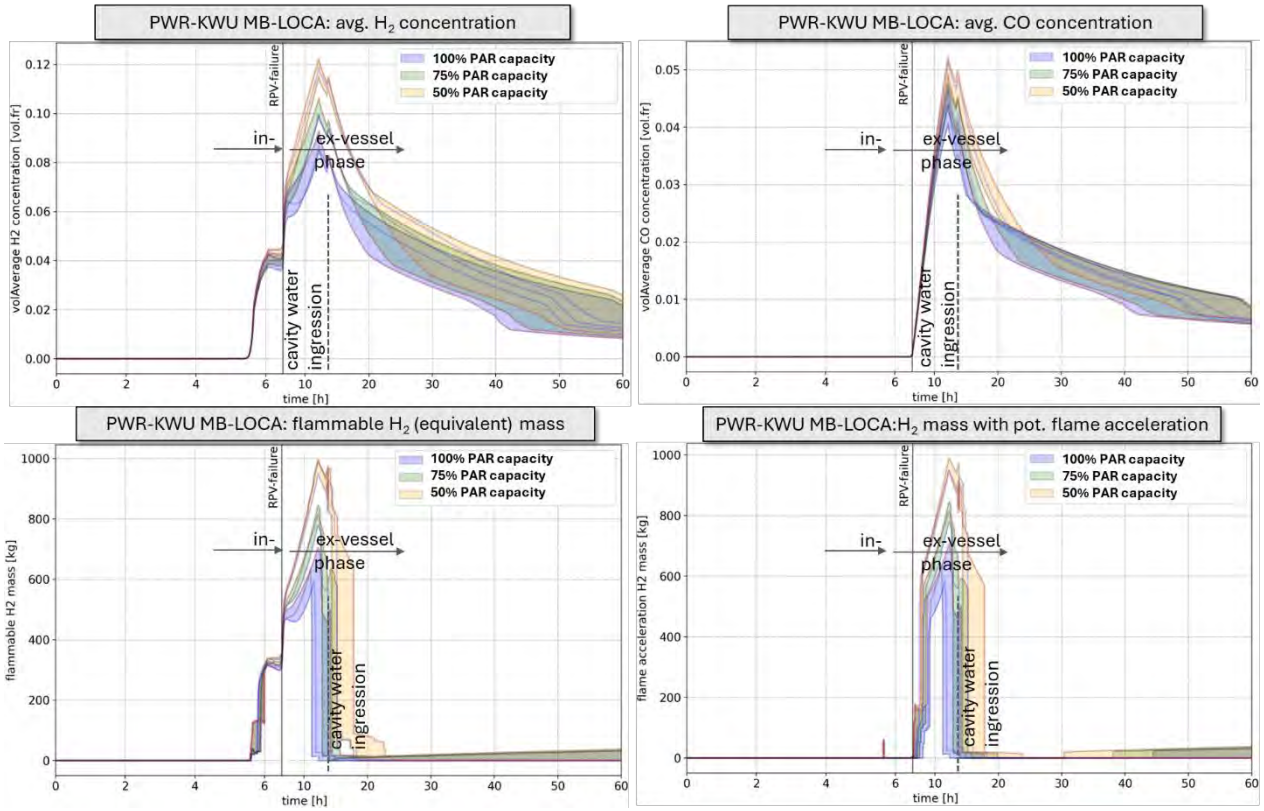

Figure 3. Average H_2 and CO concentrations in the containment and integral flammable H_2 equivalent mass for the PWR-KWU MBLOCA sequences for different PAR system capacities.

2.5. WP5: Enhancement of Severe Accident Management Guidelines

WP5 aimed to identify room for improvement of SAMGs regarding the management of combustible gases, on the basis of the experimental and computational efforts carried out in the above-mentioned WPs. Thereby, the insights from the calculations, including the late phase with CO present in the containment, are transferred into SAMGs considerations. Additionally, recommendations are given concerning possible hardware backfitting.

To make these recommendations, WP5 analyses the results of all the preceding work packages, especially the numerical analyses carried out in WP4, and the experimental results obtained within WP3. From this database, relevant aspects are pointed out, motivated and described, and the applicability to existing European pressurized water reactor types (Western-type, KWU-Type, and VVER-Type) confirmed, and the results are presented in a language commonly used in the nuclear industry framework.

In this way, WP5 formed the interface from academic research and numerical simulations into industrial application. Its outcome was documented in the AMHYCO (public) deliverable D5.1 “Generic Guidelines for SAMG Development, Minimizing the H_2/CO Combustion Risk in a Containment. Lessons learned of the AMHYCO project” (Braun et al., 2025) and can be summarized in these three fields:

a) <u>Gain in knowledge concerning simulating H_2 within a reactor containment</u>

The comparison of simulations performed on different length scales allowed to make statements concerning the connection between the gas cloud distribution within the containment and the singular point values. These findings can support the interpretation of actual measurements as displayed in the main control room, regarding the identification of a containment risk condition. The modelisation of passive autocatalytic recombiners was significantly improved, based on the experimental campaigns with PARs in WP3. Thus, in the future, they can be incorporated in

containment simulations in a much more physically accurate way. The new description includes the consumption of hydrogen as well as carbon monoxide by the PAR, the transition from oxygen-rich into oxygen lean operating conditions, the poisoning of the PAR by CO, as well as the PAR-induced ignition of the containment atmosphere by an extremely high concentration of combustible gases.

b) Improvements in severe accident management guidelines

In the simulations, a strongly negative impact of an early spray (by automatic activation) or a late re-activation of a spray (e.g., due to re-establishment of electric power) on the in-containment combustion risk was identified. Based on the WP4 simulations, the following recommendations were deduced in WP5: In case the spray is already operating, then keep it operating to at least keep the containment pressure prior to ignition low. Concerning a late reactivation, the operators shall have a mean to manually control the spray system to prevent an automatic start of the spray by re-establishing AC power, and the plant shall have appropriate means to characterize the containment atmosphere by suitable gas measurement equipment prior to manually activating the containment spray.

In the frame of WP4, numerical simulations of the PWR-KWU were performed on how the containment atmosphere, and especially its flammability, changes in case of an early and a late venting activation. The insights then were transferred to the other reactor designs. After evaluating the advantages and disadvantages of a filtered venting of the containment, it was concluded in WP5 to not recommend using the filtered containment venting system for hydrogen mitigation. The main reasoning was that a venting affects the containment atmosphere slower than a hydrogen control system based on PARs. Thus, it is beneficial to wait until the PARs have improved the hydrogen risk by consuming both H_2 and O_2 instead of activating the venting system. The results were documented in Deliverable D5.1 Chapter 5.3 and 6.4.

c) Recommendations for backfitting of hardware for long-term operation

Concerning PARs, it was shown that they are greatly beneficial regarding the mitigation of combustible gases. Even in case they would operate only with a reduced efficiency, for whatever unforeseen reason, a suitably designed system can still cope with a wide variety of accident sequences. Concerning the surveillance of the PAR operation, it turned out that often a measurement of oxygen may reveal key information about the containment atmosphere concerning a possible combustion risk state that is needed to complement the measurement of combustible gases.

Furthermore, the backfitting of a filtered venting system (FCVS) can be unconditionally recommended. Within AMHYCO WP5, it was deduced how a FCVS should be operated in the presence of combustible gases, and at which stages high-concentration of combustible gases may get in contact with oxygen-rich atmospheres.

Containment cooling systems like spraying or fan coolers are so strongly interconnected to the containment design itself that there is a low likelihood of backfitting an entirely new system. Instead, possible selective works and upgrades of the systems were evaluated. In some plant designs, the containment cooling is initiated automatically. Especially for accident sequences with a late recovery of the system, the need for manual inhibition of the system activation was identified. Further, it is strongly recommended that if a containment cooling system shall be used in accident management, then a suitable containment surveillance system shall be in place to confirm that the activation of the containment cooling system does not unnecessarily endanger the containment itself by making the atmosphere flammable.

About monitoring, AMHYCO significantly strengthened the knowledge of how to interpret point data measurements in the main control room (see Chapter 5.1) and how these relate to a containment failure risk state. Further, the optimal measurement range of a combustible gas monitoring system

was determined, and the need for such a system was deduced, depending on the plant design and anticipated usage of containment cooling systems.

3. FINAL REMARKS

The AMHYCO project went beyond the state-of-the-art of combustible gas control under severe accident conditions in several aspects. Thereby, the special focus was on closing knowledge gaps concerning combustion mixtures in the late phase of a nuclear accident. Within the scope of AMHYCO were the three dominant containment designs of pressurized water reactors in Europe: the KWU-type, the Western-type (French and Westinghouse), and the VVER-type.

The first work package established the knowledge basis, both numerically and experimentally, to understand the combustion risk of H_2, H_2O and CO mixtures in realistic severe accident conditions. Work Package 2 on one side explored the boundary conditions to be experimentally and numerically explored thereafter, as well as established a common reference plant model for the three considered PWR designs (Western, KWU-type, and VVER). In short, two different databases resulted from WP2: a database of "generic containments" for the three types of reactors and another one with more than 40 accident sequences that closely looked at the combustion risk in containment.

In Work Package 3, experimental campaigns helped, on one side, to increase the understanding of the combustion properties of H_2-CO mixtures, and, on the other side, how passive autocatalytic recombiner operate in atmospheres containing H_2 as well as CO, building an extensive database of experiments with ex-vessel representative conditions.

With improved modelling techniques based on the experimental insights in WP3 and the standardized generic plant models from WP2, in WP4 systematic containment simulations were performed by numerous codes, establishing a broad database of accidental sequences for different code approaches (LP, 3D, and CFD). This database provided insight into the numerical differences of the different codes as well as a more profound understanding of the containment atmosphere during a severe accident and the impact of existing containment cooling systems and backfitted severe-accident-related hardware. A special interest was the comparison of LP, 3D, and CFD numerical codes and how the stimulation of the hydrogen distribution on different length scales affected the results.

Finally, in WP5, all preceding experimental, theoretical, and numerical works were evaluated and condensed into proposals to improve the severe accident mitigation guidelines as well as to recommend back-fitting in existing European pressurized water reactors. The deliverable of this work package shall bring the research results into industrial application.

In the end, AMHYCO provided the community with extensive databases that broadened the knowledge as stated before the project, fulfilling and often exceeding its initially set objectives.

ACKNOWLEDGMENTS

This project has received funding from the Euratom research and training programme 2019-2020 under Grant Agreement n°945057. The content of this paper reflects only the author's view. The European Commission is not responsible for any use that may be made of the information it contains.

The following PhD students have participated in AMHYCO project and their work has been key for the success of the project: Gabriela Nobrega (CNRS/IRSN/FZJ), Laura Vastier (CNRS/IRSN), Araceli Domínguez-Bugarín (UPM), Carlos Vázquez-Rodríguez (UPM/FZJ), Luis Serra López (UPM), Miriam Müer (RUB), Johannes Hoffrichter (RUB) and Alejandra Palomino (CNRS).

REFERENCES

Bentaib, A. (2022). *D1.1 Critical assessment of key elements of combustible gases management in containment*. AMHYCO project. https://cordis.europa.eu/project/id/945057/results

Braun, M. and Reinecke, E.-A. (2025). AMHYCO engineering correlation to describe the conversion of flammable gases in Framatome passive autocatalytic recombiners. *Nuclear Engineering and Design*, 442, 114206. https://doi.org/10.1016/j.nucengdes.2025.114206

Braun, M., Reinecke, E.-A., Bentaib, A., Jiménez, G., Serra, L., Lopez López, L., Domínguez-Bugarín, A., Herranz, L. E., Fontanet, J., & Iskra, A. (2025). *D5.1 – Generic guidelines for SAMG development, minimizing the H2/CO combustion risk in a containment. Lessons learned of the AMHYCO project*. AMHYCO project. https://cordis.europa.eu/project/id/945057/results

Chaumeix, N., Nagaraju, S., Ballossier, Y., Desclaux, A., Bouton, M., & Vastier, L. (2024). *D3.1 - Synthesis and outcomes of performed experiments and numerical results related to H_2/CO/H_2O combustion*. AMHYCO project. https://cordis.europa.eu/project/id/945057/results

Ciccarelli, G., & Dorofeev, S. (2008). Flame acceleration and transition to detonation in ducts. *Progress in Energy and Combustion Science, 34*(14), 499–550.

Domínguez-Bugarín, A., Jiménez, M. A., Reinecke, E.-A., & Jiménez, G. (2022). PARUPM: A simulation code for passive auto-catalytic recombiners. *EPJ Nuclear Sciences & Technologies, 8*, 32. https://doi.org/10.1051/epjn/2022046

Domínguez-Bugarín, A., Reinecke, E.-A., Jiménez, G., Jiménez, M. A., & Gupta, S. (2025). Validation process against late phase conditions of the passive autocatalytic recombiner simulation code PARUPM as a standalone tool using experimental data from REKO-3 and THAI facilities. *Nuclear Engineering and Design, 431*, 113722.

Grosseuvres, R., Comandini, A., Bentaib, A., & Chaumeix, N. (2019). Combustion properties of H_2/N_2/O_2/steam mixtures. *Proceedings of the Combustion Institute, 37*(2), 1537–1546.

Herranz, L. E., Jiménez, G., & Nitti, F. S. (2022). Towards an optimized management of accidents. *EPJ Nuclear Sci. Technol., 8*, 43. https://doi.org/10.1051/epjn/2022019

Herranz, L. E., & Fontanet, J. (2023). *D2.2 – Identification and analysis of accident sequences posing high H2/CO combustion risk (PWR-W, PWR-VVER, PWR-KWU)*. AMHYCO project. https://cordis.europa.eu/project/id/945057/results

Herranz, L. E., Jiménez, G., & Kärkelä, T. (2025). Enhancing severe accident management through research. *EPJ Nuclear Sci. Technol., 11*, 10. https://doi.org/10.1051/epjn/2025004

Jiménez, M. A., Martín-Valdepeñas, J., Martín-Fuertes, F., & Fernández, J. (2007). A detailed chemistry model for transient hydrogen and carbon monoxide catalytic recombination on parallel flat Pt surfaces implemented in an integral code. *Nuclear Engineering and Design, 237*, 460–472.

Kelm, S., Braun, M., Bentaib, A., & Iskra, A. (2025). *D4.3 – Lessons learned during the full containment analysis of KWU, Western and VVER PWRs and quality assurance measures*. AMHYCO project. https://cordis.europa.eu/project/id/945057/results

Kelm, S. et al. (2026). Detailed assessment of combustion risk and PAR efficiency in the late phase of a severe accident within the European AMHYCO project. *Nuclear Engineering and Design*, 446 (B), 114588. https://doi.org/10.1016/j.nucengdes.2025.114588

Meynet, N., Bentaïb, A., & Giovangigli, V. (2014). Impact of oxygen starvation on operation and potential gas-phase ignition of passive auto-catalytic recombiners. *Combustion and Flame, 161*(18), 2192–2202.

Reinecke, E.-A., Kelm, S., Steffen, P.-M., Klauck, M., & Allelein, H.-J. (2016). Validation and application of the REKO-DIREKT code for the simulation of passive autocatalytic recombiner operational behavior. *Nuclear Technology, 196*(12), 355–366.

Reinecke, E., Domínguez-Bugarín, A., & Nobrega, G. (2023). *D3.2 - Synthesis and outcomes of performed experiments and numerical results related to PAR behaviour*. AMHYCO project. https://cordis.europa.eu/project/id/945057/results

Serra, L., Domínguez-Bugarín, A., Vázquez-Rodríguez, C., & Jiménez, G. (2024). *D2.1 - Data for the generic containment analysis (PWR-W, PWR-VVER, PWR-KWU)*. AMHYCO project. https://cordis.europa.eu/project/id/945057/results

Serra, L., Domínguez-Bugarín, A., Jiménez, G., Vázquez-Rodríguez, C., Braun, M., Kelm, S., Herranz, L. E. (2025). From the plant layouts to optimized LP and 3D PWR-KWU containment models for combustion risk assessment with GOTHIC 8.3(QA). Nuclear Engineering and Design, 445, 114459. https://doi.org/10.1016/j.nucengdes.2025.114459

Vázquez-Rodríguez, C., Jiménez, G., Arfinengo del Carpio, S., Bocanegra, R., Domínguez-Bugarín, A., Serra, L., Estévez-Albuja, S. & Fernández-Cosials, K. (2025). *The Preventive Methodology: A priori modification of the containment geometry to boost the computational efficiency of GOTHIC 3D models*. Nuclear Engineering and Design, 432, 113718. https://doi.org/10.1016/j.nucengdes.2024.113718

AMHYCO

Enhancing H_2 & CO Combustion Risk Management

AMHYCO project outcomes and lessons learned

Jiménez, G. (UPM), Bentaib, A. (ASNR), Herranz, L.E. (CIEMAT), Chaumeix, N. (CNRS), Kelm, S. (FZJ), Reinecke, E.-A. (FZJ), Braun, M. (FRAMATOME), Koch, M.K..(RUB), Kljenak, I.(JSI), Sevbo, O.(ENERGORISK), Visser, D.(NRG), Liang, Z.(CNL), Lazarevic, M.(LGI)

This project has received funding from the Euratom research and training programme 2019-2020 under Grant Agreement n°945057.The content of this document reflects only the author's view. The European Commission is not responsible for any use that may be made of the information it contains.

ERMSAR2026 conference

May 18-22

Madrid, Spain

AMHYCO general data

- Full Project Name: Towards An Enhanced Accident Management Of The Hydrogen/CO Combustion Risk
- EURATOM Work Programme 2019 “NFRP-02: Safety assessments for Long Term Operation (LTO) upgrades of Generation II and III reactors”
- Project No: 945057
- Start Date: 01/10/2020
- Project Duration: 48 months → 54 months
- EU contribution: 3 974 402.50 €
- 12 partners from 7 countries

AMHYCO partners

#	Participant organisation name	Country
1 (Coordinator)	Universidad Politécnica de Madrid (UPM)	Spain
2	Centro de Investigaciones Energéticas, Medioambientales y Tecnológicas (CIEMAT)	Spain
3	L'Institut de Radioprotection et de Sûreté Nucléaire (IRSN)	France
4	Centre National de la Recherche Scientifique -Orleans (CNRS)	France
5	Forschungszentrum Jülich (FZJ)	Germany
6	Framatome GmbH (FRG)	Germany
7	Ruhr-Universität Bochum (RUB)	Germany
8	Jožef Stefan Institute (JSI)	Slovenia
9	Energorisk, Ltd. (ER)	Ukraine
10	Nuclear Research and Consultancy Group (NRG)	Netherlands
11	Canadian Nuclear Laboratories (CNL)	Canada
12	LGI Consulting (LGI)	France

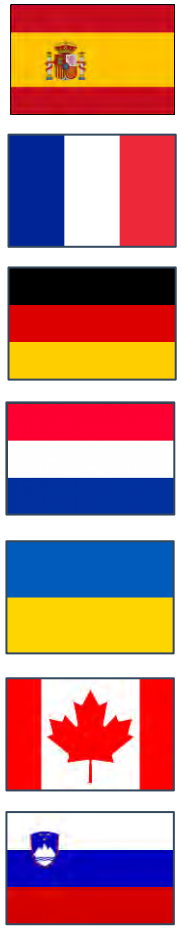

AMHYCO objectives

The AMHYCO project main objective is **to propose innovative enhancements on the way combustible gases are managed in case of a severe accident in currently operating reactors.**

To reach this main objective, the AMHYCO project has three main specific objectives:

Objective 1: To experimentally investigate phenomena that are difficult to predict theoretically: H2/CO combustion and PARs (Passive Autocatalytic Recombiners) behavior under realistic accidental conditions, taking into account their interaction with safety systems.

Objective 2: To improve the predictability of analysis tools - Lumped Parameter (LP), 3D and Computational Fluid Dynamic (CFD) codes - used for explosion hazard evaluation inside the reactor containment and providing support to SAMGs design and development.

Objective 3: To improve the Severe Accident Management Guidelines for both in-vessel and ex-vessel phases with respect to combustible gases risk management, using theoretical, simulation and experimental results.

AMHYCO workflow

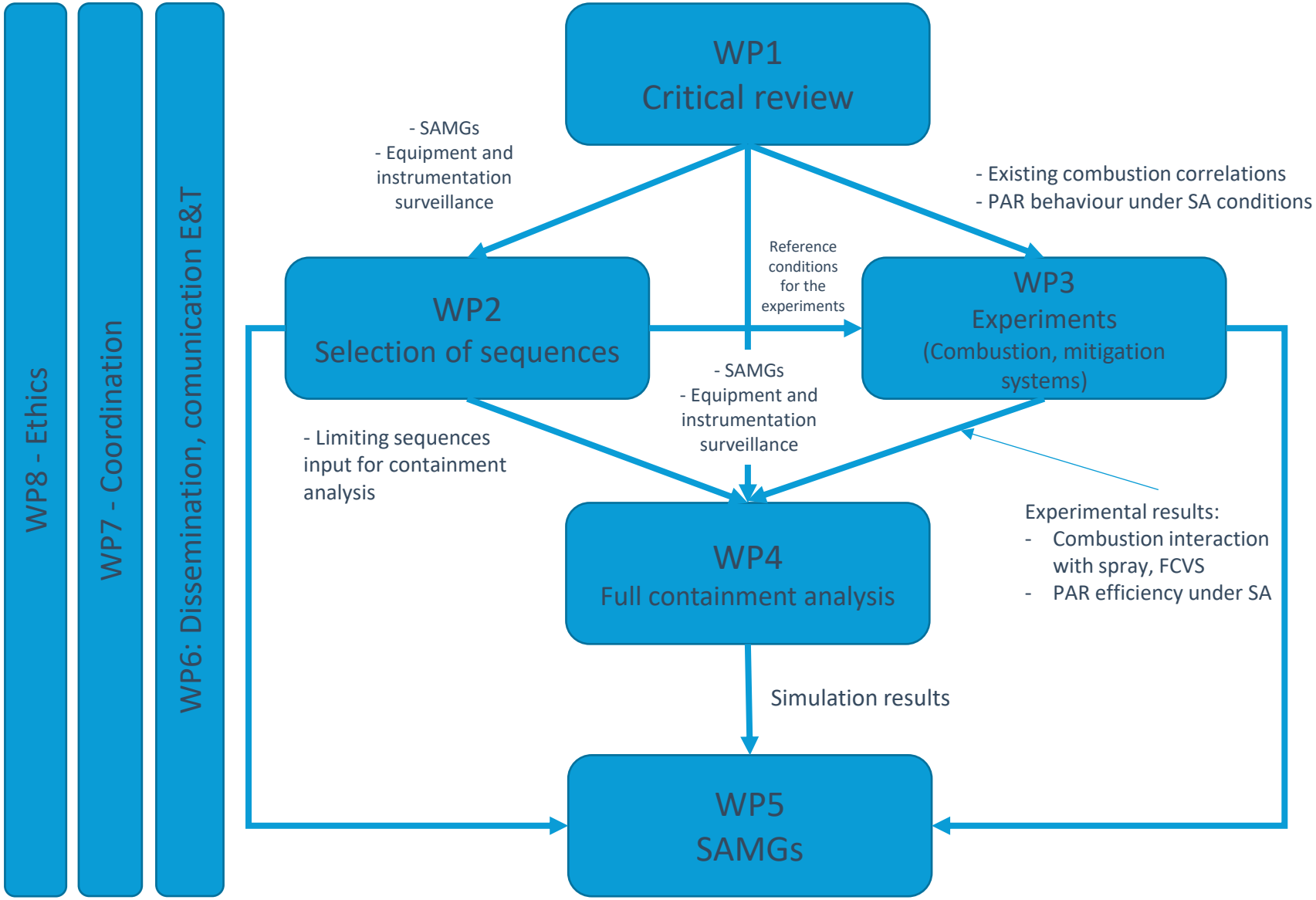

Timeline with the extension (1 Oct 2020 - 31 March 2025)

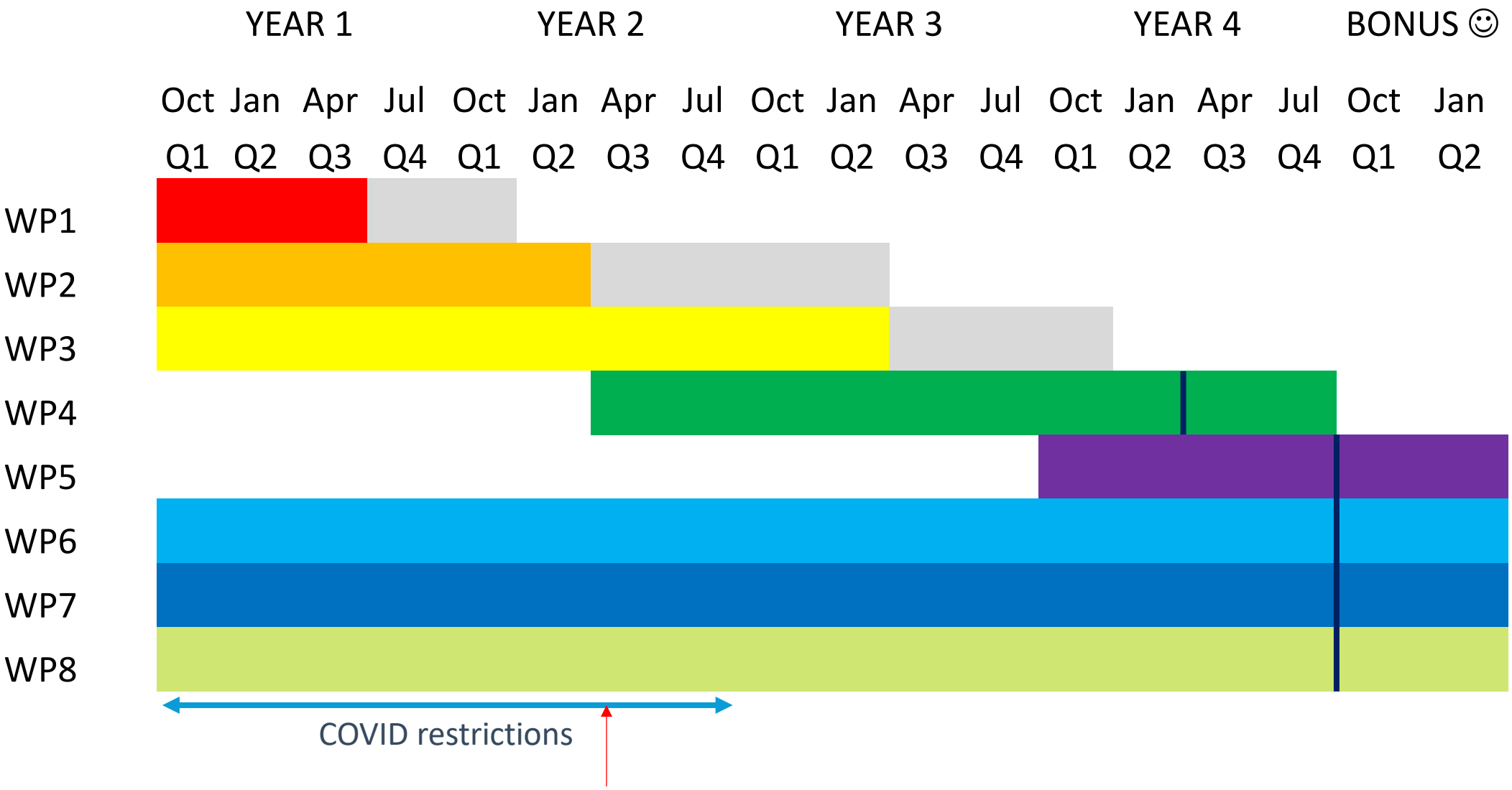

Connection with other ongoing international projects

PANDA

PAUL SCHERRER INSTITUT

PSI

THEMIS

NEA
NUCLEAR ENERGY AGENCY

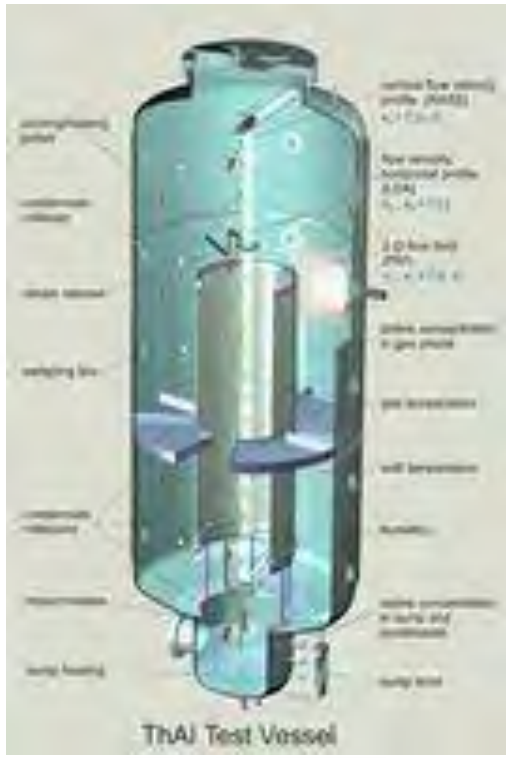

BECKER TECHNOLOGIES

SAMHYCO-NET

SAMHYCO NET

NUGENIA
Nuclear Generation II&III Alliance

Main AMHYCO lessons learned and outcomes

WP1: The need of a common knowledge basement

https://amhyco.eu/wp-content/uploads/2024/02/D1_1_Critical_assessment_of_key_elements_of_combustible_gases_management_in_containment_V1.pdf

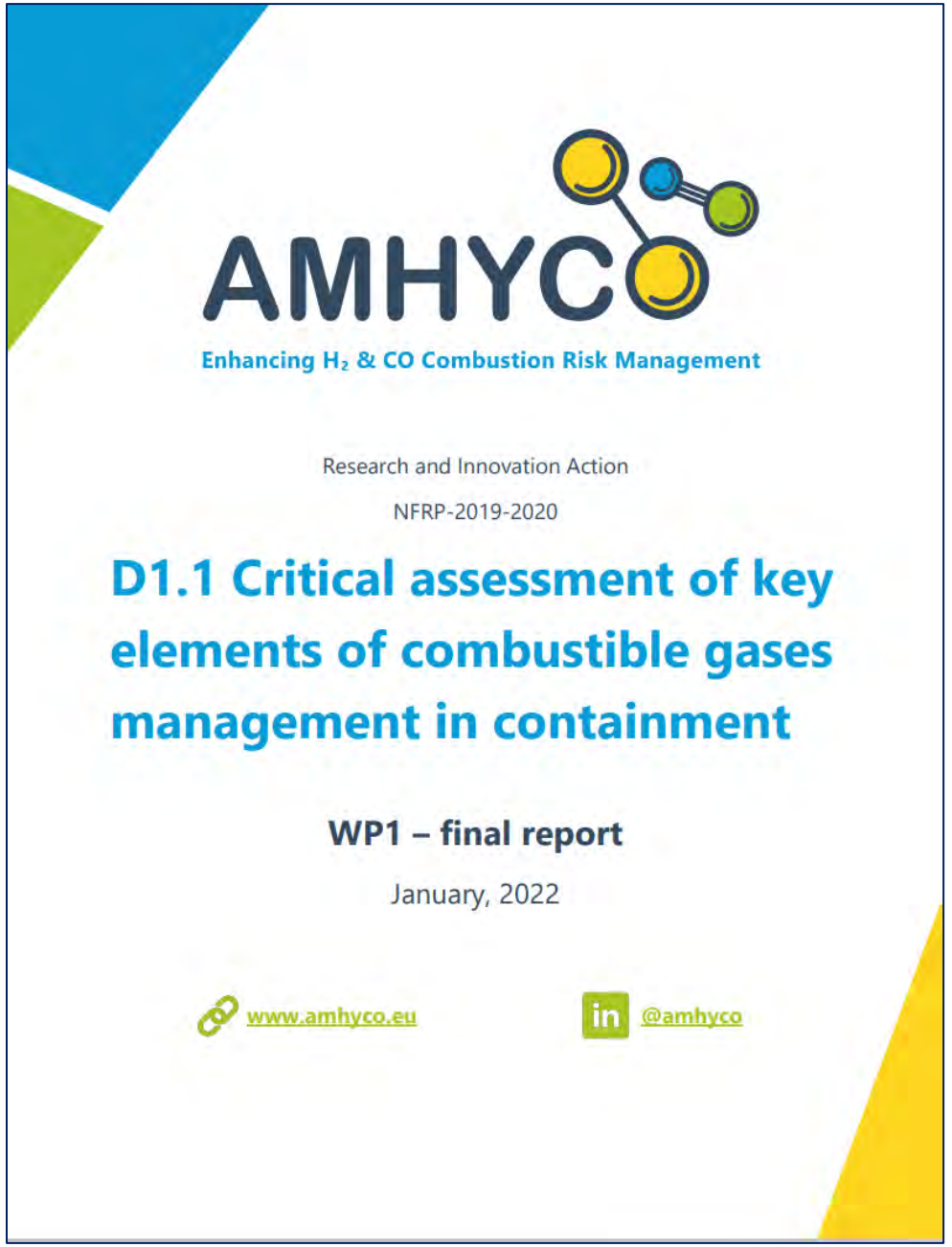

WP2: The value of a proper SA methodogy

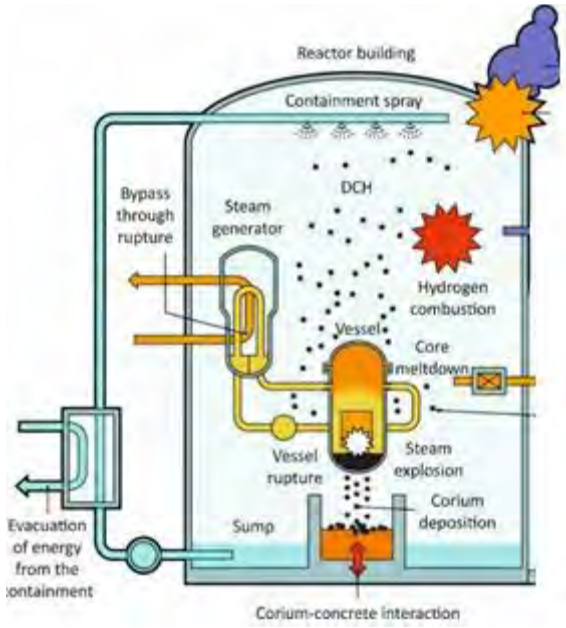

- Selection criteria
  - Figures Of Merit
    - Pre-sequence selection
      - Calculation phase
        - Selection

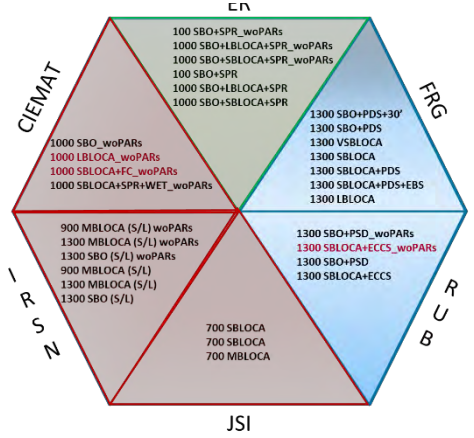

REF: Herranz et al. (2023). *Identification and Analysis of accidental sequences posing high H2/CO combustion risk (PWR-W, PWR-VVER, PWR-KWU)*. AMHYCO project

WP2: The importance of a common geometry

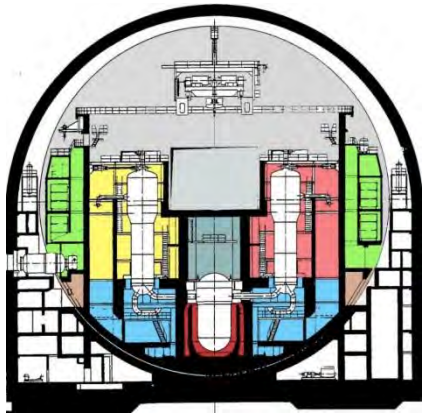

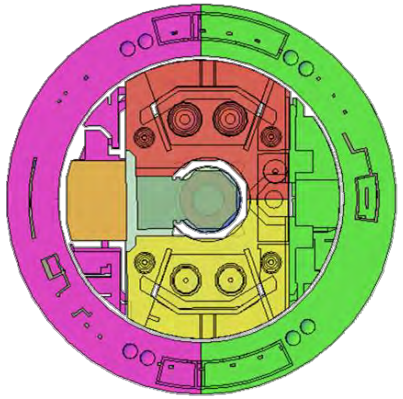

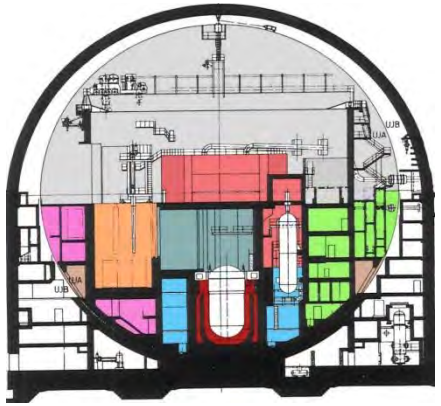

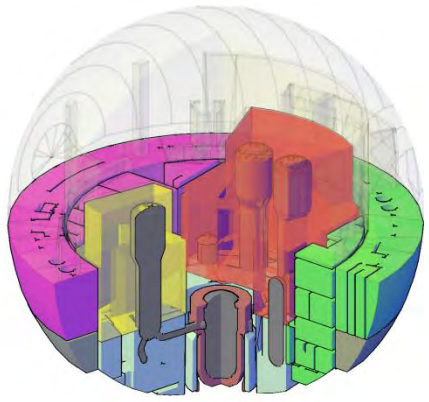

- **10 CVs: SAMHYCO +2 approach** (SFP & Reactor Room)
- **26 junctions**
- **28 pressure-sensitive doors**

Zones	Free Volume	Base Elevation	Height
	[m3]	[m]	[m]
CAVITY	250.31	-1.9	12.6
SUMP	6082.17	-1.9	12
DUCT	2668.42	6.2	5.5
SG-N	4520.74	10.1	19.2
SG-S	4446.86	10.1	19.2
ANN-E	6090.91	1.84	19.36
ANN-W	5783.02	0.35	20.85
SFP	1326.85	7.45	14.05
R-ROOM	1115.62	10.3	10.9
DOME	42653.73	21.2	29.65
TOTAL	**74938.63**		

REF: Serra et al. *D2.1 - Data for the generic containment analysis (PWR-W, PWR-VVER, PWR-KWU). AMHYCO project*

WP4: the different modelling approaches are consistent in the global values and, at the same time, complementary

WP4

LP / System codes

(most penalizing scenarios from WP2)

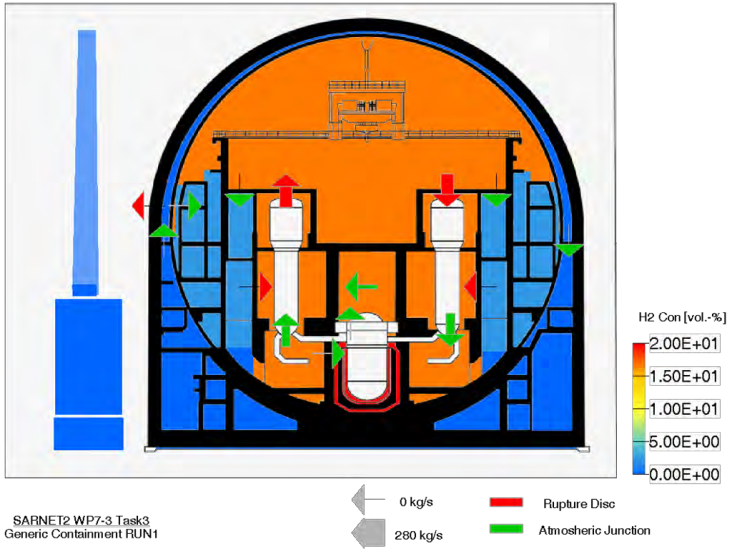

Ref: RUB

GOTHIC-3D

(Selected transients)

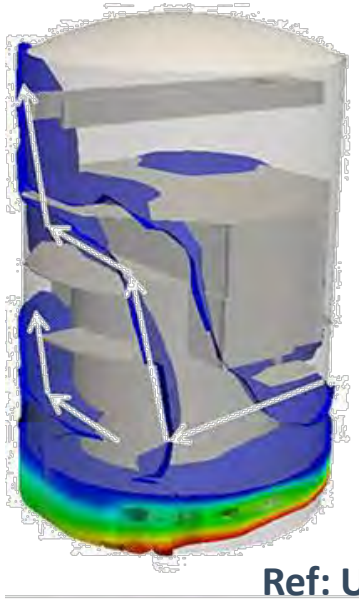

Ref: UPM

CFD

(Selected compartments)

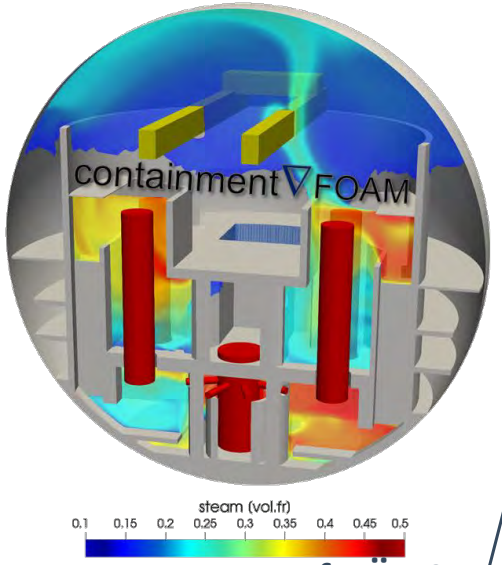

Ref: JÜLICH

REF: Serra, L. et al. From the Plant Layouts to Optimized LP and 3D PWR-KWU Containment Models for Combustion Risk Assessment with GOTHIC8.3 (QA). *Nuclear Engineering and Design*. https://doi.org/10.1016/j.nucengdes.2025.114459

WP3-WP5: the way the combustion risk at the ex-vessel phase is estimated should be rethought

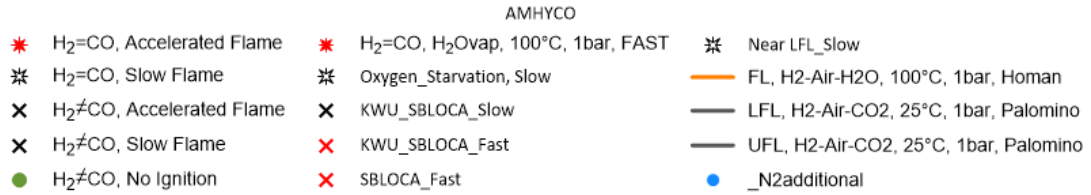

Sigma Criterion

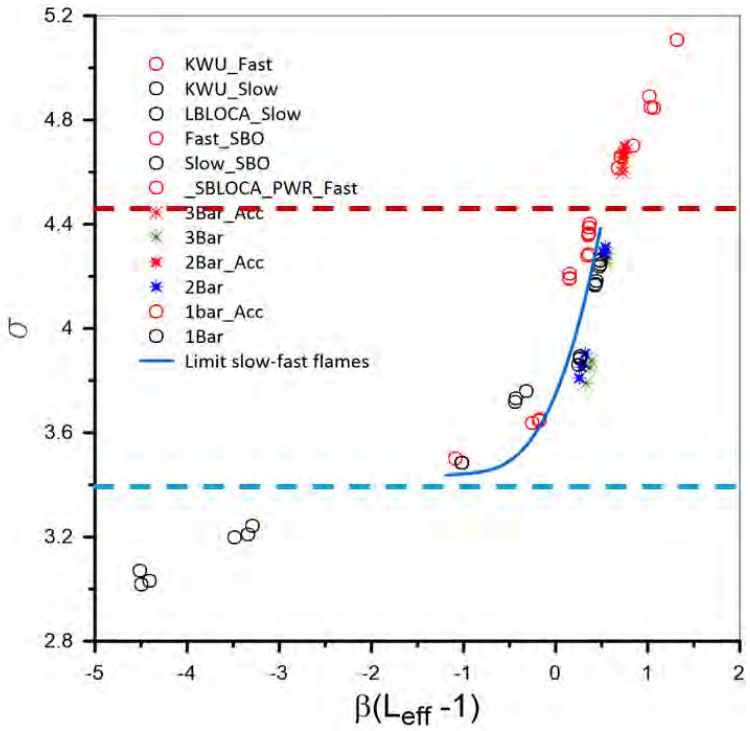

If sigma is higher that 4.5 ⇨ It is always fast flames

For sigma between 3.5 and 4.5

Estimate critical sigma and compare to the real one

If sigma > sigma* -→ Fast Flames

If sigma < sigma* → Slow flames

$$\sigma^* = 0.9 \cdot \beta \cdot \left(Le_{eff} - 1\right) + 3.9$$

For sigma below 3.5 → Slow flames

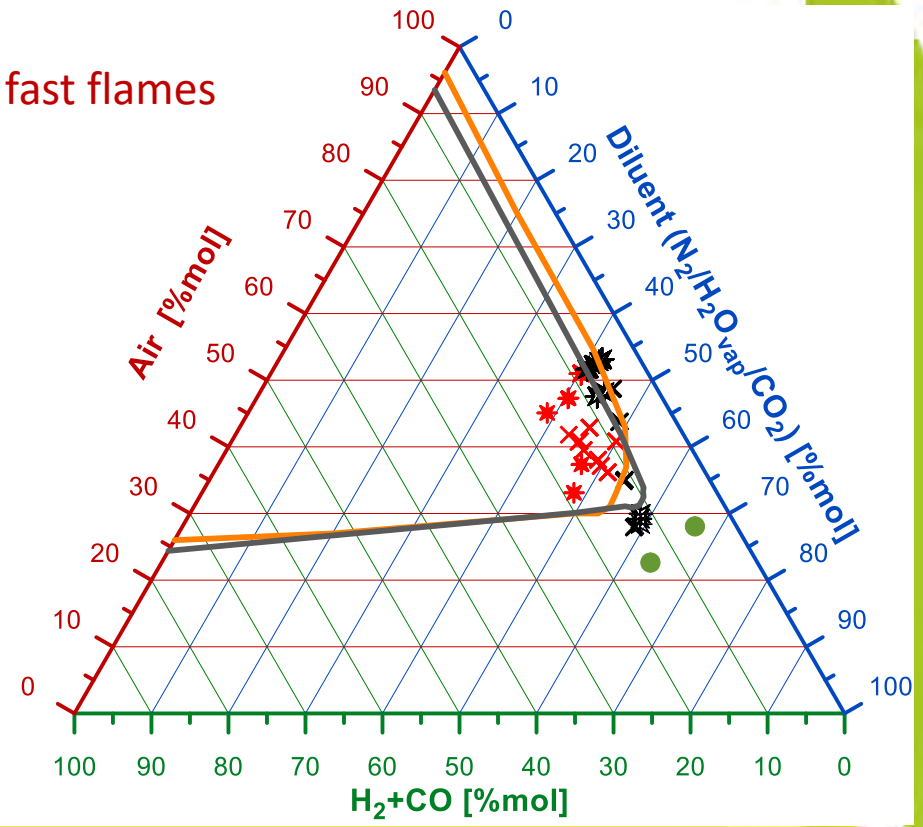

REF: Chaumeix, N., Ballosier, Y., Hamadi, A. (2025). *D4.1 – Engineering Correlations*. AMHYCO project

WP3-WP5: Now we have a clearer look of how the PARs are behaving in ex-vessel conditions

Effect of O_2 Fraction → Poisoning

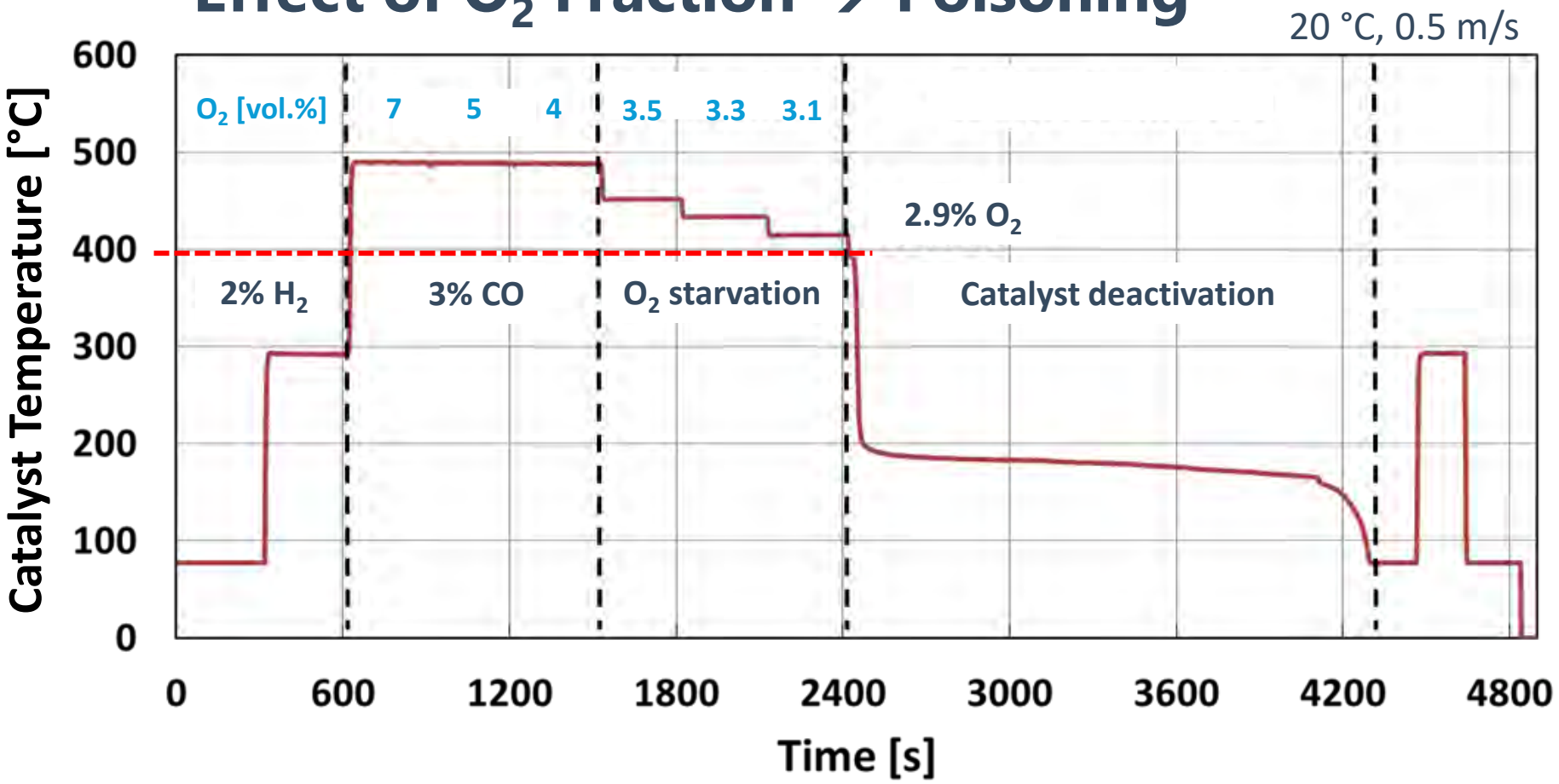

„At a certain temperature, the reaction rate steeply decreases and eventually comes to a full stop. After carbon monoxide injection is stopped, the catalyst immediately recovers and returns to full capacity."

REF: Reinecke et al. (2023). *Synthesis and outcomes of performed experiments results related to PARs behaviour*. AMHYCO project

WP4-WP5: if you don't have PARs, please buy them!!

- Assumed ‚unavailability' of a certain fraction (25%, 50%) of the PAR system

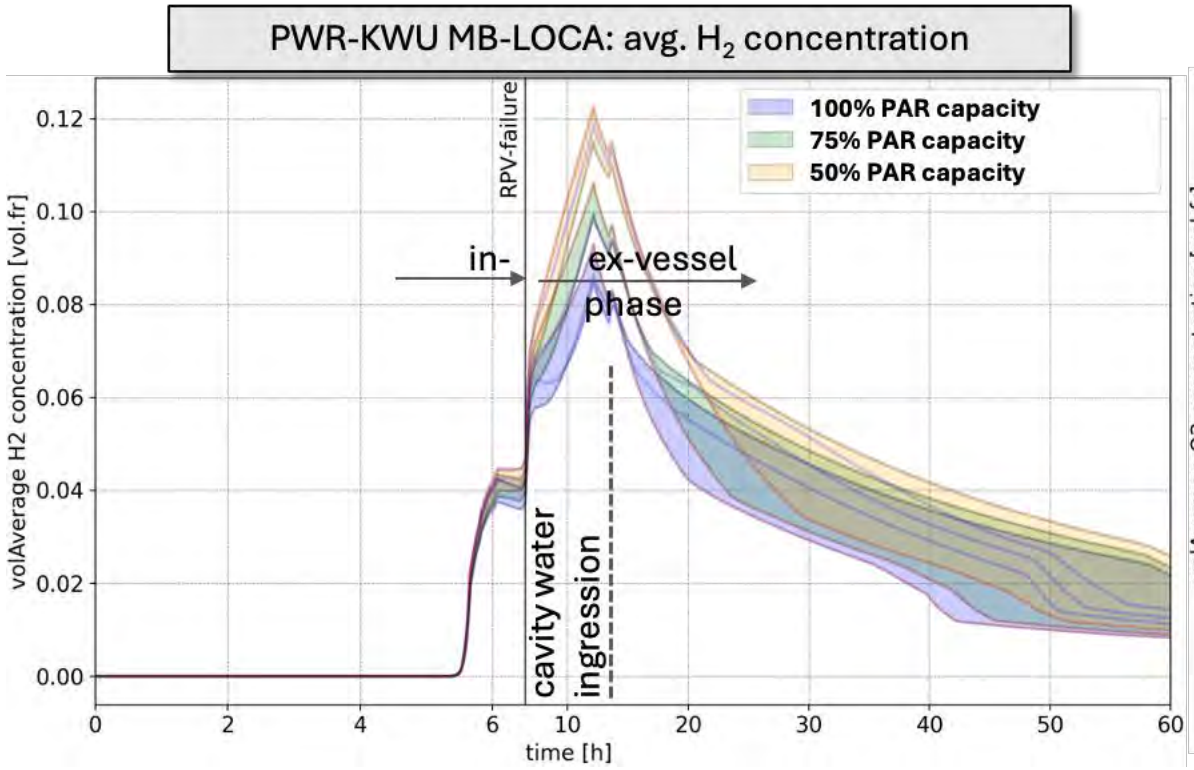

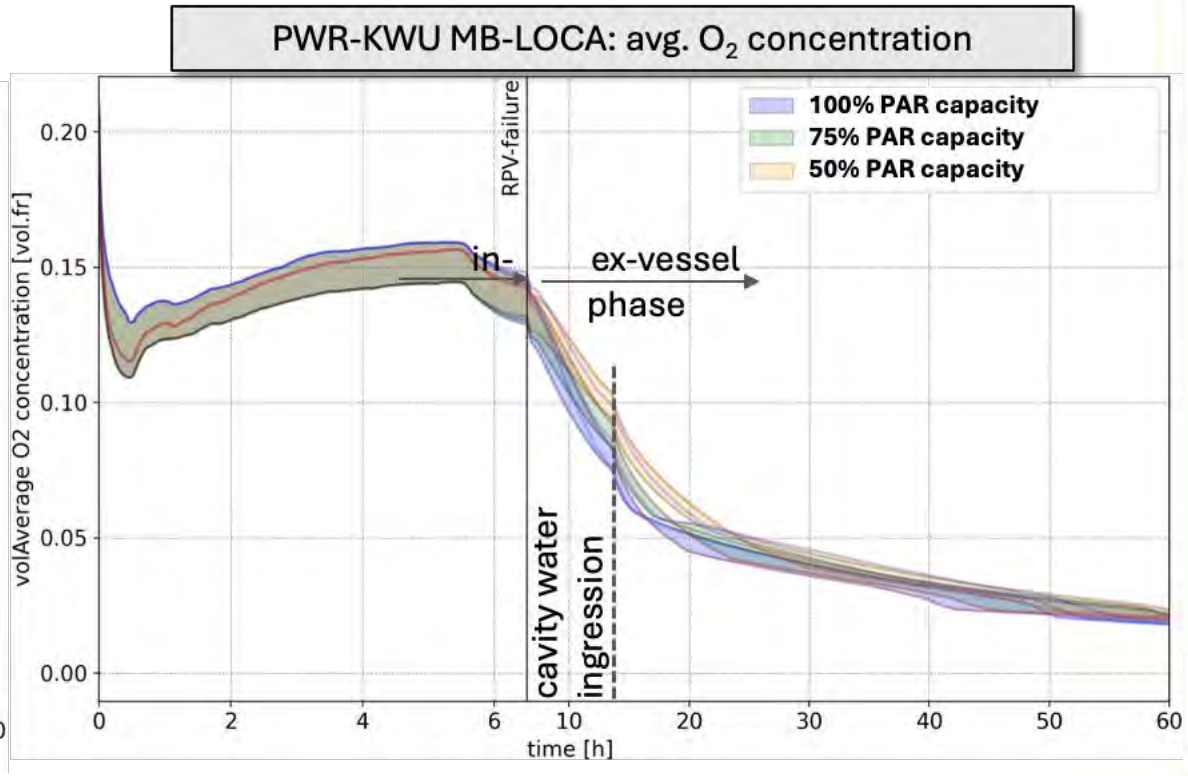

- Reduced PAR system capacity leads to higher peak H_2 concentrations.
- Differences become more apparent in ex-vessel phase but also limited by O_2 starvation

REF: Kelm, S., Braun, M., Bentaib, A., & Iskra, A. (2025). *D4.3 – Lessons learned during the full containment analysis of KWU, Western and VVER PWRs and quality assurance measures*. AMHYCO project.

WP4: local H2 accumulations are possible at the bottom part of the containment under certain conditions

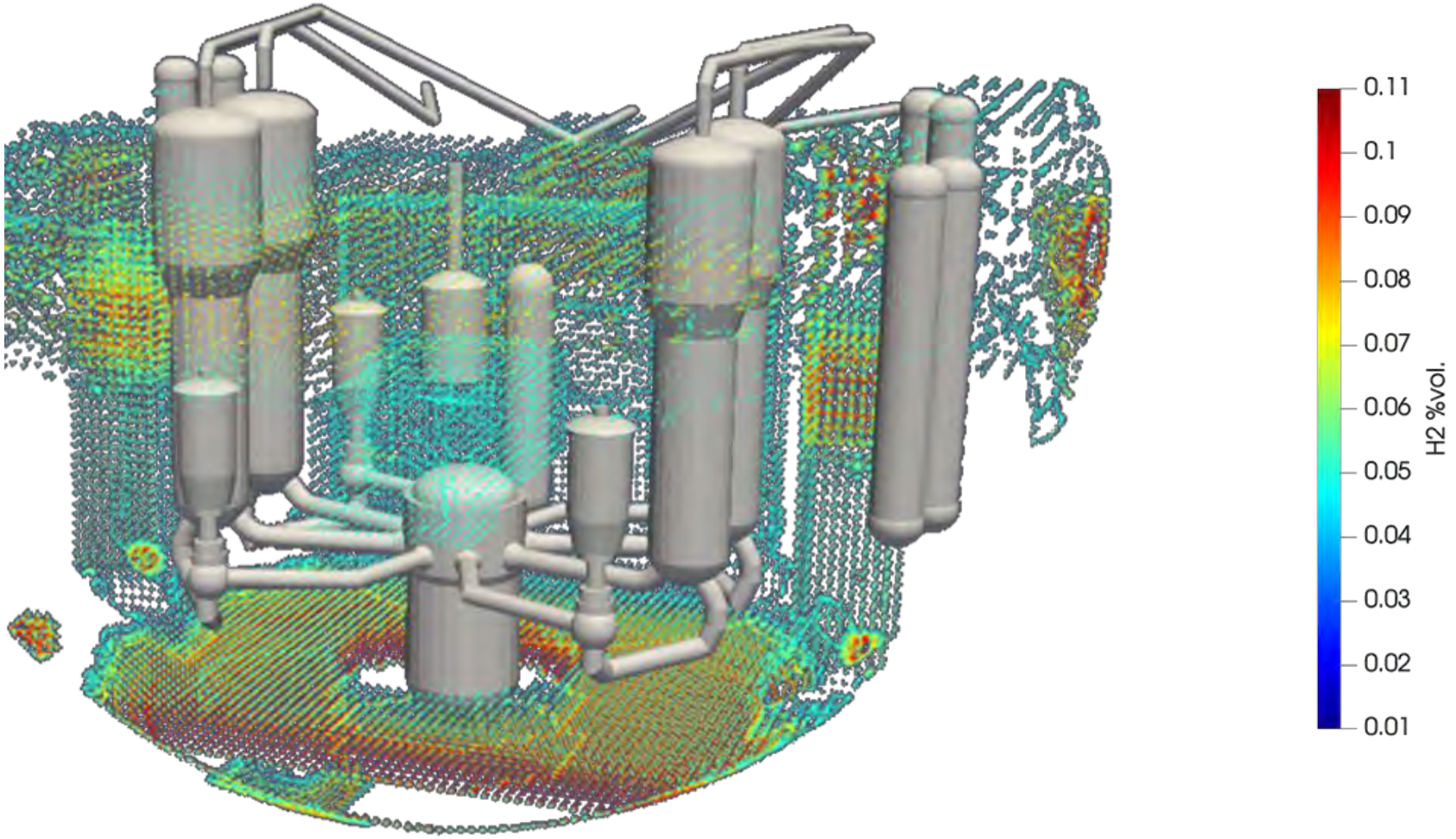

REF: Serra, L. et al. From the Plant Layouts to Optimized LP and 3D PWR-KWU Containment Models for Combustion Risk Assessment with GOTHIC8.3 (QA). *Nuclear Engineering and Design*. https://doi.org/10.1016/j.nucengdes.2025.114459

WP4-WP5: a proper spray/fan coolers operation criteria is needed for limiting the H2/CO combustion risk

- recovery of AC power enables operators to activate the sprays for pressure reduction

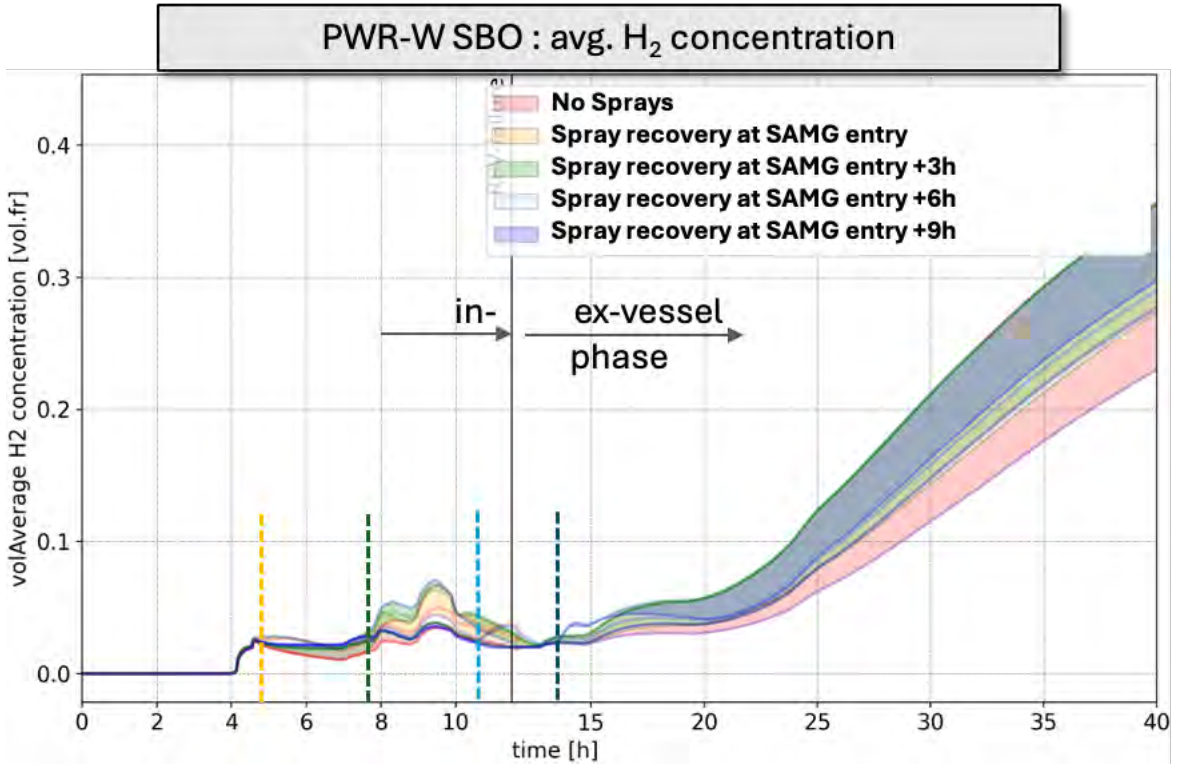

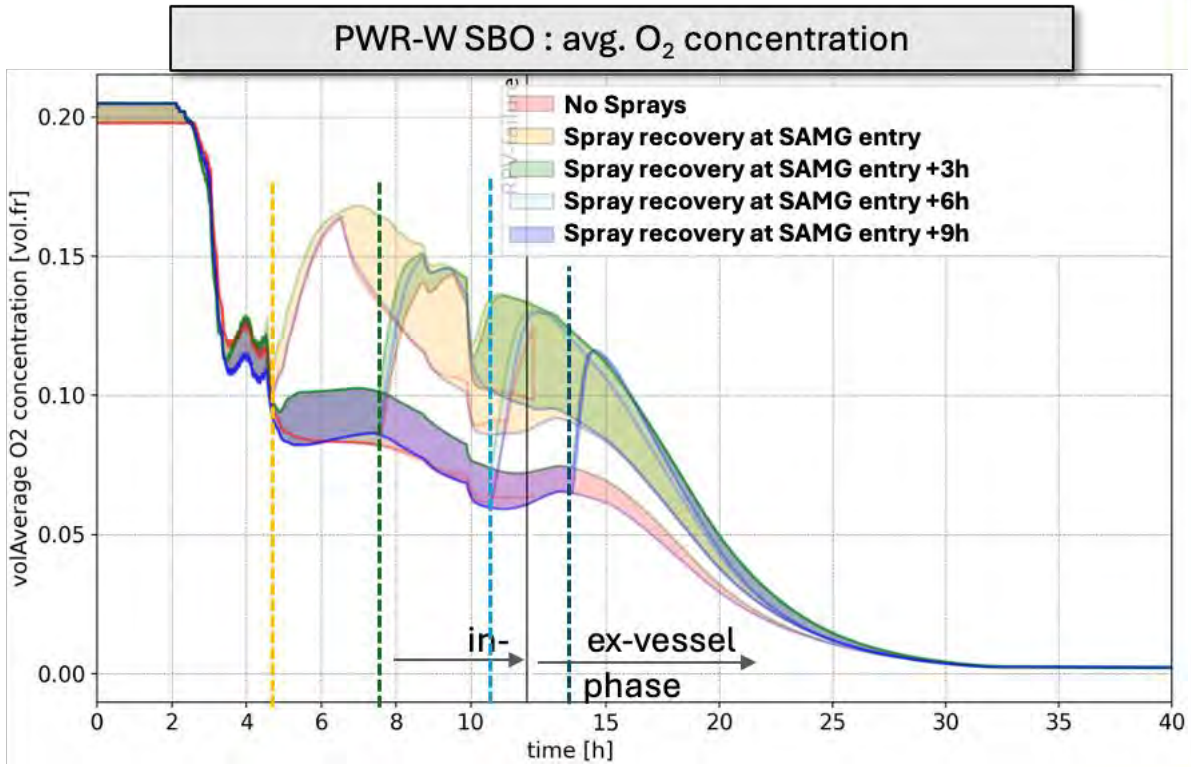

- Steam concentration mostly below inertization limit
- For late spray recovery, O_2 is consumed by the PARs (but still above O_2 limit).

*SAMG entry: depressurization of the primary system

REF: Braun, M et al. (2025). *D5.1 – Generic guidelines for SAMG development, minimizing the H2/CO combustion risk in a containment. Lessons learned of the AMHYCO project*. AMHYCO project

WP4-WP5: the equipment qualification limits should take into account 3D/CFD simulations

- EQ criterion: Evaluation of gas cloud hotter than T = 149°C, e.g. PWR-W SBO:

Dome temperature

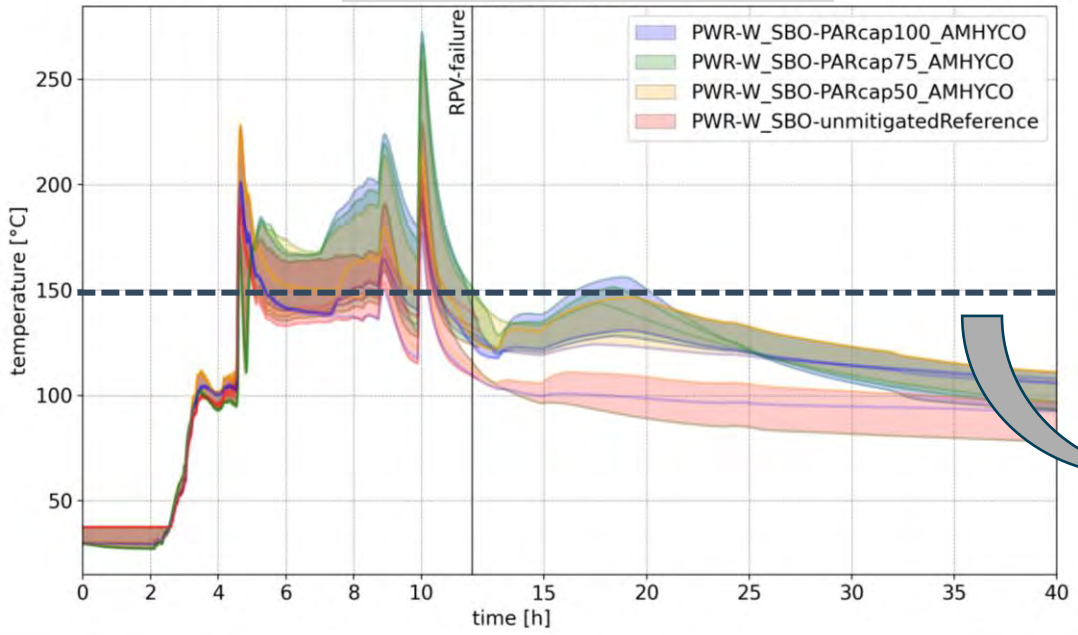

´hot cloud´

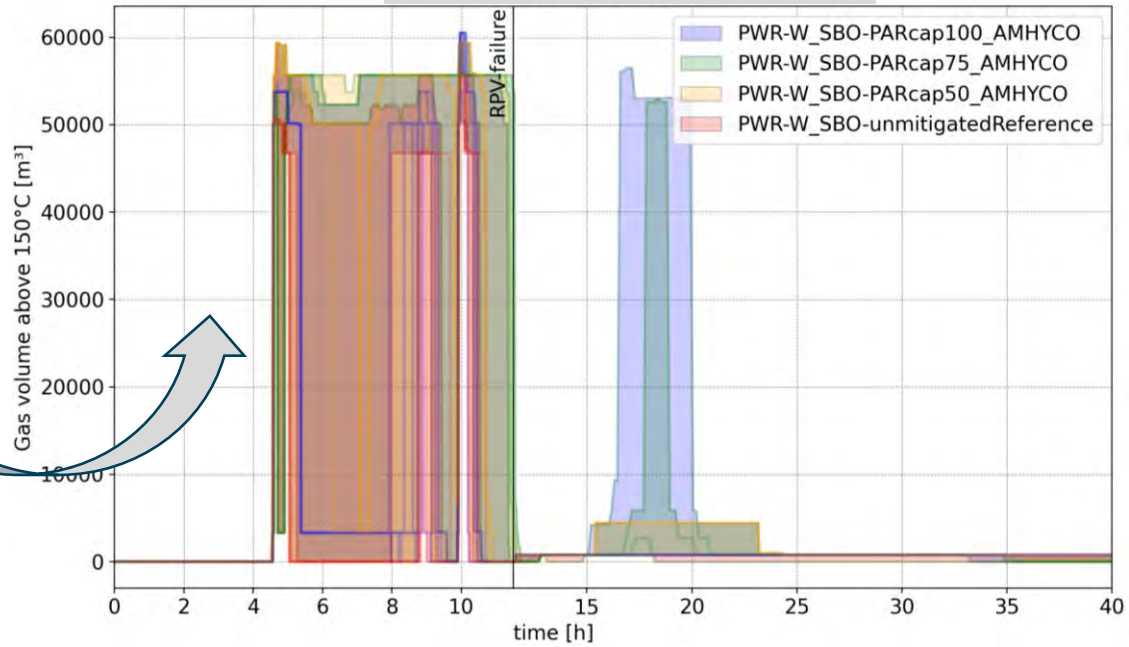

- Without containment cooling means, T_{gas} can exceed T_{lim}.in the late in-vessel and ex-vessel phases. PARs promote ‚overheating'!
- Early failures in PWR-W SBO, late failures (+50h for PWR-KWU MBLOCA and TLAP)

REF: Braun, M et al. (2025). *D5.1 – Generic guidelines for SAMG development, minimizing the H2/CO combustion risk in a containment. Lessons learned of the AMHYCO project*. AMHYCO project

WP4-WP5: containment instrument readings could bring a not totally clear idea of the global combustion risk

- Complementary 3D / CFD analysis were performed to assess heterogenities and evaluate the representativeness of available containment instrumentation
- E.g. GOTHIC analysis of PWR-KWU TLAP

O2 and CO measurements are needed!!!

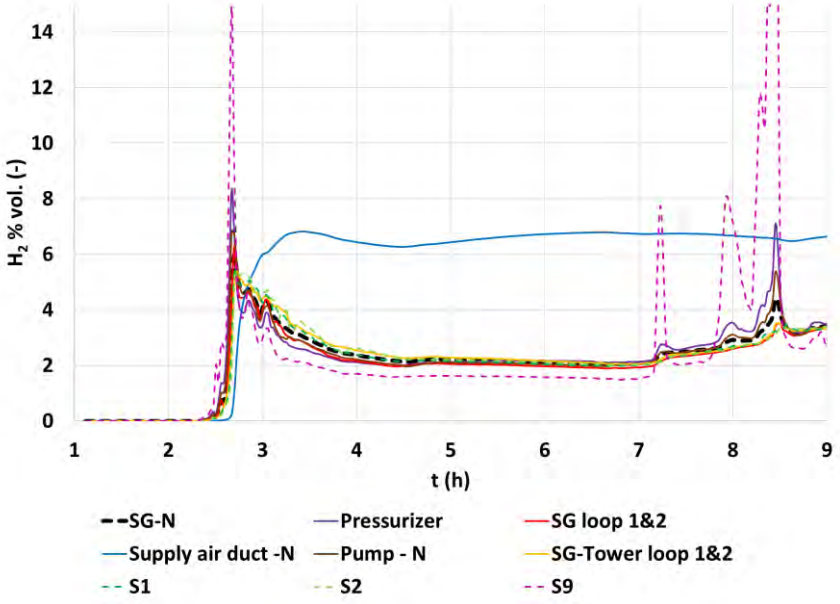

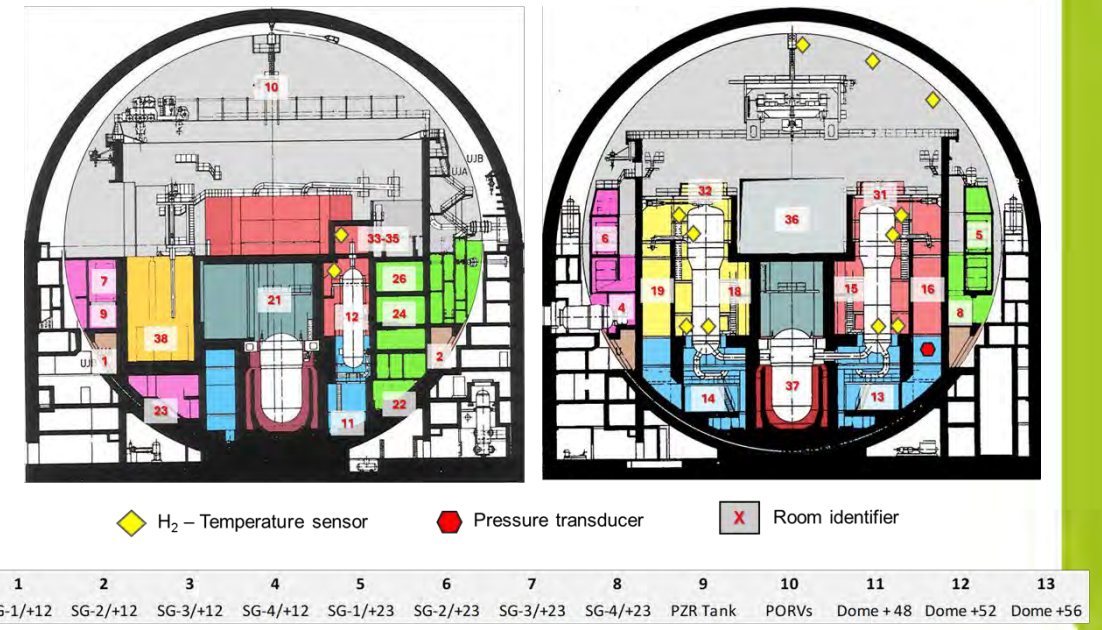

- local ‚hot spots' and temporal H_2 peaks observed near release locations and dead-ends which can cause high and fluctuating sensor readings or not be visible at all

REF: Braun, M. et al. (2025). *D5.1 – Generic guidelines for SAMG development, minimizing the H2/CO combustion risk in a containment. Lessons learned of the AMHYCO project*. AMHYCO project

ck | #189859913

WP3-WP5: AMHYCO correlation is born

$$\dot{m}_{H_2} = min\left[\nu_{H_2}, 2.0 \cdot \nu_{O_2}, 8.0\right] \cdot (k_1 \cdot p + k_2) \cdot tanh\left(\nu_{H_2} - \nu_{min}\right) \cdot c_1$$

$$c_1 = \begin{cases} 1.0 & if\ \nu_{H_2} < \nu_{O_2} \\ 0.6 & if\ \nu_{H_2} \geq \nu_{O_2} \\ 0.0 & if\ \nu_{H_2} < 2.0 \\ & or\ \nu_{O_2} < 0.25 \end{cases}$$

$$\dot{m}_{H_2} = (k_1 \cdot p + k_2) \cdot tanh\left(\nu_{H_2} - \nu_{min}\right) \cdot c_1$$

$$c_1 = \begin{cases} 1.00\ \nu_{H_2} & if\ \nu_{H_2} < \mathbf{0.84}\ \nu_{O_2} \\ \mathbf{0.84}\ \nu_{O_2} & if\ \nu_{H_2} \geq \mathbf{0.84}\ \nu_{O_2} \\ 0.0 & if\ \nu_{H_2} < 2.0 \\ & or\ \nu_{O_2} < 0.25 \end{cases}$$

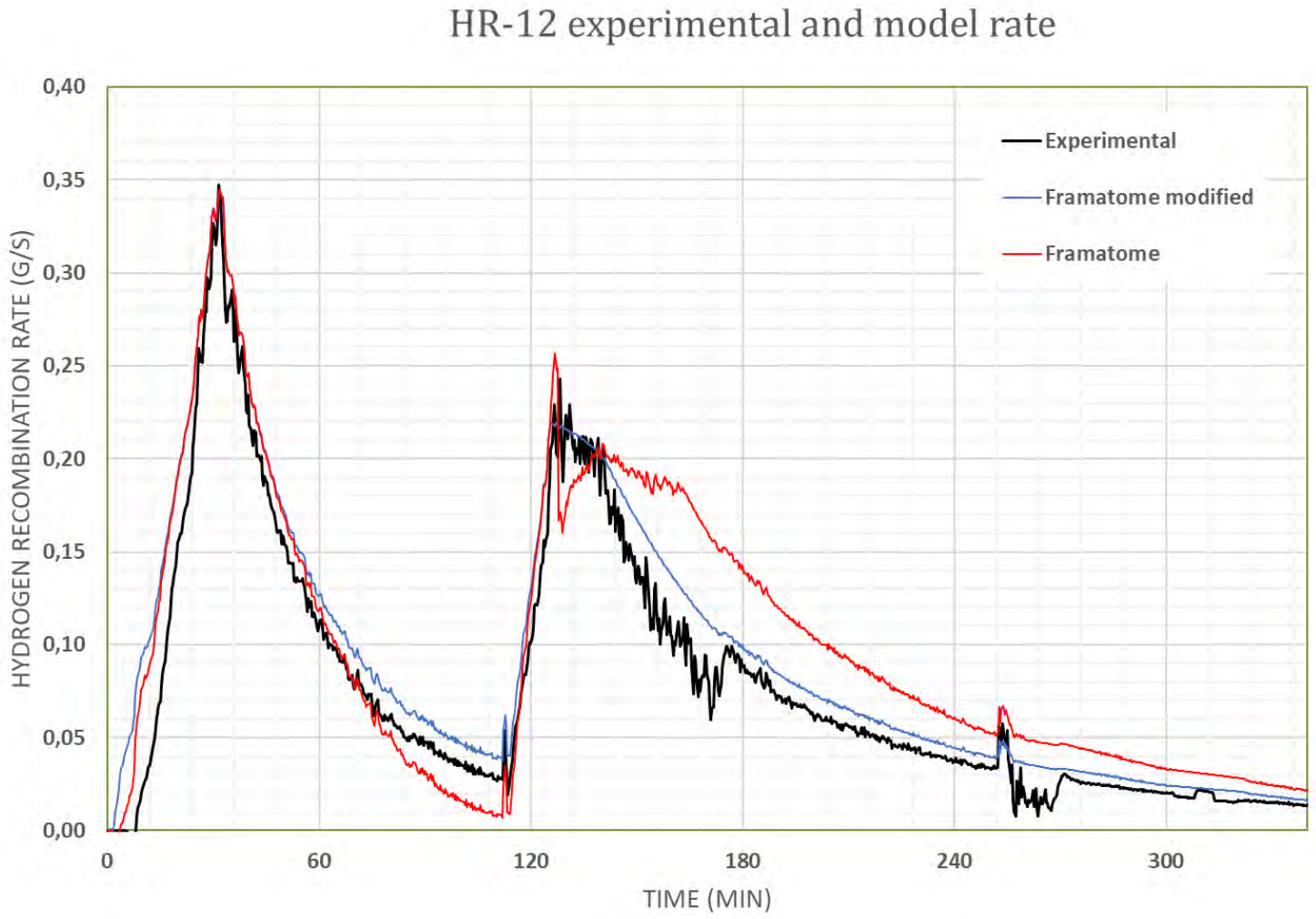

REF: Braun, M. and Reinecke, E.-A. (2025). AMHYCO engineering correlation to describe the conversion of flammable gases in Framatome passive autocatalytic recombiners.. *Nuclear Engineering and Design*. Volume 442, October 2025, 114206. https://doi.org/10.1016/j.nucengdes.2025.114206

WP6: communicate, communicate and communicate!

Conference papers published or in a pipeline: >30

Conferences: NURETH19, ENYGF2021, ICHS2021, FISA, ERMSAR2022, KERNETCHNIK2022, CSARP, NURETH23, ENYGF2023, SNE2021, SNE2022, SNE2023, ERMSAR2024, SNE2024, NUTHOS2024, SNE2025, NURETH25, ERMSAR2026…

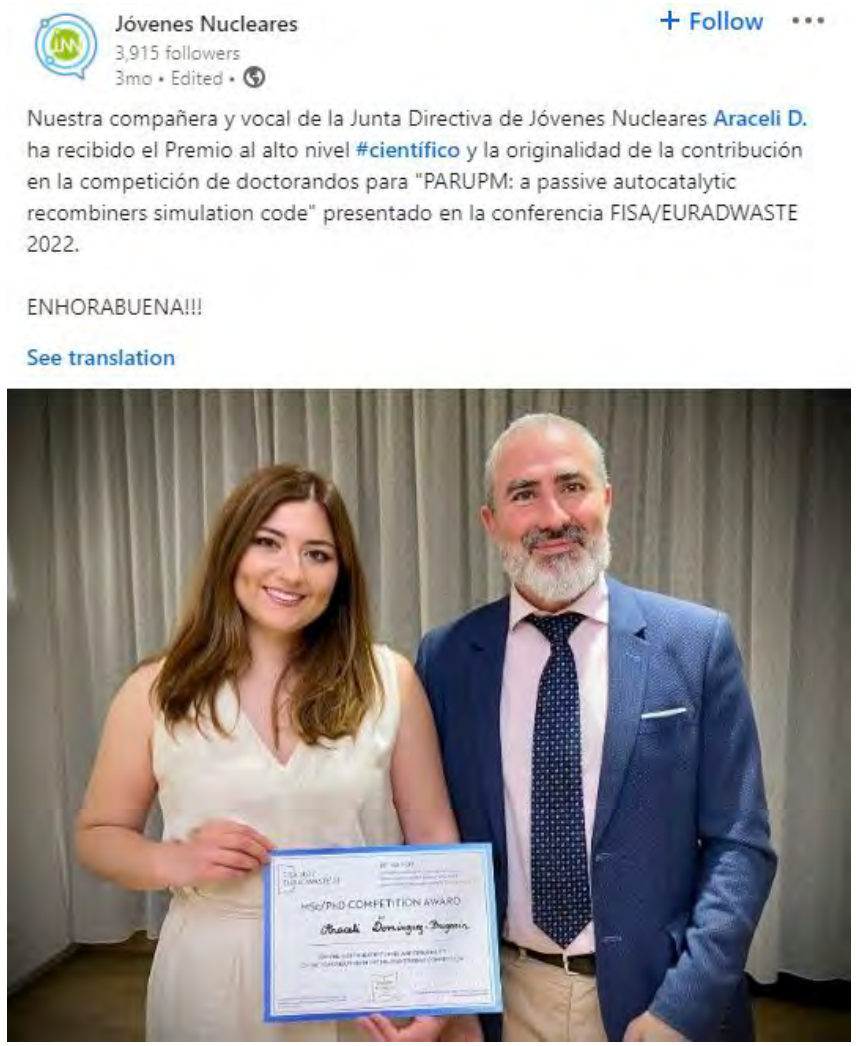

European prize for the best PhD presentation (FISA2022)

WP6: building a strong community makes the difference

UPM PhD students at FZJ

RUB PhD student at UPM

PhD mobility actions

WP6: building a strong community makes the difference

AMHYCO workshop in Madrid, February 2025

AMHYCO deliverables & publications

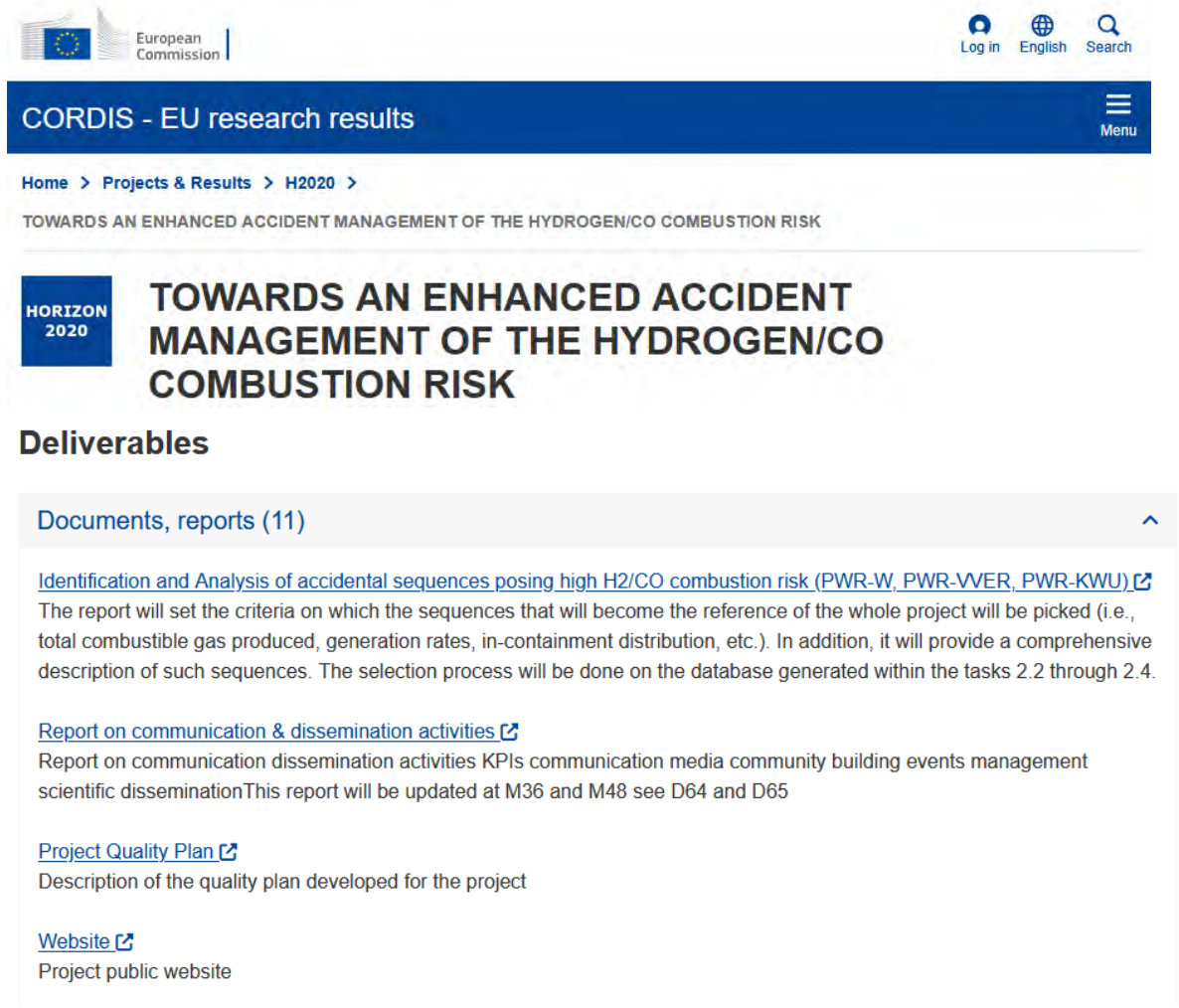

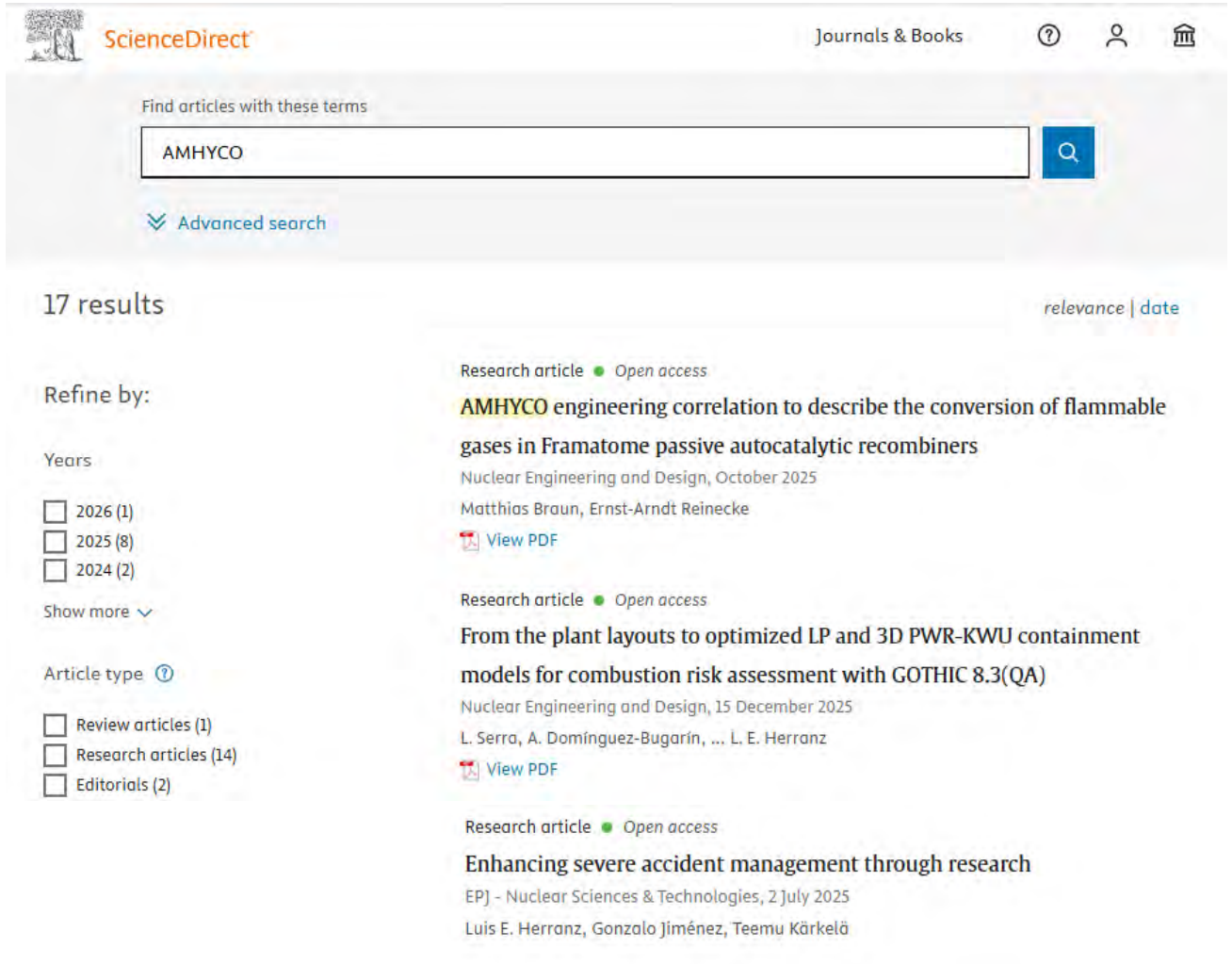

https://cordis.europa.eu/project/id/945057/results

https://www.sciencedirect.com/search?qs=AMHYCO

Also in the Project portal: https://amhyco.eu/resources/

Thank you
Connect with us for more information:

gonzalo.jimenez@upm.es

http://amhyco.eu

@amhyco

CFD ANALYSIS OF THE CONTAINMENT BEHAVIOR DURING A TLAP SEQUENCE IN A GENERIC KWU PWR WITH CONTAINMENTFOAM

Stephan Kelm, Carlos Vázquez-Rodríguez, Michael Klauck

Forschungszentrum Jülich GmbH

Wilhelm-Johnen Straße, 52425 Jülich, Germany

s.kelm@fz-juelich.de, c.vazquez-rodriguez@fz-juelich.de, m.klauck@fz-juelich.de

ABSTRACT

The European AMHYCO project (Euratom 20192020, GA No 945057) aimed at enhancing the understanding of the H_2/CO combustion risk within the containment of a nuclear power plant during a severe accident. The goals of the project were to incorporate the gained knowledge into severe accident mitigation guidelines (SAMGs) and recommend long-term operation upgrades. The analytical work comprised a consecutive analysis chain, consisting of three levels with increasing detail (system codes, 3D GOTHIC, and CFD) to assess containment pressurization, PAR efficiency, and options of individual mitigation measures regarding H_2/CO combustion risk and equipment and instrumentation survivability for three generic European PWR containment designs, namely KWU, Western (Westinghouse and French designs) and VVER.

The paper focuses on the *containmentFOAM* modeling of a KWU-PWR containment. Along with a brief introduction of the *containmentFOAM* CFD package built on OpenFOAM-11, the modeling assumptions and simplifications of the full-scale model are discussed. On this basis, the gas distribution in the containment is simulated for a Total Loss of AC Power (TLAP) sequence. The results are discussed in comparison with the system code COCOSYS also employed within AMHYCO. Due to its ability to consider momentum transfer, the CFD model reveals a different mixing mechanism close to the break. Because of the high elevation of the release location at the pressurizer relief tank, this leads to a less complete mixing in the equipment rooms and gas transport within the containment dome. While the global pressurization is not significantly affected by heterogeneous steam distribution, the evolution of a locally flammable cloud reveals a different mechanism in both approaches and the relevance of local conditions and 3D flow in the global quantification of combustion risk. To conclude, the paper summarizes the lessons learned from the full-scale CFD application and needs for further model development.

KEYWORDS

containment mixing, combustion risk, CFD, containmentFOAM

1. INTRODUCTION

The containment structure constitutes the last barrier against the release of fission products during severe nuclear accidents. Its integrity can be challenged by continuous pressurization from steam and non-condensable gas releases or by dynamic events such as combustion. Three-dimensional characteristics of the containment can influence the transport and mixing processes, and thus pressurization, combustion risk, and overall structural response to dynamic loads. Understanding these interactions is essential for accurately assessing the containment behavior under severe accident conditions.

To address these challenges, the open-source Computational Fluid Dynamics (CFD) package *containmentFOAM* has been developed since 2017 to provide highly resolved 3D simulations of the containment phenomena in large dry PWR containments [1], [2], [3]. Currently, it is extended to study containment phenomena and the effectiveness of passive safety features, e.g., for containment cooling or pressure limitation in Light-Water cooled Small Modular Reactors (LW-SMR) [4], [5].

Aligned with the conceived application of *containmentFOAM*, the European AMHYCO project (Euratom 2019–2020, GA No. 945057) [6] provided a framework dedicated to improving the understanding of hydrogen and carbon monoxide combustion risks in nuclear power plant containments during severe accidents, with the objective of supporting severe accident management guidelines and long-term operation upgrades. The project employed a hierarchical analysis approach of increasing fidelity —system codes, 3D GOTHIC, and CFD— to evaluate containment pressurization, mitigation measure effectiveness, and equipment survivability for three representative European PWR containment designs [7], [8].

Building on the AMHYCO analysis framework, this paper focuses on CFD simulations of a KWU PWR containment using *containmentFOAM*. After outlining the modeling assumptions and simplifications of the full-scale containment model, the study analyzes the distribution of condensable and non-condensable gases and investigates containment atmosphere mixing during a total loss of AC power (TLAP) with delayed depressurization, a special kind of station blackout (SBO) sequence. Results are compared with predictions obtained with the system code COCOSYS [9] to discuss plausibility of the overall transient progression but also additional insights and limitations of the CFD approach. Thus, this study complements the recent analysis done by Serra et al. [10] using the 3D 'coarse grid' CFD tool GOTHIC^{TM}. The paper concludes by summarizing key insights from the full-scale CFD application and identifying needs for further model development.

2. FULL CONTAINMENT MODELING

2.1. Accident Sequence

In this study, a total loss of AC power (TLAP) is considered as initiating event, leading to reactor scram (cf. Table 1). After the SCRAM, the decay heat is first removed by a vaporization of the secondary side steam generator (SG) inventory. Once the SG dried out after approximately one hour, pressure in the reactor cooling system (RCS) rises and the pressurizer safety valve starts cycling leading to a continuous loss of coolant to the pressurizer release tank (PRT) and, after opening of its burst discs, to the containment (steam release indicated by blue curve in Figure 1).

Time [h]	Event
0	TLAP and SCRAM
<1	SG dry-out
>1	Pressurizer safety valve cycling
1.8	Core uncovery
2.1	COT > 650°C (SAMG entry)
2.5	Onset of H_2 production
2.7	RCS depressurization (delayed)
>2.7	Hydro accumulator injection
9.1	RPV failure

Table 1: Event chronology

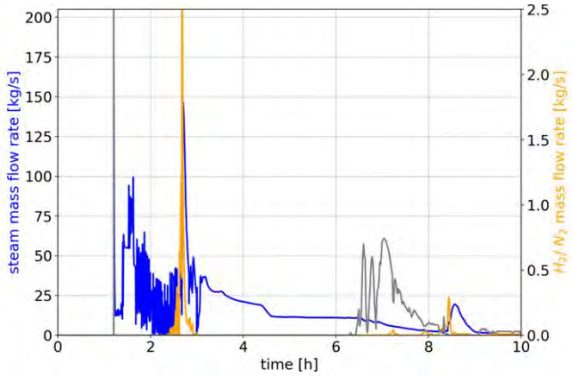

Figure 1: Mass release rates during the in-vessel phase

Later on, the continuous heat release and loss of coolant lead to core uncovery. With reaching the criterion "core outlet temperature (COT) > 650 °C", the operators switch from preventive (here assumed ineffective) accident management into mitigative accident management. However, it is assumed that they cannot proceed directly with the depressurization of the RCS as defined by the EOPs/SAMGs. Thus, when the core oxidation starts, the released H_2 initially accumulates within the RCS. After around 2.7 h, operators finally manage to initiate RCS depressurization, leading to a strong release of H_2 to the containment (orange curve in Figure 1). Along with the depressurization, the accumulators start injecting water for about 3 hours before also their N_2 inventory is injected (gray curve in Figure 1). After about nine hours, the RPV fails. However, the subsequent ex-vessel phase is not considered in this study. Energy and mass source terms are obtained from a MELCOR analysis, kindly provided by Framatome Germany within AMHYCO [11].

Before RPV failure, steam, and hydrogen are released from the RCS only via the rupture disk of the PRT. In KWU-type of containments, this tank is installed at a relatively high elevation, directly below the operating floor, see Figure 2. Considering the relatively high release location (~ +25m) in the containment and the comparably low injection momentum (compared to a MB/LB LOCA), a limited mixing in the containment and atmospheric stratification is expected and thus motivates a closer look using the CFD approach.

2.1. Geometric Model

The containment of a German KWU-type PWR consists of a spherical, free-standing steel containment with an inner diameter of ~56 m and a design pressure of 6.3 bar. Within the steel shell is a complex internal concrete structure, see Figure 2. The containment is split into two main compartments, the inner 'equipment rooms', housing the components of the RCS, and the outer rooms (e.g., service floor, dome, pipeline duct) which are accessible by plant personnel during power operation. These two compartments are primarily connected via burst foils on top of the steam generator towers, which open once a differential pressure of 30 mbar is reached. Furthermore, there are multiple doors connecting both compartments, which, however, have considerably higher opening pressure and will only be blown out during large break loss of coolant (LOCA) sequences with fast containment pressurization. In the TLAP sequence investigated in this paper, the pressurization is comparably slow, and it is assumed that only a part of the burst foils (here those on top of the northern steam generator tower 'SG-N') open. This leads to a reduced mixing in the containment compared to the sequence studied with in the AMHYCO project.

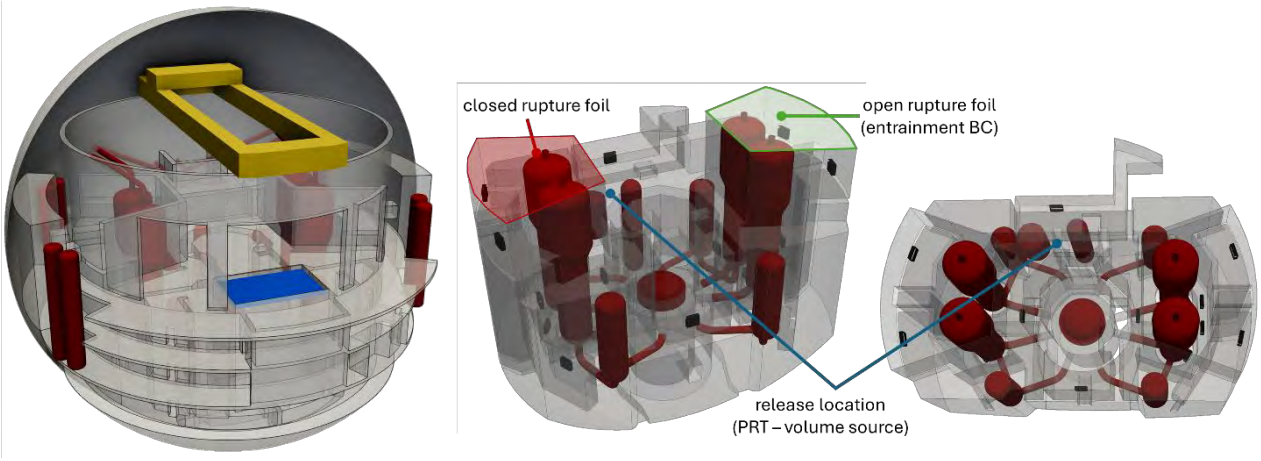

Figure 2: Full containment geometry (left), separated equipment rooms (middle/right). Black boxes represent PARs (adapted from [12])

Within AMHYCO, detailed Computational Aided Design (CAD) models have been prepared by Universidad Politécnica de Madrid (UPM) and used as a basis to derive comparable nodalisation schemes and 3D models. Furthermore, a generic system of 40 passive auto-catalytic recombiners (PAR) has been implemented [10], [12]. This 3D geometry was slightly adapted to ease meshing (e.g., removing small geometric features, thickening thin structures), while its overall heat capacity (mass * spec. heat capacity) and surface area were maintained. The nodalisation scheme used for COCOSYS corresponds to the one defined within AMHYCO and is illustrated in Figure 3 (right). It should be stressed that the nodalisation scheme was intentionally kept simple within AMHYCO, involving a limited number of control volumes (CVs), to facilitate a better comparison among the results.

2.3. Mesh

The mesh was created with the commercial software cfMesh+, which relies on the cut-cell method with cubic base cells. It uses a base mesh spacing of 40 cm and is refined towards geometric features using up to two refinement levels of 20 and 10 cm edge length. Wall shear layers near structures were resolved by five layers of prismatic cells. This proved to be an optimal mesh resolution to resolve the relevant geometric characteristics and flow features and maintain a sufficient mesh quality. A formal mesh sensitivity analysis was, however, not performed yet. The total mesh consists of approximately 10 million cells in the gas space and is illustrated in Figure 3.

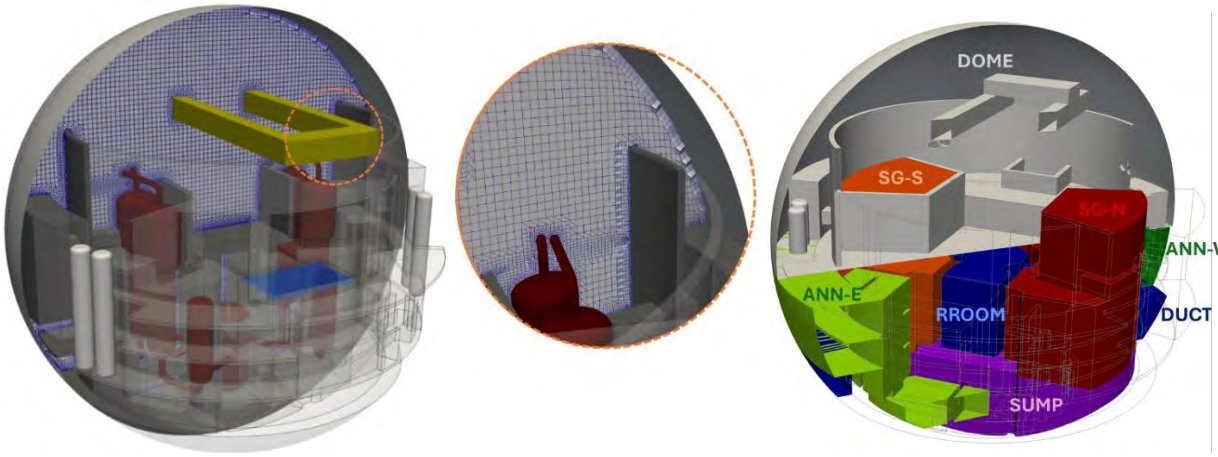

Figure 3: Discretization of the containment volume in *containmentFOAM* (left), generic nodalisation of the containment employed with COCOSYS within AMHYCO (right)

The concrete structures as well as the steel shell and polar crane are also resolved by the mesh, while other steel structures are either represented by a boundary condition (e.g., RCS components by a Robin-type boundary) or assumed to be in equilibrium with the gas phase and ignored (smaller structures such as walking grids).

2.4. Physical and Numerical Modeling

The 'baseline model set' for large dry PWR containment analysis, which was intensively validated before (e.g., [1], [2], [3], [13]), was employed. Its main characteristics are summarized in Table 2. Basically, it is based on a single-phase simplification of the containment atmosphere, where wall condensation is modeled using a diffusion layer approach [14] and bulk condensation a homogeneous equilibrium model [15]. Turbulence production and dissipation due to buoyancy forces is considered [16] and thermal radiation is simply modeled using the P_1 model, assuming the containment atmosphere to be optically thick. The rupture foils on top of the SG towers are represented by a conditional mesh connection which opens based on the

pressure difference between both sides. PARs are represented by the detailed mechanistic model *REKO-DIREKT*, developed at FZJ [17]. It was wrapped into a Functional Mockup Unit and coupled with *containmentFOAM* through its in-built Functional Mockup Interface (FMI) 2.0 interface using a domain decomposition approach.

The steam, non-condensable gases, and heat release from the PRT are efficiently treated as a volumetric source ($V \sim 1\ m^3$) without directional momentum. This is conservative since it minimizes momentum-driven mixing in the containment. The release rate, composition, and temperature are directly specified from the injection tables provided by a MELCOR simulation. All structures are represented by a conjugate heat transfer (CHT) approach and allow for condensation heat transfer except for the RCS components, which are defined as 'hot' boundaries at elevated temperature obtained from COCOSYS.

Table 2: Physical models

Physics	Model
governing equations	unsteady Reynolds-averaged Navier-Stokes equations, total energy equation, transport equation for species mass fraction
turbulent transport	k-ω based Shear Stress Transport (SST) model, including production and dissipation terms for buoyancy turbulence based on SGDH; Turbulent heat and mass transport: SGDH, Pr_t=Sc_t=0.85
multi-species transport	temperature dependent transport properties, constant specific heat capacity, ideal mixture, effective binary diffusion model, pressure and temperature dependent diffusion coefficients (Fuller model)
wall treatment and condensation	wall condensation: single phase 'diffusion-layer' approach, continuous wall functions bulk condensation: single phase homogeneous equilibrium approach, passive scalar drift-flux transport equation for fog
thermal radiation	P_1 model, gray participating mixture properties (κ_{H2O}=10 $bar^{-1}m^{-1}$, non-condensables transparent), ε_{wall} = 0.6
system models	PARs: coupling with mechanistic model REKODIREKT

The numerical schemes and settings are summarized in Table 3.

Table 3: Numerical schemes and settings

Aspect	Setting
Time step	Adaptive: 10^{-5}s ... 10^{-1}s (mean $\Delta t \sim 5e^{-3}$s)
PIMPLE loop	2 inner pressure correction loops, 2 non-orthogonality corrections, max. 10 outer loops
Convergence criteria	All equations PIMPLE residuals < 10^{-4}
Schemes	Gradients: least squares incl. gradient limiters Divergence: 2nd order with limiters Laplacian: 2nd order with limiter for non-orthogonal corrections
Time step	Adaptive: 10^{-5}s ... 10^{-1}s (mean $\Delta t \sim 5e^{-3}$s), CFL< 10
Parallelization	1024 partitions, scotch partitioner

The spatial discretization is mostly of 2nd order, while local blending towards 1st order accuracy was required for stability or boundedness. Discretization in time was 2nd order using a Crank-Nicholson scheme with 10% off-centering for stability. The time step was automatically adapted to maintain a max. CFL number below 10 and max. 5 outer PIMPLE iterations. This strategy allowed for a stable simulation of around 100 to 1500 s/day, depending on the release rate, using 1024 cores of FZJ's high-performance computing facility JURECA.

3. RESULTS

At the time of writing the paper, a simulation of the first 3 hours (11,000 s) of the accident sequence was conducted. To investigate the efficiency of the PAR system, two simulations, one with and one without PARs, were performed. Considering the mass and energy release (cf. Figure 1), the first H_2 release occurs relatively late at ~2.6 h (9,300 s). Consequently, the following discussion focuses on the steam release and pressurization as well as the distribution of H_2 and formation of a flammable gas cloud.

3.1. Steam Distribution and Pressurization

To compare *containmentFOAM* (3D) results with *COCOSYS* (1D), a volume weighted average is calculated per CV. A first impression of the results is given in Figure 4 for the DOME, which is the largest CV in the containment. Generally, the mean values obtained with *COCOSYS* and *containmentFOAM* reveal comparable trends. The wide blue bands representing min/max *containmentFOAM* values in the DOME CV showing the high local variability indicate that the gas / heat in the dome is not well mixed. Considering the two completely different code approaches to the problem, *containmentFOAM* (3D) and *COCOSYS* show a surprisingly good agreement of (averaged) results. However, the local differences in heat transfer and condensation contribute to the differences that can be observed for the mean pressure evolution.

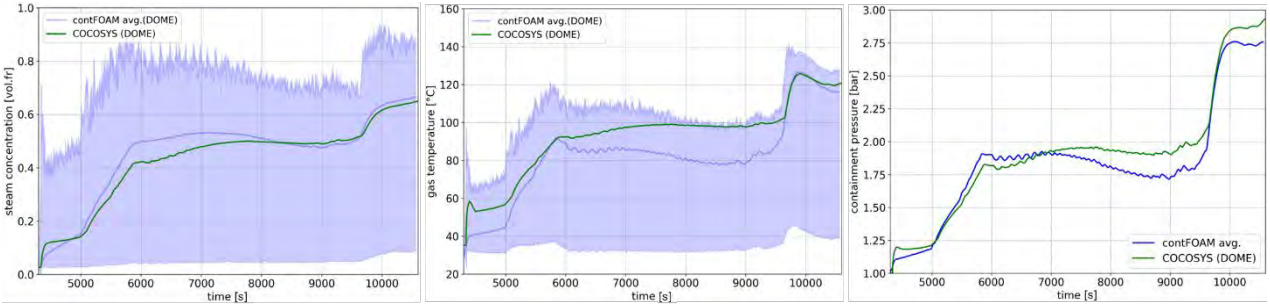

Figure 4: Comparison of steam concentration (left), gas temperature (middle) and pressure (right) in the DOME compartment

While the DOME compartment is involved in the main gas convective loop, there is less exchange with the SUMP region in the bottom of the equipment rooms during this transient in the *containmentFOAM* analysis compared to the LP model. Figure 5 illustrates this difference between both simulations. While in *COCOSYS* the predicted mean gas temperature and the steam concentration are comparable to the ones in the DOME, *containmentFOAM* predicts a considerably reduced transport of hot steam to the lower containment.

This is related to the high release elevation, the missing downward momentum, and the strong buoyancy of the released hot gases, which immediately ascend to the dome through the open rupture foils after being released. Thus, in the *containmentFOAM* analysis, the release of gases inside the equipment rooms primarily leads to a displacement of the initial atmosphere above the release location and only limited mixing below. In contrast, the coarse 1D-LP nodalisation results in a more pronounced downwards transport of steam due to the averaging along the height of the CVs ('numerical diffusion'). This is a known limitation of lumped-parameter codes.

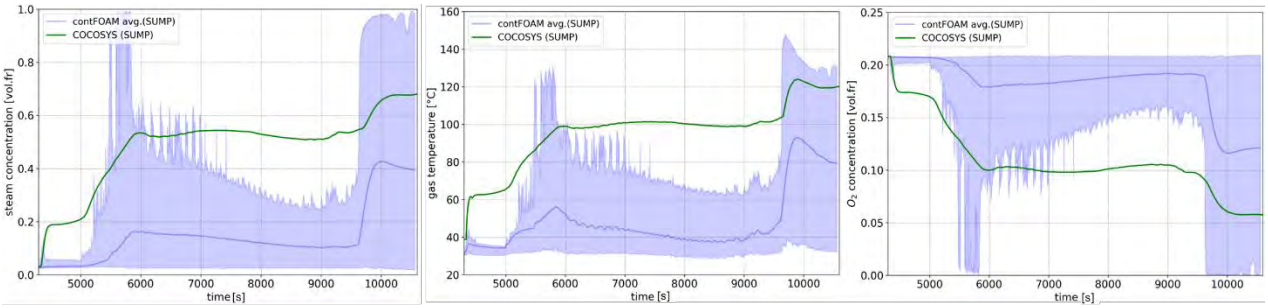

Figure 5: Comparison of steam concentration (left), gas temperature (middle) and oxygen concentration (right) in the SUMP compartment

Figure 6 illustrates the 3D distribution of steam in the containment and resulting condensation rates on the containment structures.

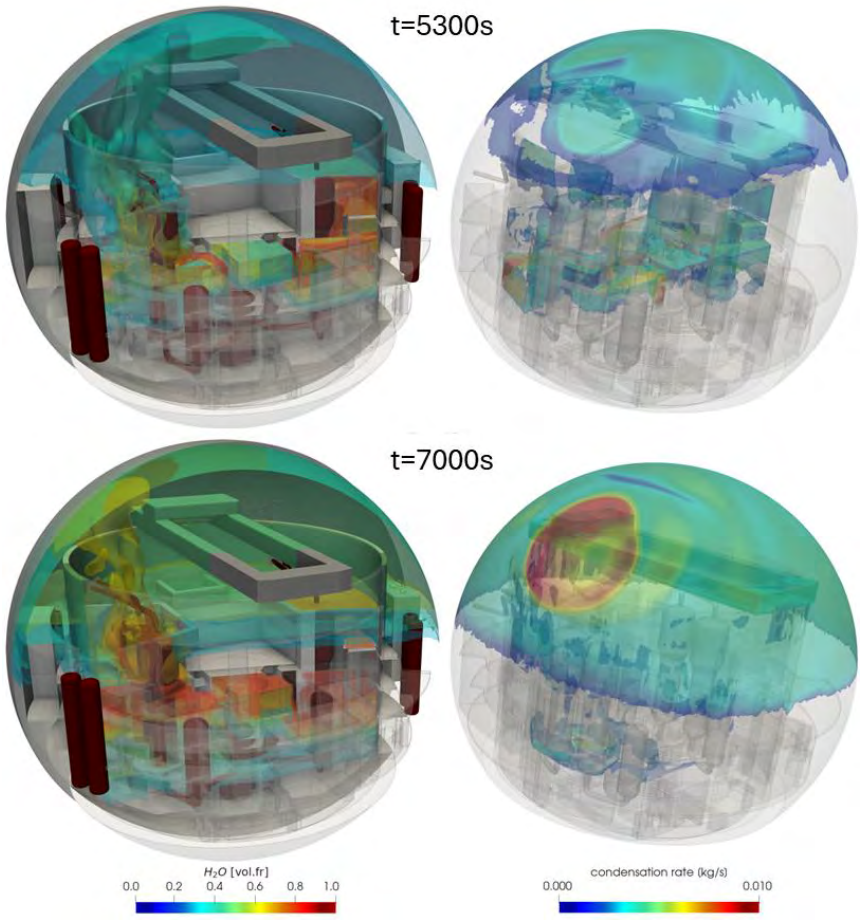

Figure 6: Steam distribution (left) and local condensation rates on structures (right)

Within the equipment rooms, a steam stratification is formed above the elevation of the PRT. Outside, in the DOME region, the stratification extends down to the upper opening of the steam generator towers. Only in these regions, significant steam condensation (>0.01 kg/m²s) occurs. Comparing the two time frames, it becomes obvious that the major condensation, which limits the pressure in the early accident phase, occurs on the containment shell, while the concrete surfaces inside the equipment rooms are heated up quickly and allow only for low condensation rates in the longer term, limited by the low heat conductivity of concrete.

3.2. H_2 Distribution and Formation of a Flammable Cloud

The observations made for steam can be extended to H_2. Primarily, in the break compartment and the DOME above, the CV averaged distribution simulated by *containmentFOAM* compares quite well with *COCOSYS* results, while the min/max band already indicates heterogeneous distribution inside the CVs. Into the region below the release elevation (SUMP) or into dead-end compartments (e.g. ANN-E) only limited transport is predicted by *containmentFOAM* and the volumetric average values are below those, obtained with the LP simulation, as illustrated in Figure 7.

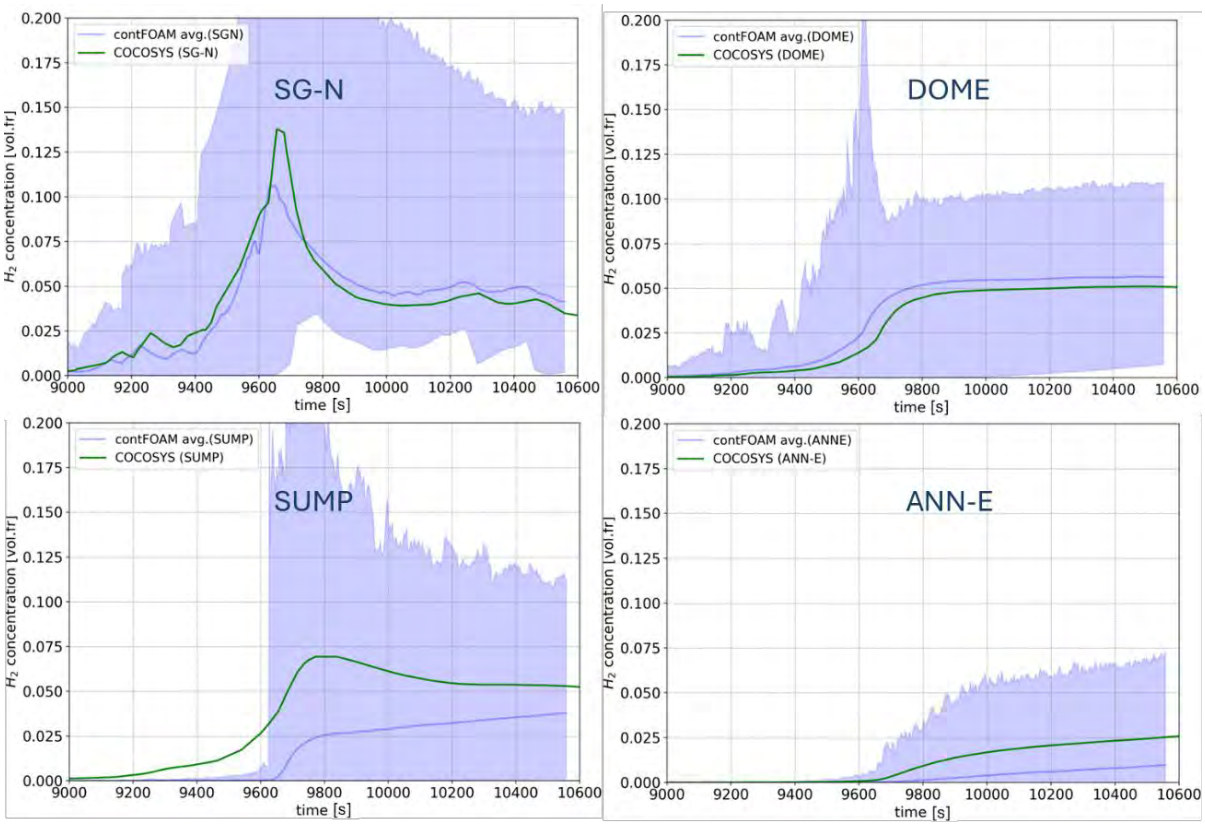

Figure 7: Comparison of H_2 distribution between different compartments: Main convective loop (top), dead-ends (bottom)

The broad blue bands indicate a heterogeneous distribution of gases within the CVs, which likely has an impact on the formation of flammable clouds. In the following, the flammable cloud was characterized using the extended flammability limits determined by CNRS within the AMHYCO project [18]. For the *containmentFOAM* analysis, the flammable cloud was both evaluated based on volumetric averages for the CVs, obtaining a LP-like quantification, as well as 'local' cell-by-cell values. The resulting evolution of the flammable volume and mass following the first H_2 release peak is compared in Figure 8. While the evolution of the flammable clouds is visibly different for the different approaches, one can stress a common point, i.e., flammability is limited to few CV's or regions. Besides, it is obvious that (i) the cell-wise and CV-wise integration of the flammable volumes does not reveal comparable trends. Furthermore, the CV-wise integration of the *containmentFOAM* results differs from *COCOSYS*. While *COCOSYS* predicts flammability in the SG-S and SUMP CV's, *containmentFOAM* reaches flammable conditions within SG-N and RROOM CVs. Looking at the cell-wise integration, the total flammable cloud(s) volume is much larger as it involves parts of the dome and sump regions, which are not globally flammable. It is also apparent that in the 'local' cell-wise integration, the flammable cloud exists for a longer duration than for the 'global' CV-wise consideration.

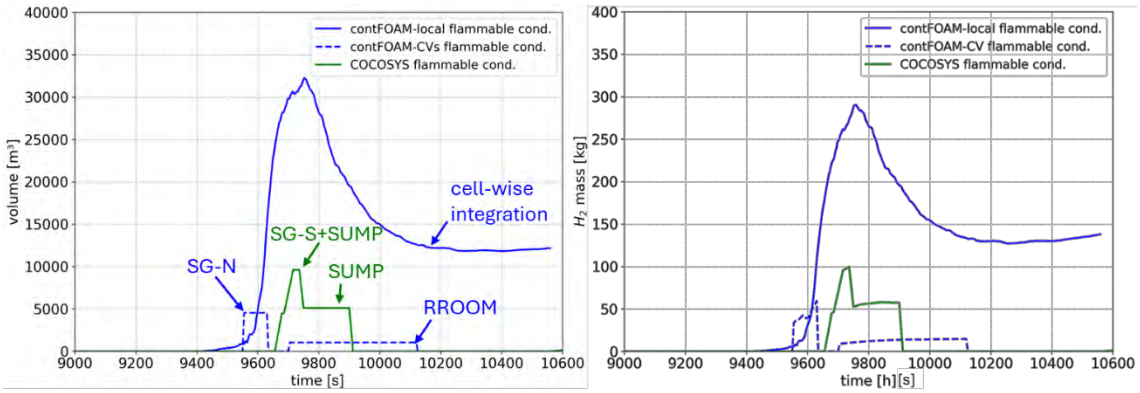

Figure 8: Comparison of flammable cloud volume (left) and H_2 mass (right)

Considering the flammable H_2 mass, considerable differences can be observed, which underlines the uncertainty associated with such a metric, evaluated by volumetric averaging for a large CV. This finding substantiates the observation made by Serra et al. [10]

The detailed build-up process of the flammable cloud is illustrated in Figure 9. Shortly after beginning of H_2 release (t = 9.600 s), the lower flammability limit (LFL) is not reached in the containment and limits the extent of the flammable cloud to a plume rising from the PRT into the dome. After a while (t = 9.900 s) the LFL is exceeded in the SG towers and DOME, but the continuous release of steam leads to a dilution of O_2 and forms an inert stratified cloud in the upper DOME.

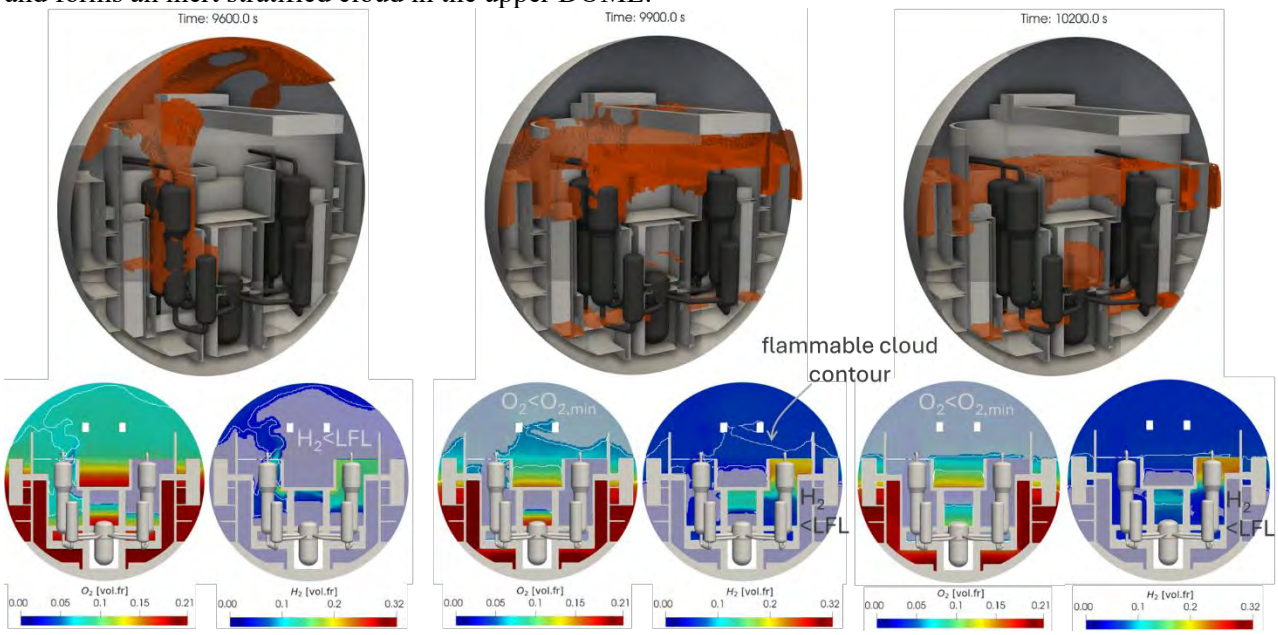

Figure 9: Visualization of flammable cloud built-up and evolution

Soon after (t=10200 s), the H_2 concentration is above the LFL in a large area of the containment, but sufficient O_2 is only available in the annular compartments and the SUMP. The resulting flammable clouds are formed in between the 'inert' O_2 lean cloud of hot injected gases and the H_2 lean initial gas mixture present in the stagnant zones. The small 2D slices at the lower half of Figure 9, coloring the areas of the containment where O_2 and H_2 are within the flammability bounds, clearly illustrate that flammable cloud (in orange) appears only where both gases are within the flammable bounds.

This situation can exist for a longer time (t > 10200 s), since the slow mass exchange between both volumes maintains flammable conditions. Looking at the same situation from the perspective of volumetric averages in large CVs, however, likely leads to 'averaging out' local flammable conditions from an 'all or nothing' viewpoint. An effect that could be potentially reduced by a refined nodalisation scheme. However, the 3D simulation also revealed considerably reduced transport of released gas to lower regions in the containment, which is difficult to reproduce using LP codes. This will affect the available O_2 concentration and thus the long-term flammability.

The implementation of a generic PAR system, consisting of 40 units, was performed in parallel to the discussed simulation and is still under investigation. It turned out that PARs, being slow-acting thermal devices, do not affect the initial peak of the flammable cloud but introduce additional local buoyancy-driven flows that enable enhanced mixing of the lower dead-end regions and the lower DOME region. Thus, the containment atmosphere mixing is promoted and O_2 is removed more effectively, leading faster to inert / O_2 lean conditions.

4. CONCLUSIONS AND FUTURE WORK

This paper presents work performed in the aftermath of the EU AMHYCO project, representing the first full-scale containment analysis based on a station blackout (SBO) sequence conducted with *containmentFOAM*. The selected sequence was chosen for detailed CFD investigation due to the elevated release location and, in comparison to LOCA scenarios, lower release mass flow rates. Consequently, pronounced stratification effects and deviations from lumped-parameter (LP) simulations were anticipated. In addition, one rupture foil on the steam generator (SG) towers remained closed during the sequence, further limiting mixing within the containment.

The applied spatial mesh resolution of approximately 10 million cells in the gas space is unprecedented for such analyses and enabled a detailed assessment of the three-dimensional distribution of steam, associated condensation phenomena, and containment pressurization. Furthermore, the distribution of hydrogen (and oxygen) was investigated, allowing to evaluate the build-up and temporal evolution of the flammable cloud.

The *containmentFOAM* results indicate that the coarse nodalisation and large control volumes used in system-level simulations tend to promote the transport of steam and non-condensable gases towards the lower sump region and annular dead-end compartments. In contrast, the resolved flow field obtained from the CFD analysis shows a significantly stronger buoyancy-driven flow towards the dome, leading to: (i) pronounced stratified conditions above the release location within the equipment rooms and above the upper openings of the SG towers in the containment dome; and (ii) visibly lower steam concentrations in the lower compartments when compared to LP results. While these differences substantially affect the local steam distribution, the resulting global containment pressurization remains in good agreement with the LP simulation. Accordingly, although wall condensation rates exhibit strong local heterogeneities, their integral effect is well comparable to the averaged rates obtained from the LP representation.

More pronounced discrepancies were observed in the hydrogen distribution and in the formation and evolution of flammable gas clouds. These result from localized mass transfer between two initially non-flammable regions, one rich in oxygen (dead-end compartment) and the other rich in hydrogen (main convective loop). Such mechanisms are difficult to represent using a coarse system-code nodalisation and therefore motivate the application of three-dimensional CFD tools such as *containmentFOAM*. It is expected that similar observations can be made for situations where dead-end compartments exist.

Nevertheless, despite notable differences in local details, both approaches yielded largely comparable results, particularly in regions characterized by sufficient mixing. Given the high computational cost of the present CFD analysis, approximately 0.5 million core-hours for 2 hours of simulated problem time, the use of CFD remains a complementary element in containment analysis. To enhance its applicability, a coupling

strategy between CFD and system codes at the compartment or control-volume level is foreseen. A first step was made within the AMHYCO project, where a one-way coupling was already successfully demonstrated, in which the dome and annular compartments were modeled at the system level and imposed as boundary conditions for a resolved CFD analysis of the equipment rooms. Furthermore, the local gas composition near the release from the pressurizer relief tank (PRT) was found to consist of pure steam, indicating the need for further development of the diffusion-layer-based wall condensation model in *containmentFOAM*. In addition, considering the phenomenology in the sump region, the current single-phase treatment should be extended to adequately represent heat and mass transfer processes involving water pools, which were found relevant within the GOTHIC™ analysis by UPM. For LP modeling, insights gained from the three-dimensional analysis should be systematically employed to refine the nodalisation scheme, reducing evaluation uncertainties regarding locally flammable conditions. While this paper only considers the LP code COCOSYS, the conclusions are transferable to other LP codes.

ACKNOWLEDGMENTS

This work is based on results obtained within the EU project AMHYCO, funded by the European Commission (Euratom 20192020, GA No 945057). We particularly thank Luis Serra-Lopez, Araceli Domínguez-Bugarín and Gonzalo Jiménez (UPM) for their efforts in creating the generic containment database and associated CAD models. Furthermore, we thank Matthias Braun (Framatome) for sharing the TLAP/SBO sequence analyzed in the paper.

We gratefully acknowledge the support of the German Federal Ministry for the Environment, Climate Action, Nature Conservation and Nuclear Safety (BMUKN) for funding code maintenance and integration of *containmentFOAM* within the national CFD reference package CF2REF (Fkz 150 1633B). We thank the John von Neumann Institute for Computing (NIC) for the computing time supercomputer JURECA at Jülich Supercomputing Centre (JSC) under projects ‘cf2app’ and ‘va4cf’. The LP simulation results were obtained using COCOSYS v2.4. COCOSYS is developed and kindly provided by GRS gGmbH, Germany.

REFERENCES

[1] S. Kelm *et al.*, “The Tailored CFD Package ‘containmentFOAM’ for Analysis of Containment Atmosphere Mixing, H2/CO Mitigation and Aerosol Transport,” *Fluids*, vol. 6, no. 3, p. 100, Mar. 2021, doi: 10.3390/fluids6030100.

[2] S. Kelm *et al.*, “Technical Scale CFD Analysis of the Pressurization and Transport Processes in the Battelle Model Containment during the ISP 37 VANAM M3 Test,” presented at the 13th International Topical Meeting on Nuclear Reactor Thermal-Hydraulics, Operation and Safety (NUTHOS 13), Hsinchu, Taiwan, Sep. 2022.

[3] S. Kelm *et al.*, “Progress in the Development of the containmentFOAM CFD Package for Analysis of Current and future LWRs,” presented at the 21nd International Topical Meeting on Nuclear reactor Thermal Hydraulics (NURETH-21), Busan, Korea, Sep. 2025.

[4] C. Vázquez-Rodríguez, K. J. X. Sturm, A. George, and S. Kelm, “Development of a LW-SMR dry containment model with containmentFOAM,” in *Proc. 5th Generation IV and Small Reactors (G4SR) Conference*, Ottawa (ON), Canada, Oct. 2024.

[5] C. Vázquez-Rodríguez and S. Kelm, “Multi-Fidelity Analysis for LW-SMR Containment Behavior in SASPAM-SA Design-II Using containmentFOAM,” in *Proc. 10th OECD/NEA Workshop on Computational Fluid Dynamics for Nuclear Reactor Safety (CFD4NRS-10),* Mito, Japan, Dec. 2025.

[6] G. Jiménez *et al.*, “AMHYCO Project – Towards and Enhanced Accident Management of the H2/CO Combustion Risk,” in *Proc. 19th International Topical Meeting on Nuclear Reactor Thermal Hydraulics (NURETH-19)*, 2022.

[7] S. Kelm *et al.*, "Detailed assessment of combustion risk and PAR efficiency in the late phase of a severe accident within the European AMHYCO project," *Nuclear Engineering and Design*, vol. 446, p. 114588, Jan. 2026, doi: 10.1016/j.nucengdes.2025.114588.
[8] G. Jiménez *et al.*, "AMHYCO Project Outcomes and Lessons Learned," in *Proc. 12h European Review Meeting on Severe Accident Research (ERMSAR2026)*, Madrid, Spain, May 2026.
[9] H.-J. Allelein, S. Arndt, W. Klein-Heßling, S. Schwarz, C. Spengler, and G. Weber, "COCOSYS: Status of development and validation of the German containment code system," *Nuclear Engineering and Design*, vol. 238, no. 4, pp. 872–889, Apr. 2008, doi: 10.1016/j.nucengdes.2007.08.006.
[10] L. Serra *et al.*, "From the plant layouts to optimized LP and 3D PWR-KWU containment models for combustion risk assessment with GOTHIC 8.3(QA)," *Nuclear Engineering and Design*, vol. 445, p. 114459, 2025, doi: 10.1016/j.nucengdes.2025.114459.
[11] M. Braun, "AMHYCO - WP2 - Core Melt Simulations for KONVOI Reactors," Framatome, D02-ARV-01-191–345, Jan. 2022.
[12] L. Serra, Domínguez-Bugarín, Vázquez-Rodríguez, and G. Jiménez, "Data for the generic containment analysis (PWR-W, PWRVVER, PWR-KWU)," AMHYCO, Deliverable D2.1, Dec. 2023.
[13] R. Ji, S. Kelm, and M. Klein, "An efficient method for input uncertainty propagation in CFD and the application to buoyancy-driven flows," *Nuclear Engineering and Design*, vol. 429, p. 113560, Dec. 2024, doi: 10.1016/j.nucengdes.2024.113560.
[14] G. V. Kumar *et al.*, "Implementation of a CFD model for wall condensation in the presence of non-condensable gas mixtures," *Applied Thermal Engineering*, vol. 187, p. 116546, 2021.
[15] A. George, S. Kelm, X. Cheng, and H.-J. Allelein, "Efficient CFD modelling of bulk condensation, fog transport and re-evaporation for application to containment scale," *Nuclear Engineering and Design*, vol. 401, p. 112067, Jan. 2023, doi: 10.1016/j.nucengdes.2022.112067.
[16] M. Kampili, G. Vijaya Kumar, S. Kelm, K. Arul Prakash, and H.-J. Allelein, "CFD simulations of stratified layer erosion in MiniPanda facility using the tailored CFD solver containmentFOAM," *International Journal of Heat and Mass Transfer*, vol. 178, p. 121568, Oct. 2021, doi: 10.1016/j.ijheatmasstransfer.2021.121568.
[17] E.-A. Reinecke, S. Kelm, P.-M. Steffen, M. Klauck, and H.-J. Allelein, "Validation and Application of the REKO-DIREKT Code for the Simulation of Passive Autocatalytic Recombiner Operational Behavior," *Nuclear Technology*, vol. 196, no. 2, pp. 355–366, Nov. 2016, doi: 10.13182/NT16-7.
[18] N. Chaumeix, Y. Ballossier, and A. Hamadi, "Engineering Correlations," AMHYCO, Deliverable D4.1, Mar. 2025.

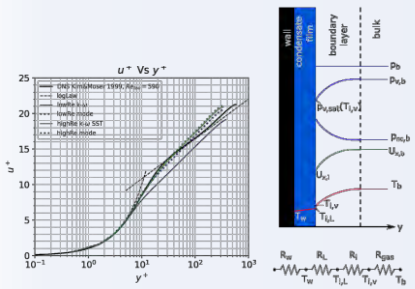

$$\frac{\partial(\rho\vec{U})}{\partial t} + \nabla\cdot(\rho\vec{U}\otimes\vec{U}) = -\nabla p + \nabla\cdot\tau + \rho\vec{g}$$

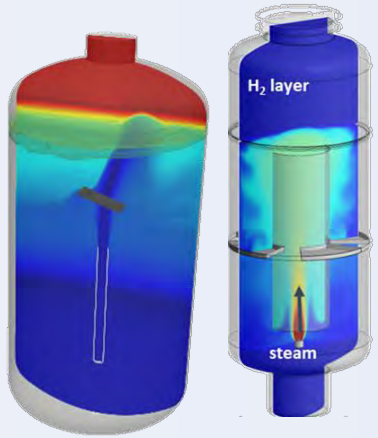

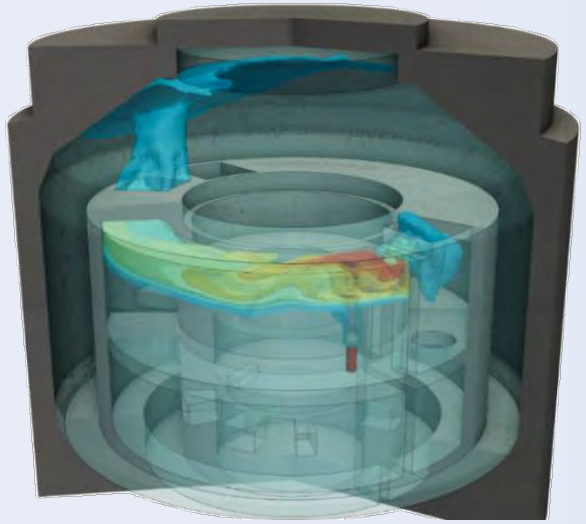

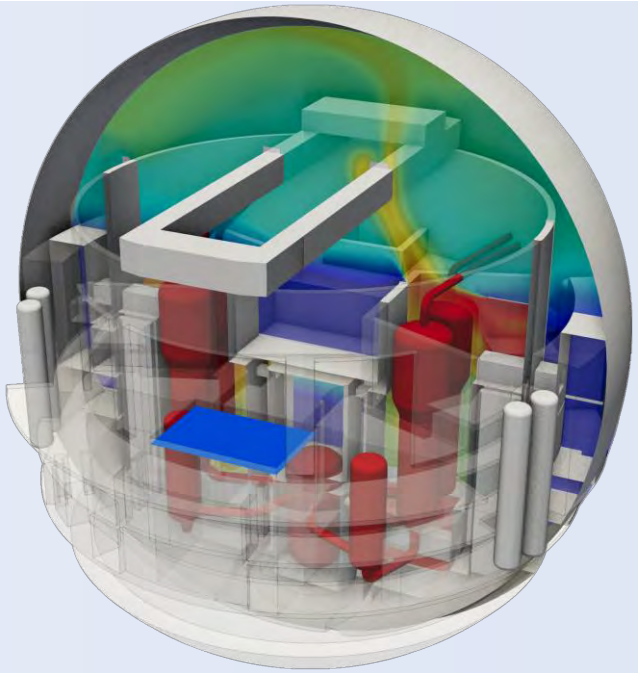

FULL SCALE CFD MODELING OF THE CONTAINMENT BEHAVIOR DURING A TLAP SEQUENCE IN A GENERIC KWU PWR

S. Kelm, C. Vázquez-Rodríguez, M. Klauck

12th European Review Meeting on Severe Accident Research Conference (ERMSAR 2026), Madrid, May. 18th-22th 2026

containment FOAM

AMHYCO

Supported by:

Federal Ministry
for the Environment, Climate Action,
Nature Conservation and Nuclear Safety

based on a decision of
the German Bundestag
Project No. 150 1633B

JÜLICH
Forschungszentrum
Mitglied der Helmholtz-Gemeinschaft

OUTLINE

- Background
- containmentFOAM CFD package
- Application to containment analysis
  - Scenario
  - Modeling approach
  - Results
- Summary and Conclusions

BACKGROUND

EU-AMHYCO 'Towards an Enhanced Accident Management of the H_2/CO combustion risk'

- Integration of CFD containment analysis in the analysis chain

LP / System codes
(most penalizing scenarios)

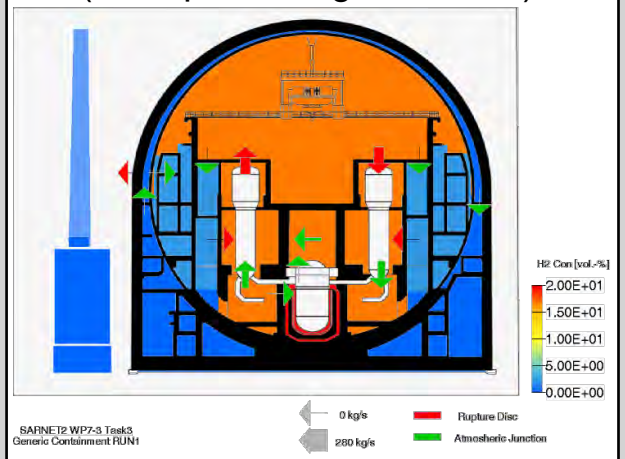

O~10 cells Ref: RUB

GOTHIC-3D
(Selected transients)

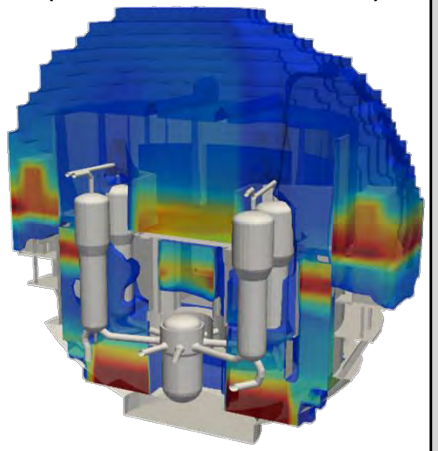

O~10^4..10^5 cells Ref: UPM

CFD
(Selected compartments)

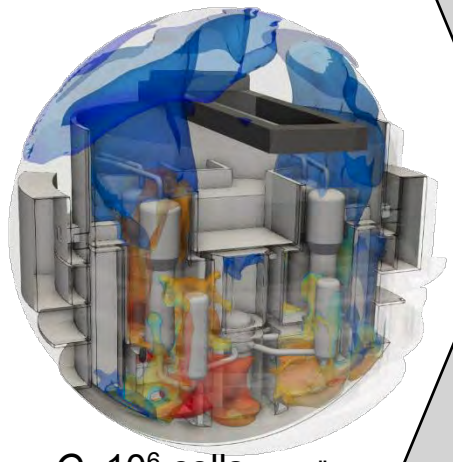

O~10^6 cells Ref: JÜLICH

- combustion risk
- effectiveness of mitigative measures
- equipment survivabilty
- instrumentation representativeness

- Focus of this talk: containmentFOAM analysis of PWR-KWU station blackout (TLAP) and comparison against COCOSYS (LP, FZJ)

Kelm, S. et al. "Detailed Assessment of Combustion Risk and PAR Efficiency in the Late Phase of a Severe Accident within the European AMHYCO Project" *Nuclear Engineering and Design,* 446, 2026, 114588

CONTAINMENTFOAM AT A GLANCE

Modeling Pressurization, Aerosol Transport and H_2/CO Gas Mixing and Mitigation

- Flows and Transport Phenomena
  - **Efficient Multi-Species Solver:** effective binary diffusion, Wilke mixture
  - **Turbulence transport**: k-ω SST model with buoyancy terms,
  - **Conjugate heat transfer,**
  - **y^+ insensitive wall treatment**, incl. surface roughness effects
  - **Wall condensation**: single phase diffusion layer model, incl. wall films,
  - **Fog formation**: single and two-phase phase drift flux model incl. PBM
  - **Aerosol transport**: single phase drift flux model, incl. decay heat,
  - **Gas radiation**: P1, gray spectral model
    Emission-based Reciprocity Monte Carlo Method, SNBCK spectral model
- Technical Systems and Components
  - **Generic system coupling** via Functional Mockup Interface
    - **PARs**: (*REKODIREKT*), **PSS , HTX, control systems** (OpenModelica)
  - **Burst discs, flaps, doors**: conditional mesh interfaces
  - **Unresolved structures**: porous media

H_2 distribution inside a dry PWR containment,
3D CAD Geometry by L. Serra-Lopez (UPM)

🕮 Kelm, S. et al. "The Tailored CFD Package 'containmentFOAM' for Analysis of Containment Atmosphere Mixing, H_2/CO Mitigation and Aerosol Transport", *Fluids* (2021) 6, no. 3: 100

CONTAINMENTFOAM – PACKAGE

Post-Processing: Flammability and combustion risk functionObject

- More than ‘just a set of specialized models’, but an application-oriented framework for pre- and postprocessing! E.g.,
  - `combustionRisk_AMHYCO` functionObject
    - For arbitrary H_2-O_2-N_2-H_2O-CO-CO_2 mixture
    - Computes flammability and potential of flame acceleration for each cell
      → visualization of isovolumes
  - Integrates:
    - Flammable volume
    - Flammable H_2 and CO mass
    - Volume of flammable cloud with potential of flame acceleration
    - According masses of H_2 and CO

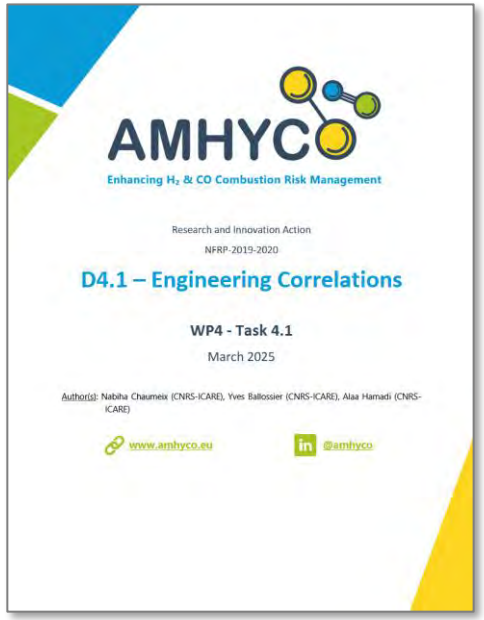

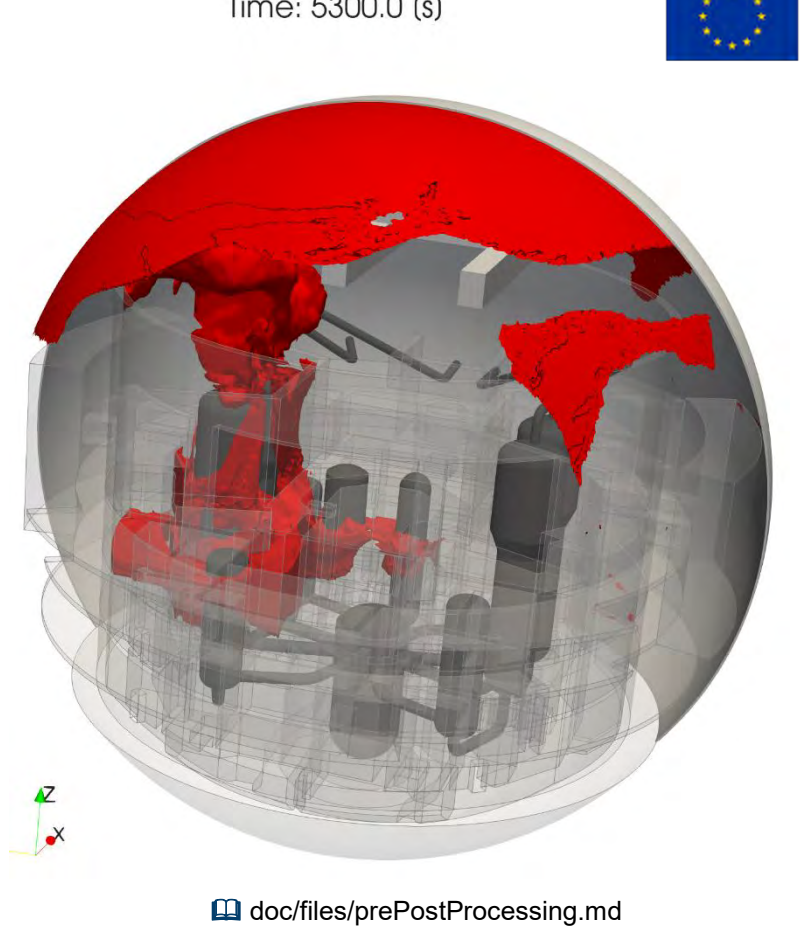

📖 doc/files/prePostProcessing.md

OUTLINE

- Update on containmentFOAM
  - systemCoupling
  - Rough wall functions
  - postprocessing
  - Documentation & support
- Application to full-scale containment analysis
  - Scenario
  - Modeling approach
  - Results
- Summary and Conclusions

APPLICATION TO CONTAINMENT ANALYSIS

PWR-KWU containment geometry

- Detailed CAD geometry as common basis for LP nodalisation and 3D containment models

  🕮 Serra, L.. et al. "From the plant layouts to optimized LP and 3D PWR-KWU containment models for combustion risk assessment with GOTHIC 8.3(QA)" *NED,* 445, 2025, 114459

- Two models:

full containment

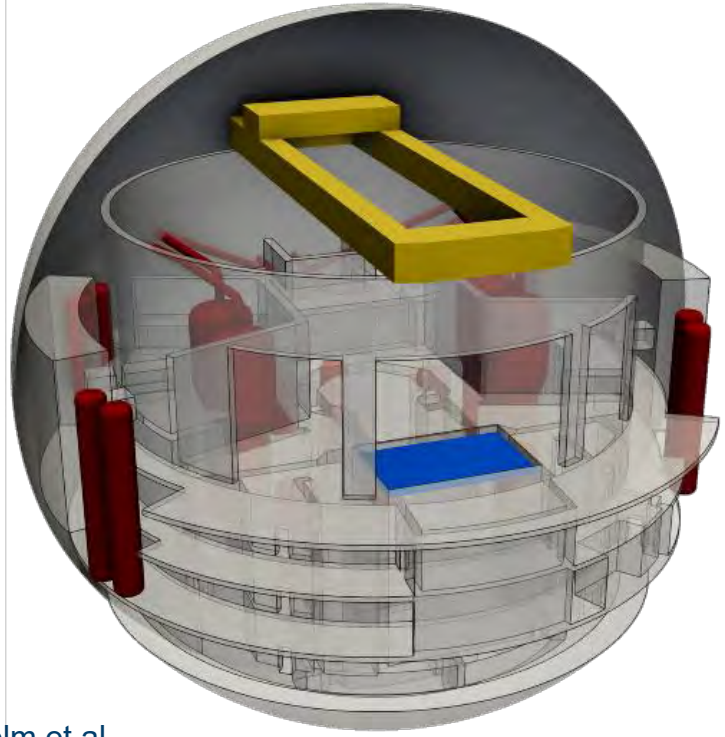

equipment rooms

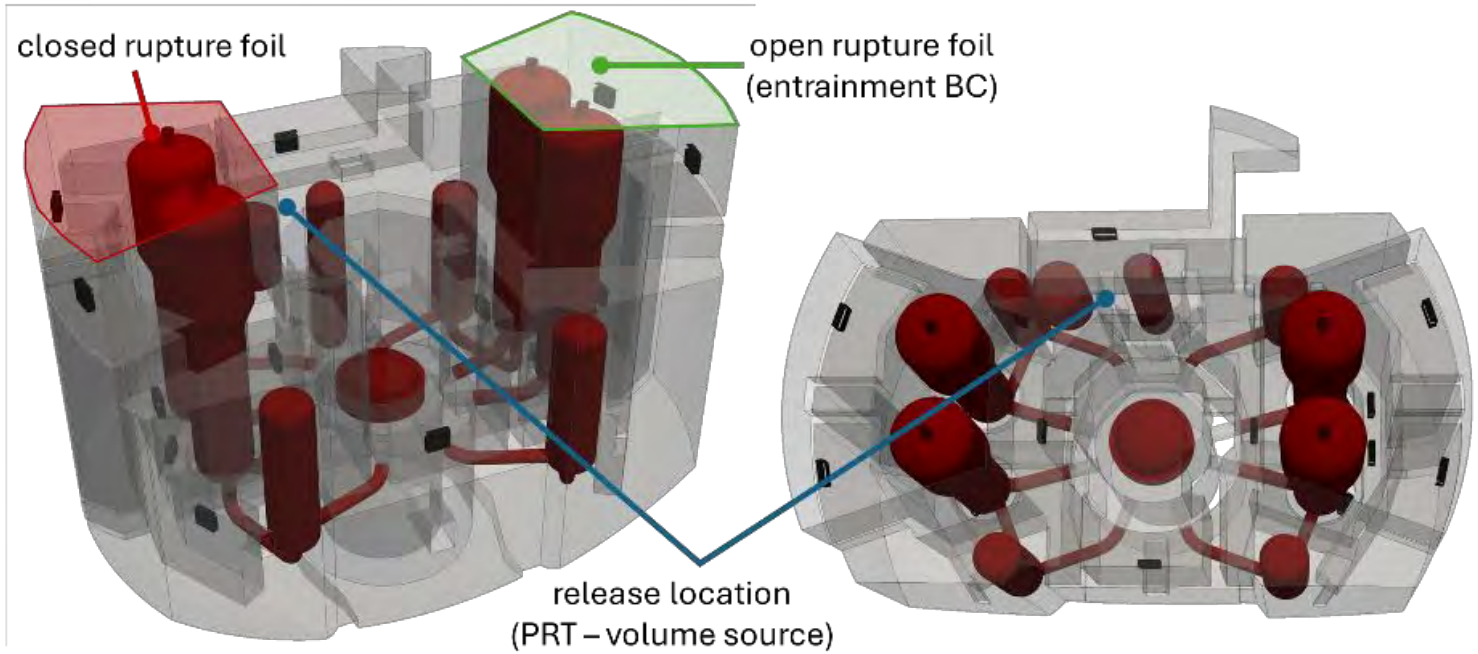

APPLICATION TO CONTAINMENT ANALYSIS

Scenario - Total loss of AC power (in-vessel phase)

- Event chronology:

Time [h]	event
0	TLAP & SCRAM
<1	SG dry-out
>1	Pressurizer safety valve cycling
1.8	Core uncovery
2.1	COT > 650°C (SAMG)
2.5	Onset of H_2 production
2.7	RCS depressurization (delayed)
>2.7	Hydro accumulator injection
9.1	RPV failure

M&E release from pressurizer release tank (MELCOR analysis by Framatome Germany)

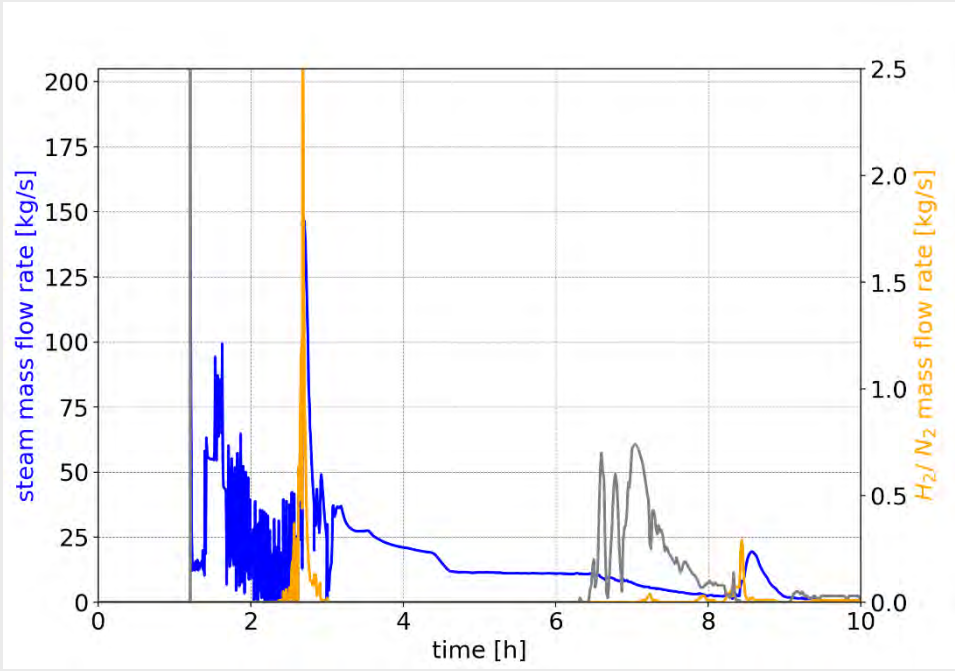

➢ High release location, low momentum → limited mixing in the equipment rooms, stratification

APPLICATION TO CONTAINMENT ANALYSIS

Geometry and Grid

- Modeling internal flow and transport processes is tightly linked to modeling (simplification) of the complex bounding geometry!
  - Mesh generation: CF-MESH+
    - Hex dominant unstructured mesh
    - max. edge length Δ=0.4m, two refinement levels (Δ =0.2 / 0.1m)
    - ➢ Geometric features of L > 0.2m can be resolved
    - 5..7 prism layers
    - ~10 Mio fluid cells
    - ~6.5 Mio solid cells
- ➢ No formal mesh sensitivity study done!

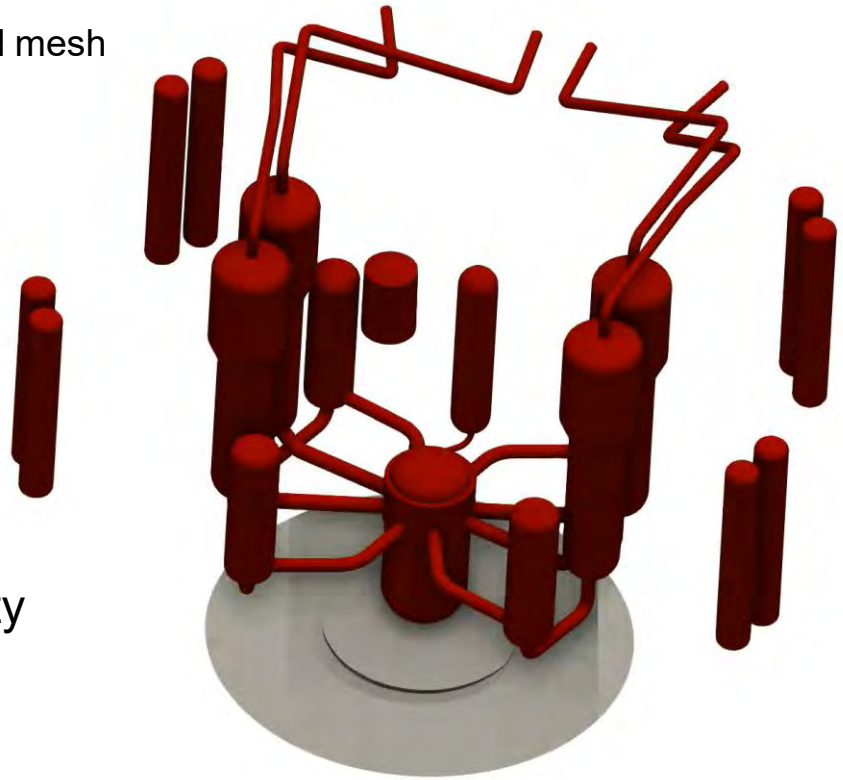

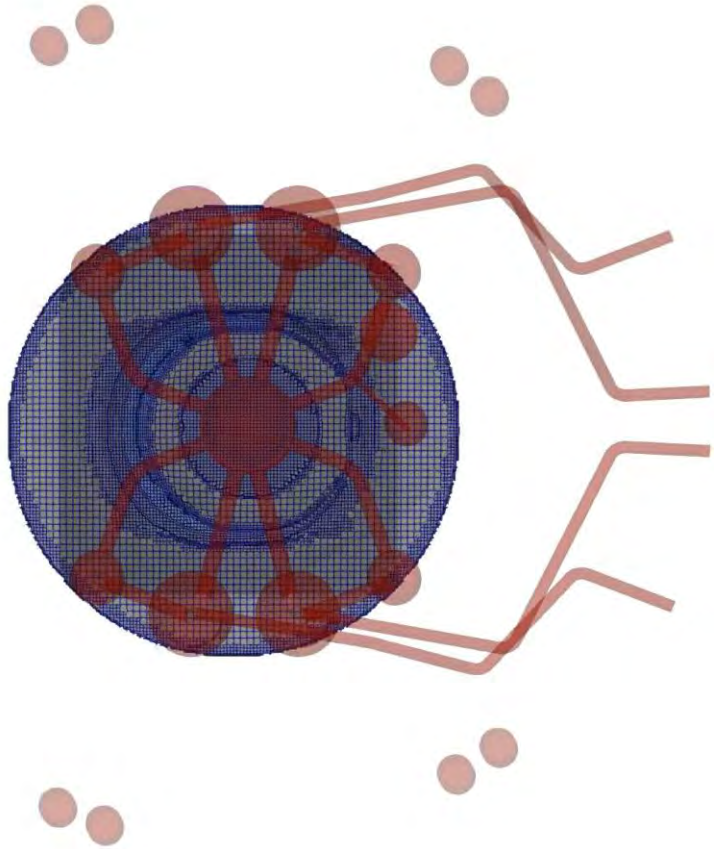

APPLICATION TO CONTAINMENT ANALYSIS

Initial and boundary conditions

- Initialization:
  - CV wise mapping from COCOSYS
- Boundary conditions:
  - M&E release: volumetric H_2O (gaseous), N_2 and H_2 source from MELCOR

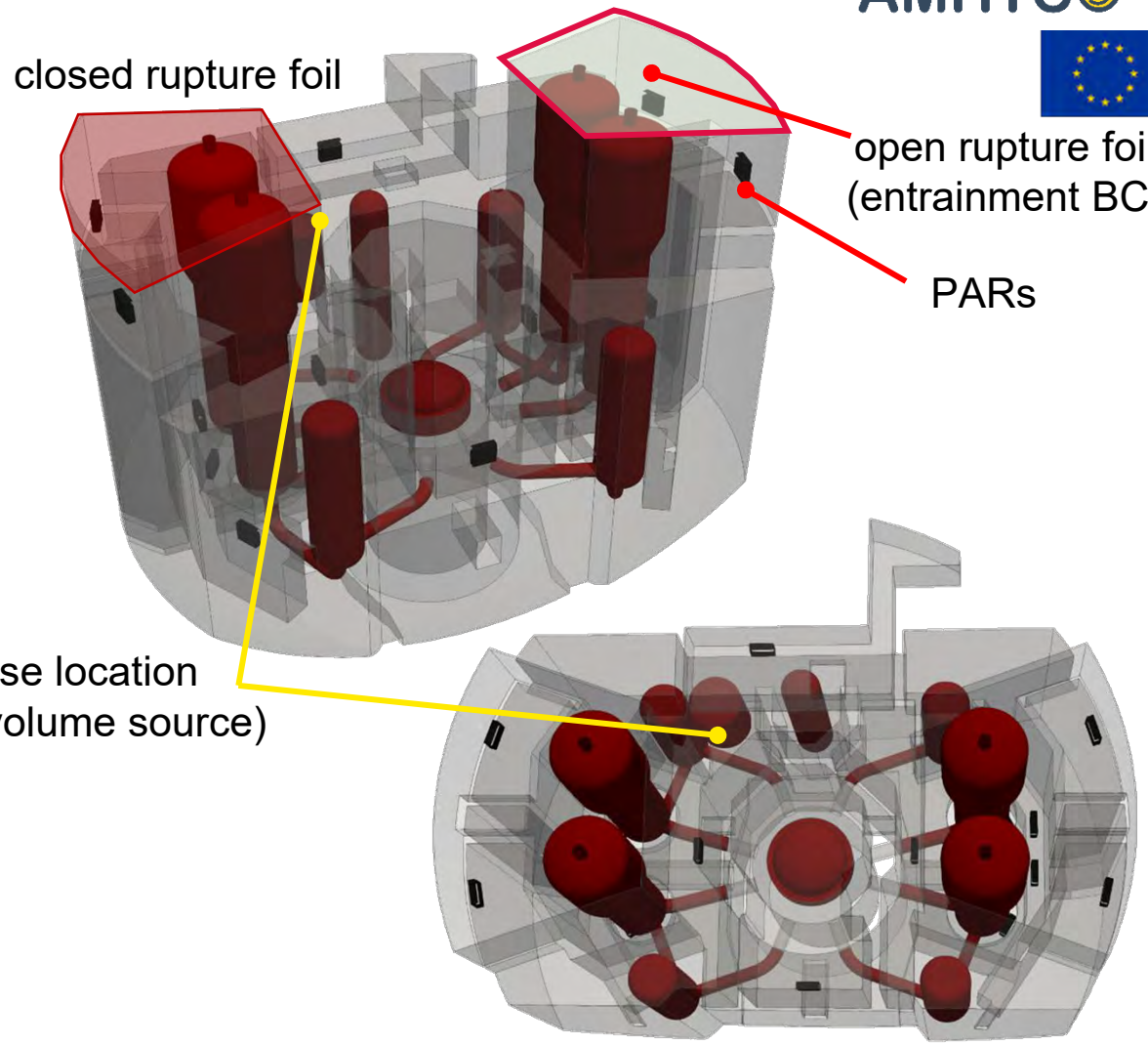

APPLICATION TO CONTAINMENT ANALYSIS

LP Modeling

- COntainment COde SYSstem (COCOSYS) developed by GRS
- Coarse nodalisation:
  - Based on the same CAD geometry
  - 8 control volumes
- Physics:
  - two-phase non-equilibrium formulation
  - water/steam release (flashing), sumps
  - Atmospheric and liquid flow paths (‘junctions’)

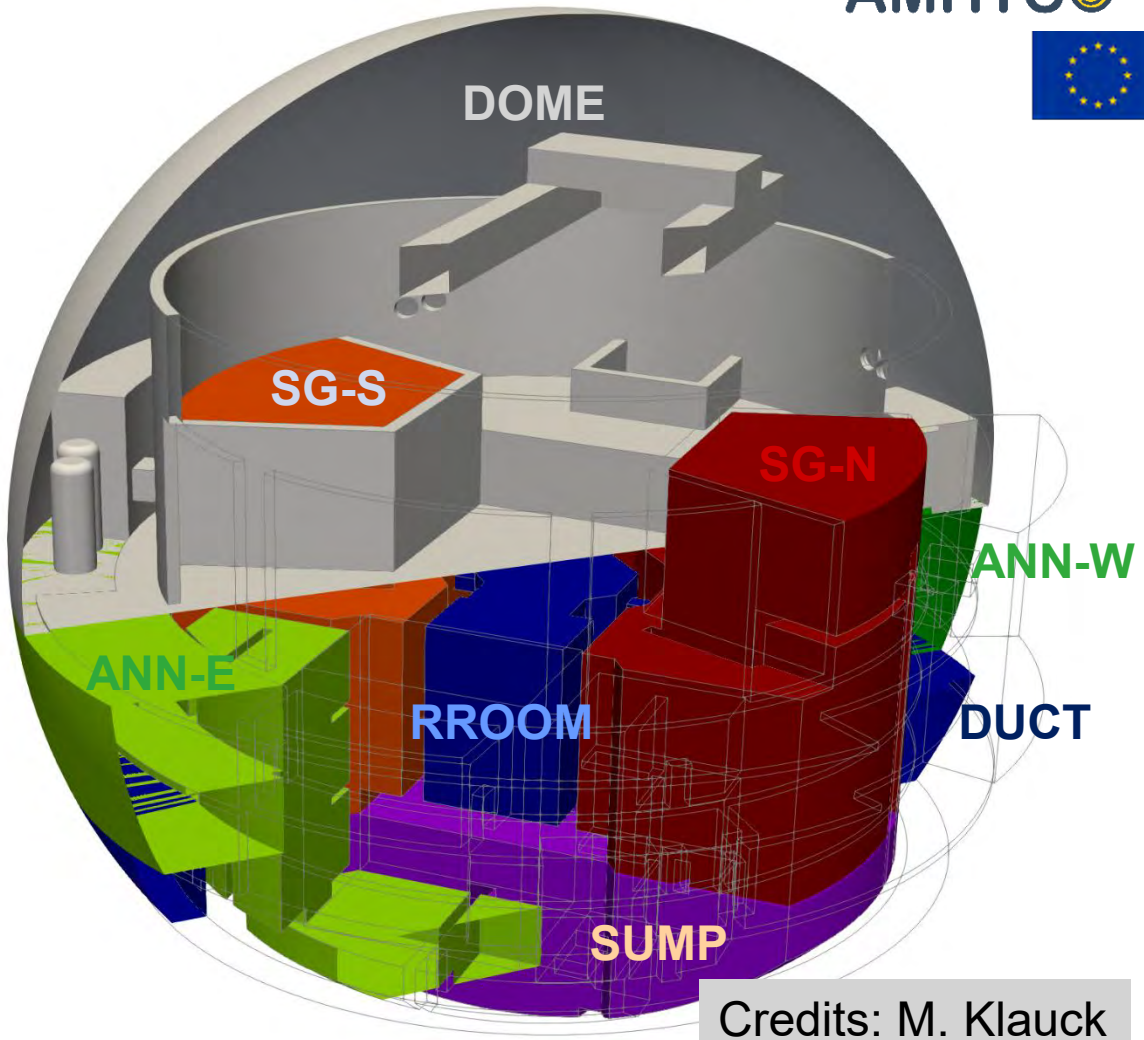

Credits: M. Klauck

APPLICATION TO CONTAINMENT ANALYSIS

Full containment - overview

- Sequence start with PRT burst disc rupture (t_0~4300s)

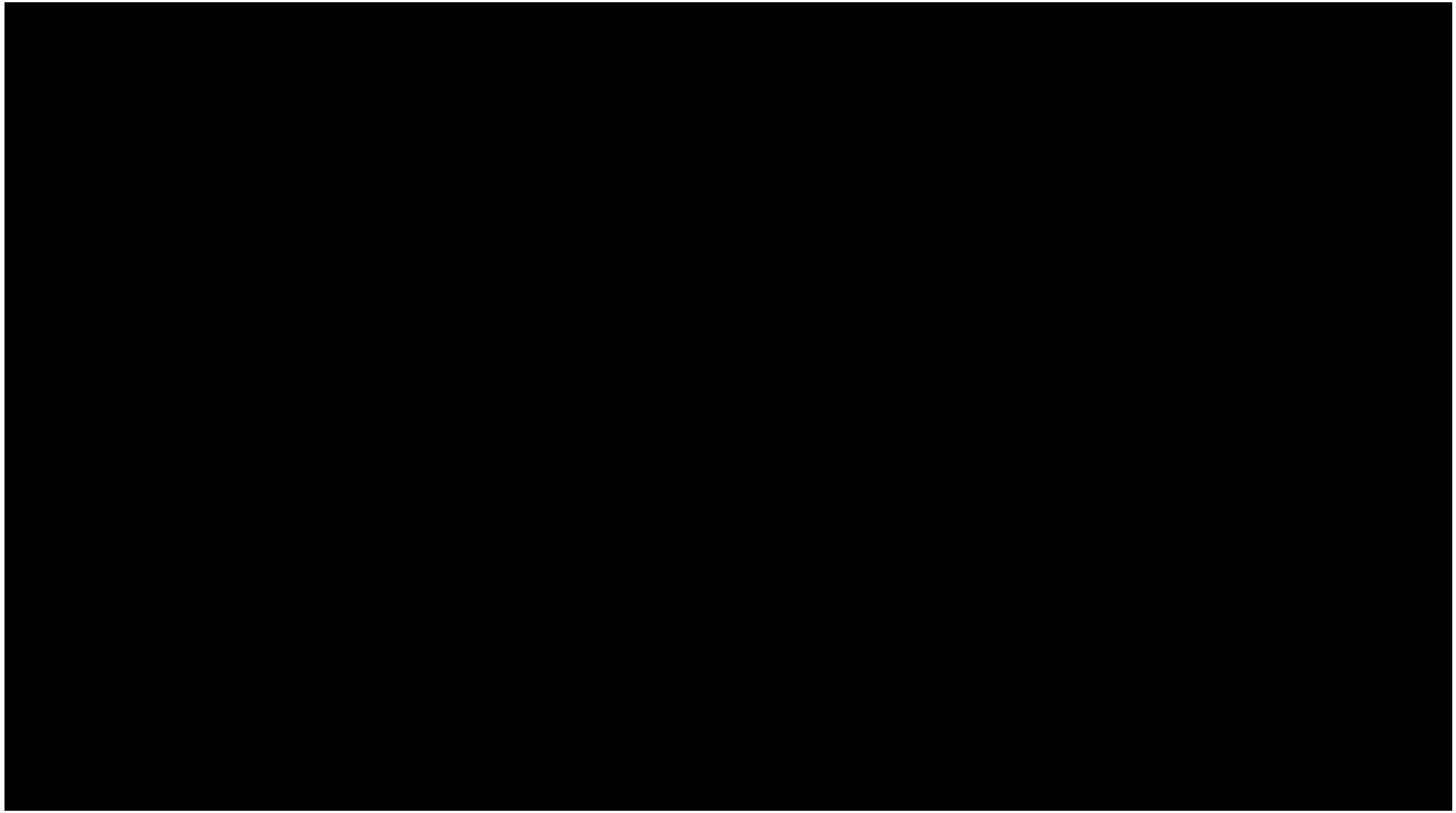

APPLICATION TO CONTAINMENT ANALYSIS

Full containment - overview

- Sequence start with PRT burst disc rupture (t_0~4300s)
- Steam stratification
- Spatially fluctuating condensation rates
  - ➢ difference to LP?

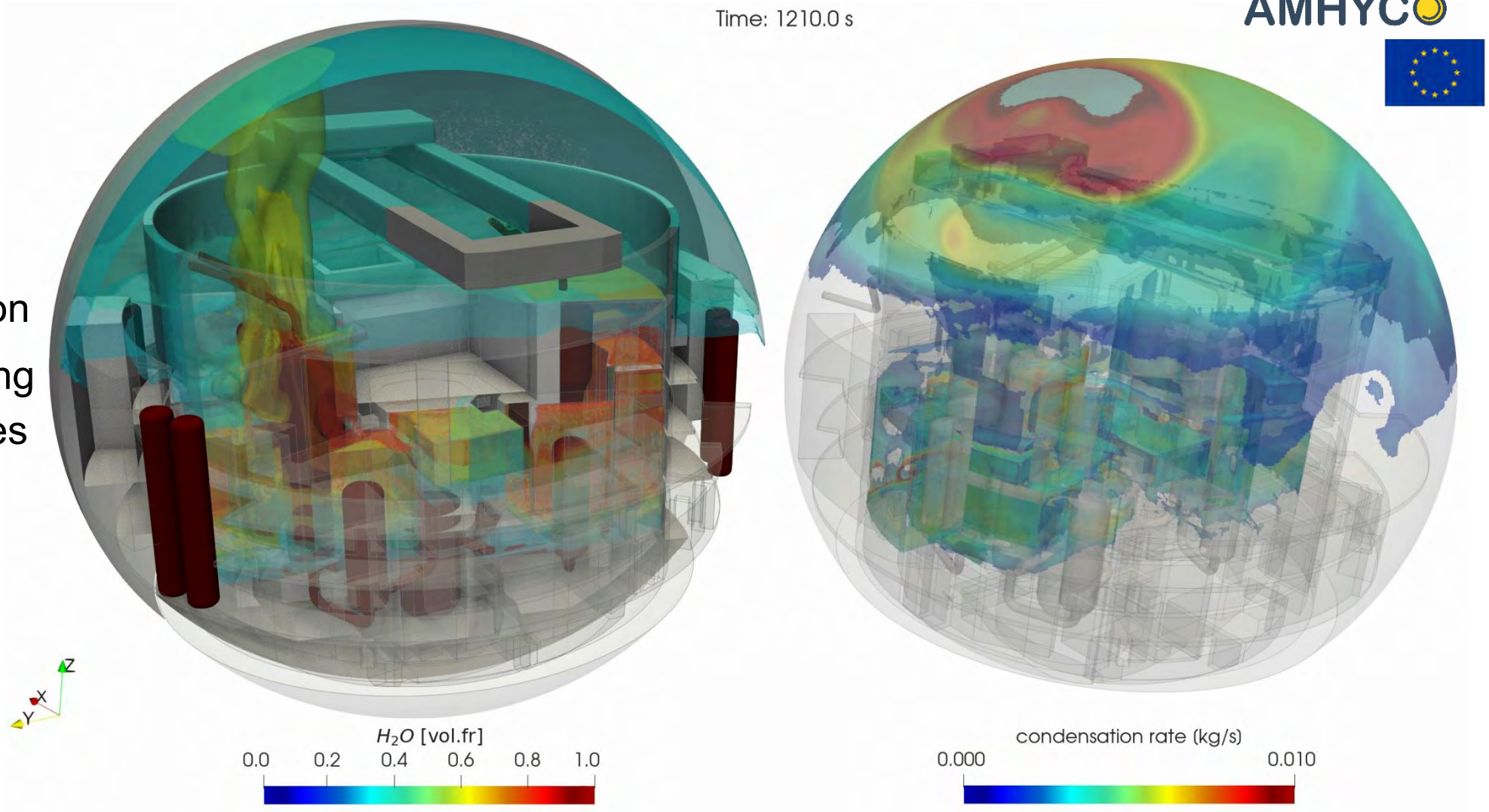

APPLICATION TO CONTAINMENT ANALYSIS

Full containment - pressurization

- Containment dome conditions

Steam concentration [vol.fr]

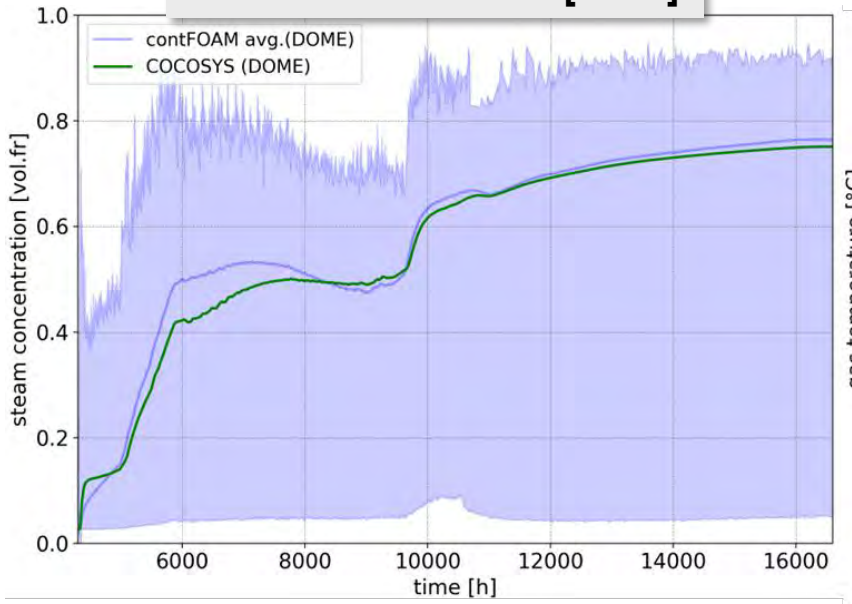

gas temperature [°C]

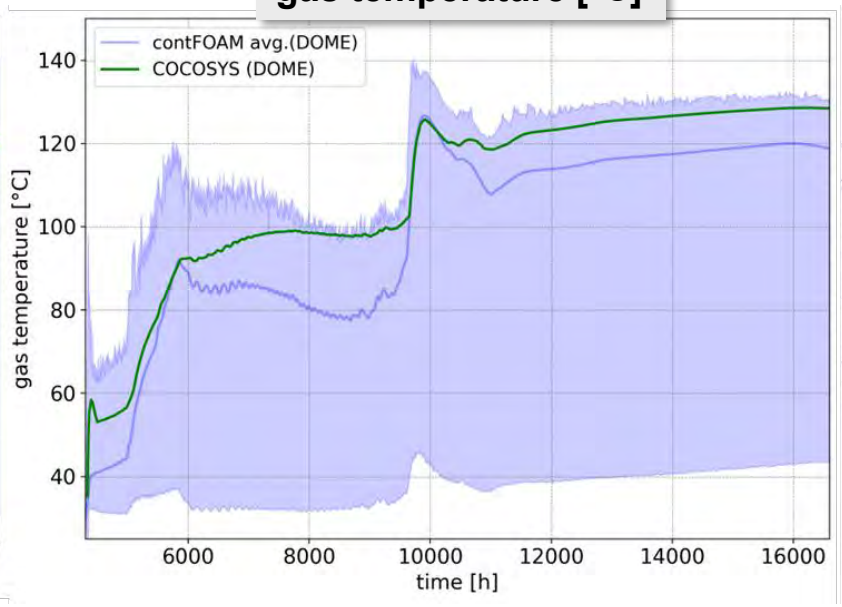

pressure [bar]

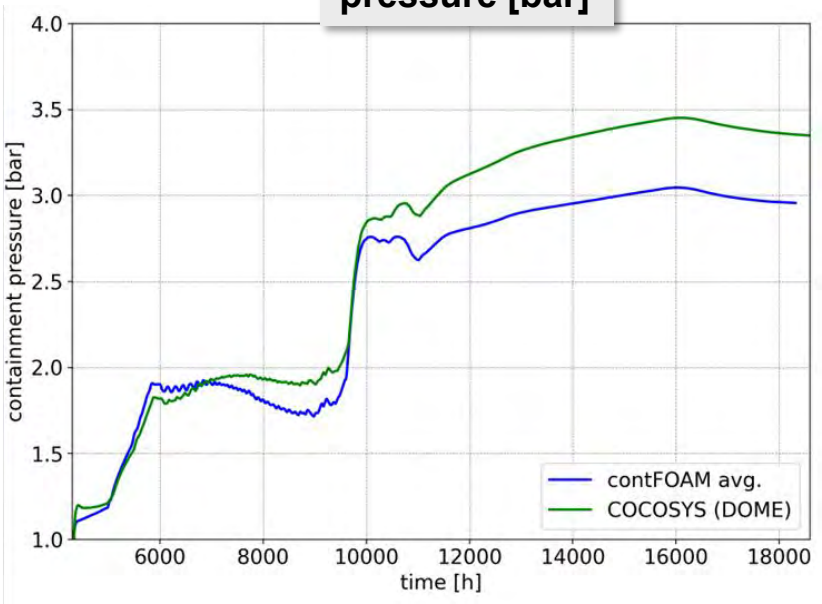

- ➢ Average CV trends well comparable with LP (COCOSYS).
- ➢ Bandwidth (min/max) indicates strong spatial heterogeneity affecting e.g., heat and mass transfer

APPLICATION TO CONTAINMENT ANALYSIS

Full containment - pressurization

- Equipment rooms stratification

Steam concentration [vol.fr]

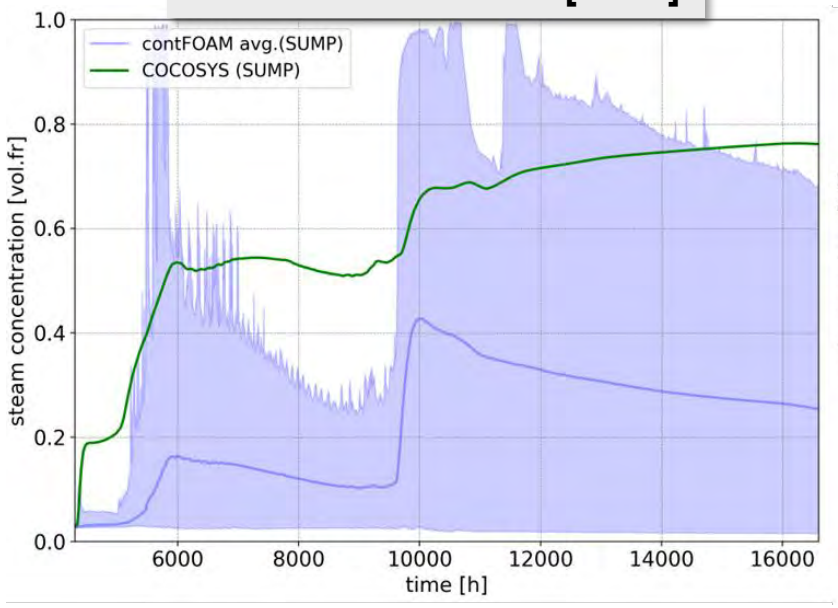

gas temperature [°C]

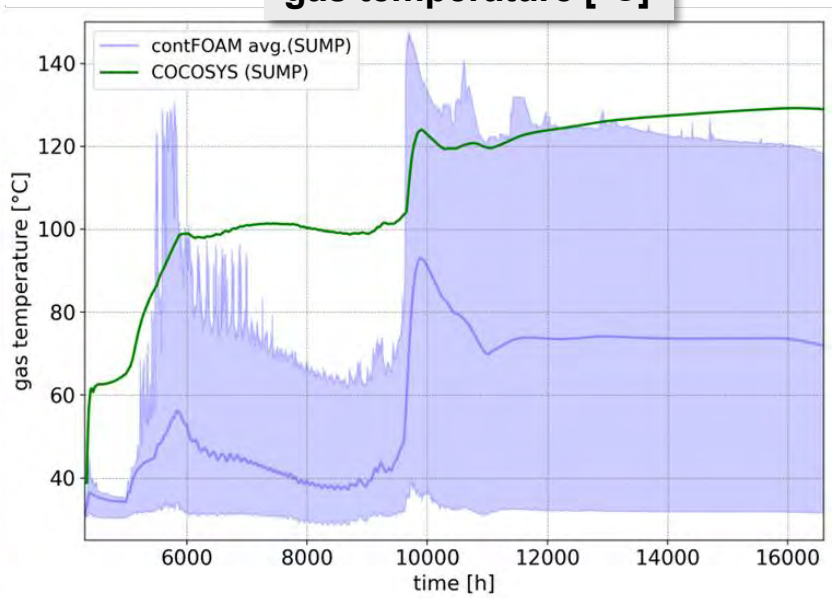

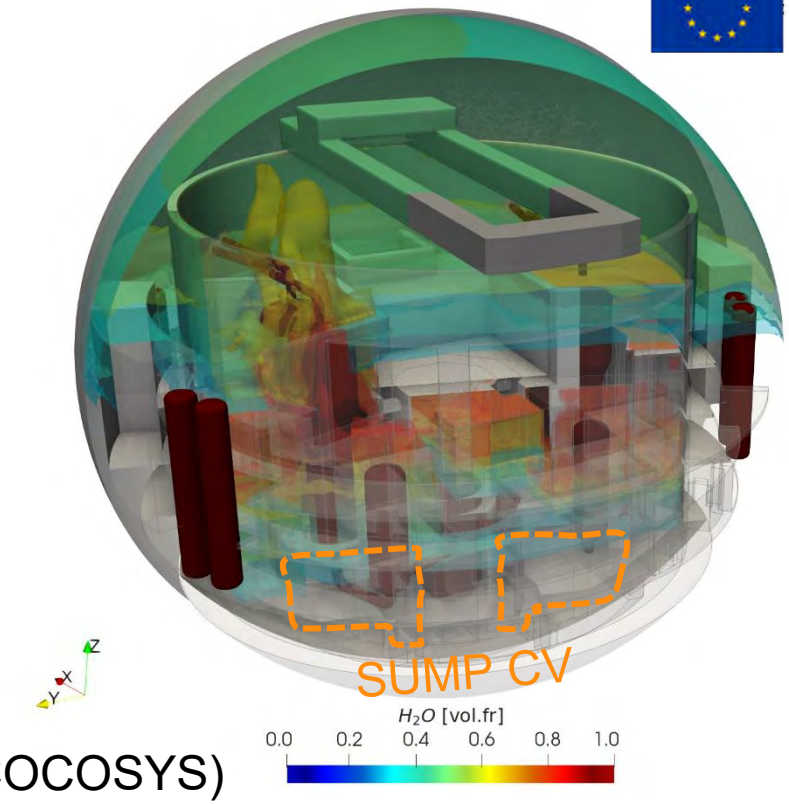

- Less transport to SUMP region and other ‘dead-end’ CVs than with LP (COCOSYS)
- Little effect on pressure (comparably small volume)
- Effect on later H_2 injection?

APPLICATION TO CONTAINMENT ANALYSIS

H_2 distribution

- Well comparable along main convective loop, but
- Deviating transport into the dead-ends / stagnant zones

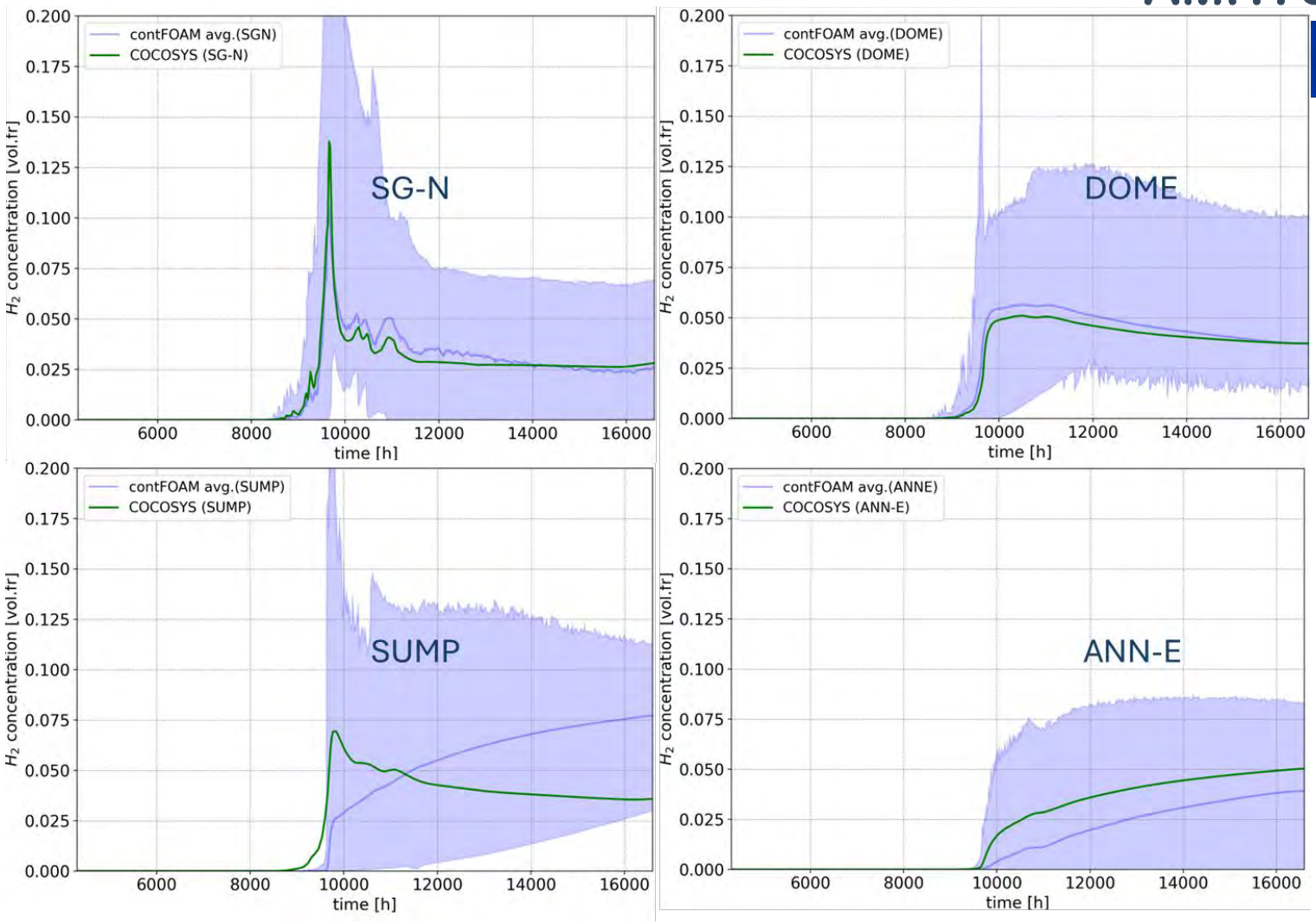

APPLICATION TO CONTAINMENT ANALYSIS

Flammability

- Cell-wise vs. CV-wise (‘all-or-nothing’) evaluation of the flammable cloud

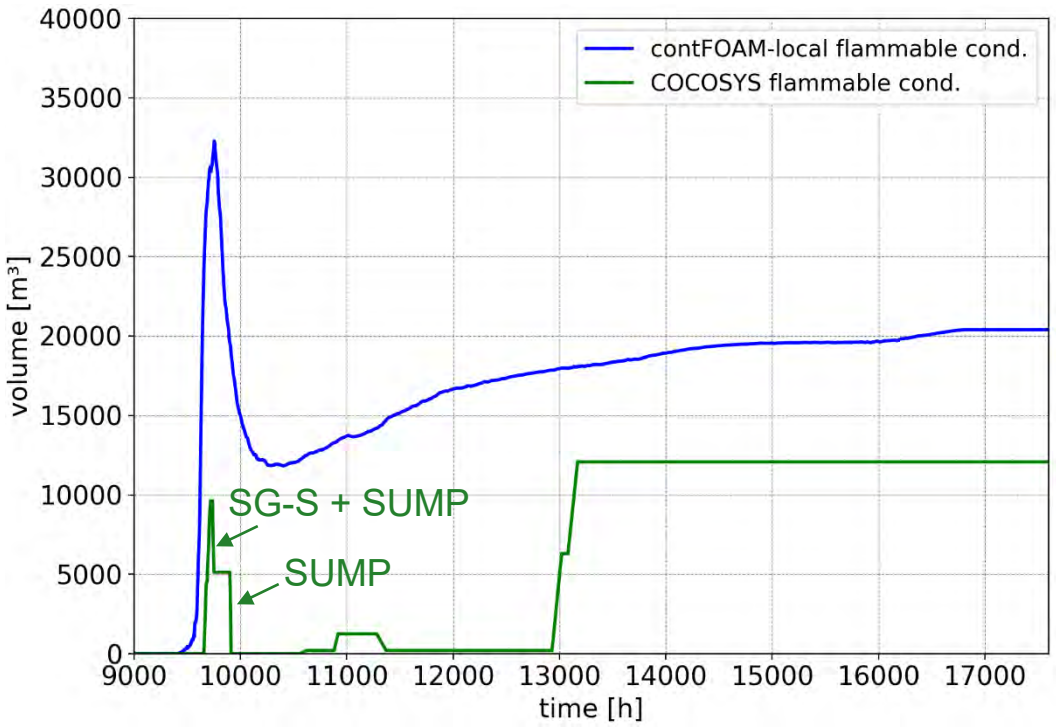

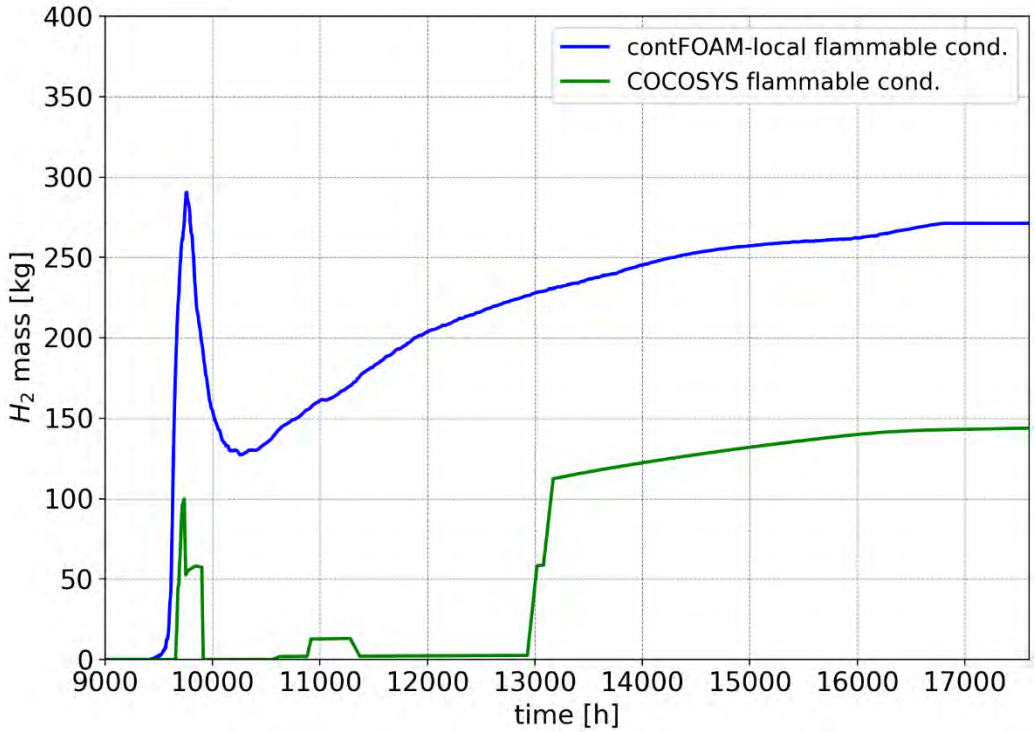

- Both codes predict no global flammability, but differences appear due to coarse nodalization

APPLICATION TO CONTAINMENT ANALYSIS

Combustion Risk

- Insights to the formation of flammable clouds

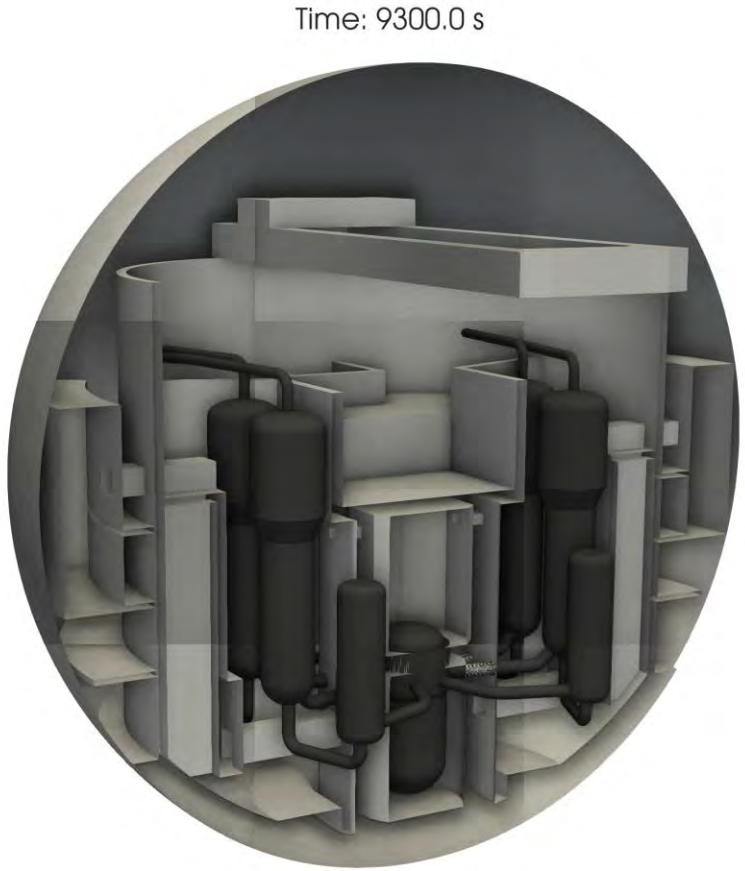

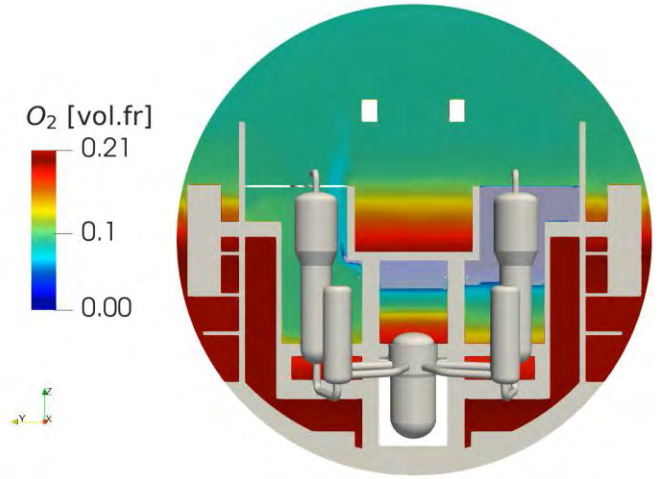

Opacity

$O_2 < O_{2,min}$

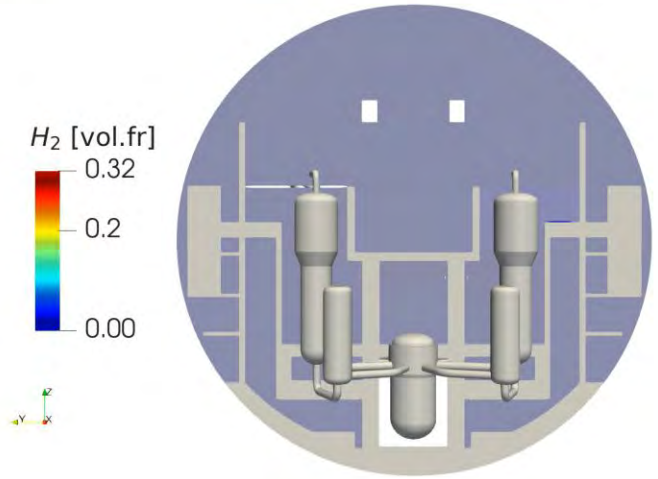

$H_2 < H_{2,min}$

APPLICATION TO CONTAINMENT ANALYSIS

Evolution of the flammable mixture

- Insights to the formation of flammable clouds..

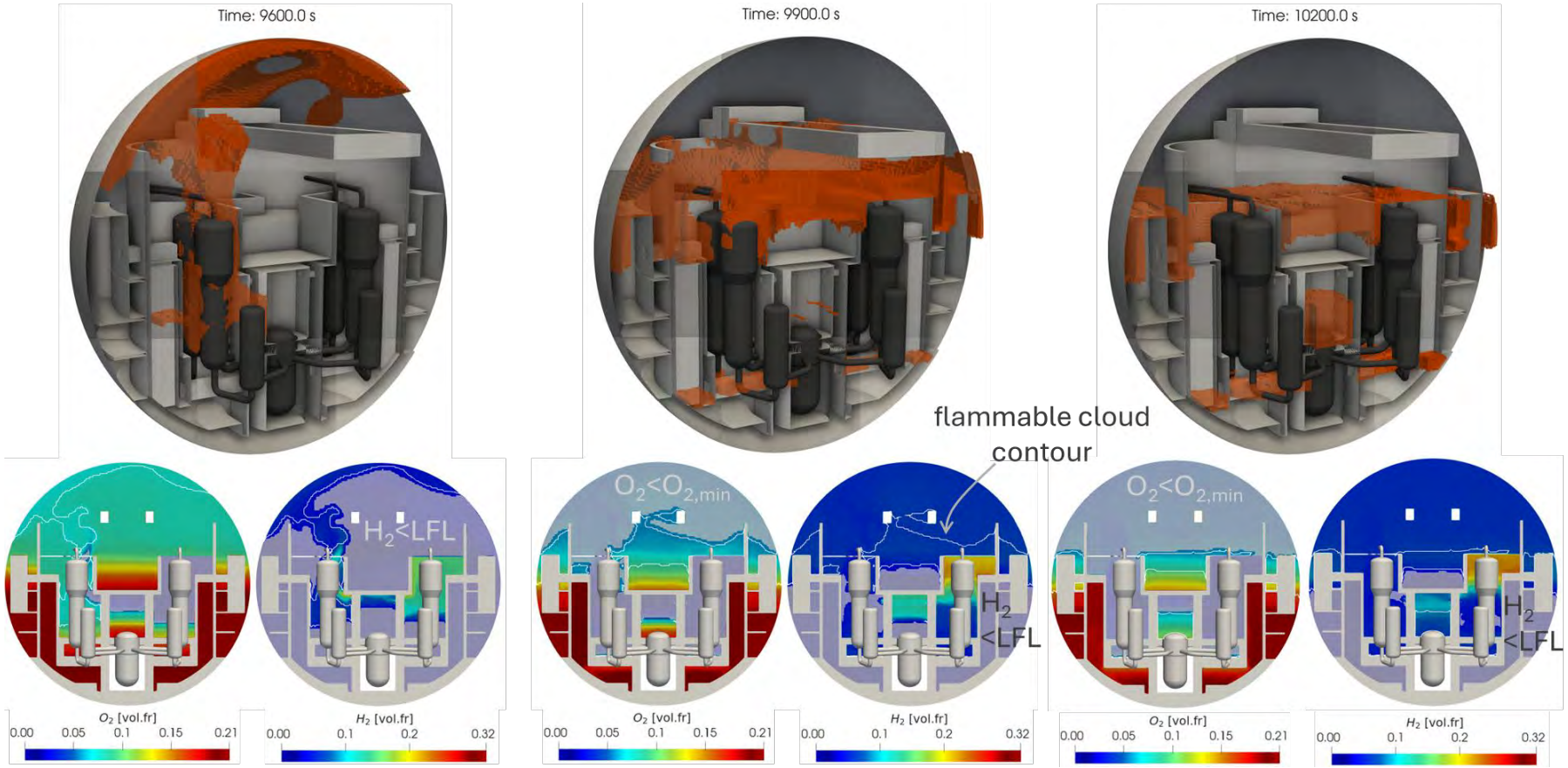

➢ ..in the transition between main convective loop (H_2 rich) and stagnant zones (O_2 rich)

SUMMARY

- Prototypic application of containmentFOAM to the in-vessel phase of a SBO sequence
  - despite notable differences in local details, both approaches yielded largely comparable results, particularly in regions characterized by sufficient mixing
  - The coarse nodalisation used in system-level simulations tends to promote the transport of steam and non-condensable gases towards the lower sump region and annular dead-end compartments
  - Flammable gas clouds are formed at the boundary between H_2 rich (main convective loop) and O_2 rich gas mixtures (stagnant regions), which is hard to capture with coarse lumped volumes
  - Full containment CFD analysis is feasible: 1024 cores, ~0.5 Mcore-h/1h transient, ~100..1500 s/day .. but still significant simplifications required (e.g., geometry, single-phase formulation) !

➢ Simulation including PARs in progress

- Needs for further model development:
  - Sump heat and mass transfer, condensation at high steam mass fractions
  - Two-way system code coupling

THE END..

- Public containmentFOAM repository
  https://go.fzj.de/containmentFOAM

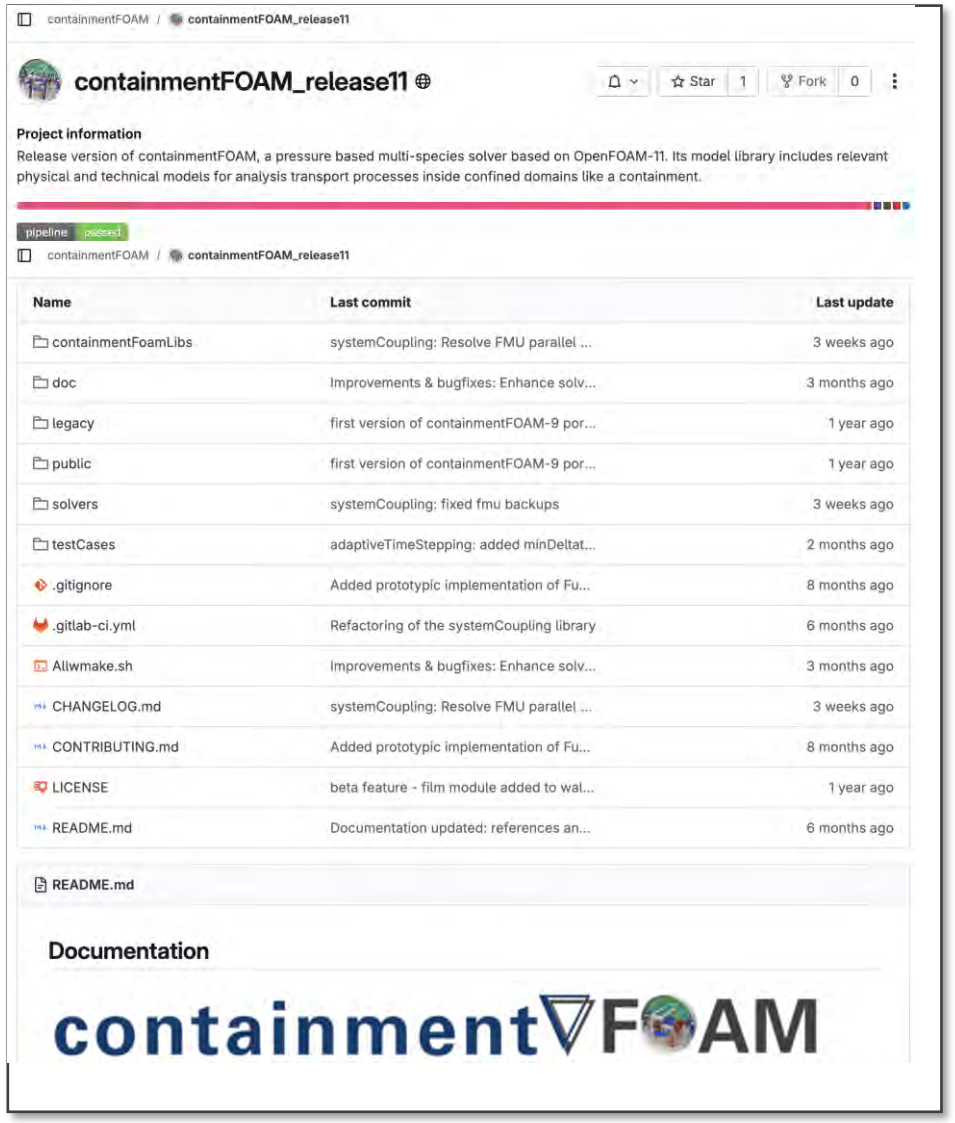

ACKNOWLEDGEMENTS

Sponsors and Projects

- German Federal Ministry for the Environment, Climate Action, Nature Conservation and Nuclear Safety (BMUKN) for funding code maintenance and integration to the national CFD reference package CF2REF (Fkz **150 1633B**) as the projects UQ4CFD (Fkz **150 1595**) and SETCOM-2 on wall condensation modeling (Fkz **150 1591**)
- Former German Federal Ministry of Economic Affairs and Energy (BMWi) and for funding projects related to further development of CFD for reactor safety application (Fkz **150 1407)** and the REKO experimental and model development program (Fkz **150 1308 / 150 1394 / 150 1470**) as well as the SETCOM projects (Fkz **1501404 / 1501489**)
- **H**elmholtz **I**nterdisciplinary Doctoral **T**raining in **E**nergy and **C**limate Research (HITEC) Graduate School, the German Academic Exchange Service (DAAD) and the Chinese Scholarship Council (CSC) for funding PhD positions and student exchange
- **IAEA O**pen-source **N**uclear **CO**des for **RE**actor Analysis (**ONCORE**) initiative, a collaborative framework for the development and application of open-source multiphysics to support research, education, and training in analysis of advanced reactor designs
- AMHYCO Project (Euratom 20192020, GA No 945057), in particular Luis Serra-Lopez, Araceli Domínguez-Bugarín and Gonzalo Jiménez (UPM) for their efforts in creating the generic containment database and associated CAD models. Matthias Braun (Framatome) for sharing the TLAP/SBO sequence.
- Dr. Berthold Schramm and Dr. Jörn Stewering (GRS) for their collaboration within the CF2REF project as well as our contributors, partners and colleagues and beta testers
- Computing time on the JURECA-DC CPU at the Jülich Supercomputing Center has been granted within the projects ‘uq4cfd’, ‘cfrun’, ‘cf2app’ and ‘va4cf’

Supported by:

Federal Ministry
for the Environment, Climate Action,
Nature Conservation and Nuclear Safety

based on a decision of
the German Bundestag

BACKUP

APPLICATIONS

EU-AMHYCO ‘Towards an Enhanced Accident Management of the H_2/CO combustion risk’

- Preparative work
  - Mesh generation:
    - 10 Mio fluid cells
    - 6.5 Mio solid cells
  - Scalability study on JURECA-dc-cpu:
    - 4 PARs
    - 12 doors/burst discs
    - SB-LOCA (1kg/s H_2/steam release)
    - ➢ Optimum ~10kCells/core (well known OpenFOAM limit, no additional bottlenecks)

JSC computing time grant ‘cfrun’ (No. 26701)

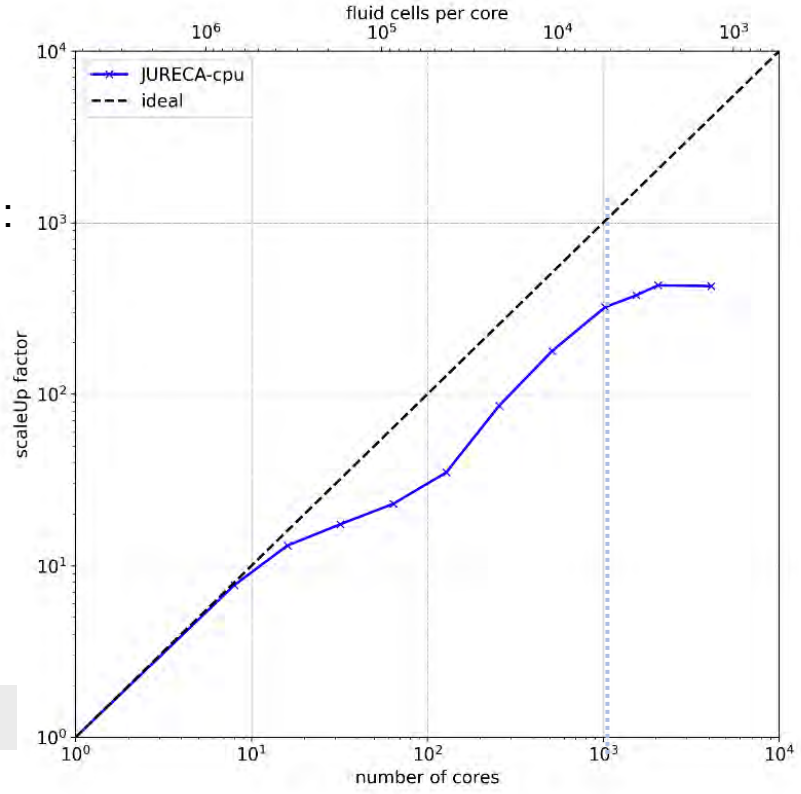

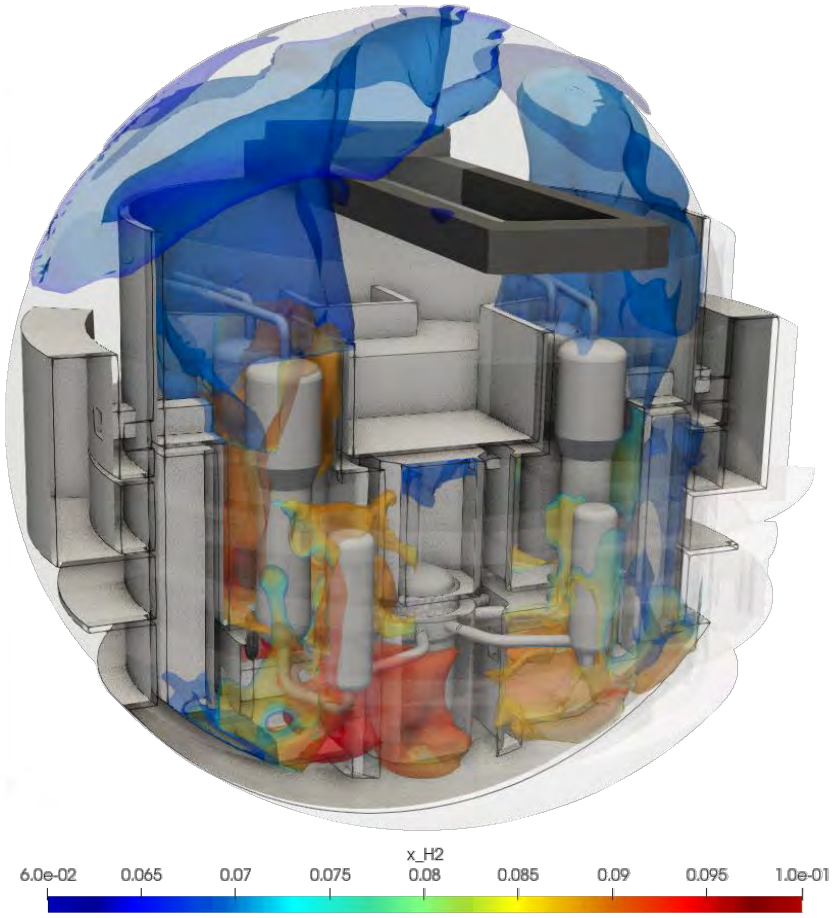

➢ Results: CFD4NRS-10 (12/2025)

UPDATES – PREPROCESSING

Field initialisation

- `setInterpolatedFields` 3D field initialization
  - Experimental data
  - Other codes

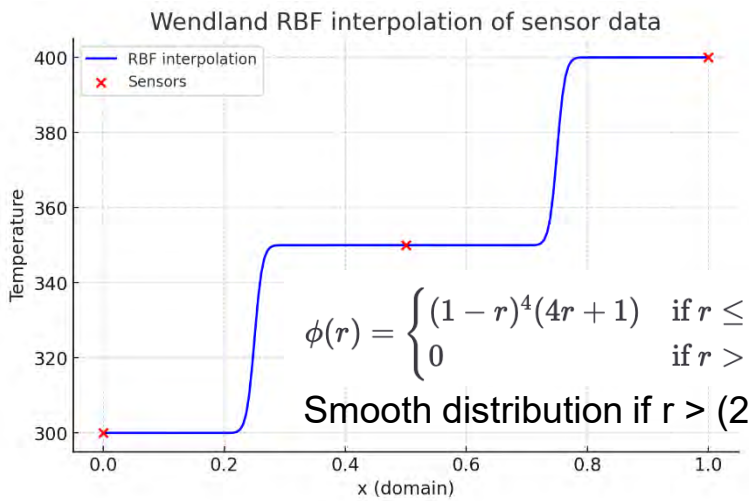

$$\phi(r) = \begin{cases} (1-r)^4(4r+1) & \text{if } r \leq 1 \\ 0 & \text{if } r > 1 \end{cases} \quad \text{where } r = \frac{\|x - x_i\|}{\text{radius}}$$

Smooth distribution if r > (2 * distance of sensors)

- Works on full mesh or cellZones
- Mapping modes (x, y, z, xy ,xz ,yz , xyz)

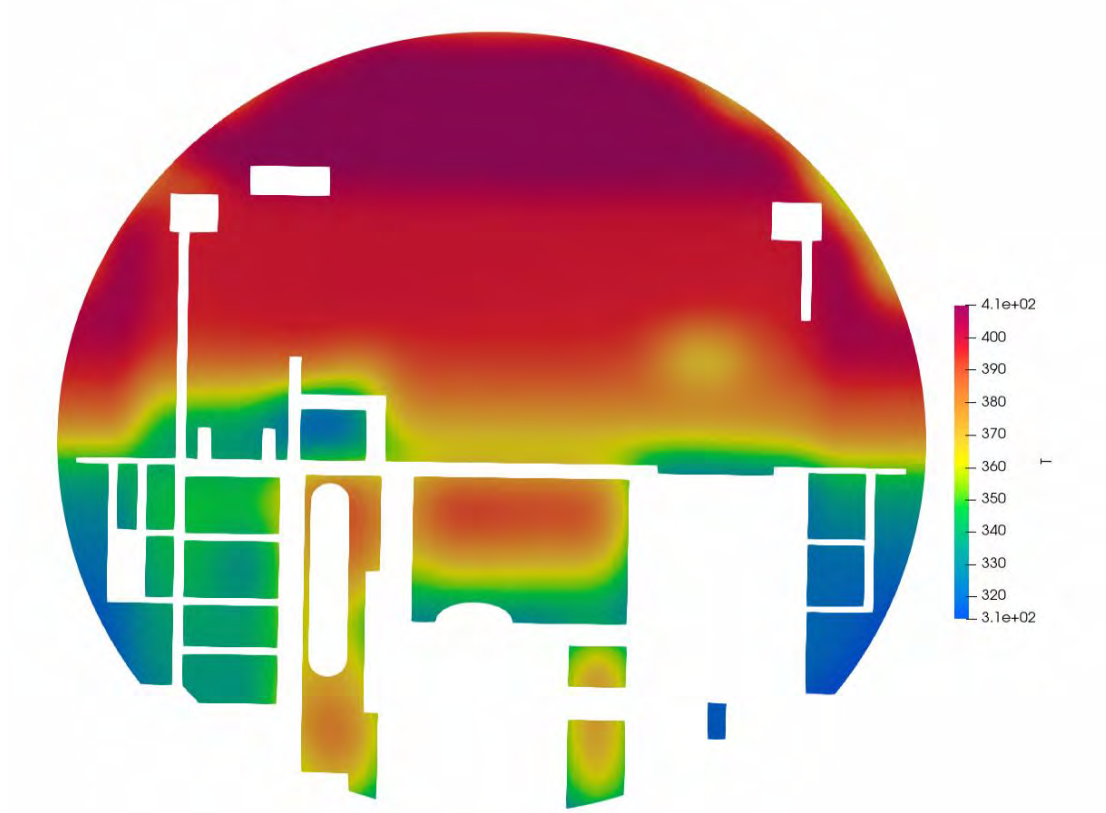

Mapped gas temperature from GOTHIC™ analysis

📖 doc/files/prePostProcessing.md

Credits: George

ETSON-AMHYCO BENCHMARK EXERCISE ON FLAME PROPAGATION IN REPRESENTATIVE REACTOR CONTAINMENT ATMOSPHERE IN CASE OF SEVERE ACCIDENT, LATE PHASES

Ahmed Bentaib[(1)], Nabiha Chaumeix[(2)], Alexandre Bleyer[(1)], Laura Gastaldo[(1)], Sina Tajfirooz [(3)], Francisco Javier Sánchez Velasco[(4)], Otón Martínez, Ramón Antonio[(4)] , Dahmani, Abderraouf[(4),] Joan Fontanet [(5)], Mantas Povilaitis [(6)], Julius Venckus [(6)] Ralf Bohm[(7)], Matthias Braun[(7)], Foad Mehdi Zadeh[(8)], Samuel Gyepi-Garbrah[(8)], Tobias Jankowski[(9)], Miriam Mueer[(9)], Berthold Schramm[(10)], Maksym Vyshemirskyi [(11)],

[(1)]ASNR, France; [(2)]CNRS, France; [(3)]NRG PALLAS, the Netherlands; [(4)]UPCT, Spain; [(5)] CIEMAT, Spain; [(6)] LEI, Lithuania; [(7)] Framatome, Germany; [(8)] CNSC, Canada; [(9)] RUB, Germany; [(10)] GRS, Germany; [(11)] SSTC, Ukraine

ABSTRACT

During a severe accident in a nuclear power plant (NPP), hydrogen (H_2) can be produced from the oxidation of fuel cladding or fuel assembly canisters and other hot metallic components. In case of failure of in-vessel corium retention, a large amount of carbon monoxide (CO) in addition to H_2 and other gases may be produced during molten corium-concrete interaction in the reactor pit. As a consequence, local concentrations of H_2 and CO can exceed the flammability limit of the gas mixture. Subsequent combustion would induce high dynamic pressure loads which could threaten the containment structures and technical equipment. Therefore, accurate and trustworthy combustion simulation is a task of primary importance in NPP accident analysis to determine local and global blast and heat loads. In particular, investigations are still necessary to increase the knowledge regarding turbulence effects on flame propagation.
In the framework of the European AMHYCO project, an experimental test campaign had been conducted with the aim to investigate the flame propagation in gaseous mixtures representing LWRs containment atmosphere during severe accident late phases. The experiments were performed on the highly instrumented ENACCEF2 facility, operated by the Institut de Combustion Aérothermique Réactivité et Environnement (ICARE) of the Centre National de la Recherche Scientifique (CNRS) in Orléans (France).
At the initiative of the AMHYCO project consortium and the European Technical Safety Organisation Network (ETSON), a code benchmark on hydrogen-carbon monoxide combustion was organised with the goal to identify the current level of the computational tools in the area of combustion simulation under conditions typical for safety considerations for NPP.
In the proposed paper, the simulation results obtained by participating organisations, using both Computational Fluid Dynamics and Lumped-Parameter computer codes, are compared to experimental results and analysed.

KEYWORDS
AMHYCO, ETSON, COMBUSTION, ENACCEF2, HYDROGEN, CARBON MONOXIDE

1. INTRODUCTION

During a severe accident (SA) in a nuclear power plant, hydrogen (H_2) can be produced from exothermic oxidation of fuel cladding or fuel assembly canisters and other hot metallic components. In case of failure of in-vessel corium retention, a large amount of carbon monoxide (CO) in addition to H_2 and other gases may be produced during molten corium-concrete interaction (MCCI) in the reactor pit. Therefore, local

concentrations of H_2 and CO can exceed the flammability limit of the gas mixture and induce strong dynamic pressure loads which may threaten the containment structures and technical equipment's, including important safety systems (SISs). The use of passive autocatalytic recombiners (PARs) considerably reduces the flammability risk of the containment atmosphere during the accidental transient. However, analyses of accidental scenarios in reactor cases show that, even in the presence of PARs, the flammability risk cannot be totally excluded during the whole accidental transient and particularly during the phases of high hydrogen production rate, which are affected by high uncertainties.

Therefore, accurate and trustworthy combustion simulation is a task of primary importance in NPP accident analysis to determine local and global blast and heat loads. Following the recommendations made in the SOAR R(99)16 [4] and the outcomes of the OECD/CCVM expert group discussions and the conclusions of ISP49 [5] and SARNET benchmarks [6], investigations are still needed to increase the knowledge regarding the effect of parameters such as turbulence level, initial temperature, initial and pressure, presence of CO, or lack of oxygen on flame propagation. In the framework of the MITHYGENE project and to this end, the new highly instrumented ENACCEF2 facility was built to address the above-mentioned issues.

To identify the current level of the computational tools in hydrogen combustion simulation under conditions typical for safety considerations for NPP, a first benchmark on hydrogen combustion was organised at the initiative of the MITHYGENE project consortium and the European Technical Safety Organisation Network (ETSON). This benchmark consisted of simulating experiments, performed in the ENACCEF2 facility, in which a homogeneous hydrogen-air mixture (for three different concentrations of hydrogen) was ignited at the tube bottom, and the subsequent flame and pressure wave propagation were measured. The benchmark blind results show that most of the used codes are able to predict qualitatively the pressure evolution inside the vessel [2]. Nevertheless, the flame speed maximum value is generally predicted with a significant deviation from the experimental results. This indicates that there are still limitations and weaknesses in the combustion models used in the different codes. These limitations concern the chemistry part, the turbulent combustion model and the coupling between the two models. An improvement of the combustion models is necessary to obtain consistent agreement between the flame regime and the pressure build-up predicted for a given configuration.

A second benchmark was organised in the framework of the SAMHYCO-NET and with the support of ETSON, as a continuation of the previous benchmark by considering more representative gas mixtures [3]. Here also, the benchmark blind results show the code's ability to predict qualitatively the pressure evolution inside the vessel and their difficulty to predict accurately the flame speed maximum. Therefore, further investigations are still needed.

Moreover, the outcomes of the international workshop on hydrogen management in NPP, held at IRSN in April 2019, underlined the need to improve the combustion models for both low hydrogen concentrations and for stratified mixtures which are more relevant for the reaction applications. Similarly, the SAMHYCO-Net outcomes pointed out the need of improving combustion models to simulate flame propagation in mixtures representative of late phases of a severe accident.

To this end, the European project AMHYCO was launched in 2020 with the objective to propose innovative enhancements on the combustible gas management procedures in case of a severe accident by addressing open issues related to the understanding of H_2 and CO phenomena involved in such an accident. To achieve this goal, an extensive experimental study has been conducted addressing different combustion phenomena including flammability limits determination, laminar and turbulent flame speed measurements and flame regime investigation the large closed ENACCEF-II facility considering different initial conditions.

From the performed experiments, three tests were selected to organize the ETSON-AMHYCO benchmark with the aim to evaluate the existing models, identify gaps in current knowledge, and derive significant

improvements in the quality and accuracy of numerical predictions of flame propagation in representative mixtures of a severe accident late phase.

The ETSON-AMHYCO benchmark was established within three main phases: STEP0, STEP1, and STEP2. STEP0 was organized as an open benchmark, while STEP1 and STEP2 were conducted as blind exercises. It is important to note that STEP2 is optional. The benchmark was started in October 2024 and lasted until February 2025. During this period, meetings were held to discuss the results and derive conclusions. This article presents and discusses the results of the submitted calculations for STEP1 and provides the main conclusions issued from the discussion during the final meeting.

2. ENACCEF2 facility

ENACCEF2 is a vertical acceleration tube of 7.65 m height and 23 cm inner diameter composed of nine cylindrical modules as shown in Figure 1. Two of these modules are equipped with large sapphire windows for imaging of the flame propagation using high speed camera.

Each module is equipped with different detectors to measure flame position and the pressure build-up during the combustion. For the benchmark needs, 2 visualization sections (sapphire windows, Figure 1-left), 27 photomultipliers (Hamamatsu), 10 pressure sensors (Kistler and PCB) and 27 shock detectors (Metal Process) were used (Figure 1-center). The initial combustible gas content along the facility is monitored using a micro-gas chromatographer (SRA instruments). Sampling of the fresh gases prior to ignition is done at 4 different heights along the facility (Figure 1-center). The gas mixture is introduced in the facility, initially under vacuum, using mass flow meters (Bronkhorst). The initial temperature is monitored using several thermocouples located at different heights along the tube. To enhance the turbulence, the lower part of ENACCEF2 is equipped with 9 annular obstacles (Figure 1-right) having a blockage ratio BR of 0.63, the separation distance between 2 consecutive obstacles was fixed to be 23 cm.

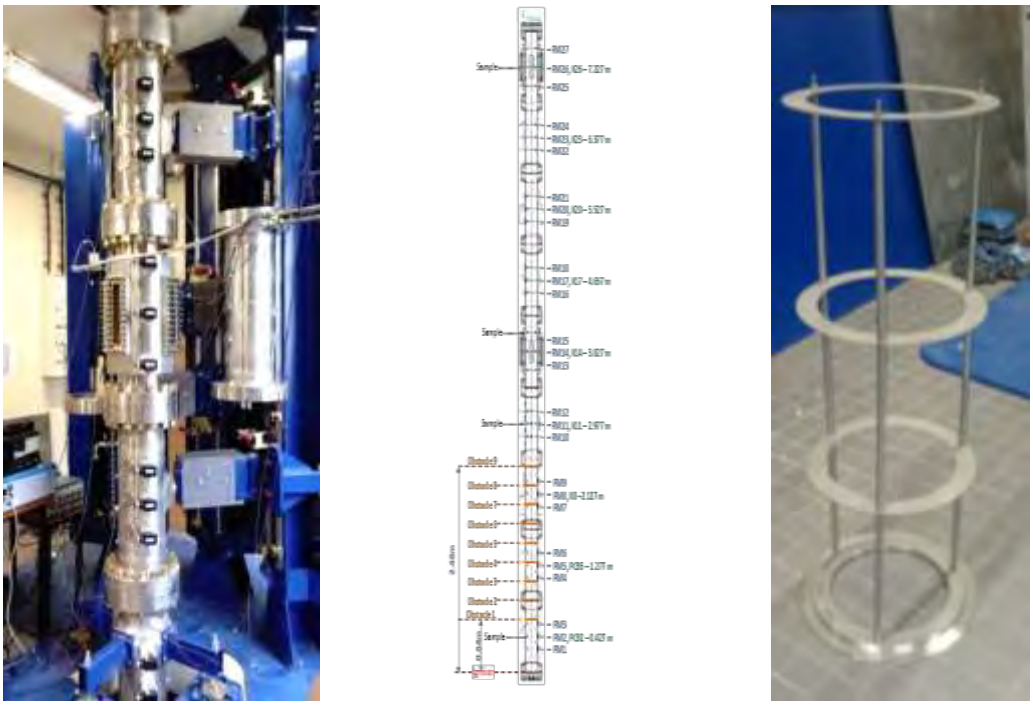

Figure 1. ENACCEF2 - left: photo, center: schematics, right: internal obstacles

3. EXPERIMENTAL RESULTS

As mentioned above, the ETSON–AMHYCO benchmark was organized in three steps based on experimental tests carried out within the AMHYCO project, using representative gas compositions and thermodynamic conditions of ex-vessel severe accident phases. The initial conditions considered are summarized in the following Table 1:

Table 1. Initial conditions of the experiments

	T_{ini} (°C)	P_{ini} (bar)	H_2O_{vap} (%mol)	CO_2(%mol)	H_2 (%mol)	CO(%mol)
STEP0	100	1	30	0	12.6±0.03	12.58±0.02
STEP1	88	2.47	20.3	16.05±0.09	7.90±0.08	7.45±0.06
STEP2	83	1.71	21.9	0	9.92±0.012	1.30±0.01

Based on the sigma criterion, all three tests fall into a flame acceleration regime, as the maximum flame velocity exceeded half the sound speed in the burned gas. Ignition is always initiated at the bottom of the facility, and the flame propagates upward through a homogeneous gas mixture. To characterize the flame propagation regime, measurements focused on flame position and pressure. Each test was performed at least three times each. The average of the recorded flame position as a function of time was then used to determine the flame velocity along the facility height, allowing the identification of acceleration and deceleration regimes. The following Figure 2 shows the flame position versus time (left graph) and the corresponding flame velocity (right), each time averaged over three experimental runs.

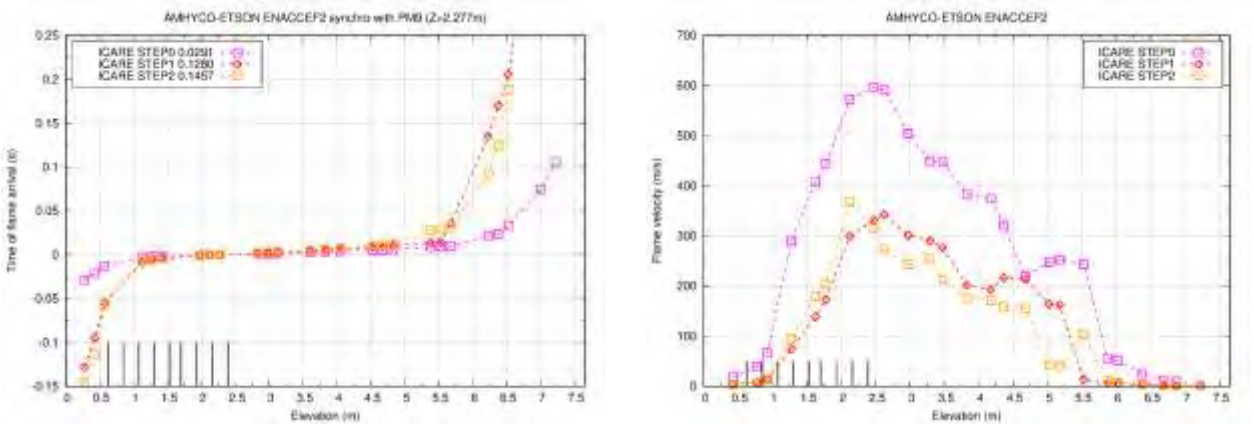

Figure 2: STEP0, STEP1 and STEP2 - average measured flame position versus time (left) and corresponding flame velocity along the facility elevation (right)

For all tests, four flame propagation phases can be distinguished:

- The first phase corresponds to the flame propagation between the ignition point and the first obstacle. During this phase, the flame propagates in a smooth tube with a maximum velocity of ~10 m/s.
- The second phase corresponds to flame propagation in the area between the first and the last obstacle. Due to turbulence induced by those obstacles, the flame front accelerates and reaches values between 340 m/s for STEP1 and 600 m/s for STEP0.
- The third phase corresponds to the flame propagation in the area just past the last obstacle. Due to the decrease of turbulence level past the last obstacles, the flame speed decreases. When the flame

becomes sub-sonic, the pressure wave detaches from the flame front and travels with speed of sound along the ENACCEF2 tube upwards. At the end of the tube, the shock wave gets reflected and starts travelling downward again. The third phase of the experiment is defined that the downward-traveling reflected shock wave did not reach the upward-traveling flame front.

- The fourth phase corresponds to the flame propagation in the upper part of the facility, after the flame front encountered the reflected shockwave. During this phase, the flame velocity is drastically slowed down due to its interaction with the reflected shockwave. The flame travels the last meter at velocities between 2 and 40 m/s.

The relative position of the shockwave can be identified in the recordings of the pressure sensors located along ENACCEF2, see Figure 3**Erreur ! Source du renvoi introuvable.**. The small black lines along the y-axis indicate the position of the obstacles in the facility. The pressure recordings are plotted in arbitrary units at the corresponding elevation of the sensor position. The upward traveling shockwave is highlighted by blue triangles, the first reflection of the shockwave by green triangles, and a secondary reflected wave by light-blue triangles. Additionally, the flame position is shown by circle-markers. When the first reflected shockwave meets the flame position, a dramatic decrease in flame velocity can be observed.

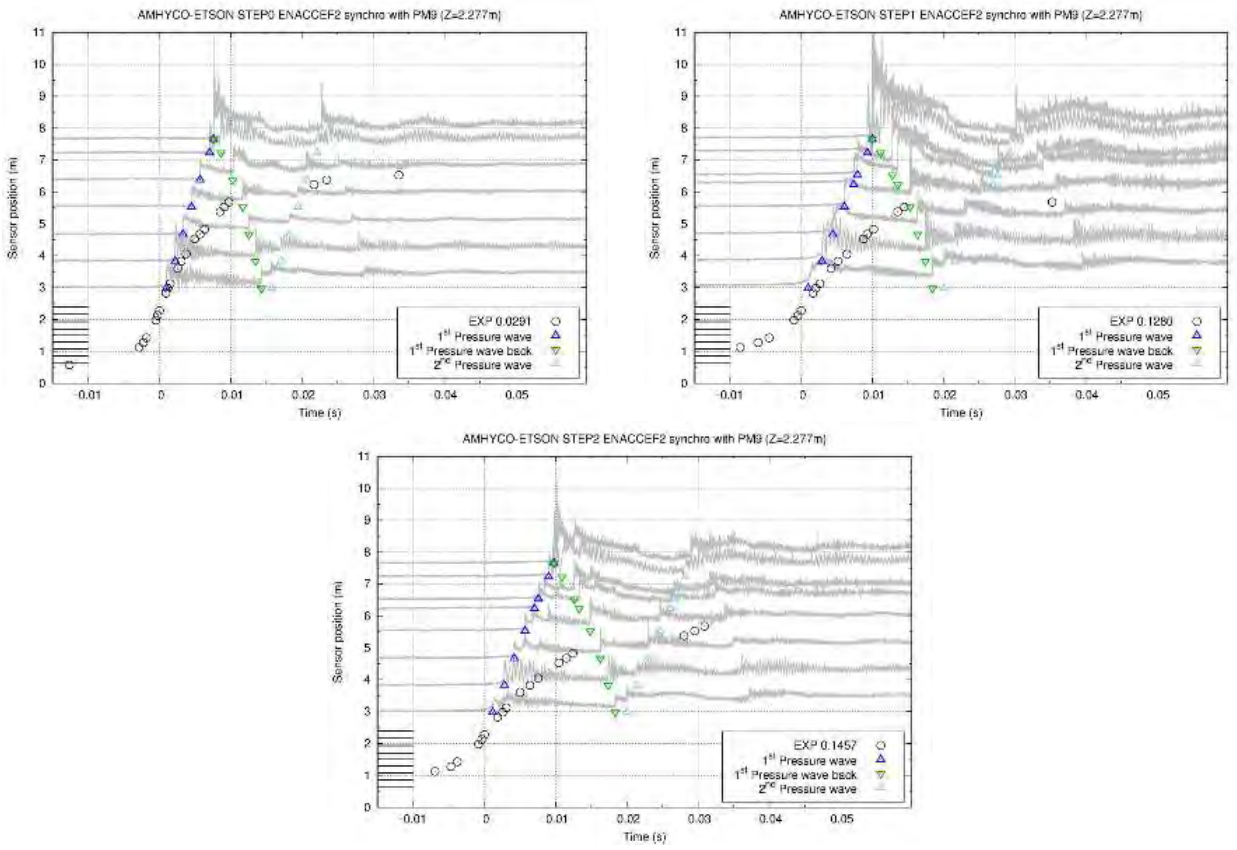

Figure 3: Pressure records in the experiment STEP0 (top-left), STEP1 (top-right), and STEP2 (bottom). The circles indicate the flame position. The blue triangles indicate the location of the pressure shock ahead the flame front, the green triangles represent the reflected shockwave.

From the experimental results presented above, we can conclude that the higher the initial fuel (CO and H_2) concentration the higher is the maximum flame velocity and the later the flame front interacts with the reflected pressure shock.

4. NUMERICAL CODES AND APPROACHES

There were eleven submitted results from nine participating organizations from 6 countries. Seven Computational Fluid Dynamics (CFD) and four Lumped-Parameter (LP) code contributions were then received. The following Table 2 presents the participating organizations and used codes.

Table 2: List of participating organizations and codes

Participants	Country	Code	Code Type	Label for graph
CNRS-ICARE	France	Experiments		ICARE-EXP
UPCT	Spain	OPENFOAM	CFD	UPCT_OPENFOAM
NRG	Netherlands	OPENFOAM	CFD	NRG_OPENFOAM
CNSC	Canada	Fluent	CFD	CNSC_Fluent
CIEMAT	Spain	MELCOR	LP	CIEMAT_Melcor
GRS	Germany	OPENFOAM	CFD	GRS_OPENFOAM
RUB	Germany	COCOSYS	LP	RUB_COCOSYS
FRG	Germany	MELCOR	LP	FRG_Melcor
ASNR	France	Fluent	CFD	ASNR_Fluent
ASNR	France	CALIF3S	CFD	ASNR_Calif
ASNR	France	ASTEC	LP	ASNR_Astec
LEI	Lithuania	OPENFOAM	CFD	LEI_OPENFOAM

The codes mentioned in Table 2 use different approaches for combustion modelling. Most of CFD combustion models are based on the burning velocity combustion approach: the flame front is then supposed to be thin, and the flame speed is obtained as a function of turbulence level and the laminar flame as for Fluent, OPENFOAM and CALIF3S codes where the burning Velocity Model (BVM model) based on a turbulent flame closure (as Zimont correlation for Fluent) is used. The chemical reaction rate is then built using the flame velocity V_{flamet}, the gas density $\bar{\rho}$ and progress variable gradient $|\nabla\tilde{c}|$ as follow: $\overline{\omega} = \bar{\rho} V_{flame} |\nabla\tilde{c}|$. The flame velocity is given by: $V_{flame} = Au' Da^{1/4}$, where A is constant. u' stands for turbulence intensity and Da for Damkhöler number [1]. However, specific modifications were incorporated into some of the models to accurately capture the Darrieus–Landau flame instability in slow combustion regime and to account for the additional effects of the Lewis number and pressure in fast flames.

As is customary in LP codes, the turbulence is not modelled, but its effects must be taken into account in flow-loss coefficients, the LP combustion models, as for ASTEC and COCOSYS codes, the correlations used to evaluate the turbulence intensity are based on the gaseous flow velocities in the atmospheric junctions between nodes (zones) (see Figure 4).

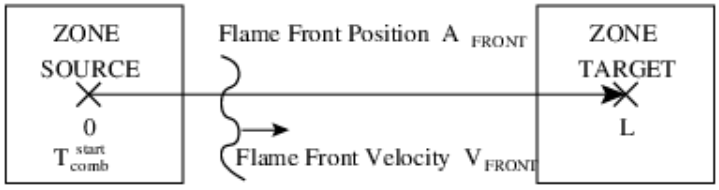

Figure 4. CPA-FRONT flame propagation principle.

The flame front burning speed is then obtained as sum of gas speed and turbulent flame speed:

$$V_{FRONT} = S_t + U_{gas}$$

where U_{gas} stands for the gas velocity in the junction and S_t represents the turbulent flame speed issued from the Peters correlation [11]:

$$S_t = S_l\,(1 + \sigma_{Peters}) \quad \text{with} \quad \sigma_{Peters} = \frac{\sqrt{\left(0.39\frac{l_t}{\delta}\right)^2 + 8\times 0.39\frac{l_t u'}{\delta S_l}} - 0.39\frac{l_t}{\delta}}{2}$$

S_l is the laminar flame speed for which several correlations are available in the ASTEC code:

- Liu-McF for the classical Liu Mac Farlane model [12]
- Liu-CNRS for the correlation developed by CNRS [13]
- USER option offering the possibility to use different correlations

u' represents the root-mean-square (RMS) velocity fluctuations given by the correlation below:

$$u' = \left|U_{gas}\right| REYFAC\ Re^{REYEXP}$$

where $Re = \frac{\rho|U_{gas}|\sqrt{S_{junc}}}{\mu}$ stands for the Reynolds number while REYFAC and REYEXP are user parameters. l_t represents the turbulence integral scale estimated based on the zone floor and the junction section area S_{junc} and δ stands for the flame thickness and μ for the dynamic viscosity.

In MELCOR [14], the flame velocity V is computed with the BURN package using the HECTR code. For a cell with characteristic length L, the combustion time associated with flame propagation is given by:

$$t_{\text{comb}} = \frac{L}{V}.$$

To account for flame acceleration and deceleration due to flame–turbulence interactions, this combustion time is modified with a user-defined factor, Frac, such that

$$t_{\text{comb,adj}} = \text{Frac} \times t_{\text{comb}}$$

The parameter Frac was calibrated along the facility height to reproduce the STEP0 experimental data, with values (from bottom to top) of 0.22, 0.04, and 0.50. By modifying Frac, the code user imposes a multiplicative increase of the internally calculated flame velocity.

For the CFD contributions, the following Table 3 summarizes the information related to numerical models, turbulence and combustion models as well as heat transfer models:

Table 3. Characteristics of CFD codes (- means "not used"; + means "used").

Partner	Label	Turbulence model	Combustion model	Laminar flame model	Ignition model	Convective heat	Radiative heat
UPCT	*UPCT-OPENFOAM*	*RANS k-ε RNG*	*PaSR.*	*28Reactions H_2-CO detailed*	*High temperature*	-	-

Partner	Label	Turbulence model	Combustion model	Laminar flame model	Ignition model	Convective heat	Radiative heat
				chemistry from [15]	*region imposed*		
NRG	*NRG-OPENFOAM*	*k-ε*	*Zimont-TFC*	*constant*	-	+	-
CNSC	*CNSC_Fluent*	*K-omega sst*	C equation + Zimont correlation	*Constant*	-	-	-
GRS	*GRS-OPENFOAM*	*SST*	*Coupled (Darrieus-Landau instability/ Dinkelacker-correlation)*	*Tabulated with additional terms for H2O concentration, temperature and pressure influsence*	*No physical model, only by initialisation*	*Heat transfer coefficient*	*fvDOM*
ASNR	*ASNR_CALIF*	*k-ω SST*	*G-equation + Zimont correlation*	*constant*	-	+	-
ASNR	*IRSN-Fluent*	*k-ω SST*	*BVM-Zimont*	*constant*	*Initialisation with burned mixture and adiabatic temperature*	+	-
LEI	*LEI-OPENFOAM*	*k-ε*	*Zimont-TFC*	*ANN trained on chem kinetics with Davis mechanism*	-	+	-

5. RESULTS OF THE SIMULATIONS AND DISCUSSIONS

Both STEP0 and STEP1 were simulated by all participants; STEP0 as an open exercise and STEP1 as a blind one. STEP2 was optional and was analyzed by few participants. For this reason, only STEP0 and STEP1 submitted results are addressed in the following sections. Following the benchmark specifications, the comparison of experimental and simulation results is performed based on:

- the flame arrival time,
- the flame velocity,
- pressure – time histories.

The STEP0 test results were provided to the participants to calibrate their models before the blind phase in STEP1 and STEP2. Figure 5 present the flame position and the flame velocity profile along the facility elevation for the STEP0 test. The small vertical lines at the bottom of the graphs indicate the position of the internal obstacles (see Figure 1). The black line represents the experiment, and the coloured lines are the simulation results of the benchmark participants.

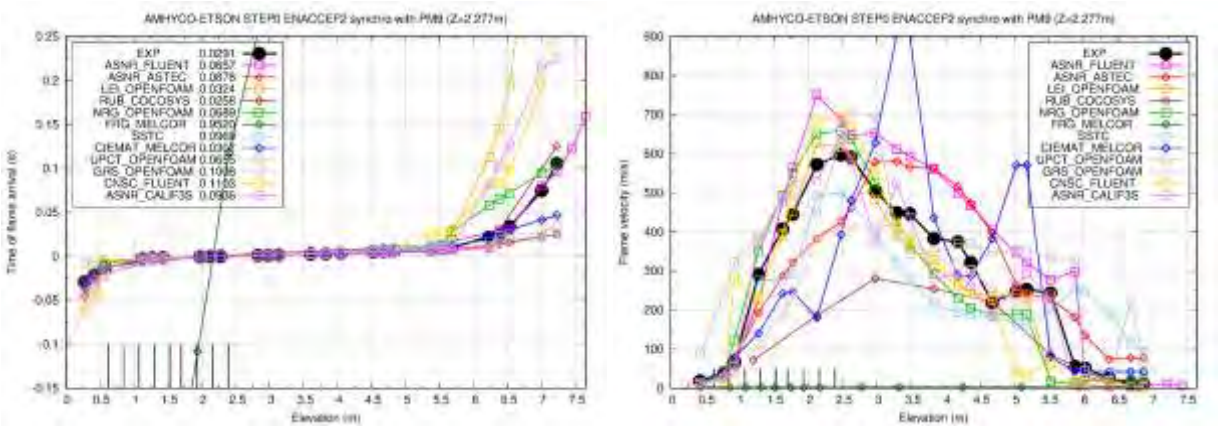

Figure 5: STEP0 - Flame position versus time (left) and flame velocity along facility elevation (right)

All codes, except one contribution with MELCOR code without time combustion calibration, are able to reproduce the main features of the combustion regimes in ENACCEF2: a 1st phase of flame acceleration before the obstacles, the very steep acceleration leading to the maximum flame speed at the end of the obstacles field and the subsequent flame deceleration. Nonetheless, large discrepancies are observed in predicting the maximum reached flame speed value and location.

In the region of flame acceleration, a pressure shock wave is created. While CFD codes can at least predict this shock wave reflection, the interaction between the flame front and the reflected shocks is not well reproduced. Figure 6**Erreur ! Source du renvoi introuvable.** compares the measured (straight black lines) and the by codes predicted pressures (straight coloured lines) at different facility elevations. The shockwave and its reflection can be observed by the relative time position of the pressure peaks. Further, in the figure also the flame front is shown as markers. The respective coloured lines represent code predictions, for a LP code on the left and for a CFD code on the right.

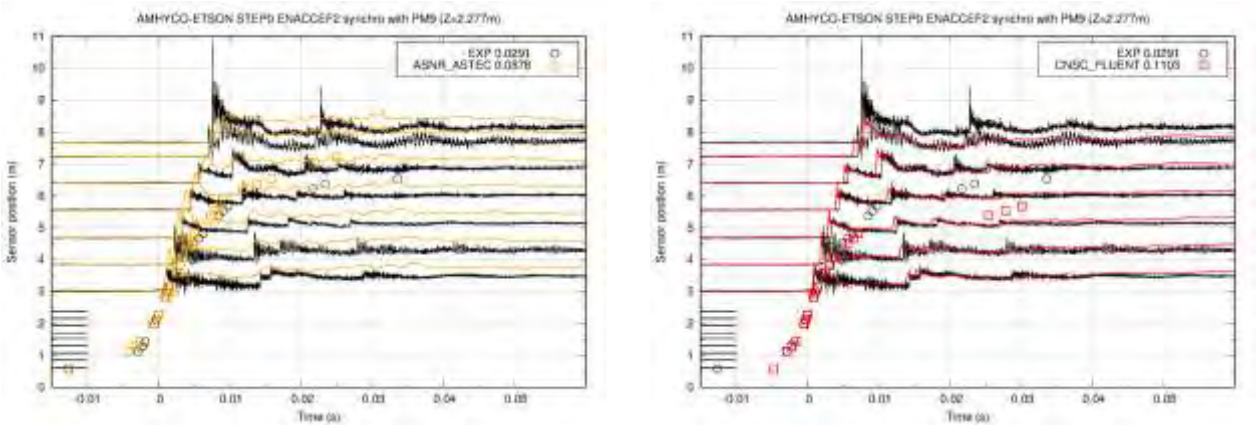

Figure 6: STEP0 - Pressure signals at different elevations (straight lines) and flame front position (markers) - comparison between experiment (black) and ASNR_ASTEC results (left, yellow) as well as CNSC_Fluent results (right, red)

The insights gained from the STEP0 test allowed participants to adjust their models in preparation for the blind STEP1 exercise. Despite this calibration phase, and because STEP1 involved different initial conditions from STEP0, discrepancies between the simulations and the experimental results persist. Nevertheless, as shown in Figure 7, most codes were able to reproduce both the acceleration and deceleration phases of the flame. The position of the peak flame speed (left figure) is reasonably well captured by most contributions. The flame speed magnitude (right figure) is still either under- or over-predicted.

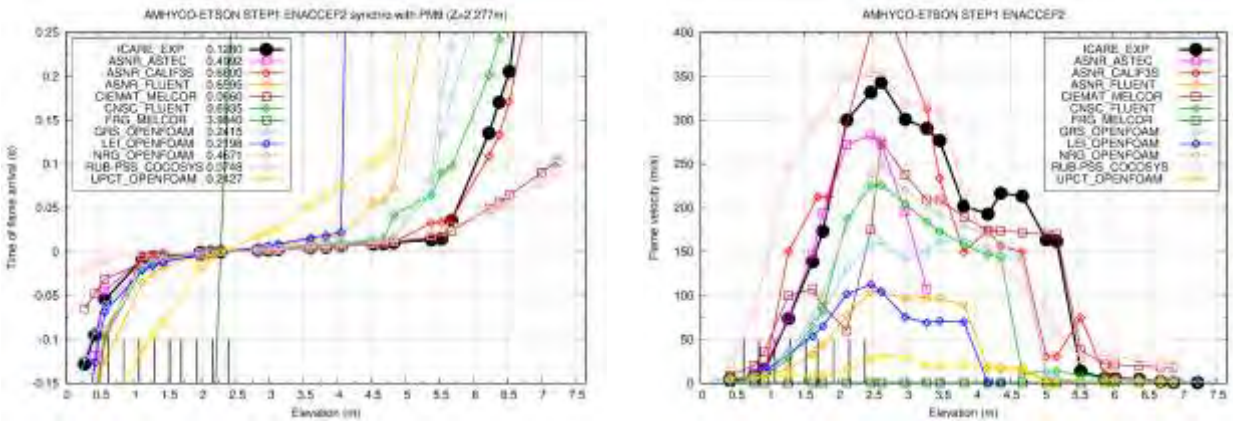

Figure 7: STEP1 - Flame position versus time (left) and flame velocity along facility elevation (right)

Moreover, the contributions that overpredict the maximum flame speed generally provide a reasonable estimate of the flame front–pressure shock interaction location. In contrast, those contributions that significantly underpredict the flame speed also predict the flame–pressure shock interaction to occur at a lower position. The pressure histories in Figure 8 below illustrate this trend for the CFD contributions.

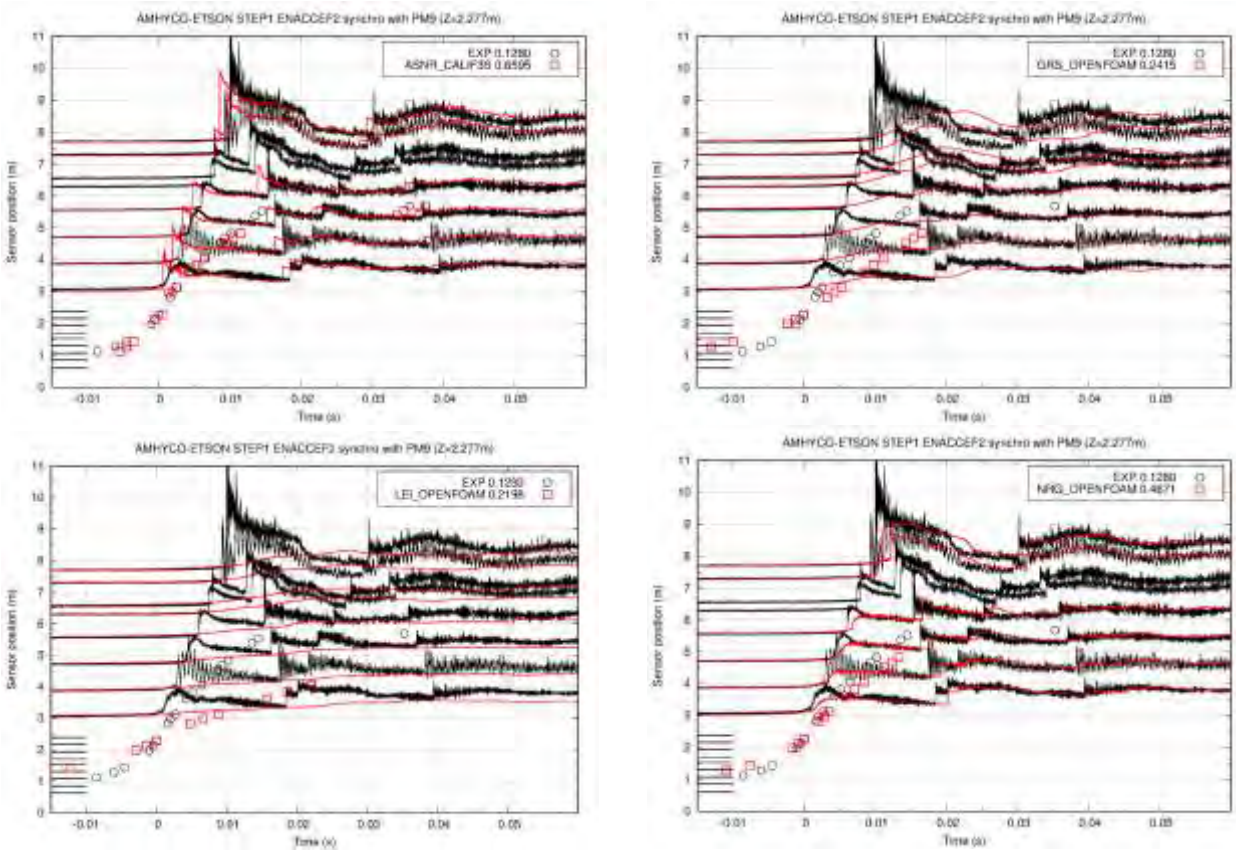

Figure 8: STEP1 - Pressure signals at different elevations (straight lines) and flame front position (markers) - comparison between experiment (black) and ASNR_CALIFS results (top-left), GRS-OPENFOAM results (top-right), LEI_OPENFOAM results (bottom-left), and NRG_OPENFOAM results (bottom-right)

6. CONCLUSIONS

The benchmark highlighted several key findings and recommendations regarding both the numerical solvers and the physical models. For the numerical solvers, it was recommended that, in addition to using an appropriate discretization scheme, pressure-based solvers should, when applicable, be corrected to account for compressibility effects. Numerical solvers, including pressure correction methods, need to be proven applicable to compressible flow; consistency and stability for compressible Euler equations, including shock solutions, should be numerically assessed. Furthermore, the use of adaptive time-stepping strategies and high-order numerical schemes was noted to improve simulation results and numerical convergence studies are necessary to reliably link results to the physical model

Regarding turbulence modelling, URANS provided acceptable predictions for the configurations considered. However, the initial turbulence level prior to ignition must be carefully specified, as it can significantly influence the overall flame behaviour.

For combustion modelling, burning velocity models (BVM) were found to yield satisfactory results, while the inclusion of detailed chemistry with CO offered no added benefit for STEP1 at the considered mesh resolution. Additionally, for lean H_2/CO mixtures, the impact of H2 and CO mass diffusivities on flame behaviour warrants further discussion.

Based on partner experience, thermal radiation is expected to have a significant influence on flame dynamics and should be investigated in future studies.

7. REFERENCES

1. G. Jimenez, L. E. Herranz, A. Bentaib, N. Chaumeix, E.-A. Reinecke, S. Kelm, M. Loeffler, M. Braun, I. Kljenak, O. Sevbo, D.C. Visser, Z. Liang, S. Balech, AMHYCO Project – Towards Advanced Accident Guidelines for Hydrogen Safety in Nuclear Power Plants, International Conference in Hydrogen Safety proceedings, 2021, ISBN 9791220094009
2. A. Bentaib & al; ETSON-MITHYGENE Benchmark on Simulations of Upward Flame Propagation Experiment in the ENACCEF2 Experimental Facility, 12th International Topical Meeting on Nuclear Reactor Thermal-Hydraulics, Operation and Safety (NUTHOS-12) Qingdao, China, October 14-18, 2018
3. A. Bentaib & al; ETSON-SAMHYCO-NET Benchmark on Simulations of Upward Flame Propagation Experiment in Representative Hydrogen-Air-Steam Mixtures of Severe Accidents Containments Atmosphere, 19th International Topical Meeting on Nuclear Reactor Thermal Hydraulics (NURETH-19) Log nr.: 35766, Brussels, Belgium, March 6 - 11, 2022
4. Flame Acceleration and Deflagration-to-Detonation Transition in Nuclear Safety, Nuclear Safety NEA/CSNI/R(2000)7, August 2000.
5. ISP-49 on Hydrogen Combustion, rapport OCDE/AEN; NEA/CSNI/R(2011)9.
6. Bentaib, A. Bleyer, N. Meynet, N. Chaumeix, B. Schramm, M. Höhne, P. Kostka, M. Movahed, S. Worapittayaporn, T. Brähler, H. Seok-Kang, M. Povilaitis, I. Kljenak, P. Sathiah, SARNET Hydrogen Deflagration Benchmarks: Main Outcomes and Conclusions, Annals of Nuclear Energy, Volume 74, December 2014, Pages 143-152, ISSN 0306-4549.
7. ANSYS FLUENT Theory Guide, Release 15.0
8. OpenFoam tutotrial, https://www.openfoam.com/documentation/tutorial-guide

9. P. Chatelard, S. Belon, L. Bosland, L. Carénini, O. Coindreau, F. Cousin, C. Marchetto, H. Nowack, L. Piar, L. Chailan, Main modelling features of the ASTEC V2.1 major version, Annals of Nuclear Energy, Volume 93, 2016, Pages 83-93,
10. OECD/NEA, ISP-49 on Hydrogen Combustion, Report NEA/CSNI/R(2011)9, 2012.
11. Peters, N., New developments in the theory of premixed turbulent combustion, Institut de l'Ecole Normale Superieure, Paris, France, 1997.
12. Liu, D., MacFarlane, R., 1983. Laminar burning velocities of hydrogen–air and hydrogen–air–steam flames. Combust. Flame 49 (1–3), 59–71.
13. Malet, F., 2005. Etude expérimentale et numérique de la propagation de flammes prémélangées turbulentes dans une atmosphère pauvre en hydrogène et humide. Ph.D. Thesis. Université d´Orléans
14. L. L. Humphries et al., 'MELCOR Computer Code Manuals Vol. 2: Reference Manual Version 2.2.18019', Sandia National Laboratories, Albuquerque, SAND2021-0241 O, Jan. 2021
15. Chelliah, H. The influence of heterogeneous kinetics and thermal radiation on the oxidation of graphite particles. Combustion and Flame 1996, 104, 81–94. https://doi.org/10.1016/0010-2180(95)00107-7.

ACKNOWLEDGMENTS

The authors acknowledge the support of the European project AMHYCO and the European Technical Safety Organisation Network (ETSON).

ETSON | EUROPEAN TECHNICAL SAFETY ORGANISATIONS NETWORK

AMHYCO

Enhancing H_2 & CO Combustion Risk Management

ETSON-AMHYCO Benchmark

EXERCICE ON HYDROGEN-CARBON MONOXIDE FLAME PROPAGATION UNDER REPRESENTATIVE OF SEVERE ACCIDENT LATE PHASES

Ahmed Bentaib, Nabiha Chaumeix, Alexandre Bleyer, Laura Gastaldo, Sina Tajfirooz , Francisco Javier Sánchez Velasco, Otón Martínez, Ramón Antonio, Dahmani, Abderraouf, Joan Fontanet, Mantas Povilaitis, Julius Venckus, Ralf Bohm, Matthias Braun, Foad Mehdi Zadeh, Samuel Gyepi-Garbrah, Tobias Jankowski, Miriam Mueer, Berthold Schramm, Maksym Vyshemirskyi

ASNR Autorité de sûreté nucléaire et de radioprotection

cnrs

NRG

Universidad Politécnica de Cartagena

CNSC CCSN Canada

Gobierno de España Ministerio de Ciencia e Innovación

Ciemat Centro de Investigaciones Energéticas, Medioambientales y Tecnológicas

SSTC NRS | State Enterprise State Scientific and Technical Center for Nuclear and Radiation Safety

Lithuanian Energy Institute

framatome

Ruhr Universität Bochum

RUB

GRS

Severe accident and hydrogen explosion in NPP

Three Mile Island nuclear Power plant

Chernobyl nuclear Power plant

Fukushima accident

Explosion in nuclear facilities may cause release of radioactive material to the environment

↓

Need to prevent the risk of explosion and limit its consequences

↓

Need to develop tools and methodologies for explosion risk assessment

Combustion modeling status
(*ISP49, SARNET and previous ETSON benchmarks outcomes*)

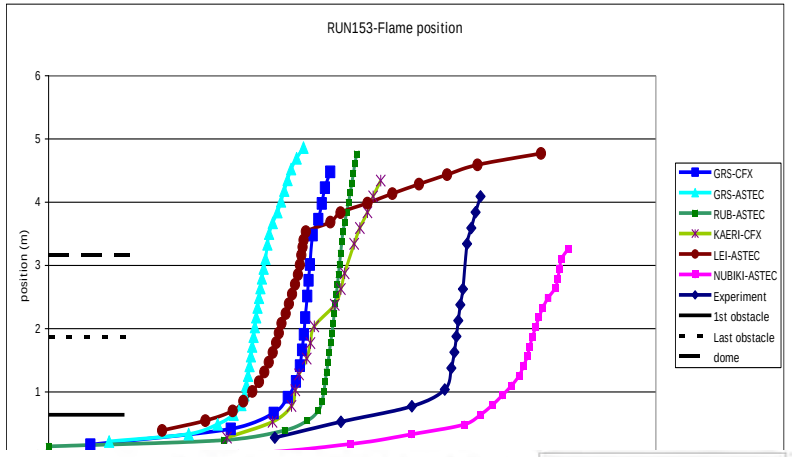

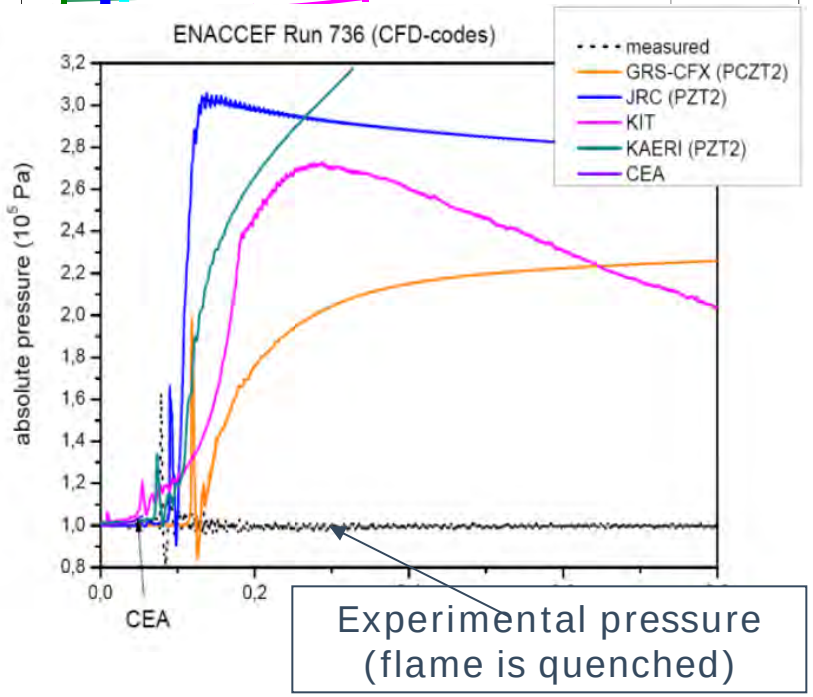

Experimental pressure (flame is quenched)

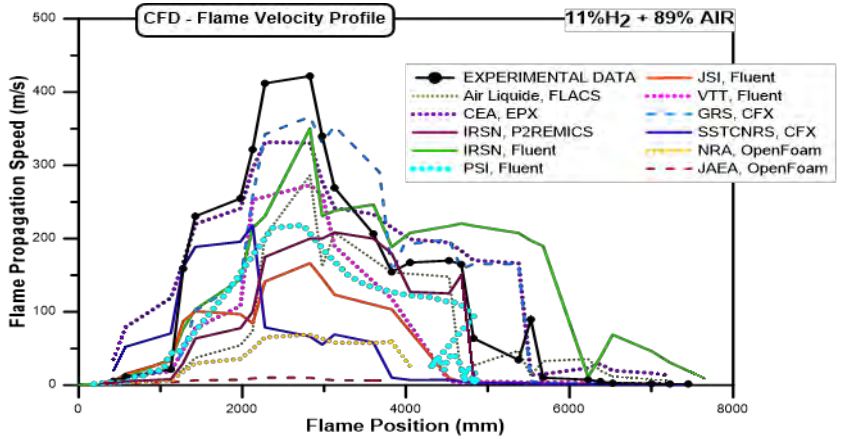

- Combustion models need to be improved to cover the entire range of flame propagation regimes (acceleration, deceleration)
- To date there is no « approved » flame quenching model, neither global, nor local (can be important for the correct prediction of combustion completeness).

Need of further investigation

Materials and methods

NEW FACILITY: ENACCEF 2

Characteristics

- h=7.65m, i.d=230mm
- T_{max}= 200°C
- P_{max}= 234 bar (without windows)
- P_{max}= 120 bar (with windows)
- **9 Annular obstacles**
  BR=0.63, x/D=1

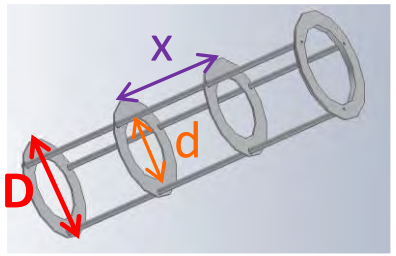

Blockage Ratio (BR)

(BR=1-(d/D)²)

Diagnostics

- 27 Photomultipliers/OH*filters
- 27 Shock Detectors
- 10 Pressure transducers
- 2 visualization sections 282*50mm
  (Schlieren visualization and PIV measurement)
- 4 Gas sampling Ports (GC analysis)
- Upward propagation
- At least 3 Runs/condition

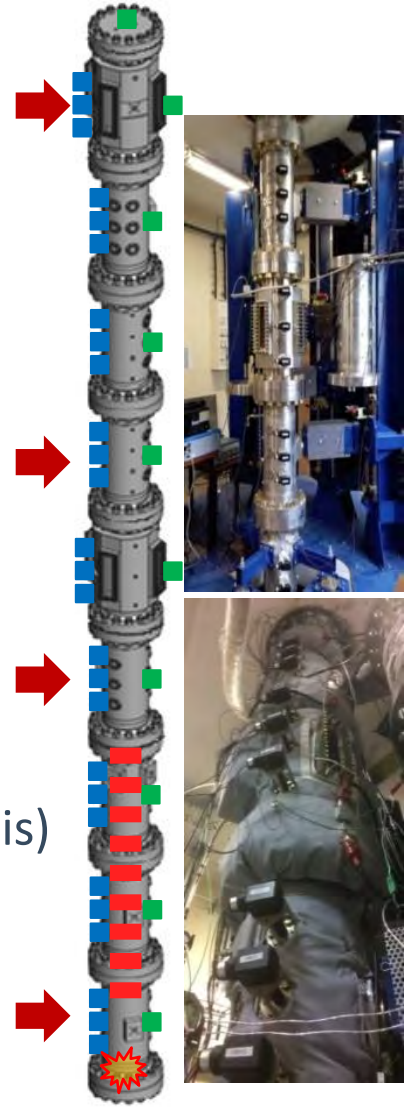

Materials and methods

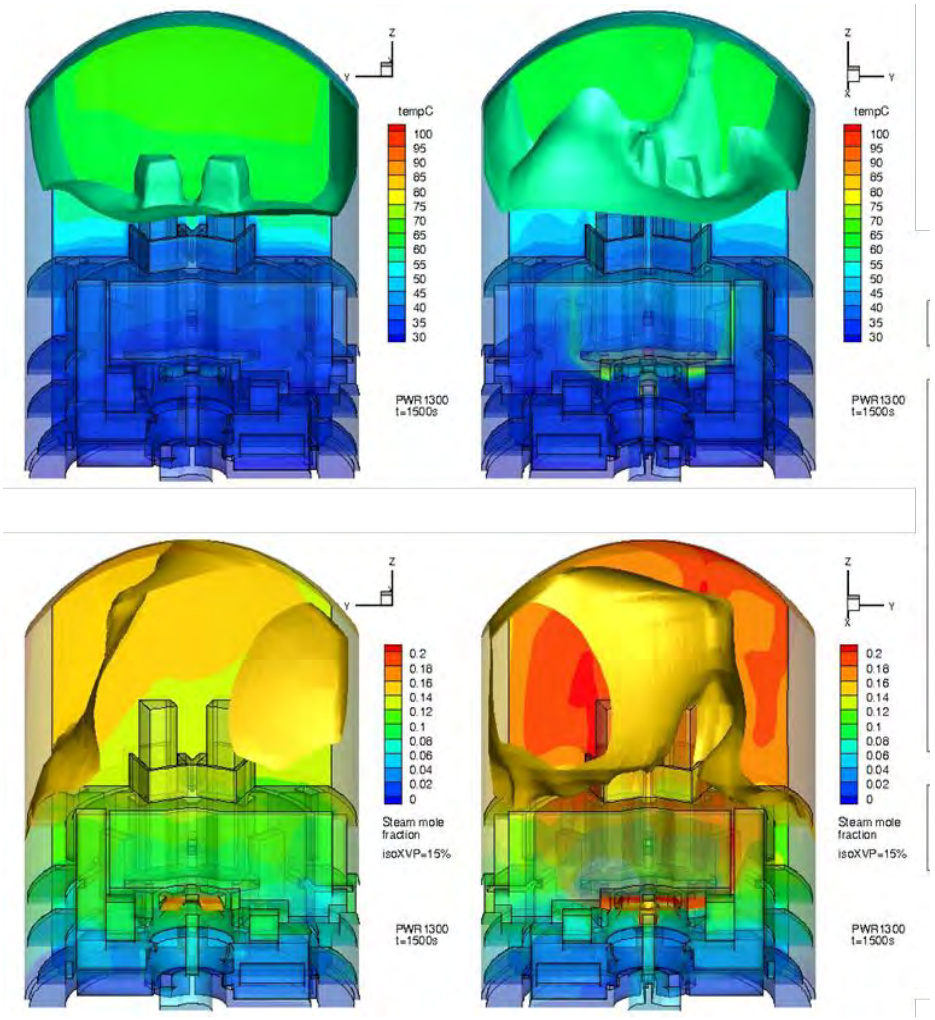

ETSON-MITHYGENE

References test : flame propagation in H2/air mixtures

Need to address more representative conditions

ETSON-SAMHYCO

Flame propagation in H2/H2O/AIR (pressure, temperature, heterogeneity)

ESTON-AMHYCO

Extension to late phase conditions
Flame propagation in H2/CO/H2O/AIR stratified mixtures (high pressure, high temperature, lack O2,..)

ETSON-MITHYGENE benchmark – Lessons learned

STEP0 → 13%vol H2, **T =23°C**, **P = 1 bar** → STEP1 → 11%vol H2, **T =25°C**, **P=1 bar** → STEP2 → 15%vol H2, **T =25°C**, **P= 1 bar**

ETSON | EUROPEAN TECHNICAL SAFETY ORGANISATIONS NETWORK — MITHYGENE

ETSON-MITHYGENE BENCHMARK

on Hydrogen Deflagration

PRELIMINARY REPORT

Prepared by

A. Bentaib[1], N. Chaumeix[2], R. Grosseuvres[1,2]
[1]IRSN, 77, av. du Général de Gaulle, 92140 Clamart, France
[2]CNRS, 3A Avenue de la Recherche, 45071 Orléans Cedex 2, France

November 2017

MITHYGENE Hydrogen deflagration Benchmark
Main outcomes and conclusions

A. **Bentaib, N. Meynet, A. Bleyer, R. Grossoeuvres**
Institut de Radioprotection et de sûreté nucléaire, 92262 Fontenay Aux Roses, France
ahmed.bentaib@irsn.fr
L. Gastaldo
Institut de Radioprotection et de sûreté nucléaire, Sain-Paul-lez durance, France
N. Chaumeix
CNRS-ICARE, UPR 3021
1C, avenue de la recherche scientifique, 45071 Orléans Cedex 2, France
chaumeix@cnrs-orleans.fr
E. Studer, S. Kudriakov
CEA, DEN, DANS/DM2S/SFME/LATF
F-91191 Gif-sur-Yvette Cedex, France
etienne.studer@cea.fr
S. Jallais, E. Vyazmina
AIR LIQUIDE R&D
Paris Saclay
Simon.jallais@airliquide.com ; Elena.vyazmina@ airliquide.com

ABSTRACT

In case of a hypothetic severe accident in a light water nuclear reactor, hydrogen could be produced during reactor core degradation and released into the reactor building. This could subsequently raise a combustion hazard. A local ignition of the combustible mixture may generate standing flames or initially slow propagating flames. Depending on geometry, mixture composition and turbulence level, the flame can accelerate or be quenched after a certain distance from the ignition point. The loads generated by the combustion process (increase of the containment atmosphere pressure and temperature) may threaten the integrity of the containment building and of internal walls and equipments. Turbulent deflagration flames may generate high pressure pulses, temperature peaks, shock waves and large pressure gradients which could seriously damage specific containment components, internal walls and/or safety equipment. The evaluation of such loads relies on codes, which in turn should be used with a high level of confidence.

Currently, turbulence effect on flame acceleration, flame deceleration and flame quenching mechanisms has not been completely well understood and further model development and validation are needed. For this purpose, hydrogen deflagration benchmark exercise had been organized in frame work of the French MITHYGENE project. This benchmark was focused on turbulence effect on flame propagation:three tests performed in the ENACCEF facility had been considered. They concern vertical flame propagation in an initially homogenous mixture with 13% hydrogen content and different geometrical configurations : 5, 9 and 16 annular obstables having the same blockage ratio (64%) to generate different levels of turbulence. This paper aims to present the Benchmark conclusions regarding the ability of CFD combustion models to predict the effect of turbulence on flame acceleration.

KEYWORDS

MITHYGENE, COMBUSTION, ENACCEF, HYDROGEN, CFD

1/17

- Codes that do not integrate explicit modelling of the flow turbulence exhibit flame speeds that are consistently overestimated.
- the modelling of turbulent effect on combustion appears to be the phenomenon on which R&D efforts must be strengthened.

ETSON-SAMHYCO benchmark – Lessons learned

STEP0
H_2 =13%vol
Steam=0%vol
Air= 87%vol
T =90°C

STEP1
H_2 =13%vol
Steam=30%vol
Air= 57%vol
T =90°C

STEP2
H_2 =13%vol
Steam=30%vol
Air= 57%vol
T =90°C
P = 2bar

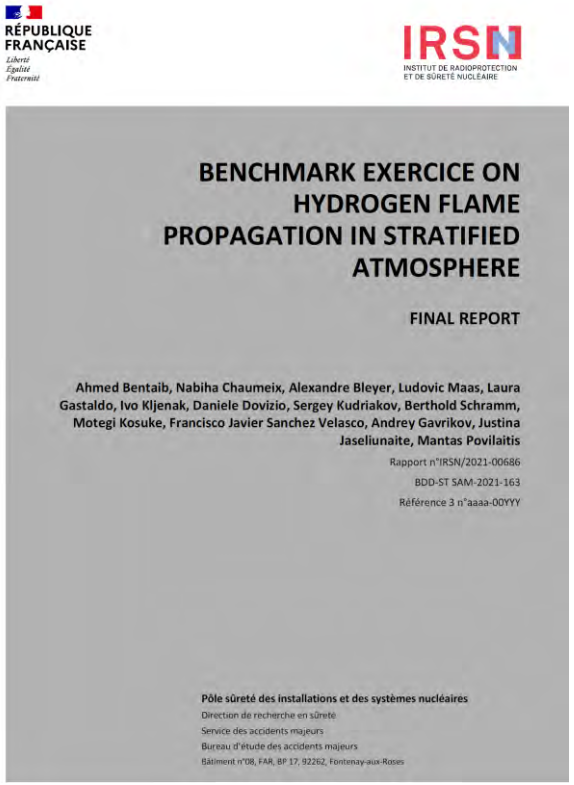
RÉPUBLIQUE FRANÇAISE
Liberté
Égalité
Fraternité

IRSN
INSTITUT DE RADIOPROTECTION ET DE SÛRETÉ NUCLÉAIRE

BENCHMARK EXERCICE ON HYDROGEN FLAME PROPAGATION IN STRATIFIED ATMOSPHERE

FINAL REPORT

Ahmed Bentaib, Nabiha Chaumeix, Alexandre Bleyer, Ludovic Maas, Laura Gastaldo, Ivo Kljenak, Daniele Dovizio, Sergey Kudriakov, Berthold Schramm, Motegi Kosuke, Francisco Javier Sanchez Velasco, Andrey Gavrikov, Justina Jaseliunaite, Mantas Povilaitis

Rapport n°IRSN/2021-00686

BDD-ST SAM-2021-163

Référence 3 n°aaaa-00YYY

Pôle sûreté des installations et des systèmes nucléaires
Direction de recherche en sûreté
Service des accidents majeurs
Bureau d'étude des accidents majeurs
Bâtiment n°08, FAR, BP 17, 92262, Fontenay-aux-Roses

The 19th International Topical Meeting on Nuclear Reactor Thermal Hydraulics (NURETH-19) Log nr.: 19001
Brussels, Belgium, March 6 - 11, 2022

ETSON-SAMHYCO-NET BENCHMARK ON SIMULATIONS OF UPWARD FLAME PROPAGATION EXPERIMENT IN REPRESENTATIVE HYDROGEN-AIR-STEAM MIXTURES OF SEVERE ACCIDENTS CONTAINMENTS ATMOSPHERE

A.Bentaib(1), N. Chaumeix(2), Gustav Nyrenstedt(2) , A. Bleyer(1), L. Mass(1) ,L. Gastaldo(1), , I. Kljenak(3), D. Dovizio(4), S. Kudriakov(5), B. Schramm(6), M. Kosuke(7), F.J.S. Velasco(8), R.A. Otón-Martínez(8), A. Gavrikov (9), J. Jaseliunaite(10), M. Povilaitis(10)

(1) IRSN, France; (2)CNRS-ICARE, France ; (3) IJS, Solvenia; (4)NRG, Netherlands; (5) CEA, France (6) GRS, Germany ; (7)JAEA, Japan; (8) UPCT, Spain; (9)IBRAE, Russia; (10) LEI, Lituania

ABSTRACT

In case of a core melt-down accident in a light water nuclear reactor, hydrogen is produced during reactor core degradation and released into the reactor building. In case of failure of in-vessel corium retention, a large amount of carbon monoxide (CO) in addition to H2 and other gases may be produced during molten core concrete interaction (MCCI). This subsequently creates a combustion hazard. A local ignition of the combustible mixture may generate standing flames or initially slow propagating flames. Depending on geometry, mixture composition and turbulence level, the flame can accelerate or be quenched after a certain distance. The pressure and temperature loads generated by the combustion process may threaten the integrity of the containment building and safety equipment. The evaluation of such loads requires validated codes which can be used with a high level of confidence. Currently, turbulence and steam effect on flame propagation mechanisms are not well reproduced by combustion models usually implemented in safety tools and further model enhancement and validation are still needed. For this purpose and at the initiative of the SAMHYCO-NET project consortium and of the European Technical Safety Organization Network (ETSON), a benchmark on hydrogen combustion was organized with the goal to identify the current level of the computational tools in the area of hydrogen combustion simulation under conditions typical for safety considerations in a Nuclear Power Plant (NPP). This benchmark is composed by four main steps with increasing difficulty starting from flame propagation in homogenous dry atmosphere and finishing with more representative conditions with (H2/H2O/O2/N2) stratified mixtures. In this paper, only experiments related to flame propagation in homogenous atmosphere are considered. The simulation results obtained by participating organizations, using both Computational Fluid Dynamics (CFD) and lumped-parameter computer codes, are compared to experimental results and analyzed. The main outcomes and lessons learned are also provided.

KEYWORDS
Benchmark, combustion, ETSON, SAMHYCO-NET, hydrogen

- Codes that do not integrate explicit modelling of the flow turbulence exhibit flame speeds that are consistently overestimated.
- Codes including explicit modelling of the flow turbulence may lead to underestimation of flame speeds.
- the modelling of turbulent effect on combustion appears to be the phenomenon on which R&D efforts must be strengthened.

ETSON-AMHYCO benchmark

Objectives: to evaluate the existing models, identify gaps in current knowledge, and derive significant improvements in the quality and accuracy of numerical predictions of flame propagation in representative mixtures of a severe accident late phase

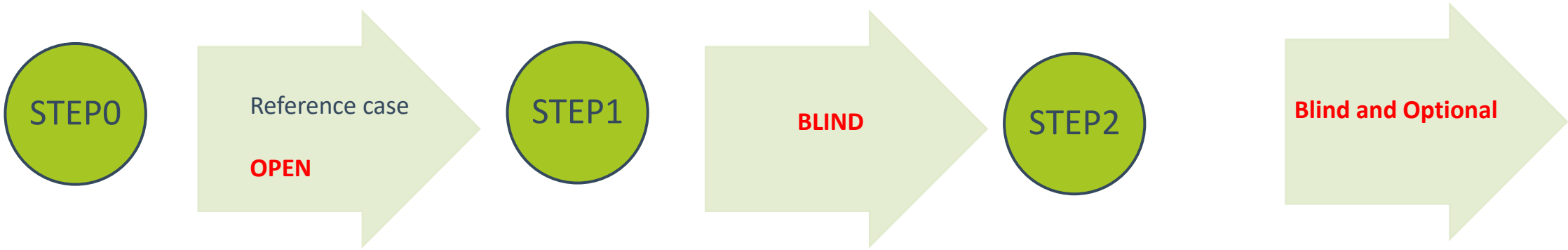

	T_{ini} (°C)	P_{ini} (bar)	H_2O_{vap} (%mol)	CO_2(%mol)	H_2 (%mol)	CO(%mol)
STEP0	100	1	30	0	12.6±0.03	12.58±0.02
STEP1	88	2.47	20.3	16.05±0.09	7.90±0.08	7.45±0.06
STEP2	83	1.71	21.9	0	9.92±0.012	1.30±0.01

ETSON-AMHYCO benchmark

Participants	Country	Code	Code Type	Label for graph
CNRS-ICARE	France	Experiments		ICARE-EXP
UPCT	Spain	OPENFOAM	CFD	UPCT_OPENFOAM
NRG	Netherlands	OPENFOAM	CFD	NRG_OPENFOAM
CNSC	Canada	Fluent	CFD	CNSC_Fluent
CIEMAT	Spain	MELCOR	LP	CIEMAT_Melcor
GRS	Germany	OPENFOAM	CFD	GRS_OPENFOAM
RUB	Germany	COCOSYS	LP	RUB_COCOSYS
FRG	Germany	MELCOR	LP	FRG_Melcor
ASNR	France	Fluent	CFD	ASNR_Fluent
ASNR	France	CALIF3S	CFD	ASNR_Calif
ASNR	France	ASTEC	LP	ASNR_Astec
LEI	Lithuania	OPENFOAM	CFD	LEI_OPENFOAM

LP modelling :

ASTEC and COCOSYS

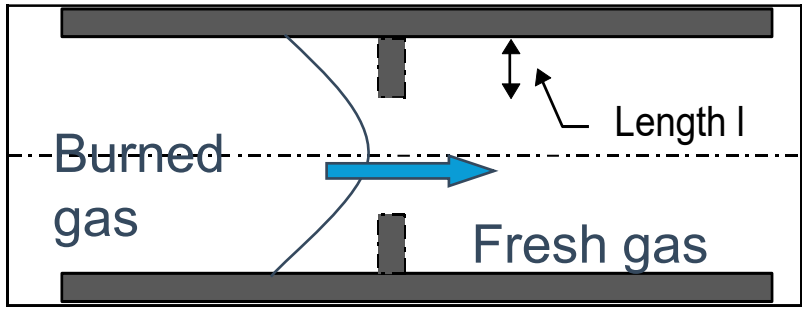

Turbulent flame velocity

(Peters correlation)

$$\frac{S_T}{S_L} = 1 + \bar{\sigma}$$

$$\bar{\sigma}^2 + 0.39.\frac{l}{l_F}\bar{\sigma} - 0.78\frac{u'.l}{S_L.l_F} = 0$$

$$u' = Cu_{gas}Re^n$$

$V_{flame} = \sigma S_T + U_{gas}$

MELCOR

V_{flame} is computed with the BURN package using the HECTR code.

$Tcomb = L\ V_{flame}$.

$Tcomb,adj = Frac \times Tcomb$

CFD modelling :

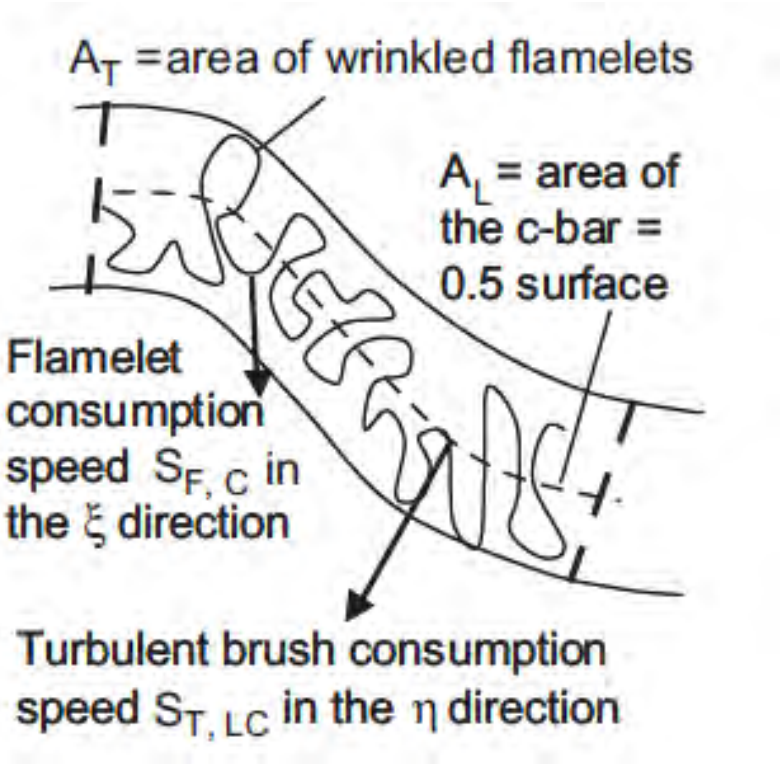

$$\frac{S_T}{S_{L0}} = \frac{A_T}{A_L}\frac{\bar{S}_{F,C}}{S_{L0}} = \frac{A_T}{A_L} I_0.$$

Combustion models use:

- Burning Velocity Model concept: *Flame front modeled using progress variable*

- The tubulent flame front velocity based on experimental correlations (Zimont, Brays, ..)

CFD modelling :

Partner	Label	Turbulence model	Combustion model	Laminar flame model	Ignition model	Convective heat	Radiative heat
UPCT	*UPCT-OPENFOAM*	*RANS k-ε RNG*	*PaSR.*	*28Reactions H_2-CO detailed chemistry*	*High temperature region imposed*	-	-
NRG	*NRG-OPENFOAM*	*k-ε*	*Zimont-TFC*	*constant*	-	+	-
CNSC	*CNSC_Fluent*	*K-omega sst*	C equation + Zimont correlation	*Constant*	-	-	-
GRS	*GRS-OPENFOAM*	*SST*	*Coupled (Darrieus-Landau instability/ Dinkelacker-correlation)*	*Tabulated with additional terms for H2O concentration, temperature and pressure influsence*	*No physical model, only by initialisation*	*Heat transfer coefficient*	*fvDOM*
ASNR	*ASNR_CALIF*	*k-ω SST*	*G-equation + Zimont correlation*	*constant*	-	+	-
ASNR	*IRSN-Fluent*	*k-ω SST*	*BVM-Zimont*	*constant*	*Initialisation with burned mixture and adiabatic temperature*	+	-
LEI	*LEI-OPENFOAM*	*k-ε*	*Zimont-TFC*	*ANN trained on chem kinetics with Davis mechanism*	-	+	-

ETSON-AMHYCO benchmark-experimental results

	T_{ini} (°C)	P_{ini} (bar)	H_2O_{vap} (%mol)	CO_2(%mol)	H_2 (%mol)	CO(%mol)
STEP0	100	1	30	0	12.6±0.03	12.58±0.02
STEP1	88	2.47	20.3	16.05±0.09	7.90±0.08	7.45±0.06
STEP2	83	1.71	21.9	0	9.92±0.012	1.30±0.01

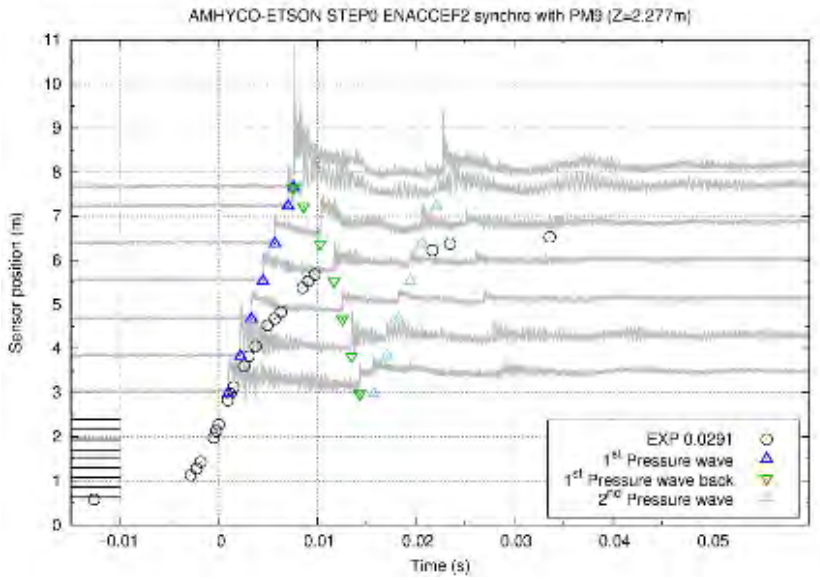

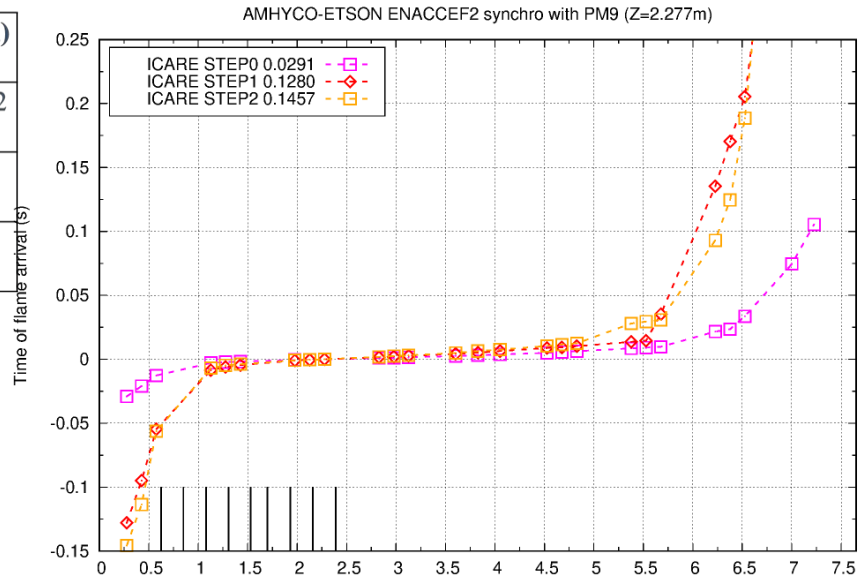

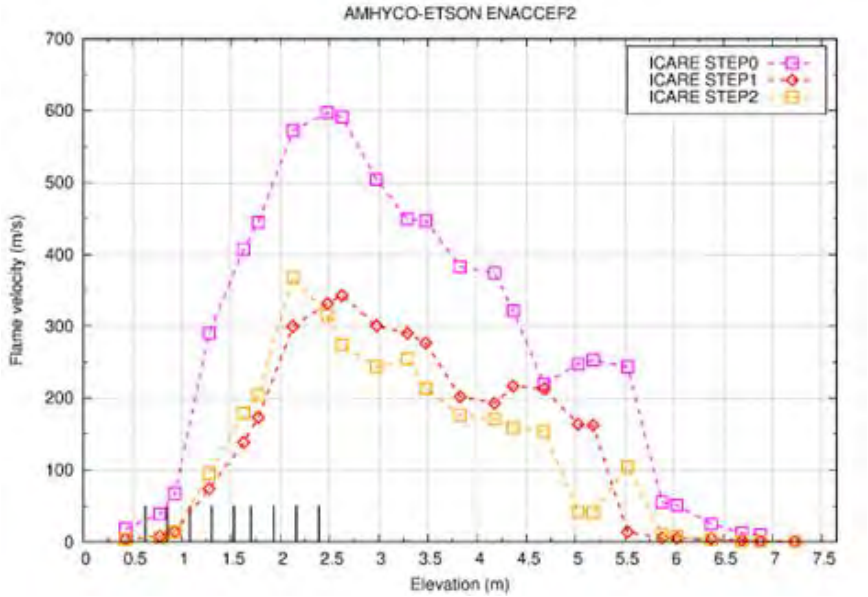

Movie of flame will be included later here

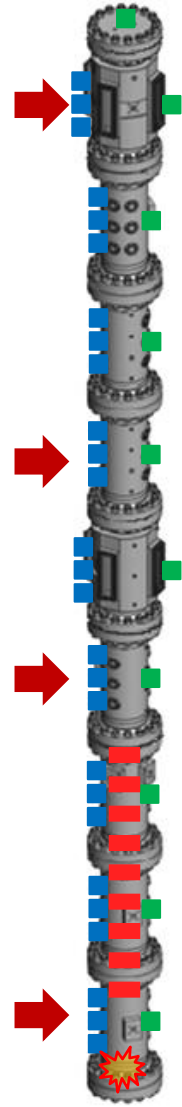

ETSON-AMHYCO benchmark-experimental results

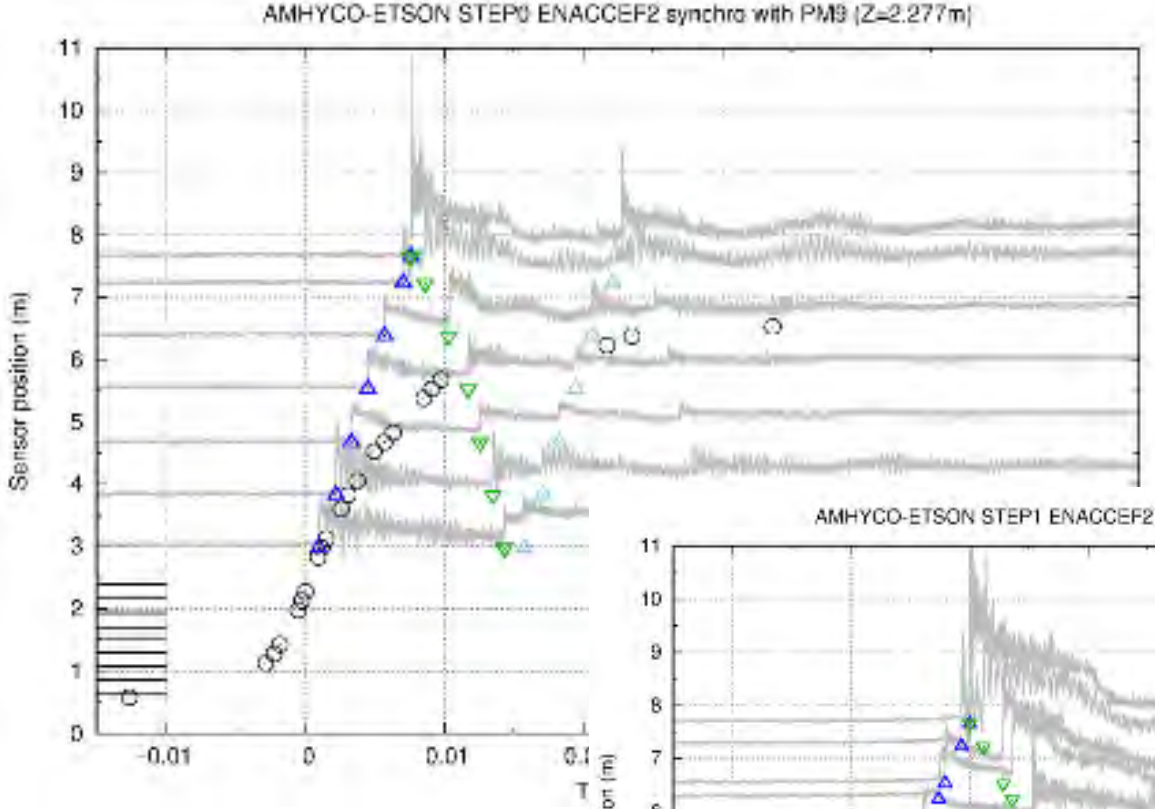

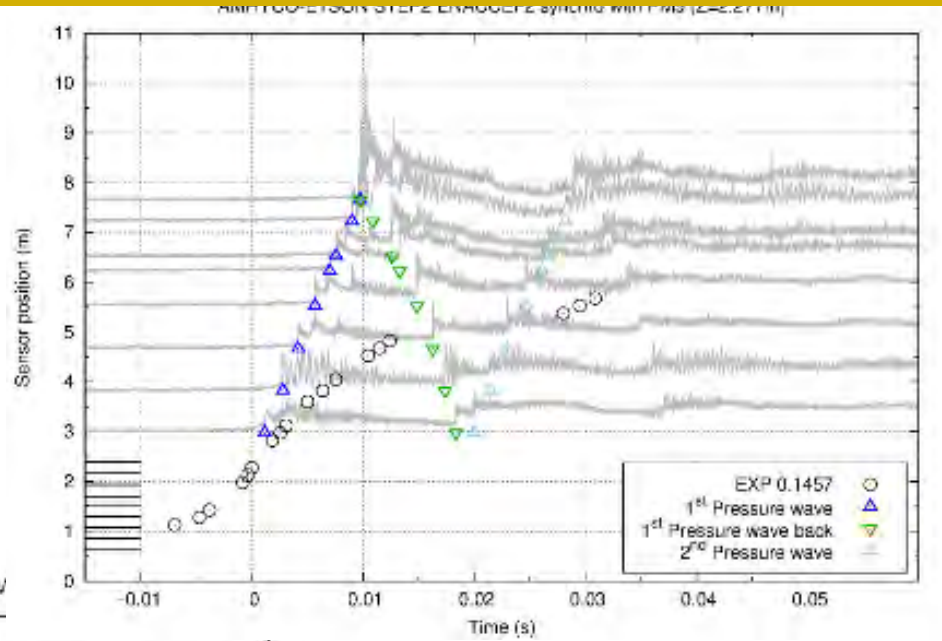

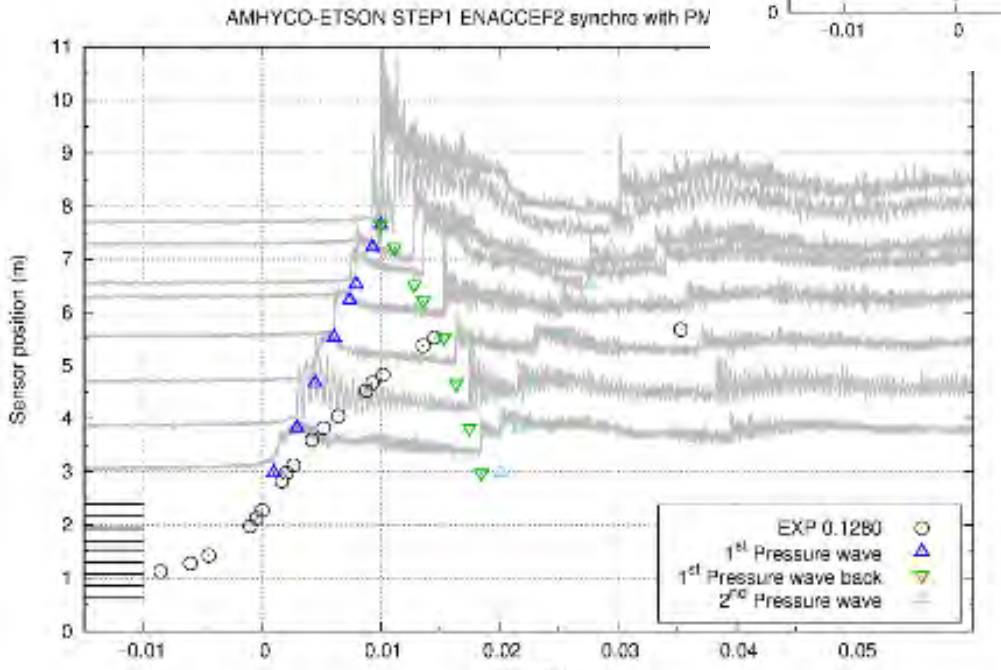

ETSON-AMHYCO: Calculation vs experiments

STEP0

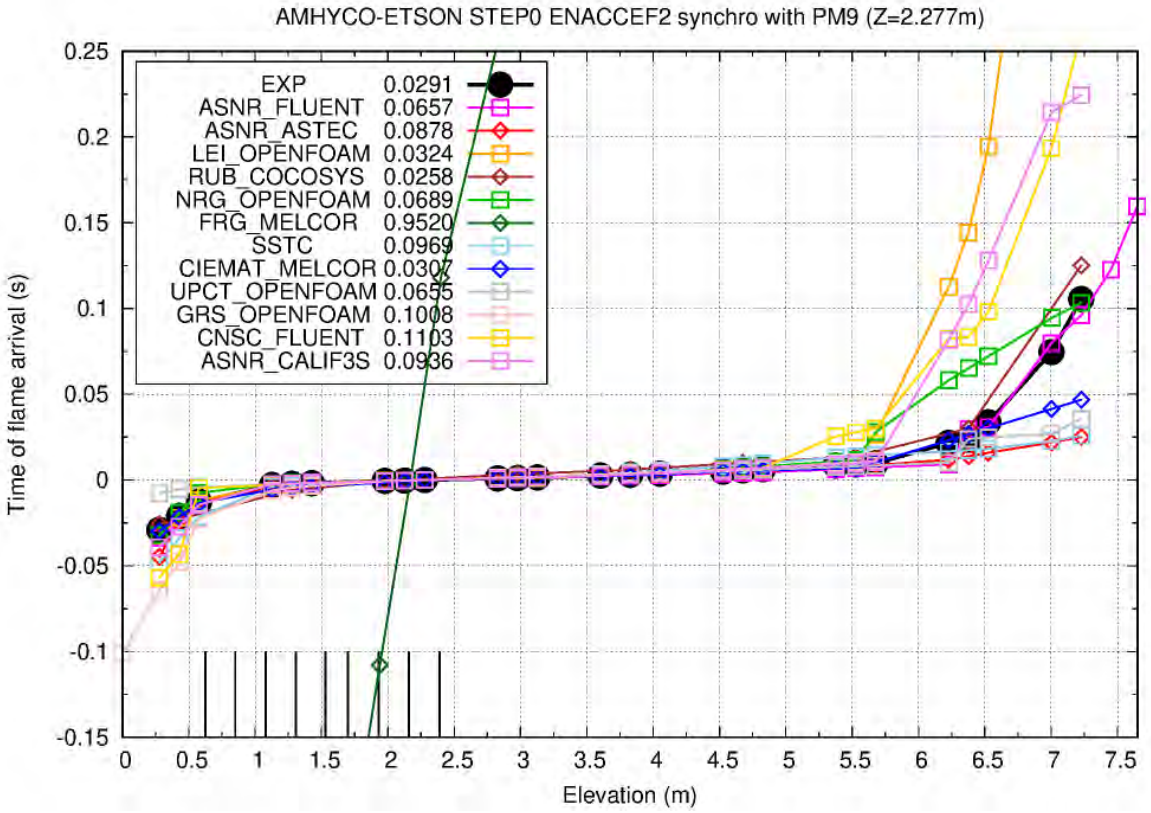

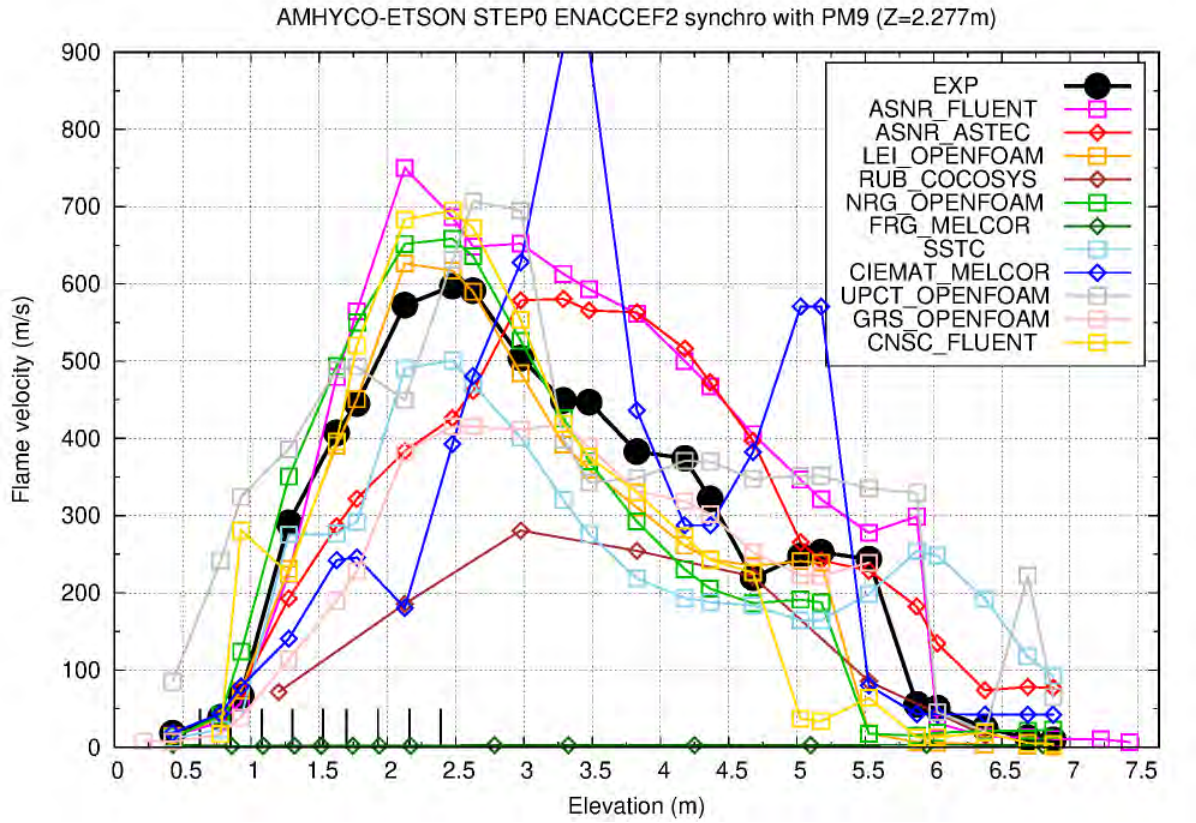

ETSON-AMHYCO: Calculation vs experiments

STEP0

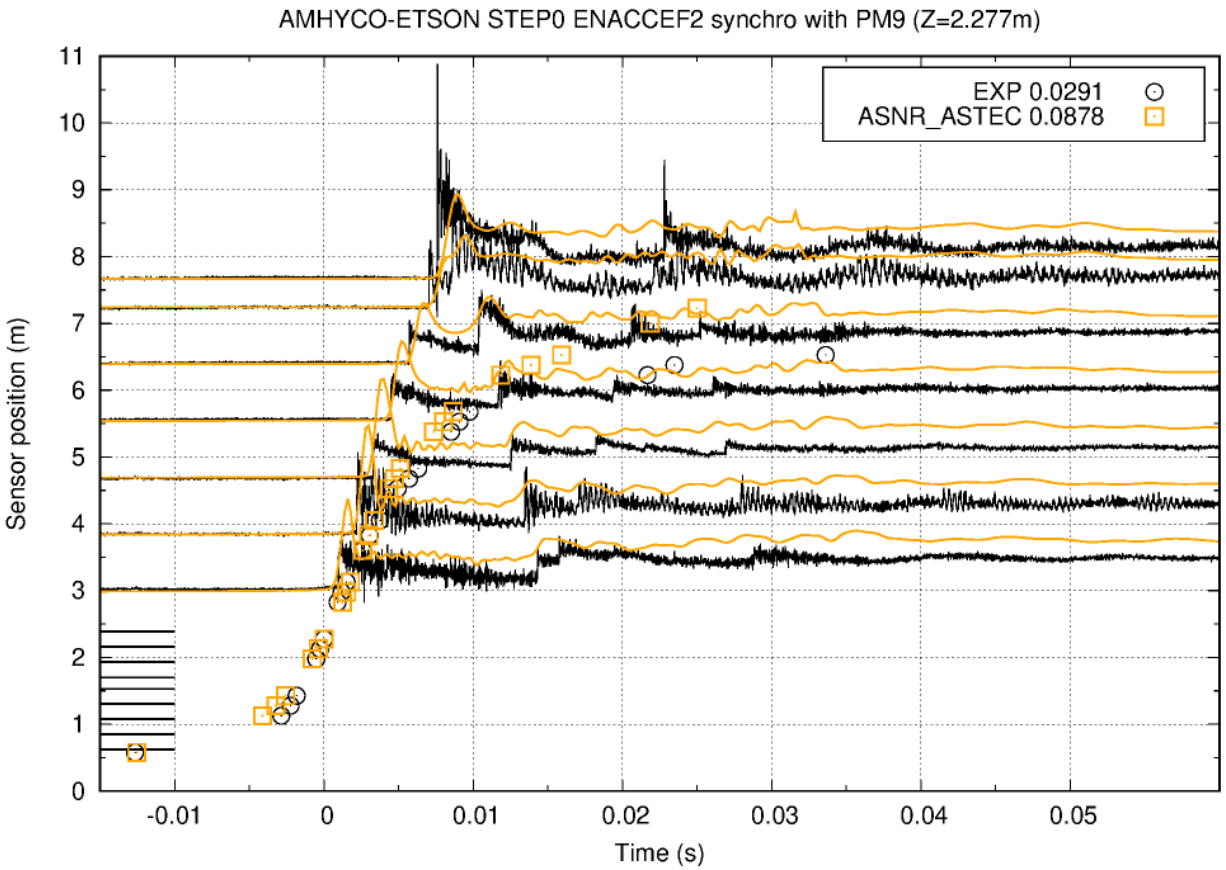

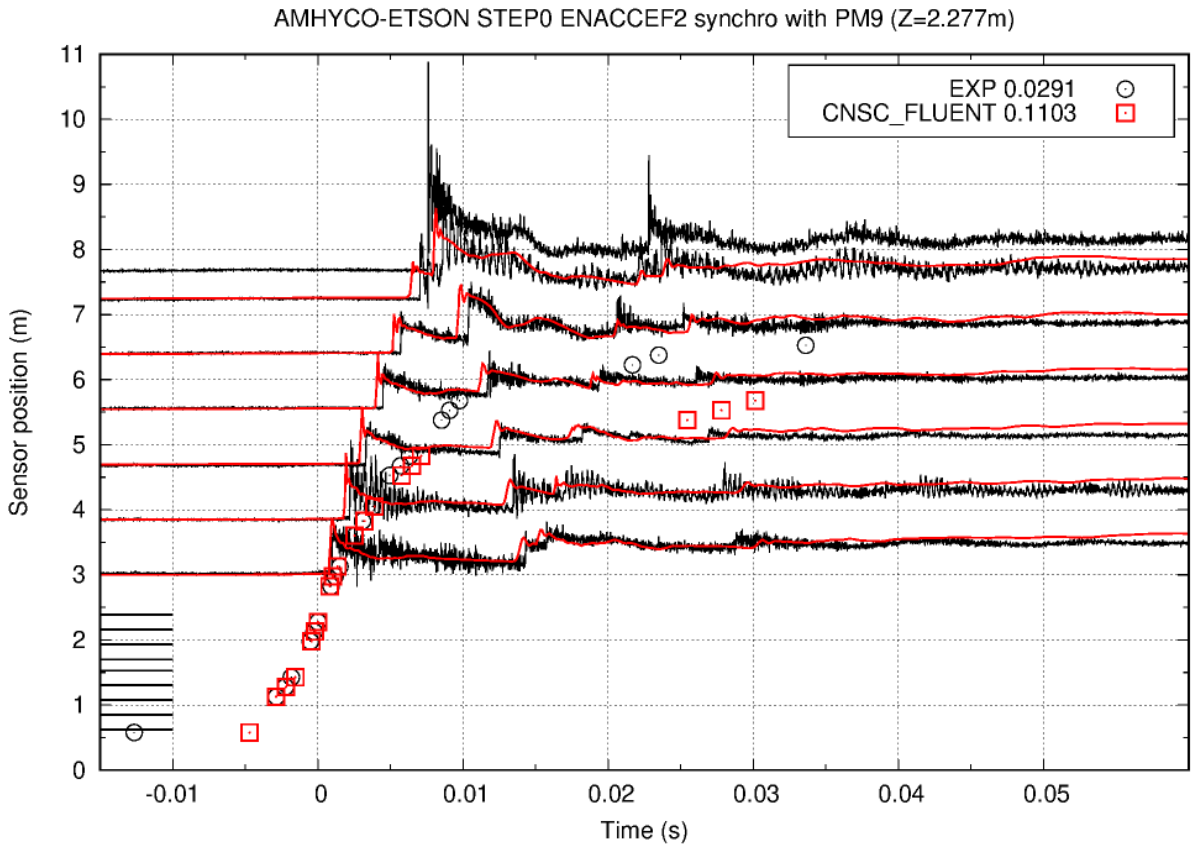

ETSON-AMHYCO: Calculation vs experiments

STEP1

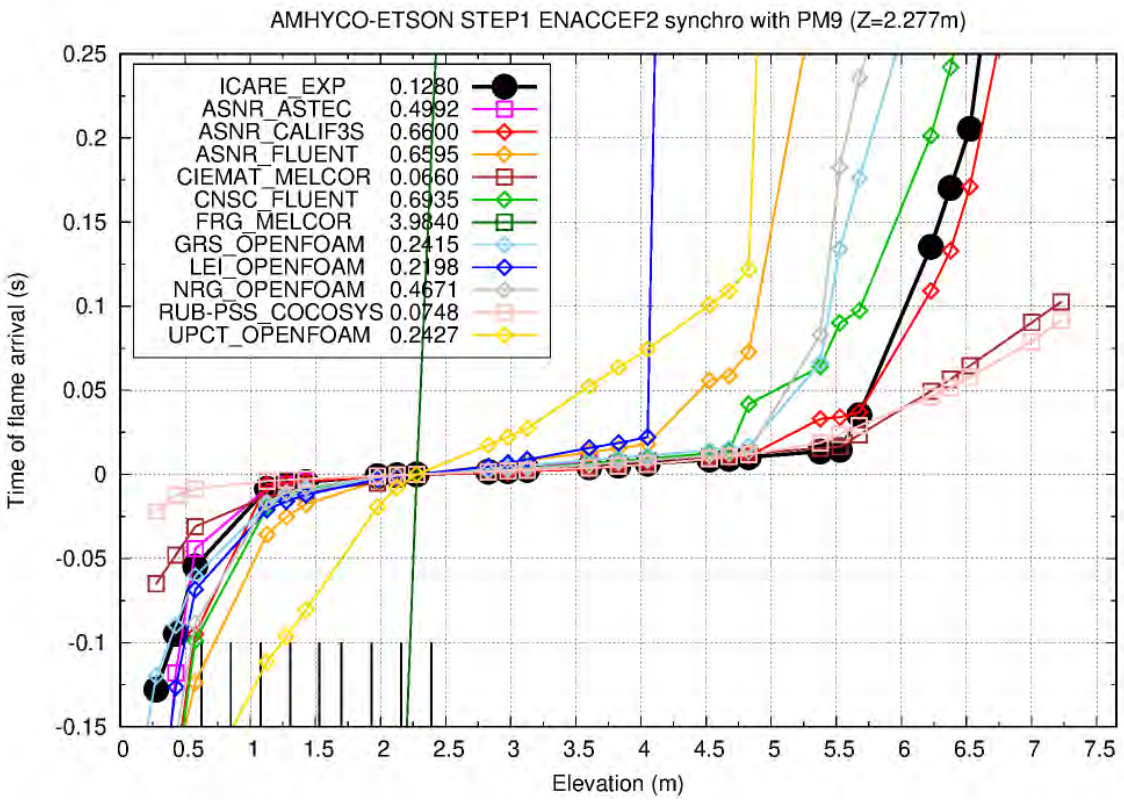

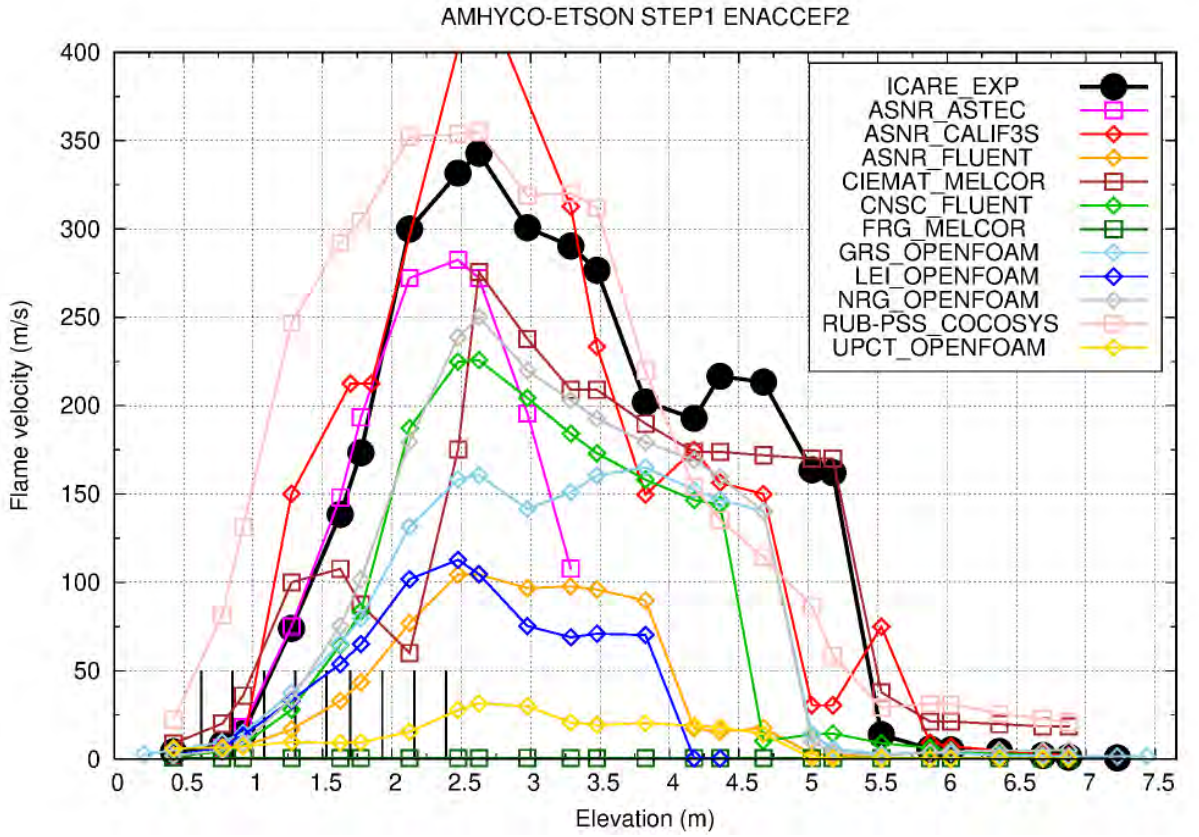

ETSON-AMHYCO: Calculation vs experiments

STEP1

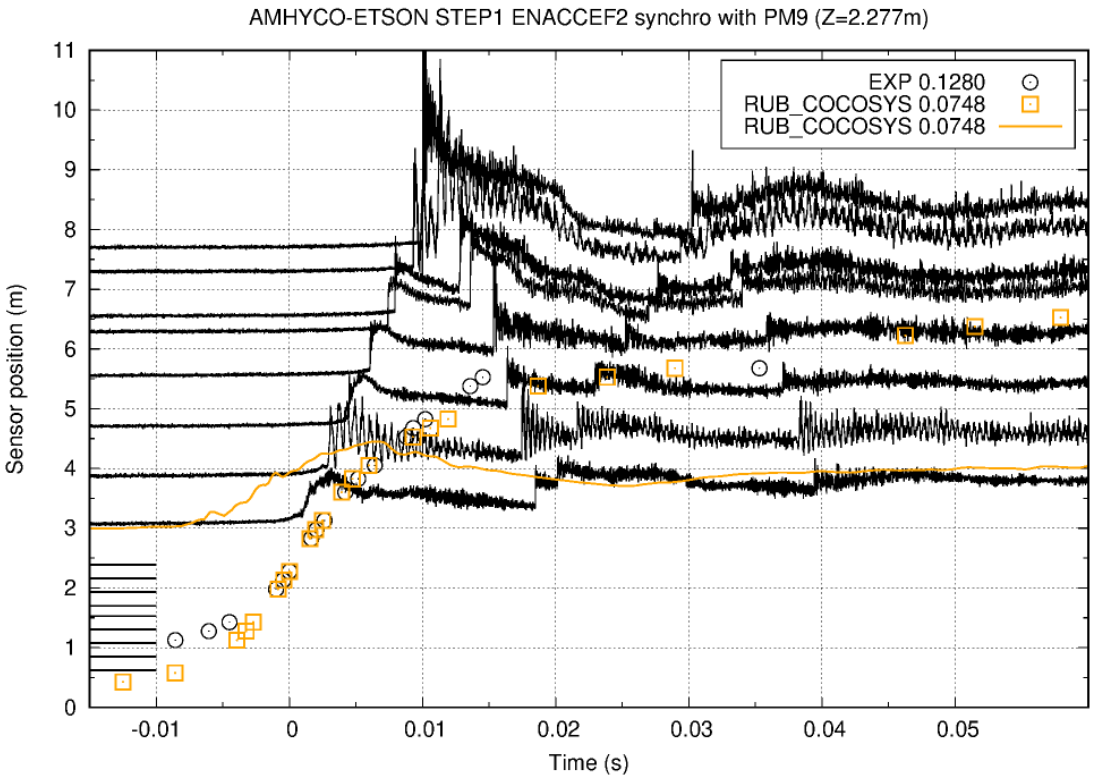

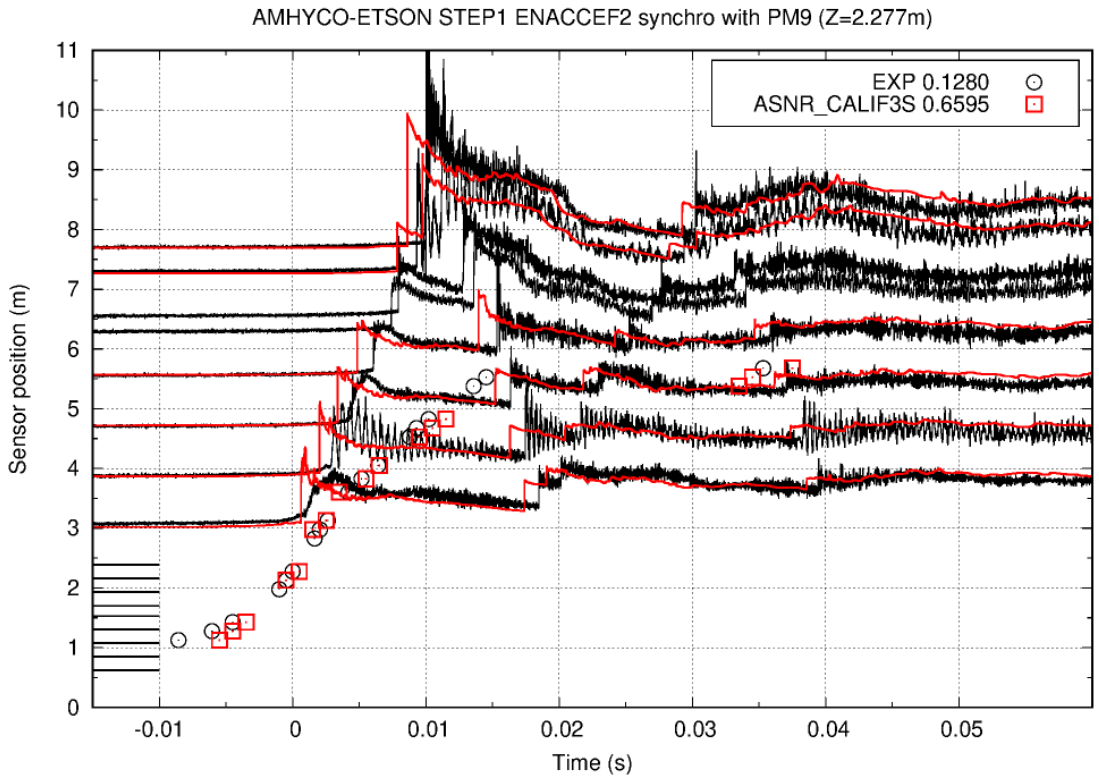

ETSON-AMHYCO: Calculation vs experiments

STEP2

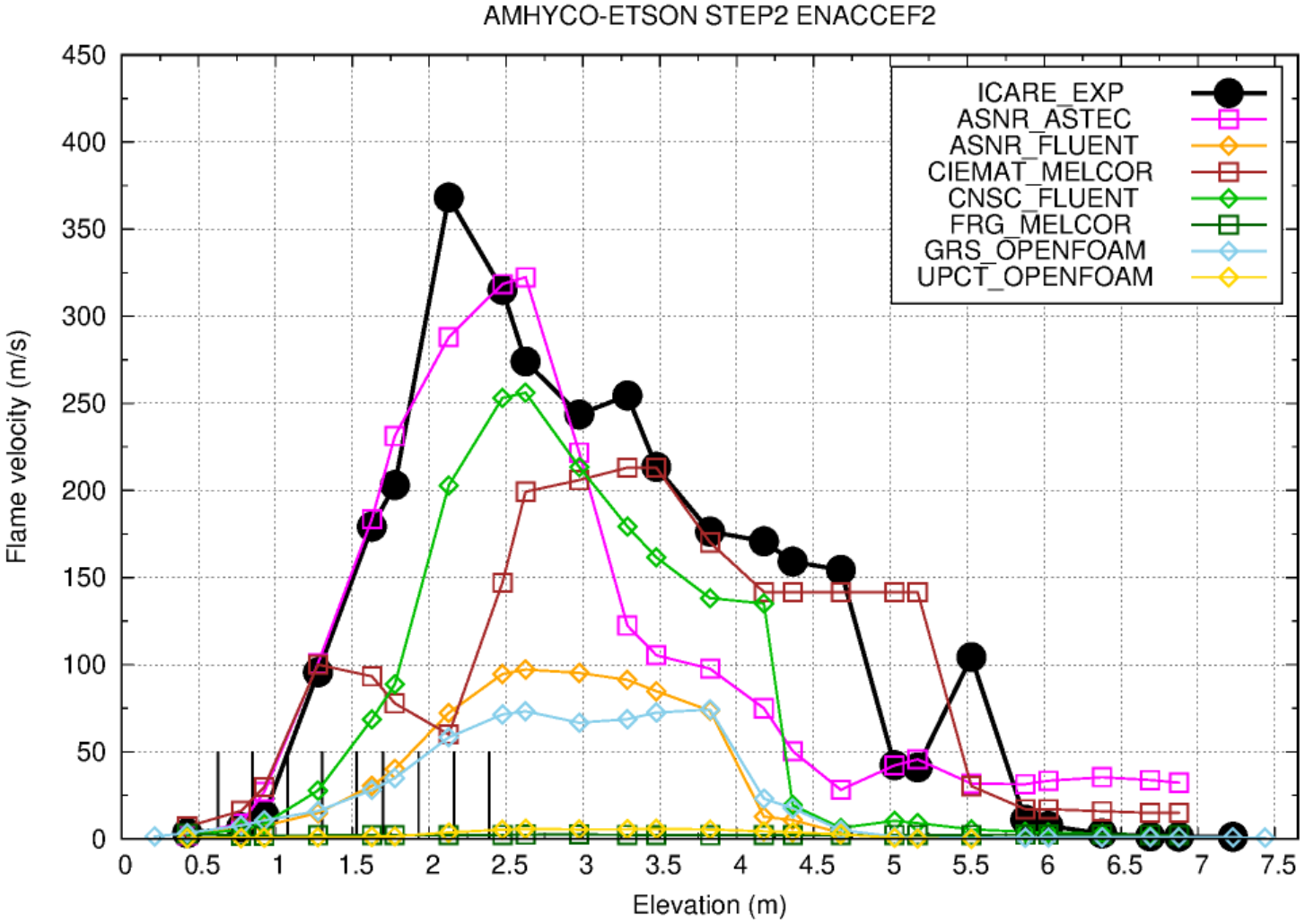

ETSON-AMHYCO: Calculation vs experiments

STEP2

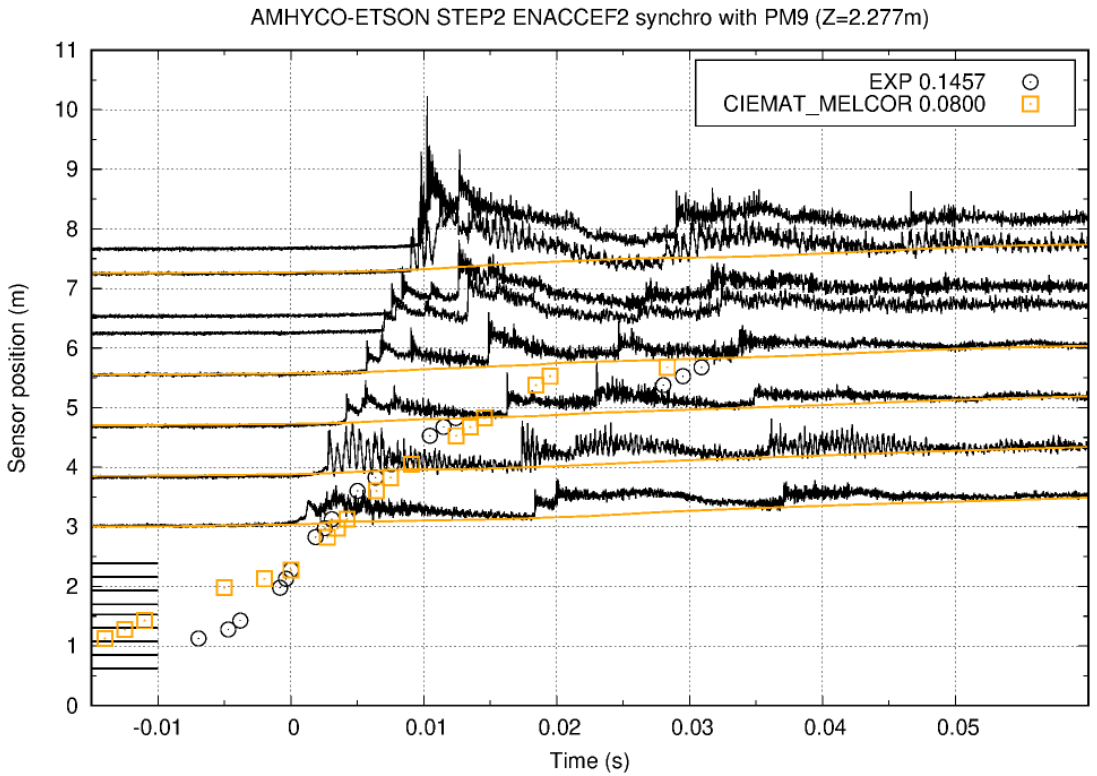

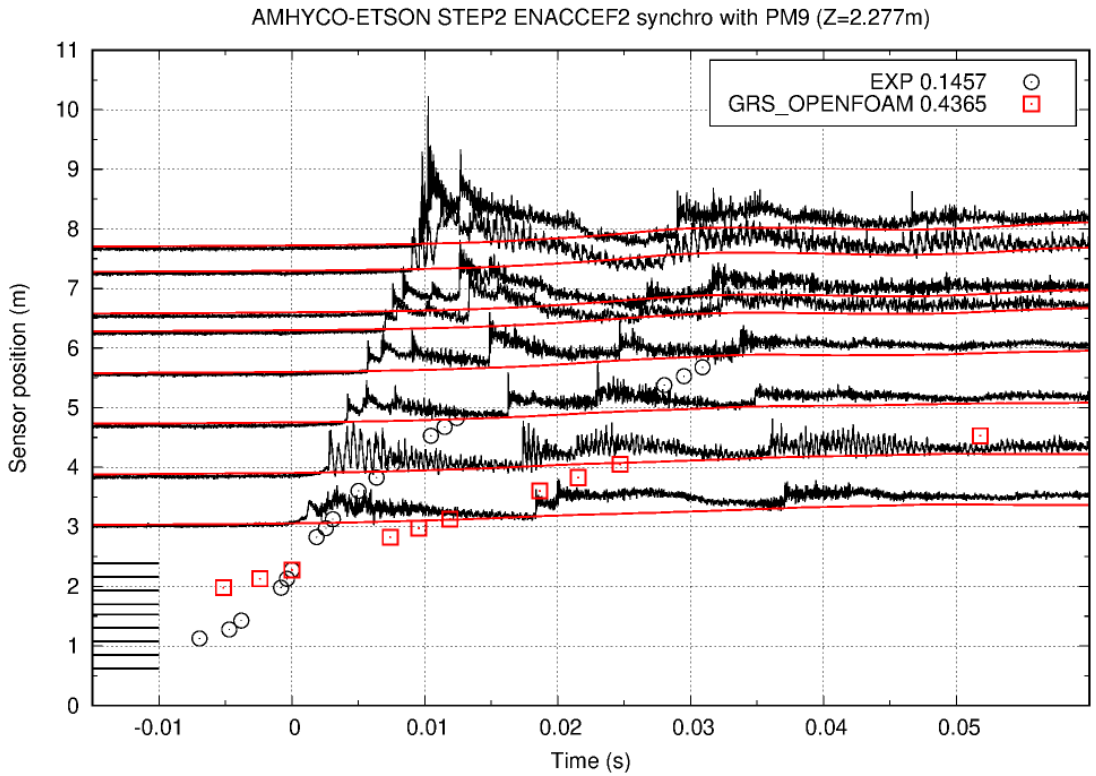

ETSON-AMHYCO: Lessons learned

Most computational codes are able to predict the phases of flame acceleration and deceleration

Combustion modelling

- Burning Velocity Models (BVM) produced satisfactory results.
- Detailed chemistry including CO did not provide additional benefits for STEP1 at the mesh resolution used.
- For lean H_2/CO mixtures, the influence of H_2 and CO mass diffusivities on flame behavior requires further discussion.

ETSON-AMHYCO: Lessons learned

Turbulence modelling

- URANS approaches provided acceptable predictions for the configurations considered.
- The initial turbulence level prior to ignition must be carefully defined, as it strongly influences overall flame behavior.

Thermal radiation

- Based on partner experience, thermal radiation is expected to significantly affect flame dynamics.
- Its influence should be examined in future studies.

ETSON-AMHYCO: Lessons learned

Numerical solvers

- Appropriate discretization schemes are essential.
- Pressure-based solvers should be corrected for compressibility effects whenever applicable.
- Numerical solvers, including pressure-correction methods, must be demonstrated to be applicable to compressible flows.
- Consistency and stability for the compressible Euler equations, including shock solutions, should be numerically verified.
- Adaptive time-stepping strategies and high-order numerical schemes were found to improve simulation accuracy.
- Numerical convergence studies are required to reliably relate simulation results to the underlying physical models.

ACKNOWLEDGMENTS

The authors acknowledge the support of the European project AMHYCO and the European Technical Safety Organisation Network (ETSON).

AMHYCO

Enhancing H_2 & CO Combustion Risk Management

ETSON | EUROPEAN TECHNICAL SAFETY ORGANISATIONS NETWORK

SUPPRESSION POOL MODELLING WITH THE CESAR THERMAL-HYDRAULIC MODULE OF ASTEC

Szogradi M., Zambaux J.-A., Bloch H., Laborde L.
Autorité de Sûreté Nucléaire et de Radioprotection (ASNR)
Centre de Cadarache B.P. 3, 13115 Saint-Paul-lez-Durance Cedex, France
marton.szogradi@asnr.fr; julie-anne.zambaux@asnr.fr; helene.bloch@asnr.fr;
laurent.laborde@asnr.fr

ABSTRACT

Free convection is a cornerstone passive safety feature of spent fuel pools and small modular reactors; thus, the adequate modelling of the related phenomena gains more and more attention to facilitate the design maturation and licensing of such nuclear units. The French Authority for Nuclear Safety and Radiation Protection (ASNR) has initiated development activities considering the CESAR thermal-hydraulic module of the ASTEC code to improve its capabilities. During the ELSMOR project potential development paths were identified with respect to containment behaviour, where direct contact condensation (DCC) was hindered as the code assumed an unsuitable (annular) flow regime in the pool. A preliminary code assessment was carried out using the results of a steam blowdown test, performed at the Blowdown and Condensation pool facility (Korea Atomic Energy Research Institute (KAERI), Republic of Korea). The conclusions of this work highlighted the need for a better depiction of DCC considering closed and open (atmospheric) volumes, along with bubble hydrodynamics. Focusing on former topic, experimental data from the SUPERCLAUDIA suppression pool facility (French Alternative Energies and Atomic Energy Commission (CEA), France) was used to reassess DCC and liquid stratification in an open tank with vertical downward steam injection in two tests. It was shown that during longer transients the blowdown pipe can play an important role in the stratification of the liquid volume of the pool. Correcting the applied flow regime in such applications, an additional model was implemented which utilizes bubbly flow instead of annular at low void fraction, enabling a more adequate depiction of DCC. An option to simplify the thermal coupling of the outer surface of pipes to the surrounding liquid volume was also added to CESAR. A modified CESAR model of interphase heat and mass exchanges was also deployed for big 0D swollen water level volumes with improved results in presence of non-condensable gas. This latter update underlined the benefits of having two separate gas temperatures in a single volume, one below the swollen water level and another above.

KEYWORDS
direct contact condensation, pool modelling, natural circulation, ASTEC

1. INTRODUCTION

Recent years have seen new light-water small modular reactor (LW SMR) projects emerging on the global stage. The design processes and anticipated regulatory reviews necessitate a rigorous review of safety analysis tools, especially with respect to passive heat removal systems. Large pools of water in which steam direct contact condensation (DCC) will occur can be found in different auxiliary and safety apparatuses, e.g. fuel storage pools and pressure suppression pools. The characteristics of these systems raise questions regarding the modelling adequacy of the related phenomena such as pool stratification, mixing and steam flow regime (jet or bubbly flow). Wang et al. [1] identified various condensation regimes during low-

pressure (< 7 bar) steam blowdown into a wet well with 28-85 °C subcooling using the high-speed video footage of bubble formation and collapse. Compiling the data allowed the researchers to define classification criteria for the different condensation regimes, however, the work covered only low steam mass flux cases. Kang & Song [2] and Choo & Song [3] investigated vertical and horizontal jets in an open pool using particle image velocimetry and a movable Pitot tube, respectively, to map the velocity field of the pool with the purpose of computational fluid dynamics (CFD) code validation. Wang et al. [1] characterized the internal circulation in the pool, driven by vertical jets, nonetheless the pressures and steam mass fluxes were once again low compared to engineering applications. Choo & Song [3] noted that the turbulent intensity around the nozzle determines the jet boundary through a momentum diffusion process in the radial direction, yet their research also relied on relatively low steam mass fluxes and small geometry hence the results are not directly applicable to larger cases. Norman & Revankar [4] conducted tests at the PUMA suppression pool facility using single or multiple horizontal jets to study the thermal mixing and stratification of the water tank. The results revealed that thermal stratification can occur under certain air flow rates, steam flow rates and pool temperature. The phenomena of mixing-to-stratification transition and vice versa were observed depending on the subcooling and steam and air flow rates. Okawa & Furuva [5] showed that lumped-parameter codes like TRACE still struggle to capture the stratification in their work considering the toroidal suppression pool of a Mark I BWR. Implementing an additional pressure loss coefficient (K-factor) on node boundaries improved the global trends albeit local effects of steam flow and condensation remained a challenge. A. Oliva et al. [6] used the CATHARE code to model transients at the SUPERCLAUDIA facility using the classic 0D approach for the water tank. Average liquid temperatures showed very good agreement with experimental trends, on the other hand, the liquid mass variation highlighted discrepancies related to DCC modelling and free surface evaporation.

The Accident Source Term Evaluation Code (ASTEC) has been developed by ASNR for severe accident analyses in various nuclear installations. This modular code can model transient scenarios from the initiating event to fission product (FP) release in the environment. The sequence of events can cover thermal-hydraulics, core degradation along with FP chemistry and transport in the containment. Due to its versatility, the code has been employed in numerous domestic and international projects by regulatory bodies, technical support organizations and industrial affiliates [7]. CESAR is the thermal-hydraulics module of ASTEC dedicated to the modelling of the reactor coolant system. During the ELSMOR Euratom project, potential development points were identified as a result of benchmark activities featuring ASTEC and MAAP [8], among which DCC in a suppression pool was noted. Addressing these modelling needs, the development of CESAR capabilities regarding this particular phenomenon has been underway and are presented here.

2. CESAR MODELLING FOR SUPPRESSION POOL

Pressure suppression pool systems are typically constituted by a big pool of water in which an injection pipe is plunged. Such devices are used to depressurize the primary circuit of a reactor by condensation of the steam injected into the water pool through the pipe. The CESAR module calculates 1D in circuits or 2D in vessel two-phase flows, with one liquid coolant and a homogeneous mix between steam and non-condensable (NC) gases. The code solves $6+n$ equations (mass balance equations for liquid, steam and n number of NC species, along with energy and momentum balance equations for each phase). To better depict large volumes where a water level is expected, e.g. in pressurizers, steam generator cavities or suppression pools, a 0D swollen water level volume can also be considered. In these big volumes, the same total pressure is assumed below and above the water level. Although there is only gas in the dry top part of the volume, there can be dispersed gas also below the water level. An additional state variable, the void fraction below the water level (α_l) in the swollen sub-volume can then be introduced. This approach still assumes that the dispersed gas is in thermal equilibrium with the continuous gas in the upper volume, which can result in unphysical gas temperatures in the tank in presence of non-condensable gas. Recent developments in the code (available from released ASTEC version 3.2) have improved this modelling by also assuming different energy and mass balance for the gas above and below the water level. This improvement is suitable for

suppression pools applications where the upper dry region can be expected to be mainly cold air while saturated steam can be expected below the water level.

In addition to the 0D pool, a 1D element is used to model the injection pipe. The wall of the pipe is also considered to be in contact with the water pool. This connection can enable condensation inside the injection pipe and boiling on the external, submerged surface of the pipe wall. In CESAR, mass transfer between liquid and steam is calculated through the interfacial heat transfers evaluated for both phases. The heat transfer is assessed between the considered phase *k* and the liquid-gas interface *i*:

$$Q_{i,k} = h \cdot A_i \cdot (T_k - T_{int}) \quad (1)$$

where h is the heat transfer coefficient, A_i is the interfacial area, T_k and T_{int} are the bulk and interface temperatures respectively (interface temperature is usually taken at saturation conditions). The heat transfer coefficient (through Nusselt number correlations) and the interfacial area are evaluated by the code depending on the flow configuration. Since the flow regimes in CESAR are mainly based on a 1D pipe configuration, the solution for large quiescent volumes might be distorted depending on the boundary conditions. In a subcooled water pool, the liquid to interface heat transfer is expected to be quite important and have a big impact on the condensation process. By default, in CESAR, in particular for low void fractions, the liquid to interface heat transfer is evaluated using the assumption of an annular flow configuration. In this case, the heat transfer coefficient is calculated using the Nusselt formula given by Shah et al. [9] while the interfacial area is given by the D_h volume hydraulic diameter as:

$$A_i = \frac{4}{D_h} \quad (2)$$

In the case of a large tank of water, as in suppression pool applications, a very small interfacial area can be expected, far from the presumed flow configuration. From the release version 3.2 of ASTEC, a new option can be applied, modifying the flow configuration detected by the code when the void fraction is small. In volumes where the option is activated, the flow is now assumed to be in the bubbly regime for low void fractions (< 0.3). The liquid to interfacial heat transfer is then evaluated using the Ranz-Marshall Nusselt number correlation for the heat transfer coefficient, and the interfacial area density is calculated using:

$$A_i = \frac{6\alpha}{d_{bub}} \text{ , where } d_{bub} = 1.73 \cdot \sqrt{\frac{\sigma}{g(\rho_{liq} - \rho_{steam})}} \quad (3)$$

where α is the void fraction and d_{bub} is the bubble diameter, σ is the surface tension, g is the gravitational acceleration, ρ_{liq} and ρ_{gas} are the liquid and gas densities, respectively.

3. TRANSIENT ANALYSES WITH CESAR

3.1. Suppression pool validation cases selection and CESAR model

The code development work revolved around two experimental facilities to cover a wider range of boundary conditions, including closed and open pools. Three tests from the literature were analyzed with CESAR:

- two long tests at ambient pressure: SUPERCLAUDIA facility [10]
- one short, pressurized test: Blowdown and Condensation (B&C) facility [11]

Heat losses were neglected in both models either due to the brief nature of the blowdown or assuming adequate insulation around the tank. The two selected facilities shared the general topology of a water tank

thus the same spatial discretization strategy was used in both cases; Fig. 1 illustrates the nodalization schemes of the models. The sparger pipe had 5 axial nodes in each case, connected to 5 wall heat structures. In the B&C model the sparger had a horizontal nozzle, and the tank was closed, whereas in the SUPERCLAUDIA model the injection was downward and the pool was open to the atmosphere. It is worth mentioning that the B&C facility employed a perforated sparger head i.e. multiple small jets along its circumference. Song et al. [12] noted that in such configurations individual jets can be lumped together, as substituting several condensation regions by one does not incur penalties in terms of steam-to-liquid momentum transfer. Air (nitrogen and oxygen) constituted the atmosphere in the tanks while no residual gas was considered in the swollen sub-volume.

Each test was run with four different water tank configurations to highlight the impact of the different modelling choices:

- *case 1*: using the standard 0D swollen water level volume with a single NC mass and gas energy balance equation for the whole water tank
- *case 2*: using the newly developed 0D volume for the water tank (with different NC mass and gas energy balance equations for both sub-volumes)
- *case 3*: case 2 with thermal coupling between the pipe and the volume
- *case 4*: case 3 with the new option modifying the flow configuration activated in the pool

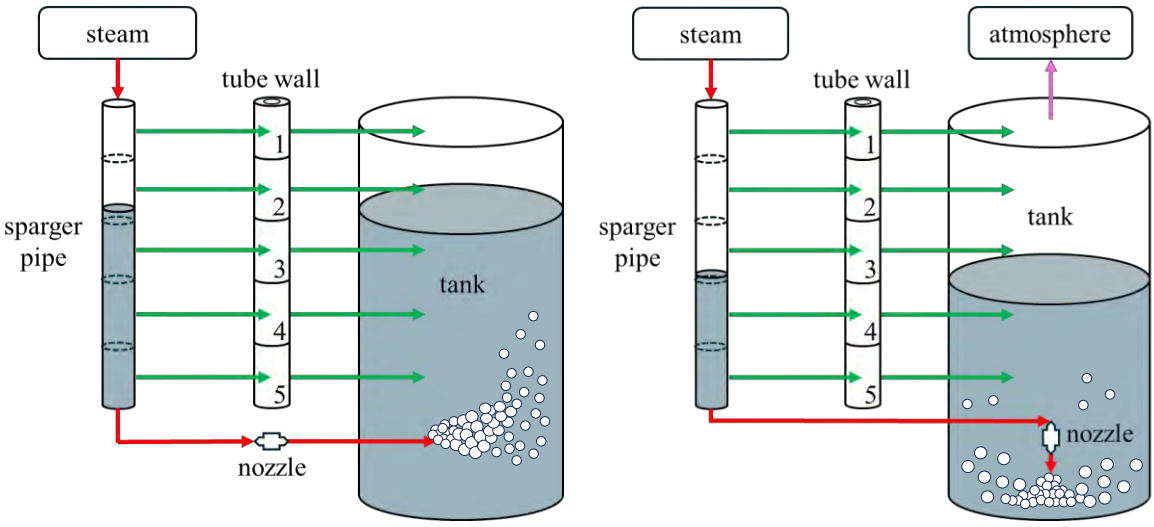

Figure 1. CESAR models of B&C KAERI (left) and SUPERCLAUDIA (right).

3.2. Pool stratification tests of the SUPERCLAUDIA facility

Avakian et al. [10] conducted steam blowdown experiments at the SUPERCLAUDIA facility of French Alternative Energies and Atomic Energy Commission (CEA). The test rig included an open and relatively small water tank. Three campaigns incorporated nine tests with varying steam pressures, nozzle diameters and nozzle head configurations. Since ref. [10] reported data on tests #3 and #5, only these two experiments were modelled in CESAR. Both runs used a constant saturated steam flow rate that slowly saturated the liquid in the atmospheric tank. The transients were terminated when the average liquid temperature reached ≈95 °C. Relevant facility parameters and test conditions are summarized in Table I.

Table I. Facility parameters and initial conditions [10].

Parameter	Value	Test conditions	Test #3 / #5
Tank inner diameter	2500 mm	Tank pressure (p_{tank})	1 bar
Tank height	1600 mm	Pressurizer pressure	45 / 100 bar
Tank free volume	7.85 m^3	Initial liq. temp. (T_{liq})	10 °C
Sparger length	1000 mm	Water level	1.03 m
Sparger elevation from tank bottom	600 mm	Liquid inventory (M_{liq})	5025 kg
Nozzle flow area on the sparger head	1.96x10^{-3} m^2	Steam flow rate ($\dot{m}_{steam}$)	76 / 167 g/s
		Transient duration	13000 / 5240 s

Fig. 2 depicts the liquid mass inventory evolution for test #3 and #5 along with the theoretical (theo.) and experimental (exp.) curves. The theoretical trend refers to full condensation while the experimental curve shows the weight measurements. In test #3, the growing discrepancy between theory and observation can be associated with the intensifying natural evaporation on the free water surface and the diminishing condensation potential of the liquid. Concerning test #5, ref. [10] called attention to the unintuitive experimental M_{liq} curve, the authors explained the surprising mass increase by the 'jet effect', the larger steam mass flux exerted an additional downward force on the bottom of the water tank, skewing the weight measurement. In case 1, condensation was very weak, whereas after switching to case 2 both tests started to show improvements compared to case 1, increasing the liquid inventory by 47 % and 135 % in tests #3 and #5, respectively. Coupling the sparger pipe with the pool (case 3) further increased condensation rates, still, quantitatively speaking the condensed steam mass was underestimated at the end by 2 % and 12 % in tests #3 and #5, respectively. Finally, by modifying the interfacial area density evaluation i.e. increasing the condensation mass transfer, the code could capture some additional inventory gain in case 4. It should yet be noted that in both tests, results are closer to the theoretical curve than to the measurement data until liquid saturation.

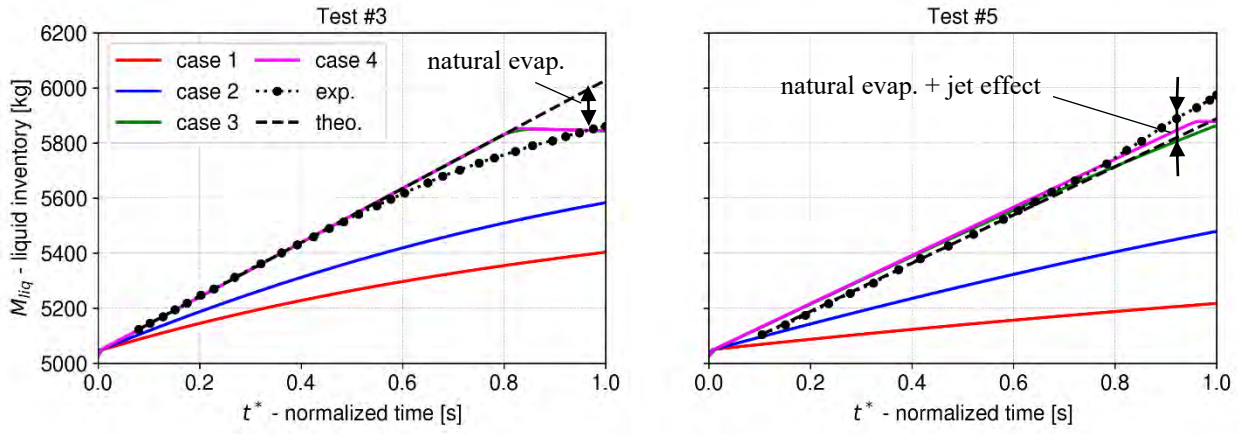

Figure 2. Liquid inventory variations in the tank.

The average liquid temperature trends are depicted in Fig. 3, where the experimental curve is the average reading of the thermocouple chain closest to the tank wall. Even though this chain was farthest from the

nozzle, its average reading can be regarded as a pool-representative T_{liq} as the variation in temperatures on all chains along the tank radius remained below 1.5 °C [10].

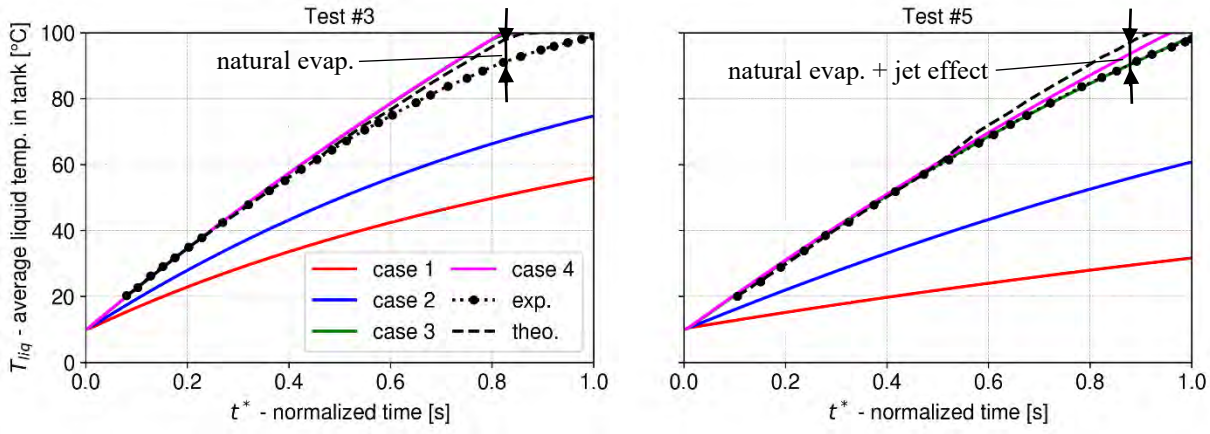

Figure 3. Liquid temperature variations in the tank.

It is interesting to note that the impact of the condensation in the sparger pipe was quite pronounced due to the length of the transients and the size of the pipe. Fig. 4 presents the total mass flow rate from vapour to liquid (positive for vaporization and negative for condensation) in the injection pipe for both experiments. The thermal coupling of the sparger pipe with the tank, when taken into account, was responsible for condensing ~87-96 % and ≈82 % of the total steam flow in tests #3 and #5, respectively. Without the coupling no condensation could take place in the pipe. The initial condensation rates could further increase as the wetted surface area of the pipe on the tank side grew, thanks to the rising water level. In test #5 the relative condensation rate was slightly lower than in test #3, this can be attributed to the higher wall temperatures of the sparger pipe due to the higher steam pressure.

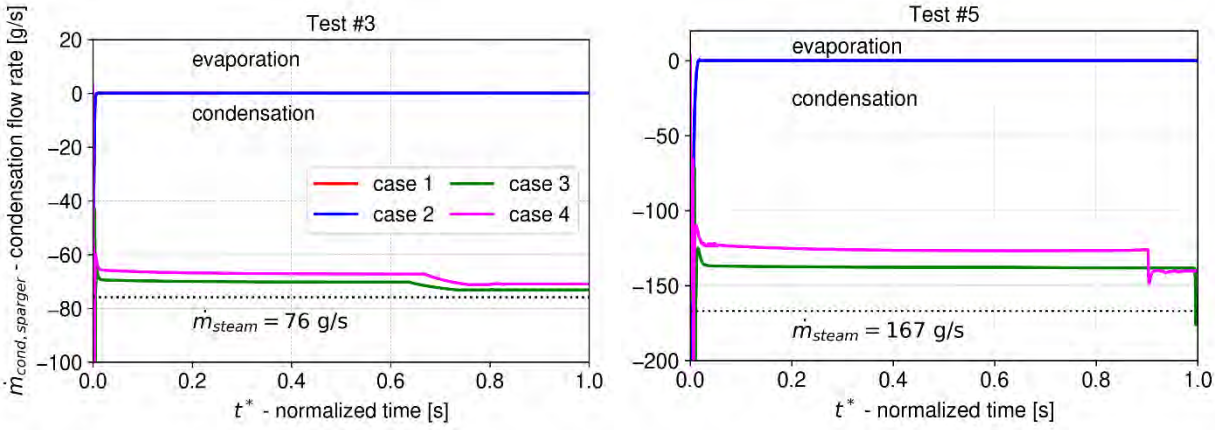

Figure 4. Condensation rates in the sparger pipe.

During the experiment the observers reported perfect condensation for the larger part of the transients, that is confirmed by the water temperature theoretical and experimental curves in Fig. 3. In the real scenario, the liquid temperature began to deviate from the ideal, nearly linear curves before the midpoint and at the

halfway point of tests #3 and #5, respectively, due to the intensifying natural evaporation on the water surface [10]. Fig. 5 depicts the phase change mass flow rates in CESAR occurring below the water level in the swollen pool volume. Case 1 showed a 0.0-1.8 g/s evaporation rate meaning that no condensation took place below the water level. Having a separate T_{gas} in the swollen volume enabled DCC to some extent, nonetheless the efficacy of this heat transfer remained unsatisfying in case 2. Due to the very efficient condensation in the sparger pipe, i.e. pipe-to-pool thermal coupling, case 3 had a much lower condensation rate in the tank compared to the previous case, as little remaining steam reaches the pool. Using the modified flow configuration in case 4 the code could capture DCC in the pool. It should be noted that the discrepancy between the steam inlet flow and the case 4 curve, until bulk saturation, corresponds to the in-pipe condensation rates given in Fig. 4, meaning complete condensation of the steam is observed in this case. Upon reaching saturation temperature in the tank, the steam started to evaporate the liquid inventory as the condensation potential dropped to zero.

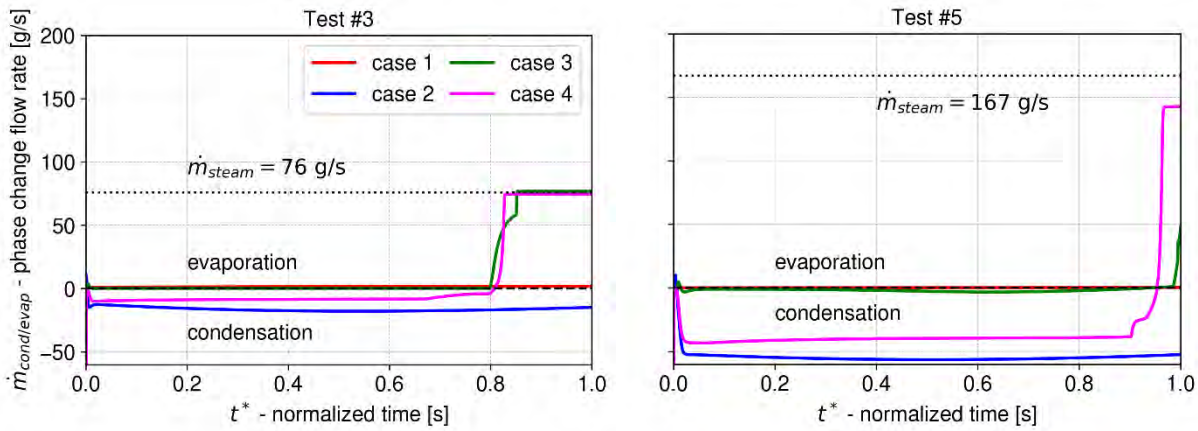

Figure 5. Phase change rates in the swollen sub-volume of the tank.

Fig. 6 shows the phase change mass flow rate at the water level in the pool. This mass flow rate is associated with the heat transfer between the free surface and the gas above the water level in the tank. The negative phase change rates in cases 1-3 (complementing the weak condensation below the water level) explain the liquid inventory gains that can be seen in Fig. 2. The cold free surface could condense some of the steam mass that broke through the water. In case 4, in the absence of steam above the water level, no substantial condensation could take place. After saturation, evaporation did occur (positive value for the phase change mass flow rate in Fig. 6). However, the flow rates only reached 1.4-1.3 g/s in tests #3 and #5, respectively, this inventory loss could not play a meaningful role in the mass balance of the tank. The liquid inventory loss due to evaporation ($\dot{m}_{evap}$) was evaluated based on M_{liq} from the experimental and theoretical curves given in ref. [10] using the following formula:

$$\dot{m}_{evap} = \frac{\Delta M_{liq,theo} - \Delta M_{liq,exp}}{\Delta t} \quad (4)$$

where $\Delta M_{liq,theo}$ and $\Delta M_{liq,exp}$ are the theoretical and experimental mass changes during Δt window. For test #3 only, the evaporation mass flow rate assessed is shown in Fig. 6 (the jet-effect observed in test #5 makes it complicated to give an estimate of the evaporation). From the experimental data, evaporation was shown to play a much more important role than what is assessed by CESAR and could explain the discrepancies observed. In order to better calculate the SUPERCLAUDIA experiments, improving the free surface evaporation model seems to be an interesting direction for further code developments.

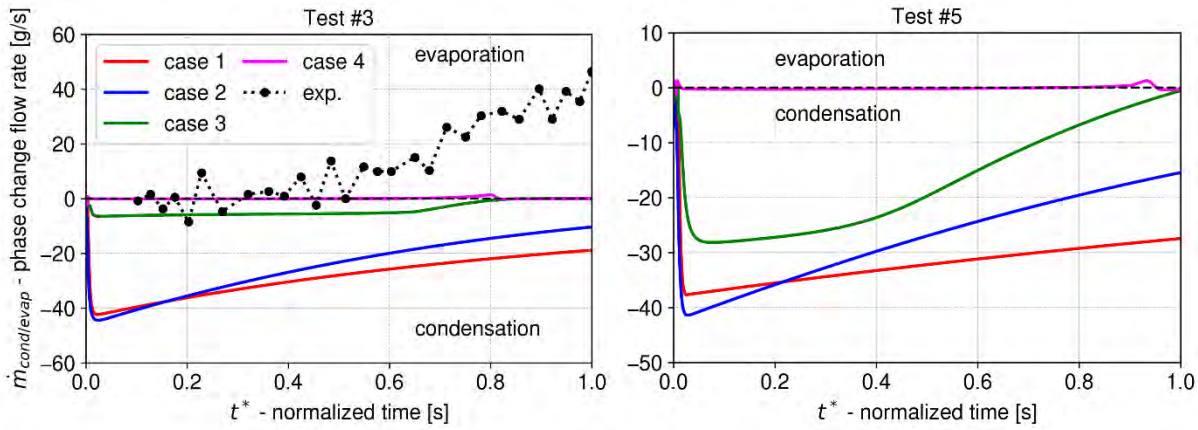

Figure 6. Free surface phase change rates in the tank.

3.3. Blowdown transient of the B&C facility of KAERI

The B&C facility of the Korea Atomic Energy Research Institute (KAERI) is a representative of the in-containment refueling water storage tank of the APR1400 [11]. Compared to the SUPERCLAUDIA facility, the pool is bigger and can pressurize. The test loop comprises a pressurizer, a piping system with a sparger and a water tank, the main parameters and initial conditions are given in Table II. The purpose of the pool mixing test was to provide input for subsequent CFD validation activities, building upon earlier research e.g. condensation regime maps and multi-hole sparger head modelling. The test procedure had two main steps: first the pressurizer was heated to produce saturated steam at 150 bar, afterwards the control valve was opened to release the steam into the water via a perforated sparger head. The calculated 60 s sequence covered a brief steady state of 4.5 s prior to injection, followed by the blowdown of 55.5 s. Transient considered here is way shorter than for the previous facility.

Table II. Facility parameters and initial conditions [11].

Parameter	Value	Initial conditions	Value
Tank inner diameter	3000 mm	Tank pressure (p_{tank})	1 bar
Tank height	4000 mm	Pressurizer pressure	150 bar
Tank free volume	28.22 m^3	Tank temperature (T_{liq})	25.60 °C
Sparger inner diameter	152.40 mm	Water level	3.02 m
Sparger length	3100 mm	Liquid inventory (M_{liq})	21244 kg
Sparger elevation from tank bottom	900 mm	Liquid volume	21.31 m^3
Nozzle flow area on the sparger head	5.52x10^{-3} m^2	Gas volume	6.91 m^3

Fig. 7 shows that, in CESAR, for cases 1-3, the water had practically no suppressive impact on the pressure balance between the tank and the pressurizer as the curves saturated around 150 bar, far above the observed experimental values provided by the pressure transducer of the tank (PT207). The liquid temperatures were underestimated for these three cases compared to thermocouple (TC635, TC705 above the sparger head in the tank). On the other hand, modification of the flow regime map in the pool volume displayed a large

impact on the results. In case 4 the maximum tank pressure was 1.30 bar, which indicated extremely efficient condensation, the injected steam could not break through the water to pressurize the tank.

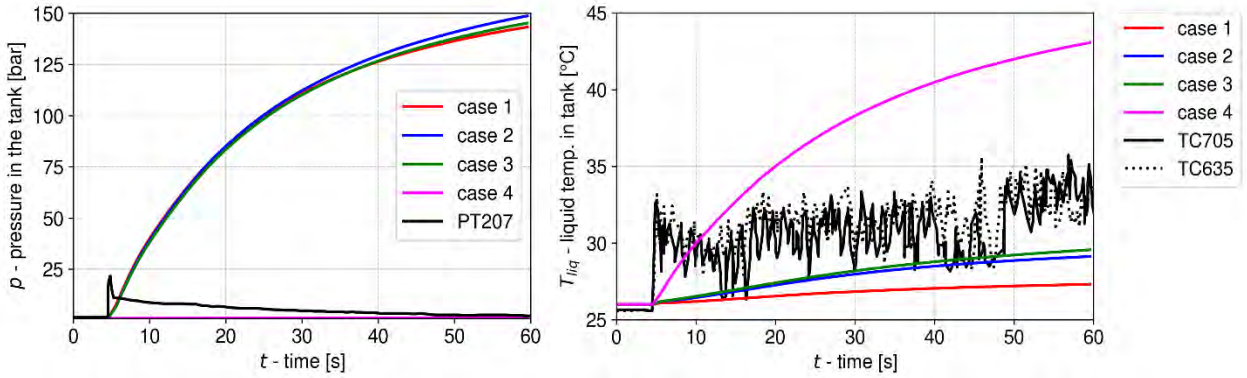

Figure 7. Pressure (left) and liquid temperature trends (right) in the tank.

Fig. 8 illustrates the phase change mass flow rates in the different parts of the system. It can be seen here that the sparger had a relatively small importance compared to SUPERCLAUDIA, only ~9.8 % of the total condensed steam mass was captured in the pipe. Free surface evaporation was a negligible factor in this case as well, as the increase of 17 °C in liquid temperature evaporated ~0.28 kg water.

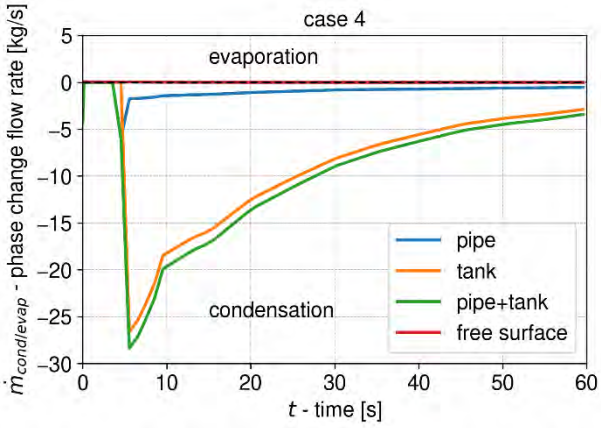

Figure 8. Phase change rates in case 4.

In case 4, due to the modification of the interfacial area evaluation, bubbles diameter becomes one of the most important parameters for the DCC. Fig. 9 illustrates this bubble diameter evolution during the test. This diameter is evaluated according to Eq. (3) and resembled rather a constant as the pressure did not vary during the transient and the water density reduction due to the warm-up was negligible. Focusing on case 4, the largest discrepancies between calculation and measurement data appeared at the beginning of the transient. Due to the large steam mass fluxes, the experiment featured a continuous vapour jet, which could raise the steam up to the free surface with small interfacial area density. With a decreasing mass flux, the jet and the bubbles could break up thereby increasing the interfacial area and the efficiency of DCC. Fig. 9 suggests that the nearly constant bubble diameter led to the overestimation of the condensation rates in the tank which prevented the pressure peak shown in the PT207 readings in Fig. 7. In other words, modelling a

jet with an approach based on the bubbly flow configuration results in the misrepresentation of the interfacial area density i.e., unrealistic heat transfer and pressure trends. The issue of wrong estimation of interfacial area could be improved by substituting the formula of d_{bub} in Eq. (3) with a model that considers jets e.g., relying on the approaches of Zeitoun [13] or Hibiki et al. [14]. Such improvements will be considered in future code developments.

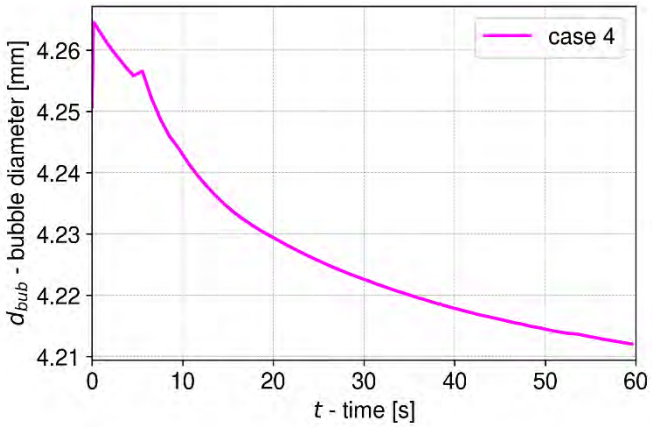

Figure 9. Bubble diameter evolution with the bubbly flow configuration in the pool.

Another point to consider is the evaluation of the heat transfer correlation used to assess the interfacial heat transfer coefficient. In case 4 the Ranz-Marshall correlation was utilized to compute the Nusselt number, which has been a popular choice in similar engineering applications yet has a very limited validity range ($Re_{bub} < 200$), most importantly; unfit for jetting. A better depiction of the heat transfer coefficient could be achieved by complementing the Ranz-Marshall correlation with other formulae, e.g. covering the transitional ($200 < Re_{bub} < 10^4$) and turbulent bubble Reynolds region ($Re_{bub} > 10^4$) with Chen & Mayinger [15] and Yang et al. [16] correlations, respectively.

4. CONCLUSIONS

Steam blowdown experiments were modelled with the CESAR thermal-hydraulic module of ASTEC, considering closed and open suppression pool facilities. The classic 0D approach with a single gas temperature in the control volume failed to capture heat transfer trends in the tank, whereas the introduction of additional state variables to distinguish the gas temperature and composition above and below the swollen water level, improved the solution profoundly. Both open- and closed-pool simulations highlighted the importance and positive impact of the flow regime correction of bubbly flow with respect to DCC. The results also underlined the impact of the thermal coupling between the injection pipe and the pool, notably during longer transients.

Concerning the SUPERCLAUDIA tests, the free surface evaporation model of CESAR was identified as a potential topic of future development. In the B&C test the pressure trend could be improved by adopting an interfacial area density or bubble diameter correlation that is fit for vapor jets in subcooled water. The turbulent nature of such applications motivates the extension of the bubble heat transfer coefficient model, which is exclusively based on the Ranz-Marshall formula. Along with these improvements of the model to be able to cover a wider range of diphasic flow configurations in the pool, additional validation work will also be pursued.

REFERENCES

1. Z. Wang et al., "Experimental investigation on the effect of direct contact condensation regime on thermal stratification", *Nucl. Eng. Des.* **421**(-), 113104 (2024).
2. H. S. Kang and Ch.-H. Song, "CFD analysis of a turbulent jet behavior induced by a steam jet discharge through a single hole in a subcooled water tank", *Nucl. Eng. Des.* **240**(9), pp. 2160-2168 (2010).
3. Y. J. Choo and Ch.-H. Song, "PIV measurements of turbulent jet and pool mixing produced by a steam jet discharge in a subcooled water pool", *Nucl. Eng. Des.* **240**(9), pp. 2215-2224 (2010).
4. T. L. Norman and S. T. Revankar, "Jet-plume condensation of steam-air mixtures in subcooled water, Part 1: Experiments", *Nucl. Eng. Des.* **240**(3), pp. 524-532 (2010).
5. R. Okawa and M. Furuva, "TRACE code demonstration of thermal stratification in BWR suppression pool", *Nucl. Eng. Des.* **355**(-), 110357 (2019).
6. A. Oliva et al., "Assessment of the CATHARE code over Superclaudia tests for a jet in a liquid water pool", *Proceedings of the 20th International Topical Meeting on Nuclear Reactor Thermal Hydraulics (NURETH20)*, pp. 5348-5357, Washington, D. C., Aug. 20–25, 2023.
7. P. Drai et al., "ASTEC V3: A comprehensive integral code for nuclear safety analysis and research – overview of recent applications and perspectives", *Proceedings of the 21st International Topical Meeting on Nuclear Reactor Thermal Hydraulics (NURETH21)*, Busan, South Korea, Aug. 31– Sept. 5, 2025.
8. J. Bittan et al., "Comparison between EDF MAAP5.04 and ASTECV3 codes on a hypothetical severe accident on the ELSMOR project E-SMR design", *Ann. Nucl. Energy* **215**(-), 111258 (2025).
9. M. M. Shah, "A general correlation for heat transfer during film condensation inside pipes", *Int. J. Heat Mass Transfer* **22**(4), pp. 547-556 (1979).
10. G. Avakian et al., "Direct contact condensation of steam injected into a water pool", *Proceedings of the 6th International Conference on Nuclear Engineering (ICONE6)*, ICONE-6025, San Diego, California, May 10–14, 1998.
11. H. S. Kang and Ch.-H. Song, "CFD analysis for thermal mixing in a subcooled water tank under a high steam mass flux discharge condition", *Nucl. Eng. Des.* **238**(3), pp. 492-501 (2008).
12. Ch.-H. Song et al., "Steam jet condensation in a pool: from fundamental understanding to engineering scale analysis", *J. Heat Transf.* **134**(3), 031004 (2012).
13. O. Zeitoun et al., "Measurement of interfacial area concentration in subcooled liquid-vapour flow", *Nucl. Eng. Des.* **152**(1-3), pp. 243-255 (1994).
14. T. Hibiki et al., "Interfacial area concentration in boiling bubbly flow systems", *Chem. Eng. Sci.* **61**(24), pp. 7979-7990 (2006).
15. Y. M. Chen and F. Mayinger, "Measurement of heat transfer at the phase interface of condensing bubbles", *Int. J. Multiph. Flow* **18**(6), pp. 877-890 (1992).
16. Q. C. Yang et al., "Experimental investigation on steam bubble interfacial heat transfer in large range Reynolds number and water subcooling", *Mod. Phys. Lett. B* **35**(3), 2150063 (2021).

SUPPRESSION POOL MODELLING WITH THE CESAR THERMAL-HYDRAULIC MODULE OF ASTEC

M. SZOGRADI, J.-A. ZAMBAUX, H. BLOCH, L. LABORDE

AUTORITÉ DE SURETÉ NUCLÉAIRE ET DE RADIOPROTECTION (ASNR), FRANCE

SOMMAIRE

01
INTRODUCTION AND CONTEXT P.03

02
SUPPRESSION POOL MODELLING P.04

03
VALIDATION ON THE SUPERCLAUDIA EXPERIMENT P.08

04
VALIDATION ON THE B&C EXPERIMENT P.12

05
CONCLUSIONS AND PERSPECTIVES P.15

01. INTRODUCTION AND CONTEXT

- Direct contact condensation
  - Spent fuel pools
  - Suppression pools → BWR, SMR (ELSMOR E-SMR, SASPAM iPWR)…

- ASTEC severe accident code for safety analysis
  - CESAR module
    - TH in RCS
    - Some containment applications → ERVC, SMR containment…
  - Previous studies have shown CESAR tends to under-estimate the pool condensation (ELSMOR project [1])
    - ➔ Improvement presented in the paper are all included in the latest ASTEC released version (v3.2)

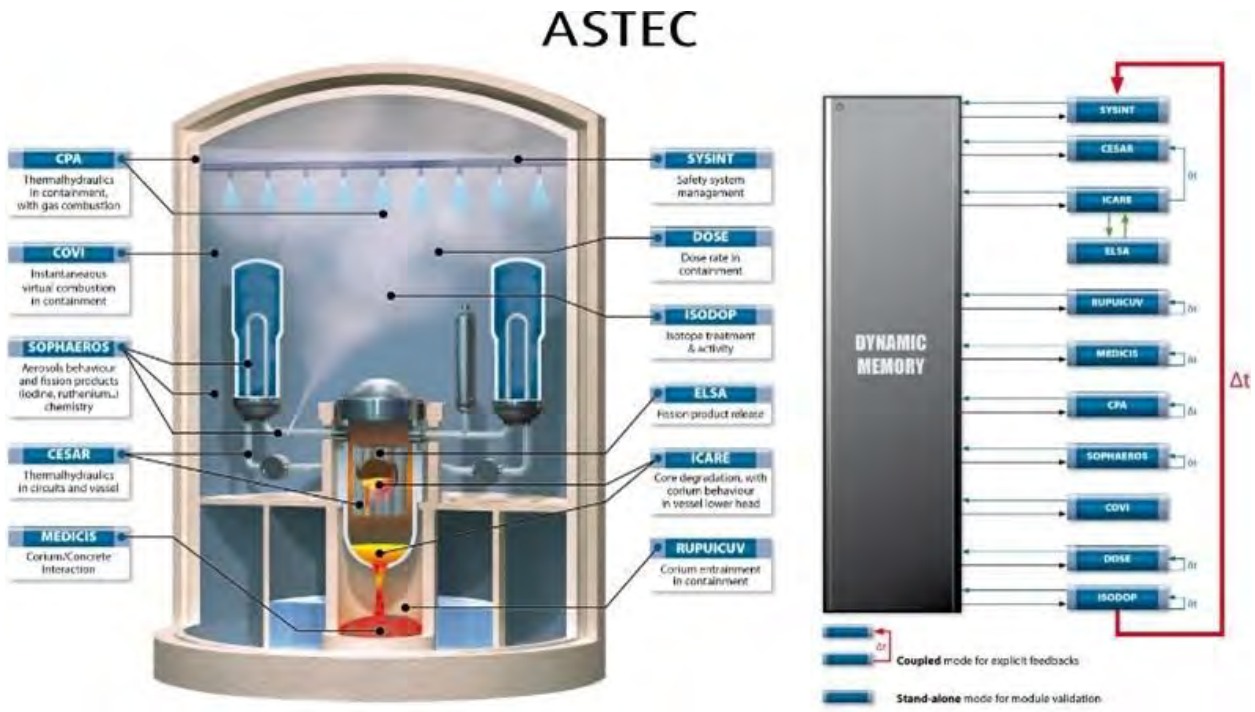

[1] Bittan et al., *Ann. Nucl. Energy (2025)*

02. SUPRESSION POOL MODELLING

❑ **Case 1** : Default modelling in CESAR using a 1D pipe and a 0D swollen water level volume

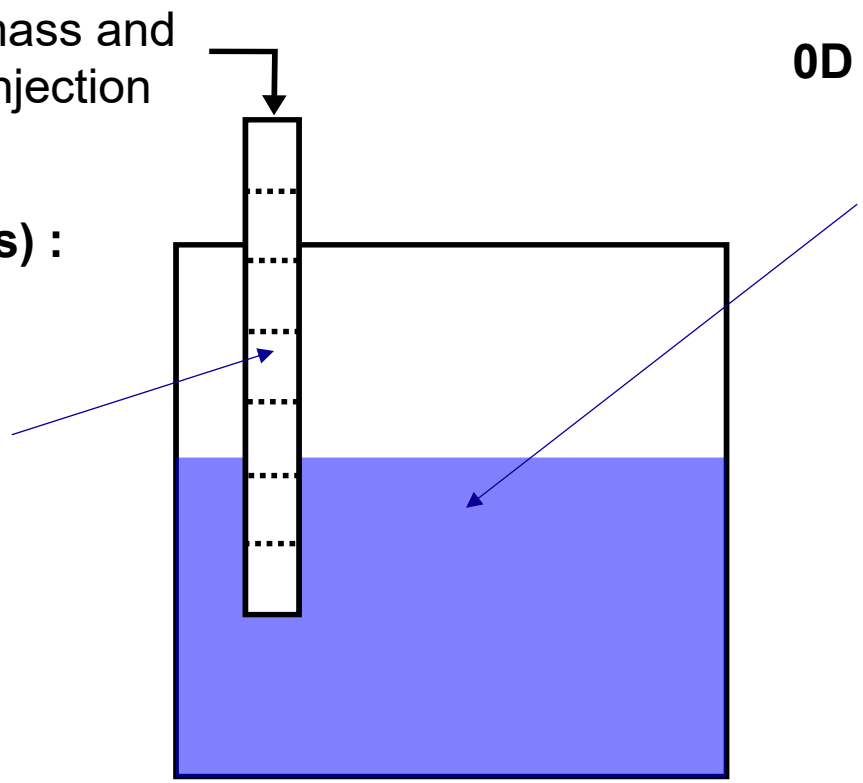

1D pipe (6 (+n) balance equations) :

- Liquid mass
- Steam mass
- Each NC gas mass
- Liquid energy
- Gas energy
- Liquid momentum
- Gas momentum

0D pool volume (5(+n) equations) :

- Liquid mass
- Global steam mass
- Global NC gas mass for each species
- Liquid energy
- Global gas energy
- Total gas mass below the water level

02. SUPRESSION POOL MODELLING

❑ **Case 2** : Application of recent CESAR improvement of the 0D swollen level volume model

- Different temperature and gas composition above and below the water level
  - → Cold air above
  - → Saturated vapour below

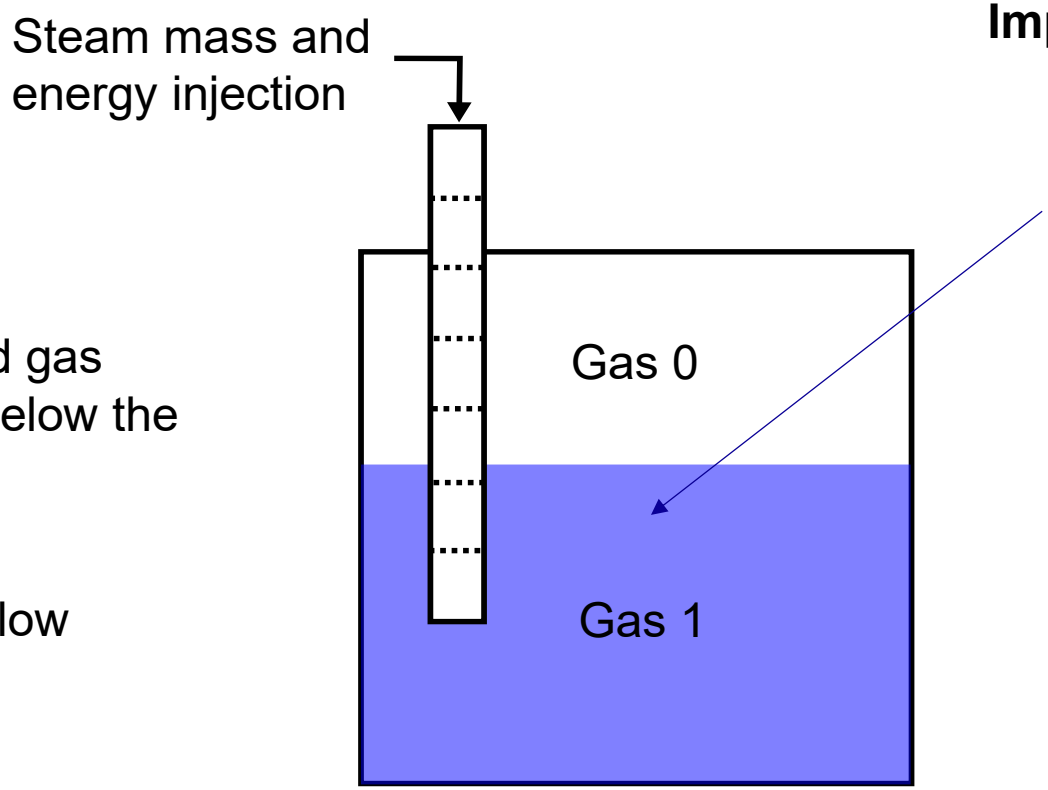

Improved 0D pool volume :

- Liquid mass
- Global steam mass
- Global NC gas mass for each species
- Liquid energy
- **Gas energy above the water level**
- **Gas energy below the water level**
- **Each NC gas mass below the water level**

➔ **6(+2n) equations**

02. SUPRESSION POOL MODELLING

❑ **Case 3** : Taking into account the thermal coupling between the pipe and the pool

- Part of the condensation can occur in the injection pipe

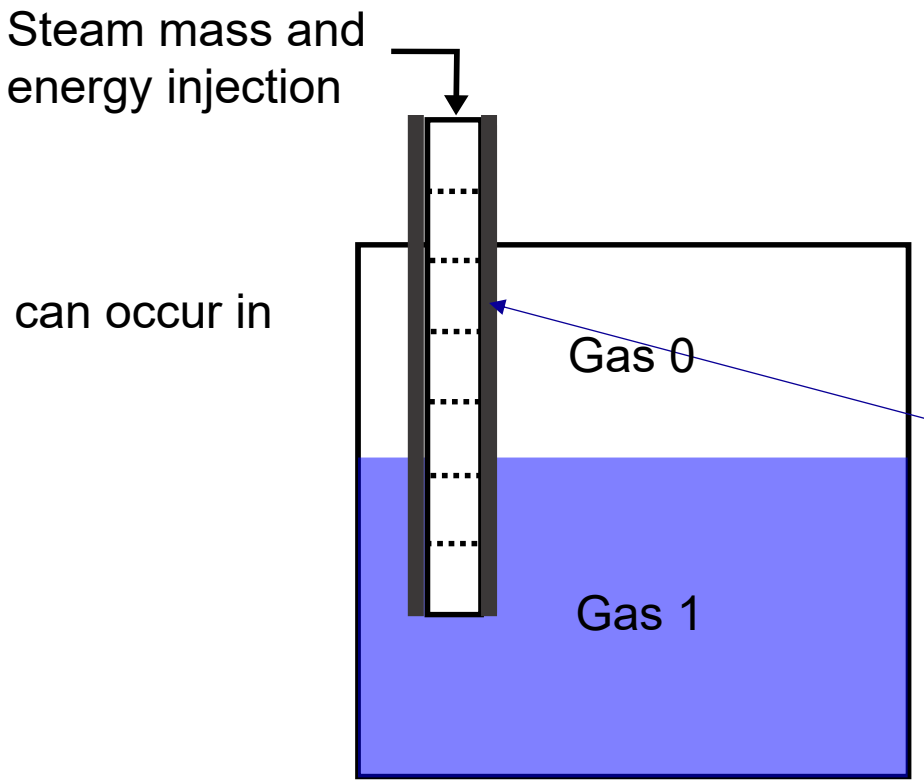

Solid wall modelling :

- Energy balance in the wall
- Heat exchange with the 1D pipe volumes and the 0D pool

02. SUPRESSION POOL MODELLING

❑ **Case 4** : Modification of the interfacial exchange below the water level in the 0D pool

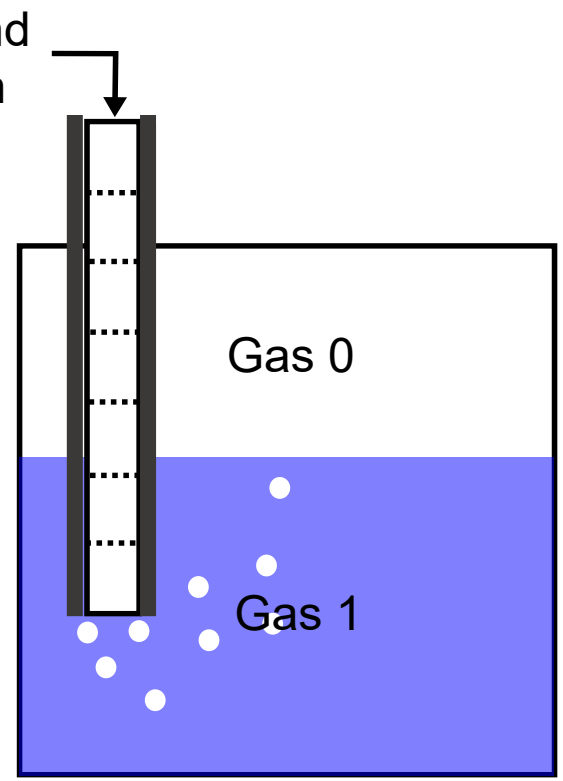

- Condensation below the water level is calculated from interfacial heat transfer evaluation

$$Q_{ik} = h\, A_i (T_i - T_k)$$

- CESAR has been written for circuit application and uses corresponding flow maps for A_i and h
- Annular configuration assumed for Q_{il} calculation in default CESAR

- Modification of the flow regime map for the pool volume :
  - ➔ Bubbly flow assumed below the water level for void fraction <0.5

	Default	New
Interfacial area Ai	$\frac{4}{D_h}$	$\frac{6\alpha}{d_{bub}}$
Heat transfer correlation	Shah [2]	Ranz and Marshall

[2] Shah, *Int. J. Heat Mass Transfer* (1979)

03. VALIDATION ON THE SUPERCLAUDIA EXPERIMENT

❑ Experiment from CEA : open tank, small volume and long transient [3]

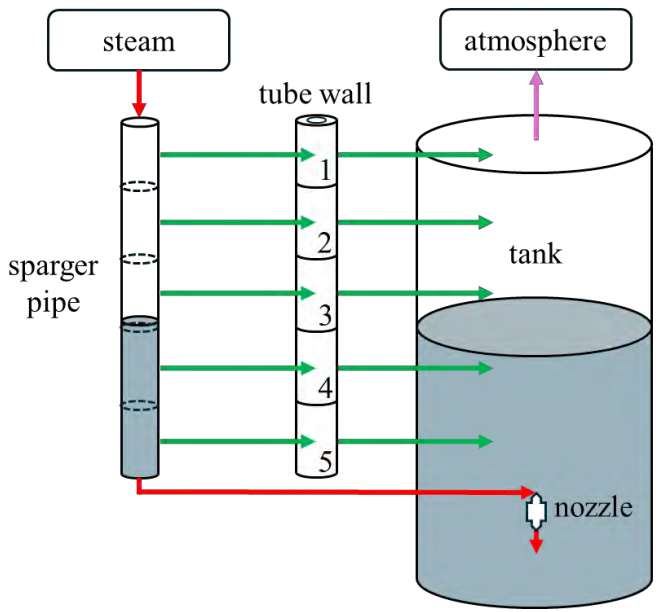

Parameter	Value	Test conditions	Test #3
Tank inner diameter	2500 mm	Tank pressure (p_{tank})	1 bar
Tank height	1600 mm	Pressurizer pressure	45 bar
Tank free volume	7.85 m^3	Initial liq. temp. (T_{liq})	10 °C
Sparger length	1000 mm	Water level	1.03 m
Sparger elevation from tank bottom	600 mm	Liquid inventory (M_{liq})	5025 kg
Nozzle flow area on the sparger head	1.96x10^{-3} m^2	Steam flow rate ($\dot{m}_{steam}$)	76 g/s
		Transient duration	13000 s

[3] Avakian et al., *ICONE6* (1998)

03. VALIDATION ON THE SUPERCLAUDIA EXPERIMENT

case 1 : default
case 2 : + improved 0D pool model
case 3 : case 2 + pipe/pool thermal coupling
case 4 : case 3 + corrected condensation

- With case 1, strong under-estimation of the condensation
- Thermal coupling between the pipe and the pool has a strong influence → where most of the condensation occurs in this case in the calculations (~90%)

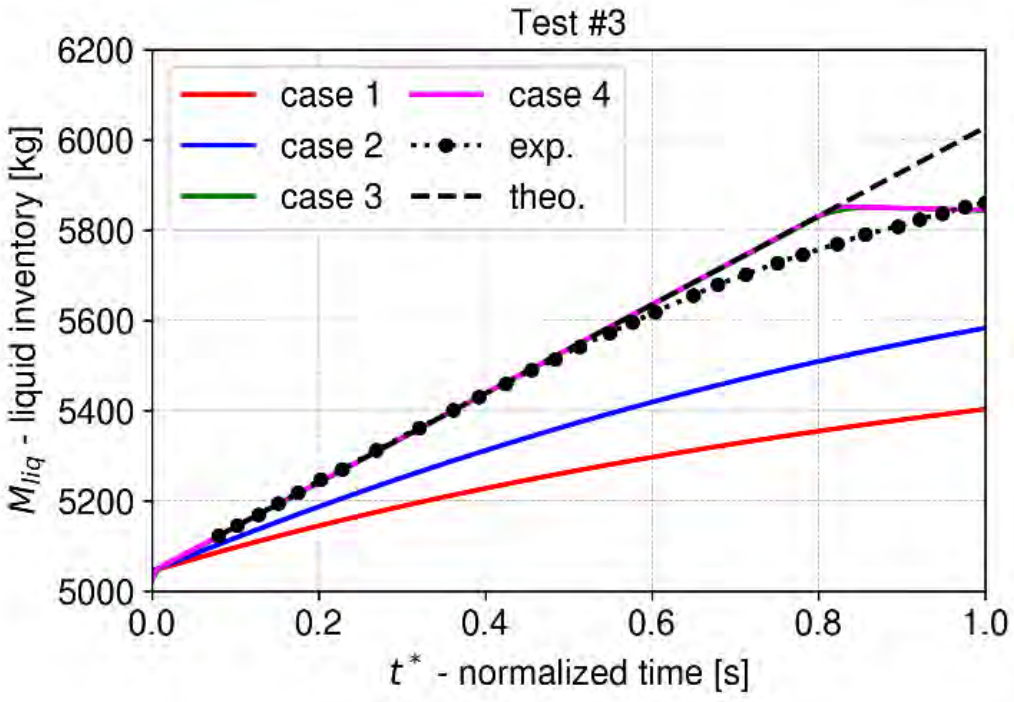

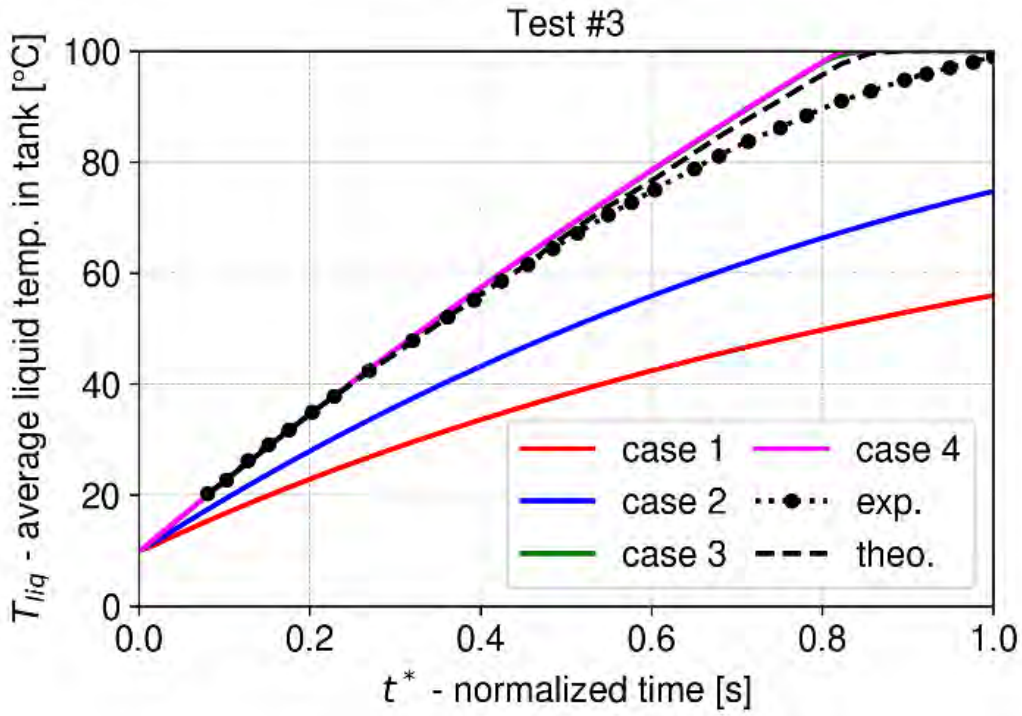

03. VALIDATION ON THE SUPERCLAUDIA EXPERIMENT

- Condensation inside the injection pipe → where most of the condensation occurs in this case in the calculations (~90%)

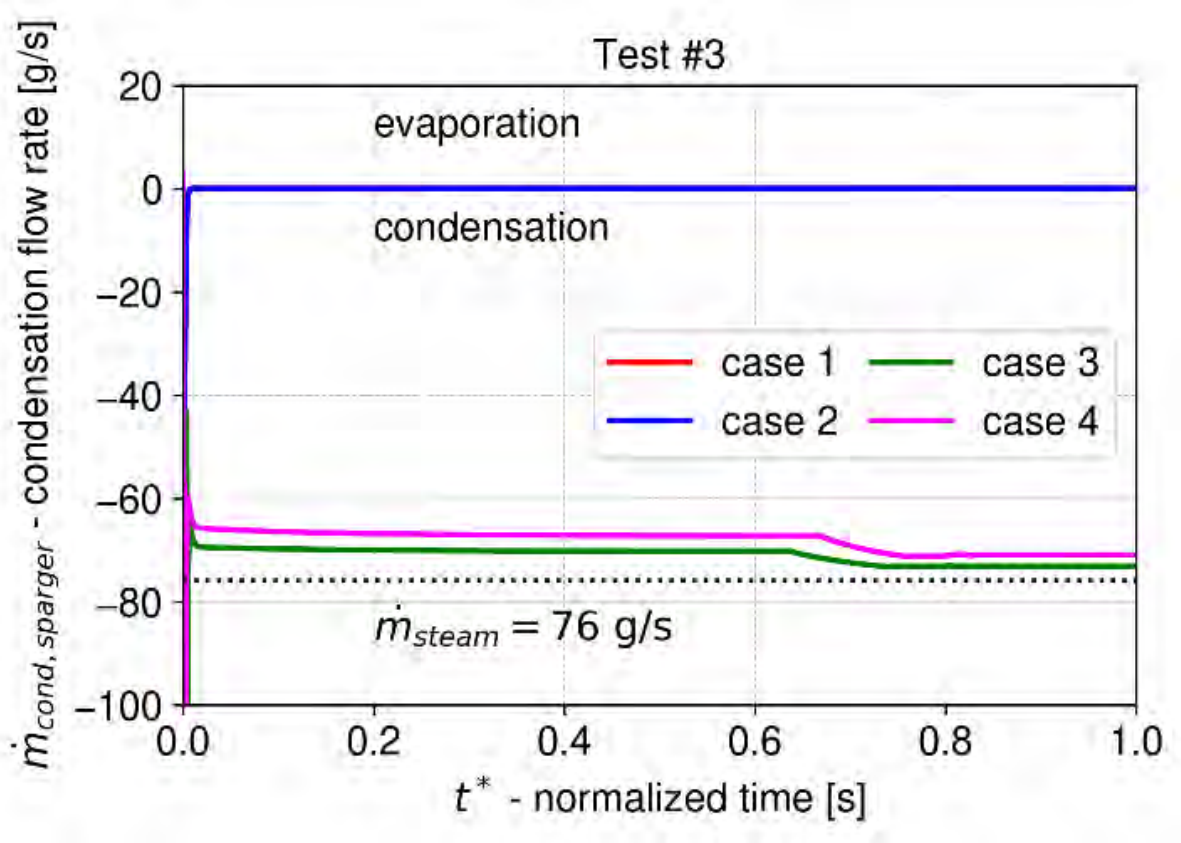

case 1 : default
case 2 : + improved 0D pool model
case 3 : case 2 + pipe/pool thermal coupling
case 4 : case 3 + corrected condensation

03. VALIDATION ON THE SUPERCLAUDIA EXPERIMENT

case 1 : default
case 2 : + improved 0D pool model
case 3 : case 2 + pipe/pool thermal coupling
case 4 : case 3 + corrected condensation
case 5 : case 4 with improved free surface heat transfer model

- End of the transient : deviation assumed to be due to evaporation at the free surface (long transient)
  - Strongly under-estimated in the calculation

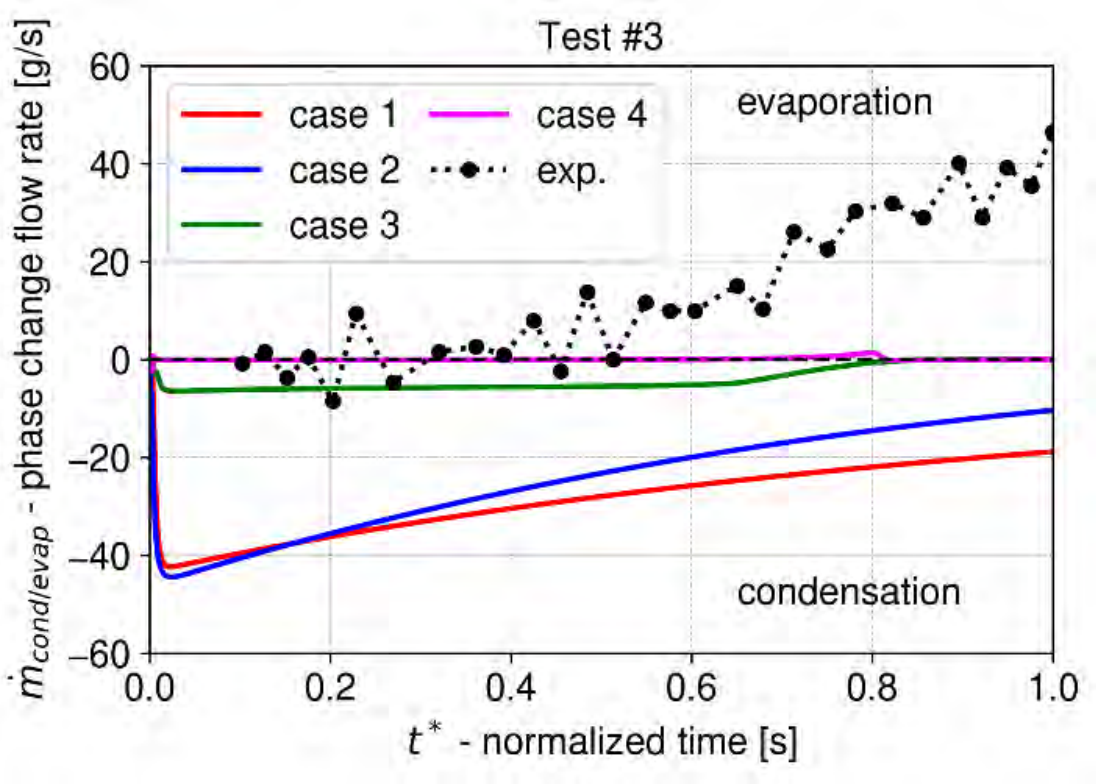

Recent development and improvement of the heat transfer model at the free surface have confirmed this hypothesis

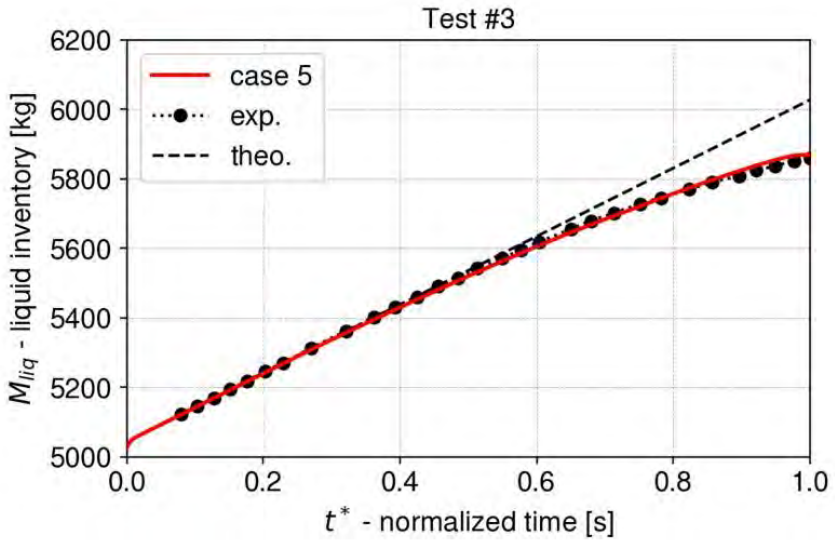

04. VALIDATION ON THE B&C EXPERIMENT

❑ Experiment from KAERI : closed tank with higher mass flow rate and smaller transient time [4]

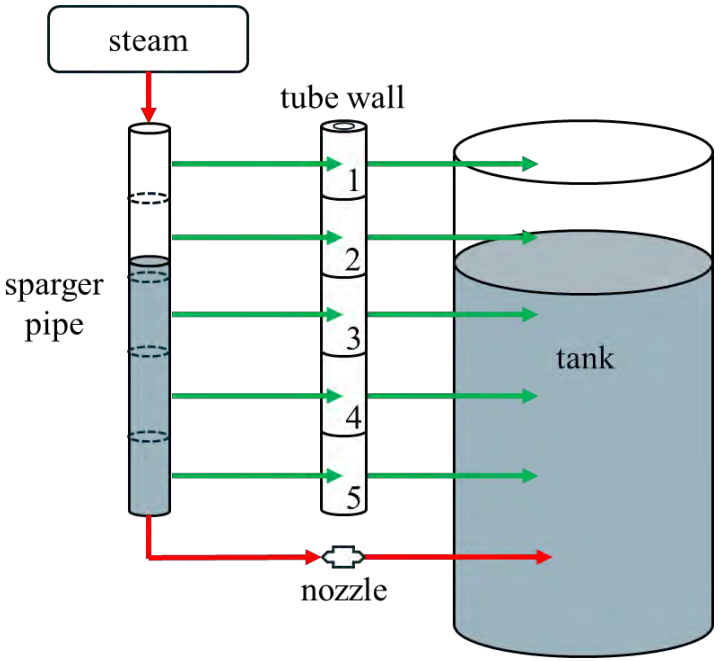

[4] Kang and Song, *Nucl. Eng. Des.* (2008)

Parameter	Value	Initial conditions	Value
Tank inner diameter	3000 mm	**Tank pressure (p_{tank})**	1 bar
Tank height	4000 mm	**Pressurizer pressure**	150 bar
Tank free volume	28.22 m^3	**Tank temperature (T_{liq})**	25.60 °C
Sparger inner diameter	152.40 mm	**Water level**	3.02 m
Sparger length	3100 mm	**Liquid inventory (M_{liq})**	21244 kg
Sparger elevation from tank bottom	900 mm		
Nozzle flow area on the sparger head	5.52×10^{-3} m^2		

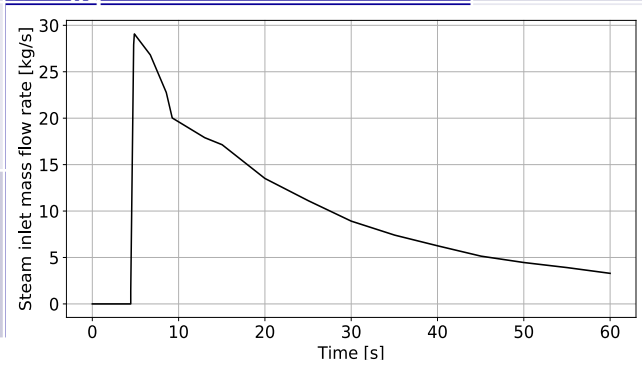

04. VALIDATION ON THE B&C EXPERIMENT

case 1 : default
case 2 : + improved 0D pool model
case 3 : case 2 + pipe/pool thermal coupling
case 4 : case 3 + corrected condensation

- Very high under-evaluation of the condensation with case 1-3
- Not much influence of the thermal coupling between the pipe and the pool → not much condensation in the pipe for this case
- Very high impact for case 4

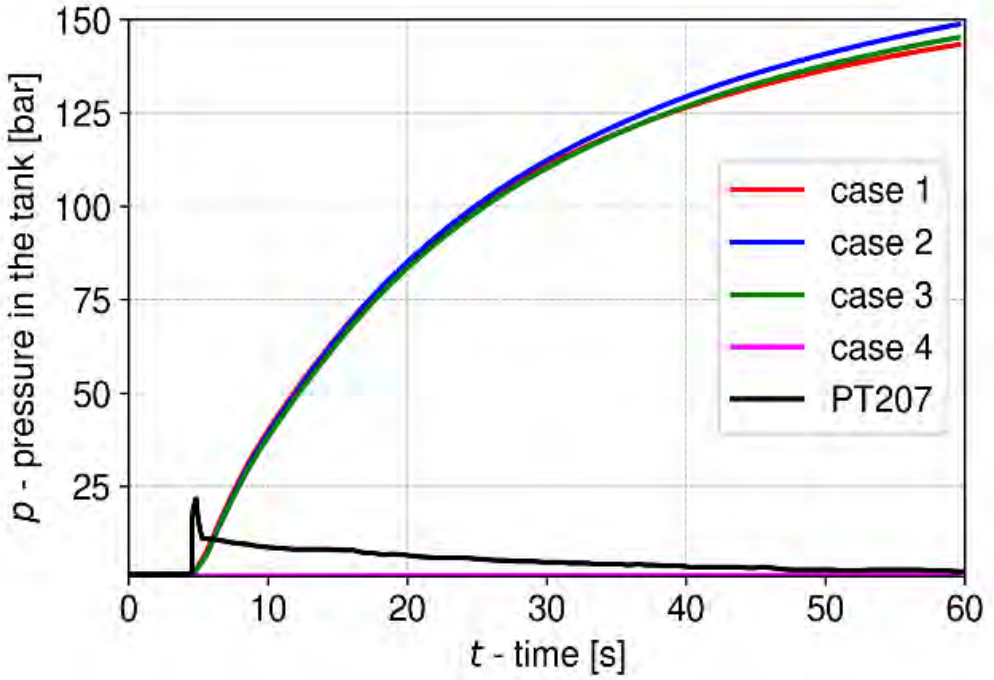

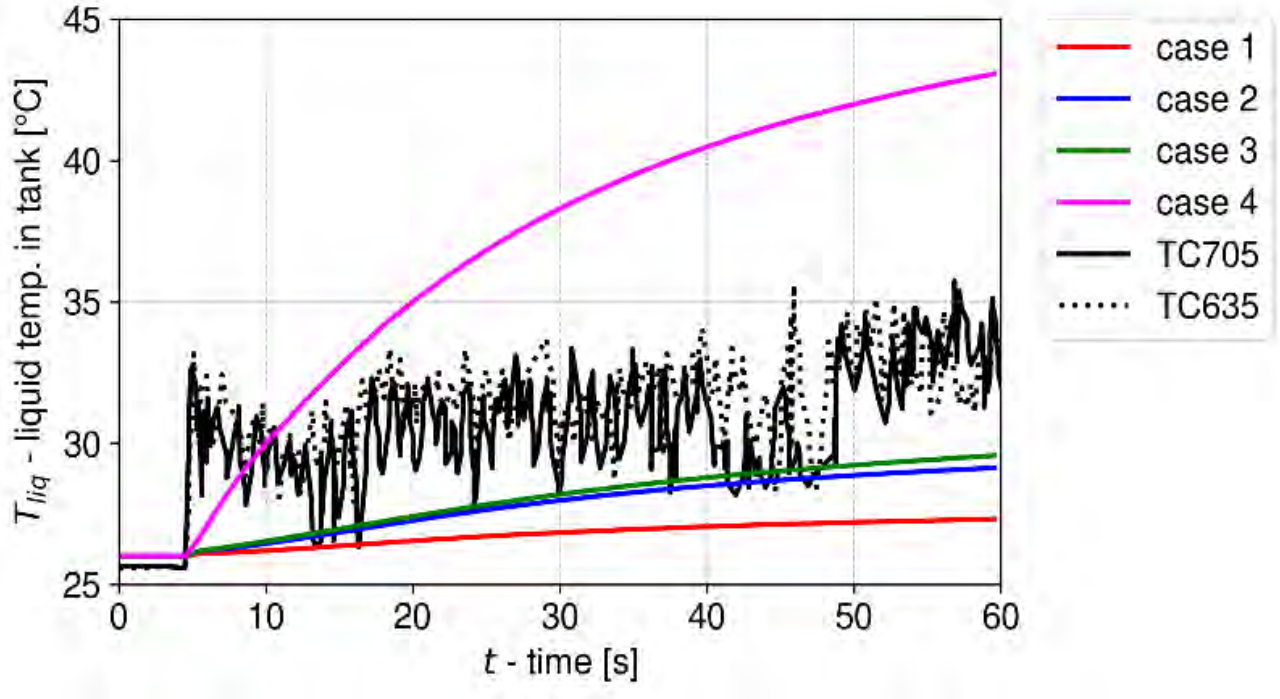

04. VALIDATION ON THE B&C EXPERIMENT

❑ Case 4 : Bubbles size around mm ➔ Ai from ~1 m^{-1} in annular configuration to ~10^3 m^{-1}

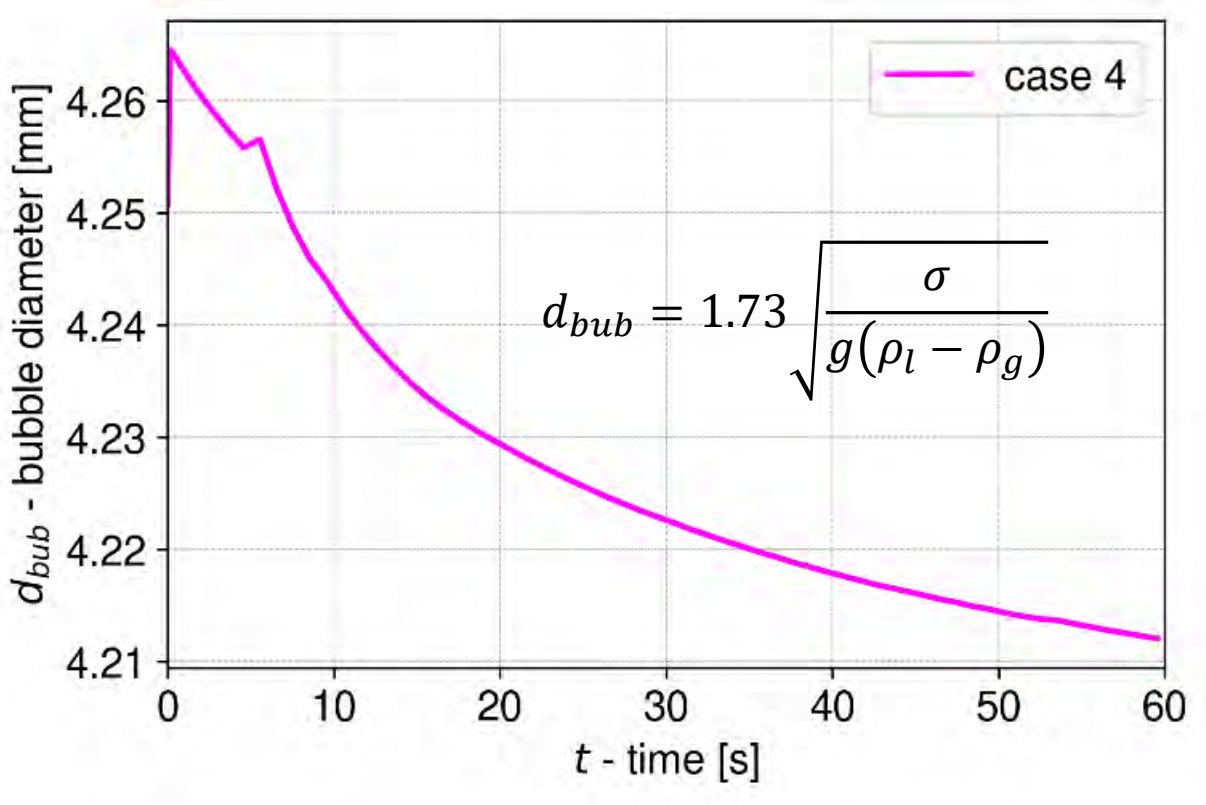

❑ Improvements planned :

- ❑ At the transient beginning, a vapour jet is expected ➔ reduction of the interfacial area
- ❑ Introduction of a more complete flow map for jet and bubbly regime
- ❑ Nusselt correlation improvement

05. CONCLUSIONS AND PERSPECTIVES

- CESAR default model does under-estimate direct contact condensation in pool configuration
  - A correct evaluation of the diphasic flow configuration and corresponding interfacial area is necessary,
  - New pool specific CESAR option available in latest released version to properly assess the liquid to interface heat transfer in bubbly flow configuration,
  - Further improvements needed to complete the flow map, including jet regime.

- In some configurations, an important part of the condensation can occur in the injection pipe : thermal coupling between the pipe and the pool should be taken into account.

- For long transients at atmospheric conditions, evaporation at the pool free surface can play an important part and should be also correctly evaluated.

THANK YOU FOR YOUR ATTENTION

VALIDATION ON THE SUPERCLAUDIA EXPERIMENT

❑ New free surface evaporation heat transfer model:

$$h_{liq} \cdot c_{p,liq}(T_{liq} - T_{int}) - h_{gas} \cdot c_{p,gas}(T_{int} - T_{gas}) = \dot{m}''_{evap} \cdot h_{fg}$$

Convection w Lloyd & Moran [1974]:

$$2.2E4 < Ra < 8.0E6: \quad h_{conv} = \frac{\lambda_f}{W} \cdot 0.54 Ra^{0.25}$$

$$8E6 < Ra < 1.6E9: \quad h_{conv} = \frac{\lambda_f}{W} \cdot 0.15 Ra^{0.333}$$

Stefan's model [2019]:

$$\dot{m}''_{evap} = Sh \cdot \frac{\rho_{gas}\mathcal{D}}{L_c} \cdot \log\left(\frac{p_{tot} - p_{v,int}}{p_{tot} - p_v}\right)$$

Bower & Saylor [2011]:

$$Sh = 0.316 \cdot Sc^{0.333} Ra^{0.306}$$

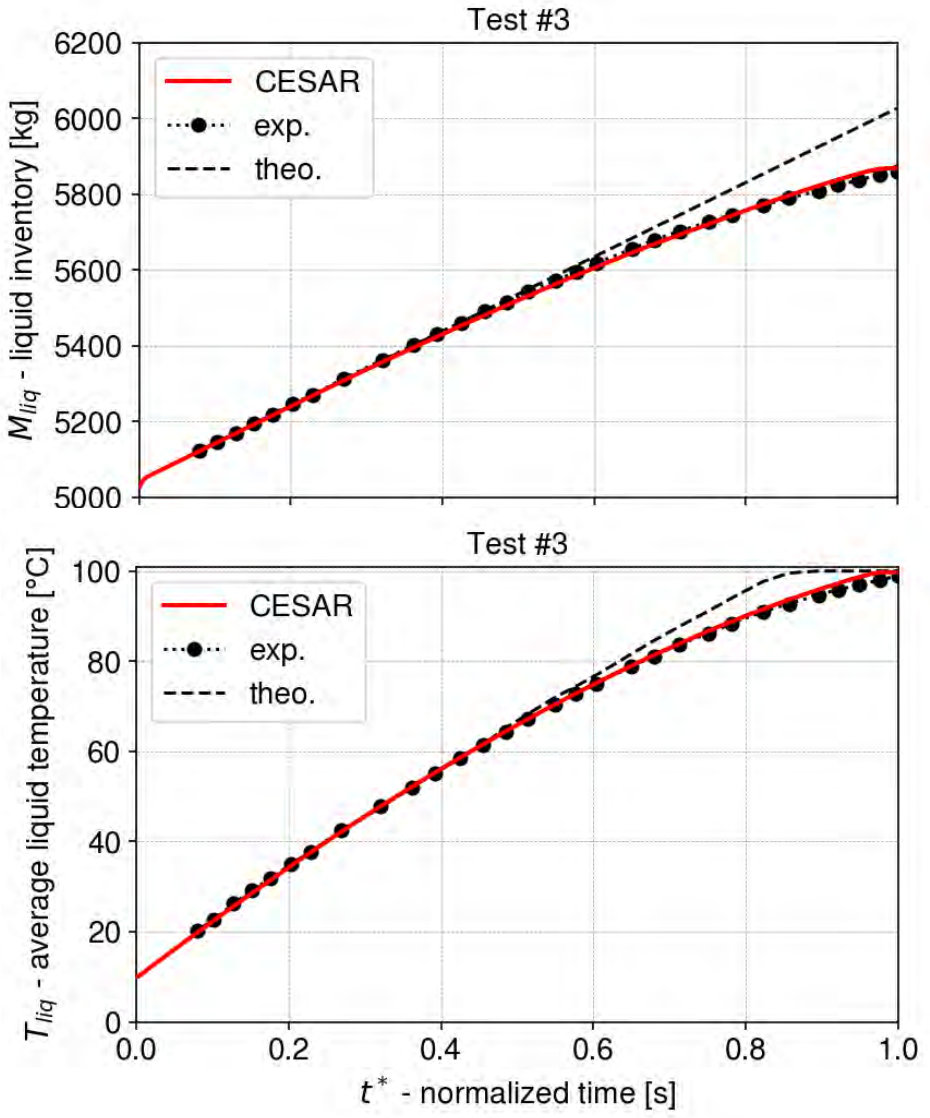

[1974] Lloyd, J. R. and Moran, W. R., Natural convection adjacent to horizontal surface of various planforms, ASME Journal of Heat and Mass Transfer, vol. 96 pp. 443-447, 1974

[2011] Bower, S. M. and Saylor, J. R., Erratum to 'A study of the Sherwood-Rayleigh relation for water undergoing natural convection-driven evaporation' Int. J. Heat Mass Transfer 52 (2009) 3055-3063], International Journal of Heat and Fluid Flow, vol. 54, p. 749, 2011

[2019] Martin, J. and Migot, B., Experimental study of the surface evaporation rate of a heated water pool at high temperature using infrared thermography, NURETH-18, 2019

The 12th European Review Meeting on Severe Accidents Research

May 18-22, 2026, Universidad Carlos III de Madrid, Madrid, Spain

TECHNICAL SESSION 4.1: EX-VESSEL CORIUM AND DEBRIS COOLABILITY

Chairs: S. Bectha (KTH), P. Piluso (CEA)

ID134	**Development of the SAFARI Code for Comprehensive Severe Accident Analysis in Nuclear Reactors: Steam Explosion Analysis Module** K. Ju Bin (Seoul National University)	Paper
ID018	**Effect of Corium Properties Uncertainties on a PWR SBO Severe Accident** L. E. Herranz (CIEMAT)	Paper Presentation
ID011	**Consideration on Floating Crusts During Molten Core Concrete Interaction** C. Journeau (CEA)	Paper Presentation

DEVELOPMENT OF THE SAFARI CODE FOR COMPREHENSIVE SEVERE ACCIDENT ANALYSIS IN NUCLEAR REACTORS: STEAM EXPLOSION ANALYSIS MODULE

Ju Bin Kim[a], Sai Raja Gopal Vadlamudi[b], Eung Soo Kim[a], Hyun Sun Park[a*]
[a] Department of Nuclear Engineering, Seoul National University, 1 Gwanak-ro, Gwanak-gu, Seoul, South Korea
* hejsunny@snu.ac.kr

[b] Institute of Fluid Dynamics, Helmholtz-Zentrum Dresden-Rossendorf (HZDR), Dresden, Germany

ABSTRACT

Steam explosions occur when molten corium comes into sudden contact with coolant during severe accidents. The resulting pressure waves can endanger containment integrity and must be assessed in accident analysis. The SAFARI project develops an integrated regulatory framework for such evaluations. It includes modules for Fuel-Coolant Interaction (FCI), Steam Explosion (SE), Molten Core-Concrete Interaction (MCCI), and Containment Thermal-Hydraulics. This paper presents the SE module.
The SE module adopts a lumped parameter model that solves mass and energy conservation equations. The thermodynamic state is determined from specific internal energy and volume, which are inverted through steam tables to obtain pressure and temperature. Near the critical point, steep nonlinear property gradients often cause instability and oscillations. To overcome this limitation, a ResNet-based deep learning surrogate was developed and integrated into the framework. It provides accurate and stable predictions of pressure and temperature in the critical region. This approach enables the code to maintain the efficiency of tabulated methods while ensuring robustness under challenging conditions.
The SE module receives initial conditions and transient mixing parameters from the FCI module to directly estimate peak pressure and impulse. Validation was performed against three benchmark steam explosion experiments: KROTOS K44, FARO L33, and TROI 13. These tests cover diverse conditions, including variations in melt composition, coolant subcooling, and geometry. The module reproduced key features such as peak pressure and impulse. This consistency across different scenarios demonstrates its robustness and versatility. Compared with mechanistic codes, it provides similar predictive accuracy with significantly lower computational cost. These results confirm that the SE module offers a reliable and efficient tool for regulatory safety evaluations. It also contributes to the establishment of an integrated severe accident analysis framework.

KEYWORDS
Steam Explosion, Parametric Model, Severe Accident, Steam Table, SAFARI code

1. INTRODUCTION

1.1. Motivation

Severe accidents in power reactors can involve core melting and relocation, potentially leading to vessel failure. Under such conditions, fuel heat up and melting may lead to relocation of molten core materials and eventual vessel failure. When molten corium is released into a wet cavity during an accident progression in ex-vessel accident, it can interact violently with the coolant. This fuel-coolant interaction, commonly referred to as FCI, involves jet breakup, premixing, and debris formation, and it can create conditions under which a steam explosion may occur [1-3]. A steam explosion is a rapid energetic event driven by fine fragmentation of molten fuel, intense heat transfer, and explosive vapor generation. The associated pressure pulse and impulse can impose high dynamic loads on surrounding structures, and therefore steam explosions remain an important issue for containment integrity and severe accident management.

Reliable assessment of steam explosion loads is required for regulatory safety evaluations and for the quantitative comparison of accident management strategies such as ex-vessel cooling. However, the steam explosion process is strongly dependent on the premixing state at the time of triggering, including fuel temperature and inventory, fragment size distribution, coolant subcooling, void fraction, and the geometric configuration of the interaction region. These parameters evolve over time during the coolability transient, and the most challenging cases are often associated with short time intervals and rapidly changing thermohydraulic conditions. Fully mechanistic multiphase codes can represent many detailed phenomena, but their computational cost and input requirements make them difficult to apply repeatedly for large parametric studies or for integration into broader severe accident analysis frameworks. This motivates the development of efficient steam explosion analysis tools that can estimate pressure and impulse over a wide range of transient conditions while maintaining physically consistent modeling assumptions.

1.2. SAFARI Project

In South Korea, the SAFARI project was initiated to establish an integrated and regulatory-oriented severe accident analysis capability. SAFARI develops a modular framework that couples key ex-vessel severe accident phenomena, including fuel-coolant interaction, steam explosion, molten core-concrete interaction, and containment thermal-hydraulics, within a consistent set of modeling assumptions and data interfaces [4]. Within this effort, the steam explosion module has been developed to provide fast and robust predictions of explosion loads using a lumped parameter approach that can accept time-dependent premixing information from the FCI module named HIPPO. The primary motivation of this development is to support systematic verification against representative benchmark experiments and to enable practical regulatory evaluations of steam explosion loads under realistic accident progression scenarios within the SAFARI framework.

2. METHODOLOGY

2.1. Model Overview

The steam explosion module called SCORPION is built on a non-equilibrium model and a lumped parameter model. The objective is to capture the mass and energy conservation equations that control pressure load generation during the short explosion transient, while keeping the computation fast enough for repeated analyses. The overall formulation is inspired by the one-dimensional lumped modeling philosophy developed in the University of Wisconsin fuel-coolant interaction program (UWFCI) [5]. Instead of resolving detailed multiphase momentum fields, the model represents the system with a small number of control volumes and tracks the time evolution of the key material masses and energies.

The coolant region is divided into a mixing zone and a slug zone as shown in Figure 1. The mixing zone is where molten fuel, fine fragments, coolant, and vapor coexist and exchange mass and energy. Fine fragmentation and rapid vapor generation are treated in this zone, and the thermodynamic state of the vapor region is determined from the evolving vapor mass, energy, and volume. The slug zone represents the upper water column that is accelerated by the pressure rise. Direct fuel-coolant interaction is not assumed in the slug zone, but mass and energy exchange with the mixing zone can occur through coolant redistribution.

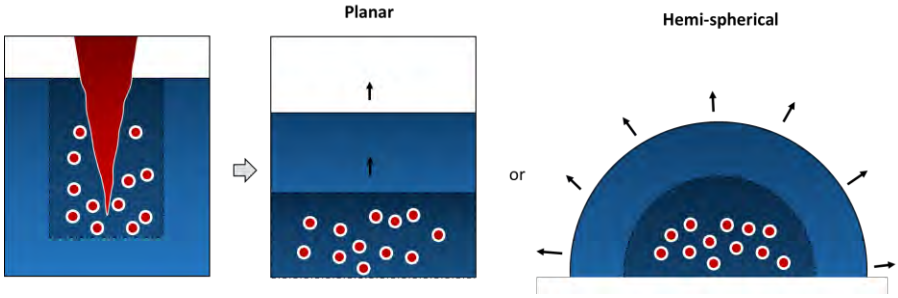

Figure 1. Conceptual illustration of mixing zone and slug zone [4].

The model tracks the masses and energies of molten fuel, fine fragments, coolant, vapor, and the slug, and it advances these quantities in time. Figure 2 provides a conceptual picture of the fragmentation process that motivates the source terms and heat transfer terms used in the conservation equations. As fragmentation proceeds, interfacial area increases and heat transfer intensifies, which accelerates vapor production and drives the pressure rise. The model is structured to reflect this causal chain in a compact form.

Time integration is performed by solving the coupled ODE system with the LSODA algorithm [7]. Pressure and temperature are obtained from the vapor specific internal energy and specific volume computed from the conserved vapor mass, energy, and volume. Momentum equations are not solved explicitly. Slug motion and the effective fragmentation process are represented using simplified kinematic relations and constraint concepts such as slug breach and acoustic limits. With this formulation, SCORPION aims to reproduce the key energetics that control pressure and impulse while maintaining computational efficiency.

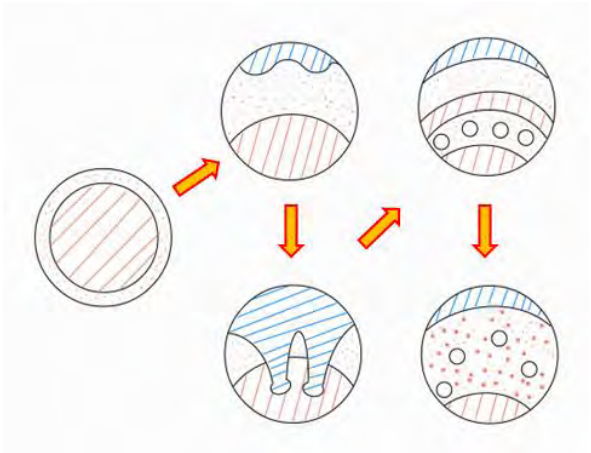

Figure 2. Conceptual illustration of fine fragmentation [6].

2.2. Governing Equations

The governing equations are written as coupled ordinary differential equations for mass and energy in the mixing and slug regions. In Eq. (1)-(10), subscripts f, fr, c, g, and s denote the molten fuel, fragmented fuel, coolant, vapor (gas), and slug-region respectively. Interfacial heat-transfer terms are written as $\dot{Q}_{lj}$, where the first subscript identifies the donor and the second the receiver. The mass conservation equations are written in Eq. (1)-(5). The mass balances represent the main conversion and exchange mechanisms. Molten fuel is converted into fine fragments by a fine fragmentation source term. Coolant is converted into vapor by rapid vaporization driven by heat transfer from the fuel and fragments. In addition, coolant can be exchanged between the mixing zone and the slug zone as the pressure driven motion redistributes coolant inventory during the transient.

$$\frac{dm_f}{dt} = -\dot{m}_{fr} \tag{1}$$

$$\frac{dm_{fr}}{dt} = \dot{m}_{fr} \tag{2}$$

$$\frac{dm_c}{dt} = -\dot{m}_g + \dot{m}_s \tag{3}$$

$$\frac{dm_g}{dt} = \dot{m}_g \tag{4}$$

$$\frac{dm_s}{dt} = -\dot{m}_s \tag{5}$$

$$\frac{dE_f}{dt} = -\dot{Q}_{fg} + \dot{m}_{fr} V_f P - \dot{m}_{fr} h_{fn} \tag{6}$$

$$\frac{dE_{fr}}{dt} = -\dot{Q}_{frg} - \dot{m}_{fr} V_f P + \dot{m}_{fr} h_{fn} \tag{7}$$

$$\frac{dE_c}{dt} = \dot{Q}_{fc} + \dot{Q}_{frc} - \dot{m}_g c_{pc}\left(T_c - T_{ref}\right) + P\dot{V}_c + \dot{m}_s c_{pc}(T_s - T_{ref}) \tag{8}$$

$$\frac{dE_g}{dt} = \dot{Q}_{fg} + \dot{Q}_{frg} - \dot{Q}_{fgc} - \dot{Q}_{frgc} + \dot{m}_g(h_{fg} + c_{pc}\left(T_c - T_{ref}\right)) - P\dot{V}_g \tag{9}$$

$$\frac{dE_s}{dt} = -\dot{m}_s c_{pc}\left(T_s - T_{ref}\right) + P\dot{V}_s \tag{10}$$

The energy conservation equations are given in Eq. (6)-(10). Heat transfer from molten fuel and fine fragments supplies energy to the coolant and vapor, while phase change introduces enthalpy transport associated with vapor generation. The expansion of the vapor region performs pressure volume work, which is included to represent the driving mechanism of the pressure pulse. These terms determine how quickly thermal energy is converted into vapor energy and how the resulting expansion produces the pressure load.

The vapor state is evaluated using variables that are naturally available in the lumped formulation. The model updates vapor mass, vapor energy, and vapor volume in time. From these conserved quantities, the vapor specific internal energy and specific volume are obtained and used to determine pressure and

temperature. This structure keeps the property evaluation consistent with the conservation equations and allows stable tracking of the thermodynamic state even when the highly energetic transients.

Overall, the conservation set provides a clear link from fragmentation and heat transfer to vapor generation and pressure loading. The equation structure is compact enough for parametric studies, yet it retains the key energetic couplings needed to predict peak pressure and impulse. This balance between physical consistency and computational simplicity is the basis for using the module in verification studies and broader severe accident analyses.

2.3. Fine Fragmentation Model

Fine fragmentation is a central process in steam explosions because it controls how much melt participates in rapid heat transfer. When coarse melt droplets or jets are broken into small particles, the total interfacial area between fuel and coolant increases sharply. This accelerates heat transfer, promotes rapid vapor generation, and amplifies the pressure load. If fragmentation is weak or ends quickly, only a limited fraction of the melt contributes to vapor production during the effective time interval, and the resulting peak pressure and impulse are reduced.

Fragmentation is commonly interpreted from two perspectives. In the hydrodynamic perspective, breakup is driven by external mechanical loading such as shock waves, strong shear, and large relative motion between phases. The breakup rate is often described using slip velocity and dimensionless groups that reflect the balance between inertia and stabilizing effects such as surface tension. In the thermal perspective, breakup is driven by thermally induced instabilities at the interfaces between melt, vapor film, and coolant. Collapse of the vapor film, local coolant penetration, and rapid rewetting can strip melt from the surface and generate fine fragments even without strong bulk acceleration.

SCORPION is implemented to allow different fragmentation options so that different assumptions can be tested under the same governing equation structure. Hydrodynamic and thermal viewpoints are both supported through alternative rate models that define the conversion of molten fuel mass into fine fragment mass. This design is useful for sensitivity studies and for comparisons against other steam explosion codes that emphasize different breakup mechanisms.

$$\frac{dm_{fr}}{dt} = 6C_{fr}m_f\sqrt{\frac{\Delta P_{fr}}{\rho_c {R_f}^2}}f(\alpha)g(\tau_{fr}) \tag{11}$$

The Tang model in the TEXAS is adopted as the default option, and the corresponding fine fragmentation rate is expressed by Eq. (11). The cutoff functions $f(\alpha)$ and $g(\tau_{fr})$ are introduced to terminate fragmentation at large void fractions and after the prescribed fragmentation time scale. The model provides a compact rate expression for the conversion of molten fuel to fine fragments and includes termination criteria that limit fragmentation when conditions become unfavorable. The fragmentation rate computed by this model directly supplies the mass source term in the governing equations, and it therefore controls the effective intensity of vapor generation and pressure loading within the lumped parameter framework.

2.4. ResNet-Based Model for Thermodynamic Property Prediction Near the Critical Point

Accurate evaluation of thermodynamic properties from specific internal energy and specific volume is essential for predicting steam explosion loads. In the original implementation, pressure and temperature were obtained by inverting the IAPWS steam tables using the vapor energy, mass, and volume from the governing equations [8]. This approach is efficient in most regions, but it becomes numerically sensitive

near the critical point, where small perturbations in state variables produce large nonlinear changes in pressure and temperature. As a result, the inversion may require very small time steps and can introduce oscillatory or nonphysical behavior, particularly when the state approaches the edge of the tabulated domain.

To overcome these limitations, a residual neural network (ResNet) surrogate was developed and integrated into SCORPION [4]. Figure 3 summarizes the architecture, which maps specific volume and specific internal energy to pressure and temperature through input normalization, a fully connected layer, and stacked residual blocks. The surrogate was trained on high resolution IAPWS-IF97 data with dense sampling in the near critical region, with normalized variables and removal of nonphysical states [8].

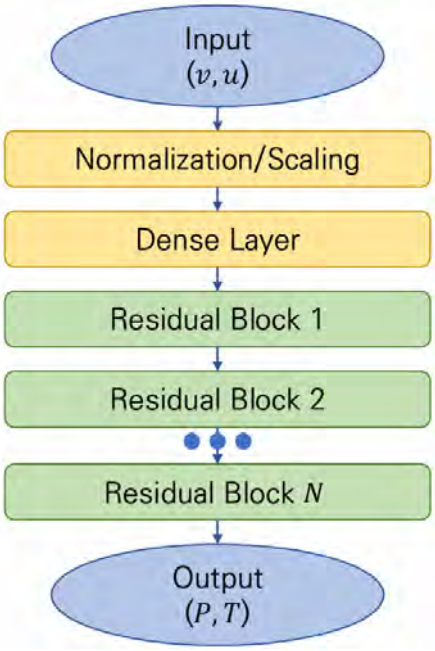

Figure 3. Network structure of the ResNet-based surrogate mapping specific volume and internal energy to pressure and temperature.

Early tests with a multilayer perceptron showed degraded accuracy in the near critical region due to steep gradients. A ResNet architecture was therefore adopted to improve both accuracy and training robustness. The network consists of an input normalization followed by multiple residual blocks with nonlinear activations and skip connections that add the block input to the block output. This residual formulation helps the network learn incremental corrections and improves convergence in deep models.

The loss function is designed to balance absolute and relative accuracy across the entire training domain. It combines mean squared error, mean absolute error, and relative error terms, with tunable weights assigned to each component. Because accurate prediction at high pressure is particularly important for severe accident analysis, an additional weighting factor is applied to samples with pressures above a specified threshold, increasing the penalty for errors in this region. The learning rate is controlled using a scheduler that reduces the rate when the validation loss stagnates, allowing coarse exploration in early epochs and fine adjustment near convergence.

Once trained, the ResNet model is incorporated into the steam explosion module through a hybrid property evaluation strategy. For states well away from the critical region, pressure and temperature are obtained from standard IAPWS steam table interpolation to retain efficiency and consistency with established data.

In the near critical region, the module evaluates pressure and temperature using the ResNet surrogate based on the current specific volume and internal energy. A smooth blending procedure is applied across the interface of the two methods to prevent abrupt changes in predicted properties. In addition, basic thermodynamic consistency checks are applied to the surrogate outputs, and table-based values are used as a safeguard when the predicted state is outside the physically admissible range.

This hybrid strategy improves numerical robustness near the critical point while preserving computational efficiency. Standalone tests confirm that the surrogate reproduces IAPWS steam table values in the near critical range with small errors. When integrated into the steam explosion calculations, the hybrid evaluation yields smoother pressure transients and more stable time integration, especially for cases with rapid energy release and high energetic cases. Overall, the combined use of conventional tables and a ResNet surrogate provides reliable property prediction in challenging near critical conditions without increasing the cost of large parametric studies.

2.5. Coupling with the FCI Module

In the SAFARI framework, the SCORPION module is coupled to the HIPPO module. HIPPO module simulates ex-vessel melt jet breakup, premixing, and debris formation in a flooded cavity, and it provides the thermohydraulic conditions that define the initial state for a potential steam explosion. This coupling enables the sequence from melt release to premixing and the subsequent explosion phase to be evaluated using consistent geometry and property assumptions.

The coupling is implemented as a one-way interface from the HIPPO module to the SCORPION module. The FCI calculation is performed first, and key premixing quantities are recorded as time-dependent outputs. These include the interacting melt mass, coolant inventory and subcooling in the mixing region, void fraction, characteristic fragment size, pool depth, and slug mass and cross-sectional area. The outputs are stored at selected times in a tabular file and used to define the initial conditions for SE calculation.

To maintain consistency between the two modules, the transferred variables are defined with clear physical meaning. Only the melt fraction that remains liquid and is in direct contact with coolant is transferred as the participating fuel, while solidified material and debris bed inventory are excluded. The mixing and slug control volumes are constructed from the pool depth and slug geometry provided by the HIPPO module so that coolant volumes and inventories remain consistent. Fragment size and void fraction are passed to the fine fragmentation and heat transfer models, and background pressure and ambient conditions are applied as boundary conditions.

This coupling strategy improves consistency and usability compared with workflows that rely on external premixing tools and manual input processing. Using premixing results directly from the HIPPO module preserves the causal link between the premixing state and explosion energetics and avoids inconsistencies caused by mismatched assumptions. The one-way interface also reduces computational cost, because the premixing calculation is performed once and its time-dependent outputs are used to define the initial and boundary conditions for the SCORPION calculation. As a result, the coupled HIPPO-SCORPION capability provides a practical and reliable basis for estimating ex-vessel steam explosion pressure and impulse.

3. RESULTS

3.1. Verification Experiments: KROTOS K44, FARO L33, TROI 13

Three OECD SERENA experiments were selected: KROTOS K44, FARO L33, and TROI 13 [1-3]. These benchmarks represent the main conditions controlling pressure and impulse generation, including melt

composition, melt inventory, melt temperature, coolant subcooling, system pressure, facility geometry, and the triggering mechanism.

KROTOS K44 provides tightly controlled initial conditions and a comparatively simple geometry, which is useful for examining how the explosion phase models reproduce peak pressure and impulse under well-defined boundary conditions [2]. FARO L33 is conducted with a prototypic corium composition under pressurized conditions and high coolant subcooling [10]. The test includes an external trigger and non-condensable gas in the cover region, which challenges the prediction of pressure rise and impulse in a deep pool. TROI 13 also employs prototypic corium, but it is characterized by a much larger melt release height and a spontaneous explosion without an external trigger [11]. This case supports an assessment of model performance under different premixing development and triggering conditions. Overall, the three benchmarks confirm the applicability of the module across a wide range of steam explosion scenarios within a unified framework.

3.2. Initial Conditions of Simulation

Table I lists the initial and boundary conditions adopted for the simulations of KROTOS K44, FARO L33, and TROI 13 [2, 10-12]. The calculations were defined to be consistent with the reported melt composition, released mass, jet diameter, system pressure, coolant subcooling, and geometric scale of each facility. For FARO L33, the released mass is reported together with the melt mass at the triggering time, and this information is used to define a representative participating inventory for the explosion phase. Using a consistent set of initial and boundary conditions enables a direct comparison of predicted peak pressure and impulse across experiments with different scales and operating conditions.

Table I. Initial and boundary conditions of experiments: KROTOS K44, FARO L33, TROI 13

Experiment	KROTOS K44	FARO L33	TROI 13
Melt Composition	Al_2O_3	80 $wt\%$ UO_2 + 20 $wt\%$ ZrO_2	70 $wt\%$ UO_2 + 30 $wt\%$ ZrO_2
Released Mass [kg]	1.45	100/25 [1)]	7.7
Release Diameter [m]	0.03	0.05	0.02
Melt Temperature [K]	2673	3070	3300
Free Fall in Gas [m]	0.43	0.77	3.8
Water Depth [m]	1.105	1.62	0.67
Pool Diameter [m]	0.20	0.71	0.60
Water Temperature [K]	363	294	292
Water Subcooling [K]	10	124	81
Pressure [MPa]	0.1	0.41	0.1
External Trigger	Yes	Yes	No

1) For FARO L33, "100/25" denotes the released melt mass and the melt mass at the triggering time, respectively.

3.3. SCORPION Simulation Results

Table II and Figures 4 to 6 summarize the SCORPION predictions for the three benchmark experiments. Rather than focusing only on peak values, the results are interpreted in the context of the defining experimental characteristics outlined in Section 3.1, including melt composition, thermohydraulic boundary conditions, facility geometry, and the triggering condition. This approach allows the verification to assess

whether the module reproduces not only the magnitude of the loads but also the expected trends and response characteristics across substantially different experimental regimes.

Table II. SCORPION analysis results for the experiments: KROTOS K44, FARO L33, TROI 13

Experiment	KROTOS K44	FARO L33	TROI 13
Peak Pressure [MPa]	27.94	9.50	6.53
Peak Impulse [kPa·s]	53.64	25.94	29.77

KROTOS K44 yields the highest predicted peak pressure and impulse among the three cases, with a peak pressure of 27.94 MPa and a peak impulse of 53.64 kPa·s. This result is consistent with the KROTOS K44 configuration, which employs a simulant alumina melt, operates under a relatively low system pressure environment, and uses a well-defined external triggering procedure in a simplified planar geometry. Under such conditions, the explosion energetics are dominated by rapid fine fragmentation and intense vapor generation within a short time interval. As a result, the pressure response rises sharply to a pronounced peak and accumulates a large impulse. The ability of SCORPION to reproduce this distinctly energetic behavior supports that the governing conservation equations and the fine fragmentation model can represent highly explosive scenarios without requiring detailed multiphase momentum resolution.

FARO L33 shows a moderated load response compared to KROTOS K44, with a predicted peak pressure of 9.50 MPa and a peak impulse of 25.94 kPa·s. FARO L33 differs from KROTOS K44 in several major aspects that directly affect steam explosion. The experiment is conducted at elevated system pressure, involves a deep pool, and uses a prototypic corium composition. Although the total released melt mass is large, the melt inventory at the triggering time can be reduced due to premixing development and solidification processes, resulting in a less concentrated energy release than in the KROTOS case. These conditions lead to a lower peak pressure and impulse. The SCORPION results follow this expected tendency by predicting a significantly reduced peak pressure relative to KROTOS K44, while still yielding a clearly developed impulse response.

TROI 13 produces the lowest peak pressure among the three cases, 6.53 MPa, while yielding a relatively large peak impulse of 29.77 kPa·s. This combination reflects the distinctive features of the TROI benchmark, which is performed with prototypic corium without an external trigger and with a larger free fall height and facility scale than the other two experiments. These factors influence premixing development and the spatial distribution of the interacting melt and coolant, often resulting in a less abrupt but more sustained pressure evolution. In such cases, the peak pressure can remain moderate while the impulse grows due to the extended duration of overpressure. The SCORPION prediction captures this qualitative behavior by producing the lower peak pressure among the three cases, while accumulating an impulse. This is an important verification point, as it indicates that the model can represent cases where the impulse is driven primarily by load duration rather than by a single extreme peak.

SCORPION shows consistent performance across the three benchmarks by reproducing distinct pressure and impulse responses that reflect the underlying differences in experimental conditions. The KROTOS K44 case exhibits a strongly energetic response representative of a low-pressure, triggered configuration with an alumina simulant melt. FARO L33 yields a more moderated load level under pressurized, deep-pool conditions with a prototypic corium melt and a limited participating inventory at the trigger. TROI 13 produces a lower peak pressure but a comparatively large impulse, consistent with its large-scale geometry, long free-fall release, and spontaneous initiation. Taken together, the results demonstrate that SCORPION can capture the relative severity and characteristic load behavior over a wide range of melt compositions,

facility scales, pressures, and triggering conditions, supporting its versatility as a steam explosion analysis tool.

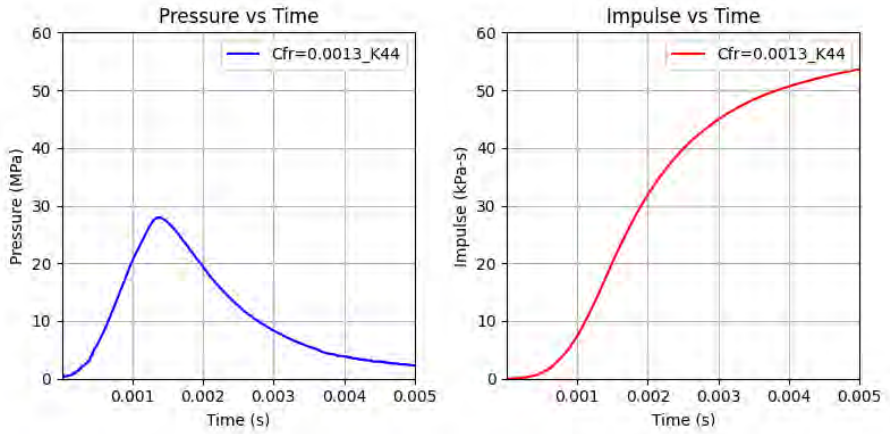

Figure 4. SCORPION simulation results for KROTOS K44: pressure and impulse.

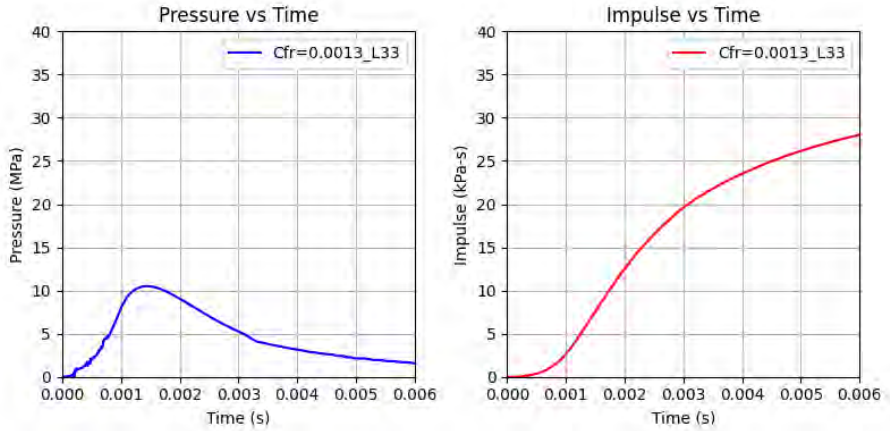

Figure 5. SCORPION simulation results for FARO L33: pressure and impulse.

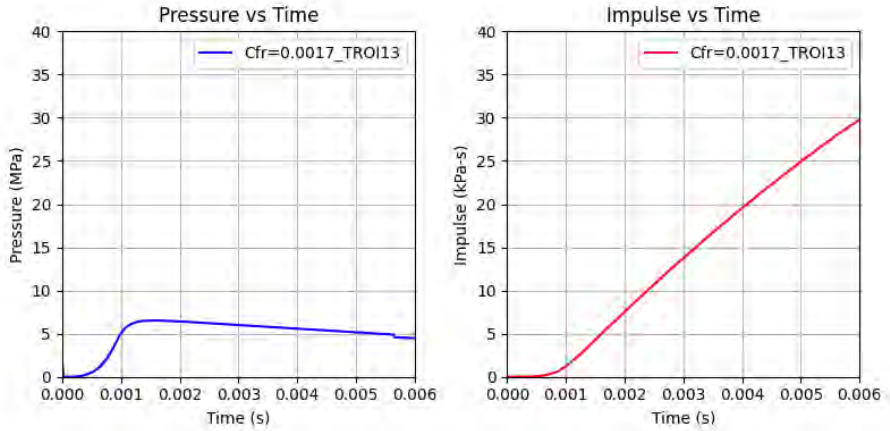

Figure 6. SCORPION simulation results for TROI 13: pressure and impulse.

3.4. Discussion on the Fragmentation Constant C_{fr}

In SCORPION, the fine fragmentation process is modeled using a lumped rate expression in which the fragmentation constant C_{fr} determines how rapidly the melt inventory is converted into fine fragments during the fragmentation time. Because fine fragmentation controls the interfacial area for heat transfer and rapid vapor generation, C_{fr} becomes a major parameter linking the premixing state to the intensity of the explosion phase. In a lumped parameter framework, C_{fr} should be interpreted as an effective parameter rather than a directly measurable material property. It represents the integrated outcome of unresolved mechanisms, including fragmentation initiation efficiency, the effective rate of droplet size reduction, and the coupling between evolving void conditions and heat transfer in the mixing region.

The case dependent C_{fr} values estimated in this study reflect that each benchmark experiment combines different melt compositions, hydrodynamic environments, and triggering conditions, which influence the effective fragmentation intensity. KROTOS K44 shows a highly energetic response under low pressure, externally triggered condition with an alumina simulant melt, while FARO L33 and TROI 13 employ prototypic corium under different system pressures and facility scales. As a result, the same fragmentation model can require different effective C_{fr} values to reproduce the observed pressure and impulse response, because the unresolved mechanisms controlling fragmentation and rapid vaporization are activated differently across experiments. C_{fr} provides a practical way to parameterize effective fragmentation rate within a consistent modeling structure, enabling systematic comparisons while preserving computational efficiency.

Although C_{fr} is empirical in nature, it does not vary arbitrarily in the present verification. The results indicate that SCORPION produces stable and physically consistent predictions within a limited band of C_{fr} values. Within this band, the pressure rise behavior and impulse accumulation trends remain qualitatively realistic, supporting the use of C_{fr} as a bounded calibration parameter for verification and sensitivity studies. Once a representative C_{fr} range is identified for a given class of experiments or accident scenarios, SCORPION can be applied efficiently to assess uncertainties and to estimate conservative envelopes of peak pressure and impulse for regulatory assessments.

4. CONCLUSIONS

In this study, the SCORPION steam explosion module within the SAFARI framework was verified using three OECD SERENA benchmark experiments, KROTOS K44, FARO L33, and TROI 13, which cover main operating conditions relevant to ex-vessel fuel-coolant interaction events. SCORPION employs a lumped parameter formulation that solves mass and energy conservation with a modular fine fragmentation treatment. It is designed to interface with the HIPPO module through a one-way coupling scheme so that time-dependent premixing information can be used as consistent initial conditions for the explosion phase. To improve numerical robustness near the thermodynamic critical point, a ResNet-based surrogate was integrated into a hybrid property evaluation scheme with the IAPWS steam tables. These initial verification results indicate that SCORPION reproduces the main pressure load characteristics of the selected experiments, including peak pressure levels, impulse trends, and transient pressure rise behavior, with consistent performance across different melt compositions, facility scales, system pressures, and triggering conditions.

Overall, the agreement obtained for the selected benchmarks suggests that SCORPION provides a computationally efficient tool for estimating steam explosion loads within an integrated severe accident analysis. The one-way coupling concept enables systematic assessments over varying premixing states without changing the core modeling structure, which is beneficial for applications requiring repeated calculations. The present results support the use of SCORPION within SAFARI for sensitivity studies and

for load estimation under representative accident progression scenarios, while additional coupled validation and code-to-code comparisons are planned to broaden the validation and benchmarking scope.

NOMENCLATURE

P : Pressure
T : Temperature
V : Volume
α : Void fraction
R_f : Radius of fuel
ρ_c : Density of coolant
v : Specific volume
u : Specific internal energy

ACKNOWLEDGMENTS

This work was supported by the Nuclear Safety Research Program through the Korea Foundation of Nuclear Safety (KoFONS) using the financial resource granted by the Nuclear Safety and Security Commission (NSSC) of the Republic of Korea. (RS-2021-KN057910)

REFERENCES

1. OECD Nuclear Energy Agency, Status Report on Ex-Vessel Steam Explosion, NEA/CSNI/R 15, OECD Publishing, Paris (2017).
2. OECD Nuclear Energy Agency, SERENA Phase I: Steam Explosion Resolution for Nuclear Applications, NEA/CSNI/R 11, OECD Publishing, Paris (2007).
3. OECD Nuclear Energy Agency, SERENA Phase II: Summary Report and Conclusions, NEA/CSNI/R(2014)15, OECD Publishing, Paris (2014).
4. Kim, J. B., Sai, R. G. V., Kim, E. S., and Park, H. S., Development of Physical Properties Prediction Model Near Critical Point Using Deep Learning, Twenty-First International Topical Meeting on Nuclear Reactor Thermal Hydraulics (NURETH-21), Busan, Republic of Korea, September 1-5, (2025).
5. J. Tang, Modeling of the complete process of one-dimensional vapor explosions, Ph. D. Thesis, University of Wisconsin (1993).
6. M. D. Oh, and M. L. Corradini. A propagation expansion model for large scale vapor explosions. Nuclear Science and Engineering, 95(3):225–240, 1987.
7. L. R. Petzold, Automatic Selection of Methods for Solving Stiff and Nonstiff Systems of Ordinary Differential Equations, SIAM Journal on Scientific and Statistical Computing, Vol. 4, No. 1, pp. 136-148 (1983).
8. Wagner, W., and Kretzschmar, H. J., International Steam Tables: Properties of Water and Steam Based on the Industrial Formulation IAPWS-IF97, Springer, Berlin (2008).
9. He, K., Zhang, X., Ren, S., and Sun, J., Deep Residual Learning for Image Recognition, Proceedings of the IEEE Conference on Computer Vision and Pattern Recognition (CVPR), pp. 770–778 (2016).
10. D. Magallon, H. Hohmann, High pressure corium melt quenching tests in FARO, NED, 155 (1995), 253-270.
11. Song, J.H., Park, I.K., Shin, Y.S., Kim, J.H., Hong, S.W., Min, B.T., and Kim, H.D., Fuel coolant interaction experiments in TROI using a UO2/ZrO2 mixture, Nuclear Engineering and Design, 222, pp. 1–15 (2003).
12. D. Magallon, I. Huhtiniemi, Experimental investigation of 150-kg-scale corium melt quenching in water, NED, 177 (1997), 321-337.

EFFECT OF CORIUM PROPERTIES' UNCERTAINTIES ON A PWR SBO SEVERE ACCIDENT

L. E. Herranz
CIEMAT, Unit of Nuclear Safety Research
Av. Complutense 40, 28040 Madrid, Spain
luisen.herranz@ciemat.es

B. Mellace, M. Angelucci, S. Paci
Department of Civil and Industrial Engineering
University of Pisa
Largo Lucio Lazzarino, 56122 Pisa, Italy
b.mellace@studenti.unipi.it, michela.angelucci@unipi.it, sandro.paci@unipi.it

ABSTRACT

During the ex-vessel phase of a severe accident in a nuclear power plant, containment integrity might be jeopardized by three main mechanisms: concrete erosion (epsilon mode), over-pressurization (delta mode), combustible gas detonation (gamma mode). All of them are tightly related to molten core-concrete interaction. This study investigates the impact of uncertainties in corium properties on key variables describing the containment scenario (i.e., pressure, gas composition, and radial and axial ablation) during a station blackout accident in a 1000 MWe pressurized water reactor. The properties analyzed are viscosity, conductivity, specific heat, density and emissivity. A stand-alone containment Best Estimate Plus Uncertainty analysis has been conducted using the MELCOR v.2.2 2025.0 code and in-house Python scripts for sampling, propagation and results processing. The Order Statistics (95/95) was used and uniform probability density functions adopted for each property. The initial and boundary conditions were taken from a MELCOR full-scope plant analysis. Under the assumption of instantaneous melt-spreading within the cavity, the results indicate a small/moderate effect of corium properties uncertainties on concrete erosion and combustion risk. Containment pressure, though, shows an observable influence, which uncertainty band ranged from -17% to +33% with respect to the best estimate value. A complementary sensitivity analysis highlighted the specific heat uncertainties as the main driver of the band scatter noted in containment pressure.

KEYWORDS
MCCI, Uncertainty Analysis, Corium properties, MELCOR

1. INTRODUCTION

Severe Accidents (SA) are low-probability, high-consequence events in which the failure of multiple safety systems can lead to the loss of core cooling and, in the most critical scenarios, to the partial or complete meltdown of the reactor core. In such conditions, molten core material (corium) may relocate to the Lower Head (LH) of the Reactor Pressure Vessel (RPV), threatening its integrity by thermal creep. In case of LH failure, the corium slumps into the cavity beneath the RPV, and it comes into contact with the pedestal and basemat concrete, leading to a Molten Core-Concrete Interaction (MCCI). As a consequence of MCCI, three major threats can jeopardize containment integrity: concrete erosion (epsilon mode); over-pressurization

(delta mode); combustible gas detonations (gamma mode) [1]. Therefore, a reliable assessment of the ex-vessel phase of a SA is of utmost relevance in nuclear safety.

To analyze these complex SAs-related scenarios, integral codes, such as MELCOR ([2], [3]) are widely used. Nevertheless, the reliability of these simulations is strongly affected by uncertainties, which may originate from physical modelling assumptions, numerical approximations, and lack of precise knowledge of boundary conditions. In this framework, the Uncertainty and Sensitivity Analysis (UaSA) approach has emerged as a fundamental instrument, as it allows combining Best Estimate (BE) simulations with a systematic quantification of uncertainties, thus providing a more comprehensive and robust basis for safety assessments [4].

The uncertainties of the corium properties reaching the pedestal in case of RPV failure, heavily associated with the materials mixture and the harsh prevailing conditions, might be substantial and affect accuracy of containment characterization during the ex-vessel phase of a SA.

The relevance of the ex-vessel phase of a SA became evident during the Fukushima Daiichi accidents and discrepancies between the forensic analysis and the in-situ observations, particularly in Unit 1, emphasized the need for better understanding ([5], [6]). International projects like ROSAU [7] (Reduction of Severe Accident Uncertainties, 2019-2024) and COPS [8] (Corium Properties for reactor Simulation and uncertainties) intended to fill existing gaps. Interestingly, the latter investigates the influence of thermo-physical properties of corium melts on SA modelling and on the analyses of corium melt stabilization strategies in a reactor.

This paper presents the major results obtained in the investigation of the influence of uncertainties in corium properties uncertainties on containment integrity in a 1000 MWe Pressurized Water Reactor (PWR) Station Blackout (SBO). Corium viscosity, conductivity, specific heat, density and emissivity have been studied, and their effect on key safety-relevant target variables (hereafter, Figures Of Merit, FOMs), including containment pressure, concrete ablation and gas flammability, have been quantitatively determined. The uncertainty and sensitivity evaluation is performed using the MELCOR v.2.2 2025.0 code in combination with in-house Python scripts for sampling, input decks creation and post-processing.

2. SCENARIO MODELLING

2.1. Containment Model

A stand-alone PWR containment model is adopted. This modelling approach is easier to handle and significantly reduces computational time, as the simulation is initiated right from the beginning of the ex-vessel phase. In this setup, corium spreading is assumed instantaneously spread over the cavity basemat at the onset of the calculation. The corium mass and energy are defined as initial conditions in the containment input deck. This approach allows excluding the complex in-vessel phenomena, which would burden the computational cost, and allowing a direct focus on the purpose of the study. The initial and boundary conditions resulting from these phenomena are imported from the corresponding full-plant MELCOR model [9]. The containment model is schematically represented in Figure 1 [10]. It consists of 11 Control Volumes (CVs), with a total volume of 61,300 m³, of which the dome CV accounts for the 76%. Further details can be found in [10].

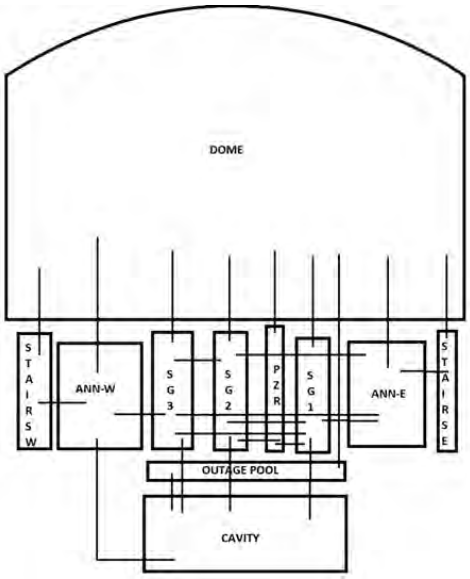

Figure 1. PWR Containment model.

2.2. Cavity Model

The cavity (CAV) package [2], derived from the CORCON Mod3 code [11], is used to set initial conditions of the corium pool and to define the cavity geometry. A 135 tons corium pool consisting of initially 78 % of oxides and 22 % of metals lay down in the cavity at the start of the simulation at 26,400 seconds (7.3 hours). Corium is treated as a single layer, according to the recommendations made by the MELCOR developers. The dimensions of pedestal walls and basemat correspond to the design parameters of a 1000 MWe Westinghouse PWR. The basemat concrete is a limestone aggregate-common sand mixture (Table I).

Table I. Limestone aggregate-common sand concrete composition in mass fraction.

SiO_2	35.80
TiO_2	0.18
MnO	0.03
MgO	0.48
CaO	31.30
Na_2O	0.082
K_2O	1.22
Fe_2O_3	1.44
Al_2O_3	3.60
Cr_2O_3	0.014
CO_2	21.15
H_2O chem	2.00
H_2O evap	2.70

The cavity is modeled as a flat-bottom cylinder. Its geometry is discretized in a set of fewer than 100 body points distributed along rays emanating from an origin located on the cavity axis. The number and position of these points were determined in accordance with the guidelines provided in the MELCOR and CORCON manuals and subsequently refined through a dedicated sensitivity analysis. The center of the reference coordinate system (R0, Z0) was defined in the middle of the eroded cavity to ensure a consistent description of the ablation profile.

Initial cavity geometry, number and position of body points are reported in Figure 2 and Table II.

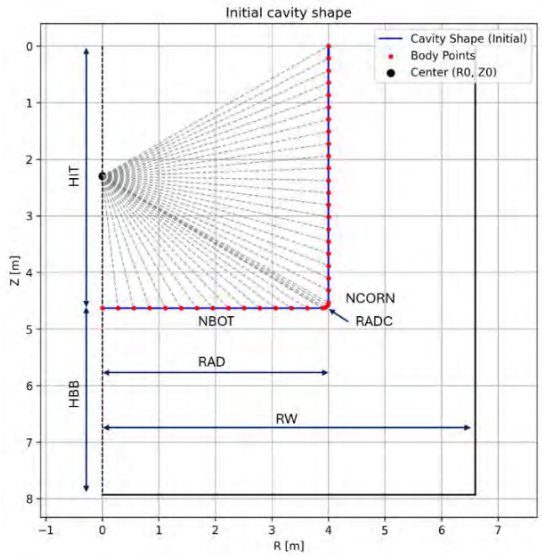

Figure 2. Cavity with body points and rays.

Total number of body points	40
NCORN points	2
NBOT points	15
(R0, Z0)	(0, 2.3)
RADC	0.1 m
HBB	3.3 m
RAD	4 m
HIT	4.6 m
RW	6.6 m

Table II. Cavity geometry and body points.

3. CORIUM PROPERTIES

The corium pool consists of a mixture of oxides and metals, mainly including UO_2, ZrO_2, FeO, Fe_2O_3, SiO_2, Al_2O_3, Zr, Fe, Cr, and Ni. Its mass and composition evolve during MCCI as a consequence of concrete ablation and chemical oxidation of metallic phases. The thermophysical properties of corium are therefore dependent on several factors, such as composition, temperature, time, corium configuration and the averaging method used to derive the overall properties from those of the individual components.

To define a consistent range for each property, the following hypotheses were introduced:

- Two representative compositions considered, a fully oxidic mixture (100% oxides) and a partially metallic mixture (containing 12% metals) ([12], [13]);
- Three characteristic temperatures considered to evaluate properties (1,700 K, 2,250 K, 2,800 K), which cover the temperature range expected during an SBO;
- No major changes in MCCI composition are assumed, which means the same corium composition is considered at the three reference temperatures;
- Corium is homogeneous. This simplification is particularly relevant for properties, such as thermal conductivity, which are strongly influenced by the configuration of the melt;
- Properties averaging was performed by applying mole fraction, mass fraction or molar volume averaging consistently with the CORCON formulation.

Table III shows the ranges found for each property.

Table III. Corium properties range.

	Averaging method	Unit of measurement	Lower bound	Upper bound
μ	Mole fraction	$kg/m \cdot s$	0.1	10

k	Mole fraction	$W/_{m \cdot K}$	1	12
$\mathbf{c_p}$	Mass fraction	$J/_{kg \cdot K}$	500	1,300
$\boldsymbol{\rho}$	Molar volume	$kg/_{m^3}$	2,800	8,000
$\boldsymbol{\varepsilon}$	Molar volume	-	0.5	1

4. UaSA METHODOLOGY

The primary objective of UaSA is to quantify the effect of input uncertainties on model outputs, and to identify the parameters that most strongly influence the system's behavior.

In this study, the uncertainty evaluation is performed using a random sampling strategy, where uncertain input parameters are sampled according to a uniform Probability Distribution Function (PDF) [14]. This assumption ensures that all values within the specified range are equally likely, given the lack of knowledge about the true PDFs of the input parameters. The uncertainty parameters are the five corium properties reported in the previous section: viscosity, conductivity, specific heat, density and emissivity. MELCOR is not enabled to change directly corium properties (except for emissivity, for which the user can set a value that remains constant throughout the simulation). However, through *ad-hoc* multipliers (M) the user can modulate property ranges as desired. In this study, Ms have been set to fit the ranges presented in Table III.

To characterize the uncertainty in the simulation outcomes, multiple code runs are required. In each run, all uncertain parameters are varied simultaneously. The minimum number of required simulations depends on the probability content and confidence level associated with the statistical tolerance limits adopted for Uncertainty Quantification (UQ). For this purpose, the Wilks non-parametric method is applied [15]. According to the Wilks' formula for a two-sided tolerance interval, at least 93 independent simulations are necessary to estimate the 95th percentile of the output distribution with a 95% confidence level. Strictly speaking, given that in the study multiple FOMs are targeted, the Wald extension [16] should be used, which yields a minimum requirement of 260 runs. Nevertheless, some scoping calculations conducted confirmed that the results coming from 93 realizations were consistent with those coming out from 260 ones. In this study the Wilk's approach was embraced to relieve the computational burden.

To evaluate the influence of input parameter values on the results, two Correlation Coefficients (CCs) are employed: Pearson and Spearman CCs. Pearson CC quantifies the linear relationship between each input parameter and the FOM, while Spearman CC measures the strength of a monotonic correlation. Both range from -1 (indicating a perfect negative linear/monotonic correlation) to +1 (indicating a perfect positive linear/monotonic correlation), while a value of 0 denotes the absence of a relationship. The p-value concept is used as well: a p-value lower than 0.05 suggests that the computed correlation between the input parameter and the output one has statistical significance.

5. RESULTS

5.1 Once-At-A-Time (OAT) Sensitivity Analysis

In this type of analysis, only one corium property is varied at a time. This approach makes it possible to determine the most appropriate value of the multiplier M to apply for each property and provides a first insight into which parameter might have the greatest influence on FOMs. However, it misses the effect of the potential interaction among different properties. Table IV displays the ranges of the individual

properties, the properties domains resulting from the BE, and the multiplier interval corresponding with the uncertainty range. As noted, uncertainty ranges encompass BE ones.

Table IV: Ranges for each property.

	Uncertainty range	Best Estimate range	Multiplier range
Viscosity [kg/ms]	0.1 – 10	0.7 – 5	0.2 – 7
Conductivity [W/mK]	1 – 12	4.5 – 12	0.33 – 1
Specific heat [J/kgK]	500 – 1,300	575 – 1,095	0.88 – 1.13
Density [kg/m^3]	2,800 – 8,000	3,300 – 7,400	0.83 – 1.07
Emissivity	0.5 – 1	-	-

The OAT sensitivity analysis showed that the corium property with the greatest influence on the dome pressure, cavity erosion and gas flammability is the specific heat, while both thermal conductivity and viscosity also appear to affect the erosion behavior. Table V summarizes these preliminary insights. To encapsulate the qualitative nature of this sensitivity analysis, a color code is chosen to reflect what has high influence (red circle), from what just makes a mild (blue circle) or no influence at all (green circle).

Table V. Corium properties influence on FOMs.

	Dome pressure	**Cavity Erosion**	**Gas Flammability**
μ	🟢	🔵	🟢
k	🟢	🔵	🟢
c_p	🔴	🔴	🔴
ρ	🟢	🟢	🟢
ε	🟢	🟢	🟢

5.2 Uncertainty Analysis (UA)

In this section, the UA for the selected three FOMs is reported: containment dome pressure, cavity erosion (through maximum cavity radius and minimum cavity altitude) and the Shapiro diagram, to assess the combustion risk.

Containment pressure (Figure 3a) displays a cumulative effect of uncertainties along time that ends up in a (-17%, 33%) interval after 2 days since the accident onset (172,800 s as calculation ending time). It is worth noting that there is a strong linear and monotonic correlation with the corium specific heat (Figure 3b). The Pearson and Spearman coefficients, evaluated at the end of the simulation, are associated with extremely low p-values (<<0.05), confirming the statistical significance of the correlation. This is interpreted as the result of a counterbalance effect of c_p on the corium temperature. On one side, a high c_p would mean a lower T_{corium}, which will result initially in less concrete erosion. But, on the other side, the amount of energy stored in the corium would be the same (regardless of its temperature) and the temperature decrease rate due to the heat transfer to concrete would be slower and last over longer time, which might eventually result in further concrete erosion and gas generation.

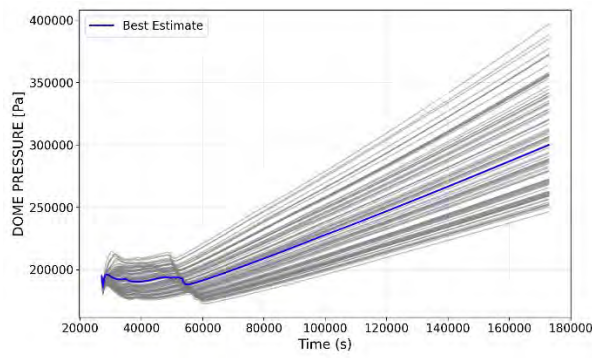

Figure 3a. Dome pressure.

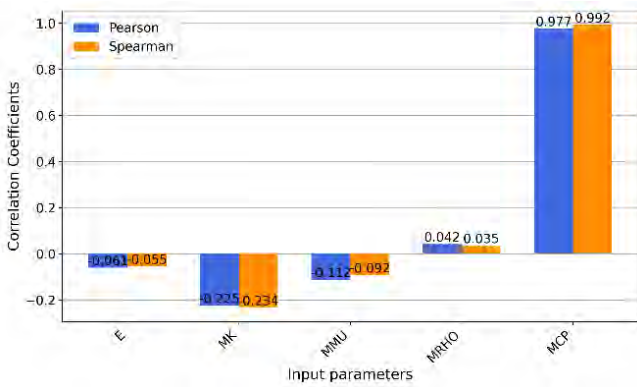

Figure 3b. CCs.

Concrete erosion scattering also shows a growing monotonically increase with time, both axially and radially, as shown in Figure 4a and Figure 5a. In both cases, the uncertainty band extends over time, although in a narrower interval with respect to the dome pressure: (5%, -5%) radially; (11%, -7%) axially. As for the sensitivity analysis, c_p seems to have the highest influence also on this FOM. The associated p-values for the Pearson and Spearman coefficients are in both cases much smaller than 0.05, confirming the statistical significance of the correlation. So, the same discussion as before might be brought up. However, it is observed that uncertainties in corium density also play a role on radial erosion with p-values of 3.4×10^{-5} (Pearson) and 1.8×10^{-4} (Spearman). While for the axial one, corium conductivity shows a statistically significant effect too with p-values of 2.9×10^{-7} (Pearson) and 7.6×10^{-8} (Spearman). The latter is consistent with a fast uniform distribution of stored thermal energy in the concrete, which would make heat transfer losses from the corium top surface more efficient and cause a faster fall of corium-concrete interfacial temperature.

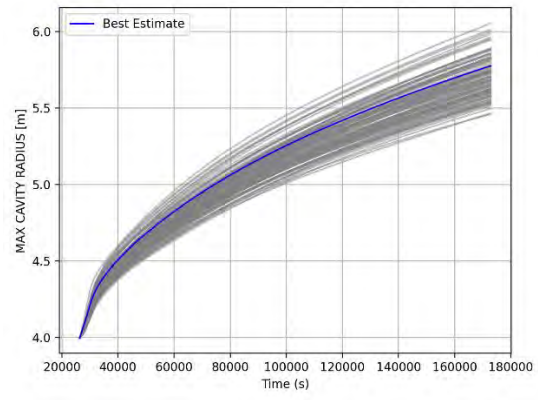

Figure 4a. Maximum cavity radius.

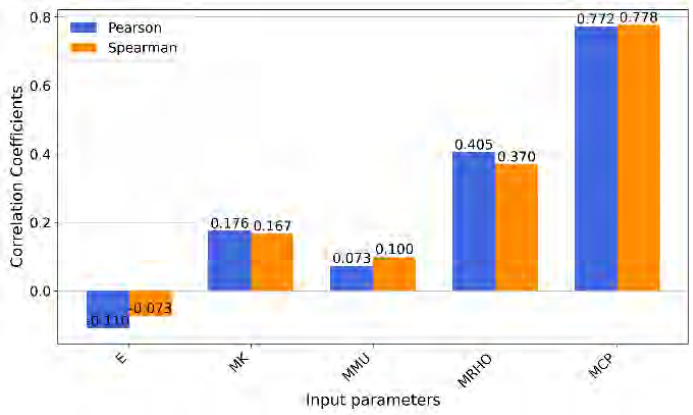

Figure 4b. CCs.

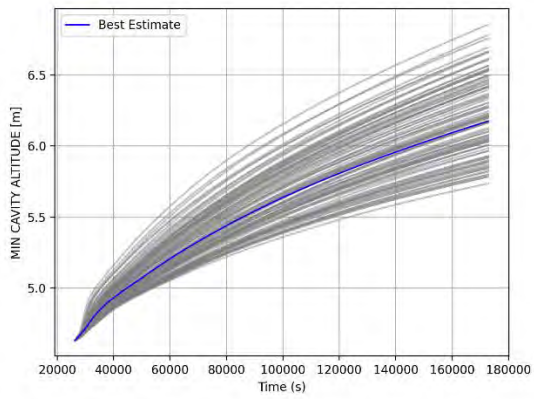

Figure 5a. Minimum cavity altitude.

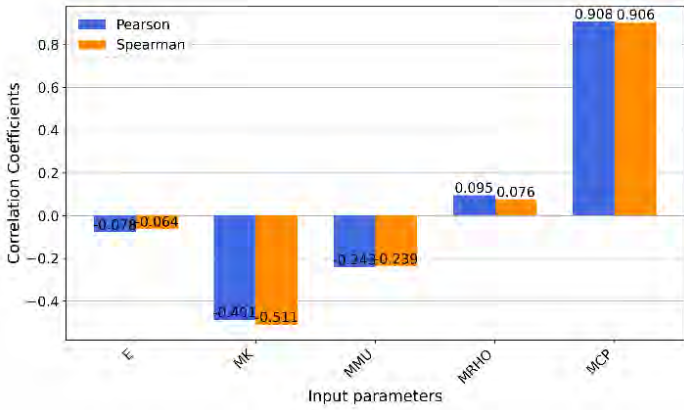

Figure 5b. CCs.

Combustion risk (Figure 6a) is observed not to change substantially due to corium properties uncertainties. At all times and in all calculations, the atmosphere gas mixture is far from the detonation limits in the diagram. If "time within flammability limits" is used as an indicator of the effect of properties uncertainties (Figure 6b), it is noted that the effect is, as in the case of erosion, pretty mild. The distribution of the time spent in the flammable region obtained from the simulations shows a negative skewness normal distribution over the range 9,000 s to 15,000 s. Almost 75% of the data points are between 12,000 s and 14,000 s: the weighted average being 12,427 s and the standard deviation is 935 s. This indicates a very moderate effect of corium properties uncertainties in the combustion risk.

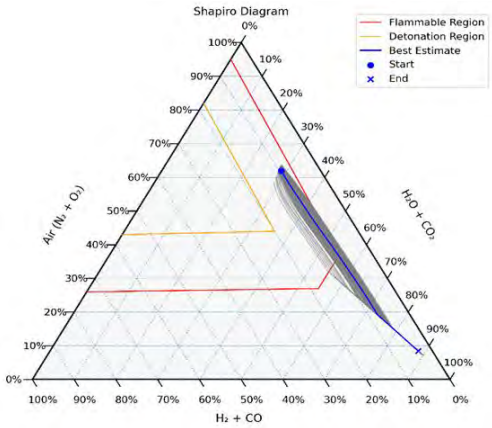

Figure 6a. Shapiro diagram.

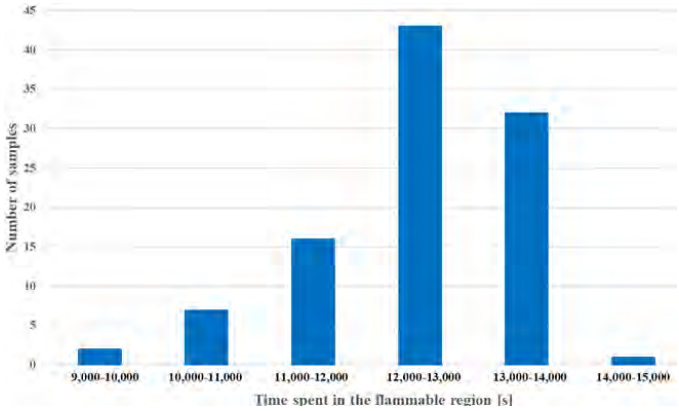

Figure 6b. Time in flammable region distribution.

Figure 6. Shapiro diagram.

Figure 7. Time spent in the flammable region.

6. MAJOR INSIGHTS

The ability of UaSA to investigate the potential effect of knowledge uncertainties on SAs footprints has been explored in this work by focusing in a specific study: the influence of uncertainties in corium thermo-physical properties on the in-containment progression of an SBO SA accident in a 1000 MWe PWR. The

insights gained are inherently associated, of course, to the NPP and scenario modelling (i.e., instantaneous melt spreading) by using a lumped parameter code (MELCOR v.2.2 2025.0) and the order statistics in the realization campaigns:

- Cavity erosion and gas flammability risk are mildly sensitive to uncertainties in corium properties. In-containment pressure, though, showed a visible effect that would translate in potential shortening of time-to-reach a given threshold;
- Among all the properties investigated, uncertainties in corium specific heat dominated any other property's effect by far.

In all the cases, the findings have been discussed to be physical grounded.

The methodology used in this work should be further proved in other scenarios and plant designs before settling down generic conclusions on the matter investigated. Nevertheless, as a high-level conclusion, the study conducted showed the usefulness of UaSA to explore areas where further research might or might not be needed.

ACKNOWLEDGEMENTS

This work is framed within the SEAKNOT project under the Grant Agreement no. 101060327. Views and opinions expressed are however those of the authors only and do not necessarily reflect those of the European Union. Neither the European Union nor the granting authority can be held responsible for them.

REFERENCES

[1] N. C. Rasmussen, 'WASH - 1400, Reactor Safety Study. An assessment of accident risk in U.S. Commercial Nuclear Power Plants', U.S. Nuclear Regulatory Commission, Oct. 1975.
[2] 'L. Humphries et al. MELCOR Computer Code Manual. Vol. 1: Primer and User's Guide. Version 2.2.18019 (2021).'
[3] 'L. Humphries et al. MELCOR Computer Code Manual. Vol. 2: Reference Manual. Version 2.2.18019 (2021).'
[4] F. d'Auria *et al.*, *Best estimate safety analysis for nuclear power plants: uncertainty evaluation*. in Safety reports series. Vienna: International Atomic Energy Agency, 2008.
[5] M. Cibula, M. Pellegrini, M. Mizokami, and S. Mizokami, 'Evaluation of Fukushima Daiichi Unit 1 Ex-Vessel Phenomenon Leveraging on Primary Containment Vessel Robotic Inspections', *Nucl. Technol.*, vol. 211, no. 3, pp. 513–530, Mar. 2025, doi: 10.1080/00295450.2024.2339578.
[6] OECD and Nuclear Energy Agency, *Benchmark Study of the Accident at the Fukushima Daiichi Nuclear Power Plant*. in Nuclear Safety. OECD, 2021. doi: 10.1787/a7af03aa-en.
[7] 'ROSAU Project'. https://www.oecd-nea.org/jcms/pl_25254/reduction-of-severe-accident-uncertainties-rosau-project
[8] 'COPS project'. https://www.oecd-nea.org/jcms/pl_100417/cops-the-corium-properties-for-reactor-simulation-and-uncertainties-cops
[9] L. E. Herranz and J. Fontanet, 'D2.2 Identification and Analysis of accidental sequences posing high H2/CO combustion risk (PWR-W, PWR-VVER, PWR-KWU)', Jul. 2023.
[10] J. Fontanet and L. E. Herranz, 'PARs Interaction with Other Safety Systems during Severe Accidents in Western PWR Containments', presented at the 21st International Topical Meeting on Nuclear Reactor Thermal Hydraulics (NURETH-21), Korea, 2025.
[11] 'D. R. Bradley et al. CORCON-MOD3: An Integrated Computer Model for Analysis of Molten Core-Concrete Interactions (1993)'.

[12] I. Khurshid, I. Afgan, and Y. Addad, 'Thermochemical Modeling of Metal Composition and Its Impact on the Molten Corium–Concrete Interaction: New Insights with Sensitivity Analysis', *Energies*, vol. 15, no. 9, p. 3387, May 2022, doi: 10.3390/en15093387.
[13] C. Journeau *et al.*, 'Two-dimensional interaction of oxidic corium with concretes: The VULCANO VB test series', *Ann. Nucl. Energy*, vol. 36, no. 10, pp. 1597–1613, Oct. 2009, doi: 10.1016/j.anucene.2009.07.006.
[14] H. Glaeser, 'GRS Method for Uncertainty and Sensitivity Evaluation of Code Results and Applications', *Sci. Technol. Nucl. Install.*, vol. 2008, pp. 1–7, 2008, doi: 10.1155/2008/798901.
[15] N. W. Porter, 'Wilks' formula applied to computational tools: A practical discussion and verification', *Ann. Nucl. Energy*, vol. 133, pp. 129–137, Nov. 2019, doi: 10.1016/j.anucene.2019.05.012.
[16] A. Guba, M. Makai, and L. Pál, 'Statistical aspects of best estimate method', *Reliab. Eng. Syst. Saf.*, vol. 80, no. 3, pp. 217–232, Jun. 2003, doi: 10.1016/S0951-8320(03)00022-X.

EFFECT OF CORIUM PROPERTIES' UNCERTAINTIES ON A PWR SBO SEVERE ACCIDENT

B. Mellace, M. Angelucci; S. Paci, L.E. Herranz*

*luisen.herranz@ciemat.es
CIEMAT

Contents

01 Background

02 Accident Scenario

03 Corium Properties

04 UaSA

05 Major Insights

01

Background

Motivation

- Containment integrity might be jeopardized in SA ex-vessel phase:
  - Concrete erosion.
  - Over-pressurization.
  - Energetic combustion (fast deflagration & detonation).

- Fukushima observations, far from “expectations”.
- Codes major discrepancies in the long run.

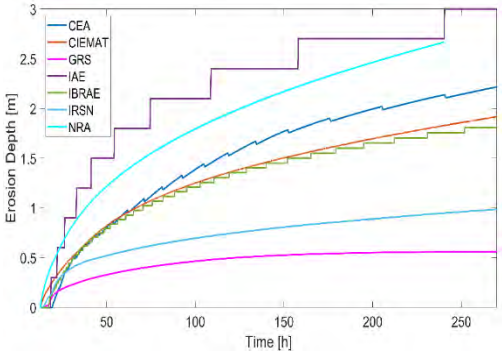

- Intl. projects on ex-vessel corium (ROSAU; **COPS**; …).
- UaSA in SA … is phasing UQ an option?

Background

Objectives & Scope

- Investigate the influence of corium properties on the containment SA scenario during the ex-vessel phase:
  - Cavity erosion
  - Pressure
  - Gas composition

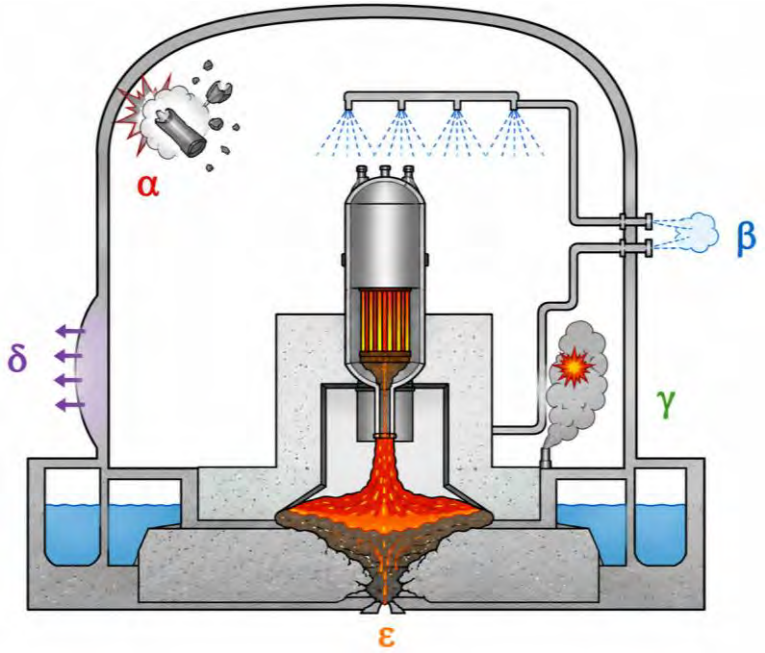

- PWR “dry cavity” (MCCI).
- UaSA approach (MELCOR + in-house Python scripts)

02 Accident Scenario

Accident Scenario

A Snapshot

- 1000 MWe W-PWR.
- Mitigated SBO.
- Dry cavity
- Corium pool: 78% ox.; 22% mtls.
- Corium total mass: 135 tons
- Limestone concrete
- Initial conditions (26,400 s = 7.3h):

P (Pa)	Tgas (K)	RH	H_2 (%)
2.66E5	457.95	0.102	8.0

SPECIES	Limestone aggregate/common sand concrete (mass%)
SiO_2	35.80
TiO_2	0.18
MnO	0.03
MgO	0.48
CaO	31.30
Na2O	0.082
K2O	1.22
$Fe2O_3$	1.44
$Al2O_3$	3.60
$Cr2O_3$	0.014
CO_2	21.15
H_2O chem	2.00
$CaCO_3$	-
Ca-OH-2	-
H_2O vap	2.70

MELCOR modelling

- MELCOR 2.2 2025.0.
- Single layer debris pool (HMX and then LOX)
- Independent containment analysis.
- Ex-vessel phase (26 – 180 ks).

CV	% of volume	% surface
Cavity	1.26%	3.90%
SG-1	2.40%	9.42%
SG-2	2.80%	9.66%
SG-3	3.11%	11.09%
ANN-E	5.39%	17.62%
ANN-W	5.64%	20.43%
PRZ	0.67%	5.32%
STAIRS-E	0.18%	0.64%
STAIRS-W	0.36%	2.13%
OUTAGE-POOL	1.92%	2.17%
DOME	76.26%	17.62%

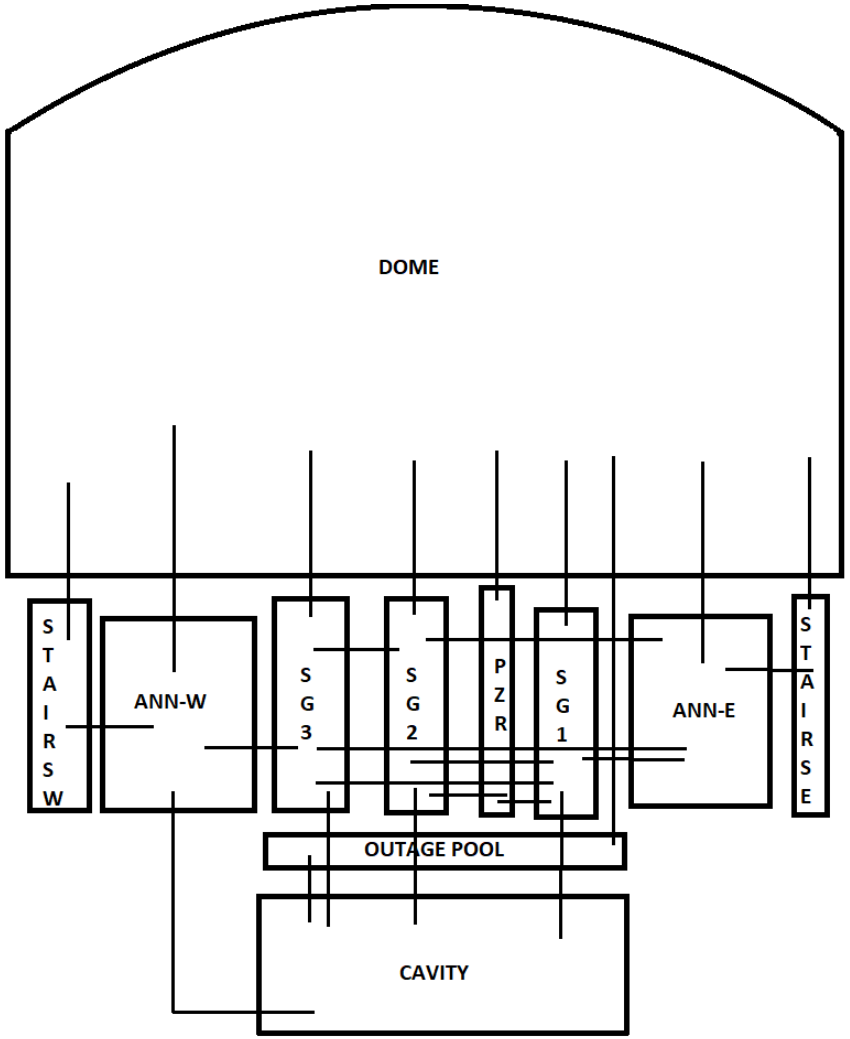

Volume = 61293 m^3
Surface area = 25120.3 m^2

Cavity modelling

- N rays = 40
- (R0, Z0) = (0, 2.3)
- N BOT = 15
- N CORN = 2
- HBB = 3.3 m
- HIT = 4.6 m
- RAD = 4 m
- RADC = 0.1 m
- RW = 6.6 m

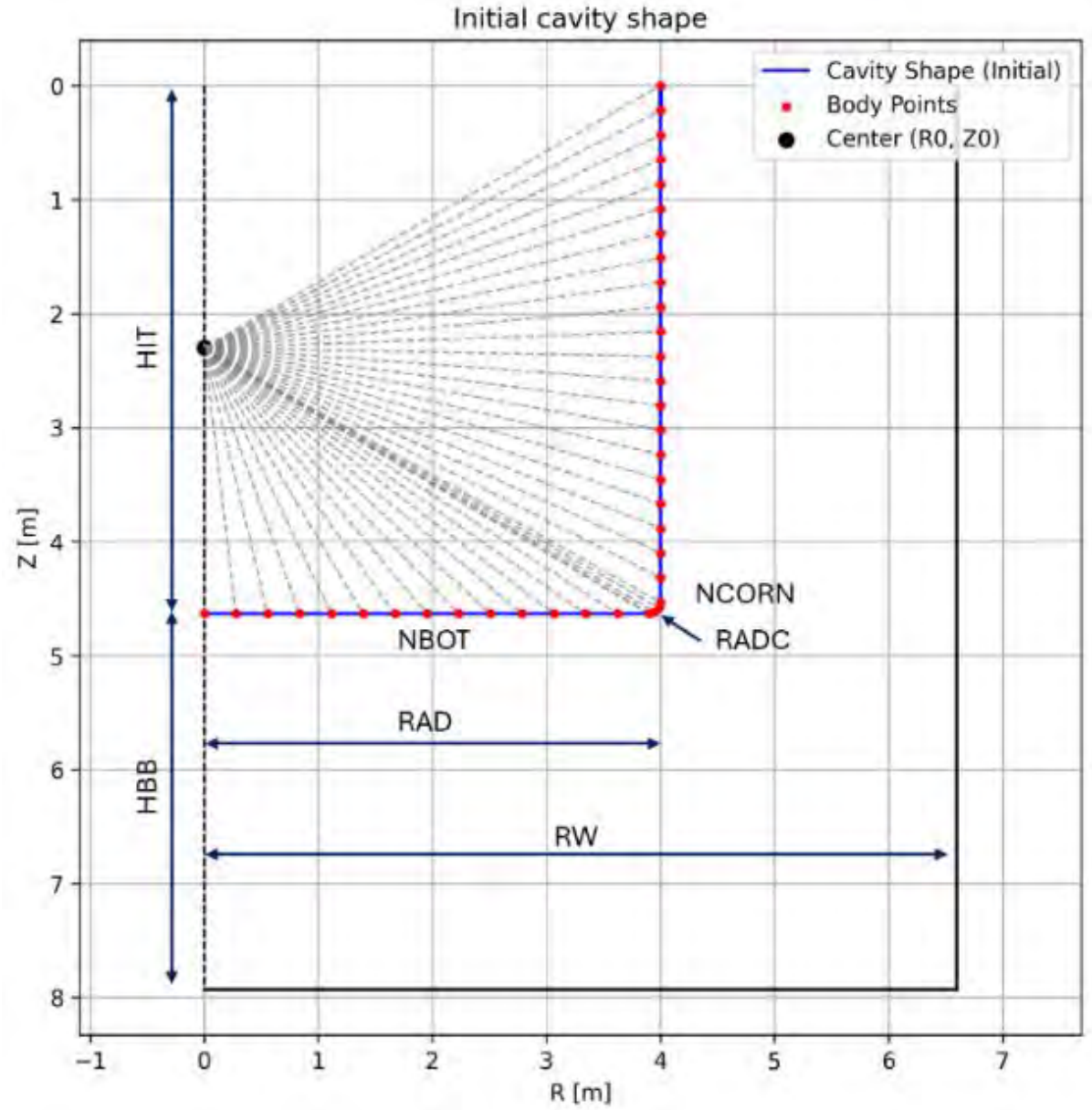

03

Corium Properties

Identification

- Viscosity, μ
- Conductivity, k
- Specific heat, c_p
- Density, ρ
- Emissivity, ε

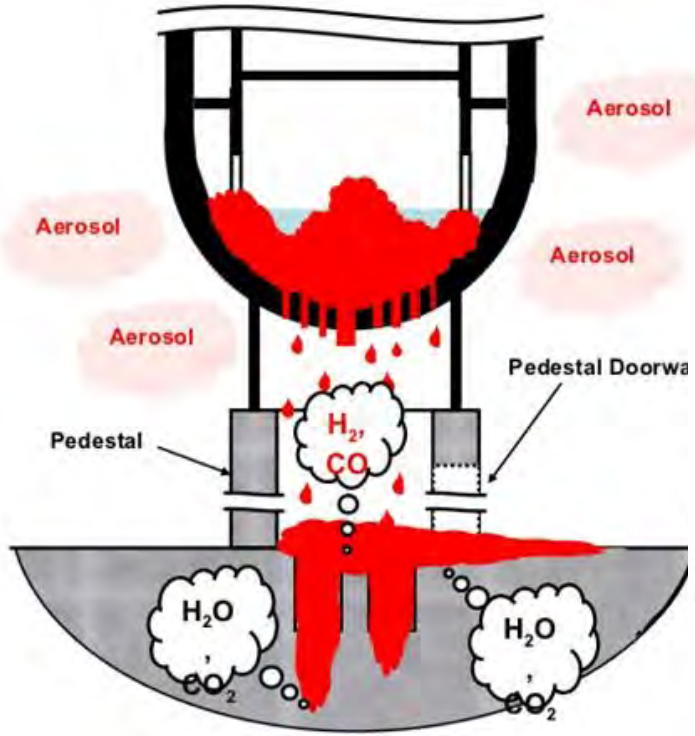

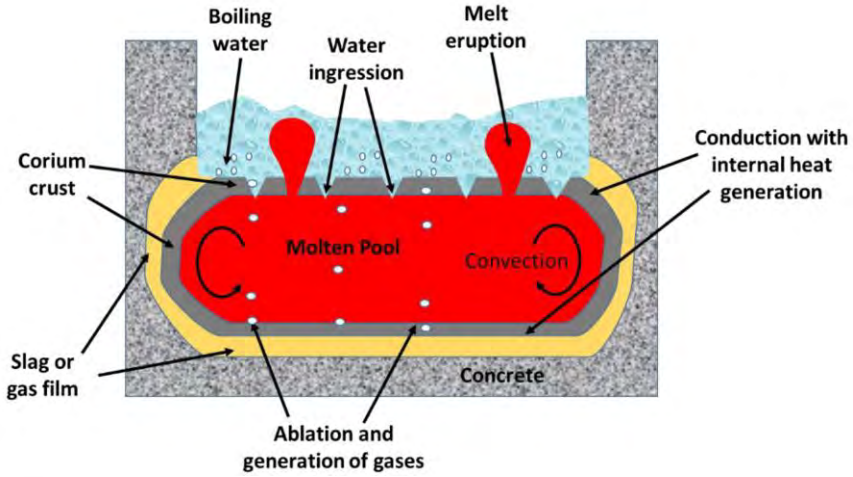

Influencing factors

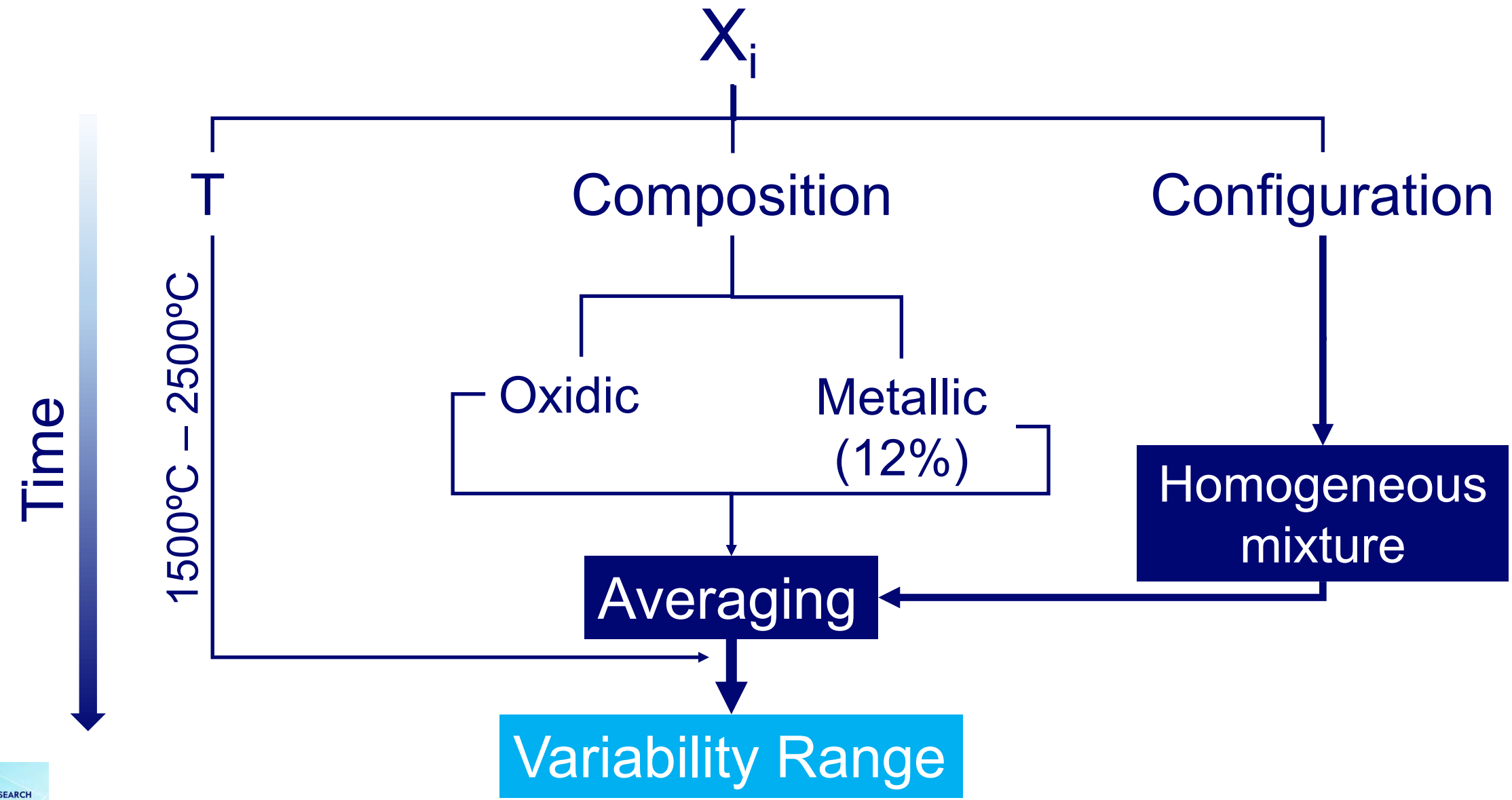

Best Estimate scenario

Corium Properties

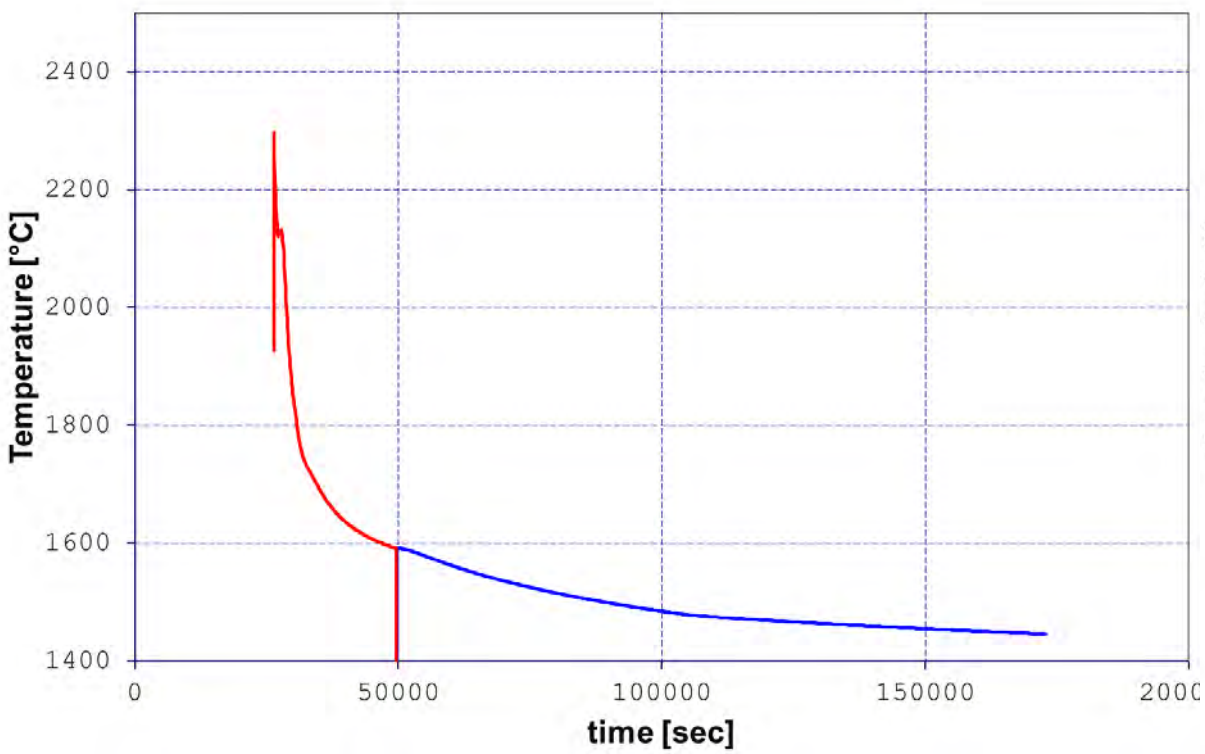

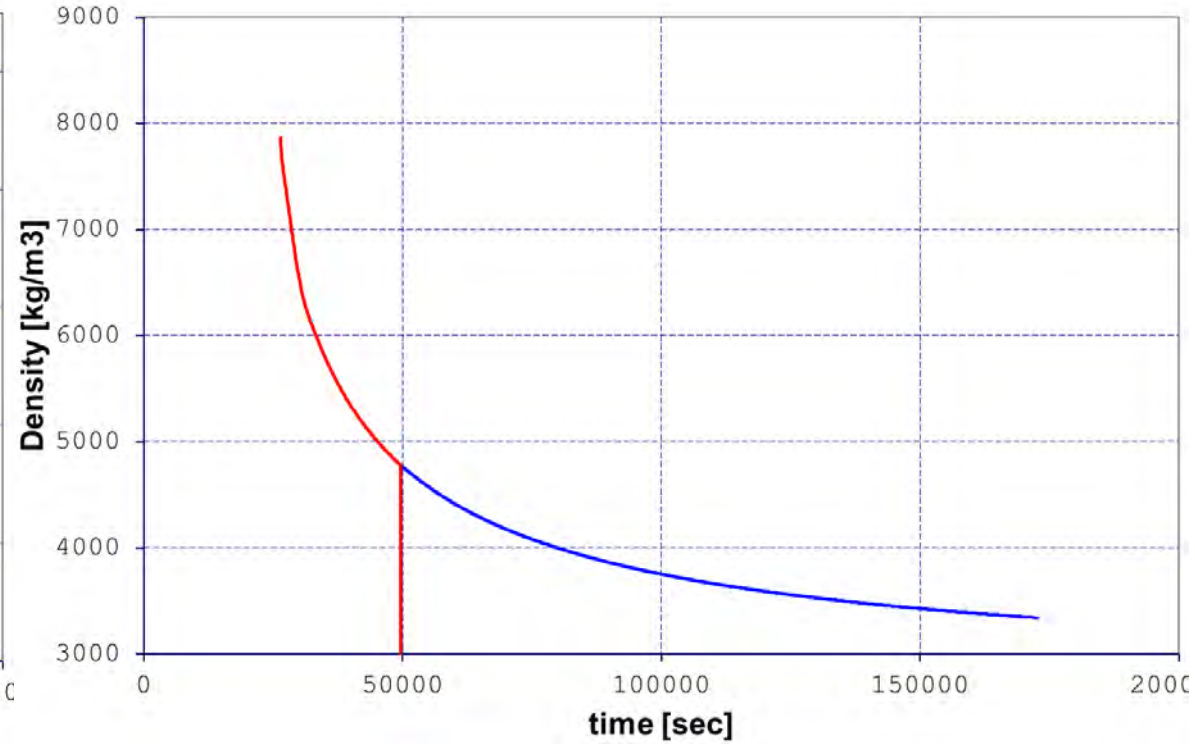

Properties ranges

	Averaging method	Unit of measurement	Lower bound	Upper bound
μ	Mole fraction	$^{kg}/_{m \cdot s}$	0.1	10
k	Mole fraction	$^{W}/_{m \cdot K}$	1	12
$\mathbf{c_p}$	Mass fraction	$^{J}/_{kg \cdot K}$	500	1,300
ρ	Molar volume	$^{kg}/_{m^3}$	2,800	8,000
ε	Molar volume	-	0.5	1

04

UaSA

Ranges Adaptation

- MELCOR v.2.2 2025.0 allows using multipliers M (SNL support!)

	Uncertainty range	BE range	Multiplier range
Viscosity [kg/m·s]	0.1 – 10	0.7 – 5	0.2 – 7
Conductivity [W/m·K]	1 – 12	4.5 – 12	0.33 – 1
Specific heat [J/kg·K]	500 – 1,300	575 – 1,095	0.88 – 1.13
Density [kg/m^3]	2,800 – 8,000	3,300 – 7,400	0.83 – 1.07
Emissivity	0.5 – 1	-	0.5 – 1

- "OAT" sensitivity

No effect
Little effect
Big effect

	Dome pressure	Cavity Erosion	Gas Flammability
μ			
k			
c_p			
ρ			
ε			

Methodology

- 95/95 Wilks approach (100 cases run).
- Random sampling within properties ranges.
- Uniform probability density functions assumed.
- In-house Python scripts to manage outputs.
- Pearson & Spearman coefficients used in the SA.

Results: Pressure

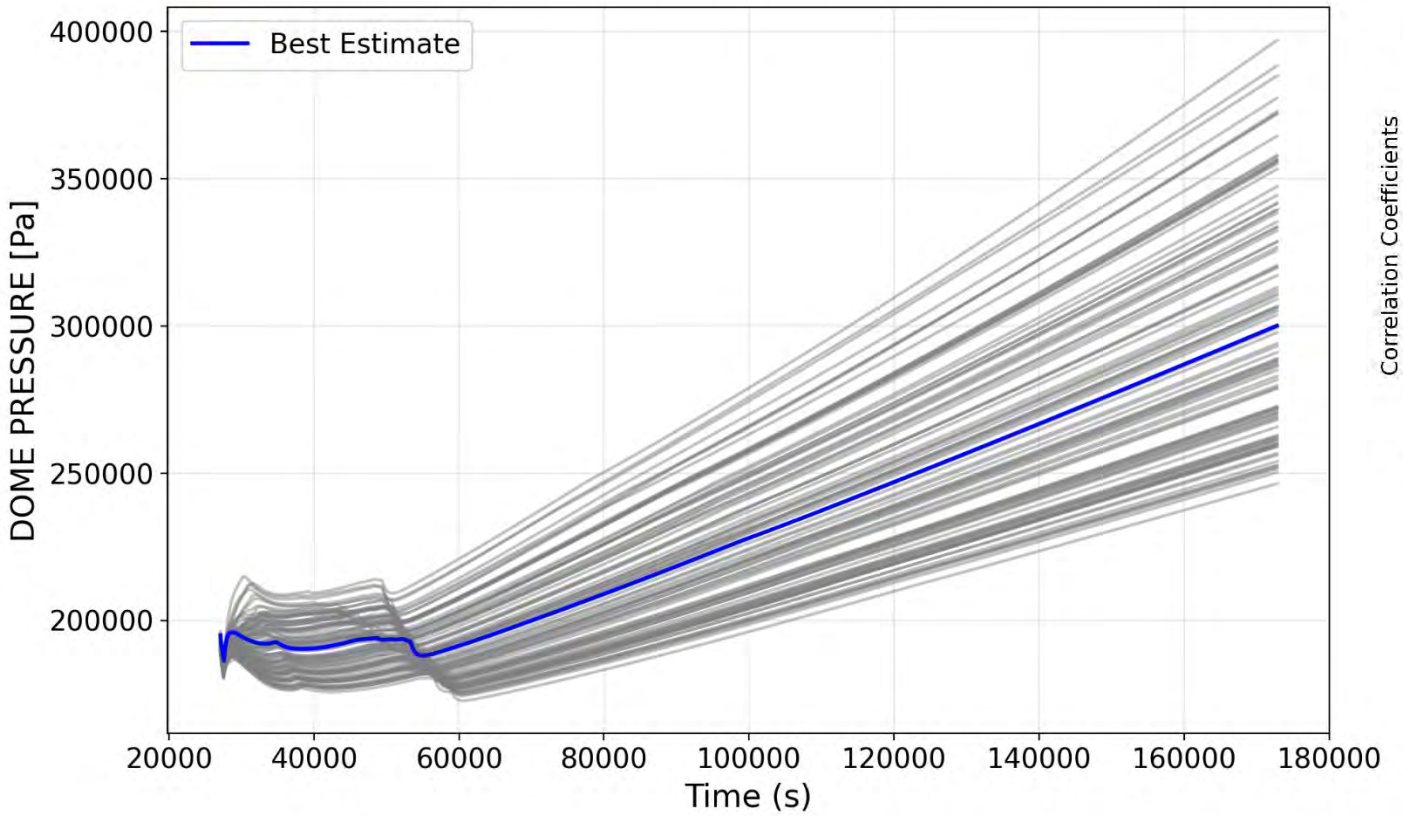

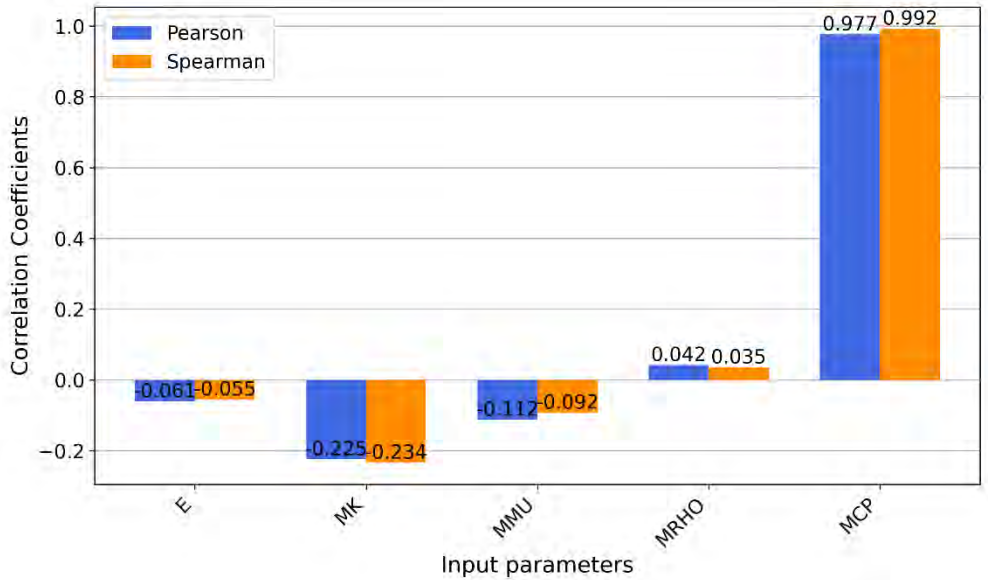

- Uncertainty band [+33%; -17%]

Results: Cavity Erosion

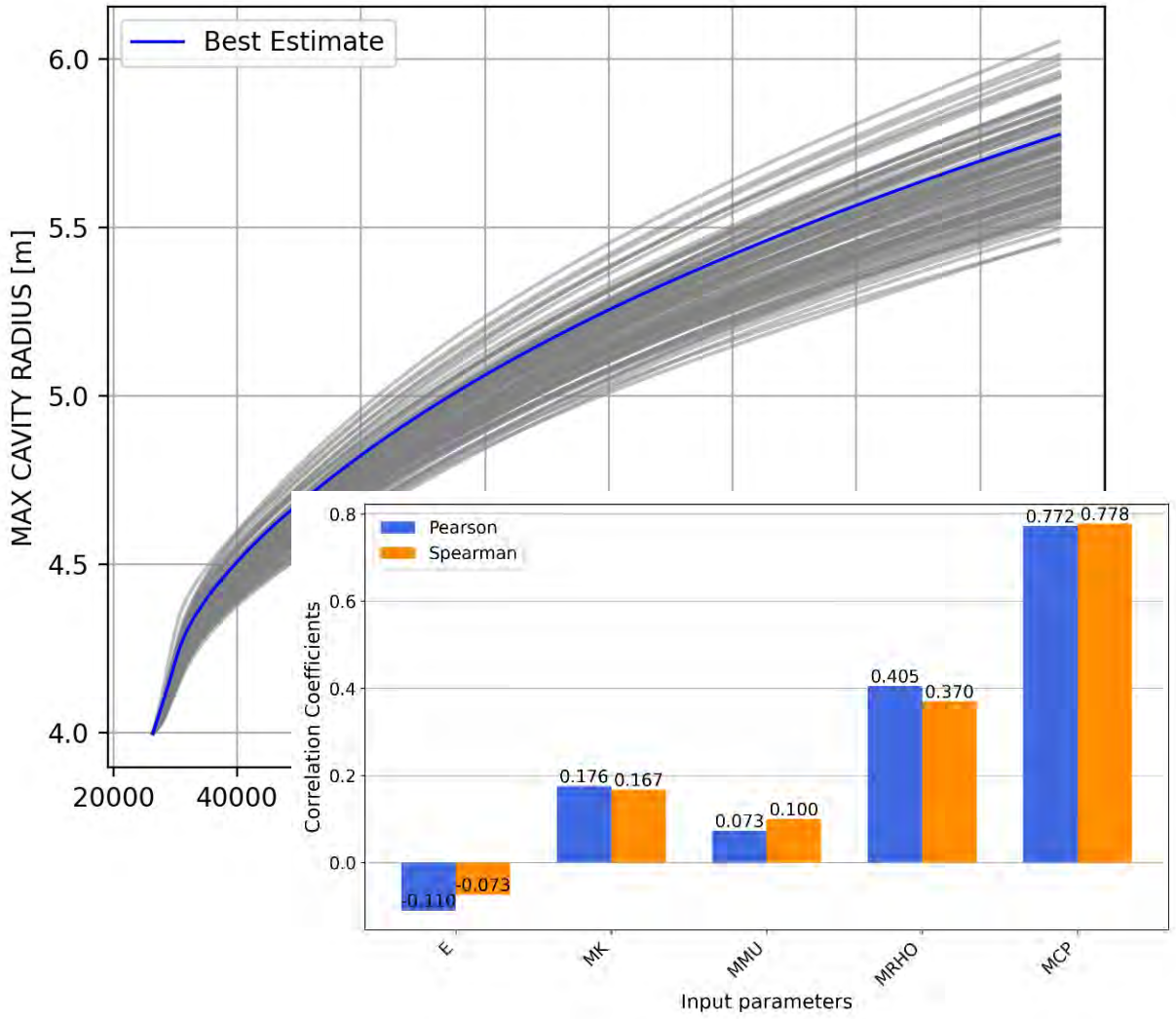

- Uncertainty band [+5%; -5%]

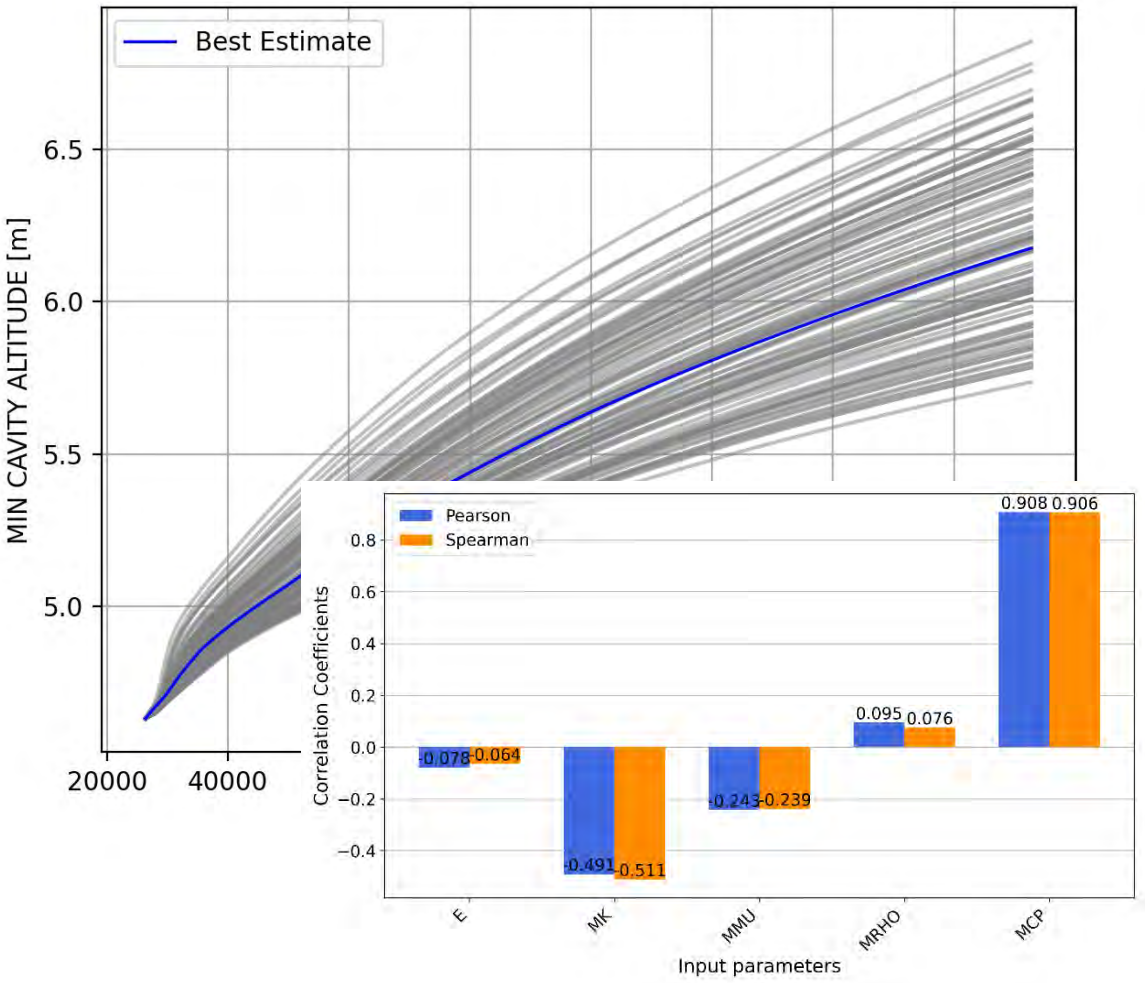

- Uncertainty band [+11%; -7%]

Results: Cavity Erosion

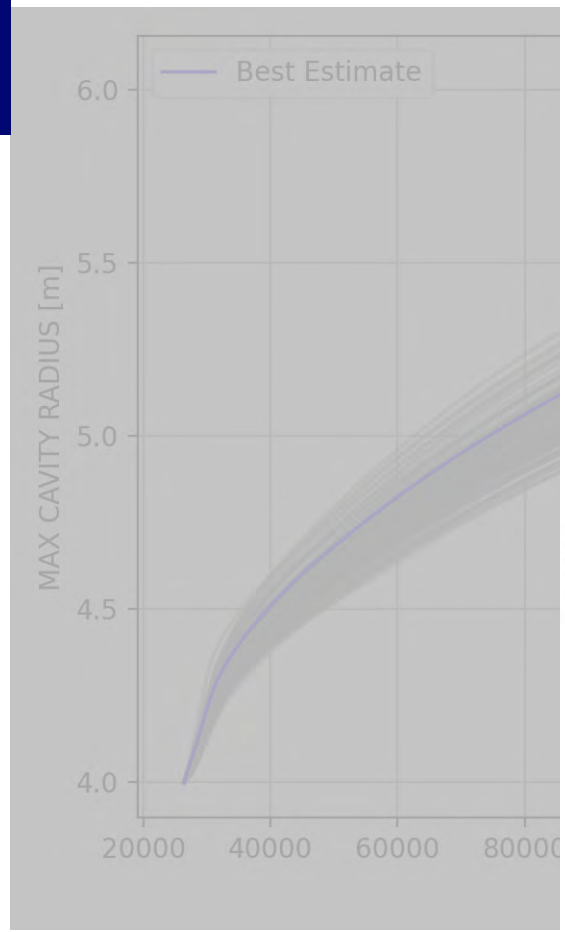

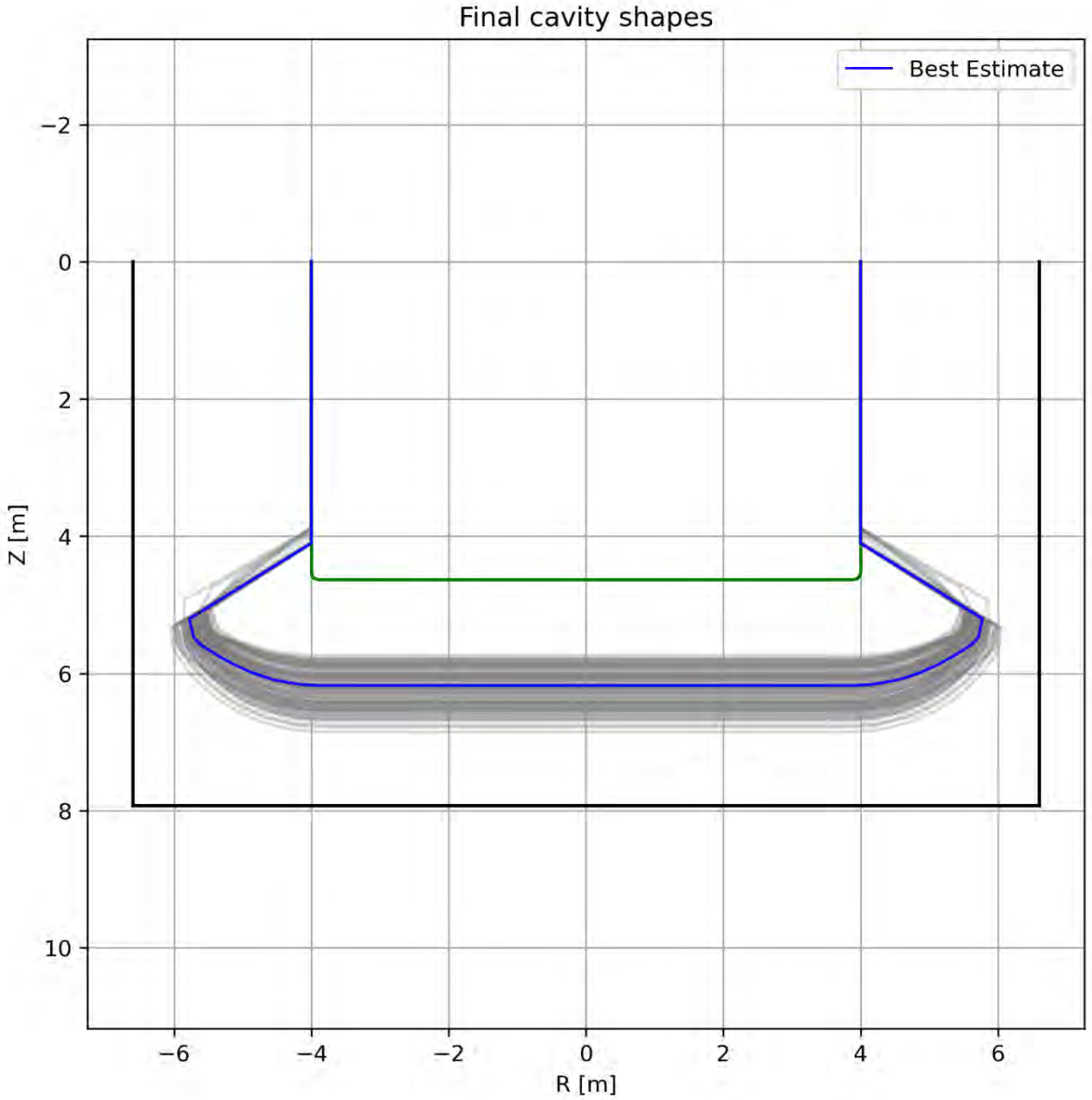

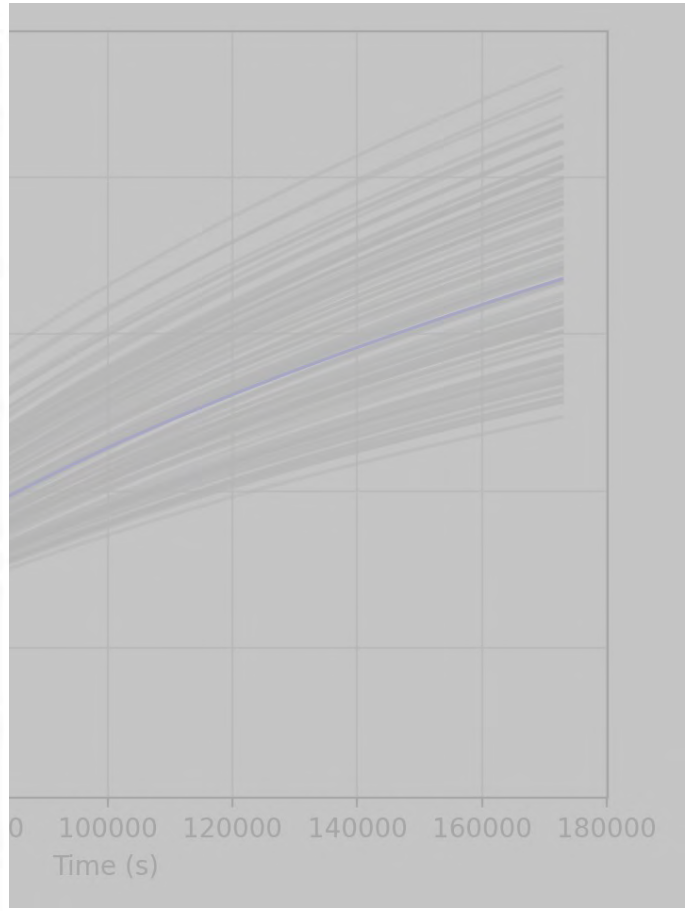

Results: Outgassing

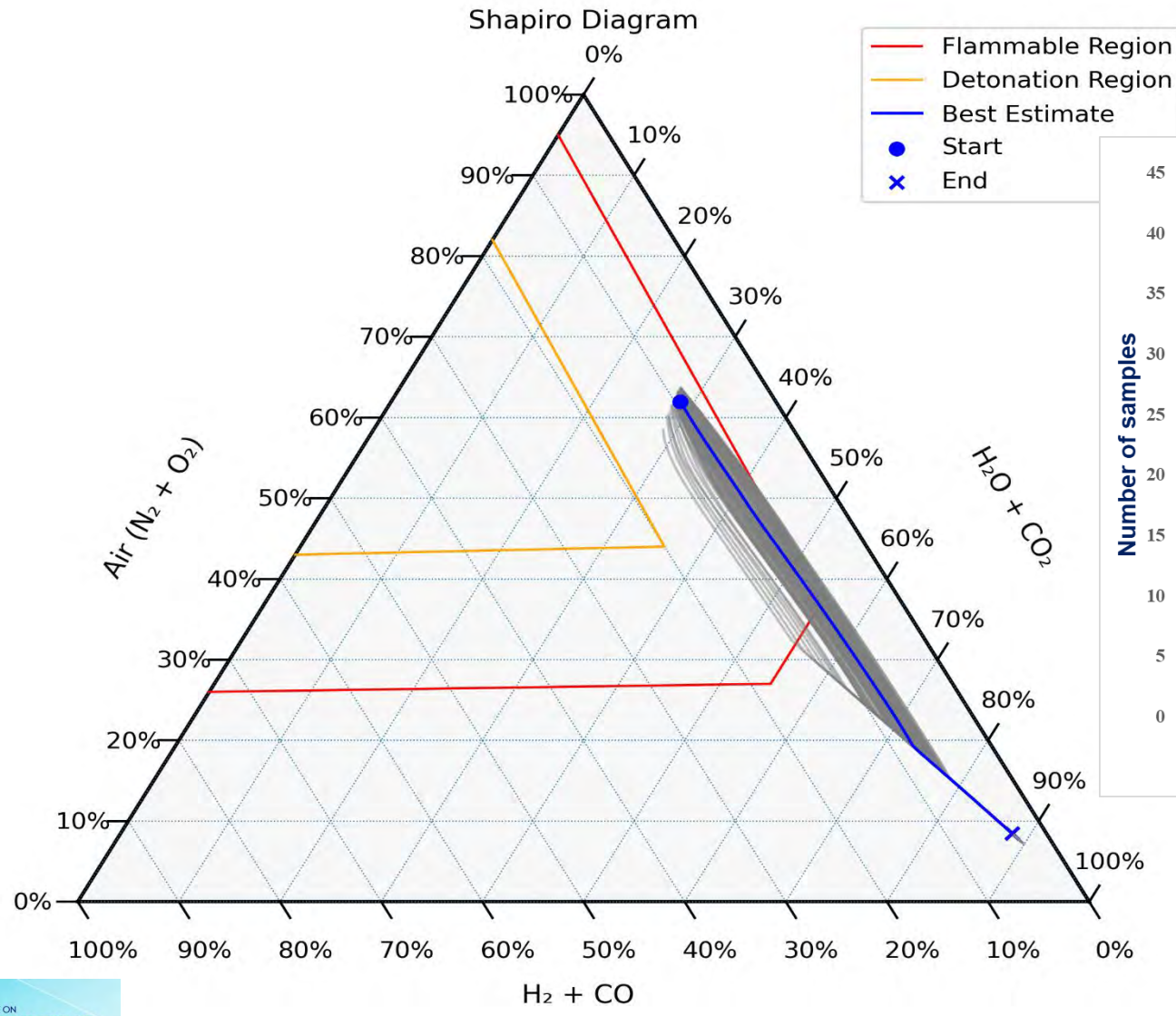

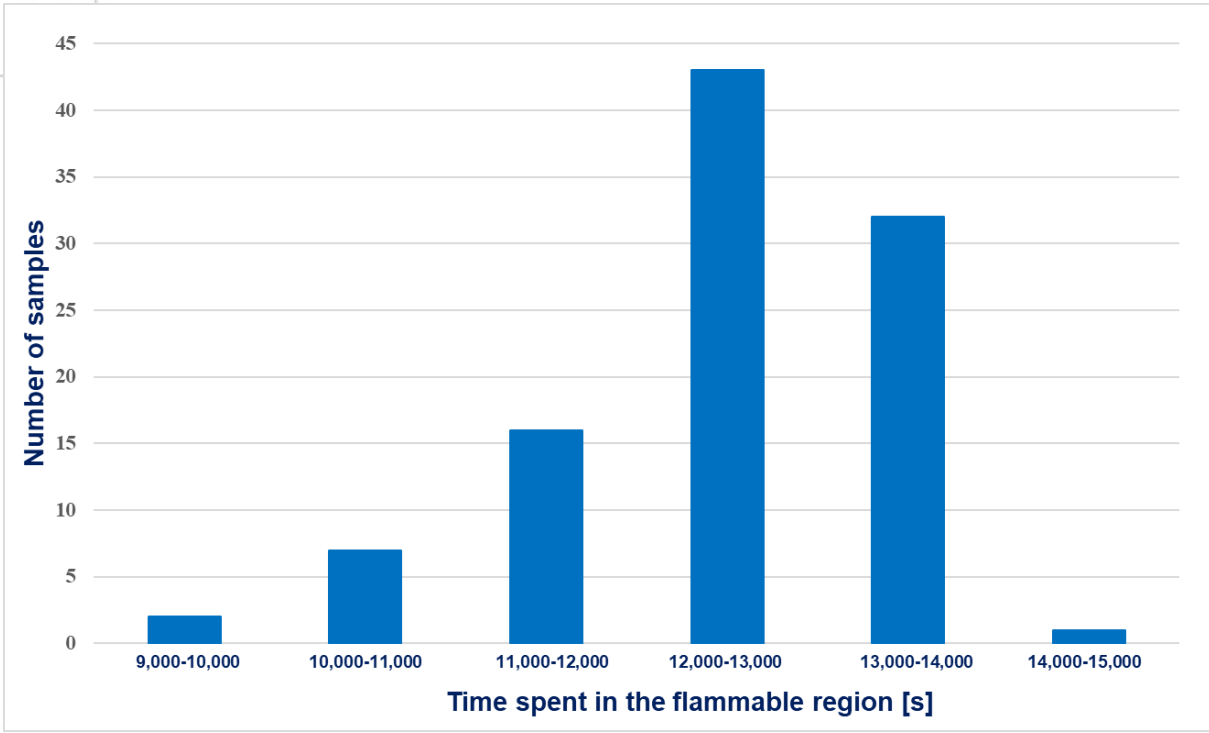

05

Major Insights

Preliminary Insights

- **A methodology** proposed to explore the relevance of corium properties on SA containment scenario in the ex-V phase.
- **Major hypos** made to set the basis of the UaSA analysis.
- A "**small/mild" effect of corium properties uncertainties** on erosion & combustion risk found.
- **Containment pressure significantly affected**, though.
- **Uncertainties in specific heat,** a big player!

Future Steps

- To consolidate the results (sensitivity to assumptions).
- To extend to other scenarios (wet cavity; Fukushima-like).

SEAKNOT

www.seaknot-project.eu

THE SEAKNOT WEBSITE

The aim of the four-year project is two-fold: to shape up a roadmap for severe accident research in the coming 10 years by means of which to achieve both a substantial reduction of remaining uncertainties and a measurable progress in the practical elimination of radiological consequences; and, no less important, to efficiently manage the knowledge and knowhow transfer to the young generation of nuclear scientists and engineers who will be involved in its implementation.

Coordinated by CIEMAT (Spain), SEAKNOT is constituted by seventeen well-known organizations from ten countries.

Funded by
the European Union

Thank you for your attention!

Università di Pisa

SEAKNOT

Ciemat
Centro de Investigaciones Energéticas, Medioambientales y Tecnológicas

UNSR

CONSIDERATIONS ON FLOATING CRUSTS DURING MOLTEN CORE CONCRETE INTERACTION

Christophe Journeau
CEA, DES, IRESNE, DTN, SMTA, LEAG
Cadarache, F-13108 Saint-Paul-lez-Durance, France
christophe.journeau@cea.fr;

ABSTRACT

In the case of Molten Core Concrete Interaction, it is commonly accepted that an anchored crust cannot remain stable at reactor pit/pedestal scale (~5-6m). Floating crust hypothesis is thus considered to study long term ex-vessel coolability by water top-flooding. Typical characteristics from Fukushima Daiichi MCCI modelling have been used to estimate crust characteristics, as well as published data from a typical PWR scenario. Melt Eruption is an important phenomenon contributing to ex-vessel coolability in flooded MCCI configuration as ejected debris are considered to be quenched and remain cooled by water pool.
Heat conduction considerations provide estimates of crust thickness (which are consistent with the 3-4 cm thickness estimated for the observed Fukushima Daiichi unit 1 pedestal shelves. A crust floatability study provides the possible floating crust potential characteristics in terms of density and porosity. It shows that a floating crust cannot withstand a large mass of ejected debris without sinking in the molten pool and remelting its lower part. This value is then compared with the ejected debris rate estimated from Ricou and Spalding model. Ejected debris cooling mode would then be limited to a short-term cooling followed by refusion (quenched at ~100°C then reintroduced in melt pool) instead of a long-term cooling by ~100°C boiling water. a new scenario can be proposed, which is currently not modelled in MCCI codes, for concretes with high gas contents as limestone-rich ones: a floating crust is formed on the top of the corium pool interacting with concrete; due to gas releases, melt eruption occurs and “volcanic vents” are formed; erupted debris droplets (typically of centimetric size) are quench in water and deposited above the crust; as the debris bed weight increases, the crust progressively sinks, remelts and is incorporated again to the molten pool.

KEYWORDS

MCCI, Crust, Melt Eruption, Coolability, Long term

1. INTRODUCTION

Terminating Molten Core Concrete Interaction (MCCI) [1] [2] is an important goal in the management of the Ex-Vessel phase during a Severe Accident. In the absence of external cooling, MCCI would continue ablating the basemat concrete for a very long time period [3]. Top flooding by water the corium concrete molten pool is considered as a means to enhance melt cooling used as a generic severe accident management strategy for ex-vessel melt stabilization in many existing plants [1].
Three main processes [1][4] have been considered that favors melt cooling even though corium thermal conductivity is relatively low and would limit cooling heat transfer:

- Water ingression in the crust [4, 5];
- Melt eruption forming particulate debris bed above the top crust [6];
- Bulk cooling in case of sudden breach of a suspended crust.

At experimental scale, crust generally anchors to the sidewall and a cavity may form between the molten pool and the crust that largely reduces upwards heat transfer in the presence of top cooling [4] even with relatively large (1.5 m) span between walls. Nevertheless, it is expected that at reactor scale, with a typical

6-meter diameter reactor pit, the crust strength would not be sufficient for it to remain in an anchored geometry for most plausible configurations [7], as the stress caused by the crust weight varies with the square of the ratio of radius over thickness. Therefore, the most expected configuration during MCCI with top flooding is that of a floating crust.
Between December 2021 and March 2022, a series of remotely operated investigations have been conducted in the pedestal of Fukushima Daiichi unit 1 [8, 9] that has shown the presence of so-called "shelves" or "terraces" [10] on the concrete wall that can be assumed to be partially anchored crust, as well as structures that are likely to be broken crusts that have fallen above the deposits that lie above the concrete substrate (Figure 1). Observing these structures that are interpreted as corium crusts, lead to reconsidering some issues about floating crusts that will be developed in this paper.

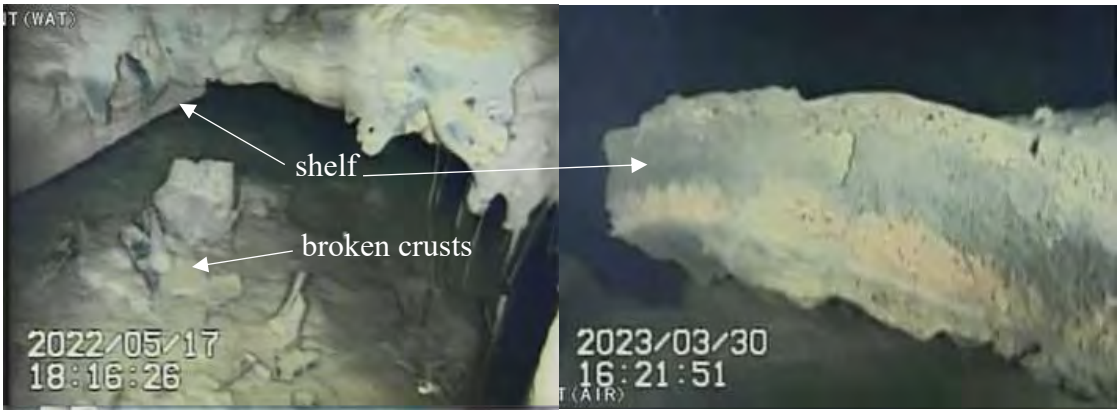

Figure 1. Remains of crusts observed during remote-operated investigation of Fukushima Daiichi unit 1. Left: "shelf" or piece of anchored crust at top, broken crusts visible at bottom ***https://photo.tepco.co.jp/en/date/2022-e/202205-e/220519-02e.html*** **;**
Right: zoom on "shelf" ***https://photo.tepco.co.jp/en/date/2023-e/202304-e/230404-01e.html***

In a first section, crust characteristics will be analysed and their floatability will be discussed. Then a section will be devoted to applications to melt eruption scenarios and a final section will focus on crust floatability during melt eruptions.

2. CRUST CHARACTERISTICS AND FLOATABILITY

Figure 2 schematically describes MCCI with water top-flooding and melt eruption. In this configuration, a floating crust is being considered, even though some small portions of an original crust at higher elevation may remain and form shelves.
From Fukushima Daiichi unit 1 MCCI benchmark [11], the melt temperature rapidly falls between 1500 and 2000 K during Molten Core Concrete Interaction, due to the mixing of the initial corium composition with molten concrete. Neglecting the effects of water ingression and of decay heat in the crust, Equation (1) determines the crust thickness by considering conductive heat transfer of the heat flux φ imposed by convection in the corium-concrete pool, between crust lower interface at a temperature in the 2000 -1500 K and its upper surface which would be around 400 K if covered by water.

$$h = \frac{k\Delta T}{\varphi} \quad (1)$$

With the thermal conductivity k of the order of 1-2 W/m²/K and an upwards heat flux in the 340- 50 kW/m² range [11], this leads to crust thicknesses between 5 and 60 mm. Actually, Cibula et al. [9] estimated from robotic observations the "shelf" (part of the crust remaining attached to the wall) thickness to 3-4 cm, which is in agreement with the simplified calculation above. Equation (1) neglects the contribution of the decay

heat present in the crust [12], which is acceptable due to the crust small thickness compared to that of the pool. Anyhow, these values must be considered as orders of magnitude, as it is difficult to estimate the actual crust thickness.

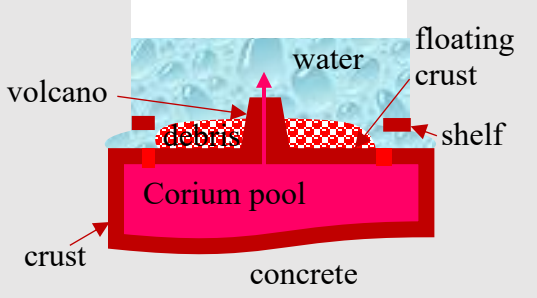

Figure 2. Schematic view of crust overlying an MCCI pool

The density of solid MCCI material is higher than that of the liquid material, as all of its constituent materials are denser in solid state compared to the corresponding liquid phases. For instance, there is about 7.5 vol% shrinkage at solidification for UO_2 [13] and 10 ±2 vol% for ZrO_2 [14, 15].
Moreover, the crust upper surface will be near water boiling point if it has been flooded by water while its lower surface will be at a temperature close to the crust-liquid interface temperature (somewhere between melt solidus and liquidus depending on model assumptions [1]). Anyhow, the crust will be colder than the molten pool and thus have a higher density due to thermal contraction.
Finally, the pool composition will evolve with the progression of concrete ablation, as concrete will mix with the oxidic phase of corium. Through this process, as molten concrete is much lighter than molten corium, there will be a continuous decrease of the molten pool density during concrete ablation.
Therefore, it is necessary to have more than 20 vol% of closed porosity in the crust than in the melt for crust to be lighter than the melt and effectively float on the pool. Indeed, open porosity would be filled by overlying water and the corresponding volume would not be accounted in considering Archimedean floatability.
These 20 vol% are quite plausible: The VB-U6 benchmark calculations [16] estimated the void fraction in the melt in the 30-50 % range at the initial minutes of the molten core-concrete interaction, so it is plausible that after solidification, similar void fractions are achieved. In less than one hour of test, the void fraction falls below 10%, implying a significant reduction of the pool height, the formation of a cavity and of an anchored crust, until it falls creating some “shelf” structures and floating crust.

3. ORDERS OF MAGNITUDE ABOUT MELT ERUPTIONS

The floating crust approach is in particular considered in the study of melt eruption in relation with concretes having a large gas content, as Limestone Common Sand concretes [1, 6] for which it is calculated to be an efficient contribution to coolability. In this approach, it is considered that thanks to entrainment by concrete-decomposition gases, corium debris are ejected through “volcanic eruptions”. The ejected droplets are then quenched in the overlying boiling water pool and accumulate as a porous particle bed atop the crust [4]. These eruptions have been observed in MCCI experiments such as e.g. ECOKATS-2 [20], MACE M3B [4] or VULCANO VBS-U1 [21] (Figure 3).
Based on Ricou and Spalding [17] correlation, Farmer [18] assumes that the superficial gas velocity j_m of the entrained melt is proportional to the superficial gas velocity j_g with a proportionality factor (entrainment rate) linked to the square root of the ratio between gas and melt densities:

$$j_m = 0.08 \left(\frac{\rho_g}{\rho_m}\right)^{1/2} j_g \qquad (2)$$

The superficial gas velocity is linked to the concrete ablation rate v by:

$$j_g = \sum_i \frac{f_i}{M_i} \cdot \varrho v \, RT/P \quad (3)$$

Figure 3. A corium "volcano" from VULCANO VBS-U1 test [21] © CEA, 2006

For a typical limestone-rich concrete such as that reported by Hengra et al. [19], f_{CO2} = 21.154 wt% and f_{H2O}=4,7 wt% while ρ = 2340 kg/m^3. At a typical corium pool temperature of 2000 K under a pressure of 3 bars, Equation (2) yields $j_g \approx 960$ v

Table I. Gas released from Limestone concrete in [19]

	CO_2	**H_2O**	**Total**
Mass fraction	21.15%	4.70%	25.85%
Density (kg/m^3)	0.79	0.32	0.63
	CO	**H_2**	**Total**
Mass after reduction (wt%)	13.5 %	1.0%	0.145
Density (kg/m^3)	0.50	0.07	0.35

In the presence of metals, steam can be reduced to hydrogen and carbon dioxide to carbon monoxide, but that would not change the superficial gas velocity as there is the total number of moles does not change during this RedOx reaction. Nevertheless, gas densities would be changed in this case. Table I synthesizes the gas densities for this case. The average gas density varies between 0.35 and 0.63 kg/m^3 in this typical case. For a typical liquid melt density of 5000 to 8000 kg/m^3, applying Equation (1) indicates that the entrainment rate j_m/j_g is typically in the 5-7.10^{-4} range and is thus consistent with coolability according to Bonnet and Seiler approach [22]. Equation (2) gives:

$$j_m \sim 0.5\text{-}0.7 \text{ v} \quad (4)$$

Ablation rates have been calculated for numerous reactor cases and reported in various publications [19, 23-27]. Table II present the range of estimated average axial ablation rates. It lies between 0.003 and 0.2 m/h. Applying (4) gives a range of melt superficial velocity between 2.10^{-3} and 2.10^{-1} m/h.
In the first hours of interaction, the superficial gas velocity is generally in the 2.5-10 cm/h range.
The surface of interaction lies between 24 m² (corresponding to a Ø5.5 m reactor pit) and 70-80 m² (corresponding to spreading from pit into a nearby compartment). Over one hour, between 5 and 60 t of debris would be forming a debris bed over the floating crust.

Table II. Ablation rates estimated from published reactor MCCI calculations with limestone-rich concretes.

Period over which estimation has been made in indicated under brackets.

Reference	Conditions	Minimum ablation rate (m/h)	Maximum ablation rate (m/h)
Cranga et al. 2010 [23]	Median value of homogeneous pool	0.01 (96-240 h)	0.08 (0-2 h)
	Median value of stratified pool	0.035 (48-96 h)	0.07 (0-48 h)
Vaitova & Stemberg 2015 [24]	VVER with limestone concrete	0.04 (32-45 h)	0.09 (0-1 h)
Yu et al. 2015 [25]	EPR with limestone concrete	----------	0.1 (0-3 h) Only published data
Stefanova et al. 2015 [26]	VVER with 26 wt% $CaCO_3$	----------	0.12 (14-30 h)
Na et al. 2021[27]	Dry MCCI	0.004 (60-330 h)	0.2 (0-1.7 h)
	Underwater MCCI	0.003 (0-6.7 h)	
Hengra et al. 2023 [19]	Dry Limestone Common Sand cavity	0.01 (28-56 h)	0.05 (0-14 h)
Fichot 2025 [12]	Limestone concrete	0.003 (60-80 h; with water ingression and eruptions)	0.015 (0-10 h; dry)

The formed debris beds have a large porosity and the debris particles have a size in the order of one centimetre that is considered coolable by boiling water [4, 22]. Termination of the concrete ablation is considered achievable when most of the corium pool is transformed into a coolable debris bed, which is possible with entrainment rates in the 10^{-4}-10^{-3} range. It has thus been suggested that addition of a thin layer of limestone concrete would accelerate stabilization [12].
This would not be operating if there were an anchored crust, because a cavity would form at between the melt surface and the anchored crust that would prevent melt eruptions from reaching above the crust. This has often been observed at laboratory scale [1, 4, 21], especially with limestone-rich concretes due to loss of volume of limestone aggregates during decarbonation. But such cavities are generally considered to be extremely unlikely at reactor scale due to the large spans for which crusts are not strong enough to stay. Broken crust are likely to have been observed at scale 1 in Fukushima Daiichi unit 1 (Figure 1 left).

4. CRUST FLOATABILITY DURING MELT EJECTION

As the crust is assumed to be floating (Figure 4), it is then necessary to estimate the quantity of debris that may lie on the crust without sinking. Let's assume a porosity of 50 vol%, which is clearly a bounding case reduces the risk of crust sinking under the weight of debris bed. It must be stressed that this porosity should also decrease thermal conductivity and thus crust thickness, but this effect is neglected here.
Taking into account shrinkage and thermal contraction, we may assume an intrinsic initial crust density of the order of 7000 kg/m^3 (i.e. 3500 kg/m^3 taking into account 50% closed porosity) and a pool density of the order of 6000 kg/m^3. In this case, about 60 % of the crust will be submerged, considering Archimedes' principle.
For a typical 35-mm thick crust, it would correspond to about 20 mm submerged and 15 mm above the molten pool level. These 15 mm will sink in the molten pool if sufficient weight is applied on top of it. This weight corresponds to the weight of displaced pool. Therefore, sinking would occur for a typical surfacic density ρ_A of 0.015 x 6000 = 90 kg/m² (i.e., a few tons over the whole MCCI area). Submersion will arrive quite rapidly in the order of 1 hour of interaction and anyhow before a significant fraction of the melt mass (of the order of 100 t). In the case of a very porous debris bed, Archimedes's force should be taken into account, reducing the apparent density of the debris by $(\rho_{debris}-\rho_{water})/\rho_{debris}$ which corresponds to 20% of added mass for the same sinking depth.

Table III: Sensitivity analysis of sinking added mass with respect to closed porosity
(Crust density : 7000 kg/m^3, Pool density: 6000 kg/m^3, pedestal diameter: 5 m)

Closed porosity	10%	20%	30%	40%	50%	60%
Porous crust density (kg/m^3)	6300	5600	4900	4200	3500	2800
Emerged height (mm) for 35-mm crust	0	2	6	11	15	19
Added mass (t) for sinking (taking into account floatability)	0	0.3	0.9	1.5	2.1	2.6

Table III presents the sensitivity of these calculations with respect to the crust porosity. It confirms that even with very high porosities, the initial crust cannot carry a significant fraction of the corium inventory without sinking. Table IV similarly presents the sensitivity of sinking with respect to the crust density. Even with crust and liquid pool having the same density (i.e., neglecting material shrinkage due to solidification and thermal contraction) and a crust closed porosity of 50%, the total mass that can be taken on the c rust without sinking is below 3 t.

Table IV: Sensitivity analysis with respect to the crust density (for a 50% closed porosity), taking the same other hypotheses than in Table III

Crust intinsic density (kg/m^3)	6000	6300	6600	7000	7500
50%-porosity crust density (kg/m^3)	3000	3150	3300	3500	3750
Emerged height (mm) for 35-mm crust	18	17	16	15	13
Added mass (t) for sinking (taking into account floatability)	2.5	2.4	2.2	2.1	1.9

Mixing of the melt pool with ablated concrete has not been considered in this order of magnitude calculation. It will reduce the melt density (but not the crust density, as crust was formed earlier) and thus increase

submersion. Independently of the exact timing of this event, it occurs that a significant fraction of the corium inventory (in the 100-ton order of magnitude) cannot stay on a floating crust without making it sink.

Figure 4. Schematic view of floating crust supporting a mass dm of debris
Arrows mark the forces applied to the floating crust

To study the behaviour of a sinking crust, it is first assumed that the system (crust + ejected debris) remains in stable horizontal position (as a raft) and debris do not roll down into the pool. The crust will thus progressively sink into the pool. In this simplified approach, the decay heat generated in the crust and the debris will be neglected, as it concerns a thickness of a few centimeters of heat-generating corium, which is negligible compared to the multi-decimeter deep pool.

At the start of the ejection process, there is an upward heat flux at the crust lower interface φ_0 following Equation (1). If a mass dm is added, it will lead to a sinking of $dh=dm/(\rho_{pool}.S.h)$. If changes of heat flux and of thermal conductivity are neglected, the flux $d\varphi$ is available to melt a mass dm' at the bottom surface of the crust in order to reach again equilibrium between convection from the pool and conduction in the crust:

$$d\varphi = k\Delta T\left[\frac{1}{h} - \frac{1}{h+dh}\right] \approx k\Delta T\frac{dh}{h^2} = \frac{k\Delta T dm}{\rho_{pool}h^2 S} \qquad (5)$$

This is valid as long as the characteristic remelting time τ is shorter than the characteristic time of mass increase due to melt eruption. Remelting of $dm'=\rho_{crust}.S.dh$ to return to the initial thickness is characterized by:

$$\tau \sim \frac{L.dm'}{d\varphi.S} = \frac{L\,\rho_{crust}\,h^2}{k\,\Delta T} \qquad (6)$$

Considering crust latent heat of the order of L= 300 kJ/kg, ρ= 7000 kg/m^3, h= 3 cm, k=1.5 W/m/K and $\Delta T \sim 2000$ K, the characteristic time is of the order of 10 minutes. This is well shorter than ejection characteristic times, so the floating crust is expected to progressively melt when it sinks because of the arrival of erupted debris.

Another plausible alternative scenario, in which there is no crust sinking, would be that, due to an uneven repartition of debris on the crust, there would be floatation instabilities and tilting of the floating crust leading to the fall of most of the debris in the pool. In this case also, there would be a rather quick return of the debris into the molten pool.

In both scenarios, heat-generating material will be temporarily removed from corium pool, (partly) quenched by water and will eventually return to the melt pool and be remelted. This will indeed provide some enhanced heat removal compared to top flooding without melt ejection. A simple way to assess the contribution of these phenomena to the overall heat balance has not been found and it is expected that more mechanistic modelling shall be carried out to determine its efficiency.

5. CONCLUSIONS

Remote-controlled investigation in Fukushima Daiichi unit 1 containment have shown the presence of structures that have been interpreted as broken crusts having fall over solidified fuel debris and of small partly-broken crusts attached to the walls (shelves). These observations have been the basis for a renewed interest in the fate of crusts during ex-vessel phases of a severe accident, in particular during top flooding with melt eruption.

Top crusts above an MCCI pool are expected to have a thickness of the order of a centimeter and must have significant porosity in order to float over the melt pool. Melt eruptions over a floating crust are considered to be an efficient way to quench a large part of the MCCI inventory as coolable particulate debris bed.

Considering typical ablation rates from reactor scale MCCI calculations reported in the literature, it occurs that the crust would sink due to the weight of the debris bed as soon as a mass of the order of a few tons (out of typical a total mass of the order of 100 t) has been deposited on the floating crust. Moreover, characteristic remelting time indicate that the remelting of the sinking crust will be significantly more rapid than that of the deposition of debris.

Therefore, a new scenario can be proposed, which is currently not modelled in MCCI codes, for concretes with high gas contents as limestone-rich ones:

- A floating crust is formed on the top of the corium pool interacting with concrete;
- Due to gas releases, melt eruption occurs and “volcanic vents” are formed;
- Erupted debris droplets (typically of centimetric size) are quench in water and deposited above the crust;
- Due to weight increase, the crust (and the overlying debris bed) progressively sinks and remelts.
- A variant would be that, instead of sinking, the crust is subject to tilting until the added debris roll out of the crust and fall back into the corium pool.

In this scenario, ejected debris cooling mode would then be limited to a short-term cooling followed by refusion (quenched at ~100°C then reintroduced in melt pool) instead of a long-term cooling of a large debris bed by ~100°C boiling water of a significant part of the inventory. Moreover, with this scenario the crust characteristics will continuously vary with composition, which may affect water ingression, as this cooling phenomenon is less efficient at high silica fractions [9].

It is thus recommended to introduce this crust sinking phenomenon in wet MCCI modelling codes to estimate the evolution of pool cooling during this plausible scenario.

NOMENCLATURE

Symbol	Variable	unit
f	Mass fraction	-
h	thickness	m
i	Gas species identifier	-
j	Superficial velocity	m/s
k	Thermal conductivity	$W.m^{-1}.K^{-1}$
L	Latent heat of fusion	J/kg
M	Molar mass	kg/mol
P	Pressure	Pa
R	Ideal gas constant	$J.K^{-1}.mol^{-1}$
S	MCCI area	m^2
T	Temperature	K
v	Ablation rate	m/s

	Greek letters	
φ	Heat flux	W/m^2
ρ	Density	kg/m^3
ρ_A	Surfacic density	kg/m^2
	Subscripts	
g	gas	
I	Concrete constituent	
m	melt	

REFERENCES

1. J.M. Bonnet, F. Robledo, M.T. Farmer, M. Cranga, C. Spengler, D. Vola, S. Basu, K. Atkhen, A. Fragette, M. Fischer, J. Foit, A. Hotta, C. Journeau, C. Marchetto, A. Morita, E. Moiseenko, F. Polidoro, Q. Zhou, *State-of-the-Art Report on Molten Corium Concrete Interaction and Ex-Vessel Molten Core Coolability*, OECD/NEA report NEA/CSNI/R(2016)15, 2017.
2. C. Journeau, P. Piluso, Molten Core Concrete Interaction, In: Konings, Rudy JM, Stoller Roger E (eds.) *Comprehensive Nuclear Materials 2nd edition*, vol. 2, pp. 499–524. Elsevier, Oxford, UK (2020). http://dx.doi.org/10.1016/B978-0-12-803581-8.11727-8
3. M. Pellegrini, C. Journeau, N. Seiler, L.E. Herranz, M. Garcia, C. Spengler, C. Bouillet, M. Barrachin, D. Luxat, L. Albright, "Analysis of the Long-Term Interaction Between Molten Core and Dry Concrete at Fukushima Daiichi Unit 1", *Nucl. Technol.* **211**, pp. 2595-2608 (2025) https://doi.org/10.1080/00295450.2024.2371267
4. M. T. Farmer, D. J. Kilsdonk, R. W. Aeschlimann, "Corium Coolability under Ex-Vessel Accident Conditions for LWRs". *Nuclear Eng. Technology*, **41**, pp. 575-602(2009).
5. M. Epstein, "Dryout heat flux during penetration of water into solidifying rock", *J. Heat Transfer*, **128**, pp. 847-850 (2006).
6. M. T. Farmer,. Phenomenological Modeling of the Melt Eruption Cooling Mechanism during Molten Corium Concrete Interaction. *Proc. ICAPP06.* Reno, Nevada, USA (2006).
7. S. Lomperski, M.T Farmer, Corium crust strength measurements, *Nucl. Eng. Des.*, **239**, pp. 2551-2561 (2009).
8. TEPCO, *Fukushima Daiichi Nuclear Power Station Unit 1 Primary Contaionment Vessel Internal Investigation. Completion of the detailed visual investigation of the perimeter of the pedestal using submesive ROV*., https://www.tepco.co.jp/en/hd/decommission/information/newsrelease/reference/pdf/2022/reference_20220523_01-e.pdf (2022)
9. M. Cibula, M. Pellegrini, M. Mizokami, S. Mizokami, "Evaluation of Fukushima Daiichi Unit 1 Ex-Vessel Phenomenon Leveraging on Primary Containment Vessel Robotic Inspections", *J. Nucl. Sci. Tech.,* **211**, pp. 513-530 (2025).
10. A.P. Pshenichnikov, "A new perspective into molten core concrete interaction for interpreting Fukushima Daiichi terrace-shaped debris", *Sci. Rep.,* **15**, 23513 (2025).
11. M. Pellegrini, C. Journeau, N. Seiler, L.E. Herranz, M. Garcia, C. Spengler, "Analysis of the Long-Term Interaction Between Molten Core and Dry Concrete at Fukushima Daiichi Unit 1", *Nucl. Tech.*, **211**, pp. 2595-2608 (2025).
12. F. Fichot, "Ex-vessel stabilization of corium: An analysis of corium-concrete interaction with top flooding for siliceous concrete", *Ann. Nucl. Ener.*, **223**, 111584 (2025).
13. J.K. Fink, "Thermophysical properties of uranium dioxide", *J. Nucl. Mater.*, **279**, pp. 1-18 (2000).
14. Q.J. Hong, S.V. Ushakov, D. Kapush, C.J. Benmore, R.J.K. Weber, A. van de Walle, A. Navrotsky, "Combined computational and experimental investigations of high temperature thermodynamics and structure of cubic UO_2 and ZrO_2", *Sci. Rep.*, **8**, 14962 (2018).
15. S. Kohara, J. Akola, L. Patrikeev, M. Ropo, K. Ohara, M. Itou, A. Fujiwara, J. Yahiro, J. T. Okada, T. Ishikawa, A. Muzino, A. Masuno, Y. Watanabe, T. Usuki, "Atomic and electronic structure of an extremely fragile liquid", *Nature Comm.*, **5**, 5892 (2014).
16. C. Journeau, J.F. Haquet, B. Letexier, A. Greco, B. Spindler, R. Gencheva, P. Groudev, D. Dimov, A. Fargette, J. Foit, B. Michel, C. Mun, T. Sevon, C. Spengler, F. Polidoro, A SARNET Benchmark on two VULCANO Molten Cre Concrete Interaction Tests, *ERMSAR-2012,* Cologne, Germany (2012).
17. F.B. Ricou, D.B. Spalding, "Measurements of Entrainment of Axisymetrical Turbulent Jets", *J. Fluid Mech.*, **11**, pp. 21-32 (1961).

18. M.T. Farmer, *The CORQUENCH Code for Modelling of Ex-Vessel Corium Coolability under Top Flooding Conditions – Code Manual – Version 4.1-beta*, Argonne Nat. Lab. Report 18/22 (2018). https://publications.anl.gov/anlpubs/2018/10/146345.pdf
19. N. H. Hengra, C.H. Song, S.J. Kim, M. Ilyas, "Assessment of corium concrete interaction and impact of water ingression mechanism using top flooding strategy for a small PWR with MELCOR 2.2", *Ann. Nucl. Ener.*, **182**, 109601 (2023).
20. H. Alsmeyer, T. Cron, G. Messemer, W. Häfner, "ECOKATS-2: A Large Scale Experiment on Melt Spreading and Subsequent Cooling by Top Flooding", *Proc. ICAPP'04 (Int. Congr. Advances nucl. Power Plants*, Pittsburgh PA, USA (2004).
21. C. Journeau, P. Piluso, J.-F. Haquet, E. Boccacio, L. Ferry, J. Monerris, G. Fritz, P. Correggio, "Oxide-Metal Corium-Concrete Interaction Test in the VULCANO facility", *Proc. OECD-NEA MCCI Seminar*, Cadarache, France (2010).
22. J.M. Bonnet, J.M. Seiler, "Coolability of Corium Spread Onto Concrete Under Water, the PERCOLA Model", 2nd CSNI Specialists Meeting on Core Debris-Concrete Interactions, OECD/NEA/CSNI R(92)10 (1992).
23. M. Cranga, B. Spindler, E. Dufour, D. Dimov, K. Atkhen, J. Foit, M. Garcia-Martin, T. Sevon, W. Schmidt, C. Spengler, "Simulation of concrete interaction in 2D geometry", *Progr. Nucl. Ener.*, **52**, pp. 76-83 (2010).
24. M. Vaitová, P. Štemberg, "Estimation of ablation depth in concrete slab under reactor during nuclear accident", *Neur. Netw. World*, **4** (15), pp. 347-367 (2015).
25. Y. Yu, J. Jiang, W. Sun, Z. Jin, Q. Zhang, "The interactions of molten core with different types of concretes in EPR severe accidents", *J. Sust. Cement-based Mater.*, **4**(1), pp. 44-53 (2015).
26. A. Stefanova, R. Gencheva, P. Groudev, M. Cranga, C. Spengler, I. Ivanov, J. Foit, P. Kotska, "Investigation of molten core-concrete interaction benchmark test for WWER 1000", *Ann. Anucl. Ener.*, **75**, pp. 742-751 (2015).
27. H. Na, S. Lee, H.-C. Kim, K.-T. Kim, „Analysis of concrete ablation depth by MCCI assuming top flooding condition of APR1400 NPP", *Ann. Nucl. Ener.*, **160**, 198363 (2021).

CONSIDERATIONS ON FLOATING CRUSTS DURING MOLTEN CORE CONCRETE INTERACTION

Christophe Journeau

Severe Accident Experimental Lab.

IRESNE Institute, CEA

Cadarache, France

Outline

1. Introduction and Context
2. Observations at Fukushima Daiichi unit 1
3. Crust Characteristics and Floatability
4. Melt Eruptions
5. Crust Floatation in presence of Melt Ejection
6. Conclusions

Introduction: Top-cooling during MCCI

- Ex-vessel phase of a Severe Accident
- Molten Core Concrete Interaction
  - Powered by decay heat
  - Ablation of concrete is to be arrested before concrete layer melt-through
- Top flooding is an accident management strategy that has been implemented in some reactors
  - Potentially after spreading (to reduce heat density)
  - Heat transfers can be enhanced by
    - Water ingression
    - Melt ejection on a floating crust
      - Ejected debris are expected to be easily coolable
        - *See Farmer, Nucl. Eng. Tech. 211 (2009) 575-602 and ICAPP2006 for more details*

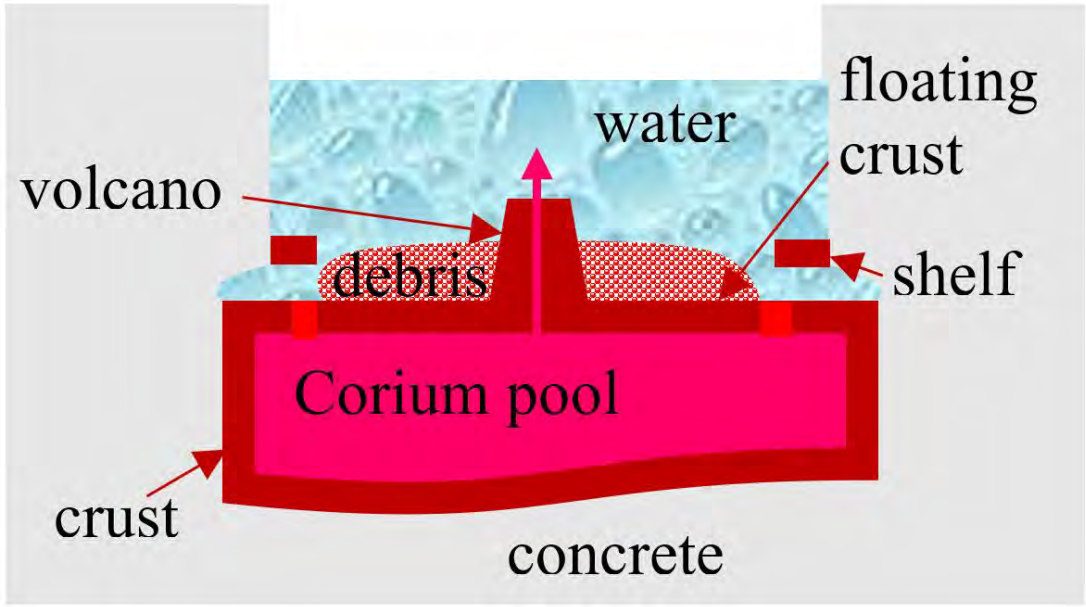

Experimental issues with crust anchoring

- At laboratory scale, during experiments, top crust often anchors to the walls
  - When gas rate decreases, pool level becomes lower and a gap appears that is reducing upwards heat transfers.
  - Top cooling efficiency is estimated during periods without this gap.
- As crust resistance varies with 1/thickness², such behavior is believed to be impossible at reactor pit/pedestal scale (5-6 m typical diameter).

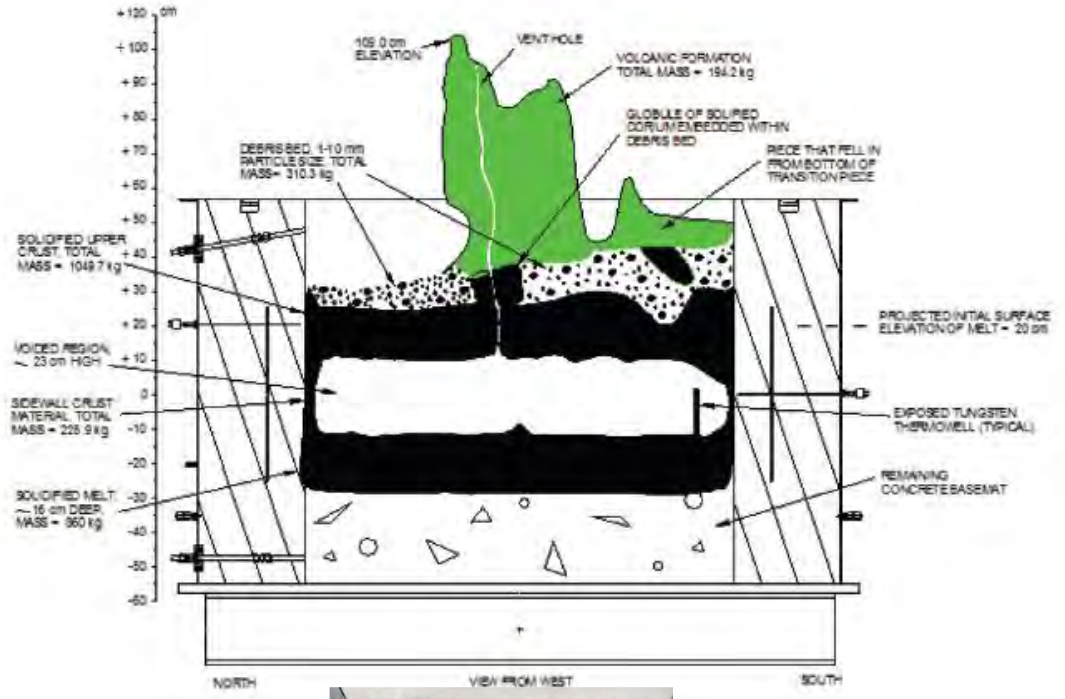

From NEA/CSNI/R(2016)15

2. Observations at Fukushima Daiichi Unit 1

Investigations between December 2021 and May 2022

- Remotely-Operated underwater Vehicle observations

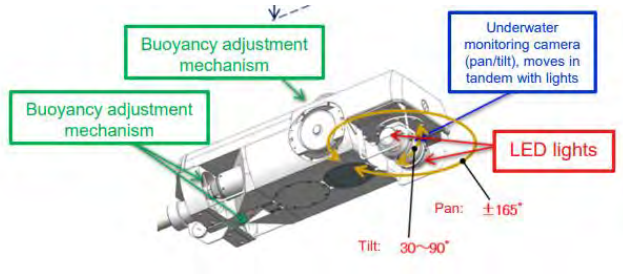

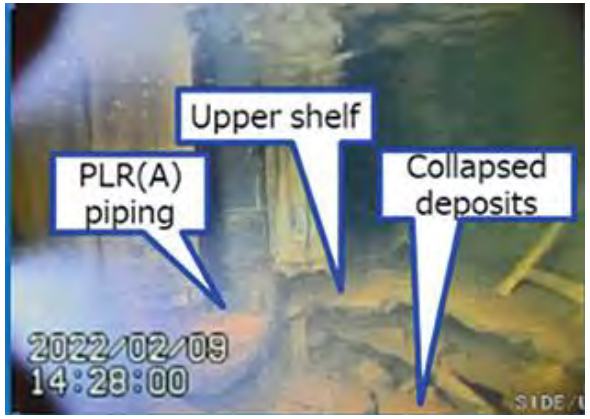

- Structures “collapsed deposits” have been found on top of deposits (likely remains of a corium spread) which have been considered to be broken crusts
- Structures called “shelves” or “terraces have been found at higher elevations that are attached to the walls
  - Interpreted as the remains of a broken anchored crust close to the walls or liner
  - Thickness 3-4 cm

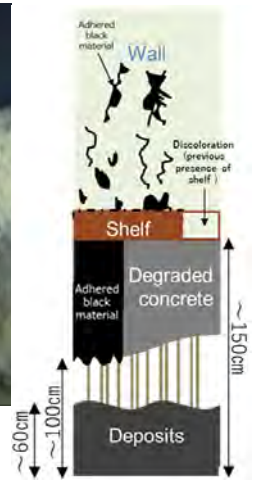

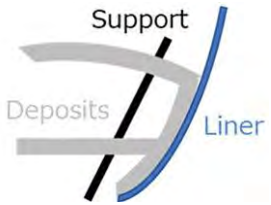

- *Images from TEPCO video archives and from Cibula et al., J.Nucl. Sci. Technol., 211 (2025) 513-530.*

3. Crust Characteristics and Floatability

Crust thickness

- Heat conduction in the crust subjected to
  - Convective heat flux at bottom
  - Imposed temperature, close to boiling point at its top surface
  - Neglecting decay heat in the crust gives:

    Thickness $h = \frac{k\Delta T}{\varphi}$
- Application:
  - Conductivity~1-2 W/m²/K
  - upwards heat flux in the 340- 50 kW/m² range [from ARC-F benchmark on 1F1]
  - Crust lower interface~2000K
  - Crust upper interface: ~430K
  - h between 5 and 60 mm
    - Fits with observed 30-40 mm

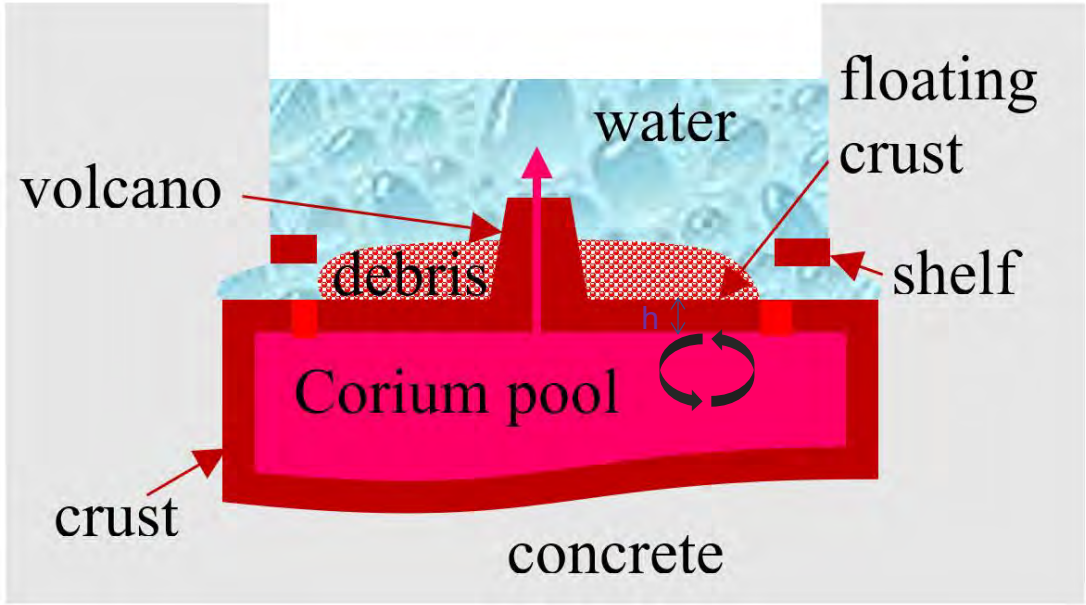

Floatability

- Solid fuel debris have a higher density than liquid pool
  - Shrinkage of 7 to 12 vol% between liquid and solid phases
  - Thermal contraction from melting point to boiling water interface temperature.
  - Liquid pool progressively mixes with lighter-density concrete
    - Affects crust and “older” ejected debris
    - Not newer eruptions
- Only solution to keep a crust afloat is to consider
  - Closed porosity in the crust
    - max ~50 vol%
    - ~20 vol% necessary
    - Calculated void fractions (are initially in the 30-50 vol%. Journeau et al, ERMSAR 2012
  - Archimedian force on particulate debris that will reduce their apparent density.

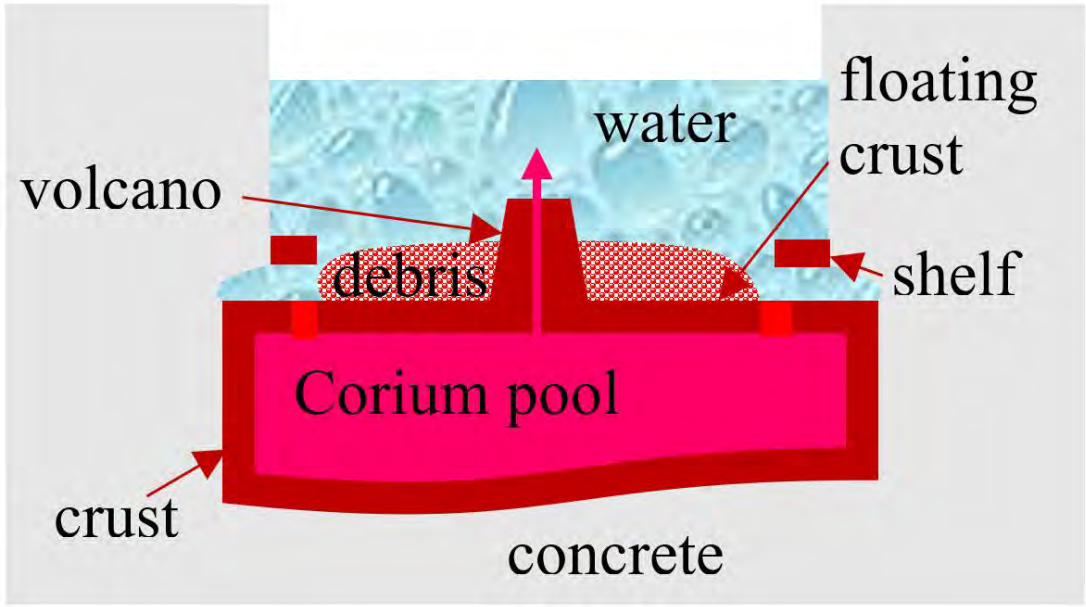

Numerical Application

- Intrinsic crust density : 7000 kg/m^3
- Crust closed porosity: bounding case of 50 vol% => Apparent density 3500 kg/m^3
- Corium pool density: 6000 kg/m^3 (taking into account mixing with some more concrete)
- Crust thickness: typically 35 mm

- Archimedes' principle
  - About 60% of the crust will be submerged
    - 20 mm below corium pool level
    - 15 mm above corium pool level

Closed porosity	10%	20%	30%	40%	50%	60%
Porous crust density (kg/m^3)	6300	5600	4900	4200	3500	2800
Emerged height (mm) for 35-mm crust	0	2	6	11	15	19

4. Melt eruptions

Melt eruptions

- Farmer adapted Ricou & Spalding correlation

$$j_m = 0.08 \left(\frac{\rho_g}{\rho_m}\right)^{1/2} j_g \qquad \text{with} \quad j_g = \sum_i \frac{f_i}{M_i} \cdot \varrho v \, RT/P$$

  - v being the concrete (average) ablation rate
  - For a typical limestone concrete, with corium at 2000 K under 3 bars, it gives j_g ~1000 v
  - For a typical corium density (5000-8000 kg/m^3) it gives
    - j_m ~ 0.5-0.7 v
- Typical ablation rates (from literature survey) in the 0.03-0.2 m/h
  - 2.5-10 cm/h generally in the first hours, then reducing.
- Considering a surface of interaction between 24 m² (Ø5 m) and 70 m² (spreading compartment) lead to formation of 5-60 t of particulate debris bed / solid volcanoes during the 1st hour.

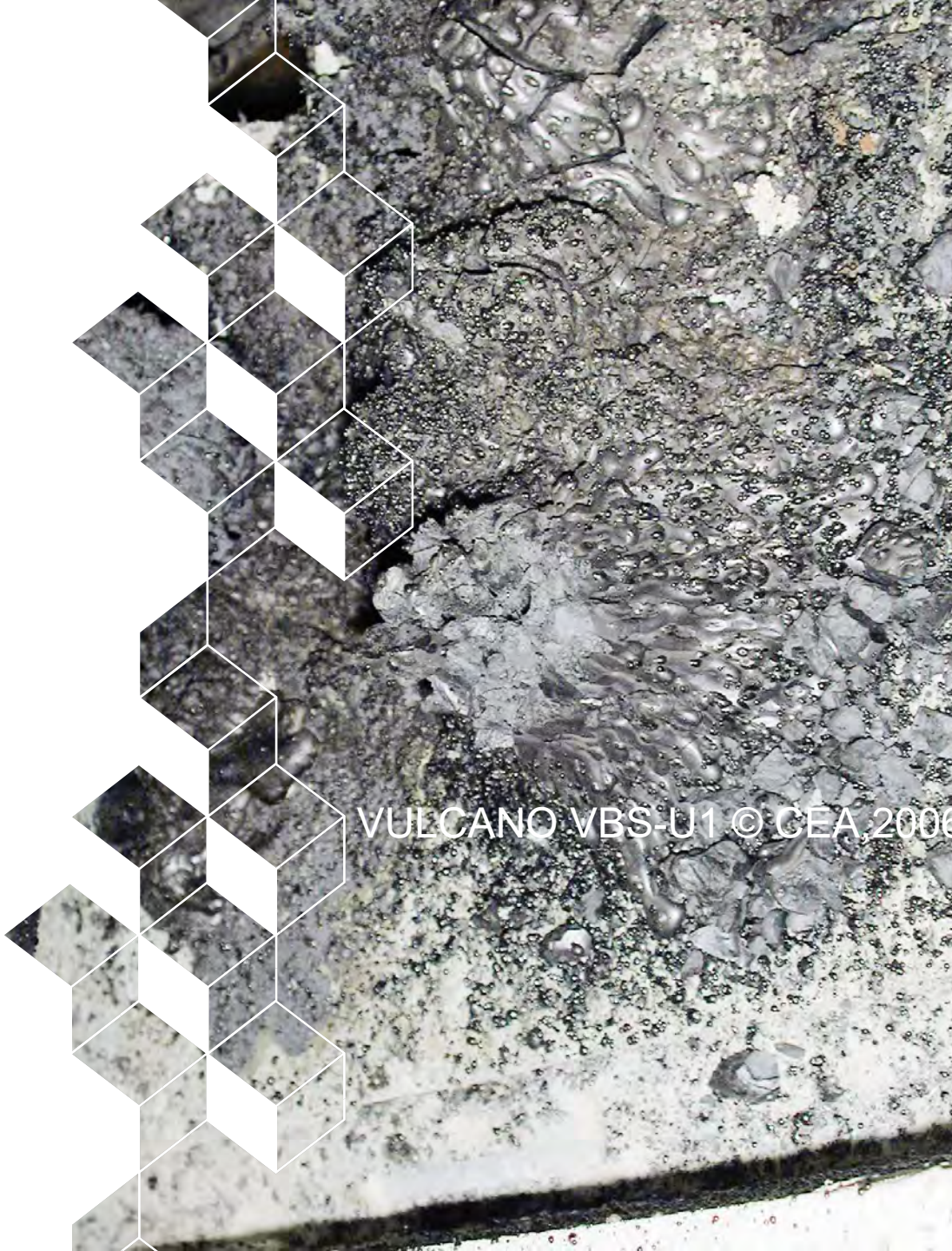

5. Crust floatation during melt ejection

Crust floatation

- Like any raft, adding a mass dm (or an equivalent mass dm' taking into account debris buoyancy) on the floating crust will make it sink of a depth dh
- Depending on the crust density and porosity, it typically takes 0.3 t to 2.6 t to completely sink the crust due to the added mass.

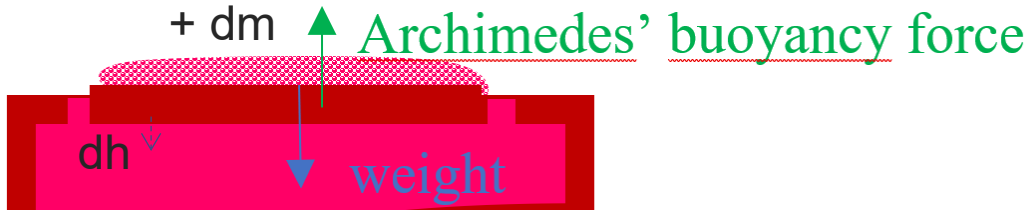

Crust intinsic density (kg/m^3)	6000	6300	6600	7000	7500
50%-porosity crust density (kg/m^3)	3000	3150	3300	3500	3750
Emerged height (mm) for 15 mm crust	18	17	16	15	13
Added mass (t) for sinking (taking into account debris floatability)	2.5	2.4	2.2	2.1	1.9

Remelting of the newly submerged crust

- Let's assume that the crust remains in stable horizontal position (as a raft with uniform distribution of added debris weight).
  - Decay heat in the crusts and debris is neglected, as well as change of heat conductivity due to the debris bed vs. crust.
- Due to increased thickness, there is an extra thermal resistance, so a flux dφ is available to remelt the extra thickness, in order to have again the thickness/thermal resistance adapted to the imposed heat flux from the pool
  - $d\varphi = k\Delta T\left[\frac{1}{h} - \frac{1}{h+dh}\right] \approx k\Delta T\frac{dh}{h^2} = \frac{k\Delta T dm}{\rho_{pool} h^2 S}$
- It is thus possible to estimate the characteristic remelting time:
  - $\tau \sim \frac{L.dm\prime}{d\varphi.S} = \frac{L\,\rho_{crust}\,h^2}{k\,\Delta T}$
  - Considering crust latent heat of the order of L= 300 kJ/kg, ρ= 7000 kg/m^3, h= 3.5 cm, k=1.5 W/m/K and ΔT ~ 2000 K, the characteristic time is of the order of 10 minutes.
    - Well shorter than the characteristic time of debris ejection.
    - Floating crust are thus expected to remelt faster than they are sinking into the corium pool so that their (thermal equivalent) thickness remains almost constant.

Scenario for uniform debris piling

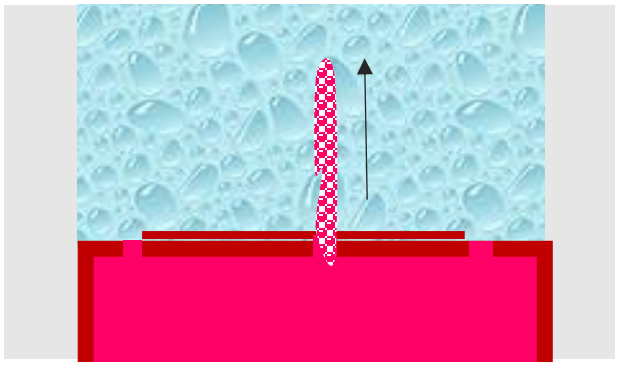

- Floating crust
- Melt eruption
- Debris are flown out of pool and quenched by the boiling water

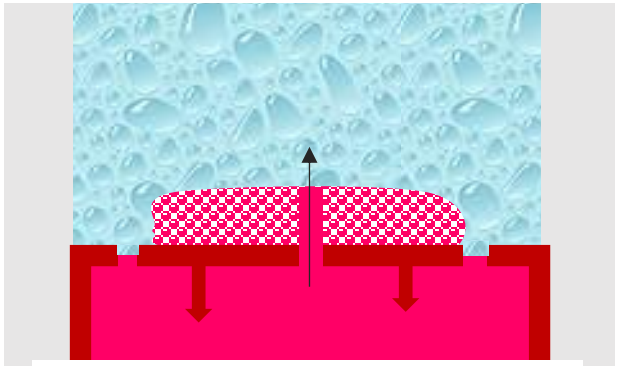

- A bed of quench particulate debris is forming above the floating crust
- Due to this extra weight, the crust progressively sinks in the molten pool

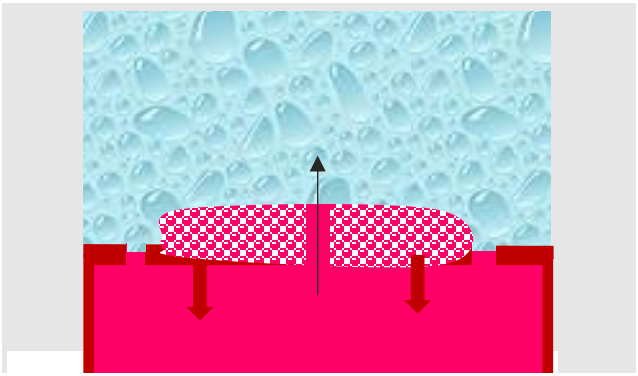

- The extra depth of submerged crust is remelted rapidly after sinking into the pool.
- The quenched debris will thus continuously remelt and reenter the molten pool.

Alternative scenario in case of non-uniform piling of particular debris

- In case of non-uniform weight distribution, the crust will not remain horizontal
  - Free particulate debris may slide/roll on the crust and fall back inside the corium pool
  - Otherwise the crust may partly remelt in an oblique geometry.
- Anyhow, as in previous scenario, after quenching in boiling water pool, the erupted debris will not remain indefinitely on the floating crust.

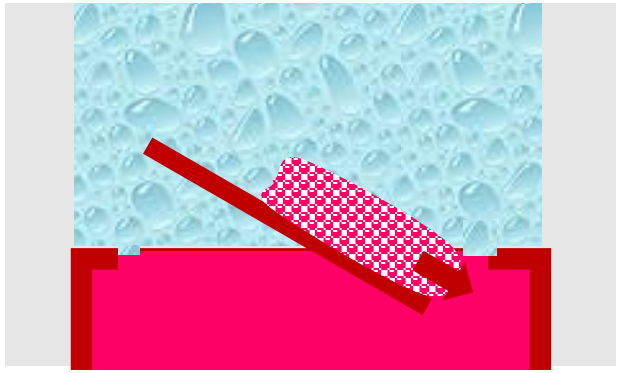

6. Conclusions

Summary - Perspectives

- Remotely-operated investigations at Fukushima Daiichi unit 1 have shown 3-4 cm thick structures that are likely to be broken solid corium crusts.
  - This has been the cause of my renewed interest in the fate of top crusts during top-flooding sequences of MCCI.
- Expected crust thickness of a few centimeters.
  - Expected to float on molten pool with typically more than 50% of crust submerged below pool surface.
- With gas-releasing concretes (e.g. limestone-rich), melt ejection above a floating crust is considered as an efficient way of cooling the MCCI melt.
- But, a floating crust will sink (or tilt) after a few tons are deposited on it.
- New scenario has been proposed in which melt eruption creates debris that are quenched and continuously remelted in the corium pool.
  - These scenarios differ from classical modelling in which the debris permanently remained cooled by the overlying water
  - More detailed modelling is now necessary to better quantify the effect of these “transient ejection” processes on the MCCI coolability, compared to the classical “permanent ejection”.

Thank you for your attention!
Any questions or comments?

CEA CADARACHE
13108 Saint-Paul-lez-Durance
France
Christophe.journeau@cea.fr
+ 33 4 42 25 70 00

The 12th European Review Meeting on Severe Accidents Research

May 18-22, 2026, Universidad Carlos III de Madrid, Madrid, Spain

TECHNICAL SESSION 3.2: SEVERE ACCIDENT SCENARIOS: SMALL MODULAR REACTORS

Chairs: M. E. Cazado (KIT), S. Brumm (JRC)

ID180	**SASPAM-SA WP5: Source Term Estimation of Generic SMR Designs** T. Hollands (GRS)	Paper Presentation
ID048	**Gas phase iodine release from iPWR pool based on MELCOR and IMPAIR calculation** M. Malicki (PSI)	Paper Presentation
ID185	**MELCOR DEC-B Transient analysis in a generic integral Pressurized Water Reactor** F. Giannetti (University of Rome 'La Sapienza')	Paper Presentation

SASPAM-SA WP5: SOURCE TERM ESTIMATION OF GENERIC SMR DESIGNS

Thorsten Hollands*
Gesellschaft für Anlagen- und Reaktorsicherheut (GRS) gGmbH
Schwertnergasse 1
50667 Köln, Germany
thorsten.hollands@grs.de

Jeremy Bittan
EDF Lab Paris-Saclay
I28 – SPC/PERICLES
7 boulevard Gaspard Monge
91120 Palaiseau, France
Jeremy.bittan@edf.fr

Fabio Giannetti
Sapienza, University of Rome
Department of Electrical and Energy Engineering (DIEE)
Nuclear Engineering Research Group (NERG)
Corso Vittorio Emanuele II, 244
00186 Rome, Italy
fabio.giannetti@uniroma1.it

ABSTRACT

Small Modular Reactors (SMR) are equipped with several especially passive safety systems to avoid severe accidents as a consequence of transients and incidents. Nevertheless, under specific initial and boundary conditions, severe accidents cannot be excluded a priori. In such cases, core degradation up to melting and relocation including fission product release possibly leading to a source term into the environment have to be taken into account.
In the frame of the EU-funded project SASPAM-SA (Safety Analyses of SMR with Passive Mitigation strategies – Severe Accident) specific severe accident scenarios were identified for two different generic SMR designs, one with a small and one with a large containment. As a consequence of the accident scenarios a specific source term can be estimated for each scenario and SMR design. Therefore, different severe accident codes like AC², ASTEC, MAAP and MELCOR were applied by several organizations. The results of the simulations are compared to evaluate the capabilities of the codes to predict a plausible accident evolution and source term estimation. Based on this comparison, representative source terms were derived for each reference scenario and SMR design, providing valuable input for the definition of emergency planning zone.

KEYWORDS
Generic SMR, Severe Accident, Source Term, Simulation Codes

1. INTRODUCTION

Small Modular Reactors (SMRs) represent a class of the innovative Nuclear Power Plants (NPP) designs to be deployed worldwide in the near future. In Europe, the technological and economical interest for SMRs has been growing in recent years. Activities are going on in several member states aiming at supporting the licensing of such systems. Among the different concepts, the Integral Pressurized Water Reactors (iPWRs) are of particular interest. They are ready to be licensed as new builds, since they integrate several evolutionary features, particularly relying in passive systems, to enhance even further the already high inherent safety. In spite of the advantageous impact of passive safety systems on the first three levels of the Defence-in-Depth (DiD) approach, a systematic a demonstration of iPWR ability to prevent and to manage Severe Accidents (SA) needs to be done (DiD levels 4-5) [1, 2].
In order to fill this gap, the HORIZON-EURATOM 'Safety Analysis of SMR with PAssive Mitigation strategies - Severe Accidents' (SASPAM-SA) project, coordinated by ENEA (Italy), was launched in 2022 and takes the contribution of 23 partners from 13 European countries [3-6]. The main objective of the SASPAM-SA project is to investigate the applicability and transfer of knowledge and know-how accumulated on the operating large-LWR reactors to the iPWRs. These activities are performed in view of European licensing needs relevant to SA and Emergency Planning Zone (EPZ) analyses. SASPAM-SA therefore aims at investigating the key elements to create a European independent point of view on the safety of iPWRs with respect to DiD levels 4 and 5 [1, 2, 3]. The expected project's outcome is to support and speed-up the licensing and siting process of iPWRs in Europe. The pillars of the SASPAM-SA project are topics not addressed in other on-going iPWR initiatives. In particular, the determination of the conditions prevailing in the Reactor Pressure Vessel (RPV) and containment under postulated SA scenarios is an essential element to support any other ongoing investigation within the project.
Two generic design-concepts are considered in SASPAM-SA. The iPWR Design-1 is characterized by a submerged containment and electric power output of ~60 MWe and the iPWR Design-2 of ~300 MWe, which employs several passive systems and a dry containment. Note that it is not the project's objective to assess the design of such concepts. One of the primary goals of SASPAM-SA is the evaluation of the capabilities of integral SA codes and Computational Fluid Dynamics (CFD) tools to simulate the key phenomena occurring in generic iPWR designs. There are differences between iPWRs and the running reactors fleet, like the tighter interaction between the different systems of iPWRs (e.g., primary, containment, and safety systems), which might question the capability of the integral codes to predict such strong thermal-hydraulic (TH) coupling. To name a few: single and two-phase natural circulation in integral RPV, thermal stratification in large pools, primary/containment coupling, in-vessel melt retention, etc. [7-10].
The SASPAM-SA results are documented in several deliverables to which this summary refers to [11]

2. GENERIC SMR DESCRIPTION

The generic iPWR Design-1 and Design-2 considered in the SASPAM-SA project are shown in Figure 1 and Figure 2 and summarized in [11]. The specifications of both designs were determined in the WP2 based on open literature and engineering judgment [7]. Such generic reactor concepts include the main iPWR design features considered in the most promising designs in the European market. Therefore, their employment in the project aims to assess more broadly the capability of codes (SA and CFD) to simulate the SA phenomena typical of iPWR.
The generic IPWR Design-1 reactor here investigated consists of a natural circulation iPWR composed of a shrouded reactor core and riser, an integrated Pressurizer (PRZ), and Helical coil Steam Generators (HSGs) within an integral RPV housed inside a steel containment. The containment is largely immersed in a large pool of water, serving as the Ultimate Heat Sink (UHS). The Emergency Core Cooling System (ECCS) in the iPWR Design-1 consists of two groups of valves allowing the coolant circulation between

RPV and containment during accident conditions: the Reactor Vent Valves (RVV) located at the top of the PRZ and Reactor Recirculation Valves (RRVs) located slightly above the active core.
The iPWR Design-2 Figure 3 is characterized by the use of several passive systems and by a dry containment. The reactor operates in forced circulation during normal operation and employs a passive mitigation strategy in accidental conditions. It consists of an integral RPV, containing the core, HSGs, primary pumps, the Control Rod Drive Mechanism (CRDM), and the PRZ. The hot water at the core outlet flows upwards in a circular riser up to the primary pumps suction located above each HSGs 4.
As mentioned above, the objective of SASPAM-SA is not the assessment of the selected generic iPWR designs. On the contrary, the goal of the project is to investigate and assess the applicability of the state-of-art computation tools to reproduce SA conditions in generic iPWRs and identify code development needs.

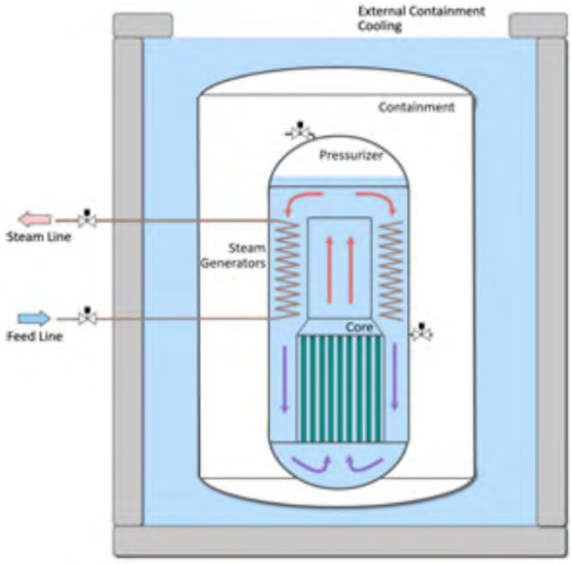

Figure 1. Design 1 layout.

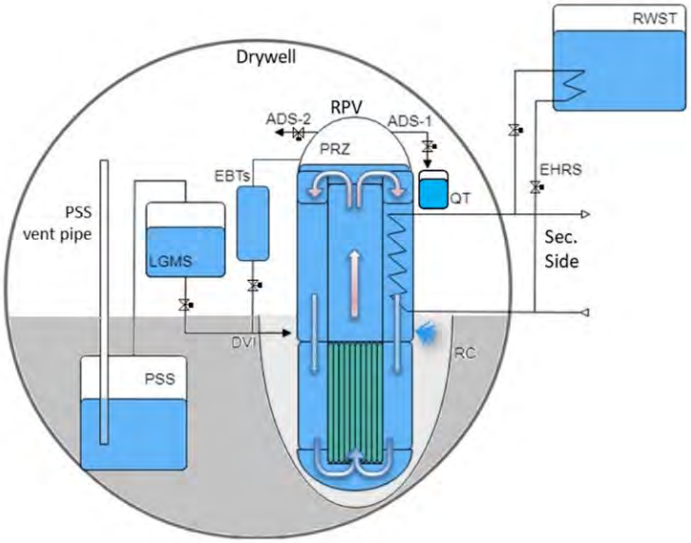

Figure 2. Design 2 layout.

3. INVESTIGATED SCENARIOS

In the following sub-chapter one scenario for each generic design will be described and the main initial and boundary conditions will be summarized.

3.1. Design 1 Scenario

A break is assumed to open at time $t_0 = 0$ s located on the Chemical and Volume Control System (CVCS) discharge line as presented in Figure 3 below.

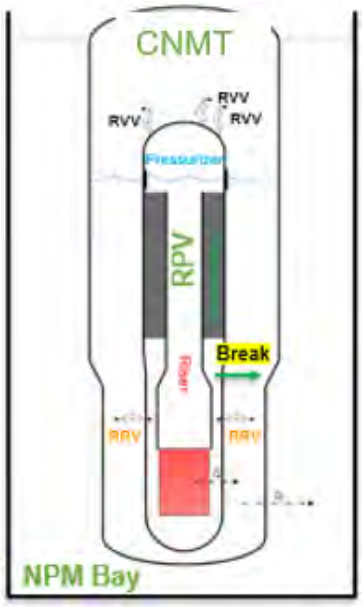

Figure 3. D1-SA1 break localization in the RCS

The break elevation is 3.5 m above the Top of Active Fuel (TAF). The break is discharging from the RCS directly into the Containment (CNMT).

The following events are assumed to happen:

- Loss of AC:
  - Loss of Feedwater (t0 + 5s – valve is open, 5s-10s valve is closing linearly),
  - Loss of CVCS (t0))
- MSIV closure (t0 + 5s – valve is open, 5s-10s valve is closing linearly)

Regarding the systems' availability and actuation:

- ECCS is activated on:
  - Pressure RPV– Pressure CNMT < 62.05 bar
  - AND CNMT Level (collapsed level in EDF MAAP5.04) >5.8 m
- 3 RVVs available (3*0.01266 m²) – Delay between threshold and signal 5s – Opening time 10s (linearly),
- 2 RRVs unavailable

Leakages

From CNMT to Reactor Building

A design leakage of $l = 0.2\%$ of volume/day is considered at P_{CNMT} = 69 bar and T_{CNMT} = 298 K. This is reasonable for this type of metallic containment.
The CNMT volume is assumed VCNMT = 200 m³. The leakage is assumed to be at the top of the CNMT above the level of water in the Reactor Building.

From Reactor Building to Environment

A break at the top of the Reactor Building (RB) is considered to allow fission products to be released into the environment. Sensitivity analyses indicate that, if the break is sufficiently large, its size does not significantly influence the magnitude of the releases to the environment.
The default considered break is 5 m².

3.2. Design 2 Scenario

The selected SA scenario is initiated by the guillotine rupture of the DVI line, along with the failure of all passive systems (Figure 4):

- EBTs,
- LGMSs,
- EHRS, and
- ADS-1.

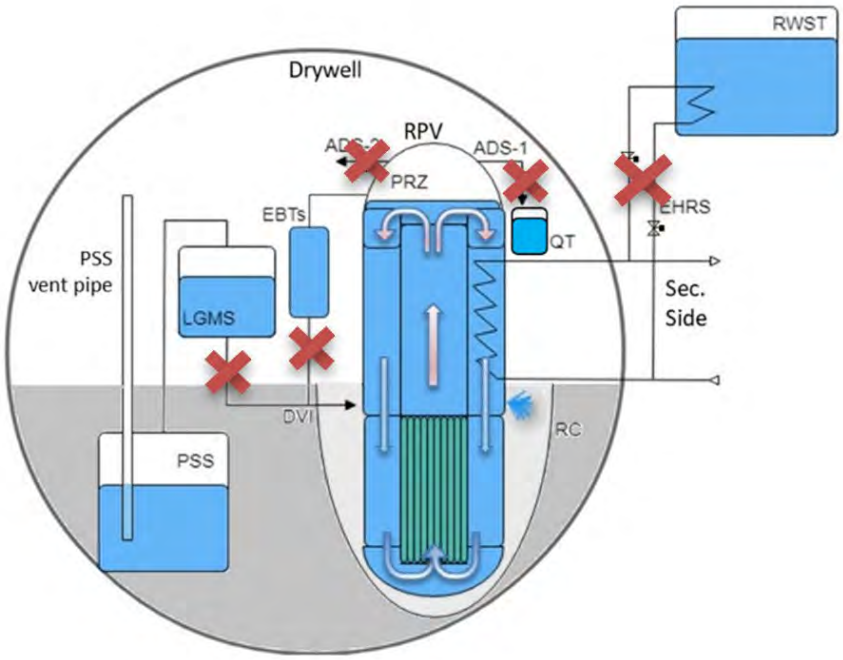

Figure 4. Schematic Scenario of Design 2.

Leakages

From DW to Environment due to design leakages
The design leakages from the containment (DW) have been modeled by "Leak" with flow area of 2.E-07 m2 (equivalent diameter of 0.504 mm) at height of 8,8885 m from the containment bottom floor. This "Leak" is modeled as an open junction with length 1.0 m.
The "Leak" has been modeled as 0.1% containment gas leaked per day at the design pressure.

From the DW Safety Valve and the Filtered Containment Venting System (FCVS) to the Environment
To avoid enormous pressure increasing in the containment it has been modeled a Safety Valve on the DW at relative elevation 10 m. The SV opens at 16 bars and closes at 8 bars. To reach the initial volumetric gas flow rate of 1.9 m^3/s, the cross-section area 0.129 m2 has been adjusted. We developed a filter system with some specific losses. As a result, the initial flow rate is around 1.9 m^3/s. The discharge loss coefficient of 0.75 is assumed. The length of the filter is 50 m.

4. Simulation Results

The progress of simulations and their analyses and evaluation differ for both designs due to complexity and variations in the systems and phenomena considered. Due to that, for design 1 core degradation as well as fission product behavior can be discussed, while for design 2 only a short comparison and evaluation for the thermal hydraulic and core degradation behavior is given.

4.1. Design 1 Results Comparison and First Evaluation

4.1.1. Core Degradation Behavior

This section provides comparison of the main phenomenological event timings obtained by the six partners (EDF, SURO, Tractebel, VTT, RUB, KIT and PSI) for the reference Severe Accident scenario. Although all partners applied the same initiating event and global boundary conditions, the results exhibit noticeable dispersion (Table I). These differences are attributed to variations in system actuation logic, nodalisation detail, code-specific modelling approaches, and assumptions regarding containment–primary coupling. Also, user experience in applying the codes can have an influence on the code performance.

Table I. Key timings – Design 1

Parameter	EDF	SURO	Tractebel	VTT	RUB	KIT	PSI
Start (t0)	0	0	0	0	0	0	0
Scram	2.9	30	3.8	3.6	–	4.3	38
RVVs opening	354	530–545	222	512	1349	297	1886
Core uncover (TAF)	6493	4555	5234	3764	–	1904	2315
H_2 onset	7949	8620	8004	7500	7057	4933	6580.32
Core completely uncovered (BAF)	20908	14190	27500	10920	–	18362	10115
First corium slump	11888	10085	27609	23671	10588	23235	8460

Vessel failure	–	–	–	–	–	-	-

4.1.2. Fission Product Release

Most of the volatile FP are released into the containment (Figure 5 and Figure 6). The overall trends are similar among partners; however, it can be observed that KIT predicts releases approximately one order of magnitude lower than the other participants.
It should also be noted that RUB and SURO report cumulative releases without accounting for radioactive decay, which may partly explain the differences in their trends.
For almost all partners, the predicted releases fall within a similar range, except for Tractebel, whose values are also around one order of magnitude lower compared to the main group.

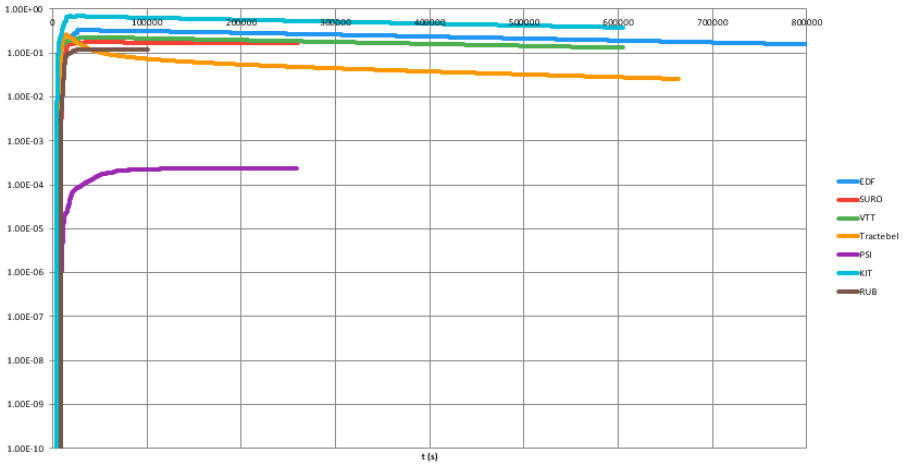

Figure 5. I131 released in Containment – Design 1.

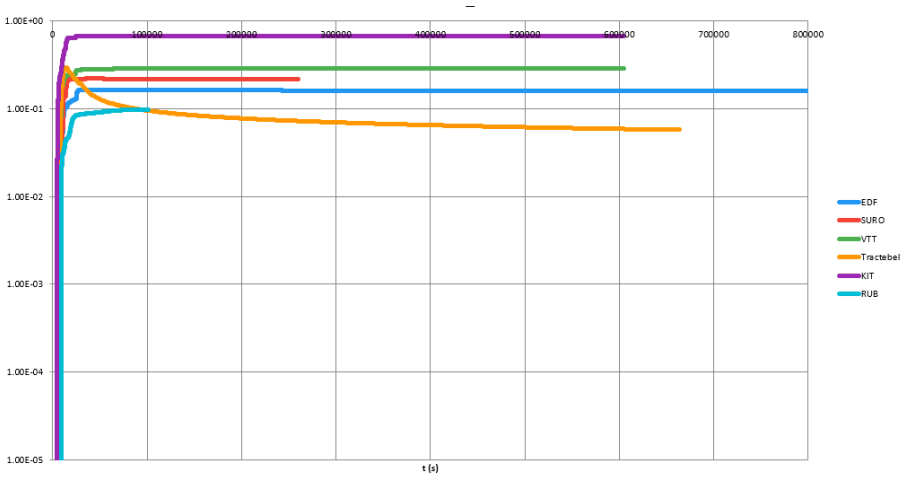

Figure 6. Cs137 released in Containment – Design 1.

Due to the very small leakage rate, the amount of fission products (FP) released to the reactor building (RB) and subsequently to the environment remains low (Figure 7 and Figure 8). For the volatile FP, most codes predict that only a few percent of the initial inventory are released to the environment. For the less volatile FP, the predicted release is on the order of 10^{-3} to 10^{-5} of the initial inventories.
It should be noted that there are significant discrepancies – sometimes several orders of magnitude – between partners regarding releases to the environment. This discrepancy did not appear for releases within

the containment. The leakage flow itself is driven by the CNMT pressure, which differs significantly between partners.

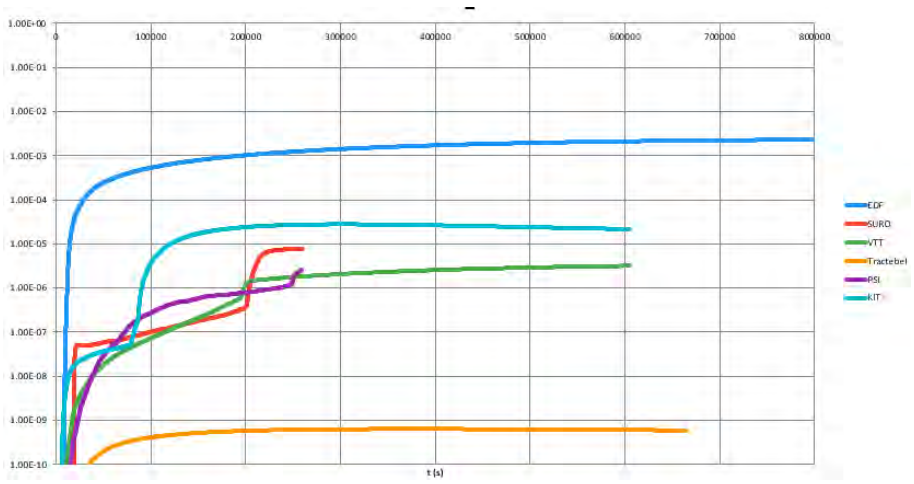

Figure 7. I131 released in Environnement – Design 1.

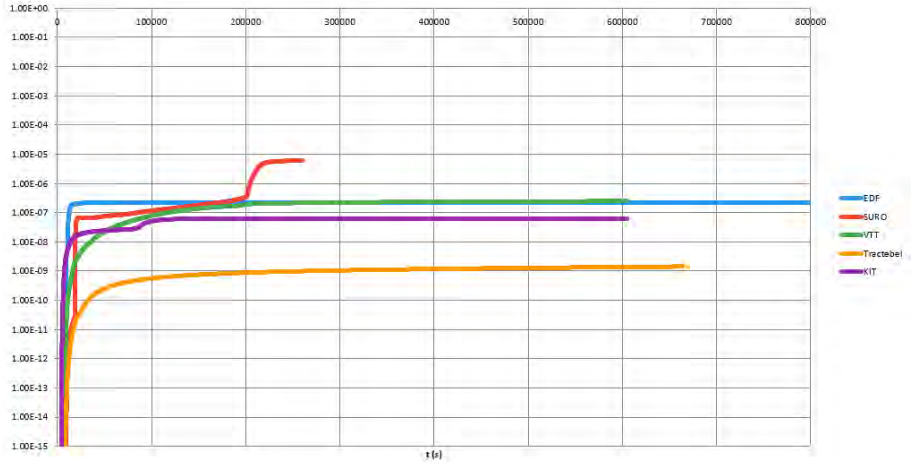

Figure 8. Cs137 released in Environnement – Design 1.

4.2. Design 2 Results Comparison and First Evaluation

The comparison of the results provided by the different partners highlights that, although some results are consistent, others exhibit significant discrepancies. The calculated RPV and containment pressure evolution (Figure 9 and Figure 10), confirming the overall alignment of the simulation approaches. However, noticeable discrepancies emerge in specific time windows, particularly during transient phases. These differences are likely related to variations in modelling assumptions, nodalization schemes, and code-specific correlations (for example the pressure's spike in primary system due to corium slump, or the peak that occurs in INRNE results at approximately 120,000). In the early phase of the transient, most partners' show a similar pressure increase rate, for containment indicating comparable initial conditions and boundary treatments. Some partners predict slightly higher peak pressures, while others exhibit a more damped response, suggesting differences in heat transfer or mass release modelling. For the maximum cladding temperature, Figure 11 shows a similar trend across all partners' calculations, with a similar heat-up phase followed by stabilization. Differences mainly appear in peak values and timing. At the end of the simulation, hydrogen production shows some variability among the partners (Figure 12), although the results remain

within the same order of magnitude, ranging approximately between 270 kg and 430 kg. An exception is observed for ENEA, whose calculation predicts significantly higher hydrogen production, reaching about 660 kg.

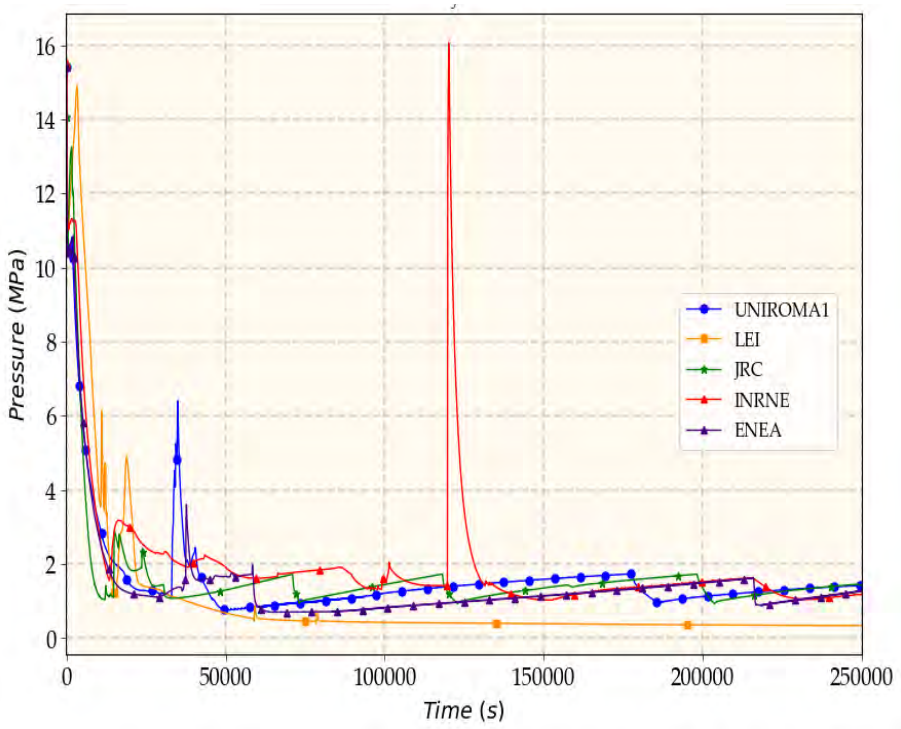

Figure 9. RPV Pressure – Design 2.

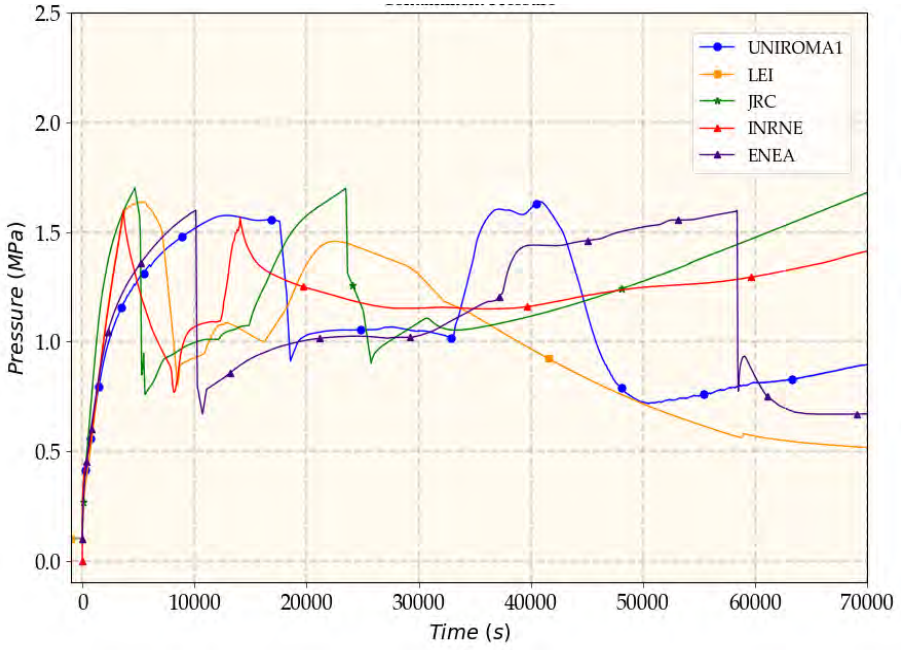

Figure 10. Containment Pressure – Design 2.

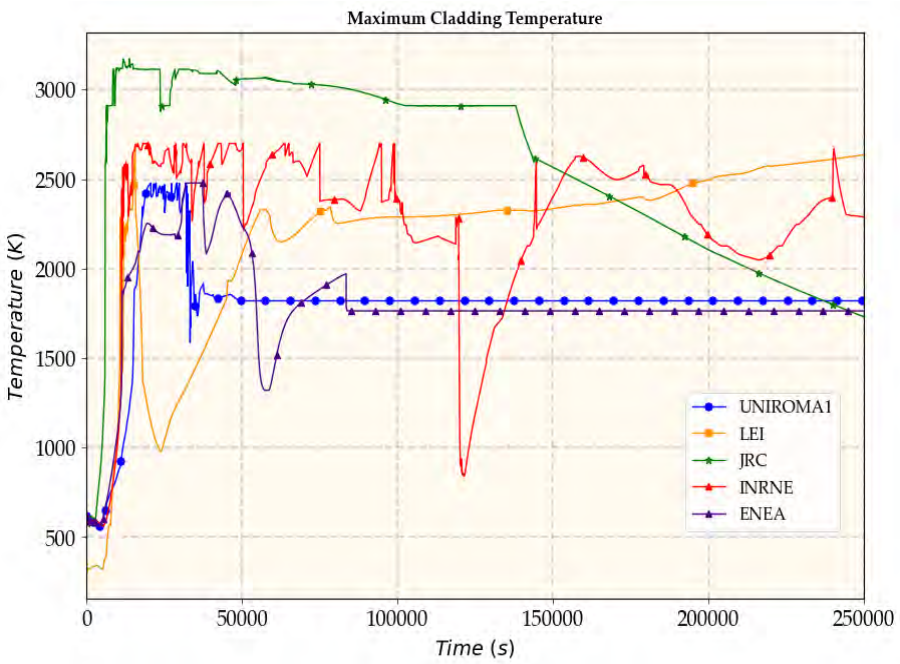

Figure 11. Maximum Cladding Temperature – Design 2.

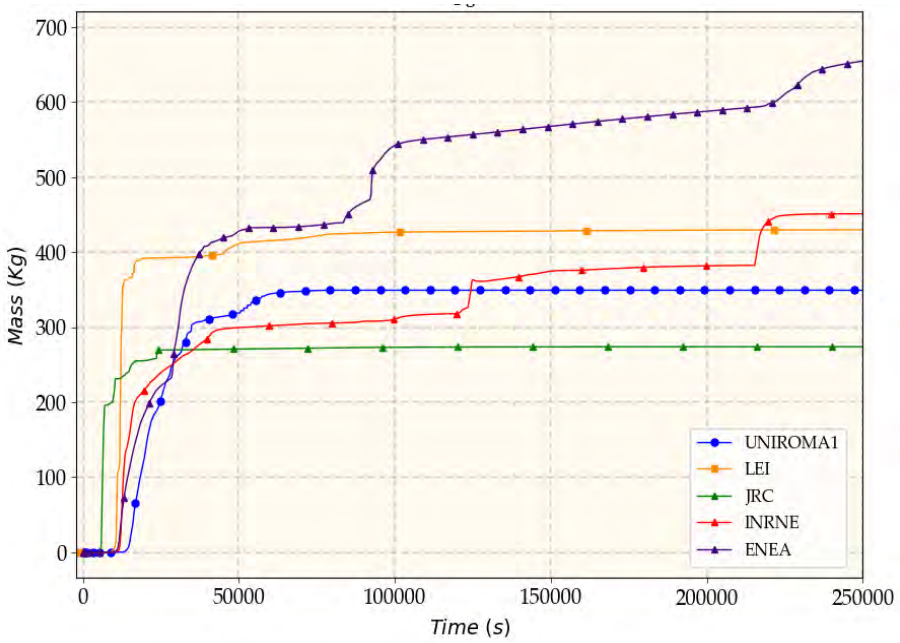

Figure 12. Hydrogen Generation – Design 2.

5. CONCLUSIONS

Design1
All partners reproduce a slow accident progression, with no vessel failure and only limited releases to the environment. Differences in predicted containment pressure and leakage modelling explain the observed variability in environmental releases. Three progression profiles clearly emerge: fast, intermediate, and slow. Overall, these results demonstrate the qualitative robustness of the simulated severe accident sequences while emphasizing the influence of modelling assumptions on quantitative outcomes. They also underscore the importance of continued efforts toward understanding and reducing inter-code differences to improve modelling consistency and enhance confidence in severe accident predictions.

Design 2
The results of the simulations show that although some results are consistent, others exhibit significant discrepancies. This can mainly be explained by different model approaches of the codes even in the core degradation and core relocation phase which has a strong impact on the containment behavior. Additionally, the detail of passive system modelling affects the containment pressure evolution and venting. Further analysis will be carried out regarding fission product behavior and source term estimation.

ACKNOWLEDGMENTS

Funded by the European Union. Views and opinions expressed are however those of the author(s) only and do not necessarily reflect those of the European Union or European Commission-Euratom. Neither the European Union nor the granting authority can be held responsible for them.

The authors thank all WP5 partners for their work and discussion as well as their contribution.

REFERENCES

1. SMR Regulators' Forum Pilot Project Report: Considering the Application of a Graded Approach, Defence-in-Depth and Emergency Planning Zone Size for Small Modular Reactors, January 2018.
2. IAEA, "Assessment of Defence in Depth for Nuclear Power Plants," SAFETY REPORTS SERIES No. 46, Vienna (2005).
3. European Commission, "Safety Analysis of SMR with PAssive Mitigation strategies - Severe Accident - SASPAM-SA Project," https://cordis.europa.eu/project/id/101059853/de, (2023).
4. https://www.saspam-sa.eu
5. https://zenodo.org/communities/saspam-sa/about
6. F. Mascari, "Safety Analysis of SMR with Passive Mitigation strategies – Severe Accident (SASPAM-SA) Horizon Euratom Project", ETSON NEWS, September 2022, https://www.etson.eu/node/290
7. IAEA, ''Natural Circulation Phenomena and Modelling for Advanced Water Cooled Reactors," IAEA-TECDOC-1677, Vienna (2012).
8. NEA/CSNI, ''Relevant thermal hydraulic aspects of advanced reactor design," Status Report, CSNI/R(1996)22, also referenced as: OCDE/GD(97)8, Paris (F) (1996).
9. OECD, "A state-of-the-art report on scaling in system thermal-hydraulics applications to nuclear reactor safety and design,'' NEA/CSNI/R(2016)14 (2017).
10. OECD, "In-vessel Code Degradation Code Validation Matrix," NEA/CSNI/R(2000)21 (2001).
11. F. Gabrielli: "Deliverable 2.2 iPWR input-deck and scenarios analyses", Safety Analysis of SMR with PAssive Mitigation strategies - Severe Accident (SASPAM-SA) (2024).

SASPAM-SA WP5: SOURCE TERM ESTIMATION OF GENERIC SMR DESIGNS

Thorsten Hollands, Jeremy Bittan, Fabio Giannetti

The 12h European Review Meeting on Severe Accident Research (ERMSAR2026)
Madrid, Spain, May 18-22, 2026

Outline

- Introduction to SASPAM-SA Project
- Generic Design Description
- Design-1
  - Investigated Scenario
  - Results
- Design-2
  - Investigated Scenario
  - Results
- Conclusion and Outlook

Introduction to SASPAM-SA Project (I)

- Small Modular Reactors (SMRs) represent a class of the innovative Nuclear Power Plants (NPP) designs to be deployed worldwide in the near future.
- In Europe, the technological and economical interest for SMRs has been growing in recent years. Activities are going on in several member states aiming at supporting the licensing of such systems.
- Among the different concepts, the Integral Pressurized Water Reactors (iPWRs) are of particular interest.
- They are ready to be licensed as new builds, since they integrate several evolutionary features, particularly relying in passive systems, to enhance even further the already high inherent safety.
- In spite of the advantageous impact of passive safety systems on the first three levels of the Defence-in-Depth (DiD) approach, a systematic a demonstration of iPWR ability to prevent and to manage Severe Accidents (SA) needs to be done (DiD levels 4-5)

Introduction to SASPAM-SA Project (II)

- In order to fill this gap, the HORIZON-EURATOM 'Safety Analysis of SMR with PAssive Mitigation strategies - Severe Accidents' (SASPAM-SA) project, coordinated by ENEA (Italy), was launched in 2022 and takes the contribution of 23 partners from 13 European countries [3-6].
- The main objective of the SASPAM-SA project is to investigate the applicability and transfer of knowledge and know-how accumulated on the operating large-LWR reactors to the iPWRs. These activities are performed in view of European licensing needs relevant to SA and Emergency Planning Zone (EPZ) analyses.
- SASPAM-SA therefore aims at investigating the key elements to create a European independent point of view on the safety of iPWRs with respect to DiD levels 4 and 5.
- The pillars of the SASPAM-SA project are topics not addressed in other on-going iPWR initiatives. In particular, the determination of the conditions prevailing in the Reactor Pressure Vessel (RPV) and containment under postulated SA scenarios is an essential element to support any other ongoing investigation within the project.

Structure of SASPAM-SA Project

- Three generic design-concepts are considered in SASPAM-SA:
  - The iPWR Design-1 is characterized by a submerged containment and electric power output of ~60 MW_e.
  - The iPWR Design-2 of ~300 MW_e, which employs several passive systems and a dry containment.
  - The BWR Design-3 of ~300 MW_e

Introduction to SASPAM-SA Project (III)

- Three generic design-concepts are considered in SASPAM-SA:
  - The iPWR Design-1 is characterized by a submerged containment and electric power output of ~60 MW_e.
  - The iPWR Design-2 of ~300 MW_e, which employs several passive systems and a dry containment.
  - The BWR Design-3 of ~300 Mw_e.

- This paper focuses only on the Designs-1 and -2 due to project progress.

- Focus of WP5 is the investigation of the containment behaviour and the source term evaluation to the environment.

Structure of SASPAM-SA Project

iPWR Design-1
Submerged containment, P~60 MWe

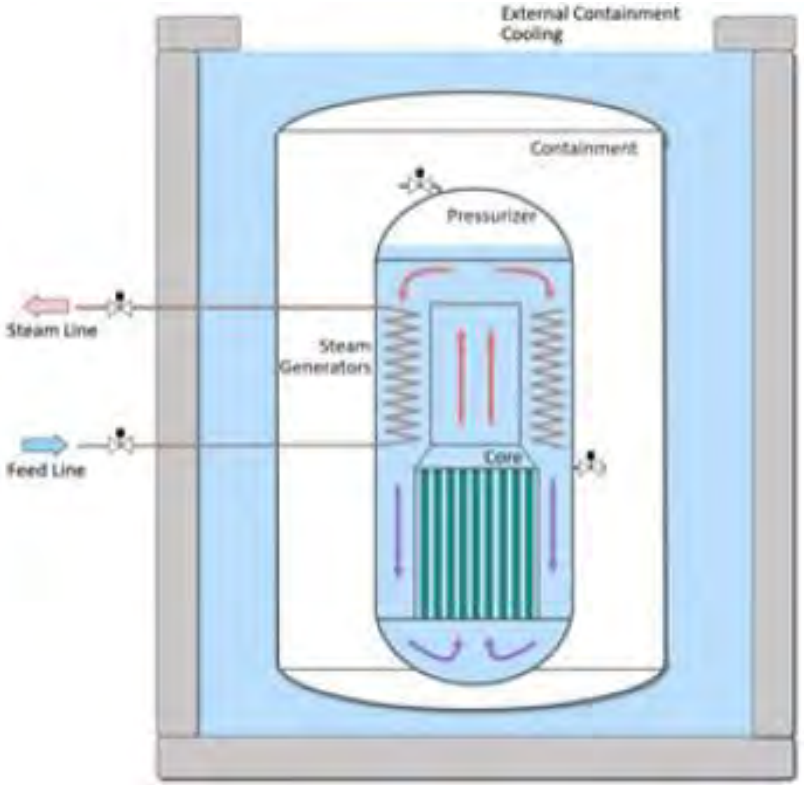

Currently generic only

Both iPWR designs **but** e.g containment safety measures differ clearly, e.g. Pressure Suppression System vs. Water Wall.

iPWR Design-2
Dry containment, several passive systems, P~300 MWe

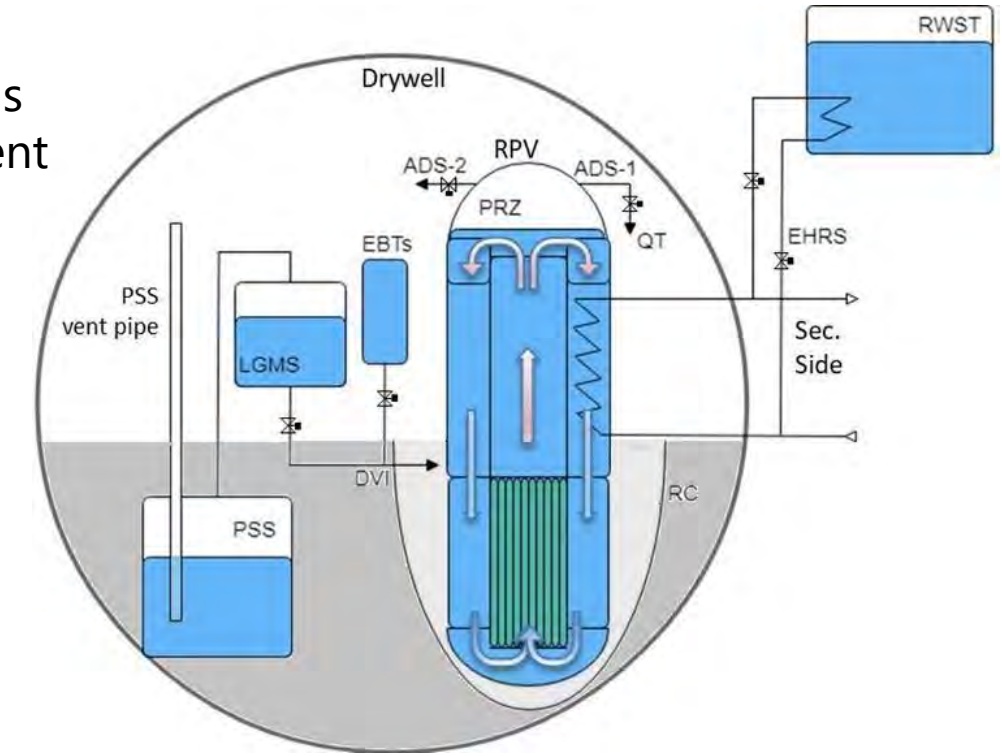

Design-1: Investigated Scenario (I)

- A break is assumed to open at time t0 = 0 s located on the Chemical and Volume Control System (CVCS) discharge line
- The break elevation is 3.5 m above the Top of Active Fuel (TAF). The break is discharging from the RCS directly into the Containment (CNMT).
- The following events are assumed to happen
  - Loss of AC
    - Loss of Feedwater (t0 + 5s – valve is open, 5s-10s valve is closing linearly),
    - Loss of CVCS (t0)
  - MSIV closure (t0 + 5s – valve is open, 5s-10s valve is closing linearly)

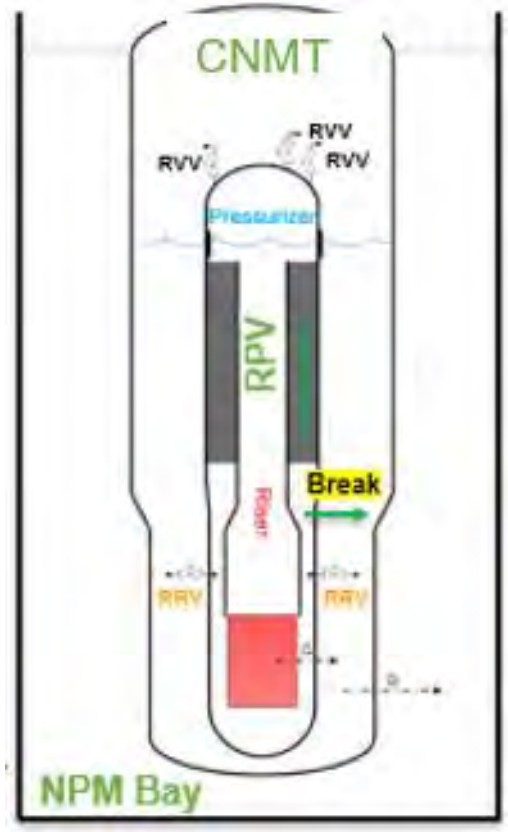

Design-1: Investigated Scenario (II)

- Regarding the systems' availability and actuation:
  - ECCS is activated on:
    - Pressure RPV– Pressure CNMT < 62.05 bar
    - AND CNMT Level (collapsed level) >5.8 m
  - 3 RVVs available (3*0.01266 m^2) – Delay between threshold and signal 5s – Opening time 10s (linearly),
  - 2 RRVs unavailable
- Leakages
  - From CNMT to Reactor Building

    A design leakage of l=0.2%" of volume/day
  - From Reactor Building to Environment

    A break at the top of the Reactor Building (RB) is considered to allow fission products to be released into the environment

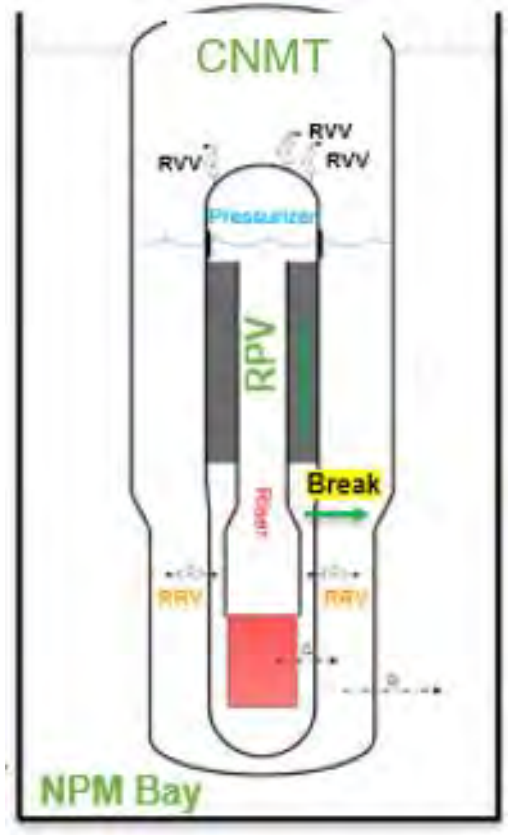

Design-1: Core Degradation Behaviour

- Main Events

Parameter	EDF MAAP	SURO MELCOR	Tractebel ASTEC	VTT MELCOR	RUB AC²	KIT ASTEC	PSI MELCOR
Start (t0)	0	0	0	0	0	0	0
Scram	2.9	30	3.8	3.6	–	4.3	38
RVVs opening	354	530–545	222	512	1349	297	1886
Core uncover (TAF)	6493	4555	5234	3764	–	1904	2315
H_2 onset	7949	8620	8004	7500	7057	4933	6580
Core completely uncovered (BAF)	20908	14190	27500	10920	–	18362	10115
First corium slump	11888	10085	27609	23671	10588	23235	8460
Vessel failure	–	–	–	–	–	-	-

Design-1: Fission Product Relative Release – I131

To Containment

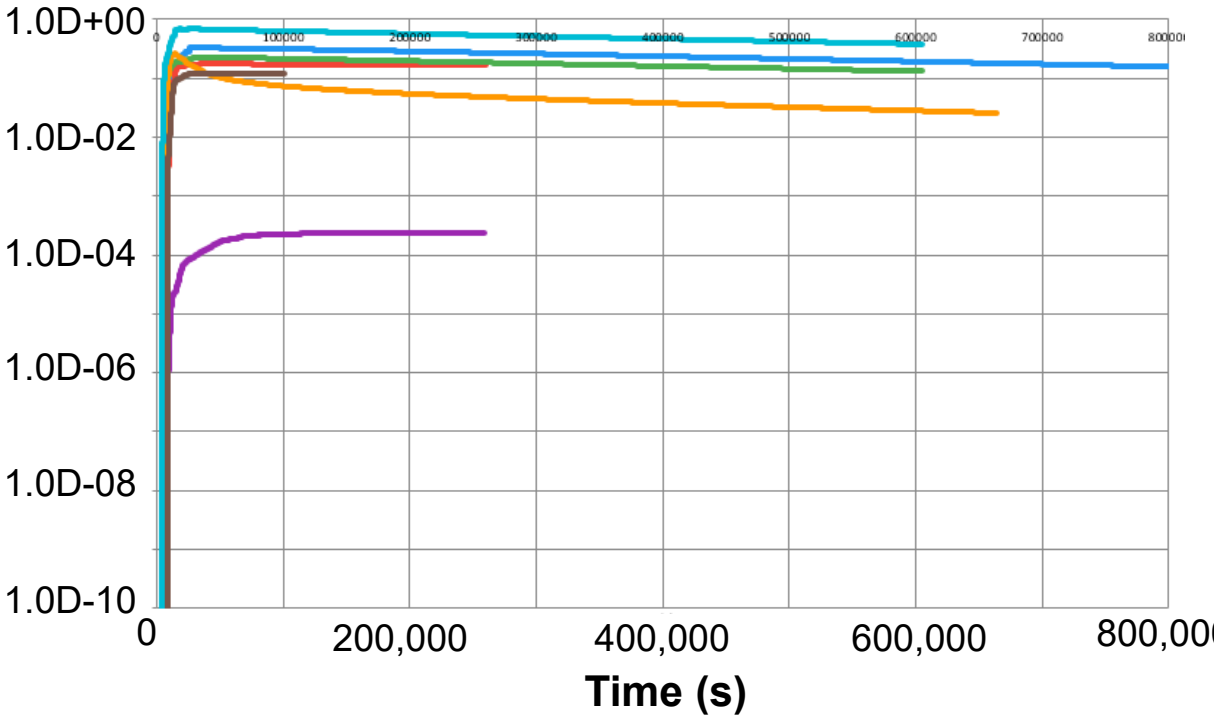

To Environment

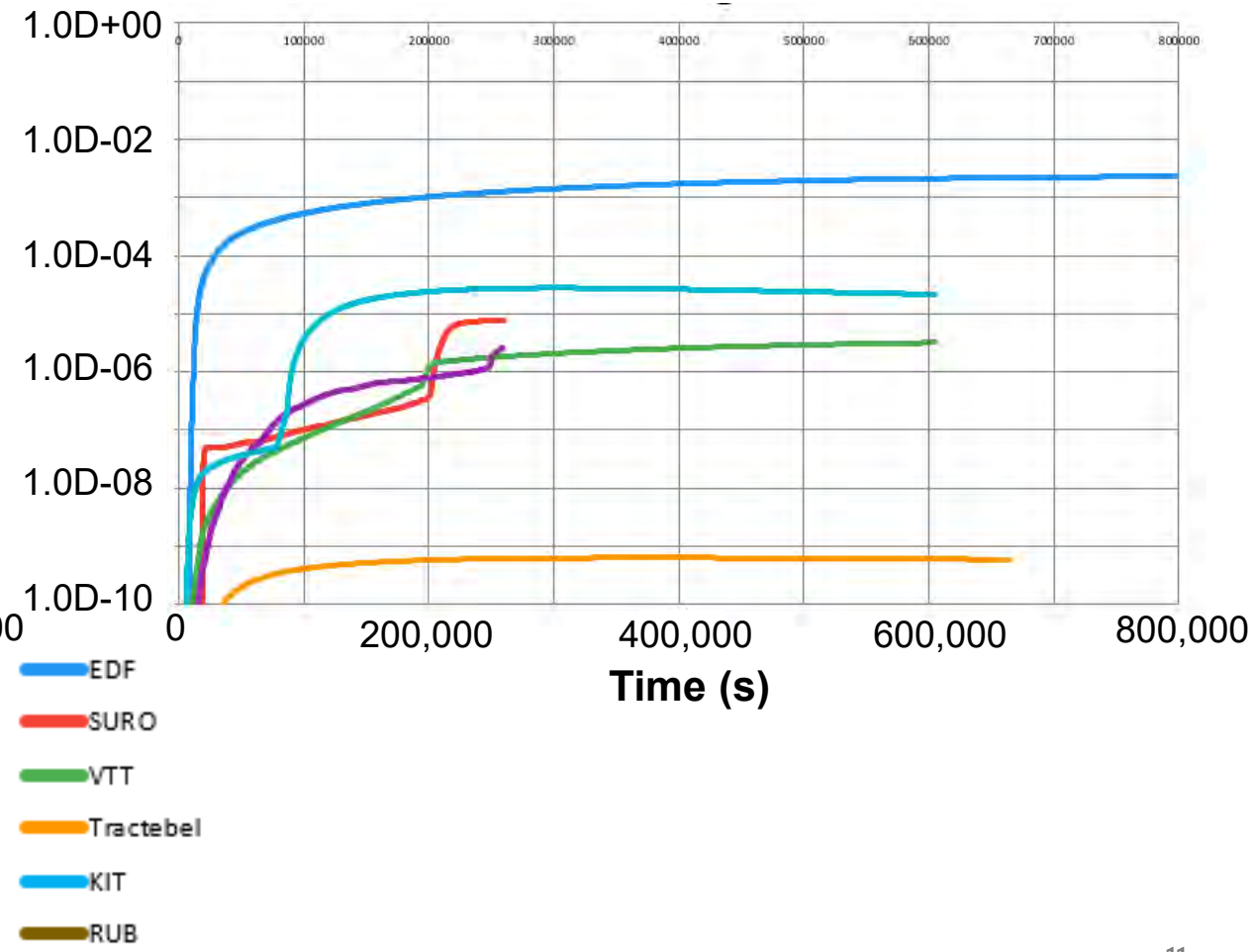

Design-1: Fission Product Relative Release – Cs137

To Containment

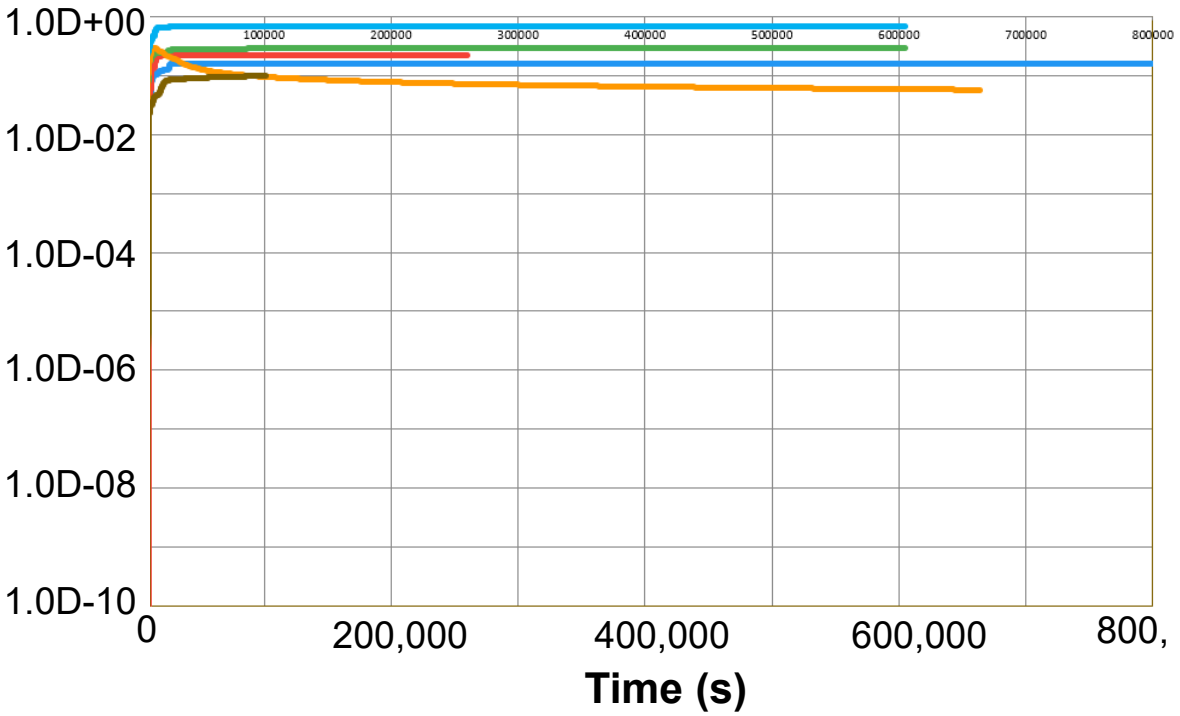

To Environment

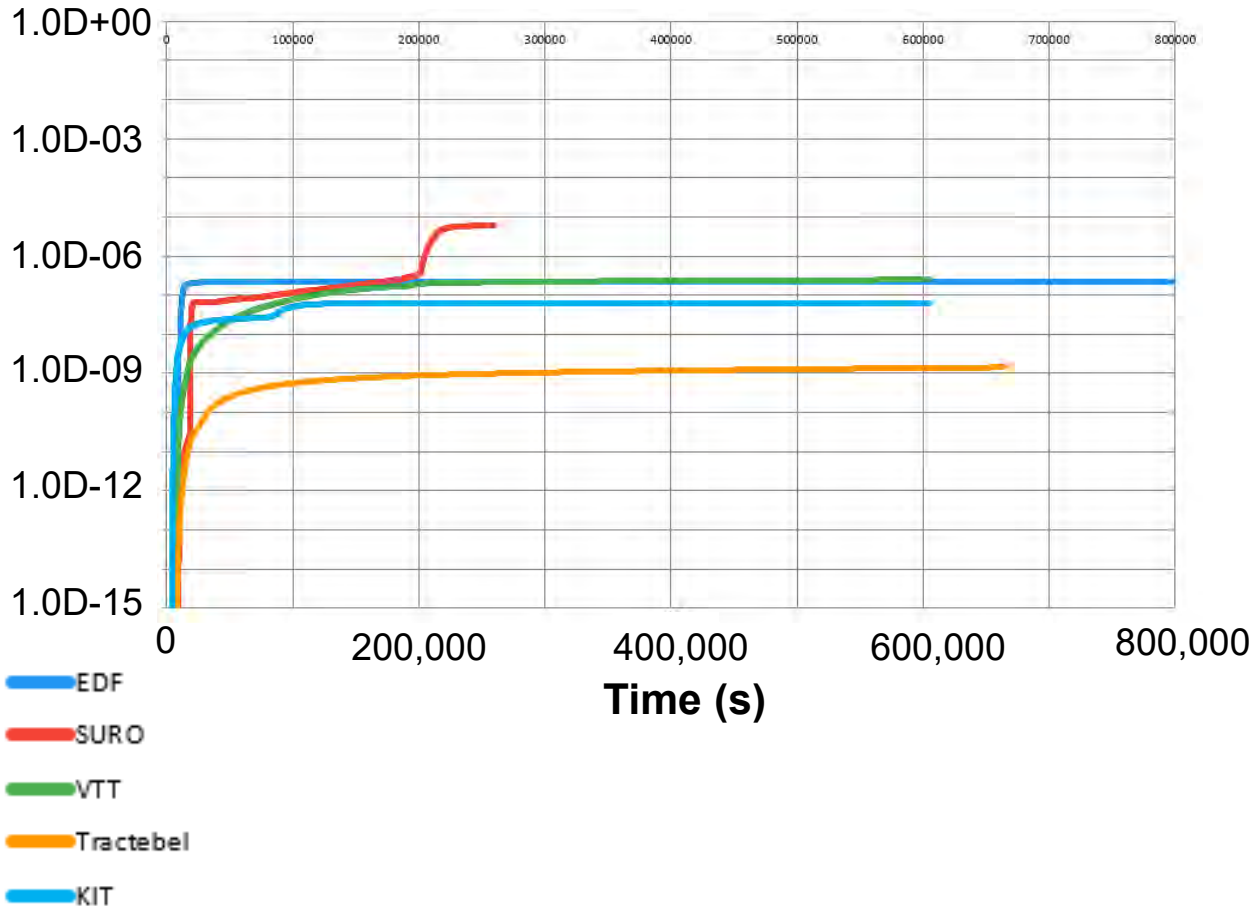

Design-2: Investigated Scenario (I)

- The selected SA scenario is initiated by the guillotine rupture of the DVI line, along with the failure of all passive systems:
  - EBTs,
  - LGMSs,
  - EHRS, and
  - ADS-1.
- Leakages
  - From DW to Environment due to design leakages
    A design leakage with flow area of 2.E-07 m^2
  - From the DW Safety Valve and the Filtered Containment Venting System (FCVS) to the Environment
    - The initial flow rate is around 1.9 m^3/s
    - The SV opens at 16 bars and closes at 8 bars

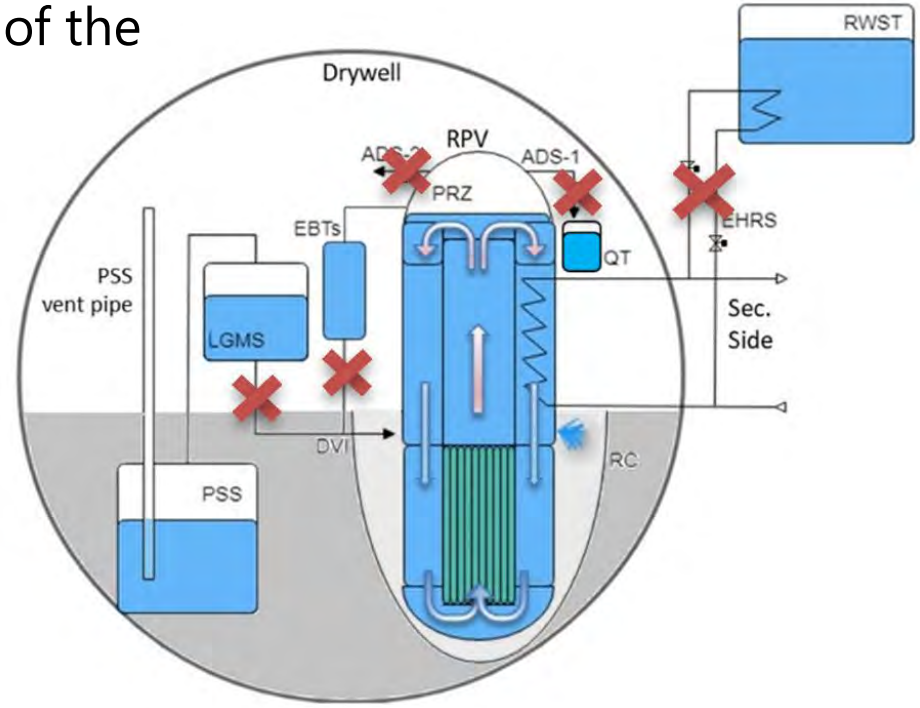

Design-2: Pressure Evolution

RPV

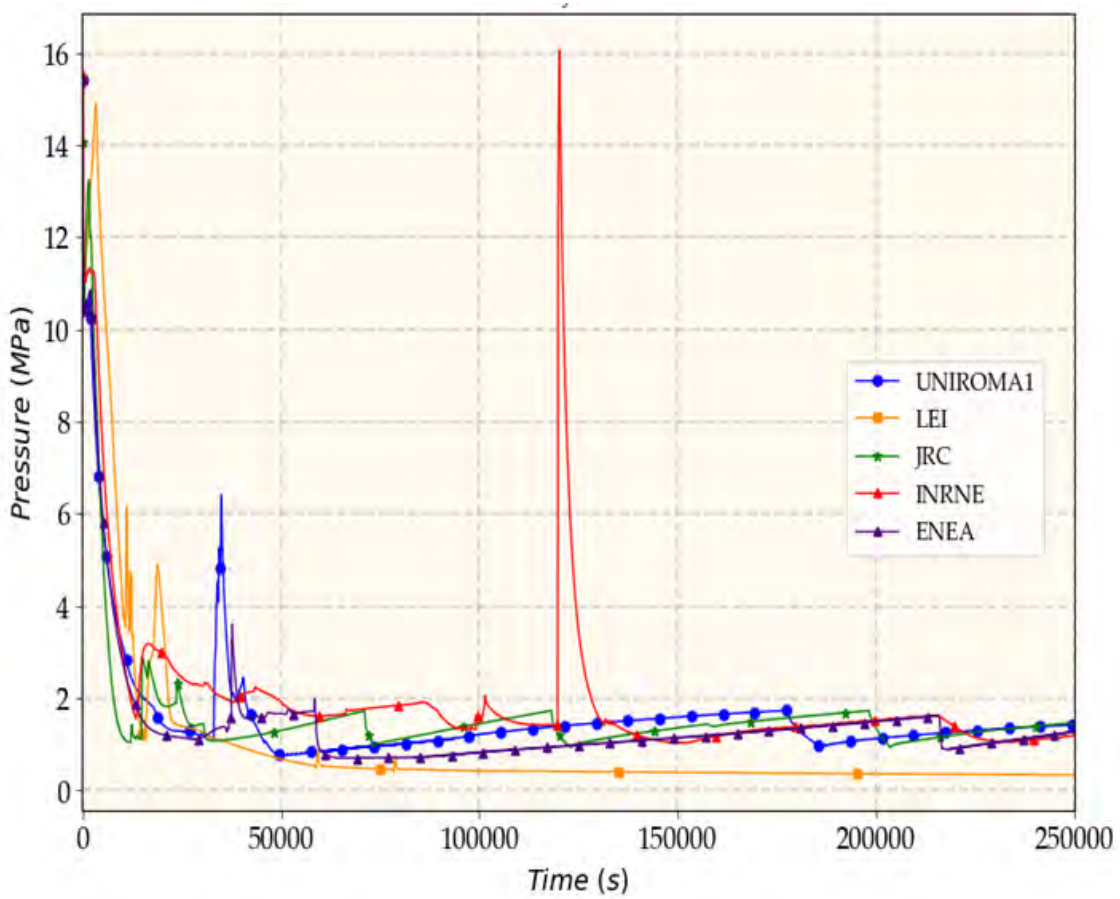

Containment

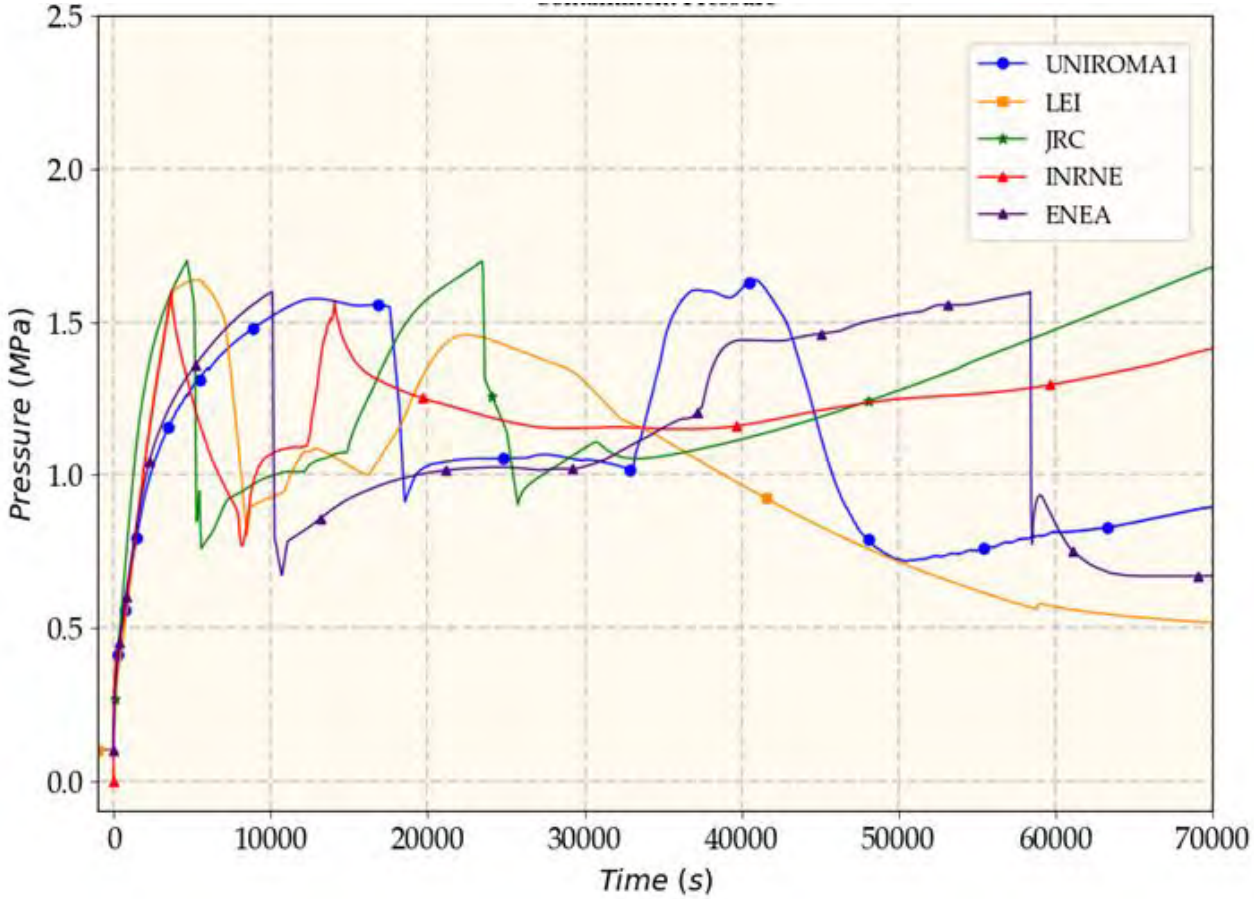

UNIROMA1	LEI	JRC	INRNE	ENEA
MELCOR	AC^2	ASTEC	ASTEC	MELCOR

Design-2: Core Degradation

Maximum PCT

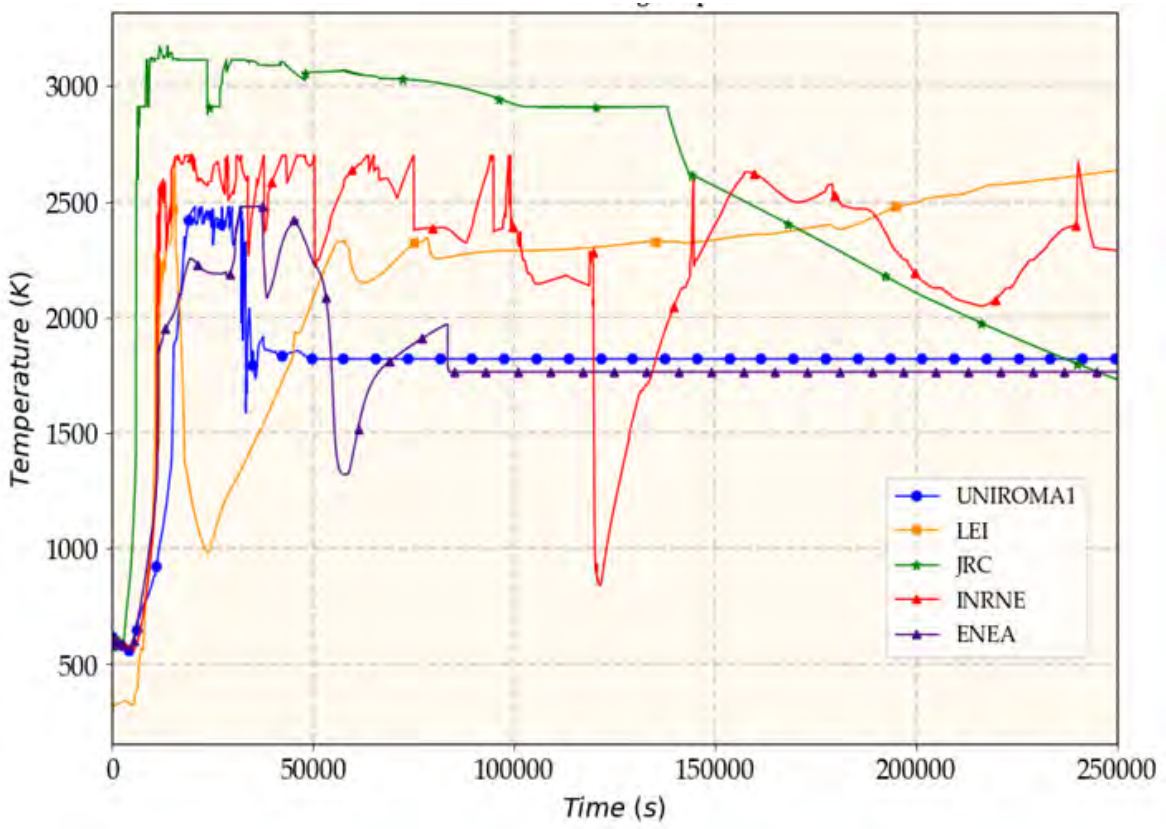

Hydrogen Generation

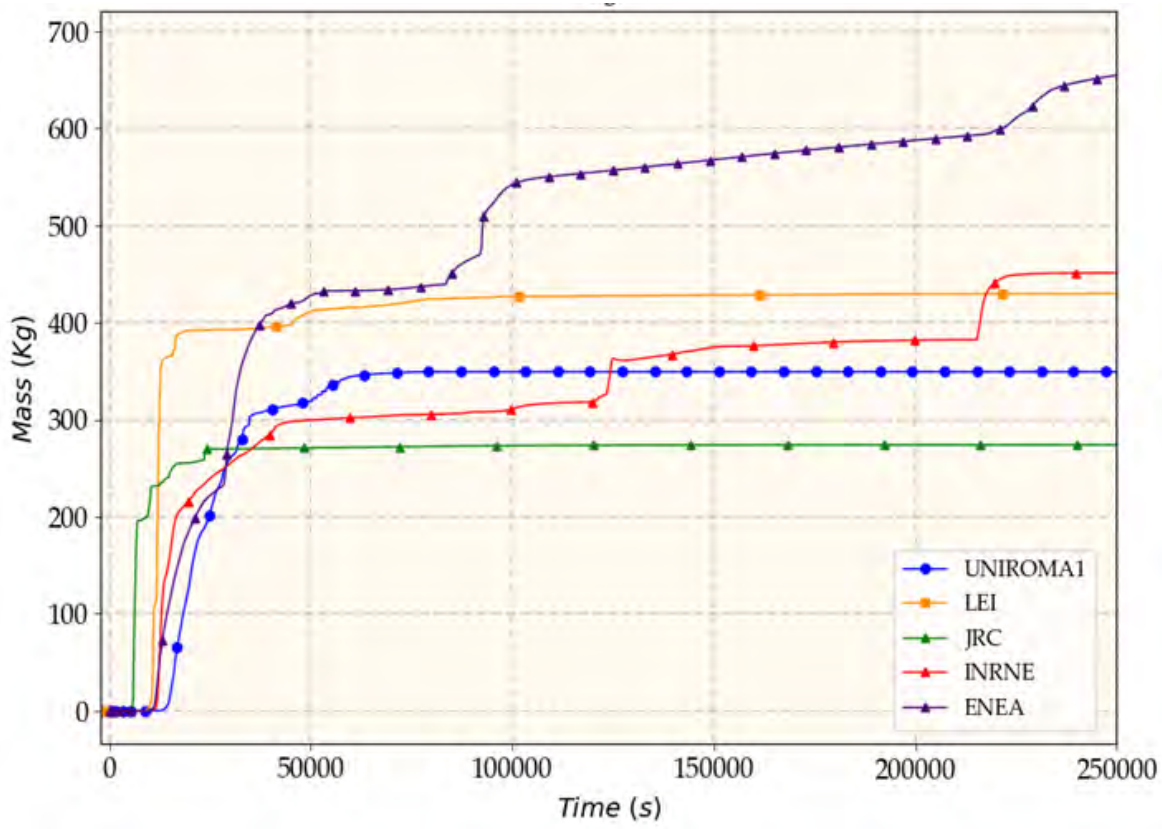

UNIROMA1	LEI	JRC	INRNE	ENEA
MELCOR	AC^2	ASTEC	ASTEC	MELCOR

Conclusion and Outlook

Design1

- All partners reproduce a slow accident progression, with no vessel failure and only limited releases to the environment. Differences in predicted containment pressure and leakage modelling explain the observed variability in environmental releases. Three progression profiles clearly emerge: fast, intermediate, and slow.
- Overall, these results demonstrate the qualitative robustness of the simulated severe accident sequences while emphasizing the influence of modelling assumptions on quantitative outcomes. They also underscore the importance of continued efforts toward understanding and reducing inter-code differences to improve modelling consistency and enhance confidence in severe accident predictions.

Design 2

- The results of the simulations show that although some results are consistent, others exhibit significant discrepancies. This can mainly be explained by different model approaches of the codes even in the core degradation and core relocation phase which has a strong impact on the containment behavior.
- Additionally, the detail of passive system modelling affects the containment pressure evolution and venting. Further analysis will be carried out regarding fission product behavior and source term estimation.

Acknowledgement/Disclaimer

SAFETY ANALYSIS OF SMR WITH PASSIVE MITIGATION STRATEGIES - SEVERE ACCIDENT

Funded by the European Union. Views and opinions expressed are however those of the author(s) only and do not necessarily reflect those of the European Union or European Commission-Euratom.

Neither the European Union nor the granting authority can be held responsible for them.

The authors thank all WP5 partners for their work and discussion as well as their contribution.

SASPAM-SA Consortium reserves all rights in this document and in the information contained therein.
Reproduction, use or disclosure to third party without express authorization is strictly prohibited.

Gas phase iodine release from iPWR pool based on MELCOR and IMPAIR calculaition

M. Malicki, T. Lind
Paul Scherrer Institute (PSI),
Forschungsstrasse 111
5232 Villigen PSI, Switzerland;
mateusz.malicki@psi.ch, terttaliisa.lind@psi.ch

ABSTRACT

The HORIZON-EURATOM SAPSAM-SA project, coordinated by ENEA (Italy), was launched in 2022 aiming at investigating the applicability and transfer of knowledge and know-how accumulated on the operating large-LWR reactors to the iPWRs, in view of the European licensing needs with respect to severe accident and Emergency Planning Zone (EPZ). Two generic iPWR concepts are considered in SASPAM-SA: the iPWR Design 1 is characterized by a submerged containment and electric power of approx. 60 MWe and the iPWR Design 2 of approx. 300 MWe, which employs several passive systems and a dry containment.
The analytical efforts by PSI were focused on Design 1. For this reactor, we investigated several DBA and severe accident scenarios. For the present work, a containment by-pass scenario was selected. In this, transport of iodine from the core to the reactor pool and subsequent potential release of gas phase iodine from the reactor pool were analysed. In the containment by-pass scenario, a break was assumed in a line below the water level of the reactor pool. Iodine concentration in the reactor pool was simulated with MELCOR, and used as an initial condition for iodine chemistry analysis using the IMPAIR code. IMPAIR accounts for formation of elemental iodine and organic iodides from iodide in water, and their subsequent release to the gas phase. In beginning of the IMPAIR calculation, all iodine in the reactor pool water was assumed in the form of iodide I-. The releases of iodine I2 and CH3I from the water to the reactor building atmosphere were analysed.

KEYWORDS
Severe accident, iPWR, MELCOR, iodine

1. INTRODUCTION

One of the key challenges in best-estimate severe accident analyses is the evaluation of the iodine source term. Due to iodine's high reactivity and complex physico-chemical behaviour during release and transport, predicting its speciation and the fraction ultimately discharged to the environment is associated with high uncertainty and remains key subject of study [1][2][3][4]. At the same time, iodine remains one of the most safety-relevant radionuclides in nuclear accidents, since it largely determines early off-site radiological consequences and directly influences emergency and mitigation measures implemented during and shortly after the accident. Under severe accident conditions, iodine released into containment/reactor pool/reactor building water may undergo complex radiation-induced chemistry. In particular, iodide can be oxidized to volatile molecular iodine (I_2) under radiolytic conditions, while the presence of organic materials may promote the formation of volatile organic iodides such as methyl iodide (CH_3I)[1]. These processes strongly affect iodine volatility, transport, and the fraction ultimately released to the environment, and therefore represent a major source of uncertainty in source term evaluation.

The SASPAM-SA project focuses on the applicability and usability of analytical methods developedfor classic Nuclear Power Plant (NPP) designs to SMRs (small modular reactors), and specifically, iPWRs (integrated pressurized water reactors) [5]. In SASPAM-SA, two designs of iPWRs are addressed, Design 1 which is characterized by a submerged containment and electric power of approx. 60 MWe and the iPWR Design 2 of approx. 300 MWe, which employs several passive systems and a dry containment. Due to unique features of iPWRs, and differences between the considered Design1 and Design2 concepts and modern Generation III/III+ reactor technologies, additional modelling approaches should be tested and assessed. One of the key distinctive features of iPWR Design1 is the presence of a Reactor Pool (RP), in which the reactor vessel is submerged. This pool may act as an Ultimate Heat Sink (UHS) and, importantly, it can also contribute to radionuclide retention if releases occur underwater. Therefore, understanding iodine behaviour in the pool is essential for realistic source term evaluation and for assessing the mitigation potential provided by this design feature.

To evaluate potential releases from a hypothetical severe accident scenario to the reactor pool, a bypass-type scenario was selected and analysed (described in the following chapters). Integral severe accident codes such as MELCOR apply a lumped-parameter approach to represent the reactor systems and containment, which enables efficient simulations but inherently limits the spatial resolution of key phenomena governing fission product transport, deposition, and resuspension. Although MELCOR includes mechanistic models for aerosol behaviour and radionuclide class transport, the prediction of iodine source term remains particularly challenging due to the complex coupling between phase transfer, water chemistry, and radiolytic reactions controlling iodine speciation and volatility [6]. As a consequence, iodine release fractions and transport predictions may remain affected by significant modelling uncertainty, especially for scenarios involving releases into water pools where, as mentioned, iodine chemistry plays a dominant role.

In this paper, the authors evaluate iodine behaviour following releases from the Reactor Coolant System (RCS) of SASPAM-SA Design 1 into the reactor pool, and subsequently through the Reactor Building (RB) towards the environment, with a particular focus on the influence of water chemistry in the pool on the overall iodine source term. To address these challenges, the European code IMPAIR was implemented to model iodine behaviour in the reactor pool, including speciation and key chemical processes similar to previous work on MELCOR and iodine behaviour [6][7]. The iodine releases are planned to be used in a follow-up work as input for atmospheric dispersion and consequence assessment using the winMACCS code. This combined, more comprehensive approach allows the pool chemistry effects to be explicitly taken into account, which is crucial for iPWR-Design1 where underwater releases and retention mechanisms may play an important role in mitigating environmental consequences.

2. MODEL AND SCENARIO DESCRIPTION

2.1. Codes

In this work two codes were applied in a sequential manner, a) MELCOR to calculate severe accident progression in iPWR (SASPAM-SA Design1), b) IMPAIR to evaluate Iodine behaviour in the reactor pool.

a) MELCOR [8][9]

MELCOR is an integral severe accident analysis code developed by Sandia National Labolatories in USA to simulate the progression of severe accidents in nuclear reactors, including thermal-hydraulic response, core degradation, reactor vessel failure, fission product release, transport, containment

behaviour. The code applies a lumped parameter approach, representing the reactor coolant system and containment as interconnected control volumes and flow paths, which enables efficient calculation of a wide range of accident scenarios. MELCOR includes models for aerosol behaviour and radionuclide class transport, however the representation of iodine chemistry and detailed pool-scrubbing mechanisms is limited, which may contribute to uncertainties in iodine speciation and source term predictions.

MELCOR input deck used in this study is adapted input deck utilized in previous SASPAM-SA work see in Figure 1 [10][11]. The iPWR is characterized by an integrated reactor pressure vessel (RPV), in which the reactor core, pressurizer, and two helicoidal steam generator loops are housed within a single vessel, eliminating the need for reactor coolant circulation pumps. The RPV is enclosed within a second pressure vessel that serves as the primary containment and is maintained under near-vacuum conditions during normal operation. The entire reactor module is located inside a reactor pool and the reactor building, providing additional passive safety features and heat removal capabilities. Main updates are added design leakage from the top of the containment pressure vessel to the reactor pool (not underwater) and updated initial inventory based on the SASPAM-SA project deliverables.

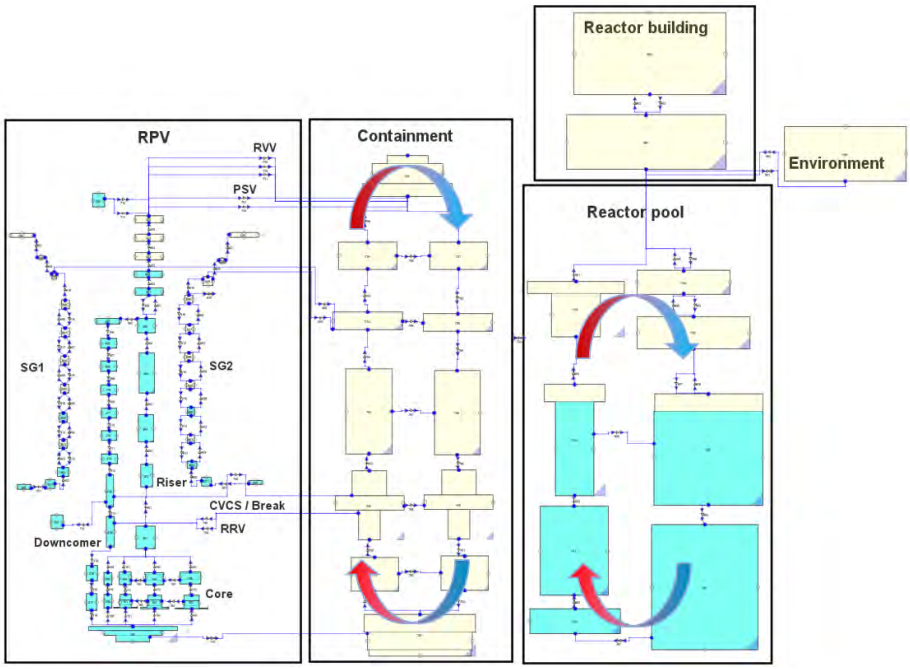

Figure 1 Schematic MELCOR nodalization of Design 1 - iPWR

b) IMPAIR [12][13]

The European iodine chemistry code Iodine Matter Partitioning And Iodine Retention (IMPAIR) is code dedicated to modelling iodine behaviour in aqueous pools under severe accident conditions, with emphasis on chemical speciation, phase partitioning, and processes governing iodine volatility [12]. Compared to MELCOR, IMPAIR allows a more mechanistic treatment of iodine transformations in water, including the influence of water chemistry and relevant reaction pathways. IMPAIR was used to calculate the release of I2 and CH3I from the reactor pool water. This code is designed to simulate iodine chemistry in a light water reactor containment under severe accident conditions, including the sump, deposition processes, and the containment atmosphere. As mentioned in [12] the model is based on 29 coupled differential equations and 69 kinetic rate constants, which describe the time dependent behaviour of multiple iodine species in both the aqueous sump and the gas phase. In addition to chemical reactions and equilibrium processes, the code accounts for key transport mechanisms such as aerosol

dynamics, mass transfer of elemental and organic iodine, and droplet carry-over during pressure relief and venting operations [12].

In this study, IMPAIR was used to evaluate iodine retention and speciation in the iPWR Reactor Pool following releases from the RCS and containment pressure vessel due to containment by-pass type scenario, providing refined source term information for subsequent transport and consequence assessment. Iodine chemistry, considering the reactions and rate constants as *given in Table I was* modeled.

Table I The iodine chemistry reactions with their rate constants and the default values used in this investigation

Gas phase wall reactions	
k_4 = 2.5E-01	Deposition velocity: I_2(g) -> I_2(dep_paint) [cm/s]
k_7 = 6.6E-06	Revolatilization of methyl iodide: I_2(dep_paint) -> CH_3I(g)
k_9 = 1.0E-04	Transfer of I^- to sump: I_2(dep_paint) -> I^-(w)
k_{53} = 2.5E-01	Deposition velocity: I_2(g) -> I_2(dep_concrete) [cm/s]
k_{54} = 6.0E-03	Transfer of I^- to sump: I_2(dep_concrete) -> I^-(w)
k_{62} = 6.0E-06	Revolatilization of I_2: I_2(dep_paint) -> I_2(g)
k_{64} = 6.0E-06	Revolatilization of I_2: I_2(dep_concrete) -> I_2(g)
Gas phase reactions	
k_{65} = 1.64E-05	Radiolytic decomposition: CH_3I(g) -> I_2(g)
Water phase reactions	
K_{11} = 3.0E0	Hydrolysis of iodine
K_{12}	Reverse reaction to k_{11}
K_{13}	Iodate formation (disproportionation)
k_{15} = 1.1E5	Iodate decomposition
k_{16} = 1.0E-07	Iodide oxidation by oxygen: I^-(w) -> I_2(w)
k_{20} = 4.0E-06	Iodide oxidation by radiolysis: I^-(w) -> I_2(w)
k_{22} = 2.5	Methyl iodide formation: I_2(w) -> CH_3I(w)
k_{24} = 3.0E-04	Radiolytic reduction: CH_3I(w) -> I_2(w)
k_{29} = 5.1E-05	Radiolytic reduction: IO_3^-(w) -> I^-(w)
k_{30} = 1.5E-07	Methyl iodide hydrolysis; H_2O
k_{32} = 5.7E-05	Methyl iodide hydrolysis: OH^- ions
k_{40} = 5.0E-01	Methyl iodide formation: HOI(w) -> CH_3I(w)
Mass transfer	
k_{35} = 1.0E-03	I_2 mass transfer at phase boundary
k_{36} = 1.0E-03	CH_3I mass transfer at phase boundary
Water phase wall reactions	
k_{17} = 5.0E-05	Deposition velocity: I_2(w) -> I_2(dep_paint) [cm/s]
k_{18} = 1.0E-07	Dissolution from immersed wall: I_2(dep_paint) -> CH_3I(w)
k_{19} = 1.0E-05	Dissolution from immersed wall: I^-(dep_paint) -> I^-(w)
k_{37} = 5.0E-05	Deposition velocity: I^-(w) -> I^-(dep_paint) [cm/s]
k_{38} = 1.0E-07	Dissolution from immersed wall: I_2(dep_paint) -> I_2(w)
k_{39} = 2.0E-05	Dissolution from immersed wall: I^-(dep_paint) -> CH_3I(w)
k_{57} = 2.0E-03	Deposition velocity: I_2(w) -> I_2(dep_concrete) [cm/s]
k_{58} = 1.0E-02	Dissolution from immersed wall: I_2(dep_concrete) -> I^-(w)
k_{69} = 1.0E-05	Dissolution from immersed wall: I_2(dep_paint) -> I^-(w)

2.2. Scenario description

The scenario implemented in MELCOR calculation is a chemical volume control system (CVCS) line break between Reactor Pressure Vessel (RPV) and reactor pool at around 7 m from the bottom of containment, which is followed by SCRAM with a partially functioning emergency core cooling system (ECCS). Only Reactor Ventilation Valves (RVV) on the top of the pressurizer were activated, which allowed some steam to condense in the containment. The break discharged the rest of the RCS coolant directly into the reactor pool. Steam condenses in the reactor pool, which heats up till saturation temperature. The reactor building filled up with steam, and as it is open to the environment (defined as

a constant control volume), exchanges the atmosphere freely. The whole scenario is calculated for 70 h.

3. RESULTS AND DISCUSSION

The accident could be divided into three phases, i) core degradation which ends with total corium relocation to the Lower Plenum (LP) at 43995 s, ii) in-vessel corium cooling when corium stays in lower plenum till 216800 s, when it is cooled by steam circulation inside RCS and outside by condensate water in the containment, and iii) vessel failure phase when corium relocates to containment pressure vessel, see Table II. After RPV failure water from the pool floods RCS and Containment.

Table II List of main events during the analysed accident scenario.

event	Time [s]	Time [h]
CVCS break	0	0.00
SCRAM	40	0.01
ECCS activation (only RVV)	514	0.14
Onset of active core uncovery	516	0.14
Onset of H2 generation	2566	0.71
Onset of fuel releases	2770	0.77
Onset of core damage	4051	1.13
Full core uncovery	531 temporar drop 4087	1.14
Onset of Core relocation to Lower Plenum	20700	5.75
RPV failure	216800	60.22
RPV and containment reflooding	239040	66.4

Seevere accident progession

In the first phase due to core uncovery and compromised cooling of RCS, core peak cladding temperature (PCT) reaches ~2500K. The core degrades entirely in less than 12.5 h (PCT drop in Figure 2). Even with the corium fully relocated to LP, one can see that vapour is extracting a significant amount of energy as the difference between inlet and outlet temperature is around 500 K until vessel failure at ~60 h when this difference decreases rapidly. The mass flow rate through the break after the flow peak at verry beginning of the transient, fluctuates during the degradation phase and the fluctuation in the circulation pattenrs cause minor back flow from pool to the RCS, see Figure 3. The natural circulation disturbance seen in Figure 4 are on the downcomer side until around 6-7 h of the transient, when the lower plenum is still under water, which blocks circulation patterns which lead to a decrease of cooling efficiency and extensive oxidation, see Figure 5. At around 6 h, corium starts to relocate to the lower plenum which cause water level in LP rapidly decreasing and opening the RCS circulation patterns. During this period, main fraction of H2 and radionuclide releases occur, see Figure 5. After ~60 h when vessel fails, rest of the water in the containment evaporates and around 66 h back flow from the pool is flooding RPV and Containment cooling down the system.

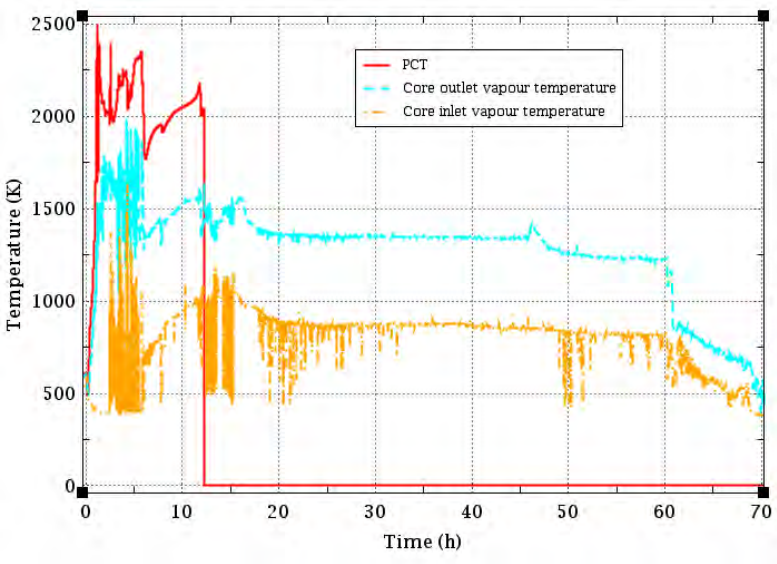

Figure 2 Temperature evolution during accident simulation, PCT, core inlet and outlet vapour temperature

This hypothetical transient was designed to provide a radionuclide source term to the reactor pool to estimate releases to the environment through the pool. The release path from RCS is a CVCS line break but besides this, there is also design leakage from containment to reactor pool (above water surface), however, as main RCS depressurization is going through the break, design leakage releases are negligible (but still added to the presented results). In this paper, the main focus is on I2 and CsI, which are modeled in MELCOR as separate classes. CsI is generated by combining I2 class and Cs class when they are released in the same core cell and timestep. In MELCOR, we can plot parameter RN1_TYCLT (Radioactive mass of a given radionuclide RN class in all control volumes of a certain type, including mass deposited on heat structures associated with the control volumes). In Figure 6, the mass of RN class 4,– I2, and RN class 16; CsI; is presented for all CVHs outside of RCS. This means it is conservatively all mass of RNs from Reactor Pool, Reactor Building and Environment. One can see that mass of I2 is extremely small as most of I2 reacted with Cs; thus it was released from the RCS as CsI. Comparing Figure 5 and Figure 6, it is clear that there is no late releases from fuel/corium but vessel failure causes additional releases to the reactor pool due to evaporation of residual water in containment and refooding of the RCS and Containment by water from the pool.

In Figure 6, the iodine released from the containment to the reactor pool as % of initial inventory (ii) is presented for I2, CsI and the total iodine. One can see that around 30% of ii is released outside of the containment pressure vessel, and the majority of those releases is done through the underwater break. In these MELCOR calculations, pool scrubbing was not turned on as the assumption was to use maximum releases for IMPAIR calculations.

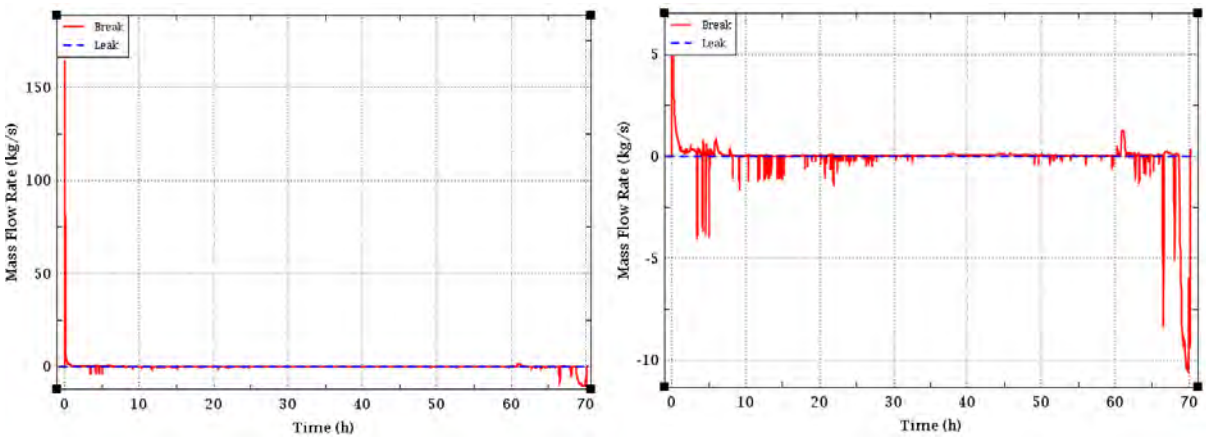

Figure 3 Mass flow rate through the break and design leackage, full scale on the left, zoom on the right.

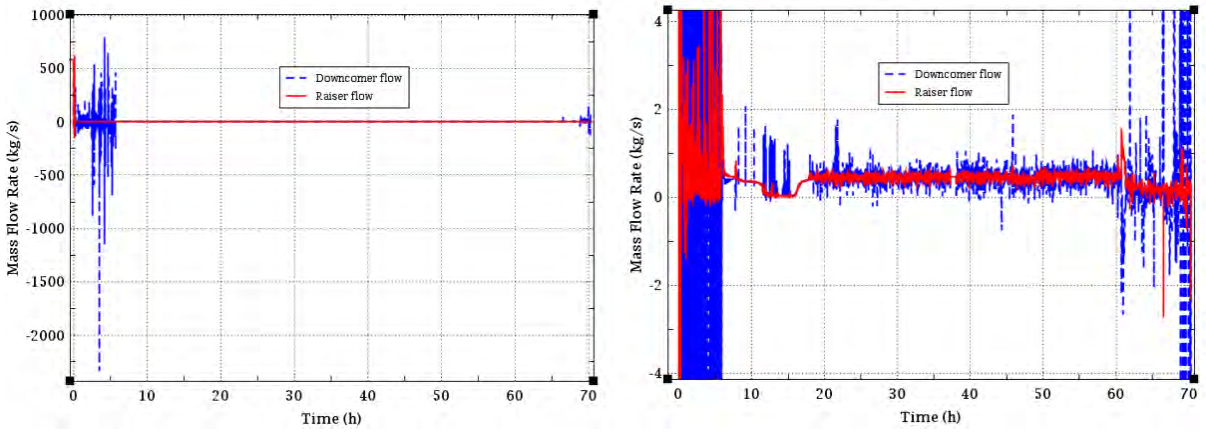

Figure 4 Mass flow rate thorught riser and downcomer (positive value - flow in design direction), full scale on the left zoom on the right.

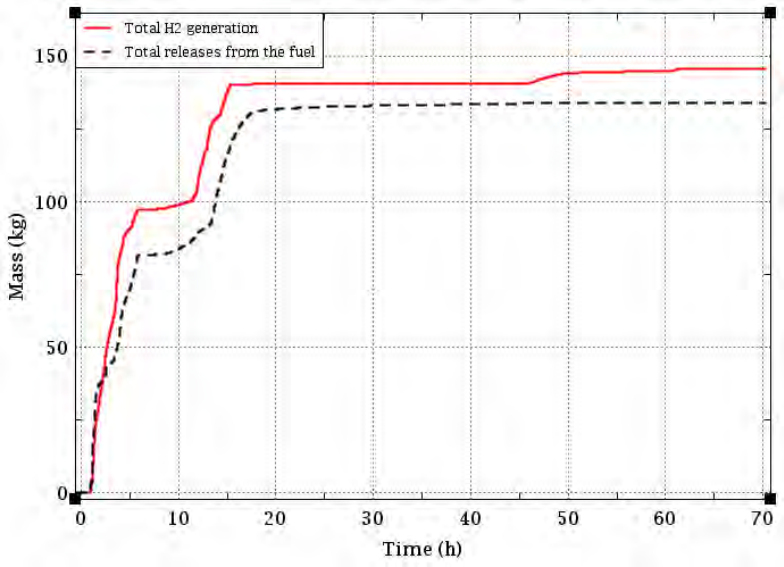

Figure 5 H_2 generation and radionuclide releases in simulated scenario.

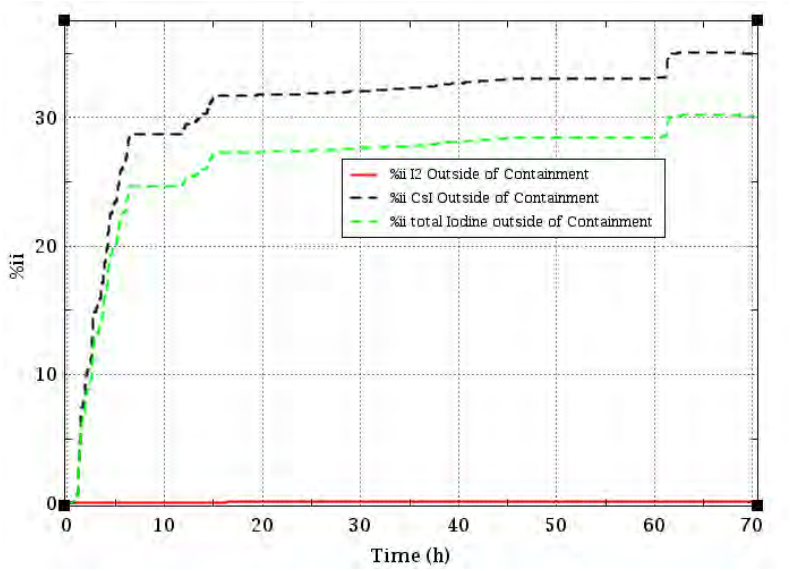

Figure 6 The % of initial inventory released from Containment for I2 and CsI and total Iodine (I2 plus I from CsI).

IMPAIR analyses

The iodine concentration in the pool water was taken from the MELCOR analysis as total iodine transported to the reator pool. The containment by-pass was assumed below the pool water level, enabling all the flow from the reactor to enter the pool. To calculate water phase reactions leading to the formation of gas phase iodine, approximately 30% of initial inventory of iodine was assumed in the pool water as shown in the above MELCOR analysis. Note that this corresponds to the total iodine mass at the end of MELCOR calculation from two RN classes, I2 and the calculated fraction of iodine from class CsI, see Figure 6 – total iodine outside of the containment. The major fraction of iodine is in the form of CsI.

Decontamination by pool scrubbing is not calculated in this first analysis, instead, all the iodine species are assumed to be scrubbed by the pool water. This assumption gives a slightly higher iodine concentration in the pool water than a best estimate using a realistic decontamination factor (DF) for iodine in the pool water which could be on the order of DF=10-100.

All iodine in the water was assumed to be in the form of iodide I- in the beginning of the calculation. This assumption is justified as the major fraction of iodine enters the pool as CsI which is soluble in water. The IMPAIR calculations were performed for 107 s (2778 hours; 114 days).

The following initial and boundary conditions were assumed:

- Water volume: 1618 m3
- Air volume: 538 m3
- Pool and air temperature T: 353 K
- Iodide in the pool water: 4.14 x 10-6 mol/l (0.30 i.i.)
- Low molecular weight organic iodides in the pool water: 1 x 10-5 mol/l
- pH = 5.0, 7.0, 9.0

- Dose rate = 3.0 kGy/h (water and air)
- Surface painted steel
- Reactor building/pool open to the environment with the leak rate of 0.0455 kg/s

The time evolution of the total gas phase iodine mass assuming pool building walls as painted steel surfaces was calculated at three pH values, 5.0, 7.0 and 9.0, Figure 7**Error! Reference source not found.**. As expected, pH had a major effect on formation of gas phase species. It is noticed that within the calculated timeframe, only a small amount of iodine is released from the pool water as gas phase species.

The main iodine species in the pool water were I- and IO3-, Figure 8. The pH dependence is observed in the rapid decrease of I- in the pool water with a low pH of 5.0 whereas with higher pH, after a rapid decrease of I- in the water, the concentration decreases only slowly, Figure 9.

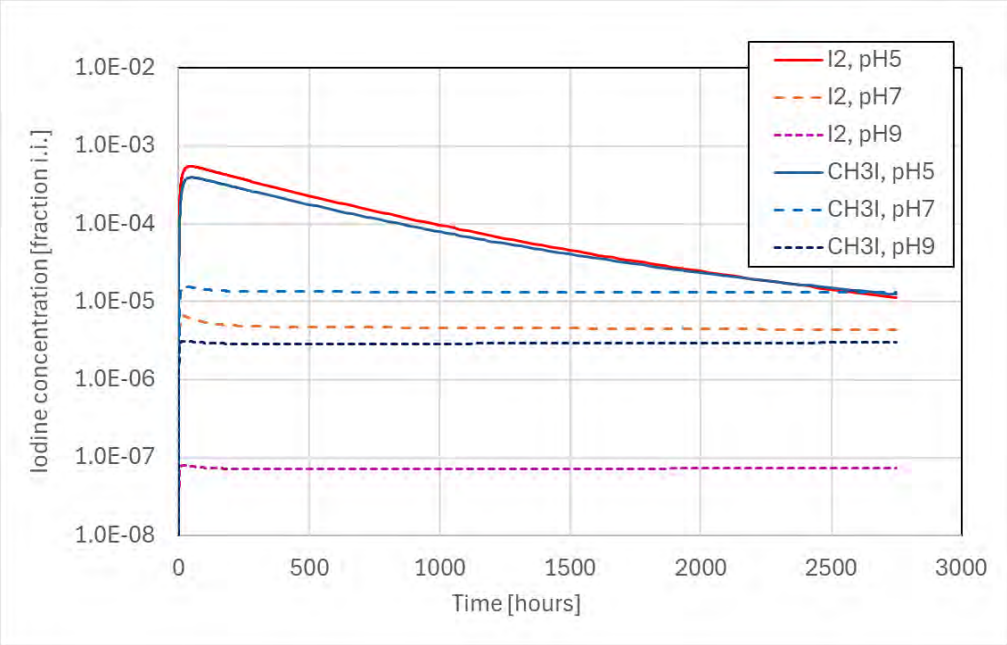

Figure 7 Evolution of Iodine concentration depends on pool pH.

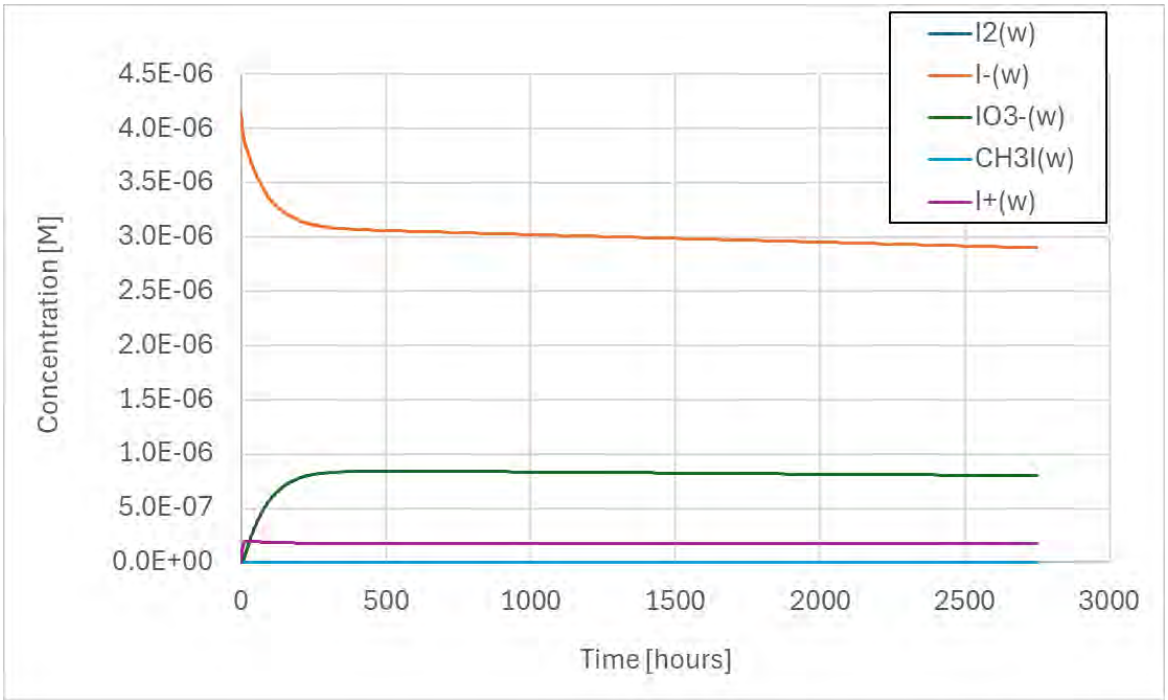

Figure 8. The main iodine species in the pool water with pH=7.0

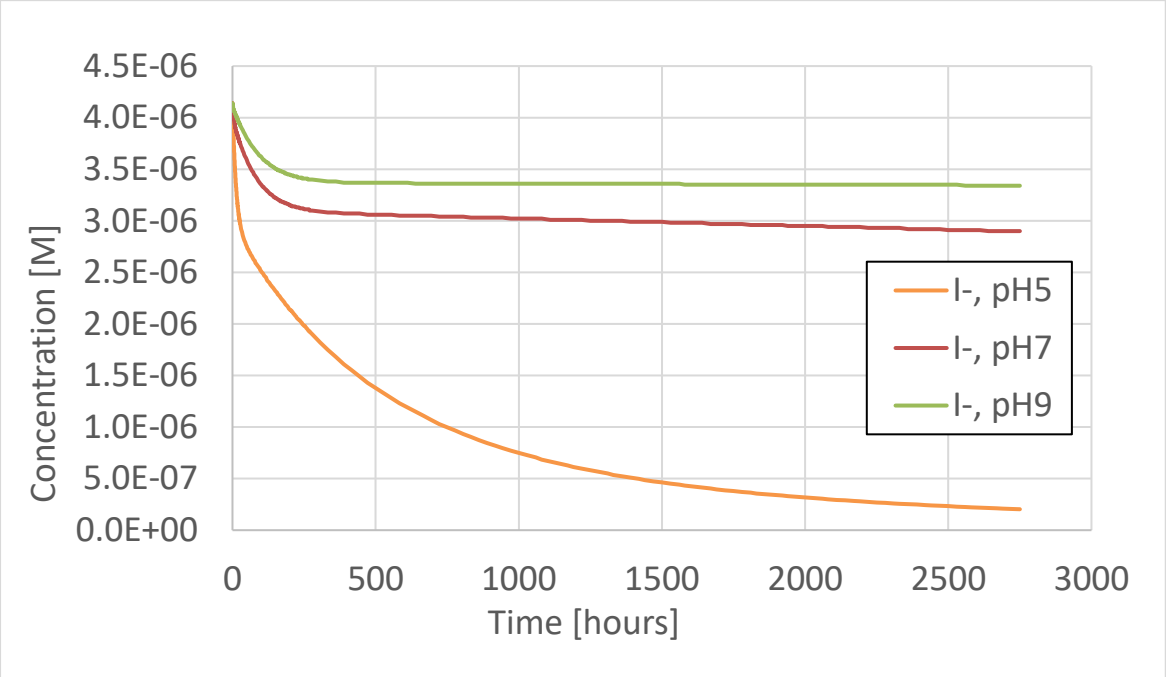

Figure 9. Time evolution of I- as the main iodine species in the pool water with pH = 5, 7 and 9

4. CONCLUSIONS

The presented analyses of a hypothetical severe accident scenario implement a bypass-type configuration in which RCS coolant is released directly into the reactor pool. The results demonstrate that MELCOR is capable of simulating this rapid accident progression and provides reasonable predictions for core degradation, in-vessel cooling, and vessel failure phases. Natural circulation within the RCS contributed to corium cooling even after core uncovery; however, due to flow blockages and unstable circulation, cooling was insufficient, ultimately leading to full core degradation and relocation

of molten material to the lower plenum. Extensive core degradation resulted in significant hydrogen and radionuclide releases, with the majority transported out of the RCS by the steam flow.

The molten pool in the lower plenum after approximately 45 h (from ~5-60h of transient) led to reactor vessel failure as a consequence of insufficient cooling caused by limited water inventory in the containment pressure vessel. Following relocation of the molten material into the containment, evaporation of the remaining condensate occurred, and after approximately 6 hours the pressure in the RCS decreased sufficiently to allow backflow from the reactor pool into the RCS. This backflow resulted in reflooding of both the RCS and the containment, effectively cooling the system.

This hypothetical scenario was used to estimate iodine releases into the reactor pool and to assess the applicability of the IMPAIR code in the evaluation of gas phase iodine release from the pool to the reactor building and the environment. In this initial analysis, all iodine released to the containment at the end of the MELCOR simulation was assumed by IMPAIR in the form of iodide (I^-) in the pool water. IMPAIR calculations were performed for three pH values (5, 7, and 9). Long-term simulations (114 days) demonstrate a strong pH dependence of iodine behaviour; however, only a small fraction of iodine was released to the gas phase within the analysed timeframe. Iodide and iodate (IO_3^-) were the dominant aqueous species, with a faster depletion of iodide observed at pH 5 compared to neutral and alkaline conditions.

ACKNOWLEDGMENTS & DISCLAIMER

Funded by the European Union

Funded by the European Union. Views and opinions expressed are however those of the author(s) only and do not necessarily reflect those of the European Union or European Commission-Euratom. Neither the European Union nor the granting authority can be held responsible for them.

Project funded by

Schweizerische Eidgenossenschaft
Confédération suisse
Confederazione Svizzera
Confederaziun svizra

Swiss Confederation

Federal Department of Economic Affairs, Education and Research EAER
State Secretariat for Education, Research and Innovation SERI

This work has received funding from the Swiss State Secretariat for Education, Research and Innovation (SERI)

Credit authorship contribution statement

M. Malicki: Methodology, Calculations, Investigation, Data curation, Writing - original draft, Visualization, Validation, T. Lind: Supervision, Writing - review & editing.

Declaration of competing interest

The authors declare that they have no known competing financial interests or personal relationships that could have appeared to influence the work reported in this paper.

Disclaimer

Described work was done as a generic scientific investigation to understand better iPWR modeling and simulation challenges related with severe accidents in such designs. It can not be used as a particular design analysis, and it should not be connected to any specific product or technical solution.

A Artificial intelligence was used to improve language correctness and clarity of the message.

REFERENCES

[1] N. Girault, L. Bosland, S. Dickinson, F. Funke, S. Güntay, L.E. Herranz, D. Powers, LWR severe accident simulation: "Iodine behaviour in FPT2 experiment and advances on containment iodine chemistry", *Nuclear Engineering and Design*, **Volume 243**, 2012, Pages 371-392, ISSN 0029-5493, https://doi.org/10.1016/j.nucengdes.2011.11.011

[2] Han-Chul Kim, Yeong-Hun Cho, Raim – "A model for iodine behavior in containment under severe accident condition", *Nuclear Engineering and Technology*, **Volume 47**, Issue 7, 2015, Pages 827-837, ISSN 1738-5733, https://doi.org/10.1016/j.net.2015.06.016

[3] G. Zablackaite, H. Shiotsu, K. Kido, T. Sugiyama, "An analytical model to decompose mass transfer and chemical process contributions to molecular iodine release from aqueous phase under severe accident conditions", *Nuclear Engineering and Technology*, **Volume 56**, Issue 2, 2024, Pages 536-545, ISSN 1738-5733, https://doi.org/10.1016/j.net.2023.10.030

[4] Nuclear energy agency committee on the safety of nuclear installations, "State of the art report on iodine chemistry", 2007, https://www.oecd-nea.org/upload/docs/application/pdf/2021-03/csni-r2007-1.pdf

[5] F. Mascari, "Safety Analysis of SMR with Passive Mitigation strategies – Severe Accident (SASPAM-SA) " Horizon Euratom Project, ETSON NEWS, September 2022, https://www.etson.eu/node/290 (accessed 21 January 2026)

[6] L. Fernandez-Moguel, A. Rydl, T. Lind, "Updated analysis of Fukushima Unit 3 with MELCOR 2.1. Part 2: Fission product release and transport analysis", *Annals of Nuclear Energy*, **Volume 130**, 2019, Pages 93-106, ISSN 0306-4549, https://doi.org/10.1016/j.anucene.2019.02.017

[7] J. Kalilainen, T. Lind, "Uncertainty quantification study on gas phase iodine release from Fukushima Daiichi accident in unit 3", *Annals of Nuclear Energy*, **Volume 166**, 2022, ISSN 0306-4549, https://doi.org/10.1016/j.anucene.2021.108740

[8] L. Humpries, R.L O. Gauntt, "MELCOR 2.2 severe accident analysis code – current status and plans for future", SAND2018-0310C,

[9] IAEA-TECDOC-1872, "Status and Evaluation of Severe Accident Simulation Codes for Water Cooled Reactors", 2019, ISBN 978-92-0-102919-5

[10] M. Malicki, T. Lind, "MELCOR 2.2 iPWR LOCA type accident analysis, PART I: Thermal-hydraulics", *Nuclear Engineering and Design*, **Volume 428**, 2024, 113433, ISSN 0029-5493, https://doi.org/10.1016/j.nucengdes.2024.113433

[11] M. Malicki, T. Lind, "MELCOR 2.2 iPWR LOCA type accident analysis, PART II: BDBA", *Nuclear Engineering and Design*, **Volume 430**, 2024, 113667, ISSN 0029-5493, https://doi.org/10.1016/j.nucengdes.2024.113667

[12] Cripps, R., Furrer, M., Hellman, S., Funke, F., "User's Handbook for the Iodine Severe Accident Behavior Code IMPAIR 2 2", PSI Report 114 (1992), ISSN 1019-0643.

[13] Guentay, S., and R. Cripps. "IMPAIR/3: A Computer Program to Analyze the Iodine Behaviour in Multi-compartments of a LWR Containment", September 1992

PSI Center for Nuclear Engineering and Sciences

Gas phase iodine release from iPWR pool based on MELCOR and IMPAIR calculations

The 12th European Review Meeting on Severe Accident Research Conference (ERMSAR 2026)

Madrid, Spain
18th – 22nd May, 2026

Mateusz MALICKI , Terttaliisa Lind : Paul Scherrer Institute
Madrid, 18 May 2026

SASPAM-SA - Design 1

- Main objective of this task was to evaluate relases from iPWR to asses potential EPZ.
- To do so, we needed to assume hipotetical bypass accident.
  - Releases directelly to the reactor pool.
  - All iodine transportet to the water

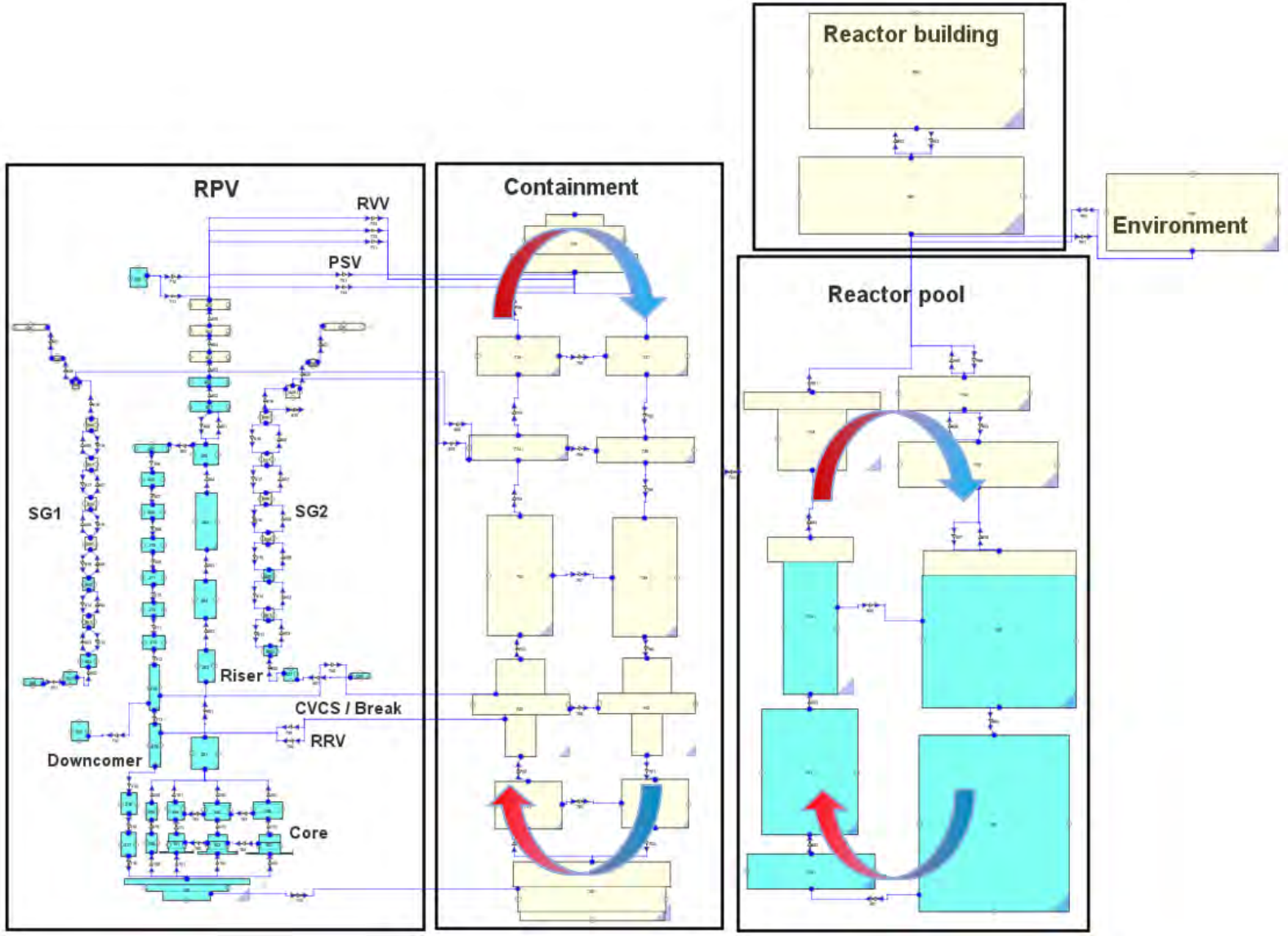

SASPAM-SA - Design 1

- Design 1 – iPWR:
  - Integral design
  - Passive safety systems
  - Submerged containment vessel
- Scenario – SBLOCA:

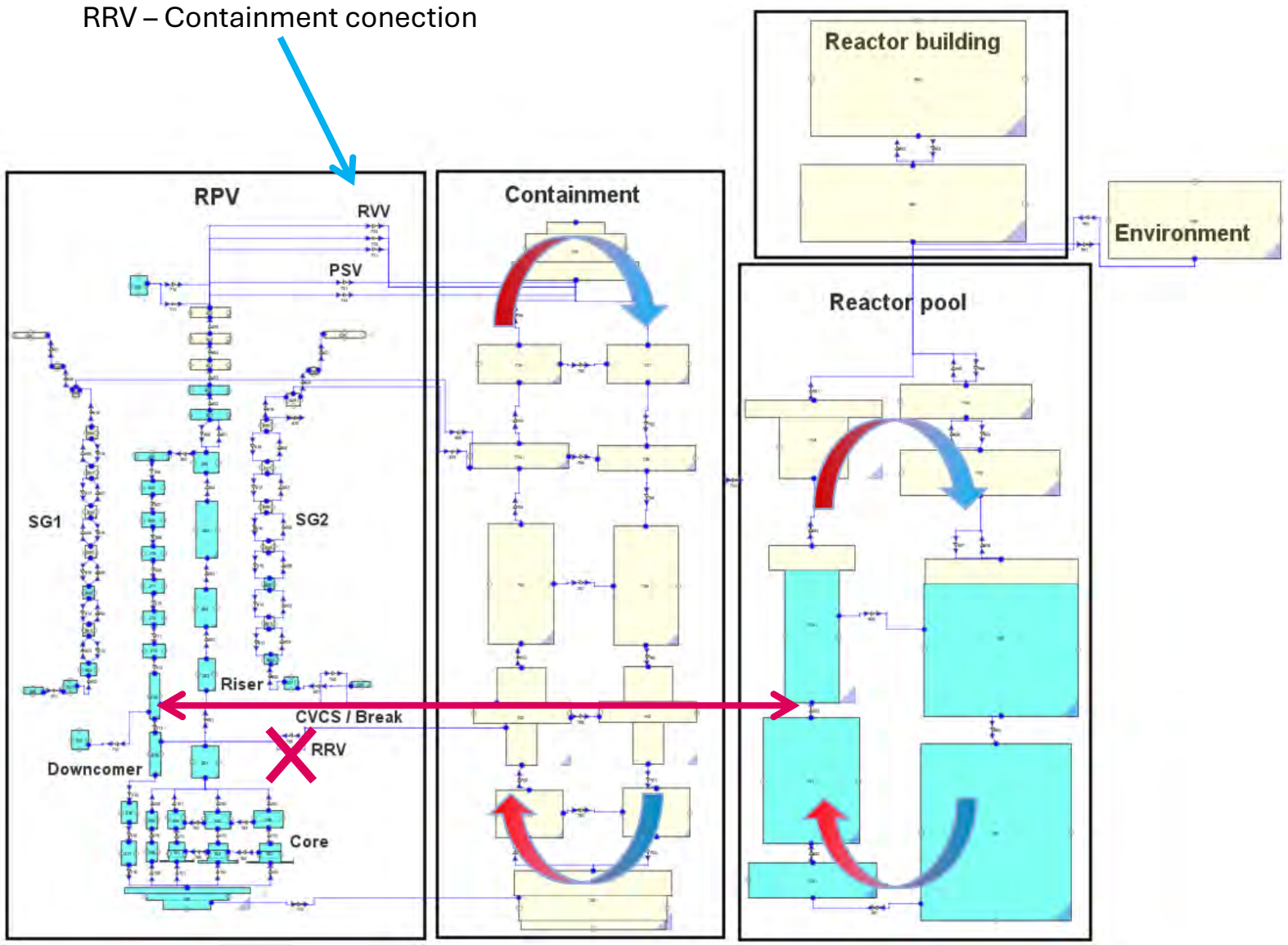

SASPAM-SA Design 1 bypass type scenario simulation

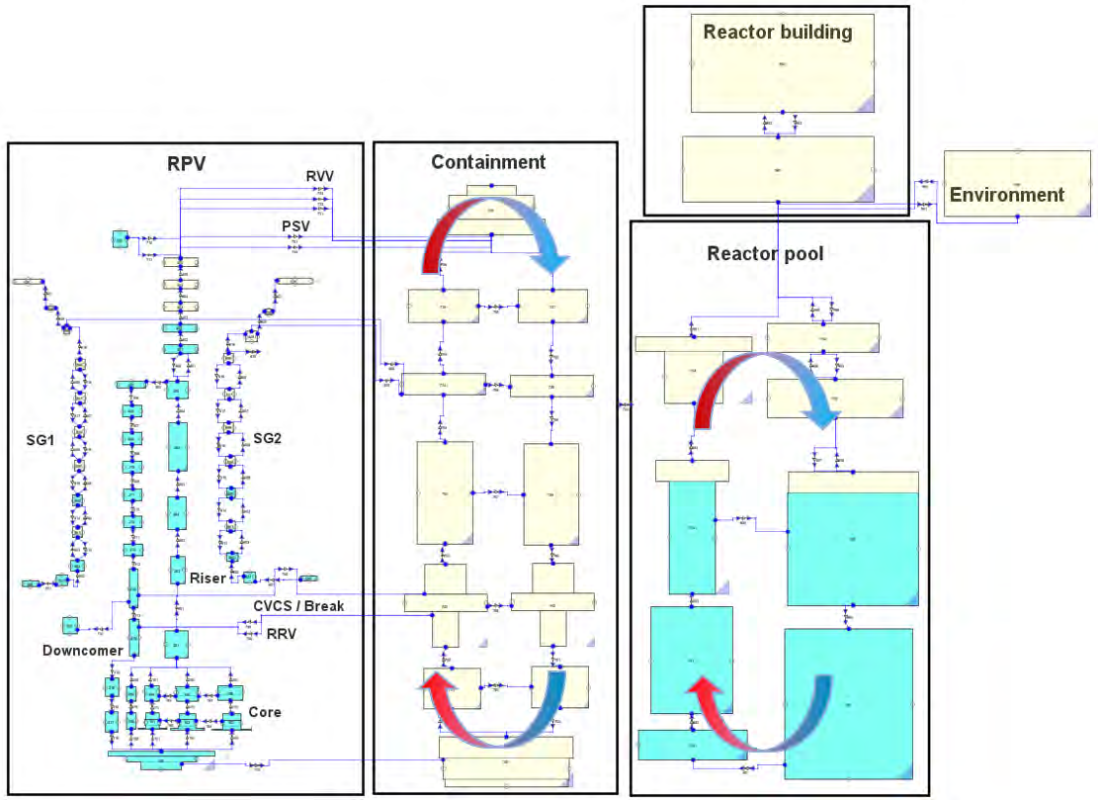

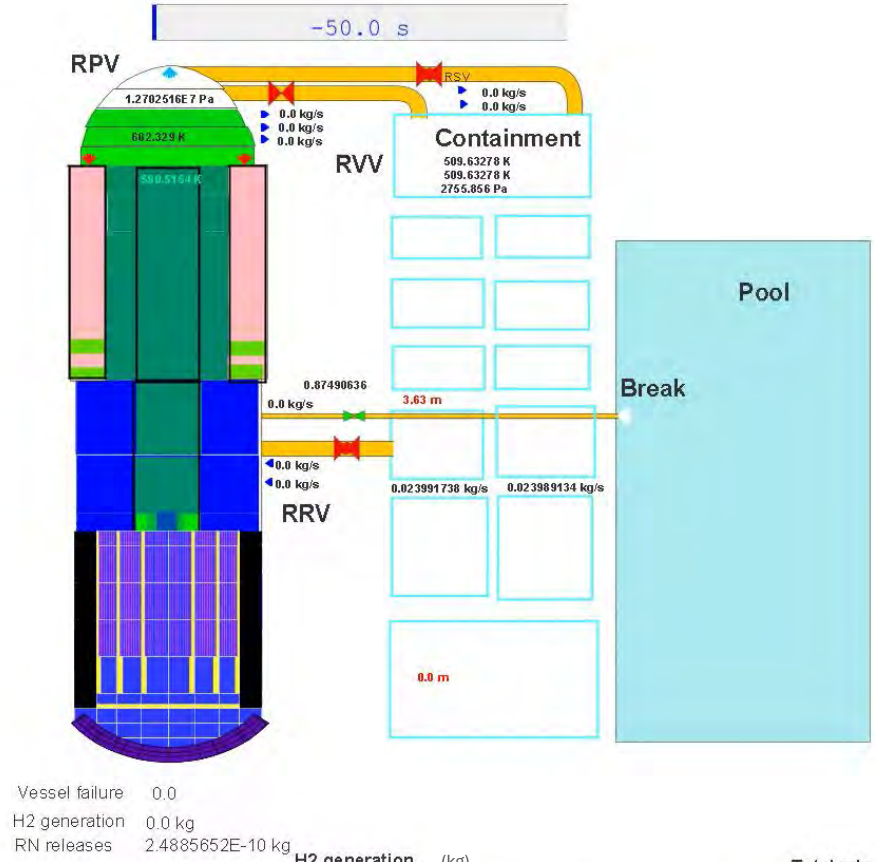

- Scenario – SBLOCA:
  - Bypass type CVCS line break from the downcomer to the reactor pool
  - RVV available
  - RRV not available

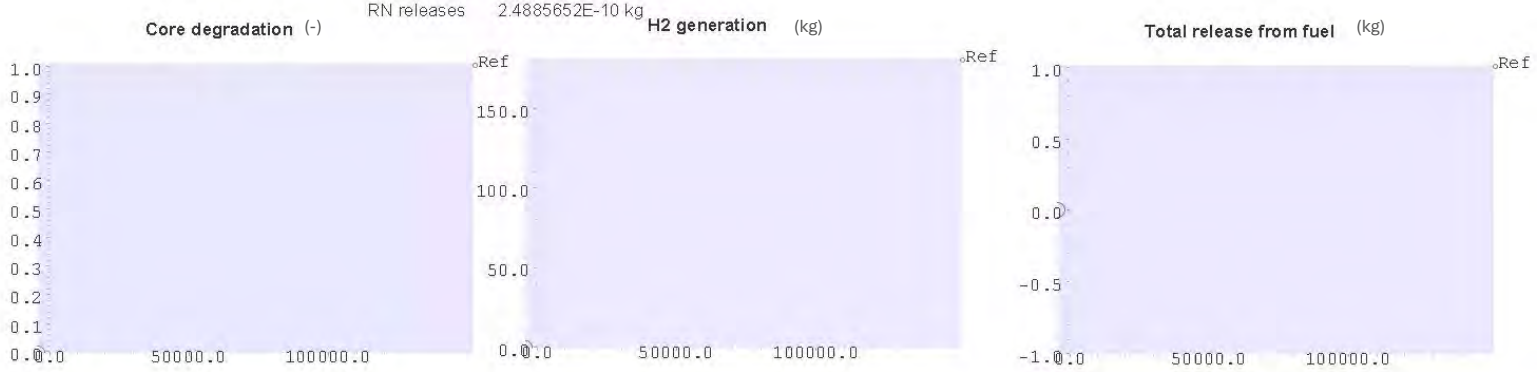

SASPAM-SA - Design 1 scenario analyses

- Scenario – SBLOCA:
  - Bypass type CVCS line break from the downcomer to the reactor pool
  - RVV available
  - RRV not available

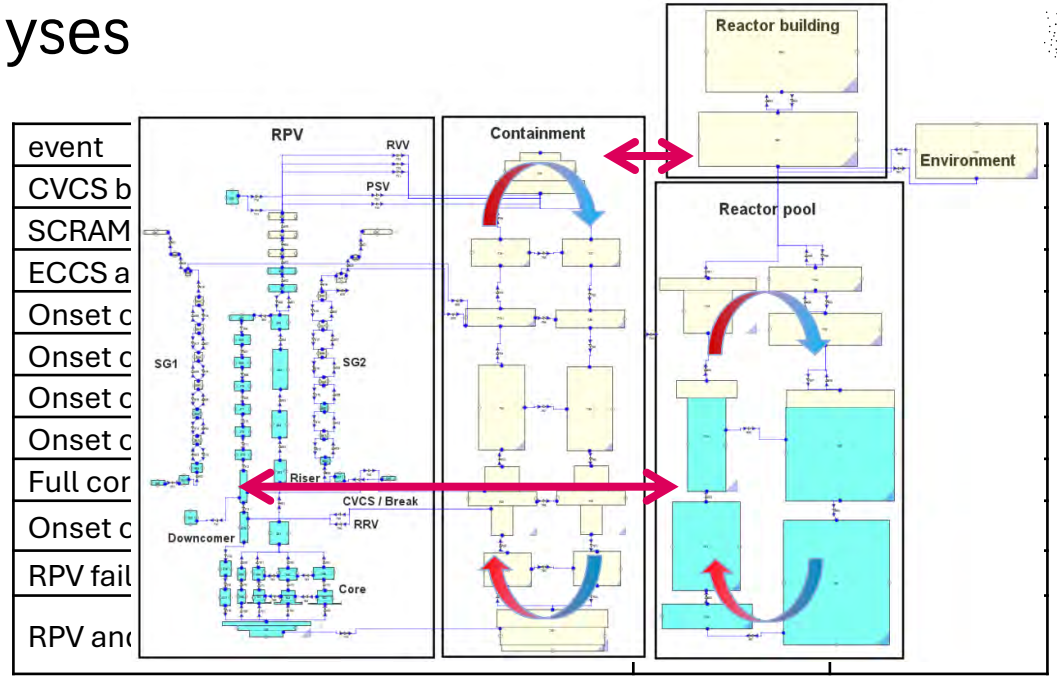

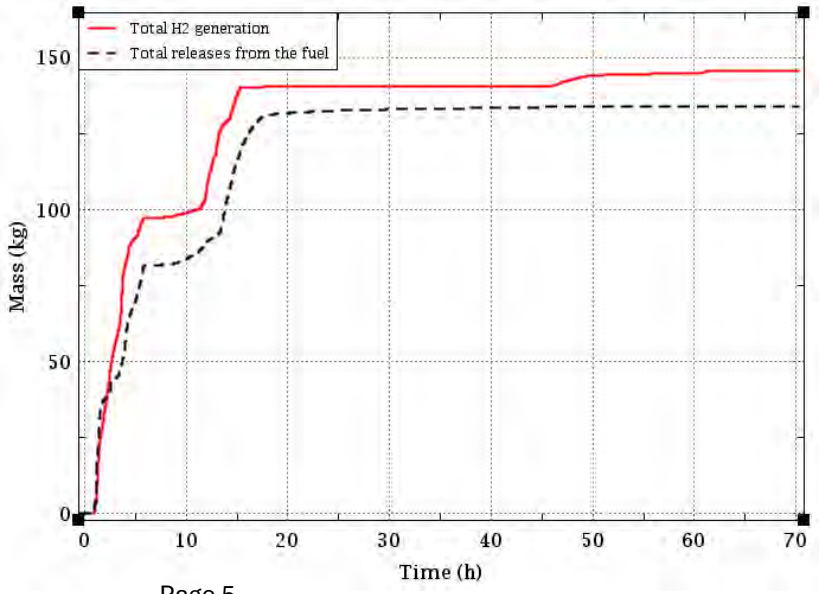

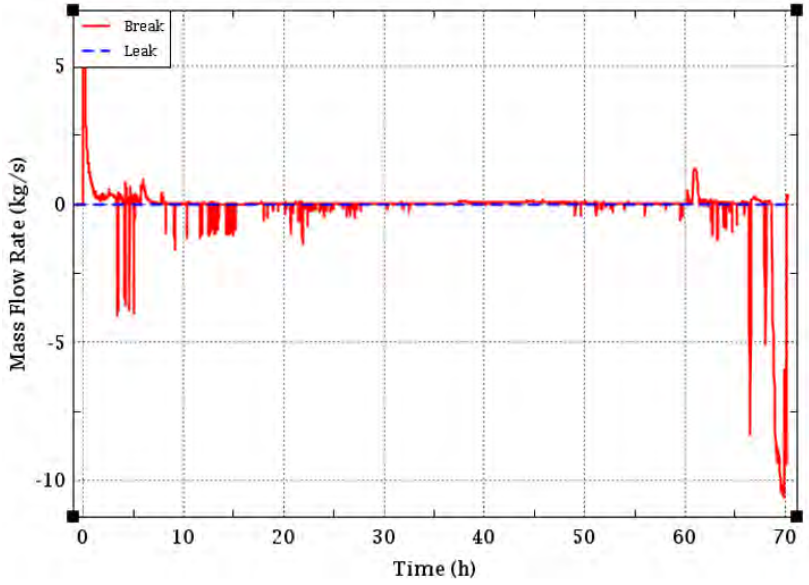

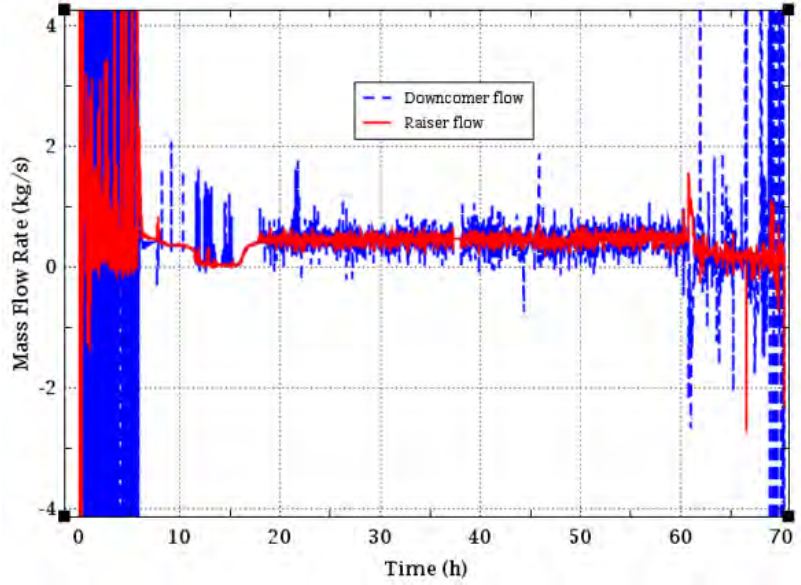

SASPAM-SA Design 1 – release analyses

IMPAIR code assumptions:

- Water volume: 1618 m^3
- Air volume: 538 m^3
- Pool and air temperature: T = 353 K
- Iodide in the pool water: 4.14×10^{-6} mol/L, corresponding to 0.30 of the initial iodine inventory
- Low-molecular-weight organic iodides in the pool water: 1×10^{-5} mol/L
- pH = 5.0, 7.0, 9.0
- Dose rate = 3.0 kGy/h in water and air
- Surface: painted steel
- Reactor building/pool open to the environment with a leak rate of 0.0455 kg/s
- Calculation time: 2778 hours, **114 days**

Scenario assumptions:

- No pool scrubbing was modeled in MELCOR; all iodine species were assumed to be scrubbed by the pool water.
- The containment bypass was assumed to be below the pool water level.
- Approximately **30%** of the initial iodine inventory was assumed to be in the pool water at the end of the transient.
- At the beginning of the IMPAIR calculation, all iodine in the water was assumed to be in the form of iodide I^-.

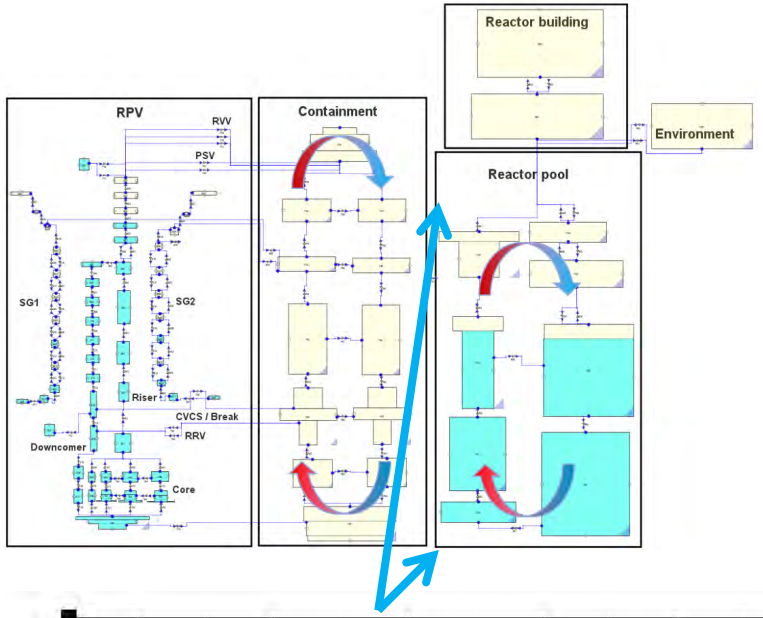

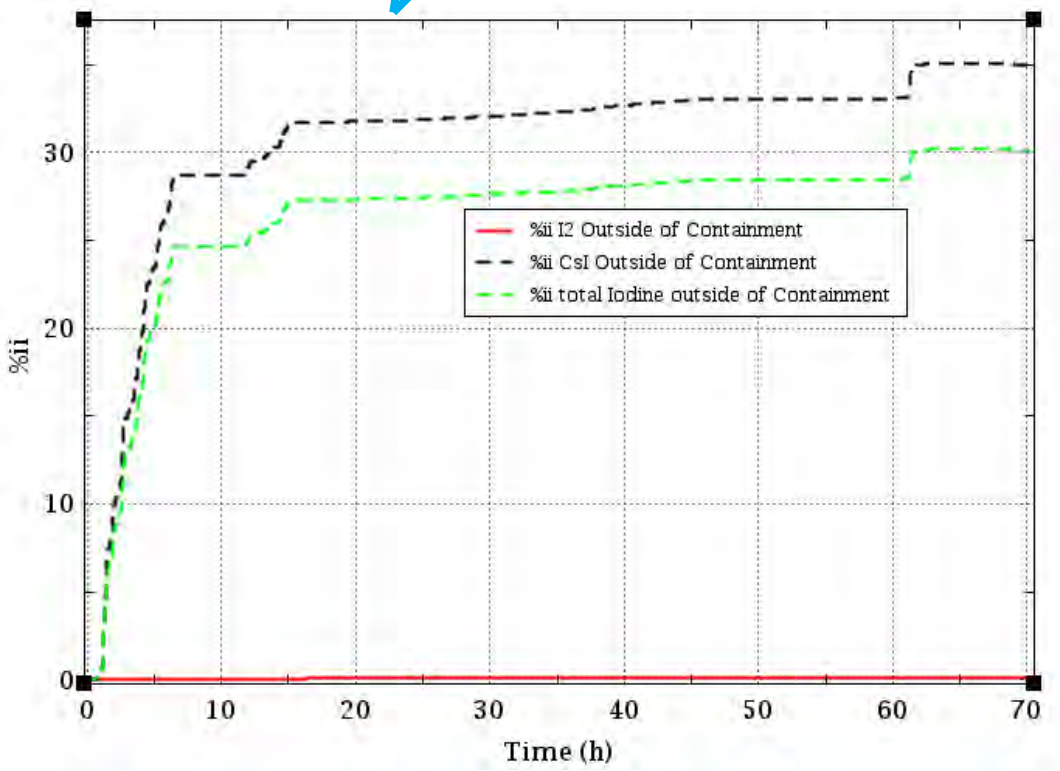

SASPAM-SA – IMPAIR analyses

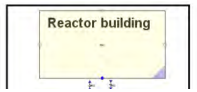

PSI

IMPAIR enables a more mechanistic simulation of iodine transformations in water by accounting for water chemistry effects and the relevant reaction pathways.

The code is designed to simulate iodine chemistry in light-water-reactor containment under severe accident conditions, including aqueous-phase processes in the sump, deposition phenomena, and iodine behavior in the containment atmosphere.

In this work, IMPAIR was used to calculate the release of I_2 and CH_3I from the reactor pool water.

The time evolution of the total gas-phase iodine mass was calculated for three pH values: 5.0, 7.0, and 9.0, assuming that the pool/building walls were painted steel surfaces.

Gas phase wall reactions	
k_4 = 2.5E-01	Deposition velocity: $I_2(g)$ -> I_2(dep_paint) [cm/s]
k_7 = 6.6E-06	Revolatilization of methyl iodide: I_2(dep_paint) -> $CH_3I(g)$
k_9 = 1.0E-04	Transfer of I^- to sump: I_2(dep_paint) -> $I^-(w)$
k_{53} = 2.5E-01	Deposition velocity: $I_2(g)$ -> I_2(dep_concrete) [cm/s]
k_{54} = 6.0E-03	Transfer of I^- to sump: I_2(dep_concrete) -> $I^-(w)$
k_{62} = 6.0E-06	Revolatilization of I_2: I_2(dep_paint) -> $I_2(g)$
k_{64} = 6.0E-06	Revolatilization of I_2: I_2(dep_concrete) -> $I_2(g)$
Gas phase reactions	
k_{65} = 1.64E-05	Radiolytic decomposition: $CH_3I(g)$ -> $I_2(g)$
Water phase reactions	
K_{11} = 3.0E0	Hydrolysis of iodine
K_{12}	Reverse reaction to k_{11}
K_{13}	Iodate formation (disproportionation)
k_{15} = 1.1E5	Iodate decomposition
k_{16} = 1.0E-07	Iodide oxidation by oxygen: $I^-(w)$ -> $I_2(w)$
k_{20} = 4.0E-06	Iodide oxidation by radiolysis: $I^-(w)$ -> $I_2(w)$
k_{22} = 2.5	Methyl iodide formation: $I_2(w)$ -> $CH_3I(w)$
k_{24} = 3.0E-04	Radiolytic reduction: $CH_3I(w)$ -> $I_2(w)$
k_{29} = 5.1E-05	Radiolytic reduction: $IO_3^-(w)$ -> $I^-(w)$
k_{30} = 1.5E-07	Methyl iodide hydrolysis; H_2O
k_{32} = 5.7E-05	Methyl iodide hydrolysis: OH^- ions
k_{40} = 5.0E-01	Methyl iodide formation: HOI(w) -> $CH_3I(w)$
Mass transfer	
k_{35} = 1.0E-03	I_2 mass transfer at phase boundary
k_{36} = 1.0E-03	CH_3I mass transfer at phase boundary
Water phase wall reactions	
k_{17} = 5.0E-05	Deposition velocity: $I_2(w)$ -> I_2(dep_paint) [cm/s]
k_{18} = 1.0E-07	Dissolution from immersed wall: I_2(dep_paint) -> $CH_3I(w)$
k_{19} = 1.0E-05	Dissolution from immersed wall: I^-(dep_paint) -> $I^-(w)$
k_{37} = 5.0E-05	Deposition velocity: $I^-(w)$ -> I^-(dep_paint) [cm/s]
k_{38} = 1.0E-07	Dissolution from immersed wall: I_2(dep_paint) -> $I_2(w)$
k_{39} = 2.0E-05	Dissolution from immersed wall: I^-(dep_paint) -> $CH_3I(w)$
k_{57} = 2.0E-03	Deposition velocity: $I_2(w)$ -> I_2(dep_concrete) [cm/s]
k_{58} = 1.0E-02	Dissolution from immersed wall: I_2(dep_concrete) -> $I^-(w)$
k_{69} = 1.0E-05	Dissolution from immersed wall: I_2(dep_paint) -> $I^-(w)$

SASPAM-SA – IMPAIR analyses

IMPAIR – iodine species:

- The main iodine species in the pool water were I^- and IO_3^-

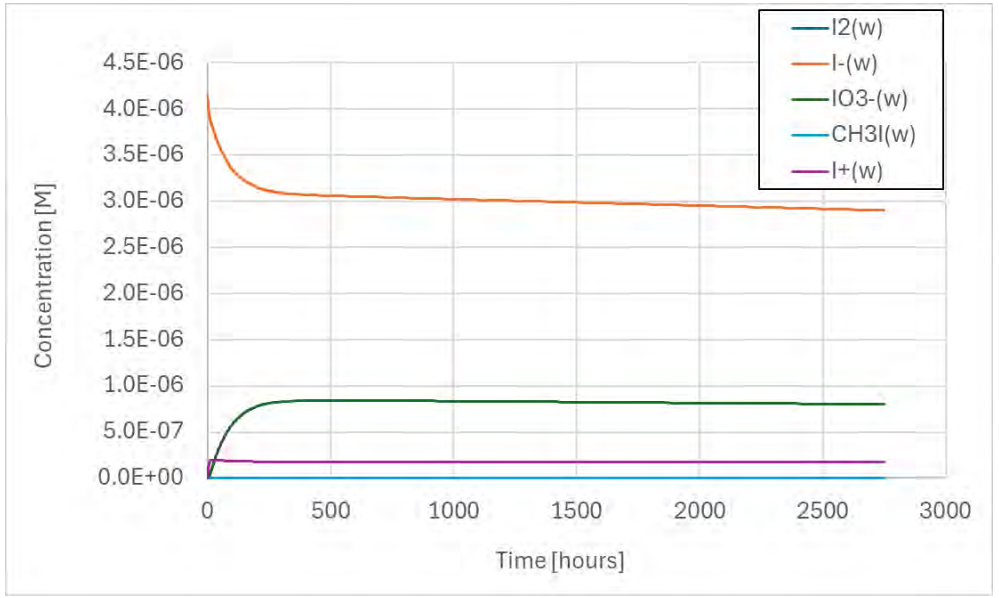

The main iodine species in the pool water with pH=7.0

IMPAIR – evolution of I^- concentration depending on pH:

- The pH dependence is observed through the rapid decrease in I^- concentration
- At a low pH of 5.0, I^- rapidly decreases in the water
- At a higher pH of 9.0, the concentration decreases only slowly

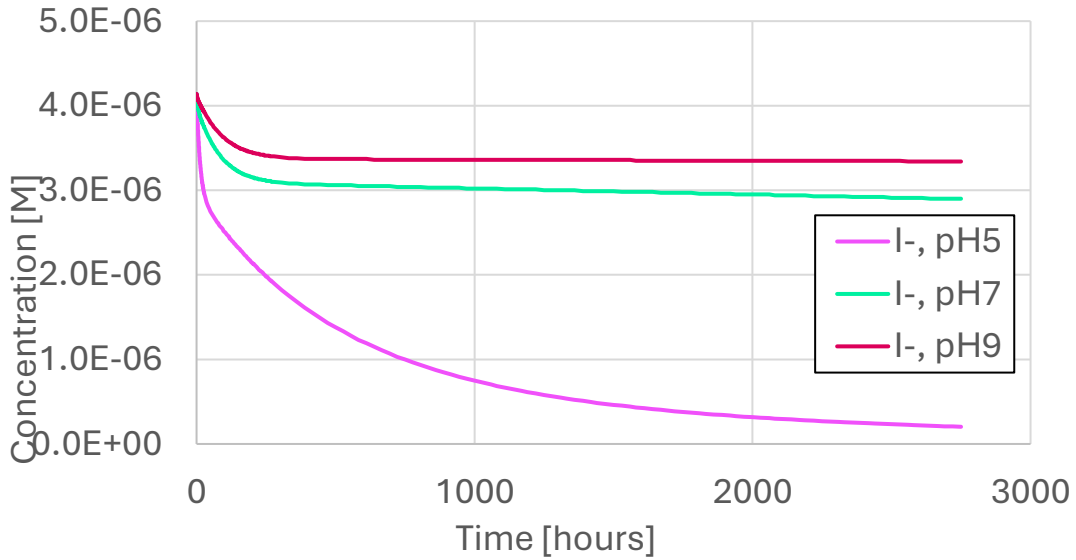

Time evolution of I- as the main iodine species in the pool water with pH = 5, 7 and 9

Conclusions

- MELCOR successfully simulated the rapid progression of the bypass-type severe accident scenario.
  - Natural circulation supported in-vessel cooling, but was insufficient to prevent full core degradation and vessel failure.
  - Reactor pool backflow after pressure reduction led to RCS and containment reflooding and effective long-term cooling.
  - The scenario provided boundary conditions for assessing iodine behaviour in the reactor pool using IMPAIR.

- IMPAIR calculations assumed iodine initially present in the pool water as iodide I^- and were performed for pH values of 5, 7, and 9.
  - IMPAIR results showed strong pH dependence of iodine chemistry, with faster I^- depletion at low pH.
  - Only a small fraction of iodine was released to the gas phase; I^- and IO_3^- remained the dominant aqueous iodine species.

ACKNOWLEDGMENTS & DISCLAIMER

Funded by the European Union. Views and opinions expressed are however those of the author(s) only and do not necessarily reflect those of the European Union or European Commission-Euratom. Neither the European Union nor the granting authority can be held responsible for them.

This work has received funding from the Swiss State Secretariat for Education, Research and Innovation (SERI)

PSI Center for Nuclear Engineering and Sciences

THANK YOU!

Mateusz MALICKI , Terttaliisa Lind : Paul Scherrer Institute

MELCOR DEC-B Transients in a generic integral Pressurized Water Reactor

M. Principato, G. Marta, and F. Giannetti*
Sapienza University of Rome, Department of Electrical and Energy Engineering DIEE – NERG research group
Corso Vittorio Emanuele II, 244, 00186 Rome, Italy
marcello.principato@uniroma1.it, giacomo.marta@uniroma1.it, fabio.giannetti@uniroma1.it

F. Mascari
ENEA
Via dei Mille 21, 40121 Bologna, Italy
fulvio.mascari@enea.it

ABSTRACT

Within the framework of the Euratom project SASPAM-SA Work packages 2 and 5, a MELCOR input deck for a generic integral Pressurized Water Reactor (iPWR) has been developed. The generic Design 2 is an iPWR, characterized by electric power of 300 MW_e, a dry containment and protected by passive safety systems. Three main Design Extended Conditions were considered, all initiating from the rupture of a Direct Vessel Injection line, causing a small break LOCA. The investigations suggested that the scenario postulate different passive systems unavailability, to investigate MELCOR capability to simulate severe accident conditions in iPWR, which is the main aim of the SASPAM-SA project. The MELCOR input deck has been developed by the Sapienza University of Rome (DIEE, NERG research group) according to best practices. The results of the analysis demonstrate that MELCOR can qualitatively replicate the expected dominant phenomena that drive the severe accident sequences. In particular, an accurate evaluation of the containment response and the adequacy of the Filtered Containment Venting System in these scenarios was also investigated.

KEYWORDS
SASPAM-SA, MELCOR, Design extended conditions, thermal-hydraulics, transient analysis

1. INTRODUCTION

Light water Small Modular Reactors (SMRs), and Integral Pressurized Water Reactors (iPWRs), are currently considered among the most mature SMR concepts for near-term deployment in Europe [1]. Their design evolution originates from large Light Water Reactors (LWRs), benefiting from extensive operational experience while introducing enhanced, largely passive safety features. Despite the improvements achieved at the early Defence-in-Depth (DiD) levels, the demonstration of iPWR robustness with respect to Severe Accident (SA) prevention and mitigation, corresponding to DiD levels 4 and 5 [2], remains a central aspect of the European licensing process. Consequently, the identification and deterministic analysis of representative SA scenarios is required to support both reactor design evaluation and regulatory review. Within this context, the Horizon Euratom Safety Analysis of SMR with PAssive Mitigation strategies-Severe Accident (***SASPAM-SA)*** project, addresses the transferability of SA knowledge, experimental data and analytical methodologies developed for large LWRs to iPWR configurations [3,4,5,6], with specific attention to European requirements for SA and Emergency Planning Zone (EPZ) analyses; SASPAM-SA is coordinated by ENEA (Italy) and involves twenty-three organizations from fourteen countries, with a total

duration of four years. Two generic iPWR reference concepts are considered in the project to support its objectives:

- *Design 1*: a low-end power iPWR configuration (about 60 MW_e) with a submerged containment.
- *Design 2*: a high-end power iPWR configuration (about 300 MW_e) characterized by a dry containment and the extensive use of passive safety systems.

These generic designs are not intended for design assessment; rather, they provide representative platforms to investigate the capability of integral SA codes and Computational Fluid Dynamics (CFD) tools to reproduce key iPWR-specific phenomena under postulated Design Basis Accident (DBA) and SA conditions. Particular attention is devoted to phenomena associated with strong thermal–hydraulic coupling between the primary system, containment and safety systems, including natural circulation, heat transfer in helicoidal steam generators, thermal stratification in large pools, and in-vessel melt retention, which may challenge the applicability of codes primarily developed for the current large LWR fleet. Given the complexity of the SASPAM-SA project and the range of its objectives, the work is structured into seven dedicated Work Packages (WPs), each addressing a specific technical or organizational aspect. Within this framework, the present paper is specifically connected to WP2, coordinated by KIT (Germany), focused on the input deck development and definition and assessment of hypothetical SA scenarios, and to WP5, coordinated by GRS (Germany), which addresses the capability of integral codes to simulate iPWR containment behavior and to evaluate the effectiveness of accident mitigation measures. The objective of this paper is to present the selected SA scenarios and to discuss the main results of containment analyses performed for the reference iPWR Design 2, highlighting key phenomenological aspects and modelling challenges.

2. iPWR DESIGN 2

The MELCOR input deck developed by Sapienza University of Rome is based on the Design 2 reference configuration adopted within the Horizon Euratom SASPAM-SA project [7,8]. This configuration represents an integral Pressurized Water Reactor with an electric output of about 300 MW_e and based on the passive safety systems considered, it is inspired by the IRIS (International Reactor Innovative and Secure) concept [8]; this configuration permits the elimination of the occurrence of some accidental sequences. The integral Reactor Pressure Vessel houses the reactor core, helical coil steam generators, the primary pumps, and the pressurizer within a single vessel; the absence of large-diameter penetrations in the vessel effectively eliminates the possibility of Large Loss-of-Coolant Accidents. The primary system is enclosed in a spherical dry containment filled with nitrogen at atmospheric pressure and subdivided into two main regions: the Drywell and the Reactor Cavity. The safety and mitigation strategy relies exclusively on passive systems that do not require external power, nevertheless, the performance of these systems is strongly governed by complex thermal–hydraulic phenomena, may still involve active initiation, and is characterized by limited operational experience; in **Errore. L'origine riferimento non è stata trovata.**, in addition to the overall reactor layout, the main safety systems are highlighted, including:

- **Emergency Heat Removal System** (EHRS), which consists of four independent natural circulation loops connected to external refueling Water Storage Tanks (RWST). Once active, it removes core power through the SGs.
- **Automatic Depressurization System** (ADS); consists of two stages, **Stage 1** includes two identical redundant trains connected to the pressurizer head through check valves, which depressurize the system by venting steam into a quench tank located in the drywell, and **Stage 2** allows pressure equalization between the containment and the RPV, located at the pressurizer top.

- **Emergency Boration Tanks** (EBT); are located in DW and inject borated water into the core by gravity via direct vessel injection (DVI, two independent lines are connected to the vessel above the core's upper plate).
- **Long-Term Gravity Make-up System** (LGMS); two tanks, located in the DW, connected to the DVI via check valves.
- **Riser-Downcomer Valves** (RI-DC): the eight connections between the riser and the downcomer are designed to allow the primary water to flow along a shorter path, bypassing the pump suction plenum, which facilitates the establishment of natural circulation in accidental phases.

For SA management, the Pressure Suppression System (PSS) plays a key role in limiting containment pressurization and supporting mitigation. The PSS enables a reverse flow mechanism that is activated when the Drywell pressure decreases below the PSS tank pressure, resulting in flooding of the reactor cavity. This facilitates external cooling of the RPV lower head and supports the In-Vessel Retention (IMVR) strategy adopted for the reference iPWR design.

2.1. MELCOR input description

The input deck has been developed with **MELCOR v2025.0.0** [9], for the creation of the input deck and for the preparation of the project database, the main geometric information has been determined by scaling the data available from the SPES-3 facility [10], by engineering evaluation or public general data available from the IRIS reactor [7,8,11] and the studies carried out by ENEA with the ASTEC code [12]. The objective of the model is to reproduce the reactor behavior under normal and accidental conditions, with a detailed thermal-hydraulic nodalization to study in depth the thermal-hydraulic phenomena related to passive systems and the phenomenology of SAs such as core degradation, radionuclide transport of radionuclides, etc [9]. Most of the structures in Design-2 will be modelled with the support of the *CVH* package, the fluid paths represented with the *FL* package will be coupled to the control volumes of the reactor, the *HS* package will be used to simulate the thermal response of the containment structures, tanks and piping; the union of these three packages represents the thermal hydraulic nodalization of the reactor. The behavior of the core and its internal structures such as fuel rods or lower head will be modeled using the *COR* package, instead with the RN package initial inventories of radionuclides in the core, cavity, and control volumes are simulated. A reactor schematization is depicted in **Figure *1* (b)** : *RPV & primary circuit*, *Secondary circuit & EHRS*, *In-containment Safety Systems and Containment (DW+RC).*

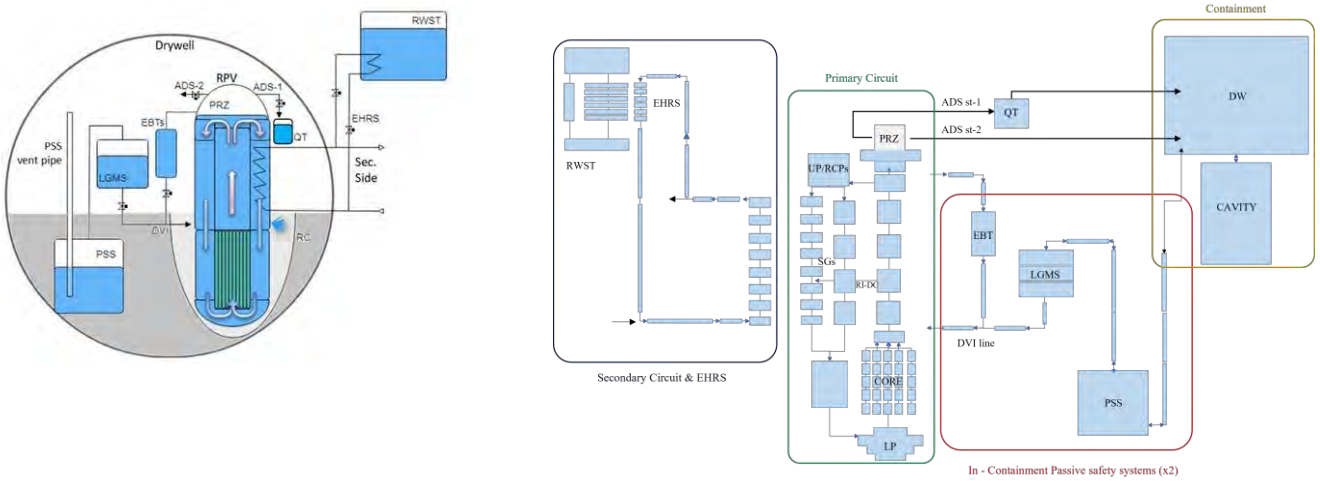

Figure 1. Design 2: conceptual scheme (a), thermal-hydraulic nodalization (b)

The iPWR reactor and its systems are represented through a slice-based nodalization strategy. The primary circuit is subdivided into 44 control volumes covering the core, bypass regions, lower plenum, downcomer, riser, pressurizer, upper plenum, and the primary side of the steam generators, including bypass zones. Passive systems such as the EBT, LGMS, PSS, and the ADS with quench tank are nodalized with dedicated control volumes, valves, and SPARC model enabled flow paths to simulate injection, venting, condensation, and radionuclide retention during accident scenarios; for the transport and deposition of radionuclides in the core, primary circuit, and containment, the RN and DCH packages are used, including the simulation of pool scrubbing and aerosol filtration processes. The stainless steel drywell, and the concrete cavity are modeled as separate single control volumes, while the containment heat structures are linked to an external volume, representing the surrounding reactor environment; to improve the simulation of condensation on the steel containment liner, the thermal structure corresponding to the DW steel liner was modified, with its geometry changed from rectangular to a spherical form; a node was added to represent the paint layer on the steel and the Film Tracking [9] model was activated to simulate the drainage of condensation, with liquid distributed between the drywell pool and the spray package (50% each). In the spray package, part of the drained liquid falls as droplets (diameter ~4 mm) into the containment volume, contributing to internal heat exchange. In addition, a venting system connected to the DW was modelled: FCVS (Filtered Containment Venting System) it provides filtered venting of the containment to mitigate radioactive releases during severe accident scenarios. The system operates when containment pressure exceeds a predefined threshold, allowing controlled release while maintaining structural integrity, the FCVS ensures that venting reduces overpressure while limiting environmental contamination.

3. SEVERE ACCIDENT ANALYSIS

The accident scenarios investigated in this work are based on a Small Break Loss of Coolant Accident (SB-LOCA) caused by a double-ended rupture of a DVI line, due to the low elevation of the break, this event constitutes a particularly demanding condition for reactor safety systems [7,8]. The injection system layout includes two independent and redundant DVI lines, identified as DVI-A and DVI-B, each connected to the corresponding safety subsystems. In the analyzed cases, DVI-A is broken, depending on the availability of the remaining safety systems, the transient may either remain within DBA conditions or evolve to a SA, which is the focus of this study. The three SAs are classified as [8]:

- SA-1: Postulated failure of **ADS-1** and **EHRS**
- SA-2: Postulated failure of **all** safety systems
- SA-3: Postulated failure of **EHRS**

The results discussed in the following sections are structured according to a sequence of *Phenomenological Windows* (PhWs), each window represents a distinct phase of the transient, characterized by the overall reactor conditions and, in particular, by the state and evolution of the core. An overview of the defined PhWs for the three analyzed transients is provided in **Table I**.

Table I. SA-1, SA-2, SA-3 Phenomenological Windows

Severe Accident	***PhW***	***Main Phenomena***	***Start** (s)*	***End** (s)*
SA-1	*PhW 1*	***Blowdown, EBT injection, Oxidation onset***	0	16364
	PhW 2	***Core Degradation, IVMR, ADS-2, Reflood***	16364	54154
	PhW 3	***FCVS operation, PSS***	54154	260000

SA-2	*PhW 1*	***Blowdown, EBT injection, Oxidation onset***	0	17645
	PhW 2	***Core Degradation, Corium Slump***	17645	42360
	PhW 3	***IVMR, FCVS operation***	42360	260000
SA-3	*PhW 1*	***Blowdown, ADS-1, EBT, LGMS, PSS***	0	10370
	PhW 2	***Oxidation onset, Core Damage, PSS***	10370	40031
	PhW 3	***FCVS operation, Core Degradation, PSS***	40031	151777
	PhW 4	***ADS-2, Reflood, FCVS***	151777	260000

3.1. SA-1

The SA-1 sequence starts with the rupture of the DVI line, which evolves into a small-break LOCA, the break triggers the SCRAM only after 27 seconds. The first phase of the SB-LOCA, known as blowdown, marks the beginning of the first phase (PhW 1) of the accident, where it is characterized by a sudden increase in pressure, leading to RCP coastdown and the opening of the RI-DC valves.

Table II. SA-1 chronological sequence

Event	*Time (s)*	*Time (h)*
Start of Transient (SoT)	0	0
SCRAM	27.98	0.01
RCP coastdown and RI-DC valves opening	109.76	0.03
EBT line opening	160.23	0.04
Water level below TAF	375	0.10
EBT-B empties	2520	0.7
Containment Design Pressure reached	2653	1.09
Time of onset H_2 production	14523	4.03
1st PSS reverse flow	16364	4.54
Onset of Core damage	21860	6.07
Water level below BAF	38920	10.81
LGMS line opening	39080	10.85
Total core degradation	40319	11.19
Molten Core Relocation in LP	41181	11.43
1st FCVS actuation	41764	11.60
2nd PSS reverse flow	42225	11.72
1st FCVS deactivation	44025	12.22
ADS-2	54154	15.04
2nd FCVS actuation	80529	22.36
3rd PSS reverse flow	80920	22.47
2nd FCVS deactivation	89032	24.73
3rd FCVS actuation	114750	31.87
3rd FCVS deactivation	123680	34.35
4th FCVS actuation	153110	42.53

4th FCVS deactivation	161020	44.72
5th FCVS actuation	194636	54.06
5th FCVS deactivation	202007	56.11
6th FCVS actuation	240297	66.74
6th FCVS deactivation	247487	68.84
End of Transient (EoT)	260000	72

As shown in **Table II**, the first EBT is actuated after only 160 seconds, since it is directly connected to the ruptured DVI line, it constitutes an additional water source for the LOCA.

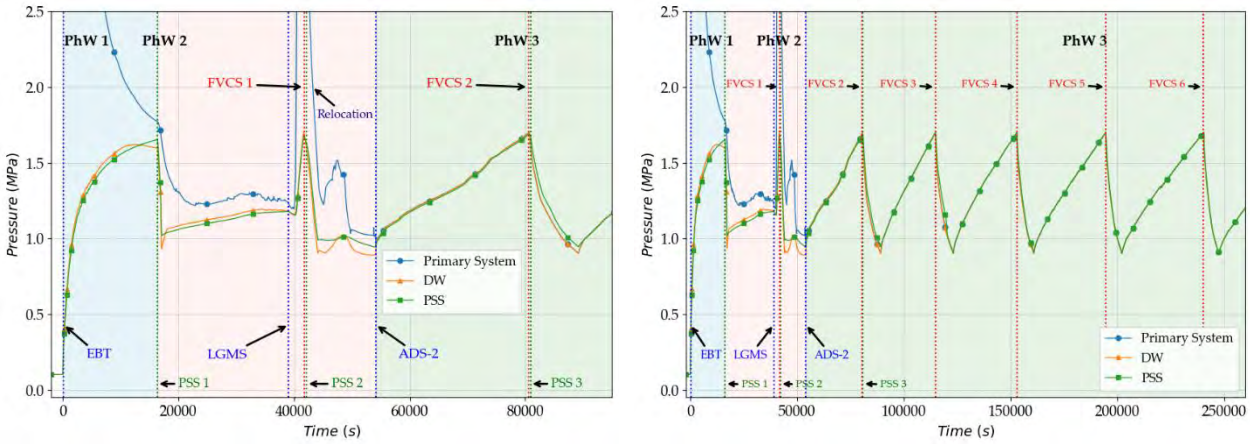

Figure 2. Pressure trends PhW 1 and PhW 2 (a), Entire simulation (b) (SA-1)

As illustrated in the figures above, the containment pressure rises, reaching the design pressure within one hour from the SOT. The steam generated inside the DW is partially sent to the PSS tanks, where it is condensed through direct liquid–steam interactions, thereby increasing the pressure in their atmosphere. This condition leads to a reverse flow from the PSS tanks back to the containment through the PSS vent pipe [7]. In this accident, three reverse flow events occur, which periodically reduce the containment pressure and contribute to flooding the reactor cavity; the first reverse flow marks the end of PhW 1. At the same time, the liquid level in the core drops dramatically, leading to PhW 2 (*cladding rupture*) only 6 hours after the DVI rupture.

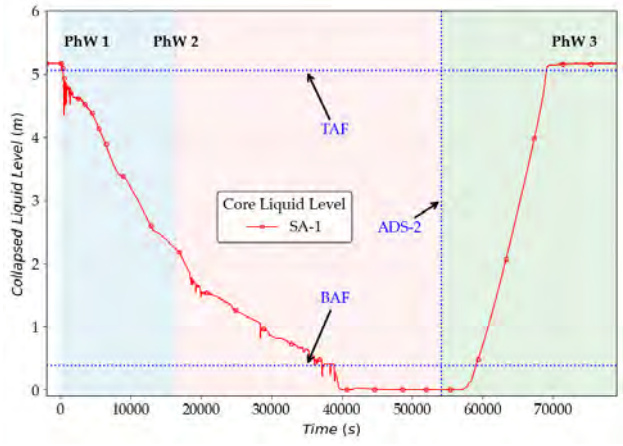

Figure 3. Core collapsed liquid level (SA-1)

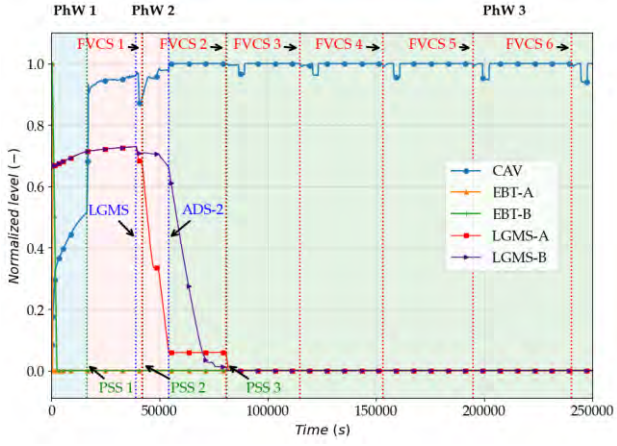

Figure 4. Collapsed normalized liquid level for EBT, LGMS and CAV (SA-1)

In PhW 2, due to the lack of ADS-1 and EHRS, the activation of the *LDPC* signal (*low RPV–containment differential pressure* [6,7]) and the consequent opening of the LGMS valves occur with a significant delay, when the core liquid level is already below the BAF (**Figure 3**) and the core is partially molten. The LGMS water injection takes place rapidly (**Figure 4**); however, this does not prevent complete melting and the relocation of the molten corium into the lower plenum (as demonstrated by the general pressure increase shown in **Figure 2**). Due to the presence of residual water in the lower plenum, the relocation causes a pressure spike in the drywell, activating the FCVS for the first time at 1.69 MPa, the venting system reduces the pressure in the DW and in the vessel, leading to a second PSS reverse flow; the valve remains open for less than one hour, until the DW pressure drops to a value of 0.85 MPa; in the final moments of PhW 2, the IVMR is achieved. The rapid emptying of the LGMS tanks activates the Low LGMS Mass signal (two LGMS tanks < 8%), which concomitantly commands the opening of the ADS-2 valves. This configuration enables controlled steam circulation between the RPV and the DW and marks the beginning of PhW 3. With the activation of the second stage of the depressurization system, the vessel is fully reflooded with water, effectively cooling the molten corium. PhW 3 is characterized by the transient behavior of the FCVS, the overall system pressures fluctuate between the two setpoint values of the FCVS. Notably, as in the first phase of the accident, the opening of the venting system valve causes the 3rd PSS reverse flow, though less pronounced than the previous two.

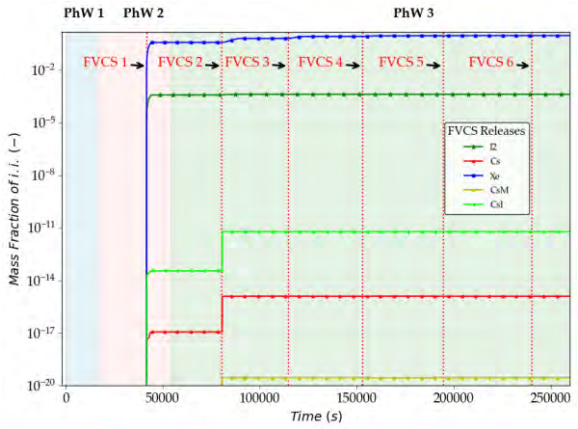

Figure 5. FCVS releases in mass fraction of initial inventory (SA-1)

The analysis of the released mass fractions respect to the initial inventory of certain classes, considering only the FCVS contribution, shows that halogen class releases are higher than those of the remaining classes because of the lower decontamination factor for elemental iodine in the FCVS. Releases are summarized in **Figure *5***, while the noble gases class (Xe) is completely released, due to their high volatility. The source term results are presented on a logarithmic scale to better highlight differences between the various classes.

3.2. SA-2

The second scenario analyzed is the more unlikely of the three. Indeed, the unavailability of all safety systems is postulated. In the **Table *III*** the main events occurring in SA-2 are listed.

Table III. SA-2 chronological sequence

Event	*Time (s)*	*Time (h)*
SoT	0	0
SCRAM	26.22	0.01

RCP coastdown and RI-DC valves opening	108.88	0.03
Water level below TAF	680	0.18
Containment Design Pressure reached	3935	1.09
Time of onset H_2 production	12803	3.55
1st PSS reverse flow	17645	4.90
Onset of Core damage	18110	5.03
Water level below BAF	31750	8.81
Corium Slump	34900	9.69
2nd PSS reverse flow	42360	11.77
Total core degradation	49636	13.78
FCVS actuation	177580	49.32
FCVS deactivation	186297	51.74
EoT	260000	72

PhW 1 starts with the rupture of DVI-A, this event triggers the SCRAM signal and the opening of the recirculation valves; the blowdown phase is very fast and similar to the one in previous case, the only source of water discharge is the vessel side broken DVI. This results in a reduction of the primary system pressure from the initial 15 MPa and produces a slightly less pronounced peak in the DW pressure (***Figure 6***) compared to the previous scenario.

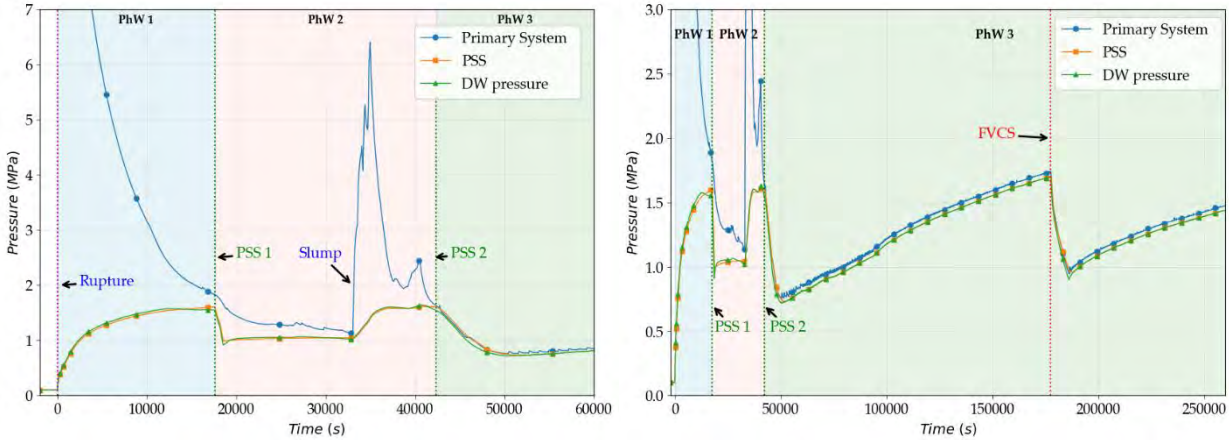

Figure 6. Pressure trends PhW 1 and PhW 2 (a), Entire simulation (b) (SA-2)

The first PSS reverse flow marks the transition to the second phase, PhW 2, of the accident: the liquid level inside the core gradually drops, leaving the core uncovered in just 9 hours: this fact, combined with the increase in cladding temperature, leads to the onset of degradation (5 hours after SOT). At the end of PhW 2, the core is completely molten and relocated within the lower plenum, from **Errore. L'origine riferimento non è stata trovata.**: we can see the presence of a corium slump, which causes a sudden pressure spike, marked in the case of the primary system (6.22 MPa). This pressure peak has a reduced impact on both the containment and the PSS, in fact, the pressure increase does not reach the threshold value required to trigger the opening of the FCVS system valve. At the conclusion of PhW-2, a second PSS reverse flow takes place, resulting in an overall pressure reduction and ensuring that the cavity remains completely flooded. This is one of the key conditions to ensure IVMR into the lower plenum. In PhW 3, the corium is already relocated to the lower plenum, and water injection into the primary system is provided solely by the flooded cavity.
After 50 hours from the onset of the transient, the thermal-hydraulic conditions of the reactor lead to an

increase in the DW pressure and to the opening of the FCVS, resulting in the release of steam and radionuclides to the environment. Compared to the previous case, releases are reduced for all the classes analyzed.

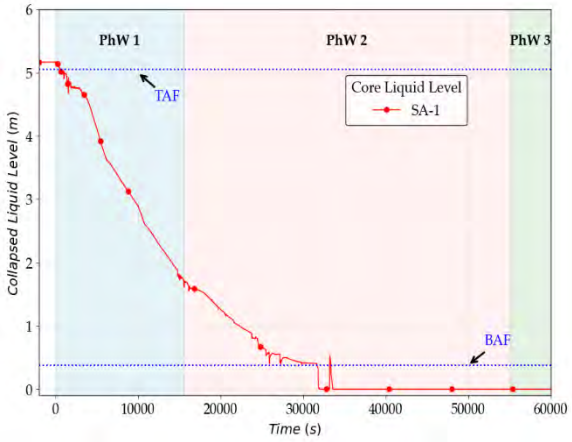

Figure 7. Core collapsed liquid level (SA-2)

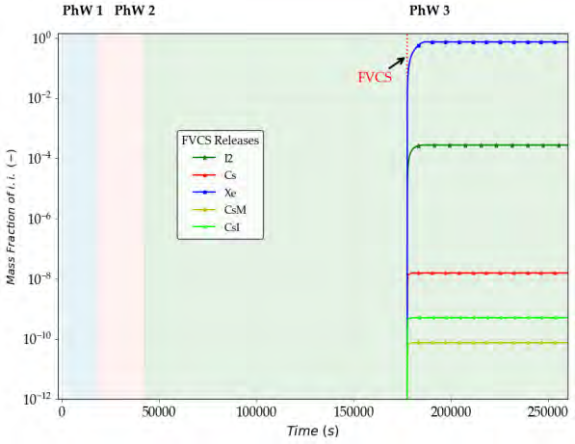

Figure 8. FCVS releases in mass fraction of initial inventory (SA-2*)*

3.3. SA-3

The last analyzed sequence postulates the failure of EHRS; the transients starts as the rupture occurs and the RCP coastdown and RI-DC valves opening is triggered. Following **Table IV**, the ADS-1 is opened and the EBT starts injecting water, the containment design pressure of 12 bar is reached earlier with respect to the other two scenarios, thanks to the triple early pathway from the vessel to the DW: the double guillotine rupture and the ADS-1. The pressurization of the containment is significantly faster, due to ADS-1 venting steam into the quench tank.

Table IV. SA-3 chronological sequence

Event	*Time (s)*	*Time (h)*
SoT	0	0.00
SCRAM	28.00	0.01
RCP coastdown and RI-DC valves opening	112	0.03
ADS-S1/EBT	166	0.04
Water level below TAF	185	0.05
Containment Design Pressure reached	918	0.25
LGMS	10370	2.88
1st FCVS actuation	19641	5.46
1st PSS reverse flow	19960	5.54
1st FCVS deactivation	20745	5.76
Time of onset H2 production	29779	8.27
Onset of core damage	40031	11.11
2nd FCVS actuation	60247	16.74
2nd PSS reverse flow	60449	16.79
2nd FCVS deactivation	62776	17.44
3rd FCVS actuation	107713	29.92

3rd PSS reverse flow	107802	29.94
3rd FCVS deactivation	114687	31.86
4th FCVS actuation	151777	42.16
ADS-S2	153000	42.50
4th FCVS deactivation	161816	44.95
5th FCVS actuation	195335	54.26
LGMS-A empty	197048	54.73
5th FCVS deactivation	203228	56.45
6th FCVS actuation	240931	66.93
6th FCVS deactivation	248364	68.99
EoT	260000	72

During PhW 1 the containment keeps pressurizing and the 1st PSS reverse flow occurs only after the 1st FCVS actuation. This system will be activated six times throughout the entire simulation (**Figure 9**). Around 3 hours after the SOT, when the primary and containment pressures are close (triggering of *low RPV-Containment differential pressure* signal), the LGMS valves open, this event marks the transition to PhW 2. In this phase's first moments, the pressure trends inside the primary, the drywell and the PSS undergo a steady state period of 3 hours, thanks to the injection of the LGMS. When the downcomer pressure becomes greater than the pressure in the LGMS, the overall system pressure gradually grows, until the value of 1.6 MPa that is the set-point for FCVS actuation; this causes a series of phenomena: the pressure in the main system drops, mass flows from the break and ADS-1 have a significant peak and the 1st PSS reverse flow is triggered, filling the reactor cavity; after this moment, the injection phenomena and pressure trends follow the opening and closing cycles of the FCVS

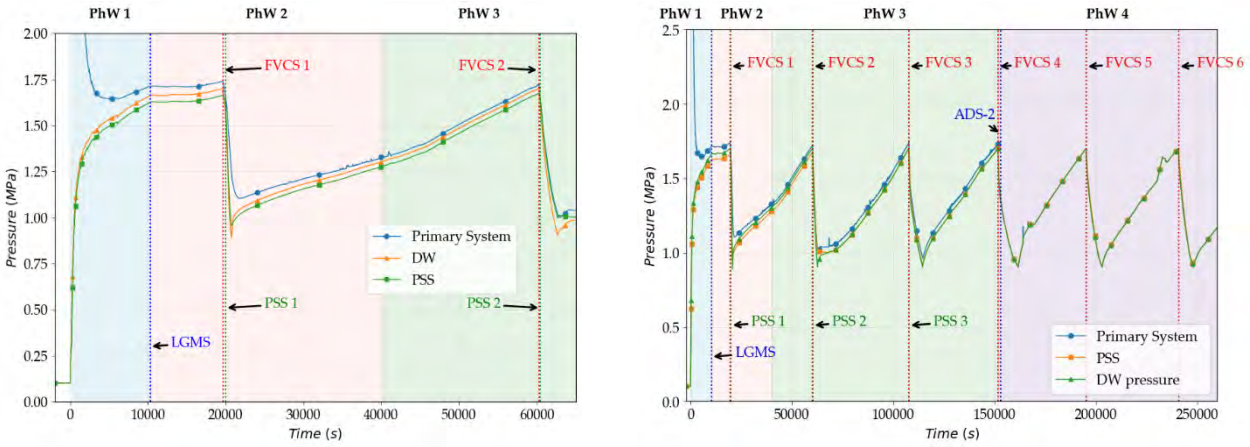

Figure 9. Pressure trends: PhW 1 (a), Entire Simulation (b) (SA-3)

Continuous FCVS cycling, as seen in 3.1, causes pressure fluctuations, which can negatively impact the reliability of the entire system, therefore, scaling of this system is considered. The **Figure 10** shows the LGMS-B tanks intermittent injection during the whole transient, following the FCVS trend, due to their pressure. Despite the operability of the injection systems and the reactor cavity contribution, the level in the core decreases, causing the core melting approximately 11 hours after SOT, beginning PhW 3 of the transient. PhW 3 is characterized by FCVS oscillations due to pressure increases caused by the greater amount of steam in the DW coming from the quench tank. The core doesn't melt completely, about 22% of the total, unlike the two previous cases, because in this phase the FCVS actuation leads to injection of LGMS

and CAV, which result in a partial reflooding of the reactor core, bringing its collapsed level to almost half the total height.

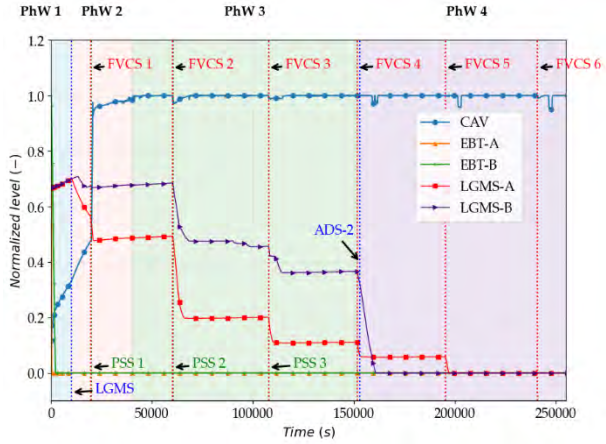

Figure 10. Collapsed normalized liquid level for EBT, LGMS and CAV (SA-3*)*

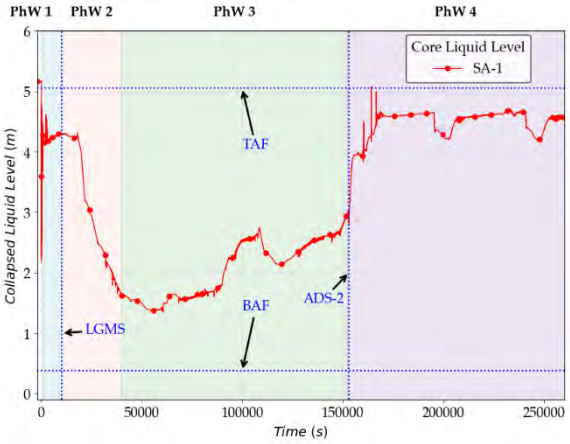

Figure 11. Core collapsed liquid level (SA-3)

When the liquid level in the LGMS-B tank reaches its minimum threshold, the ADS-2 signal is triggered, establishing a direct connection between the reactor vessel and the containment, starting PhW 4. This action leads to a substantial vessel complete reflooding, thereby restoring the core liquid level to a value close to that observed prior to the DVI line break. From this point onward, the water injections associated with the final two FCVS actuations are supplied exclusively through the cavity. The resulting collapsed liquid level, as illustrated in **Figure *11***, is sufficient to prevent further core damage for the remainder of the simulation period, extending up to 72 hours. In **Figure 12** the source term is shown. For halogens, releases are lower than SA-1 but higher than SA-2, while noble gases exhibit an overall lower release. The remaining classes, as in previous cases, show negligible releases.

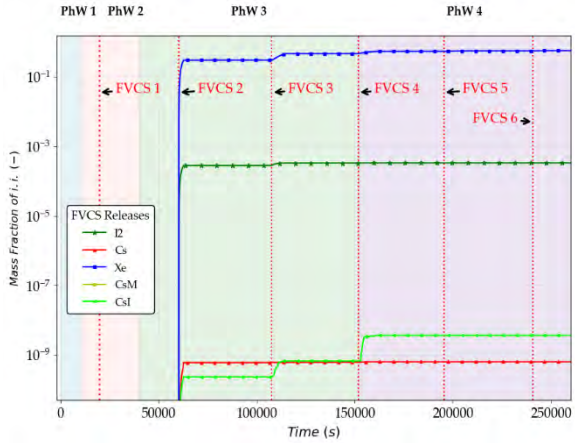

Figure 12. FCVS releases in mass fraction of initial inventory (SA-3)

4. CONCLUSION

This work presents the development and application of a MELCOR input deck for a generic iPWR Design 2 within the Horizon Euratom SASPAM-SA project. Three SA scenarios initiated by a small-break LOCA due to a DVI line rupture were analyzed, considering different configurations of passive safety system unavailability. The results indicate that MELCOR is capable of qualitatively simulating

the main phenomena expected during SA progression in an iPWR, including core degradation, corium relocation, and containment pressurization; however, quantitative assessment is currently limited by the lack of experimental validation. The analysis primarily focused on the containment response and on the role of the PSS and the FCVS, highlighting the strong coupling between depressurization, cavity flooding and pressure control; future developments will include multi-volume containment modeling to investigate these phenomena. Radionuclide releases through the FCVS were analyzed, showing that halogens are partially retained, while noble gases experience the highest release; other classes remain negligible. In addition, the potential cliff-edge effect associated with reverse flow in the PSS emerged as an aspect of interest and represents a promising topic for further investigation. Future work will therefore focus on model refinement, sensitivity analyses, a more detailed evaluation of radionuclide behavior, and comparisons with other integral and CFD codes, providing a reference for iPWR safety assessment within the SASPAM-SA framework.

ACKNOWLEDGEMNTS

The research activity is carried out by Sapienza DIAEE with the code MELCOR, in the framework of the DIAEE -ISIN agreement signed on 05/13/2020 as part of the General Arrangement between the United States Nuclear Regulatory Commission (US-NRC) and the Italian National Inspectorate for Nuclear Safety and Radiation Protection (ISIN).

Funded by the European Union. Views and opinions expressed are however those of the author(s) only and do not necessarily reflect those of the European Union or European Commission-Euratom. Neither the European Union nor the granting authority can be held responsible for them.

REFERENCES

1. IAEA, “Small Modular Reactor Catalogue 2024”, International Atomic Energy Agency, Vienna (2024).
2. IAEA, “Application of the Principle of Defence in Depth in Nuclear Safety to Small Modular Reactors, addendum to INSAG-10”, INSAG-28, International Atomic Energy Agency, Vienna (2024).
3. SASPAM-SA project website. Available at: https://www.saspam-sa.eu/
4. Horizon Euratom Safety Analysis of SMR with PAssive Mitigation strategies - Severe Accident (SASPAM-SA), available at: https://zenodo.org/communities/saspam-sa/about
5. F. Mascari, “Safety Analysis of SMR with Passive Mitigation strategies – Severe Accident (SASPAM SA) Horizon Euratom Project”, ETSON NEWS, https://www.etson.eu/node/290 (2022).
6. F.Mascari et al., “Euratom SASPAM-SA project: main ideas and first outcomes”, Proceedings of the International Conference on Small Modular Reactors and their Applications (2024)
7. M. Principato et al., “Analyses of the MELCOR capability to simulate integral PWR using passive systems in a DBA scenario” , Nucl. Eng. Des, 437, 114004, 2025. DOI: https://doi.org/10.1016/j.nucengdes.2025.114004
8. F.Gabrielli et al., “Deliverable 2.2 iPWR input-deck and scenarios analyses”, Zenodo: https://doi.org/10.5281/zenodo.14052263(2024).
9. L. Humphries, B.A. Beeny et al., “MELCOR Computer Code Manuals Vol. 1: Primer and Users’ Guide”, Sandia National Laboratories (2025).
10. M. Carelli, L. Conway, M. Dzodzo, et al., "The SPES3 experimental facility design for the IRIS reactor simulation", Sci. and Techn. of Nuclear Installations (2009).
11. “IRIS International Reactor Innovative and Secure, IRIS Plant Overview”, https://www.nrc.gov/docs/ML0336/ML033600086.pdf, (2022).

12. P. Maccari, F. Mascari, Stefano Ederli et al., “ASTEC code DBA analysis of a passive mitigation strategy on a generic IRIS SMR”, Annals of Nuclear Energy, vol.156, 108194 (2021).

12th CONFERENCE ON
SEVERE ACCIDENTS RESEARCH
May 18-22, 2026 - Madrid, Spain
ERMSAR 2026

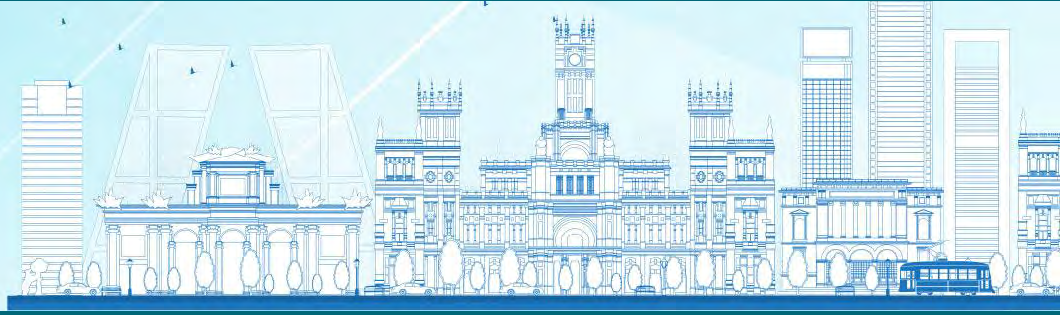

SAPIENZA
UNIVERSITÀ DI ROMA

MELCOR DEC-B Transients in a generic integral Pressurized Water Reactor

G. Marta[1], M. Principato[1], F. Mascari[2], F. Giannetti[1]

SAPAM-SA

1 Sapienza University of Rome, DIEE, NERG - Nuclear Engineering Research Group

2 ENEA NUC-ENER-SIC, Bologna Research Center

Outline

- SASPAM-SA Design-2
- Design 2 input deck summary
- Severe Accident Scenarios
- Problems and open issues
- Conclusion and future activities

SASPAM-SA Design 2

A high-end power iPWR configuration (about ***300 MW_e***) characterized by a dry containment and the extensive use of ***passive safety systems***.

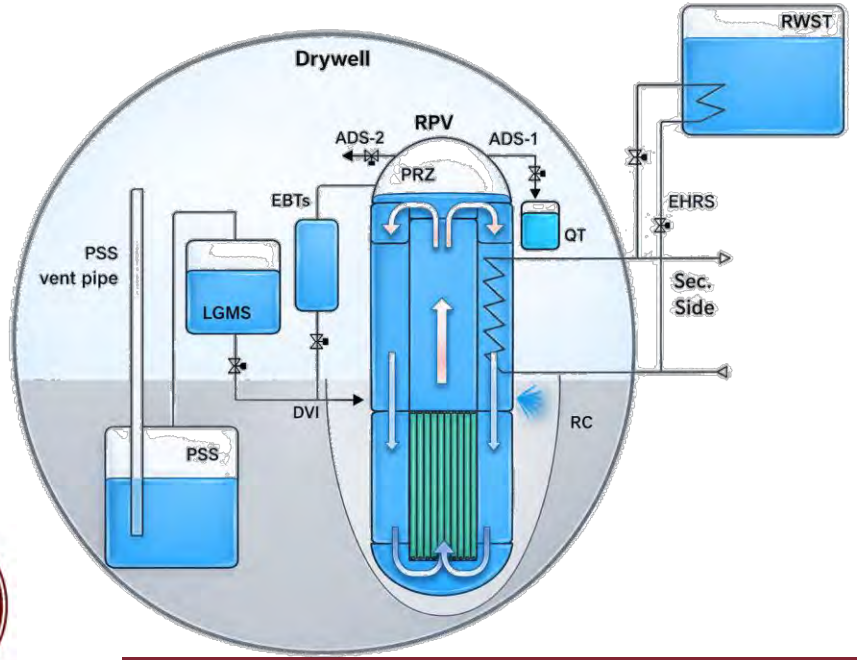

System	Safety features
EHRS	*passive cooling*
LGMS	*coolant make-up*
ADS-1	*depressurization*
ADS-2	*pressure equalization*
PSS	*pressure suppression*

Design 2 input deck summary

Secondary Circuit & EHRS

Drywell

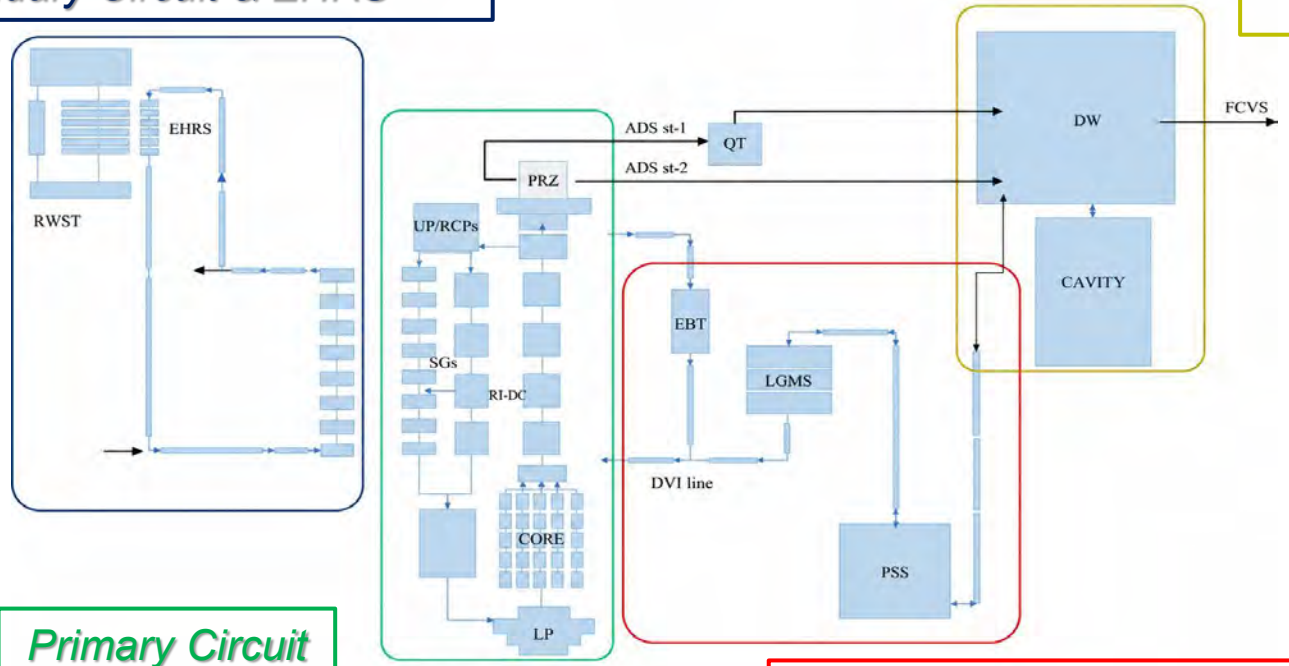

Primary Circuit

In-Containment Passive safety system

Design 2 input deck summary

Input deck modifications:

- **Filtered Containment Venting System**

Design Parameter	Value
upstream volume	*Drywell*
downstream volume	*Environment*
type	*Check valve*
cross-sectional area	*0.129 m^2*
opening pressure	*1.7 MPa*
closing pressure	*0.9 MPa*

- **DW liner condensation modeling**
  (Film Tracking Model + SPR Package)

Severe Accident Scenarios

The selected SA scenarios are initiated by the double guillotine break of **DVI line**

SA-1 (EHRS, ADS-1 ✗)

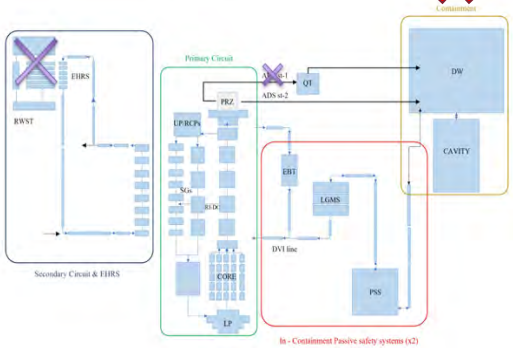

SA-2 (EHRS, ADS-1, ADS-2, LGMS ✗)

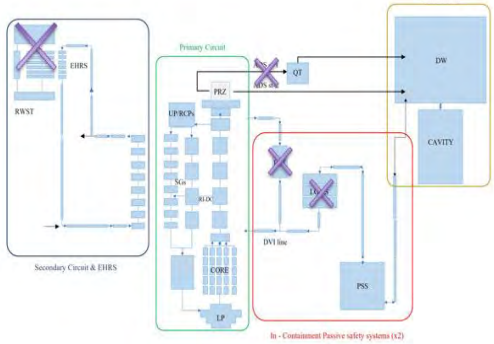

SA-3 (EHRS ✗)

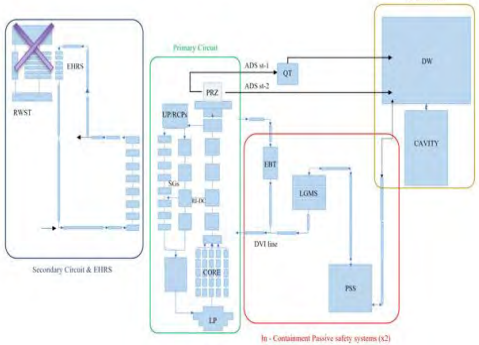

*Simulations carried out with **MELCOR 2.2 r2025.0.0**

Severe Accident Scenarios

Scenario	Postulated Failures	Mitigation Target
SA-1	ADS-1 and EHRS	Test containment coupling & PSS reverse flow
SA-2	All Safety Systems	Simulate unmitigated core degradation
SA-3	EHRS only	Evaluate effectiveness of remaining ADS-1/LGMS

Phenomenological Windows

Sequence	PhW	Main Phenomena	Start (s)	End (s)
SA-1	PhW 1	Blowdown, EBT injection, Oxidation onset	0	16364
	PhW 2	Core degradation, LGMS, PSS reverse flow, ADS-2, Reflood	16364	54154
	PhW 3	FVCS operation, PSS reverse flow	54154	260000
SA-2	PhW 1	Blowdown, EBT injection , PSS reverse flow, Oxidation onset	0	17645
	PhW 2	Core degradation, PSS reverse flow, Corium slump	17645	42360
	PhW 3	FVCS operation	42360	260000
SA-3	PhW 1	Blowdown, ADS-1, EBT ,LGMS, PSS reverse flow	0	10370
	PhW 2	Oxidation onset, PSS Reverse flow, Onset of core damage	10300	40031
	PhW 3	FVCS operation, PSS reverse flow, Core degradation	40191	151777
	PhW 4	ADS-2, Reflood, FVCS operation	151777	260000

Severe Accident Scenarios – SA1

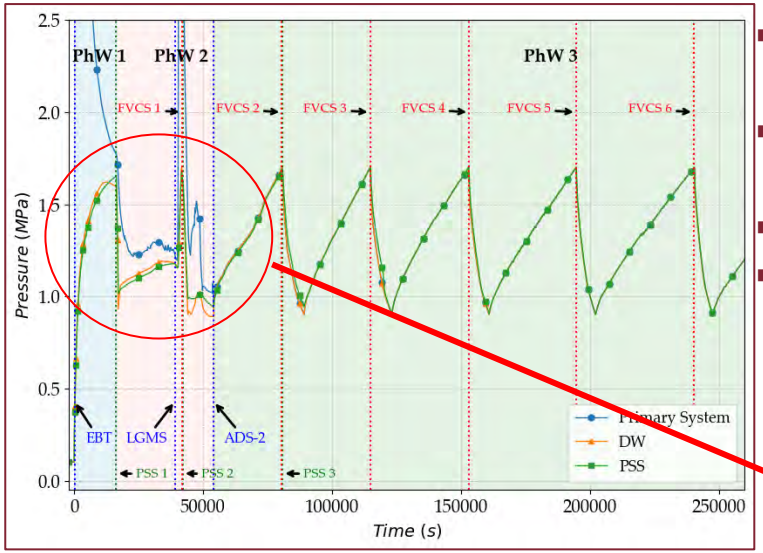

Pressure Trends

- The ADS-1 and EHRS combined failure produces a Severe Accident.
- The PSS reverse flow contributes to In-Vessel Melt Retention (IVMR) by flooding the cavity early in the transient.
- 6 FVCS actuations.
- After 15h from SOT, ADS-2 equalizes ***primary*** and ***drywell*** pressures.

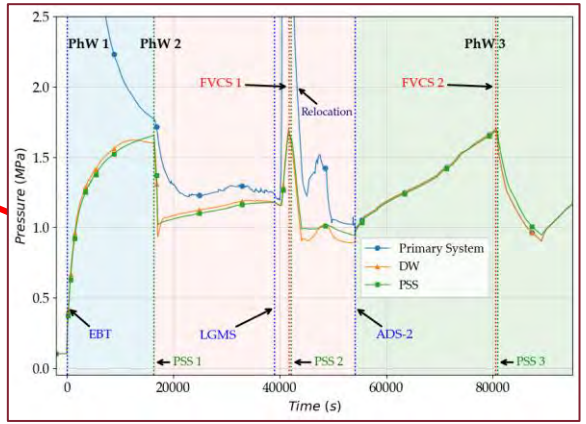

- **3 PSS reverse flows:** control the *DW pressure* contribute to flooding the *reactor cavity.*

SA1 water levels and temperature

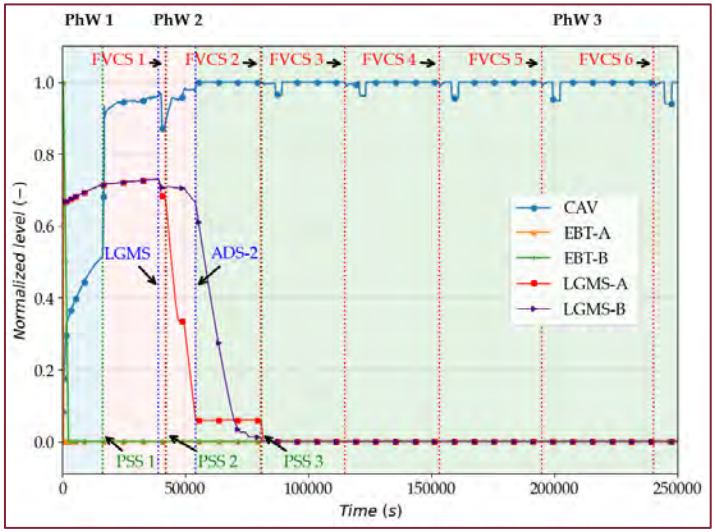

Collapsed normalized liquid level for EBT, LGMS and cavity

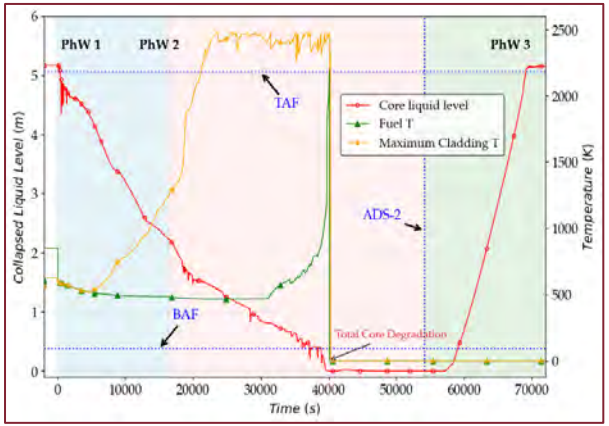

Core collapsed liquid level/Fuel and Maximum Cladding T

- At the end of simulation (72 h), the ***core level*** is above the **TAF**.

- **Reactor Cavity** results completely flood (*in all 3 scenarios*).

- **LGMS *water injection*** takes place rapidly; however, this does not prevent complete melting and the relocation of the molten corium into the lower plenum.

SA1 release frations

- The noble gases class (Xenon) are fully released.

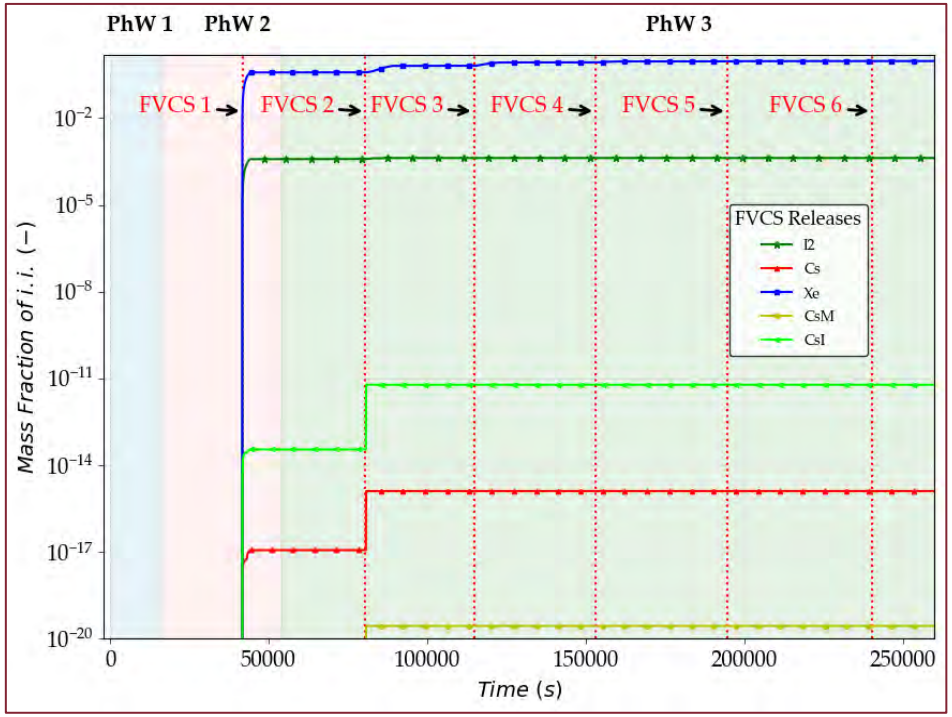

FVCS releases in mass fraction of initial inventory

- The halogen class (Iodine) releases are higher than those of the remaining classes

Severe Accident Scenarios – SA2

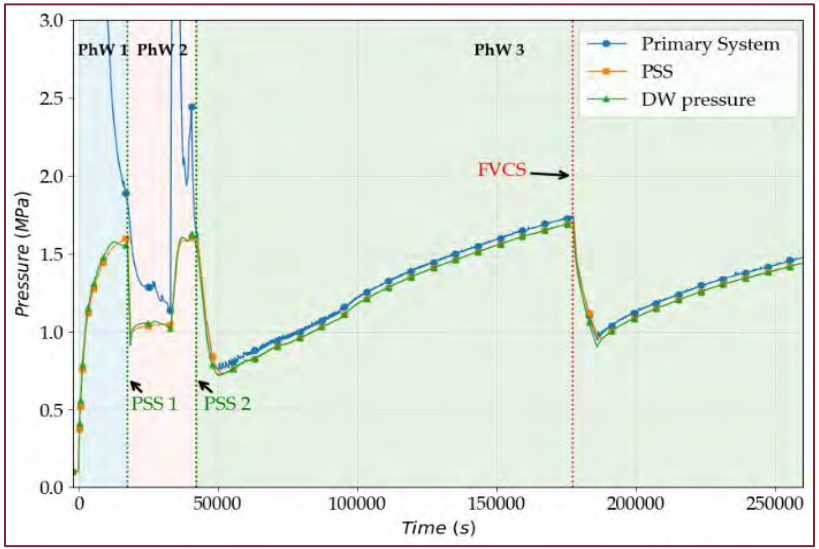

Pressure Trends

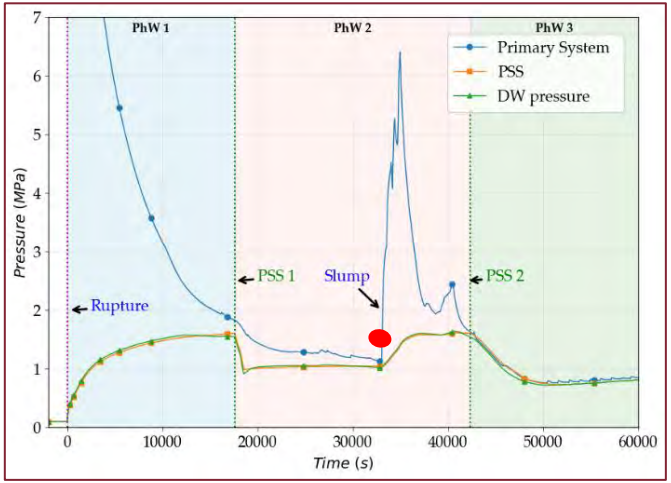

Corium Slump = spike of 6.22 MPa on Primary System pressure

(*reduced impact on DW and PSS pressures)

- The 2 PSS reverse flows reducing the DW pressure before FVCS actuation.
- 1 FVCS actuation, after 50 hours from SOT (***core is already totally molten***).

Severe Accident Scenarios – SA2

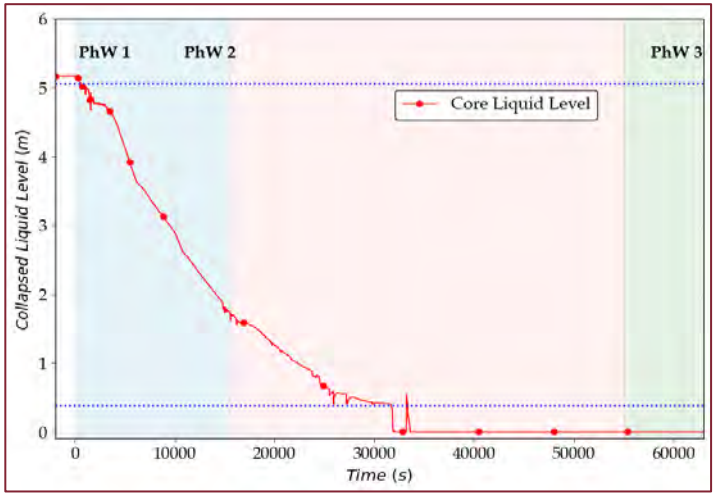

Core collapsed liquid level

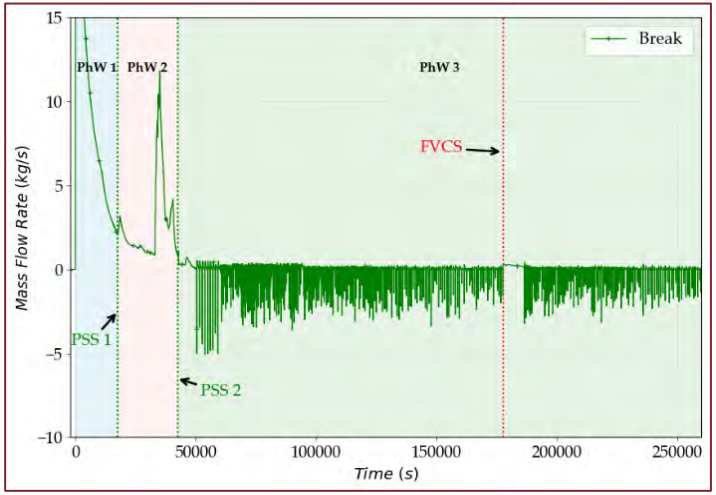

Break mass flow rate

- The ***core level*** decrease rapidly under the critical lower level (BAF), leading to *complete core degradation* in less than 7 hours from SOT.

- Water injection into the primary circuit/RPV is provided solely by the flooded **Reactor Cavity** ***(negative values on this picture)***

Severe Accident Scenarios – SA2

- Releases are reduced respect previous case; there is only one FCVS actuation.

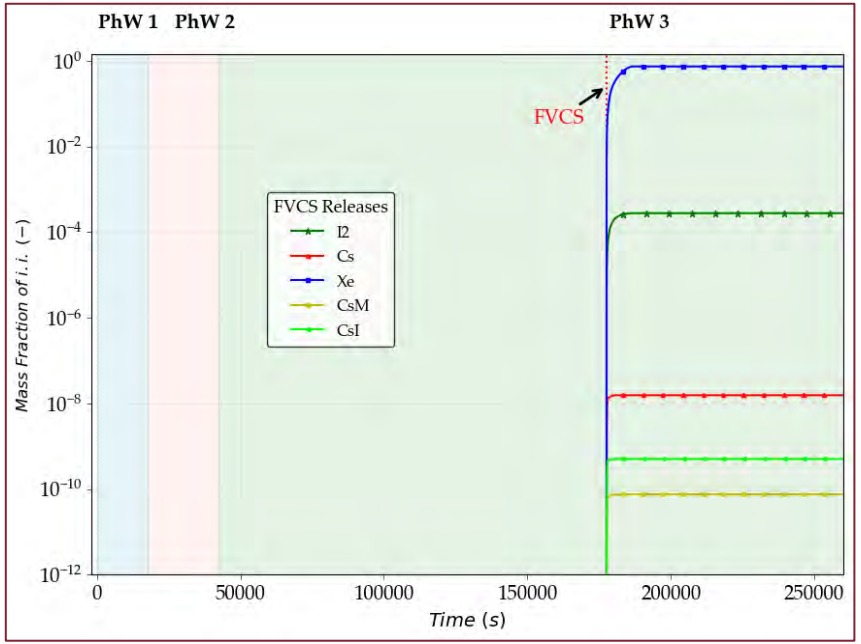

FVCS releases in mass fraction of initial inventory

Severe Accident Scenarios – SA3

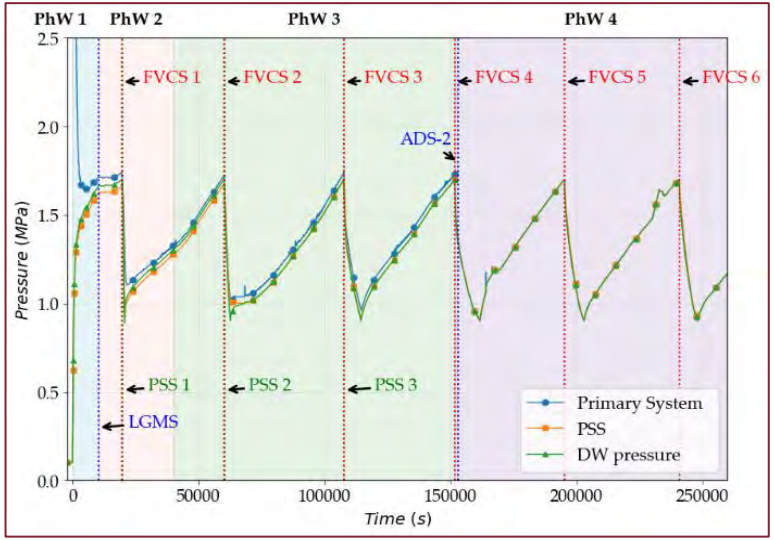

Pressure Trends

- **SA-3** has a different phenomenology; safety injection from EBT, LGMS and **Reactor Cavity** injection prevent complete core degradation.
- 6 FVCS actuations

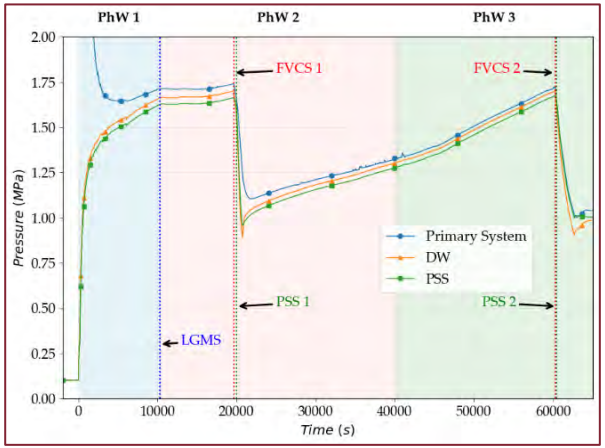

- The first FCVS actuation causes a series of phenomena: the pressure in the main system drops, mass flows from the break and ADS-1 have a significant peak and the 1st PSS reverse flow is triggered, filling the reactor cavity.

Severe Accident Scenarios – SA3

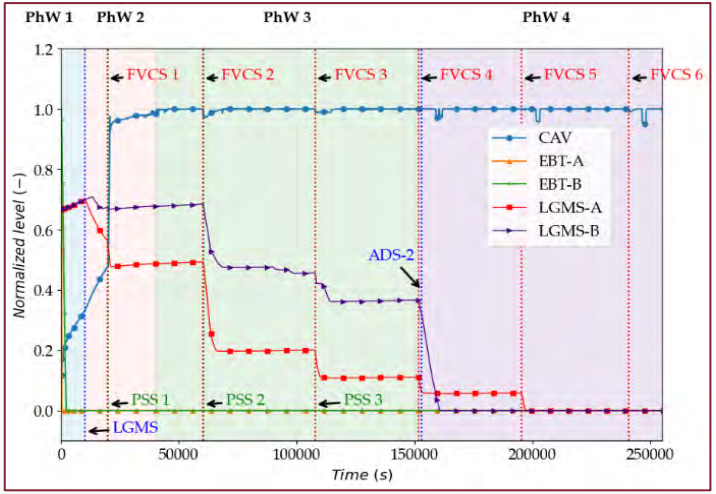

Collapsed normalized liquid level for EBT, LGMS and cavity

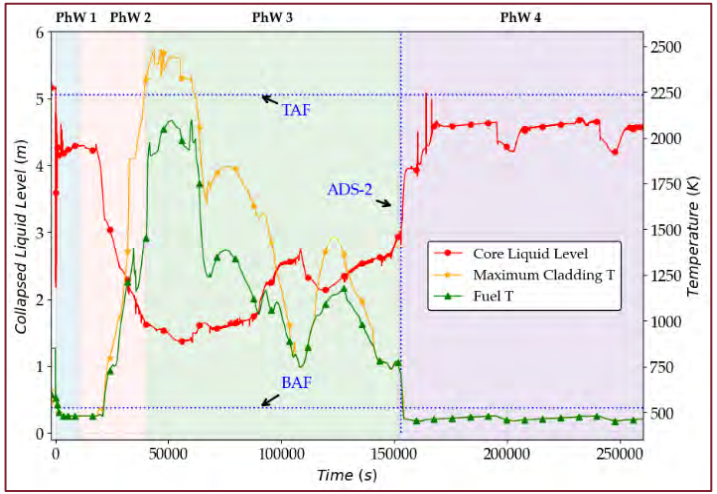

Core collapsed liquid level/Fuel and Maximum Cladding T

- The *injection* of LGMS follows the opening and closing cycles of the FCVS.
- ADS-2 actuation is delayed respect SA-1 (42.50 h).
- The water level inside the *core* ensures that only **22%** of the core is damaged.

Severe Accident Scenarios – SA3

- For halogen, releases are lower than SA-1 but higher than SA-2, while noble gases exhibit an overall lower release.

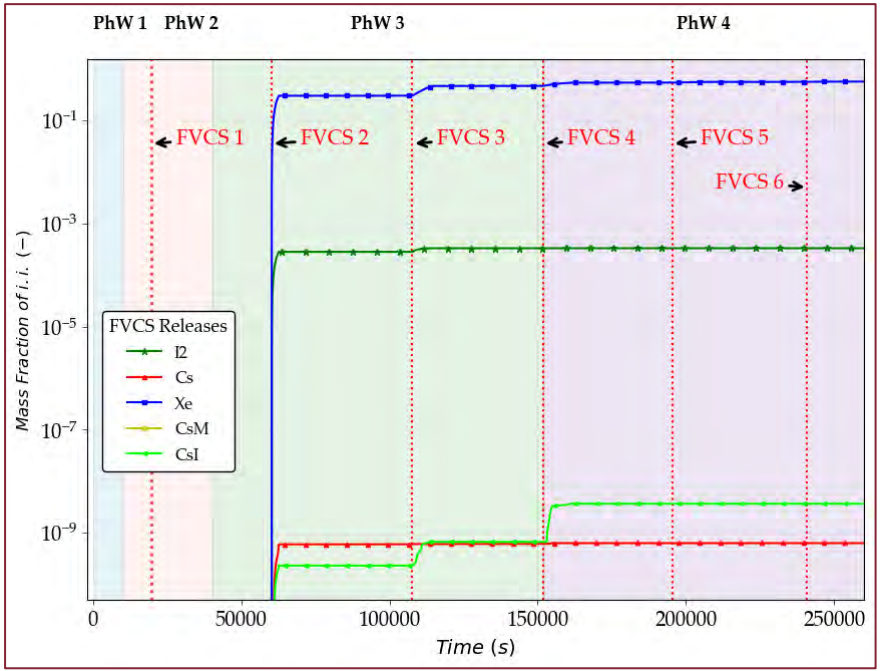

FVCS releases in mass fraction of initial inventory

Core degradation sequences

SA-1

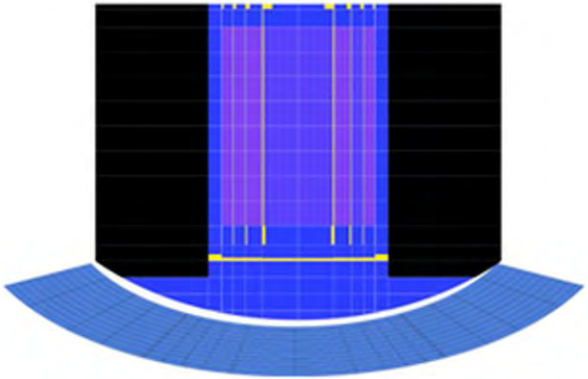

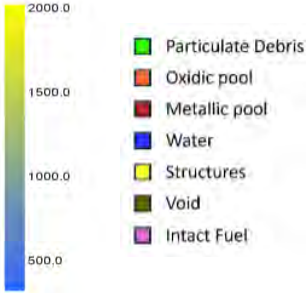

SA-3

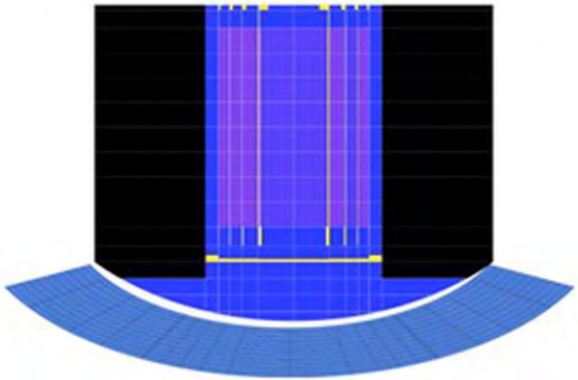

SA-2

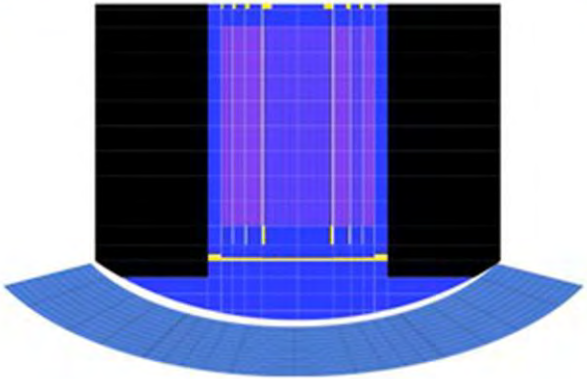

Comparative Core Degradation

Metric	SA-1 (Delayed ADS-2)	SA-2 (All failed)	SA-3 (ADS-1 active)
Time to Core Damage	6.07 hours	5.03 hours	11.11 hours
Core State	Total Melting - IVR	Total Melting -IVR	22% Damage
Corium Relocation	Yes (Lower Plenum)	Yes (Lower Plenum)	Partial (No slump)
Final Core Level	Above TAF (at 72h)	Water from break	Restored to pre-break

Problems and open issues

- The FCVS design parameters for Design-2 were adopted from a large dry containment *PWR* venting system.
- Multiple openings are observed; "large PWR" vent on a "small iPWR" containment means the pressure drops too fast when the valve opens, causing it to slam shut immediately, leading to rapid cycling: design requires iPWR-specific scaling.
- A sensitivity and uncertainty analysis is required to explore the results.

Conclusions and Future Activities

- The expected containment phenomenology in a Severe Accident Scenario are predicted using MELCOR, also using a simple containment nodalization.
- The main *passive safety* system was simulated as expected.
- *Radionuclide releases* through the FCVS showing that halogens are partially retained, while noble gases experience the highest release; other classes remain negligible.
- Potential cliff-edge effect associated with reverse flow in the PSS. The containment volumes are much smaller than a standard PWR. A slight error in predicting containment pressure could mean the difference between the cavity flooding or remaining dry.

- Future new analyses, coupling dose evaluations using HYSPLIT/WinMACCS.

Acknowledgement/Disclaimer

SAFETY ANALYSIS OF SMR WITH PASSIVE MITIGATION STRATEGIES - SEVERE ACCIDENT

Funded by the European Union

Funded by the European Union. Views and opinions expressed are however those of the author(s) only and do not necessarily reflect those of the European Union or European Commission-Euratom.
Neither the European Union nor the granting authority can be held responsible for them.

SAFETY ANALYSIS OF SMR WITH PASSIVE MITIGATION STRATEGIES - SEVERE ACCIDENT

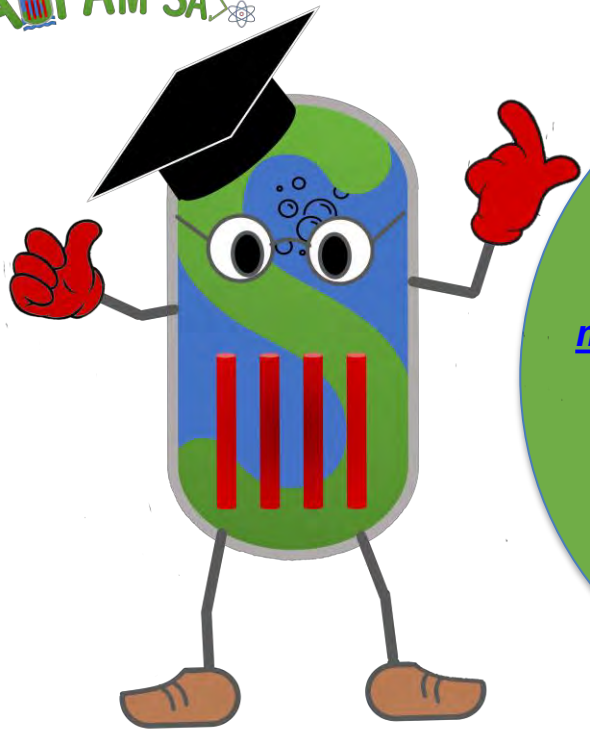

giacomo.marta@uniroma1.it

marcello.principato@uniroma1.it

fulvio.mascari@enea.it

fabio.giannetti@uniroma1.it

Thank you for listening!

VALIDATION OF THE THEORETICAL APPROACH FOR MODELLING OF THE HYDRIDE MORPHOLOGY WITH EXPERIMENTAL DATA OBTAINED FROM SPIZWURZ BUNDLE TEST

Mikhail Kolesnik*, Juri Stuckert, Mirco Grosse, Sarah Weick
Institute for Applied Materials – Applied Materials Physics (IAM-AWP), Karlsruhe Institute of Technology, Karlsruhe, Germany
mikhail.kolesnik@kit.edu

ABSTRACT

This paper presents the calibration and assessment of two complementary simulation tools using new experimental data on hydride morphology in zirconium alloy fuel cladding. The first tool is based on the numerical solution of a system of ordinary differential equations, predicting averaged microstructural quantities including the radial hydride fraction, hydride length and hydride volume density. The second, MORPHYD explicitly simulates the nucleation and diffusion-controlled growth of disc-shaped hydrides within a virtual 3D domain. In the present work, MORPHYD is applied only to 100 wppm cases because its current version is limited to precipitation-only simulations of small, non-overlapping hydrides. MORPHYD also enables the evaluation of hydride network connectivity metrics and their statistical distributions based on the Monte Carlo method, repeating the simulations a statistically significant number of times. In both approaches, hydride nucleation is described within a classical heterogeneous framework in which the defect energy for nucleation sites is defined by the user-specified distribution. Both modelling approaches were calibrated using new experimental data obtained from the SPIZWURZ bundle test on cladding tubes manufactured from Zircaloy-4 and opt. ZIRLO. The SPIZWURZ included long-term hydride reorientation experiments conducted at the LICAS facility of the Karlsruhe Institute of Technology. The test bundle consisted of 21 hydrogen-charged cladding tubes, each 2.5 meters long, which were subjected to slow, stepwise cooling over 250 days to reproduce as close as possible dry storage conditions for spent nuclear fuel. The following morphological parameters were measured experimentally across a spectrum of hydrogen concentrations and applied stresses: radial hydride fraction, hydride length and surface density, hydride continuity coefficient (HCC) and radial hydride continuity path (RHCP). The results show that, after calibration, both simulation tools reproduce the main experimental trends in hydride morphology and connectivity, supporting their further development and application for assessing hydride embrittlement of fuel rod cladding under dry storage conditions.

KEYWORDS
hydride embrittlement, zirconium alloys, dry storage, spent nuclear fuel, modelling

1. INTRODUCTION

Hydride embrittlement of zirconium claddings can pose a risk to the integrity of cladding tubes, especially during post-operational storage [1], [2]. Hydrides are capable of providing low energy brittle crack pathways, which determine the influence of hydride morphology on the degree of embrittlement [3]. Macroscale hydride morphology is the result of the agglomeration (or stacks) of microscale ones, forming a complex "cornflake" 3D surface [4], [5]. In simplified form, macroscale hydrides can be approximated as plates and specified by their length, thickness, volume density and orientation. The entire hydride network can also be characterized by its connectivity. Hydride connectivity shows the strongest correlation with the

degree of hydride embrittlement among other metrics [6]. The ductile to brittle transition is associated with percolation of brittle crack through hydrides and corresponds to the threshold of the connectivity [3].

The morphology of hydrides is determined by the alloy texture, hydrogen concentration and thermomechanical conditions during hydride precipitation and growth. The orientation of hydrides at low stresses is determined by the texture and microstructure of the alloy. However, when external stresses exceed the threshold, hydrides tend to nucleate and grow perpendicular to the external tension [7]. Temperature is another parameter that can theoretically influence the orientation of precipitating hydrides [8]. The density, length and thickness of the hydrides are strongly determined by the cooling rate. Slow cooling rates increase length and thickness and decrease number density [9].

Temperature regimes for long-term dry storage (DS) and transport of spent nuclear fuel (SNF) include the drying of fuel assemblies in storage or transport casks. During drying, the temperature of the fuel assemblies can rise to about ~ 400 °C due to decay heat in the fuel pellets, resulting in dissolution of all or a significant part of the hydrides. The hydrides will later reprecipitate as the temperature slowly decreases with the natural reduction of decay power. Meanwhile, the cladding is loaded by the internal gas pressure, creating hoop tension. These conditions can potentially lead to the precipitation of long radially oriented hydrides, increasing the degree of embrittlement. The safety assessment of DS regimes should include the prediction of hydride morphology, based on experimental investigations of embrittlement mechanisms and simulations adapted to particular conditions. Research in both directions is currently being carried out at the Karlsruhe Institute of Technology (KIT) within the framework of the SPIZWURZ project [10]. This paper presents the results of the calibration of two theoretical approaches developed for the simulation of hydride morphology in zirconium alloys on new experimental data.

2. EXPERIMENTAL CONDITIONS. SPIZWIRZ BUNDLE TEST

The experimental SPIZWURZ bundle consisted of 21 cladding tubes with a length of 2.5 m, manufactured from Zircaloy-4, opt. ZIRLO, and the duplex alloy DX-D4 and hydrogen-charged to one of two target concentrations, 100 or 300 wppm. The spatial arrangement of the rods within the bundle is shown in Fig. 1. A detailed analysis of the experimental results concerning hydride morphology, as well as a description of the SPIZWURZ experiment, can be found in [11].

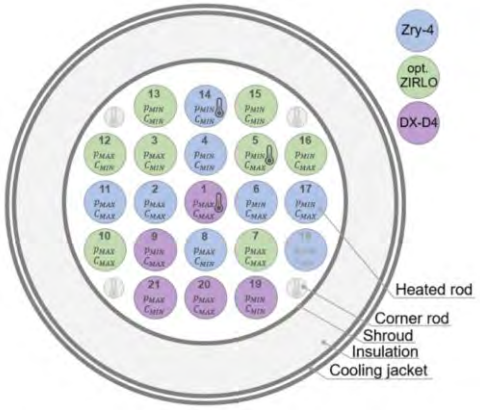

Figure 1: Schematic cross-section of the SPIZWURZ bundle. Rod arrangement

At the present stage, eight rods were selected for simulation and comparison with experimental data. These included rods 2, 4, 6, and 8 manufactured from Zircaloy-4 and rods 10, 12, 15, and 16 manufactured from opt. ZIRLO. For each alloy, the selected rods represent all combinations of the two target hydrogen

concentrations and two target internal gas pressure levels. The internal gas pressure histories applied in the simulated rods are shown in Fig. 2. Two target pressure levels, 106 and 146 bar, corresponding to approximate hoop stresses of 68 and 93 MPa, respectively.

The thermal scenario of the bundle consisted of heating up to approximately 400 °C, followed by slow, stepwise cooling. The axial temperature profiles measured by thermocouples in three instrumented rods are shown in Fig. 3*a*, where the axial coordinate of 0 mm corresponds to the beginning of the actively heated region. Fig. 3*b* presents the temperature history in the hottest axial position of rod 1 (at an elevation of 520 mm). Several abrupt temperature drops (Fig. 3*b*) are associated with unexpected power blackouts during the experiment. For the numerical simulations, smoothed temperature histories were applied, Fig. 3*b*.

The rods selected for simulations were not equipped with thermocouples; therefore, their temperature histories had to be inferred. Rods 2, 4, 6, and 8 are located symmetrically in the second layer of the bundle. Consequently, their temperature scenarios were assumed to be identical and were defined as the average of the thermocouple readings from rods 1 and 5. Rods 10, 12, 15, and 16 are located in the outer layer of the bundle; for these rods, the temperature histories were assumed to be identical to each other and equal to the thermocouple measurements obtained from rod 14, which belongs to the same layer. All temperature scenarios assumed in the simulations were smoothed in a similar way to that shown in Fig. 3*b* for the hottest zone of rod 1. These smoothed profiles remove abrupt temperature drops, short-term fluctuations of about 5 °C during holding periods, and minor non-monotonic variations, while preserving the overall thermal history and the effective cooling rates of the main cooling steps for calibration and assessment.

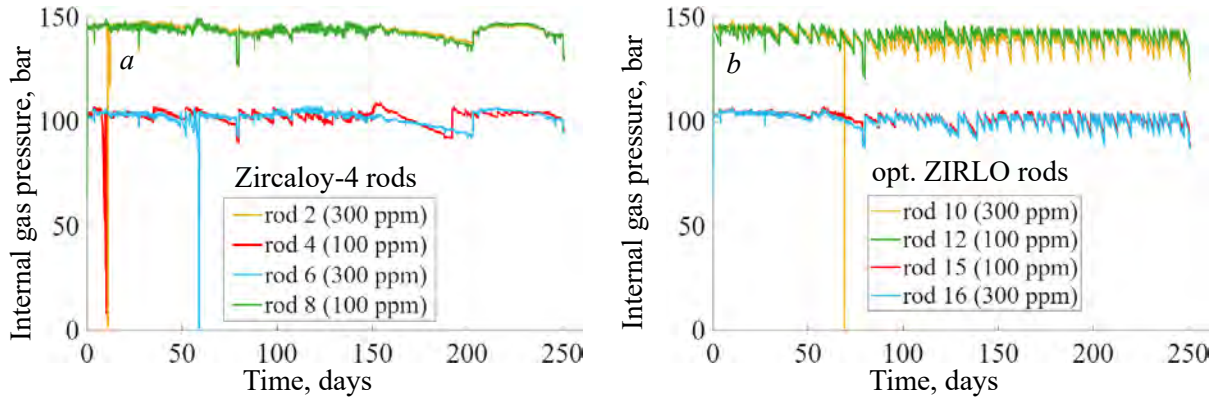

Figure 2. Internal pressure scenarios in simulated rods: a) – Zircaloy-4 rods, b) – opt. ZIRLO rods

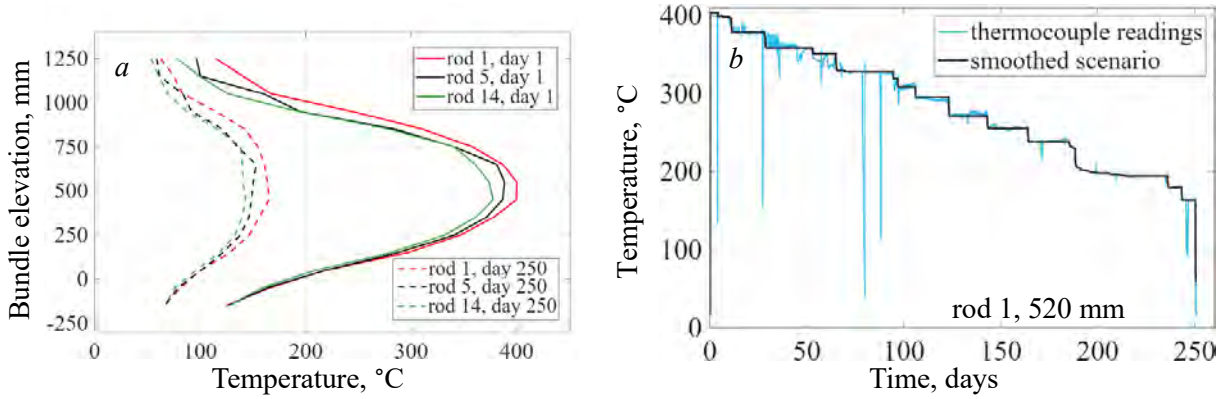

Figure 3. Bundle temperature: a) axial temperature profiles, b) temperature scenario in rod 1 at 520 mm: thermocouple readings and smoothed temperature scenario, used in simulations

3. A SIMULATION TOOL BASED ON ODE SYSTEM SOLUTION

3.1. The description of the tool

The first approach is based on the numerical solution of the system of ordinary differential equations (ODE). The simulation tool used here is based on the concept described in [12] after modernization. The ODE system has four independent variables: the hydrogen concentration in solid solution (C_s), the fraction of hydrides elongated in the radial direction (θ) and the volume density of the radial and circumferential hydrides (n_r and n_r).

The kinetics of hydrogen concentration in solid solution C_s during dissolution and precipitation of hydrides is described as the relaxation of supersaturation with a characteristic time τ_0, by analogy with [13]:

$$\frac{\mathrm{d}C_s}{\mathrm{d}t} - \frac{C_s - C_e}{\tau_0} = 0 \tag{1}$$

where C_e denotes the equilibrium hydrogen solubility, which is different for dissolution and precipitation; the characteristic time τ_0 is estimated as $\tau_0 = V_{per\ hydride}/(d \cdot D_{\mathrm{H}})$, where $V_{per\ hydride} = n^{-1}$ is the volume per hydride (n is the mean hydride concentration), and dD_{H} characterizes the diffusional-controlled sink efficiency of an average hydride, with d being the average hydride diameter and D_{H} the hydrogen diffusion coefficient.

The fraction of radially oriented hydrides θ is assumed to be constant during dissolution of hydrides and can be written as follows for precipitation [12], [13]:

$$\frac{\mathrm{d}\theta}{\mathrm{d}t} = -\frac{f_r - \theta}{C_{tot} - C_s} \cdot \frac{\mathrm{d}C_s}{\mathrm{d}t} \tag{2}$$

where C_{tot} is the total hydrogen concentration (both in solid solution and in hydride phase), and f_r is the fraction of hydrogen precipitating as a component of radially oriented hydrides at the current step [12], [13]:

$$f_r = \frac{1}{1 + f_0 \cdot \exp(-\sigma \cdot \Delta\Omega/kT)} \tag{3}$$

where f_0 and $\Delta\Omega$ are model parameters, determined the susceptibility of hydrides to reorientation.

The process of nucleation of new hydrideы on crystal lattice defects is simulated in the classical heterogeneous approximation, where the nucleation rate R is [12]:

$$R = n_0 Z j^* \cdot \exp(-\Delta G^*/kT) \tag{4}$$

where n_0 is the volume density of the nucleation sites, j^* is the hydrogen flow to the critical nucleus of the hydrides, Z is the Zeldovich factor and ΔG^* is the Gibbs energy change after the hydride nucleation, which can be written as [12]:

$$\Delta G^* = \Omega^*(g_m - \Delta\mu/v_{\mathrm{H}}) + S^*\gamma - E_d \tag{5}$$

where g_m is the mechanical deformation energy due to the volume dilatation [12], $\Delta\mu$ is the chemical energy change per unit volume, v_{H} is the atomic volume of hydrogen, γ is the metal/hydride interphase energy, Ω^* and S^* are the volume and surface area of the critical hydride nucleus, E_d is the defect energy of the nucleation sites. The defect energy of the particular nucleation site depends on the defect type and its specific features and is assumed here to be a random value with a normal distribution. The nucleation kinetics of hydride stacks at the precipitation stage is estimated as the integral over all vacant nucleation sites of the nucleation frequency from Eq. (4), [12]:

$$\frac{\mathrm{d}n}{\mathrm{d}t} = \int_{E_{d,min}}^{E_{d,max}^{frei}} Gauss(E_d) \cdot R(E_d) \cdot \mathrm{d}E_d \tag{6}$$

Gauss denotes a normal distribution over energies, with the mean value E_{d0} and standard deviation $\bar{\sigma}$. Nucleated hydrides are radial with probability equal to f_r and circumferential with probability $(1 - f_r)$:

$$\frac{\mathrm{d}n_r}{\mathrm{d}t} = f_r \cdot \mathrm{d}n, \quad \text{and} \quad \frac{\mathrm{d}n_c}{\mathrm{d}t} = (1 - f_r) \cdot \mathrm{d}n \tag{7}$$

It is assumed, that the nucleation sites with maximum defect energy are filled first, and therefore the maximum defect energy of vacant nucleation sites $E_{d,max}^{frei}$, required for the integration in Eq. (6), is [12]:

$$\frac{1 + \mathrm{erf}\left(\left(E_{d,max}^{frei}, -E_{d0}\right)/\sqrt{2} \cdot \bar{\sigma}\right)}{2} = \frac{n_r + n_c}{n} \tag{8}$$

The ODE system, including Eqs. (1), (2) and (7), is solved numerically. The main model parameters are presented in Table I in the Appendix.

3.2. Calibration and assessment of the approach based on the ODE solution

Fig. 4 present the comparison of calculated RHF on experimental data for Zircaloy-4. Two sets of numerical results are shown: blind pre-test and post-test simulations. The pre-test simulations systematically overestimate the RHF, whereas the post-test simulations exhibit significantly improved agreement with the experimental data. This discrepancy can be attributed to two main factors. First, the actual hydrogen concentrations were determined only after the experiments by destructive hot-gas extraction, which data were not available for pre-test simulations. Second, different parameter sets governing hydride reorientation (f_0 and $\Delta\Omega$ in Eq. (3)) were used in the pre-test and post-test simulations. In the pre-test simulations, these parameters were fitted using the most conservative values reported in the literature (Fig. 8*a* in [14]), which resulted in an over-conservative prediction of RHF. For the post-test simulations, the model parameters were calibrated using a larger experimental database, including the new results obtained within the SPIZWURZ experiment, leading to a substantially improved model–experiment agreement. Since SPIZWURZ data were included in calibration, these post-test simulations are used to assess calibrated model performance and identify remaining deviations and trends, rather than as fully independent validation. A noticeable deviation is seen only for rod 8. We attribute this to a likely contact between the cladding and the pellet imitator, which is supported by the abnormal deformation pattern of this tube.

Fig. 5 shows the model–experiment comparison for RHF in opt. ZIRLO. In contrast to Zircaloy-4, opt. ZIRLO exhibits a lower propensity for hydride reorientation. This behavior is captured in the model through a single alloy-dependent parameter controlling the sensitivity of hydride reorientation to applied stresses ($\Delta\Omega$ in Eq. (3)). The calculated mean absolute error (both alloys) for RHF is 0.04.

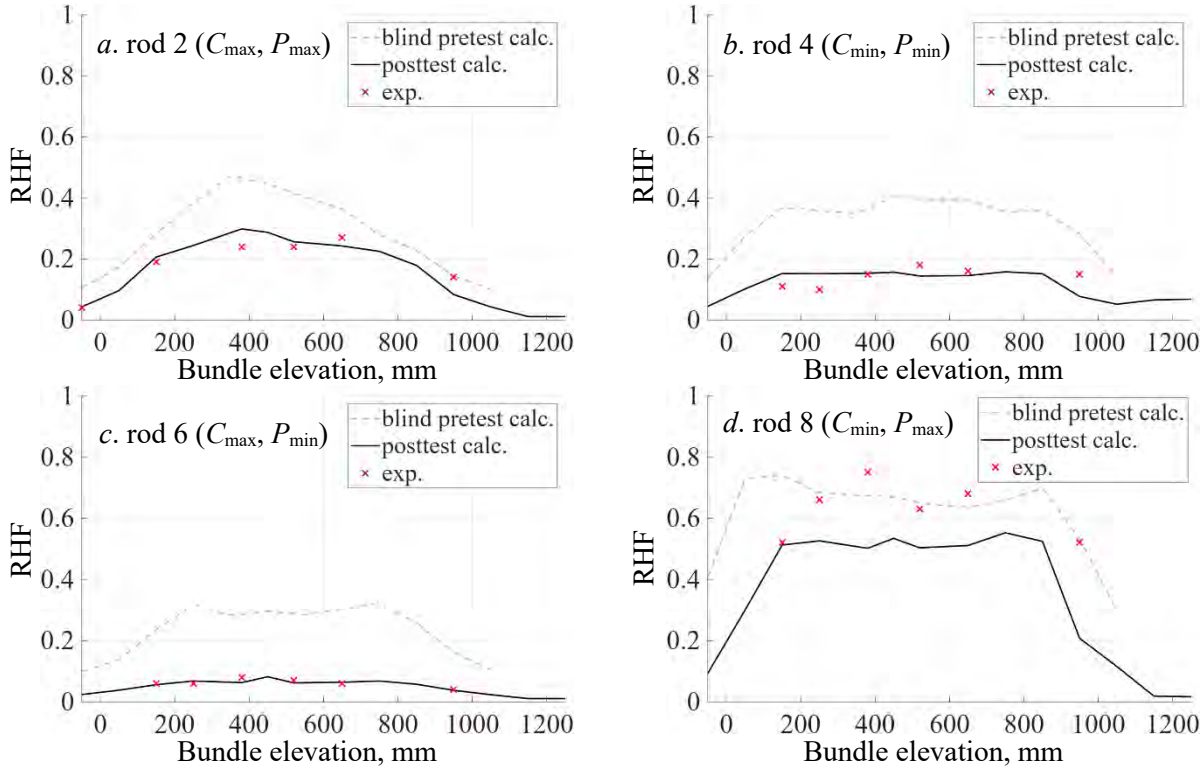

Figure 4. RHF in Zircaloy-4, model-experiment comparison; C_{max}/C_{min} corresponds to 300/100 ppm, (target concentration), P_{max}/P_{min} corresponds to 146/106 bar (target internal pressure)

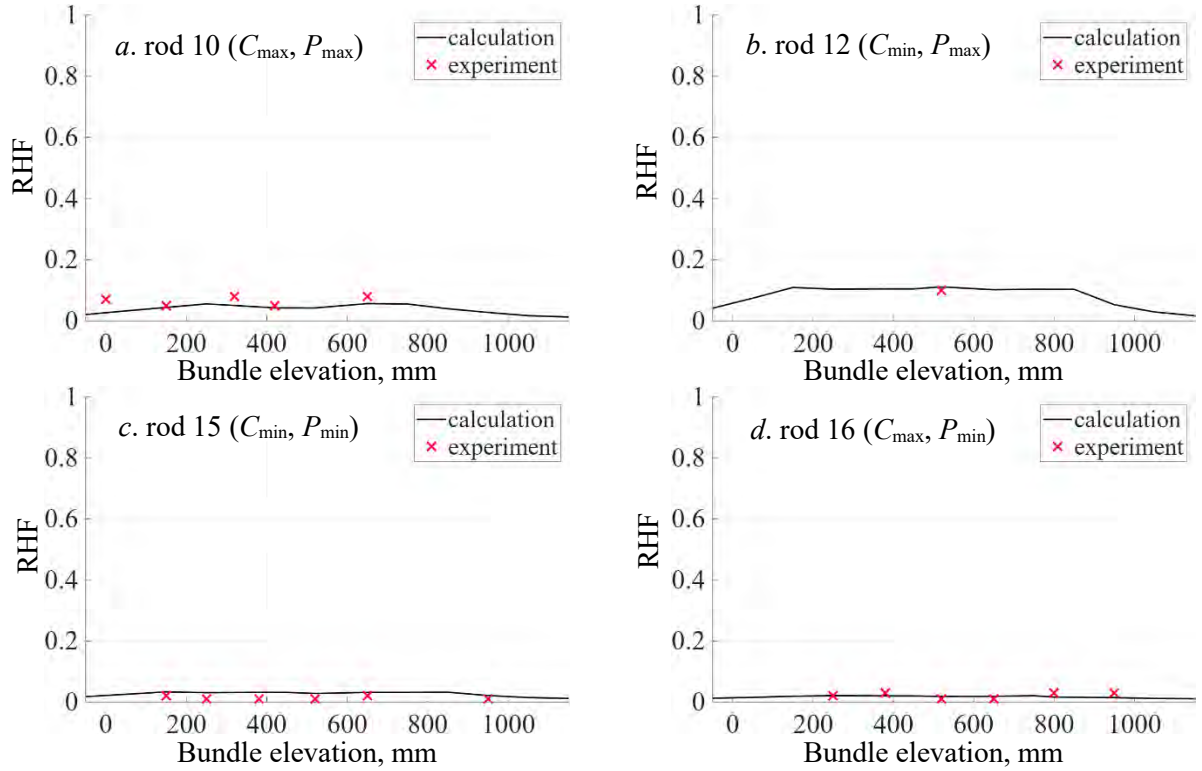

Figure 5. RHF in opt. ZIRLO, model-experiment comparison; C_{max}/C_{min} corresponds to 300/100 ppm, (target concentration), P_{max}/P_{min} corresponds to 146/106 bar (target internal pressure)

Figs. 6 and 7 compare the mean hydride length and hydride surface density for Zircaloy-4 and opt. ZIRLO. The simulated and experimentally measured values may differ by up to a factor of two, which is considered acceptable at the current stage of tool development. The calculated relative RMSE values for hydride length and hydride density are 25% and 20%, respectively. Hydride length and density are governed by the balance between the nucleation rate and the supersaturation relaxation rate and are therefore highly sensitive to uncertainties in key model parameters, including hydrogen solubility, hydrogen content, and defect-related energies. The present results were obtained using a smoothed temperature scenario (Fig. 3*b*). Compared to Zircaloy-4, opt. ZIRLO exhibits longer hydrides and a lower hydride surface density. This alloy-dependent behavior is captured in the model by assuming different densities of nucleation sites (n_0 in Eq. (4)), which may be associated with differences in crystallographic texture and in the density of high-energy grain boundaries with large misorientations.

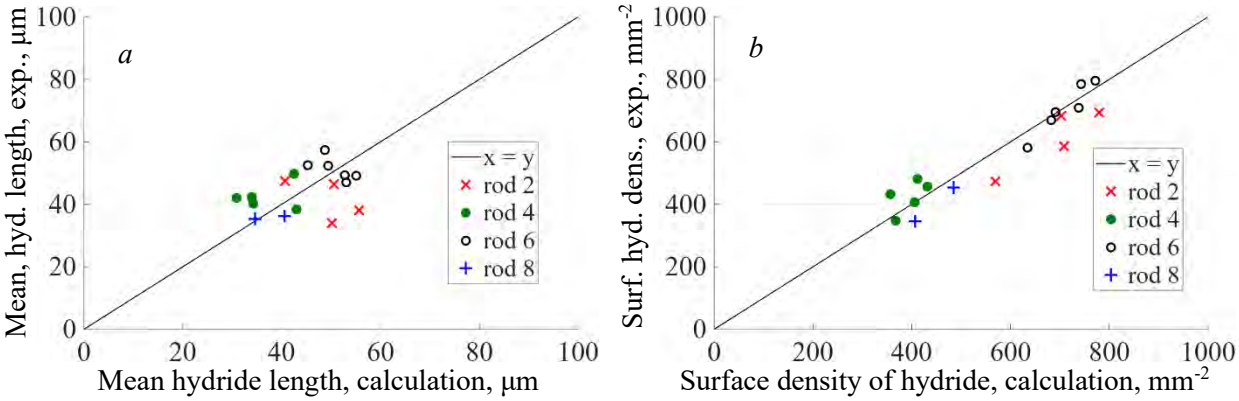

Figure 6. Experiment vs. calculation comparison in Zircaloy-4; *a*) mean hydride length, *b*) surface density of hydrides (number of hydrides per unit area on the micrograph)

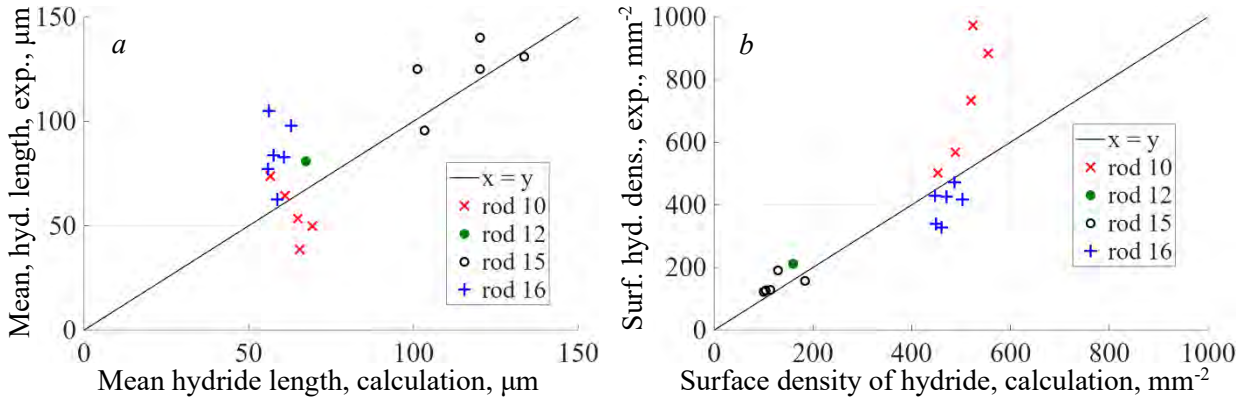

Figure 7. Experiment vs. calculation comparison in opt. ZIRLO; *a*) mean hydride length, *b*) surface density of hydrides (number of hydrides per unit area on the micrograph)

4. MORPHYD SIMULATION TOOL

4.1. The description of the tool

The numerical tool MORPHYD (an acronym of MORPHology of HYDrides), described in [15], [16], is another approach used to simulate the morphology of hydrides under the conditions of the SPIZWURZ bundle test. The physical basis of MORPHYD is very similar to the model described above; however, the

numerical realization is different. The fundamental difference is that MORPHYD simulates the nucleation and growth of disc-shaped hydrides in a virtual 3D domain. Nucleation occurs at uniformly distributed nucleation sites (defects in the crystal lattice) with a probability at the current time step τ equal to $r \cdot \tau$, where $r = R/n_0$ and R is given by Eq. (4). The orientation of the nucleated hydride is the stochastic value: the probability for radial orientation is f_r, and for circumferential orientation is $(1 - f_r)$, where f_r is determined by the Eq. (3). The growth of hydrides is determined by the diffusive flow from the solid solution to the end of the edge of the disk-shaped hydride [15], [17]. Another assumption is that each hydride can only absorb hydrogen from the space where it is the nearest hydride (in its Voronoi cell) [16]. This assumption takes into account the "clustering effect", i.e. that randomly closely related hydrides are expected to be shorter, than isolated ones due to "competition" for the hydrogen in the solid solution, needed for their growth during cooling.

Fig. 8*a* shows the MORPHYD simulation result for the hydride morphology in rod 4 at an elevation of 520 mm. Fig. 8*b* presents a cross-section of the simulated domain shown in Fig. 8*a*, which can be directly analyzed by analogy with the corresponding experimental micrographs. All MORPHYD simulation results are stochastic in nature. By repeating the simulations a statistically significant number of times, the statistical distributions of hydride morphology parameters can be evaluated using a Monte Carlo approach.

At its current stage of development, the model is limited to the simulation of the precipitation phase and is applicable only to small, non-overlapping hydrides, whose characteristic size remains smaller than the inter-hydride spacing. Consequently, MORPHYD was applied exclusively to samples with a hydrogen content of 100 ppm.

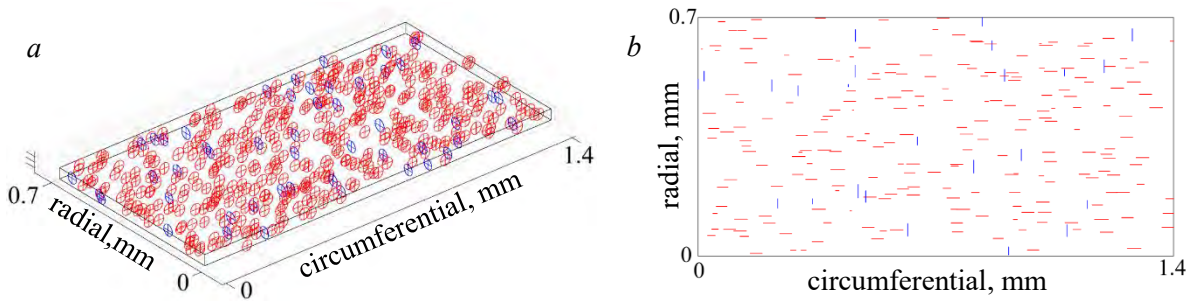

Figure 8: A single MORPHYD simulation result for rod 4 at 520 mm: *a*) disk-shaped hydrides with two orientations in a 3D domain; *b*) cross-section of the domain used for morphology analysis

4.1. Calibration and assessment of the MORPHYD

The following metrics were simulated with MORPHHYD and compared with experimental data: hydride length, hydride continuity coefficient (HCC, the sum of hydride length projected in radial direction in a 110 μm wide band, [6]) and radial hydride continuity path (RHCP, estimated as the relative reduction in calculated fracture energy for a given morphology compared to the samples without hydrides [6], [18]). By repeating the simulations at least 100 times, the statistical distribution of these morphology metrics can be estimated based on the Monte Carlo method. The calculated probability density functions (PDF) for the hydride morphology metrics in rods 4, 8, 12 and 15 at elevation 520 mm (the hottest axial zone) are compared with the experimental results on Figs. 9 – 11.

As shown in Fig. 9, the mean value and the width of the hydride length distributions obtained from simulations are in good agreement with the experimental data for both Zircaloy-4 and opt. ZIRLO. A notable

deviation is observed for rod 12, for which the simulated mean and distribution width are approximately a factor of two lower than the experimental values. Nevertheless, this discrepancy is considered acceptable at the current stage of tool development. In both experiments and simulations, the hydride length distributions are well described by a lognormal function characterized by a long-length tail [11]. In the simulations, this tail arises from the merging of several neighboring hydrides located at mutual distances smaller than approximately 5 μm, which are represented as a single elongated hydride.

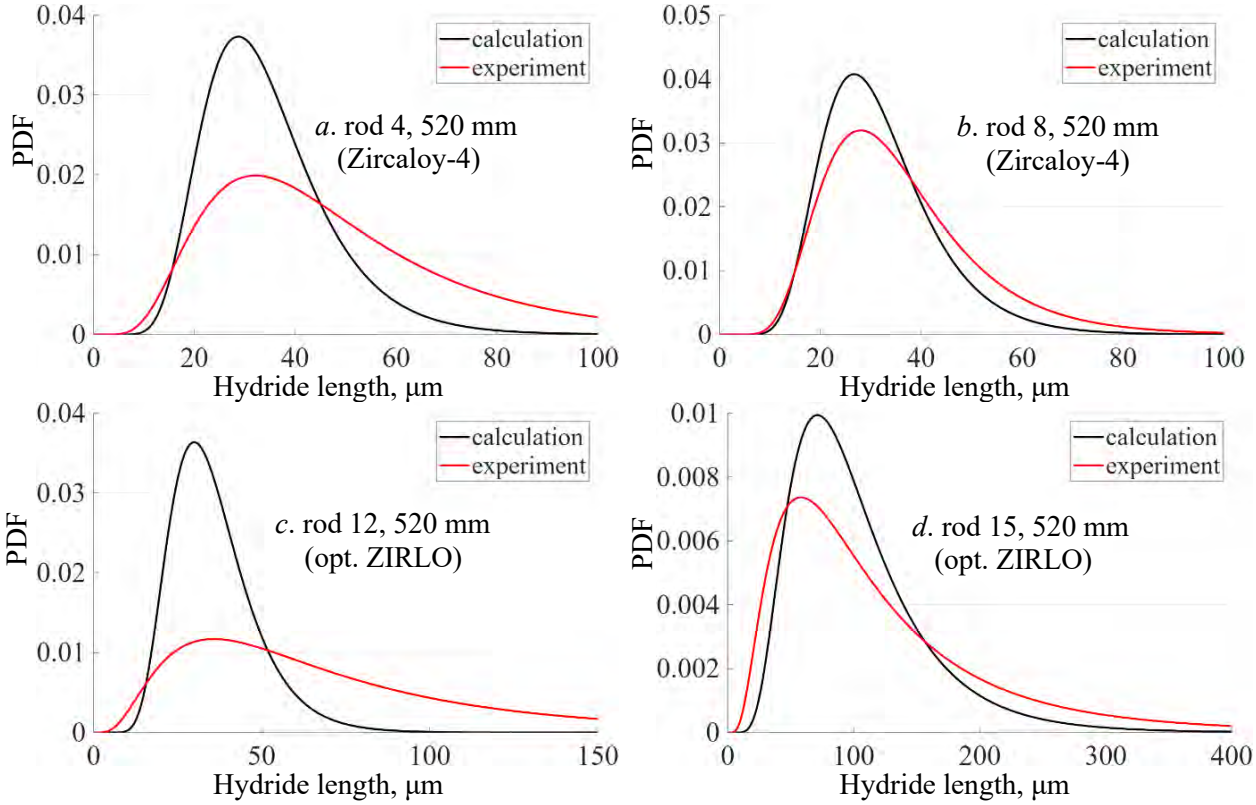

Figure 9. Statistical distributions of hydride lengths: comparison of experiment and calculation;

The calculated statistical distributions of the HCC and the RHCP are shown in Figs. 10 and 11, respectively. These distributions are compared with the corresponding experimental values obtained for the same cross-sections, which are indicated by dotted lines. The experimental HCC values are systematically higher than the mean values of the simulated distributions, whereas the experimental RHCP values are consistently lower than the corresponding simulated means. Nevertheless, when the finite width of the simulated distributions is taken into account, the experimental values remain comparable to the calculated results. The experimental value lies within the central 90% interval of the simulated distribution. Overall, the agreement between simulations and experiments is considered acceptable at the current stage of model development. Both HCC and RHCP exhibit the correct qualitative trends with increasing internal pressure and attain physically reasonable absolute values.

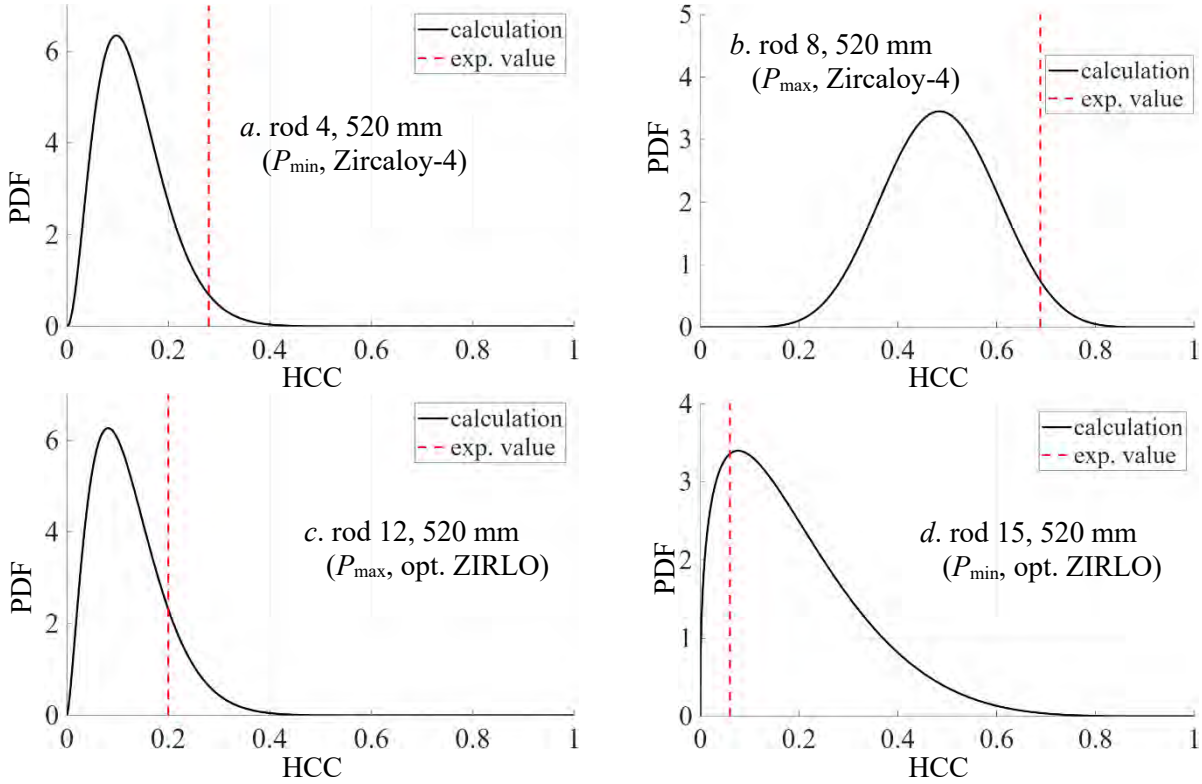

Figure 10. Calculated statistical distributions of HCC, compared with a single measurement

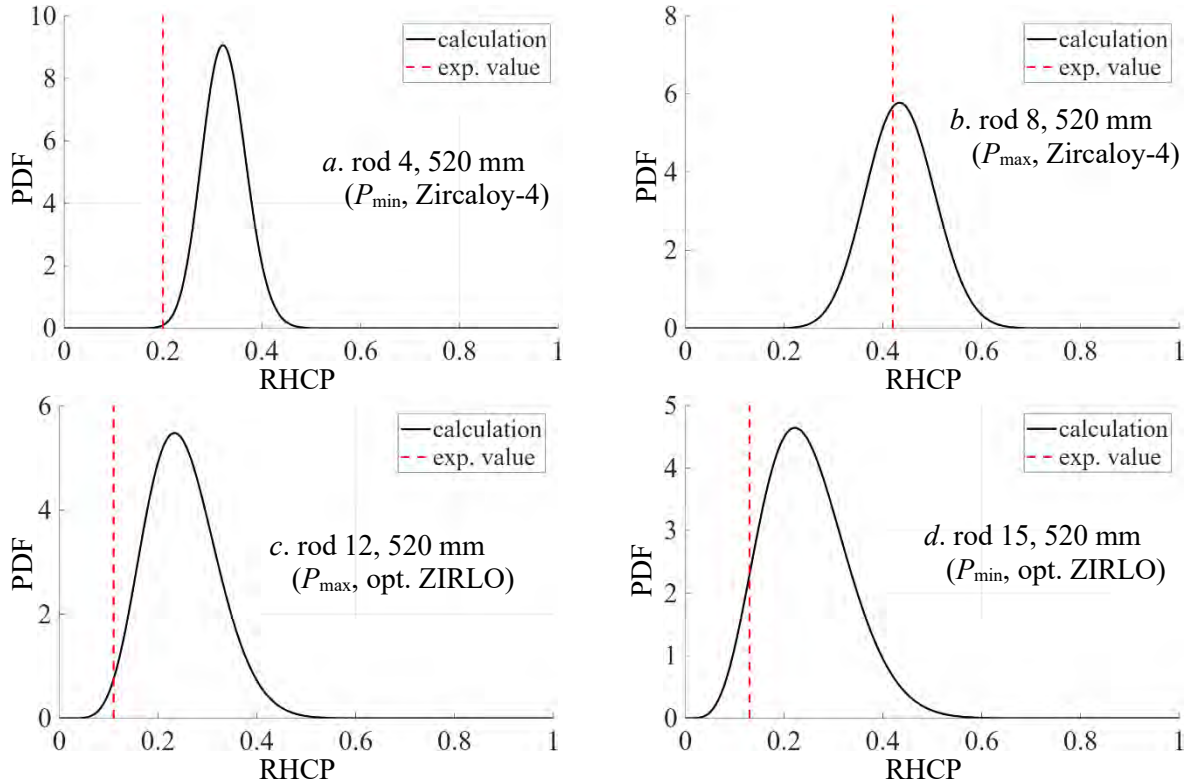

Figure 11. Calculated statistical distributions of RHCP, compared with a single measurement

5. CONCLUSION

Two numerical tools developed for the simulation of hydride morphology in zirconium alloys have been calibrated using new experimental data for Zircaloy-4 and opt. ZIRLO obtained in the SPIZWURZ test. Both numerical tools are complementary and can be used in tandem for advanced simulations.

The tool, based on the solution of the ODE system, is able to simulate the mean values of RHF, hydride length and density. The mean absolute error for RHF is 0.04, while the relative RMSE values for hydride length and density are 25% and 20%, respectively. A more systematic sensitivity analysis with respect to thermal-history assumptions and selected model parameters, including calculations with non-smoothed temperature histories, will be reported separately.

The MORPHYD tool showed the satisfactory agreement of the statistical distributions of hydride length, HCC and RHCP. The current limitations of MORPHYD are related to its precipitation stage only, the simplified description of hydride growth, and the restriction to small, non-overlapping hydrides. Therefore, the present MORPHYD assessment is limited to the 100 wppm cases.

ACKNOWLEDGMENTS

The SPIZWURZ project (FKZ RS1586A/1501609B) is funded by the Federal Ministry for the Environment, Nature Conservation, Nuclear Safety and Consumer Protection (BMUV).

REFERENCES

[1] A.T. Motta *et al.*, "Hydrogen in zirconium alloys: A review," *J. Nucl. Mater.*, **518**, pp. 440–460 (2019), DOI: 10.1016/j.jnucmat.2019.02.042.
[2] S. Suman *et al*., "Hydrogen in Zircaloy: Mechanism and its impacts," *Int. J. Hydrogen Energy*, **40** (17), pp. 5976–5994 (2015), DOI: 10.1016/j.ijhydene.2015.03.049.
[3] M. Kolesnik, "Micro-mechanisms of the ductile-to-brittle transition in hydrogenated zirconium alloys: A review and a comparison analysis of experimental data and theoretical approaches," *Eng. Fail. Anal.*, **159**, p. 108110 (2024), DOI: 10.1016/j.engfailanal.2024.108110.
[4] Q. Fang, M.R. Daymond, and A. King, "Study on the morphology of bulk hydrides by synchrotron X-ray tomography," *Mater. Charact.*, **134**, pp. 362–369 (2017), DOI: 10.1016/j.matchar.2017.11.013.
[5] M. Meyer *et al.*, "3D Hydrides Arrangement in Fuel Cladding Tubes and Timely Development of Hydrogen Relocation in Liner Cladding Investigated with Neutron Imaging," *Proceedings of TopFue 2024 reactor fuel performance conference*, Grenoble, France, 20 Sept. – 3 Oct. 2024, pp. 68–78 (2024).
[6] P.C.A. Simon *et al.* "Quantifying the effect of hydride microstructure on zirconium alloys embrittlement using image analysis," *J. Nucl. Mater.*, **547**, p. 152817 (2021), DOI: 10.1016/j.jnucmat.2021.152817.
[7] D. Hardie and M. W. Shanahan, "Stress reorientation of hydrides in zirconium-2.5% niobium," *J. Nucl. Mater.*, **55** (1), pp. 1–13 (1975), DOI: 10.1016/0022-3115(75)90132-4.
[8] M. Kolesnik, "Comparison of two kinetic approaches for modeling of radial hydride fraction in zirconium-based fuel rod cladding," *Nucl. Eng. Technol.*, 57**,** p. 103479 (2025), DOI: 10.1016/j.net.2025.103479.
[9] S.J. Min, M.S. Kim, and K.T. Kim, "Cooling rate- and hydrogen content-dependent hydride reorientation and mechanical property degradation of Zr-Nb alloy claddings," *J. Nucl. Mater.*, **441** (1-3), pp. 306–314 (2013), DOI: 10.1016/j.jnucmat.2013.06.006.
[10] M. Grosse *et al.*, "The SPIZWURZ project – Experimental investigations and modeling of the behavior of hydrogen in zirconium alloys under long-term dry storage conditions," *Nucl. Eng. Technol.*,. **56**, pp. 824–831 (2024), DOI: 10.1016/j.net.2023.09.027.
[11] M. Kolesnik, J. Stuckert, M. Grosse, and S. Weick, "Hydride morphology in zirconium cladding tubes after the SPIZWURZ bundle test . Part I : analysis of experimental data," *J. Nucl. Mater.*, **619**,

p. 156250 (2026), DOI: 10.1016/j.jnucmat.2025.156250.
[12] M. Kolesnik, T. Aliev, and V. Likhanskii, "Modeling of size, aspect ratio, and orientation of flattened precipitates in the context of Zr-H system under external stress," *Comput. Mater. Sci.*, **189**, p. 110260 (2021), DOI: 10.1016/j.commatsci.2020.110260.
[13] A.R. Massih and L.O. Jernkvist, "Stress orientation of second-phase in alloys: Hydrides in zirconium alloys," *Comput. Mater. Sci.*, **46** (4), pp. 1091–1097 (2009), DOI: 10.1016/j.commatsci.2009.05.025.
[14] Y.J. Kim, D.H. Kook, T.H. Kim, and J.S. Kim, "Stress and temperature-dependent hydride reorientation of Zircaloy-4 cladding and its effect on the ductility degradation," *J. Nucl. Sci. Technol.*, **52** (5), pp. 717–727 (2014), DOI: 10.1080/00223131.2014.978829.
[15] M. Kolesnik and T. Aliev, "Evaluating the spatial and size distributions of flat precipitates in diffusion-controlled precipitation processes," *Phys. Met. Metallogr.*, **104**, pp. 1414–1425 (2023), DOI: 10.1134/S0031918X22602074.
[16] T. Aliev and M. Kolesnik, "Evolution of an approach to the modeling of zirconium hydrides morphology based on Monte-Carlo method in 3D representation," *Lett. Mater.*, **13** (2), pp. 143–148 (2023), DOI: 10.22226/2410-3535-2023-2-143-148.
[17] T. Aliev and M. Kolesnik, "Stress concentrator at the plate-like inclusion tip as an enhancement factor of diffusion flux," *J. Phys. Commun.*, **5** (10), p. 105005 (2021), DOI: 10.1088/2399-6528/ac2a97.
[18] D. Kim, D. Kim, D. Woo, and Y. Lee, "Development of an image analysis code for hydrided Zircaloy using Dijkstra's algorithm and sensitivity analysis of radial hydride continuous path," *J. Nucl. Mater.*, **564**, p. 153647 (2022), DOI: 10.1016/j.jnucmat.2022.153647.
[19] J.J. Kearns, "Diffusion coefficient of Hydrogen in alpha Zirconium, Zircaloy-2 and Zircaloy-4," *J. Nucl. Mater.*, **43** (3), pp. 330–338 (1972), DOI: 10.1016/0022-3115(72)90065-7.
[20] J.S. Kim and Y.S. Kim, "Effect of thermal history on the terminal solid solubility of hydrogen in Zircaloy-4," *Int. J. Hydrogen Energy*, **39** (29), pp. 16442–16449 (2014), DOI: 10.1016/j.ijhydene.2014.08.018.
[21] J.S. Kim, T.H. Kim, K. Kim, and Y.S. Kim, "Terminal solid solubility of hydrogen of optimized-Zirlo and its effects on hydride reorientation mechanisms under dry storage conditions," *Nucl. Eng. Technol.*, **52** (8), pp. 1742–1748 (2020), DOI: 10.1016/j.net.2020.01.022.

APPENDIX A

Table I. Model parameters used in simulations

Alloy	Param.	Desciption	Value	Ref.
Both	D_{H}	Diffusion coefficient	$7 \times 10^{-7} \cdot \exp(-5360/T)$ [m^2/s]	[19]
	γ	hydride surface energy	0.065 [J/m^2]	[12, 13]
	v_{H}	atomic volume of H	1.7×10^{-29} [m^3]	[12]
	f_0	reorient param. from Eq. (3)	700	–
	E_{d0}	mean and standard deviation	9.6×10^{-19} [J]	–
	$\bar{\sigma}$	of defect energy norm. distr.	1.9×10^{-19} [J]	–
Zircaloy-4	C_{eq}^{TSSD}	solubility for dissolution	$2.255 \times 10^{5} \cdot \exp(-39101/RT)$ [wppm]	[20]
	C_{eq}^{TSSP}	solubility for precipitation	$8.612 \times 10^{4} \cdot \exp(-30583/RT)$ [wppm]	[20]
	n_0	nucleation site dens.	1×10^{15} [m^{-3}]	–
	$\Delta\Omega$	reorient param. from Eq. (3)	4.93×10^{-28} [m^{-3}]	–
opt. ZIRLO	C_{eq}^{TSSD}	solubility for dissolution	$7.8029 \times 10^{4} \cdot \exp(-35620/RT)$ [wppm]	[21]
	C_{eq}^{TSSP}	solubility for precipitation	$1.3256 \times 10^{5} \cdot \exp(-32824/RT)$ [wppm]	[21]
	n_0	nucleation site dens.	2×10^{14} [m^{-3}]	–
	$\Delta\Omega$	reorient param. from Eq. (3)	3.23×10^{-28} [m^{-3}]	–

Response to Reviewer#1

Accepted with no revisions

Author's response: *We sincerely thank the reviewer for the positive evaluation of our manuscript and for recommending acceptance without further revisions. We appreciate the reviewer's time and consideration.*

Response to Reviewer#2

Accepted with minor revisions

Reviewer's comment: I see several strengths. First, the topic is important and timely for dry-storage safety. Second, the two-model strategy is well motivated: the ODE tool is suitable for mean quantities along the rod, while MORPHYD addresses statistical distributions and connectivity, which are physically more relevant to embrittlement. Third, the figures on pp. 6–10 show that the models reproduce the main qualitative trends, including weaker reorientation in opt. ZIRLO and sensible pressure effects on HCC/RHCP. The manuscript is also commendably honest about current limitations: the ODE tool reaches about ±0.1 for RHF, while hydride length and density may differ by up to a factor of two, and MORPHYD is limited to precipitation-only simulations of small, non-overlapping hydrides and was applied only to 100 wppm cases.
Author's response: *We sincerely thank the reviewer for the careful and constructive evaluation of our manuscript. We are grateful for the positive comments which helped us to improve the manuscript. The detailed responses for comments are below.*

Reviewer's comment: My main concern is that the strongest "validation" result is not fully independent. The manuscript states that the post-test ODE parameter set was calibrated using a larger database that included the new SPIZWURZ results, whereas the blind pre-test simulations systematically overpredicted RHF. This is important. The paper should distinguish clearly between blind prediction and post-test calibration. As written, the term "validation" is somewhat too strong unless the authors reserve an independent subset of the data or at least tone down claims such as "reliably predict."
Author's response: *The authors are grateful to the reviewer for this important comment and agree that the present paper largely describes the calibration and assessment of the models using new experimental data rather than a fully independent validation. The manuscript has been revised accordingly. Following the reviewer's recommendation, the term "validation" has been replaced throughout the text by "calibration and assessment", where appropriate. The only exception is the title of the paper, which has been retained because it has already been included in the conference program in its current form, in order to avoid any confusion with the title used in the published conference proceedings and the conference program. Additionally, the conclusion has been corrected and the following phrase has been added to the manuscript (in the end of Page 5):*
"Since SPIZWURZ data were included in calibration, these post-test simulations are used to assess calibrated model performance and identify remaining deviations and trends, rather than as fully independent validation."

Reviewer's comment: A second concern is that the agreement assessment is still mostly qualitative. Statements such as "acceptable agreement," "±0.1 for RHF," or "factor of two" are useful, but a validation paper would be much stronger with formal error metrics: MAE/RMSE, mean relative error, bias, and perhaps confidence bands. This is especially important for MORPHYD. On pp. 9–10, the simulated HCC and RHCP distributions are compared with single experimental values, and the manuscript itself notes a systematic pattern: experimental HCC tends to be above the simulated mean, while RHCP tends to be below it. A broad simulated distribution can make a single measured value look "comparable," but that is weaker evidence than agreement in central tendency and spread.

Author's response: *We thank the reviewer for this helpful suggestion. We agree that the assessment of the model performance should be supported by quantitative error metrics where possible. In the revised manuscript, we have added quantitative metrics for the ODE-based tool. The mean absolute error for RHF is 0.04, while the relative root mean square errors for mean hydride length and hydride surface density are 25% and 20%, respectively. The corresponding comments have been added to the manuscript text in Section 3.2 and in the Conclusion.*

For MORPHYD, a direct calculation of MAE or RMSE is less straightforward because the simulations provide statistical distributions obtained from repeated Monte Carlo runs, whereas the available experimental comparison consists of single measured values for individual cross-sections. We have therefore clarified in the manuscript (above Figure 10) that the experimental value lies within the central 90% interval of the simulated distribution.

Reviewer's comment: A third issue is uncertainty propagation. The temperature histories for most rods were inferred rather than directly measured and were smoothed to remove abrupt drops and fluctuations. Because hydride precipitation is sensitive to thermal history, the paper would benefit from at least a short sensitivity analysis showing how RHF, hydride length, HCC, and RHCP change when the smoothing assumptions are varied. Likewise, several parameters in Table I appear to be fitted or user-defined rather than independently measured. The calibration workflow and uncertainty ranges should be made more explicit; otherwise it is difficult to judge how much of the agreement is physically predictive and how much comes from compensating parameter choices.

Author's response: *We thank the reviewer for this important comment. We agree that the uncertainty associated with the inferred and smoothed temperature histories is an important aspect of the present assessment. In the revised manuscript, we have clarified the purpose and limitations of the smoothing procedure (above Figure 2). The smoothing was applied to remove short-term temperature fluctuations of approximately 5 °C during the holding periods and minor non-monotonic variations, while preserving the overall thermal history and the effective cooling rates of the main cooling steps used in the experiment.*

We also agree that a systematic sensitivity analysis with respect to the temperature scenario and model parameters is highly relevant. Such an analysis has been performed as a separate follow-up study, including calculations with the original, non-smoothed temperature histories and an updated version of the model with reduced sensitivity to short-term thermal fluctuations. These results are beyond the scope of the present conference paper and will be presented at the TopFuel conference later this year. In the revised manuscript (Conclusion), we have added a short statement to make this limitation and the ongoing follow-up work explicit.

Reviewer's comment: I also think the scope limitations of MORPHYD should be stated earlier and more prominently. Page 8 explains clearly that the model is limited to the precipitation phase, to small non-overlapping hydrides, and therefore to the 100 wppm cases analyzed here. That limitation is acceptable at this stage, but it narrows the generality of the conclusions and should be visible already in the abstract and in the final take-home message."

Author's response: *We thank the reviewer for this helpful comment. We agree that the current limitations of MORPHYD should be stated more prominently. In the revised manuscript, we have added a sentence to the Abstract clarifying that the present version of MORPHYD is limited to precipitation-only simulations of small, non-overlapping hydrides and was therefore applied only to the 100 wppm cases. We have also revised the Conclusion to make this limitation visible in the final take-home message and to clarify that further model development is required before applying MORPHYD to higher hydrogen concentrations and dissolution–precipitation scenarios.*

The 12th European Review Meeting on Severe Accidents Research

May 18-22, 2026, Universidad Carlos III de Madrid, Madrid, Spain

TECHNICAL SESSION 7.1: SPENT FUEL POOLS

Chairs: A. Stakhanova (KIT), S. Paci (University of Pisa)

ID111	**Recent Activities at Canadian Nuclear Laboratories on LOCA Progression in CANDU Spent Fuel Pools** B. Dastvareh (CNL)	Paper Presentation
ID073	**Validation of the Theoretical Approach for Modelling of the Hydride Morphology with Experimental Data for Zircaloy-4 obtained from SPIZWURZ bundle Test** M. Kolesnik (KIT)	Paper Presentation

Canadian Nuclear Laboratories | Laboratoires Nucléaires Canadiens

Recent Activities at Canadian Nuclear Laboratories on LOCA Progression in CANDU Spent Fuel Pools

Behnam Dastvareh, Ph.D.
Robert David, Ph.D.
Krishna Podila, Ph.D.
Qi Chen, Ph.D.
Chris Hollingshead, Ph.D.

May 2026

Fan et al. 'Spent Fuel Response after a Postulated Loss of Spent Fuel Bay Cooling Accident', CNS Bulletin vol 33, No 3, 2012

SECTION 1

Introduction

Overview of CANDU

Key Features:

- Uses natural uranium (not enriched).
- Employs heavy water (D_2O) as the coolant and moderator.
- Reactor core is a horizontal pressure tube design rather than a pressure vessel design.
- On-power refueling—fuel can be replaced without shutting down the reactor.
- Generates tritium (a rare isotope) as a byproduct, valuable for medical research and fusion energy.
- Allows to produce medical radioisotopes (such as Cobalt-60) simultaneously with electricity, due to low-temperature moderator.

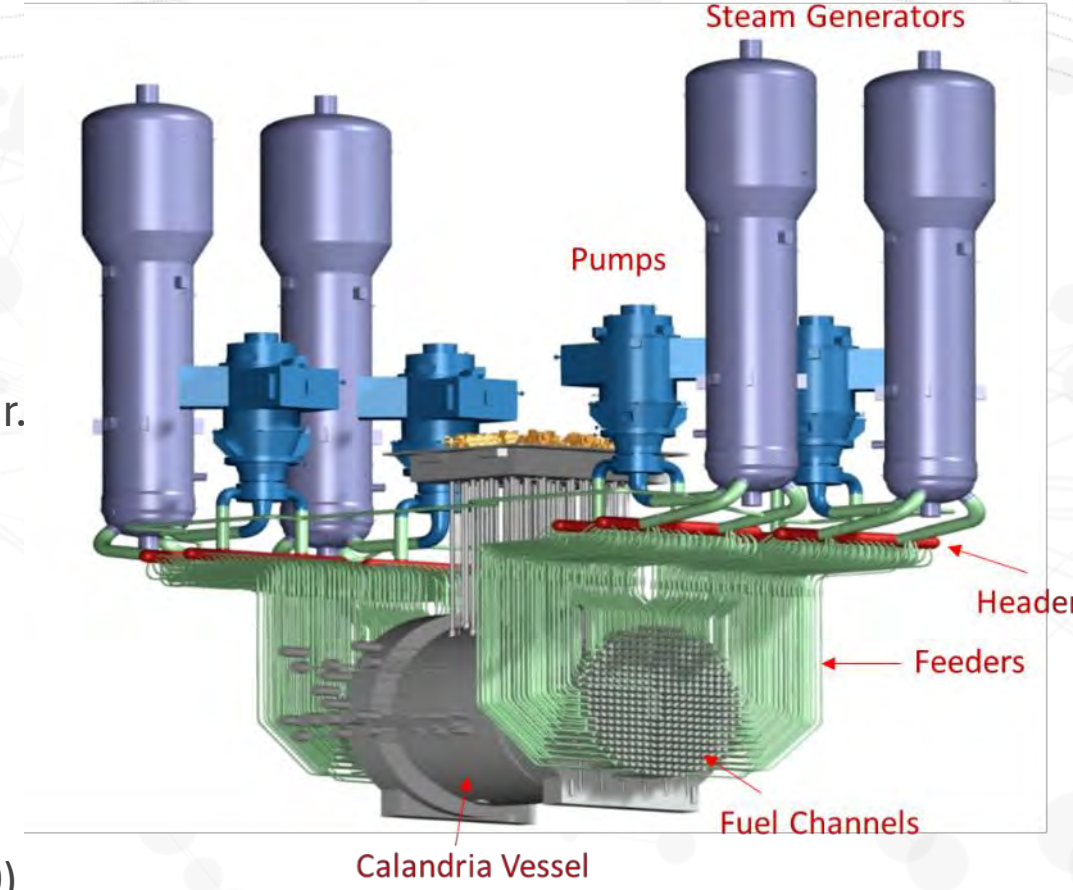

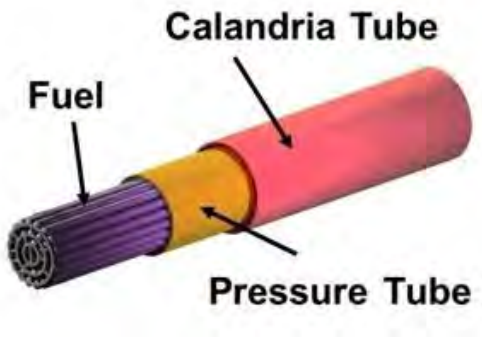

Source: Canteach.CANDU

CANDU Spent Fuel Pools (SFPs)

- CANDU fuel bundles are ~50 cm long, weigh 25 kg, and are ~10 cm in diameter
- CANDUs are refueled daily (~12-16 fuel bundle/day).
- Spent fuels continue to generate decay heat and requires cooling.
- Fuel taken from reactor is transferred to:

discharge room → reception bay → spent fuel storage bay

- In the reception bay, fuel bundles are placed in baskets
- After ~1-2 weeks, the fuel is relocated to the storage bay where bundles are transferred into trays/modules
- Criticality concerns are negligible, allowing for flexible bundle spacing.

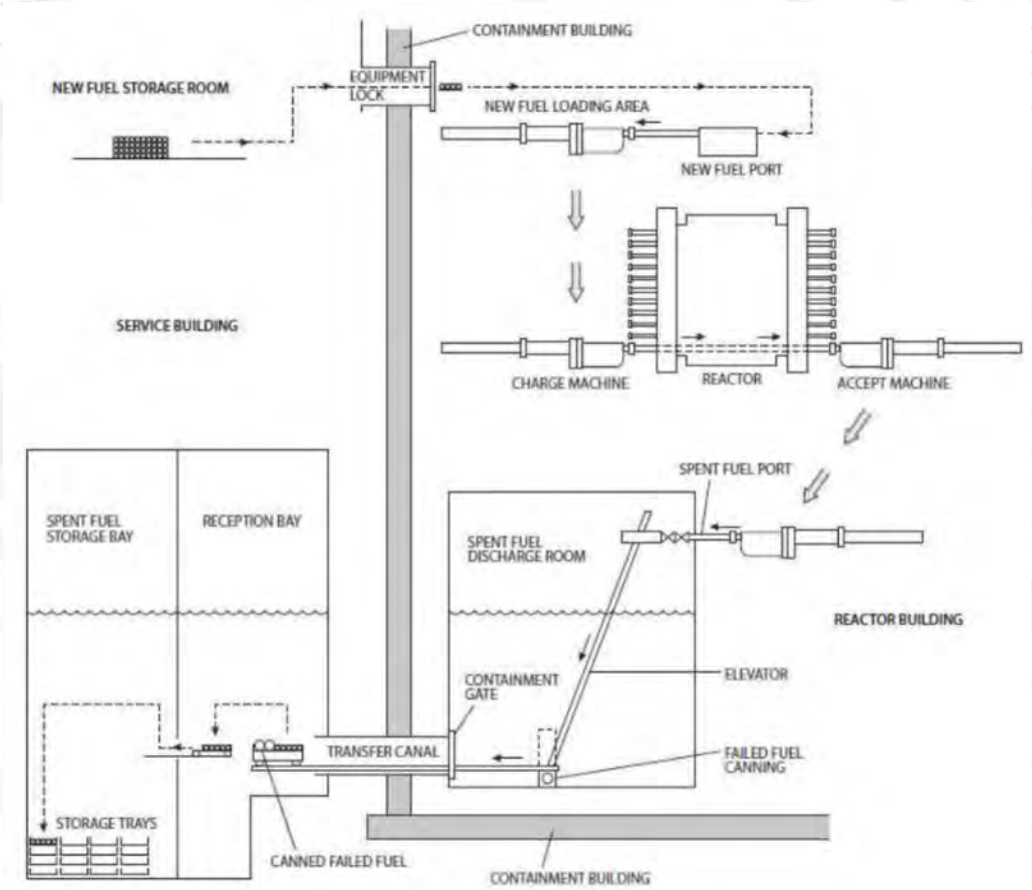

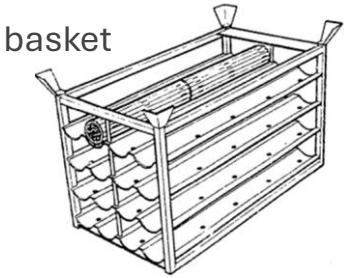

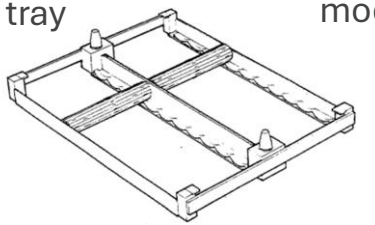

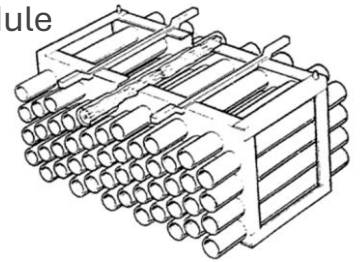

Source: The essential CANDU textbook

Motivation for SFP Accident Studies

- **SFP safety depends on active cooling**

  Prevents fuel overheating, hydrogen buildup, and radionuclide release

- **Fukushima highlighted vulnerabilities**

  water levels dropped, but emergency makeup preserved fuel coverage

- **International response**

  IAEA called for reassessment of plant resilience to extreme natural hazards, including SFPs

- **Regulatory actions**

  Global regulators, including the CNSC, addressed identified gaps

- **CNL contribution**

  ✓ Developed a PIRT [1] to identify key accident phenomena

  ✓ Initiated SFP accident analysis studies, focused on CANDU reactors

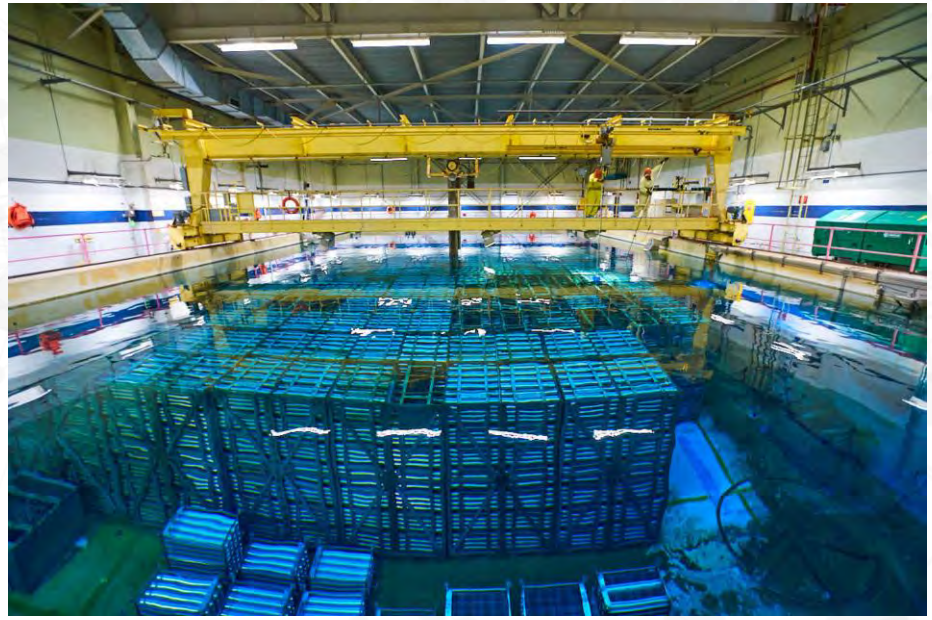

Spent nuclear fuel is stored in a pool at the Pickering Nuclear Generating Station in Pickering, Ontario. (Photo: Ontario Power Generation - Brian Pieters Corporate Visuals)

1. Phenomena Identification and Ranking Table

SECTION 2

CNL's Efforts in SFP Accident Analysis for CANDU Reactors (2022-2025)

Fuel Bay Heater Apparatus (FBHA) Experiments

Overview

Objective

- To measure the **surface temperature** of irradiated CANDU fuel bundle simulators across different power levels and under various environments (representative of LOCA [2] scenario).

Bundle Power & Test Conditions

- Typical CANDU bundle decay power decreases to ~2.6 kW after 1 days, and further to ~62 W after a year in the pool [1].
- Experiments were conducted over a range of simulated bundle power levels (500 W to 3 kW) under three environmental conditions:
  - Stagnant dry air
  - Forced dry air (flow rate of 0.013 m^3/s)
  - Steam environments (low/high steam generation rates)

2 Loss of Coolant Accident

Apparatus Design

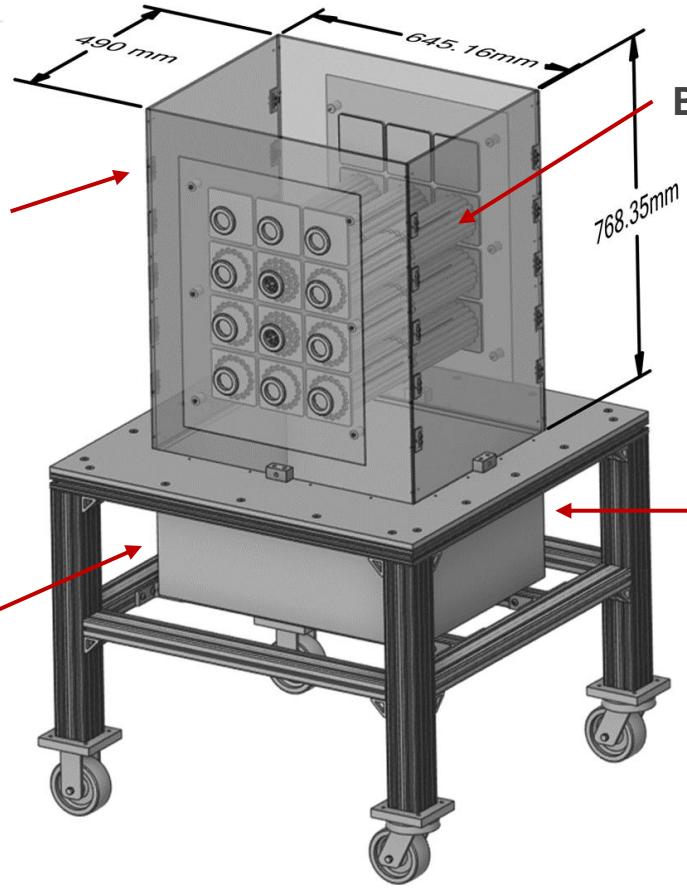

Stainless-Steel Enclosure

Bundles

Water Tank

Forced Air Supply (not shown)

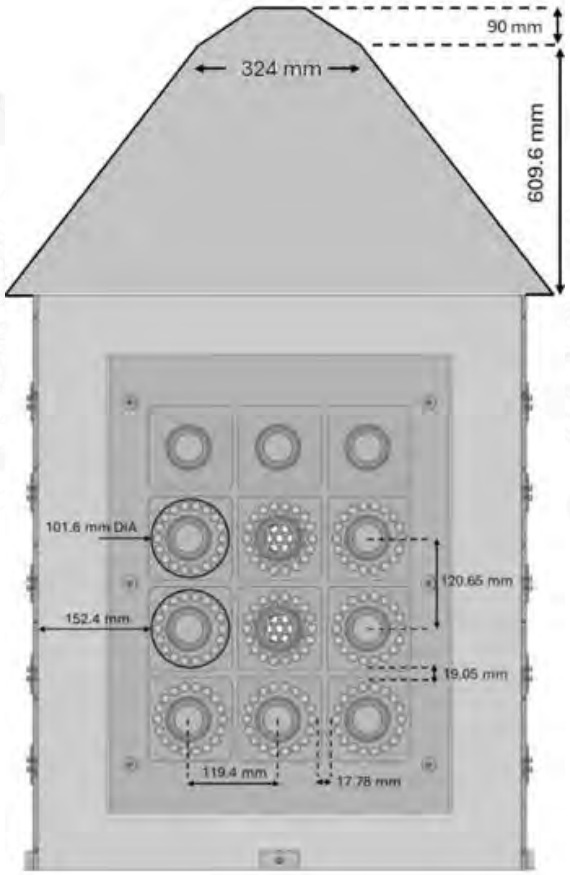

Bundles: Cartridge-heater–based simulator used to reproduce bundle heating profiles

Thermocouple Placement

- **92** TCs were embedded ~1 mm beneath the **outer surface** of the elements to measure surface temperatures of the simulated fuel elements.
- **24** TCs were deployed to monitor inter-bundle **gas** (air/steam) temperatures.
- **8** thermocouples assessed the interior apparatus **wall** temperatures.

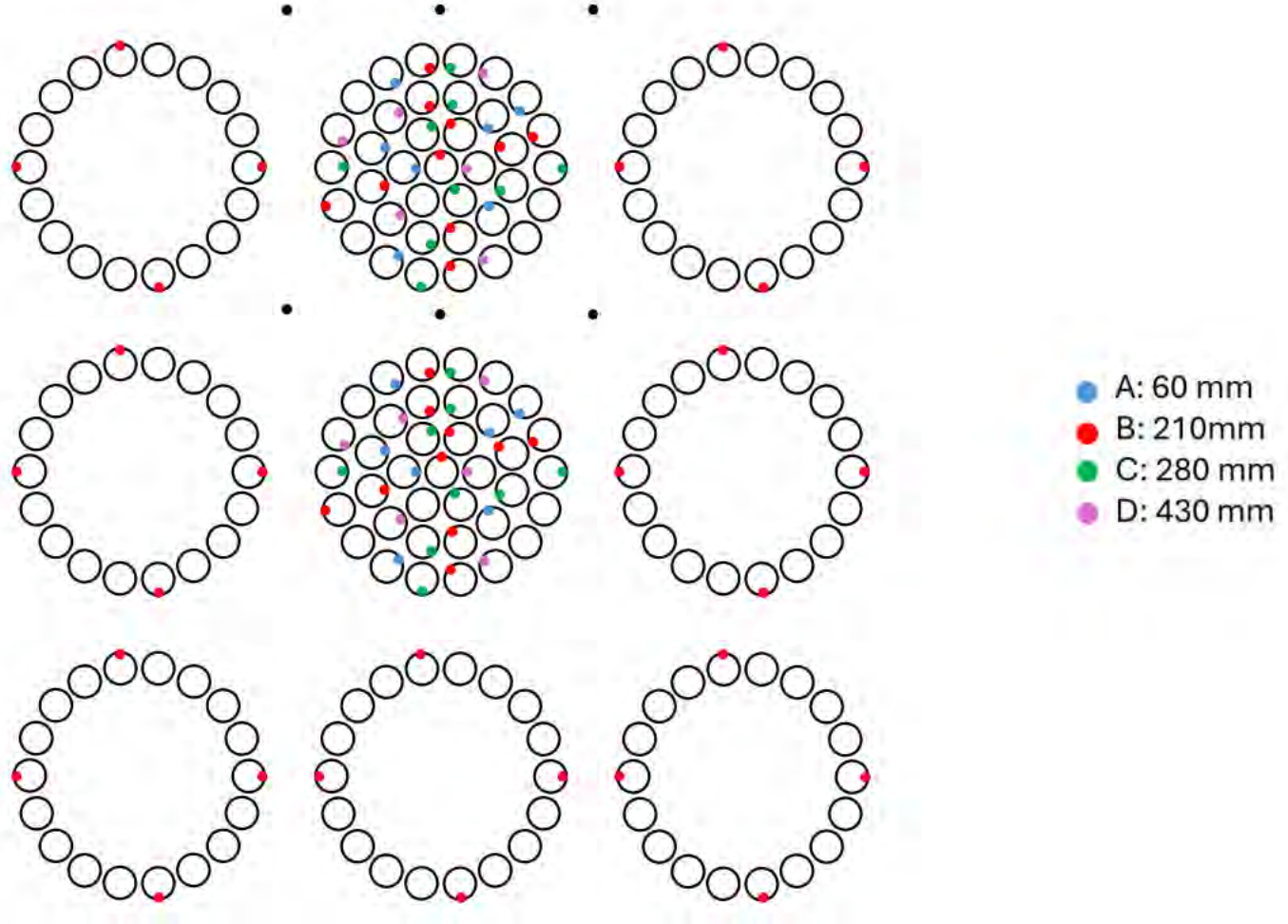

Locations of bundle (coloured) and gas (black) thermocouples. The inset illustrates the distances of thermocouples from the front edge of the bundle.

Selected Results

- The highest sheath temperatures occurred in the **stagnant air environment**, whereas the lowest were observed in the forced air environment.
- The steam generation rate had a negligible effect on sheath temperature.
- In the **top** full bundle peak temperatures were recorded at the **central element and its immediate lower vicinity**.
- In the **bottom** full bundle peak temperatures were observed at the **central element and its upper vicinity**.
- The maximum sheath temperature approached the hydrogen generation threshold (~827 °C) **at bundle power levels exceeding 2.5 kW** in the evaluated three row bundle configuration.

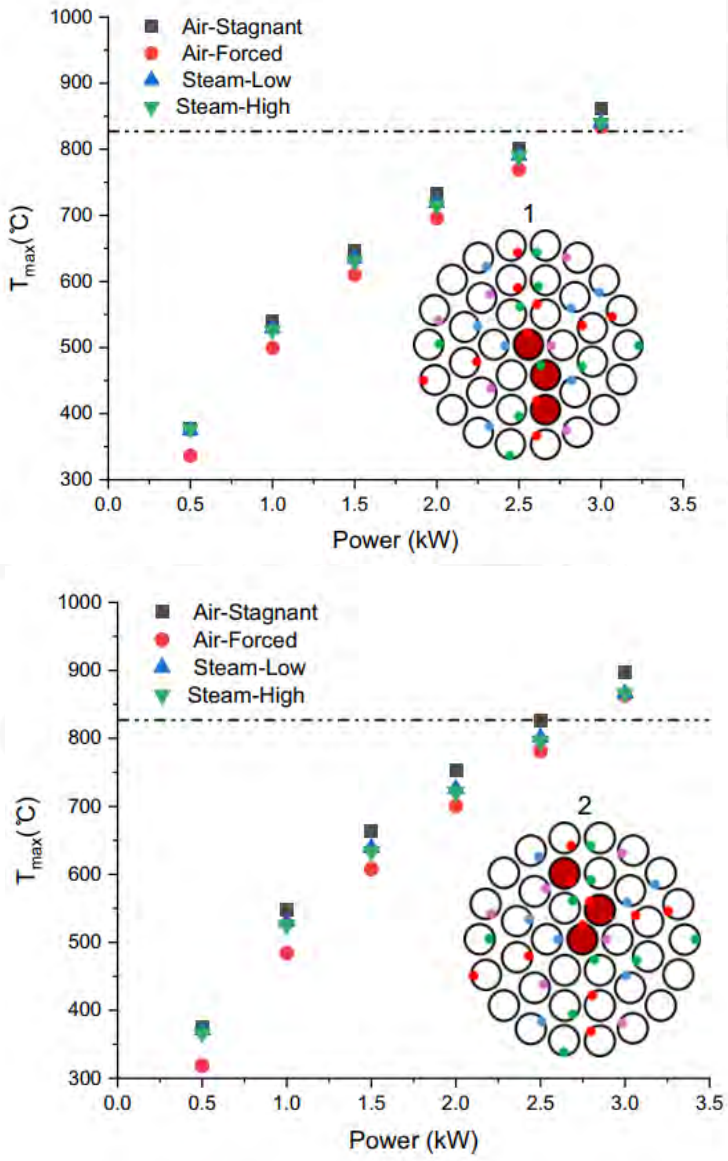

Maximum sheath temperature as a function of bundle power: (top) top full bundle; (bottom) bottom full bundle

Assessment of BAYLOCA SFP Accident Analysis Code

BAYLOCA Code Overview

- **BAYLOCA** is a fast-running, lumped-parameter accident analysis code developed for the CNSC to evaluate CANDU SFP LOCAs.
- Designed to simulate all phases of SFP accident progression, **from loss of cooling to recovery**.
- Accident evolution modeled in **four stages**:

1. Loss of pool makeup; fuel remains fully submerged
2. Pool level decreases; partial fuel uncovering begins
3. Complete loss of pool water due to boil-off or leakage
4. Cooling water restoration (can occur from any prior stage)

- User inputs include decay heat, fuel and pool geometry, building characteristics, and boundary conditions.
- Key outputs include **pool water level and temperature, fuel and gas temperatures, oxidation progression, and fission product release histories.**

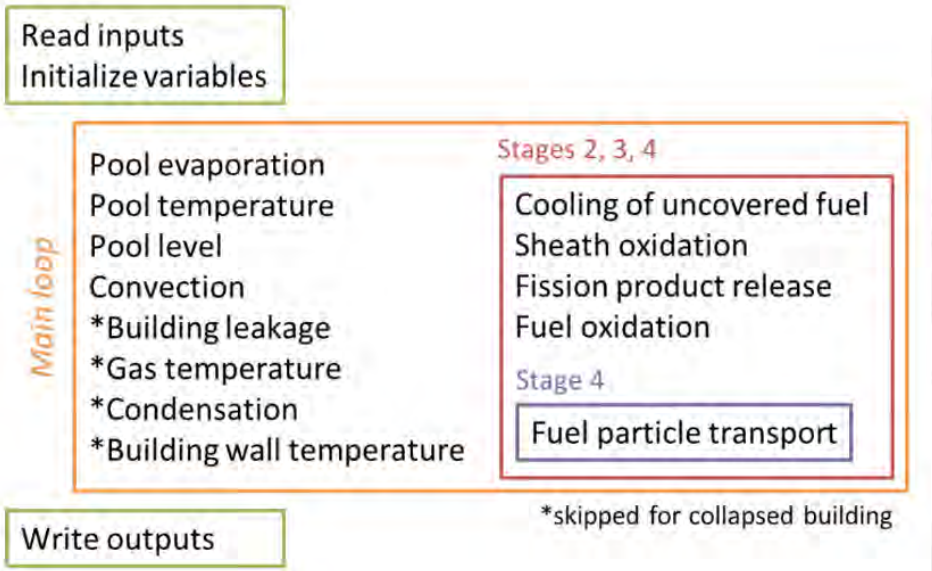

Overall view of an accident simulation

Code Assessment and Benchmarking

- Benchmarking performed against GOTHIC and CFD simulations demonstrated generally good agreement in predicted thermal-hydraulic behavior.
- Identified further refinement in:
  - ✓ convective fuel cooling
  - ✓ fission product transport
  - ✓ deposition models

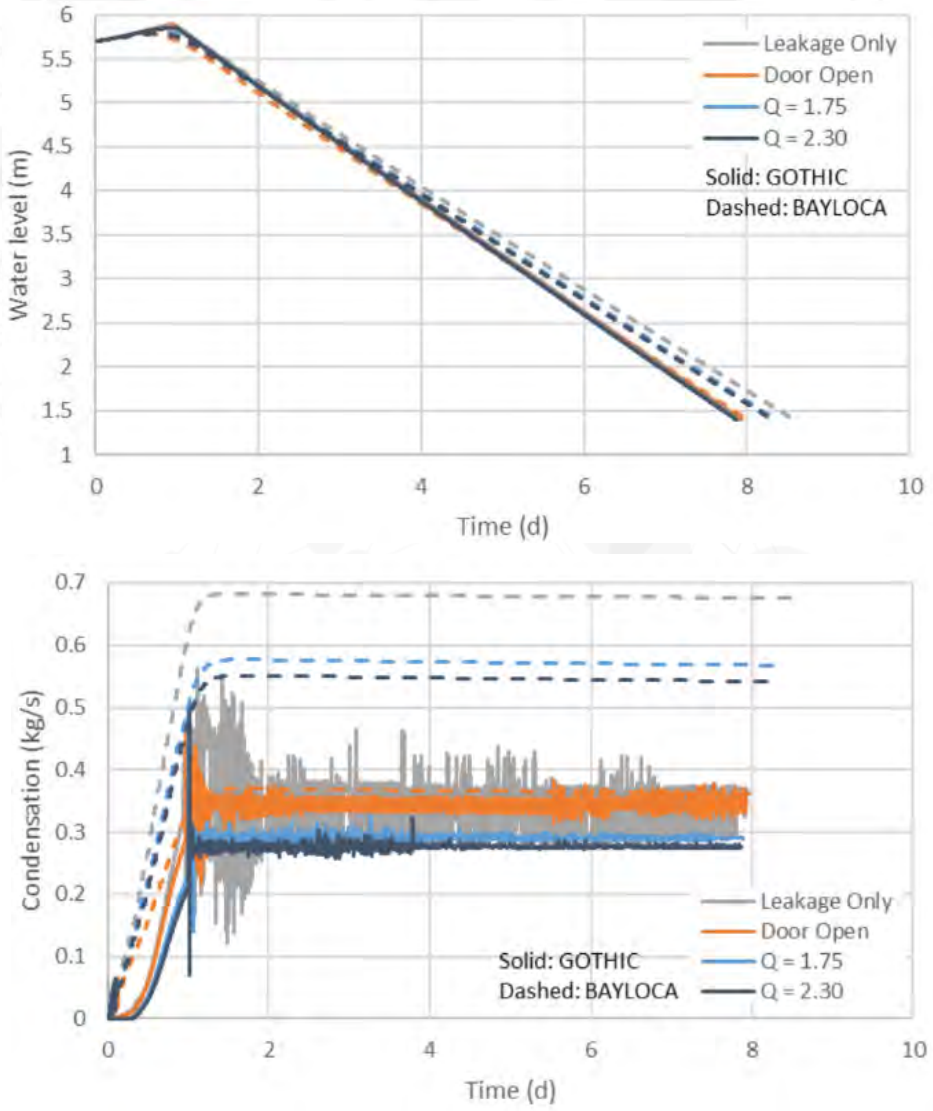

Comparison of the results between GOTHIC and BAYLOCA with similar input parameters: (top) water level in the pool, (bottom) rate of condensation

CFD Analysis of SFP Accidents

Overview and High-Level Results

- A CFD modelling capability was developed to estimate peak sheath temperatures in a CANDU SFP during a complete LOCA.
- It was intended to support the development of reduced-order, fast-running models for the BAYLOCA analysis code, and to guide experimental design.
- Simulations performed using Simcenter STAR-CCM+.
- The model represents a CANDU spent fuel module and resolves: **natural convection**, **radiative heat transfer**, and **solid conduction** within fuel bundles and structures
- Results show non-uniform temperature distributions, with the **central bundles** at row #6 experiencing the highest sheath temperatures [2].

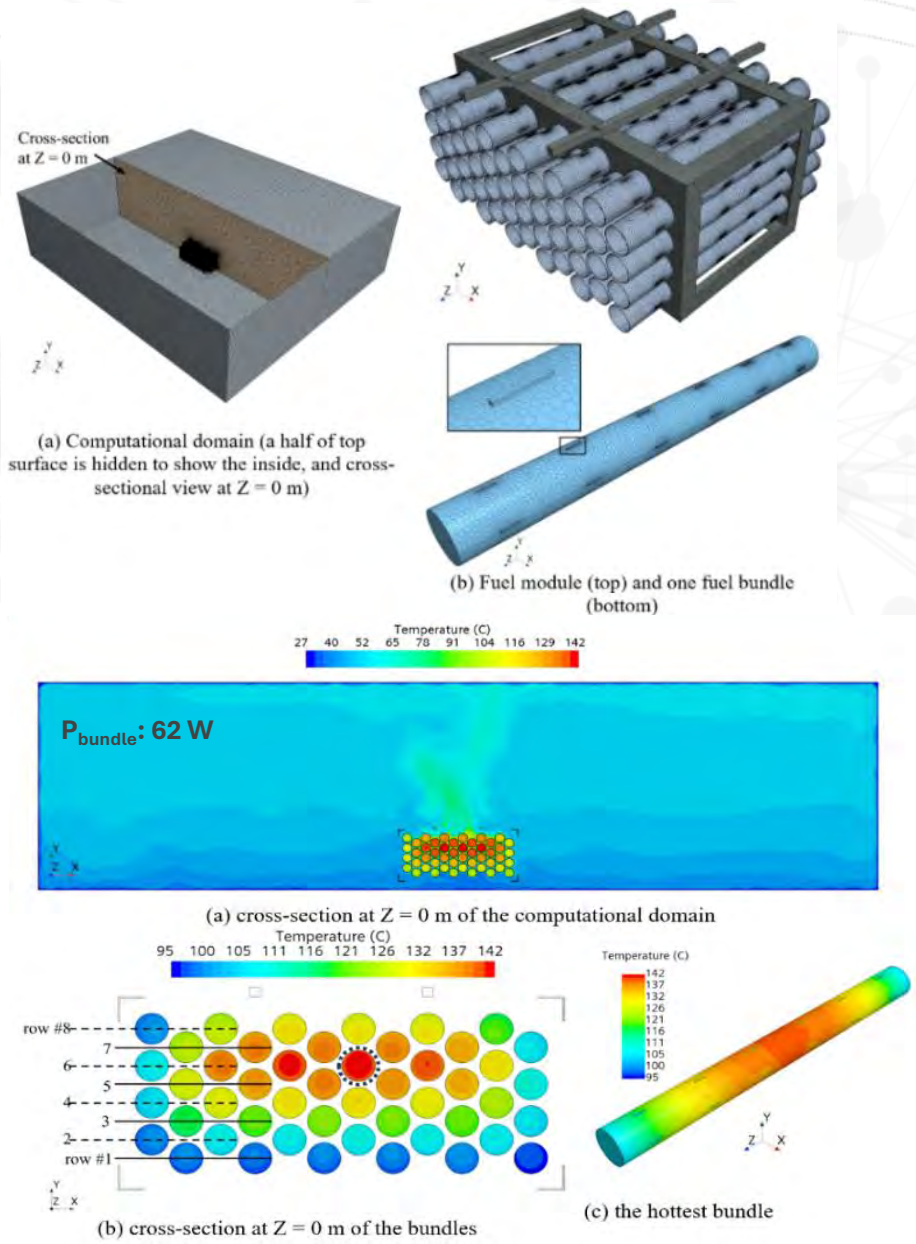

GOTHIC Analysis of SFP Accidents

GOTHIC Modelling of SFP Accident Scenarios

- GOTHIC is originally developed for containment analysis; adapted here to predict:
  - ✓ pool drainage and boil-off behaviour
  - ✓ building temperature
- Transient initiated with ~8.6 MW decay heat, decreasing with time.
- Outputs used to inform and support BAYLOCA thermal-hydraulic models.
- Model later extended to include aerosol and fission product transport:
  - ✓ Results indicate ~60% of released fission products remain inside the building, mainly deposited in liquid
  - ✓ Highlighted the conservatism of BAYLOCA's primary release assumptions (i.e. full release to environment)

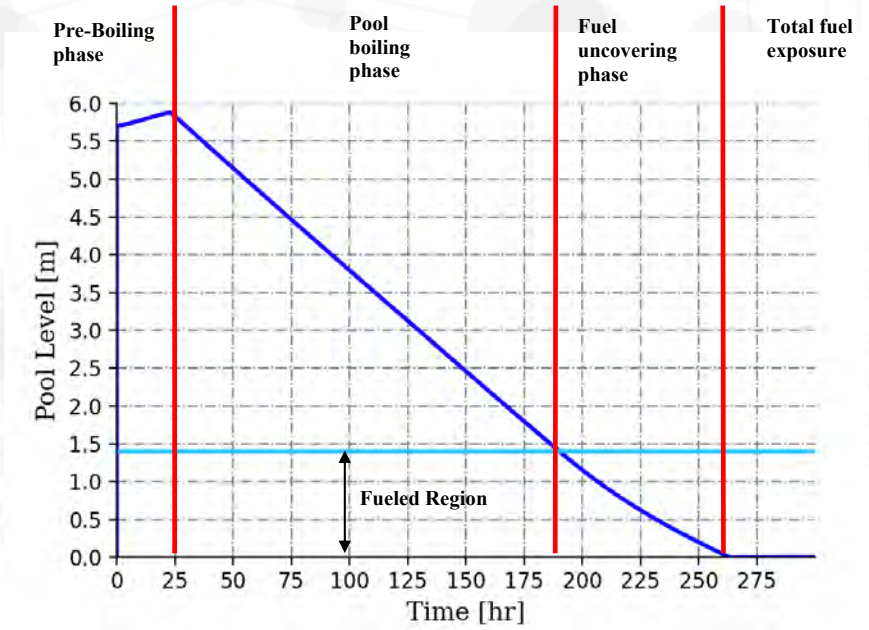

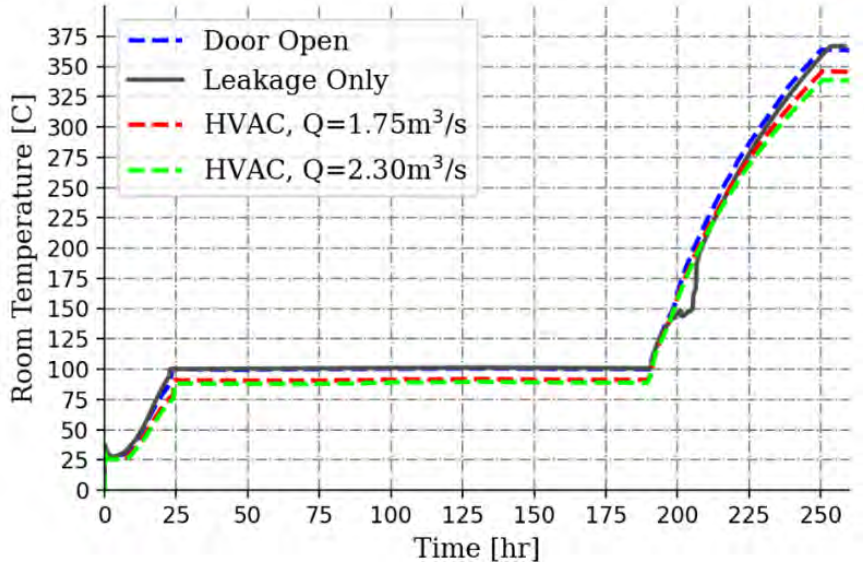

Model Insights and Identified Limitations

- Single lumped pool volume does not fully capture fuel-region porosity and internal convection.

  ➡ multiple vertically stacked pool control volumes instead of single lumped pool with.

- However, the moving liquid–vapor interface crossing the boundaries between these pool volumes during water evaporation triggers numerical instabilities.

- Current decay-heat treatment artificially returns heat from gas to the pool, suppressing gas temperatures.

  ➡ surface-based heat input above the pool as fuel becomes uncovered yielded more credible predictions.

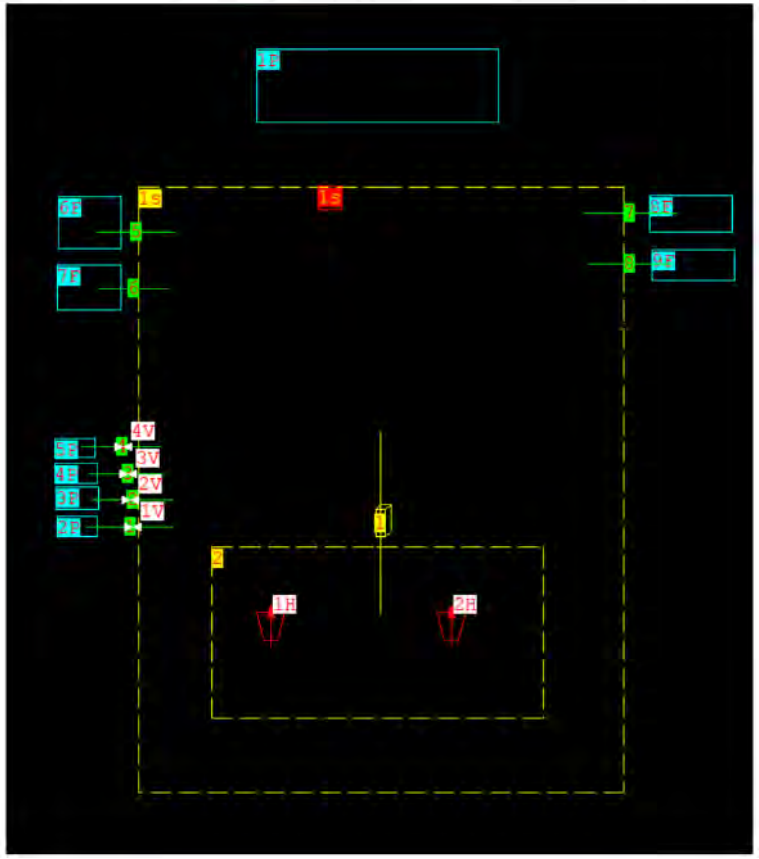

GOTHIC model of the SFP

Participation in OECD-NEA POLCA Project

OECD/NEA Pool during Loss of Cooling Accident (POLCA)

- The OECD/NEA [3] POLCA project examines the behaviour of SFPs during situations of loss of cooling through experimental analysis.

- Objectives:

✓ Enhance knowledge of SFPs in an accident scenario

✓ Improve the physical understanding of large-scale pools to provide thermal hydraulics data

✓ Support the thermal-hydraulics model development and validation for SFP during a LOCA

- Given the strong alignment with CNL objectives, CNL decided to participate in the POLCA project.

https://www.oecd-nea.org/jcms/pl_92835/assessing-the-safety-of-spent-fuel-pools-during-a-loss-of-cooling-accident

3 Economic Co-operation and Development / Nuclear Energy Agency

Summary

- **Motivation:**

Vulnerabilities of SFPs demonstrated during Fukushima accident

- **Experimental work:**

FBHA designed and commissioned. Tests measured sheath and gas temperatures under dry air, forced air, and steam conditions

- **Modeling & code development:**

✓ BAYLOCA reviewed and improved; benchmarked against GOTHIC and CFD models

✓ GOTHIC and CFD models developed to study accident progression in CANDU SFPs

- **International collaboration:**

Participation in OECD/NEA POLCA project

Acknowledgements

This Study was funded by Atomic Energy Canada Limited under the auspices of the Federal Nuclear Science and Technology Work Plan.

The research was conducted at Canadian Nuclear Laboratories by staff within the Directorates of Advanced Reactors, and Reactor Fleet and Sustainability.

References:

[1] *The Essential CANDU, A Textbook on the CANDU Nuclear Power Plant Technology*. University Network of Excellence in Nuclear Engineering (UNENE), ISBN 0-9730040.

[2] *Chen et al. CFD Modelling of a CANDU Irradiated Fuel Bay, NURETH-21, 2025*.

Appendix

Apparatus Design

Power supply and Power control

The power control panel was directly connected to the test section, distributing power to both the cartridge heaters and the immersion heater.

Data Acquisition Workstation

Recorded data from thermocouples embedded in the bundles, gas thermocouples, and power transducers.

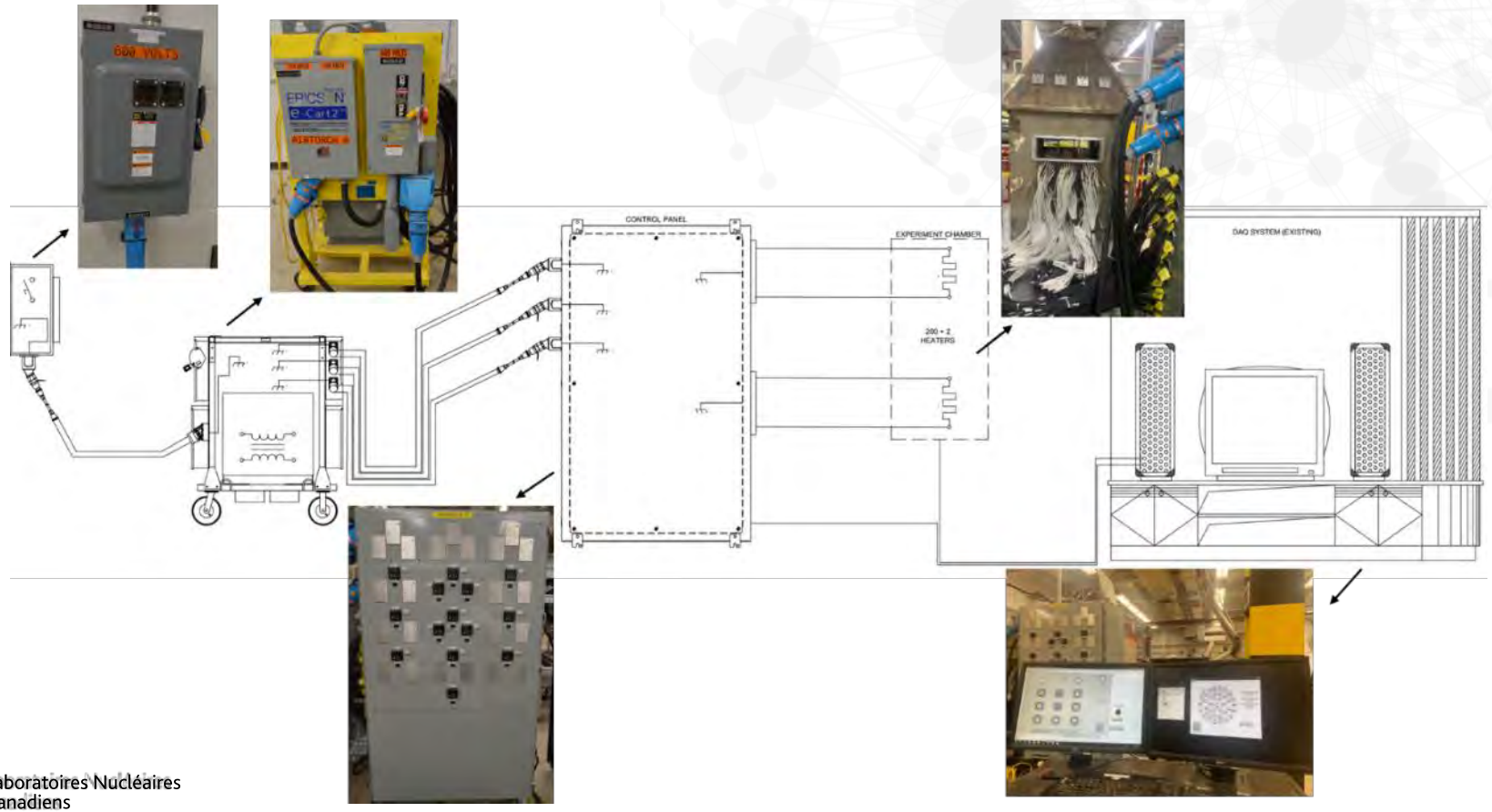

The 12h European Review Meeting on Severe Accident Research (ERMSAR2026)
Madrid, Spain, May 18-22, 2026

Log Number: 111

153-126800-CONF-011177

RECENT ACTIVITIES AT CANADIAN NUCLEAR LABORATORIES ON LOCA PROGRESSION IN CANDU SPENT FUEL POOLS

B. Dastvareh, R. David, K. Podila, Q. Chen, and C. Hollingshead
Canadian Nuclear Laboratories
286 Plant Road, Chalk River, ON, K0J 1J0, Canada
behnam.dastvareh@cnl.ca; robert.david@cnl.ca; krishna.podila@cnl.ca; qi.chen@cnl.ca;
chris.hollingshead@cnl.ca

ABSTRACT

Spent fuel pools (SFPs), located within reactor buildings, rely on active cooling systems to prevent overheating, hydrogen accumulation, and potential environmental contamination from radionuclide release. The Fukushima accident underscored the vulnerability of SFPs when cooling systems are compromised. In response, the International Atomic Energy Agency (IAEA) called on Member States to conduct national assessments of nuclear power plant designs against site-specific extreme natural hazards, explicitly including SFP structures and fuel behavior. In accordance with this guidance, Canadian Nuclear Laboratories (CNL) has undertaken studies to predict the progression of loss-of-coolant accidents (LOCA) in CANDU SFPs. This paper summarizes CNL's recent efforts in this area and presents high-level findings from these investigations.

KEYWORDS
CANDU, spent fuel pools (SFPs), loss-of-coolant accident (LOCA)

1. INTRODUCTION

1.1 Background

Spent fuel pools (SFPs), also known as irradiated fuel bays (IFBs), provide temporary storage for spent fuels removed from the reactor core until its residual heat decreases enough for safe transfer to longer-term facilities. These pools, located within or directly adjacent to reactor buildings, are typically used for temporary storage of freshly discharged fuel before transferring them to longer-term dry storage. The fuel assemblies are submerged under 5–8 meters of water, which ensures cooling and radiation shielding [1]. Figure 1 shows a typical SFP for CANDUs, which are located in connected buildings to the reactor containment and used to store spent fuel for 5-10 years of wet storage before moving to longer term dry-storage.

During a prolonged loss of coolant accident (LOCA) in SFPs, however, cladding temperatures can rise significantly and high temperature steam may interact with the cladding, accelerating oxidation and potentially leading to breakaway oxidation, an event that increases the oxidation rate by more than an order of magnitude [1]. This condition greatly raises the likelihood of fission product release, posing an immediate safety risk to both the environment and nearby populations.

The Fukushima disaster underscored the critical need for understanding the behaviour of spent fuels when cooling is lost. In response, regulators across the world, including the Canadian Nuclear Safety Commission (CNSC) made efforts to address these gaps. In support of CNSC efforts, Canadian Nuclear Laboratories (CNL) compiled a Phenomena and Identification and Ranking Table (PIRT) to identify the accident phenomena and corresponding key parameters in CANDU SFPs. The PIRT informed the development of a computer code for the CNSC called BAYLOCA (BAY Loss Of Coolant Accident) designed for SFP accident analysis [2], and laid the foundation for the series of studies on spent fuel pool

accident analysis, mainly on CANDU reactors, under the Atomic Energy of Canada Limited (AECL) Federal Nuclear Science and Technology (FNST) program. This paper summarizes CNL's efforts under the latest FNST project in this area over the last three years (2022-2025) and presents high-level findings from these investigations. For simplicity, we refer to this initiative as the SFP accident analysis project.

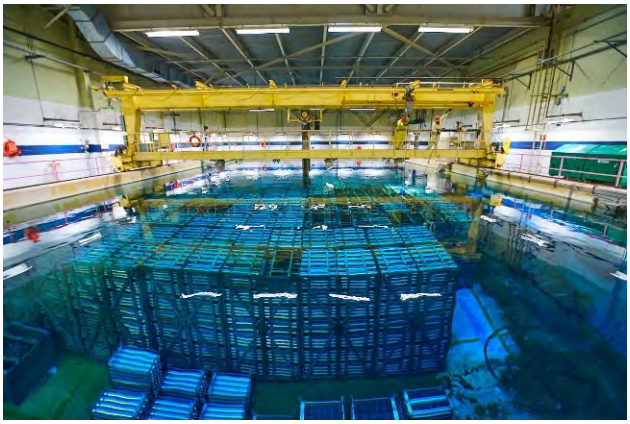

Figure 1. Spent nuclear fuel is stored in a pool at the Pickering Nuclear Generating Station in Pickering, Ontario. (Photo: Ontario Power Generation - Brian Pieters, Corporate Visuals)

1.2 Objectives and Goals of SFP Accident Analysis Project

The objective of the project was to advance the understanding of accident phenomena in CANDU SFPs and to improve insight into accident progression and its consequences. The project also aimed to enhance experimental capabilities, integrated with advanced modeling and simulation, to enable detailed analysis of accidents in CANDUs, and to support testing, benchmarking, and further development of BAYLOCA. Finally, the project sought to contribute to the global understanding of SFP accidents through active participation in international research initiatives. These objectives were pursued through several focused activities, each of which is described in the subsequent sections.

2. FUEL BAY HEATER APPARATUS (FBHA) EXPERIMENTS

CANDU fuel bundles are ~50 cm long, weigh 25 kg, and are ~10 cm in diameter. Every day during normal operation about 12-16 spent fuel bundles are received from a reactor core and stored in SFPs [3]. In response to the risk of spent fuel overheating when cooling is compromised in an accident scenario in CANDU SFPs, the FBHA was constructed, and series of experiments were conducted. As shown in Figure 2, the apparatus consists of a stainless-steel enclosure, a water tank beneath the enclosure, electrically heated simulated bundles in three rows and columns, and a hood. Inside the water tank heaters are used to generate steam.

The experiments aimed to approximate sheath and surrounding air or steam temperatures to determine heat transfer between bundles within a representative CANDU SFP tray configuration. Tests were carried out across a range of simulant bundle power levels, from 500 W to 3 kW, under stagnant dry air, blowing dry air, and steam environments. The results showed that peak sheath and gas temperatures occurred in the stagnant air environment in the middle bundle, while the lowest temperatures were observed under forced air condition. Tests conducted in steam, even over different generation rates, produced sheath temperatures that were similar to those measured under stagnant air conditions.

The maximum sheath temperature approached the hydrogen generation threshold (~827 °C) only at bundle power levels exceeding 2.5 kW. This suggests a negligible risk of hydrogen production in the evaluated three row bundle configuration, as bundle power in a CANDU SFP during the fuel uncovering phase is expected to remain significantly below 2.5 kW [4].

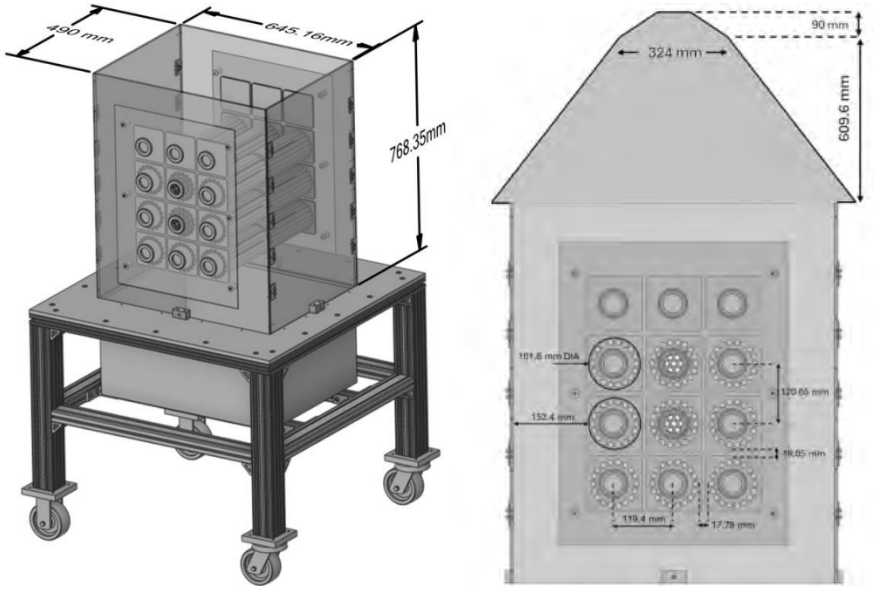

Figure 2. Schematic representation of the FBHA, illustrating its dimensions, including the stainless-steel enclosure, water tank, simulated bundles, and hood.

3. ASSESSMENT OF BAYLOCA SFP ACCIDENT ANALYSIS CODE

BAYLOCA is an independent computational tool developed for the CNSC to evaluate the progression and consequences of severe accidents in the SFPs of CANDU reactors in Canada. The code is designed for rapid execution, relying primarily on lumped-parameter models, and is capable of simulating all phases of an SFP accident. BAYLOCA represents accident evolution through four distinct stages:

Stage 1: Pool makeup is interrupted, although the spent fuel remains fully submerged.
Stage 2: The water level recedes sufficiently so that the fuels begin to be exposed to the atmosphere. In this stage some fuel assemblies are partially uncovered while others remain submerged.
Stage 3: The pool becomes completely devoid of water, either through boil-off or leakage.
Stage 4: Cooling water is restored to the pool. This stage may be entered directly from any of the preceding stages.

An overall schematic of a representative accident simulation is provided in Figure 3. User-defined inputs include initial decay heat conditions, fission product inventories, geometric and structural characteristics of the fuel stacks, pool, and building, accident-specific parameters, and ambient environmental conditions. All material properties, apart from those assigned to the building walls and roof, vary with temperature. Time-dependent outputs such as decay power, pool water temperature and height, fuel and tray temperature, gas temperature, temperature of building components, sheath and fuel oxidation, and fission product release are written to external files for subsequent post-processing. Additional detail is available in reference [2] and [5].

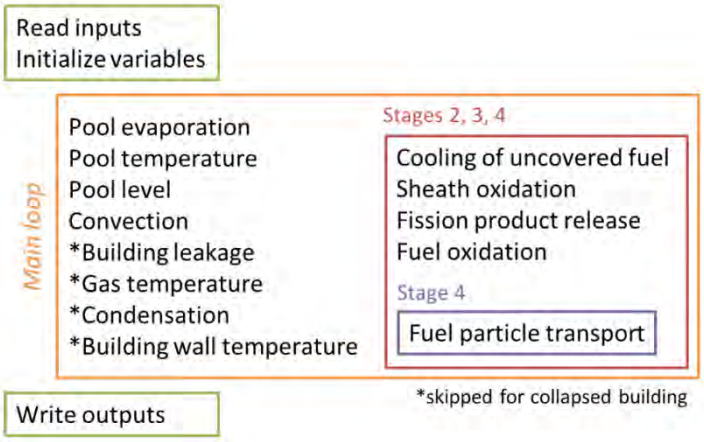

Figure 3. Overall view of an accident simulation

As part of the SFP accident analysis project, several areas for enhancement to BAYLOCA were identified, spanning phenomenological models, overall code architecture, and usability. A number of these issues have since been resolved through updates to the BAYLOCA code. Benchmarking exercises comparing BAYLOCA results with those from GOTHIC and CFD simulations demonstrated generally good agreement in thermal-hydraulic behavior, while also highlighting areas requiring further refinement, particularly with respect to fission product transport, convective fuel cooling, and deposition models within the building. Figure 4 illustrates a representative comparison between BAYLOCA predictions and GOTHIC results.

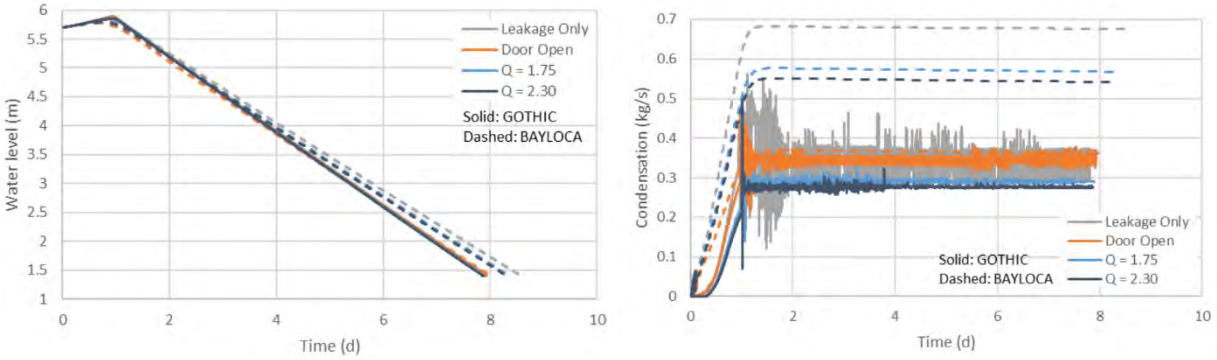

Figure 4. Comparison of the results between GOTHIC and BAYLOCA with similar input parameters: (a) water level in the pool, (b) rate of condensation.

4. CFD ANALYSIS OF SFP ACCIDENTS

A CFD modelling capability was developed in this project to estimate the peak sheath temperature in a CANDU SFP during a complete LOCA (stagnant air cooling only) [6]. Peak sheath temperature is a key indicator of accident progression and helps identify conditions under which breakaway oxidation may occur. Such conditions could threaten the integrity of the irradiated fuel bundle or lead to severe fuel damage.

A mechanistic CFD model was created using the geometric features of a CANDU spent fuel module. The model simulates flow and heat transfer within an irradiated fuel storage facility, accounting for natural convection, radiation, and solid-body conduction. The CFD simulations were performed using Simcenter STAR-CCM+. The CFD models were quantitatively evaluated and shown to capture the complex thermal-hydraulic behaviour expected in the SFP geometry at the specified decay powers.

The resulting CFD model was intended to support the development of reduced-order, fast-running models for the BAYLOCA analysis code for use in emergency response. It can also help guide experimental design by identifying conditions that warrant detailed measurement.

Figure ***5*** presents the mesh and temperature contours for a representative fuel module containing 96 irradiated fuel bundles, each decaying at 62 W in the SFP. The figure shows that the central bundles in row #6 attain the highest temperature levels within the module [6].

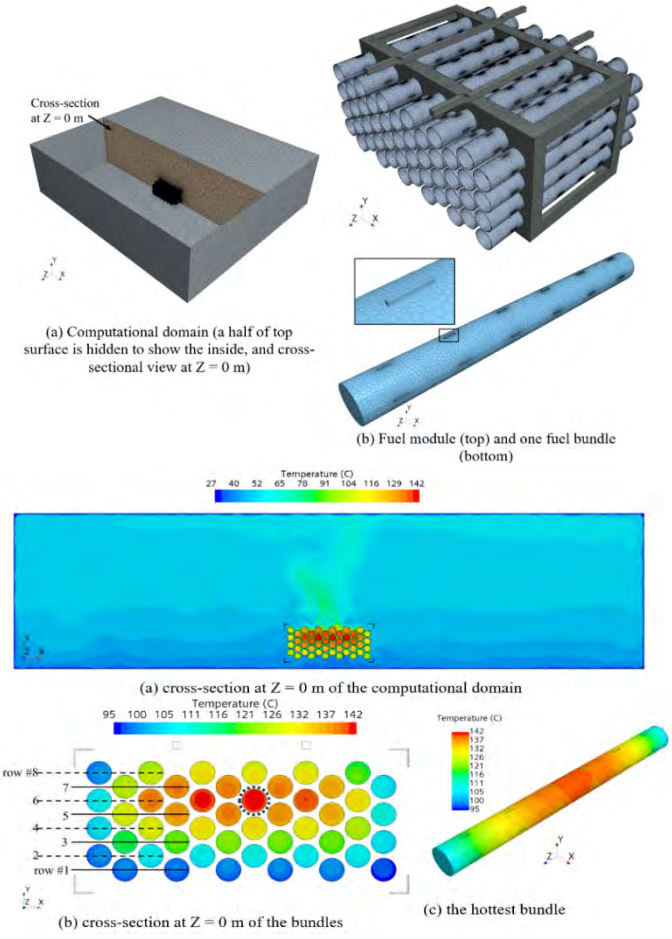

Figure 5. Mesh and temperature contours of the simulation domain, showing the pool and a fuel module containing 96 irradiated CANDU bundles, each with a decay power of 62 W [6].

5. GOTHIC ANALYSIS OF SFP ACCIDENTS

This task focused on applying the GOTHIC software, typically used for containment analyses, to simulate SFP accident scenarios and generate thermal-hydraulic data such as pool drainage behavior and building temperature responses. The results were intended to support improvements to the thermal-hydraulic models in BAYLOCA. Figure 6 presents the GOTHIC model and the predicted average building temperature for an accident scenario in a representative CANDU SFP. The building and pool dimensions were 46 × 15 × 9 m and 46 × 10 × 6 m, respectively. The analysis began with an initial decay power of approximately 8.6 MW, decreasing over time.

During the study, several limitations in GOTHIC's capability for modelling this type of scenario became evident and recommendations were made to mitigate these issues and to enhance the physical realism of future simulations. First, replacing the current single lumped pool with multiple vertically stacked pool control volumes would better capture fueled-region porosity and internal convection. However, in the version used here (GOTHIC 8.2) the moving liquid–vapor interface crossing the boundaries between these pool volumes during water evaporation triggers numerical instabilities. The issue was shared with developers to consider it for later versions. Second, the present method for applying decay heat to the gas above the pool artificially returns heat to the liquid, depressing predicted gas temperatures. Adopting a surface-based heat input just above the pool avoids this artefact and yields more credible predictions as fuel becomes exposed. Finally, because wall temperatures reach ranges where radiation becomes significant, adding radiative heat-transfer treatment to building surfaces would improve accuracy during high-temperature late phase of the accident.

The GOTHIC model was later expanded to include aerosol transport processes involving fission products. This update enabled a comparison with assumptions related to these phenomena embedded in BAYLOCA, especially those related to the conservatism of its primary release estimates. The enhanced GOTHIC simulations indicated that roughly 60% of the released fission products would remain inside the building, largely deposited in liquid accumulations. BAYLOCA 1.0 was unable to reproduce this outcome because it was designed with a conservative bias and did not include a model for fission product deposition.

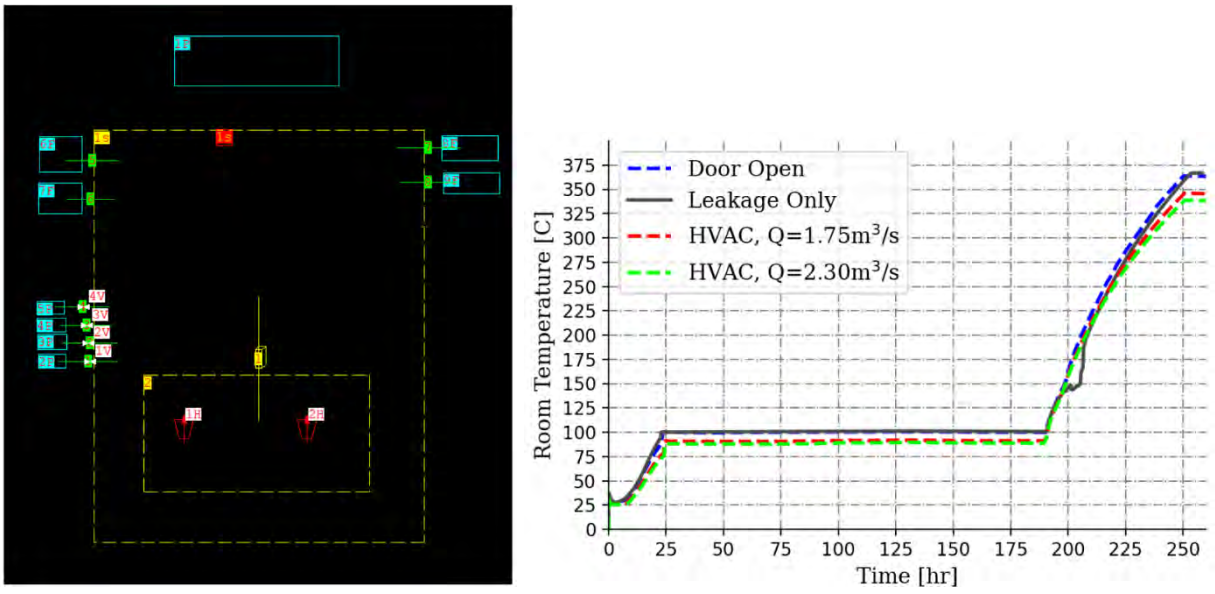

Figure 6. GOTHIC model of the SFP (left), and temperature of the building during a transient under different boundary conditions (right).

6. PARTICIPATION IN OECD-NEA POLCA PROJECT

In alignment with the objectives of the SFP accident analysis project, an international research connection was included to leverage the research and understanding of the broader community studying SFP severe accidents. This involved Canada's participation in the OECD-NEA POLCA project, which is focused on understanding LOCA scenarios in light water reactor SFP, while also generating broader insights applicable to common phenomena found in CANDU SFPs. This project aims to generate data for SFP thermal-hydraulic under accident conditions that can be used to benchmark and refine numerical modelling tools for SFP accident analysis.

7. CONCLUSION

Following the vulnerabilities revealed in SFPs during the Fukushima accident, many countries conducted research efforts in this area. As part of Canada’s response, and with the support of the CNSC, CNL initiated research efforts to improve the understanding of accident progression and consequences in SFPs, with emphasis on CANDU facilities.

As part of this effort, the FBHA was constructed to study bundle level behavior in a tray type configuration. A series of experiments were carried out to measure sheath and gas temperatures over a range of bundle powers in dry air, blowing air, and steam environments.

A comprehensive review of the BAYLOCA SPF accident analysis code was also completed, identifying several areas for improvement, including potential enhancements to phenomena models, updates to the code architecture, and improvements in the user experience. The updated code was benchmarked against results from both GOTHIC and high fidelity CFD models.

The CFD model, developed to estimate peak sheath temperatures during a complete LOCA in CANDU SFPs, demonstrated the complex heat transfer and flow patterns expected at the examined decay powers.

A thermal-hydraulic GOTHIC model was developed to simulate a LOCA scenario in a simplified SFP configuration. Several limitations in GOTHIC’s treatment of fuel exposure to air steam mixtures were identified. The model was later expanded to include aerosol and fission product transport, enabling an assessment of the conservatism of the BAYLOCA primary release assumptions.

Finally, in alignment with these efforts CNL is participating in the OECD-NEA POLCA joint project, which is designed to generate valuable data on thermal-hydraulic phenomena in a SFP under accident conditions thereby strengthening understanding and improving international capabilities for SFP safety analysis.

8. NOMENCLATURE

AECL	Atomic Energy of Canada Limited
BAYLOCA	BAY Loss Of Coolant Accident
CFD	Computational Fluid Dynamics
CNL	Canadian Nuclear Laboratories
CNSC	Canadian Nuclear Safety Commission
FBHA	Fuel Bay Heater Apparatus
FNST	Federal Nuclear Science and Technology
IAEA	Atomic Energy Agency
IFB	Irradiated Fuel Bay
LOCA	Loss-Of-Coolant Accident
LWR	Light Water Reactor
NEA	Nuclear Energy Agency

OECD	Organization for Economic Development
PIRT	Phenomena and Identification and Ranking Table
POLCA	Pool during Loss of Cooling Accident
SFP	Spent Fuel Pool

9. ACKNOWLEDGMENTS

This work was supported by Atomic Energy of Canada Limited's Federal Nuclear Science & Technology program. The authors thank Justin Spencer, Jason Wu, and Penny Neal for manuscript review. The authors also acknowledge the contributions of Ray Dickson, Kurt Stoll, Kevin Krkljus, Michael Callaghan, and Aidan Rutledge for design, construction and execution of the experiments.

10. REFERENCES

1. Organization for Economic Development-Nuclear Energy Agency (OECD-NEA), "Status Report on Spent Fuel Pools under Loss-of-Cooling and Loss-of-Coolant Accident Conditions: Final Report," NEA, OECD Publishing, Paris, (2015).
2. J. S. Bell, K. Stoll, R. David, J. Wu, A. Vasic, and S. Groulx, "Degraded cooling of spent fuel bundles in irradiated fuel bays," *presented at the 40th Annual Conference of the Canadian Nuclear Society and 45th Annual CNS/CNA Student Conference*, (2021).
3. Editor-in-Chief Wm. J. Garland, *The Essential CANDU, A Textbook on the CANDU Nuclear Power Plant Technology*. University Network of Excellence in Nuclear Engineering (UNENE), (2017).
4. H. Z. Fan, R. Aboud, E. Choy, W. Zhu, and H. Liu, "Spent fuel response after a postulated loss of spent fuel bay cooling accident," *Canadian Nuclear Society Bulletin*, vol. 33, (2012).
5. R. David, J. S. Bell, R. S. Dickson, A. C. Morreale, and H. V. Yan, "BAYLOCA: A Severe Accident Code for CANDU Irradiated Fuel Bays," *presented at the 44th Annual CNS Conference*, Toronto, Canada, Jun. (2025).
6. Q. Chen, K. Podila, and A. Morreale, "CFD Modelling of a CANDU Irradiated Fuel Bay," in *Proceedings of 21st International Topical Meeting on Nuclear Reactor Thermal Hydraulics (NURETH-21)*, BEXCO Busan, Korea, Sep. (2025).

Karlsruhe Institute of Technology

Institute for Applied Materials

Validation of the Theoretical Approach for Modelling of the Hydride Morphology with Experimental Data Obtained from SPIZWURZ Bundle Test

M. Kolesnik, J. Stuckert, M. Grosse, S. Weick

12th European Review Meeting on Severe Accident Research (ERMSAR 2026), Madrid, Spain

Institute for Applied Materials; Program NUSAFE

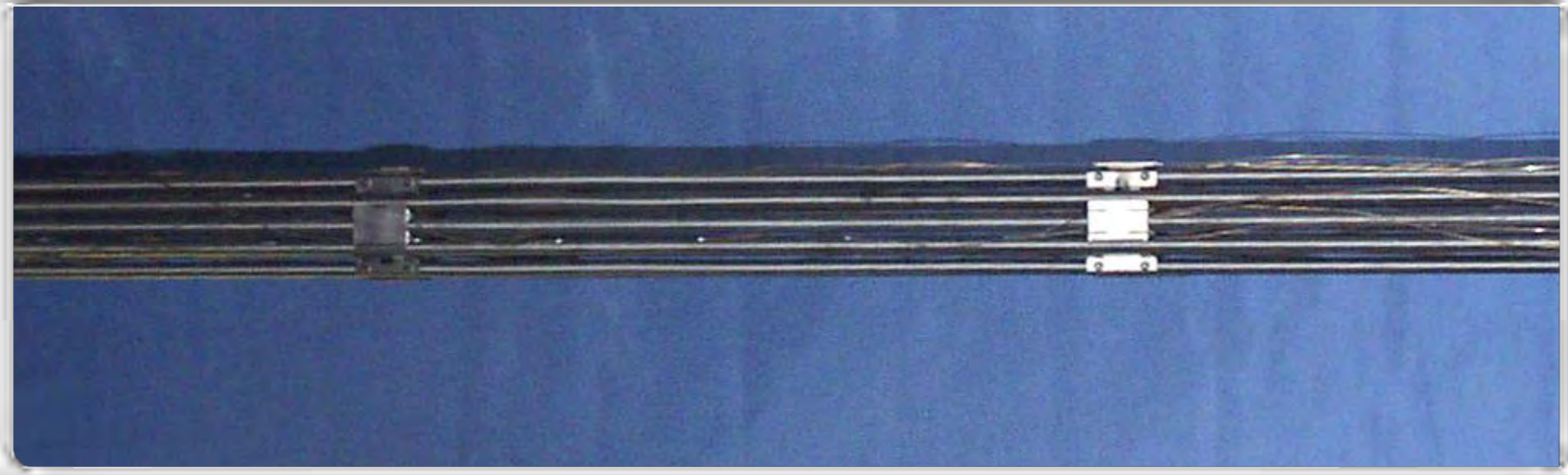

Hydrogen embrittlement of zirconium alloys
the role of hydrides

1. Plastic flow localization

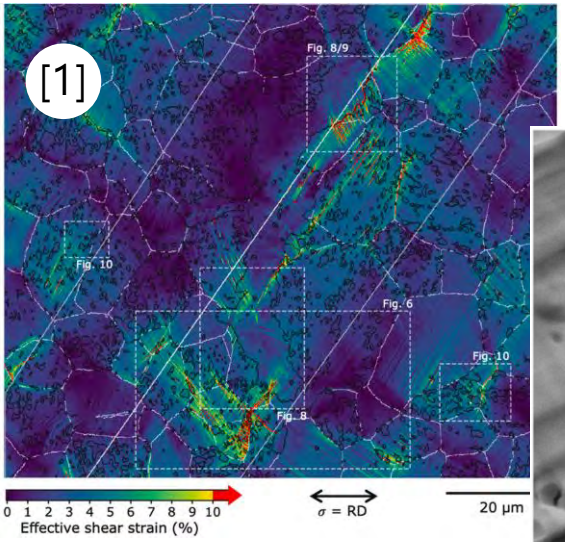

2. Crack nucleation sites

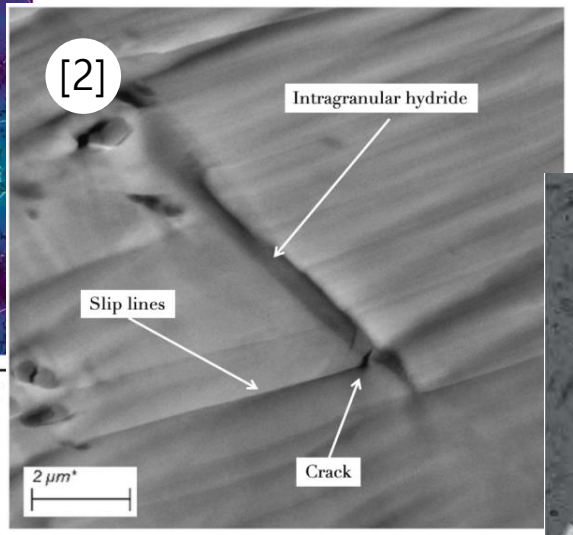

3. Pathways for brittle crack growth

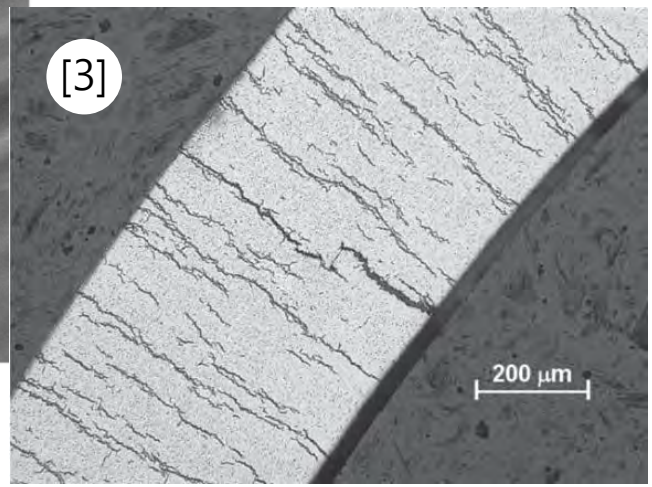

Necessary condition of ductile-to-brittle transition:
hydride morphology can provide a continuous path through the specimen

[1] R. Thomas *et al. Acta Mater.*, 261 (2023) 119327; DOI: 10.1016/j.actamat.2023.119327
[2] L. Reali *et al. J. Mech. Phys. Solids*, 147 (2021) 104219; DOI: 10.1016/j.jmps.2020.104219
[3] M. Billone *et al. J. Nucl. Mater.*, 433 (2013) 431 - 448; DOI: 10.1016/j.jnucmat.2012.10.002

Hydrogen embrittlement of zirconium alloys
hydride morphology metrics

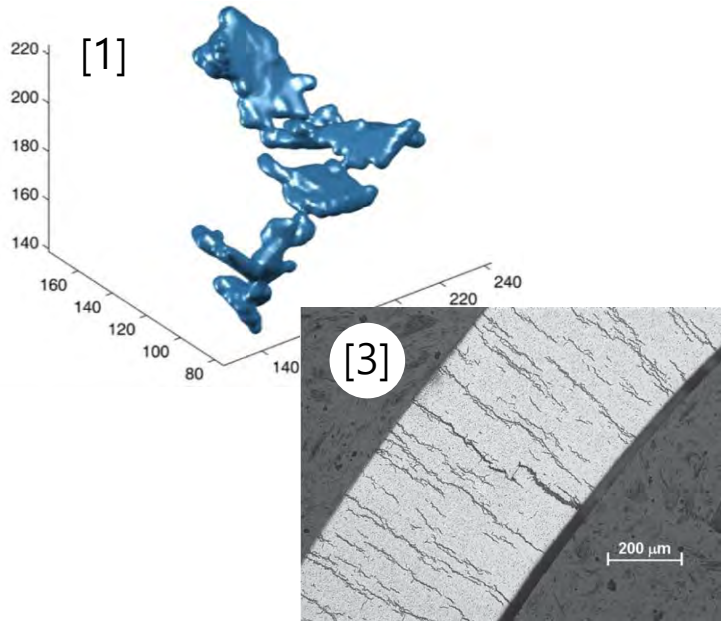

Morphology metrics in simplified 2D approximation:

1. orientation
2. length
3. spacing

Integral morphology metrics: continuity of hydrides

Accumulated Hydride Length (AHL)

Hydride Continuity Coefficient (HCC)

Radial Hydride Continuity Factor (RHCF)

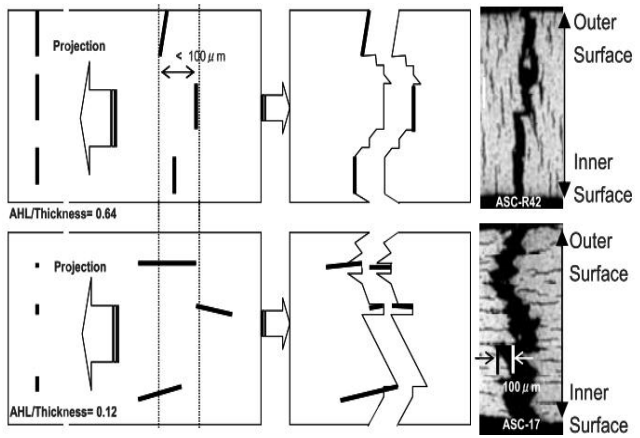

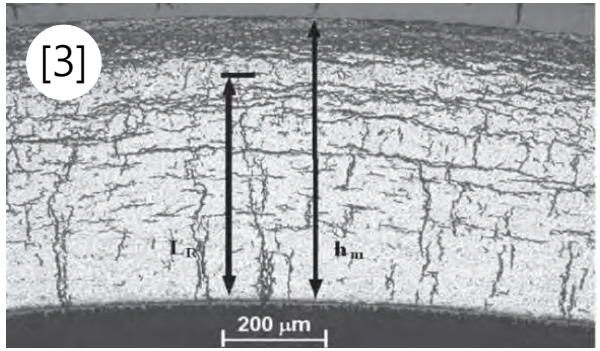

The morphology of the hydrides is controlled by the texture and microstructure of the alloy, as well as by the thermomechanical history

[1] Fang *et al. Mat. Charact.*., 134 (2017) 362–369; DOI: 10.1016/j.matchar.2017.11.013
[2] M. Nakatsuka and S. Yagnik *J. ASTM int.* 8 (2010); DOI: 10.1520/JAI102954
[3] M. C. Billone *et. al. J. Nucl. Mat.* 433 (2013) 431-448; DOI: 10.1016/j.jnucmat.2012.10.002

Hydride reorientation
in conditions of dry storage of spent nuclear fuel

Karlsruhe Institute of Technology

The scheme of spent fuel dry storage

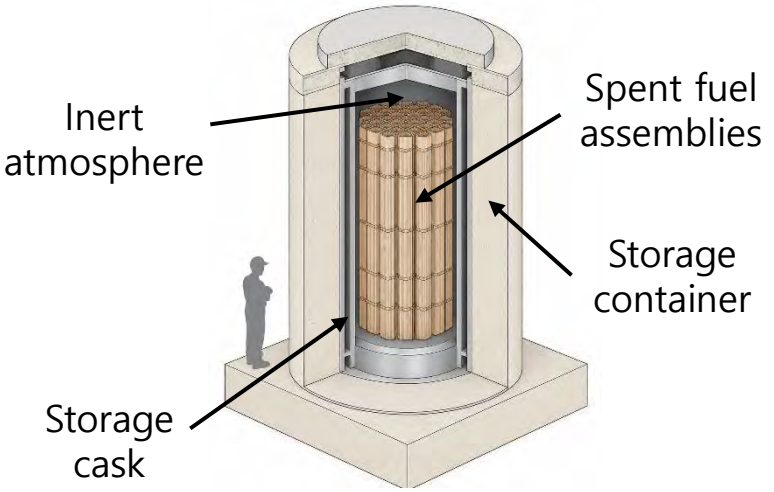

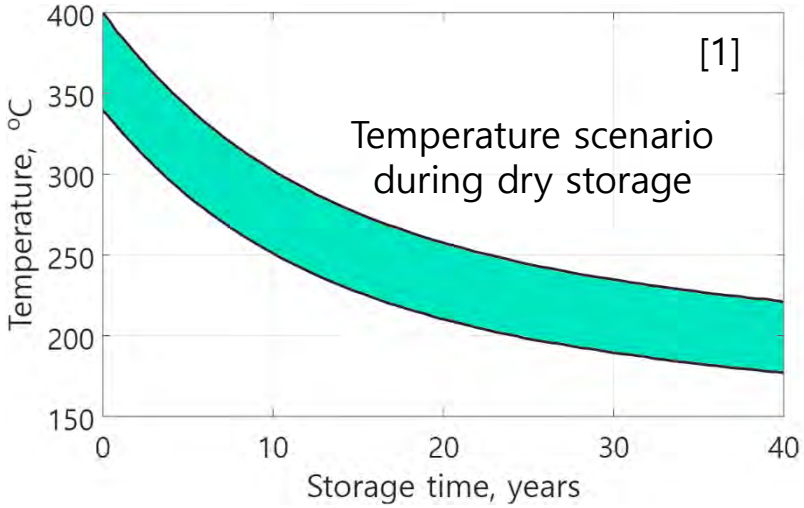

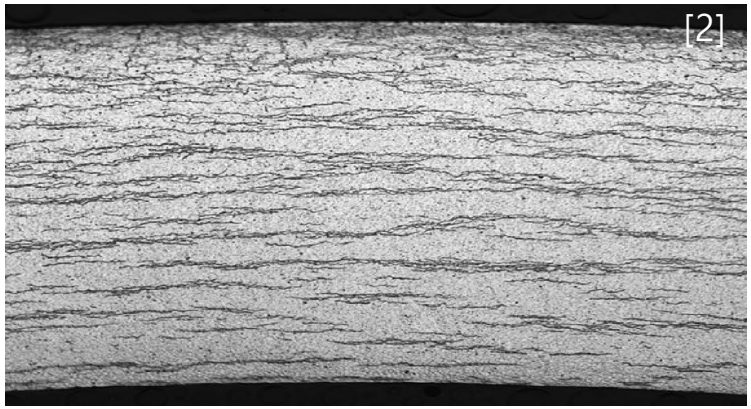

Tangential hydride orientation in fuel claddings after in-reactor operation

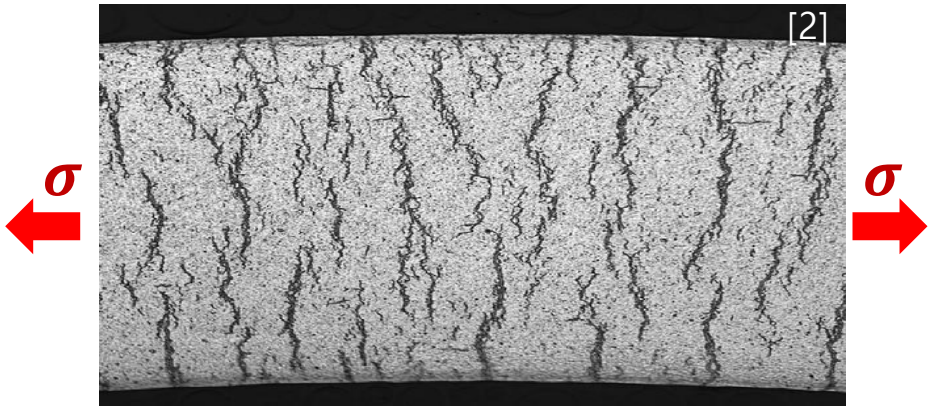

Possible hydride reorientation in the presence of tangential tensile stresses

[1] J. Rashid and A. Machiels, LWR fuel performance meeting, San Francisco, September 30 – October 3, 2007
[2] H.C. Chu et al. *J. Nucl. Mater.* 362 (2007) 93-103, DOI: 10.1016/j.jnucmat.2006.11.008

SPIZWURZ bundle test
experimental conditions

SPIZWURZ samples (long-term dry storage of spent nuclear fuel simulation):
8 hydrogenated cladding tubes (Zircaloy-4 and opt. ZIRLO), loaded by internal gas pressure, subjected to thermocycle with slow stepwise cooling

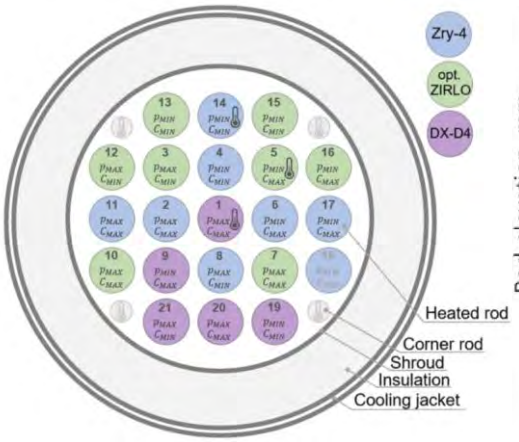

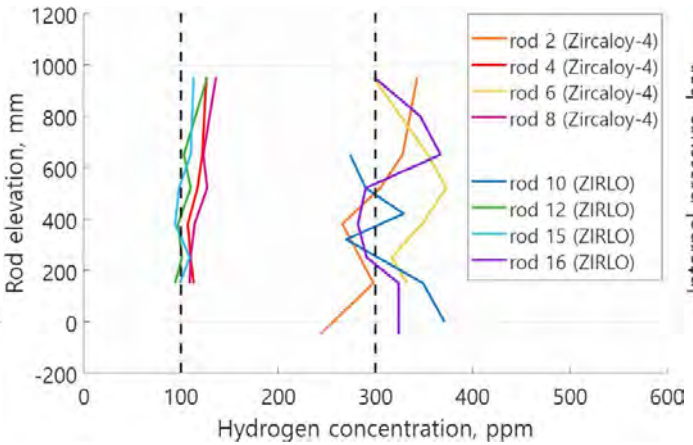

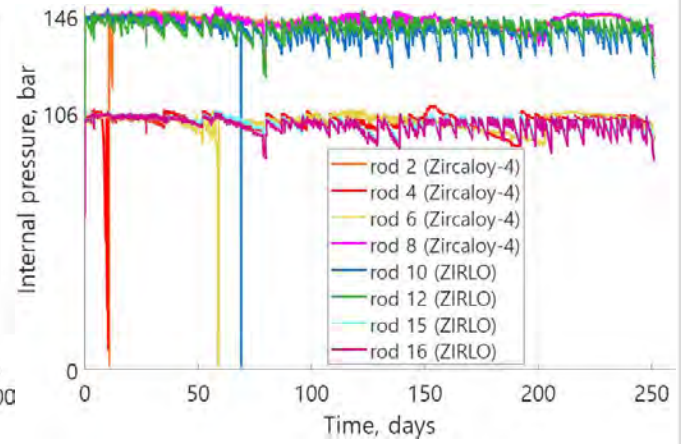

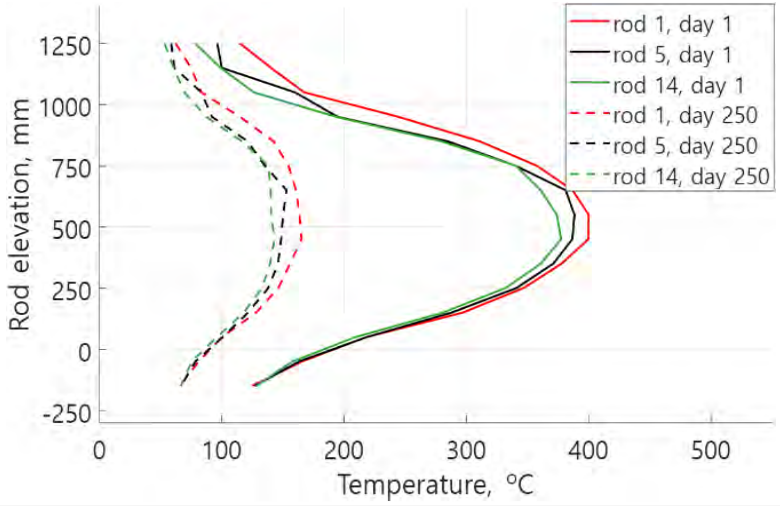

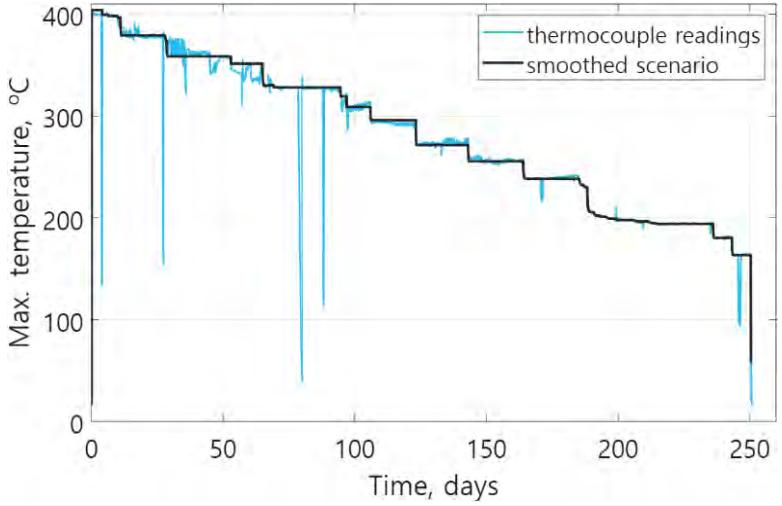

Model based on ODE system solution
model description

1. Diffusion growth of hydrides:
H concentration in solution C_s tends to its equilibrium value C_e with characteristic time τ_0

$$1)\quad \frac{\mathrm{d}C_s}{\mathrm{d}t} - \frac{C_s - C_e}{\tau_0} = 0$$

$$\tau_0 = \frac{\Delta}{\alpha^2 D_{\mathrm{H}}}$$

2. Orientation of hydrides:
Accumulated radial hydride fraction θ evolution is determined by the instantaneous fraction of radially-oriented hydrides precipitated on the current time step f_r

$$2)\quad \frac{\mathrm{d}\theta}{\mathrm{d}t} = \frac{\theta - f_r}{C_{tot} - C_s} \cdot \frac{\mathrm{d}C_s}{\mathrm{d}t}$$

$$f_r = \frac{1}{1 + f_0 \cdot \exp\left(-\sigma \cdot \Delta\Omega / kT\right)}$$

3 and 4. Nucleation of hydrides:
Approximation of classical heterogeneous nucleation theory on predefined nucleation sites with normally distributed defect energies.

$$3)\quad \frac{\mathrm{d}n_r}{\mathrm{d}t} = f_r \cdot \frac{\mathrm{d}n}{\mathrm{d}t}$$

$$4)\quad \frac{\mathrm{d}n_t}{\mathrm{d}t} = \left(1 - f_r\right) \cdot \frac{\mathrm{d}n}{\mathrm{d}t}$$

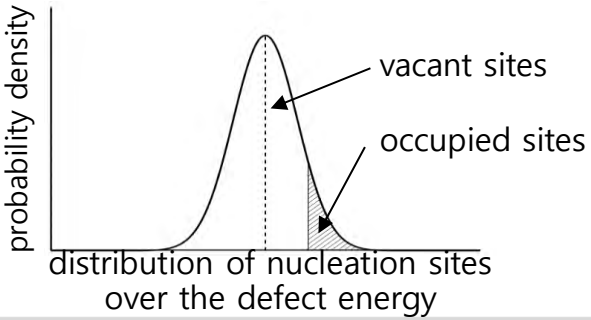

$$\frac{\mathrm{d}n}{\mathrm{d}t} = \int_{E_{d,\min}}^{E_{d,\max}^{frei}} \varphi\left(E_d\right) \cdot n_{\max} \cdot R\left(E_d\right) \cdot \mathrm{d}E_d$$

$$R\left(E_d\right) = Zj^* \cdot \exp\left(-\Delta G\left(E_d\right)^* / kT\right)$$

$$\Delta G\left(E_d\right) = \Omega_n \left(g_m - \Delta\mu / v_{\mathrm{H}}\right) + S_n \gamma - E_d$$

Model based on ODE system solution
simulation results 1

Rods 2, 4, 6 and 8 (Zircaloy-4):
located symmetrically within the bundle and have all possible combinations of hydrogen content (100 and 300 ppm) and internal pressure (106 and 146 bar)

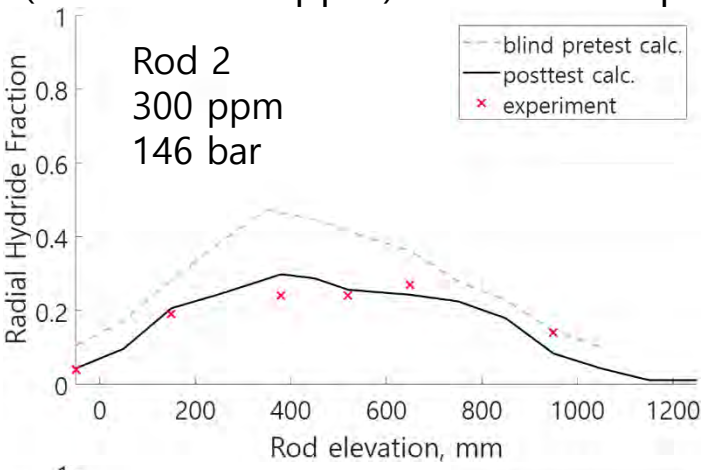

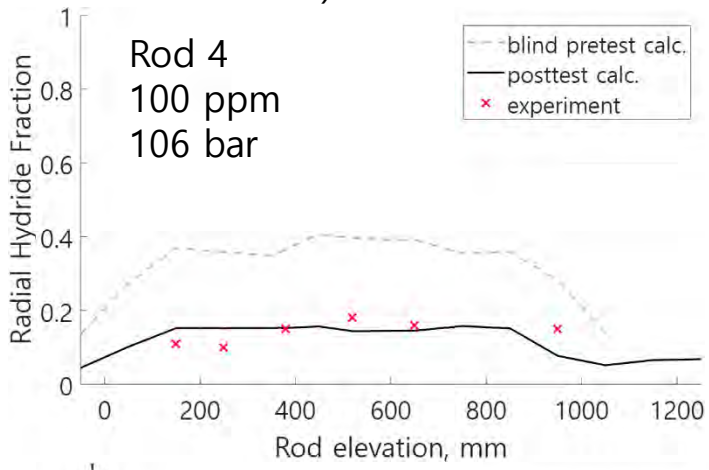

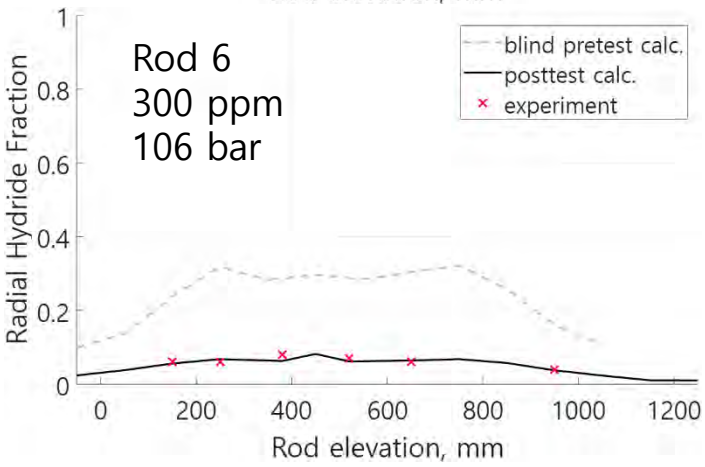

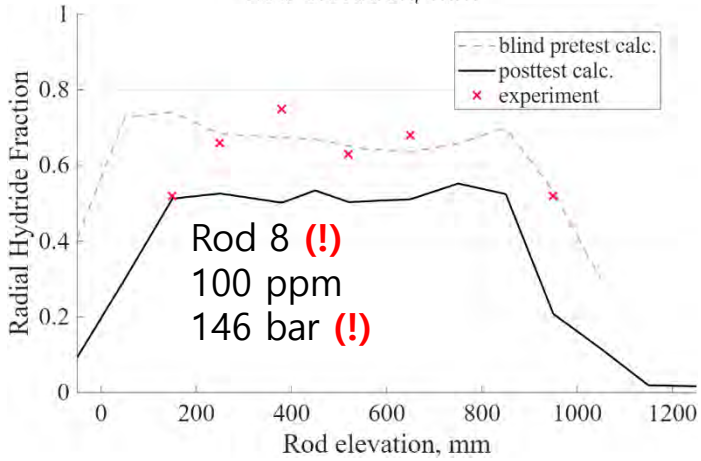

The difference in pre- and post-simulations originates from:
(i) the actual H concentration and (ii) the datasets used to fit the model parameters

Model based on ODE system solution
simulation results 2

Rods 10, 12, 15 and 16 (opt. ZIRLO):
located symmetrically within the bundle and have all possible combinations of hydrogen content (100 and 300 ppm) and internal pressure (106 and 146 bar)

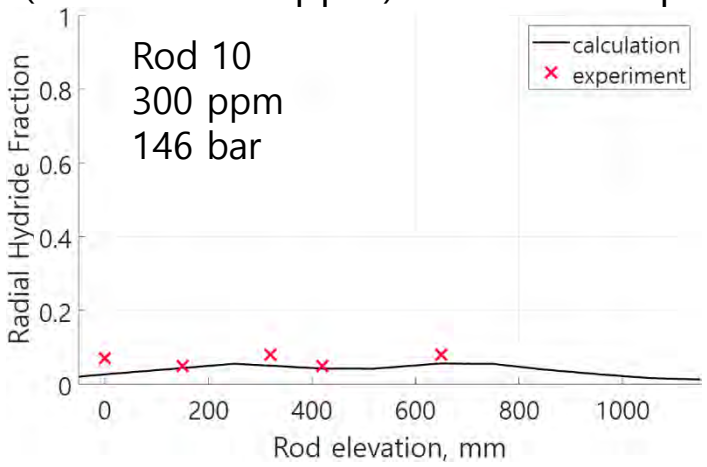

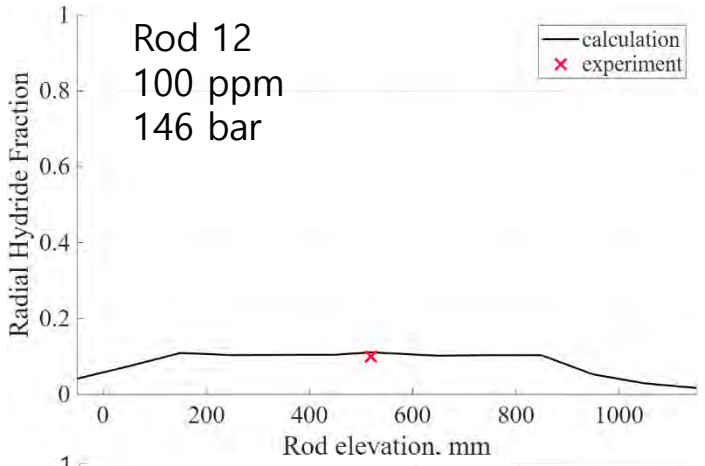

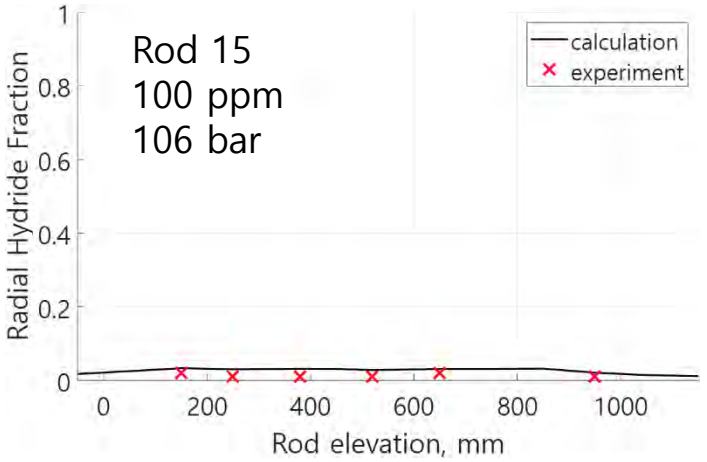

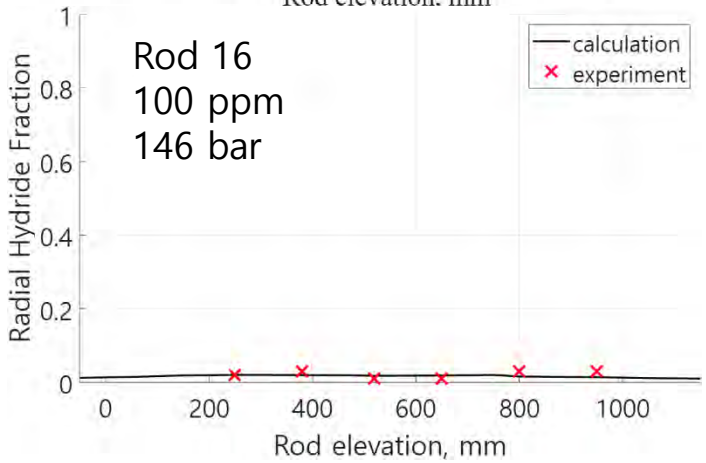

Tendency to reorientation in opt. ZIRLO is lower than that in Zircaloy-4. Possible explanation is the difference in texture and grain structure

Model based on ODE system solution
simulation results 3

Experiment-to-calculation comparison:
mean hydride length and surface density of hydrides

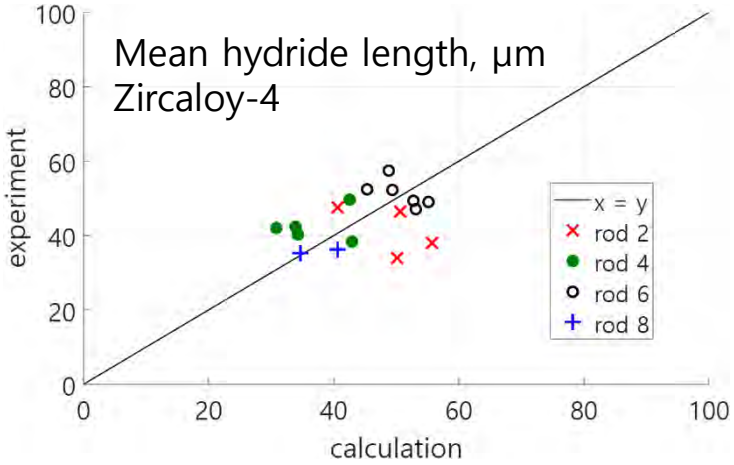

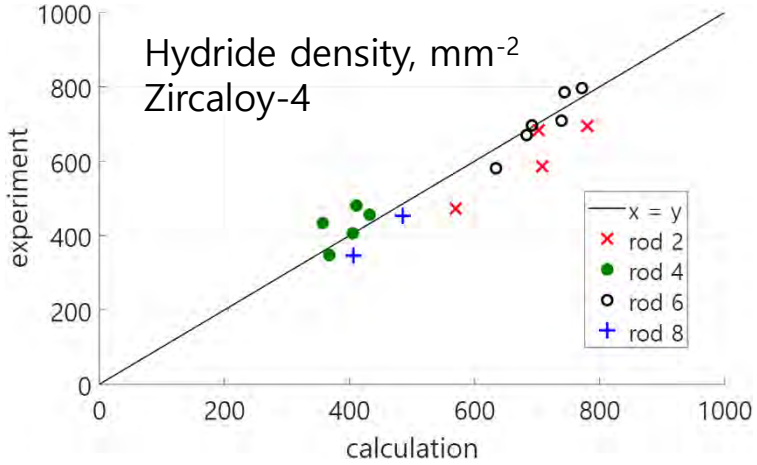

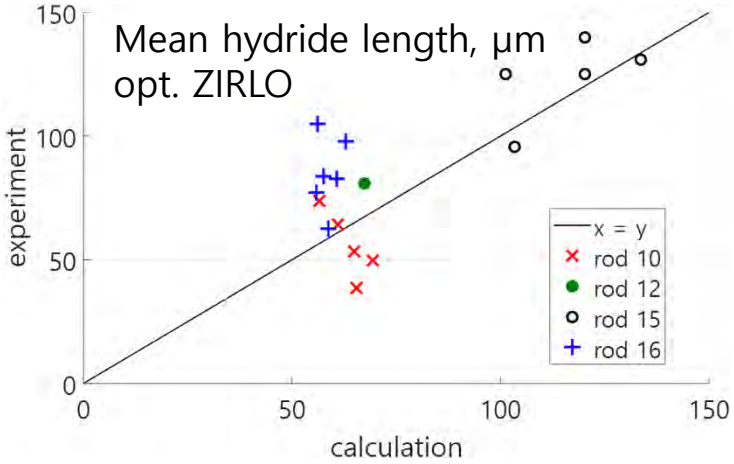

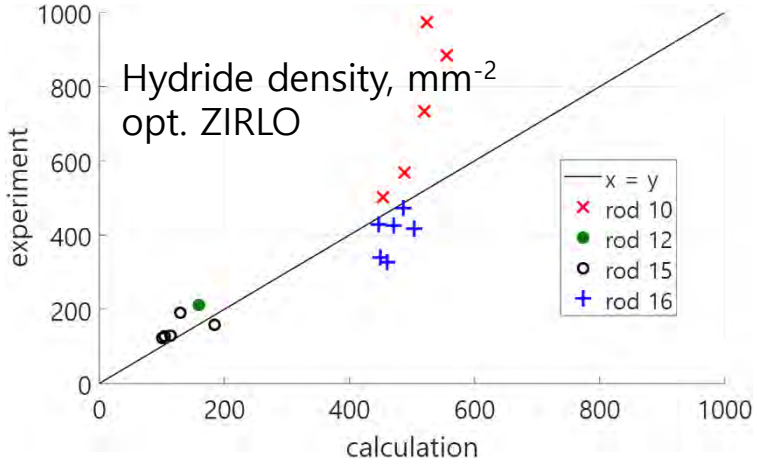

Mean hydride length in Zircaloy-4 is lower and hydride density is higher than in ZIRLO

MORPHYD module
the model description

Nucleation and growth of hydrides

- disk-shaped hydrides
- pre-defined nucleation sites
- classical nucleation theory
- diffusional growth
- competition of neighboring hydrides for the hydrogen in solid solution

Cross-section analysis

- morphology analysis as with experimental cross-sections
- any hydride morphology metric
- statistical analysis of metrics

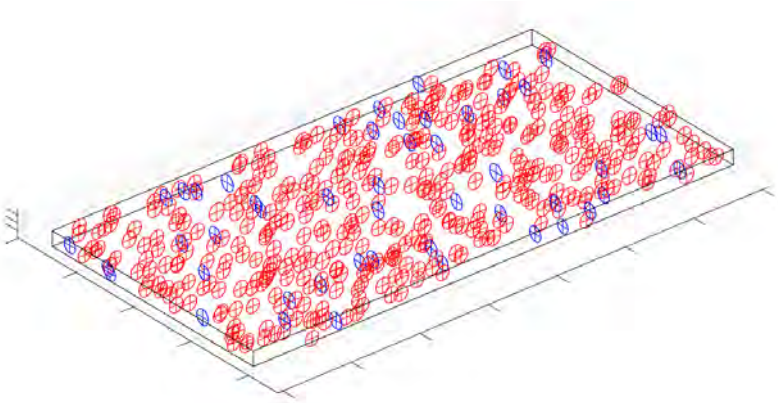

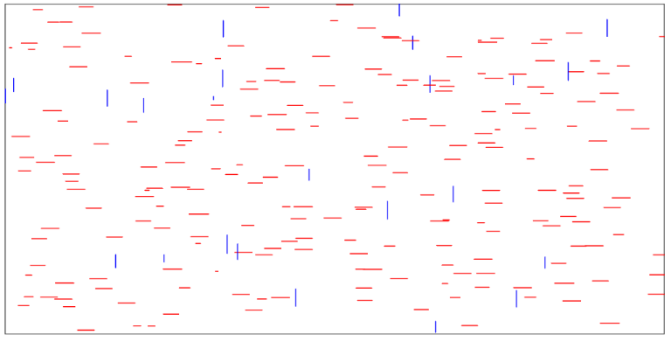

Current limitations of the MORPHYD module:

(i) precipitation only (no dissolution), (ii) valid for small hydrides

[1] M. Kolesnik and T. Aliev, *Phys. of Met. and Metal.* 104 (2023) 1414-1425, DOI: 10.1134/S0031918X22602074
[2] T. Aliev and M. Kolesnik, *Let. on Mater.* 13 (2023) 143-148, DOI: 10.22226/2410-3535-2023-2-143-148

MORPHYD module
comparison with experiment 1

Hydride length distribution (at elevation 520 mm in the hottest axial zone)

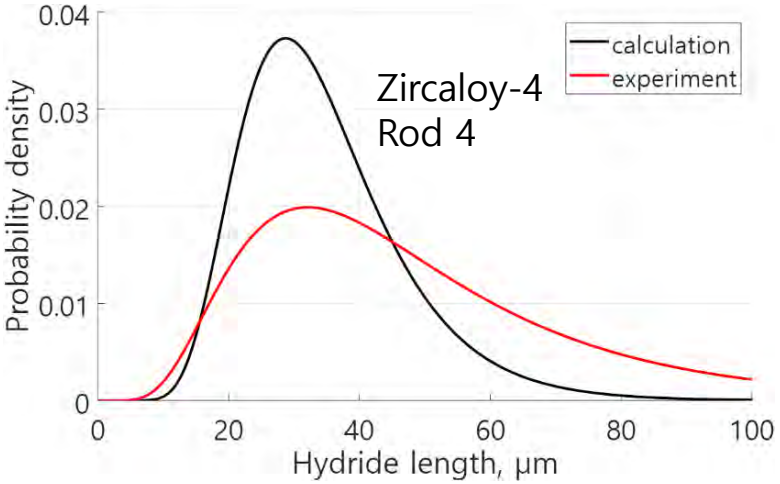

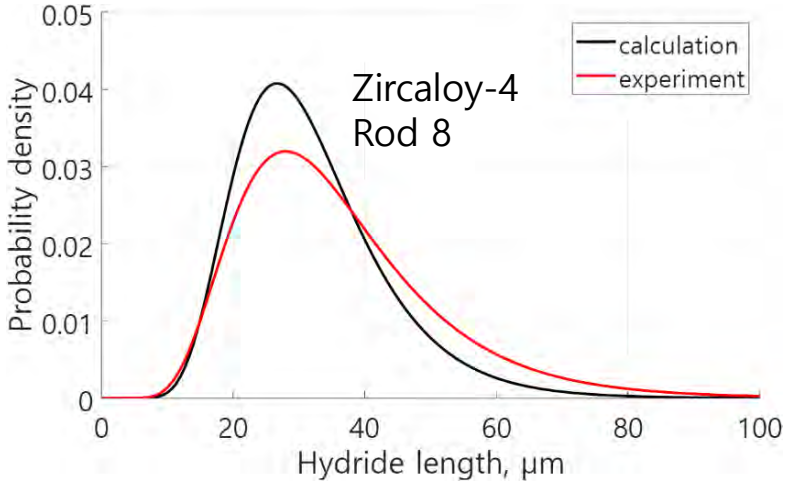

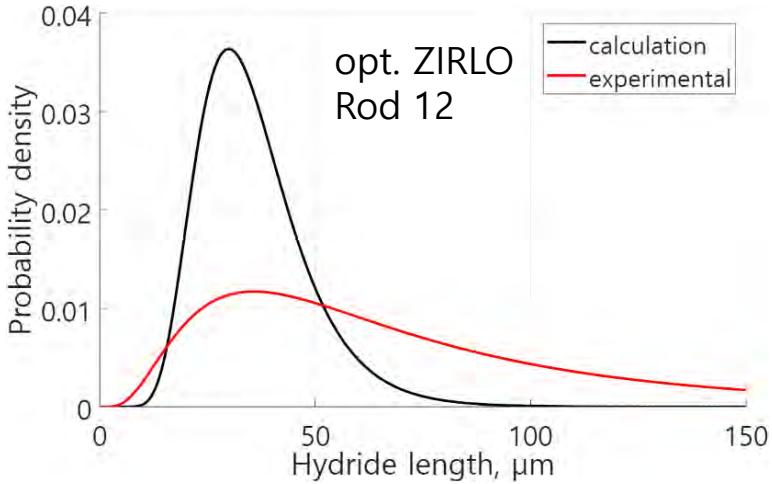

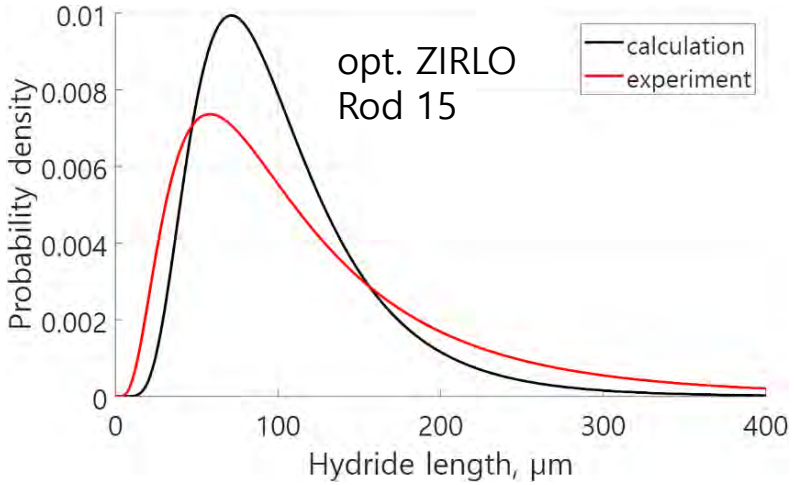

MORPHYD module
comparison with experiment 2

Hydride Continuity Coefficient (HCC) – the total projection of hydride lengths on radial direction in a 110-μm band (at elevation 520 mm in the hottest axial zone)

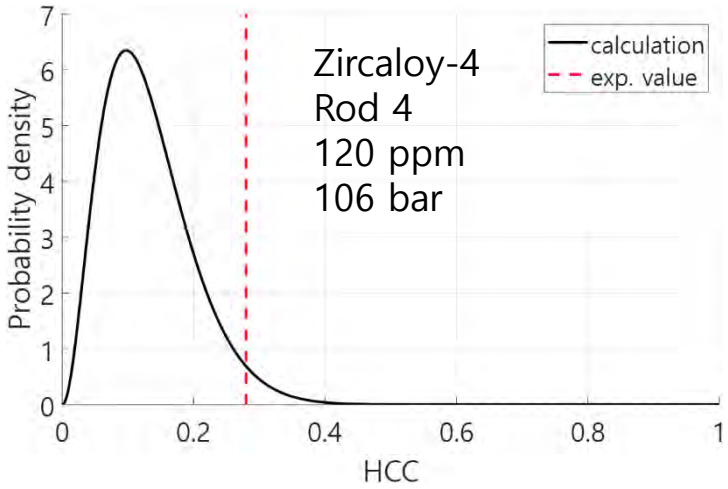

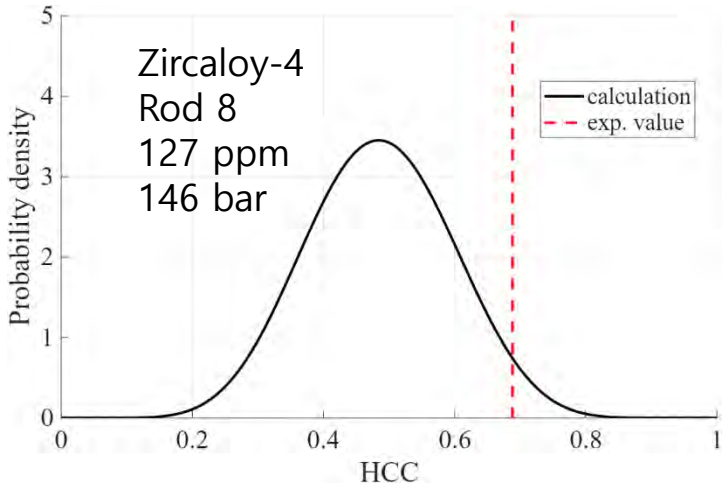

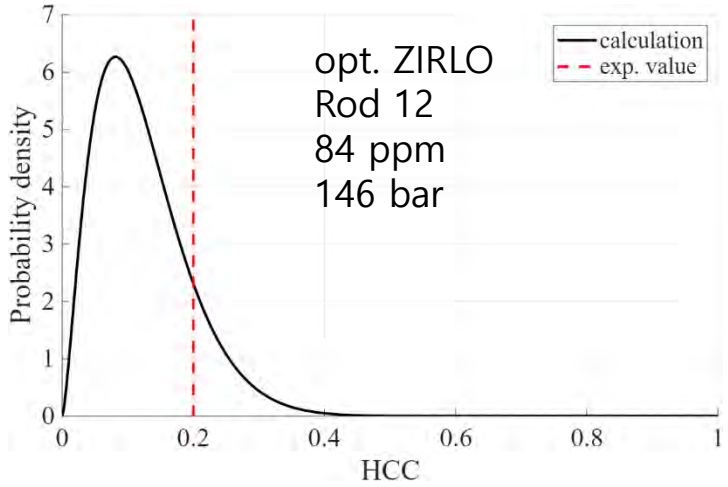

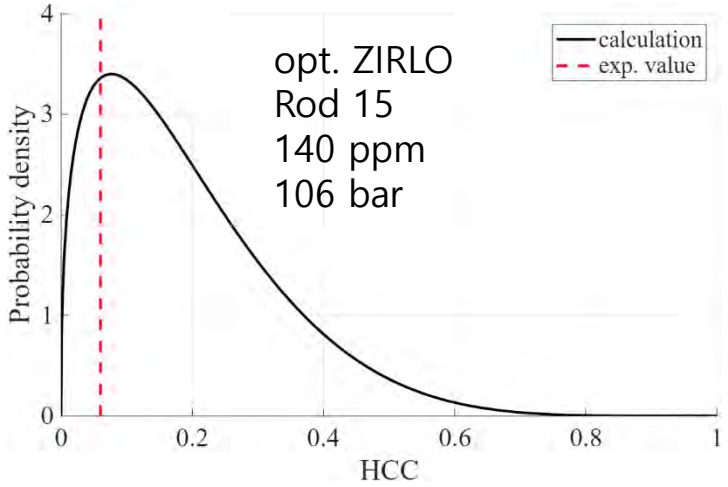

MORPHYD module
comparison with experiment 3

Radial Hydride Continuity Path (RHCP) – the estimated relative reduction of the fracture energy (at elevation 520 mm in the hottest axial zone)

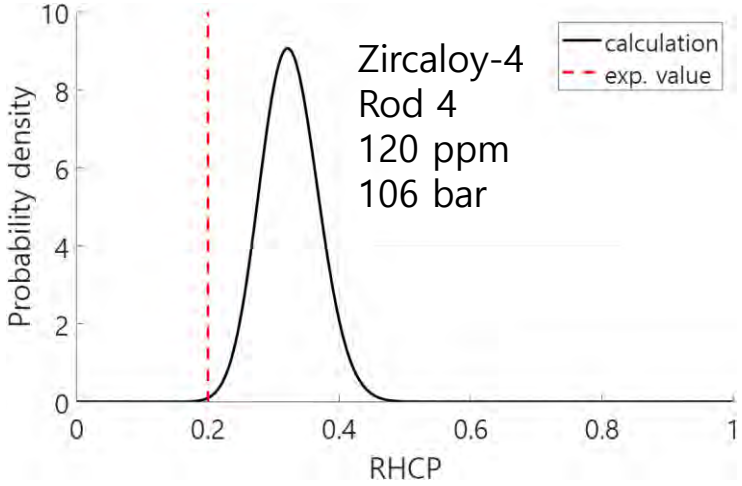

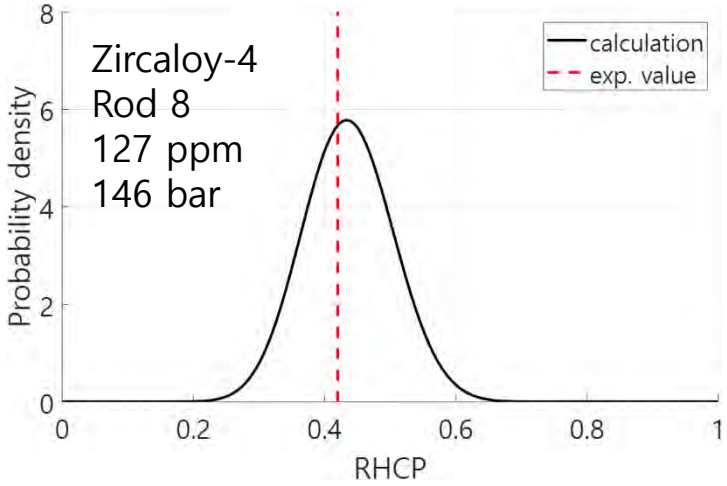

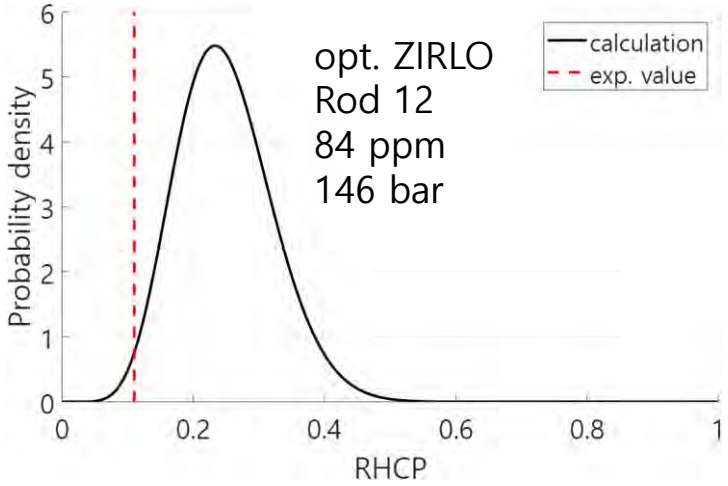

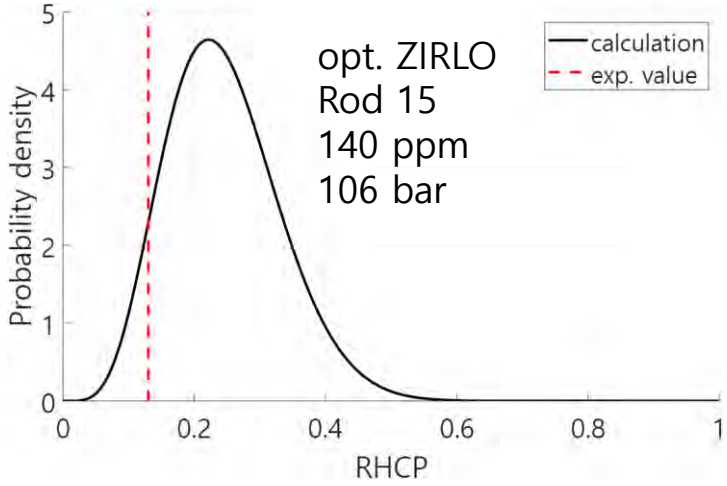

Conclusion

- Two complementary numerical tools have been calibrated using new data from SPIZWURZ experiment for Zircaloy-4 and opt. ZIRLO.
- The ODE-based tool reasonably predicts mean morphology parameters: RHF, hydride length and hydride density.
- MORPHYD reproduces statistical distributions of hydride length and integral hydride morphology metrics.
- Safety-relevant assessment can be supported by the tandem use of both approaches, with MORPHYD applied within its current validity limits.

Thank you for your attention

https://www.iam.kit.edu/awp/english/163.php

http://quench.forschung.kit.edu/

The 12h European Review Meeting on Severe Accident Research (ERMSAR2026)
Madrid, Spain, May 18-22, 2026

Log Number: 111

153-126800-CONF-011177

RECENT ACTIVITIES AT CANADIAN NUCLEAR LABORATORIES ON LOCA PROGRESSION IN CANDU SPENT FUEL POOLS

B. Dastvareh, R. David, K. Podila, Q. Chen, and C. Hollingshead
Canadian Nuclear Laboratories
286 Plant Road, Chalk River, ON, K0J 1J0, Canada
behnam.dastvareh@cnl.ca; robert.david@cnl.ca; krishna.podila@cnl.ca; qi.chen@cnl.ca;
chris.hollingshead@cnl.ca

ABSTRACT

Spent fuel pools (SFPs), located within reactor buildings, rely on active cooling systems to prevent overheating, hydrogen accumulation, and potential environmental contamination from radionuclide release. The Fukushima accident underscored the vulnerability of SFPs when cooling systems are compromised. In response, the International Atomic Energy Agency (IAEA) called on Member States to conduct national assessments of nuclear power plant designs against site-specific extreme natural hazards, explicitly including SFP structures and fuel behavior. In accordance with this guidance, Canadian Nuclear Laboratories (CNL) has undertaken studies to predict the progression of loss-of-coolant accidents (LOCA) in CANDU SFPs. This paper summarizes CNL's recent efforts in this area and presents high-level findings from these investigations.

KEYWORDS
CANDU, spent fuel pools (SFPs), loss-of-coolant accident (LOCA)

1. INTRODUCTION

1.1 Background

Spent fuel pools (SFPs), also known as irradiated fuel bays (IFBs), provide temporary storage for spent fuels removed from the reactor core until its residual heat decreases enough for safe transfer to longer-term facilities. These pools, located within or directly adjacent to reactor buildings, are typically used for temporary storage of freshly discharged fuel before transferring them to longer-term dry storage. The fuel assemblies are submerged under 5–8 meters of water, which ensures cooling and radiation shielding [1]. Figure 1 shows a typical SFP for CANDUs, which are located in connected buildings to the reactor containment and used to store spent fuel for 5-10 years of wet storage before moving to longer term dry-storage.

During a prolonged loss of coolant accident (LOCA) in SFPs, however, cladding temperatures can rise significantly and high temperature steam may interact with the cladding, accelerating oxidation and potentially leading to breakaway oxidation, an event that increases the oxidation rate by more than an order of magnitude [1]. This condition greatly raises the likelihood of fission product release, posing an immediate safety risk to both the environment and nearby populations.

The Fukushima disaster underscored the critical need for understanding the behaviour of spent fuels when cooling is lost. In response, regulators across the world, including the Canadian Nuclear Safety Commission (CNSC) made efforts to address these gaps. In support of CNSC efforts, Canadian Nuclear Laboratories (CNL) compiled a Phenomena and Identification and Ranking Table (PIRT) to identify the accident phenomena and corresponding key parameters in CANDU SFPs. The PIRT informed the development of a computer code for the CNSC called BAYLOCA (BAY Loss Of Coolant Accident) designed for SFP accident analysis [2], and laid the foundation for the series of studies on spent fuel pool

accident analysis, mainly on CANDU reactors, under the Atomic Energy of Canada Limited (AECL) Federal Nuclear Science and Technology (FNST) program. This paper summarizes CNL's efforts under the latest FNST project in this area over the last three years (2022-2025) and presents high-level findings from these investigations. For simplicity, we refer to this initiative as the SFP accident analysis project.

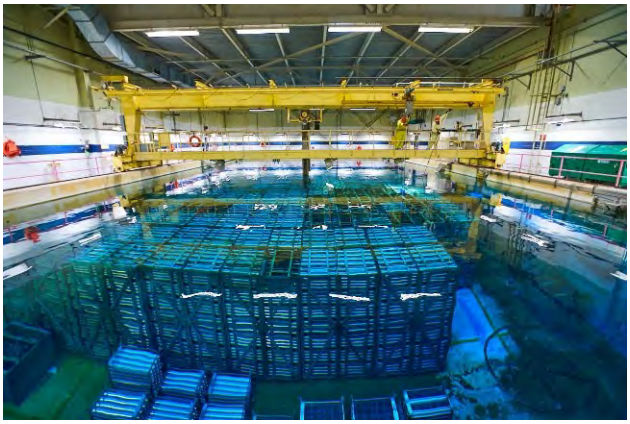

Figure 1. Spent nuclear fuel is stored in a pool at the Pickering Nuclear Generating Station in Pickering, Ontario. (Photo: Ontario Power Generation - Brian Pieters, Corporate Visuals)

1.2 Objectives and Goals of SFP Accident Analysis Project

The objective of the project was to advance the understanding of accident phenomena in CANDU SFPs and to improve insight into accident progression and its consequences. The project also aimed to enhance experimental capabilities, integrated with advanced modeling and simulation, to enable detailed analysis of accidents in CANDUs, and to support testing, benchmarking, and further development of BAYLOCA. Finally, the project sought to contribute to the global understanding of SFP accidents through active participation in international research initiatives. These objectives were pursued through several focused activities, each of which is described in the subsequent sections.

2. FUEL BAY HEATER APPARATUS (FBHA) EXPERIMENTS

CANDU fuel bundles are ~50 cm long, weigh 25 kg, and are ~10 cm in diameter. Every day during normal operation about 12-16 spent fuel bundles are received from a reactor core and stored in SFPs [3]. In response to the risk of spent fuel overheating when cooling is compromised in an accident scenario in CANDU SFPs, the FBHA was constructed, and series of experiments were conducted. As shown in Figure 2, the apparatus consists of a stainless-steel enclosure, a water tank beneath the enclosure, electrically heated simulated bundles in three rows and columns, and a hood. Inside the water tank heaters are used to generate steam.

The experiments aimed to approximate sheath and surrounding air or steam temperatures to determine heat transfer between bundles within a representative CANDU SFP tray configuration. Tests were carried out across a range of simulant bundle power levels, from 500 W to 3 kW, under stagnant dry air, blowing dry air, and steam environments. The results showed that peak sheath and gas temperatures occurred in the stagnant air environment in the middle bundle, while the lowest temperatures were observed under forced air condition. Tests conducted in steam, even over different generation rates, produced sheath temperatures that were similar to those measured under stagnant air conditions.

The maximum sheath temperature approached the hydrogen generation threshold (~827 °C) only at bundle power levels exceeding 2.5 kW. This suggests a negligible risk of hydrogen production in the evaluated three row bundle configuration, as bundle power in a CANDU SFP during the fuel uncovering phase is expected to remain significantly below 2.5 kW [4].

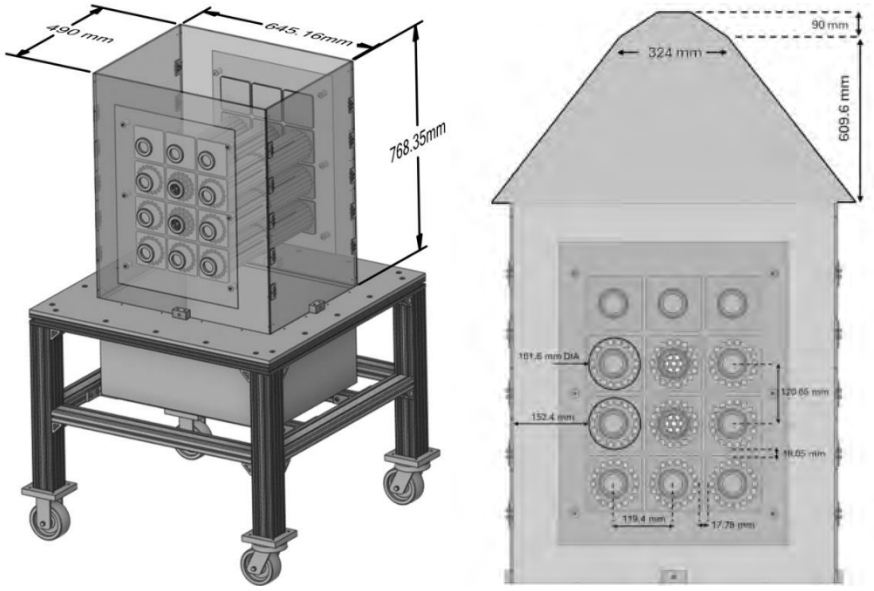

Figure 2. Schematic representation of the FBHA, illustrating its dimensions, including the stainless-steel enclosure, water tank, simulated bundles, and hood.

3. ASSESSMENT OF BAYLOCA SFP ACCIDENT ANALYSIS CODE

BAYLOCA is an independent computational tool developed for the CNSC to evaluate the progression and consequences of severe accidents in the SFPs of CANDU reactors in Canada. The code is designed for rapid execution, relying primarily on lumped-parameter models, and is capable of simulating all phases of an SFP accident. BAYLOCA represents accident evolution through four distinct stages:

Stage 1: Pool makeup is interrupted, although the spent fuel remains fully submerged.
Stage 2: The water level recedes sufficiently so that the fuels begin to be exposed to the atmosphere. In this stage some fuel assemblies are partially uncovered while others remain submerged.
Stage 3: The pool becomes completely devoid of water, either through boil-off or leakage.
Stage 4: Cooling water is restored to the pool. This stage may be entered directly from any of the preceding stages.

An overall schematic of a representative accident simulation is provided in Figure 3. User-defined inputs include initial decay heat conditions, fission product inventories, geometric and structural characteristics of the fuel stacks, pool, and building, accident-specific parameters, and ambient environmental conditions. All material properties, apart from those assigned to the building walls and roof, vary with temperature. Time-dependent outputs such as decay power, pool water temperature and height, fuel and tray temperature, gas temperature, temperature of building components, sheath and fuel oxidation, and fission product release are written to external files for subsequent post-processing. Additional detail is available in reference [2] and [5].

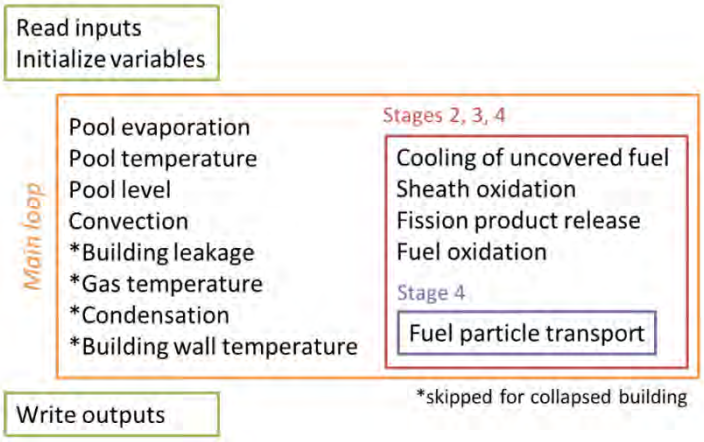

Figure 3. Overall view of an accident simulation

As part of the SFP accident analysis project, several areas for enhancement to BAYLOCA were identified, spanning phenomenological models, overall code architecture, and usability. A number of these issues have since been resolved through updates to the BAYLOCA code. Benchmarking exercises comparing BAYLOCA results with those from GOTHIC and CFD simulations demonstrated generally good agreement in thermal-hydraulic behavior, while also highlighting areas requiring further refinement, particularly with respect to fission product transport, convective fuel cooling, and deposition models within the building. Figure 4 illustrates a representative comparison between BAYLOCA predictions and GOTHIC results.

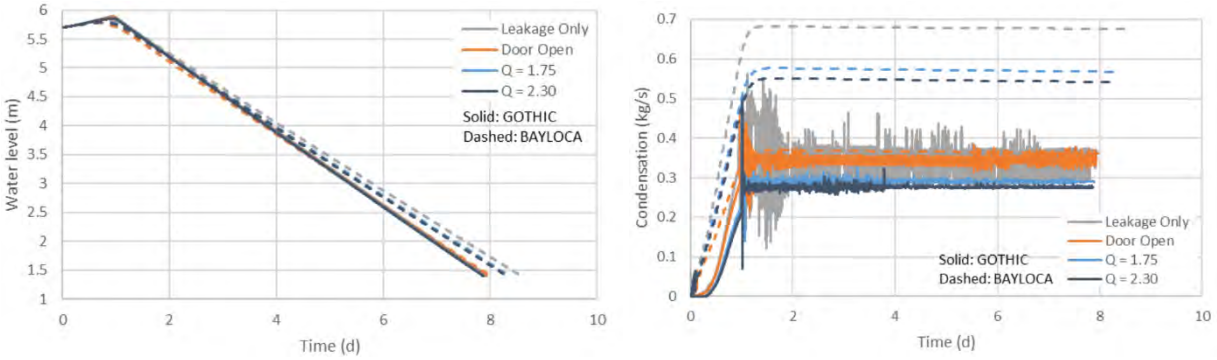

Figure 4. Comparison of the results between GOTHIC and BAYLOCA with similar input parameters: (a) water level in the pool, (b) rate of condensation.

4. CFD ANALYSIS OF SFP ACCIDENTS

A CFD modelling capability was developed in this project to estimate the peak sheath temperature in a CANDU SFP during a complete LOCA (stagnant air cooling only) [6]. Peak sheath temperature is a key indicator of accident progression and helps identify conditions under which breakaway oxidation may occur. Such conditions could threaten the integrity of the irradiated fuel bundle or lead to severe fuel damage.

A mechanistic CFD model was created using the geometric features of a CANDU spent fuel module. The model simulates flow and heat transfer within an irradiated fuel storage facility, accounting for natural convection, radiation, and solid-body conduction. The CFD simulations were performed using Simcenter STAR-CCM+. The CFD models were quantitatively evaluated and shown to capture the complex thermal-hydraulic behaviour expected in the SFP geometry at the specified decay powers.

The resulting CFD model was intended to support the development of reduced-order, fast-running models for the BAYLOCA analysis code for use in emergency response. It can also help guide experimental design by identifying conditions that warrant detailed measurement.

Figure ***5*** presents the mesh and temperature contours for a representative fuel module containing 96 irradiated fuel bundles, each decaying at 62 W in the SFP. The figure shows that the central bundles in row #6 attain the highest temperature levels within the module [6].

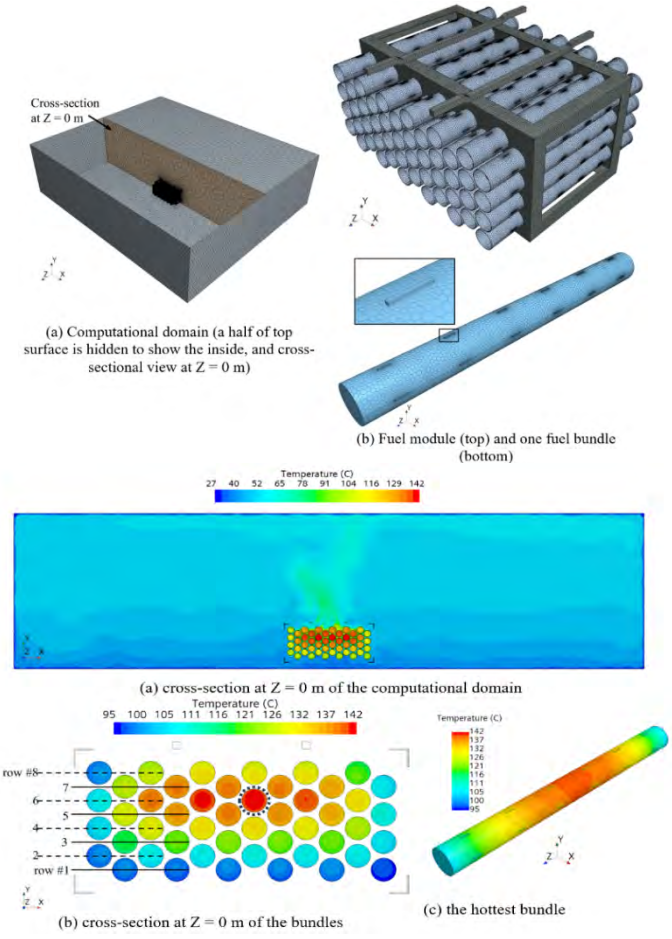

Figure 5. Mesh and temperature contours of the simulation domain, showing the pool and a fuel module containing 96 irradiated CANDU bundles, each with a decay power of 62 W [6].

5. GOTHIC ANALYSIS OF SFP ACCIDENTS

This task focused on applying the GOTHIC software, typically used for containment analyses, to simulate SFP accident scenarios and generate thermal-hydraulic data such as pool drainage behavior and building temperature responses. The results were intended to support improvements to the thermal-hydraulic models in BAYLOCA. Figure 6 presents the GOTHIC model and the predicted average building temperature for an accident scenario in a representative CANDU SFP. The building and pool dimensions were 46 × 15 × 9 m and 46 × 10 × 6 m, respectively. The analysis began with an initial decay power of approximately 8.6 MW, decreasing over time.

During the study, several limitations in GOTHIC's capability for modelling this type of scenario became evident and recommendations were made to mitigate these issues and to enhance the physical realism of future simulations. First, replacing the current single lumped pool with multiple vertically stacked pool control volumes would better capture fueled-region porosity and internal convection. However, in the version used here (GOTHIC 8.2) the moving liquid–vapor interface crossing the boundaries between these pool volumes during water evaporation triggers numerical instabilities. The issue was shared with developers to consider it for later versions. Second, the present method for applying decay heat to the gas above the pool artificially returns heat to the liquid, depressing predicted gas temperatures. Adopting a surface-based heat input just above the pool avoids this artefact and yields more credible predictions as fuel becomes exposed. Finally, because wall temperatures reach ranges where radiation becomes significant, adding radiative heat-transfer treatment to building surfaces would improve accuracy during high-temperature late phase of the accident.

The GOTHIC model was later expanded to include aerosol transport processes involving fission products. This update enabled a comparison with assumptions related to these phenomena embedded in BAYLOCA, especially those related to the conservatism of its primary release estimates. The enhanced GOTHIC simulations indicated that roughly 60% of the released fission products would remain inside the building, largely deposited in liquid accumulations. BAYLOCA 1.0 was unable to reproduce this outcome because it was designed with a conservative bias and did not include a model for fission product deposition.

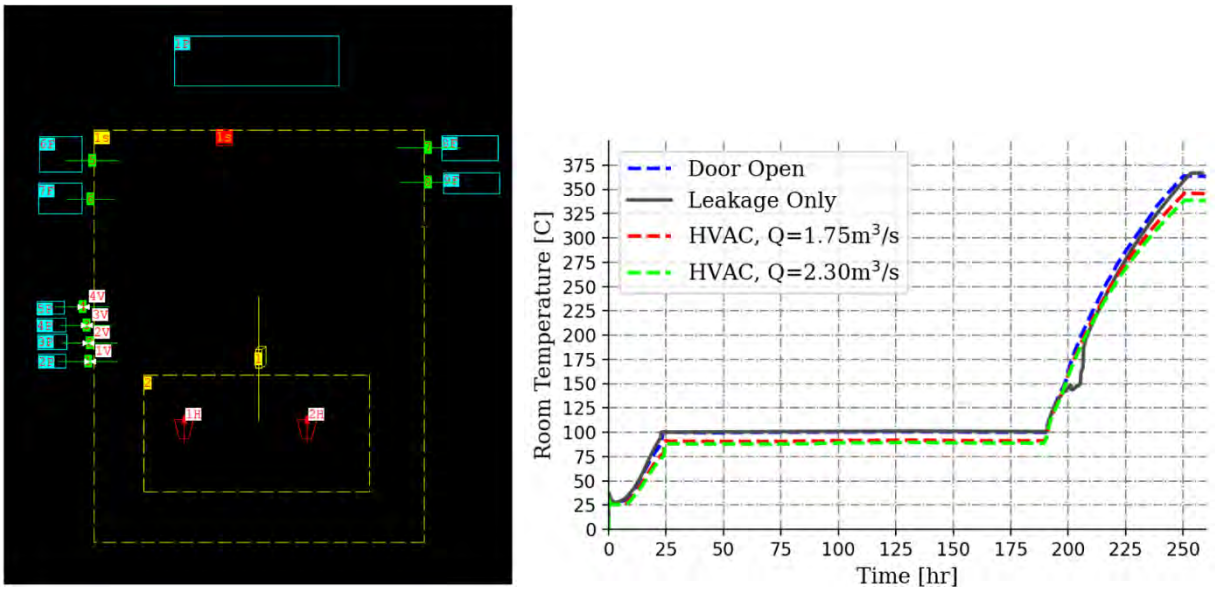

Figure 6. GOTHIC model of the SFP (left), and temperature of the building during a transient under different boundary conditions (right).

6. PARTICIPATION IN OECD-NEA POLCA PROJECT

In alignment with the objectives of the SFP accident analysis project, an international research connection was included to leverage the research and understanding of the broader community studying SFP severe accidents. This involved Canada's participation in the OECD-NEA POLCA project, which is focused on understanding LOCA scenarios in light water reactor SFP, while also generating broader insights applicable to common phenomena found in CANDU SFPs. This project aims to generate data for SFP thermal-hydraulic under accident conditions that can be used to benchmark and refine numerical modelling tools for SFP accident analysis.

7. CONCLUSION

Following the vulnerabilities revealed in SFPs during the Fukushima accident, many countries conducted research efforts in this area. As part of Canada’s response, and with the support of the CNSC, CNL initiated research efforts to improve the understanding of accident progression and consequences in SFPs, with emphasis on CANDU facilities.

As part of this effort, the FBHA was constructed to study bundle level behavior in a tray type configuration. A series of experiments were carried out to measure sheath and gas temperatures over a range of bundle powers in dry air, blowing air, and steam environments.

A comprehensive review of the BAYLOCA SPF accident analysis code was also completed, identifying several areas for improvement, including potential enhancements to phenomena models, updates to the code architecture, and improvements in the user experience. The updated code was benchmarked against results from both GOTHIC and high fidelity CFD models.

The CFD model, developed to estimate peak sheath temperatures during a complete LOCA in CANDU SFPs, demonstrated the complex heat transfer and flow patterns expected at the examined decay powers.

A thermal-hydraulic GOTHIC model was developed to simulate a LOCA scenario in a simplified SFP configuration. Several limitations in GOTHIC’s treatment of fuel exposure to air steam mixtures were identified. The model was later expanded to include aerosol and fission product transport, enabling an assessment of the conservatism of the BAYLOCA primary release assumptions.

Finally, in alignment with these efforts CNL is participating in the OECD-NEA POLCA joint project, which is designed to generate valuable data on thermal-hydraulic phenomena in a SFP under accident conditions thereby strengthening understanding and improving international capabilities for SFP safety analysis.

8. NOMENCLATURE

AECL	Atomic Energy of Canada Limited
BAYLOCA	BAY Loss Of Coolant Accident
CFD	Computational Fluid Dynamics
CNL	Canadian Nuclear Laboratories
CNSC	Canadian Nuclear Safety Commission
FBHA	Fuel Bay Heater Apparatus
FNST	Federal Nuclear Science and Technology
IAEA	Atomic Energy Agency
IFB	Irradiated Fuel Bay
LOCA	Loss-Of-Coolant Accident
LWR	Light Water Reactor
NEA	Nuclear Energy Agency

OECD	Organization for Economic Development
PIRT	Phenomena and Identification and Ranking Table
POLCA	Pool during Loss of Cooling Accident
SFP	Spent Fuel Pool

9. ACKNOWLEDGMENTS

This work was supported by Atomic Energy of Canada Limited's Federal Nuclear Science & Technology program. The authors thank Justin Spencer, Jason Wu, and Penny Neal for manuscript review. The authors also acknowledge the contributions of Ray Dickson, Kurt Stoll, Kevin Krkljus, Michael Callaghan, and Aidan Rutledge for design, construction and execution of the experiments.

10. REFERENCES

1. Organization for Economic Development-Nuclear Energy Agency (OECD-NEA), "Status Report on Spent Fuel Pools under Loss-of-Cooling and Loss-of-Coolant Accident Conditions: Final Report," NEA, OECD Publishing, Paris, (2015).
2. J. S. Bell, K. Stoll, R. David, J. Wu, A. Vasic, and S. Groulx, "Degraded cooling of spent fuel bundles in irradiated fuel bays," *presented at the 40th Annual Conference of the Canadian Nuclear Society and 45th Annual CNS/CNA Student Conference*, (2021).
3. Editor-in-Chief Wm. J. Garland, *The Essential CANDU, A Textbook on the CANDU Nuclear Power Plant Technology*. University Network of Excellence in Nuclear Engineering (UNENE), (2017).
4. H. Z. Fan, R. Aboud, E. Choy, W. Zhu, and H. Liu, "Spent fuel response after a postulated loss of spent fuel bay cooling accident," *Canadian Nuclear Society Bulletin*, vol. 33, (2012).
5. R. David, J. S. Bell, R. S. Dickson, A. C. Morreale, and H. V. Yan, "BAYLOCA: A Severe Accident Code for CANDU Irradiated Fuel Bays," *presented at the 44th Annual CNS Conference*, Toronto, Canada, Jun. (2025).
6. Q. Chen, K. Podila, and A. Morreale, "CFD Modelling of a CANDU Irradiated Fuel Bay," in *Proceedings of 21st International Topical Meeting on Nuclear Reactor Thermal Hydraulics (NURETH-21)*, BEXCO Busan, Korea, Sep. (2025).

The 12th European Review Meeting on Severe Accidents Research

May 18-22, 2026, Universidad Carlos III de Madrid, Madrid, Spain

TECHNICAL SESSION 1.2: SEVERE ACCIDENT SCENARIOS - UNCERTAINTY AND SENSITIVITY ANALYSES

Chairs: L. Tiborcz (GRS), F. Giannetti (University of Rome 'La Sapienza')

ID006	**Employment of relative time scale in the U&S analysis of the MBLOCA scenario in a generic KONVOI NPP** A. Stakhanova (KIT)	Paper Presentation
ID009	**Calibration of the Postulated Scenario of Fukushima-Daiichi Unit 1 through the Application of Uncertainty Quantification** L. E. Herranz (CIEMAT)	Paper Presentation
ID026	**Integrated Severe Accident Analysis for a VVER-1000: Accident Progression, Uncertainty Quantification, and Radiological Consequences Assessment** M. Angelucci (University of Pisa)	Paper Presentation

EMPLOYMENT OF RELATIVE TIME SCALE IN THE U&S ANALYSIS OF THE MBLOCA SCENARIO IN A GENERIC KONVOI NPP

A. Stakhanova, F. Gabrielli, V.H. Sanchez-Espinoza

Karlsruhe Institute of Technology, KIT, Hermann-von-Helmholtz-Platz 1, Eggenstein-Leopoldshafen, Germany

anastasia.stakhanova@kit.edu; fabrizio.gabrielli@kit.edu; victor.sanchez@kit.edu

ABSTRACT

This work presents the results of uncertainty and sensitivity analysis (U&Sa) performed using a modified approach – introducing a relative time scale instead of an absolute time scale. All simulations have been done with the European reference Accident Source Term Evaluation Code (ASTEC) **[1]**, developed by ASNR (formerly IRSN) and representing a Medium Break Loss of Coolant accident (MBLOCA) with the activation of the Filtered Containment Venting System (FCVS) in a generic KONVOI NPP **[2]**. The U&Sa was performed with KArlsruhe Tool for Uncertainty and Sensitivity Analysis (KATUSA) **[2]**, developed by KIT. The paper shows the modified approach to perform U&Sa of the SA simulations, discuss the results and remaining questions. The simple statistics for the fission product (FP) release into the containment and environment as well as correlation coefficients between the release values and the selected uncertain input parameters (UPs) are presented in the paper. The difference in the correlation coefficients values as a result of using the different time scale types is discussed.

KEYWORDS

ASTEC, KATUSA, Sensitivity analysis, Severe accident, Uncertainty analysis

1. INTRODUCTION

U&Sa in the nuclear safety field plays important role in analyzing the potential consequences **[3, 4, 5]** of severe accidents and allows a closer look on the variations in the SA progression and the release to the environment. The SA codes used to perform such simulations have a lot of uncertainties **[6, 7]** in their models of various physical processes. In addition to it, other uncertainties exist, for example, related to the reactor model. All this leads to significant differences in the simulations output, which should be analyzed and taken into account.

Currently, the standard approach **[8]** in the field includes the following steps:

- Identifying the uncertain input parameters and the output of interest;
- Sampling input parameters inside the defined range of values;
- Running certain number of simulations with the selected code;
- Computing the correlations between input and output parameters.

Often the output of interest is a single value like, for example, peak cladding temperature or final release value of a given fission product, but it could be also a parameter changing over time, when the goal is to look at changes of the selected parameter over time and how the uncertain input parameters can influence those changes at the different stages of the severe accident progression.

This paper focus at one particular issue that SA simulation results have quite different progression in time depending on the values of the uncertain input parameters, which could require different way of how these results are approached and analyzed.

The analyzed data is the results of the MBLOCA SA scenario simulations with the ASTEC code, which were obtained earlier and presented **[2]**, where in some cases the conditions of activating the FCVS were fulfilled. That subset of simulations – with the activated FCVS – is analyzed in the current work. This group of simulation is particularly interesting due to the very late activation of the FCVS – for some simulations it happens at time point, when other simulations have already reached the time of a basemat rupture. That makes U&Sa quite tricky, raising the question, how to analyze correctly such ensemble of simulations at the same time keeping as much data as possible for analysis.

This work tries to answer this question introducing the so-called "relative time scale" option, where data from different simulations is aligned on the time scale from 0 to 1. This allows to analyze the results not between given time points t_1 and t_2, removing all data lying outside of this time window, but to look at the data between two selected events – one of them will be always located at 0 point at the relative time scale, and the other – at 1.

The paper is organized in the following way:

- ***Chapter 2*** provides a shortened description of the computational framework – ASTEC KONVOI NPP model and the KATUSA tool. For a more detailed description, see the previous works **[2, 9]**;
- ***Chapter 3*** describes the idea of the relative time scale approach;
- ***Chapter 4*** at the beginning shows how much data could be lost in case of using the standard approach with the absolute time scale, then presents the results of the U&Sa obtained with using the relative time scale option and comparing them with the previous ones;
- ***Chapter 5*** discusses the results of the performed analysis and the differences in the results obtained with two different approaches.

2. COMPUTATIONAL FRAMEWORK

The same computational framework described here has been used for our previous works **[2, 9]**. For this paper no new simulations have been made, the data presented in **[2]** has been re-used instead. All simulation results were acquired using the ASTEC code and KATUSA tool. The generic KONVOI-1300 NPP model has been used as input for the ASTEC code.

The ASTEC model of the KONVOI-1300 NPP is shown at ***Figure 1***. The reactor core in ASTEC model is divided in six cylindrical rings plus two additional channels representing the downcomer and the bypass. Each core channel consists of fuel rods, control rods, grid spacers and plates. The containment is divided into 26 rooms plus an auxiliary building. The containment and the annulus are connected with each other and with the environment by means of fans. Two filtering systems are modelled - the annulus air extraction system (AAES) connects the annulus to the environment and is always available; the Filtered Containment Venting System (FCVS) connects the containment and the environment. The FCVS is activated as Severe Accident Management (SAM) action when the absolute pressure in the containment reaches 6.3 bar, and it is deactivated when the absolute pressure in the containment is equal to 3.65 bar. The goal of this SAM is the containment depressurization aiming at avoiding containment rupture.

The KATUSA tool developed at KIT **[2, 9, 10]** consists of the following six modules:

- *Sampling*: Two algorithms are available - Simple Random Sampling (SRS) or Latin Hypercube Sampling (LHS). The uncertain input parameters can be pre-correlated;

- *Organize simulations*: This part of the tool run multiple ASTEC simulations using the number of cores provided by the user. Each simulation has its own input deck with a corresponding set of uncertain input parameters values;
- *Identify failed simulations*: Failed runs are identified to be exclude from further analysis;
- *Collect data from non-failed simulations*: User provides the list of figure-of-merit (FoM), which will be extracted from all non-failed samples and stored in a database;
- *Adjust time grid and interpolate the data*: The collected data are interpolated onto a common time grid for further U&Sa and then stored in the database;
- *Perform U&Sa*: For each selected FoM, simple statistics (minimum, mean, maximum, 5th, 50th, and 95th percentiles values) and time-dependent correlation coefficients can be computed.

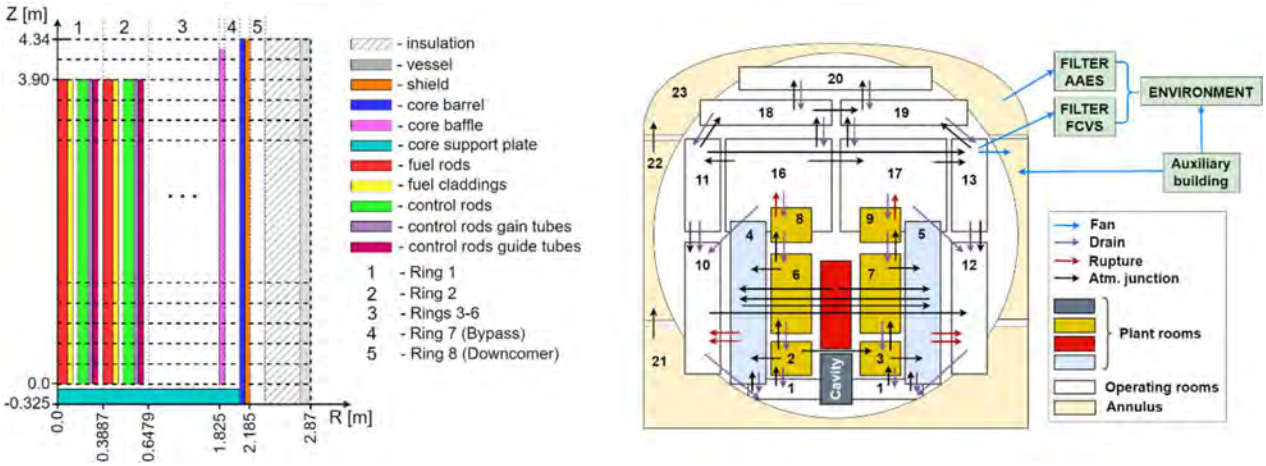

Figure 1. Core (left) and containment (right) nodalization of the ASTEC model of a generic KONVOI NPP (dimensions not in scale) [11, 12].

All details about the selected uncertain input parameters are provided in the ***Appendix A*** to avoid unnecessary repetitions.

3. ABSOLUTE AND RELATIVE TIME SCALE

This section explains the current approach to perform U&Sa used in KATUSA tool and how it could be changed. On ***Figure 2*** is shown how the data extracted for U&Sa in the current version of KATUSA tool. During the adjusting time grid and interpolating the data step (see above in the ***Section 2***) it is specified between which characteristic events the data should be extracted. For example, one wants to analyze the data between the start of fission product (FP) release and up to the basemat rupture – in that case, the starting point of the data extraction will be the maximum time of the start of FP release and the minimum time of the basemat rupture among all considered simulations. This leads to the exclusion some of the data from analysis – namely, all the data after the minimum time of the basemat rupture will not be taken into account, because this particular simulation is finished, and analysis couldn't be continued.

Figure 2. Current approach for data extraction implemented in KATUSA.

In addition to it, at every given time step the simulations considered in U&Sa are experiencing the different stages of the SA progression. For example, see on ***Figure 3*** – "Sample 1" hasn't yet reached the time point, when 20 tons of corium are relocated to the lower plenum, while the "Sample 2" has already passed the lower head vessel failure event.

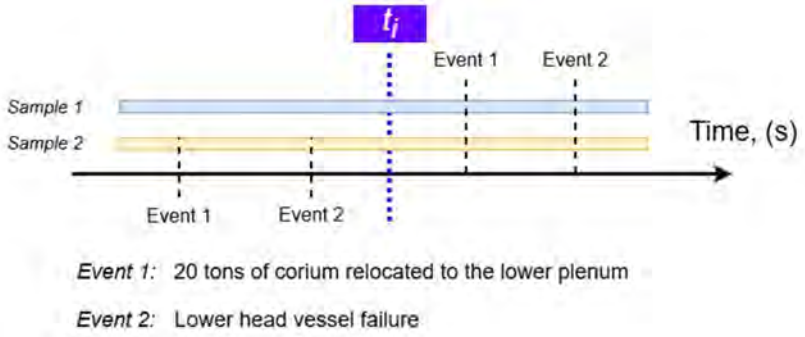

Figure 3. Samples with the different SA progression used in U&Sa.

On the idea of the relative time scale ***Figure 4*** is illustrated. For example, firstly the data between "Event 1" and "Event 2" is taken for analysis. Instead of using the approach shown on the ***Figure 2***, here the data between two considered events is taken from each sample and interpolated on one time scale from 0 to 1. After that, the data between "Event 2" and "Event 3" could be analyzed in the same manner. Therefore, any number of the characteristic events could be considered in the analysis.

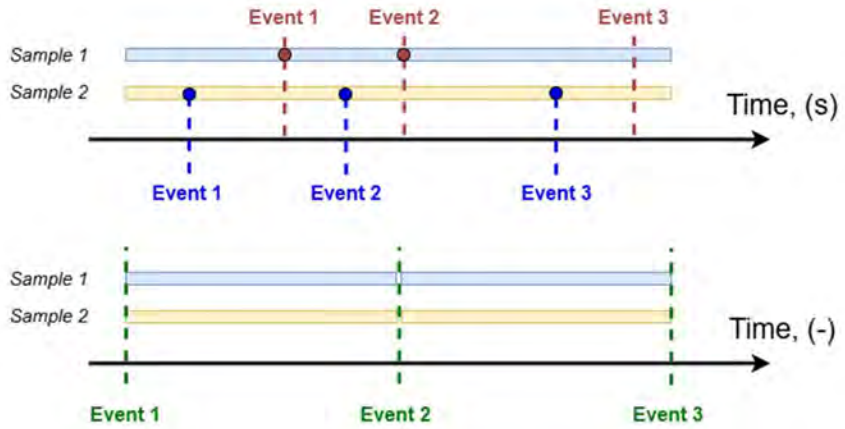

Figure 4. Absolute and relative time scale schemes.

4. RESULTS OBTAINED WITH THE RELATIVE TIME SCALE

Initially for our previous work **[2]** the two sets of the MBLOCA scenario simulations with the activation of the FCVS were performed with the 300 simulations in each set. For the current analysis these sets were combined and divided into two sub-sets by the presence of the FCVS activation. As a result, there are 97 simulations with the activated FCVS and 477 simulations where conditions of FCVS activation haven't been reached – these two sub-sets are analyzed separately. From initial 600 simulations 26 have failed and are not considered in the U&Sa.

On ***Figure 5*** is shown how time of characteristic events is distributed for two sub-sets of simulations (with and without FCVS activation). Start of FP release usually happens between ~450 s and ~700 s, most likely closer to 500 s. The time of LHVF has a wider spread – mostly it happens between ~17 000 s and 30 000 s, but there are couple of samples in the set (without FCVS activation) with much shorter degradation phase. The FCVS activation time is spreading from ~170 000 s up to ~370 000 s. Time of the basemat rupture mostly lying between ~220 000 s and ~360 000 s, and couple of samples have much shorter and much longer SA progression time.

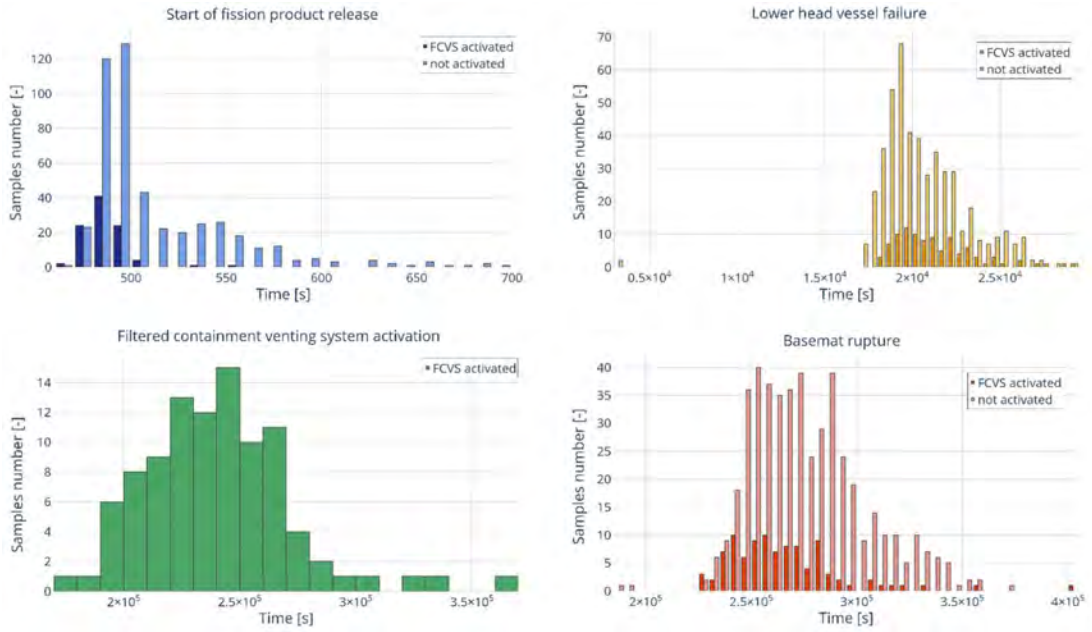

Figure 5. Distribution of the characteristic events in time for simulations with and without FCVS activation.

In this paper the main focus will be on the subset of simulations with the activated FCVS due to the following reasons:

1) Time of the FCVS activation in our simulations could be very close to the time of basemat rupture;
2) After FCVS activation, the changes in FP release (for example, Xe release into the environment) happens very fast (see example on the left upper part of the ***Figure 8***), which in combination with 1) makes U&Sa more complicated.

On ***Figure 6*** is shown how the basemat rupture time and time of FCVS activation are distributed. For subset of simulations without FCVS activation couple of samples could be excluded (see two marked samples on the left), due to their particularly short SA progression time, leaving majority of the samples for further analysis. On the contrary, for the subset with FCVS activation, the minimum basemat rupture time is marked with the vertical line, and one can see that only part (not even half) of the samples with be used for further analysis in that case. All other data will be lost if U&Sa is performed with absolute time scale.

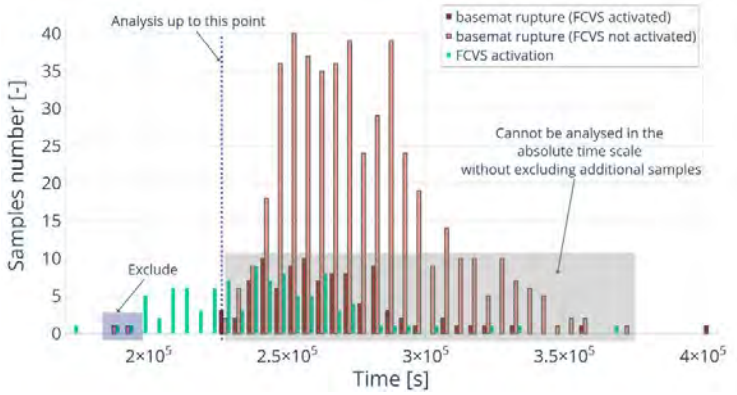

Figure 6. Distribution of the basemat rupture time and time of FCVS activation. Data not included in analysis with absolute time scale option is marked.

According to what is presented above on the ***Figure 6***, the amount of lost data will be quite significant, which is shown on ***Figure 7***. Therefore, the attempt was made to perform U&Sa in a different way without losing the data.

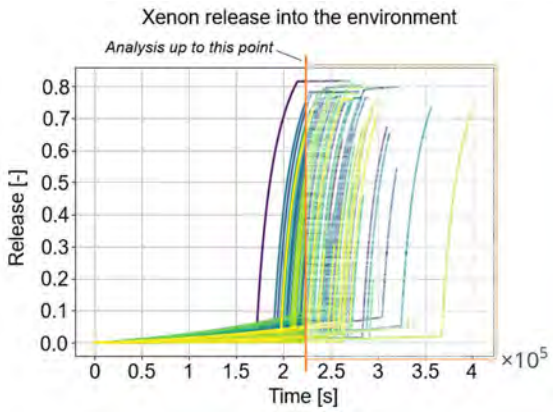

Figure 7. Data lost in the U&Sa with the absolute time scale for set of simulations with the FCVS activated.

Below the results of the U&Sa for the subset of simulations with activated FCVS will be presented. The Spearman correlation coefficients for this set are calculated for the Xenon, Cesium and Barium release using absolute and the relative time scales options.

On ***Figure 8*** all 97 simulations, where FCVS was activated, are shown on one plot. Thin solid lines represent the simulations used for analysis. The thick dashed lines are the excluded simulations. The reason for exclusion was that the activation of the FCVS in these cases happened on the last or one to the last time

step leaving to room for analyzing separately the time window between the FCVS activation and the basemat rupture. The details for the excluded samples are presented in ***Table 1***.

Table I. Excluded samples with the FCVS activation shortly before the basemat rupture

Sample index (from 97 samples set)	FCVS activation time, (s)	Basemat rupture time, (s)
6	238603.0	239803.0
21	238765.0	240065.0
37	269791.0	271591.0
56	244093.0	245393.0
69	243824.0	244524.0
70	257986.0	258286.0
75	264649.0	266149.0
83	330874.0	331674.0

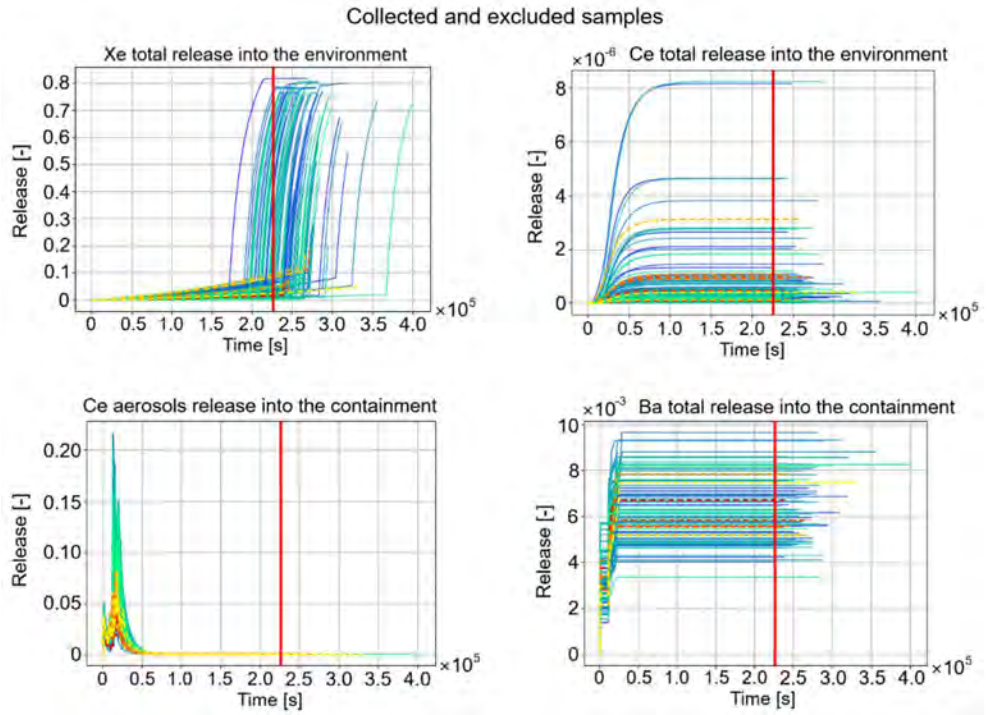

Figure 8. Xe, Cs, Ba release into the containment in time. Analyzed and excluded samples.

To check the effect from exclusion some of the simulations from the set, the comparison of the Spearman correlation values has been done between the case, where no samples were excluded and the case where 8 samples were excluded. The results are shown on the ***Figure 9***. As a results, no significant changes have been observed for the Spearman correlation values between the considered FP release and the most important uncertain input parameters.

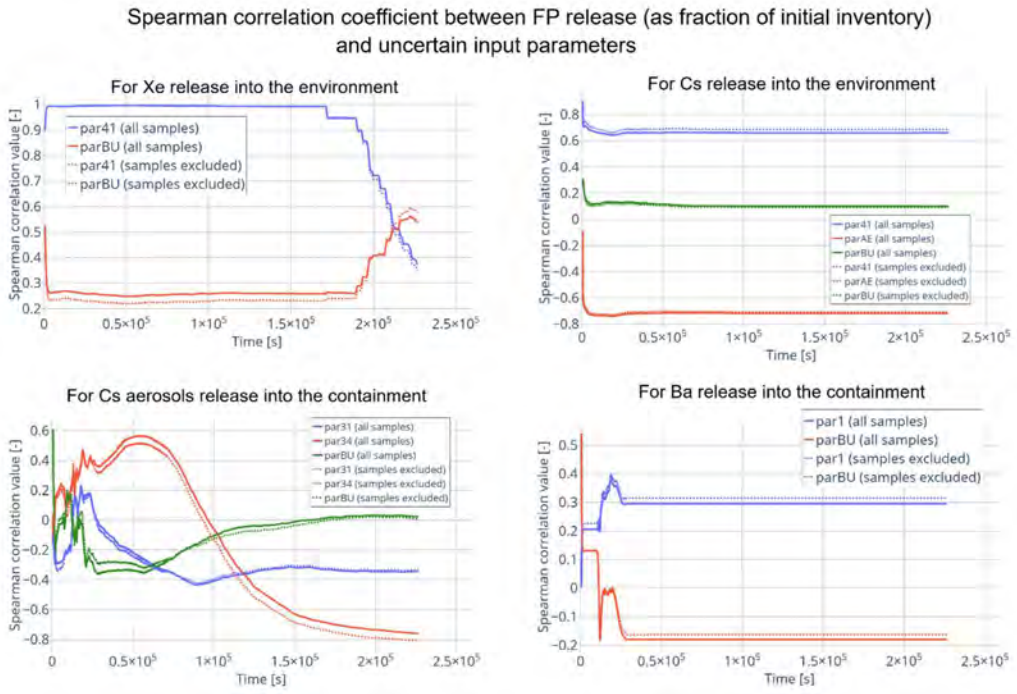

Figure 9. The Spearman correlation values in time for Xe, Cs and Ba release. With and without samples exclusion.

After confirming that exclusion of particular small group of simulations will not lead to any significant changes in the results, the Spearman correlation values were calculated both on the absolute and relative time scales. Below, on ***Figures 10 – 13*** results are shown for Xe, Cs and Ba release. The figures are presented in the following manner:

- Left subplot: correlation values are calculated on the absolute time scale from start of FP release up to basemat rupture. The time zones where LHVF, FCVS activation and basemat rupture can happen are colored and highlighted with text. The analysis on the absolute time scale performed up to the minimum time of the basemat rupture (see the scheme on ***Figure 2***).
- Right subplot: the relative time scale option is used for analysis. The start of FP release for every considered simulation is considered as "0", and the basemat rupture time – as "1" (see the scheme on the ***Figure 4***). The time zones where LHVF and FCVS activation can happen are colored and highlighted with text.

In addition, the time scale could be divided into zones to investigate the influence of the uncertain input parameters on the FP release inside each zone. These results are not presented here due to the paper size limit.

Moving to the relative time scale allows to avoid losing of the data (as it was shown on the ***Figure 7***) and to analyze the time period between the FCVS activation and the basemat rupture time for all simulations.

Xenon release into the environment according to our previous analysis **[2]** is mostly governed by the two UPs – *par41* related to the leakage rate between containment and environment and *parBU* related to the burnup level. From the ***Figure 10*** one can see that correlation coefficient values for *par41* computed with the relative time scale option show the same pattern as for the absolute time scale. But for *parBU* the rising effect closer to the end of the process is not observed anymore.

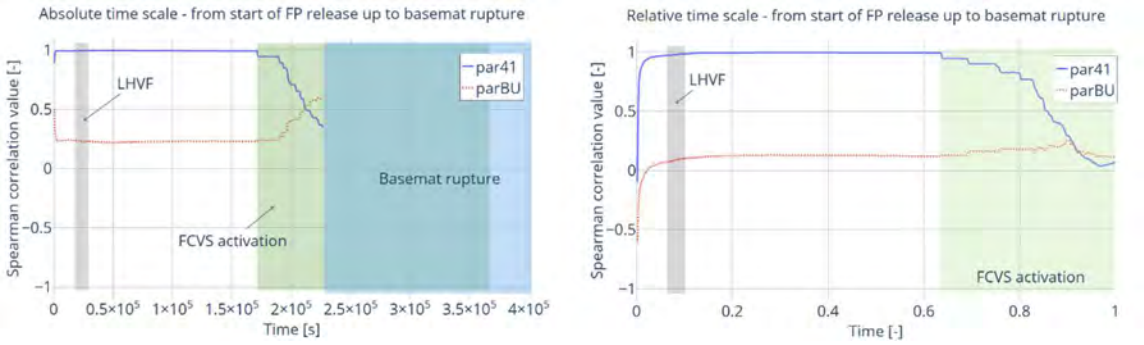

Figure 10. Spearman correlation values for the Xe release into the environment on the absolute and relative time scales.

For Cesium aerosols release into the containment was found that the most influencing parameters are *par31* and *par34* related to the aerosol behavior, and *parBU* related to the burnup level. It could be seen from ***Figure 11***, that Spearman correlation values for *par31* and *par34* for absolute and relative time scale options are quite similar, while for *parBU* the relative time scale option gives higher values up to FCVS activation region.

For Cesium release into the environment three UPs play a role – *par41*, *parBU* which were mentioned already, and *parAE* related to the filter efficiency for aerosols. For these parameters no significant changes in values has been observed between the relative and absolute time scales options, which is depicted on the ***Figure 12***.

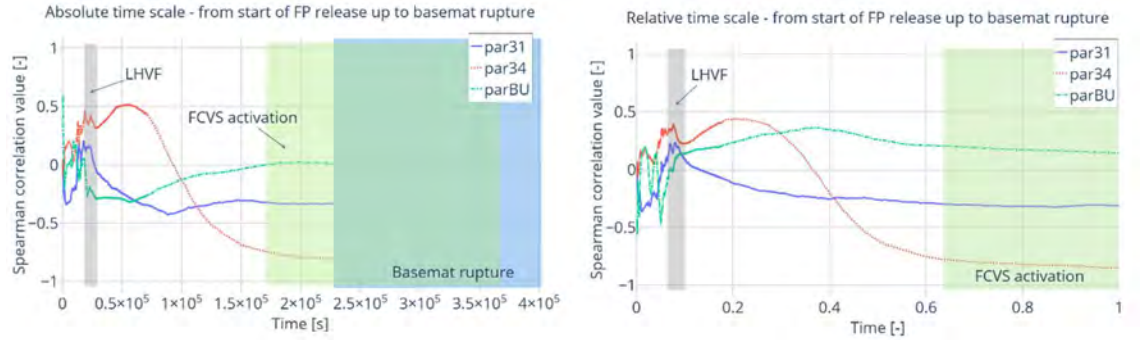

Figure 11. Spearman correlation values for the Cs aerosols release into the containment on the absolute and relative time scales.

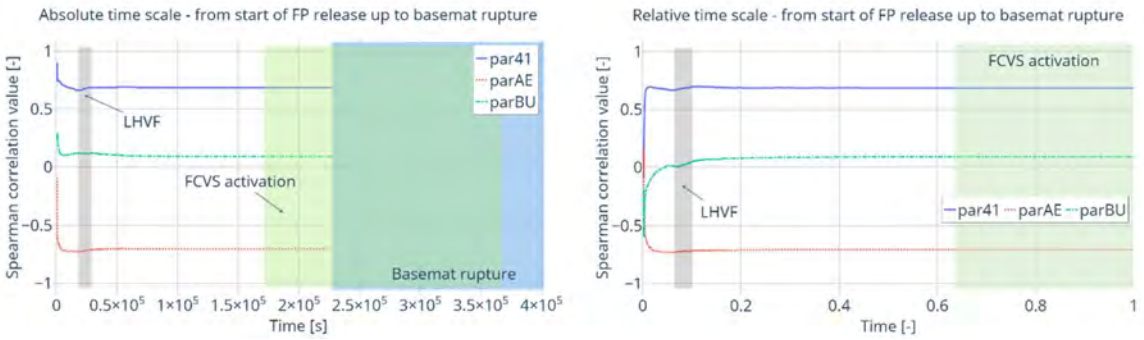

Figure 12. Spearman correlation values for the Cs release into the environment on the absolute and relative time scales.

For Barium release into the containment the main parameters as were found previously are the *parBU* and *par1* related to the model governing release from the fuel pellets. In this analysis also no significant differences have been found between the two different time scale options, at least after the LHVF event.

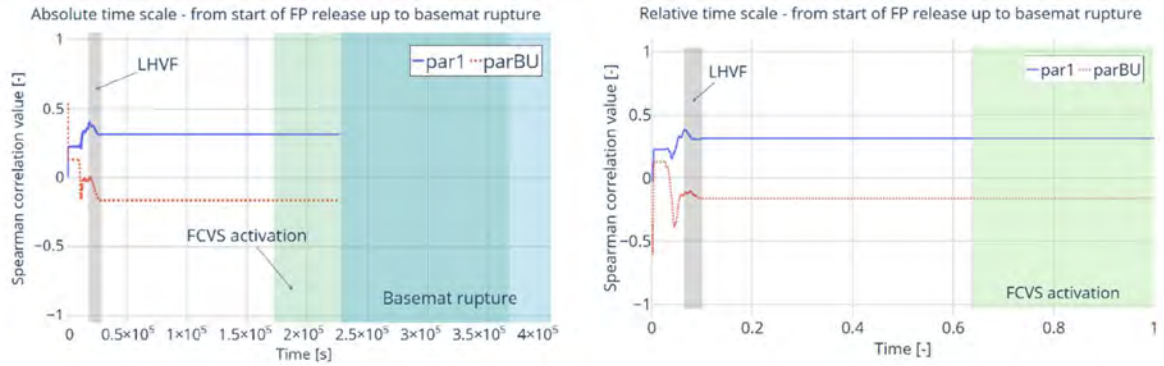

Figure 13. Spearman correlation values for the Ba release into the containment on the absolute and relative time scales.

5. CONCLUSIONS

In this paper the new "relative time scale" option for performing the U&Sa is introduced. This approach, comparing to the one used in our previous works, allows to reduce to the minimum exclusion of the data. This is quite relevant for the U&Sa of the SA simulations, which could have significant differences in the SA progression and timing of the main characteristic events. In this work the different option to look at such type of data is tested on the previously acquired set of the simulations of the MBLOCA SA scenario with the activation of FCVS. The activation of that system happens very late in the course of the SA progression, and some simulations could already reach the basemat rupture, while the others are still haven't reached the FCVS activation time. All these make U&S analysis quite tricky and lead potentially to exclusion a lot of samples from already not very large set of simulations (just 97 samples in total). That lead to the idea to look at this data at the different angle and to introduce the so-called "relative time scale", where the time of one characteristic event is set to "0", the time of the other event – to "1", and all the data interpolated to this time scale, helping to preserve as much data as possible.

To illustrate this approach the Spearman correlation coefficients have been calculated for the Xe, Cs and Ba release into the environment and containment, and comparison of the results between the "relative" and "absolute" time scale option have been made. Mostly the data are in a very good agreement, except maybe the very first time steps, which could have just numerical reasons, due to the very small release values at the beginning of the time scale. In addition to it, the Spearman correlation values for the *parBU* (related to the burn-up level) show some difference for the Xe release into the environment, and also for the Cs aerosols release into the containment. In these cases, the difference is observed along the whole SA progression and could not be attributed to the small release values.

REFERENCES

1. P. Chatelard, and L. Laborde, "ASTEC V2. 2 code validation: Illustrative results and main outcomes", *Nuclear Engineering and Design,* **413**, p.112547 (2023).
2. A. Stakhanova, F. Gabrielli, V.H. Sanchez-Espinoza, E.M. Pauli, A. Hoefer, "Uncertainty and sensitivity analysis of the ASTEC source term results of a MBLOCA scenario with the activation of

severe accident management actions in a generic KONVOI plant", *Proceedings of ERMSAR2024*, Stockholm, Sweden, 13-16 May, 2024, Paper 001, pp. 695-707 (2024).

3. K. Chevalier-Jabet, F. Cousin, L. Cantrel. and C. Séropian, "Source term assessment with ASTEC and associated uncertainty analysis using SUNSET tool", *Nuclear Engineering and Design*, **272**, pp.207-218 (2014).
4. E. Pauli, A. Hoefer, A. Stakhanova, F. Gabrielli, V.H. Sanchez-Espinoza, "Prediction of the Radiological Consequences of a Severe Accident Scenario in a Generic KONVOI Nuclear Power Plant", *Proceedings of ERMSAR2022*, Karlsruhe, Germany, 16-19 May, 2022, Paper 311, pp. 338-350 (2022).
5. X. Zheng, H. Itoh, H. Tamaki, and Y. Maruyama, "An integrated approach to source term uncertainty and sensitivity analyses for nuclear reactor severe accidents", *Journal of Nuclear Science and Technology*, **53**(3), pp.333-344 (2016).
6. P. Maccari, A. Bersano, S. Ederli, F. Gabrielli, and F. Mascari, "Validation and uncertainty analysis of ASTEC in early degradation phase against QUENCH-06 experiment", *Nuclear Engineering and Design*, **414**, p.112600 (2023).
7. F. Mascari, M. Massone, G. Agnello, M. Angelucci, S. Paci, M. D'Onorio, and F. Giannetti, "Phebus Fpt1 Uncertainty Application With the Melcor 2.2 Code", In *Proceedings of the NURETH-19 Meeting*. ANS (2022)
8. H. Glaeser, "GRS method for uncertainty and sensitivity evaluation of code results and applications", *Science and Technology of Nuclear Installations*, *2008*(1), p.798901.
9. A. Stakhanova, F. Gabrielli, V.H. Sanchez-Espinoza, A. Hoefer, and E.M. Pauli, "Uncertainty and sensitivity analysis of the ASTEC simulations results of a MBLOCA scenario in a generic KONVOI plant using the FSTC tool", *Annals of Nuclear Energy*, **192**, p.109964 (2023).
10. A. K. Mercan, "Impact of Uncertainties of Nuclear Severe Accidents on Radiological and Nuclear Dispersion Predictions", *Hacettepe Journal of Biology and Chemistry*, **52**(5), pp.305-314 (2024).
11. I. G. García-Toraño, "Further development of Severe Accident Management Strategies for a German PWR Konvoi Plant based on the European Severe Accident Code ASTEC," Dissertation, Karlsruher Institut für Technologie, Fakultät für Maschinenbau (2017).
12. F. Gabrielli, et al., "Impact of Realistic Fuel Inventories on the Radiological Consequences of a Severe Accident Scenario in a Generic Konvoi Plant by Means of the ASTEC Code," *Proceedings of the KERNTECHNIK*, Leipzig, Germany, 21-22 June, 2022.
13. T. Ikeda, et al., "Analysis of core degradation and fission products release in Phebus FPT1 test at IRSN by detailed severe accidents analysis code, IMPACT/SAMPSON," *Nuclear Science and Technology,* **40**(8), pp.591-603 (2003).
14. G. Brillant, C. Marchetto, W. Plumecocq, "Fission product release from nuclear fuel I. Physical modelling in the ASTEC code," *Annals of Nuclear Energy,* **61**, pp.88-95 (2013).
15. G. Brillant, C. Marchetto, W. Plumecocq, "Fission product release from nuclear fuel II. Validation of ASTEC/ELSA on analytical and large-scale experiments," *Annals of Nuclear Energy,* **61**, pp.96-101 (2013).
16. G. Pastore, et al., "Uncertainty and sensitivity analysis of fission gas behavior in engineering-scale fuel modelling," *Journal of Nuclear Materials,* **456**, pp.398-408 (2015).
17. K.W. Song, et al., "Sintering of mixed UO2 and U3O8 powder compacts," *Journal of nuclear materials,* **277**, pp.123-129 (2000).
18. Y. Pontillon, et al., "Lessons learnt from VERCORS tests: Study of the active role played by UO2–ZrO2–FP interactions on irradiated fuel collapse temperature," *Journal of nuclear materials,* **344**, pp.265-273 (2005).
19. Nuclear Regulatory Commission (NRC). "State-of-the-art reactor consequence analyses (SOARCA) project: Sequoyah integrated deterministic and uncertainty analyses". Nuclear Regulatory Commission, NUREG/CR-7245, Technical report (2018).

20. P. Hofmann, P., et al., "ZrO2 dissolution by molten Zircaloy and cladding oxide shell failure. New experimental results and modelling," Forschungszentrum Karlsruhe, FZKA 6383, Technical report (1999).
21. Nuclear Regulatory Commission (NRC). "State-of-the-Art Reactor Consequence Analyses Project: Uncertainty Analysis of the Unmitigated Long-Term Station Blackout of the Peach Bottom Atomic Power Station". Nuclear Regulatory Commission, NUREG/CR-7155, SAND2012-10702P, Technical report (2012).
22. J.C. Helton, et al., "Uncertainty and sensitivity analysis of a model for multicomponent aerosol dynamics," *Nuclear technology,* **73**, pp.320-342 (1986).

APPENDIX A

In this Appendix the detailed information about eighteen selected UPs is provided. Their meaning and corresponding PDFs, as well as the links to the literature are given in ***Table A-I***. The UPs could be divided into following group according to their meaning:

- *par1*, *par2*, *par5*, and *par5a* are related to the ASTEC code ELSA model for simulation of the the fission product release;
- *par14*, *par15*, and *par16* are related to the fuel cladding integrity criteria;
- *par31* - *par37* are from ASTEC SOPHAEROS and CPA calculation models simulating the behavior of the aerosols in the reactor coolant system and in the containment;
- *par41* governs the uncertainty of the leakage rate from the containment to the annulus;
- *parBU* related to the fuel burnup level, namely the number of effective full power days;
- *parAE* and *par12* characterize the performance of the FCVS: filter efficiency for aerosols and filter efficiency for gaseous iodine, respectively.

On ***Figure A-1*** the correlations between UPs are shown.

Table A-I. Uncertain input parameters: meaning, probability density functions, references

Par.	PDF	PDF parameters	Description	Reference
par1	Normal	$\mu = 5.0$, $\sigma = 30\%$	Correction factor for the ratio S/V of the fuel pellets due to roughness	**[13, 14, 15]**
par2	Normal	$\mu = 0.03$, $\sigma = 30\%$	Correction factor for the ratio S/V of the fuel pellets for the limited steam access	**[13, 14, 15]**
par5	Normal	$\mu = 1.2E\text{-}5$, $\sigma = 30\%$	Geometrical diameter of the grain	**[16, 17]**
par5a	Triangular	mode = 2.0E-6, min = 1.6E-6 max = 3.4E-6	Standard deviation of geometrical diameter of the grain	**[16, 17]**
par14	Normal	$\mu = 2500.0$, $\sigma = 10\%$	Threshold Temperature of the cladding Dislocation [K]	**[18, 19]**
par15	Normal	$\mu = 2300.0$, $\sigma = 10\%$	Threshold Temperature of the oxide layer Dislocation [K]	**[20]**
par16	Normal	$\mu = 250.0E\text{-}4$, $\sigma = 20\%$	Threshold thickness of the oxide layer [mm]	**[20]**
par31	Uniform	min = 2.975, max = 4.025	Particle mean thermal conductivity (J/m/K)	Engineering judgement

par32	Uniform	min = 714.0, max = 966.0	Average specific heat (J/kg K) of the aerosol	Engineering judgement
par33	Triangular	mode = 3000.0, min = 2610.0, max = 10000.0	Particle mean density (kg/m3)	**[21]**
par34	Triangular	mode = 1.1E-8, min = 1.0E-8, max = 2.0E-07	Particle minimum geometrical radius (m)	**[22]**
par35	Triangular	mode = 1.99E-5, min = 5.0E-6, max = 2.0E-5	Particle maximum geometrical radius (m)	**[22]**
par36	Triangular	mode = 1.0, min = 0.9, max = 1.0	Shape factor relative to particle coagulation	**[21]**
par37	Beta	$\alpha = 1.0$, $\beta = 5.0$, min = 1.0, max = 3.0	Shape factor relative to Stokes velocity	**[19]**
par41	Uniform	min = 1.0, max = 30.0	Coefficient for the leakage rate between containment and annulus	Engineering judgement
parBU	Uniform	min = 10.0, max = 328.0	Effective full power days	Engineering judgement
parAE	Truncated Log-normal	min=0.9, max=0.9995	Filter efficiency for Aerosols	Truncated Log-normal
parI2	Truncated Log-normal	min=0.9, max=0.999	Filter efficiency for Gases (I2)	Truncated Log-normal

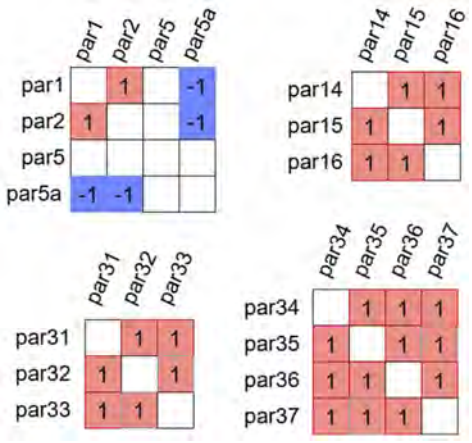

Figure A-1. Correlations between UPs.

The 12th European Review Meeting on Severe Accident Research (ERMSAR-2026), Madrid, Spain. May 18-22, 2026

EMPLOYMENT OF RELATIVE TIME SCALE IN THE U&S ANALYSIS OF THE MBLOCA SCENARIO IN A GENERIC KONVOI NPP

Stakhanova A, Gabrielli F, Sanchez-Espinoza V. H - Karlsruhe Institute of Technology (KIT)

Table of content

- Previous work
- Computational framework
- Problem description
- Proposed solution
- Results of U&S analysis with the relative time scale
- Conclusions and outlook

Previous work

Karlsruhe Institute of Technology

Previous work - MBLOCA with SAM - described in:

A. Stakhanova et al., “Uncertainty and Sensitivity Analysisof the ASTEC Source Term Results of a MBLOCA Scenariowith the Activation of Severe Accident Management Actionsin a Generic KONVOI Plant,” Proc. ERMSAR2024, Paper001, p. 695, Stockholm, Sweden, May 13–16, 2024

B. Stakhanova, A., Gabrielli, F., Sanchez Espinoza, V.H., Pauli, E.M. and Hoefer, A., 2025. Uncertainty and Sensitivity Analysis of the ASTEC Source Term Results of a MBLOCA Scenario with the Activation of Severe Accident Management Actions in a Generic Konvoi Plant. *Nuclear Technology*, pp.1-18. https://doi.org/10.1080/00295450.2025.2544372

A:

- Set of 300 MBLOCA simulations (with 48 simualtions where FCVS was activated) analyzed as a whole – ERMSAR-2024 conference
- Results between MBLOCA and MBLOCA+FCVS activation were compared

B:

- Relative time scale is introduced
- Relative time scale is applied to the FP release in environment and containment results
- Results between MBLOCA and MBLOCA+FCVS activation were compared

Computational framework

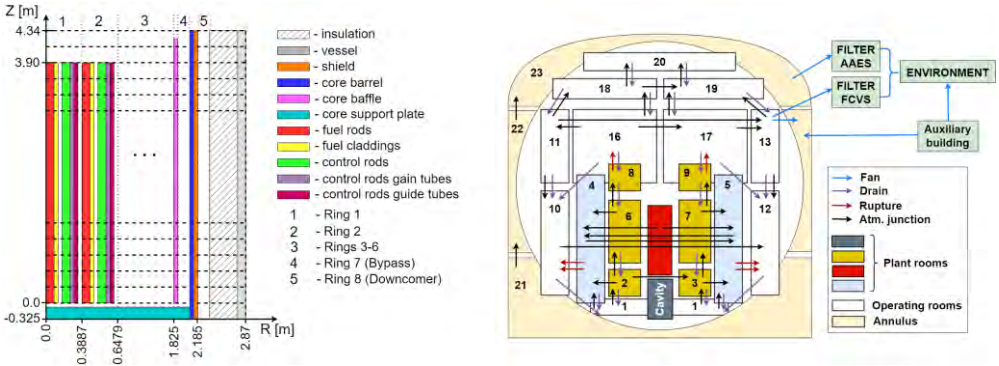

Figure 1. Core (left) and containment (right) nodalization of the ASTEC model of a generic KONVOI NPP

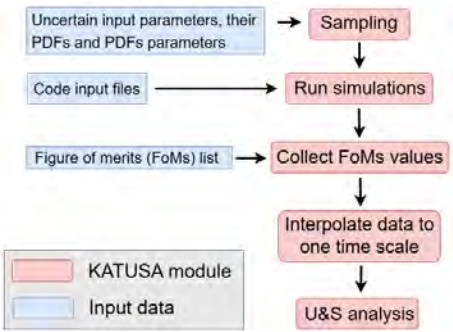

Figure 2. KATUSA tool scheme

- ASTEC code
- KATUSA tool for U&S analysis
- KONVOI-1300
- MBLOCA scenario
- 600 simulation in total -> 97 with FCVS activation are analyzed
- 18 uncertain input parameters, some of them are correlated

Problem description

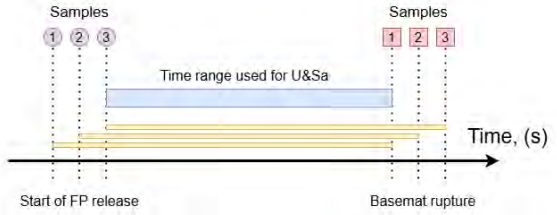

Figure 3. Approach for data extraction used in previous works

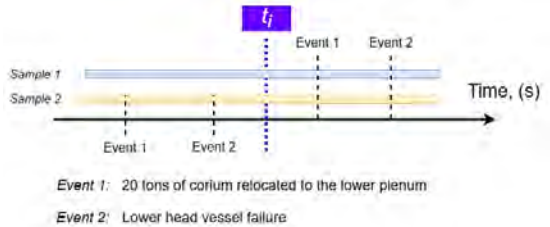

Figure 4. Samples with the different SA progression used in U&Sa

- In the previous works the U&S analysis was made on the absolute time scale.
- Between two considered events the data analysed as it is shown on the ***Figure 3***.
- For any time point different realisations of the SA scenario could be at the different stages of the SA progression – ***Figure 4***.

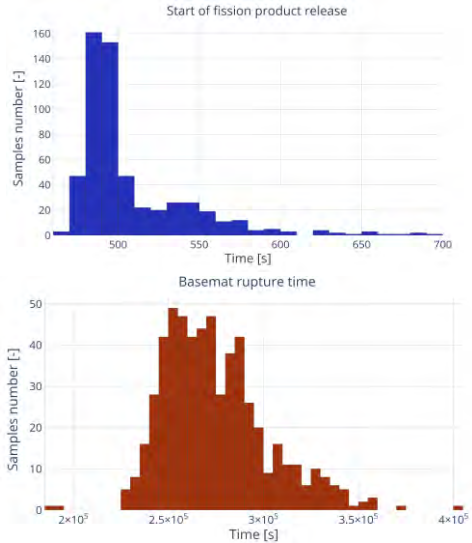

Figure 5. Distribution of the characteristic events in time

- The range between the earliest and the latest start of FP release – usually in our simulations [400, 700] s
- The range for the time of basemat rupture is much broader - ***Figure 5.***

Problem description

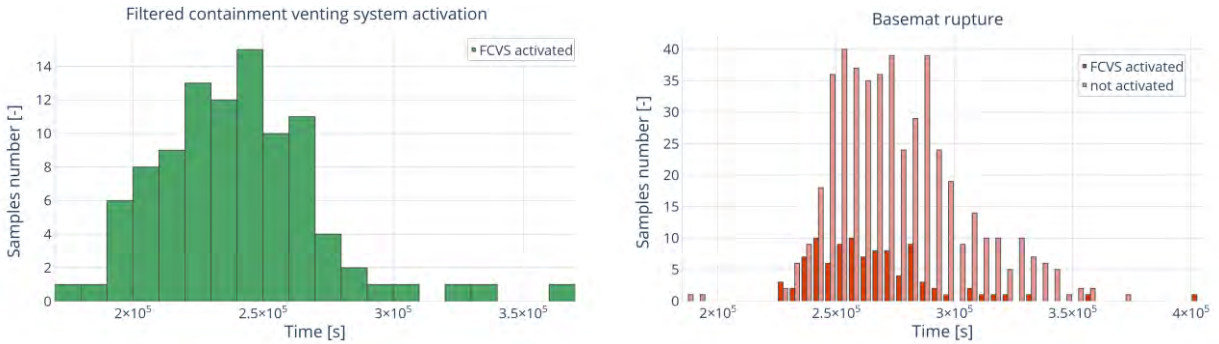

Figure 6. Distribution of the characteristic events in time

Due to the late activation of the filtered containment venting system (FCVS) – ***Figure 6***:

1) Stop analysis, for example, at ~ 250 000 s – it will lead to loss of the part of the time scale, where FCVS is activated for significant number of samples – ***Figure 7***

2) Extend the time range for analysis – exclude a lot of sample (including onces with FCVS activation)

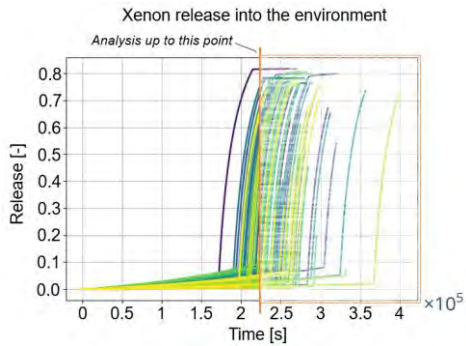

Figure 7. Data lost in the U&Sa with the absolute time scale for set of simulations with the FCVS activated.

Proposed solution

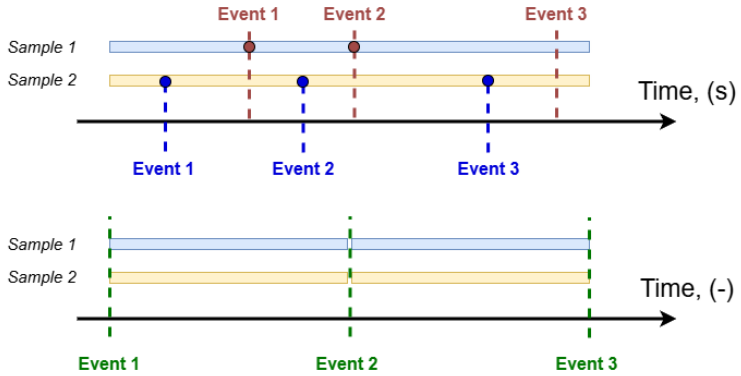

Figure 8. Absolute and relative time scales schemes

Proposed solution is to align all simulated SA progressions to the common relative time scale – ***Figure 8***.

- Take start of FP release as time point „0“ and basemat rupture as time point „1“
- Divide time scale into parts. For example, analyze first the part between start of FP release and lower head vessel failure (LHVF), then between LHVF and basemat rupture

Results of U&S analysis

- In total 600 MBLOCA simulations were performed to collect enough cases with FCVS activation
- 97 cases with FCVS
- 8 cases (from 97) were excluded due to the FCVS activation happened right before the basemat rupture - ***Figure 9***
- Spearman correlation coefficients were calculated on the absolute time scale to check the effect from excluded samples - ***Figure 10***

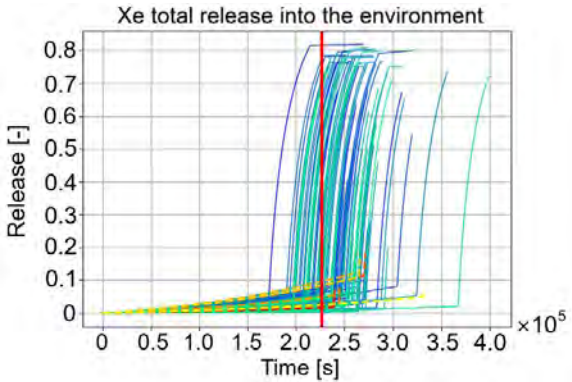

Figure 9. Xe release into the containment in time. Analyzed and excluded samples.

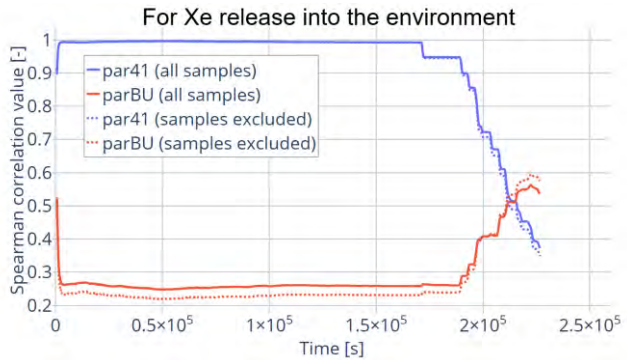

Figure 10. The Spearman correlation values in time for Xe, release. With and without samples exclusion.

Results of U&S analysis

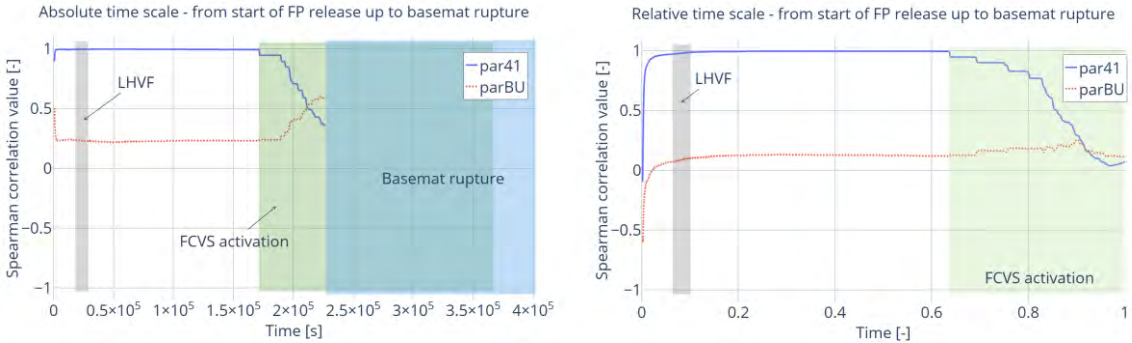

Figure 11. Spearman correlation values for the Xe release into the environment on the absolute and relative time scales.

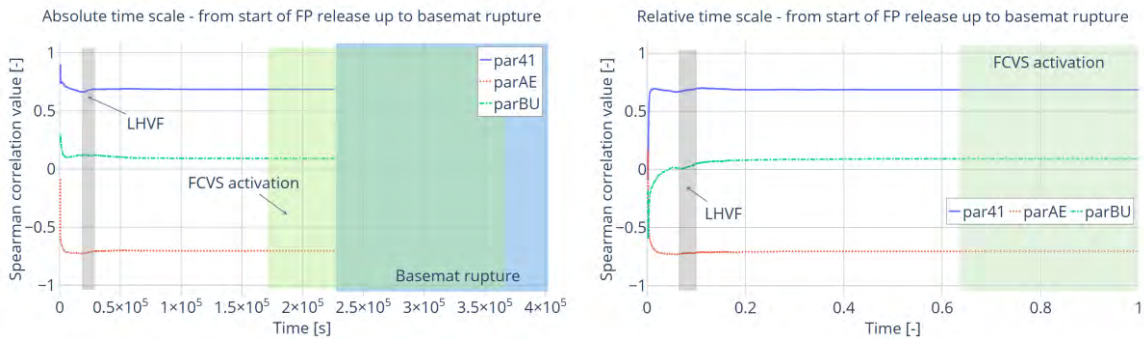

Figure 12. Spearman correlation values for the Cs release into the environment on the absolute and relative time scales.

Results of U&S analysis

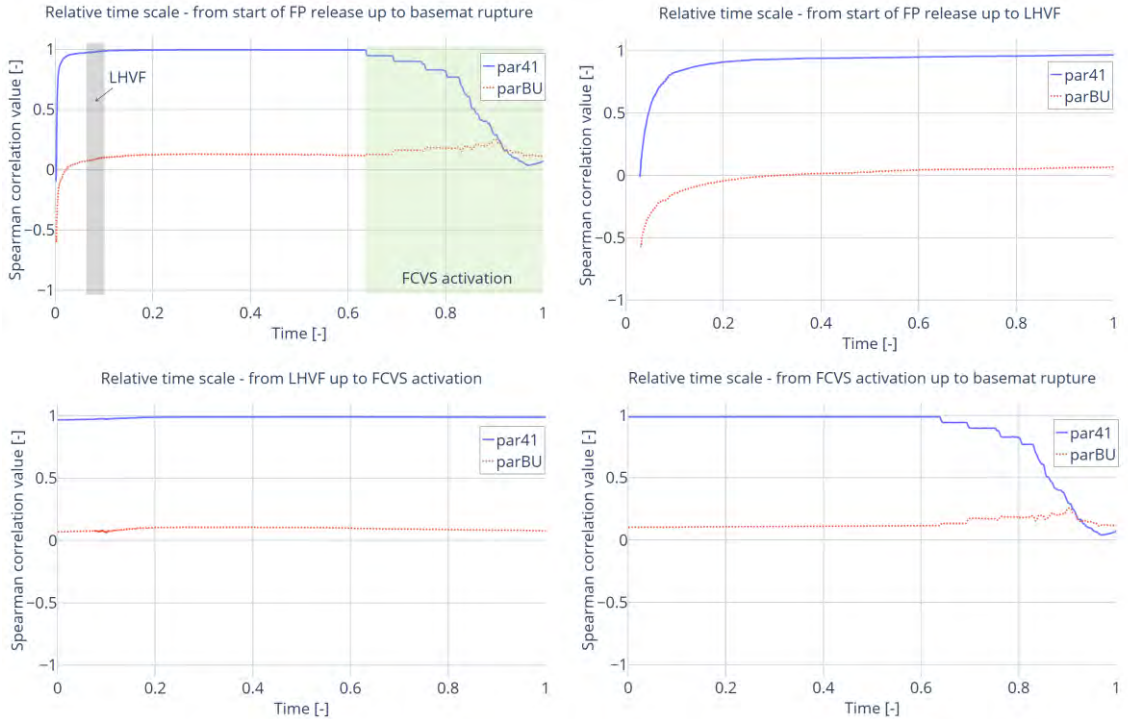

Figure 13. Spearman correlation values for the Xe release into the environment on the relative time scale. Example of dividing time scale into parts between characteristic events

Conclusions and outlook

- Previous work of analyzing results of MBLOCA SA scenario with FCVS activation is continued
- Relative time scale option is used to perform U&S analysis
- Focus on the simulations where FCVS was activated to show the need of the relative time scale option
- Time scale could be divided into zones between characteristic events

- Relative time scale option could be further tested
- Other options of time scales alignment could be considered

Thank you for your attention!

Contacts: KIT, INR; Stakhanova Anastasia, anastasia.stakhanova@kit.edu

CALIBRATION OF THE POSTULATED SCENARIO OF FUKUSHIMA DAIICHI UNIT 1 THROUGH THE APPLICATION OF UNCERTAINTY QUANTIFICATION

L.E. Herranz, M. Garcia, T. Lugo
CIEMAT
Avenida Complutense 40, 28040 Madrid (Spain)
luisen.herranz@ciemat.es; monica.gmartin@ciemat.es; tamara.lugo@ciemat.es

ABSTRACT

A thorough understanding of the accidents unfolding at the Fukushima Daiichi site in Japan on March 11th 2011, is a sound path to optimize accident management. This has been the ultimate goal of the BSAF, ARC-F and FACE projects, conducted under the OECD frame. CIEMAT focused on the Unit 1 accident and postulated a scenario that fitted the in-Reactor Pressure Vessel (RPV) and in-Primary Containment Vessel (PCV) pressure footprints with MELCOR 2.2.9607 (2017). Further code versions, though, caused significant changes in the estimates and raised the need to re-build a plausible scenario. Based on MELCOR 2.2.r2024 (2024), this paper describes the rationale underneath the scenario postulated and how an *ad-hoc* application of Uncertainty and Sensitivity Analysis (UaSA) turned it into a valuable tool to assess its consistency. Even though the hypotheses made in the scenario resulted in trends consistent with data, their magnitude and timing did not capture them, even if uncertainty bands are considered. An interpretation of consistencies and differences is included in this paper.

KEYWORDS
Forensic Analysis, Severe Accident, Uncertainty Quantification, Fukushima-Daiichi

1. INTRODUCTION

The Fukushima Daiichi accident, occurred in Japan on 11 March 2011, has revived the interest for the analysis of severe accidents. Despite the low probability of this type of events, Fukushima Daiichi has brought forward two irrefutable facts: the occurrence of highly unlikely accidents is possible; and, in the event of such an accident, their consequences might be long lasting and of sizeable dimensions, with worldwide impact in many regards. Consequently, grasping a thorough understanding of the accident unfolding has been in the spotlight as a way to gain insights for mitigation and prevention of these accidents.

Since 2012, the international OECD/BSAF project [1] adopted a forensic approach to find out defensible scenarios that could explain the evolution of the accident at the units 1 through 3 of the Fukushima Daichii Nuclear Power Plant. In this frame, CIEMAT focused on the Unit 1 accident and chased postulated malfunctions and failures in equipment and components that resulted in variables evolutions consistent with the data recorded, particularly in-RPV and in-PCV pressure footprints. MELCOR 2.2.9607 (2017) was used at the time [2].

The continuous code development, however, has entailed changes that resulted in significant differences in the MELCOR estimates with respect to the previous versions. This triggered a new campaign of calculations to test how the postulated scenario should be modulated (i.e., keeping the major assumptions and hypotheses, but varying some of the parameter settings) to keep a data-predictions match at least as good as in earlier calculations: a scenario re-calibration. This paper describes the rationale underneath the scenario

postulated and how an *ad-hoc* application of Uncertainty and Sensitivity Analysis (UaSA) turned into a valuable tool to assess its consistency.

2. BEST ESTIMATE CALCULATIONS

2.1. MELCOR basic model

The plant is modelled with the MELCOR 2.2. code [3], [4] through 109 control volumes, 215 flow paths and 137 heat structures. The model is completed with around 180 user functions describing aspects like valves and safety systems operation or water injection along the sequence.

The RPV nodalization includes the steam-dome, dryers, separators, shroud dome, annulus and the lower plenum whereas the core is split axially in 7 nodes and radially in 4 rings giving 56 control volumes, which account for the corresponding channels and bypasses. The in-shroud region is set with 4 radial nodes and 8 axial nodes, the core plate is defined with 1 node and 3 nodes describe the lower plenum (LP) (Fig. 1a).

The PCV nodes have been distributed as follows (Fig. 1b): 9 nodes for the Dry Well (DW), 8 circumferential nodes for the Wet Well (WW) and 8 nodes for the vents between DW and WW. Cavity is modelled through 2 interconnected cavities (one for the pedestal region and the other to the DW floor outside the pedestal) (Fig. 1c). Finally, the reactor building is modeled through 19 control volumes, 25 flow paths and 58 heat structures (Fig. 1d). A detailed description of the model can be found at [2].

Given the analytical nature of this paper, it is worth highlighting that the plant model has been kept with no changes in all the calculations reported.

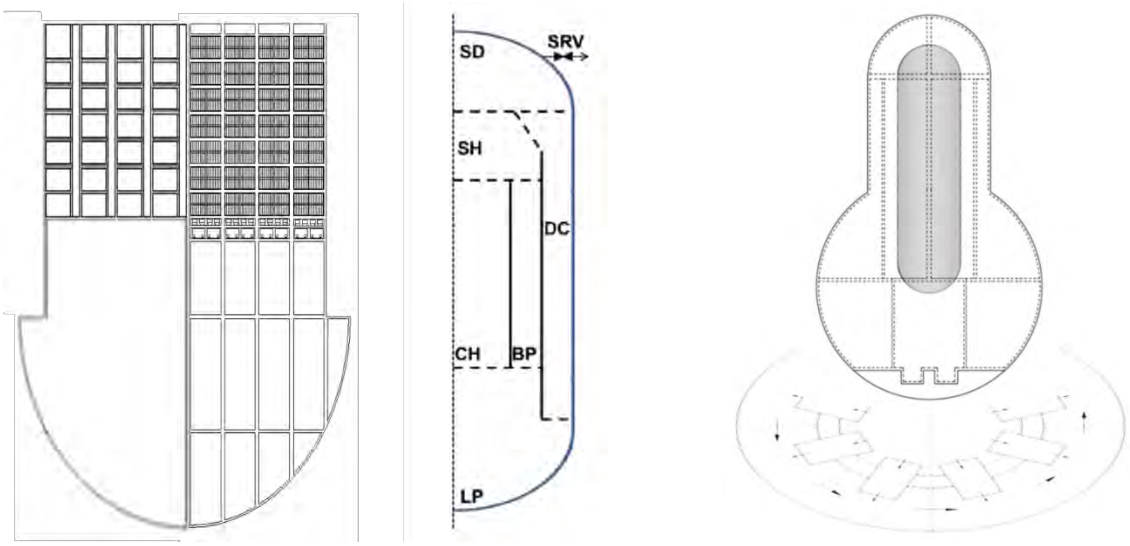

a) RPV. b) DW & WW.

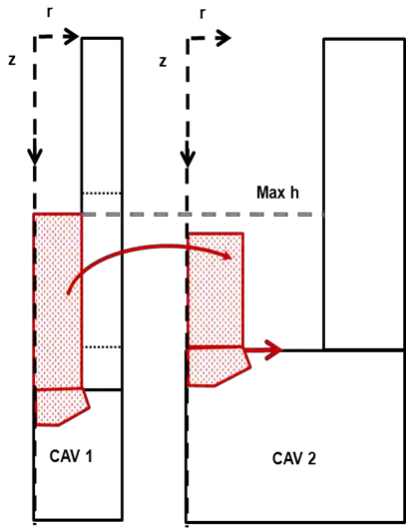

c) Cavity.

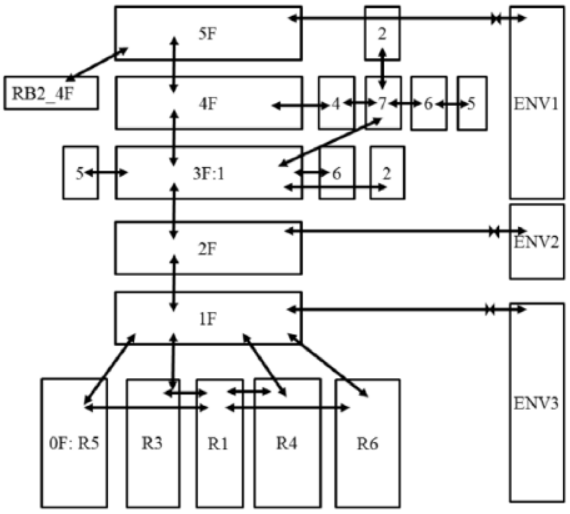

d) Reactor building.

Figure 1. 1F1 MELCOR nodalization.

2.2. Key Scenario Hypothesis

Scarcity of data along the first 12 h since the accident onset is crucial. During this time interval core extensively degraded and resulted in RPV and PCV failures. The information available is not enough to identify neither timing nor the mechanisms responsible for the RPV failure, which eventually determined to a good extent the in-containment pressure evolution and final failure. In other words, a forensic approach (i.e., building a full scenario out of few footprints) is indispensable to ascertain defensible scenarios that could explain the accident unfolding. This forensic approach was based on two variables recorded during this period: in-RPV pressure and in-PCV pressure. Some other signals did complement these two variables, like in-core water level or dose rates in PCV. However, their accuracy limited their use to qualitative comparisons.

The main fundamental hypotheses considered in the proposed scenario are as follows [2], [5]:

- The isolation condenser is modelled as an energy sink with an imposed efficiency to fit the RPV pressure oscillations reported during the first 50' of the accident.
- The 4 SRVs are modelled as valve-controlled flow paths (just one SRV operated during the accident).
- Two RPV leaks are considered: through the SRV gaskets when the SRV location reaches 723 K (steam and hydrogen) and from the LP (water), as a collateral damage of the quake.
- A DW flange failure is assumed at high containment pressure and a temperature (> 755 K).
- PCV venting (~24 h).
- Reactor building major failure imposed right after the venting.
- A "perfect" vertical stratification in the suppression pool under the injection point is assumed.
- No water injection is modelled during the first 24 h of the accident.

Given the goal of this work, the calculation time was restricted to the first 24 h since the quake event.

2.3. Results across MELCOR versions

The continuous MELCOR code development [6], [7], [8] has meant internal changes in models and settings that has correspondingly resulted in changes in predictions. Figs. 2a and 2b synthesize the estimates coming

from different versions of MELCOR for the in-RPV and the in-PCV pressures during the first 24 h of the accident. As observed, there are major differences with respect to the "reference version" (9607 in the plots). First, RPV failure time (sharp pressure drop down to less than 1 MPa) has been brought forward at least 4 h (Fig. 2a). As a consequence, the in-PCV evolution (Fig. 2b) has moved up as well and the tendency shown by the reference calculation has been lost both in timing and in the magnitude of pressure spike, at approx. 12 h in the reference calculation, caused by the RPV failure. Note that only the version r2024.0.3 was capable to describe the quasi steady-state drawn by data after 12 h (around 0.75 MPa); the 21402 version got there too, but at much later times (20 h).

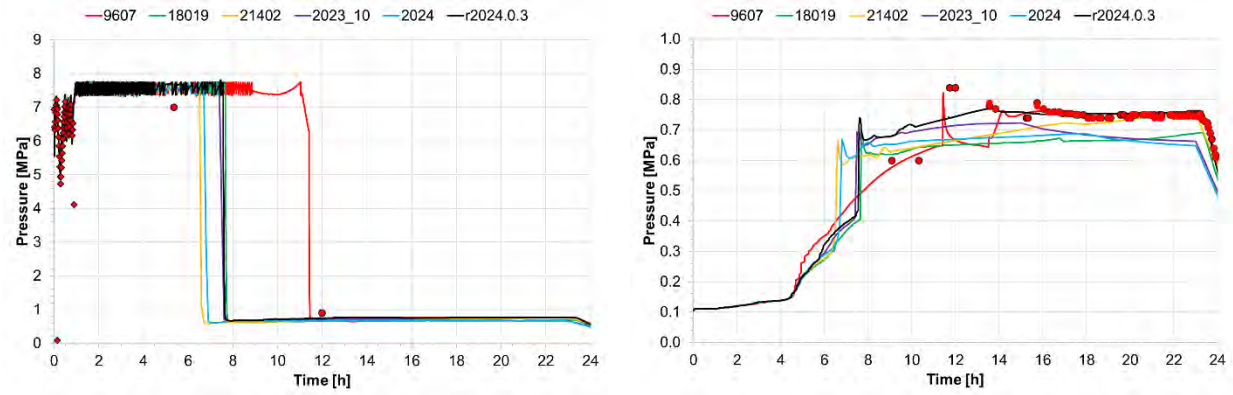

a) in-RPV pressure. b) in-PCV pressure.

Figure 2. MELCOR versions update.

2.4. MELCOR Latest Version´s Best Estimate

As a result of the differences found, a re-calibration of the postulated scenario has been proposed by using the last code version released at the time these calculations were made (MELCOR 2.2.r2024.0.3). Three factors have been explored in these studies (Table I): the dimensions of the leaks from the primary system; the thermal setpoint failure limit of RPV lower plenum penetrations; and the description of the materials interactions while core degradation. Given the complex in-core phenomenology, the parametric results of each of the three factors explored (neither their combination) showed a clear non-linear effect on the in-PCV pressure. In Figure 3, the MELCOR calculation with the above version for the parameters as set in the reference case (RC, red line) and in the Best Estimate (BE, blue line) case are shown; in grey, some of the intermediate parametric calculations done are displayed for completeness.

Table I. Parameters of the scenario re-calibration.

Parameter	Value range	RC	BE
Time of LP leakage (h)	0-1	1	0
LP leakage diameter (m)	$0 - 5 \cdot 10^{-3}$	$2 \cdot 10^{-3}$	$3.5 \cdot 10^{-3}$
Gasket failure diameter (m)	$10^{-2} – 3 \cdot 10^{-2}$	$2 \cdot 10^{-2}$	$2 \cdot 10^{-2}$
Penetrations failure setpoint (K)	1153 – 1673	1153	1400
Materials-interaction modelling	INT/EUT	INT	EUT

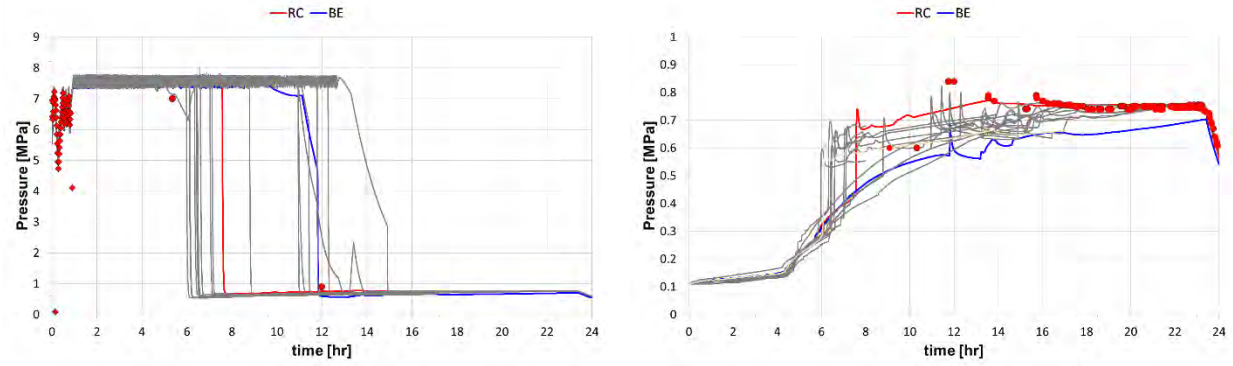

a) in-RPV pressure. b) in-PCV pressure.

Figure 3. Scenario re-calibration.

In-RPV pressure is shown in Fig. 4a. After the IC operation for about 45' since the quake, the data recorded does not allow a true comparison with estimates, since just a couple of data points, at around 5 h (7 MPa) and at 12 h (less than 1 MPa) were recorded. Namely, primary system depressurization occurred in between 5 and 12 h, which is a broad "blind-interval" from the in-RPV perspective. According to the MELCOR estimates, during the in-vessel phase, more than 500 kg of H_2 were produced (Fig 4b), mostly via Zr oxidation (87.7%), the remaining coming from SS oxidation (11.8 %) (Fig. 4b).

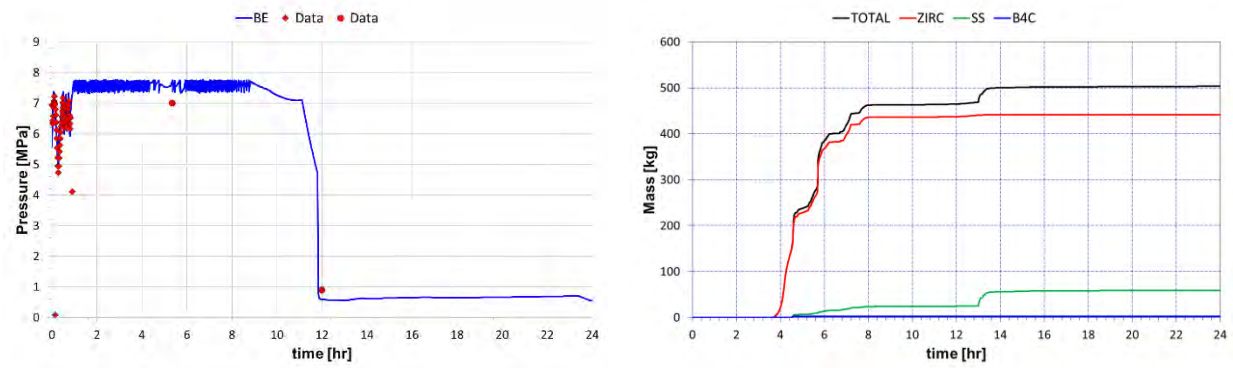

a) In-RPV pressure. b) In-vessel H_2 production.

Figure 4. Core degradation.

As for the in-containment P evolution (Fig. 5a), no data existed for 9 h and, then, from about 12 h on, recordings allow a thorough description of the variable. A pressure spike of about 0.25 MPa occurred from 10.5 h to a bit earlier than 12 h. At that moment, the loss of PCV tightness slightly depressurized the DW which slowly moved down to a steady state high pressure (at around 0.75 MPa), where it got quasi-steady because of the continuous generation of gases from the molten corium interaction with concrete (MCCI). Figure 5b shows the continuous additional generation of about 300 kg of H_2 until 24 h, and more than 400 kg of CO, from the oxidation of remaining metals in the corium deposited in the reactor cavity.

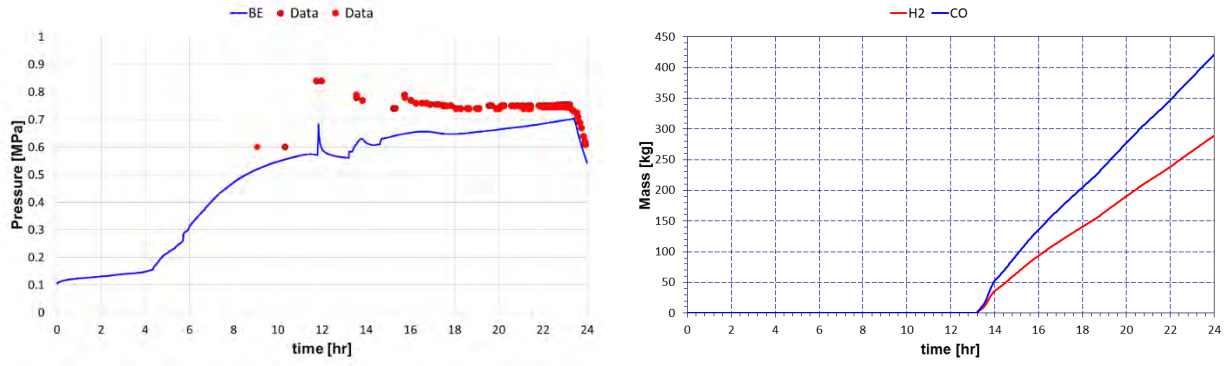

a) In-PCV pressure. b) Ex-vessel gases generation from MCCI.

Figure 5. In-PCV evolution.

Assuming BE predictions reasonably capture the data trends available, the Fukushima Daiichi Unit 1 scenario evolved as follows: after reactor scram (earthquake time), RPV was initially controlled by IC cooling for about 45' and, once the SBO occurred and the IC is lost, RPV pressure oscillated around the lowest setting of one of the SRV (7.5 MPa) for about 11 h. At 11.8 h, in-RPV pressure sharply decreased due to the RPV lower head rupture through penetrations. A small leak of water from RPV into the DW makes in-PCV rise slowly during the first 4 h and, then, faster when steam leaks into the DW through the SRV gasket leaking (723 K setting) makes in-PCV rise steadily from about 4 h to near 12 h, where the RPV failure causes a sudden pressure increase.

Two major deviations, though, weaken this scenario as a plausible one to explain the accident unfolding: the containment pressure peaks at a value 0.15 MPa below the data recorded and decreases fast, while data shows a sort of plateau held for a few tens of minutes; the steady state value drawn by data after 15 h is never reached in MELCOR estimates. Nevertheless, it might be worth investigating how uncertainties in the postulated scenario might affect the data-estimates comparison.

3. UaSA APPLICATION

3.1. Input Parameters

Based on previous forensic and sensitivity analyses, the chosen uncertain input parameters and their characterization are shown in the next table (Table II).

Table II. Uncertain parameters.

Parameter	Short description	Reference value	Range of Variation	PDF Type	Ref.
$Area_{LP_BREAK}$ (m^2)	Area of the LP break	$9.62 \cdot 10^{-6}$	$7.85 \cdot 10^{-7}$/$1.96 \cdot 10^{-5}$	Uniform	Sensitivity studies
$Area_{GASKT_LEAK}$ (m^2)	Area of the gasket leak	$3.14 \cdot 10^{-4}$	$1.77 \cdot 10^{-4}$/$3.14 \cdot 10^{-4}$	Uniform	Sensitivity studies
$T_{solidus}$ (Zr/SS EUT) (K)	Solidus temperature of the eutectic pair	1210	1100/1400	Uniform	[4]
$T_{solidus}$ (Zr/INC EUT) (K)	Solidus temperature of the eutectic pair	1210	1100/1400	Uniform	[4]
$T_{solidus}$ (UO_2/ZrO_2 EUT) (K)	Solidus temperature of the eutectic pair	2450	2200/2650	Uniform	[4], [9]

Parameter	Short description	Reference value	Range of Variation	PDF Type	Ref.
T_{P_FAIL} (K)	Penetration failure temperature	1273	1000/1671	Uniform	[4], [10]
STRAIN	Total strain assumed to cause failure in the LP	0.18	0.15/0.3	Uniform	

Note that the Probability Density Function (PDF) was subject to a parametric analysis. A second realization campaign was carried out with a triangular PDF to check the sensitivity to the uniform approximation, and no major differences resulting. Because of that, we decided to apply the uniform PDF according to the principle of maximum entropy.

3.2. Realization Campaigns

The methodology used for UQ is based on the Wilks's order statistics method [11]. Each FOM (Figure of Merit) is evaluated independently assuming it is a scalar variable (neglecting time dependence). Thus, for a tolerance interval with a 95% coverage and 95% confidence, it is necessary a sample of at least 93 code runs. To achieve this, a campaign was carried out with 250 samples, of which 180 run successfully (crash rate of 28%).

The selected FOMs in this study are the in-RPV pressure, the in-PCV pressure and the time of the vessel failure; the ending time of calculation is 24 h after the accident. Even though the main uncertainty analysis is carried out at 24 h, it is interesting to look at the time evolution of the considered FOMs. As can be seen from the dispersion plots (Fig. 6), all calculations follow the same global trends but with substantial differences in the timing of vessel failure, which heavily conditions the transient evolution in the PCV. In the case of in-PCV pressure it is noted that the upper bound of the uncertainty band covers the steady state after 15 h and there are some calculations peaking over 0.8 MPa, although at different times than the data records. This is also displayed in the PDF distributions of RPV time failure and in PCV maximum pressure (Fig. 7). In other words, uncertainties in the dimensions of leaking points, temperature settings for RPV failure and thermal thresholds describing the materials interactions might respond to some of the deviations noted, making the postulated scenario still defensible, although the most favorable scenarios seem not to have a high probability.

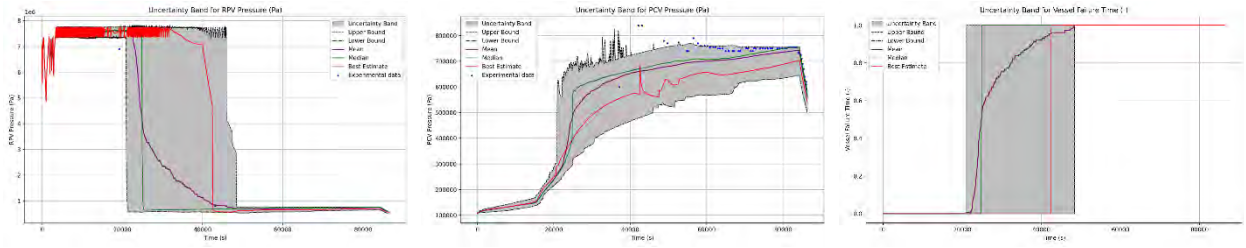

a) In-RPV pressure. b) In-PCV pressure. c) Time of vessel failure

Figure 6. Dispersion plots for selected FOMS.

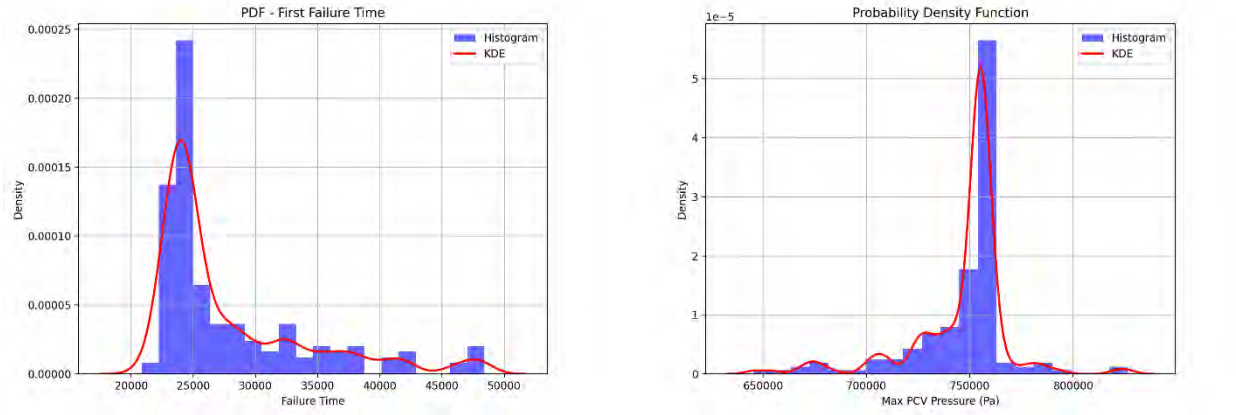

a) RPV failure time b) Maximum PCV pressure

Figure 7. Probability Density Functions key FOMS.

3.3. Sensitivity Analysis

Pearson's and Spearman's CCs have been considered as a first approach for sensitivity analysis of the RPV failure time (Fig. 8) and the in-PCV pressure at the ending time (Fig. 9). From the analysis, it is noted that RPV failure is notably affected by the size of the LP leak and, to less extent, by the temperature set for the lower head temperature and the UO_2-ZrO_2 eutectic temperature. In the case of the PCV maximum pressure, a high sensitivity to the LP leak size is found too, with the UO_2-ZrO_2 eutectic temperature also affecting.

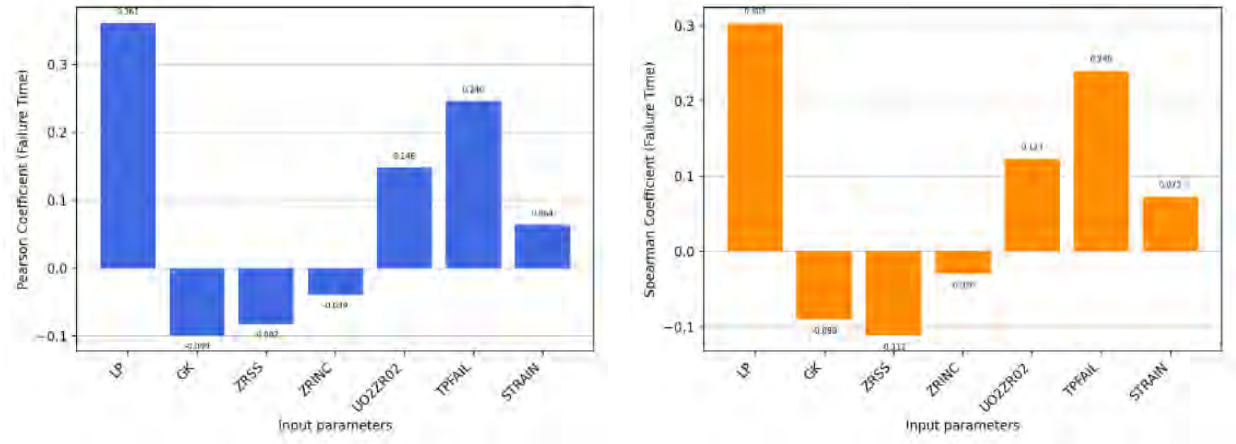

a) Pearson b) Spearman

Figure 8. Correlation coefficients of RPV failure time.

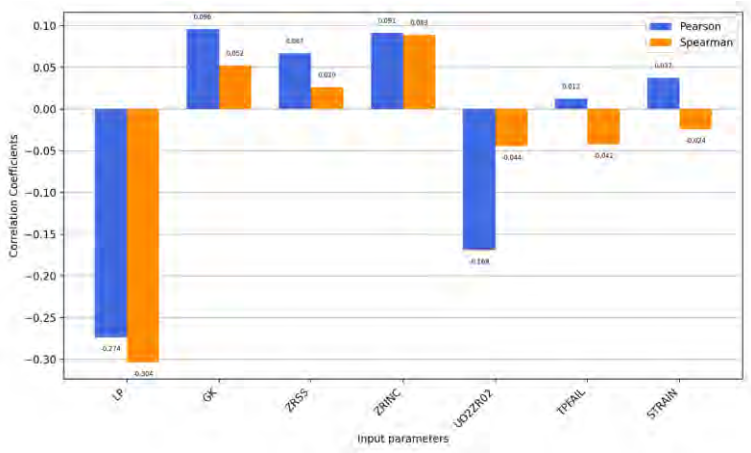

Figure 9. Pearson & Spearman coefficients for maximum in-PCV pressure.

In short, further studies should set reasonable values for the rest of uncertain variables in this study and focus on the liquid leak from the cooling system to the drywell and the eutectic temperature of UO_2-ZrO_2.

4. MAIN INSIGHTS

The existing footprints recorded during the Fukushima Daiichi accident during the first 24 h after the earthquake in Unit 1 pose a forensic challenge to SA analysts. However, capturing the main features of the scenario might provide valuable insights into SA management. The results shown in previous section allow reaching the following conclusions:

- The MELCOR code is mature enough to become a useful "forensic analytical tool". The integration of multiple phenomena, the thorough models and code validation done over years and the enhancement of the numerical robustness achieved, do support this statement. However, as any other SA code, the analyst should be aware that MELCOR has also drawbacks and limitations that are inherent to the extreme complexity of the SA scenarios, particularly when used as a forensic tool in search for the prevailing boundary conditions.
- Recalibration of the initially postulated SA scenario of Fukushima Daiichi Unit 1 highlighted that such a scenario might still be defensible based on the tendencies observed in the PCV, not so much on quantitative terms. The UaSA application reinforced this idea by exploring over 100 combinations of the uncertain variables consider key for the scenario postulated.
- The size of the liquid leak between the cooling system and drywell, the eutectics modeling (particularly, UO_2-ZrO_2 interactions) during core degradation and, to less extent, the size of the SRV gasket failure, are the factors that might influence more in the postulated scenario.

By no means, the work described above intends to conclude that the scenario postulated is the right one for Unit 1. Alternative scenarios that meet the same accident footprints have been proposed by other authors [12].

ACKNOWLEDGMENTS

The authors are grateful to partners in Fukushima OECD related projects for the insightful discussions; particularly to Marco Pellegrini, who led some of the earliest studies on forensic analysis. The authors wish to thank CSN for the support given to this work through the collaboration set for severe accident research (APIAS project).

REFERENCES

[1] M. Pellegrini *et al.*, "Main Findings, Remaining Uncertainties and Lessons Learned from the OECD/NEA BSAF Project," *Nuclear Technology*, vol. 206, no. 9, pp. 1449–1463, Sep. 2020, doi: 10.1080/00295450.2020.1724731.

[2] L. E. Herranz and C. López, "Challenges and sensitivities in the modelling of Fukushima Daiichi Unit 1 unfolding with MELCOR 2.2," *Annals of Nuclear Energy*, vol. 141, p. 107348, Jun. 2020, doi: 10.1016/j.anucene.2020.107348.

[3] L. L. Humphries *et al.*, "MELCOR Computer Code Manuals Vol. 2: Reference Manual Version 2.2.18019," SAND2021-0241 O, Jan. 2021.

[4] L. L. Humphries *et al.*, "MELCOR Computer Code Manuals Vol. 1: Primer and Users' Guide Version 2.2.19018," SAND2021-0252 O, Jan. 2021.

[5] L. E. Herranz, C. López, J. Fontanet, and E. Fernández, "Lessons learned from the Fukushima analysis: the modelling of severe accidents in Nuclear Power Plants," presented at the NURETH-16 International Topical Meeting on Nuclear Reactor Thermal Hydraulics, Hyatt Regency Chicago, Sep. 2015.

[6] L. L. Humphries, J. Phillips, R. C. Schmidt, B. A. Beeny, D. Louie, and N. E. Bixler, "MELCOR Code Change History (Revision 14959 to 18019)," Sandia National Laboratories (SNL-NM), Albuquerque, NM (United States), SAND--2020-14302, Dec. 2020. doi: 10.2172/1756139.

[7] L. Humphries, B. Beeny, T. Haskin, L. Albright, and F. Gelbard, "MELCOR Code Change History: Revision 18019 to 21402," Sandia National Laboratories (SNL-NM), Albuquerque, NM (United States), SAND2022-0114, Dec. 2021. doi: 10.2172/1855048.

[8] L. I. Albright *et al.*, "Material Interactions in Severe Accidents – Benchmarking the MELCOR V2.2 Eutectics Model for a BWR-3 MARK-I Station Blackout: Part I – Single Case Analysis," *Nuclear Engineering and Design*, vol. 382, p. 111292, Oct. 2021, doi: 10.1016/j.nucengdes.2021.111292.

[9] M. Stempniewicz, "Analysis of Reactor Vessel Lower Head Penetration Tube Failure," in *Proceedings of the Workshop on in-vessel core debris retention and coolability*, 1999, pp. 386–398. Accessed: Feb. 11, 2026. [Online]. Available: https://inis.iaea.org/records/afqyb-b1e28

[10] L. L. Humphries *et al.*, "OECD Lower Head Failure Project Final Project Report," OECD, csni-r2002-27 Volume 1-Integral Experiments and Material Characterization, 2002. Accessed: Feb. 11, 2026. [Online]. Available: https://www.oecd-nea.org/jcms/pl_17888/lower-head-failure-project-final-project-report?details=true

[11] S. S. Wilks, "Determination of Sample Sizes for Setting Tolerance Limits," *The Annals of Mathematical Statistics*, vol. 12, no. 1, pp. 91–96, Mar. 1941, doi: 10.1214/aoms/1177731788.

[12] L. E. Herranz *et al.*, "Overview and outcomes of the OECD/NEA benchmark study of the accident at the Fukushima Daiichi NPS (BSAF) Phase 2 – Results of severe accident analyses for Unit 1," *Nuclear Engineering and Design*, vol. 369, p. 110849, Dec. 2020, doi: 10.1016/j.nucengdes.2020.110849.

GOBIERNO DE ESPAÑA
MINISTERIO DE CIENCIA, INNOVACIÓN Y UNIVERSIDADES

Ciemat
Centro de Investigaciones Energéticas, Medioambientales y Tecnológicas

Calibration of the Postulated Scenario of Fukushima-Daiichi Unit 1 Through the Application of UQ

Luis E. Herranz*, M. Garcia, T. Lugo

*luisen.herranz@ciemat.es
Unit of Nuclear Safety Reseach
Departament of Nuclear Fission
CIEMAT

12th European Review Meeting on Severe Accident Research (ERMSAR2026)
May 18-22, 2026, Madrid, Spain

Contents

01 Framework

02 BE Calculations

03 UaSA Application

04 Main Insights

01

Framework

Framework

The International Context

BSAF phase 1

- *6 days simulation*
- *"PCV bounded":*
  1. *Th's*
  2. *Core degradation*
  3. *MCCI*

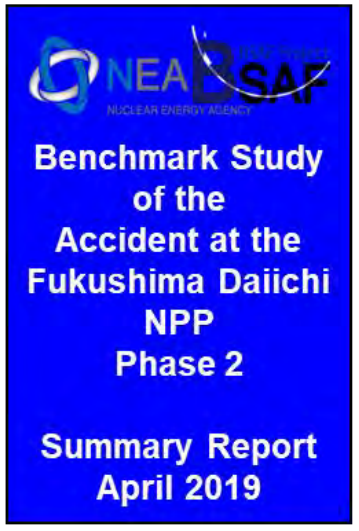

BSAF phase 2

- *21 days simulation*
- *R/B "bounded":*
  1. *Th's*
  2. *Core degradation*
  3. *MCCI*
  4. *Source term*

ARC-F

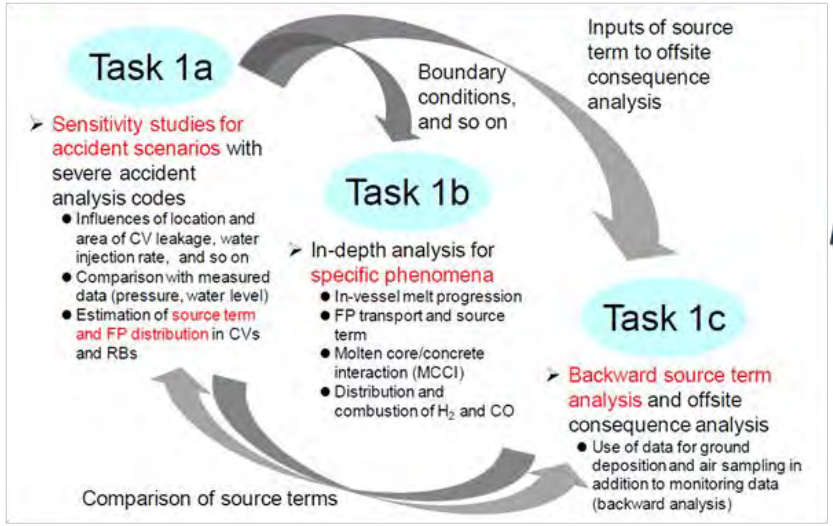

FACE

Framework

FACE project

OECD/NEA FACE project (2022-2026): Fukushima-Daiichi Nuclear Power Station Accident Information, Collection and Evaluation project.

Scope 1: In-depth discussions of accident progression.

- **Task 1a: FP behavior and associated accident scenarios**
- Task 1b: H_2 leakage, transport and combustion
- Task 1c: MCCI and melt progression for conditions of MCCI
- Task 1d: Backward ST estimation

1F1 scenario characterization

Framework

Objectives & Scope

- **Objective**

  Forensic analysis of Fukushima Unit 1: a search for a defensible scenario

- **Tool**

  - MELCOR 2.2 (SNL, UNRC).
  - UaSA

- **Scope**

  - Re-calibration of the possible scenario in 1F1

02

BE Calculations

MELCOR base model

GOBIERNO DE ESPAÑA
MINISTERIO DE CIENCIA, INNOVACIÓN Y UNIVERSIDADES
Ciemat
Centro de Investigaciones Energéticas, Medioambientales y Tecnológicas
UNSR

CORE

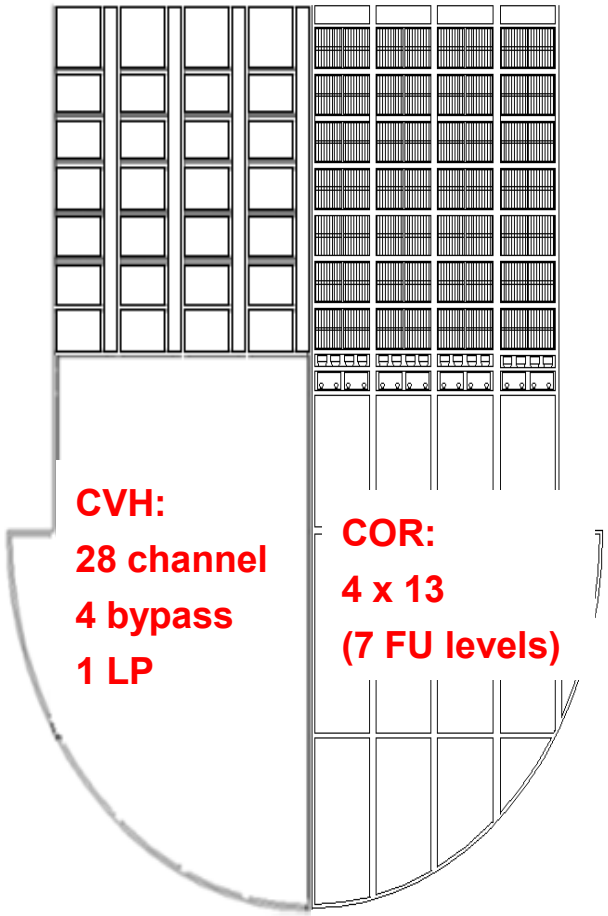

RPV

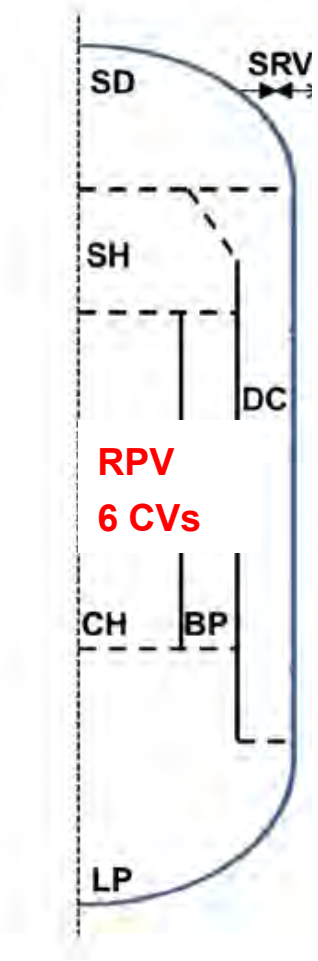

PCV

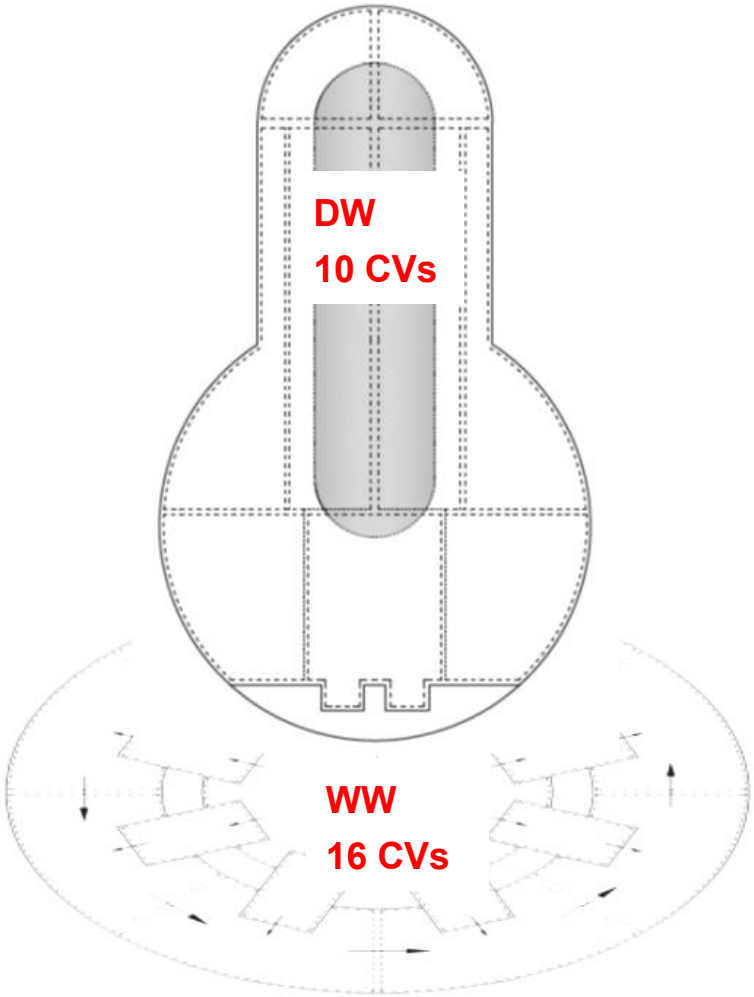

CAVITY

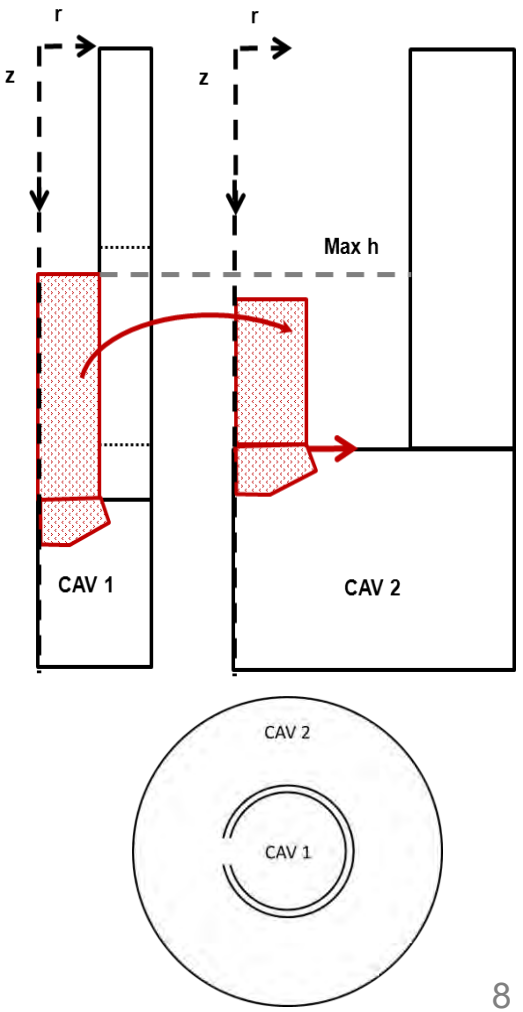

Key Hypothesis

Hypotheses setting

- SRVs (4;1 on).
- IC effect fitting.
- RCS leakages (GK & LP).
- No water injection till 10 days.
- Vertical stratification in the suppression pool.
- DW flange failure.
- PCV venting (~ 24 h).
- *End calculation time = 24 h*

BE Calculations

Across MELCOR versions

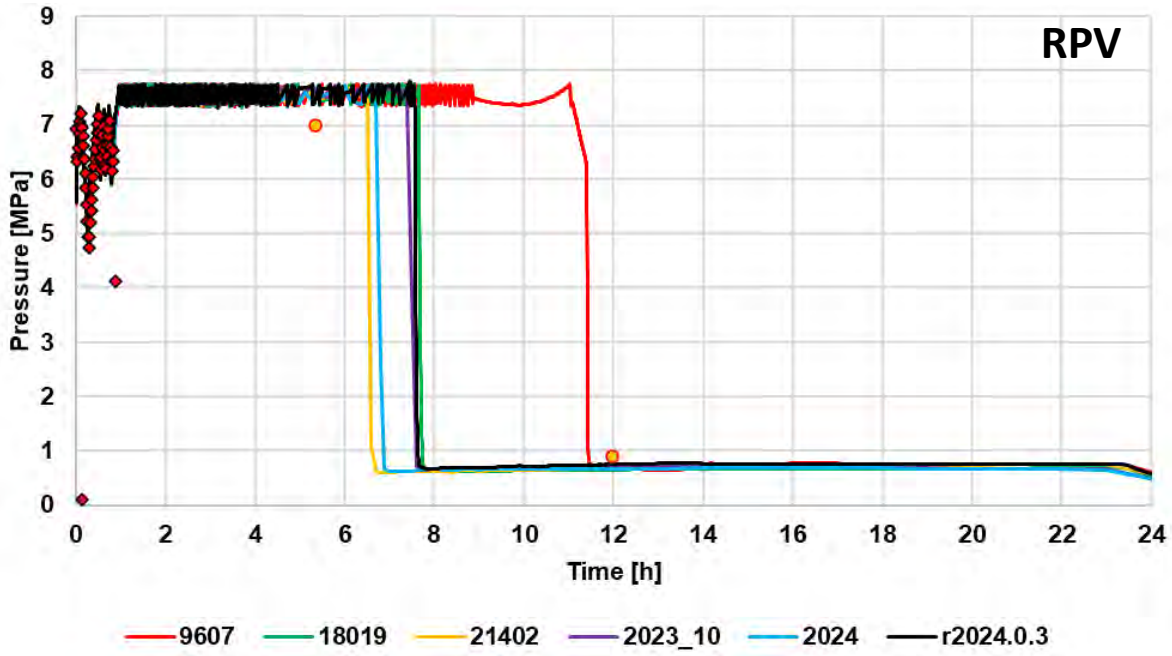

Significant variation in accident progression!

Scenario re-calibration r2024.0.3 based on P_{RPV} & P_{DW}

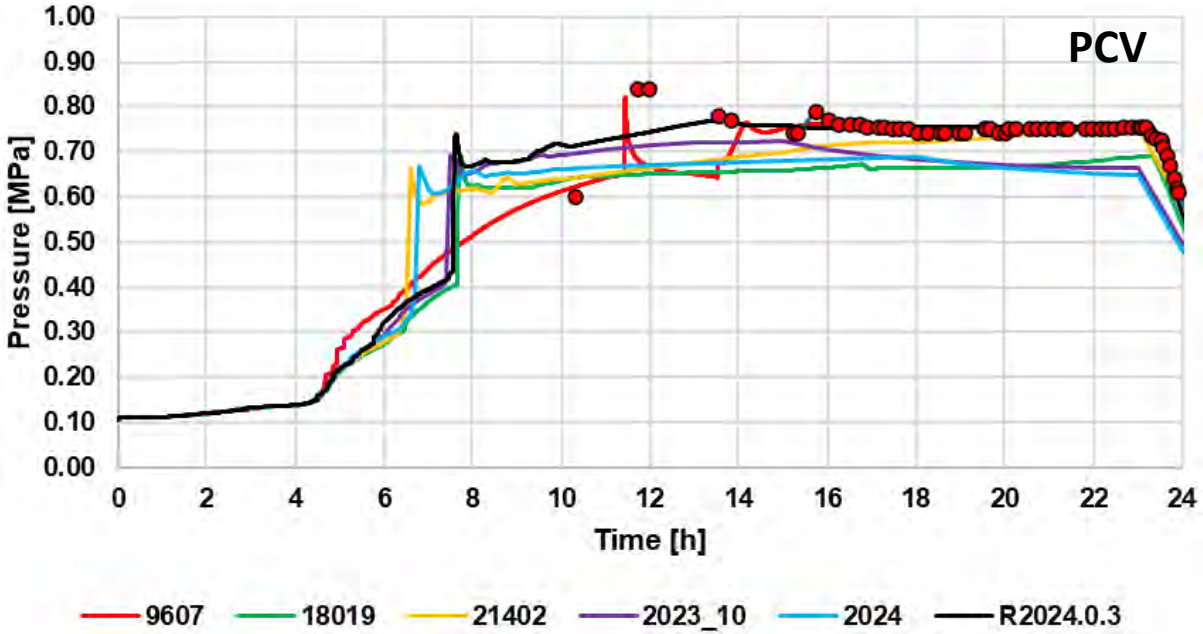

MELCOR BE

Scenario re-calibration r2024.0.3

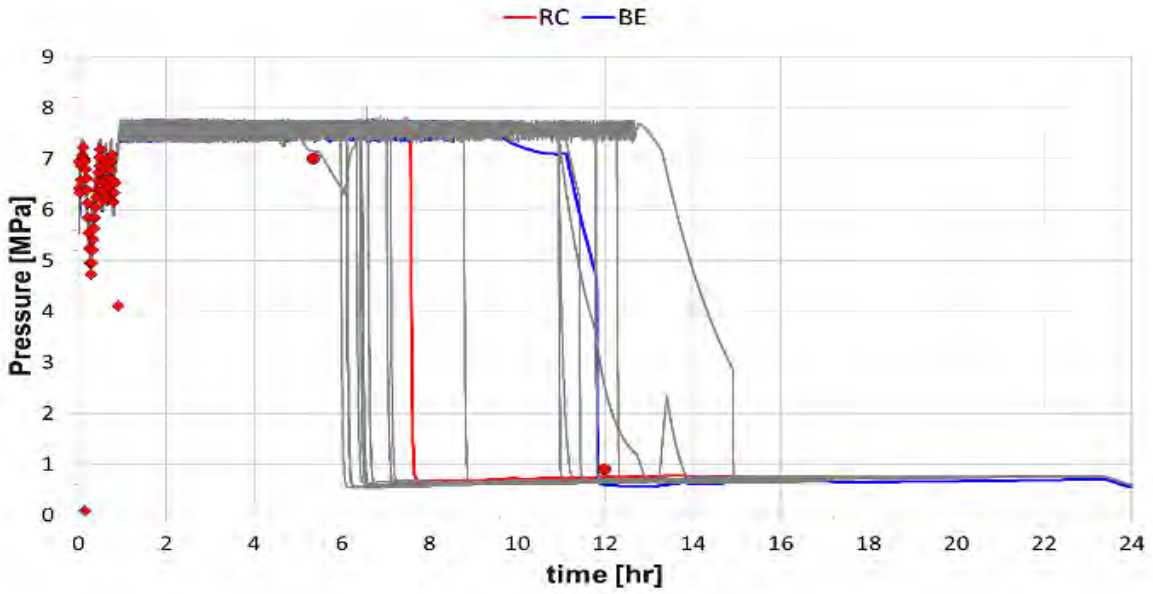

In-RPV pressure

Parameter	Value range	RC	BE
Time of LP leakage (h)	0-1	1	0
LP leakage diameter (m)	$0 - 5 \cdot 10^{-3}$	$2 \cdot 10^{-3}$	$3.5 \cdot 10^{-3}$
Gasket failure diameter (m)	$10^{-2} – 3 \cdot 10^{-2}$	$2 \cdot 10^{-2}$	$2 \cdot 10^{-2}$
Penetrations failure setpoint (K)	1153 – 1673	1153	1400
Materials-interaction modelling	INT/EUT	INT	EUT

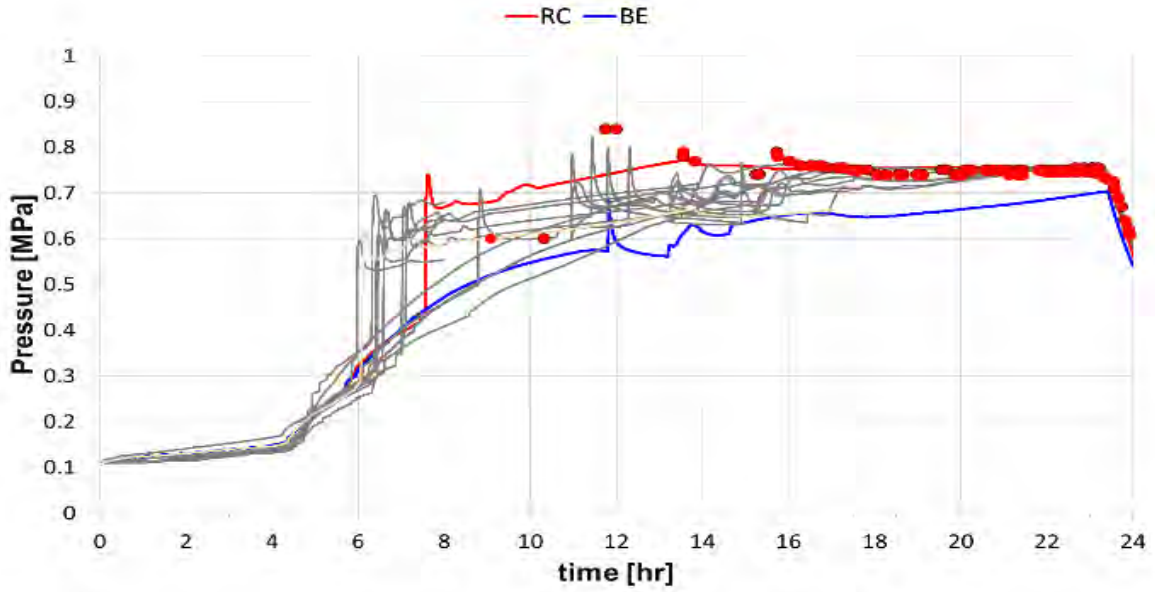

In-PCV pressure

BE Calculations

MELCOR BE

GOBIERNO DE ESPAÑA
MINISTERIO DE CIENCIA, INNOVACIÓN Y UNIVERSIDADES
Ciemat
Centro de Investigaciones Energéticas, Medioambientales y Tecnológicas

Core degradation

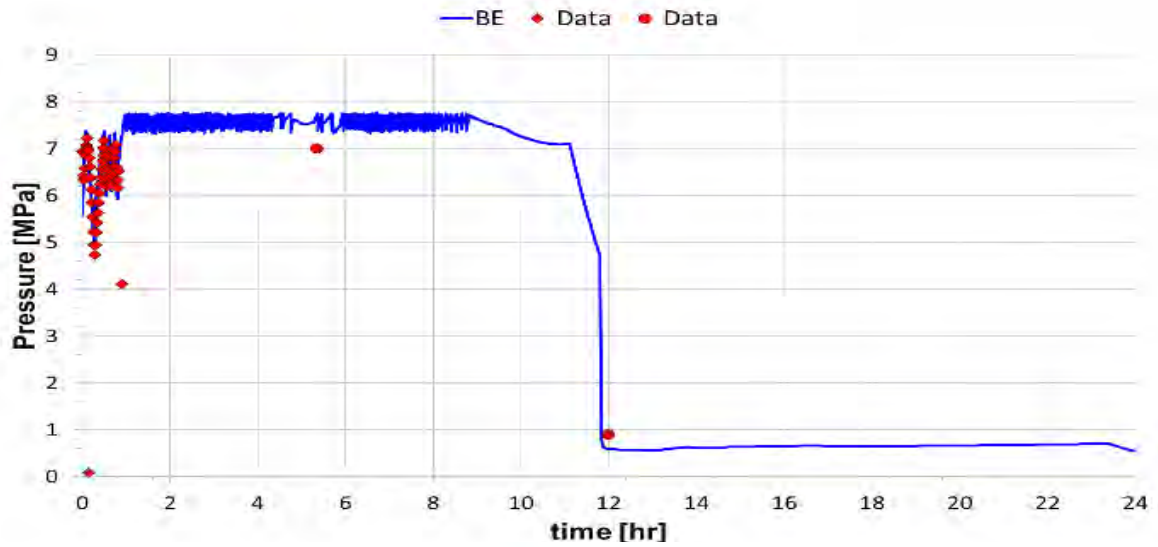

In-PCV Evolution

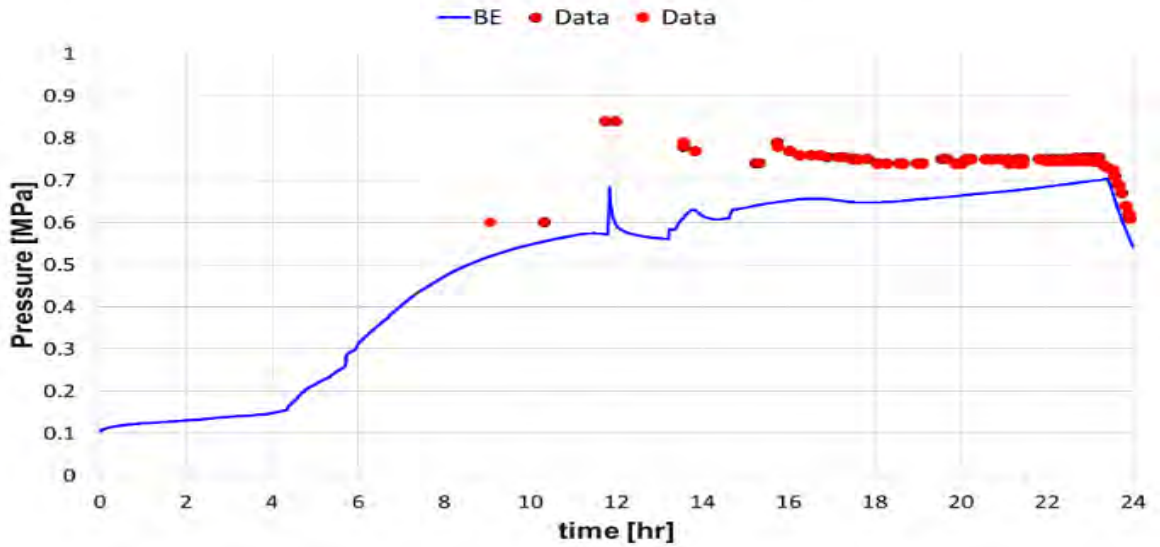

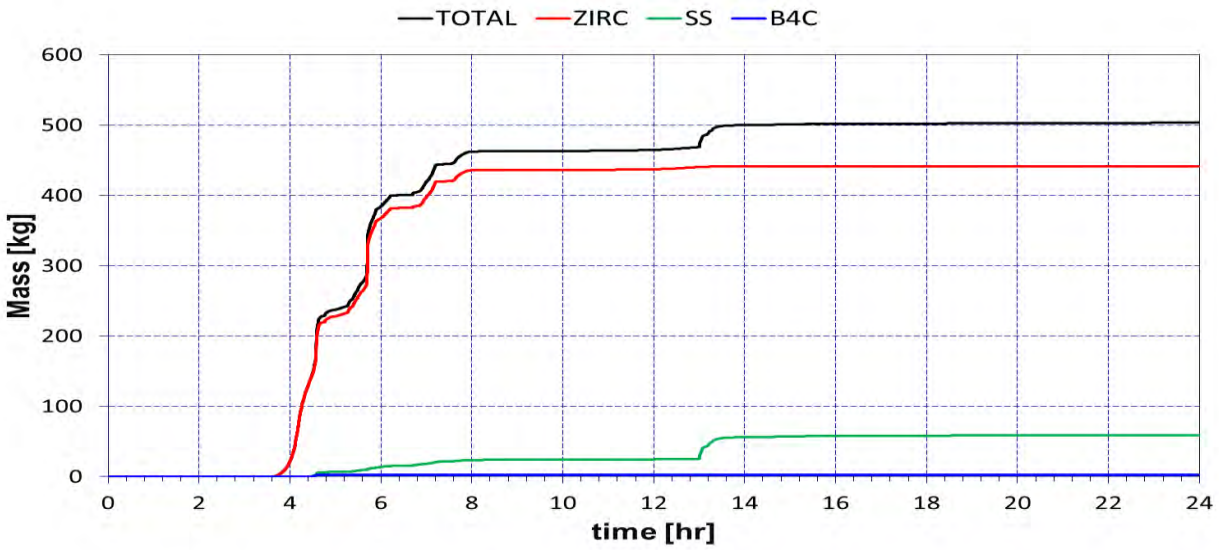

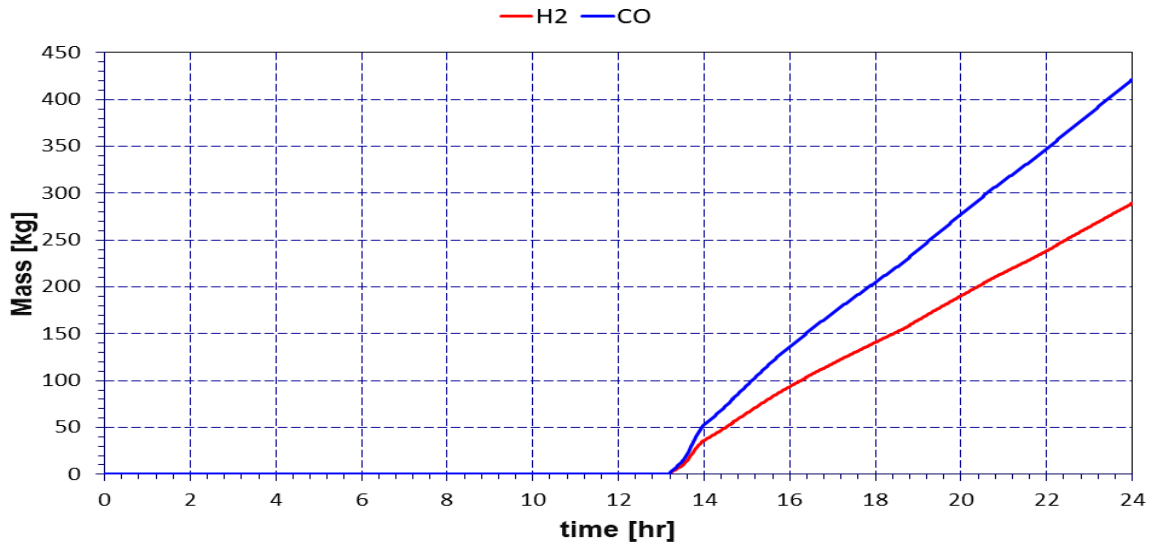

03

UaSA Application

- Order Sts. – double side (95/95) – 93 runs – SRS method – 7 UPs
- FOMs: P_{RPV}, P_{PCV}, $RPV_{liqlevel}$, t_{FAIL} (RPV)

Parameter	Default	LB	UB	PDF	Ref.
$Area_{LP_BREAK}$ (m^2)	$9.62 \cdot 10^{-6}$	$7.85 \cdot 10^{-7}$	$1.96 \cdot 10^{-5}$	Uniform	Sensitivity studies
$Area_{GASKT-LEAK}$ (m^2)	$3.14 \cdot 10^{-4}$	$1.77 \cdot 10^{-4}$	$3.14 \cdot 10^{-4}$	Uniform	Sensitivity studies
$T_{solidus}$ (Zr/SS EUT) (K)	1210	1100	1400	Uniform	Humphries L.L. *et al.*, 2021. *MELCOR Manuals.*
$T_{solidus}$ (Zr/INC EUT) (K)	1210	1100	1400	Uniform	Humphries L.L. *et al.*, 2021. *MELCOR Manuals.*
$T_{solidus}$ (UO_2/ZrO_2 EUT) (K)	2450	2200	2650	Uniform	Humphries L.L. *et al.*, 2021. *MELCOR Manuals.*
T_{P_FAIL} (K)	1273.15	1000	1671	Uniform	Humphries L.L. *et al.*, 2021. *MELCOR Manuals; M. M. Stempniewicz M., 1998. Analysis of Reactor Vessel Lower Head Penetration Tube Failure.*
LP Strain	0.18	0.15	0.3	Uniform	Humphries et al., 2021. MELCOR Manuals; Humphries et al., 2022. OECD Lower heaf failure project final report.

UaSA Application

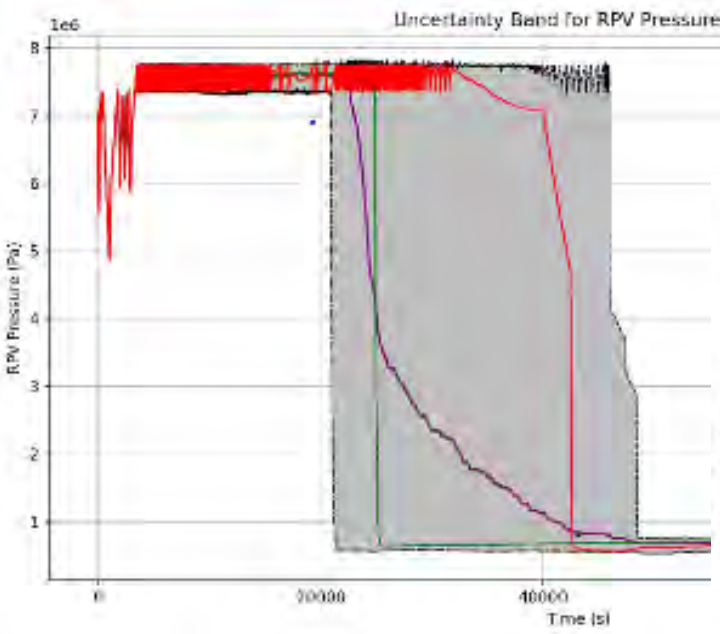

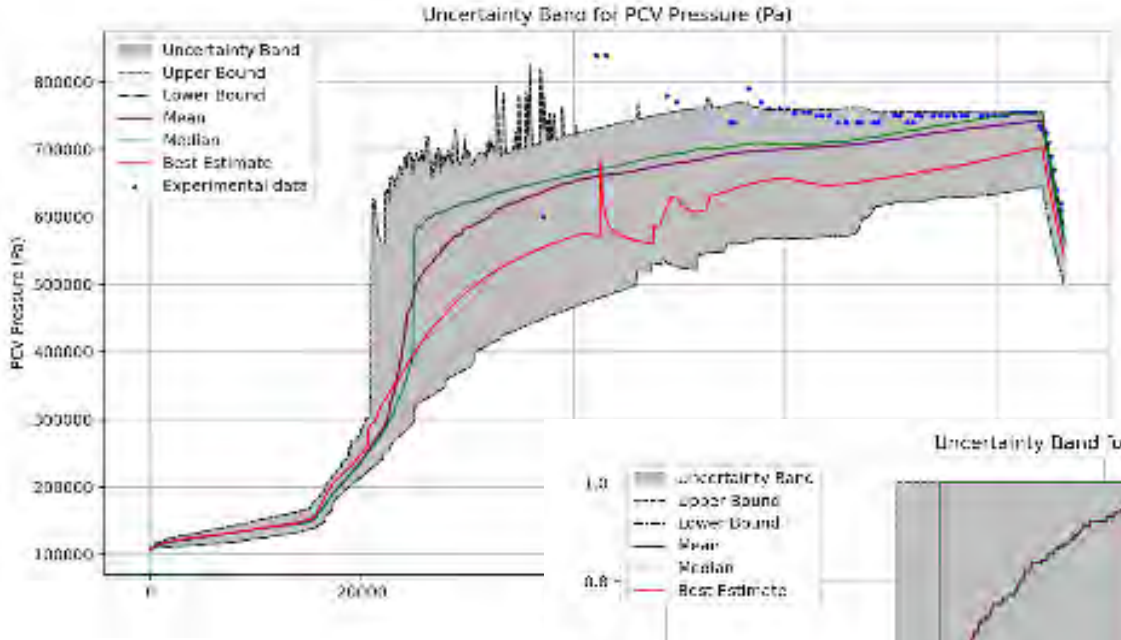

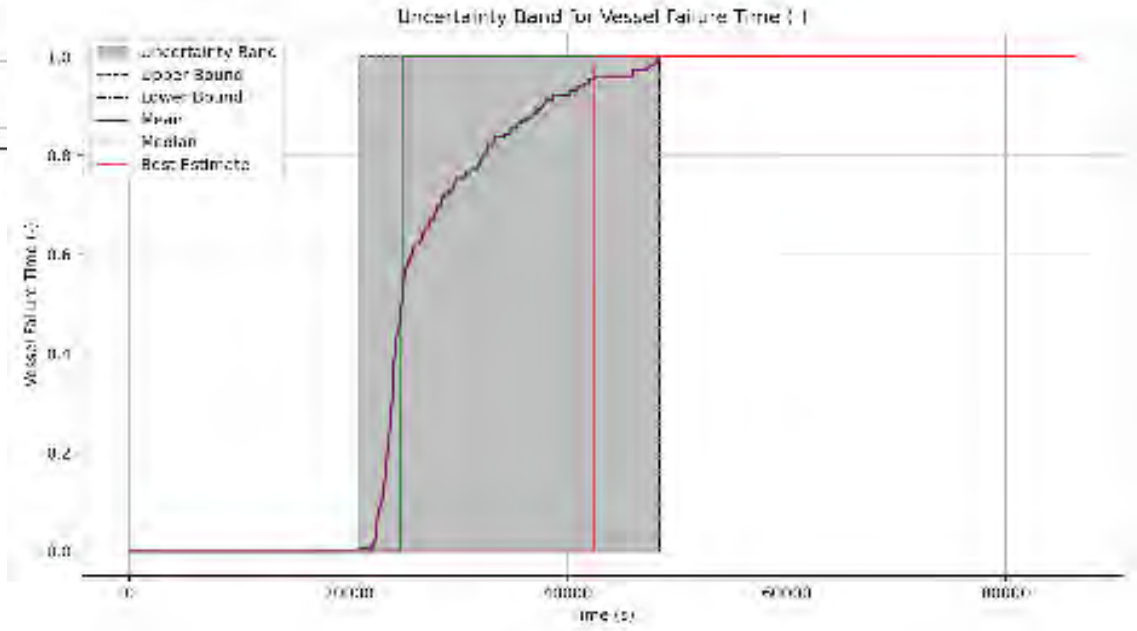

PDF: Uniform

Total samples: 250

Crashed: 70

Successful: 180

Crash rate: 28%

UaSA Application

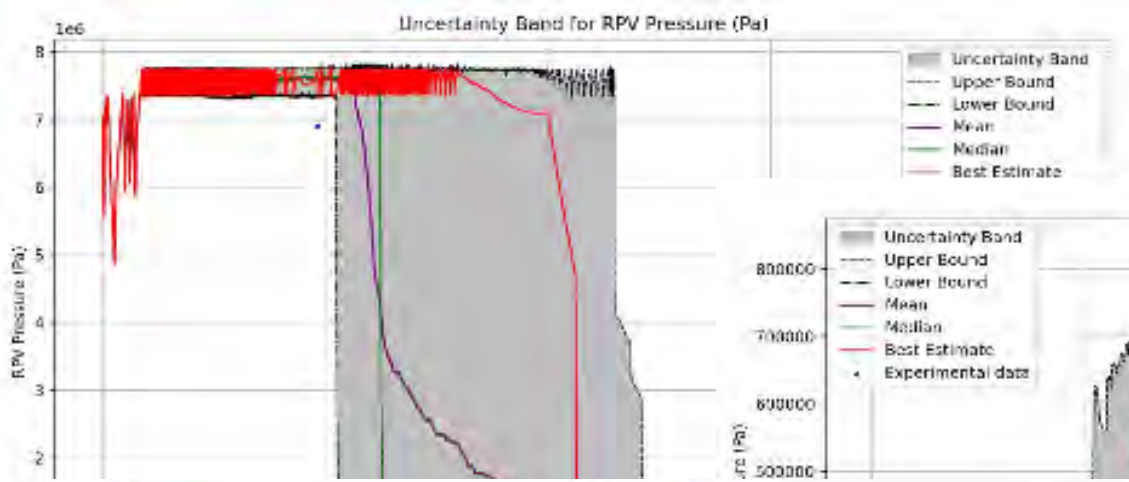

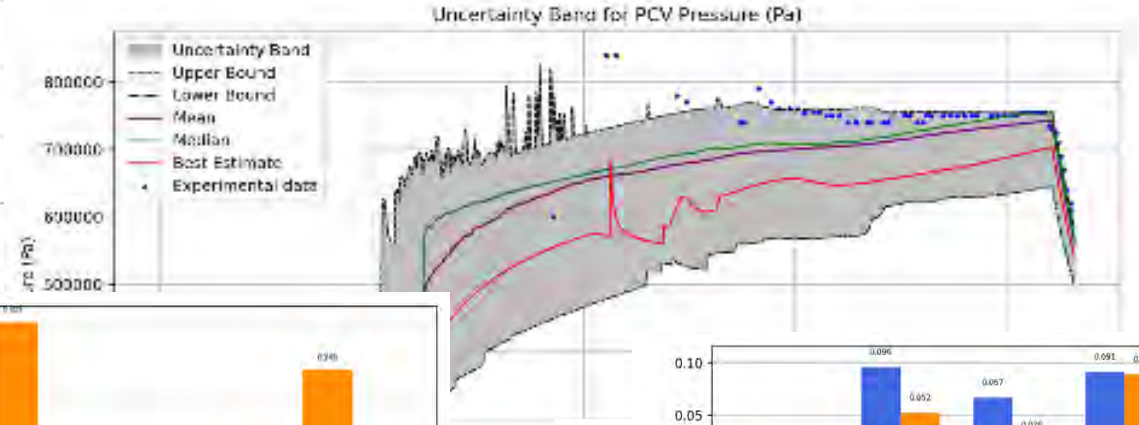

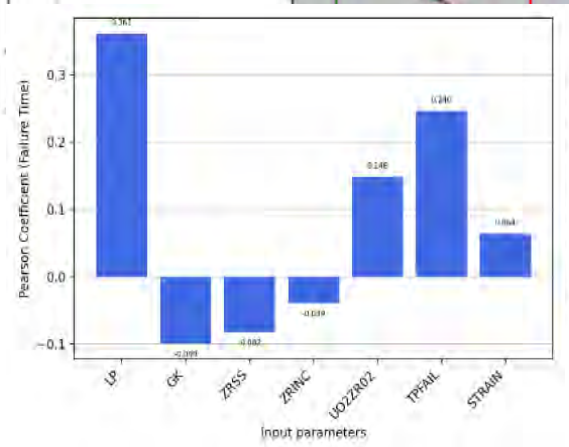

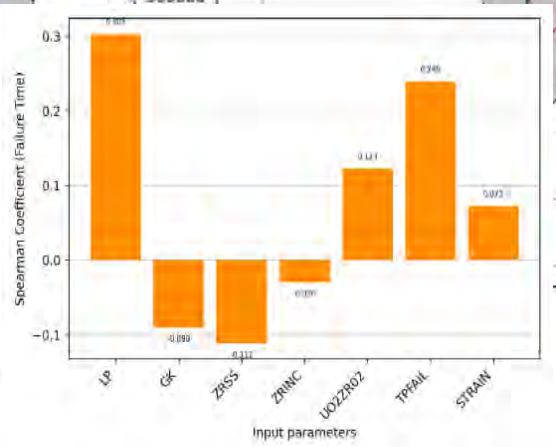

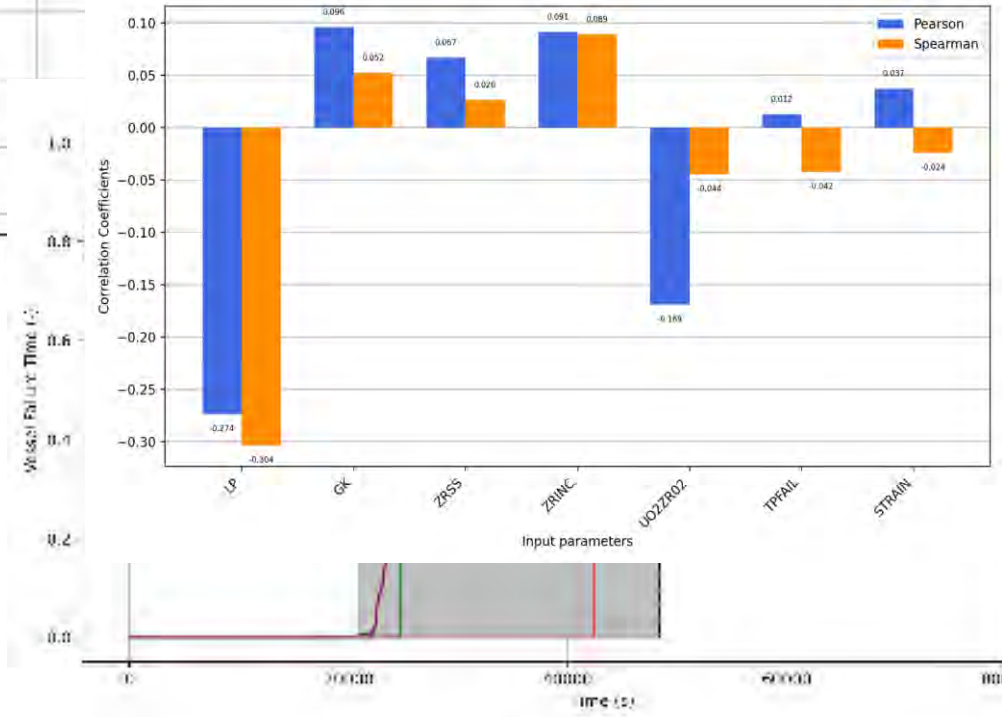

PDF: Uniform

Total samples: 250

Crashed: 70

Successful: 180

Crash rate: 28%

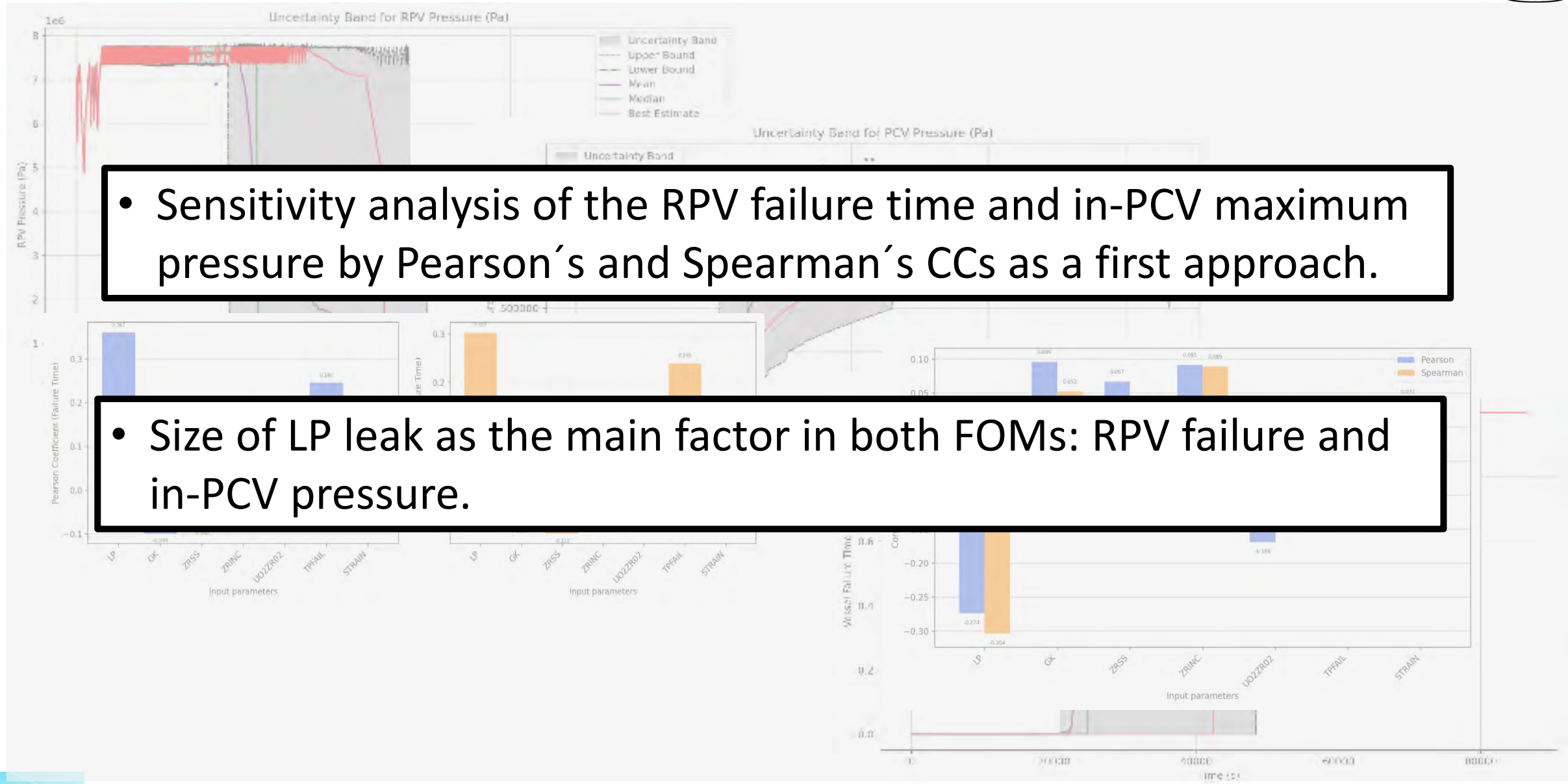

- Sensitivity analysis of the RPV failure time and in-PCV maximum pressure by Pearson´s and Spearman´s CCs as a first approach.

- Size of LP leak as the main factor in both FOMs: RPV failure and in-PCV pressure.

04

Main Insights

Main Insights

- Accident scenario **“forensic analysis”** is an essential tool.
- As codes keep evolving, it is indispensable **to credit** them along the way. “Hands & brain” needed for the purpose!
- Postulated scenario as a defensible scenario after the UaSA application.
- Size of liquid leak (cooling system/DW) and the eutectic model during core degradation as the most influencing factors.
- Next steps:
  - **Consolidate the model and focus on FP transport & H_2 leaking.**

Thank you for your attention!

Unit of Nuclear Safety Research
Department of Nuclear Fission
CIEMAT
luisen.herranz@ciemat.es

INTEGRATED SEVERE ACCIDENT ANALYSIS FOR A VVER-1000: ACCIDENT PROGRESSION, UNCERTAINTY QUANTIFICATION, AND RADIOLOGICAL CONSEQUENCES

Michela Angelucci, Livia Marzullo, Sandro Paci
University of Pisa
Largo Lucio Lazzarino, 56126 Pisa, Italy
michela.angelucci@unipi.it; l.marzullo@studenti.unipi.it; sandro.paci@unipi.it

Anastasia Stakhanova, Onur Murat, Fabrizio Gabrielli
Karlsruhe Institute of Technology
Hermann-von-Helmholtz-Platz 1, Eggenstein-Leopoldshafen, Germany
anastasia.stakhanova@kit.edu; fabrizio.gabrielli@kit.edu

ABSTRACT

Nuclear safety aims at the protection of people, society and environment from the consequences of hypothetical accidents in Nuclear Power Plants (NPPs). This is particularly true in the case of Severe Accidents (SAs) with partial or complete core meltdown and potential radioactive release to the environment. In such conditions, a rigorous assessment of accident progression, Source Term (ST), and radiological consequences is essential for the development of accident management strategies guidelines and for emergency preparedness.
The present study investigates a hypothetical Large Break Loss of Coolant Accident (LBLOCA) in the hot leg during a Station Blackout (SBO) sequence for a generic VVER-1000 reactor. The analysis relies on the integral SA code ASTEC (v3.1.1) to simulate accident progression, fission products release from the core, and ST to the external environment. The KATUSA tool and the JRODOS decision support system are then used for uncertainty and sensitivity analysis and for radiological dispersion and consequence evaluation under different meteorological conditions, respectively. As a case-study, the radiological consequences analysis has been performed taking into consideration the location of Zaporizhzhia NPP area in southeastern Ukraine.
The integrated use of a SA code, an Uncertainty Analysis (UA) tool, and a consequence assessment system provides a comprehensive computational framework for SAs analysis. The results from the UA reveal that the uncertainty band for the total activity released to the environment is not negligible. In a complementary way, sensitivity analysis points out containment leakage area and fuel burnup as the factors driving the ST variability. Moreover, atmospheric dispersion and consequences analyses indicate limited off-site radiological consequences, in both winter and summer seasons, under maximum release conditions.

KEYWORDS
SEVERE ACCIDENT, VVER, UNCERTAINTY QUANTIFICATION, ASTEC, JRODOS

1. INTRODUCTION

Nuclear safety aims at the protection of people, society and the environment from the consequences of hypothetical accidents occurring in Nuclear Power Plants (NPPs) [1]. This objective becomes especially relevant in the case of Severe Accidents (SAs), characterized by partial or complete core melting and potential release of radioactive material to the environment.

In such scenarios involving core degradation and possible radioactive release, the timely and reliable estimation of the Source Term (ST) represents a key element to support decision-making by the emergency teams. In fact, the ST determines magnitude, composition and timing of radioactive releases, which, in turn, affect atmospheric dispersion, radiological consequences and the effectiveness of the protective actions.

In this context, simulation tools capable of evaluating the progression of the accident itself and the resulting ST, together with the assessment of the off-site radiological impact, play a fundamental role. However, despite the significant progresses achieved in the development and advancement of integral SA codes, some uncertainties still remain and affect the prediction of a SA sequence evolution and the ST release [2]. On this account, Uncertainty and Sensitivity Analysis (UaSA) represents an essential complement to Best-Estimate (BE) SA simulations. By quantifying the variability of key output variables and identifying the parameters driving the associated uncertainty, this type of analysis provides a more robust basis for scenario interpretation and for strengthening emergency preparedness and response capabilities.

The present work proposes and applies an integrated analysis framework that systematically combines SA simulations, Uncertainty Quantification (UQ), and radiological consequences assessment. More precisely, the framework integrates the capabilities of the European Accident Source Term Evaluation Code (ASTEC) [3], developed by ASNR, the KArlsruhe Tool for Uncertainty and Sensitivity Analysis (KATUSA) [4], and the Java Real-Time On-line Decision Support (JRODOS) system [5], the last two being developed by KIT. The calculation platform is applied to a hypothetical Large Break Loss of Coolant Accident (LBLOCA) on the hot leg occurring in conjunction with a Station Blackout (SBO) in a generic VVER (Vodo-Vodyanoi Energetichesky Reaktor)-1000 NPP. The selected scenario is representative of high-risk sequences [6] and is characterized by rapid system depressurization and challenging conditions for accident management.

The objectives of this study are threefold: to simulate the progression of the selected SA and to estimate the corresponding radiological ST using an updated version of the ASTEC model of a generic VVER-1000 NPP assessed at KIT [7]; to quantify uncertainties and sensitivities affecting key Figures of Merit (FoMs), with particular emphasis on the activity released to the environment; and to evaluate the off-site radiological consequences for a representative site by coupling the ST results with atmospheric dispersion calculations performed with JRODOS. Through this integrated approach, the work aims to provide a comprehensive assessment of SA consequences and to highlight the added value of uncertainty-informed analyses for emergency preparedness and radiological risk evaluation.

2. ACCIDENT SCENARIO AND METHODOLOGY

2.1. Reference Plant and Accident Scenario

VVERs are Pressurized Water Reactors (PWRs) of Soviet design, in which light water is used both as coolant and neutron moderator, operating according to principles similar to those of Western PWRs. They constitute a significant fraction of the global nuclear reactor fleet, with numerous units currently in operation and more than 20 under construction worldwide. In particular, more than 30 VVER-1000 units are in operation nowadays, mainly in Russia, China and Eastern Europe [8].

Given their widespread deployment and their relevance within the international nuclear fleet, the analysis of SAs scenarios for VVER-1000 reactors is of particular interest. For this reason, the analyses presented in this work refer to a generic VVER-1000/V320 NPP, representative of generation II VVER designs currently in operation.

The selected accident sequence is a LBLOCA (more specifically, a double ended guillotine break) occurring on the hot leg, combined with a SBO condition (hereafter, LBLOCA+SBO). The SBO assumption implies

the loss of both off-site and on-site AC power supplies, resulting in the unavailability of active safety systems and significantly challenging the removal of decay heat from the reactor core. In addition, no Severe Accident Management (SAM) actions and no Filtered Containment Venting Systems (FCVS) are considered in the analysis. This choice represents a conservative assumption, aimed at evaluating the potential ST and radiological consequences in the absence of mitigation measures.

The LBLOCA+SBO sequence has been selected based on Probabilistic Risk Analysis (PRA) insights, which identify LOCA combined with SBO conditions among the sequences associated with the highest core damage frequencies for VVER-1000 reactors [6]. Such scenarios are characterized by rapid system depressurization, early core uncover, and limited opportunities for operator intervention, making them particularly relevant for SA analysis and emergency preparedness assessments.

2.2. Integrated Computational Framework

The assessment of SA progression, ST and associated uncertainties, as well as off-site radiological consequences, is performed by means of an integrated computational framework that combines three complementary tools: the SA code ASTEC, the UaSA tool KATUSA, and the decision-support system JRODOS. Each tool addresses a specific stage of the analysis chain, ensuring continuity from the starting of the accidental sequence to the evaluation of the radiological impact.

ASTEC is an integral code developed to model a SA, from the initiating event up to the release of radioactive material to the environment. The code addresses both in-vessel and ex-vessel phenomena, including core heat-up and degradation, Fission Products (FPs) release and transport, containment thermal-hydraulics, and ST evaluation. In this work, the ASTEC code (v3.1.1) is mainly used to carry out a BE simulation, with the prediction of the timing, magnitude, and isotopic composition of the radiological ST associated with the LBLOCA+SBO scenario.

KATUSA is a tool developed at Karlsruhe Institute of Technology (KIT) for performing UaSA through the propagation of input uncertainties. The tool manages the entire process, from initial input parameters' sampling and input deck preparation, through the automatic execution of multiple ASTEC calculations, to the post-processing of the results, including the computation of simple statistics and Correlation Coefficients (CCs) [9]. In the present study, KATUSA is employed to quantify the uncertainty affecting key ST-related FoMs when varying several input parameters. In addition, the tool is also used to identify the parameters that influence the most the variability of the predicted ST, thus providing insights into the dominant drivers of uncertainty.

JRODOS is a system dedicated to the assessment of atmospheric dispersion and radiological consequences following an accidental radioactive release. It uses the isotopic release data as input to simulate radionuclide transport, deposition, and dose to the population, accounting for site characteristics and meteorological conditions. This allows the evaluation of off-site radiological impact in terms of environmental contamination and effective doses. While JRODOS is typically applied in combination to ST data derived from a BE ASTEC simulation, in present work the effective dose assessment is performed using the maximum activity release, as resulting from the UaSA analysis.

Further details on each step and the corresponding results are provided in the next sections.

The overall analysis workflow is schematically represented in Figure 1.

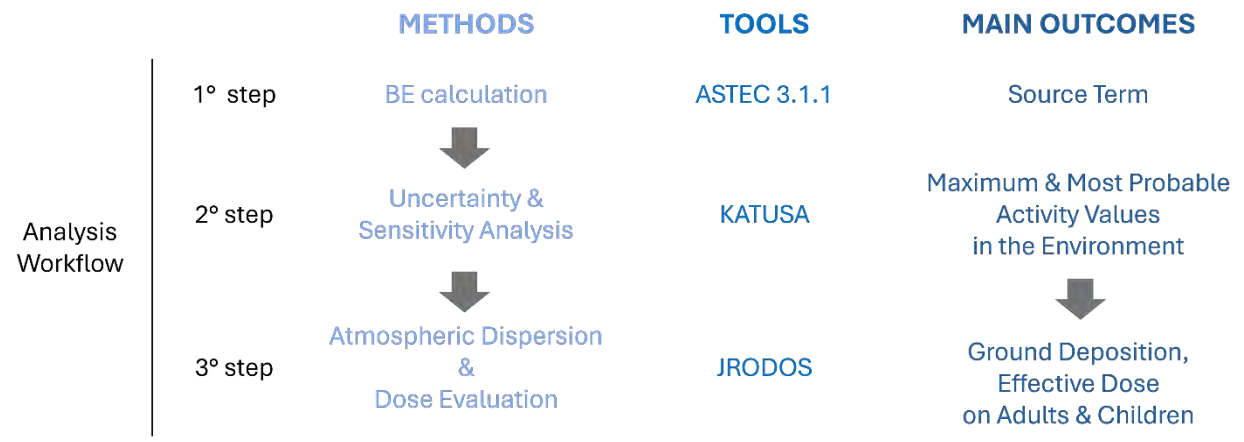

Figure 1. Analysis Workflow

3. SEVERE ACCIDENT PROGRESSION AND SOURCE TERM

3.1. Accident Progression

As introduced in the previous sections, the SA scenario investigated in this work is a hypothetical LBLOCA+SBO occurring on the hot leg of a VVER-1000 reactor. The accident sequence has been simulated using ASTEC v3.1.1, starting from an integral plant nodalization originally developed for ASTEC v2.2 [7] and subsequently adapted to a more recent version of the code.

The accident is initiated by the instantaneous double-ended guillotine break on the hot leg, which causes a rapid depressurization of the primary circuit and the discharge of coolant into the containment. The reactor is assumed to scram at the initiation of the event, while the SBO condition leads to the loss of off-site and on-site AC power and, consequently, to the unavailability of active safety systems. Main coolant pumps coast down shortly after the initiating event, resulting in the early loss of forced circulation.

Following the primary pressure decrease, water injection from the hydro-accumulators partially compensates for the coolant inventory loss and temporarily delays core heat-up. However, after the depletion of accumulator inventory, heat removal from the core becomes inadequate. As a consequence, the core progressively uncovers, and a rapid increase in fuel and cladding temperatures take place. Therefore, cladding oxidation starts, accompanied by significant hydrogen generation and FPs release from the fuel.

With the progression of the accident, extensive core degradation occurs, with molten materials relocating downward through the core region and accumulating in the lower plenum. The interaction between molten materials and residual coolant contributes to additional oxidation processes and further hydrogen production. The continued heat-up of the lower head ultimately leads to reactor pressure vessel failure, allowing the relocation of corium into the containment cavity.

After vessel failure, ex-vessel phenomena dominate the transient. Molten Core Concrete Interaction (MCCI) takes place in the cavity, generating additional thermal power and non-condensable gases, which affect containment pressure and composition. The progressive ablation of the concrete of the cavity eventually leads to basemat failure.

The main events characterizing the accident progression and their corresponding occurrence times are summarized in Table 1.

Table I. Main events characterizing the accident progression - timing

Event	Time (s)
Large break on the hot leg	0.0
Reactor scram	0.0
Main coolant pumps' coast down	0.0
Turbine trip	1.6
Accumulator injection - starting	5.1
Accumulator injection - ending	111.8
Onset of FPs release	456.2
First material slump in the lower plenum	1081.8
Lower head failure	3377.9
Basemat failure	106705.0

3.2. Source Term Results

The conducted BE analysis resulted in the evaluation of the ST, both in-containment and in the environment. Figure 2 shows the time evolution of the total activity transported to the containment and the one released to the environment during the accident progression.

Following core heat-up and fuel degradation, FPs are released from the fuel and transported through the primary system and to the containment. Due to the location of the break on the hot leg, the steam generator is effectively bypassed. As a consequence, a significant fraction of the released FPs is transported directly into the containment. Nevertheless, partial retention occurs within the primary system and the containment. As a result, the activity in the containment atmosphere reaches approximately 1.0E+19 Bq at the end of the transient.

Part of the activity transported to the containment is subsequently released into the environment. Retention mechanisms within the containment, including deposition on containment walls and internal structures, limit the activity available for release. Nevertheless, since no FCVS is considered, the activity released to the environment directly depends on the containment inventory and on the leakage characteristics. A total activity of around 6.0E+15 Bq is released to the environment.

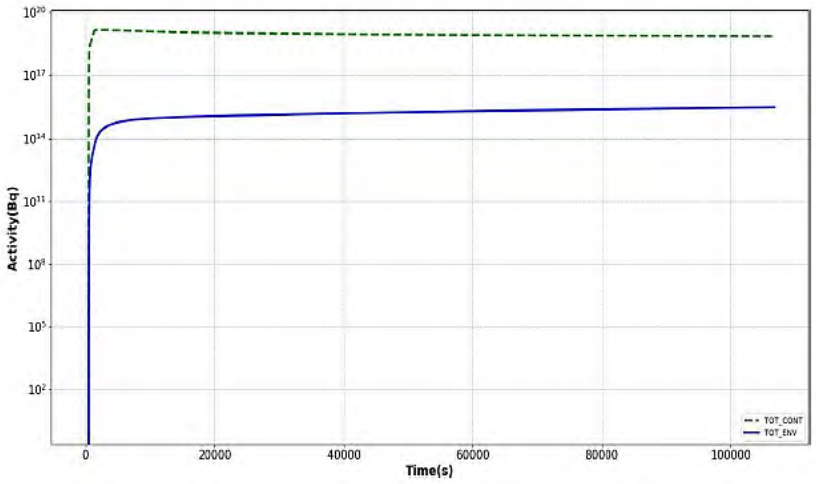

Figure 2. Activity transported to the containment and released to the environment

The resulting environmental ST is characterized by an early release dominated by noble gases, following by the release of volatile radionuclides, such as cesium and iodine, which are particularly relevant for radiological consequences. More specifically, following inhalation or ingestion, iodine accumulates in the thyroid increasing cancer risk, while cesium contributes to long-term contamination and both external and internal exposure.

The isotope-wise activity released in the environment at the end of the transient is shown in Figure 3. As it can be seen, xenon and iodine exhibit the dominant activity levels among the represented radionuclides.

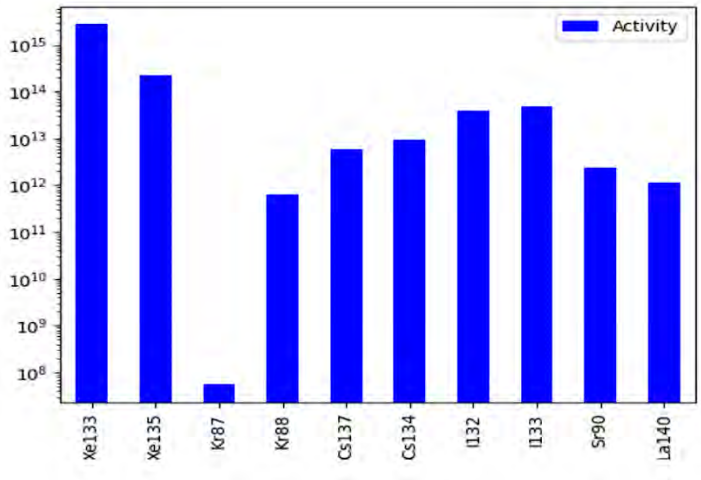

Figure 3. Isotope-wise activity in the environment

4. UNCERTAINTY AND SENSITIVITY ANALYSIS

4.1. Uncertainty Analysis Setup

In order to account for uncertainties affecting the prediction of the ST, an UaSA is performed using KATUSA, coupled with ASTEC, with particular emphasis on ST-related FOMs.

The Uncertainty Analysis (UA) is carried out by means of a total of 150 ASTEC simulations, generated through a random sampling of selected input parameters. For each run, KATUSA automatically prepares the corresponding ASTEC input deck, executes the calculation, and extracts the relevant output variables.

A set of uncertain input parameters is selected based on their relevance to FPs release, transport and behavior in the containment under SA conditions. More specifically, the selected parameters include quantities related to aerosol behavior, containment leakage, and fuel burnup. For each parameter, an appropriate variation range as well as a Probability Distribution Function (PDF) are defined. Their characterization is mainly based on literature review, engineering judgement, and the experience gained from the MUSA project [2], [10], [11].

The list of selected input parameters, together with their corresponding variation ranges and PDFs, is reported in Table II.

Table II. Input parameters - characterization

Parameter	Description	Reference Value	Variation Range	PDF
frho	Particle mean density (kg/m3)	3000.0	2610.0 10000.0	Triangular Mode: 3000.0
fR_max	Particle max radius (m)	1.995E-5	5.0E-6 2.0E-5	Triangular Mode: 1.995E-5
fR_min	Particle min radius (m)	1.1E-8	1.0E-8 2.0E-7	Triangular Mode: 1.1E-8
fspheat	Particle mean specific heat (J/kgK)	840.0	71.0 960.0	Uniform
fv_stks	Shape factor relative to Stokes velocity	1.0	1.0 3.0	Beta Alpha: 1.0 Beta: 5.0
p_bu	Effective full power days	164.0	10.0 320.0	Uniform
f_leak	Containment leakage area (multiplier)	1.0	0.8 1.2	Uniform

4.2. Uncertainty Analysis Results

The UA results are presented in terms of activity released to the environment, which is selected as primary FoM. This FoM is directly relevant for the assessment of the radiological consequences, since it constitutes a key input for dispersion and dose calculations.

Figure 4 shows the uncertainty band associated with the total activity released to the environment as obtained from the UA runs. The results show that the predicted ST exhibits a non-negligible variability, which reflects the combined effect of the selected uncertain input parameters. In particular, the activity released to the environment spans over a range between a minimum value of 3.9E+15 Bq and a maximum value of 7.2E+15 Bq.

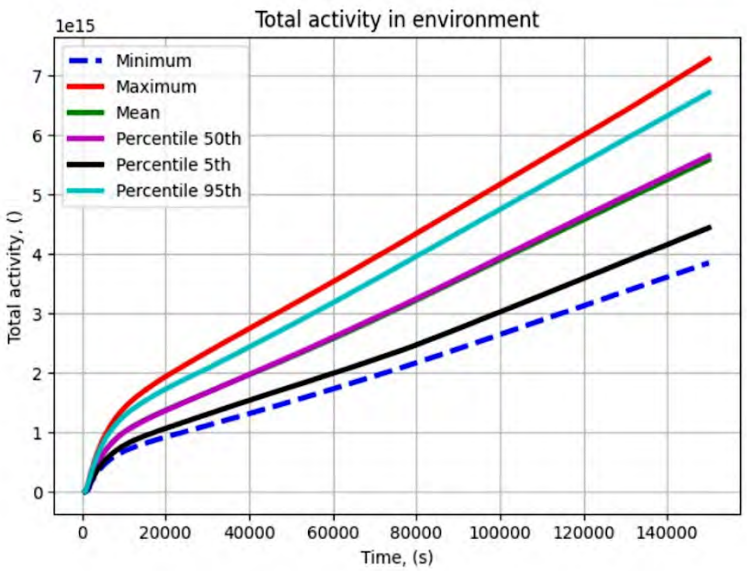

Figure 4. Activity Released to the environment – uncertainty band

Focusing on the final step of the UQ, it is additionally possible to derive a probability distribution of the total activity in the environment. As it can be observed in Figure 5, the distribution is asymmetric, and it is characterized by a clear peak, which identifies the most probable value, while the upper tail corresponds to less frequent but more severe release scenarios.

It is worth noting that the BE simulation result (≈ 6.0E+15 Bq), as presented in Section 3.2, lies close to the most probable value of the uncertainty distribution (6.18E+15 Bq), indicating a good representativeness of the BE calculation within the uncertainty space explored. On the other hand, the maximum release scenario exceeds the BE value to some degree, underlining the importance of accounting for uncertainty when evaluating potential radiological consequences.

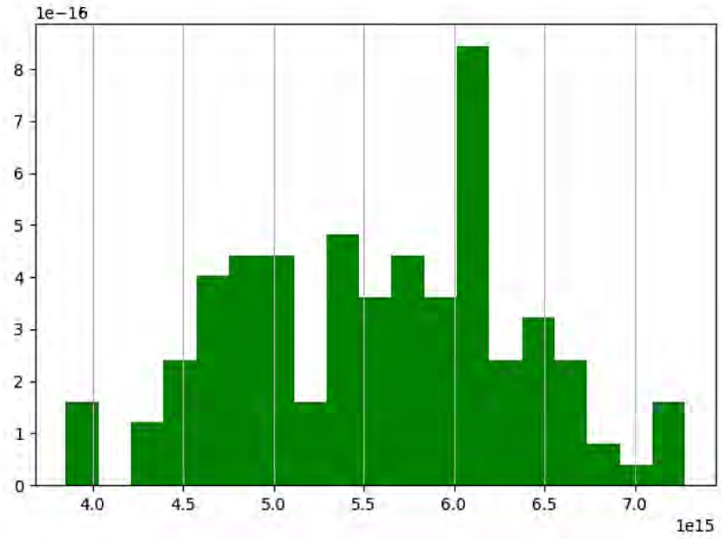

Figure 5. Probability distribution of the total activity in the environment at the last step pf the UA

4.3. Sensitivity Analysis Results

In complement to the UA, a sensitivity analysis is performed with the aim of identifying the input parameters with the strongest influence on the studied FoM, namely the activity released to the environment. For this purpose, a correlation-based sensitivity metric is employed. In particular, the Spearman CC is adopted to account for monotonic relationships between each uncertain input parameter and the FoM.

The sensitivity analysis indicates that the containment leakage area and the fuel burnup play a dominant role in driving the variability of the environmental ST, whereas the influence of the remaining parameters is comparatively limited. The strong sensitivity associated with the containment leakage area reflects its direct role in governing the transfer of radioactive material from the containment to the environment once containment integrity is lost. Similarly, fuel burnup directly affects the initial FPs inventory in the core and, consequently, the amount of radioactive material available for release during a SA scenario. The combined influence of these two parameters explains the majority of the spread observed in the UA results.

Figure 6 presents the Spearman CC obtained by considering the activity released to the environment as the FoM and the containment area leakage as input parameter. Figure 7 shows the Spearman CC for the same FoM when accounting for the fuel burnup as input parameter.

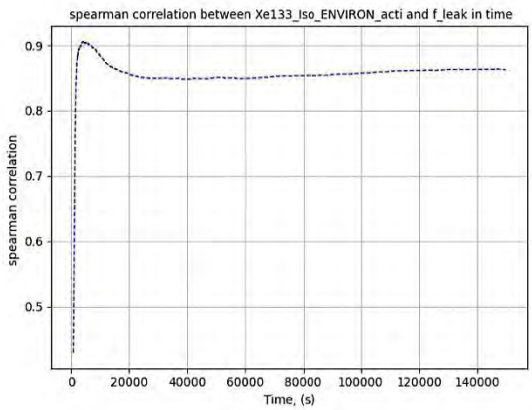

Figure 6. Spearman CC – activity to the environment vs containment leakage area

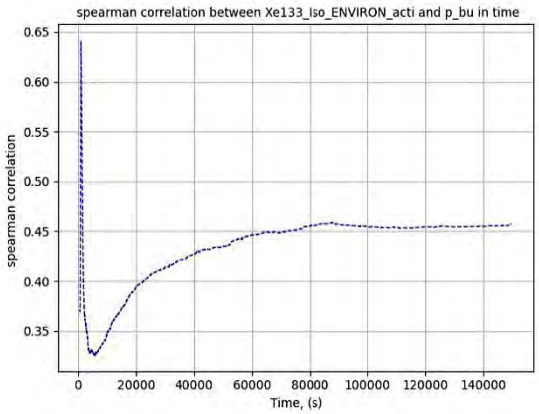

Figure 7. Spearman CC – activity to the environment vs fuel burnup

5. RADIOLOGICAL CONSEQUENCES ASSESSMENT

5.1. Dispersion Analysis Setup

Based on the results of the UA presented in Section 4.2, two representative ST scenarios are identified: the most probable release and the maximum release of activity to the environment. While both scenarios are worthy of further investigation and provide valuable information, the present radiological consequence assessment focuses on the maximum release scenario, which represents a bounding case and ensures a conservative evaluation of off-site radiological impact.

The analysis is carried out using the JRODOS decision-support system. The time-dependent, isotope-wise ST associated with the maximum release scenario, as obtained from the ASTEC-KATUSA coupling, is provided as input to JRODOS for the simulation of atmospheric dispersion, radionuclide deposition, and population exposure.

In addition to ST-related data, JRODOS requires detailed geographical and demographic information for the considered NPP site. As a case-study, the location of Zaporizhzhia NPP (ZNPP), located in southeastern Ukraine, is selected as a representative site. Moreover, to account for the influence of atmospheric conditions on radionuclide transport and deposition, two different meteorological scenarios are considered, representative of summer and winter conditions, respectively.

The JRODOS calculations are performed over a domain covering approximately 640000 km^2, with a total population of about 37.6 million inhabitants. The dispersion simulations are carried out over a time window of 42 hours starting from the onset of radioactive release. No emergency countermeasures, such as sheltering, evacuation, or administration of KI pills, are assumed in the simulations, in order to maintain the conservative analysis framework. For reference, the adopted intervention criteria consider sheltering when the effective dose exceeds 10 mSv and evacuation when the effective dose exceeds 50 mSv, while KI administration is considered when thyroid dose thresholds of 100 mSv for adults and 10 mSv for children are exceeded.

5.2. Radiological Impact Results

The radiological consequences assessment results for the maximum release scenario are presented in terms of ground deposition of aerosol and effective doses to the adult population, considering both summer and winter meteorological conditions.

Figure 8 shows the spatial distribution of the total aerosol distribution at the end of the calculation, in summer conditions. The deposition reached a maximum value of 1.89E+4 Bq/m^2, with decreasing values at increasing distance from the release point. The estimated lifetime effective doses to the population, evaluated considering cloud shine, ground shine, and inhalation pathways, remain limited over the considered area. As shown in Figure 9, the estimated lifetime effective dose for adults is well below the adopted intervention thresholds, showing a maximum value of 2.49E-1 mSv.

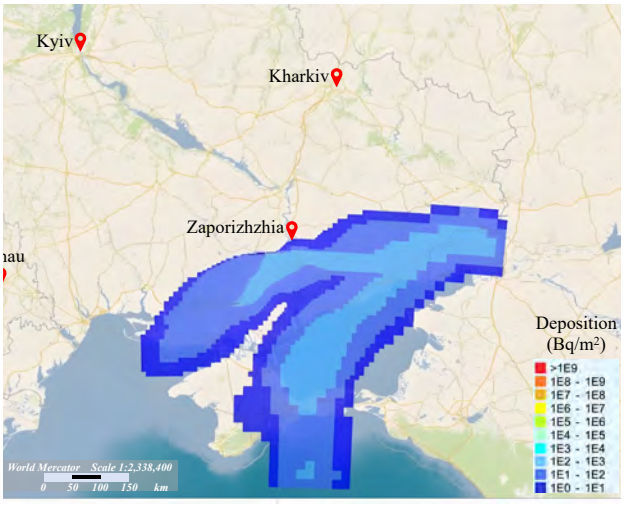

Figure 8. Ground deposition of aerosol at the end of the calculation – summer

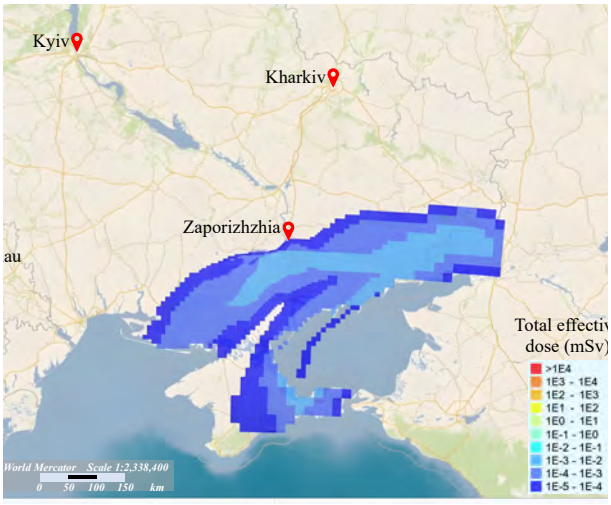

Figure 9. Effective dose for adults - summer

In winter, the deposition pattern differs (Figure 10), consistently with a more stable atmosphere, and resulting in a plume that follows the wind direction more clearly. In this case, the aerosol ground deposition reaches a higher maximum value of 7.7E+4 Bq/m^2. A corresponding increase is observed for the lifetime effective dose for the adult population, that reaches a value of 9.69E-1 mSv (Figure 11). Nevertheless, even considering these less favorable conditions, the calculated effective dose remains below the criteria for sheltering and evacuation.

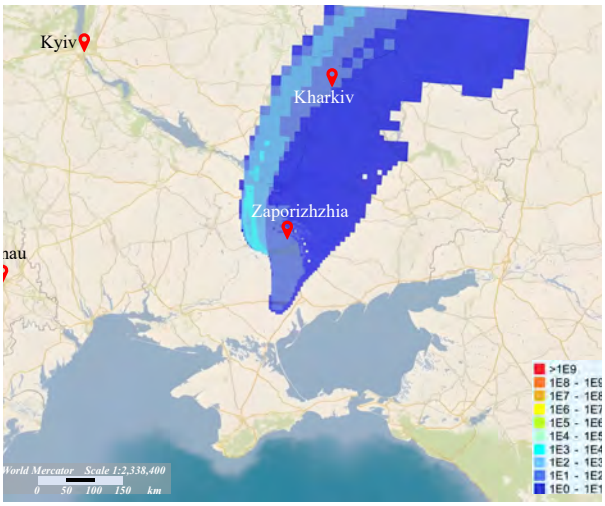

Figure 10. Ground deposition of aerosol at the end of the calculation – winter

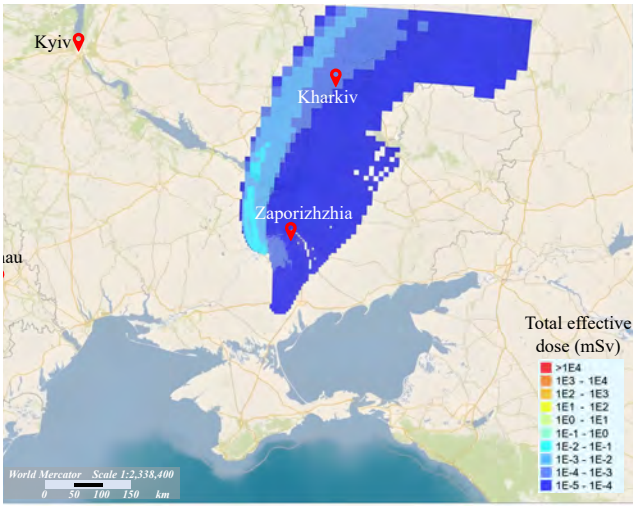

Figure 11. Effective dose for adults - winter

6. CONCLUSIONS

In this work, an integrated computational framework combining SA simulation, UaSA, and radiological consequence assessment has been applied to a hypothetical LBLOCA+SBO scenario in a generic VVER-1000 NPP, under conservative assumptions (no mitigation measures and FCVS have been modeled). The results demonstrate the consistency and robustness of the adopted framework, which allows the systematic evaluation of accident progression, radiological ST, and off-site consequences within a unified and coherent analysis chain.

The integrated analysis provides some meaningful insights:

- The study demonstrates the importance of UaSA in SA ST evaluation. The uncertainty propagation highlights a non-negligible variability in the activity released to the environment and shows that BE results, while representative of the most probable outcome, do not fully capture the range of possible releases. The identification of containment leakage area and fuel burnup as the dominant contributors to ST variability provides valuable physical insight and underlines the need to explicitly account for these parameters when assessing radiological risk;
- The radiological consequence assessment, performed under conservative assumptions and focusing on the maximum release scenario, indicates that the off-site radiological impact remains limited, with effective doses to the population staying below intervention thresholds even under unfavorable meteorological conditions.

In short, the integrated approach adopted in this work is relevant for emergency preparedness and planning, as it provides not only BE predictions but also uncertainty-informed results that can be directly used in decision-support tools. Moreover, the framework offers a flexible basis for future analyses. Possible extensions of the present work include the modeling of SAM strategies and containment mitigation systems, the application to different site locations and with meteorological conditions, and the investigation of additional accident scenarios and alternative FoMs. Such developments would further enhance the applicability of the computational framework and its value for safety analysis and emergency response support.

ACKNOWLEDGMENTS

This work is framed within the SEAKNOT project under the Grant Agreement no. 101060327. Views and opinions expressed are, however, those of the authors only and do not necessarily reflect those of the European Union. Neither the European Union nor the granting authority can be held responsible for them.

REFERENCES

[1] IAEA, “Fundamental Safety Principles: Safety Fundamentals,” 2006.
[2] S. Brumm *et al.*, “Uncertainty quantification for severe-accident reactor modelling: Results and conclusions of the MUSA reactor applications work package,” *Ann. Nucl. Energy*, vol. 211, p. 110962, Feb. 2025, doi: 10.1016/j.anucene.2024.110962.
[3] ASNR, “The ASTEC software system | ASNR.” Accessed: Jan. 23, 2026. [Online]. Available: https://research-assessment.asnr.fr/astec-software-system
[4] V. H. Sanchez-Espinoza *et al.*, “KIT reactor safety research for LWRs: Research lines, numerical tools, and prospects,” *Nucl. Eng. Des.*, vol. 414, p. 112573, Dec. 2023, doi: 10.1016/J.NUCENGDES.2023.112573.

[5] A. Wengert, "JRodos: an off-site emergency management system for nuclear accidents," Karlsruhe, 2017.
[6] USNRC, "Kalinin VVER-1000 Nuclear Power Station Unit 1 PRA (Beta Project). NUREG/IA-0212, Vol.1," 2005. Accessed: Jan. 23, 2026. [Online]. Available: www.nrc.aov/readinq-rm/doc-collections/nuregs
[7] A. Kağan Mercan, F. Gabrielli, V. Hugo Sanchez-Espinoza, and W. Raskob, "Analysis of the consequences of a LBLOCA with SBO severe accident in a generic VVER-1000 by means of ASTEC and JRODOS codes," *Nucl. Eng. Des.*, vol. 400, no. November, 2022, doi: 10.1016/j.nucengdes.2022.112078.
[8] IAEA, "Nuclear Power Reactors in the World (2025 Edition)," INTERNATIONAL ATOMIC ENERGY AGENCY, 2025. doi: 10.61092/IAEA.1G28-W3UK.
[9] A. Stakhanova, F. Gabrielli, V. H. Sanchez-Espinoza, E. M. Pauli, and A. Hoefer, "UNCERTAINTY AND SENSITIVITY ANALYSIS OF THE ASTEC SOURCE TERM RESULTS OF A MBLOCA SCENARIO WITH THE ACTIVATION OF SEVERE ACCIDENT MANAGEMENT ACTIONS IN A GENERIC KONVOI PLANT," *Proceeding of the ERMSAR2024*, 2024.
[10] F. Mascari *et al.*, "Main outcomes of the Phebus FPT1 uncertainty and sensitivity analysis in the EU-MUSA project," *Ann. Nucl. Energy*, vol. 196, no. October 2023, 2024, doi: 10.1016/j.anucene.2023.110205.
[11] L. E. Herranz *et al.*, "Major Achievements of the EC MUSA Project," *Nucl. Technol.*, pp. 1–11, Feb. 2025, doi: 10.1080/00295450.2024.2444081.

12th CONFERENCE ON
SEVERE ACCIDENTS RESEARCH
May 18-22, 2026 – Madrid, Spain
ERMSAR 2026

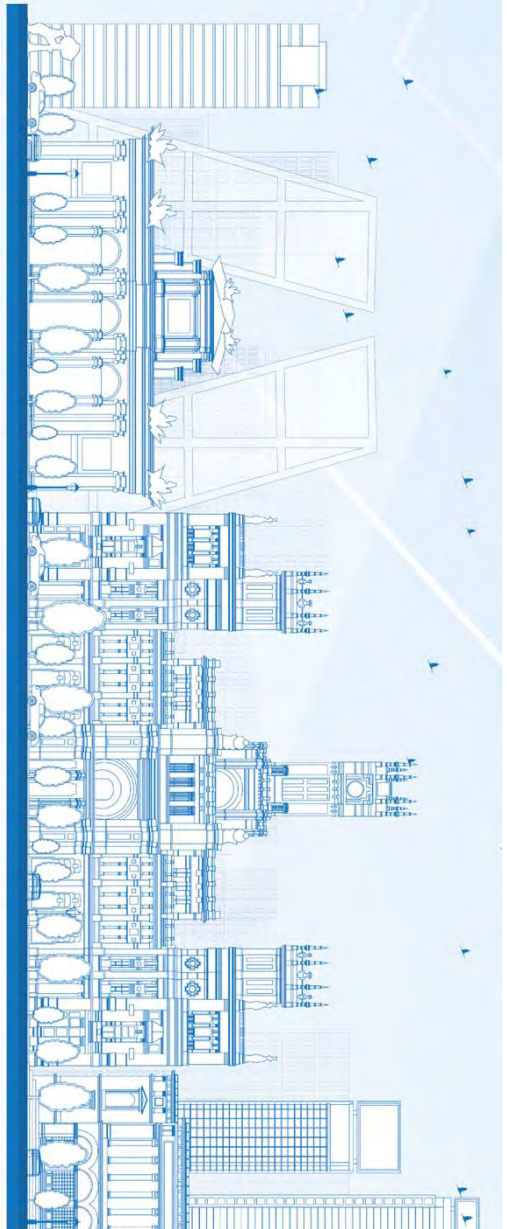

INTEGRATED SEVERE ACCIDENT ANALYSIS FOR A VVER 1000

ACCIDENT PROGRESSION, UNCERTAINTY QUANTIFICATION AND RADIOLOGICAL CONSEQUENCES

M. Angelucci, L. Marzullo, A. Stakhanova,
O. Murat, F. Gabrielli, S. Paci

KIT

UNIVERSITÀ DI PISA

ACKNOWLEDGEMENTS

This work is framed within the SEAKNOT project under the Grant Agreement no. 101060327. Views and opinions expressed are, however, those of the authors only and do not necessarily reflect those of the European Union. Neither the European Union nor the granting authority can be held responsible for them.

CONTENTS

MOTIVATION & OBJECTIVE

COMPUTATIONAL FRAMEWORK

RESULTS

CONCLUSIONS

MOTIVATION

THE OBJECTIVE OF NUCLEAR SAFETY IS «TO PROTECT PEOPLE AND ENVIROMENT FROM HARMFUL EFFECTS OF IONIZING RADIATION».

THIS IS PARTICULAR RELEVANT IN THE CASE OF SEVERE ACCIDENTS, WITH CORE MELTDOWN AND POTENTIAL RADIOACTIVE RELEASE.

IN SUCH SCENARIOS, THE TIMELY AND RELIABLE ESTIMATION OF THE SOURCE TERM IS A KEY ELEMENT FOR EMERGENCY DECISION-MAKING AND RADIOLOGICAL CONSEQUENCES ASSESSMENT.

MOTIVATION

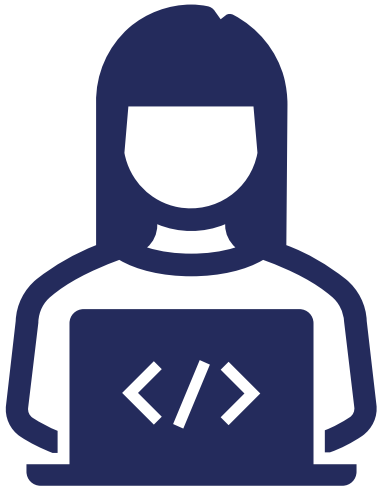

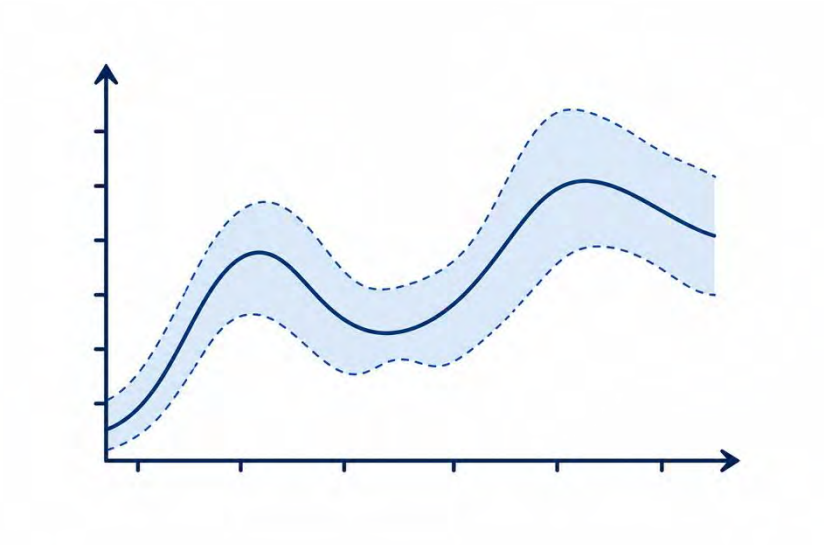

UNCERTAINTY IN THE SOURCE TERM PREDICTION DIRECTLY PROPAGATES INTO EMERGENCY DECISION-MAKING AND RADIOLOGICAL CONSEQUENCE ASSESSMENT

OBJECTIVE

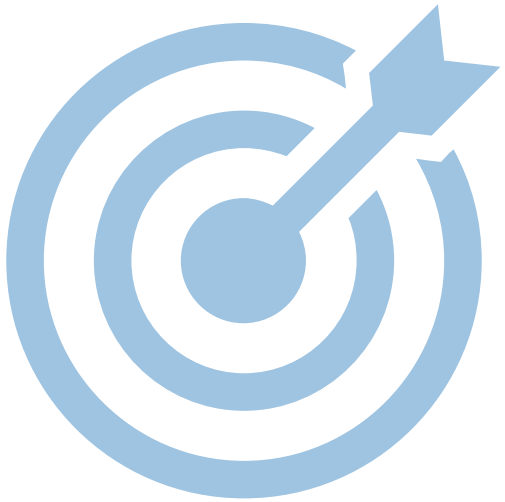

INTEGRAL ANALYSIS FRAMEWORK:

- SA SIMULATIONS
- UNCERTAINTY QUANTIFICATION
- RADIOLOGICAL CONSEQUENCES ASSESSMENT

IMPORTANCE OF UNCERTAINTY-INFORMED ANALYSIS

VVER1000/320

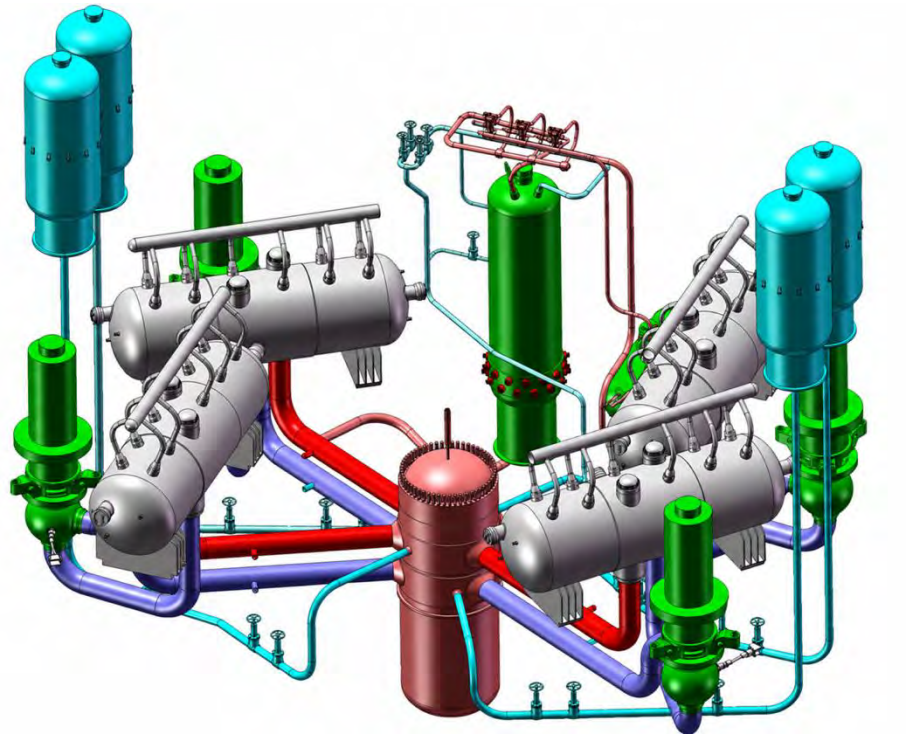

[1]

~30 VVER1000 UNITS
IN OPERATION NOWADAYS

RUSSIA, CHINA AND
EASTERN EUROPE

REPRESENTATIVE OF
GEN.II VVER REACTORS

ACCIDENT SCENARIO

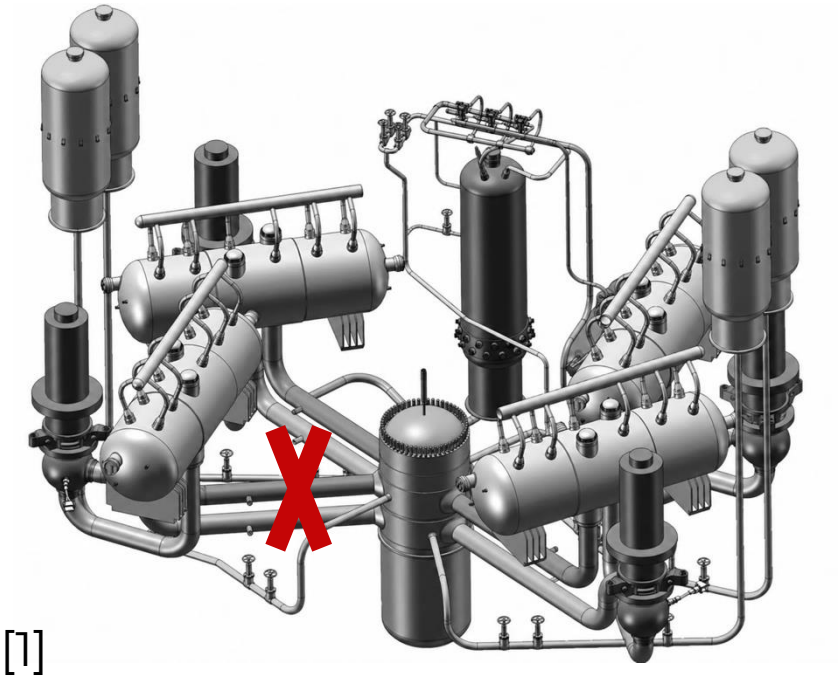

[1]

LBLOCA on the hot leg

SBO – no AC power supply
no active safety systems

NO SAM actions

NO FCVS

INTEGRATED FRAMEWORK

ASTEC

SEVERE ACCIDENT SIMULATION

KATUSA

UNCERTAINTY & SENSITIVITY ANALYSIS

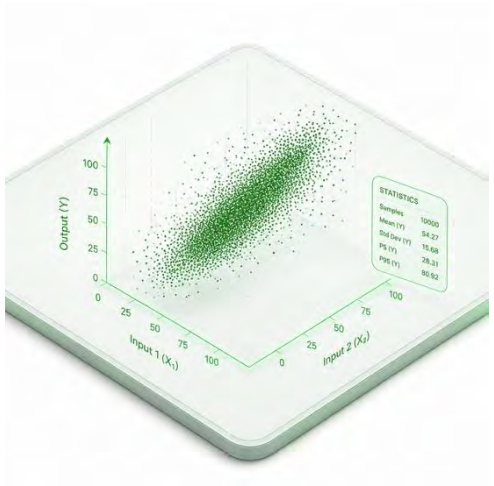

JRODOS

ATMOSPHERIC DISPERSION & DOSE ASSESSM.

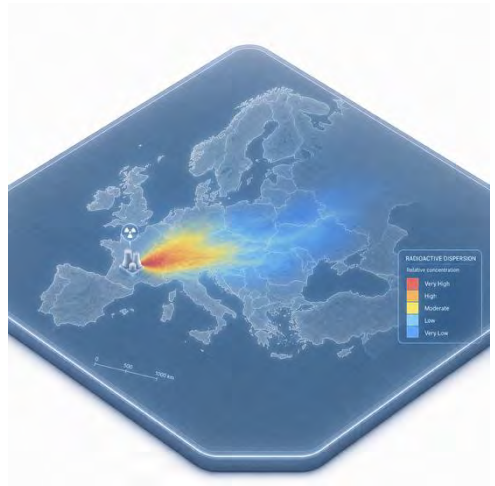

ASTEC MODEL

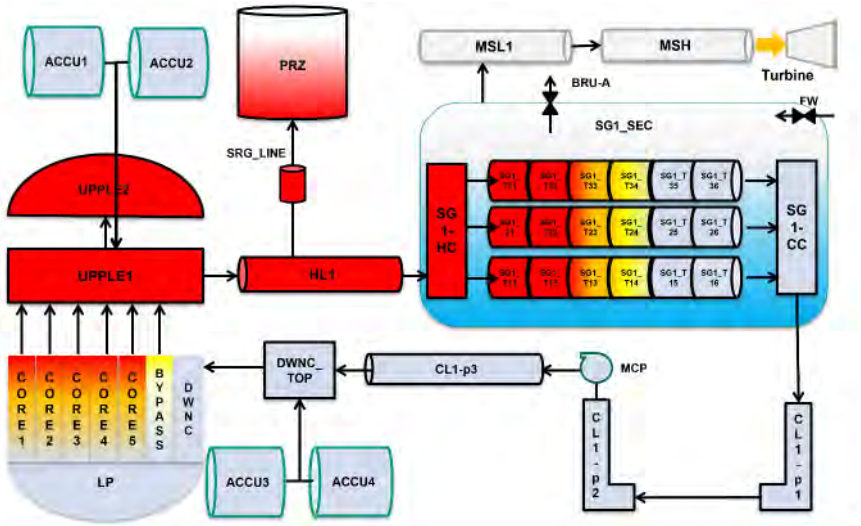

[2]

CONTAINMENT

FPs RELEASE
& TRANPORT

ASTEC 3.1.1

IN-VESSEL
& EX-VESSEL

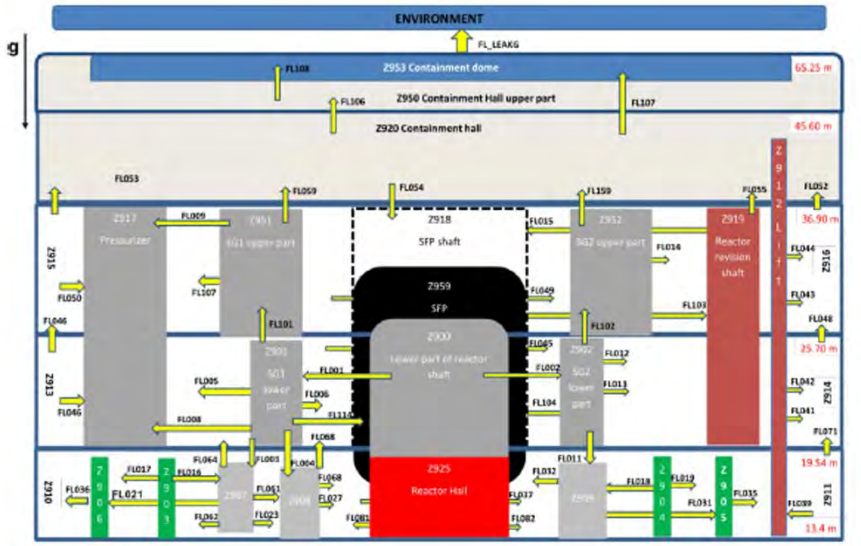

TIMELINE – ACCIDENT PROGRESSION

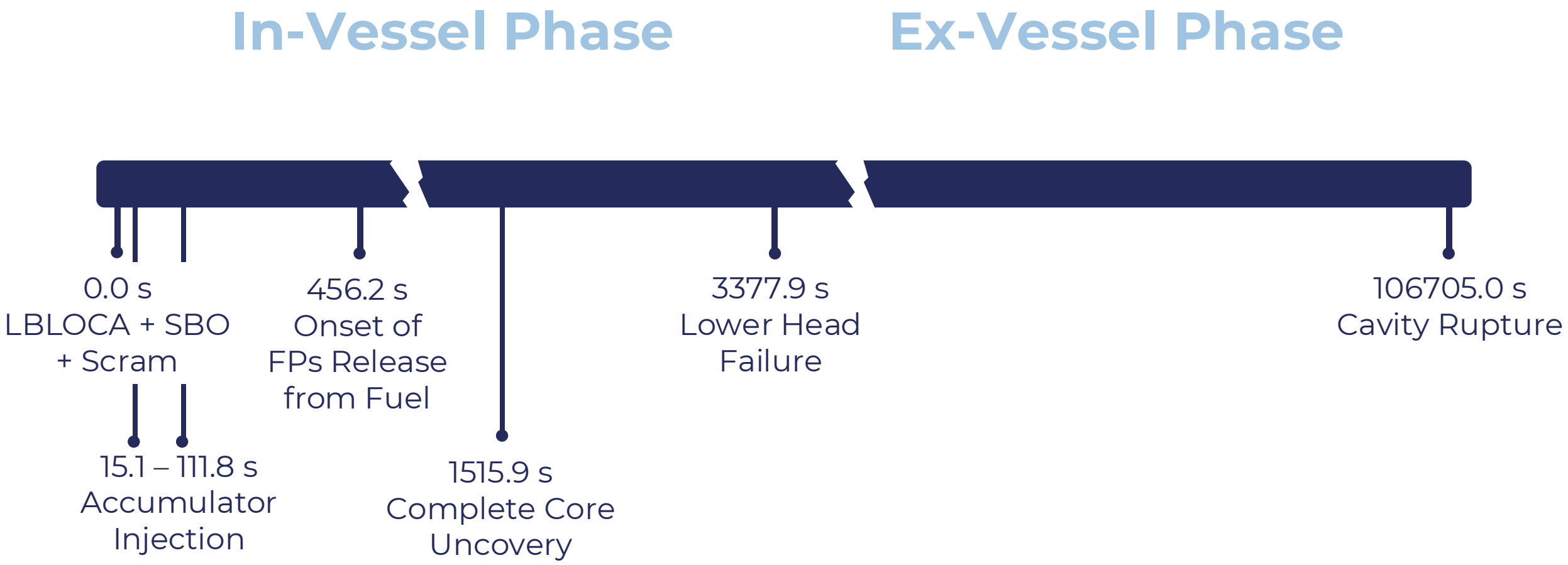

SOURCE TERM

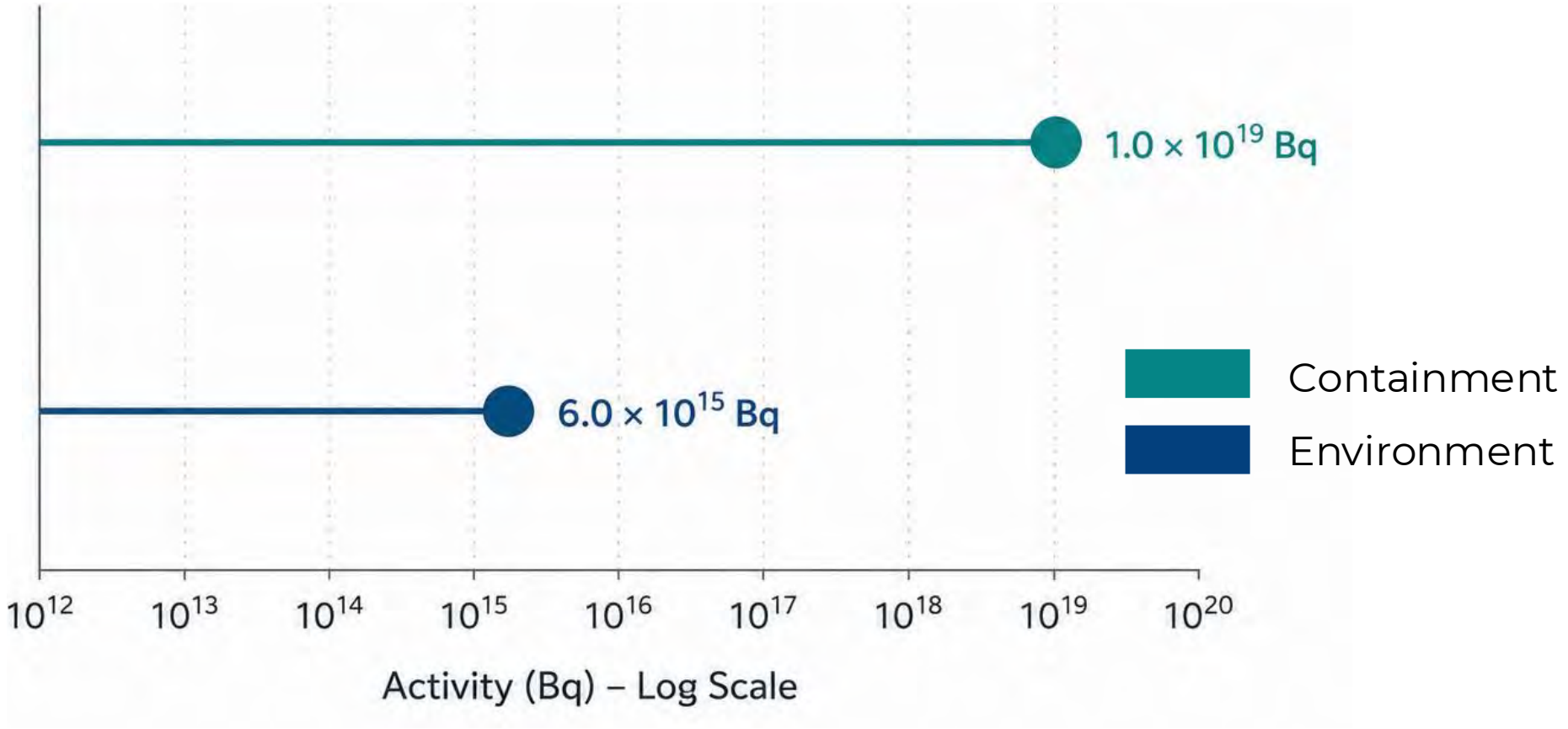
1.0 × 10^19 Bq
6.0 × 10^15 Bq
10^12
10^13
10^14
10^15
10^16
10^17
10^18
10^19
10^20
Activity (Bq) – Log Scale
Containment
Environment

ISOTOPE DISTRIBUTION

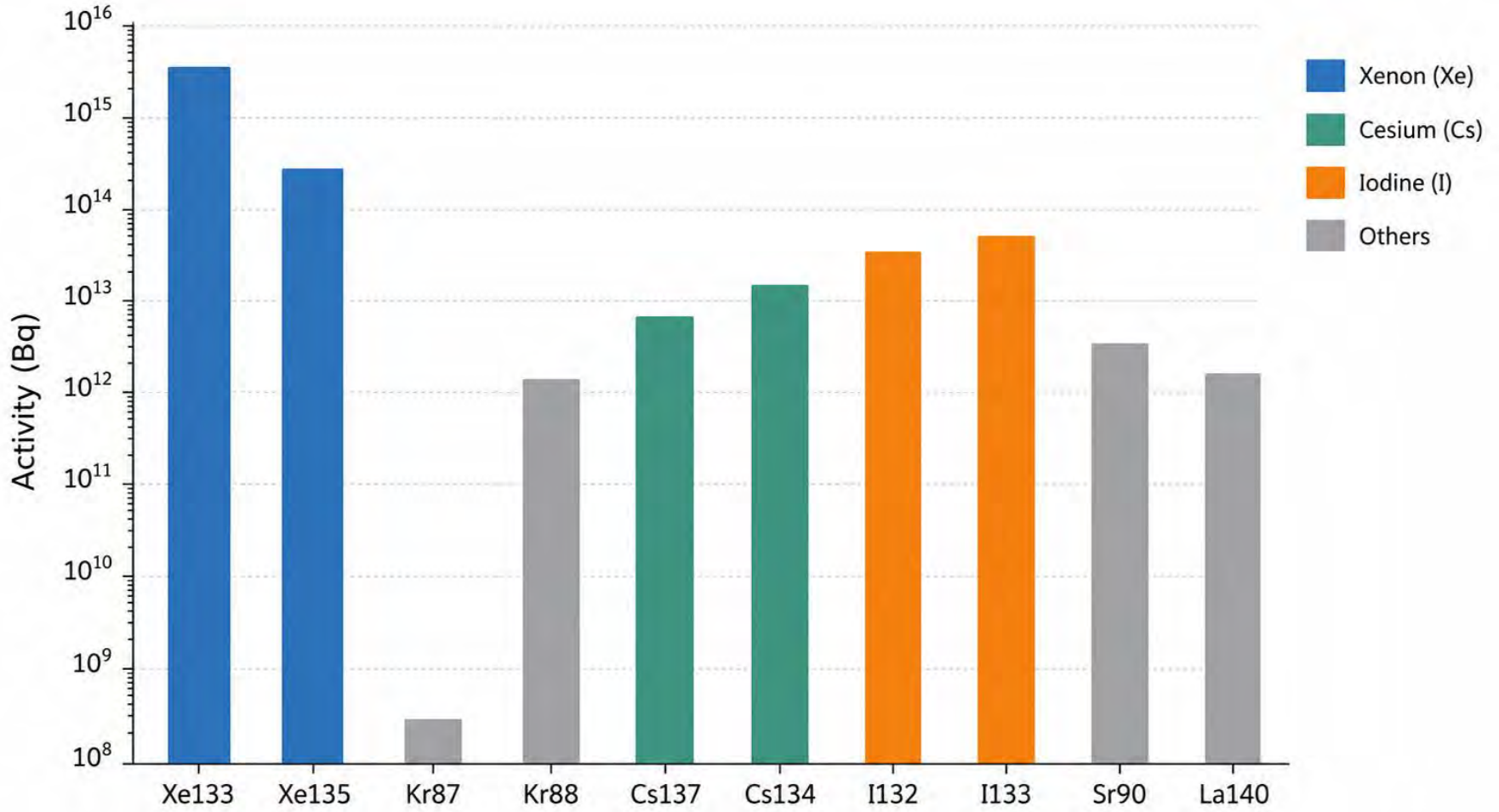

UA SETUP

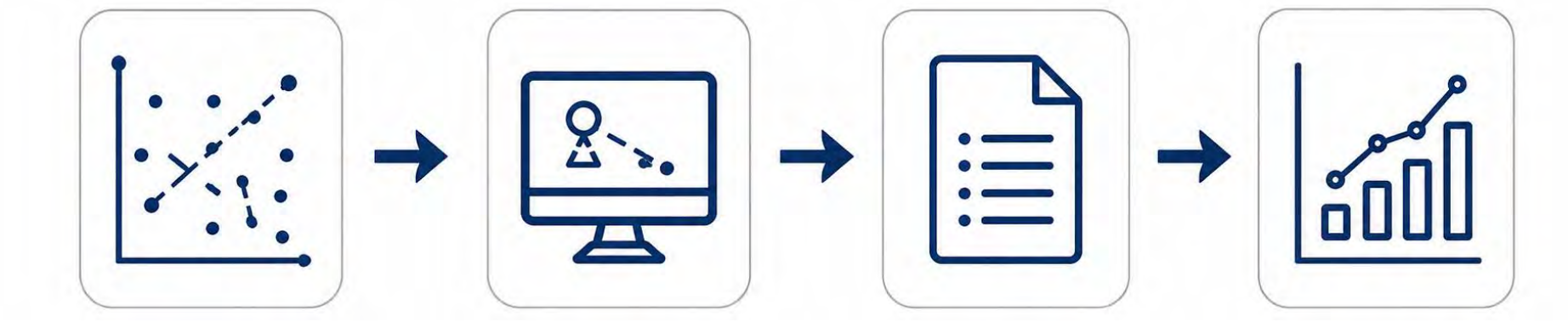

1. SAMPLING

2. ASTEC SIMULATIONS

3. FOMs EXTRACTION

4. STATISTICS & CORRELATIONS

UA SETUP

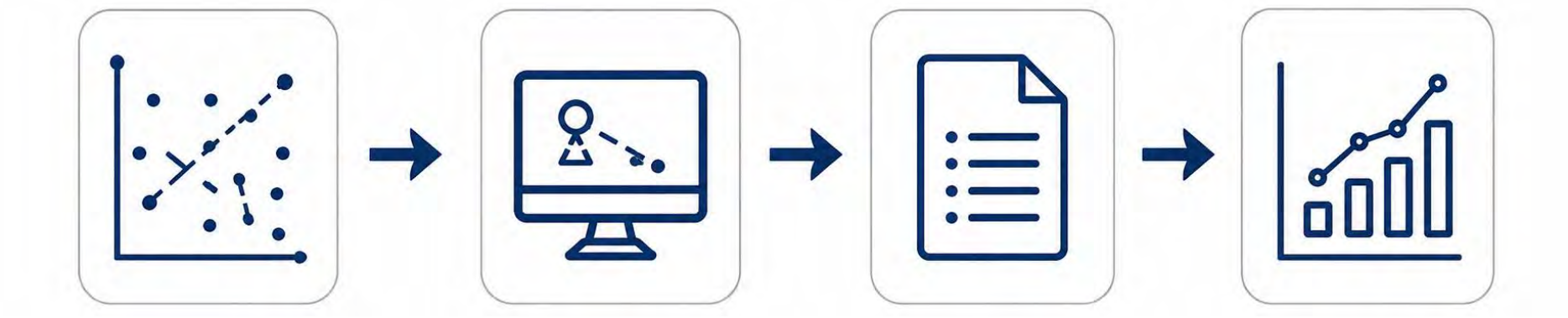

I. SAMPLING → 2. ASTEC SIMULATIONS → 3. FOMs EXTRACTION → 4. STATISTICS & CORRELATIONS

INPUT UNCERTAIN PARAMETERS

- AEROSOL BEHAVIOR
- FUEL BURNUP
- CONTAINMENT LEAKAGE

UA SETUP

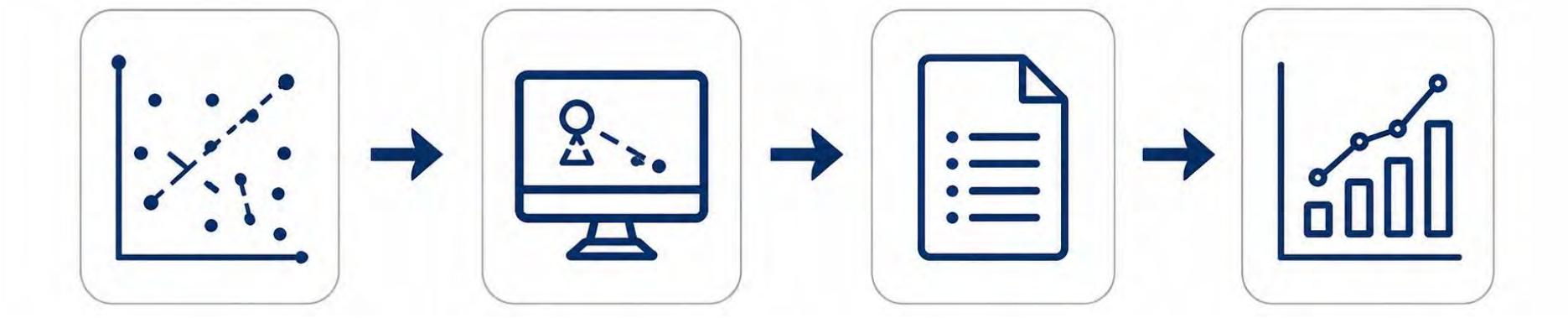

I. SAMPLING

2. ASTEC SIMULATIONS

3. FOMs EXTRACTION

4. STATISTICS & CORRELATIONS

150 RUNS

FAILED CALCs EXCLUDED

UA SETUP

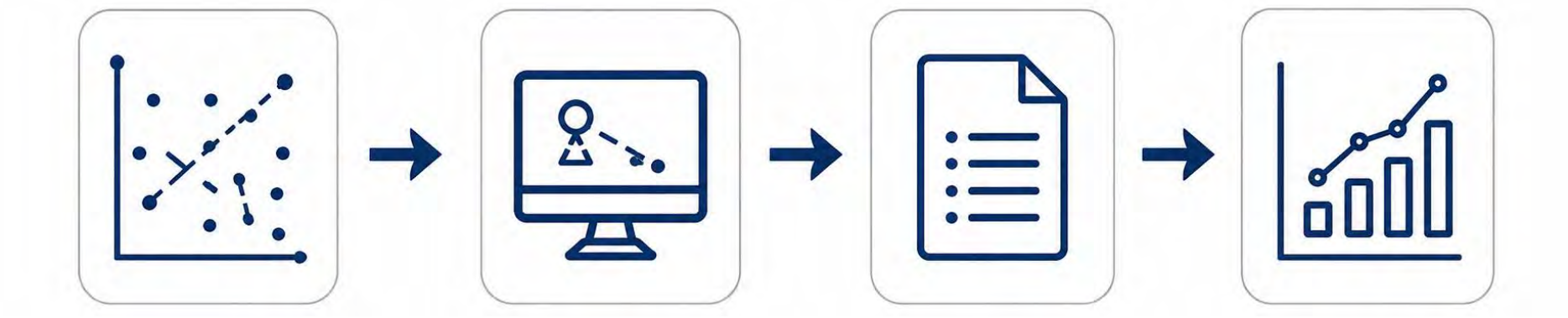

I. SAMPLING

2. ASTEC SIMULATIONS

3. FOMs EXTRACTION

4. STATISTICS & CORRELATIONS

FIGURES OF MERIT

ONSET OF FP RELEASE

ACTIVITY TO THE ENVIRONMENT

ISOTOPE DISTRIBUTION

UA SETUP

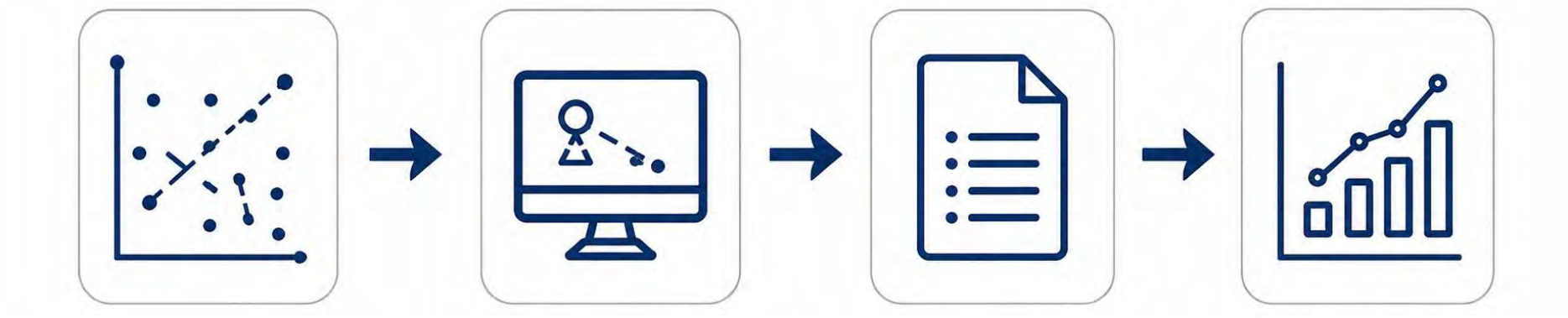

I. SAMPLING

2. ASTEC SIMULATIONS

3. FOMs EXTRACTION

4. STATISTICS & CORRELATIONS

CORRELATION COEFFICIENTS

PEARSON CC

SPEARMAN CC

UA RESULTS: UNCERTAINTY BAND

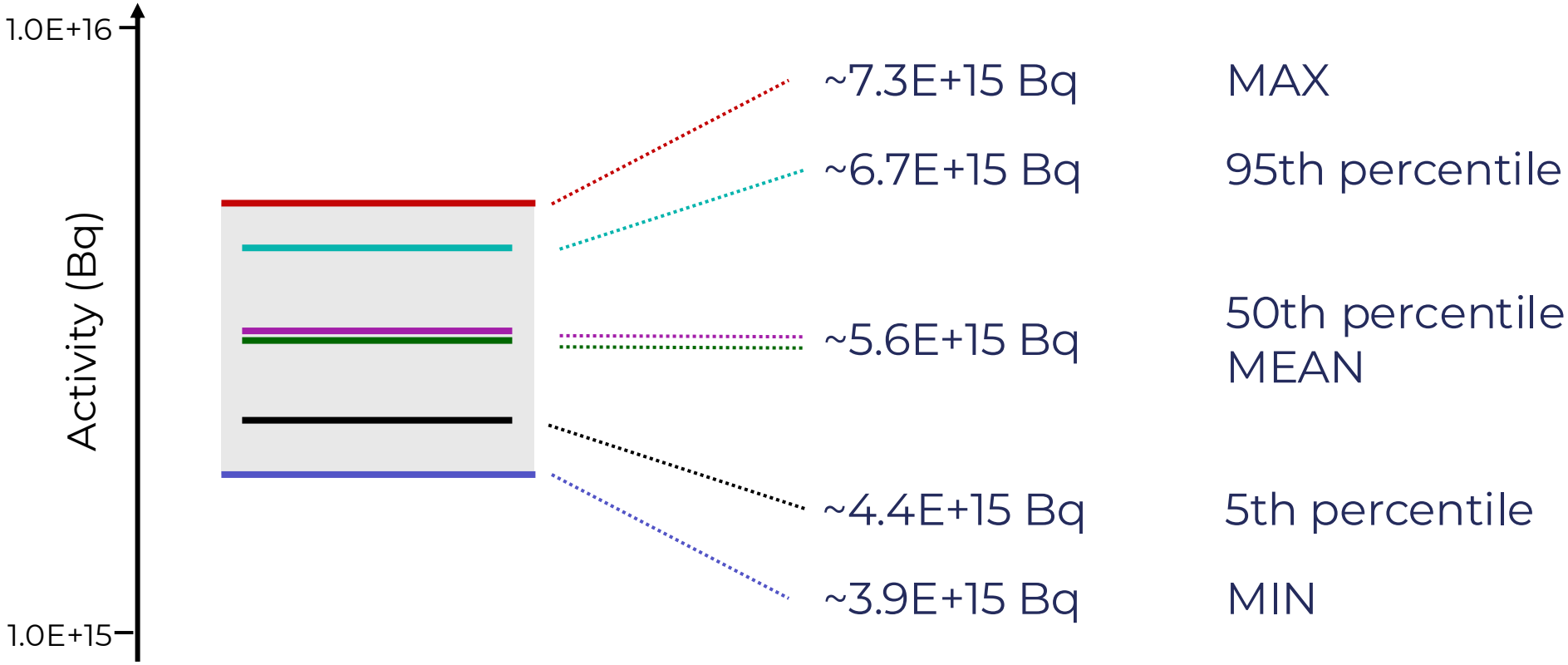

UA RESULTS: UNCERTAINTY BAND

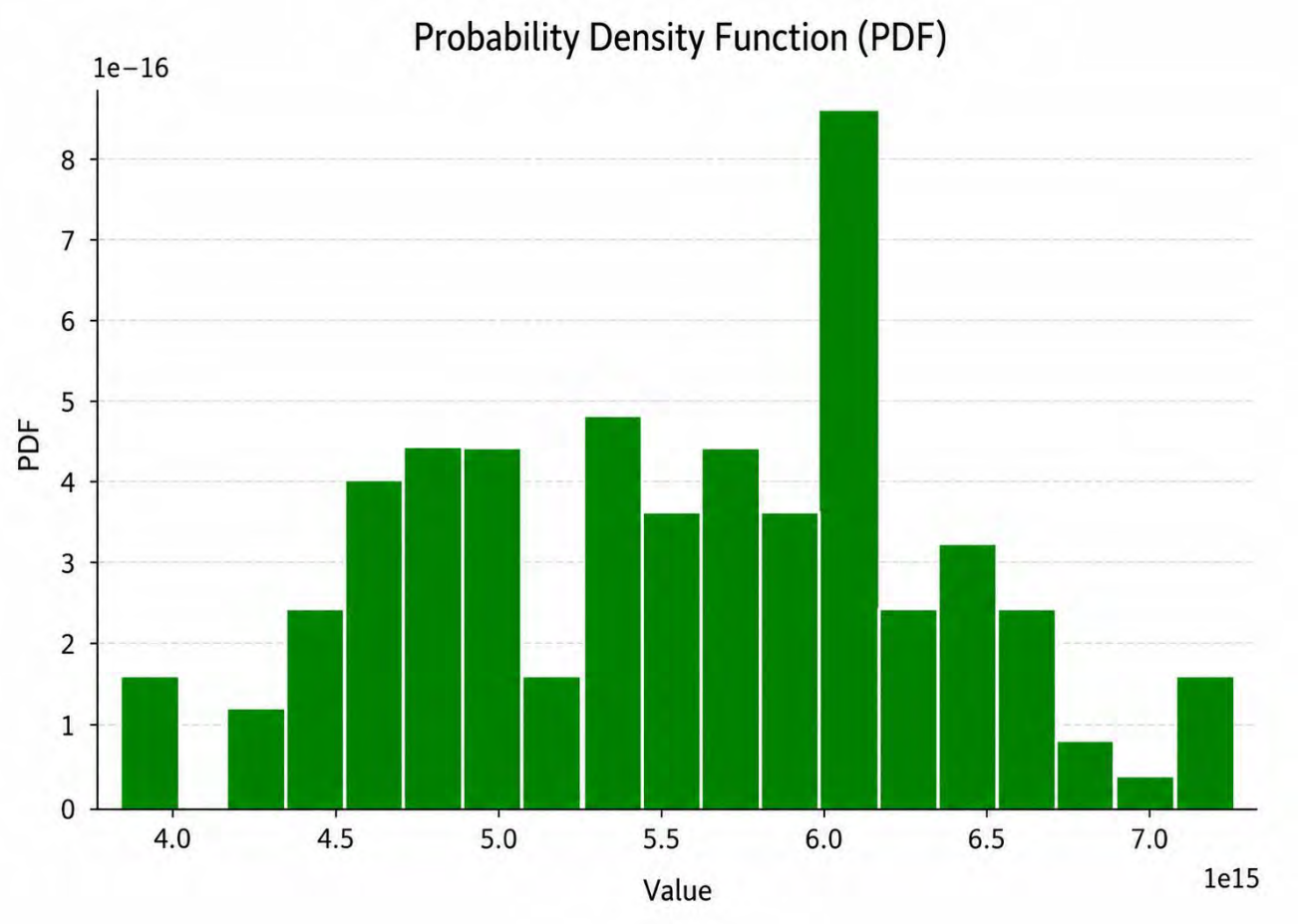

MOST PROBABLE VALUE
6.18E+15 Bq

MAXIMUM VALUE
7.28E+15 Bq

SENSITIVITY ANALYSIS

FOM:
ACTIVITY TO THE ENVIRONMENT

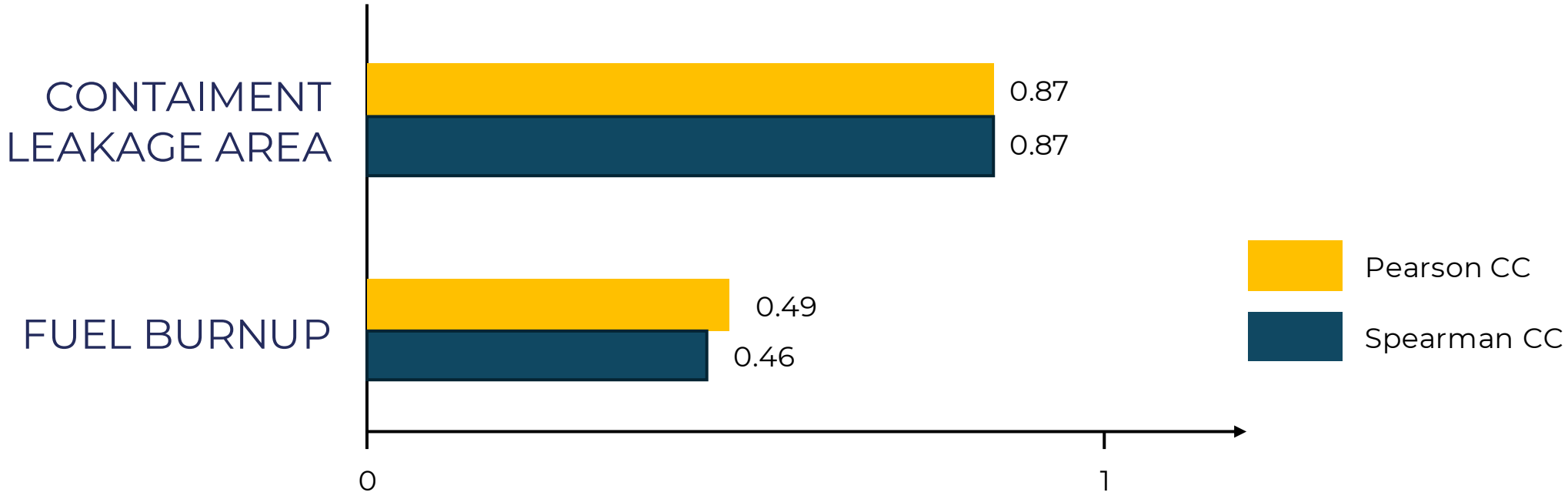

JRODOS SETUP

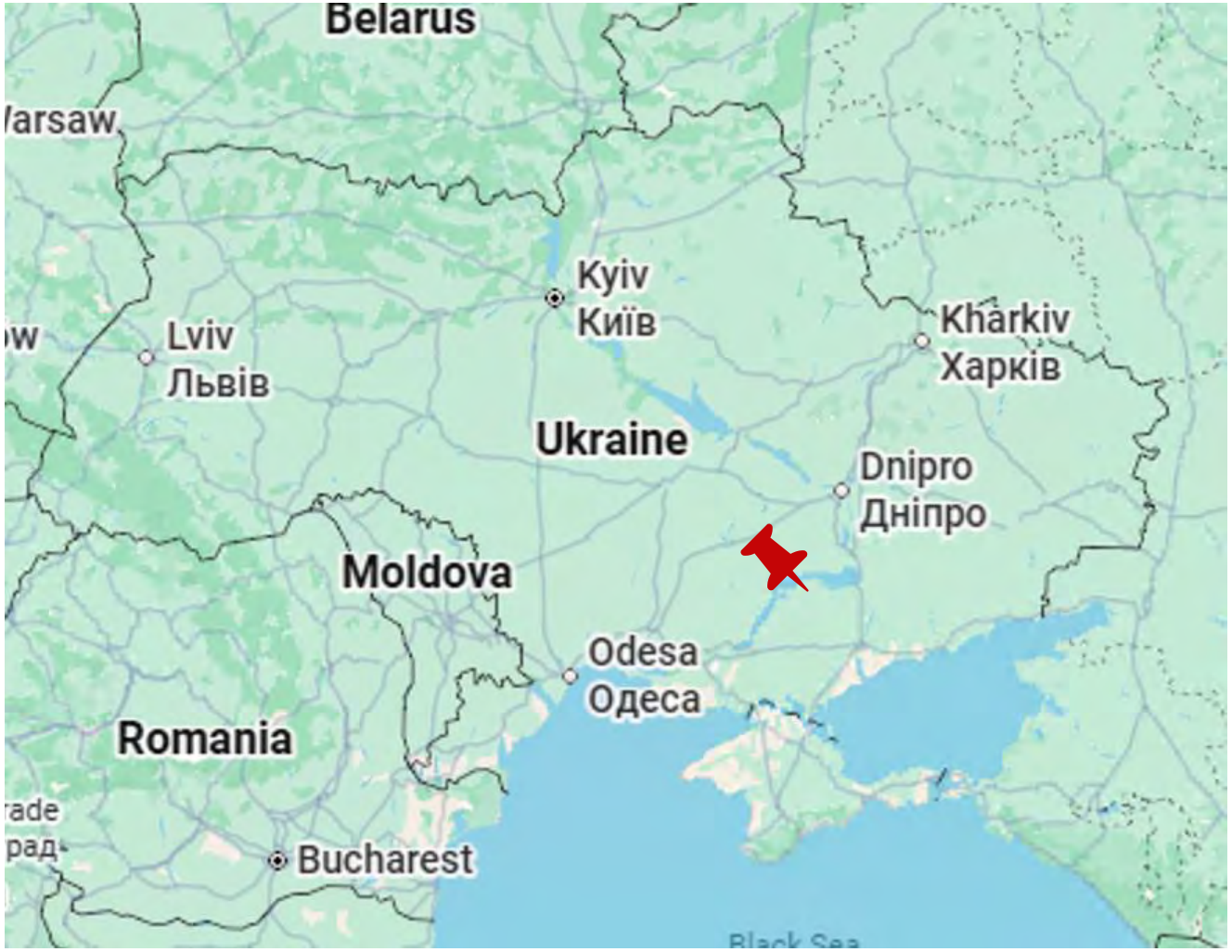

LOCATION:
ZAPORIZHZIA NPP

METEOROLOGY:
SUMMER & WINTER

AREA:
640000 KM^2

POPULATION:
37630232 INHABITANTS

CALCULATION TIME:
42 HOURS

GROUND DEPOSITION

SUMMER

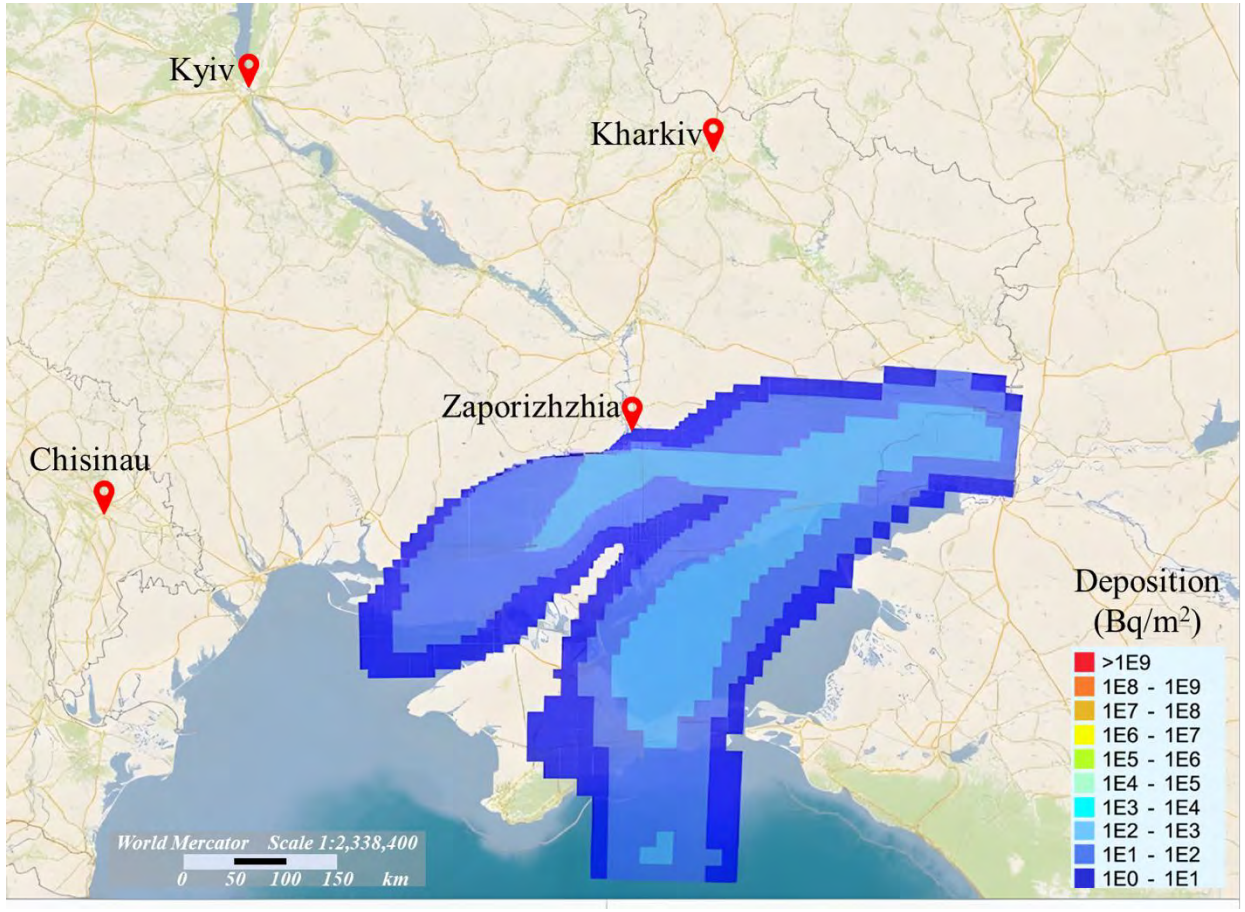

WINTER

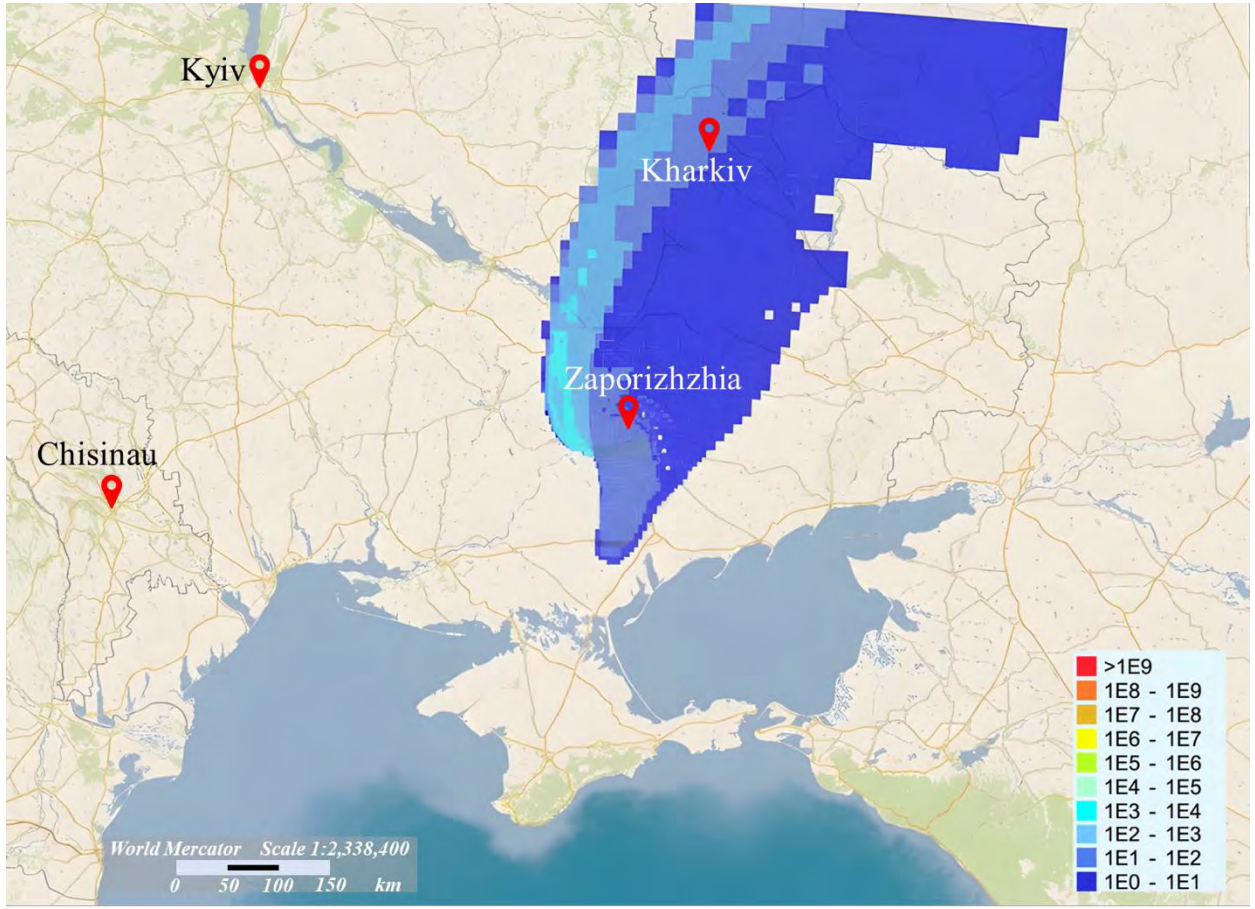

EFFECTIVE DOSE (lifetime)

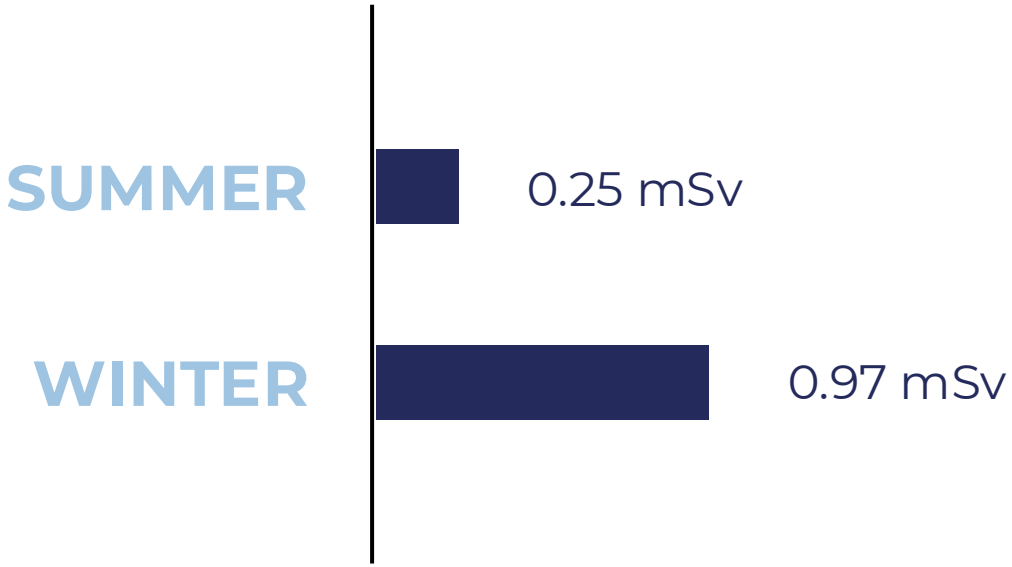

INTERVENTION THRESHOLDS	
10 mSv	SHELTERING
10 mSv	KI ADMINISTRATION (CHILDREN)
50 mSv	EVACUATION
100 mSV	KI ADMINISTRATION (ADULTS)

CONCLUSIONS

- THE INTEGRATED ASTEC-KATUSA-JRODOS FRAMEWORK ALLOWS THE SYSTEMATIC EVALUATION OF ACCIDENT PROGRESSION, RADIOLOGICAL SOURCE TERM, AND OFF-SITE CONSEQUENCES WITHIN A UNIFIED AND COHERENT ANALYSIS CHAIN.

- THE STUDY REITERATES THE IMPORTANCE OF UNCERTAINTY AND SENSITIVITY ANALYSIS IN THE ASSESSMENT OF THE SOURCE TERM.

- UNCERTAINTY-INFORMED RESULTS MIGHT BE DIRECTLY USE IN DECISION-MAKING TOOLS.

OUTLOOK
FUTURE WORK

SAM STRATEGIES

CONTAINMENT MITIGATION SYSTEMS

DIFFERENT SITE LOCATIONS

DIFFERENT METEOROLOGICAL CONDITIONS

DIFFERENT ACCIDENTAL SCENARIOS

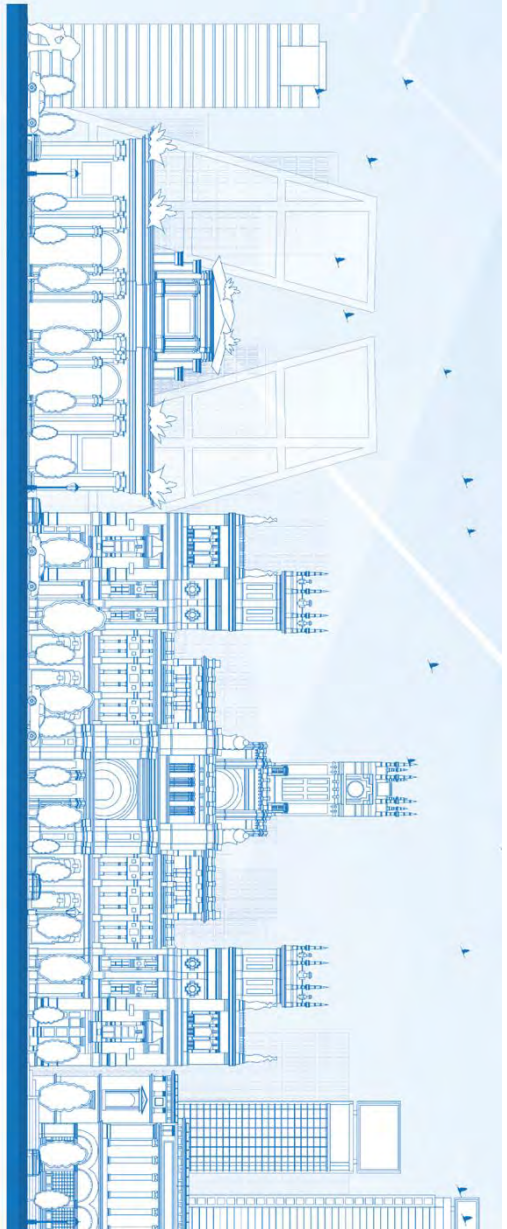

THANK YOU FOR YOUR ATTENTION!!

michela.angelucci@unipi.it

https://www.linkedin.com/in/michela-angelucci-02829114b

References

[1] Z. Tabadar, S. Aghajanpour, M. Jabbari, M. Khaleghi, M. Hashemi-Tilehnoee, Thermal-hydraulic analysis of VVER-1000 residual heat removal system using RELAP5 code, an evaluation at the boundary of reactor repair mode, 2018
[2] https://publikationen.bibliothek.kit.edu/1000167141

INPUT PARAMETERS

Parameter	Description	Reference Value	Variation Range	PDF
frho	Particle mean density (kg/m3)	3000.0	2610.0 10000.0	Triangular Mode: 3000.0
fR_max	Particle max radius (m)	1.995E-5	5.0E-6 2.0E-5	Triangular Mode: 1.995E-5
fR_min	Particle min radius (m)	1.1E-8	1.0E-8 2.0E-7	Triangular Mode: 1.1E-8
fspheat	Particle mean specific heat (J/kgK)	840.0	71.0 960.0	Uniform
fv_stks	Shape factor relative to Stokes velocity	1.0	1.0 3.0	Beta Alpha: 1.0 Beta: 5.0
p_bu	Effective full power days	164.0	10.0 320.0	Uniform
f_leak	Containment leakage area	1.0	0.8 1.2	Uniform

The 12th European Review Meeting on Severe Accidents Research

May 18-22, 2026, Universidad Carlos III de Madrid, Madrid, Spain

TECHNICAL SESSION 2.2: IN-VESSEL CORIUM AND DEBRIS COOLABILITY

Chairs: X. Gaus-Liu (KIT), F. Fichot (ASNR)

ID066	**Direct numerical evaluation of core equivalent conductivity: a comparative analysis of open rod and flat plate assemblies** R. Le Tellier (CEA)	Paper Presentation
ID151	**Experimental Investigation of Debris-Bed Formation for Optimizing Core-Catcher Design** T. Mashiko (University of Tokyo)	Paper Presentation
ID115	**A comparison of EATF and Zircalloy-4 cladding behaviour under severe accident conditions from 1600°C till 1970°C in steam/argon atmosphere** P. Piluso (CEA)	Paper Presentation

DIRECT NUMERICAL EVALUATION OF CORE EQUIVALENT CONDUCTIVITY: A COMPARATIVE ANALYSIS OF OPEN ROD AND FLAT PLATE ASSEMBLIES

R. Le Tellier
CEA, DES, IRESNE, DTN, Cadarache
F-13108 Saint Paul-lez-Durance, France
romain.le-tellier@cea.fr

E. Saïkali, A. Calloo
Université Paris Saclay, CEA, DES, ISAS, DM2S
F-91191, Gif-sur-Yvette, France
elie.saikali@cea.fr; ansar.calloo@cea.fr

ABSTRACT

Radiation is an important mode of heat transfer when investigating loss of coolant accidents in light water nuclear reactors. For small reactors, it plays a decisive role as a mode of heat exchange in some phases of accidents, even overtaking gas convection. However, modelling radiative heat transfer in a reactor core is not straightforward because of its complicated geometry. Accordingly, in codes that simulate the accident sequence, approximate lumped parameter models are used. In very general terms, they are built from a combination of net radiation enclosure models and equivalent conductivity models. Regarding the latter homogenization approach, valid for an optically thick medium, different approximate models have been proposed in the literature with a specific focus on open rod geometries (typical of Pressurized Water Reactors). Little interest have been shown in cores composed of closed flat plate assemblies despite the fact that they can be found in various reactor designs ranging from material testing reactors to space thermal propulsion reactors. In the present work, the equivalent conductivity is evaluated by direct numerical simulations of conjugate radiative and conductive heat transfer modes on spatial domains representative of both types of core geometries. A comparison is provided, taking also into account the approximate model in use in the RADR model of the ASTEC code. In addition, the effects of the lattice heterogeneities due to guide tubes and control rods in the open rod case are analyzed.

KEYWORDS
Radiative heat transfer, conduction, equivalent conductivity

1. INTRODUCTION

Loss-of-Coolant Accidents (LOCAs) represent critical design-basis events for light water nuclear reactors. During such accidental transients, radiative heat transfer becomes a pivotal mechanism for heat dissipation, as the liquid coolant can no longer effectively remove heat from the core. For small reactors, currently under active development all over the world, this mode of heat transfer is especially significant as its relative importance in comparison with heat removed by gas convection is increased. Because of the complex

dependency of Zircaloy cladding oxidation to temperature (with a strong escalation typically above 1800K), bifurcations in the core degradation transients can be observed depending on the heat removal; accordingly, it is sensitive to radiative heat transfer as illustrated, for instance, in [1].

Modeling radiative heat transfer in a reactor core is not straightforward because of its complicated geometry that can evolve with time during core degradation. Accordingly, in codes that simulate the accident sequence, approximate lumped parameter models are used. In very general terms, they are built from a combination of net radiation enclosure models (e.g. total exchange surface method [2]) and effective conductivity models (such as Rubiolo model proposed in [3, 4] and implemented in the RADR model of the ASTEC code [5]). While the former are used to describe the radiation between opaque and diffuse surfaces through a fluid for well-defined geometrical configurations, the latter are diffusion models based on a porous medium approach. Regarding the net radiation enclosure models, in thermalhydraulics system codes and severe accident codes, they are based on lumped surfaces and can yield highly inaccurate results because of the uniform surface temperature approximation on the one hand and the uniform radiosity surface assumption on the other hand. While the latter bias can be mitigated by correction factors [6] or suppressed by the Gebhart method [7], the former one remains and, as further analyzed in [8], can be predominant when the solid conductivity is low. Regarding the effective conductivity approach, it is valid for an optically thick medium (at the scale of the representative volume element used for homogenization). If this condition is met in reactor cores, its accuracy is dependent on the modelling of the equivalent conductivity $\underline{\underline{Ke}}$ associated with the anisotropic Fourier law $\boldsymbol{q} = -\underline{\underline{Ke}}\boldsymbol{\nabla} T$ with $\boldsymbol{q}$ the total heat flux vector and T the temperature field. It should also be noted that such an approach can be inadequate when the boundary effects are important *i.e.* the temperature jump between the porous medium and the enclosing boundary is large [3].

On the one hand, different approximate models for $\underline{\underline{Ke}}$ have been proposed in the literature with a specific focus on open rod geometries (typical of Pressurized Water Reactors – PWR) in the context of nuclear cores. Little work has been reported for cores composed of closed flat plate assemblies despite the fact that they can be found in various reactor designs ranging from Material Testing Reactors (MTR) (e.g. [9]) to space thermal propulsion reactors (see, for instance [10]). One noticeable exception is the work reported in [11] where Rubiolo model has been partially extended to such geometries.

On the other hand, a "brute force" approach to evaluate this conductivity is to simulate conjugate radiative and conductive heat transfer modes on a spatial domain representative of the core geometrical pattern under investigation. While this method is computationally intensive, it can be considered as a "reference" method useful for the validation of approximate algebraic models. It was used in [3] for instance.

The present work is focused on the comparison of $\underline{\underline{Ke}}$ radial component (*i.e.* in the plane perpendicular to the extrusion axis of the prismatic core) between a standard PWR (open rod geometry) and a plate assembly-based MTR. The equivalent conductivity is evaluated by direct numerical simulations on spatial domains representative of both cores. This analysis is supplemented by results obtained with Rubiolo model and its partial extension to the case of closed flat plate assemblies in [11]. The paper is organized as follows. First, numerical models and tools are introduced in Section 2 and illustrated on a validation test case taken from [3] in Section 3. Then, the configurations of interest associated with the two core types under consideration are presented in Section 4. The corresponding numerical results are discussed in Section 5. Finally, Section 6 gives short conclusions and perspectives.

2. METHODS

In this section, the two different methods that have been used to evaluate the equivalent conductivity of a 2D porous medium composed of opaque and grey solids (conductivity K_s, total emissivity ε_s) in a transparent

fluid (conductivity λ_g) are introduced. The "reference" method is based on the direct numerical simulation of conjugate radiative and conductive heat transfer modes on a spatial domain representative of the porous medium; in the remainder, the conductivity obtained with such an approach will be referred to as an apparent conductivity and denoted *Ka*. The Rubiolo model is an approximate algebraic model proposed in [3, 4] for a regular Cartesian lattice of cylindrical rods and partially extended to the case of closed flat plate assemblies in [11]; in the remainder, the associated equivalent conductivity is denoted *Ke*.

2.1. Direct numerical simulation approach

In order to evaluate the apparent conductivity, simulations of both radiative and conductive heat transfers on a 2D rectangular two-phase spatial domain $\mathcal{D}$ (see Figure 1) are performed considering the following boundary conditions:

$$\begin{aligned} T &= T_0 - \frac{\delta T}{2} \text{ and } \varepsilon = 1 && \text{on } \Gamma_L \\ T &= T_0 + \frac{\delta T}{2} \text{ and } \varepsilon = 1 && \text{on } \Gamma_R \\ \boldsymbol{\nabla} T \cdot \boldsymbol{n} &= 0 \text{ and specular reflection} && \text{on } \Gamma_U \cup \Gamma_B \end{aligned}$$

where T is the temperature, ε the emissivity, and $\boldsymbol{n}$ the outward normal on the domain boundary. With such symmetry boundary conditions at the top and the bottom, an infinite lattice along the *y*–axis is simulated in such a way that the apparent conductivity along the *x*–axis can be evaluated as:

$$Ka(T_0) = \frac{L_X \int_{\Gamma_L \cup \Gamma_R} |\boldsymbol{q} \cdot \boldsymbol{n}| \, ds}{2 L_Y \delta T} \tag{1}$$

where $\boldsymbol{q}$ is the total heat flux (conduction and radiation accounted in), L_X (resp. L_Y) is the domain length along the *x*–axis (resp. *y*–axis). In this approach, $\mathcal{D}$ is associated with a solid-fluid geometrical pattern deemed representative of the porous medium under consideration. Taking a unit emissivity on Γ_L and Γ_R (black boundaries), the boundary effect on the temperature gradient, in comparison with an infinite medium along the *x*–axis, is mitigated. This is the approach that was used for the partial validation of Rubiolo model presented afterwards in [3].

The coupled conduction-radiative heat transfer calculations were performed with the TrioCFD code [12], an open-source code (`https://triocfd.cea.fr/`) based on the TRUST numerical platform [13] (`https://cea-trust-platform.github.io/`), referred to as TRUST/TrioCFD. For our present applications, it couples conduction in the fluid and solid phases to radiation between the solid surfaces (considered as opaque, grey and diffuse) through the transparent fluid. The heat conduction equation is solved over triangular meshes considering a first order finite volume-element discretization. For radiative heat transfer, the radiosity equations are solved for a given partitioning of the solid surfaces. The associated view factors are obtained either from exact formulas (for the simple case of a rectangular cavity) or using the pyMCRAD numerical tool based on a Monte-Carlo Ray-Tracing method [8]; they are provided to TRUST/TrioCFD as input parameters. In practice, from a unique description of the geometry and the associated surface partitioning, the view factors are calculated (with pyMCRAD in the general case) and a meshing of the volumes is carried out with the gmsh tool [14]. From there, TRUST/TrioCFD calculations are performed. For more detail, the reader is referred to [8] where such calculations with these numerical tools have been first reported.

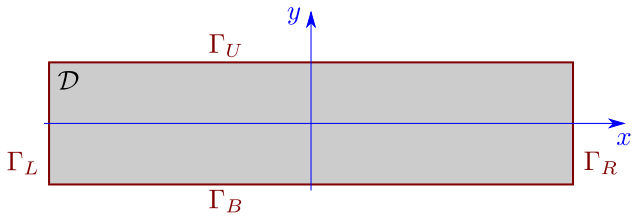

Figure 1. Notations associated with the geometrical domain $\mathcal{D}$ considered for coupled radiation-conduction calculations.

2.2. Rubiolo model

This algebraic model is based on a thermal resistance formalism where the possible coupling between radiative and conductive heat transfer modes is taken into account (contrarily to simpler models where they are supposed to act independently). For the sake of conciseness, the formulation of Rubiolo model is presented in Appendix A. For the purpose of this paper, the following model features should be kept in mind:

- This model is obtained considering a homogeneous solid phase in such a way that, when this phase is heterogeneous, it should be first replaced by an equivalent homogeneous medium characterized by an equivalent conductivity K_s. Considering the heterogenous nature of a fuel pin or a flat plate assembly, this homogenization step is crucial. To do so, a model was proposed and validated in [3] for a typical fuel pin geometry (a fuel rod in a clad with a gaseous gap, taking into account radiation through the gas). In [11], the same thermal resistance approach based on an electrical analogy was followed for flat plate assemblies and 2×2–arrangement of such assemblies; no validation was proposed.
- While this model formulation is rather general and does not depend directly on the porous medium structure, it requires closure laws that, in principle, should be defined on a case-by-case basis depending on the phase topology. In [3], the different closures were obtained for a regular Cartesian lattice of identical cylinders. If some closures are simply algebraic laws (some obtained under simplifying hypotheses), the closures associated with the equivalent conductive Kt and radiative Kr conductivities have been obtained in a precise way from the numerical simulations of closure problems. In the extension of this model to a regular Cartesian lattice of identical squares (for the flat plate assemblies) in [11], the associated closure problems were not solved to obtained new laws; the closure laws for the cylinders case were transposed.

In the case of open rod geometries (where all the rods are identical), the validation in [3] showed that the bias introduced by this model is lower than 10%. It is worth noting that, in the frame of this model, the difference in conductivity between an infinite lattice and a finite lattice can also be estimated.

3. VALIDATION TEST CASE

In order to validate the use of the pyMCRAD and TRUST/TrioCFD tools for evaluating the apparent conductivity of a geometric pattern, the case of a 10–rod pattern reported in [3] has been revisited. The associated analysis is summarized in this section.

For the evaluation of view factors, the surfaces of the rods are partitioned into 16, while the surfaces Γ_L and Γ_R are partitioned into 8. For TRUST/TrioCFD, the triangular mesh was generated considering a uniform characteristic mesh size of 0.2mm.

Before presenting the comparison results, several remarks should be made:

- First, it should be noted that in [3], as the tool used (CASTEM2000) did not allow for the treatment

of specular reflection conditions (for the evaluation of view factors), the geometric pattern considered had 4 rows of rods along the y–axis to minimize boundary effects (associated with the isotropic nature of the reflection on Γ_U and Γ_B) without significantly increasing the domain size. The associated bias (not present in our simulations with specular conditions) is said to be less than 2% in [3].

- In terms of boundary conditions for evaluating Ka at temperature T_0, in [3], it is considered $T = T_0$ on Γ_L and $T = T_0 + \delta T$ on Γ_R, which leads to an offset of $\delta T/2$ compared to our results where a centered difference was favored.
- In [3], the partitioning of the surfaces is comparable to the one used in the present paper, while the mesh is significantly coarser (about 3.5 times) but for second-order finite elements. The discretization error is said to be less than 1% in [3]. Our calculations suggest that this is indeed the case when the temperature (and conductivity) is sufficiently high, with a bias increasing as T_0 decreases.

Considering $\delta T = 50$K and varying T_0 in a range between 400K and 2800K (as in [3]), the apparent conductivity obtained with pyMCRAD and TRUST/TrioCFD is illustrated in Figure 2b in comparison with the results from [3] and the equivalent conductivity Ke of the infinite lattice calculated with Rubiolo model. If we compare the apparent conductivities, we can see that the relative difference is less 2%, except for the lowest temperature (below 1200K) where it increases to approximately 5%. Given the previous remarks on the calculations performed in [3] and adding the fact that the results from [3] were extracted by digitizing Figure 3.18 from [3] in PDF format, these results are deemed satisfactory and validate the combined tools pyMCRAD and TRUST/TrioCFD. The relative difference w.r.t. Rubiolo model is, at the most, of about 10% with an underestimation (resp. overestimation) of the conductivity for the highest (resp. lowest) temperature. It is worth noting that, in this case, the relative difference between the finite-size geometric pattern and an infinite lattice, as evaluated in the frame of Rubiolo model, is about -5% at 1900K and tends to be reduced when the temperature increases.

λ_g [W.m^{-1}.K^{-1}]	K_s [W.m^{-1}.K^{-1}]	ε_s [–]
0.01	10.0	0.5

(a) 10×1– homogeneous rod pattern – fuel pins in red – length is 5.01cm, pitch is 0.50cm.

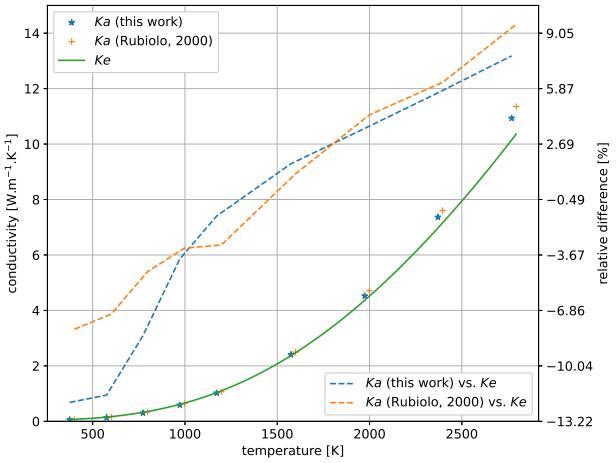

(b) Apparent and equivalent conductivities as a function of temperature.

Figure 2. Verification test case adapted from [3].

4. APPLICATION TEST CASES

For the intended comparative analysis between open rod and closed flat plate assemblies, the two considered assemblies are depicted in Figure 3. In terms of geometry, while the 17×17–rod open assembly (see Figure 3a) is a standard PWR assembly, the 24–flat plate closed assembly is taken from the fictitious MTR core proposed in [15] (previously considered for radiative heat transfer analysis in [8]). The pins and plates that compose theses two assemblies are depicted in Figure 4. In the case of the 17×17–rod open assembly,

two cases will be considered afterwards regarding the guide tube pins: either the guide tube is empty or an AgInCd pin is inserted inside.

In terms of materials, for the sake of comparison, in the 24–flat plate closed assembly, the same UO_2 and Zircaloy materials as in the 17×17–rod open assembly have been considered for the fuel and cladding of the plates.[1] The UO_2, Zircaloy and steel conductivity laws (as a function of temperature) are depicted in Figure 5a while AgInCd conductivity was taken constant equal to $60\text{W.m}^{-1}\text{.K}^{-1}$; all these data were taken from [16].

For the calculations performed afterwards, the different assembly elements have been homogenized following a thermal resistance approach based on an electrical analogy. For the cylindrical pins, the approach proposed in [3] (where radiative heat transfer through the gas gaps is taken into account) was followed and the conductivity laws obtained for the equivalent homogenized pins are illustrated in Figure 5b. For the plates (considered to be composed of layered infinite slabs), the analogy is very straightforward but, contrarily to the cylindrical pins where the equivalent conductivities can be considered isotropic, one has to distinguished between the conductivity parallel to the plate axis (denoted "fuel plate $\|$") and the one perpendicular to the plate axis (denoted "fuel plate $\perp$") as they significantly differ (see Figure 5b). Accordingly, in all subsequent calculations where plates are involved and can be oriented vertically or horizontally, an anisotropic thermal conductivity $\underline{\underline{K_s}}$ is considered with diagonal components $\underline{\underline{K_{s,xx}}} \neq \underline{\underline{K_{s,yy}}}$.

The different geometric patterns that have been considered for apparent conductivity calculations are depicted in Figure 6. For the open rod assembly, because of the guide tube pins location in the assembly, a pattern limited to three layers of pins was deemed sufficient for this study where the guide tube impact is studied. Regarding the closed plate case, different patterns have been studied in order to study the impact of the assemblies orientation in the core. The different test cases are summarized in Table I. The $2 \times 2-$ assembly case with a checkerboard arrangement is the one studied in [11]. This limited set of cases has been constructed in order to:

- Assess the effect of the heterogeneities introduced in the open rod lattice because of the guide tubes, either empty or with an AgInCd pin inserted.
- Assess the anisotropy effect for patterns of flat plate assemblies.
- Compare, for both types of assemblies, the evaluated apparent conductivities to the equivalent conductivities obtained with Rubiolo model.

In all cases, an emissivity ε_s of 0.8 has been taken, a value representative of oxidized Zircaloy.

■ ***Nota Bene*** In the remainder, the apparent and equivalent conductivities are evaluated over the $[250, 2750]$K temperature range for comparison purpose. Obviously, during a core heat-up transient, many important phenomena occur in such a way that geometrical configurations of Table I are not maintained over such a large temperature range as materials degrade and melt (typically above 1800K). In addition, AgInCd melting point is about 800°C. Accordingly, the quantitative results that have been obtained here should not be transposed directly to an actual accident transient. ■

In terms of meshing, a characteristic mesh size of 1mm has been used in all cases. For the view factors evaluation was considered as follows. The external surface of all rods (resp. square assemblies and flat plates) was partitioned in 16 (resp. 4×4). Γ_L and Γ_R were partitioned accordingly in such way that all partitioned surfaces have approximately the same area. A limited parametric analysis on these discretization parameters, not reported here, was carried out in such a way that the associated bias was found limited (to about 2% at the most).

[1] In [15], different materials are used for such a MTR core.

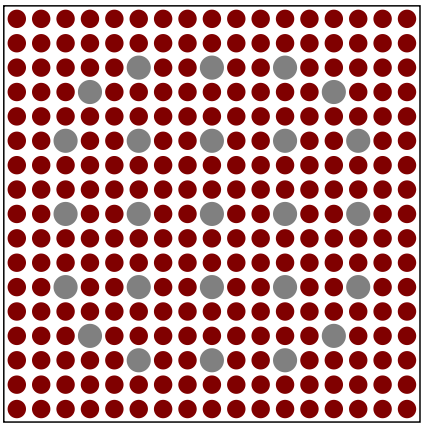

(a) 17 × 17–rod open assembly – fuel pins in red, guide tube pins in gray – length is 21.504cm, pitch is 1.26cm.

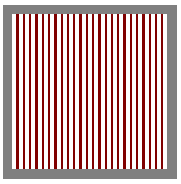

(b) 24–flat plate closed assembly – fuel plates in red, canister wall in gray – length is 9cm with a 0.5cm-thick canister wall.

Figure 3. The two assembly geometries considered (relative scale is preserved).

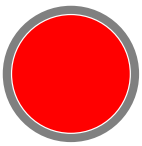

(a) Fuel pin (radii $\{0.4096, 0.418, 0.475\}$cm).

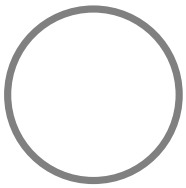

(b) Guide tube (radii $\{0.5725, 0.6225\}$cm).

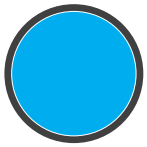

(c) AgInCd pin (radii $\{0.43, 0.437, 0.484\}$cm).

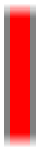

(d) Fuel plate (8-cm length – 1/8 shown – fuel thickness 0.14cm, clad thickness 0.038cm).

Figure 4. Geometries of the different assembly elements (relative scale is preserved) – UO_2 in red, AgInCd in cyan, Zircaloy in gray and steel in dark gray.

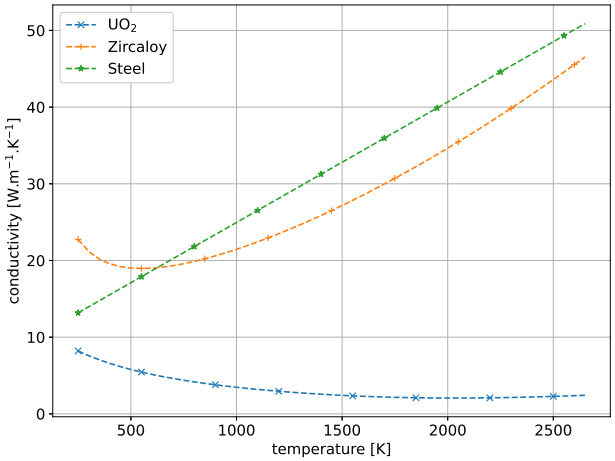

(a) Materials conductivities.

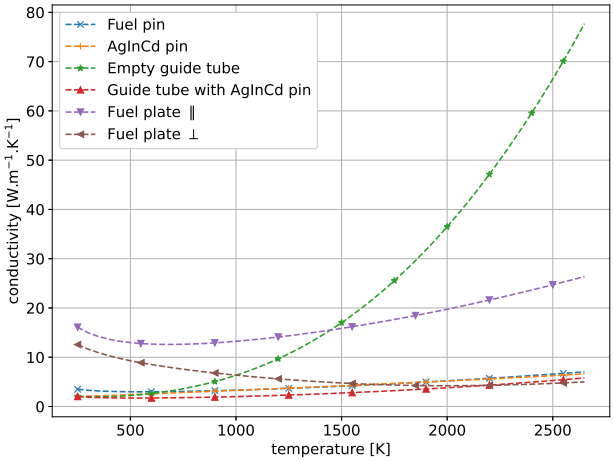

(b) Equivalent homogeneous pins and plates conductivities.

Figure 5. Conductivities as a function of temperature for the different materials and equivalent homogeneous pins and plates.

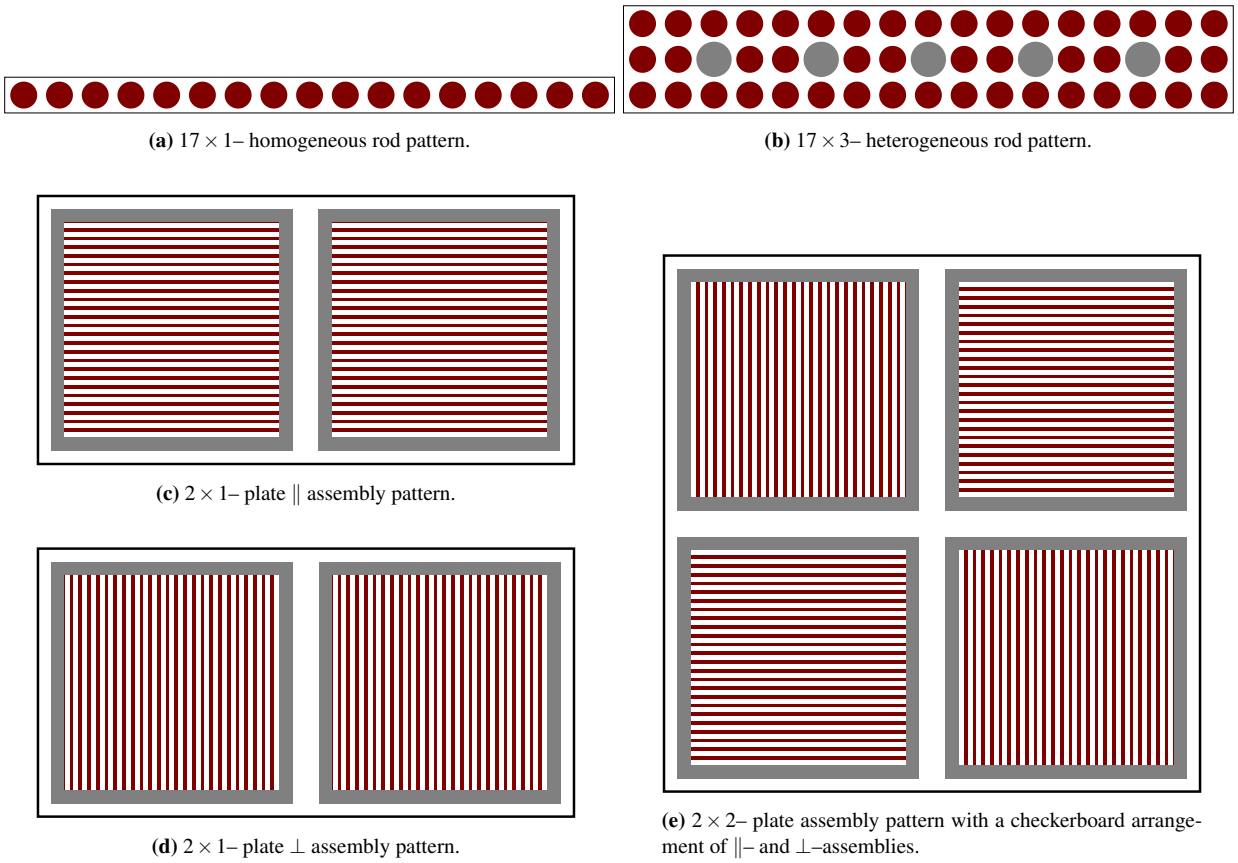

(a) 17×1– homogeneous rod pattern.

(b) 17×3– heterogeneous rod pattern.

(c) 2×1– plate $\parallel$ assembly pattern.

(d) 2×1– plate $\perp$ assembly pattern.

(e) 2×2– plate assembly pattern with a checkerboard arrangement of $\parallel$– and $\perp$–assemblies.

Figure 6. Geometrical patterns considered for the apparent conductivity evaluation (relative scale is preserved) – $\parallel$ assembly (resp. $\perp$ assembly) denotes an assembly with plates oriented along the x–axis (resp. y–axis) – in addition, a 4×2–pattern of flat plate assemblies has been used but is not shown.

Table I. The different test cases for apparent conductivity calculations.

Case	Geometrical pattern	Conductivities laws (cf. Figure 5)
$17 \times 1 -$ rod	Figure 6a	fuel pin
$17 \times 3 -$ rod, empty GT	Figure 6b	fuel pin, empty guide tube
$17 \times 3 -$ rod, AgInCd GT	Figure 6b	fuel pin, guide tube with AgInCd pin
$2 \times 1 -$ $\parallel$ assembly	Figure 6c	fuel plate $\perp$, fuel plate $\parallel$, steel
$2 \times 1 -$ $\perp$ assembly	Figure 6d	fuel plate $\perp$, fuel plate $\parallel$, steel
$2 \times 2 -$ assembly	Figure 6e	fuel plate $\perp$, fuel plate $\parallel$, steel

5. NUMERICAL RESULTS AND DISCUSSION

In Figure 7a, the apparent conductivity, as calculated with the pyMCRAD and TRUST/TrioCFD tools, is illustrated as a function of temperature for the three open rod cases. First, it is observed that the heterogeneity associated with the empty guide tubes (case $17 \times 3 -$ rod, empty GT) has a limited impact on the conductivity, with a variation between -3.5% and -1% compared to the homogeneous lattice case $17 \times 1 -$ rod. This effect is actually the combination of two opposing trends: if the guide tubes have a significantly higher conductivity than the fuel rods, they also have a larger radius that reduces heat transfer by radiation through

the gas. Next, when considering AgInCd pins in the guide tubes (case $17 \times 3 - \text{rod, AgInCd GT}$), a more significant decrease in Ka is observed compared to the case $17 \times 1 - \text{rod}$ (up to -12% at 2750K). Indeed, as seen in Figure 5b, the presence of AgInCd pins in the guide tubes drastically reduces the conductivity of the equivalent rod such that, compared to a fuel rod, there is both a lower conductivity of the solid phase and a reduced direct heat exchange by radiation through the gas. It is worth comparing these variations to the effect associated with the lattice size that, in the $17 \times 1 - \text{rod}$ case, can be estimated in the frame of Rubiolo model as discussed previously. It is found that the relative difference between the finite lattice and an infinite lattice is about -5% at 500K with a reduction to -2% at 2750K.

On the overall, considering that AgInCd melts at about 800°C, one may conclude that the lattice heterogeneities due to guide tubes and control rods in such an open rod configuration have a limited impact and that the use of Rubiolo model in such cases does not introduce a significant additional bias in comparison with the homogeneous lattice case.

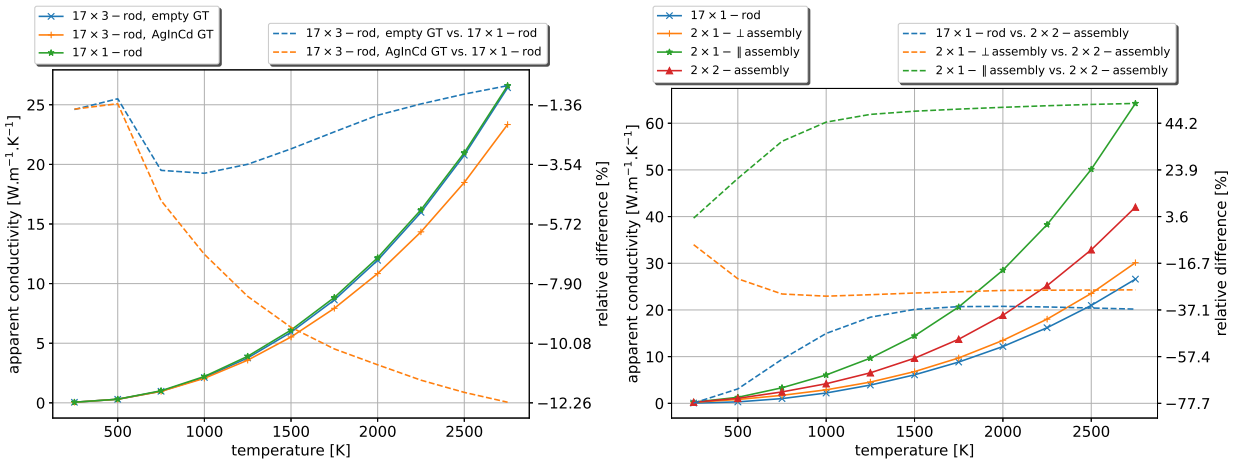

(a) Open rod cases.

(b) Flat plate assembly cases.

Figure 7. Apparent conductivities as a function of temperature for the different test cases.

The conductivity results for the flat plate assembly cases are depicted in Figure 7b where Ka in the $17 \times 1 - \text{rod}$ case has also been plotted for the sake of comparison. In any cases, the flat plate assembly patterns exhibit a significantly higher conductivity than the open rod pattern: in the upper temperature range (above 1500K), the conductivity relative increase between the $17 \times 1 - \text{rod}$ case and the $2 \times 2 - \text{assembly}$ case is about 35%. Then, comparing the $2 \times 1 - \parallel$ assembly and $2 \times 1 - \perp$ assembly cases, as expected, it is observed that when the plates are parallel to the heat flux, the apparent conductivity is higher. The difference increases when the temperature increases in such a way that, at 2750K, the conductivity of the $2 \times 1 - \parallel$ assembly case is 50% higher than in the $2 \times 1 - \perp$ assembly case. As expected again, the conductivity in the $2 \times 2 - \text{assembly}$ case is somewhere in between the parallel and perpendicular plate cases. It is worth comparing these variations to the effect associated with the number of assemblies considered in the geometric pattern. To do so, an additional calculation of a 4×2–pattern (the 2×2– plate assembly pattern being replicated along the x–axis) has also been performed. A noticeable conductivity increase was observed above 750K when the pattern x–axis length is doubled, reaching about 6% at 2750K.

Finally, the apparent conductivity for the homogeneous open rod case and the different flat plate assembly cases are compared to the equivalent conductivities obtained with Rubiolo model (and its adaptation to flat plate assembly cores in [11]) for the associated configurations in Figure 8b. The solid phase equivalent conductivities Ks used in Rubiolo model in the different plate assembly cases are depicted in Figure 8a.

Regarding the open rod lattice, the difference between Ka and Ke follows a consistent trend w.r.t. the observations made in the verification case (see Figure 2b in Section 3) *i.e.* Ke is lower (resp. greater) than Ka for $T_0 > 750$K (resp. $T_0 < 750$K) with an underestimation in the high temperature range that is slightly more severe (about 16% at 2750K). When considering the plate assembly cases $2 \times 1-\parallel$ assembly and $2 \times 1-\perp$ assembly, Ke is higher than Ka over the whole temperature range and the trends are differents. In the $2 \times 1-\parallel$ assembly case, the overestimation is maximum at 500K (about 30%) and largely decreases when the temperature is increased. In the $2 \times 1-\perp$ assembly case, while the overestimation is comparable in the low temperature region, the bias steadily increases when the temperature increases above 1000K to reach about 35% at $T_0 = 2750$K. In the $2 \times 2-$ assembly case, error compensation is at play with Rubiolo model in such a way that Ke underestimates Ka for $T_0 < 2250$K with a difference that decreases when the temperature increases in such a way that it is almost zero at $T_0 = 2250$K. Accordingly, the difference in conductivity between the open rod and flat plate assembly configurations in the high temperature range is higher when Ke is considered in comparison to Ka estimation.

On the overall, one may conclude that Rubiolo model's partial extension to flat plate assembly configurations in [11], while giving the correct trends, introduces a noticeable additional bias in comparison with the open rod case. To reduce it (to a level comparable to the open rod case), the closure laws for equivalent conductive Kt and radiative Kr conductivities should be improved by solving the associated closure problems in the actual geometry of such configurations (a regular Cartesian lattice of identical squares).

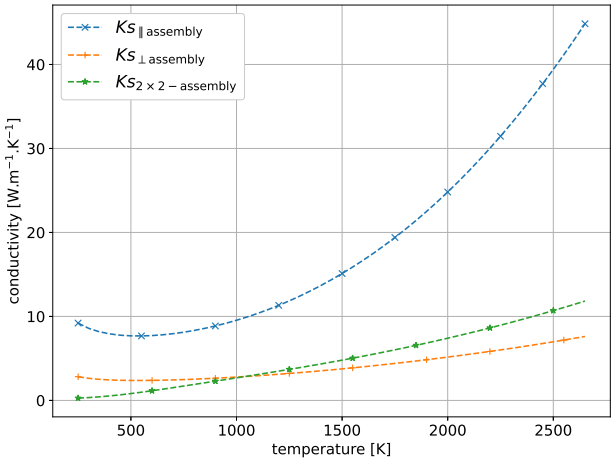

(a) Homogenized assemblies equivalent conductivities as used in Rubiolo model for evaluating Ke.

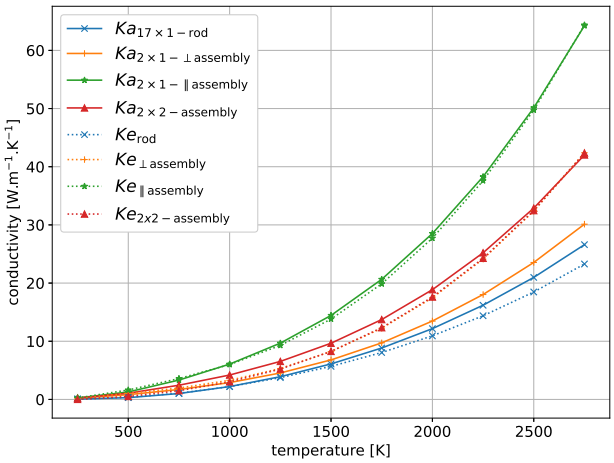

(b) Apparent and equivalent conductivities.

Figure 8. Apparent and equivalent conductivities as a function of temperature in all test cases.

6. CONCLUSIONS AND PERSPECTIVES

In this study, we have evaluated and compared the equivalent thermal conductivity in open rod and closed flat plate assemblies, two types of geometries commonly found in nuclear reactors. To do so, direct numerical simulations and the approximate Rubiolo model were considered. Our results show that the apparent conductivity varies significantly between these two types of assemblies, with higher conductivities observed in flat plate assemblies. Additionally, we found that the heterogeneities introduced by guide tubes in open rod assemblies have a limited impact on conductivity, except in the presence of AgInCd rods inside, which significantly reduces conductivity. In flat plate assembly configurations, it was shown that the partial extension of Rubiolo model (initially proposed for open rod cores) from [11] gives the correct trends but that the associated bias is noticeably increased in comparison with the open rod case.

A direct perspective to this work would be to construct, for flat plate assembly configurations, closure laws for the equivalent conductive and radiative conductivities at play in Rubiolo model in order to reduce this bias. It could be achieved through numerical simulations performed with the same pyMCRAD and TRUST/TrioCFD tools used in this study. From a broader perspective, the validation of lumped parameter models using an equivalent conductivity approach should now be tackled considering core-wise stationary calculations. Once again, pyMCRAD and TRUST/TrioCFD tools could be used for obtaining "reference" solutions. It should be noted that, because of performance issue, the pyMCRAD is limited to 2D configurations for the time being. Another tool, based on the Intel® Embree library, is under development for calculating view factors in 3D [17]. Performing such coupled conduction and radiation transport calculations in 3D is also a strong perspective.

REFERENCES

[1] M. Malicki, P. Darnowski, and T. Lind, "An iPWR MELCOR 2.2 Study on the Impact of the Modeling Parameters on Code Performance and Accident Progression," *Energies*, vol. 17, no. 13, p. 3279, Jan. 2024, number: 13 Publisher: Multidisciplinary Digital Publishing Institute.

[2] H. C. Hottel and A. F. Saforim, *Radiative transfer*. McGraw-Hill, 1967.

[3] P. Rubiolo, "Modélisation du transfert thermique dans un milieu poreux : application aux réacteurs nucléaires en situation accidentelle," Ph.D. dissertation, Aix-Marseille 1, Jan. 2000.

[4] P. Rubiolo and J. M. Gatt, "Modeling of the radiative contribution to heat transfer in porous media composed of spheres or cylinders," *International Journal of Thermal Sciences*, vol. 41, no. 5, pp. 401–411, Apr. 2002.

[5] M. Zabiégo, F. Fichot, and P. Rubiolo, "Modeling of Radiative Heat Transfer during a PWR Severe Accident," *Nuclear Technology*, vol. 154, no. 2, pp. 194–214, May 2006.

[6] J. Munthe Andersen and H. Abel-Larsen, "CORECOOL. Model description of the programme," Risø National Laboratory, Roskilde, Denmark, Report 87-550-0565-9, 1978.

[7] B. Gebhart, "Surface temperature calculations in radiant surroundings of arbitrary complexity – for gray, diffuse radiation," *International Journal of Heat and Mass Transfer*, vol. 3, no. 4, pp. 341–346, 1961.

[8] R. Le Tellier, J. Costa Sallés, and C. Brayer, "A comprehensive analysis of lumped enclosure models' biases for evaluating inter-assembly radiative heat transfer in accident simulation," *Nuclear Engineering and Design*, vol. 433, p. 113870, Mar. 2025.

[9] Y. Sudo, H. Ando, H. Ikawa, and N. Ohnishi, "Core Thermohydraulic Design with 20% LEU Fuel for Upgraded Research Reactor JRR-3," *Journal of Nuclear Science and Technology*, vol. 22, no. 7, pp. 551–564, 1985.

[10] C.-S. Lin and G. Youinou, "Design and Analysis of a 250 MW Plate-Fuel Reactor for Nuclear Thermal Propulsion," KnowVille, USA, Apr. 2020.

[11] M. Zabiégo, "Radiative Heat Transfer in a Plate-Fuel Reactor Core," in *Proc. of CHT-08 ICHMT International Symposium on Advances in Computational Heat Transfer*, Marrakech, Morocco, 2008.

[12] P.-E. Angeli, U. Bieder, and G. Fauchet, "Overview of the TrioCFD code: Main features, V&V procedures and typical applications to nuclear engineering," in *NURETH 16 - 16th International Topical Meeting on Nuclear Reactor Thermalhydraulics*, Chicago, United States, Aug. 2015.

[13] E. Saikali, A. Bruneton, P. Ledac, and R. Bourgeois, "TRUST: the HPC open-source CFD platform – from CPU to GPU," *EPJ Nuclear Sciences & Technologies*, vol. 11, p. 53, 2025.

[14] C. Geuzaine and J.-F. Remacle, "Gmsh: A 3-D finite element mesh generator with built-in pre- and post-processing facilities," *International Journal for Numerical Methods in Engineering*, vol. 79, no. 11, pp. 1309–1331, 2009, _eprint: https://onlinelibrary.wiley.com/doi/pdf/10.1002/nme.2579.

[15] S. Nicolas, A. Noguès, L. Manifacier, and L. Chabert, "A dummy core for V&V and education & training purposes at technicatome: In and ex-core calculations," in *Proc. of 18th International Group on Research Reactors (IGORR) Conference*, Sydney, Australia, 2017.

[16] IAEA, Ed., *Thermophysical Properties of Materials for Nuclear Engineering: A Tutorial and Collection of Data*. IAEA, 2008.

[17] L. Bulgarelli, A. Calloo, E. Saïkali, and R. Le Tellier, "A Monte Carlo Ray-Tracing Algorithm for Estimating View Factors for Thermal Analysis of Reactor Cores," in *Proc. of PHYSOR 2026 - The International Conference on Physics of Reactors*, Torino, Italy, 2026.

APPENDIX A. Equivalent conductivity model for a porous medium

In order to evaluate the equivalent conductivity Ke along a direction $\vec{e}$, Rubiolo model proposed in [3] starts from a representative layer of the porous medium as depicted in Figure 9. The conductivity of the solid (resp. gas) phase is denoted K_s (resp. λ_g) while the solid surface emissivity is denoted ε_s. The porosity of the layer is p and its average temperature T. From there, the layer equivalent conductivity Ke is expressed in terms of the equivalent conductive Kt and radiative Kr conductivities as follows:

$$Ke = K_g + Kr^0 + \left(R_s + \left(\frac{Kr - Kr^0}{1 - R_s\left(Kr - Kr^0\right)} + \frac{Kt - K_g}{1 - R_s\left(Kt - K_g\right)} \right)^{-1} \right)^{-1} \tag{2}$$

with $K_g = \lambda_g \frac{S_g}{S}$, $Kr^0 = \lim_{K_s \to 0} Kr$ and $R_s^{-1} = \lim_{T \to +\infty} \left(Kr - Kr^0\right)$. This expression is general and is *a priori* applicable to any geometry where the heat exchanges can be described considering the following modes acting in parallel: thermal conduction through the gas phase alone (K_g term in Eq. 2), radiation through the gas phase alone (Kr^0 term in Eq. 2), conduction in the radiative solid and coupled conduction and radiation through the gas (the third term in Eq. 2).

Regarding radiative heat transfer, in [3], the following expression have been proposed for Kr:

$$Kr = 4\left(\frac{2 - (\hat{a} + 2\hat{r})}{\hat{a} + 2\hat{r}} \right) \sigma T^3 L \tag{3}$$

with $\hat{a} = a(1-\varphi)$, $\hat{r} = r + \varphi(r_0 - r)$, $r_0 = \lim_{\varepsilon_s \to 0} r$. Function φ takes into account the solid temperature inhomogeneity in the layer under the assumption that, at any point $\vec{r}$ in the solid phase, $T_s(\vec{r}) = \varphi T_s^0(\vec{r}) + (1-\varphi) T_s^\infty(\vec{r})$ where $T_s^0(\vec{r}) = \lim_{K_s \to 0} T_s(\vec{r})$ and $T_s^\infty(\vec{r}) = \lim_{K_s \to +\infty} T_s(\vec{r}) = T$. Accordingly, it should enforce $\lim_{K_s \to 0} \varphi = 1$ and $\lim_{K_s \to \infty} \varphi = 0$. Accordingly, one has:

$$Kr^0 = 4\left(\frac{1 - r_0}{r_0} \right) \sigma T^3 L \tag{4}$$

From there, in order for R_s^{-1} to remain finite when $T \to +\infty$, φ should be such that: $\exists \alpha > 0$,

$$\varphi = 1 - \frac{\alpha}{4\sigma T^3} + o\left(\frac{1}{4\sigma T^3} \right) \tag{5}$$

Under these conditions, R_s can be expressed as:

$$R_s = \frac{2\left(r_0\right)^2}{\alpha\left(2(r - r_0) - a\right)} \tag{6}$$

This model is general and can be applied to any geometry provided that the four following closures are obtained: $\frac{S_g}{S}$, Kt, φ and associated α, (a, r) and associated r_0. Moreover, the following asymptotic behaviours are enforced:

- $\lim_{K_s \to +\infty} Ke = Kt + Kr$ provided that $\lim_{K_s \to +\infty} R_s = 0$

- $\lim_{K_s \to 0} Ke = \lambda_g + Kr^0$ provided that $\lim_{K_s \to 0} R_s = +\infty$ and $\lim_{K_s \to 0} Kt = \lambda_g$
- $\lim_{\varepsilon_s \to 0} Ke = Kt + Kr^0$ provided that $\lim_{\varepsilon_s \to 0} Kr = Kr^0$ *i.e.* $\lim_{\varepsilon_s \to 0} \varphi = 0$
- $\lim_{T \to 0} Ke = Kt$

For a uniform Cartesian arrangement of cylindrical (resp. square) solids, $\frac{S_g}{S} = 1 - \sqrt{\frac{4}{\pi}(1-p)}$ (resp. $\frac{S_g}{S} = 1 - \sqrt{(1-p)}$).

For φ, under simplifying hypotheses, [3] proposes to use for a cylinder of diameter d (or a slab of thickness d):

$$\varphi = \left(1 + \frac{2K_s}{4 + \varepsilon_s \sigma T^3 d}\right)^{-1} \tag{7}$$

in such a way that $\alpha = \frac{2K_s}{\varepsilon_s d}$.

For K_t, a correlation has been proposed in [3] from the numerical simulation of conductive heat transfer in the 2D-unit cell associated with the cylinder lattice for various porosity and conductivity ratio K_s/λ_g values. In a similar way, correlations for a, r have been obtained from numerical simulation of radiative heat transfer in the gas phase of a 2D-unit cell varying ε_s and p (and imposing a zero solid temperature).

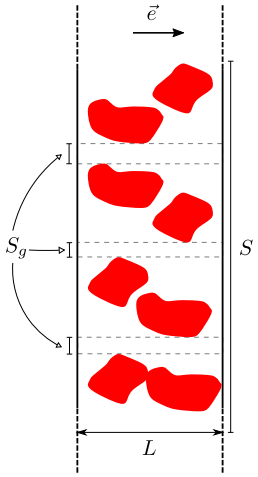

Figure 9. Layer of the porous medium – the solid phase is in red – thickness L, total and "free" cross-sectional areas S and S_g respectively.

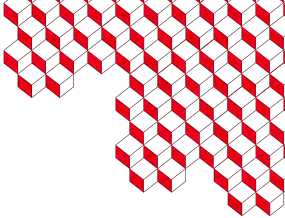

Direct numerical evaluation of core equivalent conductivity: a comparative analysis of open rod and flat plate assemblies

The 12th European Review Meeting on Severe Accidents Research (ERMSAR2026), Madrid, Spain, May 18–22, 2026

R. Le Tellier [1] (romain.le-tellier@cea.fr) E. Saïkali [2] A. Calloo [2]

[1] CEA, DES, IRESNE, DTN, CADARACHE
[2] UNIVERSITÉ PARIS SACLAY, CEA, DES, ISAS, DM2S

Outline

Introduction

Problem Statement

Methods

Application Test Cases

Numerical Results

Conclusions & Perspectives

1. Introduction

Context and problem statement

Context

Radiative heat transfer crucial for heat dissipation during LOCA in LWRs

- For small reactors, the accident progression can be very sensitive to the heat removal from the core [MDL24]
- Bifurcations in the core degradation transients because of the complex dependency of Zircaloy cladding oxidation to temperature

Its modeling is complex due to the intricate geometry of reactor cores

- Approximate lumped parameter models are used in accident simulation codes
- Built from a combination of net radiation enclosure models and effective conductivity models
- Equivalent conductivity $\underline{\underline{Ke}}$ associated with the anisotropic Fourier law $\boldsymbol{q} = -\underline{\underline{Ke}}\boldsymbol{\nabla} T$
  (N.B. valid for an optically thick medium – at the scale of the representative volume element used for homogenization)

Problem Statement

- Different models in the literature for $\underline{\underline{Ke}}$ mainly focused on open rod geometries (PWRs)
- In particular, Rubiolo model [Rub00, RG02] as implemented in the RADR model [ZFR06] of the ICARE module of the ASTEC code
  - Rather general formulation that requires geometry-dependent closures
  - Obtained in practice only for a regular Cartesian lattice of identical cylinders

→ **In a standard 17×17 PWR assembly, what is the impact of the guide tubes on $\underline{\underline{Ke}}$?**

- Little work for closed flat plate assemblies
  - Found in various designs ranging from material testing reactors to space thermal propulsion reactors
  - Rubiolo model partially extended to such geometries [Zab08] but no validation

→ **How $\underline{\underline{Ke}}$ varies for closed flat plate assemblies?**

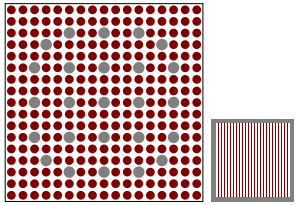

Nota Bene

- Focus here on the radial component of $\underline{\underline{Ke}}$ to investigate these two questions
- Radiation between opaque solids through a transparent medium

2. Methods

Direct numerical simulation approach and Rubiolo model

Methods - Direct Numerical Simulation Approach

- "Reference" approach for evaluating the equivalent conductivity
- Simulate radiative and conductive heat transfer modes in two-phase spatial domain $\mathcal{D}$:

$$T = T_0 - \frac{\delta T}{2} \text{ and } \varepsilon = 1 \quad \text{on } \Gamma_L$$

$$T = T_0 + \frac{\delta T}{2} \text{ and } \varepsilon = 1 \quad \text{on } \Gamma_R$$

$$\nabla T \cdot \boldsymbol{n} = 0 \text{ and specular reflection} \quad \text{on } \Gamma_U \cup \Gamma_B$$

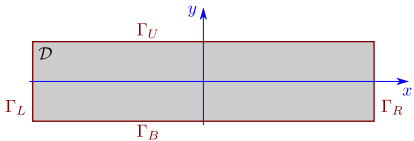

FIGURE 2: Geometrical domain $\mathcal{D}$: L_X (resp. L_Y) is the domain length along the x–axis (resp. y–axis)

- Evaluate the apparent conductivity (Ka) along the x–axis from $\boldsymbol{q}$ the total heat flux on $\Gamma_L \cup \Gamma_R$:

$$Ka(T_0) = \frac{L_X \int_{\Gamma_L \cup \Gamma_R} |\boldsymbol{q} \cdot \boldsymbol{n}| \, ds}{2 L_Y \delta T}$$

- TRUST/TrioCFD code [SBLB25] for conduction/radiation coupled calculation
  - Triangular meshes, finite volume-element discretization with anisotropic conductivity handling
  - View factors obtained by Ray-Tracing Monte-Carlo method [LTCSB25] or analytical formulas

Methods - Rubiolo Model

- Algebraic model based on thermal resistance formalism for describing a porous medium
  - Opaque homogeneous solid (conductivity K_s, emissivity ε_s)
  - Transparent fluid (thermal conductivity λ_g)
  - Porosity p
- Requires: K_s (solid homogenization) and closures laws that depend on the phase topology
  - S_g/S
  - Equivalent conductive Kt and radiative Kr conductivities
- Kt and Kr closures laws + validation $\rightarrow$ available for a regular Cartesian lattice of identical cylinders (RADR model in ASTEC)
- For closed flat plate assemblies: partial adaptation (only K_s) [Zab08] and no validation

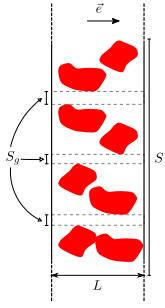

Methods - Verification test case (adapted from [Rub00])

- *Ka* evaluated in [Rub00] with CASTEM2000

λ_g [W.m^{-1}.K^{-1}]	K_s [W.m^{-1}.K^{-1}]	ε_s [–]
0.01	10.0	0.5

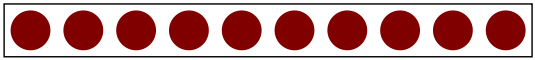

FIGURE 3: 10 × 1– homogeneous rod pattern – fuel pins in red – length is 5.01cm, pitch is 0.50cm

- Very good agreement between both *Ka* evaluations
- *Ke* with Rubiolo model vs. *Ka*: a limited underestimation ($\approx$ 10%)

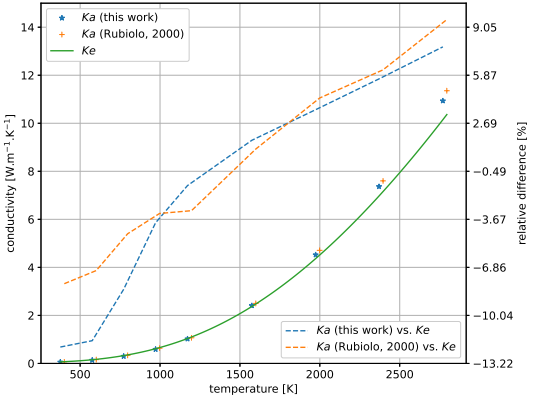

FIGURE 4: Apparent and equivalent conductivities as a function of temperature

3. Application Test Cases

Assemblies - Geometries and Materials

- Standard 17 $\times$ 17 PWR assembly
- 24–flat plate closed assembly from fictitious MTR core proposed in [NNMC17]

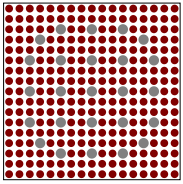

(A) fuel pins in red, guide tube pins in gray

(B) fuel plates in red, canister wall in gray

(A) Fuel pin

(B) Guide tube

(C) AgInCd pin

(D) Fuel plate

(UO_2 in red, AgInCd in cyan, Zircaloy in gray and steel in dark gray)

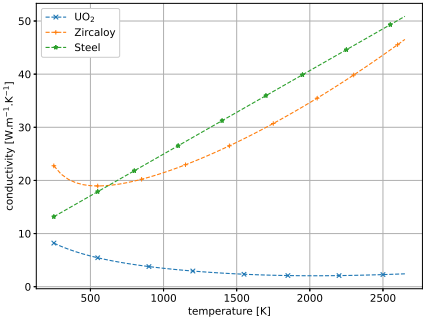

FIGURE 7: Materials conductivities

- conductivity of AgInCd: 60W.m^{-1}.K^{-1}
- all material data taken from [IAE08]
- $\varepsilon_s = 0.8$ (oxidized Zy)

Geometrical Patterns and Test Cases

- Assembly elements homogenization

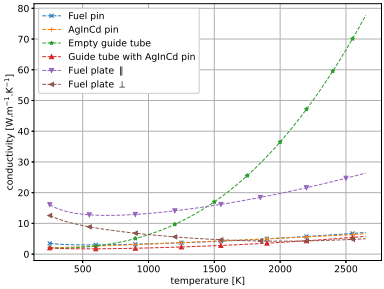

- Selected test cases
  - $17 \times 1 - \mathrm{rod}$ (homogeneous)
  - $17 \times 3 - \mathrm{rod},\ \mathrm{empty\ GT}$ (empty guide tube)
  - $17 \times 3 - \mathrm{rod},\ \mathrm{AgInCd\ GT}$(AgInCd pin in guide tube)
  - $2 \times 1 - \parallel \mathrm{assembly}$ (plates parallel to heat flux)
  - $2 \times 1 - \perp \mathrm{assembly}$ (plates perpendicular to heat flux)
  - $2 \times 2 - \mathrm{assembly}$ (checkerboard arrangement)
  - $4 \times 2 - \mathrm{assembly}$ (checkerboard arrangement)

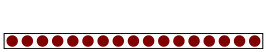

(A) 17×1– homogeneous rod pattern

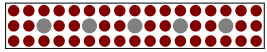

(B) 17×3– heterogeneous rod pattern

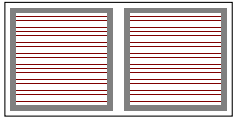

(C) 2×1– plate $\parallel$ assembly pattern

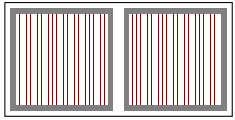

(D) 2×1– plate $\perp$ assembly pattern

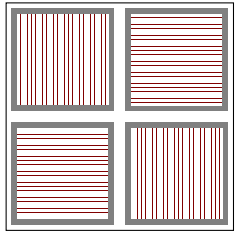

(E) 2×2– plate assembly pattern

3. Numerical Results

Numerical Results - Open Rod Cases

Ka in the open rod cases: what is the impact of the guide tubes?

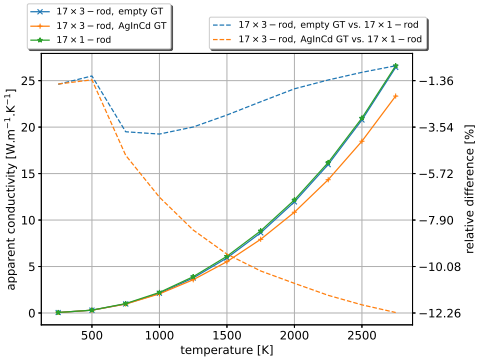

FIGURE 9: Apparent conductivities as a function of temperature: open rod cases

- Heterogeneities due to empty guide tubes
  → a very limited impact on conductivity (-3.5% to -1%)
- AgInCd pins in guide tubes
  → a more significant decrease in *Ka* (down to −12%)
- Taking into account that AgInCd melts at about 800 °C
  → lattice heterogeneities have a limited impact

→ considering the homogeneous lattice case probably sufficient in accident scenario codes

Numerical Results - Flat Plate Assembly Cases

Ka in plate assemblies: how does it compare with the open rod case?

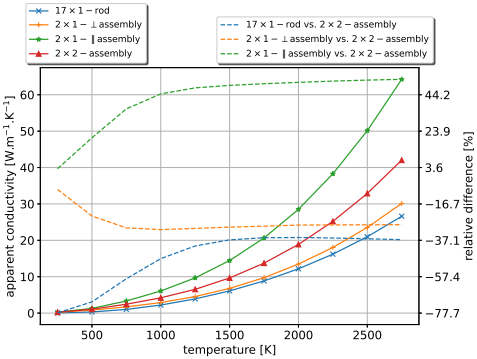

FIGURE 10: Apparent conductivities as a function of temperature: flat plate assembly cases

- Higher conductivity compared to open rod cases
- Strong anisotropy effect: conductivity is higher when plates are parallel to the heat flux
- $2 \times 2 - \mathrm{assembly}$ somewhere in between the parallel and perpendicular plate cases

N.B. Pattern size effect $4 \times 2 - \mathrm{assembly}$ (not shown) vs. $2 \times 2 - \mathrm{assembly}$: limited increase (a few %) in *Ka*

Numerical Results - Comparison with Rubiolo model

Ke (Rubiolo model) vs. *Ka*

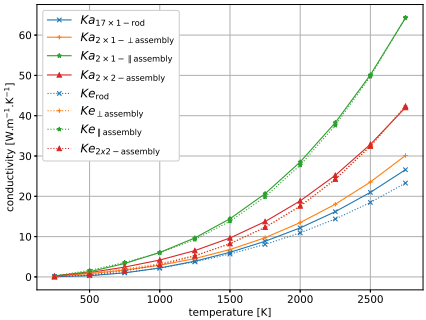

FIGURE 11: Apparent and equivalent conductivities – $Ke_{\perp\text{ assembly}}$ and $Ke_{2\times2\text{ assembly}}$ almost indistinguishable

- Open rod lattice: same trend as in the verification case with an underestimation slightly more pronounced (up to $\approx$ 16%)
- K_s as used in Rubiolo model for evaluating *Ke* in the plate assembly cases (following [Zab08])

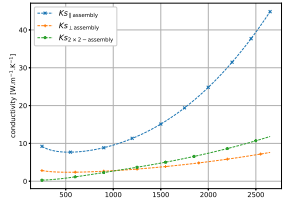

- $2\times1-\parallel\text{assembly}$ and $2\times1-\perp\text{assembly}$:
  - *Ke* $>$ *Ka* over the whole temperature range
  - at 500K: about 30% bias
  - above 1000K: bias $\nearrow$ (resp. $\searrow$) in $\perp$ (resp $\parallel$) case
- in $2\times2-\text{assembly}$ case: error compensation at play with *Ke* very close to $2\times1-\perp\text{assembly}$ case

$\rightarrow$ correct trend but noticeable additional bias in comparison with the open rod case

Conclusions & perspectives

- Evaluation and comparison of equivalent conductivity in open rod and closed flat plate assemblies using direct numerical simulations and Rubiolo model
- Main findings:
  - Limited impact of heterogeneities introduced by guide tubes in open rod assemblies
  - Flat plate assemblies compared to open rod assemblies: higher conductivity and strong anisotropy
  - Partial extension of Rubiolo model in [Zab08]: noticeable additional bias in comparison with the open rod case
- Perspectives:
  - Improve Rubiolo model application to flat plate assemblies: construct closure laws for K_t and K_r conductivities in such a configuration
  - Use direct numerical simulations for the thorough validation of lumped parameter models that describe radiative heat transfer in accident codes
  - Extend the direct numerical simulation approach to 3D configuration: tool for calculating view factors in 3D under development [BCSLT26] using the Intel® Embree library

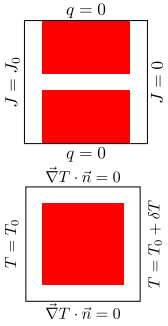

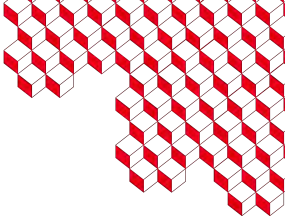

Thanks! Any questions?

References I

[BCSLT26] Lorenzo Bulgarelli, Ansar Calloo, Elie Saïkali, and Romain Le Tellier. A Monte Carlo Ray-Tracing Algorithm for Estimating View Factors for Thermal Analysis of Reactor Cores. In *Proc. of PHYSOR 2026 - The International Conference on Physics of Reactors*, Torino, Italy, 2026.

[IAE08] IAEA, editor. *Thermophysical Properties of Materials for Nuclear Engineering: A Tutorial and Collection of Data*. IAEA, 2008.

[LTCSB25] R. Le Tellier, J. Costa Sallés, and C. Brayer. A comprehensive analysis of lumped enclosure models' biases for evaluating inter-assembly radiative heat transfer in accident simulation. *Nuclear Engineering and Design*, 433:113870, March 2025.

[MDL24] Mateusz Malicki, Piotr Darnowski, and Terttaliisa Lind. An iPWR MELCOR 2.2 Study on the Impact of the Modeling Parameters on Code Performance and Accident Progression. *Energies*, 17(13):3279, January 2024. Number: 13 Publisher: Multidisciplinary Digital Publishing Institute.

References II

[NNMC17] S. Nicolas, A. Noguès, L. Manifacier, and L. Chabert. A dummy core for V&V and education & training purposes at technicatome: In and ex-core calculations. In *Proc. of 18th International Group on Research Reactors (IGORR) Conference*, Sydney, Australia, 2017.

[RG02] P. Rubiolo and J. M. Gatt. Modeling of the radiative contribution to heat transfer in porous media composed of spheres or cylinders. *International Journal of Thermal Sciences*, 41(5):401–411, April 2002.

[Rub00] Pablo Rubiolo. *Modélisation du transfert thermique dans un milieu poreux : application aux réacteurs nucléaires en situation accidentelle*. PhD thesis, Aix-Marseille 1, January 2000.

[SBLB25] Elie Saikali, Adrien Bruneton, Pierre Ledac, and Remi Bourgeois. TRUST: the HPC open-source CFD platform – from CPU to GPU. *EPJ Nuclear Sciences & Technologies*, 11:53, 2025.

References III

[Zab08] Magali Zabiégo. Radiative Heat Transfer in a Plate-Fuel Reactor Core. In *Proc. of CHT-08 ICHMT International Symposium on Advances in Computational Heat Transfer*, Marrakech, Morocco, 2008.

[ZFR06] M. Zabiégo, F. Fichot, and P. Rubiolo. Modeling of Radiative Heat Transfer during a PWR Severe Accident. *Nuclear Technology*, 154(2):194–214, May 2006.

EXPERIMENTAL INVESTIGATION OF DEBRIS-BED FORMATION FOR OPTIMIZING CORE-CATCHER DESIGN

Tomonari Mashiko*, Yihua Xu, Ryo Yokoyama,
Yohei Kano, Shuichiro Miwa, Koji Okamoto
The University of Tokyo
Corresponding Address
tomonari4212@g.ecc.u-tokyo.ac.jp; xuyh@vis.t.u-tokyo.ac.jp; yokoyama@vis.t.u-tokyo.ac.jp;
yhkano@g.ecc.u-tokyo.ac.jp; miwa@n.t.u-tokyo.ac.jp; okamoto@n.t.u-tokyo.ac.jp

ABSTRACT

Large-scale three-dimensional experiments were performed to investigate debris-bed formation during underwater sedimentation of sub-millimeter particles under conditions relevant to sodium-cooled fast reactor (SFR) core disruptive accidents. Solid particles with different diameters and densities were released into a water pool through nozzles of varying diameters, and their settling, spreading, and deposition behaviors were recorded using high-speed imaging.
The resulting debris-bed shape was quantified using several geometrical indicators, including inner diameter, fan diameter, outer diameter, maximum height, outer slope angle and inner slope angle. Dimensionless parameters representing granular-jump intensity, particle–fluid coupling, and momentum injection were introduced to interpret the observed trends. A clear transition in the dominant formation mechanisms was identified around a Stokes number of unity, separating fluid-coupled and inertia-dominated regimes.
Based on these findings, regime-wise empirical correlations were developed for key geometrical indicators. The proposed framework embeds experimentally observed physical tendencies into invariant dimensionless parameters and provides quantitative insight into debris-bed formation behavior, contributing to debris-bed study and core-catcher design for SFR safety evaluation.

KEYWORDS
SFR, Debris bed formation, CDA, Experimental study

1. INTRODUCTION

In a core disruptive accident (CDA) of a sodium-cooled fast reactor (SFR), molten core materials are fragmented through melt–sodium interaction and subsequently relocated to the lower plenum by passing through internal flow paths such as control rod guide tubes [1]. Due to the high boiling point and thermal conductivity of liquid sodium, stable film boiling is unlikely; instead, direct liquid–liquid contact is expected, leading to rapid quenching and fragmentation into fine debris with characteristic sizes on the order of 0.1–1.0 mm [1].
The fragmented debris particles settle and accumulate on the core-catcher system installed at the bottom of the reactor vessel [2]. The final debris bed shape strongly affects coolability, recriticality risk, and in-vessel retention performance [3,4]. Therefore, understanding debris-bed formation mechanisms and identifying governing parameters are essential for SFR safety evaluation.
Previous experimental studies have investigated debris-bed formation using sedimentation experiments. The Japan Atomic Energy Agency (JAEA) and Kyushu University conducted a series of three-dimensional experiments focusing on the effects of nozzle diameter, particle density, and drop height [5–7]. Cheng et al. performed large-scale quasi-two-dimensional experiments and identified multiple flow regimes based on

particle–fluid interaction mechanisms [8]. However, limitations in experimental scale, particle size range, and dimensionality reduce the applicability of these studies to realistic SFR accident scenarios.
Motivated by these gaps, the present study conducts large-scale three-dimensional sedimentation experiments using sub-millimeter particles to clarify debris-bed formation mechanisms and to construct physically interpretable empirical correlations based on dimensionless analysis.

2. MATERIALS AND METHODS

2.1 Experimental apparatus and simulant materials

Figure 1 shows a schematic of the experimental apparatus. Experiments were conducted in a transparent acrylic tank with internal dimensions of 60 cm × 60 cm × 120 cm. Solid particles were released from a hopper through nozzles with diameters of 24 mm and 30 mm into a quiescent water pool with a fixed water depth of 90 cm.
Three types of particles—stainless steel, zirconia, and alumina—were used as debris simulants. Particle diameters ranged from 0.3 to 2.0 mm. Particle properties and experimental conditions are summarized in Table **1** and Table **2**. In all experiments, a constant bulk particle volume of 3.0 L was used.
High-speed cameras were installed near the nozzle and near the bottom of the tank to capture particle entry and deposition processes. Additional cameras recorded the global spreading behavior and final debris-bed shape.

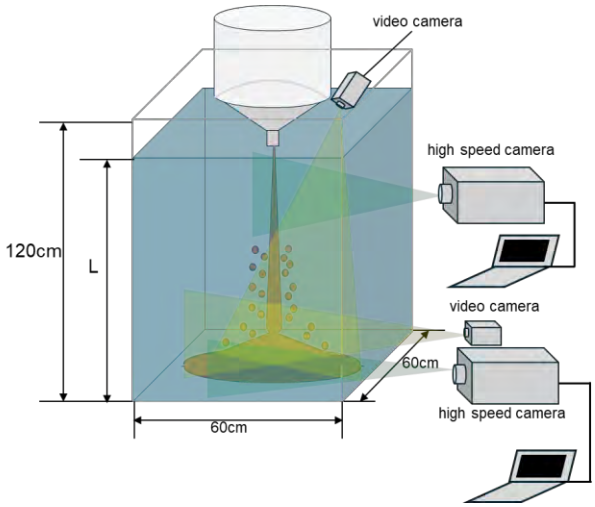

Figure 1. The schematic of the experimental apparatus

Table 1. Particle properties

Materials	Density ρ_p [kg/m³]	Particle diameter d [mm]
Al_2O_3	3600	2.0
		1.0
		0.5
ZrO_2	6000	2.0
		1.0
		0.5
SS	7800	2.0
		1.0
		0.3

Table 2. Experimental conditions

Particle volume V [L]	Nozzle diameter D_{nozzle} [mm]	Water height H [cm]
3.0	24, 30	90

2.2 Experimental procedure and characteristic velocities

Particles were released instantaneously by removing a retaining pin at the hopper outlet. After entering the water as a coherent group, particles settled through the water column, spread radially near the bottom, and accumulated to form a debris bed. Selected test conditions were repeated to confirm experimental repeatability. The Mean Absolute Percentage Error (MAPE) in the measured geometrical indicators were within approximately ±5.21–17.4%, depending on the parameter, as summarized in Table 3. Based on this assessment, the systematic trends discussed in the following sections are significantly larger than the experimental scatter.
The initial exit velocity at the nozzle, $\mathbf{v}_i$, was estimated using the continuity equation,

$$\mathbf{v}_i = \frac{4Q}{\pi D_{\text{nozzle}}^2}, \tag{1}$$

where Q is the average discharge flow rate.
A terminal velocity $\mathbf{v}_t$was defined as a characteristic velocity scale describing particle motion near the bottom region. This velocity scale was used consistently in the definition of dimensionless parameters without attempting detailed modeling of the settling process.

Table 3. Experimental uncertainty of the measured geometrical indicators, quantified by MAPE from repeated test conditions.

Geometrical indicator	MAPE [%]
D_{inner}	14.2
D_{fan}	7.95
D_{outer}	6.14
h_{max}	5.21
θ_{out}	17.4
θ_{in}	15.0

3. RESULTS AND DICUSSIONS

3.1 Debris bed morphology and geometric indicators

Figure **2** shows representative debris-bed shapes observed in the experiments. Three typical morphologies were identified: volcano, concave, and flat-topped beds, depending on particle size, density, and injection conditions.
To quantitatively characterize these shapes, five geometrical indicators were defined as shown in Figure 3: inner diameter D_{inner}, fan diameter D_{fan}, outer diameter D_{outer}, maximum height h_{max}, inner slope angle θ_{in} and outer slope angle θ_{out}. These indicators were selected to separately represent impact-induced spreading near the center region, lateral particle transport, and stabilization behavior at the bed periphery.
To enable comparison across different experimental conditions and to extract physically meaningful trends, the characteristic lengths were nondimensionalized using $V^{1/3}$, where V is the total particle volume released in each experiment, as defined previously. Since $V^{1/3}$ represents the characteristic length scale of the deposited debris volume, this normalization allows the geometrical indicators to be evaluated independently of the absolute amount of released particles.
Accordingly, the diameters D_{inner} , D_{fan} , and D_{outer} were normalized as $D^*_{\text{inner}} = D_{\text{inner}}/V^{1/3}$, $D^*_{\text{fan}} = D_{\text{fan}}/V^{1/3}$, and $D^*_{\text{outer}} = D_{\text{outer}}/V^{1/3}$. The maximum bed height was similarly nondimensionalized as $h^*_{max} = h_{\text{max}}/V^{1/3}$. The outer slope angle θ_{out}, the inner slope angle θ_{in} are inherently dimensionless geometrical quantities and were therefore used directly without normalization.

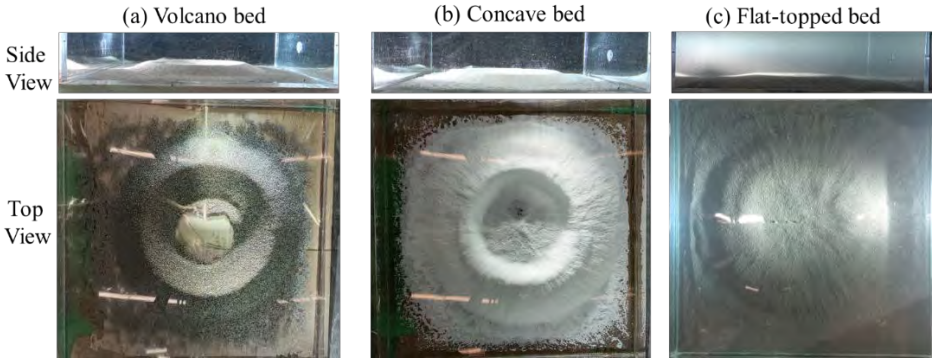

Figure 2. Representative debris bed shape observed in the present experiments. The upper figures show side views, and the bottom figures show top views on each debris bed shape. (a) volcano-shaped bed (material: SS, $\boldsymbol{d = 1.0}$mm, $\boldsymbol{D}_{\text{nozzle}} = \boldsymbol{24}$mm), (b) concave bed (material: ZrO_2, $\boldsymbol{d = 0.5}$mm, $\boldsymbol{D}_{\text{nozzle}} = \boldsymbol{24}$mm), and (c) flat-topped bed (material: SS, $\boldsymbol{d = 0.3}$mm, $\boldsymbol{D}_{\text{nozzle}} = \boldsymbol{20}$mm).

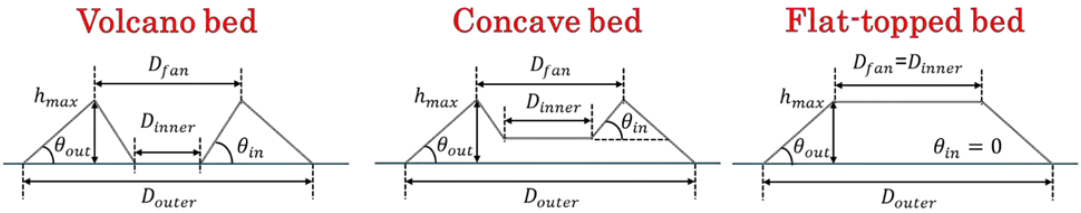

Figure 3. The geometrical definition of each debris bed shape ($\boldsymbol{D_{inneer}, D_{fan}, D_{outer}, h_{max}, \theta_{in}, \theta_{out}}$)

3.2 Inner diameter $\boldsymbol{D}_{\text{inner}}$

After particle impact on the bottom surface, a clear radial spreading pattern was observed, leaving a central cavity as shown in Figure 4. This behavior is characteristic of a granular jump, in which the vertical momentum of the particle group is abruptly converted into horizontal motion upon interaction with the bottom surface [9]. The resulting cavity defines the inner diameter D_{inner}, which represents the spatial extent of this momentum conversion process.

To quantify the intensity of the granular jump, a Froude number was introduced as

$$Fr_t = \frac{\mathbf{v}_t}{\sqrt{gD_{\text{nozzle}}}}, \tag{2}$$

where D_{nozzle} represents the characteristic length scale of momentum injection and $\mathbf{v}_t$ is a representative particle velocity near the bottom region. From a physical perspective, Fr_t expresses the ratio between particle inertia and the restoring effect of gravity during bottom impact.

In addition, a Stokes number was defined to characterize particle–fluid coupling during impact,

$$St_i = \frac{\rho_p d}{C_d \rho_l D_{\text{nozzle}}}, \tag{3}$$

where the drag coefficient C_d was evaluated using the Schiller–Naumann correlation [10]. This parameter reflects the relative importance of particle inertia compared with fluid drag during rapid deceleration and redirection at the bottom surface.

Figure 5 (a) shows the relationship between the normalized inner diameter D^*_{inner} and Fr_t. The data exhibits two distinct regimes separated around $St_i \approx 1$, as summarized in Figure 5(b). Within each regime, D^*_{inner}

increases monotonically with increasing Fr_t, indicating that the cavity size is governed primarily by the strength of the granular jump.
In the low-St_i regime, particle motion remains strongly coupled to the surrounding fluid, and the extent of radial spreading is controlled by fluid-driven momentum redistribution. In contrast, in the high-St_i regime, particle inertia dominates the impact process, leading to a more direct conversion of vertical momentum into lateral motion. Despite the difference in dominant mechanisms, D_{inner} consistently reflects the magnitude of momentum conversion at bottom impact.
These results demonstrate that D_{inner} is a sensitive geometrical indicator that directly captures the dominant momentum-conversion mechanism during the granular jump.

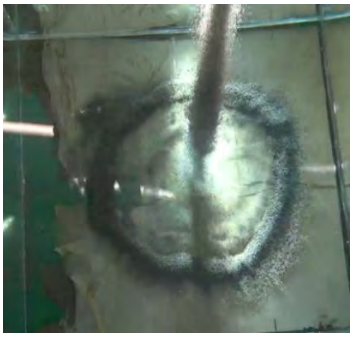

Figure 4. Top-view visualization of particles spreading near the bottom surface 2.5 sec after release. The granular jump causes lateral expansion of the particle group and leaves a central cavity that defines the inner diameter D_{inner} (material: SS, d=1.0mm, D_{nozzle}=24mm).

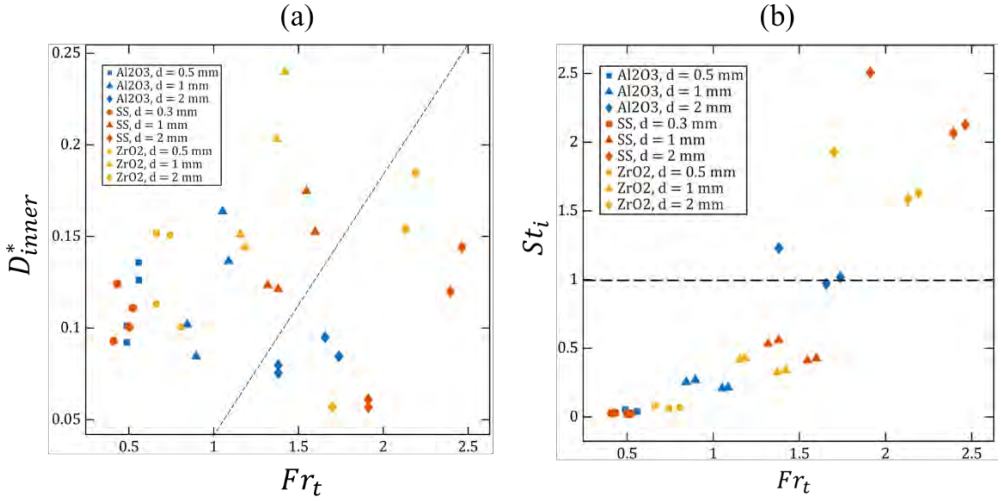

Figure 5. (a) Relationship between the normalized inner diameter $D^*_{\text{inner}}$and the Froude number Fr_t. (b) Relationship between the Stokes number St_i and Fr_t, indicating a regime transition around $St_i = 1$. Symbols represent experimental data for different particle materials and diameters.

3.3 Fan diameter D_{fan}

Figure 6 (a) shows a strong correlation between the normalized fan diameter D^*_{fan} and the normalized inner diameter D^*_{inner}, indicating that cavity formation and upper region spreading are closely linked phenomena. This correlation suggests that the granular jump not only determines the size of the central cavity but also controls the subsequent redistribution of particles above the cavity region.

Figure 6 (b) presents the relationship between D^*_{fan} and Fr_t. Like D^*_{inner}, two distinct regimes are observed. In the low-St_i regime, D^*_{fan} increases strongly with Fr_t, reflecting fluid-coupled momentum redistribution. In this regime, particles redirected by the granular jump remain strongly influenced by the liquid flow, resulting in enhanced spreading in the upper region.
In the high-St_i regime, D^*_{fan} continues to increase with Fr_t, although the underlying mechanism changes. Here, particle–particle interactions play a more dominant role, and the spreading reflects a combination of direct inertial motion and subsequent collisions rather than fluid-driven transport alone.
These observations indicate that D_{fan} serves as a complementary geometrical indicator to D_{inner}, capturing the extent to which the granular jump influences particle redistribution beyond the immediate impact zone.

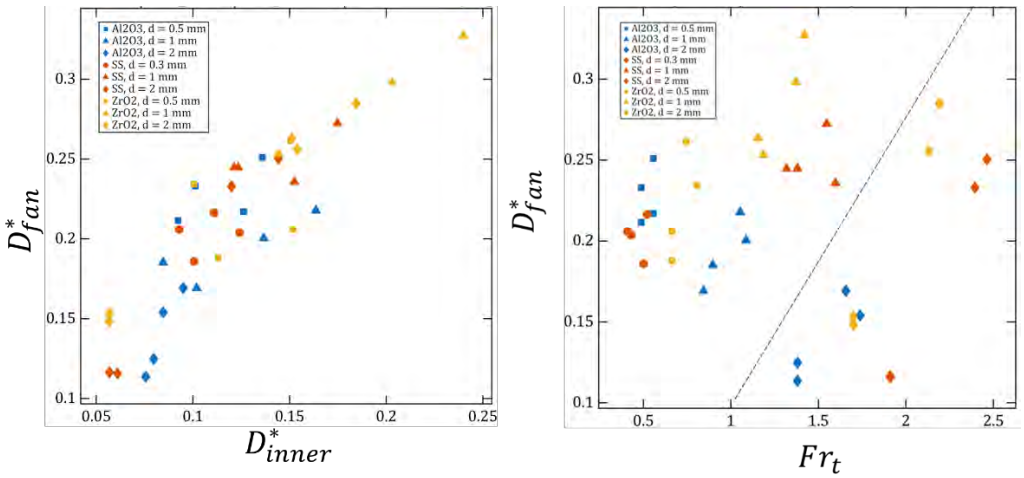

Figure 6. (a) Relationship between the normalized fan diameter D^*_{fan} and the normalized inner diameter D^*_{inner}. (b) Relationship between D^*_{fan} and Fr_t. Symbols represent experimental data for different particle materials and diameters.

3.4 Outer diameter D_{outer}

To clarify the dominant velocity scale governing the lateral extent of the outer region, two Reynolds numbers were examined. Previous debris-bed studies have emphasized the role of particle inertia in lateral spreading behavior [8]. Following this perspective, a Reynolds number based on particle settling motion near the bottom was first considered.
This Reynolds number is defined using the representative settling velocity $\mathbf{v}_t$ as

$$Re_{Dt} = \frac{\rho_l \mathbf{v}_t D_{\text{nozzle}}}{\mu_l}, \tag{4}$$

which characterizes the relative importance of inertial and viscous effects associated with particle motion in the near-bottom region.
In addition to settling inertia, the initial momentum of the particle jet acts as a driving source for both particle motion and the surrounding liquid flow. During injection, a portion of the particle momentum is transferred to the liquid, generating a large-scale flow field that can significantly influence lateral particle transport. To account for this particle–flow coupling, a second Reynolds number based on the initial momentum injection near the nozzle was introduced and defined as

$$Re_{Mi} = \frac{\sqrt{\frac{M_i}{\rho_l}}}{\nu}, \tag{5}$$

where ν is the kinematic viscosity of water. Here, M_i denotes the initial momentum of the particle jet, given by

$$M_i = \rho_p \mathbf{v}_i^2 \, \pi \left(\frac{D_{\text{nozzle}}}{2} \right)^2 . \tag{6}$$

Figure 7 compares the dependence of the normalized outer diameter D^*_{outer} on these two Reynolds numbers. In Figure 7(a), where the data are organized using Re_{Dt}, substantial scatter remains and no clear systematic trend is observed. Notably, the largest lateral spreading occurs at smaller Re_{Dt}, corresponding to weaker terminal settling inertia. This behavior indicates that the lateral extent of the outer region cannot be explained solely by particle settling dynamics near the bottom.

In contrast, Figure 7(b) presents D^*_{outer}as a function of Re_{Mi}, revealing a much clearer data collapse. This indicates that the lateral extent of the outer deposition region is governed primarily by the momentum injected near the nozzle rather than by the terminal behavior of individual particles.

The improved collapse with Re_{Mi}suggests that the spreading of the outer region is driven by the flow field generated through particle–fluid momentum transfer during the injection process. The initial particle jet imparts momentum to the surrounding liquid, inducing a radial flow that transports particles laterally toward the periphery. Consequently, the outer region spreading is not controlled by terminal settling inertia characterized by Re_{Dt}, but is instead dominated by flow-induced transport associated with the initial momentum injection, as represented by Re_{Mi}.

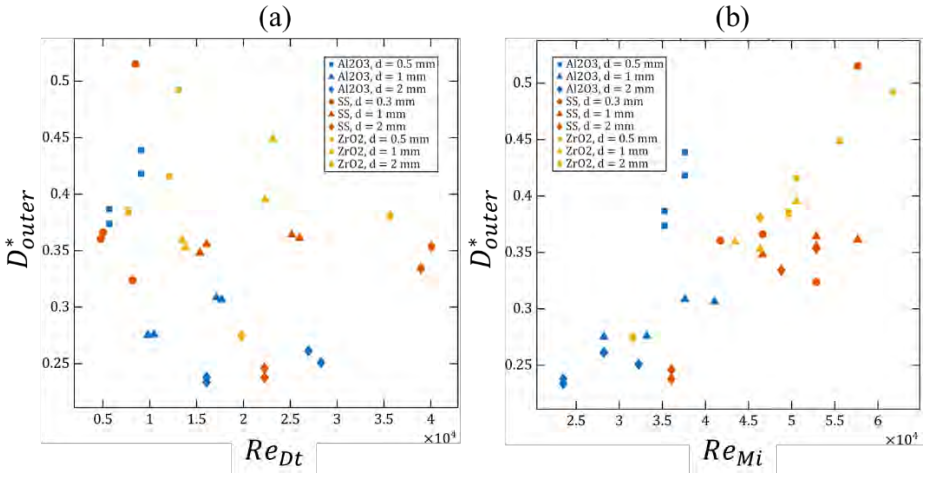

Figure 7. Relationship between the normalized outer diameter $\boldsymbol{D^*_{\text{outer}}}$ and Reynolds numbers based on (a) the representative terminal velocity, $\boldsymbol{Re_{Dt}}$, and (b) the initial jet momentum, $\boldsymbol{Re_{Mi}}$.

3.5 Maximum height h_{max}

Figure 8(a) and (b) show the relationship between the normalized maximum bed height $h_{\text{max}}$and the Stokes number $St_i$for two nozzle diameters. For both cases, a clear transition is observed around $St_i \approx 1$, indicating a change in the dominant mechanism governing vertical bed development.

In the low-St_i regime, h_{max}increases with increasing St_i. Particle motion in this regime remains strongly coupled to the surrounding fluid, and increasing particle inertia reduces the effectiveness of flow-induced lateral redistribution after bottom impact. As a result, particles tend to accumulate near the central region, promoting vertical piling and leading to an increase in the maximum bed height.

In the high-St_i regime, granular-jump dynamics dominate, and the evolution of $h_{\text{max}}$is governed by how particle momentum is redistributed near the bottom. As particle inertia increases, granular-jump-induced collisions occur closer to the bed center, enhancing particle–particle interactions and promoting lateral redistribution toward the fan region. For conditions in which particle supply and momentum injection are

spatially distributed over a wider area, this redistribution limits further central accumulation, resulting in plateau or decreasing trends in $h_{\max}$.
Overall, $h_{\max}$reflects a balance between inertia retention during bottom impact and the scale-dependent redistribution of particle mass near the bed. Its evolution is therefore controlled not only by particle dissipation, but also by how the spatial distribution of particle momentum governs the partitioning between vertical piling and lateral spreading.

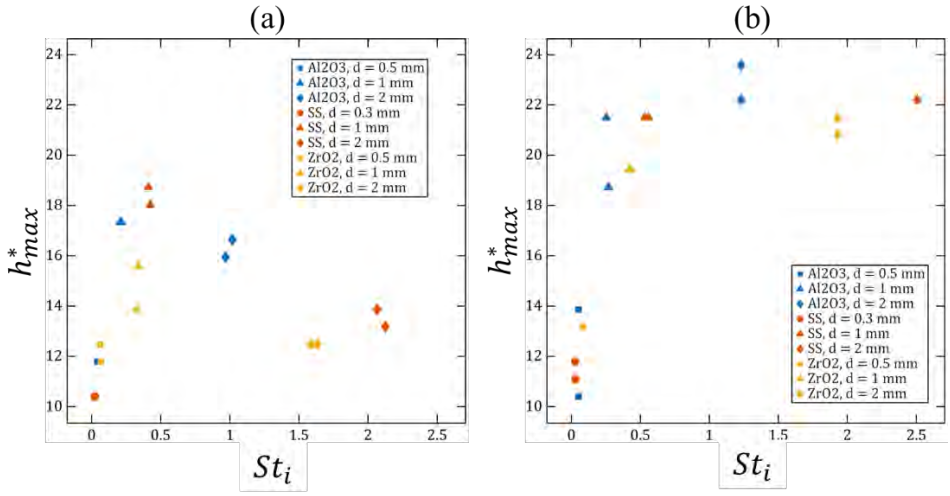

Figure 8. Relationship between the normalized maximum bed height h^*_{max} and the Stokes number St_i for (a) $D_{\text{nozzle}} = 24$mm and (b) $D_{\text{nozzle}} = 30$mm. In both cases, two regimes are observed around $St_i \approx 1$, indicating a transition in the dominant bed-formation mechanism.

3.6 Outer slope angle θ_{out}

Figure 9 (a) and (b) show the relationship between the outer slope angle θ_{out} and the Stokes number St_i for two nozzle diameters. The similarity of the trends for different nozzle diameters indicates that θ_{out} is a relatively robust geometrical indicator with weak dependence on injection scale.
In the low-St_i regime, θ_{out}increases with increasing St_i. As particle inertia becomes more significant relative to viscous forces, particles arriving at the outer region are less easily rearranged by the surrounding fluid. Consequently, steeper slopes can be maintained without significant fluid-induced reworking.
In the high-St_i regime, θ_{out} decreases with further increases in St_i. Under these conditions, collision-driven redistribution and inertial avalanching dominate near the bed periphery. Particles arriving at the outer region retain sufficient momentum to destabilize local packing, leading to enhanced rearrangement and gentler slopes.
These results indicate that θ_{out} captures the stabilization mechanism at the bed periphery and reflects the competition between fluid-induced reworking and inertia-driven redistribution.

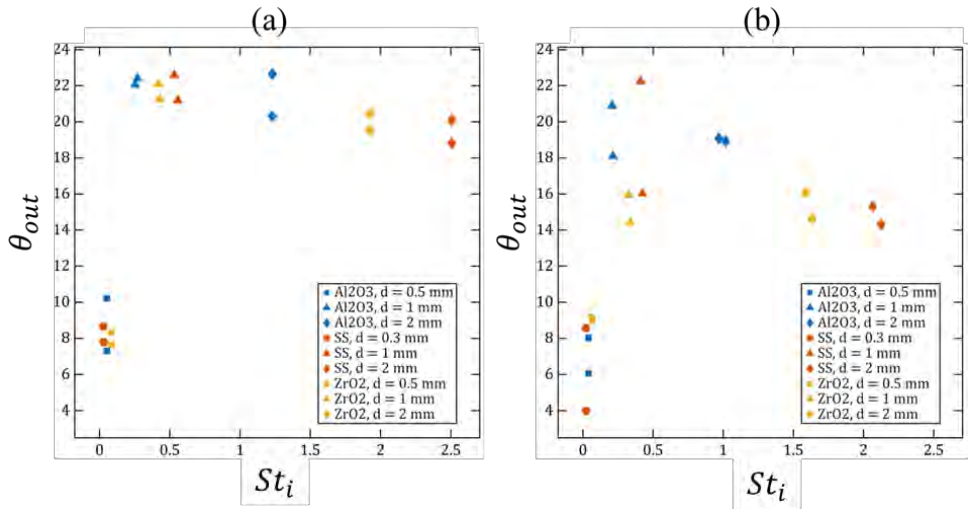

Figure 9. Relationship between the outer slope angle θ_{out} and the Stokes number St_i for (a) $D_{\mathrm{nozzle}} = 24\mathrm{mm}$ and (b) $D_{\mathrm{nozzle}} = 30\mathrm{mm}$. In both cases, two regimes are observed around $St_i \approx 1$.

3.7 Inner slope angle θ_{in}

Figure 10 (a) and (b) show the dependence of the inner slope angle θ_{in} on the Stokes number St_i for two nozzle diameters. For both cases, θ_{in} increases in the low-St_i regime ($St_i < 1$), where particle motion remains strongly coupled to the surrounding fluid. As St_i increases, particles increasingly retain vertical momentum during settling, enabling weak granular jumps at bottom impact. Consequently, a larger fraction of particles contributes to inner-slope formation near the center, leading to a gradual increase in θ_{in}.
Around $St_i \approx 1$, a transition in the dominant formation mechanism of the inner slope is observed, beyond which the behavior of θ_{in} depends strongly on the nozzle diameter. For the larger nozzle diameter, θ_{in} decreases monotonically in the high-St_i regime. In this case, particle supply and momentum injection are spatially distributed over a wide area, and granular-jump-induced particles are preferentially redistributed laterally rather than accumulating near the center. As a result, inner-slope geometry is governed primarily by lateral redistribution, and the effect of spreading leads to a progressive reduction in θ_{in}.
In contrast, for the smaller nozzle diameter, θ_{in} exhibits a non-monotonic trend in the high-St_i regime. Immediately above $St_i \approx 1$, energetic particle impacts concentrated near the bed center disrupt the formation of a stable inner slope, resulting in a sharp decrease in θ_{in}. With further increases in St_i, the inward displacement of the granular-jump location becomes more pronounced, and particle collisions occur while a larger fraction of inertia is retained. Under these conditions, enhanced particle accumulation and collision-induced rearrangement promote packing and frictional stabilization near the center, leading to a recovery and subsequent increase in θ_{in}.
Overall, these results indicate that θ_{in} reflects a regime-dependent balance between lateral redistribution and central stabilization, analogous to the behavior observed for the maximum bed height. While inner-slope formation is dominated by redistribution for the larger nozzle diameter, scale-dependent collision inertia and packing effects play an increasingly important role for the smaller nozzle diameter, making θ_{in} a sensitive indicator of granular-jump onset and particle redistribution geometry.

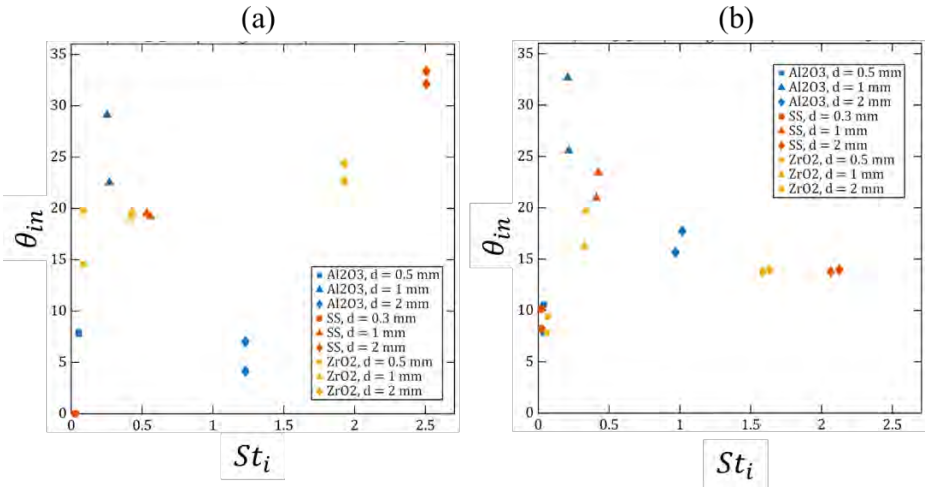

Figure 10. Relationship between the inner slope angle $\boldsymbol{\theta_{in}}$ and the Stokes number $\boldsymbol{St_i}$ for (a) $\boldsymbol{D_{nozzle}} = \mathbf{24}$mm and (b) $\boldsymbol{D_{nozzle}} = \mathbf{30}$mm.

4. EMPRICAL CORRELATIONS

Based on the detailed analysis in Section 3, this section examines whether the dominant tendencies governing debris-bed formation can be quantitatively embedded into a predictive description of the outer slope angle θ_{out} as a physically meaningful and condition-independent quantity.

As discussed in Section 3, θ_{out} is established through granular-jump-induced momentum conversion near the bottom, subsequent particle transport toward the outer region, and particle rearrangement and stabilization at the bed periphery. To represent these mechanisms in a dimensionless framework, Fr_t is adopted to characterize granular-jump intensity, Re_{Mi} to account for flow-driven particle transport, and the Stokes number St_i to describe particle–fluid coupling. In addition, a buoyancy parameter $Bu = (\rho_p - \rho_l)/\rho_l$ is introduced to represent the effect of density difference driving sedimentation.

The results in Section 3 revealed a clear regime transition around $St_i \approx 1$. Since the dominant physical mechanisms differ across this boundary, separate empirical correlations were constructed for the low- and high-St_i regimes. The resulting correlations are given as follows:

$$\theta_{\text{out}} = 2.23 \times 10^9 \, Fr_t^{0.77} \, Re_{Mi}^{-1.80} \, St_i^{0.16} \, Bu^{0.51} (St_i < 1), \tag{7}$$

$$\theta_{\text{out}} = 6.34 \times 10^4 \, Fr_t^{0.13} \, Re_{Mi}^{-0.82} \, St_i^{-0.016} \, Bu^{0.20} (St_i \gtrsim 1). \tag{8}$$

Figure 10 shows that the proposed correlations reproduce the experimental values of $\theta_{\text{out}}$with small errors, yielding a mean absolute percentage error of 12.1% in the low-St_i regime and 3.16% in the high-St_i regime, both smaller than the experimental repeatability.

The fitted exponents provide a consistency check between the proposed correlations and the experimentally observed trends discussed in Section 4. The Stokes number shows a positive exponent in the low-St_i regime and a near-zero to slightly negative exponent in the high-St_i regime, reflecting the transition from particle–fluid interaction–dominated behavior to particle–particle interaction–dominated redistribution.

The nozzle-based Reynolds number Re_{Mi} exhibits a negative dependence in both regimes, indicating that enhanced flow-driven lateral spreading reduces the outer slope angle irrespective of the dominant interaction regime. The buoyancy parameter Bushows a positive dependence, consistent with the role of density contrast in promoting inertia-driven particle rearrangement.

The influence of the Froude number Fr_t is pronounced in the low-St_i regime due to granular-jump-induced momentum conversion but becomes weak in the high-St_i regime, suggesting a secondary role once particle

motion is inertia-dominated. Overall, although empirical, the correlations capture the dominant physical mechanisms governing the outer slope formation in a physically consistent manner.

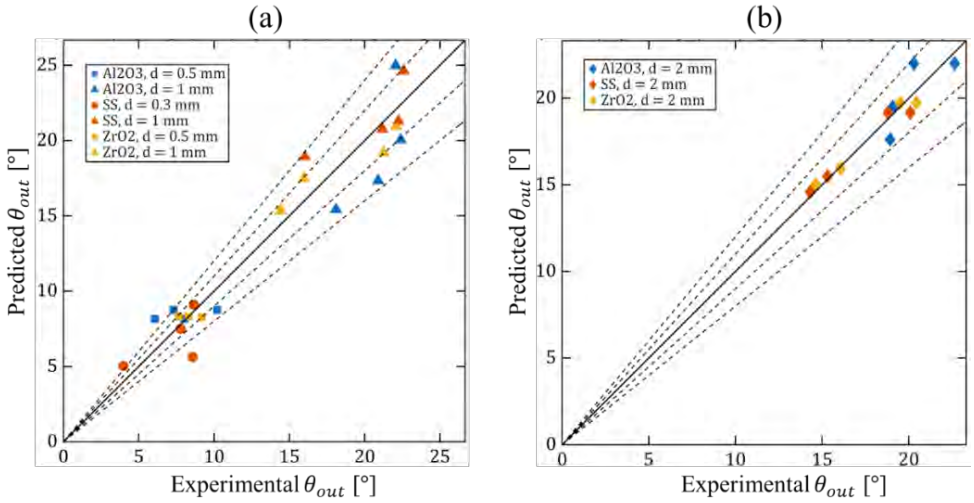

Figure 11. Comparison between predicted and experimental values of the outer slope angle $\boldsymbol{\theta_{out}}$ obtained from the regime-wise empirical correlations; (a) data points with $\boldsymbol{St_i < 1}$and (b) data points with $\boldsymbol{St_i \gtrsim 1}$. Solid lines indicate the parity line, while dashed lines represent ±10% and ±20% deviation from the experimental values. MAPE on each graph is 12.12% in (a), 3.16% in (b).

5. CONCLUSIONS

Large-scale three-dimensional experiments were conducted to investigate debris-bed formation during underwater sedimentation of fine particles under conditions relevant to CDA in sodium-cooled fast reactors. By systematically analyzing debris-bed shape together with appropriate dimensionless parameters, the dominant formation behaviors and their underlying physical mechanisms were identified.

The experiments showed that debris beds can be classified into three representative morphologies—volcano, concave, and flat-topped—and that debris-bed formation is governed by regime-dependent mechanisms with a clear transition around a Stokes number of unity. At low Stokes numbers, particle motion is strongly coupled to the surrounding fluid, and granular-jump-induced momentum conversion promotes lateral particle transport, leading to central cavity formation and influencing both bed height and outer slope geometry. At high Stokes numbers, particle inertia dominates, particle–particle interactions and inertial redistribution become more important, and the influence of fluid-driven transport diminishes.

Among the geometric indicators examined, the outer slope angle $\theta_{\mathrm{out}}$was identified as a relatively robust characteristic with weak dependence on experimental scale and debris volume. Based on this regime distinction, empirical correlations for θ_{out}were developed, reproducing the experimental data within approximately ±13%, which is smaller than the experimental repeatability error. The fitted exponents are consistent with the experimentally observed trends in each regime, supporting the physical relevance of the selected dimensionless parameters.

Although direct extrapolation to reactor conditions is limited by the simplified experimental configuration, the proposed framework provides a physically consistent and scalable basis for debris-bed assessment. Future work should extend the approach to more realistic conditions, including non-spherical particles, modified bottom geometries, and forced or background convection, which are expected to affect granular-jump behavior and near-bottom momentum redistribution. The present findings contribute to the refinement of predictive models and to the design and safety assessment of core catcher systems in SFRs.

NOMENCLATURE

Bu buoyancy parameter, $(\rho_p - \rho_l)/\rho_l$ [–]
C_d drag coefficient [–]
D_{inner} inner diameter of debris bed [m]
D_{fan} fan diameter of debris bed [m]
D_{outer} outer diameter of debris bed [m]
D_{nozzle} nozzle diameter [m]
Fr_t Froude number based on terminal velocity, $\mathbf{v}_t/\sqrt{gD_{\mathrm{nozzle}}}$ [–]
h_{max} maximum debris bed height [m]
Re_{Dt} Reynolds number based on terminal velocity [–]
Re_{Mi} Reynolds number based on initial jet momentum [–]
St_i Stokes number characterizing particle–fluid coupling [–]
$\mathbf{v}_i$ particle velocity at nozzle exit [m s^{-1}]
$\mathbf{v}_t$ representative terminal velocity near bottom region [m s^{-1}]
V total particle volume released [m^3]
θ_{in} inner slope angle of debris bed [deg]
θ_{out} outer slope angle of debris bed [deg]

Greek symbols
ρ_l liquid density [kg m^{-3}]
ρ_p particle density [kg m^{-3}]
μ liquid dynamic viscosity [Pa s]
ν liquid kinematic viscosity [m^2 s^{-1}]

ACKNOWLEDGMENTS

This work is funded by JSPS KAKENHI grant number JP24K22849. This work was supported by JAEA Nuclear Energy S&T and Human Resource Development Project Grant Number JPJA24H24020026

REFERENCES

[1] Suzuki, T., et al., *Fragmentation behavior of molten core materials in sodium*, Nucl. Eng. Des., 272 (2014) 245–257.
[2] Tentner, A.M., Parma, E., Wigeland, R., *Core disruptive accident analysis and core catcher concepts for SFRs*, Nucl. Eng. Des., 240 (2010) 3663–3676.
[3] Sudha, K., Harvey, J., *Debris bed coolability in fast reactor severe accidents*, Nucl. Eng. Des., 241 (2011) 365–376.
[4] Polidoro, F., Parozzi, F., *In-vessel retention and debris bed cooling issues in fast reactors*, Ann. Nucl. Energy, 45 (2012) 114–123.
[5] Tagami, H., et al., *Three-dimensional sedimentation experiments on debris bed formation*, Ann. Nucl. Energy, 111 (2018) 474–486.
[6] Shamsuzzaman, M., et al., *Experimental study on debris bed characteristics for sedimentation behavior of solid particles*, Ann. Nucl. Energy, 111 (2018) 474–486.
[7] Sheikh, M., et al., *Effect of mixed particle size on debris bed formation*, Nucl. Eng. Des., 330 (2018) 402–414.
[8] Cheng, X., et al., *Large-scale experiments on debris bed formation and flow regimes*, Nucl. Eng. Des., 312 (2017) 233–245.
[9] Boudet, J.F., et al., *Granular jump dynamics*, Phys. Rev. Lett., 99 (2007) 114301.
[10] Schiller, V.L., Naumann, A., *A drag coefficient correlation*, Z. Ver. Dtsch. Ing., 77 (1935) 318–320.

Experimental Investigation of Debris-Bed Formation for Optimizing Core-Catcher Design

ERMSAR 2026

May 19th , 2026

Session 2.2 In-vessel Corium and debris coolability

M2 Tomonari Mashiko,
Yihua Xu, Ryo Yokoyama, Yohei Kano, Miwa Shuichiro, Koji Okamoto

Table of contents

1. Background and objective
2. Methods for 3D DBF experiments
3. Results: Terminal bed shape
4. Discussion on each geometric parameter
    1. D_{inner}
    2. D_{outer}
    3. θ_{out}
5. Developing empirical correlations (θ_{out})
6. Summary

Table of contents

1. Background and objective
2. Methods for 3D DBF experiments
3. Results: Terminal bed shape
4. Discussion on each geometric parameter
    1. D_{inner}
    2. D_{outer}
    3. θ_{out}
5. Developing empirical correlations (θ_{out})
6. Summary

Background

ULOF (Unprotected LOss of Flow)

→***What happens when the coolant flow is lost in SFR?***

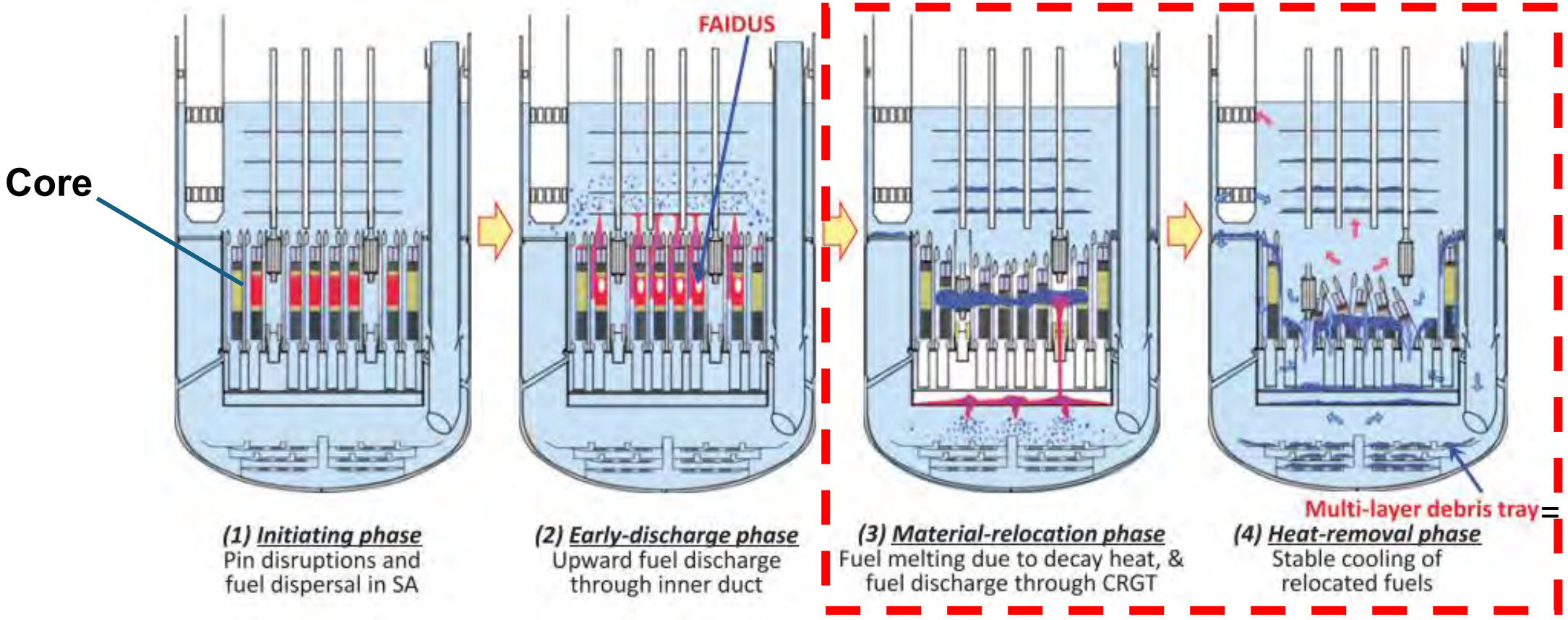

[ref] T. Suzuki, et al., JNST Vol.51, No. 4, pp.493-513(2014)

Background

(3) Material Relocation Phase

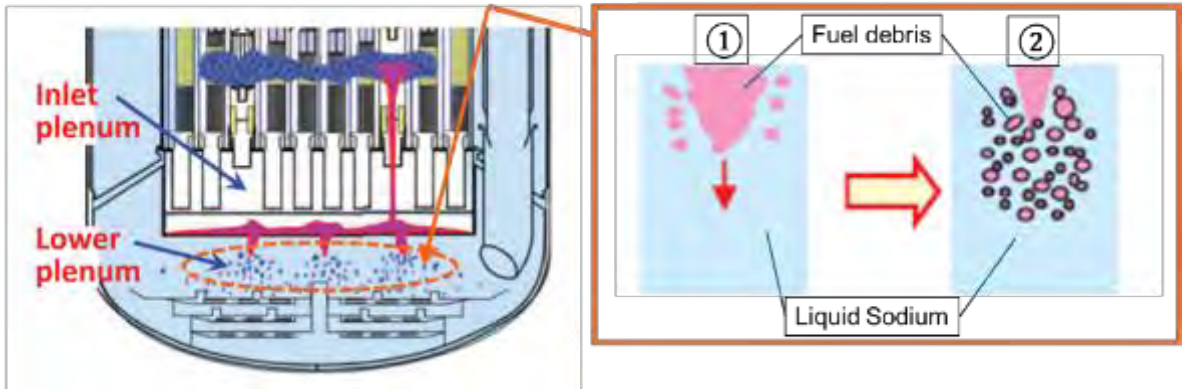

① **Fuel debris is quenched** by **liquid sodium**
② It becomes **tiny particle**
(Diameter: 0.1~1.0mm)←***sub-millimeter particles***

(4) Heat Removal Phase

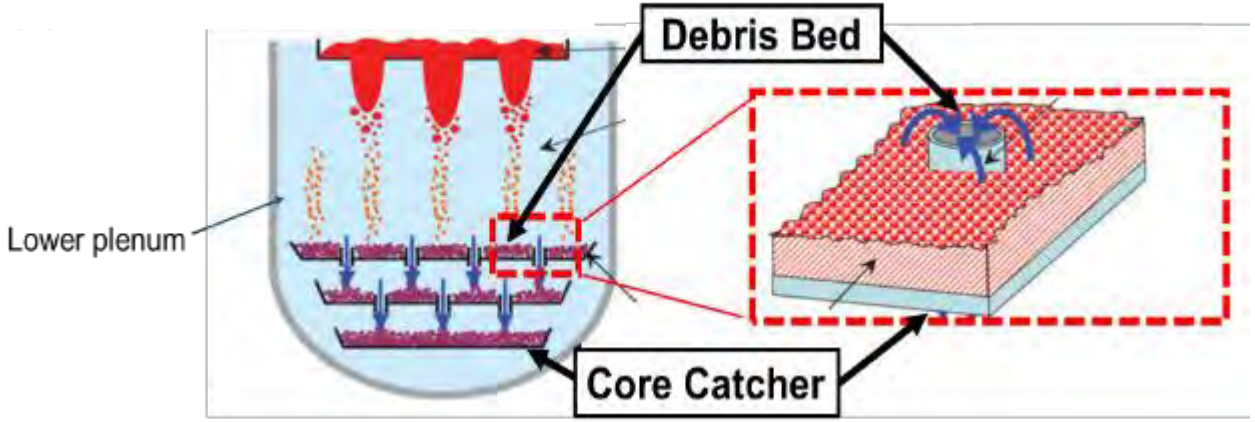

- **Debris accumulates** on the ***Core Catcher*** and is **cooled by** ***natural circulation***
- **The coolability** depends on **the debris bed shape**

Debris bed formation is important for the coolability and safety

[ref] T. Suzuki, et al., JNST Vol.51, No. 4, pp.493-513(2014)

Background

The physics of two-phase flow of liquid(sodium) and solid(debris particles) is **complicated**…

Debris bed formation is investigated **experimentally** **using metal particles and water**

DBF in SFR

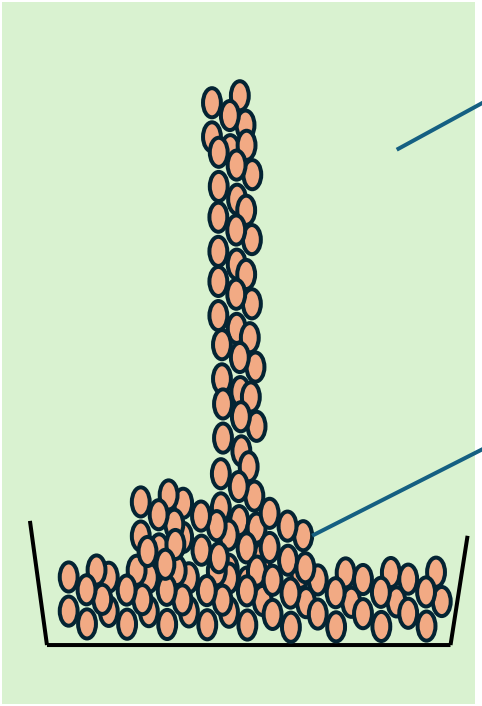

Liquid sodium ⇔ Water

Debris particles ⇔ Metal particles

DBF experiment

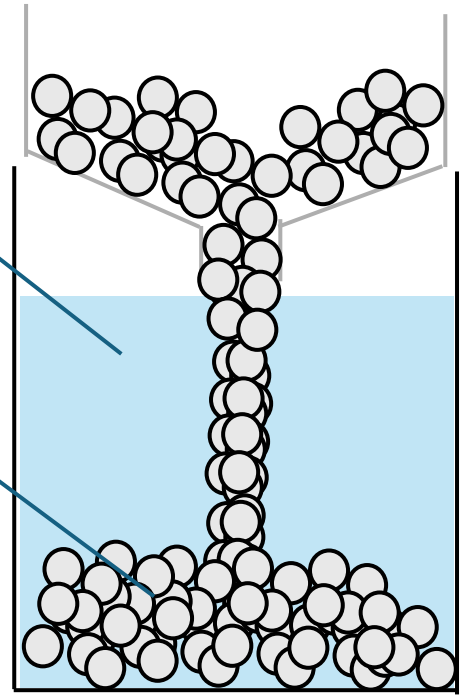

Previous Study (2D DBF experiment)

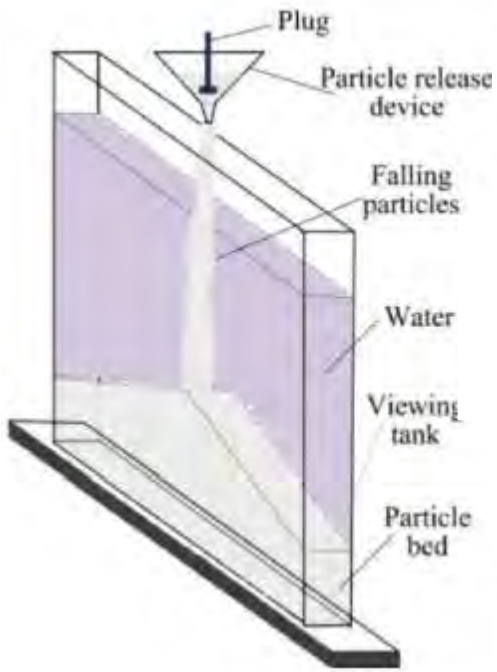

Fig. The experimental facility

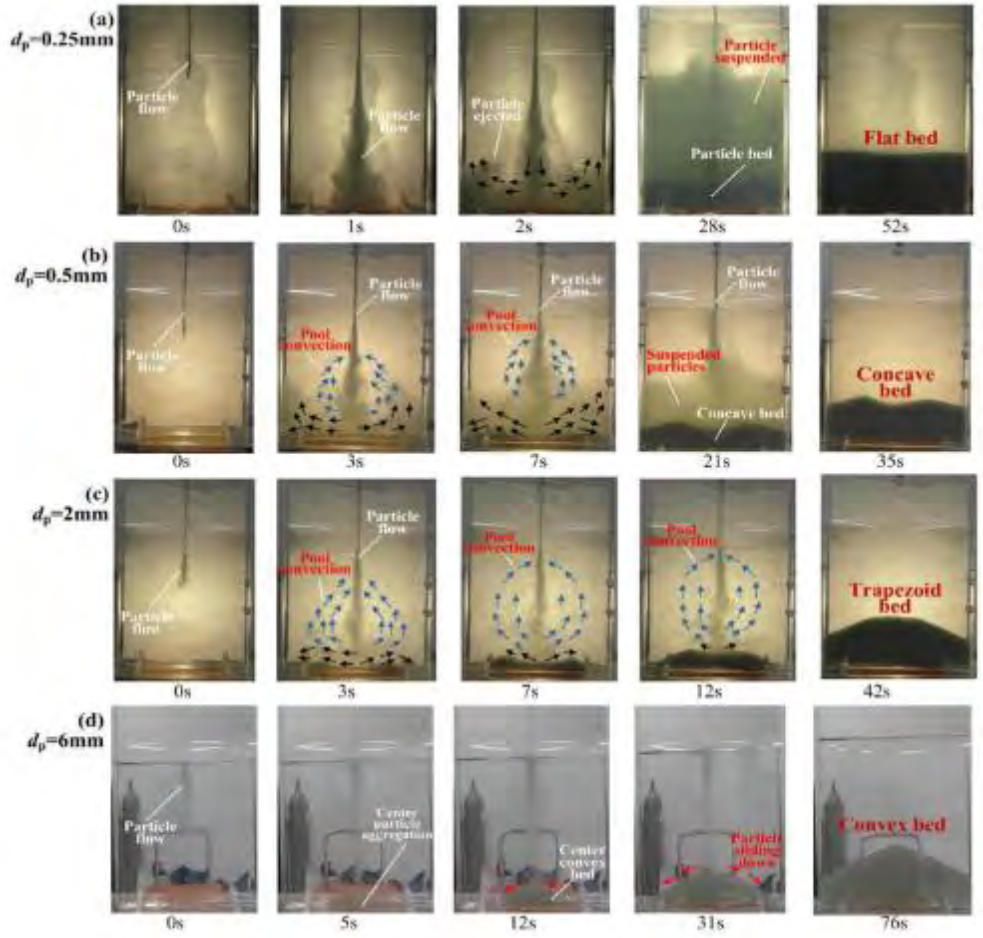

Fig. The results of the 2D DBF experiment

Previous Study

2D Large-scale DBF experiments using sub-millimeter particles

Important factors for debris bed shape

- **Particle diameter**
- The balance; **inertia vs convection**

These results can be applied to ***3D***?

[ref] Cheng, S.et al.,. Ann. Nucl. Energy 109, 658–666.

Objective

＜Objective＞

By **clarifying the debris bed formation mechanism** through **3D experiment**, **the debris bed formation behavior** can be understood, contributing to the evaluation of **the integrity of core catcher systems in SFRs**.

Experiment to get insights

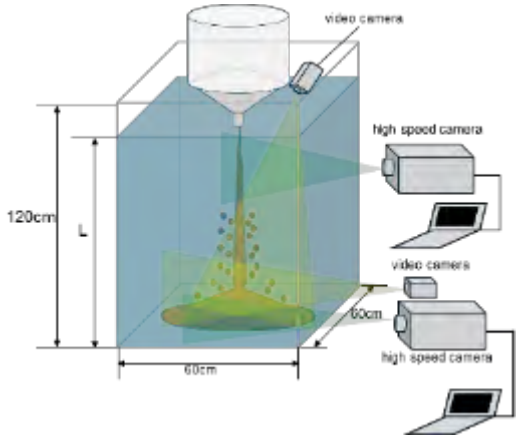

Analyzing underlying physics

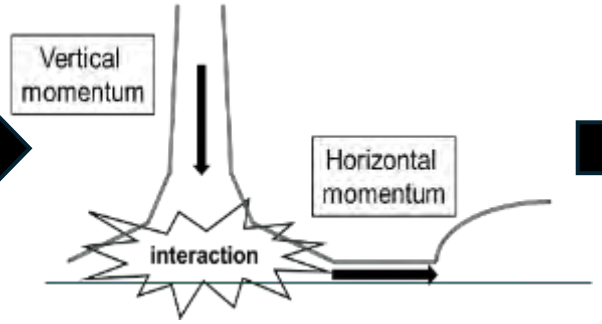

Developing empirical correlations

$$\theta_{\mathrm{out}} = 1.47 \times 10^{8}\, Fr_t^{0.63}\, Re_{Mi}^{-1.54}\, St_i^{0.19}\, Bu^{0.46}$$

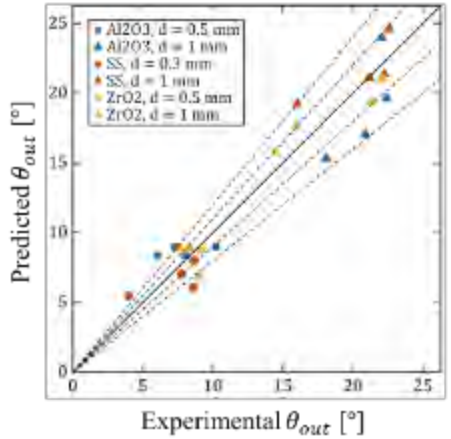

Evaluating the actual scenario

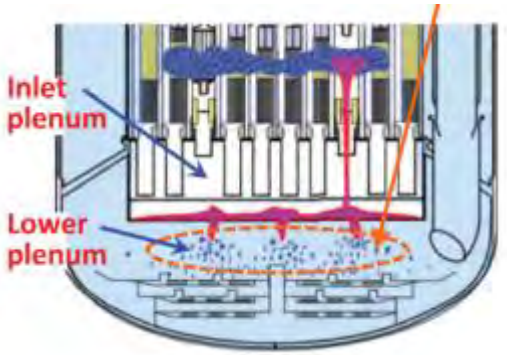

[ref] T. Suzuki, et al., JNST Vol.51, No. 4, pp.493-513(2014)

Table of contents

1. Background and objective
2. Methods for 3D DBF experiments
3. Results: Terminal bed shape
4. Discussion on each geometric parameter
    1. D_{inner}
    2. D_{outer}
    3. θ_{out}
5. Developing empirical correlations (θ_{out})
6. Summary

Method

Procedures

① Setting particles into hopper
② Releasing particles into water
③ Measuring the DBF behavior

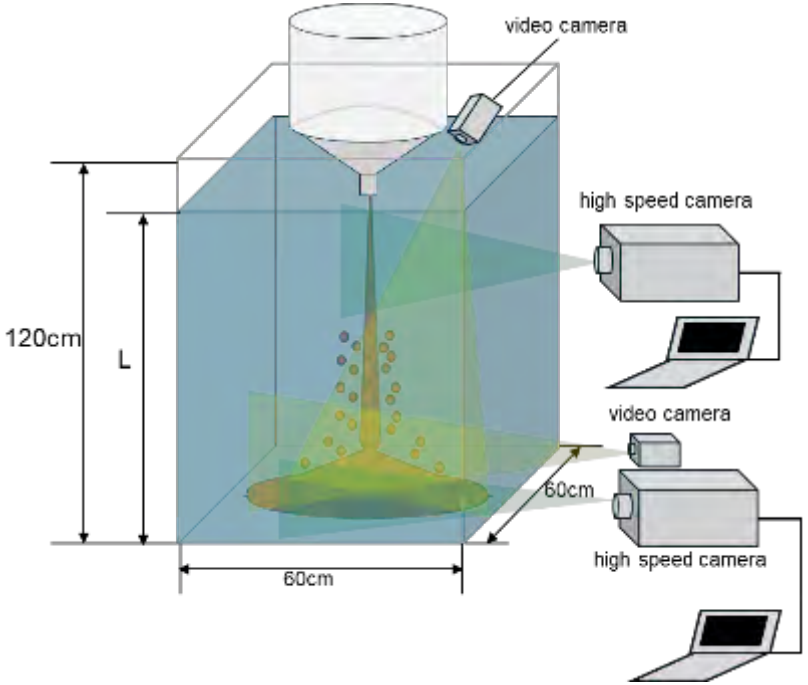

Fig. The Schematic of the experimental facility

Initial Variables

① **Particle Diameter d**

0.5mm 1mm 2.0mm

② **Particle Density ρ_p**

SS
(7900kg/m³)

ZrO_2
(6070kg/m³)

Al_2O_3
(4000kg/m³)

③ **Nozzle Diameter D_{nozzle}**

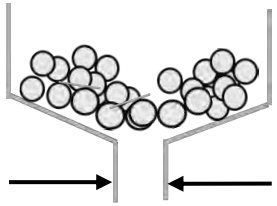

$D_{nozzle} = 24, 30$ mm

Movie of the experiment

Table of contents

1. Background and objective
2. Methods for 3D DBF experiments
3. Results: Terminal bed shape
4. Discussion on each geometric parameter
    1. D_{inner}
    2. D_{outer}
    3. θ_{out}
5. Developing empirical correlations (θ_{out})
6. Summary

Terminal bed shape

Volcano	Concave bed	Flat-topped
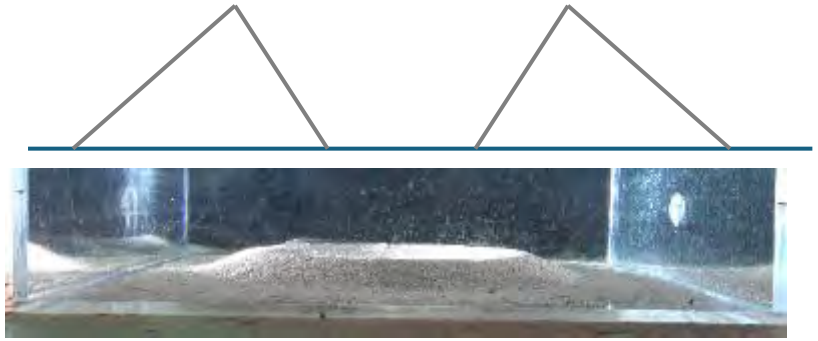	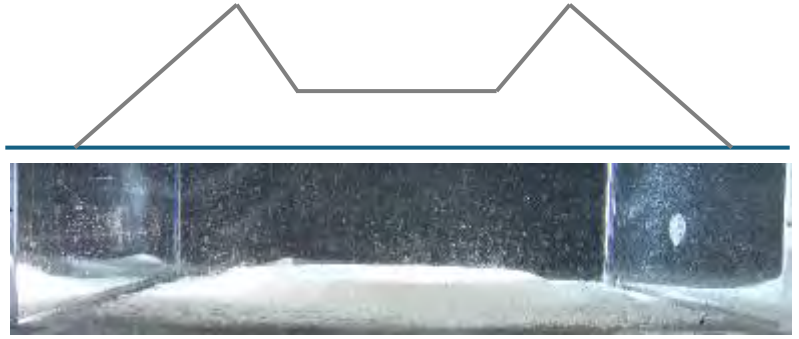	
d = 1.0mm, Stainless	d = 0.5mm, ZrO2	d = 0.3mm, Stainless

Terminal bed shape

UTokyo

Volcano	Concave bed	Flat-topped

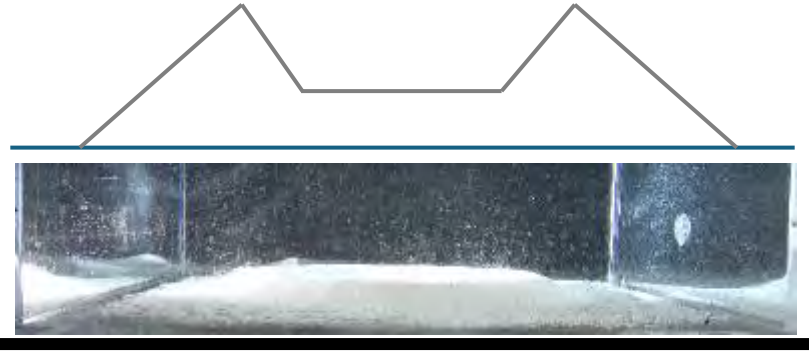

Which parameters influence the bed geometry?
What's the underlying physics?

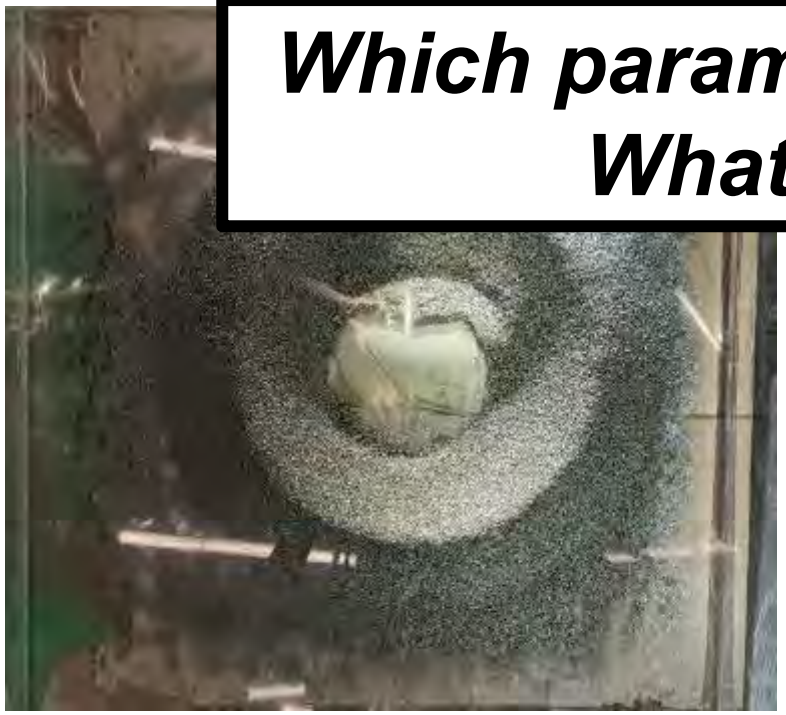

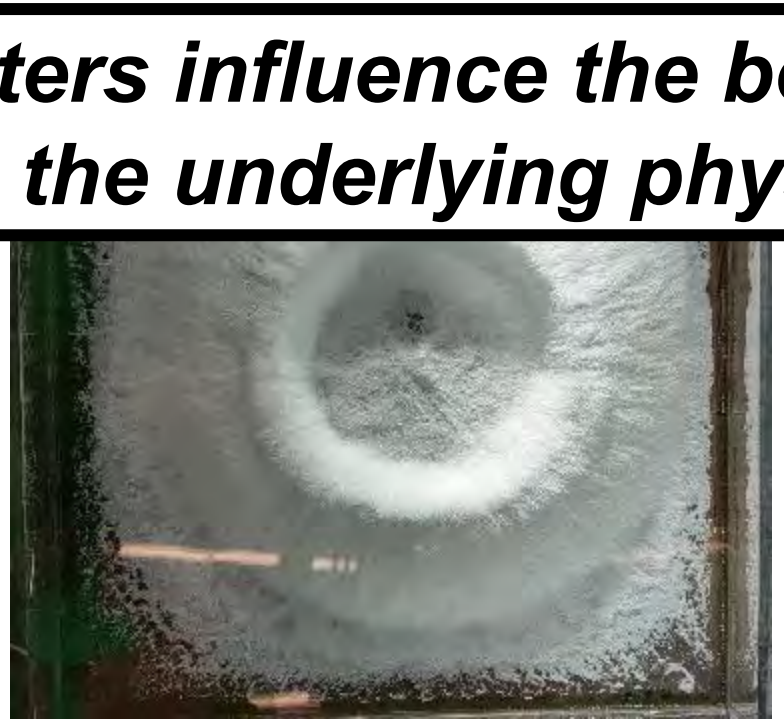

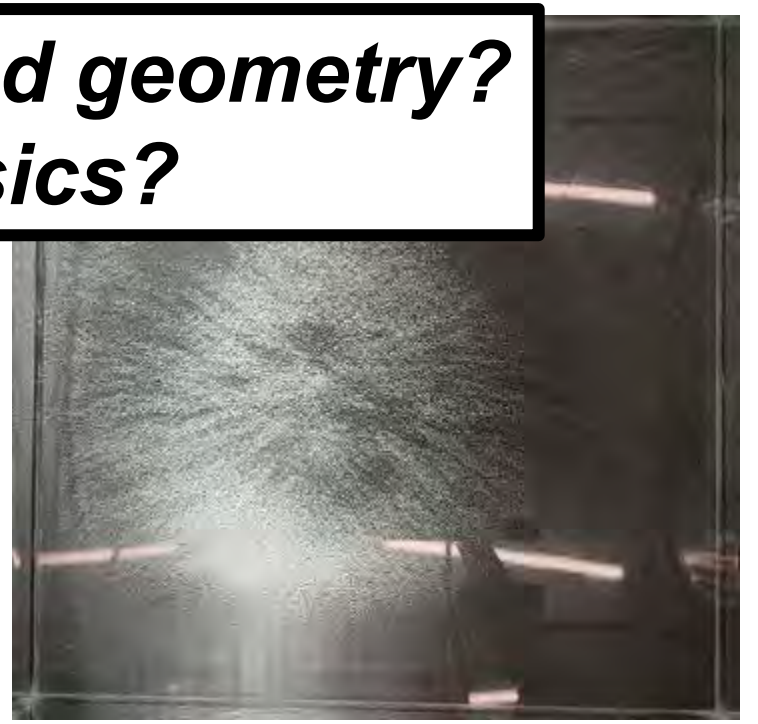

d = 1.0mm, Stainless

d = 0.5mm, ZrO2

d = 0.3mm, Stainless

Measured values

Volcano

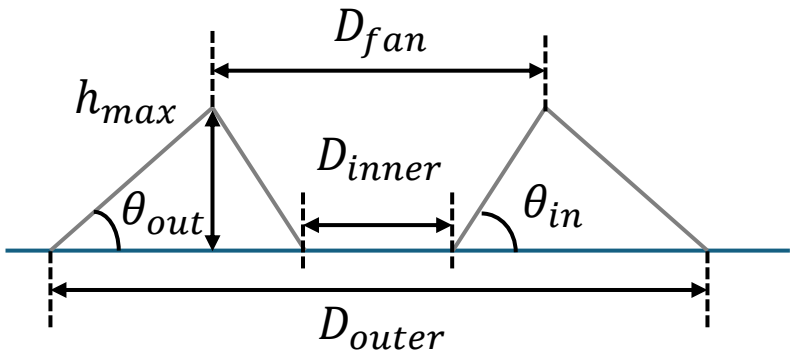

Concave bed

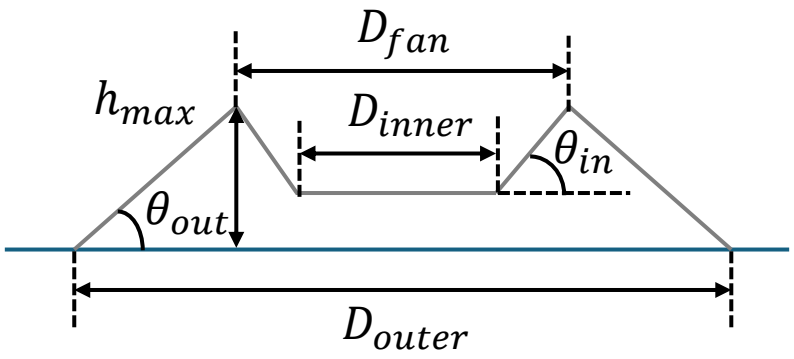

Flat-topped

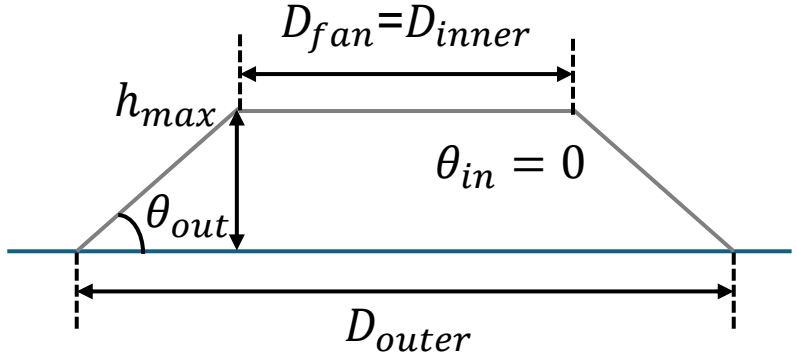

Dimensionless

$$D^*_{inner} = \frac{D_{inner}}{V^{\frac{1}{3}}} \quad D^*_{fan} = \frac{D_{volcano}}{V^{\frac{1}{3}}} \quad D^*_{outer} = \frac{D_{outer}}{V^{\frac{1}{3}}} \quad h^*_{max} = \frac{h_{max}}{V^{\frac{1}{3}}}$$

$V = initial\ particles\ volume$ (3.0L)

Table of contents

1. Background and objective
2. Methods for 3D DBF experiments
3. Results: Terminal bed shape
4. Discussion on each geometric parameter
    1. D_{inner}
    2. D_{outer}
    3. θ_{out}
5. Developing empirical correlations (θ_{out})
6. Summary

Discussion ~D^*_{inner}

Volcano

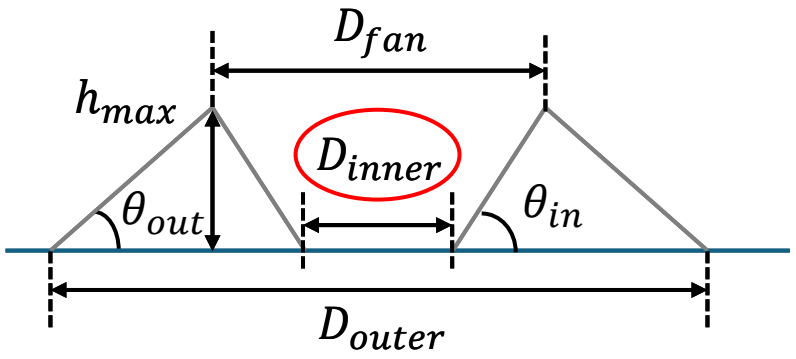

Concave bed

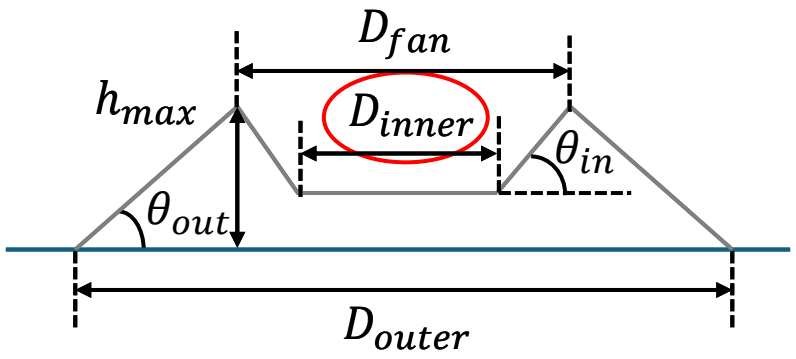

Flat-topped

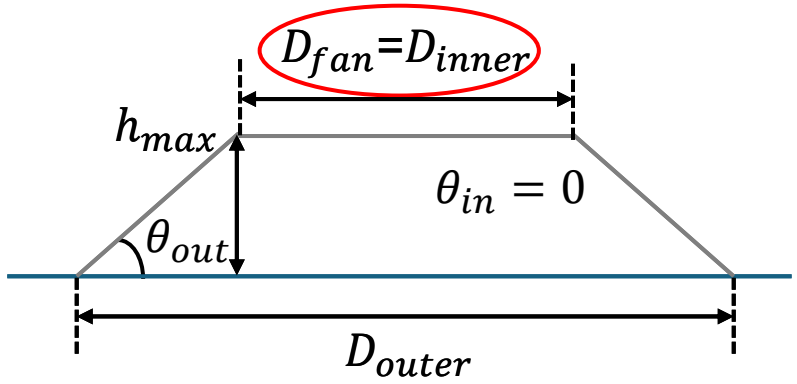

Dimensionless

$$D^*_{inner} = \frac{D_{inner}}{V^{\frac{1}{3}}} \quad D^*_{fan} = \frac{D_{volcano}}{V^{\frac{1}{3}}} \quad D^*_{outer} = \frac{D_{outer}}{V^{\frac{1}{3}}} \quad h^*_{max} = \frac{h_{max}}{V^{\frac{1}{3}}}$$

$V = initial\ particles\ volume$ (3.0L)

Discussion ~$D^*_{inner} = \frac{D_{inner}}{\frac{1}{V^3}}$~

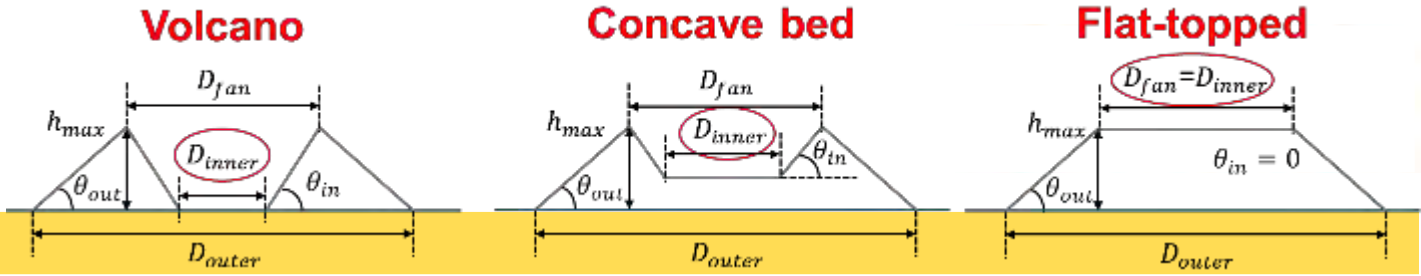

D_{inner} is generated by "***Granular jump***"?

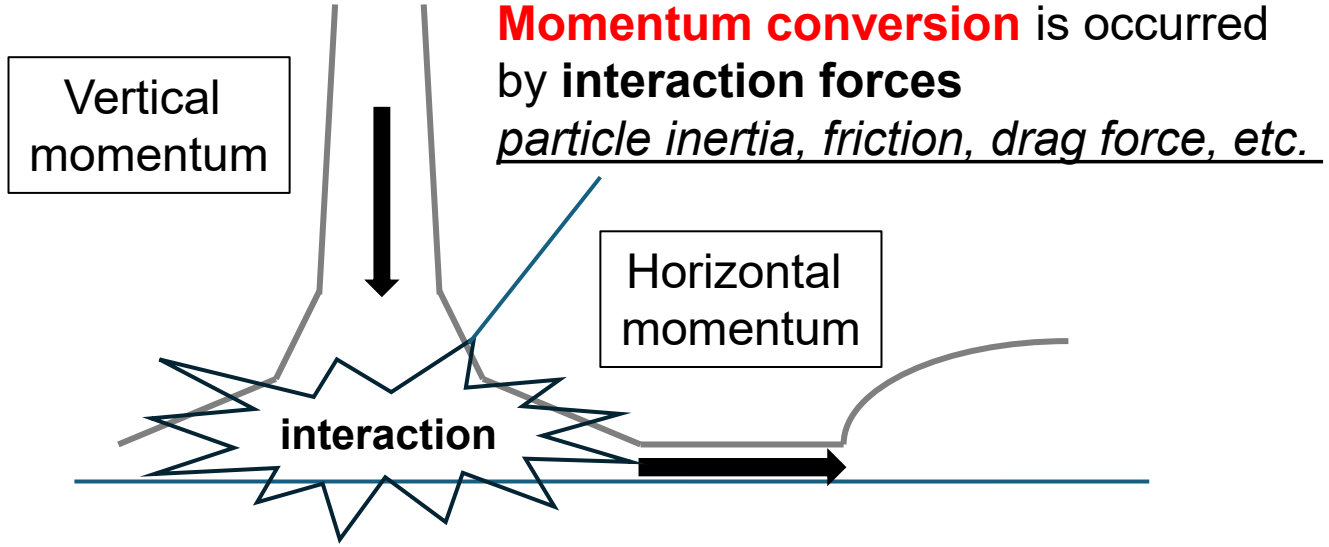

The intensity of jump is governed by Fr number

Discussion ~$D^*_{inner} = \frac{D_{inner}}{V^{\frac{1}{3}}}$~

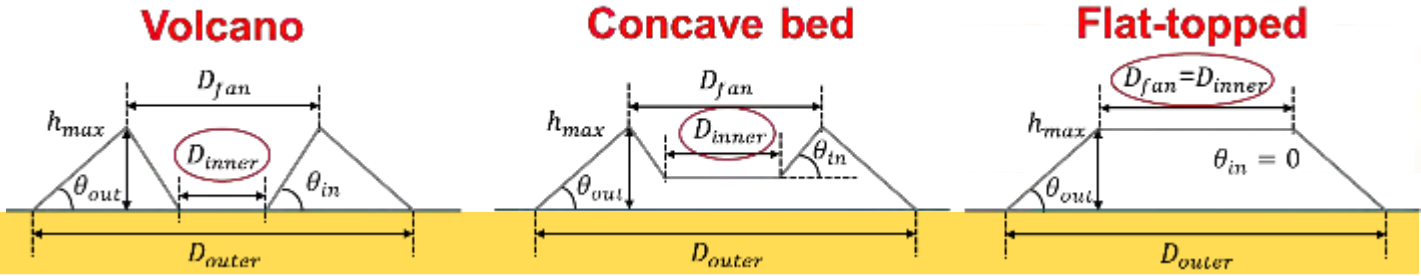

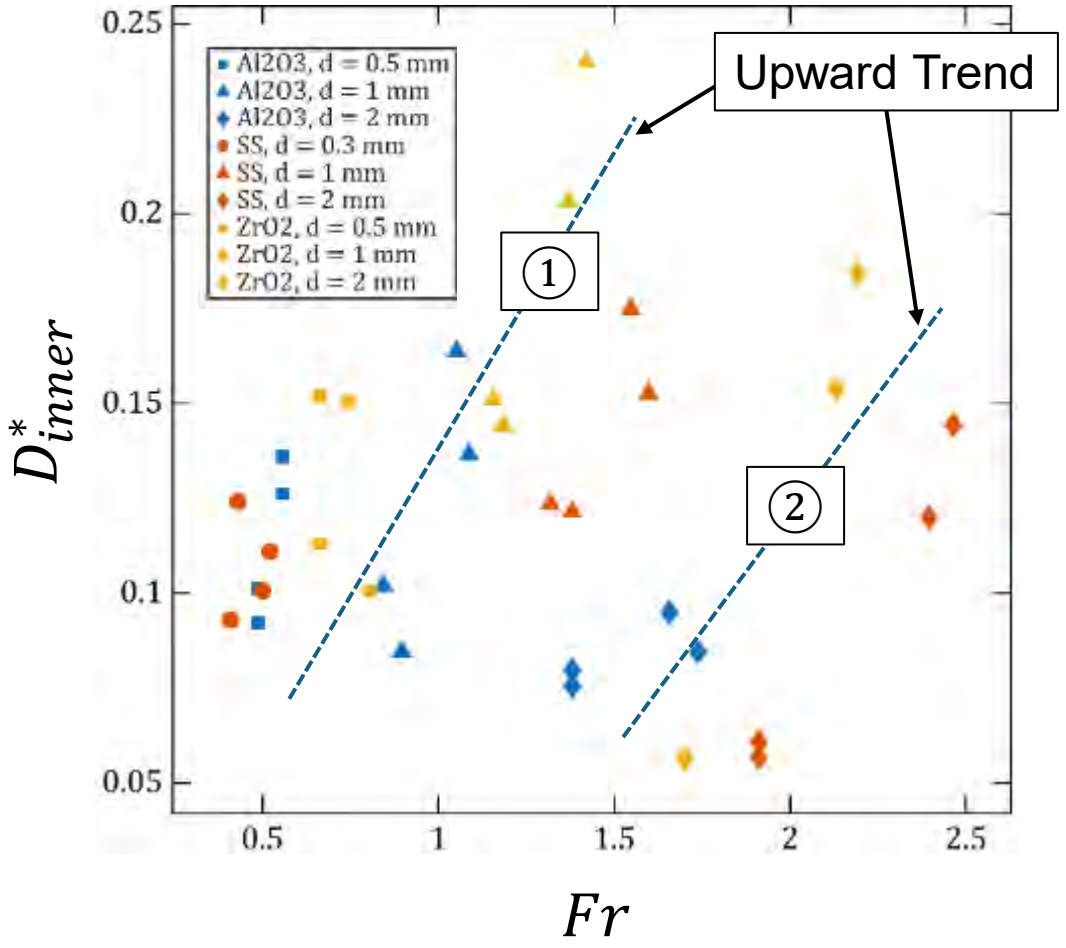

$$Fr = \frac{v_t}{\sqrt{gD_{nozzle}}}$$

v_t = particle terminal velocity
D_{nozzle} = nozzle diameter

- **Two regimes** exist…
  - ① Particle size: **less than 1mm**
  - ② Particle size: **2mm**

- D_{inner} **is in proportion to** Fr on each regime

D_{inner} **is governed by the intensity of granular jump (**Fr**)**

Fig. The relationship between Fr and D^*_{inner}

Discussion ~$D^*_{inner} = \frac{D_{inner}}{V^{\frac{1}{3}}}$~

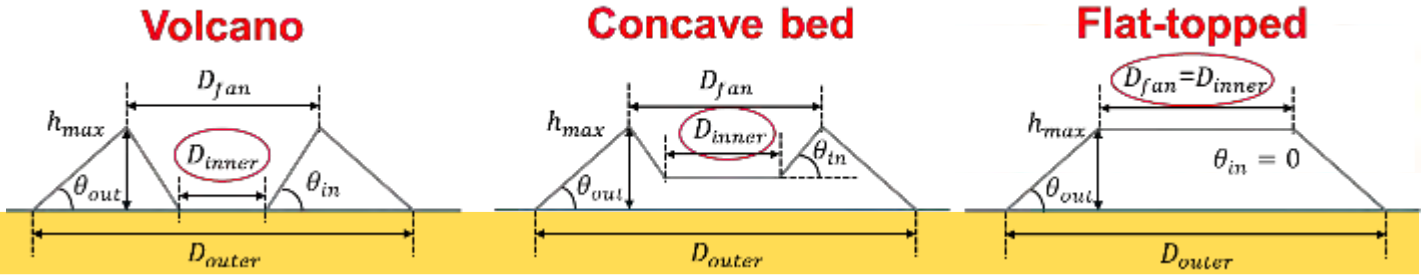

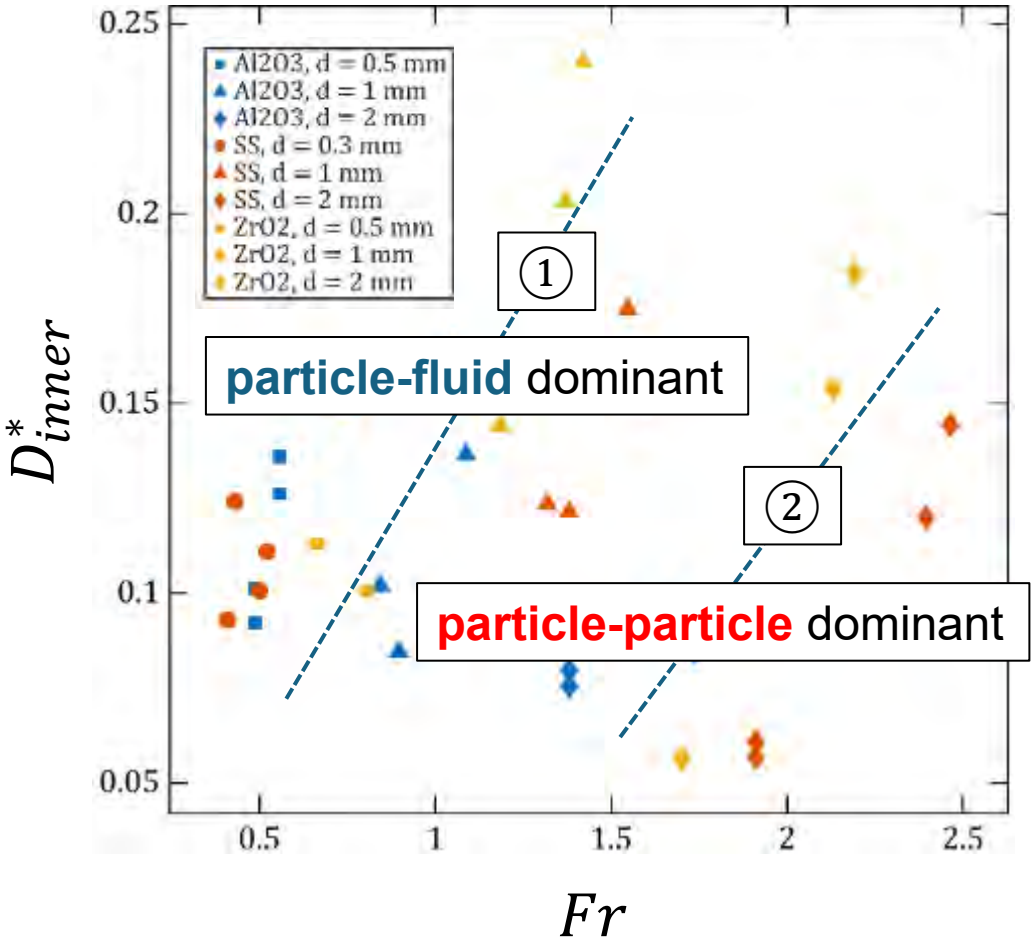

Why two regimes exist?

Introducing St number

$$St = \frac{\rho_p d}{C_d \rho_f D_{nozzle}}$$

C_d: drag coeffiecent
ρ_f: fluid density

➡ Particle motion is { **coupled to the fluid** ($St < 1$) / **inertia-dominated** ($St > 1$) }

① Particle size: **less than 1mm** ($St < 1$)
→**particle-fluid interaction dominated**

② Particle size: **2mm** ($St > 1$)
→**particle-particle interaction dominated**

Different dominant forces lead to different momentum conversion process and regime separation

Fig. The relationship between Fr and D^*_{inner}

Discussion ~D^*_{outer}

Volcano

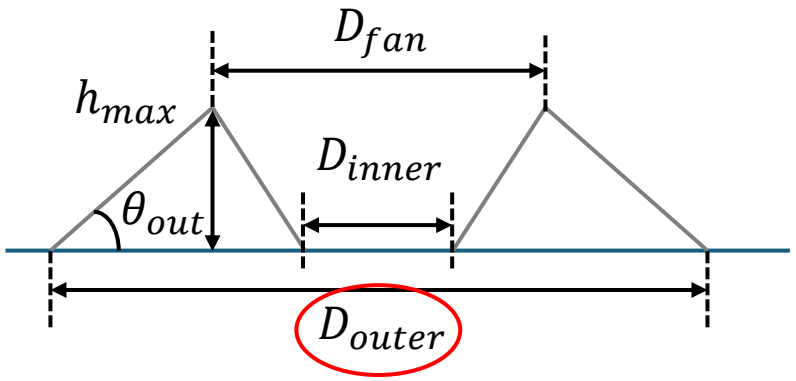

Concave bed

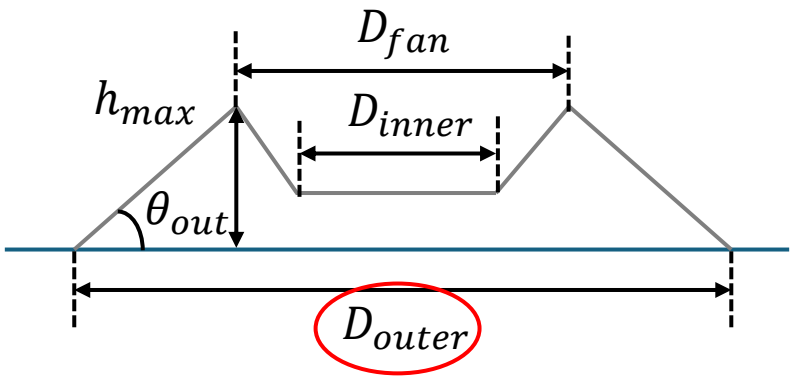

Flat-topped

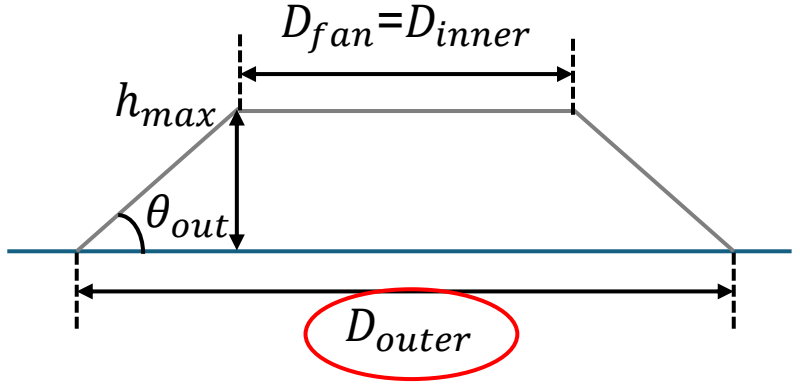

Dimensionless

$$D^*_{inner} = \frac{D_{inner}}{V^{\frac{1}{3}}} \quad D^*_{fan} = \frac{D_{volcano}}{V^{\frac{1}{3}}} \quad D^*_{outer} = \frac{D_{outer}}{V^{\frac{1}{3}}} \quad h^*_{max} = \frac{h_{max}}{V^{\frac{1}{3}}}$$

$V = initial\ particles\ volume$ (3.0L)

Discussion ~$D^*_{outer} = \frac{D_{outer}}{\frac{1}{V^3}}$~

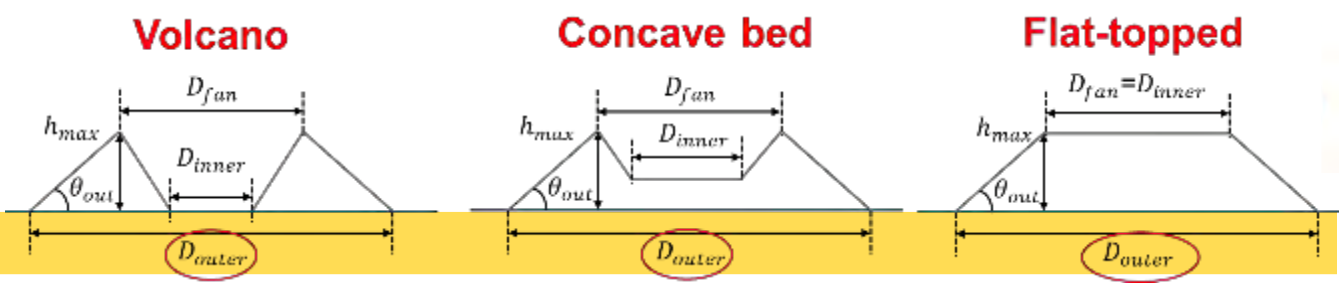

Low Re → low residual inertia

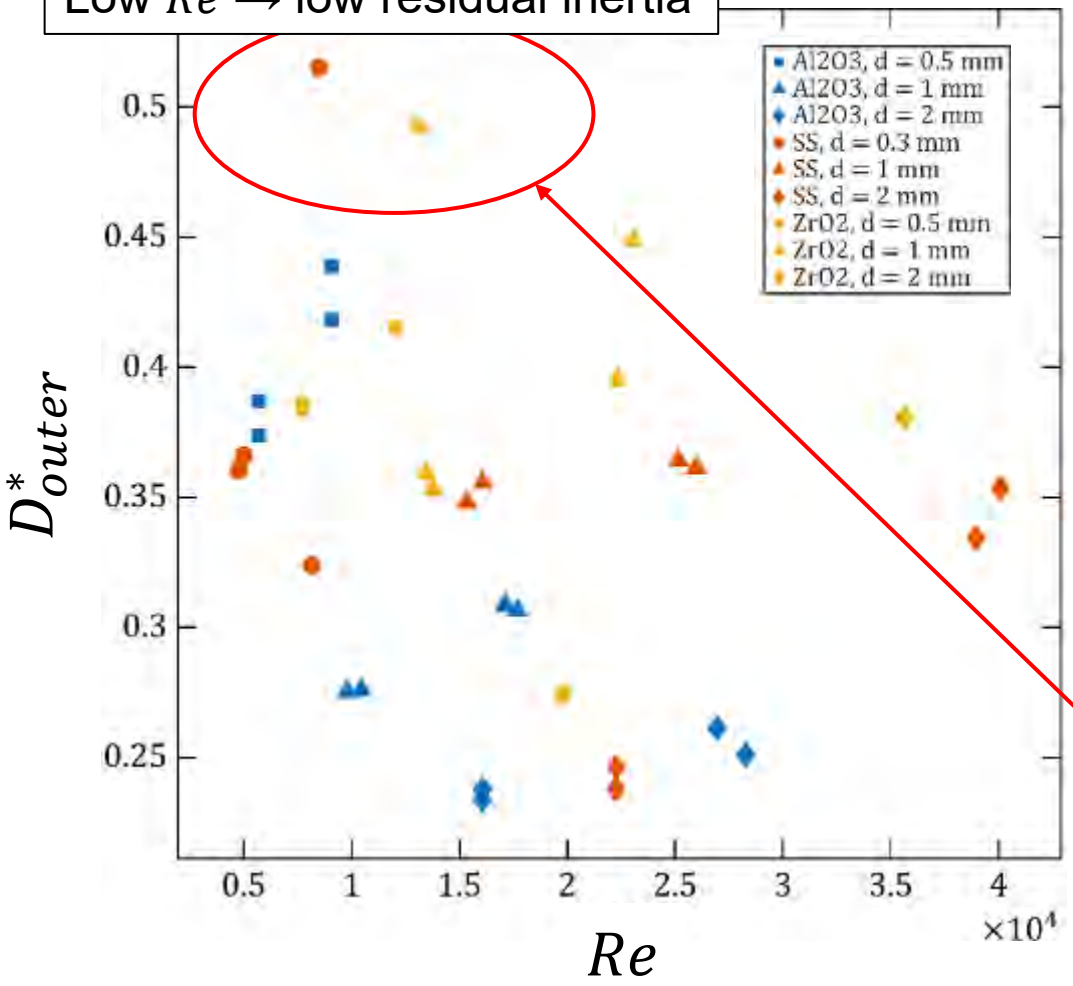

D_{outer} is **the maximum particle spreading**
→***Particle Inertia*** *vs* ***Fluid viscosity*** *is important?*

$$Re = \frac{\rho_f v_t D_{nozzle}}{\mu} = \frac{Inertia\ of\ particles}{Viscosity\ of\ fluid}$$

$v_t = terminal\ velocity$
$\mu = dynamic\ viscosity\ of\ fluid$

Re → **the residual inertia** just before falling

However, why these case with low Re spreads the most?

Fig. The relationship between Re and D^*_{outer}

Discussion ~$D^*_{outer} = \frac{D_{outer}}{\frac{1}{V^{\frac{1}{3}}}}$~

D^*_{outer} is in proportion to Re_{M0}

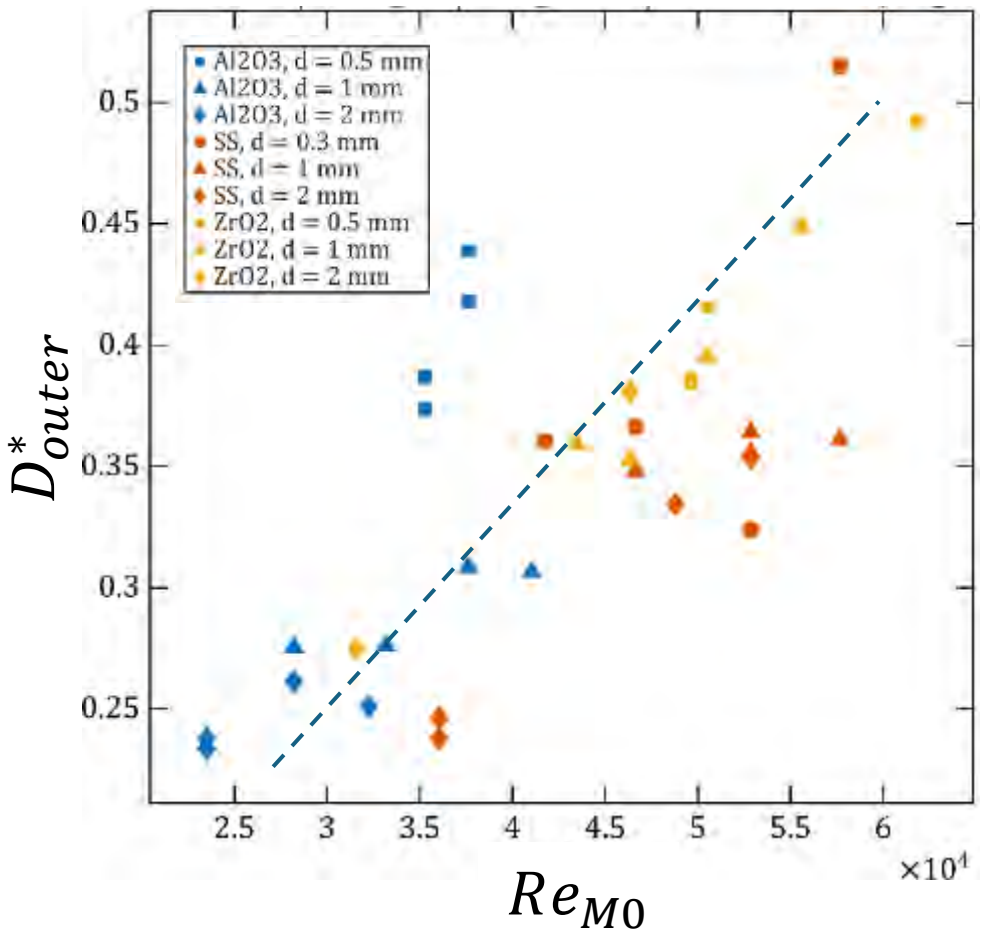

$$Re_{M0} = \frac{\sqrt{M_0/\rho_l}}{\nu}$$

M_0 = Initial momentum

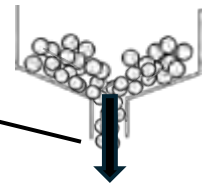

Initial momentum M_0 vs fluid viscosity μ

Initial momentum M_0=
(particle momentum) + (**fluid flow momentum**)

Re is unable to track this parameter
Particle spreads with the "flow"

The balance of
"Flow", Inertia vs Fluid viscosity
is important for the diffusion, D_{outer}

Fig. The relationship between Re_{M0} and D^*_{outer}

Discussion ~θ_{out}~

Volcano

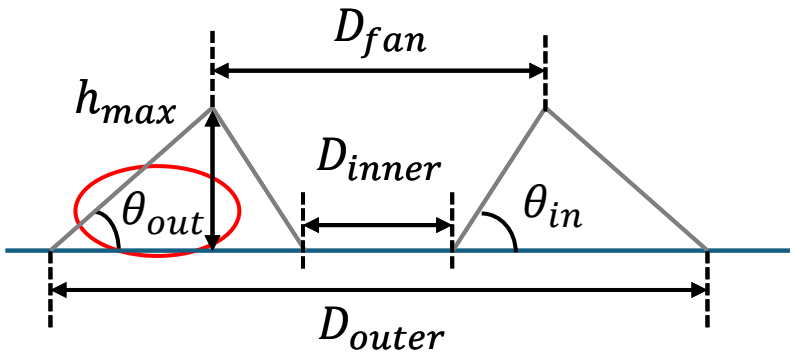

Concave bed

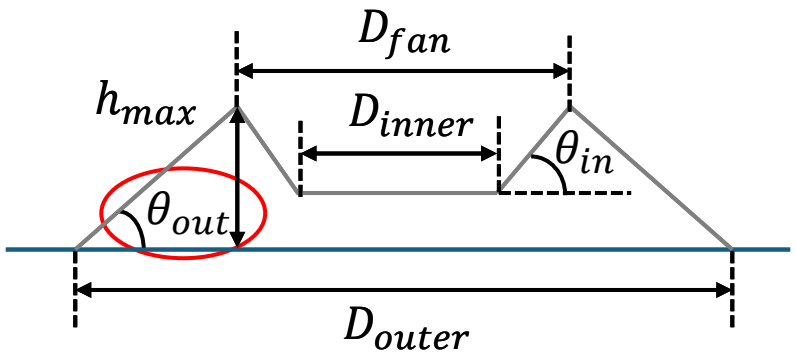

Flat-topped

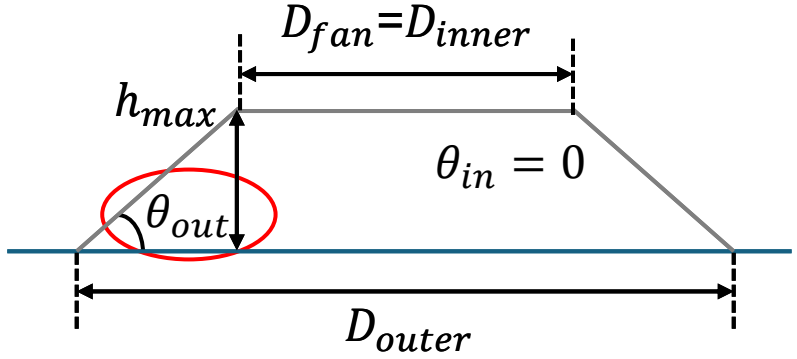

Dimensionless

$$D^*_{inner} = \frac{D_{inner}}{V^{\frac{1}{3}}} \quad D^*_{fan} = \frac{D_{volcano}}{V^{\frac{1}{3}}} \quad D^*_{outer} = \frac{D_{outer}}{V^{\frac{1}{3}}} \quad h^*_{max} = \frac{h_{max}}{V^{\frac{1}{3}}}$$

$V = initial\ particles\ volume$ (3.0L)

Discussion ~θ_{out}~

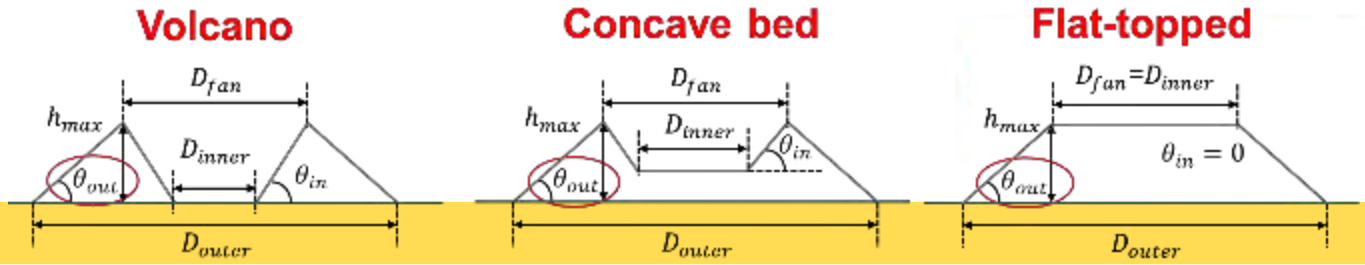

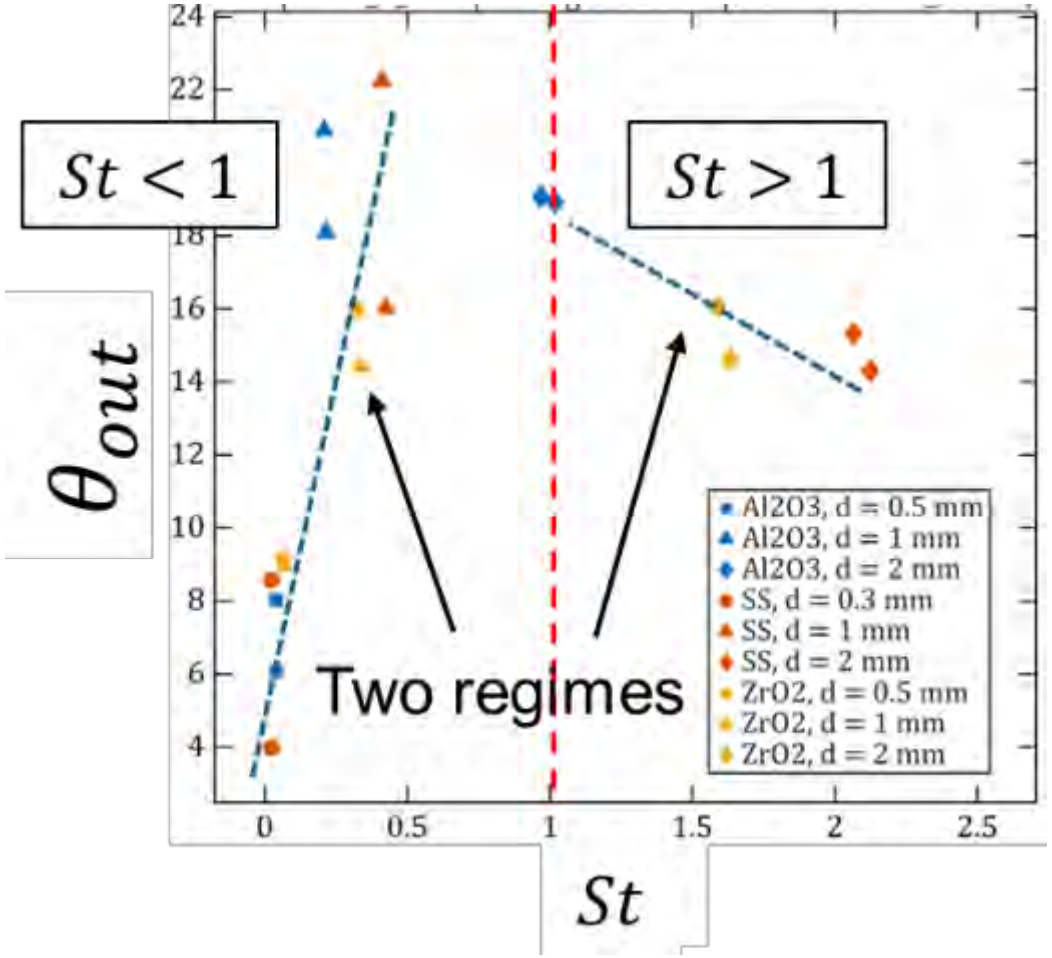

$St < 1$ (**particle-fluid interaction** dominated)

$\theta_{out} \uparrow$ = particles become **less influenced by the fluid** maintaining the steeper slope

$St > 1$ (**particle-particle interaction** dominated)

$\theta_{out} \downarrow$ = promoting **rearrangement by particle interaction** relaxing the slope

θ_{out} is controlled by particle mobility under fluid and particle forces governed by St

Fig. The relationship between St and θ_{out}

Summary of the discussion

Volcano

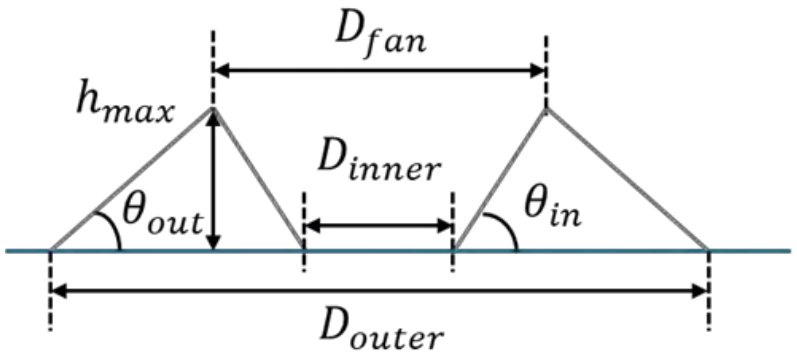

Concave bed

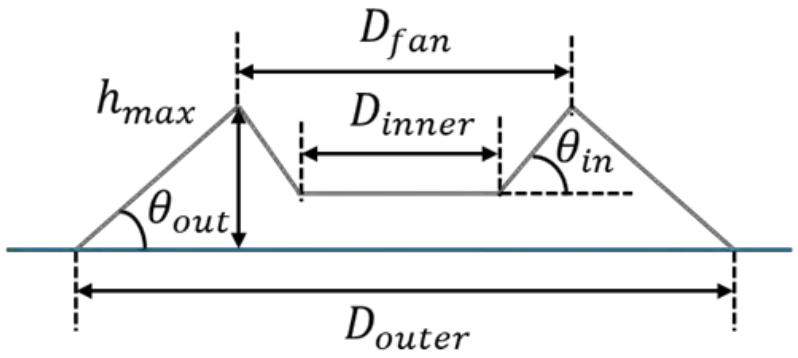

Flat-topped

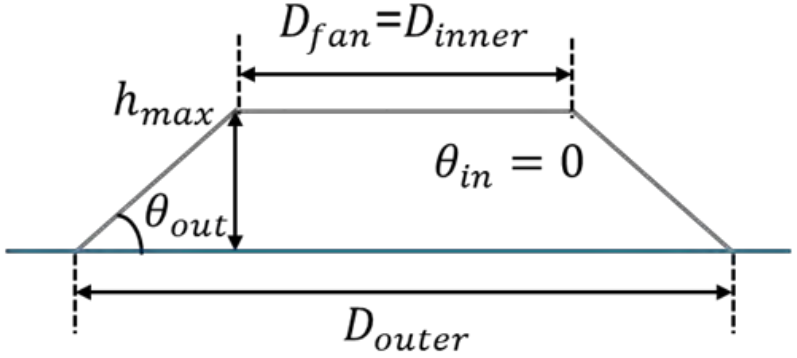

D_{inner}

- D_{inner} is generated by "**Granular jump**" and **its intensity is determined by Fr**
- **St governs the dominant forces** and the momentum conversion process during Granular jump

D_{outer}

- D_{outer} is affected by the balance **"flow", inertia and fluid viscosity,** which is governed by **Re_{M0}**

θ_{out}

- θ_{out} is controlled by **particle mobility under fluid and particle forces** governed by **St**

Summary of the discussion

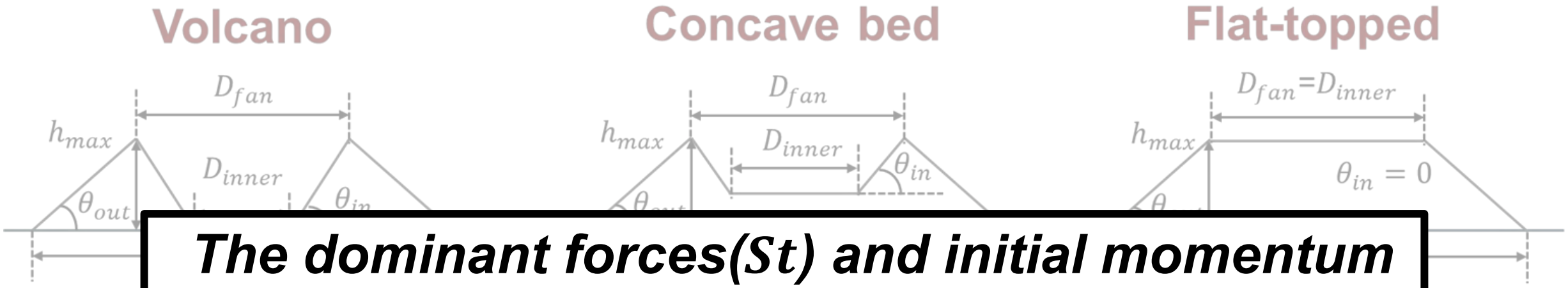

The dominant forces(St) and initial momentum influence the DBF behavior (e.g., granular jump)

D_{inner}

- St **governs the dominant forces** and the momentum conversion process during Granular jump

D_{outer}

- D_{outer} is affected by the balance **"flow", inertia and fluid viscosity,** which is governed by Re_{M0}

θ_{out}

- θ_{out} is controlled by **particle mobility under fluid and particle forces** governed by St

Table of contents

1. Background and objective
2. Methods for 3D DBF experiments
3. Results: Terminal bed shape
4. Discussion on each geometric parameter
    1. D_{inner}
    2. D_{outer}
    3. θ_{out}
5. Developing empirical correlations (θ_{out})
6. Summary

Developing empirical correlation ~θ_{out}~

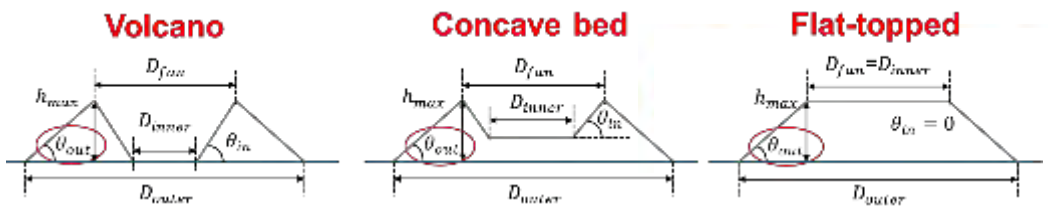

$\boldsymbol{\theta_{out}}$

- Universal, **debris-volume-independent** parameter
- Developed by **the multiple physical phenomena**

The defined empirical correlation

$$\theta_{out} = K(St)^a(Fr)^b(Re_{M0})^c\left(\frac{\rho_p - \rho_l}{\rho_l}\right)^d$$

Inertia vs Fluid coupling **Jump intensity** **Diffusion** **Buoyancy effect**

Depending on St, **the dominant physics of θ_{out} is different**

Different correlations are required on each St regime

Developing empirical correlation ~θ_{out}~

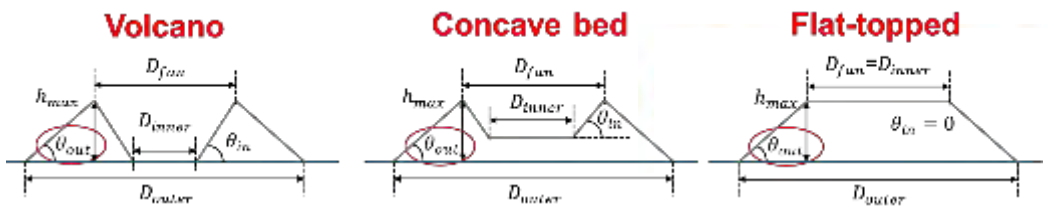

$St < 1$: particle-fluid interaction

MAPE: 13.9%

$$\theta_{out} = 1.47 \times 10^{8}\, St_i^{0.19} Fr_t^{0.63} Re_{M0}^{-1.54} Bu^{0.46}$$

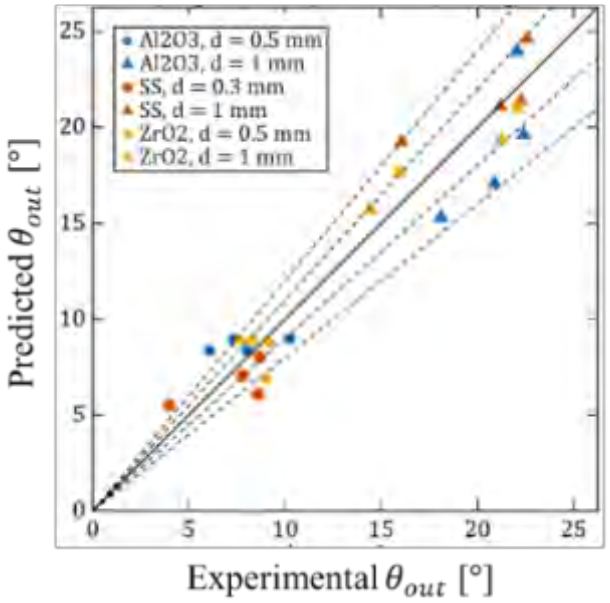

$St > 1$: particle-particle interaction

MAPE: 3.2%

$$\theta_{out} = 1.09 \times 10^{5} St_i^{0.045} Fr_t^{0.27} Re_{M0}^{-0.87} Bu^{0.14}$$

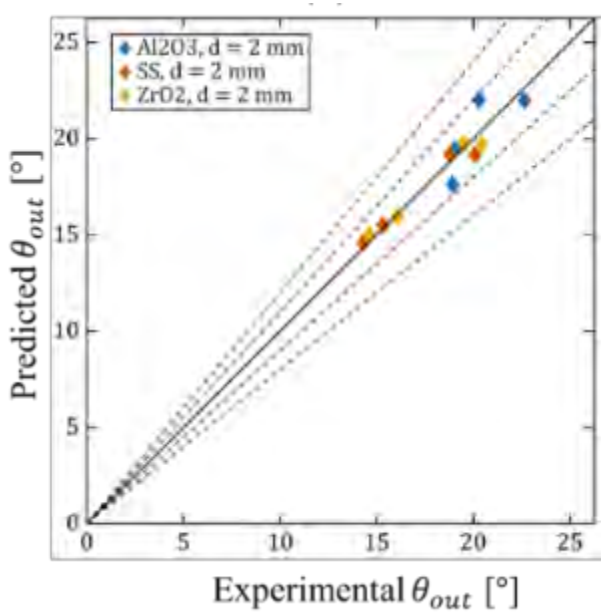

Error is relatively small ➡ **Proposed physics is quantitatively well captured**

Fig. The comparison of predicted and experimental θ_{out}

Table of contents

1. Background and objective
2. Methods for 3D DBF experiments
3. Results: Terminal bed shape
4. Discussion on each geometric parameter
    1. D_{inner}
    2. D_{outer}
    3. θ_{out}
5. Developing empirical correlations (θ_{out})
6. Summary

Summary

Background
- In severe accidents of SFRs, molten core materials relocate and solidify on the core-catcher, **forming a debris bed**
- **Understanding its formation mechanism** is essential for designing core-catcher system **with optimal coolability**

Previous Studies
- 2D experiments highlighted the importance of **particle diameter** and the balance between **inertia** and **convection**
- However, their applicability to **3D configurations** remained unclear

This Study
- Conducted **3D debris bed formation experiments** with various particle sizes, densities, and nozzle conditions.
- Observed three typical bed shapes: **volcano**, **concave**, and **flat-topped**, depending on parameters

Summary

Discussion

- $\boldsymbol{D_{inner}}$ is dominated by **granular jump** and two regimes exist due to the **different conversion mechanism**
- $\boldsymbol{D_{outer}}$ is governed by the balance between **flow, inertia and fluid resistance**
- $\boldsymbol{\theta_{out}}$ is governed by **particle mobility under fluid and particle forces**, governed by $\boldsymbol{St}$

Empirical correlation

- Empirical correlation for θ_{out} was developed using dimensionless parameters representing **underlying physics**
- The proposed correlations reproduce the experimental data with **small prediction errors**.

Future Work

- Effects of realistic initial conditions (**polydispersity, surface roughness, convection**)
- Detailed analysis of **falling jet** and **granular jump**
- Simulating DBF behavior **with elastoplastic model**

Acknowledgement

This work was supported by JAEA Nuclear Energy S&T and Human Resource Development Project Grant Number JPJA24H24020026

Reference

Cheng, S., Wang, S., Jiang, G., Yu, J., Qian, Y., Gong, P., Cui, J. "Development and analysis of a regime map for predicting debris bed formation behavior." *Ann. Nucl. Energy 109*, 2017: 658-666.

Suzuki, T, et al. "A scenario of core disruptive accident for Japan sodium-cooled fast reactor to achive in-vessel retension." *J. Nucl. Sci. Technol. 51* (J. Nucl. Sci. Technol.), 2014: 493–513.

Thank you for your attention!

Terminal Velocity v_t

→**Terminal velocity v_t** needs to be calculated **in advance** as **an input parameter**

<The theory of particles terminal velocity>

①Calculating the terminal velocity of single particle $\boldsymbol{v_{single}}$
(If Re is high, C_d is about 0.44)

$$v_{single} = \sqrt{\frac{4}{3}\frac{(\rho_p - \rho_f)}{\rho_f C_d} g d_p}$$

②**Modifying v_{single} by liquid fraction ε** and obtaining v_t
(If Re is high, n is about 2.35)

$$\boldsymbol{v_t = \frac{v_{single}}{\varepsilon^n}, \varepsilon = \text{liquid fraction}}$$

<How to get the liquid fraction ε>

① Based on the PIV data, obtaining **actual ε**
② Assuming $\boldsymbol{\varepsilon = f(d, D_{nozzle}, H, Re, Fr, \ldots)}$, developing **the correlation by regression**
③ Applying **ε correlation** to other cases and calculating it

[ref] Di Felice, R. (1994). The voidage function for fluid-particle interaction systems. *International journal of multiphase flow*, *20*(1), 153-159.

A comparison of EATF and zircalloy-4 cladding behaviour under severe accident conditions from 1600°C till 1970°C in steam/argon atmosphere

Pascal Piluso, Mehdi Nasselahsen, and Jules Delacroix*
CEA, DES, IRESNE, DTN, SMTA, LEAG.
Cadarache F-13108 Saint-Paul-Lez-Durance, France.
mehdi.nasselahsen@cea.fr; pascal.piluso@cea.fr; jules.delacroix@cea.fr

Emmanuel de Bilbao and Sawsen Youssef
CNRS, CEMHTI UPR3079
Univ. Orléans
F-45071 Orléans, France
emmanuel.debilbao@univ-orleans.fr; sawsen.youssef@univ-orleans.fr

ABSTRACT

In the frame of Severe Accidents studies, different ways of mitigation are currently proposed all over the world by the nuclear community. One possible way of mitigation concerns the use of new cladding concepts: the Enhanced Accident Tolerant Fuel (E-ATF) could avoid severe accidents thanks to the increase of a supplementary coping time in comparison with the current cladding such as zircalloy-4. Among the different EATF cladding under development and qualification, the chromium coated zircalloy has shown a high interest for the nuclear industry. The formation of a chromium oxide protective layer has been presented as being very resistant under steam conditions at high temperature.
The VITOX facility-PLINIUS severe accident facility at CEA-Cadarache has been recently developed in order to perform experiments simulating severe accidents conditions representative of reactor case from 1600°C till 1970°C under steam non starvation conditions. This paper presents experimental tests, calibration, instrumentation, results and analyses performed in the VITOX facility for EATF (chromium coated zircalloy) and zircalloy-4. Mechanistic oxidation behaviors of both cladding EATF and zircalloy-4 are presented, oxidation kinetics and hydrogen production laws are proposed and discussed.

KEYWORDS
EATF, zircalloy-4, oxidation by steam, hydrogen production, oxidation kinetics

1. INTRODUCTION

After the severe accidents that occurred in the three reactors of the Fukushima-Daiichi nuclear power plant in Japan in 2011, the development of new fuels Accident Tolerant Fuels (ATF) has become a priority worldwide to improve on the one hand safety and on the other hand increase the performance of the fuel in the reactor under normal conditions, notably the burn-up [1-3].
To meet these objectives, several strategies have been developed for the ATF either around the UO_2 nuclear fuel or around the cladding. For the ATFs with new cladding concepts, several ways have been explored:

change the cladding (for example replace it with a silicon carbide cladding), make surface deposits on the zircalloy cladding either on the inner side or on the external side [4]. For the external layer, several material solutions have been proposed from pure metallic phases till full oxidic phases [5].
In this paper, only the so-called E-ATF (Enhanced Accident Tolerant Fuel) cladding with chromium on zircalloy-4 is presented. Indeed, the latter offer a very good compromise: a minor modification of the fuel cladding with a specific surface treatment that will produce E-ATF. This option offers no drastic changes for the operation of the reactor but with a high potential gain considering the burn-up.
Classical zircalloy-4 and E-ATF claddings have been used for this study in order to better understand and qualify their respective behavior under severe accident conditions, i.e at high temperature between 1600°C and 1970°C under steam and non-starvation conditions, especially regarding oxidation kinetics and hydrogen production. In a first part, the main oxidation phenomena involved for zircalloy alloys are shortly reminded. In the second part, VITOX facility is described and then in the last part, some results are presented for zircalloy-4 and E-ATF claddings.

2. BEHAVIOR UNDER NORMAL, INCIDENTAL AND ACCIDENTAL CONDITIONS FOR ZIRCALLOY CLADDING AND EATF

Under normal conditions, the zirconium alloy will oxidize (stress corrosion, 330°C, 155 bars) and a thin oxide layer will form on the surface.
There are typically two oxidation regimes [6]:

- A first so-called pre-transient regime where a layer of black, adherent zirconium oxide will form. The oxidation law is a parabolic law, governed by the diffusion of oxygen through the formed oxide layer. At the beginning of oxidation, the zirconia grains are equiaxed. Then, during the anionic growth of the oxide layer, the zirconia grains grow into an elongated shape perpendicular to the metal/oxide interface.
- A second post-transient regime occurs when the zirconium oxide layer undergoes compressive stresses due to differences in bulk density (zirconium, zirconium oxide) causing the formation of cracks. Oxygen can then penetrate more quickly at the oxide/metal interface through the cracks formed and thus access the metal/oxide interface more quickly. A second layer of protective oxide is then formed and a new parabolic kinetics begins again, and so on.

The kinetics of oxidation presents itself as a succession of parabolic regimes (Figure 1), each parabolic domain ending on the cracking of the oxide layer. In all cases, the oxidation reaction at the water/cladding interface is as follows:

$$Zr_{(s)} + 2H_2O_{(liq)} \rightarrow ZrO_{2(s)} + 2xH_{2(g)} + 4(1-x)\,H \qquad \text{(Equation 1)}$$

Under LOCA conditions for a PWR fuel, two distinct kinetic regimes depending on the temperature domain are identified:

- **Temperature below 1800 K:** ***"slow" process of oxidation***
  - Swelling of the zircaloy cladding by creep due to overpressure inside the fuel
  - Phenomenon of «ballooning»
  - Risk of local rupture (1200K)
  - Beginning of oxidation at 1300K-1400K, strongly exothermic reaction aiding the rise of thermal runaway (*breakaway*):

$$Zr(s) + 2\,H_2O_{(g)} \rightarrow ZrO_2\,(s) + 2\,H_2 \quad (\Delta H = -555\text{kJ/mol}) \qquad \text{(Equation 2)}$$

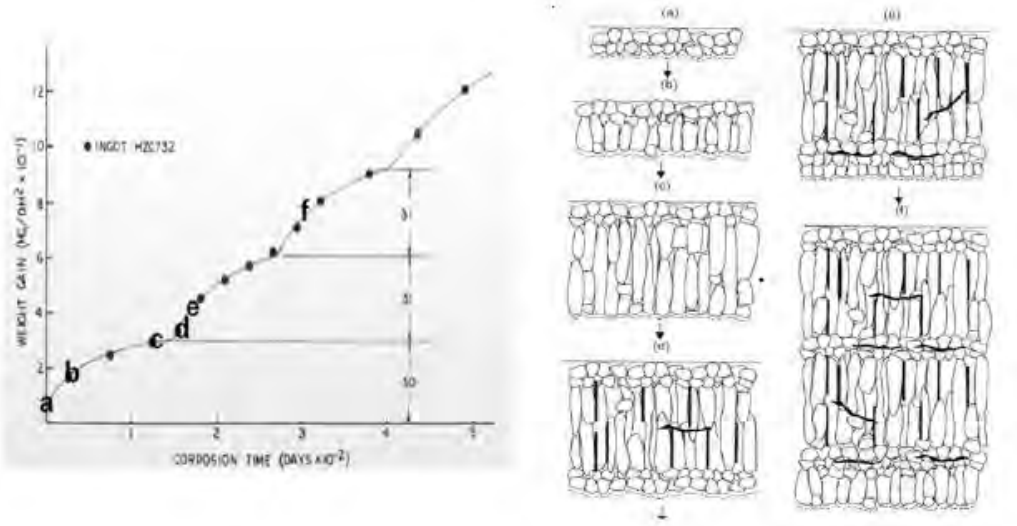

Figure 1: Oxidation regimes of the zirconium alloys cladding- Normal PWRs conditions [7].

The oxidation kinetics of zircaloy, after a transient phase, follows a parabolic type distribution expressed as [8]:

$$\mathbf{e = k_{ox}\sqrt{t}} \qquad \text{(Equation 3)}$$

- e: oxide thickness (m)
- k_{ox}: parabolic oxidation constant ($m/sec^{0.5}$)
- t: time

It has to be stressed that the parabolic constant can be expressed according to an oxidized thickness (ex-situ measurement), but usually the oxidized thickness can be non-uniform and can vary in a large manner of several tens %, hence a difficulty to estimate correctly k_{ox}. For these reasons, in the frame of this work, another approach to describe parabolic behavior is proposed to avoid this source of uncertainties.

- **For temperatures above 1800 K:** ***a "rapid" external oxidation promoting a "thermal runaway" of the zircalloy oxidation reaction***
  - Acceleration of oxidation kinetics with a factor 10 to 20 for the oxidation constant
  - Zirconia layer rupture beyond 2300 -2500 K

At the end, we can note that only extrapolation are proposed for the parabolic constant above 2000K with 2 laws with high differences as it ca be seen on the figure 2.

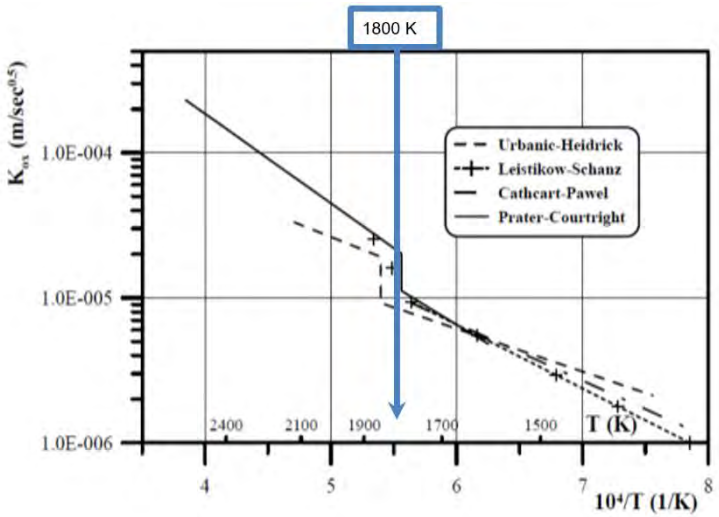

Figure 2: Oxidation parabolic constants for the zirconium alloys cladding- LOCA PWRs conditions [8].

Under normal conditions, E-ATF chromium protected cladding seem to provide an obvious benefit, notably by blocking the oxidation of the cladding thanks to the formation of Cr_2O_3 thin layer which stops oxidation phenomena of zircaloy alloys at low temperatures (360°C, 150 bars). This gain should eventually allow new features to be added to nuclear fuel, notably with higher burn-ups [9-10].
In incidental conditions, the primary objective for E-ATF is to demonstrate improved performance against current fuels up to the threshold temperature of 1500K (1200°C), qualification criterion for BDBA studies (Beyond Design Basis Accident).
Beyond incidental conditions, it would be possible with the ATF not to reach the thermal runaway temperature by "*sufficiently slowing down the oxidation and hydrogen production and assuming to recover means of water injection into the vessel after a "certain time*" as shown in Figure 3 proposed by [11].
In this ideal vision of ATFs, the entry into severe accidents with corium formation and significant hydrogen production would therefore be excluded for LOCA scenarios.

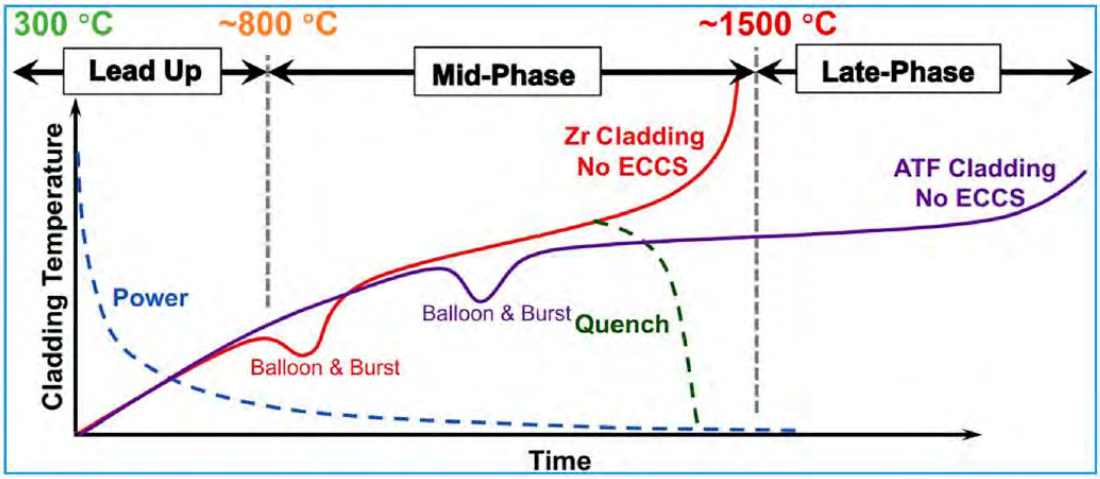

Figure 3: General overview of coolant–limited accident progression inside an LWR core [11].

For nuclear safety demonstration, the determination of the coping time to be able to recover cooling and water injection after a LOCA is crucial: if effective cooling can be recovered within this time, the accident will not escalate into a severe accident. However, if effective cooling cannot be restored regardless of the coping time, as in the Fukushima Daiichi accident, the severe accident will continue to progress. Under these conditions, - as it was the case for Fukushima-Daiichi severe accident- the severe accident will go on. Under these conditions, it is essential to assess whether chromium-coated E-ATF claddings perform better or worse than zircaloy-4 claddings.
Above 1600K (1300°C), the Cr-Zr interdiffusion is highly activated with the formation at the Cr/Zr interface of $Zr(Cr,Fe)_2$ intermetallic compounds [12]. Between 1600K and 1800K, the existence of an eutectic at low temperature at 1613K between Cr and $Zr(Cr,Fe)_2$ will generate a liquid phase [12]. This liquid phase, even if it represents a limited quantity, will modify surface properties and could accelerate candling-type phenomena at low temperatures. However, available data remain very limited at higher temperatures, and no studies are available to our knowledge on E-ATF behavior above 1900K under non–steam-starvation conditions.

3. EXPERIENCES

3.1. VITOX experimental facility

Steam oxidation experiments on Zircaloy alloys and E-ATF were conducted in the VITI facility, part of the PLINIUS Severe Accident Platform at CEA Cadarache. The VITI facility features an induction-heated furnace capable of reaching temperatures up to 2700 °C.
The VITOX (**VITI-OX**idation) configuration [13,14] has been especially develop in order to perform analytical oxidation experiments on different families of alloys at solid and liquid states with oxygen or steam and measuring on line hydrogen production and oxygen (see figure 4). For solid configuration, the sample is placed inside the crucible with the possibility to use different geometries from plates to cylinders. The design of the high-temperature cell ensures a convenient exposure of the sample to steam flow.
This assembly is confined within a so-called separating tube, all components being made of yttria-stabilised zirconia, which prevents oxidation especially of the susceptor from steam exposure. These protected components surrounding the separating tube are the susceptor and the thermal shield, made of tungsten and porous graphite, respectively. The susceptor is electromagnetically coupled to the inductor, and is heated by the resulting Joule effect in link with eddy currents. In turn, the susceptor heats the high-temperature cell up to the target temperature by radiative heat transfer. The thermal shield ensures thermal homogeneity at sample scale, by limiting thermal losses.

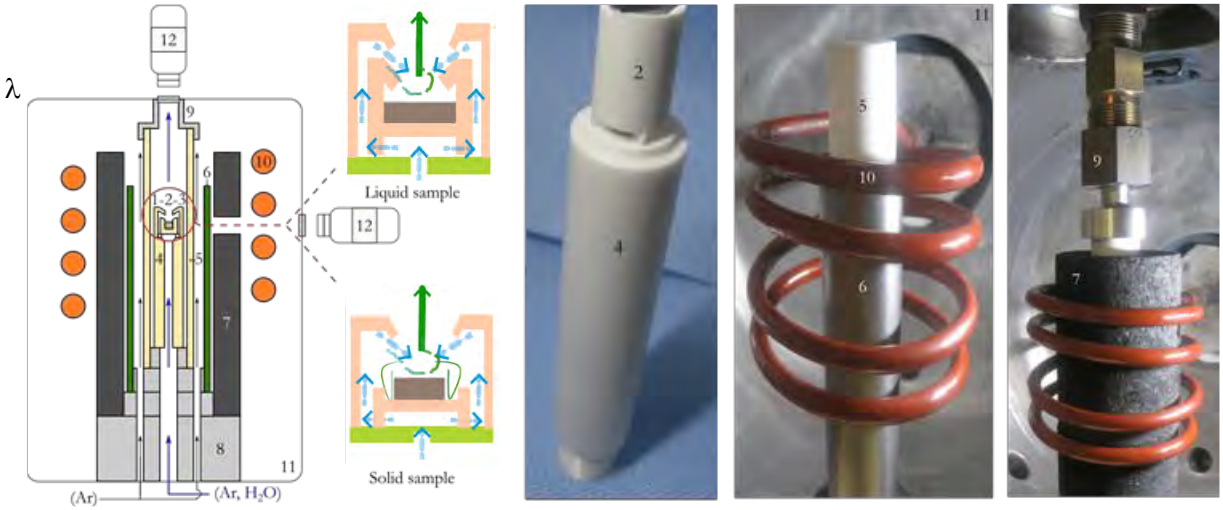

Figure 4: Experimental layout of VITOX facility. Labels: 1) 316Nb Sample, 2) Crucible, 3) Lid, 4) Support, 5) Separating tube, 6) Susceptor, 7) Thermal shield, 8) Injector, 9) Sampling rod, 10) Inductor, 11) Confinement vessel, 12) Video-pyrometers.

All the experiments are carried out inside a water-cooled confinement vessel, for the sake of controlling working atmosphere quality. Steam is generated by means of a Controlled Evaporation Mixing (CEM) unit, and flows through heated and insulated gas lines up to the injector in the lower (and cooler) part of the experiment. This injector also allows for argon gas circulation around the separating tube, providing an additional and dynamic confinement of potential steam leaks through the separating tube. The residual gases after interaction with the sample are collected downstream by means of a sampling rod connected to the separating tube. At the exhaust, a cold trap condensates residual steam, followed by hydrogen analyser. Video-pyrometers (bi-chromatic,λ_1= 0.95µm and λ_2= 1.05µm) are located either on top or on the side of the vessel and focus on the sample or on the susceptor wall, respectively. They allow for sample and susceptor monitoring during the tests, along with temperature measurements by infrared thermometry.

The instrumentation used in VITOX experiments is detailed Table I, along with related features.
The confinement vessel is first placed under primary vacuum by pumping. Argon is then injected into the furnace until 1.3 bar (absolute pressure), with a flow rate of 2 L/min. This preliminary step is cycled until the initial oxygen concentration is reduced below 30 vol.ppm to limit initial oxidation during the heating process. Heating is then initiated under a static argon atmosphere at a rate of approximately 20 ◦C/ min. Above 800°C, residual oxygen within the vessel is pumped by the graphite of the thermal shield. Once the working temperature reached and stabilized, a molar composition of 10 % H_2O and 90 % Ar for steam oxidation tests is injected in the test tube. The injection flow rate for both oxidant mediums is set at 2.60 L/min (see Figure 5).

Table I. VITOX Instrumentation

Denomination	Measurement range and accuracy
CEM Unit Bronkhorst® W-303B	Ar flow-rate $Q_{Ar} \in [1.2; 60]$ L/min. H_2O flow-rate $Q_{H_2O} \in [12; 600]$ g/h. Temperature $T_{CEM} \in [20; 200]$ °C. Manufacturer accuracy: 1% reading.
Videopyrometers Keller® PA40	Temperatures T_{K1} (susceptor) and T_{K2} (sample) $\in [800; 3000]$ °C. Two-colour pyrometers. Manufacturer accuracy: 1% reading.
Hydrogen analyzer AP2E® Proceas	Hydrogen concentration $[H_2](t) \in [0 ; 5]$ % vol. LOD = 5 ppm vol. Manufacturer accuracy : 1% reading.
Precision scale Sartorius® MCA524P -2S00-U QP99	Mass $m \in [0; 520]$ mg. Manufacturer accuracy: 0.1 mg.

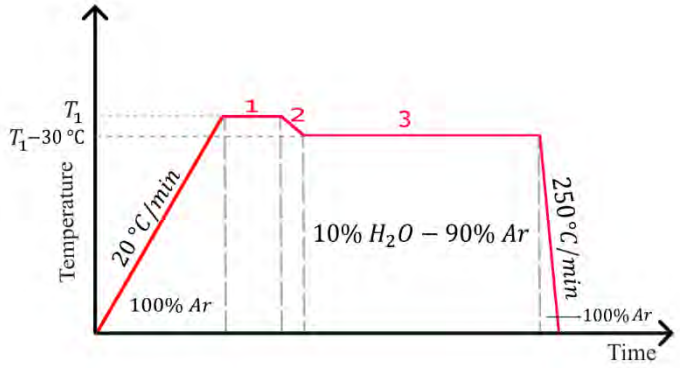

Figure 5: Thermal treatment for VITOX-test - Heating up (20°C/min) till the temperature plateau - 1 Stabilization under Ar 2- Steam injection 3- Oxidation plateau under steam

The weight gain during VITOX oxidation tests is obtained by tracking the mass balance of the gas injected into and the gas leaving the oxidation chamber. This approach allows indirect measurement. The tracking of the weight gain, standardized to the reactive surface and measured in g/cm², is established as a function of an adjustment factor k, set to align the in-situ mass reading at time "tf " with the actual mass, measured after a "tf " duration test.
For oxidation tests under steam atmosphere, it is assumed that one mole of oxygen adsorbed at the surface of the sample is equivalent to one mole of hydrogen released out of the sample.
One could define the weight gain per reactive surface unit as in equation 4:

$$W(t) = {}^{k}/_{S} \times \int_0^t C(H_2)(u).du \quad ; \quad k = \frac{m_{t_f} - m_i}{\int_0^{tf} C(H_2)(u).du} \qquad \text{(Equation 4)}$$

- W(t): weight gain of the sample, (g/cm²)
- C(H_2): volumetric concentration of in-situ released hydrogen at "t" instant, (vol.%)
- S: reactive surface of the sample, (cm²)
- t: time, (s)
- k: adjustment factor, (g/s.vol. %)
- m_i: initial mass of the sample, (g)
- m_{tf}: final mass of the sample, weighed after a "tf " duration test, (g)

Hydrogen mass release can be deduced from Eq. (4), taking the following form as formulated with Eq. (5):

$$m_{H_2}(t) = \frac{M_{H_2}}{M_o} \times W(t) \qquad \text{(Equation 5)}$$

- M_O: molar mass of oxygen, (g/mol)
- M_{H2} : molar mass of hydrogen, (g/mol)

3.2. VITOX experimental grid

In order to determine oxidation kinetics under Ar-H_2O gas of zircalloy-4 and E-ATF at solid state, different temperature representative of severe accident conditions have been chosen.

Table II. VITOX experimental grid for zircalloy-4 and E-ATF at solid state

Cladding	Temperature (°C)	Duration (sec.)	Gas composition (mol.%)
Zircalloy-4 (Cylinder, thickness 2 mm)	1600	1800	Ar (90%)-Steam (10%)
	1700	1800	Ar (90%)-Steam (10%)
	1800	1800	Ar (90%)-Steam (10%)
E-ATF (Plate, thickness 0,67 mm)	1600	600	Ar (90%)-Steam (10%)
	1700	600	Ar (90%)-Steam (10%)
	1800	600	Ar (90%)-Steam (10%)

4. RESULTS AND DISCUSSION

4.1. Zircalloy-4 oxidation at solid state

In order to compare the results obtained in this study with those of the literature regarding steam oxidation of zircaloy-4 alloy, the parabolic constant k_p has been chosen as reliable parameter. The reaction rate constants were determined using a modified parabolic model, which accounts for a 200-second threshold corresponding to an "incubation phase".The description of the parabolic law is carried out according to equation 6:

$$W(t) = \sqrt{(t - t_i) \cdot k_p + b}, \qquad \text{(Equation 6)}$$

- W(t): weight gain of the sample, (g/cm²)
- t_i: incubation period (s)
- k_p: parabolic constant (g^2/cm^4.sec.)

- b: square of the mass at the establishment of the parabolic regime (g^2/cm^4)

The experimental kinetics obtained using this approach are shown in Figure 6. In the first instants of reaction, oxidation does not follow parabolic behavior, hence the need to introduce an incubation time t_i. Moreover, oxidation kinetics increase significantly with rising temperature. At 1800 °C, complete oxidation of the sample occurs approximately 400 seconds earlier than at 1700 °C.

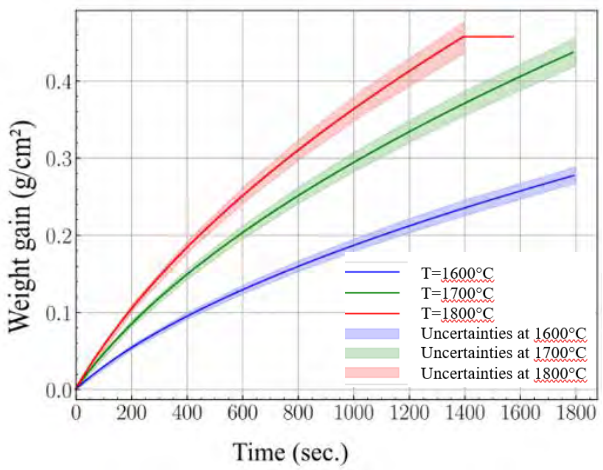

Figure 6: Weight gain for zircalloy-4 under steam at 1600, 1700, 1800°C in VITOX facility

The temperature dependence of the parabolic rate constant is shown in Figure 7, highlighting differences between the VITOX experiments and literature data [15,16]. The uncertainty in the parabolic constants k_p reported by Prater et al. [16] and Urbanic et al. [15] was calculated by accounting for the contribution of temperature, as proposed by the respective authors. The same approach was similarly applied to the VITOX data, indicating a substantial reduction in uncertainties and a more precise determination of the parabolic rate constants. The newly proposed values for the zircaloy-4 oxidation parabolic constants are higher than those reported in the literature [15,16], indicating faster oxidation kinetics.

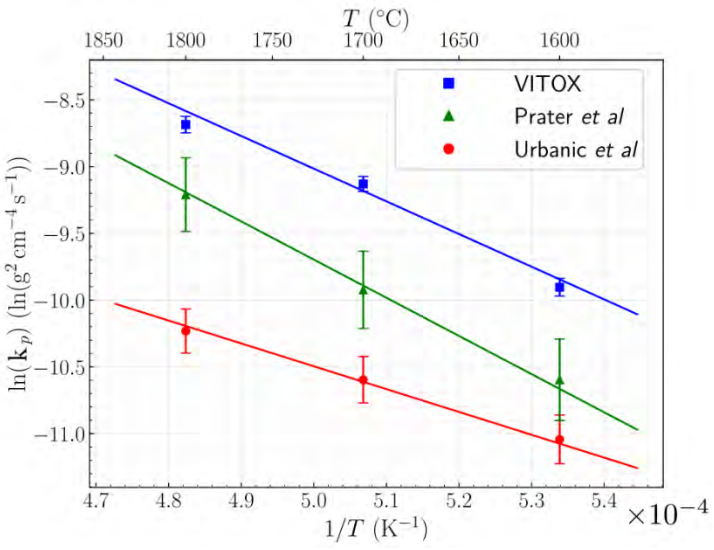

Figure 7: Evolution of the parabolic constants for zircalloy-4 for VITOX and Urbanic et al. [15] and Prater et al. [16].

In the first study reported by Prater *et al.*[16], the parabolic rate constant may be affected by the non-uniform oxide/metal interface, which can disturb the accurate determination of the effective oxide thickness. In the second study by Urbanic *et al.*[15], the total weight gain was calculated assuming the only formation of zirconia, thereby neglecting the contribution of the Zr(O) phase. Moreover, steam-starvation conditions are likely to have occurred in this experiment [15]. These methodological and experimental limitations can provide a plausible explanation to the deviation of the parabolic rate evolution between VITOX data and those of the literature [15,16].
The activation energy obtained from the VITOX data exhibits a reduced uncertainty range compared to the literature [15,16], showing a difference of approximately 55 % relative to Urbanic *et al.* [15] and about 10 % relative to Prater *et al.* [16]. (Table III).

Table III. Activation energy and their uncertainties for zircalloy-4 steam oxidation

	Urbanic et al. [15]	**Prater et al. [16]**	**VITOX**
Activation energy (J/mol)	200 300	224 000	131 000
Relative uncertainty (%)	8	19	32

4.2. E-ATF oxidation at solid state

The steam oxidation of the E-ATF alloy follows parabolic kinetics from the early instants of reaction over the temperature range 1600°C - 1800 °C. The maximum oxide weight gain is consistent across all temperatures, reaching approximately 0.16 g/cm². This value is obtained after 600 seconds at 1600 °C, 260 seconds at 1700 °C, and 150 seconds at 1800 °C (Figure 8).

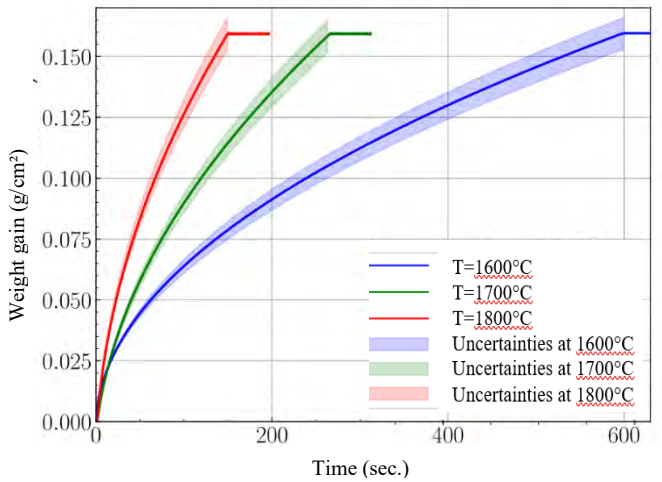

Figure 8: Weight gain E-ATF under steam at 1600, 1700, 1800°C in VITOX facility

In order to investigate the oxidation mechanism of E-ATF under steam conditions, a blank test was first conducted under argon atmosphere to characterize the distribution of metallic phases prior to steam injection. SEM–EDS analyses revealed the formation of a zirconium-rich dendritic phase and an inter-dendritic chromium-rich phase. The atomic fraction of chromium at the external interface was approximately 30.26 %. The presence of such microstructure indicates the complete consumption of chromium to form a Zr–Cr eutectic phase at 1600 °C [12]. Upon steam injection, oxidation of the Zr–Cr

eutectic phase induces the formation of an α-Zr(O) layer at the external interface, along with inward migration of the remaining eutectic into the bulk of the sample. Subsequent oxygen diffusion leads to progressive consumption of α-Zr(O) and the formation of zirconia throughout the sample. Chromium released during oxidation of the Zr–Cr eutectic precipitates within the internally formed zirconia, ultimately leading, after complete zirconium consumption, to a biphasic layer composed of chromia Cr_2O_3 and zirconia ZrO_2 (Figure 9).

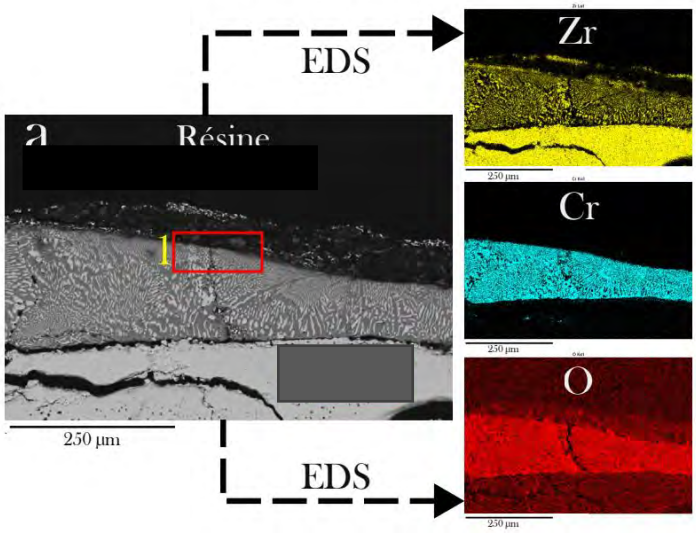

Figure 9: BSD image of the upper part of the E-ATF sample after oxidation under steam at 1800 °C and EDS acquisitions of the elements Zr, Cr and O-Eutectics-Upper part

At both 1700 °C and 1800 °C, oxidation of the E-ATF alloy results in the formation of a lamellar microstructure and spherical inclusions of both zirconia and chromia phases, likely indicating the formation of a Zr-Cr-O eutectic phase (Figure 10). Final state is slightly different at 1600°C.

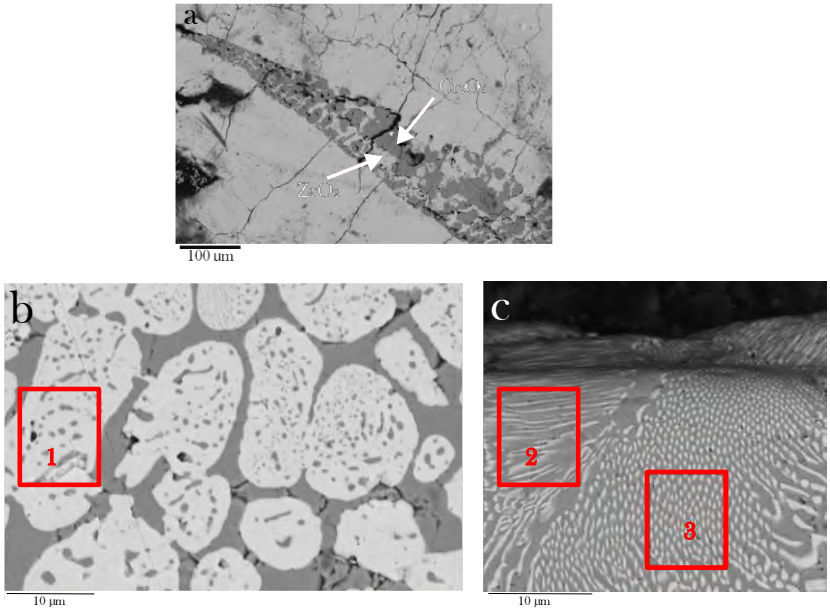

Figure 10: (a) - BSD image of biphasic layer of zirconia and chromia. (b-1) – BSD image of submicrometric inclusions of chromia within zirconia cells. (c-1) – lamellar microstructure of zirconia in chromia layer. (c-2) – inclusions of zirconia in chromia layer-

4.3. Comparison Zircalloy-4/E-ATF oxidation at solid state

For the first time, it has been possible to study the oxidation of E-ATF at temperature representative of severe accident conditions. As seen in the previous section, E-ATF oxidation kinetic follows a parabolic trend between 1600 °C and 1800 °C. It is possible to do a direct comparison between E-ATF and zircalloy-4. Figure 11 presents the activation energies established from parabolic constants. The activation energy of the E-ATF alloy corresponds to a value of 220.000 kJ/mol whereas it is about 203.000 kJ/mol for zircalloy-4.

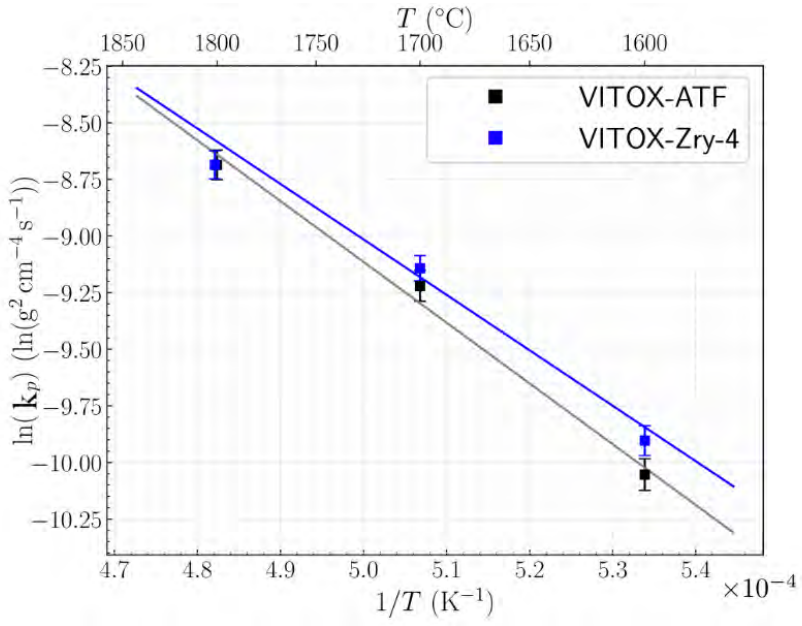

Figure 11: evolution of the oxidation parabolic constants for zircalloy-4 and E-ATF

These new results show that the coupling between the steam oxidation and the formation of an eutectic liquid phase for EATF leads to a macroscopic behavior close to zircaloy 4 at temperature above 1600°C, the activation energy being the same order of magnitude for both cladding. The impact of the formation of a liquid phase on the mechanical behavior of the cladding pin is not today clearly understood and will need complementary studies to assess if it moderates or accelerates the degradation and delocalization phenomena.

5. CONCLUSIONS

After Fukushima accidents, a lot of efforts has been done all over the world to develop and qualify new tools for mitigation in the frame of severe accident management. One important way of mitigation concerns the E-ATF for which different concepts have been proposed. One concept concerns the chromium coating protective layer on zircalloy. This new family of E-ATF cladding should offer a coping time to manage the severe accident.

In order to quantify the steam oxidation effect on both zircalloy-4 and E-ATF, a specific facility has been developed, the VITOX facility (**VIT**I-**Ox**idation), to follow on-line hydrogen production and oxidation kinetics under non steam starvation conditions. The new methodology proposed more reliable results for zircalloy-4 steam oxidation studies. A more rapid kinetic of zircalloy-4 above 1600°C is proposed in this work in comparison with the previous literature [16].

The behavior of E-ATF shows above 1600°C in isothermal conditions a behavior close to zircalloy-4 under steam non starvation conditions, meaning the total disappearance of the chromium protective effect. The

impact of formation of a liquid phase due to the formation of a eutectic seems to play an effect at second order on the oxidation mechanism.
The process of E-ATF manufacturing seems to play a negligible effect on oxidation phenomena and hydrogen production.
Transitory conditions for zircalloy-4 and E-ATF have to be studied and compared to complete the knowledge concerning the oxidation and hydrogen production mechanism at temperature above 1600°C and in non-starvation conditions.

ACKNOWLEDGMENTS

The authors gratefully thank Martin Steinbrueck (KIT) for the E-ATF materials and for the very fruitful discussion on steam oxidation of zircalloy-4 and EATF.

REFERENCES

1. F. Goldner, « Development strategy for advanced LWR fuels with enhanced, accident tolerance, Present. to Enhanc. Accid. Toler. LWR Fuels », *Natl. Metrics Work.* Oct. (2012).
2. G. Kim, J.H. Yang, W.J. Kim, Y.H. Koo, « Development status of accident tolerant fuel for light water reactors in Korea », *Nucl. Eng. Technol*. **48**, (2016).
3. K.A. Terrani, « Accident tolerant fuel cladding development: promise, status,and challenges *», Journal of Nuclear Materials,* **501** (2018).
4. **IAEA-TECDOC-1921**, « Analysis of Options and Experimental Examination of Fuels for Water Cooled Reactors with Increased Accident Tolerance (ACTOF) », (2020).
5. B.A. Pint, K.A. Terrani, Y. Yamamoto, L.L. Snead, «Material selection for accident tolerant fuel cladding», *Metall. Mater. Trans.* **E.2** pp190-196 (2015).
6. A. Nechaev « Corrosion of zirconium alloys in nuclear power plants », IAEA, Vienna, IAEA-**TECDOC-684**: 1–177, (1993).
7. A. T. Motta, A. Yilmazbayhan, R. J. Comstock, J. Partezana, G. P. Sabol, B. Lai, Z. Cai. « Microstructure and Growth Mechanism of Oxide Layers Formed on Zr Alloys Studied with Micro-Beam Synchrotron Radiation ». *Journal of ASTM International*, **2**, Paper ID: JAI12375, (2005).
8. G. Schanz, B. Adroguer, A. Volchek , « Advanced treatment of zircaloy cladding high-temperature oxidation in severe accident code calculations: Part I. Experimental database and basic modeling», *Nuclear Engineering and Design,* 232 (2004).
9. C. Tang, M. Stueber, H. Juergen Seifert and M. Steinbrueck, « Protective coatings on zirconium-based alloys as accident-tolerant fuel (ATF) claddings », *Corros Rev*; **35(3):** 141–165, (2017).
10. J.-C. Brachet et al., « Early studies on Cr-Coated Zircaloy-4 as enhanced accident tolerant nuclear fuel claddings for light water reactors», *Journal of Nuclear Materials*, **517,** 268-285 (2019).
11. S.J Zinkle, K.A.; Terrani, J.C.; Gehin, L.J Ott, L.L Snead, « Accident tolerant fuels for LWRs: A perspective», *Journal of Nuclear Materials,* **448**, 374–379 (2014).
12. J.C. Brachet, T. Guilbert, M. Le Saux, J. Rousselot, G. Nony, C. Toffolon-Masclet, A. Michau, F. Schuster, H. Palancher, J. Bischoff, J. Augereau, E. Pouillier, « Behavior of Cr-coated M5 claddings during and after high temperature steam oxidation from 800°C up to 1500°C (LOss-of-coolant accident & design extension conditions) », *Proceedings of WRFPM/TOPFUEL 2018,* 30 Sept. – 04 Oct, Prague, Czech Republic, (2018).
13. P. Piluso, S. Thilliez, J. Delacroix, E. de Bilbao and J. Poirier, « Iron and zirconium oxidation at liquid state under Ar-O_2 and Ar-H_2O gas mixtures in severe accident conditions», *The 10th European Review Meeting on Severe Accident Research* (ERMSAR2022), Log Number: 319 Akademiehotel, Karlsruhe, Germany, May 16-19, (2022).
14. M.Nasselahsen, S.Thilliez, J. Delacroix, S. Youssef, L. Brissonneau, J. Poirier, P. Piluso, E. de Bilbao « Iron and 304L-stainless steel oxidation under oxygen and steam atmosphere at high temperature from

1350°C to 1600°C», *Journal of Nuclear Materials*, **Volume 619**, January 2026, 156270, https://doi.org/10.1016/j.jnucmat.2025.156270 (2026).
15. VF. Urbanic and TR. Heidrick. « High-temperature oxidation of zircaloy-2 and zircaloy-4 in steam». *Journal of Nuclear Materials*, **75**(2) :251–261, (1978).
16. JT. Prater and EL. Courtright, «Oxidation of zircaloy-4 in steam at 1300 to 2400°C», *Zirconium in the Nuclear Industry*. ASTM International, (1987).

A comparison of EATF and zircalloy-4 cladding behaviour under severe accident conditions from 1600°C till 1800°C in steam/argon atmosphere

Pascal Piluso, Mehdi Nasselahsen, and Jules Delacroix
CEA, DES, IRESNE, DTN, SMTA, LEAG.
Cadarache F-13108 Saint-Paul-Lez-Durance, France.
mehdi.nasselahsen@cea.fr; pascal.piluso@cea.fr; jules.delacroix@cea.fr

Emmanuel de Bilbao and Sawsen Youssef
CNRS, CEMHTI UPR3079
Univ. Orléans
F-45071 Orléans, France
emmanuel.debilbao@univ-orleans.fr; sawsen.youssef@univ-orleans.fr

Contents

1. Behavior under severe accident conditions for zircalloy and E-ATF claddings

2. VITOX facility: an efficicient and reliable tool for steam oxidation studies from solid to liquid state

3. Results and discussion on zircalloy-4 and E-ATF

4. Conclusion and perspective

1. Behavior under severe accident conditions for zircalloy and E-ATF claddings

Early in-vessel degradation

Under LOCA conditions for a PWR fuel, two distinct kinetic regimes for zircalloy cladding oxidation

- ✓ **For temperature below 1800 K (1527°C):** *"slow" process of oxidation*
- ✓ **For temperatures above 1800 K (1527°C)**: *a "rapid" external oxidation promoting a "thermal runaway" of the zircallov oxidation reaction* [1]

$Zr + 2\,H_2O \rightarrow ZrO_2 + 2\,H_2$ $\quad \Delta H = -6.4$ MJ/kg of Zr

- Formation of ZrO_2 and α-Zr(O) layers on cladding
- Production of H_2 : 1 Kg of Zr ⇒ ~ 0.5 m^3 (STP) of H_2
- Highly exothermic reaction & highly dependent on temperature
  - Oxidation rate controlled by oxygen diffusion in ZrO_2
  - Parabolic kinetics if unlimited steam supply

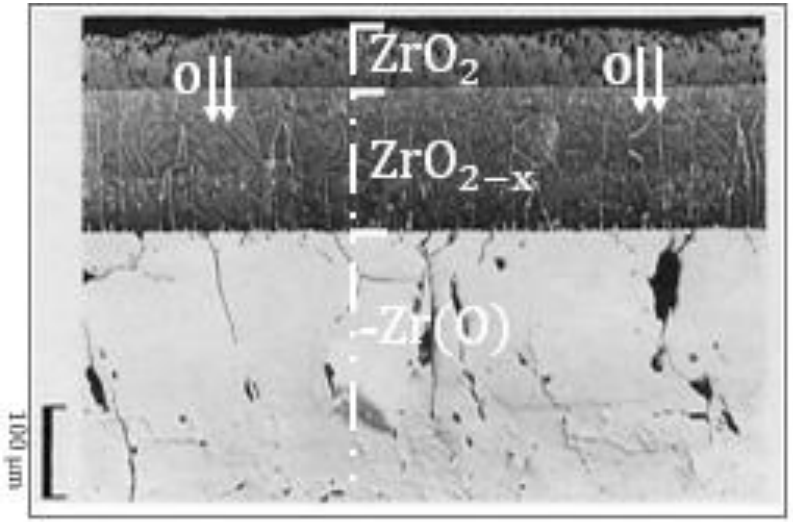

$$e = k_{ox}\sqrt{t}$$

- e: oxide thickness (m)
- k_{ox}: parabolic oxidation constant (m/$sec^{0.5}$)
- t: time

1. F, Fichot, SAP-2025, Early In-vessel Core Degradation, SAP-2025, FZJ, Germany

Zircalloy cladding oxidation at high temperature

✓ **Parabolic constant kp: Arhenius Law**

$$k_p = A \times e^{-Ea/RT}$$

Authors	Temperature (°C)	Kinetics	Ea (kJ/mol)
Urbanic *et al.* [1]	*1500 – 1850*	*Parabolic*	*138,00*
Prater *et al.* [2]	*1500 – 2400*	*Parabolic*	*220,00*

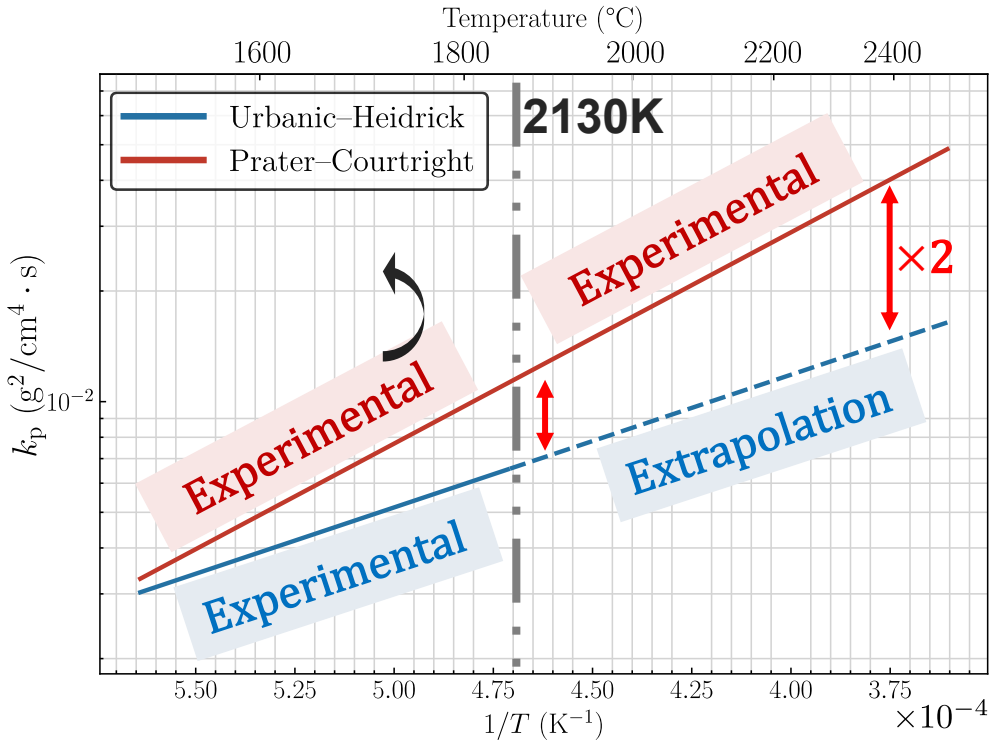

- Few experimental data for oxidation>1800K
- Acceleration of oxidation kinetics with a **factor 10 to 20 ?** for the oxidation constant kp
- Extrapolation proposed for the parabolic constant above 1800K

1. *VF. Urbanic and TR. Heidrick. « High-temperature oxidation of zircaloy-2 and zircaloy-4 in steam». Journal of Nuclear Materials, 75(2) :251–261, (1978).*
2. *JT. Prater and EL. Courtright, «Oxidation of zircaloy-4 in steam at 1300 to 2400 °C», Zirconium in the Nuclear Industry. ASTM International, (1987).*

E-ATF chromium protected cladding

- **For BDBA studies** (Beyond Design Basis Accident),E-ATF: improved performance against current fuels up to the threshold temperature of 1500K (1200°C)[1]

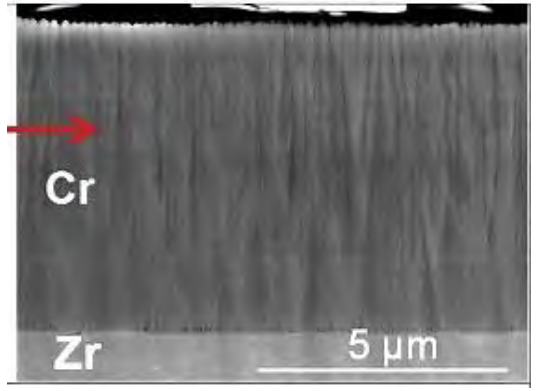

- **For LOCA studies (Loss of Coolant)**, the coping time to be able to recover cooling and water injection is crucial: if effective cooling can be recovered within this time, the accident will not escalate into a severe accident

- For E-ATF in LOCA conditions, no data

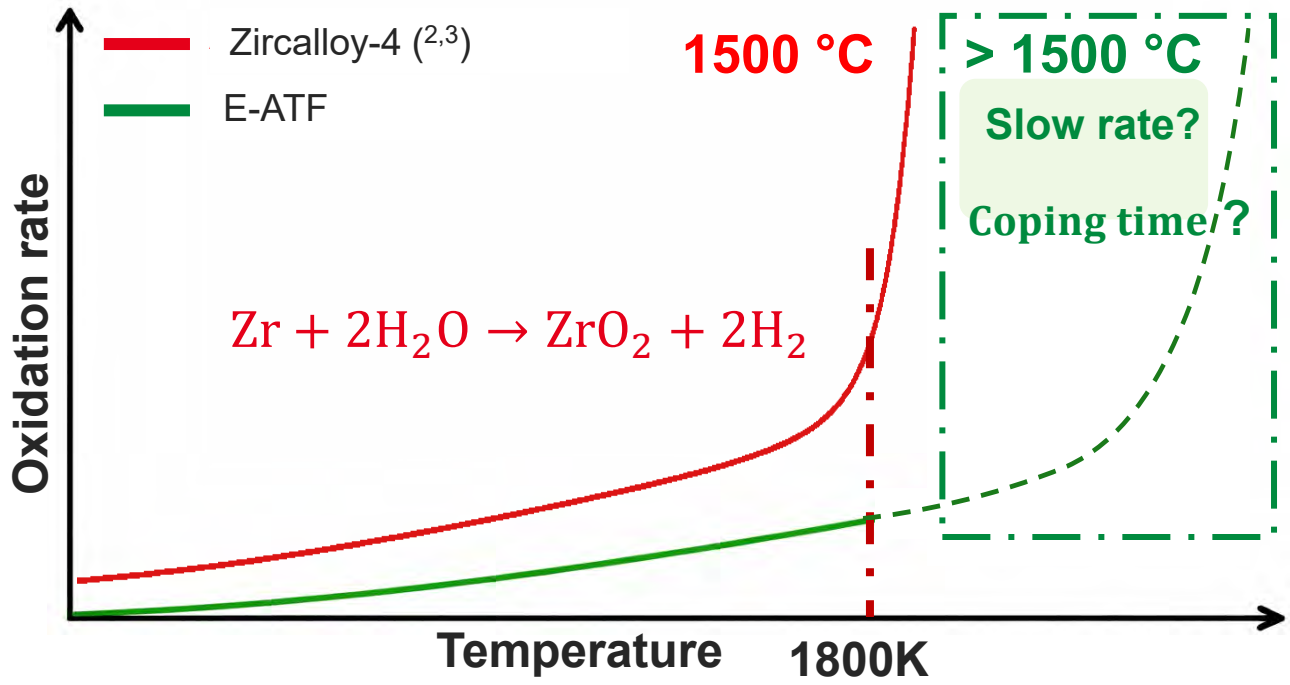

1. J.C. Brachet et al.. Corrosion Science, 2020.
2. VF. Urbanic and TR. Heidrick. « High-temperature oxidation of zircaloy-2 and zircaloy-4 in steam». Journal of Nuclear Materials, **75**(2) :251–261, (1978).
3. JT. Prater and EL. Courtright, «Oxidation of zircaloy-4 in steam at 1300 to 2400 ℃», Zirconium in the Nuclear Industry. ASTM International, (1987).

2. VITOX facility: an efficicient and reliable tool for steam oxidation studies from solid to liquid state

VITOX: heating process

1)Zircalloy Sample 2) Crucible 3) Lid 4) Support 5) Separating tube 6) Susceptor
7) Thermal shield 8) Injector 9) Sampling rod 10) Inductor 11) Confinement vessel 12) Video-pyrometers

VITOX: hydrogen measurement

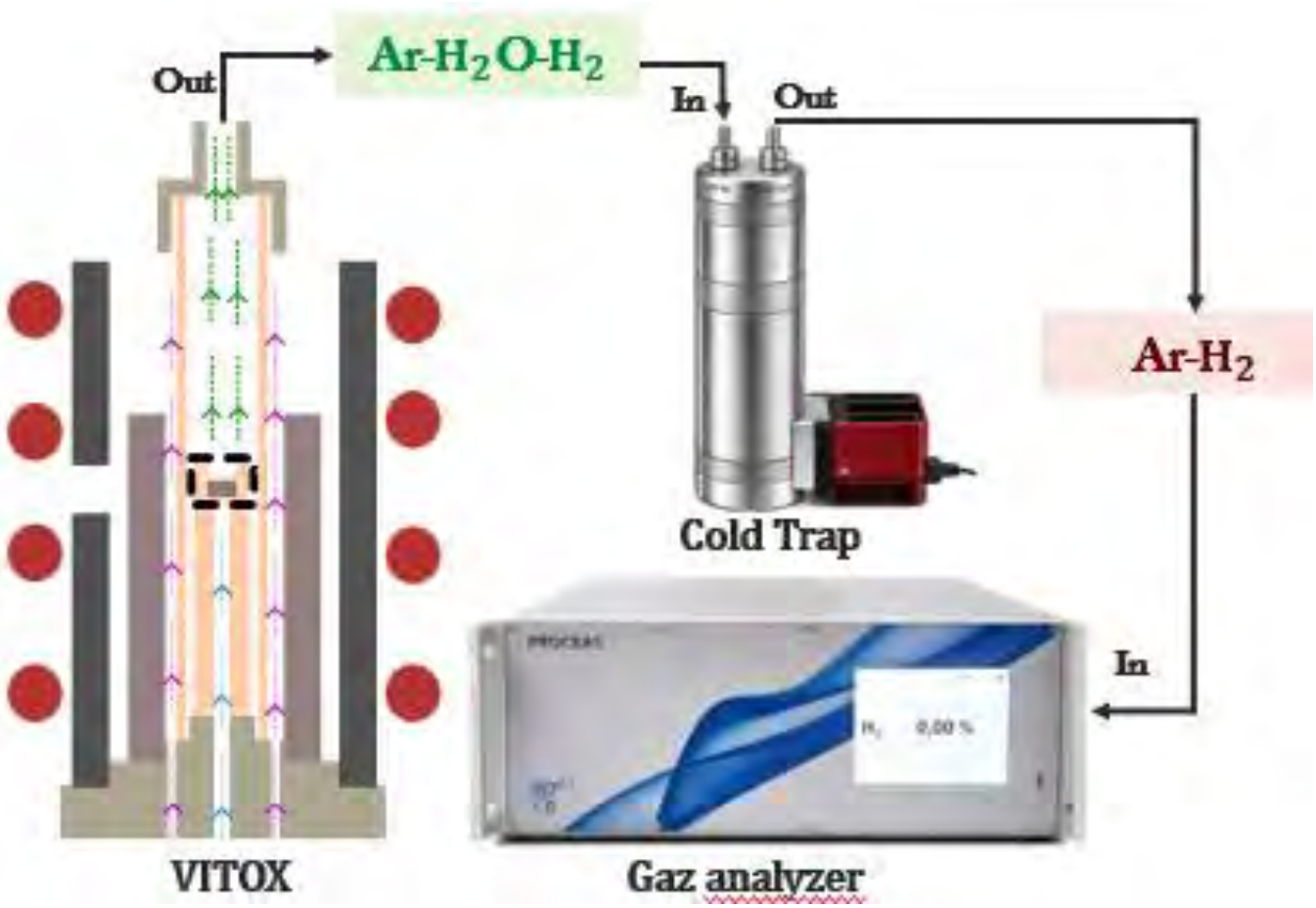

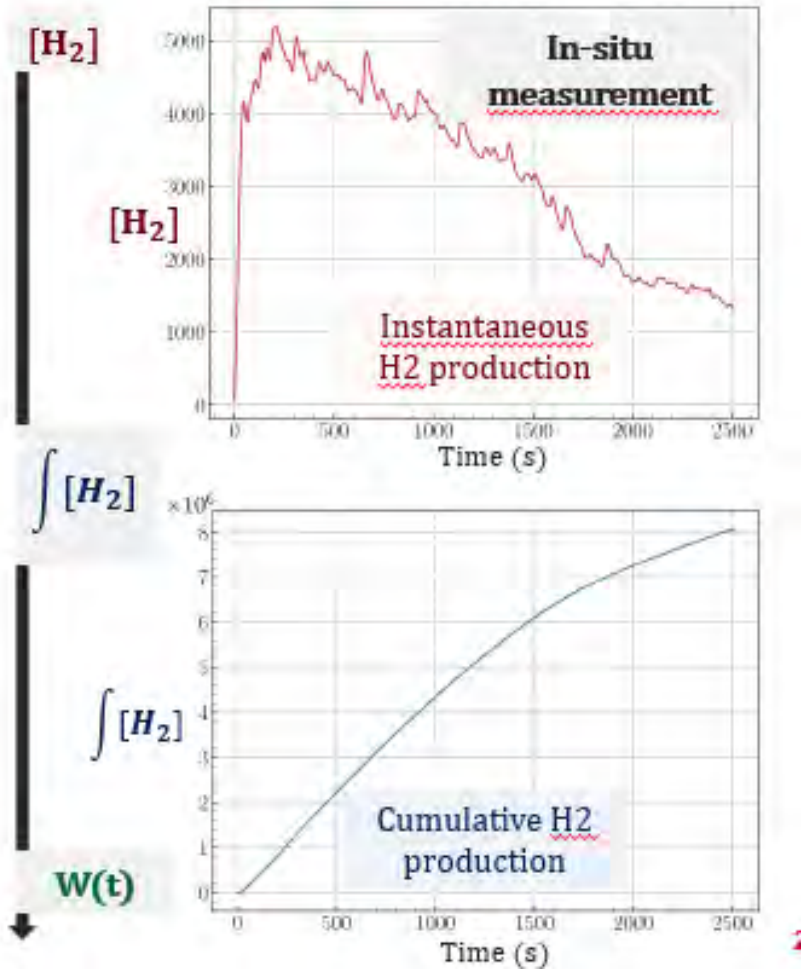

VITOX-test: steam oxidation experimental procedure

- **Heating up (20°C/min) till the temperature plateau**
  1. Stabilization under Ar
  2. Steam injection
  3. Oxidation plateau under steam

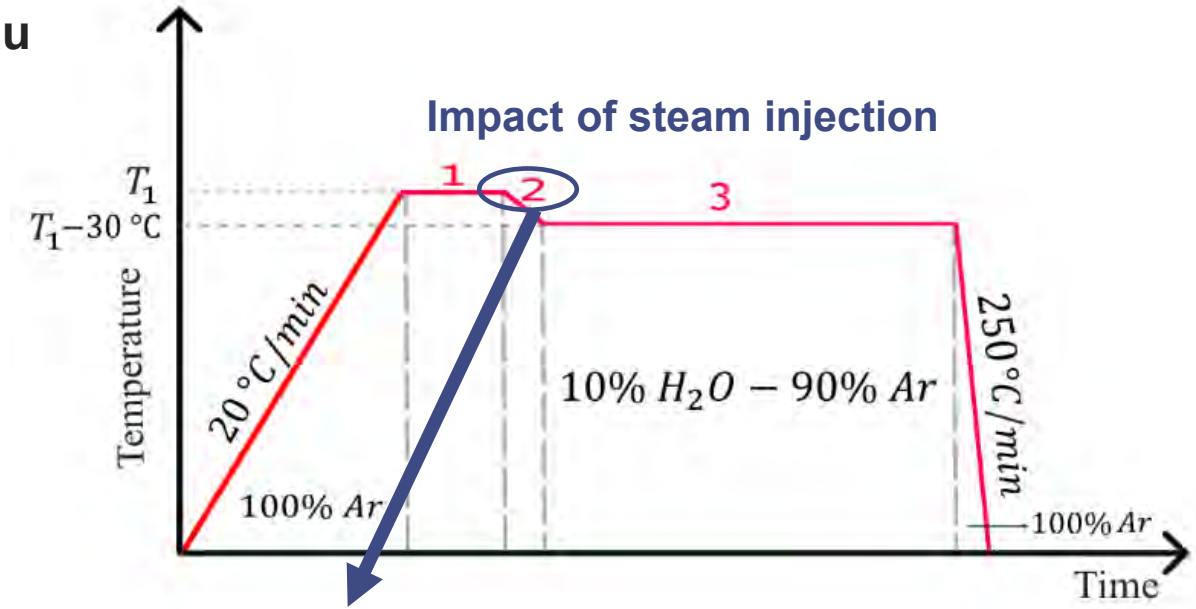

$$W(t) = {}^{k}/_{S} \times \int_0^t C(H_2)(u).du \quad ; \quad k = \frac{m_{t_f} - m_i}{\int_0^{t_f} C(H_2)(u).du}$$

$$m_{H_2}(t) = \frac{M_{H_2}}{M_o} \times W(t)$$

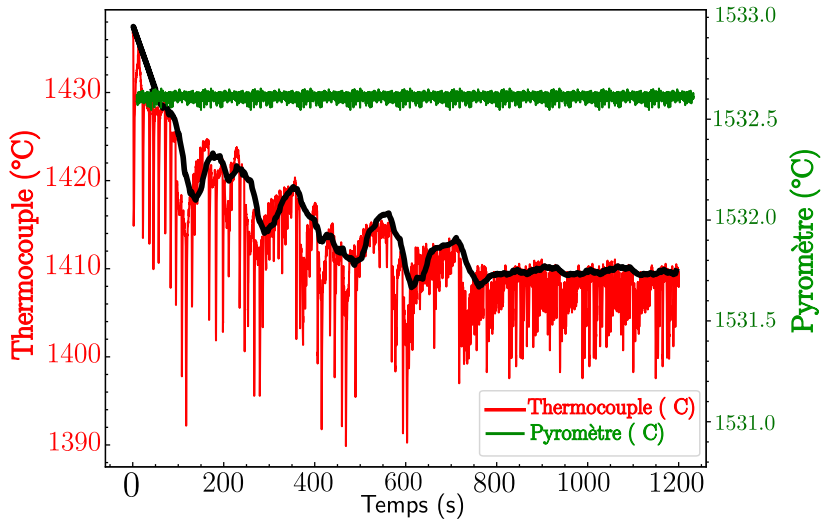

VITOX experimental grid: zircalloy-4 and E-ATF at solid state

Cladding	Temperature (°C)	Duration (sec.)	Gas composition (mol.%)
Zircalloy-4 (Thickness 2 mm)	1600	1800	Ar (90%)-Steam (10%)
	1700	1800	Ar (90%)-Steam (10%)
	1800	1800	Ar (90%)-Steam (10%)
E-ATF (Thickness 0,67 mm)	1600	600	Ar (90%)-Steam (10%)
	1700	600	Ar (90%)-Steam (10%)
	1800	600	Ar (90%)-Steam (10%)

3. Results and discussion on Zircalloy-4 and E-ATF

Zircalloy-4 oxidation at solid state (1/2)

- **Experimental approach with incubation time**

- **Incubation phase: no parabolic behaviour**

$$W^2(t) = (t - \mathbf{t_i}) \times \mathbf{k_p} + \mathbf{W_0^2}\ (\mathbf{t_i})$$

- W(t): weight gain of the sample, (g/cm²)
- t_i: incubation period (s)
- k_p: parabolic constant (g²/cm⁴.sec.)
- W_0: mass at the establishment of the parabolic regime (g²/cm⁴)

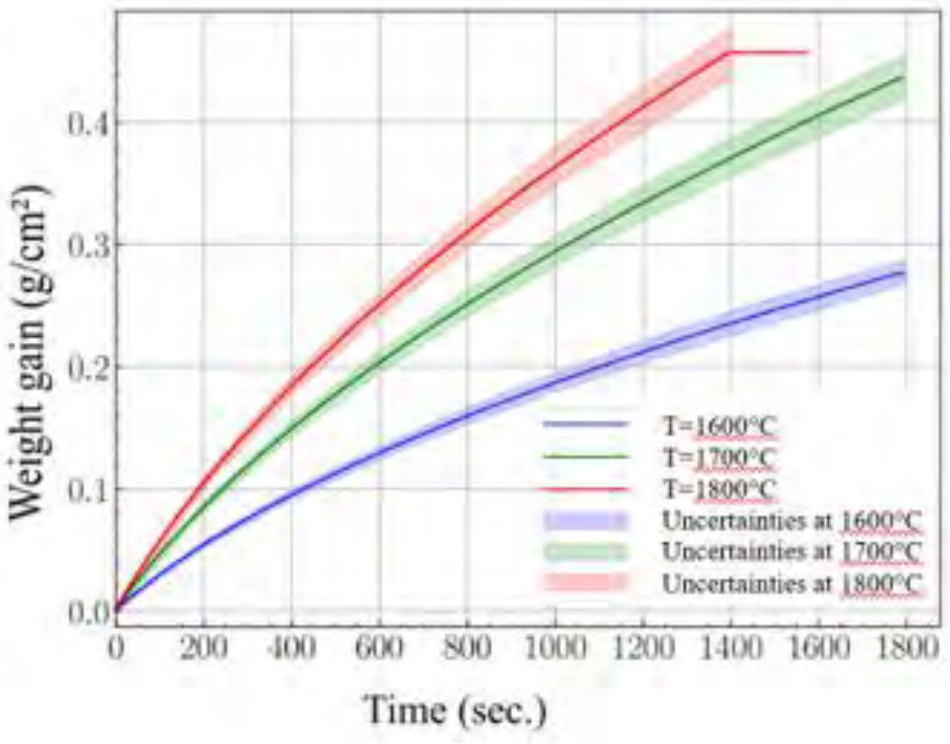

Zircalloy-4 oxidation at solid state (2/2)

- Prater *et al* : the parabolic rate constant may be affected by the non-uniform oxide/metal interface, which can disturb the accurate determination of the effective oxide thickness

	VITOX	Prater et al. [2]	Urbanic et al. [1]
Activation energy (J/mol)	203 000	224 000	131 000

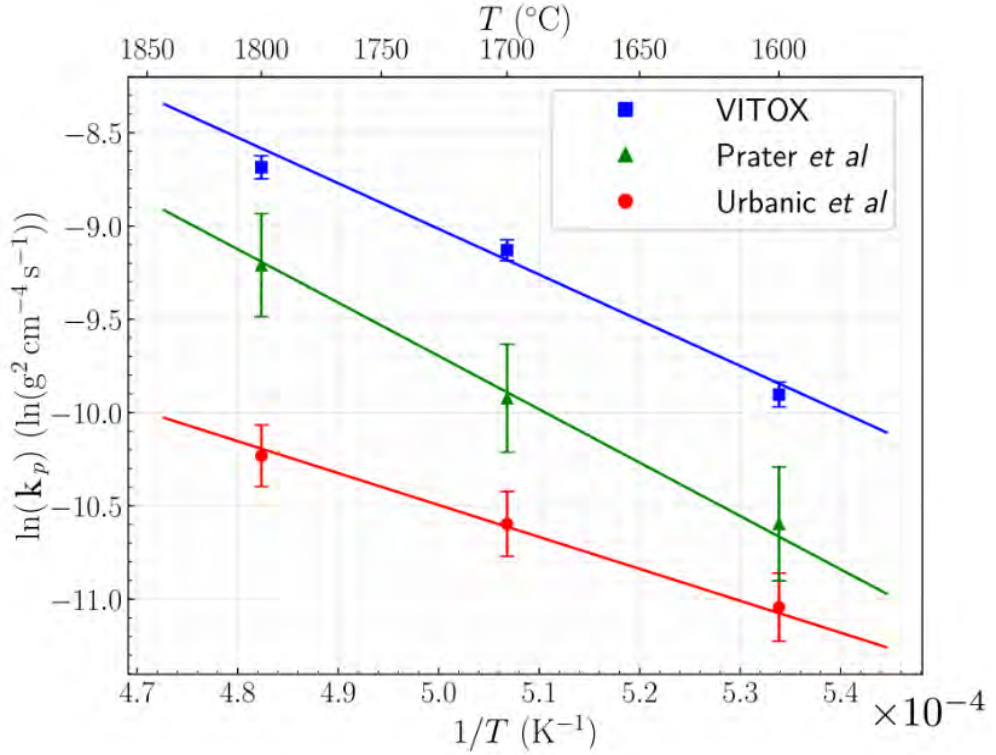

T (°C)	VITOX ($g/cm^2.s^{0,5}$)	Prater *et al.*[1] ($g/cm^2.s^{0,5}$)	Difference (%)
1600	$7{,}07 \times 10^{-3}$	$4{,}91 \times 10^{-3}$	**30**
1700	$1{,}08 \times 10^{-2}$	$7{,}02 \times 10^{-3}$	**35**
1800	$1{,}30 \times 10^{-2}$	$9{,}70 \times 10^{-3}$	**25**

1. *VF. Urbanic and TR. Heidrick. « High-temperature oxidation of zircaloy-2 and zircaloy-4 in steam». Journal of Nuclear Materials,* ***75****(2) :251–261, (1978).*
2. *JT. Prater and EL. Courtright, «Oxidation of zircaloy-4 in steam at 1300 to 2400 ℃», Zirconium in the Nuclear Industry. ASTM International, (1987).*

E-ATF oxidation at solid state (1/2)

No incubation time, **immediately parabolic**

$$W^2(t) = \mathbf{k_p} \times t$$

The maximum oxide weight gain is consistent across all temperatures 0.16 g/cm².

- 600 seconds at 1600 °C,
- 260 seconds at 1700 °C,
- 150 seconds at 1800 °C

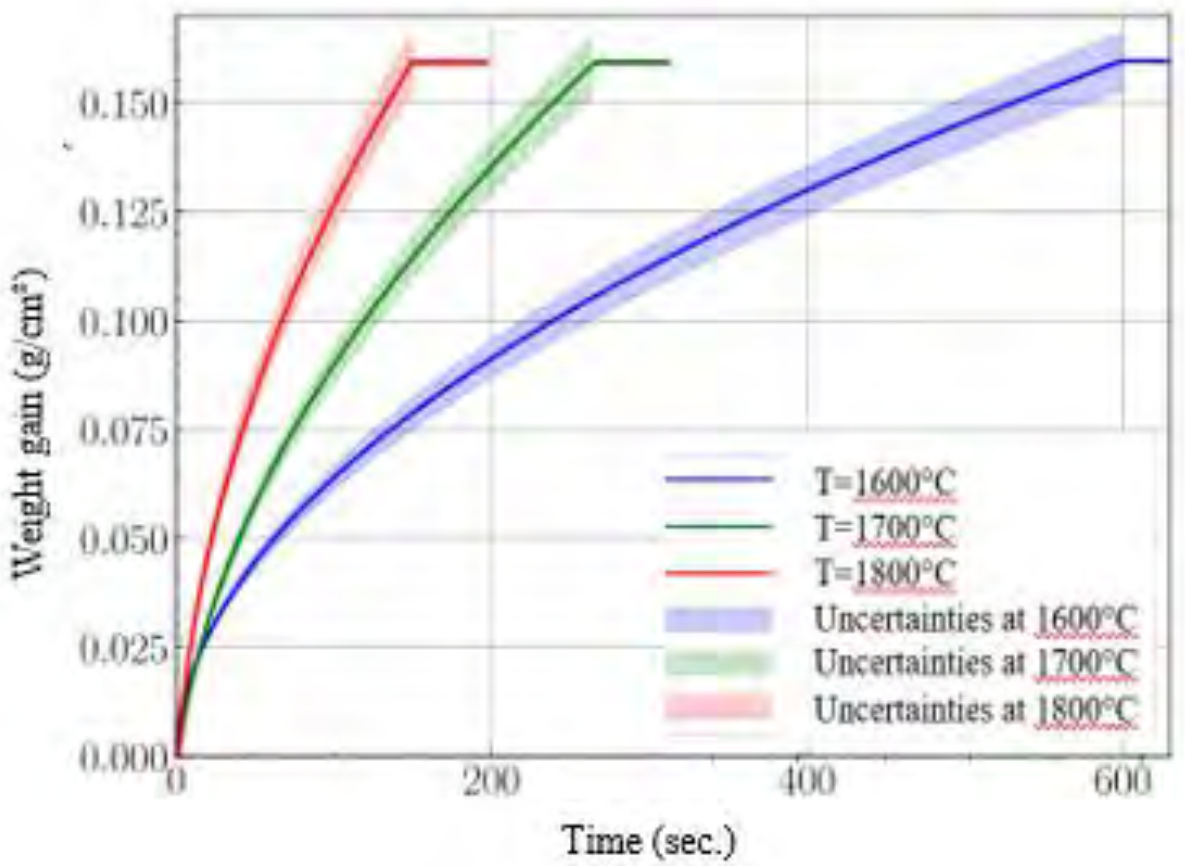

E-ATF oxidation at solid state (2/2)

SEM - EDS

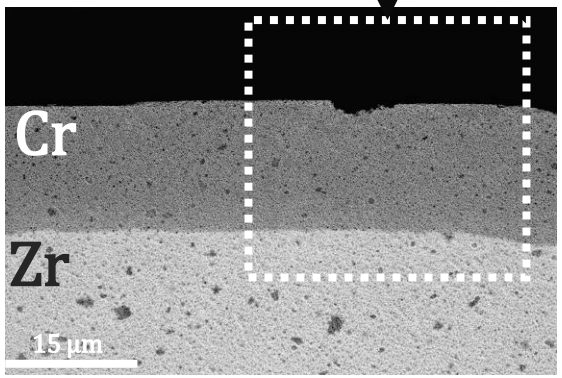

Initial state

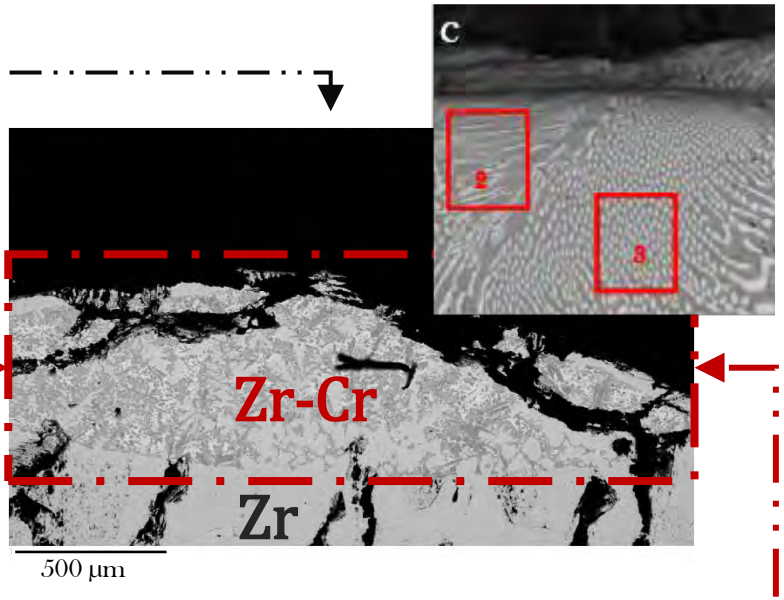

[Cr]=30,26 %at.

Dendritic zone

Interdendritic zone

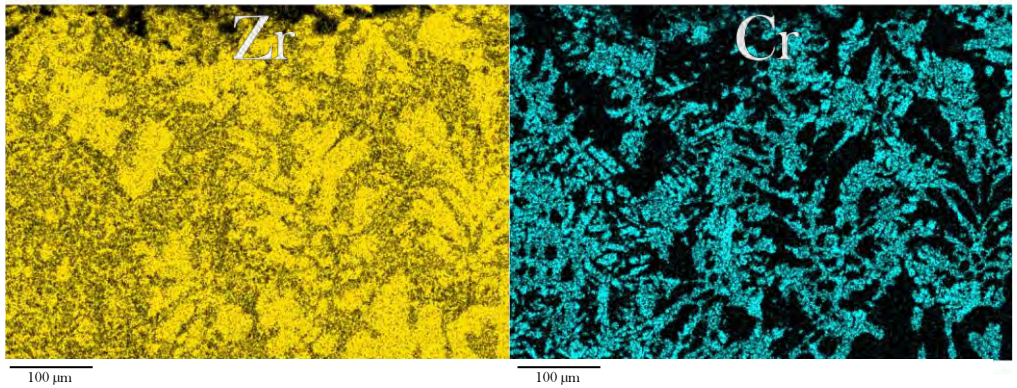

Phase diagram Zr-Cr

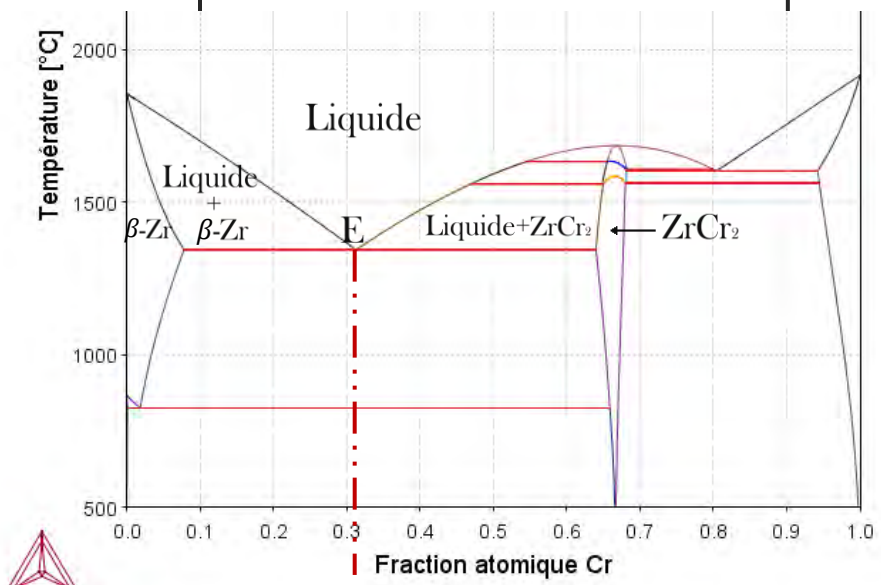

[Cr]=31,04 %at: eutectic composition.

T_{eut} = **1340 °C** ⟺ Liq = **Zr + $ZrCr_2$**

Solidification

Comparison Zircalloy-4 and E-ATF

- Oxidation kinetics and parabolic constants

T (°C)	**E-ATF** ($g/cm^2.s^{0,5}$)	Zircaloy-4 ($g/cm^2.s^{0,5}$)	**Difference (%)**
1600	$6{,}56 \times 10^{-3}$	$7{,}07 \times 10^{-3}$	**7**
1700	$9{,}95 \times 10^{-3}$	$1{,}08 \times 10^{-2}$	**8**
1800	$1{,}30 \times 10^{-2}$	$1{,}30 \times 10^{-2}$	**< 1**

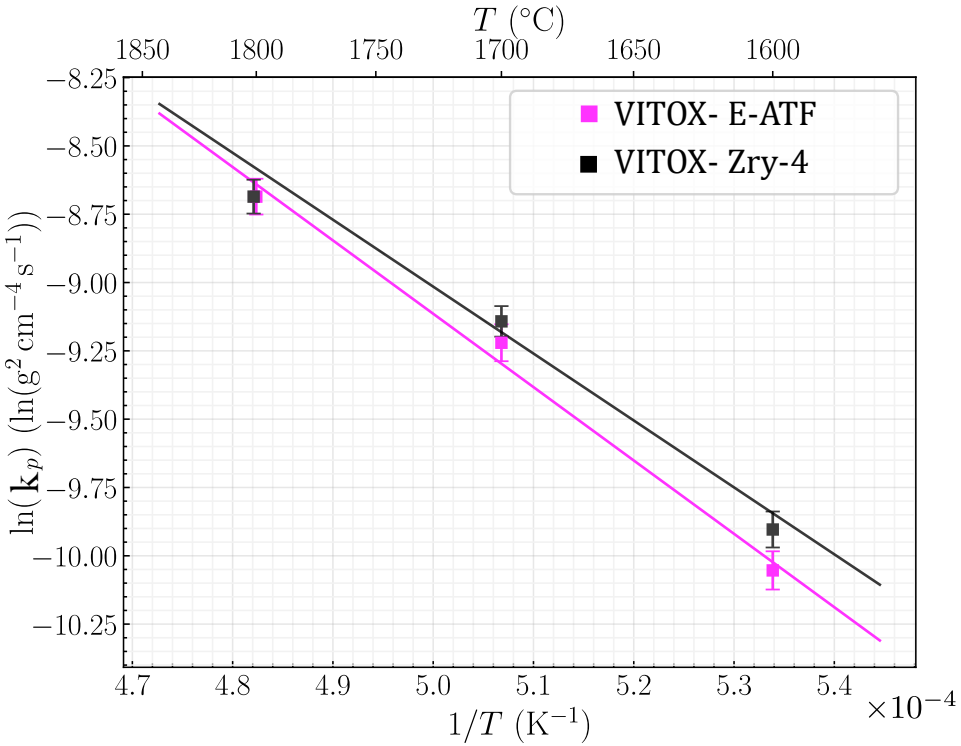

- **Total chromium consumption of the deposition layer at 1600°C**
- **Formation of a Zr-Cr eutectic liquid at the external interface**
- **Preferential formation of zirconia at external interface**
- **Parabolic constants comparable to zircalloy-4**

4. Conclusion and perspective

Conclusion and perspective

- **PLINIUS platform: development of VITOX facility (VITI-Oxidation), specifically designed to follow on-line hydrogen production and oxidation kinetics under non steam starvation conditions.**
- **New kinetics laws at temperature for zircalloy 4 above 1600°C: more rapid kinetics than those proposed in the literature.**
- **E-ATF protected by chromium layer: in isothermal conditions, behavior close to zircalloy-4 under steam non starvation conditions, meaning the total disappearance of the chromium protective effect.**
- **Formation of a liquid phase due to the formation of a eutectic: limited effect on oxidation mechanisms.**
- **E-ATF manufacturing process: limited effect on oxidation mechanisms.**
- **Perspectives: transitory conditions for zircalloy-4 and E-ATF (oxidation and hydrogen production).**

Thank you for your time and attention

The authors gratefully thank Martin Steinbrueck (KIT) for the E-ATF materials and for the very fruitful discussion on steam oxidation of zircalloy-4 and EATF.

The 12th European Review Meeting on Severe Accidents Research

May 18-22, 2026, Universidad Carlos III de Madrid, Madrid, Spain

TECHNICAL SESSION 3.3: SEVERE ACCIDENT SCENARIOS - SMALL MODULAR REACTORS

Chairs: F. Mascari (ENEA), M. Malicki (PSI)

ID117	**Investigation of Severe Accident Progression in Integral PWR SMRs** G. Acharya (KTH)	**Paper** **Presentation**
ID107	**Evaluation of Hypothetical Severe Accident Progression with ATF Cladding in Generic Integral PWR Designs in the Frame of the SASPAM-SA Project** M. E. Cazado (KIT)	**Paper** **Presentation**
ID164	**Comparative Analysis of Containment Behavior in a Generic iPWR Design under Postulated BDBA Conditions Using ASTEC v3.1.2 and MELCOR v2.2 codes** E. Cilia (ENEA)	**Presentation**
ID046	**SASPAM-SA: Assessment of existing experimental data in WP3** T. Lind (PSI)	**Paper** **Presentation**

INVESTIGATION OF SEVERE ACCIDENT PROGRESSION IN INTEGRAL PWR SMRS

Govatsa Acharya, Dmitry Grishchenko, and Pavel Kudinov
KTH Royal Institute of Technology, Division of Nuclear Science and Engineering,
Albanova University Center, 10691 Stockholm, Sweden.
govatsa@kth.se; dmitrygr@kth.se; pkudinov@kth.se

ABSTRACT

The development and deployment of Small Modular Reactors (SMRs), specifically integral Pressurized Water Reactors (iPWRs), promise enhanced safety and flexibility in nuclear power generation. However, understanding the behavior of these reactors during severe accidents, particularly the core degradation and source term — the release and transport of radioactive materials — remains a critical area of investigation. This study focus on the core degradation phenomena in iPWR SMRs. Unlike large traditional reactors, the integrated design of iPWR SMRs, with their smaller cores, compact primary systems, and passive safety features, introduces unique factors that affect the progression of core degradation and the resulting source term. MELCOR v2.2.r2023.0 is used to model severe accident scenarios in a 160MWth submerged containment natural circulation PWR. A Design Basis Accident (DBA) involving loss of coolant accident (LOCA) occurring in the chemical volume control system (CVCS) discharge line inside the CNT, with expected functioning of emergency core cooling system (ECCS) is analyzed. Progression during additional design extension conditions were also assessed. The role of LOCA break sizes is analyzed to assess its impact on mitigating core degradation. Preliminary results reveal that the compact design and passive features of iPWR SMRs can significantly alter the dynamics of core degradation and fission product behavior compared to traditional reactors. These findings provide valuable insights for refining source term models specific to iPWR SMRs and contributes to the broader understanding of severe accident phenomena in advanced reactor designs and supports the development of safety guidelines tailored to SMRs.

KEYWORDS
SMR, MELCOR, severe accident analysis, submerged containment design, LOCA, SGTR

1. INTRODUCTION

There is growing interest in deploying Small Modular Reactors (SMRs) to cater to growing energy demands by large data centers and industries, and to replace energy sources with large carbon footprint increasingly due to their ability in meeting flexible power needs [1]. SMRs enjoy better safety features, including inherent, passive, integral safety features, than conventional reactors, drawing to its appeal [2]. SMRs also promise simplification and standardization making it economically feasible. Among over 70 designs of SMRs available from the last 60 years of development [2], Integral Pressurized Water Reactors (iPWRs) are of interest. These are designs where the reactor primary circuit is housed together as an integral component [4]. This integral design, with a smaller core, promises “safety by design” and when scaled can effectively cater to flexible power demands with load-following operability. Although advancements have been made in different SMR technologies , with a few reactors already in operation or under construction in Russia and China, certain technical aspects are in focus pertaining, but not limited to, instrumentation, control and human factor engineering, development of new codes and standards for license and operation, source term for multiple module plants and establishment of emergency planning zones during accidents [3]. Discussions with regulators regarding elimination of public evacuations are ongoing.

With international interest in the technology and technical aspects needing more knowledge, EURATOMs SASPAM-SA project, the frame under which this study is undertaken, commenced in 2022 in order to address these challenges and support European licensing needs relevant to analysis of severe accidents (SA) and emergency planning zones (EPZ) [5]. Due to certain uniqueness of the designs of iPWRs, the capability of system codes and analytical tools to analyze the complex phenomenon in the reactor during an adverse event is a challenge that is being addressed by many studies [11][12][13][14]. Hydrogen explosions [6], forced and natural circulation passive safety [7][8], in-vessel cooling and debris retention [9], containment phenomena and behaviour [10] are some of the aspects in focus for SMR design analysis. Typically, SA codes such as MELCOR or ASTEC, are used in modelling accidents and are validated against experiments. These integral codes were designed for use in large reactor analysis. When new phenomena, such as in SMRs, where extensive experimental data are unavailable, use of system codes may include uncertainties based on modelling or design choices. This requires adequate knowledge of code capabilities and shortcomings, motivating current research.

Recently, generic designs of iPWRs were analyzed where a design basis accident (DBA) and some design extension conditions (DEC) were simulated [5][15][16]. The thermal-hydraulic characterization during the accident progression, conditions of vessel and containment, show counter intuitive behaviour of peak cladding temperature (PCT) when compared to large-PWRs. Capability of MELCOR in stable and accurate simulation of iPWR during loss of coolant accident (LOCA) was demonstrated [17][18]. The conservative source term behaviour in iPWR during severe accidents was recently analyzed in a complementary study [19]. In this study, SA analysis for a generic iPWR design is performed for accident scenarios with focus on core degradation and further T/H characterization, as part of activities in the SASPAM-SA project.

2. iPWR MODEL DESCRIPTION

The generic iPWR design under consideration is of the submerged containment type, where the integral reactor vessel is housed inside a larger containment which is submerged inside a pool of water, shown in Figure 1(a). The MELCOR model is a development of input deck developed by [15][16]. The specifications were based on available open literature. The iPWR is a 160MWth, naturally cooled integral reactor with 2 helical tube steam generators (HTSG). The reactor pressure vessel (RPV) is contained inside a containment vessel (CNT) to maintain core cooling in case of potential loss of reactor vessel integrity. The primary system operating pressure is 8.3MPa and CNT is almost a vacuum. In case of accidents the, steam generators (SGs) are isolated and emergency core cooling system (ECCS), comprising of 3 reactor ventilation valves (RVVs) at the top of RPV and 2 reactor recirculation valves (RRVs) at elevation above top of active fuel (TAF), is activated which opens the RVVs to vent steam into the containment, and the RRVs which establishes coolant circulation between the reactor coolant system (RCS) and the containment side transferring decay heat to the reactor pool (RP) acting as the ultimate heat sink (UHS). The core has 37 17x17 fuel assemblies, about half the height of typical PWR assemblies located at the bottom of the RPV. Above the core, a cylindrical riser tube terminates in the pressurizer (PRZ). The downcomer, an annular region surrounding the riser, houses the two HTSGs in the upper part and the core in the lower part. The HTSG consists of a set of tube bundles with separate feedwater inlet and steam outlet lines. The MELCOR model of the iPWR, shown in Figure 1(b), comprises of control volumes (CVs) representing parts of RPV, SGs, CNT, RP, reactor building and the environment, and flowpaths (FLs) representing connections between CVs. Details of packages used to develop inputs in MELCOR can be found in the guides [15][16].

The T/H behaviour is dependent on the assumptions and choices made in nodalization of these CVs and properties of FLs. Here, the RPV has 5 CVs for the riser, 5 CVs for the PRZ, 7 CVs for SG primary side, 5 CVs for the downcomer, 8 CVs for the core channel and bypass, and 1 CV for the lower plenum (LP). Heat structures (HS) transfer heat between CVs, here, cylindrical HS are defined between RPV and CVN axially, and hemispherical HS are defined at top and bottom of RPV.

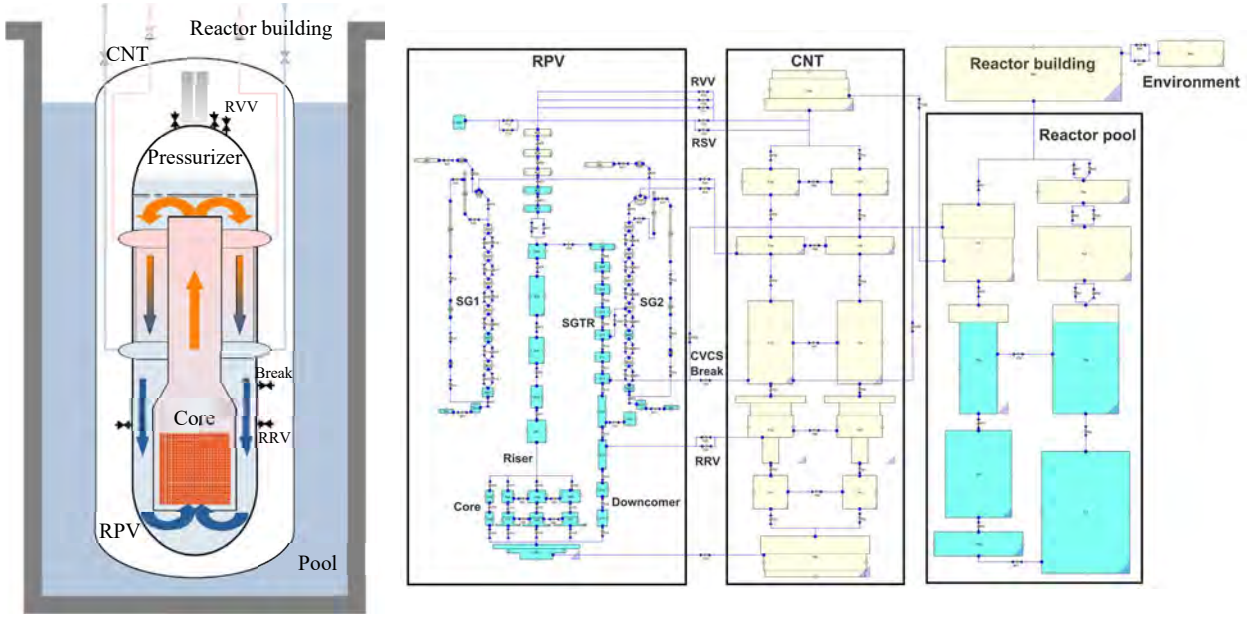

(a) Generic design. (b) MELCOR nodalization.

Figure 1. Schematic of the generic iPWR design (based on [15]).

The CNT is defined by 12 CVs, separately for the cold and hot side to support natural convection, to reduce instabilities in simulations, while RP has 8 CVs. The SG is a bundle of once through HTSG, whose secondary side has 2 sets with 7 CVs each. The heat transfer inside is modelled using HelicalSG HS in MELCOR. HSs also exist for the CNT designed to support natural convection in the pool. FLs exist between CVs in the core, riser, downcomer, SGs and CNT. A leakage FL is added to the top of CNT with the top of RP, and the flow rate is controlled by a tabular depending on pressure differences. The core is modelled in the COR package, as 4 rings radially and 10 levels axially. Active core is in the central 3 rings and levels 6-9, the lower plate in level 4 and lower plenum in levels 1-3. 2 reactor safety valves (RSV) are included to protect RPV from over-pressure. Decay heat tables based on ANS73 standard are implemented. The radionuclide transport is handled by the RN package, where hygroscopic and chemisorption models are activated. Revised CORSOR-Booth high burnup model is used for fission product (FP) release.

2.1. Accident Scenarios

The DBA and DEC scenarios studied here are given in Table 1 below. The SA identified in SASPAM-SA were based on potential severity of consequences and not on probability of occurrence. A LOCA in chemical volume and control system (CVCS) discharge line, 1.6” diameter, is assumed to be the initiator in DBA, with fully functioning ECCS. Postulated DECs, referenced as in the table, include spurious opening of the RVV and RRV either with fully or partially functioning ECCS. In order to analyze non-LOCA type scenarios in the CNT, a 13mm tube rupture in the SG and loss of feedwater leading to loss of heat sink (LOHS) are included. Unavailability of RRVs during an accident voids natural circulation in the CNT.

The conditions for activation of the ECCS (ECCS signal) are as follows. RVVs and RRVs open simultaneously after 15s of both these conditions being met:

1. High containment water level – above 5.8m,
2. Low RCS pressure – pressure difference between PRZ and CNT is below 6.2MPa.

Table I. Accident scenarios considered for analysis.

Scenario ID	Initiator	ECCS availability		Comments
		RVV	RRV	
DBA	CVCS discharge LOCA	Yes	Yes	1.6” LOCA in CVCS discharge to CNT
DBAN	CVCS discharge LOCA	No	No	1.6” LOCA in CVCS discharge to CNT
SA1	CVCS discharge LOCA	Yes	No	1.6” LOCA in CVCS discharge to CNT
SA1o	CVCS discharge LOCA	Yes 1	No	1.6” LOCA in CVCS discharge to CNT
SA2	Spurious opening of 1 RVV	Yes 2	No	2.5” RVV opening of 1 RVV
SA2N	Spurious opening of 1 RVV	No	No	2.5” RVV opening of 1 RVV
SA3	Spurious opening of 1 RRV	No	Yes 1	2.5” RRV opening of 1 RRV
SA3N	Spurious opening of 1 RRV	No	No	2.5” RRV opening of 1 RRV
SA4	CVCS discharge LOCA	Yes	Yes	1.6” LOCA in CVCS to RP
SA4N	CVCS discharge LOCA	No	No	1.6” LOCA in CVCS to RP
SA5	CVCS discharge LOCA	Yes	Yes	1.6” LOCA in CVCS to CNT, breach in CNT to RP
SA5N	CVCS discharge LOCA	No	No	1.6” LOCA in CVCS to CNT, breach in CNT to RP
SA6	SG tube rupture (SGTR)	Yes	Yes	No steam line isolation, feedwater line isolated
SA6N	SG tube rupture (SGTR)	No	No	No steam line isolation, feedwater line isolated
SA7	Loss of heat sink (LOHS)	Yes	Yes	Steam line and feedwater line isolated

In open literature (for instance NuScale), activation of RRVs have inadvertent actuation block (IAB), wherein RRVs open only after IAB clears (pressure difference between PRZ and CNT is < 6.2MPa). While in LOCA type situation this may imply RRVs open almost simultaneously with RVVs, in actuality that may not be the case. The sensitivity of timing of RVV and RRV activation on the accident progression is performed in a separate study, where RRVs open only after RVVs open with set delay time and low RCS condition is met. In this study, the sensitivity of accident progression on size of break is analyzed by considering 12 CVCS break size diameters from 0.1cm to 4.4cm in the absence of ECCS. On a spectrum, DBAN scenario would be the 11th case with 4cm diameter LOCA and LOHS would be the 0th case with no LOCA. In the case of SGTR accident (SA6), where there is no loss of coolant to the CNT, condition 1 is not satisfied. Hence, it is assumed ECCS is activated upon fulfilling condition 2.

From the perspective of FP release pathway to the environment: DBA/DBAN, SA1/SA1o, SA2/SA2N, SA3/SA3N, SA7 cases have a leakage FL from the containment to the reactor building, SA4/SA4N, SA5/SA5N cases have, in addition to leakage, direct/indirect FL from the RPV to the reactor building, and in the case of SA6/SA6N FPs trace a pathway from RPV into the turbine CVs through ruptured SG tube, which in this study is considered to be outside the containment pressure boundary and hence part of the environment.

3. RESULTS

Here, results of MELCOR simulations are presented with timing of events, T/H considerations, and core behaviour. All accident scenarios were run using MELCOR v2.2.r2023 for 72h. In some of the figures presented, the range is shortened for better readability. Table 2 shows the timing of reactor trip signal, ECCS signal, core uncovery and core damage process.

3.1. Thermal-hydraulic Behaviour

DBA and DBAN: In LOCA type scenarios where coolant is lost directly to CNT (CVCS line break or spurious opening of valves), reactor trips between 4 and 44s. In the case of DBA, once the reactor trips,

depressurizes into and fills the CNT, ECCS is activated at 520s. This initiates circulation of coolant between RPV and CNT, enabling removal of decay heat. The elevation of CVCS break is at 9m, and RRV at 5.6m. Water fills the containment, subsequently, decay heat boils the water and steam produced escapes majorly through the RVVs and the break, see Figure 2(a). The released steam condenses on the CNT walls and collects adding to circulating pool below. In the RRVs, Figure 2(b), both positive and negative flow are observed, indicating convection of the coolant. Figure 2(c) shows the collapsed liquid levels in the RPV and the CNT, where at ~10.5m after the start of accident, levels on either side of the RPV are stabilized. One can observe the heat transfer rates, Figure 2(d), from the core to the water (in blue) coinciding with decay heat (in yellow), indicating successful cooling and expected behaviour of ECCS. The fuel and cladding temperature during this scenario can be observed in Figure 3(a).

Table II. Timing of events during the accident scenarios.

Scenario ID	SCRAM	High CNT level	ECCS signal	Core uncovery	Gap release	PD formation	Relocation to LH	Core plate failure	LH failure
DBA	19	520	520	-	-	-	-	-	-
DBAN	19	520	-	4950	12782	13728	-	-	-
SA1	19	520	520	4610	12419	13386	-	-	-
SA1o	19	520	520	4995	12990	14197	-	-	-
SA2	4	8640	8640	20256	32517	33600	53618	55170	-
SA2N	4	8640	-	20239	32410	33530	51722	51721	-
SA3	7	60	61	174	5111	6038	-	-	-
SA3N	7	60	-	620	6097	6955	12830	-	-
SA4	44	-	815	848	3300	4178	10426	12057	232843
SA4N	44	-	-	1814	7412	8565	13071	13071	33682
SA5	19	775	775	3591	29725	31742	65800	65806	-
SA5N	19	775	-	2310	9238	10478	15834	15834	-
SA6	30	-	1380	-	-	-	-	-	-
SA6N	30	-	-	27350	40220	42934	72145	79230	84320
SA7	23	-	-	-	-	-	-	-	-

SCRAM - safety control rod axe man/reactor trip; PD - particulate debris; LH - RPV lower head.

With absence of ECCS, in DBAN, circulation of water is not established, steam mainly flows outwards, till level in RPV reaches the break elevation that is filling the CNT. Then the water surrounding the core boils off slowly, because steam can only escape from the break (not through RVVs). Core starts uncovering at 4950s. Subsequently, (i) once the level falls below the core in the LP, it takes a longer time to boil into steam, (ii) there is no direct core cooling by water, and (iii) the heat from the core is removed by steam and by conduction across lower head (LH) to water in CNT. The cladding is exposed to steam, undergoing oxidation and generating hydrogen and oxidation heat in the process. This further accelerates degradation of the fuel rods, ultimately leading to failure of cladding due to high temperature, see Figure 3(b) the first failure of cladding occurs around 5h. When this happens, irrespective of the axial level where the failure occurs, FPs in the entire fuel-cladding gap are released, at 12782s. Formation of particulate debris (PD) – resulting from collapse of fuel rods and other components – follows at 13728s.

Fuel and cladding in the upper levels start melting and relocating downwards by gravity (candling). If the molten mass is cooled, it may refreeze onto other intact material forming conglomerate debris (DC). With insufficient cooling, more such intact material degrades, relocating downwards. This mixture of molten material, particulate debris and conglomerate debris would then relocate onto the core support plate.

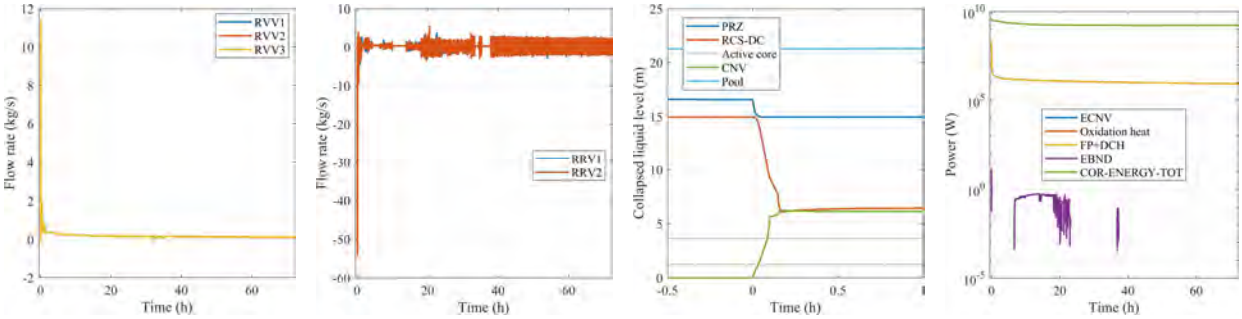

(a) RVV flow rate. (b) RRV flow rate. (c) Collapsed liquid levels. (d) Rate of heat transfers.

Figure 2. Evolution of T/H properties during DBA scenario. ECNV: convective heat transfer, FP+DCH: fission power and decay heat, EBND: conductive heat transfer (to HSs), COR-ENERGY-TOT: total energy handled in COR package.

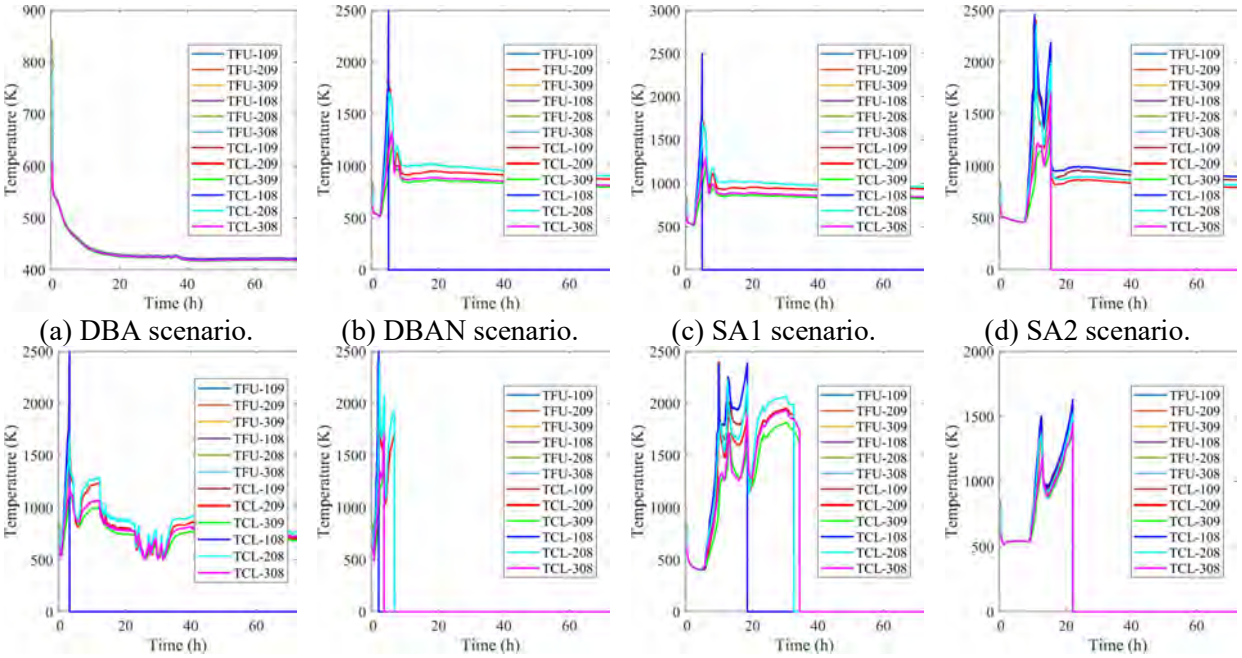

(a) DBA scenario. (b) DBAN scenario. (c) SA1 scenario. (d) SA2 scenario.

(e) SA3N scenario. (f) SA4 scenario. (g) SA5 scenario. (h) SA6N scenario.

Figure 3. Fuel and cladding temperature in the top 2 axial levels. TFU: cell fuel temperature, TCL: cell cladding temperature.

SA1 and SA1o scenarios. SA1/SA1o scenario have progressions similar to DBAN, except that with the availability of RVVs, loss of coolant inventory from the reactor vessel is accelerated. In DBAN, SA1 and SA1o, the opening at RVVs and the break, create a circulation pattern of steam around the core, cooling it for a longer period preventing degradation, without large relocation to the LH, see Figure 4(a) and (b) for mass of steam in the core and LP regions.

SA2, SA2N, SA3 and SA3N scenarios. In the case of SA2, SA2N, SA3 and SA3N, the loss of coolant occurs via the opening of larger ECCS valves (2.5" v/s 1.6" of CVCS) – SCRAM is quicker. However, with opening of RVV loss of RCS is through steam escaping out at top of RPV, whilst with opening of RRV, loss is through water flowing out at just above active core level: latter case sends faster ECCS signal at 61s compared to 8640s of the former scenarios. It is observed, quiet expectedly, that core uncovery in SA2 and

SA2N happens much later than SA3 and SA3N, see Figure 5(a), when boiling of water in RPV starts there is smaller quantity of water inside RPV so uncovery is faster. Irrespective of availability of ECCS, during SA2/SA2N, failure of the core support plate and debris collection in the LP is observed.

With twice the larger area in SA3 compared to SA3N for escaping steam, uncovery is almost twice as fast. One thing to be noted here is that, if the total inventory of RCS were to be transferred to the CNT, it would fill to a level above RRV elevation (lower than CVCS break elevation). Therefore, when water starts collecting in CNT, there is counter-current flow of escaping steam and incoming water in the RRVs. This can be sensitive to accident progression, because any slight change in T/H conditions can lead to large change in water level inside the RPV, subsequently causing variations in core cooling. Between SA3 and SA3N, a variation of flow area is shown to either induce debris relocation to LH (at 12830s in SA3N) or not (in SA3), suggesting a limiting area of flow that avoids relocation of debris. Figure 6(a) and (b) show the mass of steam in RPV during SA3 and SA3N. Unavailability of ECCS, for a brief period at ~3.5h during SA3N accident causes sufficient cooling deficit conditions in the LP and core regions leading to debris relocation to LP, see Figure 3(e) the drop of cladding material temperature in the innermost ring of the top axial level of the core.

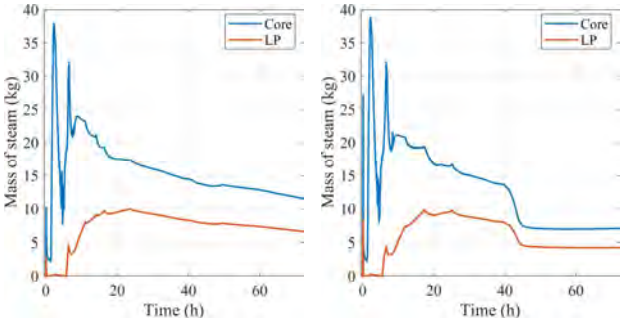

(a) DBAN scenario. (b) SA1 scenario.

Figure 4. Mass of steam inside RPV.

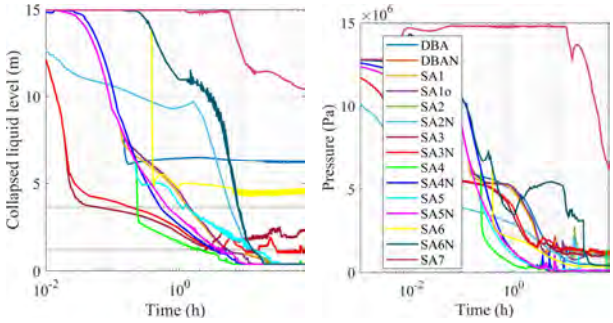

(a) Collapsed liquid level. (b) Pressure.

Figure 5. Water level and pressure in the RPV for all cases. Black horizontal lines: Active core.

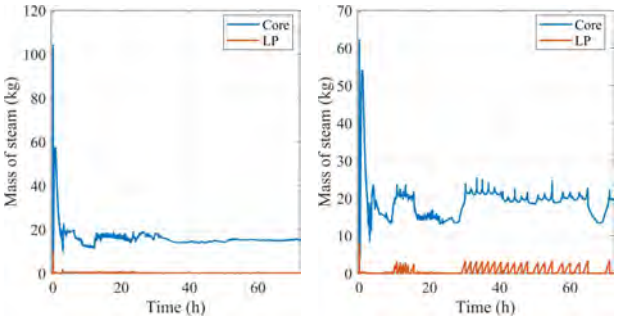

(a) SA3 scenario. (b) SA3N scenario.

Figure 6. Mass of steam inside RPV.

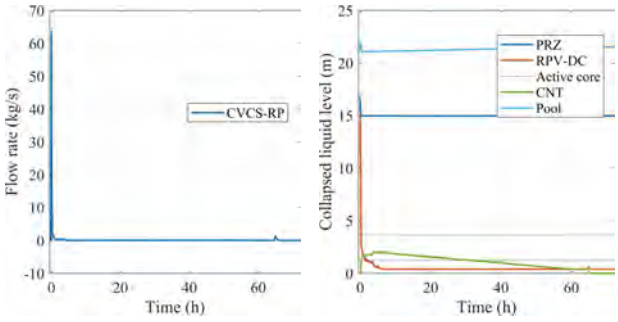

(a) Flow rate. (b) Collapsed liquid level.

Figure 7. Flow rate of the break and liquid level during SA4 scenario.

SA4 and SA4N scenarios. In these scenarios, the containment is bypassed and the coolant is lost directly from the downcomer to the reactor pool. The flow rates through the break and the liquid level are shown in Figure 7(a) and (b). SA4 has the fastest complete core uncovery, by 2h liquid level is below bottom of active fuel (BAF). As seen in Table II, these scenarios have the earliest onset of debris formation and gap releases amongst all the cases considered. As seen in Figure 7(b), before ECCS activation level at 815s, CNT is

filled due to steam escaping the RPV through safety valves by overpressure. After ECCS activation, CNT is filled by water, and the liquid inventory in the RPV and CNT has reached such low levels that activating ECCS does not establish circulation through the RRVs. ECCS is therefore unable to prevent the eventual core degradation and relocation at 10426s. Subsequently, the support plate fails at 12057s. In the case of SA4N, this relocation is observed at 13071s, instantly followed by support plate failure. Expectedly, this scenario leads to a failure of the LH 232843s for SA4 and 33682s for SA4N due to insufficient cooling of the debris pool. This is one of the most severest of scenarios, where time period from core uncovery to vessel failure is less than 10h.

SA5 and SA5N scenarios. In these two scenarios, the core is partially covered with water for most of the 72h, and the natural circulation inside RPV is restricted. In the case of SA5, a break in CVCS line causes LOCA and simultaneously a flow is established from the CNT to the reactor pool, so that coolant can escape as steam directly to the reactor building, leading to loss of coolant inventory in the reactor, see Figure 8(b). Until 20h, the coolant from the RPV flows into the CNT, post which, total mass of liquid water (that could sustain core cooling) in the CNT starts reducing. Compared to DBAN scenario, the coolant temperatures inside the CNT in SA5 is lower, see Figure 9(a) and (b) (where TLIQ: liquid temperature, TSAT: saturation temperature of the liquid). Because in the case of DBAN, the containment pressure boundary is not breached, the pressure in the CNT is high compared to SA5, where the pressure is almost atmospheric, see Figure 5(b) (red line). Correspondingly, in Figure 9(a), the water saturation temperature in the CNT is higher (purple line) and the water in CNT does not boil (yellow line). However, in the case of SA5, saturation temperature of water in CNT is lower, accelerating conversion to steam and loss to the RP. The flow rate of the pathway leading out of the CNT is shown in Figure 10(a). A maximum of 6kg/s flow rate of steam is initially observed, due to high CNT pressure, which gradually reduces to atmospheric. A small peak at ~18h is observed due to pressure spike caused by core degradation.

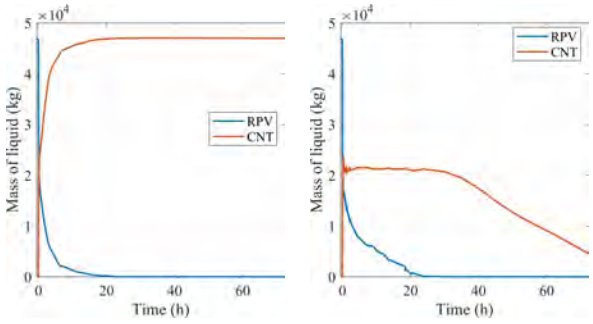

(a) DBAN scenario. (b) SA5 scenario.

Figure 8. Mass of coolant inside the CNT boundary.

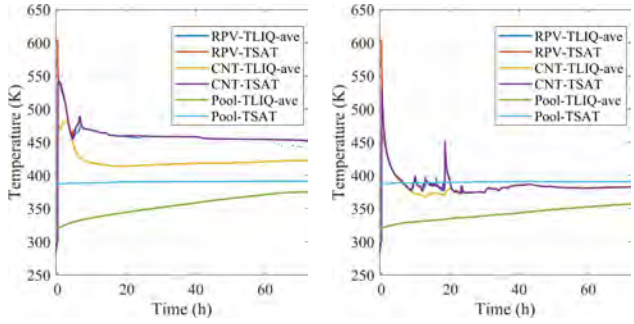

(a) DBAN scenario. (b) SA5 scenario.

Figure 9. Water temperature in RPV, CNT and RP.

SA6 and SA6N scenarios. In the case of SA6 and SA6N, with rupture of a single tube of the SG and opening a containment bypass pathway to the turbines, SCRAM occurs late at 30s, because the depressurization caused in RPV is slow (also the pressure in the CNT is unaffected as it is bypassed, similar to SA4/SA4N case) to trigger reactor trip. Another point to note is that in SA6N, since CNT is bypassed, water does not accumulate there, just as in the case of SA4N. The flow rate of steam through the tube rupture is shown in Figure 10(b). Negative values indicate flow into the SG. Flow rate peaks to ~9.3kg/s initially due to high primary side pressure, see Figure 5(b) (light green line). The depressurization due to flow into SG is insufficient to balance pressure generated by superheated steam, the reactor safety valves are triggered at 14.75MPa pressure. This causes steam to flow into the CNT, that condenses and flows to the bottom (which is why liquid temperature increase in CNT is observed in Figure 11(a) (purple line)). The RSV closes once primary reaches 14.7MPa. Once the primary side is sufficiently depressurized, boiling water in the core increases the pressure, sufficiently higher than in other SA cases, at ~5.5MPa. Core uncovery starts at 27350s, the longest it takes amongst all SA cases where core is uncovered, because of the time needed for

evaporation of entire RCS inventory and RPV dryout. Gap release occurs at 40220s and relocation of debris to LH at 72145s. The core support plate fails at 79230s and roughly 1.2h later at 84320s the LH fails. Once the LH fails, the CNT is instantly pressurized and water inside is vaporized.

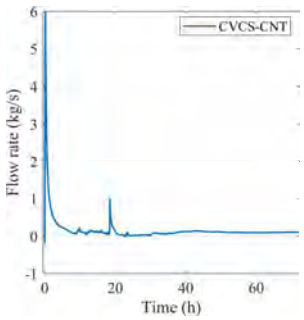

(a) SA5 scenario.

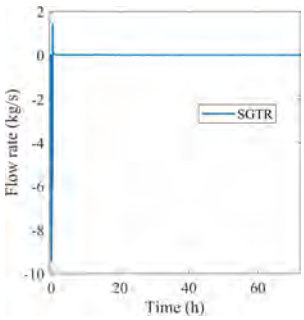

(b) SA6 scenario.

Figure 10. Flow rate of the break pathways.

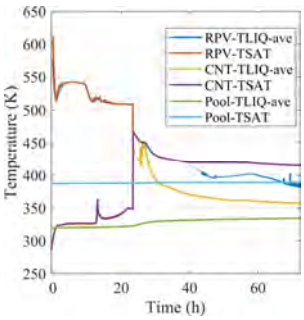

(a) Water temperatures.

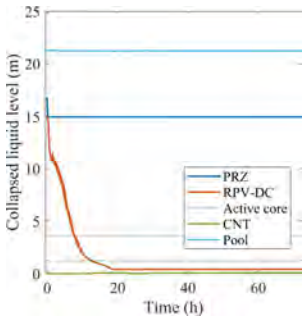

(b) Collapsed liquid level.

Figure 11. T/H properties during SA6N scenario.

SA7 scenario. In the case where no LOCA or SGTR event occurs, and only the feedwater flow is stopped leading to loss of heat sink (LOHS), the primary pressure increases once the reactor trips at 23.2s. There is no vent for the steam being generated by the boiling of water, and the RPV pressure increases beyond 14.75MPa, triggering the RSV, see Figure 5(b) (dark blue line). This vents out steam continuously for >10h as liquid level in the RPV drops and in the CNT increases. Once the CNT water level surrounds the active fuel region (after ~10h), this creates stronger direct heat transfer from the core to the RP, which hitherto was filled with air and steam, thus a weaker heat transfer. Once this happens, the temperatures of the fuel gradually reduce because of higher rate of removal of decay heat, and the pressure inside the RPV reduces further, and eventually venting in the RSV stops. No core uncovery is observed until the end of 72h at which time the primary pressure is about 10MPa. This scenario is similar in many ways to a very small sized LOCA at the top of RPV.

Effect of LOCA break sizes. To analyze effect of break sizes, a spectrum of scenarios is considered with 12 sizes uniformly spaced between 0.1cm and 4.4cm (Case-001 to Case-012). Firstly, the effect in DBAN is presented, followed by SA4N and SA5N. The ECCS is assumed unavailable in all scenarios. The reference scenarios (DBAN, SA4N and SA5N) would be equivalent to 11th case with a break size of 4cm. The T/H and accident progression parameters for these accident scenarios are shown in Figure 12, Figure 13 and Figure 14.

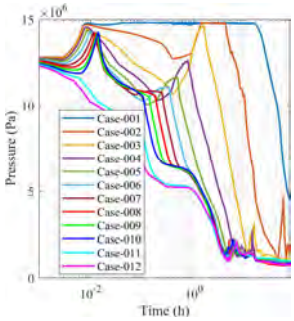

(a) RPV pressure.

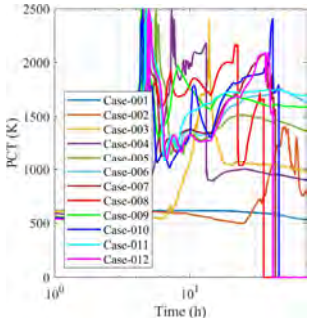

(b) PCT.

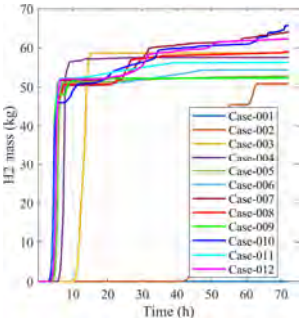

(c) H_2 generation.

Figure 12. SA characterization for DBAN cases with varying break sizes.

For varying sizes during DBAN, reactor trip causes the RCS pressure to increase, and in cases lacking sufficient break flow area, pressure does not fall. The smaller size of the LOCA break does not lead to loss of pressure in the RPV, as does larger LOCA. This leads to initial venting via RSV. In the case of 001 the RSV does not close until sufficient loss of steam into the CNT. In the case of 002 and 003, after closing of RSV, the rising pressure by the boiling of water and insufficient loss of water to CNT for circulation, reactivates the RSV briefly. Other cases lead to higher depressurization and subsequent uncovery of the core is expectedly faster with increasing size. Core degradation phenomenon is not linear. Cases 010, 008 and 007 lead to complete damage of the core (indicated by the vertical drop in PCT signal in the plot). Case 009 leads only to ~10% damaged core. In the former cases, complete dryout and steam starvation is observed. However, the size of break in Case 009 (diameter of 3.275cm) is sufficient to circulate steam inside the RPV and transfer the decay heat to the water in the CNT. PCT is also lower in 009, than 010 and 008 for instance. Such non-trivial behavior needs to be verified by further analysis and experimental observations.

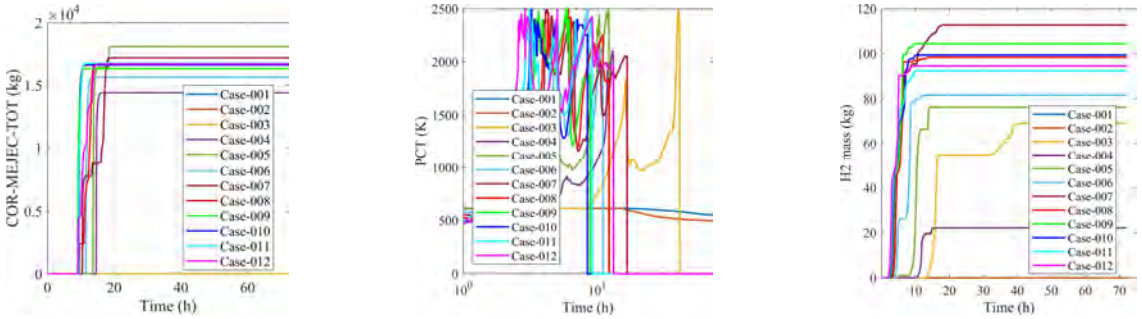

(a) Core debris mass ejection. (b) PCT. (c) H_2 generation.

Figure 13. SA characterization for SA4N cases with varying break sizes.

In the case of SA4N with varying break flow sizes, pressure trends match the case of DBAN, however the downstream control volume is the reactor pool instead of the CNT, which leads to loss of debris cooling capacity with empty CNT. Consequently, what is observed is that Cases 001 and 002 because of small break size, retains sufficient coolant inventory saving the core from uncovery. All other larger break sizes lead to complete uncovery and core degradation, and except for Case 003, lead to RPV failure and debris ejection to the CNT at 9-15h after onset of LOCA. Between Case 003 and Case 004 corresponding to break size 0.89cm and 1.29cm lies the limiting size that can avoid complete RPV failure. Roughly 14-18tons of debris is ejected from the RPV to the CNT. Largest debris ejection is observed for Case 005 at ~18tons where almost all debris formed is ejected, whereas in other cases, some conglomerate and particulate debris remain in the core. Total H_2 generation for Case 007 is the largest at ~113kg. Generally SA4N cases lead to almost twice the amount of H_2 generation compared with DBAN. However, in DBAN the hydrogen accumulates inside the CNT whereas in SA4N cases it flows out to the reactor building.

In the case of SA5N with changing the break sizes, it is seen from Figure 14(b) that all considered sizes lead to complete core damage. The RPV pressure follows a typical evolution as seen from DBAN case, with the variations arising from subsequent loss of steam from the varying sized break CNT to the RP. Because there is an intermediate control volume between RPV and the RP enough steam circulation is possible to maintain debris cooling to prevent RPV failure, even in Case 012 with the largest break size. Similar to SA4N cases, total H_2 generation extends from ~62kg for Case 001 to a maximum of ~120kg for Case 006. Largely, all the hydrogen is transferred along with steam into the reactor building and very small amounts are retained in the CNT itself. Complete core uncovery is observed to occur between ~3.5h to ~5.5h and correspondingly, complete core damage between ~7.2h to ~70h. This indicates a double-sided LOCA break inside the CNT is able to retain the debris inside the RPV without failing the LH for 72h irrespective of the size of break, unlike a break inside the RPV itself (SA4N). A similar analysis on the effect of size of tube rupture during SGTR (SA6N) is in progress and will be presented in the future.

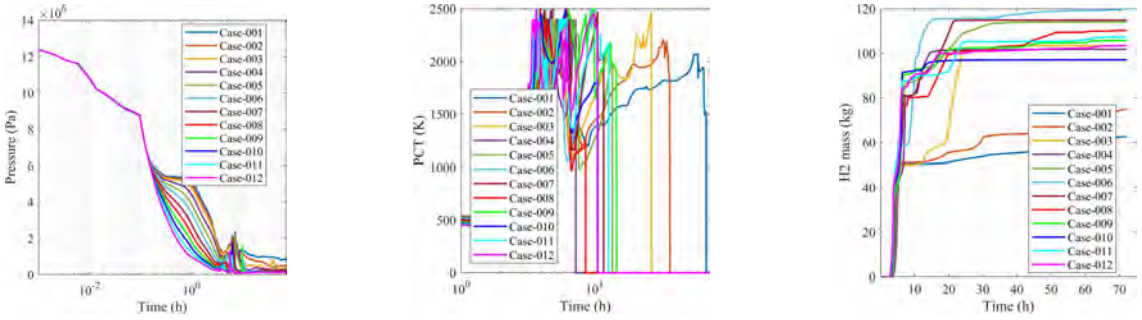

(a) RPV pressure. (b) PCT. (c) H_2 generation.

Figure 14. SA characterization for SA5N cases with varying break sizes.

3.2. Core Degradation

The mass of solid and molten debris for scenarios with uncovery and damaged core (DBAN, SA2, SA3, SA3N, SA4, SA4N, SA5, SA5N and SA6N) are presented in Figure 15. As mentioned before, following uncovery, the cladding is oxidized and ultimately fails in absence of cooling. This starts fuel oxidation and, with increasing temperature of the fuel-cladding (UO_2/ZrO_2) eutectic mixture, can melt and candle. Presence of oxide layer in the cladding can contain the molten ZrO_2 inside the shell. Any failure of material component forms particulate debris that slumps to the bottom of core. The overall damage fraction of the core (defined as fraction of fuel that is no longer intact due to loss of support, liquefaction or melting) for all scenarios is shown in Figure 17(a). In the case of DBAN, since the commencement of PD formation, 2200kg of DC and 2000kg of PD are formed in the core region. Until 72h, this debris is oxidized slowly without reaching component failure temperature, as the circulating steam cools the core without further degradation. When the core support plate fails, the falling debris (if water exists in the LP) can be quenched. Oxidation of the core components generates about 60kg of H_2 at the end of 72h. SA1 has similar magnitudes and behaviour of debris masses and is not shown in the figure, however it generates the least H_2 among the cases considered, about 55kg.

In the cases of SA2, SA3 and SA3N, initial damage of core is similar (~10% damage fraction), resulting in the formation of 3000kg, 2100kg and 2750kg of PD and 2100kg, 2750kg and 2100kg of DC in the core region respectively. It is also interesting to note that in SA3, the total damage fraction is 10%, the top 2 axial levels of the central ring have failed, whereas in SA3N, the damage fraction is 0.2%, with major failure in any of the core cells. However, in both the cases, comparable PD and DC are formed, mainly due to damage of the cladding. This is the effect of, as noted earlier, limiting area of the RRV that keeps the core partially covered with counter-current flow in partially activated ECCS. SA2 generates about 70kg, SA3 59kg and SA3N slightly higher 68kg of H_2 at the end of the simulation. Due to failure of the support plate, about 4500kg and 80kg debris are relocated to the LP in SA2 and SA3N respectively.

By 10h due to insufficient cooling of the core, about 16tons of PD+DC have relocated to the lower plenum and around 4tons form a molten pool during SA4 generating about 110kg of H_2. The debris remain as such without any further relocation due to sufficient water in the CNT transferring the decay heat until about 65h when the CNT is dry around the LP region effectively removing major heat transfer. Subsequent to RPV failure all debris, around 18tons, is ejected to the CNT vessel. In the case of SA4N at 10h, due to unavailability of water in the CNT, any debris relocation to LP almost instantly fails the RPV and ejects about 17tons of debris. This scenario generates about 92kg of H_2 by oxidation. In the case of SA5, at ~10h about 10tons of PD+DC forms in the core region which relocates to the LP at ~20h. Some of the debris is quenched forming almost forming about 2tons of DC in the LP. From about 32h onwards the water in the CNT falls below TAF and due to insufficient cooling more debris relocation occurs, forming 4.5tons molten pool in the LP and an additional 18tons of PD+DC generating about 165kg H_2. The, now rapidly evaporating, water in the CNT keeps extracting decay heat until 72h preventing further degradation.

With SA6, ECCS is activated upon satisfaction of the ECCS low pressure condition. However, the loss of coolant inventory through the tube rupture is slow that core is never uncovered by 72h. In SA6N, with high pressure conditions – about 5MPa until 10h (full core uncovery) followed by about 3MPa, which is the highest among all cases considered in this study during early core degradation – water inventory in the RPV is lost completely by 20h forming about 1000kg of PD in the core. Once the core plate fails at 72145s, further core damage is observed reaching 100% by 22h, which drives relocation to the LP forming about 14.2tons of PD+DC. This is massive relocation causes instant lowerhead failure ejecting 15tons of debris to the CNT with a breach area of 0.045m^2, which subsequently cooled by the reactor pool. In total, during this accident about 64kg of H_2 is generated.

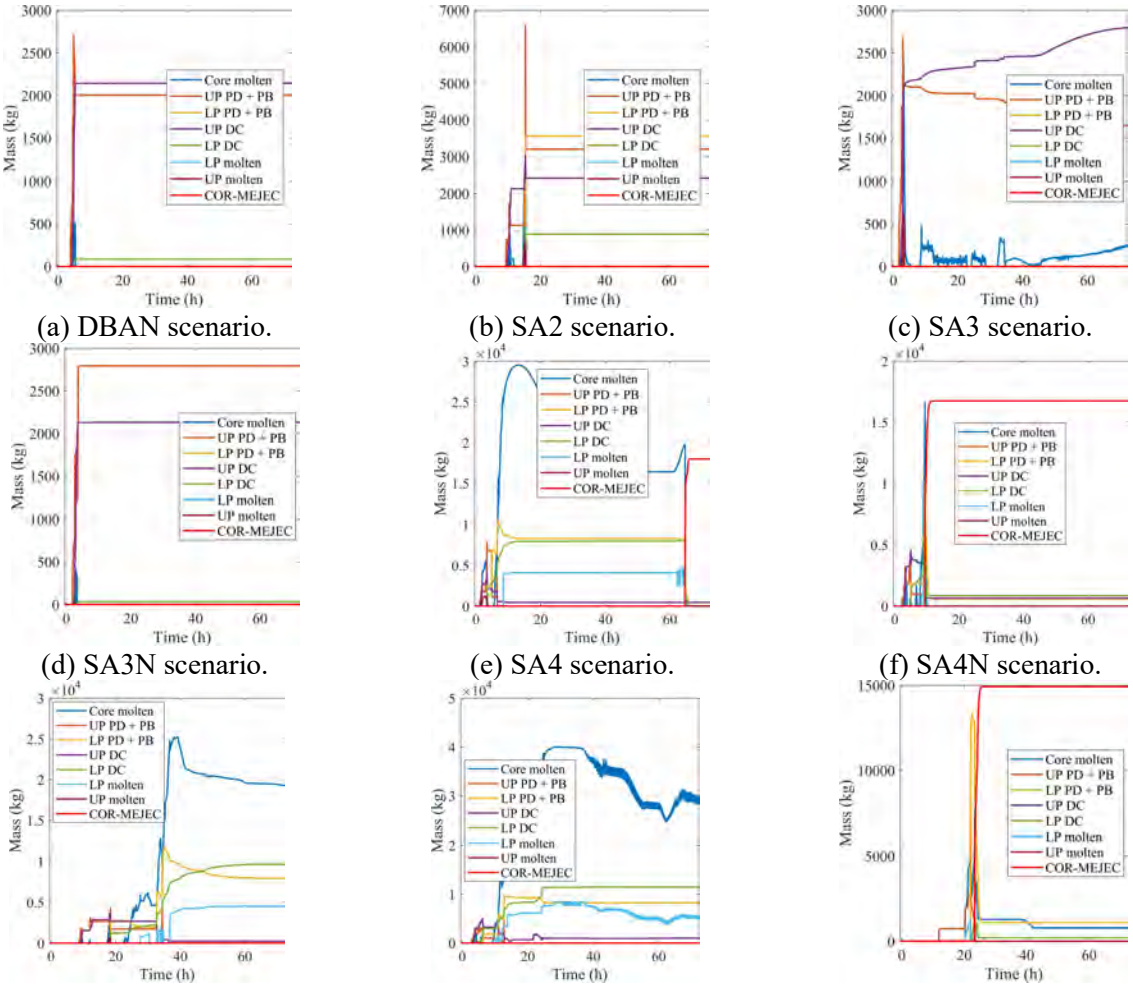

(a) DBAN scenario. (b) SA2 scenario. (c) SA3 scenario.

(d) SA3N scenario. (e) SA4 scenario. (f) SA4N scenario.

(g) SA5 scenario. (h) SA5N scenario. (h) SA6N scenario.

Figure 15. Solid and molten debris mass formation during the postulated accident scenarios.

A point of observation is that, with the failure of LH in this design as observed during SA4, SA4N and SA6N, the distance between LH and CNT vessel is small, ~0.4m. This can cause plugging of the breach by the ejected debris. Experimental evidence may be necessary to accurately describe the porosity of the debris and flow characteristics of molten material through the breach. Once the LH fails, pressure in the CNT equalizes with the RPV in cases with unavailable ECCS. The ejected debris may interact with the CNT support structures, melting the steel. At the moment the CAV package in MELCOR that represents the CNT is setup in the Design 1 deck as concrete and will be upgraded to include other appropriate material. The water that is retained or relieved through safety valves in CNT, quenches the hot debris and decay heat is transferred to the RP eventually. The temperature evolution of the RP is shown in Figure 16. The pool

temperature, acting as the UHS, is indicative of effective core cooling. It can be observed that 3 different "type" of behaviour is observed. First, CNT is filled with no out-flow: either due to LOCA (or SGTR) or activation of ECCS and there is no flow path from the CNT (DBA, DBAN, SA1, SA1o, SA2, SA2N, SA3, SA3N, SA6, SA7). Second, CNT is filled with out-flow: either due to LOCA (SA5 and SA5N) or activation of ECCS (SA4) and open flow path to the pool. Third, CNT is completely bypassed: either due to LOCA directly to the pool (SA4N) or SGTR with no ECCS activation (SA6N). Since the last 2 types have cases with RPV failure, it can be expected that SA5 and SA5N that do not lead to failure within 72h may indeed fail beyond this period without accident management strategies. Furthermore, analysis on the effect of delayed activation of ECCS during these accidents is underway.

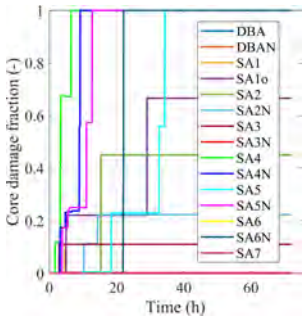

(a) Core damage fraction.

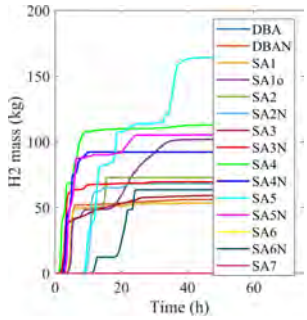

(b) H_2 generation.

Figure 17. Core degradation properties for all scenarios.

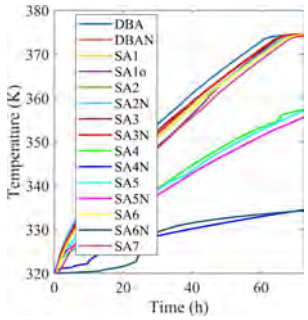

Figure 16. Temperature of reactor pool for all scenarios.

4. CONCLUSIONS

The work presented in this study aimed to demonstrate capability of system SA code MELCOR in successfully simulating postulated DBA and severe accidents in a submerged containment type generic iPWR. In the DBA scenario, the code demonstrates its ability to simulate passive safety (natural circulation) to prevent core uncovery. Several DEC scenarios involving spurious opening of RVV or RRV, loss of heat sink, and SG tube rupture were simulated with MELCOR. The code can qualitatively and quantitatively address specific phenomena affecting SMRs. The need to verify code accuracy in simulating natural convection with flow constraints, and behavior of debris accumulation in the vessel lower head were identified. Largely, all SA scenarios behave similarly in 3 groups, for their ability to transfer decay heat from the core to the reactor pool. The delay in activating ECCS, and filling of the containment vessel can affect this transfer, leading to severe core damage (DBA with ECCS v/s DBAN without ECCS, SA2 with ECCS v/s SA2N without ECCS). When the break of the primary system is closer to the core, fraction of core damage also depends on the area of the break (SA3N vs SA3, latter with twice the area). Together with delay, the capacity of ECCS can induce non-linear effects on SA phenomena. Non-LOCA accidents such as SGTR can be a challenge for iPWR, that have design and size constraints. The helical tube SGs are susceptible to inadvertent operational degradation leading to rupture. Under such a scenario, the behavior of the reactor systems was shown to be non-trivial. STR and cases with CNT bypassed almost certainly lead to full core damage with high likelihood of RPV failure. This necessitates analysis of severe accident measures in mitigating ex-vessel accident progression.

The size of break in the CVCS was shown to affect core degradation. In regions with extreme, coupled interactions in the core, the accident may progress differently with minor changes in the conditions (Case 009 v/s Case 008 and 010). The presence of small amounts of circulating steam inside the RPV significantly altered the reactor conditions. MELCOR code's capability to handle such situations needs to be addressed with further sensitivity and uncertainty studies. As was demonstrated with counterintuitive behavior of LOCA break sizes, advanced search algorithms could be employed to identify input domains that can lead to a SA. These results support further tasks of SASPAM-SA in best estimate analysis and assessments of emergency planning zones.

ACKNOWLEDGMENTS

Funded by the European Union. Views and opinions expressed are those of the author(s) only and do not necessarily reflect those of the European Union or European Commission-Euratom. Neither the European Union nor the granting authority can be held responsible for them.

This work is supported by ROAAM+ project funded by Swedish Radiation Safety Authority. The authors are thankful to Mateusz Malicki and Terttaliisa Lind from PSI for providing the MELCOR input deck for iPWR design.

REFERENCES

1. IAEA. Small Modular Reactors, Advances in SMR Developments. In: International Conference on Small Modular Reactors and Their Applications, 21-25 October, Vienna, Austria, 2024.
2. IAEA. Advances in Small Modular Reactor Technology Developments, A Supplement to: IAEA Advanced Reactors Information System (ARIS). International Atomic Energy Agency, Vienna, Austria, 2020.
3. NEA. Small Modular Reactors: Challenges and Opportunities. NEA No. 7560, Nuclear Energy Agency – OECD, 2021.
4. Handbook of Small Modular Nuclear Reactors. 2nd Edition. Eds: Daniel T. Ingersoll and Mario D. Carelli. Woodhead Publishing, 2020.
5. Fabrizio Gabrielli, et al.: Analysis of postulated severe accidents in generic integral pwr small modular reactors in the frame of the horizon euratom saspam-sa project. In: The 11th European Review Meeting on Severe Accident Research, May, KTH Royal Institute of Technology, Stockholm, Sweden, 2024.
6. Fangnian Wang, et al.: Investigations of hydrogen hazard mitigation by deliberate ignition in small modular reactor during severe accident using GASFLOW-MPI. Annals of Nuclear Energy, 179, pp. 109392, 2022.
7. Siniša Šadek, et al.: Small break LOCA studies for different layouts of passive safety systems in the IRIS reactor. Nuclear Engineering and Design, 431, pp. 113745, 2025.
8. A. Fakhraei, et al.: Safety analysis of an advanced passively-cooled small modular reactor during station blackout scenarios and normal operation with RELAP5/SCDAP. Annals of Nuclear Energy, 143, pp. 107470, 2020.
9. Qingan Xiang, et al.: Research on debris in-vessel cooling and retention behavior for the small modular reactor ACP100. Progress in Nuclear Energy, 134, pp. 103641, 2021.
10. Dening Eric Jia, et al.: GOTHIC and MELCOR benchmarking of the CNL strong condensation containment apparatus experiments. Nuclear Engineering and Design, 427, pp. 113440, 2024.
11. F. Mascari, et al.: Small modular reactors and insights on passive mitigation strategy modeling. Nuclear Engineering and Design, 401, pp. 112088, 2023.
12. Luis E. Herranz, et al.: Overview of key thermal–hydraulic phenomena in severe accident unfolding: Current knowledge and further needs. Nuclear Engineering and Design, 407, pp. 112256, 2023.
13. Michaël Montout, et al.: PASTELS project - overall progress of the project on experimental and numerical activities on passive safety systems. Nuclear Engineering and Technology, 56 (3), pp. 803-811, 2024.
14. Longze Li, et al.: MELCOR severe accident analysis for a natural circulation small modular reactor. Progress in Nuclear Energy, 100, pp. 197-208, 2017.
15. Mateusz Malicki, T. Lind: MELCOR 2.2 iPWR LOCA type accident analysis, PART I: Thermal-hydraulics. Nuclear Engineering and Design, 428, pp. 113433, 2024.
16. Mateusz Malicki, T. Lind: MELCOR 2.2 iPWR LOCA type accident analysis, PART II: BDBA. Nuclear Engineering and Design, 430, pp. 113667, 2024.
17. L.L. Humphries, et al.: MELCOR Computer Code Manuals Vol. 1: Primer and Users' Guide Version 2.2.r2023. SAND2023-10997 O, Sandia National Laboratories, Albuquerque, NM, USA, 2023.
18. L.L. Humphries, et al.: MELCOR Computer Code Manuals Vol. 2: Reference Manual Version 2.2.r2023. SAND2023-10994 O, Sandia National Laboratories, Albuquerque, NM, USA, 2023.
19. G. Acharya, D. Grishchenko, P. Kudinov: Investigation of Source Term During Severe Accidents in Integral PWR SMRs. In: The 21st International Topical Meeting on Nuclear Reactor Thermal Hydraulics, August, Busan, Korea, 2025.

INVESTIGATION OF SEVERE ACCIDENT PROGRESSION IN INTEGRAL PWR SMRS

12th European Review Meeting on Severe Accident Research (ERMSAR2026)
Madrid, Spain, May 18-22, 2026

Govatsa Acharya, Dmitry Grishchenko, Pavel Kudinov
Division of Nuclear Science and Engineering,
KTH Royal Institute of Technology,
Stockholm, Sweden

EU SASPAM-SA Project

- Increasing global interest in deploying SMRs has necessitated activities in support of licensing such reactors – particularly iPWRs.
- There is also a need for demonstrating ability of iPWRs to prevent and manage SAs.
- Can knowledge and experience in operating large LWRs be applied to iPWRs?
  - Main objective of HORIZON-EURATOM '**S**afety **A**nalysis of **S**MR with **PA**ssive **M**itigation strategies - **S**evere **A**ccidents' project launched in 2022.
- Key Outcomes:
  - Support iPWR licensing process by demonstration needed for the safety.
  - Speed up the licensing and siting process of iPWRs in Europe.
- Key Highlights:
  - Applicability of large LWR reactor knowledge and know-how to the near-term deployment iPWR, in view of SA and EPZ analyses, will be assessed and consolidated.
  - Identify the research priorities in terms of methodology, code development and experimental needs.
  - Support regulators in decision-making as well as Industry and TSOs in assessing the applicability of iPWR safety features.

BELGIUM: EC-JRC, TRACTEBEL-ENGIE
BULGARIA: INRNE, TUS
CZECH REPUBLIC: SURO
FINLAND: VTT
FRANCE: CNRS, EDF, IRSN
GERMANY: KIT, FZJ, GRS, RUB
ITALY: ENEA, UNIROMA1, POLIMI, SINTEC
LITHUANIA: LEI
ROMANIA: RATEN
SWEDEN: KTH
SWIZERLAND: PSI
SPAIN: CIEMAT
UKRAINE: SSTC-NRS

23 PARTNERS FROM 13 EUROPEAN COUNTRIES, COMPOSED OF: UNIVERSITIES, RESEARCH INSTITUTES, TSO, INDUSTRIAL AND ENGINEERING ORGANIZATIONS

F. Gabrielli, et al., (2024)

Work Packages: KTH Contributions

Current

Develop and assess generic but representative iPWR SA code input-decks and to identify plausible SA scenarios.

2.1

Review the existing experimental database, to assess its applicability to iPWR, to propose methods to apply existing data to iPWR, and to identify new experimental needs.

3.1, 3.2

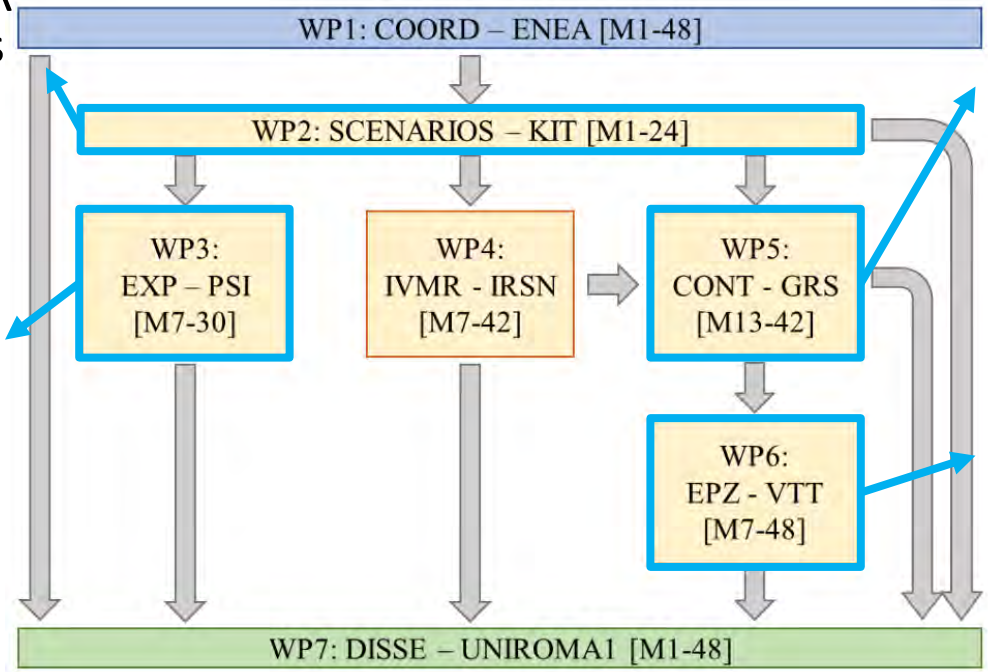

Assess the codes to simulate the main containment behaviour (TH, FP and aerosol) and characterize the efficiency of passive measures for accident mitigation.

5.1, 5.2

Provide EPZ size and extension for selected SA scenarios coupling the results of ST codes to radiological consequences tools.

6.2, 6.3, 6.4

G. Acharya, et al., (2025)

Generic iPWR – Design 1

- Submerged containment type 160MWth iPWR.
  - ~8.3MPa RPV.
  - CNT ~vacuum.
- Natural circulation in case of accidents involving LOCA.
  - ECCS - RVV (3) and RRV (2) – open establishing circuit.
    - High CNT water level - 5.8m.
    - Low RPV pressure – 6.2MPa ΔP.

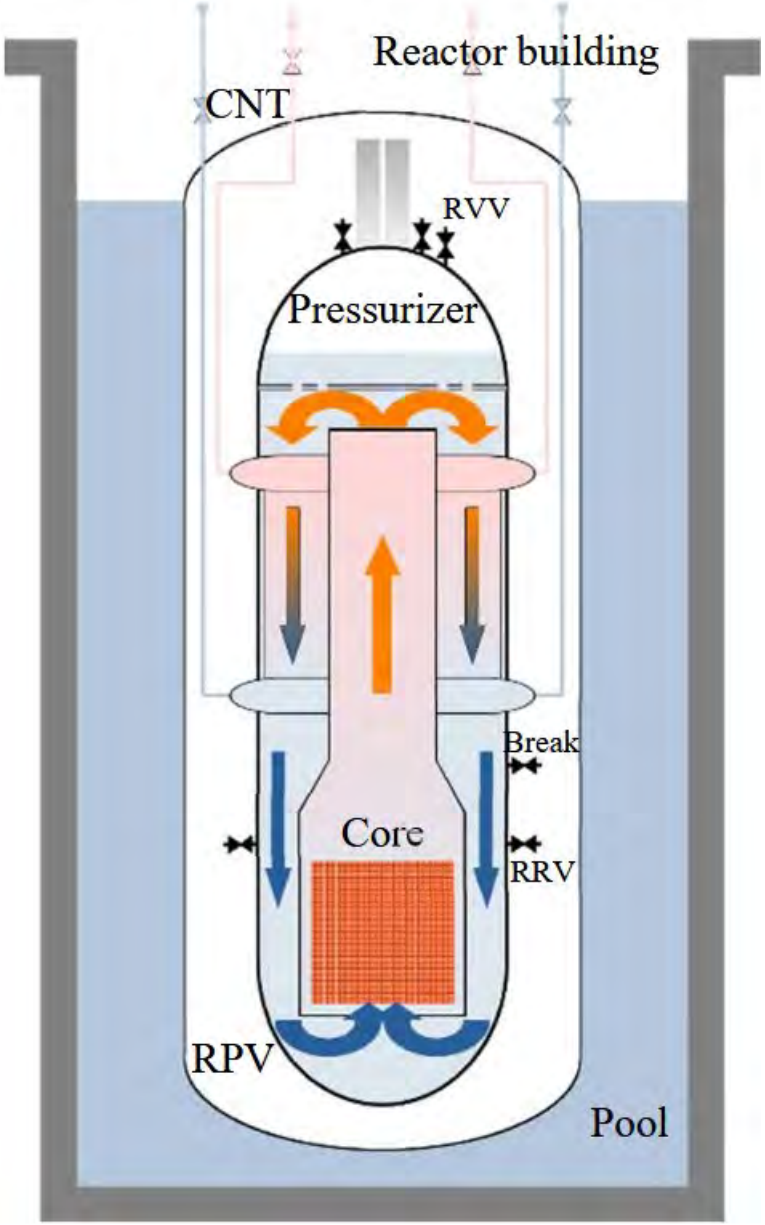

MELCOR Nodalization

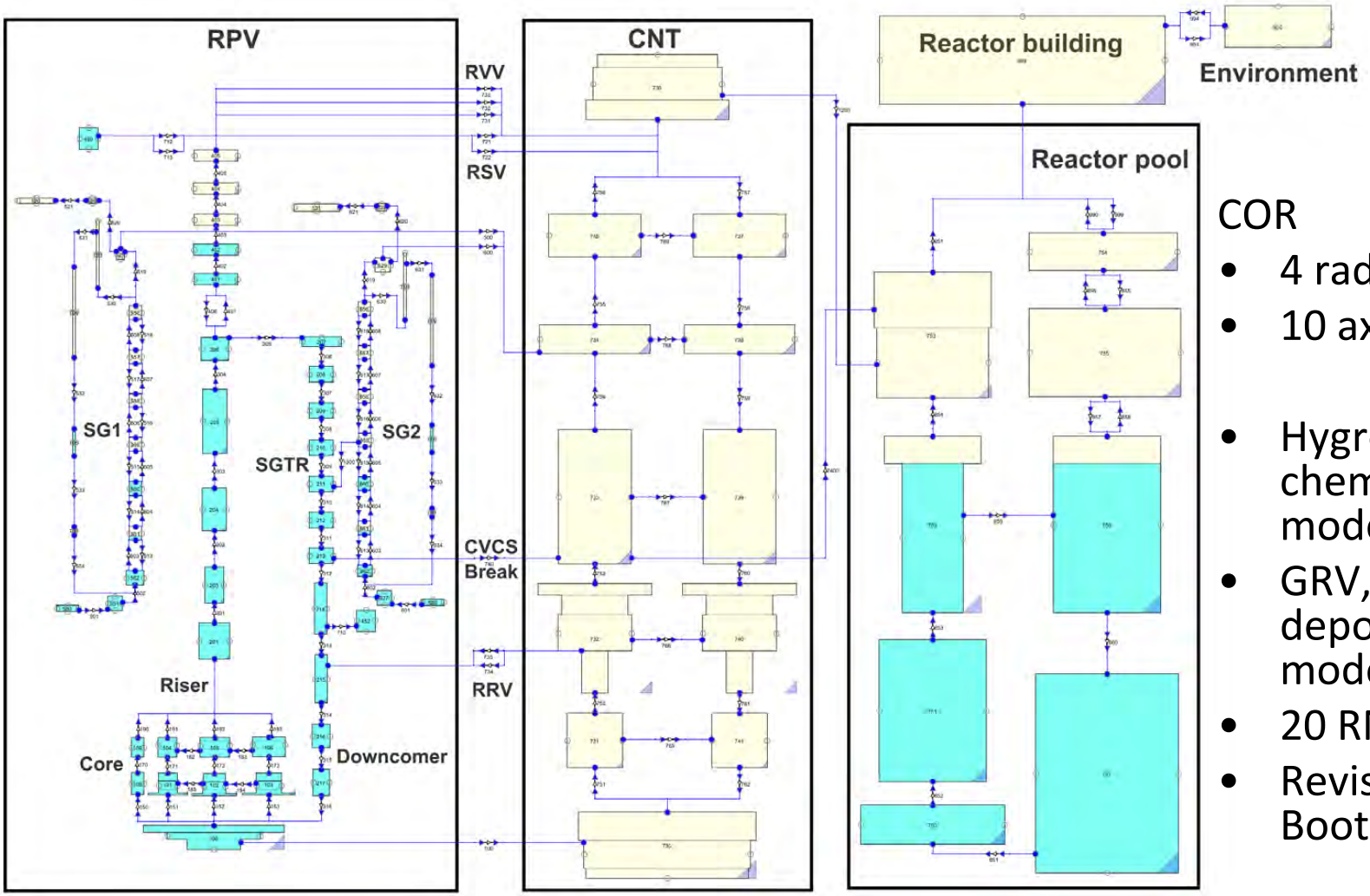

COR

- 4 radial
- 10 axial

- Hygroscopic and chemisorption models ON.
- GRV, THM, DIF deposition models OFF.
- 20 RN Class.
- Revised CORSOR-Booth model.

- v2.2.r2023

M. Malicki, et al., (2024)

SA Scenarios Considered

Scenario ID	Initiator	ECCS availability		Comments
		RVV	RRV	
DBA	CVCS discharge LOCA	Yes	Yes	1.6” LOCA in CVCS discharge to CNT
DBAN	CVCS discharge LOCA	No	No	1.6” LOCA in CVCS discharge to CNT
SA1	CVCS discharge LOCA	Yes	No	1.6” LOCA in CVCS discharge to CNT
SA1o	CVCS discharge LOCA	Yes 1	No	1.6” LOCA in CVCS discharge to CNT
SA2	Spurious opening of 1 RVV	Yes 2	No	2.5” RVV opening of 1 RVV
SA2N	Spurious opening of 1 RVV	No	No	2.5” RVV opening of 1 RVV
SA3	Spurious opening of 1 RRV	No	Yes 1	2.5” RRV opening of 1 RRV
SA3N	Spurious opening of 1 RRV	No	No	2.5” RRV opening of 1 RRV
SA4	CVCS discharge LOCA	Yes	Yes	1.6” LOCA in CVCS to RP (outside CNT)
SA4N	CVCS discharge LOCA	No	No	1.6” LOCA in CVCS to RP (outside CNT)
SA5	CVCS discharge LOCA	Yes	Yes	1.6” LOCA in CVCS to CNT, breach in CNT to RP
SA5N	CVCS discharge LOCA	No	No	1.6” LOCA in CVCS to CNT, breach in CNT to RP
SA6	SG tube rupture (SGTR)	Yes	Yes	No steam line isolation, feedwater line isolated
SA6N	SG tube rupture (SGTR)	No	No	No steam line isolation, feedwater line isolated
SA7	Loss of heat sink (LOHS)	Yes	Yes	Steam line and feedwater line isolated

- 15 scenarios selected - not considering probability of occurrence, but only expected severity of consequences.

SA Scenarios – FP Pathways

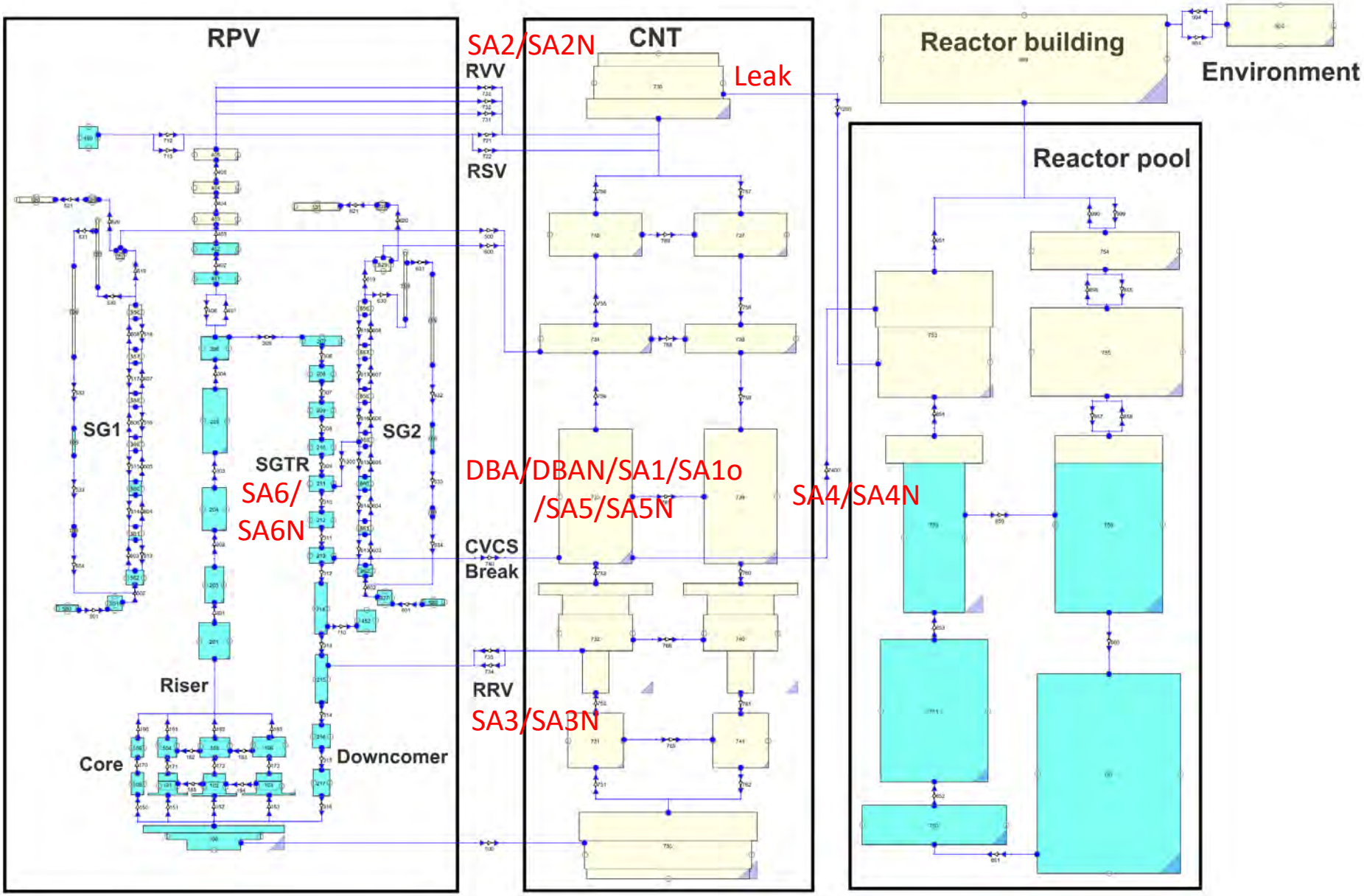

Results

Scenario ID	SCRAM	High CNT level	ECCS signal	Core uncovery	Gap release	PD formation	Relocation to LH	Core plate failure	LH failure
DBA	19	520	520	-	-	-	-	-	-
DBAN	19	520	-	4950	12782	13728	-	-	-
SA1	19	520	520	4610	12419	13386	-	-	-
SA1o	19	520	520	4995	12990	14197	-	-	-
SA2	4	8640	8640	20256	32517	33600	53618	55170	-
SA2N	4	8640	-	20239	32410	33530	51722	51721	-
SA3	7	60	61	174	5111	6038	-	-	-
SA3N	7	60	-	620	6097	6955	12830	-	-
SA4	44	-	815	848	3300	4178	10426	12057	232843
SA4N	44	-	-	1814	7412	8565	13071	13071	33682
SA5	19	775	775	3591	29725	31742	65800	65806	-
SA5N	19	775	-	2310	9238	10478	15834	15834	-
SA6	30	-	1380	-	-	-	-	-	-
SA6N	30	-	-	27350	40220	42934	72145	79230	84320
SA7	23	-	-	-	-	-	-	-	-

Results – DBA, DBAN, SA1

DBA DBAN SA1

Liquid level

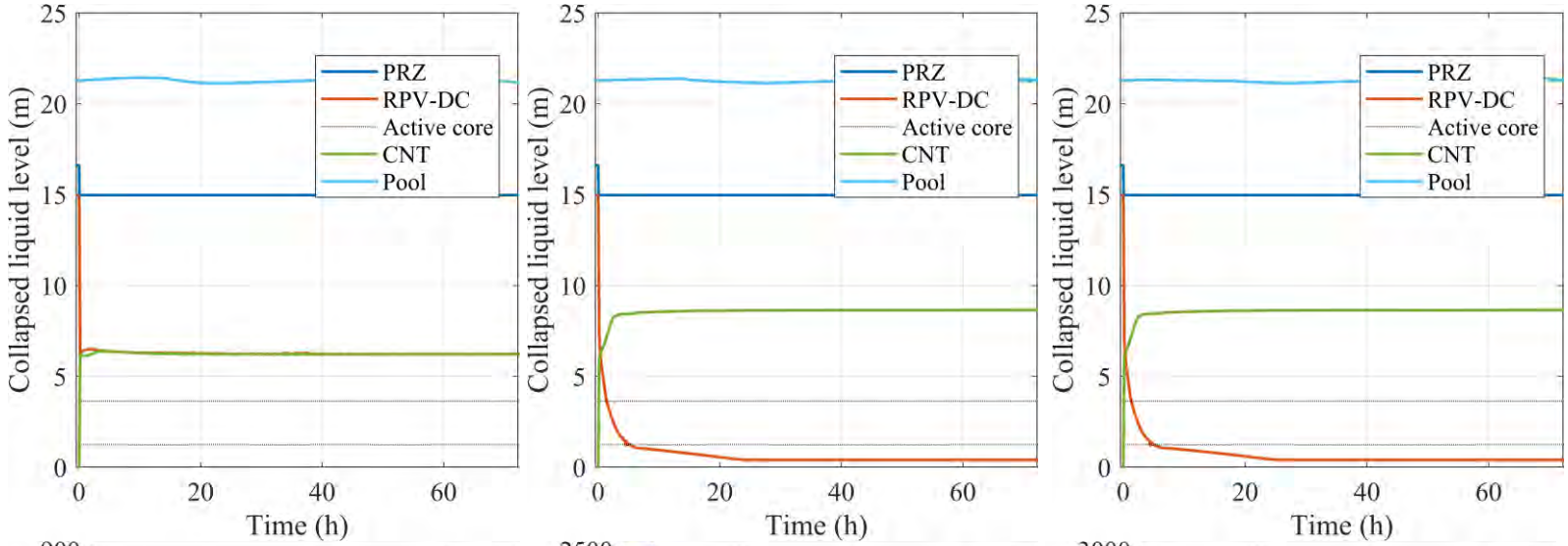

Fuel temperature

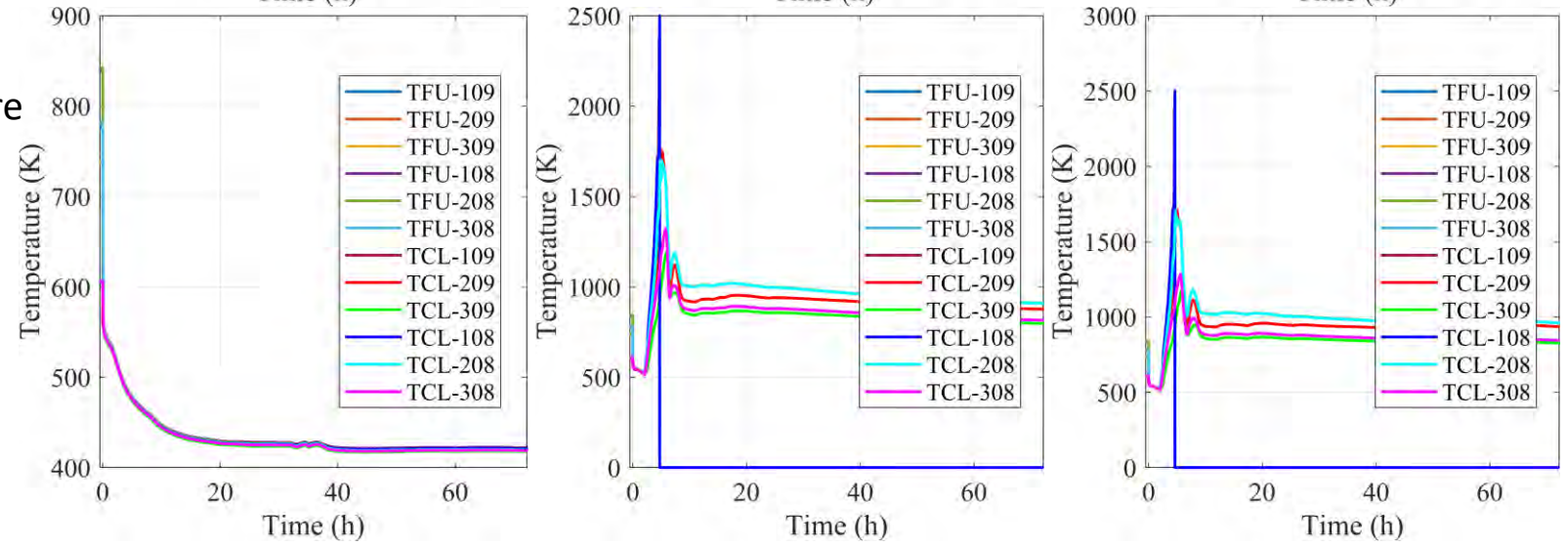

Results – SA2, SA3, SA3N

SA2 SA3 SA3N

Liquid level

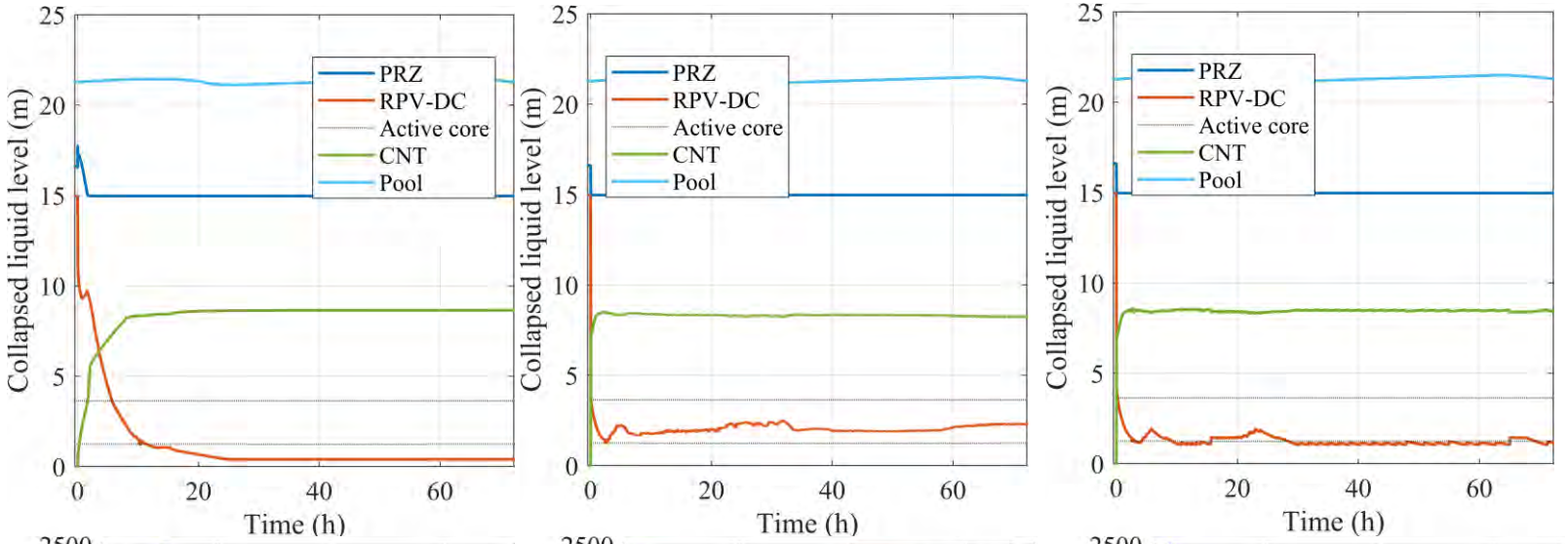

Fuel temperature

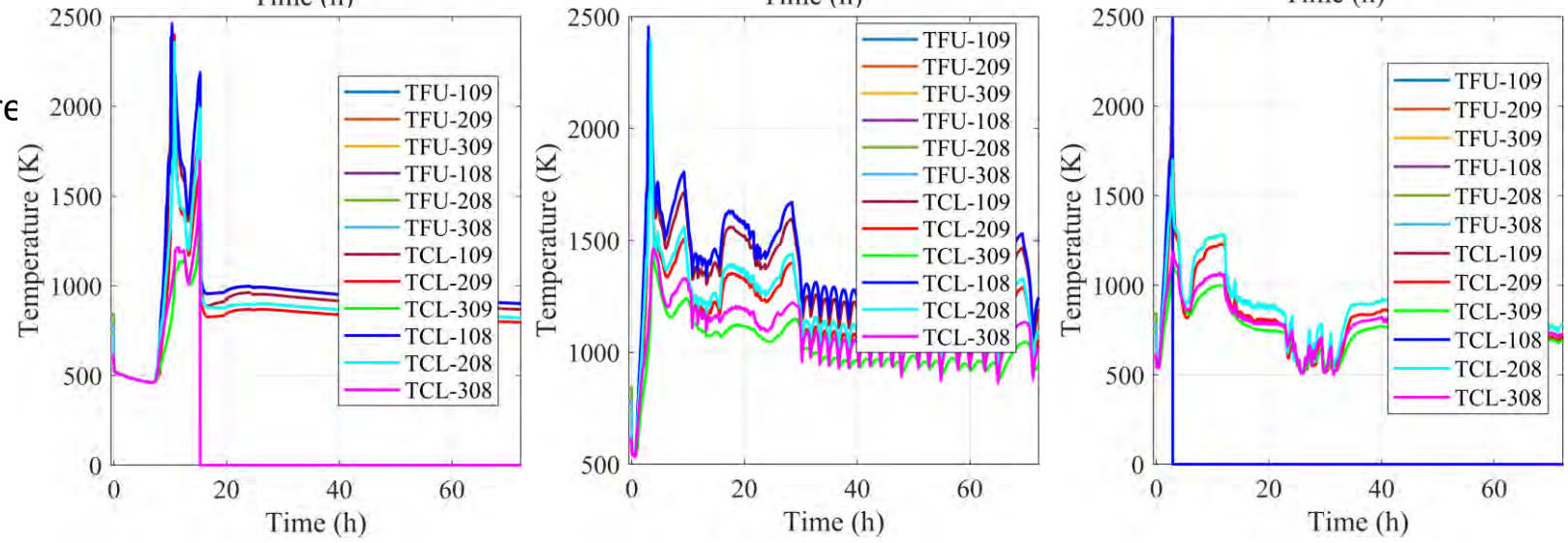

Results – SA2, SA3, SA3N

- With twice the larger area (2 RRVs available) in SA3 compared to SA3N for escaping steam, uncovery is almost twice as fast.
- Counter-current flow of escaping steam and incoming water in the RRVs.
  - Can lead to higher uncertainty in core cooling, oxidation heat and hydrogen generated.
- SA3 no relocation of debris to the LP, SA3N there is relocation at 12830s.

Results – SA4, SA4N

SA4 SA4N

Liquid level

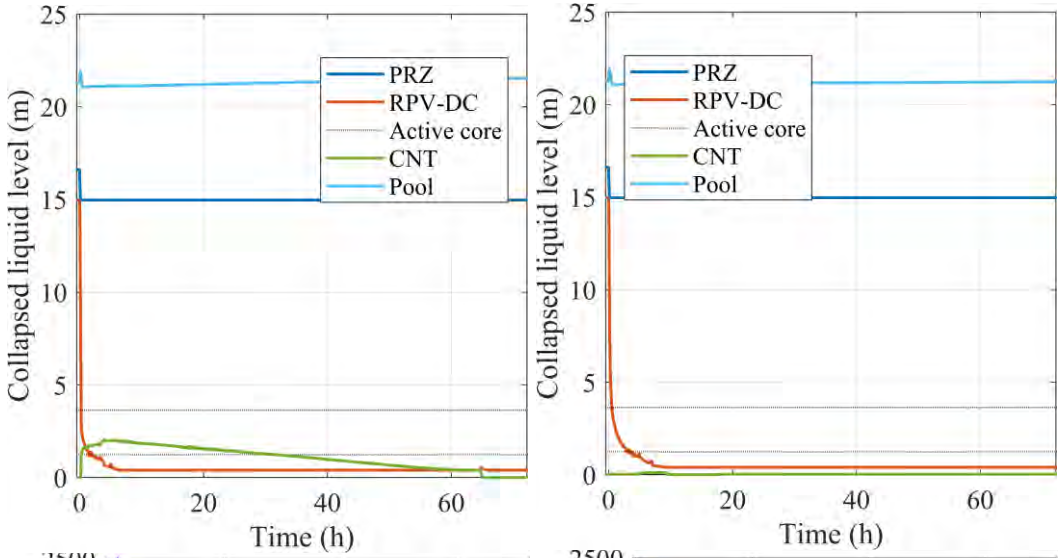

Fuel temperature

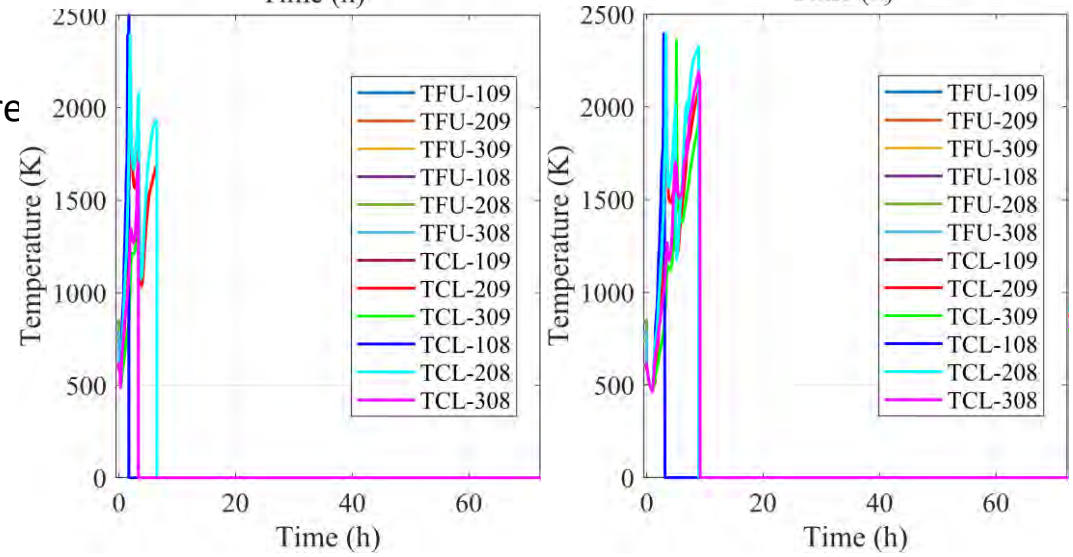

- CNT is bypassed, coolant lost directly to RP.
- Fast core uncovery, <2h level below BAF.
- One of the severest scenarios, with direct pathway for FPs.

Results – SA5, SA5N

SA5 SA5N

Liquid level

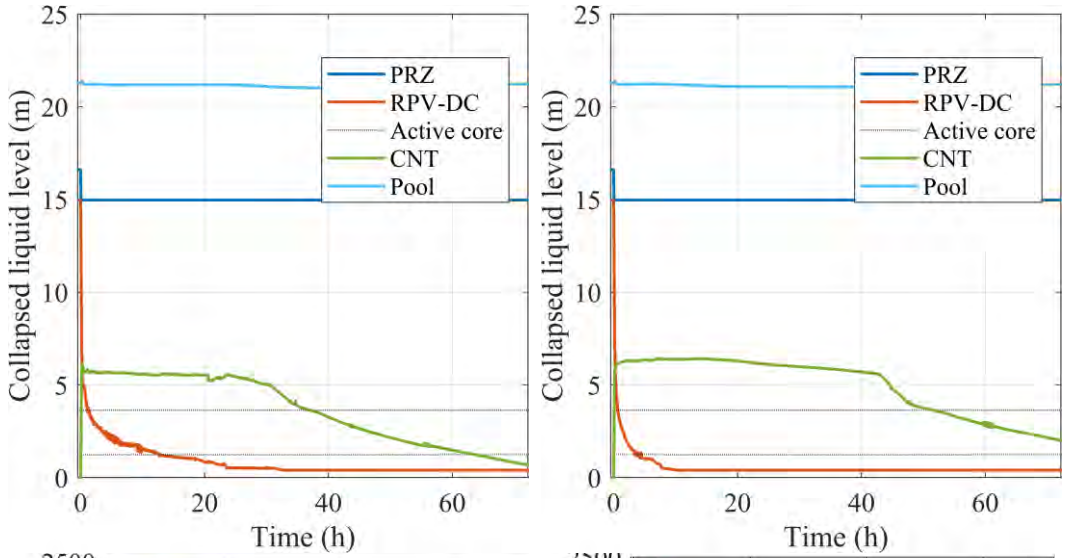

Fuel temperature

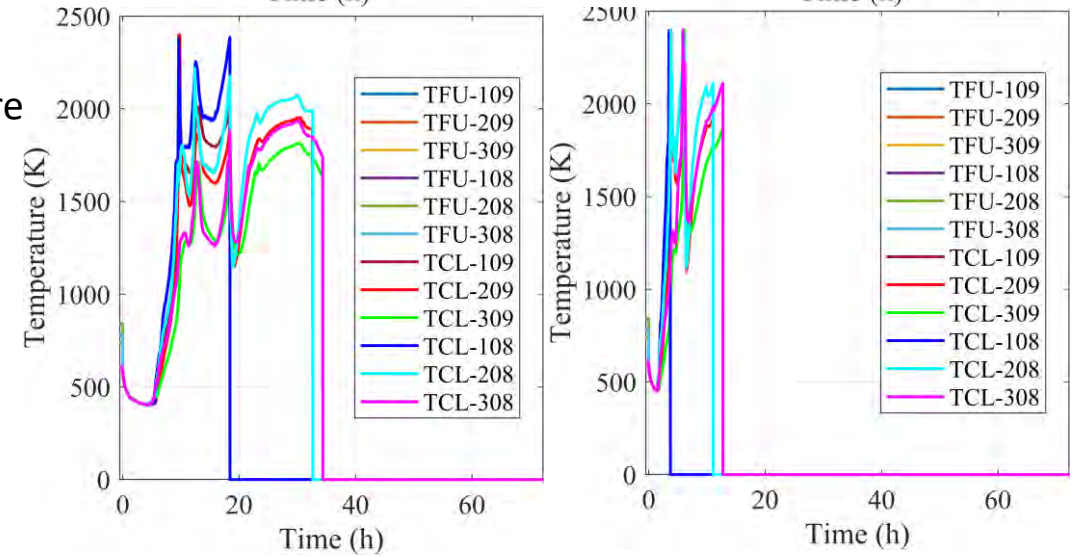

- Similar to SA4/SA4N, coolant inventory depletes with loss of steam to RP/RB.
- While relocation of debris to LP is observed, no failure of LH is observed.
  - Until 72h, steam circulation is able to prevent LH failure.

Results – SA6, SA6N

SA6 SA6N

Liquid level

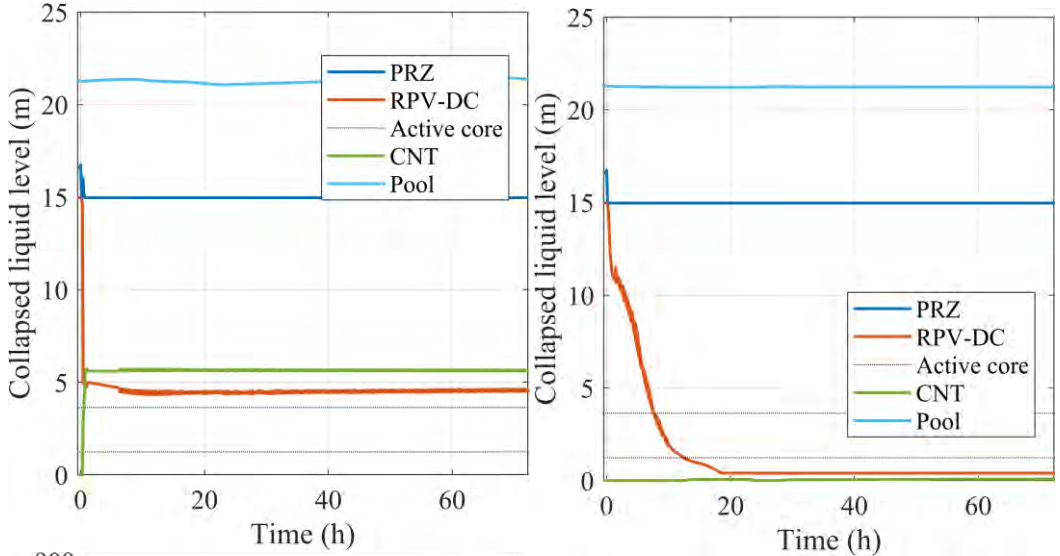

Fuel temperature

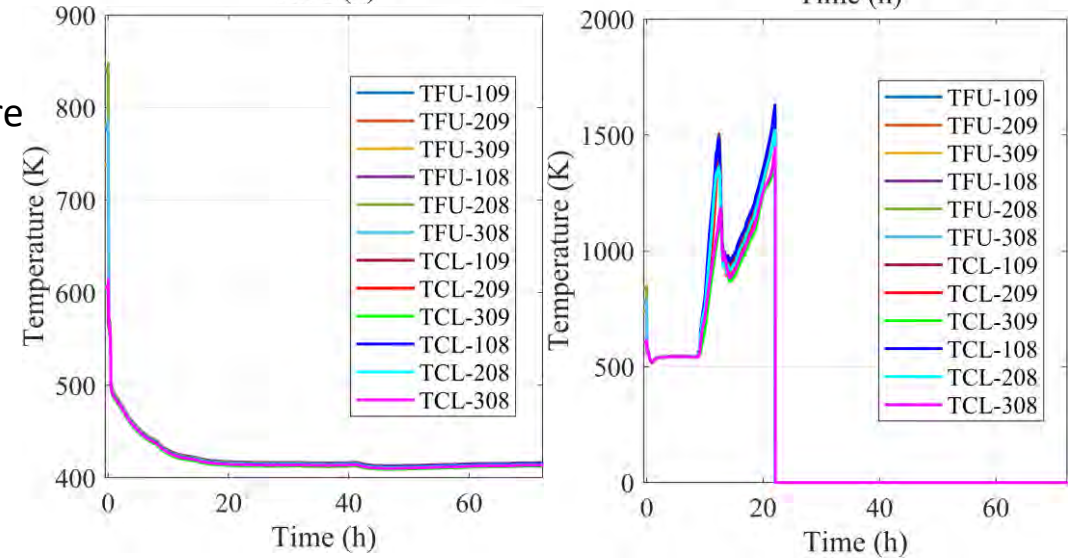

- SA6 similar to DBA, no core damage.
- SAN, coolant inventory lost through SG secondary side.
- IN SA6N, RSV are activated, leading to steam condensing in the CNT despite ECCS unavailable.

Results – Core Degradation

DBAN

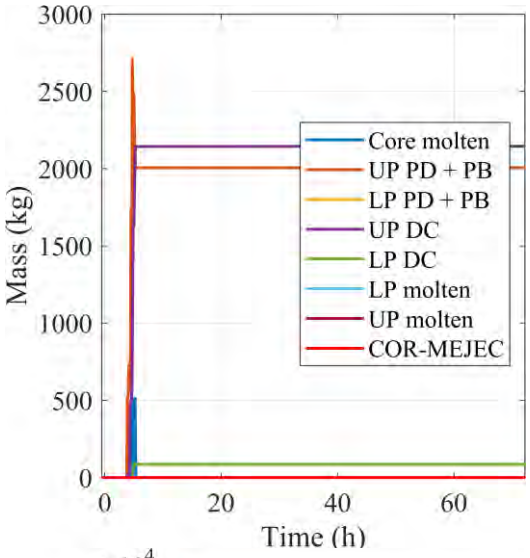

SA2

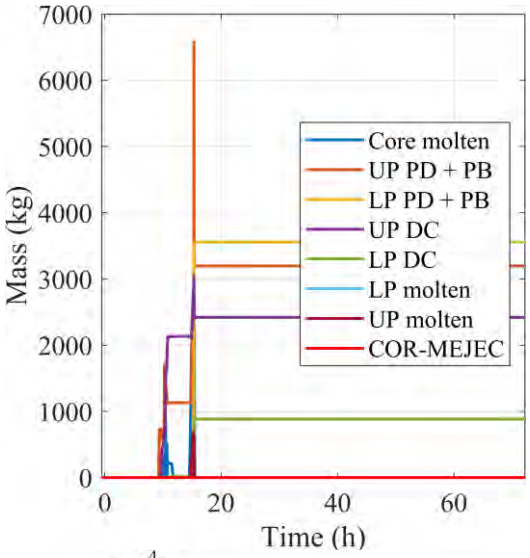

SA3

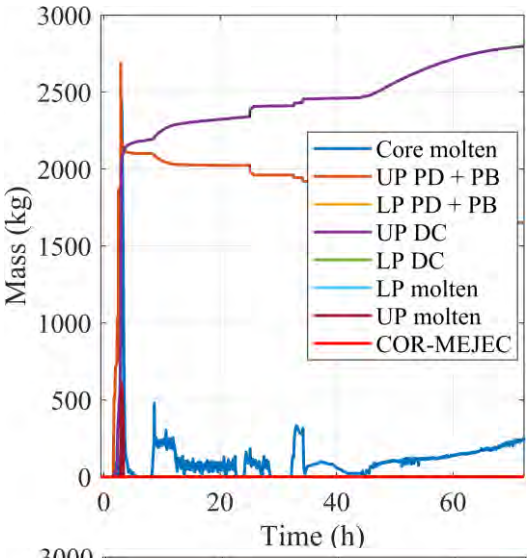

SA4

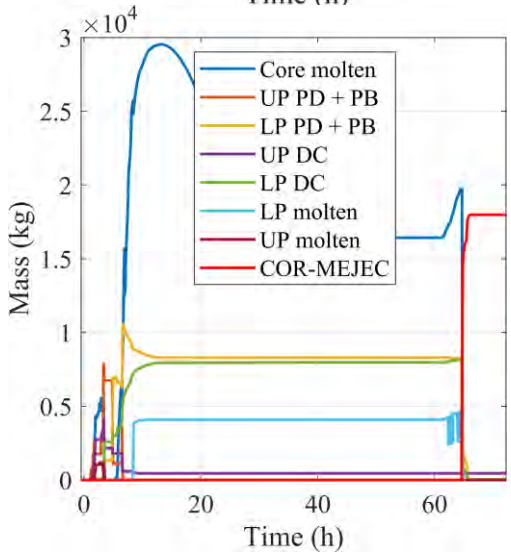

SA4N

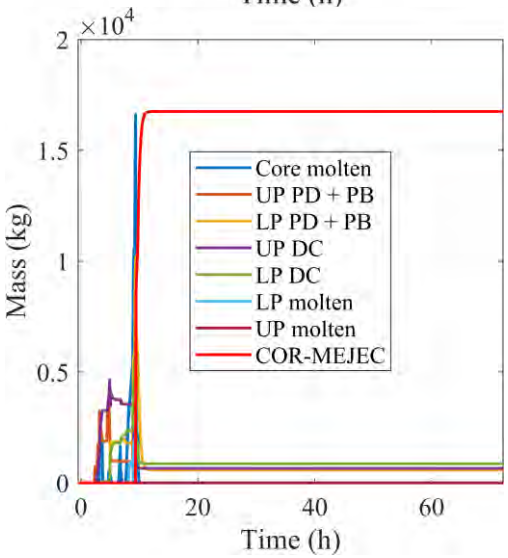

SA3N

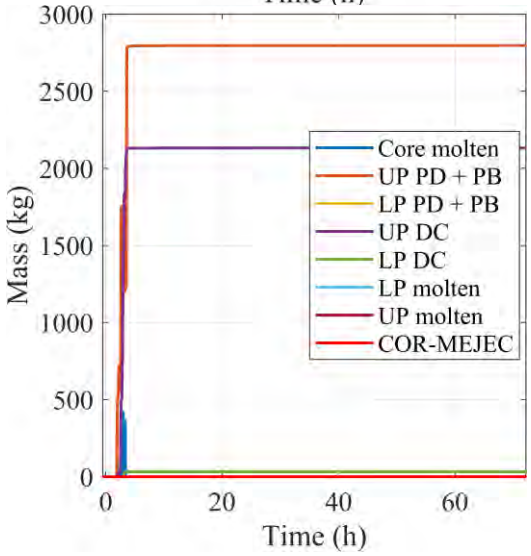

Results – Core Degradation

SA5

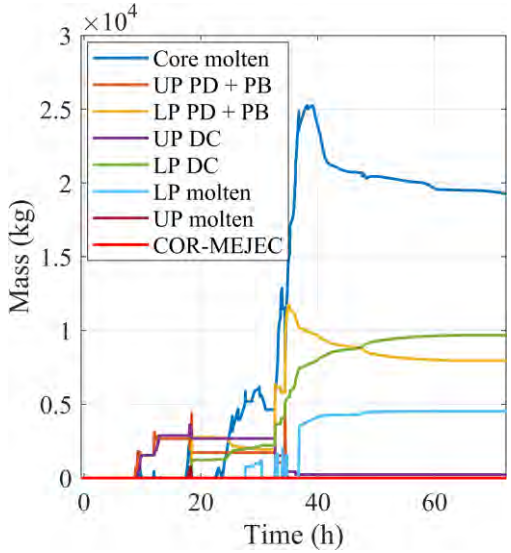

SA5N

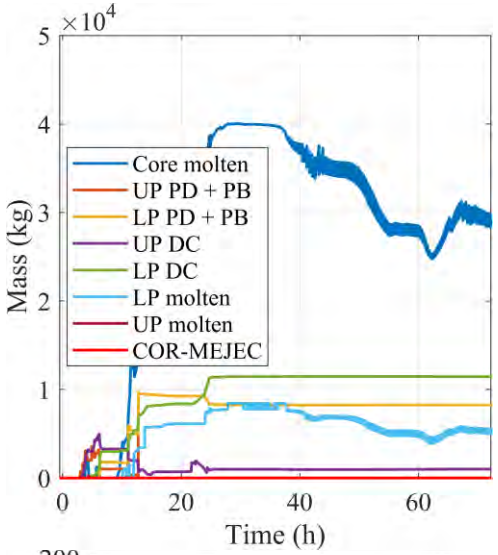

SA6N

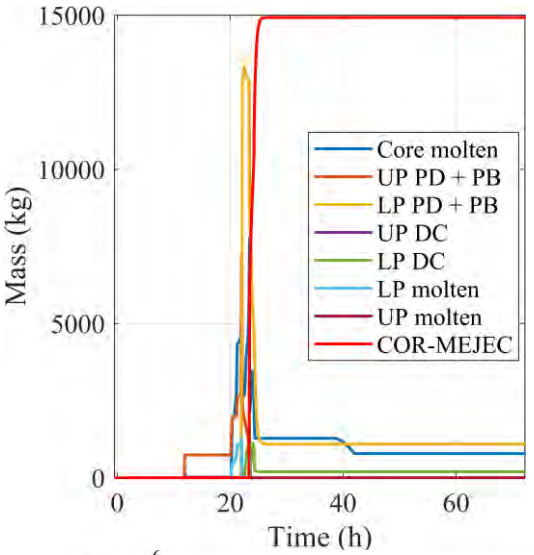

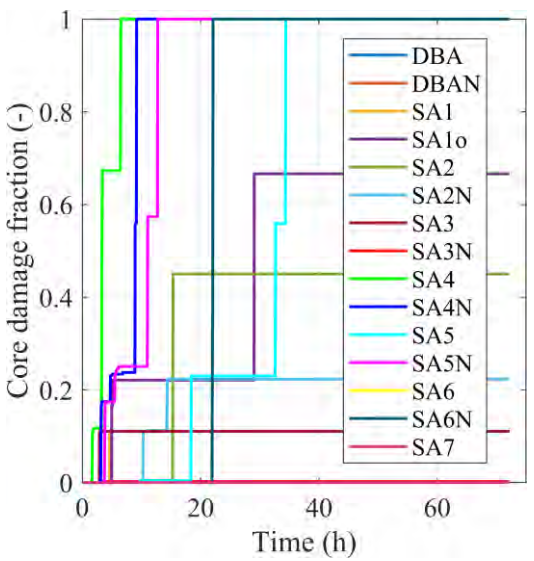

Core damage fraction

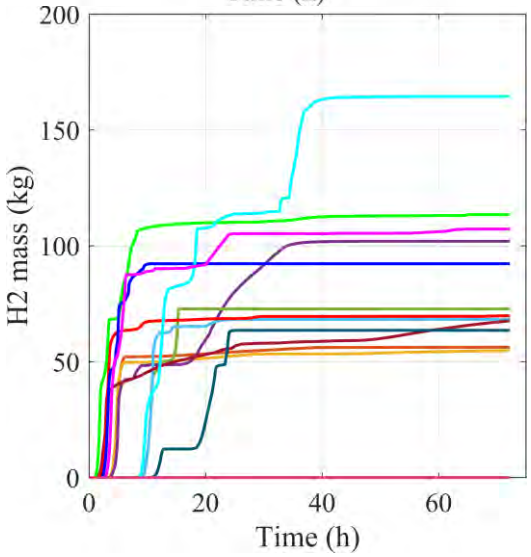

Hydrogen generated

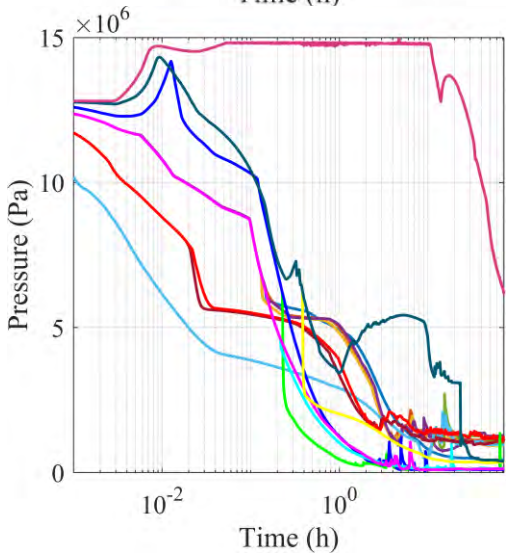

RPV pressure

Results – Core Degradation

SA5

Mass ejected from RPV

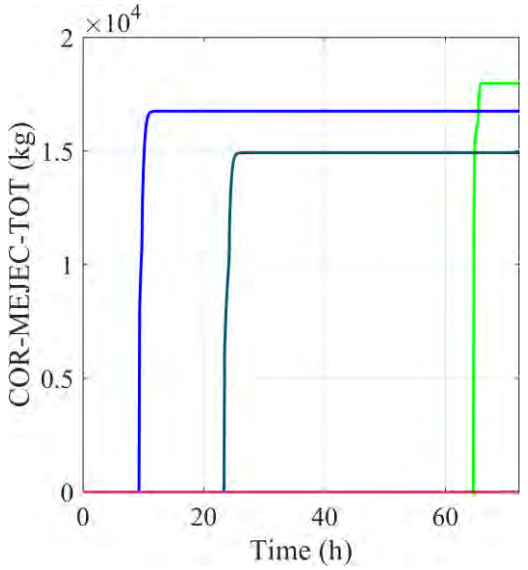

RP temperature

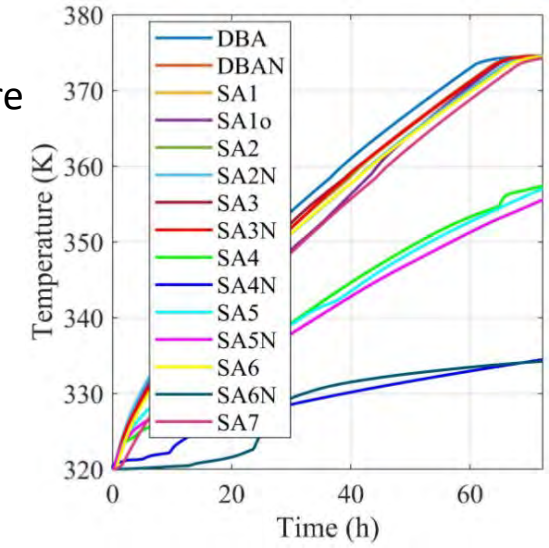

- With failure of LH in this design as observed during SA4, SA4N and SA6N, the distance between LH and CNT vessel is small, ~0.4m.
  - can cause plugging of the breach by the ejected debris.
- Current input deck considers the CNT as concrete in the CAV package in MELCOR and will be upgraded to include other appropriate material.
- SA5 and SA5N that do not lead to failure within 72h may indeed fail beyond this period without accident management strategies.

Results – Effect of Break Sizes: DBAN

	Area
1	7.85E-07
2	1.94E-05
3	6.27E-05
4	1.31E-04
5	2.24E-04
6	3.41E-04
7	4.83E-04
8	6.50E-04
9	8.42E-04
10	1.10E-03
11	1.30E-03
12	1.60E-03

Core damage fraction

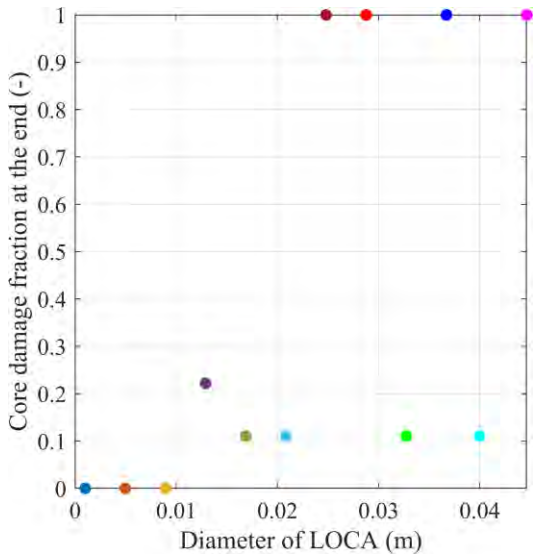

Pressure

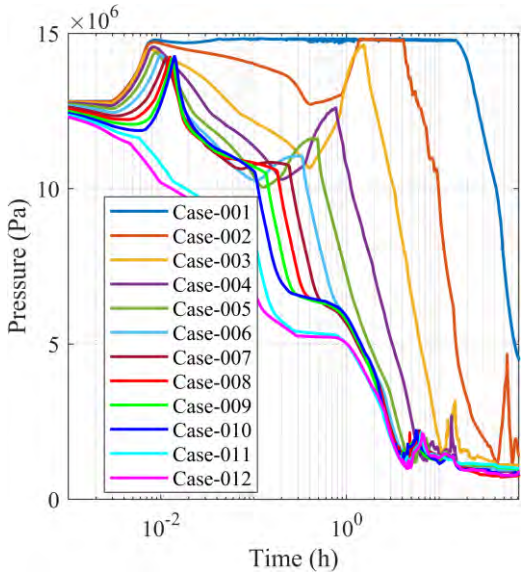

Hydrogen generated

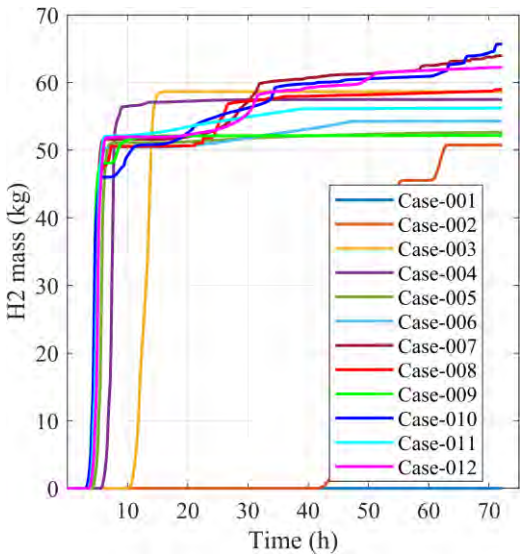

- Very small sizes cause activation of RSV, as LOCA does not cause sufficient depressurization.
  - In 002 and 003, after closing of RSV, the rising pressure by the boiling of water and insufficient loss of water to CNT for circulation, reactivates the RSV.
- Cases 012, 010, 008 and 007 lead to complete damage of the core.
  - Cases 009 and 010 lead to only 10% core damage, with the break sizes allowing for sufficient steam circulation that prevents complete core damage. In other cases, complete dryout of the core is observed.

Results – Effect of Break Sizes: SA4N

	Area
1	7.85E-07
2	1.94E-05
3	6.27E-05
4	1.31E-04
5	2.24E-04
6	3.41E-04
7	4.83E-04
8	6.50E-04
9	8.42E-04
10	1.10E-03
11	1.30E-03
12	1.60E-03

Core damage fraction

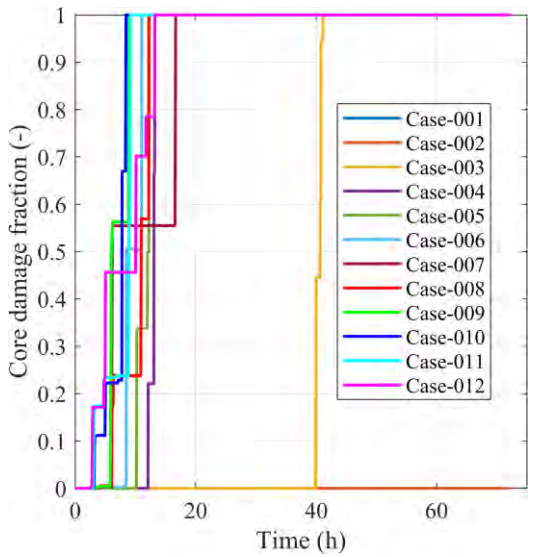

Pressure

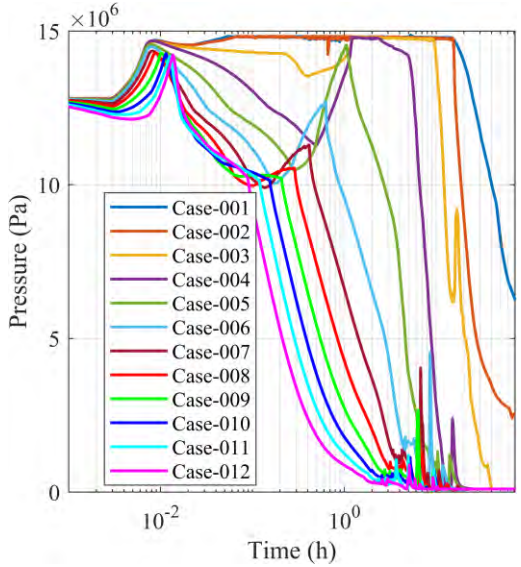

Hydrogen generated

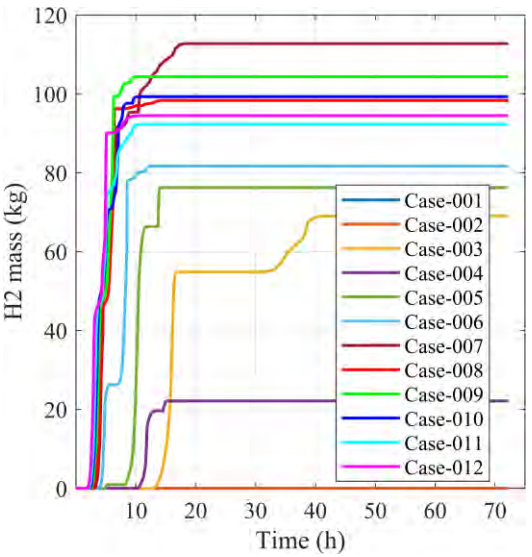

- All cases from 003 onwards lead to complete core degradation and 004 onwards to RPV failure.
- ~14-18tons of debris is ejected to the CNT. Largest is observed for 005.
- Generally, SA4N cases lead to almost twice the amount of H2 generation compared with DBAN

Results – Effect of Break Sizes: SA5N

	Area
1	7.85E-07
2	1.94E-05
3	6.27E-05
4	1.31E-04
5	2.24E-04
6	3.41E-04
7	4.83E-04
8	6.50E-04
9	8.42E-04
10	1.10E-03
11	1.30E-03
12	1.60E-03

Core damage fraction

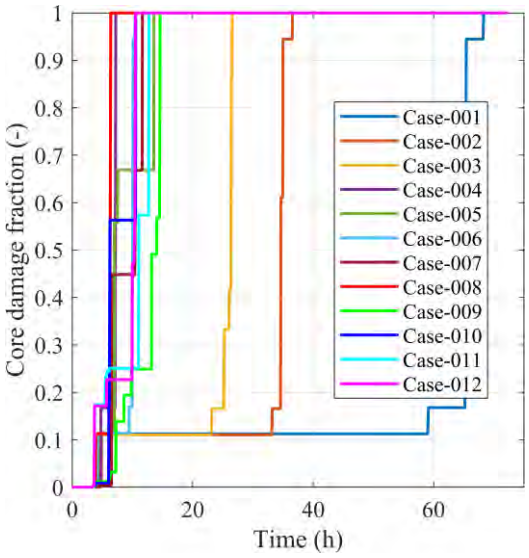

Pressure

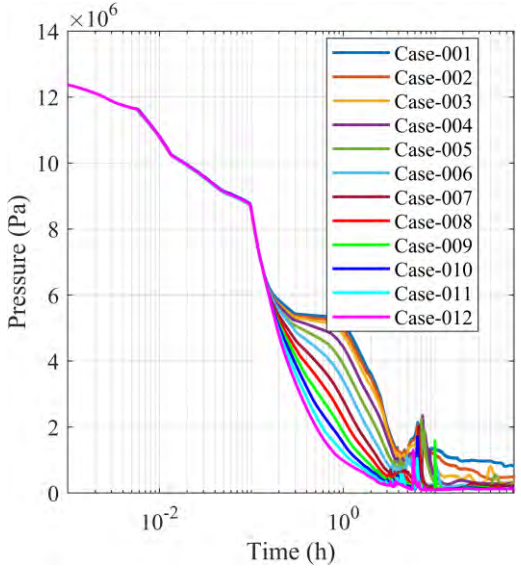

Hydrogen generated

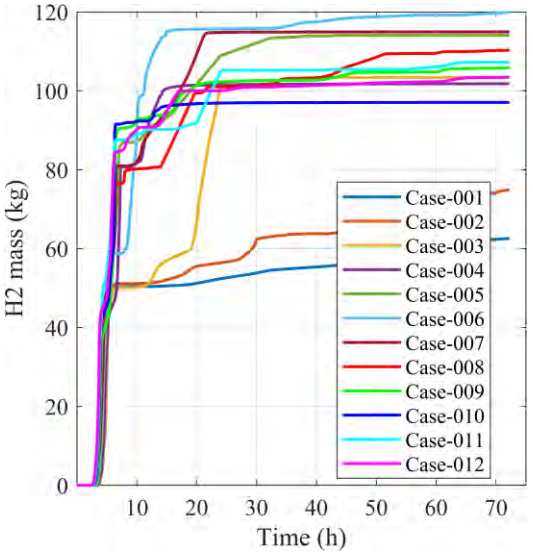

- Enough steam circulation is possible to maintain debris cooling to prevent RPV failure, even in case 012.
- Hydrogen mass generated is similar to SA4N cases.

Summary and Outlook

- As contribution to SASPAM-SA project MELCOR is used to simulate postulated accidents.
- Several scenarios leading to SA were simulated. The code can qualitatively and quantitatively address specific phenomena affecting SMRs.
- The need to verify code accuracy in simulating natural convection with flow constraints, and behavior of debris accumulation in the vessel lower head were identified.
- Largely, all SA scenarios behave similarly in 3 groups, for their ability to transfer decay heat from the core to the reactor pool.
  - The delay in activating ECCS, and filling of the containment vessel can affect this transfer, leading to severe core damage (DBA with ECCS v/s DBAN without ECCS, SA2 with ECCS v/s SA2N without ECCS).
- SGTR and cases with CNT bypassed almost certainly lead to full core damage with high likelihood of RPV failure.
- The size of break in the CVCS was shown to affect core degradation. In regions with extreme, coupled interactions in the core, the accident may progress differently with minor changes in the conditions.
- Advanced search algorithms could be employed to identify input domains that can lead to a SA – under development.
- Further parametric analysis for DBAN, SA4N, SA5N are in progress – feeds to WP6 assessment of emergency planning zones.

Thank you for your attention.

Funded by the European Union. Views and opinions expressed are those of the author(s) only and do not necessarily reflect those of the European Union or European Commission-Euratom. Neither the European Union nor the granting authority can be held responsible for them.

This work is supported by ROAAM+ project funded by Swedish Radiation Safety Authority. The authors are thankful to Mateusz Malicki and Terttaliisa Lind from PSI for providing the MELCOR input deck for iPWR design.

References

1. F. Gabrielli, et al., “Deliverable 2.2 iPWR input-deck and scenarios analyses”, https://doi.org/10.5281/zenodo.14052263, (2024).
2. M. Malicki, T. Lind, “MELCOR 2.2 iPWR LOCA type accident analysis, PART I: Thermal-hydraulics”, Nuclear Engineering and Design, 428, 113433 (2024).
3. G. Acharya, et al., “Investigation of Source Term During Severe Accidents in Integral PWR SMRs”, NURETH21, Busan, Korea (2025).

KTH
VETENSKAP
OCH KONST

EVALUATION OF HYPOTHETICAL SEVERE ACCIDENT PROGRESSION WITH ATF CLADDING IN GENERIC INTEGRAL PWR DESIGNS IN THE FRAME OF THE SASPAM-SA PROJECT

M. E. Cazado, F. Gabrielli, and V. H. Sánchez-Espinoza
Karlsruhe Institute of Technology (KIT)
Hermann-von-Helmholtz-Platz, 1, 76344 Eggenstein-Leopoldshafen, Germany
mauricio.cazado@kit.edu; fabrizio.gabrielli@kit.edu; victor.sanchez@kit.edu

F. Mascari
ENEA, FSN-SICNUC-SIN
Via Martiri di Monte Sole 4, Bologna, Italy
fulvio.mascari@enea.it

J. Krieger, G. T. Stahlberg, M. K. Koch
Ruhr-Universität Bochum, PSS
Universitätsstrasse 150, 44801 Bochum, Germany
julia.krieger@pss.rub.de; gregor.stahlberg@pss.rub.de; marco.koch@pss.rub.de

T. Sevón
VTT Technical Research Centre of Finland
Kivimiehentie 3, Espoo, Finland
tuomo.sevon@vtt.fi

P. Maccari
ENEA, NUC-ING-PST
C.R. Brasimone, Camugnano, Italy
pietro.maccari@enea.it

M. Valincius, A. Kaliatka
Lithuanian Energy Institute
Breslaujos str. 3, 44403 Kaunas, Lithuania
mindaugas.valincius@lei.lt; algirdas.kaliatka@lei.lt

M. Principato, G. Marta, F. Giannetti
Sapienza University of Rome
Corso Vittorio Emanuele II 244, 000186 Rome, Italy
marcello.principato@uniroma1.it; giacomo.marta@uniroma1.it; fabio.giannetti@uniroma1.it

ABSTRACT

Small Modular Reactors (SMRs), particularly integral Pressurized Water Reactor (iPWR) designs, are emerging as a viable option for providing flexible, scalable and inherently safer nuclear power generation to meet the global energy demand. To further enhance the safety margins of these systems in the event of an accident, Advanced Technology Fuel (ATF) materials have been proposed as alternative to traditional

zirconium-based fuel cladding. Specifically, FeCrAl alloys are gaining interest due to their superior high-temperature oxidation resistance and ability to reduce the hydrogen generation, as demonstrated in separate effect experiments and in the QUENCH-19 bundle test conducted at the Karlsruhe Institute of Technology (KIT) in 2018.

In this framework, the HORIZON-EURATOM SASPAM-SA project, initiated in 2022 and coordinated by ENEA (Italy), aims to address fundamental knowledge gaps in the modelling and understanding of severe accident (SA) progression in generic iPWR designs. Among the tasks within the project, one focuses on assessing the performance of integral codes to simulate postulated SA scenarios involving FeCrAl as a cladding material. Within Work Package 2, coordinated by KIT (Germany), numerical analyses were conducted using the ASTEC, AC^2 and MELCOR codes to investigate the behaviour of two generic iPWR designs under SA conditions, comparing the performance of FeCrAl with conventional Zircaloy.

All codes demonstrated an overall capability to simulate the reduction of H_2 production in the early stage of the SA scenarios associated to the use of FeCrAl as cladding material. The incorporation of FeCrAl also led to delays in the onset of high-temperature transients. Although some differences were observed across the codes based on each model implementation, and the current models available for FeCrAl present limitations and uncertainties at advanced degradation stages, the general trends consistently highlight the potential of FeCrAl to mitigate risk and enhance safety.

KEYWORDS
Severe Accident Analysis, Small Modular Reactors, Advanced Technology Fuels (ATF), FeCrAl Cladding

1. INTRODUCTION

Small Modular Reactors (SMRs) have been gaining significant attention as a next-generation nuclear option due to their modular deployment strategies, versatile markets applications, such as remote or industrial settings, and improved safety features [1]. Alongside plant-level innovations, enhancements to the fuel system are being explored to strengthen safety margins during beyond-design-basis conditions. Advanced Technology Fuels (ATFs), previously termed Accident-Tolerant Fuels, represent an important component of this effort as they are designed to delay core degradation and maintain the overall reactor integrity during Severe Accident (SA) scenarios, thus providing extended time for emergency and operator actions [2]. Fe-based alloy, such as FeCrAl, are among the most promising concepts (along with Cr-coated Zr and SiC) due to their superior oxidation resistance in high-temperature steam environment and balanced mechanical properties when compared to Zircaloy [3-5].

Many SMR designs, particularly Integral Pressurized Water Reactors (iPWRs), feature passive safety functions that reinforce the initial levels of the defense-in-depth (DiD) principle. However, regulatory expectations also require the demonstration of independent safety analysis prevention and mitigation capabilities (DiD level 4) and adequate support for offsite emergency response (DiD level 5). This requires dedicated analytical studies under postulated SA conditions [6, 7]. Within this context, the EU-funded SASPAM-SA project (Safety Analysis of SMRs with PAssive Mitigation Strategies - Severe Accidents), which was initiated in 2022 and is being coordinated by ENEA (Italy), is addressing this need by evaluating how knowledge from large commercial LWRs can be transferred to iPWR concepts [8-10]. As part of the SASPAM-SA project, a specific study was conducted to evaluate the influence of ATF cladding on SA progression in two generic iPWR configurations. The main objective of this research is not to assess the designs or to stablish a formal benchmark, but rather to evaluate modelling capabilities and how integral codes simulate critical in-vessel phenomena. This particular study involved the collaborative efforts of six international organizations (ENEA, KIT, LEI, RUB, UNIROMA1 and VTT) using three system codes (ASTEC, AC^2 and MELCOR).

This paper summarizes the results of the comparative study of SA sequence simulations using FeCrAl and Zircaloy as cladding materials. This work highlights the different modelling approaches and code implementations used for the ATF cladding, and discusses the key finding in terms of hydrogen generation and timing of events in the two generic SMRs designs analyzed.

2. GENERIC iPWR DESIGNS DESCRIPTIONS

The evaluation conducted within the SASPAM-SA project considered two representative iPWR concepts. These generic designs were defined using publicly available data and expert engineering judgment to cover the main design features considered in the most promising concepts to be deploy in the near-term future [11, 12]. Both selected concepts integrate the reactor core, steam generators, and pressurizer within a single Reactor Pressure Vessel (RPV). This integral configuration enhances safety by eliminating large-diameter external loop piping, thereby removing the possibility of Large Break Loss-of-Coolant Accidents (LB-LOCA) common in traditional PWRs. While the project goal is not to evaluate these specific designs, they serve as the reference cases to assess the capabilities of integral codes in simulating key phenomena during hypothetical accidents. In Figure 1, schematic representations of Design-1 and -2 are presented.

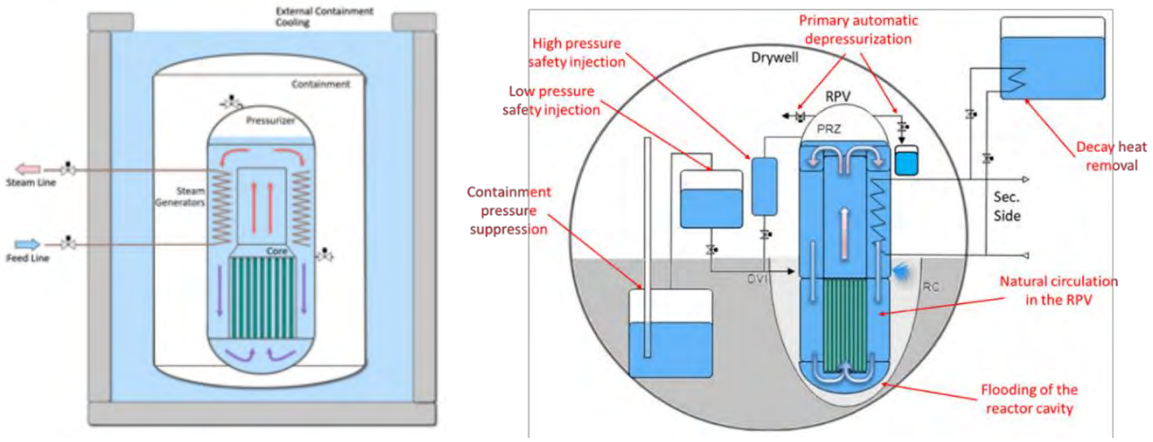

Figure 1. Representation of the generic iPWR Design-1 (left) and Design-2 (right).

2.1. Generic iPWR Design-1

The generic Design-1 is a 160 MWth natural circulation iPWR, characterized by a submerged containment. The generic design studied consists on an integral RPV housing a shrouded core, a riser, a pressurizer, and two helical tube steam generators. The core consists of 37 fuel assemblies arranged in a 17×17 configuration with an active height of approximately 2 m. Finally, the RPV is within a steel containment vessel that is submerged in a large external pool of water, which serves as the ultimate heat sink. The interior of the containment is maintained at a near-vacuum atmosphere to promote steam condensation in the event of steam release from the RPV.

The primary passive safety system is the Emergency Core Cooling System (ECCS), which improves heat removal in case of accident by using the Reactor Vent Valves (RVs) located at the top of the RPV and Reactor Recirculation Valves (RRs) positioned in the downcomer above the core level. During an accident sequence, these valves establish a natural circulation flow path: steam is vented to the containment, condensed on the walls cooled by the external pool, and then returned to the RPV through the RRs.

2.2. Generic iPWR Design-2

The generic Design-2 represents a larger power generation unit with a thermal output of 1000 MWth. Unlike Design-1, this reactor operates under forced circulation during normal conditions, using primary coolant pumps integrated within the RPV alongside the core, steam generators, control rod drive mechanisms, and pressurizer. Design-2 employs a dry containment concept and incorporates passive mitigation strategies to manage design basis and severe accidents. The main passive features are described below:

- After the primary pump trip, coolant flow is sustained by **Natural Circulation** in the RPV, with riser-downcomer connections ensuring flow even at reduced coolant levels;
- **Decay Heat Removal** is achieved via natural circulation between the steam generators and a submerged heat exchanger in an elevated pool;
- The Primary **Automatic Depressurization System** (ADS) reduces the RPV pressure to enable the activation of passive safety injection systems;
- **High-Pressure Safety Injection** uses a natural circulation loop between the RPV and dedicated tanks of borated water, while **Low-Pressure Safety Injection** relies on gravity-driven flow from elevated tanks through direct vessel injection (DVI) lines;
- **Containment Pressure Suppression** mitigates the pressure buildup by directing steam into a large pool of water through the DryWell (DW) connections;
- **Flooding of the Reactor Cavity** is automatically initiated under SA conditions to provide external cooling of the lower head, thereby supporting in-vessel melt retention.

3. ATF MATERIAL AND MODELLING STRATEGIES

The development of ATF cladding materials has become a critical area of research to improve safety margins in the event of a SA. Under off-normal conditions, such as LOCAs, the reactor core may become exposed to high-temperature steam, triggering several degradation mechanisms [13, 14]. Even though zirconium-based alloys are still an effective material under normal operating conditions, they show certain limitations at high temperatures. Zircaloy cladding can experience ballooning and bursting between 973 K and 1373 K due to internal pressurization, and undergo fast exothermic oxidation reactions in steam environment. These reactions generate substantial heat, accelerating further temperature increase, and produce large quantities of hydrogen, thus increasing the risk of combustion or detonation [3, 13-15]. Following the Fukushima-Daiichi accident, significant efforts have been directed towards identifying cladding concepts that can mitigate these phenomena by delaying the onset of rapid oxidation and reducing hydrogen release during core degradation.

ATF developments for cladding can be broadly classified into three main categories:

- **Surface-modified zirconium alloys**, including metallic and ceramic coatings, which improve early-phase oxidation behaviour while retaining the Zircaloy substrate;
- **Non-zirconium metallic alloys**, such as FeCrAl, which rely on protective and adherent oxides that show higher oxidation resistance;
- **Ceramic-based composite**, mainly SiC/SiC, which offer excellent chemical stability but face mechanical, joining and manufacturing challenges at industrial scale.

Among these options, FeCrAl alloys have emerged as a promising metallic ATF cladding due to their balanced formability, mechanical strength and demonstrated performance in high-temperature steam. Their superior oxidation resistance comes from the formation of a dense, adherent Al_2O_3 scale, which maintains oxidation rates several orders of magnitude lower than Zircaloy below 1673 K. However, at higher temperatures, scale failure triggers the rapid formation of Fe-rich oxides with accelerated kinetics [3]. Although there are some challenges with FeCrAl, such as higher thermal neutron absorption, these can be mitigated by reducing the thickness of the cladding or increasing the fuel enrichment. Current optimization

focuses on balancing the content of chromium and aluminium to prevent embrittlement while retaining the high oxidation resistance [3, 4, 13, 14]. This has led to the development of several specific candidates, such as the B136Y3 alloy, which was selected as the reference material for this study, as it has been extensively studied through separate-effect and bundle tests at the QUENCH facility at the Karlsruhe Institute of Technology in Germany [3, 16].

A key aspect of the modelling task was that each partner had full autonomy over the level of detail included in the modelling and implementation strategies within each code framework. Three integral codes were used for testing ATF in the two generic iPWRs: ASTEC, AC² and MELCOR for Design-1 by KIT, RUB and VTT respectively, and for Design-2 by ENEA, LEI and UNIROMA1 respectively. The modelling approaches adopted for each code and partner are briefly described below.

3.1. ASTEC Modelling Strategy

At the time of the study, ASTEC V3.1 did not include a dedicated FeCrAl model; however, efforts are currently underway to its development [17]. To perform the simulations, partners used the MDB structure to overwrite the Zr oxidation correlation with the temperature-dependent parabolic FeCrAl law derived from experimental data [3]. The kinetics rate of the parabolic law presents an Arrhenius form $A \times \exp(-Q/RT)$, in which $R = 8.31446$ J/molK, and the A and Q constants are listed in Table I. Two variants were applied:

- **Oxidation-only substitution**, retaining default zirconium thermophysical and thermodynamic properties to isolate the effect of oxidation kinetics;
- **Extended substitution**, including FeCrAl thermophysical and thermodynamic updates [4], while still relaying on Zr-based corium oxidation models in late degradation phases.

Table I. Arrhenius constants for FeCrAl oxidation kinetics.

Temp. Range	A [$\mathrm{kg^2/m^4 s}$]	Q [$\mathrm{J/mol}$]	comments
873 K ≤ T < 1173 K	5.376×10^{-3}	1.847×10^{5}	θ-alumina kinetics
1173 K ≤ T < 1273 K	4.692×10^{-12}	0.0	-
1273 K ≤ T < 1648 K	5.018	2.877×10^{5}	α-alumina kinetics
T ≥ 1648 K	2.4×10^{8}	3.527×10^{5}	Fe-oxide kinetics

Both implementations of Design-1 were tested by KIT. For Design-2, ENEA used the oxidation-only approach. In all cases, the core geometry remained unchanged.

3.2. AC² Modelling Strategy

ATF modelling capabilities were included into AC² since version 2023.1. This implementation assumes the formation of a single protective α-Al_2O_3 layer during FeCrAl oxidation, i.e., Fe-rich oxide formation after alumina scale failure is not explicitly represented in the current study. The reaction kinetics follow a parabolic rate law analogous to zirconium oxidation models and are calculated using an Arrhenius-type equation incorporating a reduction factor to account for the effects of steam starvation. Different modelling options are available:

- **Option 20**: kinetics based on KANTHAL material. Arrhenius constants: $A = 3.1\ \mathrm{kg^2/m^4 s}$ and $Q = 2.785 \times 10^5\ \mathrm{J/mol}$;
- **Option 21**: identical formulation as option 20 with empirically increased constants;
- **Option 22**: user-defined oxidation parameters.

In addition to these release-version capabilities, recent AC^2 developments [18] introduced multi-component oxidation models to further improve the physical representation of FeCrAl oxidation under SA conditions, including the transition at 1648 K. However, evaluations with the new models are not included in this work.

Material property data must be user-defined if other than the standard Zircaloy is used. Design-1, modelled by RUB, was tested using Option 21, adopting fuel rod geometries and specific FeCrAl parameters from literature [19] while missing data were derived from Zircaloy or iron databases. In contrast, LEI applied Option 20 to Design-2, keeping cladding properties identical to the reference zirconium case.

3.3. MELCOR Modelling Strategy

In MELCOR, a generalized oxidation model based on Arrhenius equations is used. For this model, user-defined constants must be specified for each temperature range. The properties of both the FeCrAl alloy and a unified FeCrAl oxide are provided in the MELCOR Material Properties. However, these can be overwritten by the user in the input interface.

In the simulations conducted by VTT for Design-1, experimental data from Kim et al. [3] was used to fit an Arrhenius equation for two temperature ranges. Nevertheless, the oxidation heat release remained based on the default MELCOR Zr oxidation framework. Since the heat release associated with Zr oxidation is expected to be larger than that of FeCrAl oxidation for early degradation regime, this assumption may conservatively overestimate the local heat generation and, as a consequence, the cladding temperature.. The Arrhenius constants used are:

- $T \leq 1573\ K$: $A = 1.66 \times 10^{-2}$ $\mathrm{kg^2/m^4 s}$ and $Q/R = 22334$ K;
- $T \geq 1673\ K$: $A = 2.48 \times 10^{8}$ $\mathrm{kg^2/m^4 s}$ and $Q/R = 39282$ K;
- The code performs an interpolation between the two temperature limits for which the coefficients are undefined.

For Design-2, simulated by UNIROMA1, FeCrAl properties for both the metallic and oxide phases were implemented from Field et al. [19], and oxidation kinetics rate constants were applied based on experimental data [3]. For both designs, the cladding thickness was the same as the Zr reference material in order to keep the core geometry.

4. POSTULATED ACCIDENT SCENARIOS

To evaluate the performance of the integral codes when implementing ATF cladding materials, hypothetical accident sequences were postulated for the two generic iPWR designs used in this study. These scenarios involve system failures leading to core uncovery and subsequent heat-up, thereby initiating the oxidation processes relevant to the study of FeCrAl performance.

Regarding the core conditions, the partners adopted two different assumptions. Some used the SASPAM-SA database [20] that includes decay heat data and isotopic inventories for 60 MWd/tU, while others considered a fission product inventory derived from a scaled PWR core and applied a decay heat curve based on the ANS73 standard [21] with or without a 20% power increase.

4.1. Hypothetical Scenario for Design-1

The postulated SA sequence consists of a break in the Chemical and Volume Control System (CVCS) discharge line, combined with a loss of AC power. The break, which had a diameter of ~0.04 m, was located above the top of the active fuel (TAF), creating a path between the downcomer and the containment vessel. The elevation was set to between 3.5 and 6.5 m above the TAF, depending on the modelling assumptions adopted by each participant.

The postulated sequence begins with a loss of AC power, followed by the Main Steam Line closing after 5 s. The ECCS actuates when the pressure difference between the containment and the RPV falls below 6.2–6.9 MPa (depending on the partner), and when the containment water level exceeds about 5.8 m, i.e., above the elevation of the RRs. The RVs remain functional, whereas both RRs are assumed to be unavailable and remain closed.

4.2. Hypothetical Scenario for Design-2

For Design-2, the initiating event of the SA sequence is a guillotine break of one Direct Vessel Injection (DVI) line, combined with the failure of the Emergency Heat Removal System (EHRS), while all other safety systems remain available. Following the DVI break, the increase in the containment pressure rises the plant safety signal. About 5 s later, the reactor scrams, the secondary system is isolated, and the primary pressure control system is shut down. As the pressurizer (PRZ) level decreases below its low-level set-point (< ~14%), a signal initiates reactor coolant pump (RCP) coastdown and RI-DC valve opening. Continued depressurization leads to a low-pressure signal (PRZ pressure < ~11.7 MPa), triggering Emergency Boration Tank (EBT) injection and ADS Stage-1 actuation.

When the pressure difference between the RPV and the containment falls below ~0.05 MPa, the Long-term Gravity Make-up System (LGMS) activates. If the mass in one LGMS tank drops below about 8%, a low-mass signal triggers ADS Stage-2. The sequence leads to sustained primary depressurization and safety injection, while the failed EHRS prevents decay-heat removal, enabling a SA progression.

5. SELECTED RESULTS AND DISCUSSIONS

The selected results of the SA transients performed using the ASTEC, AC² and MELCOR codes for Designs -1 and -2 are presented below. The results primarily focus on hydrogen production and peak cladding temperature evolution. These quantities were selected because the FeCrAl implementations currently used in this study still rely, to different extent, on Zr-based degradation models, which are expected to be more applicable during the initial degradation phase, when oxidation kinetics dominate the response and the cladding preserves its rod-like geometry. However, after cladding failure, FeCrAl-specific effects on melting, relocation, and interactions with UO_2 and other core materials are not yet fully represented in the SA codes. Therefore, late-phase results should therefore be interpreted with caution.

5.1. Results for iPWR Design-1

For all codes, the initial thermohydraulic progression of the SA sequence follows the same overall dynamics for FeCrAl and the Zircaloy reference cases during the initial phase of the transient. Following the break initiation, the primary coolant is discharged into the containment vessel. However, even when the ECCS signal is triggered, the unavailability of the RRs prevents coolant recirculation, leading to progressive core uncovery, increasing the cladding temperature, and ultimately initiating core degradation. A detailed description of the accident progression can be found in [12, 22]. Key sequence parameters are provided in Table II.

The timing of the ECCS signal varied across the codes, primarily due to the modelled break elevations. AC² showed activation ~360 seconds earlier, while the FeCrAl implementation in ASTEC and MELCOR produced no significant differences on the ECCS timing or on key parameters such as the maximum water level and pressure in containment. The deviations observed in AC² are attributed to geometric modifications and to the conservative decay heat assumption (ANS-73 +20%) applied to the specific input deck, whereas the core geometry remained unchanged in the ASTEC and MELCOR models. Despite some differences, the impact of FeCrAl on the initial thermohydraulic sequence is not significant.

Core uncovery begins as the coolant is discharged into the containment and the RRs stuck closed. While MELCOR and ASTEC show small differences for TAF and BAF (Top and Bottom of Active Fuel) timings, AC² reports earlier occurrences by approximately 640 s and 3730 s, respectively. Following the onset of core uncovery, a gradual temperature increase is observed among all codes up to approximately two hours. After this period, a rapid escalation in temperature is triggered; however, the timing of this escalation's onset and subsequent evolution depends on the cladding material and the code-specific implementation. In ASTEC, the oxidation-only substitution (FeCrAl-1) delays the time at which the cladding reaches 1648 K by ~28 min compared to the Zr case. When both the oxidation kinetics and the material properties are modified (FeCrAl-2), the delay increases to approximately 35 min. A similar behaviour is observed with MELCOR, in which the FeCrAl case presents a delay of ~20 min. This delay occurs despite the conservative Zr-like oxidation enthalpy assumed in MELCOR (Section 3.3), suggesting that slower reaction kinetics dominate the thermal escalation during this phase. In contrast, AC² shows a near-linear FeCrAl temperature increase, reaching 1648 K ~3 min earlier than in the Zr case. This difference in behaviour is likely to be influence by the specific AC² modelling assumptions and input-deck conditions, including the FeCrAl oxidation kinetics implementations

Table II. iPWR Design 1: Progression of the postulated SA sequence with FeCrAl and Zircaloy.

Event/Parameter	ASTEC – KIT			AC2 – RUB		MELCOR – VTT	
	FeCrAl-1	FeCrAl-2	Zr	FeCrAl	Zr	FeCrAl	Zr
Scram time (s)	4.3	4.3	4.3	0	0	4	4
ECCS signal (s)	935	938	934	4177	4537	513	512
Max. water level in Containment (m)	9.76	9.65	9.75	8.28	8.56	8.35	8.32
Pmax in Cont. (MPa)	2.65	2.65	2.65	4.94	4.83	4.68	4.67
TAF uncovered (s)	3817	3833	3851	5493	6130	3960	4050
BAF uncovered (s)	23000	22382	22483	11519	15254	10290	10920
Clad at 1648 K (s)	11090	11510	9400	10000	10180	9480	8280
Total H_2 gen. (kg)	48.9	28.1	64.0	10.95	72.4	69.0	90.0
1st corium slump in the LP (s)	29350	30460	29515	15521	11050	25245	23671
Corium in the LP (kg)	7630	9020	5771	6585	8460	3112	2967

The most significant effect of FeCrAl concerns the hydrogen generated during core degradation, in particular during the early degradation phase. The hydrogen has multiple sources, including the oxidation of cladding, corium, and structural materials. Figure 2 (left) presents a comparison for the total H_2 generated in the core during the first 30000 s of the transient for FeCrAl and Zr claddings. Compared to the Zr case, the implementation of FeCrAl cladding results in a reduction in hydrogen production. In both ASTEC and MELCOR, the onset of rapid hydrogen escalation is delayed by approximately 35 (FeCrAl-2) and 20 min, respectively. This is consistent with the delayed temperature escalation. However, AC² does not show a rapid hydrogen escalation phase for FeCrAl. Although an overall reduction in hydrogen production is achieved with FeCrAl, the late-phase results should be interpreted with caution due to the modelling limitations when cladding integrity is lost. Since corium oxidation models are Zr-based (e.g., UZOXMAG in ASTEC), their application to iron-based alloy such as FeCrAl is uncertain. Thus, Figure 2 (right) shows the cumulative hydrogen generated only before the cladding reaches 1648 K, when the modelling results are more reliable. As can be seen in this figure, implementing FeCrAl results in a 72% reduction in hydrogen for ASTEC FeCrAl-2 (compared to 67% with FeCrAl-1), a 95% reduction for AC², and an 81% reduction

for MELCOR. The observed reductions are consistent with the superior steam oxidation resistance of FeCrAl. Its kinetics are orders of magnitude slower than those of Zircaloy while the protective alumina scale remains intact. Following the alumina scale failure, the behaviour is governed by rapid iron oxidation. Although the cladding retains a rod-like geometry at 1648 K, the subsequent degradation process differs from that of Zircaloy due to FeCrAl's different melting temperature and melt interaction behaviour. This affects the timing and kinetics of material relocation into the melt, significantly impacting late-phase evolution. As previously mentioned, no model dedicated to FeCrAl was developed in the SA codes for advanced degradation phase. This should be addressed in future studies.

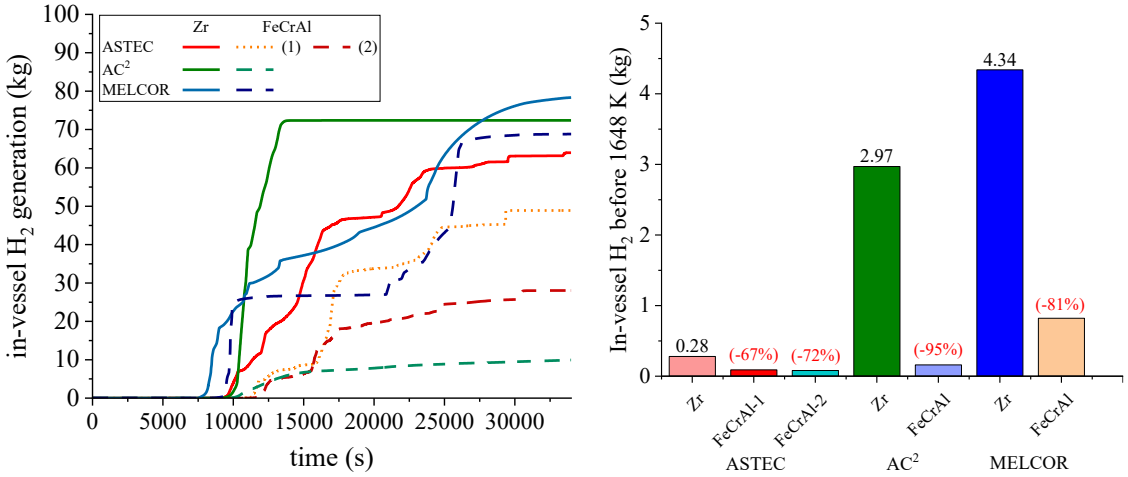

Figure 2. Selected results for Design-1. *Left*) Total H_2 generation during SA sequence. *Right*) Cumulative H_2 before reaching a peak cladding temperature of 1648 K.

It is worth noting that none of the simulations performed with either FeCrAl or Zr cladding led to vessel failure.

5.2. Results for iPWR Design-2

As previously mentioned, the scenario evaluated for Design-2 is initiated by a guillotine break of one of the DVI lines with the unavailability of the EHRS while all other safety systems operate normally. Early safety actions, such as SCRAM, RCP coastdown, opening of the RI-DC valves, actuation of the EBT and ADS-1 show no or negligible difference between the FeCrAl and Zr simulations. The main results are summarized in Table III.

Once the event is initiated, the pressure in the containment experiences a rapid increase, reaching the design pressure at ~670–800 s, depending on the code. In ASTEC and MELCOR, containment failure is assumed, whereas in AC², a venting valve modelled on specific threshold values is used. As the RPV depressurizes, the water level gradually decreases while the cavity accumulates water. The core uncovers and reaches the TAF at ~1715–5830 s, triggering degradation and hydrogen generation. No significant differences between FeCrAl and Zr simulations were observed in ASTEC or AC², while MELCOR predicts the TAF to be reached ~24 minutes earlier for FeCrAl. Notable differences in the timing of the temperature escalation are observed depending on the cladding material used. In general, it was observed that FeCrAl delays the temperature escalation dynamics. In ASTEC, the use of FeCrAl introduces a significant delay of about 4900 s (1.4 hours) before the 1648 K cladding temperature onset is reached. In contrast, in AC², the delay is much smaller (less than 500 s). In MELCOR, the Zircaloy case shows a clear rapid escalation starting at ~24900 s (6.9 hours), whereas the FeCrAl case shows a nearly linear temperature increase without a sudden jump. It reaches 1648 K roughly 8800 s (2.4 hours) later than the Zircaloy case.

Figure 3 shows the FeCrAl and Zr comparisons of total H_2 generated in the vessel during the transient on the left, and the H_2 mass accumulated before reaching 1648 K on the right. In all cases, the use of FeCrAl results in a delayed onset of rapid oxidation and lead to notable reductions in the hydrogen generated. These differences are associated with the dynamics of temperature escalation and the slower kinetics of steam oxidation of FeCrAl during the early to intermediate phases. As mentioned above for Design-1, significant uncertainties arise as the core degradation progresses and FeCrAl interacts with other core materials, for which no dedicated models are applied yet. To highlight the effects of the cladding in the early phase, prior to cladding loss of integrity, the right-hand plot presents the in-vessel H_2 mass at the time the PCT reaches 1648 K. While ASTEC and AC² predict reductions exceeding 95% in the early phase, MELCOR shows a significantly more conservative reduction of only 17%. For ASTEC and AC², the reduction up to this transition temperature exceeds 95%, whereas in MELCOR it is about 17%. This deviation could be attributed to each specific ATF implementation and core degradation modelling strategies.

Table III. iPWR Design 2: Progression of the postulated SA sequence with FeCrAl and Zircaloy.

Event/Parameter	ASTEC - ENEA		AC2 - LEI		MELCOR-UNIROMA1	
	FeCrAl	Zr	FeCrAl	Zr	FeCrAl	Zr
Scram time (s)	25	25	45	45	27	27
RCP-Coastdown (s)	105	105	162	162	157	157
RI-DC valves opening (s)	105	105	162	162	157	157
EBT Actuation (s)	311	311	227	227	173	172
Containment Design Pressure reached (s)	800	800	801	801	670	670
TAF uncovered (s)	5830	5830	5260	5360	1720	3130
BAF uncovered (s)	-	-	-	-	113400	63000
Cladding at 1648 K (s)	18170	13250	14020	13550	33670	24880
LGMS Actuation (s)	21880	18590	10270	10270	11320	10350

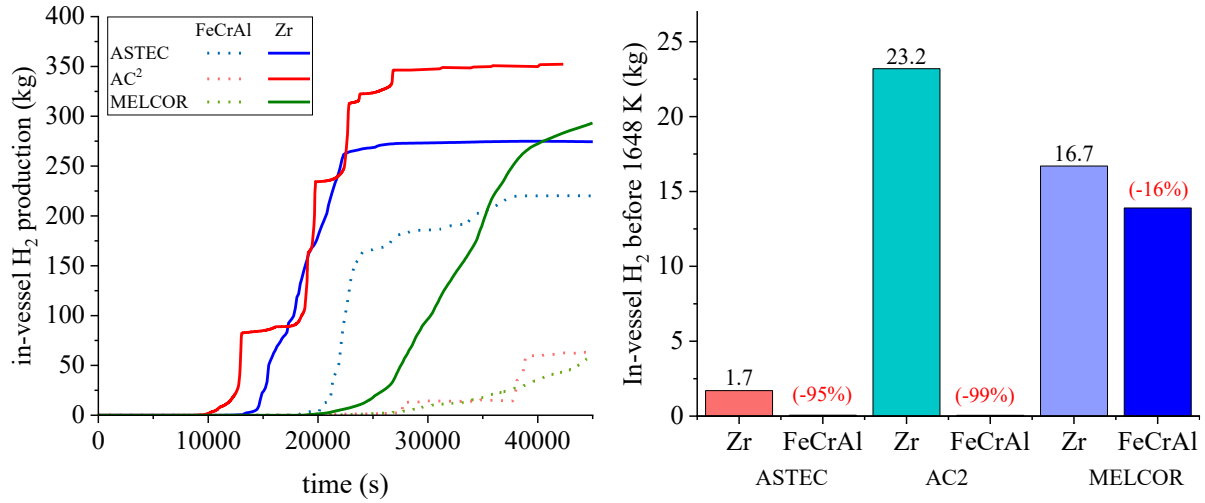

Figure 3. Selected results for Design-2. *Left*) Total H_2 generation during SA sequence. *Right*) Cumulative H_2 before reaching a peak cladding temperature of 1648 K.

Despite the existing uncertainties and the differences in codes and FeCrAl implementations, there is consistent indication that this material can provide a delay the onset of core degradation and reduce the associated hydrogen generation to some extent.

6. CONCLUSIONS

As part of the SASPAM-SA project, SA analyses were performed for two generic iPWR configurations to assess the impact of ATF cladding based on FeCrAl alloys in comparison with conventional Zircaloy. The integral codes ASTEC, AC², and MELCOR were employed to simulate postulated scenarios and quantify FeCrAl effects on key phenomena, such as hydrogen generation, cladding temperature escalation, and the timing of early core degradation processes.

Overall, the codes demonstrated the capability to implement different FeCrAl modelling approaches and to reproduce the main thermal-hydraulic phenomena of SA progression in both designs. Replacing Zircaloy with FeCrAl had no major impact on global thermal-hydraulic variables during the early stage of degradation, aside from minor discrepancies attributed to modelling assumptions such as break elevation, nodalization, or boundary conditions. The main differences between the Zircaloy and FeCrAl cases were observed in the oxidation-driven phenomena, where FeCrAl led to reduced hydrogen production, delayed onset of rapid temperature increase, and a slower transition into early degradation phases. These effects are consistent with the superior steam oxidation resistance of FeCrAl during the period in which the protective alumina layer remains intact.

The performance of each code depended on the modelling strategy adopted. ASTEC and MELCOR mainly implemented the oxidation kinetics of FeCrAl, with optional updates to selected material properties, AC² offered several oxidation formulations based on a single temperature range in the version used. In addition, a common limitation of the codes is their reliance on Zr-based models for late degradation phases, reducing result reliability once cladding integrity is lost due to the lack of dedicated FeCrAl models for high-temperature thermomechanical phenomena, relocation, and corium interaction. Despite these limitations, the simplified implementations were adequate for demonstrating the potential benefits of FeCrAl. The analyses suggest that, while it does not prevent core damage, FeCrAl behaves as an accident-delaying cladding material by extending the time period before severe degradation and significantly reducing hydrogen production during the early phase.

Although recent developments have aimed to improve high-temperature behaviour, further development and validation of dedicated FeCrAl models for late in-vessel degradation are needed to strengthen safety assessments and simulation capabilities, including UO_2 interaction and melt formation.

ACKNOWLEDGMENTS

Funded by the European Union

Funded by the European Union. Views and opinions expressed are, however, those of the author(s) only and do not necessarily reflect those of the European Union or European Commission - Euratom. Neither the European Union nor the granting authority can be held responsible for them.

REFERENCES

1. IAEA, “Design Safety Considerations for Water Cooled Small Modular Reactors Incorporating Lessons Learned from the Fukushima Daiichi Accident,” *IAEA-TECODC-1785*, Vienna (2016).

2. IAEA, "Analysis of Options and Experimental Examination of Fuels for Water Cooled Reactors with Increased Accident Tolerance (ACTOF)," *IAEA-TECDOC-1921*, Vienna (2020).
3. C. Kim, C. Tang, M. Große, Y. Maeng, C. Jang and M. Steinbrück, "Oxidation mechanism and kinetics of nuclear-grade FeCrAl alloys in the temperature range of 500-1500 °C in steam," *Journal of Nuclear Materials*, **564**, pp. 153696 (2022).
4. P. Aragón, F. Feria and L. E. Herranz, "Modelling FeCrAl cladding thermo-mechanical performance. Part I: Steady-state conditions," *Progress in Nuclear Energy*, **153**, pp. 104417 (2022).
5. IAEA, "Accident Tolerant Fuel Concepts for Light Water Reactors," *Proceedings of a Technical Meeting held at Oak Ridge National Laboratories*, United States of America, 13-16 October (2014).
6. IAEA, "Assessment of Defence in Depth for Nuclear Power Plants," *Safety Reports Series No. 46*, Vienna, Austria (2005).
7. S. Magruder, D. Jackson, K. Thomas, K. Herviou, P. Dupuy, M. Devos and S. Cook, "SMR Regulators' Forum Pilot Project Report: Considering the Application of a Graded Approach, Defence-in-Depth and Emergency Planning Zone Size for Small Modular Reactors," *IAEA International Conference on Topical Issues in Nuclear Installation Safety*, Vienna, Austria, pp. 103-107 (2018).
8. SASPAM-SA, "Safety Analysis of SMR with PAssive Mitigation strategies Severe Accident," https://www.saspam-sa.eu (2022)
9. L. E. Herranz, L. Poubeau, L. Chailan and L. Mascari, "Looking ahead to Severe Accident Reseach," *EPJ Nuclear Sciences and Technologies*, **11** (2025).
10. F. Mascari et al., "Horizon Euratom SASPAM-SA Project: Main Ideas and First Outcomes," *International Conference on Small Modular Reactors and their Applications*, Vienna, Austria (2024).
11. SASPAM-SA, "Milestone 2.1: Generic Data on Design 1 and Design 2," (2023).
12. F. Gabrielli, "Deliverable 2.2 - iPWR input-deck and scenarios analyses," SASPAM-SA (2024).
13. Y. Yamamoto, B. Pint, K. Terrani, K. Field, Y. Yang and L. Snead, "Development and property evaluation of nuclear grade wrought FeCrAl fuel cladding for light water reactors," *Journal of Nuclear Materials*, **467**, pp. 703-716 (2015).
14. C. Tang, A. Jianu, M. Steinbrueck, M. W. A. Grosse and H. J. Seifert, "Influence of composition and heating schedules on compatibility of FeCrAl alloys with high-temperature steam," *Journal of Nuclear Materials*, **511**, pp. 496-507 (2018).
15. P. Aragon, F. Feria and L. E. Herranz, "Modelling FeCrAl cladding thermo-mechanical performance. Part II: Comparative analysis with Zircaloy under LOCA conditions," *Progress in Nuclear Energy*, **163** (2023).
16. J. Stuckert, M. Grosse and M. Steinbrueck, "Results of the bundle test QUENCH-19 with FeCrAl claddings," *Scientific Report NUSAFE 3574*, Karlsruhe Institute of Technology (2022).
17. Z. I. Jiménez, F. Gabrielli, M. E. Cazado, V. H. Sánchez-Espinoza, L. Laborde, L. Carenini and P. Drai, "ASTEC FeCrAl Model Validation and Application," *12th ASTEC Users' Club Meeting*, Fontenay-aux-Roses (2025).
18. L. Lovasz, T. Löher and I. Steudel, "Simulation of TMI-2 accident with ATHLET-CD/AC2 with and without using ATF," *Proceedings of the International Conference Nuclear Energy for New Europe*, Bled, Slovenia (2025).
19. K. G. Field, M. A. Snead, Y. Yamamoto and K. A. Terrani, "Handbook on the Material Properties of FeCrAl Alloys for Nuclear Power Production Applications (FY18 Version: Revision 1)," ORNL, United States (2018).
20. SASPAM-SA, "Deliverable 2.1: Fuel inventory of the iPWR Design-1 and Design-2," (2024).
21. A. C. Thadini, "Attachment 1. Appendix K Decay Heat Standard - Research Information Letter 0202, NRC/RES-ML021720702," NRC (2002).
22. F. Gabrielli et al., "Analysis of postulated Severe Accidents in Generic Integral PWR Small Modular Reactors in the frame of the Horizon Euratom SASPAM-SA project," *Proceedings of the 11th European Review Meeting on Severe Accidents Research (ERMSAR2024)*, Stockholm (2024).

SAFETY ANALYSIS OF SMR WITH PASSIVE MITIGATION STRATEGIES - SEVERE ACCIDENT

Evaluation of Hypothetical Severe Accident Progression with ATF Cladding in Generic Integral PWR Desings in the Frame of the SASPAM-SA Project

Mauricio E. Cazado, F. Gabrielli, V. H. Sánchez-Espinoza (KIT)
F. Mascari (ENEA), J. Krieger, G. T. Stahlberg, M. K. Koch (RUB), T. Sevón (VTT), P. Maccari (ENEA), M. Valincius, A. Kaliatka (LEI), M. Principato, G. Marta, F. Giannetti (UNIROMA1)

Karlsruher Institut für Technologie (KIT)

Content

SAFETY ANALYSIS OF SMR WITH PASSIVE MITIGATION STRATEGIES - SEVERE ACCIDENT

- Introduction & Motivation
- Generic iPWR Designs
- ATF Concept: FeCrAl
- ATF Modelling Strategies
- Accident Scenarios Selected
- Results
- Conclusions

SASPAM-SA Consortium reserves all rights in this document and in the information contained therein. Reproduction, use of disclosure to third party without express authorization is strictly prohibited.

Introduction & Motivation

SAFETY ANALYSIS OF SMR WITH PASSIVE MITIGATION STRATEGIES - SEVERE ACCIDENT

- **SMRs** are a promising innovation, offering modular deployment, versatile applications, and clean and reliable energy solutions.
- **iPWR** are based on well-proven and established LWR technology, with enhanced safety features.
- **SA analysis** are still required to support:
  - Defense-in-Depth assessment,
  - Accident Management strategies, and
  - Emergency Planning considerations.
- ATF concepts aim to improve safety margins during off-normal and accident conditions.

Delay degradation

Reduce H_2 generation

SASPAM-SA Consortium reserves all rights in this document and in the information contained therein. Reproduction, use of disclosure to third party without express authorization is strictly prohibited.

Introduction & Motivation

SAFETY ANALYSIS OF SMR WITH PASSIVE MITIGATION STRATEGIES - SEVERE ACCIDENT

Several activities to support possible license need:

SASPAM-SA: Safety Analysis of SMR with Passive Mitigation strategies – Severe Accident

- Investigates SA progression in generic iPWR concepts,
- Evaluates the transferability of knowledge from large LWR to iPWR,
- Dedicated task on ATF

Scope of the present ATF study: Integral-code assessment of FeCrAl vs. Zircaloy in-vessel behavior

Partners	KIT	RUB	VTT	ENEA	LEI	UNIROMA1
Design	1			2		
Code	ASTEC	AC2	MELCOR	ASTEC	AC2	MELCOR

SASPAM-SA Consortium reserves all rights in this document and in the information contained therein. Reproduction, use of disclosure to third party without express authorization is strictly prohibited.

Generic iPWR Designs

SAFETY ANALYSIS OF SMR WITH PASSIVE MITIGATION STRATEGIES - SEVERE ACCIDENT

iPWR Design-1

Submerged containment, P~60 MWe

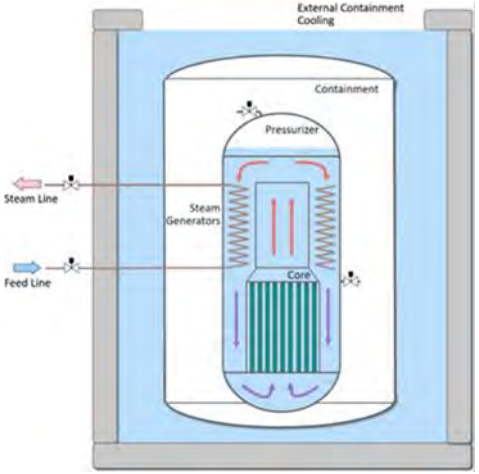

iPWR Design-2

Dry containment, several passive systems, P~300 MWe

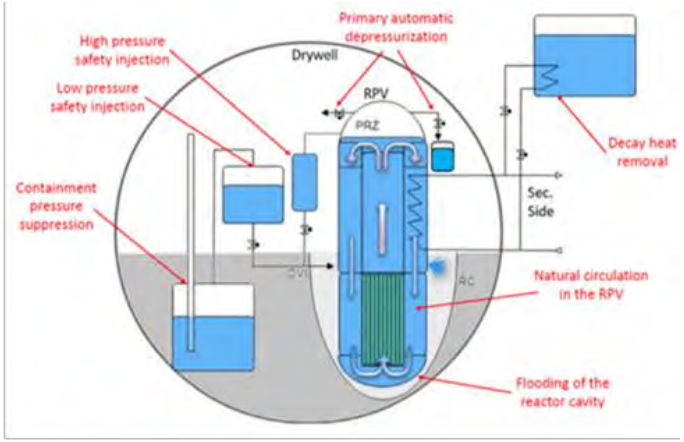

- The designs incorporate the main safety features of the most promising concepts ready for deployment in the European market
- It is not the objective of the task to assess the design of such concepts

SASPAM-SA Consortium reserves all rights in this document and in the information contained therein. Reproduction, use of disclosure to third party without express authorization is strictly prohibited.

ATF Concept: FeCrAl

FeCrAl alloys

Nuclear grade FeCrAl: 10 – 13 wt% Cr and 5 – 6 wt% Al. Additional additives to improve oxidation resistance and mechanical properties: Mo and Y.

Advantages

- Superior mechanical properties compared to Zr alloy.
- Superior oxidation resistance at high temperatures: formation of protective Al_2O_3
- Lower hydrogen generation under steam oxidation.

Challenges

- Higher neutron absorption cross-section than Zircaloy: cladding thickness must be reduced.
- Tritium permeability due to lack of hydrogen isotopes trapping, but lower than pure Fe.
- FeCrAl with high Cr content is susceptible to irradiation embrittlement.
- Interaction between UO_2 and FeO forming an Eutectic at ~1335°C

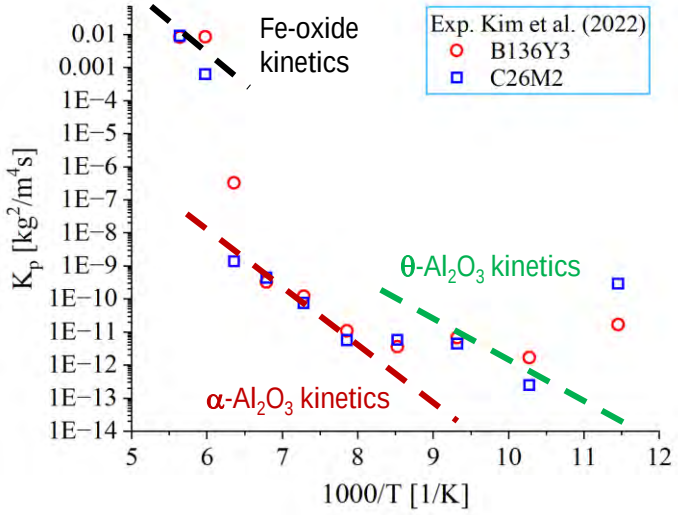

Parabolic rate constants of B136Y3 and C26M2 as a function of temperature with the parabolic constants of Fe-oxide , α-alumina and θ-alumina (Kim, 2022).

≤1300°C: Aluminum oxidation
>1400°C: Iron oxidation dominates the reaction

SASPAM-SA Consortium reserves all rights in this document and in the information contained therein. Reproduction, use of disclosure to third party without express authorization is strictly prohibited.

ATF Modelling Strategies

Each Partner had full autonomy over the level of detailed included in the modelling and implementation strategies within each code framework: ASTEC, AC^2 and MELCOR.

ASTEC

- No FeCrAl built-in models in the version used (under development by KIT and ASNR – See Presentation by Z. Balbuena - KIT).
- MDB structure used to implement FeCrAl properties in place of Zr-based properties: Oxidation kinetics and material properties.

AC^2

- Formation of a single protective α-Al_2O_3 layer during FeCrAl oxidation. Fe-rich oxide formation after alumina failure not explicitly treated in the version used.
- Different options for oxidation kinetics of FeCrAl. Material property data is user-defined.

MELCOR

- Generalized oxidation model.
- Default FeCrAl and FeCrAl oxide properties that can overwritten.

Late phase degradation still rely, to different extent, on Zr-based models

SASPAM-SA Consortium reserves all rights in this document and in the information contained therein. Reproduction, use of disclosure to third party without express authorization is strictly prohibited.

Accident Scenarios Selected

SAFETY ANALYSIS OF SMR WITH PASSIVE MITIGATION STRATEGIES - SEVERE ACCIDENT

Design 1

SA-1: 100% break on the CVCS makeup line (high elevation to avoid reverse flow)

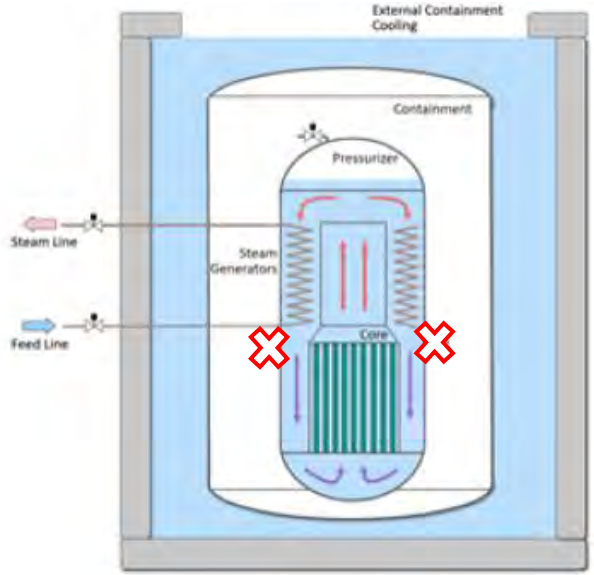

Design 2

SA-3: Unavailability of EHRS system

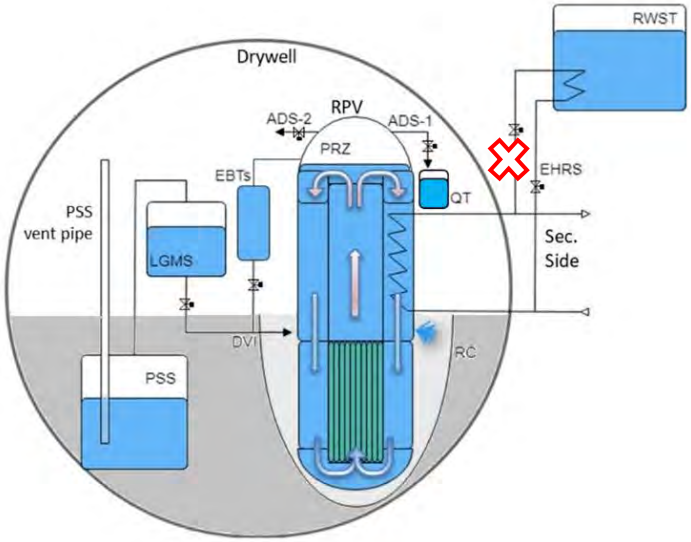

SASPAM-SA Consortium reserves all rights in this document and in the information contained therein. Reproduction, use of disclosure to third party without express authorization is strictly prohibited.

Accident Scenarios Selected

Main FoM

- Hydrogen generation
- Peak Cladding Temperature
- Timing of key degradation event

✓ FeCrAl implementation mainly affects oxidation kinetics.

✓ A reference temperature of 1648 K was used for early-phase comparison, corresponding to the transition in FeCrAl oxidation behaviour.

✓ After cladding failure, FeCrAl-specific melting, relocation, and interactions with UO_2 are not fully represented → Simulations still rely on Zr-based models.

SASPAM-SA Consortium reserves all rights in this document and in the information contained therein. Reproduction, use of disclosure to third party without express authorization is strictly prohibited.

Results – Design 1

- Initial thermal-hydraulic progression is similar for FeCrAl and Zircaloy.
- FeCrAl has no major effect on: ECCS signal timing, Maximum containment water level and pressure.

Partners /Code	**KIT - ASTEC**			**RUB - AC2**		**VTT - MELCOR**	
Cladding	Zr	FeCrAl1	FeCrAl2	Zr	FeCrAl	Zr	FeCrAl
Clad at 1648 K (s)	9400	11090	11510	10180	10000	8280	9480
Delay -1648 K	~28 – 35 min			Slightly earlier		~ 20 min	
Total H_2 (kg)	64	48.9	28.1	72.4	10.95	90	69
H_2 reduction	~23 – 56%			~85%		~23%	

SASPAM-SA Consortium reserves all rights in this document and in the information contained therein. Reproduction, use of disclosure to third party without express authorization is strictly prohibited.

Results – Design 1

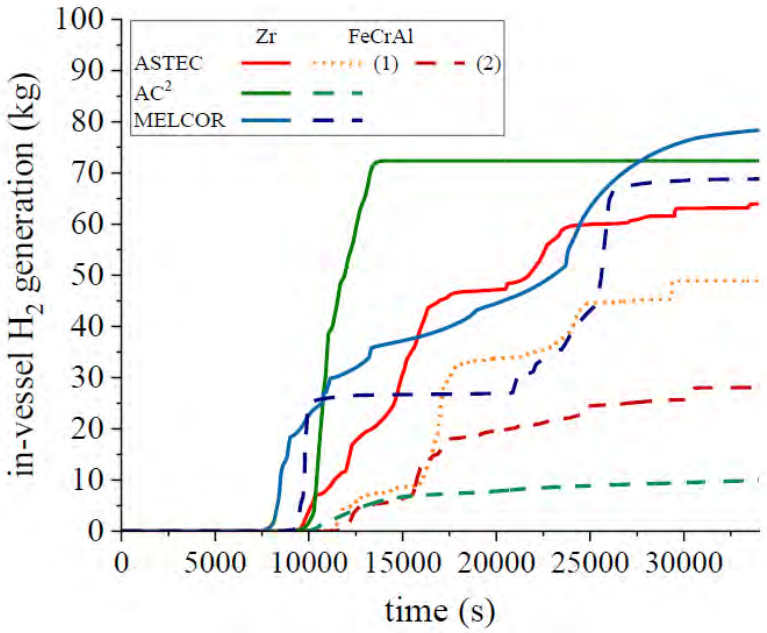

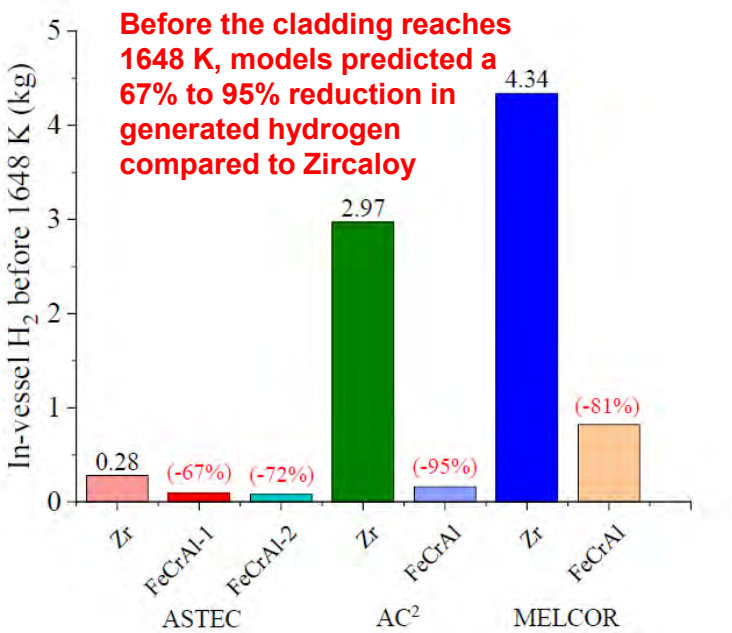

Selected results for Design-1. *Left*) Total H_2 generation during SA sequence. *Right*) Cumulative H_2 before reaching a peak cladding temperature of 1648 K.

SASPAM-SA Consortium reserves all rights in this document and in the information contained therein. Reproduction, use of disclosure to third party without express authorization is strictly prohibited.

Results – Design 2

- Early safety actions show negligible differences between FeCrAl and Zircaloy.
- Similar to Design-1, FeCrAl significantly delayed the temperature escalation dynamics

Partners /Code	ENEA - ASTEC		LEI - AC2		UNIROMA1 - MELCOR	
Cladding	Zr	FeCrAl	Zr	FeCrAl	Zr	FeCrAl
Clad at 1648 K (s)	13250	18170	13550	14020	24880	33670
Delay -1648 K	~82 min		~8 min		~ 146 min	

For Design 2, depending on the code, the time taken to reach the 1648 K threshold was delayed by up to 2.4 hours when using FeCrAl

SASPAM-SA Consortium reserves all rights in this document and in the information contained therein. Reproduction, use of disclosure to third party without express authorization is strictly prohibited.

Results – Design 2

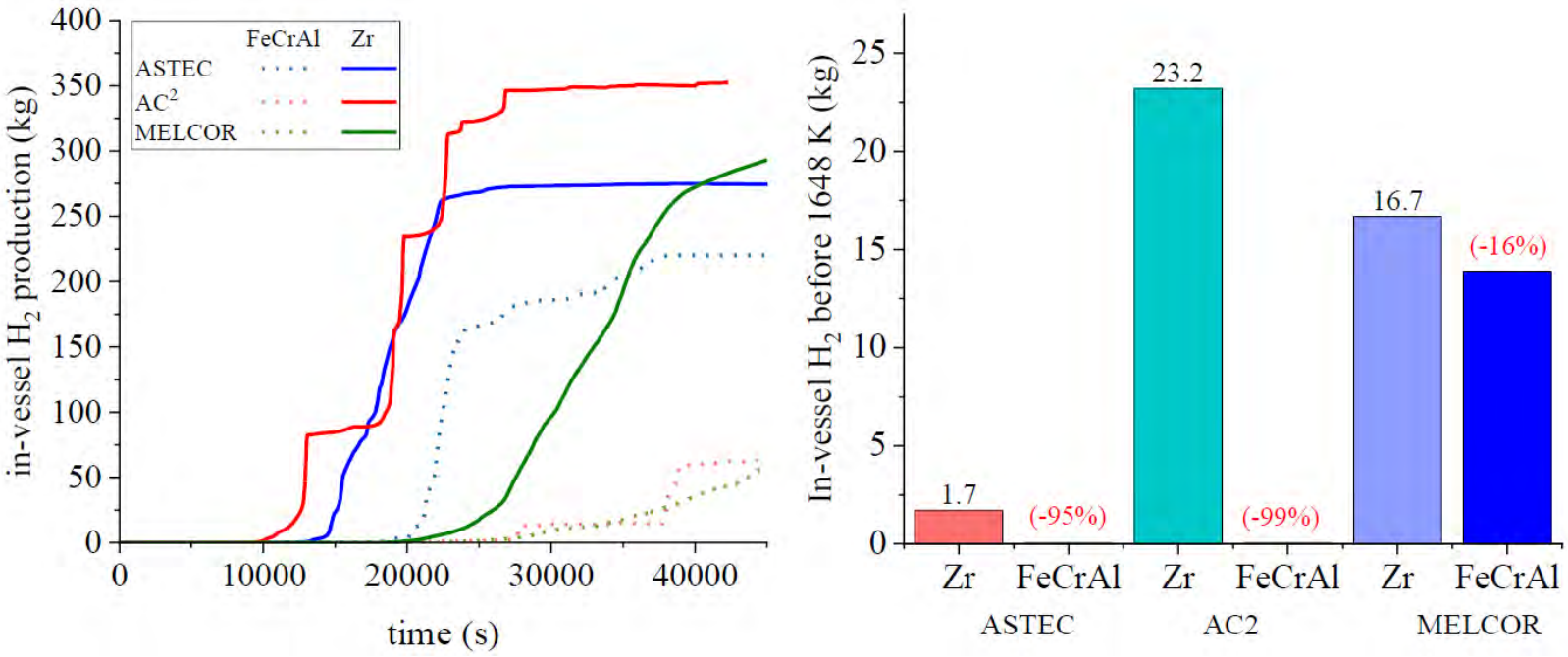

Selected results for Design-2. *Left*) Total H_2 generation during SA sequence. *Right*) Cumulative H_2 before reaching a peak cladding temperature of 1648 K.

SASPAM-SA Consortium reserves all rights in this document and in the information contained therein. Reproduction, use of disclosure to third party without express authorization is strictly prohibited.

Conclusions

- Within SASPAM-SA, SA analyses of two generic iPWRs assessed FeCrAl ATF cladding against Zircaloy.
- Overall, the codes implemented different FeCrAl approaches and reproduced the main SA thermal-hydraulic trends: **FeCrAl had limited impact on early global TH behaviour**, with expected differences mainly due to modelling assumptions.
- The performance of each code depended on the modelling strategy adopted.
- The implementations were adequate for demonstrating the potential benefits of FeCrAl: **reduction of H_2 production and delay of rapid temperature rise before cladding failure**.
- Dedicated FeCrAl late-degradation models, including UO_2 interaction and melt formation, require further development and validation.

SASPAM-SA Consortium reserves all rights in this document and in the information contained therein. Reproduction, use of disclosure to third party without express authorization is strictly prohibited.

Acknowledgement/Disclaimer

Funded by the European Union

Funded by the European Union. Views and opinions expressed are, however, those of the author(s) only and do not necessarily reflect those of the European Union or European Commission-Euratom.
Neither the European Union nor the granting authority can be held responsible for them.

SASPAM-SA Consortium reserves all rights in this document and in the information contained therein. Reproduction, use of disclosure to third party without express authorization is strictly prohibited.

ALMA MATER STUDIORUM
UNIVERSITÀ DI BOLOGNA

COMPARATIVE ANALYSIS OF CONTAINMENT BEHAVIOR IN A GENERIC IPWR DESIGN UNDER POSTULATED BDBA CONDITIONS USING ASTEC V3.1.2 AND MELCOR V2.2 CODES

M. Savini, G. Grippo, E. Cilia*, F. Mascari

UNIBO – Department of Industrial Engineering

ENEA - Research Center

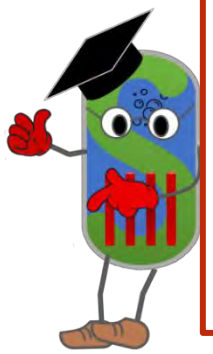

The present **activity** has been **conducted in the framework of the Horizon Euratom SASPAM-SA project**. The project is coordinated by ENEA and 23 organization from 14 countries are involved.

SASPAM-SA

Funded by the European Union

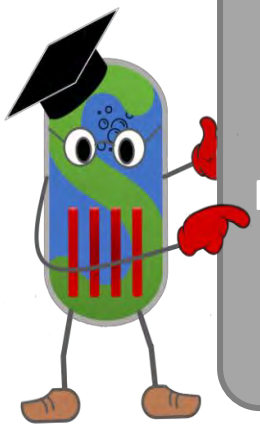

TARGET OF THE PROJECT

- Identification of **plausible postulate SA scenarios** for **iPWR** designs;
- Identification of the **conditions** in the **vessel** and in the **containment** that **characterize iPWR scenarios** and differ significantly from those in large-LWRs;
- Study the **applicability** of the **existing experimental database** to **iPWR** and identify **new experimental needs**;
- Assess the **capability** of internationally recognized **European and Non-European computational tools** (largely used in Europe) to **describe the behaviour** of the most promising **iPWR designs** during **SA scenarios** and to **predict** the resulting **radiological impact** on- and off-site.

ALMA MATER STUDIORUM
UNIVERSITÀ DI BOLOGNA

Generic iPWR Design2 and selected sequences

Design 2

Several passive systems, a dry containment (with a RC) and an electric power of about 300 MWe.

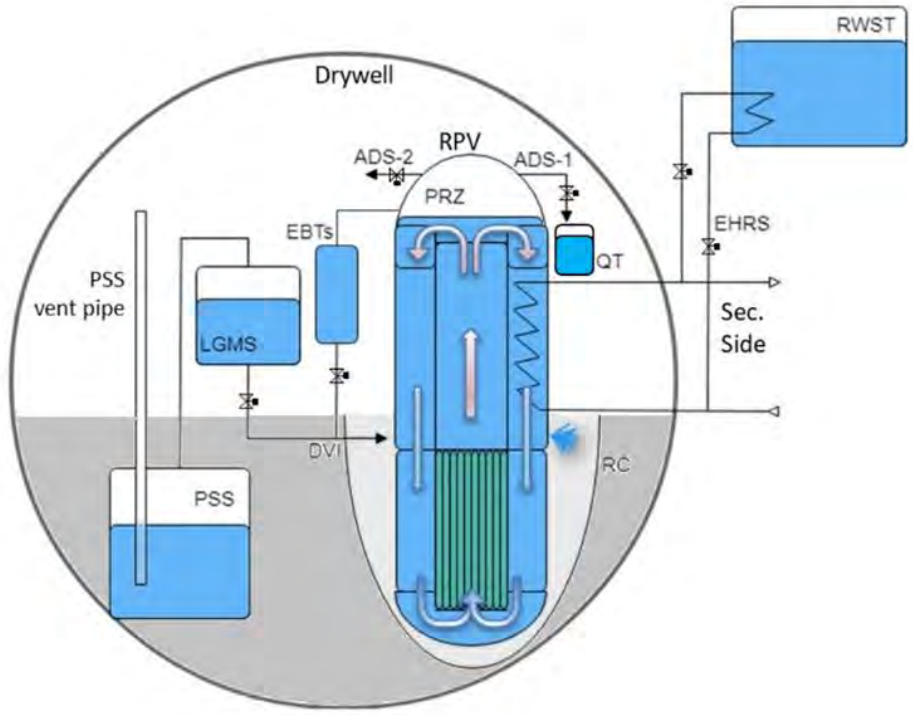

- The reactor operates in **forced circulation during normal operation** and employs a **passive mitigation strategy in accidental transients**.
- It consists of an **integral RPV**, which contains the core, a compact SG, the Control Rod Drive Mechanism (CRDM), the primary pumps and the **pressurizer included in the upper head**.

- To develop the **ASTEC and MELCOR input-deck**, a **reference database** was needed.
- Considering the **characteristics of Design 2 reactor type** and the selected passive systems, a **generic IRIS SMR type has been considered as reference** for this analysis.
- During the development of the MELCOR and ASTEC nodalization, **no proprietary data have been used.**
- The **main geometric information** has been **determined by scaling the data available from the SPES-3 facility**, by engineering evaluation or public general data available for the IRIS reactor.

ALMA MATER STUDIORUM
UNIVERSITÀ DI BOLOGNA

Generic iPWR Design2 and selected sequences

DBA

After the qualification of the steady state, the DBA scenario selected is the guillotine break of one Direct Vessel Injection (DVI) line, considering the availability of all safety systems.

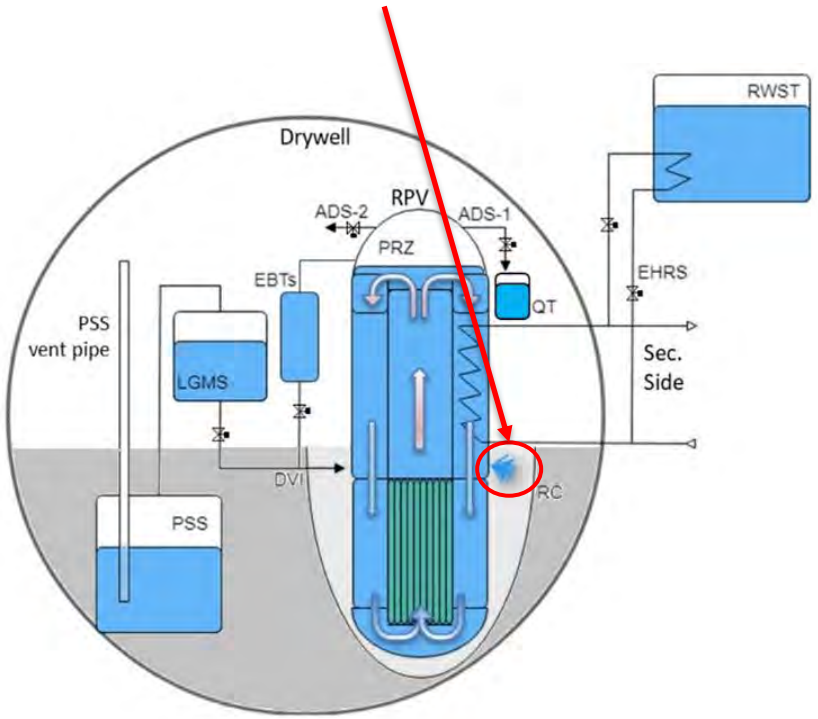

SA1

The first SA scenario postulated is the guillotine break of one Direct Vessel Injection (DVI) line, considering the postulated unavailability of EHRS and ADS-1 systems (through the assumed not opening of the related actuation valves).

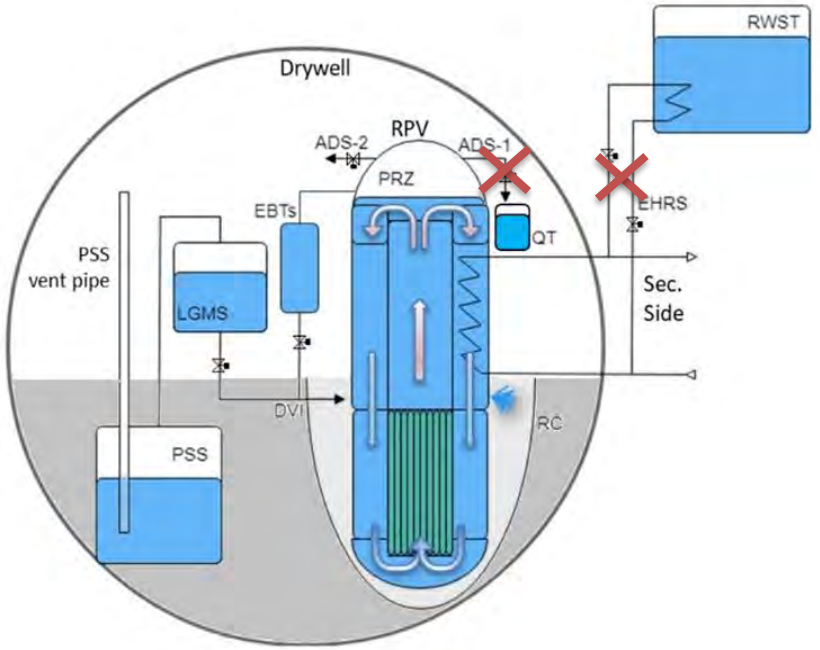

ALMA MATER STUDIORUM
UNIVERSITÀ DI BOLOGNA

Why containment modelling matters for iPWR SA analysis

- **The considered Integral PWRs** (iPWRs) **rely on a strong thermal-hydraulic coupling** between **RPV, containment and passive safety systems**.
- In the new advanced passive reactor designs**, it is not possible to consider the RCS as a boundary condition for the containment**; instead, it is necessary to consider the physical behavior of the containment coupled with the physical behavior of the RCS during the transient evolution:
    - the containment is not simply a receiving volume for mass and energy released from the primary system. It actively influences the pressure evolution, liquid redistribution, steam condensation.

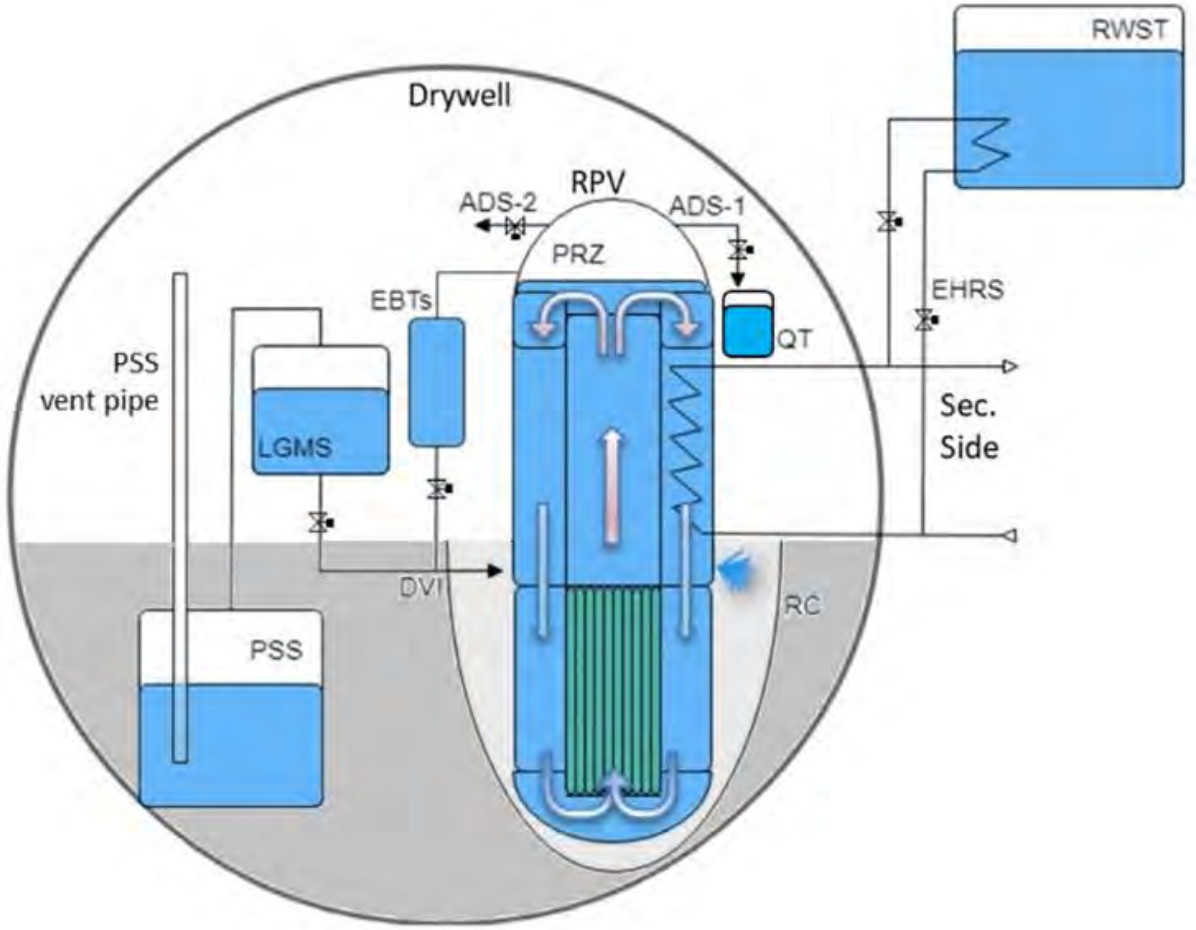

ALMA MATER STUDIORUM
UNIVERSITÀ DI BOLOGNA

Previous ASTEC containment nodalization: limitation identified in first analyses

Calculations with the previous ASTEC nodalization showed a limitation in predicting the draining of water from the DW to the RC due to **liquid hold-up in DW** regions.

This nodalization limitation in liquid redistribution affected:

- **RC level**
- **DW liquid inventory**
- **Break reverse flow**

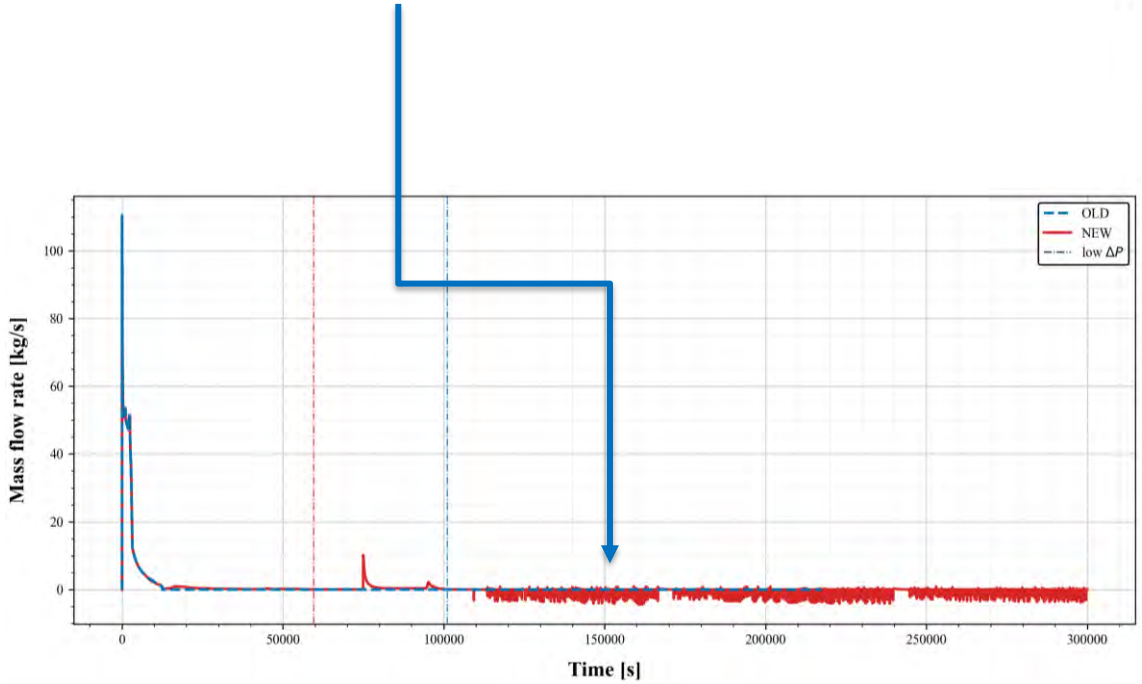

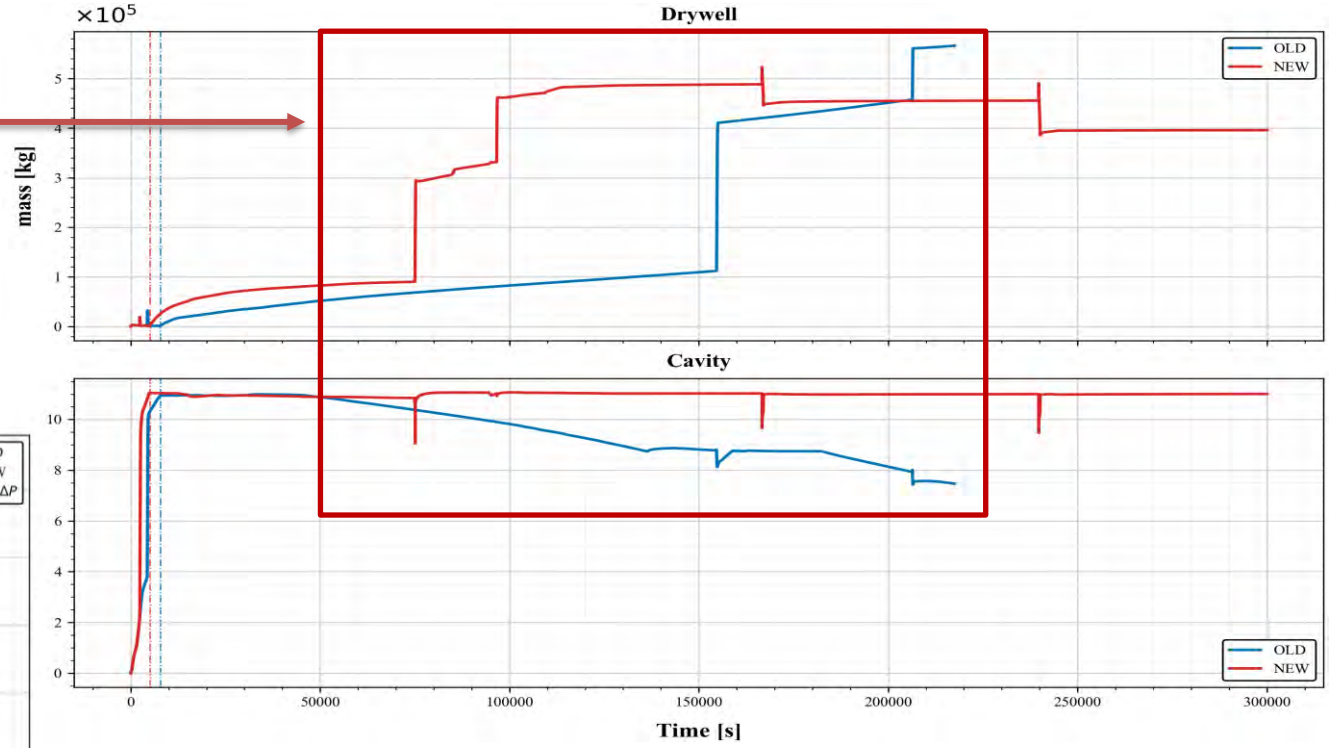

ALMA MATER STUDIORUM
UNIVERSITÀ DI BOLOGNA

Updated RC–DW hydraulic representation

A gravity-driven path has been added between the DW and the lower RC region.

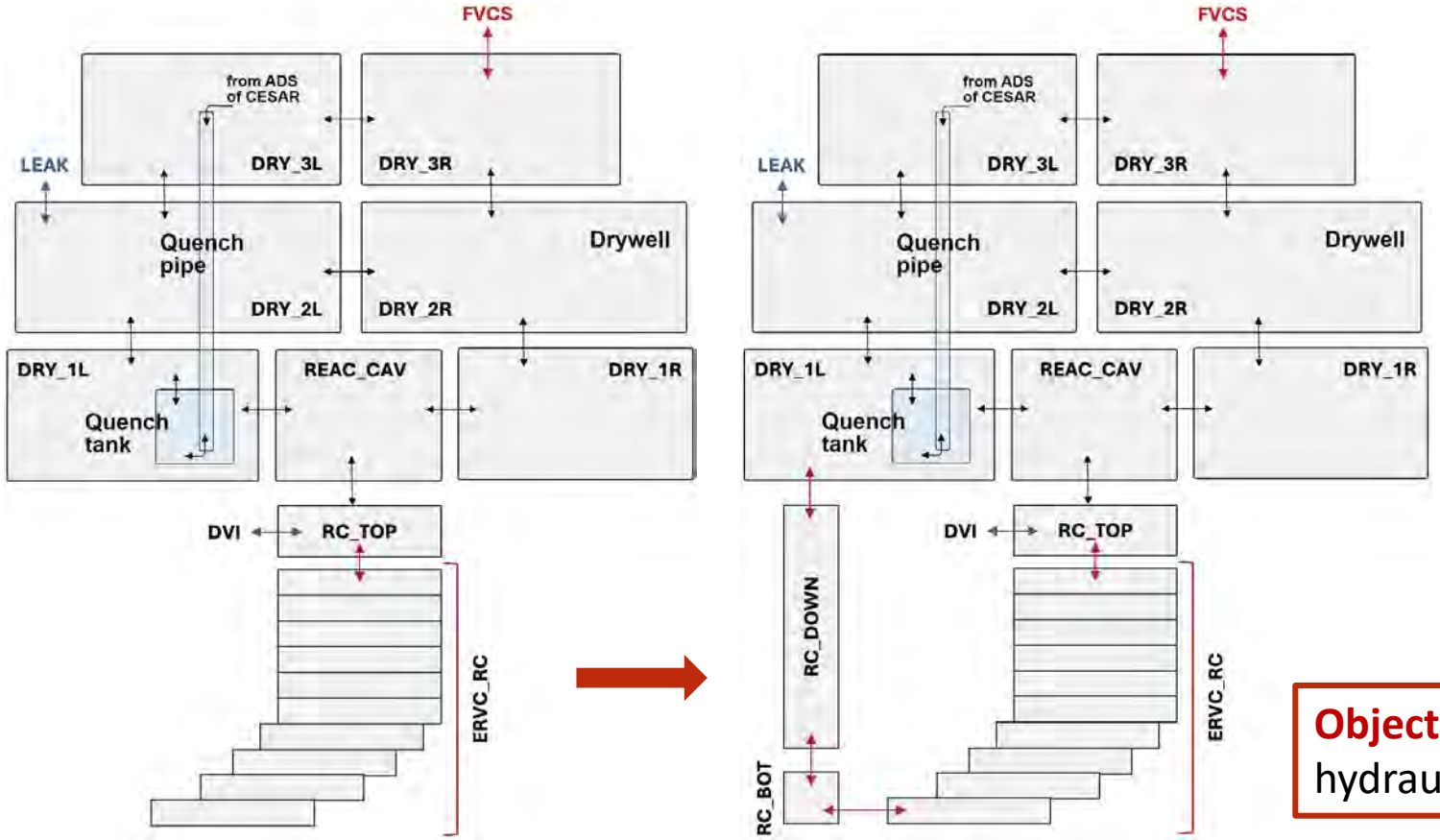

Added CESAR volumes:

- RC_BOT;
- RC_DOWN.

RC_DOWN is connected to DRY_1R, providing a downcomer-like drainage path.

The modification preserves the global RC capacity while allowing water accumulated in the DW to be redistributed toward the cavity more consistently.

Objective: correct containment-side thermal hydraulics prediction

ALMA MATER STUDIORUM
UNIVERSITÀ DI BOLOGNA

DBA consistency check

The updated input cannot be used directly for SA1 without checking its impact on the **reference DBA response**.

The DBA check **verifies whether the RC–DW update**:

- **improves liquid redistribution**;
- **preserves** primary **depressurization behaviour**;
- **preserves EHRS heat removal (not directly connected)**
- **preserves final core cooling**;

Comparison was performed **among**:

- MELCOR;
- previous ASTEC input (v0);
- updated ASTEC input (v1).

Event	MELCOR	ASTEC_v0	ASTEC_v1
High DW pressure signal	41.0	20.0	17.7
Low PRZ level signal	122.0	65.0	67.5
Low PRZ pressure signal	148.0	158.0	158.8
Low DP RPV–containment signal	1884.0	1398.0	1320.7
1st RPV–DW pressure equalization	2000.0	1584.0	1486.3
1st PSS vent injection	3010.0	5534.0	4038.2
2nd RPV–DW pressure equalization	3315.0	6606.0	4283.6
2nd PSS vent injection	5405.0	n.a.	n.a.
Core level reaches TAF	3000.0	5500.0	8950.0
Cavity level reaches DVI elevation	3950.0	6600.0	7278.1
Low LGMS mass signal	12265.0	12902.0	13179.2

ALMA MATER STUDIORUM
UNIVERSITÀ DI BOLOGNA

DBA check: pressure equalization and break-flow reversal

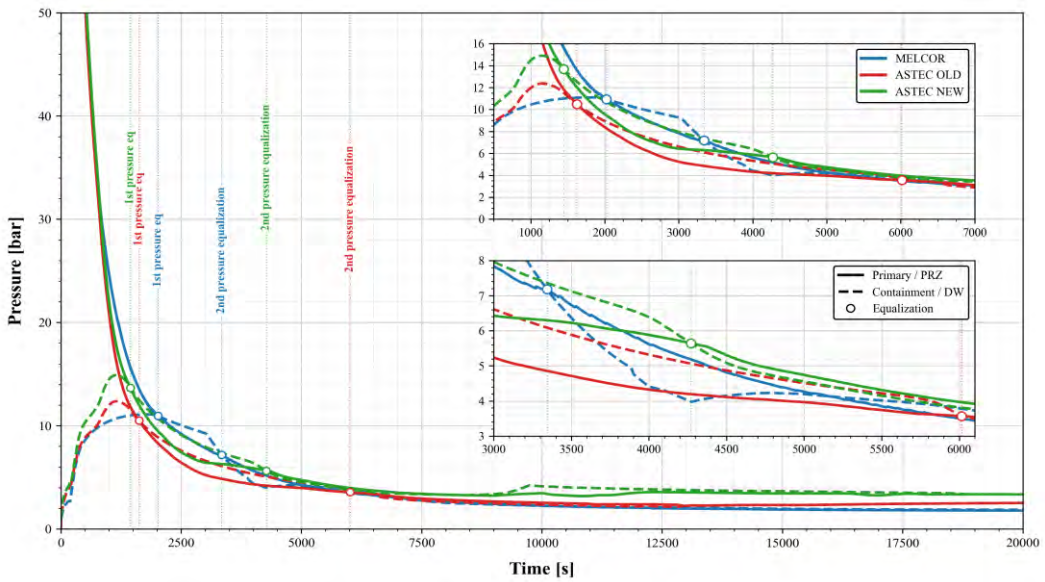

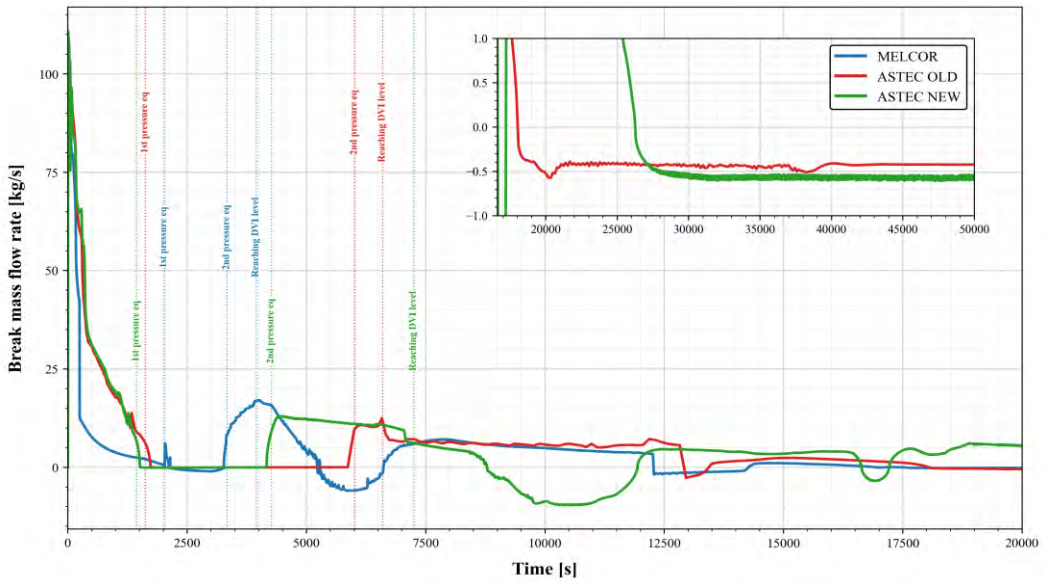

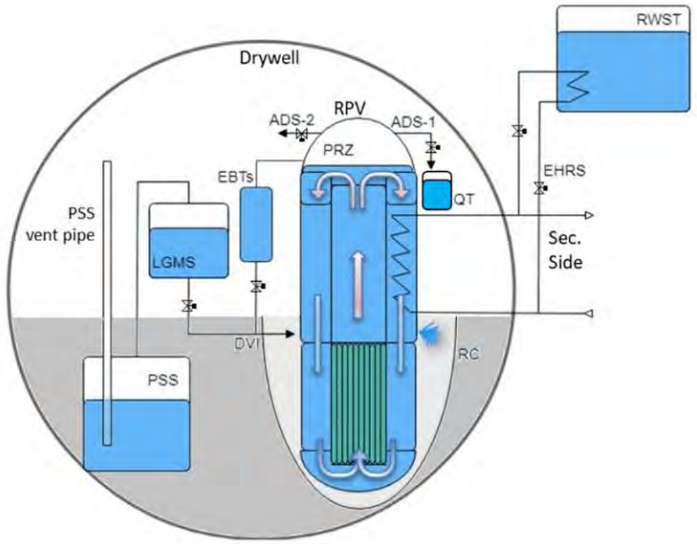

- Updated ASTEC nodalization preserves the global DBA pressure response.
  - First RPV–DW pressure equalization: ~1490s in updated ASTEC.
  - Second pressure equalization: ~4280s in updated ASTEC.
- Break reverse flow occur after the second pressure equalization and RC level rise.
- Compared with the previous ASTEC input, the updated input improves the prediction of
  - cavity filling;
  - Break reverse flow.
- It is to note that the second equalization is anticipated with respect to the previous analyses

ALMA MATER STUDIORUM
UNIVERSITÀ DI BOLOGNA

DBA check: final safety outcome is preserved

ASTEC v1 predicts a **slower and more progressive RC filling**.

- Cavity level reaches DVI elevation at ~7280s.
- Core level reaches TAF later, at ~8950s.

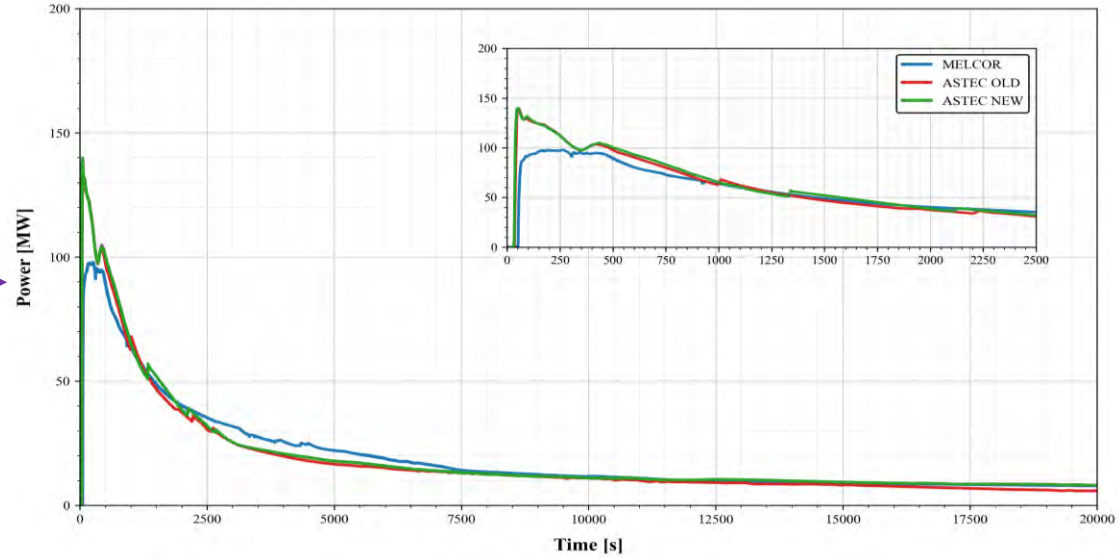

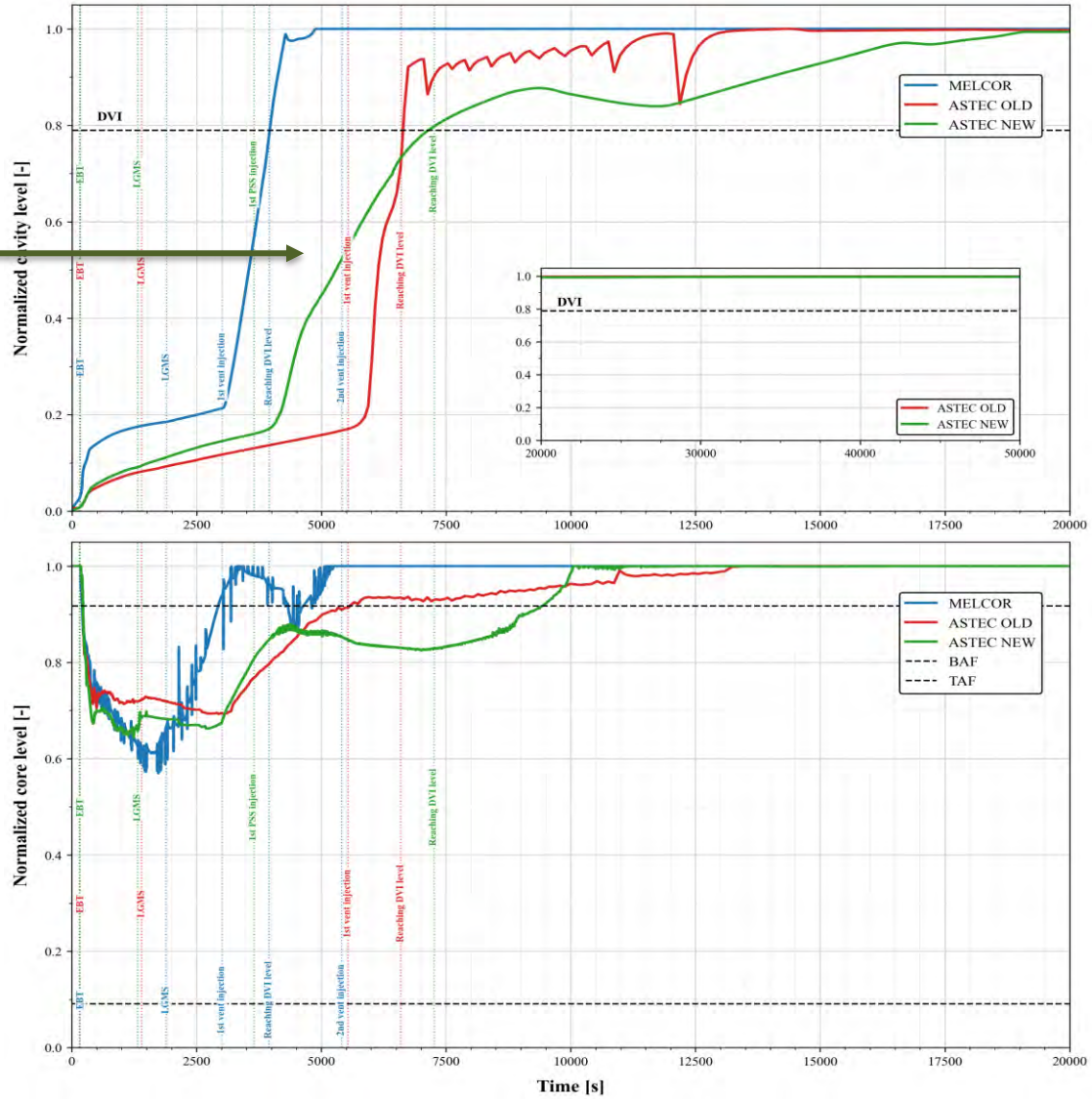

However, **the final DBA outcome is unchanged**:

- core remains sufficiently cooled;
- no SA progression occurs;
- **EHRS heat removal** is essentially **unaffected**.

The update acts mainly **on containment liquid redistribution, not on the heat removal function of the EHRS**.

ALMA MATER STUDIORUM
UNIVERSITÀ DI BOLOGNA

SA1 BDBA sequence: dominant phenomenology

- **SA1 SoT** from the same **DVI guillotine break**
- **EHRS unavailable**: decay heat is not effectively removed through the secondary side.
- **ADS-1 unavailable**: affect primary depressurization.

Transient governed by:

- the **break discharge**
- RPV–DW pressure coupling;
- passive injection availability;
- core heat-up and oxidation;

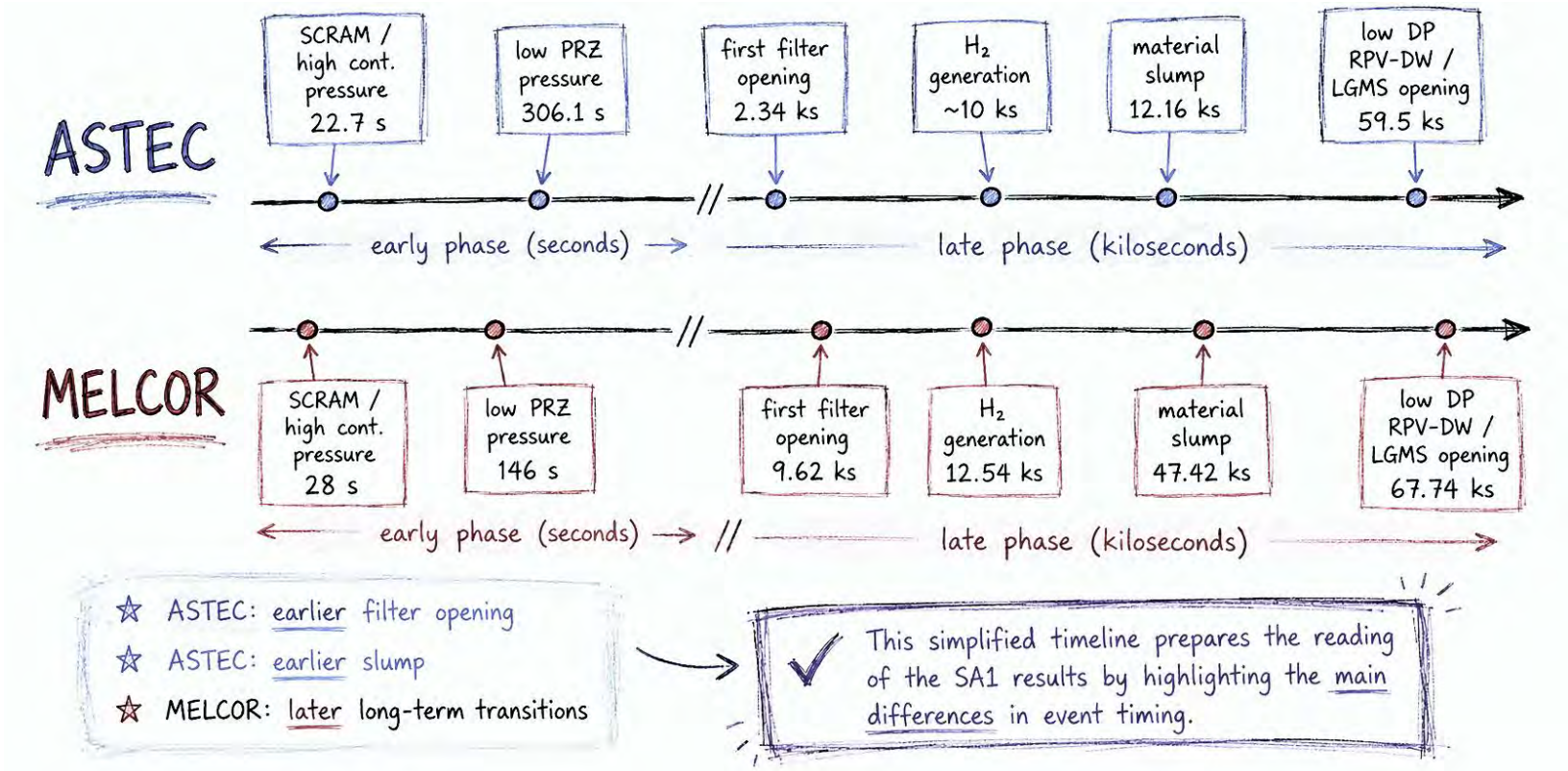

ALMA MATER STUDIORUM
UNIVERSITÀ DI BOLOGNA

SA1: RPV–DW pressure coupling

- Both codes predict rapid containment pressurization after the DVI break. Pressure cycling is associated with filter actuation
- Both codes predict the long term RPV/containment coupling

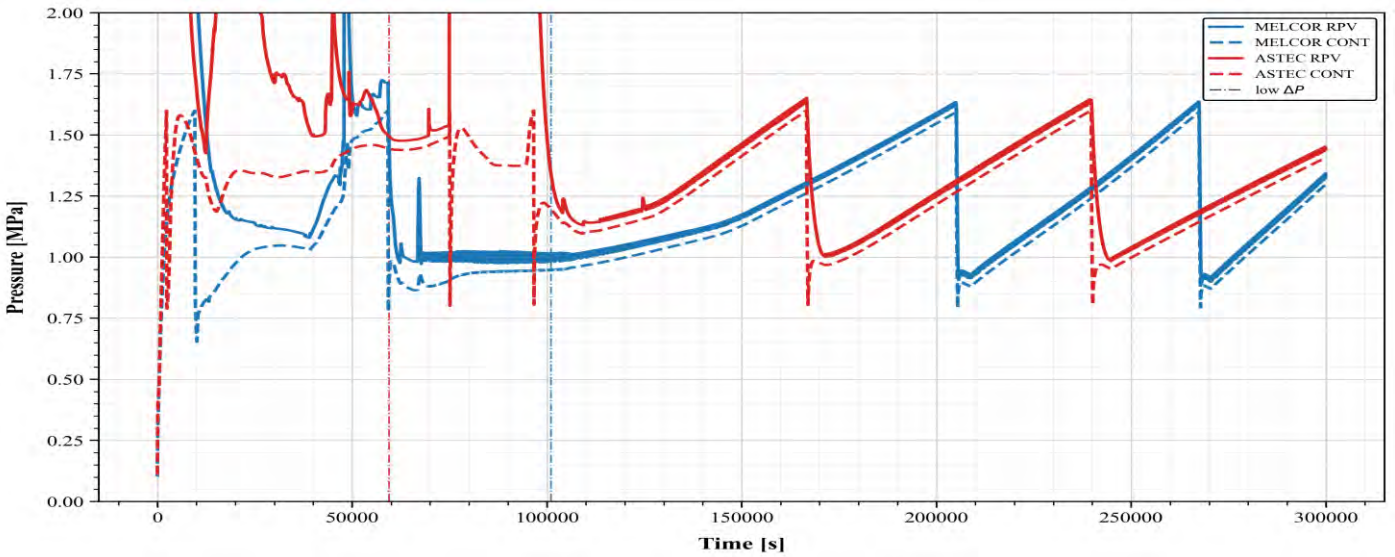

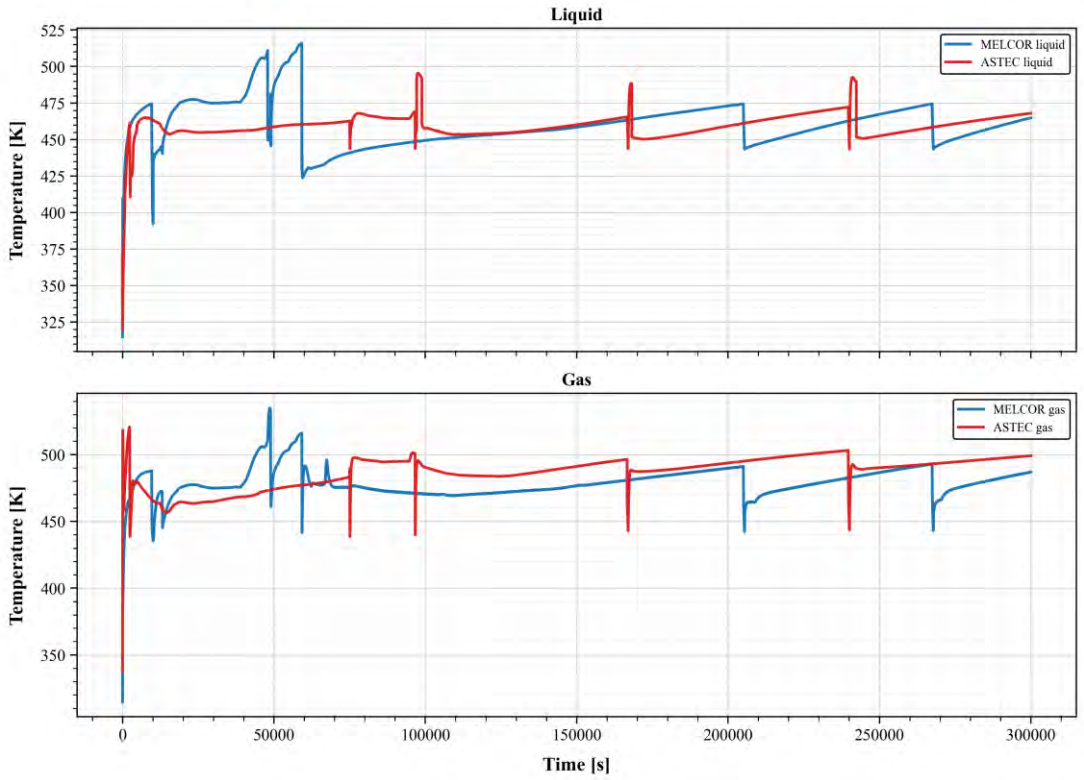

- Gas and liquid temperatures remain broadly in the 450–500 K range for both the code with some quantitaive discrepancies

ALMA MATER STUDIORUM
UNIVERSITÀ DI BOLOGNA

SA1: water redistribution and core uncovery

- Both codes predict an **initial break discharge followed by low/oscillating flow and reverse-flow** phases.
- **The updated ASTEC** input **avoids** the previous **DW liquid hold-up**.
- **The full filling of the RC allow reverse flow through the DVI break over the long term**.

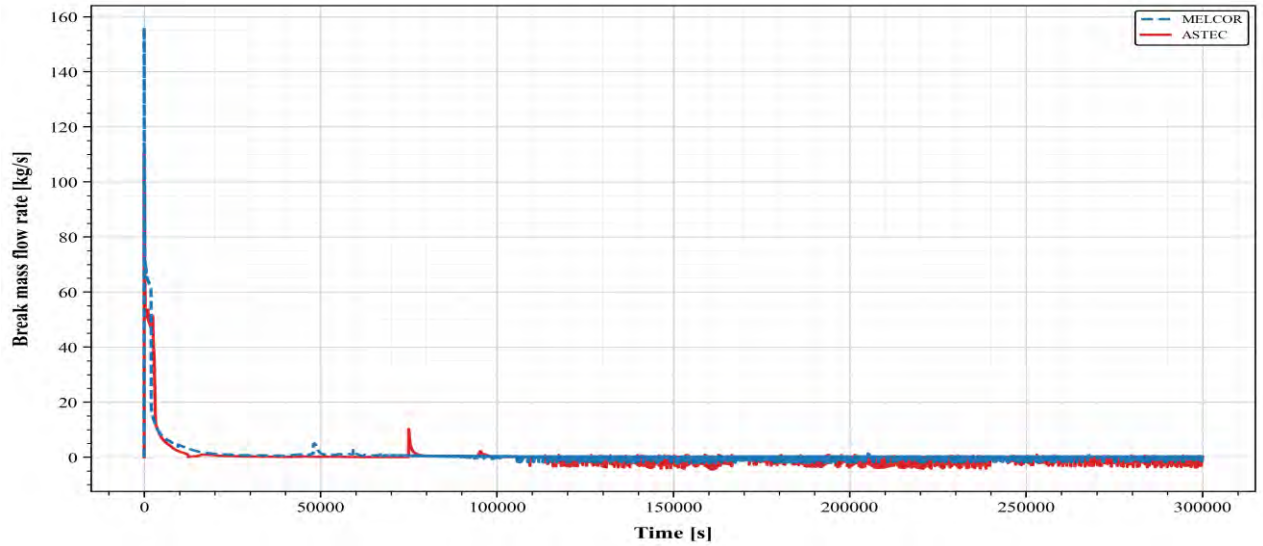

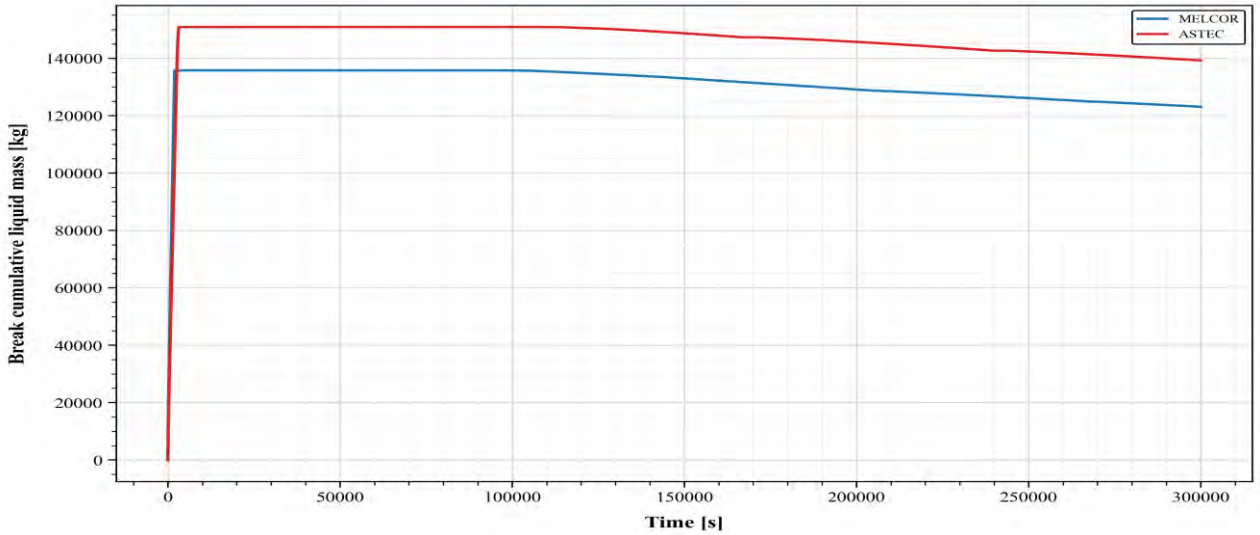

ALMA MATER STUDIORUM
UNIVERSITÀ DI BOLOGNA

SA1: degradation timing and hydrogen production

- Both codes predict the **same qualitative progression in terms of degradation phenomena:** core uncovery; heat-up; oxidation; material degradation; H_2 generation.
  - **ASTEC anticipates** cladding failure/**degradation** and **H_2 production**.
  - **MELCOR** predicts a **delayed degradation** sequence.

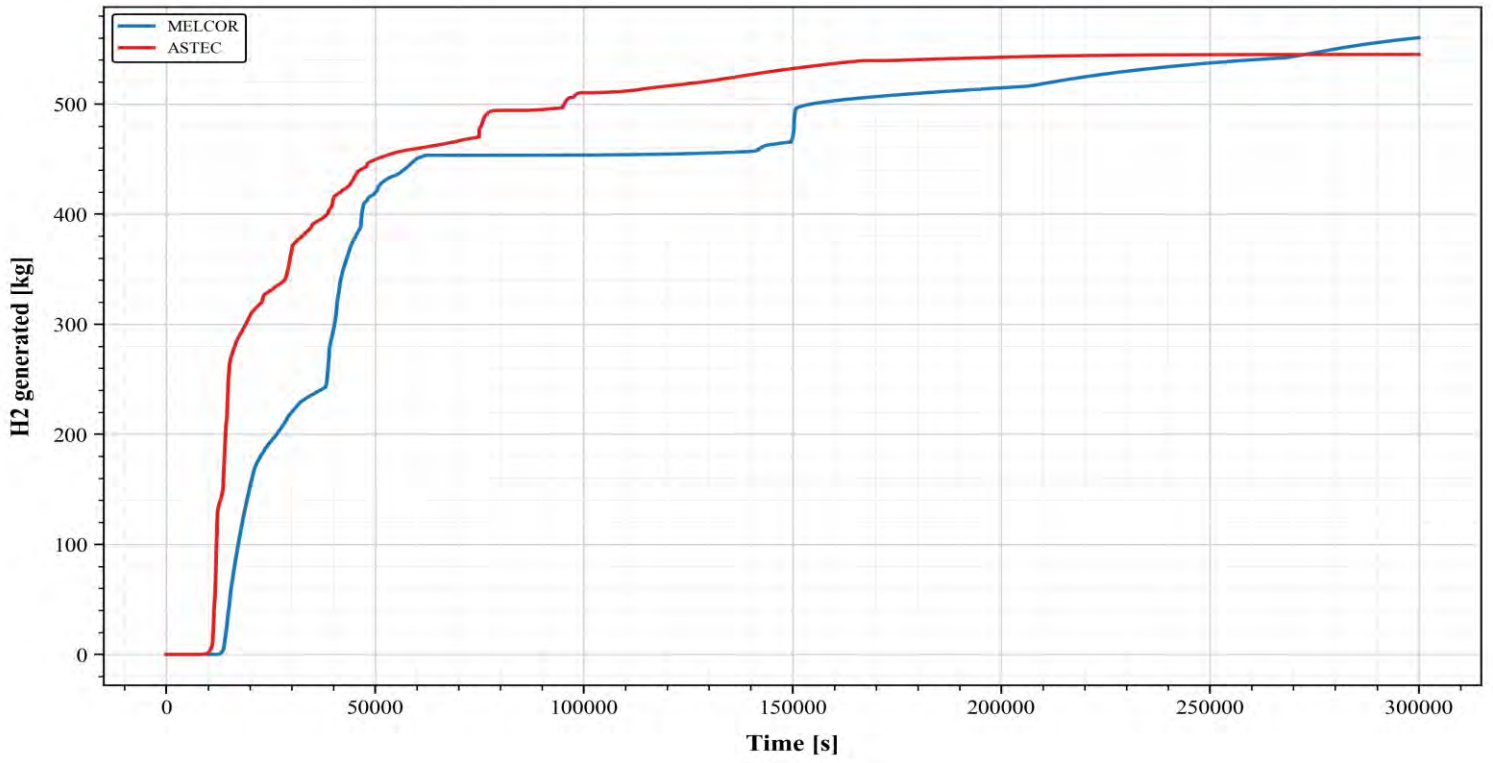

- Despite these differences the final cumulative H_2 mass is comparable, above 500 kg.

ALMA MATER STUDIORUM
UNIVERSITÀ DI BOLOGNA

Conclusions and future remarks

- The previous ASTEC input showed a containment-RC liquid-redistribution limitation under SA1-like conditions.
- The updated RC–DW hydraulic path restores a more physical consistent gravity-driven transfer of water toward the reactor cavity.
- DBA consistency check confirms that the update modifies some timing (of thermal-hydraulic phenomena within the containment) but preserves global DBA safety outcome.

ASTEC and MELCOR are in qualitative agreament in reproducing SA1 progression, but with quantitative discrepancy in:

- Containment-RPV coupling timing;
- liquid redistribution;
- Degradation behaviour timing;

Future work:

- extend the comparison to other BDBA sequences;
- more detailed studies on the condensation behaviour.

ALMA MATER STUDIORUM
UNIVERSITÀ DI BOLOGNA

ALMA MATER STUDIORUM
UNIVERSITÀ DI BOLOGNA

Credits:

Marcello Savini

Presented by Erik Cilia

marcello.savini2@unibo.it
erik.cilia@unibo.it

www.unibo.it

SASPAM-SA: Assessment of existing experimental data in WP3

T. Lind[1], G. Grippo[2], F. Mascari[3], M. Garcia[4], L.E. Herranz[4], N. Chaumeix[5], M. Klauck[6], E. Reinecke[6], J. Denis[7], A. Bentaib[7], D. Grishchenko[8], P. Kudinov[8], M. Constantin[9], M. Vyshemirskyi[10], D. Gumenyuk[10], I. Ivanov[11], T. Kärkelä[12]

[1] Paul Scherrer Institute (PSI), Switzerland; terttaliisa.lind@psi.ch
[2]University of Bologna, [3]ENEA, Italy, [4]CIEMAT, Spain, [5]CNRS, France, [6]Forschungszentrum Jülich GmbH (FZJ), Germany, [7]ASNR, France, [8]KTH, Sweden, [9]RATEN, Romania, [10]SSTC, Ukraine, [11]TUS, Bulgaria, [12]VTT, Finland

ABSTRACT

The HORIZON-EURATOM SAPSAM-SA project, coordinated by ENEA (Italy), was launched in 2022 aiming at investigating the applicability and transfer of knowledge and know-how accumulated on the operating large-LWR reactors to the iPWRs, in view of the European licensing needs with respect to severe accident and Emergency Planning Zone (EPZ). Two generic iPWR concepts are considered in SASPAM-SA: the iPWR Design 1 is characterized by a submerged containment and electric power of approx. 60 MWe and the iPWR Design 2 of approx. 300 MWe, which employs several passive systems and a dry containment.

Extensive scientific test programs have been carried out for today's LWRs over the past few decades, which have contributed to understanding and assessing the phenomena associated with postulated severe reactor accidents. One of the key objectives of SASPAM-SA is to evaluate the relevance and applicability of the existing experimental database to iPWR. The emphasis was on SASPAM-SA Designs 1 and 2, but for specific phenomena, considerations were extended to generic light-water iPWRs. The applied methodology relies on i) determining the main phenomena to be assessed, ii) identifying available experimental facilities and data for the identified phenomena, iii) using data from WP2 for the geometry of Designs 1 and 2, as-well-as for severe accident scenarios and relevant boundary conditions, iv) comparing the experimental data with the data for iPWR, and v) assessing the applicability to iPWR analysis.

Based on the review, the applicability of the data for iPWR analysis has been assessed. Experimental data needs from previous tests, or from new investigations, are identified for phenomena for which no applicable data are available or for which the database is not sufficient, but are considered of significant importance for iPWR analysis. This work is conducted in collaboration with the EU-SEAKNOT project. Recommendations for future experimental data needs are given.

Introduction

Safety assessments of nuclear power plants need reliable, validated analysis methods. Typically, those analysis methods involve the use of accident analysis codes, which can have different levels of scale and detail in the modelling of the phenomena involved. For Severe Accidents (SA), the complex, interconnected, and interdisciplinary phenomena during the accident progression typically require a certain amount of empirism to be applied in the modelling. For validation of the models, experimental data from separate effect scale to integral effect scale all the way to real accident data are used. For this validation, an extensive database has been generated over decades of

experimental efforts. Most of the available data have been produced to represent large Light-Water Reactor (LWR) features and conditions. Recent development of various Small-Modular Reactor (SMR) concepts, many of them using LWR technology, has brought with it the need to validate the codes developed for large-LWRs for use to carry out safety analysis of light-water SMRs.

To assess if the data generated for large LWRs are applicable to SMRs, the experimental facilities and conditions need to be compared to the design features and accident conditions in SMRs. SASPAM-SA project addressed this issue by first developing a methodology for assessment of the applicability of the data and then by reviewing data for different SA phenomena using the methodology (Lind et al., 2024). The focus was on two selected generic iPWR (integrated Pressurized Water Reactor) designs. The main SA phenomena for investigation were selected to be: 1) in-vessel, 2) ex-vessel, 3) containment, and 4) source term topics. Once the work was started, it was decided to include natural circulation in the investigation as its own topic due to its decisive importance in many light-water small modular reactor designs.

Natural circulation is not, strictly speaking, a SA phenomenon; however, it significantly affects the SA progression, especially during the initial phase of the transient. It is treated here as many of the light-water SMR designs increasingly use natural circulation during normal operation and / or in safety systems. The present activity aimed to assess if the existing experimental data for natural circulation are applicable to iPWRs; in order to achieve such goals, both Integral Effect Test Facilities (IETF) and Separate Effects Test Facilities (SETF) have been considered and, moreover, several open access experiments have being reviewed focusing on the thermal-hydraulic of integral Reactor Pressure Vessel (RPV), the primary/containment coupling and the passive systems operation that affect the SA progression As most of the safety analysis tools have been developed for active systems using experimental data for active systems, the validity of the tools for passive systems needs to be assessed. As natural circulation is generally driven by small forces caused by temperature and density differences, it is also highly dependent on the particular geometries and Thermal-Hydraulic (TH) properties. Thereby, the experimental data used for code validation should be produced under conditions closely resembling specific SMR geometries and TH conditions.

In-vessel phenomena. For in-vessel phenomena, reflooding of a rod-like geometry, as well as several phenomena related to core degradation, debris bed, melt formation and lower head failure were reviewed. Many light-water SMR designs foresee fuel rods and assemblies closely resembling large LWR designs, but many times with shorter length of the fuel rods. The different length has mainly an effect on the TH behaviour of the core, including cooling of an over-heated core. The core degradation phenomena at later stages of core heat-up can be expected to be rather similar to large LWRs as long as similar fuel is used. In the later stages of the core degradation, the large amount of structures consisting of stainless steel would affect debris melting and melt pool characteristics.

Ex-vessel phenomena. Ex-vessel phenomena were included in the analysis to a limited extent even though no ex-vessel scenarios were identified in WP2 analyses. SMRs are typically designed for in-vessel retention of the melt. Therefore, ex-vessel phenomena are not expected to be of significant importance. However, adopting a conservative defence-in-depth approach, selected ex-vessel phenomena were included in this work. The containment designs in different light-water SMRs differ considerably. In many designs, the containment is a steel structure in which, therefore, molten-core concrete interaction would not take place. Instead, challenge to the containment would be more similar to the reactor pressure vessel lower head with a molten pool or debris in which the hot corium will react with the stainless steel. In the SMR, the steel content would be expected to be high.

Containment. Gas distribution with focus on hydrogen can be affected by several factors associated with the thermal hydraulics of the containment. Firstly, the effects of inertia (forced convection) and buoyancy (natural convection), which accompany the release of gas, need to be quantified to

estimate the amount of gas mixed by the release and the possible development of a stratified atmosphere in the dome region of the containment. Secondly, the mixing process depends on sink/source terms of mass and/or energy, condensation in bulk and on the walls and evaporation in the sump and on the walls. Both can induce a natural convection flow that transports the gases and enhances mixing. The geometry of the containment can also play an important role in gas distribution. Depending on the design, there may be dead-end compartments that can impede mixing and induce stratification. Finally, accident management systems such as sprays, venting and coolers can also influence gas distribution.

For containment phenomena with focus on hydrogen risk, inert and steam rich containment atmospheres as well as high containment pressures pose distinctly different boundary conditions compared to large LWRs. During a SA in a LWR, large amounts of hydrogen can be generated and released into the containment during reactor core degradation. Additional burnable gases (H_2 and CO) may be released into the containment in case of corium/concrete interaction. This could subsequently raise a combustion hazard. As the Fukushima Daiichi accidents revealed, hydrogen combustion could cause high pressure spikes that could challenge the reactor buildings and lead to the failure of surrounding buildings. To prevent the gas explosion hazard, most of the mitigation strategies adopted by European countries are based on the implementation of Passive Autocatalytic Recombiners (PARs). Thereby, their experimental validation space was assessed in this work.

Finally, data for hydrogen combustion risk was assessed. The hydrogen release can form a combustible mixture depending on different parameters, namely: (i) the H_2 content compared to the oxidant, (ii) the thermodynamic conditions, (iii) the ignition source that could lead to the combustible mixture. When a flammable mixture is ignited, several regimes of combustion can be reached, each of these regimes is characterized by the flame speed which in turns will lead to an overpressure in a confined environment. The phenomena of interest for safety analysis are:

- the flammability limits and their variation with the thermodynamic conditions and the presence of diluents
- Flame propagation and the impact of the environment through well-characterized initial turbulence
- Flame propagation in confined vessel laden with obstacles to characterize flame acceleration in a complex environment and determine the propensity of a given mixture to undergo a fast combustion regime responsible of substance pressure loads on equipment and infrastructures.

Assessment in this work was carried out with the focus on these phenomena.

Source term. Finally, source term issues ranging from aerosol characteristics to aerosol transport, pool scrubbing and iodine chemistry were reviewed and analysed. The containments in light-water SMRs are many times much smaller than in larger LWRs, and are planned for much higher pressures. At the same time, there is typically a large amount of water present compared to the reactor power. Many containments are either at a very low pressure or inertized. These features will result in containment conditions distinctly different from large LWRs with a large pressure range, high humidity and reducing conditions. The small geometrical dimensions would also affect the formation and transport of radionuclides.

Designs and SA scenarios

The main objectives of this work were to assess the relevance and applicability of the existing experimental database to iPWR, and to identify the need for new experiments. The emphasis of the review was on SASPAM-SA Designs 1 and 2 (Mascari et al., 2024; Herranz et al, 2025), Figure 1, but for specific phenomena, considerations were extended to generic light-water iPWRs.

The generic iPWR Design-1 investigated consists of a natural circulation iPWR composed of a shrouded reactor core and riser, an integrated Pressurizer (PRZ), and two Helical coil Steam Generators (HSGs) within an integral RPV housed inside a steel containment. The containment is largely immersed in a large pool of water, serving as the ultimate heat sink. The Emergency Core Cooling System (ECCS) in the iPWR Design-1 consists of two groups of valves allowing the coolant circulation between RPV and containment during accident conditions: the Reactor Vent Valves (RVV) located at the top of the PRZ and Reactor Recirculation Valves (RRVs) located slightly above the active core.

The generic iPWR Design-2 investigated is characterized by the use of several passive systems and by a dry containment. The reactor operates in forced circulation during normal operation and employs a passive mitigation strategy in accident conditions. It consists of an integral RPV, containing the core, eight HSGs, eight primary pumps, the Control Rod Drive Mechanism (CRDM), and the PRZ. The hot water at the core outlet flows upwards in a circular riser up to the primary pumps suction located above each HSGs.

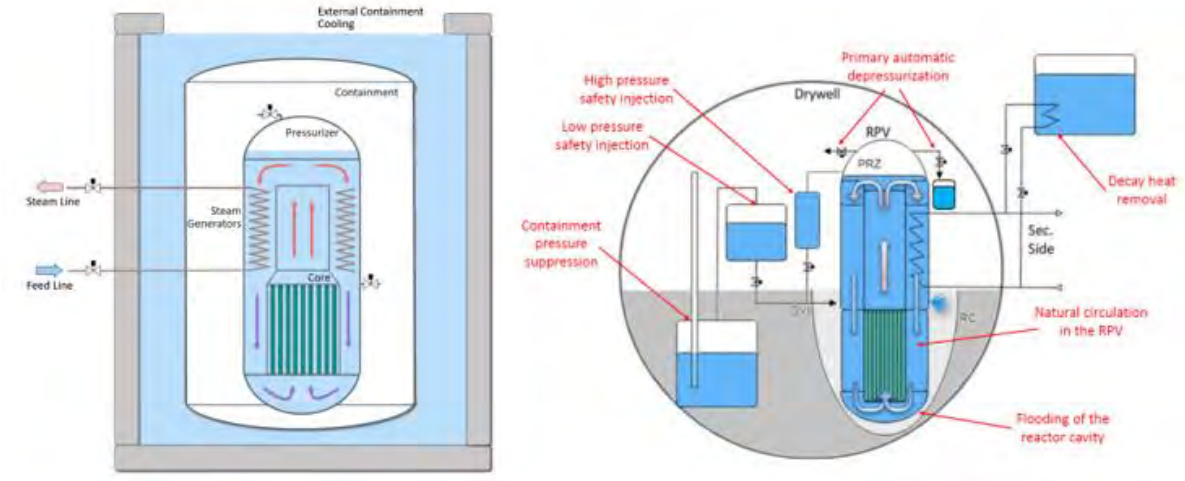

Figure 1. The designs 1 (on the left) and 2 (on the right) used in the SASPAM-SA project (figure from SASPAM-SA)

Several design basis and beyond design basis accident scenarios were postulated in two designs, Design-1 and Design-2 (Gabrielli et al., 2024; Gabrielli et al., 2026). The main parameters relating to the phenomena selected to be investigated were extracted from the analyses and compared to those in the experiments. The reader is referred to Habrielli et al., 2026 for further details of the accident scenarios.

Experimental data analysis

Natural circulation

As most of the safety analysis codes have been developed based on data for active safety systems, the applicability of the data and existing models for passive systems and natural circulation needs to be assessed. Several main parameters affect natural circulation behavior: 1) geometry: e.g. elevation between the source and sink or piping diameters; 2) phases: single phase/two phase; 3) conditions: pressure and temperature fields; 4) pressure losses and heat losses; 5) non-Condensable gas content (NCG).

In both Design 1 and 2, natural circulation is adopted:

- Design 1: During normal operation and accident conditions in the RPV and in the primary/containment coupling

- Design 2: During accident conditions in the RPV and in passive safety systems while in normal operation the plant works in forced circulation.

For review of natural circulation data, the OSU-MASLWR facility (Mascari et al., 2012) was selected based on scaling and other design criteria. In the selected facility, several experimental tests have been performed investigating different types of phenomenology. For the present work, the test DOE OSU-MASLWR-001 and DOE OSU-MASLWR-003B were analysed for primary-containment coupling, . In first instance, the experimental data range has been verified to evaluate the applicability to the design, considering the selected figures of merit (containment and primary pressure), and, subsequently, the dimensionless number conservation for the phenomenon of interest has been evaluated.

For passive systems, existing data for natural circulation from test 7 in the PERSEO facility (in-Pool Energy Removal System for Emergency Operation) (Mascari et al, 2023) was selected. The analysis methodology applied to the PERSEO test data follows the same approach used for the OSU-MASLWR tests. The work has been focused on comparing the EHRS operation in Design 2 during DBA conditions with the experimental data from PERSEO facility. The SA sequences have not been considered in this analysis since they are characterized by EHRS unavailability.The analysis highlights the general applicability of the OSU-MASLWR experimental data for characterizing Design 1, and of PERSEO data for characterizing in-pool decay heat removal systems as in Design 2. At the same time, it underlines the limited transferability of OSU-MASLWR data to Design 2, due to the fundamentally different system configuration and decay heat removal mechanisms.Needs for future testing to improve the accuracy of code results have been identified. Increasing the instrumentation to locally characterize the phenomena of interest, such as condensation, is crucial. For instance, the addition of wall thermocouples to measure in/out containment wall temperatures and parametric oxygen analyzers to estimate non-condensable gas concentrations would provide more detailed insights into the physical processes occurring during natural circulation. These measurements are particularly important for ensuring that the observed phenomena are accurately captured, especially in scenarios where, even if there is a geometrical similarity, the physical interactions are not fully replicated. . On the other hand, considering the existing experimental databases, the analysis'results underscores the importance of careful scaling considerations when applying such data to advanced reactor designs. While current experimental databases provide valuable insights, their application requires a thorough understanding of their limitations, particularly regarding the representation of passive safety features and natural circulation phenomena under various operating conditions.

In-Vessel phenomena

Rod-like geometry. To assess the applicability of existing data for in-vessel hydrogen generation, oxidation behaviour, cladding failure, temperature data, and the influence of reflooding of a rod-like geometry to iPWRs, data from the QUENCH facility were compared with iPWR SA conditions with focus on test QUENCH-06. The experimental data obtained from QUENCH-06 were found to be directly applicable to iPWR SMR. There are no major differences between the fuel assemblies of large PWR and iPWR. The hydrogen production, oxidation behavior, cladding failure, temperature data, and the influence of reflooding may be used in the current limits of uncertainties (experimental, simulation models).

The need of new experiments is rather necessary for a more detailed understanding of the phenomena and their correlations than to obtain basic knowledge (that is the same for large reactors and iPWR). The future efforts for the experimental work will support both cases.

The reflooding case is of interest especially for the large values of the flowrate since QUENCH-06 does not offer data for such case. The existing data may be extrapolated for reasonable range of the parameters both in case of large PWR and iPWR.

Particulate debris bed spreading and coolability. The debris bed coolability is among the critical factors for the integrity of the RPV. Therefore, the main goal of the experimental work in PDS tests at KTH was to provide data for model development for the assessment of uncertainty in the debris self-spreading for achieving a coolable state of the debris bed. Phenomena of particulate debris spreading caused by upward two phase (water and gas) flow was of interest. The analysis showed that the experimental data for particulate debris bed spreading and coolability from PDS tests can be used for the development of a model to predict self-leveling of a non-agglomerated debris bed. The data are relevant to a limited set of scenarios where such beds can be formed either inside the primary vessel or inside the containment vessel. In conventional LWR ex-vessel debris bed coolability is dependent on debris be agglomeration and particle size distribution. There is no obstruction for water access to the debris bed. In case of Design 1 iPWR, the reactor vessel lower head and reactor support skirt are positioned directly on top of and around the debris bed, effectively obstructing water recirculation through the debris bed.

Melt propagation in a porous bed. The REMCOD experiments studied melt propagation through debris beds of different morphologies (e.g., ceramic, metallic, glass particles) and with different thermal properties. The tests show that melt penetration into debris is influenced by particle size, material, and morphology. Solidification (crust formation) was a significant factor in halting melt penetration, and different materials (glass, ceramics, metal) had different effects on the melt behavior. The REMCOD data for melt propagation in a porous bed was found to be relevant in understanding how debris mixtures in iPWRs might behave under severe accident conditions, including the remelting and potential plugging of coolant channels. In addition, the REMCOD experiments were found to provide data on how molten material can remelt and spread through cold debris beds, which is relevant for predicting how molten core material might spread across containment structures or through the reactor cavity in iPWRs.

Melt jet underwater. The goal of DEFOR-MG experiments was to provide an experimental study on underwater phenomena of melt jet structure interaction, breach ablation, plugging, melt jet release and fragmentation. The DEFOR-MG tests highlight different modes of vessel breach, including variations in breach size, melt composition (oxidic vs. metallic), and melt superheat. These failure modes are relevant to both large LWRs and SMRs, as they can lead to varying melt discharge rates and debris bed configurations that influence cooling and the potential for containment failure.

The DEFOR-MG test results highlight key phenomena such as melt fragmentation, nozzle ablation, and debris bed coolability, which are crucial in the confined and integrated structure of SMRs. The findings offer essential data for the optimization of passive safety features, the prevention of containment failure, and the mitigation of SAs in iPWRs. The findings on potential energetic steam explosions due to inadequate quenching are relevant to both LWRs and iPWRs. SMRs with smaller containment volumes could be more vulnerable to pressure spikes if effective melt quenching does not occur.

In-vessel melt pool formation. The data and results related to the in-vessel melt pool formation were reviewed from the LIVE-L1 and LIVE-L3 experiments performed within the LACOMERA project. The LIVE experiments provided significant information on the melt pool behavior during cooling of the outer RPV surface with air followed by the flooding of the lower head.

Materials. In the series of LIVE experiments, the test vessel wall was made of stainless steel (AISI316Ti, material number X6CrNiMoTi17-12-2). Similar material (stainless steel) was adopted in the Design-1 and Design-2 (also confirmed by the material properties section on the input deck of the facilities).

Size. In the series of LIVE experiments, test vessel has outer diameter equal to 1 m, with wall thickness 0.025 m. The geometry differences between Design 1, 2 and LIVE vessel showed that results of experiments cannot be directly applied for Design 1 and 2 from the point of view of melt in-vessel coolability.

Range of parameters. The results of the performed analyses demonstrated that the parameter range of the LIVE-L1, L3, L3A experiments may be partially applicable for in-vessel coolability analysis of Designs 1 and 2.

Ex-Vessel phenomena

As already mentioned, a limited review and assessment of ex-vessel data was conducted despite the fact that no ex-vessel scenarios were identified in SA analyses in SASPAM-SA. The data and results related to the debris coolability and Molten Core Concrete Interaction (MCCI) were assessed from experiments carried out in the OECD-MCCI project. The primary goal of the experiments was to provide data on the behavior of molten corium interacting with concrete under various conditions, focusing on the ability to cool the corium using water flooding, and the effects of corium and concrete interaction on containment structures. Additional goals were to investigate different cooling strategies during SAs, crust break-up and debris cooling after the crust break-up.

Related to iPWRs, the experimental data from MCCI-1, MCCI-2, and MCCI-6 tests were found to provide a solid foundation for understanding core-concrete interactions and coolability in nuclear reactors. For iPWR-specific applications, the data would need to be supplemented with additional experiments with prototypical materials and geometries, or scaled appropriately to account for the differences in design, operational parameters, and advanced safety features of iPWRs.

Containment phenomena

The main containment phenomena considered in this work were related to hydrogen risk: hydrogen distribution, flammability, and mitigation using PARs. In the following, this work is described.

Hydrogen distribution

Several experimental programs have been carried out to investigate the effect of the main phenomena on the hydrogen distribution considering different scales. The data from TOSQAN (e.g., Pocheron et al., 2007; Lemaitre and Pocheron, 2008, Malet et al., 2010) THAI (e.g., OECD/NEA, 2014)), MISTRA (e.g., Studer et al., 2006), and PANDA (e.g., Auban et al., 2004; Paladino et al., 2008) facilities have been reviewed. In these facilities, various experimental programs were performed under OECD/NEA auspices or in the framework of European or national projects.

The data issued from the experimental programs mentioned above covers a large domain of representative conditions of SA in large LWRs. The range of the addressed conditions in the performed tests can be summarized as follow:

- Temperature between 20°C and 150°C,
- Steam concentration between 0 and 70%vol
- Hydrogen concentration between 0 and 20%vol
- Pressure between 0.1 and 0.4 MPa.

iPWR containments with design conditions with pressures above 1.0 MPa, temperatures above 150°C, and steam contents above 70 vol-% are foreseen. These conditions have not been covered in the past experimental programs.

Hydrogen mitigation with PARs

Starting in the 1980s, PAR performance has been studied in a series of test campaigns over the years. Based on these investigations, the PAR response to different pressures, gas mixtures, humidity, temperature and the presence of inhibitors has been broadly assessed.

The following test series were considered for this review noting that for most of these programs, full data sets are not publicly available:

- CTF and LSVCTF (AECL, Canada): Fundamental and qualification tests with AECL PARs (1983-2018) [Koroll et al., 1996]

- KALI-H2 (CEA/EPRI/EDF, France): Fundamental and qualification tests with Areva and NIS PARs (1995-1998) [Braillard et al., 1997]
- H2PAR (IPSN/EDF, France): Impact of core melt aerosols and catalyst poisons with AECL, Areva, and NIS PARs (1995-1999) [Rongier and Studer, 1996]
- Surtsey Vessel (Sandia NL, USA): Fundamental and qualification tests with NIS PARs (1997-1998) [Blanchat and Malliakos, 2000]
- BMC (Battelle, Germany): Several aspects of PAR performance with Areva and NIS PARs (1991-1996) [Kanzleiter, 1997]
- REKO (FZJ, Germany): Single-effect and reaction kinetics tests with generic catalysts/PARs (since 2001) [Reinecke et al., 2010]
- THAI (Becker Technologies, Germany): Several aspects of PAR performance with AECL, Areva, and NIS PARs (since 2003) [Gupta et al., 2013]

The review showed that, in general, the operating behavior of PARs can be considered to be well understood. Furthermore, a comprehensive experimental database is available, which is specifically relevant to large LWR containments with state-of-the-art recombiner models and the accident conditions to be expected there. However, a conclusive statement on the applicability of the existing PAR knowledge and the available test data to iPWR is not yet possible without reservation. If, for example, air ingress into the containment is postulated in the course of the accidnt, significantly different accident conditions would have to be expected compared to large LW-PWRs. Depending on the point in time of the air ingress, the change in atmospheric gas composition would follow different paths, so that a combustible gas composition may also develop under certain circumstances (see Figure 2).

For these possible transients, experimental data for PAR operation at pressures > 0.5 MPa, for the startup behavior under extremely humid conditions and/or oxygen depletion, as well as for fast H_2 feed rates into comparatively small containment volumes are not available. Furthermore, it should be noted that, due to geometric constraints, significantly more compact PAR models may have to be developed for iPWRs and that a substantial database exists so far mainly for rather large-scale PARs. The release of H_2 and O_2 by radiolysis could also play a more significant role in smaller containments and might necessitate different PAR designs.

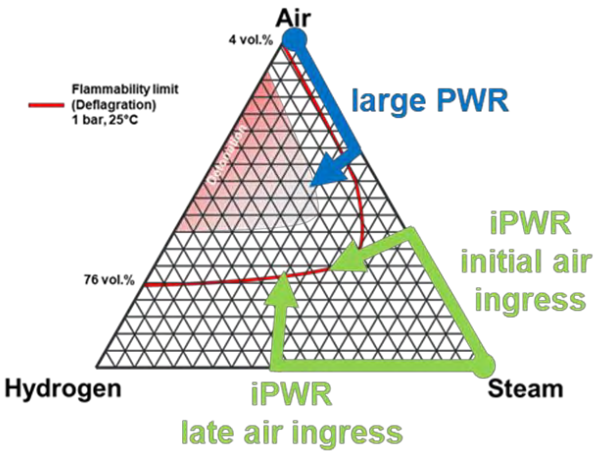

Figure 2. Qualitative progression of gas compositions for different accident scenarios

Combustion risk

The hydrogen risk in LWRs has been addressed over roughly 2 decades through both experimental and simulation investigations. To conduct the analysis of the available data, the following programs have been considered and for which part of the data is publicly available:

- Integral large-scale experiments on hydrogen combustion for SA code validation-HYCOM, a joint research project was carried out in the EU Fifth Framework Programme, concerning hydrogen risk in a nuclear power plant [Breitung et al. 2005],
- IRSN/CNRS research programs on experimental investigation of flammability domain [Cheikhravat et al. 2015], impact of water spray [Joseph-Auguste et al. 2009] and solid particles (graphite and tungsten) [Sabard et al. 2013]
- IRSN/CNRS research programs on H2 safety criteria [Bleyer etal. 2012], [Bentaib et al. 2014]
- PIA-MITHYGENE, a national program on post-Fukushima accident [Bentaïb et al. 2014b]
- THAI, run by Becker Technology with some combustion activities (ISP 49: H2 combustion based on OECD THAI hydrogen deflagration tests)
- Several benchmarks SARNET, ETSO-MITHYGENE, ETSON-SAMHYCO-NET [Bentaib et al., 2014, 2018, 2022]

The description of the flammability limits and the behavior of the flame close these limits are very important for the analysis of the combustion risk applicable to iPWRs. If the temperature domain is close to iPWRs, the pressure is rather limited. From the literature data, the flammability limit of H_2-air diluted or not with steam does not vary linearly with the pressure and data are needed by extending these studies to higher pressures > 1.0 MPa. For iPWR, Fig. 2 illustrates that the mixture will be close to the upper flammability limit. In this case, the flame will lead to a complete combustion with pressure peaks that are substantially higher than the ones reached when the mixture is close to the lower flammability limit.

The codes may use turbulent combustion models that have been validated for lean mixtures. However, rich mixtures behave differently when submitted to turbulence. Indeed, lean mixtures are prone to thermo-diffusive instabilities that enhance the burning speed while rich mixtures are not. Moreover, the increase of the initial pressure is responsible for the occurrence of the hydrodynamic instabilities that modify substantially the burning rate in presence of turbulence.

Regarding combustion regimes, most of the research has focused on lean mixtures (H_2 lean, O_2 rich) for a limited range of temperatures (25 to 140°C) and limited to 0.1 MPa. When considering the Beyond Design Basis Accident (BDBA) in an iPWR, if an air ingress is possible leading to the formation of rich H_2 mixtures (lean O_2), the flame dynamic is completely different, and only limited data is available in the literature. Moreover, the initial pressure can be more than 1.0 MPa and can reach 2.0 MPa during the transient. In this domain of pressure, there is no data in the literature.

Source term

Experimental data for source term were reviewed in the area of aerosol characteristics, aerosol transport in humid / condensing atmosphere, pool scrubbing, and iodine chemistry.

Aerosol characteristics

Aerosol characteristics have a decisive influence on the transport of fission products. This has been investigated in primary circuit conditions covering temperatures from 300 K to 1700 K (e.g., Gouëllo et al., 2020; Kärkelä et a., 2014; Kärkelä et al., 2017). The work has resulted in a unique database describing also the shape of particles, which usually differs from the spherical shape – often assumed (as a simplification) in computer code calculations.

The importance of particle dynamic shape factor on fission product transport and mitigation is similarly applicable to conventional large LWRs as well as to the innovative LW-SMRs (iPWR). In general, the computer codes used for safety analysis assume spherical particles. Particle shape can typically be accounted for by using a shape factor. Accurate knowledge of the particle shape at various stages of accident is difficult to obtain, thus it is a notable source of uncertainty related to particle transport. It is likely that at least insoluble particles differ from the spherical shape during a SA, and therefore, dynamic shape factor higher than 1.0 (spherical particle) should be considered in the analysis work.

Aerosol transport in humid atmosphere

Experimental data for aerosol transport and mitigation were reviewed with the focus on high-humidity, condensing conditions and hygroscopic aerosols. A brief summary of the findings is given below.

Aerosol transport in the containment was investigated in the experimental programs in the AHMED (Mäkynen et al., 1997) and DIANA facilities (Kalilainen et al., 2016). The main aim of the AHMED experimental program was to determine the depletion of both inert and hygroscopic aerosols in the containment under high humidity conditions to understand the reasons for the observed large discrepancies between the results from model calculations and measurements carried out in large scale experiments. The experiments demonstrated the influence of humidity and hygroscopic growth of particles on depletion from the containment atmosphere emphasizing the importance of these phenomena in iPWR containments.

Aerosol deposition in heat exchangers, both in-tube and outside of them, as addressed in the experimental programs in AIDA (no references found in the open literature) and CESANE (Friesen et al., 2001) facilities was shown to have a significant detrimental effect on the heat transfer and on the flow patterns in the heat exchanger. Unfortunately, experimental data from the AIDA program are not available in sufficient detail. CESANE data have limited applicability as the geometrical and other design parameters have a decisive impact on the aerosol deposition and thereby its effect on the heat transfer. Due to the importance of natural circulation and the potential aerosol effects on it, the aerosol deposition in condensing atmosphere is of considerable importance.

The ARTIST experiments for aerosol retention in the U-tube steam generator during steam generator tube rupture SAs were found not to be applicable to present iPWR designs which employ helical coil once-through steam generators.

Pool scrubbing

Fission product retention in water ponds, i.e., pool scrubbing, is known to be an efficient way to mitigate potential source term to the environment. A vast investigation has been done over decades to thoroughly understand the multi-physics that govern this complex process. As a result, a large database has been produced under the anticipated conditions in large LWRs (Herranz et al., 2022). In this work, the database was complemented with additional recent experimental data. The experimental data were found to be sufficient to cover the SA conditions as analysed in the SASPAM-SA project. However, it was observed that experimental data at high injection gas temperatures and velocities, as well as with light non-condensable gases would be beneficial to cover future data needs. Particular attention should be paid to the scaling issues in the pool scrubbing experiments.

Iodine chemistry in the containment

An extensive program has been carried out in the EPICUR facility to provide experimental data for the development and validation of iodine chemistry models in a reactor containment in an accident situation.

Approximately thirty tests were performed by IRSN between 2005 and 2010 as part of the ISTP. The aim of these tests was to study the behavior of iodine in the containment and the effect of irradiation on i) the volatile iodine released from the sump; ii) the formation of organic iodides from the iodine deposited on the painted surfaces of the containment, whether submerged or above ground; iii) the formation of iodine oxides from gaseous iodine and their stability.

About thirty tests were performed by the IRSN as part of the international STEM AND STEM2 programs for the period 2011-2019. In particular, the effects of irradiation on i) the stability of iodine aerosols (CsI, AgI, iodine oxides, etc.) (e.g., Bosland and colombani, 2020); ii) the interactions between iodine and aged paints (e.g., Bosland and Colombani, 2020), taking into account the extension of reactor life; iii) revolatilisation of iodine in the long term after an accident.

In the MiRE and PASSAM (Albiol et al., 2018) programs with the aim of improving the management of radioactive releases in the event of a nuclear accident, around fifteen tests were carried out. The MiRE program (2013-2022) focused on the study of materials capable of trapping radioactive iodine in conditions close to those of an accident, while PASSAM (2013-2016) evaluated existing filtration systems, focusing on gaseous iodine. Together, these projects have made it possible to strengthen filtration solutions to limit the consequences of nuclear accidents.

Finally, eight tests were carried out by the IRSN as part of the international ESTER program. The aim of these tests was to identify additional sources of organic iodine formation, in particular i) in the presence of volatile organic compounds (VOCs): methane, acetone and ethylene; and ii) on different substrates: cables, quartz coupons, galvanized steel and stainless steel.

These tests provide an extensive database of iodine behaviour in the containment of a large-LWR. However, the expected reducing conditions in the containment of a iPWR have not been addressed in these tests. As chemistry of fission products is known to be strongly affected by the gas atmosphere, iodine chemistry data under reducing conditions would be of great importance.

Concluding words

In this work, the applicability of existing experimental data from large LWRs to be used for safety analysis of iPWRs was assessed. The emphasis was on SASPAM-SA Designs 1 and 2, but for specific phenomena, considerations were extended to generic light-water SMRs. The methodology relies on i) determining the main phenomena to be assessed, ii) identifying available experimental facilities, including scaling considerations, and data for the identified phenomena, iii) using data from analyses made in SASPAM-SA for the severe accident scenarios to determine the boundary conditions, iv) comparison of the experimental data with the data for iPWR, and v) classification of the data based on their applicability to iPWR analysis.

Based on the analysis, the data which can be used for iPWR analyses were assessed for natural circulation, in-vessel phenomena, ex-vessel phenomena (limited extent due to absence of such scenarios in WP2 analyses), containment, and source term. Experimental data needs are identified for the phenomena to which no applicable data are available or to which the database is not sufficient, but which are considered of significant importance for iPWR analysis.

ACKNOWLEDGEMENT

Co-Funded by the European Union. Views and opinions expressed are however those of the author(s) only and do not necessarily reflect those of the European Union or European Commission-Euratom. Neither the European Union nor the granting authority can be held responsible for them.

Project funded by

Schweizerische Eidgenossenschaft
Confédération suisse
Confederazione Svizzera
Confederaziun svizra

Swiss Confederation

Federal Department of Economic Affairs,
Education and Research EAER
State Secretariat for Education,
Research and Innovation SERI

References

T. Albiol, L. Herranz, E. Riera, C. Dalibart, T. Lind, A. Del Corno, T. Kärkelä, N. Losch, B. Azambre, C. Mun, L. Cantrel, 2018. Main results of the European PASSAM project on severe accident source term mitigation. Ann. Nucl. Energy, 116. https://doi.org/10.1016/j.anucene.2018.02.024.

O. Auban, R. Zboray, D. Paladino, "Investigation of Large-Scale Gas Mixing and Stratification Phenomena related to LWR Containment Studies in the PANDA Facility", Nuclear Engineering and Design, Volume 237, Issue 4, Pages 409-419 February 2007.

Bentaib, A., Bleyer, A., Meynet, N., Chaumeix, N., Schramm, B., Höhne, M., Kostka, P., Movahed, M., Worapittayaporn, S., Brähler, T., Seok-Kang, H., Povilaitis, M., Kljenak, I., Sathiah, P., 2014. SARNET hydrogen

deflagration benchmarks: Main outcomes and conclusions. Annals of Nuclear Energy, ERMSAR 2013 conference of the SARNET network 74, 143–152. https://doi.org/10.1016/j.anucene.2014.07.012

Bentaib, E. Studer, N. Chaumeix, S. Magne, E. Reinecke, D. Pinet, MITHYGENE project Towards the improvement of hydrogen risk assessment models and safety management procedures, Int. Workshop on Nuclear Safety and Severe Accident (NUSSA-2014) Sept. 3-5, 2014, Chiba, Japan

Bentaïb, A., Chaumeix, N., Grosseuvres, R., Alexandre, B., Gastaldo, L., Ludovic, M., Jallais, S., Vyazmina, E., Kudriakov, S., Studer, E., Dehbi, A., Berthold, S., Veikko, T., M, F., Tadej, H., Ivo, K., Yu, M., Trianti, N., Sato, M., Murgatroyd, J., Povilaitis, M., 2018. ETSON-MITHYGENE benchmark on simulations of upward flame propagation experiment in the ENACCEF2 experimental facility, in: 12th International Topical Meeting on Reactor Thermal-Hydraulics, Operation, and Safety (NUTHOS-12). Qingdao City, Shandong Province, China.

Bentaib, A., Chaumeix, N., Nyrenstedt, G., Bleyer, A., Maas, L., Gastaldo, L., Klejnak, I., Dovizio, D., Kudriakov, S., Schramm, B., Motegi, K., Otón-Martínez, R.A., Danilin, A., Gavrikov, A., Jaseliunaite, J., Povilaitis, M., 2022. ETSON-SAMHYCO-NET benchmark on simulations of upward flame propagation experiment in representative hydrogen-air-steam mixtures of severe accidents containments atmosphere, in: The 19th International Topical Meeting on Nuclear Reactor Thermal Hydraulics (NURETH-19). Brussels (virtual), Belgium.

Bleyer, A., Taveau, J., Djebaïli-Chaumeix, N., Paillard, C.E., Bentaïb, A., 2012. Comparison between FLACS explosion simulations and experiments conducted in a PWR Steam Generator casemate scale down with hydrogen gradients. Nuclear Engineering and Design 245, 189–196. https://doi.org/10.1016/j.nucengdes.2012.01.010

Bosland, Loic, and Juliette Colombani. "Review of the potential sources of organic iodides in a NPP containment during a severe accident and remaining uncertainties." Annals of Nuclear Energy 140 (2020): 107127.

Bosland, Loic, and Juliette Colombani. "Study of the radiolytic decomposition of CsI and CdI2 aerosols deposited on stainless steel, quartz and Epoxy painted surfaces." Annals of Nuclear Energy 141 (2020): 107241.

Breitung, W., Dorofeev, S., Kotchourko, A., Redlinger, R., Scholtyssek, W., Bentaib, A., L'Heriteau, J.-P., Pailhories, P., Eyink, J., Movahed, M., Petzold, K.-G., Heitsch, M., Alekseev, V., Denkevits, A., Kuznetsov, M., Efimenko, A., Okun, M.V., Huld, T., Baraldi, D., 2005. Integral large scale experiments on hydrogen combustion for severe accident code validation-HYCOM. Nuclear Engineering and Design 235, 253–270. https://doi.org/10.1016/j.nucengdes.2004.08.063

Cantrel, Laurent, et al. "Research works on iodine and ruthenium behavior in severe accident conditions." Journal of Nuclear Engineering and Radiation Science 4.2 (2018): 020903.

Cheikhravat, H., Goulier, J., Bentaib, A., Meynet, N., Chaumeix, N., Paillard, C.-E., 2015. Effects of water sprays on flame propagation in hydrogen/air/steam mixtures. Proceedings of the Combustion Institute 35, 2715–2722. https://doi.org/10.1016/j.proci.2014.05.102

E. Friesen, J. Meseth, S. Guentay, D. Suckow, J. López Jiménez, L. Herranz, V. Peyres, G.F. De Santi, A. Krasenbrink, M. Valisi, L. Mazzocchi, 2001. Containment behaviour in the event of core melt with gaseous and aerosol releases (CONGA). Nucl. Eng. Design, 209, 253-262. https://doi.org/10.1016/S0029-5493(01)00408-3.

F. Gabrielli, 'ANALYSIS OF POSTULATED SEVERE ACCIDENTS IN GENERIC INTEGRAL PWR SMALL MODULAR REACTORS IN THE FRAME OF THE HORIZON EURATOM SASPAM-SA PROJECT', May 13, 2024, Zenodo. doi: 10.5281/zenodo.12594257.

Gouëllo, M., Hokkinen, J., Kärkelä, T., 2020. Advances in the understanding of molybdenum effect on iodine and caesium reactivity in condensed phase in the primary circuit in nuclear severe accident conditions, In: Nuclear Engineering and Technology. 52, 8, p. 1638-1649.

G. Grippo, 'COMPARISON OF A DBA SEQUENCE IN A GENERIC iPWR BETWEEN MELCOR AND ASTEC CODES', May 13, 2024, Zenodo. doi: 10.5281/zenodo.12579696.

L. E. Herranz, F. Sánchez, and S. Gupta, 2022. Validation Matrix for Pool Scrubbing Models. Nucl. Technol., doi: 10.1080/00295450.2022.2122679.

L. E. Herranz, B. Poubeau, L. Chailan, Lionel, F. Mascari, Looking ahead to severe accident research, EPJ Nuclear Sciences and Technologies, Volume 11, art. no. 28, 2025 https://doi.org/10.1051/epjn/2025025

Joseph-Auguste, C., Cheikhravat, H., Djebaïli-Chaumeix, N., Deri, E., 2009. On the use of spray systems: An example of R&D work in hydrogen safety for nuclear applications. International Journal of Hydrogen Energy, 2nd International Conference on Hydrogen Safety 34, 5970–5975. https://doi.org/10.1016/j.ijhydene.2009.01.018

Kalilainen, J., Rantanen, P., Lind, T., Auvinen, A., Dehbi, A, 2016. Experimental investigation of a turbulent particle-laden flow inside a cubical differentially heated cavity. J. Aerosol Sci. https://doi.org/10.1016/j.jaerosci.2016.06.001.

Kärkelä, T., Kajan, I., Tapper, U., Auvinen, A., Ekberg, C., 2017. Ruthenium transport in an RCS with airborne CsI, In: Progress in Nuclear Energy. 99, p. 38-48.

Kärkelä, T., Vér, N., Haste, T., Davidovich, N., Pyykönen, J., Cantrel, L., 2014. Transport of ruthenium in primary circuit conditions during a severe NPP accident, In: Annals of Nuclear Energy. 74, p. 173-183.

Lind et al., 2024. SASPAM-SA: Assessment of the relevance and applicability of existing experimental databases to iPWR. Paper 057 tt the The 11th European Review Meeting on Severe Accident Research (ERMSAR2024), KTH, Stockholm, Sweden, May 13-16, 2024.

Malet J., Porcheron E., Vendel J. OECD International Standard Problem ISP-47 on containment thermal-hydraulics - Conclusions of the TOSQAN part, Nuclear Engineering and Design, Vol. 240, pp. 3209–3220, 2010.

F. Mascari, G. Vella, B. G. Woods, F. D'Auria, Analyses of the OSU-MASLWR Experimental Test Facility. Hindawi Publishing Corporation, Science and Technology of Nuclear Installations Volume 2012, Article ID 528241, 19 pages, doi:10.1155/2012/528241.

F. Mascari, et al., OECD/NEA/CSNI/WGAMA PERSEO benchmark: Main outcomes and conclusions, Nuclear Eng. and Design, Volume 405, 15 April 2023, 112220.https://doi.org/10.1016/j.nucengdes.2023.112220

Mascari et al., 2024. Horizon Euratom SASPAM-SA project: Main ideas and first outcomes. IAEA International Conference on Small Modular Reactors and their Applications, 21–25 October 2024, Vienna, Austria.

Mäkynen, J., Jokiniemi, J.K., Ahonen, P.P., Kauppinen, E.I., Zilliacus, R. AHMED experiments on hygroscopic and inert aerosol behaviour in LWR containment conditions: experimental results. Nucl. Eng. Design 178 (1997), pp. 45-59.

OECD/NEA, Status Report on Hydrogen Management and Related Computer Codes, NEA/CSNI/R(2014)8, June 2014.

D. Paladino, R. Zboray, P. Benz, M. Andreani, Three-gas mixture plume inducing mixing and stratification in a multi-compartment containment, Nuclear Engineering and Design 2008.Lemaitre P., Porcheron E. Analysis of heat and mass transfers in two-phase flow by coupling optical diagnostic techniques. Exp. Fluids, Vol. 45, pp. 187–201, 2008.

Porcheron E., Lemaitre P., Nuboer A., Rochas V., Vendel J. Experimental investigation in the TOSQAN facility of heat and mass transfers in a spray for containment application. Nuclear Engineering and Design, Vol. 237, pp. 1862-1871, 2007.

J. Sabard, Y.-C. Hsu, M. Idir, N. Chaumeix, A. Bentaib, (2013). "Impact of Graphite dust on the explosion properties of H2/O2/N2 mixtures", Proceedings of the 24th ICDERS, July 28-August 2, 2013, Taipei, Taiwan

Studer E., MagnaudJ.P., DabbeneF., TkatschenkoI., International Standard Problem on Containment Thermal-hydraulics ISP47: Step 1 – Results from the MISTRA Exercise, Nuclear Engineering and Design 237 (5), 536–551, 2006.

PSI Center for Nuclear Engineering and Sciences

SASPAM-SA: Assessment of existing experimental data in WP3

Applicability of large-PWR data to iPWR

The 12th European Review Meeting on Severe Accident Research (ERMSAR 2026)

May 18–22, 2026, Madrid, Spain

T. Lind / PSI, G. Grippo and F. Mascari / ENEA, M. Garcia and L.E. Herranz / CIEMAT, N. Chaumeix / CNRS, M. Klauck and E. Reinecke / FZ Jülich, J. Denis and A. Bentaib / ASNR, D. Grishchenko and P. Kudinov / KTH, M. Constantin / RATEN, M. Vyshemirskyi and D. Gumenyuk / SSTC NRS, I. Ivanov / TUS, T. Kärkelä / VTT

In this presentation

- **SASPAM-SA project**
- **Aims of WP3: Applicability of experimental data**
- **Designs 1 and 2 and postulated severe accident scenarios**
- **Evaluated experimental data**
  - Natural circulation
  - In-vessel
  - (Ex-vessel)
  - Containment
  - Source term
- **Identified data needs**

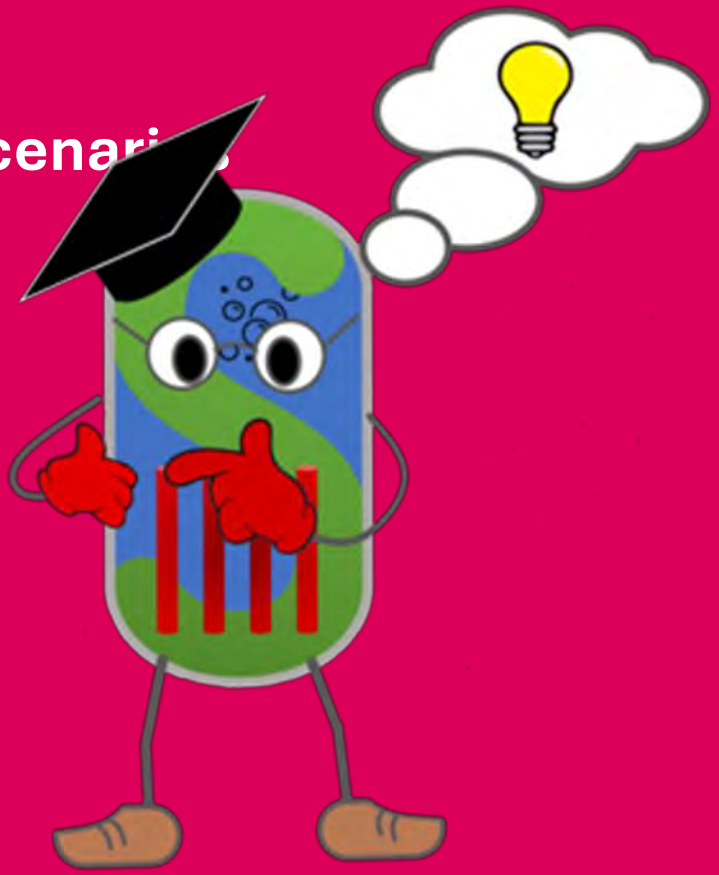

SASPAM-SA: Safety Analyses of SMR with Passive Mitigation strategies – Severe Accident

- Investigate **the applicability and transfer of the operating large-LWR reactor knowledge** and know-how to the near-term deployment of integral PWR (iPWR), in the view of Severe Accident (SA) and Emergency Planning Zone (EPZ) European licensing analyses needs
- To be **supportive for the iPWR licensing process** by bringing up key elements of the safety demonstration
- To **speed up the licensing** and siting process of iPWRs in Europe
- Dedicated actions on **Accident Tolerant Fuels (ATF) and In-Vessel Melt Retention (IVMR)**

Work package 3: Applicability of the existing data to iPWR

- Phenomena:
  - Natural circulation
  - In-vessel
  - (Ex-vessel)
  - Containment
  - Source term
- Select facilities and tests
- Compare boundary conditions of experiments to severe accident conditions of Designs 1 and 2
- Identify conditions in which data are not available

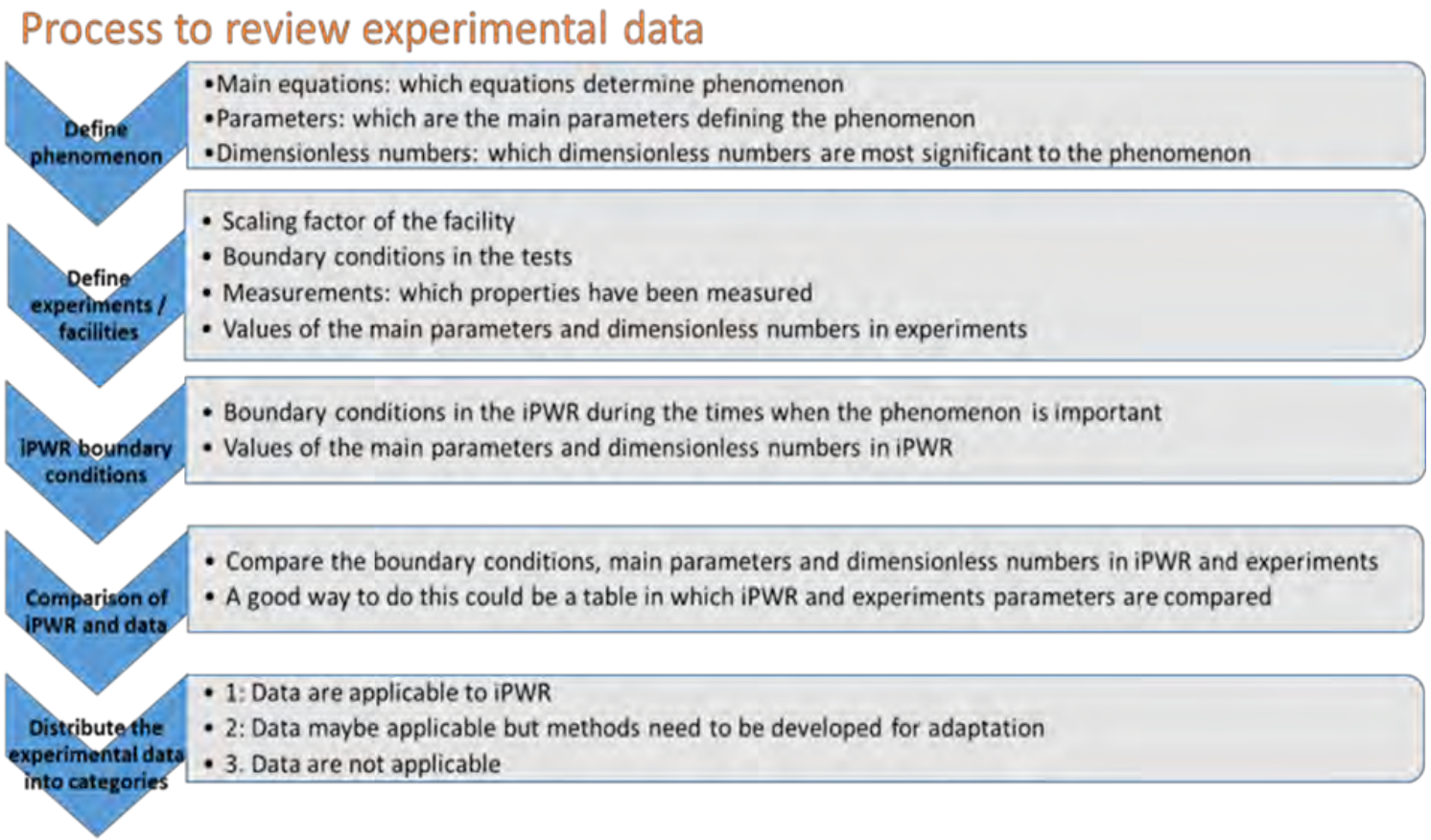

Work package 3: Applicability of the existing data to iPWR

Partner	In-vessel	(Ex-vessel)	Containment	Source term
ENEA	Natural circulation			
KTH	Debris, liquid melt, FCI			
RATEN	Re-flooding of rod-like geometry	Corium spreading and cooling		
SSTC NRS	In-vessel coolability	Ex-vessel coolability		
TUS	Melt pool formation			
ASNR (IRSN)			H_2 distribution	Iodine chemistry
CNRS			H_2 combustion risk	
FZJ			H_2 mitigation with PAR	
VTT				Aerosol properties
PSI				Aerosol transport
CIEMAT				Pool scrubbing
CNL			Joined the project in 2025	

SASPAM-SA Design 1

- **SA-1:**
  - A break in the Chemical and Volume Control System (CVCS) make-up line combined with a loss of AC power
  - The Reactor Vent Valves (RVVs) are operational
  - The Reactor Relief Valves (RRVs) stuck closed. The break discharges directly into the containment
  - The break height was varied, and reverse flow was either allowed or suppressed depending on the modelling approach
- **SA-2:**
  - Inadvertent opening of one RVV (5”) and loss of AC power
  - Two RVVs are available and actuated as in SA-1
  - Both RRVs are unavailable
  - This configuration prevents water recirculation from the containment to the RPV
- **SA-3:**
  - A smaller break (1.7”) in the pressurizer vent line with a loss of AC power
  - The remaining RVVs are available and actuated as in SA-1
  - The RRVs are unavailable

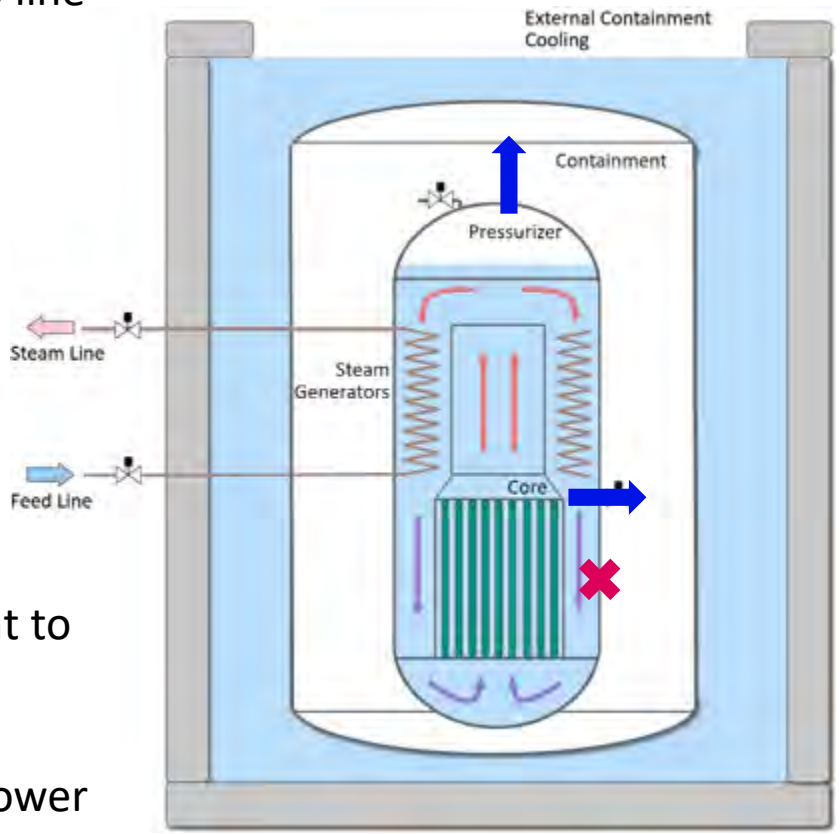

SASPAM-SA Design 2

- **SA-1:**
  - A guillotine break of one Direct Vessel Injection (DVI) line together with the unavailability of the Emergency Heat Removal System (EHRS) due to failure of the corresponding valves to open.
- **SA-2:**
  - DVI break, combined with the unavailability of both the EHRS and the Automatic Depressurization System (ADS) due to valve failure
- **SA-3:**
  - DVI break together with the unavailability of all safety systems as a result of the failure of the associated valves to open

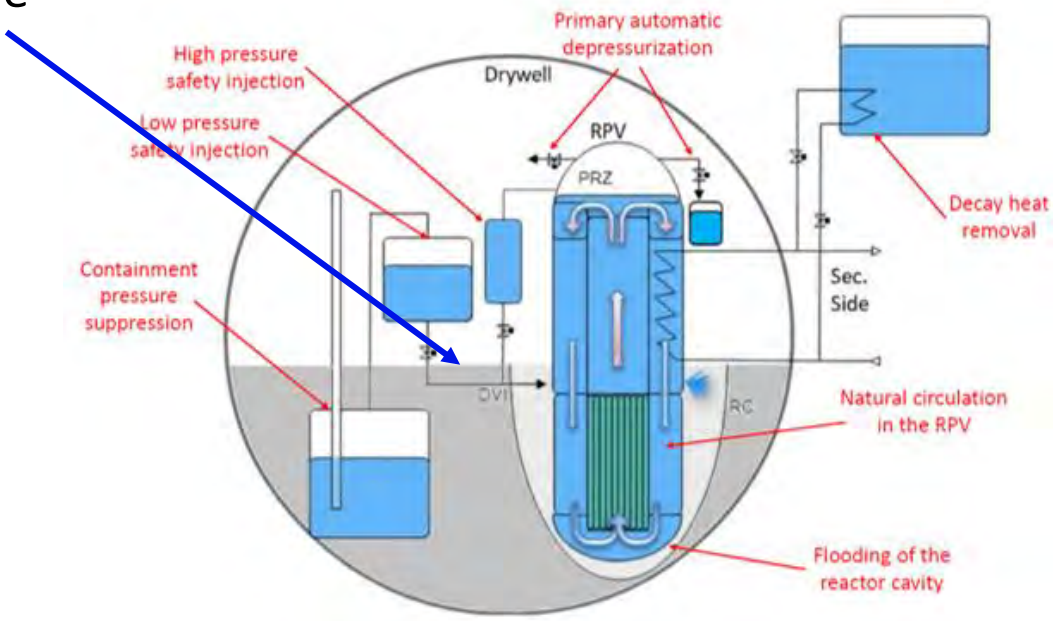

Natural circulation

- **Design 1:**
  - During normal operation and accidental conditions
  - In the Reactor Pressure Vessel (RPV) and in the primary/containment coupling (MASLWR-001, 003B)
- **Design 2:**
  - During accidental conditions (PERSEO)
  - In the RPV and in the passive systems (e.g., decay heat removal system)

- MASLWR facility for primary/containment coupling
- PERSEO facility passive safety systems

- Primary containment coupling with different SBLOCA dimensions
- Compact steam generator in different operating conditions
- Natural circulation in an integral PWR at low flow rates
- EHRS at different accidental conditions

OSU-MASLWR facility

[NUREG/IA-0466]

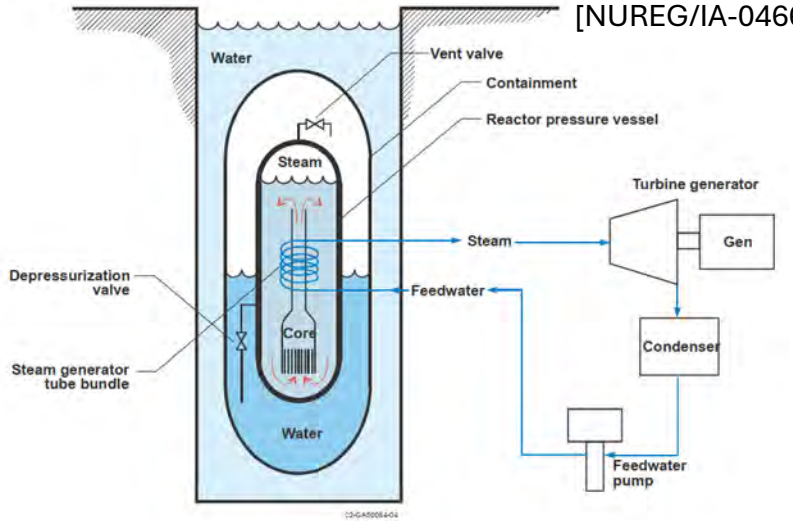

PERSEO facility – In-operation layout

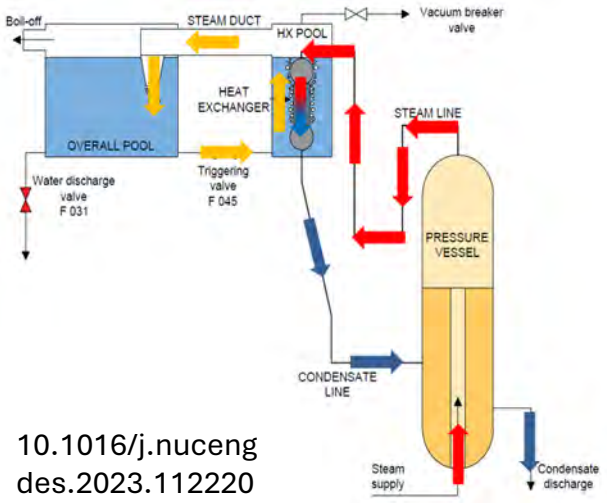

10.1016/j.nucengdes.2023.112220

In-vessel – oxidation and coolability of rod-like geometry

- **QUENCH-06 test**
  - The core heat-up and reflooding at temperatures above 2000 K
  - Pre-oxidation behavior without severe damage to the rods due to reflooding with water
  - Cladding oxidation and hydrogen generation
- **Applicability**
  - **No major differences** between the fuel assemblies of large PWR and iPWR
  - Hydrogen production, oxidation behavior, cladding failure, temperature data, and the influence of reflooding may be used in the current limits of uncertainties (experimental, simulation models)

Reflooding data at large flowrates may not be readily available

QUENCH facility

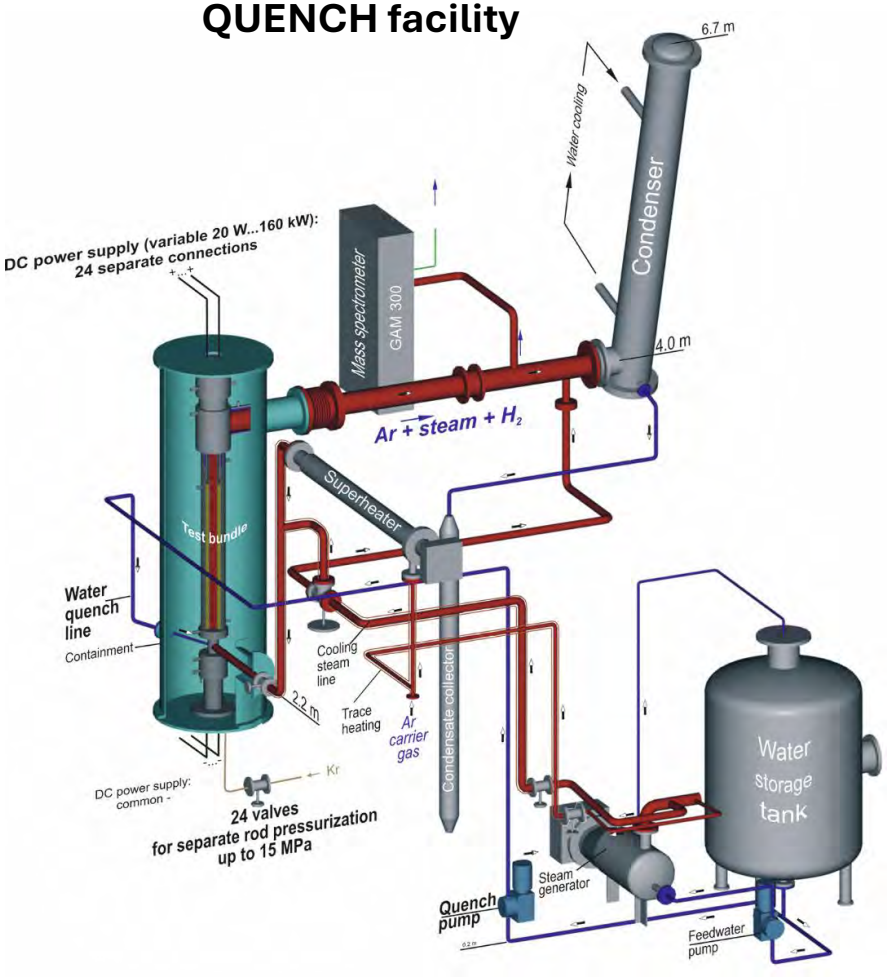

https://www.iam.kit.edu/awp/english/163.php

In-vessel – debris bed, melt propagation and FCI

- **KTH experiments:**
  - Debris formation and agglomeration – DEFOR facility
  - Particulate debris spreading – PDS facility
  - Melt propagation in a porous debris bed – REMCOD facility
  - Lower head failure, breach ablation and plugging during melt release – DEFOR-MG facility
  - Steam explosion in stratified melt-coolant configuration
- Parametric tests with simulant materials for phenomenological understanding and model development

REMCOD

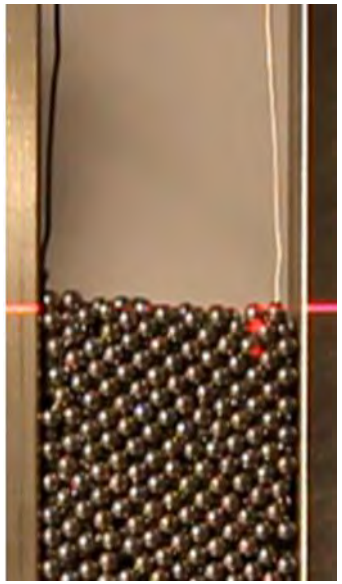

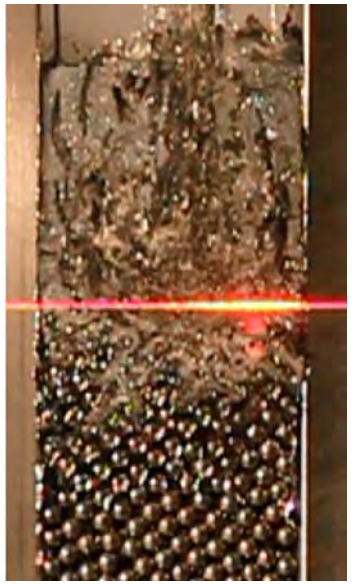

- Underwater melt release and debris bed formation (agglomeration) in a shallow water pool
- Debris coolability with obstructions to water circulation
- Remelting and melt relocation into a dry lower head at low volumetric power
- The effect of steam explosion in a small containment

Pictures: KTH

In-vessel – melt pool formation

- **LIVE experiments:**
  - For lower plenum phenomena related to in-vessel cooling of a molten core LIVE (Large-scale Tests on In-vessel Melt Relocation and Retention), i.e., LIVE-1, -2, -L3A, L4 and L5L
  - LIVE-L1: melt pour is central
  - LIVE-L3: melt pour is lateral near to wall
  - The LIVE3D test facility simulates the lower plenum of a water-cooled reactor pressure vessel and investigates the transient and steady state thermal-hydraulics and heat transfer of solid and liquid corium under various accident scenarios.

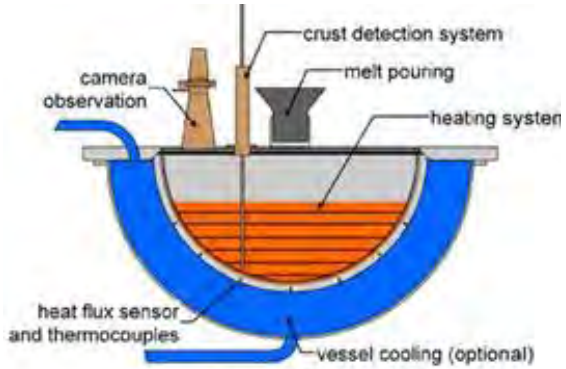

Figure 1: LIVE test vessel

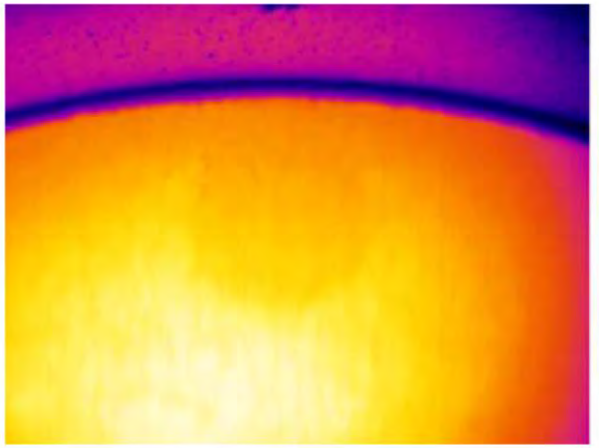

Thermal image of the melt surface in LIVE-L1

Parametric understanding, not aiming to replicate SMR conditions: confined geometry, large amount of steel, abundant water cooling, etc.

Pictures: KTH

Containment – hydrogen distribution

- **Facilities**
  - TOSQAN (e.g., Pocheron et al., 2007; Lemaitre and Pocheron, 2008, Malet et al., 2010)
  - THAI (e.g., OECD/NEA, 2014))
  - MISTRA (e.g., Studer et al., 2006)
  - PANDA (e.g., Auban et al., 2004; Paladino et al., 2008)
- **The range of addressed conditions:**
  - Pressure 0.1-0.4 MPa
  - Temperature 20-150°C,
  - Steam content 0-70%vol
  - Hydrogen concentration 0-20%vol
- **iPWR containments with design conditions:**
  - Pressures > 1.0 MPa
  - Temperatures > 150°C
  - Steam contents > 70 vol-%

MISTRA

THAI+

Containment – hydrogen combustion risk

- Research programs at **IRSN (ASNR) and CNRS**:
  - Fundamental flame properties of H_2-Air-diluents (steam, He, CO_2)
  - Self-acceleration of H_2 based flames
  - Acceleration of the flame in a turbulent medium
  - Safety criteria for H_2 based mixtures applicable to nuclear power plant

- Different configurations:
  - Homogeneous mixtures
  - Homogeneous gradients (positive and negative)
  - Upward and downward propagation
  - Initial H_2= 4-20 mol-%
  - Initial T= 25-140°C
  - Initial p = 1 bar
  - Water vapor = 0-30%
  - He-CO_2 = 0-40%
  - Effect of water spray

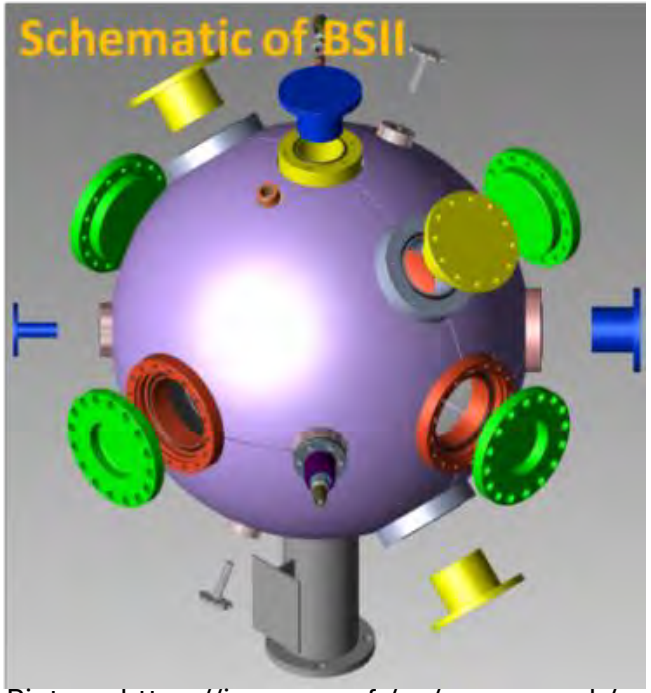

Picture: https://icare.cnrs.fr/en/en-research/en-facilities/en-ct-spherical-bombs/

- Potential air ingress leading to formation of **fuel-rich** mixtures (lean O_2)
  ⇒ Different flame dynamic
  ⇒ Only scarce data available
- **Initial pressure from10 bar to 20 bar** during the transient
  ⇒ At this pressure, no data in the literature

Containment – hydrogen mitigation with PARs

- **Facilities**
  - **CTF and LSVCTF** (AECL, Canada): [Koroll et al., 1996]
  - **KALI-H2** (CEA/EPRI/EDF, France): [Brailard et al., 1997]
  - **H2PAR** (IPSN/EDF, France): [Rongier and Studer, 1996]
  - **Surtsey Vessel** (Sandia NL, USA): [Blanchat and Malliakos, 2000]
  - **BMC** (Battelle, Germany): [Kanzleiter, 1997]
  - **REKO** (FZJ, Germany): [Reinecke et al., 2010]
  - **THAI** (Becker Technologies, Germany): [Gupta et al., 2013]
- In general, the operating behavior of PARs can be considered to be well understood
- A comprehensive experimental database available, specifically relevant to large LWR containments and the accident conditions to be expected there

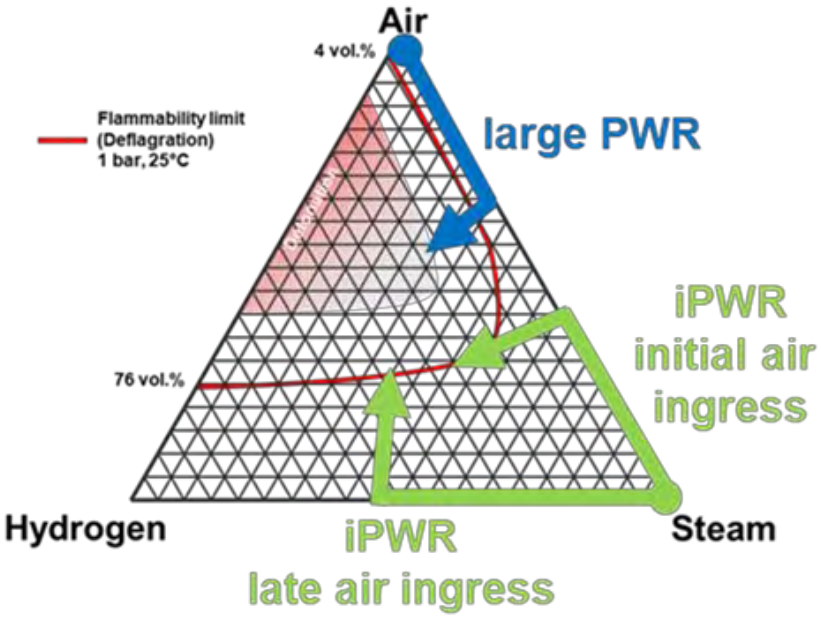

iPWR containments:

- Pressures > 0.5 MPa
- Startup under extremely humid conditions and/or oxygen depletion
- Fast H_2 feed rates into small containment volumes
- Significantly **more compact PAR models** may have to be developed for iPWRs

Note: Air ingress!

Source term – aerosol characteristics

- **VTT experimental programs for aerosol characteristics**
  - Primary circuit experimental studies simulated fission product behavior when transporting from high temperatures to low temperatures (from primary circuit to containment conditions)
  - Various shapes in primary circuit conditions
  - Effect of humidity on particle shape

- iPWRs high humidity and small containments
  - Collapse of chain-like agglomerates
  - Particle hygroscopic growth
  - Transport in confined geometries dependent on particle characteristics: size, density, shape

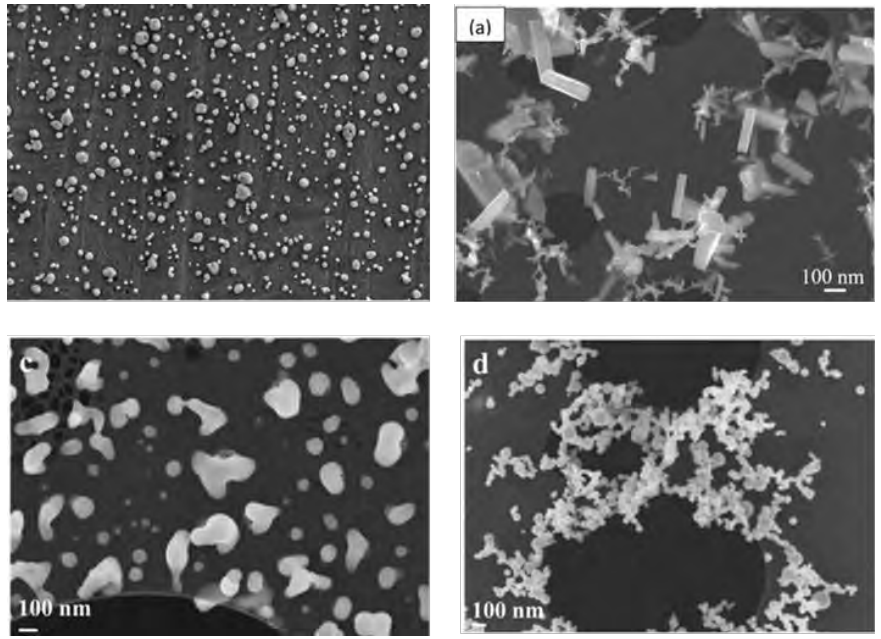

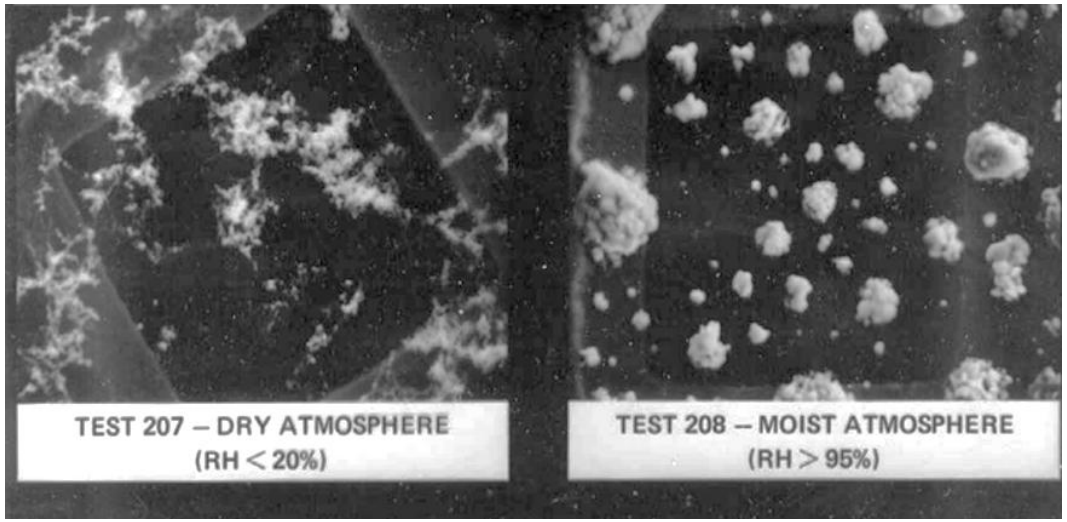

Pictures: VTT and NEA/CSNI/R(2009)5

Source term – aerosol transport in condensing conditions

- **AIDA:** Effect of aerosol deposition in PCCS
- **CESANE:** Effect of aerosol deposition on heat transfer, influenced by:
  - Aerosol characteristics: size, shape, composition, concentration
  - Gas atmosphere (steam and NC content)
  - Temperature gradient, heat exchanger power
  - Heat exchanger geometry, esp. entry effects
- **PCC-VTT:** In-tube diffusio-phoresis in condensing conditions
- **AHMED:** Aerosol deposition in containment under humid conditions
- **DIANA:** Aerosol transport in natural circulation – dry conditions
- **ARTIST:** Aerosol deposition during SGTR severe accident
- **FCVS projects:** Large containment conditions

AIDA and CESANE showed that aerosol deposition had a significant effect on:

- Heat transfer
- Pressure drop in the heat exchanger → Flow distribution

Data not readily available

AIDA data

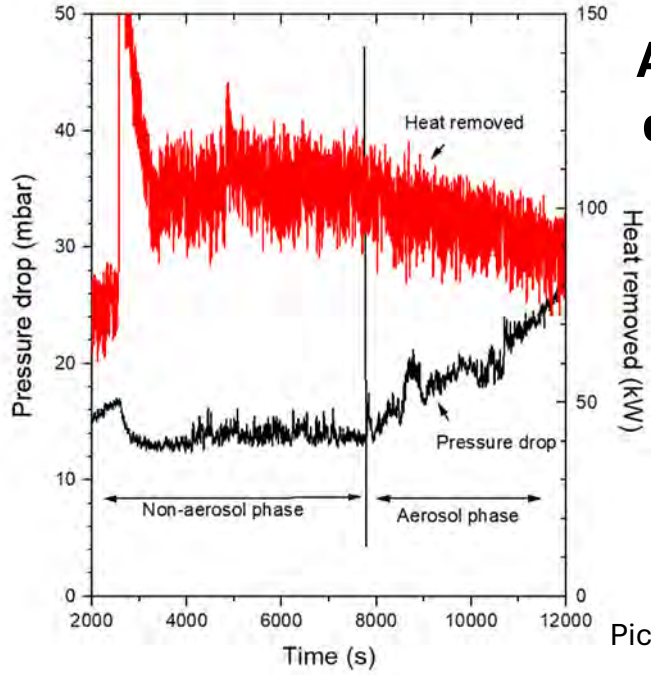

Pictures: PSI

CESANE data

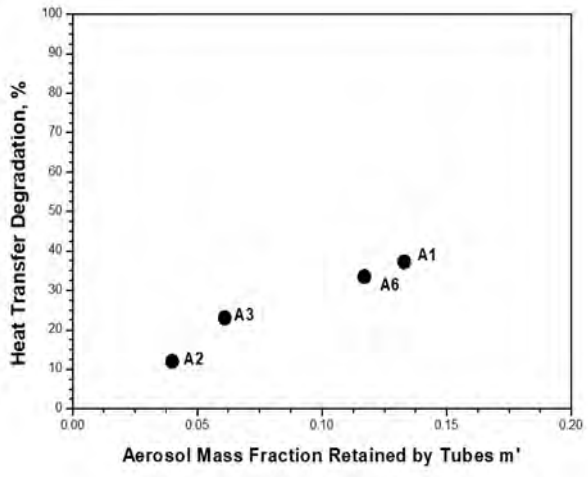

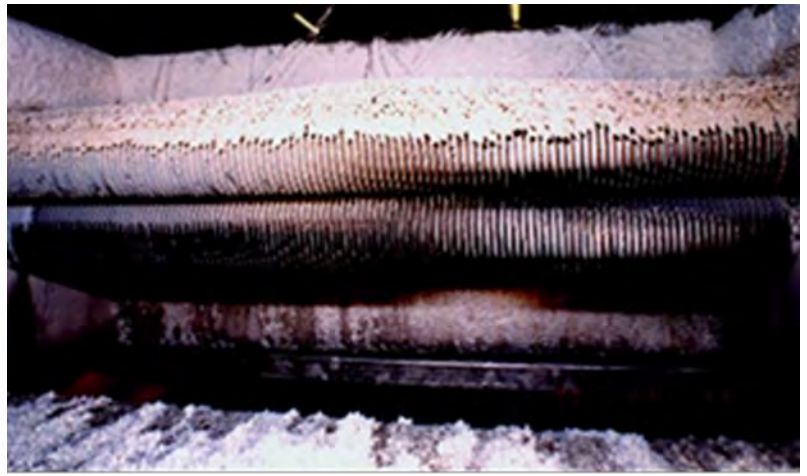

Source term – pool scrubbing

- **Data from over 20 experimental programs in 1960-2016 (Herranz et al., 2022)**
- **Extended by experiments in 2016-2024**
  - 27 additional references, > 350 experiments
  - 8% of the total number of tests are considered qualified for validation and about 36% are seen as useful for understanding
    - FCVS performance oriented (36%)
    - Hydrodynamics oriented (43%)
    - Other Factors (21%). For example, vapor scrubbing or incomplete test characterization

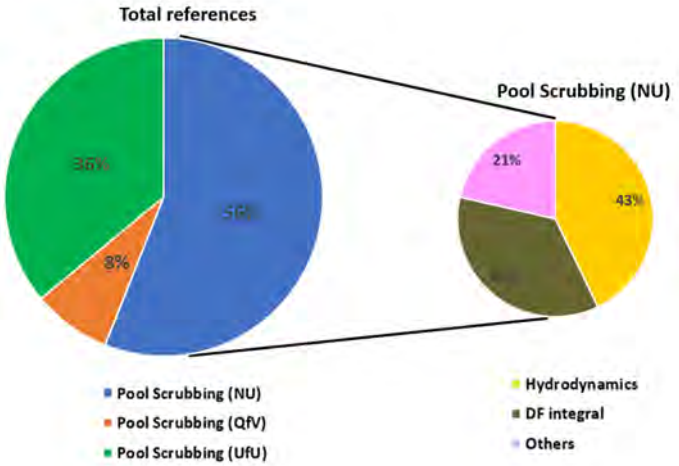

Picture: CIEMAT

Data base might be needed to be extended:

- **Higher gas injection temperatures**. The hot condition would enhance thermo-phoretic depletion at the pool inlet region
- Presence of **light non-condensable gases** (i.e., H_2 or He as a surrogate gas). Inner bubble hydrodynamics might be affected by the substantial difference in terms of molecular weight of NC. *This observation applies to both iPWRs and LWRs*
- ***Facility scaling should be paid attention to***

Source term – iodine chemistry

- **Data from:**
  - ISTP – 30 tests in 2005-2010
    - volatile iodine released from the sump
    - formation of organic iodides from the iodine deposited on the painted surfaces (submerged and not)
    - formation of iodine oxides from gaseous iodine and their stability
  - STEM and STEM2 – 30 tests in 2011-2019
    - stability of iodine aerosols (CsI, AgI, iodine oxides, etc.);
    - interactions between iodine and aged paints for LTO
    - revolatilisation of iodine in the long term after an accident
  - MiRE and PASSAM – 15 tests in 2013-2022
  - ESTER – 8 tests in 2020-2025, sources for organic iodine formation
    - in the presence of volatile organic compounds (VOCs): methane, acetone and ethylene
    - on different substrates: cables, quartz coupons, galvanized steel and stainless steel

EPICUR facility

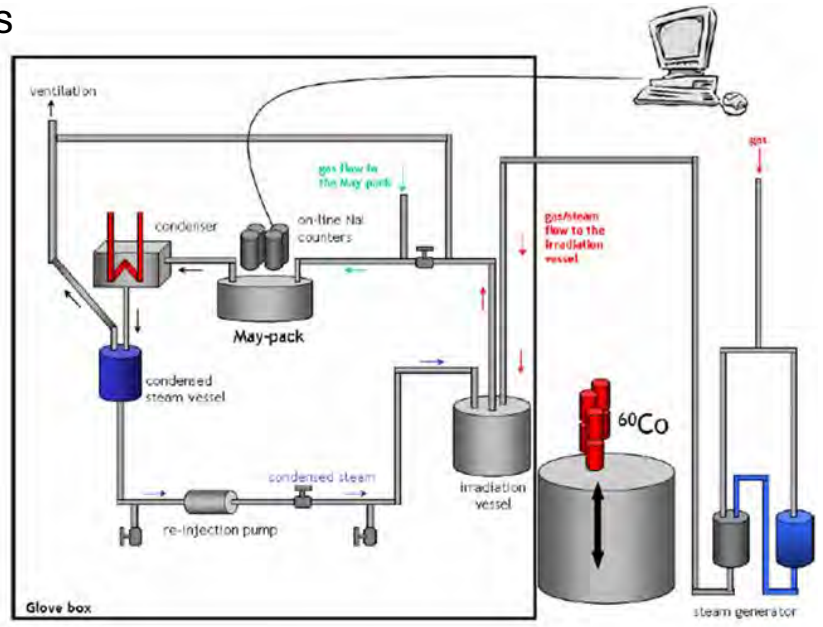

Iodine behaviour under reducing or low-oxygen conditions of iPWR containments has not been investigated

Concluding words

- Experimental data were reviewed by 11 organizations for:
  - Natural circulation (1 partner)
  - In-vessel and ex-vessel (ex-vessel limited) (4 partners)
  - Containment (3 partners)
  - Source term (4 partners)
- **LWR data are applicable in most of domains addressed**. Some prevailing boundary conditions would require extensions of the existing databases
- Those experimental data needs for iPWR were identified

Acknowledgements

A big thank you to all the SASPAM-SA partners and especially to Fabrizio Gabrielli for providing accident analysis data used in this work.

Funded by the European Union. Views and opinions expressed are however those of the author(s) only and do not necessarily reflect those of the European Union or European Commission-Euratom. Neither the European Union nor the granting authority can be held responsible for them.

Funded by the European Union

This work has received funding from the Swiss State Secretariat for Education, Research and Innovation (SERI)

Project funded by

Schweizerische Eidgenossenschaft
Confédération suisse
Confederazione Svizzera
Confederaziun svizra

Swiss Confederation

Federal Department of Economic Affairs, Education and Research EAER
State Secretariat for Education, Research and Innovation SERI

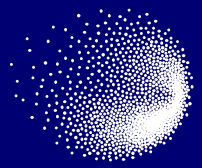

PSI Center for Nuclear Engineering and Sciences

THANK YOU!

The 12th European Review Meeting on Severe Accidents Research

May 18-22, 2026, Universidad Carlos III de Madrid, Madrid, Spain

TECHNICAL SESSION 3.4: SEVERE ACCIDENT SCENARIOS - SMALL MODULAR REACTORS

Chairs: S. Brumm (JRC), F. Rocchi (ENEA)

ID148	**Assessment of Emergency Planning Zone for iPWRs within the Horizon Euratom SASPAM-SA Project** M. Ilvonen (VTT)	Paper Presentation
ID191	**Performance Assessment of Passive Safety Systems and Identification of Conditions Leading to Design Extension Scenarios** E. Cilia (University of Bologna)	Paper Presentation
ID119	**Effect of Delayed Recovery of ECCS during Severe Accidents in Integral PWR SMRs** G. Acharya (KTH)	Paper Presentation
ID181	**Investigation of In Vessel Melt Retention by a stand-alone Lower Plenum ASTEC model of integral-PWR design#1 in the SASPAM-SA project** S. Brumm (JRC)	Paper Presentation

ASSESSMENT OF EMERGENCY PLANNING ZONE FOR iPWRs WITHIN THE HORIZON EURATOM SASPAM-SA PROJECT

[1]Ilvonen M., [2]Rocchi F., [3]Murat O., [4]Acharya G., [5]Slavickas A., [6]Casartelli E. S., [7]Kyrylenko Y., [8]Ivanov I., [9]Giannetti F., [10]De la Rosa Blul J. C., [2]Guglielmelli A., [2]Mascari F

[1]VTT, Finland; [2]ENEA, Italy; [3]KIT, Germany; [4] KTH, Sweden; [5]LEI. Lithuania; [6]POLIMI, Italy; [7]SSTC-NRS, Ukraine; [8]TUS, Bulgaria; [9]Sapienza University of Rome, Italy. [10]European Commission Joint Research Centre, The Netherlands

Corresponding Address:
P.O. BOX 1000, FI-02044 VTT
mikko.ilvonen@vtt.fi

ABSTRACT

The Horizon Euratom SASPAM-SA project (Safety Analysis of SMR with PAssive Mitigation strategies – Severe Accidenft) analyzes the applicability of current state-of-the-art severe accident codes against hypothetical generic iPWR designs in the view of the needs of the European licensing processes. In addition to work packages related to code analysis capabilities, current experiments' applicability to iPWRs, and containment analyses, WP6 (on Emergency Planning Zone – EPZ) considers the offsite dispersion and doses caused by radioactive releases from postulated severe accidents, thus representing the last phase of calculations. Twelve partners are working to achieve numerical, quantitative results about the geographic extent of off-site dose consequences, affecting the final decision on EPZ.

Initially, a set of varyingly conservative calculations were performed, based on atmospheric source terms ranging from maximum possible quantities down to smaller release estimates from pure 'expert judgement' or some quite simple analytical work. The codes used included JRODOS, MACCS, HotSpot, RASCAL, GENII and ARANO. The first phase mainly served to test the calculation capabilities of the codes used at the participating institutions.

In the current phase, more refined 'BE' STs produced within WP5 ('Containment') are being used to avoid exceedingly conservative results due to lack of release knowledge, i.e. detailed data about actual nuclide content, activities, temporal release rate trend, effective release height etc.

Generally, it is expected that SMR smaller inventories and longer delays before any atmospheric release might lead to smaller dose consequence footprints than those for existing large LWR plants. That could facilitate the acceptance of SMR plant sites near densely populated areas. Finally, it is expected, at the end of the project, that results from WP6 can be used to understand limits, if any, of the current codes and/or methods and approaches in producing sound and reliable data for EPZ extents of iPWRs.

KEYWORDS
EPZ, Severe Accident, SMR, atmospheric dispersion, offsite doses

1. INTRODUCTION TO WP6 (EPZ)

The Horizon Euratom SASPAM-SA project (Safety Analysis of SMR with PAssive Mitigation strategies – Severe Accident) [1,2,3], coordinated by ENEA (Italy), analyzes the applicability of current state-of-the-art Severe Accident (SA) codes against hypothetical generic integral Pressurized Water Reactor (iPWR) designs in the view of the needs of the European licensing processes. In addition to Work Packages (WP) related to code analysis capabilities [4,5], current experiments' applicability to iPWRs [6], and containment analyses [3], WP6 (Emergency Planning Zone, EPZ), considers the offsite dispersion and doses caused by radioactive releases from postulated SAs, thus representing the last phase of calculations. In order to maximize the knowledge transferability and impacts of the project, two generic design-concepts, characterized by different evolutionary innovations in comparison with larger operating reactor, were selected for analyses.

The overall objective of WP6 is to provide evaluations of size and extension of EPZ for selected SA scenarios, eventually (during latter half of SASPAM-SA project) coupling the results of BE Source Term (ST) codes to radiological consequences tools. One of the most important features of iPWRs is the possibility of their siting near densely populated areas thanks to the (claimed) increased inherent safety, the assumedly lower radiological impact, and possibly reduced size of the region affected by releases (dose consequences footprint). The need to demonstrate these features using quantitative results is addressed by WP6 which attempts to provide a sound basis for the assessment of EPZ. WP6 will produce recommendations on rigorous and justified methodology for iPWR EPZ 'right-sized' determination. However, the size is not necessarily universally the same in all countries due to domestic regulations, for all kinds of plants or for all sites. Furthermore, for the EPZ, SASPAM-SA is strictly considering radiological consequences only ('off-site doses footprint area'), leaving out any possible social, political, logistics etc. factors. It can be postulated that the EPZ cannot be smaller than the area defined by the purely radiological considerations.

The structure of WP6 is the following:
- Task 6.1: Critical review of existing EPZ methodology
- Task 6.2: Preliminary conservative offsite dose assessments
- Task 6.3: Offsite doses & EPZ by Best Estimate (BE) approach
- Task 6.4: Conclusions on iPWR EPZ & recommendations on methodology

This paper considers mainly the first two tasks of WP6, specifically the review of current methodologies (Task 6.1) and the conservative assessments of EPZ (Task 6.2). VTT (Finland) is leading the work in WP6.

Task 1 (methodology review) is devoted to the analyses of the methods already available for large Light Water Reactors (LWR) to understand their applicability to iPWR. It included also preparatory work in relation to the following task such as an analysis of the suitability of codes linked to the problem of near range atmospheric dispersion and the effect of nearby buildings.

Task 2 (preliminary / conservative dose calculations) was devoted to develop first estimates of STs relying on publicly available data or conservative hypothesis based on initial inventory evaluated in WP2, and to calculate EPZs using simplified and conservative methods. This provides background technical results to be used as a comparison set for the BE tasks.

2. CRITICAL REVIEW OF THE EXISTING METHODOLOGY FOR EPZ DETERMINATION

The work carried out within Task 6.1 focused on a comprehensive review of the existing methodologies, relevant to the definition of EPZs for integral iPWR. The activities were jointly conducted by ENEA, JRC, LEI, POLIMI, SSTC NRS, TUS, Università di Roma, and VTT, combining expertise from multiple European and international institutions.

The review work included the following subtopics:

- Analysis of the methods already available for large-LWR to understand their applicability to iPWR.
- Preparatory work in relation to the following task such as an analysis of the suitability of codes linked to the problem of near range atmospheric dispersion and the effect of nearby buildings.
- Study of country-specific regulations on EPZ & protective measures, IAEA guidelines on those & outcomes of the SMR Regulators' Forum [13], and outcomes of relevant IAEA CRP projects.
- Analysis of current EPZ approaches (large PWR or other) and their applicability to smaller iPWRs.
- Review of simulation tools and recommendations for suitable, possibly harmonized methods for iPWR SMR EPZ.
- Overview of short range dispersion special approaches & phenomena.
- Consideration of risk-informed methodology for the calculation of the EPZ size for an iPWR SMR.

The activities by WP6 partners included examination of the features of several available dispersion and dose projection tools, including their near-range capability which is important for SMRs, if exceedance of dose limits is only expected in the near-range. Current regulations and methodologies for EPZ were studied to serve as groundwork both for the quantitative calculations and the expected methodology recommendations.

The review of EPZ-related regulations covered e.g. Bulgaria, Finland, Lithuania, Ukraine, and the USA. The implications of the International Atomic Energy Agency (IAEA) and European Union (EU) standards and directives for several EU countries were considered. The codes for release through water volumes (like reactor pool) were SPARC-90 for pool scrubbing and IMPAIR for iodine chemistry and release. For the atmospheric dispersion and dose calculations, e.g. JRODOS, MACCS, HotSpot, or the VTT in-house code ARANO were used.

2.1. Current regulations on EPZ & protective measures

SASPAM-SA WP6 performed a comprehensive review of EPZ[1] regulations and methodologies across multiple countries and international frameworks. In the EU, the bases are directives (Basic Safety Standards 2013/59/Euratom [7] and European Nuclear Safety Directive 2014/87/Euratom [8]) which set overarching goals for emergency management but do not prescribe specific EPZ distances. Instead, member states define zones based on national policies, laws and risk assessments.

Country-specific approaches vary significantly. Belgium mandates evacuation planning within 10 km and sheltering/iodine prophylaxis within 20 km, while Bulgaria uses a tiered system (Precautionary Action Zone[2] – PAZ – 2 km, Urgent Protective Actions Zone[3] – UPZ – conditionally 30 km, and a long-term zone, without fixed outer boundary because its extent is determined by monitoring results and conditions after an event) integrated into the disaster protection legislation. Finland used to prescribe 5 km precautionary and

[1] **Emergency Planning Zone (EPZ)**: The precautionary action zone (PAZ) and the urgent protective action planning zone (UPZ) [10].

[2] **Precautionary Action Zone (PAZ)**: An area around a facility for which emergency arrangements have been made to take urgent protective actions in the event of a nuclear or radiological emergency to avoid or to minimize severe deterministic effects off the site. Protective actions within this area are to be taken before or shortly after a release of radioactive material or an exposure, on the basis of prevailing conditions at the facility [10].

[3] **Urgent Protective Actions Zone (UPZ)**: An area around a facility for which arrangements have been made to take urgent protective actions in the event of a nuclear or radiological emergency to avert doses off the site in accordance with international safety standards. Protective actions within this area are to be taken on the basis of environmental monitoring — or, as appropriate, prevailing conditions at the facility [10].

20 km planning zones, supported by STUK regulations and detailed rescue plans, but shifted to a flexible scheme with the STUK Emergency Decree Y/2/2024 [12]. France in 2019 expanded its EPZ for sheltering and iodine pills from 10 km to 20 km to improve public preparedness. Other European nations (Czech Republic, Hungary, Lithuania, Slovakia, Slovenia, Spain) adopt similar concentric-zone models, typically ranging from 3–5 km for immediate actions to 30 km or more for extended measures, often aligned with IAEA guidance. Ukraine is in the process of harmonizing national rules with EU and IAEA standards.

Internationally, Canada applies flexible, case-by-case EPZ sizing, while the U.S. has shifted to a performance-based, risk-informed approach for SMRs and new technologies, formalized in updated NRC regulations (final new rule 2023). This method considers accident scenario likelihoods, together with the STs, potentially reducing EPZs to very small distances for advanced designs.

Overall, trends indicate some movement towards risk-informed, site-specific EPZ sizing, especially for SMRs, balancing safety, practicality, and societal factors. For example, the UK Nuclear Regulatory Review by Fingleton, 2025 [11], strongly emphasizes simplification of regulations together with management and proportionality of risks. Protective actions, such as evacuation, sheltering, iodine prophylaxis, and food restrictions, are most universally planned based on dose criteria and operational intervention levels.

2.2. Future development – Finland example

Finland's regulations are evolving related to SMRs, starting with the determination of EPZ (consisting of PAZ and UPZ). STUK emphasizes that SMR safety should be assessed case by case, as their lower power and passive safety features can reduce risks compared to traditional nuclear power plants. This flexibility may allow SMRs to be located closer to urban areas, provided safety is demonstrated.

A major legislative reform is underway, but EPZ rules were updated earlier through STUK Regulation Y/2/2024 (effective February 2024) [12] to support urban planning. Previously fixed EPZ distances — PAZ at 5 km and UPZ at 20 km — are now flexible, based on dose criteria. For PAZ, radiation dose outside the zone must remain below 1 Sv within 10 hours. Inside PAZ, efficient precautionary evacuation is planned to prevent early deterministic health effects. Outside UPZ, dose remaining below 10 mSv within 48 hours is required, to not necessitate sheltering indoors there. Licensees must demonstrate compliance using realistic SA scenarios, though probabilistic risk assessment is not required. SASPAM-SA WP6 is facing the same fundamental problem: How to choose the accident scenarios for EPZ determination purposes? However, a further step towards risk-informed approach may be expected with the recent STUK information that the accident and release scenario for UPZ may be less severe than that for PAZ. The approach prioritizes safety performance regarding emergency preparedness rather than prescribing reactor design / technology, actually so aligning with IAEA EP&R high-level guidelines and STUK emergency regulations ('VAL' guides).

2.3. IAEA and the SMR Regulators' Forum

WP6 outlined IAEA guidelines for emergency preparedness and response planning, with protective measures for nuclear facilities, which are not yet specifically focusing on SMRs. The IAEA defines five Emergency Preparedness Categories (EPC), with Category I posing the highest offsite health risks. SMRs generally fall between Categories I–III, suggesting potential for reduced emergency planning compared to large LWRs, though enhanced safety needs to be demonstrated.

Key standards include GSR Part 7 (2015; possibly to be updated) [10], which sets 26 requirements for preparedness and response, covering hazard assessment, protective actions, public communication, and medical response [10]. It applies to all reactor types, including small or next-generation designs. Supporting documents such as EPR-NPP-PPA (2013) [9] provide practical guidance on protective actions and EPZ

sizing, though currently presented methods remain deterministic and rather simplified, often based on worst-case scenarios.

The IAEA recommends concentric EPZ zones called PAZ near the plant for immediate measures once release is expected and UPZ for rapid protective actions. Post-Fukushima, recommended planning area increased significantly, with Extended Planning Distances (EPD)[4] up to 100 km and Ingestion and Commodities Planning Distance (ICPD)[5] up to 300 km.

The SMR Regulators' Forum (2015–2018) [13] addressed challenges in applying EPZ concepts to SMRs, advocating a graded, site-specific approach that considers design features and possible accident scenarios with smaller inventories, passive safety features and possibly slower accident progression. While smaller EPZs for SMRs are possible, current IAEA methodologies are mainly those for large reactors, lacking adaptation for SMR-specific safety innovations. Future guidance should integrate lessons from modern studies, emphasizing optimization and justification principles.

2.4. IAEA CRP projects

WP6 reviewed results from two IAEA Coordinated Research Projects (CRPs) focused on EPZs for SMRs. The earlier CRP (I25001, 2010) [14] examined small reactors without on-site refueling, producing TECDOC-1652 [15], which addressed reactor characteristics and emergency planning, proposing a methodology to redefine EPZs using Probabilistic Risk Assessment (PRA) and deterministic dose evaluations. The approach aimed to reduce EPZ size for innovative SMRs while maintaining safety level.

The later CRP (I31029, 2018–2021) [16] involved participants from 12 countries, aiming to establish technical bases for EPZ sizing for SMRs, particularly relevant for urban or industrial heat applications. Objectives included:

1. defining criteria for EPR based on SMR safety features (e.g. smaller STs, enhanced safety systems),
2. developing methodologies linking SMR design to offsite arrangements, and
3. contributing to future IAEA guidance on EPZ determination.

Research focused on modelling radioactive inventories, STs, and off-site dose assessments to compare against national and international protective action levels. While most participants calculated reference accident cases for specific SMR designs, broader methodological discussions also occurred. A TECDOC summarizing these findings is still pending publication.

2.5. Different safety approaches: risk-informed, generic vs. specific etc.

WP6 also discussed the characterization and classification of various methodologies for determining EPZs for nuclear installations, particularly with regard to their applicability for SMRs. Two main categories can be described as generic and specific. Generic approaches apply fixed distances based on conservative assumptions without considering plant-specific details, relying on bounding calculations for STs and atmospheric dispersion. These methods are simple and widely used but often overly conservative and

[4] **Extended Planning Distances (EPD)**: The extended planning distance is the distance within which arrangements at the preparedness stage (before an emergency) need to be made to monitor the dose rates from deposition [9].

[5] **Ingestion And Commodities Planning Distance (ICPD)**: distance at which urgent restrictions are placed on the consumption and distribution of local produce, wild-grown products (e.g. mushrooms and game), milk from grazing animals or rainwater that need to be implemented before or shortly after a release in order to: (a) significantly reduce the risk of an increase in the thyroid cancer incidence due to radiation induced cases, and (b) to reduce doses in excess of the generic criteria given in Table 23 of [9].

misaligned with smaller inventories and advanced safety features of modern SMR designs. Specific methodologies, by contrast, incorporate plant-specific safety analyses, accident scenarios, and plant PRA, offering tailored EPZs that reflect actual design and safety features. Within specific approaches, deterministic methods use bounding SA scenarios, while probabilistic methods employ Level 2 PRA results to estimate accident frequencies together with consequences. Hybrid or risk-informed approaches combine deterministic dose calculations with probabilistic insights to balance conservatism and practicality.

WP6 also attempted to classify some national and international EPZ practices, including IAEA guidelines, UK's REPPIR 2019 [17] framework, and examples from France, Belgium, Slovakia and the Netherlands. Probabilistic and mixed approaches can significantly reduce EPZ size, potentially to site boundaries, by leveraging SMR safety features. However, these methods are computationally demanding and require regulatory maturity and ultimately, for best acceptance, harmonized probability thresholds across jurisdictions. WP6 work includes a SWOT analysis for deterministic (see Table I), probabilistic, and mixed approaches, highlighting trade-offs in implementation complexity, exploitation of SMR inherent safety features, conservatism, and alignment with EU and global practices. While deterministic methods remain straightforward and widely understood, probabilistic and mixed approaches, though challenging, offer opportunities for optimized EPZs and broader SMR deployment, provided harmonization and technical capability are achieved.

Table I. SWOT Analysis for the Deterministic Approach (ENEA)

	Strengths +	**Weaknesses -**
Internal Factors	• Easy to implement (no need for PSA-2) • Easy to check and verify • Well known and established	• Not exploiting, in ST use, the inherent safety features of some SMRs • Over-conservative in results
	Opportunities +	**Threats -**
External Factors	• Depends only on Intervention Levels, which should be harmonized in EU • Easy to implement in different EU countries, even in those with lower background in PSA	• Results not supportive of SMR non-electric uses • Not aligned with USA, UK or Canada practice • Considered too much old-fashioned? • Perhaps not reaching the goal of EPZ harmonization in EU for a given design

2.6. SMR-specific dispersion and exposure considerations

If expecting to find exceedance of dose limits in SMR cases nearer to the plant than currently typical for large LWRs, it is more important than before to have physically realistic modelling of atmospheric dispersion in the near-field, with still a lot of influence from ST parameters and possible building etc. obstacles. For larger plants, such distances have been included in the EPZ anyway. Some particularities of near-field dispersion that were identified in WP6 work can be listed as follows:

- Many SMR designs locate the reactor underground, or at least the size of the building is smaller than for large NPPs. Possibly the initial heat content is smaller. These factors will make the effective release height smaller, meaning a more concentrated radioactive cloud in the nearby areas. Furthermore, the possible offsite adverse effects are inherently located more pronouncedly in the

nearby areas only, because of the small source. Potential siting near population centres makes it very important to study those near-field effects in great detail.
- Building wake: Turbulent eddies around buildings provide more initial spread.
- Stack-tip downwash (buildings and other structures causing downwards transfer of activity concentrations)
- Cloud rise (plume rise): Initial upward momentum and heat content make the release rise higher than stack height right at the starting point. Even when iPWR plants are not expected to have tall stacks, the effect may not be negligible, depending on how the release enters the atmosphere.
- Near-field dispersion parameters: Weather mast measurements may be more reliable near the source than NWP (numerical weather prediction) model, but more masts than one single would make the data even more reliable and complete.
- Very narrow plume: It takes some time for the release to spread in the lateral and vertical directions, and when e.g. using the Gaussian model, choice of appropriate parameters is very important.
- Urban / industrial terrain: Terrain roughness may decrease wind speeds locally and induce turbulence. Furthermore, spread directions may favour street 'canyons' etc.

In many dose pathways (exposure modes), there are potentially some specific considerations to perform an accurate assessment of doses, originating specifically from the siting and small size of SMR plants:
- Cloudshine: In many codes, the so-called 'semi-infinite uniform' approximation of the radioactive cloud is used. Then the radiation source is a uniformly distributed concentration [18] in a half-space (or practically, a half-sphere). With SMR plants, we are interested in the close surroundings, and it is important to consider the cloudshine source in all of its possible physical reality / realizations: In some cases, a long, narrow plume extending as such relatively far (even several kilometers) from the source (cf. the LINCON code used to generate cloud gamma dose conversion coefficients for ARANO). In urban environment, big buildings may provide considerable shielding effect against external radiation.
- Groundshine: In population centers and in industrial settings, deposition will not accumulate only on ground surface and vegetation, but to a relatively large extent also on the surfaces of buildings. They will become an additional source of radiation. Their decontamination is usually laborious. On the other, buildings provide some shielding for more faraway radiation source.
- Inhalation: In urban environment, with a large population in a large number of buildings, the inhalation dose caused by inhaled radionuclides indoors is a particularly important consideration. Air-tightness and ventilation systems of the buildings determine how much activity will be inhaled indoors. Depending on the systems, it may be possible to considerably reduce the internal dose commitment.
- Ingestion: Traditionally, and with regard to usually defined representative person, the conservative assumption of all consumed foodstuff being produced locally, very near the target population, has been used. However, this is seldom true in today's world, where foodstuff are routinely transported over great distances before being offered to consumers. It is even less true for SMR surrounding environment which may be urban or industrial, and in any case the area affected by significant deposition is expected to be smaller.

3. OFFSITE DOSE ASSESSMENTS BEFORE CONTAINMENT CALCULATIONS

In the SASPAM-SA project, two hypothetical generic iPWR designs were defined to be considered in detail in all WPs and phases of the project:
- Design 1: A generic iPWR characterized by a submerged containment and electric power of about 60 MWe;
- Design 2: A generic iPWR characterized by the use of several passive safety systems, a dry containment and an electric power of about 300 MWe.

Several SASPAM-SA project partners working in WP6 (ENEA, JRC, KIT, KTH, LEI, POLIMI, SSTC NRS, TUS, UNIROMA, VTT) selected one of the designs to study with regard to potential atmospheric radioactive releases and offsite doses. In the conservative phase of the project, detailed SA code calculations of the phenomena in reactor core and containment were in most cases not used.

Each partner had the freedom to select representative accident scenarios to study, including both Design Basis Accidents (DBAs) and SAs. The selection of scenarios common to the project was defined by WP2 and had various postulated breaks in piping, malfunctions of valves and failures of safety systems. The scenarios enable performing varied assessments of radionuclide behaviour and containment performance, which is the topic of WP5. The diversity of cases ensured that the study so far captured a broad spectrum of released amounts of radionuclides. The selection of scenarios is crucially important for EPZ determination purposes. In WP6, it was concluded that some consideration should be paid to the probabilities of the scenarios, in order to not use e.g. only extremely unlikely cases to calculate the dose consequence footprint areas.

STs are affected by assumed fuel burnup, which was available from WP2 for 20 to 60 MWd/kg in steps of 2.5 MWd/kgU; higher burnup means more accumulation of long-lived isotopes. From WP2, there was the inventory of 304 nuclides available [19]. Fractions of inventory released to the atmosphere usually depend on nuclide chemical group. The atmospheric release may happen at temporally variable release rates. Simple offsite dose codes typically only accept a uniform rate; more sophisticated codes can use any temporal evolution. Obviously, released amounts of activity have a very big and direct effect on off-site doses, the exact effect depending on nuclide. For final phases of SASPAM-SA, the releases will come from WP5 results. In previous studies it was typically found that the biggest uncertainty in offsite doses (and so also in the EPZ sizing) is coming from the (poor) knowledge of the ST, while also other, subsequent uncertainties do exist.

The preliminary / conservative analyses by WP6 partners considered a broad range of input parameters, like the variability in ST evaluations. Fuel burnup values ranged from 15 to 60 MWd/kgU, representing conditions from early to extended core reloading. Radionuclide inventories used included 2 – 71 species, mostly ensuring coverage of key fission products and activation products relevant to safety assessments. Atmospheric release fractions were highly dependent on chosen scenario and expert judgement by partner, spanning from fraction 1e-5 to whole inventory, depending on nuclide, reflecting both conservative (or even extremely conservative) SA release assumptions and more realistic ones, and also more probable design-basis accident conditions. These ranges provided a good readiness basis for evaluating containment performance and radiological consequences under diverse accident scenarios.

As an example of the initial conservative phase of WP6, the atmospheric source term used in the LEI analyses was developed by applying a simplified large PWR methodology consistent with U.S. NRC RG 1.183 [20] and with the source term evaluation approaches discussed by Mitrakos, 2022 [21]. In this LEI specific approach, a prompt LOCA driven release without delay was assumed, using standard PWR release fractions for noble gases, iodines, and aerosols. Radionuclide behaviour in the containment was calculated through a time dependent balance of release, decay, deposition, and a conservative leakage rate of 0.65 % d^{-1}. This methodology produced nuclide specific released fractions like in Fig. 1 below.

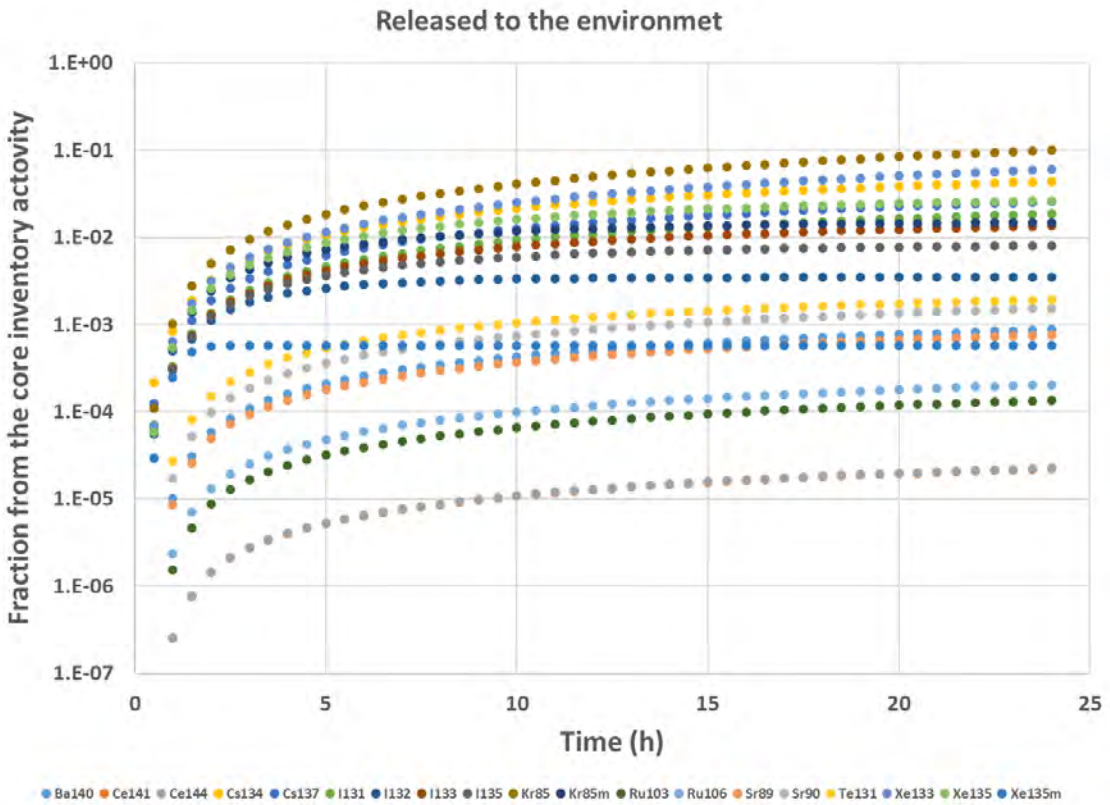

Figure 1. Nuclide-specific cumulative released fractions to the environment of the core inventory of Design-2. A sample case from the initial conservative phase approach by LEI, to illustrate some of the source term features needed for the subsequent atmospheric dispersion modelling.

In addition to released amounts of activity, STs must be described by also a number of other release parameters, like effective release height (or distribution on various atmospheric transport starting heights), and release duration, with possible temporal variations of nuclide-specific release rates. Effective release height is typically defined by height of stack or containment breach hole, increased by the effect of plume rise by momentum and buoyancy. Several off-site dose codes use the inventories at reactor shutdown time, corrected by the so-called delay time (time for radioactive chain decay and various other decontaminating processes between shutdown and start of atmospheric release). Decay inherently continues also during release duration and atmospheric dispersion. All the mentioned release parameters have a major effect on off-site doses; their increase leads to doses decreasing).

The modelling of atmospheric ST in WP6 incorporated a wide range of temporal and spatial release parameters, reflecting different assumptions on possible accident progression. Release delay times varied from the unrealistic zero to more than one day, depending on assumptions made about containment integrity and safety systems response. Effective release heights ranged from ground level for containment bypass or venting scenarios to more than 100 m for stack discharges with cloud rise, influencing the subsequent atmospheric dispersion patterns. Release durations spanned from rapid emissions lasting for one hour to prolonged releases over several days, corresponding to severe accident conditions with only a gradual leakage. These variations represent coverage of potential off-site radiological consequences on many levels of severity.

Assumed iPWR site in WP6 could be anything from operating NPP site to proposed newbuild site and a completely hypothetical one. The partners mostly selected representative locations within their countries, typically existing nuclear sites or candidate SMR deployment areas, while also ensuring realistic dispersion and population data. Off-site doses generally depend on site-specific environment and weather conditions. As the source of weather data, both Numerical Weather Prediction (NWP) reanalysis (data assimilation of past prediction data with observations) and site mast measurements were used, with the size of the data set chosen according to the needs of deterministic or statistical study. For near field calculations (as expectedly most interesting and typical for small iPWR), local weather mast measurements may be better representative than numerical data with large grid cells. Meteorological inputs for WP6 work were obtained from national weather services, site-specific historical datasets, or publicly available databases such as ERA5 reanalysis, providing wind speed, direction, temperature, and stability classes (one point or 3D) for dispersion modelling.

The code tools of WP6 implement physical models for atmospheric dispersion and off-site dose projection. They typically have a large number of possibly user-tunable parameters, like dry deposition velocity, washout coefficient, dose and dose rate conversion factors, shielding factors, breathing rates etc. Partners used their chosen set of dose criteria, i.e. limits of projected (or averted) dose, above which actions should be implemented to reduce doses to people. When using statistical / long-term weather data, also confidence levels are chosen, meaning the fractile (percentile), e.g. 95 %, of all values such that the dose was lower (or EPZ smaller) in 95 % of all cases, called P95 in short. In WP6 so far, the partners used a mix of established calculation tools for ST and dispersion modelling, including RODOS, MACCS, RASCAL, GENII, HotSpot, ARANO, and as well as some in-house / national methodologies. As for the radiation dose criteria, evaluations were based on standard IAEA or national regulatory limits for public exposure, typically expressed in terms of e.g. effective dose (mSv) for short-term health effects. With statistical weather, meteorological sampling applied percentile-based confidence levels, most commonly 95%, to ensure conservative enough estimates of doses under varying atmospheric conditions.

4. CONCLUSIONS

Generally SASPAM-SA WP6 on iPWR EPZ was, even in the conservative assessments phase, able to demonstrate that the EPZ for iPWR could potentially be reduced from that of large LWRs. Conservative and deterministic assessment of off-site doses is basically usable also for SMRs. Also the IAEA SMR Regulators' Forum Pilot project report [13] concludes about EPZ that '*the IAEA safety requirements and methodology for determining the EPZ size are effective in establishing an emergency preparedness and planning program*'. After the conservative assessments phase of SASPAM-SA WP6, the calculations using a BE ST will show if further reduction of iPWR EPZ seems feasible. This will depend on assumed mitigative strategies to reduce the emissions from the containment to outside atmosphere. If only very near-range doses turn out to be decisive for EPZ size, then probably some improvements to near-field dispersion and dose models would be recommended.

A possibly justifiable way to further reduce the iPWR EPZ size (even with conservative STs) is to replace the so far most used deterministic worst-case methodology, to a risk-informed approach. This is however outside the scope of the present SASPAM-SA project, in lack of the full spectrum of STs and their associated probabilities from PSA level 2. For future projects, some knowledge of the order of magnitude of Design Extension Condition (DEC)-A and DEC-B frequencies / probabilities could be useful. Some nuclear regulators are considering or going to consider a risk-informed methodology, meaning to take into account also the probabilities of accident sequences and the associated offsite consequences, not only their magnitudes.

In future projects, creating an EPZ database for DEC-A and DEC-B can be recommended. The US 'traditional' EPZ distances (10 / 50 miles) originate in part as kind of generalization of the results of the

influential WASH-1400 study (1975) [22] where several NPPs and also SA sequences for them were considered. Likewise for the EPZ determination of present iPWR (and other SMRs) it would be beneficial that several plant types and SA releases be considered. Also, there is no one single 'correct' off-site consequence code that calculates the most reliable results. To draw conclusions that are useful for regulators and operators willing to site their plant, it would be good to have much more results than just single plant type – single accident scenario – single ST – single approach to EPZ calculation.

Co-location of SMRs presents many cases: colocation of several modules / units, siting reactor(s) in a populated city, or reactor(s) in industrial area (like oil refinery, hydrogen production, fertilizers, steel, etc). There are events like common cause failure, or e.g. industrial accident affecting nuclear plant, or nuclear radioactive release affecting the industry, thus also the possibility of simultaneous conventional and nuclear emergency. Too high dose rates and contamination may slow down emergency management efforts. Also there are some new considerations to calculate dispersion, deposition and external / internal doses when accidents happens in built environment. Those would be good to study more in more detail.

NOMENCLATURE

BE	Best Estimate
CRP	Coordinated Research Project
DBA	Design Basis Accident
DEC	Design Extension Conditions
EDP	Extended Planning Distances
EPC	Emergency Preparedness Categories
EPZ	Emergency Planning Zone
EU	European Union
IAEA	International Atomic Energy Agency
ICPD	Ingestion And Commodities Planning Distance
iPWR	Integral Pressurized Water Reactor
LWR	Light Water Reactors
NPP	Nuclear Power Plant
PAZ	Precautionary Action Zone
PRA	Probabilistic Risk Assessment
PWR	Pressurized Water Reactor
SA	Severe Accident
SASPAM-SA	Safety Analysis of SMR with PAssive Mitigation strategies – Severe Accident
SMR	Small Modular Reactor
ST	Source Term
UPZ	Urgent Protective Actions Zone
WP	Work Packages

ACKNOWLEDGMENTS

Funded by the European Union

Funded by the European Union. Views and opinions expressed are however those of the author(s) only and do not necessarily reflect those of the European Union or European Commission-Euratom. Neither the European Union nor the granting authority can be held responsible for them.

The authors would like to thank Prof. Rositza Kamenova-Totzeva (National Center of Radiobiology and Radiation Protection, Sofia, Bulgaria) for her valuable review of the manuscript and her constructive contribution regarding the conservative assessment of TUS.

REFERENCES

1. https://zenodo.org/communities/saspam-sa/about
2. F. Mascari et al., *Horizon Euratom SASPAM-SA project: main ideas and first outcomes*, in Proceedings of the International Conference on Small Modular Reactors and their Applications, 21–25 October 2024, Vienna, Austria (2024)
3. Herranz L.E., Poubeau B., Chailan L., Mascari F., *Looking ahead to severe accident research* (2025) EPJ Nuclear Sciences and Technologies, 11, art. no. 28, DOI: 10.1051/epjn/2025025
4. Gabrielli, F. (2024). *Analysis of postulated severe accidents in generic integral PWR small modular reactors in the frame of the horizon euratom SASPAM-SA project*. The 11th European Review Meeting on Severe Accident Research (ERMSAR2024), KTH, Stockholm, Sweden. Zenodo.
5. Principato, M. (2024). *In vessel melt retention 0d model for integral pressurized water reactors*. The 11th European Review Meeting on Severe Accident Research (ERMSAR2024), KTH, Stockholm, Sweden. Zenodo
6. Lind, T. (2024). *SASPAM-SA: Assessment of the relevance and applicability of existing experimental databases to iPWR*. The 11th European Review Meeting on Severe Accident Research (ERMSAR2024), KTH, Stockholm, Sweden. https://doi.org/10.5281/zenodo.12645051
7. Directive 2013/59/Euratom - protection against ionising radiation | Safety and health at work EU-OSHA
8. Council Directive 2014/87/Euratom of 8 July 2014 amending Directive 2009/71/Euratom establishing a Community framework for the nuclear safety of nuclear installations, Directive - 2014/87 - EN - EUR-Lex
9. *EPR-NPP public protective actions 2013, Actions to Protect the Public in an Emergency due to Severe Conditions at a Light Water Reactor*, 2013, IAEA, Vienna, Austria Actions to Protect the Public in an Emergency due to Severe Conditions at a Light Water Reactor | IAEA
10. IAEA Safety Standards, *Preparedness and Response for a Nuclear or Radiological Emergency*, General Safety Requirements No. GSR Part 7, 2015, Vienna, Austria. P_1708_web.pdf
11. J. Fingleton, Nuclear Regulatory Review, UK, 2025
12. *Radiation and Nuclear Safety Authority Regulation on the Emergency Arrangements of a Nuclear Power Plant,* STUK Y/2/2024, STUK Y/2/2024 | Regulation | Stuklex
13. SMR Regulators' Forum Pilot Project Report: Report from Working Group on Emergency Planning Zone January 2018, APPENDIX IV - SMR RF Report_29.01.2018
14. Small Reactors Without On-Site Refuelling | IAEA
15. IAEA-TECDOC-1652: Small Reactors without On-site Refuelling: Neutronic Characteristics, Emergency Planning and Development Scenarios Final Report of an IAEA Coordinated Research Project | IAEA, IAEA, 2010, Vienna, Austria
16. Development of Approaches, Methodologies and Criteria for Determining the Technical Basis for Emergency Planning Zone for Small Modular Reactor Deployment | IAEA
17. Radiation (Emergency Preparedness and Public Information) Regulations 2019 (REPPIR) - HSE
18. ICRP, Dose coefficients for external exposures to environmental sources. ICRP Publication 144. Ann. ICRP 49(2) (2020).
19. Gabrielli, F. (2024). Fuel inventory of the iPWR Design-1 and Design-2. Zenodo. https://doi.org/10.5281/zenodo.14052163
20. U.S. Nuclear Regulatory Commission, Alternative Radiological Source Terms for Evaluating Design Basis Accidents at Nuclear Power Reactors, Regulatory Guide 1.183, Washington, D.C. (2000).
21. D. Mitrakos, Radiological impact and emergency zones for small iPWR with different approaches for source term calculation, Progress in Nuclear Energy, Vol. 145, 104123 (2022). DOI:10.1016/j.pnucene.2022.104123.
22. OFFICIAL EXHIBIT - RIV000147-00-BD01 - NUREG-75/014 (WASH-1400), Reactor Safety Study: An Assessment of Accident Risks in U.S. Commercial Nuclear Power Plants (1975).

SAFETY ANALYSIS OF SMR WITH PASSIVE MITIGATION STRATEGIES - SEVERE ACCIDENT

ASSESSMENT OF EMERGENCY PLANNING ZONE FOR iPWRs WITHIN THE HORIZON EURATOM SASPAM-SA PROJECT

ERMSAR2026, 19 May 2026, Madrid

Mikko Ilvonen / VTT (WP6 lead)
& WP6 Partner Institutes

Rocchi F, Murat O, Acharya G, Slavickas A, Casartelli E S, Kyrylenko Yu, Ivanov I, Giannetti F, De la Rosa Blul H C, Guglielmelli A, Mascari F

VTT Nuclear Energy (Finland)

WP6 (EPZ) introduction

SAFETY ANALYSIS OF SMR WITH PASSIVE MITIGATION STRATEGIES - SEVERE ACCIDENT

- Assessment of EPZ zones for iPWRs within the Horizon Euratom SASPAM-SA Project
- SASPAM-SA project (Safety Analysis of SMR with PAssive Mitigation strategies – Severe Accident)
- Applicability of current state-of-the-art severe accident codes against hypothetical generic iPWRs
- WP6 (EPZ) considers the offsite dispersion and doses caused by radioactive releases from SA.
- Initially, a set of varyingly conservative calculations were performed.
- The codes used in WP6 included JRODOS, MACCS, HotSpot, RASCAL, GENII and ARANO.
- In the current phase, more refined Best Estimate BE source terms from WP5 ('Containment') are being used to avoid exceedingly conservative results.
- Detailed SA code (WP5) data about actual nuclide content, activities, temporal release rate trend, effective release height etc.
- General expectation is that SMR smaller inventories and longer delays before any atmospheric release might lead to smaller dose consequences.
- Acceptance of SMR plant sites near (or even in) densely populated areas?
- WP6 attempts to understand limits, if any, of the current codes and/or methods and approaches in producing sound and reliable data for EPZ extents of iPWRs.

SASPAM-SA (2022-2026) WP connections

SAFETY ANALYSIS OF SMR WITH PASSIVE MITIGATION STRATEGIES - SEVERE ACCIDENT

Safety Analysis of SMR with PAssive Mitigation strategies – Severe Accidents

Adapt existing LLWR safety knowledge to iPWRs in Europe

- **Experiments, SA codes, dispersion & off-site doses**

Two generic iPWR designs:

- **D1: Characterized by a sub-merged containment and ~60 MWe**
- **D2: Several passive systems, dry containment, ~300 MWe**

WP5: From mechanistic modelling of containment phenomena to atmospheric releases

WP6: Study capability to assess extent of EPZ zones (PAZ and UPZ) needed for iPWR site

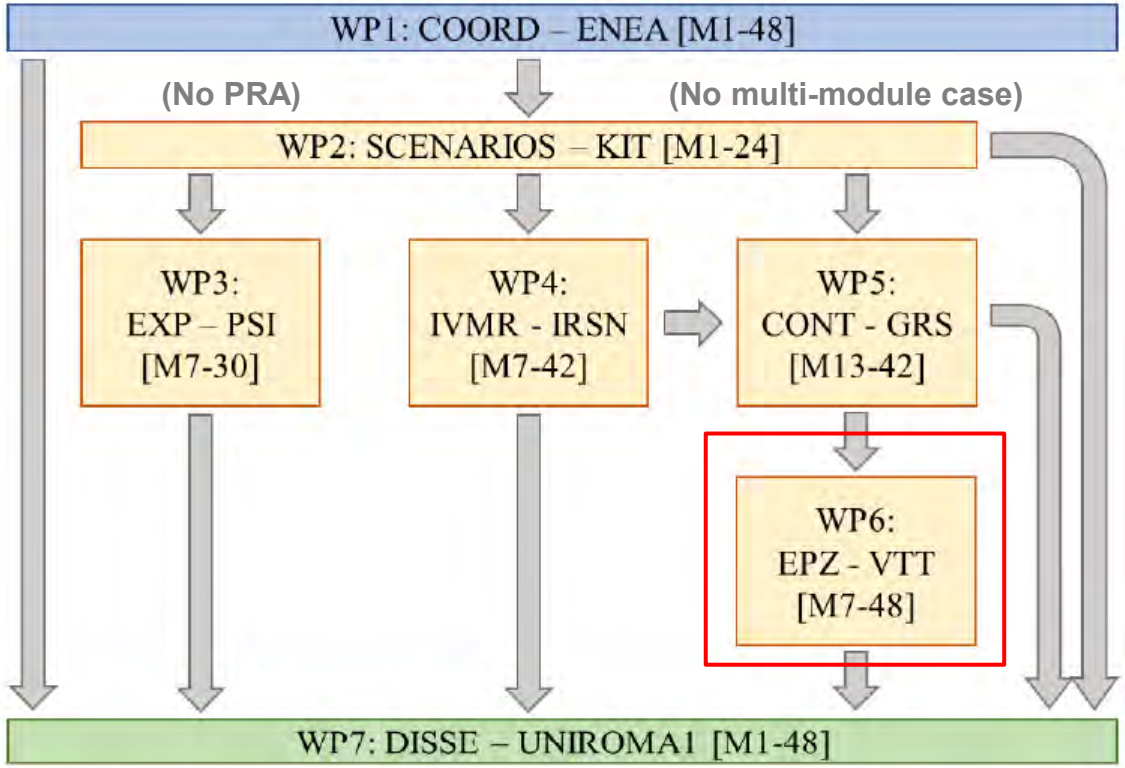

Figure 5 SASPAM-SA project diagram and WP interconnections.

EPZ: Emergency planning zone

(IAEA)

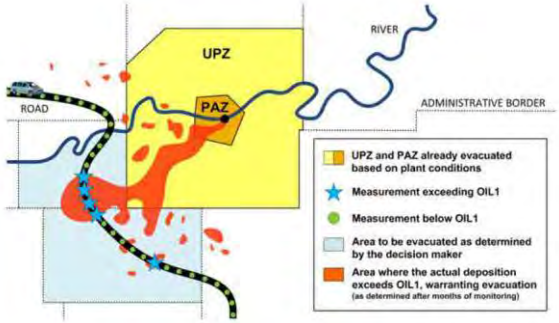

- PAZ (precautionary action zone): smaller, inner zone
- UPZ (urgent protective actions planning zone): larger, outer zone
- Avoid or minimize severe deterministic effects / avert doses offsite

- Why important to determine?
  - PAZ: Urban planning (in city plan area) starts well in advance
  - EPZ will affect actual siting decision
  - EP&R (Emergency preparedness & response) planning
  - DiD Level 5, independently: Off-site emergency response to mitigate radiological impact
  - People want to know their potential radiological risks (not technical details)
- Benefits from potentially reduced EP&R / EPZ:
  - Siting closer to densely populated areas, particularly important for heat
  - Overall decreased cost of maintaining emergency preparedness
- Potential justification:
  - Small inventory, potentially easier heat transfer, advanced safety features (often passive)
  - With various time delays, Early Release unlikely

Tasks of WP6 (SMR EPZ)

SAFETY ANALYSIS OF SMR WITH PASSIVE MITIGATION STRATEGIES - SEVERE ACCIDENT

- SASPAM-SA, 2022-2026, possible extension to 31 March 2027, coordinator ENEA
- Structure of SASPAM-SA WP6 (EPZ), Task lead VTT / Ilvonen
  - Task 6.1: Critical **review** of existing EPZ methodology
    - Partners: ENEA, LEI, POLIMI, SSTC NRS, TUS, UNIROMA1, VTT, JRC
  - Task 6.2: Preliminary **conservative offsite dose** assessments
    - Partners: ENEA, CIEMAT, KIT, KTH, LEI, POLIMI, PSI, SSTC NRS, TUS, UNIROMA1, VTT, JRC
  - Task 6.3: Offsite doses & EPZ by **best estimate (BE)** approach
    - Partners: ENEA, KIT, KTH, LEI, PSI, SSTC NRS, TUS, UNIROMA1, VTT
  - Task 6.4: Conclusions on iPWR EPZ & **recommendations on methodology**
    - Partners: ENEA, KIT, KTH, LEI, POLIMI, PSI, SSTC NRS, TUS, UNIROMA1, VTT, JRC
  - CNL (Canada) joined during project by amendment

WP6 review of EPZ methodologies

Relation of IAEA documents with EPZ determination – by ENEA, JRC, TUS, VTT

1. GSR Part 7 (2015): 'Preparedness and Response for a Nuclear or Radiological Emergency'
   - Establishes requirements for an adequate level of preparedness and response for a nuclear or radiological emergency, irrespective of its cause; "**What should be achieved**"
   - Appendix II has tables of generic limits expressed as doses
2. GS-G-2.1 (2007): 'Arrangements for preparedness for a nuclear or radiological emergency'
   - Recommendations on implementation of specific safety requirements
   - "**What should be done and how**"
3. EPR NPP PPA (2013): 'Actions to Protect the Public in an Emergency due to Severe Conditions at a Light Water Reactor' – IAEA EPR Series publication
   - Basic information and criteria needed by a decision maker in order to protect the public during an emergency involving SA in LWR); applies to reactors with power > 100 MWth
   - Appendix I: Basis for the suggested size and protective actions within the emergency zones and distances: "Zone size calculations are very uncertain and based on very simple assumptions"

WP6 review of EPZ methodologies

SAFETY ANALYSIS OF SMR WITH PASSIVE MITIGATION STRATEGIES - SEVERE ACCIDENT

Relation of IAEA documents with EPZ determination – by ENEA, JRC, TUS, VTT

- IAEA guidelines and examples of methodologies to estimate the EPZ are suited for large LWRs.
- For SMR guidance on practical implementation, focus should be put on specific technologies.
- Technology neutrality should be foreseen for higher-level documents, like Safety Requirements.
- Information from MSs to start discussion: Consultancy Meetings, CRPs and the production of TECDOCs
- TECDOC from CRP I31029 (2018-21, 'SMR EPZ methods') has been in preparation.
- Not considering the principles of justification and optimization >> national, site/society dependent
- Possible differences in STs between SMRs and large LWRs >> effectiveness of countermeasures?

- The IAEA EPZ reference approach can be found in IAEA document EPR-NPP PAA 2013, Appendix I:"Basis for Suggested Size and Protective Actions within the Emergency Zones and Distances".
- In this approach plant-specific feature as well as meteorological conditions, presence of buildings, terrain complex morphology are not taken into account.
- It is based on a deterministic safety analysis postulating conditions for a Severe Accident (SA) and Radiological Consequences (RC) event.

Country review: Still mostly fixed EPZ sizes

- **Country-specific EPZ regulations – by ENEA, JRC, LEI, SSTC NRS, TUS, VTT, CNL**
- **Considered 17 countries & EU level**

EU (Directives 2013/59 and 2014/87)
Belgium regulation (10 / 20 km)
Bulgaria emergency planning system
Canada regulation
Czech regulation (5-10 / 13-20 km)
Finland offsite dose limits and EPZ size
France regulation (5 / 20 km)
Hungary regulation (30 km)
Italy
Lithuania current regulations on EPZ (5 / 30 km)
Netherlands regulation (5 / 10 / 20 km)
Romania regulation (10 km)
Slovakia regulation (5-10 / 20-30 km)
Slovenia regulation (10 km)
Spain regulation (10 km)
Sweden (5 / 25 km)
Ukrainian requirements for EPZ sizing
USA

- Mostly fixed EPZ zone sizes, made for large LWR.
- Flexibility can be found in USA, Canada, UK and Finland.

Finland's EPZ in new (2024) regulations

SAFETY ANALYSIS OF SMR WITH PASSIVE MITIGATION STRATEGIES - SEVERE ACCIDENT

- 2. The precautionary action zone (PAZ) shall be defined in such a way that, in the event of an accident, there is a high probability that there will be no need to evacuate the population beyond the PAZ and that the necessary evacuation measures can be effectively carried out inside the PAZ in order to prevent or limit severe deterministic effects of ionising radiation. In order to enable effective evacuation, the PAZ shall be subject to land use restrictions.
- 3. When determining the size of the PAZ, it shall be demonstrated that, in the event of an accident, the radiation dose of an unprotected person outside the PAZ will not exceed 1 Sv within 10 hours of the start of exposure.
  - (Note: 1 Sv in 10 h appears in Table II.1 of IAEA GSR Part 7 for red bone marrow.)
- 4. The emergency planning zone (EPZ) shall be determined in such a way that, in the event of an accident, there is a high probability that there will be no need for the population to shelter indoors outside the EPZ.
- 5. When determining the size of the EPZ, it shall be demonstrated that, in the event of an accident, the radiation dose of an unprotected person outside the EPZ will not exceed 10 mSv within 48 hours of the start of exposure. The EPZ can be limited to a maximum distance of approximately 20 km.
  - (Note: 10 mSv in 2 d has long been the threshold for sheltering in STUK VAL regulations.)

- How to practically implement the new flexibility of STUK Y/2/2024 (Feb 2024) ?
  - Licence applicant must present and justify the size of EPZ for their plant.
  - Flexible scheme facilitates early start of urban planning for SMR projects.
  - For the EPZ size, possible assumptions (What should be the accident scenarios ?):
    - Large amount of released radioactive material is in the containment
    - There is some breach or by-pass of the containment
  - That is clearly, multiply failing management of a severe accident.
  - More detailed 'lower-level' regulations are expected to appear later during the legislation reform process – 2026?

New Decree (2026) additionally states:

- Early releases: Must have 5 h from accident start for protective measures
- Outside PAZ, Cs-137 deposition must remain less than 400 kBq/m2 (suffices to avoid evacuation, i.e. 20 mSv/week)

Choices for flexible EPZ approaches

- Probabilistic (cf. PSA levels 1-2-3) vs. deterministic ('worst plausible / maximum credible' scenario & possibly 'worst weather case, with stable atmosphere and low wind speed'
  - Probabilistic approach to atmospheric source term (ST) has all the release parameters (nuclide-specific activities etc.) but also some information of the expected frequency of such a release to happen.
  - Probabilistic approach to dispersion uses a large number of weather conditions, e.g. site hourly measurements for several years, and uses each of them to calculate offsite doses resulting from one given source term >> result is probability distribution of dose (or rather, doses, via pathway, at distance & integration time).
  - The combined approach could be completely deterministic, completely probabilistic, or hybrid (mixed) of the two.
  - IAEA IEC: 'Probabilistic can be used as complementary to deterministic'
- Consequence based (dose / health effect)
  - Predicted – averted – residual dose (as basis for choosing protective measures) ?
  - Look at only individual doses (STUK / Finland), or make a difference by using population dose (manSv, based on population distribution), even when individual doses the same?
- Risk-informed (US NRC new ruling 2023); Risk based (probability x consequence)

Deterministic / probabilistic approaches

SAFETY ANALYSIS OF SMR WITH PASSIVE MITIGATION STRATEGIES - SEVERE ACCIDENT

Comparison of different approaches to NPP offsite safety – by JRC, ENEA in WP6

-- SWOT analysis for the deterministic approach, by ENEA:

	Strengths +	Weaknesses -
Internal Factors	• Easy to implement (no need for PSA-2) • Easy to check and verify • Well known and established	• Not exploiting, in source term used, the inherent safety features of some SMRs • Over-conservative in results
	Opportunities +	Threats -
External Factors	• Depends only on Intervention Levels, which should be harmonized in EU • Easy to implement in different EU countries, even in those with lower background in PSA	• Results not supportive of possible SMR non-electric uses, like small district heat-only reactor • Not aligned with USA, UK or Canada practice • Considered too much old-fashioned? • Perhaps not reaching the goal of EPZ harmonization in EU for a given design

-- SWOT analysis for the probabilistic approach (full-scope PSA-3), by ENEA:

	Strengths +	Weaknesses -
Internal Factors	• Full exploitation of declared improved and inherent features of some SMRs • Proper estimation of safety margins • Possible limitation of EPZ to site boundaries	• Difficult to implement • Enormously time-demanding, especially if considering the use of microscale ATM dispersion • Too little experience among EU regulators?
	Opportunities +	Threats -
External Factors	• Possible important role in SMR massive deployment • In line with USA, UK and Canada practice	• Are EU regulatory bodies ready for it? • Depends on decision on probability thresholds: is EU harmonized on this?

Practical work: Off-site doses footprint area

SAFETY ANALYSIS OF SMR WITH PASSIVE MITIGATION STRATEGIES - SEVERE ACCIDENT

- Out of scope of SASPAM-SA:
  - (Comprehensive hazard assessment, internal / external)
  - (Comprehensive listing of initiating events, or PIEs in PSA terminology)
- Preceding work packages of SASPAM-SA:
  - WP2: Selection of accident scenarios to consider
  - WP5: Containment phenomena, atmospheric source term, release parameters
- WP6 (iPWR EPZ):
  - Atmospheric physics of dispersion and offsite doses (external / internal pathways)
  - Computer codes for dispersion and offsite doses chosen in WP6
  - Site data, weather data (data source, location, time span, resolution)
  - exposure pathways, target organs, age groups, breathing rates, shielding factors, etc. etc.
  - Looking at projected, averted, or residual dose; Confidence level (e.g. P95 = 95 %)
  - Generic dose limits, protective actions, EPZ (PAZ and UPZ) sizes proposed
  - ‘Validation’ by code inter-comparisons; Uncertainties, ‘unknown unknowns’

Phenomena affecting an atmospheric release and off-site doses

SAFETY ANALYSIS OF SMR WITH PASSIVE MITIGATION STRATEGIES - SEVERE ACCIDENT

IAEA-TECDOC-379 (Atmospheric dispersion models for application in relation to radionuclide releases)

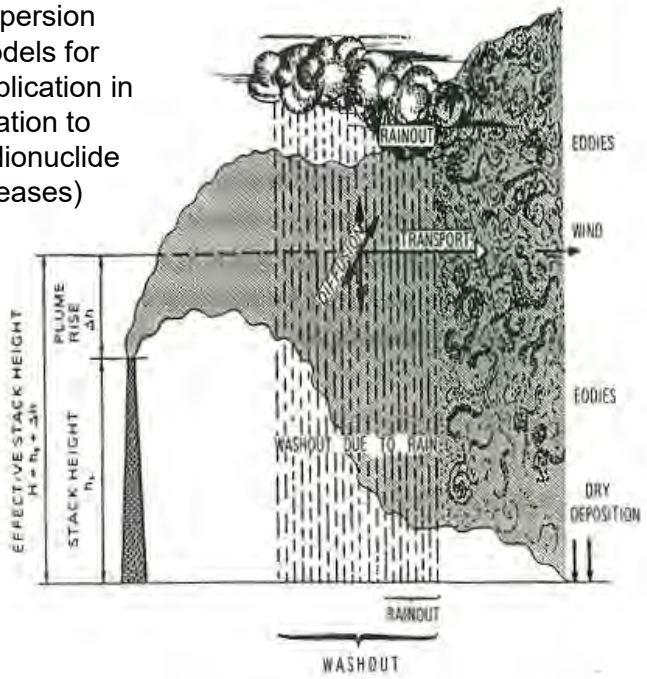

FIG.1. Behaviour of effluents released to the atmosphere.

Sandia National Laboratories: MACCS Accident Consequence Model

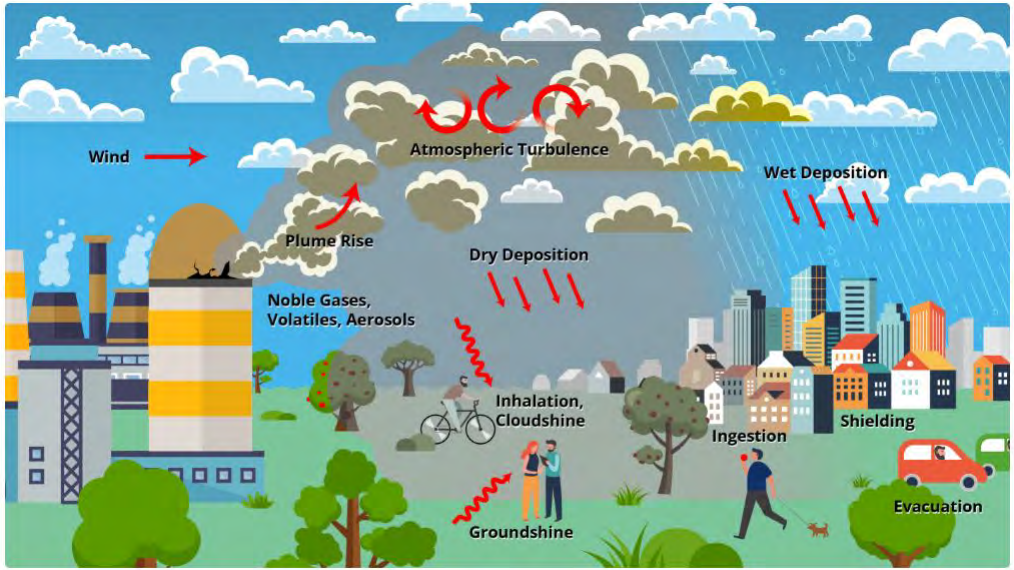

MACCS Data Flow

For EPZ in WP6, we consider: cloudshine, groundshine and inhalation

Near-field dispersion is very important

- Small initial heat content of release, small reactor building, possibly underground >> Effective release height smaller, meaning a more concentrated radioactive cloud in the near range.
- Small core >> Possible adverse offsite effects are inherently located pronouncedly in the near range.
- Siting in or near population centers makes it very important to study near-field effects in more detail.
- Building wake and stack tip / building downwash: Structures may cause immediate downwards transfer of activity, while turbulent eddies around buildings also provide more initial spread.
- Cloud rise (plume rise): Initial upward momentum, heat content >> How much rise by buoyancy?
- Near-field dispersion parameters: Weather mast measurements may be more reliable near the source than analysis fields from NWP (numerical weather prediction) model. Single point sufficient very near.
- Very narrow plume cases: It takes some time for the release to spread in the lateral and vertical directions, and when e.g. using the Gaussian model, choice of appropriate parameters is important.
- Cloudshine source is not uniform. Dry deposition and inhaled concentrations when touching ground.
- Urban / industrial terrain: Terrain roughness may decrease wind speeds locally and induce turbulence. Furthermore, spread directions may favor street ‘canyons’ etc.

- In SASPAM-SA WP6, detailed study of some of these done by SSTC NRS and CNL

WP6 collects a calculation database

- Other SASPAM-SA WPs, like WP2 and WP5, also collect calculation parameters / Key Figures of Merit from the cases calculated by all partners
- For the Conservative calculations phase (Task 6.2), WP6 partners could use their own estimates of the atmospheric source term and release parameters.
- Therefore, various choices appeared, ranging from pure expert judgement or literature-based release fractions to simple analytical calculations or actual mechanistic modelling by dedicated SA codes
- For the Best Estimate phase (BE, Task 6.3, on-going), all WP6 partners are using source term data from WP5 (Containment): The chosen scenarios and mechanistically calculated releases as function of time, for specific dose-relevant nuclides.
- The calculation databases will remain as a valuable asset for future projects as a comprehensive reference.

WP6 collects a calculation database

Scenarios, Source terms, Release parameters, Site and Weather data

	A	B	C	D	E
1	Partner	Case #	Design	Scenario	

	A	B	C	D	E	F	G	H	I	J	K	L	M	N	O
1	Partner	Case #	Number of nuclides	List of nuclides	%ii: Noble gases	%ii: Iodine nuclides	%ii: Alkaline metals	%ii: Earth alkalines	%ii: Metalloids	Released activity I-131 (Bq)	activity Cs-137 (Bq)	I_2 (% of iodine)	CsI (% of iodine)	CH_3I (% of iodine)	
2															

	A	B	C	D	E	F	G
1	Partner	Case #	Delay after SCRAM	Release duration	Constant or varying release rate	Effective release height	

	A	B	C	D	E	F	G	H	I	J	K	L	M
1	Partner	Case #	Site	Weather: Mast / 3D NWP	Weather data source	Weather time span	Horizontal resolution	Vertical resolution	Time resolution	Environment description	Roughness parameter	Mast turbulence method	

SAFETY ANALYSIS OF SMR WITH PASSIVE MITIGATION STRATEGIES - SEVERE ACCIDENT

WP6 collects a calculation database

SAFETY ANALYSIS OF SMR WITH PASSIVE MITIGATION STRATEGIES - SEVERE ACCIDENT

Dose codes and criteria; Doses and EPZ extents

	A	B	C	D	E	F	G	H	I	J	K	L
1	Partner	Case #	Dispersion code	Dose code	Code provider	Lagrangian / Euler / CFD	Dry deposition velocities	Grid resolution	External DCF set used	Internal DCF set used	Breathing rates	Shielding factors

	A	B	C	D	E	F	G	H	I
	Partner	Case #	External dose criteria	Internal dose criteria	Country	Regulator	Regulation codes	Weather cases confidence level	

	G
	Target organs / Effective dose

	Partner	Case #	External pathways considered	Internal pathways considered	Target age groups

	G	H
1	PAZ protective measure	UPZ protective measure	PAZ population	UPZ population

	Partner	Case #	PAZ extent (m)	UPZ extent (m)

WP6 Task 6.2: Chosen designs & scenarios

SAFETY ANALYSIS OF SMR WITH PASSIVE MITIGATION STRATEGIES - SEVERE ACCIDENT

- Design-1: iPWR characterized by a submerged containment and electric power of about 60 MWe
- Design-2: iPWR, several passive systems, dry containment, electric power of about 300 MWe

Listing of scenarios, available from SASPAM-SA WP2:

iPWR Design-1:

DBA-1: Loss of AC (Feedwater, DHRS, CVCS), ECCS activated, Break on CVCS discharge line (10%)
DBA-2: Loss of AC (Feedwater, DHRS, CVCS), ECCS activated, Break on CVCS discharge line (20%)
DBA-3: Loss of AC (Feedwater, DHRS, CVCS), ECCS activated, Break on CVCS discharge line (35%)
DBA-4: Loss of AC (Feedwater, DHRS, CVCS), ECCS activated, Break on CVCS discharge line (100%)
SA-1: break on CVCS, Loss of AC, partial ECCS activation (both RRVs fail)
SA-2: spurious opening of 1 RVV, Loss of AC, partial ECCS activation (both RRVs fail)
SA-3: high venting break, Loss of AC, partial ECCS activation (both RRVs fail)

iPWR Design-2:

DBA-1: Guillotine break of one Direct Vessel Injection (DVI) line, considering the availability of all safety systems
SA-1: guillotine break of one Direct Vessel Injection (DVI) line, considering the unavailability of EHRS and ADS-1 systems
SA-2: guillotine break of one Direct Vessel Injection (DVI) line, considering the unavailability of all safety systems
SA-3: guillotine break of one Direct Vessel Injection (DVI) line, considering the unavailability of EHRS system

WP6 Task 6.2: Chosen designs & scenarios

SAFETY ANALYSIS OF SMR WITH PASSIVE MITIGATION STRATEGIES - SEVERE ACCIDENT

Design-1: iPWR characterized by a submerged containment and electric power of about 60 MWe

Design-2: iPWR, several passive systems, dry containment, electric power of about 300 MWe

- SA-2: Guillotine break of one Direct Vessel Injection (DVI) line, unavailability of all safety systems

Partner	Design	Scenario
KIT	Design-1	Total release (whole inventory) of selected FPs
LEI	Design-2	NUREG 1.183 LOCA
SSTC NRS	Design-1	3 cases, varying inventory & release fractions
TUS	Design-2	DBA-1, SA-2
JRC	Design-2	SA-2
VTT	Design-1	108 ‘artificial cases’, separately for nuclide groups, vary release fractions
ENEA	Design-2	SA-2 (= ‘R11’)
POLIMI	Design-2	SBLOCA (inside / outside containment)
KTH	D1, BWR	D1: DBAN, SA1, SA2, SA2N, SA3, SA3N, SA5, SA6
UNIROMA	Design-2	DBA-1, SA-2

WP6 Task 6.2: Nuclides & activities (Bq)

Source terms (for Task 6.3 BE, from WP5):

- Burnup: Available from WP2 for from 20 to 60 MWd/kg in steps of 2.5 MWd/kgU
- Nuclides: WP2 / 304 nuclides available (spreadsheet format)
- Fractions of inventory released to atmosphere: Should usually depend on nuclide chemical group
- Release rates: Simple codes only accept uniform rate; more sophisticated, temporal evolution

- Obviously, released activities have very big & direct effect on off-site doses (depending on nuclide).
- Over the years, in usual cases, it was found that the biggest uncertainty in offsite doses (and so the EPZ sizing) is actually coming from the (poor) knowledge of the source term, while also other, subsequent uncertainties do exist.

WP6 Task 6.2: Nuclides & activities (Bq)

SAFETY ANALYSIS OF SMR WITH PASSIVE MITIGATION STRATEGIES - SEVERE ACCIDENT

Source terms chosen by WP6 partners in the Conservative phase (Task 6.2)

- Partners were completely free to choose their own degree of conservativeness when creating the source terms for atmospheric dispersion. (Some also just tested their code tools with some ST.)
- For on-going Task 6.3 BE (Best Estimate), source terms come from WP5 (Containment).

Partner	Burnup	Nuclides	Atm. release fractions
KIT	60 MWd	22	1.0 (whole inventory)
LEI	20, 40, 60	19	1e-5 < fraction > 0.1 (depending on nuclide)
SSTC NRS	15+30+45	26	6.8e-5 < fraction < 0.988 (depending on nuclide)
TUS	20, 40, 60	40	Kr, Xe 100 %, less volatiles 10 % or 1 %
JRC	N/A	I-131, Cs-137	(2e16 Bq, 2e14 Bq)
VTT	40	29	2.08e-4 < fraction < 0.32 (depending on nuclide)
ENEA	45	< 60	2e-5 < fraction < 2e-2 (depending on nuclide)
POLIMI	40	17	(to CNT) Kr, Xe 100 %, halogens 0.4, others 0.002-0.3
KTH		MELC. classes	For Cs and I, up to 10 % / 12 %
UNIROMA		71 (CR-7270)	(time-dependent rate)

WP6 Task 6.2: Delay, duration, h_{eff}

Release parameters (for Task 6.3 BE, from WP5):

- Delay time: Time for chain decay & decontaminating processes between reactor shutdown and start of atmospheric release
    - (Of course, decay continues also during release duration and atmospheric dispersion.)
- Effective release height: Height of stack / breach hole + plume rise by momentum / buoyancy
- Release duration; possibly temporally variable release rates for each specific nuclide
- All these release parameters have major effect on off-site doses (increase >> doses decrease).

WP6 Task 6.2: Delay, duration, h_{eff}

Release parameters chosen by WP6 in the Conservative phase (for Task 6.3 BE, from WP5):

Partner	Delay time	Eff. release height	Duration
KIT	(no delay)	100 m	24 h
LEI	< 60 min	10 m	24 h
SSTC NRS	16.2 h	Ground / 10 m	10 min / 6 h
TUS	1 h	Ground level	1 h
JRC	4.77 h (37 h)	20 m	5 h (23 h)
VTT	1 h – 10 d	20 / 60 / 120 m	1 h – 10 d
ENEA	6.5 h	10 / 50 m	5 h
POLIMI	1.7 / 24 (+ 8 h)	1 m	24 h
KTH	(dep. on scen.)	5 – 34 m	Up to 70 h
UNIROMA		0 m and 20 m	

WP6 Task 6.2: Site and weather

Site: Could be anything: operating NPP, proposed for iPWR, or completely hypothetical

- However, off-site doses generally depend on site-specific environment & weather conditions

Weather data: source can be NWP or mast; choice of data set size for deterministic or statistical study

- For near field, local weather mast measurements may be better than numerical with large grid cells
- Note: 1° = appr. 100 km (east-west depending on latitude)
- Reanalysis = data assimilation of past prediction data with observations

WP6 Task 6.2: Site and weather

SAFETY ANALYSIS OF SMR WITH PASSIVE MITIGATION STRATEGIES - SEVERE ACCIDENT

Partner	Site	Weather data
KIT	KIT campus	NOMAD (NOAA), 1 year (2021), resolution 0.5°
LEI	Kaunas / thermal	single point, 5 distinct cases
SSTC NRS	3 (near Kyiv)	single point (2019-2022); WRF 0.05° 2023-2024
TUS	Kozloduy VVER site	D; NIMH (Bulgaria), Kozloduy met. stations, Meteoblue (US)
JRC	(fictitious)	ECMWF reanalysis, hi-res 10x10 km, 30 d (June 2022), n=120
VTT	(no specific)	single point, 84 different combinations
ENEA	(Arkansas Unit 1)	single point, 2 cases (A-1.8 m/s and C-3.6 m/s-rain)
POLIMI	NW Italy	default values from on-site data 1959-2013, stab. A to F
KTH	3 sites in Sweden	2020, hourly (SMHI, Vattenfall, Copernicus data)
UNIROMA	Southern Europe	One year, hourly (8760 sequences)

WP6 Task 6.2: Codes, criteria, conf. level

Code tools: Implement physical model(s) for atmospheric dispersion and off-site dose projection

- Lots of parameters: v_{dry}, $c_{washout}$, DCFs, shielding factors, breathing rates, …

Dose criteria: Limits of projected (or averted) dose, above which actions should be implemented to reduce doses to people

- TEDE = Total Effective Dose Equivalent
- Generic dose limits may also be specified as organ-specific doses

Confidence levels: (with statistical / long-term weather data): The fractile (percentile), e.g. 95 %, of all values such that the dose was lower (or EPZ smaller) in 95 % of all cases; called P95.

WP6 Task 6.2: Codes, criteria, conf. level

SAFETY ANALYSIS OF SMR WITH PASSIVE MITIGATION STRATEGIES - SEVERE ACCIDENT

'Conservative analyses of iPWR EPZ extent'

WP6 partner	Code	Dose criteria	Confidence levels
KIT	JRODOS (main developer)	TEDE 10/100 mSv (SSK)	(365 days considered)
LEI	RODOS	TEDE 100 mSv	N/A (deterministic cases)
SSTC NRS	JRODOS, HotSpot	(several, from NRBU-97)	P90, P95, P99
TUS	Excel / PC-CREAM	Red m. 1 Gy, inh. 100 mSv	N/A
JRC	JRODOS	10 / 50 mSv (GS-G-2.1)	'boundary method' (max_{cell})
VTT	ARANO (in-house devel.)	STUK UPZ 10 mSv / 48 h	P95 shown from cum.distr.
ENEA	RASCAL	IAEA GSR Part 7, App. II	N/A
POLIMI	GENII FRAMES	Evacuation (by 5 countries)	N/A
KTH	MACCS	SSM: UPZ 0.1 Sv, PAZ 1 Gy	95 / 99.5 %
UNIROMA	MACCS	IAEA shelt / evac / ITB	95 %

VTT: Parametric study, ARANO code

Seen in a 'wishlist' of SASPAM-SA End User Group (EUG):

- Harmonize methods for defining the EPZ
- How to properly select the source term from a range of accident analyses?
- How to define conditions for spreading of radioactive materials in the environment?
- Treatment of several years of weather data with a resolution of one hour

Attempt to 'partially answer' these questions: Start with a kind of sensitivity study.

How to choose relevant / plausible values for release parameters? Customarily (FI / large LWR):

- Time from initiating event to off-site alert: 30 min
- Time from initiating event to start of release could be 0.5 h – 4 h – or more
- Duration of release: hours - days (highest release rate most usually during the first hours)
- In highest-consequence weather, distance of 5 km could usually be reached in 15 – 60 min
- Exposure time to cause deterministic effects off-site: worst case, a few hours; usually more

For the ARANO study, for iPWR, extened these assumptions also towards the less conservative.

VTT: Iodine isotopes, effect of duration

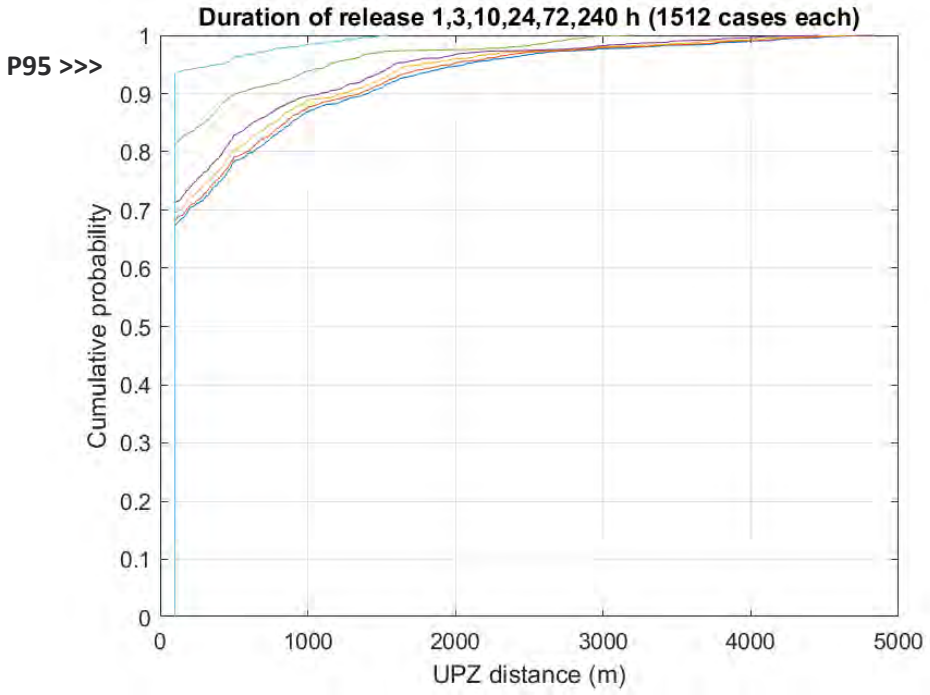

Design-1, 0.1 % of iodine isotopes (of D1 inventory)

Cumulative probability distributions of EPZ distance (Finland STUK limit 10 mSv / 48 h)

Duration of release 1 / 3 / 10 / 24 / 72 / 240 h. Other release parameters and weather may take on range of values >> probability distribution of EPZ. (Results would change with site-specific weather.)

Guide to ordering of curves:

1. **blue (blue): 1 h**
2. **red (red): 3 h**
3. **yellow (yellow): 10 h**
4. **magenta (magenta): 24 h**
5. **green (green): 72 h**
6. **cyan (cyan): 240 h**

Figure. Dependence of the Design-1 UPZ (i.e. EPZ outer bound) distance on release duration (DU), when release contains only iodine (atmospheric release fraction 0.001 of core shutdown inventory). STUK (Finland) 10 mSv criterion was used. Shown are the cumulative probability distributions of EPZ distance for each DU. The 95 % percentiles (P95 values) of UPZ distance are: **2060 m, 1976 m, 1760 m, 1579 m, 1143 m, 375 m**

VTT: Iodine isotopes, P95 EPZ (m) for iodine

SAFETY ANALYSIS OF SMR WITH PASSIVE MITIGATION STRATEGIES - SEVERE ACCIDENT

In this plot, we show (for each value of the six varied parameters) the 95 % percentile value of the EPZ distance, as extracted from the previously shown cumulative probability distributions.

Important to note:

- The '0.1 % of iodine' is completely hypothetical, but assumed to be a conservative fraction for Design-1 with large water pool.
- The '95 %' is a confidence choice.
- However, weather here is not for any real site, and the P95 values would change for real site-specific weather (will be in BE phase).

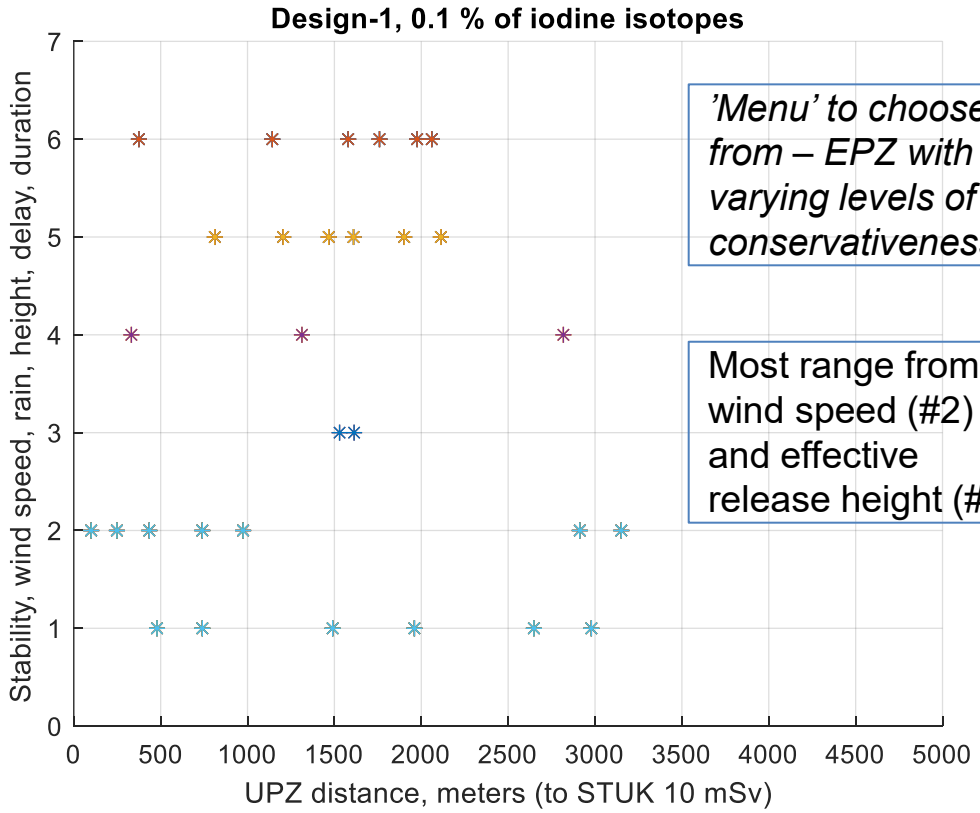

'Menu' to choose from – EPZ with varying levels of conservativeness…

Most range from wind speed (#2) and effective release height (#4).

Release data from WP5 (Containment)

- Responsibilities:
  - WP5: GRS (Hollands); cf. ERMSAR2026 presentation #180 (Monday pm)
  - Design-1: EDF (Bittan)
  - Design-2: UNIROMA (Giannetti)
- STs (corium > containment > atmosphere) for the BE phase (Task 6.3) available:
  - PSI (Malicki), Design-1 SA-1 (MELCOR)
  - Tractebel (Di Giuli), Design-1 Case-1 (ASTEC)
  - VTT (Sevón), Design-1 SA-1 and SA-2 (MELCOR)
  - KIT (Gabrielli), D1 (ASTEC)
  - EDF (Bittan), Design-1 Case-1 (MAAP)
  - SURO, D1 (MELCOR)
  - KTH, D1 (MELCOR)
- For each accident scenario considered, a consolidated ‘best estimate’ source term for WP6 (EPZ)
- Scenario selection (likelihood?) for EPZ might depend on country-specific risk acceptance
- In WP6, we emphasize a plausible scenario (and not very improbable ones)

Release data from WP5 (Containment)

D1 SA-1: Break on CVCS, loss of AC, partial ECCS activation (both RRVs fail)

WP5, Design-1 scenarios considered:

1. SA-1 (as defined in WP2): Reference case, featuring a leakage from the containment (CNMT) to the reactor building (RB) at 0.2% of volume per day (under 69 bar and 298K), and a break from the RB to the environment (5 m²)
2. Bypass scenario, based on SA-1, but with the break occurring directly into the RB. It assumes the availability of reactor recirculation valves (RRVs) and reactor vent valves (RVVs), leading to CNMT dry-out and eventual vessel failure.

- Regarding Figures of Merit, the activity of key isotopes like Cs, I, Xe, Kr and the total activity released to the environment as primary metrics
- Expressed in Bq or as a fraction of the initial inventory (burnup chosen)
- Most important for doses, include iodine and cesium (at least ^{131}I and ^{137}Cs)

Releases, VTT MELCOR calculations for D1

SAFETY ANALYSIS OF SMR WITH PASSIVE MITIGATION STRATEGIES - SEVERE ACCIDENT

SA-1: break on CVCS, both RRVs fail
SA-2: spurious opening of 1 RVV, both RRVs fail
Opposite of SA-2: spurious opening of 1 RRV, all RVVs fail
Containment bypass through broken CVCS line, RRVs and RVVs operate normally:

- Almost 10 % of cesium escaped in first 10 h (HUGE RELEASE, even when smaller inventory)

- Scenarios' VTT results plotted (Tuomo Sevón) >>>
- Cs release into the environment

- VTT D1 SA-1 result chosen:
  - WP5 >> WP6 (EPZ)

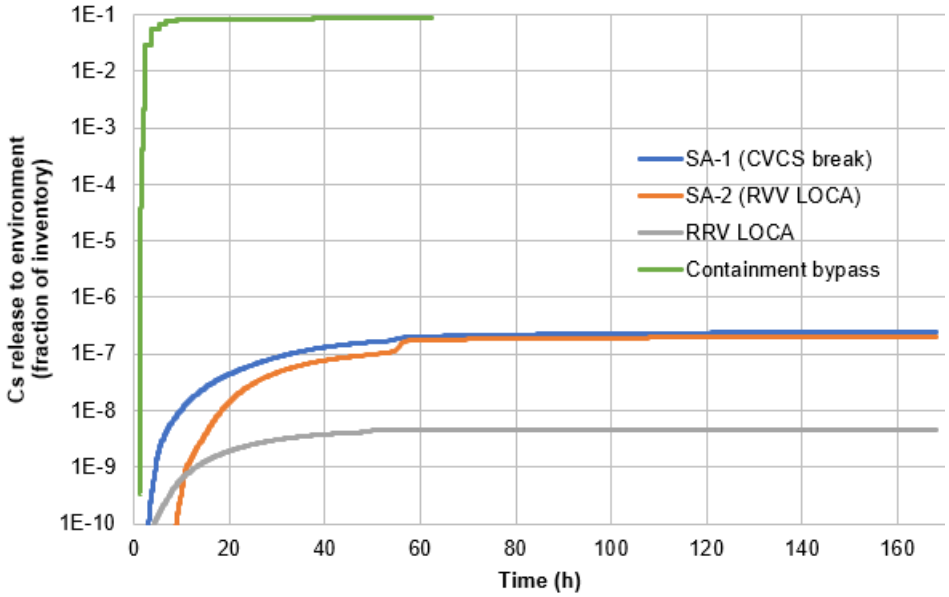

D1 bypass releases, ARANO, 10 % alkali

- Offsite doses and EPZ (VTT ARANO code)

- Fraction 0.1 of D1 core inventory alkali metals
- Cs-137 inventory = 4.184e+16 Bq
- HUGE RELEASE with bypass case, even when small reactor inventory

- ARANO parametric study results
- Parameters 1-3: stability class, wind speed, rain
- Parameters 4-6: release height, delay after shutdown, duration of release (Very little effect from height, because large distances.)
- This was with hypothetical weather; Task6.3 will be real site weather

- Dose criterion: 10 mSv / 48 h (cloudshine, groundshine, inhalation commitment)
- == Finland STUK criterion for UPZ, found in regulation STUK/Y/2024

- What is the realistic frequency (1 / reactor-year) that such a case (with containment bypass through broken CVCS line) would happen at all?

File 'upz_dist_P95_values_alkali_frc_0.1.txt'

```
alkali UPZ param 1 value 1 P95_dist 7064.24
alkali UPZ param 1 value 2 P95_dist 8495.33
alkali UPZ param 1 value 3 P95_dist 13500
alkali UPZ param 1 value 4 P95_dist 19170.4
alkali UPZ param 1 value 5 P95_dist 22540.4
alkali UPZ param 1 value 6 P95_dist 29449.5
alkali UPZ param 2 value 1 P95_dist 25935.5
alkali UPZ param 2 value 2 P95_dist 25905.5
alkali UPZ param 2 value 3 P95_dist 20188
alkali UPZ param 2 value 4 P95_dist 19357.6
alkali UPZ param 2 value 5 P95_dist 16667.6
alkali UPZ param 2 value 6 P95_dist 13206.1
alkali UPZ param 2 value 7 P95_dist 11043
alkali UPZ param 3 value 1 P95_dist 23720.2
alkali UPZ param 3 value 2 P95_dist 18387.2
alkali UPZ param 4 value 1 P95_dist 19943.6
alkali UPZ param 4 value 2 P95_dist 19780.7
alkali UPZ param 4 value 3 P95_dist 19626.4
alkali UPZ param 5 value 1 P95_dist 19932
alkali UPZ param 5 value 2 P95_dist 19899.6
alkali UPZ param 5 value 3 P95_dist 19893.4
alkali UPZ param 5 value 4 P95_dist 19872.5
alkali UPZ param 5 value 5 P95_dist 19819.4
alkali UPZ param 5 value 6 P95_dist 19597
alkali UPZ param 6 value 1 P95_dist 21100.9
alkali UPZ param 6 value 2 P95_dist 20996.7
alkali UPZ param 6 value 3 P95_dist 20679.1
alkali UPZ param 6 value 4 P95_dist 20174.2
alkali UPZ param 6 value 5 P95_dist 15945.8
alkali UPZ param 6 value 6 P95_dist 7886.08
```

Comparison of partner calculations for D1

Design 1 is generic iPWR with a submerged containment and electric power of about 60 MWe

Scenario SA-1: break on CVCS, both RRVs fail

- Atmospheric environment source terms for: Kr-85, Xe-131m, Xe-133, Xe-135, I-131, I-133, I-135, Cs-134, Cs-136, Cs-137, Te-127, Te-129m, Te-132, Sr-90, Ba-140
- Comparison plots of partners' SA-1 results (by EDF / Bittan)
- Design 1, SA-1: ^{131}I released into the environment >>>
- VTT D1 SA-1 result (green) chosen:
  - Transfer from WP5 >> WP6 (EPZ)
  - VTT mostly close to the mean values
- WP6: Reference scenario and possibly BE + sensitivity

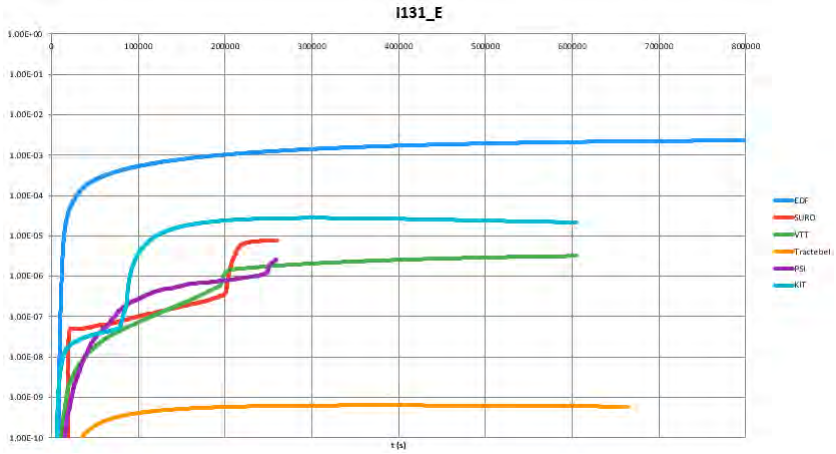

- Releases: Orders of magnitude differences
- Modelling in codes, assumptions made
- Condensation models, nodalisation etc.
- 'User effect', even when same code ?

- SASPAM-SA is interfacing with another current EU project (EASI-SMR)
- Our WP5 results help in defining atmospheric release fractions in EASI-SMR

SAFETY ANALYSIS OF SMR WITH PASSIVE MITIGATION STRATEGIES - SEVERE ACCIDENT

WP6 T6.3: Sites, Helsinki metropolitan area

SAFETY ANALYSIS OF SMR WITH PASSIVE MITIGATION STRATEGIES - SEVERE ACCIDENT

- Industrial / fossil plant locations
- Inland: Ämmässuo
- Coastal: Suomenoja, Salmisaari, Vuosaari
- (Sites hypothetical at the moment)

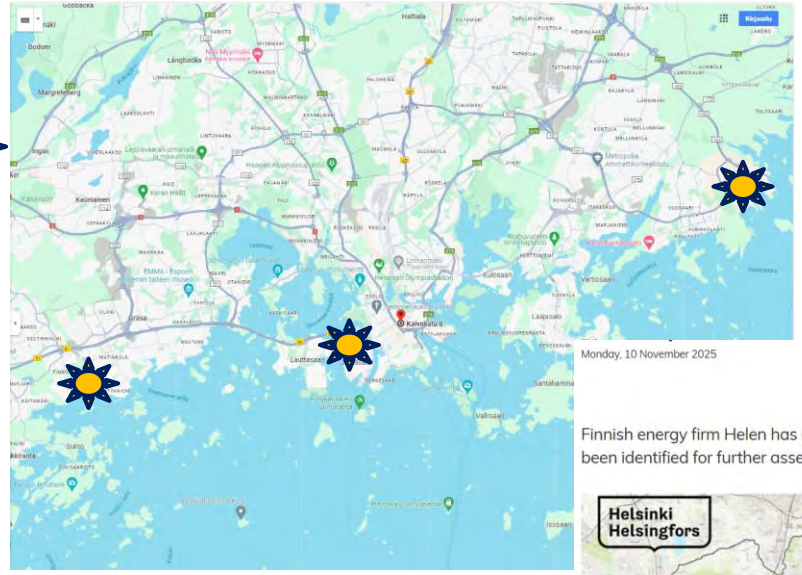

Monday, 10 November 2025

Finnish energy firm Helen has announced that three potential sites in Helsinki have been identified for further assessment for locating a small nuclear power plant.

(image: Helen)

- However, Helen (Helsinki Energy) announced in 2025 three prospective sites for their SMR project >>>

WP6 T6.3 VTT: Vuosaari, Helsinki

SAFETY ANALYSIS OF SMR WITH PASSIVE MITIGATION STRATEGIES - SEVERE ACCIDENT

- One of Helen tentative sites is Vuosaari in eastern Helsinki:
- 60.220 N, 25.171 E (a current fossil power plant site) >>>

- Weather data from observations or analysis?
- Weather data from FMI for 5 years (2020-2024), total 43848 hourly conditions, from model analysis fields
- Top: Wind speed & direction
- Bottom: Rain and stability class distributions
- Parameters usable in codes ARANO, VALMA and MACCS.

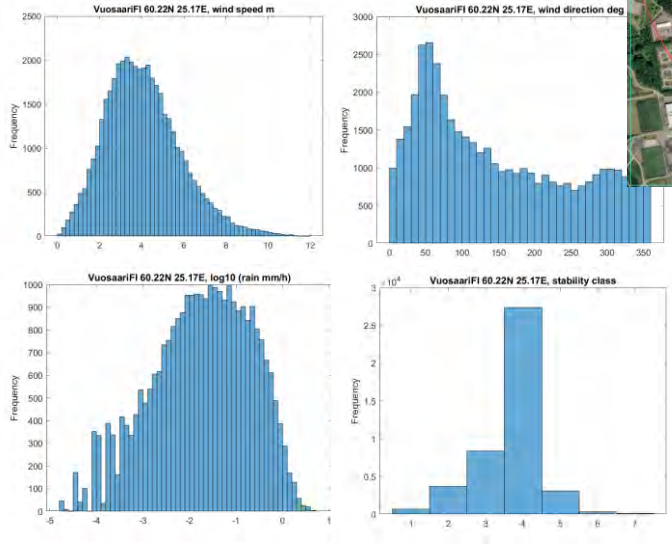

WP6 conclusions: Regulatory frameworks

SAFETY ANALYSIS OF SMR WITH PASSIVE MITIGATION STRATEGIES - SEVERE ACCIDENT

- Suitability of overall procedures in WP6, regulatory framework etc. (those reviewed or the one work was based on): Technically mostly fairly reasonable, but most regulators still fix EPZ.
- Clearly, small / advanced reactors deserve flexible, consequence-oriented approach.
- Regulatory frameworks already with risk metrics are better applicable to passive SMR.

- What is 'safe enough'? >> Suffice it to show that final risk level the same or lower than LLWR ?
- EPZ is ultimately a political / societal / regulator decision, with enough margins
- What we calculated in WP6 should rather be called e.g. 'off-site doses footprint area'

- Can nuclear EP&R ever be harmonized even within the EU? (Cf. IAEA NHSI)
- Urge / trigger international organizations to consider SMR in more detail, more practical level (IAEA, EU Industrial Alliance; regulator side HERCA, WENRA, ENSREG)

- What is the 'share' of each DiD level in achieving the final offsite safety level?
- Frequent comment from IAEA colleagues: EP&R (DiD level 5) / EPZ is not a design issue, but by definition, 'beyond what was ever considered explicitly during design'

WP6 conclusions: Probabilities and risk

SAFETY ANALYSIS OF SMR WITH PASSIVE MITIGATION STRATEGIES - SEVERE ACCIDENT

- Probability of DEC-A and DEC-B (i.e. just order of magnitude) is important because many regulators are going to consider some risk-informed methodology.
- In SASPAM-SA, however, full spectrum of STs and their PSA-2 probabilities can not be available.
- CNL: SASPAM is missing accident likelihood assessments. Maybe we can give it a shot as call our guesses 'expert judgement' ?
- An accident scenario with multiple failures of systems can be extremely unlikely to ever happen! So is it then appropriate to be used as basis for emergency planning?

- ENEA: Even in a very conservative manner and with a purely deterministic, worst-case method, the EPZ could be reduced a lot w.r.t. large LWRs, e.g. in some cases to about 1-3 km.
- The calculations using a BE Source Term and a refined atmospheric ATM code (JRODOS) will indicate whether the EPZ size could be further reduced or not.
- The overall EPZ methodology might be shifted from a deterministic, worst-case approach, to a risk-informed one.
- On the use of PRA: Passive systems may be more difficult; sometimes partially functioning; very low probabilities are usually most uncertain.

WP6 conclusions: Uncertainties

SAFETY ANALYSIS OF SMR WITH PASSIVE MITIGATION STRATEGIES - SEVERE ACCIDENT

- The 'Conservative' phase quantitative values (distances) are preliminary and very conservative.
- There are obvious reasons for spread of results & possible outliers.

- Uncertainties exist at every step: Source term, atmospheric dispersion, dose assessment.
  - Uncertainties regognized qualitatively; quantification practically not possible.
  - Most probably the source term uncertainties dominate over dispersion and doses.
- Release is decisive: large or not, early or not? Precautionary, or urgent protection needed?
- ENEA: For example, a mitigative strategy to protect the containment (passive FCV) in Design-2, could lead to substantial reduction of source term.

WP6 conclusions: Number of cases

- WP6 can answer the main question: The current dispersion and off-site dose codes and methodologies are generally applicable, provided that no built area or very near range.
- More cases should be calculated to better answer the quantitative question 'SMR EPZ size'.
- We cannot say anything nearly certain about iPWR EPZ extent (numbers, km) based on the 'Conservative phase' work; better after the BE phase.

- 'SMR EPZ size' cannot be generic; must be plant- or design-specific
- Generic EPZ does not exist. SASPAM-SA has shown that a realistic source term is critical. Realistic reactor & containment design and environment are needed.

- Recommended follow-up: Create a 'generic' but representative EPZ database under key DECA and DECB conditions, applying the best practices and recommendations identified in SASPAM-SA, including the iPWR designs, a generic BWR and LDR Lite
- After current SASPAM-SA, there is much better readiness to do more cases, as people already have set up their calculation systems – then for EPZ, we could basically 'plug in' more different DEC-A and DEC-B release source terms.

Conclusions: Codes, Built environments

SAFETY ANALYSIS OF SMR WITH PASSIVE MITIGATION STRATEGIES - SEVERE ACCIDENT

- WP6 was generally satisfied with SMR EPZ methodology used:
  - Choices of codes, calculation parameters, practical steps followed, etc.
- To answer the main questions of SASPAM-SA: The codes were mostly found to be appropriate. Current dispersion & dose codes are applicable when the EPZ is still relatively large.
- What we are changing for Task 6.3 BE work: Will generally be various refinements.
- Old, classic methodology seems usable also for SMRs (cf. the conclusions of the IAEA SMR Regulators' Forum Pilot Project report on EPZ).

- With very small source term, and consequently emphasis of very near range, the usual dispersion & doses methodology might not be sufficient, perhaps requiring microscale modeling.
- Co-location has many cases: co-location of several modules / units, reactor(s) in a populated city, or reactor(s) in industrial area (like oil refinery, hydrogen production, fertilizers, steel, etc).
- Recommended to develop methods to account for the near-field effects in atmospheric dispersion.
- Recommended to develop more high-fidelity short range / built environment modelling.
- See next slide: Some ideas for built area dispersion and doses modelling.

Built area modelling: descriptive parameters

Values / distributions (per grid cell) of the following could be used to guide simple models, once high-fidelity simulations have been performed e.g. by LES or CFD.

- 3D geometry of buildings etc. >>>
  - Roughness length
  - Ground surface elevation
  - Building height over ground
  - Number of buildings, area fraction covered by buildings
  - Height-to-width ratio of buildings
  - Building frontal areas; actual (detailed shape) surface area
- Surface cover / materials >>>
  - Grass / other vegetation / street materials
  - Building surface materials
  - Albedo
- 2D geometry of streets / city blocks / buildings >>>
  - Distribution of street directions (0 – 180 degrees), street widths
  - For example, 'Manhattan street network' – bimodal direction distribution
  - Building facade / lateral side directions
- For radiation doses, also >>>
  - Building types (one-family … block)
  - Sky view (not obscured by buildings) fraction
  - HVAC / ventilation air intake height
  - Concrete thickness / shielding factors of the floors

Acknowledgement/Disclaimer

Funded by the European Union

Funded by the European Union. Views and opinions expressed are however those of the author(s) only and do not necessarily reflect those of the European Union or European Commission-Euratom.
Neither the European Union nor the granting authority can be held responsible for them.

SAFETY ANALYSIS OF SMR WITH PASSIVE MITIGATION STRATEGIES - SEVERE ACCIDENT

Contact / WP6:
Mikko Ilvonen
VTT Nuclear Energy
Finland
mikko.ilvonen@vtt.fi

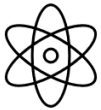

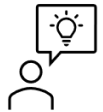

Some additional backup slides >>>

- Some additional slides next, intentionally left to be viewed

Classifications of EPZ methodology

- Fixed (so far in most countries) / or flexible (UK, Finland, US, Canada)
- Generic / or generalized (specific to case: plant, design, site characteristics)
- Prescriptive ('how must be done') / or performance-based
    - US NRC final new rule 2023: technology-neutral, consequence-oriented, performance-based, dose-based, risk-informed
- Deterministic / probabilistic / mixed (regarding source term / weather conditions)
- Choice of accident scenarios (and thus ST) for EP&R: worst possible, worst plausible, 'limiting case', large spectrum of, frequency limit etc.
    - JRC in WP6: 'RCM based EPZ', CoP 'Cone of Plausibility'
- Level of conservativeness vs. best estimate; validation, uncertainties
- Additionally: Other than offsite dose footprint considerations
    - Practical arrangements for protection, geographical features
    - Political, risk perception, safety margins, public acceptance, NIMBY

Generic vs. generalized EPZ methodology

SAFETY ANALYSIS OF SMR WITH PASSIVE MITIGATION STRATEGIES - SEVERE ACCIDENT

Generic methodology: not plant-specific (accident evolution, radiological release, site-specific meteorological data, etc.)

- Source term evaluation
- EPZ distance evaluation
  - Criteria driven by protective actions: Action-specific thresholds, e.g. Germany 10 km evac. & 100 km ITB
  - Criteria driven by reference doses: Single generic threshold, e.g. US: 0.05 Sv whole body, 0.25 Sv thyroid

Generalized methodology: design/plant-specific; safety analysis, accident selection, ST evaluation, criteria for EPZ distance

- Source term evaluation
  - Deterministic approach: set of representative, bounding severe accidents
  - Probabilistic approach: plant-specific PRA level 2 >> spectrum of scenarios (release category & frequency)
- EPZ distance evaluation
  - Based on bounding scenarios (WP6): e.g. Belgian dispersion model, parameters for standard scenarios
  - Based on frequency limitation
  - Based on risk (reduced to level of tolerable risk)
  - Risk-informed approach

Frequent comment from IAEA colleagues: EP&R / EPZ is not a design issue, but by definition, beyond what was considered

Off-site dispersion & dose assessment, EPZ

SAFETY ANALYSIS OF SMR WITH PASSIVE MITIGATION STRATEGIES - SEVERE ACCIDENT

Release

Dispersion, chain decay

Doses

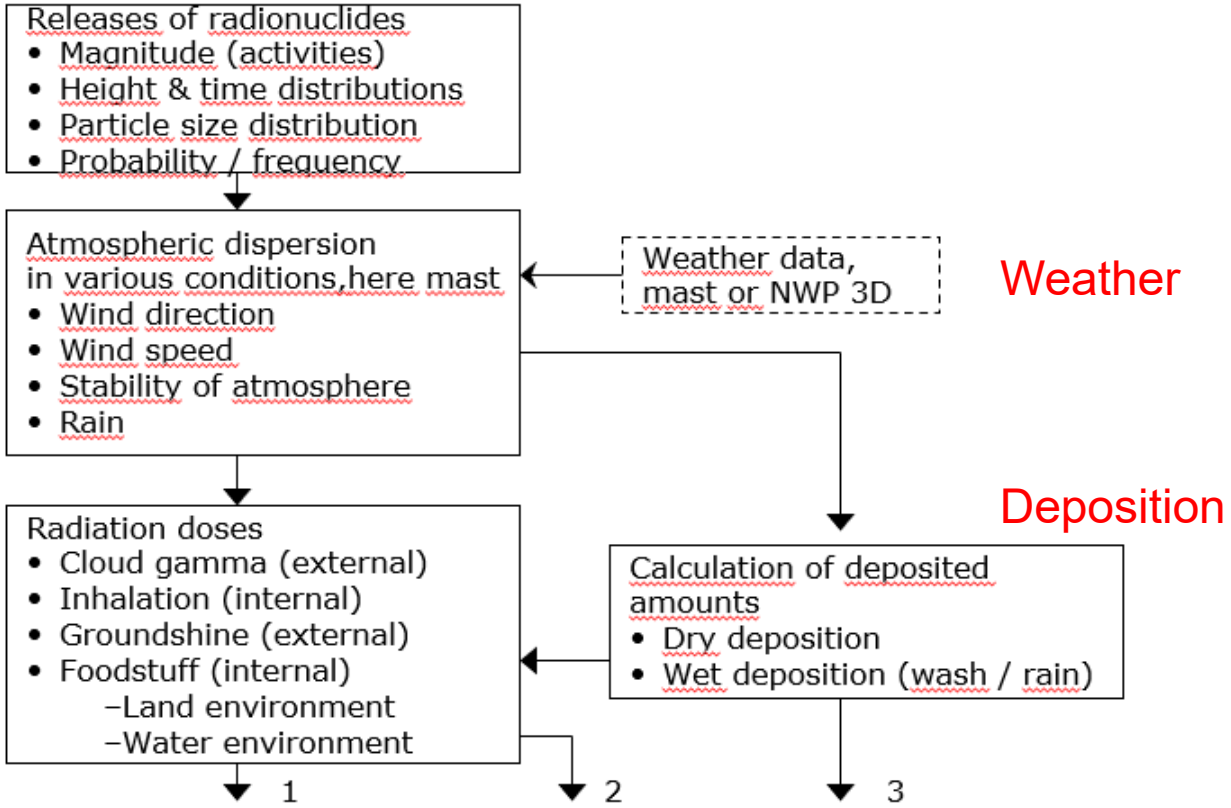

Health & economic consequences

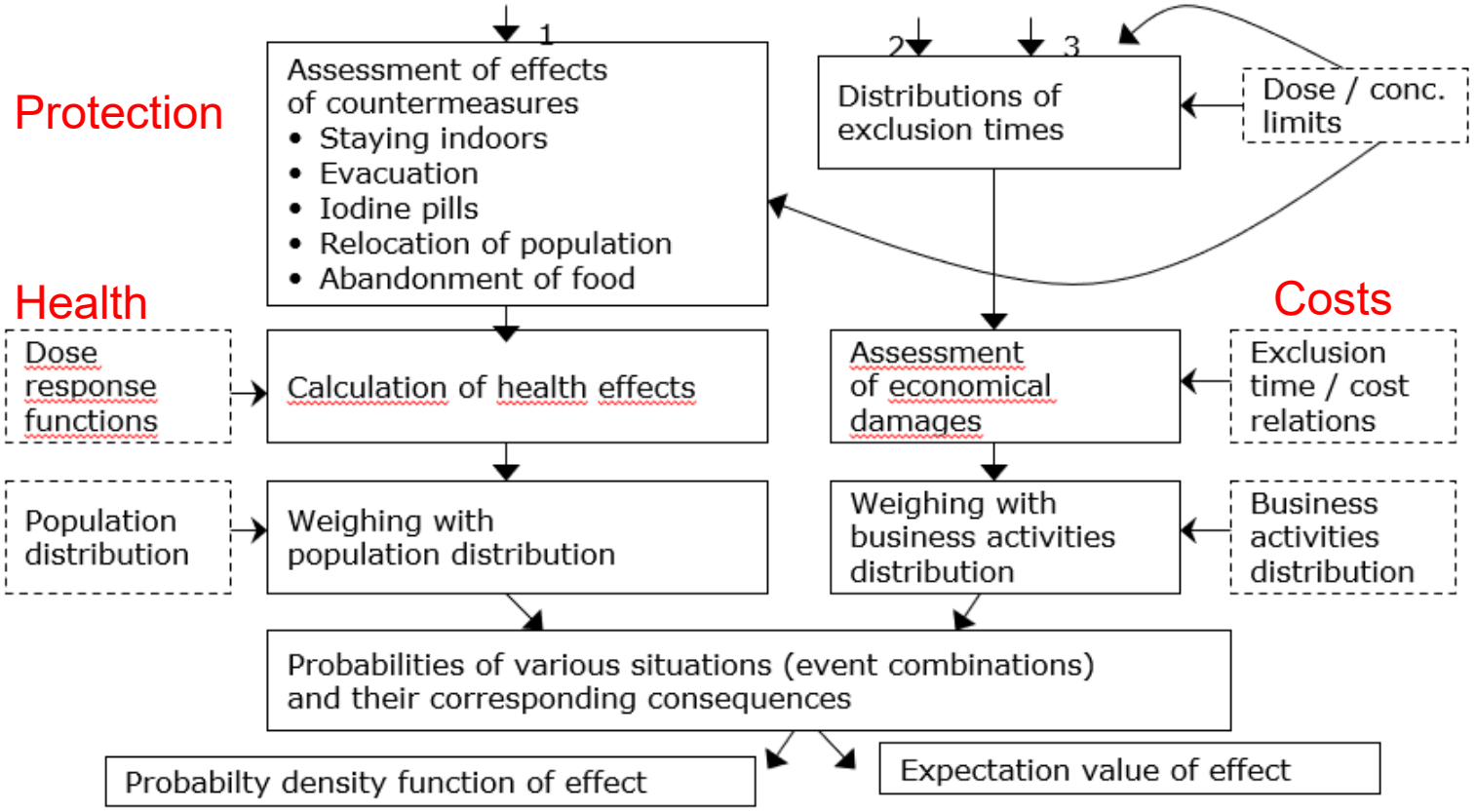

WP6: Steps done for Conservative phase

SAFETY ANALYSIS OF SMR WITH PASSIVE MITIGATION STRATEGIES - SEVERE ACCIDENT

- Review of published data on iPWR inventories and atmospheric source terms
- Interfacing with WP2 to receive scenarios and calculated reactor core radionuclide inventories
- Creation of conservative atmospheric source terms based on inventories: nuclides, activities, duration, height, …
- Selection of dispersion and dose codes to use for offsite consequences
- Selection of sites / site specific data (as required by dose code)
- Selection of weather data source, resolution, location & time period
- Performing offsite dose assessment calculations: codes' most important parameter values listed, including:
- -exposure pathways, target organs, age groups, breathing rates, shielding factors, etc. etc.
- Selecting the set of generic dose criteria (or possibly OILs) to initiate protective measures
- Selecting predicted offsite doses according to desired confidence level (P95 etc)
- Finding conservative EPZ distances according to criteria & confidence
- Identification and possible ranking of uncertainty sources
- Recommendation of suitable procedures to be used in Task 6.3

WP6 T6.3 VTT: Vuosaari, Helsinki

Vuosaari weather data for 5 years (2020-2024), total 43848 hourly conditions

Tables show frequencies of cases with dispersion direction toward inland area.

Table row: Stability class

(1 = A unstable to 6 = F (stable)

Column: Wind speed from < 2 m/s to > 10 m/s, at 2 m/s intervals

Most typical, independent of rain, was neutral D (4) and wind speed from 2 to 6 m/s.

Vuosaari: Site = 5, rain < 0.1 mm/h

1	189	6	0	0	0	0
2	400	833	116	0	0	0
3	283	1653	1512	230	0	0
4	369	4301	3526	900	90	2
5	575	812	4	0	0	0
6	257	26	0	0	0	0

Vuosaari: Site = 5, rain > 0.1 mm/h

1	48	0	0	0	0	0
2	59	78	28	0	0	0
3	51	248	281	32	0	0
4	49	319	422	227	61	10
5	47	24	0	0	0	0
6	6	0	0	0	0	0

PERFORMANCE ASSESSMENT OF PASSIVE SAFETY SYSTEMS AND IDENTIFICATION OF CONDITIONS LEADING TO DESIGN EXTENSION SCENARIOS

Erik Cilia
University of Bologna
Department of Industrial Engineering
Via dei colli 16, 40136, Bologna
erik.cilia@unibo.it

Fulvio Mascari
ENEA, Research Center Bologna, NUC-ENER-SIC
Via dei Mille 21, 40121, Bologna
fulvio.mascari@enea.it

ABSTRACT

To enhance the safety of nuclear power plants, advanced reactor designs such as Small Modular Reactors (SMRs) adopt Passive Safety Systems (PSSs). These systems aim to improve the inherent safety of the plant while reducing system complexity and overall plant costs. However, since PSS operation relies on relatively low driving forces, such as natural circulation and gravity injection, their reliability must be assessed under all conditions that may occur during accident scenarios to ensure proper functioning.
In this work, a reliability analysis of an Emergency Heat Removal System (EHRS), representative of a PSS that passively removes residual core heat via natural circulation, was conducted using the REPAS methodology. This probabilistic–deterministic framework enables the assessment of PSS reliability, supporting the characterization of performance and the identification of conditions that guarantee correct operability. The methodology was applied considering a generic integral-PWR SMR design in which a small break-LOCA was simulated. The MELCOR code has been used, and a set of runs was performed, each corresponding to a different realization of uncertain parameters sampled through a Monte Carlo procedure. The uncertainty space covered thermal-hydraulic conditions that can affect the PSS operation, with particular emphasis on non-condensable gas (NCG) inventory, valves opening ratio, loss coefficients and tube roughness of the EHRS in-pool heat exchanger and liquid level in pools. This study investigates the scenarios leading to SA conditions, assessing the impact of NCG accumulation on EHRS performance, and identifying the boundary conditions associated with passive system functional failure. In this view, the SA scenarios are collectively characterized to highlight the behavior and conditions driving the transition from Design Basis Accidents (DBAs) to Design Extension Conditions (DECs). This first sensitivity analysis shows that NCG inventories as small as about 0.6% of the total EHRS volume are sufficient to drive the analyzed system into SA conditions within the simulated transient, confirming NCG accumulation as a critical factor for passive systems relying on natural circulation.

KEYWORDS
Passive Safety Systems; EHRS; Severe Accident; SMR; Non-Condensable Gas.

1. INTRODUCTION

Nuclear reactors safety is a fundamental aspect of nuclear technology development, particularly in the case of Small Modular Reactors (SMRs). Among them, integral Pressurized Water Reactors (iPWRs) are considered for near-term deployment. These designs build upon established reactor technology while incorporating evolutionary modifications to enhance inherent safety, including the integration of Passive Safety Systems (PSSs) that operate without reliance on external power or active components. One key PSS in these designs is the Emergency Heat Removal System (EHRS), which provides residual decay heat removal from the core during accident conditions.

Unlike mechanical failures, which involve physical damage or malfunction of components, functional failures occur when a PSS is unable to perform its intended safety function despite all components operating correctly. In fact, PSS performance relies on natural driving forces, such as natural circulation and gravity, which are sensitive to initial and boundary conditions. As a result, even small deviations in system parameters or operational conditions can significantly affect the ability of a PSS to fulfill its safety function [1].

To investigate these effects, this work leverages results from a previous application of the Reliability Evaluation of Passive Systems (REPAS) methodology [2] [3], a probabilistic–deterministic framework designed to assess PSS performance and identify conditions that may lead to functional failures. In the prior REPAS study [4], a set of uncertainty parameters was selected to represent key influences on the EHRS, including Valve Opening Ratio (VOR), heat exchanger tube roughness, Non-Condensable Gas (NCG) content, and pool water inventory. These parameters are used in the present work to systematically analyze the behavior of the EHRS under off-nominal conditions, revealing the operational limits and vulnerabilities that may lead to functional failures.

The present paper focuses on a detailed analysis of scenarios in which off-nominal EHRS operation leads the reactor into Severe Accident (SA) conditions, identifying the factors and mechanisms that drive the system toward functional failure. Following this analysis, a sensitivity study is conducted to investigate the influence of the NCG content on EHRS performance, highlighting its role as a critical factor in system response. Deterministic calculations of the reactor response under these conditions are carried out using the MELCOR code [5] [6], a fully integrated SA simulation tool capable of modelling thermal-hydraulic behavior, as well as degradation phenomena affecting the reactor pressure vessel during a SA.

2. REFERENCE REACTOR AND TRANSIENT

2.1. Reactor Design

The reference reactor considered in this study is a generic iPWR with an electrical power of approximately 300 [MWe], representative of a SMR concept [7] [8]. The selected configuration corresponds to the so-called *Design 2* (**Figure 1**), developed within the Horizon Euratom SASPAM-SA project [7] [8] [9] [10], and is adopted here as a reference layout for the assessment of accident mitigation strategies based on PSSs. The plant layout features a dry containment (composed by Drywell, DW and Reactor Cavity, RC) and an integral Reactor Pressure Vessel (RPV), which houses the reactor core together with the main primary system components. These include compact Steam Generators (SGs), the control rod drive mechanisms, the primary coolant pumps, and the pressurizer, which is integrated into the upper head of the vessel. The integral configuration reduces primary loop complexity and enhances system compactness.

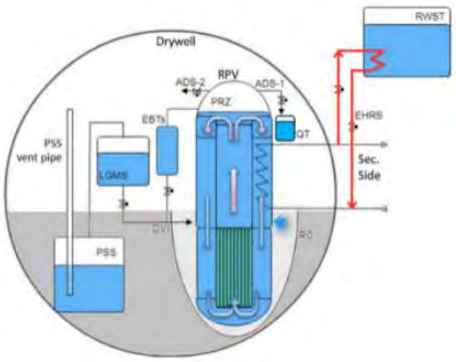

Figure 1. Generic iPWR design considered with the EHRS circuit highlighted in red.

The safety strategy adopted by the design relies extensively on passive safety systems. The systems considered include the Emergency Heat Removal System (EHRS), the Automatic Depressurization System (ADS), the Emergency Borated Tank (EBT), the Pressure Suppression System (with the acronym PSS in **Figure 1** and **Figure 4**), and the Long-term Gravity Make-up System (LGMS), as well as the possibility of reactor cavity flooding for SA mitigation. During normal operation, the reactor operates under forced circulation, while passive systems are activated to manage and mitigate accidental transients.
This reference design provides the basis for the development of the MELCOR input model described in Section 3, which is used to simulate the plant response under SA conditions.

2.2. Reference Transient

The reference scenario considered in this work is a Design Basis Accident (DBA) and specifically the reference transient is a small break-LOCA [11], identified as one of the most challenging scenarios for the considered iPWR design. The postulated initiating event is a double-ended guillotine break of one of the two Direct Vessel Injection (DVI) lines, i.e., the safety injection lines that deliver emergency coolant directly into the reactor vessel, with the availability of all passive safety systems, including the EHRS which removes residual decay heat via natural circulation to the RWST pool.
Long-term core cooling is ensured by the combined action of the EHRS, steam condensation in the DW, and the water inventory accumulated in the RC. For the analyzed conditions, the core remains covered throughout the transient (see the core level trend in **Figure 2**), with no onset of core degradation or hydrogen production, confirming the effectiveness of the passive mitigation strategy for the selected reference scenario. This is confirmed by **Figure 3**, which shows the power balance over the transient. The figure highlights the decay power generated in the core, the power transferred from the core to the primary coolant, from the primary system to the secondary system, and finally from the secondary system to the EHRS, showing that the generated power is fully removed throughout the transient.
By the end of the simulated 50000 s, the reference case has reached nearly stationary conditions on the main figures of merit (core level, decay-heat removal balance), so that the effectiveness of the passive mitigation strategy can be regarded as firmly established for this scenario. The 50000 s time window was adopted throughout the present study as a compromise, in view of the computational cost of the detailed nodalization, most notably the explicit modeling of the two EHRS trains as separate hydraulic loops (Section 3).

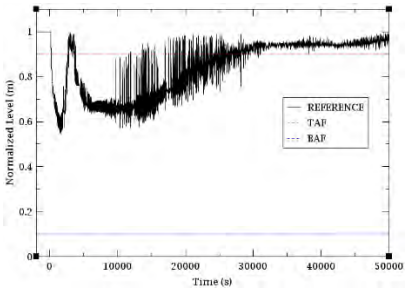

Figure 2. Normalized core coolant level of the core.

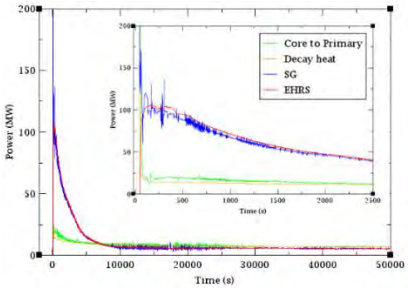

Figure 3. Power balance of the system during the transient.

3. MELCOR CODE AND NODALIZATION

The calculations in this work are performed using the integral SA code MELCOR, developed by Sandia National Laboratories for the U.S. Nuclear Regulatory Commission. MELCOR simulates the behaviour of light water reactors under steady-state and transient conditions, with a focus on SA sequences. It models thermal–hydraulic phenomena, core degradation, reactor pressure vessel and containment response, and estimates the radioactive source term.

In the present work, MELCOR version 2023 is used, and the input deck was developed using SNAP [12], which facilitates model construction and post-processing. A detailed description of the code and its models can be found in [5] [6].

The nodalization, developed by ENEA within the SASPAM-SA project for a generic iPWR design, is based on a generic design derived from IRIS [13] and balances computational efficiency and accuracy in representing thermal–hydraulic and core degradation phenomena. It has been developed exclusively using publicly available information, without reliance on proprietary data, by scaling experimental data from the SPES-3 facility [14] and through engineering evaluations based on open literature sources.

The Reactor Pressure Vessel and primary system are subdivided into hydraulic regions (reactor core, Lower/Upper Plenum, core bypass, riser, downcomer, pressurizer, SG primary side and bypass), modelled through control volumes and flow paths, while heat transfer is handled via associated heat structures. Pressure losses and thermal contributions from internal components are included.

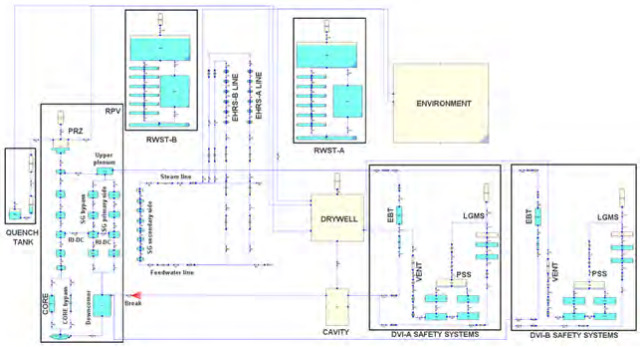

Figure 4. MECLOR CVH nodalization [4].

Passive safety system lines (EBT, Pressure Suppression System, PSS vent, LGMS) are represented independently. The EHRS is simplified to two equivalent heat exchanger lines thermally coupled to Refuelling Water Storage Tanks (RWSTs). SGs are represented as a single equivalent unit with multiple control volumes on primary and secondary sides. The reactor core is modelled as a single hydraulic control volume coupled to the COR package, which adopts multi-level axial and radial discretization. The containment uses separate control volumes for the reactor cavity and drywell; the reactor cavity couples

with the CAV package, while the drywell is thermally coupled to the environment. The postulated break connects the downcomer and containment via relevant safety system lines.
A schematic view of the MELCOR CVH nodalization for the considered iPWR design is shown in **Figure 4**. The model consists of 130 control volumes, 145 flow paths, and 139 heat structures [4].

4. REPAS APPLICATION & MAIN RESULTS

The REPAS methodology estimates the probability of failure of a passive system to perform its mission by accounting for uncertainties in physical and geometric parameters that may compromise the expected thermal-hydraulic phenomena. The general objective of the methodology is to analytically characterize the performance of a passive system, verify its proper functioning, and enable comparisons with active systems or alternative passive concepts.
The roadmap of the methodology can be summarized as follows: system characterization and definition of the Target Mission (TM); identification of the uncertain parameters and their probability distributions; development of the input deck and execution of the reference calculation; definition of the Failure Criteria (FCs); execution of a simulation campaign with a sample size sufficient to achieve a statistically meaningful characterization of system performance; and reliability estimation through comparison of the outcomes with the FCs.
In the present application, the system under investigation is the EHRS of the iPWR Design 2 (**Figure 1**), whose TM is the transfer of decay heat from the core to an external pool under accident conditions. Based on engineering judgement, the uncertain parameters considered most relevant for our application were the loss coefficient (k), surface roughness of the EHRS-HXs tubes, VOR, NCG fraction, and pool initial water level. Each parameter was assigned a variability range and a probability distribution.
After the execution of the reference transient, the results of the calculation were then used to define the FCs for the EHRS, one for each FOM: cladding temperature > 600 K after system activation, collapsed coolant level in the core < 1/2 of the active core height, and EHRS removed power < 70 MW.
A set of N simulations was then performed, each characterized by different values of the uncertain parameters sampled through a Monte Carlo technique. The minimum sample size N required to ensure the selected statistical confidence and probability levels was determined through Wilks' formula [15] for the one-sided tolerance interval, resulting in a minimum required sample size of N=124 simulations. The adopted statistical target consists of a confidence level of 0.95 and a probability content of 0.95, considering three figures of merit.
For the present REPAS application, 150 MELCOR runs were executed; however, 24 runs were excluded due to numerical failures. **Figure 5** shows the time-dependent profiles of the maximum cladding temperature (first FOM), in which seven simulations exceeded the defined FC. The simple rank correlation diagram reported in **Figure 6** highlights the relative influence of uncertain parameters on the maximum cladding temperature.

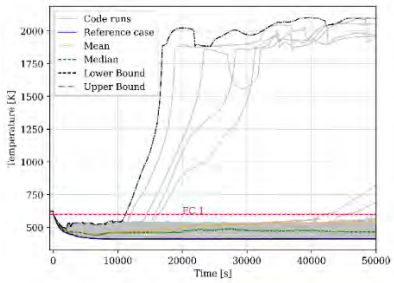

Figure 5. Max cladding temperature for the REPAS calculations.

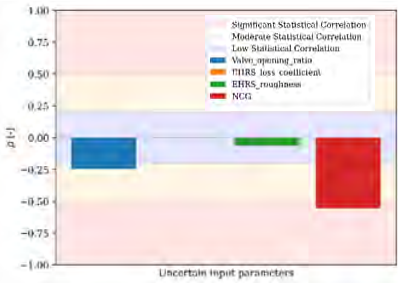

Figure 6. Simple rank correlation coefficient for the maximum cladding temperature.

These results indicate that the NCG fraction[1] and VOR are the most influential parameters affecting system reliability.
Finally, the REPAS methodology concludes by comparing the simulation outcomes with the defined FCs, allowing the reliability of the EHRS to be quantified in terms of selected FOMs, i.e., as the probability of system failure associated with the occurrence of the sampled scenarios.

5. ANALYSIS OF SEVERE ACCIDENT CASES

After the application of the REPAS methodology, more than one hundred simulations were analyzed, from which five cases were identified as evolving into SA conditions. The progression of these cases is illustrated in **Figure 7**, showing the temporal evolution of the Maximum Cladding Temperature, and in **Figure 8**, reporting the normalized core collapsed coolant level.

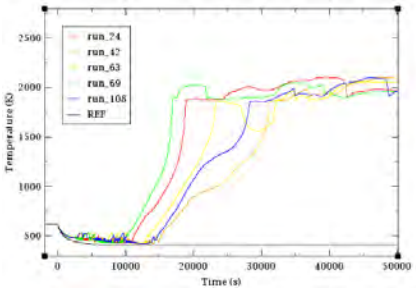

Figure 7. Max cladding temperature for the five SA cases and for the reference.

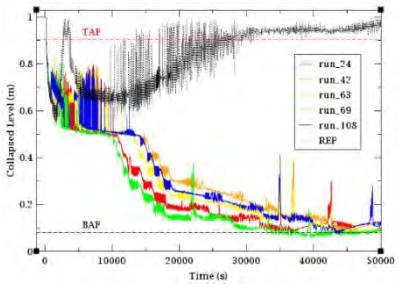

Figure 8. Normalized core coolant level for the five SA cases and for the reference.

Figure 7 shows the increase in cladding temperature for all five cases, followed by stabilization in the range of 1800–2000 K, indicating cladding failure and exceeding the safety criteria defined in [16], according to which the cladding temperature during a LOCA should not exceed 1400 K. **Figure 8** shows the evolution of the collapsed liquid level in the core, indicating that, in all five cases, the curves remain consistently below the Top of Active Fuel (TAF), leaving the active core region almost entirely uncovered.
Following the application of the REPAS methodology, the uncertainty parameters having the greatest influence on the three FOMs, namely the maximum cladding temperature, the minimum core level, and the maximum power removed by the EHRS, were identified by means of the Simple Rank Correlation Coefficient, calculated using Spearman's rank correlation [17]. The most influential parameters were found to be the EHRS circuit VOR, and the amount of NCG present in the EHRS-HXs.
For completeness, **Table 1** reports the percentage deviations from the reference values of all uncertainty parameters considered in the analysis for the five SA cases. The table includes the two parameters identified as the most influential by the Spearman correlation analysis, as well as the three less influential ones, namely the initial liquid level in the RWST pool, the pressure loss coefficient and the surface roughness of the EHRS-HXs piping.
The positive and negative values in **Table 1** are to be understood as percentage increases and decreases, respectively, with respect to the nominal value of each parameter considered, , except for NCG, whose value

[1] Additional clarification is required regarding the sampling approach adopted for the NCG fraction. Due to the method used to provide input data into the code, it is not straightforward to directly sample the NCG amount. Since the initial quantity of NCG inside the EHRS tubes affect the initial water inventory, the initial water level in the EHRS was used as a surrogate sampling variable. Consequently, a high liquid level in EHRS heat exchangers (EHRS-HXs) corresponds to a low NCG fraction, whereas a low liquid level indicates a higher NCG presence. As a result, correlations involving NCG in the Spearman diagrams must be interpreted inversely.

represents the nitrogen volume fraction within the sampled control volume (one out of the six composing the EHRS-HX of each EHRS train; each of 0.07 m³).

Table 1. Percentage deviation of uncertainty parameters from their nominal values.

Run id	$\Delta k_{\%}$	$\Delta RWST\ lev_{\%}$	$\Delta NCG_{\%}$	$\Delta VOR_{\%}$	$\Delta roughness_{\%}$
24	+53.22	-52.29	+64.59	-45.65	-1.16
42	+13.86	-24.3	+96.43	-0.19	-2.47
63	+10.33	-34.08	+80.06	-90.28	-2.42
69	+66.13	-59.61	+41.38	-51.95	+1.6
108	+34.6	-28.93	+85.86	-72.19	-1.82

From the uncertainty parameter deviations reported in **Table 1**, it is possible to understand why runs 69 and 24 represent the most severe cases (in terms of the three FOMs considered in this work) from a safety perspective, whereas runs 108 and, in particular, 42 are the least severe.

Table 1 shows that runs 69 and 24 exhibit medium-to-high deviations across almost all uncertainty parameters considered with surface roughness representing the only limited variation. By contrast, the other cases are characterized by large deviations for selected parameters but do not show the same simultaneous occurrence of multiple unfavorable conditions. Among them, run 69 is particularly challenging, as **Figure *7*** and **Figure *8*** indicate that it is the SA case in which the cladding temperature sharply increases, and the core water level significantly drops earliest in time. Runs 42 and 108, on the other hand, exhibit a delayed onset of both phenomena.

To illustrate the magnitude of these differences, cladding temperature begins at approximately 9000 s for run 69 versus 14000 s for run 42, and the second rapid decrease of the core water level (following the initial break-induced drop) occurs shortly after 10000 s for run 69 versus around 14500 s for run 42.

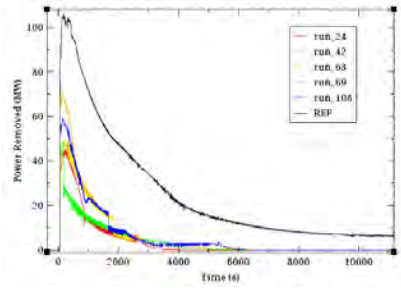

Figure 9. Max EHRS power removed for the five SA cases and for the reference.

Figure 9 shows the time evolution of the maximum power removed by the EHRS system. The graph indicates that all initial peaks of maximum power removal in the SA cases are lower than that observed in the reference calculation, where the PSS operates correctly, and the maximum power removed reaches 106.5 MW. Once again, the most penalizing cases are runs 24 and 69, which exhibit a maximum power removed around 48 MW. In particular, run 69 shows the fastest decline in the power curve, confirming it as the most severe case among those analyzed.

Before concluding this paragraph, some consideration is warranted for run 42. Based on the data reported in **Table 1** for this run, the critical events, namely the sharp increase in cladding temperature and the significant reduction of the core liquid level, occur later than in the other runs, particularly compared to the most severe cases, 69 and 24. The same data also reveal the significant contribution of NCG to the passive system failure. Aside from minor deviations in the pressure loss coefficient and surface roughness, the EHRS valve is nearly fully open (VOR = 99.81%), the RWST pool liquid level is moderately reduced (less than a quarter below its nominal value), and the NCG volume fraction is 96.43% of the sampled control volume. Thus, even though four out of the five uncertainty parameters do not deviate drastically from their

reference values, the elevated presence of NCG alone leads the transient to reach SA. This observation justifies the sensitivity study on NCG in the EHRS-HXs presented in the following section.

6. SENSITIVITY STUDY

Based on the conclusions drawn in the previous section, the present analysis focuses on a more detailed investigation of the effects of NCG on the performance of the EHRS passive safety system. The significant role played by NCG in driving the system toward SA conditions is consistent with the well-established degradation of condensation heat transfer in the presence of NCG [18], which impairs vapor transport to the condensing surface and reduces heat exchanger effectiveness, a particularly critical effect for systems relying on natural circulation as the sole driving force. For this reason, a dedicated sensitivity study is carried out by varying the NCG inventory in the EHRS-HXs across a progressively wider range of configurations. During the REPAS application, the sampling of the NCG inventory was restricted to one control volume per EHRS train out of the six composing the pool-immersed EHRS-HX. To better assess the impact of this modeling assumption, a preliminary sensitivity analysis was performed by varying the NCG volume fraction within these two control volumes (one per EHRS train) considered in the REPAS sampling. Specifically, five cases were defined with increasing NCG fractions, namely 85% (NCG_1), 90% (NCG_2), 95% (NCG_3), 98% (NCG_4), and 100%, corresponding to a fully gas-filled control volume (NCG_5). **Figure 10** and **Figure 11** show the time evolution of the maximum cladding temperature and the power removed by the EHRS, respectively, for the five NCG_cases and for the reference calculation.

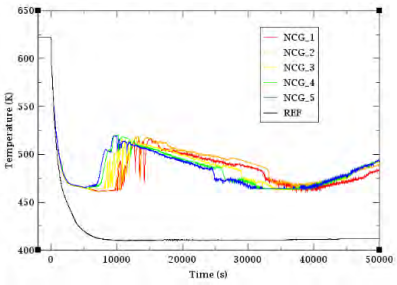

Figure 10. Max cladding temperature for the five NCG_cases and for the reference.

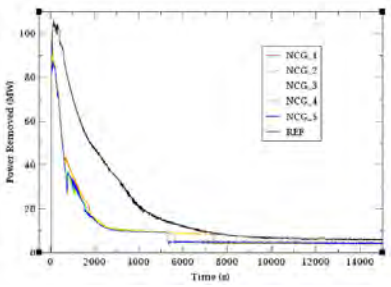

Figure 11. Max EHRS power removed for the five NCG_cases and for the reference.

From **Figure 10** and **Figure 11** it emerges that, despite the NCG volume fraction in the sampled control volume, none of the simulated scenarios reach SA conditions within the simulated time window, although a monotonic increase of the cladding temperature is observed in all cases after about 38000 s. In particular, **Figure 10** shows that the maximum cladding temperature remains below 520 K in all cases after the post-SCRAM temperature drop, indicating that the fuel cladding integrity is preserved over the simulated interval; however, the non-stationary trend suggests that a long-term evolution toward SA conditions cannot be excluded on the basis of the present calculations alone.

Nevertheless, increasing the NCG fraction progressively degrades EHRS performance, as reflected in the trends of removed power shown in **Figure 11**. The final power drop occurs at progressively later times, with the minimum power removed reached first in NCG_5 (5345 s from the start of the transient), followed by NCG_4 (5635 s), NCG_3 (6205 s), NCG_2 (7205 s), and NCG_1 (7385 s), respectively. This corresponds to a total delay of approximately 34 minutes between the earliest and latest cases, highlighting the impact of increasing NCG content on the timing of EHRS performance degradation. It is worth underlining that in these sensitivity cases the minimum removed power is around 4.5 MW, while in the reference case is around 5.5 MW. In particular, the continued rise of the cladding temperature observed around 38000 s indicates that these cases have not yet reached a stationary condition at 50000 s; extended simulations are therefore required to conclusively assess whether this first set of configurations ultimately avoids SA conditions.

With regard to the core collapsed coolant level, the water level decreases following the small-break LOCA and, due to the partial effectiveness of the EHRS, does not fully recover to nominal values. Nevertheless, for all five NCG_cases considered in this initial sensitivity study, the level remains below the TAF but consistently above the Bottom of Active Fuel (BAF).
Since none of the NCG configurations in the first set proved excessively penalizing for the system under investigation, the analysis was extended with an additional set of five simulations. Five new cases, labeled NCG_6 through NCG_10, were defined by progressively adding one more EHRS-HX control volume fully occupied by NCG per EHRS train. Specifically, case NCG_6 includes, in addition to the fully gas-filled volume considered in NCG_5, a second heat exchanger volume filled with NCG. This procedure was continued up to NCG_10, in which all heat exchanger volumes (i.e., the entire EHRS-HXs) are fully filled with NCG. **Figure 12** and **Figure 13** show the time evolution of the maximum cladding temperature and the core collapsed coolant level, respectively, for these additional five NCG sensitivity cases.

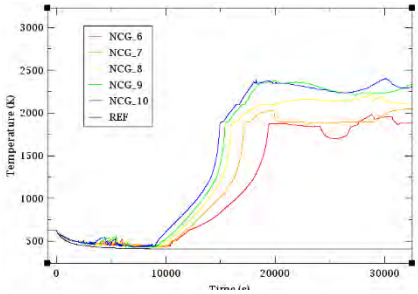

Figure 12. Max cladding temperature for the additional five NCG_cases and for the reference.

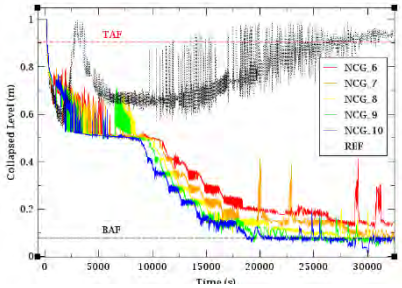

Figure 13. Normalized core coolant level for the additional five NCG_cases and for the reference.

The cladding temperature trends reported in **Figure 12** indicate that all five cases evolve into SA conditions. A combined inspection of **Figure 12** and **Figure 13** shows that the onset of cladding temperature escalation occurs concurrently with a rapid reduction of the core coolant level. This behavior is observed at progressively earlier times as the NCG inventory increases, from approximately 10300 s for NCG_6 to 9000 s for NCG_10. Beyond 30000 s, the core water level in all five cases stabilizes around the BAF. Finally, **Figure 14** and **Figure 15** show the EHRS removed power and circuit mass flow rate for these cases and for the reference.

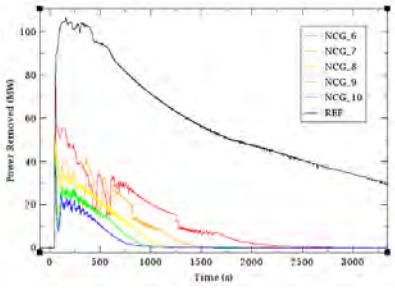

Figure 14. Max EHRS power removed for the additional five NCG_cases and for the reference.

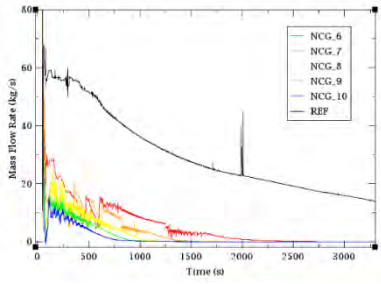

Figure 15. EHRS Mass flow rate for the additional five NCG_cases and for the reference.

A comparison between the EHRS removed power and the circulating mass flow rate shows that the temporal trends of these two quantities are qualitatively very similar within each analyzed case. This behavior is consistently observed across all scenarios from NCG_6 to NCG_10, confirming that the EHRS heat removal capability is directly governed by the natural circulation established in the loop: as the circulating mass flow rate drops, the power removed from the core drops accordingly. For all cases in the second set (NCG_6 through NCG_10), both the EHRS removed power and the circulating mass flow rate decrease rapidly to near-zero values, though at different instants. Moving from the least penalizing scenario (NCG_6) to the

most unfavorable one (NCG_10), the time at which these minima are reached occurs progressively earlier, indicating an earlier loss of EHRS effectiveness with increasing NCG inventory.
A direct comparison between cases NCG_5 and NCG_6 further highlights the impact of NCG accumulation on EHRS performance. In case NCG_5, where only one of the six heat exchanger control volumes is fully filled with NCG, the system does not evolve into SA conditions. Although the circulating mass flow rate undergoes a faster and more pronounced reduction compared to the reference case, it stabilizes shortly after 5000 s at an approximately constant value of about 2 kg/s. Conversely, in case NCG_6, where two heat exchanger control volumes are completely filled with NCG, the system evolves into SA conditions, and the circulating mass flow rate drops below 1 kg/s before 2000 s. In the present configuration, a single heat exchanger control volume corresponds to approximately 0.214% of the total EHRS volume; accordingly, the transition from NCG_5 to NCG_6 results in an NCG volume fraction of 0.86%, sufficient to drive the system into SA conditions.
To obtain a first estimate of the NCG volume fraction leading to a DBA-to-DEC transition, an additional sensitivity cycle is performed to investigate the system behavior for NCG fractions between those of NCG_5 and NCG_6. Five additional cases are therefore defined, labeled NCG_5-2, NCG_5-4, NCG_5-6, NCG_5-8, and NCG_5-9. Starting from the NCG_5 configuration, in which the first of the six heat exchanger control volumes per EHRS train is fully occupied by nitrogen, the second control volume is progressively filled with NCG at increasing fractions of 20%, 40%, 60%, 80%, and 90%, respectively, thus bridging the gap between NCG_5 and NCG_6.
Figure 16 and **Figure 17** show the time evolution of the maximum cladding temperature and the power removed by the EHRS, respectively, for these last five NCG sensitivity cases.

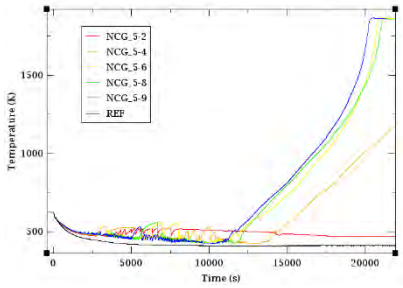

Figure 16. Max cladding temperature for the last five NCG cases and for the reference.

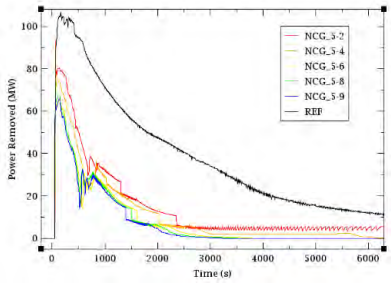

Figure 17. Max EHRS power removed for the last five NCG cases and for the reference.

Figure 16 and **Figure 17** show that, among the five additional sensitivity cases, only NCG_5-2 does not reach SA conditions within the simulated time window. As clearly visible in **Figure 16**, cases NCG_5-4 through NCG_5-9 all exhibit a sharp escalation of the maximum cladding temperature, confirming the onset of core degradation. This behavior is corroborated by **Figure 17**, which shows that only NCG_5-2 maintains a non-negligible removed power, sufficient to ensure adequate heat removal from the core and to prevent the transition to SA over the analyzed time span. In all other cases, the removed power progressively drops to zero, with the collapse occurring earlier as the NCG fraction in the second heat exchanger control volume increases.
The present sensitivity study provides an indication of the volume fraction of NCG that may drive the system into SA conditions within the simulated time window. The least penalizing case evolving into SA is NCG_5-4: a nitrogen volume fraction of approximately 0.6%[2] of the total EHRS system volume is therefore sufficient to lead the system to SA within 50000 s. It should be emphasized that this figure represents a sufficient, rather than strictly minimum, NCG inventory

[2] This value is computed as the ratio between the total NCG volume present in both EHRS trains in case NCG_5-4 and the total EHRS volume.

for SA onset, since the lower-NCG_cases (NCG_1–NCG_5 and NCG_5-2) display non-stationary trends at 50000 s whose long-term outcome cannot be conclusively assessed from the present calculations.
This result, combined with the findings of the previous sensitivity sets, provides a first characterization of the EHRS response to increasing NCG content within the 50000 s simulation window, progressively narrowing the NCG inventory range within which SA onset is observed, from the initial case-to-case resolution of the first two sets down to the finer resolution achieved in the present one.

7. CONCLUSIONS

This work presents a detailed analysis of severe accident scenarios emerging from a prior application of the REPAS methodology to the EHRS of a generic iPWR SMR design, with focus on the role of NCG accumulation in driving functional failures of the passive safety system. Beyond the methodological application itself, the study shows how the combined REPAS–MELCOR approach can be exploited to investigate how specific governing parameters drive the transition from DBA to DEC conditions through the progressive loss of passive system functionality.
Among the cases identified in the REPAS campaign, five evolved into SA conditions. Their analysis revealed that the Valve Opening Ratio (VOR) and the Non-Condensable Gas (NCG) fraction within the EHRS-HXs are the most influential parameters, with their simultaneous unfavorable combination as the primary driver toward core degradation. A dedicated sensitivity study, based on deterministic MELCOR simulations with progressively increasing NCG inventory, showed that small amounts of NCG can impair natural circulation in the EHRS and degrade its heat removal capability, consistent with the degradation of condensation heat transfer reported in the open literature. Rather than aiming at the quantitative identification of a precise NCG threshold for SA onset, which would require a more extensive analysis, this study demonstrates that small quantities of NCG on the tube side can affect the passive system mission. Extending the simulated transients well beyond the 50000 s considered here is essential to properly quantify the long-term impact of NCG on the EHRS performance in the present model and represents the natural continuation of this work.

NOMENCLATURE

ADS: Automatic Depressurization System; **BAF**: Bottom Active Fuel; **DBA**: Design Basis Accident; **DEC**: Design Extension Condition; **DVI**: Direct Vessel Injection; **DW**: DryWell; **EBT**: Emergency Borated Tank; **EHRS**: Emergency Heat Removal System; **EHRS-HX**: EHRS-Heat Exchanger; **FC**: Failure Criterion; **FOM**: Figure Of Merit; **iPWR**: integral Pressurizer Water Reactor; **LGMS**: Long-term Gravity make-up System; **NCG**: Non-Condensable Gas; **RC**: Reactor Cavity; **REPAS**: Reliability Evaluation of Passive Safety systems; **RPV**: Reactor Pressure Vessel; **RWST**: Refuelling Water Storage Tank; **SA**: Severe Accident; **SG**: Steam Generator; **SMR**: Small Modular Reactor; **TAF**: Top Active Fuel; **TM**: Target Mission; **VOR**: Valve Opening Ratio.

ACKNOWLEDGMENTS

Funded by the European Union

Funded by the European Union. Views and opinions expressed are however those of the author(s) only and do not necessarily reflect those of the European Union or European Commission-Euratom. Neither the European Union nor the granting authority can be held responsible for them.

ENEA carried out the research activity with MELCOR code and SNAP, obtained in the framework of the ENEA-ISIN agreement signed on March 23rd 2020 as part of the General Arrangement between the United

States Nuclear Regulatory Commission (US-NRC) and the Italian National Inspectorate for Nuclear Safety and Radiation Protection (ISIN).

This work has been partially supported by the ENEN2plus project (HORIZON-EURATOM-2021-NRT- 01-13101061677) founded by the European Union.

REFERENCES

1. L.Burgazzi, "Reliability evaluation of passive systems through functional reliability assessment," *Nuclear Technology* **144.2**, pp. 145-151 (2003).
2. F. D'Auria, and G.M. Galassi, "Methodology for the evaluation of the reliability of passive systems," pp. 1-34 (2000).
3. J.Jafari, F. D'Auria, H. Kazeminejad, and H. Davilu, "Reliability evaluation of a natural circulation system," *Nuclear Engineering and Design* **224.1**, pp. 79-104 (2003).
4. L. Tempesta, "Application Of The REPAS Methodology To Analyze The Reliability Of The EHRS In The Decay Heat Removal Strategy For An SMR," Master's thesis, University of Bologna, (2024).
5. L.L. Humphries, B. Beeny, F. Gelbard, D. Louie, and J. Phillips, *MELCOR Computer Code Manuals Volume 1: Primer and Users' Guide*. No. SAND-2015-6691R. Sandia National Lab. (SNL-NM), Albuquerque, NM, United States (2015).
6. L.L. Humphries, B. Beeny, F. Gelbard, D. Louie, J. Phillips and H. Esmaili, *MELCOR Computer Code Manuals Vol. 2: Reference Manual version 2.2.* Sandia National Lab. (SNL-NM), Albuquerque, NM, United States (2017).
7. M. Principato, F. Giannetti, M. Imperatori, M. D'Onorio, M. Garcia, L.E. Herranz, A. Bersano, F. Mascari, «Analyses of the MELCOR capability to simulate integral PWR using passive systems in a DBA scenario,» *Nuclear Engineering and Design,* vol. 437, n. 114004, 2025.
8. SASPAM-SA, «Deliverable 2.2: iPWR input-deck and scenarios analyses,» 2024.
9. "SASPAM-SA," https://zenodo.org/records/10046740 (2023).
10. L. E. Herranz, B. Poubeau, F. Mascari and L. Chailan, "Looking ahead to severe accident research," EPJ N-Nuclear Sciences & Technologies 11: 28, 2025.
11. G. Grippo, "Comparison Of A DBA Sequence In A Generic IPWR Between MELCOR And ASTEC Codes," doi: 10.5281/zenodo.12579696. (2024).
12. Applied Programming Technology, Inc., *Symbolic Nuclear Analysis Package (SNAP) User's Manual*, (2021).
13. «INTERNATIONAL REACTOR INNOVATIVE AND SECURE, IRIS Plant Overview,» October 2002.
14. M. Carrelli, L. Conway, M. Dzodzo, A. Maioli, L. Oriani, G. Storrick, B. Petrovic, A. Achilli, G. Cattadori, C. Congiu, R. Ferri, M. Ricotti, D. Papini, F. Bianchi, P. Meloni, S. Monti, F. Berra, D. Grgic, G. Yoder, A. Alamberti, «The SPES3 experimental facility design for the IRIS reactor simulation,» Science and Technology of Nuclear installations, vol. vol2009, n. 579430, 2009.
15. S.S. Wilks, "Determination of sample sizes for setting tolerance limits," *The Annals of Mathematical Statistics* **12.1**, pp. 91-96, (1941).
16. International Atomic Energy Agency (IAEA), *Safety Margins of Operating Reactors-Analysis of Uncertainties and Implications for Decision Making*. International Atomic Energy Agency, (2003).
17. K.A. Gamble, L.P. Swiler, «Uncertainty Quantification and Sensitivity Analysis Applications to Fuel Performance Modeling,» SAND2016-4597C, 2016.
18. J. Huang, J. Zhang and L. Wang, "Review of vapor condensation heat and mass transfer in the presence of non-condensable gas," *Applied thermal engineering* **89**, pp. 469-484, (2015).

Italian National Agency for New Technologies,
Energy and Sustainable Economic Development

PERFORMANCE ASSESSMENT OF PASSIVE SAFETY SYSTEMS AND IDENTIFICATION OF CONDITIONS LEADING TO DESIGN EXTENSION SCENARIOS

The 12th Conference on SEVERE ACCIDENTS RESEARCH – ERMSAR 2026, 18 – 22 May 2026, Madrid, Spain

Erik Cilia[1], Fulvio Mascari[2]

[1]University of Bologna, Italy
[2]ENEA, Bologna, Italy

Purpose of the study

In this work, a reliability analysis of a **Decay Heat Removal System (DHRS)** was performeed strarting from a previous **REPAS** application and exending it with a sensitivity analysis.

- **DHRS** is a fundamental system to **remove the decay power** from the core;
- It works in **Natural Circulation (NC);**
- There are valves that connect system to the reactor vessel ➔ **need the activation**;
- **His failure can lead to Design Extension Condition**.

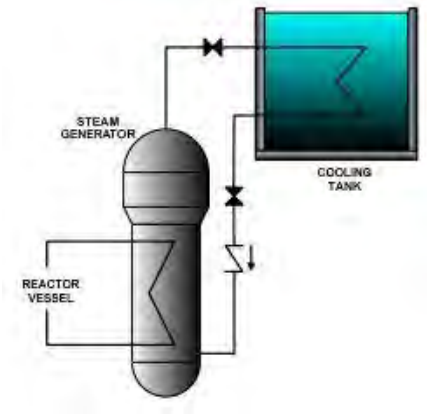

The present activity has been conducted in the framework of the Horizon Euratom **SASPAM-SA project**. The project is coordinated by ENEA and 23 organization from 14 countries are involved.

Funded by the European Union

REPAS methodology

REPAS methodology was developed for the evaluation of the reliability of passive systems.

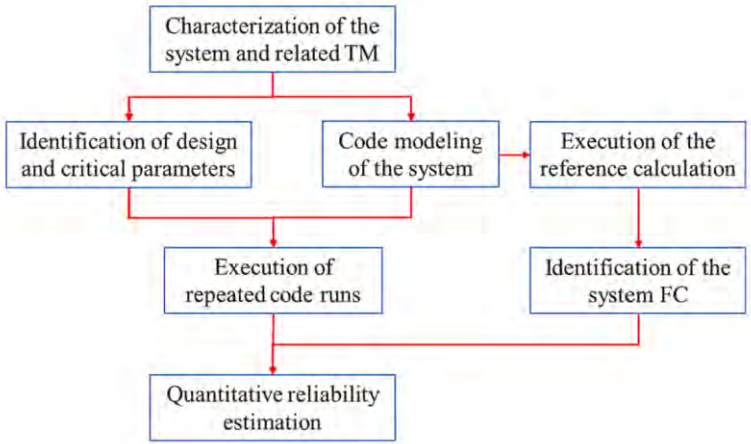

Main steps of the method:

- Characterization of the design of the system, its operating conditions and **Target Mission (TM),**
- Identification of design and critical parameters, with their reference values, ranges of variability and probability distributions,
- Code modeling of the system and execution of the reference calculation.
- Identification of the system **Failure Criteria (FC),**
- Execution of repeated code runs,
- Quantitative reliability estimation.

Generic iPWR Design

The **iPWR** here considered is characterized by the use of several passive systems, by a dry containment and a power of about 300 MWe:

- The reactor operates in **forced circulation during normal operation** and employs a passive mitigation strategy in accidental transients;
- It consists of an **integral RPV**, which contains the core, a compact SGs, the Control Rod Drive Mechanism (CRDM), the primary pumps and the pressurizer included in the upper head;
- The hot water at the core outlet flows **upward in a circular riser** up to the primary pumps suction. The flow path continues through the annular region of the DC, outside the core, to the LP and then back to the core.

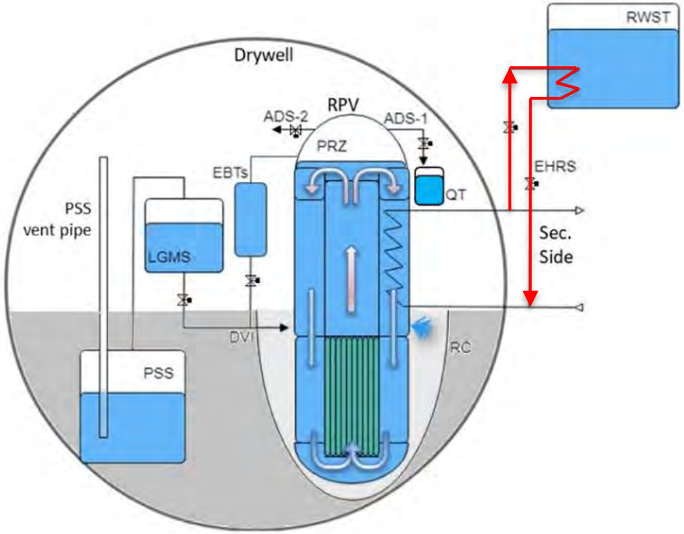

MELCOR nodalization

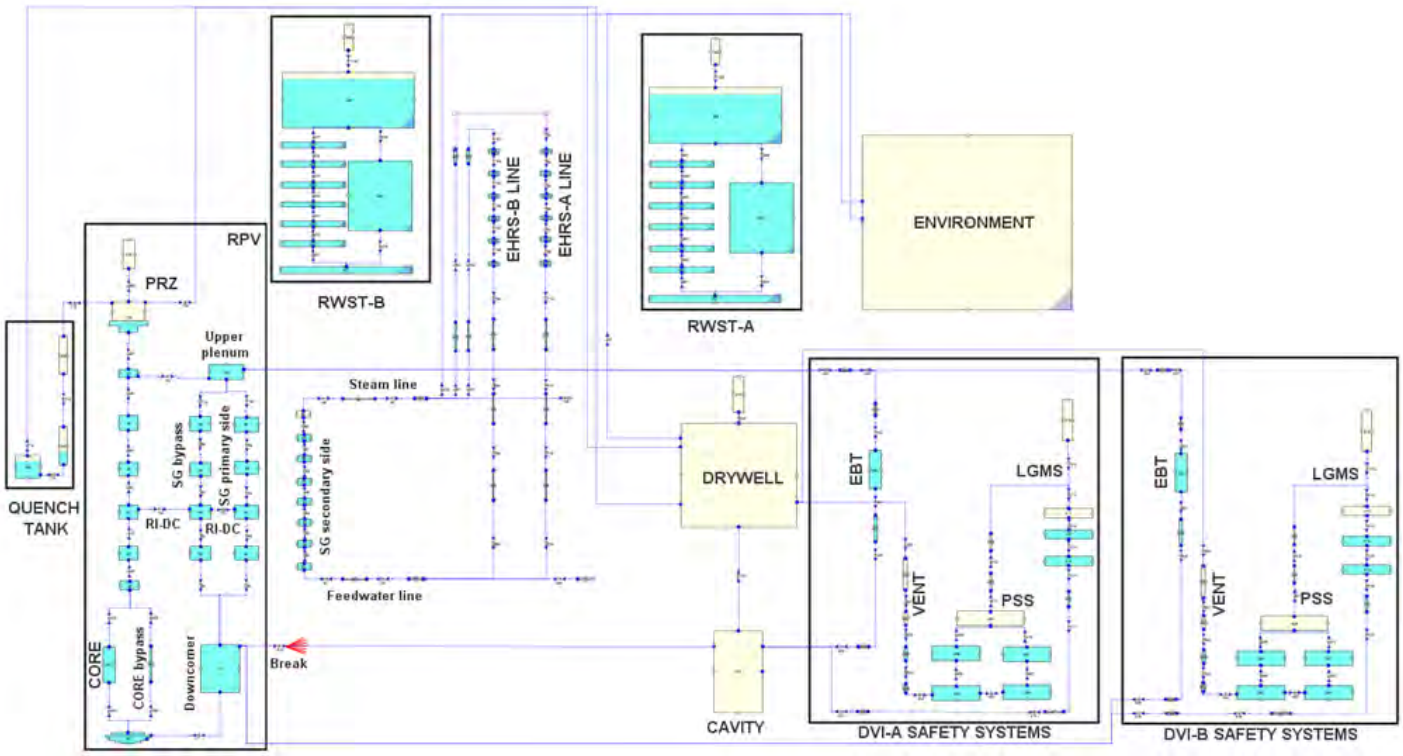

Reference Transient

DBA scenario: Guillotine break of one Direct Vessel Injection (DVI) line, considering the availability of all safety systems.

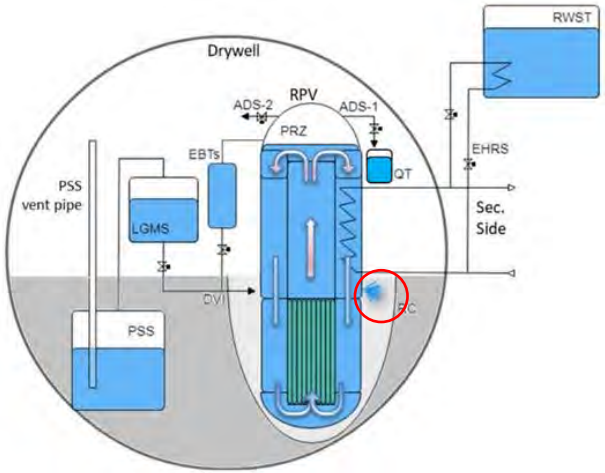

BREAK OF DVI LINE

High Containment Pressure signal
- SCRAM
- Secondary system isolation
- EHRS actuation

Low PRZ level signal
- RCP coastdown
- RI-DC valves opening

Low PRZ pressure signal
- EBTs actuation
- ADS stage-1 actuation

Low DP RPV-Containment signal
- LGMSs actuation

Low LGMS mass signal
- ADS stage-2 actuation

REPAS application

Among the **150 MELCOR simulations** performed, **5 resulted** into a **Severe Accident.**

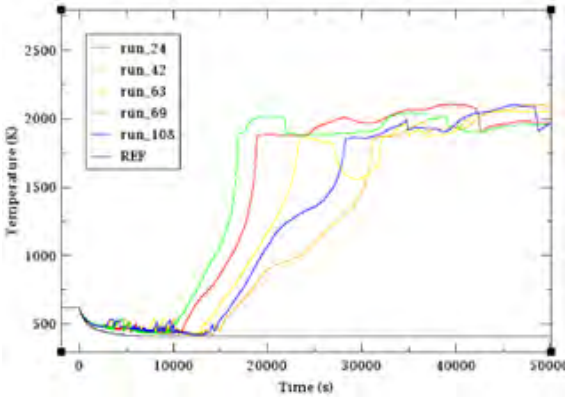

Max Cladding temperature

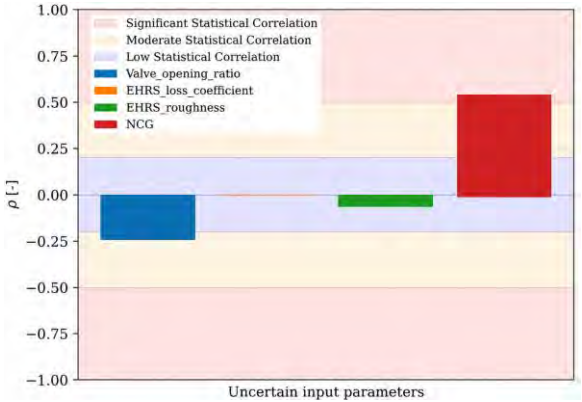

Simple rank correlation coefficient

Uncertain parameters

Parameter	Nominal value	PDF
Loss coefficient (k)	0.6	Stepwise
Surface roughness	5 E-05 m	Normal
Valve Opening Ratio (VOR)	1	Stepwise
Non-Condensable Gas (NCG) fraction	0	Stepwise
RWST initial level	2 m	Stepwise

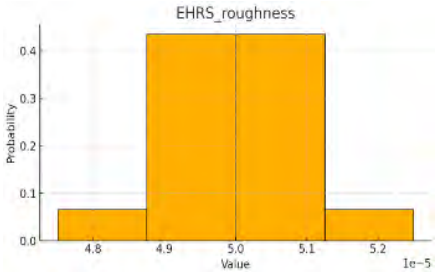

Sensitivity Analysis

Three separate sensitivity analysis campaigns were carried out, each comprising five different calculations, with the aim of identifying the threshold level of NCG that leads to SA.

1° Sensitivity calculations set:

- **NCG_1**: 85% vol. of N_2 for the considered control volume (for each line)
- **NCG_2**: 90% vol. of N_2 for the considered control volume (for each line)
- **NCG_3**: 95% vol. of N_2 for the considered control volume (for each line)
- **NCG_4**: 98% vol. of N_2 for the considered control volume (for each line)
- **NCG_5**: 100% vol. of N_2 for the considered control volume (for both line)

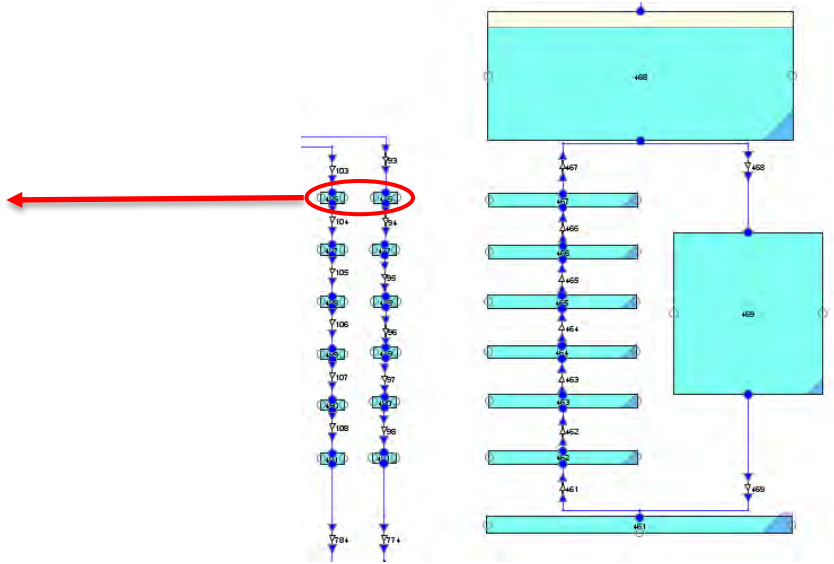

Sensitivity Analysis

Three separate sensitivity analysis campaigns were conducted, each consisting of five different calculations.

1° Sensitivity calculations set:

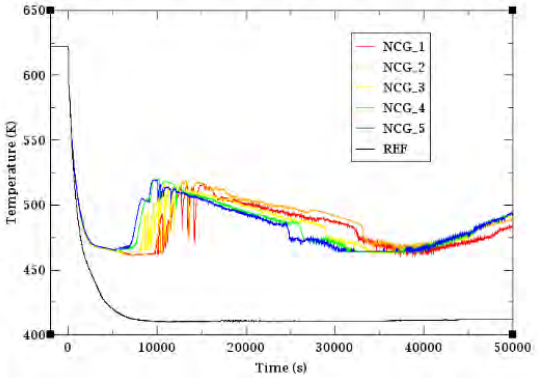

Max Cladding temperature

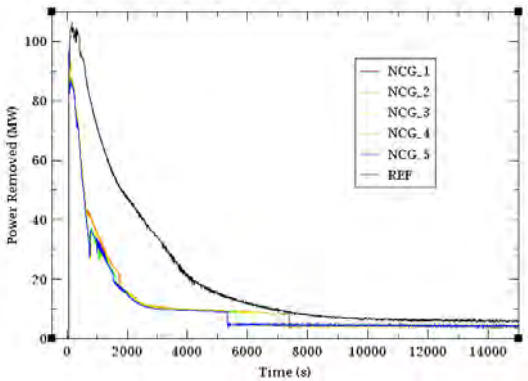

EHRS power removed

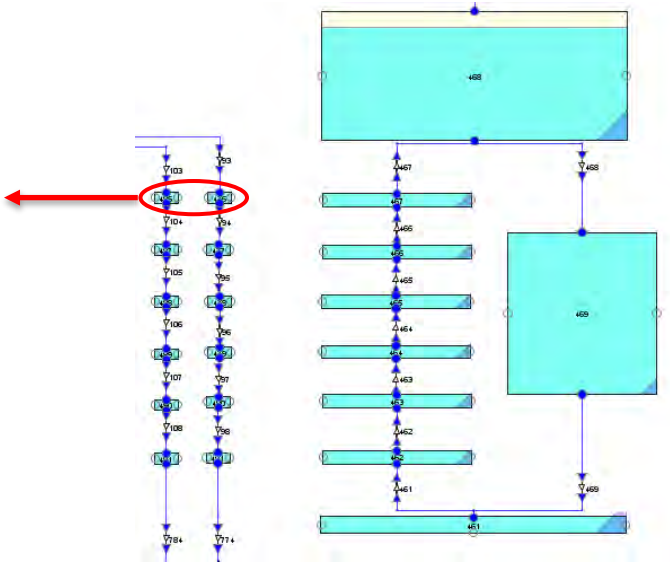

Sensitivity Analysis

Three separate sensitivity analysis campaigns were carried out, each comprising five different calculations, with the aim of identifying the threshold level of NCG that leads to SA.

2° Sensitivity calculations set:

- **NCG_6**: Two control volumes full of N_2 (for each line)
- **NCG_7**:Three control volumes full of N_2 (for each line)
- **NCG_8**: Four control volumes full of N_2 (for each line)
- **NCG_9**: Five control volumes full of N_2 (for each line)
- **NCG_10**: Six control volumes full of N_2 (for each line)

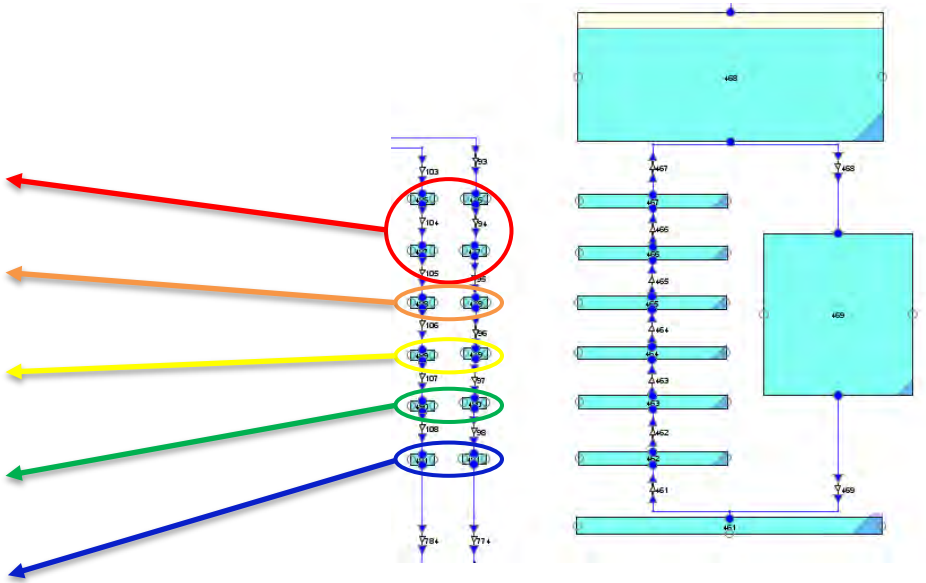

Sensitivity Analysis

Three separate sensitivity analysis campaigns were carried out, each comprising five different calculations, with the aim of identifying the threshold level of NCG that leads to SA.

2° Sensitivity calculations set:

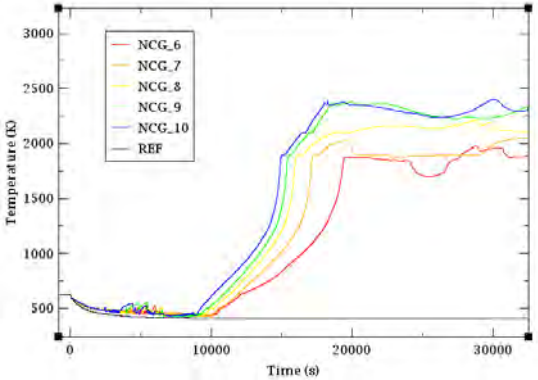

Max Cladding temperature

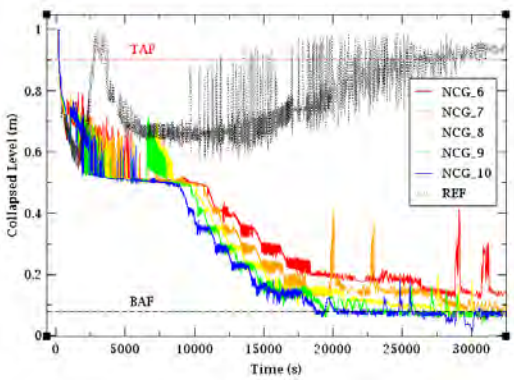

Collapsed core coolant level

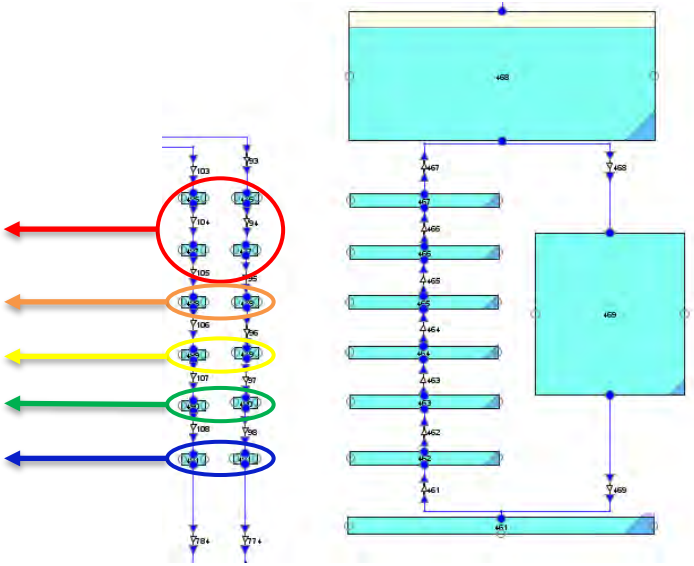

Sensitivity Analysis

Three separate sensitivity analysis campaigns were carried out, each comprising five different calculations, with the aim of identifying the threshold level of NCG that leads to SA.

3° Sensitivity calculations set: Starting with the first control volume filled with N_2, we proceed by adding increasing amounts to the second volume only.

- **NCG_5-2**: 20% vol. of N_2 for the 2° control volume considered(for each line)
- **NCG_5-4**: 40% vol. of N_2 for the 2° control volume considered (for each line)
- **NCG_5-6**: 60% vol. of N_2 for the 2° control volume considered (for each line)
- **NCG_5-8**: 80% vol. of N_2 for the 2° control volume considered (for each line)
- **NCG_5-9**: 90% vol. of N_2 for the 2° control volume considered (for both line)

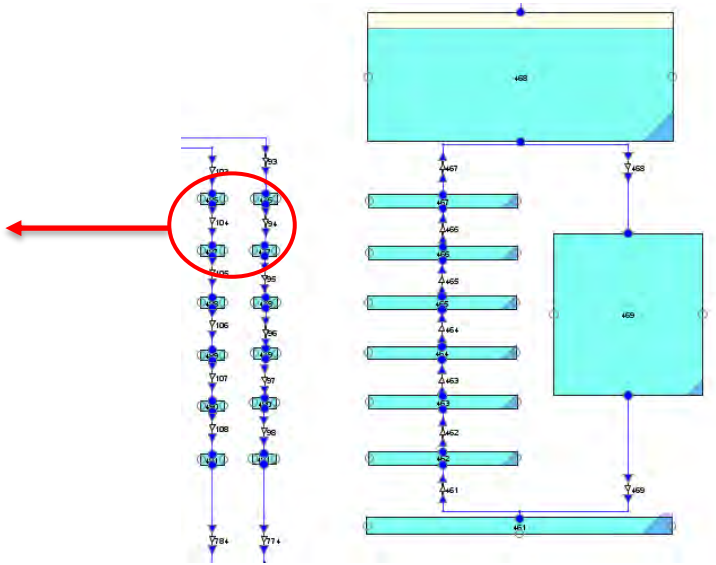

Sensitivity Analysis

Three separate sensitivity analysis campaigns were carried out, each comprising five different calculations, with the aim of identifying the threshold level of NCG that leads to SA.

3° Sensitivity calculations set: Starting with the first control volume filled with N_2, we proceed by adding increasing amounts to the second volume only.

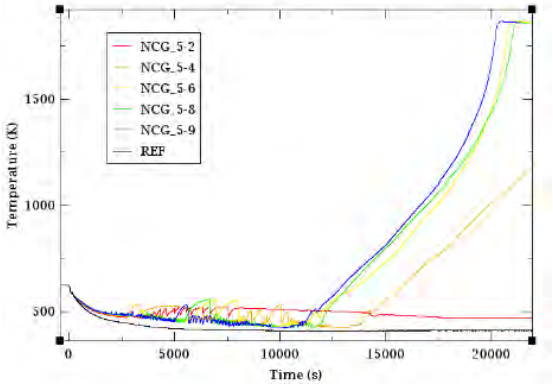

Max Cladding temperature

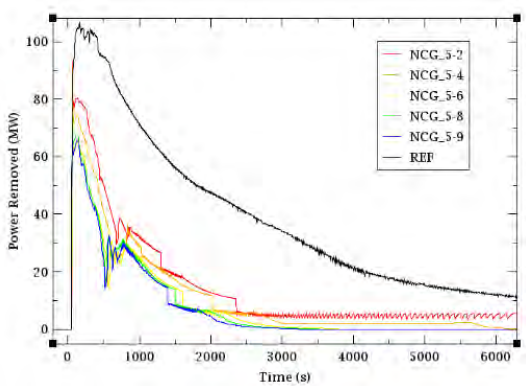

Power removed

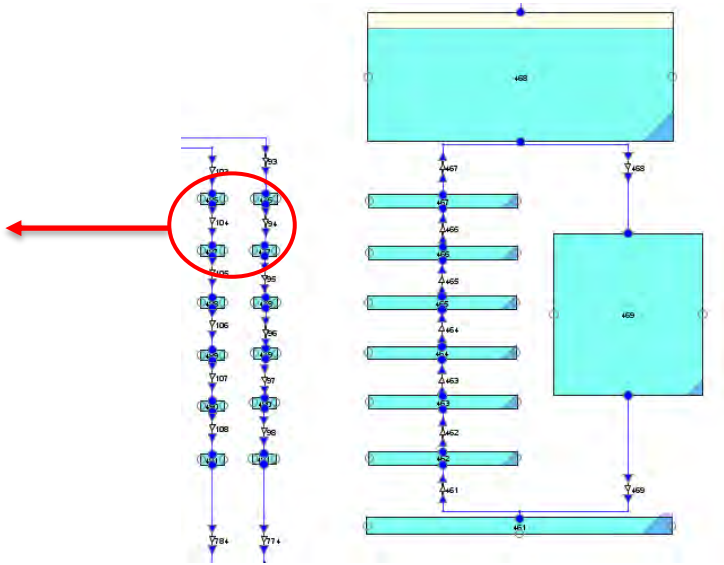

Conclusions

- The **REPAS** methodology, applied together with **MELCOR**, was used in a **generic iPWR** SMR under **SB-LOCA** conditions to investigate **EHRS** behavior and characterize the **transition from DBA to DEC** and SA scenarios.
- Five scenarios evolved into SA conditions. **The most influential parameters** were the Valve Opening Ratio (**VOR**) and the accumulation of **NCGs** inside the EHRS-HXs, which strongly degraded natural circulation and condensation heat transfer.
- The sensitivity study showed that **increasing NCG content progressively reduced EHRS heat removal capability**, leading to earlier coolant level decrease and core degradation. In the present model, an **NCG fraction of about 0.6%** of the total EHRS volume was **sufficient to trigger SA conditions within 50000 s**.
- Extending the simulated transients well beyond the 50000 s considered here is essential to properly quantify the long-term impact of NCG on the EHRS performance in the present model.

Acknowledgment/Disclaimer

Funded by the European Union

Funded by the European Union. Views and opinions expressed are however those of the author(s) only and do not necessarily reflect those of the European Union or European Commission-Euratom.
Neither the European Union nor the granting authority can be held responsible for them.

ENEA carried out the research activity with MELCOR code and SNAP, obtained in the framework of the ENEA-ISIN agreement signed on March 23rd 2020 as part of the General Arrangement between the United States Nuclear Regulatory Commission (US-NRC) and the Italian National Inspectorate for Nuclear Safety and Radiation Protection (ISIN).

This work has been partially supported by the ENEN2plus project (HORIZON-EURATOM-2021-NRT-01-13101061677) founded by the European Union.

Thank you for your attention

erik.cilia@unibo.it

EFFECT OF DELAYED RECOVERY OF ECCS DURING SEVERE ACCIDENTS IN INTEGRAL PWR SMRS

Govatsa Acharya, Dmitry Grishchenko, and Pavel Kudinov
KTH Royal Institute of Technology, Division of Nuclear Science and Engineering,
Albanova University Center, 10691 Stockholm, Sweden.
govatsa@kth.se; dmitrygr@kth.se; pkudinov@kth.se

ABSTRACT

The Emergency Core Cooling System in an Integral Pressurized Water Reactor promises enhanced safety of the reactor during transients and accidents. In particular, during Loss of Coolant Accidents, this system enables long-term cooling of the reactor, by way of opening of the 3 Reactor Ventilation Valves at the top of the Reactor Pressure Vessel and 2 Reactor Recirculation Valves above the core thereby establishing a natural circulation loop. The ECCS actuation signal is typically triggered when the Module Protection System at high containment water level and low differential pressure between RPV and containment vessel. In this study, operation of these valves with delayed manual actuation and opening is simulated using MELCOR for 72h. Time delays for opening of RVVs and RRVs were uniformly sampled in a period up to 27,000s after the initiating event that includes Loss of Coolant Accident and Steam Generator Tube Rupture. The focus of this paper is the core degradation progression and the thermal-hydraulic properties in the containment vessel. The core cooling process is sensitive to the full availability of ECCS, and it can be fully achieved if RRVs are open within about 15,000s irrespective of timing of RVVs opening. Debris properties and hydrogen generation due to oxidation are also characterized, and timing of melt relocation is found to be sensitive to timing of ECCS activation. These findings are important for in-vessel debris coolability, risk-performance and risk-informed assessment of passive safety features in Small Modular Reactors, and aid in better understanding of code capabilities and uncertainties involved in severe accident analysis.

KEYWORDS
SMR, MELCOR, severe accident analysis, submerged containment design, LOCA, SGTR

1. INTRODUCTION

Small Modular Reactors (SMRs) have a large growing interest in the international community to cater to growing energy demands by large data centers and industries, and to replace energy sources with large carbon footprint increasingly due to their ability in meeting flexible power needs [1]. SMRs enjoy better safety features, including inherent, passive, integral safety features, than conventional reactors, drawing to its appeal [2]. SMRs also promise simplification and standardization making it economically feasible. An innovative safety component of the passively safe SMRs is the Emergency Core Cooling System (ECCS). The ECCS in these SMRs propose 2 sets of redundant valves comprising of 3 independent Reactor Ventilation Valves (RVVs) at the top of the Reactor Pressure Vessel (RPV) that discharges into the Containment Vessel (CNT) and 2 independent Reactor Recirculation Valves (RRVs) just above the core [36] that lets water in to the RPV thereby establishing a natural circulation loop. Unlike conventional Pressurized Water Reactors (PWRs), where ECCS comprises of several safety injection tanks and pumps that inject borated water in case of Anticipated Operational Occurrences (AOOs) and postulated accidents like Loss-of-Coolant Accidents (LOCAs), ECCS in Integral PWRs (iPWRs) are much smaller and simpler in operation [4]. iPWRs, such as the NuScale reactor, in order to simplify and adhere to regulations on system reliability [3], have developed novel engineered systems such as Inadvertent Actuation Block (IAB) feature

to the main ECCS valves [37]. Achieving low Core Damage Frequency (CDF $<10^{-9}$/year) and Large Release Frequency (LRF $< 10^{-10}$/year) [5][38], demands exceptional reliability and innovative systems to ensure effective accident mitigation even in the absence of offsite power.

Single Failure Criteria (SFC) is an important issue that has received attention in the case of functioning of the ECCS valves. ECCS is "considered to be designed against an assumed single failure if a single failure of any active or passive component does not result in the loss of the capability of the system to perform its safety functions" according to Appendix A to 10 CFR Part 50 [39], and during the audit by the US NRC the design itself was revised [39]. This issue was also reviewed in innovative-SMR design [40] as it aims to satisfy stringent safety criteria for Standard Design Approval. [6] also examined single failure accident conditions initiated by partial failures of the ECCS stuck closed. [7] performed safety assessment assuming ideal operating conditions with no safety degradation due to component level failures in i-SMRs, which then was recently followed by another assessment assuming partial valve failures [8]. This also highlighted multi-valve failure being a driver for accelerated core heat-up and hydrogen generation.

Degraded ECCS function in traditional PWRs due to blockages and clogging have been a part of reactor safety assessments [9][10][11][12]. Such blockages were identified as a relevant issue after the Barsebäck-2 accident in 1992 [13], with accumulation of fibrous material potentially hampering core cooling. It is a possibility that, even if SFC is resolved in iPWRs, there may be other such instances, even if conditions are extrapolated from traditional PWRs, that may jeopardize the ability of the ECCS valves to operate as intended, effectively leading to uncovery and subsequent damage of the core.

In response to growing international interest and technical knowledge gaps, the EURATOM SASPAM-SA project – the framework for this research – was launched in 2022 to tackle these issues and support European licensing requirements for severe accident (SA) analysis and emergency planning zone (EPZ) evaluation [14]. The distinct designs of iPWRs present challenges for system codes and analytical tools in simulating complex reactor phenomena during off-normal events, a difficulty explored in multiple studies [20][21][22][23]. Key focus areas include hydrogen explosions [15], forced and natural circulation passive safety [16][17], in-vessel cooling and debris retention [18], containment phenomena and behaviour [19]. Severe accident codes like MELCOR and ASTEC, typically employed to model accidents and validated against experimental data, were originally developed for large reactors. Applying these integral codes to novel phenomena in SMRs – where extensive experimental data are scarce – can introduce uncertainties rooted in modeling assumptions or design decisions. This underscores the need for thorough understanding of code strengths and limitations, which drives ongoing investigation.

Recent analyses of generic iPWR designs have simulated design basis accidents (DBAs) and certain design extension conditions [14][24][25]. Studies have shown MELCOR's ability to perform stable and accurate simulations of iPWRs during LOCAs [26][27][28]. The complete core degradation phenomena and conservative source term behaviour in iPWR during several severe accident scenarios were analyzed in complementary studies [29][30]. In the present study, the consequences of delayed activation of ECCS on thermal-hydraulic and core degradation during SAs in a generic iPWR is studied using MELCOR code.

2. iPWR MODEL DESCRIPTION

Here the generic iPWR design in consideration is of the submerged containment type, where the integral reactor vessel is housed inside a larger containment which is submerged inside a pool of water, shown in Figure 1(a). Specifications for the development of the model are gathered from open literature and do not represent any specific reactor design. The study therefore provide a largely qualitative set of results. The MELCOR v2.2.r2023.0 model used here has undergone several modifications from the original input deck developed by [24][25]. The iPWR is a 160MWth, naturally cooled integral reactor with 2 helical tube steam generators (HTSG). The RPV is contained inside a CNT to maintain core cooling in case of potential loss

of reactor vessel integrity. The primary system operating pressure is 8.3MPa and CNT is almost at vacuum. The core has 37 17x17 fuel assemblies, about half the height of typical PWR assemblies located at the bottom of the RPV. Above the core, a cylindrical riser tube terminates in the pressurizer (PRZ). The downcomer, an annular region surrounding the riser, houses the two HTSGs in the upper part and the core in the lower part. The HTSG consists of a set of tube bundles with separate feedwater inlet and steam outlet lines. The MELCOR model of the iPWR, shown in Figure 1(b), comprises of control volumes (CVs) representing parts of RPV, SGs, CNT, RP, reactor building and the environment, and flowpaths (FLs) representing connections between CVs. Details of packages used to develop inputs in MELCOR can be found in the guides [26][27]. As done in many other studies, the MELCOR model lacks the Decay Heat Removal System (DHRS), for conservativeness and mainly as the scenarios modelled are of LOCA-type SA where DHRS may be insignificant [31].

The T/H behaviour is dependent on the assumptions and choices made in nodalization of these CVs and properties of FLs. In case of accidents the steam generators (SGs) are isolated and ECCS is activated which establishes coolant circulation between the reactor coolant system (RCS) and the containment side transferring decay heat to the reactor pool (RP) acting as the ultimate heat sink (UHS).

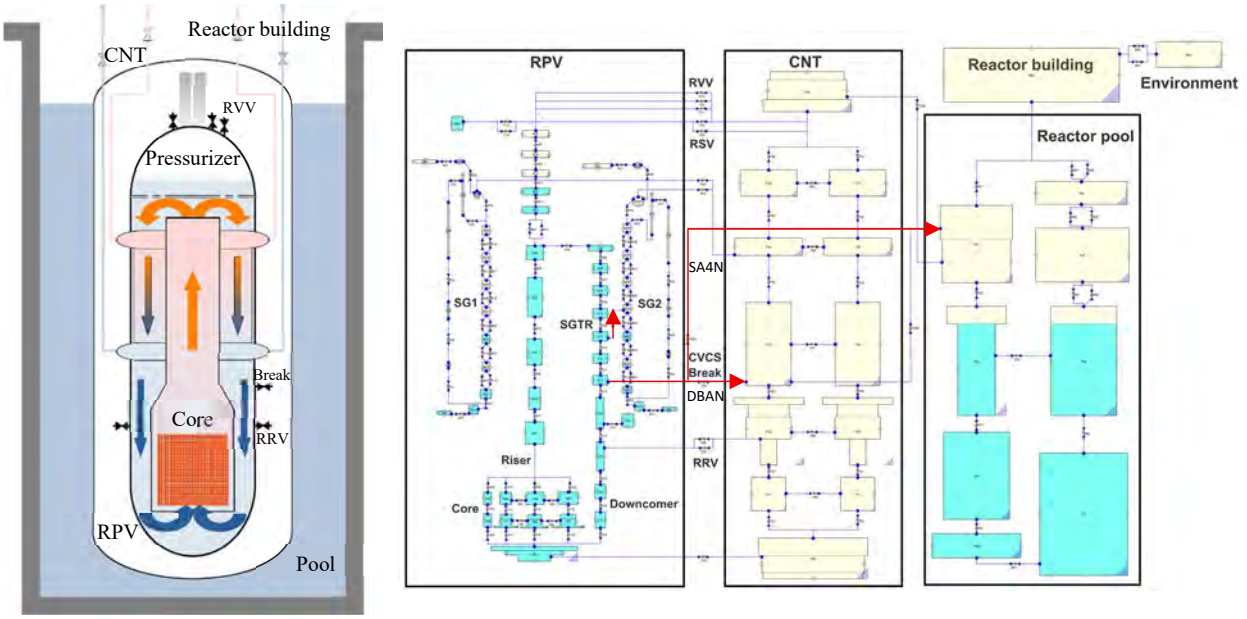

(a) Generic design. (b) MELCOR nodalization.

Figure 1. Schematic of the generic iPWR design (based on [24]).

The CNT is defined by 12 CVs, separately for the cold and hot side to support natural convection, to reduce instabilities in simulations, while RP has 8 CVs. The SG is a bundle of once through HTSG, whose secondary side has 2 sets with 7 CVs each. The heat transfer inside is modelled using HelicalSG HS in MELCOR. HSs also exist for the CNT designed to support natural convection in the pool. FLs exist between CVs in the core, riser, downcomer, SGs and CNT. A leakage FL is added to the top of CNT with the top of RP, and the flow rate is controlled by a tabular depending on pressure differences. The core is modelled in the COR package, as 4 rings radially and 10 levels axially. Active core is in the central 3 rings and levels 6-9, the lower plate in level 4 and lower plenum in levels 1-3. 2 reactor safety valves (RSV) are included to protect RPV from over-pressure. Decay heat tables based on ANS73 standard are implemented. The radionuclide transport is handled by the RN package, where hygroscopic and chemisorption models are activated. Revised CORSOR-Booth high burnup model is used for fission product (FP) release.

2.1. Emergency Core Cooling System

The ECCS valves comprise the main valve, IAB valve, and two solenoid (trip and reset) valves. The reset valve links fluid from the Chemical and Volume Control System (CVCS) to pressurize the interior of the ECCS valve. It opens only when fluid is supplied, remains closed during normal operation in a fail-closed state. Conversely, the trip valve serves to depressurize the ECCS valve by connecting it to the CNT during accident conditions; it is normally closed but assumes a fail-open state [36].

The main valve opens in response to the pressure differential between the main chamber and the CNT. During normal operation, pressure inside the ECCS compresses a spring, which holds the main valve closed. The IAB valve, normally open, permits pressure equalization between the main chamber and the ECCS valve. It is actuated by the pressure difference between the RPV and the ECCS valve. When this differential exceeds ~9 MPa, RPV pressure compresses the IAB valve's spring, thereby isolating the pressure connection between the main chamber and the ECCS valve [36].

ECCS activation is controlled by the Module Protection System (MPS). There are a few conditions to be met for the actuation of the ECCS, however not all are applicable in the generic model. The only conditions defined for ECCS actuation are the following,

1. High CNT level – >5.8m.
2. Low PRZ-CNT pressure difference – <6.2MPa.

When both conditions are met, both RVVs and RRVs are set to open after an opening delay of 15s. Additionally, the ECCS can be manually operated in the control room.

2.2. Accident Scenario Definitions

The SA initiating events considered here is based on the preliminary results obtained from conservative reference scenarios run in [29][30]. In particular it was observed that, within 72h of the initiating event, LOCA type scenario in the Chemical Volume and Control System (CVCS) discharge line outside the CNT (SA reference ID SA4/SA4N) and SG Tube Rupture (SGTR) accident (SA reference ID SA6N) leads to failure of the RPV lowerhead. Similar LOCA scenario inside the CNT, with a CNT bypass line so that mass transfer from the CNT to the reactor building (RB) can occur (SA reference ID SA5N), leads to RPV dryout with imminent lowerhead failure, just after 72h. In all the cases it was assumed that ECCS is unavailable. It should be noted that for SA6N and SA5N ECCS was assumed to be unavailable. In cases where it is available, RPV failure could be possible long after 72h and not before. However in the case of SA4 despite ECCS being available the scenario leads to rapid RPV failure. The DBA scenario considered was the CVCS LOCA inside the CNT with all ECCS valves functional. A case with non-functional ECCS (SA reference ID DBAN) showed that RPV can be devoid of water, however core remains in partially damaged state for a long period of time without undergoing further degradation.

Considering these facts, in this paper DBAN, SA4N and SA6N are simulated (reference cases defined in Table I) – which represent different types of SA scenarios with ECCS failure at the beginning of the accident – whereby, after a brief delay, ECCS function is recovered manually by the operators. Readers are directed to [30] for more details of the reference cases of these scenarios. Here the scenarios with delayed ECCS recovery is identified as DBAN-ECCS, SA4N-ECCS and SA6N-ECCS. Such risk-informed analyses have been performed in probabilistic safety assessment (PSA) of large reactors, such as the Nordic Boiling Water Reactors (BWRs), where operators can manually activate pumps, valves, etc. to recover safety systems and study the impact of timing on essential core degradation characteristics [32][33][34]. A typical block diagram for the event description is provided in Figure 2. Note that RVV is assumed to be recovered before RRV. ECCS failure can be pinned to mechanical or electrical factors. Although their likelihood to fail is small, the consequences if they do can be extreme, and lessons from Fukushima accident is a reminder to anticipate the worst case scenario that can result in core damage [35].

Table I. Accident scenarios considered for analysis.

Scenario ID	Initiator	ECCS availability		Comments
		RVV	RRV	
DBAN	CVCS discharge LOCA	No	No	1.6” LOCA in CVCS discharge to CNT
SA4N	CVCS discharge LOCA	No	No	1.6” LOCA in CVCS to RP (outside CNT)
SA6N	SG tube rupture (SGTR)	No	No	No steam line isolation, feedwater line isolated

The scenario begins with an initiating event (LOCA or SGTR), followed by reactor scram and isolation of CNT and SG (in the case of LOCA). DHRS is unavailable, ECCS valves fail to function initially and steam can escape through the RSV cycling when RSVs are activated if necessary to prevent overpressure. Either just before or after uncovery and onset of core damage, RVVs are recovered by the operators with a delay (t_{RVV}) followed by recovery of RRVs (t_{RRV}). Time delays for both RVVs and RRVs are uniformly sampled in [0, 27000]s for all scenarios and all MELCOR simulations are run for 72h from initiating event using a MATLAB setup that restarts crashed simulations with automatic time-step refinement.

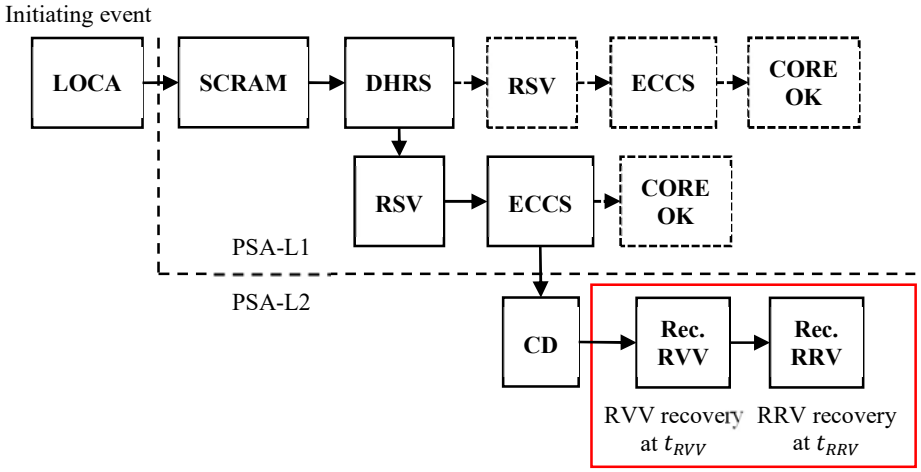

Figure 2. Block diagram for potential core damage in absence of ECCS and recovery of RVV and RRV function. CD: core damage.

From the perspective of FP releases to the environment: DBAN-ECCS considers only the leakage path from the CNT to the RP – essentially CNT is isolated even if core damage occurs, and small releases can be expected which represents RC1; SA4N-ECCS considers large releases directly to the RP and the environment as CNT is bypassed which represents RC2; and SA6N-ECCS again represents RC2 which considers a combination of core damage and CNT bypass scenario, where it is conservatively assumed that any FP collected beyond SG control volumes (turbine CVs) are part of the environmental source term. Typically, a scenario defined by loss of support systems account for a large fraction of CDF and LRF.

3. RESULTS

Here, results of MELCOR simulations are presented with T/H considerations, core behaviour and timing of events. All accident scenarios were run using MELCOR v2.2.r2023 for 72h.

3.1. Results of the Reference Cases – DBAN, SA4N and SA6N

Table II shows the timing of reactor trip signal, ECCS signal, core uncovery and core damage process for the reference cases. As seen, in the case of SA4/SA4N and SA6/SA6N, as the CNT is bypassed, the high

CNT level condition is not met, and a modification is made especially for SA4 and SA6, where the ECCS is activated even when just the pressure difference condition is satisfied. In these 2 cases, it is observed that the core damage is minimized for a long time. In the case of SA4, the lowerhead (LH) indeed fails much later than when ECCS does not activate. In the scenario with SGTR and functioning ECCS, the core remains covered for the duration of 72h. And in the case with failure of ECCS, a failure of the LH is observed at ~24h. While in SA4N there is a period of ~6h between failure of the core plate and failure of LH, there is only ~1.5h between the two events in SA6N. The time of recovery of ECCS [0, 27000]s extends across the core degradation progression for DBAN and SA4N, and only until core uncovery for SA6N. Another observation is that events (except for the failure of RPV) in SA4N occur later than in SA4 where ECCS functions as expected, indicating that activating ECCS may sometimes accelerate core degradation as the core uncovery is quicker in those conditions.

Table II. Timing of events during the reference accident scenarios [30].

Scenario ID	SCRAM	High CNT level	ECCS signal	Core uncovery	Gap release	PD formation	Relocation to LH	Core plate failure	LH failure
DBA	19	520	520	-	-	-	-	-	-
DBAN	19	520	-	4950	12782	13728	-	-	-
SA4	44	-	815	848	3300	4178	10426	12057	232843
SA4N	44	-	-	1814	7412	8565	13071	13071	33682
SA6	30	-	1380	-	-	-	-	-	-
SA6N	30	-	-	27350	40220	42934	72145	79230	84320

SCRAM - safety control rod axe man/reactor trip; PD - particulate debris; LH - RPV lower head.

3.2. Delayed ECCS Recovery in DBAN Scenario

The 28 cases resulting from the sampling of the time of delays are shown for reference in Figure 3(a). The collapsed liquid level and the pressure in the RPV are presented in Figure 3(b) and (c). As seen, initially 3 different trajectories evolve as a result of availability of the RVV, numbers marked on the figure, and subsequent delays result in continuation of the trajectories and bifurcations occur only later upon activation of the RRVs. Correspondingly the pressure evolves according to different sets of trajectories, initially linked to depressurization with the loss of coolant inventory in the RPV and subsequent boiling and evaporation related pressurization. For the first few cases, the ECCS activates before the core is uncovered and hence SA is averted, however in the succeeding cases, core is either partially or fully exposed before the RRV is activated, whereby the coolant that is lost to the CNT is circulated back to the RPV (seen as vertical jumps in the liquid level). As a result, those cases where the RVV opens at time t = 0s (001, 002, 004, 007, 011, 016, 022), are saved from any form of core damage, even if the core is partially uncovered. Cases 012, 013 and 014, corresponding to RRV activating at t = 18000s, see very minor damage (<0.3%) following uncovery, oxidation and failure of the cladding in the central topmost ring of the fuel assemblies. Here, the core is not fully uncovered. Any further delay in opening of the RRV result in low core damage (11-17%) with small fraction of the debris being relocated to the LP, as the core is fully uncovered for at least an hour before activation of RRV.

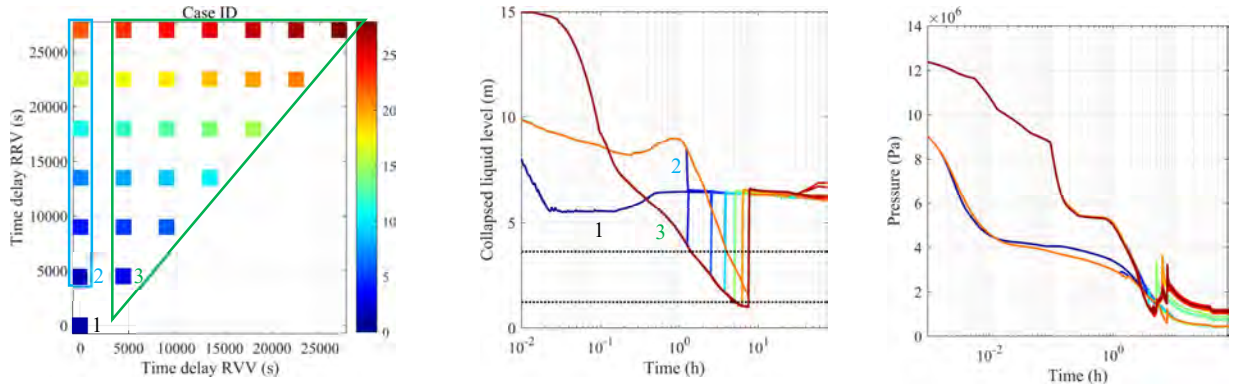

(a) Case ID as a function of RVV and RRV opening times.

(b) Collapsed liquid level in the RPV. Dashed lines represent active core region.

(c) Pressure in the RPV.

Figure 3. Evolution of T/H properties during DBAN-ECCS scenario. Colors represent the case corresponding to a particular set of RVV and RRV delays.

Hydrogen mass generated as a result of oxidation of the structures and cladding is presented in Figure 4(a). Most of the hydrogen mass is generated in cases from late activation of RVVs (>4500s) and RRVs (>18000s), thereby slower loss of coolant inventory and for longer period of time, similar to progression in TMI wet-core scenario. Figure 4(b) and (c) show the debris (combined particulate (PD) and conglomerate debris (DC)) properties in the core region at the time of failure of the core support structures (SS). Cases where damage occurs with early opening of RVVs (<18000s), at the time of SS failure, have slightly larger fraction of debris above the support plate than cases where RVVs open at a later time (>18000s). This is because the SS fails at a slightly later time compared to cases with late RVV activation, which likely enhances natural circulation and thus produces better core cooling. The oxidic mass fraction also corroborates this fact, given that cases with early opening of RVVs have a higher oxidic fraction as the core stays at uncovered state longer until SS failure. Upon SS failure, some mass of debris relocates to the LP, where the remaining water quenches any falling molten material. This causes the pressure to rise, seen as secondary peaks in the RPV, see Figure 3(c). Because all the coolant inventory stays within the CNT, though this debris relocates to the LP, it is cooled by surrounding water in the RPV and the CNT, arresting further degradation. The debris mass that has relocated to the LP at the end of simulation, shown in Figure 5(a), indicates that late opening of RVVs results in larger relocation (>3400kg) subsequent to the failure of support plate compared to early opening.

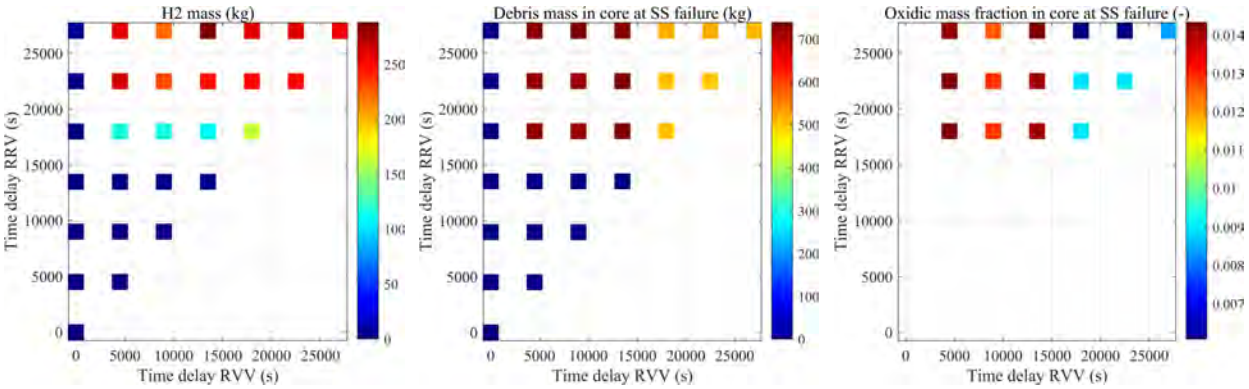

(a) Hydrogen generation in the core.

(b) Total debris in core region at SS failure.

(c) Oxidic mass fraction in the core region at SS failure.

Figure 4. Core properties during DBAN-ECCS scenario. SS: support structures.

Figure 5(b) presents the final oxidic mass fraction in the core region, showing that late opening of RRVs (>25000s) combined with early opening of RVVs (<18000s), provide the core a combination of long period of uncovery and sufficient amount of steam circulation to enhance oxidation of the cladding and the structures, and corresponding hydrogen generation (see Figure 4(a)). Figure 5(c) shows the total convective heat transfer from the core as a function of time of activation of RVVs and RRVs. The COR package uses Lipinski dryout correlation to compute the limiting heat transfer rate from the porous particulate debris bed and in case any of the axial levels give more heat transfer rates than the limit, no convection is calculated for debris or structures below this level. This is also the case when debris undergoes quenching at this limiting rate, no convection from other components to the water pool is considered [26][27]. Early ECCS activation results in large decay heat removal by convection to the CVH package, however when the RRVs are activated late (>18000s) a reduction in convective heat transfer is observed. The least heat removal coincides with the scenario that leads to some of the highest hydrogen generation (Case 025). Once the RRVs are activated, all the debris above the core support plate is quenched by reflooding.

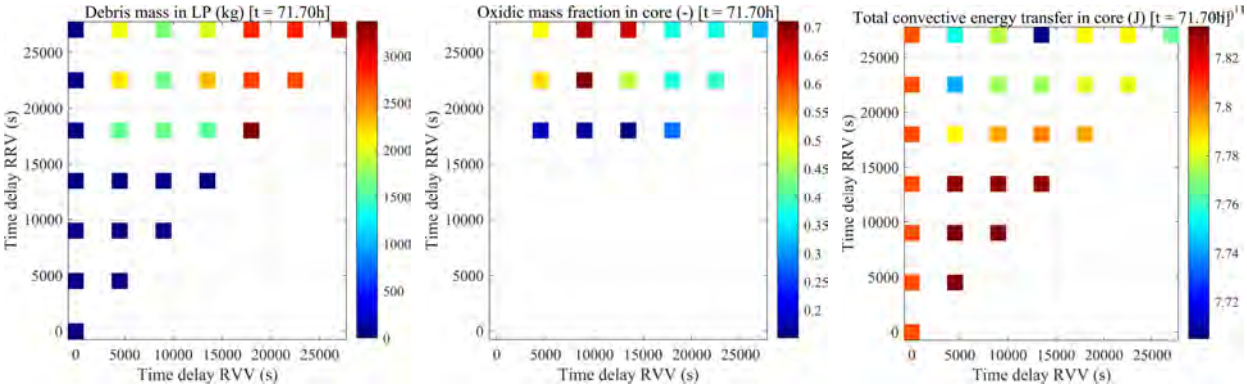

(a) Total debris in core region at 72h.

(b) Oxidic mass fraction in the core region at 72h.

(c) Total convective energy transfer from the core.

Figure 5. Properties during DBAN-ECCS scenario.

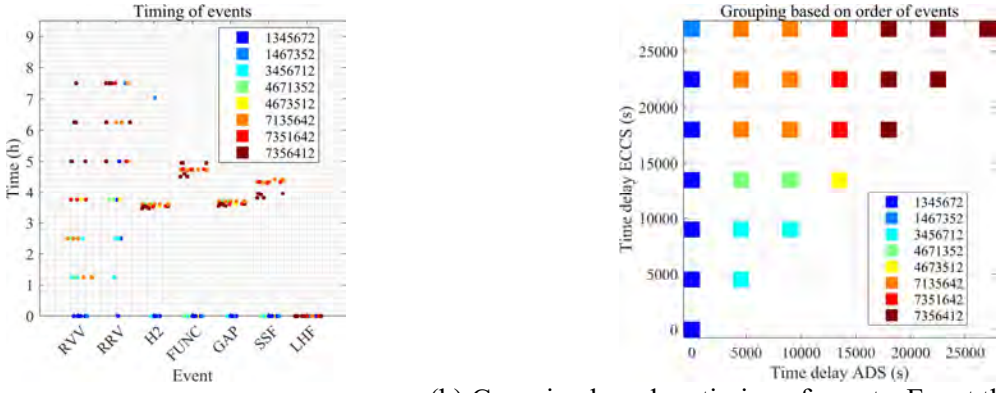

(a) Timing of events in 1-7.

(b) Grouping based on timing of events. Event that occurs first is placed first in the group ID.

Figure 6. Timing of major events during DBAN-ECCS scenario. 1 RVV: time of activation of RVV, 2 RRV: time of activation of RRV, 3 H2: time of commencement of H2 generation, 4 FUNC: time of full core uncovery, 5 GAP: time of onset of gap release, 6 SSF: time of failure of SS, 7 LHF: time of failure of LH.

Figure 6(a) shows the timing of major events (activation of RVVs and RRVs, commencement of oxidation, full core uncovery, gap release, failure of SS and failure of the LH) for all the considered scenarios. Figure 6(b) shows the grouping of the cases based on the order of the above events. This is a concise way of expressing clusters of cases that behave similarly during the accident. Whenever RVVs are activated early,

a SA is prevented from occurring: groups **1345672**, **1467352**, 3456**712** (here the first 5 events i.e. 3rd, 4th, 5th, 6th 7th events do not occur at all, they have t = 0s) and 467**1352** (here the first 3 events i.e. 4th, 6th, 7th events do not occur, they have t = 0s) avoid any core damage. Group 467**3512** has delayed activation of RVV and RRV, and despite uncovery of core, oxidation of cladding once ECCS is activated at 13500s, it ceases core damage and is the latest time for the operator to activate ECCS to maintain an intact core in this type of accident scenario.

3.3. Delayed ECCS Recovery in SA4N Scenario

The collapsed liquid levels in the RPV and the CNT for the 28 delayed scenarios of SA4N-ECCS are presented in Figure 7(a) and (b). Similar to the DBAN-ECCS scenario, 3 sets of evolution of parameters are observed corresponding to different rates of loss of coolant from the RPV (break is outside the CNT). Unlike the DBAN-ECCS scenarios, for some cases (set 3) RVVs and RRVs are activated at such late times that, the water that is eventually collected/condensed in the CNT will never circulate back into the RPV as the liquid level never reaches the height of RRV valves (5.6m). Consequently, no natural circulation is established and there is no heat transfer from the core debris in the lower parts of the RPV to the UHS, leading to core damage due to inadequate core inventory. Core degradation further proceeds with LH attack by the molten melt in the and its failure with ejection of debris to the CNT. The pressure evolution is shown in Figure 7(c).

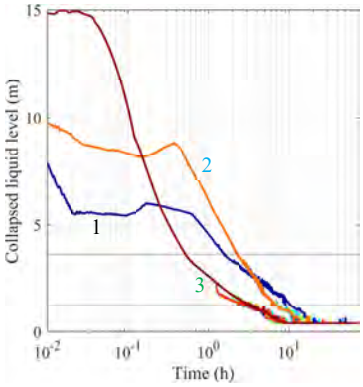

(a) Collapsed liquid level in the RPV. Dashed lines represent active core region.

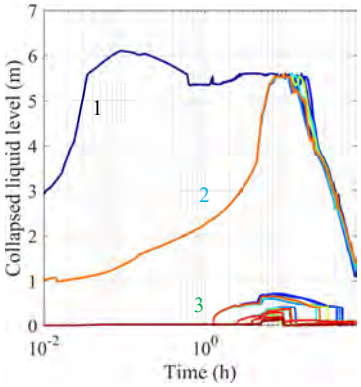

(b) Collapsed liquid level in the CNT. RRV is at 5.6m.

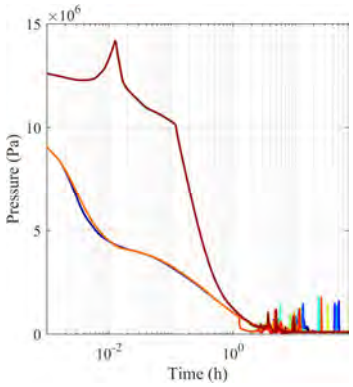

(c) Pressure in the RPV.

Figure 7. Evolution of T/H properties during SA4N-ECCS scenario. Colors represent the case corresponding to a particular set of RVV and RRV delays, as in Figure 3(a).

Figure 8(a) shows the total hydrogen generated as a function of RVV and RRV activation times. In this type of scenario where the RPV is losing coolant directly to outside the CNT, late opening of RVV valves have no drastic effect on oxidation in the core. Largest hydrogen mass is generated when the RVVs open at 4500s, and increases with increasing delay of RRV opening times. In this scenario, opening of RRV only serves to circulate steam from the CNT to the RPV, thereby increasing oxidation of the core materials, eventually expelling steam to the RB via the break. Early activating of RVVs (>4500s) also leads to the formation of larger amounts of debris in the core just before SS failure, as seen in Figure 8(b). This is likely due to loss of coolant to the CNT which does not enhance core cooling, but only exacerbates core degradation. Consequently, by the time SS fails and the debris relocation has taken place, due to lack of RPV LH cooling by surrounding water in the CNT, solid debris that is quenched in the water present in the LP evaporates all the water, increasing its temperature, and undergoes melting to form a pool in the LH. The total mass of this debris pool just before failure of the RPV LH is shown in Figure 8(c). Late ECCS activation (>13500s), results in slightly smaller amount of melt in the LP, compared to cases with early RVV activation (<9000s).

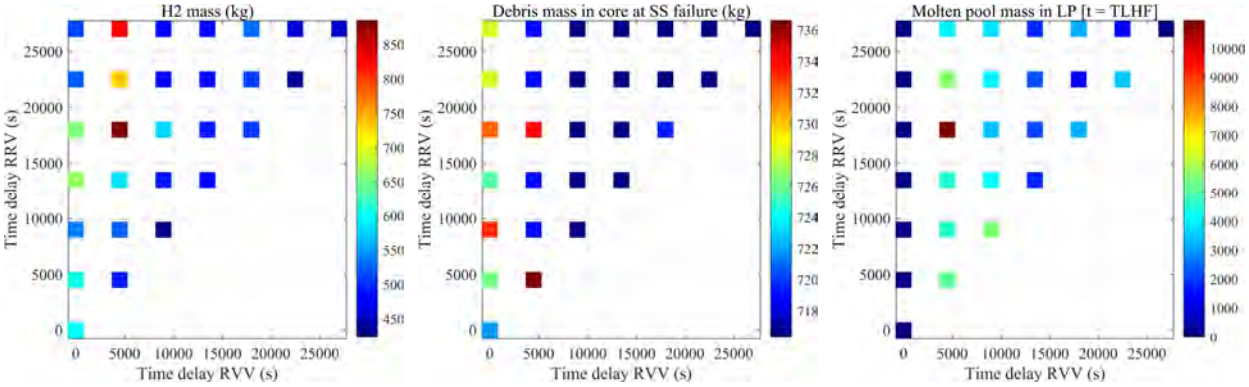

(a) Hydrogen generation in the core.

(b) Total debris in core region at SS failure.

(c) Molten mass in the LP at RPV failure.

Figure 8. Core properties during SA4N-ECCS scenario. SS: support structures.

SA4N being one of the few scenarios leading to RPV failure, can expect roughly 10-22ton of debris mass being ejected from the RPV, as shown in Figure 9. MELCOR by default assumes both solid and molten debris is ejected to the cavity. Based on the size of the breach and porosity of the debris in the LH, if any, there is likely a mixture of the two being ejected, and this would necessitate further sensitivity study using codes and experimental verification. Except for the cases with RVVs activating at t = 0s, all cases observe RPV failure. It is likely that if the simulations extended a few hours beyond 72h, these cases would also lead to failure once the coolant in the CNT would evaporate, see Figure 7(b). As with delayed RVVs activation affecting the molten debris in the LP, similar effect can be made out for mass of debris ejected to the CNT. Based on the timing of events, in Figure 10(a), it is seen that late ECCS activation, leads to early LHF (~10h), and subsequently time of LHF for cases with early ECCS activation can extend from 24-50h. Another observation regarding the timing of onset of oxidation and gap release of FPs is that these events occur roughly in 3 groups as predicted by MELCOR. Earliest hydrogen generation (at ~2h) can be expected from cases with late (>13500s) ECCS activation. Onset of hydrogen generation at ~6h is expected from RVVs activation at t = 0s and delayed RRVs activation (>22500s), while earliest ECCS activation (RVVs at t = 0s and RRVs < 22500s) result in the late oxidation. Consequently, based on the order of timing of these events, cases can be grouped as shown in Figure 10(c). From the perspective of arresting SA progression in SA4N like accident, operators may either recover RVVs instantly, irrespective of availability of RRVs, or delay the activation of ECCS to let the coolant evaporate by itself than accelerate it.

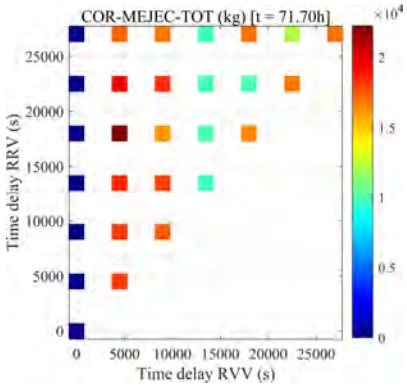

Figure 9. Total debris mass ejected upon RPV failure.

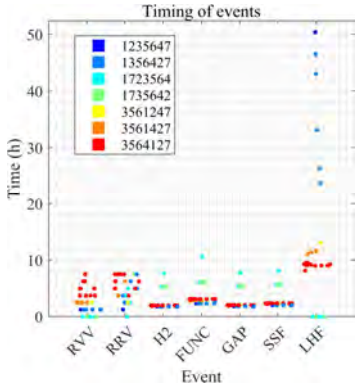

(b) Timing of events in 1-7.

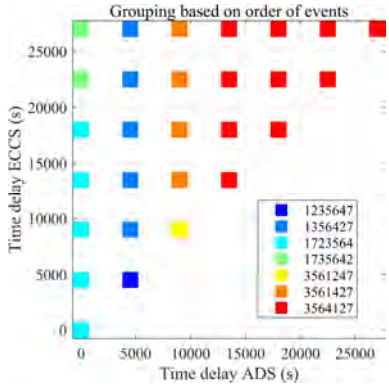

(c) Grouping based on timing of events. Event that occurs first is placed first in the group ID.

Figure 10. Timing of major events during SA4N-ECCS scenario.

3.4. Delayed ECCS Recovery in SA6N Scenario

The time evolution of the liquid levels in the RPV and the CNT are provided in Figure 11(a) and (b). Similar to the previous scenarios, three different trajectories are observed for the collapsed liquid levels, however unlike the previous accidents (SA4N particularly), cases in set 3 lead to the core being partially flooded with water once the RRVs are open. Water inside the RPV evaporates into the CNT where it condenses, up to the level of the RRVs. Because the flow out through the small SGTR is governed by the pressure difference across the primary and secondary sides, once the RVVs are open, the primary side instantly depressurizes, seen as vertical drops in the pressure evolution in Figure 11(c), leading to loss in flow rate through the tube rupture. In essence, small quantities of water may trickle down the RRVs, get instantly vapourized in the core, flow out through the open RVVs and circulate back. This keeps the core partially wet for extended periods. For cases with late ECCS opening (>13500s, Cases 010, 014, 015, 019, 020, 021, 025, 026, 027, 028), water from the CNT may not be able to circulate back in through the RRVs to even partially cover the core and thus complete core may be uncovered. For cases with extreme delays (> 22500, Cases 021, 027, 028), water in the CNT is too low to replenish the core.

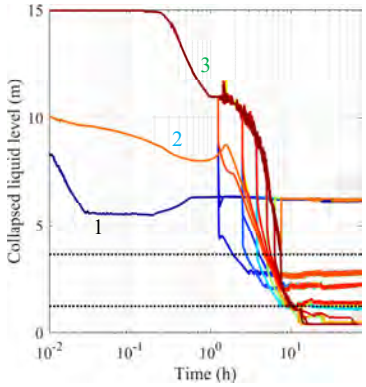

(a) Collapsed liquid level in the RPV. Dashed lines represent active core region.

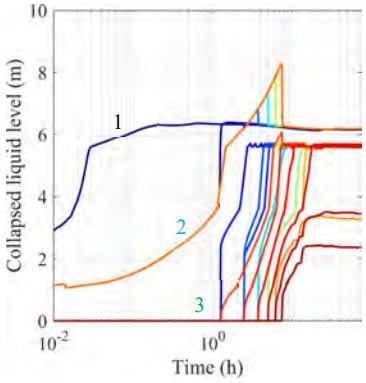

(b) Collapsed liquid level in the CNT. RRV is at 5.6m.

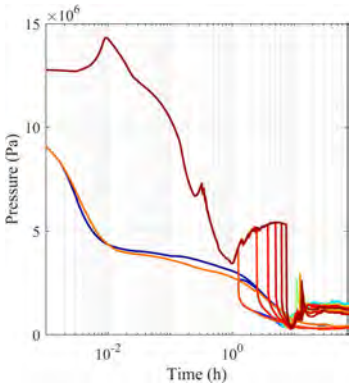

(c) Pressure in the RPV.

Figure 11. Evolution of T/H properties during SA6N-ECCS scenario. Colors represent the case corresponding to a particular set of RVV and RRV delays, as in Figure 3(a).

As a result of inadequate core cooling, cases with late ECCS opening (>13500s) see oxidation of the core producing about ~350-580kg of hydrogen, as shown in Figure 12(a). Unlike, the late RRV activation cases in DBAN-ECCS that produce hydrogen in the core, only those cases with late RRV and RVV activation undergoes oxidation. As shown in Figure 12(b), roughly 700kg of debris can be seen in the core region at the time of SS failure, corresponding to the same case of activation of ECCS. When the debris relocates to the LP, shown in Figure 13, further accident progression is arrested by the water pool in the LP. Case 010, results in largest hydrogen generated as well as some of the highest mass of debris relocated, mainly due to the fact that, early RRV activation combined with inability of water circulation and complete core uncovery for extended period oxidizing, melting and relocation of the debris. Consequently, this case has the least oxidic mass remaining in the core at end of the simulation, as shown in Figure 12(c).

Unlike, SA4N-ECCS cases, there is no complete loss of coolant from the CNT. Therefore, the operation of ECCS within this period [0, 27000]s, successfully manages in-vessel retention of the debris and prevents ex-vessel accident progression, which was the case in SA6N [30]. The maximum fraction of damaged core is around 70% (for the extremely delayed Case 028). While operator intervention was considered early in the accident progression (before core uncovery, see SA6N in Table II), it may be necessary to also investigate actions in the later phase of the accident, where severity of core damage state may worsen the situation. In tandem, it is also worthy to investigate the effect of size of SGTR on the accident progression.

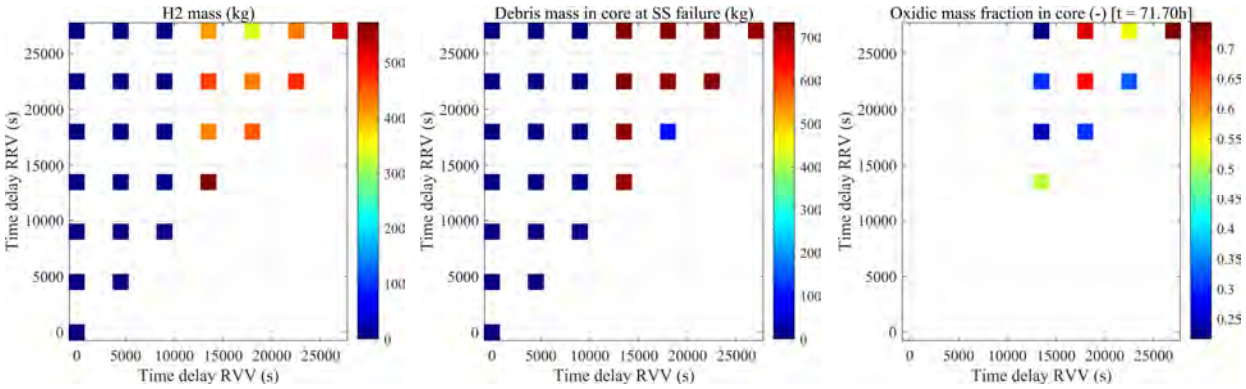

(a) Hydrogen generation in the core. (b) Total debris in core region at SS failure. (c) Oxidic mass fraction in the core region at 72h.

Figure 12. Core properties during SA6N-ECCS scenario. SS: support structures.

Finally, the timing of major events and grouping according to the order of these events are presented in Figure 14(a) and (b). Onset of gap release and oxidation, in the case of DBAN-ECCS was restricted to ~3.4-3.8h and in the case of SA4N-ECCS restricted to 3 different time periods: ~2h, ~5h and ~8h. While in the case of SA6N-ECCS, these two events occur between 6-8h after the start of the accident, and the least ordered groups of events occur (4 v/s 8 and 7 in the former 2 scenarios). Phenomenologically, the grid based uniform sampling method may give a quick way of exploring the input space. As was noted earlier, expanding the operator intervention space to include late accident phase, may vastly increase the number of calculations. This will necessitate use of other methods, such as genetic algorithms, to reduce the user effect in identifying scenarios that can lead to SA and non-trivial scenarios. One such scenario can be identified (as red in color) in Figure 14(b). For instance, Case 015, does not experience failure of the SS while nearby cases all have SS failure in 6.2-8.2h. This may likely be a one off outlier or a result of time-step refinement when the code restarts after a crash and possibly missing cliff-edge effects in SS failure models.

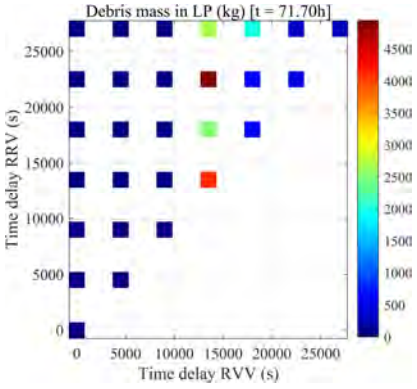

Figure 13. Debris mass in the LP at 72h.

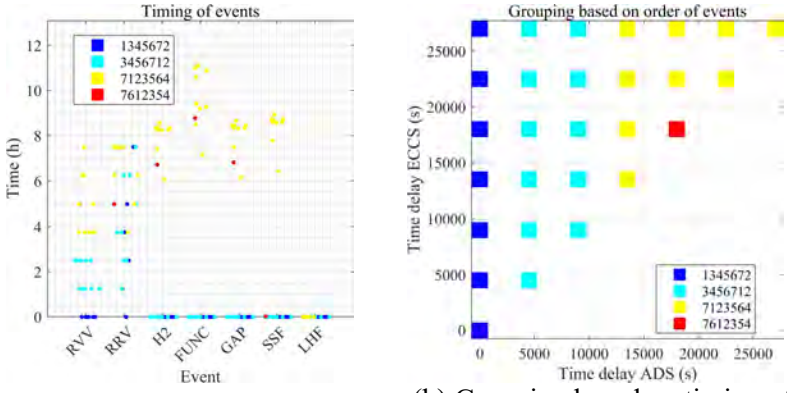

(a) Timing of events in 1-7.

(b) Grouping based on timing of events. Event that occurs first is placed first in the group ID.

Figure 14. Timing of major events during SA6N-ECCS scenario.

4. CONCLUSIONS

In this study, mitigation of SA progression in a generic iPWR by considering delayed recovery of ECCS was presented. The effect delayed activation of RVVs and RRVs have on debris properties, oxidation, integrity of the RPV and in-vessel melt retention strategy of submerged SMRs have been assessed using MELCOR code. Three different accident scenarios were assessed for the effect of the delayed ECCS

function. Different operation domains were identified that leads to specific set of events that may leads to severe core damage and relocation.

It was observed that in the case of DBAN-ECCS, late RRV activation can result in large debris formation and hydrogen generation, irrespective of time of activation of RVVs. However as the coolant inventory remains within the CNT, RPV failure is not observed for any time of delay. In the case of SA4N-ECCS, all cases where RVVs are not activated along with LOCA, lead to RPV failure and debris in ex-vessel state. This is also the scenario where largest oxidation of the cladding and structures takes place. Early activation of RVVs may postpone RPV failure at a cost of large amounts of hydrogen being generated. In the case of SA6N-ECCS, all delayed RVV activation scenarios lead to core damage, without RPV failure.

The reliability analysis of ECCS with operator actions have shown, in most cases, dominating sequences for core damage are inability of RRVs to open early, or inability of water inventory in the CNT to establish natural circulation through the RRVs. It has already been shown in [30] that size of break effect the speed of accident progression, it has to be investigated how the accident proceeds with capacity of ECCS severely reduced along with operator delays. This assessment, along with the sensitivity analysis, will be performed in a separate future study.

ACKNOWLEDGMENTS

Funded by the European Union. Views and opinions expressed are those of the author(s) only and do not necessarily reflect those of the European Union or European Commission-Euratom. Neither the European Union nor the granting authority can be held responsible for them.

This work is supported by ROAAM+ project funded by Swedish Radiation Safety Authority. The authors are thankful to Mateusz Malicki and Terttaliisa Lind from PSI for providing the MELCOR input deck for iPWR design.

REFERENCES

1. IAEA. Small Modular Reactors, Advances in SMR Developments. In: International Conference on Small Modular Reactors and Their Applications, 21-25 October, Vienna, Austria, 2024.
2. IAEA. Advances in Small Modular Reactor Technology Developments, A Supplement to: IAEA Advanced Reactors Information System (ARIS). International Atomic Energy Agency, Vienna, Austria, 2020.
3. Handbook of Small Modular Nuclear Reactors. 2nd Edition. Eds: Daniel T. Ingersoll and Mario D. Carelli. Woodhead Publishing, 2020.
4. Welter Ket al.: Unique safety features and licensing requirements of the NuScale small modular reactor. Frontiers in Energy Research, 11, 2023.
5. H.O. Kang, et al.: Light water SMR development status in Korea. Nuclear Engineering and Design, 419, pp. 112966, 2024.
6. M.A. Allaf, et al.: Transient behavior of the NuScale 250-MW(thermal) power module with Cr-Coated Zr cladding during a severe accident. Nuclear Technology, pp. 1-14, 2025.
7. C.H. Song, et al.: MELCOR Analysis for Core Coolability by Flooding Safety System Applicable for i-SMR. Transactions of the Korean Nuclear Society Spring Meeting, Jeju, Korea, pp. 67-74, 2023.
8. C.H. Song, et al.: Safety implications of multiple passive safety valve failures in an i-SMR design. Progress in Nuclear Energy, 191, pp. 106065, 2026.
9. R. Rubio, . Jimenez: Potential issues related to emergency core cooling system strainers performance at boiling water reactors: Application to Cofrentes NPP (Spain). Nuclear Engineering and Design, 275, pp. 11-16, 2014.
10. Strålsäkerhetsmyndigheten: Fibre Clogging in Nuclear Power Plants An Investigative Study on the Filter Mat Forming and Retention of Fibres on Screens of Various Design. Report 2020:07, SSM, Sweden, 2020.
11. F. D'Auria, G.M. Galassi: Methodology for the Evaluation of the Reliability of Passive Systems. DIMNP NT, 420 (00) 2000.
12. A. Bersano: Application of REPAS to analyze the sump clogging issue following a LOCA and its impact on the reliability of the ECCS long-term core cooling function. Nuclear Engineering and Design, 417, pp. 112877, 2024.
13. R.E. Löfstedt: The Barsebäck nuclear plant case. Energy Policy, 24(8), pp. 689-696, 1996.
14. F. Gabrielli, et al.: Analysis of postulated severe accidents in generic integral pwr small modular reactors in the frame of the horizon euratom saspam-sa project. In: The 11th European Review Meeting on Severe Accident Research, May, KTH Royal Institute of Technology, Stockholm, Sweden, 2024.

15. Fangnian Wang, et al.: Investigations of hydrogen hazard mitigation by deliberate ignition in small modular reactor during severe accident using GASFLOW-MPI. Annals of Nuclear Energy, 179, pp. 109392, 2022.
16. Siniša Šadek, et al.: Small break LOCA studies for different layouts of passive safety systems in the IRIS reactor. Nuclear Engineering and Design, 431, pp. 113745, 2025.
17. A. Fakhraei, et al.: Safety analysis of an advanced passively-cooled small modular reactor during station blackout scenarios and normal operation with RELAP5/SCDAP. Annals of Nuclear Energy, 143, pp. 107470, 2020.
18. Qingan Xiang, et al.: Research on debris in-vessel cooling and retention behavior for the small modular reactor ACP100. Progress in Nuclear Energy, 134, pp. 103641, 2021.
19. Dening Eric Jia, et al.: GOTHIC and MELCOR benchmarking of the CNL strong condensation containment apparatus experiments. Nuclear Engineering and Design, 427, pp. 113440, 2024.
20. F. Mascari, et al.: Small modular reactors and insights on passive mitigation strategy modeling. Nuclear Engineering and Design, 401, pp. 112088, 2023.
21. Luis E. Herranz, et al.: Overview of key thermal–hydraulic phenomena in severe accident unfolding: Current knowledge and further needs. Nuclear Engineering and Design, 407, pp. 112256, 2023.
22. Longze Li, et al.: MELCOR severe accident analysis for a natural circulation small modular reactor. Progress in Nuclear Energy, 100, pp. 197-208, 2017.
23. Zhexi Guo, Sicong Xiao: Thermal hydraulic study of NuScale iPWR passive containment cooling behaviour during loss-of-coolant accident. International Journal of Advanced Nuclear Reactor Design and Technology, 7(2), pp. 100-109, 2025.
24. Mateusz Malicki, T. Lind: MELCOR 2.2 iPWR LOCA type accident analysis, PART I: Thermal-hydraulics. Nuclear Engineering and Design, 428, pp. 113433, 2024.
25. Mateusz Malicki, T. Lind: MELCOR 2.2 iPWR LOCA type accident analysis, PART II: BDBA. Nuclear Engineering and Design, 430, pp. 113667, 2024.
26. L.L. Humphries, et al.: MELCOR Computer Code Manuals Vol. 1: Primer and Users' Guide Version 2.2.r2023. SAND2023-10997 O, Sandia National Laboratories, Albuquerque, NM, USA, 2023.
27. L.L. Humphries, et al.: MELCOR Computer Code Manuals Vol. 2: Reference Manual Version 2.2.r2023. SAND2023-10994 O, Sandia National Laboratories, Albuquerque, NM, USA, 2023.
28. M. Principato, et al.: Analyses of the MELCOR capability to simulate integral PWR using passive systems in a DBA scenario. Nuclear Engineering and Design, 437, pp. 114004, 2025.
29. G. Acharya, et al.: Investigation of Source Term During Severe Accidents in Integral PWR SMRs. In: The 21st International Topical Meeting on Nuclear Reactor Thermal Hydraulics, August, Busan, Korea, 2025.
30. G. Acharya, et al.: Investigation of Severe Accident Progression in Integral PWR SMRs. In: The 12th European Review Meeting in Severe Accident Research, May, Madrid, Spain, 2026.
31. NuScale Power, LLC: Containment Response Analysis Methodology. Topical Report TR-0516-49084-NP, NuScale Power, LLC, 2019.
32. S. Galushin, P. Kudinov: Sensitivity analysis of debris properties in lower plenum of a Nordic BWR. Nuclear Engineering and Design, 332, pp. 374-382, 2018.
33. S. Galushin, P. Kudinov: Analysis of core degradation and relocation phenomena and scenarios in a Nordic-type BWR. Nuclear Engineering and Design, 310, pp. 125-141, 2016.
34. S. Galushin, P. Kudinov: Analysis of the Effect of Severe Accident Scenario on Debris Properties in Lower Plenum of Nordic BWR Using Different Versions of MELCOR Code. Science and Technology of Nuclear Installations, 2019, pp. 5310808, 2019.
35. IAEA: Design Safety Considerations for Water Cooled Small Modular Reactors Incorporating Lessons Learned from the Fukushima Daiichi Accident. International Atomic Energy Agency, Vienna, Austria, 2016.
36. L.L.C. NuScale Power: NuScale Standard Plant Design Certification Application, Chapter Six Engineered Safety Features, Revision 5. Oregon, United States of America (2020).
37. L.L.C. NuScale Power: NuScale Standard Plant Design Certification Application, Chapter Seven Instrumentation and Controls, Revision 5. Oregon, United States of America (2020).
38. L.L.C. NuScale Power: NuScale Standard Plant Design Certification Application, Chapter Nineteen Probabilistic Risk Assessment and Severe Accident Evaluation, Revision 5. Oregon, United States of America (2020).
39. U.S. NRC: Application Of The Single Failure Criterion To NuScale Power LLC's Inadvertent Actuation Block Valves. SECY-19-0036 (1994).
40. D. Choi, et al.: Review of Failure Modes and Effects of IAB Valves in NuScale. Transactions of the Korean Nuclear Society Spring Meeting Jeju, Korea, May 22-23 (2025).

EFFECT OF DELAYED RECOVERY OF ECCS DURING SEVERE ACCIDENTS IN INTEGRAL PWR SMRS

12th European Review Meeting on Severe Accident Research (ERMSAR2026)
Madrid, Spain, May 18-22, 2026

Govatsa Acharya, Dmitry Grishchenko, Pavel Kudinov
Division of Nuclear Science and Engineering,
KTH Royal Institute of Technology,
Stockholm, Sweden

Background: Risk Oriented Accident Analysis Methodology+

- ROAAM+ framework is being developed at KTH for risk assessment in Nordic BWR, It addresses uncertainties in:
  - Scenarios – aleatory.
  - Phenomena – epistemic.
- ROAAM+ is a risk analysis framework which is comprised of:
  - Detailed full models (FMs) – for key information about physics.
  - Coupled Fast-running surrogate models (SMs) – for sensitivity, uncertainty and failure domain analysis.
- ROAAM+ connect SA scenario with in-vessel, ex-vessel accident progression and ultimately release to environment.
- Latest analysis highlighted importance of ex-vessel phenomena:
  - Debris bed coolability – needs deep pool of water in cavity.
  - Steam explosion risks – necessitates reinforcement of hatch doors in the cavity.
- Need to further develop and demonstrate failure domain identification methodology.

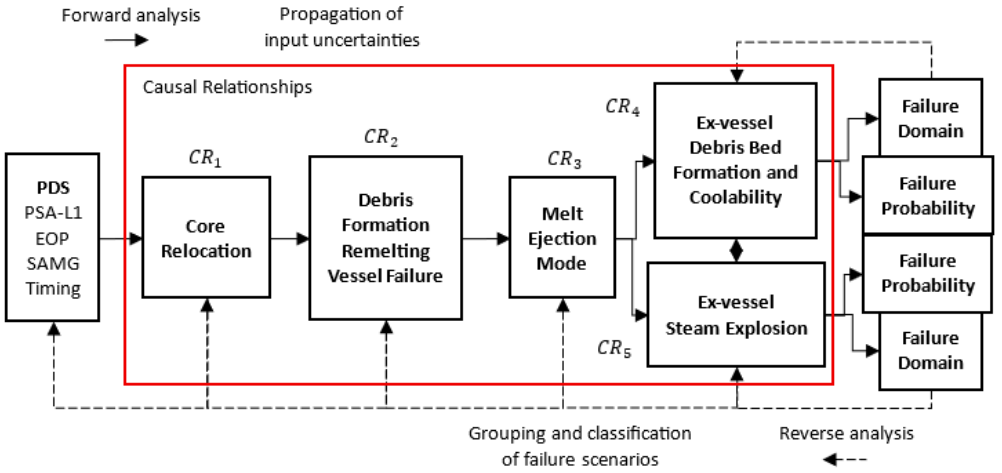

Current ROAAM+ framework for Nordic BWR. The top layer of the framework is shown, that decomposes the various phenomenon into multistage causal relationships (CRs) propagating uncertainties from the initial plant damage state (PDS) to the ex-vessel phenomenon, represented by SMs within an envelope of bounding assessment. EOP: emergency operating procedure, SAMG: SAM guidelines.

Work Packages: KTH Contributions

G. Acharya, et al., (2026)

Develop and assess generic but representative iPWR SA code input-decks and to identify plausible SA scenarios.

2.1

Review the existing experimental database, to assess its applicability to iPWR, to propose methods to apply existing data to iPWR, and to identify new experimental needs.

3.1, 3.2

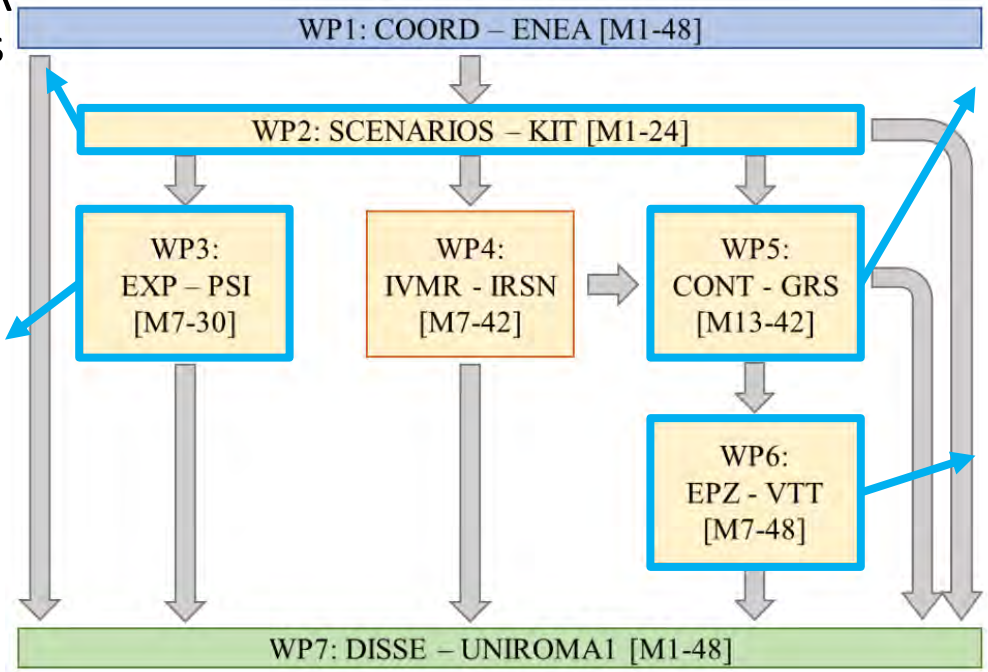

Assess the codes to simulate the main containment behaviour (TH, FP and aerosol) and characterize the efficiency of passive measures for accident mitigation.

5.1, 5.2

Provide EPZ size and extension for selected SA scenarios coupling the results of ST codes to radiological consequences tools.

6.2, 6.3, 6.4

G. Acharya, et al., (2025)

Motivation and Goals

- Reduction of user effect in the selection of scenarios that can lead to severe accidents.
- Genetic algorithm based scenario space/failure domain identification is under development.
  - Efficient surrogate modelling approaches can replace expensive SA code (MELCOR) full model simulations.
  - Need for a training database.
- Ultimate goals:
  - Define a set of events (failure/recovery of the systems etc.) and ranges of possible timing for those events.
  - Sample in the space of the possible scenarios (each scenario is created by different combinations and timing of the events).
  - For each scenario (automatically generated using genetic algorithm) run FM code to find out if such scenario will lead to
    - core damage and
    - release of fission products.

Current Study Objectives

- Investigation of degraded ECCS function and partial recovery of RVVs and RRVs in a generic iPWR.
  - Analysis of events and timing of those events during representative accident scenarios.
  - Creation of a training database for development of SMs.

SASPAM-SA Generic iPWR Design 1

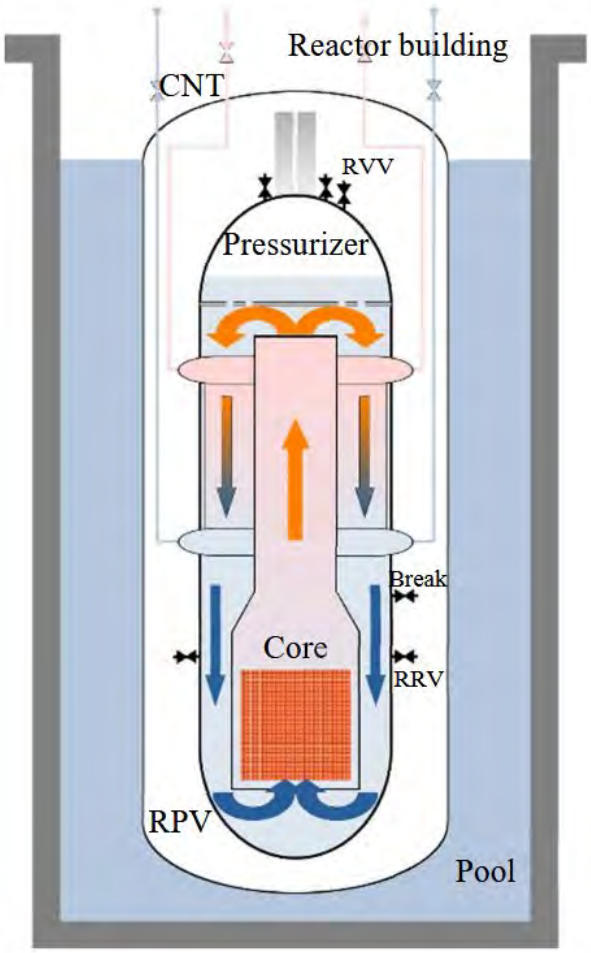

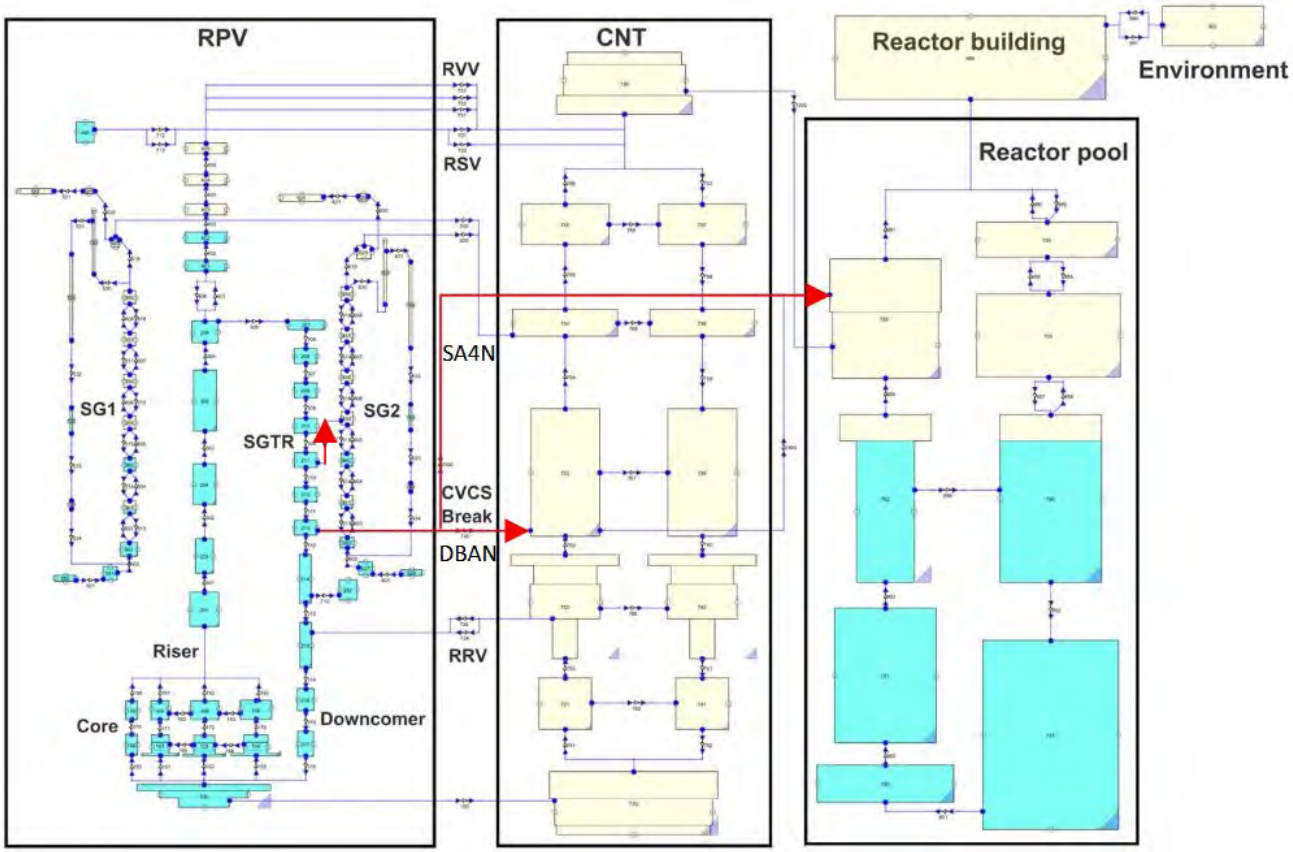

M. Malicki, et al., (2024)

Design 1: ECCS Description

- ECCS activation is controlled by the Module Protection System (MPS). There are a few conditions to be met for the actuation of the ECCS, however not all are applicable in the generic model.
- The only conditions defined for ECCS actuation are the following,
  - High CNT level – >5.8m.
  - Low PRZ-CNT pressure difference – <6.2MPa.
- When both conditions are met, both RVVs and RRVs are set to open after an opening delay of 15s.
- Additionally, the ECCS can be manually operated in the control room > manual operator delay + 15s.

Design 1: Accident Scenarios Description

- 3 accident scenario families considered

Scenario ID	Initiator	ECCS availability		Comments
		RVV	RRV	
DBAN	CVCS discharge LOCA	No	No	1.6" LOCA in CVCS discharge to CNT
SA4N	CVCS discharge LOCA	No	No	1.6" LOCA in CVCS to RP (outside CNT)
SA6N	SG tube rupture (SGTR)	No	No	No steam line isolation, feedwater line isolated

  - Identified here as DBAN-ECCS, SA4N-ECCS and SA6N-ECCS.

Time delays for recovery of ECCS are selected with a uniform grid sampling strategy in the range [0, 27000s] subjected to $t_{RRV} > t_{RVV}$.
28 cases per accident scenario are sampled.

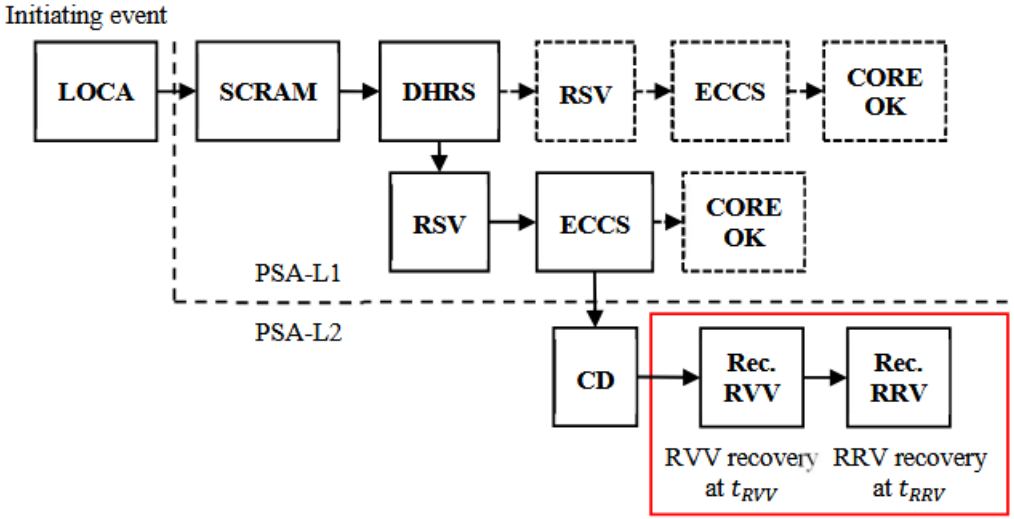

Figure 2. Block diagram for potential core damage in absence of ECCS and recovery of RVV and RRV function. CD: core damage.

Results: Reference Scenarios

Scenario ID	SCRAM	High CNT level	ECCS signal	Core uncovery	Gap release	PD formation	Relocation to LH	Core plate failure	LH failure
DBA	19	520	520	-	-	-	-	-	-
DBAN	19	520	-	4950	12782	13728	-	-	-
SA4	44	-	815	848	3300	4178	10426	12057	232843
SA4N	44	-	-	1814	7412	8565	13071	13071	33682
SA6	30	-	1380	-	-	-	-	-	-
SA6N	30	-	-	27350	40220	42934	72145	79230	84320

SCRAM - safety control rod axe man/reactor trip; PD - particulate debris; LH - RPV lower head.

- CNT bypass scenarios (SA4[N]/SA6[N]) leads to no activation of ECCS – control logic is altered.
- DBAN – no debris relocation, no LH failure
- SA4/SA4N – early relocation to LP, no ECCS leads to quicker LH failure than with ECCS.
  - SA4N events occur later than in SA4 – activating ECCS may faster core degradation.
- SA6N – Core uncovery is slower, however time from relocation to LP to LH failure is very short.

Results: DBAN-ECCS

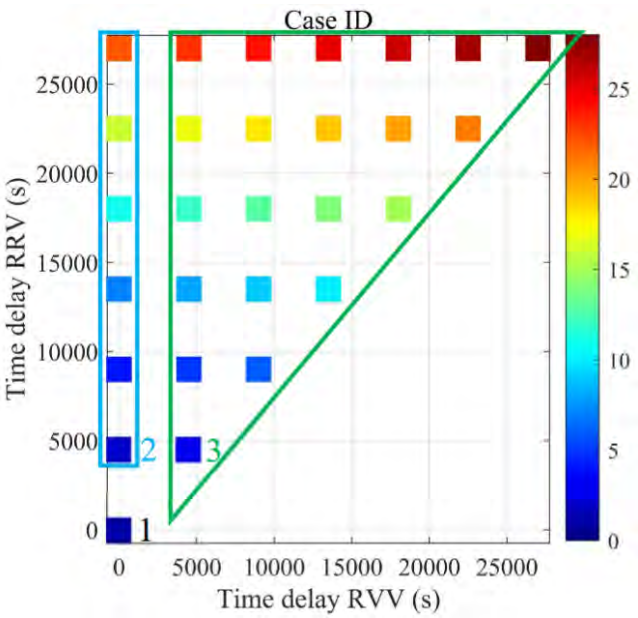

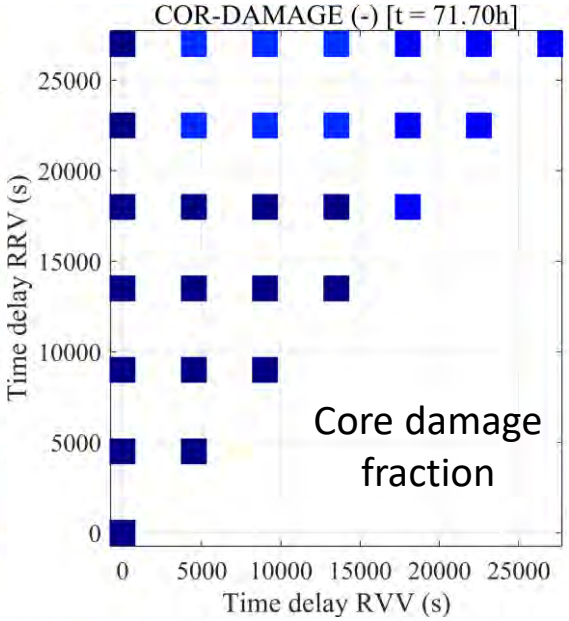

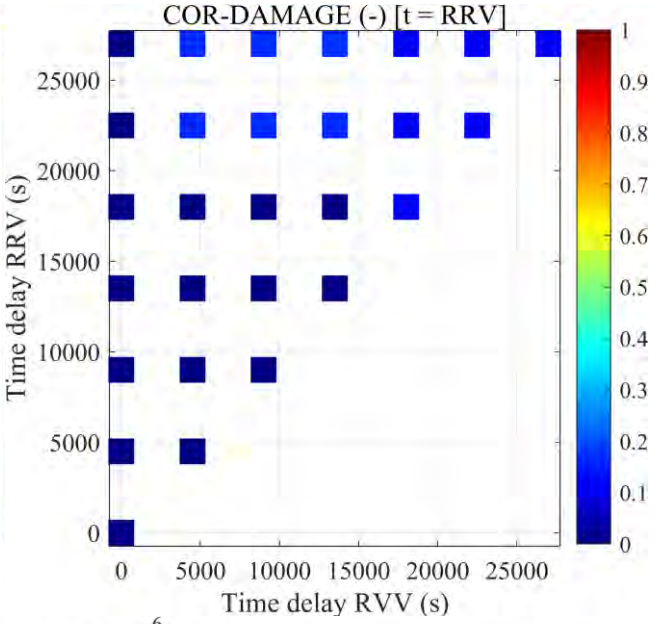

Core damage fraction

Coloured representation of case IDs.

Collapsed liquid level

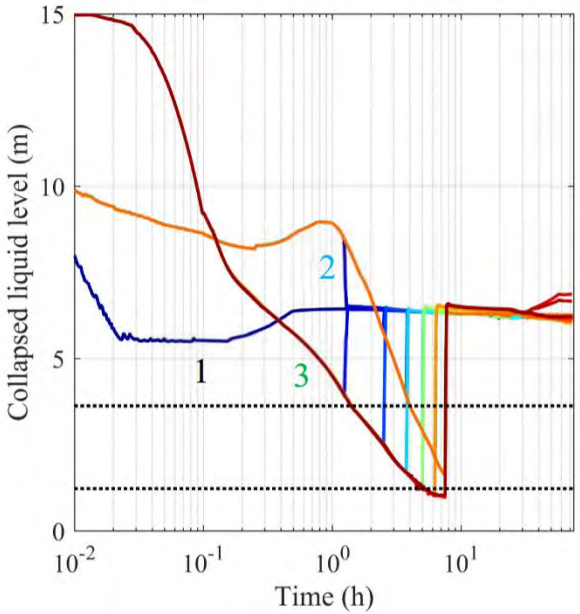

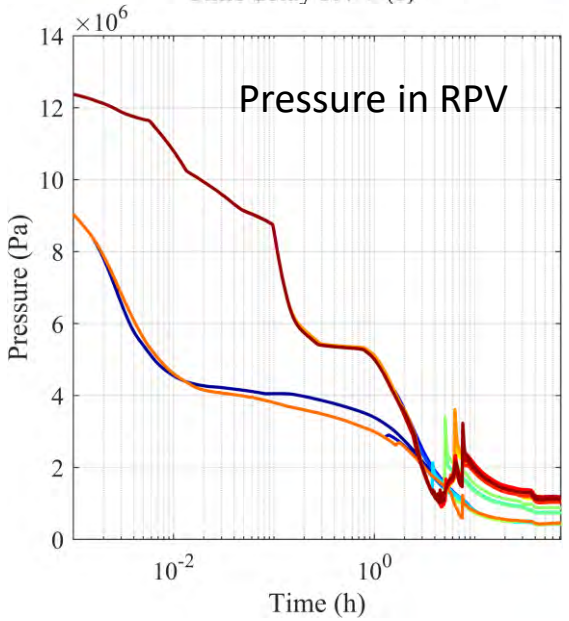

Results: DBAN-ECCS

- For the first few cases, the ECCS activates before the core is uncovered and hence SA is averted.
- However, in the succeeding cases, core is either partially or fully exposed before the RRV is activated.
- Most hydrogen generated in cases with t_{RVV}>4500s and t_{RRV}>18000s.

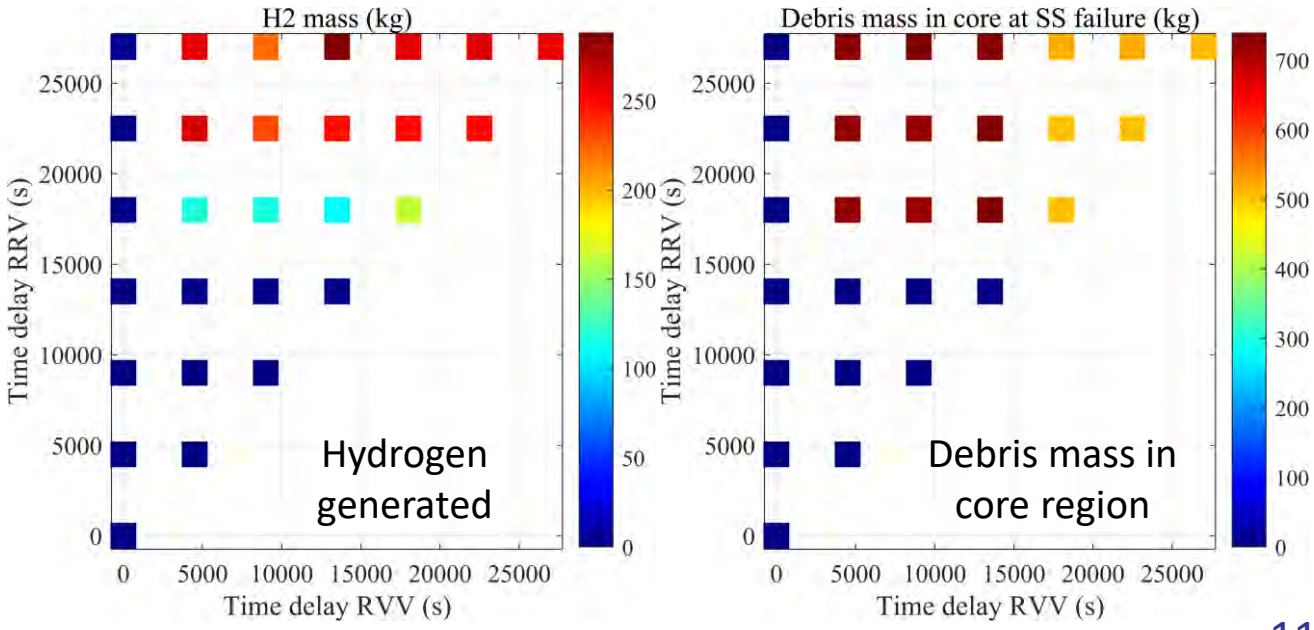

Results: DBAN-ECCS

- Cases where damage occurs with early opening of RVVs (<18000s), at the time of SS failure, have slightly larger fraction of debris above the support plate than cases where RVVs open at a later time (>18000s).
  - SS fails at a later time compared to cases with late RVV activation > larger accumulation of debris.

- Cases with early opening of RVVs have a higher oxidic fraction as the core stays at uncovered state longer until SS failure.
- Late opening of RVVs results in larger relocation (>3400kg) subsequent to the failure of support plate compared to early opening.

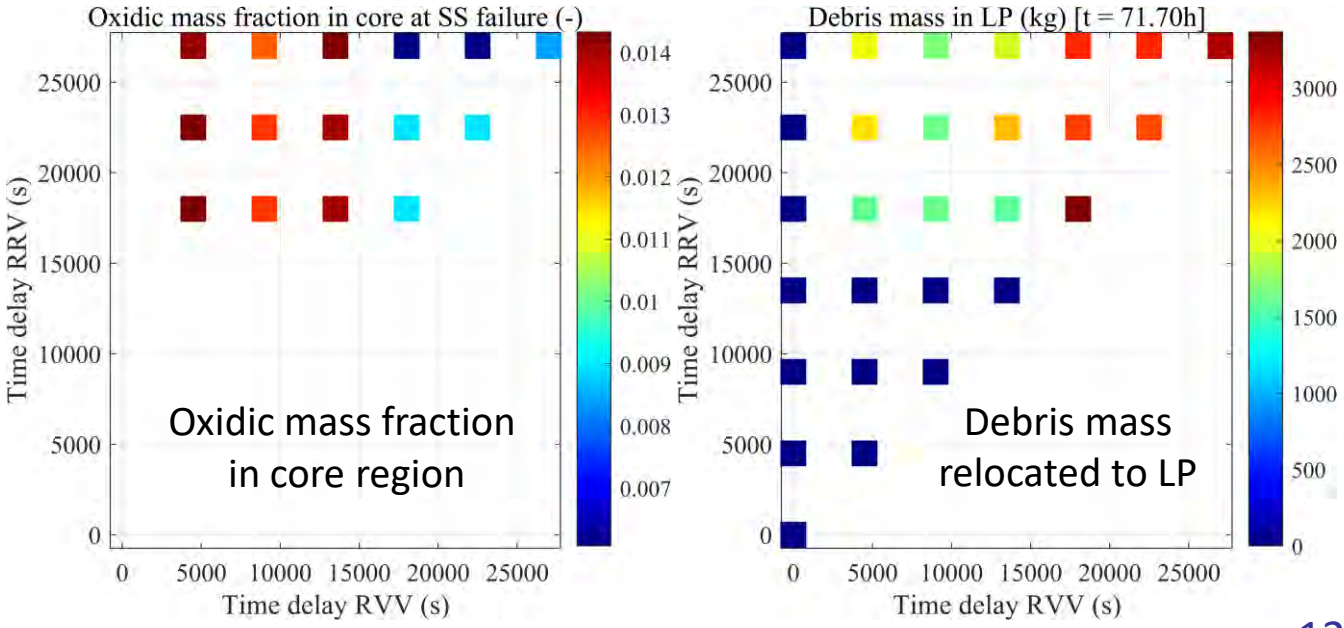

Results: DBAN-ECCS

- Grouping according to order of events: expresses clusters of cases that behave similarly during the accident.
- Whenever RVVs are activated early, a SA is prevented from occurring.
- 13500s is the latest time for the operator to activate ECCS to maintain an intact core in this type of accident scenario.

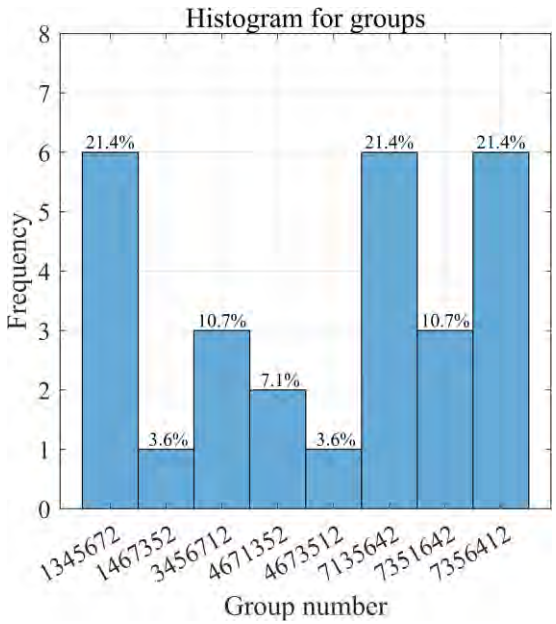

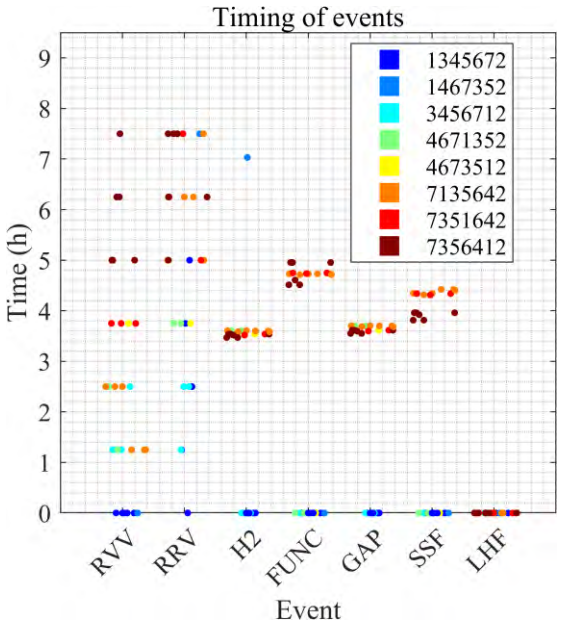

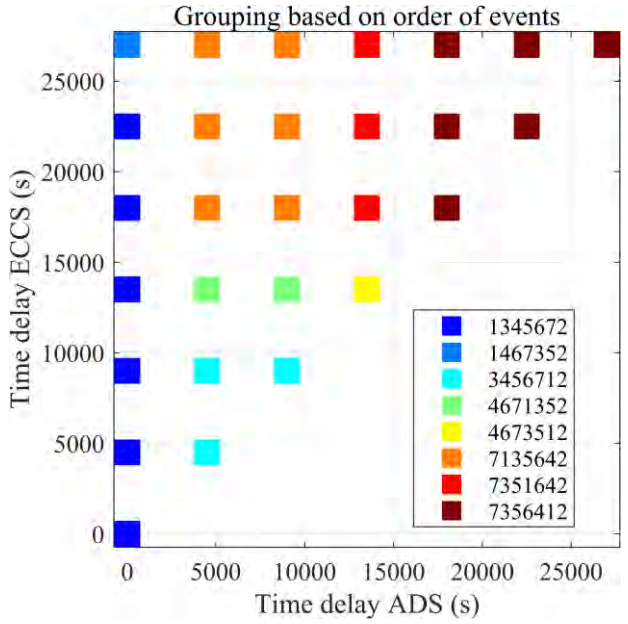

Results: SA4N-ECCS

- Similar to the DBAN-ECCS scenario, 3 sets of evolution of parameters are observed corresponding to different rates of loss of coolant from the RPV.
- Unlike the DBAN-ECCS scenarios, for some cases (set 3) RVVs and RRVs are activated at such late times that, the water that is eventually collected/condensed in the CNT will never circulate back into the RPV.
- Core degradation further proceeds with LH attack by the molten melt in the and its failure with ejection of debris to the CNT.

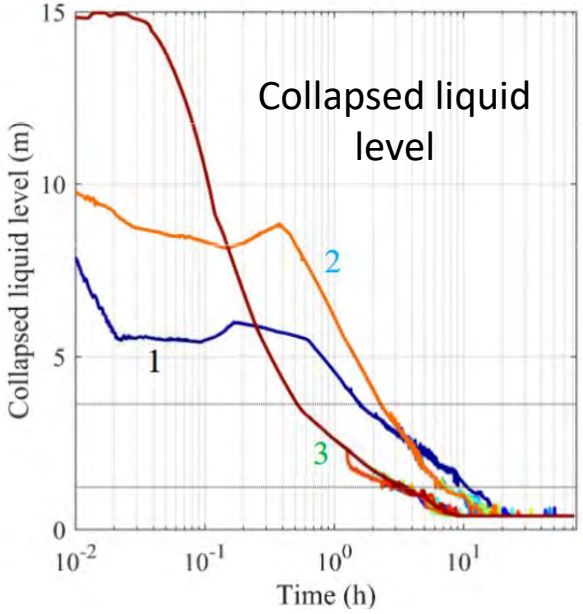

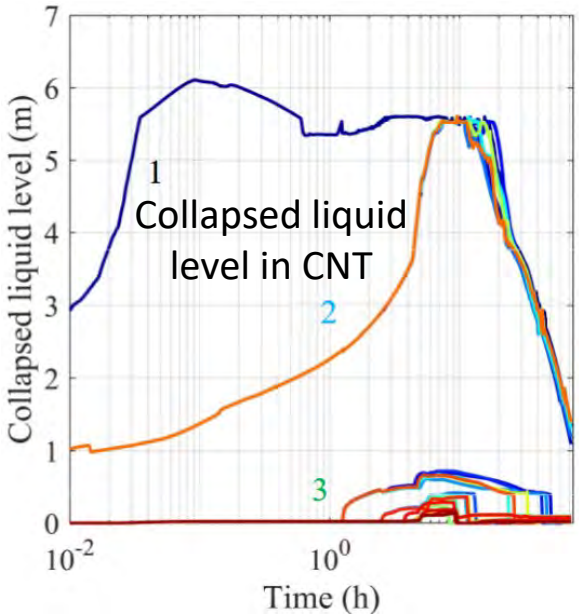

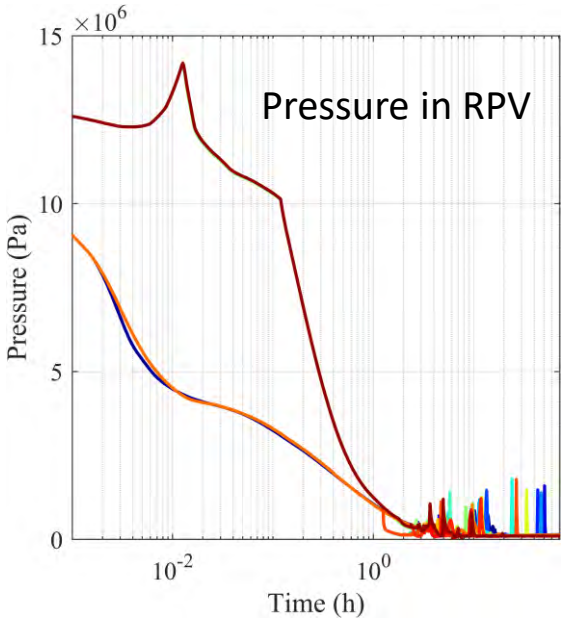

Results: SA4N-ECCS

- Late opening of RVV valves have no drastic effect on oxidation in the core.
- Largest hydrogen mass is generated when the RVVs open at 4500s.
- Essentially, opening of RRV only serves to circulate steam from the CNT to the RPV.
- Early activating of RVVs (>4500s) also leads to the formation of larger amounts of debris in the core just before SS failure.
- SA4N being one of the few scenarios leading to RPV failure, can expect roughly 10-22ton of debris mass being ejected from the RPV.

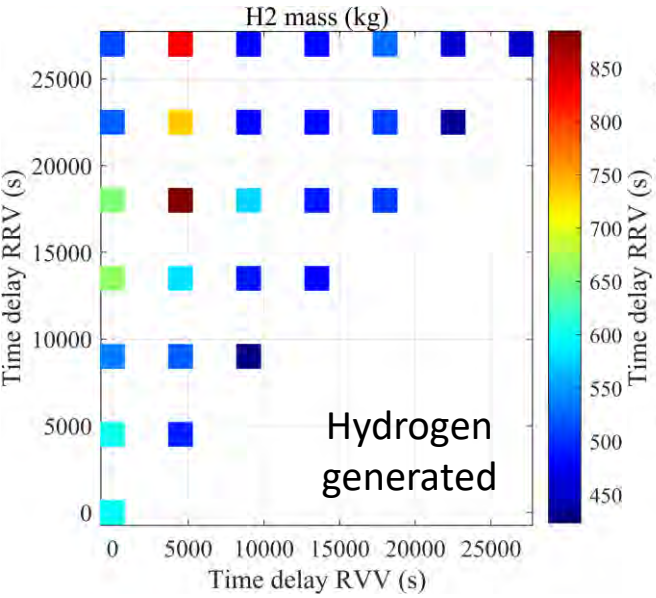

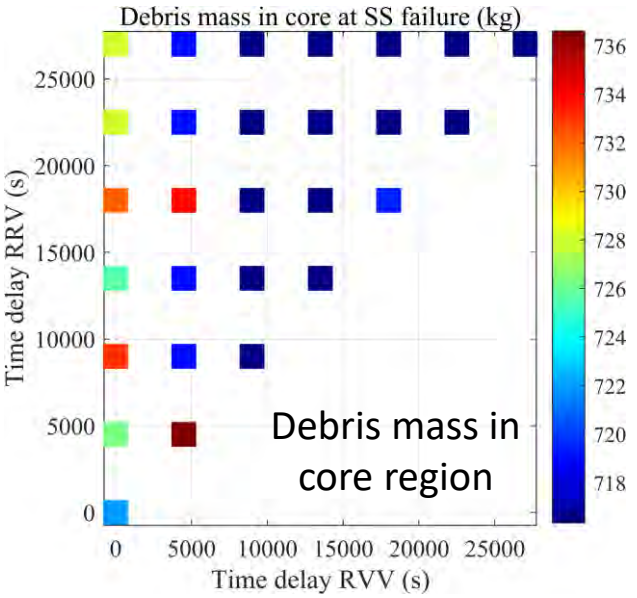

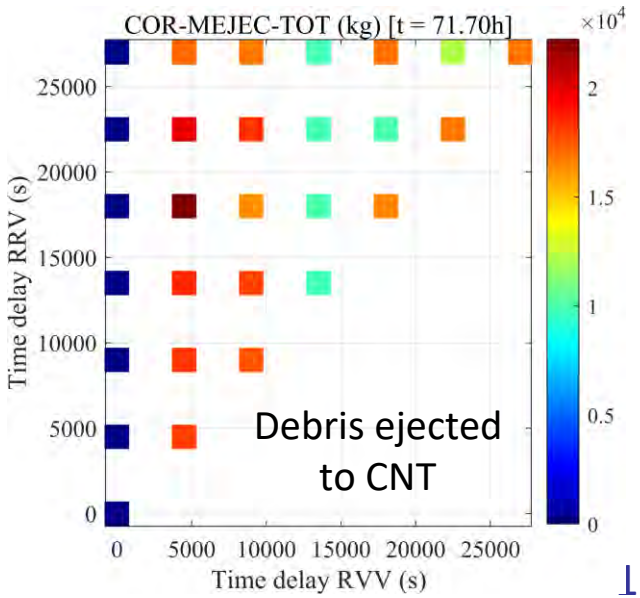

Results: SA4N-ECCS

- Grouping according to order of events: late ECCS activation, leads to early LHF (~10h), and subsequently time of LHF for cases with early ECCS activation can extend from 24-50h.
- From the perspective of arresting SA progression in SA4N like accident, operators may either recover RVVs instantly, irrespective of availability of RRVs, or delay the activation of ECCS to let the coolant evaporate by itself than accelerate it, i.e. keep the core covered for as long as possible > needs further cases and analysis of results.

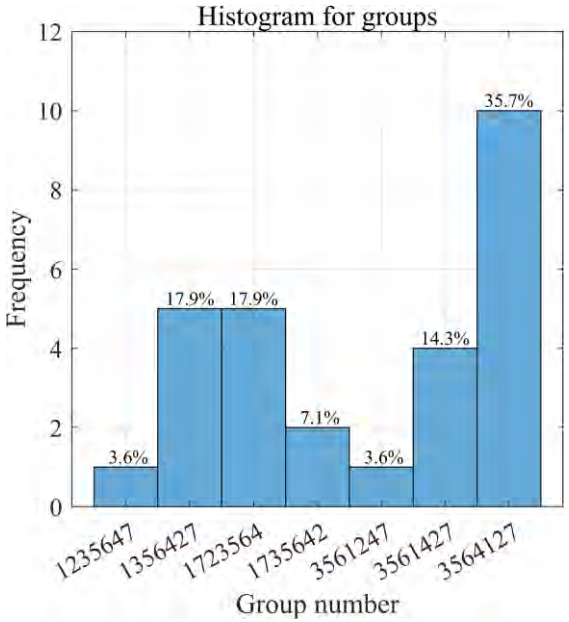

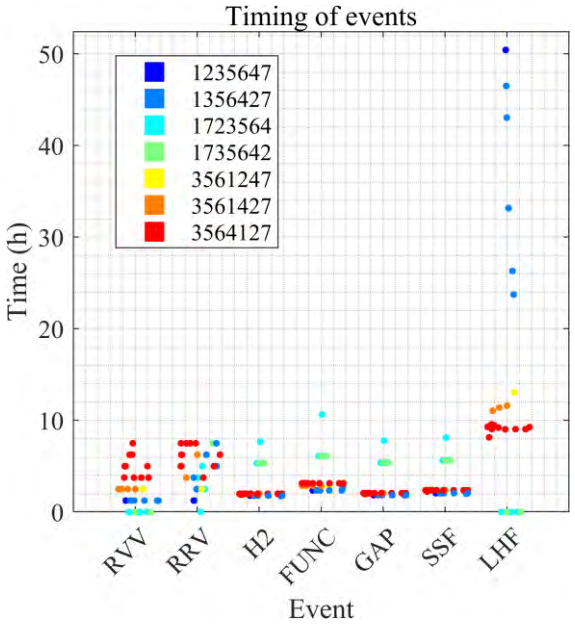

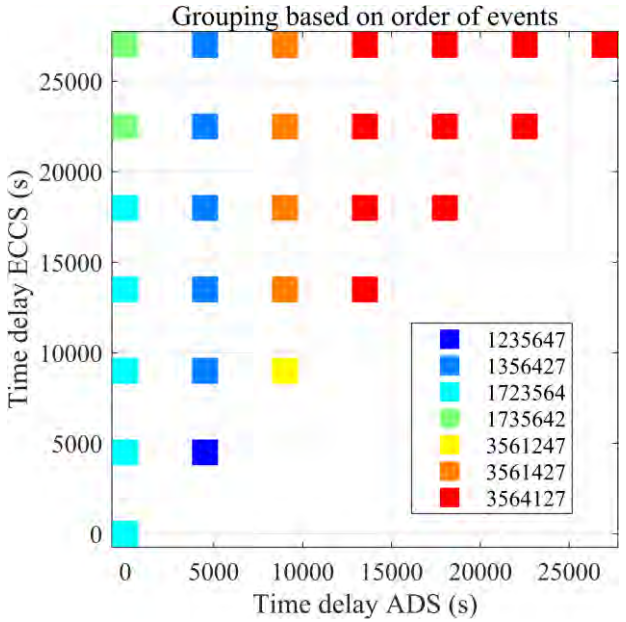

Results: SA6N-ECCS

- Similar to the previous scenarios, 3 different trajectories are observed for the collapsed liquid levels.
- However, unlike the previous accidents (SA4N particularly), cases in set 3 lead to the core being partially flooded with water once the RRVs are open.
- For cases with late ECCS opening (>13500s, Cases 010, 014, 015, 019, 020, 021, 025, 026, 027, 028), water from the CNT may not be able to circulate back in through the RRVs to even partially cover the core and thus complete core may be uncovered.
- For cases with extreme delays (> 22500, Cases 021, 027, 028), water in the CNT is too low to replenish the core.

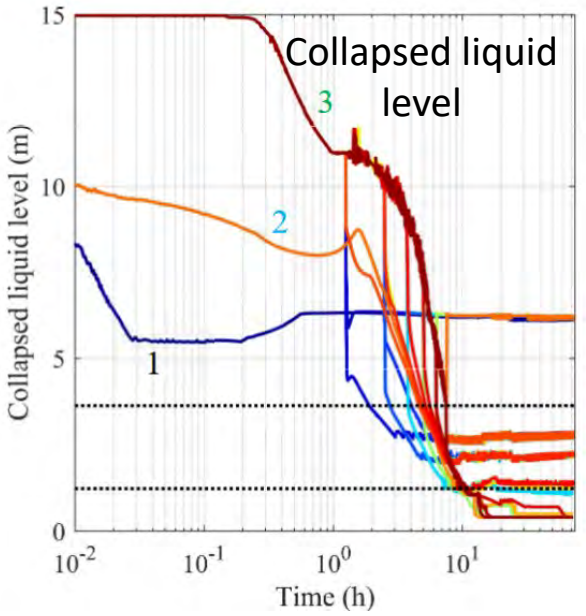

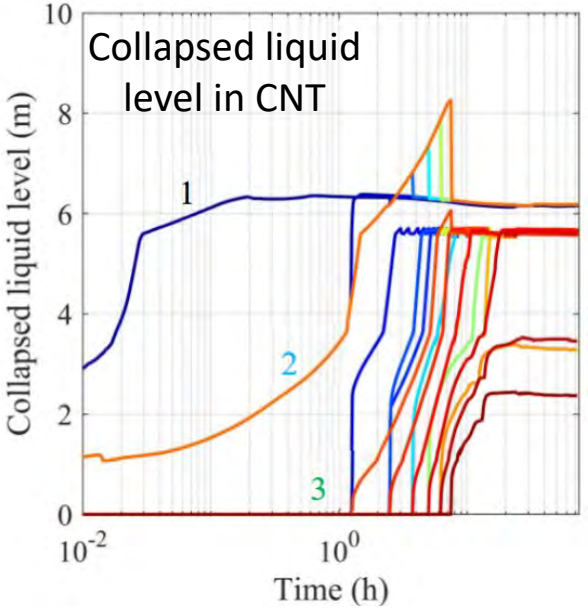

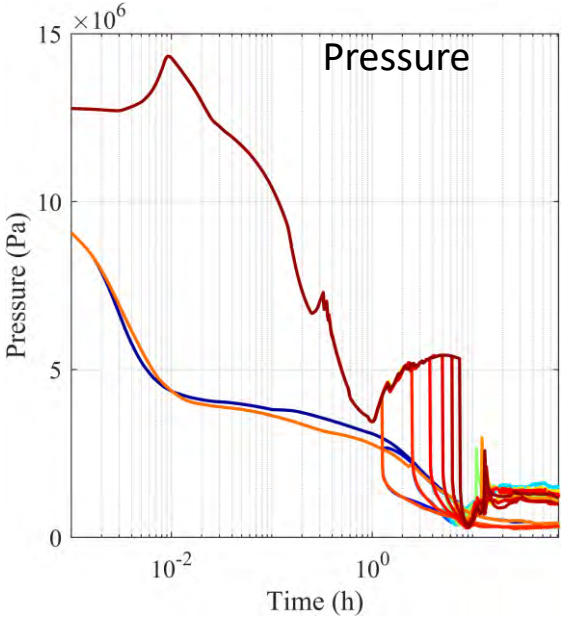

Results: SA6N-ECCS

- As a result of inadequate core cooling, cases with late ECCS opening (>13500s) see oxidation of the core producing about ~350-580kg of hydrogen.
- Only those cases with late RRV and RVV activation (>13500s) undergoes oxidation.
- Unlike, SA4N-ECCS cases, there is no complete loss of coolant from the CNT.
- Therefore, the operation of ECCS within this period [0, 27000]s, successfully manages in-vessel retention of the debris and prevents ex-vessel accident progression, which was the case in SA6N.
  - it may be necessary to also investigate recovery actions in the later phase of the accident (>27000s), where severity of core damage state may worsen the situation.

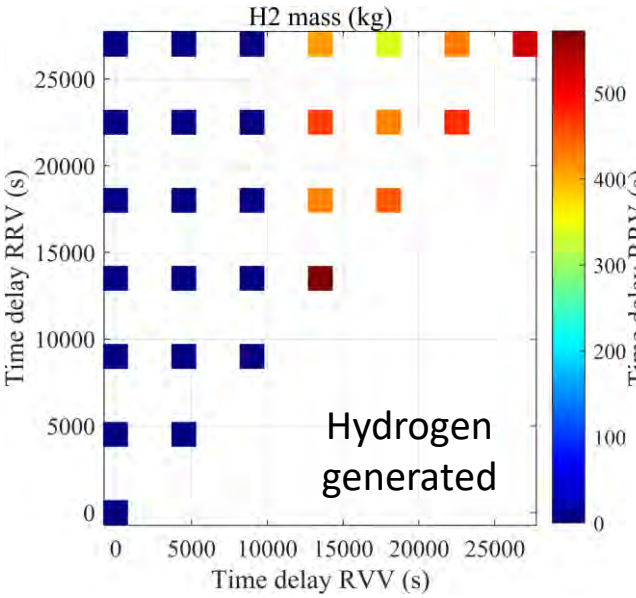

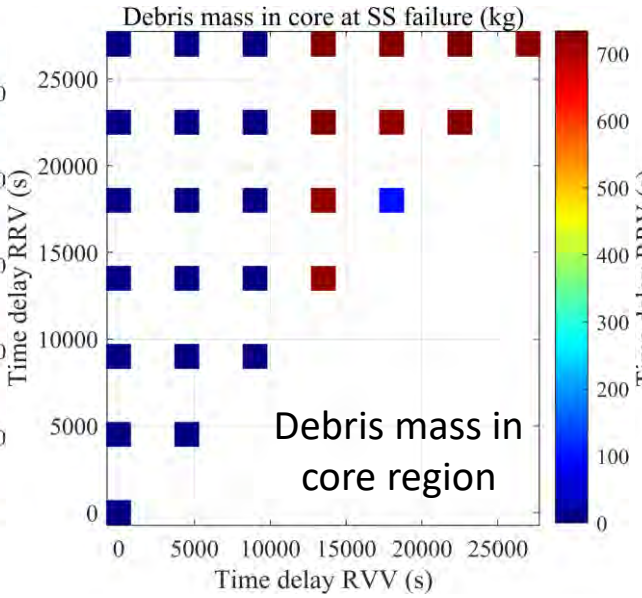

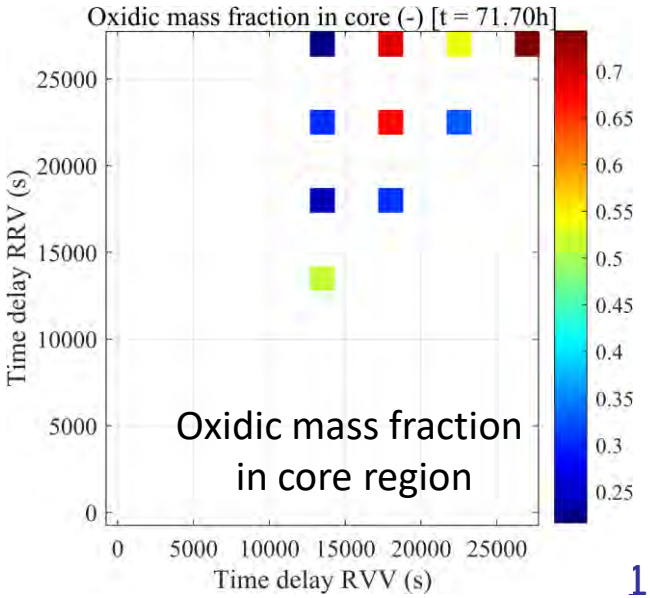

Results: SA6N-ECCS

- Grouping according to order of events: least ordered groups of events occur (4 v/s 8 and 7 in the former 2 scenarios).
- Case 015, does not experience failure of the SS while nearby cases all have SS failure in 6.2-8.2h.
  - This may likely be a one-off outlier or a result of time-step refinement when the code restarts after a crash and possibly missing cliff-edge effects in SS failure models, and may warrant further analysis to resolve potential uncertainties.

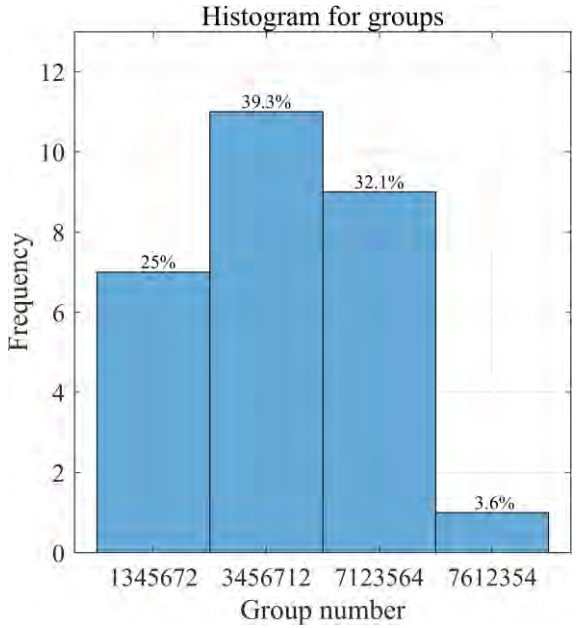

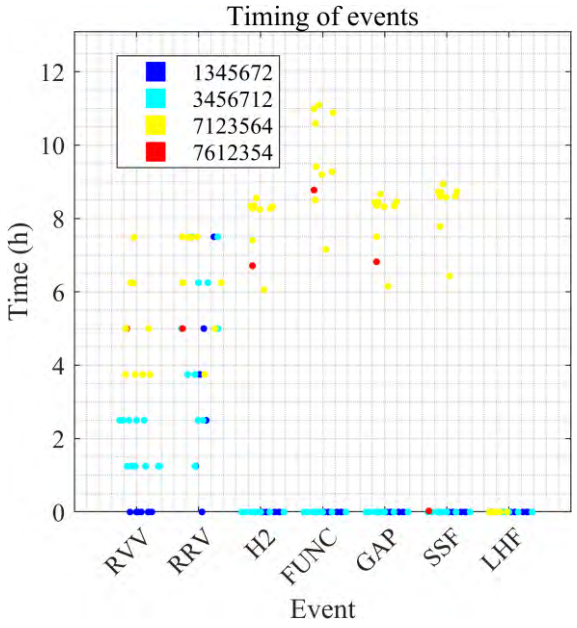

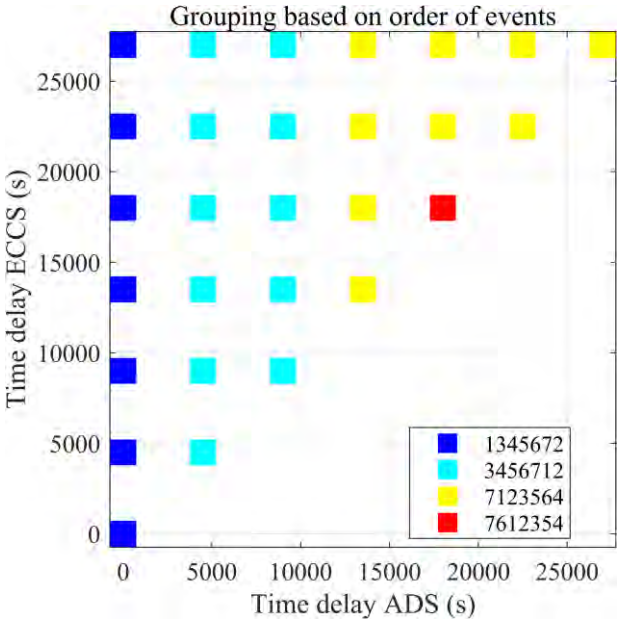

Summary and Outlook

- Mitigation of SA progression in a generic iPWR by considering delayed recovery of ECCS was presented.
- Three different accident scenarios were assessed for the effect of the delayed ECCS function.
- Different operation domains were identified that leads to specific set of events that may leads to severe core damage and relocation.
- In the case of DBAN-ECCS, late RRV activation can result in large debris formation and hydrogen generation, irrespective of time of activation of RVVs. However, as the coolant inventory remains within the CNT, RPV failure is not observed for any time of delay.
- In the case of SA4N-ECCS, all cases where RVVs are not activated along with LOCA, lead to RPV failure and debris in ex-vessel state.
- In the case of SA6N-ECCS, all delayed RVV activation scenarios lead to core damage, without RPV failure.
- The reliability analysis of ECCS with operator actions have shown, in most cases, dominating sequences for core damage are inability of RRVs to open early, or inability of water inventory in the CNT to establish natural circulation through the RRVs.
- Data valuable for the development of GA based search algorithm for SA domain identification and training of surrogate models.

Thank you for your attention.

Funded by the European Union. Views and opinions expressed are those of the author(s) only and do not necessarily reflect those of the European Union or European Commission-Euratom. Neither the European Union nor the granting authority can be held responsible for them.

This work is supported by ROAAM+ project funded by Swedish Radiation Safety Authority. The authors are thankful to Mateusz Malicki and Terttaliisa Lind from PSI for providing the MELCOR input deck for iPWR design.

References

1. M. Malicki, T. Lind, “MELCOR 2.2 iPWR LOCA type accident analysis, PART I: Thermal-hydraulics”, Nuclear Engineering and Design, 428, 113433 (2024).
2. G. Acharya, et al., “Investigation of Source Term During Severe Accidents in Integral PWR SMRs”, NURETH21, Busan, Korea (2025).
3. G. Acharya, et al., “Investigation of Severe Accident Progression in Integral PWR SMRs”, ERMSAR2026, Madrid, Spain (2026).

KTH
VETENSKAP
OCH KONST

INVESTIGATION OF IN-VESSEL MELT RETENTION BY A STAND-ALONE LOWER PLENUM MODEL OF INTEGRAL-PWR DESIGN #1 IN THE SASPAM-SA PROJECT, USING THE ASTECv3 CODE

S. Brumm
European Commission Joint Research Centre
Directorate G – Nuclear Safety and Security
Westerduinweg 3
NL – 1755LE Petten
stephan.brumm@ec.europa.eu

ABSTRACT

Within Work Package 4 of the SASPAM-SA project, funded under the Horizon-EURATOM programme, some established severe accident codes are assessed as to their capability of modelling In-Vessel Corium Melt Retention in two candidate Small Modular Reactor designs. Project participants were asked to set up a Best-Estimate-Plus-Uncertainty analysis by simulating accident transients in a stand-alone Lower Plenum model, with a set of agreed initial and boundary conditions.
This paper reports results of analyses that have been carried out around the task set in SASPAM-SA, with the Severe Accident code ASTEC V3.1.2 and its Uncertainty-Analysis front end SUNSET, for the integrated PWR design #1 of SASPAM; an external reactor vessel cooling loop driven by natural convection is part of the model to explore the functioning of the "ERVC pipe" feature of ASTEC. Five Uncertainty and Sensitivity Analyses of 500 simulations each have been carried out, three for an initial set of 15 uniformly distributed uncertain model variables and two where this set of uncertain input parameters has been varied to target the investigation. Their results have been evaluated regarding their impact on the residual thickness of the partly ablated Reactor Pressure Vessel wall, on the forming of a heavy-metal layer at the bottom of the Corium pool, and on other target model outputs. The global sensitivity of these target values has been analysed by correlation-based (Pearson coefficients) and by variance-based (Sobol' indices) methods.
The results discussed indicate that the code produces plausible results for the melt retention scenario. It is shown that natural convection in the ASTEC model of the external reactor vessel cooling loop is established and that all residual heat is removed through the vessel wall and to the ultimate heat sink. ASTEC simulations provide plausible results for the interaction of the different uncertain-parameter assumptions and vessel ablation. The initial mass of UO_2, by determining the amount of residual heat, and the heat resistance of the cooling path are examples of this. The paper underlines that the method of simulating the lower plenum during In-Vessel Melt Retention is credible. It must be stressed that the assumptions in the stand-alone model are conservative and that the degree of ablation computed cannot be taken at face value. For that goal, a comprehensive model will be applied in future work

KEYWORDS
IVMR, ASTEC, SASPAM-SA, sensitivity analysis

1. INTRODUCTION

In the context of developing and licensing the Small Modular Reactors that are expected to cover some of the energy needs of the future, it is important to insist on high nuclear safety standards including the resilience against severe accidents. The research carried out and tools developed for SA analyses in past decades have naturally been focused on large reactor concepts. Current research in the field is addressed to the question of whether existing SA codes cover with sufficient accuracy the phenomena that could take place in, and are thus applicable to, SMR. This is particularly important for an integrated PWR design that is a strong evolution of large reactor designs, with potential changes to the importance of physical phenomena; and example mentioned often is a higher reliance on condensation when passing residual heat to the ultimate heat sink. One of the situations of interest is the attack on the RPV after the hypothetical case of a reactor core melting and dropping into the Lower Plenum.
In terms of evaluating the results of SA simulations, Uncertainty Analysis has been increasingly made use of starting almost a decade ago, see e.g. [1] and [2] that are in the field of IVMR; the MUSA project [3] that was dedicated to broadly investigating UaSA application in SA simulation and Source Term evaluation; and [4] that added a detailed UaSA to extend the original SOARCA study on accident consequences. The approach to generating simulation data from the SA model requires the random perturbation of selected parameters, with the difference that sensitivity analysis does not demand the knowledge of realistic uncertainties of those parameters. In the SA context, running detailed simulations represents a large effort: one simulation in ASTEC can take more than 24 hours, multiplied by 100 simulations carried out by most contributors in MUSA. Also, code “failures” (typically reaching the minimum time step) for some UP combinations were experienced and complicate the analyses further. The sensitivity analyses carried out in MUSA used correlation techniques to attribute the sensitivity of target outputs.
This paper reports on the analyses carried out for the SMR design #1 considered as one of two designs in the Horizon-Europe project SASPAM-SA [5]. In the Work Package 4 of this project, the contributing partners agreed to run stand-alone Lower Plenum models addressed at analysing In-Vessel Melt Retention, using a range of SA codes used by different research groups. Boundary conditions for simulating a reference case and for setting up an Uncertainty and Sensitivity Analysis were agreed. This application follows the scheme broadly explored in [6].
For the work reported, analyses have been carried out with the severe accident code ASTEC V3. In addition to the SASPAM-agreed analysis, some changes related to the uncertain parameters were made and additional UaSA were run to broaden the interpretation of the results. Also, the submodel in the ASTEC code that is crucial for computing the Corium layer configuration in the Lower Plenum was given a closer look by establishing the effect of uncertainties in its key parameters. The post-processing and interpretation of results added to the commonly used Pearson correlation coefficients a recent algorithm that calculates first-order variances and covariances: so-called Sobol’ indices [7].
In the first section of the paper, the analysis approach is set out in terms of the input deck and in explaining the cases considered and evaluation methods applied. The results are then reported first for a best estimate reference simulation, and in further sections for the different sensitivity analyses. The paper closes with Conclusions and Acknowledgements.

2. ANALYSIS DESCRIPTION

2.1. Model Input Deck

The model used is based on an input deck for the stand-alone Lower Plenum of a PWR1000 reactor that is included in the ASTEC V3.1.2 software distribution. This has been adapted to fit the Design #1 considered in SASPAM-SA in that

- the overall size of the Lower Plenum was adapted to Design #1;
- the shape of the LP was changed to semi-ellipsoidal (from semi-spherical as coded in the original input deck);
- masses of materials in the Corium pool were revised.

For the Corium pool, a phase separation model based on interface equilibrium for oxide and metal layers was chosen.
The input deck was extended by adding an ERVC loop, including a containment volume and heat flux connections between the loop and a surrounding pool that serves as ultimate heat sink.
Main initial conditions of this model are constant temperatures in each of the entities RPV steel, oxide layer, top metal layer, and ERVC loop.
The simulation starts from a LP filled with two layers: one with UO_2, Zr, ZrO_2 (according to the chosen level of Zr oxidation), at a temperature of 2700 K, and a top layer of steel at 1700 K. This means that the make-up of the metallic and oxide layers of the pool is an initial condition and is changing towards an equilibrium found by that model. Residual heat generation is defined by the specific heat of U, either in its oxidic or its metallic form. The migration of species means that according to the evolution of the equilibrium residual heat is produced in both oxide and metal layers.

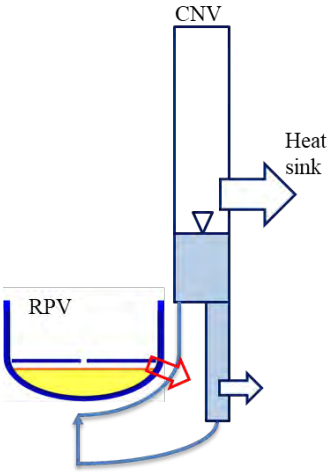

Figure 1. Lower Plenum with External Reactor Vessel Cooling loop.

The boundary conditions of the model are:

1. The only connection between the LP and the ERVC loop is the heat transfer through the LP wall. The connection between RPV and CNV that would be created by an opening pressure relief valve at the top of the RPV is neglected. However, it is assumed that, at this stage of the accident, the containment is filled with water to a certain level.
2. The heat removal to the ultimate heat sink (a pool in which the containment vessel is situated) is defined by heat exchange surface, a heat transfer coefficient and the temperature of the heat sink.
3. For the containment atmosphere, it is assumed that hydrogen as a non-condensable gas is present, at 10 bar initial pressure. Hydrogen explosion is no objective of the analysis and is not modelled.
4. The metallic top layer experiences radiative heat losses, but rather than setting a boundary condition, these losses are calculated by ASTEC's RADCAV model that calculates the radiation between the metal surface and the structures present: these are the core support plate and the RPV walls above the Corium pool.

2.2. Reference Case and Sensitivity Analysis

Table I displays the data agreed in SASPAM-SA WP4.2 for key input parameters in the reference case and in the subsequent UaSA; it is appended by 4 parameters that are mostly related to the ERVC loop. All UP in the UaSA were assumed to be uniformly distributed between the minimum and maximum values provided in the table.
The UaSA was run with the help of the SUNSET tool that is part of the ASTEC software distribution. The SUNSET tool managed the generation of random uniform input parameter distributions for 500 simulations in each of the analyses below. The random generator was initialized with a different 5- or 6-

digit integer number, and the statistical independence of the input demonstrated by the insignificant values of the input correlation matrix.
For the post-processing of the data in Microsoft® Excel®, Python routines were developed to convert the SUNSET output. The statistical evaluation of the data was carried out by two different methods: (i) by computing Pearson correlation coefficients using functions provided by Excel®. It was assumed that the largest part of the accordance of outputs and random inputs is linear; (ii) by a global sensitivity analysis by variance decomposition as offered by the software tool SIML@B [8]. The software implements a recent algorithm [9] to compute Sobol' indices [7] and identify the input uncertainties whose variances contribute most to the variance of the MRVT. For this paper it is important to know that S_i are normalized variance contributions of individual UP, while ST_i are total contributions that also include covariances between different UP.

Five different UaSA are discussed in the following:

1. The original UaSA as agreed in SASPAM-SA WP4
2. Acknowledging that treating initial masses of UO2, Zr and steel as statistically independent does not reflect the physical reality of a molten core, and thus moving to initial conditions where the bulk of Zr and steel is a function of the (random) amount of UO2 and only a part of 10 – 20% of Zr and steel is modelled as an statistically independent variation.
3. The UaSA submitted within WP4.2 of SASPAM-SA that deviated from 2. by the amount of steel in the simulation.
4. Realising that ASTECs submodel for the corium pool is key to whether a HM layer forms in addition to the light metal and the oxide layer, an UaSA with 4 parameters of the SEPALOWE taken as UP in a separate analysis
5. Synthesizing the previous analyses, an UaSA where the UP found significant in 1. and 4., are kept while all others are taken at their constant reference value.

Table I. Reference data and uncertainty ranges for uncertain parameters

Parameter	Name	Reference	Minimum	Maximum
Geometry of LP				
Thickness of vessel (cm)	thives0	0.12	0.10	0.14
Degradation				
Mass of UO2 in LP (t)	mmm0	9.	4.5	9.
Mass of Zr in LP (t) (U/Zr ratio is constant)	mmzr0	2.5	0.9	2.5
Zr fraction oxidized in LP	rzrox0	0.5	0.3	0.8
Mass of Steel (t) in LP	mmu0	4.0	1.5	4.5
Power per unit mass of UO2 (W/kg)	powe_i0	190	178	200
Containment				
Pressure (bar)	pCNV0	12	11	13
Material properties				
Oxide conductivity (W/K/m)	condox0	2.0	1.0	3.0
Molten steel conductivity (W/K/m)	condst0	20	20	40
Vessel conductivity (W/K/m)	condves0	30	25	35
Metal emissivity (-)	emissliq	0.5	0.2	0.8
ERVC loop and core support plate				
Temperature UHS [K]	tpool	323.15	303.15	343.15
HTC to UHS [W/m2/K]	htcpool	1000	1000	2000
ERVC thickness factor	etf	1.0	0.8	1.2
Initial temp. of core support plate [K]	Tplt	873	560	1100

3. REFERENCE CASE RESULTS

Figure 2 illustrates the temperature distribution in the Lower Plenum, and the ablation of the RPV wall, at the end of the simulation at 20,000 s. Ablation of the wall has taken place, and the residual thickness is down to 5.85 cm from the initial 12 cm.
Figure 2(bottom) adds the information of how the mass of 3 material layers in the lower plenum is evolving; it confirms that the initial configuration of 2 layers evolves into 3 layers at the slump of the top metal layer to the bottom of the LP, at about 1,650 s, and that that bottom HM layer is disappearing over time. The melting of the core support plate and thus the addition of 1,500 kg of steel to the pool takes place between 2500 and 3500 s into the transient.
Other steady-state results of the reference case are:

- Heat generation and removal in the system are balanced.
- The passive ERVC loop is functioning. After a transient phase, and starting from a small initial value, the flow is 36.5 kg/s.
- The composition of the light metal layer is mostly steel at about 4,200 kg, but also about 1,400 kg of U and a bit less than 500 kg of Zr.

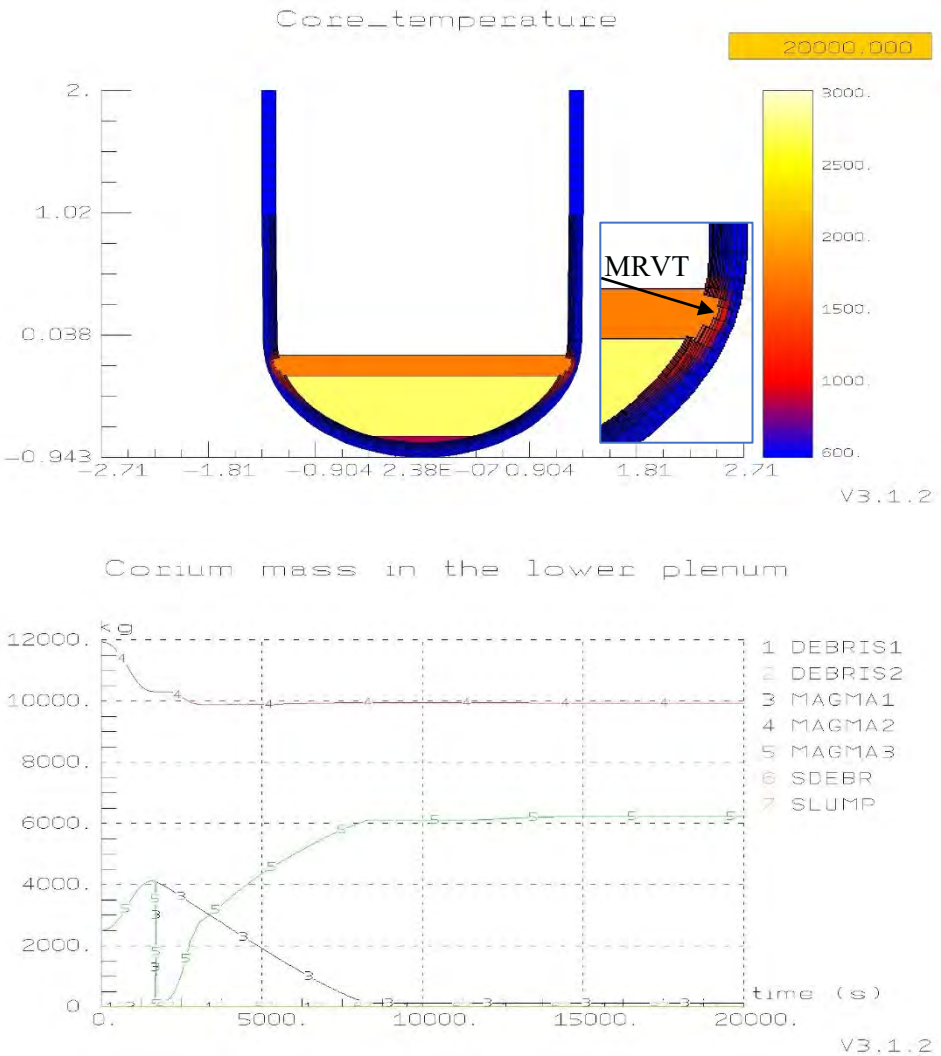

Figure 2. Reference case. Temperature field in RPV and Corium pool at steady state (top); evolution of the mass of the different layers of the Corium pool (bottom).

4. UNCERTAINTY AND SENSITIVITY ANALYSIS RESULTS

4.1. SASPAM-agreed Case (random-generator initializer: 52447)

In this case, uncertain parameters were selected according to Table I. The evolution of residual wall thickness for the first 100 simulations is displayed in Figure 3 alongside the reference case. Under the assumptions made, considerable wall ablation is to be expected; after some ablation, the heat resistance of the remaining wall thickness is small enough to pass heat without the inside of the RPV wall exceeding melting temperature. In all 500 simulations, the residual thickness stays above 2.8 cm.

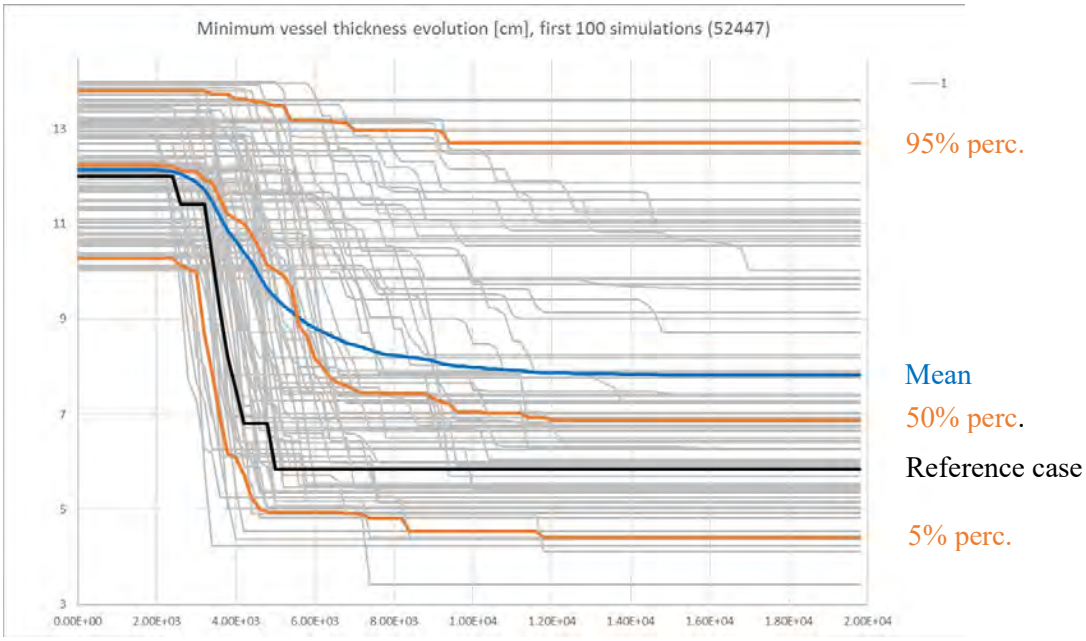

Figure 3. Horsehair diagram of minimum residual vessel thickness

Table II shows statistics of key simulation outputs at 20,000 s that is taken as steady state. The main message is that the uniformly distributed uncertain parameters are providing significant perturbation to the IVMR model output. In 262 out of the 500 simulations a HM layer exists at the end of the transient. Pearson coefficients computed for a broad set of outputs are displayed in Table III; at 500 samples, CC larger than 0.088 are significant (p-value < 0.05). They suggest that initial material masses and Zr oxidation degree significantly influence the physics in the lower Plenum: heights *HMAG* and densities *RHO* of Corium layers; the occurrence of a HM third layer in addition to oxide layer and top metal layer; power lost from the layers through the wall, *Pex*, and through radiation, *Prad3*; the crust thickness of the oxide layer *crstox*; and, ultimately, the residual thickness $s_{v,rem}$ of the RPV at the location with the largest ablation. This ablation is also correlated to the vessel conductivity and top-layer emissivity.

Table II. Means and ranges of outputs at steady state in the SASPAM-SA WP4.2 case

Output	5% perc.	mean	95% perc.
MRVT [cm]	4.689	8.033	12.811
HF top metal to inside RPV [kW/m^2]	373.944	943.215	1436.939
HF oxide to inside RPV [kW/m^2]	34.402	60.973	98.521
Relative difference with CHF	40.2%	68.6%	93.4%
Thickness of top metal layer [m]	0.000	0.112	0.172
Thickness of oxide layer [m]	0.257	0.396	0.511
Oxide crust thickness RPV wall [cm]	2.429	6.931	10.129
Top crust thickness [cm]	0.000	0.077	0.333
Power lost by radiative HF	9.7%	20.2%	36.3%

Oxide/Metal density ratio	0.906	0.988	1.045
Containment pressure [bar]	6.91	7.57	8.40

Table III. Pearson correlation coefficients for selected model outputs.

	vessthimin	crstox	Pex2	Pex3	Prad3	HMAG1	HMAG2	HMAG3	RHO1	RHO2	RHO3	3rd_layer
thives0	0.194	0.063	0.065	-0.031	0.058	-0.073	0.001	0.075	-0.008	0.017	-0.053	-0.006
mmm0	-0.651	-0.601	-0.749	-0.477	-0.282	-0.153	0.608	0.034	0.001	0.344	0.166	-0.102
mmzr0	0.088	0.069	0.022	0.315	-0.178	0.459	-0.083	-0.211	0.226	-0.851	-0.029	0.357
rzrox0	-0.038	-0.026	-0.247	-0.191	0.123	-0.466	0.567	0.083	-0.426	-0.211	-0.704	-0.430
mmu0	0.324	0.009	-0.086	-0.307	0.220	-0.406	0.313	0.815	-0.621	-0.093	-0.290	-0.580
powe_i0	-0.081	-0.100	-0.115	-0.075	-0.048	0.007	0.012	0.024	0.012	-0.083	-0.065	0.021
pCNV0	-0.044	-0.016	-0.026	-0.045	0.013	-0.029	0.047	-0.002	-0.009	-0.046	0.051	-0.023
condox0	0.075	0.424	-0.052	0.016	0.100	-0.041	-0.013	0.020	-0.029	0.063	-0.023	-0.012
condst0	-0.046	0.309	0.274	-0.116	0.054	0.015	-0.066	0.008	0.027	0.132	0.034	0.023
condves0	0.245	0.015	-0.001	0.009	0.056	0.029	-0.020	-0.047	0.041	0.012	0.021	0.032
emissliq	0.304	-0.012	-0.037	0.225	-0.295	-0.015	0.021	0.023	-0.036	-0.033	0.027	-0.030
tpool	0.057	0.080	0.021	0.060	-0.040	-0.031	0.001	-0.007	-0.044	0.023	0.020	-0.050
htcpool	-0.040	0.016	-0.013	-0.043	0.074	-0.039	0.002	0.028	0.028	0.047	0.016	0.013
Tplt	0.087	-0.001	0.004	0.048	-0.045	0.010	0.004	-0.007	-0.037	0.008	-0.025	-0.045
etf	-0.026	-0.064	-0.080	-0.023	-0.011	-0.068	0.077	0.007	-0.066	-0.027	0.009	-0.077

While not shown here, it is no surprise that the temperatures along the vessel wall – highest in the elements that are close to the interface of oxide and top metal layer – are strongly correlated with the ultimate heat sink temperature *tpool*.

Table IV. Global Sensitivity Analysis by Sobol' indices for the minimum residual vessel thickness

Variances			Covariances		
S_2	mmm0	0.44 ± 0.03	$S_{3,4,5}$	mmzr0, rzrox0, mmu0	0.02
S_5	mmu0	0.11 ± 0.02	$S_{3,5}$	mmzr0, mmu0	0.03
S_{11}	emissliq	0.08 ± 0.02	$S_{4,5}$	rzrox0, mmu0	0.01
S_{10}	condves0	0.06 ± 0.02			
S_1	thives0	0.03 ± 0.01	Relative Training Error		0.16098
S_3	mmzr0	0.01 ± 0.01	Sample Variance of vessthimin		7.135

Table IV shows how the variance of the MRVT can be attributed to the UP. The order of significance is identical to the Pearson CC, with the benefit that the values are easier to interpret – 44% of the output variance are explained by *mmm0*. Capturing second-order effects, the covariances are less important in this application. However, in case of *mmzr0* the overall impact dominated by the covariances. The table shows that the "training error" is relatively large at about 16%: the variances calculated explain only 84% of the output variance.

4.2. SASPAM-agreed Case with Modification (337249)

The UaSA simulations were set up with the reference, minimum and maximum values defined in Table I. However, for the initial masses of UO_2, Zr and steel, equations were introduced to limit their statistical independence:

$$m_{Zr} = \frac{2.5}{9} m_{UO2} - \Delta m_{Zr} \quad (1)$$

$$m_{steel} = \frac{4.5}{9} m_{UO2} - \Delta m_{steel} - m_{CSP} \quad (2)$$

where the uncertain parameters m_{UO2} [4.5 t, 9 t], Δm_{Zr} [0 t, 0.35 t] and Δm_{steel} [0 t, 0.7 t] are all uniformly distributed in the intervals given, and m_{CSP} = 1.5 t is the mass of the core support plate. The justification for this limitation is the fact that a molten core will always consist of a mix of UO2, Zr and steel that resembles the intact core. Random deviations from this mix can be assumed, but an independence where

e.g. a maximum amount of UO_2 meets the minimum amount of Zr and steel seems far-fetched. The adhoc equations lead to ranges m_{Zr} and m_{steel} that agree with minima/maxima in the original case in Table I.

Key results computed in the modified approach are displayed in Table V. Most notably, the 5% and 95% percentile values are less extreme than in the original case; particularly for the HF in the top metal layer. Furthermore, the mean value of HF in the top metal layer is significantly different. Most other mean values are similar, as is the number of cases where a HM layer is formed: 256 out of 500. Comparing Pearson coefficients with those of the SASPAM-agreed case shows the same patterns, but weaker.

Table V. Key results' ranges for the modified case, again at 20,000 s.

Output	5% perc.	mean	95% perc.
MRVT [cm]	4.978	7.624	11.112
HF top metal to inside RPV [kW/m^2]	508.007	679.529	921.409
HF oxide to inside RPV [kW/m^2]	35.399	63.786	100.645
Relative difference with CHF	48.5%	71.0%	93.6%
Thickness of top metal layer [m]	0.079	0.125	0.168
Thickness of oxide layer [m]	0.284	0.412	0.536
Oxide crust thickness/ RPV wall [cm]	2.747	6.754	9.869
Top crust thickness [cm]	0.000	0.055	0.307
Power lost by radiative HF	9.9%	18.6%	28.9%
Oxide/Metal relative density	0.942	0.995	1.036
Containment pressure [bar]	6.92	7.60	8.43

4.3. SASPAM-agreed Case with Modification and High Steel Content (94271)

These results shown above differ from the JRC results submitted in WP4.2 of SASPAM-SA, where the modifications (1), (2) were made but where, in addition, the "steel mass in the LP" of Table I was taken as the initial steel mass; this meant that, together with the melted core support plate, the amount of steel was 1.5 t larger. Here, it is briefly touched to understand the impact on the results.

Table VI. Key results' ranges for the modified case with large steel content, at 20,000 s.

Output	5% perc.	mean	95% perc.
MRVT [cm]	7.160	9.927	12.526
HF top metal to inside RPV [kW/m^2]	402.891	497.055	611.673
HF oxide to inside RPV [kW/m^2]	37.393	65.227	101.651
Relative difference with CHF	65.2%	77.0%	88.4%
Thickness of top metal layer [m]	0.133	0.180	0.223
Thickness of oxide layer [m]	0.354	0.442	0.532
Oxide crust thickness/ RPV wall [cm]	2.729	6.624	9.759
Top crust thickness [cm]	0.000	0.108	0.388
Power fraction lost by radiative HF	12.1%	17.3%	23.2%
Oxide/Metal relative density	0.982	1.022	1.078
Containment pressure [bar]	6.95	7.62	8.50

The strong correlation of a 3rd layer and the initial steel mass mmu0, -0.58 as shown in Table III, indicates that this would have a big impact. And indeed, in the submitted results, a 3rd layer was only formed in 7 of 500 simulations.

Table VI displays key results of this UaSA; the most notable differences with Table V are indeed linked to the much higher amount of steel present: the top metal layer is thicker, and as a consequence heat flux and vessel ablation are smaller.

4.4. A closer look into the Corium-pool model (111111)

The lower plenum model of the severe accident code is undoubtedly at the centre of predicting the attack of the Corium pool at the RPV. In particular, the heat distribution and the effect of a light top metal layer focussing heat on a small part of the RPV wall determine whether vessel ablation will lead to RPV failure. Of the Corium phase separation and stratification models offered by ASTEC, the interface equilibrium model [10, 11] as the most recent and developed, has been used.

Table VII. Choice of uncertain parameters and their intervals in the SEPALOWE model.

Parameter	Name	Default	Minimum	Maximum
SEPALOWE model				
Threshold for beginning of stratification inversion [%]	tresh	5.0	4.0	6.0
Heat exchange oxide/moving metal [%]	frac	100	80	100
Species diffusion coefficent	diff	1.E-8	8.E-9	12.E-9
Height ratio of interaction zones	coef	0.1	0.08	0.12

Parameters in the model that can be selected by the user, and that were taken as uncertain parameters, are:

- the threshold of density difference (in percent) before a heavier upper layer slumps through a lower layer, initialising a stratification inversion
- a parameter determining the heat exchange between a moving (rising or slumping) metal species and the oxide layer, ranging between 0 and 100% - the latter meaning instantaneous thermal equilibrium
- the species diffusion coefficient
- the height ratio of the top to bottom interaction zones between layers that are characteristic for the interface equilibrium model

The ranges of the uniform distributions assumed are shown in Table VII. The UaSA is similar to previous analyses, with the same key outputs. The input uncertainties lead to output variations (not displayed here) that are small in terms of the physical problem. As in the analyses shown earlier, the overall result is a bifurcation where 74% (369/500) of simulations end up with 3 layers (i.e. including a HM layer at the LP bottom), and 26% (131/500) with 2 layers (just light metal and oxide layer).
The GSA is applied to get information on how the model parameters influence the results:

- the Sobol' indices in Table VIII tell that the appearance of a third layer is exclusively linked to parameter *tresh* that defines at which density difference between two layers slumping occurs.
- When just looking at results of the 3-layer branch of the bifurcation, the MRVT is mainly sensitive to parameter *frac* that determines the heat exchange of the slumping/rising metal fraction with the surrounding oxide layer; see Table VIII (right).
- The parameters *diff* and *coef* are insignificant in these analyses.

Table VIII. Individual S_i and total Sobol' indices ST_i provided by SIMLAB [4, 5]. Sensitivity of the occurrence of a heavy metal layer (left); sensitivity of residual wall thickness in the 369 cases where a HM layer is formed (right)

Name	S_i	$\pm\Delta S_i$	ST_i	$\pm\Delta ST_i$
tresh	0.85	± 0.02	0.85	± 0.02
frac	0.00	± 0.00	0.00	± 0.00
diff	0.00	± 0.00	0.00	± 0.00
coef	0.00	± 0.00	0.00	± 0.00

Name	S_i	$\pm\Delta S_i$	ST_i	$\pm\Delta ST_i$
treshval	0.07	± 0.02	0.12	± 0.03
fracval	0.67	± 0.04	0.70	± 0.04
diffval	0.00	± 0.00	0.01	± 0.01
coefval	0.01	± 0.01	0.01	± 0.01

4.5. Combination of significant UP from SASPAM and SEPALOWE analyses (123457)

To conclude, it seems interesting to combine the previous analyses to get an importance ranking among UP linked to initial conditions and those linked to the lower plenum model. UP selected for are: *mmm0*, *mmzr0*, *rzrox0*, *mmu0*, *condves0* and *emissliq* from Table I and *tresh*, *frac* from Table VII.
The key output values turn out to be close to those of the original SASPAM-SA WP4.2 analysis in Table II. The sensitivity of the MRVT as the target value of the analysis as expressed by Sobol' indices and Pearson correlation coefficients is displayed in Table IX. 41% of the variance in $s_{v,rem}$ is due to *mmm0*, followed by 22% due to *mmu0*. The correlation coefficients support the top of the ranking, without telling which one of *mmu0*, *condves0* and *emissliq* is second-ranked. However, the CC tell that larger *mmm0* reduces MRVT while larger *mmu0*, *condves0* and *emissliq* lead to larger MRVT.

Table IX. Sensitivity of residual wall thickness to the UP. Sobol' indices of the GSA (left); Pearson correlation coefficients (right).

Number	Name	Si	±ΔSi	STi	±ΔSTi
1	mmm0	0.41	± 0.04	0.41	± 0.04
2	mmzr0	0.01	± 0.01	0.07	± 0.02
3	rzrox0	0	± 0.00	0.07	± 0.02
4	mmu0	0.14	± 0.03	0.22	± 0.04
5	condVES0	0.07	± 0.02	0.07	± 0.02
6	emissliq	0.08	± 0.02	0.08	± 0.02
7	treshval	0	± 0.00	0	± 0.00
8	fracval	0	± 0.00	0	± 0.00

	vessthimin
mmm0	-0.607
mmzr0	0.080
rzrox0	-0.019
mmu0	0.285
condVES0	0.278
emissliq	0.291
treshval	0.003
fracval	0.015

As in the previous UaSA, the overall result shows a bifurcation; 49% (243/500) of simulations end up with 3 layers and 51% (257/500) with 2 layers. To go into further detail of this behaviour and its link to wall ablation, the results have been separated and the two branches looked at separately.
The comparison of results for the 2 branches reveals some interesting points:

- Most importantly, the mean of $s_{v,rem}$ is smaller in cases with a HM layer and the minimum remaining wall thickness of that branch is 3.31 cm, as compared to 4.9 cm for the 2-layer branch.
- In the branch with HM layer, there are cases with disappearing top metal layer. A closer look at the data confirms that, in this problem set-up, 14 simulations do not feature a top metal layer at tend = 20,000 s. Also, huge heat fluxes in the top metal layer (4.55 MW/m2 as 95% percentile, and even 10.6 MW/m2 in the most extreme case of simulations with HM layer) are computed. This is the sign of singular, unphysical cases that occur when the (random) UO_2 and Zr masses are large and coincide with a small initial steel mass.
- The fact that there is a steel fraction in the HM layer is indicated by a top metal layer mean height of 8.6 cm with HM layer, when it is 13.9 cm without.

Table X shows how MRVT is correlated to the uncertain parameters. Next to the known importance of the UO_2 mass for both branches, the marked difference is the positive effect of the steel mass mmu0 in the 2-layer branch, while no correlation is shown in the branch with HM layer. Apparently, the consumption of steel in the HM layer annihilates the influence.
It is seen as a sign of robustness that the parameters of the Corium layer separation model that had a visible effect in the previous UaSA are insignificant when compared to the effect of initial conditions.

Table X. Pearson correlation coefficients for the minimum vessel thickness as target value. 2 layers (oxide, light metal) (left); 3 layers (oxide, light metal, heavy metal) (right).

	vessthimin
mmm0	-0.662
mmzr0	0.096
rzrox0	-0.184
mmu0	0.434
condVES0	0.354
emissliq	0.344
treshval	-0.048
fracval	0.009

	vessthimin
mmm0	-0.613
mmzr0	0.188
rzrox0	-0.046
mmu0	0.050
condVES0	0.223
emissliq	0.267
treshval	0.021
fracval	0.023

5. CONCLUSIONS

Based on the UaSA within SASPAM-SA WP4 for a stand-alone model, this paper has explored several variations of the uncertain parameter base to highlight sensitivities of key model outputs and in particular the MRVT at steady-state, when ablation has stopped. In addition to the thermal-hydraulic modelling of the cooling loop, the modelling of the stratification evolution of the Corium pool in the Lower Plenum has been the focus. For the evaluation of statistical dependencies in the simulation data, a variance-decomposition technique was applied in addition to Pearson correlation coefficients.

The list of conclusions is multi-faceted. Starting with the input deck, the pipe element offered by ASTEC for a simple implementation of ERVC worked well for modelling the natural convection mechanism. The model was robust and results delivered were found plausible.

The analyses of vessel ablation suggest that it is most sensitive to the mass of UO_2; this is of little surprise, as this mass is the dominating factor in defining the amount of residual heat in the system. The MRVT also shows sensitivity to the mass of steel in the Lower Plenum, to the emissivity of the top metal layer and to vessel wall conductivity, as pointed out in the paper.

The comparison of the effect of uncorrelated vs. correlated, and physically more realistic, initial masses demonstrates that the former leads to more simulations with extreme, unrealistic, results. 5% and 95% percentile show the difference, while the mean of key outputs is not diverging very much. Also important, the MRVT in any of the simulations is found to be 2.8 cm, as compared to 3.3 cm when the more realistic material ratios are used.

The formation of a HM layer in ASTEC has been the subject of several sensitivity analyses. It has been demonstrated that within the Corium pool model, the formation depends entirely on the density difference threshold that defines the onset of metal slump or rise through the oxide layer. When looking at the broader SASPAM-SA analyses, Pearson correlation coefficients and the number of simulations ending up with a HM layer suggest that high steel content reduces the likelihood of a HM layer.

It has been shown that the presence of a HM layer tends to increase the heat flux in the top metal layer, simply by incorporating part of the steel in the system in the HM layer.

In the final UaSA, the combination of initial-condition UP with Corium pool model UP showed that the results are sensitive to the former – in particular again mass of steel -, not the latter. This is regarded as a positive sign that there are no over-sensitivities in the Corium pool model that show up in simulations using that submodel.

The evaluation of UaSA results with two different methods demonstrated that correlation coefficients and Sobol' indices identify the same most significant sensitivities. It highlighted that Sobol' indices, by attributing variance to the different uncertain parameters, are easier to interpret and are providing a more detailed picture of direct and, by covariances, joint influences on the target quantities. The initial Zr mass is an example of such joint influence, see Table IV. Correlation coefficients have the useful property of indicating positive/negative direction of an influence, which is useful information for scrutinizing results.

This stand-alone model is limited in addressing some effects that are likely to influence heat removal, the most important being the simplification of not modelling the RPV to containment connection that exists through the pressurizer release valves. Ablation results are also strongly dependent on the assumption of initial material masses in the Corium pool – in the existing complex large ASTEC model

of design #1 those masses would be the result of the modelled core melting process and could be very different. However, that analysis is very challenging due to the computational effort and the smaller robustness than the stand-alone model and has been set aside until now.

NOMENCLATURE

CC	Correlation Coefficient
CNV	Containment Vessel
ERVC	External Reactor Vessel Cooling
GSA	Global Sensitivity Analysis
HF	Heat Flux
IVMR	In-Vessel Melt Retention
LP	Lower Plenum
MRVT	Minimum Remaining Vessel Thickness
PWR	Pressurised Water Reactor
RPV	Reactor Pressure Vessel
SA	Severe Accident
SMR	Small Modular Reactor
UaSA	Uncertainty and Sensitivity Analysis
UP	Uncertain Parameter

ACKNOWLEDGMENTS

The collaboration with colleagues in SASPAM-SA WP4 is the basis for this paper. L. Carénini of ASNR has supported this work with valuable feedback on the SEPALOWE model of ASTEC and on early results. By making available and providing training for the SIMLAB tool for calculating Sobol' indices, R. Rossati and her colleagues of the European Commission's unit JRC.S.3 have helped adding this analysis to the paper.
This work was carried out in the context of the Horizon-EURATOM-funded project SASPAM-SA. The work reported in this paper has been entirely funded by direct EURATOM means of the European Commission's Joint Research Centre.

REFERENCES

1. E. Moiseenko, A. Filippov et al. "BEPU Evaluations in IVMR for VVERs: Melt Pool Behaviour and Thermomechanics of the Ablated Vessel". Best Estimate Plus Uncertainty International Conference (BEPU 2018), Lucca, Italy (2018).
2. L. Carénini et al., "IVMR modelling with transient effects during molten pool formation and stabilization – Outcomes from models' comparison performed in the IAEA CRP J46002", Annals of Nuclear Energy, Volume 218 (2025). https://doi.org/10.1016/j.anucene.2025.111365 .
3. L. E. Herranz et al., "Major Achievements of the EC MUSA Project", Nuclear Technology (2025). https://doi.org/10.1080/00295450.2024.2444081.
4. S.T. Ghosh et al., "State-Of-the-Art Reactor Consequence Analyses project: Uncertainty Analyses for Station Blackout Scenarios", Nucl. Technol., 207, pp. 441–451 (2021), DOI: https://doi.org/10.1080/00295450.2021.1875737 .
5. F. Mascari et al., "Horizon-EURATOM SASPAM-SA project: main ideas and first outcomes", Proceedings of IAEA "International Conference on Small Modular Reactors and their Applications", 21–25 October 2024, Vienna, Austria (2024).
6. S. Brumm et al., "Uncertainty Quantification for Severe-Accident Reactor Modelling: Set-up and First Results of the Horizon-2020 Project MUSA", Ann. Nucl. Energy, 191, 109919 (2023); https://doi.org/10.1016/j.anucene.2023.109919.
7. I.M. Sobol', "Sensitivity estimates for nonlinear mathematical models", Math. Mod. and Comput. Exp., Vol 1, 407-414 (1993).
8. https://web.jrc.ec.europa.eu/rapps/pub/simlab
9. Q. Shao et al., "Bayesian sparse polynomial chaos expansion for global sensitivity analysis", Comput. Methods Appl. Mech. Engrg. 318 (2017).
10. F. Fichot and L. Carénini. "Some consequences of material interactions for in-vessel melt retention". In ICAPP Conference, Nice, France (2015).
11. L. Carénini and F. Fichot, "The impact of transient behavior of corium in the lower head of a reactor vessel for in-vessel melt retention strategies", Proceedings of ICONE24 conference, Charlotte, USA (2016).

European Commission

Investigation of IVMR by a stand-alone Lower Plenum ASTEC model of iPWR design#1 in the SASPAM-SA project

Stephan Brumm, JRC

ERMSAR 2026, 19-5-2026, #181

Content

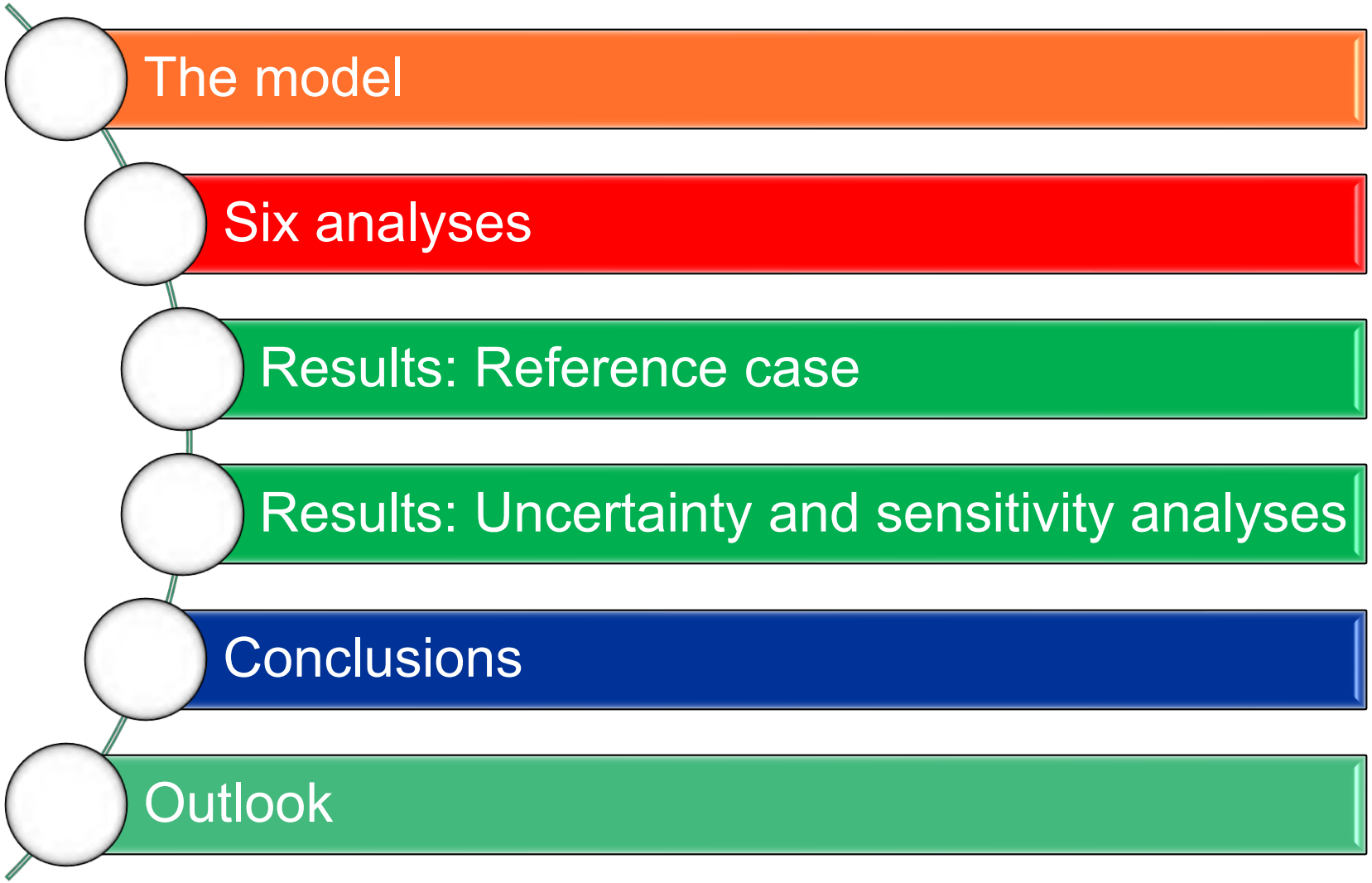
The model
Six analyses
Results: Reference case
Results: Uncertainty and sensitivity analyses
Conclusions
Outlook

The stand-alone model

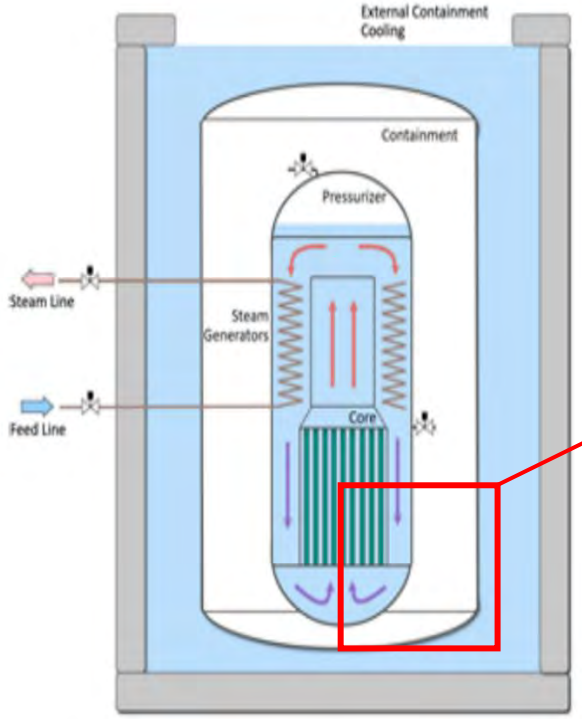

Integrated Pressurized Water Reactor design #1

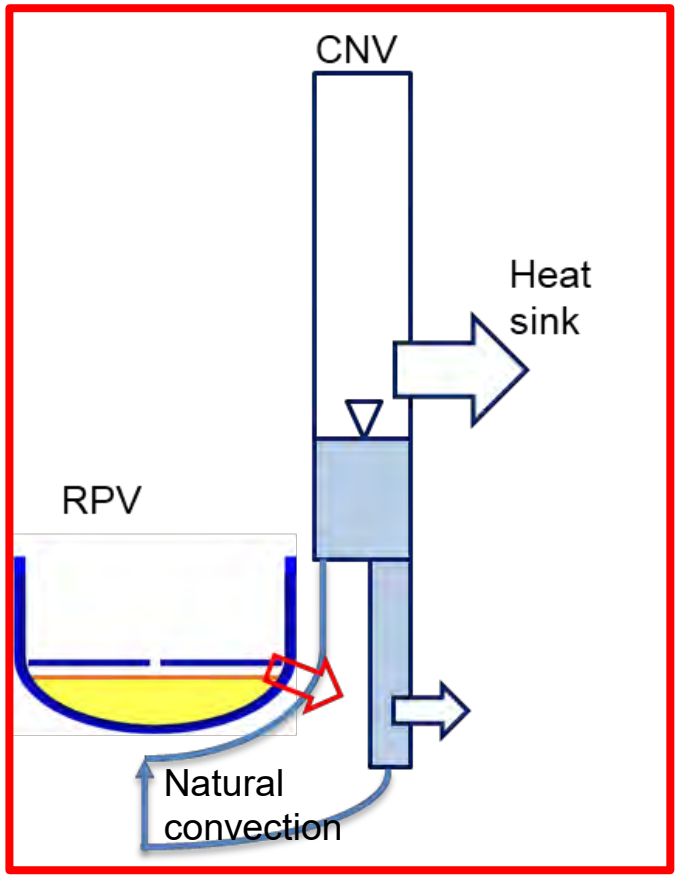

Severe Accident. Model of molten core in the Lower Plenum (yellow) and natural convection cooling

- ASTEC V3.1.2
- Initial conditions: material masses in the two-layered molten pool; residual power; thermal hydraulics
- Residual heat melts the wall of the reactor pressure vessel
- Investigate how sensitive the key output is to uncertain input parameters
- Key output: residual vessel thickness

Six analyses

- SASPAM-SA's objective to demonstrate capability and/or shortcomings of SA codes when applied to SMR
- Run different SA codes with an agreed set of inputs

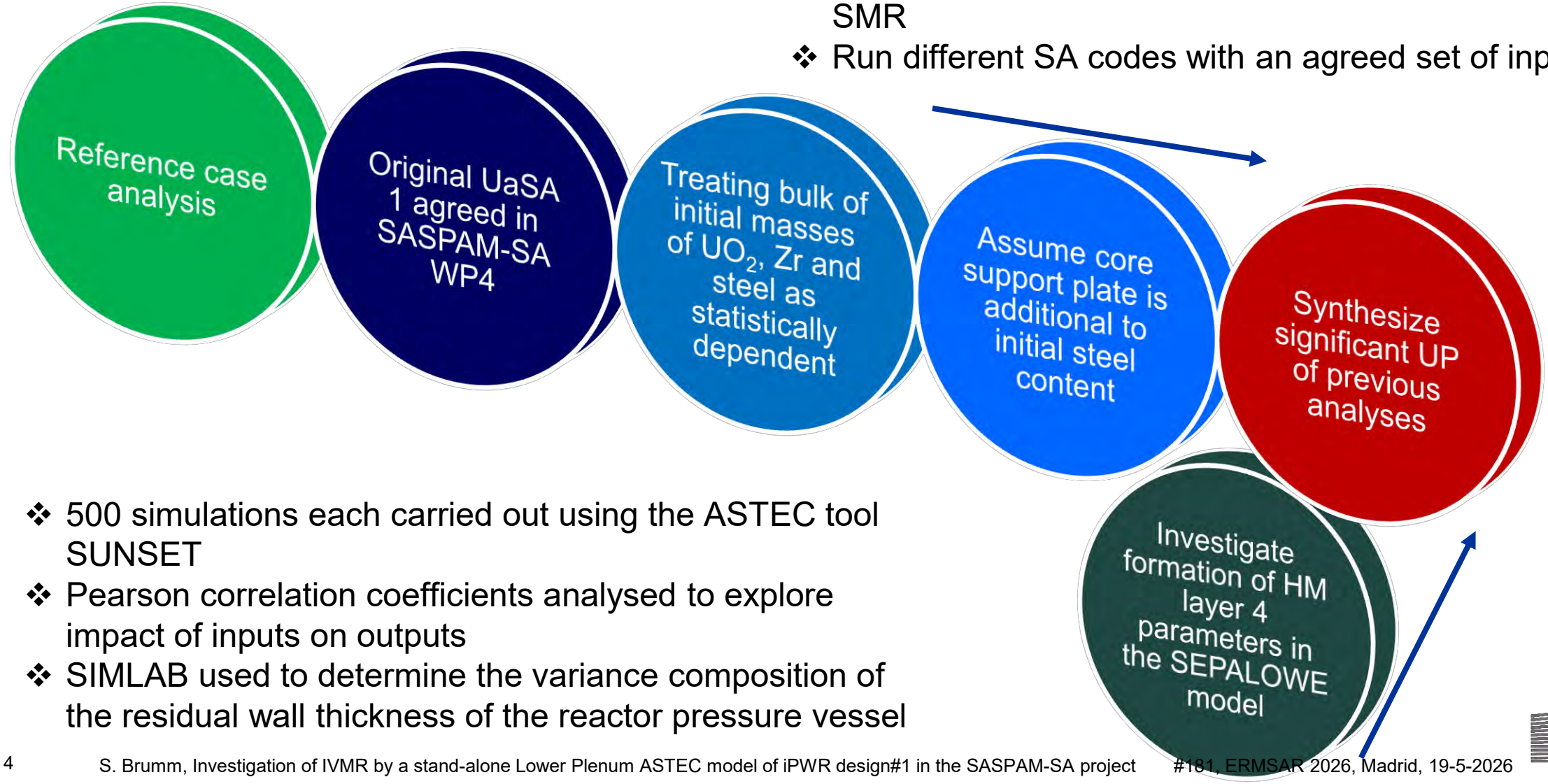

- 500 simulations each carried out using the ASTEC tool SUNSET
- Pearson correlation coefficients analysed to explore impact of inputs on outputs
- SIMLAB used to determine the variance composition of the residual wall thickness of the reactor pressure vessel

SAPAM-SA WP4: uncertain inputs and output

Parameter	Variable name	Reference/ Best est.	Minimum	Maximum
Geometry				
Thickness of vessel (cm)	THI_VES0	0.12	0.10	0.14
Degradation				
Mass of UO2 in LP (t)	mmm0	9.	4.5	9.
Mass of Zr in LP (t) (U/Zr ratio is constant)	dmmzr0	2.5	0.9	2.5
Zr fraction oxidized in LP	rzrox0	0.5	0.3	0.8
Mass of Steel (t) in LP	dmmu0	4.0	1.5	4.5
Power per unit mass of UO2 (W/kg)	powe_i0	190	178	200
Containment				
Pressure (bar)	pCNV0	12	11	13
Material properties				
Oxide conductivity (W/K/m)	condOX0	2	1	3
Molten steel conductivity (W/K/m)	condST0	20	20	40
Vessel conductivity (W/K/m)	condVES0	30	25	35
Metal emissivity (-)	emissliq	0.5	0.2	0.8
Material properties				
Temperature UHS [K]	tpool	323.15	303.15	343.15
HTC to UHS [W/m2/K]	htcpool	1000	1000	2000
ERVC thickness factor	ETF	1.0	0.8	1.2
Initial temperature of core support plate [K]	Tplt	873.	560.	1100.

Output:
Residual thickness of the Reactor Pressure Vessel

Reference case

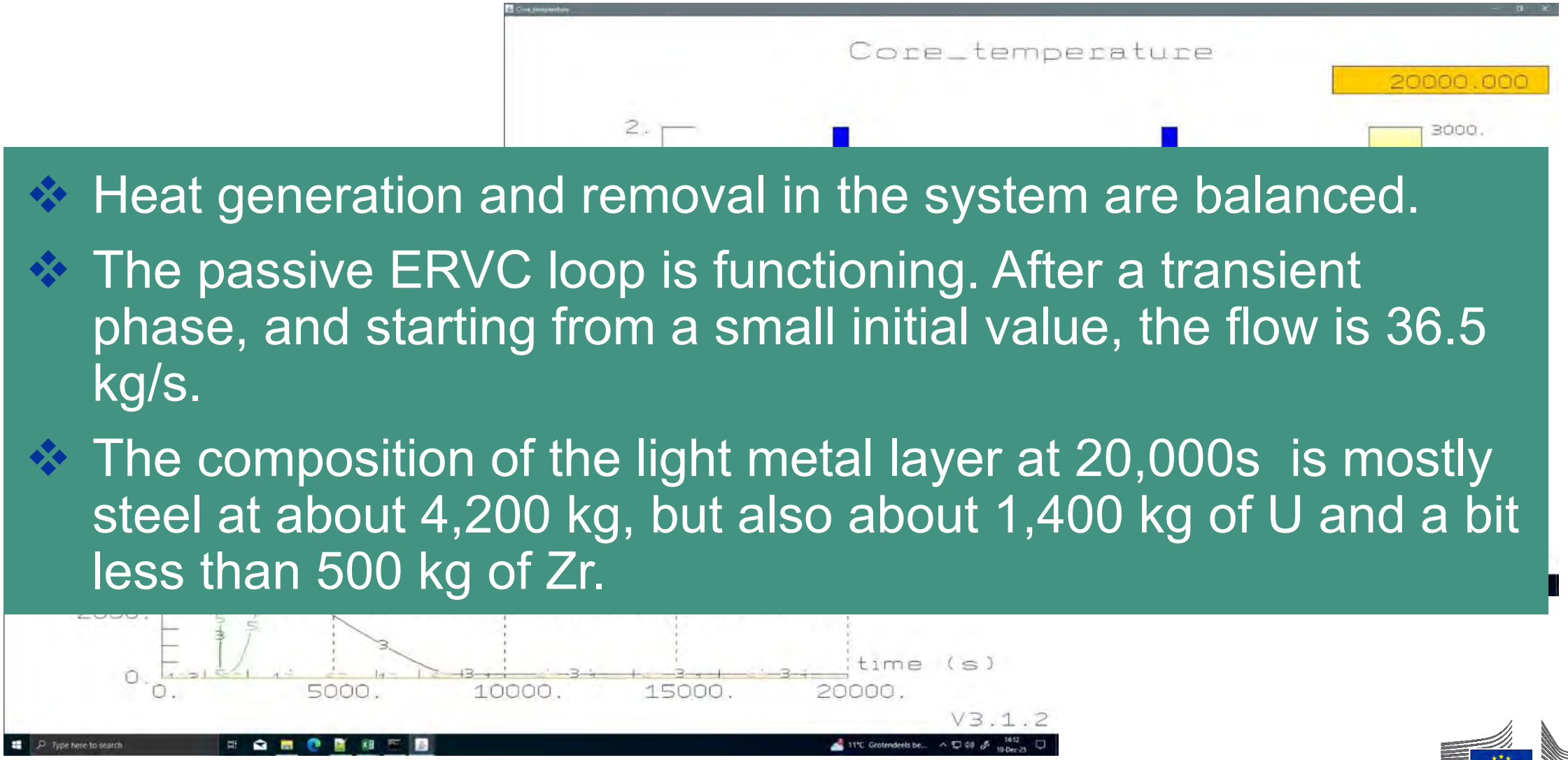

- Heat generation and removal in the system are balanced.
- The passive ERVC loop is functioning. After a transient phase, and starting from a small initial value, the flow is 36.5 kg/s.
- The composition of the light metal layer at 20,000s is mostly steel at about 4,200 kg, but also about 1,400 kg of U and a bit less than 500 kg of Zr.

UaSA simulation: horsehair diagram

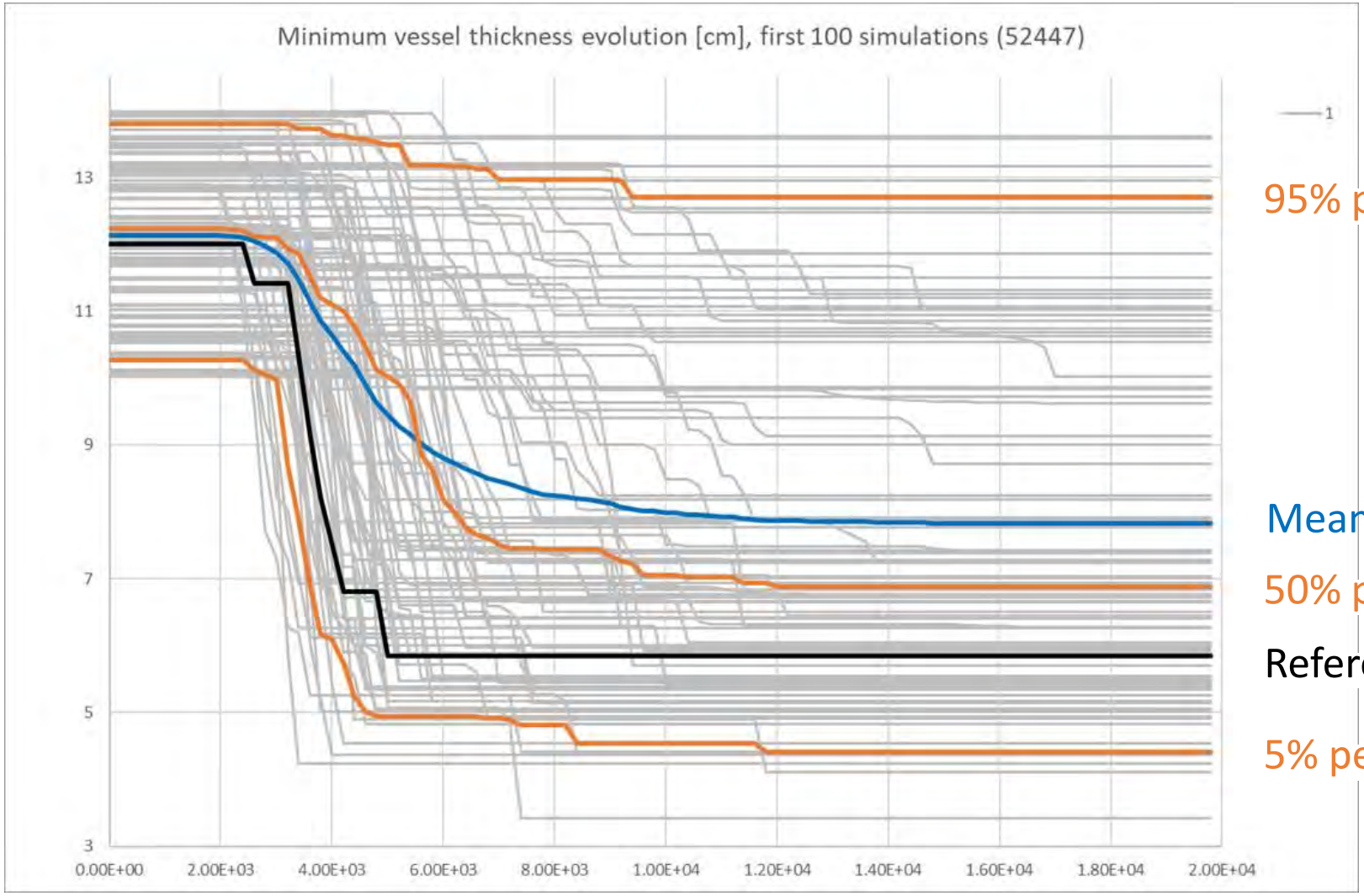

UaSA simulation: correlation coefficients

Key outputs →

Uncertain inputs ↓

	vessthimin	crstox	Pex2	Pex3	Prad3	HMAG1	HMAG2	HMAG3	RHO1	RHO2	RHO3	3rd_layer
thives0	0.194	0.063	0.065	-0.031	0.058	-0.073	0.001	0.075	-0.008	0.017	-0.053	-0.006
mmm0	-0.651	-0.601	-0.749	-0.477	-0.282	-0.153	0.608	0.034	0.001	0.344	0.166	-0.102
mmzr0	0.088	0.069	0.022	0.315	-0.178	0.459	-0.083	-0.211	0.226	-0.851	-0.029	0.357
rzrox0	-0.038	-0.026	-0.247	-0.191	0.123	-0.466	0.567	0.083	-0.426	-0.211	-0.704	-0.430
mmu0	0.324	0.009	-0.086	-0.307	0.220	-0.406	0.313	0.815	-0.621	-0.093	-0.290	-0.580
powe_i0	-0.081	-0.100	-0.115	-0.075	-0.048	0.007	0.012	0.024	0.012	-0.083	-0.065	0.021
pCNV0	-0.044	-0.016	-0.026	-0.045	0.013	-0.029	0.047	-0.002	-0.009	-0.046	0.051	-0.023
condox0	0.075	0.424	-0.052	0.016	0.100	-0.041	-0.013	0.020	-0.029	0.063	-0.023	-0.012
condst0	-0.046	0.309	0.274	-0.116	0.054	0.015	-0.066	0.008	0.027	0.132	0.034	0.023
condves0	0.245	0.015	-0.001	0.009	0.056	0.029	-0.020	-0.047	0.041	0.012	0.021	0.032
emissliq	0.304	-0.012	-0.037	0.225	-0.295	-0.015	0.021	0.023	-0.036	-0.033	0.027	-0.030
tpool	0.057	0.080	0.021	0.060	-0.040	-0.031	0.001	-0.007	-0.044	0.023	0.020	-0.050
htcpool	-0.040	0.016	-0.013	-0.043	0.074	-0.039	0.002	0.028	0.028	0.047	0.016	0.013
Tplt	0.087	-0.001	0.004	0.048	-0.045	0.010	0.004	-0.007	-0.037	0.008	-0.025	-0.045
etf	-0.026	-0.064	-0.080	-0.023	-0.011	-0.068	0.077	0.007	-0.066	-0.027	0.009	-0.077

UaSA simulation: Global Sensitivity Analysis by Sobol' indices

« The variance of the minimum residual vessel thickness at 20,000 s is made up by … »

Variances			Covariances		
S_2	mmm0	0.44	$S_{3,4,5}$	mmzr0, rzrox0, mmu0	0.02
S_5	mmu0	0.11	$S_{3,5}$	mmzr0, mmu0	0.03
S_{11}	emissliq	0.08	$S_{4,5}$	rzrox0, mmu0	0.01
S_{10}	condves0	0.06			
S_1	thives0	0.03	Relative Training Error		0.16098
S_3	mmzr0	0.01	Sample Variance of vessthimin		7.135

SIMLAB tool: https://web.jrc.ec.europa.eu/rapps/pub/simlab

Algorithm: Shao et al., "Bayesian sparse polynomial chaos expansion for global sensitivity analysis"

Conclusions

- Reference case: the model meets expectations
- Scenario-specific:
  - Initial mass of UO_2, and thus residual heat, is the largest impact on vessel ablation
  - Initial mass of steel affects strongly the probability of a heavy metal layer (neg. correlation) and, indirectly, vessel ablation (pos. correlation)
  - Compared to initial conditions, the overall sensitivity of HM layer to SEPALOWE model parameters is not significant
- Evaluation:
  - Variance attribution (Sobol' indices) provides a detailed picture of how uncertain inputs impact the uncertainty of the target variable
  - Covariances add to the picture
  - Correlation coefficients support the plausibility check by predicting negative/positive correlation
- General:
  - ASTEC is capable of simulating IVMR in SMR
  - Validation of models more important for SMR than for large reactors needs to be explored

Outlook

- The stand-alone model relies on assumptions (i.c., b.c.) and simplifications; results will be more credible from a more complete model
- The large ASTEC iPWR #1 model by Tractebel, used in SASPAM-SA WP2, has been run as a best estimate case, with significant deviation from the stand-alone model
  - For comparison: t_0 = 0 s; t_{slump} = 24,000 s; t_{end} = 44,000 s
  - 10 - 15% of the core is not slumping into the LP
  - With volatile FP and non-slump accounted, the residual heat in the Corium pool is 73% of total
  - The core support plate is not melting after the Corium slump
  - The Corium pool consists of an oxide layer and a heavy metal layer
- While this comparison will be further explored, the first indication is that the stand-alone model initial conditions are very conservative

Fill in copyright information.

Thank you

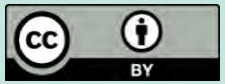

© European Union 2026

Unless otherwise noted the reuse of this presentation is authorised under the CC BY 4.0 license. For any use or reproduction of elements that are not owned by the EU, permission may need to be sought directly from the respective right holders.

Slide 3: iPWR #1 scheme, source: SASPAM-SA

The 12th European Review Meeting on Severe Accidents Research

May 18-22, 2026, Universidad Carlos III de Madrid, Madrid, Spain

TECHNICAL SESSION 5.2: HYDROGEN RISK AND CONTAINMENT BEHAVIOR

Chairs: S. Kelm (FZJ), G. Jiménez (Universidad Politécnica de Madrid)

ID092	**PARs for Hydrogen Measurement in Nuclear Containments in Severe Accidents** L. Gardner (CNL)	Paper Presentation
ID093	**Development of a database for PAR model validation based on THAI experiments and its application in the framework of the AMHYCO project** E.-A. Reinecke (FZJ)	Paper Presentation
ID069	**Fission product behavior and Source Term Impacts in Ex-Vessel Phase using THAI Test Data: the OECD/NEA THEMIS Project** K. Dieter (Becker Technologies GmbH)	Paper Presentation
ID078	**Development status of the flammability risk monitoring system in severe accidents** Y. Na (KAERI)	Paper Presentation

The 12h European Review Meeting on Severe Accident Research (ERMSAR2026) **Log Number: 092**
Madrid, Spain, May 18-22, 2026

PARS FOR HYDROGEN MEASUREMENT IN NUCLEAR CONTAINMENTS IN SEVERE ACCIDENTS

Gardner L* and Ibeh B
Canadian Nuclear Laboratories
Corresponding Address
lee.gardner@cnl.ca;blessing.ibeh@cnl.ca

ABSTRACT

Monitoring nuclear containment atmosphere in severe accidents is essential for accident management. However, most nuclear plants do not have hydrogen measurement capabilities because the methods for hydrogen detection are limited and have constraints due to power requirements. Any hydrogen measurement technology adopted for use in the containment must meet certain sensing, certification/regulatory, environmental, and power requirements. Passive autocatalytic recombiners (PARs) have been installed in many reactor containments where they mitigate hydrogen explosion risks by utilizing catalysts to facilitate the recombination reaction between hydrogen and oxygen (from air). PARs are not only optimally located in the containment area, where hydrogen may be present during an accident, but are also qualified as a safety system in containments. In addition, PARs can simplify the approach to hydrogen sensing in containment, since they do not need gas sampling lines and have the potential to not require containment boundary penetrations or power. When the PAR is activated, there is a quantitative relationship between the catalyst temperature and the hydrogen concentration in the environment. To determine the local hydrogen concentration, the PAR catalyst temperature can be measured and transmitted wirelessly outside of the containment building. This study outlines the use of PARs as a reliable approach to hydrogen concentration measurements in post-accident containments. The details of the proof-of-concept experiments used for this study are presented. Its applicability and operating range are also discussed.

KEYWORDS
PAR, hydrogen, recombiner, sensor, catalyst

1. INTRODUCTION

The accumulation of hydrogen (H_2) within the reactor containment building at nuclear power plants (NPPs) during a severe accident has long been a concern for the nuclear industry given the potential for the formation of combustible H_2-air mixtures that can lead to explosions. Such explosions can cause severe damage to critical equipment and the reactor containment building itself, resulting in the potential for release of fission products into the environment. It is, therefore, important for NPPs to be able to measure and monitor H_2 concentration within the reactor containment building during accidents [1]. A suitable H_2 measurement technique can provide real time data on H_2 concentrations and its distribution giving operators important insight that not only enhances the safe operation of NPPs, but also their ability to make critical accident management decisions should a severe accident scenario unfold.

In Canada, the H_2 concentration in the reactor containment building is only measured at Point Lepreau Nuclear Generating Station (PNGS), where gas is drawn from a single sample location to a remote analyzing cabinet outside the containment boundary [2]. Outside of Canada, similar methods to PNGS are employed

for H_2 detection, as well as other technologies including catalytic bead-type sensors and electrochemical sensors. The shortcomings of these measurement approaches are their limited numbers in reactor containment buildings potentially giving a false representation of the H_2 distribution, and their power requirements, which will be lost if a station blackout scenario occurs [2].

Numerous H_2 sensing/measurement technologies have been deployed in non-nuclear applications; however, it is unknown whether they can be successfully deployed in a reactor containment building to accurately measure H_2 concentrations. To effectively function in the post-accident atmosphere, these H_2 measuring technologies must be able to operate under high temperature (i.e., >100 °C) and high humidity, be resistant to radiation and have low drift [1]. In addition, the need to power the sensor will add additional requirements to ensure the operation during all situations, including station blackout.

Passive autocatalytic recombiners (PARs) are already present in many reactor containment buildings where they serve to mitigate H_2 explosion risk should an accident unfold. PARs are not only strategically located where H_2 may be present but also qualified for operation in NPPs. Numerous PARs (i.e., 15 to 30) are installed in CANDU reactor containment buildings. So, if utilized as a network of H_2 sensors, they can provide a reasonable estimate of the H_2 distribution, compared to, for example, a single measurement location currently employed in some NPPs. PARs are radiation resistant/tolerant and utilize noble metals to catalyse the exothermic reaction between H_2 and air (oxygen, O_2). It is the exothermic nature of the recombination reaction between H_2 and O_2 that results in an increase in catalyst temperature that can be correlated with H_2 concentration. This relationship has formed the basis of the concept of the present work to use the PAR as a H_2 sensing/measuring device in NPPs.

There are, however, two main challenges that must be addressed before the PAR can be used as a H_2 measurement device in reactor containment buildings. The first is to develop a sufficiently accurate and reliable correlation between PAR catalyst temperature and H_2 concentration. The second is to establish a reliable method of transmitting the acquired catalyst temperature signal out of the reactor containment building. This difficulty arises from the limitations of using powered technologies in reactor containment buildings and the challenge of transmitting a signal through the ~1 m thick concrete reactor containment building boundary. Once outside of the boundary, it is assumed that conventional means to transmit the signal can be used.

This paper will introduce the conventional methods used for H_2 measurement and discuss their limitations, and present experimental results from proof of concept and concept development testing to demonstrate the potential for the application of the PAR as a H_2 sensor.

2. BACKGROUND

2.1. Hydrogen measurement in containment

An assessment of commercially available H_2 sensor technologies was performed to investigate their suitability for deployment in reactor containment buildings of NPPs. Such H_2 measurement devices/technologies must meet sensing, certification/regulatory, environmental, and power requirements. Additional considerations may include operational lifetime, reliability, reproducibility, and any unique/specific requirements as may be necessary for a particular utility or reactor containment building within which they will be deployed.

Thermal conductivity, electrochemical, resistance-based (e.g., catalytic bead sensors), optical and work function-based sensing technologies were reviewed for use in nuclear containment buildings. Key factors considered in the assessment of H_2 sensors for any given scenario (nuclear or non-nuclear) have been classified into two broad categories, namely, deployment matrices and operational matrices [4]. Deployment matrices are typically one-time considerations that include capital costs, control wiring, electronic interface, cost of installation, commercial maturity, placement, physical size and power requirements. Operational

metrics pertain to on-going and recurring requirements that include calibration requirements, consumables, device to device repeatability, maintenance effects, mechanical stability, minimum analyte volume, operation lifetime, orientation effect and warm-up/start-up time [4].

Notwithstanding the abovementioned general requirements, an attempt to develop specific requirements for H_2 concentration measurement in CANDU containment buildings was made by assembling the range of conditions that the H_2 sensor may be exposed to during a severe accident. These conditions have been identified and grouped into the following specific requirements:

I. Sensing Requirements

It is imperative that the H_2 sensing device is able to have a range of measurement with reasonable accuracy that includes the lower flammability limit (LFL) of H_2-in-air (4 vol.%). The desired range of measurement for H_2 extends to the limit that the PAR could induce a H_2 ignition. Thus, the maximum H_2 concentration is 7 vol.% (in dry conditions) with an accuracy to within ± 0.5 vol.% [1][5].

II. Certification/Regulatory Requirements

The H_2 sensing device must meet the requirements stipulated in relevant codes and standards (e.g., CSA N290.3 [6] and N290.6 [7]) related to control systems, safety systems, instrumentation and requirements for monitoring and display of plant status in the event of a severe accident.

III. Environmental Requirements

H_2 sensors should be robust enough to withstand chemical interference, presence of poisons and radiation that may be present in the containment building environment. For radiation tolerance, the sensor must withstand the presence of gamma, beta and neutron radiation. For chemical interference, the sensor must retain functionality in the presence of steam (100% relative humidity/RH), H_2, helium, O_2 (to very low levels) and fission products. The sensor must be able to be operational at ambient temperatures up to 200 °C and at high temperatures up to 500 °C for very short periods of time (e.g., potentially from H_2 combustion). The presence of carbon monoxide is not considered as its release in severe accident scenarios for CANDU reactors is precluded by in-vessel retention.

IV. Power Requirements

The power requirements should be low enough to be supplied by technologies such as power harvesting in the containment or by batteries that can last from installation to the next routine shut down (during which time the battery can then be replaced).

V. Others

Operational lifetime, reliability, reproducibility and any other specific requirement imposed by the reactor containment that will be hosting the H_2 sensor must be considered.

A summary of the desirable range of values for some of the key parameters is presented in Table I. It is worth mentioning that although the commercially available H_2 sensors/detectors find applications in a wide range of industries and circumstances where high accuracy is required, the review of their methods of operation and limitations indicate that most of them would not be suitable for deployment in the reactor containment building of a NPP without compromising requirements or significant modifications that may end up impacting their functionality when all the factors for suitability are considered. Most commonly, the power requirements for the H_2 sensing technologies limit their use in scenarios where a station is without power. Furthermore, other common issues found with deploying commercial H_2 sensors to nuclear containment buildings include sensitivity toward high humidity and radiation environments.

Table I. Summary of sensor parameters and range of requirements.

Parameter/ Variable	Range	Comments	Ref.
Ambient Temp.	15 – 300 °C	Should not lose functionality from prolonged exposure at max. temp.	[2]
Transient Temp.	Up to 500 °C	Should not lose functionality from brief exposure to max. temp.	[2]
H_2 Conc.	Up to 10 vol.%	Must measure up to 10 vol.% (in dry conditions) with an error of ±0.5 vol.% (to avoid detonation range)	[1]
O_2 Conc.	0 - 20 vol.%	If sensor requires O_2 to function, it must also function at low O_2 vol.% (i.e., < 1 vol.%)	[1]
Steam	Up to 100 vol.%	In the presence of inert gas and diminishing O_2	[1]
Pressure	Up to 400 kPa(g)	Must retain functionality up to design pressure of containment	[2]
Radiation (total integrated dose)	20 Mrad	Presence of beta/gamma/neutron radiation - 1000 krad/h for 200 h	[8]
Energy	Capable of operating for extended periods	Battery or energy harvesting	[1]
Lifetime	>2 years	Based on the outage frequency	
Accuracy	± 0.5%	Must retain high accuracy within measurement range	[1]
Response time	≤ 2 s	Lag between temp. detection transmission and receiving must be small	[1]

2.2. PAR as a hydrogen sensor: adoptability and technical feasibility

PARs facilitate the catalytic oxidation of H_2 to water. The catalysts, as well as the appropriate design of PARs, have been extensively investigated with numerous publications available in open literature. While it is not the aim of this paper to focus on the intended function of PARs, it is important to point out the key attributes that have made this technology a key presence in the containment structures of NPPs worldwide.

The general attributes of PARs that are fundamental to their use as a H_2 sensor include their optimal locations in the containment building for contact with H_2 in the event of an accident, their radiation resistance/tolerance, their qualification as a safety system in NPPs, and their operation without a power supply. Notwithstanding these attributes, PARs still require O_2 to function and contaminants like volatile organic compounds (VOCs) can impair its function if present in the containment. These VOCs may evolve into the containment atmosphere from insulation materials, paints or other organic materials (greases, solvents, oils, lubricants, etc.) that may be used during maintenance operations in NPPs.

The principle of the application of the PAR as a H_2 sensor is based on the relationship between catalyst temperature and H_2 concentration. It is well understood that the exothermic recombination reaction between H_2 and O_2 yield a measurable increase in catalyst temperature. In fact, for many experiments performed on PARs, based upon the H_2 concentration, the catalyst temperature is a predictable value that has been an indicator of whether the catalyst condition is acceptable, or the experiment is performed correctly. It is known that the PAR catalyst temperature increases with an increase in the H_2 concentration and PAR self-starts at low H_2 concentration (i.e., <2 vol.% H_2 in air) [5]. However, very little (if any) research has been conducted on using the PAR catalyst as a method to monitor H_2 concentration within containment and no publications in open literature have been found.

In addition, resistance-based H_2 sensors known as catalytic bead sensors use catalyst technology and the temperature rise of the catalyst to derive a H_2 concentration. Therefore, the catalyst temperature-H_2 concentration relationship is considered as a reliable method for H_2 concentration determination once the catalyst temperature is measured with some precision and accuracy. Furthermore, Liang et. al. [2] identified that PARs were instrumented with thermocouples to "inform on a tendency of H_2 production and H_2 concentrations inside the containment" in France and Japan. The fact that PARs are already installed in reactor containments and the numerous shortcomings of existing H_2 sensing technologies makes the use of PARs as a H_2 sensing technique an option worth investigating.

2.3. Methods for signal transmission

Two schemes to transmit the catalyst temperature signal out of the containment building were investigated. The first method is to run thermocouple wire directly from the PAR to and through the containment boundary. The advantage to this approach is that a thermocouple signal (over a relatively short distance) does not require power, as it is generated by the temperature difference typically between two metals. The biggest drawback is the need to be run wiring throughout containment and through the containment boundary. The second approach is to connect a thermocouple to a wireless transmitter in a location near the PAR, then receive the catalyst temperature signal outside the containment boundary with a wireless receiver unit. The main advantage to this scheme is the minimal use of wires, which eliminates any concerns regarding passing wires throughout the containment building and boundary. The major drawback is that this type of technology has not been widely qualified for use in NPPs. There is also the challenge of supplying adequate power to the wireless device.

3. PROOF OF CONCEPT/PRELIMINARY TESTING

3.1. PAR catalyst temperature versus hydrogen concentration

The surface temperature of the AECL PAR catalyst plate has consistently been monitored in a large portion of tests on the full-size PAR in the large-scale vented combustion test facility (LSVCTF) at CNL's Whiteshell Laboratories (WL). A description of the LSVCTF can be found elsewhere [5]. The catalyst plate located in the centre of the PAR has always been instrumented with three Type-K thermocouples, since it typically experiences the highest temperatures, with measurements taken at the horizontal centre of the plate in the top, middle and bottom sections. The method includes strapping the thermocouple to the plate by tack welding ribbons of stainless-steel shim stock to the catalyst plate. Prior to tack welding, the catalyst is sand blasted from the plate to allow a reliable thermal contact between the shim stock and the plate. Fig. 1 shows a photo of a PAR catalyst plate with the three thermocouples attached.

The H_2 concentration sampling and analysis approaches have not changed significantly over the duration of the full-scale PAR testing. The locations where the gas samples were taken have been consistent. H_2 concentration measurements are sequentially taken from four or five different locations within the LSVCTF combustion chamber. The standard gas sampling locations are at the inlet and outlet of the PAR, and at the top and middle locations in the room. For the current evaluation, only the PAR inlet sample location was investigated, since it has the strongest relationship to the PAR catalyst temperatures due to its proximity to the catalyst plates. The PAR inlet sample line was located in the centre of the PAR inlet, approximately 20 cm below the inlet of the PAR.

Figure 1. Photograph of a PAR catalyst plate instrumented with thermocouples at the top, middle and bottom locations when tested at the LSVCTF.

Forty-six (46) experiments were selected for the evaluation, after meeting a small set of criteria to ensure that the PAR geometry, catalyst material, facility instrumentation and experimental conditions were consistent. The experimental data were processed and plotted, and a second order/quadratic polynomial curve fit was applied to provide an equation that could be used to relate the three catalyst plate temperature locations with the PAR inlet H_2 concentration. A measured PAR catalyst plate temperature can therefore be correlated with the corresponding PAR inlet H_2 concentration by using the developed polynomial equation.

An analysis of the accuracy of the three catalyst plate temperatures was also performed to select the best location on the catalyst plate (top, middle or bottom) to use as a H_2 sensor. An error of 5% and 10% was applied to the full-scale H_2 concentration value. The full-scale value of 6.5 vol.% H_2 was used, since above this concentration the likelihood of the PAR inducing a H_2 ignition increases significantly. The error associated to each equation was 0.33 vol.% and 0.65 vol.% for 5% and 10% error, respectively. The figures for bottom, middle and top catalyst plate temperature measurement locations with the polynomial fit and errors are given in Fig. 2. Residual analysis of the curve fitting indicate that curves fit the data well (data not shown here).

Based on the information shown in Fig. 2., the temperature measurement location that has the least amount of error is at the top of the catalyst plate. Some of the data for the temperature measured at the top of the catalyst plate falls outside of the 10% error lines; however compared with the fit of the bottom and middle catalyst plate temperature measurements, the top has the least amount of data outside of the 10% error lines. Therefore, the catalyst temperature measurement at the top of the catalyst plate was selected as the measurement location moving forward.

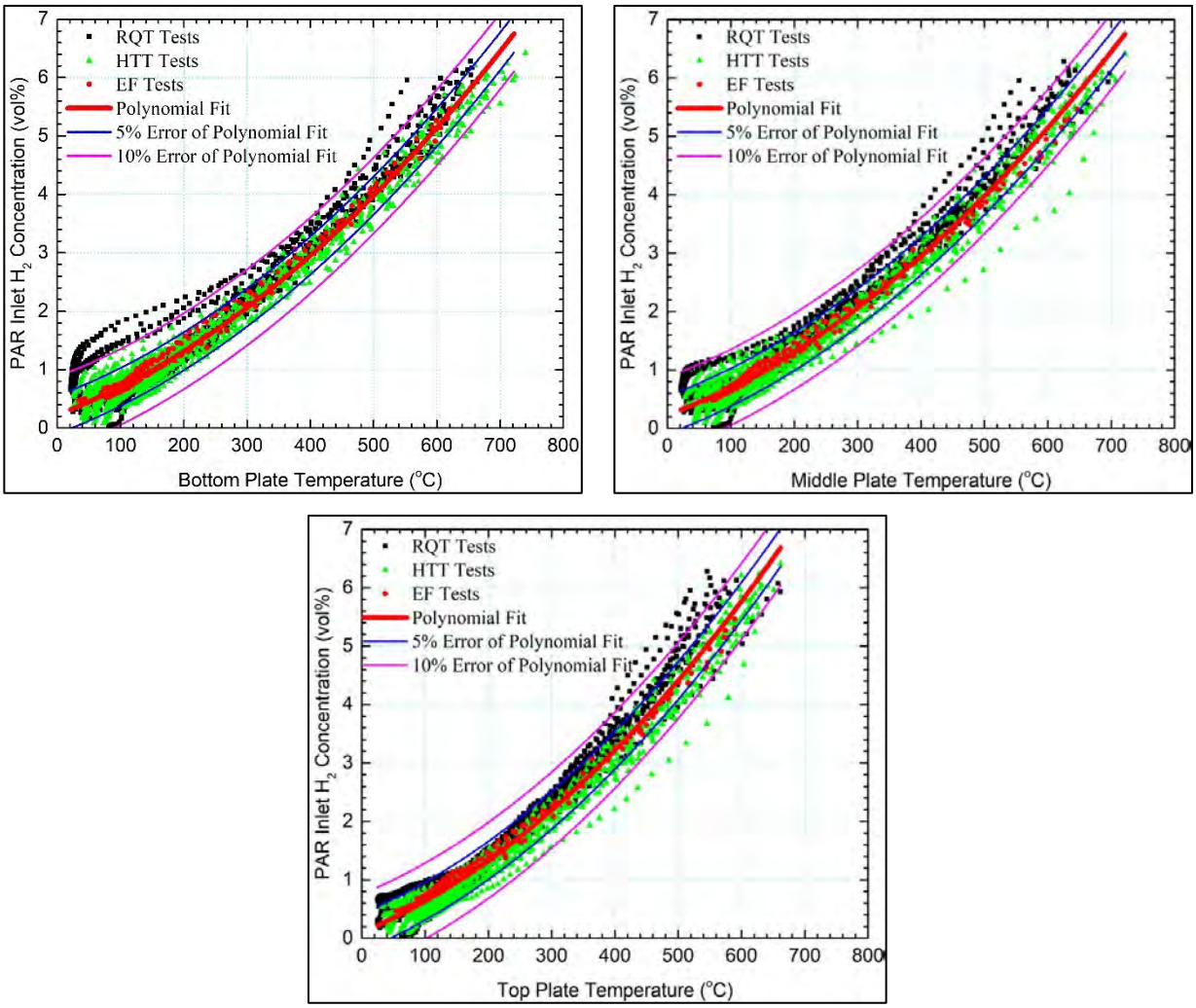

Figure 2. Data of inlet H_2 concentration vs. bottom (top left), middle (top right) and top (bottom left) catalyst plate temperatures with 2nd order polynomial fit and 5% and 10% error applied to the polynomial.

3.2. Wireless signal transmission

Wireless sensor networks are feasible options for monitoring various equipment or environment conditions in NPPs. They have the main advantages of low cost and high flexibility when compared to wired networks. Wireless sensor nodes are mostly powered by chemical batteries with fixed energy densities and replacing depleted batteries frequently is a shortcoming for its (wireless) adoption. Usually, a wireless sensor network consumes a lot of power to function while in continuous active mode, which shortens the battery and sensor lives significantly. To decrease the power consumption, wireless sensor networks can be programmed so that they can *wake-up* periodically for the transmissions and stay in *sleeping* mode between transmissions. Moreover, a low power consumption of a wireless sensor node also enables the use of conventional batteries with minimum power management for long-term operation.

An industrial wireless high temperature sensor network tool was purchased and used to validate the use of a wireless sensor network to monitor the PAR catalyst plate temperatures reliably in the reactor containment building. This wireless sensor network was selected because of its unique features, including long

communication range and ability to sense high temperatures (i.e., use of Type K thermocouples). The system consists of a transmitter, receiver and Labview-based software to adjust the sensor parameters and record the temperature data. The transmitter and receiver form a wireless sensor network for remote temperature sensing governed by a low power operation DigiMesh protocol. Each module has a Radio Frequency (RF) device and an adapter board enclosed in a polycarbonate box with an external RF antenna of 2.1 dBi (dBi is the amount of focus applied by an antenna with respect to an Isotropic Radiator). With polycarbonate enclosures, both modules have an operating temperature range of -20 to +85 °C.

The wireless transmitter is powered by four AA batteries and has a Type K thermocouple connector next to the RF antenna. The transmitter can provide measurements for temperatures up to 980 °C with an accuracy of ±1.1 °C. The RF device within the transmitter has a power efficient sleeping mode and can deliver up to 500,000 transmissions from four AA batteries. The user can also configure its sleeping mode by changing the transmission frequency which can increase the battery life for up to 10 years. The receiver module is a wireless-to-USB modem that connects to the computer through USB for data processing and its RF device can be powered using an external power supply (5 V to 32 VDC). With on-board RF antennas, the RF devices in the modules have a 3.2 km of line-of-sight communication range that can be increased up to 45 km using high gain antennas.

3.2.1. Power consumption

An important factor in using wireless sensing networks in reactor containment buildings is the power requirements for such networks and how such power is to be provided. To verify the power consumption of the wireless transmitter in all its possible states, it was necessary to perform a real time power consumption study on the wireless transmitter when it performs remote temperature sensing at given program settings. The information gained can also be useful to run the wireless transmitter with an optimized program to achieve the desired battery life.

The power consumption analysis with two AA batteries found that it is unable to power the wireless transmitter for the period of time (years) that is required for an NPP. Since it consumes only a few milliwatts less power in the sleep mode compared to the active mode, the analysis estimated that the transmitter would not last more than a month. Nonetheless, the power requirement (~75 mW) of the active mode is quite low given that the PAR on its own does not require power. When the power requirement for wireless transmission is compared with the power requirements of other H_2 sensing technologies [1], it is more feasible to adopt this approach as a method for measuring H_2 concentration in containment.

Further effort is required toward modifying the firmware of the RF device to set it at the lowest possible power consumption in sleep. Further analysis will be performed to determine the power consumption at the lowest power level, which is expected to decrease the power consumption from milliwatts to microwatts when the wireless transmitter is in sleep mode. An evaluation will also be performed to determine the lifetime of the battery at the lowest power setting at a range of transmission frequencies. An alternative option to this is to use more batteries to provide more power to the transmitter.

3.2.2. Wireless transmission

The Hydrogen Safety Test Facility (HSTF) at Chalk River Laboratories (CRL), described in Ref. [9], was used to determine if a thermocouple signal could be wirelessly transmitted through a significant boundary (e.g., vessel and concrete wall). The HSTF spherical test vessel has a carbon steel wall thickness of 12.7 mm (0.5 inches), and the walls to the laboratory are approximately 1 m thick concrete, which are considered to be representative of the inner liner and walls of the containment building.

The wireless transmitter was attached to the inside wall of the HSTF. The receiver module of the wireless sensor network was coupled to a laptop equipped with the LabVIEW software and placed outside the lab

concentre wall, approximately 5 m away from the sealed HSTF vessel. The experiment was performed at dry conditions (no steam was used to alter the relative humidity). Three catalysts coupons of 4 cm by 6 cm were installed in a scaled PAR housing. Two thermocouples (Type K) were attached to the middle catalyst coupon, one feeding the data acquisition system and the other feeding the wireless transmitter.

Fig. 3 shows the results from the experiment, demonstrating that both catalyst temperature measurements are in excellent agreement. Fig. 3 also shows an excellent match between the hydrogen concentration and catalyst temperature. The test demonstrated that it is possible to transmit catalyst plate temperature through a 12.7 mm thick carbon steel and approximately 1 m thick concrete boundary wirelessly to a receiver.

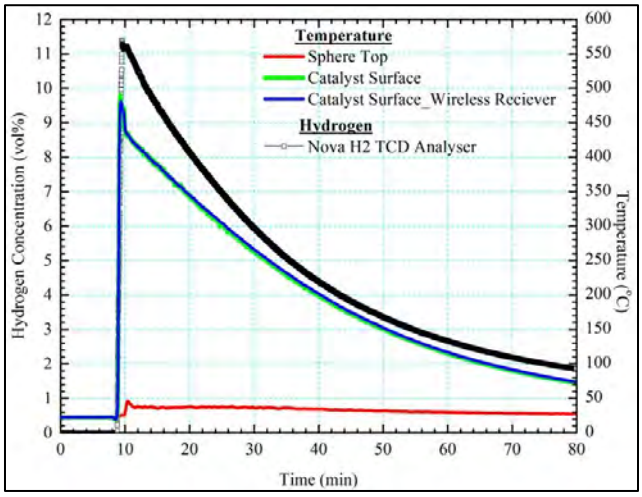

Figure 3. Temperature (wireless and wired data acquisition) and H_2 concentration profile for PAR experiment through metal and concrete boundary.

4. ADVANCED TESTING

After experimentally establishing the potential use of PAR as a H_2 sensor, the next step was to ensure that such use of PARs (and relevant accessories like transmitters and suitable power sources) can meet the requirements for deployment into CANDU containment. A series of tests were performed to experimentally validate the use of PARs together with a transmitting device for H_2 sensing in containment, such that it retains functionality under same qualification requirements already met by the AECL PAR. A summary of the results from the tests are provided in Table II and discussed in the Sections 4.1 to 4.6.

Table II. Summary of results comparing PAR as a H_2 sensor versus qualification requirements.

Requirements		Test Results	
Parameter/ Variable	**Range**	**(Pass / Fail, or successfully tested range)**	**Comments**
Ambient Temp.	15 – 150 °C	Partial Pass	Tests covered up to 100 °C. Modifications needed to transmitter housing and further testing to 150 °C for extended periods
Transient Temp.	Up to 500 °C	Pass	
H_2 Conc.	0.6 - 10 vol.%	Partial Pass	PARs will measure H_2 up to ~7 - 8 vol.% when they will ignite H_2 and limit H_2 concentration in containment building to less than ~8 vol.%
O_2 Conc.	0.6 - 20 vol.%	Fail	The min. O_2 concentration identified is 0.6 vol% but is dependent on the H_2 concentration.
Steam	Up to 100 vol.%	Partial Pass	Accuracy is not affected by steam concentration. Environmental tests on the transmitter covered up to 55 vol.%. Further testing needed to cover up to 100 vol.% for extended periods
Pressure	Up to 250 kPag	Partial Pass	Transmitter passed transient pressure tests. Further tests needed to qualify transmitter under static pressure conditions
Radiation (total integrated dose)	20 Mrad	Fail	Modifications needed to transmitter housing to protect internal electronics from radiation or modify electronics to better handle radiation.
Energy	Capable of operating for extended periods	Not Tested	Modifications to firmware and analysis needed to ensure the transmitter can operate long term without replacing batteries or additional batteries
Lifetime	≥ 2 years	Not Tested	
Accuracy	± 0.5%	Not Tested	
Response time	≤ 2 s	Fail	The PAR as a H_2 sensor response time was found to range from 1 - 2 min

4.1. High ambient temperature

The wireless temperature transmitter was assessed for high temperature (100 °C) for extended periods of time (days). This parameter is to ensure that the transmitter can survive the containment building post-accident ambient temperature.

Originally, a value of 150 °C was planned for the exposures to cover the envelope of containment building temperatures in accident scenarios; however, standard lithium batteries (such as, Energizer Ultimate Lithium Batteries) have a maximum temperature rating of 60 °C. Thus, alternative batteries with an extended temperature range (Tadiran TLH-5903 Lithium Batteries) were used in the wireless temperature transmitter that have a maximum temperature rating of 125 °C. Due to these limitations, the wireless transmitter was exposed to 100 °C, so that the maximum temperature of the battery was not exceeded. It should be noted that the high temperature batteries were hard wired to the wireless temperature transmitter because of the design of the high temperature batteries.

Exposures were performed by installing the transmitter in an oven and operating the oven for about 8 h per day. The exposure was performed this way to observe the wireless transmitter and prevent any fires or damage to the oven. The wireless transmitter was exposed to 100 °C in the oven for 11 days and a total of 65.5 hours. The transmitter remained functional throughout the exposure period with no physical or functional degradation found.

A method to expose the wireless transmitter to higher ambient temperatures (e.g., 150 °C), but not expose the battery to such temperatures, could be to insulate the transmitter housing. However, the heat generated by the electronics would also need to be considered before insulating the housing to prevent heating the transmitter from the inside. In general, the PAR as a H_2 sensor has come close to meeting the ambient temperature parameter identified in Table III without making significant modifications to the transmitter housing.

4.2. Transient temperature and pressure

The wireless temperature transmitter was installed inside the HSTF during H_2 combustion tests. In the experiment the transmitter was exposed to a brief pressure transient with an overpressure greater than 100 kPa. High frequency temperature measurements were not made; however, it is expected that the temperature transient from the H_2 combustion was well above 300 °C. Once the H_2 combustion was initiated, the temperature and pressure would instantaneously rise in the vessel, and decay over approximately one minute

These experiments provided a simulated H_2 combustion exposure to the wireless transmitter, and no damage or noticeable effects were found on the transmitter housing or electronics enclosed in the temperature transmitter. These results satisfy the requirements identified of the transient temperature parameter in Table II.

4.3. Steam exposure

4.3.1 Sensor Accuracy

The correlation developed between H_2 concentration and catalyst temperature included experimental data with initial RH ranging from 5 – 100% at 20 – 25 °C. In addition, data from more than 20 experiments conducted at steam concentrations ranging from 0.6 vol% to 44.7 vol% were reviewed to investigate if the steam concentration impacted the catalyst temperature measurement. It was found that the steam concentration does not impact the PAR catalyst temperature. Therefore, the accuracy of the H_2 concentration measurement by the PAR as a H_2 sensor is not affected by steam concentration.

4.3.2 Environmental

To investigate the effect of a high steam concentration on the wireless temperature transmitter, tests were performed to expose the wireless temperature transmitter to high temperature and high humidity. With the recombiner installed in the HSTF, H_2 was injected into the vessel with the expectation for the recombination reaction to increase the temperature and humidity inside the vessel. In these tests, H_2 was injected during two periods to allow the H_2 concentration to be consumed and the steam concentration and temperature in the vessel to increase. After the second H_2 injection, the humidity was above 70% for the entire 80 minutes and the ambient temperature increased from approximately 50 °C to approximately 85 °C near the end of the test. The RH decreased as a result of the ambient temperature increase. The steam concentration at the beginning of the test (e.g., 100% RH and 50 °C) was calculated to be approximately 12 vol.% and toward the end of the test (e.g., 70% RH and 85 °C) was approximately 55 vol.%. The wireless temperature

transmitter was exposed to the maximum steam concentration for approximately 30 – 40 minutes in each test.

In both tests the transmitter stopped functioning about midway through the test. Upon inspection after testing, it was found that the unit had failed due to a faulty battery connection in the transmitter. As a result, the transmitter did not have sufficient power to continue to operate. This issue occurred in both high steam concentration tests and is attributed to the higher temperature causing the battery connectors to loosen and cause a weak connection to the battery. This issue can be resolved by adding additional support or hard wiring the battery to the transmitter, as was done in the ambient temperature tests. In general, the wireless temperature transmitter could operate in the high humidity environment as the exposure to the steam was not found to damage the transmitter; however, the duration of the exposure to high humidity environment over the two tests was only about one hour. A longer-term exposure would provide further confidence in the capability of the system to operate in such environments.

The results of these experiments provide confidence and a step towards meeting the requirements identified in Table II; however, the wireless temperature transmitter does not fully satisfy the requirements identified in Table II regarding the steam parameter. More tests to expose the transmitter to higher steam concentrations and for longer durations are required to meet the identified requirement.

4.4. Radiation dose

The wireless temperature transmitter was exposed to gamma radiation in one of CNL's Nordion Gammacells with a cobalt-60 source providing a dose rate of 0.0291 Mrad/h. Three separate attempts were made where a wireless temperature transmitter was placed inside of the Gammacell and was briefly exposed to gamma radiation. In all three cases, upon checking the wireless temperature transmitter signal with the receiver, it was found that the transmitter was not responding. After the transmitter was removed from the Gammacell, an inspection on the wireless transmitter and batteries was performed. In all three cases it was found that the batteries remained functional, while the temperature transmitter had failed. It was assumed that the electrical components (semiconductor) had failed due to exposure to radiation from the Gammacell [10].

The three exposure time periods were 20.0, 287.3 and 24.2 hours. Therefore, a minimum exposure dose of 0.58 Mrad was received by the wireless temperature transmitters and resulted in a failure of the transmitter. This result indicated that the wireless transmitter has a very low tolerance for radiation exposure compared with the required dose of 37 Mrad identified in Table II.

A method to potentially prevent the internal electronics' exposure to radiation is to replace the transmitter housing with a housing made from a material that has radiation shielding properties, such as lead. The wireless signal could still be accessed through the antenna, which is threaded into the transmitter housing.

4.5. Oxygen concentration

Many tests were performed with the PAR under low O_2 conditions [11]. The limits of PAR operation were identified in these tests, where if the O_2 concentration is less than H_2 concentration, the PAR recombination rate becomes reduced. The reduction in recombination rate will impact the catalyst temperature, which in turn will impact the correlated H_2 concentration if the PAR was used as a H_2 sensor. Therefore, the minimum O_2 concentration for the PAR as a H_2 sensor is related to the H_2 concentration. The minimum H_2 concentration is about 0.6 vol%. Therefore, the minimum O_2 concentration is 0.6 vol%, but may be a greater value depending on the H_2 concentration.

The O_2 concentration parameter in Table I suggests that the sensor must operate at O_2 concentrations down to 0 vol.%. Thus, the PAR as a H_2 sensor does not meet this requirement. On the other hand, self-start was

found to be minimally affected by low O_2 concentration [11]. Thus, it can be assumed that the response time of the PAR as a H_2 sensor is not affected by low O_2 concentration.

4.6. Response time

Response time of the PAR is defined here as the time for the PAR to respond to the local H_2 concentration after it has self-started. This definition does not include the PAR self-start. This is an important distinction, as the self-start parameter is dependent on the degradation level of the catalyst, post-accident containment temperature and the local H_2 concentration. However, if it is assumed that the initial post-accident temperature or hydrogen concentration are high, or the catalyst degradation level is low, the PAR is expected to self-start with minimal delay as the hydrogen is released.

To assess the response time, tests performed at room conditions were reviewed to determine the response time of the PAR, which will provide insight into the PAR as a H_2 sensor. An example of the delay time for the PAR to start functioning and attain the temperature that would align with the catalyst plate temperature and the local H_2 concentration is provided in Fig. 4 for a test performed in the HSTF. H_2 is injected into the facility multiple times to determine the minimum H_2 concentration required for the PAR to self-start. After the fourth injection, at about 1.2 vol.% H_2, the PAR self-starts, and the response time of the PAR can be assessed. The final H_2 injection is complete, and the mixing fan is turned off at 46 minutes. The PAR catalyst temperature immediately begins to increase when the fans are turned off and reaches a 10 °C increase in about 1.5 minutes. The 10 °C increase signifies a notable rise in the hydrogen concentration and is considered a 'response' from the PAR. Data from large-scale tests in the LSVCTF was also reviewed and a similar range of data was found. Thus, for new or regenerated catalyst plates, a response time for the PAR as a H_2 sensor can be considered to range from 1 - 2 minutes, which is well above the required response time of less than 2 seconds identified in Table II.

To determine the response time of the PAR as a H_2 sensor more accurately, a series of tests could be performed where the wireless temperature transmitter and point-type H_2 sensors are installed in the HSTF. H_2 injections would then be performed to pre-selected H_2 concentrations. The test would then compare the response time of the PAR as a H_2 sensor against the point-type sensors.

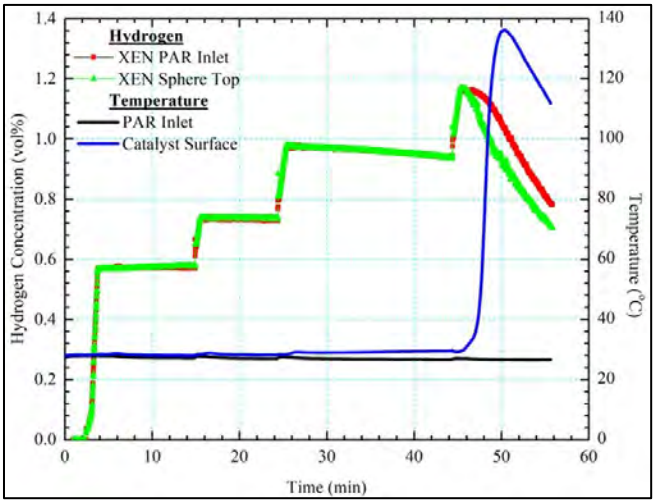

Figure 4. Self-start test demonstrating response time of PAR as a H_2 sensor.

5. SUMMARY

Many different approaches to measure H_2 in air are commercially available or in development for utilization for non-nuclear applications. As part of the review, it was determined that due to power requirements for commercially available H_2 sensors (i.e., > 1 Watt), and the power limitations in the reactor containment building (i.e., < 100 mW), the PAR that has been installed in NPPs for H_2 mitigation during an accident, has a very valuable complementary applicability as a H_2 sensor.

An empirical equation had been developed, relating the PAR catalyst plate temperature to the local H_2 concentration. This relationship can be utilized to estimate the local H_2 concentration in the reactor containment building during an accident requiring transmission of the temperature signal outside of the reactor containment building either by a hardwired approach using cables or wirelessly using a suitable wireless network. It has been demonstrated that a wireless signal can be transmitted and received across a boundary representative of the reactor containment building wall. It was also found that using thermocouple specifications and appropriate attachment methods the response time and stability of the temperature measurement can be improved.

To continue to develop the PAR as a H_2 sensor concept, more testing and qualification is required. Investigations into the static pressure, humidity, but mainly radiation resistance of the wireless temperature transmitter, would provide significant confidence in the ability of the transmitter to withstand nuclear reactor containment building post-accident conditions.

6. REFERENCES

1. J. Gu, “Hydrogen Detection in Nuclear Power Plants: Comparison of Potential, Existing, and Innovative Technologies” *Electrical Power Research Institute (EPRI) Report*, 3002002107 (2013).
2. Z. Liang, M. Sonnenkalb, A. Bentaib, M. Sangiorgi, “Status Report on Hydrogen Management and Related Computer Codes”, *NEA/CSNI report*, NEA/CSNI/R(2014)8 (2014).
3. T. Hubert, L., Boon-Brett, G. Black, U. Banach, “Hydrogen sensors – A review,” *Sensors and Actuators B* **157**, pp. 329-352 (2011).
4. R. Ortiz Cebolla, E. Weidner, W. Buttner, C. Bonato, “Summary Report for a Hydrogen Sensor Workshop - Hydrogen Safety Sensors and their use in Applications with Hydrogen as an Alternative Fuel,” EUR 28852 EN, *Publications Office of European Union*, Luxembourg (2017).
5. L. Gardner, Z. Liang, T. Clouthier and R. MacCoy, “A large-scale study on the effect of ambient conditions on hydrogen recombiner-induced ignition,” *International Journal of Hydrogen Energy*, 2021. **46**(23), pp. 12594-12604.
6. CSA Group, “Requirements for the Containment System of Nuclear Power Plants”, CSA N290.3:16 (R2021).
7. CSA Group, “Requirements for Monitoring and Display of Nuclear Power Safety Functions in the Event of an Accident”, N290.6:16 (R2021).
8. CSA Group, “Environmental Qualification of Equipment for Nuclear Power Plants”, CSA N290.13:25 (2025).
9. L.B. Gardner, B. Ibeh, J. Murphy, J. Allain, S. Yeung and C. Chenard, “Hydrogen recombination scaling experiments at CNL’s hydrogen safety test facility,” *Nuclear Engineering and Design*, **377** (2021).
10. T.P. Kaloni, J. Patel, B. Ellis, H. Fritzsche, E. Torres, “Computational simulation on radiation damage in GaAs-based betavoltaic cells,” *Radiation Physics and Chemistry*, **238** (2026).
11. L. Gardner, B. Ibeh, J. Murphy, M. Thomas, S. Cotosman, “PAR performance under oxygen-limited conditions,” *The 19th International Topical Meeting on Nuclear Reactor Thermal Hydraulics (NURETH-19)*, Brussels, Belgium, March 6-11, 2022.

PARs for Hydrogen Measurement in Nuclear Containments in Severe Accidents

Lee Gardner (lee.gardner@cnl.ca) and Blessing Ibeh

European Review Meeting in Severe Accident Research
2026 May 18-22

Canadian Nuclear Laboratories | Laboratoires Nucléaires Canadiens

Background - Hydrogen Measurements for Nuclear Containment

- Current Status
  - Common approach: sampling systems connected to gas analysis equipment
  - Alternatives: in-situ sensors (catalytic bead, electrochemical, thermal conductivity)
- Type of Sensors Reviewed
  - Thermal conductivity, electrochemical, resistance-based (e.g., catalytic bead sensors), optical and work function-based sensing technologies
- Limitations
  - Power
  - Cross-sensitive or require oxygen
  - Signal transmission
  - Limited number in containment
  - Qualification

Background – Sensor Requirements in Accidents (CANDU)

Parameter/ Variable	Range	Comments
Ambient Temperature	15 – 300 °C	
Transient Temperature	Up to 500 °C	
H_2 Concentration	Up to 10 vol.%	With error of ±0.5 vol.% (to avoid detonation range)
O_2 Concentration	0 - 20 vol.%	If sensor requires O_2, must function at low O_2 (i.e., < 1 vol.%)
Steam	Up to 100 vol.%	In the presence of inert gas and diminishing O_2
Pressure	Up to 400 kPa(g)	Retain functionality up to design pressure of containment
Radiation (total integrated dose)	20 Mrad	Beta/gamma/neutron - 1000 krad/h for 200 h
Energy	Can operate for extended periods	Source from battery or energy harvesting
Lifetime	>2 years	Based on the outage frequency
Accuracy	± 0.5%	
Response time	≤ 2 s	

PAR as a Hydrogen Sensor - Concept

- Heat generated from exothermic recombination reaction
- Catalyst instrumented with thermocouples, provide temperature measurements
- Measured catalyst temperature can be correlated with H_2 concentration

IR Image of Operating PAR

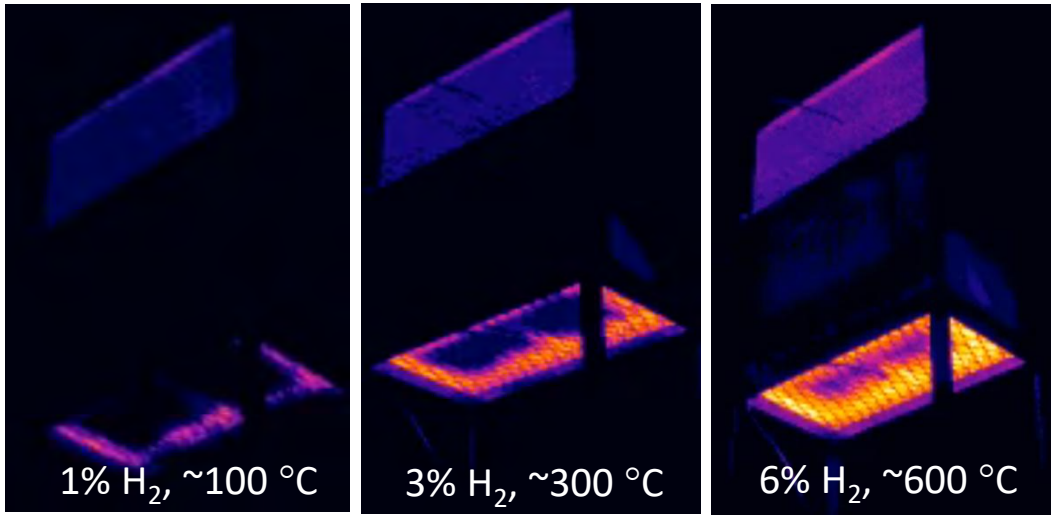

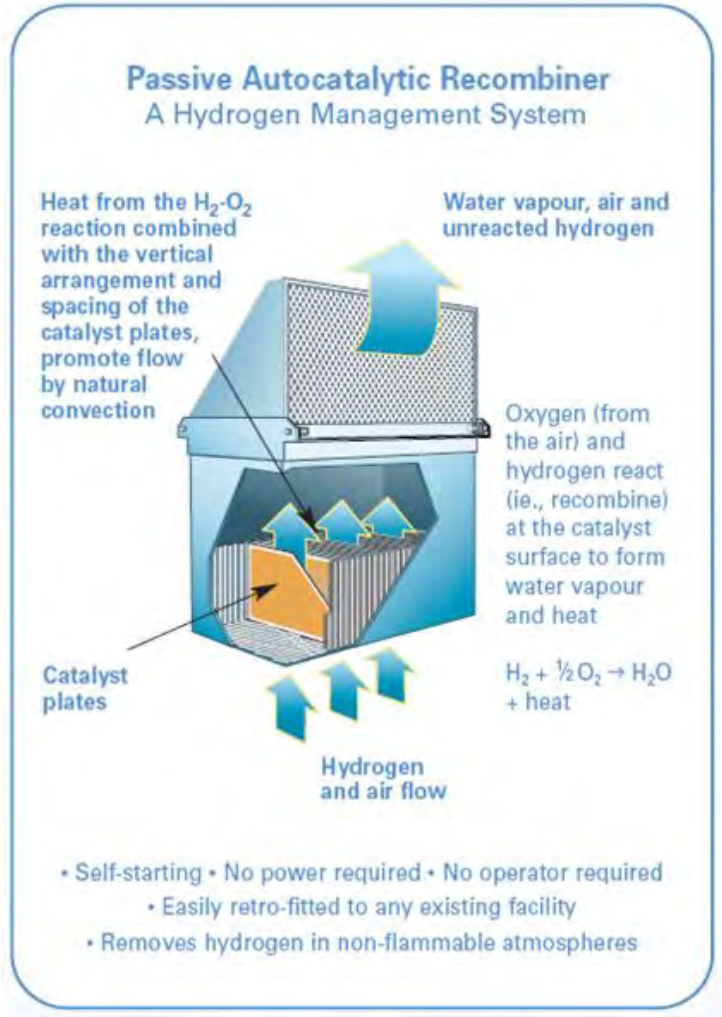

PAR as Hydrogen Sensor - Feasibility

Adoptability

- PAR already installed in containment
- Very little or no power needed for signal transmission
- PAR qualified for nuclear containment & SAs
  - PAR operation in SAs studied extensively

Signal Transmission

- Wired (thermocouple wire)
  - \+ No power needed
  - \- Penetration through containment boundary

- Wireless (transmitter/receiver)
  - \+ No penetration through containment boundary needed
  - \- Wireless transmitter for nuclear containment are under development
  - \- Power required for transmitters

Proof of Concept/Preliminary Testing

- Catalyst temperatures measured at 3 locations (top, middle, bottom in horizontal centre)
- Data used from 46 large-scale experiments
- Best fit was found in the top catalyst plate location

Catalyst Plate

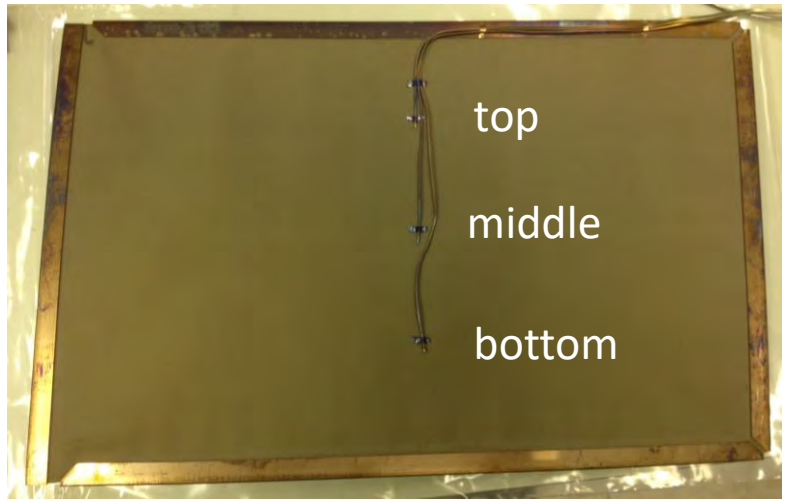

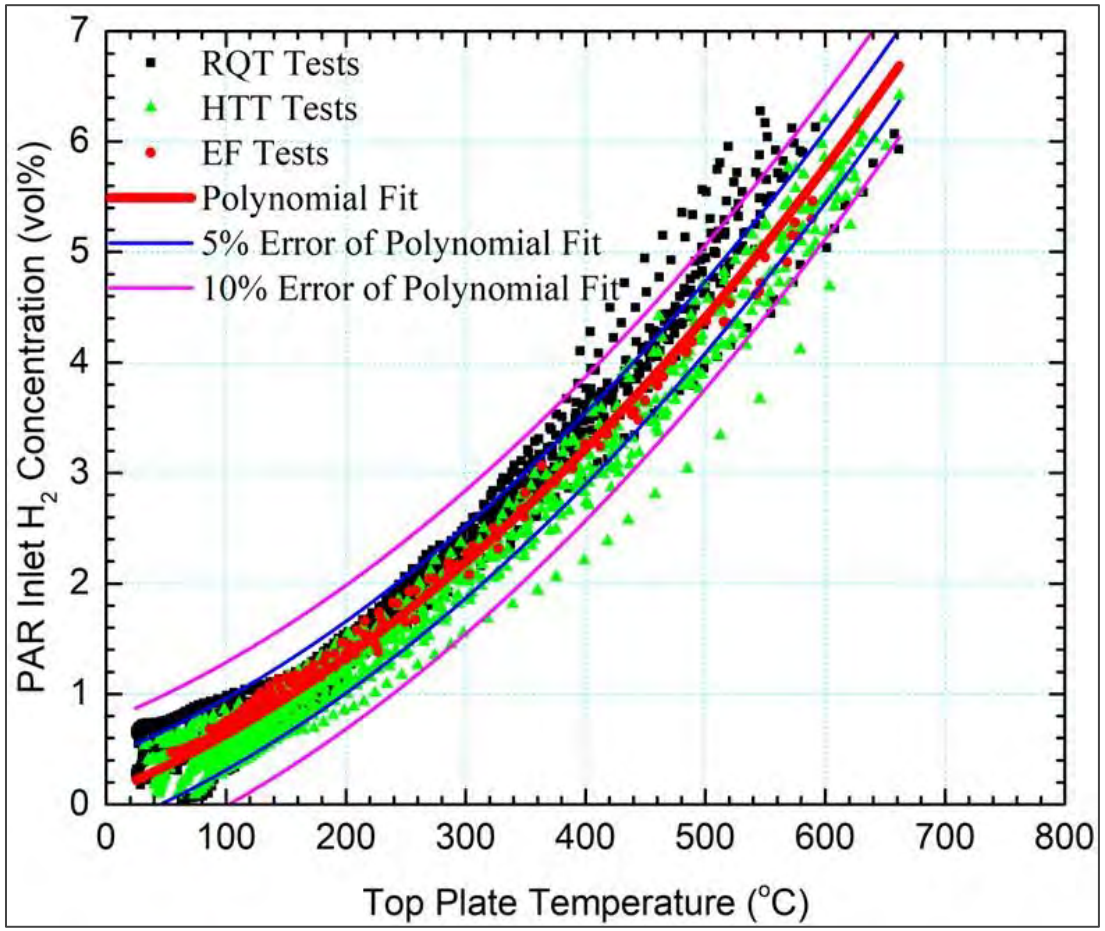

Proof of Concept/Preliminary Testing

Wireless Transmission

- Power Consumption Analysis
  - 2 AA batteries were insufficient to power transmitter
  - Firmware can be modified to set transmitter to sleep between transmissions

- Wireless Transmission Boundary Tested
  - 12.7 mm thick carbon steel
  - 1 m thick concrete

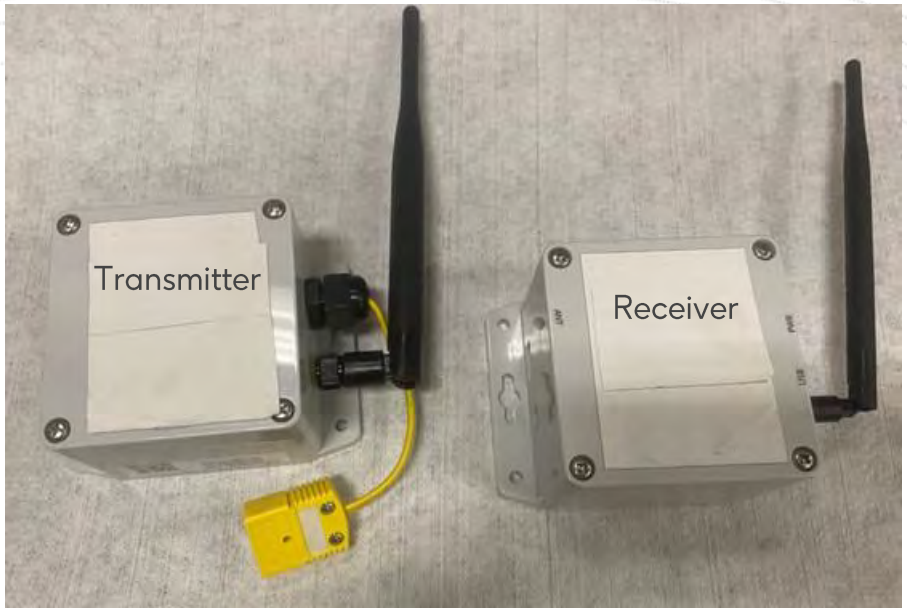

Commercial Wireless Thermocouple Transmitter/Receiver

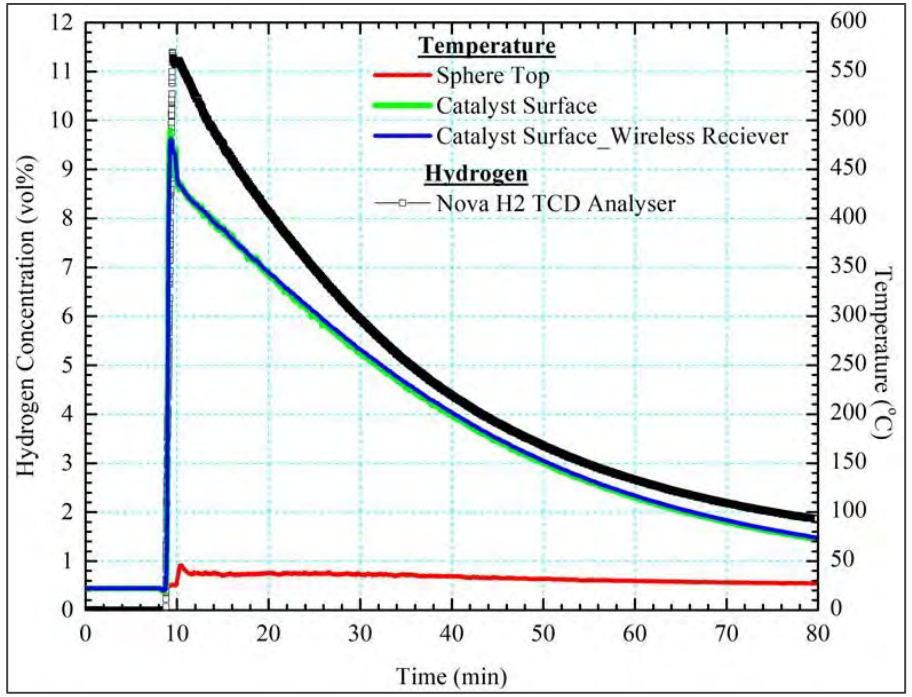

Advanced Testing

Requirements		Test Results	
Parameter/ Variable	**Range**	**(Pass / Fail, or successfully tested range)**	**Comments**
Ambient Temp.	15 – 150 °C	Partial Pass	Tests up to 100 °C. Modifications needed to transmitter housing & further testing to 150 °C for extended periods
Transient Temp.	Up to 500 °C	Pass	
H_2 Conc.	≤ 10 vol.%	Partial Pass	PARs measure H_2 up to ~7 - 8 vol.% when they can ignite H_2
O_2 Conc.	0 - 20 vol.%	Fail	The min. O_2 conc. identified is 7 vol.%
Steam	Up to 100 vol.%	Partial Pass	Tests covered up to 55 vol.%. Further testing needed to cover up to 100 vol.% for extended periods
Pressure	Up to 250 kPag	Partial Pass	Transmitter passed transient pressure tests. Further tests needed to qualify transmitter under static pressure conditions
Radiation (total integrated dose)	20 Mrad	Fail	Modifications needed to transmitter to protect electronics from radiation or modify electronics
Energy	Capable of operating for extended periods	Not Tested	Modifications to firmware & analysis needed to ensure the transmitter can operate long term without replacing or additional batteries
Lifetime	≥ 2 years	Not Tested	
Accuracy	± 0.5%	Not Tested	
Response time	≤ 2 s	Fail	The PAR as H_2 sensor response time range from 1 - 2 min

Advanced Testing

High Ambient Temperature

- Wireless transmitter installed in ventilated oven
- Exposed to 100 °C for 65.5 h
- No physical or functional degradation found

Transient Temperature & Pressure

- Wireless transmitter connected to thermocouples attached to recombiner catalyst in HSTF
- H_2 combustion test performed in HSTF
- Overpressure >100 kPa
- Max. temperature > 300 °C
- No physical damage or noticeable effects to transmitter

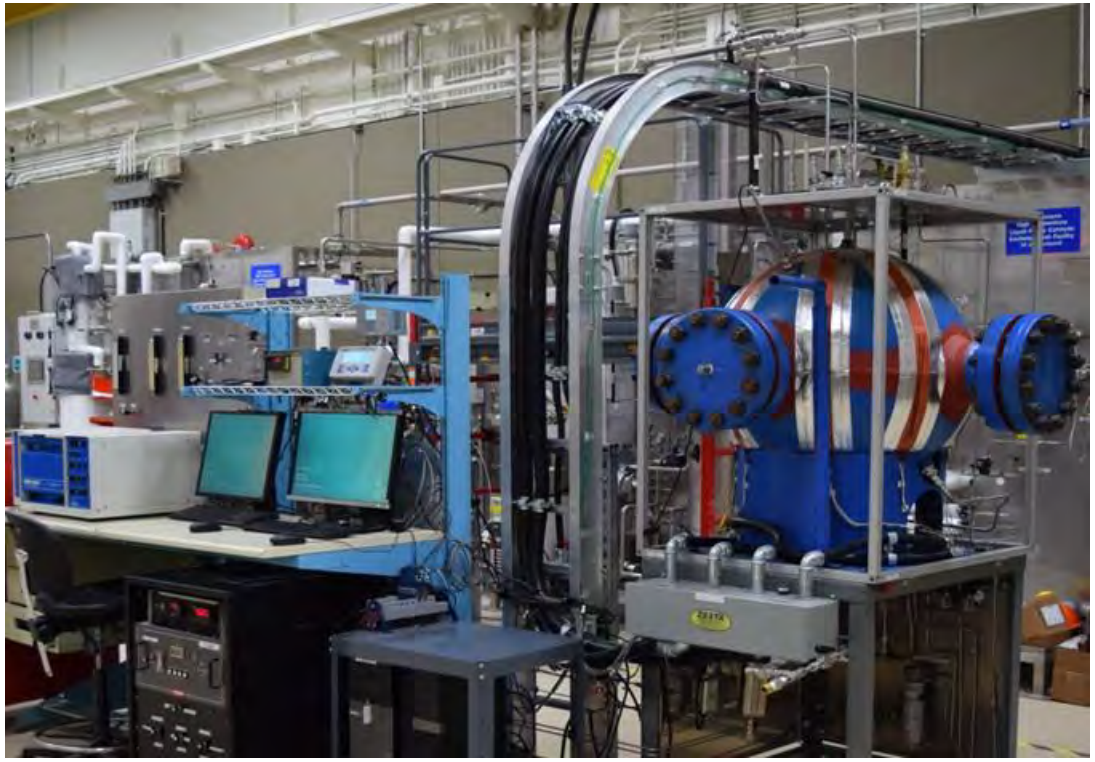

Hydrogen Safety Test Facility (HSTF)

Advanced Testing

Steam Exposure

- Wireless transmitter connected to thermocouples attached to recombiner catalyst in the HSTF
- Multiple tests performed in HSTF. Each with multiple H_2 injections to increase steam concentration
- Wireless transmitter exposed to 55 vol% steam
- High temperature caused issues with battery connections
  - Modifications made to battery housing

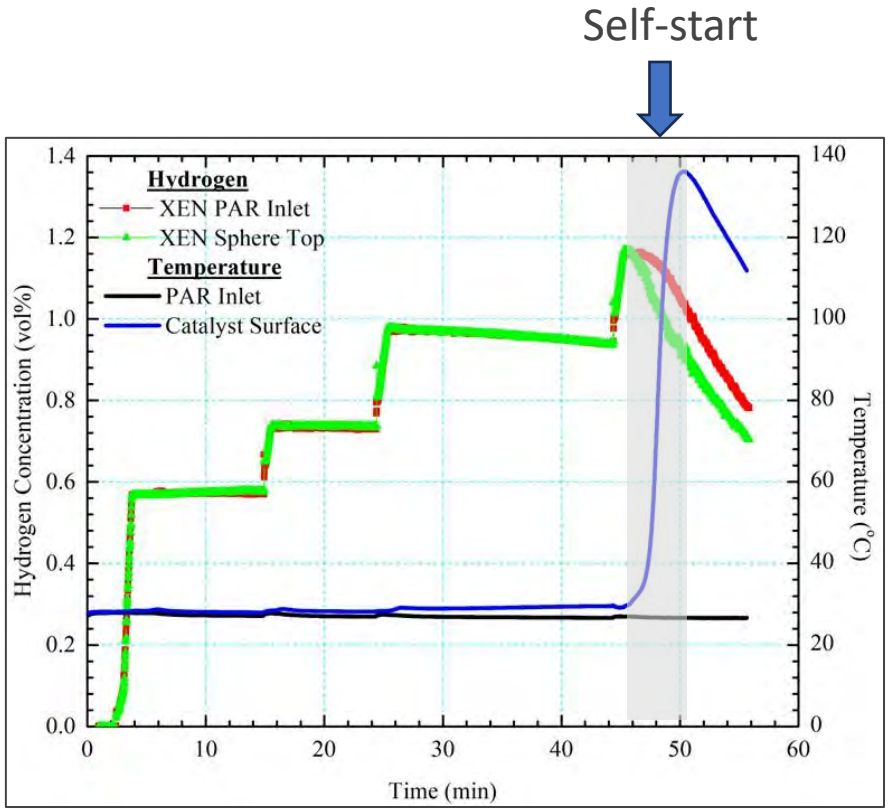

Response Time

- Time for PAR to respond to local H_2 conc. after start-up
- Does not include PAR start-up time
  - many factors impact start up (containment conditions, etc.)
- 10 °C catalyst temperature rise in 1.5 min (in example)
- Data from large-scale tests reviewed: response time is 1 – 2 min

Advanced Testing

Radiation Dose

- Wireless transmitter exposed to gamma radiation
- Three exposure attempts made. All found that transmitter had failed due to semiconductor failure.
- Exposure periods were 20.0, 287.3 and 24.2 h
- Minimum dose = 0.58 Mrad

CNL's Gamma cell Facility

Oxygen Concentration

- Historical work[1] reviewed to assess minimum O_2 concentration
- PAR requires O_2 to operate
- PAR operates with as low as 0.1 vol% O_2
  - Temperature correlation needs to adapt for O_2 limiting conditions

[1] L. Gardner, B. Ibeh, J. Murphy, M. Thomas, S. Cotosman, "PAR performance under oxygen-limited conditions," *The 19th International Topical Meeting on Nuclear Reactor Thermal Hydraulics (NURETH-19)*, Brussels, Belgium, March 6-11, 2022.

Summary & Future Work

- PAR as a H_2 sensor has potential for H_2 detection and measurement in containment for SAs
- Potential for low cost and simplified adoption
- Further work is needed on wireless transmission in containment
  - Prevent radiation from failing semiconductors
  - Improve power consumption
- Further work on correlation behaviour in oxygen limiting conditions and extend steam and pressure exposure limits
- Demonstration/evaluation in NPP containment?

FISSION PRODUCT BEHAVIOR AND SOURCE TERM IMPACTS IN EX-VESSEL PHASE USING THAI TEST DATA: THE OECD/NEA THEMIS PROJECT

K. Dieter, J. Treufo, M. Freitag, E. Schmidt, M. Colombet, B. von Laufenberg
Becker Technologies GmbH
Neckarstraße 12-14, 65239 Hochheim, Germany
dieter@becker-technologies.com; treufo@becker-technologies.com; freitag@becker-technologies.com; eike.schmidt@becker-technologies.com; colombet@becker-technologies.com; von.laufenberg@becker-technologies.com

G. Langrock, F. Funke
Framatome GmbH, Erlangen, Germany
gert.langrock@framatome.com; friedhelm.funke@framatome.com

ABSTRACT

Gaseous iodine released into the containment during hypothetical severe accidents in light water reactors could be oxidized by air radiolysis products, forming gaseous iodine oxides (IO_x). Such aerosols are considered source-term relevant because these very fine particles can remain airborne long-term or can be easily resuspended from structures. The OECD/NEA THEMIS project aimed to investigate phenomena where the knowledge base for safety assessment has not been sufficiently developed and to provide data for code-model validation of lumped parameter and computational fluid dynamics codes for reactor applications. The test Iod-36 aimed to quantify the adsorption and agglomeration of IO_x onto nuclear background aerosols. Silver was used as the mid and long-term phase accident aerosol. The test Iod-37 focused on the thermal stability of gas-borne IO_x and the potential conversion of IO_x to I_2 under accident typical temperatures, ranging from 80 °C up to 140 °C. Both tests were executed in the technical-scale THAI$^+$ test facility with an initial temperature of 80 °C and a relative humidity of 50 %. Ozone was used to promote the formation of IO_x inside the vessel and the molecular iodine was injected once the preconditioning phase was completed. Several instruments were installed to monitor iodine gas concentration, ozone concentration, iodine surface depletion and thermohydraulic parameters such as pressure, humidity and temperature. The agglomeration of IO_x with background reactive silver aerosols (Iod-36) led to the removal of iodine from the vessel atmosphere correlated with the settling process of the larger silver particles. The results of Iod-37 showed that for an increasing temperature, the formation of gaseous iodine could be observed.

KEYWORDS
THAI, severe accident, fission products, source term, iodine oxides

1. INTRODUCTION

Gaseous molecular iodine (I_2) released into the containment during hypothetical severe accidents in light water reactors (LWRs) could be oxidized by air radiolysis products, forming gaseous iodine oxides (IO_x) [1]. IO_x can form aerosols which can behave differently from I_2. The conversion from gaseous I_2 into IO_x by air radiolysis products was measured in lab-scale investigations, e.g. [1], [2], [3], [4] and in technical scale tests using the THAI$^+$ test facility, e.g. Iod-13 and Iod-14, [5], [6]. IO_x aerosols are considered source-term relevant because these fine particles can remain airborne long-term or can easily be resuspended from

structures [7]. Furthermore, IO_x compounds can thermally decompose at high gas temperatures. Additionally, factors such as humidity and temperature have been the focus of recent investigations to study the formation and stability of different IO_x compounds and aerosol species [8], [9] [10].

The OECD/NEA THEMIS project aimed to investigate phenomena where the knowledge base for safety assessment has not been sufficiently developed and to provide data for code-model validation of Lumped Parameter (LP) and Computational Fluid Dynamics (CFD) codes for reactor applications. The investigations focused on processes and phenomena occurring in the late phase of severe accidents. Specifically, source-term-related issues such as the depletion or further chemical reactions of IO_x particles with nuclear background aerosols (test Iod-36) and the thermal stability of IO_x at high temperatures (test Iod-37) were investigated [11].

Test Iod-36 aimed to investigate the adsorption and agglomeration of IO_x onto nuclear background aerosols, which are considered to be chemically reactive with respect to iodine. Some candidates for aerosols that are known to be representative for the mid and long-term phase of an accident were Ag, CsI and CsOH, from which silver (Ag) was chosen for this test due to the potential advantages for the measurement system and quality of the experimental data in the $THAI^+$ test facility. The investigation included the adsorption of IO_x particles onto the Ag aerosol and their impact on depletion mechanisms, such as aerosol deposition onto horizontal and vertical vessel surfaces. The thermo-hydraulic conditions were set to be representative of prototypical accident conditions in terms of gas atmosphere (air-steam mixture) and aerosol characteristics (size distribution and mass concentration) [7]. Test Iod-37 focused on the thermal stability of gas-borne IO_x and the potential conversion of IO_x to I_2 under accident-typical gas temperatures, ranging from 80 °C up to 140 °C [12].

Both tests were performed at approximately 50 % relative humidity, which is high enough to ensure representativeness of severe accident conditions and low enough prevent possible deliquescence of IO_x in the investigated temperature range of test Iod-37 [13]. The thermal stability of the formed IO_x was investigated by measuring IO_x as aerosol and inorganic iodine as gaseous species.

2. FACILITY DESCRIPTION

The technical-scale $THAI^+$ test facility consists of the THAI test vessel (TTV) and the Parallel Attachable Drum (PAD) as shown in Figure 1. The PAD vessel is connected to the TTV through a lower and upper pipe that can be removed for different configurations. For the execution of the tests Iod-36 and Iod-37, the TTV was used in a standalone configuration. For this purpose, the TTV was closed and the inner cylinder was removed. The dimensions of the TTV are 3.15 m in diameter and 9.3 m in height, leading to an inner volume of 60 m^3. The TTV is made of stainless steel and it is completely covered by 120 mm mineral wool for thermal insulation. The cylindrical part of the TTV is double walled with a 16.5 mm gap that is filled with thermal oil for wall heating and/or cooling. The remaining vessel wall sections can be electrically heated to achieve the desired temperature. The maximum admissible overpressure of the TTV is 14 bar at a corresponding temperature of 180 °C.

The facility is equipped with the necessary supply systems for steam, compressed air, nitrogen, oxygen, light gas (helium), combustible gases (hydrogen and carbon monoxide), aerosols and gaseous iodine. An advanced instrumentation and data acquisition system is installed to monitor the relevant physical quantities with high spatial and temporal resolution.

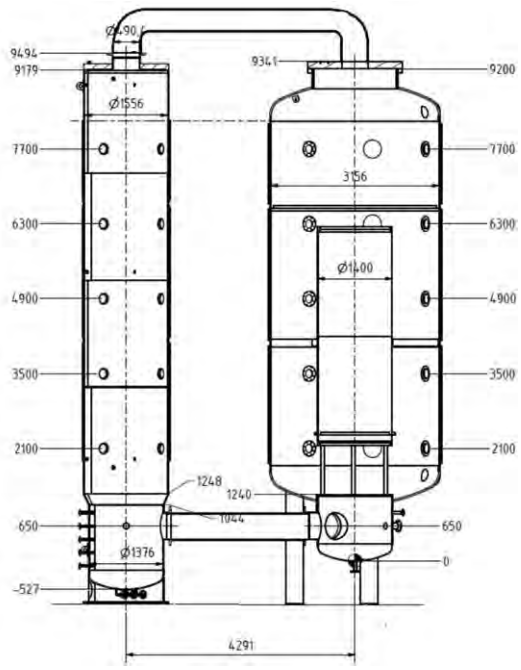

Figure 1: THAI$^+$ configuration and dimensions (mm) of the THAI$^+$ test facility.

1. EXPERIMENTAL METHODOLOGY

The experimental configuration of the TTV, i.e. injection locations and sensor positions, was similar for both tests Iod-36 and Iod-37. However, the main difference between both tests was the absence of the fluidized bed Ag aerosol injection in test Iod-37 (see Figure 2). The specified initial conditions of both tests are given in Table 1.

Table 1: Specified initial tests conditions

Test ID	Initial conditions	Iodine and Ozone injection	Ag-Aerosol concentration
Iod-36	1.5 bar, ~ 80 °C superheated, r.H. 50 %, 0.24 bar steam partial pressure	< 1 g I_2 O_3/I_2 molar ratio: 20… 30	> 1 g/m^3
Iod-37	1.5 bar, ~ 80 °C superheated, r.H. 50%, 0.24 bar steam partial pressure	< 1 g I_2 O_3/I_2 molar ratio: 20… 30	None

1.1. IO_x behavior and the interaction with nuclear background aerosol (Iod-36)

The test procedure for the test Iod-36 consisted of a preconditioning phase followed by the main test phases as listed below:

- Preconditioning phase to establish initial conditions within the TTV, including heating of the vessel and steam injection to generate a relative humidity of approx. 50 %
- Ozone injection to establish a dedicated ozone concentration in the vessel
- I_2 gas injection following the THAI standard procedure

- IO_x formation and measurement
- Background Ag aerosol injection and measurement of IO_x-Ag-aerosol coagulation and depletion

The heating of the vessel was controlled by the oil flow in the vessel mantles and the electrical heating circuits. The ozone was generated by an ozoniser OT-020 from Lenntech with a nominal flow rate between 8 to 10 g/h. I_2 was injected using pre-heated nitrogen as carrier gas at an elevation of H = 8.4 m. The injected gaseous molecular iodine was radiolabeled with I-123. Ag aerosol particles were injected through a 9 mm inner diameter pipe near the centerline at an elevation of H = 1.9 m (only test Iod-36). Steam was injected with an upwards directed injection tube at an elevation of H = 1.13 m at the vessel centerline, provided by an electrical 108 kW steam generator. Air was injected in horizontal direction towards the vessel center at an elevation of H = 3.5 m and it was provided by the THAI$^+$ test facility compressed air supply system (dehumidified and free of oil).

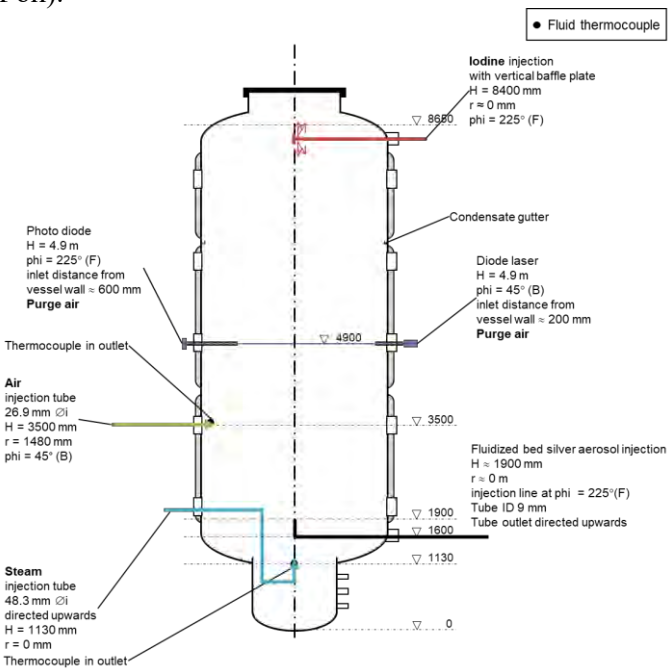

Figure 2: Test configuration – Iodine, Ag aerosol, air and steam injection; laser absorption system (test Iod-36).

The sampling and measurement system consisted of the following equipment:

- 6 gas scrubbers were used to measure iodine concentrations in the gas phase (see positions in Figure 3). The absorber liquid of the gas scrubbers was an aqueous solution of 0.1 mol/L sodium hydroxide and 0.5 wt% sodium thiosulfate (pH = 13). Sampling times were between 2 and 5 minutes at flow rates of 1 l/min inside the vessel, driven by the pressure difference between vessel and environment.
- 2 external gas scrubbers were used to measure the ozone concentration with a phosphate buffered KI solution as solvent.
- 2 Maypack filtering stations were used to measure iodine concentrations in the gas phase.
- 2 Bulk filters were used to measure aerosol mass concentration. Each filter was equipped with 47 mm borosilicate glass microfibers and one cascade impactor station to separate 10 particle size classes.

- 1 laser light extinction measurement (photo diode) was used to provide a continuous, in-line and non-intrusive measurement of the aerosol concentration.
- Aerosol measurements were conducted using a scanning mobility particle sizer (SMPS) from GRIMM Aerosol Technik (model SMPS+C 5416 with L-DMA) which is comprised of a differential mobility analyzer (DMA) and a condensation particle counter (CPC).
- An additional ozone and iodine measurement was performed by wide spectral light absorption spectroscopy (LASI-SPEC).
- 2 lead-shielded NaI scintillation detectors were used to monitor the I-123 radiation inside the vessel.
- Several thermal hydraulic instruments to record humidity, pressure, fluid and surface temperature.

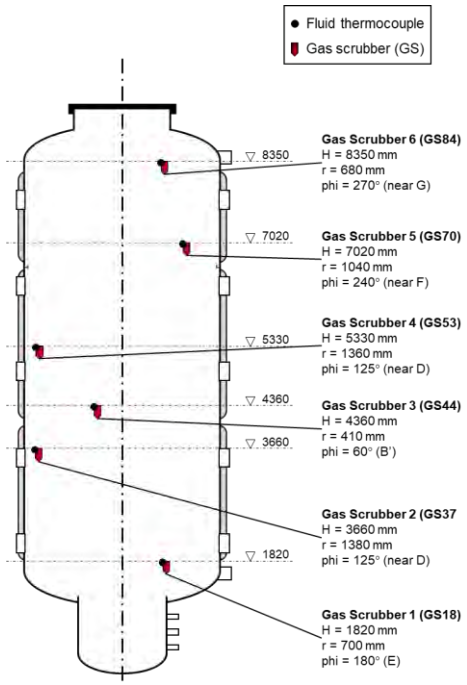

Figure 3: Test configuration – Positions of the gas scrubbers (tests Iod-36 and Iod-37).

1.2. IO_x stability under high temperature (Iod-37)

The test configuration and instrumentation used in test Iod-37 were the same as in test Iod-36, except for test Iod-37 not having an Ag injection phase. However, the positions of the injections shown in Figure 2 and the positions of the gas scrubbers in Figure 3 remained the same.

The test procedure for the test Iod-37 was conducted as follows:

- Preconditioning phase to establish initial conditions within the TTV, including heating of the vessel and steam injection to generate a relative humidity of approx. 50 %
- Ozone injection to establish a dedicated ozone concentration in the vessel
- Short I_2 gas injection following the THAI standard procedure
- IO_x formation and measurement
- Long term heating of the facility at full power up to 140 °C and steam injection to maintain 50 % r.H., 1.8 bar steam partial pressure

2. RESULTS AND DISCUSSION

2.1. IO_x behavior and the interaction with nuclear background aerosol (Iod-36)

The average gas temperature in the TTV was approx. 80 °C before the first steam injection. The relative humidity measured was about 50 % on average, showing sufficient homogeneity within the plenum of the vessel. The injection of ozone did not significantly change the vessel pressure and temperature due to the low amount. The injection of I_2 together with the nitrogen carrier gas slightly increased the pressure. However, it did not influence the gas temperature which stayed constant at around 80 °C. The Ag aerosol injection slightly increased the pressure due to the air carrier gas. After this step, the pressure remained quasi constant and it only changed slowly due to the gas sampling measurements (i.e. CNC, sampling filter, impactor, Maypack and gas scrubber measurement) and by the dry purging air used to prevent particle deposition at the optical extinction probe.

The gas phase iodine concentration measured with the gas scrubbers is shown in Figure 4. Following the injection of I_2, the first gas scrubber measurements show comparatively low but increasing iodine concentrations. This phenomenon has also been observed in previous tests including iodine and ozone like Iod-14 or Iod-37. One possible explanation for this phenomenon is insufficient retention of the formed iodine oxides by the absorber solution ($Na_2S_2O_2$/NaOH). It is most likely that the oxidation process of iodine, the formation of water-soluble species, such as HIO_3, I_2O_4, I_2O_5 or I_4O_9 and their coagulation, had not yet been completed shortly after the I_2 injection. It is also possible that non-dissolvable intermediate IO_x species, such as IO or IO_2, had formed. Following the start of the Ag injection, the total iodine concentration measured with the gas scrubbers shows a steady, nearly exponential decrease. This effect was more pronounced at lower measurement positions, as the aerosol particles settled under the influence of gravity. However, a comparative analysis of earlier tests (e.g. test Iod-26 from the OECD/NEA THAI-2 project) showed that Ag aerosols are highly effective at removing iodine oxides and gaseous iodine, which is most likely caused by agglomeration and sedimentation [14]. The test confirmed that reactive background aerosols can play a significant role in reducing airborne iodine in accident scenarios.

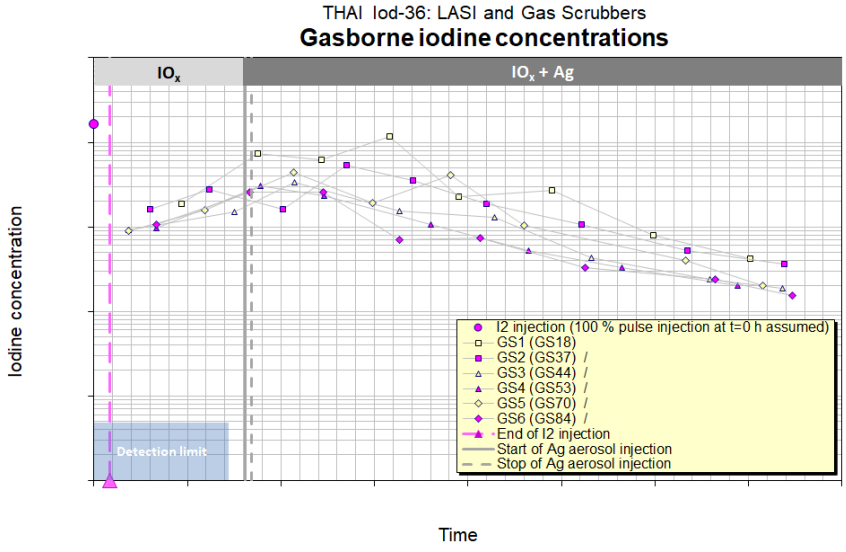

Figure 4: Iod-36: Gasborne iodine concentrations from gas scrubbers.

The surface loading of iodine on the steel coupon was obtained from the conversion of the corrected count rate measured by the online detector OS21D (see Figure 5). The measured raw value was corrected by the contribution of iodine in the gas phase between the glass and the steel coupon, based on total iodine measured by the Maypacks. The measurement curve in Figure 5 shows that some iodine was deposited on the vertical steel coupon in the first phase of the test, a process that was then enhanced by the injection of the Ag aerosol.

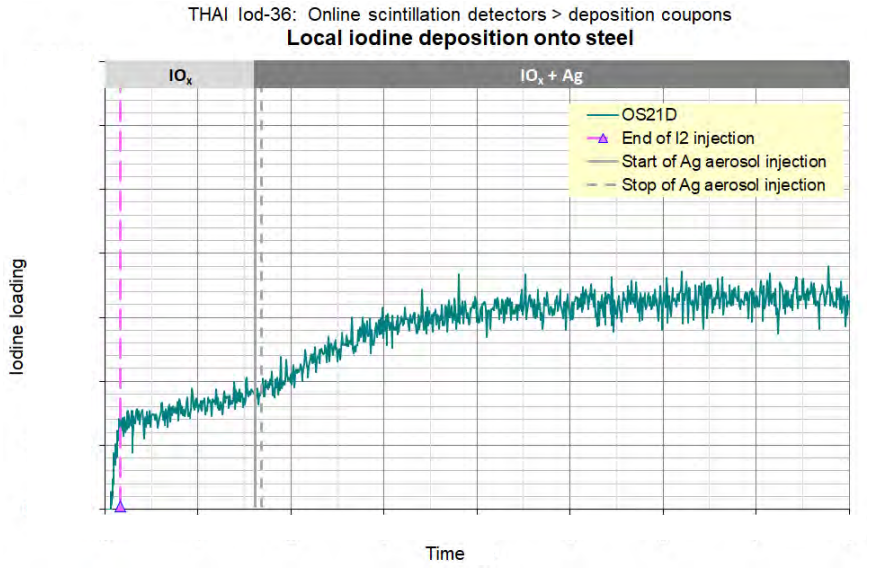

Figure 5: Iod-36: Local iodine loadings on steel deposition coupon (linear scale).

2.2. IO_x stability under high temperature (Iod-37)

The test Iod-37 examined the thermal stability of IO_x formed by the reaction of I_2 and ozone in a humid atmosphere. The average gas temperature in the TTV was about 80 °C prior to the first steam injection. The pressure increased after the first steam injection. The relative humidity was mostly about 50%, indicating that the plenum region was sufficiently well mixed. The injection of ozone did not have an significant impact on the vessel pressure or temperature, but the injection of iodine, the following steam injection and the gas heating increased the pressure. Approximately 1 hour after the start of the I_2 injection, the vessel heated up at an almost linear rate until reaching a gas temperature of up to 140 °C. As the vessel gas temperature increased, the particle number concentration decreased, most likely due to agglomeration. At the end of the test, the vessel pressure decreased due to gas temperature reduction and gas sampling procedures.

The gasborne iodine concentrations measured using the gas scrubbers are shown in Figure 6. Similarly to former iodine/ozone tests as well as the measurement results in test Iod-36, the iodine concentrations initially increased slowly, most likely attributed to the limited scrubbing efficiency caused by the small particle size of the newly formed IO_x. Over time, the IO_x particles agglomerated and the scrubbing efficiency improved, resulting in a more effective retention. The ozone concentrations, which were monitored using both LASI and external gas scrubbers, decreased at a nearly linear rate with the iodine injection, proving that the molecular I_2 was oxidized. Approximately 1 to 1.5 hours after the I_2 injection, the concentrations stabilized at a comparatively low level which persisted throughout the temperature increase from 80 °C to 140 °C.

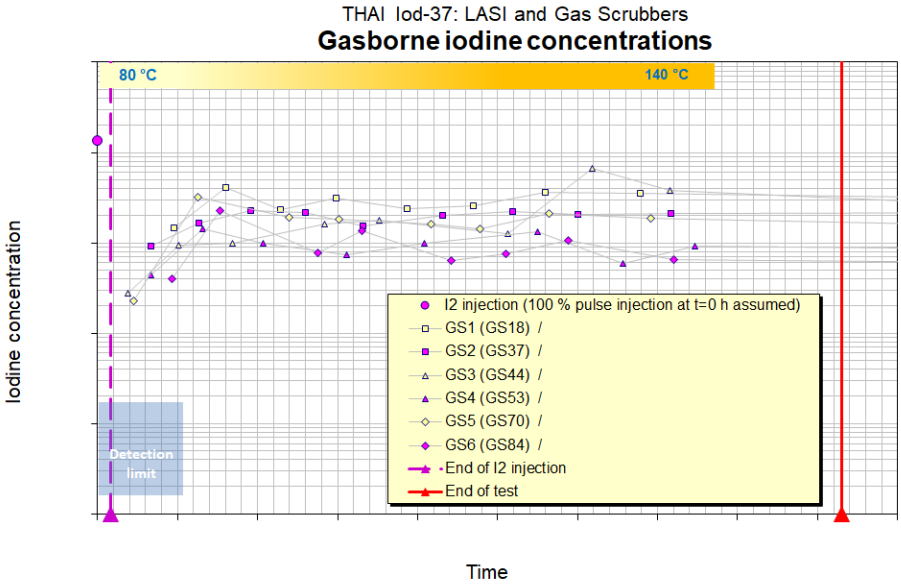

Figure 6: Iod-37: Gas-borne iodine concentrations from gas scrubbers.

Maypack filter measurements indicated that most of the iodine was present in the form of an aerosol, which is consistent with the measurement results for rapid formation of IO_x. Aerosol concentrations declined only slightly during the first 1 to 1.5 hours. As the temperature increased, the concentration of inorganic gaseous iodine began to rise, most probably due to the thermal decomposition of IO_x (see Figure 7). This decomposition process seemed to dominate the competing I_2/steel surface reactions, confirming that elevated temperatures promote the conversion of aerosol-bound IO_x into gaseous iodine species under the tested conditions. These findings emphasize the thermal instability of IO_x and its potential remobilization at high temperatures, which is an important consideration for source term assessments in late-phase severe accidents.

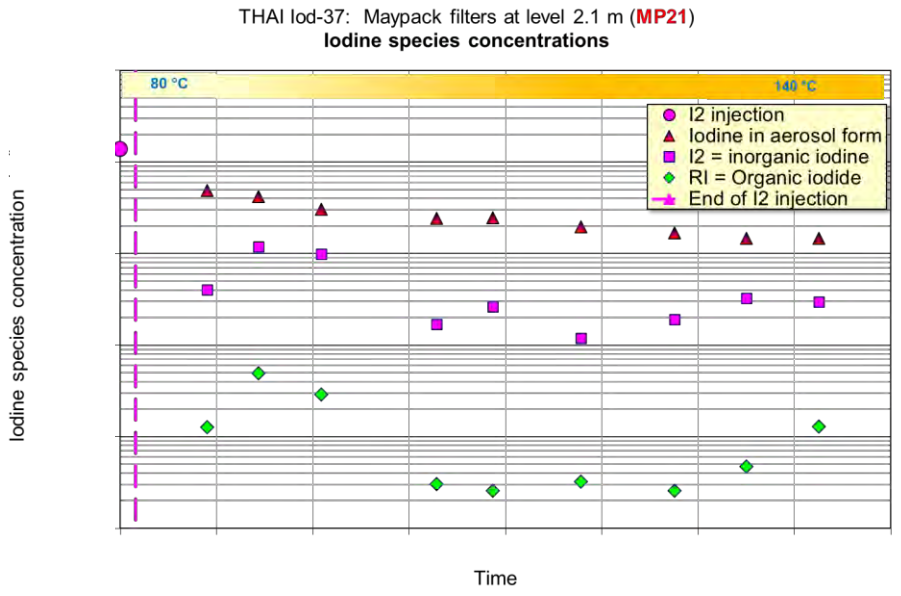

Figure 7: Iod-37: Iodine species concentrations from Maypack filters.

3. SUMMARY AND CONCLUSIONS

This paper reports the results of the THAI test Iod-36 and test Iod-37 performed in the frame of the OECD/NEA THEMIS project by Becker Technologies and with the support of Framatome on the iodine specific measurements. On one hand, the objective of test Iod-36 was to study the formation of IO_x particles and their interaction and adsorption onto containment typical nuclear background aerosols, considered to be chemically reactive with iodine. Therefore, Ag was chosen as representative background aerosol. On the other hand, the objective of test Iod-37 was to study the formation and long-term thermal stability of IO_x particles at elevated gas temperatures ranging from 80 to 140°C.

The initial conditions and preconditioning phases of both tests were set to be similar. The initial gas temperature and relative humidity established in test Iod-36 and test Iod-37, prior to the ozone and I_2 injection phases, were approximately 80 °C and 50 %. In both tests, the IO_x particle formation was initiated by a short injection of gaseous I_2 into an ozone containing atmosphere. After these test phases, test transients and the corresponding results of the tests differ from each other. In the case of test Iod-36, Ag was injected into the vessel at a constant temperature, while in test Iod-37 the vessel was heated up to a maximum temperature of up to 140°C without Ag being present. In test Iod-36, the formation and particle agglomeration of IO_x was measured before the injection of Ag aerosol, whereas in test Iod-37, the formation and particle agglomeration of IO_x was measured before the heating phase.

Gas scrubbers and Maypack filters were the main instrumentations to monitor the gasborne iodine concentration, while scintillation detectors were used to measure the iodine deposition at the steel coupons. Several thermohydraulic sensors were used to monitor the pressure, temperature and humidity. The ozone over I_2 ratio in both tests was set to be larger than 10. Measurements of total atmospheric iodine concentrations and iodine loadings on stainless steel were provided for both tests.

In test Iod-36, the gas scrubbers showed that the iodine concentration decreased steadily and nearly exponentially until the end of the test with the addition of Ag aerosols in the vessel atmosphere. This trend was also observed in prior tests performed at the THAI$^+$ test facility, which demonstrates that the removal rate of IO_x from the containment atmosphere is governed by the settling of the Ag aerosol particles. The activity measurements indicated that the activity went from IO_x particles to the depleted particles with the Ag injection. This confirms that reactive background aerosols can play a critical role in reducing airborne iodine in severe accident scenarios. This does not necessarily mean that IO_x aerosols have chemically reacted with Ag aerosol, because the settling mechanism might be accompanied by a coagulative or adsorptive mechanism. The Ag aerosol concentration was monitored by laser extinction and at the end of the test more than 90 % of the initial airborne Ag was depleted.

In test Iod-37, upon injection, iodine rapidly formed IO_x particles, with particle concentrations increasing sharply before gradually declining, primarily due to agglomeration. Measurements of atmospheric iodine species, total atmospheric iodine concentrations and iodine loadings on stainless steel consistently indicate that iodine was quickly converted into stable, aerosol-bound IO_x particles shortly after injection. The total concentration of airborne iodine persisted in the atmosphere over extended periods, maintaining a relatively constant level even during heating. However, the analysis of the Maypack filter measurements showed that fraction of iodine aerosol decreased slowly, while the fraction of inorganic iodine species increased at elevated temperatures. This shift is attributed mainly to the thermal decomposition of IO_x, which becomes more significant than competing surface reactions that remove gaseous iodine.

ACKNOWLEDGMENTS

The financial support provided by the countries who participated in the OECD/NEA THEMIS project is greatly acknowledged. Funding by the Federal Republic of Germany, represented by the Federal Ministry

for the Environment, Nature Conservation, Nuclear Safety and Consumer Protection (BMUV) under project number 1501613 is greatly acknowledged. Responsible for the contents of this publication are the authors. In accordance with the agreement of the THEMIS project management board, the full project results are subject to non-disclosure until 31 December 2027. The results presented in this publication were approved for public release and have been prepared in a manner that preserves confidentiality, for example using anonymized or blinded axes in graphical representations.

REFERENCES

1. L. Bosland et al., “PARIS project: Radiolytic oxidation of molecular iodine in containment during a nuclear reactor severe accident. Part 1. Formation and destruction of air radiolysis products – experimental results and modelling”, Nuclear Engineering and Design 238, 3542–3550, 2008.
2. A.C. Vikis et al., “Reaction of iodine with ozone in the gas phase”, J. Phys. Chem. 89, 812–815, 1985.
3. F. Funke et al., “Radiolytic oxidation of molecular iodine in the containment atmosphere”, In: OECD Workshop on Iodine Aspects of Severe Accident Management, Vantaa, Finland, May 18–20, pp. 79–89, 1999.
4. L. Bosland et al., “PARIS project: Radiolytic oxidation of molecular iodine in containment during a nuclear reactor severe accident: Part 2. Formation and destruction of iodine oxides compounds under irradiation – Experimental results modelling”, Nuclear Engineering and Design, 241(9), 4026-4044, 2011.
5. F. Funke et al., “Iodine oxides in large-scale THAI tests”, Nuclear Engineering and Design, 245, 206-222, 2012.
6. S. Dickinson et al., “Experimental and modelling studies of iodine oxide formation and aerosol behaviour relevant to nuclear reactor accidents”, Annals of Nuclear Energy, 74, 200-207, 2014.
7. M. Freitag et al., “IOx behaviour in containment atmosphere: interaction with nuclear background aerosol Test Iod-36”, Technical Report no. 1501613 – TR – Iod-36 (Framatome report number D02-ARV-01-229-515), 1 Becker Technologies GmbH, Eschborn, Germany, 2 Framatome GmbH, Erlangen, Germany, December 2023.
8. D. K. Smith et al., “The water–iodine oxide system: a revised mechanism for hydration and dehydration”, RSC Adv., 2017, 7, 10183, 2017.
9. J. C. Gómez Martín et al., “Insights into the Chemistry of Iodine New Particle Formation: The Role of Iodine Oxides and the Source of Iodic Acid”, J. Am. Chem. Soc., 144, 9240 – 9253, 2022.
10. O. Leroy et al., “Study of the stability of iodine oxides (IxOy) aerosols in severe accident conditions”, Annals of Nuclear Energy 181, 109526, 2023.
11. S. Gupta et al., “OECD/NEA THEMIS Project: THAI Experiments on Mitigation measures and source term issues to support analysis and further Improvement of Severe accident management measures (Public Version)”, Report No. 1501613-FR-2 (Final Report), Becker Technologies GmbH, Hochheim am Main, Germany, December 2024.
12. G. Langrock et al., “IOx behaviour in containment atmosphere: thermal stability Test Iod-37”, Technical Report no. 1501613 – TR – Iod-37 (Framatome report no. D02-ARV-01-229-514), 1 Framatome GmbH, Erlangen, Germany, 2 Becker Technologies GmbH, Eschborn, Germany, November 2023.
13. R. Kumar et al., “Physical properties of iodiate solutions and the deliquescence of crystalline I2O5 and HIO3”, Atmos. Chem. Phys. 10, 12251-12260, 2010.
14. Funke, F; et al.: Deposition of molecular iodine on aerosol particles Iod-26 (Test using reactive aerosol Ag), Technical Report 150 1420–Iod-26-FR Becker Technologies, Germany, November 2013.

DEVELOPMENT OF A DATABASE FOR PAR MODEL VALIDATION BASED ON THAI EXPERIMENTS AND ITS APPLICATION IN THE FRAMEWORK OF THE AMHYCO PROJECT

Ernst-Arndt Reinecke*, Claudia Druska
Forschungszentrum Jülich GmbH
52425 Jülich, Germany
e.-a.reinecke@fz-juelich.de; c.druska@fz-juelich.de

Matthias Braun
Framatome GmbH
Paul-Gossen-Str. 100, 91052 Erlangen, Germany
matthias.braun@framatome.com

ABSTRACT

The installation of passive autocatalytic recombiners (PARs) for hydrogen risk mitigation inside the containment is a world-wide standard for light-water reactors. Numerical PAR models enable the simulation of PAR operation under severe accident conditions. In combination with containment simulation codes, they are a valuable tool for demonstrating the efficient reduction of combustible gas accumulations and for evaluating mitigation strategies.
A comprehensive experimental program conducted within the OECD/NEA projects THAI and THEMIS provided extensive test data on PAR performance that model developers use to demonstrate the performance of their codes. However, due to the transient character of these tests, analyses have often been limited to selected tests, while a comprehensive review of the entire validation results has been difficult to achieve.
As part of the European AMHYCO project, a database of quasi-steady state measurement points was derived from these transient experiments. This new database enables the performance of PAR models to be validated for the boundary conditions of the entire test program. Furthermore, a critical analysis of measured and derived data was performed, enabling an assessment of uncertainties.
The new database was used to assess the validity of numerical PAR models used in AMHYCO analyses. First, the mechanistic code REKO-DIREKT was validated. Then, the performance of an engineering correlation for Framatome PARs under late-phase conditions was evaluated, before model improvements were implemented and confirmed.

KEYWORDS
Hydrogen mitigation, Passive autocatalytic recombiners (PAR), model validation, validation database

1. INTRODUCTION

In the context of protecting nuclear power plants from the consequences of accident-related massive hydrogen and carbon monoxide releases, the European AMHYCO project (2020-2025) focused particularly on the late phase of severe accidents in light water reactors (LWR). Here, the molten corium-concrete interaction (MCCI) can be a source of significant amounts of gaseous products, of which carbon monoxide

* Corresponding author

is of particular interest, being another combustible gas like hydrogen [1]. Consequently, the project addressed open issues related to the understanding of the impact of carbon monoxide on both hydrogen combustion phenomena and hydrogen mitigation by PARs under the conditions of the late accident phase.

The installation of 40-60 passive autocatalytic recombiners (PARs) inside the containment has become a key element in the hydrogen mitigation strategy of most western LWRs. Consequently, in AMHYCO specific attention was focused on understanding the performance of PARs under the challenging conditions of ex-vessel conditions. These conditions include specifically oxygen-lean conditions and involve the presence of carbon monoxide. For these conditions, only sparse knowledge was publicly available. Hence, the overall target was to advance the predictive capabilities of numerical PAR models, which were used in scenario analyses, to obtain a realistic picture of the PAR behaviour.

The further advancement of numerical PAR models was supported by an experimental program performed in the REKO facilities at Forschungszentrum Jülich [2]. Besides this AMHYCO-internal experimental campaign, the project made also use of data from the international OECD/NEA THAI projects. For this purpose, a specific database was extracted from selected THAI experiments that provided an additional validation step for the advanced PAR models towards the ultimate goal of the modelling activities in AMHYCO.

2. DATABASE GENERATION

The following section outlines the requirements for test data for PAR modelling (see also Figure 1, right) and describes the composition of the AMHYCO THAI database. The PAR models used within the project were the Framatome engineering correlation [3], the mechanistic models REKO-DIREKT (Forschungszentrum Jülich, Germany) [4] and PARUPM (Universidad Politécnica de Madrid, Spain) [5], and the CFD model SPARK developed by IRSN, France [6] (Figure 1, left).

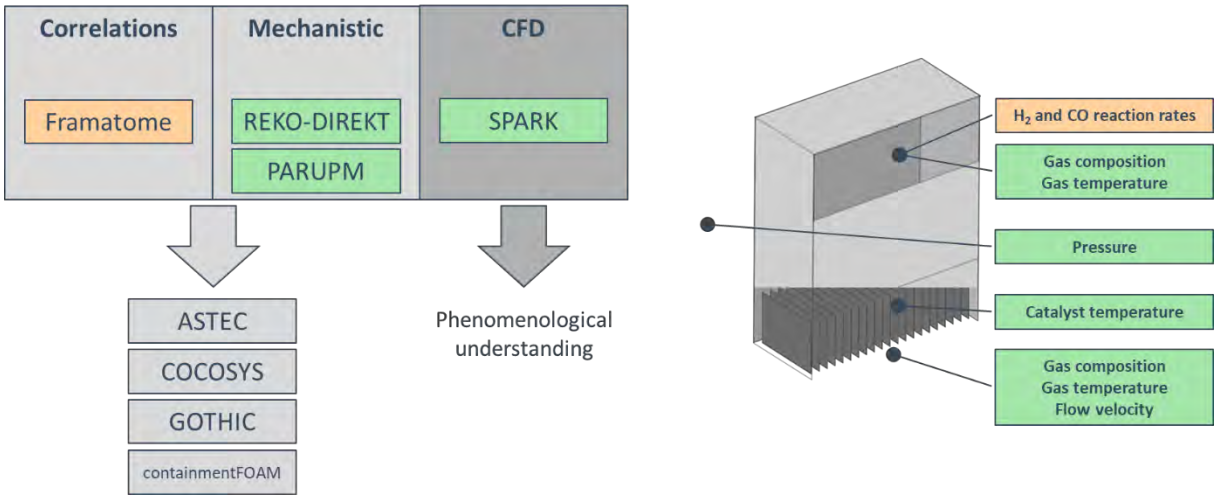

Figure 1. PAR models used in AMHYCO (left), data required for PAR model validation (right).

2.1. Requirements for a PAR Database

The minimum goal of the most fundamental PAR models is to predict the recombination rate of hydrogen based on the conditions of the atmosphere in the vicinity of the respective PAR. These conditions are typically

- pressure,
- gas temperature,
- and the composition of the gas mixture.

In severe accident scenario simulations, this information is available regardless of whether lumped parameter or CFD tools are used. Engineering correlations have become most widely established, e.g. for PARs by Framatome, CNL, or NIS [3]. These are relatively easy to implement due to their mathematical simplicity and require only minimal computing time. More complex PAR models provide further information beyond the recombination rate, such as

- catalyst temperature,
- outlet gas temperature,
- outlet gas composition,
- and the gas flow velocity,

at the price of increasing complexity and computational cost.

Within the scope of the AMHYCO project, another important step in model development was the consideration of the conversion of carbon monoxide to carbon dioxide inside PARs, which occurs specifically in the late accident phase. The corresponding conversion rates are also required for model validation. However, since the test data from the corresponding OECD/NEA projects for carbon monoxide are not yet publicly available, they cannot be presented here.

2.2. The AMHYCO THAI Database

The THAI facility operated by Becker Technologies in Eschborn/Germany is the centrepiece of several ambitious experimental programs conducted under the auspices of the OECD/NEA [7]. The experiments address various accident phenomena inside LWR containments and cover a wide range of thermophysical boundary conditions. Of specific interest for the AMHYCO project were experiments on the operational behaviour of Framatome PARs. A total of around 50 experiments were conducted with this PAR type. Framatome PARs thus represent the devices with the largest available independent database worldwide.

The PAR experiments were performed with a single PAR inside the THAI vessel with a volume of approx. 60 m^3. The experiments are of transient nature, which means that the boundary conditions of PAR operation are continuously changing. When hydrogen is fed into the vessel and the PAR starts operation, there is a continuous change of the hydrogen concentration – increasing during the injection phase, decreasing during the depletion phase. Additionally, due to the energy release, gas temperature inside the vessel atmosphere increases continuously. In the past, the validation of PAR models against these transient data has always been performed using single selected experiments. By this approach, the general view at strengths and weaknesses of models was lost.

In AMHYCO, the generation of a database of quasi-steady state measurement points derived from the transient THAI experiments aimed at providing a validation database, which allows to gain an overview of the PAR model performance for the entire experimental program rather than only comparing single transient experiments with model calculations. The database is suited for testing both, correlation model and detailed PAR models.

Figure 2 shows the progression of the hydrogen concentration at the PAR inlet over time of a typical THAI HR test sequence (here: HR-3). After reaching the initial atmosphere conditions (pressure, temperature, humidity, a prototypical test involves the following steps:

- hydrogen injection until reaching approx. 6 vol.% (1st injection phase)
- stop of injection and subsequent depletion of hydrogen by the PAR (1st depletion phase)
- hydrogen injection until ignition occurs (2nd injection phase)
- stop of injection and subsequent depletion of hydrogen by the PAR (2nd depletion phase)

Instead of evaluating the entire time evolution of the experiment, only some quasi-steady state measurement points were identified as indicated by the coloured circles in Figure 2. The measurement values were averaged for 60 s around these selected measurement points.

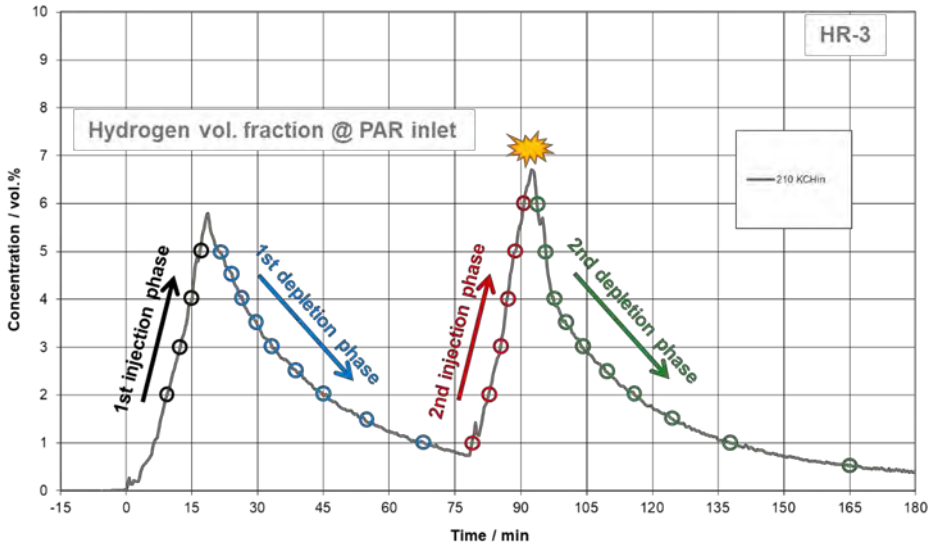

Figure 2. Progression of the hydrogen concentration in a typical PAR test sequence.

Figure 3 and Figure 4 show the obtained averaged flow velocity through the PAR and the hydrogen outlet concentration over the inlet hydrogen concentration for all four experimental phases. During both injection phases (black and red circles) as well as during the first measurement points of the first depletion phase (blue circles for concentrations above 3 vol.%) the PAR performance is not yet well developed. It takes until the second depletion phase until the PAR is in quasi-steady state operation. Based on this observation, the database considers only data from the second depletion phase (green circles).

The following data values were taken from the second depletion phases to serve as PAR model input conditions, see Figure 1 (right):

- Total pressure in bar
- Gas temperature in °C at the PAR inlet

  As the temperature measurement at the PAR inlet is significantly influenced by the heat radiation from the hot catalyst sheets [8], the value from a different thermocouple has been selected (HR-1 - HR-28: 067 BTF21H12; HR-51ff: 118 BTF13B07). These thermocouples are mounted at a similar elevation inside the THAI vessel as the PAR, but being located on the opposite side of the inner cylinder they are well shielded against heat radiation.

- Gas composition (hydrogen, oxygen, steam, later carbon monoxide and carbon dioxide) in vol.% at the PAR inlet

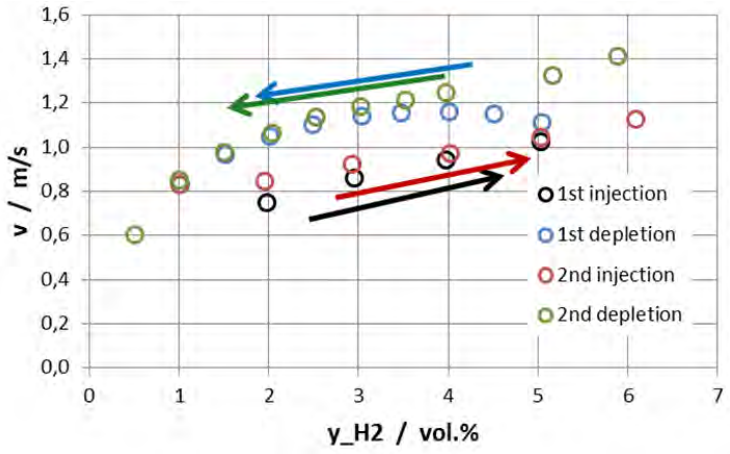

Figure 3. Experimental phases and selected measurement points for the flow velocity.

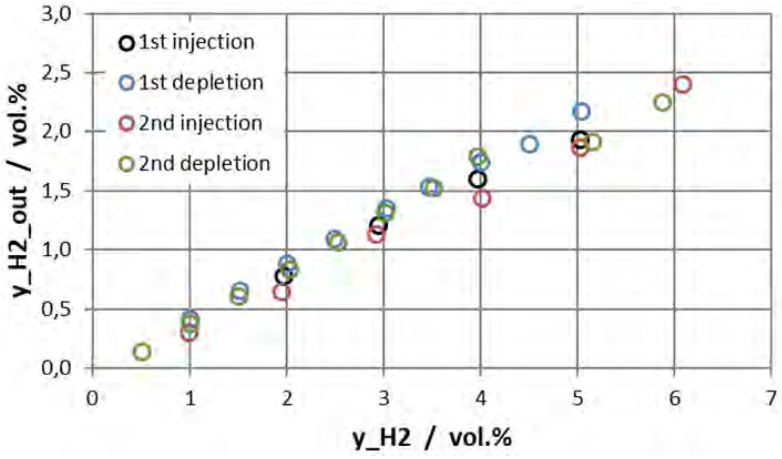

Figure 4. Experimental phases and selected measurement points for the outlet hydrogen concentration.

The following data values were derived to be used for the PAR models to validate the calculation results (PAR model output), see Figure 1 (right):

- Gas temperature in °C at the PAR outlet

  The outlet temperature is measured at three different positions in THAI. As PAR models don't consider the temperature distribution in the PAR outlet cross section, the average value has been calculated.
- Gas composition (hydrogen, oxygen, steam, in later tests carbon monoxide and carbon dioxide) in vol.% at the PAR outlet

  Like for the gas temperature, the outlet gas concentrations are measured at three different positions in THAI. Again, PAR models require averaged values for the PAR outlet. Due to the

unclear measurement signal of one of the three measurement positions (in [8] it is suggested, that buoyant backflow occurs at the measurement gas probe at the lower edge of the PAR outlet), the user selects between an average of either the two remaining sensor values or all three values. The discrepancy between both options provides a measure for the measurement uncertainty.

- Flow velocity in m/s
- Recombination rates (for hydrogen, later also for carbon monoxide) in g/s

  Two different equations are used to calculate the recombination rates. The official equation proposed in the THAI project is based on a hydrogen mass balance of the catalyst section and uses the measurement values of the hydrogen concentration at the PAR inlet and outlet ($y_{H2,in}$ and $y_{H2,out}$), pressure (p), flow velocity (v) and gas temperature at the PAR inlet (T_{in}) with the PAR inlet cross section (A_{in}), and the specific ideal gas constant for hydrogen (RH2):

  $$\dot{r}_{H2} = \left(y_{H2,in} - y_{H2,out}\right) \cdot (p \cdot v \cdot A_{in})/(R_{H2} \cdot T_{in}) \quad (1)$$

  This equation omits the reduction of the outlet molar flow. Hence, an alternative value for the recombination rate was added to the database, which is calculated according to a molar balance of the catalyst section:

  $$\dot{r}_{H2} = \left(y_{H2,in} - y_{H2,out}\right)/\left(1 - 0.5 \cdot y_{H2,out}\right) \cdot (p \cdot v \cdot A_{in})/(R_{H2} \cdot T_{in}) \quad (2)$$

  Furthermore, Equation 2 uses the cross section of the instrumentation inlet channel instead of the PAR inlet cross section. Due to the uncertainties with regard to inlet temperature and outlet gas composition (see above), each of both equations is calculated with different values: (i) official inlet temperature and average outlet concentrations of three values; (ii) alternate inlet temperature and average outlet concentrations of three values; (iii) alternate inlet temperature and average outlet concentrations of two values. The six different values for the recombination rate are used to obtain uncertainty bars for the recombination rates (see example in Figure 5).
- Catalyst temperatures in °C at three vertical positions of the catalyst sheet
  (low = 1 cm, mid = 7 cm, up = 13 cm)

  For measurements values from different catalyst sheets at identical positions, average values are provided. Similar as for the recombination rates, the measurement discrepancies are used to obtain uncertainty bars for the catalyst temperature values.

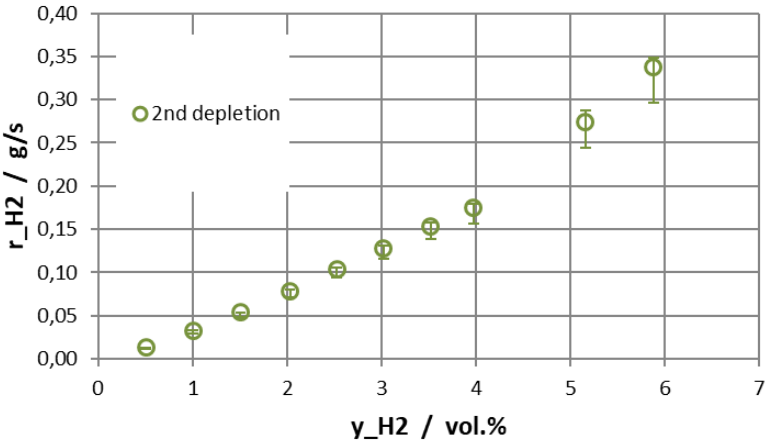

Figure 5. Example for recombination rates with uncertainty bars.

Table I gives an overview of selected tests from the THAI HR program for Framatome PARs that were selected to be included in the AMHYCO database due to their suitability to obtain quasi-steady state data.

The tests that were omitted had different objectives, some of which involved significant transients. The selected tests cover a comprehensive range of boundary conditions, with pressure between 1 bar and 3 bar, gas temperature between 25 °C and 117 °C, and up to 60 vol.% steam, and both oxygen-rich and oxygen-lean gas mixtures. Overall, the database consists of 132 quasi-steady state measurements.

Table I. HR tests selected for the AMHYCO database

Test number	Pressure	Temperature	Humidity
HR-1, HR-2	1.0 bar	25 °C	Dry
HR-13		86 °C	60 vol.% steam
HR-3, HR-28, HR-51	1.5 bar	25 °C	Dry
HR-7		74 °C	25 vol.% steam
HR-9		90 °C	47 vol.% steam
HR-11		97 °C	60 vol.% steam
HR-5	3.0 bar	25 °C	Dry
HR-12, HR-52, HR-53		117 °C	60 vol.% steam

3. MODEL VALIDATION

In the framework of the AMHYCO project, a total of four PAR models have been advanced according to the databases developed in the experimental program. The new AMHYCO THAI database was specifically used to further advance the Framatome engineering correlation and to validate the REKO-DIREKT code.

3.1. Advancement of the Engineering Correlation for Framatome PARs

Based on progress made within the AMHYCO project and its predecessor, the SAMHYCO-NET project [9], the engineering correlation for Framatome PARs was further developed. A detailed description of the new so-called AMHYCO correlation is given in reference [10]. One focus of the advancement was on the refinement of the recombination rate predictions for oxygen-lean conditions. The new THAI database proved to be a very useful basis for identifying model deficiencies as well as demonstrating the progress made.

Figure 6 (top) shows a plot of the hydrogen recombination rates obtained with the existing engineering correlation against the recombination rates obtained from the THAI database. The experiments performed under oxygen-rich conditions are marked with open symbols, while experiments performed under oxygen-lean conditions are represented by filled symbols. While the original correlation performs well under oxygen-rich conditions, a significant uncertainty (over- as well as underprediction) is visible for oxygen-lean conditions. This was a relevant point for the AMHYCO project as oxygen-lean conditions are expected to be present during almost the entire ex-vessel phase of the accident scenarios to be analysed.

The observed uncertainty was significantly reduced by the new AMHYCO correlation. The comparison of recombination rates with the AMHYCO THAI database (Figure 6, bottom) demonstrates the successful improvement of the correlation as well as the suitability of the new database to support targeted model advancement.

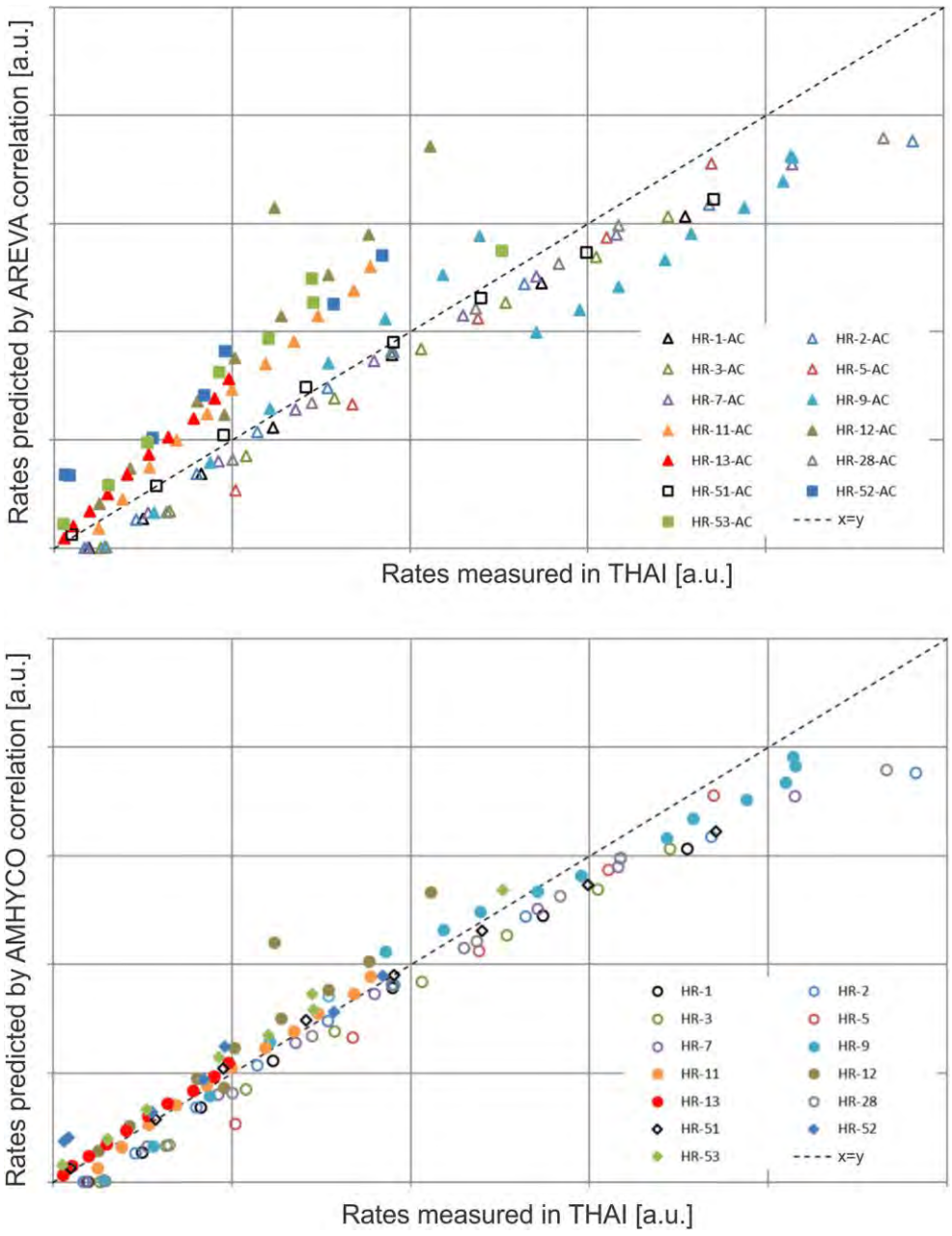

Figure 6. Comparison of calculated recombination rates with the AMHYCO THAI database (top: original correlation, bottom: new AMHYCO correlation) [10]

The rates for carbon monoxide recombination (not included here) show a comparable trend. The corresponding validation data, which involve new experiment from the OECD/NEA THEMIS project, cannot be shown in the present paper due to contractual reasons.

3.2. Validation of REKO-DIREKT

REKO-DIREKT is a mechanistic PAR model that provides several additional information on PAR performance data, such as the catalyst temperature distribution and an internal model to calculate the chimney flow velocity. It can be used for arbitrary PAR geometries. Having been developed with in-house single-effect experiments, the AMHYCO THAI database was used to validate the model.

Figure 7 shows the comparison of calculated hydrogen outlet concentrations with the values from the THAI database. The database allows for quantification of the agreement by calculating statistical deviations. In this example, the results confirm the overall good prediction of the hydrogen outlet concentration for the entire pressure range. Similarly, it is confirmed that the oxygen conditions (rich or lean) have no influence on the quality of the results.

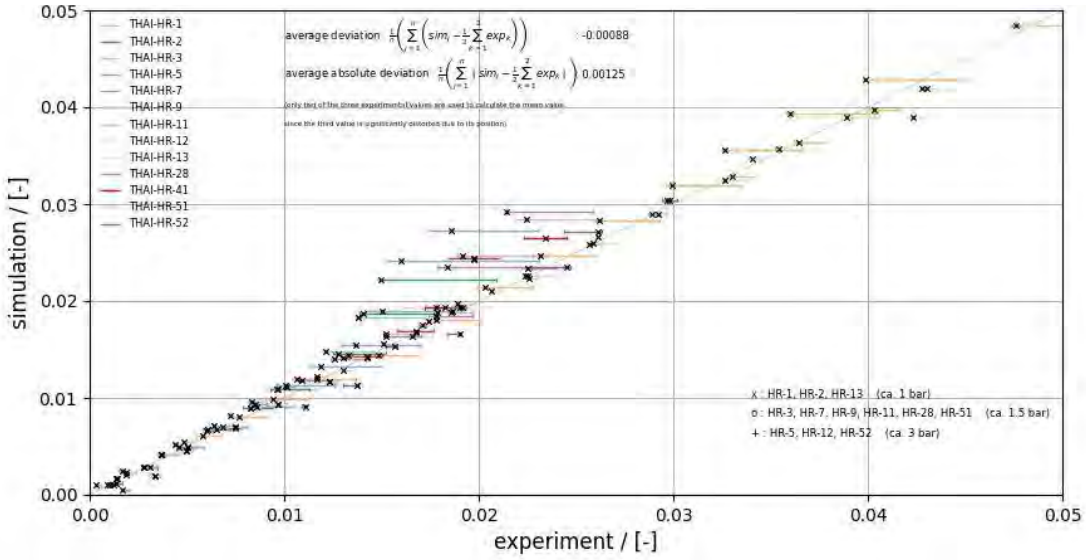

Figure 7. Calculated outlet hydrogen concentration (REKO-DIREKT) compared with values from the AMHYCO THAI database.

A specific feature of REKO-DIREKT is the calculation of the temperature profile along the catalyst sheets. A comparison of calculated and measured values is shown in Figure 8. Again, the quality of the results is independent from the pressure. Overall, the agreement is good, although the calculated temperature values are systematically too high.

As these examples show, the AMHYCO database supports consistent model improvements for PAR models. Model adjustments that lead to an improvement in the code can be immediately tested and evaluated in the way demonstrated.

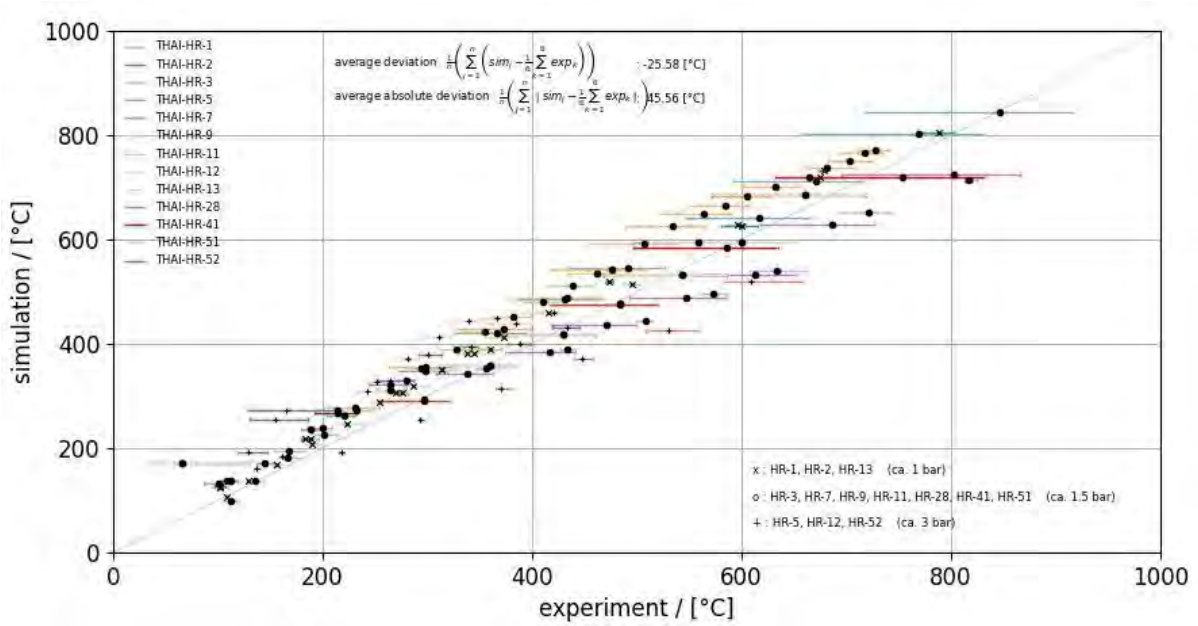

Figure 8. Calculated catalyst temperatures (REKO-DIREKT) compared with data from the AMHYCO THAI database.

4. CONCLUSIONS

PAR models are a valuable tool to assess the efficiency of the hydrogen mitigation strategy for severe accidents in LWRs. Part of the work within the AMHYCO project has specifically focused on advancing and validating PAR models with regard to the boundary conditions of the late phase of a severe accident. Careful validation of the advanced PAR models is mandatory for reliable scenario simulations.

In AMHYCO, a database was developed that consists of quasi-steady state measurement data from the transient PAR experiments performed in the framework of the OECD/NEA THAI projects. The database allows to simultaneously compare PAR model calculations with the entire range of boundary conditions studied in the experiments. Optional evaluation paths for some variables, e.g. the recombination rate or the outlet concentration, allow to assess uncertainties beyond the measurement accuracies based on the respective measurement devices.

The new AMHYCO THAI database represents a significant improvement compared to the consecutive validation of PAR models against single experiments. By this, model deficiencies can be more conveniently and more precisely identified, and the accuracy of the PAR model can be quantitatively assessed. Both aspects have been successfully demonstrated with the engineering correlation for Framatome PARs and the mechanistic PAR code REKO-DIREKT for generic PARs.

The AMHYCO project has also been studying the effect of carbon monoxide-induced catalyst poisoning and the corresponding relevant boundary conditions and gas mixtures. The future development of the database aims to include these aspects as well as introducing new experiments performed as the OECD/NEA THEMIS project continues.

ACKNOWLEDGMENTS

The AMHYCO project has received funding from the Euratom research and training programme 2019-2020 under Grant Agreement n◦945057. The content of this paper reflects only the author's view. The European Commission is not responsible for any use that may be made of the information it contains.

The financial support of the participating countries to the OECD/NEA THAI projects is gratefully acknowledged. The data for the tests HR-51 to HR-52 are part of the THAI-VI national project, which was funded by the German Federal Ministry for Economic Affairs and Energy under grant number 1501547, on the basis of a decision by the German Bundestag.

REFERENCES

1. M. Petit, H. Alsmeyer, V. Gustavsson, In-vessel and ex-vessel hydrogen sources, part ii: GAMA perspective statement on ex-vessel hydrogen sources, NEA/CSNI/R(2001)15.
2. E.-A. Reinecke, G. Nobrega, A. Bentaib, A. Domínguez-Bugarín, G. Jiménez, M. Braun, S. Struth, C. Druska, M. Klauck, Outcomes of the experimental and numerical work on the operational behavior of passive auto-catalytic recombiners in the late phase of a severe accident in the framework of the AMHYCO project, *Proc. 11th European Review Meeting on Severe Accident Research (ERMSAR2024)*, Stockholm, Sweden, May 13-16, 2024.
3. Reinecke, E.-A., Bentaib, A., Kelm, S., Jahn, W., Meynet, N., Caroli, C., Open issues in the applicability of recombiner experiments and modeling to reactor simulations, *Progress in Nuclear Energy* **52** (2010) 136-147.
4. E.-A. Reinecke, S. Kelm, P.-M. Steffen, M. Klauck, H.-J. Allelein, Validation and application of the REKO-DIREKT code for the simulation of passive auto-catalytic recombiners (PARs) operational behavior, *Nuclear Technology* **196/2** (2016) 355-366.
5. A. Domínguez-Bugarín, C. Vázquez-Rodríguez, L. Serra, S. Kelm, E.-A. Reinecke, Gonzalo Jiménez, Miguel Ángel Jiménez, S. Gupta, Validation of the PARUPM and GOTHIC 8.3 code coupling using THAI hydrogen recombination tests, *Annals of Nuclear Energy* **226** (2026) 111855.
6. N. Meynet, A. Bentaïb, V. Giovangigli, Impact of oxygen starvation on operation and potential gas-phase ignition of passive auto-catalytic recombiners. *Combustion and Flame* **161/8** (2014) 2192-2202.
7. S. Gupta, M. Freitag, G. Poss, THAI experimental research on hydrogen risk and source term related safety systems, *Frontiers in Energy* **15** (2021) 887-915.
8. E.-A. Reinecke, S. Kelm, B. Simon, M. Klauck, H.-J. Allelein, Interpretation of the entire OECD/NEA-THAI HR test series including AREVA and AECL PARs using the code REKO-DIREKT, *OECD/NEA THAI2 Final Seminar*, Frankfurt/Main, Germany, November 18-19, 2014.
9. E.-A. Reinecke, J. Fontanet, L.E. Herranz, Z. Liang, L. Maas, O. Mazurok, J.-S. Park, D.C. Visser, M. Hupp, S. Gupta, PAR model development exercise in the framework of SAMHYCO-NET, *Nuclear Engineering and Design* **399** (2022) 112035.
10. M. Braun and E.-A. Reinecke, AMHYCO engineering correlation to describe the conversion of flammable gases in Framatome passive autocatalytic recombiners, *Nuclear Engineering and Design* **442** (2025) 114206.

DEVELOPMENT OF A DATABASE FOR PAR MODEL VALIDATION BASED ON THAI EXPERIMENTS AND ITS APPLICATION IN THE FRAMEWORK OF THE AMHYCO PROJECT

ERNIE REINECKE, CLAUDIA DRUSKA, MATTHIAS BRAUN (FRAMATOME GMBH, ERLANGEN)

ERMSAR 2026 | MADRID, SPAIN | MAY 18-22, 2026

Mitglied der Helmholtz-Gemeinschaft

JÜLICH Forschungszentrum

OUTLINE

Development of a Database for PAR Model Validation based on THAI Experiments and its Application in the Framework of the AMHYCO Project

- Background
- Needs for PAR Model Development
- Database Generation
- Adding Uncertainties
- Model Validation
  - Framatome Engineering Correlation
  - REKO-DIREKT
- Conclusions

BACKGROUND: PARS

Passive Auto-Catalytic Recombiners (PARs)

- PARs are qualified safety systems for conditions of nuclear power plant accidents for flameless conversion of hydrogen.
- Due to the exothermal reaction, a buoyancy-driven flow is induced through the chimney on top of the catalyst section.
- Being an entirely passive safety measure, PARs will operate even in case of SBO and without operator's interaction.

Framatome (France)

AECL/CNL (Canada)

NIS (Germany)

RET (Russia)

Ceracomb (Korea)

OUTLET
Air, produced vapor and residual hydrogen leaving the PAR box

CHIMNEY
Amplification of the buoyancy effect due to exothermal reaction

CATALYST SECTION
$H_2 + ½\ O_2 \Rightarrow H_2O$ + heat
$CO + ½O_2 \rightarrow CO_2$ + heat

INLET
Hydrogen and air entering the PAR box

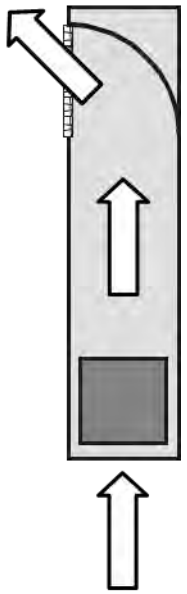

BACKGROUND: SEVERE ACCIDENT – LATE PHASE

Mitigation of the Combustion Risk under Challenging Conditions

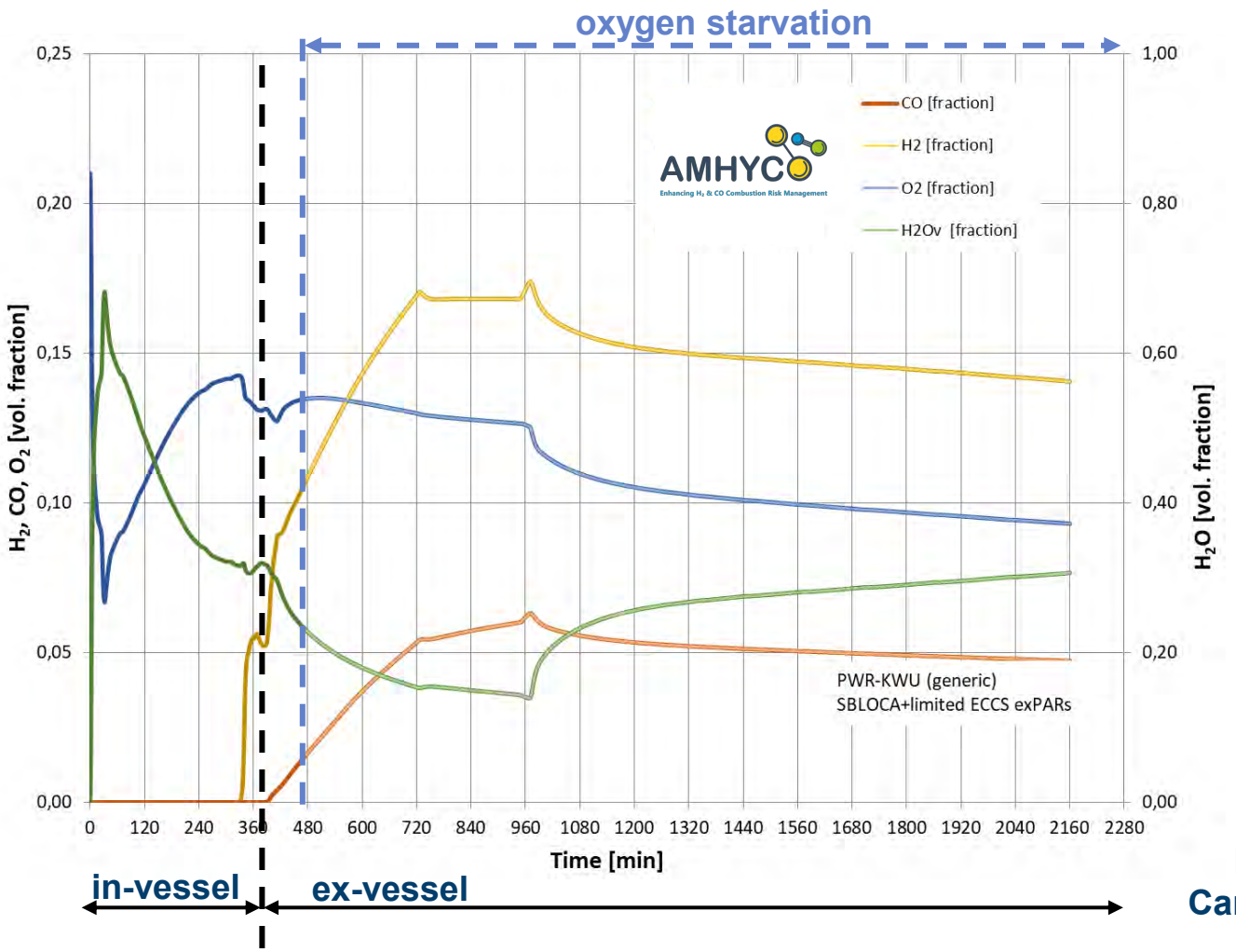

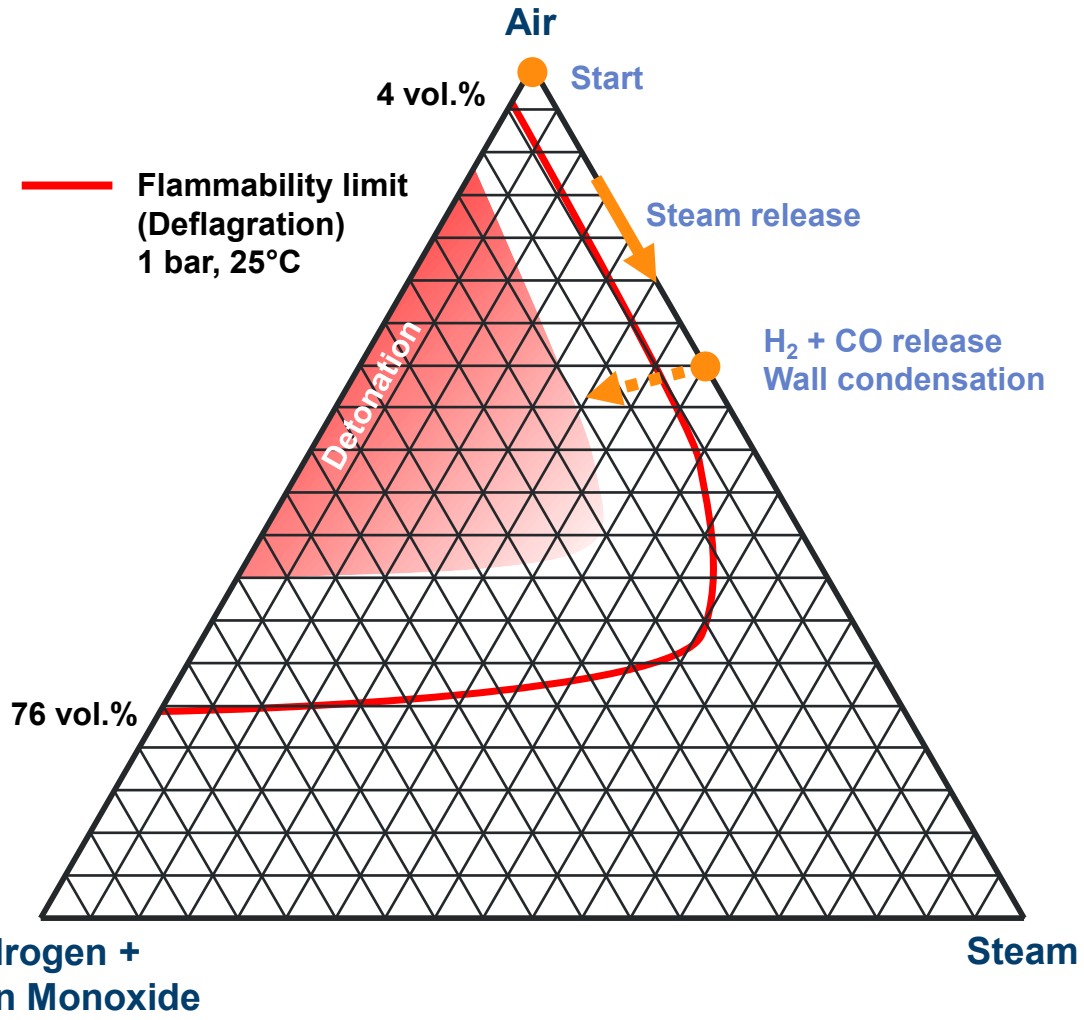

BACKGROUND: AMHYCO – WP3

Objective: Realistic PAR Behavior in Accident Simulations

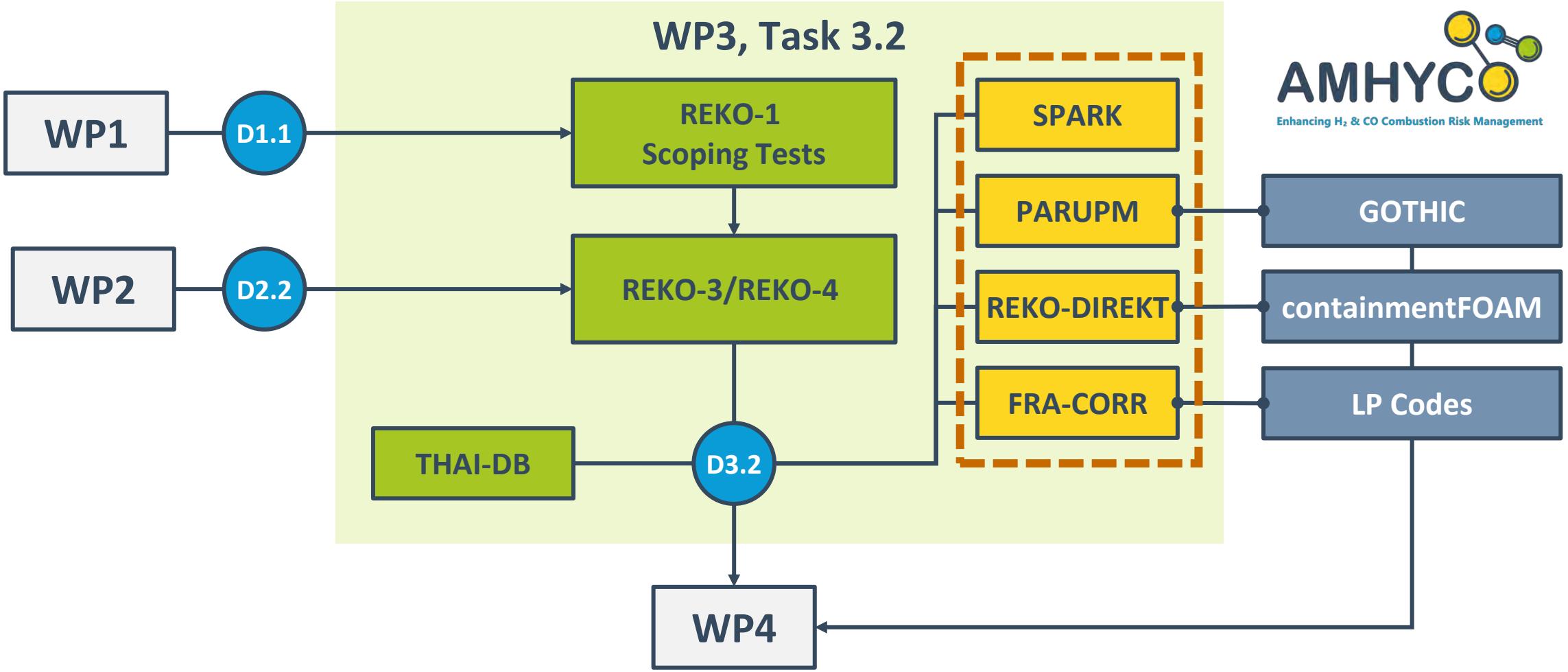

BACKGROUND: PAR CODES

Model Strategies

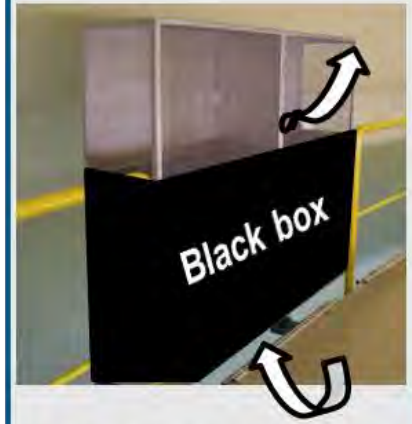

Rate Correlations (Manufacturers)

- Integral recombination rate

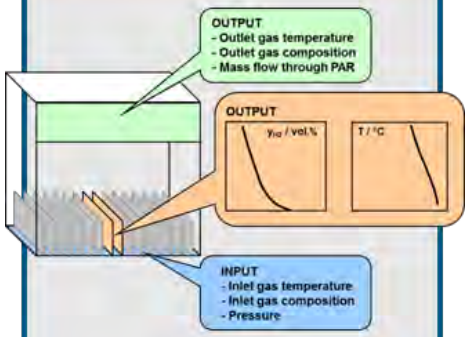

REKO-DIREKT (JÜLICH)

+ addition of
- Local recombination rate
- Local catalyst temperature
- Chimney flow

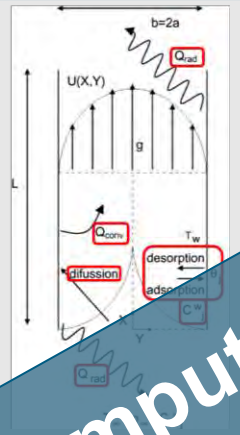

ARUPM (UPM)

+ addition of
- Surface reaction

ANSYS-CFX (JÜLICH)

+ addition of
- Temperature field
- Concentration field
- 3D flow & transport phenomena

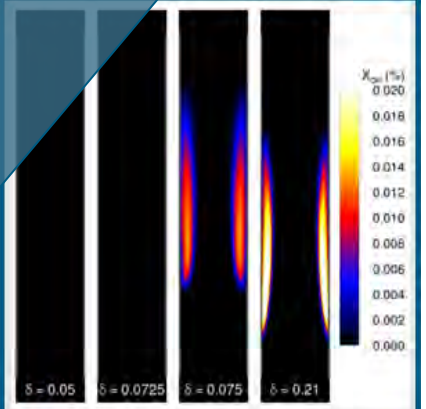

SPARK (IRSN)

+ addition of
- Gas phase chemistry
- Surface chemistry
- Multi-component transport

Level of detail & computational cost

NEEDS FOR PAR MODEL DEVELOPMENT

PAR Models in AMHYCO and their Purposes

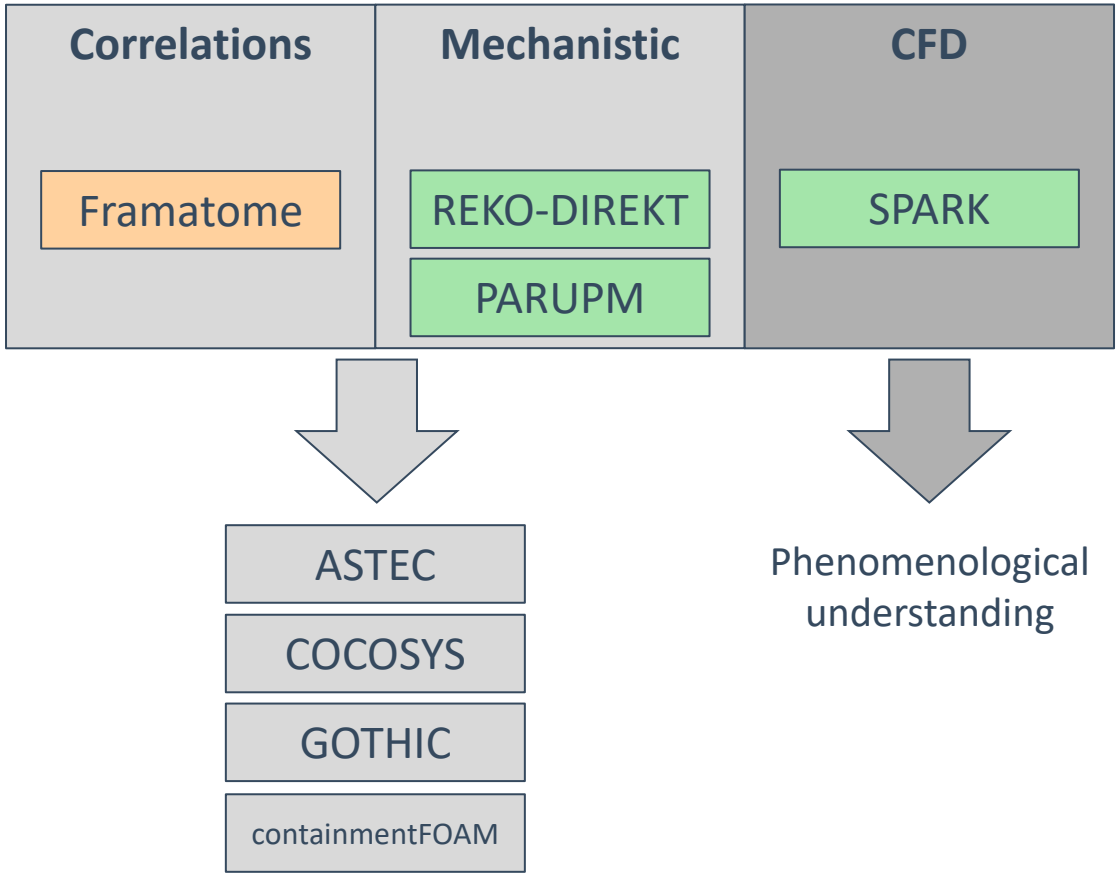

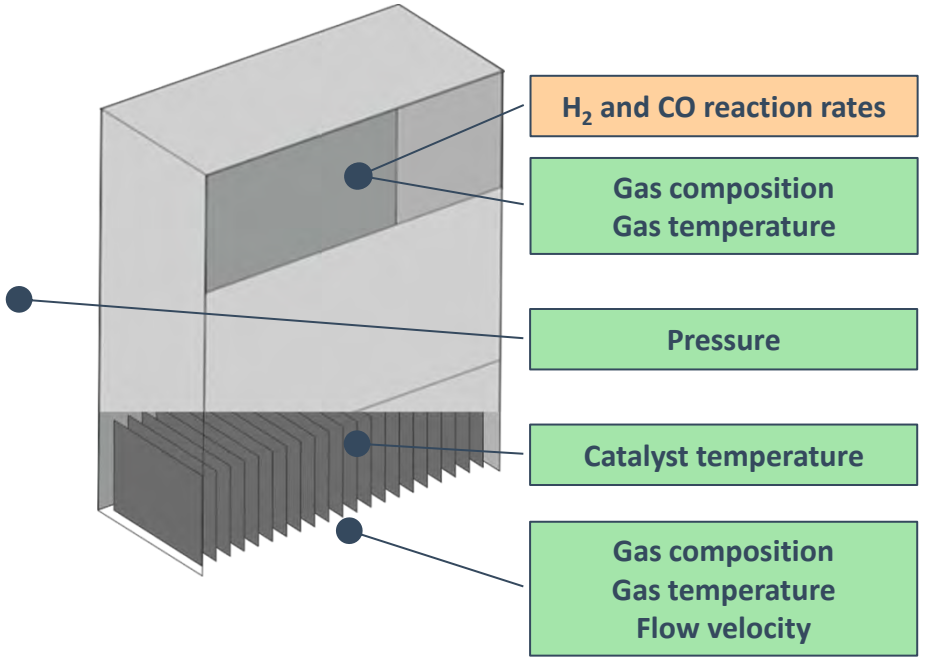

NEEDS FOR PAR MODEL DEVELOPMENT

Available PAR Experiments

THAI

- Transient measurements
- Natural flow conditions

➔ **Need for (quasi-) steady state data**

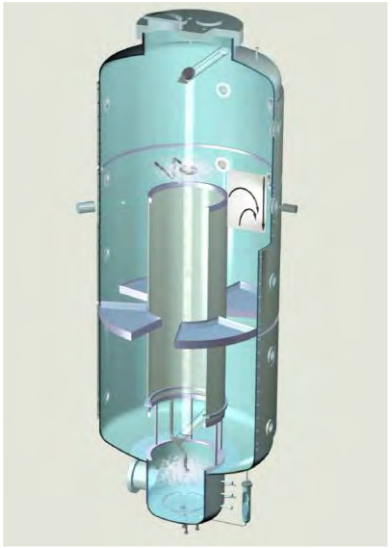

REKO-3

- Steady state measurements
- Forced flow conditions

➔ **Need for „realistic“ inlet parameters**

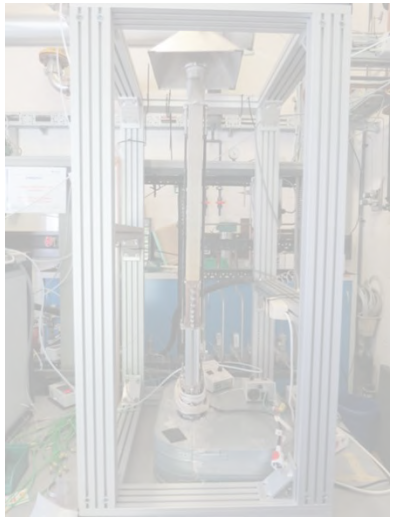

GENERATING THE AMHYCO THAI-DB

PAR Experiments: HR Series

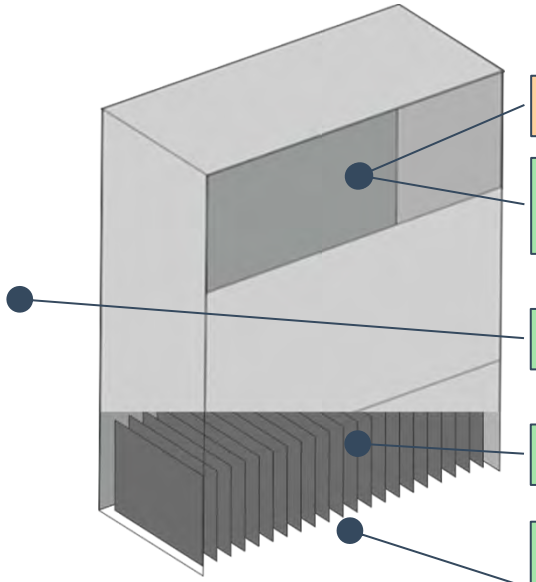

H_2 and CO reaction rates

Gas composition
Gas temperature

Pressure

Catalyst temperature

Gas composition
Gas temperature
Flow velocity

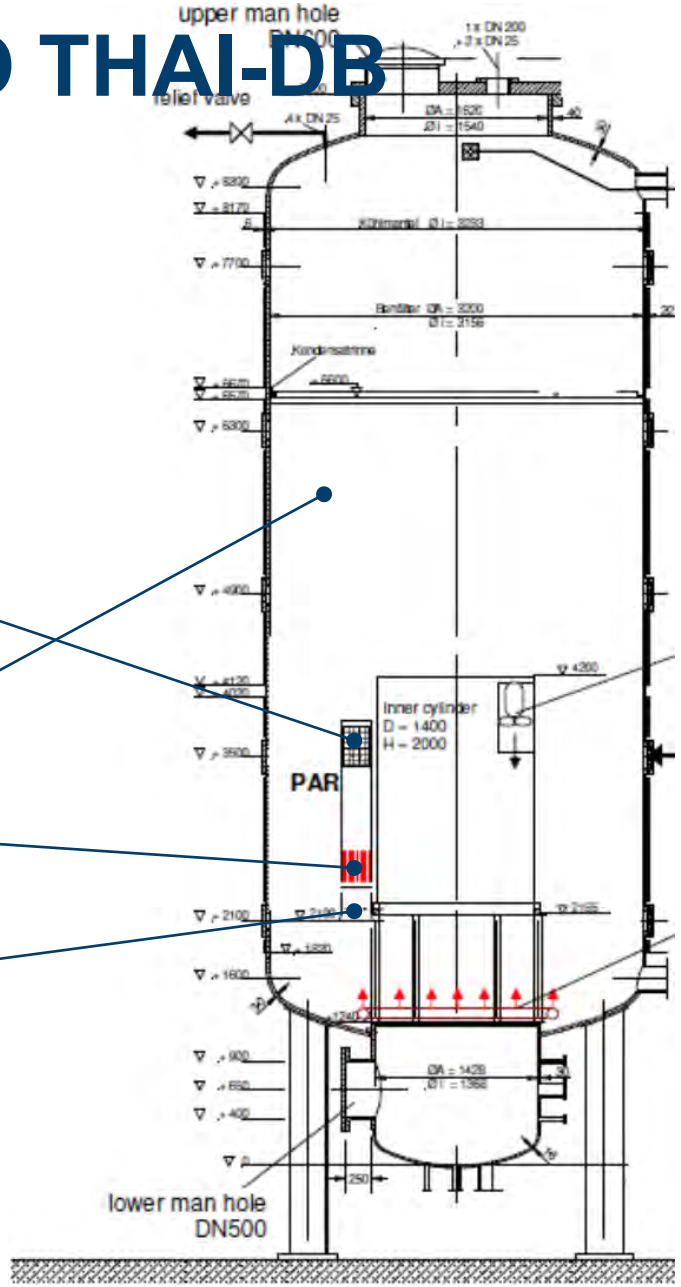

GENERATING THE AMHYCO THAI-DB

Analysis of Experimental Phases and Data Point Selection (Average over 1 min)

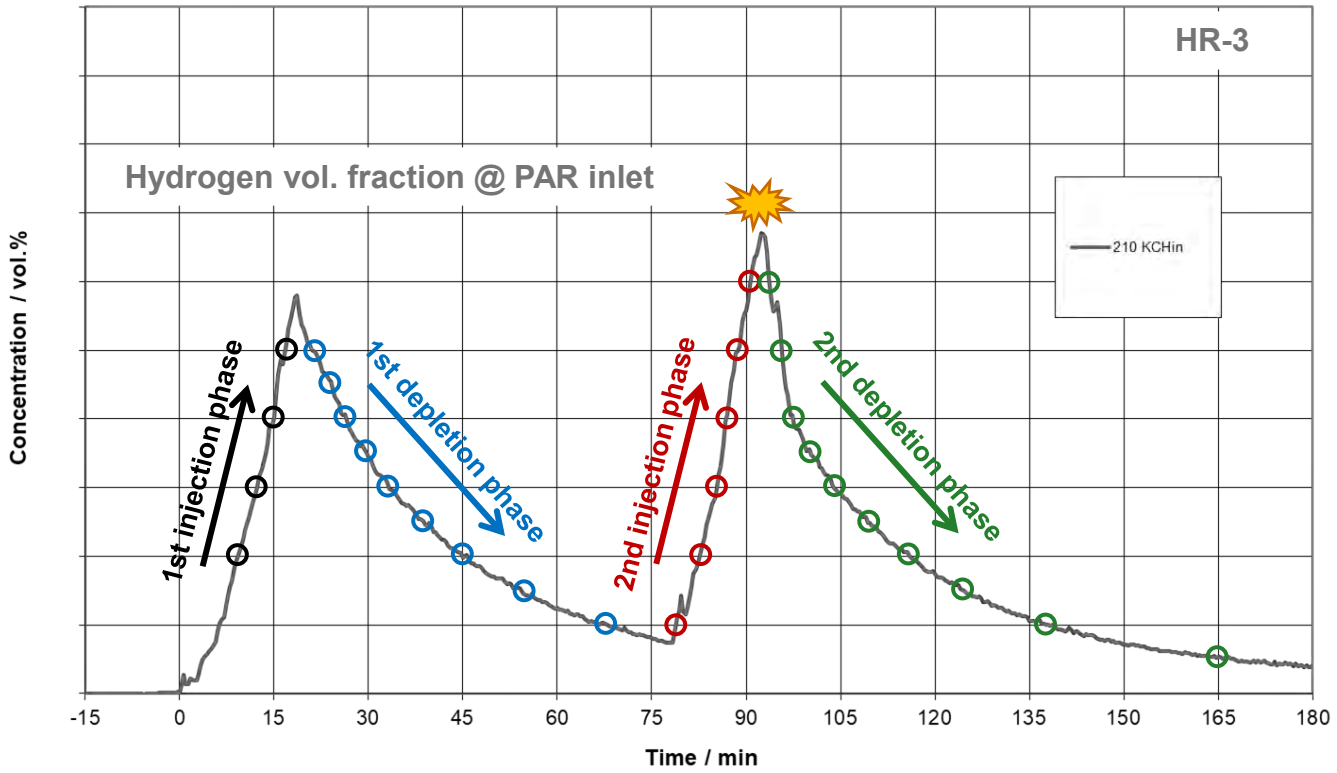

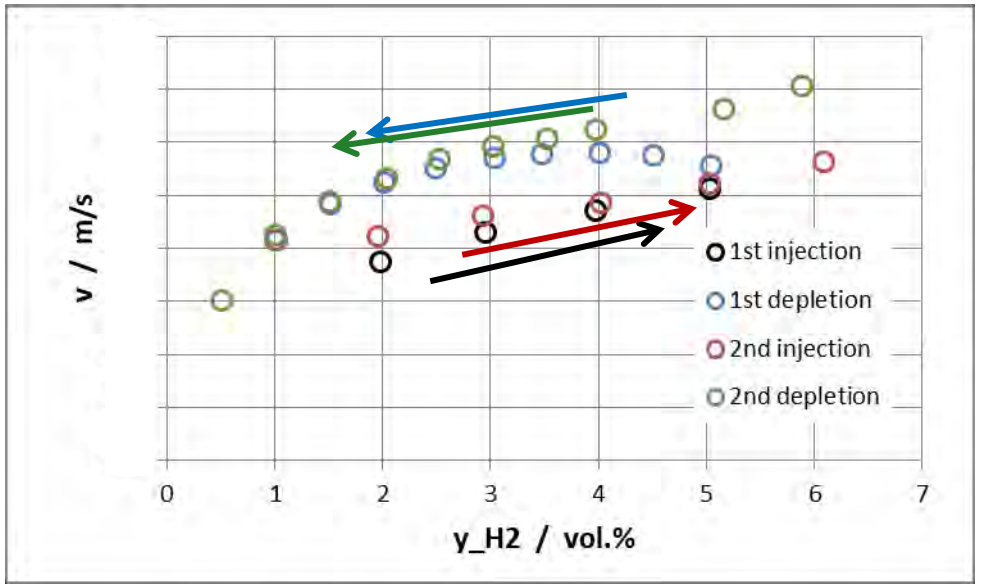

Calculation of recombination rate:

$$M_{H2} = \frac{(C_{H2in} - C_{H2out}) \cdot P \cdot V_{in} \cdot A_{in}}{R_{H2} \cdot T_{in}}$$

➔ **Database considers only 2nd depletion phase**

GENERATING THE AMHYCO THAI-DB

Example: Catalyst Temperature

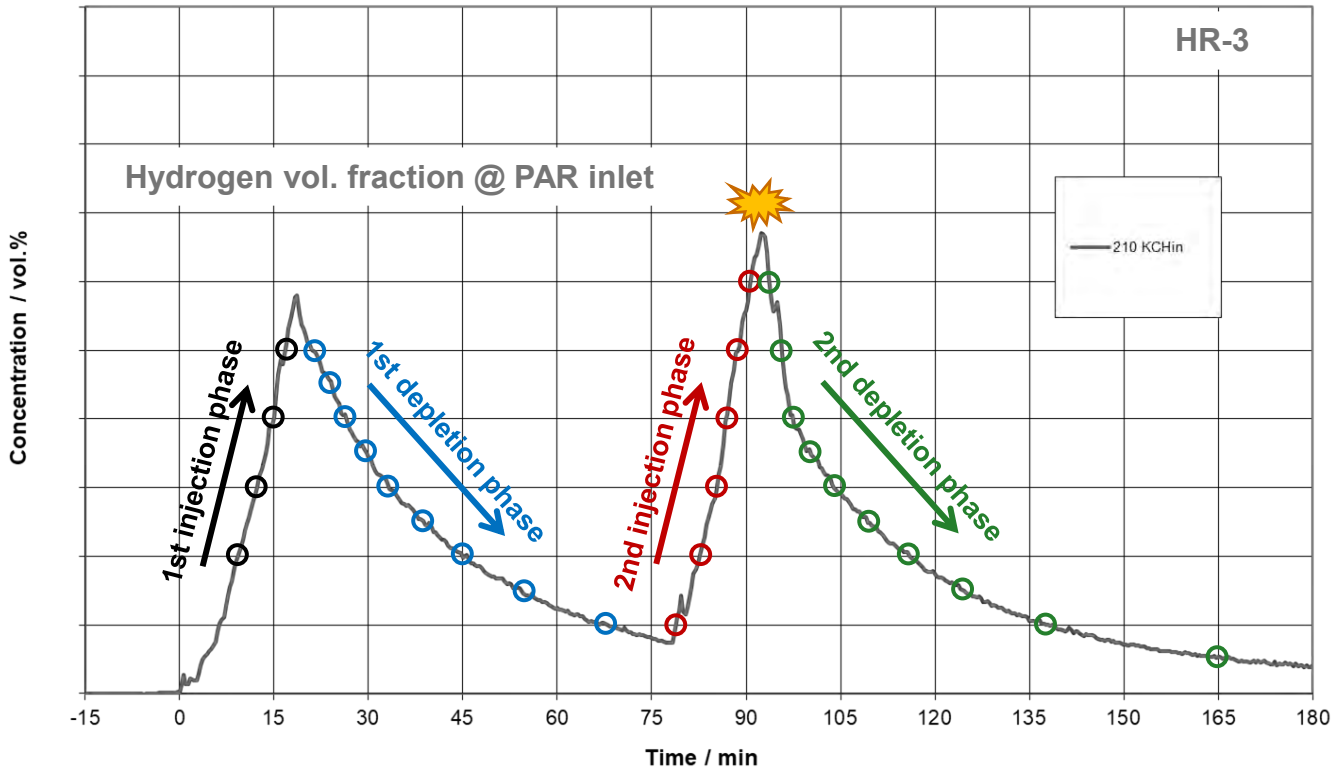

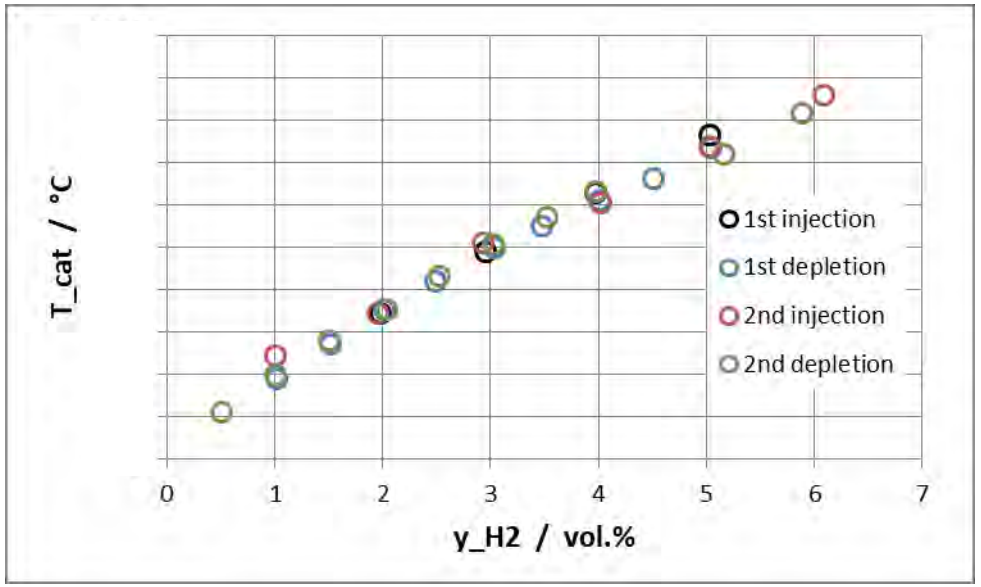

Catalyst temperature less problematic due to low thermal inertia of the catalyst sheets

GENERATING THE AMHYCO THAI-DB

Selection of HR Tests

Test number	Pressure	Temperature	Humidity
HR-1, HR-2	1.0 bar	25 °C	Dry
HR-13		86 °C	60 vol.% steam
HR-3, HR-28, HR-51	1.5 bar	25 °C	Dry
HR-7		74 °C	25 vol.% steam
HR-9		90 °C	47 vol.% steam
HR-11		97 °C	60 vol.% steam
HR-5	3.0 bar	25 °C	Dry
HR-12, HR-52, HR-53		117 °C	60 vol.% steam

➔ 132 quasi-steady state measurement points

ADDING UNCERTAINTIES

Optional Decisions by Users

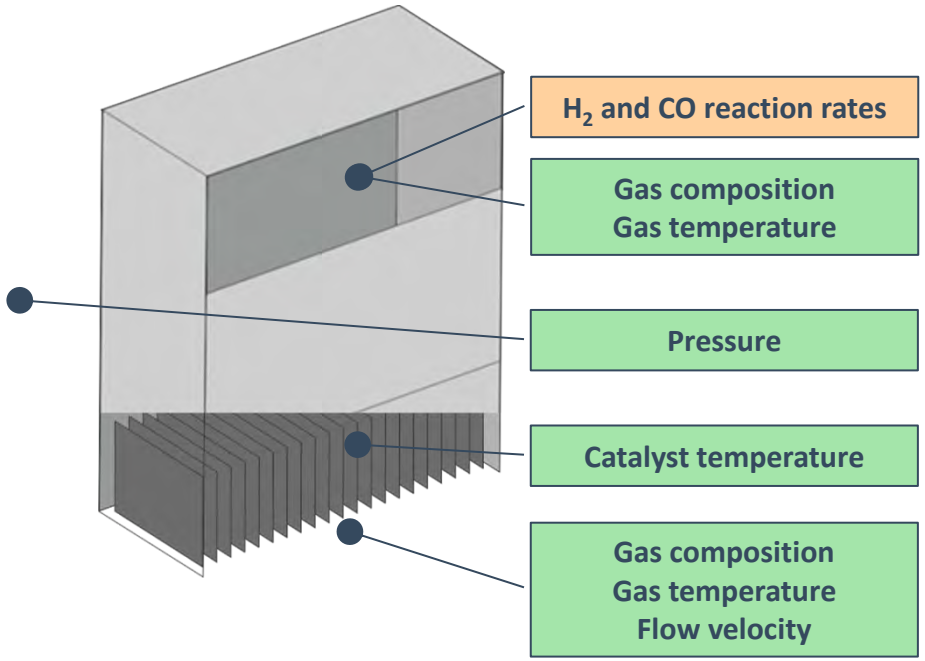

Adding uncertainties

- Inlet gas temperature
- Outlet concentration
- Recombination rate
- Catalyst temperature
- Outlet gas temperature

ADDING UNCERTAINTIES

Inlet Gas Temperature

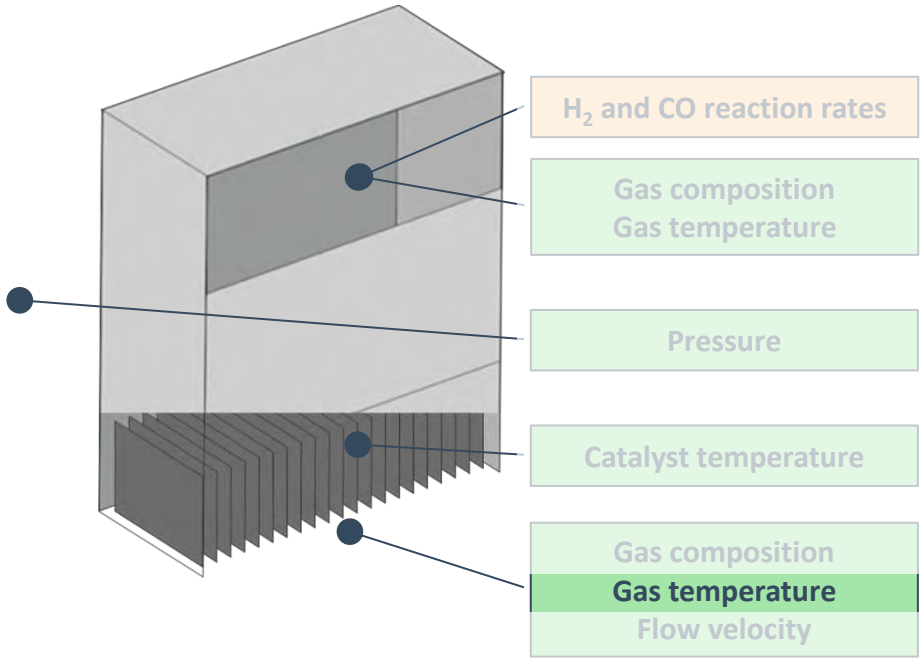

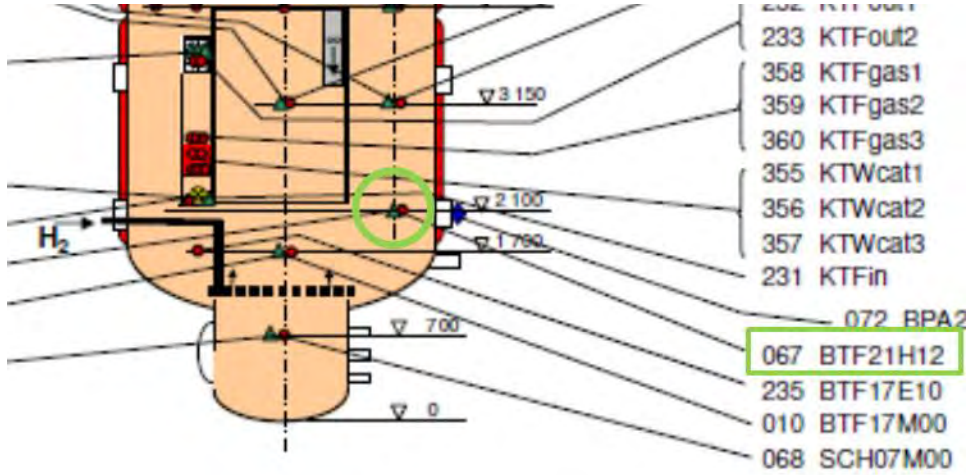

ADDING UNCERTAINTIES

Inlet Gas Temperature

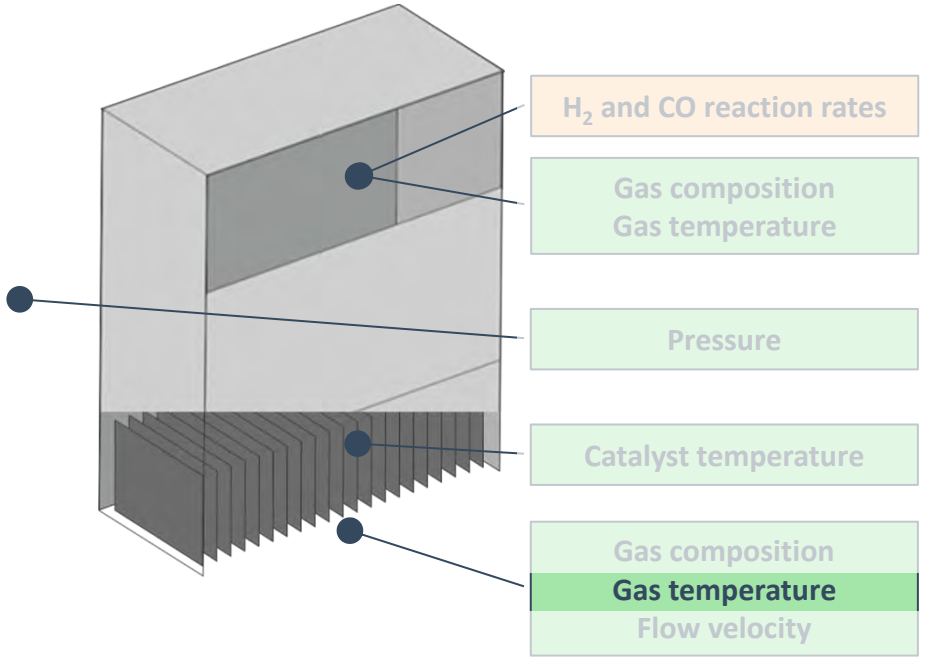

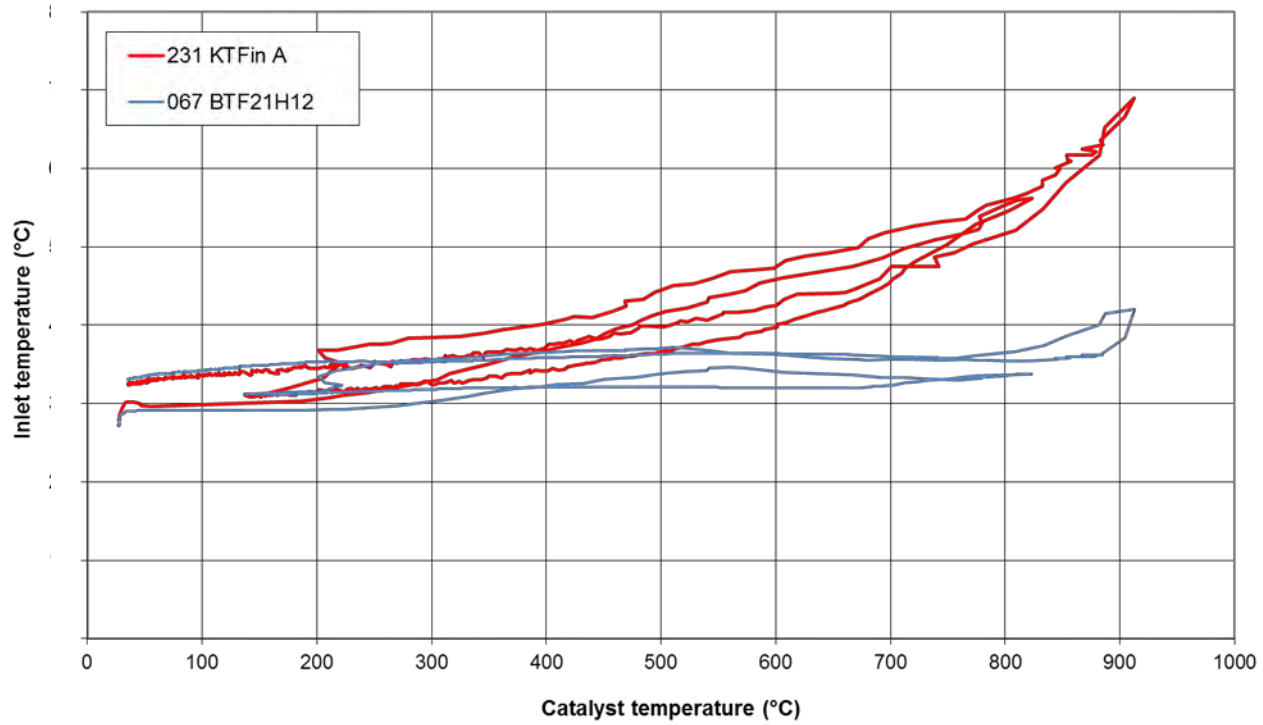

➔ **Optional: use of BTF21H12 instead of KTFin**

ADDING UNCERTAINTIES

Outlet Gas Composition

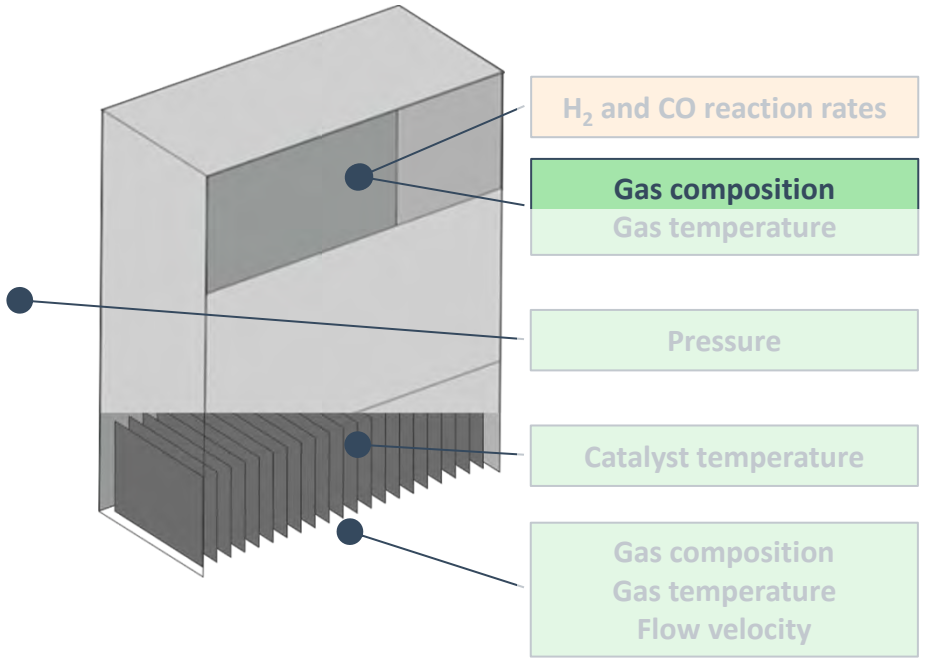

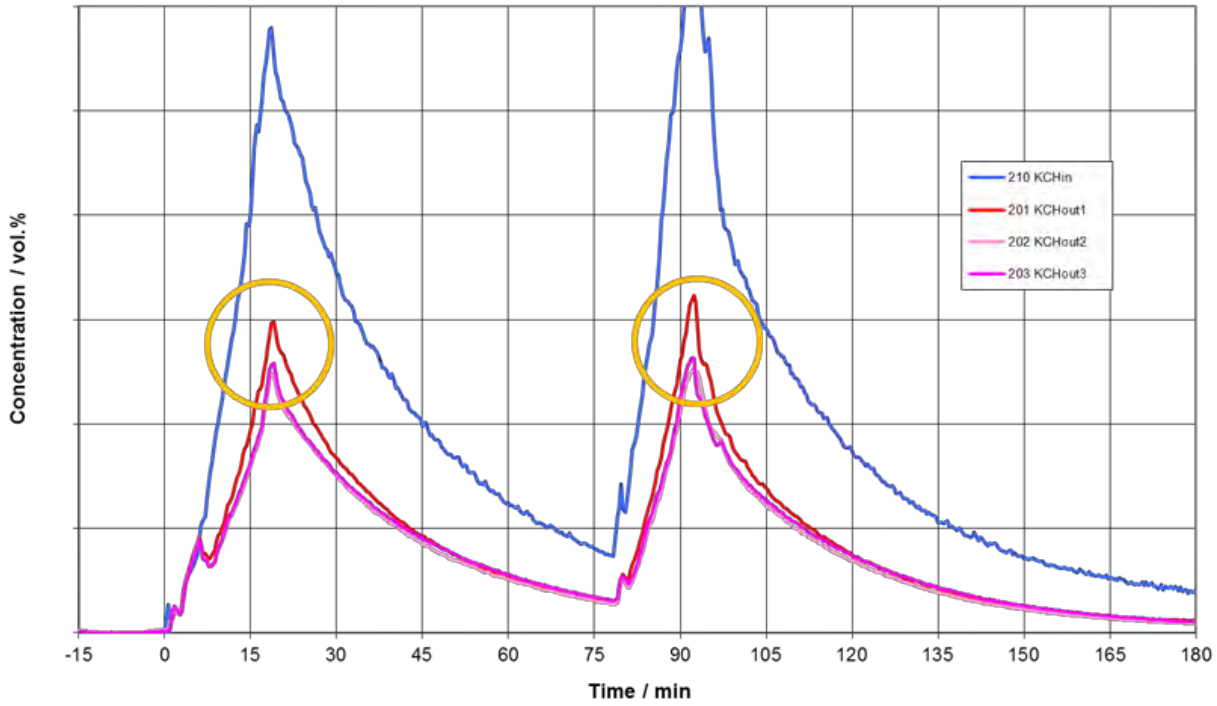

ADDING UNCERTAINTIES

Outlet Gas Composition

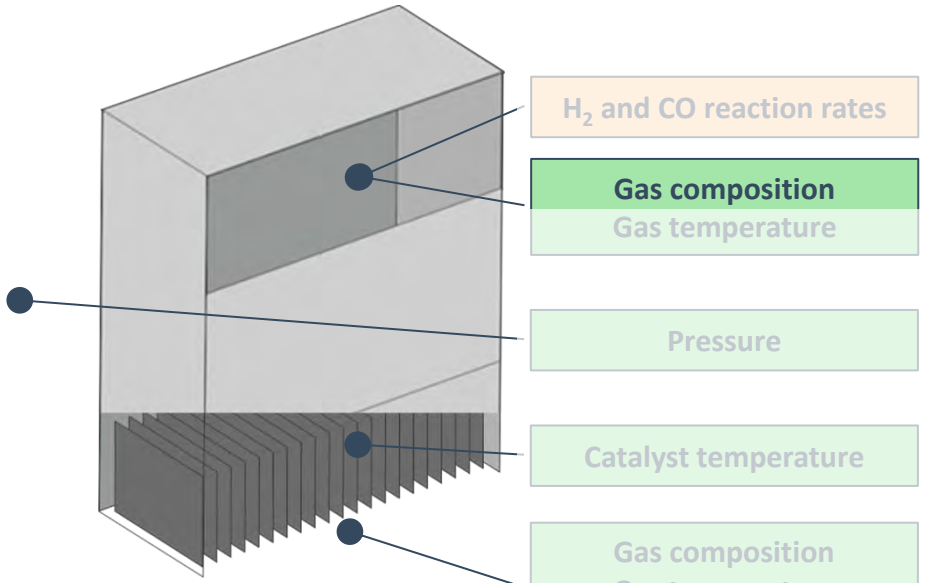

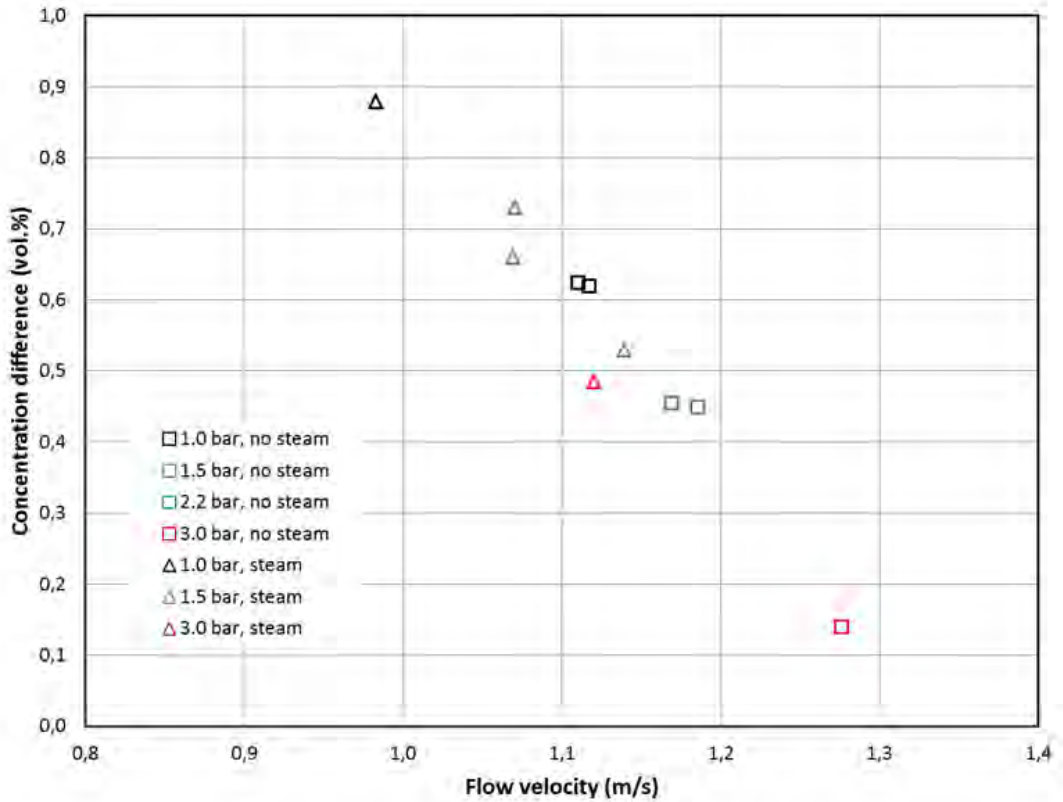

➔ **Optional: sensor KCHout1 disregarded**

ADDING UNCERTAINTIES

Catalyst Temperatures and Outlet Gas Temperatures

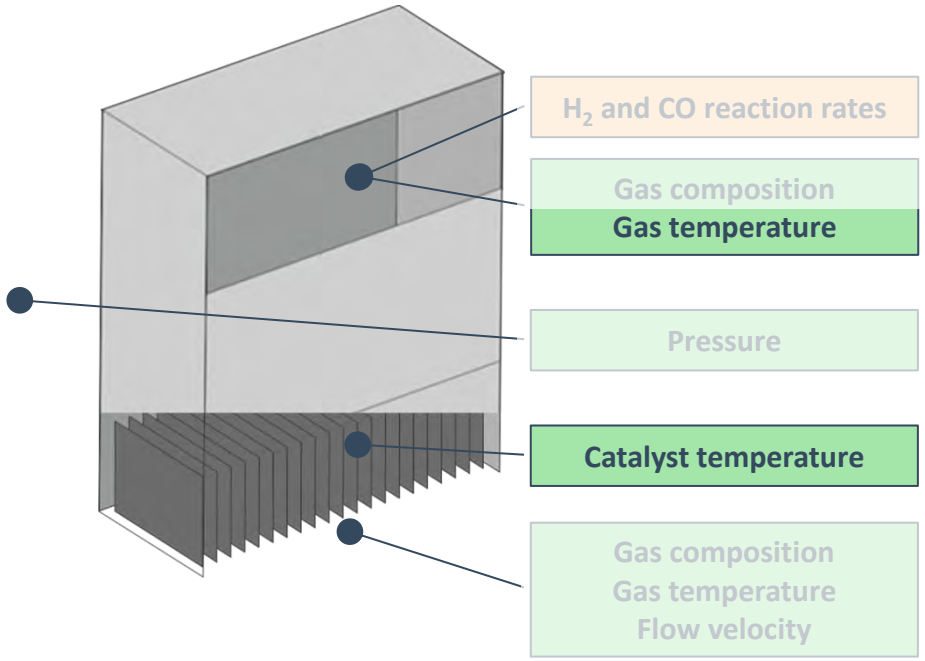

Measurements at up to 3 positions

➔ **Average values with uncertainty**

ADDING UNCERTAINTIES

Recombination Rates

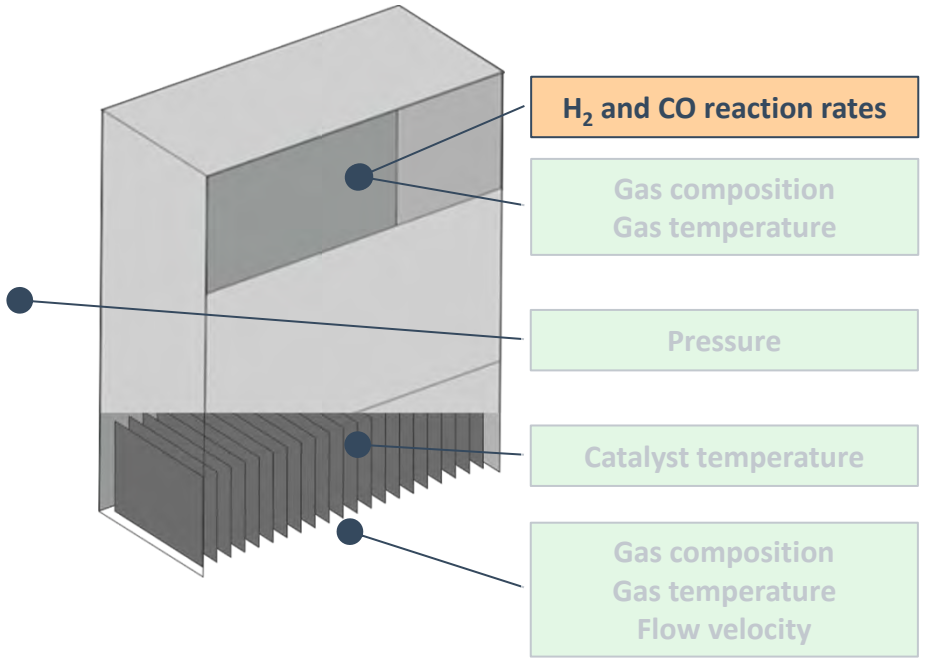

Option 1:

$$\dot{r}_{H2} = \left(y_{H2,in} - y_{H2,out}\right) \cdot \frac{p \cdot v \cdot A_{in}}{R_{H2} \cdot T_{in}}$$

Option 2:

$$\dot{r}_{H2} = \frac{\left(y_{H2,in} - y_{H2,out}\right)}{\left(1 - 0.5 \cdot y_{H2,out}\right)} \cdot \frac{p \cdot v \cdot A_{in}}{R_{H2} \cdot T_{in}}$$

+ optional use of inlet temperature and outlet gas concentration

➔ **6 „alternative“ recombination rates**

ADDING UNCERTAINTIES

Recombination Rates

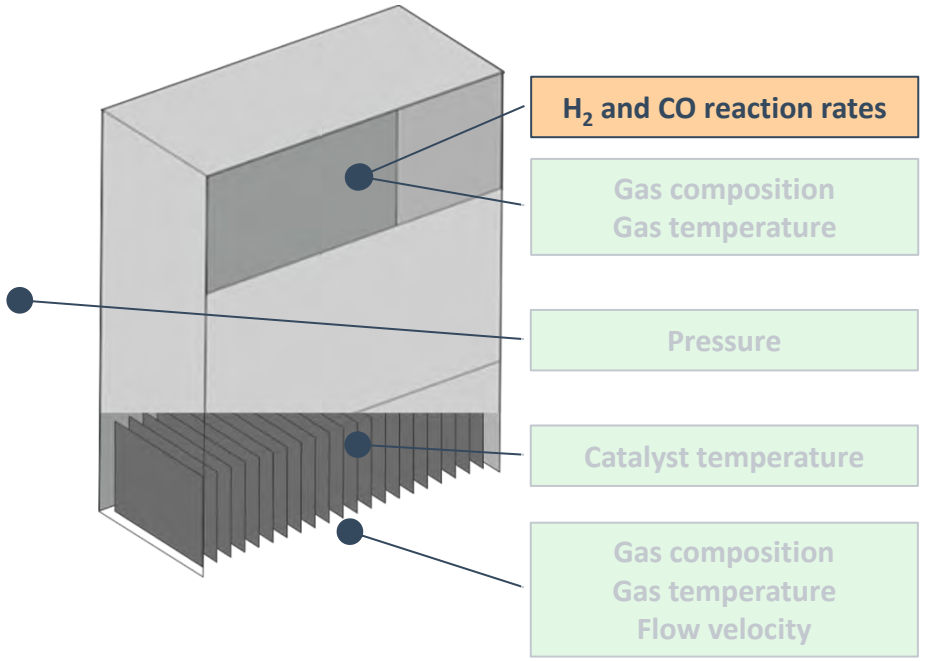

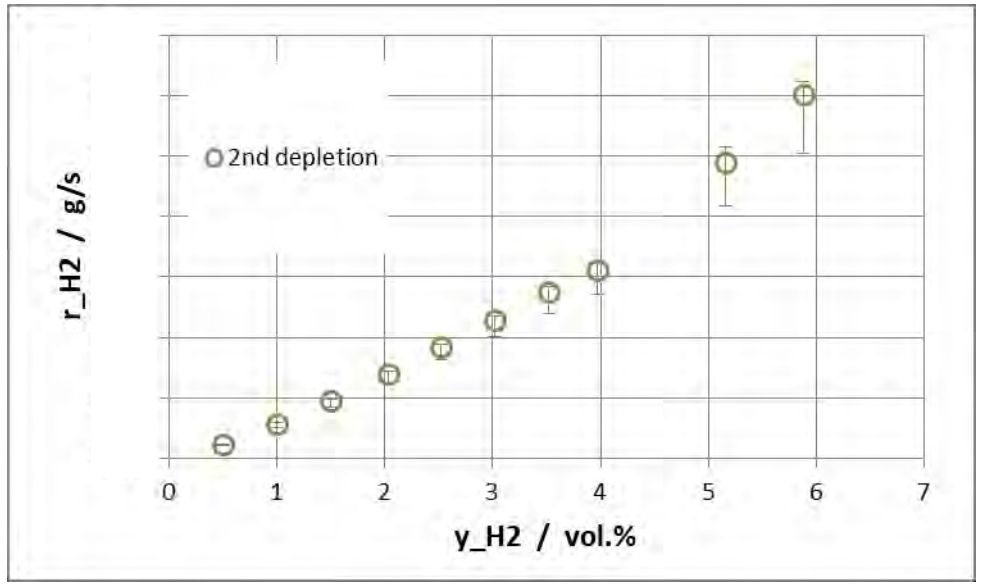

Uncertainty estimation by means of different calculation schemes and assumptions

➔ 6 „alternative“ recombination rates

MODEL VALIDATION

Optimization of the Framatome Engineering Correlation

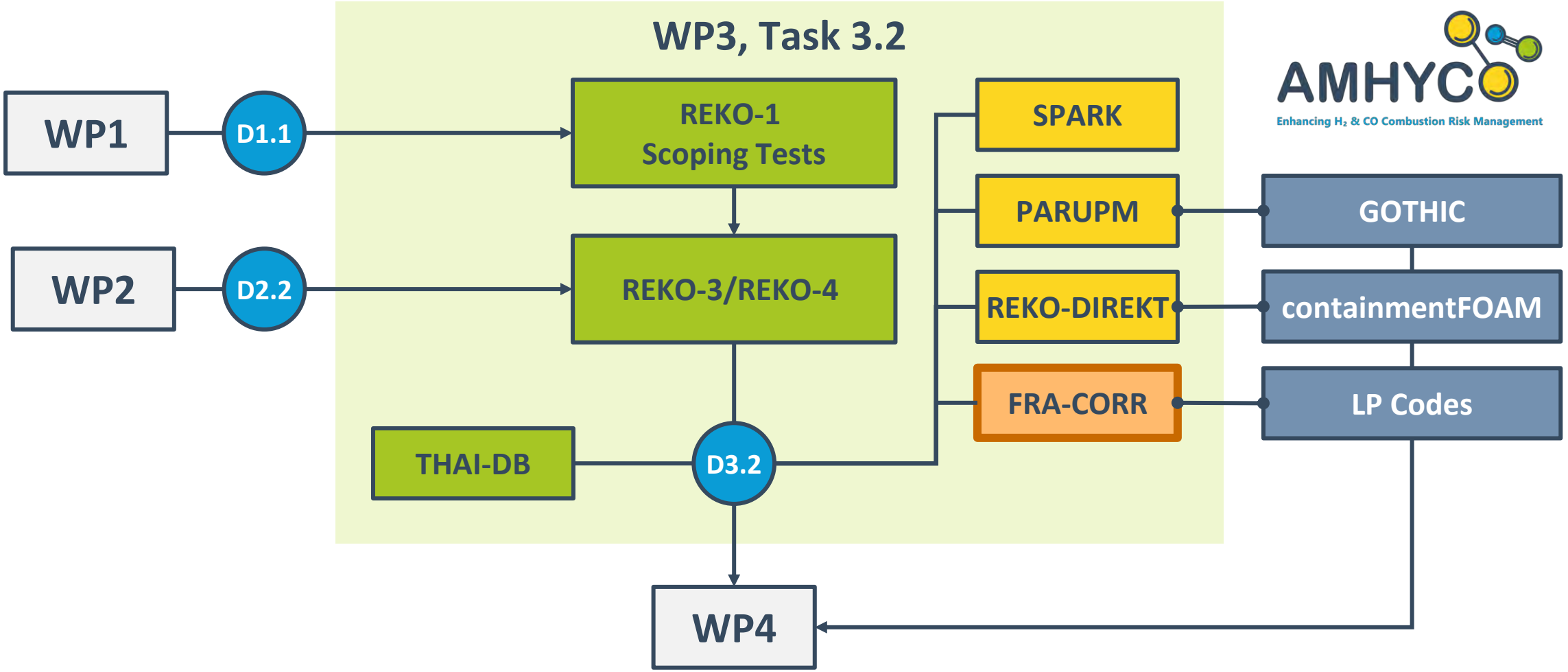

MODEL VALIDATION

Optimization of the Framatome Engineering Correlation

Initial Framatome Correlation

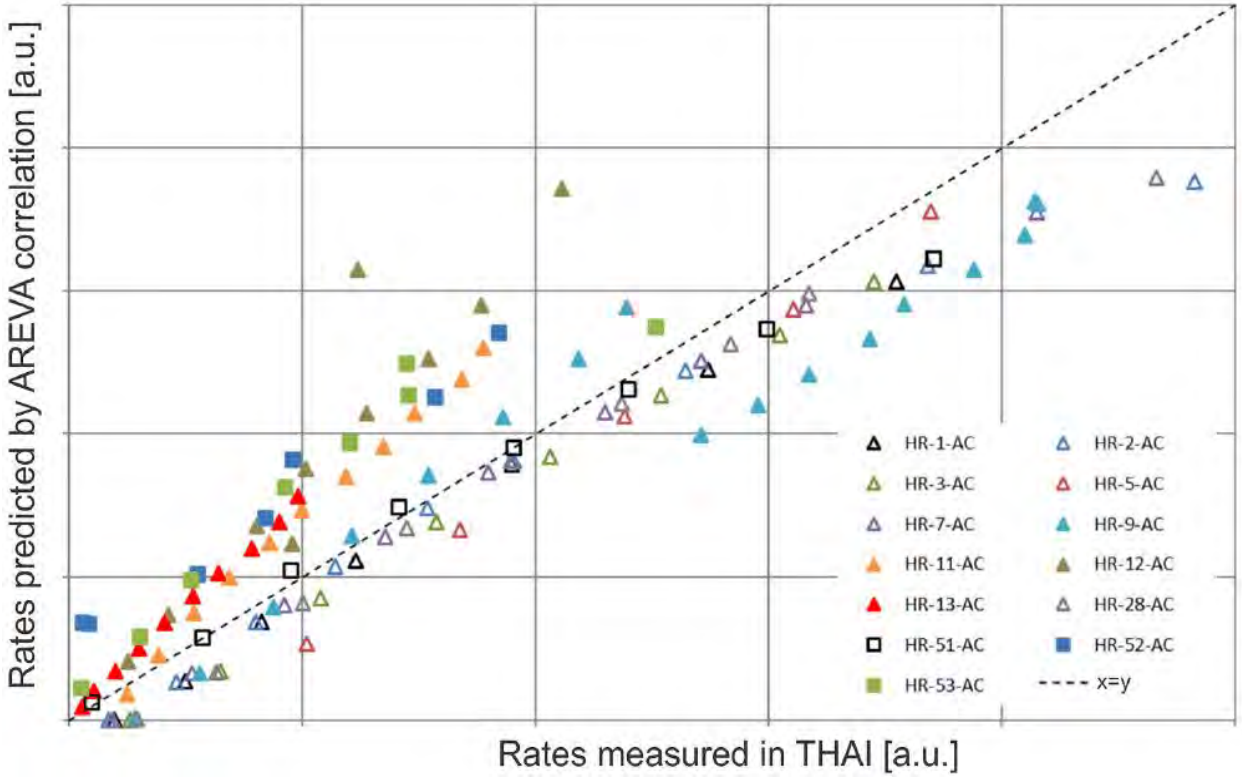

Enhanced AMHYCO Correlation

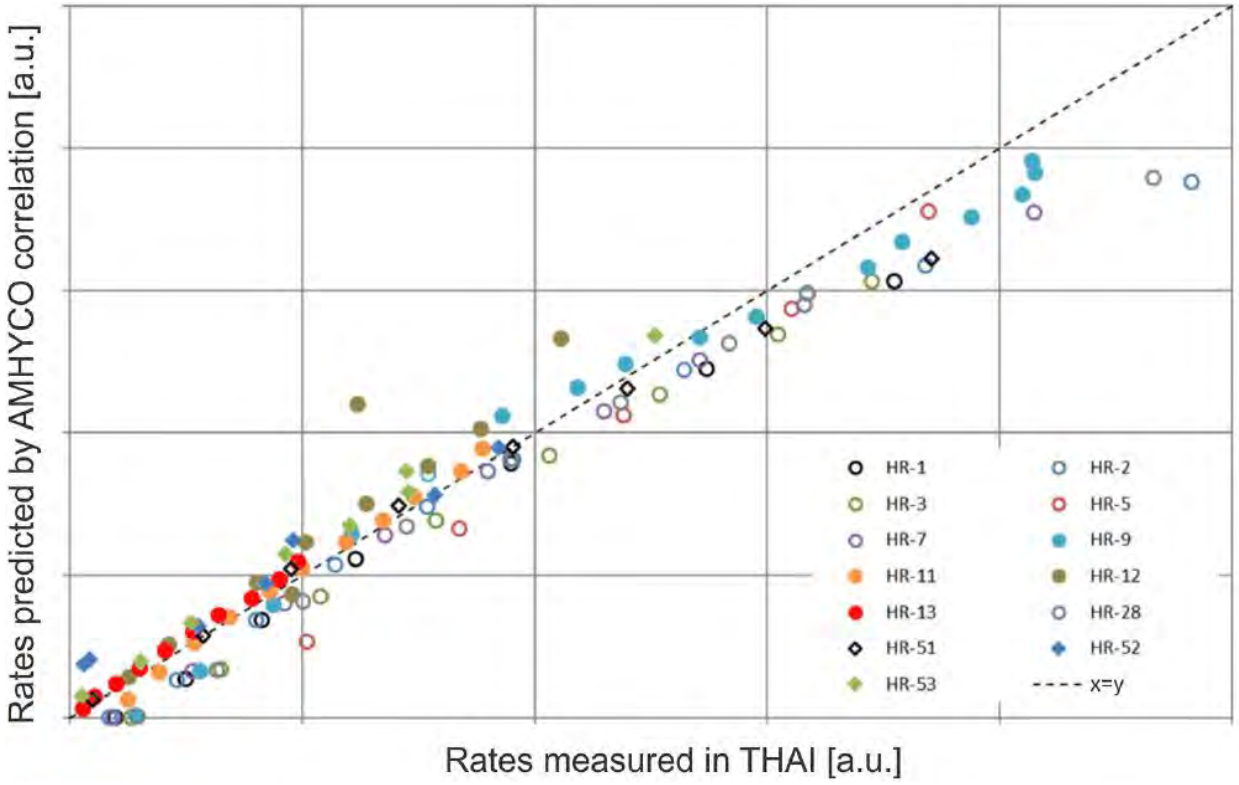

Braun and Reinecke: AMHYCO engineering correlation to describe the conversion of flammable gases in Framatome passive autocatalytic recombiners Nuclear Engineering and Design 442 (2025) 114206, https://doi.org/10.1016/j.nucengdes.2025.114206

MODEL VALIDATION

REKO-DIREKT Validation

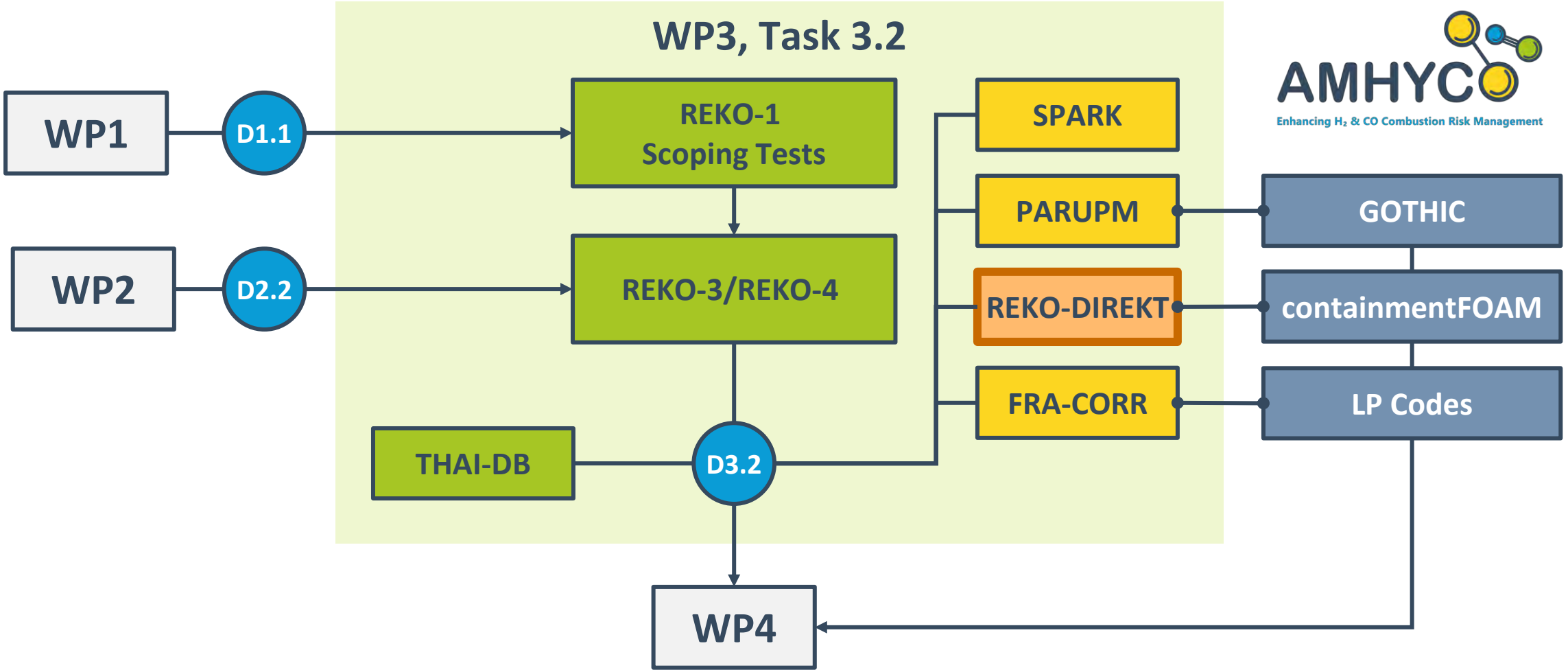

MODEL VALIDATION

REKO-DIREKT: Catalyst Temperature

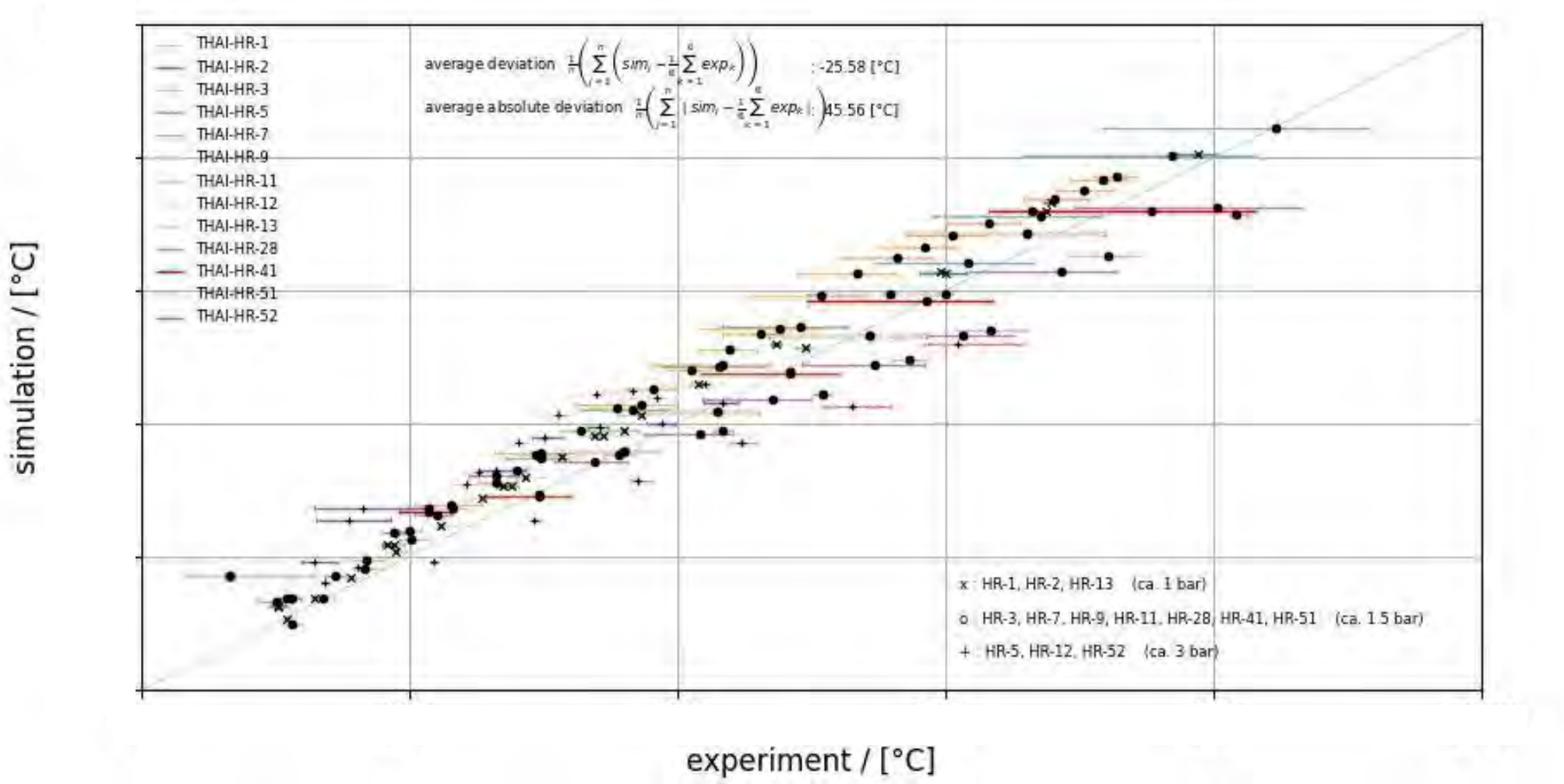

MODEL VALIDATION

REKO-DIREKT: Hydrogen Outlet Concentration

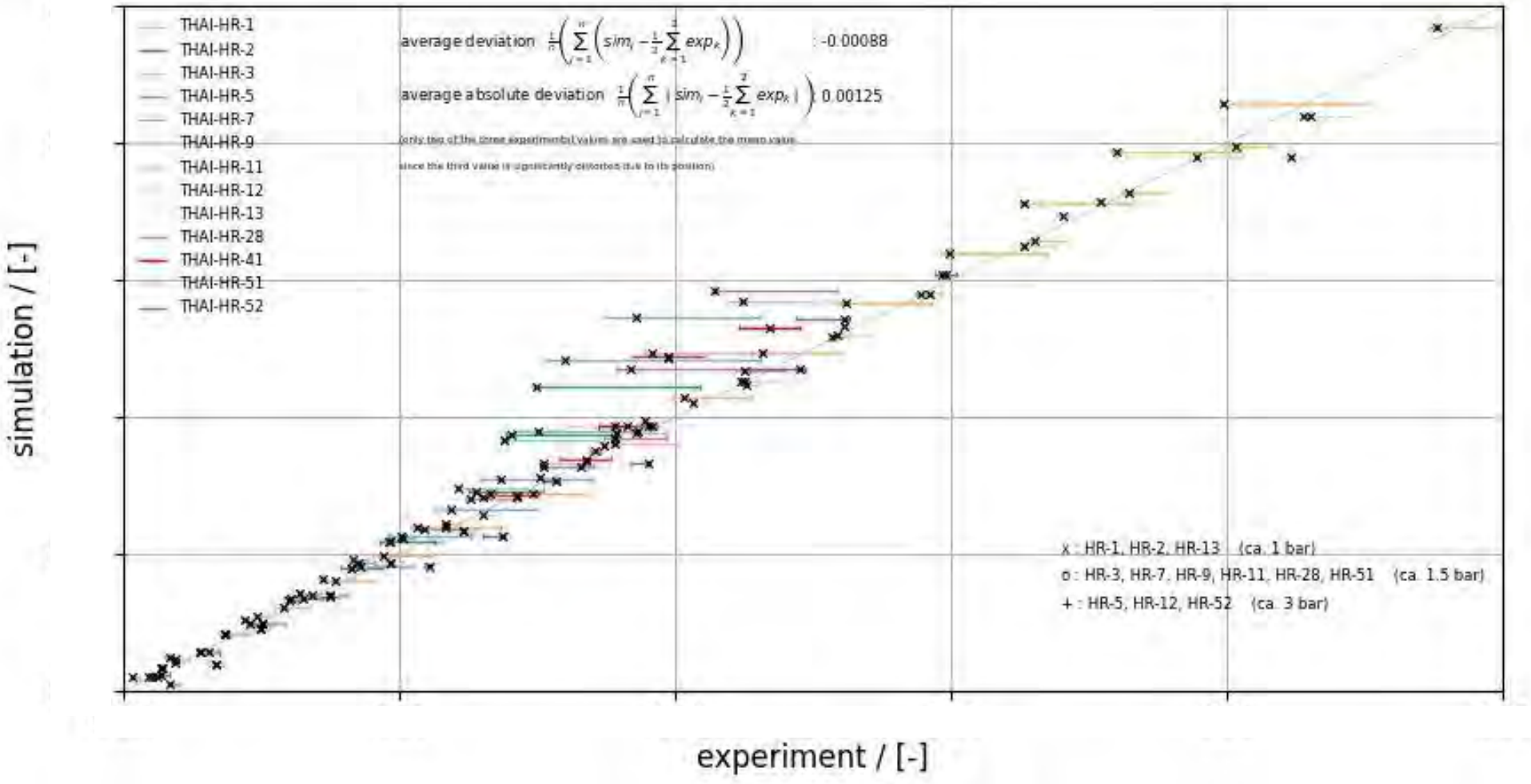

MODEL VALIDATION

REKO-DIREKT: Inlet Flow Velocity

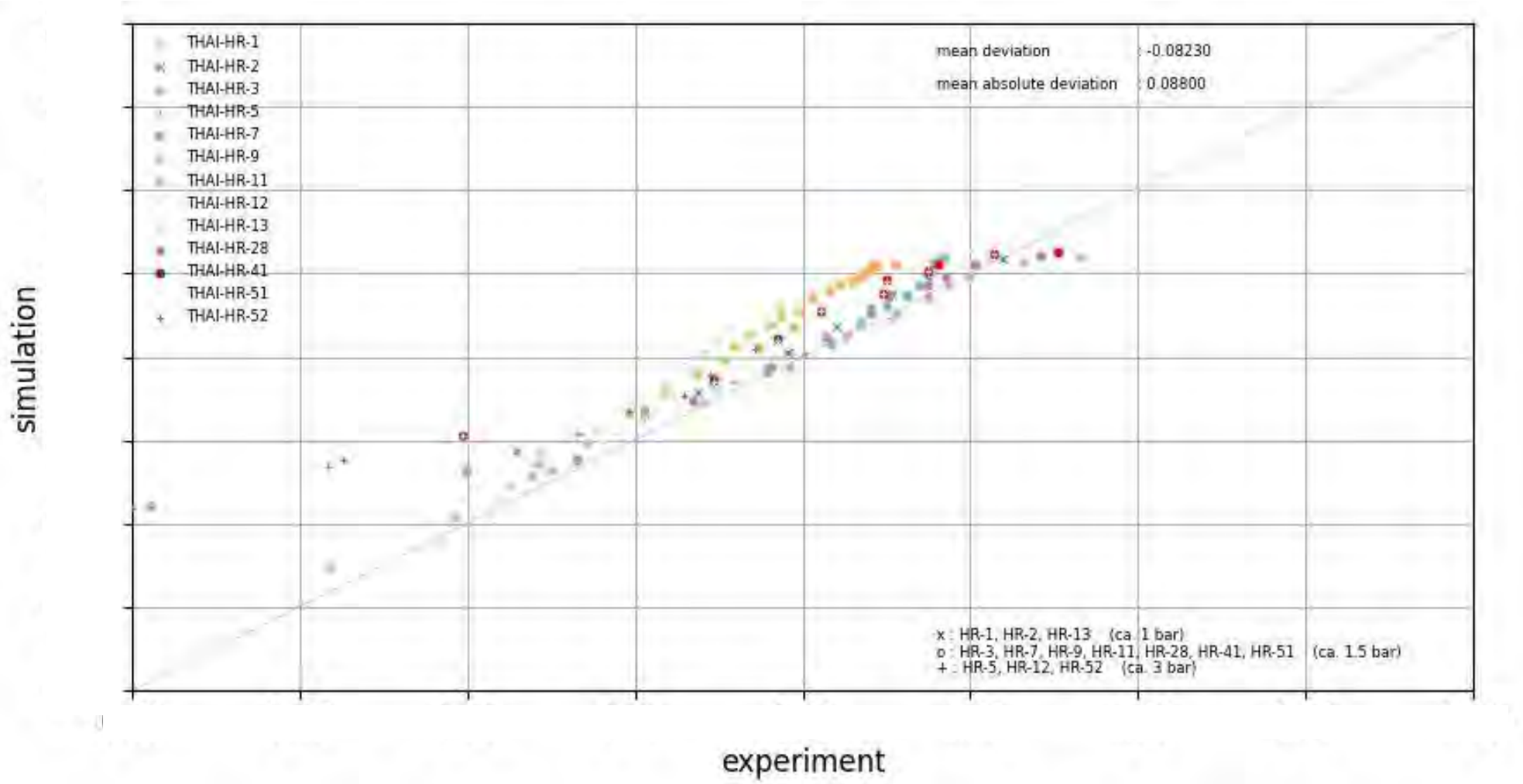

MODEL VALIDATION

REKO-DIREKT: Recombination Rate

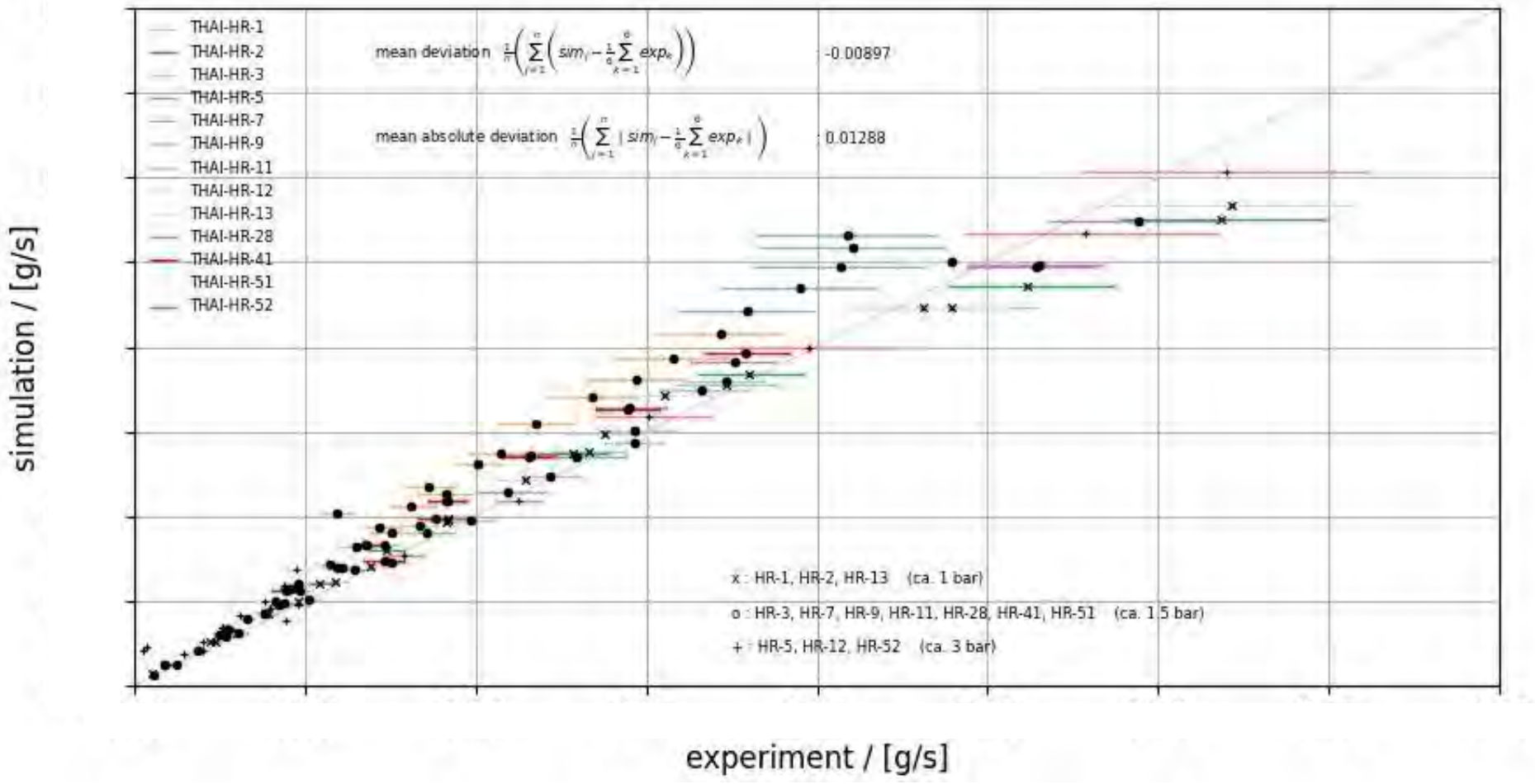

CONCLUSIONS

Development of a Database for PAR Model Validation based on THAI Experiments and its Application in the Framework of the AMHYCO Project

- In AMHYCO, a database was developed that consists of quasi-steady state measurement data from the transient PAR experiments performed in the framework of the OECD/NEA THAI projects.
- The database allows to simultaneously compare PAR model calculations with the entire range of boundary conditions studied in the experiments.
- Optional evaluation paths for some variables, e.g. the recombination rate or the outlet concentration, allow to assess uncertainties beyond the measurement accuracies based on the respective measurement devices.
- Database application has been demonstrated with the engineering correlation for Framatome PARs and the mechanistic PAR code REKO-DIREKT for generic PARs.

ACKNOWLEDGEMENTS

AMHYCO has received funding from the Euratom research and training programme 2019-2020 under Grant Agreement n°945057. The content of this paper reflects only the author's view. The European Commission is not responsible for any use that may be made of the information it contains.

AMHYCO Partners

Thank you
Connect with us for more information:

gonzalo.jimenez@upm.es

http://amhyco.eu

@amhyco

ACKNOWLEDGEMENTS

The financial support of the participating countries to the OECD/NEA THAI projects is gratefully acknowledged. The data for the tests HR-51 to HR-52 are part of the THAI-VI national project, which was funded by the German Federal Ministry for Economic Affairs and Energy under grant number 1501547, on the basis of a decision by the German Bundestag.

AMHYCO Partners

THANK YOU FOR YOUR KIND ATTENTION !

FISSION PRODUCT BEHAVIOR AND SOURCE TERM IMPACTS IN EX-VESSEL PHASE USING THAI TEST DATA: THE OECD/NEA THEMIS PROJECT

K. Dieter, J. Treufo, M. Freitag, E. Schmidt, M. Colombet, B. von Laufenberg

Becker Technologies GmbH, Germany

G. Langrock, F. Funke

Framatome GmbH

On behalf of:

Federal Ministry
for the Environment, Nature Conservation,
Nuclear Safety and Consumer Protection

of the Federal Republic of Germany

Introduction

Introduction

Background and Motivation

- Gaseous iodine released into the containment during hypothetical severe accidents in LWR could be oxidized by air radiolysis products
  - Iodine oxides (IO_x) can be formed
  - Aerosols are considered source-term relevant
    - ➢ long-term airborne
    - ➢ can be resuspended from structures

Objective

- Gain experimental data for LP and CDF code validation
- Improve knowledge base for safety assessment

Aim

- Iod-36 aimed to quantify the adsorption and agglomeration of IO_x onto nuclear background aerosols
  - Silver was used as the mid and long-term phase accident aerosol
- Iod-37 focused on the thermal stability of gas-borne IO_x and the potential conversion of IO_x to I_2
  - accident-typical gas temperatures ranging from 80 up to 140 °C

Experimental setup

Experimental setup

- THAI$^+$: Thermal-hydraulics, Hydrogen, Aerosols, Iodine, + Multi-compartment
- 2 vessel configuration
  - 14 bar at 180 °C max
  - 10 bar at 250 °C max
- System can be heated or cooled independently via three thermal oil mantles (accuracy +/- 1 °C)
- Access trough flanges for (optical) measurement systems
- Approved for H_2, CO and radiolabeled I_2 in combination with deflagrations

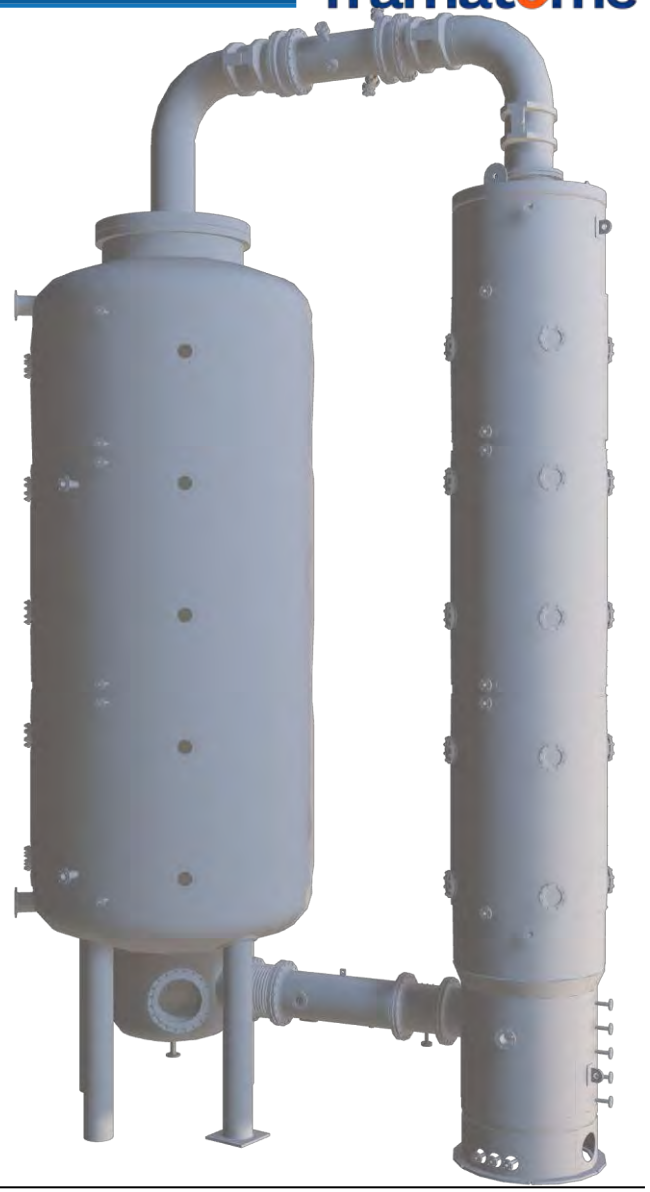

Experimental setup

- THAI$^+$: Thermal-hydraulics, Hydrogen, Aerosols, Iodine, + Multi-compartment
- 2 vessel configuration
  - 14 bar at 180 °C max
  - 10 bar at 250 °C max
- System can be heated or cooled independently via three thermal oil mantles (accuracy +/- 1 °C)
- Access trough flanges for (optical) measurement systems
- Approved for H_2, CO and radiolabeled I_2 in combination with deflagrations

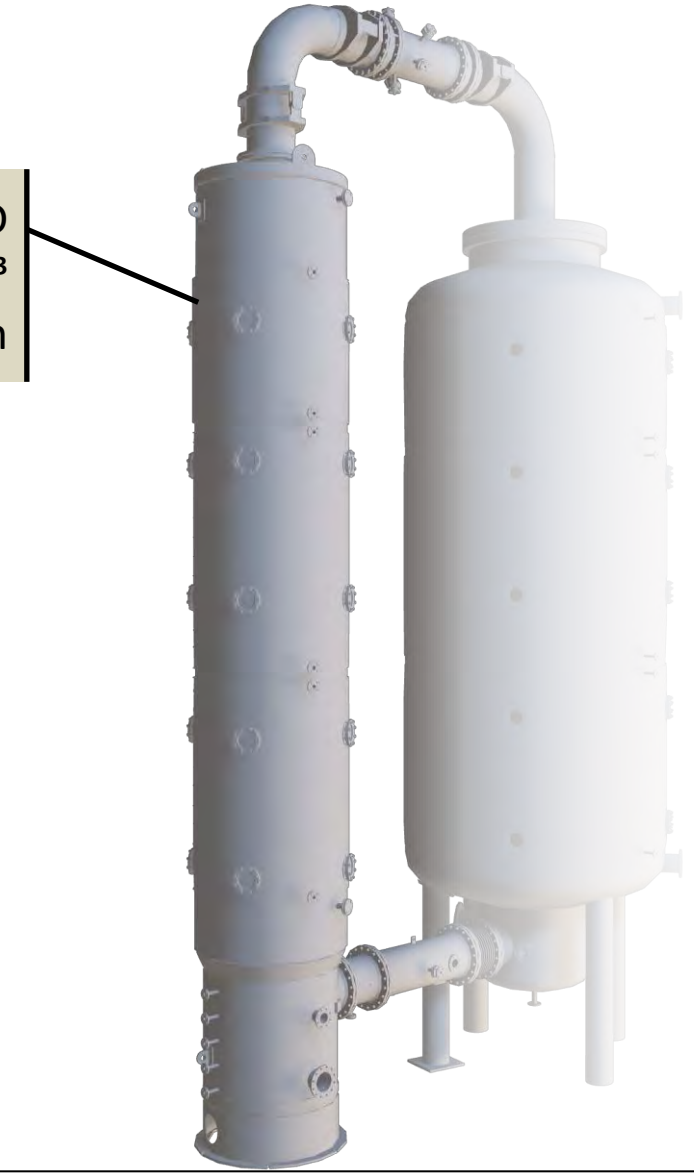

Experimental setup

- THAI$^+$: Thermal-hydraulics, Hydrogen, Aerosols, Iodine, + Multi-compartment
- 2 vessel configuration
  - 14 bar at 180 °C max
  - 10 bar at 250 °C max
- System can be heated or cooled independently via three thermal oil mantles (accuracy +/- 1 °C)
- Access trough flanges for (optical) measurement systems
- Approved for H_2, CO and radiolabeled I_2 in combination with deflagrations

Experimental setup

Aerosol and iodine

- 6x internal and 2x external gas scrubbers
- 2x Maypacks
- scanning mobility particle sizer
- 2x bulk filters and impactors
- LASI-SPEC & laser extinction
- 2x lead-shielded NaI scintillation detectors pointing at coupons

Thermal hydraulics

- Temperature (fluid and surface)
- Pressure
- Humidity
- Gas concentration measurement system

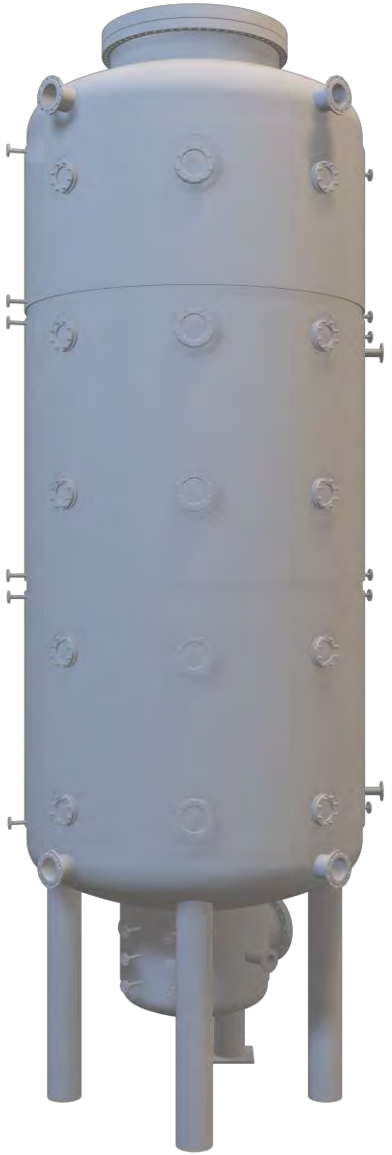

Test procedure

Test procedure

- Preconditioning phase 1
  - Temperature: 80 °C
  - 50 vol.-% of superheated steam
  - Pressure: 1.5 bar

- Preconditioning phase 2
  - Injection of ozone
  - Injection of gaseous I_2
    - ➢ IO_x formation and measurement

- Main phase **Iod-36**
  - Injection of Ag aerosol

- Main phase **Iod-37**
  - Long-term heating up to 140 °C

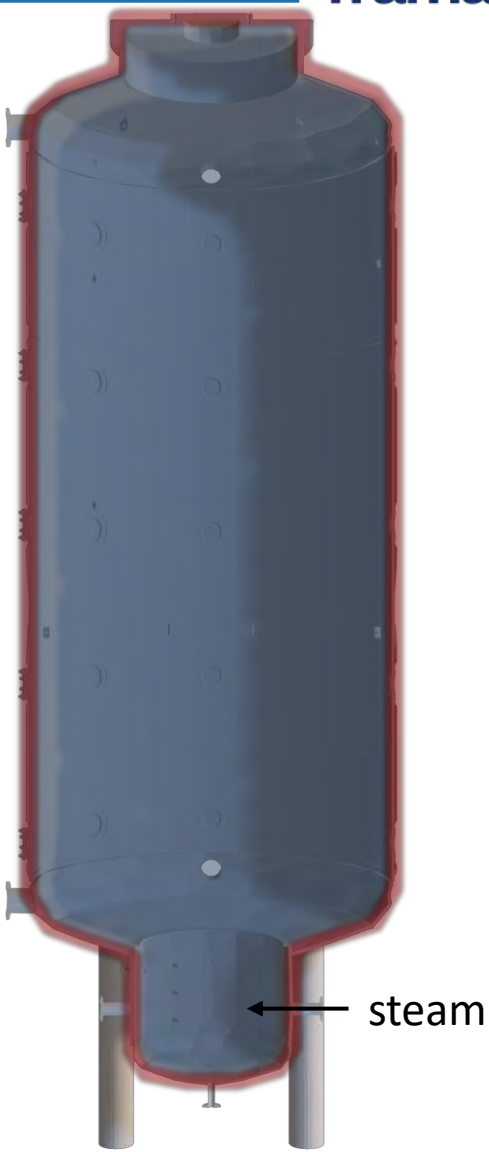

Test procedure

- Preconditioning phase 1
  - Temperature: 80 °C
  - 50 vol.-% of superheated steam
  - Pressure: 1.5 bar

- Preconditioning phase 2
  - Injection of ozone
  - Injection of gaseous I_2
    - ➢ IO_x formation and measurement

- Main phase **Iod-36**
  - Injection of Ag aerosol

- Main phase **Iod-37**
  - Long-term heating up to 140 °C

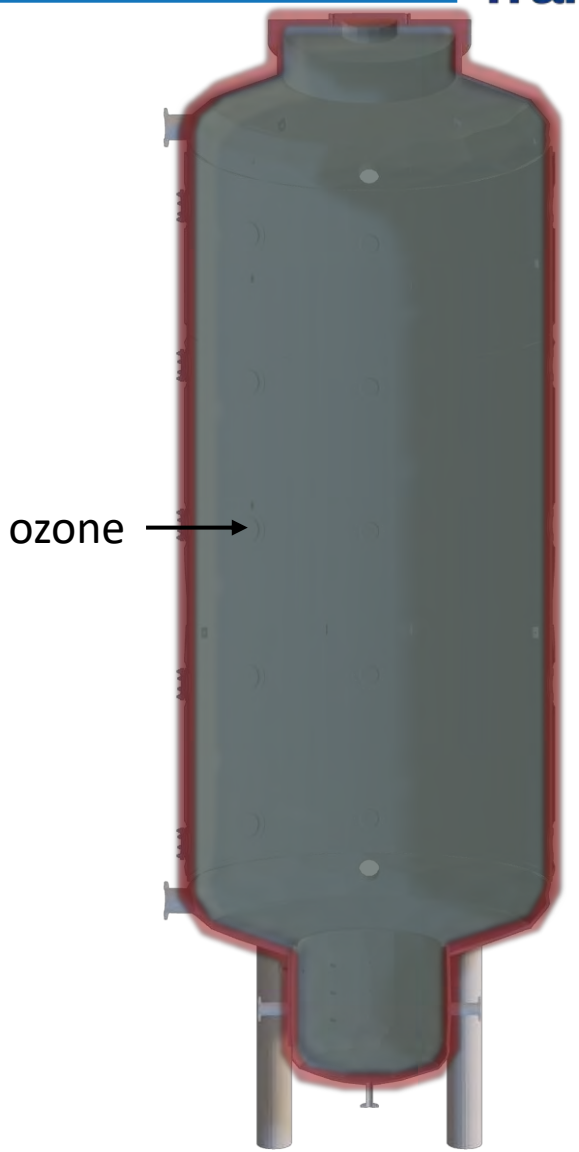

Test procedure

- Preconditioning phase 1
  - Temperature: 80 °C
  - 50 vol.-% of superheated steam
  - Pressure: 1.5 bar

- Preconditioning phase 2
  - Injection of ozone
  - Injection of gaseous I_2
    - ➢ IO_x formation and measurement

- Main phase **Iod-36**
  - Injection of Ag aerosol

- Main phase **Iod-37**
  - Long-term heating up to 140 °C

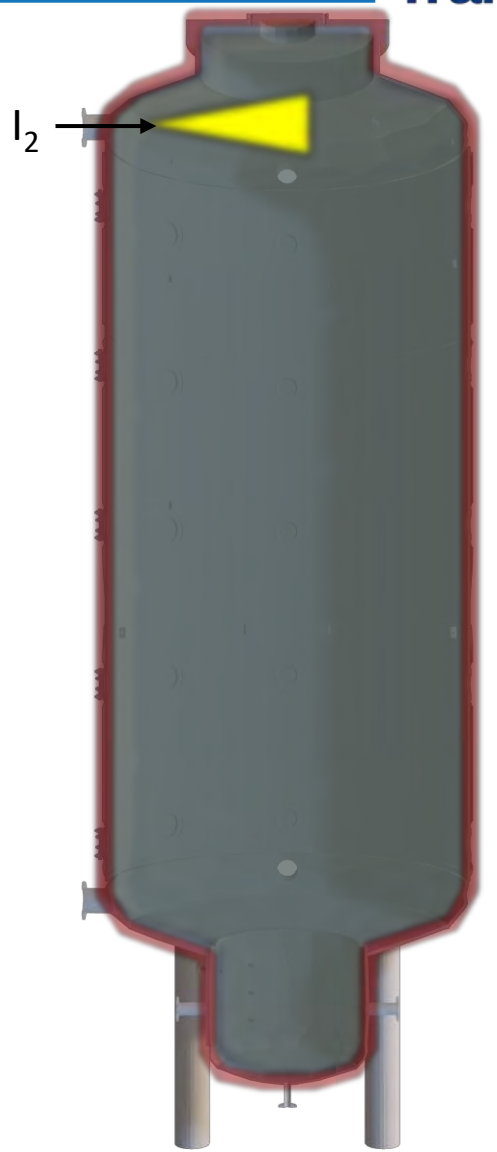

Results Iod-36

Results Iod-36

- Initial gas scrubber measurements showed low but increasing iodine concentrations
- Possible reasons
  - Incomplete oxidation
  - Coagulation of iodine species after I_2 injection
  - Formation of intermediate non-soluble IO_x species (e.g. IO, IO_2)
- After Ag aerosol injection, iodine concentration decreased steadily and nearly exponentially
- Stronger reduction observed at lower measurement positions due to particle settling
- Main removal mechanisms
  - Agglomeration
  - Sedimentation
- Conclusion
  - Reactive background aerosols can significantly reduce airborne iodine during accident scenarios

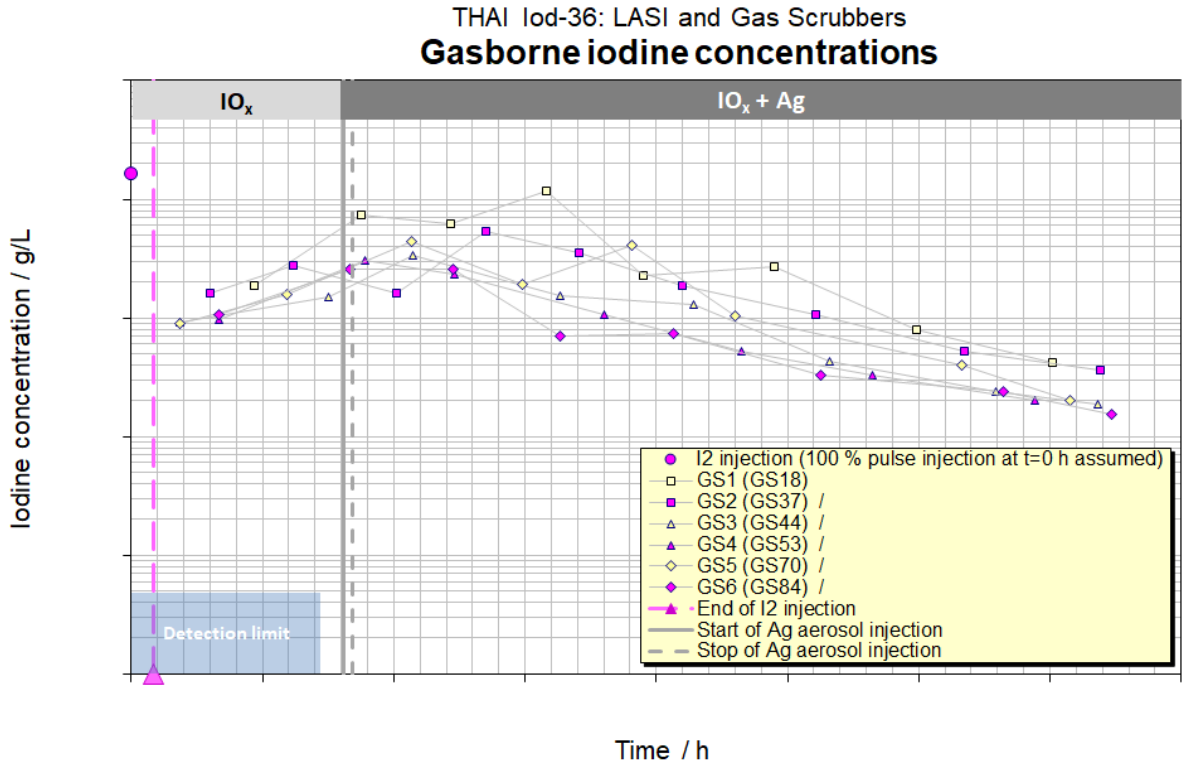

Results Iod-36

- Surface iodine loading determined from corrected count rate measured by online detector OS21D
- Raw detector signal corrected for
  - Contribution of gaseous iodine between glass and steel coupon
  - Total iodine concentration measured by Maypack systems
- Measurement results showed
  - Initial iodine deposition on the vertical steel coupon during early test phase
  - Deposition process significantly enhanced after Ag aerosol injection
- Results indicate that Ag aerosols promote iodine removal from the gas phase and increase surface deposition

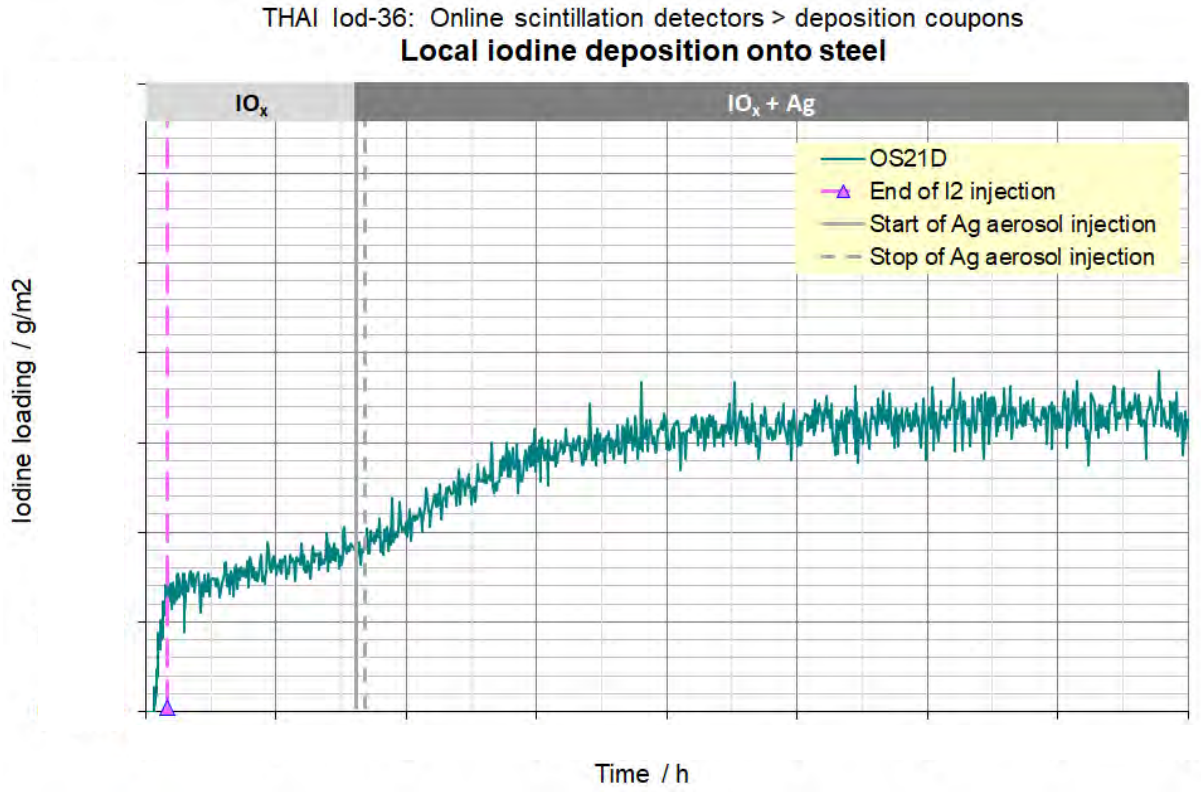

Results Iod-37

Results Iod-37

- Ozone concentration decreased nearly linearly during iodine injection
  - Succesfull oxidation of molecular I_2
- Gas scrubber measurements showed initially slow increase in airborne iodine concentration
- Likely explanation
  - Newly formed IOx particles were initially very small
  - Reduced scrubbing efficiency at early stages
- Over time
  - IO_x particles agglomerated
  - Scrubber retention efficiency improved
- About 1 - 1.5 hours after I_2 injection
  - Iodine concentrations stabilized at a low level
  - Low concentration persisted during heating from 80 °C to 140 °C

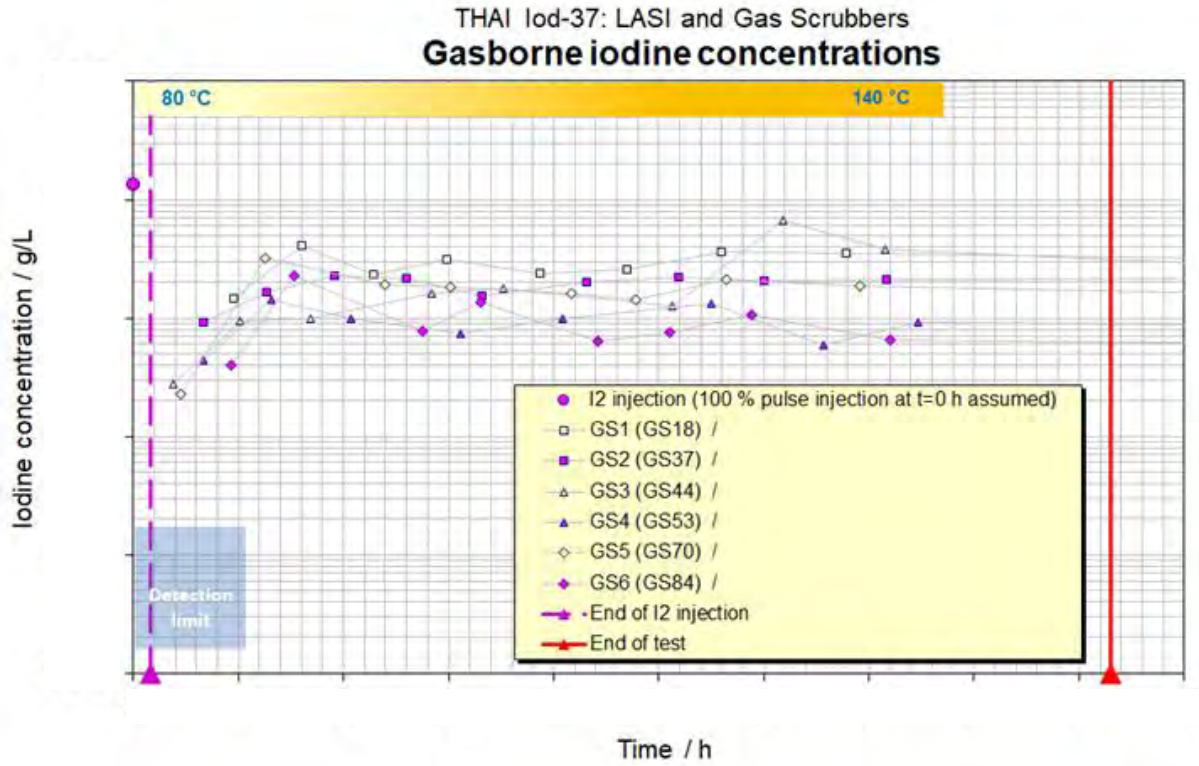

Results

- Maypack measurements showed that most iodine was present as aerosol-bound IO_x
- Confirms rapid formation of iodine oxide particles after I_2/ozone reaction
- Aerosol concentration decreased only slightly during the first 1 - 1.5 hours
- With increasing temperature
  - Concentration of inorganic gaseous iodine increased
  - Most likely caused by thermal decomposition of IO_x
- Decomposition process dominated over competing I_2/steel surface reactions
- Key conclusion
  - Aerosol-bound IO_x exhibits significant thermal instability
  - High temperatures can increase airborne iodine release (remobilization)
- Important implication for
  - Source term assessment
  - Late-phase severe accident analysis

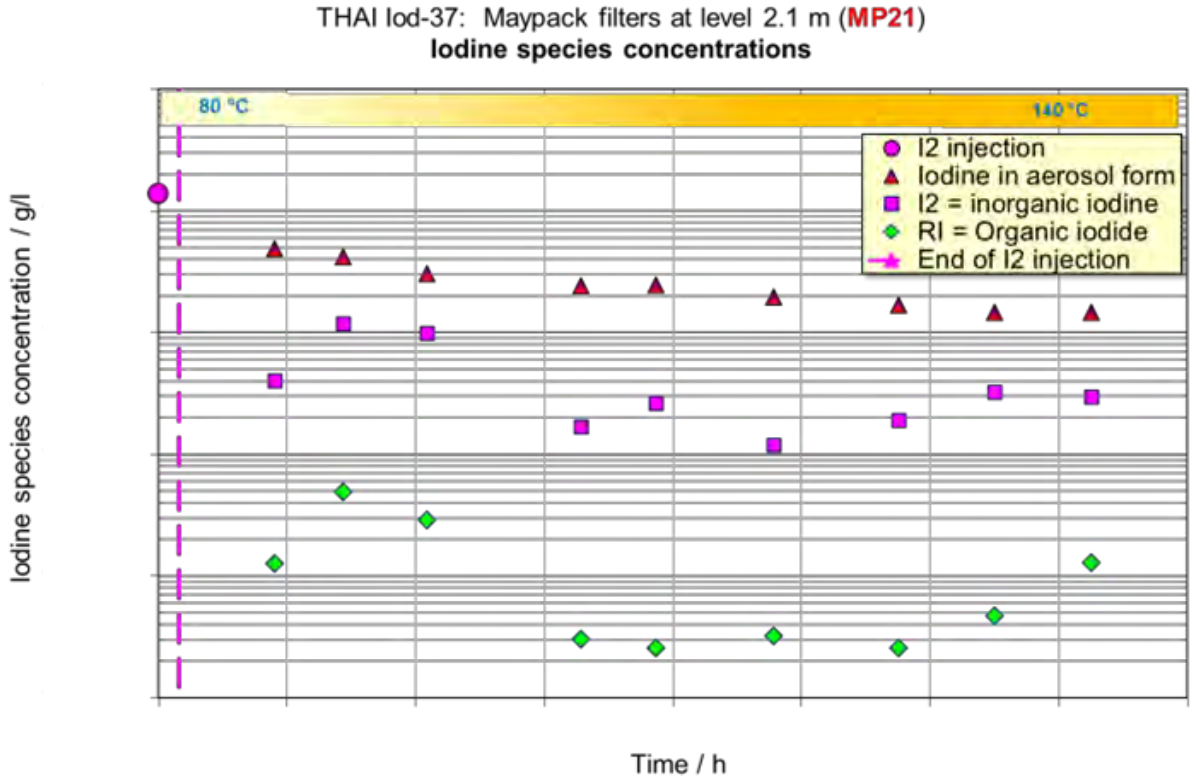

Summary and conclusions

Summary and conclusions

- Formation and behavior of iodine oxide particles (IO_x) under severe accident conditions was investigated
- Test Iod-36 (with Ag aerosol)
  - Ag aerosols strongly reduced airborne iodine concentration
  - Removal mainly caused by
    - Aerosol settling
    - Agglomeration and/or adsorption effects
  - More than 90 % of airborne Ag aerosol was depleted by the end of the test
  - Reactive background aerosols can significantly mitigate airborne iodine in containment atmospheres
- Test Iod-37 (thermal stability study)
  - IO_x initially formed stable aerosol-bound iodine species
  - Particle concentrations decreased over time mainly due to agglomeration
  - Elevated temperatures (80 - 140 °C) promoted thermal decomposition of IO_x
  - Increasing fraction of inorganic gaseous iodine observed at high temperatures
- Findings are highly relevant for severe accident source term assessments and containment safety analyses

Acknowledgements

The financial support provided by the countries who participated in the OECD/NEA THEMIS project is greatly acknowledged.

Funding by the Federal Republic of Germany, represented by the Federal Ministry for the Environment, Nature Conservation, Nuclear Safety and Consumer Protection (BMUV) under project number 1501613 is greatly acknowledged.

On behalf of:

Federal Ministry
for the Environment, Nature Conservation,
Nuclear Safety and Consumer Protection

of the Federal Republic of Germany

Backup

Backup

DEVELOPMENT STATUS OF THE FLAMMABILITY RISK MONITORING SYSTEM IN SEVERE ACCIDENTS

Youngsu Na, Seongho Hong, Ki-Han Park, Jin-Hyeok Kim, Jeong-Yun Oh, and Changwan Kang
Korea Atomic Energy Research Institute
989-111 Daedeok-daero, Yuseong-gu, Daejeon, 34057, Korea
ysna@kaeri.re.kr; hsh4004@kaeri.re.kr; kihan@kaeri.re.kr; jinhyeok@kaeri.re.kr; ojy@kaeri.re.kr; kcw508@kaeri.re.kr

ABSTRACT

We are developing a flammability risk monitoring system for real-time tracking of the flammability of combustible gases that threaten the integrity of containment buildings during severe accidents. Previous sampling methods for measuring hydrogen concentration during accidents have functional limitations, such as time delays associated with gas transport. In this study, we are designing a modular sampling system to overcome these limitations and developing a non-sampling concentration assessment method that utilizes the catalyst temperature response of passive autocatalytic recombiners (PARs) installed within the containment building. Performance evaluations of the sampling-based measurement system have demonstrated an accuracy of less than 0.1 vol.% within a hydrogen concentration range of 0.1 to 9.0 vol.%, while maintaining stable control of gas sensor operating temperature and pressure, even under simulated accident conditions. Experiments on the hydrogen recombination behavior of PARs are currently being conducted in an 80 m³ severe accident simulation facility, and a correlation equation for non-sampling hydrogen concentration assessment is under development. The data processing algorithm converts dry hydrogen concentrations, obtained via the sampling method, into actual wet concentrations under accident conditions. When combined with hydrogen concentrations obtained by the PAR-operation-based non-sampling method and compared with flammability limits, this can provide real-time combustion hazard information during an accident. This flammability risk monitoring system is expected to enhance the effectiveness of combustible gas control strategies during severe accidents.

KEYWORDS
Severe accident, Hydrogen, Flammability, Monitoring system

1. INTRODUCTION

In a severe accident, hydrogen and carbon monoxide are generated during core degradation and molten core-concrete interaction (MCCI). These gases, if released into the upper containment building and mixed with atmospheric oxygen, can form an explosive mixture. Hydrogen, in particular, possesses a low ignition energy and a wide flammability range. The dynamic and thermal loads produced during its combustion pose a significant threat to the structural integrity of the containment building. Consequently, accurately assessing the combustion risk of these flammable gases in real-time is a crucial countermeasure for enhancing nuclear power plant safety within accident mitigation strategies.

Currently, most operational nuclear power plants utilize sampling-based instrumentation to measure hydrogen concentration by drawing atmospheric air from within the containment building to an external measurement unit. [1] While this sampling method offers the advantage of protecting concentration sensors from high-temperature steam and radioactive aerosols inside the containment, it introduces uncertainties

due to inherent delays. Specifically, there is a suction time delay caused by the length of the sampling pipeline and the flow rate, as well as a response time delay attributable to the free volume of the pre-processing equipment. Consequently, these delays prevent the instrumentation from providing an immediate, real-time reflection of the conditions within the containment building. Furthermore, safety concerns have been raised regarding the sampling pipeline itself, as it could potentially serve as a bypass leakage path for radioactive materials.

To address these limitations, we are developing a monitoring system that integrates two distinct approaches, as illustrated in Figure 1. Firstly, a sampling system has been designed and is currently undergoing performance evaluation. This design incorporates functional modularization to minimize suction time delay and utilizes a pool scrubbing method to reduce steam condensation trap and filter housing volume. Secondly, the research aims to leverage the dozens of passive autocatalytic recombiners (PARs) already installed within the containment building as a non-sampling tool for hydrogen concentration assessment. The thermal reaction occurring on the catalyst surface during PAR operation exhibits a strong correlation with the ambient hydrogen concentration. This correlation enables the real-time acquisition of hydrogen concentration data from various locations within the containment, even in the absence of sampling lines.

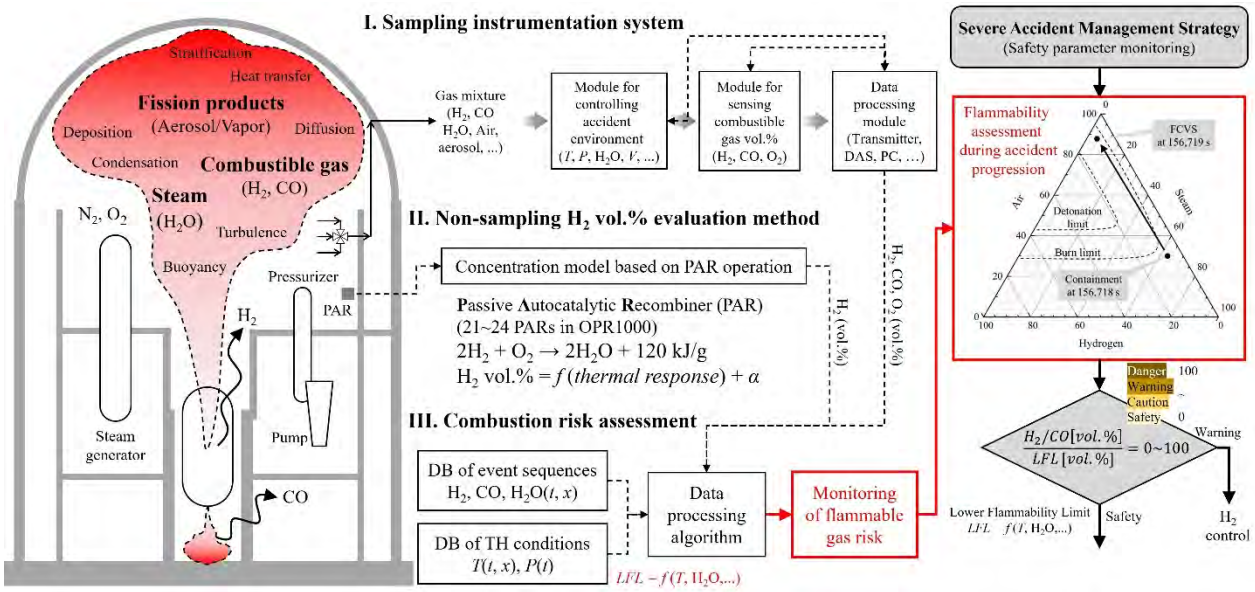

Figure 1. Conceptual Diagram for the Development of a Flammable Gas Risk Monitoring System.

This paper presents the results of performance validation for an advanced sampling module and outlines the current development status of a PAR-based non-sampling concentration assessment method, which is being implemented in a large-scale experimental facility simulating severe accident environments. Furthermore, a data processing algorithm is under development to convert dry hydrogen concentrations obtained from the sampling module into actual wet concentrations relevant to accident conditions. This algorithm will also facilitate real-time monitoring of flammable gas hazards by comparing the calculated hydrogen concentrations, derived from the PAR-based non-sampling method, with the flammability limits. This integrated technology is expected to provide critical data for determining optimal mitigation strategies within severe accident management guidelines.

2. MODULAR SAMPLING INSTRUMENTATION SYSTEM

To ensure reliability in severe accident environments, the sampling-based measurement system employs a modular design comprising an environmental control module and a flammable gas concentration sensing

module. As depicted in Figure 2, the environmental control module draws a gas mixture from the experimental vessel (or containment building), subjects it to a pre-treatment process, and then discharges it back into the vessel (or containment building). During this process, a portion of the gas is directed to the concentration sensing module via pressure control [2]. Notably, to mitigate the inherent time delay, a functional limitation of conventional sampling systems, the design incorporates a mechanism to optimize the suction flow rate by controlling the rotational speed of the circulation pump.

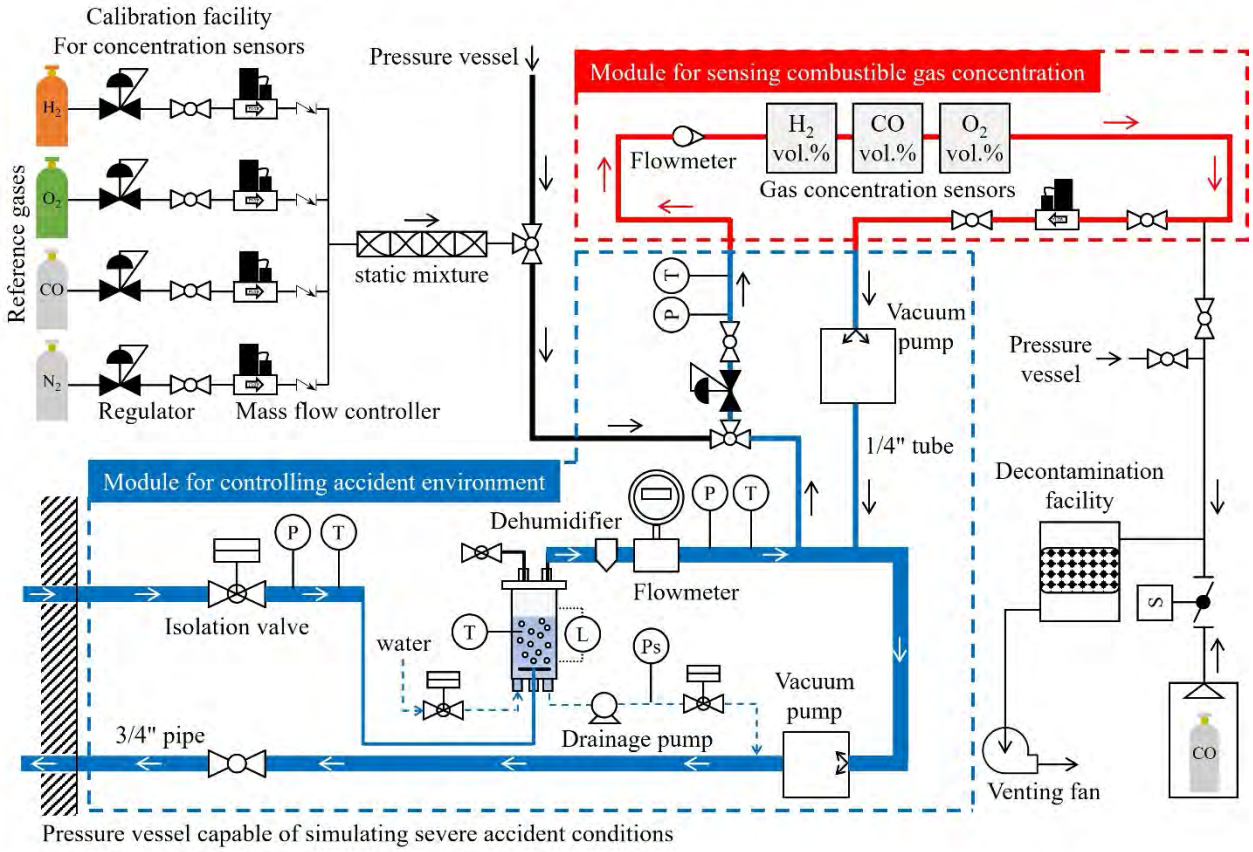

Figure 2. Conceptual Diagram of the Modular Instrumentation System and Performance Evaluation Test Facility.

The pool scrubbing technology employed in the environmental control module serves to protect sensor integrity by condensing superheated steam and removing aerosolized fission products. Concurrently, it minimizes hydrogen concentration dilution and reaction time delays attributed to the volume of the condensation trap and aerosol filter housing. To enhance aerosol removal efficiency, the nozzle within the pool was designed as a sparger, featuring 48 uniformly distributed 1.5 mm diameter holes.

The concentration sensing module incorporates three types of sensors, arranged in series, for monitoring hydrogen, carbon monoxide, and oxygen concentrations. A thermal conductivity sensor was selected to measure hydrogen concentration over a range of 0 to 100 vol.%. For carbon monoxide and oxygen concentrations, an optical sensor and a paramagnetic sensor were chosen, respectively. To ensure precise sensor measurements, the sampling flow rate is maintained at a constant 1 l/min using a mass flow controller.

The environmental control module and the concentration sensing module were designed, as shown in Figure 3, and subsequently fabricated into cabinet-type enclosures for individual performance evaluation.

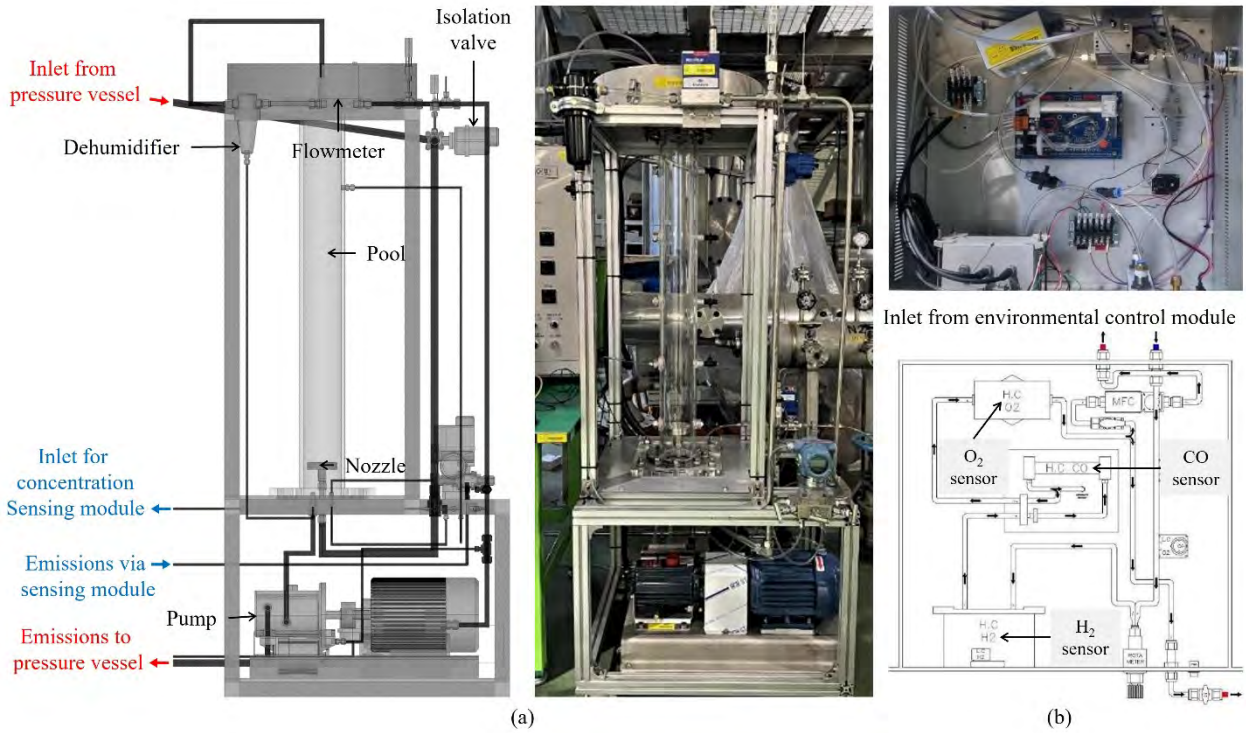

Figure 3. Design and Fabrication of the Modular Measurement System: (a) Environmental Control Module Drawing (Left) and Assembled Unit (Right), (b) Concentration Sensing Module Drawing (Bottom) and Assembled Unit (Top).

3. NON-SAMPLING EVALUATION METHOD BASED ON PAR OPERATION

To address the risks of leakage in sampling lines and the limitations of measurement locations, a non-sampling concentration assessment method is being developed, which utilizes the operational characteristics of passive autocatalytic recombiners (PARs) installed within containment buildings. The PAR unit was designed as a catalytic body coated with platinum (Pt) at a concentration of 60 g/ft³, integrated into a lattice structure, and housed within a chimney intended to generate buoyancy-driven flow [3]. The catalytic body has dimensions of 93.5 mm in width, 190 mm in length, and 25 mm in height. Its lattice structure features a cell density of 36 cpsi (cells per square inch), with a wall thickness of 0.7 mm between cells. Each individual cell measures 3.5 x 3.5 mm^2, resulting in a total of 990 cells. The exothermic reaction that occurs when hydrogen and oxygen recombine on the catalyst surface is closely correlated with the surrounding hydrogen concentration. This allows for the inverse calculation of hydrogen concentration around a PAR by measuring the temperature rise with thermocouples affixed to the catalyst surface.

Figure 4 illustrates the experimental setup within the SPARC (Spray-Aerosol-Recombiner-Combustion) facility, operated by the Korea Atomic Energy Research Institute (KAERI). A Passive Autocatalytic Recombiner (PAR) was installed inside a cylindrical SPARC vessel measuring 3.4 m in diameter, 9.5 m in height, and with a volume of 80 m³. Hydrogen recombination experiments using the PAR were subsequently conducted under simulated severe accident conditions, involving controlled hydrogen injection. [3] Initial thermohydraulic conditions for hydrogen injection were determined based on severe accident scenario calculations of a small-break loss-of-coolant accident (SBLOCA) in a Korean Standard Nuclear Power Plant (OPR1000) using the MELCOR code. For the hydrogen recombination experiments, conditions within a pressure range of 1.32 to 1.93 bar and steam-saturated temperatures from 60.4 to 88.3 °C were selected. [4] Following the transient region characterized by a rapid increase in catalyst temperature, the correlation between the catalyst surface temperature and the hydrogen concentration around the PAR was observed.

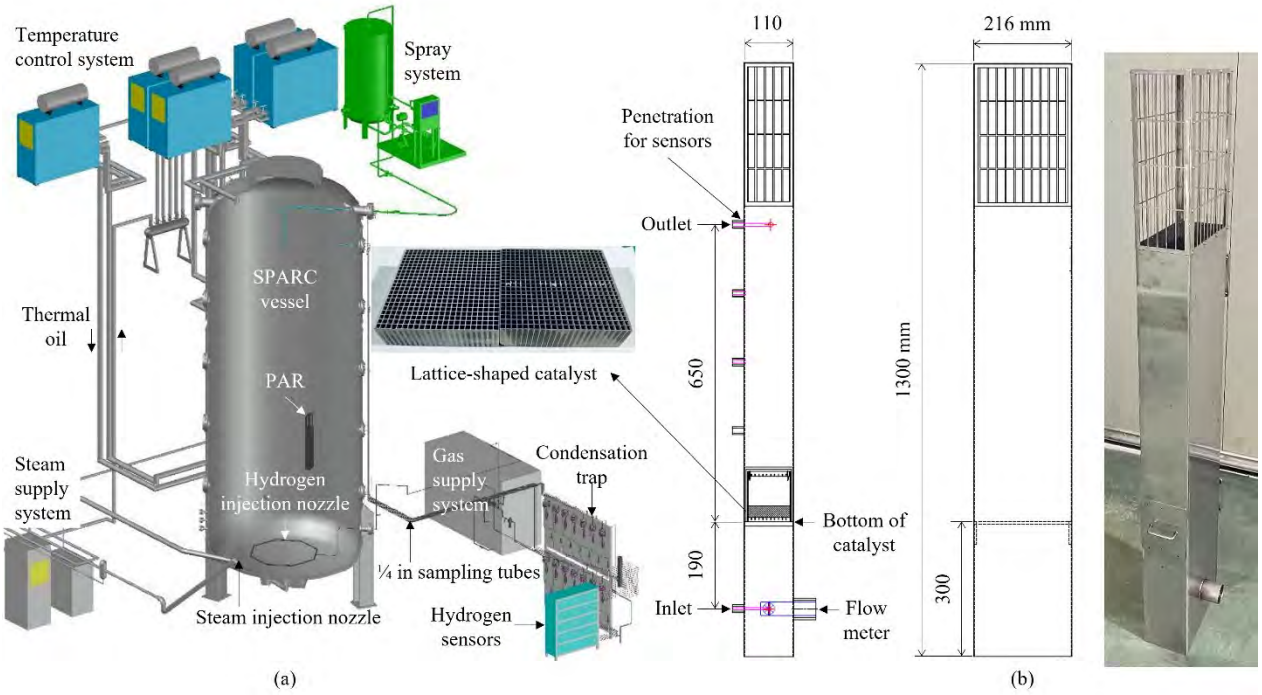

Figure 4. (a) PAR Installed within the SPARC Vessel; (b) Fabrication Diagram and Photograph of the PAR.

4. INTEGRATED DATA PROCESSING ALGORITHM

The raw data acquired from the sampling system represents a dry hydrogen concentration, with steam removed during the preprocessing stage. Consequently, it is essential to convert this to a wet concentration, reflecting the actual conditions within the containment building. This conversion to a wet concentration is performed using Equation 1, which calculates the steam concentration based on relative humidity and saturated vapor pressure, subsequently incorporating this into the dry hydrogen concentration. [3]

$$(C_h)_w = \left(1 - \frac{C_s}{100}\right)(C_h)_d \quad (1)$$

We developed Python 3.11-based code that automates time-delay compensation and wet hydrogen concentration conversion processes. The wet hydrogen concentration, measured through a sampling method, and the hydrogen concentration calculated using a non-sampling method based on PAR operation, are both utilized in a flammability assessment algorithm to diagnose combustion risk. By comparing the experimentally derived correlation for the flammability limits of hydrogen-steam-air mixtures [5] with the hydrogen concentrations obtained using both sampling and non-sampling methods, a hazardous percentage for the current atmospheric conditions can be determined.

5. RESULTS

5.1. Accuracy and Interference Characteristics of Sensing Modules

Figure 5 illustrates the performance evaluation of the concentration sensing module utilizing a standard gas. The thermal conductivity-based hydrogen sensor demonstrated an accuracy with less than 0.1 vol.% error

within the range of 0.1 to 9.0 vol.%. [2] Notably, in concentrations exceeding 2.0 vol.%, the residual standard deviation remained stable at approximately 0.1.

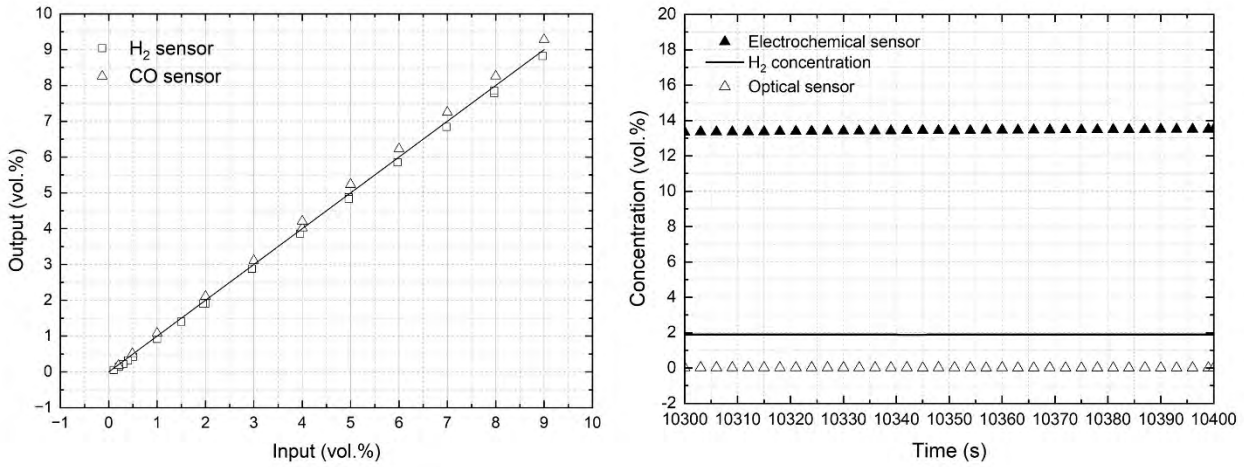

Figure 5. Hydrogen/Carbon Monoxide Sensor Accuracy (Left) and the Effect of Gas Interference on the Carbon Monoxide Sensor (Right).

In an evaluation of gaseous interference effects on carbon monoxide concentration sensors based on their measurement principles, injecting 2 vol.% hydrogen gas into the sensing module caused electrochemical carbon monoxide sensors to exhibit a false concentration reading of approximately 13.44 vol.%. In contrast, the optical carbon monoxide sensor employed in this system maintained an error of less than 0.02 vol.%, irrespective of hydrogen concentration. This demonstrates the suitability of optical sensors for late severe accident environments where both hydrogen and carbon monoxide are produced simultaneously.

5.2. Stability of Environmental Control under Transient Conditions

The performance of the environmental control module was validated under rapid pressure rise conditions of 0.9 kPa/s, which are more severe than those stipulated for major accident scenarios. Despite a sharp increase in experimental vessel pressure from 1.07 bar to 2.0 bar, the inlet pressure of the sensing module was consistently maintained at 1.09 bar by the pressure regulator. Furthermore, even when the inlet temperature to the water bath rose to 42.1 °C, owing to the intake of the 60 °C atmosphere from within the experimental vessel, the gas exiting the water bath was cooled to 23.7 °C. This successfully met the operational temperature requirement for the sensor, which is below 25 °C.

5.3. Time Delay and Response Time Analysis

By simplifying only the pool scrubber section of the environmental control module in the sampling system and evaluating the time delay as show in Figure 6, it was observed that the physical intake delay time (td)—defined as the period from the initiation of hydrogen injection until the sensor outputs the hydrogen concentration—remained constant at approximately 26 to 27 seconds (Figure 7). However, the response time (tr), which is the duration required for the hydrogen sensor's output to increase proportionally to the injected hydrogen concentration after the initial output, varied from 13 seconds (for a free volume ratio of 0.41) to 32 seconds (for a free volume ratio of 1.0, representing a water tank filled with air). This response time was found to be directly proportional to the free volume ratio of the water tank, which serves as a pre-treatment facility. In a comparative experiment, a bypass pipeline with an equivalent volume to the water bath was employed. This configuration resulted in a slight increase in the suction delay time to 35 seconds due to the extended pipeline length, while the reaction time was significantly reduced to 5 seconds. This observation suggests that gas drawn into the water bath tank follows a specific path through the free volume

of the bath and that optimizing the design of the water bath tank and the water level is a critical parameter for the real-time monitoring performance of sampling-based measurement systems.

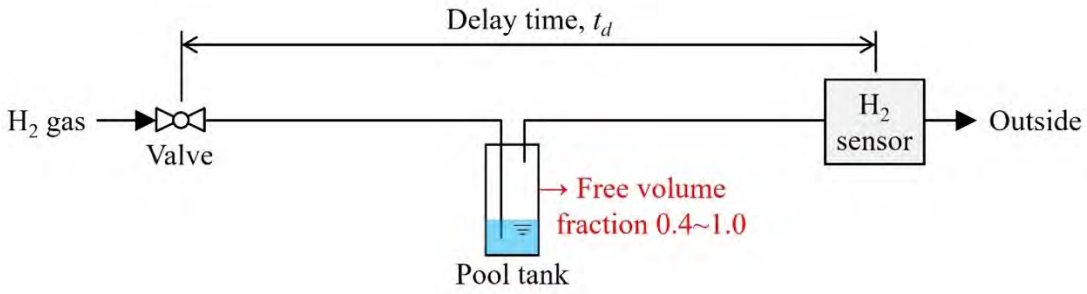

Figure 6. Conceptual Diagram of the Time Delay Evaluation Facility for a Sampling-Based Measurement System.

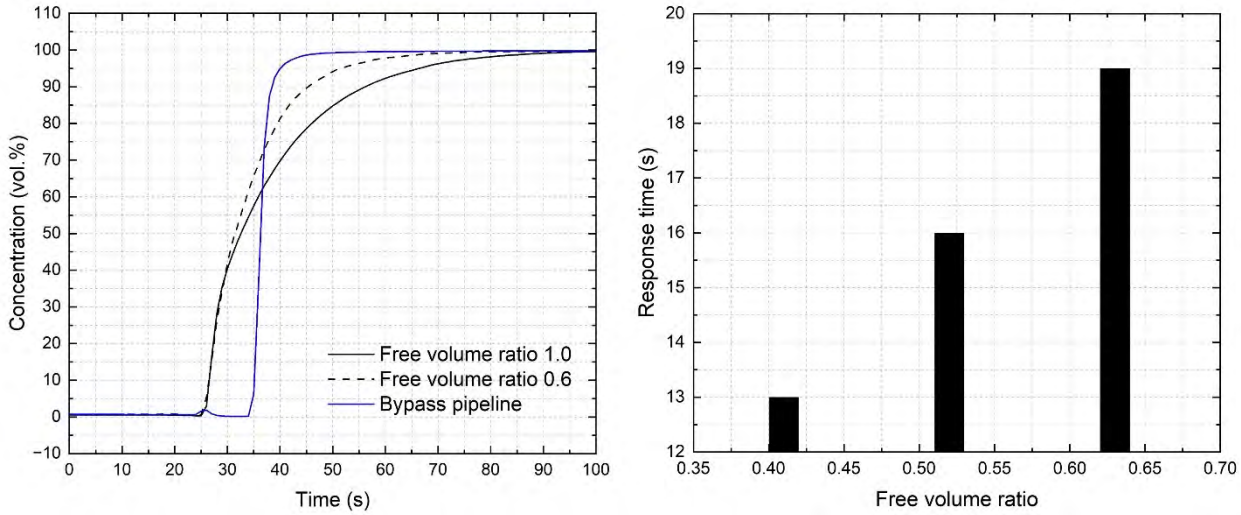

Figure 7. Intake delay and Response Time as Functions of Free Volume Ratio in a Water Tank.

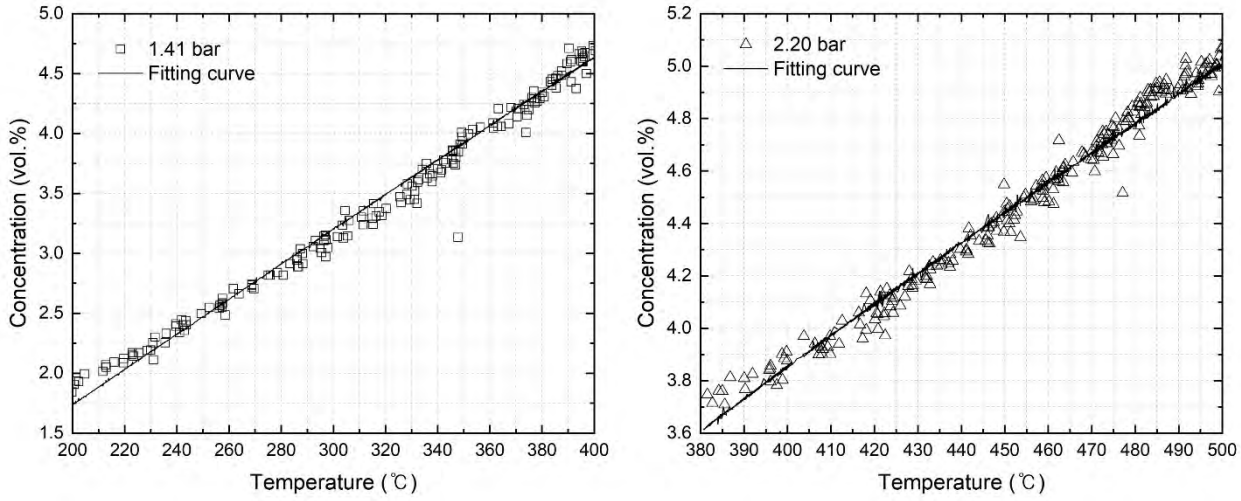

Figure 8. Correlation Between Hydrogen Concentration around the PAR and Catalyst Temperature: 1.41 bar (Left) and 2.20 bar (Right).

5.4. Validation of PAR-based Hydrogen Estimation

Experiments on hydrogen recombination conducted at the SPARC facility validated the effectiveness of the PAR-based hydrogen concentration assessment method across an average pressure range of 1.41 to 2.2 bar and an average ambient temperature range of 64.4 to 94.6 °C. A linear correlation was observed between the catalyst surface temperature and the hydrogen concentration around the PAR, as depicted in Figure 8.

6. CONCLUSIONS

We are currently developing a flammability risk monitoring system specifically designed for severe accidents, comprising three key components: advanced sampling instrumentation, PAR-based non-sampling hydrogen concentration assessment, and a data processing algorithm. This paper presents a preliminary evaluation of the performance and validity of certain individual system components.

Firstly, the environmental control module consistently maintained the operational temperature and pressure of its sensors, even within accident conditions. The implementation of pool scrubbing can effectively mitigate the time delay issues previously caused by concentration dilution within conventional condensation traps and filter housings. Both hydrogen and carbon monoxide sensors demonstrated high accuracy.

Second, experiments on hydrogen recombination conducted within a severe accident simulation environment revealed a linear correlation between the thermal response of the PAR catalyst surface and the hydrogen concentration around the PAR. This finding suggests that PARs could potentially serve as a type of non-sampling sensor to augment concentration data at various locations within a containment building.

Third, the data processing algorithm can compensate for time delays during the sampling process and convert dry hydrogen concentrations to wet concentrations by accounting for the steam removed during sampling. By comparing the hydrogen concentrations obtained from both the sampling-based measurement system and the PAR-operation-based non-sampling method with the flammability limit in real time, a quantitative risk index can be generated.

These findings will contribute to the real-time provision of combustible gas hazard levels in severe accidents, enabling the preemption of potential adverse effects that could arise during spray operations.

ACKNOWLEDGMENTS

This work was supported by the National Research Foundation of Korea (NRF) grant funded by the Korea government (Ministry of Science and ICT) (No. RS-2022-00144368).

REFERENCES

1. OECD/NEA, “Status Report on Hydrogen Management and Related Computer Codes,” *NEA/CSNI/R(2014)8* (2014).
2. Youngsu Na, Jin-Hyeok Kim, Changwan Kang, and Seongho Hong, “Assessment of Monitoring Performance for Hydrogen Concentration in Severe Accidents,” *Proceedings of the 21th International Topical Meeting on Nuclear Reactor Thermal Hydraulics (NURETH)*, Busan, Korea, August 31~September 5 (2025).
3. Youngsu Na, “Analysis of Hydrogen Recombination Rates of Lattice-Shaped Catalysts Under Varying Concentrations of Hydrogen,” *Nuclear Technology* (2025). (Published online)
4. Youngsu Na, “Mixing of hydrogen-steam buoyancy jets released into the upper atmosphere of the containment building,” *Nuclear Technology*, **211**, pp. 273-285 (2025).
5. Billy W. Marshall, “Hydrogen:Air:Steam flammability limits and combustion characteristics in the FITS vessel,” *NUREG/CR-3468* (1986).

12th Conference on Severe Accidents Research (ERMSAR 2026)
May 18-22, 2026, Madrid, Spain

Session 5.2 Hydrogen risk and Containment behavior

Development status of the flammability risk monitoring system in severe accidents

Real-time hydrogen monitoring based on the thermal response of a PAR

Youngsu Na*
Seongho Hong, Ki-Han Park, Jin-Hyeok Kim, Jeong-Yun Oh, and Changwan Kang

*Corresponding author: ysna@kaeri.re.kr

Limitations of H_2 Sampling Measurements in Severe Accidents

Measurement of H_2 vol.% during accidents

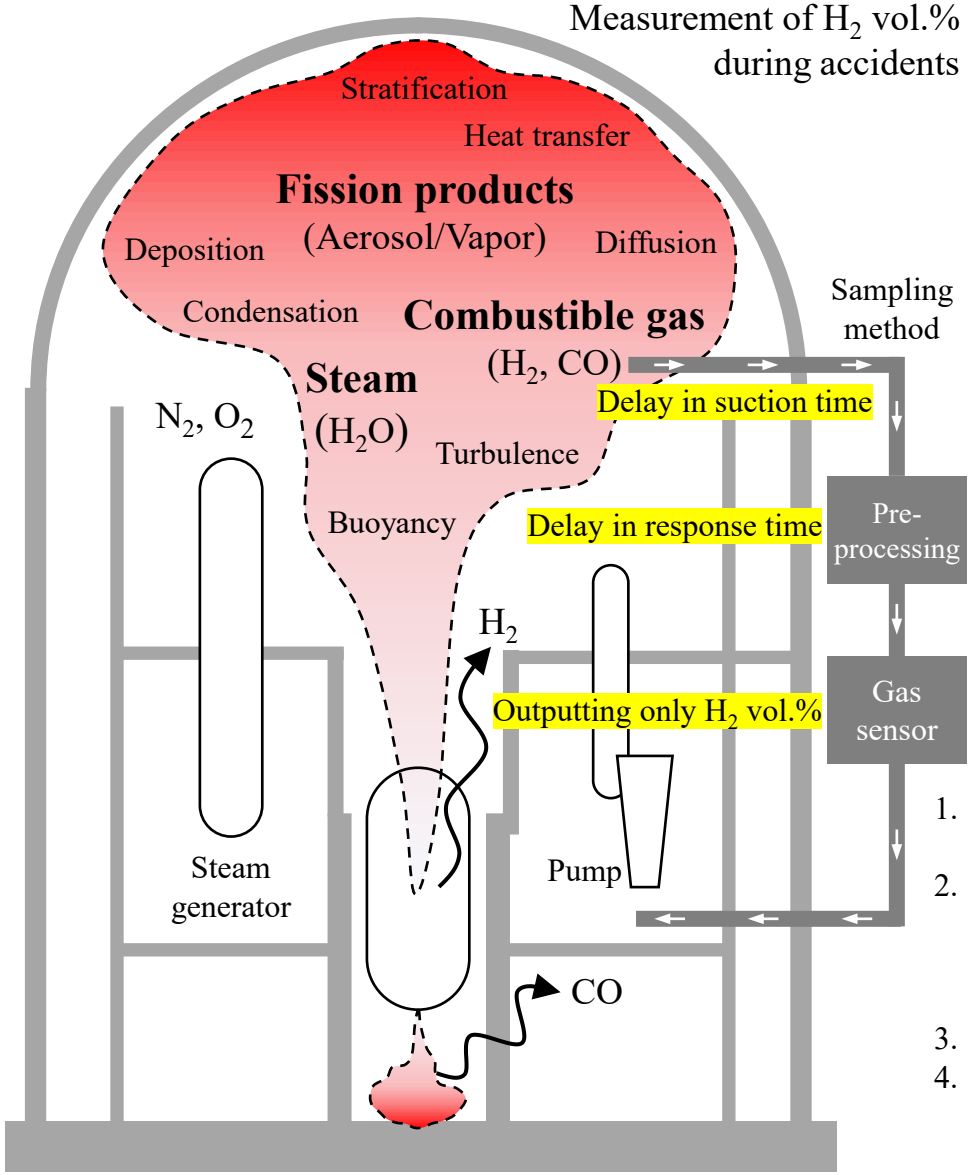

Countries	Measurement method[1]
Belgium	Sampling, ~20 vol.%
Canada	Sampling(#1), iodine, noble gases
Finland	Sampling(#4)
France	PAR+TCs, Raman spectroscopy under development[2]
Germany	Sampling(#10)
Japan	Sampling, portable, PAR, etc.
Korea	Pressure/Temperature, Sampling[3]
Netherlands	Sampling
Spain	Sampling(#2), catalyst reaction(#11)
Switzerland	Sampling, detectors inside containment
Sweden	Sampling

1. OECD/NEA, Status Report on Hydrogen Management and Related Computer Codes, NEA/CSNI/R(2014)8 (2014).
2. A. Bentaïb et al., "THE COMOS SYSTEM - AN INNOVATIVE MONITORING SYSTEM FOR CONTAINMENT ATMOSPHERE IN SEVERE ACCIDENT" EPJ Nuclear Sci. Technol. (Submitted, 2025).
3. KHNP, Hanul Unit 3, 4 Final Safety Analysis Report (1998).
4. Y. Na, "Analysis of Hydrogen Recombination Rates of Lattice-Shaped Catalysts Under Varying Concentrations of Hydrogen", *Nuclear Technology*, **212** (2026) 1019-1034.

H_2 recombination tests in SA conditions[4]

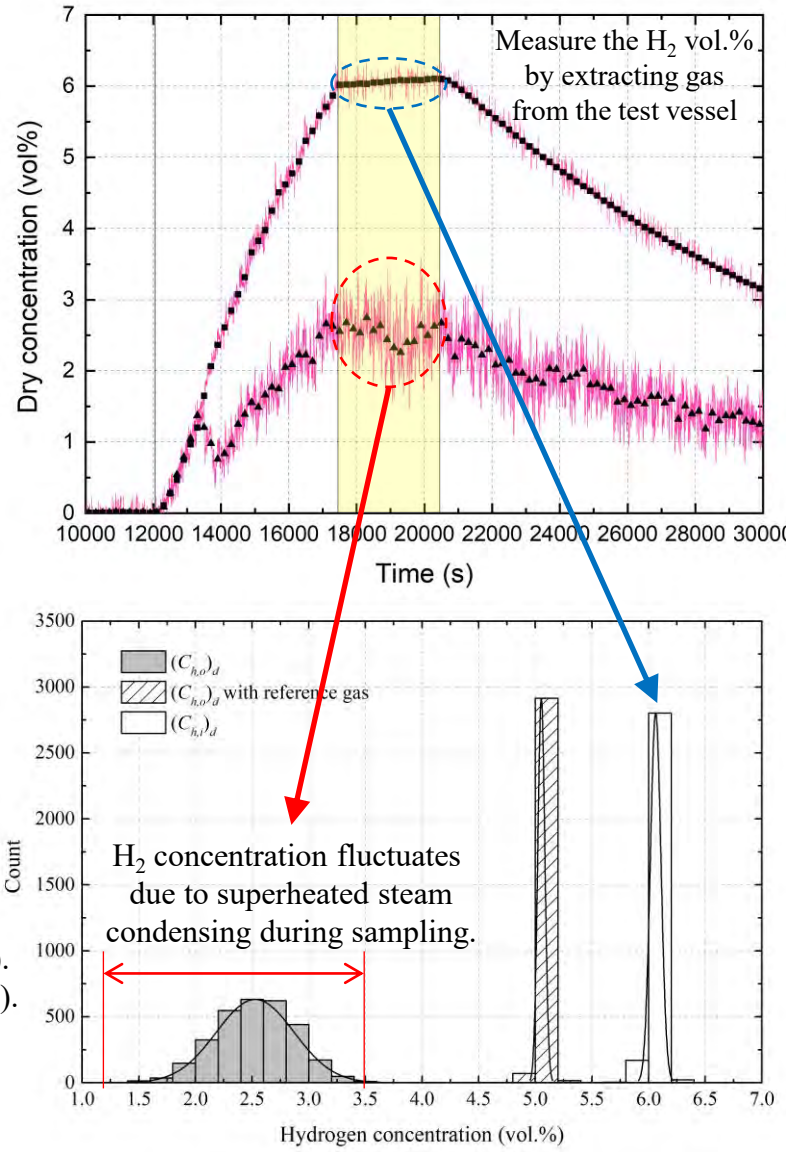

Development of Flammability Risk Monitoring System

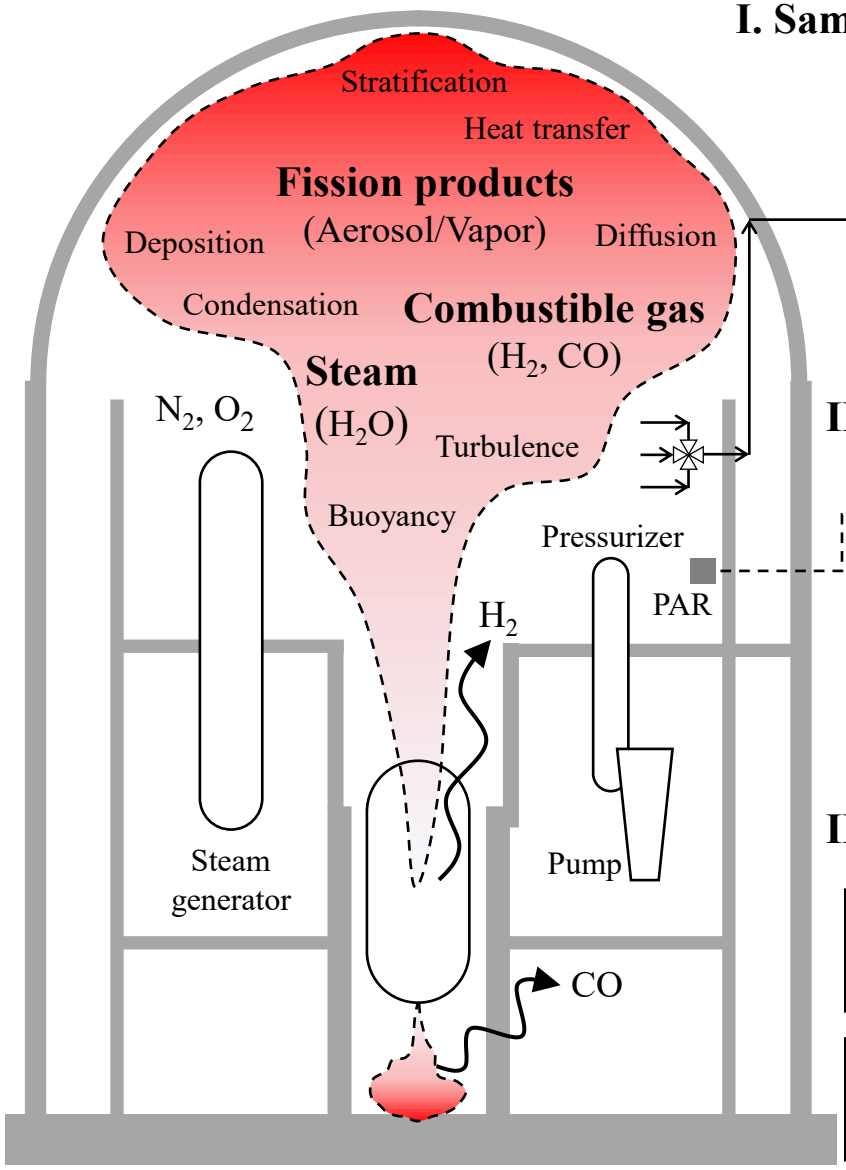

I. Sampling instrumentation system

Gas mixture (H_2, CO H_2O, Air, aerosol, ...)

→ Module for controlling accident environment (T, P, H_2O, V, ...)

↔ Module for sensing combustible gas vol.% (H_2, CO, O_2)

→ Data processing module (Transmitter, DAS, PC, …)

Delay time ▼

II. Non-sampling H_2 vol.% evaluation method

Concentration model based on PAR operation

Passive **A**utocatalytic **R**ecombiner (PAR)
(21~24 PARs in OPR1000)

$2H_2 + O_2 \rightarrow 2H_2O + 120$ kJ/g

H_2 vol.% = f (*thermal response*) + α

H_2 (vol.%)

H_2, CO, O_2 (vol.%)

III. Combustion risk assessment

DB of event sequences
H_2, CO, $H_2O(t, x)$

DB of TH conditions
$T(t, x)$, $P(t)$

Data processing algorithm

Monitoring of flammable gas risk

$LFL = f(T, H_2O,...)$

Severe Accident Management Strategies
(Safety parameter monitoring)

Flammability assessment during accident progression[5]

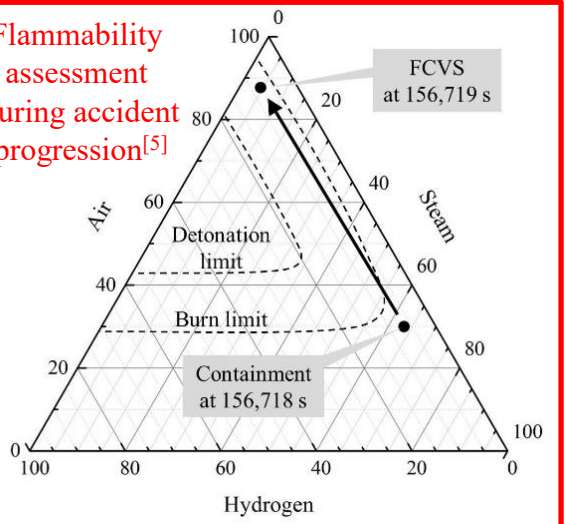

Danger 100
Warning ~
Caution
Safety 0

$\frac{H_2/CO[vol.\%]}{LFL\,[vol.\%]} = 0\sim100$

Warning

Lower Flammability Limit
$LFL = f(T, H_2O,...)$

Safety

H_2 control

5. Y. Na, "The Hydrogen Issue in the Initial Operation of a Filtered Containment Venting System", *Nuclear Technology*, **195** (2016), 329-334.

I. Sampling instrumentation system

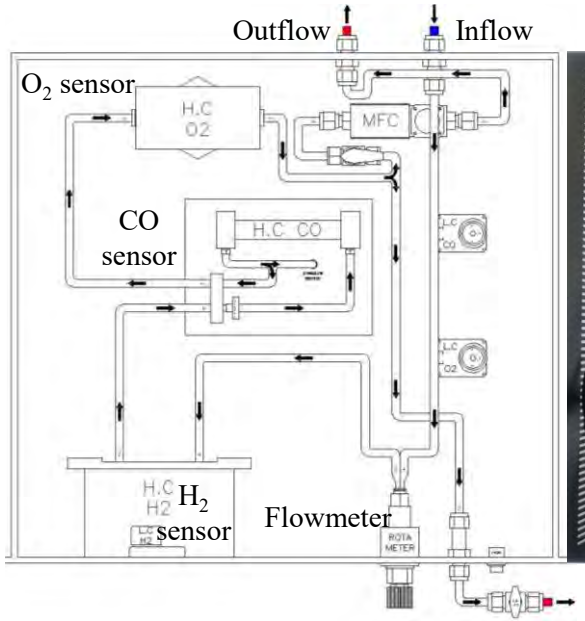

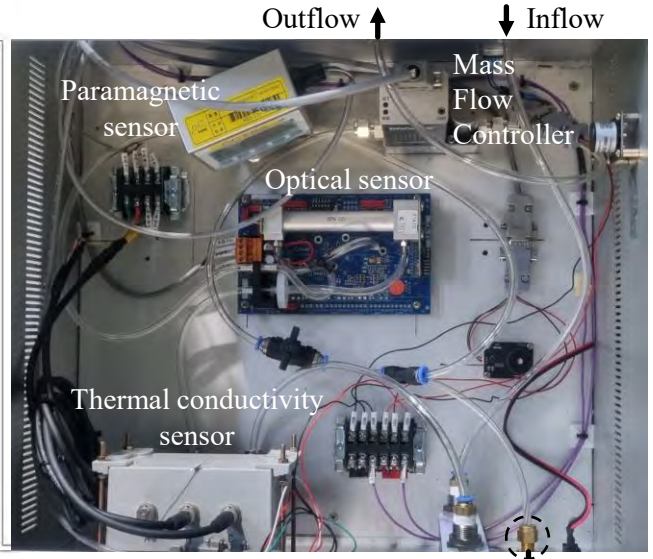

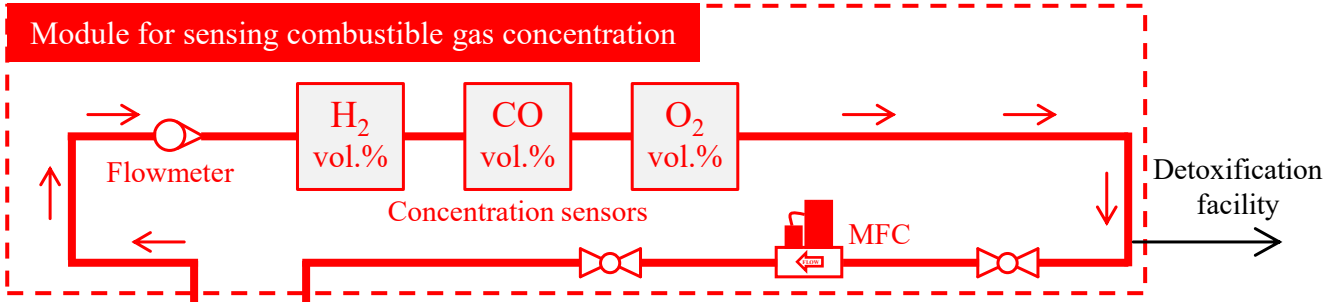

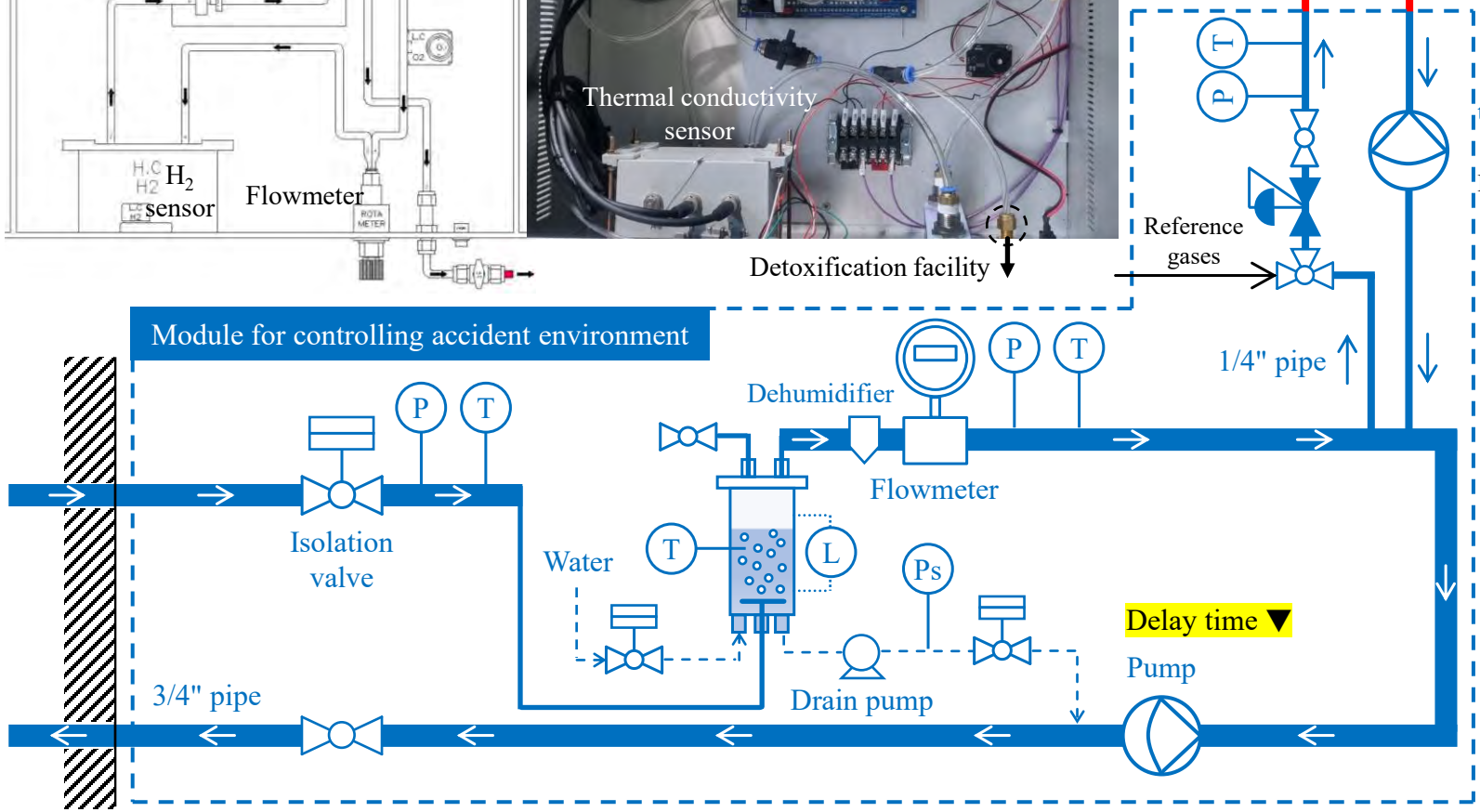

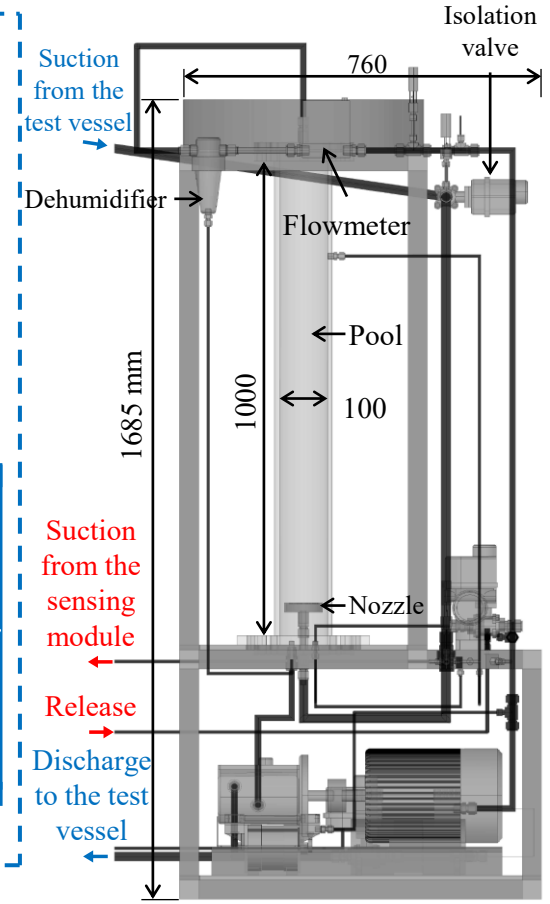

Test vessel capable of simulating severe accident conditions

Performance of a sampling instrumentation system

Pressure 1.5~2.0 bar → ≤ 1.1 bar
Temperature 22~60 ℃ → ≤ 24 ℃
Flow rate 34~70 l/m → 1 l/m

Detoxi-fication facility

① Gas mixture

Test vessel capable of simulating severe accident conditions

Temperature control, steam, and aerosol removal

Data processing module

Module for sensing combustible gas concentration

⑤ Gas sensors

Calibration facility

⑦ Discharge to the test vessel

Modular monitoring system

Module for controlling accident environment

② Isolation valve

④ Dehumidifier

③ Pool

⑥ Pump

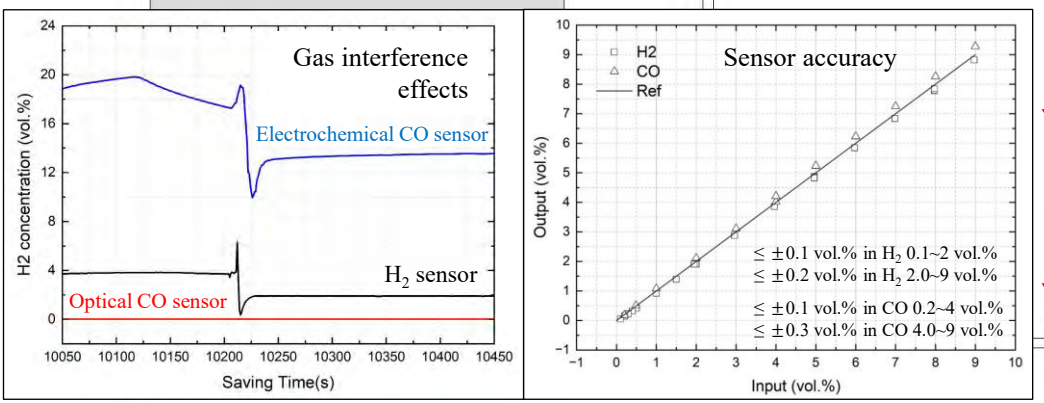

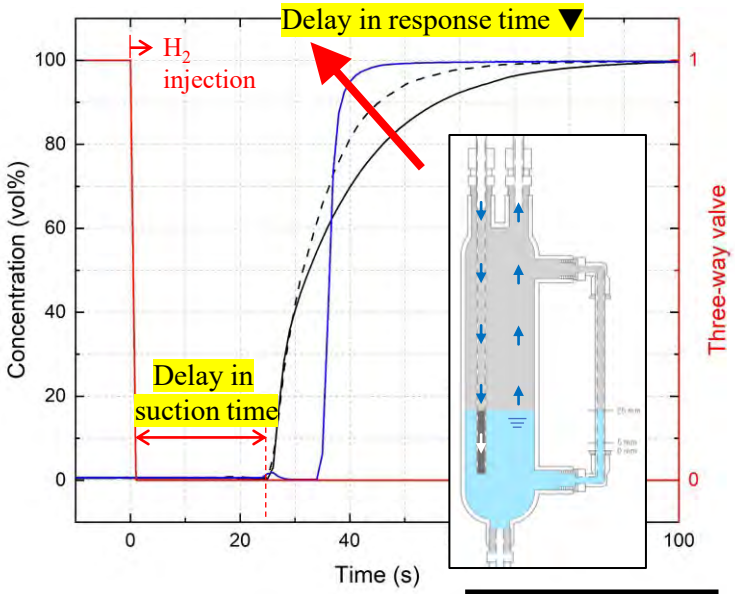

Modular pool scrubbing

(test scheduled)

Decontamination factor

Nozzle exit

Bubble rise

$$DF = DF_1 \times DF_2 \times DF_3 \times DF_4$$

Condensation

Inertial impaction (d_p)

Gravity(d_p), diffusion, Centrifugal

Condensation, Gravity, Diffusion, Centrifugal $= f(d_p)$

$$DF_{CS} = DF_1 \times DF_{2,d} \times DF_{3,d} \times DF_{4,d}$$

$$DF_{I2} = DF_1 \times DF_4 \text{ (Early accident)}$$

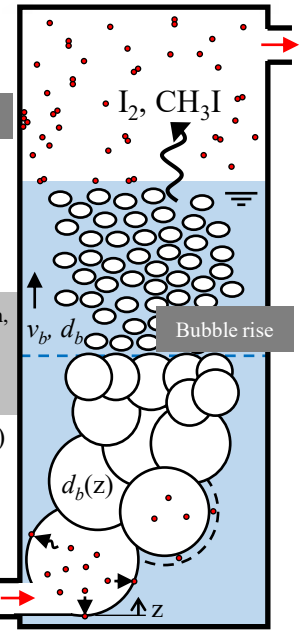

II. Non-sampling H_2 vol.% evaluation method

Hydrogen recombination tests

Lattice-shaped catalyst
Cell 36 cpsi, Pt 60 g/ft^3
KE-7580 made by
Heesung Catalysts corp.

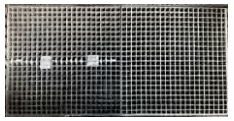

PAR housing
216 x 110 x 1300 mm
SUS304, 1.5 t

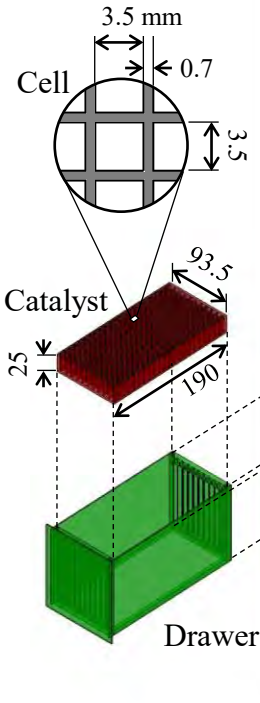

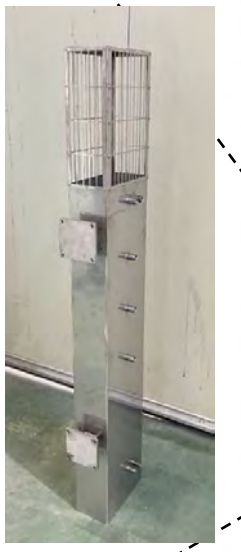

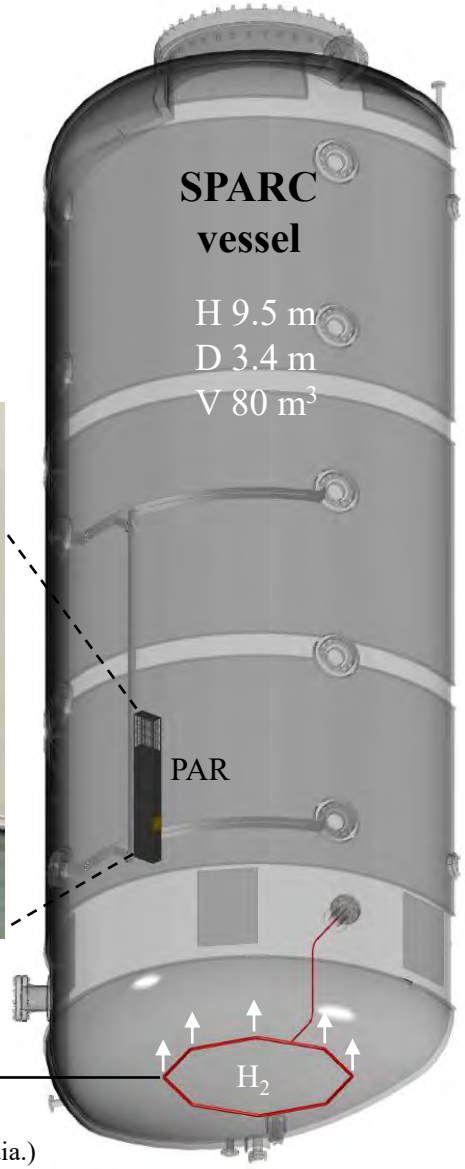

Accident environment[6]

Variables	Range
Pressure(kPa)	101~500
Temperature(K)	301~409
H_2O(vol.%)	0~65.6
O_2(vol.%)	21.0~5.5
H_2(vol.%)	0~4.0
CO(vol.%)	0~4.0(MCCI)
Aerosol(g/m^3)	0~5 / 1~5 μm

LOCA in OPR1000 calculated by MELCOR code

Initial conditions of H_2 injection

Variables	Values
Pressure(bar)	1.34
Temperature(°C)	61.9
Relative humidity(%)	100

H_2 concentration at PAR inlet[4]

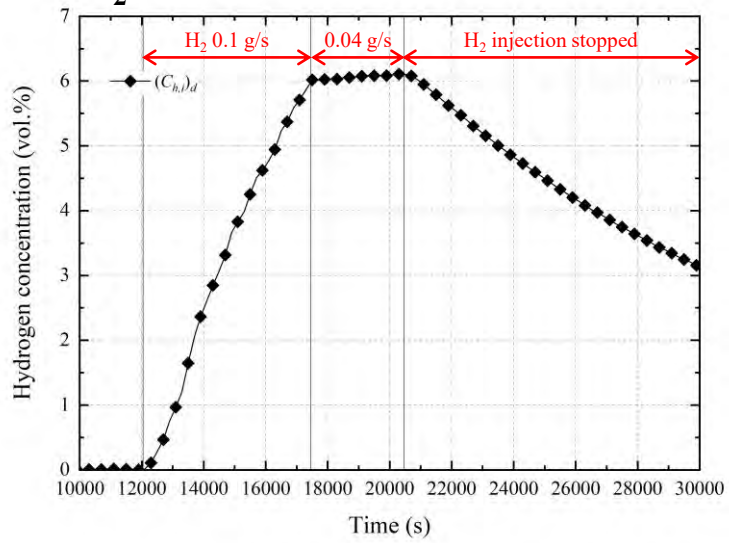

Thermal response = f (H_2 vol.% around PAR)

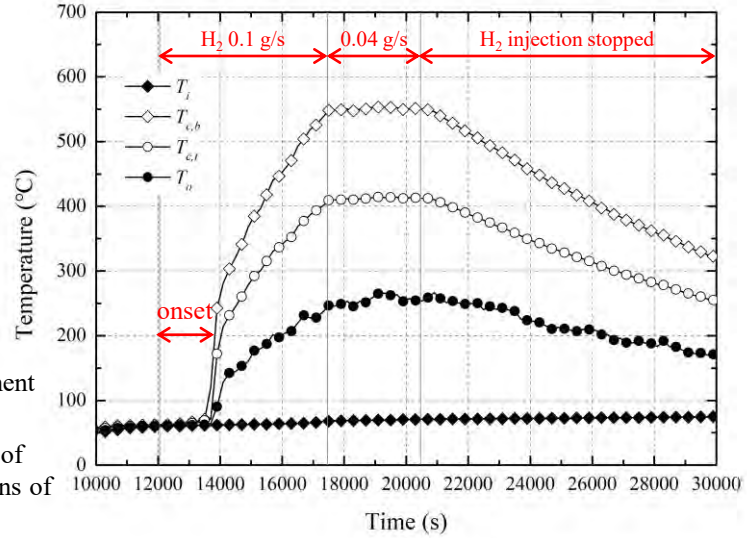

6. Y. Na, "Mixing of hydrogen-steam buoyancy jets released into the upper atmosphere of the containment building," *Nucl. Technol.* **211** (2025) 273-285.
4. Y. Na, "Analysis of hydrogen recombination rates of lattice-shaped catalysts under varying concentrations of hydrogen," *Nucl. Technol.* **212** (2026) 1019-1034.

Experimental conditions from severe accident analysis

Hydrogen generation

$Zr + 2H_2O \rightarrow ZrO_2 + 2H_2 + 6.5$ MJ/kg

Oxidized Zr mass(kg/m^2)

$$\frac{d(W^2)}{dt} = K(T) = 29.6e^{\frac{-16820}{T}}$$

Reaction rate constant

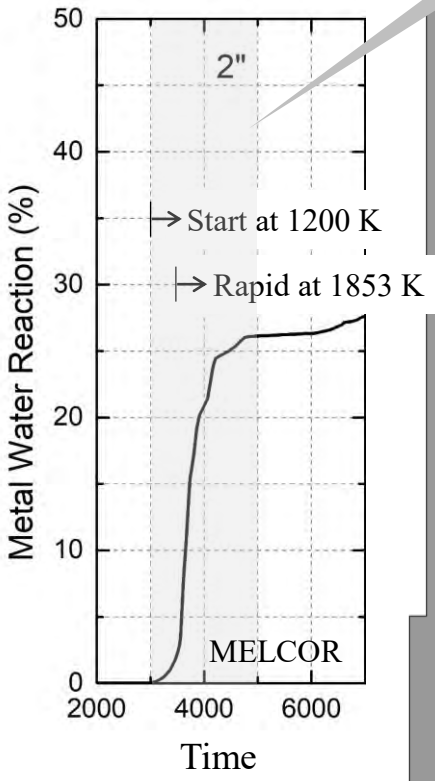

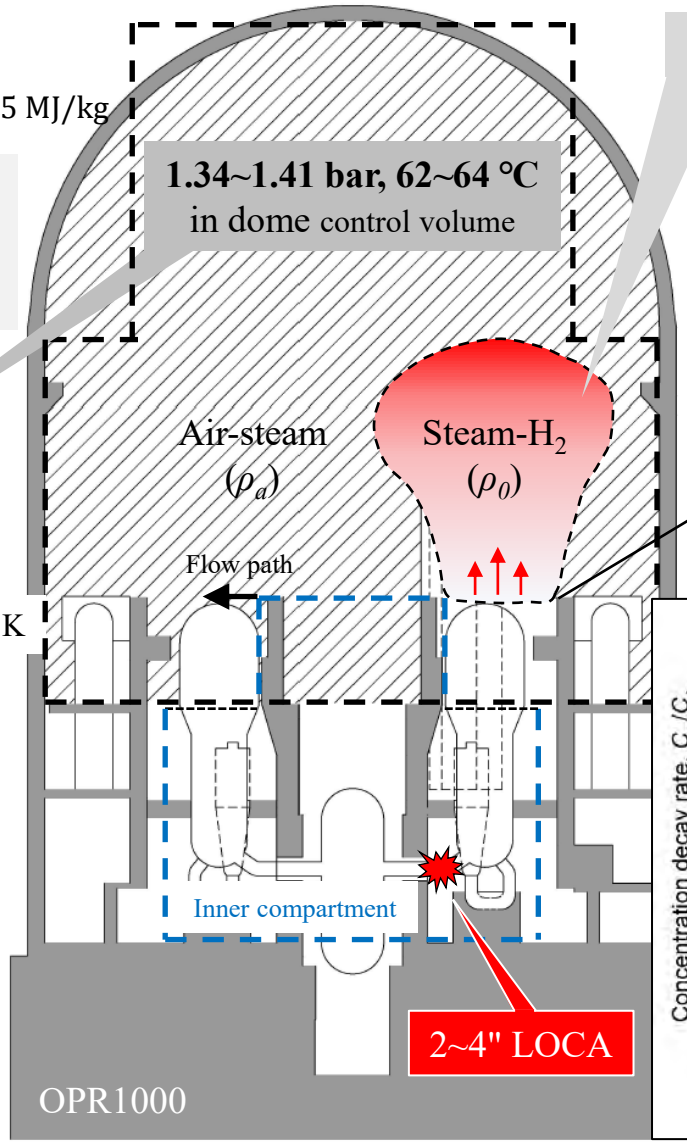

Simplified steam-H_2 release to buoyancy jet[6]

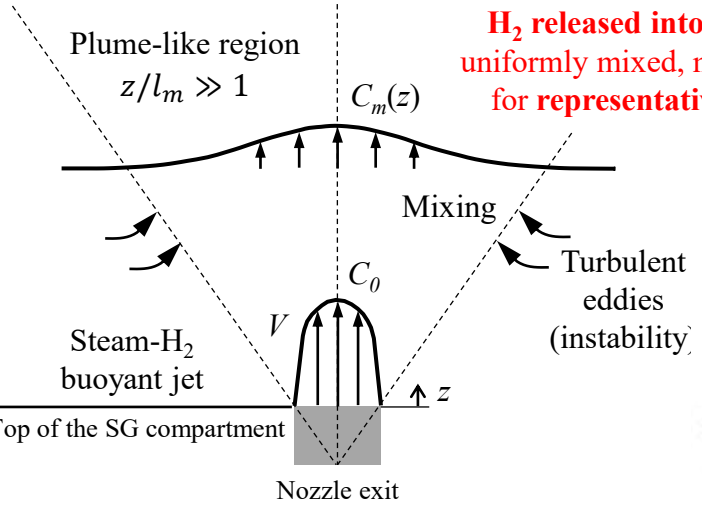

H_2 released into the dome is uniformly mixed, making it ideal for **representative sampling**

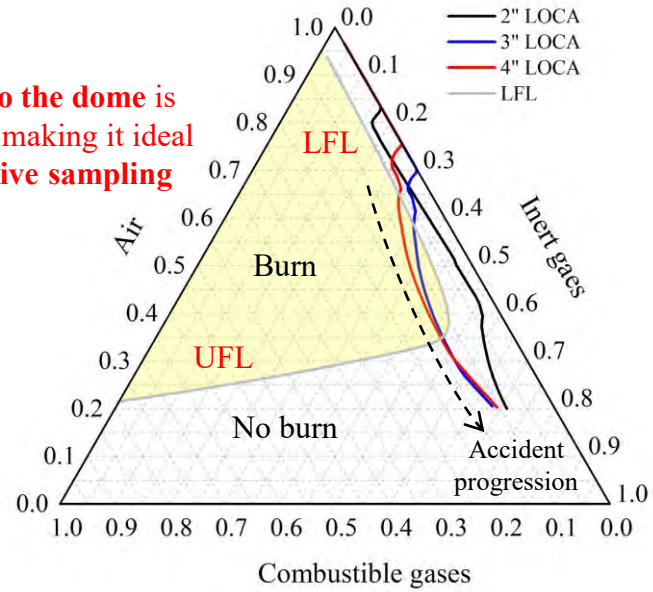

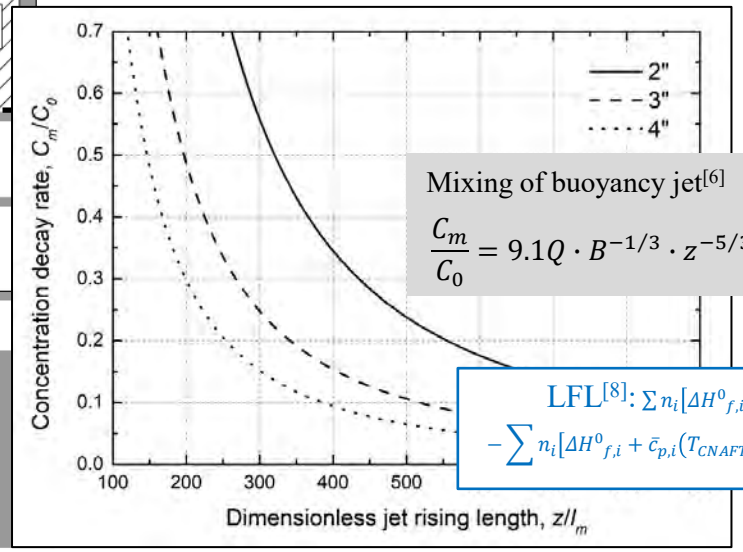

Mixing of buoyancy jet[6]

$$\frac{C_m}{C_0} = 9.1Q \cdot B^{-1/3} \cdot z^{-5/3}$$

LFL[8]: $\sum n_i[\Delta H^0{}_{f,i} + \bar{c}_{p,i}(T_i - T_{ref})]_{reactants} - \sum n_i[\Delta H^0{}_{f,i} + \bar{c}_{p,i}(T_{CNAFT} - T_{ref})]_{products} = Q_{rad,1}$

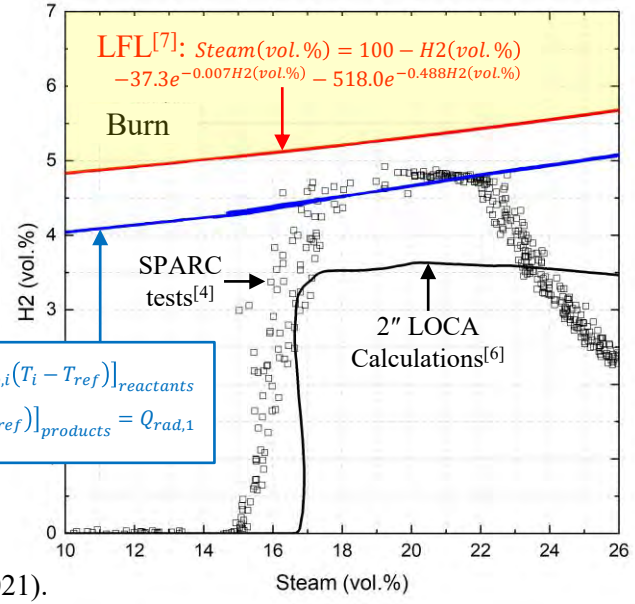

7. Billy W. Marshall, Hydrogen:Air:Steam flammability limits and combustion characteristics in the FITS vessel, NUREG/CR-3468, (1986).
8. J. Jeon et al., A mechanistic analysis of H_2O and CO_2 diluent effect on hydrogen flammability limit considering flame extinction mechanism, *NET*, **53**, (2021).

Linear proportional relationship between C_{H2} and T_c

Mass transport of H_2 on **PAR** catalyst surface

$$J_{H2} = h_m(C_{H2} - C_c) \quad + \quad Q = J_{H2} \cdot A \cdot \Delta H \quad \rightarrow \quad Q_l = h \cdot A(T_c - T_g) \quad \rightarrow \quad C_{H2} \propto T_c$$

Energy transport of **PAR** catalyst reaction

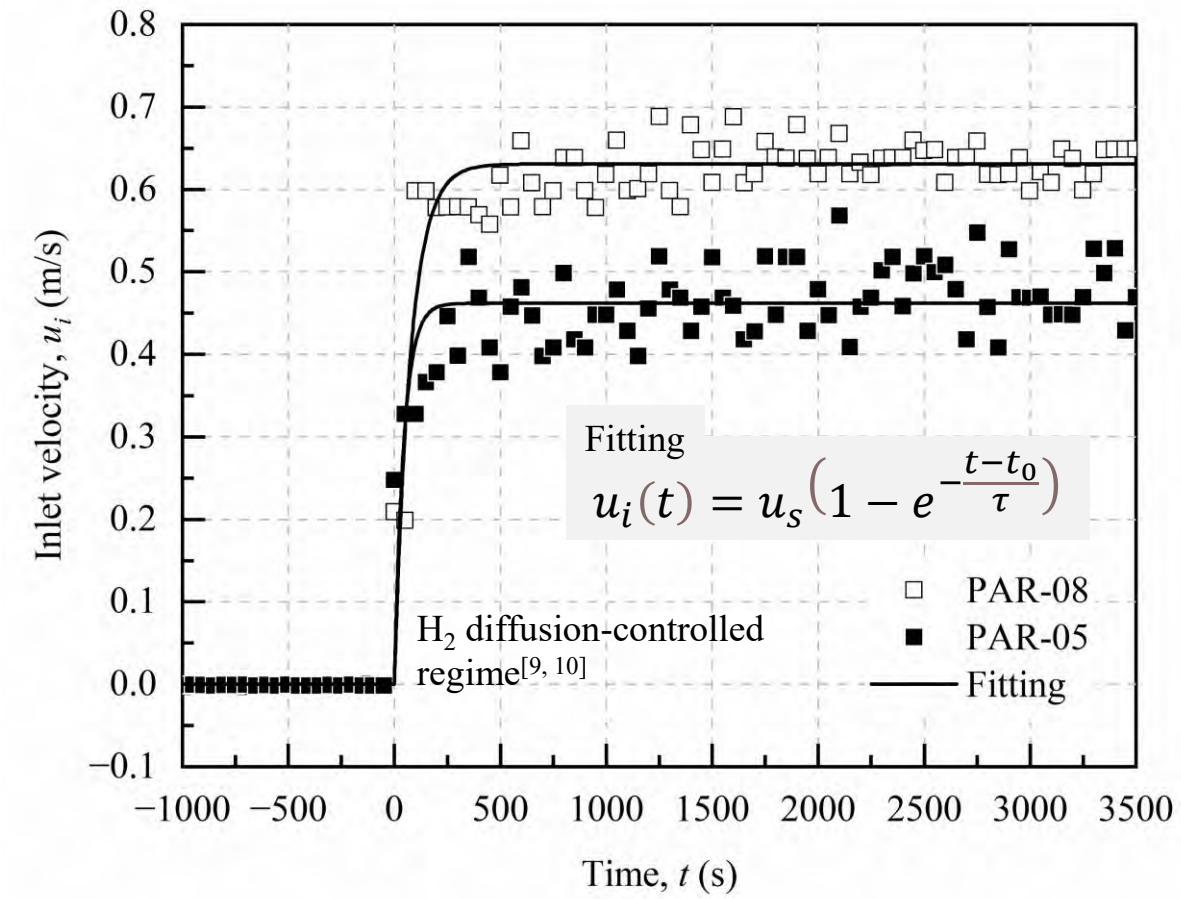

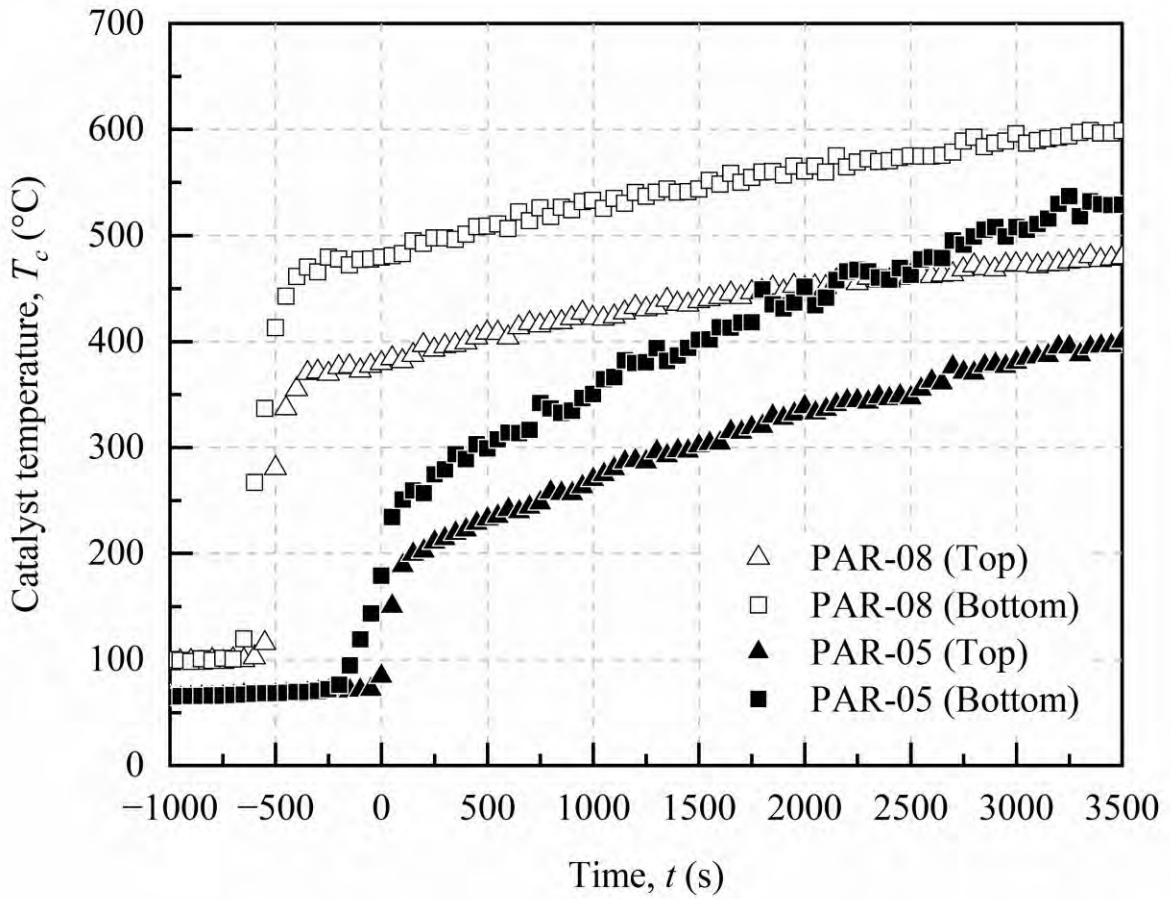

9. J. Böhm, Modelling of processes in catalytic recombiners, Forschungszentrum Jülich GmbH, Jülich, Germany, 2007. (in German)
10. S. Kelm, W. Jahn, E.-A. Reinecke, Operational behaviour of catalytic recombiners - experimental results and modelling approaches, in: OECD/NEA & IAEA Workshop on Experiments and CFD Codes Application to Nuclear Reactor Safety (XCFD4NRS), Grenoble, France, September 10-12, 2008.

Real-time H_2 concentration monitoring using a PAR

Correlation[11] $C_{H2} = \left(S_1 \cdot \frac{P}{T} + S_2\right) T_{c,b} + \left(I_1 \cdot \frac{P}{T} + I_2\right)$

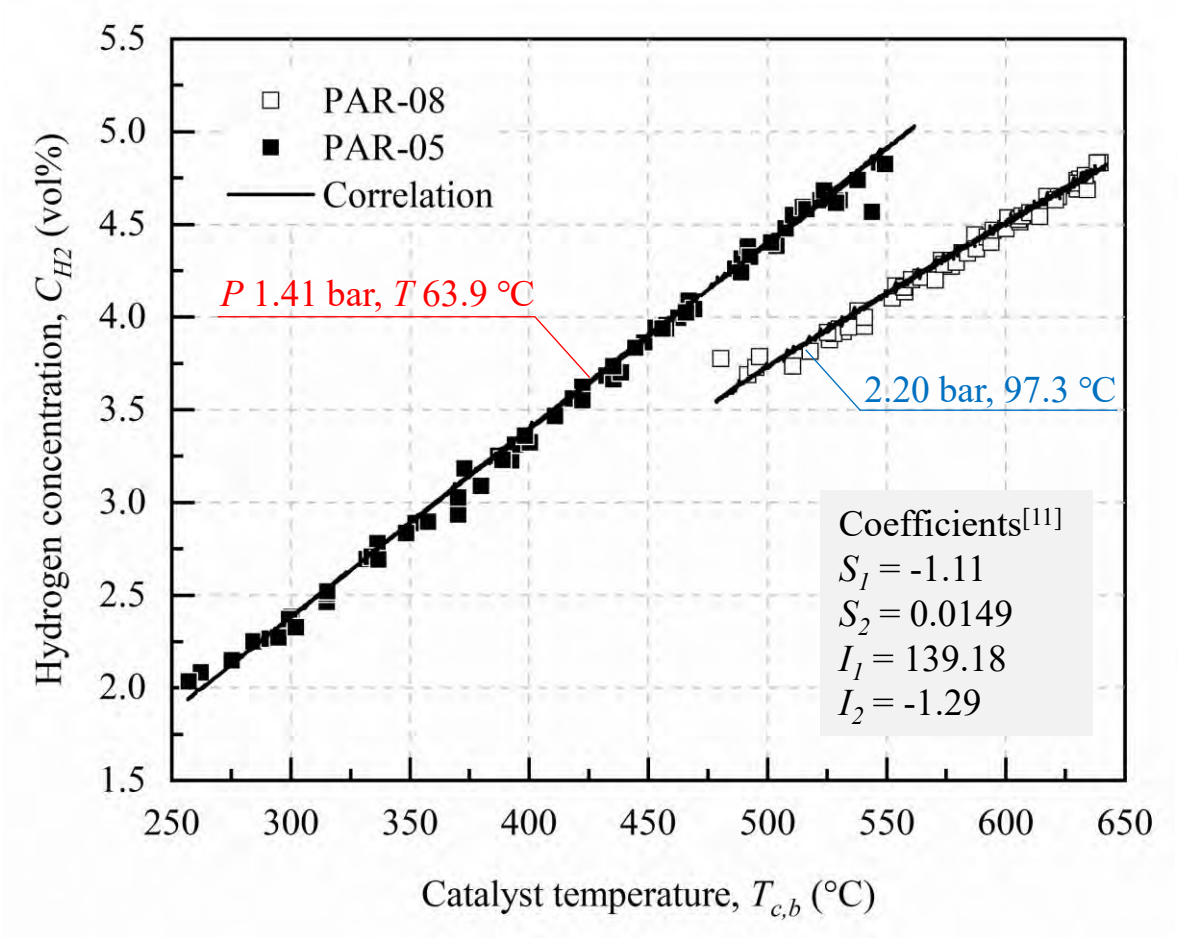

III. Combustion risk assessment

Utilization of PAR-based H_2 concentration backup monitoring

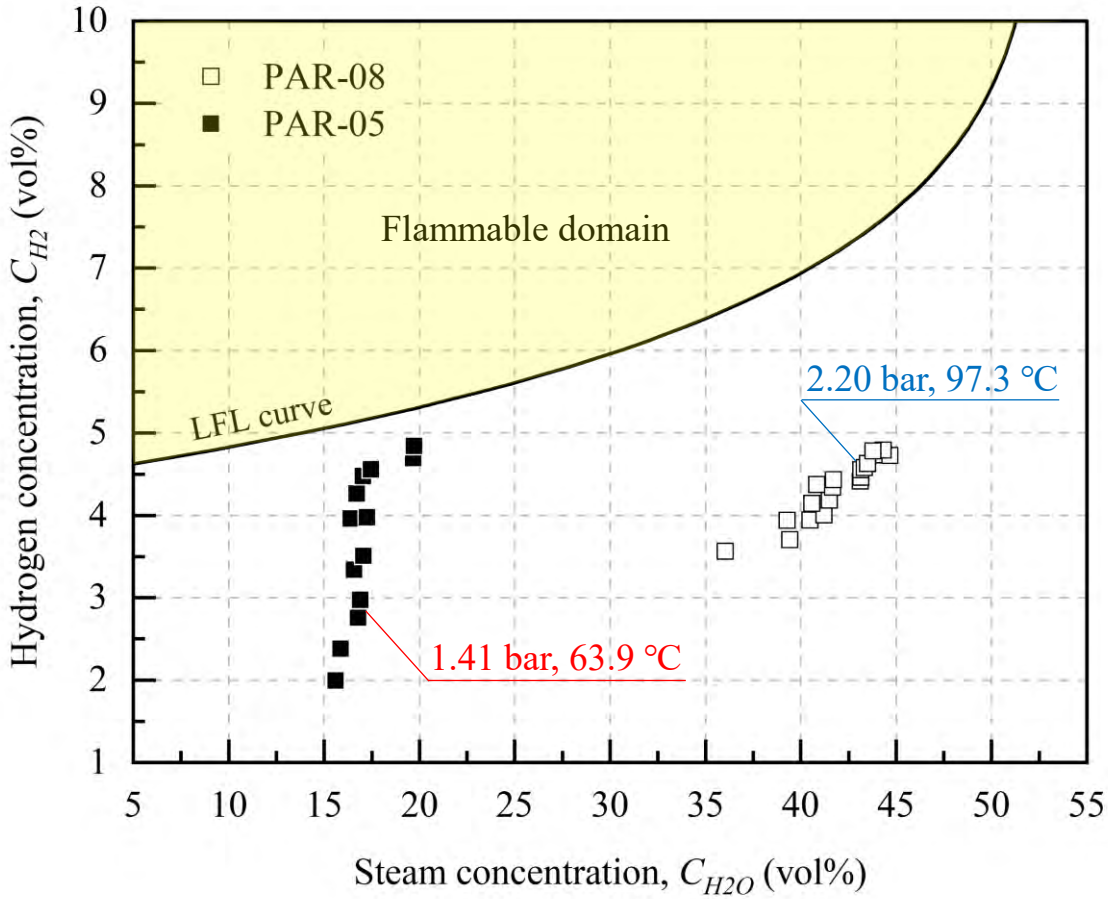

11. Y. Na, Real-Time Hydrogen Monitoring Based on the Thermal Response of Passive Autocatalytic Recombiners During Severe Accidents, TBD.

Flammability risk monitoring system under development

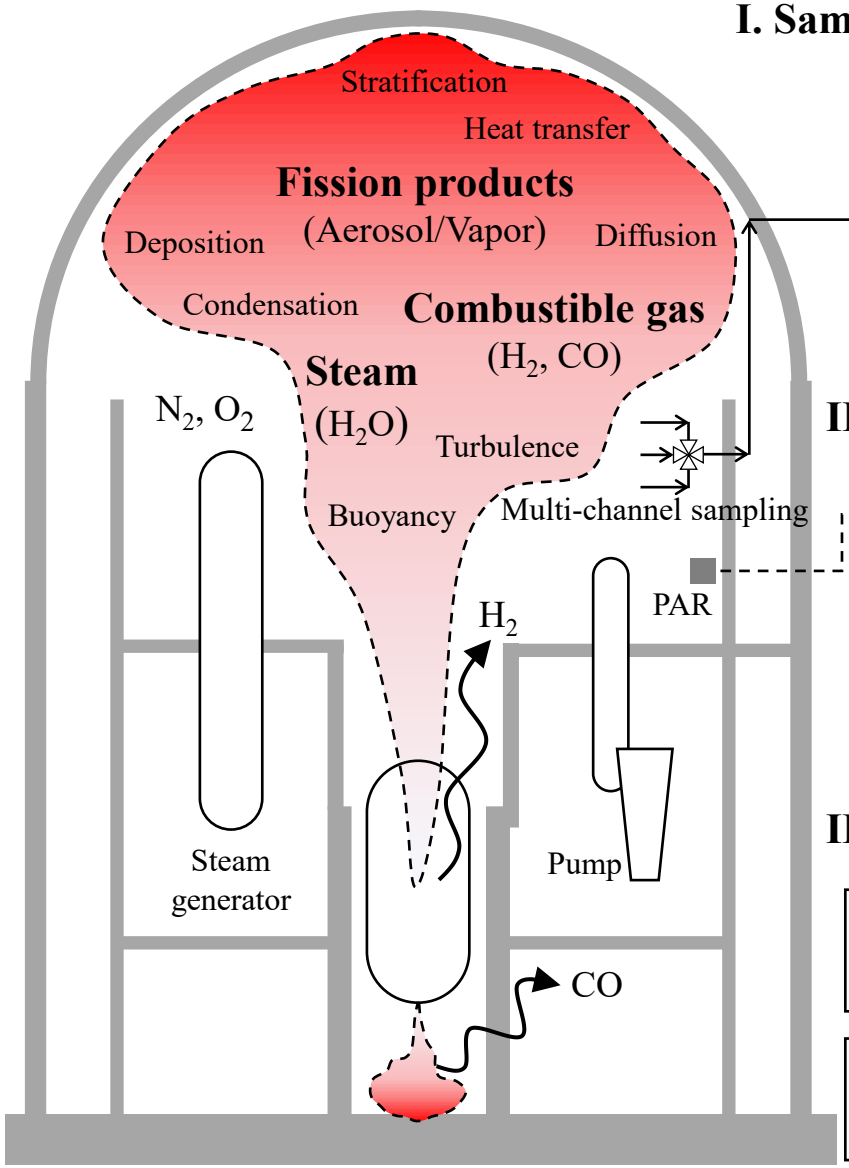

I. Sampling instrumentation system

Gas mixture (H_2, CO H_2O, Air, aerosol, ...)

→ Module for controlling accident environment (T, P, H_2O, V, ...)

↔ Module for sensing combustible gas vol.% (H_2, CO, O_2)

→ Data processing module (Transmitter, DAS, PC, …)

II. Non-sampling H_2 vol.% evaluation method

Concentration model based on PAR operation

Passive **A**utocatalytic **R**ecombiner (PAR)
(21~24 PARs in OPR1000)

$2H_2 + O_2 \rightarrow 2H_2O + 120$ kJ/g

H_2 vol.% = f (*thermal response*) + α

H_2 (vol.%)

H_2, CO, O_2 (vol.%)

III. Combustion risk assessment

DB of event sequences
H_2, CO, $H_2O(t, x)$

DB of TH conditions
$T(t, x)$, $P(t)$

→ Data processing algorithm

$LFL = f(T, H_2O,...)$

→ Monitoring of flammable gas risk

The comprehensive performance test will be completed by 2026.

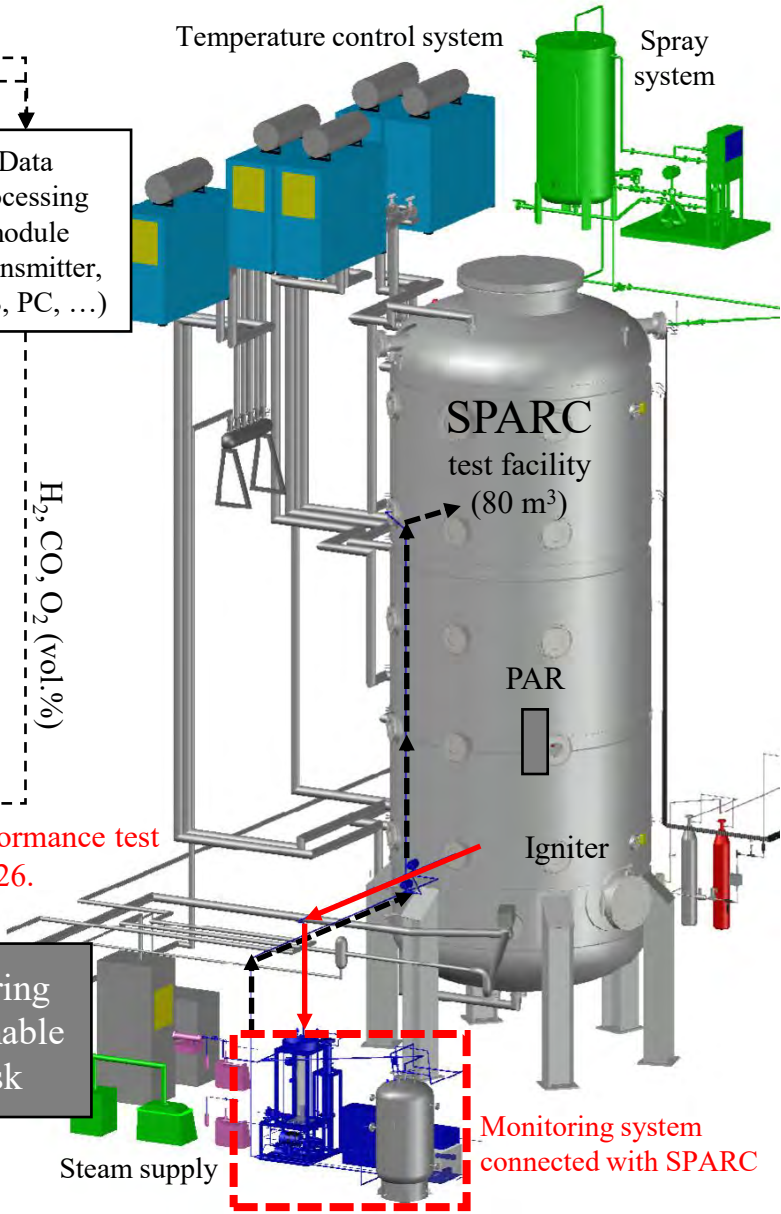

The 12th European Review Meeting on Severe Accidents Research

May 18-22, 2026, Universidad Carlos III de Madrid, Madrid, Spain

TECHNICAL SESSION 6.2: SOURCE TERM

Chairs: T. Lind (PSI), T. Kärkelä (VTT)

ID195	**Developing a Concept for the Prediction of Long-Term Radionuclide Leaching from Corium in Post-Accident Scenarios** T. Jankowski (RUB)	Paper Presentation
ID031	**FissiOn pRoducts bEhavior under SeverE accident with New fuel concepts The OECD/NEA FORESEEN Project** A.-C. Grégoire (ASNR)	Paper Presentation
ID201	**Scaling Effects in Iodine Retention for Filtered Containment Venting: Experimental Findings and Safety Implications** S. Gupta (Framatome GmbH)	Paper Presentation
ID182	**A Deep Learning Surrogate Model for Rapid Prediction of Atmospheric Radioisotope Dispersion** O. Murat (KIT)	Paper Presentation

DEVELOPING A CONCEPT FOR THE PREDICTION OF LONG-TERM RADIONUCLIDE LEACHING FROM CORIUM IN POST-ACCIDENT SCENARIOS

Florian Krist, Tobias Jankowski and Marco K. Koch
Ruhr-Universität Bochum,
Plant Simulation and Safety Group (PSS)
Universitätsstr. 150, 44801 Bochum
krist@pss.rub.de, jankowski@pss.rub.de and koch@pss.rub.de
ORCID-ID: 0000-0002-4089-5801, 0000-0001-5506-0498 and 0000-0001-7260-5250

ABSTRACT

The decommissioning of the Fukushima Daiichi Nuclear Power Plant presents an exceptional challenge in long-term safety management, specifically regarding the stabilisation and treatment of the "Liquid Source Term". In frame of the EU project SCORATES, investigations focus is on improving understanding of the post-operation liquid source term, with the aim of enhancing strategies to mitigate and monitor the release of radionuclides into the environment. Leaching phenomena from different scientific fields are analysed with regard to their suitability for the modelling of severe accident scenarios and especially the long-term liquid source term. Different approaches from the literature are presented and discussed as well as past investigations in the frame of the decontamination intentions of the damaged TMI-2 nuclear power plant.

Leaching mechanisms are being investigated in order to develop a model that takes into account the relevant phenomena and enables predictions to be made about the mass of released radionuclides into the aqueous phase depending on specific boundary conditions. Given that no established leaching models yet exist, the basic concept here is to develop a framework for the future model by incorporating several validated sub-models from different disciplines, each representing a specific sub-phenomenon. Temperatures, composition and surface area of corium, the liquid, its pH value and redox potential are included in the model development as relevant influencing factors.

KEYWORDS
Review, Fission Product Behaviour, Liquid Source Term, Leaching, Model Development

1. INTRODUCTION

Ensuring safe long-term cooling after a meltdown event is a major technical challenge. A current key issue regarding the post-operation at Fukushima Daiichi nuclear power plant is the potential and actual leaching rates of radionuclides from the solidified materials of the degraded nuclear reactor into the surrounding liquid. In the frame of the decommissioning activities, a huge amount of contaminated water needs to be treated. As the damaged reactors were cooled by injection of water, these amounts of water were exposed to contamination. As part of the EC Euratom SOCRATES project, comprising a consortium of 18 institutions from nine countries, the knowledge and modelling of long-term leaching of radionuclides from molten core material is being enhanced.

Data from the accident at Three Mile Island's Unit 2 (TMI-2) nuclear power plant demonstrate the scale of this challenge, with large amounts of the core inventory found outside the reactor core. In the frame of the decontamination efforts at the damaged TMI-2 reactor, investigations have been conducted regarding the

distribution of fission products within and outside the reactor cooling system. Analyses of TMI-2 samples confirmed that the majority of released radionuclides, except for ^{90}Sr and ^{144}Ce, were found dispersed in the basement water and sediment. Specifically, measurements showed that 59 % of the ^{3}H, 2.7 % of the ^{90}Sr, 15 % of the ^{129}I, 20 % of the ^{131}I and 42 % of the ^{137}Cs that were initially present in the core could be found outside the core in the reactor building after the accident. [1, 2]

Further, it was investigated how long contaminated components would need to remain in the water in order to be decontaminated. Although it became apparent that the decontamination periods were impractical, it was also found that there was a continuous increase in ^{90}Sr in the cooling circuit, which was attributed to leaching within the RPV. Figure 1 shows the normalised in-vessel measurement values for ^{90}Sr compared ^{137}Cs, as well as the radioactive isotopes detected outside the primary circuit. Following the accident, the reinjection of water and subsequent exchange within the primary system was expected to decrease the concentration of radioactive isotopes, as observed with ^{137}Cs. However, an increase in the concentration of ^{90}Sr was measured during the first 18 months after the accident, before it eventually dropped as well. [1]

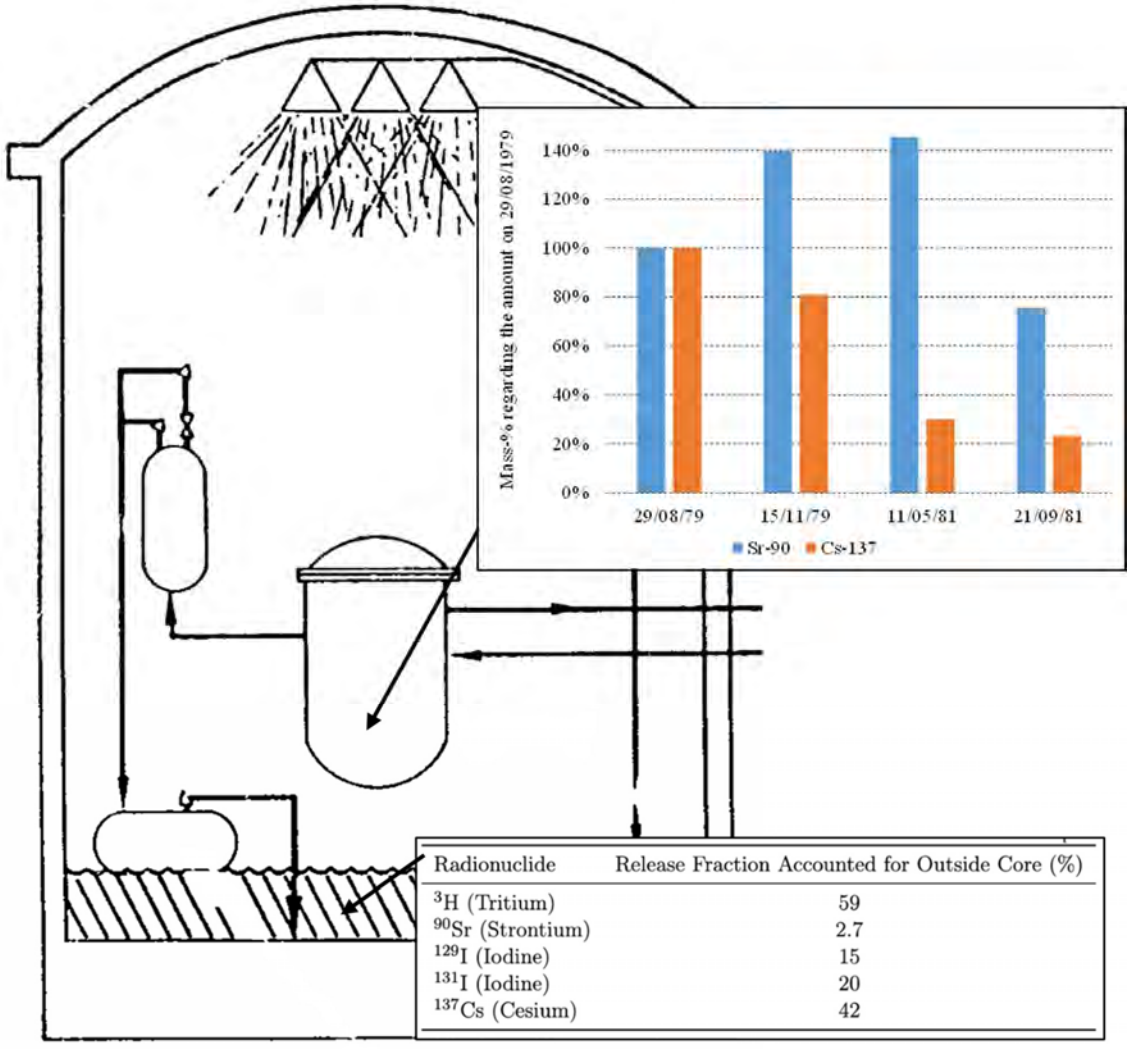

Radionuclide	Release Fraction Accounted for Outside Core (%)
^{3}H (Tritium)	59
^{90}Sr (Strontium)	2.7
^{129}I (Iodine)	15
^{131}I (Iodine)	20
^{137}Cs (Cesium)	42

Figure 1. TMI-2 Reactor building source term measurements, based on [1]

Leaching can essentially be described as a function of the kinetic and thermodynamic interactions occurring at the debris-water interface over decades. In severe accident scenarios, the heterogeneity of corium – comprising fuel isotopes, cladding, structural metals and concrete ablation products – presents a challenge to standardized prediction methods. Decommissioning strategies must account for these complex material identities to design effective water treatment. Furthermore, the evolution of the debris physical state – from highly porous to dense solidified ingots – serves as the primary boundary condition for kinetic modelling. [3–6]

In this paper a brief material characterisation to account for specific material properties is given (chapter 2), which is necessary for a fundamental description of the mechanisms related to leaching (chapter 3). Chapter 4 introduces a conceptual framework for the relevant sub-phenomena, which will support the development of leaching models in later stages of the SOCRATES project. The paper includes a brief discussion of uncertainties (chapter 5) and concludes with a summary of the analysis (chapter 6).

2. PHYSICAL AND CHEMICAL CHARACTERIZATION OF CORIUM DEBRIS

The material structure of corium and debris resulting from a reactor core meltdown, particularly in the context of the Fukushima Daiichi accident, is characterized by extreme heterogeneity and a complex two-phase architecture at both the macroscopic and molecular levels. At the macroscopic level, the materials can be considered as corium, i.e. the material that forms during the melting of the fuel elements in the reactor core, and as debris, i.e. the resolidified product resulting from the interaction of molten corium with structural materials or concrete. Debris can be categorised as either in-vessel, interacting with reactor internals (like in TMI-2), or ex-vessel, resulting from the molten core-concrete interaction (MCCI) when the melt reaches the concrete basement. Macroscopic fragments range from dense, stony blocks to highly porous, friable materials. Unlike the glass-like debris found at Chernobyl, which showed a high degree of homogeneity, Fukushima's ex-vessel debris is a complex MCCI product with distinct phase partitioning. In this work, investigations focus on debris resulting from MCCI with silicate concrete, which is typically used in western pressurised water reactors, cf. [7, 8]. [3, 9]

In general, MCCI debris can be considered as a two-phase system consisting of a silicate-rich glassy matrix and various crystalline inclusions. The amorphous phase of the debris is represented by a multioxide silicate with a complex chemical structure that inherits its composition from the ablated concrete (primarily SiO_2, Al_2O_3, and CaO). This matrix is characterized by a network of Si-O-Si bridging bonds and Si-O-M bonds (where M is Al, Ca, or Fe). This phase is significantly more soluble than the crystalline fuel inclusions. During interaction with water, it undergoes incongruent dissolution, where divalent (Ca^{2+}) and trivalent (Al^{3+}) ions are released faster than the tetravalent silicon network, potentially leading to the formation of a silicon-enriched hydrated surface layer [3, 9]

Embedded within the relatively soluble glassy matrix are chemically more stable crystalline structures, where $(U, Zr)O_2$ solid solutions are the predominant crystalline phases consisting of an isomorphic mixture of uranium and zirconium oxides. Previous studies investigated MCCI-representative samples. In [5] a heterogeneous sample was prepared in which the fragments were mainly composed of U (between 64 and 86 wt%), Zr (between 0.5 and 7.5 wt%) and a more homogeneous sample in which the main elements were U (approximately 52 wt%) and Zr (approximately 16.5 wt%). In [9] five debris compositions were produced, each with a different ratio of core to cement components, shown in Figure 2. Investigations show that the $(U, Zr)O_2$ phase in the samples tend to adopt a fluorite structure and can occur as cubic phase dendrites or tetragonal crystallites. Structural materials from the reactor (stainless steel and Inconel) contribute to the formation of metallic and oxide phases. These appear as spinels, specifically $Fe(Fe, Cr, Ni)_2O_4$, which are isomorphic mixtures containing iron, nickel, and chromium [3, 5, 9]

The leaching behaviour of corium is intrinsically linked to the microscopic heterogeneity existing between its amorphous glassy phases and crystalline inclusions. The phase boundaries between the silicate-rich glassy phases and crystalline phases of $(U, Zr)O_2$ solid solutions and Fe-Cr-Ni spinels govern the macroscopic release of radionuclides since the glassy silicate phase often dissolves at rates that are orders of magnitude higher than those of the chemically stable fuel-bearing inclusions. In synthesized Fukushima-type debris, heavy metal silicates are rarely detected, suggesting that uranium and zirconium oxides do not participate significantly in the silicate network. This lack of interaction leaves radionuclides trapped within a relatively soluble silicate glass, while the bulk of the uranium remains in a poorly soluble crystalline state. Consequently, the macroscopic leaching rate represents an average of these individual phase contributions. [2, 3, 5, 9]

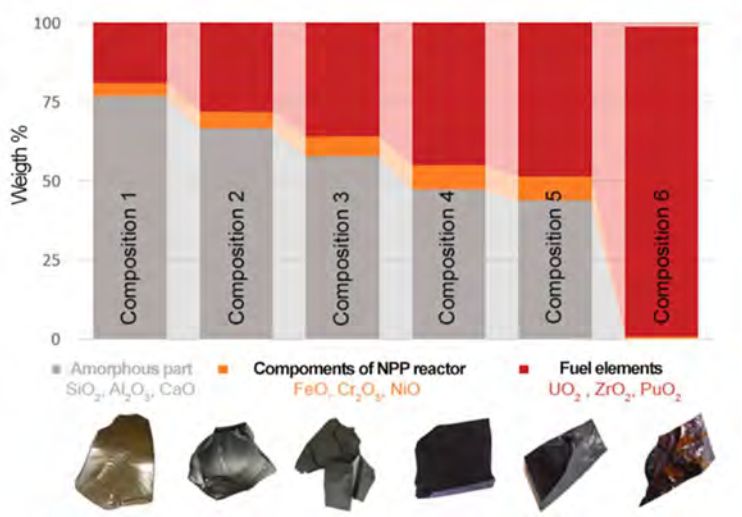

Figure 2. Compositions of synthesized ex-vessel debris samples [9]

3. LEACHING PHENOMENA

Leaching of corium and debris can be described as a multi-stage process governed by various physical and chemical mechanisms. This process is typically divided into several distinct phases, ranging from immediate mobilization to long-term structural evolution. The classification into several characteristic phases here is based on findings from studies with different research focuses on the ageing processes of corium and debris in aqueous environments including studies on vitrified waste. The classification applies to leaching from MCCI debris. The limits of the validity of the conclusions must be critically examined in further studies.

a. Initial Phase: Rapid Release and Surface Wash-off

The first stage of interaction between the debris and water is characterized by the rapid mobilisation of radionuclides located on the external surface or within accessible pores and cracks. Depending on the context this phase is referred to as surface wash-off or the release of the "Instant Release Fraction" (in context of spent fuel) and involves the near-instantaneous dissolution of soluble fission product deposits, such as cesium and iodine compounds. While critical for experimental validation, this fraction is expected to be more limited in corium than in spent fuel due to the high temperatures reached during the melting process, which may have already volatilized a large proportion of these inventories. [1, 10, 11]

b. Early Matrix Alteration: Interdiffusion and Hydrolysis

Once the surface-accessible inventory is depleted, the leaching process enters a stage where the solid matrix begins to degrade. Water molecules penetrate the matrix, while mobile modifier ions (such as Calcium in MCCI debris) exchange with hydronium ions (H_3O^+) from the solution. Simultaneously, the chemical bonds

of the silicate network (in MCCI debris) undergo hydrolysis. Investigations on Fukushima-type debris show, that the dissolution may be incongruent, as discussed in chapter 2. [3, 12]

c. Transition Phase: The Rate Drop

As the leaching progresses, experimental studies on nuclear waste suggest a significant decrease in release rates, possibly by several orders of magnitude. There are two primary scientific perspectives on possible reasons for this rate drop [3, 13]:

1. Chemical Affinity: This approach suggests that the rate decreases as the concentration of silicon in the solution approaches a saturation limit (thermodynamic control) [12].
2. Diffusion Barrier: This view argues that the hydrated surface layer reorganizes into a dense, passivating Interfacial Diffusion Barrier (IDB) that physically inhibits further transport of water and ions [3].

As an integrated approach consideration should be given to couple these mechanisms, suggesting that affinity controls silicon distribution while the IDB governs the diffusive resistance for mobile elements like Cs.

d. Long-Term Phase: Residual Rate and Surface Etching

The system eventually reaches a quasi-steady state known as the residual rate. For MCCI debris, this phase is described as a surface etching process. As the relatively soluble glassy silicate matrix erodes, the surface becomes enriched with a "dusty layer" of low-soluble crystalline oxides, such as $(U, Zr)O_2$ and spinels. This enrichment is critical for long-term assessments, as it governs the properties of the debris surface over decades of underwater storage. [3, 9]

e. Potential Late Phase: Resumption of Alteration

Investigations on vitrified waste show that under specific environmental conditions, a sudden acceleration of leaching can occur long after the rate drop. This phenomenon, referred to as “Resumption of Alteration”, is systematically linked to the precipitation of secondary phases, particularly zeolites (e.g., scolecite). These phases consume silicon and aluminium from the solution and the IDB, effectively stripping the protective properties of the alteration layer and allowing the matrix to dissolve rapidly once more. [12, 13]

4. SUB-MODEL FRAMEWORK

Prediction of the liquid source term requires a fundamental understanding of all relevant sub-phenomena related to any kind of radionuclide release into the aqueous phase. While leaching comprises the time-dependent physical-chemical pathways of solid-state degradation, such as interdiffusion and matrix hydrolysis, the liquid source term is considered as the integrated outcome of all mobilisation processes under specific boundary conditions. This framework develops a multidisciplinary concept breaking down the liquid source term modelling into five primary sub-phenomena, each influenced by the thermochemical boundary conditions. The approaches describing the sub-phenomena are focused on leaching-related mechanisms, whilst also considering rapid mobilization of labile inventories during early-stage, the initial "wash-off". [5]

4.1. Initial Surface Wash-off and Labile Inventory

The initial contact between fuel debris and the aqueous environment is dominated by the “surface wash-off”, which comprises radionuclides located on accessible surfaces and within open pores [11]. TMI-2 measurements provided the first large-scale empirical data on the initial wash-off of radionuclides, documenting that volatile fission products were primarily dispersed in the building’s basement water and sediment [1]. This surface wash-off is critical for model validation and experimental data interpretation, as it accounts for the concentration spikes observed in the early stages of experimental leaching tests [10]. Diagnostic diagrams, which plot normalized release rates against time, typically reveal initial spikes that are

several orders of magnitude higher than steady-state dissolution [14]. These spikes represent the dissolution of fine particulates and the removal of loosely bound ions, such as ^{137}Cs, from the debris surface [3]. Quantifying this labile inventory is essential for immediate safety assessments during debris retrieval and handling. Data from TMI-2 suggests that these surface-accessible radionuclides constitute the main part of the initial liquid source term [1]. While these rapid effects are transient, they establish the chemical baseline for long-term matrix degradation [14]. Furthermore, sea salt interactions can enhance this initial release by altering the ionic strength and ion-exchange kinetics at the debris surface [15]

4.2 Diffusion and Geometrical Kinetics

The transport of dissolved radionuclides within corium is driven by diffusion, necessitating a shift towards mechanistic kinetic modelling. The molecular diffusion coefficient D_i cannot directly be applied here, as it is only valid for diffusion in free solution, not within a porous solid. Different phenomena limit the effective transport [16]. These include interdiffusion of water molecules into the silicate matrix, ion exchange between radionuclides and protons from the cooling water, and the hydrolysis of the Si-O-Si bonds in the silicate network. The "combined resistances" method addresses the simultaneous diffusion of water into the matrix and the outward migration of dissolved species [17]. In the non-stationary and three-dimensional case, Fick's second law applies [3]:

$$\frac{\partial C_i}{\partial t} = D_{i,\text{eff}}\,\nabla^2 C_i, with \quad D_{i,\text{eff}} = \frac{D_i}{R_i}, \tag{1}$$

where C_i is the concentration of the diffusing radionuclide i in the pore fluid and $D_{i,\text{eff}}$ the effective diffusion coefficient which is derived by the molar diffusion coefficient in the solution D_i and the retention factor R_i. The retention factor is an effective parameter that summarises various physico-chemical processes that decelerate transport and includes morphological factors describing the micro-structure of the debris. [3]

In this approach, the geometry of the corium is considered in a simplified form. For spherical geometry, the analytical solution for the differential equation describing the diffusion-controlled release from an object with an initial uniform concentration C_0 and boundary condition $C = 0$ at the surface (infinite reservoir, negligible reverse dissolution) is given (see [16]):

$$M_{diff,i}(t) = m_{0,i}^{\text{diff}} \cdot \frac{S_A}{V} \cdot \sqrt{\frac{D_{eff,i}\,t}{\pi}} \tag{2}$$

Here, the factors involved are the mass of radionuclide i remaining in the body after the instant release $m_{0,i}^{\text{diff}}$, the surface area S_A and the volume of the corium object V. The equation applies to small time scales and demonstrates the characteristic √-behaviour of the diffusion-controlled phase. The surface-to-volume ratio is a key parameter for real corium, but one that is difficult to determine in cases of non-uniform porosity. For long time scales, when the concentration in the solid has decreased significantly, the release approaches an exponential decay behaviour. The short-time approximation (√-regime) is considered valid for time scales ranging from days to years in a first approach.

4.3. Matrix Dissolution

Once the diffusive depletion of the readily accessible inventory is well advanced, the rate of matrix dissolution controls further radionuclide release. Long-term radionuclide release is thus governed by the dissolution of the silicate matrix or crystalline phases of $(U, Zr)O_2$ solid solutions [17]. The Normalized Mass Loss $N_{L,i}$ represents the mass of the total solid matrix that must theoretically be dissolved in order to

reach the measured concentration of a radionuclide C_i in the solution (assuming congruent dissolution) and can therefore be considered a measure of matrix stability [3]:

$$N_{L,i} = \frac{C_i V}{f_i S_A}. \quad (3)$$

By incorporating the surface-to-volume ratio and – with the mass fraction f_i in the solid matrix – the specific inventory, $N_{L,i}$ allows the comparison of the stability of different materials and the mobility of different radionuclides, independent of the specific sample geometry.

For the $(U,Zr)O_2$ matrix, the driving force is oxidative dissolution by radiolysis products, in particular H_2O_2. The dissolution-controlled phase is characterised by linear time dependence. For the $(U,Zr)O_2$ matrix, the dissolution-controlles release under oxidising conditions can be described (for $C \ll C_{sat}$) with the rate of matrix dissolution R_{Matrix} (see [12]). To determine the release rate of a radionuclide i, the dissolution rate normalised to the reactive surface area is multiplied by the given surface area S_A and corrected by the concentration ratio of the radionuclide relative to uranium in the matrix $\frac{c_i}{c_U}$:

$$M_{diss,i}(t) = \frac{c_i}{c_U} \cdot R_{Matrix} \cdot S_A \cdot t. \quad (4)$$

Regarding MCCI debris, perspectively, the breaking of Si-O-Si bonds and the subsequent formation of internal silanol groups should be examined. Surface Complexation Models (SCM) and Surface Precipitation Models (SPM) allow for the mathematical description of interfacial reactions [17]. The kinetic rates derived from these models provide the maximum release potential before thermodynamic attenuation occurs [see 3, 14].

4.4. Thermodynamic Affinity and Interfacial Diffusion Barriers (IDB)

The “rate drop” phenomenon, where leaching rates decrease significantly over time, is governed by chemical saturation and the formation of Interfacial Diffusion Barriers (IDB) [12]. As the concentration of dissolved Si and Al in the leachate approaches equilibrium, the thermodynamic affinity for further dissolution diminishes. Secondary mineral layers, such as gel layers or protective re-condensed silica, act as transport barriers that isolate the bulk material from the solution. While the bulk dissolution rate slows, local chemical environments can still drive the migration of specific high-mobility elements. The IDB model is essential for predicting the stabilization of debris under static storage conditions. The interaction between thermodynamic saturation and protective layer growth determines the transition from kinetic to residual leaching regimes. [3, 9, 12, 13]

4.5. Redox Dynamics and Radiolysis Effects

The radiation field within the debris affects chemical stability through radiolysis of water [18]. Alpha-radiolysis generates reactive oxidants like H_2O_2 which enhance the oxidative dissolution of the $(U,Zr)O_2$ matrix [14]. This process is effectively countered by “chemical buffering” from structural materials like metallic iron [19]. Metallic iron serves as a reducing agent, consuming radiolytic oxidants and maintaining a low redox potential (Eh), which reduces the mobility of redox-sensitive actinides [18]. Diagnostic diagrams illustrate that the presence of Fe can lower the fractional release rates of uranium by several orders of magnitude [14]. Models that ignore these dynamics likely overestimate the long-term leaching of fuel isotopes in high-activity environments [19].

4.6. Influence of Environmental Variables: Sea Salt and pH

Fukushima's environmental context, characterized by seawater exposure, requires specific sub-modelling of salt-debris interactions. Seawater alters radionuclide solubility by providing complexing agents and increasing the ionic strength of the leachate. Furthermore, the pH of the system, which ranges from acidic to highly alkaline depending on concrete interaction, strongly influences dissolution rates. Experiments show that Si and Al release rates are minimized at neutral pH but increase significantly under acidic and basic conditions. These pH-dependent dissolution profiles directly control the exposure of fuel-bearing phases to the aqueous environment. Including these variables in the predictive model enables site-specific effects to be considered. [3–5, 15]

5. DISCUSSION OF UNCERTAINTIES

Uncertainties in leaching prediction involve the risk of leaching "resumption" caused by secondary phase precipitation, such as zeolites. Zeolite formation consumes dissolved silica, lowering the saturation level and driving further matrix degradation. The altering processes influencing the leaching behaviour is schematically shown in Figure 3. Additionally, mechanical degradation, including cracking and exfoliation, can increase the effective surface area (S_A) beyond geometric estimates. Such structural failures potentially lead to release rates significantly higher than those predicted by initial models. Validation is achieved by comparing model predictions with suitable experimental data or the observed chemical composition of the Fukushima reactor cooling water. Long-term irradiation effects on the $(U,Zr)O_2$ solid solution also remain a subject of active study. [3, 5, 9, 13]

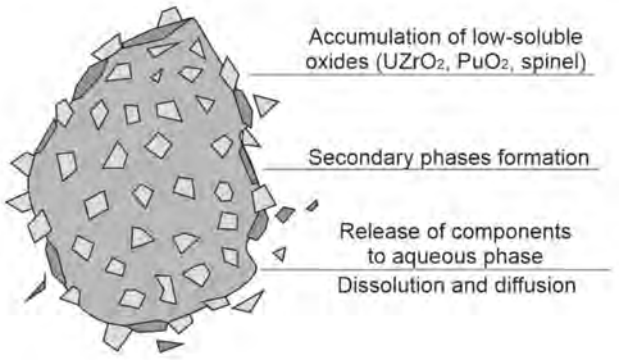

Figure 3. Altering processes influencing the leaching behaviour [9]

6. CONCLUSION

This paper addresses the technical challenge of predicting the liquid source term after core melt accidents such as those at Fukushima Daiichi or TMI-2. The overall objective is to improve the mitigation and monitoring of the release of radionuclides into the cooling water during decommissioning. The pronounced material heterogeneity of the corium, consisting of fuel, claddings, structural metals and concrete ablation products, prevents the application of standardised prediction methods. Corium debris, especially from the melt-concrete interaction, is considered as a complex two-phase system consisting of an amorphous, glass-like silicate matrix (based on concrete components) and embedded chemically more stable crystalline phases, such as the $(U,Zr)O_2$ matrix or Fe-Cr-Ni spinels. The glass phase shows a higher solubility than the crystalline components and is subject to incongruent dissolution. The leaching process is described in terms of five mechanistic phases. These take into account the rapid mobilisation of the labile inventory, early matrix dissolution up to long-term effects.

The methodology proposed for the prediction of long-term radionuclide leaching from Fukushima corium debris is based on a multidisciplinary approach that integrates physical, chemical, and mathematical sub-models. The model framework is intended to bridge the gap between laboratory-scale data and long-term/multi-scale projections. By incorporating matrix dissolution, redox dynamics, and environmental variables, the framework aims to become a reliable tool for decommissioning safety assessments. The integration of the sub-models should consider the complex material structure.

ACKNOWLEDGMENTS

SOCRATES has received funding from the Euratom research and training programme 2024-2028 under Grant Agreement n°101163745. The content of this paper reflects only the author's view. The European Commission is not responsible for any use that may be made of the information it contains.

REFERENCES

[1] C. V. McIsaac and D. G. Keefer, "TMI-2 Reactor Building Source Term Measurements: Surfaces and Basement Water and Sediment," EG&G Idaho, Inc., Idaho Falls, Idaho 83415, USA GEND-042, 1984.

[2] W. J. Gray and D. M. Strachan, "UO2 Matrix Dissolution Rates and Grain Boundary Inventories of Cs, Sr, and Tc in Spent LWR Fuel," Pacific Northwest Laboratory, Richland, Washington 99352, USA PNL_SA--18268, 1990.

[3] V. G. Rumynin *et al.,* "Analytical models for predicting the behavior of the Fukushima fuel debris during laboratory tests and long-term storage," *Journal of Nuclear Materials*, vol. 568, p. 153895, 2022, doi: 10.1016/j.jnucmat.2022.153895.

[4] T. Sasaki, Y. Takeno, T. Kobayashi, A. Kirishima, and N. Sato, "Leaching behavior of gamma-emitting fission products and Np from neutron-irradiated UO 2 –ZrO 2 solid solutions in non-filtered surface seawater," *Journal of Nuclear Science and Technology*, vol. 53, no. 3, pp. 303–311, 2016, doi: 10.1080/00223131.2015.1055315.

[5] A. Nakayoshi, C. Jegou, L. de Windt, S. Perrin, and T. Washiya, "Leaching behavior of prototypical corium samples: A step to understand the interactions between the fuel debris and water at the Fukushima Daiichi reactors," *Nuclear Engineering and Design*, vol. 360, p. 110522, 2020, doi: 10.1016/j.nucengdes.2020.110522.

[6] D. W. Akers, R. K. Mccardell, M. L. Russell, and G. Worku, "TMI-2 Core materials and fission product inventory," *Nuclear Engineering and Design*, vol. 118, no. 3, pp. 451–461, 1990, doi: 10.1016/0029-5493(90)90046-Z.

[7] D. Jacquemain, *Nuclear Power Reactor Core Melt Accidents*. Erscheinungsort nicht ermittelbar: EDP SCIENCES, 2015. [Online]. Available: https://directory.doabooks.org/handle/20.500.12854/79011

[8] J.-M. Bonnet *et al.,* "State-of-the-Art Report on Molten Corium Concrete Interaction and Ex-Vessel Molten Core Coolability," Organisation for Economic Co-Operation and Development, Nuclear Energy Agency - OECD/NEA, Committee on the Safety of Nuclear Installations - CSNI, 46, quai Alphonse Le Gallo, 92100 Boulogne Billancourt (France) NEA--7392, 2017. [Online]. Available: https://inis.iaea.org/records/s1r4a-t4m78

[9] K. B. Rozov *et al.,* "The development of a long-term predictive model of the changes in debris properties during interaction with aqueous solutions. Thermodynamic–kinetic modeling," *Progress in Nuclear Energy*, vol. 158, p. 104599, 2023, doi: 10.1016/j.pnucene.2023.104599.

[10] R. O. Abdel Rahman, A. A. Zaki, and A. M. El-Kamash, "Modeling the long-term leaching behavior of (137)Cs, (60)Co, and (152,154)Eu radionuclides from cement-clay matrices," *Journal of hazardous materials*, vol. 145, no. 3, pp. 372–380, 2007, doi: 10.1016/j.jhazmat.2006.11.030.
[11] D. Serrano-Purroy *et al.,* "Instant release fraction and matrix release of high burn-up UO2 spent nuclear fuel: Effect of high burn-up structure and leaching solution composition," *Journal of Nuclear Materials*, vol. 427, 1-3, pp. 249–258, 2012, doi: 10.1016/j.jnucmat.2012.04.036.
[12] T. Ma *et al.,* "A mechanistic model for long-term nuclear waste glass dissolution integrating chemical affinity and interfacial diffusion barrier," *Journal of Nuclear Materials*, vol. 486, pp. 70–85, 2017, doi: 10.1016/j.jnucmat.2017.01.001.
[13] M. Fournier, S. Gin, and P. Frugier, "Resumption of nuclear glass alteration: State of the art," *Journal of Nuclear Materials*, vol. 448, 1-3, pp. 348–363, 2014, doi: 10.1016/j.jnucmat.2014.02.022.
[14] D. W. Shoesmith, "Fuel corrosion processes under waste disposal conditions," *Journal of Nuclear Materials*, vol. 282, no. 1, pp. 1–31, 2000, doi: 10.1016/S0022-3115(00)00392-5.
[15] M. Takano and T. Nishi, "High temperature reaction between sea salt deposit and (U,Zr)O2 simulated corium debris," *Journal of Nuclear Materials*, vol. 443, 1-3, pp. 32–39, 2013, doi: 10.1016/j.jnucmat.2013.06.039.
[16] C. G. Benson, T. v. Berlepsch, F. Funke, H. Hein, M. K. Koch, M. S. Newland: Late Phase Source Term Phenomena: Review of Immersed Core Processes, 5th Euratom Framework Programme AEAT/RINT/0315, 2001.
[17] F. Faraji, A. Alizadeh, F. Rashchi, and N. Mostoufi, "Kinetics of leaching: a review," *Reviews in Chemical Engineering*, vol. 38, no. 2, pp. 113–148, 2022, doi: 10.1515/revce-2019-0073.
[18] M. Odorowski *et al.,* "Effect of metallic iron on the oxidative dissolution of UO2 doped with a radioactive alpha emitter in synthetic Callovian-Oxfordian groundwater," *Geochimica et Cosmochimica Acta*, vol. 219, pp. 1–21, 2017, doi: 10.1016/j.gca.2017.08.043.
[19] T. Frohne, R. A. Diaz-Bone, G. Du Laing, and J. Rinklebe, "Impact of systematic change of redox potential on the leaching of Ba, Cr, Sr, and V from a riverine soil into water," *J Soils Sediments*, vol. 15, no. 3, pp. 623–633, 2015, doi: 10.1007/s11368-014-1036-8.

RUB

RUHR-UNIVERSITÄT BOCHUM

Developing a Concept for the Prediction of Long-Term Radionuclide Leaching from Corium in Post-Accident Scenarios

Florian Krist, Tobias Jankowski and Marco K. Koch

ERMSAR 2026 | Madrid | 19.05.2026

PSS Plant Simulation and Safety
Prof. Dr.-Ing. Marco K. Koch

OUTLINE

- **Motivation**
  - Relevance for Source Term Analysis
  - Findings from TMI-2
- **Properties of Debris**
  - Situation at Fukushima Daichii
  - Phase composition and Structure
- **Leaching: Governing Parameters and Boundary Conditions**
- **Model Framework**
  - Basic Ideas, Approaches
  - Uncertainties, Limitations

PSS Plant Simulation and Safety
Prof. Dr.-Ing. Marco K. Koch
RUHR UNIVERSITÄT BOCHUM
RUB

Source Term Analysis

- Possible fission products (FP) release during and after a severe accident
- Early Accident Phase
  - Release of volatile FP (e.g. Kr, Xe, I)
- Late Accident Phase
  - Relocation of core material, formation of debris beds
  - Possible RPV failure
  - Release of semi and low volatile FP (e.g. Mo, Ba, Sr)
- Long-Term
  - Fukushima Daiichi: 15 years of water cooling
  - Continuous flow of contaminated water requiring complex treatment
  - Release of radionuclides from debris through leaching (e.g. Cs, Sr, actinides)

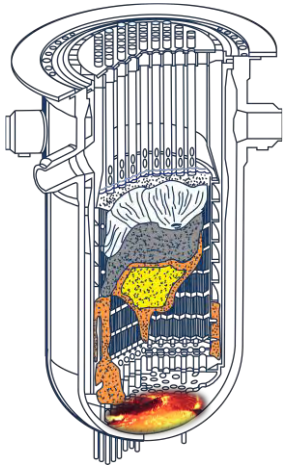

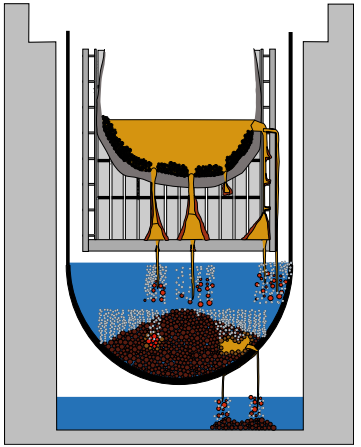

PSS Plant Simulation and Safety
Prof. Dr.-Ing. Marco K. Koch
RUHR UNIVERSITÄT BOCHUM
RUB

FINDINGS FROM TMI-2

- Species dispersed outside the core
- Increase in ^{90}Sr despite water exchange
- ➢ Element-specific characteristics

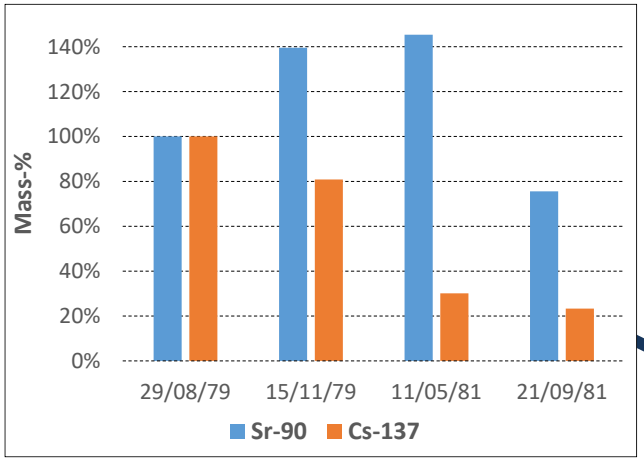

Radionuclide	Release fraction accounted for outside core
^{3}H	59
^{90}Sr	2.7
^{129}I	15
^{131}I	20
^{137}Cs	42

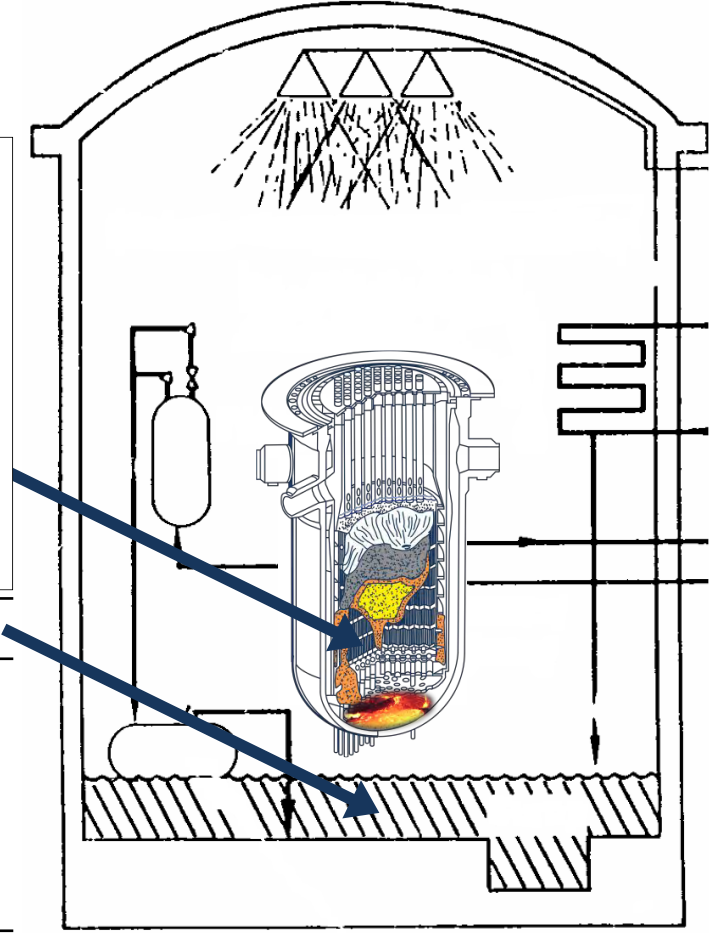

Debris at Fukushima Daiichi
Three Units, Differeent Situations

Unit	Matrix	Localisation
1	MCCI multioxide silicate matrix with crystalline fuel inclusions	Mainly Ex-vessel
2	Crystalline $(U,Zr)O_2$	Mainly In-vessel
3	Both caracteristics (1 & 2)	In- and ex-vessel

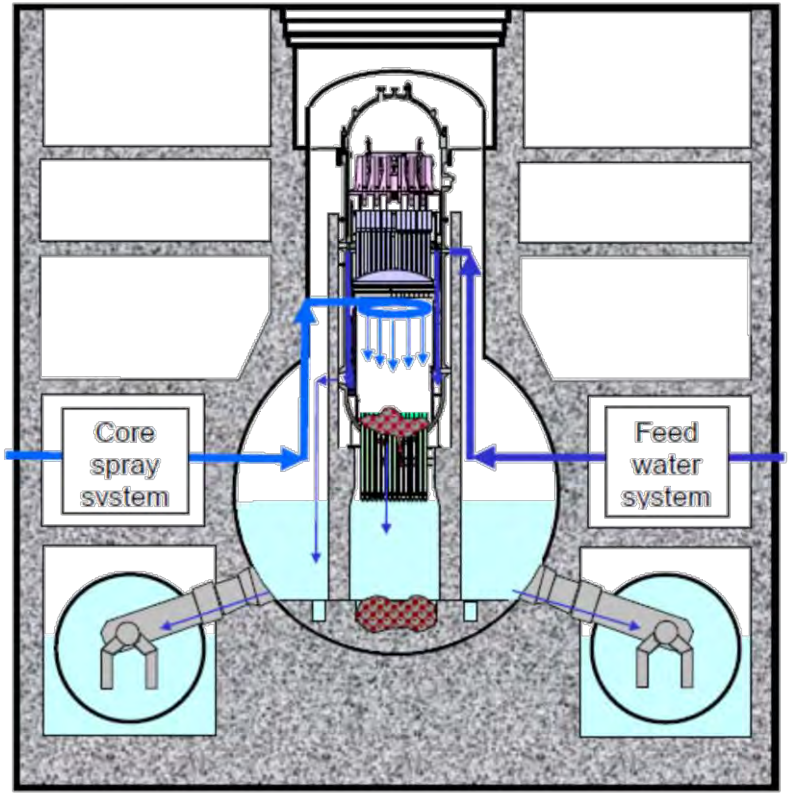

Fukushima Daiichi Unit 3; Source: TEPCO, 2015

PSS Plant Simulation and Safety
Prof. Dr.-Ing. Marco K. Koch
RUHR UNIVERSITÄT BOCHUM
RUB

MCCI Debris

Phase composition and Structure

In-vessel

- **Oxidic Phases**
  - $(U,Zr)O_{2-x}$
  - ZrO_2
  - UO_{2+x} / U_3O_8
  - FeO / Fe_3O_4 / Fe_2O_3
- **Metallic Phases**
  - Fe-Cr-Ni
  - Zr
  - Fe-Zr intermetallics
  - (e.g. Fe_2Zr)

Ex-vessel

- **Silicate Phases**
  - CaSiO3
  - Ca2SiO4
  - CaAl2O4

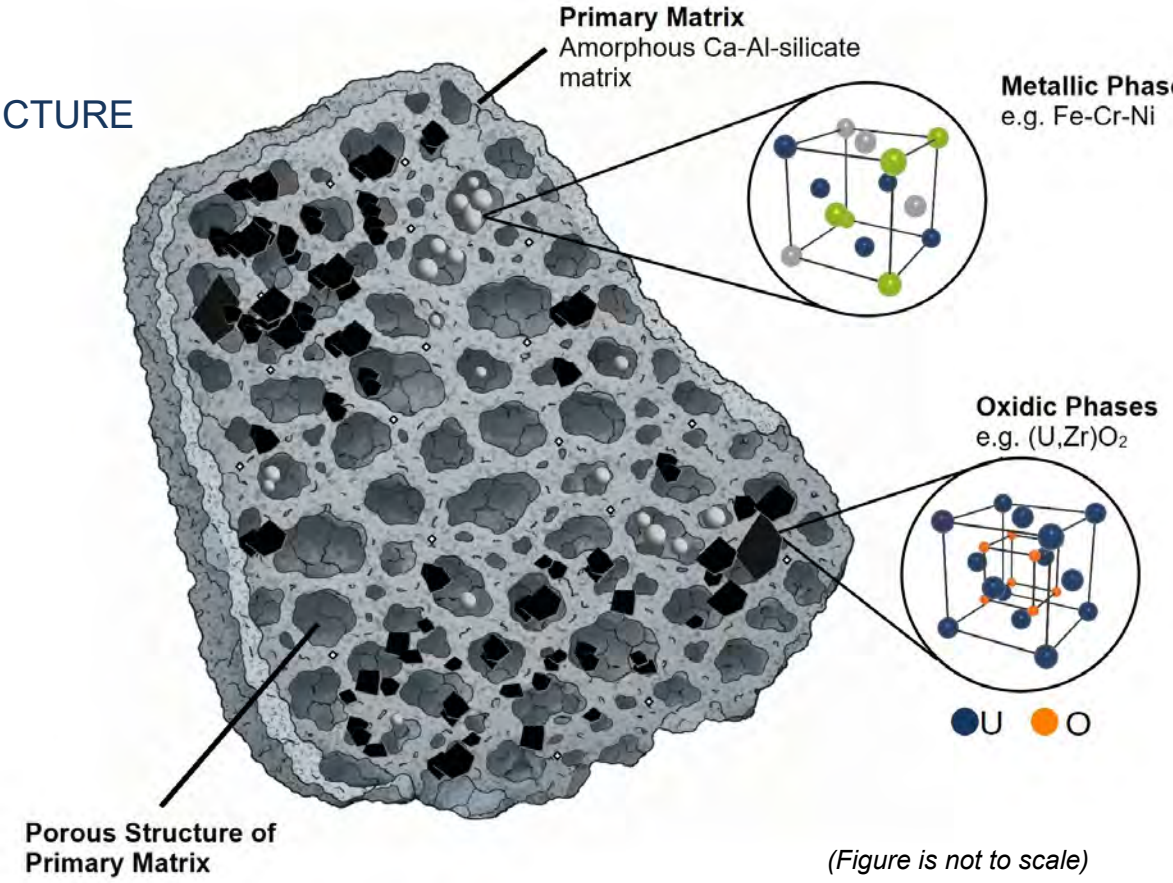

(Figure is not to scale)

PSS Plant Simulation and Safety
Prof. Dr.-Ing. Marco K. Koch
RUHR UNIVERSITÄT BOCHUM
RUB

Leaching: Governing Parameters and Boundary Conditions

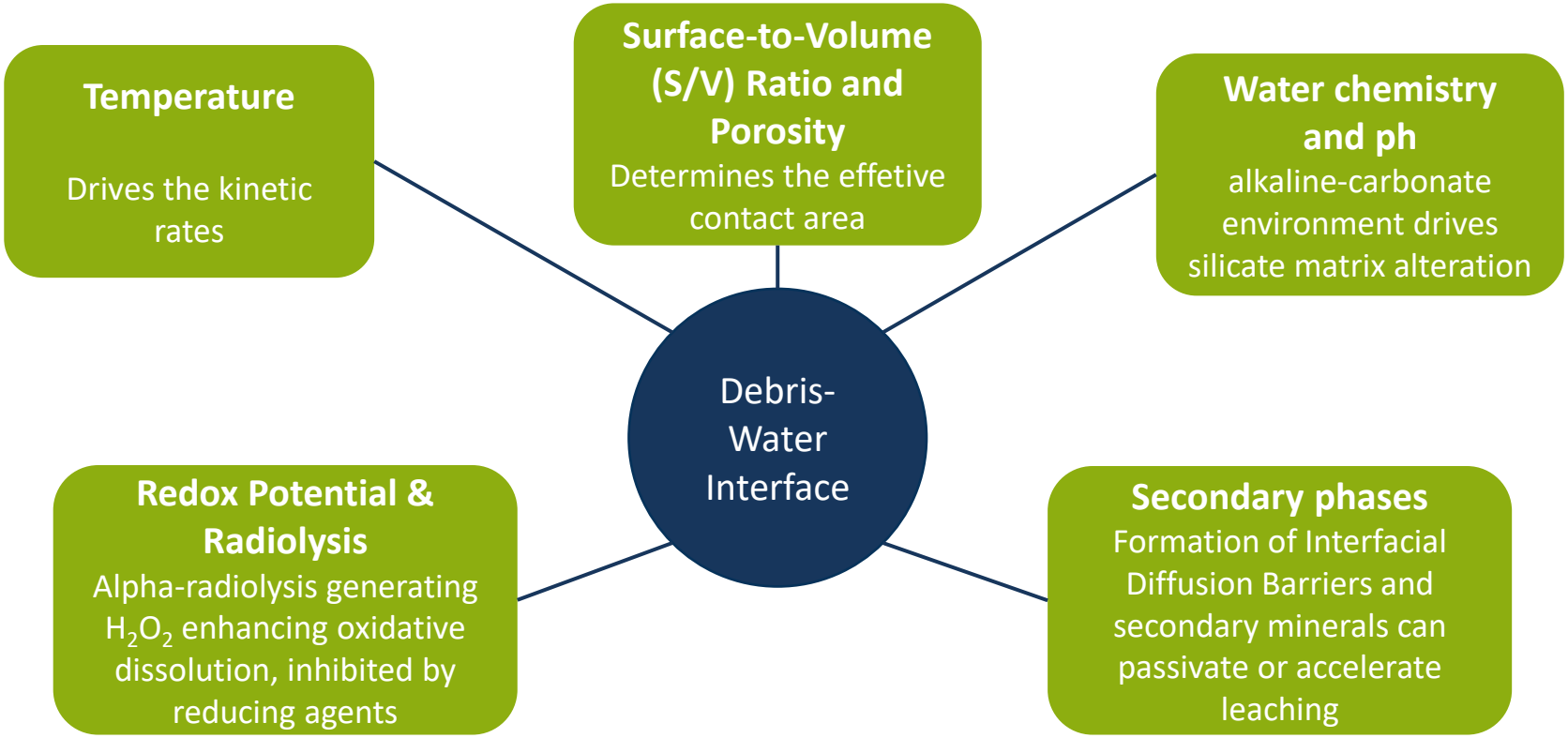

PSS Plant Simulation and Safety
Prof. Dr.-Ing. Marco K. Koch
RUHR UNIVERSITÄT BOCHUM
RUB

Model Framework: Basic Ideas

Instant Release (Surface Wash-off)	Diffusion-Controlled Release	Dissolution-Controlled Release
• Rapid mobilisation of species on surfaces	• Slow migration of species along grain boundaries and pore networks • Kinetics: Follow a characteristic $\sqrt{t}$ dependence	• Oxidative dissolution of debris matrix • Kinetics: Linear dependence over time

$$M_{total,i}(t) = M_{IR,i} + M_{diff,i}(t) + M_{diss,i}(t)$$

- Each term representing a different release mechanisms
- Parameters should be derived from independant thermodynamic and strucural variables

PSS Plant Simulation and Safety
Prof. Dr.-Ing. Marco K. Koch
RUHR UNIVERSITÄT BOCHUM
RUB

Model Framework: Mathematic Approaches

Instant Release

Variable: $f_{IR,i}$
Instant Release Fraction

- Determined by intertial history, volatility of species and accessible porosity

$$M_{IR,i} = f_{IR,i} \cdot m_{0,i}$$

Diffusion

Variable: $D_{\mathrm{eff},i}$
Effective Diffusion Coefficient

- Governed by internal tortuosity, pore networks and temperature
- Scales with S/V ratio

$$M_{diff,i}(t) = m_{0,i}^{\mathrm{diff}} \cdot \frac{S}{V} \cdot \sqrt{\frac{D_{\mathrm{eff},i} \cdot t}{\pi}}$$

Dissolution

Variable: R_{Matrix}
Fractional Matrix Dissol. Rate

- Governed by redox potential and H_2O_2 concentration
- Opposing mechanisms: oxidative dissolution and chemical buffering by structural metals

$$M_{diss,i}(t) = \frac{c_i}{c_U} \cdot R_{Matrix} \cdot S \cdot t$$

PSS Plant Simulation and Safety
Prof. Dr.-Ing. Marco K. Koch
RUHR UNIVERSITÄT BOCHUM
RUB

Model Framework
Representing Element-specific Release Profiles

Type A: e.g. Cs

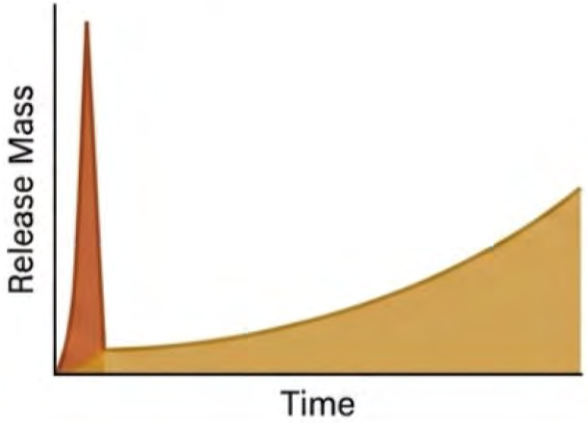

Type B: e.g. U

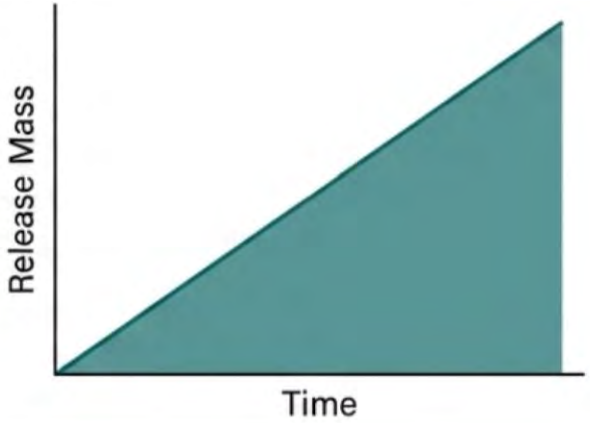

Type C: e.g. Sr

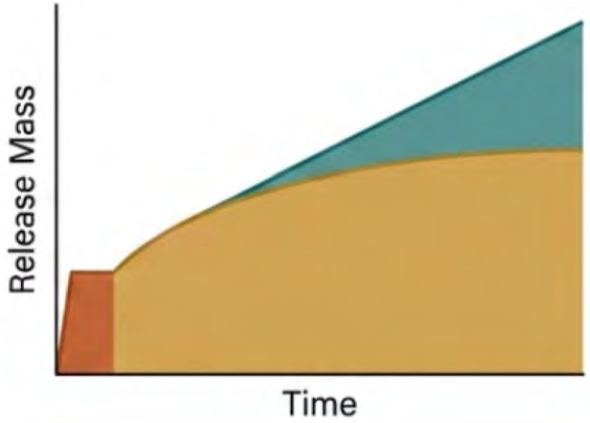

PSS Plant Simulation and Safety
Prof. Dr.-Ing. Marco K. Koch
RUHR UNIVERSITÄT BOCHUM
RUB

Model Framework: Parameter and Uncertainties

Parameter	Reference value	Range	Source
$f_{IR,Cs}$	20 - 35 %	5 - 50 %	Kirishima et al. 2015
$f_{IR,U}$	0,05 - 0,1 %	< 0,5 %	Kirishima et al. 2022
D_{eff}	10^{-9} m²/s	10^{-9} - 10^{-11} m²/s	Riba et al. 2020
R_{Matrix}	10^{-6}-10^{-7} /d	10^{-5} - 10^{-8} /d	Nakayoshi et al. 2020
S/V	material-specific	Factor of 100	Benson et al. 2001

- Overall uncertainty: roughly 3 orders of magnitude
- Challenges for the acquisition of reliable material data

PSS Plant Simulation and Safety
Prof. Dr.-Ing. Marco K. Koch
RUHR UNIVERSITÄT BOCHUM
RUB

Model Framework:
Limitations and systematic uncertainties

- Temperature range: 20 – 100 °C
- Homogenity assumption
  - Model approach assumes debris to be chemically and structurally homogeneous to allow for LP code integration, neglecting the micro-heterogeneity of the phases
- Missing spatial resolution
  - Averaging out local saturation effects
- Simplified chemistry
  - Neglection of secondary phases (e.g. zeolites)
  - pH changes treated via static adjustments rather than dynamic equilibrium
- Handling the uncertainty band of parameters

PSS Plant Simulation and Safety
Prof. Dr.-Ing. Marco K. Koch
RUHR UNIVERSITÄT BOCHUM
RUB

CONCLUSION

- Review of leaching mechanisms and debris properties
  - Element-specific release paths
  - Heterogeneity of debris as a major challenge
- Development of a conceptional framework for modeling of leaching rates of radionuclides
  - Three physically transparent terms
  - Parameters derivable from literature
  - Possibility of extension the model to include boundary conditions not yet considered/investigated
- Validation needs
  - Long-term experiments (>1 year)
  - Investigation on the temperature dependence of $(U,Zr)O_2$ dissolution rate
  - D_{eff}: Measurement with known porosity/tortuosity

PSS Plant Simulation and Safety
Prof. Dr.-Ing. Marco K. Koch
RUHR UNIVERSITÄT BOCHUM
RUB

ACKNOWLEDGMENT

SOCRATES has received funding from the Euratom research and training programme 2024-2028 under Grant Agreement n°101163745. The content of this paper reflects only the author's view.

The European Commission is not responsible for any use that may be made of the information it contains

Funded by
the European Union

Supported by:

Federal Ministry
for the Environment, Climate Action,
Nature Conservation and Nuclear Safety

based on a decision of
the German Bundestag

Thank you for your attention!

Florian Krist
krist@pss.rub.de

Tobias Jankowski
jankowski@pss.rub.de

Marco K. Koch
koch@pss.rub.de

RUHR-UNIVERSITÄT BOCHUM
PSS Plant Simulation and Safety
Prof. Dr.-Ing. Marco K. Koch

Building: IC | Floor 2
Universitätsstr. 150 | D-44801 Bochum

pss.rub.de

Photos: © RUB

FissiOn pRoducts bEhavior under SeverE accident with New fuel concepts THE OECD/NEA FORESEEN PROJECT

Grégoire A.C.[a], Alvarez C., Denis J.[a], Cantrel L.[a]

Autorité de Sûreté Nucléaire et de Radioprotection, PSN-RES/SEREX/L2EC, F-13115, Saint-Paul-lez-Durance, France.
anne-cecile.gregoire@asnr.fr; coralie.lemaoutalvarez@asnr.fr; jean.denis@ansr.fr; laurent.cantrel@asnr.fr

ABSTRACT

With the growing interest in advanced design fuels and particularly Cr/Al-doped fuel, Cr-containing cladding and the consideration of Fe-Cr-Al claddings on the longer-term, ASNR and the Source Term (ST) community partners have decided to launch an international OECD research initiative, called FORESEEN (2026-2029), to investigate the effects of chromium and aluminium on the behaviour of fission products under severe accident conditions and their potential impacts on ST.

A comprehensive set of research though OECD international and EU-programs investigated the source term and fission products behaviour of "historic" Light Water Reactor. Nevertheless, recent reviews on the State of the Art on Light Water Reactor Accident-Tolerant Fuels (NEA 7317, NUREG/CR-7283 and NEA 7576 reports) pointed out the lack of knowledge about behaviour of advanced fuels during severe accident. The objective of the FORESEEN project is to assess whether the presence of Cr and Al might affect the behaviour of FPs during their transportation in the RCV as well as on their behaviour in sump and containment, thereby impacting the source term. The impact of chromium itself has to be assessed considering vaporisation of activated ^{51}Cr or formation of the highly toxic Cr-VI oxidation state. The FORESEEN project is organized in two axis: i/ FP transportation in the RCV. Tests will be carried out at ASNR's CHIP facility to study Cr and Al interaction with the main volatile FPs and its impact on deposition and transport ii/ FP chemistry in the containment. Experiments at the ASNR's EPICUR facility, under irradiation, will focus on Cr and Al influence on FP behaviour in the containment/sump, including liquid phase and aerosol chemistry.

Beyond improving the understanding of the underlying phenomenology, the main objective is to extend the validation database and, if needed, update the SA simulation tools to cover these new fuels.

KEYWORDS

Advanced Fuel, Chromium, Aluminium, severe accident, source term

1. INTRODUCTION

Among the various designs of advanced fuel, chromium-doped fuel has received particular attention from manufacturers. Its increased grain size is expected to mitigate pellet-clad interaction and reduce Fission Gas Release (FGR) during reactor operation [1], and potentially under LOCA conditions [2]. Similarly, chromium-coated and Fe-Cr-Al claddings are being considered to enhance fuel protection during accidents. However, international assessments have identified significant knowledge gaps regarding the behavior and release of chromium and aluminum under severe accident (SA) conditions [3],[4].

Releases of chromium and aluminum from doped fuel or from Cr- and Al-containing claddings are expected under SA scenarios involving extended core degradation. The potential release of these elements and their interactions with other fission products during transport through the reactor coolant system (RCS) represent key concerns [5]. The chromium and aluminum content in such a core can be substantial; for example, chromium may reach several hundred kilograms in the case of Cr-doped fuel and Cr-coated claddings, Aluminium is present in smaller quantities than chromium, typically up to a few tens of kilograms, though the amount can be higher if Fe-Cr-Al claddings are used. These amounts are higher than the quantities of fission products present in spent fuel, such as caesium (~150–200 kg), molybdenum (~200 kg) and iodine (~10–20 kg) [6]. Significant chromium /aluminium release could have multiple consequences, including chemical or radiological toxicity following the release of activation product such as ^{51}**Cr** ($t_{1/2}$ = 27 days). Cr and Al high reactivity may also alter the physico-chemical behavior of other volatile fission products (Cs, Mo, I), potentially modifying the source term released into the containment and, possibly, the environment.

Over the past decades, extensive experimental and modelling research has significantly advanced our understanding of fission product behavior. This knowledge has been incorporated into simulation tools such as ASTEC, MELCOR, and AC², enabling the estimation of releases during the short- and medium-term phases of an accident scenario. Such ST evaluations support effective accident management plan and the application of countermeasures to protect populations. The central challenge is to determine how the presence of chromium and aluminum may affect the transport of radioactive fission products into the containment and in which extent they will modify long term behavior in the containment building.

In this view, ASNR has submitted the international OECD project **FORESEEN (2026-2029)** to investigate the effects of chromium and aluminium on fission product behaviour under severe accident conditions. The findings will inform the development of severe accident simulation tools, to accurately model these new fuel and cladding types. To investigate this range of phenomena, the **FORESEEN** project is structured around two complementary axes.

- **Axis 1** focuses on fission product transport within the reactor coolant system (RCS). Experiments will be conducted at ASNR's **ACCRAS** and **CHIP** facilities, aiming to evaluate the interactions of chromium and aluminium with fission products and their influence on deposition and transport behaviour.
- **Axis 2** addresses fission product chemistry within the containment building. Tests performed at the **EPICUR** facility, under irradiation, will examine the effects of chromium and aluminium on the liquid source term considering precipitation, vaporization, or solubilization of fission products in the sump—as well as on aerosols within the containment.

The objectives, work plan, as well as the current state of the art and identified knowledge gaps, are described in further detail below.

2. FP TRANSPORTATION IN THE RCV IN PRESENCE OF CHROMIUM AND ALUMINIUM

2.1. Chromium and aluminium volatilization and reactivity in RCS conditions during a SA

The release of Cr species from the degraded core according to SA scenarios can be significant in the temperature range (1400-2000°C) where the volatilization of the main FPs (Cs, I Mo) is observed [3]. Cr_2O_3 volatilisation under reducing conditions is mentioned in the literature ([7] to [14]) whereas in oxidizing conditions (under air or air/water vapour), the formation of volatile Cr- species (as Cr(VI) as oxide or oxo-hydroxide) is well known ([7] to [13],[15]). Simulation at thermodynamic equilibrium (NUCLEA Tool box

calculations, Figure 1.1) indicates indeed that in pure steam conditions Cr vaporization becomes significant from 1450°C on (1% of Cr vaporized), at 1550°C it amounts up to 8% and is completed just above 1700°C. $Cr^{(IV)}O_2$ dominates in the vapour phase, but $Cr^{(VI)}O_3$ and $Cr(VI)O_2(OH)$ species can be formed too. In Steam/air mix, vaporization starts at 1200°C, is completed close to 1600°C and $Cr(VI)O_3$ is the main vaporized species. In the solid phase (below 1500-1600°C) Cr_2O_3 remains the most stable species.

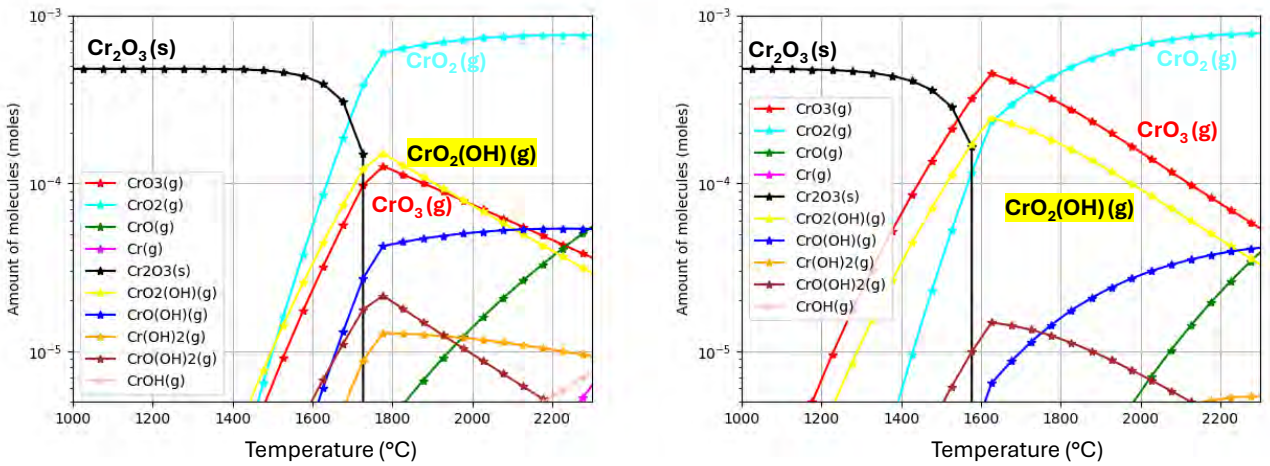

Figure 1: Predicted chromium species at thermodynamic equilibrium as a function of temperature (1000–2200 °C) in steam (left panel) and steam/air atmosphere (right panel).
*Simulations were performed using the **NUCLEA Toolbox** with dataset **DB SGSUB_23-1** under the following initial conditions: Cr = 50 mg, P = 1 bar. For the steam-only case (left panel), the molar ratio $n_{steam}/n_{Cr} \approx 1.7$, with argon added to maintain the same non-condensable gas volume as in the steam/air case. For the steam/air case (right panel), the atmosphere consists of 80% steam / 20% air, with $n_{steam}/n_{Cr} \approx 1.7\times10^4$ and $n_{O2}/n_{Cr} \approx 800$.*

Depending on the atmospheric and temperature conditions, substantial amounts of vaporized chromium species can be transported in the reactor coolant system (RCS) alongside the main volatile fission products (I, Cs, Mo, Te) and control rod materials (SIC, B_4C), with which they may react. Chromium's reactivity with iodine is not considered as a major mechanism. In contrast, chromium is known to react with caesium to form caesium chromates ($Cr_xCs_yO_z$) under oxidative atmospheres [16], though the formation of Cs–Cr species cannot be excluded in experiments simulating TMI-2 [17] and the Fukushima-Daiichi accident conditions [18]. Chromium can also react with molybdenum to produce chromium molybdates such as $CrMoO_4$ or $Cr_2O_3\cdot3(MoO_3)$, the latter potentially forming even in steam environments [19]. The formation of other metallic chromates involving silver, cadmium, or indium is likewise possible [20],[21].

This high chemical reactivity can significantly alter the nature of species released into the containment vessel. The effect is particularly important because chromium can indirectly influence iodine behavior:

- Chromium may act as a sink for Cs, Cd, or Ag, reducing the scavenging effect of these elements on iodine and thereby promoting gaseous iodine transport through the RCS.
- Chromium can also act as a molybdenum scavenger, preventing the formation of other metallic molybdates (e.g., Cs, Ag, Cd…), which may promote the formation of metallic iodides.

In high-temperature steam environments (>1000 °C), Fe-Cr-Al exhibits superior performance compared to a Cr_2O_3 protective layer due to the formation of a stable, corundum-type α-Al_2O_3 oxide layer. This layer

generally forms a uniform, columnar-grained protective coating across the surface [22], even though Cr_2O_3 tends to evaporate above 1000 °C [23].

For alumina, in steam-rich atmospheres, it was observed that solid alumina can react to form the volatile $Al(OH)_3$ species at elevated temperatures [24]. According to experimental measurements presented by Opila et al.[24], partial pressures of $Al(OH)_3$ in the 1600-1800°C range (0.1 to 1 Pa) are of the same order of magnitude as those of the volatile fission products released in the RCS in severe accident conditions (lower bound). Therefore, reactivity of volatile aluminum compounds with other volatile species (FPs or control rod material) cannot be ruled out.

The Al-Cs system is not reactive [25]. On the contrary, the formation of aluminium molybdates ($Al_2(MoO_4)_3$) by solid reaction between $Al(OH)_3$ and molybdenum oxide above 973K is reported by Matsumoto et al [26]. Knowing that Mo chemistry governs the overall behavior of Cs-chemistry and thus of I- chemistry [27], [28], the possible influence of Al should be investigated. In addition, reactivity between aluminium oxide and borates species cannot be excluded in conditions prevailing in the RCS in SA, as expected from the Al_2O_3-B_2O_3 binary diagram [29]. Finally, direct reaction of iodine with aluminium metal can be expected [30] resulting in the formation of AlI_3 compounds (strong exothermic reaction), even in the presence of a protective layer of Al_2O_3.

2.2. Experimental work proposal

The proposed work aims at two primary objectives: (i) to generate the knowledge necessary for developing chemical models that account for chromium reactivity under RCS conditions, and (ii) to validate these models to ensure confidence in their application to reactor scenarios. To achieve these objectives, the experimental strategy combines **analytical-scale experiments**—partly conducted within an ongoing PhD project—with **semi-integral tests** to be carried out in the CHIP facility.

Under the high-temperature conditions prevailing in the reactor coolant system (RCS), thermal reactions dominate over radiolytic processes; therefore, experiments will be conducted using natural simulants for both fission products and chromium.

2.2.1 Analytical tests

These tests will be conducted in the **ACCRAS** device (Figure 5), designed as a high temperature open flow reactor. Since surface conditions can influence chemical reactivity, the main line (alumina tube) will be modified (i) to minimize unwanted high-temperature reactions—achieved by lining the high-temperature zone (1500–1100 °C) with yttria-stabilized zirconia (Zr-Y8), which is unreactive with chromium oxide vapors, unlike alumina; and (ii) to reproduce surface conditions at lower temperatures (900–150 °C) representative of the RCS during a severe accident, using pre-oxidized stainless steel or Inconel surfaces.

Chemical system with increasing complexity, involving up to three elements of interest, will be investigated. First, volatilization/ transport behaviour of chromium or aluminium alone in specific atmosphere (reducing or oxidising) will be considered. Mix with precursors representative of the main volatile fission products (Cs, Mo, …) will be then studied. All species will be vaporized from crucibles placed directly in the line. Vaporization temperature and atmospheric composition will be adjusted to achieve different Cr or Al/FP ratios (either in excess or default), thereby covering all relevant scenarios. The same thermal gradient will be applied across all tests to ensure consistent conditions.

Concerning aluminium reactivity, the effect of boron is of particular interest, as boron aluminates may form under these conditions. On the contrary, air is not included in the test atmosphere, as it promotes the formation of alumina—a highly refractory and relatively unreactive compound.

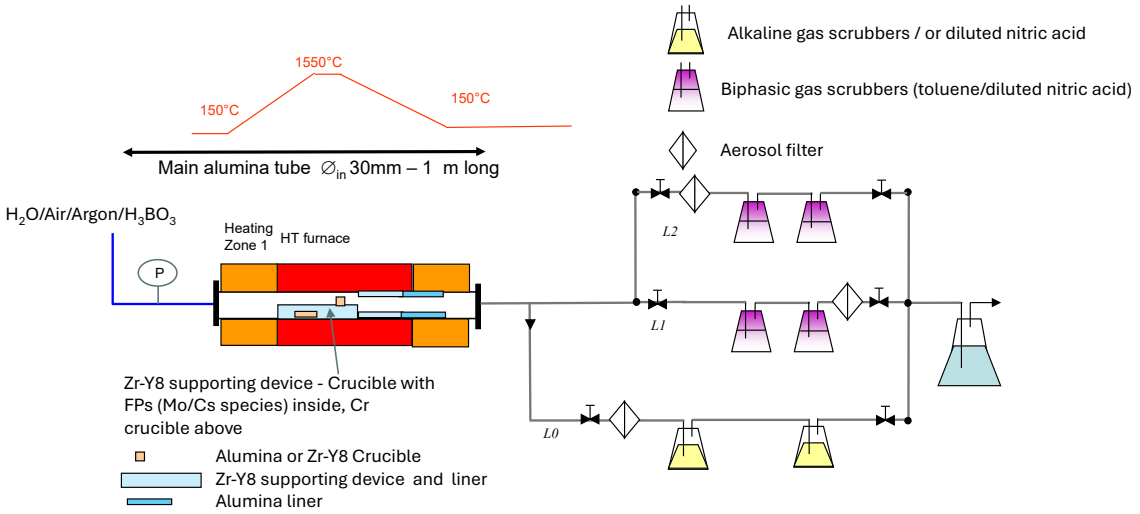

Figure 5: the ACCRAS test device.

The data obtained will include the elemental distribution along the line (deposition and transport) and, as far as possible, the chemical nature of the deposited and transported species (surface characterisation techniques such SEM -EDX, XRD ...). Deposition profiles along the thermal gradient will be determined using collecting plates—Zr-Y8 or alumina plates in the high-temperature zone, and stainless steel or Inconel at lower temperatures. These experiments will subsequently be simulated using the SOPHAEROS module of the ASTEC code.

The key advantage of these analytical-scale tests is their ability to provide accurate and comprehensive data for a simplified chemical system involving up two or three elements if CsI is included as a precursor of caesium. However, they do not address coupled effects, such as the competitive influence of chromium on caesium or molybdenum reactivity and the resulting indirect consequences for iodine transport.

2.2.2 Semi-integral tests: CHIP facility

The CHIP facility consists of a high-temperature furnace, a thermal gradient tube (TGT), and associated instrumentation (Figure 6). Semi-integral tests involve the simultaneous injection of various fission products (FPs) and/or control rod materials, such as silver or boron, into the CHIP line along with chromium. Chromium and aluminium species will be vaporized directly in the high-temperature zone. The possibility of external injection—using an aerosol generator and transport through a separate line to the high-temperature zone—will also be explored.

Four tests are planned. Two of these will investigate the influence of chromium and/or aluminium on the transport of key FPs (I, Cs, Mo) alone in steam atmosphere. Element ratios will be selected to be as representative as possible of severe accident scenarios, with Cr or Al/FP ratios defined based on prior results from analytical tests. Results will be compared with the MoCsI reference test [27]. The third test will

consider the addition of control rod elements (Ag, Cd) and compared to the **CHIP+ test** [28]. The last test will be defined according to results obtained during the project from analytical and semi-integral tests.

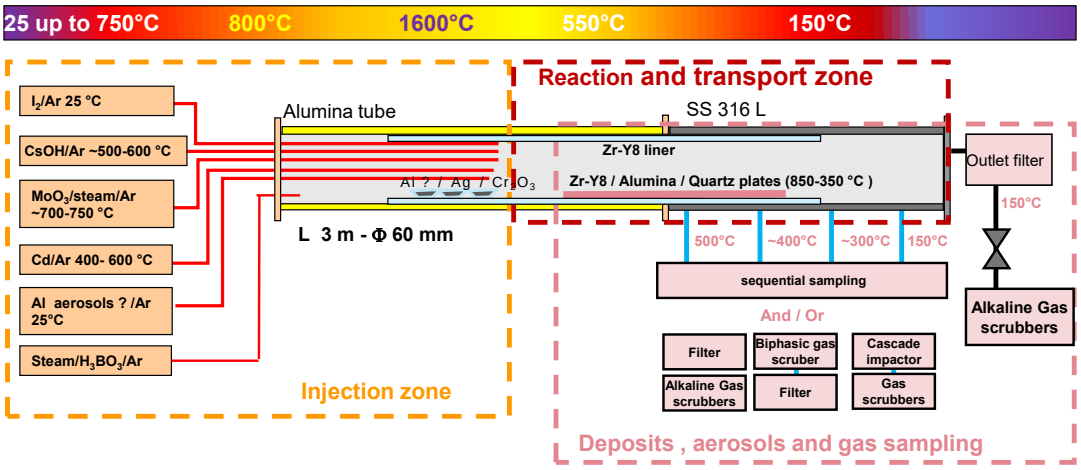

Figure 6: Scheme of the CHIP line - configuration for FP transport studies.

The measured data will include the amount of each element deposited along the TGT, the fraction of gas and aerosol transported at low temperatures, the chemical speciation of iodine (gaseous molecular iodine, other gaseous iodine species, and iodine aerosols), and the aerosol size distribution. Special attention will be given to molybdenum and iodine chemistry with deposited species analyzed using XRD or Raman spectroscopy to identify potential aluminium molybdate, aluminium borates or aluminium iodides compounds, such as and to assess any effects on caesium chemical speciation.

3. FP BEHAVIOUR IN THE CONTAINMENT IN PRESENCE OF CHROMIUM AND ALUMINIUM

The objective is to investigate key phenomena occurring in the containment that may influence accident consequences and management strategies. These include the formation of precipitates, the partitioning between soluble and insoluble species, the chemistry of chromium and aluminium under irradiation, and the agglomeration of metallic particles.

For defining the initial chemical composition for these studies, information on chromium and aluminium releases—both in terms of quantities, chemical forms, and speciation—into the containment will be supported by simulations, in complement to the experimental results obtained in Axis 1. This includes other possible sources – such as containment structural material leaching.

3.1 Chromium and aluminium reactivity in the containment conditions during a SA

To complement the state of the art developed for Axis 1, which focus on gaseous and condensed phases, this section presents key information on the chemistry of chromium and aluminium in aqueous solution, as a preliminary step to studying its impact on containment sump chemistry.

Chromium can exist in several oxidation states, most commonly +2, +3, and +6. The +3 state (Cr(III)) is the most stable, while the +4 and +5 states are relatively rare. Cr(VI) compounds are strong oxidizing agents, whereas Cr(II) acts as a reducing agent. Generally, Cr(III) oxides are poorly soluble, while Cr(VI) species are highly soluble and chemically toxic [31]. Pourbaix diagrams representing the dominant chromium

species in aqueous solution, as a function of pH and redox potential were established at 25°C[32] [33] and 100°C [32]. These diagrams highlight the predominance of insoluble chromium oxide (Cr_2O_3) under most conditions. However, under oxidizing conditions, chromium species in the +VI oxidation state can form [34] and become dominant across the full pH range. Such conditions can be assumed as H_2O_2 generated by radiolysis is known to be a strong oxidant. The oxidation–reduction potential of chromium ($E°(Cr^{3+}/Cr_2O_7^{2-})$ = 1.33 V/ENSH) is comparable to that of ruthenium ($E°(RuO_2/RuO_4)$ = 1.39 V/ENSH), underscoring its strong oxidizing potential. The relative fractions of Cr(III) and Cr(VI) depend on pH, dose rate (which influences the redox potential), and temperature. As for aluminium, only one oxidation state is stable in aqueous media (III).as soluble Al^{3+} ions in acidic media or AlO_2^- in strong alkaline media. In the pH 4-8 range, the dominant species is the poorly soluble Al_2O_3 oxide.

Only limited data are currently available on the chemistry of fission products with chromium and aluminium in aqueous phase. Regarding caesium chemistry, reference [35] indicates the possible formation of highly soluble caesium chromate (Cs_2CrO_4) and less soluble caesium dichromate ($Cs_2Cr_2O_7$). A preliminary review of geochemical databases integrated in tools such as PHREEQC—including NEA, Thermoddem, Thermochimie, and LLNL databases ([36] to [39]), —reveals the presence of precipitated species such as strontium chromate ($SrCrO_4$), chromium triiodide (CrI_3), and strontium iodide (SrI_2), and caesium alumino-silicates but no thermodynamic data for caesium chromate species.

These considerations raise several key questions regarding the influence of chromium and aluminium on fission product chemistry in the containment and, consequently, on the source term:

- What is the chemical speciation of chromium in the containment atmosphere and liquid phases in the short and medium term?
- What is the impact of chromium (particularly Cr(VI)) and aluminium on caesium chemical speciation in solution? Could caesium chromates form? and would this alter the soluble/insoluble fraction of caesium in the liquid phase?
- How might chromium and aluminium affect strontium chemistry? Given that strontium is generally soluble, could the elements influence its soluble/insoluble partitioning in the liquid phase?
- Finally, could chromium impact iodine chemistry in the liquid phase and thereby affect the volatilization of gaseous iodine in the containment atmosphere?

The objectives of Axis 2 is therefore to investigate the behaviour of chromium and aluminium in the liquid phase at around 100°C and under controlled radiation conditions, through experiments using boric acid and sodium hydroxide solutions together with main soluble FPs (Cs, Mo, I, Sr). Soluble and insoluble fractions of Cs and Sr will be investigated, and the potential impact of chromium on iodine volatility assessed.

3.2 Experimental works (EPICUR facilities and laboratory-scale tests)

To address these questions, seven experimental tests are proposed on the EPICUR facility (Figure 8), complemented by laboratory-scale tests involving various analytical techniques (XRD, ICP-MS, SEM-EDX, etc.).

The EPICUR facility is initially devoted to study iodine reactivity under radiolysis and allow the use of labelled iodine (^{131}I) to monitor iodine releases by on-line γ-spectrometry achieving thus very low detection

limits. It is composed of i/ a panoramic irradiator that delivers an average gamma dose rate of several kGy.h^{-1}, ii/ an irradiation stainless steel vessel (4.8 liters) adapted for both liquid or solid samples, itself connected to iii/ a specific iodine filtering device (May pack system). This May pack system contains different species-selective filters for the retention of iodine aerosols, molecular iodine or organic iodides. The volatile species produced in the irradiation vessel are transferred to this May-pack device with an adapted gas flow. On-line gamma measurements are provided by 4 NaI (Tl) counters placed above each stage of filters of the May-pack device. The irradiation vessel is equipped with a pH probe that is directly in contact with the fluid. Preparation and post-test operations of labelled samples are performed in a dedicated radiochemistry laboratory, adjacent to the EPICUR facility.

Several long duration (2-3 days) tests will be conducted in a boric acid–sodium hydroxide solution at pH 7 Firstly, the reactivity of chromium alone will be investigated, to quantify the formation of hexavalent chromium (Cr(VI)) under irradiation, starting from chromium oxide powder. The following tests will consider chromium influence on caesium and iodine chemistry by performing tests in presence of caesium hydroxide and caesium iodide while maintaining the other conditions unchanged. The objective is to determine the soluble fraction of caesium (formation of insoluble caesium chromate species?) and the volatile fraction of iodine formed. Then after, the role of additional presence of strontium under similar conditions will be considered. A second series of tests will investigate the impact of aluminium on molybdenum solubility. Outputs of Axis 1 work will help to define the most relevant precursors to consider. Same conditions (buffer, duration, temperature) as for the previous tests will be applied. The fraction of soluble /insoluble species will be evaluated.

The last test series will investigate the stability under irradiation of multi-component aerosols in the Cr–Cs–I system in the gas phase. Previous results from the STEM2 programme have shown that the decomposition of multi-component aerosols can significantly influence the concentration of gaseous iodine, making this analysis particularly relevant.

In parallel, laboratory-scale tests will be conducted at ~100°C without irradiation. In these tests, the behaviour of chromium/aluminium will be examined in the presence of hydrogen peroxide to simulate radiolysis products, with the objective of obtaining complementary data on the influence of temperature, pH, and redox potential on their chemistry.

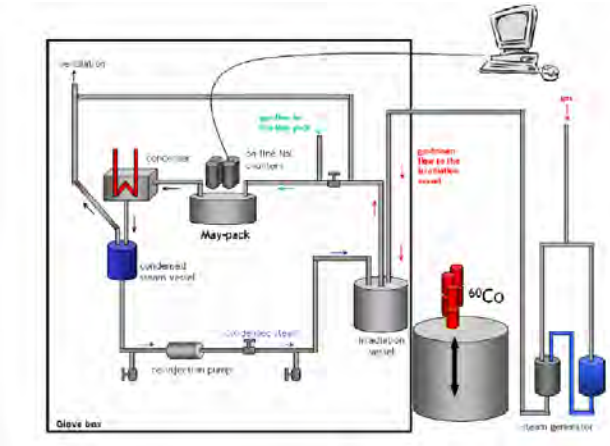

Figure 8: Schematic view of the ASNR - EPICUR facility.

4. CONCLUSIONS

After the Fukushima Daichii Accident, growing interest was put in advanced fuel concepts which involve Cr/Al-doped fuel, Cr-containing cladding and on the longer term, Fe-Cr-Al claddings. Chromium-doped fuel is expected to mitigate pellet-clad interaction and reduce Fission Gas Release (FGR) during reactor operation, and potentially under LOCA conditions. Similarly, chromium-coated and Fe-Cr-Al claddings are being considered to enhance fuel protection during accidents.

Nevertheless, recent reviews on the State of the Art on Light Water Reactor Accident-Tolerant Fuels (NEA 7317, NUREC/CR-7283 and NEA 7576 reports) pointed out the lack of knowledge about the behaviour of these new fuel concept during severe accident. To address this issue, ASNR and several partners have launched an international OECD research initiative, called FORESEEN (2026-2029), to investigate the effects of chromium and aluminium on the behaviour of fission products under severe accident conditions. The FORESEEN project aims to assess whether the presence of Cr and Al may affect the behaviour of FPs during their transportation through the RCV (axis 1) and on their behaviour in the sump and containment (axis 2). The programme has two primary objectives: (i) to generate the knowledge necessary for developing chemical models that account for chromium reactivity under RCS conditions, and (ii) to validate these models to ensure confidence in their application to reactor scenarios. To achieve these objectives, the experimental strategy combines analytical-scale experiments with semi-integral tests.

Analysis of experimental results and their interpretation will be conducted within the Analytical Working Group (AWG). Its primary objective is to propose adaptations to existing source term models to account for the effects of chromium and aluminium on fission product behaviour. Benchmarks and sensitivity analyses will be proposed and conducted.

The outcomes of the OECD FORESEEN program will support partners in enhancing/consolidating their models/safety view and reducing uncertainties on source term assessments for the new fuel/cladding concepts.

ACKNOWLEDGMENTS

ASNR's acknowledges the OECD and EPRI, INL, VTT, KINS, KENTECH university, NRA, SSM, GRS partners for their support and fruitful discussion to elaborate the OECD FORESEEN project.

REFERENCES

[1] C. Delafoy, I. Arimescu, "Developments in fuel design and manufacturing in order to enhance the PCI performance of AREVA NP's FUEL", OECD/NEA Workshop: Pellet-Clad Interaction (PCI) in Water-Cooled Reactors, Lucca, Italy 22-24 June 2016

[2] C. Delafoy et al., "Benefits of FRAMATOME's E-ATF evolutionary solution: Cr-coated cladding with Cr_2O_3-doped fuel", Topfuel 2018

[3] NUREG/CR-7283, "Phenomena Identification Ranking Tables for Accident Tolerant Fuel Designs Applicable to Severe Accident Conditions", 2021

[4] State-of-the-Art on Light Water Reactor Accident-Tolerant Fuels, NEA 7317 (2018)

[5] M. Khatib-Rahbar, « Phenomena identification ranking tables for accident tolerant fuel designs applicable to severe accident conditions », NUREG/CR-7283, ERI/NRC 21-204, 2021.

[6] D. Jacquemain, Les accidents de fusion du cœur des réacteurs nucléaires de puissance - État des connaissances, IRSN. edp sciences, 2013.

[7] A. Yamauchi, « Evaporation of Cr_2O_3 in atmosphere containing H2O », 2003, Oxidation of Metals 59(5/6)

[8] Steinbruck, « High-temperature oxidation and quenching of chromium-coated zirconium alloy ATF cladding tubes with and w/o pre-damage », 2022, J. Nuclear Materials 559 153470

[9] J-C. Brachet, « High temperature steam oxidation of chromium-coated zirconium-based alloys : Kinetics and process », 2020, Corrosion Science 167 108537

[10] H. Yeom, « High temperature oxidation and microstructural evolution of cold spray chromium coatings on Zircaloy-4 in steam environments », 2019, J. Nuclear Materials 526 151737

[11] L. Royer, « On the oxidation and nitridation of chromium at 1300°C », 2010, Oxid Met 74, p. 79-92.

[12] X. Han, « An interesting oxidation phenomenon of Cr coatings on Zry-4 substrates in high temperature steam environment », 2019, Corrosion Science 156, p. 117-124.

[13] M. Syrtanov, « High-temperature steam oxidation of accident-tolerant Cr/Mo-Coated Zr Alloy at 1200-1400°C », 2023, Coatings (13) 191. https://doi.org/10.3390/coatings13010191

[14] Peres et al., « High temperature chromium volatilization from Cr_2O_3 powder and Cr2O3-doped UO2 pellets in reducing atmospheres », Journal of Nuclear Materials 423, p. 93-101, 2012, doi: 10.1016/J.JNUCMAT.2012.01.001.

[15] B. B. Ebbinghaus, « Thermodynamics of Gas Phase Chromium Species: The chromium oxides, the chromium oxyhydroxides, and volatility calculations in waste incineration processes », 1993, Combustion and Flame 93 : 119-137

[16] D.C. Fee et al. « Phase equilibria in the Cs-Cr-O System », J. Nucl. Mat. 84, 1979, p. 286-294. https://doi.org/10.1016/0022-3115(79)90169-7

[17] R.A. Lorenz and J.L. Collins, « Release and transport of fission product caesium in the TMI-2 accident ». CONF-860911—19 (1986). https://inis.iaea.org/records/pfjsj-f8942

[18] I.W. Ngarayana et al., « Interaction of Caesium Hydroxide with Oxide Layers Under Simulated Light Water Reactor Severe Accident ». Nucl. Sc. and Engineering 198, p. 818-824 (2024). https://doi.org/10.1080/00295639.2023.2227829

[19] Bühler et al., « Preparation and Characterization of a New Ternary Chromium (III)–Molybdenum(VI) Oxide $Cr_{2-2x}Mo_xO_3$ », J. of Solid State Chemistry, 140, 1998, p. 350-353. https://doi.org/10.1006/jssc.1998.7899

[20] B.M. Abu-Zied. « Preparation of cadmium chromite spinel: a combustion approach ». Colloids Surf. A: Physicochem. Eng. Asp 211, 2002, p. 27-42. https://doi.org/10.1016/S0927-7757(02)00221-2

[21] AAH. El-Bassuony et al., « Synthesis, characterization, magnetic and antimicrobial properties of silver chromite nanoparticles », J. Mater. Sci.: Mater. Electron. 31, 2020, p. 3662-3673. https://doi.org/10.1007/s10854-020-02924-8

[22] L. Joyce et al., « Oxidation behaviour of PM-C26M FeCrAl alloy in low-temperature steam 400 – 900 °C », Nuclear Materials and Energy 43 (2025) 101953

[23] R.B. Rebak, V.K. Gupta, M. Larsen, « Oxidation characteristics of two FeCrAl alloys in air and steam from 800°C to 1300°C », JOM 70 (2018) 1484–1492, https://doi.org/10.1007/s11837-018-2979-9.

[24] Elizabeth J. Opila, "Alumina Volatility in Water Vapor at Elevated Temperatures", J. Am. Ceram. Soc., 87(9), p. 1701–1705 (2004).

[25] J. Sangster and A.D. Pelton, Al-Cs evaluation contributed by, Centre de Recherche en Calcul Thermochimique, Ecole Polytechnique, P.O. Box 6079, Station A, Montréal, Quebec, Canada, H3C 3A7. This work was supported by ASM International. Literature searched through 1988. Dr. Pelton is the Alloy Phase Diagram Program Co-Category Editor for binary alkali alloys.

[26] Y. Matsatmuto and R. Shimanouchi (2025), Synthesis of $Al_2(MoO_4)_3$ by Two Distinct Processes, Hydrothermal Reaction and Solid-State Reaction (2025), https://doi.org/10.1016/j.proeng.2016.06.507

[27] Grégoire A.-C., Kalinainen J., Cousin F., Mutelle H., Cantrel L., Auvinen A., Haste T., Sobanska S. (2015). « Studies on the role of molybdenum on iodine transport in the RCS in nuclear severe accident conditions », Annals of Nuclear Energy, 78, 117–129. https://doi.org/10.1016/j.anucene.2014.11.026

[28] Grégoire A.C., Sobanska, S., Tornabene C., Talage D., Mamede A.S., Morin S., Cantrel L. (2022). Influence of SIC control rod material on iodine release in nuclear severe accident – Chemical reactivity in thermal conditions of RCS, Annals of Nuclear Energy, 162, 108900. https://doi.org/10.1016/j.anucene.2021.108900

[29] P.J.M Gielisse and W.R. Fortier, The System Al_2O_3-B_2O_3, Nature, Vol 195, pp69-70 (1962).

[30] D. Zschätzsch et al.(2021). Corrosion of metal parts on satellites by iodine exposure in space Journal of Electric Propulsion . https://doi.org/10.1007/s44205-022-00014-

[31] Argonne National Laboratory (2007), https://remm.hhs.gov/ANL_ContaminantFactSheets_All_070418.pdf

[32] B. Berverskog and I. Puigdomenech (1997), Revised Pourbaix diagrams for chromium at 25°C – 300°C, Pergamon Corrosion Science, Vol. 39, No. 1, pp. 43-57.

[33] S. K. Sharma et al (2014), Heavy metals in water, their adverse health effects and Biosorptive removal: A review, Int. J. Chem. VOL 3 (1) (2014): PP 132 – 149

[34] Jialiang et al. (2021), A review of the formation of Cr(VI) via Cr(III) oxidation in soils and groundwater https://doi.org/10.1016/j.scitotenv.2021.145762

[35] P. A. G. O`Hare and J. Boerio (1975), Standard enthalpy of solution and formation of caesium chromate. Derived thermodynamic properties of the aqueous chromate, bichromate, and dichromate ions, alkali metal and alkaline earth chromates, and lead chromate, J. Chem. Thermodynamics 1975, 7, 1195-1204

[36] THERMODDEM https://thermoddem.brgm.fr/databases

[37] THERMOCHIMIE https://www.thermochimie-tdb.com/

[38] LLNL https://seaborg.llnl.gov/resources/geochemical-databases-modeling-codes

[39] NEA https://www.oecd-nea.org/dbtdb/tdbdata/

ASNR Autorité de sûreté nucléaire et de radioprotection

Fission Products behavior under severe accident with new fuel concepts : THE OECD/NEA FORESEEN PROJECT

Grégoire A.C., Alvarez C., Denis J., Cantrel L.

EMRSAR 2026 – MADRID, MAY 18-22

FORESEEN OECD PROJECT

FissiOn pRoducts bEhavior under SeverE accidEnt with New fuel concepts

OECD/NEA JOINT PROJECT CONCERNING S/T RELATIVE TO ATF FUEL IN SA CONDITIONS

OPERATED BY ASNR

WITH THE FOLLOWING PARTNERS AT THAT TIME: EPRI, NRA, VTT, KINS, KENTECH, SSM

STARTED APRIL 2026 – DURATION 4 YEARS

"It is far better to foresee even without certainty than not to foresee at all."
Henri Poincaré 1854-1912

SA BEHAVIOR OF ATF FUEL

PROPOSAL BUILT FROM CONCLUSIONS OF SOAR & PIRT

- State-of-the-Art on Light Water Reactor Accident-Tolerant Fuels, NEA 7317 (2018)
- Phenomena Identification Ranking Tables for Accident Tolerant Fuel Designs Applicable to Severe Accident Conditions, NUREG/CR-7283 (2021)
- WGFS TOP-ATF which included Source Term issue

These reports pointed out the lack of knowledge about behavior of ATF in severe accident conditions.

The FORESEEN should deepen the:

➔ impact of chromium and aluminium on fission product release (Cr-doped fuel and Cr-coated Zr& Fe-Cr-Al claddings)

➔ role of these elements on transport and containment chemistry

And thus, extent the validation database of the SA simulation tools to these new designs of fuel for ST assessment

THE MAIN EXPECTED PHENOMENA ARE :

- Formation of chromium or aluminum based species modifying the Cs & Mo chemistry and indirectly the iodine one
- Chemistry/transport through the RCS and in the containment

CHROMIUM AND ALUMINIUM IN ATF FUEL

LARGE AMOUNTS :

Chromium: several hundred of kilograms in the case of Cr-doped fuel and Cr-coated claddings

Aluminium in smaller quantities : up to a few tens of kilograms, though the amount can be higher if Fe-Cr-Al claddings are used

In comparison the quantities of fission products present in spent fuel amounts up to :

Caesium ~150–200 kg,

Molybdenum ~200 kg

Iodine ~15–20 kg

Cr AND Al: DIRECT AND INDIRECT EFFECT ON THE SOURCE TERM

- Cr dopant could have antagonist effects on fission product release from degraded fuel (increase the fission product path for release & increase their diffusion coefficient)
- Cr and Al volatility (cladding) can be significant above 1400 °C
- Literature or past post-accident analysis (TMI, Chornobyl, Fukushima-Daichii) show possible interaction between Cr or Al and several FP like Mo and Cs ➔ indirect impact on the gaseous iodine formation with antagonist effects
- Under neutron irradiation, ^{50}Cr (13% of natural Cr) form ^{51}Cr which is a γ-emitter with a half-life of 27,7 d and high mass activity (3,4 10^{15} bq/g) – impact of the volatilized Cr on ST
- Cr exists with several oxidation states (principally Cr-III and Cr-VI) with different impact on solubility : Cr-III under oxide form is rather insoluble whereas Cr-VI is soluble.
- Cr-VI is highly toxic and may be formed by oxidative radiolysis of Cr-III

FORESEEN PROJECT OBJECTIVES

GAIN KNOWLEDGE AND EXTENT CAPABILITY OF EXISTING SIMULATION TOOLS TO COVER THESE NEW FUELS AND ASSESS ST FOR EACH PHASE OF THE SEVERE ACCIDENT

FPs release from irradiated fuel samples : Cr or Al impact on kinetics, species and quantities of FP releases ? ➔ to be addressed in a second phase

AXIS 1 focuses on the chemistry/transport of fission products within the reactor coolant system (RCS) Experiments will be conducted on dedicated facilities hosted at ASNR, aiming to evaluate the interactions of chromium and aluminium with fission products and their influence on deposition and transport behaviour.

AXIS 2 addresses the chemistry of fission products within the containment building

Tests performed at the EPICUR facility will examine the effects of chromium and aluminium on the liquid source term considering precipitation, vaporization, or solubilization of fission products in the sump—as well as on aerosols within the containment.

AXIS -1 – FP transportation in the rcs in presence of chromium and aluminium

Chemical reactivity and transport in the RCS:

- ☞ **Amounts of FPs deposited inside the RCS**
- ☞ **Chemical speciation of FPs reaching the containment (Gazeous /Aerosol form)**
- ☞ **Intensively studied over the past decades with a focus on iodine chemistry**
- ☞ **Role of Mo: governs the overall behaviour of Cs-chemistry and thus of I- chemistry**

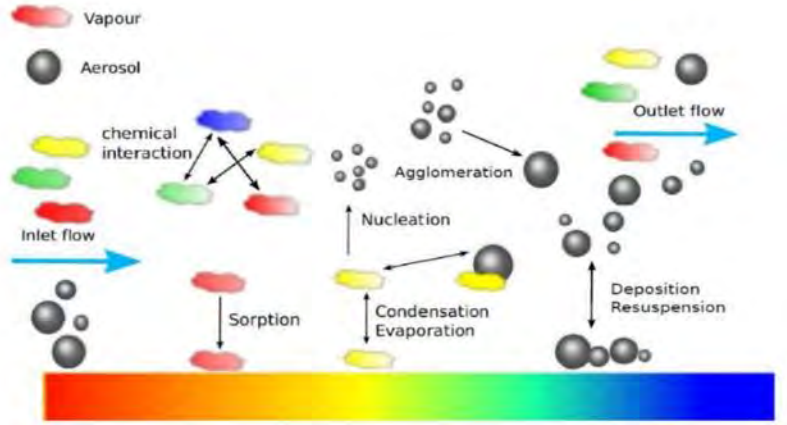

RCS transport : main phenomena to be taken into account

Source : https://research-assessment.asnr.fr/sites/en/files/2024-02/TransportEtChimieDesPF_ASTEC2.jpg.pngportEtChimieDesPF_ASTEC2.jpg.png (834×506)

AXIS 1 – SCIENTIFIC ISSUES

What should be the role of Cr and Al in the RCS chemistry and in which extent it may affect the transport of the FPs (Cs, Mo) and control rod material (Cd, Ag) ?

What would be the consequences for the release of gaseous iodine species at the break

↗ (if Cr act as a Cs, Cd or Ag sink) or ↘ (if Cr or Al acts mainly as Mo sink) ?

Cr Volatility

- **Steam : Vaporization > 1450°C, completed above 1700°C, mainly as Cr(IV)**
- **Air/Steam : Vaporization > 1200°C, completed above 1600°C, mainly as Cr(VI)**

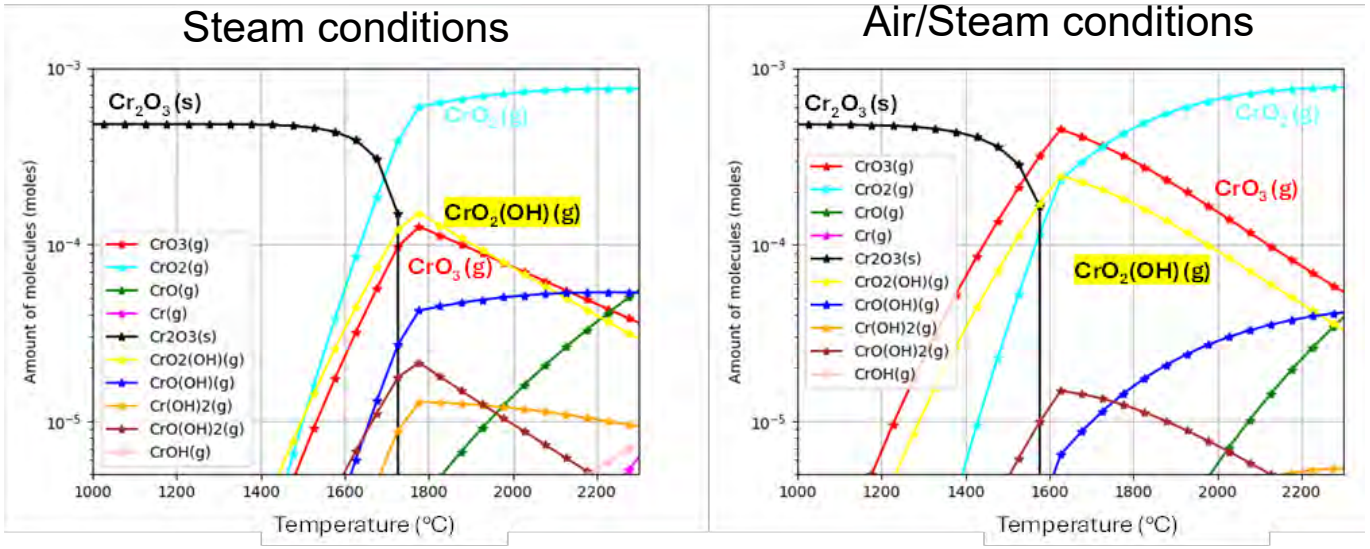

*Simulations were performed using the **NUCLEA Toolbox** with dataset **DB SGSUB_23-1** under the following initial conditions: Cr = 50 mg, P = 1 bar. For the steam-only case (left panel), the molar ratio $n_{steam}/n_{Cr} \approx 1.7$, with argon added to maintain the same non-condensable gas volume as in the steam/air case. For the steam/air case (right panel), the atmosphere consists of 80% steam / 20% air, with $n_{steam}/n_{Cr} \approx 1.7\times10^{4}$ and $n_{O2}/n_{Cr} \approx 800$.*

Al Volatility

- **In high-temperature steam environments (>1000 °C), Fe-Cr-Al exhibits a protective layer due to the formation of a stable, corundum-type α-Al_2O_3 oxide layer**
- **In steam-rich atmospheres, solid alumina can react to form the volatile $Al(OH)_3$ species**

CHROMIUM AND ALUMINUM REACTIVITY IN RCS CONDITIONS

- **Cr-Cs-O and Al-Cs-O systems: Various $Cr_xCs_yO_z$ forms cited in lit.** [2]/some available in thermo DB (as SGPS: **$Cr_2^{(VI)}Cs_2O_7$)**/ not predicted in steam conditions by Facstage calculations / Cs-Cr species formation not excluded in experiments reproducing TMI2[3] and FD [4] SA conditions **. No Al-Cs species referenced ➔ Cr can act as a Cs sink**

- **Cr-MoO_3 system: $Cr_2O_3.3(MoO_3)$ or $CrMoO_4$** cited in literature [1] but not present in thermodynamic data base (SGPS), **$Cr_2O_3.3(MoO_3)$** can be expected in steam conditions (Cr^{III}) **➔ Cr can act as a Mo sink**

- Chromite/Chromate species cited in the literature : **$CdCr_2O_4$, $Ag_2Cr_2O_4$** [5;6]

- **Al-MoO_3:** system expected to be highly reactive – formation of $Al_2(MoO_4)_3$ from $Al(OH)_3$ and MoO_3 precursor occurs above 973K [7] – MoO_3 used a MCC for Al metal surface protection [8]

- **Al_2O_3 –B_2O_3 system:** aluminoborates can form at high temperature entering in competition with cesium borate formation [8]

Oxidative conditions promotes the formation of stable alumina

[1] Bühler et al., J. of Solid State Chemistry (1998), [2] D.C. Fee et al., J.Nucl.Mat.(1979); [3] Lorenz and Collins, CONF-860911—19 (1986) [4] Ngarayana et al., Nucl. Sc. And Engineering (2024); [5] B.M. Abu-Zied, Colloids and Surfaces A: Physicochem. Eng. Aspects 211 (2002) ; [6]AAH. El-Bassuony et al., Journal of Materials Science: Materials in Electronics (2020) [7] Matsatmuto et al, (2025), Synthesis of Al2(MoO4)3 by Two Distinct Processes, Hydrothermal Reaction and Solid-State Reaction https://doi.org/10.1016/j.proeng.2016.06.507 [8] P.J.M Gielisse and W.R. Fortier, The System Al_2O_3-B_2O_3, Nature, Vol 195, pp69-70 (1962).

Axis 1: two complementary experimental approaches

Analytical tests

- ☞ Devoted to study Cr or Al transport at high temperature in a simple configuration
- ☞ Influence of carrier gas composition: steam and/or steam/air and/or steam/boric acid/air
- ☞ Interaction with main volatile FPs (Mo or Cs) : investigation of the conditions enhancing reactivity / identification of deposited/transported species
- ☞ Comparison with simulation at thermodynamic equilibrium – identification of needed data

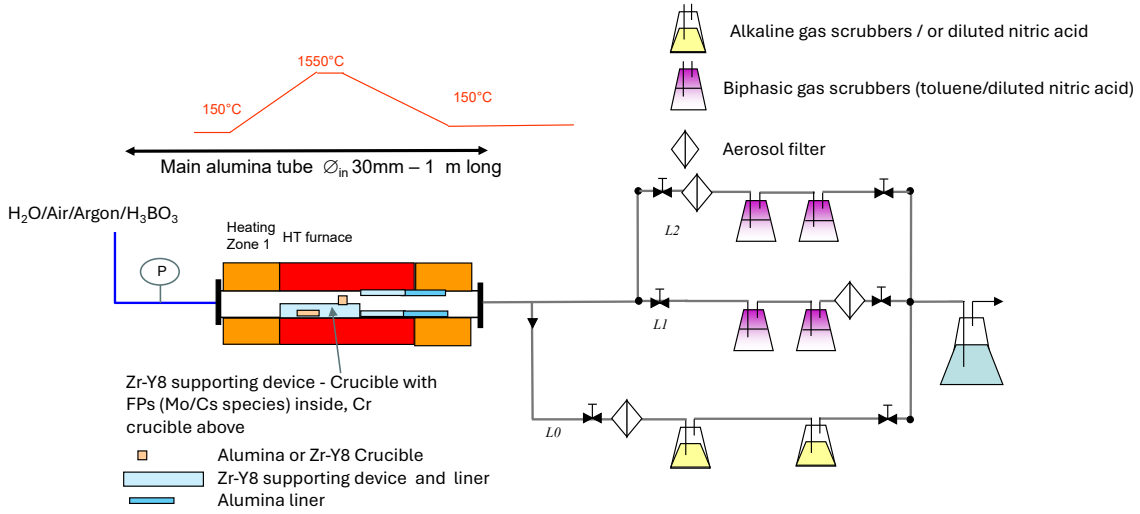

ACCRAS line configuration allows to vaporizes only **two different precursors** in the main line

Carrier gaz (involving up to O_2, H_2O, Boric acid, N_2, Ar) is injected at the main flange inlet

Axis 1: two complementary experimental approaches

Semi integral tests (CHIP experimental set up)

☞ Tests for studying coupled effects on the most representative chemical composition featuring the main volatile FPs and control rod material

☞ Assess influence of Cr/Al on FP transport in more realistic conditions (element ratio, atmosphere conditions)

☞ First tests with Cr of Al + Mo-Cs-I chemical system, then tests with additional injection of CR elements (Ag, Cd, B)

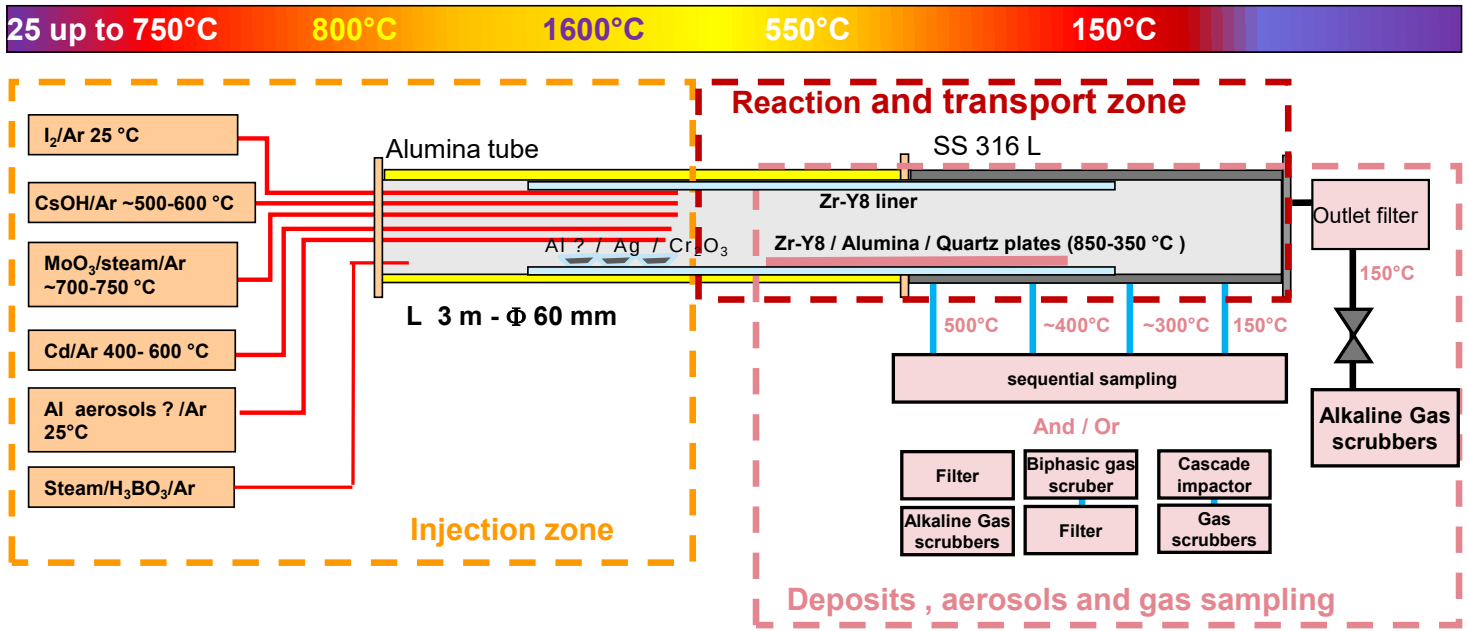

AXIS -2 – FP behaviour in the containment

Introduction

- **Containment chemistry involves gaseous / solid / aqueous phases in steam/ hydrothermal conditions (short term) and radiolytic environment**
  ➔ numerous interdependent phenomena

- **Chromium/Aluminium may affect fission product chemistry in the containment**
  - **Modification of sump chemistry with potential impact on gaseous source term (iodine)**
  - **Insoluble form may be deposited on surfaces leading to higher dose impact on structures (pumps, sump filters …)**

- **Long-Term Severe Accident Management issues:**
  - **Ensure permanent safety and environmental protection against the mid-term consequences involving liquid source terms**
  - **Fission product speciation resulting of chemical process is essential for the development of appropriate accident mitigation devices and measures**
  - **Cooling functions (water recirculation) to be maintained at long term**

- **FORESEEN project complements SOCRATES project (2024), integrating the impact of chromium and aluminium (ATF fuel)**

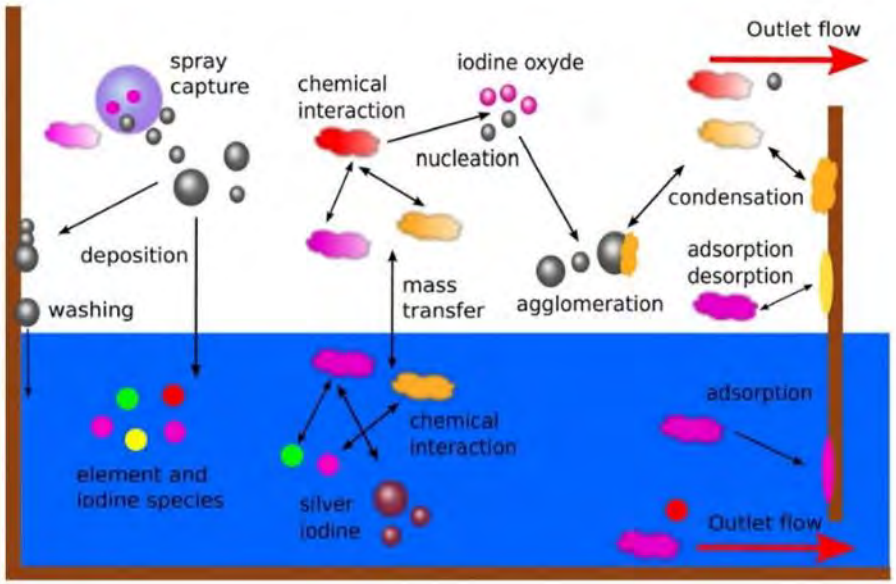

https://research-assessment.asnr.fr/sites/en/files/2024-02/TransportEtChimieDesPF2_ASTEC2.jpg.png

CHROMIUM /ALUMINIUM REACTIVITY IN AQUEOUS SOLUTION

- Chromium can exist in several oxidation states, most commonly +2, +3, and +6
  - Hexavalent - Cr (VI): soluble and highly toxic
  - Trivalent - Cr(III) rather insoluble if under oxide form

  - pH and redox potential diagrams (25°C and 100°C) : insoluble chromium oxide (Cr_2O_3) dominant species under most conditions
  - Hexavalent chromium species may be formed following radiolysis in the containment conditions production of oxidative species (mainly H_2O_2) may oxidize Cr(III) into Cr(VI)[1]

- Aluminium : only one oxidation state is stable in aqueous media (+3)

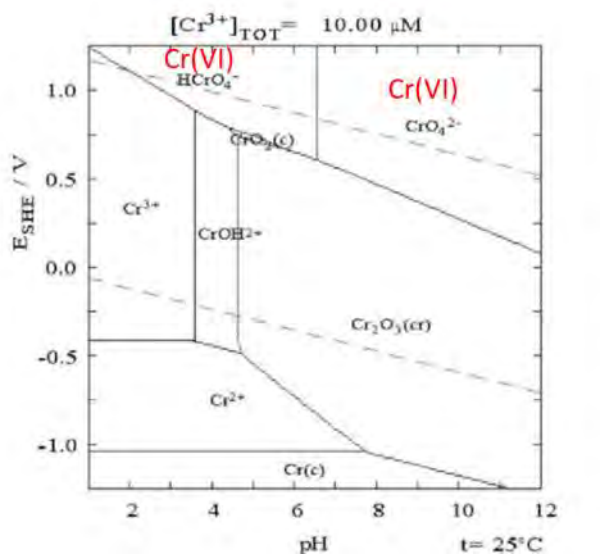

Pourbaix diagram of Chromium [7]

- Chemistry of fission products with chromium and aluminium in aqueous phase : limited literature data .

  - Caesium chemistry : possible formation of highly soluble caesium chromate (Cs_2CrO_4) and less soluble caesium dichromate ($Cs_2Cr_2O_7$) [2]. Pollucite formation ?

  - Preliminary review of geochemical databases integrated in tools such as PHREEQC—including NEA, thermoddem, thermochimie, and LLNL databases [3-6] : presence of minerals such as strontium chromate ($SrCrO_4$). Formation of Aluminium borates ?

[1] Jialiang et al. (2021), DOI 10.1016/j.scitotenv.2021.145762 ; [2] P. A. G. O`Hare and J. Boerio (1975), J. Chem. Thermodynamics, 7, 1195-1204; [3] THERMODDEM https://thermoddem.brgm.fr/databases; [4] THERMOCHIMIE https://www.thermochimie-tdb.com/ ;[5] LLNL https://seaborg.llnl.gov/resources/geochemical-databases-modeling-codes [6] NEA https://www.oecd-nea.org/dbtdb/tdbdata/ [7] B. Berverskog and I. Puigdomenech (1997), Pergamon Corrosion Science, Vol. 39, No. 1, pp. 43-57

Axis 2 – scientific issues

Scientific issues:

- **Chemical speciation of Cr and Al inside the containment at short/middle term in gas and liquid phases**
- **Direct impact of cesium chemistry (aerosol composition – cesium solubility)**
- **Direct impact of strontium chemistry (liquid phase - strontium chromate, strontium solubility)**
- **Indirect impact on iodine chemistry to be assessed (volatility)**

Data of Cr and Al releases (amounts, chemical forms and speciation) inside the containment will be provided from simulations in complements of experimental data of Axis 1 (Cr doped fuel + cladding and/or iron-chromium-aluminum (FeCrAl) alloys)

Technical proposal to study Cr and Al behaviour in CV conditions

Investigate the behaviour of Cr and Al in the aqueous phase at 100°C under controlled irradiation conditions together with main soluble FPs (Cs, Mo, I, Sr). Study of Cs and Sr solubility and the potential impact on iodine volatility .

TESTs in EPICUR irradiator facility

- Long duration (2-3 days) tests in a boric acid–sodium hydroxide solution at pH 7
- Reactivity of chromium (Cr_2O_3) : quantify the formation of hexavalent chromium (Cr(VI)) under irradiation
- Chromium influence on caesium and iodine chemistry : tests in presence of caesium hydroxide and caesium iodide while maintaining the other conditions unchanged . Investigate soluble fraction of Cs and iodine volatility
- The same with addition of strontium ($Sr(OH)_2$)
- Impact of aluminium on molybdenum solubility
- Stability under irradiation of multi-component aerosols in the Cr–Cs–I system in the gas phase

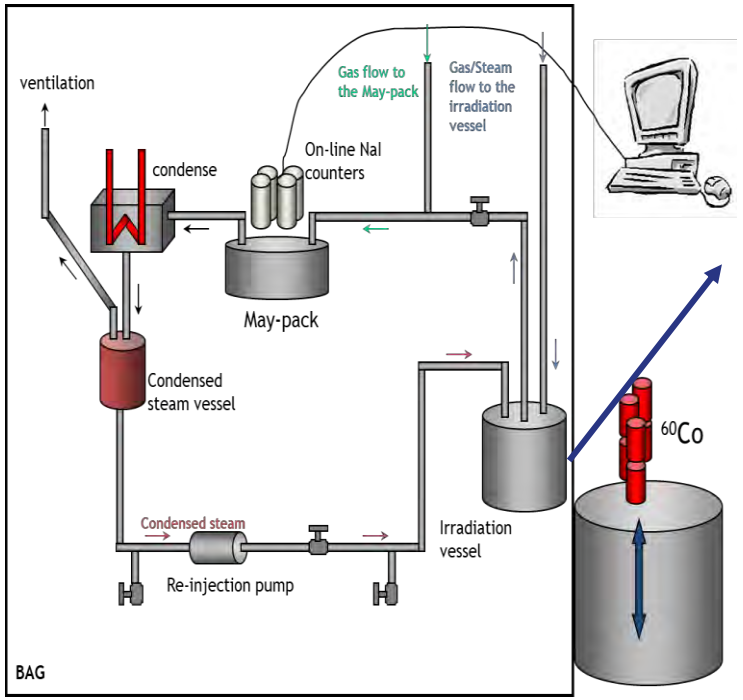

Complementary tests outside EPICUR (High pressure / high temperature reactor)

- Same conditions
- Hydrogen peroxide to simulate irradiation effect

CONCLUSION / PERSPECTIVES

The FORESEEN project aims to assess if Cr and Al may affect the behaviour of FPs during their transportation through the RCV (axis 1) and on their behaviour in the sump and containment (axis 2) – with to primary objectives :

(i) to generate knowledge necessary for developing chemical models that account for chromium reactivity under RCS conditions,

(ii) to validate these models to ensure confidence in their application to reactor scenarios. To achieve these objectives, the experimental strategy combines analytical-scale experiments with semi-integral tests.

Analysis and interpretation of experimental results will be conducted within the **Analytical Working Group (AWG)** with the objective

(i) to propose adaptations to existing source term models to account for the effects of chromium and aluminium on fission product behaviour with a focus on Cr transport / deposit in the RCS in presence of the other main FPs

(ii) To benchmark different simulations tools

ASNR's acknowledges OECD and EPRI, INL, VTT, KINS, KENTECH university, NRA, SSM, GRS partners for their support and fruitful discussion to elaborate the OECD FORESEEN project.

To get further information and interest to join the project, please contact:
laurent.cantrel@asnr.fr

Thank you for your attention

SCALING EFFECT IN IODINE RETENTION FOR FILTERED CONTAINMENT VENTING: EXPERIMENTAL FINDINGS AND SAFETY IMPLICATIONS

Sanjeev Gupta, Norbert Losch, Maria Miklautsch, Sebastian Buhlmann
Framatome GmbH
Seligenstaedter Strasse 100, Karlstein, 63791, Germany
Sanjeev.Gupta@framatome.com, Norbert.Losch@framatome.com,
Maria.Miklautsch@framatome.com, Sebastian.Buhlmann@framatome.com

ABSTRACT

Filtered Containment Venting Systems (FCVS) allow controlled depressurization and filtration of the containment atmosphere during severe accidents, reducing overpressure and radiological releases. Following the Fukushima-Daiichi accident and the associated challenges with controlled venting, efforts were intensified to improve iodine retention - particularly for organic iodine species. In response, Framatome developed and qualified a dedicated adsorbent section designed to enhance gaseous iodine retention in its existing FCVS applications.

The development and qualification efforts comprised laboratory-scale pre-qualification and subsequent performance verification in the technical-scale JAVA-PLUS facility. The qualification program demonstrates that iodine retention in FCVS adsorbent stages depends on both chemical kinetics and thermo-hydraulic system behavior. Laboratory tests establish intrinsic adsorption performance and material robustness, but do not account for hydrodynamic non-idealities present at full scale. Large-scale testing shows that retention efficiency is strongly influenced by flow distribution, temperature homogeneity, and gas-solid contact, leading to non-linear scaling effects. Adsorption efficiency emerges as a system property, shaped by the interaction of material characteristics and reactor geometry. The observed differences due to scale effects were further analysed using CFD simulations, which confirmed that flow distribution and residence time in the actual design are at least as favourable as in the JAVA-PLUS facility, supporting the transferability of test results.

This paper presents the main outcomes of these efforts, discusses key parameters influencing iodine retention under various operating conditions, highlights key factors for qualification programmes and summarizes practical experiences and lessons learned from retrofit projects considering both dry- and wet-filtration systems installed in NPPs.

KEYWORDS
FCVS, Iodine retention, Adsorbent, Scaling, Reactor application, Experiments, CFD

1. INTRODUCTION

Filtered Containment Venting Systems (FCVS) are implemented in many nuclear power plants as a final severe accident management measure to preserve containment integrity. During severe accident scenarios, decay heat, hydrogen generation, and steam production may lead to a progressive increase in containment pressure. FCVS enable controlled depressurization of the containment atmosphere while filtering

radioactive materials, thereby reducing the risk of containment failure and limiting radiological releases to the environment.

Several FCVS concepts are deployed worldwide, including dry sand-bed filters, metallic dry filters, wet scrubbers, and hybrid filters (e.g. metal-sand-bed) [1]. Wet FCVS rely on scrubbing processes in alkaline solutions to remove aerosols and water-soluble gaseous species. For aerosols, the current FCVS designs have reached a high degree of maturity, and extensive experimental qualification programmes have demonstrated decontamination factors (DFs) – generally defined as ratio of the total mass of a contaminant entering a filtered containment venting system to the mass exiting it - typically exceeding 10^3, including scenarios with high steam fractions and transient severe accident conditions [1]. In contrast to aerosols, gaseous iodine remains a key challenge for FCVS. Iodine is radiologically important due to its volatility and high biological uptake. Under severe accident conditions, iodine can be present in different chemical forms, including aerosol-bound iodides, molecular iodine (I_2), hydrogen iodide (HI), and organic iodides. While wet scrubbing is effective for molecular iodine and hydrogen iodide, organic iodine, most commonly represented by methyl iodide (CH_3I) is only weakly soluble and largely unaffected by conventional scrubbing or standard dry filtration stages. Furthermore, the retention or release of gaseous radionuclides (mainly iodine) from water pools is governed by physical and chemical processes that differ significantly from those affecting aerosol retention in water pools (“pool scrubbing”) [2]. This is because the release of gaseous radionuclides from the pool surface can be largely independent of the mass flow of gaseous radionuclides injected into the pool water, due to other processes occurring in the pool, such as hydrolysis, interactions with surfaces, and the effects of impurities.

Post-Fukushima research has highlighted the potential importance of organic iodine in the residual iodine source term during containment venting. International and European programmes, such as EC-PASSAM project [2], identified organic iodine formation and retention as major contributors to source-term uncertainty. As a consequence, expectations for FCVS performance increasingly include not only high aerosol DFs but also demonstrable retention of gaseous iodine, particularly organic iodine.

To meet the increased expectations for gaseous iodine mitigation, recent FCVS designs and retrofit concepts - already implemented in several nuclear power plants worldwide (such as the Gösgen NPP in Switzerland) - include dedicated adsorbent stages downstream of the primary aerosol retention components. This requires the selection of materials and system configurations compatible with severe accident conditions, including high temperature, high steam content, and fully passive operation. Silver-based zeolites are commonly used for this purpose due to their chemical affinity for organic iodine and their stability in steam-rich environments. The present paper focuses primarily on the performance of wet FCVS systems, particularly configurations incorporating an upstream wet scrubber. However, it also highlights findings and design considerations that could be relevant for application in dry filter technologies - especially regarding the design of an upstream adsorbent stage for gaseous iodine retention.

This paper outlines the testing approach used to select and qualify an additional adsorbent material specifically to enhance gaseous iodine retention in the FCVS system. The new adsorbent stage is designed to be installed downstream of the existing wet (venturi scrubber) and dry (metal fiber filter) filtration stages in a standard FCVS. It is designed to be easily retrofitted into already operating FCVS installations, offering fully passive and reliable operation without the need for active controls or external power. The testing methodology integrates laboratory-scale pre-screening of adsorbent materials, performance verification in the technical-scale JAVA PLUS facility, and supporting computational fluid dynamics (CFD) analyses to assess the suitability of candidate materials for reactor-scale application, with a primary focus on gaseous iodine capture. Particular emphasis is placed on understanding scale effects, identifying key parameters governing iodine retention, and demonstrating the relevance of technical scale experiments under representative boundary conditions to ensure an optimal FCVS iodine retention performance at reactor scale under typical severe accident conditions.

2. DEVELOPMENT AND QUALIFICATION PHASE - REQUIREMENTS

The development and qualification of the adsorbent filter section followed a structured two-phase experimental program designed to meet the requirements of FCVS operation at NPPs following a severe accident. In the first phase, small-scale laboratory tests were conducted to screen candidate adsorbent materials and evaluate the selected material under a range of accident-relevant conditions, including high temperatures, steam-saturated atmospheres, and other relevant conditions such as the effect of containment impurities. Particular emphasis was placed on ensuring that the adsorbent provided sufficient retention for organic iodine with a target decontamination factor (DF) > 50, or retention efficiency > 98%. The adsorbent material also needed to ensure maintaining the requested high retention for molecular iodine (DF > 1000). Additionally, the selected materials were evaluated for chemical and mechanical stability under aging and thermal cycling, and for consistent performance without degradation due to exposure to chemically active gases. To ensure reproducibility and reliability of the test results, the DFs were independently verified by independent experts (TÜV) by employing their own test facilities.

In the second phase, the selected adsorbent's performance was validated in a large-scale test facility replicating the geometric and thermal characteristics of a real FCVS system. This allowed for assessment of the adsorbent's behavior under representative flow rates, pressure conditions, and environmental stresses, to confirm its suitability for field application. The qualification campaign ensured that the adsorbent met all operational and safety requirements, including long-term stability and consistent performance under both normal and accident conditions.

As part of qualification testing, the design requirements for the additional adsorbent stage considered both initial and final containment pressures (up to 8 bar) to preserve containment integrity during venting, including operation in steam-saturated atmospheres at the end of venting at relatively lower pressure (down to 1.5 bar), ensuring robust system performance over complete venting cycle. The adsorbent stage was originally qualified for retrofitting to the Framatome wet FCVS. Later on, conditions relevant to dry filters were also tested. Therefore, the adsorbent material needed to be verified to be chemically and mechanically stable under radiation exposure, high steam content, and in the presence of potential inhibitor gases (e.g. HNO_3, NO_x, HCl) without significant degradation of retention capability. Further, decay heat from gaseous iodine and aerosols must be quantified for FCVS qualification; including this heat load in adsorbent design ensures thermal stability and retention efficiency. Long-term stability under passive stand-by conditions and compatibility with FCVS operational lifetimes (≥20 years) were set as additional requirements.

3. EXPERIMENTAL RESULTS

3.1. Laboratory scale tests

The laboratory-scale qualification program was conducted to (i) pre-select suitable adsorbent materials, (ii) quantify retention efficiencies for CH_3I and I_2 under representative thermal hydraulic conditions as expected during a severe accident (SA), and (iii) verify material robustness against typical severe accident stressors, including elevated temperatures, high humidity, and radiological loads.

Several zeolite variants were evaluated as candidate adsorbent materials. The zeolite variants had different pore structures and sizes, depending on the specific type of zeolite used. One of the parameters varied in the candidate material was the molar SiO_2/Al_2O_3 ratio, in addition to the amount and form of silver. The laboratory scale tests were conducted independently by a third party (TÜV) using their own test facility.

The schematic diagram of the adsorbent test section used for testing at Framatome is shown in Fig. 1. Parametric investigations were performed in testing apparatus consisting of fixed-bed columns typically comprising adsorption columns with bed volumes of approximately 5–20 mL and bed heights of a few

centimetres. Tests were conducted under controlled steam–gas mixtures (0–100 % steam), temperatures of approximately 80–160 °C, and at ambient pressure. Organic iodine was introduced as CH_3I, generally at concentrations on the order of 10^{-8} mol L^{-1}, and for duration of about 1h.

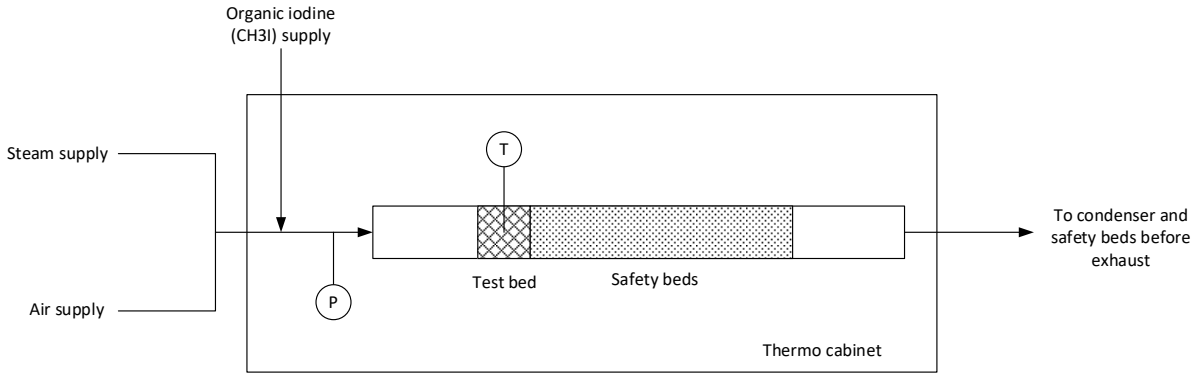

Figure 1: Exemplary schema of the laboratory scale test facility

As part of the material screening phase, 26 adsorbent materials were tested under standardized conditions representative of normal FCVS venting, using a steam-air mixture, fixed flow rate, and a superheating margin of approximately 13 K. Under these reference conditions, a widespread organic iodine retention performance was observed, with measured decontamination factors for CH_3I differing by more than one order of magnitude between the lowest- and highest-performing materials. Based on these results, four adsorbents were selected for further comparative evaluation under varying operating conditions, including both FCVS equilibrium states with high superheating and end-of-venting scenarios characterized by low superheating (Fig. 2, top).

The results confirmed residence time and superheating as the dominant parameters for CH_3I retention. Increasing residence time from approximately 0.1s to 1.0s resulted in a systematic increase in decontamination factor, while a reduction of superheating from ~13 K to below 5 K led to a pronounced decrease in retention efficiency for all candidates. Temperature variations within the investigated range of 120 - 160 °C had a secondary influence compared with residence time and superheating. The four selected materials were compared on the basis of performance index (k) defined as:

$$K - Value = \frac{\log D\,F}{t}$$

where,
k = Performance index [s^{-1})
DF = Decontamination factor [-]
t = Residence time [s]

Out of the two best performing candidates, the final selection was based on the specific structural details demonstrating higher hydrothermal stability with higher resistance against condensing conditions and high humidity. Extended parametric and sensitivity testing of the selected adsorbent showed no significant loss of organic iodine retention during long-term operation up to 120 h, after exposure to 10 vol% hydrogen, or after radiation doses up to 5000 kGy. Thermal stability tests up to 300 °C confirmed preservation of mechanical integrity and adsorption functionality.

The finally selected adsorbent material (Sorbent 3) was then subject to detailed DF investigations. Under investigated conditions, organic iodine DF were typically in the range of 10^2 to 10^3, depending predominantly on superheating and residence time. Molecular iodine retention exceeded CH_3I retention under identical boundary conditions (Fig. 2, bottom). Importantly, even at low superheating (≤ 2 K),

adsorption performance degraded gradually rather than abruptly, and no cliff-edge behavior was detected across the investigated parameter space.

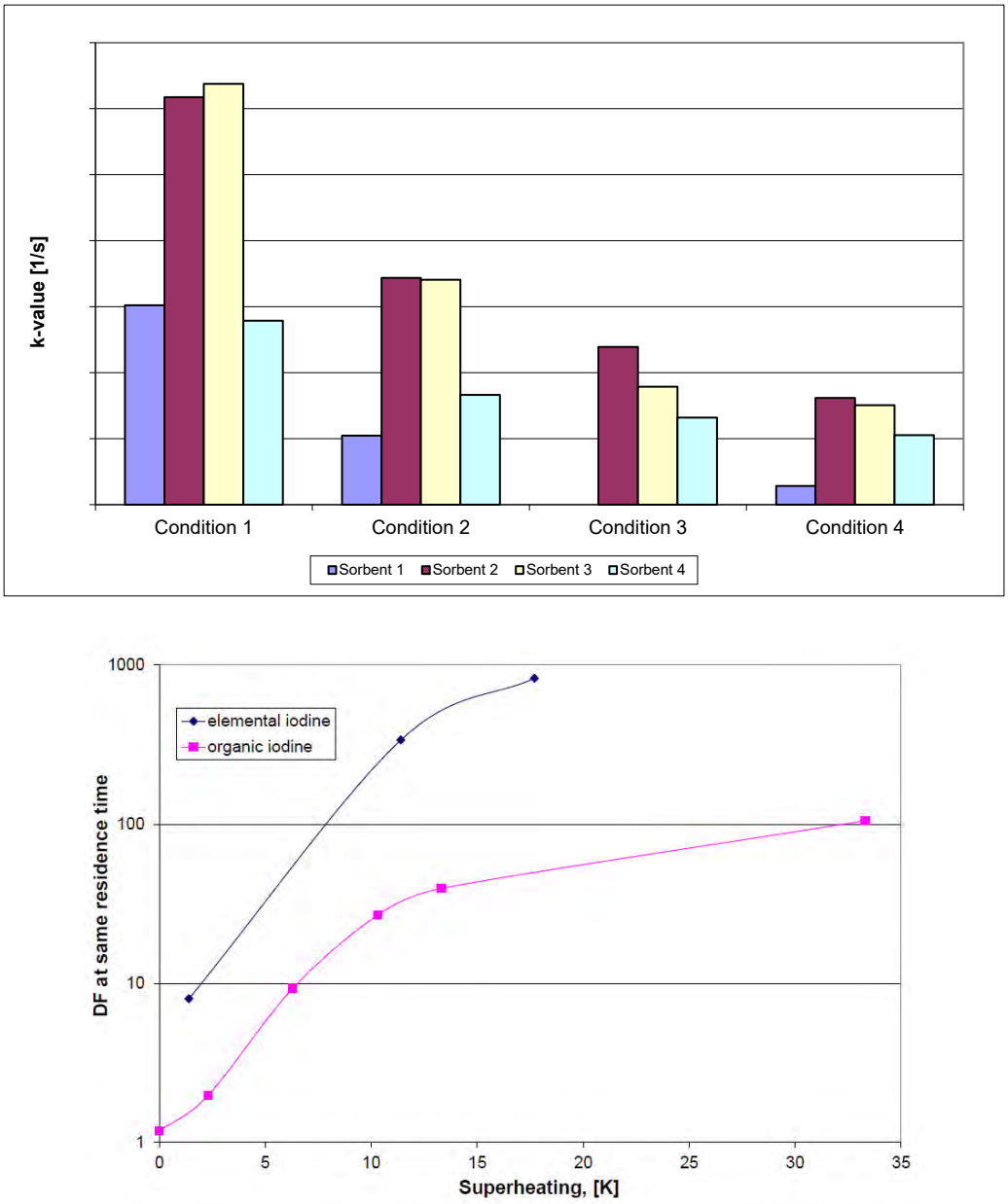

Figure 2: K-value comparison for 4 candidate materials (top); gaseous iodine retention (bottom)

3.2. Technical scale tests at JAVA-PLUS facility

The JAVA test facility, which represents the Framatome FCVS system, was extended to JAVA-PLUS by adding a third retention stage, the adsorbent section, see Fig. 3a. The adsorbent section in JAVA PLUS has a height of approximately 2 m, a diameter of about 1.2 m (Fig. 3a & 3c). The selected dimension and mass of the absorbent allowed investigation of scale-dependent thermal-hydraulic effects, which were not possible at the laboratory scale tests discussed in section 3.1. The required superheating in the adsorbent section can be generated by isenthalpic throttling at the throttling orifice (Fig. 3a). The facility allows transient operation, including start-up phases, pressure decay during venting, and operation near the

saturation, where condensation may occur. The operating characteristics of the JAVA PLUS test facility are shown in Table 1.

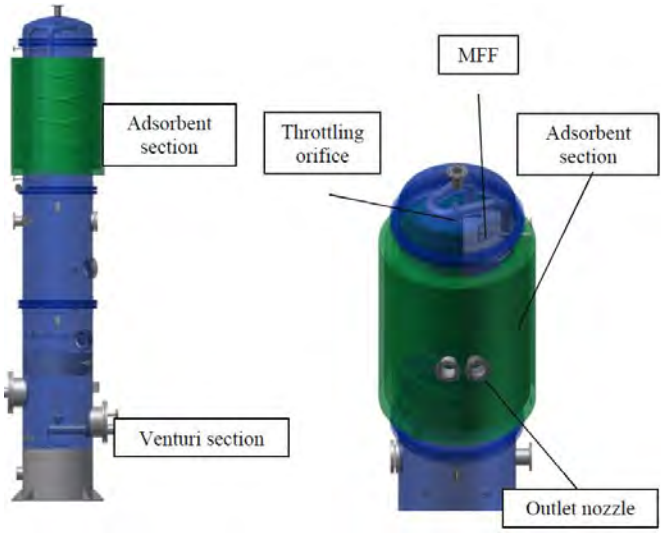

(a)JAVA PLUS test facility with the adsorbent section

(b) Lower section of the JAVA PLUS facility

(c) Adsorbent section (picture)

Figure 3: JAVA PLUS test facility

Table 1: Operating characteristics of the JAVA PLUS test facility

PARAMETER	VALUE
Pressure Before Venturi Scrubber Inlet	1 – 10 bara
Temperature	Up to 200 °C
Gas Composition	Steam / air mixtures in the range: 0 % - 100 % steam
Liquid Phase Composition	Demineralized water, sodium thiosulfate, sodium hydroxide
Scaling Factor Compared to Typical FCVS installed in a NPP	Height: 1/1 Volume: 1/3 Mass flow: 1/3
Mass Flow	Up to 2 kg/s (steam and air mixture) - steam 1.5 kg/s - air 0.5 kg/s
Volume of Test Facility	8 m^3
Height of Adsorbent Section	2 m
Diameter of Adsorbent Section	1.2 m

The test matrix covered:

- Pressure: from approximately 5 bar (a) at vent opening down to 1.5 bar(a) at end of venting
- Temperature: up to 160 °C at the adsorbent inlet
- Thermodynamic state of the gas-mixture: adjustable by water injection at JAVA facility inlet: near-saturation conditions at the metal-fibre filter inlet, and slightly superheated conditions at inlet to the adsorbent section.
- Residence time: mean values in the order of 0.3–1.5 s, depending on flow regime
- Superheating: from >10 K down to <5 K above the dew point
- Transient operation: vent opening, transient start-up and depressurization phases

Large-scale tests revealed that decontamination factors (DF) for CH_3I were systematically lower than laboratory values, typically reduced by a factor of 10 to 100 for comparable superheating and residence times. Nevertheless, the target DF > 50 was confirmed under worst-case conditions, with values exceeding 100 under medium and high-pressure conditions. The primary reason for the observed differences in DFs is expected to be due to the nearly ideal hydrodynamic conditions in laboratory experiments - such as uniform velocity profiles, minimal radial temperature gradients, short bed heights, and high surface-to-volume ratios- which allow adsorption to be governed mainly by reaction kinetics and effective gas-solid contact, resulting in high apparent DFs. In contrast, large-scale systems inherently exhibit geometric and hydrodynamic non-idealities that are suppressed in laboratory setups, leading to lower observed decontamination factors in industrial applications.

Similar to the laboratory scale tests, superheating and residence time emerged as the primary parameters controlling CH_3I retention. Empirical correlations from JAVA PLUS tests confirmed a linear relationship between normalized k-value and superheating, with deviations observed below 5 K (Fig. 4), mainly due to condensation risks near the dew point.

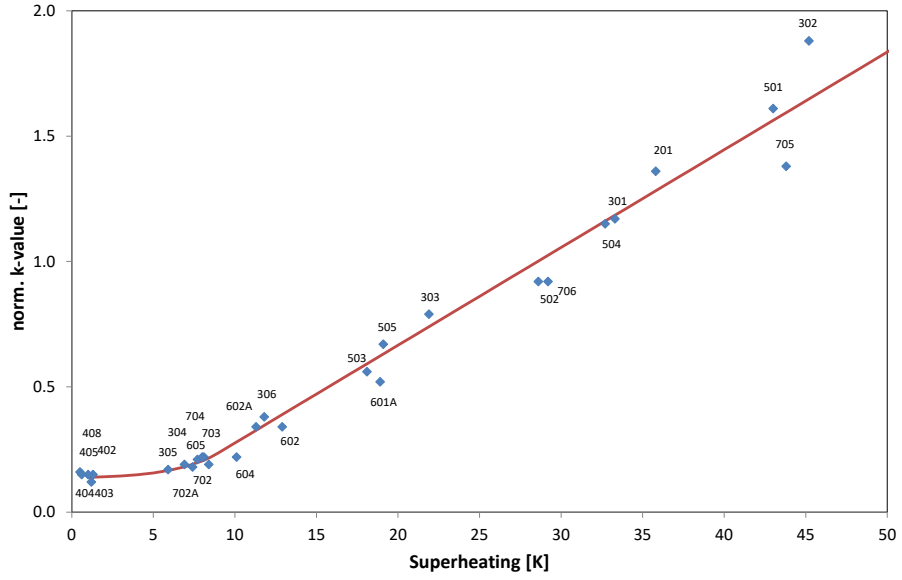

Figure 4: Dependency of normalized k-value on superheating of JAVA PLUS results

Secondary influences included temperature, gas composition, flow distribution, and wall heat losses. Temperature variations affected retention indirectly by altering saturation conditions. Gas composition influenced absolute temperature, but superheating remained nearly unchanged for similar pressures. Flow distribution and wall heat losses, negligible at laboratory scale, had a measurable impact on adsorbent utilization at technical scale.

Based on JAVA PLUS testing, superheating and residence time are confirmed as the principal parameters governing CH_3I retention, forming the basis for reactor-scale design and performance evaluation of the adsorbent section. The vent gas volume flow rate is dictated by operational variables (mass flow rate, composition, pressure, density), while adsorbent volume is fixed by section geometry. Normalized residence time, calculated proportional to actual residence time, is used to account for these factors. Attaining a target DF, therefore requires a minimum residence time in the adsorbent section. Fig.5 shows a viewgraph correlating normalized residence time and superheating, with a design curve for DF = 50. This systematic approach enables precise evaluation and optimization of adsorbent performance under varying reactor-scale operational conditions.

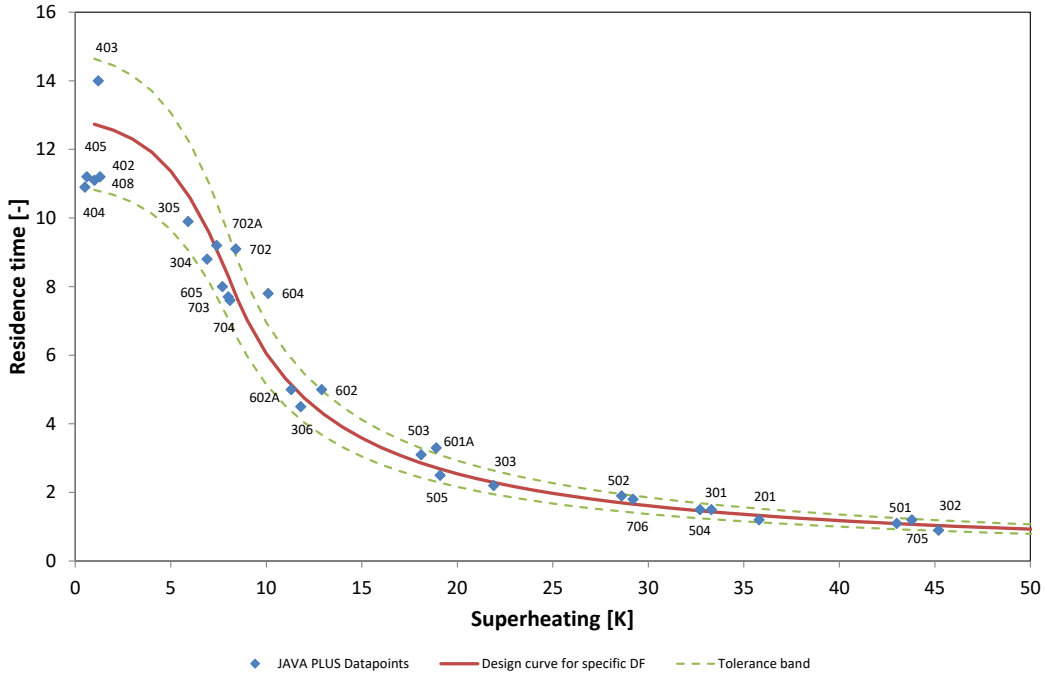

Figure 5: Normalized residence time depending on superheating for design DF valve of 50

4. SCALING EFFECTS AND EXTRAPOLATION OF RESULTS TO REACTOR SCALE

Comparing laboratory and technical-scale JAVA PLUS tests shows that CH_3I retention in FCVS adsorbent stages depends on both chemical reactions, system flow and temperature conditions. Laboratory tests measure basic adsorption and chemical stability, but do not include flow and temperature variations found at larger scale. In technical-scale systems, retention efficiency is mainly affected by flow distribution, temperature uniformity, and gas -solid contact.

The abovementioned factors cause non-linear scaling effects that cannot be described by mean residence time alone. Technical-scale systems have wider residence-time distributions, so some parts of the flow have less contact with the adsorbent, reducing overall retention. Comparison of the superheating versus residence time in Fig. 6 show that large-scale tests need longer residence times to reach the same retention efficiency as small-scale tests. This is due to uneven flow and temperature profiles. Optimization at the JAVA PLUS facility improved flow and temperature uniformity, which increased retention efficiency (see Fig. 6).

However, it is not possible to fully reproduce small-scale conditions in large-scale systems. In real applications, uneven flow is typical. This means that scaling challenges are not limited to residence time. It is important to consider realistic boundary conditions, flow variations, and the resulting thermal-hydraulic inhomogeneities when designing and evaluating large-scale systems.

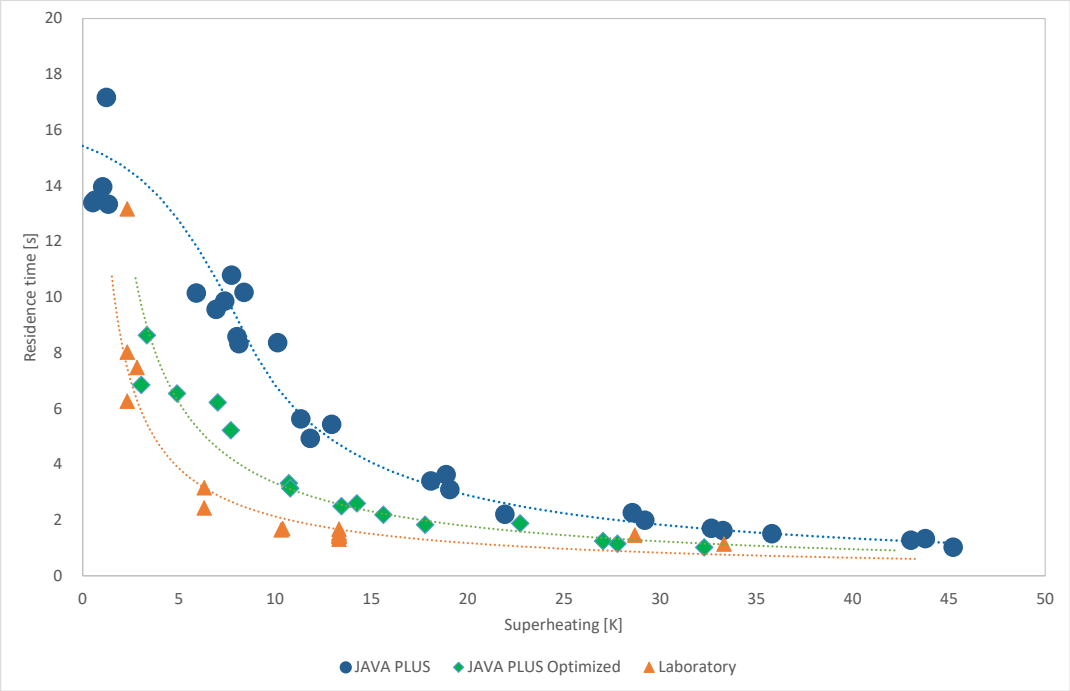

Figure 6: Comparison of results from small-scale and JAVA PLUS with and without optimized flow conditions

CFD analysis, utilizing CFD code ANSYS FLUENT version 14.5, was conducted to bridge the findings from technical-scale tests at the JAVA PLUS facility with the design of reactor-scale adsorbent stages. The simulations utilized Gambit version 2.4.6 as the preprocessor to generate a hybrid mesh with approximately 19.2 million cells. The k-ω SST turbulence model and a second-order discretization scheme were employed to improve solution accuracy.

The CFD analysis simulations showed that flow inside the JAVA PLUS adsorbent section is not uniform. Inlet and outlet geometry, along with internal structures, lead to preferential flow paths especially near the vessel walls (see Fig. 7 top), which revealed clear temperature inhomogeneity at the inlet and throughout the adsorbent bed. Velocity profiles from the CFD simulations highlighted low-velocity regions. The design of the inlet and outlet was identified as the main cause of flow maldistribution. Based on these findings, the adsorbent section design was optimized, such as by adapting an optical traveling length along the wall relative to the bed depth. Additionally, specific measures – such as adding baffle plates - were implemented and tested in the JAVA PLUS (see Fig. 6 in previous section) facility. These actions resulted in improved flow uniformity and iodine retention during the testing campaign.

Another important outcome from the CFD evaluation is that mean residence time alone does not capture the real behavior at larger scale. Instead, the shape and width of the residence-time distribution (RTD) are crucial. A broader RTD means that some portions of the gas pass through the adsorbent with much shorter contact times, mainly due to velocity gradients caused by the inlet design and geometric constraints. These short contact times are responsible for lower CH_3I retention and explain why technical-scale decontamination factors are lower than those measured in laboratory setups, even when nominal conditions are similar.

Figure 7 (bottom) presents the inflow conditions of the adsorbent section in the JAVA PLUS test facility and in a separate adsorbent vessel (representative of the solution for retrofit solutions for different venting systems). The influence of different parameters was evaluated and analyzed. As relevant value for comparison the standard deviation of residence time within sorbent bed was found. As the two most relevant influencing factors the depth of sorbent bed and therewith the pressure loss of the sorbent bed as well as in- and outflow were identified. As result of the analysis, it was validated that the distribution of residence time in the applied or real design is better or equal to the JAVA PLUS sorbent section to allow transfer of the test results.

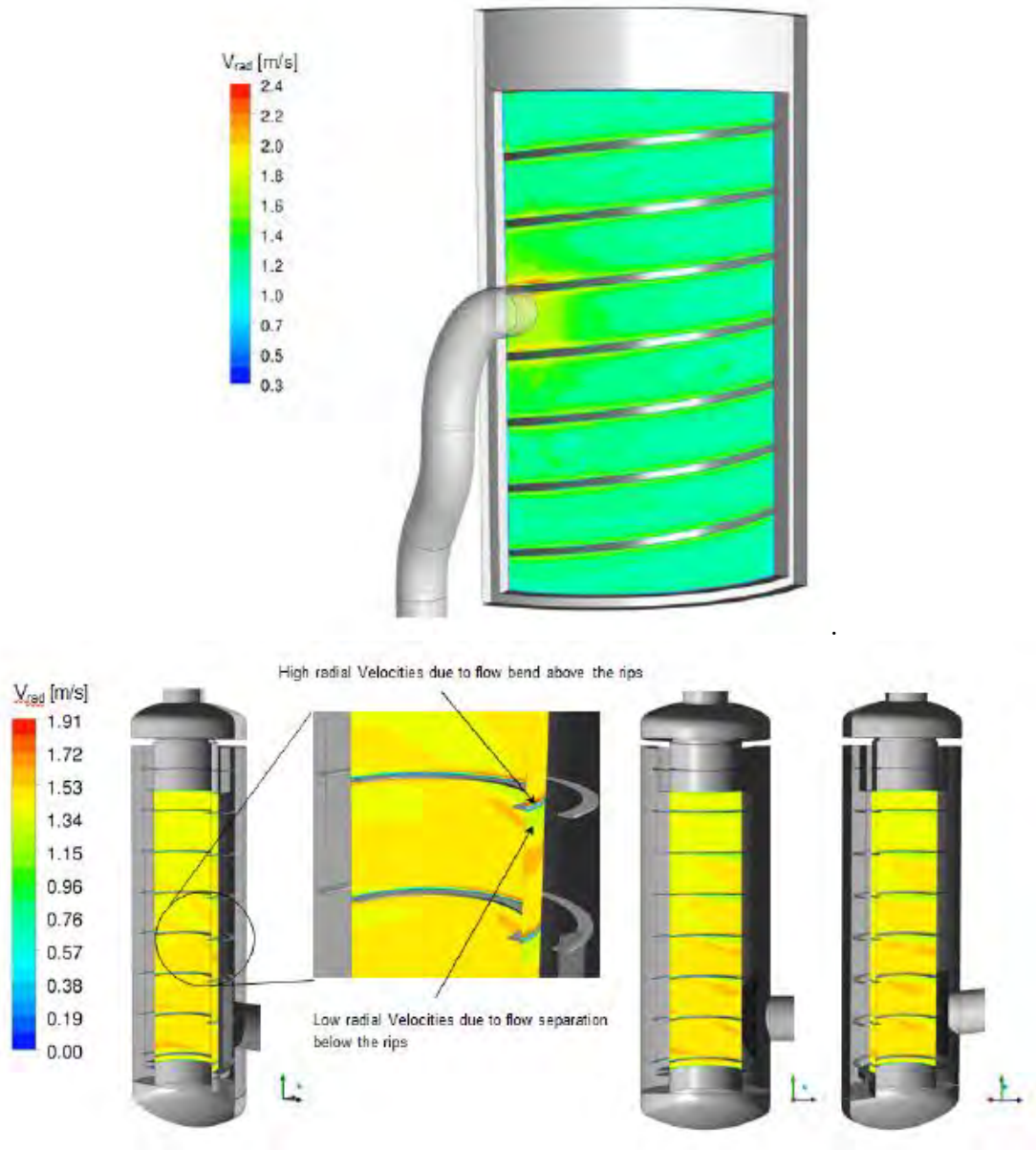

Figure 7: Inflow conditions of the adsorbent section of the JAVA PLUS test facility (top), real-scale retrofitting vessel (bottom)

Finally, transient CFD simulations were used to analyse vent opening and pressure decay phases, during which rapid changes in flow rate and pressure can temporarily reduce local superheating or modify flow

distribution. These analyses quantified the duration and spatial extent of limiting conditions and demonstrated that such transients remain bounded within the qualification envelope established by the technical-scale testing programme.

The safety implication from scaling effects arises when laboratory data are used for adsorbent design, leading to underestimated bed thickness or mass. Under severe accident venting conditions - high steam, variable flow, transient superheating—this can cause earlier iodine breakthrough and reduced DF. Gaseous iodine, especially CH_3I, dominates the volatile fraction not retained by filters, so its release depends on realistic, large-scale retention performance. A tenfold drop in DF as observed between laboratory scale and JAVA PLUS tests, implies a tenfold increase in released organic iodine activity, directly impacting off-site dose projections and Emergency Planning Zone (EPZ) sizing. Adsorbent sizing must therefore use full-scale k-values from representative conditions, with conservative residence time and avoidance of condensation-sensitive designs, as scaling directly determines adsorbent mass, bed geometry, and iodine source term for emergency planning.

5. STANDARD FCVS SYSTEM WITH RETROFIT POTENTIAL OF ADSORBENT SECTION

The Framatome FCVS concept (Fig. 8 & Table 2) is based on a modular system architecture designed to ensure effective retention of aerosols and gaseous iodine species, including both elemental and organic iodine, under severe accident conditions. Primary filtration stages provide high and stable aerosol retention, while downstream iodine retention stages are integrated to meet defined acceptance criteria without adversely affecting the hydraulic performance or passive operation of the venting system over the relevant range of pressure, temperature, and steam conditions.

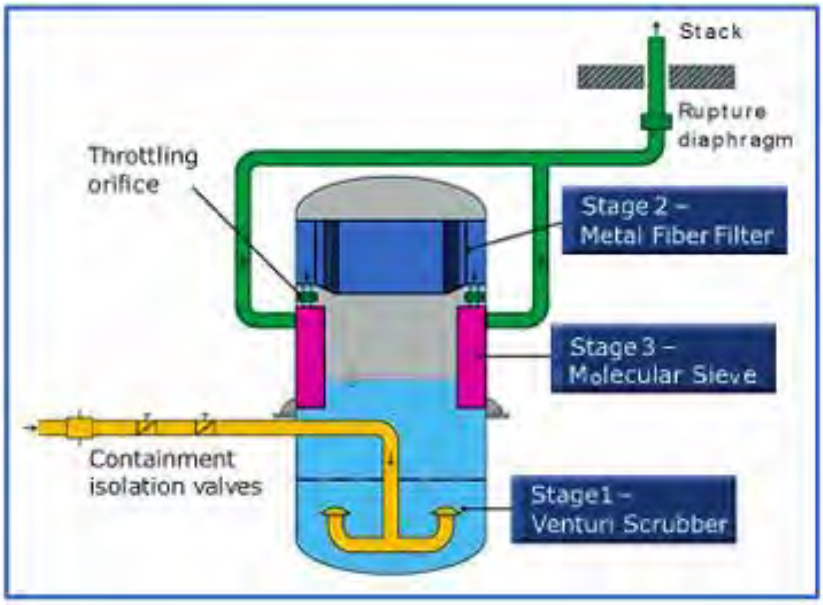

Figure 8: Schematic of Framatome FCVS system

Table 2: Main design features of Framatome FCVS

Main stages	Function	Operating characteristics	Retained species
Stage 1 – Venturi scrubber	Primary filtration	• Operation at near-containment pressure • Gas acceleration in venturi nozzles • Injection into scrubbing liquid • Passive heat transfer to liquid	• Aerosols • Elemental iodine
Stage 2 – Metal fiber filter	Secondary filtration	• Removal of fine and re-suspended aerosols • Droplet and condensate separation • Low pressure drop design	• Fine aerosols • Liquid droplets
Stage 3 – Silver-doped molecular sieve	Gaseous iodine filtration (optional)	• Silver-doped zeolite bed • Chemisorption forming AgI • Modular integration / retrofit	• Gaseous iodine • Organic iodine

The current paper presents performance results for an FCVS configuration incorporating an upstream wet scrubber. In such a configuration, the scrubber provides efficient aerosol removal, significant quenching of the gas stream, and partial retention of soluble iodine species, thereby substantially reducing aerosol loading, gas temperature, and chemical aggressiveness at the inlet of the downstream dry adsorbent stage. As a consequence, parameters such as particulate fouling, excessive pressure drop due to dust accumulation, and direct exposure to peak thermal-hydraulic conditions do not represent dominant design drivers for the adsorbent section. In particular, aerosol-induced clogging, untreated acid gas spikes, and uncontrolled condensation effects are mitigated upstream, limiting their impact on residence time requirements, hydrothermal stability margins, and long-term adsorbent performance.

However, the testing campaign also included performance testing with only upstream dry filter section without wet filtration stage. In such situation, the adsorbent stage will probably be directly exposed to acid gases without prior quenching and decontamination. In any case, aerosols will not reach the adsorbent section because there is always an aerosol filter positioned before it. This filter may take the form of filter mesh, cartridges, or a sand bed. Furthermore, the amount of iodine within the specified ranges does not actually have any impact. The system design is based on kinetic considerations. This means that even if no iodine is retained in the preceding section, the required quantity of adsorbent does not increase, as there is always sufficient buffer available. Nevertheless, the design requirements for the dry filtration stage become more stringent in terms of aerosol pre-separation (higher DF for particulates), thermal conditioning to ensure sufficient superheating and avoid condensation within the bed and increased chemical resistance against HCl/HNO_3. Moreover, structural and hydraulic design must consider higher pressure drop and fouling risks, as well as enhanced decay heat management within the adsorbent bed.

The operational experience with the Framatome FCVS installed in NPPs has been accumulated through routine periodic inspections. Samples have been collected and analyzed at intervals of 1 to 5 years, resulting in a consistent operational record spanning more than a decade. Throughout this period, no decrease in iodine retention has been observed, demonstrating stable and reliable adsorbent performance under the tested conditions.

Conclusions

This paper summarizes the main outcomes of testing done towards developing a dedicated gaseous iodine retention stage for FCVS systems installed worldwide. While conventional filtration systems achieve high aerosol decontamination factors, their efficiency for volatile iodine species, particularly organic iodide remains limited, necessitating complementary retention mechanisms.

Framatome's systematic development approach combined laboratory-scale qualification—demonstrating intrinsic DF for organic iodine (CH_3I) well above 50 under broad range of typical severe accident conditions. For this purpose, industrial-scale verification under representative thermo-hydraulic conditions were carried out. Large-scale testing confirmed the robustness of the selected silver-impregnated zeolite and highlighted the critical importance of full-scale validation to capture hydrodynamic scaling effects.

Overall, the study underlines that for dimensioning of FCVS adsorbent stages, conservative DF values must therefore be based on large-scale verification results. Laboratory data remain indispensable for material selection, parametric understanding, and development of design correlations, but cannot serve as sole performance validation.

CFD analyses provided valuable insights into flow distribution, temperature homogeneity, and residence time behavior, supporting optimized reactor-scale implementation. The modular adsorbent concept enables flexible integration and backfitting across diverse FCVS configurations within the existing nuclear power plant fleet.

Importantly, adding an adsorbent stage for gaseous iodine retention is a technically feasible backfit for existing nuclear power plants, regardless of the original FCVS design. Whether the current system uses a dry aerosol filter or a wet scrubber, a dry adsorbent module can be integrated as a modular add-on without major changes to the primary venting approach.

REFERENCES

1. OECD/NEA, Status Report on Filtered Containment Venting, NEA/CSNI/R(2014)7.
2. T. Albiol, L. Herranz, E. Riera, C. Dalibart, T. Lind, A. Del Corno, T. Kärkelä, N. Losch, B. Azambre, C. Mun, L. Cantrel, "Main results of the European PASSAM project on severe accident source term mitigation", Annals of Nuclear Energy, 116 (2018), pp. 42-56.

framatome

SCALING EFFECT IN IODINE RETENTION FOR FILTERED CONTAINMENT VENTING: EXPERIMENTAL FINDINGS AND SAFETY IMPLICATIONS

SANJEEV GUPTA, NORBERT LOSCH, MARIA MIKLAUTSCH, SEBASTIAN BUHLMANN

The 12h European Review Meeting on Severe Accident Research (ERMSAR2026)

Log Number: 201, Madrid, Spain, May 18-22, 2026

C1 - Framatome Restricted - . - Framatome know-how

Export Control - AL : N / ECCN : N

Confidentiality

[X] **This document contains Framatome's know-how**

EXPORT CONTROL

AL = N	ECCN = N

Goods labeled with "AL not equal to N" are subject to European or German export authorization when being exported within or out of the EU.
Goods labeled with "ECCN not equal to N or EAR99" are subject to U.S. reexport authorization. Even without a label, or with label: "AL:N" or "ECCN:N" or "ECCN:EAR99," authorization may be required due to the final whereabouts and purpose for which the goods are to be used.

FRAMATOME'S INFORMATION PROTECTION RULES

[X] C1 -This document and any and all information contained therein and/or disclosed in discussions supported by this document are **restricted**.

[ ] C2 : This document and any and all information contained therein and/or disclosed in discussions supported by this document are sensitive and **Framatome confidential,** such as its disclosure, alteration or loss are detrimental with a significant-to-high impact for Framatome.

The document, if disclosed, and any information it contains are intended for the sole attendees. The disclosure or reference to such information or document shall be made only on a proper judgment basis and by mentioning expressly "this information shall not be disclosed / transferred without prior consent".

[ ] C3 –This document and any and all information contained therein and/or disclosed in discussions supported by this document are classified **Framatome Secret**.

Each one must commit to keep secret any written or oral information disclosed during the meeting. It is forbidden to disclose it to any legal entity and any individual (including within Framatome) without prior consent of the meeting chairman.

This document and any and all information contained therein and/or disclosed in discussions supported by this document, are confidential, protected by applicable intellectual property regulations and contain data subject to trade secrets regulations. Any reproduction, alteration, disclosure to any third party and/or publication in whole or in part of this document and/or its content is strictly prohibited without prior written express approval of Framatome. This document and any information it contains shall not be used for any other purpose than the one for which they were provided. Legal and disciplinary actions may be taken against any infringer and/or any person breaching the aforementioned obligations.
© Framatome – All rights reserved

Background: FCVS in severe accident management

- Filtered Containment Venting Systems (FCVS) are implemented as a final severe accident management measure to preserve containment integrity.
- During severe accidents, decay heat, hydrogen generation and steam production may progressively increase containment pressure.
- FCVS enable controlled depressurization while filtering radioactive materials, such as:
  - Aerosols
  - Iodine

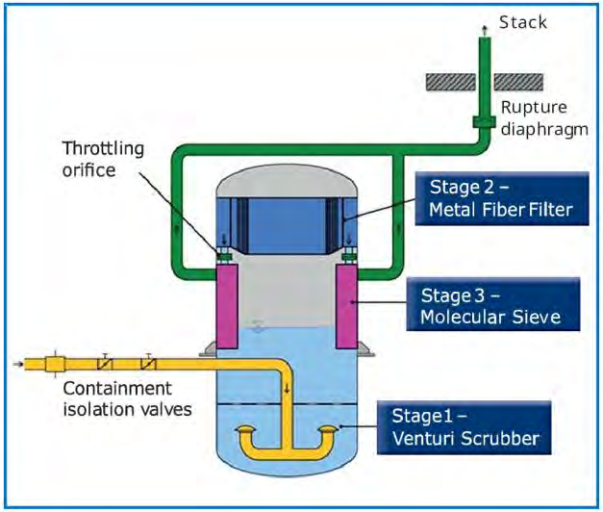

Framatome FCVS PLUS with - Venturi scrubber, metal fiber filter and iodine filtration stage

 © Framatome - All rights reserved

C1 - Framatome Restricted - . / Framatome know-how / Export Control - AL : N ECCN : N

Background: Gaseous iodine retention

- During Venting iodine is released by 3 transport mechanism from the containment:
  - **Aerosol-bound iodides** — Efficient aerosol filtration in mature filter design
  - **I_2 / HI** — Efficient retention by wet scrubbing and sorbent filter
  - **Organic iodides (e.g. CH3I)** — Largely unaffected by conventional scrubbing and aerosol filters

- Research projects, like EC-PASSAM, identified organic iodine formation and retention as major contributors to source-term uncertainty.
- Post-Fukushima research:
  Organic iodine is highlighted as an important iodine source term during venting.
- Safety authorities increasingly request FCVSs with qualified organic iodine retention

 © Framatome - All rights reserved

Framatomes FCVS PLUS qualification program:

- **Objective**:
  Develop and qualify a additional filter section to enhance gaseous iodine retention in existing FCVS applications→ ***Organic Iodine DF > 50***
- **Scope**
  - **Laboratory tests**: screen candidate adsorbent materials and evaluate the selected material under a range of accident-relevant conditions
  - **Large-scale** (JAVA-PLUS) tests: verification of the selected adsorbent materials in a large-scale test facility replicating the geometric and thermal-hydraulic characteristics of a real FCVS system
  - **CFD analysis** to support in experimental set-up design and assessment towards extrapolation of test results to reactor scale venting systems.

Screening	Lab qualification	JAVA-PLUS	CFD
26 adsorbent variants	**CH_3I / I_2 DFs**	**Technical-scale validation**	**Test-design calculations, reactor-scale extrapolation**

Laboratory scale tests

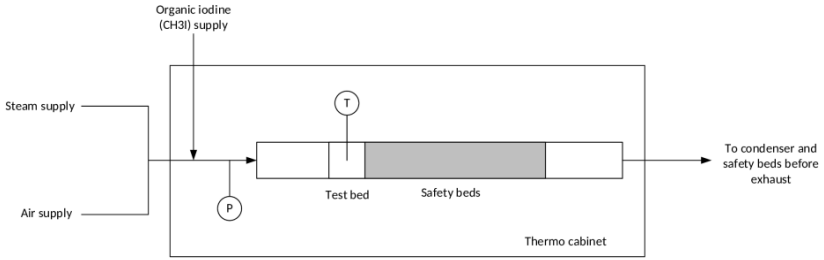

An exemplary sketch of laboratory scale set-up

Performance comparison

$$k = \frac{ln(DF)}{t}$$

Where:
k = performance index [1/s]
DF = decontamination factor [-]
t = residence time [s]

Typical laboratory parameters

- Fixed-bed columns with sorbent beds
  - Diameter: ~2.5 cm
  - Bed height: ~2.5 cm
- Parametric testing
  - 0 - 100% steam/air
  - 60 - 120 °C (condensing & superheated)
  - Flow velocity
  - …
- Organic iodine is continuously injected at stable conditions for about 1h (tracered test)
- Tests conducted independently by TÜV to verify decontamination factors
  - Values verified by in-house laboratory testing

Laboratory scale tests – Results

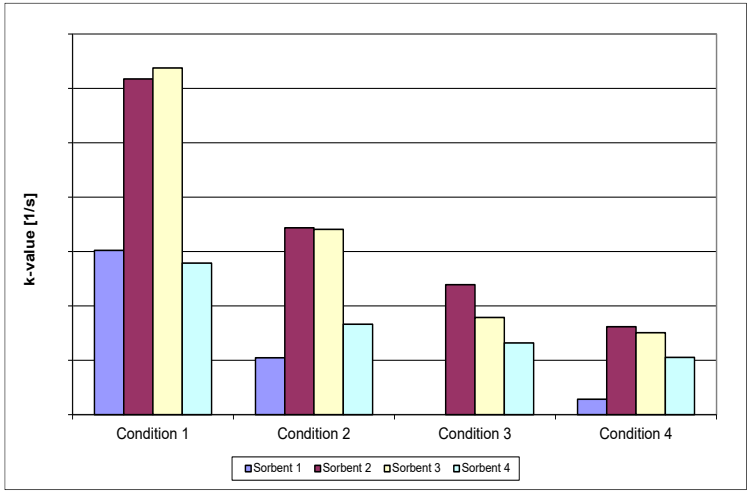

$k = \ln(DF)/t$

Figure 2 (top): K-value comparison for four candidate materials

- 26 adsorbent materials were screened under standardized conditions
  - Silver zeolite are best adapted
- CH_3I DFs differed by more than one order of magnitude between the lowest- and highest-performing materials.
- 4 adsorbents were selected for further comparison under FCVS start-of-cycle and end-of-venting conditions.

→ **Residence time and superheating are the dominant parameters for CH_3I retention.**

Final selection was based on performance and higher hydrothermal stability

Technical scale tests – JAVA-PLUS

- **Test facility parameters**
  - Total height: 8 m
  - Height sorbent section: 2 m
  - Diameter: 1.2 m
  - Mass flow Scale: ~ 1:3
- **Operating conditions for tests**
  - Gas flow rate: up to 1.5 kg/s
  - Gas phase composition: steam-air mixture
  - Inlet pressure: 1.5 – 8 bar abs
  - Pressure in the adsorbent stage: up to 2 bar abs
  - Temperature: 50 – 180°C
  - Transient
    - Venting cycle (depressurization of containment)
    - Start-up transient

framatome

 © Framatome - All rights reserved

C1 - Framatome Restricted - . / Framatome know-how / Export Control - AL : N ECCN : N

JAVA-PLUS tests – Large scale results

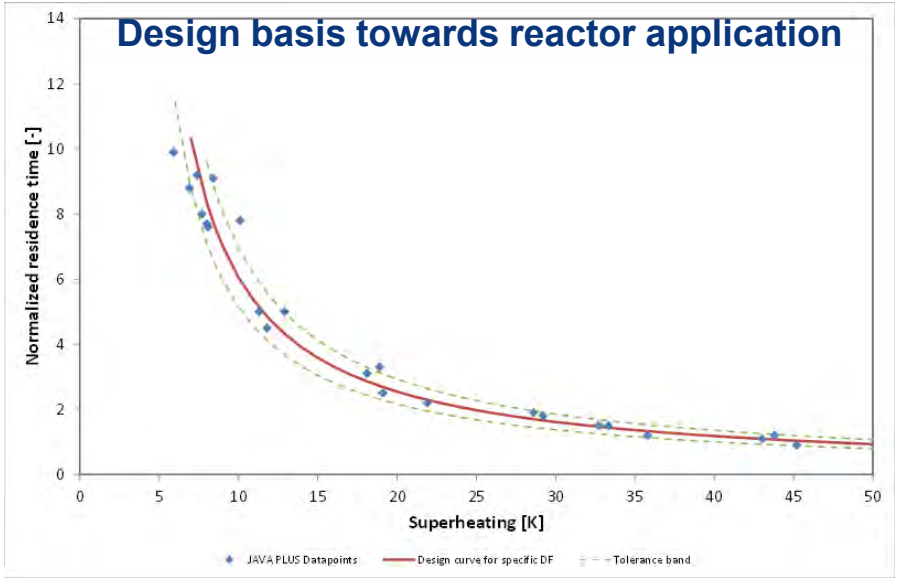

Normalized residence time for design DF = 50

The lower the superheating, the higher the needed residence time to reach the same DF

1st Conclusions from testing

- Confirmation: DF is mainly dependent of
  - Residence time
  - superheating
- Target DF requires a minimum residence time in the adsorbent section
  - Amount of silver sorbent needs to be adjusted to reach target DF

$$k = \frac{ln(DF)}{(t/t_{normalized})}$$

Scale comparison – Lab & Large scale

Laboratory scale testing	Large Scale Testing
Sorbent Volume ~ 0.0015 L Flow cross section ~ 0.0005 m²	Sorbent Volume ~ 80 L Flow cross section ~ 1.7 m²
Scaling factor ~ 1:90 000	Scaling factor ~ 1:3
Even/ideal flow distribution ideal inlet flow conditions **Even/ideal temp. distribution** heated in a heating cabinet	**Realistic flow and temp. distrib.** Real. design / geometry / flow dyn.
- Inhouse Testing - Independent 3rd party Testing	- JAVA Large scale testing

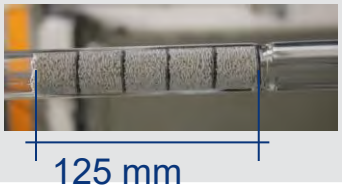

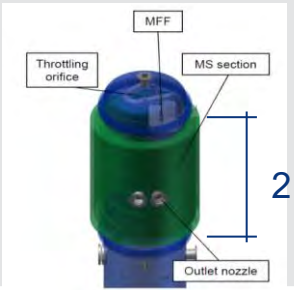

Organic Iodine DFs in JAVA-PLUS were systematically lower than laboratory values:

Factor of 10–100 for comparable conditions

 © Framatome - All rights reserved
C1 - Framatome Restricted - . / Framatome know-how / Export Control - AL : N ECCN : N

Scaling – Results

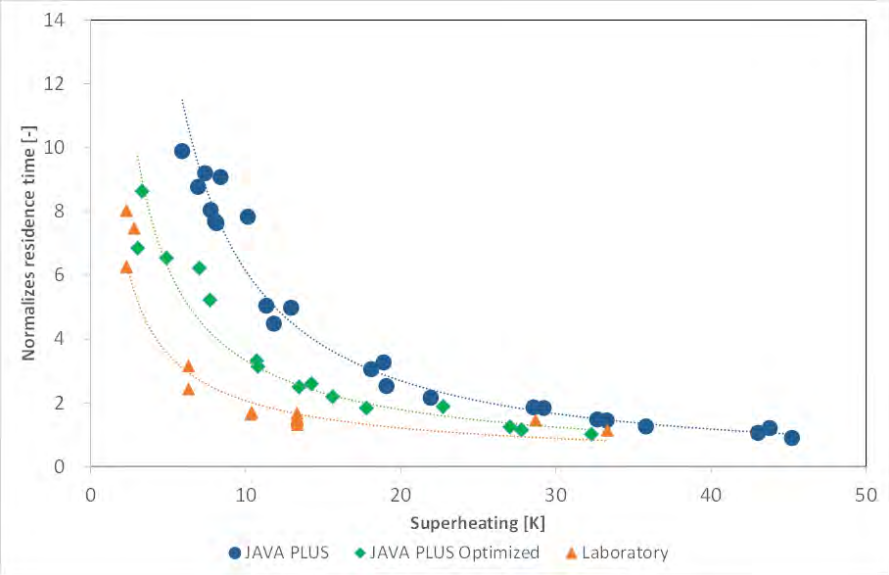

DF = 50
Small-scale and JAVA-PLUS results with and without optimized conditions

Comparison of
- Laboratory tests
- Large scale tests (not optimized)
- Large scale tests (optimized)

➢ Technical-scale systems show
  - non-ideal flow distribution (residence time distribution)
  - temperature inhomogeneity

→ *i.e. expected conditions for real FCVS operation in a NPP*

➢ At low superheating (≤2 K), performance degraded gradually. No cliff-edge behavior was detected

Key point
Technical-scale tests need longer residence times to reach the same retention efficiency as small-scale tests

CFD analysis: flow distribution and residence-time behavior

CFD code ANSYS FLUENT 14.5 with a hybrid mesh of about 19.2 million cells and k-ω SST turbulence model.

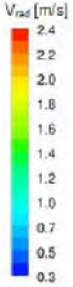

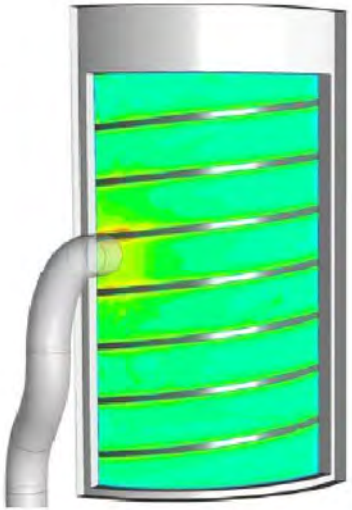

Flow conditions of JAVA-PLUS adsorbent section

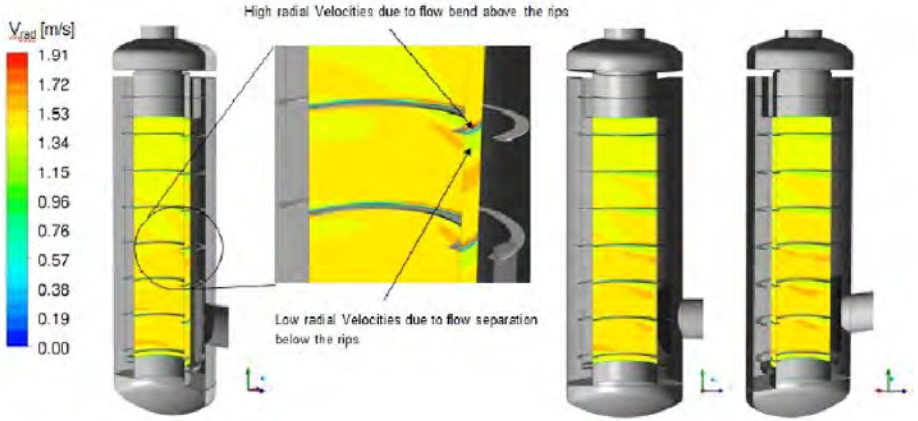

Real-scale retrofitting vessel

→ **Aeras with higher gas speed feature lower residence time => local DF reduction (filter gap!)**

→ **The real/applied designs used for show similar or better residence-time distribution as in the JAVA PLUS sorbent section, supporting transferability of the JAVA PLUS test results to the real design**

 © Framatome - All rights reserved
C1 - Framatome Restricted - . / Framatome know-how / Export Control - AL : N ECCN : N

Safety implication of scaling effects

→ Using laboratory data alone can underestimate needed adsorbent bed volume

- Under severe accident venting - high steam, variable flow and transient superheating - undersized beds may cause reduced DF.
- A tenfold drop in DF implies a tenfold increase in released organic iodine activity
- Released volatile iodine directly affects off-site dose projections and Emergency Planning Zone sizing.
- Adsorbent sizing should use full-scale k-values from representative conditions with conservative residence time.

FCVS dimensioning principle

Laboratory scale test data is indispensable for material selection and parametric understanding.

Laboratory data is not sufficient as sole performance validation for upscaling (factor << 10)

Scaling directly determines adsorbent mass, bed geometry and iodine source term

 © Framatome - All rights reserved

Conclusions

- A dedicated adsorbent stage is necessary to complement FCVS filtration for volatile iodine, particularly organic iodide.
- Technical-scale JAVA-PLUS tests confirmed robustness and exposed hydrodynamic scaling effects that reduce observed DFs relative to laboratory tests by factor 10 - 100
- Conservative FCVS adsorbent design should be based on large-scale verification.
- The modular adsorbent concept is a technically feasible backfit for existing NPPs with wet or dry FCVS configurations.

Main outcome
Iodine retention in FCVS adsorbent stages is a system property shaped by material behavior, thermal-hydraulics and reactor geometry

Large scale tests data are a key for reactor application

framatome

Merci

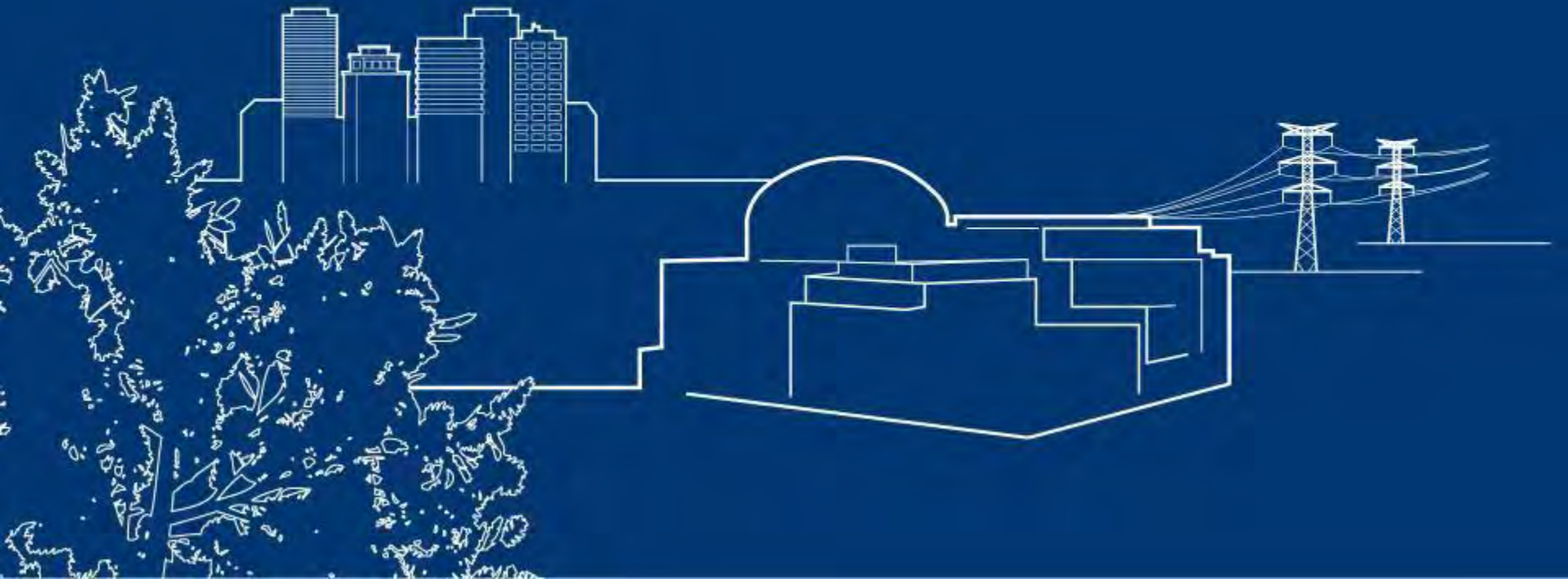

Any reproduction, alteration, transmission to any third party or publication in whole or in part of this document and/or its content is prohibited unless Framatome has provided its prior and written consent.

This document and any information it contains shall not be used for any other purpose than the one for which they were provided.

Legal and disciplinary actions may be taken against any infringer and/or any person breaching the aforementioned obligations.

A Deep Learning Surrogate Model for Rapid Prediction of Atmospheric Radioisotope Dispersion

Onur Murat, Fabrizio Gabrielli, Victor Hugo Sánchez-Espinoza
Karlsruhe Institute of Technology
Hermann-von-Helmholtz-Platz 1, 76344, Eggenstein-Leopoldshafen, Germany
onur.murat@kit.edu; fabrizio.gabrielli@kit.edu; victor.sanchez@kit.edu

ABSTRACT

Rapid and accurate prediction of the atmospheric radionuclide dispersion is critical for emergency response following a severe accident in Nuclear Power Plant (NPP). Java based Real-time Online DecisiOn Support System (JRODOS) code was developed at the Karlsruhe Institute of Technology (KIT) to analyze radiological consequences of the radionuclides dispersions. In order to complete a single simulation in JRODOS, weather condition data was on selected time frame processed by the code and selected atmospheric dispersion model applied to calculate the movement and deposition of the radionuclide material over a selected region. Based on the source term and duration of the release, one simulation can take minutes and this computational cost makes multi-year extensive risk assessments costly in terms of calculation power and time. In order to overcome this problem an Artificial Neural Network (ANN) was trained on a dataset of simulations generated by JRODOS for a reference arbitrary plant location at KIT Campus North, assuming a constant release source term. The network learns the complex, non-linear relationship between meteorological input parameters and the resulting radiological dose rate maps. This surrogate model accurately reproduces the dispersion consequences and reduces the analysis time from minutes to seconds. Additionally, the model can provide more information about dispersion span by considering a larger timeframe dataset and weather conditions around the plant. This acceleration allows for the consideration of multiple calendar years which strengthens emergency preparedness by enabling faster evaluation of potential outcomes under a wide range of weather conditions. Further results will be shown and discussed in the paper.

KEYWORDS
Severe Accident, JRODOS, Machine Learning, Neural Network, Radionuclide Dispersion

1. Introduction

In the event of radiological dispersion caused by the nuclear emergencies such as severe accidents, priority of the authorities is to accurately predicts the trajectory of the release and put the emergency plans into action. For this purpose, regulatory bodies rely on advance decision support systems. The European Java based Real-time Online DecisiOn Support System (JRODOS) [1], developed by the Karlsruhe Institute of Technology (KIT), stands as European standard tool for regulators and it is currently operational in many countries. JRODOS integrates meteorological forecasts by including source term and complex atmospheric dispersion models to calculate radiological dispersion over a selected domain in any place over the globe and draw conclusions for protective measures such as sheltering, evacuation, iodine tablet distribution.

JRODOS relies on the Gaussian puff models and Lagrangian particle models to resolve and simulate radioactive plume dispersion and how the cloud interacts with topography and wind fields. Even though simulation results bring accurate calculation, these physical calculations can be computationally expensive. Especially considering statistical analysis which involves thousands of individual analyses on selected domain is highly time consuming. In a previous work [2] it was showed that in order to create a dispersion map to better understand possible consequences around the selected plant by including large span of weather

conditions, significant amount of time is required and yet the results were still not mature enough to draw a generic conclusion on the selected region.

In order to create a connection between computational speed and physical accuracy, advancements on machine learning applications offers promising alternative of data-driven Artificial Neural Network (ANN) models. The network can learn complex behavior between weather parameters by training an ANN with precalculated numerous of simulation. Despite the dispersion models in the JRODOS or in any other dispersion code, trained ANN does not solve physical equations, but it performs matrix multiplications to predict the phenomena and this brings significant speed boost to the simulations.

Previous work on ANN applications focused on spatial dose rate interpolation and integration of the virtual reality in order to reduce exposure of doses inside facilities [3]. Expanding from facility level to environmental releases, estimation of the effective doses in case of Loss of Coolant Accidents also predicted by using multi-layer perceptron models and dose predictions showed acceptable up to certain level [4]. After that, radiological releases on NPP level were further investigated by taking advantage from GPU based accelerations on multi-layer perceptron to reduce training time [5]. More recently, focus has been given to the capturing the temporal dynamics of radioactive plumes and tracking extreme points on the grid and exploration whole body doses [6]. Furthermore, integration of machine learning with established code like HotSpot has enabled to investigate different severe accident scenarios and to predict effective doses to make comparison between different transients [7].

In this study, an ANN model has been developed and trained with pre-defined datasets of JRODOS simulations. After construction of the ANN model, validation of the prediction has been performed with test cases and the capability of the model has been proven. The selected base case in JRODOS and the methodology of the ANN structure and training procedure is given Section 2. After that comparison between ANN model and JRODOS simulations are presented for the evaluate model prediction capability and conclusion and next steps are described afterwards.

2. Methodology of Artificial Neural Network Model Construction

The initial step in constructing an ANN is the establishment of a database to train the model. A set of 1000 JRODOS simulation have been completed to create a database around the selected NPP location. A fictitious power plant location in the KIT Campus North has been selected and grid has been established within a 100 km radius. Simulations were for a time period of 24 hours with 30-minute time steps by using RIMPUFF dispersion model. The starting time of the dispersions in each simulation randomly selected within the calendar year 2021. Early countermeasures and prevention actions have not been considered for the simulations and the stack height of the release point has been selected as 150 meters. Weather data for the simulations has been provided by the American NOMAD servers which are hosted by the U.S. National Oceanic and Atmospheric Administration. Source term has been selected by the one of the pre-defined constant releases in the bank of the JRODOS library. Details about the released isotopes are given in the Table I. All isotopes are defined to be released within a single time interval (30 minutes) in the simulations.

Table I. Total released activity to the atmosphere within 30 minutes time interval.

Isotope	Activity (Bq)	Isotope	Activity (Bq)
Cs-134	1.1E+15	Kr-87	9.0E+15
Cs-136	4.7E+14	Kr-88	1.8E+17
Cs-137	6.5E+14	Sr-90	4.7E+13
I-131	9.5E+15	Sr-91	6.4E+14
I-132	1.3E+16	Te-131m	1.1E+15
I-133	1.5E+16	Te-132	1.3E+16
I-135	7.0E+15	Xe133	4.6E+18
Kr-85	2.4E+16	Xe-135	2.1E+18
Kr-85m	1.5E+17		

Numerical weather prediction files, known as GRIB files, from the American NOMAD servers provide global weather data with a resolution of 0.5 degrees in latitude and longitude grid [8]. Files contains complex and non-standardized structures of data as well as vertical layers of atmosphere over the whole globe. In order to create a basic model to test the methodology, the number of parameters selected has been kept as low as possible. In this way, the ANN model parameter size and training effort has been kept as minimum. The parameters that have been selected for investigation are as follows: the U-Component and V-Component of the wind at the level of the stack height; the temperature of the atmosphere at the stack height level and surface pressure level. These parameters have been selected from each of 1000 simulations that have been performed to create a simulation database. Since the single grid point is not enough to capture the parameter behavior, selection of parameters were extracted over the KIT Campus Nord spatial domain. GRIB files have resolution of 0.5 degrees, which corresponds to the around 50 km size of meshes. A 5x5 grid (two neighbors in every direction) has been used to extract the parameters every grid point, and feature matrix has been constructed for each time step. The general layout of the matrix is given in Equation 1. Each row in the matrix corresponds to a single time line over the 25 grid points for four selected parameters.

The total effective gamma dose rate results of the performed simulations have been utilized to establish the result matrix, which is given in Equation 2. JRODOS can provide wide range of dispersion analysis results which can be used in the machine learning algorithms. However, for the purpose of the simplicity, only a global parameter of the total effective gamma dose rate has been selected. Each simulation has been subdivided into 48 snapshot points of the time step, and each 30-minute time step points have been considered as an independent sample. In this way, total number of the result with their corresponding time stamp increased to 48.000 for 1000 simulation. After that, 90% of the simulations and the corresponding weather parameters have been separated to create a training set and remaining 10% of the data has been used as a test set in order to evaluate the prediction capability of the model after trained on the training set.

Following the construction of the matrices, the multilayer perceptron regression model is established. The input layer consists of 100 nodes, the function of which is to store selected weather parameters in the feature matrix. Afterwards, three hidden layers follows with 512, 1024 and 2048 nodes and the final output layer consist of 8056 nodes. These nodes at the output layer corresponds each mesh point in the described grid over the KIT Campus North domain. Each operation in the hidden layers applies rectified linear unit (ReLU) activation function to the parameters to catch up the non-linear behavior of the database.

The training operation of the model starts with feeding input matrix from the rows of the feature matrix. In order to ensure that gradient updates of the selected parameters are maintained at a comparable level, it is also necessary to normalize the input parameters. Since the pressure values are in the range of six-digit

numbers and temperature levels are in one or two digits at most, their contribution to the results with equal gradients will not be the same and consequently, the model can have unrealistic biases for certain parameters. After operation with their assigned weights and activation function, all parameters pass through to the final output layer to construct the total effective gamma dose rates in each mesh point on the grid. Subsequently, a comparison is made between the ANN prediction and the results of the JRODOS simulation, which are stored in the result matrix. The loss of the model prediction is then determined. Following backward pass operation applies optimization algorithm to update the weights of the approximately 19 million parameters in the network. This process is repeated iteratively in an attempt to minimize the loss function. General layout of the network structure is given in Figure 1.

$$X = \begin{matrix} u_{t_0}^{0} \dots u_{t_0}^{24} \\ \vdots \\ u_{t_43199}^{0} \dots u_{t_43199}^{24} \end{matrix} \quad \begin{matrix} v_{t_0}^{0} \dots v_{t_0}^{24} \\ \vdots \\ v_{t_43199}^{0} \dots v_{t_43199}^{24} \end{matrix} \quad \begin{matrix} T_{t_0}^{0} \dots T_{t_0}^{24} \\ \vdots \\ T_{t_43199}^{0} \dots T_{t_43199}^{24} \end{matrix} \quad \begin{matrix} P_{t_0}^{0} \dots P_{t_0}^{24} \\ \vdots \\ P_{t_43199}^{0} \dots P_{t_43199}^{24} \end{matrix} \tag{1}$$

$$y = \begin{matrix} dose_{t_0}^{mesh_0} & \dots & dose_{t_0}^{mesh_8055} \\ \vdots & \vdots & \vdots \\ dose_{t_43199}^{mesh_0} & \dots & dose_{t_43199}^{mesh_8055} \end{matrix} \tag{2}$$

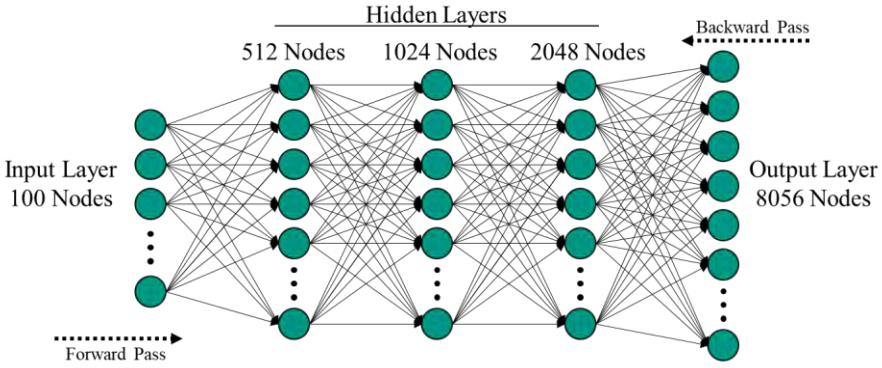

Figure 1. Structural layout of the Neural Network for the JRODOS surrogate model.

Furthermore, a validation strategy has been implemented to the ANN structure to check the model estimations in every training loop to evaluate the model performance. The standard application of the ANN structure involves the utilization of the training dataset, with the training loss being calculated using known historical data. However, trained model may calculate a low level of training loss and it may estimate unrealistic results for the test dataset. One potential explanation for this phenomenon could be an excessive number of iterations over the training set, leading to overfitting of the known data. In order to overcome this problem, at the end of every one full pass-through of the training set, the averaged mean squared error of the entire test set has been saved as validation loss and it was tracked over the ongoing loops. This result gives the evolution of the model to predict the test cases and gives the performance of the ability to predict new dataset that the model has never seen before. Early stopping functionality, which tracks the validation loss, automatically terminates the training loops when model began the overfit.

3. Results

The initial strategy of the training resulted in a model that predicts safe averages over the entire grid but fails to captures extreme points. Due to fact that the radiological dispersion plume only gets peak points on very limited number of mesh points over the domain, the rest of the points on the grid receives a zero or a very small dose value. For this reason, initial guess of zeros or very small numbers for the entire grid provides reasonable level of loss value in general and the model does not search for any improvement in order to catch peak points.

In order to overcome this issue during training a logarithmic transformation was applied to the target output matrice (y) in order to teach gradients and shape of the dose map over the grid effectively without being overwhelmed between magnitude differences between peak points and the overall average. Specifically, a log(1+x) function was utilized to handle zero-value total effective gamma dose rates, preventing undefined negative infinity errors. Furthermore, a dynamic penalty weighting factor has been calculated based on the magnitude of the actual target value and this weight has been multiplied by mean square error for loss calculation in the training loops. Consequently, the model has been punished heavily for underestimating high magnitude dose rate peaks and this approach forces the ANN not to pass extreme peak points.

The training of the model has been established by using CPU and GPU units separately. The training has been completed within a timeframe of approximately 20 hours, utilizing an 12th generation Intel i9-12900 CPU. It took around 15 minutes with a NVIDIA GeForce GTX 1050 Ti GPU. The total effective gamma dose rate prediction of the ANN model has been achieved in approximately 0.08 seconds. This is very fast compared to the JRODOS simulations during the production of training cases where each simulation required around 2 minutes and 15 seconds.

Regarding the temporal mechanics of the model, the current ANN model is designed as a direct, instantaneous mapping function rather than a time-series forecasting model. The ANN predicts the spatial dose rate map at any specific time step t utilizing the meteorological conditions and source term parameters available at that exact time t. It does not utilize a sliding time window or a historical memory of meteorological conditions. Because the network architecture is a standard Feedforward Neural Network (Multi-Layer Perceptron), it treats each temporal slice independently. Consequently, the predicted dose distribution at time t is calculated strictly as a localized function of the atmospheric and release state at that moment.

In order to evaluate the ANN dynamic performance over a continuous release scenario, a full 24-hour simulation sequence was selected from the database for direct comparison, given in Figure 2. The X-axis of the plotted figures corresponds to the meshing points of the JRODOS grid at the selected KIT Campus North NPP location, while the Y-axis corresponds to the total effective gamma dose rate. The results demonstrate a good agreement between the JRODOS simulations and the ANN predictions in terms of level of dose rate. ANN successfully captures the overall magnitude of the dose rates as well as the complex spatial distribution over the computational grid. The point-by-point mesh comparisons indicate that the neural network accurately reproduces the transport and dispersion patterns as they evolve over the 24-hour period.

In order to represent the performance of the model in general, the predictions of the ANN model and the JRODOS results of a randomly selected cases from the test sets are presented in Figure 3. The model predicts elevated dose values where the JRODOS simulations registers a plume and dose reading. This indicates that the model has internalized the complex and non-linear behavior of the dispersion dynamic. The model successfully produces the plume's footprint however, the level of dose rates is often overestimated. Since the weighting factor are applied where the dose peaks are read for the losses, an over estimation can be seen at the peak points between 0-1000 mesh points for case #1338 and #336 in the Figure 3. Last case #1952 shows the highest dose reading levels among the randomly selected cases. The number of readings in that

case over the grid is not crowded as other cases and this shows that plume did not travel too far but stays around the NPP. Consequently, very high dose rates compare to other cases have been recorded for the case #1952. Since this kind of release cases are rare among the training set, the ANN model could not catch this scenario and overlooked the penalty loss on this case as long as the overall average is getting better in total.

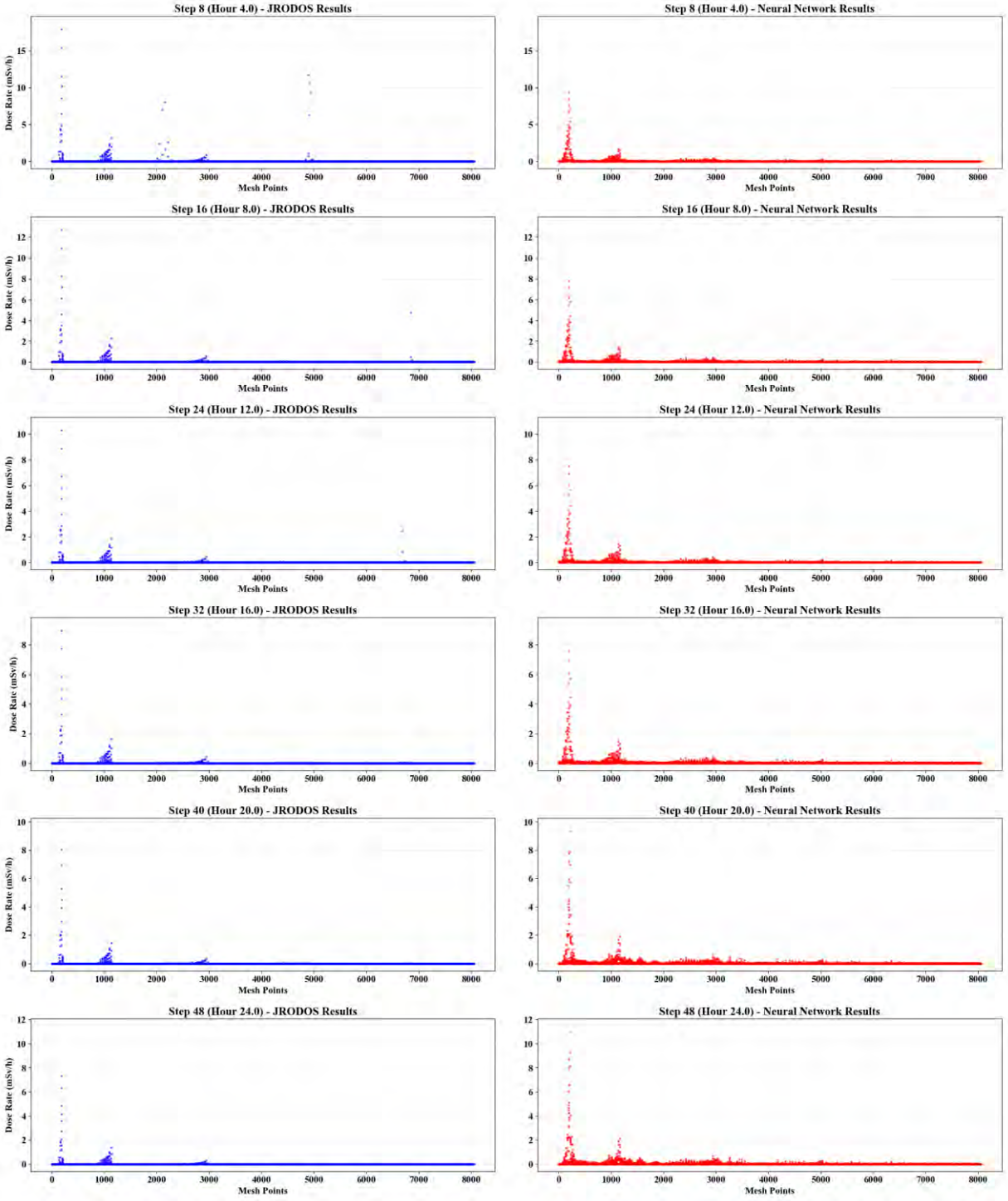

Figure 2. Comparison of selected 24h simulation steps between JRODOS and Neural Network predictions.

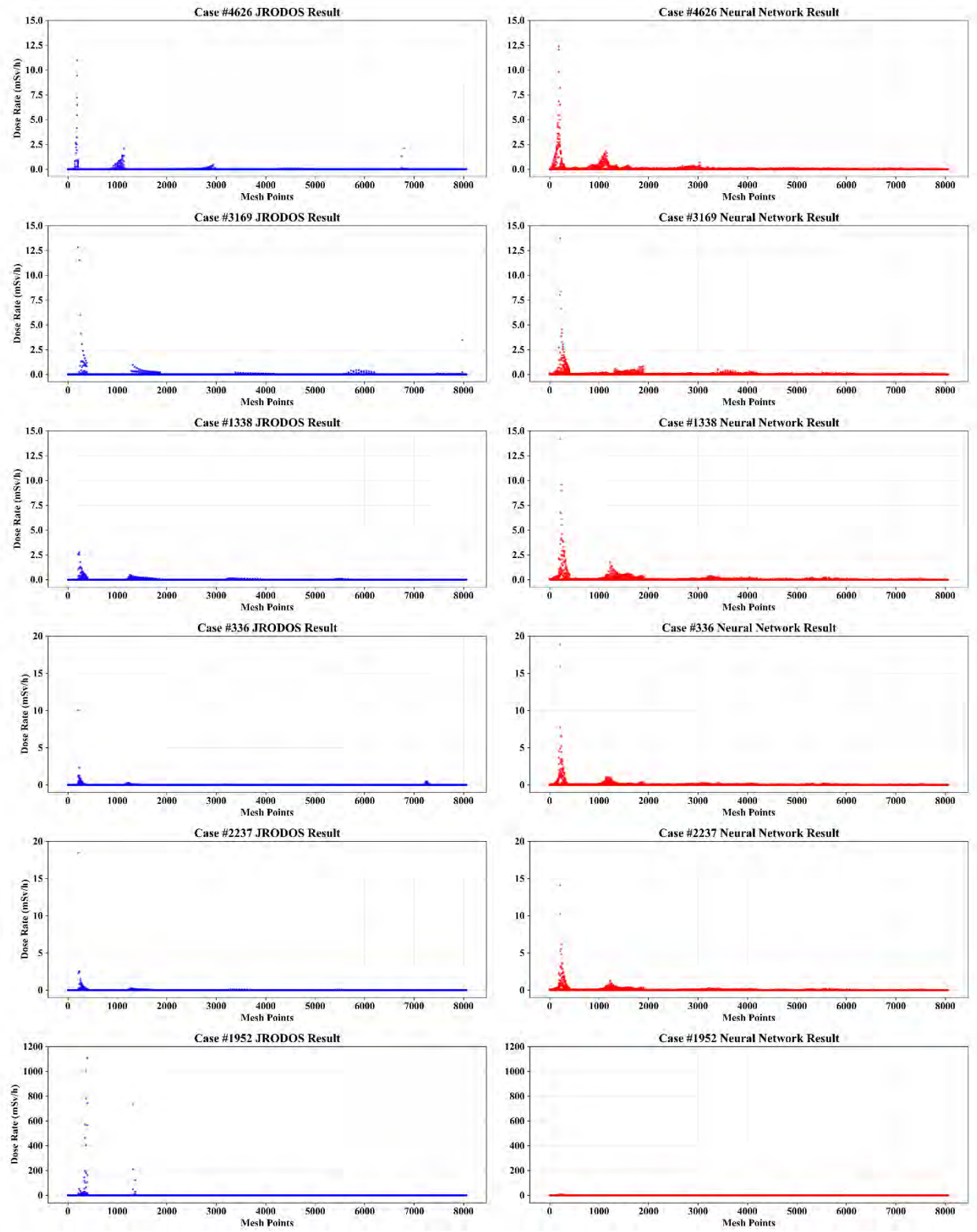

Figure 3. Comparison between JRODOS simulation results and Neural Network predictions for random selected time instants of the evaluation cases.

The application of the ANN model demonstrated that it provides significant speed up for dispersion calculations. This achievement is not only important to rapidly evaluate possible consequences over the considered regions, but it also provides ability to create massive number of calculations to enlarge the result databank in order to take into account larger span of weather conditions. Since the beginning of the 20th century human activities plays an important role in the dynamics of the atmosphere, meteorological conditions are rapidly changing and new conditions need to be taken into account to incorporate current and possible future conditions of the atmosphere. In order to show rate of changes in the atmosphere; weather parameters extracted from European Climate Data Store Copernicus [9] and average of the temperature for month of February in Figure 3 is pictured over the KIT Campus Nord region enclosed by latitude 48°-50° North and longitude 7°-10° East coordinates for each calendar year from 1940 to 2025. It can be seen that average temperature is getting higher and hottest recordings on average in February are being observed. This might end up result of dispersion which has never been unpredicted before considering recorded conditions in history. All those rates of changes will continue to contribute to the variation of extreme weather conditions in the future. Dispersion analyses based on the previous recorded conditions on the considered region will not be enough to correctly determine consequences. For this reason, including large variety of conditions and extrapolation will be necessary by taking into account expected future conditions to create more comprehensive emergency plans. Consequently, the computational speed advantage of ANN models will be an important asset for expanding risk databases and conducting forward-looking emergency planning.

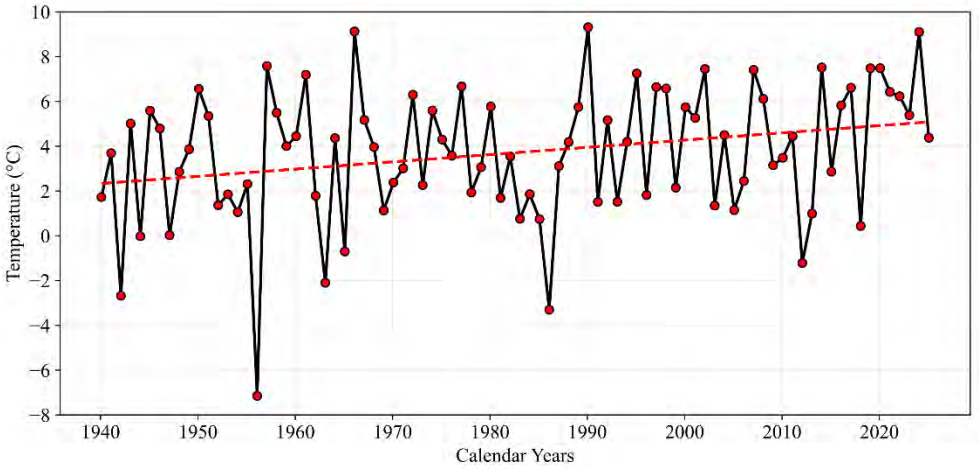

Figure 3. Monthly average of temperatures for February in the KIT Campus North.

4. Conclusion

A calculation methodology based on the use of ANN has been developed to speed up the radionuclide dispersion analysis. The ANN model has been trained with built training database and validated against the JRODOS using by the test samples. Since the radioactive isotope dispersion into the atmosphere is the last step to evaluate public and environmental safety during severe accident progression, estimation of the transfer of the particles provides roadmap to better preparation of emergency planning and mitigation strategies. The ANN application accelerates simulation process significantly and, in this way, large number of weather conditions can be utilized to picture possible consequences on the selected region. It is clear that the conditions in the atmosphere rapidly changing and this method can be used to predict future conditions and produce a dispersion analysis and outcome map.

Future improvement on the ANN model will focus on source term release data, which are derived from severe accident codes, in order to refine the result space for nuclear applications. This enhancement is particularly important for Small Modular Reactors which are intended to be deployed diverse industrial and public locations. Environmental Impact Assessments and Emergency Planning and Response strategies can be enhanced significantly by utilizing ANN models to accelerate the evaluation of radiological dispersion analyses.

It can be stated that, prediction capability of ANN models is as good as the data quality used for the training. Consequently, the current model generally overlooks the rare and extreme dispersion scenarios over the region. Expanding both training database and considered weather parameters and iteration of the model with enlarged database, the prediction accuracy of ANN will be better equipped to recognize and accurately predict these rare cases.

REFERENCES

[1] I. Ievdin, D. Trybushny, M. Zheleznyak, and W. Raskob, "RODOS re-engineering: aims and implementation details," *Radioprotection*, vol. 45, no. 5, pp. S181–S189, 2010, doi: 10.1051/radiopro/2010024.

[2] O. Murat, F. Gabrielli, and V. H. Sanchez-Espinoza, "Source term dispersion analysis and construction of the probabilistic dispersion map around the Peach Bottom Unit-2 plant using the ASTEC and JRODOS codes," *Annals of Nuclear Energy*, vol. 215, p. 111277, Jun. 2025, doi: 10.1016/j.anucene.2025.111277.

[3] A. C. A. Mól and C. A. F. Jorge, "Radiation dose rate map interpolation in nuclear plants using neural networks and virtual reality techniques," *Annals of Nuclear Energy*, 2011.

[4] C. M. D. N. A. Pereira, R. Schirru, K. Gomes, and J. L. Cunha, "Artificial Neural Networks for Radiation Dose Prediction in Nuclear Emergencies-Preliminary Investigations," in *Proceedings of 2016 International Conference on Modeling, Simulation and Optimization Technologies and Applications (MSOTA2016)*, Xiamen, China: Atlantis Press, 2016. doi: 10.2991/msota-16.2016.98.

[5] F. S. M. Desterro, M. C. Santos, K. J. Gomes, A. Heimlich, R. Schirru, and C. Mna. Pereira, "Development of a Deep Rectifier Neural Network for dose prediction in nuclear emergencies with radioactive material releases," *Progress in Nuclear Energy*, vol. 118, p. 103110, Jan. 2020, doi: 10.1016/j.pnucene.2019.103110.

[6] M. A. G. S. Filho, M. C. Santos, and C. M. N. A. Pereira, "Exploring LSTM-based prediction for radioactive plume atmospheric dispersion in nuclear power plant emergencies: A preliminary study," *Nuclear Engineering and Design*, vol. 419, p. 112982, Apr. 2024, doi: 10.1016/j.nucengdes.2024.112982.

[7] M. Najar, N. N. M. Maglas, H. Wang, Z. Qiang, and M. M. M. Ali, "Enhancing radiological risk evaluation through AI and HotSpot code integration: A Comparative study of LOCA and SGTR," *Radiation Physics and Chemistry*, vol. 230, p. 112580, May 2025, doi: 10.1016/j.radphyschem.2025.112580.

[8] G. K. Rutledge, J. Alpert, and W. Ebisuzaki, "NOMADS: A Climate and Weather Model Archive at the National Oceanic and Atmospheric Administration," *Bull. Amer. Meteor. Soc.*, vol. 87, no. 3, pp. 327–342, Mar. 2006, doi: 10.1175/BAMS-87-3-327.

[9] Copernicus Climate Change Service (2023): ERA5 monthly averaged data on single levels from 1940 to present. Copernicus Climate Change Service (C3S) Climate Data Store (CDS)., doi: 10.24381/cds.f17050d7.

A Deep Learning Surrogate Model for Rapid Prediction of Atmospheric Radioisotope Dispersion

12th European Review Meeting on Severe Accident Research Conference
ERMSAR2026
May 18-22, 2026 - Madrid, Spain

Onur Murat, Fabrizio Gabrielli, Victor Hugo Sanchez Espinoza
Karlsruhe Institute of Technology
Institute for Neutron Physics and Reactor Technology
Reactor Physics and Dynamic Group
Hermann-von-Helmholtz Platz 1, 76344 Eggenstein-Leopoldshafen

Content

1. Motivation
2. Tool: JRODOS
3. Artificial Neural Network (ANN) Surrogate Approach
4. Database & Setup
5. ANN Architecture and Training
6. Results
7. Importance of ANN Application
8. Conclusion

Motivation

- In the event of a severe accident, emergency response authorities require fast and accurate predictions of radionuclides.
  - Emergency Management Guidelines
  - Identification of Emergency Planning Zones
- Comprehensive risk assessments covering multiple calendar years and thousands of weather scenarios are computationally prohibitive.

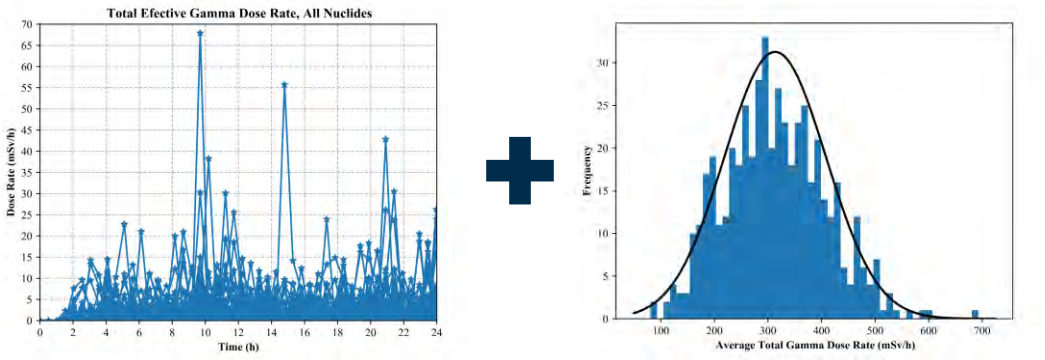

JRODOS Simulation of large batches requires
years of CPU time

60,000 simulation + Central Limit Theorem
25 days CPU time

- A surrogate model is needed that can reproduce the Code (JRODOS) quality dispersion maps in a fraction of the time.

What is JRODOS?

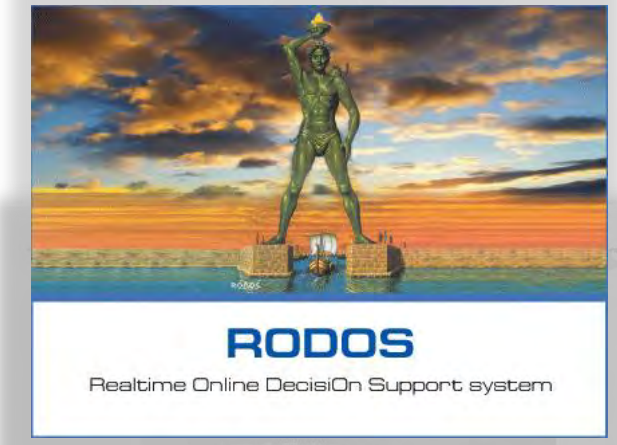

- JRODOS (Java-based Real-time Online Decision Support) System is the European standard tool for radiological emergency management, currently operational in regulatory bodies across many countries.
- The system integrates meteorological forecast data with user-defined source terms and advanced atmospheric dispersion models to calculate radionuclide transport and deposition over any region on the globe.
- Simulation outputs guide protective actions such as population sheltering, evacuation zone definition, and iodine tablet distribution.
- JRODOS relies on physically rigorous Gaussian puff and Lagrangian particle models, which accurately capture plume behavior and topographic interactions but at significant computational cost.

Artificial Neural Network (ANN) Surrogate Approach

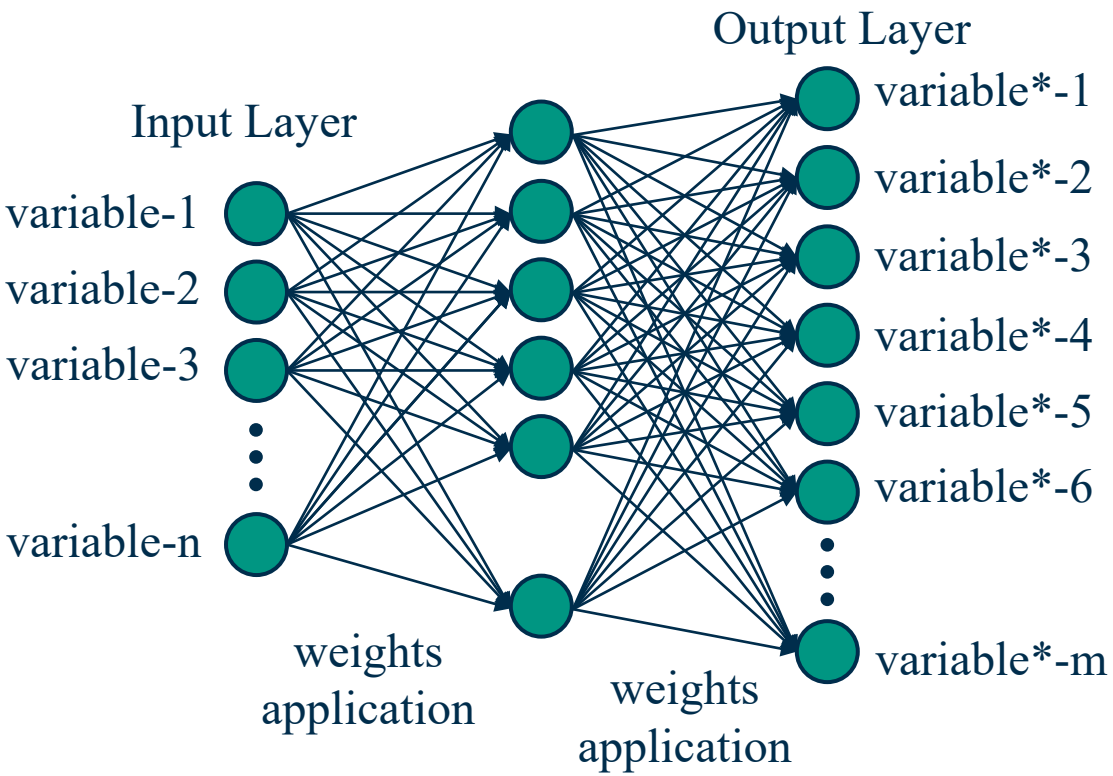

- JRODOS or any other dispersion tool deals with differential equations, wrappers and libraries.

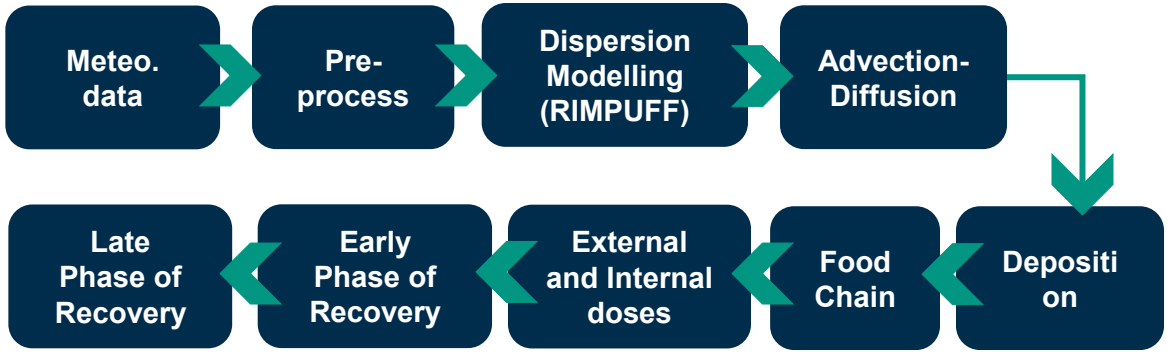

- An Artificial Neural Network (ANN) can be trained on a large database of pre-computed JRODOS simulations.
  - No equations are solved at runtime, only a series of fast matrix multiplications
- This acceleration makes it feasible to evaluate dispersion consequences across thousands of weather scenarios and multiple calendar years

Database and Setup

Isotope	Activity (Bq)	Isotope	Activity (Bq)
Cs-134	1.1E+15	**Kr-87**	9.0E+15
Cs-136	4.7E+14	**Kr-88**	1.8E+17
Cs-137	6.5E+14	**Sr-90**	4.7E+13
I-131	9.5E+15	**Sr-91**	6.4E+14
I-132	1.3E+16	**Te-131m**	1.1E+15
I-133	1.5E+16	**Te-132**	1.3E+16
I-135	7.0E+15	**Xe133**	4.6E+18
Kr-85	2.4E+16	**Xe-135**	2.1E+18
Kr-85m	1.5E+17		

- 1,000 JRODOS simulations was generated using a fictitious NPP location at KIT Campus North.
  - 100 km radius
  - 30 minutes time-steps over 24 hours simulation windows
- Radionuclides discharged into the atmosphere within a single 30-minute interval from a stack height of 150 meters.
- Weather data from U.S. NOAA NOMADS servers in GRIB format at 0.5-degree spatial resolution.
  - Random sampling of analysis starting time in year 2021
- 4 atmospheric parameters were extracted over a 5×5 grid centered on the plant.
  - U, V component of wind
  - Temperature
  - Surface pressure
- The dataset was divided into **90% for training** and **10% for testing.**

ANN Architecture and Training 1/2

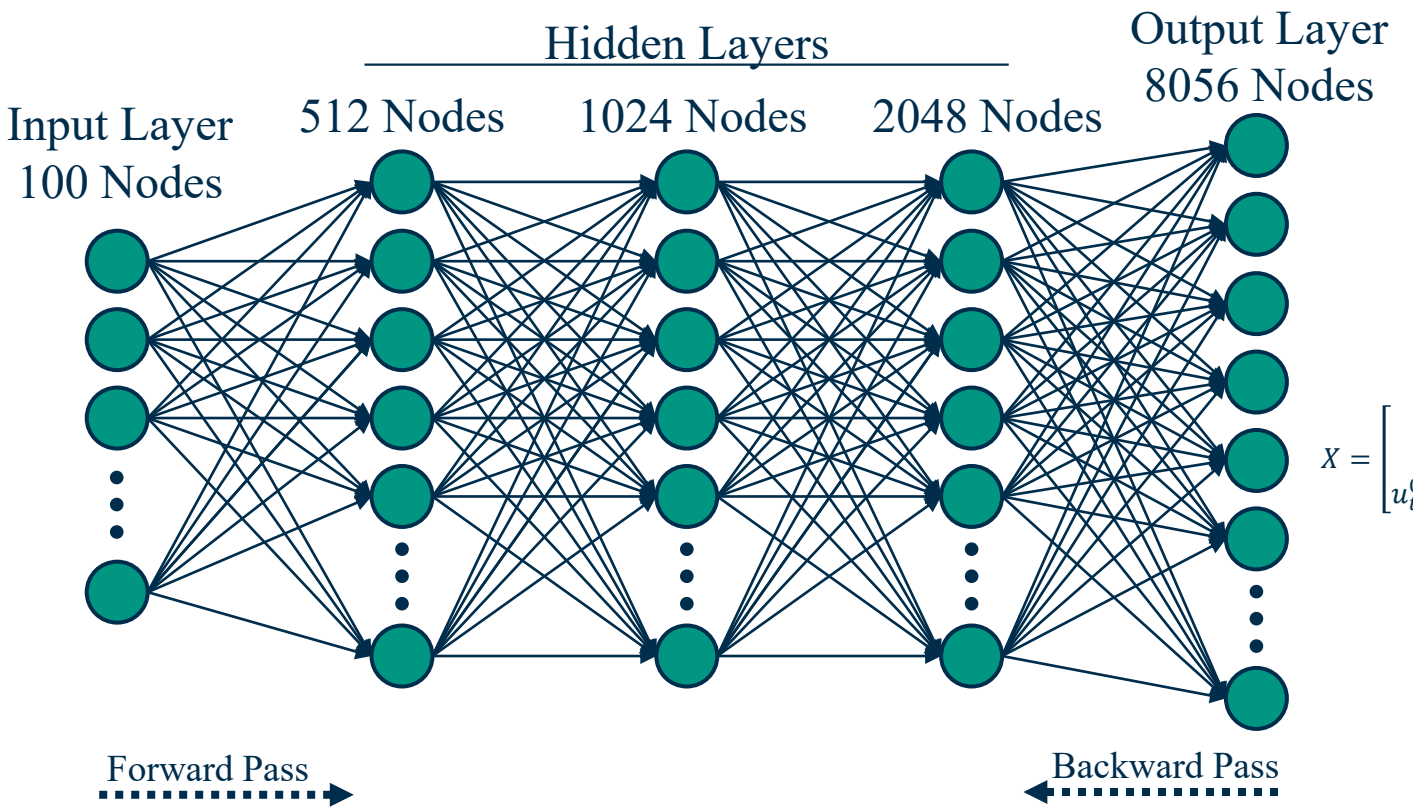

- Multilayer Perceptron (MLP) regressor with around 19 millions trainable parameters.
  - 100 nodes for meteorological input.
  - 8,056 output nodes for dose rate values corresponding to every mesh.

$$X = \begin{bmatrix} u^{0}_{t_0} \dots u^{24}_{t_0} & v^{0}_{t_0} \dots v^{24}_{t_0} & T^{0}_{t_0} \dots T^{24}_{t_0} & P^{0}_{t_0} \dots P^{24}_{t_0} \\ \vdots & \vdots & \vdots & \vdots \\ u^{0}_{t_47999} \dots u^{24}_{t_47999} & v^{0}_{t_47999} \dots v^{24}_{t_47999} & T^{0}_{t_47999} \dots T^{24}_{t_47999} & P^{0}_{t_47999} \dots P^{24}_{t_47999} \end{bmatrix}$$

$$y = \begin{bmatrix} dose^{mesh_0}_{t_0} & \dots & dose^{mesh_8055}_{t_0} \\ \vdots & \vdots & \vdots \\ dose^{mesh_0}_{t_47999} & \dots & dose^{mesh_8055}_{t_47999} \end{bmatrix}$$

ANN Architecture and Training 2/2

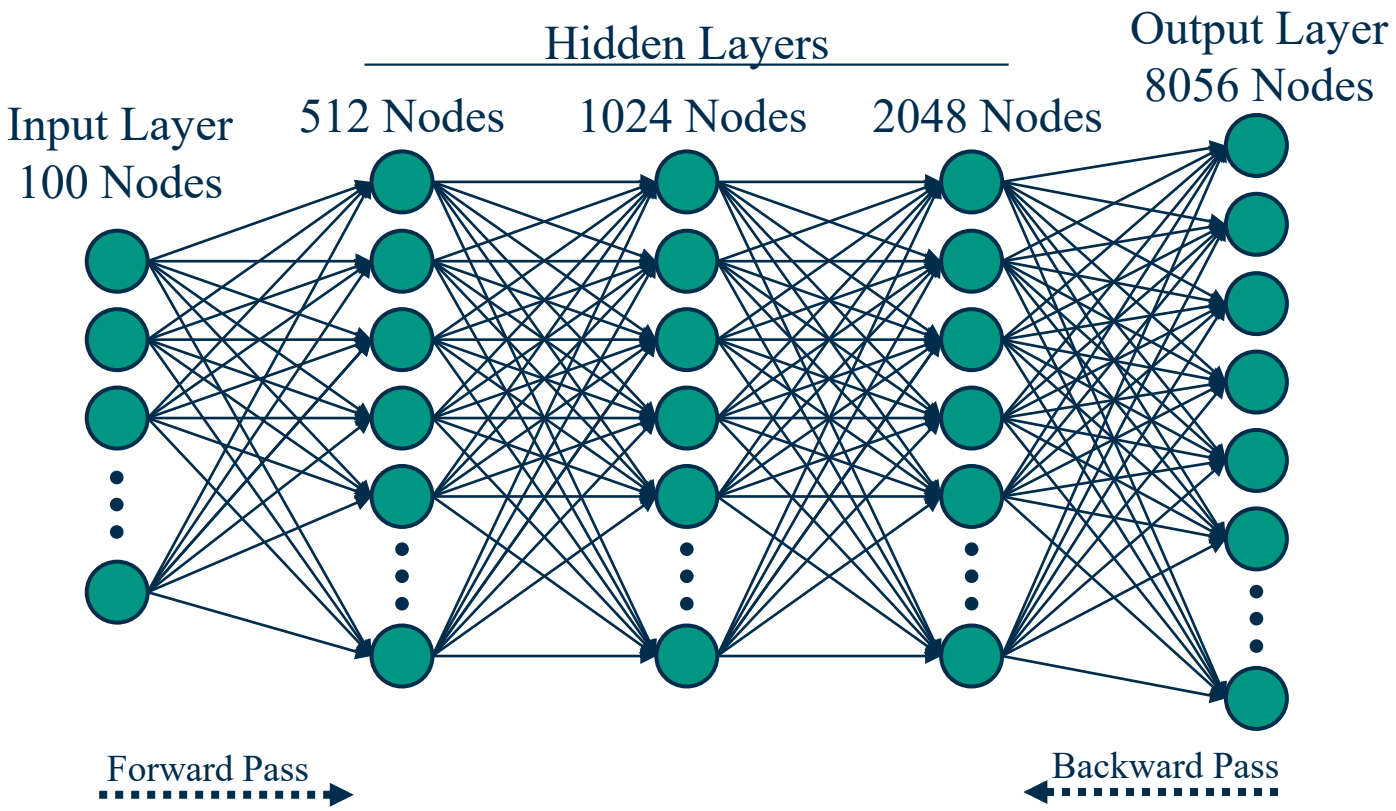

- ReLU activation functions are applied throughout the hidden layers to capture the non-linear behavior of the dispersion physics.
- Input parameters are normalized to prevent large-magnitude values like surface pressure from dominating gradient updates.
- Overfitting prevention: early stopping based on validation loss.

intel ~20 hours

NVIDIA ~15 minutes

Training Challenges and Solutions

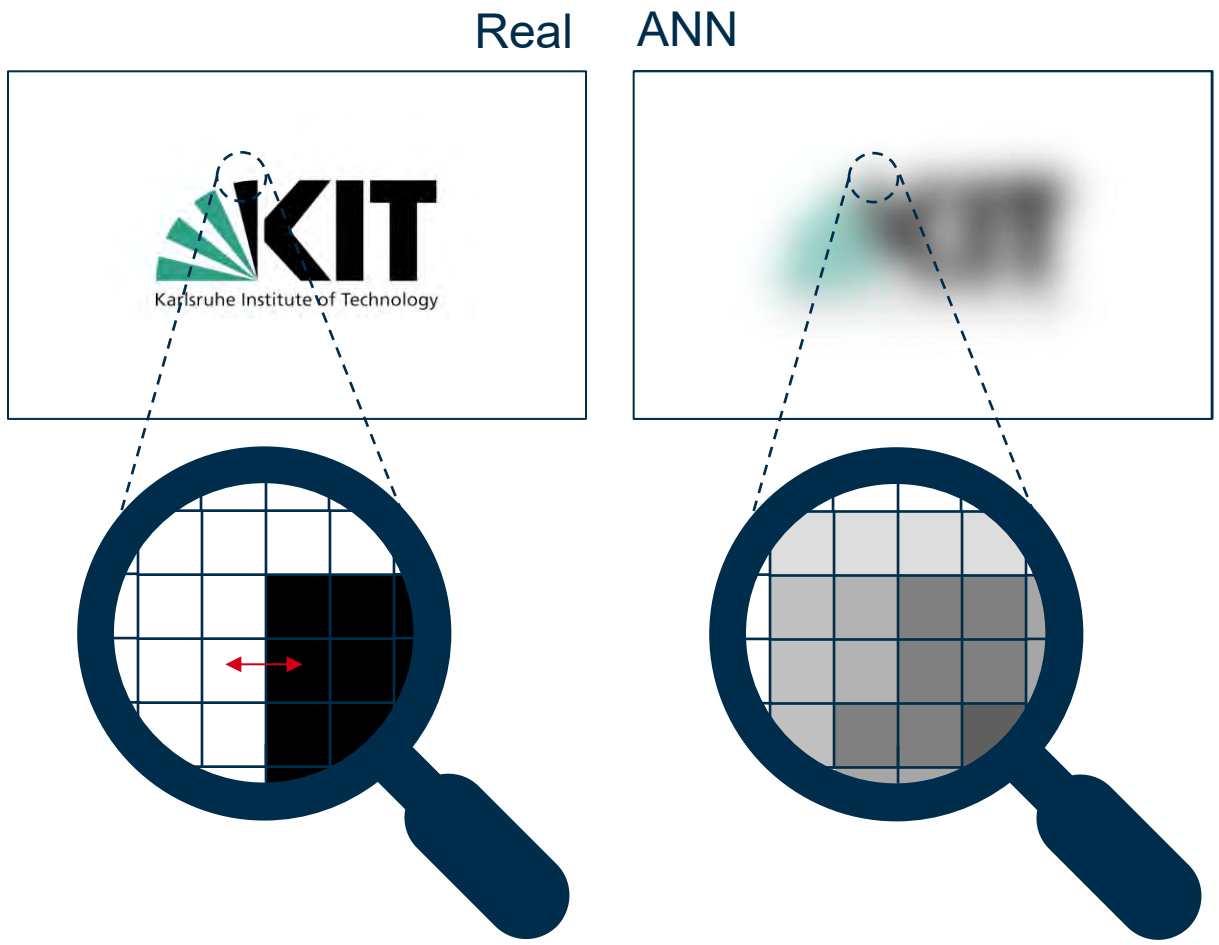

- Radioactive dispersion affects only a small fraction of the grid at any time.
  - Most grid points have near-zero dose → model learns to predict zeros.
- **Logarithmic scaling:** compressing the dynamic range and allowing the network to learn the shape.

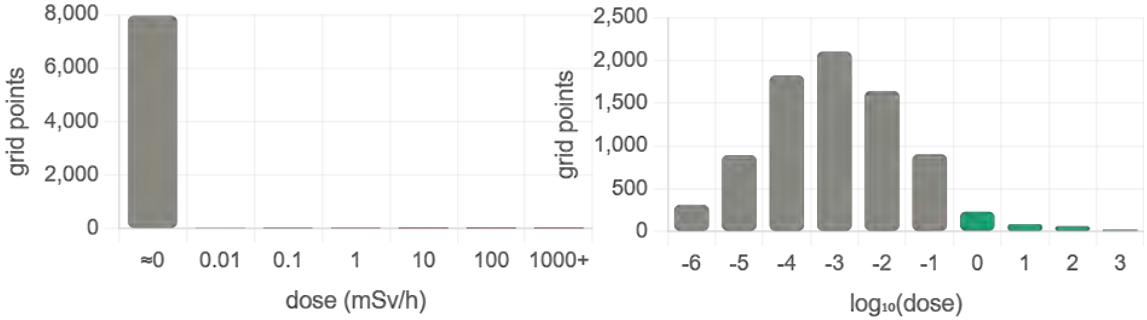

- **Penalty weighting:** penalty for underestimation of peak dose points.

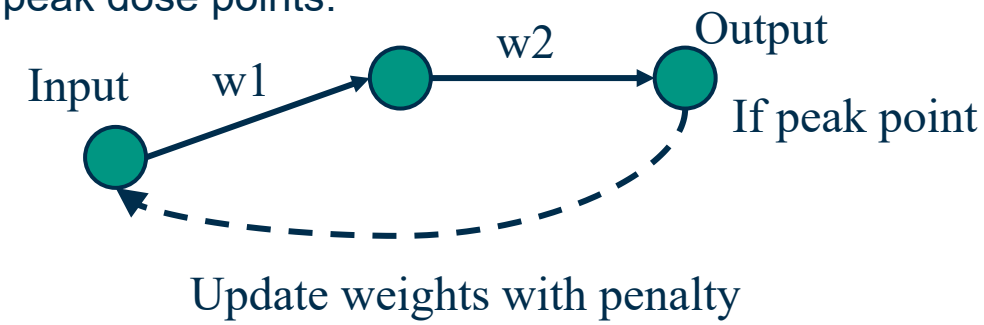

Results: JRODOS vs ANN Prediction

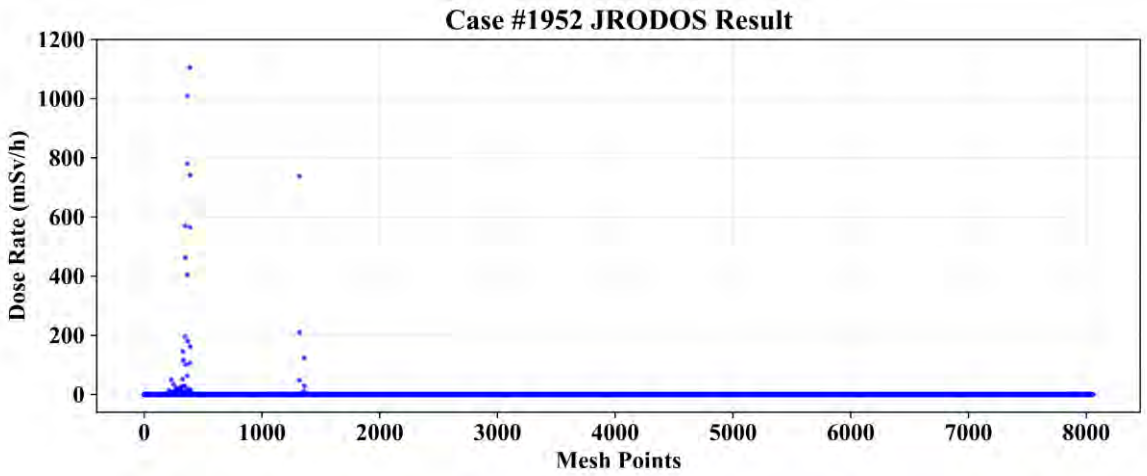

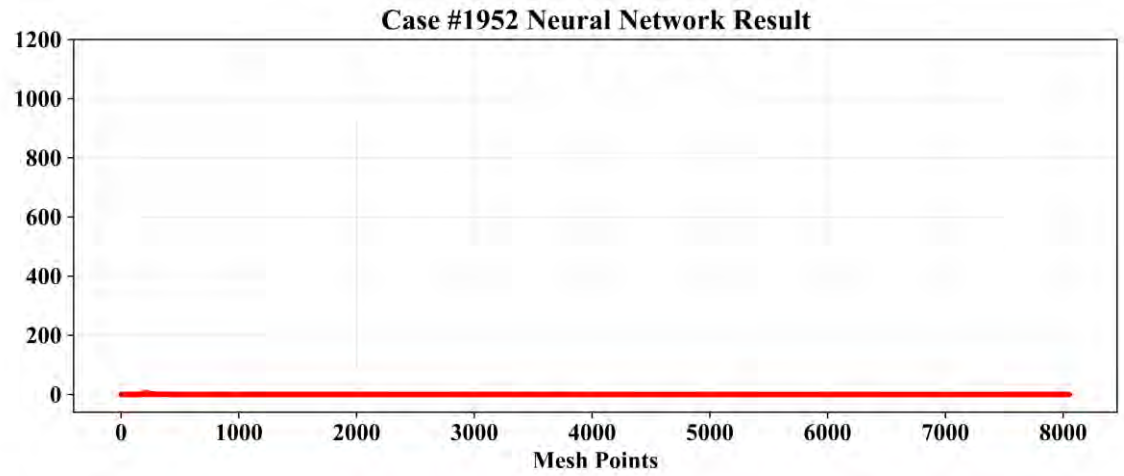

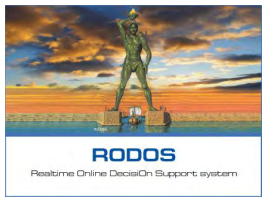

~135 seconds

ANN **~0.08 seconds**

- The ANN model successfully identifies the spatial location and general footprint of the radioactive plume across the majority of test cases.
- For most test cases, dose rate predictions show good agreement with JRODOS results, with some tendency to overestimate peak values which is consequence of the penalty weighting.
- Model currently fails to capture cases where the plume remains close to the release point and does not travel far result in very high localized dose readings.

Why is it important? Climate Change

PROGRAMME OF THE EUROPEAN UNION

opernicus
Europe's eyes on Earth

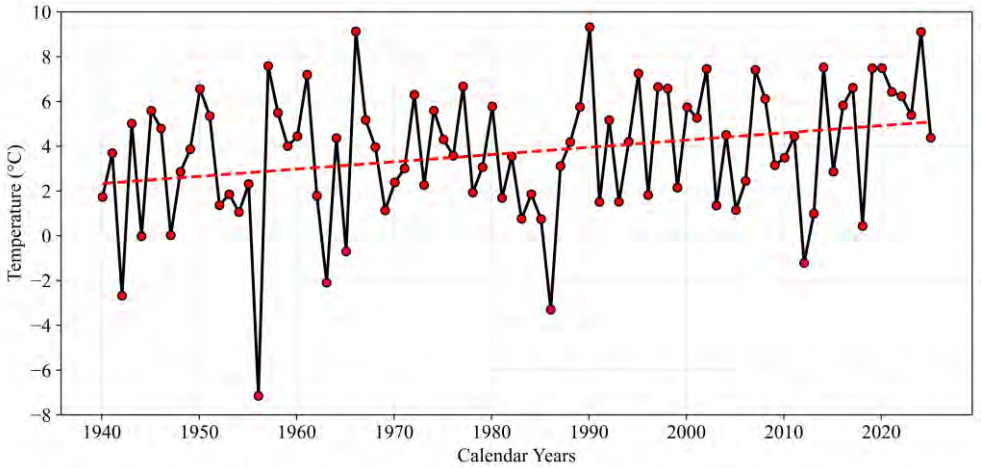

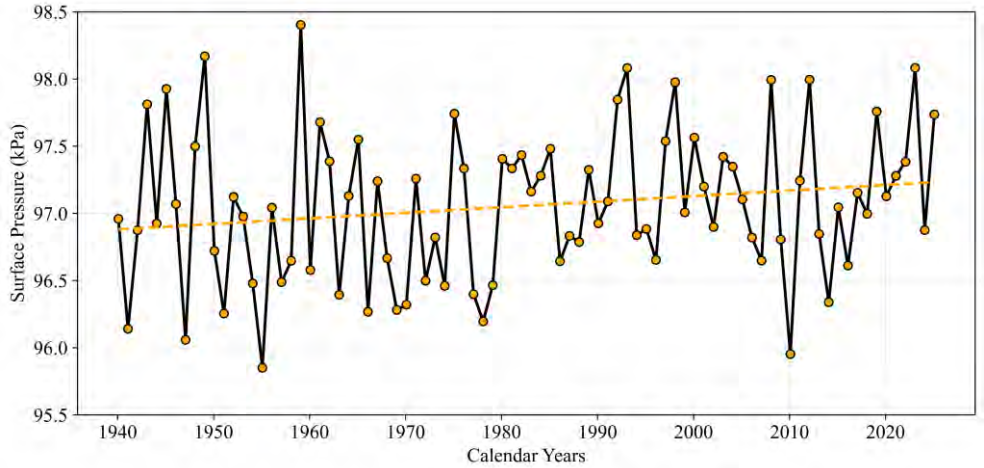

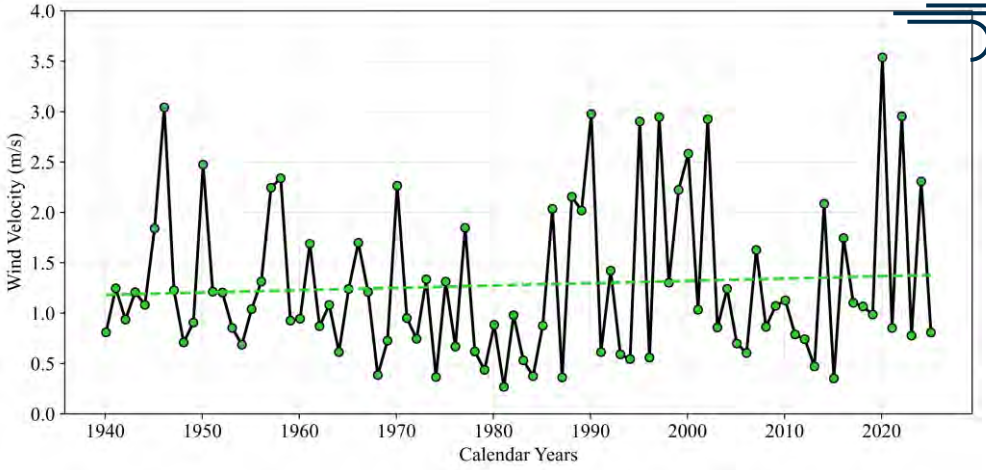

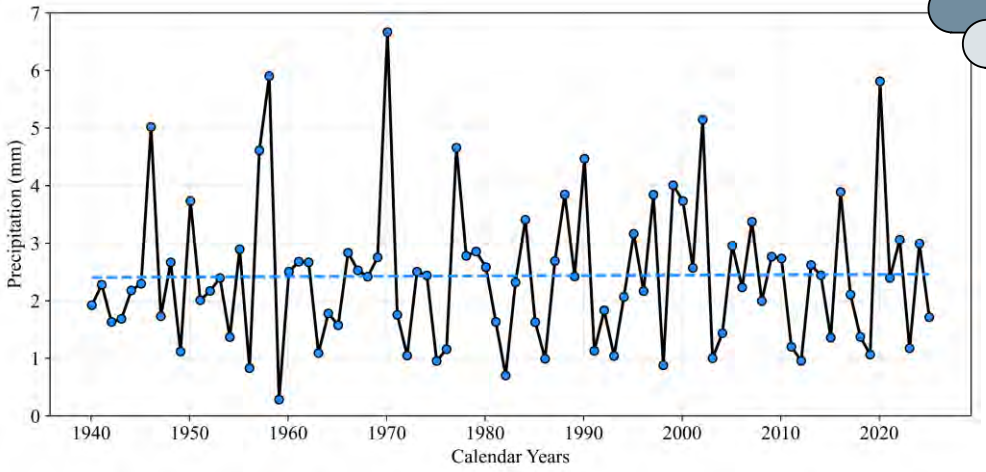

Conclusion

- A deep learning surrogate model was successfully developed and validated against JRODOS, reducing dispersion prediction time from over 2 minutes to less than 0.1 seconds.
- The ANN accurately captures plume location and footprint across a wide range of meteorological conditions, demonstrating the viability of data-driven surrogate models as a complement to physics-based dispersion codes.
- The speed advantage opens the door to comprehensive multi-year, multi-scenario statistical assessments that significantly strengthen nuclear emergency preparedness and planning.
- The model will be extended for variable source terms derived from severe accident simulation codes. Scenario-specific dose predictions for different accident progressions is going to be considered.
- Investigation of application to Small Modular Reactor (SMR) siting studies, Environmental Impact Assessments, and Emergency Planning Zone definition is in agenda.
- The model accuracy will be improved iteratively for high-consequence, low-probability dispersion events through targeted data augmentation and advanced loss function design.

Thank you for your attention

Onur Murat

onur.murat@kit.edu

The 12th European Review Meeting on Severe Accidents Research

May 18-22, 2026, Universidad Carlos III de Madrid, Madrid, Spain

PLENARY SESSION: EXPECTATIONS FROM SA R&D (ROUND TABLE)

Chair: A. Bentaib (NEA)

Expectations from SA R&D. A Regulator Point of View M. Sánchez (CSN)	Presentation
Notes to the Severe Accident Research Community Based on the Experience of the Fukushima Daiichi Accident T. Fuketa (NDF; NRA)	Presentation
L. Borondo Arribas (Iberdrola)	Presentation
Severe Accident in NPP Research and Application A. Giner (Westinghouse)	Presentation

CSN CONSEJO DE SEGURIDAD NUCLEAR

Plenary Session 2: Expectations from SA R&D.

Miguel Sánchez Perea
(msp@csn.es)
Modeling and Simulation Branch (MOSI)
Nuclear Safety Council (CSN)
C/ Pedro Justo Dorado Dellmans, 11, 28040-Madrid (Spain)

My Conjecture of Answers

"ERMSAR2026-Informed Attendees Answers"

CSN CONSEJO DE SEGURIDAD NUCLEAR

Plenary Session 2: Expectations from SA R&D. A Regulator Point of View

Miguel Sánchez Perea
(msp@csn.es)
Modeling and Simulation Branch (MOSI)
Nuclear Safety Council (CSN)
C/ Pedro Justo Dorado Dellmans, 11, 28040-Madrid (Spain)

CSN CONSEJO DE SEGURIDAD NUCLEAR

Regulatory Interest in SA R&D

- Severe Accident R&D (SAR&D) is essential worldwide for **evidence-based nuclear regulation**, **continuous safety improvement**, and **increased knowledge of severe accident.**
- SAR&D enhances the capability of regulators ensuring that NPPs are designed, operated, and maintained with **robust defense-in-depth measures against low-probability-high-consequence events**, as well.
- Regulatory Decision-Making processes rely on (well validated, V&V) **Dynamic Simulation Computational Tools** (and the associated plant models), **Risk Assessment** (Level 2&3 PSA in the case of SA) **methods**, and **Uncertainty Quantification (UQ) methods** (hopefully!).
- **Experimental and analytical research** remain essential to reduce uncertainties and improve severe accident management strategies.
- Licensing frameworks for advanced reactor designs (NEI 18-04, 10CFR53, …) will increasingly depend on **validated models**, **PSA methodologies**, and **uncertainty-informed decision-making**

Improvement of Tools and Methods

Dynamic Simulation Computational Tools and V&V

- Regulators rely on validated severe accident integral codes for independent safety assessments.
- Validated computational tools improve confidence in predictions and safety evaluations.
- Feedback from experiments to simulation codes is essential to continuously improve model accuracy and predictive capabilities.
- Experimental R&D programs provide essential data for Verification and Validation (V&V) activities.

Risk Assessment (Level 2 & 3 PSA)

- PSA methodologies help regulators prioritize safety improvements according to risk significance.
- Containment event trees and release categories support evaluation of plant risk profiles.
- Subsidiary analytical tools of L2PSA methods need to be well validated against experimental results.
- SAR&D provides models and input data for Level 2 Probabilistic Safety Assessments (PSA).
- SAR&D results enhance the understanding and delineation of dominant accident sequences and overall plant risk.

Uncertainty Quantification (UQ)

- Experimental and analytical research remain essential to reduce uncertainties.
- SAR&D provides data/knowledge to characterize uncertainties in the phenomena/parameters.
- Development of Systematic UQ Methodologies, including comprehensive PIRT studies, (i.e., a potential "Severe Accident Uncertainty Handbook") would significantly enhance safety assessments.
- Inverse UQ (IUQ) methods would improve the characterization of uncertain inputs to UQ (parameters/phenomena).
- *Advanced reactor licensing frameworks (NEI 18-04, 10CFR53, ...) will increasingly depend on "Validated Models, PSA Methodologies, and Uncertainty-informed" decision-making.*

CSN CONSEJO DE SEGURIDAD NUCLEAR

Summary of Expectations

- **Experimental Programs** to provide essential data for V&V and improvements of SA simulation tools.
  - Need for international collaboration in supporting experimental facilities, data bases, expertise, ….
- **Development and Deployment of Systematic UQ Methodologies for SA**, including comprehensive PIRT studies to enhance SA safety assessments and RIDM.
  - **Inverse UQ (IUQ) methods** to improve the characterization of uncertain inputs to UQ (parameters/phenomena).
- **Extensive use of AI and ML techniques** in any of the pillars.
- Eventual **applicability of IDPSA methods to SA analysis** (e.g., advanced reactor designs)
  - To address the mutual interactions between disturbances (e.g., failures of the equipment, human actions, stochastic physical phenomena) and the corresponding transients (i.e., deterministic response).
  - To compute consistently the tight coupling of the Scenarios, their Consequences (deterministic), and their Frequency (probabilistic) (i.e., all the three ingredients of Risk).
  - All the three ingredients intrinsically uncertain: IDPSA a consistent and integrated treatment of the different sources of uncertainties.

CSN CONSEJO DE SEGURIDAD NUCLEAR

Plenary Session 2: Expectations from SA R&D: A Regulator Point of View

Thank you for your attention!

Miguel Sánchez Perea
(msp@csn.es)
Modeling and Simulation Branch (MOSI)
Nuclear Safety Council (CSN)
C/ Pedro Justo Dorado Dellmans, 11, 28040-Madrid (Spain)

CSN CONSEJO DE SEGURIDAD NUCLEAR

Regulatory Use of SAR&D

Regulatory Use of SAR&D (1/3)

Development of Regulatory Frameworks

- SAR&D supports development of regulations for BDBAs, DECs, containment performance, and severe accident management.
- Advanced reactor licensing frameworks (NEI 18-04, 10CFR53, ...) will increasingly depend on validated models, PSA methodologies, and uncertainty-informed decision-making.

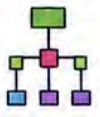

Risk-Informed Decision Making

- Provides PSA input for risk-informed and performance-based regulation using metrics such as LERF.
- Advanced reactor licensing frameworks (NEI 18-04, 10CFR53, ...) will increasingly depend on validated models, PSA methodologies, and uncertainty-informed decision-making.

Licensing and Safety Review

- Support verification of vendor analyses and evaluation of SA mitigation systems and associated SA guidelines using SA codes and Risk methods.

Validation of Safety Analysis Codes

- Experimental SAR&D data support the improvement of simulation tools (ASTEC, MELCOR, MAAP, ...), and the subsidiary analytical tools on L2 PSA methods.
- Experimental investigations improve understanding of degraded core behavior.
- SAR&D analyzes in-vessel and ex-vessel core melt progression phenomena, evaluate melt retention strategies, core catcher requirements and debris coolability.

Regulatory Use of SAR&D (2/3)

Accident Management and SAMGs Review

- Contributed to the development and validation of Severe Accident Management Guidelines (SAMGs).
- Help to evaluate whether operators can effectively mitigate core damage progression.
- Help to analyze containment protection strategies and accident mitigation actions, e.g., supporting the assessment of combustible gases control, depressurization, and containment protection strategies
- Research also investigates possible negative effects of mitigation actions.
- Understanding uncertainties helps avoid unrealistic overly conservative approaches.

Containment Performance and Combustion Risk Mitigation

- Experimental programs support combustible gases (hydrogen, and CO) generation, transport and combustion.
- Helps to defines requirements for PARs, igniters, and venting systems under SA conditions and supports their safety evaluations
- Experimental SAR&D data support the improvement of simulation tools (ASTEC, MELCOR, MAAP, ….), and the subsidiary analytical tools on L2 PSA methods

Source Term Evaluation and Emergency Planning

- Experimental and analytical programs improve source term realism for emergency planning and offsite consequence assessment.
- Simulation tools support the definition of emergency planning zones and protective actions, and help to evaluate evacuation timing, sheltering, and iodine distribution strategies.
- Results strengthen public communication and emergency response coordination.
- Research also investigates possible negative effects of mitigation actions.
- Understanding uncertainties helps avoid unrealistic overly conservative approaches.

Regulatory Use of SAR&D (3/3)

Post-Accident Monitoring and Instrumentation

- Help to define survivable instrumentation requirements for SA management decision-making.
- Help in the characterization and guarantee of proper functioning of the instrumentation under SA challenging levels

Post-Fukushima Enhancements and SFP Safety

- Post-Fukushima SAR&D strengthened the deployment and optimization of:
  - ❑ SBO mitigation (and other DEC-A),
  - ❑ mobile equipment (FLEX),
  - ❑ associated guidelines (EDMGs and FSGs) deployment,
  - ❑ filtered containment vents,
  - ❑ beyond-design-basis preparedness, ...
- Spent Fuel Pool (SFP) studies improved cooling and makeup water strategies.

International Collaboration and Harmonization

- EU, OECD/NEA and IAEA cooperation improves consistency and sharing of SAR&D knowledge.
- Accomplish international compromises in supporting experimental facilities, data bases, expertise, ...
- Help to fulfill commitments aimed at maintaining national expert groups in SA.

Inspection, Oversight, and Enforcement

- Help to focus oversight on systems critical for SA mitigation and BDBA readiness.

Notes to the Severe Accident Research Community Based on the Experience of the Fukushima Dai-ichi Accident

NDF **Toyoshi FUKETA** UTokyo

Nuclear Damage Compensation and Decommissioning Facilitation Corporation

May 19, 2026

Plenary Session 2 'EXPECTATIONS FROM SA R&D'

TEPCO Fukushima Dai-ichi Accident

Pre-accident

- ✓ Overconfidence: Safety myth
- ✓ Belief among industries, regulators, and academia in “sufficient knowledge of NPP risks”

Reality revealed

- ✓ Critical gaps in knowledge and risk awareness
- ✓ Inability to take effective actions

Post-accident global consensus

- ✓ Recognition of the need for enhanced safety measures
- ✓ Commitment to additional actions for strengthening NPP resilience

Peace-time preparedness

- ✓ Once an accident occurs, numerous self-proclaimed experts emerge, and their misleading views can compromise critical decision-making.
- ✓ Prior to the accident, there was a tendency in our society to discourage SA studies for fear of inciting public unease over nuclear energy.
- ✓ Establishing public recognition of credible information sources before a crisis is essential.
- ✓ An authoritative entity is essential to filter out dubious technical claims with a firm stance.

Analyzing accident scenarios takes the highest priority

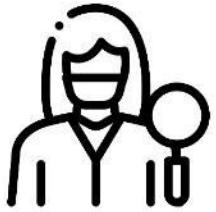

- ✓ While understanding individual phenomena is important, prioritizing accident progression and scenarios is critical.
- ✓ Once an accident occurs, public attention shifts to what happens next, and authorities are immediately required to estimate the worst-case scenario.
- ✓ Many people now seem to be trying to believe that SAs can be practically eliminated by design. However, new accident scenarios should be considered for new designs.
- ✓ Research into detecting the onset and progression of phenomena is also essential.

Magnitude of consequence

- ✓ The greatest damage of the F-1 accident is the long-term relocation due to environmental contamination.
- ✓ Accident consequences cannot be assessed solely by radiation exposure.
- ✓ Is LRF, Large Release Frequency, an adequate indicator for large-scale releases?
  There may be ethically unacceptable consequences that must not be exceeded, regardless of probability.

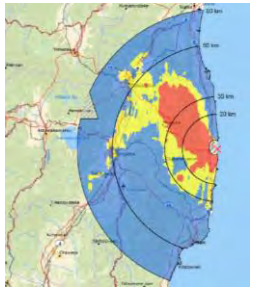

- ✓ The long-term post-accident response largely determines the magnitude of damage.

Recommendation, e.g.,

- ✓ Establish the technical basis for the practical elimination of major radioactive release in advanced reactors and define its requirements.
- ✓ Evaluate severe accident measures for existing plants, incorporating Fukushima insights and long-term operation plans.
- ✓ Identify containment-threatening scenarios in advanced systems, considering diverse safety designs and concepts.
- ✓ Develop advanced instrumentations for SA monitoring and management.
- ✓ Organize a framework with the widest possible community to lead collaborative experimental projects around structured collaborative experimental research platforms.

Innovation requires strong and independent regulatory body

Under-regulation

- ✓ Cause fundamental threat to market stability
- ✓ Increase “Weakest link” risk

  Devastate the entire industry due to a failure by a single poor competitor

Strong and independent regulator

- ✓ Provide objective evaluation of diverse technologies
- ✓ Ensure a level playing field to foster healthy competition
- ✓ Enable the best concepts and companies to prevail

ERMSAR 2026

Lourdes Borondo

Head of Nuclear Safety and Quality, Cofrentes NPP, IBERDROLA

IBERDROLA NUCLEAR GENERATION ASSETS

C.N. GAROÑA
DESMANTELAMIENTO
PROPIEDAD 50%

C.N. ASCÓ I (PWR)
TARRAGONA
1.032 MW
PROPIEDAD 0%

C.N. ASCÓ II (PWR)
TARRAGONA
1.027 MW
PROPIEDAD 15%

C.N. TRILLO (PWR)
GUARDALAJARA
1.066 MW
PROPIEDAD 49%

C.N. VANDELLÓS II (PWR)
TARRAGONA
1.087 MW
PROPIEDAD 28%

C.N. VANDELLOS I
DESMANTELAMIENTO
PROPIEDAD 21%

C.N. ALMARAZ I (PWR)
CÁCERES
1.049 MW
PROPIEDAD 53%

C.N.ALMARAZ II (PWR)
CÁCERES
1.044 MW
PROPIEDAD 53%

C.N. COFRENTES (BWR)
VALENCIA
1.092 MW
PROPIEDAD 100%

C.N. JOSE CABRERA
DESMANTELAMIENTO
PROPIEDAD 0%

IBERDROLA OWNS 43% OF SPANISH NUCLEAR ASSETS

Internal Use

LEVEL 2 PROBABILISTIC SAFETY ASSESSMENT

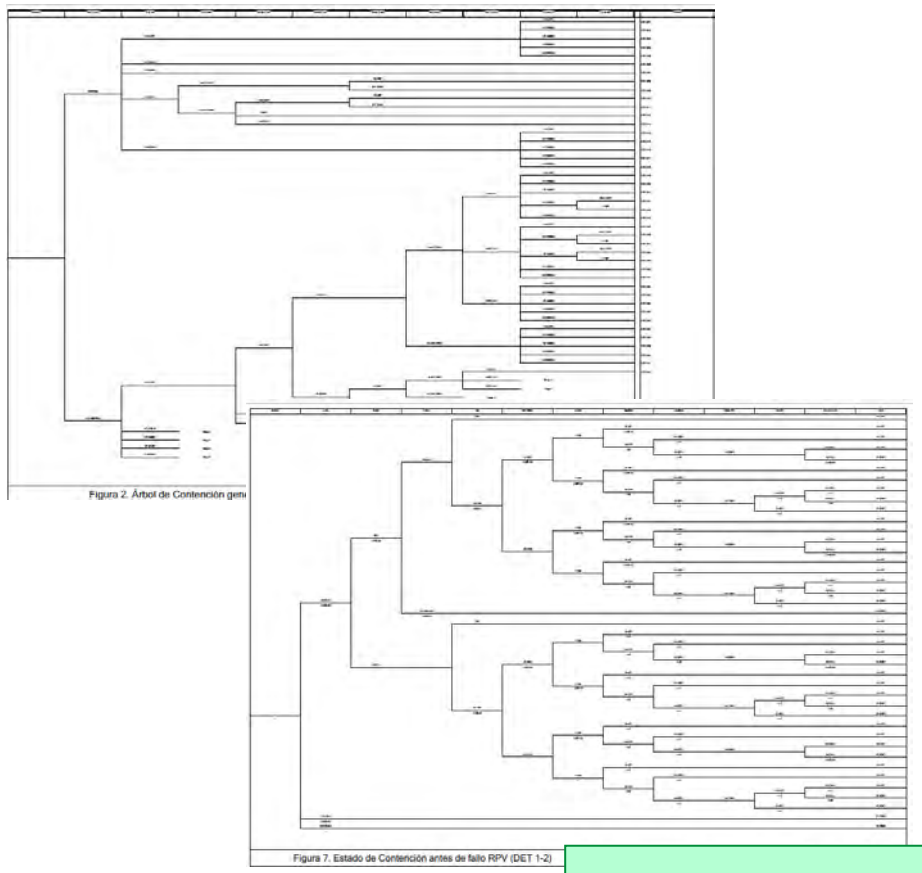

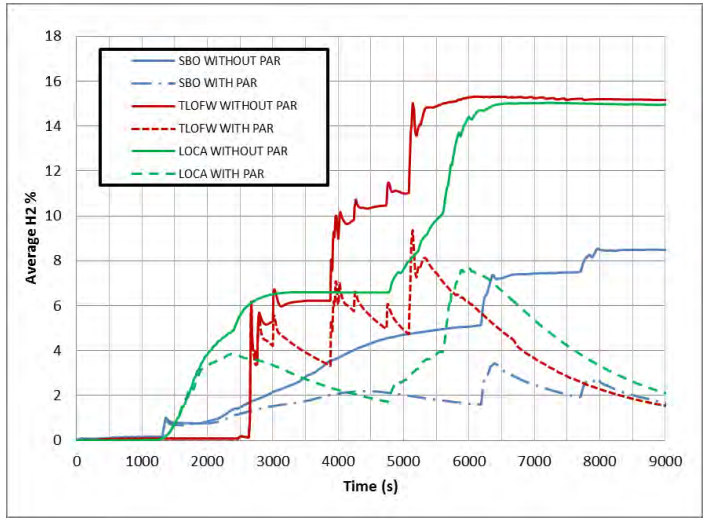

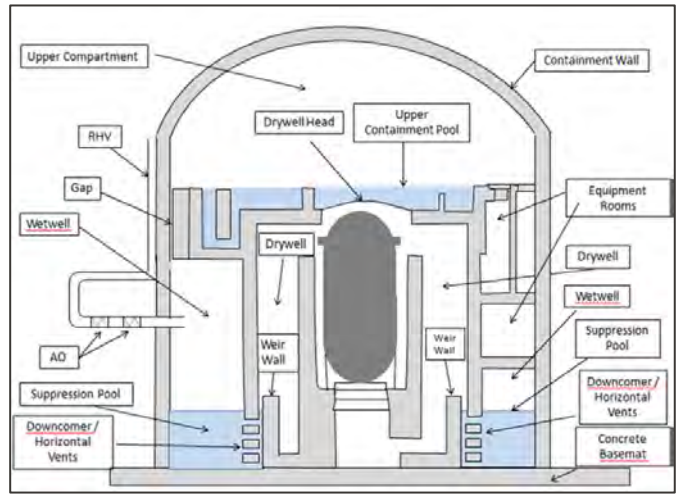

MAAP for limiting H2+CO release rates

GOTHIC-3D model (>3600 nodes) for gases distribution in containment

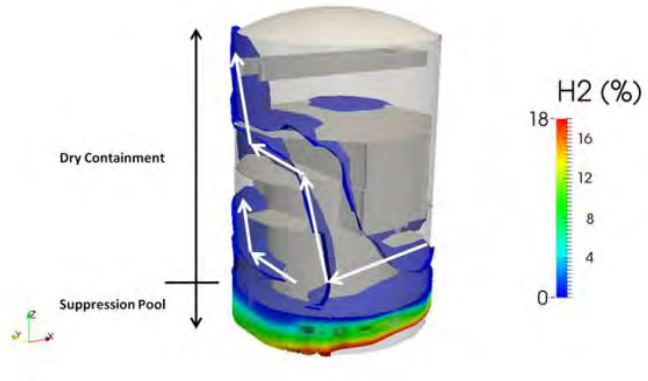

Internal Use

SEVERE ACCIDENT MANAGEMENT GUIDELINES

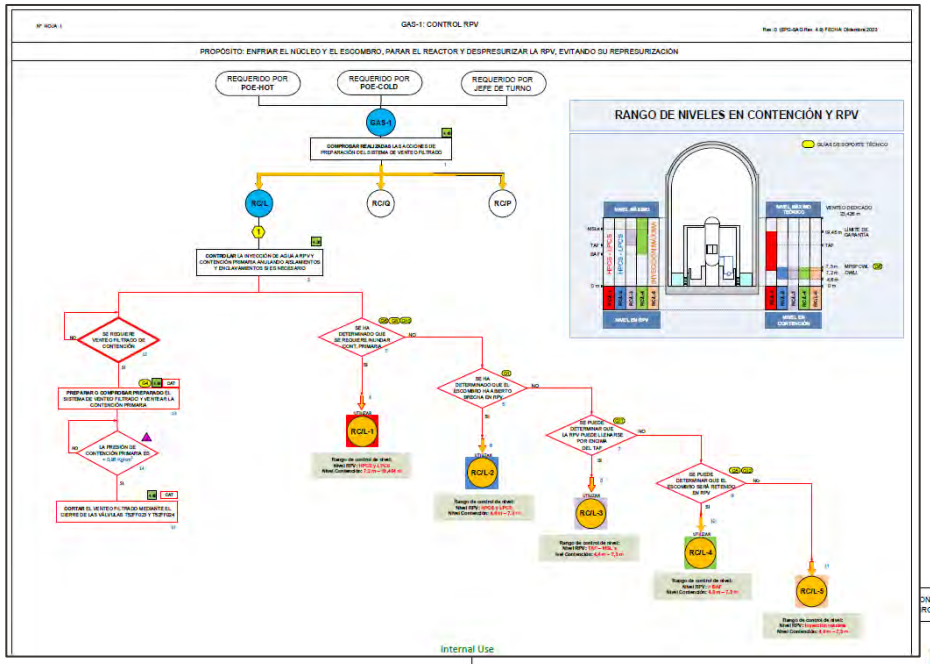

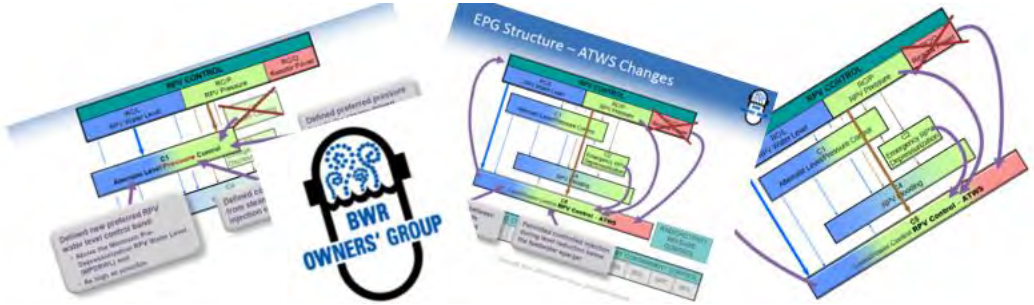

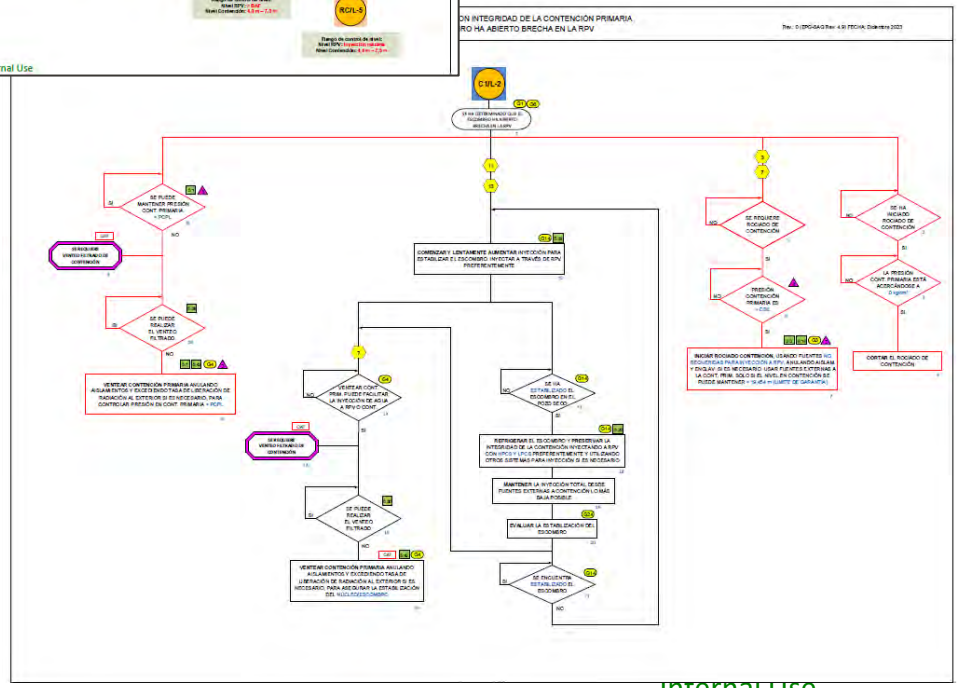

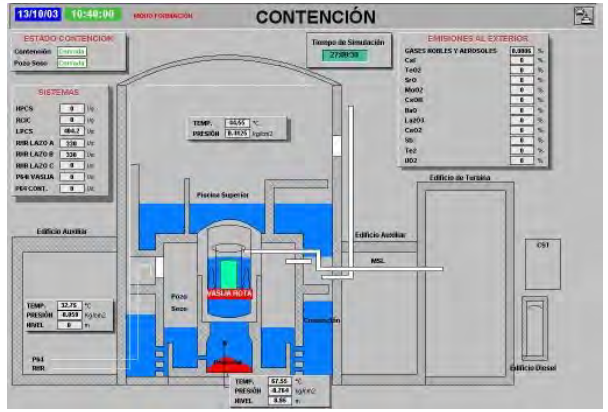

Internal Use
Internal Use

REINFORCED EMERGENCY MANAGEMENT SYSTEM

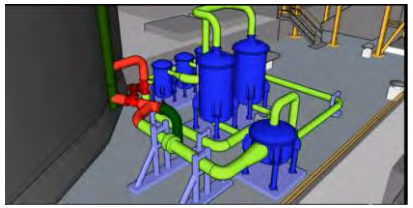

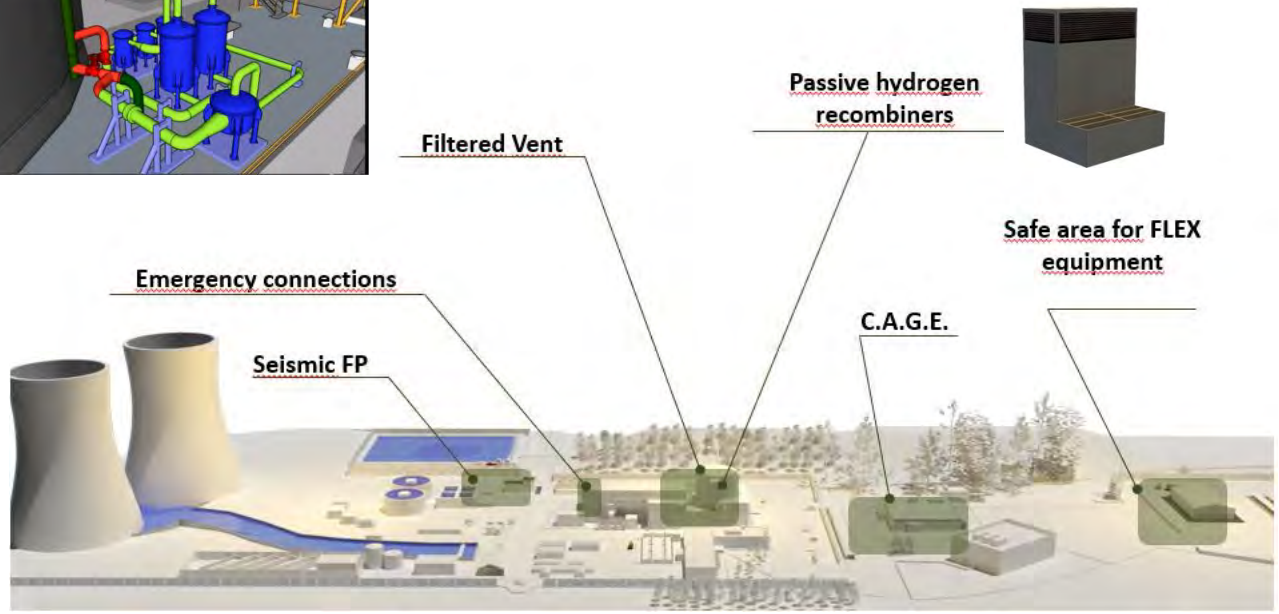

Large Scope Emergency Drills

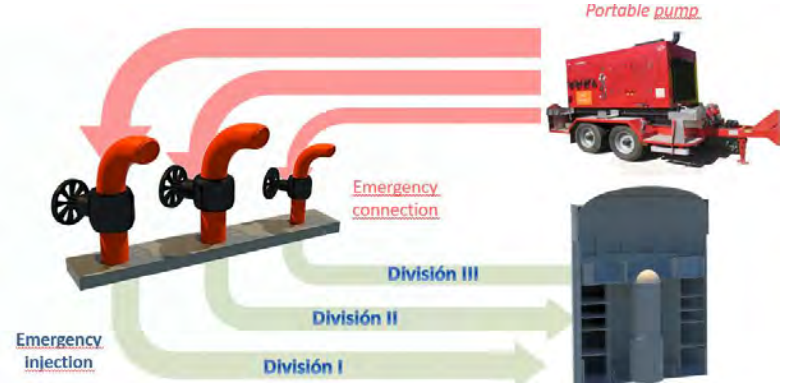

ACCOUNTABILITY

TEAMWORK

LEADERSHIP

THANK YOU

IBERDROLA

Severe Accident in NPP Research and Application

Amparo Giner González

Westinghouse Proprietary Class 2 | © 2025 Westinghouse Electric Company LLC. All Rights Reserved.

Information included in this material is proprietary and confidential and cannot be disclosed or used for any reason beyond the intended purpose without the prior written consent of Westinghouse Electric Company LLC

Westinghouse Experience supporting SAMGs Implementation

Extensive support to utilities worldwide:

- Development of SAMGs
- Maintenance and periodic review
- Updates incorporating latest industry practices

Based on industry generic SAMG frameworks:

- Owners Groups (PWROG, BWROG)

Proven capabilities:

- Plant-specific adaptation
- Integration with EOPs and plant procedures
- Validation, implementation, and training

Value delivered:

- Alignment with international standards
- Continuous improvement of SAMG strategies

Westinghouse Proprietary Class 2 | © 2025 Westinghouse Electric Company LLC. All Rights Reserved.

Westinghouse Proprietary Class 2 | © 2025 Westinghouse Electric Company LLC. All Rights Reserved.

Information included in this material is proprietary and confidential and cannot be disclosed or used for any reason beyond the intended purpose without the prior written consent of Westinghouse Electric Company LLC

The 12th European Review Meeting on Severe Accidents Research

May 18-22, 2026, Universidad Carlos III de Madrid, Madrid, Spain

POSTER SESSION		
ID015	**MAAP5 Analysis of High-Pressure Severe Accidents in a Small Modular Reactors** Byung Jo Kim (KEPCO E&C)	Abstract Poster
ID019	**Development and Evaluation of an Ablation-Resistant Basemat Concrete for Severe Accident Mitigation in LWRs** E. Chen (CNPE)	Abstract Poster
ID023	**Aerosol Removal Behavior by Containment Spray** B. Lee (KAERI)	Abstract
ID025	**Development of performance verification test methodology for passive radioactive material filtration system** K.H. Park (KAERI)	Abstract Poster
ID027	**Experimental analysis of molten salt aerosol in tank of confined volume: evaporation, airborne and deposition.** Jun-young Kang (KAERI)	Abstract
ID029	**Additional primary depressurized line (APDL) for NPP Units with VVER-440/V-213** O. Mykhailenko (ES Group LLC)	Abstract Poster
ID030	**SOCRATES EU project on liquid source term during a severe nuclear accident – WP 3: Boundary evolution conditions in the bulk liquid phase** A.-C. Grégoire (ASNR)	Abstract Poster
ID032	**Preliminary Experimental Study on the Elemental Iodine Adsorption Filter for a Passive Radioactive Material Filtration System** J. Jung (KAERI)	Abstract Poster
ID035	**Re-examination of the VULCANO VE-U9 Corium Spreading Test Using a Novel Pressure-Substitution Implicit Solver and Crust Fracture Model** R. Yokoyama (University of Tokyo)	Abstract
ID047	**SOCRATES: Leaching behaviour of radionuclides in severe accidents** T. Lind (PSI)	Abstract Poster
ID015	**MAAP5 Analysis of High-Pressure Severe Accidents in a Small Modular Reactors** Byung Jo Kim (KEPCO E&C)	Abstract Poster

ID055	**Containment of Radioactive Water Large Volumes and Concept of a Long-Term Containment Cooling System with Steam Condensing Heat Exchanger for NPPs with VVER-1000 Reactors** O. Mazurok (ES Group LLC)	Abstract Poster
ID056	**Implementation and Analytical Justification of Long-Term Containment Cooling System with Additional Spray Circuit, Heat Exchangers, and Turbine-Driven Pumps for NPPs with VVER-440 Reactors** V. Ivanov (ES Group Europe s.r.o.)	Abstract Poster
ID063	**Analysis of Postulated Design Basis Accidents in General Integral PWR Small Modular Reactors: Outcomes on Integral Codes' Modelling Capabilities from the Horizon Euratom SASPAM-SA Project** F. Gabrielli (KIT)	Poster
ID070	**Three-Dimensional Numerical Prediction of Natural Convection in Corium Pools Using Advanced RANS Turbulence Models** Alsalman Shahad (KFPUM)	Abstract
ID077	**Recalescence Behavior of Molten Refractory Oxides during Fast Cooling by Aerodynamic Levitation** Y. Gong (CNPE)	Abstract Poster
ID085	**High-Temperature Interactions of Corium, Steel, and Boron Carbide: Experimental Simulation of Fukushima Daiichi Unit 3** B. Mészáros (Centrum Výzkumu Řež)	Abstract Poster
ID089	**Detection, Segmentation, and Reconstruction of Overlapping Bubbles in Pool Scrubbing Experiments at the SAAB Facility** Y. Wu (FZJ)	Abstract Poster
ID090	**Experimental Study of Molten Corium–Serpentinite Concrete Interaction Using Cold Crucible Induction Melting** B. Nikolaiev (Centrum Výzkumu Řež)	Abstract
ID094	**Effect of Pt Coating Methods on Hydrogen Recombination Activation for Passive Autocatalytic Recombiners** Dae-Hyun Kim (Chosun University)	Abstract Poster
ID095	**Study of prototypical corium at solid state containing fission products: crystallographic and microstructural analysis, impact on weathering and leaching mechanisms** T. Mourier (CEA)	Abstract Poster
ID098	**Computational Thermodynamic Study of the Ex-Vessel Molten Corium** Y. Du (KTH)	Abstract Poster
ID101	**Evaluation of accident tolerant fuel using MELCOR2.2 on representative accident sequences in typical Japanese PWR**	Abstract

	M. Sekine (NRA)	Poster
ID106	**QUENCH-19: Bundle Experiment on ATF FeCrAl Claddings under Severe Accident Conditions** D. Schaefer (KIT)	Abstract Poster
ID116	**Experimental investigation of top-flooding of corium in the MERELAVA facility** S. Renaudière de Vaux (CEA)	Abstract Poster
ID118	**MELCOR Analysis of the Nordic BWR Pressure Suppression Pool During SBO Accident** G. Acharya (KTH)	Abstract Poster
ID122	**Assessing the Capabilities of MELCOR V2.2 against the QUENCH-19 Bundle Test with FeCrAl Cladding** M. E. Cazado (KIT)	Abstract Poster
ID124	**The PIANOFORTE CATAPULT Project: Comprehensive Assessment and Preparedness for Emerging Nuclear Technologies** F. Gabrielli (KIT)	Abstract Poster
ID127	**ASSAS project: Creating Infrastructure and Training Database for Surrogate Models for a Severe Accident Simulator** A. Stakhanova (KIT)	Poster
ID141	**3D Estimation Diagrams of Units 1–3 at the Fukushima Daiichi Nuclear Power Station Updated in 2025** T. Yamashita (JAEA)	Abstract Poster
ID142	**SOCRATES Horizon Euratom project on liquid source term** T. Kärkelä (VTT)	Abstract Poster
ID158	**Comparison of Monte Carlo and Wilks' Methods for Uncertainty Quantification of a Severe Accident in a PWR** P. Darnowski (Warsaw University of Technology)	Abstract Poster
ID162	**Development of the SAFARI Code for Comprehensive Severe Accident Analysis in Nuclear Reactors: Framework and Methodology.** Hyun Sun Park (Seoul National University)	Abstract
ID166	**Impact of FeCrAl Cladding Material on the Progression of a Severe Accident in a Generic BWR Mark-I NPP: analysis of a SBO Scenario with the ASTEC Code** O. Murat (KIT)	Abstract Poster
ID167	**Study of the Impact of Polydisperse Droplet Distribution in the Spray System Using GOTHIC-3D** C. Gabicagogeascoa (Universidad Politécnica de Madrid)	Abstract Poster
ID169	**Investigating Severe Accident Scenarios for NNRs: Developing the GIROSCOPE Methodological Framework for EP&R**	Abstract

	A. Wawrzyńczak-Szaban (NCBJ)	Poster
ID193	**3D Simulation of Debris Bed Quenching with Top-Flooding for FLOAT Experiments** J. Kokalj (JSI)	Abstract Poster
ID202	**MELCOR Severe Accident Analysis in LDR-lite: a District Heating Reactor** M. Principato (PSI)	Abstract Poster
ID204	**Analysis of IVMR through ERVC for i-SMR using CINEMA Computer Code** Rae-Joon Park (KEARI)	Abstract Poster
ID205	**Analysis of Spreading Distance in Spill Out Accident of Molten Salt Reactor** Rae-Joon Park (KAERI)	Abstract Poster
ID208	**Development of a Fission Product Mitigation System for Severe Accident Conditions in Small Modular Reactors** Jaehoon Jung (KAERI)	Abstract Poster

MAAP5 ANALYSIS OF HIGH-PRESSURE SEVERE ACCIDENTS IN A SMALL MODULAR REACOTRS

Byung Jo Kim, Yong Ju Cho, and Dong Min Park
KEPCO Engineering & Construction Co.
269 Hyeoksin-ro, Gimcheon-si, Gyeongsangbuk-do, Republic of KOREA
bjokim@kepco-enc.com; cyongju93@kepco-enc.com; ko44355@kepco-enc.com

ABSTRACT

The safety assessment of Small Modular Reactors (SMRs) requires rigorous analysis of severe accident scenarios, particularly high-pressure transients, which pose greater challenges in compact designs compared to conventional PWRs with large containments. This study evaluates a high-pressure severe accident in a PWR-type SMR using the MAAP5 code, focusing on a total loss of feedwater (TLOFW) event. Results show that despite core uncovery and entry into a severe accident phase, the reactor maintains long-term coolability through inherent passive mechanisms. Natural circulation within the reactor vessel and passive heat removal via the external vessel wall prevent significant core damage. The passive containment cooling system effectively transfers heat to the emergency cooling tank, maintaining containment integrity. Hydrogen generation is minimal, and the high steam environment precludes combustion risk. The analysis demonstrates that the SMR's passive safety systems effectively mitigate high-pressure accident progression, ensuring stable cooling and enhanced safety without operator intervention.

KEYWORDS
SMR, high-pressure, passive safety, severe accident

1. INTRODUCTION

Small Modular Reactors (SMRs) possess inherent safety characteristics that fundamentally reduce the likelihood of severe accidents, owing to their lower thermal power, integral design, and reliance on passive safety systems, compared to large-scale nuclear power plants. These features enable long-term decay heat removal without external power or operator intervention, thereby enhancing resilience under multiple failure accident scenarios, including high-pressure severe accidents.

A variety of SMR designs have been proposed worldwide. According to the OECD/NEA SMR Dashboard [1], designs incorporating passive cooling systems are receiving significant attention. In particular, designs such as NuScale [2] and i-SMR [3], which employ passive heat removal systems that circulate internal atmosphere and condensed water between the Reactor Vessel (RV) and the Containment Vessel (CV), offer favorable characteristics for long-term cooling. However, due to the relatively small free volume of SMRs compared to large Pressurized Water Reactors (PWRs), high-pressure conditions are more likely to persist during the progression of a severe accident. This increases the significance of high-risk accident sequences such as High-Pressure Melt Ejection (HPME) and Direct Containment Heating (DCH).

In this study, a high-pressure severe accident scenario is analyzed using the Modular Accident Analysis Program (MAAP5.06) [4] for an SMR design incorporating passive safety systems. The primary system responses, pressure evolution, fuel damage timing, and performance of passive safety equipment are

evaluated. The objective is to quantitatively assess the SMR's response characteristics under high-pressure severe accident conditions and to derive design insights for enhancing safety.

2. DESIGN CHARACTERISITCS OF SMALL MODULAR REACTOR

The SMR analyzed in this study features an integral design, with the reactor core, pressurizer, steam generator, and reactor coolant pumps housed within a single RV. The RV is enclosed by a steel CV, which provides structural and radiological protection. At the upper part of the CV, heat exchangers for the Passive Containment Cooling System (PCCS) are installed and connected to an external water source in the Emergency Cooling Tank (ECT). The PCCS removes heat from the CV's internal atmosphere. Condensate formed on the heat exchanger surface falls by gravity into the annular gap between the RV outer wall and the CV inner wall, forming a condensate pool. This pool provides long-term passive cooling of the RV outer surface. A pressurizer located at the top of the RV is equipped with two Pressurizer Safety and Relief Valves (PSRVs) and an Emergency Depressurization Valve (EDV), which function to mitigate Reactor Coolant System (RCS) overpressure during transient or accident conditions. Additionally, an Emergency Recirculation Valve (ERV) is installed on the lower side of the RV. This valve allows the condensate pool water to be naturally recirculated back into the core region, supporting accident mitigation through passive cooling.

3. SELECTED SEQUENCE

Among various initiating events that could lead to a high-pressure severe accident, a Total Loss of Feedwater (TLOFW) is selected for analysis due to its rapid accident progression and high decay heat load. The scenario assumes a simultaneous loss of both main and passive auxiliary feedwater systems, followed by failure of automatic opening of the EDV and ERV - representing a conservative and challenging condition. Under this scenario, RCS overpressure control relies solely on the cycling operation of the two PSRVs, while the CV is cooled passively by the PCCS. The total simulation period extends for 7 days (168 hours) from the initiation of the transient.

4. CALCULATION RESULTS AND ANALYSIS

Immediately after the TLOFW event, the reactor coolant pumps (RCPs) trip and a reactor scram are assumed, leading to a rapid rise in RCS temperature and pressure. Approximately 400 seconds after the initiating event, the PSRVs open for the first time, discharging coolant and steam into the CV. The valves close again at 488 seconds, and subsequently cycle based on pressure setpoints. As shown in Figure 1, the RCS pressure is maintained within a range of 14.0 to 17.2 MPa due to the PSRV cycling. By 10.6 hours (38,304 seconds), the RCS pressure no longer reaches the PSRV opening setpoint, and discharge ceases. The total cumulative mass released through the PSRVs is approximately 141 tons, with a peak mass flow rate of up to 31 kg/s during initial discharge.

As the RCS inventory decreases, the water level in the RV gradually drops. The top of the core becomes uncovered at 13,761 seconds (~3.8 hours), and the water level stabilizes, leaving approximately 75% of the core height exposed (Figure 2). Although the severe accident entry conditions are initiated at 30,597 seconds (~8.5 hours), the maximum fuel temperature does not exceed 1,125 K and gradually decreases over time. This indicates that significant core melt or structural failure does not occur. A strong natural circulation flow is established between the uncovered core and the upper plenum, with a peak natural circulation flow rate of 10 kg/s.

The PCCS functions as designed, forming a condensate pool of approximately 8.2 m depth at the bottom of the CV, which effectively cools the RV outer wall (Figure 2). The outer tube wall temperature of the PCCS heat exchanger remains 80 to 100 K lower than the bulk CV atmosphere temperature, enabling continuous

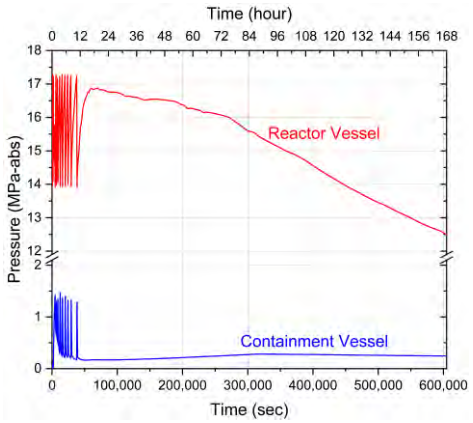

Figure 1. RCS and CV pressure transients during the 7-day accident sequence.

condensation. The condensation rate peaks at 50 kg/s initially and stabilizes at around 29 kg/s during long-term operation (Figure 3). The ECT water temperature increases gradually and reaches saturation at approximately 86 hours (3,096 minutes), after which evaporation begins (Figure 3). However, sufficient water inventory remains at the end of the 7-day period, ensuring that the CV is protected from overpressure threats (Figure 1). This confirms that the PCCS heat removal capacity is sufficient to manage decay heat over the long term.

The total hydrogen generated over the 7-day period is approximately 24 kg, which corresponds to about 12% of the theoretical maximum from complete cladding oxidation. The hydrogen is uniformly distributed within the CV. Given the extremely high steam concentration (over 95%) and low oxygen and hydrogen concentrations, the risk of hydrogen combustion is deemed negligible.

5. SUMMARY

This study evaluates the response of a passive-safety-based Small Modular Reactor (SMR) under high-pressure severe accident conditions. A conservative scenario involving total loss of feedwater and failure of emergency depressurization and recirculation systems was analyzed using the MAAP5.06 code over a 7-day period.

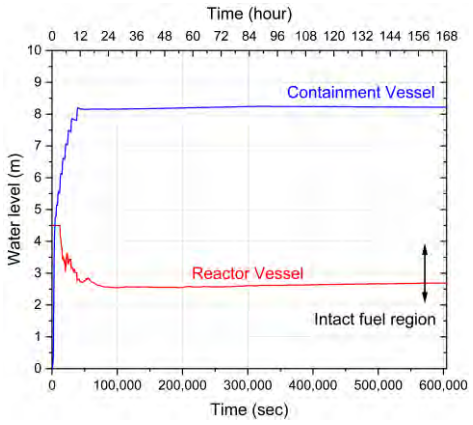

Figure 2. Core water level and condensate pool formation in the CV.

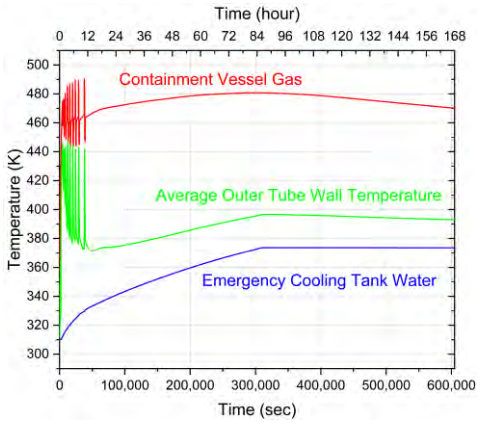

Figure 3. CV atmosphere temperature, PCCS heat exchanger outer wall temperature, and ECT water temperature.

The results show that RCS pressure is effectively controlled through the cycling operation of the PSRVs. The PCCS functions as intended, forming and maintaining a condensate pool that provides sustained passive cooling of the RV outer wall. This, combined with natural circulation within the core region, effectively suppresses fuel temperature rise. Although the core becomes largely uncovered (~75%), no significant core melt or structural failure is observed, and the maximum fuel temperature remains below 1,125 K.
Hydrogen generation is limited to 24 kg (~12% of full oxidation), and the high steam concentration and low oxygen environment within the CV eliminate the risk of hydrogen combustion.

These findings demonstrate that, even under severe and conservative assumptions, the inherent safety features and passive cooling systems of the SMR effectively mitigate accident progression. In particular, the prevention of RV rupture under high pressure and the sustained long-term heat removal capability confirms that SMRs can provide a high level of safety during severe accident scenarios.

This study provides valuable insights for the development of high-pressure severe accident management strategies and the design validation of passive safety systems in SMR applications.

ACKNOWLEDGMENTS

This work was supported by the Korea Institute of Energy Technology Evaluation and Planning (KETEP) and the Ministry of Climate, Energy & Environment (MCEE) of the Republic of Korea (No.RS-2025-02318177).

REFERENCES

1. OECD/NEA, The NEA Small Modular Reactor Dashboard: Third Edition (2025).
2. S. J. Weber and E. M. Mullin, “Severe Accident Phenomena: A Comparison among the NuScale SMR, Other Advanced LWR Designs, and Operating LWRs,” *Nuclear Technology*, **206:9**, pp.1351-1360 (2020)
3. C. H. Song, J. Song, S. J. Kim, “Evaluation of accident mitigation capability of passive core and containment cooling systems of i-SMR under representative LOCA and non-LOCA conditions,” *Nuclear Engineering and Technology*, **57**, pp. 103556 (2025)
4. EPRI, MAAP5.06 User’s Manual (2021)

12th CONFERENCE ON
SEVERE ACCIDENTS RESEARCH
May 18-22, 2026 - Madrid, Spain
ERMSAR 2026

MAAP5 ANALYSIS OF HIGH-PRESSURE SEVERE ACCIDENTS IN A SMALL MODULAR REACTOR

Byung Jo KIM, Yong Ju CHO, and Dong Min PARK
KEPCO Engineering and Construction Co., KOREA

1. Background and Motivation

In the event of a severe accident in a Small Modular Reactor (SMR), there exists a potential threat of radioactive material release to the environment. Compared to conventional large-scale pressurized water reactors (PWRs), the free volume of the Containment Vessel (CV) in an SMR is approximately one-tenth to one-twentieth that of a conventional large PWR, which may increase the risk of containment overpressurization during high-pressure severe accidents.

Key Concern: The substantially smaller CV free volume in SMRs means that high-pressure severe accidents may pose a greater risk of containment over-pressurization and potential failure compared to large conventional PWRs.

This study evaluates the progression and consequences of a high-pressure severe accident in a PWR-type SMR using the MAAP5, with particular focus on the effectiveness of passive safety features.

2. Methodology and Assumptions

The severe accident progression in an SMR under high-pressure conditions was simulated using the MAAP5 (Modular Accident Analysis Program, Version 5) code.

MAAP5 Code | PWR-type SMR | Passive Safety | Containment Vessel Integrity

Key Assumptions:

- High-pressure transient initiated with loss of main feed water system.
- Only the Passive Containment Cooling System (PCCS) is assumed to remain available.
- All other passive safety systems (e.g., Passive Auxiliary Feedwater System, Passive Emergency Core Cooling System) are assumed to fail.
- No operator action is credited throughout the transient.

Initiating Event (Loss of Main Feed water) → Passive Systems Fail (except PCCS) → High-Pressure Transient → Core Damage → PCSS Mitigation

3. MAAP5 Nodalization Schematic

Reactor Vessel (RV) | **Containment Vessel (CV)**

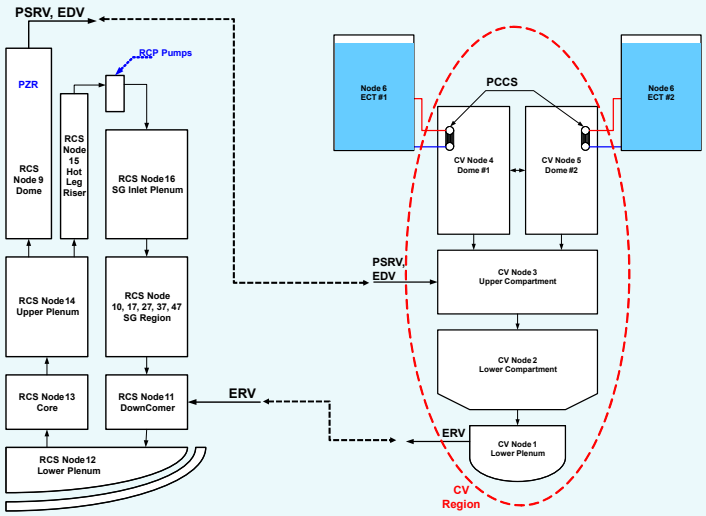

4. Accident Progression

Phase 1 – High Pressure Blowdown & Core Damage:

- Following the initiating event, RCS pressure remained at an elevated level within the automatic open/close pressure band of PSRV (Pressurizer Safety Relief Valve).
- RCS inventory was discharged through the PSRV cycling, leading to the core uncovery and onset of severe accident conditions.

Phase 2 – PCCS Mitigation & Accident Termination:

- PCCS forms a condensate pool on the external surface of the RV.
- Combined with natural circulation inside the RV and passive heat sink, large-scale core melting and relocation to the lower head were prevented.

5. Analysis Results

Primary System Pressure Transient:

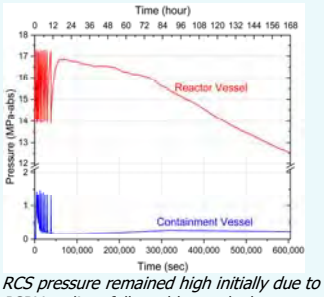

RCS pressure remained high initially due to PSRV cycling, followed by gradual depressurization as passive cooling progressed.

Core Water Level and Condensed Pool Level:

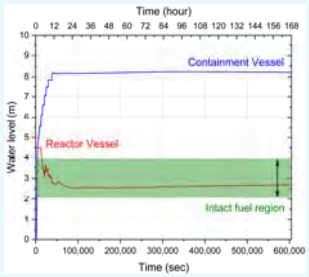

Although core level decreased initially, condensate accumulation on the RV exterior contributed to long-term heat removal.

Temperature Drop across Heat Transport Medium:

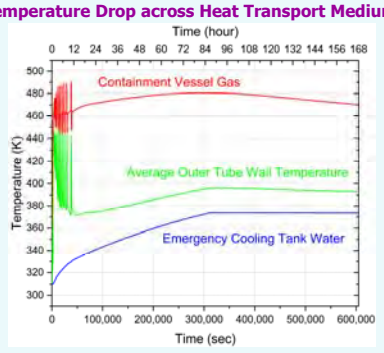

The maintained temperature gradient indicates continued passive heat transfer from the RV to the containment-side cooling path.

6. Conclusions

Summary of Findings

- A high-pressure severe accident was initiated by loss of main feed water with only PCCS available.
- MAAP5 was used to analyze a accident in SMR.
- PCCS-induced external RV cooling and natural circulation mitigated accident progression.
- Passive heat removal mechanisms provided sustained long-term cooling.
- No high-pressure failure of the RV or CV was predicted under assumed conditions.

★ The results indicate strong passive accident mitigation capability without credited operator action.

Development and Evaluation of an Ablation-Resistant Basemat Concrete for Severe Accident Mitigation in LWRs

Chen Erhui (1), Zhang Li (1), Li Nan (2), Pei Jie (2), Li Wei (2), Yuan Yidan (2)

(1) China Nuclear Power Engineering Co., Ltd., (2) China Nuclear Power Engineering Co.,Ltd.

Type of abstract: Poster
Subject area: Ex-vessel corium interactions and coolability
Keywords: ablation-resistant concrete; basemat concrete; COLOR facility; MCCI; severe accident

During a severe accident in a light water reactor, molten corium may enter the reactor cavity and erode the basemat concrete through molten core–concrete interaction (MCCI), potentially threatening containment integrity through basemat penetration and overpressure. Previous studies have shown that the concrete type and its material properties are critical factors affecting both the ablation rate and gas generation. This work presents a systematic method for screening ablation-resistant concrete, developed from practical engineering requirements and a corium–concrete erosion model. Based on CALPHAD thermodynamic calculations, an optimal composition enriched in MgO and Al_2O_3 was identified. Mechanical tests and thermodynamic analyses confirm that the designed concrete meets nuclear-grade structural strength standards while exhibiting a high melting point and large melting enthalpy. One-dimensional MCCI experiments conducted in the COLOR facility, using ZrO_2–Zr–Fe as a corium simulant, show that its ablation rate is significantly lower than that of conventional siliceous concrete, demonstrating strong potential for application in severe accident mitigation.

12th CONFERENCE ON
SEVERE ACCIDENTS RESEARCH
May 18-22, 2026 - Madrid, Spain
ERMSAR 2026

Development of an Ablation-Resistant Basemat Concrete for Severe Accident Mitigation in LWRs

Erhui Chen, Li Zhang, Nan Li, Jie Pei, Wei Li, Yidan Yuan*

Introduction

During severe accidents of LWRs, molten corium may enter the reactor cavity and erode the basemat concrete through molten core–concrete interaction (MCCI), potentially threatening containment integrity through basemat penetration and over-pressure. Concrete type and properties are known to critically influence MCCI outcomes. Therefore, modifying the concrete mix design to reduce the ablation rate and limit non-condensable gas production represents an effective strategy for MCCI mitigation.

Research Objectives

- **Screening:** develop a systematic screening criteria for ablation-resistant concrete
- **Selection:** perform thermodynamic calculations to identify high-performance candidate formulations
- **Simulation:** evaluate the selected concrete via MAAP5
- **Validation:** via experimental MCCI test (In Progress)

Screening Methodology

During the MCCI phase, the novel concrete is designed to:

- Reduce the ablation rate
- Suppress non-condensable gases (H_2,CO,CO_2)
- Lower the melt pool temperature
- Promote homogenization or layer inversion (metal layer below oxide layer) through oxidation

Additional requirements: C40 strength grade and adequate workability for construction.

Based on a one-dimensional ablation model for concrete (Fig.1), the concrete ablation rate is given by:

$$v_{abl} = \begin{cases} \dfrac{h\left(T_F - T_{F,m}\right) + q_v x_{cr} - k_{cn}\dfrac{T_{dc} - T_0}{\delta}}{\rho_{cn}\Delta H_{cn}}, & \text{with crust} \\ \dfrac{h\left(T_F - T_{dc}\right) - k_{cn}\dfrac{T_{dc} - T_0}{\delta}}{\rho_{cn}\Delta H_{cn}}, & \text{without crust} \end{cases}$$

T_F : corium temperatur $T_{F,m}$: liquidus temperature of corium

T_{dc} : melt temperature of concrete T_0 : initial temperature of concrete

ΔH_{cn}: melt enthalpy of concrete (from T_0 to T_{dc})

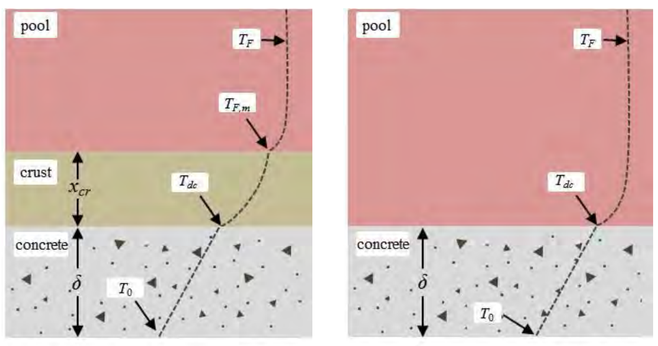

Fig.1 1D concrete ablation model (left: with crust, right: without crust)

According to the above equation, the concrete ablation rate decreases with:

- Higher melt temperature of concrete
- Higher melt enthalpy of concrete
- Higher density of concrete
- Higher thermal conductivity of concrete
- Lower convection heat transfer coefficient
- Lower melt pool temperature
- Higher liquidus temperature of corium-concrete mixture

Screening Assumptions and Tools:

- Thermodynamic equilibrium between molten corium and concrete with representative decay heat
- No transient, no kinetics, no external cooling (adiabatic system)

The properties and thermal equilibrium of various candidate concrete formulations are evaluated using Thermo-Calc software and NUCLEA database.

Ablation-Resistant Basemat Concrete

The composition of concrete is dominated by various oxides. To identify an optimal formulation, binary and ternary combinations were prepared from a set six common oxides (Fe_2O_3, Al_2O_3, CaO, SiO_2, MgO, SrO). Based on the screening criteria, the novel formulation characterized by a **MgO-Al_2O_3 rich system (M3)** was identified. This composition was compared against an ordinary siliceous concrete (**P1**, listed in Table 1).

Table 1 concrete	P1 compositions
MgO	1.04
Al_2O_3	12.39
Fe_2O_3	2.09
SiO_2	63.07
CaO	8.56
SrO	0.06
K_2O	3.69
Na_2O	2.66
MnO_2	0.06
TiO_2	0.29
Cr_2O_3	0.03
CO_2	0.5
H_2O	5.16

Key Property Enhancements (M3 vs. P1, see Table 2)

Compare to P1, the novel M3 concrete offers:

- Increased compressive strength
- Higher liquidus/solidus/melt temperature
- Higher melt enthalpy and specific heat.
- Greater heat conductivity and density.

Table 2 properties comparison between P1 and M3

Property	P1	M3	units
Slump	160	140	mm
Compressive strength (28d)	68.6	92.1	MPa
Splitting tensile strength (28d)	5.6	5.7	MPa
Specific heat	0.97	1.1	kJ/(kg▪K)
Thermal conductivity	2.38	5.56	W/(m▪K)
Density	2580	2950	kg/m^3
Porosity	7.2%	12.9%	--
Liquidus T *	1620.5	2940.4	K
Solidus T *	1411	1577.7	K
T_{dc} *	1562.2	2846.2	K
ΔH_{cn} *	2.0×10^6	5.1×10^6	J/kg

* : calculated from Thermo-Calc with NUCLEA database

MAAP5 Simulation Parameters

- **Accident scenario:** double-ended cold leg LOCA (1000MWe Zion-like PWR) with dry cavity
- **PRV failure:** at 5686s after accident initiation
- **Corium state**: detailed in Table 3, with a residual decay heat of 43.5MW.

MCCI Mitigation Results

- **Ablation resistance:** M3 demonstrates a dramatic reduction in erosion rate compared to P1 **(2.22cm/h vs. 9.82cm/h)**.
- **Gas generation:** limited gas production due to the absence of carbonate aggregates in both P1 and

Table 3 corium composition at lower plenum when RPV fails	
	Mass/t
UO_2	63.8
ZrO_2	5.2
Zr	8.0
SS	0.7

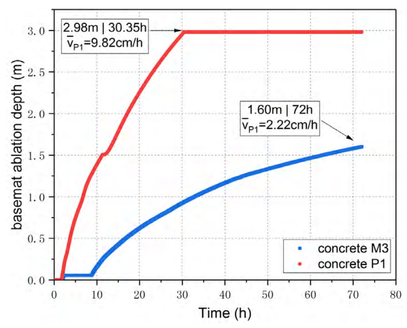

Fig.2 basemat ablation depth of P1 and M3

Experimental setup

Facility: The COLd crucible for cOrium behavior Research (COLOR) facility

- Principle: high-frequency induction heating within a cold crucible,
- Corium material: simulant (ZrO_2) or prototype melt
- Key data and Instrumentation:
  - Melt Temperature: via infrared pyrometer; a tung-sten rod is utilized for crust breaking
  - Ablation Rate: K/C thermocouples embedded in the concrete
  - Gas Generation: via mass spectrometer
  - Post-test Analysis : XRF/SEM/XRD

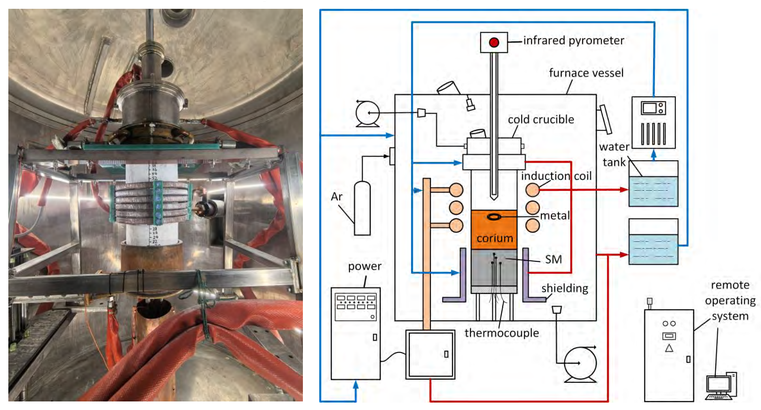

Fig.3 COLOR facility and schematic diagram

Table 4 design parameter of COLOR facility

Melting temperature	> 2800℃
Melt mass	20 kg
Cold crucible (copper)	Diameter: 217 mm Height: 616 mm
Furnace vessel	Double-layer stainless steel Diameter : 2m, Height: 2m
Power	Maximum 500 kW
Frequency range	100~150 kHZ
Atmosphere	Vacuum / Ar

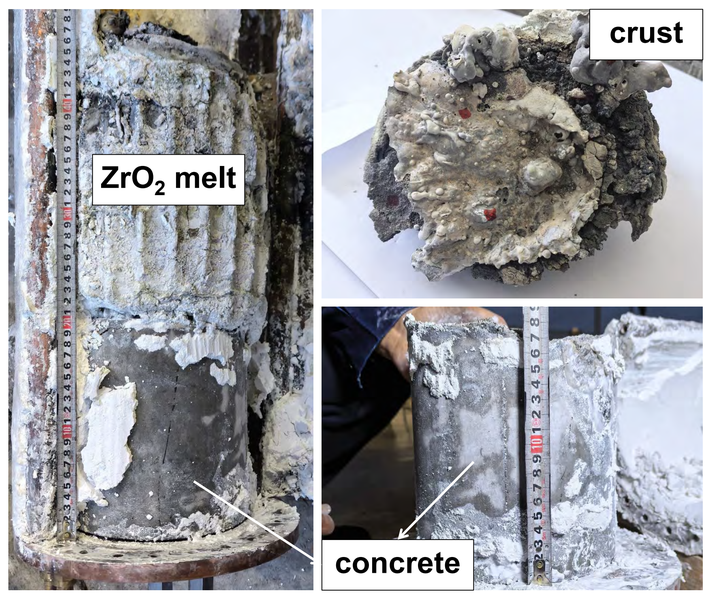

Fig.4 pre-test result

Conclusions

- Established a systematic screening method for ablation-resistant concrete.
- Identified a high-performance MgO-Al_2O_3 rich system through thermodynamic calculations.
- Confirmed that the designed concrete meets nuclear-grade structural strength standards while exhibiting a higher melting point and larger melting enthalpy.
- MAAP5 simulations demonstrate that the designed concrete significantly reduces the ablation rate during MCCI.
- Validation one-dimensional MCCI experiments are currently underway.

CNNC Key Laboratory for Severe Accident Research in Nuclear Power Safety
China Nuclear Power Engineering Co., Ltd, Beijing, China

Erhui Chen **Email:** cheneh@cnpe.cc
chenerhui97@163.com
*yidanyuan2010@aliyun.com

AEROSOL REMOVAL BEHAVIOR BY CONTAINMENT SPRAY

Byeonghee Lee* and Kwang Soon Ha
Korea Atomic Energy Research Institute
Daedeokdaero 989-111, Yuseong, Daejeon, Korea, 34057
*leebh@kaeri.re.kr; tomo@kaeri.re.kr

ABSTRACT

Aerosol behavior by water spray were experimentally investigated to examine the fission product removal in containment by spray system. The test facility is composed of a vessel, a spray system with different nozzles, and two multi-stage impactors to measure the aerosol concentration by size. The test vessel was initially filled with air with 0.7 μm SiO_2 aerosol particles until the particle density saturated, and then the inlet and the outlet of the vessel were closed. The aerosol concentration decreases slowly by time by different mechanisms, mainly by the gravitational settling. Meanwhile, the aerosols agglomerates and therefore the number of larger particles increases. After keeping the vessel isolated for a moment, water sprayed from the nozzle at the vessel top. The spray droplets wash out the aerosol, resulting in an abrupt drop of aerosol concentration in the vessel. The spray nozzle was designed such that the droplet size and the mass flow rate per covering area are the same as that in the operating nuclear power plant, OPR1000. In addition to the reference nozzle, nozzles having different characteristics in terms of droplet diameter and the mass flow rate per area were also tested. 5 different tests including no-spray case were conducted with the facility. The aerosol removal becomes faster as the mass flow rate increases, however, the removal rate seemed not influenced by the droplet size. The model for the spray decontamination in containment was formulated, and the calculation results were compared with the tests.

KEYWORDS
Containment spray, Aerosol, Fission product, Droplet, Decontamination

1. INTRODUCTION

Containment spray system is an engineering safety feature of nuclear power plants, to decrease the temperature and pressure also to remove fission products during accidents. Also, the spray also removes airborne fission products. The airborne fission products released by an accident are either deposited on structures or wall surfaces by different deposition mechanisms, such as gravitational settling, thermophoresis, and diffusion. In addition to those mechanisms, the spray water droplets absorb aerosols in their falling trajectory, removing the aerosols effectively.

In the mechanism of aerosol removal by spray, the droplet size determines the falling speed, and the mass flow rate of the spray is related to the population of droplets. Both of them affects the aerosol removal efficiency. At the same time, the aerosol removal rate differs by the particle size.

In this article, the aerosol behavior in containment were examined experimentally by using a vessel and a spray system. The aerosol concentration in the vessel were measured by particle size along time, with different spray nozzles. The experimental results were then compared with the model calculation considering the mechanisms of aerosol removal by droplets.

2. AEROSOL-SPRAY EXPERIMENT

2.1. Experimental Facility

Figure 1 shows the schematic of ART (Aerosol Retention Test with spray) facility for spray-aerosol experiments. The test vessel is designed to simulate a reactor containment, with an inner diameter of 1580 mm and a height of 2080 mm. The volume of the vessel is about 3.5 m^3. The aerosol concentration was measured by using ELPI (electrical low-pressure impactor, DEKATI) at two different positions, top and bottom in the vessel. The sampling nozzles are vertically aligned, and the distance between the nozzles is 700mm. A containment spray-simulating nozzle is installed at the top of the vessel.

In the beginning of the test, the carrier gas (air) with aerosols is injected into the vessel until the aerosol concentration in the vessel is saturated, and then the inlet and the outlet of the vessel were closed. The vessel was kept isolated for a while to observe the change of the aerosol concentration without spray, and then the spray is activated at the top of the vessel. Then, the water spray washes out aerosols and the aerosol concentration in the vessel decrease rapidly. Throughout the tests, the aerosol concentration by size were monitored and recorded with the ELPI.

Table 1 shows the specification of the aerosol nozzles installed in existing OPR1000 nuclear power plant and the nozzle used in the experiment, which is designed such that the flow rate per area and the droplet diameter are the same as those of OPR1000 [1]. The nozzle in the table is a reference nozzle which simulate the actual plant condition, and there are other nozzles which are different in droplet size and flow rate.

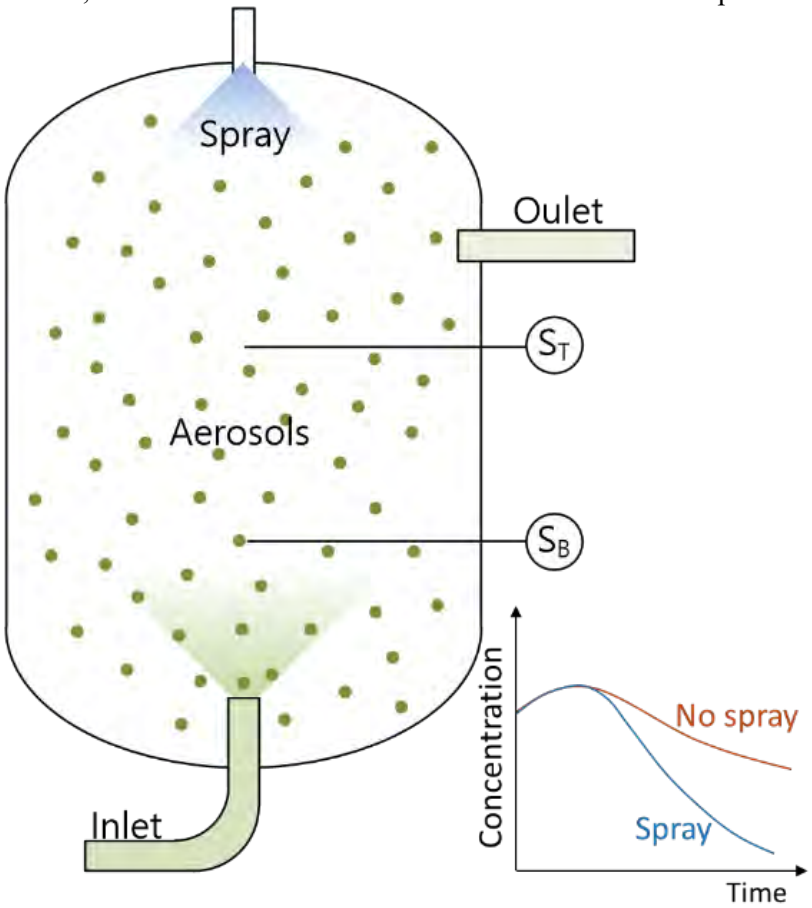

Figure 1. Schematic of ART experimental facility

Table I. Spray variables for ART reference nozzle

Variable	OPR1000	ART(Ref.)
$D_{droplet}$ (μm)	295	300
Flow rate (slpm)	57.6	17.2
Area per nozzle (m^2)	6.58	1.96
Flow rate per area (slpm/m^2)	8.8	8.8

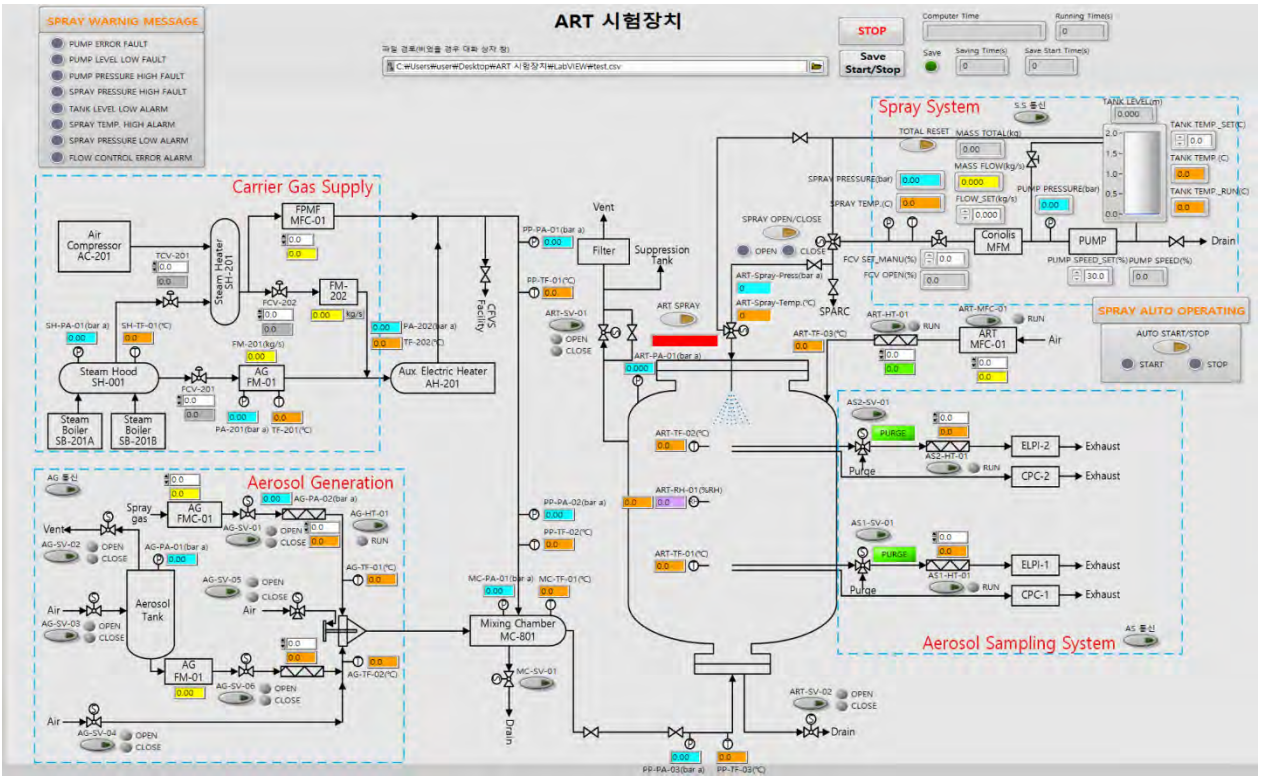

Figure 2. Control panel of ART experimental facility

Figure 2 shows the control panel of ART facility. The facility is composed of a carrier gas supply system, an aerosol generation system, a test vessel, two aerosol sampling systems, and a spray system. The carrier gas supply system provides air or steam at a temperature of the experimental condition. The aerosols are airborne by ejecting aerosol-dispersed ethanol together with heated air in the mixing chamber of the aerosol supply system. The temperature of the mixing chamber was set to be higher than the boiling temperature of ethanol, and the temperatures of pipes and the vessel were set to be the experimental condition. The spray system supplies water at the designated temperature and flow rate to the spray nozzle. The two sampling nozzles were connected from the vessel to the ELPI, via the diluter unit to decrease the aerosol concentration down to the allowed range of the ELPI.

2.2. Experimental Conditions

Table 2 shows the test matrix which shows the characteristics of the spray nozzles for each test cases. The variables of the test are droplet size and flow rate of the spray, which are affecting the aerosol removal characteristics. The first case, NSA, was performed to examine the aerosol behavior in the vessel without spray. Depending on the spray nozzle, the droplet diameter is 200 μm, 300 μm, or 500 μm, and the flow rate is 5.0 slpm or 17.2 slpm.

Table 3 shows the thermal-hydraulic conditions of experiments. The carrier gas in the experiments is air to eliminate the effect of condensation of steam. The aerosol particles are SiO_2 with diameter of 0.7 μm from a previous review about the aerosol particle characteristics during a severe accident, which was AMMD of 1-2 μm [2]. The gas temperature was kept identical at the inlet, vessel, and outlet. The temperature of the spray water was also the same as the gas temperature, to remove the effect of thermophoresis during the experiment.

Table 2 Test matrix of ART experiments

No.	Test Name	Spray	Droplet size (μm)	Flow rate (slpm)
1	**NSA**	X	N/A	
2	**SA300H**	O	300	17.2
3	**SA500H**		500	17.2
4	**SA300L**		300	5.0
5	**SA200L**		200	5.0

Table 3 Experimental Condition

Condition	Value
Experimental gas	Air
Temperature (°C)	60
Pressure (bar abs)	1
Filling mass flow (slpm)	200
Aerosol particle	SiO_2
Aerosol particle diameter (μm)	0.7

3. RESULTS

2.1. Aerosol Behavior without Spray

Figure 3 shows the mass concentrations of the aerosol at the top and at the bottom of the vessel. All the test cases except non-spray case (NSA) were presented, to show the overall aerosol behavior during the experiments. NSA test case is not presented here, because the aerosol behaviors before the spray represent the non-spray case. The aerosol concentration increases during the injection period, and then decreases slowly after the vessel is isolated by closing the inlet and the outlet.

When the spray is activated, the aerosol concentration decreased abruptly because the particles were washed out by the spray droplets. In the figure, the total mass concentration is higher at the top then that at the bottom. The higher aerosol concentration at the top is observed in all test cases, because the aerosol containing gas were injected from the bottom of the vessel, pushing the aerosols toward the top of the vessel.

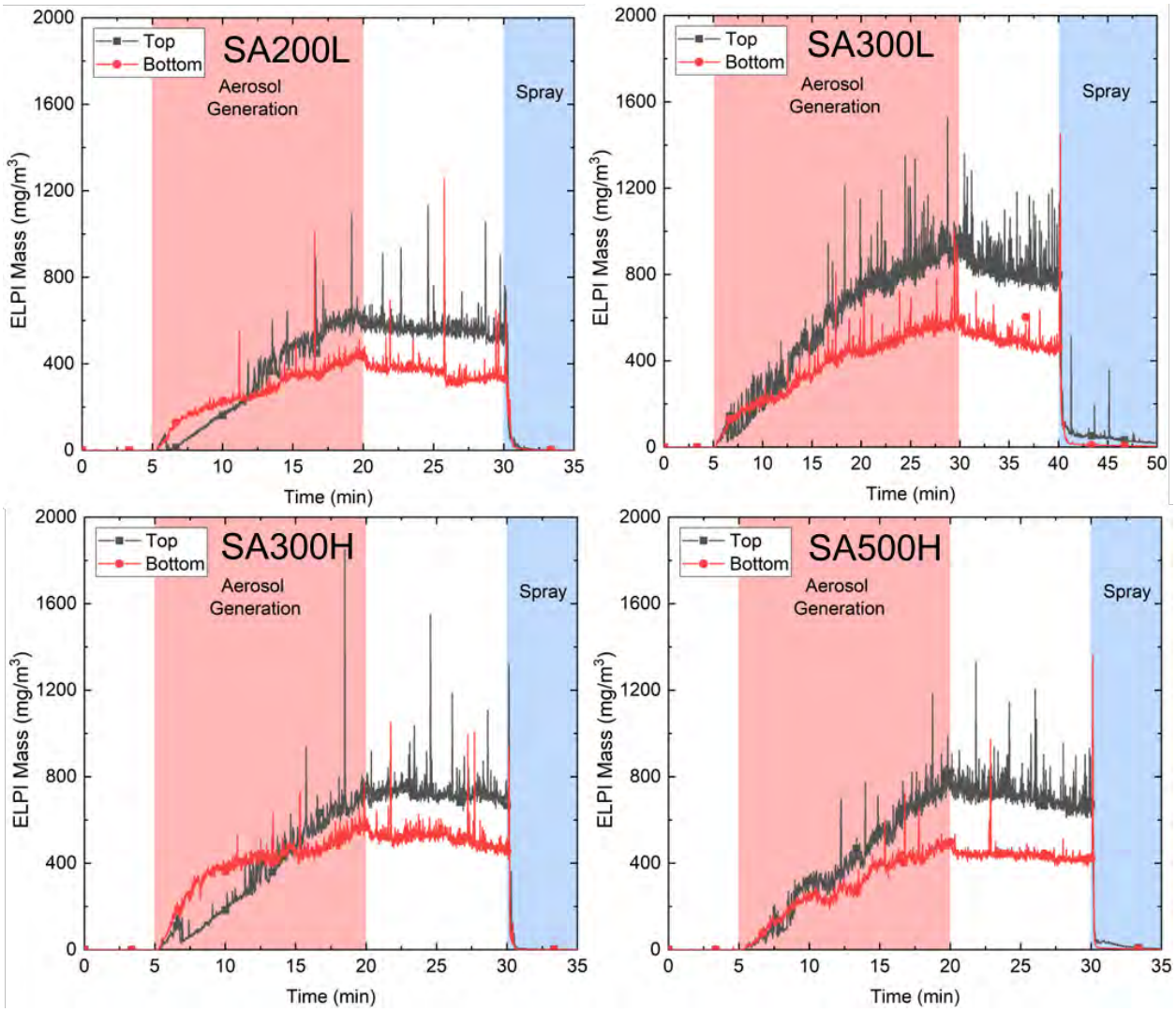

Figure 3. Overall mass concentrations of tests

Figure 4 shows the mass concentration and the number density of the aerosol at the top and at the bottom of the vessel for SA300H test. The overall aerosol behaviors before the spray are almost similar in the other tests because the test conditions are identical in every test except the spray variables. The aerosol behaviors after the spray are not visible well in the figures due to the abrupt decreases of the concentration, therefore they will be analyzed in the next chapter.

ELPI measured the aerosol concentration by 14 different size bin. Among them, the dominant size bins in terms of the mass and the number concentration, 0.75 μm, 1.2 μm, 2 μm, and 3 μm, are presented here. Note that the aerosols injected into the vessel were monodispersed SiO_2 particles with diameter of 0.7 μm. Therefore, the larger particles in the figures are considered as the result of particle agglomeration. One of the evidence of the agglomeration is that the concentration of 3 μm particles at the vessel top increases slowly after the vessel isolation, which means that the injected aerosols agglomerate and become larger. As the results of the agglomeration, the 2 μm particles had the highest mass concentration, whereas the 0.75 μm particles had the highest number density.

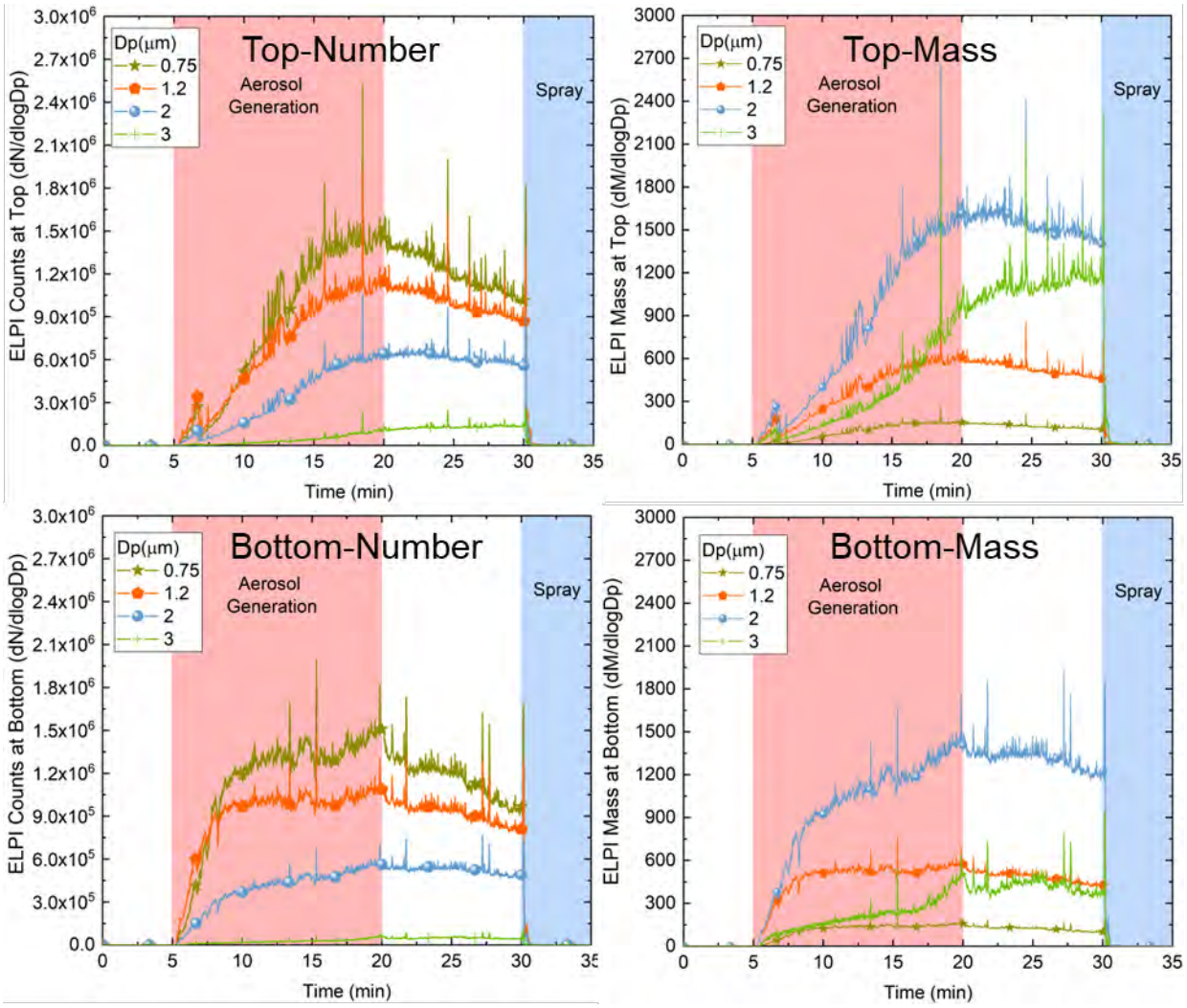

Figure 4. Mass and number concentration by aerosol size in SA300H test

Without a spray, two important aerosol deposition mechanisms are a gravitational settling and a diffusion [3]. The deposition velocity by gravitational settling is

$$v_{grav} = \frac{d_p^2 \rho_p g C_m}{18\mu} \quad (1)$$

where d_p is particle diameter, ρ_p is particle density and μ is dynamic viscosity of air. And the deposition velocity by diffusion is

$$v_{diff} = \frac{kTC_m}{3\pi\mu d_p \delta} \quad (2)$$

where k is Boltzmann constant, T is temperature, and δ is diffusion boundary layer thickness assumed to be 10 μm. The Cunningham slip correction is given by

$$C_m = 1 + \frac{2\lambda}{d_p}\left[1.257 + 0.4\exp\left(-\frac{1.1 d_p}{2\lambda}\right)\right] \quad (3)$$

where λ is the mean free path which can be calculated by

$$\lambda = \frac{\mu}{\rho_g}\sqrt{\frac{\pi M}{2RT}} \quad (4)$$

where M is molecular weight and R is gas constant. The thermophoresis is not important in this experiment due to the isothermal condition in the vessel.

Table 4 shows the deposition velocities of aerosol particles by gravitational settling and those by diffusion. For the particle size from 0.75 to 3 μm, deposition velocity of gravitational settling is more than 10 times larger than that of diffusion. Therefore, the aerosol behavior is dominated by the gravitational settling. Even for the largest 3 μm particle, the deposition velocity, which means the falling velocity of aerosol is only 0.68 mm/s, therefore the aerosol concentration decreases very slowly. This explains the slow decrease of aerosol concentration in the experiment before the spray activation.

Table 4 Deposition velocity of aerosol particle

		Particle size (μm)			
		0.75	1.2	2	3
Deposition velocity (m/s)	Grav. settling	5.0E-5	1.2E-4	3.1E-4	6.8E-4
	Diffusion	4.1E-6	2.4E-6	1.3E-6	8.7E-7
Time to travel 1 m by gravitational settling (hr)		5.5	2.3	0.9	0.4

2.1. Aerosol Behavior without Spray

Figure 5 shows the aerosol concentration decrease by the spray activation. In all cases, the aerosol concentration decreases abruptly upon the spray activation, however, the rate of decrease varies among cases. In general, the cases with smaller spray flow rate shows slower decrease of aerosol concentration. However, the droplet size seems not very Relative for the aerosol removal. Larger droplets wash out more aerosol particle on its falling trajectory, however, the number of spray droplets decreases as the droplet volume increases for the same flow rate of the spray, which compensate each other. It is note that, the decreasing rate seems not depend on the aerosol particle size.

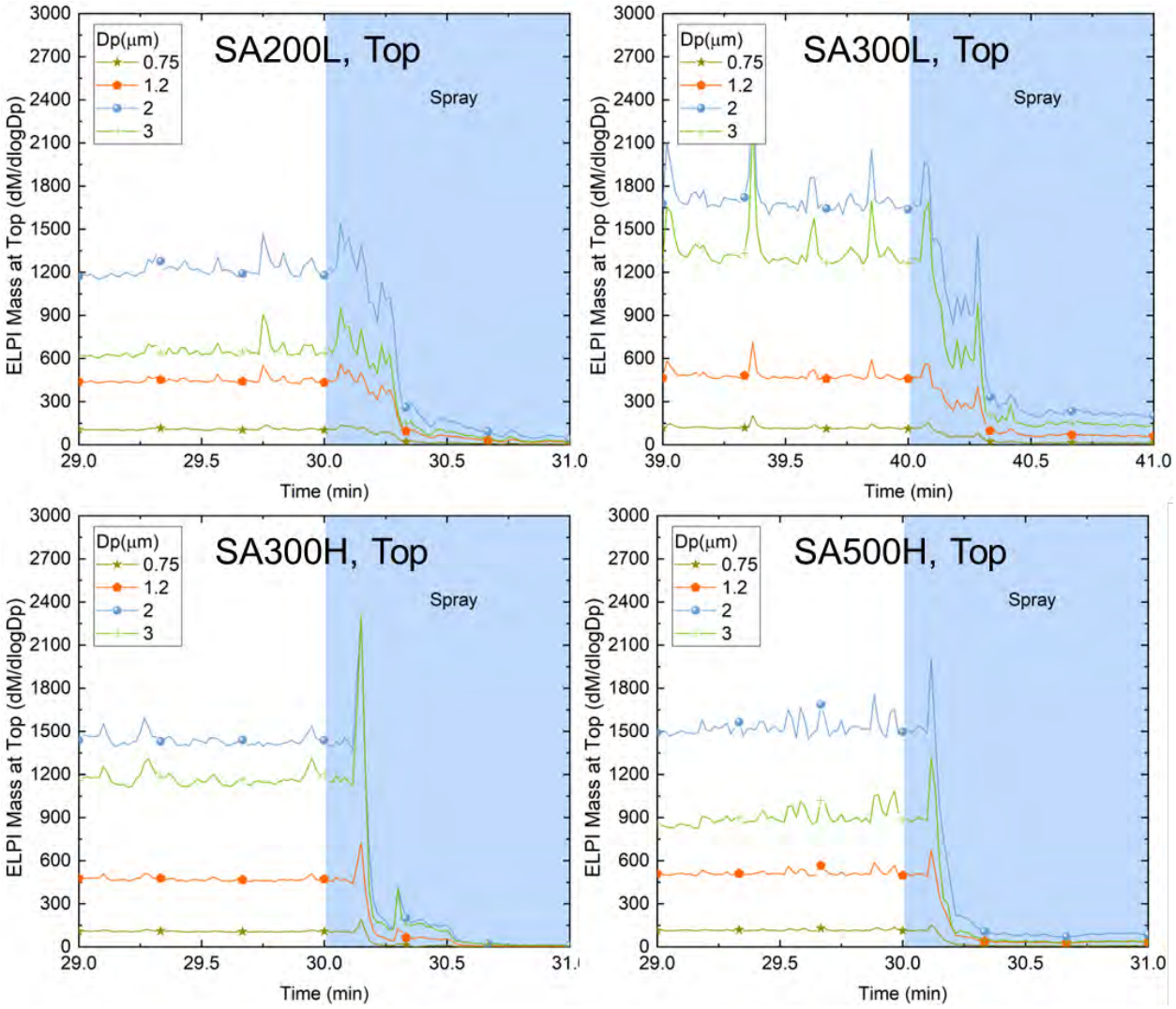

Figure 5. Mass and number concentration by aerosol size in SA300H test

The aerosol removal by spray can be formulated as a first-order rate equation [4]

$$\frac{dM_k}{dt} = -\lambda_{k,i} M_k \tag{5}$$

Where M_k is the particle mass of size k and $\lambda_{k,i}$ is the removal rate constant of the particle size k by the droplet size i. The removal rate constant is

$$\lambda_{k,i} = \frac{3F_i h E_{i,j}}{4Vr_i} \tag{6}$$

Where F_i is the volumetric flow rate for droplet size i, $E_{i,j}$ is the collection efficiency for droplet size k, h is the fall height of the droplet, V is the control volume, and r_i is the droplet radius.

The dominant mechanism of aerosol removal by spray droplets depends on the droplet size. When the droplet size is larger than 10 μm, inertial impaction and interception are dominant mechanisms of aerosol removal, and the other mechanisms such as diffusiophoresis or diffusion are negligible.

The collection efficiencies of interception depend on the flow regime around the droplet,

$$\varepsilon_{in,vis} = (1+l)^2\left[1 - \frac{3}{2(1+l)} + \frac{1}{2(1+l)^3}\right] \quad \text{(for viscous flow)} \tag{7}$$

$$\varepsilon_{in,pot} = (1+l)^2 - (1+l) \quad \text{(for potential flow)} \tag{8}$$

The collection efficiencies of impaction also depend on the flow regime, and that for potential flow is

$$\varepsilon_{im,pot} = \left[\frac{Stk}{Stk+0.5}\right]^2 \quad \text{for Stk}\geq 0.2 \tag{9}$$

and $\varepsilon_{im,pot}$ is 0 for Stk≤0.0834, and is linearly interpolated for 0.0834<Stk<0.2. The collection efficiency of impaction for viscous flow is

$$\varepsilon_{im,vis} = \left[1 + \frac{0.75 log_e(2Stk)}{Stk-1.214}\right]^{-2} \quad \text{for Stk}>1.214 \tag{10}$$

and is zero otherwise. Stk is the Stokes number,

$$Stk = \frac{2r_p^2 \rho_p (v_d - v_p)}{9\mu r_d} \tag{11}$$

where v_d and v_p are the terminal velocities of the droplet and particle, respectively, and μ is the gas viscosity. When the flow is between potential and viscous regime, the collection efficiency can be interpolated by

$$\varepsilon_x = \frac{\varepsilon_{x,vis} + \varepsilon_{x,pot}(\frac{Re}{60})}{1+(\frac{Re}{60})} \tag{12}$$

where Re is the droplet Reynolds number.

A terminal velocity of a droplet is important parameter to estimate the collection efficiency. The terminal velocity of a sphere can be calculated theoretically, however, the terminal velocity of droplet is not simply calculated by that because of the flow inside the droplet. Instead, the terminal velocity of a droplet can be

estimated by empirical equations or experimental results. The terminal velocities of droplets with diameter of 200 μm, 300 μm, and 500 μm are approximately 0.8 m/s, 1.2 m/s and 2.0 m/s, respectively [5].

Figure 6 shows the comparison between the calculation and the experiment for the tests at the vessel top. The calculation shows that the concentration of small particles decreases slower than that of large particles, whereas the experiment shows that decreasing rates of the aerosol concentration seem identical for every sizes. In addition, the decreasing rate of aerosol concentration in the experiments are even faster than that of largest particle in the calculation. That is, there are removal mechanisms of aerosol particles other than the impaction and the interception of droplet. However, a thermophoresis is not plausible for the experiment because the vessel wall and gas temperature are the same. The diffusion or diffusiophoresis are also not probable due to the large droplet size.

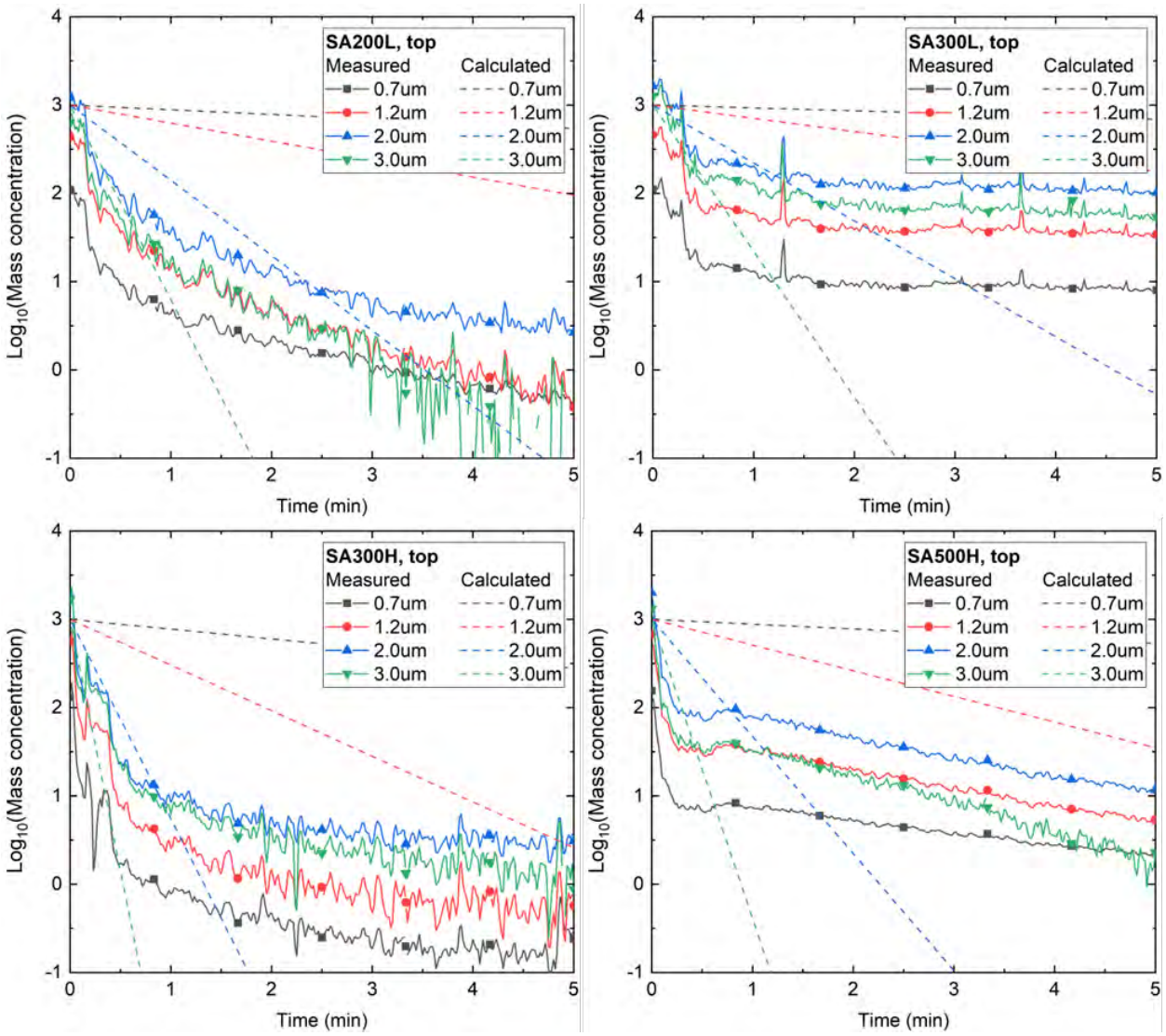

Figure 6. Calculation and measurement of aerosol removal by spray

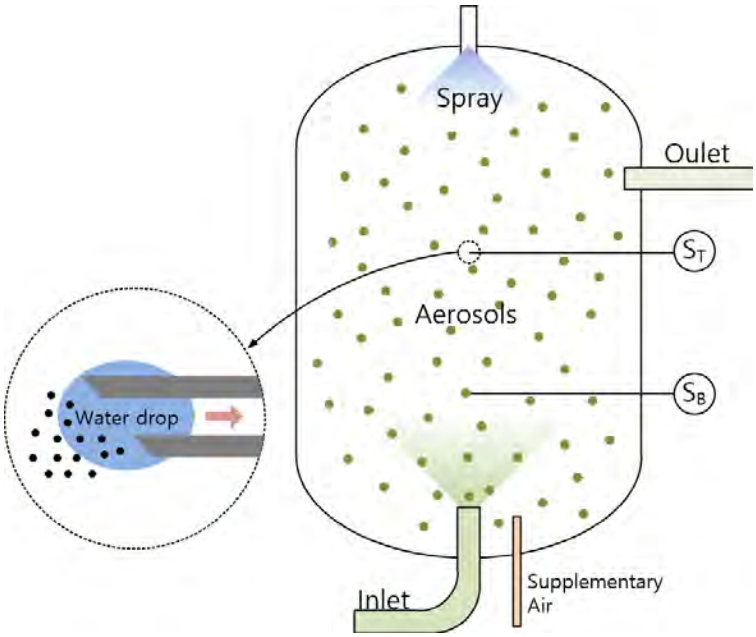

Figure 7. Water trap at sampling nozzle inlet

Figure 7 shows the one possible reason why the aerosol concentrations showed the same decreasing rate regardless of the particle size. By the spray, the inlets of the sampling nozzles are wet, which forms water traps. All aerosol particles drawn through the sampling port subsequently pass through the water trap. Then, the aerosols are removed mostly by the water trap before they reach the ELPI.

One solution to prevent the aerosol removal by water trap at the sampling nozzle inlet is to alternate between sampling and spraying. Water is sprayed for a few to several seconds and then the spray is stopped, and then the aerosol sampling started for a few tens of seconds. Currently, the alternating between sampling and spraying is under examination. After that, the experiments will be conducted again with the method.

4. CONCLUSIONS

Aerosol removal behavior by water spray were tested for different spray conditions with ART experimental facility. The test vessel was filled with the SiO_2 aerosol particles with diameter of 0.7 μm, and then the vessel is isolated for a while by closing the inlet and outlet. The aerosol concentration decreases slowly mainly by gravitational settling, and then decreases abruptly when the spray is activated. Meanwhile, the aerosols were agglomerates and therefore the particles of 2 μm showed the highest mass concentration, although the 0.75 μm particles showed the highest number density. The deposition velocity by gravitational settling were calculated to be less than 1 mm/s even for the largest particles, therefore the concentration decreases very slowly without spray.

The aerosol removal by spray, on the other hand, was calculated for the dominant removal mechanisms, impaction and interception. The removal rates were calculated for the experimental condition, for the different particle sizes. The calculation showed that the concentration of small particles decreases slower than that of large particles. However, the experiments showed almost identical removal rates of particles regardless the size, which do not correspond the calculation. The possible explanation of the phenomena is the formation of water trap at the inlet of the sampling nozzle. To avoid the aerosol capture by the water trap, the method of alternating the spray and the sampling is currently under examination, and the tests will be performed again with the method.

ACKNOWLEDGMENTS

This work was supported by the National Research Foundation of Korea (NRF) grant funded by the Korean government (Ministry of Science and ICT) (RS-2022-00144202).

REFERENCES

1. Korea Hydro-Nuclear Power Cooperation (KHNP), “Final Safety Analysis Report (FSAR) of Shin-Kori Unit 1 & 2,” Chapter 6 Engineering Safety Feature (2018)
2. M.P. Kissane, “On the nature of aerosols produced during a severe accident of a water-cooled nuclear reactor,” *Nucl. Eng. Des.* **238,** pp. 2792-2800 (2008)
3. F.M. Gelbard and S. Durbin, “Comparing the MELCOR Aerosol Deposition Model with Exact Analytical Solution,” SAND2024-03561R, Sandia National Laboratory, (2024)
4. L. L. Humphries et. al., “MELCOR Computer Code Manuals Vol. 2: Reference Manual Version 2.2.11932,” SAND2018-13560, Sandia National Laboratory, (2018)
5. R. Gunn and G. D. Kinzer, “The terminal velocity of fall for water droplets in stagnant air,” *J. Meteorol.* **6**, pp. 243-248 (1949)

DEVELOPMENT OF PERFORMANCE VERIFICATION TEST METHODOLOGY FOR PASSIVE RADIOACTIVE MATERIAL FILTRATION SYSTEM

Kihan Park, Sungho Hong, and Jaehoon Jung*
Korea Atomic Energy Research Institute (KAERI)
989-111 Daedeok-daero, Yuseong-gu, Daejeon, Korea
kihan@kaeri.re.kr; hsh4004@kaeri.re.kr; jhjung@kaeri.re.kr

ABSTRACT

During the severe accident in nuclear power plants (NPPs), lots of radioactive materials are released into the containment building. To prevent the containment overpressure failure and reduce release of radioactive materials into the environment, the filtered containment venting system (FCVS) installed outside the containment building was developed. In Korea, to more enhance the safety of NPPs, a passive radioactive material filtration system is being developed. This another system installed in the containment building aims to minimize release of radioactive materials into the environment by capturing radioactive materials in both airborne and gaseous phases within the containment. It consists of two main components, which are the passive fluid induction component and the fission product filtration component. To evaluate and verify the performance of this system, the development of a reasonable and reliable test methodology is essential. This paper introduces several test methods using simulants conducted by KAERI and the supporting evidence.

KEYWORDS
Filtration, Radioactive material, Aerosol, Iodine, Organic iodide

1. INTRODUCTION

Severe accidents at NPPs lead to the release of significant amounts of radioactive materials inside the containment building. A passive radioactive material filtration system, designed for installation in the containment building to capture the radioactive materials in both airborne and gaseous phases, is currently under development in Korea [1]. It is in the shape of a rectangular duct, which consists of a hydrogen catalyst, an aerosol filter, and an iodine adsorbent [2]. The exothermic reaction caused by hydrogen recombination in the catalyst induces natural convection from the bottom to the top of the duct.

KAERI is developing the test methodology to conduct verification tests on the system's radioactive materials reduction performance using simulants (SiO_2, I_2, CH_3I). This paper reviews relevant literature on capturing methods to measure the simulant concentrations, and proposes the performance verification test methods.

2. SIMULANT MEASURING METHODS

2.1. Silicon Dioxide (SiO_2)

Spherical monodisperse non-disintegrating SiO_2 particles are representative simulant of nuclear aerosols [3]. A common method for measuring the mass concentration of particulate matter in a gas is to collect the particles from the sampled gas using a filter and measure the change in the filter weight. Considering the high-temperature steam environment within the containment building during a severe accident, the sampling strategy of EPA Method 5, which prevents condensation utilizing a heated sampling train, provides a relevant framework for developing a suitable measurement procedure. Regarding the filter weight measurement, variations in humidity and temperature can affect the gravimetric measurement of the particulate matter by altering the mass of the filters [4]. Thus, the filters should be conditioned identically before both the pre- and post-sampling weighing.

2.2. Iodine (I_2)

There are two methods for capturing I_2 in the sampling gas: liquid trapping method, solid adsorption method. In the former, a specific aqueous solution, such as ascorbic acid or sodium hydroxide (NaOH) solution, is used to collect and convert iodine into iodide ion (I^-) and iodate ion (IO_3^-) [5]. Regarding the latter, although there are many studies on development of adsorbents for I_2, especially silver-exchanged zeolite showed complete retention of I_2 up to 900 ℃ regardless of the oxidizing or reducing condition in the presence of hydrogen [6]. The I_2 captured by silver-exchanged zeolite has the form of silver iodide (AgI) and silver iodate ($AgIO_3$); the latter decomposes to form AgI at temperatures exceeding 190 ℃ [7]. Although AgI is highly stable and insoluble, appropriate pretreatment before analysis, for example the elution reaction using aqueous sodium sulfide (Na_2S), results in dissolution of I^- into the solution [8]. Therefore, I_2 concentration can be measured using ion selective electrode (ISE), ion chromatograph (IC) or inductively coupled plasma-mass spectrometry (ICP-MS).

2.3. Methyl Iodide (CH_3I)

There are two methods for capturing CH_3I in the sampling gas: liquid trapping method, solid adsorption method. In the former, a specific nonpolar solvent, such as toluene, is used to dissolve CH_3I. Due to the high volatility of CH_3I, several precautions are required for handling: low-temperature capture is more effective, and upon completion of capture, the samples must be sealed and analyzed as quickly as possible, and airtightness should be maintained using headspace vials and gas-tight syringes during sample extraction for analysis [9]. CH_3I concentration can be measured gas chromatography-flame ionization detector (GC-FID) or gas chromatography-mass spectrometry (GC-MS). Regarding the latter, silver-exchanged zeolite captures CH_3I through the decomposition reaction, resulting in the formation of AgI and subsequent organic byproducts such as methanol, dimethyl ether, alkanes, and alkenes [7]. The AgI analysis method noted above can be used to determine the CH_3I concentration. Meanwhile, activated carbon is the only adsorbent media for normal atmosphere cleanup systems mentioned in NRC Regulatory Guide (RG) 1.140, which specifies that its CH_3I removal performance must be tested according to ASTM D3803 and pass the specified criteria. For example, triethylenediamine (TEDA)-impregnated AC showed 98.4% adsorption efficiency for CH_3I under the conditions of 70 ℃ temperature, 90 % relative humidity (RH), and 15 ppm CH_3I concentration [10]. Because TEDA-impregnated AC captures CH_3I through physical adsorption and chemical reaction, a chemical extraction method is necessary as thermal desorption cannot fully desorb the captured CH_3I for measuring the concentration [11].

3. PERFORMANCE VERIFICATION TEST METHODS

KAERI plans to conduct performance verification tests for the passive radioactive material filtration system in two ways: in-line test, in-vessel test. The former is to install the system in a pipeline with carrier gas flows containing a simulant, and then measure the simulant concentrations at the system's inlet and outlet. The

latter is to install the system inside a pressure vessel with an internal volume of 80 m^3, and then measure the concentrations at several points inside the vessel.

3.1. In-line Test Method

The in-line test method is used to obtain the decontamination factor (DF) and pressure drop of the filtration system for each simulant. The carrier gas consists of air and steam, and contains at a time a single species of simulant. However, this method is not suitable for verifying the radioactive material reduction performance as a passive system. Due to the absence of hydrogen in the carrier gas, the flow inducement part does not operate. Criteria for sampling location selection and sampling system design could be referenced from ANSI/HPS N 13.1, and CFD analysis would be performed concurrently.

3.2. In-vessel Test Method

The in-vessel test method is used to verify the radioactive material reduction performance as a passive system in a defined space. Air, steam, hydrogen, and simulants can be injected into the vessel. A key challenge in this method is how to estimate the mean simulant concentration within the vessel from a limited number of sampling locations. The interior of the vessel would be virtually partitioned into several regions. The simulant concentration measured from the sampling point in each region could be assumed to be representative of the mean concentration of that region.

The mean concentration of a simulant in the vessel ($\overline{C_{tot}}$) is :

$$\overline{C_{tot}} = \sum C_i V_i \,/\, \sum V_i \tag{1}$$

where C_i is the simulant concentration in the i-th region, and V_i is the volume in the i-th region.

CFD analysis could be employed to validate this estimation method of the mean concentration in the vessel.

ANSI/AHAM AC-1, which is the standard for measuring performance of portable household air cleaners, provides a relevant framework for verifying the performance of the filtration system. This standard defines the method for measuring the CADR (Clean Air Delivery Rate) value, a key performance indicator of air cleaners. KAERI plans to evaluate the performance of the filtration system using the CADR value.

The mean concentration of a simulant in the vessel over time is :

$$\overline{C_{tot}}(t) = C_0 e^{-kt} \tag{2}$$

where C_0 is the initial concentration of a simulant in the vessel, and k is the decay rate constant.

Sampling should be initiated and terminated simultaneously across all sampling points. Due to the difficulty in real-time measurement of the simulant concentration, sampling is carried out at fixed time intervals and subsequently analyzed offline. The concentration trends over the test period would be then estimated from these results.

The method for calculating CADR is :

$$CADR = V\left(k_{on} - k_{off}\right) \tag{3}$$

where V is volume of the test chamber, k_{on} is the decay rate when the filtration system is operating, and k_{off} is the decay rate when the filtration system is not operating.

4. CONCLUSIONS

KAERI is developing the test methodology for the performance evaluation and verification of a passive radioactive material filtration system, currently under development in Korea, using simulants (SiO_2, I_2, CH_3I). Various literatures for measuring simulant concentrations were reviewed: a filter-based gravimetric method for SiO_2, and both liquid trapping and solid adsorption methods for I_2 and CH_3I. For verifying the performance for the filtration system, two methods are proposed. The in-line test is conducted by installing the system in a pipeline with carrier gas flows containing a simulant and measuring the simulant concentrations at the inlet and outlet to obtain the DF and pressure drop of the filtration system for each simulant. The in-vessel test is conducted by installing the system inside a pressure vessel with an internal volume of 80 m^3 and measuring the simulant concentrations at several points to calculate the mean concentration in the vessel over time and determine the CADR value, providing a quantitative performance indicator for the filtration system.

ACKNOWLEDGMENTS

This work was supported by the Korea Institute of Energy Technology Evaluation and Planning (KETEP) and the Ministry of Climate, Energy & Environment (MCEE) of the Republic of Korea (Grant No. RS-2025-02318177).

REFERENCES

1. J. Jung, S. Hong, J. Kim, and C. Kang, “Preliminary Experiment on the Elemental Iodine Capture Filter Performance for Filtration System,” *Trans. KNS Autumn Meet.*, Changwon, Korea, October 24-25, 2024 (2024).
2. J. Kim, K. Choi, J. Jung, and Y. Na, “Performance Simulation of a Catalyst in a Passive Radioactive Material Reduction System,” *Trans. KNS Autumn Meet.*, Changwon, Korea, October 30-31, 2025 (2025).
3. A. Dehbi, D. Suckow, T. Lind, S. Guentay, S. Danner, and R. Mukin, “Key Findings from the Artist Project on Aerosol Retention in a Dry Steam Generator,” *Nucl. Eng. Technol.* **48**(4), pp. 870-880 (2016).
4. K. Widziewicz-Rzońca and M. Tytła, “Water Sorption by Different Types of Filter Media Used for Particulate Matter Collection Under Varying Temperature and Humidity Conditions,” *Int. J. Environ. Res. Public Health* **17**(14), 5180 (2020).
5. S. Kutsuna and N. Kaneyasu, “A laboratory study on the uptake of gaseous molecular iodine by clay minerals at different relative humidities,” *Environ. Sci.: Atmos.* **2**(5), pp. 1041-1059 (2022).
6. H. Zhang, X. Kou, L. Liu, N. Cerboni, K. Tokoi and R. Eichler, “Gaseous radioactive iodine retention on silver-loaded zeolites under varying temperatures and atmospheric conditions,” *Journal of Radioanalytical and Nuclear Chemistry* **334**(10), pp. 7087-7096 (2025).
7. J. Huve, A. Ryzhikov, H. Nouali, V. Lalia, G. Augé, and T. J. Daou, “Porous sorbents for the capture of radioactive iodine compounds: a review,” *RSC Advances* **8**(51), pp. 29248-29273 (2018).
8. A. Yadav, S. Chong, B. J. Riley, J. S. McCloy, and A. Goel, “Iodine Capture by Ag-Loaded Solid Sorbents Followed by Ag Recycling and Iodine Immobilization: An End-to-End Process,” *Ind. Eng. Chem. Res.* **62**(8), pp. 3635-3646 (2023).
9. T. J. Kim, M. Kim, D. Kim, S. H. Jung, and J. W. Yeon, “Concentration Determination of Volatile Molecular Iodine and Methyl Iodide,” *Bull. Korean Chem. Soc.* **39**(6), pp. 824-828 (2018).
10. S. Kitani, T. Noro, and T. Kohara, “Removal of methyl iodide by impregnated charcoals from flowing air under humid condition,” *J. Nucl. Sci. Technol.* **9**(4), pp. 197–202 (1972).
11. G. I. Park, I. T. Kim, J. K. Lee, S. K. Ryu, and J. H. Kim, “Effect of Temperature on the Adsorption and Desorption Characteristics of Methyl Iodide over TEDA-Impregnated Activated Carbon,” *Carbon Letters* **2**(1), pp. 9–14 (2001).

12th CONFERENCE ON
SEVERE ACCIDENTS RESEARCH
May 18-22, 2026 - Madrid, Spain
ERMSAR 2026

DEVELOPMENT OF PERFORMANCE VERIFICATION TEST METHODOLOGY FOR PASSIVE RADIOACTIVE MATERIAL FILTRATION SYSTEM

Kihan Park[a*], Sungho Hong[a], Jaehoon Jung[a]
[a]Korea Atomic Energy Research Institute (KAERI), 989-111 Daedeok-daero, Yuseong-gu, Daejeon, Korea
Corresponding author: kihan@kaeri.re.kr

1. Introduction

- **During the severe accident in nuclear power plants (NPPs),**
  lots of radioactive materials are released into a containment building. To prevent the containment overpressure failure and reduce release of radioactive materials into the environment, it has been developed that the filtered containment venting system (FCVS) which is installed outside the containment building. jet pool scrubbing.
- **To capture the airborne radioactive materials,**
  A passive radioactive material filtration system, designed for installation in the containment building, is currently under development in Korea.
- **To evaluate and verify the performance of this system,**
  KAERI is developing the test methodology to conduct verification tests on the system's radioactive materials reduction performance using simulants (SiO_2, I_2, CH_3I). This poster reviews relevant literature on capturing methods to measure the simulant concentrations, and proposes the performance verification test methods.
- **Keywords :** Filtration, Radioactive material, Aerosol, Iodine, Organic iodide

2. Passive Radioactive Material Filtration System

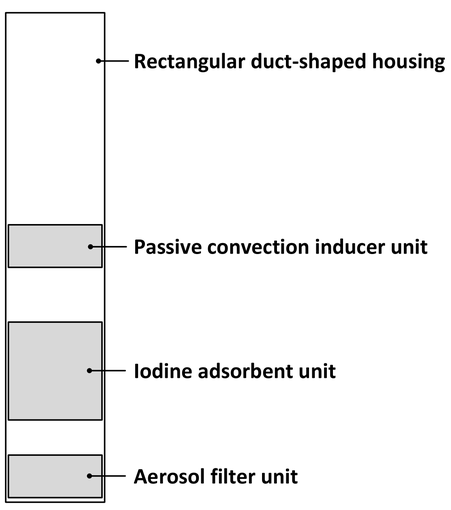

Fig. 1. Schematic diagram of passive radioactive material filtration system

- The system features a rectangular duct shape, consisting of a passive convection inducer unit, an aerosol filter unit, and an iodine adsorbent unit.
- The passive convection inducer unit consists of a hydrogen catalyst, where the exothermic reaction driven by hydrogen recombination induces natural convection from the bottom to the top of the duct.
- The aerosol filter unit utilizes a metal fiber filter to capture particulate radioactive materials.
- The iodine adsorbent unit employs silver-exchanged zeolite to capture gaseous iodine and organic iodide.
- To evaluate and verify the system's performance in reducing radioactive materials using simulants (SiO_2, I_2, CH_3I), it is essential to measure their concentrations.
- Considering the extreme environment within the containment building during a severe accident and the use of stimulant mixtures, the simulants were captured in stages over specific intervals for post-test concentration measurements.

3. Simulant Concentration Measuring Methods

Silicon Dioxide (SiO_2)

- Spherical monodisperse non-disintegrating SiO_2 particles are representative simulant of nuclear aerosols.
- A common method for measuring the mass concentration of particulate matter in a gas is to collect the particles from the sampled gas using a filter and measure the change in the filter weight.
- Given the high-temperature steam conditions in the containment building, the sampling strategy of EPA Method 5, which determines particulate matter emissions from stationary sources using a heated sampling train to prevent condensation, provides a relevant framework for developing a suitable measurement procedure.
- Regarding the filter weight measurement, variations in humidity and temperature can affect the gravimetric measurement of the particulate matter by altering the mass of the filters. Thus, the filters should be conditioned identically before both the pre- and post-sampling weighing.

Iodine (I_2)

- There are two methods for capturing I_2 in the sampling gas: liquid trapping method, solid adsorption method. In the former, a specific aqueous solution, such as ascorbic acid or sodium hydroxide (NaOH) solution, is used to collect and convert iodine into iodide ion (I^-) and iodate ion (IO_3^-).
- In the latter, although there are many studies on development of adsorbents for I_2, especially silver-exchanged zeolite showed complete retention of I_2 up to 900 ℃ regardless of the oxidizing or reducing condition in the presence of hydrogen.
- The I_2 captured by silver-exchanged zeolite has the form of silver iodide (AgI) and silver iodate ($AgIO_3$); the latter decomposes to form AgI at temperatures exceeding 190 ℃.
- Although AgI is highly stable and insoluble, appropriate pretreatment before analysis, for example the elution reaction using aqueous sodium sulfide (Na_2S), results in dissolution of I^- into the solution.
- Therefore, I_2 concentration can be measured using ion selective electrode (ISE), ion chromatograph (IC) or inductively coupled plasma-mass spectrometry (ICP-MS).

Methyl Iodide (CH_3I)

- There are two methods for capturing CH_3I in the sampling gas: liquid trapping method, solid adsorption method. In the former, a specific nonpolar solvent, such as toluene, is used to dissolve CH_3I.
- Due to the high volatility of CH_3I, several precautions are required for handling: low-temperature capture is more effective, and upon completion of capture, the samples must be sealed and analyzed as quickly as possible, and airtightness should be maintained using headspace vials and gas-tight syringes during sample extraction for analysis.
- CH_3I concentration can be measured gas chromatography-flame ionization detector (GC-FID) or gas chromatography-mass spectrometry (GC-MS).
- In the solid adsorption method, silver-exchanged zeolite captures the iodine species from CH_3I via a decomposition reaction to form stable AgI, thereby allowing the CH_3I concentration to be determined through the aforementioned AgI analysis method.
- Meanwhile, activated carbon (AC) is the only adsorbent media for normal atmosphere cleanup systems mentioned in NRC Regulatory Guide (RG) 1.140, which specifies that its CH_3I removal performance must be tested according to ASTM D3803 and pass the specified criteria.
- For example, triethylenediamine (TEDA)-impregnated AC showed 98.4% adsorption efficiency for CH_3I under the conditions of 70 ℃ temperature, 90 % relative humidity (RH), and 15 ppm CH_3I concentration.
- Because TEDA-impregnated AC captures CH_3I through physical adsorption and chemical reaction, a chemical extraction method is necessary as thermal desorption cannot fully desorb the captured CH_3I for measuring the concentration.

4. Performance Verification Test Methods

In-line Test Method

- The in-line test method is used to obtain the decontamination factor (DF) and pressure drop of the filtration system for each simulant.
- The carrier gas consists of air and steam, and contains at a time a single species of simulant. However, this method is not suitable for verifying the radioactive material reduction performance as a passive system. Due to the absence of hydrogen in the carrier gas, the flow inducement part does not operate.
- Criteria for sampling location selection and sampling system design could be referenced from ANSI/HPS N 13.1, and CFD analysis would be performed concurrently.

In-vessel Test Method

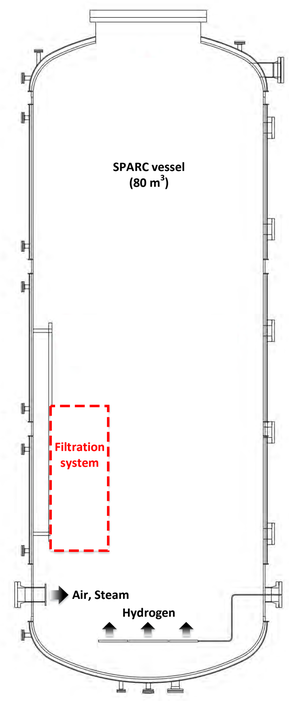

Fig. 2. Schematic diagram of in-vessel test method

- The in-vessel test method is used to verify the radioactive material reduction performance as a passive system in a defined space, such as 80 m^3 SPARC vessel at KAERI. Air, steam, hydrogen, and simulants can be injected into the vessel.
- To estimate the mean simulant concentration within the vessel from a limited number of sampling locations, the interior would be partitioned into several virtual regions. The simulant concentration measured at a specific sampling point within each region would then be taken as a representative value for its respective region.
- The mean concentration of a simulant in the vessel ($\overline{C_{tot}}$) is :

$$\overline{C_{tot}} = \sum C_i V_i \,/\, \sum V_i$$

where C_i is the simulant concentration in the i-th region, and V_i is the volume in the i-th region.

- CFD analysis could be employed to validate this estimation method of the mean concentration in the vessel.
- ANSI/AHAM AC-1, which is the standard for measuring performance of portable household air cleaners, provides a relevant framework for verifying the performance of the filtration system. This standard defines the method for measuring the CADR (Clean Air Delivery Rate) value, a key performance indicator of air cleaners.
- KAERI plans to evaluate the performance of the filtration system using the CADR value.

- The mean concentration of a simulant in the vessel over time is :

$$\overline{C_{tot}}(t) = C_0 e^{-kt}$$

where C_0 is the initial concentration of a simulant in the vessel, and k is the decay rate constant.

- Sampling should be initiated and terminated simultaneously across all sampling points. Due to the difficulty in real-time measurement of the simulant concentration, sampling is carried out at fixed time intervals and subsequently analyzed offline.
- The concentration trends over the test period would be then estimated from these results.
- The method for calculating CADR is :

$$CADR = V\left(k_{on} - k_{off}\right)$$

where V is volume of the test chamber, k_{on} is the decay rate when the filtration system is operating, and k_{off} is the decay rate when the filtration system is not operating.

5. Conclusions

- KAERI is developing the test methodology for the performance evaluation and verification of a passive radioactive material filtration system, currently under development in Korea, using simulants (SiO_2, I_2, CH_3I).
- Various literatures for measuring simulant concentrations were reviewed: a filter-based gravimetric method for SiO_2, and both liquid trapping and solid adsorption methods for I_2 and CH_3I.
- For verifying the performance for the filtration system, two methods are proposed. The in-line test is conducted by installing the system in a pipeline with carrier gas flows containing a simulant and measuring the simulant concentrations at the inlet and outlet to obtain the decontamination factor (DF) and pressure drop of the filtration system for each simulant.
- The in-vessel test is conducted by installing the system inside a pressure vessel with an internal volume of 80 m^3 and measuring the simulant concentrations at several points to calculate the mean concentration in the vessel over time and determine the CADR value, providing a quantitative performance indicator for the filtration system.

Acknowledgements

This work was supported by the Korea Institute of Energy Technology Evaluation and Planning (KETEP) and the Ministry of Climate, Energy & Environment (MCEE) of the Republic of Korea (Grant No. RS-2025-02318177).

Evaporation of molten salt for MSR application

Jun-young Kang, Sung Il Kim, Sang Mo An, Seong Ho Hong, Keun Sang Choi, and ChangWan Kang
Korea Atomic Energy Research Institute (KAERI)
Daejeon, 34057, Rep. of Korea
kkang0620@kaeri.re.kr;

ABSTRACT

Present study is to report the preliminary result about molten salt evaporation. Simulant salt (NaCl-KCl, 5:5) of which temperature is from 600 to 800 C is evaporated under atmospheric pressure. As salt gas undergoes rapid condensation, and turns into an aerosol form. Present study evaluated the evaporated mass flux, particle shape and chemical composition using SEM/EDS. The evaporation characteristics can be utilized as boundary conditions for future experiments evaluating airborne/wall-deposited aerosol behavior using a tank.

KEYWORDS
Molten Salt Reactor (MSR), Aerosol, Condensation, Evaporation, Deposition

1. INTRODUCTION

When molten salt is heated above its melting point, significant amounts of salt vapor are generated due to evaporation. If the molten salt contains fission products, the molten salt vapor and aerosols can serve as major carriers for the transport of fission products. Therefore, a test apparatus was constructed to develop a methodology for evaluating the evaporation and aerosol behavior of molten salts using surrogate salts, with the aim of extending this methodology to assess the radiation source release due to aerosol formation in salt spill accident of a Molten Salt Reactor (MSR) system.

To design test apparatus for evaluating salt aerosols, a prior research analysis on molten salt evaporation, wall deposition, and aerosol behavior was conducted as follows. The vapor pressure of molten salts is relatively low, so experimental studies related to molten salt evaporation have largely been conducted under vacuum conditions. For NaCl-KCl, a melting point around 650°C, it has been reported that a weight loss of approximately 30% occurs after 1 hour of evaporation under vacuum at 770°C [**1**]. The behavior of molten salt evaporation under atmospheric pressure is significantly suppressed due to the low vapor pressure of molten salts, and it is known that evaporation of single NaCl gradually begins at temperatures above 1095K [**2**]. Therefore, it is evident that a molten salt heating system capable of maintaining high temperatures for extended periods is required to evaluate the vapor generation and aerosol behavior due to molten salt evaporation. Implementing vacuum conditions is considered an ideal scenario that does not closely resemble the atmospheric conditions inside the containment vessel of an actual MSR. For aerosol behavior evaluation, test designs based on atmospheric pressure conditions are required. However, the evaporation rate under atmospheric pressure is expected to be significantly lower than under vacuum, potentially requiring extended test durations (over 1 hour). There are no predictive correlations for the evaporation rate of molten salts according to prior research, and this test aims to determine the evaporation rate by measuring the mass loss due to evaporation at different temperatures relative to the initial molten salt mass.

Preceding research on the wall deposition due to the condensation of molten salt vapor is quite limited. When molten salt vapor condenses on surfaces, irregular nucleation leading to crystalline wall deposits is observed, which differs from the aggregation forms of mono-dispersed particles. Additionally, it has been

experimentally reported that the condensation mechanisms from vapor to liquid or vapor to solid depend on the molten salt temperature and the ambient air temperature [**3**]. This prior research is an individual-effect study involving the insertion of a condensation tube into a relatively small (O.D. 20 mm) test apparatus, and it does not include evaluations of the airborne aerosol and deposition behaviors on wall surfaces in a large volume similar to an MSR containment vessel.

Major research on the characterization of molten salt aerosols primarily focuses on developing non-contact aerosol measurement techniques for the application of MSR systems. The most significant advantage of non-contact aerosol measurement techniques is their ability to provide real-time aerosol characterization and elemental analysis even under high radiation and harsh reactor environments. (1) The U.S. Argonne National Laboratory (ANL) conducted evaluations of aerosol behavior by evaporating CsI salt (melting point 632°C) using an optical light scattering aerosol spectrometer [**4,5**]. This non-contact aerosol characterization methodology involves irradiating aerosol particles with a light source and evaluating their scattering properties, enabling the assessment of aerosol diameter (0.1-10 microns) and number concentration. CsI salt was used due to its higher vapor pressure compared to chlorides, resulting in a relatively higher evaporation rate. The aerosol transport gas was argon. The key results indicated that aerosols with diameters below 1 micron were predominantly measured, and the volume-average particle concentration was approximately 65,000 P/cm³, equating to a mass-average particle concentration of 1.2 mg/cm³ considering the CsI density of 4.5 g/cm³, which is a significantly high value. (2) The U.S. Oak Ridge National Laboratory (ORNL) used Laser-induced breakdown spectroscopy (LIBS) to evaluate aerosol characteristics generated from NaNO3-KNO3 molten salt [**6,7**]. LIBS enables aerosol concentration measurement based on the scattering properties of aerosol particles when irradiated with a laser, providing the advantage of real-time elemental composition assessment of aerosols while aerosol diameter distribution cannot be measured. Based on this, evaluations of this methodology were conducted using inert gases (Xe, Kr) and aerosols (Cs), and various individual-effect tests are being reported for direct application to MSR systems. Summarizing the preceding research, the evaluation of molten salt aerosol characteristics primarily employs non-contact optical methodologies, clearly revealing their pros and cons. A notable disadvantage is that the detection limit and uncertainty are significantly high under conditions of low aerosol formation, and uncertainties arising from non-contact methods (focus, calibration, and difficulty in absolute quantification) exist. Therefore, test under present study intends to apply a contact aerosol measurement methodology using an Electrical Low Pressure Impactor (ELPI). ELPI is advantageous for quantifying aerosol diameter distribution and number concentration, and has the benefit of elemental and chemical analysis through sample recovery.

Based on the analysis of existing researches, the aerosol characterization methodology was established, and the test apparatus was designed and constructed, which is divided into two types: (I) Evaporation rate measurement and (II) Aerosol behavior characterization. Present study introduces the design progress of test apparatus as well as preliminary result of salt evaporation.

2. MATERIAL AND METHOD

Experimental investigations about salt evaporation and aerosol dynamics are conducted through two independent tests: (1) measurement of evaporation rates at steady-state molten salt temperatures, and (2) characterization of airborne/wall-deposited aerosols at steady-state molten salt temperatures. First, the evaporation rate measurement test involves evaluating the change in molten salt mass due to evaporation over a set period, without a simulated containment vessel tank atop the furnace. Metal crucible containing molten salt includea a gas transfer line (diameter 1/4", length approximately 3.5m) between the furnace and the crucible to preheat the carrier gas (nitrogen), ensuring that the temperature of the molten salt, gas line, and carrier gas remains consistent throughout the experiment. This prevents local cooling of the molten salt and its gas due to the gas convection or heat loss. The evaporation mass is measured using a filtering device installed at the exit port of the crucible cover. The crucible, with an inner diameter of 78mm and height of

190mm, is a cylindrical design and is welded rather than bolted to prevent molten salt vapor leakage during the test. The filtering device consists of a condenser, a filter (WHATMAN GF/F, glass fiber, 500°C, 0.7 um), and a scrubber. The main role of the condenser is to condense the molten salt vapor into aerosols. The filter captures aerosol particles, and the scrubber collects any residual aerosols not captured by the filter through liquid sparging.

For the evaluation of airborne/wall-deposited aerosols, a tank installed atop the furnace simulates the containment vessel of an MSR, allowing for the condensation and aerosol formation of molten salt vapor due to volume expansion. The tank has a diameter and height of 0.6m and is cylindrical. Airborne aerosol concentration (#N) and size distribution within the tank can be evaluated using an ELPI. The aerosol deposition mass on the tank bottom surface due to gravitational settling or on the side walls due to thermophoresis can also be assessed.

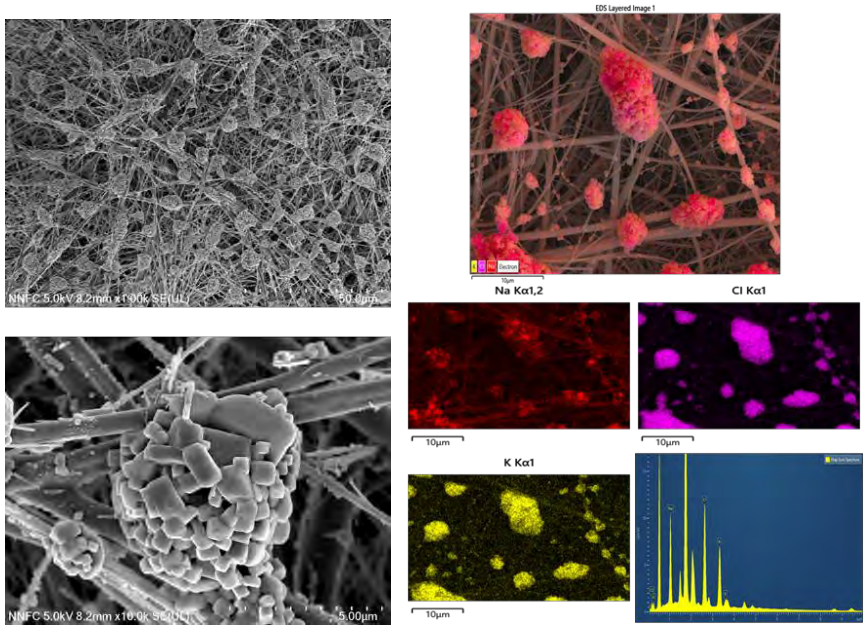

Figure 1. SEM/EDS images about salt aerosol particles captured in the filter (NaCl-KCl 5:5, 600C)

3. RESULTS AND DISCUSSION

The molten salt evaporation rate measurement is performed sequentially at four different temperature cases (800°C, 700°C, 650°C, and 600°C). Initially, the furnace power is gradually increased to form a molten salt pool inside the crucible. Once the temperature of the molten salt sample exceeds the melting point and begins to form a molten salt pool, a carrier gas (nitrogen) is injected into the pool at a constant flow rate to create a uniformly heated molten salt. The furnace power is then adjusted to control the molten salt temperature. When the molten salt reaches the target temperature, a pressure test (1.5 bar) is conducted first to determine the leak rate, which can introduce errors in the evaporation rate measurement. After confirming the leak rate through the pressure test, the evaporation rate is measured under steady-state temperature conditions at 800°C, with measurement conditions set at a duration of 1800 seconds or a maximum crucible pressure of 1.5 bar. Once the 800°C experiment is completed, the furnace power is adjusted to change the molten salt temperature (700°C, 650°C, 600°C), and the measurements are repeated.

As temperature increases, the amount of molten salt vapor generated by evaporation also increases, leading to a corresponding increase in evaporation mass. The evaporation mass per unit area is approximately 15 mg/m2-s at 800°C, indicating that a significant amount of salt vaporizes and can form aerosols despite the

relatively low vapor pressure of the molten salt. The collected evaporation mass was measured through a three-stage process involving a condenser, filter, and scrubber, with most of the molten salt aerosol being captured by the filter. Interestingly, although the amount is relatively small compared to above the melting point, some evaporation mass was still collected below the melting point. Even though solidified salt has a lower diffusion coefficient compared to its molten state, under the test conditions, which are significantly higher than room temperature, salt vaporization can occur, enabling aerosol formation. This finding is consistent with previous studies. Analysis of the collected molten salt aerosol particles revealed that they formed crystalline structures with sizes on the order of 1 micron, significantly smaller than the original salt particles during the initial filling. SEM analysis of the molten salt aerosol particles within the filter showed that they consisted of agglomerations of hundreds of nanoparticles, indicating substantial agglomeration. As temperature increased, the evaporation mass of the molten salt increased, indicating a corresponding increase in aerosol generation. With higher temperatures, the molten salt aerosol particles formed porous layers by agglomerating. EDS analysis confirmed that the primary components of the collected aerosol particles matched the major constituents of the surrogate salt used in the test. However, the initial molar ratio of the binary salt was different from the molar ratio of the captured aerosol, which can be attributed to the relatively higher evaporation flux of KCl compared to NaCl [**1**]. Through this preliminary test, the evaporation behavior of molten salt near the melting point was quantitatively evaluated, providing boundary conditions for future experiments (airborne aerosol characterization) with the tank.

4. CONCLUSIONS

Present study into the evaporation and aerosol behavior of molten salts provides a comprehensive understanding of their dynamics under various temperature conditions. The experiments, conducted at 800°C, 700°C, 650°C, and 600°C, demonstrated a notable increase in evaporation mass with rising temperatures, reflecting the increasing vaporization of molten salts. Even below the melting point, a measurable amount of evaporation occurred, suggesting that vaporization is possible despite the relatively low vapor pressure of molten salts. Analysis of collected molten salt aerosol particles revealed crystalline structures with sizes on the order of 1 micron, and primary components of the collected aerosol particles matched the constituents of the surrogate salt used in the tests.

ACKNOWLEDGMENTS

This work was supported by the National Research Foundation of Korea (NRF) grant funded by the Korea government (MSIT) (RS-2023-00261295).

REFERENCES

1. L.L.Wang et al., Vacuum evaporation of KCl-NaCl salts: Part II. Vaporization-rate model and experimental results, 1996
2. A.M.Laptev et al., Sublimation rate of solid NaCl powders and evaporation rate of liquid NaCl upon heating in vacuum and air, 2024
3. M.Brostrom et al., Condensation in the KCl-NaCl system, 2013
4. S.Thomas, Method for real-time salt aerosol concentration and size measurements for molten salt reactor safety assessment, ANL/CFCT-24/25, 2024
5. S.Shahbazi et al., State of knowledge on aerosols and bubble transport for mechanistic source term analysis of molten salt reactors, ANL/NSE-22/47, 2022
6. H.B.andrews, Monitoring nobel gas (Xe,Kr) and aerosols (Cs,Rb) in a molten salt reactor surrogate off-gas stream using laser-induced breakdown spectroscopy (LIBS), 2022
7. Z.B.Kitzhaber et al., Sparge sampling of molten salts for online monitoring via laser-induced breakdown spectroscopy, 2025

12th CONFERENCE ON SEVERE ACCIDENTS RESEARCH
May 18-22, 2026 - Madrid, Spain
ERMSAR 2026

Additional Primary Depressurized Line (APDL) for NPP Units with VVER-440/V-213

Mykhailenko O., Mazurok O. (Ph.D.), Ivanov V., Tiurin A., Pustovit P.
Energy Safety Group LLC, Kyiv, Ukraine.
Ing. Vicena I., Ing. Kossuth R., Ing. Bachorík O.
VÚEZ, a.s., Levice, Slovakia

ENERGY SAFETY GROUP

Introduction

To minimize the consequences of Severe Accident (SA) with core damage, the In-Vessel Melt Retention (IVMR) system has been implemented at Rivne NPP Units 1 and 2 with VVER-440/V-213 (RNPP-1,2) in Ukraine. This system is designed to retain the melt in the Reactor Pressure Vessel (RPV) and prevent the SA from progressing to the ex-vessel stage by creating a closed natural circulation loop for external RPV cooling. For this purpose, water is supplied to the reactor cavity and the reactor vessel is submerged in water up to the support embeds, while the steam generated during cooling returns to the Steam Generator (SG) box and condenses.

The implementation of the IVMR system for RNPP-1,2 was carried out by Energy Safety Group LLC (ES Group), together with VÚEZ, a.s.

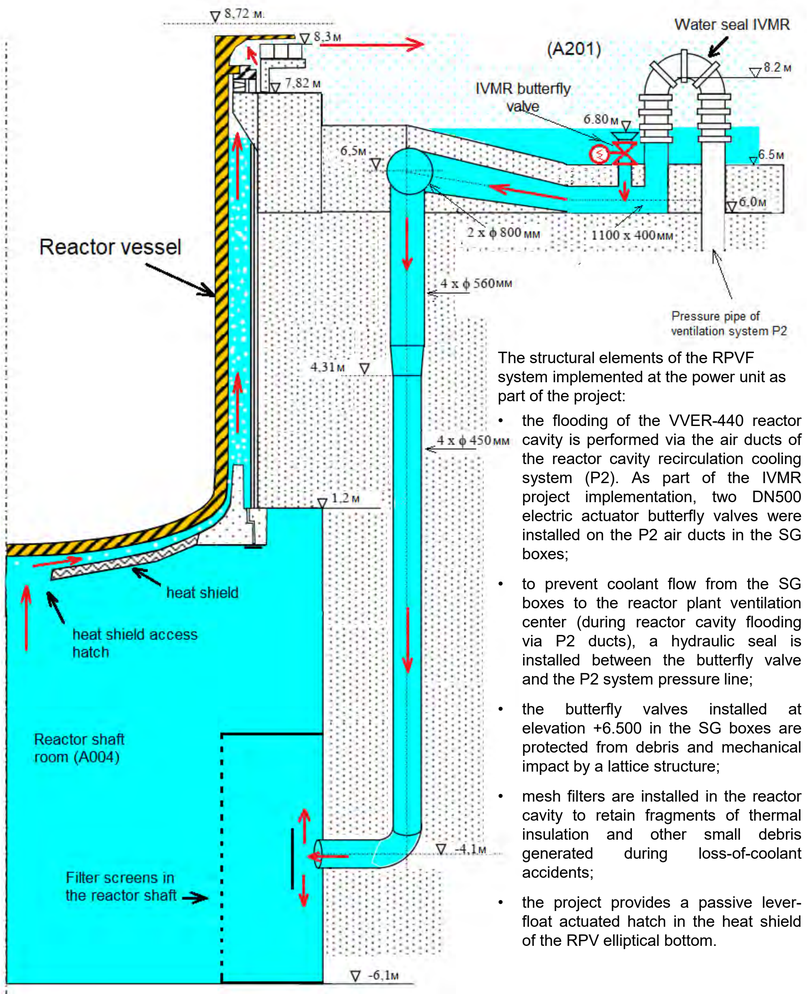

The structural elements of the RPVF system implemented at the power unit as part of the project:

- the flooding of the VVER-440 reactor cavity is performed via the air ducts of the reactor cavity recirculation cooling system (P2). As part of the IVMR project implementation, two DN500 electric actuator butterfly valves were installed on the P2 air ducts in the SG boxes;
- to prevent coolant flow from the SG boxes to the reactor plant ventilation center (during reactor cavity flooding via P2 ducts), a hydraulic seal is installed between the butterfly valve and the P2 system pressure line;
- the butterfly valves installed at elevation +6.500 in the SG boxes are protected from debris and mechanical impact by a lattice structure;
- mesh filters are installed in the reactor cavity to retain fragments of thermal insulation and other small debris generated during loss-of-coolant accidents;
- the project provides a passive lever-float actuated hatch in the heat shield of the RPV elliptical bottom.

The results of the analytical justification showed that in the event of an accident with a total power unit blackout and a sealed primary circuit, the conditions for starting the IVMR system occurred. The IVMR system is put into operation upon reaching a core outlet temperature of 450 °C, which is a condition for transitioning to the Severe Accident Management Guidelines (SAMG).

In the event of further SA development, to reduce the load on the reactor vessel in case of a sealed primary circuit, it is necessary to simultaneously perform primary circuit depressurization to preserve the integrity of the reactor vessel. Therefore, upon reaching the conditions for transitioning to the SAMGs, the relevant SAMG procedures provide for actions aimed at reducing the primary circuit pressure to values less than 6 kgf/cm². For this, the staff must ensure power supply and manually open the Pressurizer Safety Valves (PRZ SVs), the valves on the PRZ SV bypass line, and the valves of the Emergency Gas Removal System (EGRS valves).

In the event of an accident with a total power unit blackout and a sealed primary circuit, the conditions for starting the IVMR system and performing primary circuit depressurization occur after ≈(11÷12.5) hours. Without the use of external power sources, by this time the accumulator batteries will be discharged, which will not allow depressurization of the primary circuit using the existing design-basis means. Moreover, the PRZ SVs, the valves on the PRZ SV bypass line, and the EGRS valves are not qualified for SA conditions; therefore, the question of their effective use remains open even if power supply becomes available.

Consequently, ES Group, together with VÚEZ, a.s., has developed a solution to enhance the safety of the unit by introducing the Additional Primary Depressurized Line (APDL), in compliance with the SAMG-2 requirement for primary circuit depressurization.

The APDL valve does not require electrical power to remain open, unlike PRZ SVs, and will open once the conditions for primary depressurization are met, subsequently remaining in the open position.

The main purpose of implementing the APDL is the ability to perform primary circuit depressurization, to preserve the integrity of the reactor vessel and ensure reliable operation of the IVMR system during a SA with core damage, in the event when the existing primary circuit depressurization means (PRZ SVs and EGRS) become unavailable.

The object of modification is the primary circuit pressure compensation system at RNPP-1,2. The modification involves implementation of the APDL by installing new equipment (not included in the original design) at RNPP-1,2. The implementation of the APDL does not duplicate the design-basis systems (PRZ SVs and EGRS). The introduction of the APDL significantly expands the capabilities and reliability of staff actions for primary circuit depressurization under SA conditions.

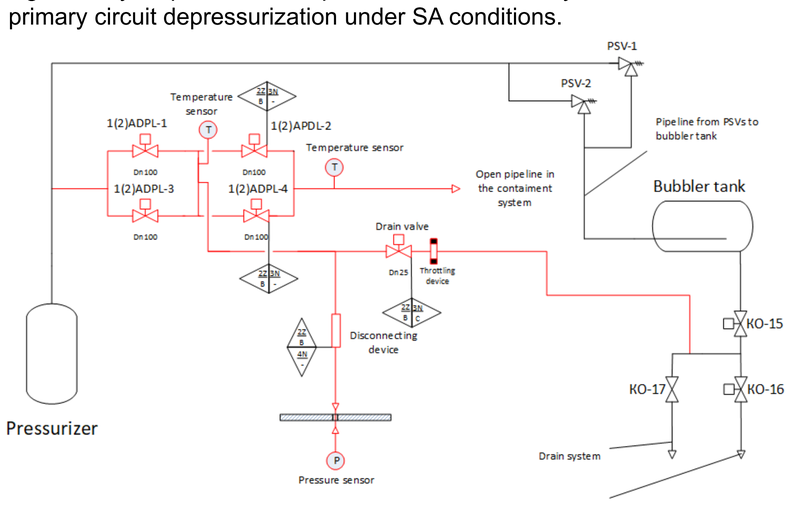

Technological diagram of the APDL for RNPP-1,2

APDL Concept

The APDL for RNPP-1,2 provides the following functions:

- primary circuit depressurization in the course of a SA, when existing primary circuit pressure reduction means (PRZ SVs, the valves on the PRZ SV bypass line, and EGRS valves) will be unavailable;
- preservation of reactor vessel integrity due to the reliable functioning of the IVMR system;
- reliable maintenance of primary circuit pressure at a low level (less than 6 kgf/cm²) on a long-term basis without additional staff actions;
- enhances the overall safety of the unit by utilizing equipment qualified for SA conditions, that allows for performing actions in accordance with SAMG-2 for primary circuit depressurization.

Short description of APDL

The main APDL pipeline (DN100) is a cut-in on the pipeline connecting the pressurizer and the PRZ SVs. The main APDL pipeline is divided into two identical lines to ensure the reliability of APDL operation.

On each of the lines, there are two consecutively connected main APDL valves – 1(2)APDL-1÷4 (DN100), which are in the closed position under normal operating conditions. The sequential arrangement of the two valves 1(2)APDL-1÷4 ensures reliable isolation of the high-pressure side.

The medium is discharged into the premises of the bubbler tank and pressurizer A527/1(2) through the open part of the pipeline. The medium discharge pipeline to the containment premises gradually increases in diameter from DN100 to DN125, and then to DN150. This is done to reduce the dynamic impact of the steam-gas jet discharged by the APDL.

A drain pipeline is also included for collecting and diverting operational leakages caused by the design-basis tightness limits of the main APDL valve. The drain pipeline is connected to the leak detection system of the primary circuit and has connection with the drain system. On the drain pipeline, a normally closed drain valve and a throttling device are installed to reduce the parameters of the leakages received from the main APDL valves to the operating parameters of the organized leakage system of the primary circuit.

The APDL incorporates measuring instruments that ensure monitoring of equipment parameters at a level sufficient for the APDL's functionality.

The APDL is equipped with the Process Control System (PCS), which is designed to control the APDL valves based on operator commands from the main control room (MCR)/emergency control room (ECR), display the valve status, and measure the temperature and pressure.

When the IVMR system is operating, the primary circuit depressurization must be continuous. Thus, the primary circuit depressurization through the PRZ SVs will require constant power supply to the pulse valve solenoids to hold the PRZ SVs in the open position.

The APDL valve does not require electrical power to remain open. The APDL valve opens once the conditions for primary circuit depressurization are met and subsequently remains in the open position.

The APDL valve can be controlled only from the MCR and ECR. This ensures direct operator control of the APDL valve, without the need for additional actions.

The main APDL valves are qualified for SA conditions.

APDL refers to a protective safety system, classification designation of the APDL as a whole – 23 and seismic category I .

Based on placement conditions, the APDL components are classified as items located at the NPP in the containment.

Parameters of the APDL environmental

№	Parameter Name	Value
1	Pressure, kgf/cm²	2,5
2	Temperature, ºC	127
3	Medium	steam-water mixture
4	Humidity, %	100
5	Chemical composition	primary circuit coolant
6	Dose rate, R/h	4,85×10⁴

Operating medium parameters of the APDL

№	Parameter Name		Value
1	Pressure, kgf/cm² (abs.)	NOC	up to 140
		SA	up to 140
2	Temperature, ºC	NOC	up to 335
		SA	up to 450 (inclusive)
3	Hydrostatic test pressure, kgf/cm²	up to 165	
4	Medium	steam, water, steam-water mixture, nitrogen	
5	pH	from 4,2 to 10,3	
6	Boric acid concentration, g/dm³	from 0 to 20	
7	Hydrogen concentration, mg/dm³	from 2,2 to 4,5	
8	Chloride ion concentration, mg/dm³	up to 0,005	
9	Total activity, Ci/L	up to 10^{-1}	
10	Corrosion product concentration, mg/dm³	up to 1	
11	Ammonia concentration, mg/dm³	more than 3,0	

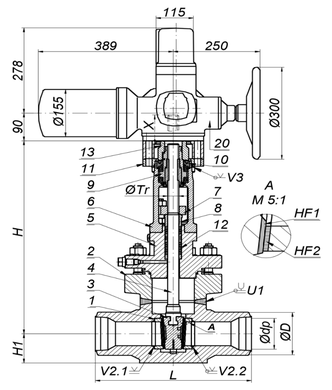

Main valve – a wedge gate valve with an integrated electric actuator

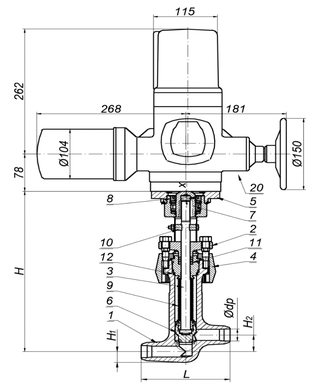

Drain valve – a bellows-sealed valve with an integrated electric actuator

The APDL has a flow capacity of 64 kg/s, corresponding to the combined flow rate of two PRZ SVs (the flow through one PRZ SV is 32 kg/s). This capacity is sufficient to reliably reduce and maintain the primary circuit pressure at a low level.

For all SA scenarios considered, the pressure in the containment remains below the design limit of 2.5 kgf/cm² (abs). Due to the presence of passive autocatalytic recombiners in the containment, conditions leading to hydrogen detonation do not develop during the APDL operation.

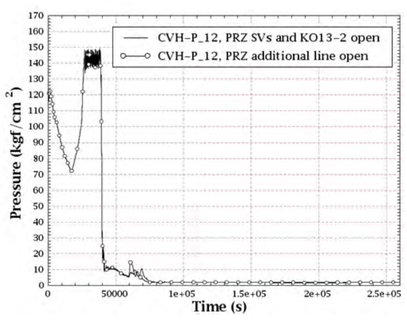

Primary circuit pressure (comparison of the APDL and PRZSVs)

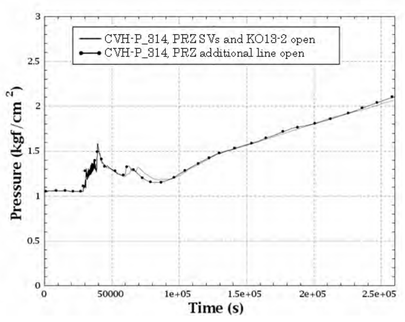

Pressure in containment (comparison of the APDL and PRZSVs)

APDL Process Control System (PCS)

A PCS was developed for the APDL, which implements the control of the APDL valves according to the commands of the MCR/ECR operator, visualization of the valve status, and measurement of temperature and pressure.

The PCS performs the following functions:

- formation of APDL valve control commands considering the position of the valve control keys, the position of the limit switches and the closing torque clutch;
- reception of signals from temperature and pressure sensors;
- exchange of digital communication channels with the "Black Box" / IOS and the signal of the unified time system;
- continuous automatic archiving, signaling, display and registration of technological and electrical parameters during the operation of the APDL equipment;
- automatic diagnostics, archiving, signaling and display of data on the technical condition of the APDL equipment;
- notification of malfunctions;
- notification of unauthorized access attempts;
- protection against unauthorized access;
- prevention of personnel errors;
- performs diagnostics and self-monitoring.

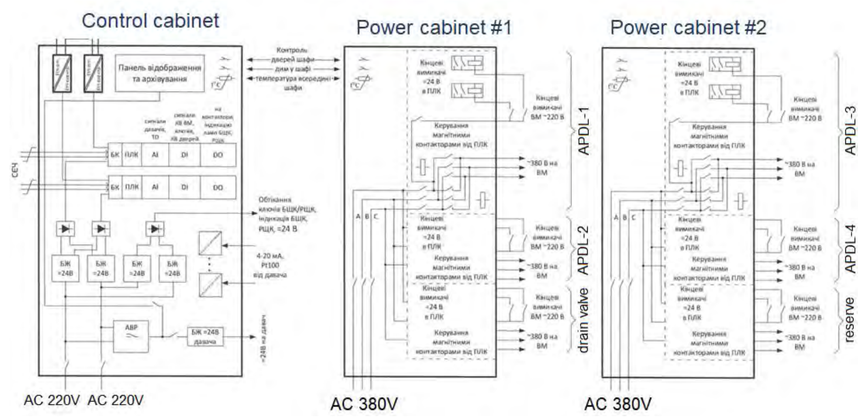

Structural diagram of the APDL PCS

APDL operation

During normal operation and Design Extension Conditions (Category A), the APDL remains in standby mode in a "ready for operation" state. The main APDL valves and the drain APDL valve are operable and in the closed position.

The APDL must be put into operation in accordance with the SAMG-2 requirement for primary circuit depressurization and should start no later than the start-up of the IVMR system.

For successful depressurization of the primary circuit, it is sufficient to open at least two consecutive main APDL valves (1(2)APDL-1÷4) in a combination that enables discharge of the medium from the primary circuit. That is, these can be combinations using one of the parallel lines or opening the corresponding valves in cross-combinations.

General Conclusions

- The implementation of the APDL significantly expands the capabilities and reliability of staff actions specifically under SA conditions.
- The APDL equipment is designed for operation throughout the progression of a SA, and the implementation scheme ensures a high level of reliability, ensuring continued APDL functionality even in the presence of single failures.
- The system allows performance of actions in accordance with SAMG-2 for primary circuit depressurization using equipment qualified for the corresponding operating conditions.
- It ensures the reliable operation of the IVMR system.

12th CONFERENCE ON
SEVERE ACCIDENTS RESEARCH
May 18-22, 2026 - Madrid, Spain
ERMSAR 2026

ADDITIONAL PRIMARY DEPRESSURIZED LINE (APDL) FOR NPP UNITS WITH VVER-440/V-213

Mykhailenko O., Mazurok O. (Ph.D.), Ivanov V., Tiurin A., Pustovit P. - Energy Safety Group LLC, Kyiv, Ukraine.
Ing. Vicena I., Ing. Kossuth R., Ing. Bachorík O. - VÚEZ, a.s., Levice, Slovakia

ENERGY SAFETY GROUP

Introduction

To minimize the consequences of Severe Accident (SA) with core damage, the In-Vessel Melt Retention (IVMR) system has been implemented at Rivne NPP Units 1 and 2 with VVER-440/V-213 (RNPP-1,2) in Ukraine. This system is designed to retain the melt in the Reactor Pressure Vessel (RPV) and prevent the SA from progressing to the ex-vessel stage by creating a closed natural circulation loop for external RPV cooling. For this purpose, water is supplied to the reactor cavity and the reactor vessel is submerged in water up to the support embeds, while the steam generated during cooling returns to the Steam Generator (SG) box and condenses.

The implementation of the IVMR system for RNPP-1,2 was carried out by Energy Safety Group LLC (ES Group), together with VÚEZ, a.s.

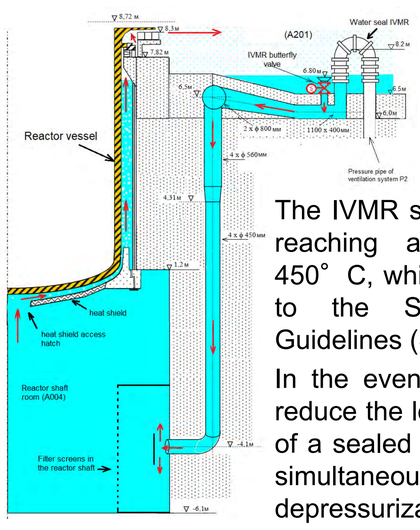

The results of the analytical justification showed that in the event of an accident with a total power unit blackout and a sealed primary circuit, the conditions for starting the IVMR system occurred.

The IVMR system is put into operation upon reaching a core outlet temperature of 450° C, which is a condition for transitioning to the Severe Accident Management Guidelines (SAMG).

In the event of further SA development, to reduce the load on the reactor vessel in case of a sealed primary circuit, it is necessary to simultaneously perform primary circuit depressurization to preserve the integrity of the reactor vessel. Therefore, upon reaching the conditions for transitioning to the SAMGs, the relevant SAMG procedures provide for actions aimed at reducing the primary circuit pressure to values less than 6 kgf/cm². For this, the staff must ensure power supply and manually open the Pressurizer Safety Valves (PRZ SVs), the valves on the PRZ SV bypass line, and the valves of the Emergency Gas Removal System (EGRS valves).

In the event of an accident with a total power unit blackout and a sealed primary circuit, the conditions for starting the IVMR system and performing primary circuit depressurization occur after ≈(11÷12.5) hours. Without the use of external power sources, by this time the accumulator batteries will be discharged, which will not allow depressurization of the primary circuit using the existing design-basis means. Moreover, the PRZ SVs, the valves on the PRZ SV bypass line, and the EGRS valves are not qualified for SA conditions; therefore, the question of their effective use remains open even if power supply becomes available.

Consequently, ES Group, together with VÚEZ, a.s., has developed a solution to enhance the safety of the unit by introducing the Additional Primary Depressurized Line (APDL), in compliance with the SAMG-2 requirement for primary circuit depressurization.

The APDL valve does not require electrical power to remain open, unlike PRZ SVs, and will open once the conditions for primary depressurization are met, subsequently remaining in the open position.

The main purpose of implementing the APDL is the ability to perform primary circuit depressurization, to preserve the integrity of the reactor vessel and ensure reliable operation of the IVMR system during a SA with core damage, in the event when the existing primary circuit depressurization means (PRZ SVs and EGRS) become unavailable.

The object of modification is the primary circuit pressure compensation system at RNPP-1,2. The modification involves implementation of the APDL by installing new equipment (not included in the original design) at RNPP-1,2. The implementation of the APDL does not duplicate the design-basis systems (PRZ SVs and EGRS). The introduction of the APDL significantly expands the capabilities and reliability of staff actions for primary circuit depressurization under SA conditions.

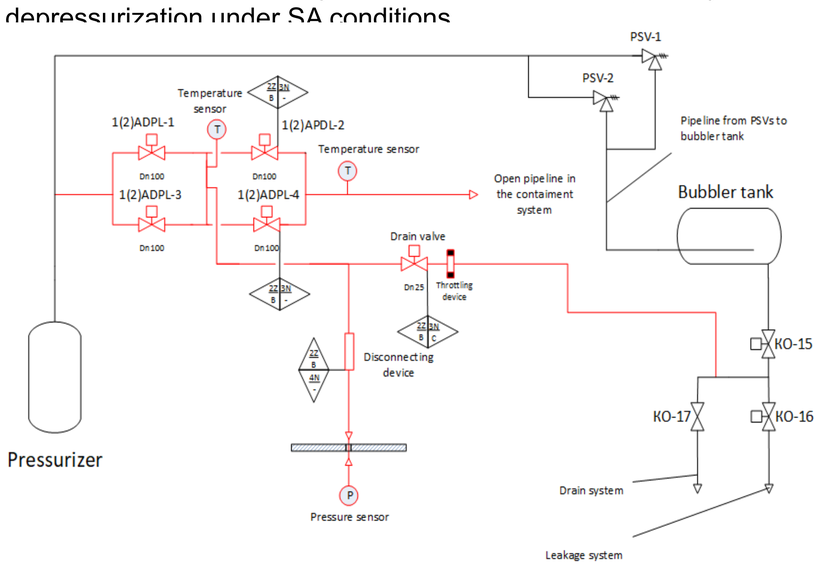

Technological diagram of the APDL for RNPP-1,2

APDL Concept

The APDL for RNPP-1,2 provides the following functions:

- primary circuit depressurization in the course of a SA, when existing primary circuit pressure reduction means (PRZ SVs, the valves on the PRZ SV bypass line, and EGRS valves) will be unavailable;
- preservation of reactor vessel integrity due to the reliable functioning of the IVMR system;
- reliable maintenance of primary circuit pressure at a low level (less than 6 kgf/cm²) on a long-term basis without additional staff actions;
- enhances the overall safety of the unit by utilizing equipment qualified for SA conditions, that allows for performing actions in accordance with SAMG-2 for primary circuit depressurization.

Short description of APDL

The main APDL pipeline (DN100) is a cut-in on the pipeline connecting the pressurizer and the PRZ SVs. The main APDL pipeline is divided into two identical lines to ensure the reliability of APDL operation. On each of the lines, there are two consecutively connected main APDL valves – 1(2)APDL-1÷4 (DN100), which are in the closed position under normal operating conditions. The sequential arrangement of the two valves 1(2)APDL-1÷4 ensures reliable isolation of the high-pressure side.

The medium is discharged into the premises of the bubbler tank and pressurizer A527/1(2) through the open part of the pipeline. The medium discharge pipeline to the containment premises gradually increases in diameter from DN100 to DN125, and then to DN150. This is done to reduce the dynamic impact of the steam-gas jet discharged by the APDL.

A drain pipeline is also included for collecting and diverting operational leakages caused by the design-basis tightness limits of the main APDL valve. The drain pipeline is connected to the leak detection system of the primary circuit and has connection with the drain system. On the drain pipeline, a normally closed drain valve and a throttling device are installed to reduce the parameters of the leakages received from the main APDL valves to the operating parameters of the organized leakage system of the primary circuit.

The APDL incorporates measuring instruments that ensure monitoring of equipment parameters at a level sufficient for the APDL's functionality. The APDL is equipped with the Process Control System (PCS), which is designed to control the APDL valves based on operator commands from the main control room (MCR)/emergency control room (ECR), display the valve status, and measure the temperature and pressure.

When the IVMR system is operating, the primary circuit depressurization must be continuous. Thus, the primary circuit depressurization through the PRZ SVs will require constant power supply to the pulse valve solenoids to hold the PRZ SVs in the open position. The APDL valve does not require electrical power to remain open. The APDL valve opens once the conditions for primary circuit depressurization are met and subsequently remains in the open position.

The APDL valve can be controlled only from the MCR and ECR. This ensures direct operator control of the APDL valve, without the need for additional actions. The main APDL valves are qualified for SA conditions. APDL refers to a protective safety system, classification designation of the APDL as a whole – 23 and seismic category I . Based on placement conditions, the APDL components are classified as items located at the NPP in the containment.

Parameters of the APDL environmental

№	Parameter Name	Value
1	Pressure, kgf/cm²	2,5
2	Temperature, ºC	127
3	Medium	steam-water mixture
4	Humidity, %	100
5	Chemical composition	primary circuit coolant
6	Dose rate, R/h	$4{,}85\times10^4$

Operating medium parameters of the APDL

№	Parameter Name		Value
1	Pressure, kgf/cm² (abs.)	NOC	up to 140
		SA	up to 140
2	Temperature, ºC	NOC	up to 335
		SA	up to 450
3	Hydrostatic test pressure, kgf/cm²		up to 165
4	Medium		steam, water, steam-water mixture, nitrogen
5	pH		from 4,2 to 10,3
6	Boric acid concentration, g/dm³		from 0 to 20
7	Hydrogen concentration, mg/dm³		from 2,2 to 4,5
8	Chloride ion concentration, mg/dm³		up to 0,005
9	Total activity, Ci/L		up to 10^{-1}
10	Corrosion product concentration, mg/dm³		up to 1
11	Ammonia concentration, mg/dm³		more than 3,0

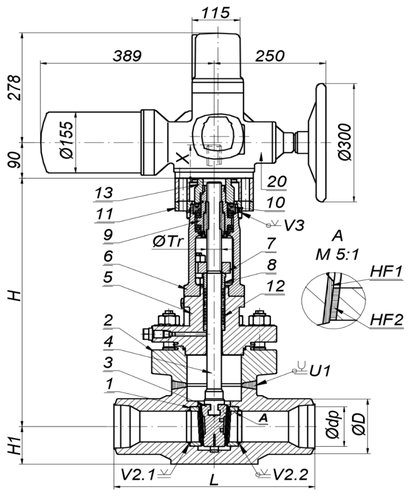

Main valve – a wedge gate valve with an integrated electric actuator

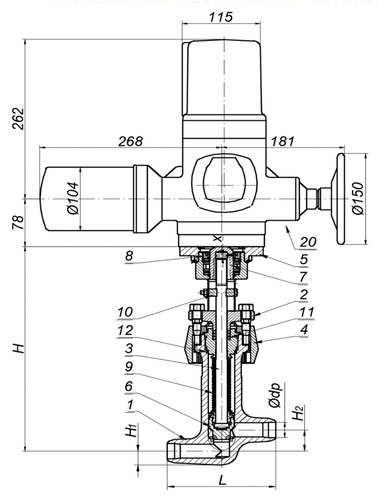

Drain valve – a bellows-sealed valve with an integrated electric actuator

The APDL has a flow capacity of 64 kg/s, corresponding to the combined flow rate of two PRZ SVs (the flow through one PRZ SV is 32 kg/s). This capacity is sufficient to reliably reduce and maintain the primary circuit pressure at a low level.

For all SA scenarios considered, the pressure in the containment remains below the design limit of 2.5 kgf/cm² (abs). Due to the presence of passive autocatalytic recombiners in the containment, conditions leading to hydrogen detonation do not develop during the APDL operation.

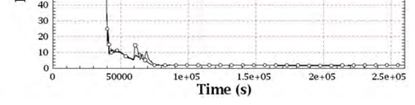

Primary circuit pressure (comparison of the APDL and PRZSVs)

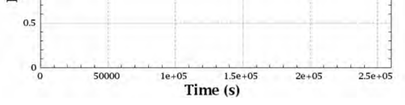

Pressure in containment (comparison of the APDL and PRZSVs)

APDL Process Control System (PCS)

A PCS was developed for the APDL, which implements the control of the APDL valves according to the commands of the MCR/ECR operator, visualization of the valve status, and measurement of temperature and pressure.

The PCS performs the following functions:

- formation of APDL valve control commands considering the position of the valve control keys, the position of the limit switches and the closing torque clutch;
- reception of signals from temperature and pressure sensors;
- exchange of digital communication channels with the "Black Box" / IOS and the signal of the unified time system;
- continuous automatic archiving, signaling, display and registration of technological and electrical parameters during the operation of the APDL equipment;
- automatic diagnostics, archiving, signaling and display of data on the technical condition of the APDL equipment;
- notification of malfunctions;
- notification of unauthorized access attempts;
- protection against unauthorized access;
- prevention of personnel errors;
- performs diagnostics and self-monitoring.

APDL operation

During normal operation and Design Extension Conditions (Category A), the APDL remains in standby mode in a "ready for operation" state. The main APDL valves and the drain APDL valve are operable and in the closed position.

The APDL must be put into operation in accordance with the SAMG-2 requirement for primary circuit depressurization and should start no later than the start-up of the IVMR system.

For successful depressurization of the primary circuit, it is sufficient to open at least two consecutive main APDL valves (1(2)APDL-1÷4) in a combination that enables discharge of the medium from the primary circuit. That is, these can be combinations using one of the parallel lines or opening the corresponding valves in cross-combinations.

General Conclusions

- The implementation of the APDL significantly expands the capabilities and reliability of staff actions specifically under SA conditions.
- The APDL equipment is designed for operation throughout the progression of a SA, and the implementation scheme ensures a high level of reliability, ensuring continued APDL functionality even in the presence of single failures.
- The system allows performance of actions in accordance with SAMG-2 for primary circuit depressurization using equipment qualified for the corresponding operating conditions.
- It ensures the reliable operation of the IVMR system.

SOCRATES EU project on liquid source term during a severe nuclear accident – WP 3: Boundary evolution conditions in the bulk liquid phase

Grégoire A.C., Derbali M., Denis J.
Autorité de Sûreté Nucléaire et de Radioprotection, PSN-RES/SEREX/L2EC,
F-13115, Saint-Paul-lez-Durance, France.Corresponding Address
Anne-cecile.gregoire@asnr.fr; mouna.derbali-interim@asnr.fr; jean.denis@asnr.fr

Kärkelä T.
VTT Technical Research Centre of Finland,
Kivimiehentie 3, 02044 VTT, Espoo, Finland
teemu.karkela@vtt.fi

Sarraf R.
NUVIA,
280, avenue Napoléon Bonaparte – CS6002, F-92506 RUEIL-MALMAISON, France
riad.sarraf@nuvia.com

ABSTRACT

During normal operations in a Nuclear Power Plant, strict control of water chemistry is essential to prevent corrosion and preserve the integrity of components. In case of a severe accident, contaminated water present in containment sump or in spent fuel pools can harm system operations (by oxidation, corrosion or clogging processes) and compromise post-accident cooling capacities. Within the SOCRATES Horizon Euratom project, the objective of work package 3 is to investigate, through laboratory-scale tests, the intricacies of liquid chemistry in such complex situation. The focus is made on understanding how common materials in nuclear facilities interact with fission products when immersed in liquids.
Experiment test matrix will be based on a meticulous inventory of debris that could potentially be present in water during accidents. These encompass concrete or metallic particles, fragments of glass fibre insulation, paint chips arising from erosion or corrosion processes. Dissolution of such debris releases elements like silicon, calcium, metallic cations into aqueous media. Boundary conditions of the liquid present after a severe accident occurring in NPP (chemical buffer, pH, temperature) as well as inventories of key radionuclides will be defined based on the outputs of SOCRATES work package 2.
Laboratory-scale tests will be performed to characterize pool chemistry evolution in terms of pH, redox potential, soluble compounds, precipitates/colloids formation. Chemical and physical behaviours of debris and sludges, together with stable isotopes representative of highly soluble fission products (cesium and strontium) will be investigated. Particular attention will be given to how thermal and radiolytic stresses influence debris dissolution/degradation and next interactions with Cs and Sr. Furthermore, experiments will actively assess the kinetics of evolution in liquid properties by monitoring precipitate formation and size evolution.
These experiments will provide critical insights into the long-term fate of cesium and strontium in liquid phase following severe nuclear accidents.

KEYWORDS
SOCRATES, severe accident, liquid source term, caesium, strontium

1. INTRODUCTION

In the aftermath of Fukushima Daiichi NPP accident, open questions were raised related to long-term management of SA. Depending on SA scenario, huge volumes of water released from the RCS and from the emergency core cooling systems are collected in the lower parts of the reactor containment building. If these volumes exceed the capacity of the sump and recirculating pumps, flooding of the CV basement occurs, inducing contamination in areas that are difficult to access. Such large inventories were observed in the case of TMI-2 accident, when CV basement was flooded by ~2500 m^3 of contaminated water [1]. Contaminated water (debris, soluble/insoluble radionuclides) can harm system operations (by oxidation, corrosion, clogging processes) resulting in possible leakage leading to ground water contamination and having consequences on degraded fuel coolability and post-accident management.
In this view, needs have been identified for exploring comprehensively the chemistry and behavior of the liquid source term that arises from aerosols (including the most soluble radionuclides as Cs and Sr) and debris sedimentation in the water, from material leached from the containment walls and from interaction with immersed surfaces.
Within the SOCRATES program, the objective of WP3 is to investigate by laboratory scale tests, the intricacies of liquid chemistry in such complex situations and delving deep into how common materials in nuclear facilities react with fission products when immersed in liquids.

2. TEST BOUNDARY CONDITIONS

The term boundary conditions encompass all the parameters used to characterize the liquid phases found in the lower part of the containment vessel (sump in PWR or lower drywell/wetwell for BWR) or spent fuel pools, in the short and long term in SA conditions. It includes

- physical parameters as temperature and pressure evolution of the atmosphere in contact with the liquid phase.
- identification of the various chemical buffers (e.g., boric acid/soda, trisodium phosphate) to regulate pH; a comprehensive inventory of debris that could potentially be present in water during accident: concrete or metallic particles, fragments of glass fiber insulation, paint chips arising from erosion or corrosion processes. Debris dissolution introduces elements like silicon, calcium, and metallic cations.
- chemical parameters such as pH and redox potential, which results of the liquid phase composition evolution (taking account of chemical buffer, water radiolysis, material leaching, radionuclides release from degraded core, water supply).

Based on past accident data [1-3], on literature review on debris leaching in LOCA situation [4-5] and on literature review on cesium and strontium behaviour in accidental conditions [5] and their reactivity [6-8], the most likely conditions that can prevail in the liquid phase at mid/long term after a severe accident are summarized below.

Sump water temperature evolves rapidly in the hours following the accident initiation [1-3]. At short term (few hours after accident sequence), sump liquid temperatures up to 140°C can be still expected if the containment vessel remains pressurized (up to 5 bars). At long term, the temperature of the water collected in the lower parts of the containment vessel depends on the final state of the reactor (e.g. in-vessel corium or ex-vessels corium) and the possibility to operate closed recirculating cooling loops or not. A reasonable estimate of the temperature of water collected in the sump lies in the 40-80°C range.

Sump/basement water pH in the short term depends on the buffering agent used (soda, boric acid, sodium tetraborate, trisodium phosphate…) and the injection scenarios [3]. In order to stabilize halogen species (iodine) in the liquid phase, the objective is to maintain high pH conditions in the sump phase despite the release of highly soluble acidic species in the containment atmosphere following air radiolysis (nitric acid) and thermal/radiolysis degradation of cable insulation (hydrochloric acid). At short term, some scenarios predict acidic conditions (6.5-7.0), but final pH in the 7.8-8.7 range are expected in most scenarios with sodium tetraborates dissolution whatever the contribution of the acidic species generated in the containment

atmosphere. At long term, sump pH evolution will be linked to post accident operations, with the objective of maintaining slightly alkaline conditions (pH in between 8.5 and 9).

To the best of our knowledge, there is no publication related to long term impact of water radiolysis on sump water composition in SA conditions. Water radiolysis is expected to produce ROS (reactive oxygenated species) among them H_2O_2 is identified as the most stable in the long term (for timescales ranging from minutes to days). Expected H_2O_2 concentrations range from 10^{-8} up to 10^{-4} mol/l [9]. Generation of nitric acid following the radiolysis of nitrogen dissolved in water in equilibrium with air leads to a slow acidification of the liquid phase [10-11]. As oxidative species, ROS and HNO_3 are expected to play a role on sump chemistry in the long-term.

Dissolution behaviour and reactivity (e.g. secondary phase formation) of debris was investigated in LOCA situation [4-5] for different sump conditions. Final average cation concentration lies in between several dozen up to several hundred ppm for Si, Ca, Al but remains limited for Zn, Fe. In boric acid/soda buffer solution (pH 8.5), the formation of secondary phase featuring silica and calcium borates (colemanite) and zinc silicates (willemite) or zinc oxides was evidenced in analytical tests [5]. Enhanced precipitation processes are observed in the lower temperature range (40-60°C). In presence of borates ions, formation of borates species may compete with the formation silicate or carbonate phases.

Cesium is one of the main fission products in spent fuel. Its mass can amount up to 150-400 kg depending on the total initial fuel mass and fuel burn up [3]. Cesium is volatile and its fractional release during a severe accident can exceed 80% of its initial core inventory [3]. Main Cs released/transported forms up to the containment vessel are CsOH, CsI which are quite soluble in aqueous acidic or alkaline media. Aqueous phase contamination occurs following aerosol sedimentation/entrainment and containment vessel wall washing following the activation of emergency core cooling systems. Long-lasting low continuous contamination can also occur, following leaching of the degraded core, resulting in very high Cs contamination levels with concentration up to several dozen of ppm. Very low fractions of Cs are found in the basement sludges or deposited on the concrete immersed walls for both TMI-2 [1] and Chornobyl accidents (in between 0.2% and 4% of total Cs inventory found in the basements). Although representing a small fraction of cesium released from degraded core, the mass deposited or absorbed on surfaces poses a challenge for decontamination operations, inducing high dose rates preventing any human intervention. In the hydrothermal conditions prevailing in the sump liquid phase, several Cs- containing secondary phases can be hypothesized: pollucite [6], cesium aluminophosphate, Cs borates crystal [7].

Fission product Sr mass in a core amounts up to 50-130 kg depending on the total initial fuel mass and fuel burn up [3]. Strontium is considered as non-volatile with releases during a severe accident of less than 1% of its initial core inventory [3], these releases occur when high temperature are reached in the degraded core – mainly during the second oxidation phase. SrO is the main released/ transported form, but other species are not excluded. Important Sr deposition is expected to occur on the RCS walls; As a consequence of its low volatility, early Sr incomes in the liquid phase are low compared to that of Cs: only 0.7% of initial Sr core inventory were found in the liquid phase after TMI-2 accident [1] and 3.3% for the FD accident (Unit 2 - sampling of end of March 2011 [2]). Over time, a continuous strontium supply in the liquid phase is expected resulting from RCS surfaces washing and core leaching. Sr is mainly found in the bulk liquid, expected as hydrated Sr^{2+} cation. A higher Sr fraction than for Cs is found in the solid phase (sludges). Indeed, the formation of low soluble strontium carbonates (strontianite), strontium silicates and strontium borates upon mild heating in alkaline media is reported by [8].

3. CONCLUSION / PERSPECTIVE

Laboratory-scale tests will be performed at VTT and ASNR to characterize pool chemistry evolution in terms of pH, redox potential, soluble compounds, precipitates/colloids formation. Chemical and physical behaviour of debris and sludges together with stable isotopes of caesium and strontium will be investigated. Of particular interest is understanding how thermal/radiolytic stresses influences debris

dissolution/degradation and next interactions with Cs and Sr. Furthermore, experiments will actively assess the kinetics of liquid properties evolution by monitoring precipitate formation and size evolution.

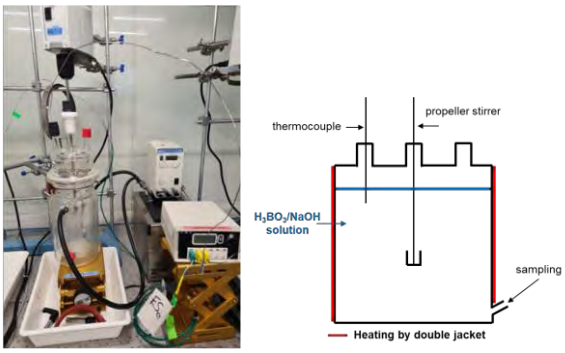

Figure 1 : typical batch device for study of sump reactivity.

To produce reliable data set on sump chemistry evolution, experimental work will consider chemical system with increasing complexity: analytical test devoted to better understand element reactivity will be firstly conducted, phenomenological tests will be performed in a second phase. Experiments' boundary conditions will be based on the parameters. Long-duration tests (from several hours up to several weeks) will be performed in batch conditions.

ACKNOWLEDGMENTS

The SOCRATES project has received funding from the European Union's Horizon Europe research and innovation programme under Grant Agreement No 101163745

REFERENCES

1. McIsaac C.V. et al. (1984). TMI-2 reactor building source term measurements, surface and basement sediments, GEND-042.
2. Grambow B. et al. (2022). Ten year after the NPP accident at Fukushima: review on fuel debris behavior in contact with water, JNST. 59:1, 1-24
3. "Jacquemain D, Coordinator (2015). Nuclear Power Reactor Core Melt accident, current state of knowledge, edp science isbn: 978-2-7598-1835-8.
4. Dallman J. et al. (2006). Integrated Chemical effects tests project: consolidated data report NUREG /CR - 6914n Vol 1.
5. Le Maout-Alvarez C. (2023). Etude expérimentale des effets chimiques sur le colmatage des filtres dans l'industrie nucléaire, Thesis, University of Lorraine, in french.
6. MacLaren I. et al. (1999). Hydrothermal Synthesis of Pollucite ($CsAlSi_2O_6$) Powders, *J. Am. Ceram. Soc.,* **82** [11] 3242–44.
7. Dumanli F. T.S. el al. (2023). Characterization, thermal dehydration kinetic, and thermodynamic study of synthesized cesium borate ($CsB_5O_8{\cdot}4H2O$), Inorganic and Nano-Metal Chemistry 53, 2023 - Issue 3,
8. Liu Z.H. et al. (2006). Synthesis and thermochemistry of $SrB_2O_4{\cdot}4H_2O$ and SrB_2O_4, Thermochimica Acta 448, 59–62.
9. Joseph J.M. et al. (2008). A combined experimental and model analysis on the effect of pH and O_2(aq) on g-radiolytically produced H_2 and H_2O_2, Radiation Physics and Chemistry 77, 1009– 1020,
10. Dey G.R. (2011). Nitrogen compounds' formation in aqueous solutions under high ionizing radiation: An overview, Radiation Physics and Chemistry 80, 394–402.
11. Jegou C. et al. (2007). Spent fuel UO_2 matrix alteration in aqueous media under oxidizing conditions, Radiochimica acta, 95, 513-522.

12th CONFERENCE ON
SEVERE ACCIDENTS RESEARCH
May 18-22, 2026 - Madrid, Spain
ERMSAR 2026

SOCRATES EU PROJECT ON LIQUID SOURCE TERM DURING A SEVERE NUCLEAR ACCIDENT – WP 3: BOUNDARY EVOLUTION CONDITIONS IN THE BULK LIQUID PHASE – Experimental Phase

Grégoire A.C., Derbali M., Denis J. (ASNR), Kärkelä T. (VTT), Sarraf R. (Nuvia)

A. Context – Objectives

In case of a severe accident, huge volume of water released from the RCS and from the emergency core cooling systems are collected in the reactor containment building – flooding of the CV basement (TMI-2 and FD accidents)

- Such contaminated water (Debris, RN) can harm system operations (by oxidation, corrosion, clogging etc.) resulting in possible leakage leading to ground water contamination and having consequences on degraded fuel coolability.
- **Presence of specific (soluble/insoluble) impurities may affect radiolytic and corrosion reactions as well as precipitation processes and fission products chemistry** (e.g. chlorine affecting iodine chemistry) and play a role on the kinetics of these processes.

Needs for exploring comprehensively the chemistry and behaviour of the liquid source term that arises from aerosols (incl. soluble RNs such as Cs and Sr), debris sedimentation in the water, material leached from the containment walls and from interaction with immersed surfaces

SOCRATES WP3 : laboratory scale tests – conditions representative of boundary conditions of bulk liquid phase in SA situation

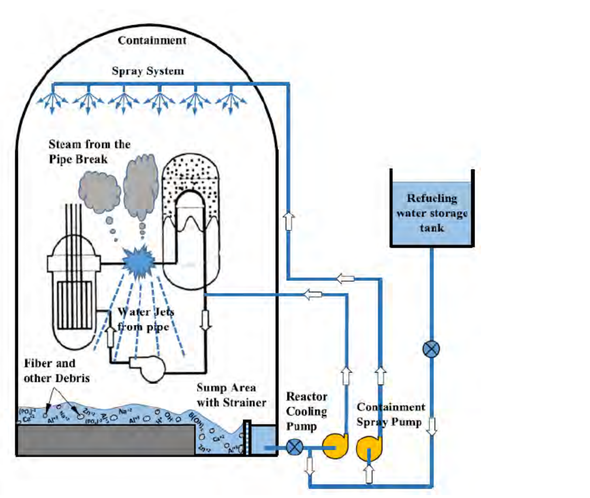

Scheme of recirculation loop in the NPP
[**Trigeol** , J.F. et al (2021). https://irsn.hal.science/irsn-04113763/document]

B. Bulk Liquid phase boundary conditions

Thermal – Hydraulics

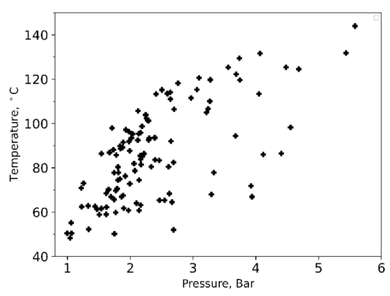

Sump temperature and CV pressure – ASTEC simulations of SA scenarii on a 1300 MWe PWR (Nowack et al., 2025).

Sump composition and pH

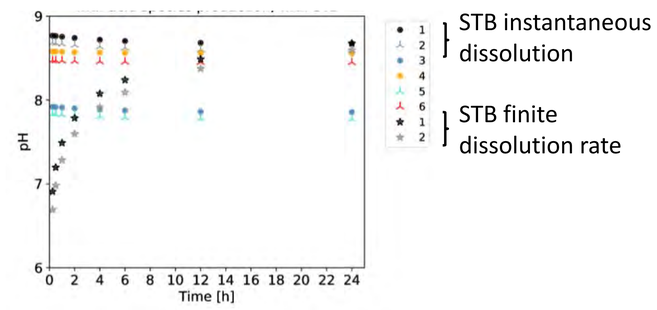

Sump pH evolution ASTEC simulations of a SA on a 1300 MWe PWR scenarii (1-6) involving water from RCS and supply tanks . Scenario 1-2 : Sodium Tetra Borate baskets

Temperature	100-130°C for studies reproducing early post-accident phase (1-2 days) 40-80 °C for studies focused on long term evolution phase (weeks up to months)
pH	pH ~ 4 - 5 for early post-accident phase (several hours after accident) pH > 7 for long term phases, experiments up to pH 9 can be considered
Main water Radiolysis product	H_2O_2 estimated level 10^{-6} up to 10^{-4} mol/L
Buffering media	NaOH/Boric acid/STB [Na] 2000-5000 ppm, [B] 2000-5000 ppm
Cl	10 to 15000 ppm (high bound value = sea water as coolant/ lower bond value = HCl production from atmosphere radiolysis of cable insulation)
Mg	6-1000 ppm (high bound value linked to use of sea water as coolant)
K	20-300 ppm
Sulfates	<2000 ppm
Carbonates	Equilibrium with air atmosphere
Nitrates	Air/Water radiolysis product

Review of material immersed / leached in the sump containment

Debris leaching	Large concentration ranges / local inhomogeneities
Ca (concrete)	10-100 ppm
Si (concrete, insulation)	30-450 ppm
Al (dry glue)	5 ppm (400 ppm if metallic surfaces)
Zn (galvanized steel)	5-50 ppm
Fe (galvanized steel)	1-10 ppm

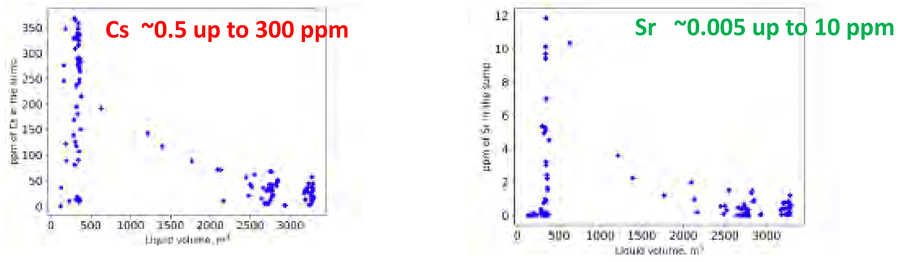

Cs, Sr concentrations (ppm) in the sump as a function of liquid final volume at the end of ASTEC simulations of SA scenarii on a 1300 MWe PWR (Nowack et al., 2025).

C. Experiment strategy (Grégoire et al., 2025)

Characterize pool chemistry evolution in terms of pH, redox potential, precipitates and colloids formation

Several subtask to investigate pool chemistry step by step

- **Evaluate long term corrosion of immersed debris (insulation, paints) and surfaces (metallic and concrete) ; Si, Ca, Zn, Fe source term role of buffer, pH , temperature and radiolysis**
- **Bulk solution reactivity of elements from debris : simple chemical system up to complex mix involving Ca, Cs, Zn, Fe in pure water or tap water or NaOH/boric acid/ STB – role of temperature, pH, Boron species and radiolysis**
- **Bulk solution reactivity with Cs and Sr**
- **Investigation of Cs and Sr adsorption on immersed debris surface (bare/painted concrete surfaces)**
- **Phenomenological tests involving Cs and/or Sr : long-term trials are planned. Two tests (allowing up to 3 x 5 days irradiation duration) scheduled in ASNR-EPICUR facility in 2027**

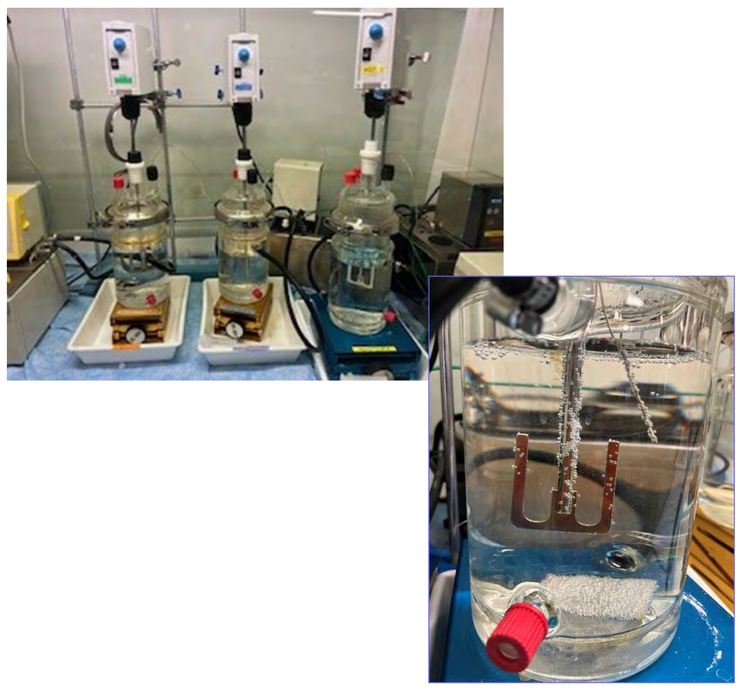

Work performed at ASNR and VTT

Reference : Grégoire et al.(2025), Test conditions for liquid phase study, D3.1 report, EU-SOCRATES Programme; Nowack H., et al. (2025), Nowack H., et al. (2025), Review of SA code capabilities, D2.2 report, EU-SOCRATES program; Le Maout-Alvarez C. (2023). Etude expérimentale des effets chimiques sur le colmatage des filtres dans l'industrie nucléraire, Thesis, University of Lorraine.

Preliminary Experimental Study on the Elemental Iodine Adsorption Filter for a Passive Radioactive Material Filtration System

Jaehoon Jung*, Seongho Hong, Jinheok Kim, Kihan Park, Jeongyun Oh, Seokgyu Jeong, and Chang Wan Kang
Korea Atomic Energy Research Institute (KAERI)
989-111 Daedeok-daero, Yuseong-gu, Daejeon, Korea
jhjung@kaeri.re.kr

ABSTRACT

After the Fukushima accident, various safety systems have been developed to enhance the safety of nuclear power plants. To further strengthen safety, a passive radioactive material filtration system is being developed for operation inside the containment building to minimize environmental impacts during severe accidents. The system consists of a passive gas entrainment system and a fission product mitigation system. To enhance its effectiveness, the performance and characteristics of each subsystem must be systematically evaluated and optimized. For this purpose, KAERI is preparing aerosol, elemental iodine, and organic iodine tests. Among these efforts, this paper specifically introduces the elemental iodine experiment, including the experimental facility and preliminary results.
An elemental iodine test setup was established to evaluate the removal efficiency of an iodine adsorption filter. Preliminary experiments were conducted to investigate the effects of parameters such as pressure and velocity on the first-stage adsorption filter. The results provided insights into performance trends and limitations of the first design. Based on these findings, improvements to the filter design are currently in progress. This paper presents the overall filtration system, the elemental iodine experimental facility, and key findings from the preliminary tests.

KEYWORDS
Severe accident, Filtration, Radioactive material, Iodine

1. INTRODUCTION

After the Fukushima accident, lots of safety systems have been developed, and the safety of domestic nuclear power plants (NPPs) has also improved. To further improve the safety of NPPs, it is necessary to develop a radioactive material filtration system which operates in containment to minimize damage caused by release of radioactive material to the environment during the severe accident.
The goal of this project is the development of a passive radioactive material filtration system which can be applied to the operating NPPs[1]. It consists of two main components, the passive fluid induction system and a fission product filtration system. To evaluate the performance of the radioactive filtration system in the containment using the severe accident analysis code, it is necessary to develop the fission product removal efficiency model. Also, to optimize the system, we need to understand the characteristics of each component.
KAERI is preparing for the aerosol, elemental and organic iodine tests to understand the characteristics of each component. This paper introduces the elemental iodine test set up for obtaining the elemental iodine removal efficiency and characteristics of adsorbents.

2. EXPERIMENT FACILITY FOR IODINE TEST

Figure 1 presents a schematic diagram of experimental facility used for iodine mitigation performance evaluation. The facility consists of three main subsystems: 1. Performance test section, 2. Thermal-hydraulic system (gas supply, cooling, storage, and discharge), 3. Fission product simulation and measurement system The gas supply system is designed to simulate thermal-hydraulic conditions relevant to severe accidents. In a mixing chamber, the supplied gas is mixed with simulated fission products (iodine) before entering the performance test section. After passing through the performance test section, the exhaust gas is cooled, treated to remove aerosols and iodine, and finally discharged to the atmosphere.

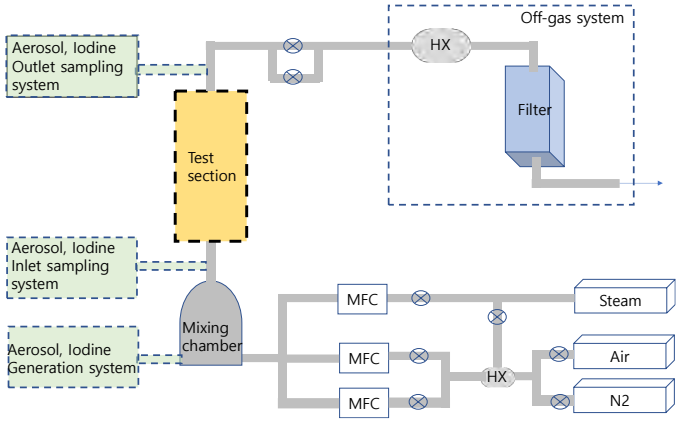

Figure 1. Schematic of experimental setup

2.1. Thermal-Hydraulic System

The gas supply system provides air as the primary test fluid using a steam boiler and an air compressor (Table 2). A receiver tank is installed downstream of the supply system to reduce flow pulsations and ensure stable gas delivery. Gas flow rate and pressure are controlled using flow meters and control valves.
The experiments were conducted at pressures ranging from 1.5 to 5 bar, with face velocities of approximately 0.2 to 1.0 m/s for a filter size of 305 × 305 mm. To accommodate a wide range of flow rates, the injection line was branched, as shown in Fig. 1. Additionally, the outlet line was divided into two branches to facilitate pressure control under low-flow conditions.
Although most iodine is removed in the performance test section, residual contaminants may remain in the exhaust gas. Therefore, the exhaust passes through a water-filled scrubber system, followed by HEPA and charcoal filters, before being released to the atmosphere.

2.2. Performance Test Section

The performance test section includes the iodine mitigation system to be evaluated. To minimize scaling effects, the iodine adsorption filter installed in the test section has the same dimensions and installation configuration as the actual filter used in the mitigation system. To evaluate the performance limits of the filter, differential pressure across the filter was also measured.

2.3. Iodine Generation and Measurement System

The iodine generation system is shown in the left part of Fig.2, and the iodine sampling system is shown in the right part.
To simulate iodine released during severe accidents, an iodine injection system was developed. Solid iodine crystals (up to 50 g) were heated to generate gaseous elemental iodine, which was then transported into the main test system using nitrogen or air as a carrier gas[2].

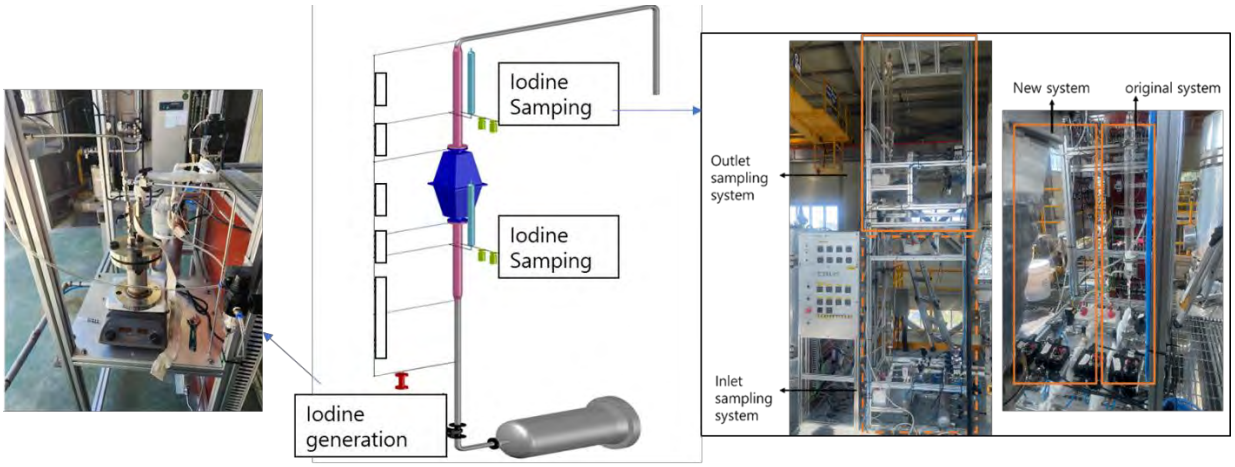

Figure 2. Iodine Generation and Measurement System

Iodine concentrations at the inlet and outlet of the test section were measured. The sampling flow rates and pressure were controlled using needle valves. To prevent steam condensation and reduce iodine losses on cold surfaces, the sampling lines were maintained at elevated temperatures.
Elemental iodine was collected using liquid gas scrubber columns equipped with coolant jackets. The coolant jackets prevented evaporation of the scrubber solution during the sampling. After the primary scrubber, an additional scrubber was installed to confirm complete iodine collection [3].
The collected samples were analyzed using iodide ion-selective electrodes (ISE). Ascorbic acid was added to the scrubber solution to reduce molecular iodine (I_2) to iodide ions (I^-). Although the ISE system can provide near real-time trends of iodine concentration, its sensitivity to temperature variations limits its accuracy. Therefore, precise measurements were obtained through post-test calibration under controlled temperature conditions.

3. PRELIMINARY TEST RESULTS AND DISCUSSION

3.1. System Performance Verification

Several preliminary experiments were conducted to characterize system behavior and support detailed test planning. The test conditions are summarized in Table 1. Inlet pressures upstream of the iodine injection nozzle ranged from 1.5 to 5 bar(g), and gas velocities were between 0.5 and 0.8 m/s. During the experiments, gas temperature, wall temperature, absolute pressure, gauge pressure, differential pressure, and sampling flow rates were measured along the test section.
The preliminary tests confirmed that pressure, temperature, and steam and air velocity were well controlled. In addition, stable operation of the iodine generation and sampling systems was verified.

3.2. Discussion

The relationships between decontamination factor (DF), pressure, gas velocity, and test gas composition were analyzed. The DF is defined as the ratio of the iodine concentration at the inlet and outlet.
Air-only conditions: Increasing pressure from 1.5 to 3 bar had little effect on DF, whereas increasing pressure to 5 bar resulted in approximately a 50% reduction in DF. This trend is attributed to the increased mass flow rate, which reduces the residence time required for iodine-adsorbent interaction.
Air–steam mixture: When both air and steam were used, DF decreased significantly as pressure increased from 1.5 to 3 bar, while further pressure increase to 5 bar had a minor effect.

Effect of steam fraction: At 1.5 and 5 bar, steam had little influence on DF. However, at 3 bar, DF decreased noticeably with steam addition. Comparison of air-only, air/steam = 5:5 wt%, and air/steam = 3:7 wt% conditions at 3 bar showed a clear trend of decreasing DF with increasing steam content.
The observed phenomena at 3 bar suggest complex interactions among pressure, steam content, and adsorption kinetics. Additional experimental and theoretical investigations are required, which are planned for future studies.

Table I. Preliminary Test Results

Test No.	Test Results						
	Pressure	Air flow rate (kg/s)	Steam flow rate (kg/s)	Inlet concentration (ppm)	Outlet concentration (ppm)	DF	Pressure difference (Pa)
1	1.5	0.062	0.000	18.45	0.77	**24.11**	217.50
2	1.5	0.015	0.033	22.65	0.88	**25.83**	370.1
3	3	0.025	0.061	9.04	1.30	**6.97**	917
4	3	0.043	0.094	5.72	0.70	**8.23**	1080.11
5	5.09	0.040	0.093	4.83	0.36	**13.37**	762.53
6	3.07	0.051	0.051	25.43	1.45	**17.60**	253.54
7	5.11	0.040	0.094	7.19	0.66	**10.84**	280.40
8	3.07	0.025	0.063	17.53	1.94	**9.05**	231.53
9	3.04	0.122	0.000	5.21	0.19	**26.82**	316.90
10	5.04	0.194	0.000	2.57	0.22	**11.80**	431.95

4. CONCLUSIONS

An experimental facility was developed to evaluate the iodine removal performance of an adsorbent-based mitigation system under simulated severe accident conditions. Thermal-hydraulic tests confirmed stable control of pressure, temperature, gas velocity, and iodine generation and sampling systems.
Preliminary results indicate that pressure and steam content significantly affect iodine removal performance, particularly at intermediate pressure conditions. Future experiments will focus on a wider range of operating conditions to develop a predictive model for iodine removal efficiency.

ACKNOWLEDGMENTS

This research was supported by the National Research Foundation of Korea (NRF) funded by the Ministry of Science and ICT. (RS-202200144064).

REFERENCES

List references here, according to their first use in the paper. Include the following information (as applicable). Do not include these sentences in the full paper.

1. J. Jung, D.S, and S.H. Kim, “Preliminary Evaluation on Radioactive Material Filtration System Effectiveness under Development”, T*ransactions of the Korean Nuclear Society Spring Meeting*, Jeju, Korea, May 18-19, 2023.
2. J. Jung, J. B. Lee, and H.Y. Kim, “Experimental Investigation of Iodine Decontamination Performance of a Filtered Containment Venting System in ARIEL Facility”, *Proceedings of the International Conference Nuclear Energy for New Europe*, Bled, Slovenia, Sep 11-14, 2017.
3. J. Jung, S. Jeong, and C.W. Kang, “Preliminary Experimental Study on the Elemental Iodine Removal Performance of Adsorbent for Filtration System”, T*ransactions of the Korean Nuclear Society Autumn Meeting*, Changwon, Korea, Oct 24-25, 2024.

12th CONFERENCE ON
SEVERE ACCIDENTS RESEARCH
May 18-22, 2026 - Madrid, Spain
ERMSAR 2026

Preliminary Experimental Study on the Elemental Iodine Adsorption Filter for a Passive Radioactive Material Filtration System

Jaehoon Jung [a]*, Seongho Hong[a], Jinheok Kim[a], Kihan Park[a], Jeongyun Oh[a], Seokgyu Jeong[a], and Chang Wan Kang[a]
[a]Korea Atomic Energy Research Institute, Yuseong-gu, Daejeon, Korea
*Corresponding author: jhjung@kaeri.re.kr

Introduction

1. Introduction

- After the Fukushima accident, lots of safety systems have been developed, and the safety of domestic nuclear power plants(NPPs) has also improved. To further improve the safety of NPPs, it is necessary to development of radioactive material filtration system which operates in containment to minimize damage caused by release of radioactive material to the environment during the severe accident.
- The goal of this project is the development of a passive radioactive material filtration system which can be applied the operating nuclear power plants. Before developing the passive radioactive material filtration system development, it is needed to confirm the effect of fission product removal efficiency when applying the radioactive material filtration system inside containment.
- KAERI is preparing for the aerosol, elemental and organic iodine tests to understand the characteristics of each component. This paper introduces the elemental iodine test set up for obtaining the elemental iodine removal efficiency and characteristics of adsorbents.

Experimental setup

2. Thermal-Hydraulic System

Experimental setup

- Figure 1 presents a schematic diagram of experimental facility used for iodine mitigation performance evaluation. The facility consists of three main subsystems:
  - 1. Performance test section,
  - 2. Thermal-hydraulic system
  - 3. Fission product simulation and measurement system

Thermal-Hydraulic System

- The gas supply system provides air as the primary test fluid using a steam boiler and an air compressor. Gas flow rate and pressure are controlled using flow meters and control valves.
- The experiments were conducted at pressures ranging from 1.5 to 5 bar, with face velocities of approximately 0.2 to 1.0 m/s for a filter size of 305 × 305 mm.
- The exhaust passes through a water-filled scrubber system, followed by HEPA and charcoal filters, before being released to the atmosphere.

Fig. 1 Schematic diagram of test set up

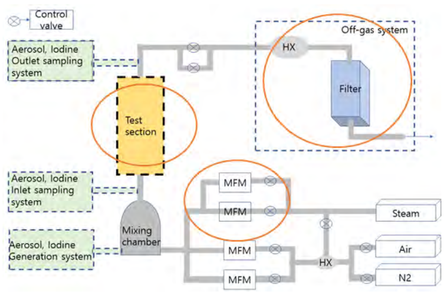

Table. 1 Capacity of test facility

Parameter	Value
Maximum operating pressure	10 bar a
System temperature	25 ~ 200 °C
Steam generator capacity	5000 kg/hr
Nitrogen generator capacity	1800 kg/hr
Air supply capacity	1800 kg/hr
핵분열 생성물 관련 성능	
Aeorosol Concnetration (SiO2)	$\mu g/m^3$~10 g/m^3
Elemental iodine(I_2) concentration	max. ~1000 ppm
Organic iodine(CH_3I) concentration	Max. ~1000 ppm

Table. 2 Test facility

Part	System	Main Equipment
Test Part	Performance Test Components	Performance Test Components
Thermal-hydraulic Part	Gas Supply System	Steam Boiler Unit
		Air Compressor Unit
		Air Heater
		Air Reservoir
		Steam Ejector
	Storage & Drain System	Suppression Tank
		Charcoal& HEPA filter
	Cooling System	Steam Condenser
		Circulation Pump
		Cooling Tower
Aerosol/Iodine Generation Parts	Aerosol/Iodine generation & Measuring System	Aerosol/Iodine Injector
		Sampling Bottle & system

3. Performance Test Section

Performance Test Section

- The performance test section includes the iodine mitigation system to be evaluated.
- To minimize scaling effects, the iodine adsorption filter installed in the test section has the same dimensions and installation configuration as the actual filter used in the mitigation system.
- To evaluate the performance limits of the filter, differential pressure across the filter was also measured.

Iodine Generation and Measurement System

- Solid iodine crystals (up to 50 g) were heated to generate gaseous elemental iodine, which was then transported into the main test system using nitrogen or air as a carrier gas
- Iodine concentrations at the inlet and outlet of the test section were measured.
- The sampling flow rates and pressure were controlled using needle valves.
- Elemental iodine was collected using liquid gas scrubber columns equipped with coolant jackets. The coolant jackets prevented evaporation of the scrubber solution during the sampling.
- The collected samples were analyzed using iodide ion-selective electrodes (ISE).

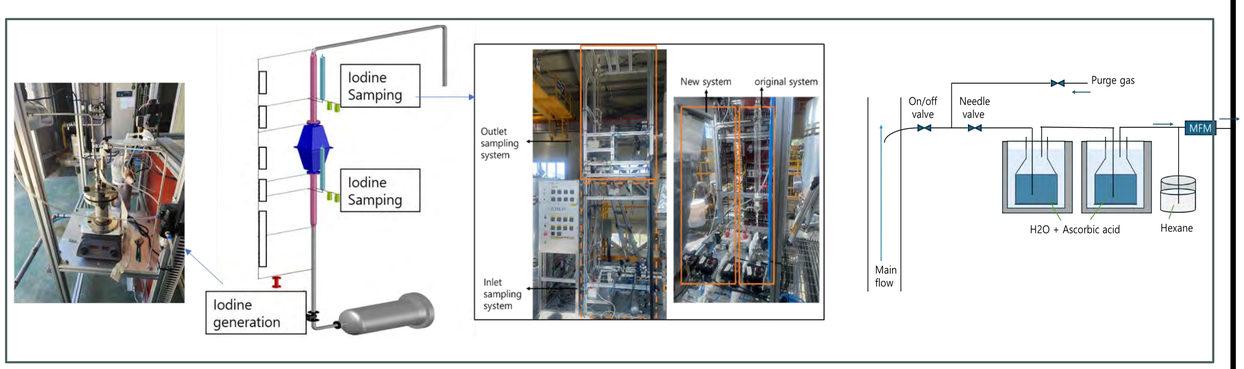

Fig. 2 Elemental iodine generation and sampling system

Preliminary test results

4. System Performance Verification

- The test conditions are summarized in Table 3. Inlet pressures upstream of the iodine injection nozzle ranged from 1.5 to 5 bar(g), and gas velocities were between 0.5 and 0.8 m/s. During the experiments, gas temperature, wall temperature, absolute pressure, gauge pressure, differential pressure, and sampling flow rates were measured along the test section.
- The preliminary tests confirmed that pressure, temperature, and steam and air velocity were well controlled. In addition, stable operation of the iodine generation and sampling systems was verified.

Table. 3 Preliminary Test Results

Test No.	Test Results						
	Pressure	Air flow rate (kg/s)	Steam flow rate (kg/s)	Inlet concentration (ppm)	Outlet concentration (ppm)	DF	Pressure difference (Pa)
1	1.5	0.062	0.000	18.45	0.77	**24.11**	217.50
2	1.5	0.015	0.033	22.65	0.88	**25.83**	370.1
3	3	0.025	0.061	9.04	1.30	**6.97**	917
4	3	0.043	0.094	5.72	0.70	**8.23**	1080.11
5	5.09	0.040	0.093	4.83	0.36	**13.37**	762.53
6	3.07	0.051	0.051	25.43	1.45	**17.60**	253.54
7	5.11	0.040	0.094	7.19	0.66	**10.84**	280.40
8	3.07	0.025	0.063	17.53	1.94	**9.05**	231.53
9	3.04	0.122	0.000	5.21	0.19	**26.82**	316.90
10	5.04	0.194	0.000	2.57	0.22	**11.80**	431.95

Fig. 3 Experimental results at 3 bar

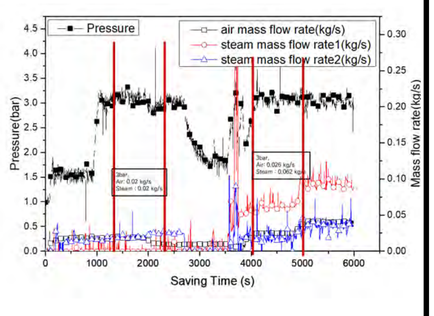

5. Discussion & Conclusions

- The relationships between decontamination factor (DF), pressure, gas velocity, and test gas composition were analyzed. The DF is defined as the ratio of the iodine concentration at the inlet and outlet.
- Air-only conditions: Increasing pressure from 1.5 to 3 bar had little effect on DF, whereas increasing pressure to 5 bar resulted in approximately a 50% reduction in DF. This trend is attributed to the increased mass flow rate, which reduces the residence time required for iodine-adsorbent interaction.
- Air–steam mixture: When both air and steam were used, DF decreased significantly as pressure increased from 1.5 to 3 bar, while further pressure increase to 5 bar had a minor effect.
- Effect of steam fraction: At 1.5 and 5 bar, steam had little influence on DF. However, DF decreased with steam addition at 3 bar. Comparison of air-only, it showed a clear trend of decreasing DF with increasing steam content.
- The observed phenomena at 3 bar suggest complex interactions among pressure, steam content, and adsorption kinetics. Additional experimental and theoretical investigations are required, which are planned for future studies.

Acknowledgements

This research was supported by the National Research Foundation of Korea (NRF) funded by the Ministry of Science and ICT. (RS-202200144064).

Re-examination of the VULCANO VE-U9 Corium Spreading Test Using a Novel Pressure-Substitution Implicit Solver and Crust Fracture Model

***Ryo Yokoyama, Shunichi Suzuki, and Koji Okamoto**
The University of Tokyo
Corresponding Address
yokoyamaryo395@g.ecc.u-tokyo.ac.jp; s_suzuki@n.t.u-tokyo.ac.jp; okamoto@n.t.u-tokyo.ac.jp

Christophe Journeau
Commissariat à l'énergie atomique et aux énergies alternatives (CEA)
Address
christophe.journeau@cea.fr

ABSTRACT
Lessons learned from the Fukushima Daiichi Accident (1F), where molten corium spread across the ex-vessel floor, underscore the importance of understanding corium spreading behavior for both accident reconstruction and the design of core-catcher systems. Recent experiments, notably the VULCANO VE-U9 test at CEA Cadarache, have shown that substrate conditions significantly affect corium spreadability. These studies also revealed that crust breaching can occur during spreading, adding complexity to melt–substrate interactions. However, the underlying mechanism of crust breaching remains insufficiently explored. In this work, the VULCANO VE-U9 experiment is re-examined using a novel particle-based approach coupled with a crust breaching model based on the Drucker–Prager yield criterion. A pressure-substitution implicit solver was developed to efficiently handle the highly viscous corium flow. When the yield function exceeded zero, the model reduced viscosity to represent crust fracture and subsequent flow. Simulations reproduced the grinding-like motion of viscous corium and successfully captured crust breaching at the advancing front due to compressive stress surpassing the yield strength. The proposed model reproduces fundamental breaching phenomena without artificial adjustments. To improve agreement with experimental observations, sensitivity analyses of key parameters—such as internal friction angle and cohesion constant—are recommended, as these govern the yield stress magnitude.

KEYWORDS
Corium Spreading; Crust formation; Solidification; Fukushima Accident; Core-Catcher

1. INTRODUCTION
High-temperature, highly viscous corium spreading is one of the crucial ex-vessel phenomena during a hypothetical nuclear severe accident, as it can determine the initial condition of the debris and the subsequent accident progression, such as molten core–concrete interaction (MCCI) [1,2]. Recently, the VULCANO VE-U9 experimental program observed prototypic corium spreading over sacrificial concrete and ablation-resistant ceramic substrates to investigate the role of MCCI in spreading dynamics [3]. A grinding-type motion of the corium can be seen over the ablation-resistant ceramic substrates, whereas a sliding motion of the corium is observed over the sacrificial concrete substrates. The low-viscosity lubricating boundary layer generated locally by MCCI enhances the spreadability of the corium. Furthermore, in the ablation-resistant ceramics experiment, crust breaching at the advancing front of the corium is observed, causing re-spreading of the corium encapsulated inside the crust. To gain deeper insight into the VULCANO VE-U9 experiments, a Lagrangian Moving Particle Hydrodynamics (MPH) model, which is one of the mesh-free particle methods, is developed and applied to simulate the experiments [4,5]. In this model, appropriate slip and no-slip boundary conditions are implemented to mimic the substrate-dependent spreading morphologies. However, the present methods cannot simulate crust-breaching behavior. Although a

previous study proposed a crust-breaching model based on the von Mises stress, this approach has uncertainties because the yield stress is manually prescribed and the von Mises equivalent stress is a scalar invariant that does not retain the directionality of the stress state or the difference between tensile and compressive failure modes [6]. In the context of the compression-dominated crust breaching that is observed in the experiment, a more suitable and physically consistent crust breaching model is indispensable.
In this study, we re-examine the VULCANO VE-U9 corium spreading experiment on ablation-resistant ceramics by introducing a crust-breaching model. In the previous MPH method, a pressure–viscosity simultaneous implicit solver was employed, in which the unknown pressure and velocity fields are solved implicitly and simultaneously. In contrast, the present study adopts a pressure-substitution implicit solver, in which only the unknown velocity field is solved implicitly while the pressure is substituted, leading to a lower computational burden than the original algorithm.

2. Numerical model

2.1 Control Equations

The governing equations consist of the momentum equation

$$\rho_0 \frac{\mathrm{D}\mathbf{u}}{\mathrm{D}t} = -\nabla \mathrm{P} + \mu \nabla^2 \mathbf{u} + \rho_0 \mathbf{g}, \tag{1}$$

Pressure equation for the incompressible control

$$\mathrm{P} = -\lambda \nabla \cdot \mathbf{u} + \kappa \frac{\Delta \rho}{\rho_0}, \tag{2}$$

And the energy conservation equation

$$\frac{\mathrm{DH}}{\mathrm{D}t} = k \nabla^2 T + \dot{Q}, \tag{3}$$

where ρ_0, $\mathbf{u}$, P, μ, $\mathbf{g}$, λ, κ, H, k, T, and $\dot{Q}$ correspond to the density, pressure, dynamic viscosity, gravity ac celeration, bulk viscosity, bulk modulus, enthalpy per unit volume, thermal conductivity, temperature, and volumetric heat source term, respectively. When Eq.(2) is substituted into Eq.(1), the following equation, whose unknown value is only $\mathbf{u}$, can be obtained.

$$\rho_0 \frac{\mathrm{D}\mathbf{u}}{\mathrm{D}t} = \lambda \nabla (\nabla \cdot \mathbf{u}) - \kappa \nabla \left(\frac{\Delta \rho}{\rho_0} \right) + \mu \nabla^2 \mathbf{u} + \rho_0 \mathbf{g}, \tag{4}$$

If we discretize Eq.(4) with the MPH method framework, the following linear matrix equation can be obta ined.

$$\rho_0 \frac{\mathbf{u}^{k+1}}{\Delta t} = -2\mu(dim+2) \sum_j \left(\frac{\mathbf{u}_j^{k+1} - \mathbf{u}_i^{k+1}}{|\boldsymbol{r}_{ij}|} \cdot \mathbf{e}_{ij} \right) \mathbf{e}_{ij} w'_{ij} -$$

$$\sum_j \left(\lambda \sum_l \left(\mathbf{u}_l^{k+1} - \mathbf{u}_i^{k+1} \right) \cdot \mathbf{e}_{li} w'_{li} + \lambda \sum_l \left(\mathbf{u}_l^{k+1} - \mathbf{u}_i^{k+1} \right) \cdot \mathbf{e}_{il} w'_{il} \right) \mathbf{e}_{ij} w'_{ij}$$

$$= \rho_0 \frac{\mathbf{u}^k}{\Delta t} - \kappa \sum_j \left((n_j - n_0) + (n_i - n_0) \right) \mathbf{e}_{ij} w'_{ij} + \rho_0 \mathbf{g}, \tag{5}$$

In which unknown velocity $\mathbf{u}^{k+1}$ is solved by CG (Conjugated Gradient) solver.

2.1 Crust Breaching model

The present crust-breaching model assumes that the structural collapse occurs when the local stress exceeds the yield strength defined by the Drucker–Prager yield criterion. Once a particle is identified as a breached crust element, its rheological behavior is switched from solid-like to elasto-viscous fluid, in which the flowability is governed by the local shear rate. Firstly, the local stress of the crust is assumed as

$$\boldsymbol{\sigma} = 2\mu \boldsymbol{\varepsilon} - \mathrm{P}\mathbf{I}, \tag{6}$$

where $\boldsymbol{\sigma}$, $\boldsymbol{\varepsilon}$, and $\mathbf{I}$ are Cauchy stress tensor, strain rate tensor, and identity tensor, respectively. From the Cauchy stress tensor, the second invariant of stress J_2 can be calculated as

$$J_2 = \sqrt{\frac{1}{2}(\boldsymbol{\sigma} + \mathrm{P}\mathbf{I}) : (\boldsymbol{\sigma} + \mathrm{P}\mathbf{I})}. \quad (7)$$

As the yield stress, the following Drucker–Prager yield criterion is employed:

$$f_p = \sqrt{3J_2} - (\alpha_\phi \mathrm{P} + \kappa), \quad (8)$$

where

$$\alpha_\phi = \frac{3\,tan\phi}{\sqrt{9 + 12tan^2\phi}}$$
$$\kappa = \frac{3c}{\sqrt{9 + 12tan^2\phi}}. \quad (9)$$

Here ϕ and c are the internal friction angle and the cohesion. In the present simulation, the yield criteria are set following conditions as it likely occurs compression conditions.

$$Breached\ Crust = \begin{cases} f > 0 \\ and \\ tr(\boldsymbol{\varepsilon}) < 0 \end{cases}, \quad (10)$$

Once the crust breaching occurs, the following simple elastoviscous model is applied to the breached particle.

$$\mu_{eff} = \frac{\alpha_\phi \mathrm{P} + \kappa}{2\dot{\boldsymbol{\gamma}}}, \quad (11)$$

where $\dot{\gamma}$ is shear rate which is calculated as

$$\dot{\boldsymbol{\gamma}} = \sqrt{2\boldsymbol{\varepsilon} : \boldsymbol{\varepsilon}}. \quad (12)$$

3. 2D VULCANO VE-U9 simulation

The present study simulated a two-dimensional configuration of the VULCANO VE-U9 experiment. Simulations were performed both with and without activation of the crust-breaching model for comparison. The simulation results are summarized in Figure 1, where the color label represents the solid fraction. Up to 8.0 s, the spreading behavior of the corium is similar in both cases, while crust breaching is observed at 12.0 s. The disruption occurs only at the advancing front position due to the compressive stress present there. After 12.0 s, the corium encapsulated within the crust re-spreads from the breaching point. Subsequently, the spreading gradually ceases due to a combination of reduced inertial force and cooling from radiative heat transfer at the free surface. The spreading length at the advancing front is also summarized in Figure 1. Pink and green markers indicate the simulation results, while the blue line represents the experimental data. In the experiment, re-spreading occurred around 17.0 s, whereas it occurred at 12.0 s in the simulation. Since the current crust breaching model includes sensitivity parameters such as the internal friction angle and cohesion constant, which determine the yield criteria, it is necessary to perform sensitivity analyses with respect to these parameters to better match the experimental results. In the experiment, a 16% extension in spreading distance was observed, compared to 12% in the simulation. The results indicated that the present method can simulate the crust breaching behavior without any artificial approximation while the sensitivity analyses are essential to mimic the timing of the crust breaching behavior.

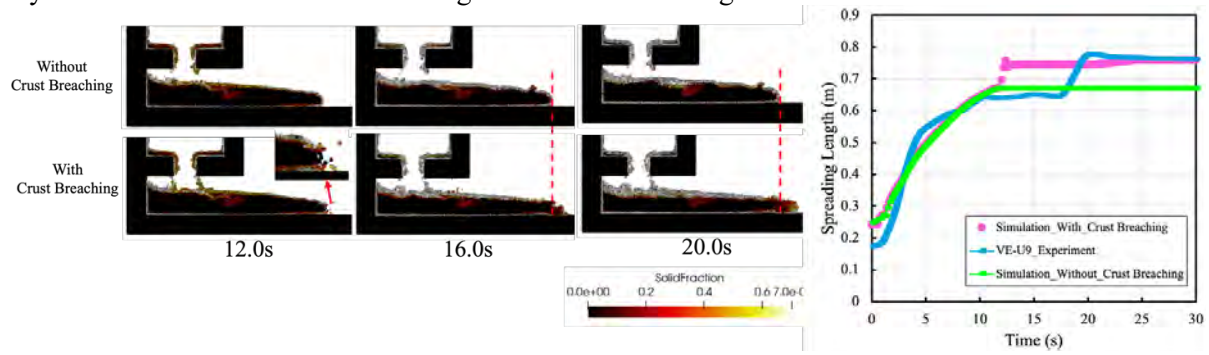

Figure 1 (left) snapshots of the spreading behavior with/without crust breaching model (right) spreading length at the advancing front position

4. CONCLUSIONS

This study presents corium spreading simulations that incorporate a crust breaching model together with a pressure-substitution implicit calculation method to re-examine the VULCANO VE-U9 experiment, where crust breaching behavior was observed on a ceramic substrate. The crust breaching model is based on the Drucker–Prager yield criterion, which defines crust failure when the local stress exceeds the yield threshold under compressive conditions. Once breaching occurs, the affected particles are treated as an elasto-viscous fluid whose viscosity depends on the local shear rate, enabling realistic representation of post-fracture flow. Two-dimensional simulations of the VULCANO VE-U9 configuration were conducted. The proposed approach successfully reproduced crust breaching at the advancing front and the characteristic stop-and-go spreading behavior frequently observed in experiments. Unlike previous studies, this model captures the fundamental physics of crust breaching without relying on artificial adjustments or empirical tuning. A quantitative comparison of spreading length revealed that the simulation achieved a 12% extension, slightly underestimating the experimental observation of approximately 16%. These discrepancies highlight the need for sensitivity analyses of key parameters—such as internal friction angle and cohesion constant—which govern the yield stress and thus influence the timing of crust failure.
Overall, the present method demonstrates strong potential for simulating physics-based crust breaching phenomena during corium spreading, providing a more robust framework for accident analysis and core-catcher design.

ACKNOWLEDGMENTS

This work is founded by JSPS KAKENHI grant number JP24K22849 This work was supported by JAEA Nuclear Energy S&T and Human Resource Development Project Grant Number JPJA24H24020026

REFERENCES

1. T. Theofanous, H. Yan, M. Podowski, C. Cho, D. Powers, T. Heames, J. Sienicki, C. Chu, B. Spencer, J. Castro, Y. Rashid, R. Dameron, J. Maxwell, D. Powers, “The Probability of Mark-I Containment Failure by Melt-attack of the Liner,” Division of Systems Research, Office of Nuclear Regulatory Research, U.S. Nuclear Regulatory Commission, Washington DC (1993).
2. T. Dinh, M. Konovalikhin, B. Sehgal, “Core melt spreading on reactor containment floor,” *Prog. Nucl. Energy*, **36**, pp. 405-465 (2000). https://doi.org/10.1016/S0149-1970(00)00088-3
3. M. Johnson, A. Denoix, V. Bouyer, H. Goda, H. Kamohara, J. Takeuchi, L. Brissonneau, C. Journeau, “High-temperature ex-vessel corium spreading: Part 1: Experimental investigations on ceramics and sacrificial concrete substrates,” *J. Nucl. Sci. Technol.,* **59**, pp. 446-458 (2021). https://doi.org/10.1080/00223131.2021.1977199
4. M. Kondo, T. Fujiwara, I. Masaie, J. Matsumoto, “A physically consistent particle method for high-viscous free-surface flow calculation,” *Comput. Part. Mech.*, **9**, pp. 265 (2022). https://doi.org/10.1007/s40571-021-00408-y
5. R. Yokoyama, M. Kondo, S. Suzuki, S. Miwa, M. Pellegrini, M. Johnson, A. Denoix, V. Bouyer, C. Journeau, K. Okamoto, “A Lagrangian approach to ex-vessel corium spreading over ceramics and concrete substrates using a moving particle hydrodynamics,” *Nucl. Eng. Des.*, **399**, 112029 (2022). https://doi.org/10.1016/j.nucengdes.2022.112029
6. Jubaidah, Umazume, Y., Takahashi, N., Li, X., Duan, G., Yamaji, A., “2D MPS method analysis of ECOKATS-V1 spreading with crust fracture model,” *Nucl. Eng. Des.*, **379**, 111251 (2021). https://doi.org/10.1016/j.nucengdes.2021.111251

SOCRATES: Leaching behaviour of radionuclides in severe accidents

Lind Terttaliisa (1), Kärkelä Teemu (2), de Vecchy Jon (3), Barrachin Marc (3), Journeau Christophe (4), Delacroix Jules (4), Autillo Matthieu (4), Andrikopoulos Christos (5), Herranz Luis Enrique (6), AT KHEN Kresna (7), Nichenko Sergii (8), Serrano Purroy Daniel (9), Rehrmann Jonas (10), Gumenyuk Dmytro (11)

(1) Paul Scherrer Institute, Switzerland, (2) VTT, (3) ASNR, (4) CEA, (5) Chalmers University of Technology, (6) CIEMAT, (7) EdF, (8) ETH Zürich, (9) EU-JRC, (10) Ruhr Universität Bochum - PSS, (11) SSTC

Type of abstract: Poster
Subject area: Source term issues
Keywords: Liquid source term, corium, leaching, experiments, radionuclides

The HORIZON-EURATOM SOCRATES project addresses critical gaps in our understanding of the liquid source term during severe nuclear accidents. In addition, it offers innovative solutions to mitigate and better assess the release of radionuclides into the environment. This topic has gained significant interest after the Fukushima Daichi nuclear power plant accident as a result of the large volumes of contaminated water to be treated, and the behaviour of radionuclides in the water. The aim of SOCRATES is to directly contribute to the mid-to-long-term accident management of nuclear power plants, enhancing safety, environmental protection, and safe waste management.

The main objective of the Work Package 4 is to investigate the source and formation of liquid phase contamination. The first tasks are to identify boundary conditions and key parameters for the leaching of radionuclides from the fuel, and to define test matrix for the experimental research. For this, literature survey has been carried out and documented. In the next phase, leaching experiments with different materials will be carried out by following a process of step-by-step progress from “simple experiments” to “more complex experiments”. The materials used in the experimental work are: i) inactive ceramic material models with representative fission product species, ii) simulated fuel pellets, and iii) prototypic, uranium-containing corium debris and TMI-2 corium.

The results of the literature survey will be presented with the aim of summarizing existing data on debris leaching and any other relevant leaching data, as well as depicting the test conditions to be used in the leaching tests. The planned leaching tests will also be briefly described.

12th CONFERENCE ON
SEVERE ACCIDENTS RESEARCH
May 18-22, 2026 - Madrid, Spain
ERMSAR 2026

SOCRATES: LEACHING BEHAVIOUR OF RADIONUCLIDES IN SEVERE ACCIDENTS

T. Lind[1], T. Kärkelä[2], J. Devecchy[3], M. Barrachin[3], C. Journeau[4], J. Delacroix[4], M. Autillo[4], C. Andrikopoulos[5], L.E. Herranz[6], K. At Khen[7], S. Nichenko[8], D. Serrano-Purroy[9], S. Utsunomiya[10], J. Rehrmann[11], D. Gumenyuk[12]

[1]Paul Scherrer Institute, [2]VTT, Finland, [3]ASNR, France, [4]CEA, France, [5]Chalmers, Sweden, [6]CIEMAT, Spain, [7]EDF, France, [8]ETH Zürich, Switzerland, [9]EC-JRC, Germany, [10]Kyushu University, [11]RUB PSS, Germany, [12]SSTC NRS, Ukraine

SOCRATES project

The HORIZON-EURATOM SOCRATES project addresses critical gaps in our understanding of the liquid source term during severe nuclear accidents. In addition, it offers innovative solutions to mitigate and better assess the release of radionuclides into the environment. This topic has gained significant interest after the Fukushima Daichi nuclear power plant accident as a result of the large volumes of contaminated water to be treated, and the behaviour of radionuclides in the water. The aim of SOCRATES is to directly contribute to the mid-to-long-term accident management of nuclear power plants, enhancing safety, environmental protection, and safe waste management.

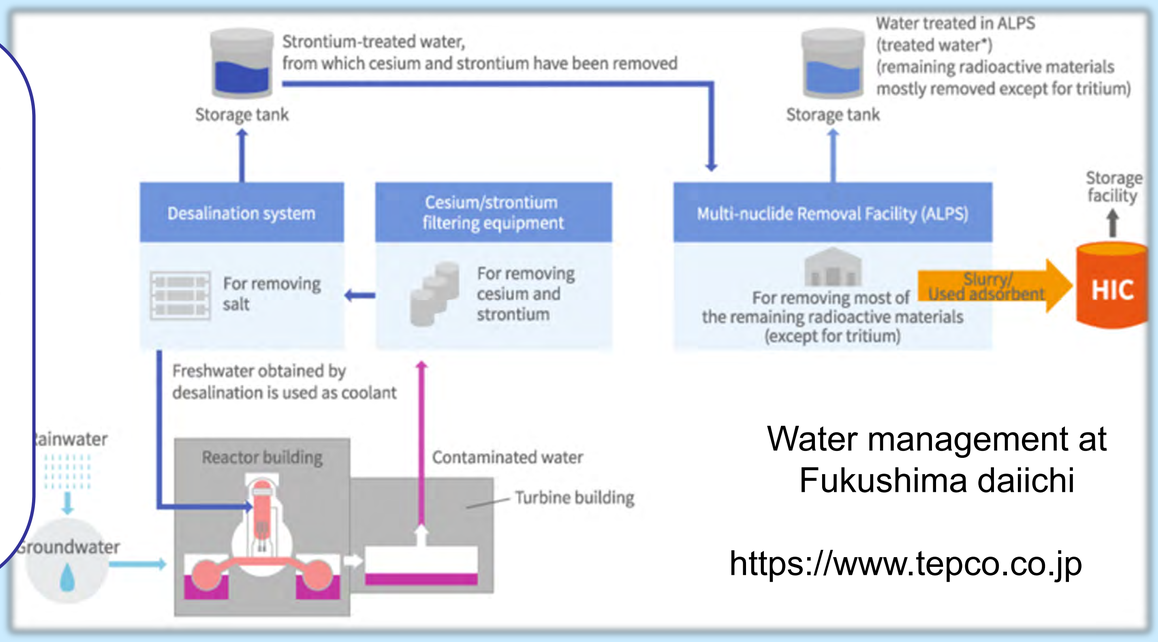

Water management at Fukushima daiichi

https://www.tepco.jp

An example of the experimental facilities: VITI at CEA

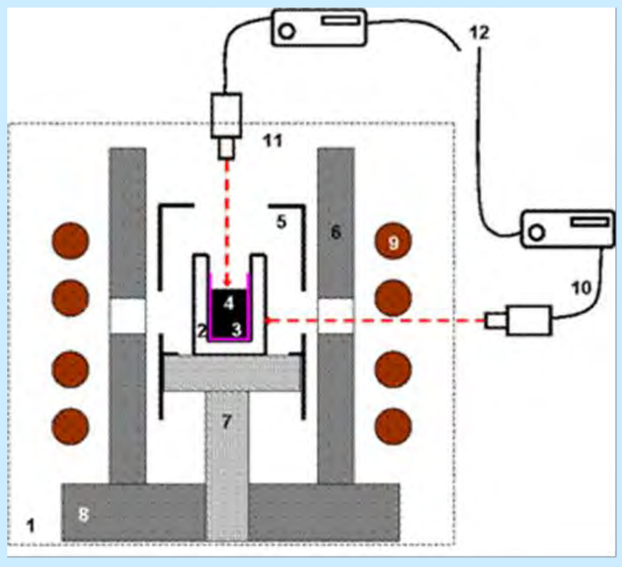

WP4: Leaching experiments

The objective of the WP4 is to experimentally investigate the source and formation of liquid phase contamination:

- to identify boundary conditions and key parameters for the leaching of radionuclides from the fuel
- to define test matrix for the experimental research by carrying out a literature search and summary
- to conduct leaching experiments with different materials:
  - inactive ceramic material models with fission product species
  - simulated fuel pellets
  - prototypic, uranium-containing corium debris
  - TMI-2 corium.

LEACHING TESTS

Experimental data for leaching of radionuclides in water include leaching tests of simulant materials for both in-vessel and ex-vessel corium as well as leaching tests with corium collected from the TMI-2 and Chornobyl plants. The results for in-vessel corium show that the atmosphere under which the simulant debris is synthesized has a decisive effect on the leaching behaviour of actinides, oxidizing conditions during synthesis resulting in increased leaching. Similarly, leaching in seawater increases dissolution rate as compared to distilled or pure water. Volatile fission products, e.g., Cs, have a much higher leachability than actinides.

TMI-2 corium samples collected from two different locations, i.e., molten core and lower crust, showed no major differences between the samples or water composition. Comparison of leaching behaviour of TMI-2 corium with that of spent nuclear fuel revealed that the U dissolution rate from both TMI samples was two orders of magnitude higher than dissolution from spent fuel in deionized water. Dissolution of Cs did not vary much between different samples.

An example of the experimental facilities: cyclone at ASNR

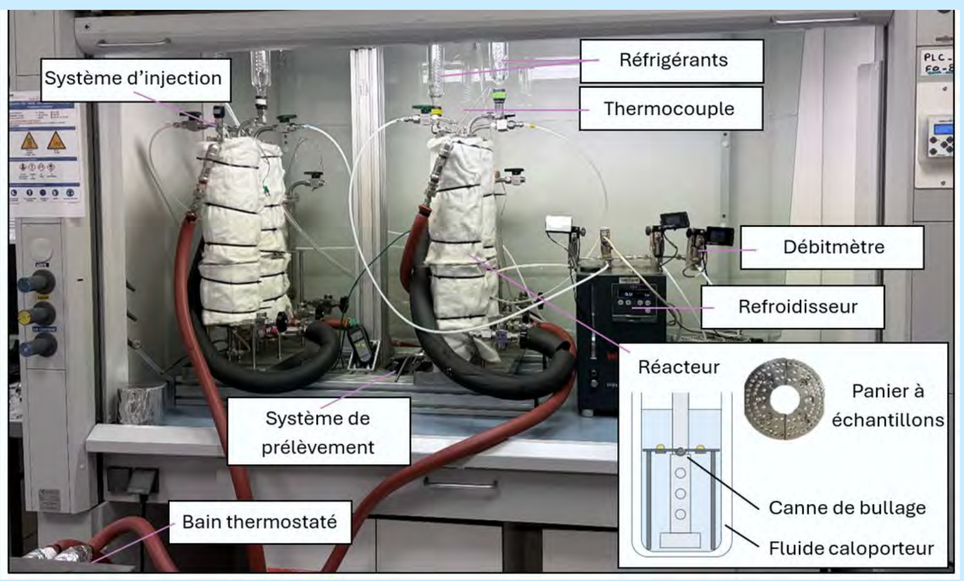

DATA FROM PAST ACCIDENTS

According to the available data, large fractions of Cs and I were found in contaminated water in TMI-2 (up to 50% of initial inventory) and Fukushima Daiichi (20-70% of initial inventory for units 2 and 3), whereas significantly smaller fractions of 137Cs and 90Sr were analysed in the water in Chronobyl plant (3-10% of initial inventory). In the long term, the main contributors to the water activity were different isotopes of Cs and Sr as well as tritium, the other radionuclides being less important to the activity in water.

Project funded by
Schweizerische Eidgenossenschaft
Confédération suisse
Confederazione Svizzera
Confederaziun svizra
Swiss Confederation
Federal Department of Economic Affairs, Education and Research EAER
State Secretariat for Education, Research and Innovation SERI

The Associated Partner PSI is funded by the Swiss State Secretariat for Education, Research and Innovation (SERI).

Funded by the European Union. Views and opinions expressed are however those of the author(s) only and do not necessarily reflect those of the European Union or European Atomic Energy Community (Euratom). Neither the European Union nor Euratom can be held responsible for them.

Funded by the European Union

12th CONFERENCE ON SEVERE ACCIDENTS RESEARCH
May 18-22, 2026 - Madrid, Spain
ERMSAR 2026

CONTAINMENT OF RADIOACTIVE WATER LARGE VOLUMES AND CONCEPT OF A LONG-TERM CONTAINMENT COOLING SYSTEM WITH STEAM CONDENSING HEAT EXCHANGER FOR NPPS WITH VVER-1000 REACTORS

O. Mazurok (Ph.D.), O. Mykhailenko, V. Ivanov, A. Tyurin, A. Hanenko, Yu. Vorobyov
ES Group LLC, Kyiv, Ukraine
E. Kostov (Ph.D.), Á. Pérez-Salado Kamps (Ph.D.), V. Pashynskyi, C. Hartmann (Ph.D.), Hans Troselius, O. Hessler
Westinghouse Electric Germany GmbH, Mannheim, Germany

The Issue of Radioactive Water Accumulation During Severe Accident Management

The problem of accumulation and management of significant volumes of radioactive water during severe accidents (SA) is associated with the need for continuous cooling of nuclear fuel in the reactor core, regardless of the extent of fuel damage. The volumes of accumulated radioactive water depend on the design features of the power units, the selected SA management strategy, and the characteristics of the nuclear power plant (NPP) site.

Conceptually, two approaches can be identified for managing large volumes of radioactive water generated during SA:

- storage outside the containment in dedicated tanks;
- long-term retention of radioactive water within the containment, followed by its gradual purification.

Disadvantages of Storing Radioactive Water in Tanks Outside the Containment

At the destroyed Fukushima Daiichi NPP more than 1.34 million tons of radioactive water have accumulated as a result of the operation of open-loop cooling systems. Further storage of radioactive water in additional tanks at the Fukushima Daiichi NPP site has revealed the disadvantages of this method, including limitations on tank capacity, risks of leakage, and radioactive contamination of the environment.

In general, the concept of storing radioactive water in tanks outside the containment is suboptimal for the following reasons:

- the need to establish dedicated areas with a large number of tanks for radioactive water storage;
- the need for an extensive system of technological connections;
- risks of leakage and radioactive contamination of the environment;
- risks of personnel radiation exposure when storing water outside the containment;
- potentially significant financial costs, taking into account all stages of work (procurement, testing, long-term storage, and maintenance).

Radioactive water storage tanks at the Fukushima Daiichi NPP

Closed-Loop Cooling Using Design-Basis Systems

The type of coolant circulation in the reactor core cooling circuit has a significant impact on the volume of radioactive water accumulated during SA: open (as implemented at the Fukushima Daiichi NPP) and closed.

A closed circulation loop using design-basis Emergency Core Cooling Systems (ECCS) at VVER-1000 power units can reduce the amount of radioactive water through repeated circulation of the coolant within the containment. However, at the ex-vessel stage of SA, the use of the design-basis ECCS will lead to the leaching of highly radioactive fuel-containing materials from the corium and their subsequent accumulation in ECCS equipment.

The design-basis ECCS of VVER-1000 reactors are not qualified for SA conditions. Therefore, use of the ECCS in SA will involve certain risks and disadvantages:

- contamination of the cooling circuit with radioactive particles of corium due to direct contact of the coolant (water) with corium;
- clogging of filters in ECCS pump suction lines, damage to ECCS pump seals by mechanical particles;
- heating and potential additional degradation of ECCS equipment due to residual heat release from corium particles;
- inability to maintain ECCS equipment due to high radiation levels.

This may result in a failure of the ECCS pumps and the occurrence of radioactive water leaks in non-leak-tight areas of the reactor compartment.

Closed-Loop Water Exchange and Purification

To extend the operating time of the ECCS equipment during SA, water exchange and purification of the closed cooling loop can be applied. However, this mode also has certain limitations:

- coolant purification via water circulation will result in the accumulation of additional radioactive water of approximately 240–720 m³/day;
- design-basis water purification systems are not designed to treat highly radioactive water containing corium particles, resulting in loss of their operability and inability to perform maintenance;
- formation of highly radioactive waste containing corium particles.

According to the results of calculations based on coolant water circulation, all potentially available tank capacity will be completely filled within 9-34 days (for various NPPs with VVER-1000 power units, based on water exchange calculations for only one affected power unit). At the same time the volume of tanks in the reactor building of a single (affected) power unit is about 1900 m³. The total volume of tanks in the NPP's special buildings and affected power unit is about 7400-10600 m³.

Increasing capacity for receiving, processing, and disposing of radioactive water beyond design limits does not solve the problem of long-term heat removal from the corium. A more optimal approach is to develop and implement measures that prevent large amounts of radioactive water from leaving the containment.

Concept of the Long-Term Containment Cooling System for VVER-1000

An alternative closed-loop option is proposed for implementation – the use of a steam-gas mixture in the cooling circuit, which is formed within the containment in the corium flooding area. Advantages:

- higher heat removal efficiency due to boiling;
- no leakage of liquid radioactive coolant containing corium particles outside the containment and the possibility of system maintenance;
- long-term retention of radioactive water within the containment without further increase in water volumes.

It should be noted that following the accident at the Fukushima Daiichi NPP, a significant number of safety improvement measures have been implemented at all NPPs in Ukraine. These measures are aimed at increasing the resilience of NPPs to external hazards and extended design-basis conditions. However, at least the following interrelated issues remain unresolved, which affect the ability to manage SA:

- proper handling of large volumes of radioactive water generated during SA, when applying a strategy of accident management involving water injection into the containment and its subsequent discharge outside;
- ensuring long-term (72 hours after the start of the accident) heat removal and pressure relief from the containment at the ex-vessel stage of the accident, and preventing exceedance of containment temperature and pressure limits and potential containment failure;
- cooling of the corium in the ex-vessel stage during SA, since there are currently no clear research conclusions regarding the feasibility of retaining the melt within the reactor vessel for VVER-1000 power units.

At VVER-1000 power units the Containment Filtered Venting System (CFVS) has already been implemented. The CFVS prevents containment failure under accident conditions by automatically opening when the containment pressure reaches 5.0 kgf/cm² (abs) (design limit), followed by operator control. However, operation of the CFVS does not ensure long-term heat removal from the containment (beyond 72 hours), and the containment temperature reaches the accident condition limit of 250 °C.

Containment Medium Parameter Limits for VVER-1000

Containment limit parameters	Design basis accident «LB-LOCA»	SA	FCVS operation during SA
Temperature, °C	150	250	Increasing
Pressure (abs.), kgf/cm²	5,0	5,0	5,0

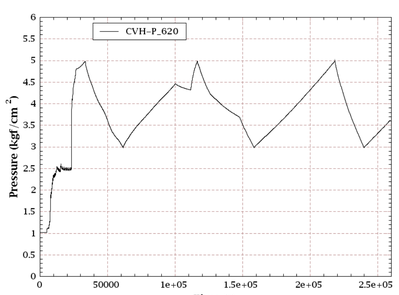

Containment Pressure during CFVS Operation

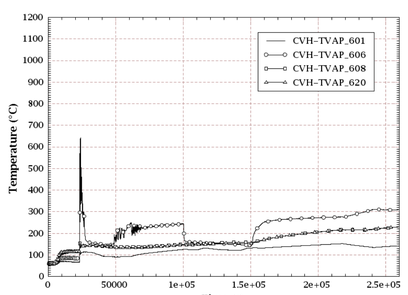

Containment Temperature during CFVS Operation

However, the introduction of the Long-Term Containment Cooling System (LTCCS) will resolve the above-mentioned safety issues.

Currently, ES Group and Westinghouse are jointly implementing the LTCCS at Rivne NPP Units 1,2 with VVER-440 reactors, and a separate LTCCS concept is being developed for NPP with VVER-1000 (LTCCS-1000).

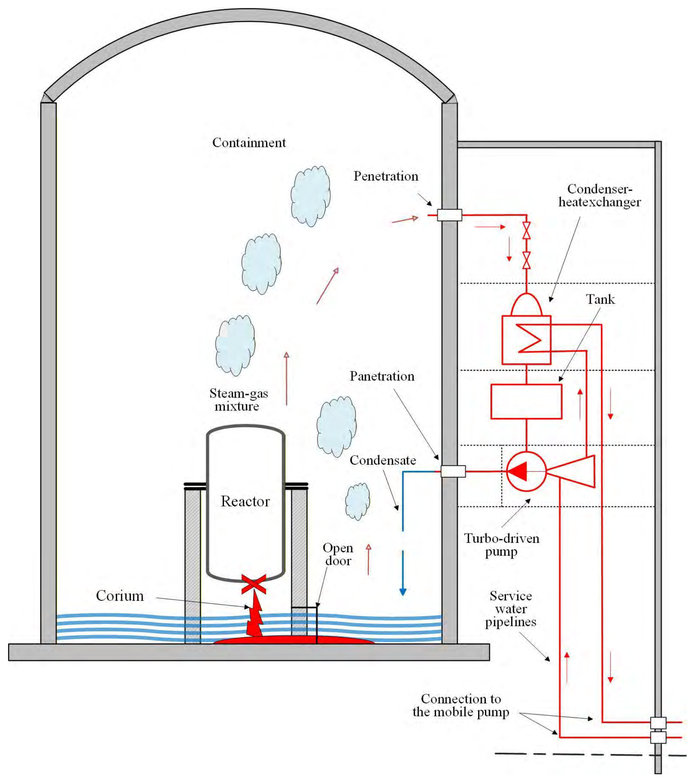

General Diagram of the LTCCS-1000

The main function of the LTCCS-1000 power units is to maintain the containment integrity by:

- reducing the adverse effects of corium on the containment base slab;
- preventing exceedance of permissible pressure and temperature limits in the containment through heat removal from the corium.

The LTCCS-1000 operational concept Includes:

- the heat source in the containment during the ex-vessel phase of SA is corium located in the reactor cavity;
- the primary purpose of the LTCCS is to remove heat from the corium and to reduce pressure and temperature in the containment;
- prevention of an increase in the volume of radioactive water by the LTCCS through closed-loop circulation and removal of the steam-gas mixture from the containment;
- independence from other systems during accident management;
- capability to function alongside the FCVS;
- activation of the LTCCS during the ex-vessel phase of SA.

Design and Operation of the LTCCS-1000

The LTCCS-1000 power units consists of two loops.

The first loop operates using a pump unit driven by a hydraulic turbine. The turbine-driven pump and heat exchanger are located outside the containment in the reactor building.

The LTCCS-1000 is designed to use a turbine-driven pump similar to that implemented in the LTCCS at Rivne NPP Units 1,2 with VVER-440 reactors.

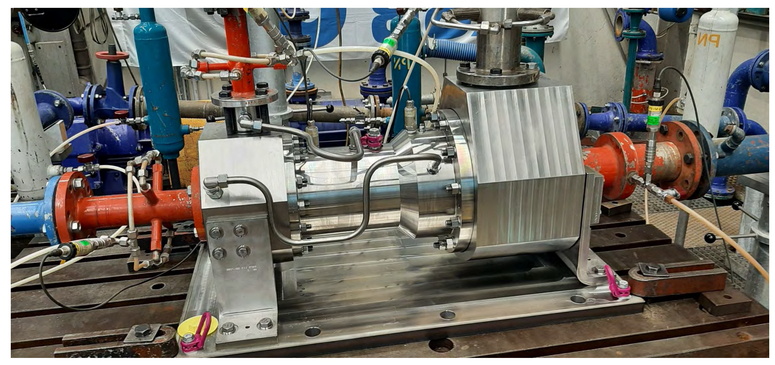

Turbine-driven pump by KSB SE & Co. KGaA

During the ex-vessel phase of SA, the water covering the corium heats up and evaporates inside the containment. Due to the excess pressure in the containment, the steam is directed through the first loop of the LTCCS to the heat exchanger for condensation and cooling. The condensate is collected in an intermediate tank and then, using the turbine-driven pump, returned to the containment. This configuration provides a closed circulation loop for the steam-water coolant and prevents mechanical impurities containing highly radioactive corium fragments and debris from entering the LTCCS equipment. Full water coverage of the corium, achieved by creating a "pool" on the containment base slab, ensures uniform cooling over the entire corium spreading area compared to sprinkler-based cooling.

The second loop of the LTCCS is a "clean" technical water circuit that does not come into direct contact with radioactive fission products. Separate mobile pump units are planned to supply water to the second loop. Initially, the technical water is used as the working fluid to drive the turbine of the turbine-driven pump. The technical water is then supplied to the LTCCS heat exchanger to cool the steam coming from the containment. The pressure in the second loop is maintained higher than in the first loop. This prevents the potential leakage of radioactive water through the LTCCS equipment, its entry into the reactor building, and subsequently into the environment. The removed heat is dissipated into an open water reservoir near the power unit.

Preliminary Calculation Results

Preliminary calculations were performed for the VVER-1000/V-320 design model.

- The LTCCS reduces and stabilizes containment pressure and temperature below design limits during an accident.
- The number of CFVS cycles is reduced after the LTCCS is activated.

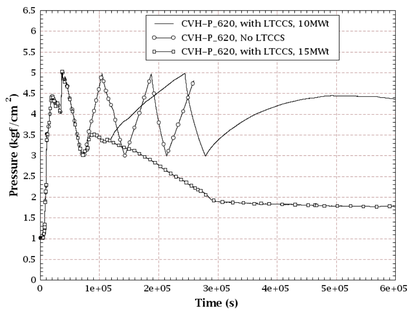

Containment Pressure for the "Total Station Blackout" Scenario

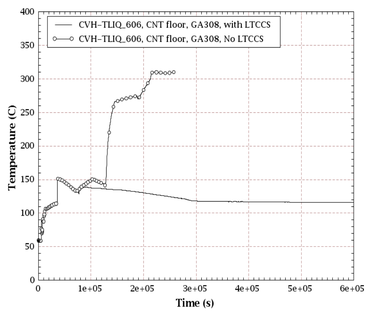

Containment Temperature for the "Total Station Blackout" Scenario

- Stopping further forced pressure relief from the containment via the CFVS significantly slows down the decrease of the water level in the retention pool due to evaporation.
- After 3–5 days, the LTCCS capacity can match the residual heat generation, depending on the selected equipment.
- By reducing containment pressure during the LTCCS operation, the release of radioactivity into the environment is decreased.
- The LTCCS capacity can be regulated by adjusting the blowdown opening after the condenser (blowdown into the scrubber).
- Before the LTCCS operation, additional water must be supplied to the containment to raise the level above the corium layer.
- The LTCCS operation in the late phases of SA does not affect hydrogen safety. Most of the hydrogen in the containment has already been recombined by passive autocatalytic recombiners (PARs), and the LTCCS does not condense steam within the containment atmosphere.

Conclusions (Advantages of the LTCCS-1000)

- Long-term cooling and prevention of containment failure.
- Removal of only the steam-gas mixture from the containment, with no significant carryover or accumulation of highly radioactive corium particles in the LTCCS equipment.
- Prevention of an increase in radioactive water volume by LTCCS closed-loop circulation, retaining existing radioactive water inside the containment.
- No need for additional storage tanks for radioactive water.
- Capability for long-term management of radioactive water at later stages of accident mitigation.
- Independence of the LTCCS from other plant systems.
- Possibility of using standardized design solutions on serial power units with VVER-1000/V-320 reactors.
- The LTCCS-1000 concept can be applied similarly to power units of VVER-1000/V-302,V-338 designs (South Ukraine NPP).

12th CONFERENCE ON
SEVERE ACCIDENTS RESEARCH
May 18-22, 2026 - Madrid, Spain
ERMSAR 2026

CONTAINMENT OF RADIOACTIVE WATER LARGE VOLUMES AND CONCEPT OF A LONG-TERM CONTAINMENT COOLING SYSTEM WITH STEAM CONDENSING HEAT EXCHANGER FOR NPPS WITH VVER-1000 REACTORS

O. Mazurok (Ph.D.), O. Mykhailenko, V. Ivanov, A. Tyurin, A. Hanenko, Yu. Vorobyov, Energy Safety Group (ES Group)
E. Kostov (Ph.D.), Á. Pérez-Salado Kamps (Ph.D.), V. Pashynskyi, C. Hartmann (Ph.D.), Hans Troselius, O. Hessler, Westinghouse Electric Company (WEC)

The Issue of Radioactive Water Accumulation During Severe Accident Management

Accumulation and management of significant volumes of radioactive water during severe accidents (SA) is associated with continuous cooling of nuclear fuel/debris. Accumulated radioactive water volume depends on the design features and SA management (SAM) strategy for nuclear power plant (NPP).

Disadvantages of Storing Radioactive Water in Tanks Outside the Containment

At Fukushima Daiichi NPP (Fukushima-1) more than 1.34 million tons of radioactive water have accumulated after operation of open-loop cooling systems. The concept of radioactive water storage in tanks outside the containment has features:

- special areas with many tanks;
- extensive system of technological connections;
- risks of leakage and contamination of the environment;
- risks of personnel radiation exposure;
- potentially significant financial long-term costs.

Radioactive water storage tanks at the Fukushima-1

Closed-Loop Cooling Using Design-Basis Systems

Closed loop cooling with Emergency Core Cooling Systems (ECCS) at VVER-1000 power units can reduce the amount of radioactive water. However, ECCS operation has some features:

- needs considerable electric energy supply;
- cooling circuit contamination by corium particles;
- possible clogging of ECCS filters, pump seals damage;
- ECCS equipment failure due to decay heat in circle;
- inability to perform maintenance actions for ECCS equipment;
- risk of leaks outside containment in case of ECCS failures.

Closed-Loop Water Exchange and Purification Limitations

Water exchange and purification of the closed ECCS cooling loop can be applied, but with following limitations:

- additional radioactive water accumulation by 240–720 m³/day;
- tank capacities will be exhausted within 9-34 days;
- water purification systems are not designed to treat highly radioactive water containing corium particles;
- highly radioactive waste formation with corium particles.

Unresolved SAM Issues for VVER-1000 (Ex-vessel Phase)

Safety improvements have been implemented at Ukrainian NPPs following Fukushima accident. Some issues remained unresolved:

- handling of large radioactive water volumes after SAM strategies application;
- ensuring long-term (beyond 72 hours) containment heat removal and pressure control at SA ex-vessel phase;
- large mass of post-accident hydrogen in containment;
- corium/debris cooling during SA ex-vessel phase.

All VVER-1000 units are equipped with Containment Filtered Venting System (CFVS) with scrubber or dry filter with passive opening at pressure 5.0 kgf/cm² (abs) (design limit), followed by operator control. However, CFVS operation does not ensure long-term containment heat removal (beyond 72 hours).

Concept of the Long-Term Containment Cooling System (LTCCS) for VVER-1000 (Ex-vessel Phase)

An alternative closed-loop system is proposed for implementation. Main subsystem is steam-gas mixture condensing circuit (containment atmosphere cooling), and auxiliary is a containment water cooling circuit (containment pool cooling). Advantages are:

- high heat removal efficiency due to boiling over core debris (steam circuit);
- corium stabilization outside the reactor pressure vessel (RPV)
- containment pressure decrease to nearly atmospheric values;
- containment water temperature decrease less than 100 ºC (water circuit);
- functional independence from DBA equipment;
- long-term radioactive water retention within the containment;
- system components maintenance availability;

Implementation of LTCCS resolves the above-mentioned safety issues. Currently, ES Group and WEC are jointly implementing the LTCCS at Rivne NPP Units 1,2 with VVER-440 reactors, and a separate LTCCS concept is being developed for NPP with VVER-1000 (LTCCS-1000).

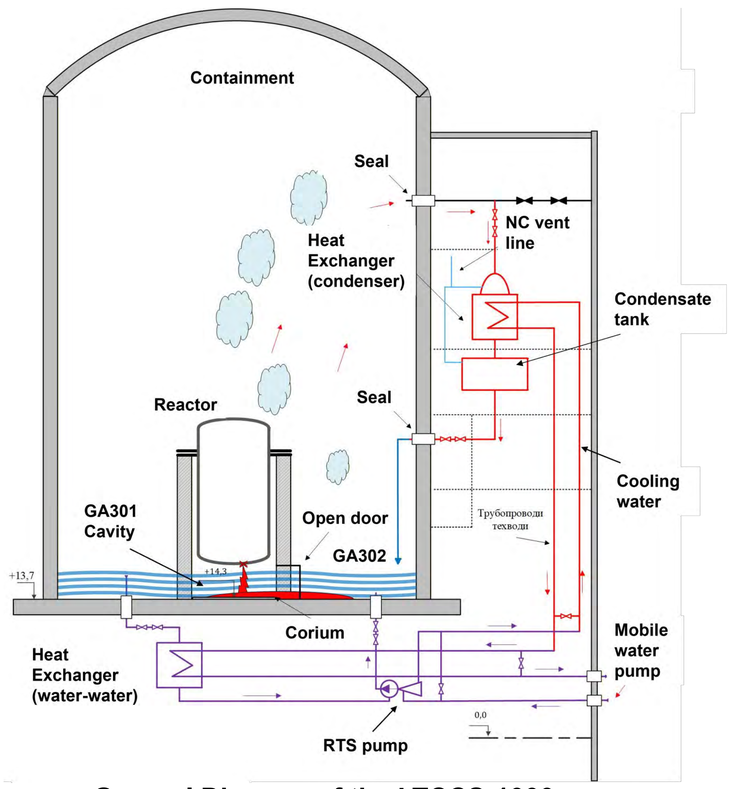

General Diagram of the LTCCS-1000

LTCCS-1000 concept accounts for :

- removal of non-condensable (NC) gases (to support condensation) including hydrogen;
- integration with the CFVS;
- dry reactor cavity prior RPV failure (prevent steam explosions);
- heat removal both from the corium and the spent fuel pool (SFP);
- long-term containment floor water cooling;
- reducing the adverse effects of corium on the base slab.

Design and Operation of the LTCCS-1000

The LTCCS-1000 consists of two containment circuits (steam and water) and cooling water loop. The water circuit operates using a pump unit driven by a hydraulic turbine. The condenser, turbine-driven (RTS) pump and heat exchanger are located outside the containment in the reactor building.

The turbine-driven pump for LTCCS-1000 is similar to the implemented one for LTCCS at Rivne NPP with VVER-440 reactors.

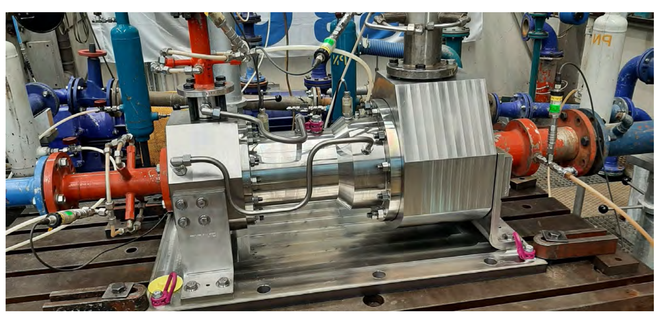

Turbine-driven pump

LTCCS Operation for VVER-1000 (Ex-vessel Phase)

Functioning of “contaminated” containment circuits:

- corium spreading on the containment floor;
- corium is flooded with cooling water (some water added);
- boiling over core debris produces steam and increases containment pressure;
- steam condenses in condenser (steam circuit);
- NCs are vented after condenser through CFVS;
- condensate is drained/pumped back to containment;
- containment water is cooled via heat exchanger by turbine-driven pump (water circuit);

Functioning of “clean” circuit (external cooling circuit/circuits):

- mobile water source unit;
- first supplies water to condenser cooling;
- secondly supplies water to heat exchanger and RTS pump;
- hot water discharges to environment;
- cooling circuit can be split in two separate ones.

Example analysis for unit blackout with SAM actions:

- LTCCS total capacity matches decay heat after 3–5 days;
- radioactivity release is decreased;
- LTCCS condensation capacity initially is controlled by NC venting after condenser (to CFVS scrubber);
- LTCCS operation fully resolves late containment hydrogen problem.

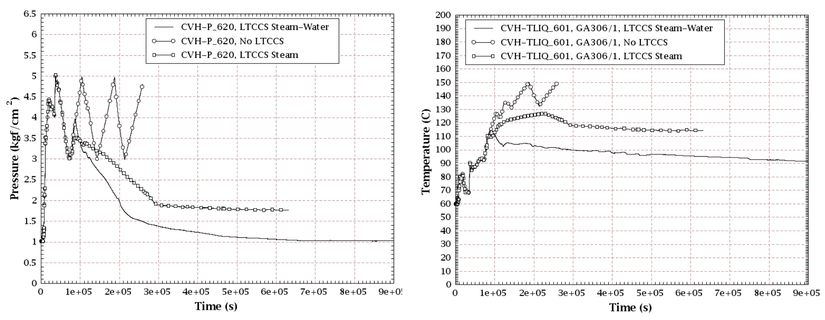

a) **b)**

Containment pressure (a) and containment water temperature (b) for cases with LTCCS water-steam circuits operation, without LTCCS and with LTCCS steam circuit only operation

LTCCS Specific Design

LTCCS specific design is under development by considering:

- external cooling circuits amount (see fig. below);
- coolable corium spreading issues;
- condenser aerosol load;
- number of turbine-driven pumps and water heat exchangers;
- SFP cooling line;
- long-term water balance in containment;
- system specifications and initiation criteria.

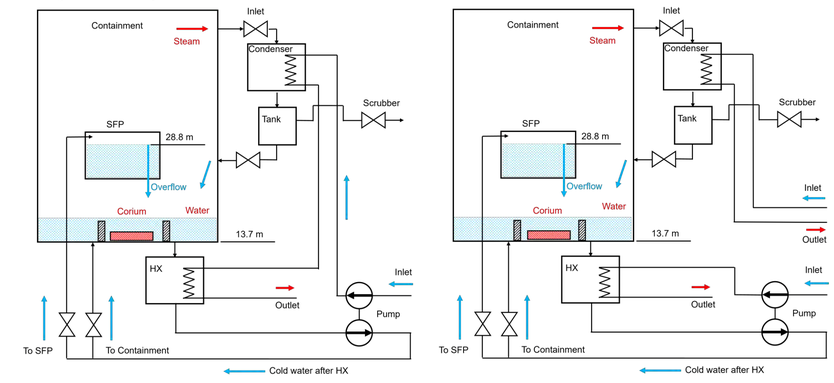

a) **b)**

Some LTCCS concept design schemes with common external cooling circuit (a) and two separate external circuits (b)

Conclusions for LTCCS-1000

- long-term cooling and prevention of containment failure;
- radioactive water storage inside containment;
- late post-accident hydrogen problem resolved;
- SFP cooling resolved;
- open-ready containment conditions after LTCCS operation;
- no need for additional storage tanks for radioactive water;
- independence of LTCCS from other plant systems.

12th CONFERENCE ON SEVERE ACCIDENTS RESEARCH
May 18-22, 2026 - Madrid, Spain
ERMSAR 2026

Implementation and Analytical Justification of Long-Term Containment Cooling System with Additional Spray Circuit, Heat Exchangers, and Turbine-Driven Pumps for NPPs with VVER-440 Reactors

Ivanov Vadym, Mazurok Oleksandr (Ph.D.), Vorobyov Yuriy, Tiurin Artem, Mykhailenko Oleksandr
ES Group LLC, Kyiv, Ukraine.
Kostov Emil (Ph.D.), Pérez-Salado Kamps Álvaro, Hartmann Christoph (Ph.D.), Troselius Hans
Westinghouse Electric Germany GmbH, Mannheim, Germany

ENERGY SAFETY GROUP

Introduction

To minimize the consequences of a severe accident (SA) with core damage, the In-Vessel Melt Retention (IVMR) system has been implemented at power units 1 and 2 of the Rivne Nuclear Power Plant (RNPP) with VVER-440/V-213 reactors. This system is designed to retain the melt within the reactor pressure vessel (RPV) and prevent progression of a SA to the ex-vessel phase by creating a closed natural circulation loop for external RPV cooling.

During operation of the IVMR system at RNPP power units 1&2, the pressure and temperature limits in the containment are not exceeded for 72 hours. However, the containment pressure and temperature continue to rise steadily due to the lack of heat removal from the containment. This inevitably results in further violation of containment design limits after 72 hours.

To prevent containment parameters from exceeding their design limits, the Long-Term Containment Cooling System (LTCCS) is used to ensure adequate heat removal from the containment.

The primary objective of the LTCCS is to maintain the containment integrity and ensure the reliable and efficient operation of the IVMR system.

ES Group and Westinghouse jointly developed and delivered this innovative system to improve the safety of the Ukrainian VVER-440 units during severe accidents and the long-term post-accident period.

The LTCCS is a supplementary system designed to enhance the safety of RNPP power units 1&2 under accident conditions. During normal operation, the LTCCS is in standby mode.

Requirements

The LTCCS belongs to safety systems, classified as a whole as Safety Class 2L (confinement-related system) and Seismic Category I.

Design functions of the LTCCS:

- maintain containment temperature and pressure over a long period of time (up to 6 months), ensuring that these parameters remain below their maximum design limits of 127 °C and 2.5 kgf/cm² (abs);
- provide removal of the decay heat (capacity not less than 4 MW) from the containment over a long period of time;
- maintain containment integrity and minimize the release of radioactive products outside the containment by reducing the parameters in the accident localization area (ALA);
- ensure the reliable and efficient operation of the IVMR system.

Design requirements to the LTCCS:

- operation of the LTCCS for 6 months (short-term stops are allowed, but they should not affect the design functions);
- operating pressure of the LTCCS secondary circuit must be higher than the operating pressure in both the primary circuit and the containment to prevent the leakage of radioactive products outside the ALA.

Layout

The LTCCS consists of two loops/circuits:

- primary circuit – contaminated. The primary circuit components are in the containment rooms. The working medium of the primary circuit is a radioactive coolant (boron solution) accumulated in containment rooms during accidents;
- secondary circuit – “clean” (non-contaminated). The secondary circuit components are in the containment rooms, reactor building and industrial site of the RNPP. The working medium (water) is not contaminated.

The LTCCS consists of three channels that have the same number of components. Common to all three channels are the Additional Spray Circuit and the water intake point in the containment.

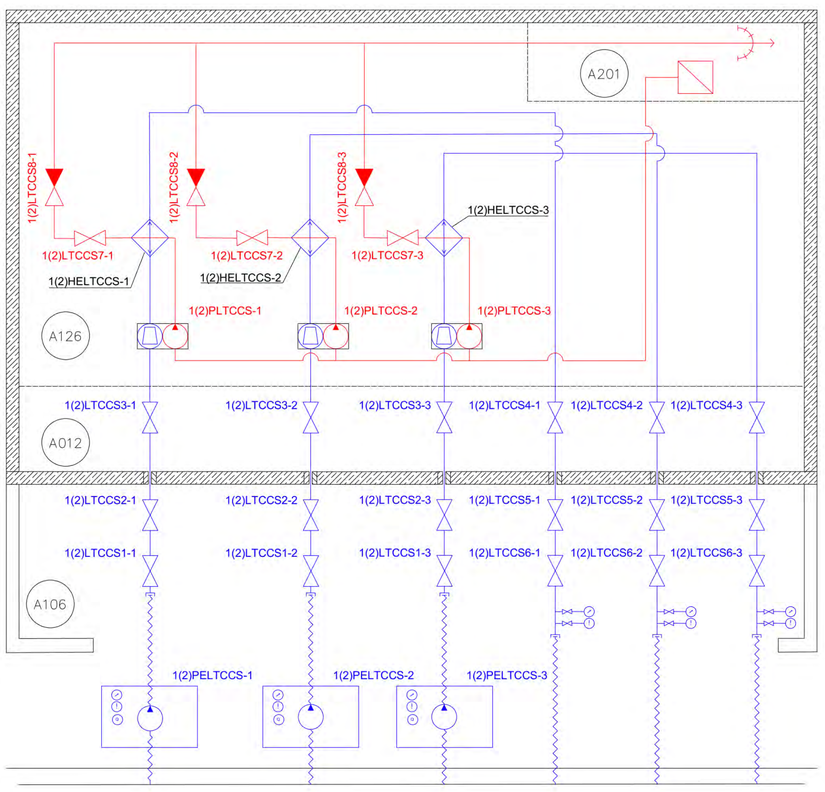

Process Flow Diagram of the LTCCS for Units No. 1,2 of RNPP

Short description of the LTCCS

The primary circuit coolant is pumped from the containment by a dynamic pump unit with a hydraulic drive turbine - Reactor-Turbine-Sump-Pump (RTS pump), cooled down in heat exchangers and then sprayed through the nozzles of the Additional Spray Circuit to reduce both pressure and temperature inside the containment.

The primary circuit of the LTCCS comprises the pump part of the RTS pumps 1(2)PLTCCS-1(2,3), heat exchangers 1(2)HELTCCS-1(2,3) (coolant side), shut-off valves 1(2)LTCCS7-1(2,3) and check valves 1(2)LTCCS8-1(2,3).

The primary circuit with contaminated water is located only in the containment. The active element of the primary circuit is the RTS pump. The RTS pump is actuated by the water flow supplied to the turbine

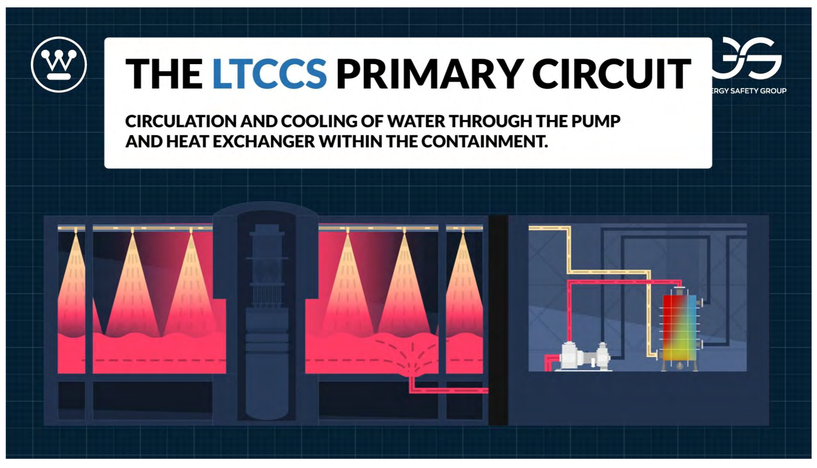

Primary circuit of the LTCCS

The secondary circuit of the LTCCS comprises the intermediate pump units 1(2)PELTCCS-1(2,3), flexible hoses, hermetic penetrations, localizing valves 1(2)LTCCS1,2,3,4,5,6-1(2,3), turbine part of the RTS pumps 1(2)PLTCCS-1(2,3), heat exchangers 1(2)HELTCCS-1(2,3) (cooling water side).

The secondary circuit is designed to ensure the proper functioning of the primary circuit. Service water is drawn from an open reservoir located near the power unit by an external pump station, supplied to the turbine of the RTS pump and further directed to the heat exchanger (to cool the primary coolant). The secondary circuit water is then returned to the open reservoir.

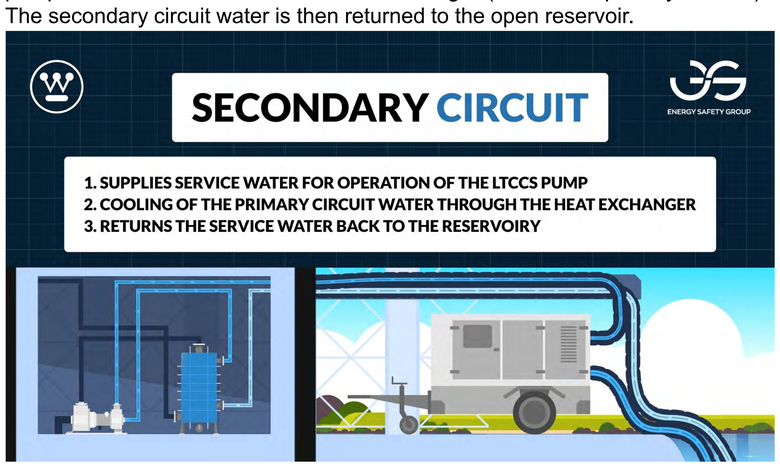

Secondary circuit of the LTCCS

The RTS pump, manufactured by KSB SE & Co. KGaA, is the heart of the LTCCS, which circulates radioactive coolant inside the containment.

The RTS pump consists of a pump and turbine parts, with the turbine and pump impellers connected by a common shaft. Water flow rotates the turbine, which drives the pump part.

The pump section is part of the LTCCS primary circuit, while the turbine section is part of the secondary circuit. A mechanical seal separates the turbine and pump parts of the RTS pump to prevent contaminated water from entering the turbine part if the pump is stopped or running.

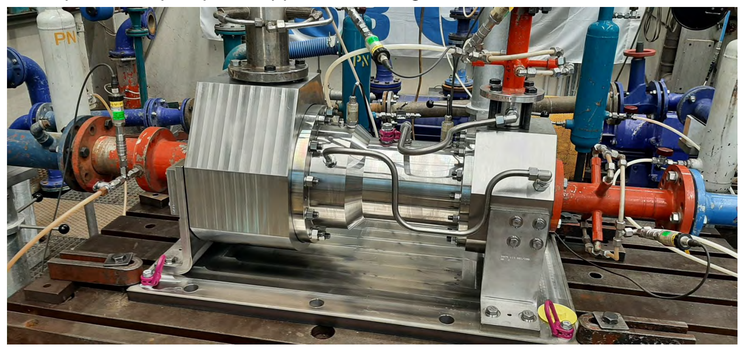

RTS Pump

External pump units (mobile pump stations) located outside the power unit near an open reservoir are used to supply water to the secondary circuit of the LTCCS. Water is supplied to and returned from the system through flexible hoses.

The external pump units can be taken out of service on a train-by-train basis for scheduled maintenance and refueling while the LTCCS is in operation, thereby ensuring continuous operation of the system. It is sufficient to operate two out of three LTCCS channels to maintain containment parameters within acceptable limits after 3 days.

Cooling of the LTCCS primary circuit is performed using a plate heat exchanger with a welded housing.

The advantages of this solution are relatively small dimensions of the equipment with a sufficient heat exchange surface. This allows new equipment to be installed in the limited space available inside the containment and transported to the installation site.

A heat capacity of 2.2 MW per train has been selected to maintain an operational efficiency margin of the heat exchanger in the event of internal surface contamination over a period of 6 months.

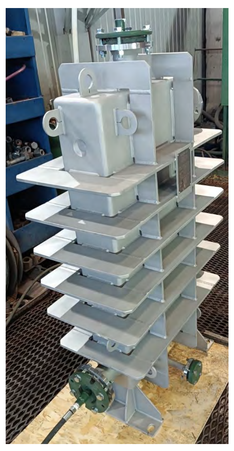

Environmental conditions in containment

№	Parameter Name	Value
1	Pressure, kgf/cm²	2,5
2	Temperature, ºC	127
3	Medium	steam-water mixture

Working medium

№	Parameter Name	Value
	Primary circuit	
1	Medium	boric acid solution 16-20 g/l
2	Temperature, ºC	up to 127
	Secondary circuit	
3	Medium	service water
4	Temperature, ºC	5÷45

Main technical parameters of components

№	Parameter Name	Value
	RTS pump (3 units included in LTCCS)	
1	Pump part (primary circuit)	
1.1	Drive type	hydraulic (from turbine part)
1.2	Nominal head, m	20
1.3	Nominal flow rate, m³/h	67
2	Turbine part (secondary circuit)	
2.1	Nominal head, m	68
2.2	Nominal flow rate, m³/h	57
	Heat exchangers (3 units included in LTCCS)	
1	Heat capacity, MW	2,2
2	Coolant temperature (primary circuit), °C	127
3	Cooling water temperature (secondary circuit), °C	45
	Intermediate pump units (3 units included in LTCCS)	
1	Nominal head, m	140
2	Nominal flow rate, m³/h	57
	Nozzles (8 pieces included in LTCCS)	
1	Spray angle, °	120
2	Total flow rate through the nozzle group, m³/h	201
3	Maximum flow rate through the nozzle, l/min	630

Analytical justifications of the LTCCS

The analytical justification of the thermal-hydraulic behavior of the LTCCS, reactor, and containment was performed using the MELCOR and RELAP calculation codes.

Acceptance criteria for the LTCCS operation applied in the justification analysis:

- Containment pressure during accident progression is less than the design limit of 2.5 kgf/cm² (abs.);
- Minimum water level in the SG boxes is at least 6.85 m;
- Ratio of gas mixture components in the containment on the Shapiro-Moffett diagram does not enter the detonation region;
- In case of a spontaneous hydrogen combustion, containment pressure is less than 2.5 kgf/cm² (abs.);
- Containment pressure is reduced to less than 1.1 kgf/cm² (abs.) and is maintained consistently below this value (strong criterion);
- Containment pressure is steadily decreasing (weak criterion);
- Containment water temperature in the SG boxes (corridors to the IVMR suction) is reduced below 90ºC and maintained consistently below this value (strong criterion);
- Containment water temperature in the SG boxes (corridors to the IVMR suction) is steadily decreasing (weak criterion).

Results of the Analytical justification

The LTCCS (3 channels) heat removal capacity for a maximum cooling water temperature of 45°C and a nominal flow rate of 67 m3/h matches the decay heat in 3-6 days at containment water temperatures in the range of 95 °C÷110 °C.

Cooling water with 25 °C temperature after 3 days can equalize the LTCCS capacity to the decay heat at a containment water temperature of 95 °C, and for 6 days at the temperature of 80 °C. Stable operation of three LTCCS channels reduces the pressure in the containment to atmospheric level.

With two LTCCS channels in operation, the containment parameters may begin to decrease after 6-8 days. Lower cooling water temperatures would help this happen earlier. In this case the containment pressure increases maximally to 1.4÷1.5 kgf/cm² that is less than the design limit. Therefore, operation of the LTCCS with two channels is also successful but needs a longer stabilization time.

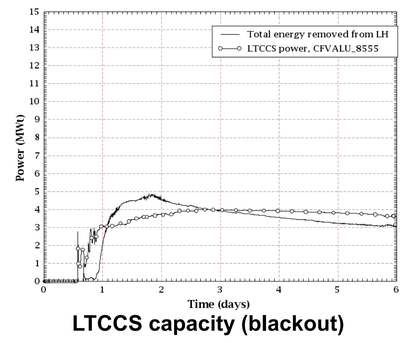

LTCCS capacity (blackout)

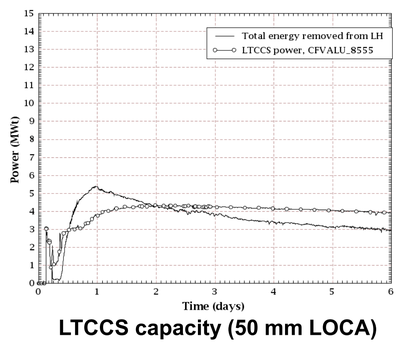

LTCCS capacity (50 mm LOCA)

In all calculated accident sequences with a timely start-up of the IVMR system and simultaneous operation of the LTCCS, the criterion of a maximum containment pressure less than 2.5 kgf/cm² (abs) is met. After the IVMR and LTCCS systems start, the containment pressure decreases and later temporarily rises to 1.2÷1.4 kgf/cm² (abs) before the final decrease.

A late LTCCS start-up with high containment pressure is followed by a more rapid decrease in containment parameters and a successful reduction of pressure to less than 1.1 kgf/cm² (abs).

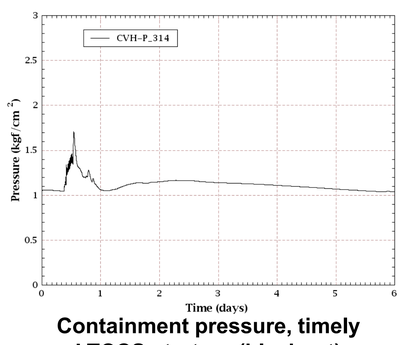

Containment pressure, timely LTCCS start-up (blackout)

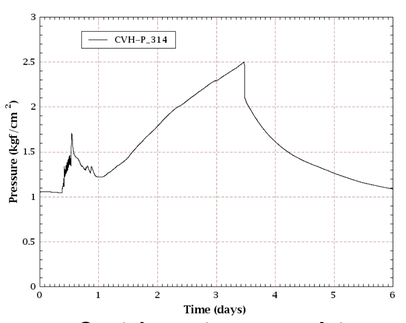

Containment pressure, late LTCCS start-up (blackout)

The containment water temperature follows the containment pressure behavior. After the IVMR and LTCCS timely start-up and the initial temperature decrease, it rises temporarily to 96÷101 °C. Water temperatures are slightly higher for the primary circuit breaks of any size. Afterwards, the water temperature decreases continuously that might be significantly prolonged in time. A late LTCCS start-up is followed by a more rapid decrease in water temperature and successful heat removal.

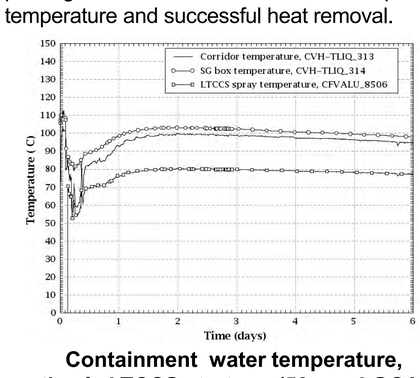

Containment water temperature, timely LTCCS start-up, (50 mm LOCA)

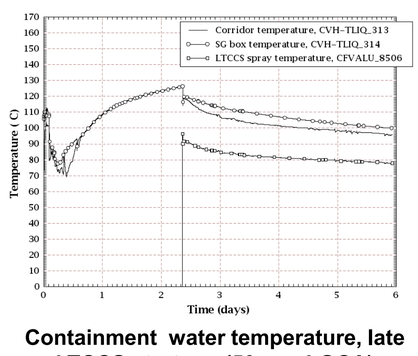

Containment water temperature, late LTCCS start-up, (50 mm LOCA)

Hydrogen safety

Operation of the LTCCS causes condensation of water vapor inside the containment and a corresponding increase in the fraction of non-condensable gases (including hydrogen). To ensure hydrogen safety during the LTCCS operation, an optimal reconfiguration of the existing passive autocatalytic recombiners (PAR) was determined through iterative calculations. A modified layout of installed PARs was proposed, and installation locations for four additional PAR modules of NIS-PAR-44KKH type, supplied as part of the LTCCS delivery set, were specified.

As a result, conditions for hydrogen detonation during the LTCCS operation are avoided inside the containment. The long-term hydrogen safety is improved in the spray tower. Localized hydrogen combustion associated with vapor condensation is temporarily and may occur only in areas where PARs installation is impossible. The containment pressure in case of hydrogen combustion at any time during the accident progression is estimated to be less than the design limit of 2.5 kgf/cm² (abs).

Conclusions of the LTCCS Analytical Justification

1. The LTCCS significantly expands the capabilities and reliability of stabilizing and bringing the containment and reactor to a safe state during severe accidents.

2. The three-channel LTCCS design makes it possible to reduce the containment pressure and temperature along with the IVMR system operation. The LTCCS heat removal capacity in realistic cases can be equal to residual core power in 3 days.

3. With two of the three LTCCS channels in operation, the conservative analysis indicates that the containment pressure and temperature begin to decrease after 6-8 days. Lower cooling water temperatures shift this effect to earlier times. No violation of the containment pressure limit is expected for any configuration.

4. All LTCCS acceptance criteria selected for the justification analysis are met.

5. The release of activity to the environment is reduced compared to cases without the LTCCS operation due to lower containment pressure and removal of aerosols by the LTCCS sprays.

12th CONFERENCE ON
SEVERE ACCIDENTS RESEARCH
May 18-22, 2026 - Madrid, Spain
ERMSAR 2026

IMPLEMENTATION AND ANALYTICAL JUSTIFICATION OF LONG-TERM CONTAINMENT COOLING SYSTEM WITH ADDITIONAL SPRAY CIRCUIT, HEAT EXCHANGERS, AND TURBINE-DRIVEN PUMPS FOR NPPS WITH VVER-440 REACTORS

Ivanov Vadym, Mazurok Oleksandr (Ph.D.), Vorobyov Yuriy, Tiurin Artem, Mykhailenko Oleksandr, Energy Safety Group (ES Group)
Kostov Emil (Ph.D.), Pérez-Salado Kamps Álvaro, Hartmann Christoph (Ph.D.), Troselius Hans, Westinghouse Electric Company (WEC)

Introduction

To minimize the consequences of a severe accident (SA) with core damage, the In-Vessel Melt Retention (IVMR) system has been implemented at power units 1&2 of the Rivne Nuclear Power Plant (RNPP) with VVER-440/V-213 reactors. This system is designed to retain the melt within the reactor pressure vessel (RPV) and prevent progression of a SA to the ex-vessel phase by creating a closed natural circulation loop for external RPV cooling.

During operation of the IVMR system at RNPP power units 1&2, the pressure and temperature limits in the containment are not exceeded for 72 hours. However, the containment pressure and temperature continue to rise steadily due to the lack of heat removal from the containment. This inevitably results in further violation of containment design limits after 72 hours.

To prevent containment parameters from exceeding their design limits, the Long-Term Containment Cooling System (LTCCS) is used to ensure adequate heat removal from the containment.

The primary objective of the LTCCS is to maintain the containment integrity and ensure the reliable and efficient operation of the IVMR system. ES Group and WEC jointly developed and delivered this innovative system to improve the safety of the Ukrainian VVER-440 units during severe accidents and the long-term post-accident period.

The LTCCS is a supplementary system designed to enhance the safety of RNPP power units 1&2 under accident conditions. During normal operation, the LTCCS is in standby mode.

Requirements

Design functions of the LTCCS:

- maintain containment temperature and pressure over a long period of time (up to 6 months), ensuring that these parameters remain below their maximum design limits of 127 ºC and 2.5 kgf/cm² (abs);
- provide removal of the decay heat (capacity not less than 4 MW) from the containment over a long period of time;
- maintain containment integrity and minimize the release of radioactive products outside the containment by reducing the parameters in the accident localization area (ALA);
- ensure the reliable and efficient operation of the IVMR system.

Design requirements to the LTCCS:

- operation of the LTCCS for 6 months (short-term stops are allowed, but they should not affect the design functions);
- operating pressure of the LTCCS secondary circuit must be higher than the operating pressure in both the primary circuit and the containment to prevent the leakage of radioactive products outside the ALA.

Layout

The LTCCS consists of two loops/circuits:

- primary circuit – contaminated. The primary circuit components are in the containment rooms. The working medium of the primary circuit is a radioactive coolant (boron solution) accumulated in containment rooms during accidents;
- secondary circuit – “clean” (non-contaminated). The secondary circuit components are in the containment rooms, reactor building and industrial site of the RNPP. The working medium (water) is not contaminated.

The LTCCS consists of three channels that have the same number of components. Common to all three channels are the Additional Spray Circuit and the water intake point in the containment.

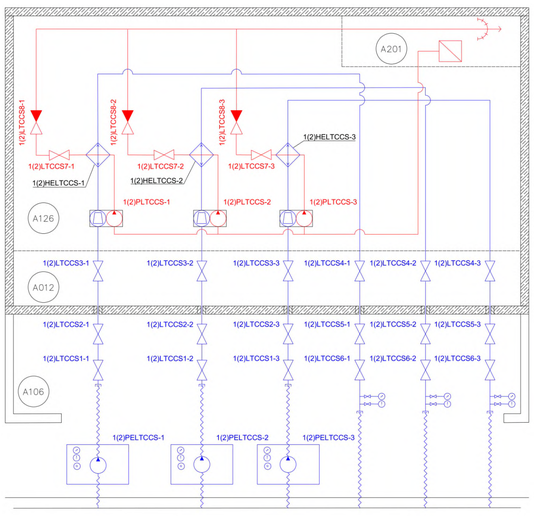

Process Flow Diagram of the LTCCS for RNPP-1,2

Short description of the LTCCS

The primary circuit coolant is pumped from the containment by a dynamic pump unit with a hydraulic drive turbine - Reactor-Turbine-Sump-Pump (RTS pump), cooled down in heat exchangers and then sprayed through the nozzles of the Additional Spray Circuit to reduce both pressure and temperature inside the containment.

The primary circuit of the LTCCS comprises the pump part of the RTS pumps, heat exchangers (coolant side), shut-off and check valves.

The primary circuit with contaminated water is located only in the containment. The active element of the primary circuit is the RTS pumps. The RTS pump is actuated by the water flow supplied to the turbine.

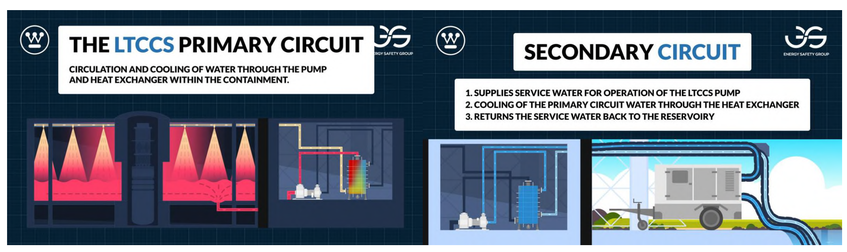

Primary circuit of the LTCCS **Secondary circuit of the LTCCS**

The secondary circuit of the LTCCS comprises the intermediate pump units, flexible hoses, hermetic penetrations, localizing valves, turbine part of the RTS pumps, heat exchangers (cooling water side).

The secondary circuit is designed to ensure the proper functioning of the primary circuit. Service water is drawn from an open reservoir located near the power unit by an external pump station, supplied to the turbine of the RTS pump and further directed to the heat exchanger (to cool the primary coolant). The secondary circuit water is then returned to the open reservoir.

The RTS pump, manufactured by KSB SE & Co. KGaA, is the heart of the LTCCS, which circulates radioactive coolant inside the containment.

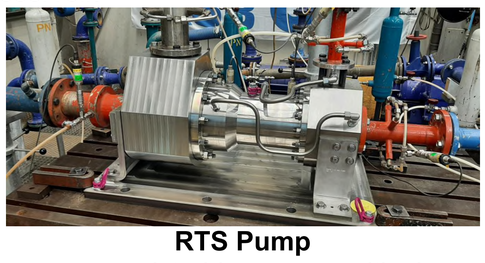

RTS Pump

The RTS pump consists of a pump and turbine parts, with the turbine and pump impellers connected by a common shaft. Water flow rotates the turbine, which drives the pump part.

The pump section is part of the LTCCS primary circuit, while the turbine section is part of the secondary circuit. A mechanical seal separates the turbine and pump parts of the RTS pump to prevent contaminated water from entering the turbine part if the pump is stopped or running.

Environmental conditions in containment

№	Parameter Name	Value
1	Pressure, kgf/cm²	2,5
2	Temperature, ºC	127
3	Medium	steam-water mixture

Working medium

№	Parameter Name	Value
	Primary circuit	
1	Medium	boric acid solution 16-20 g/l
2	Temperature, ºC	up to 127
	Secondary circuit	
3	Medium	service water
4	Temperature, ºC	5÷45

Main technical parameters of components

№	Parameter Name	Value
	RTS pump (3 units included in LTCCS)	
1	Pump part (primary circuit)	
1.1	Drive type	hydraulic (from turbine part)
1.2	Nominal head, m	20
1.3	Nominal flow rate, m³/h	67
2	Turbine part (secondary circuit)	
2.1	Nominal head, m	68
2.2	Nominal flow rate, m³/h	57
	Heat exchangers (3 units included in LTCCS)	
1	Heat capacity, MW	2,2
2	Coolant temperature (primary circuit), °C	127
3	Cooling water temperature (secondary circuit), °C	45
	Intermediate pump units (3 units included in LTCCS)	
1	Nominal head, m	140
2	Nominal flow rate, m³/h	57
	Nozzles (8 pieces included in LTCCS)	
1	Spray angle, °	120
2	Total flow rate through the nozzle group, m³/h	201
3	Maximum flow rate through the nozzle, l/min	630

Results of the Analytical justification of the LTCCS

The analytical justification of the thermal-hydraulic behavior of the LTCCS, reactor, and containment was performed using the MELCOR and RELAP calculation codes.

The LTCCS (3 channels) heat removal capacity for a maximum cooling water temperature of 45 ºC and a nominal flow rate of 67 m³/h matches the decay heat in 3-6 days at containment water temperatures in the range of 95 ÷ 110 ºC.

Stable operation of three LTCCS channels reduces the pressure in the containment to atmospheric level.

Cooling water with 25 ºC temperature after 3 days can equalize the LTCCS capacity to the decay heat at a containment water temperature of 95 ºC, and for 6 days at the temperature of 80 ºC. With two LTCCS channels in operation, the containment parameters may begin to decrease after 6-8 days. Lower cooling water temperatures would help this happen earlier. In this case the containment pressure increases maximally to 1.4÷1.5 kgf/cm² that is less than the design limit. Therefore, operation of the LTCCS with two channels is also successful but needs a longer stabilization time.

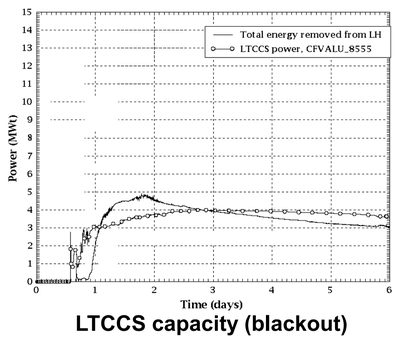

LTCCS capacity (blackout)

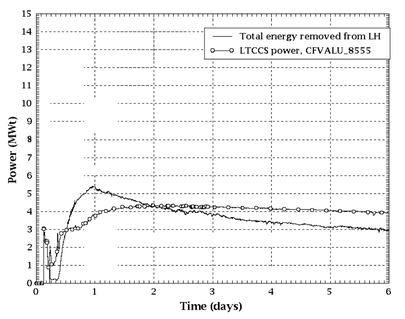

LTCCS capacity (50 mm LOCA)

In all calculated accident sequences with a timely start-up of the IVMR system and simultaneous operation of the LTCCS, the criterion of a maximum containment pressure less than 2.5 kgf/cm² (abs) is met. After the IVMR and LTCCS systems start, the containment pressure decreases and later temporarily rises to 1.2÷1.4 kgf/cm² (abs) before the final decrease.

A late LTCCS start-up with high containment pressure is followed by a more rapid decrease in containment parameters and a successful reduction of pressure to less than 1.1 kgf/cm² (abs).

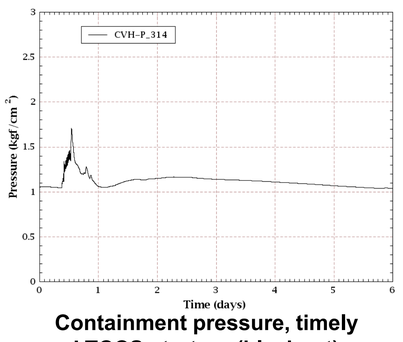

Containment pressure, timely LTCCS start-up (blackout)

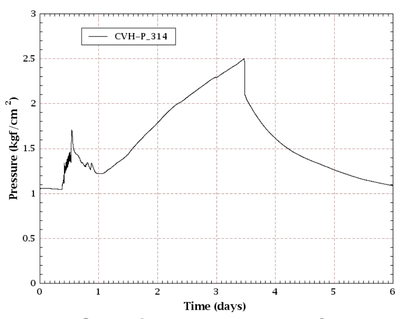

Containment pressure, late LTCCS start-up (blackout)

The containment water temperature follows the containment pressure behavior. After the IVMR and LTCCS timely start-up and the initial temperature decrease, it rises temporarily to 96÷101 ºC. Water temperatures are slightly higher for the primary circuit breaks of any size. Afterwards, the water temperature decreases continuously that might be significantly prolonged in time. A late LTCCS start-up is followed by a more rapid decrease in water temperature and successful heat removal.

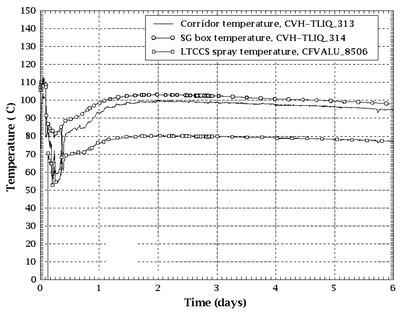

Containment water temperature, timely LTCCS start-up (50 mm LOCA)

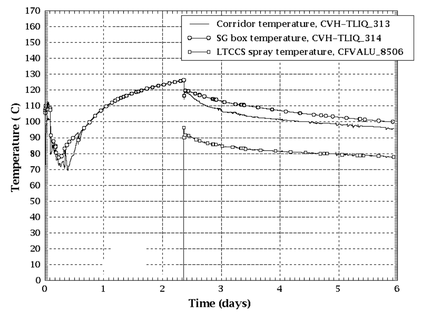

Containment water temperature, late LTCCS start-up, (50 mm LOCA)

Conditions for hydrogen detonation during the LTCCS operation are avoided inside the containment. The long-term hydrogen safety is improved in the spray tower. Localized hydrogen combustion associated with vapor condensation is temporarily and may occur only in areas where PARs installation is impossible. The containment pressure in case of hydrogen combustion at any time during the accident progression is estimated to be less than the design limit of 2.5 kgf/cm² (abs).

Conclusions of the LTCCS Analytical Justification

1. The LTCCS significantly expands the capabilities and reliability of stabilizing and bringing the containment and reactor to a safe state during severe accidents.
2. The three-channel LTCCS design makes it possible to reduce the containment pressure and temperature along with the IVMR system operation.
3. With two of the three LTCCS channels in operation, the conservative analysis indicates that the containment pressure and temperature begin to decrease after 6-8 days. No violation of the containment pressure limit is expected for any configuration.
4. All LTCCS acceptance criteria selected for the justification analysis are met.
5. The release of activity to the environment is reduced compared to cases without the LTCCS operation due to lower containment pressure and removal of aerosols by the LTCCS sprays.

12th CONFERENCE ON
SEVERE ACCIDENTS RESEARCH
May 18-22, 2026 - Madrid, Spain
ERMSAR 2026

Analysis of Postulated Design Basis Accidents in General Integral PWR Small Modular Reactors: Outcomes on Integral Codes' Modelling Capabilities from the Horizon Euratom SASPAM-SA Project

F. Gabrielli[1], M. E. Cazado[1], V.H. Sanchez-Espinoza[1], F. Mascari[2], P. Maccari[2], G. Grippo[2,3], G. Agnello[2], M. Di Giuli[4], J. Bittan[5], N. Bakouta[5], M. Malicki[6], T. Lind[6], M. Principato[6], M. Makarenko[7], Yu. Yesipenko[7], O. Zhabin[7], D. Gumenyuk[7], C. Vázquez-Rodríguez[8], S. Kelm[8], M. Klauck[8], E.-A. Reinecke[8], M. K. Koch[9], J. Krieger[9], G. Stahlberg[9], T. Jankowski[9], M. Garcia Martin[10], L. E. Herranz[10], [11]N. Reinke, A. Bentaib[12], L. Carénini[13], J.-C. de la Rosa Blul[14], A. Kaliatka[15], M. Valincius[15], M. Constantin[16], F. Giannetti[17], T. Sevon[18], P. Groudev[19], G. Acharya[20], K. Mahmoud[20], P. Kudinov[20], D. Grishchenko[20]

[1]KIT (Germany), [2]ENEA, [3]UNIBO (Italy), [4]Tractebel Engineering (Belgium), [5]EDF (France), [6]PSI (Switzerland), [8]SSTC NRS (Ukraine), [8]FZJ (Germany), [9]RUB PSS (Germany), [10]CIEMAT (Spain), [11]GRS GmbH (Germany), [12] OECD/NEA (France), [13]ASNR (France), [14]JRC(Netherlands), [15]LEI (Lithuania), [16]RATEN (Romania), [17]Sapienza University of Rome (Italy), [18]VTT (Finland), [19]INRNE (Bulgaria), [20]KTH (Sweden)

Motivation

- 'Safety Analysis of SMR with PAssive Mitigation strategies - Severe Accidents' (SASPAM-SA) project (2022-2026), coordinated by ENEA (F. Mascari) - 23 partners from 13 European countries
  - assessing the applicability of knowledge gained from large Light Water Reactors (LWRs) to iPWRs, supporting licensing and siting activities and contributing to a European, independent perspective on iPWR safety for DiD levels 4 and 5

WP2 (SCENARIO): Objectives

- **Evaluating the capabilities of state-of-art European and non-European integral SA codes and Computational Fluid Dynamics (CFD) tools to simulate the key phenomena occurring in generic iPWR designs**
- Methodology:
  - iPWR Design-1 and Design-2 database (generic designs, decay heat) based on open-literature
  - Assessment of generic, but representative, SA and CFD codes' datasets
  - Postulating Design Basis Accident (DBA) and SA sequences
  - Analysis the postulated DBA and SA scenarios
  - No PSA assessments employed in postulating the scenarios (generic designs)
  - Codes' datasets shared among the partners upon request

The generic iPWR Design-1 and Design-2

iPWR Design-1 (P~60 MWe)
Submerged containment

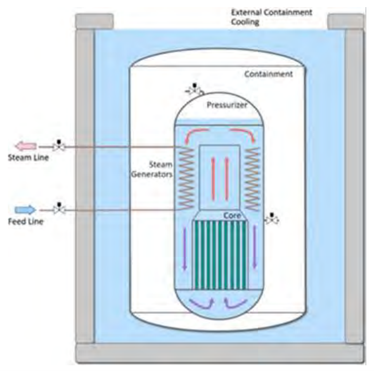

iPWR Design-2 (P~300 MWe)
Dry containment, several passive systems

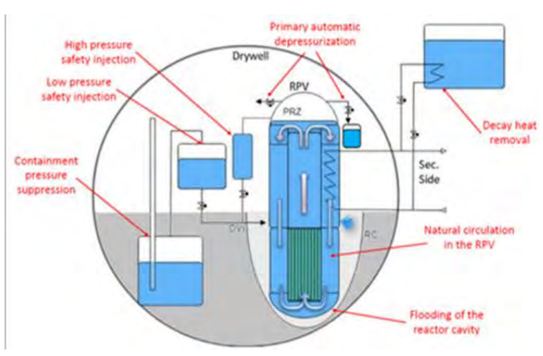

Codes, Partners, and Contribution

Code	Partners	Contribution/Role
ASTECv3.1 (CPA)	KIT	Contribution to a new dataset
ASTECv2.2 (CESAR)/ v3.1 (CPA)	Tractebel	Dataset sharing
MELCORv2.2	PSI/KTH	Dataset sharing/Use
EdF-MAAP5.04	EdF	New dataset
AC²	RUB	New dataset
ANSYS CFX	SSTC NRS	New dataset
AC²	GRS	AC2 user support
ASTEC	ASNR	ASTEC user support
—	RATEN	Support in the definition of the scenarios

Code	Partners	Contribution/Role
ASTECv3.1	ENEA	Dataset sharing
MELCORv2.2	ENEA, UNIROMA1 /CIEMAT, KTH	Dataset sharing/Use
MAAP5.06	JRC	New dataset
AC²	LEI	New dataset
CAD and containmentFOAM	FZJ	New dataset
AC²	GRS	AC2 user support
ASTEC	ASNR	ASTEC user support
—	RATEN	Support in the definition of the scenarios

iPWR Design-1: Results

- **Postulated DBA scenario: Chemical and Volume Control System (CVCS) make-up line break with loss of AC (different break sizes: 10%, 20%, 35%, and 100%)**
- Transient progression: Loss of FDW, Reactor SCRAM, Isolation of the MSL
  - Activation of the ECCS: (RPV –CNMT pressure < 62 bar) & CNMT level > 5.8 m, Opening of 3 RVVs and 2 RRVs

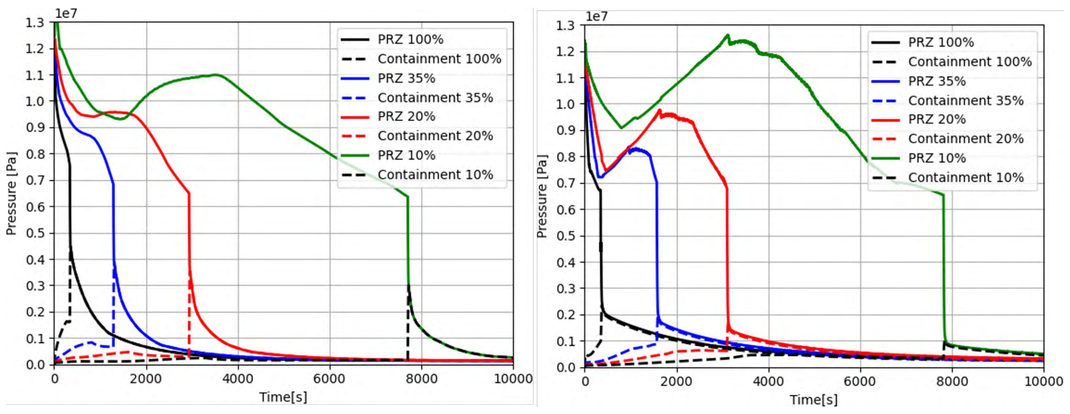

RPV and CNMT pressure computed by ASTECv3.1 (left) and EdF-MAAP (right)

iPWR Design-1 – key events during the DBAs (break size, 100%, 35%, 20%, and 10%)

Parameter/Event	ASTECv3.1 (KIT)	ASTECv2.2 CESAR (Tractebel)	ASTECv3.1 CPA (Tractebel)	EdF-MAAP (EdF)	MELCORv2.2 (PSI)	AC² (RUB)	MELCORv2.2 (KTH)
Actuation of the ECCS (s)	339 1286 2933 7696	259 1142 2427 6612	319 1213 2736 6117	349 1571 3100 7814	339/341 1060/1035 1830/1815 4380/4705	1439 1741 2568 3850	510
Max. liquid level in the CNMT [m]	6.6 6.8 6.9 7.2	6.8 7 7.2 7.5	7.1 7 7.9 7.9	8.1 8.2 8.3 8.5	6.8 7 6.9 6.9/6.5	5.8 5.8 5.9 6.3	6.3
Min. liquid level above TAF [m]	0.8 0.9 0.8 0.9	2.7 1.5 1.4 0.8	1.8 1.4 1.2 0.96	0.8 0.8 0.9 1.8	1.3 0.6 0.5/0.6 0.6/0.9	- - - -	4.7
Max. CNMT Pressure [MPa]	4.47 3.85 3.54 3	5.4 4.8 4 3.1	4.8 4 3.6 2.9	2.5 2 1.7 1.1	5.9/6.0 6.7/7.0 6.8/7.2 6.6/7.3	5.2 4.7 4.7 5.3	

iPWR Design-2: Results

- **Postulated DBA scenario: double-ended break of the Direct Vessel Injection (DVI) line, considering the availability of all safety systems**
- The scenario represents a serious and challenging safety concern for generic iPWR Design-2
- The response strategy depends on the activation of passive safety systems based on the established signal triggers

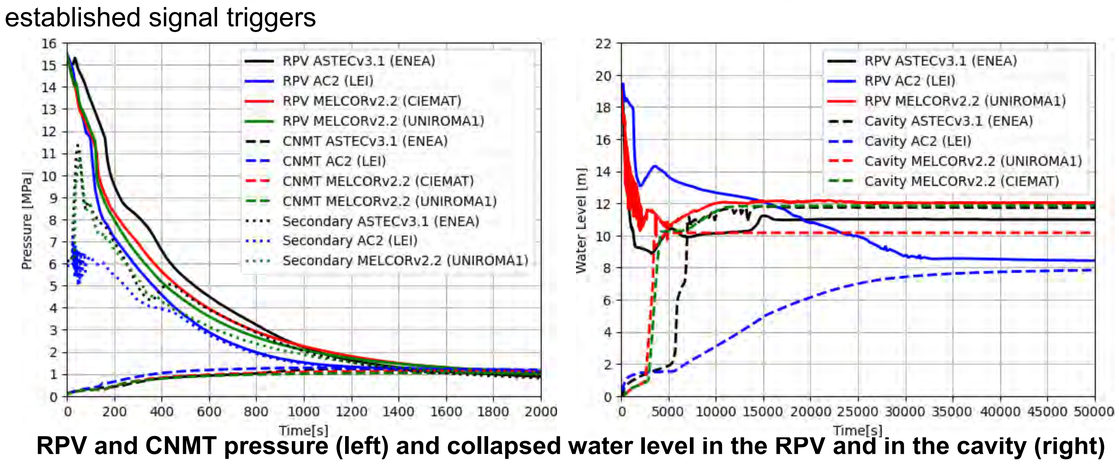

RPV and CNMT pressure (left) and collapsed water level in the RPV and in the cavity (right)

iPWR Design-2: relevant phenomenological events during the postulated DBA

Parameter/Event	ASTECv3.1 (ENEA)	MELCORv2.2 (UNIROMA1)	MELCORv2.2 (CIEMAT)	MAAP 5.06 (JRC)	AC² (LEI)
High CNMT pressure set-point [s]	**20**	**27**	**28**	**31**	**28**
Low PRZ level signal [s]	**68**	**88**		**50**	**62**
Low PRZ pressure signal [s]	**160**	**109**	**108**	**170**	**92**
Actuation of EBT [s]	165		112	121	97
Actuation of ADS-1 [s]	168	117	128		100
Low DP RPV-CNMT signal [s]	**1466**	**1780**	**1750**	**1274**	**1904**
Actuation of LGMS [s]	1470		1770	1279	1909
Low LGMS mass signal [s]	**13459**	**13620**	**11030**	**25920**	**14301**
Start of reverse flow in the PSS [s]	4950	2850	4170	5050	15400*
Actuation of ADS-2 [s]	13460	13620		25920	14301*
Collapsed Max. liquid level in the CNMT [m]	11.7		11.8		8.4
Collapsed Min. level in the core from LP bottom [m]	3.84	2.98	4.52		5.5
Core TAF refilled - collapsed [s]	5500	1000	5650	4320	

Conclusion

- **The codes are able to predict the key TH phenomena during DBA scenarios** (e.g., single and two-phase natural circulation in RPV, primary/CNMT natural circulation coupling, energy removal from the external pool)
- **Good agreement among the codes**, e.g., timing of activation of the safety systems and results of the key TH figures-of-merit

Acknowledgements

Funded by the European Union. Views and opinions expressed are however those of the author(s) only and do not necessarily reflect those of the European Union or European Commission-Euratom. Neither the European Union nor the granting authority can be held responsible for them

This work has received funding from the Swiss State Secretariat for Education, Research and Innovation (SERI)

Three-Dimensional Numerical Prediction of Natural Convection in Corium Pools Using Advanced RANS Turbulence Models

Alsalman Shahad (1), Alasif Abdullah (2), Siddiqui Osman, Shams Afaque

(1) King Fahad University of Petroleum and Minerals (KFUPM), (2) King Fahd University of Petroleum & Minerals (KFUPM)

Type of abstract: Poster
Subject area: In-vessel corium and debris coolability
Keywords: Severe accidents, corium pool, CFD, turbulence modeling, RANS

In the event of a severe nuclear accident, the reactor core is subjected to extreme thermal conditions leading to melting of the structural elements. This molten material is called corium and its accumulation at the lower plenum of the reactor pressure vessel (RPV) is often referred to as the corium pool. This corium pool continues to generate energy due to radioactive material, while the heat is rejected through the walls of the lower plenum and resulting in a strong natural convection regime at a very high Rayleigh number (Ra). In-vessel melt retention is one of the key accident management strategies, and a thorough understanding of this high Ra number natural convection within the corium pool is essential for studying the integrity of the RPV.

However, a proper understanding of such a high Ra flow regime in the corium pool is extremely challenging for an off-the-shelf Reynolds Averaged Navier Stokes (RANS) based Computational Fluid Dynamics (CFD) approach. Therefore, a thorough investigation of these RANS based modelling approaches must be performed to assess their prediction capabilities. In this study, a wide range of RANS turbulence models are tested and validated against an available reference database. Two commonly used commercial software are selected to perform this validation study, i.e. Simcenter STAR-CCM+ and Ansys Fluent. The study has shown that off-the-shelf RANS models are not capable of accurately predicting the strong buoyancy forces that appear at very high Ra flows. Hence, a much more sophisticated modeling of turbulent heat flux is needed which should take into account the complex flow behaviour exhibited in the corium pool. In a nutshell, the validation efforts performed in this research work establish a foundation to study and investigate severe accident scenarios and support the development of reliable strategies for in-vessel melt retention and nuclear safety in general.

Recalescence Behavior of Molten Refractory Oxides during Fast Cooling by Aerodynamic Levitation

Gong Yaopeng (1)

(1) China Nuclear Power Engineering Co. Ltd.

Type of abstract: Poster
Subject area: Other applications (fusion reactors, interim SNF storage, Accident Tolerant Fuels (ATFs), etc
Keywords: recalescence behavior□refractory oxides□aerodynamic levitation□fast cooling□melting point

During the rapid cooling process of molten crystals, when the temperature drops to a deeply undercooled state, the material's temperature quickly rises back to near the melting point in a short time due to the release of latent heat during the solidification process, accompanied by a luminescence phenomenon. This is a possible method for measuring the melting point of refractory materials. Based on the containerless installation ALSEE(Aerodynamic Levitation-laSer heating installation for mElt propErties), recalescence behavior of Al2O3, ZrO2 and Y2O3 were described in the study and a discussion on different recalescence temperatures under various gas environments was conducted. Besides, phase transformation analysis of the cooling process was performed through thermo-dynamic calculation, so as to compare with the approximate melting point obtained from the experiment. This work lays the foundation for the performance verification of refractory materials used in nuclear power industry

12th CONFERENCE ON
SEVERE ACCIDENTS RESEARCH
May 18-22, 2026 - Madrid, Spain
ERMSAR 2026

Recalescence behavior of molten refractory oxides during fast cooling by aerodynamic levitation

Yaopeng GONG, Li ZHANG, Zhiqiang DONG, Yidan YUAN*
Email: gongyp@cnpe.cc, yidanyuan2010@aliyun.com
CNNC Key Laboratory for Severe Accident Research in Nuclear Power Safety, China Nuclear Power Engineering Co., Ltd., Beijing, China

Introduction

During the rapid cooling of a high-temperature liquid drop, the temperature of the drop falls into an undercooling region. Thereafter, the temperature increases rapidly back to the melting temperature due to the nucleation and release of heat of fusion. This phenomenon is referred to as recalescence. Density [1] and isobaric heat capacity [2] can be measured during the process of cooling, while melting temperature and heat of fusion [3] can be measured according to the recalescence behavior. This study presents the melting temperature and heat of fusion measurements of molten refractory oxides using aerodynamic levitation, a non-contact technique for property measurements. This method can be applied to the measurements of corium components, thereby enriching the experimental thermodynamic data of corium and facilitating the accurate prediction of corium behavior under severe accident scenarios [4].

Experimental Setup

The experimental setup, called ALSEE (Aerodynamic Levitation-laSEr hEating installation for melt properties), is developed at China Nuclear Power Engineering Co., Ltd. for the precise thermophysical and thermodynamic property measurements of corium (see Figure 1). Aerodynamic levitation was achieved by a conical converging-diverging nozzle, enabling the levitation of a spherical sample in the diameter range of 2 to 3 mm. Argon gas was chosen as the levitating gas due to its inert nature. Sample heating was performed using two CO_2 laser devices. Temperature of the sample was measured by a 2-color pyrometer with the uncertainty of 0.5%. Sample behavior was observed using a high-speed camera.

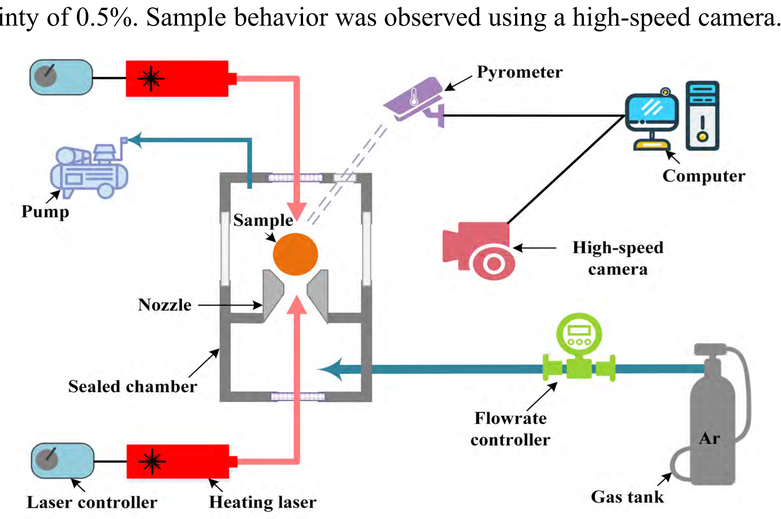

Figure 1. Schematic view of ALSEE facility

Melting Temperature Measurement

The temperature during rapid cooling is shown in Figure 2. A 2-color pyrometer operates by evaluating the ratio of the spectral radiant brightness of the target object at two selected wavelengths which is independent of the object emissivity. An increase in image brightness corresponds to a rapid rise in sample temperature during nucleation. The recalescence temperature is considered to be the melting temperature. As shown in Figure 2, the measured melting temperature of 2323.95K for Al_2O_3 is in good agreement with the reference value of 2327K [5], with the error of 3.05K less than the measurement uncertainty(0.5%). Therefore, it is convincing to measure melting point based on the recalescence phenomenon for oxides.

Figure 3 shows the result of ZrO_2 and a Fe_2O_3-CaO mixture. The melting temperature of 2973.6K for ZrO_2 is also close to the reference value of 2988K [1]. The melting temperature of Fe_2O_3-CaO is 1633K, which is in good agreement with the thermodynamic calculation(TC) results using Thermo-Calc 2023a software with the OXDEMO database.

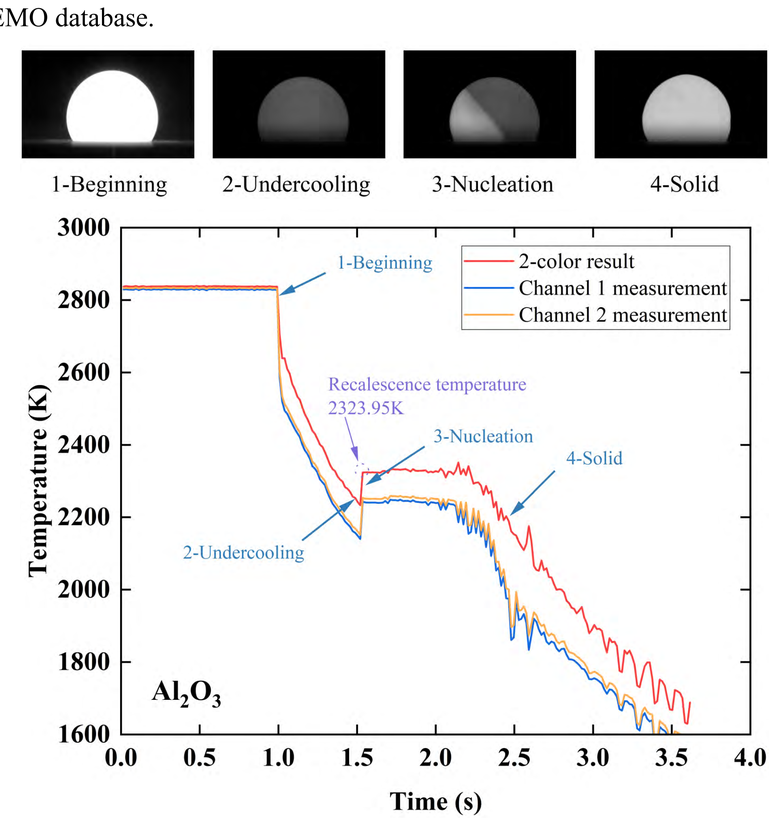

Figure 2. Recalescence behavior of Al_2O_3

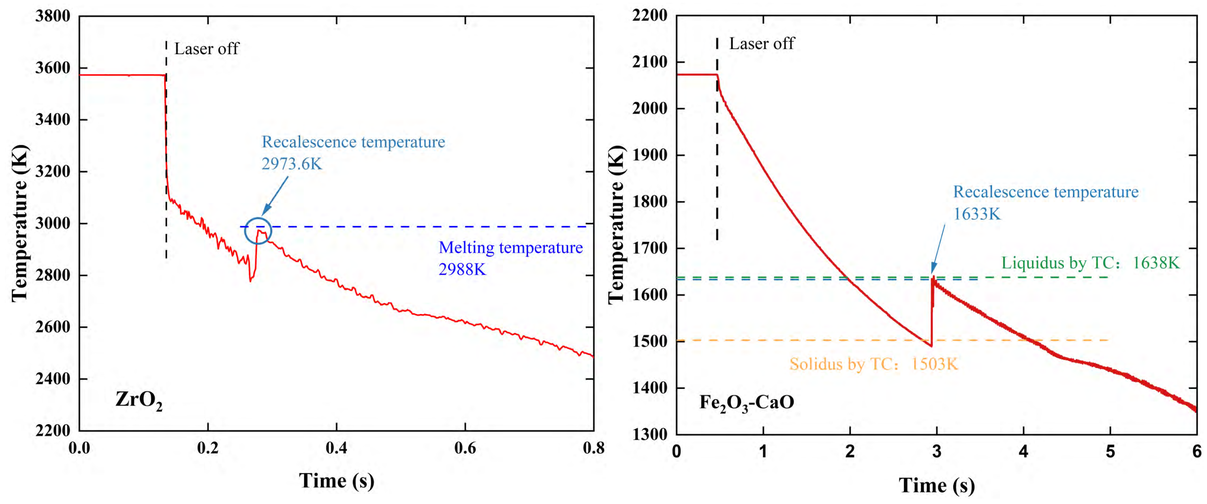

Figure 3. Recalescence behavior of ZrO_2 and Fe_2O_3-CaO

Heat of fusion Measurement

For the sample, the total heat lost during cooling in argon gas can be expressed in general as:

$$m\int C_p dT = A\int\left[\varepsilon\sigma(T^4 - T_{amb}^4) + h(T - T_g)\right]dt$$

Prior to solidification, the sample undergoes a temperature increase to T_m following nucleation. When the heat of fusion released by solidification is balanced with radiation and heat transfer, the sample temperature stays at the metling temeprature, showing a plateau in the temeprature profile, as shown in Figure 4. The heat of fusion is experssed as follows:

$$\Delta H_f = C_p\Delta T + \frac{A}{m}\int\left[\varepsilon\sigma(T^4 - T_{amb}^4) + h(T - T_g)\right]dt$$

As temperature difference during nucleation ΔT increases, plateau duration Δt decreases. When Δt decreases to zero, the hypercooling limit (the maximum of ΔT, ΔT_{hyp}) is reached. The heat of fusion is all consumed to elevate the sample temperature up to T_m. Therefore, the heat of fusion can be determined by:

$$\Delta H_f = C_p\Delta T_{hyp}$$

The measurement results for Al_2O_3 are given in Figure 4. The relationship between Δt and ΔT is obtained through linear fitting of experimental data. ΔT_{hyp} is calculated to be 672K when Δt equals to 0. Considering the isobaric capacity of 153.5 J/(mol·K) for liquid Al_2O_3 [6], the heat of fusion is calculated to be 103.0 kJ/mol, showing small deviations from the published value of 109.0 kJ/mol [6]. The measurement uncertainty is about 9.5 kJ/mol. The measurement errors may source from the limited number of experimental data points, the subjective determination of plateau time, and the impact of impurities inside samples on the recalescence behavior.

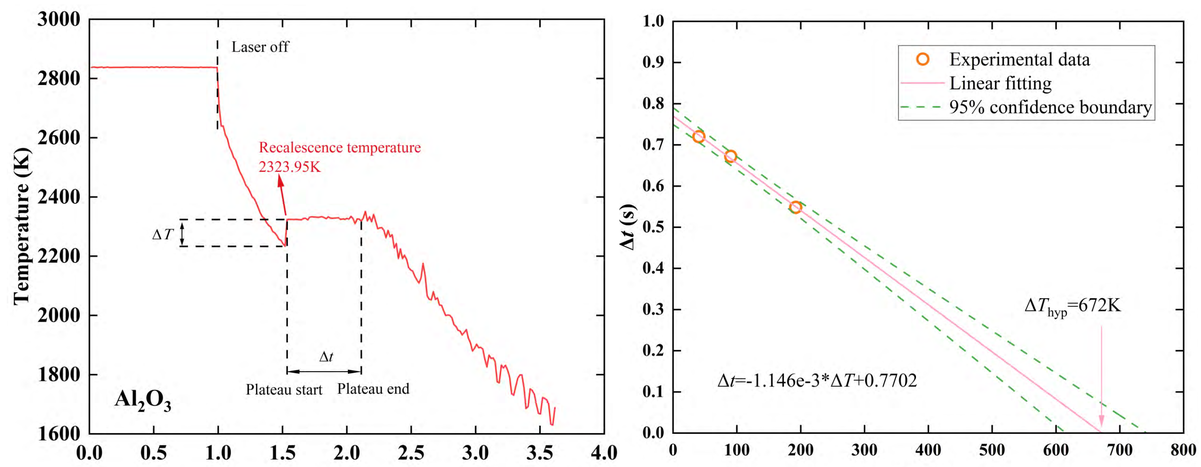

Figure 4. Heat of fusion measurement of Al_2O_3

Conclusion

This study shows the ability of ALSEE measuring melting temperature and heat of fusion by analyzing the recalescence behavior during the fast cooling. The measurement of melting temperature is convincing while the design of the experiment need to be modified to enhance reliability for heat of fusion measurement.

References

[1] Kondo T, Muta H, Kurosaki K, et al. Density and viscosity of liquid ZrO2 measured by aerodynamic levitation technique[J]. Heliyon, 2019, 5(7): e02049.
[2] Sun Y, Muta H, Ohishi Y. Multiple-gas cooling method for constant-pressure heat capacity measurement of liquid metals using aerodynamic levitator[J]. Review of Scientific Instruments, 2021, 92(9): 095102.
[3] Kawamoto K, Goto T, Kobatake H. Development of heat-of-fusion measurement for metals using a closed-type aerodynamic levitator[J]. ISIJ International, 2024, 64(7): 1155-1161.
[4] Gong Y, Zhang L, Yuan Y, et al. Thermophysical properties of UO2-ZrO2 melt measured by aerodynamic levitation[J]. Journal of Nuclear Materials, 2024, 602: 155356.
[5] Langstaff D, Gunn M, Greaves G N, et al. Aerodynamic levitator furnace for measuring thermophysical properties of refractory liquids[J]. Review of Scientific Instruments, 2013, 84(12): 124901.
[6] Paradis P F, Ishikawa T, Saita Y, et al. Non-contact thermophysical property measurements of liquid and undercooled alumina[J]. Japanese Journal of Applied Physics, 2004, 43(4A): 1496-1500.

High-Temperature Interactions of Corium, Steel, and Boron Carbide: Experimental Simulation of Fukushima Daiichi Unit 3

Mészáros Bence (1), Sklenka Jana (1), Čížková Karin (1), Itoh Ayumi (2), Hrbek Jan (1), Paukov Mykhaylo (3), Kobayashi Yoshinao (2), Tyrpekl Václav (4)

(1) Centrum Výzkumu Řež, (2) Institute of Science Tokyo, (3) Researcher, (4) Faculty of Science, Charles University

Type of abstract: Poster
Subject area: In-vessel corium and debris coolability
Keywords: corium, cold crucible, material analysis. IVMR, induction heating

The 2011 accident at the Fukushima Daiichi Unit 3 boiling water reactor (BWR-4, Mark I) resulted in extensive core degradation. To replicate the accident conditions during the in-vessel phase, we conducted experiments using induction melting in a cold crucible, observing the interaction between partially oxidized corium, stainless steel, and boron carbide. Our previous work validated these experiments by comparing the produced aerosols with samples from the actual accident site. Building on this, the present study investigates material characteristics of solidified corium melt to support decommissioning efforts at the Fukushima Daiichi Unit 3 reactor. The rapid solidification following the gas-producing reaction of the corium with B4C prevented significant phase separation, resulting in a well-mixed metallic/oxidic melt. Analysis of the cross-section of the solidified ingot using scanning electron microscopy with energy-dispersive X-ray spectroscopy revealed a relatively homogeneous composition within the oxidic regions, while the metallic areas were heterogeneous. These findings offer crucial insights into the post-accident state of the core melt and can inform the development of effective decommissioning strategies.

12th CONFERENCE ON
SEVERE ACCIDENTS RESEARCH
May 18-22, 2026 - Madrid, Spain
ERMSAR 2026

HIGH-TEMPERATURE INTERACTIONS OF CORIUM, STEEL, AND BORON CARBIDE: EXPERIMENTAL SIMULATION OF FUKUSHIMA DAIICHI UNIT 3

Bence Mészáros (bence.meszaros@cvrez.cz), Jana Sklenka, Karin Čížková, Ayumi Itoh, Jan Hrbek, Mykhaylo Paukov, Yoshinao Kobayashi, Václav Tyrpekl

Introduction

- The Fukushima Daiichi accident highlighted the importance of understanding corium behaviour for accident management and decommissioning activities.
- Effective severe accident mitigation strategies, including in-vessel and ex-vessel melt retention, require reliable experimental data on prototypic corium materials.
- Experimental research on corium is challenging due to its complex composition, high temperatures, and multiphase behaviour.
- Induction skull melting (cold crucible) enables preparation and investigation of high-temperature prototypic corium under representative conditions.
- This work presents experimental studies of Fukushima Unit 3 prototypic corium prepared in a cold crucible, followed by elemental, phase, and microstructural characterization of the resulting ingots.

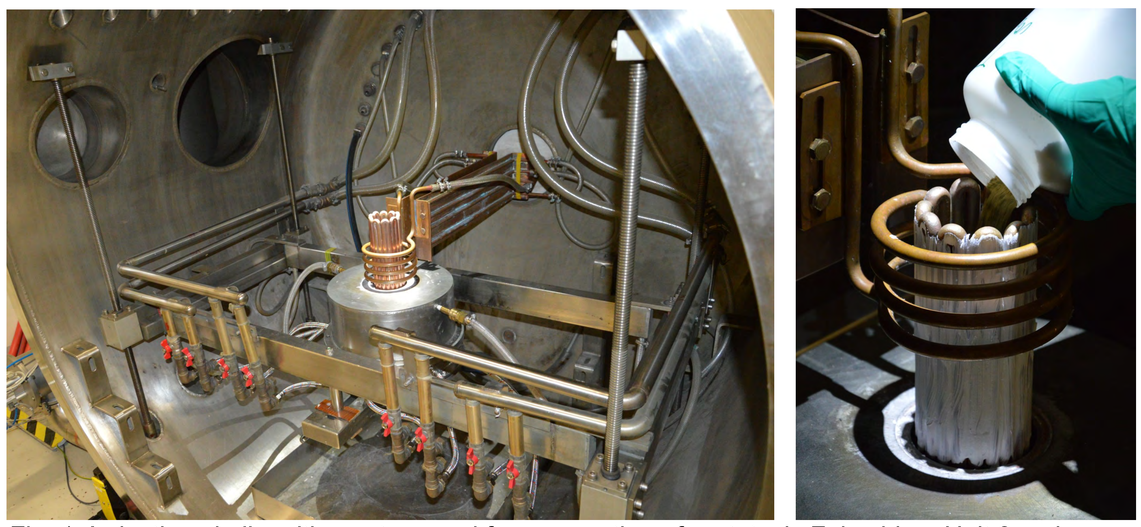

Fig. 1: Induction skull melting setup used for preparation of prototypic Fukushima Unit 3 corium.

Experimental section

- Two induction skull melting experiments (T-1 and T-2) were performed to prepare prototypic sub-oxidized Fukushima Unit 3 corium.
- Corium was prepared in a segmented water-cooled copper cold crucible under a protective argon atmosphere.
- Metallic zirconium was gradually added to the molten oxide pool to achieve sub-oxidized corium conditions representative of severe accident scenarios (C43 and C65).
- In T-1 interaction with stainless steel were conducted to simulate reactor material interactions during accident progression.
- In T-2 interaction with stainless steel and B_4C were conducted.
- Resulting ingots were sectioned and prepared for detailed characterization.
- Microstructural and elemental analyses were performed using SEM/EDS, while phase composition was determined by X-ray diffraction (XRD).

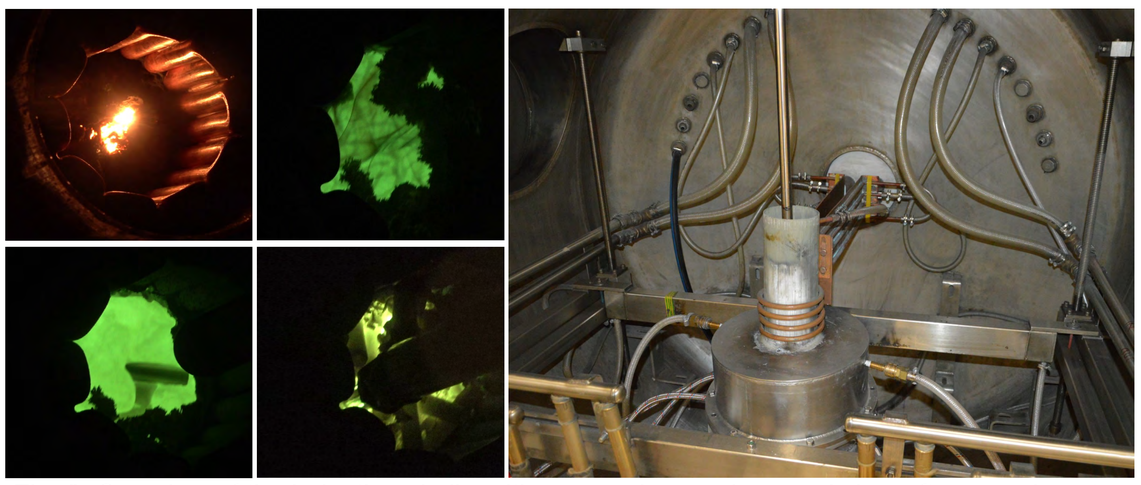

Fig. 2: Overview of the induction skull melting procedure and general view after experiment.

Table 1: Corium compositions of T-1 and T-2 experiments.

	experiment	T-1 (C43)	T-2 (C65)
	component	mass [g]	mass [g]
input components	UO_2	434.6	455.0
	ZrO_2	164.0	168.3
starting material	Zr	5.0	4.8
additives	Zr	170.7	73.9
	stainless steel	13.1	10.1
	B_4C	-	4.2

Acknowledgements

The presented work has been realized with in Institutional Support by the Ministry of Industry and Trade of the Czech Republic. The presented results were obtained using the CICRR infrastructure, which is financially supported by the Ministry of Education, Youth and Sports project LM2023041.

This work was supported by the Japan Atomic Energy Agency's Nuclear Energy S&T and Human Resource Development Project funded by Japanese government with the Grant Number of JPJA21F21461577.

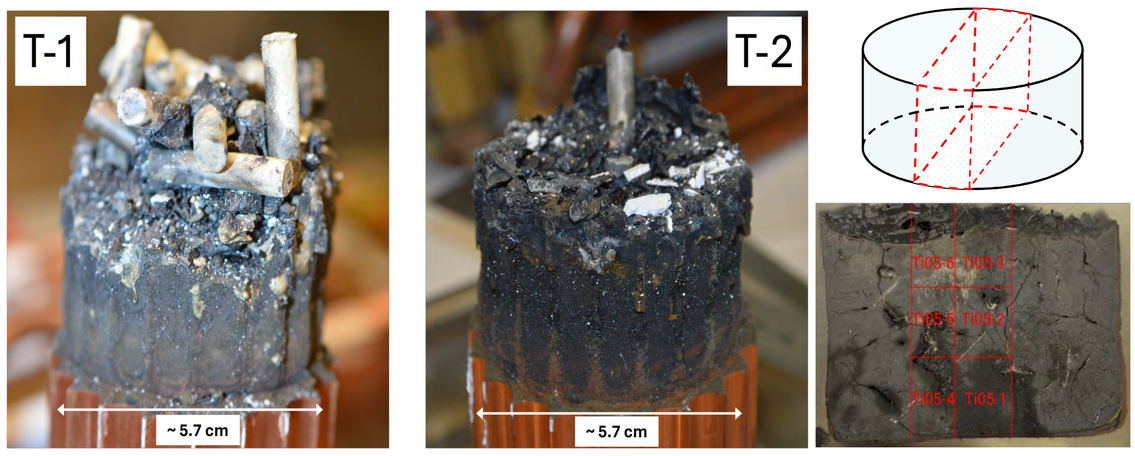

Fig. 3: Solidified corium ingots after corium–steel interaction experiments.

Results

- Prototypic sub-oxidized corium corresponding to Fukushima Unit 3 was successfully prepared using induction skull melting technology.
- Corium–steel interaction occurred at temperatures between corium solidus and liquidus temperatures.
- Stainless steel interaction remained localized in T-1.
- In T-2, metallic interaction zones extended through a much larger volume.
- Cr–Mn spinel phases formed due to oxidation of steel components.
- B_4C caused intensive gas generation and enhanced melt convection.
- Melt stirring induced by B_4C redistributed metallic phases throughout the ingot.
- Oxidation of B_4C enhanced uranium reduction within the melt.
- B_4C may accelerate severe accident progression through enhanced melt mixing and uranium reduction.
- Zr-rich U–Zr–O solid solutions similar to TMI-2 debris were identified.
- Separate ZrO_2 formation may indicate zirconium solubility limitations in suboxidized corium.

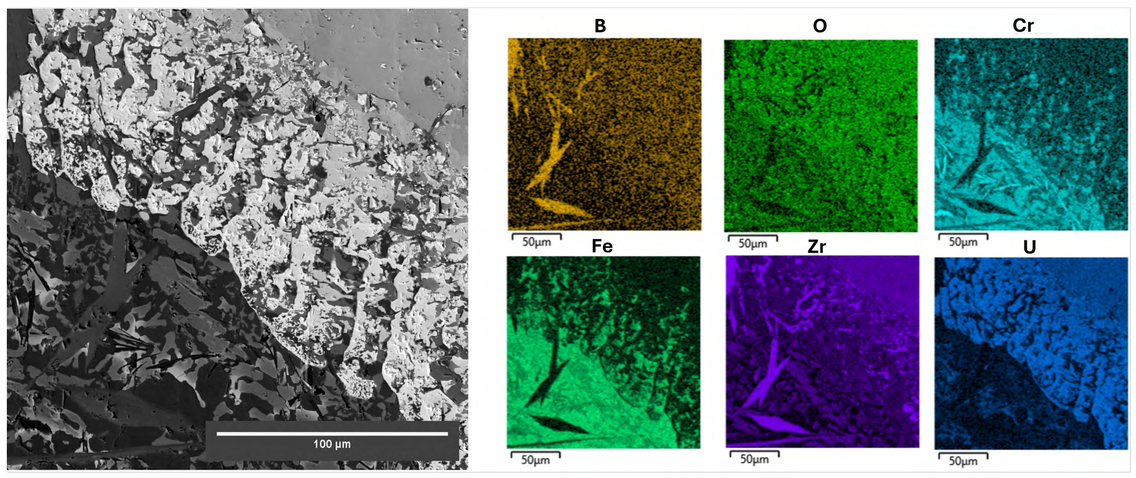

Fig. 4: Influence of B_4C on phase formation and metallic alloy evolution during corium interaction.

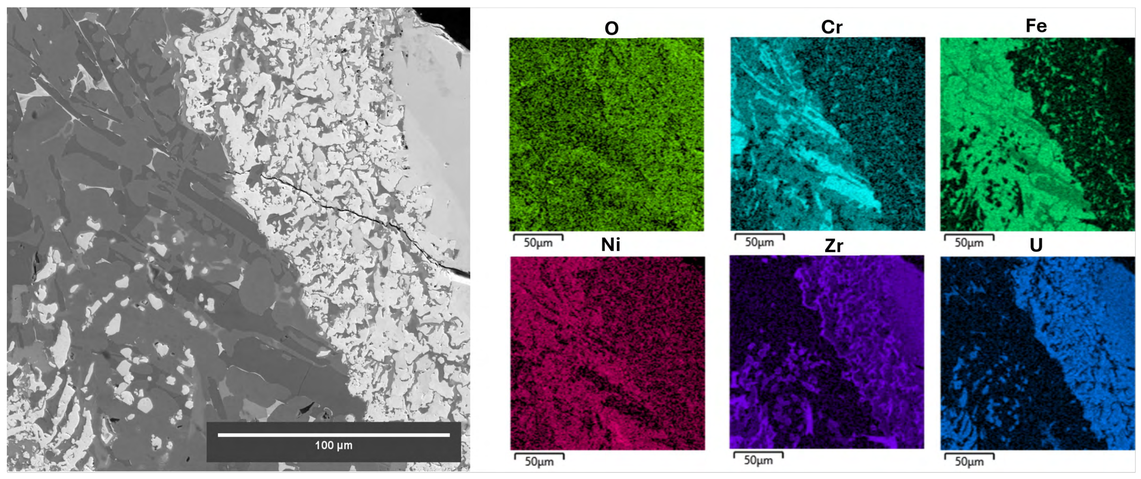

Fig. 5: SEM image and EDS elemental maps of the interaction zone between corium and stainless steel showing formation of metallic alloys and oxidic phases.

Conclusion

- Prototypic sub-oxidized corium representative of Fukushima Daiichi Nuclear Power Plant Unit 3 was successfully synthesized using induction skull melting technology under severe accident conditions.
- The experiments demonstrated that corium–stainless steel interaction occurred between corium solidus and liquidus temperatures.
- Addition of B_4C significantly modified melt behavior by enhancing gas generation, melt convection, and uranium reduction.
- Separate ZrO_2 formations were identified, indicating possible zirconium solubility limitations in suboxidized corium.
- The results provide new experimental insight into early-stage corium evolution and demonstrate the strong influence of B_4C on severe accident progression and corium–steel interaction phenomena.

CVŘ | Research Centre Řež

Detection and Segmentation of Overlapping Bubbles in Pool Scrubbing Experiments at the SAAB Facility

Yihui Wu, Michael Klauck
Forschungszentrun Jülich GmbH
524258 Jülich, Germany
y.wu@fz-juelich.de; m.klauck@fz-juelich.de

ABSTRACT

Pool scrubbing is considered one of the most effective mechanisms for mitigating fission product release during severe accidents in NPP. The efficiency of this process is governed by bubble hydrodynamics, as the rising bubbles and their interaction with aerosol particles determine the overall removal performance. Consequently, accurate characterization of bubble parameters – including diameter, size distribution, rise velocity, and relaxation time – is essential for reliable prediction of the decontamination factor (DF). Despite the availability of various physical models, discrepancies between simulations and experimental data remain significant, largely due to uncertainties in bubble parameters. In recent years, machine learning has been widely applied to bubble imaging to improve parameter estimation. While most existing models perform well on trained datasets acquired under simplified laboratory conditions, their accuracy decreases under complex boundary conditions such as high void fractions, turbulence, significant overlapping, and large-scale pool facilities. In this overview, we present an extended U-Net model, that has been retrained on experimental images from the SAAB facility at Forschungszentrum Jülich. The bubbles images in this dataset are taken under more realistic and challenging boundary conditions. First preliminary results show a promising prediction on bubble binary segmentation, highlighting its potential to enhance bubble characterization in complex multiphase flow experiments.

KEYWORDS
Pool scrubbing, Bubble hydrodynamics, Machine learning, Images processing

1. INTRODUCTION

The simulation of aerosol removal phenomena and the reliable prediction of DFs in pool scrubbing processes have gained increasing interest in recent years. Over the past decades, many experimental projects, including THAI, POSEIDON and SAAB [1-4], have focused on understanding the physical behavior of pool scrubbing better. However, several issues remain unsolved. DFs assessed from different facilities under similar experimental conditions often differ by several orders of magnitude, making meaningful comparison difficult and challenging the validation of simulation results. Besides, most pool scrubbing models (SPARC-B/98 within COCOSYS or MELCOR) rely on simplified input parameters. These simplifications cause discrepancies between experimental observations and numerical predictions [5, 6]. To improve simulation results, it is therefore essential to employ reliable, clean, and CFD-grade input bubble information as much as possible.

In recent years, machine learning has seen extensive exploration and rapid development in science applications, offering a promising bridge between experimental and numerical studies. In particular, deep learning has proven effective for bubble identification and segmentation [7-9] and is regarded as a potential approach for obtaining reliable bubble physical parameters to enhance simulation accuracy. Haas et al. [8]

have proposed a faster, region-based convolutional neural network detector (RCNN) to locate bubbles by identifying anchor points with the corresponding bubble bounding boxes, together with a shape-regression CNN assuming elliptical bubble geometries. Kim et al. [10] presented a slightly modified Mask R- for automatic bubble detection, demonstrating high accuracy at low gas volume fractions; however, its robustness under diverse experimental conditions remains limited. Cui et al. [11] achieved bubble detection and segmentation at gas contents up to 20% using the Mask R-CNN model and applied spherical reconstruction for submillimeter-scale bubbles. Hessenkemper et al. [9] evaluated three different CNN-based methods − Double U-Net, StarDist, and Mask R-CNN − for identifying and segmenting overlapping bubbles using synthetic images and tested two methods (ellipse fitting and radial distance correction) to recover hidden parts of overlapped bubbles.

The literature review reveals several open challenges that remain to be addressed:

- Accuracy remains insufficient at high gas content, especially for heavily overlapping bubbles.
- Current bubble-detection models are not universally applicable and are often sensitive to change in experimental conditions and configurations.
- Existing models are primarily trained by the datasets derived from small-scale facilities and lack data from large-scale experiments.
- Bubble reconstruction typically relies on ellipse fitting, which is not well suited for irregular bubbles.

In this extended abstract, we present the preliminary results for a binary segmentation task using the U-Net model with a ResNet-32 backbone. Images acquired from the large-scale SAAB Facility [4,12] (Figure 1, l eft) provided by the ongoing NAMPS project (German national project conducted by IATF-KIT, grant no. 1501652) are used for training and validation. Our work aims to address aforementioned challenges through more robust deep CNN techniques.

1. U-NET ARCHITECTURE

The U-Net architecture has been widely proven as an effective solution for image segmentation tasks. Inspired by the model developed by our colleagues at HZDR, we employ a PyTorch-based U-Net with a ResNet-34 backbone to perform bubble-image segmentation in our work.

For bubble hydrodynamic experiments, the camera and illumination system are positioned opposite each other, as shown in Figure 1 (middle). Images are recorded under various hydrodynamic conditions with different gas-injection velocities. The resulting recordings capture swarms of bubbles, often overlapping and associated with relatively high gas void fractions. Figure 1 (right) presents an example of a captured image. It is noted that bubble image shows inhomogeneous illumination distribution, which is a limitation of the SAAB facility itself. The center of the image is overexposed, while the surrounding areas appear darker. Considering significant bubble overlaps makes bubbles identification and segmentation to be challenged.

The task is firstly considered as a binary segmentation problem in which the background is labeled as 0 and the objects (bubbles) as 1. The encoder adopts a pretrained ResNet-34 consisting of six stages for hierarchical feature extraction. The initial learning rate is set to 2×10^{-4} and the weight decay to 1×10^{-4}. The decoder follows the standard U-Net structure with skip connections linking encoder and decoder layers. During training, the loss function is defined as a weighted combination of the Dice loss and the Focal loss, with weights of 0.7 and 0.3, respectively. The Focal loss parameters α and γ are set to 0.25 and 2, consistent with recommended values in literature. The complete loss function is given in Eq. (1):

$$\min L = 0.7\left(1 - \frac{2\sum(py)+\varepsilon}{\sum p+\sum y+\varepsilon}\right) + 0.3\left(-\alpha(1-p)^{\gamma} y \log p - (1-\alpha)p^{\gamma}(1-y)\log(1-p)\right) \quad (1)$$

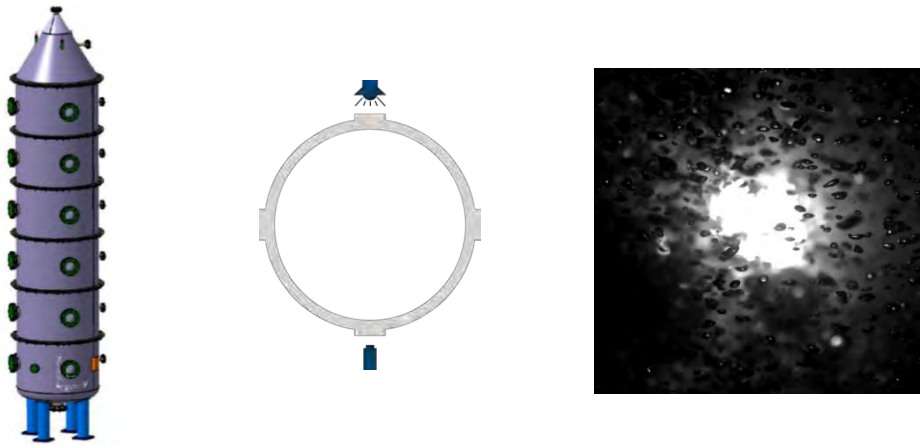

Figure 1. Overview of the SAAB facility vessel (left), orientation of the high-speed camera and illumination system (middle), and representative example of a captured bubble image (right).

2. PRELIMINARY RESULTS AND FIRST CONCLUSIONS

In our binary segmentation study, we increased the input cropped image size from 256×256 to 512×512 and explored a range of training configurations. The experimental parameters included the use of data augmentation, different batch sizes (8, 16, 32), various segmentation architectures (U-Net, U-Net++, FPN, SegFormer, PAN), different pre-trained backbones (ResNet-34, EfficientNet-B7, mit-b2), multiple weighted loss-function combinations, and different dropout rates, with the goal of achieving the best F1 and IoU scores. Our best preliminary results were obtained using a U-Net with a mit-b2 backbone, an input image size of 512×512, data augmentation enabled, a dropout rate of 0.2, a batch size of 16, and a Dice–Focal loss weighting of 0.7 to 0.3. The best F1 score achieved was 0.8229 at a threshold of 0.4747. The corresponding IoU at this optimal threshold was 0.70, indicating that the resulting model is reasonably effective and suitable for further investigation.

Figure 3 shows the training and validation loss, as well as the IoU curves, over the training epochs. It is noted that during the decreasing of training loss, the validation loss also decreases and eventually stabilizes, indicating no clear signs of overfitting. However, the IoU scores still have potential for improvement. Figure 2 illustrates the differences between the predicted masks and the ground truth. It can be observed that some errors come from missed bubbles (false negatives), while others result from incorrectly predicted bubbles (false positives) highlighting the necessity to further improve the manual mask annotations, which is expected to increase both the training IoU and the overall model accuracy. Nevertheless, the preliminary prediction results for the 1024×1024 bubble images are a promising first attempt. The next step will be to extend the current binary segmentation approach to a bubble-classification segmentation capable of identifying overlapping bubble situations.

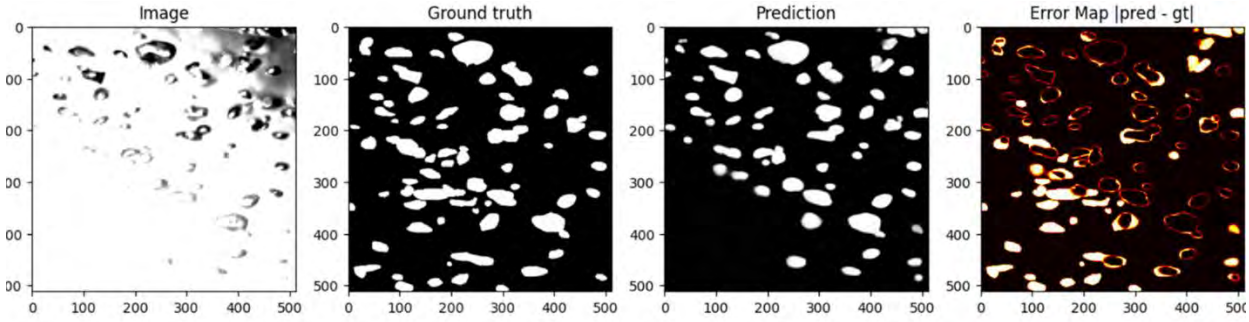

Figure 2. The error map between prediction masks and ground truth.

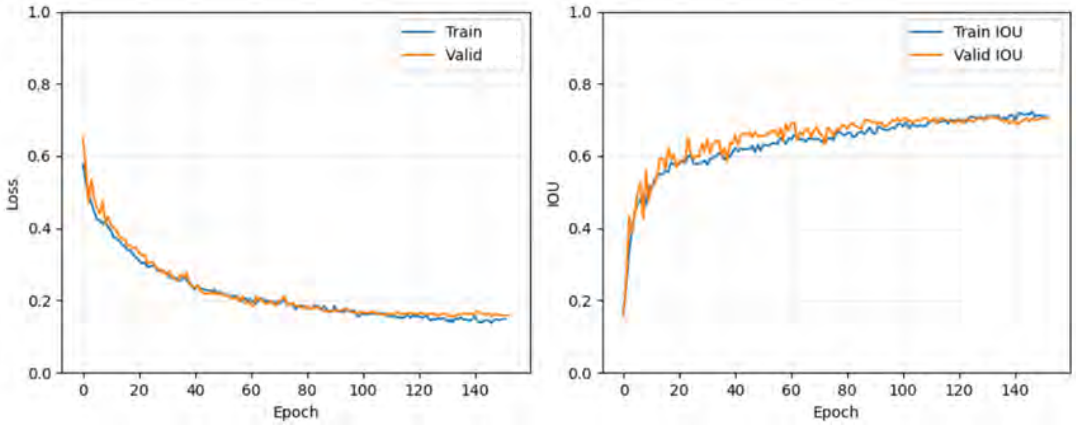

Figure 3. Loss curve and IoU curve.

ACKNOWLEDGMENTS

This work was funded by the German Federal Ministry of Research, Technology and Space (BMFTR, grant no. 02NUK101) on the basis of a decision by the German Bundestag.

REFERENCES

1. S. Gupta et al., "THAI test facility for experimental research on hydrogen and fission product behaviour in light water reactor containments," *Nuclear Engineering and Design* **294**, pp. 183-201 (2015).
2. A. Dehbi, D. Suckow and S. Guentay, "The effect of liquid temperature on pool Scrubbing of aerosols," *Arerosol Sci.* **28**, pp. 2 (1997).
3. J. Kobalz and H.-J. Allelein, "SAAB Test Facility – Separate Effect Tests on Pool Scrubbing Phenomena," *PASSAM Final Workshop on source term mitigation of severe accidents*, Paris, France, February 27, 2017.
4. H.-J. Allelein et al., *Severe Accident Aerosol Behavior II final report*, German national project, grant no. 1501551, RWTH Aachen University (2023).
5. S. Gupta et al., "Integration of pool scrubbing research to enhance Source-Term calculations (IPRESCA) project–Overview and first results," *Nuclear Engineering and Design* **404**, pp. 112189 (2023).
6. W. Kikuchi et al., "Experimental Study of Aerosol Behavior During Pool Scrubbing: Part 2 — Decontamination of Aerosol Particle in Two Phase Flow," *26th International Conference on Nuclear Engineering*, London, England, July 22-26, 2018.
7. Y. Fu and Y. Liu, "BubGAN: Bubble generative adversarial networks for synthesizing realistic bubbly flow images," *Chemical Engineering Science*, **204**, pp. 35-47 (2019).
8. T. Haas et al., "BubCNN: Bubble detection using Faster RCNN and shape regression network," *Chemical Engineering Science*, **216**, pp:115467 (2020).
9. H. Hessenkemper et al., "Bubble identification from images with machine learning methods," *International Journal of Multiphase Flow*, **155**, pp. 104169 (2022).
10. Y. Kim and H. Park, "Deep learning-based automated and universal bubble detection and mask extraction in complex two-phase flows," *Scientific Reports*, **11**(1): pp: 940 (2021).
11. Y. Cui et al., "A deep learning-based image processing method for bubble detection, segmentation, and shape reconstruction in high gas holdup sub-millimeter bubbly flows," *Chemical Engineering Journal*, **449**, pp. 137859 (2022)
12. M. Klauck et. al., "The SAAB Project: Experimental Studies on Several Phenomena Related to the Assessment of Aerosol Behavior in Severe Accidents, " *Proc. 20th International Topical Meeting on Nuclear Reactor Thermal Hydraulics (NURETH-20),* Washington, D.C, USA, August 20–25, 2023 pp. 4073-4085 (2023).

12th CONFERENCE ON
SEVERE ACCIDENTS RESEARCH
May 18-22, 2026 - Madrid, Spain
ERMSAR 2026

DETECTION AND SEGMENTATION OF OVERLAPPING BUBBLES IN POOL SCRUBBING EXPERIMENTS AT THE SAAB FACILITY

Yihui Wu, Michael Klauck, Forschungszentrum Jülich GmbH, Germany

Introduction & Motivation

Challenges: The simulation of aerosol removal phenomena and the reliable prediction of DFs in pool scrubbing processes have gained increasing interest in recent years. DFs assessed from different facilities under similar experimental conditions often differ by several orders of magnitude, making meaningful comparison difficult and challenging the validation of simulation results. Most pool scrubbing models (SPARC-B/98 within COCOSYS or MELCOR) rely on simplified input parameters, which cause discrepancies between experimental observations and numerical predictions. [1, 2]

Approach: Deep learning has proven effective for bubble identification and segmentation and is regarded as a potential approach for obtaining reliable bubble physical parameters to enhance simulation accuracy [3, 4]. In the CNN-OBA project, we apply a well-established U-Net architecture with various pre-trained encoders for binary segmentation. The bubbles image data were obtained from the large-scale SAAB Facility within the NAMPS project. This approach aims to provide more robust bubble physical parameters, ultimately enhancing the predictive capability of pool scrubbing simulations.

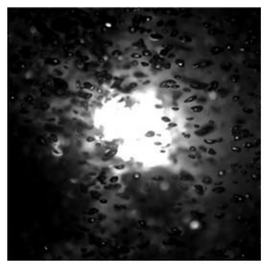

Hydrodynamic Experiments

Modular SAAB facility: [5]

- **flexibility:** various gas injection geometries (upward, downward, and sideways)
- **scalability:** pool height 0.5-5.5 m; heating options up to boiling conditions
- **setup:** camera and illumination system in a counter-position

Experimental conditions:

- various **hydrodynamic conditions** with different gas-injection velocities
- focusing on the **swarms of bubbles**

Key technical challenges:

- **overlapping bubbles**: relatively high gas void fractions up to 30%
- **illumination limitation:** inhomogeneous distribution (center overexposure dark periphery)
- **segmentation difficulty:** challenging to conventional image processing and existed models

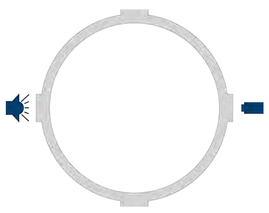

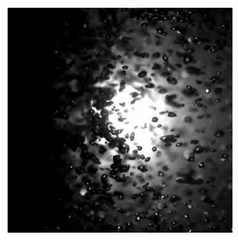

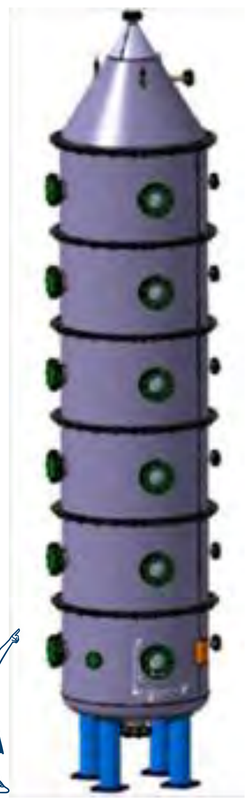

Machine Learning (U-Net Architecture[6])

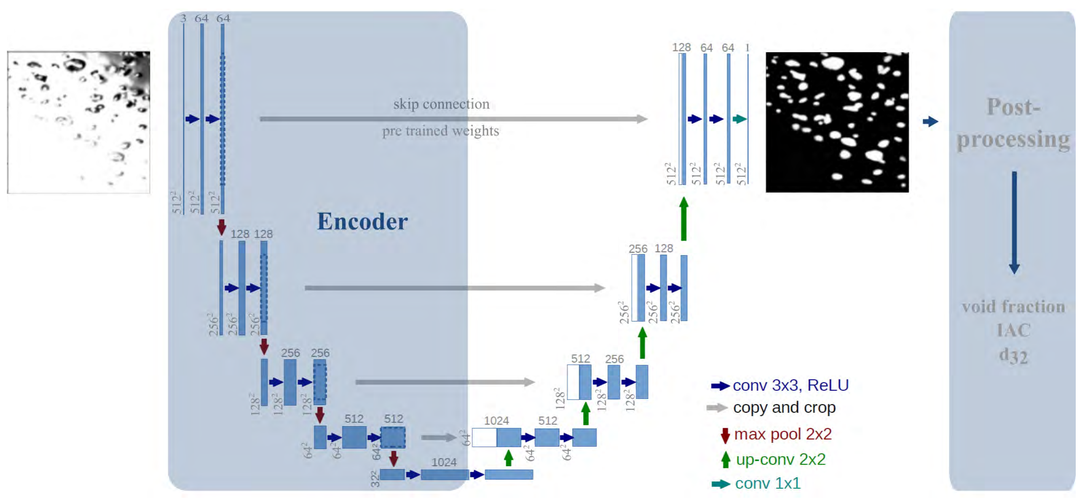

Task: Binary segmentation (0: Background, 1: Bubbles) with manually labeled annotation (CVAT)

Pre-processing: Resize / crop from 1024 x 1024 images

Augmentation: flipping, rotation, contrast, noises (only for training sets)

Encoder Backbone options: ResNet34, Mit-b2 (SegFormer), EfficientNet-b7

- initialized with ImageNet-pretrained weights to accelerate convergence

Loss function: $\mathcal{L}_{loss} = 0.7\mathcal{L}_{Dice} + 0.3\mathcal{L}_{focal}(\alpha = 0.25, \gamma = 2)$ with **Adam optimizer**

Hyperparameters: Learning Rate: 0.0002| Weight decay: 0.0001| Dropout: 0.2 | Batch size: 16

Results

Ablation: Larger training patches improve performance

Encoders:

- SegFormer encoder achieves the best results (modern Transformer backbone)
- pure U-Net also achieves relatively high performance

Metrics: Dice and IoU indicate robust learning of bubble boundaries

Error source: Performance mainly limited by low-quality manual annotations

Encoder Backbone	Input sizes	Dice	IoU
UNet	512×512	0.8101	0.6809
ResNet-34	512×512	0.8048	0.6735
SegFormer mit-b2_L	512×512	**0.8229**	**0.6978**
EfficientNet-b7	512×512	0.7989	0.6651
SegFormer mit-b2_S	128×128	0.8062	0.6808

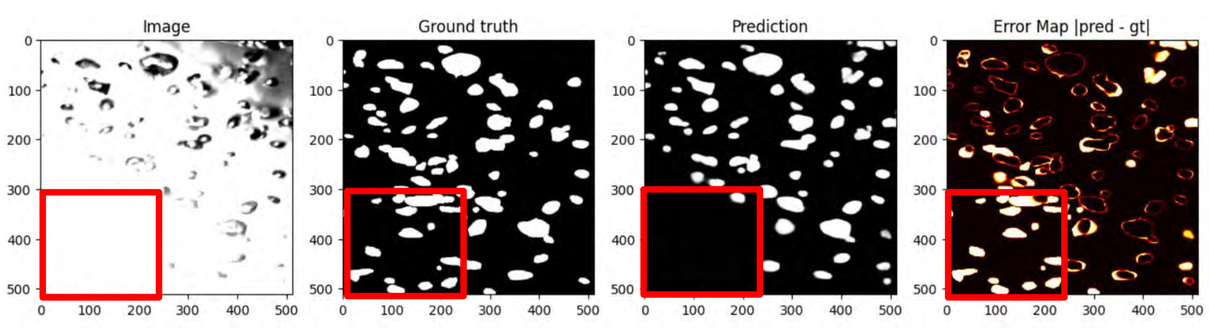

Outlook

High Fidelity Ground Truth:

- implementing semi-automated labeling tools and human cross verification
- reducing the labeling image size from 1024×1024 resolution to 128×128

Synthetic Inputs: 3D-bubble modeling to provide bubble physical information ground truth, enabling rigorous validation of segmentation model post-processing

Beyond Binary: Instance-Level Segmentation

- focusing on decoupling overlapping bubbles and acquiring bubbles size distribution information at highly void fraction (swarm flow)

Physics-coupled Post-Processing:

- **bubble parameters**: Sauter mean diameter (d_{32}), local void fraction (α), , Interfacial Area Concentration (IAC)
- **SPARC-98 integration**: providing physical and statistical based bubble information for pool scrubbing simulation

Paper contribution to NUTHOS-15 conference (Sept. 28 - Oct. 02, 2026, in Kashiwa-no-ha, Japan):

- Wu et al., “A CNN-based Approach for Bubble Segmentation in Pool Scrubbing”

References

1. S. Gupta et al., "Integration of pool scrubbing research to enhance Source-Term calculations (IPRESCA) project–Overview and first results," *Nuclear Engineering and Design* **404**, pp. 112189 (2023).
2. W. Kikuchi et al., "Experimental Study of Aerosol Behavior During Pool Scrubbing: Part 2 — Decontamination of Aerosol Particle in Two Phase Flow," *26th International Conference on Nuclear Engineering*, London, England, July 22-26, 2018.
3. H. Hessenkemper et al., "Bubble identification from images with machine learning methods," *International Journal of Multiphase Flow*, **155**, pp. 104169 (2022).
4. Y. Kim and H. Park, "Deep learning-based automated and universal bubble detection and mask extraction in complex two-phase flows," *Scientific Reports*, **11**(1): pp: 940 (2021).
5. M. Klauck et. al., "The SAAB Project: Experimental Studies on Several Phenomena Related to the Assessment of Aerosol Behavior in Severe Accidents, " *Proc. 20th International Topical Meeting on Nuclear Reactor Thermal Hydraulics (NURETH-20),* Washington, D.C, USA, August 20–25, 2023 pp. 4073-4085 (2023).
6. O. Ronneberger et. al., (2015). "U-net: Convolutional networks for biomedical image segmentation, " *International Conference on Medical image computing and computer-assisted intervention,* pp. 234-241, Cham: Springer international publishing.

Acknowledgements

This research was funded by the German Federal Ministry of Research, Technology and Space (Bundesministerium für Forschung, Technologie und Raumfahrt BMFTR). Project title: “Convolutional Neural Networks for Overlapping Bubble Analysis with respect to Pool Scrubbing (CNN-OBA),” grant number 02NUK101.

The authors would like to express their gratitude to Prof. Xu Cheng from KIT-IATF for kindly providing the image data from the NAMPS project funded by the German Federal Ministry for the Environment, Climate Action, Nature Conservation and Nuclear Safety (Bundesministerium für Umwelt, Klimaschutz, Naturschutz und nukleare Sicherheit), grant no.1501652.

Federal Ministry of Research, Technology and Space

Federal Ministry for the Environment, Climate Action, Nature Conservation and Nuclear Safety

Experimental Study of Molten Corium–Serpentinite Concrete Interaction Using Cold Crucible Induction Melting

Nikolaiev Borys (1)

(1) CVŘ

Type of abstract: Poster
Subject area: Ex-vessel corium interactions and coolability
Keywords: Cold crucible induction melting Molten corium-concrete interaction

Molten corium concrete interaction (MCCI) is a key phenomenon during the ex-vessel phase of severe accidents of nuclear power plants. Research in this topic is essential for improving safety protocols and aiding decommissioning efforts for nuclear power plants. Study of the interaction between corium and serpentinite concrete has historically been neglected compared to other concrete types. This study thus focused on investigating the interaction between prototypic oxidic corium and serpentinite concrete using induction melting in a cold crucible. Off-gas composition was studied and post-test material analyses using X-Ray diffraction (XRD) and scanning electron microscopy (SEM) were performed. The gained knowledge will serve to increase safety during severe accidents.

EFFECT OF PT COATING METHODS ON HYDROGEN RECOMBINATION ACTIVATION FOR PASSIVE AUTOCATALYTIC RECOMBINERS

Dae-Hyun Kim, Dong-Wook Oh*
Department of Mechanical Engineering
Chosun University
17, Chosundae 1-gil, Dong-gu, Gwangju, Korea 61452
rlaeogus1995@naver.com; dwoh@chosun.ac.kr

Youngsu Na
Korea Atomic Energy Research Institute
111, Daedeok-daero 989 Beon-gil, Yuseong-gu, Daejeon, Korea 34057
ysna@kaeri.re.kr

ABSTRACT

The mitigation of hydrogen in nuclear containment buildings during a severe accident relies heavily on passive autocatalytic recombiners (PARs). Inside a PAR, hydrogen and oxygen react on platinum-based catalysts that are coated on a plate or mesh structure. Effective operation of PARs requires the initiation of recombination at hydrogen concentrations as low as 1 vol.%, a concentration significantly below the lower flammability limit of hydrogen in air (4 vol.%). Achieving this low-concentration activation hinges on the development of practical techniques for coating the expensive platinum catalysts onto the metallic or ceramic substrates. In this study, the recombination performance and activation conditions of three catalyst types were experimentally investigated in a laboratory-scale PAR device. Two of the catalysts were flat stainless-steel plates coated with platinum via sputtering and electroplating, respectively. The third, serving as a reference, was a commercial honeycomb-type catalyst (KE-7580, Heesung Catalysts Corp.) in which the catalyst material is wash-coated onto a cordierite mesh. To evaluate the activation characteristics, the flat-plate catalysts were preheated to surface temperatures of up to 250°C, and their activity was evaluated by observing the surface temperature increase and maintenance due to the exothermic reaction upon the supply of hydrogen–air mixtures with hydrogen concentrations ranging from 4 to 6 vol.%. In contrast, the honeycomb catalyst was tested under ambient conditions, and its performance was assessed by measuring the catalyst surface temperature and the hydrogen concentrations at the inlet and outlet to calculate the catalytic removal rate. This study aims to experimentally determine the operational activation limits of these catalysts, thereby contributing to the enhancement of catalyst plate performance for PARs.

KEYWORDS
Passive autocatalytic recombiner, Hydrogen recombination, Catalyst reaction, Catalyst coating methods

1. INTRODUCTION

Hydrogen mitigation within nuclear power plant containment buildings is an important aspect of safety management for preventing the risk of gas explosions that may occur during severe accidents. The initiation

of PAR operation generally occurs at low hydrogen concentrations below the flammability limit, and this early activation characteristic is important for suppressing hydrogen accumulation during the early phase of an accident. Therefore, the catalytic activation characteristics under low hydrogen concentration conditions are an important factor in evaluating PAR performance. The activation behavior of PAR catalysts depends not only on the chemical composition of the catalyst but also on the surface structure [1]. Previous studies have focused on optimizing reaction efficiency within porous supports with large specific surface areas, whereas studies directly addressing activation limits in densely formed catalytic layers remain relatively limited [2,3]. In this study, the activation characteristics of a commercial honeycomb catalyst and plate-type catalysts coated with platinum via sputtering and electroplating were experimentally compared. The catalytic activation was examined as functions of the preheating temperature of plate-type catalysts and hydrogen concentration, and the effects of surface structural differences on reaction activation under low hydrogen concentration conditions were elucidated through comparisons of catalyst surface structures and platinum distributions using SEM–EDX analysis.

2. EXPERIMENTS AND RESULTS

Three types of catalysts were used to compare activation characteristics depending on the coating method. The commercial honeycomb catalyst KE-7580 consisted of a cordierite support with a cell density of approximately 46 CPSI and was coated with Pt on the surface. The sputtered catalyst was fabricated by depositing a 30 μm-thick Ti layer on a stainless steel plate to prevent oxidation and subsequently depositing Pt to a thickness of 100 μm. The electroplated catalyst was fabricated by electroplating Pt onto a Ti plate to a thickness of 0.5 μm. The plate-type catalysts had an area of 100×100 mm^2 and a thickness of 1.5 mm. Catalyst activation tests were conducted in a lab-scale PAR test facility as shown in Figure 1. The hydrogen–air mixture flow rate and concentration were controlled using mass flow controllers (MFC), and the mixture was uniformly mixed using a static mixer before entering the bottom of the test facility. The plate-type catalysts were preheated to a surface temperature of 250~300°C using a hot air blower to determine the activation limit and the gas mixture was then introduced. Thermocouples were attached at the center of the plate surface and at positions 25 mm above and below the center and catalyst activation was identified from surface temperature changes induced by the exothermal reaction. The honeycomb catalyst was tested at ambient temperature without separate preheating. Thermocouples were attached to the upper and lower surfaces of the honeycomb channels to measure temperature changes during the reaction and the hydrogen concentration was measured 100 mm downstream of the catalyst. The hydrogen removal rate and recombination performance were analyzed by comparing the concentration differences between the inlet and outlet for different hydrogen concentrations and flow rates.

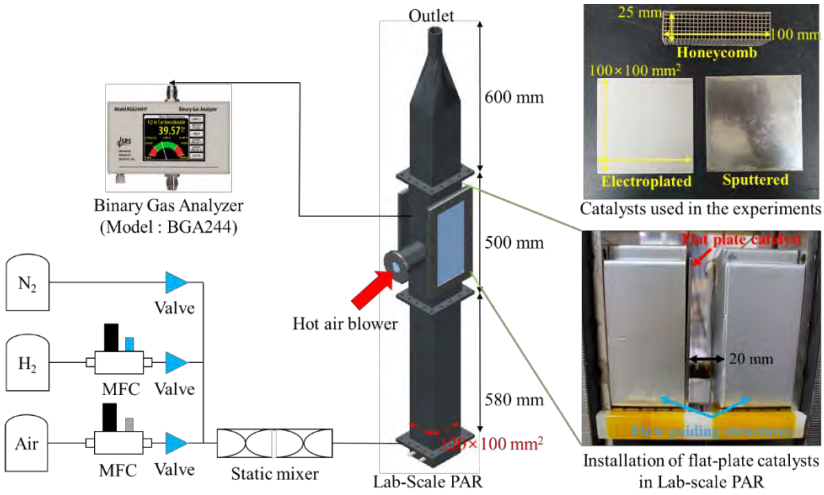

Figure 1. Schematic of a lab-scale PAR experiment.

Figure 2 shows the surface temperatures of the plate-type catalysts as functions of the preheating temperature and hydrogen concentration. The sputtered catalyst maintained a surface temperature above approximately 180℃ at the lower region due to the exothermic reaction after the surface was preheated to 250℃ and 6 vol.% hydrogen was subsequently introduced as shown in Figure 2(a). However, at the same hydrogen concentration the surface temperature continuously decreased and the reaction was not activated even after the gas mixture was introduced when the preheating temperature was increased to 300℃. In contrast, when the plate-type catalyst was preheated to 300℃ and the gas mixture was subsequently introduced at the same hydrogen concentration, the surface temperature fell below 100℃ and the reaction was not activated. Therefore, the sputtered catalyst may exhibit transient reactions but does not achieve stable activation. The electroplated catalyst showed catalytic reactions only at a hydrogen concentration of 6 vol.% after preheating to 300℃, and the surface temperature was maintained at approximately 250℃ as shown in Figure 2(b). Therefore, lower hydrogen concentrations are considered to require higher activation energy for the initiation of the reaction. The honeycomb catalyst was activated upon hydrogen injection at ambient temperature without a separate preheating process and the outlet hydrogen concentration decreased even at a low inlet hydrogen concentration of 1 vol.% as shown in Figure 3(a). Figure 3(b) and (c) show the surface temperature and hydrogen removal rate for different flow conditions. As the hydrogen concentration increased, the catalyst surface temperature rose due to exothermic reactions, while the hydrogen removal rate decreased because the amount of hydrogen supplied per unit time increased and the removable fraction became relatively smaller. In contrast, an increase in flow rate reduced the surface temperature by shortening the residence time and limiting the effective reaction on the catalyst surface while the hydrogen removal rate increased due to enhanced mass transfer. In contrast, an increase in flow rate reduced the surface temperature by shortening the residence time and limiting the effective reaction on the catalyst surface, while the hydrogen removal rate was analyzed to increase as mass transfer was enhanced and reactants were more effectively supplied to the catalyst surface.

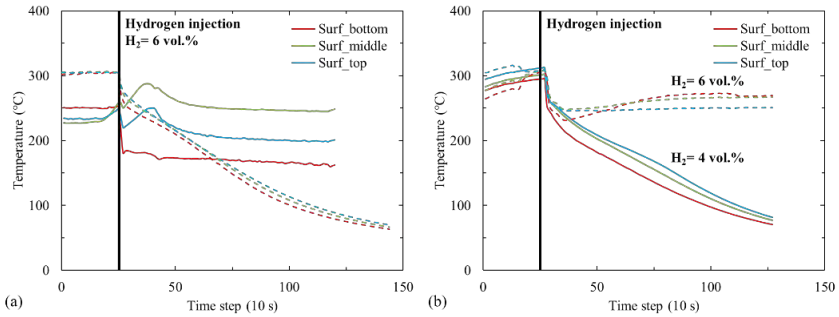

Figure 2. Surface temperature results of plate type catalysts under hydrogen and air mixture injection after preheating (a) sputtered plate preheated to 250, 300℃ with 6 vol% hydrogen injection, (b) electroplated plate preheated to 300℃ with 4, 6 vol% hydrogen injection.

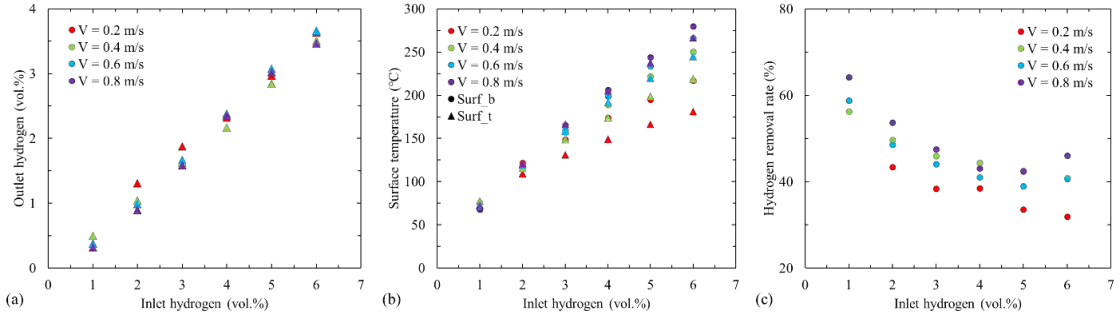

Figure 3. Experimental results of honeycomb catalyst according to inlet velocity and hydrogen concentration (a) outlet hydrogen concentration (b) surface temperature (c) hydrogen removal rate.

Figure 4 shows the Pt distribution on the catalyst surfaces from SEM–EDX analysis displayed in red. The honeycomb catalyst exhibits a porous surface structure with Pt present on the surface, providing diffusion pathways for gas penetration into the catalyst and a large effective reaction area. The sputtered catalyst shows a dense Pt distribution in the form of a thin film, and the electroplated catalyst exhibits locally aggregated Pt particles. As a result, the limited gas diffusion pathways and effective reaction areas of the plate-type catalysts limit the occurrence of catalytic reactions.

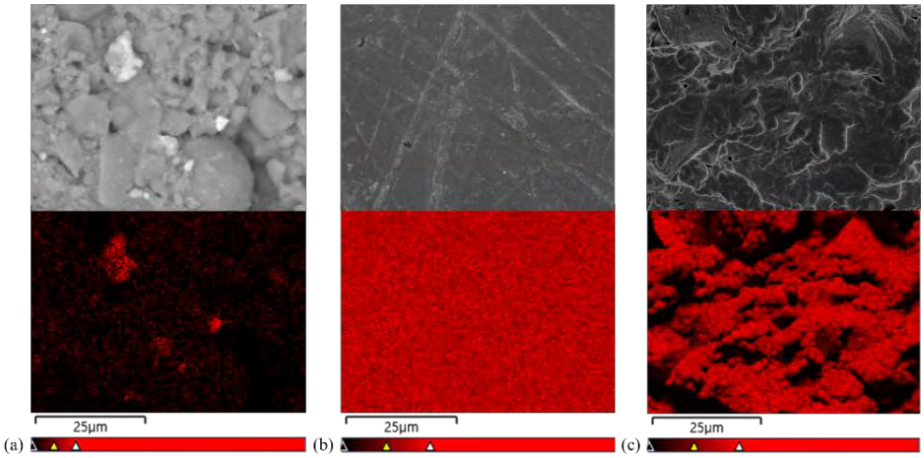

Figure 4. SEM-EDX analysis results of catalyst surfaces according to coating methods (a) honeycomb catalyst (b) sputtered catalyst (c) electroplated catalyst.

3. CONCLUSIONS

In this study, the activation characteristics of PAR catalysts were compared according to Pt coating methods. The honeycomb catalyst initiated catalytic reactions at ambient temperature and low hydrogen concentration conditions, whereas the sputtered and electroplated plate-type catalysts exhibited limited activation despite high-temperature preheating. SEM–EDX analysis showed that the honeycomb catalyst featured a porous structure with well-distributed Pt, providing sufficient gas diffusion pathways and a large reaction area, whereas the sputtered and electroplated catalysts exhibited dense surface structures with localized Pt distribution, resulting in structural limitations unfavorable for activation. These findings suggest that the initiation behavior of PAR catalysts under low hydrogen concentration conditions is more strongly influenced by surface structure and diffusion characteristics than by the Pt coating method itself.

ACKNOWLEDGMENTS

This work was supported by the National Research Foundation of Korea (NRF) grant funded by the Korean government (Ministry of Science and ICT) (No. RS-2022-00144368) and Korea Institute of Energy Technology Evaluation and Planning(KETEP) and the Ministry of Trade, Industry & Energy(MOTIE) of the Republic of Korea (No. RS-2024-00397362).

REFERENCES

1. E.A. Reinecke, et al., “Studies on innovative hydrogen recombiners as safety devices in the containments of light water reactors,” *Nuclear Engineering and Design*, **230**(1-3), pp. 49-59 (2004).
2. A.E. Kozhukhova, et al., “Catalytic Hydrogen Combustion for Domestic and Safety Applications: A Critical Review of Catalyst Materials and Technologies,” *Energies*, **14**(16), pp. 4897 (2021).
3. A.E. Kozhukhova, et al., “AThermally Conductive Pt/AAO Catalyst for Hydrogen Passive Autocatalytic Recombination,” *Catalysts*, **11**(4), pp. 491 (2021).

12th CONFERENCE ON
SEVERE ACCIDENTS RESEARCH
May 18-22, 2026 - Madrid, Spain
ERMSAR 2026

EFFECT OF PT COATING METHODS ON HYDROGEN RECOMBINATION ACTIVATION FOR PASSIVE AUTOCATALYTIC RECOMBINERS

Dae-Hyun Kim[1], Youngsu Na[2], Dong-Wook Oh[1]
[1] Chosun University, Korea. [2] Korea Atomic Energy Research Institute, Korea.

1. INTRODUCTION

● **Passive autocatalytic recombiner (PAR)**

- In the event of a severe accident at a nuclear power plant, a large amount of **hydrogen is produced** by a reaction of high-temperature water vapor and zircaloy, which is a shell material for nuclear fuel rods.
- Hydrogen can be ignited with very little energy at low concentrations (below 4% vol.), so if hydrogen accumulates in the upper region of the containment due to buoyancy, there is a risk of explosion.
- **PAR**s prevent hydrogen explosions in nuclear power plants by reducing the hydrogen concentration within the combustible limit range through the passive catalytic recombination of hydrogen and oxygen.

▸ To compare **hydrogen recombination activation** characteristics depending on **Pt coating methods** and catalyst surface structures, and to **interpret the relationship between surface characteristics and reaction activation** under ambient-temperature and low-concentration hydrogen conditions.

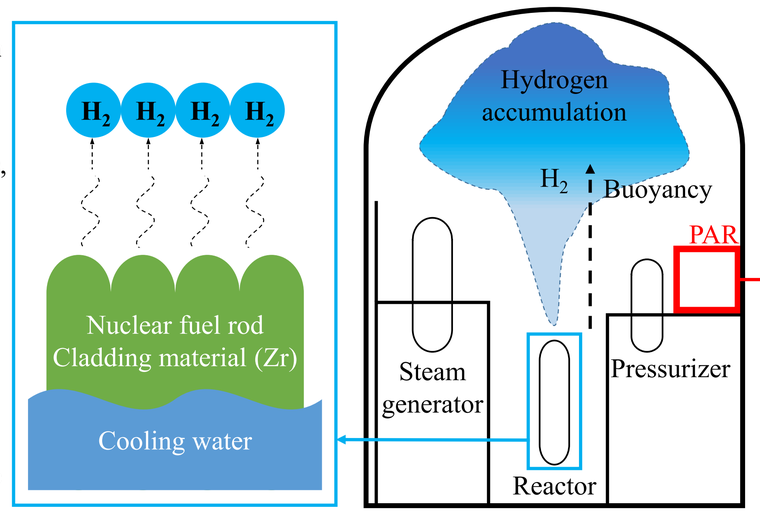

Hydrogen production process

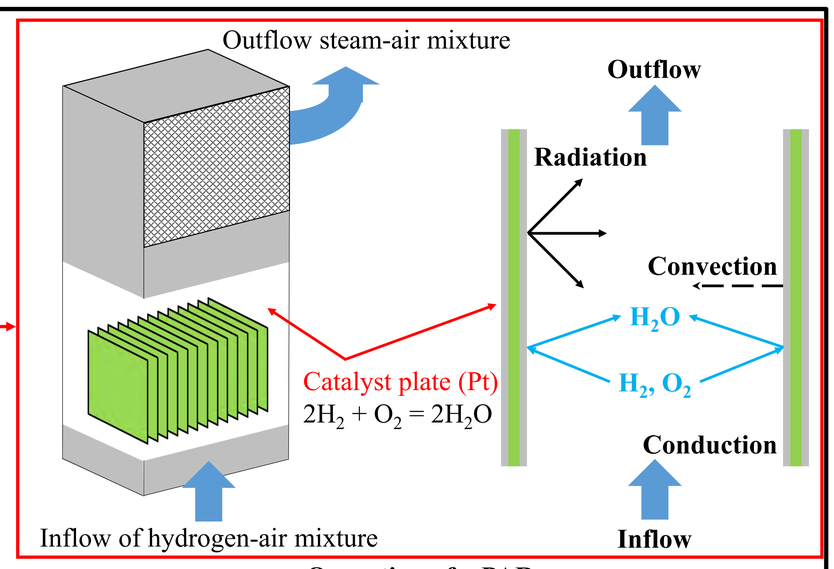

Operation of a PAR

2. EXPERIMENTAL METHOD

● **Lab-scale PAR catalytic activation experiment**

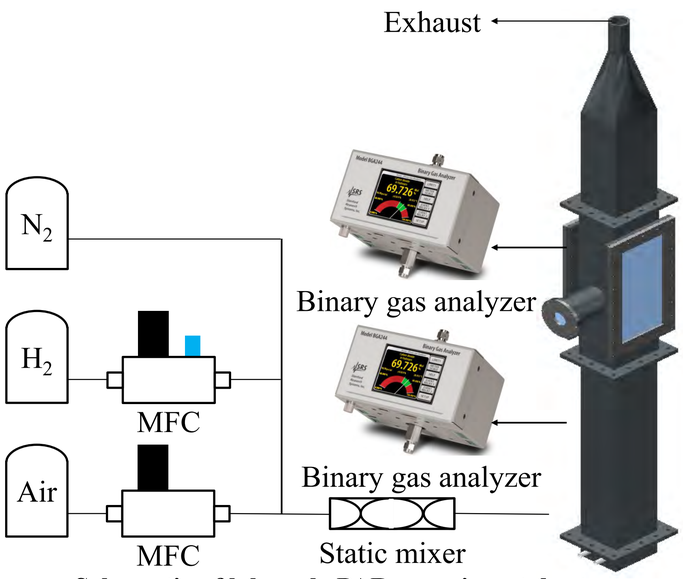

Schematic of lab-scale PAR experimental setup

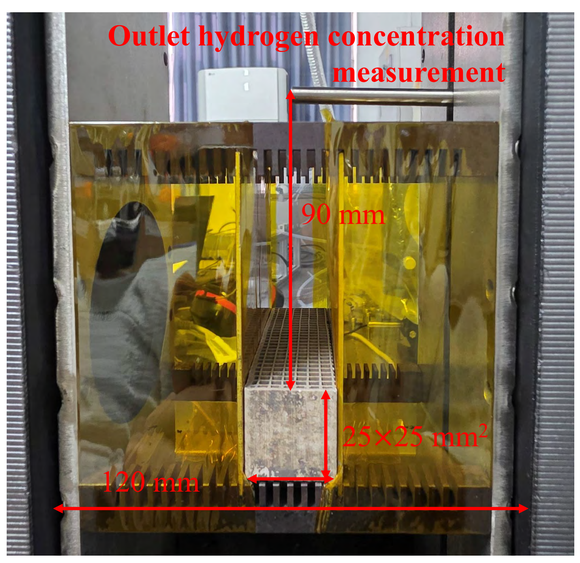

Installation of Lattice type catalyst

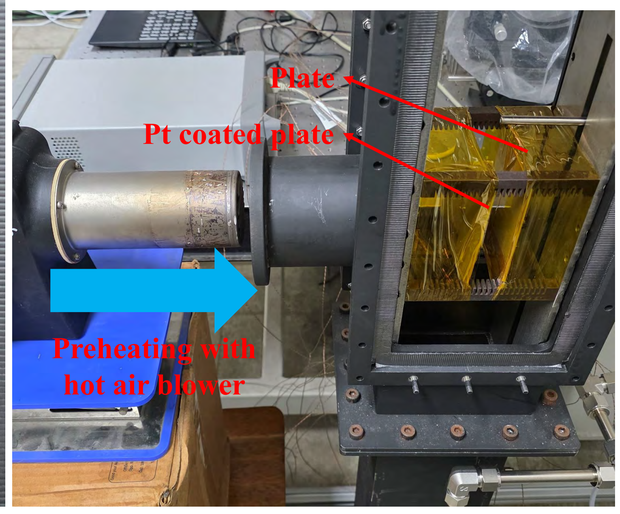

Plate catalyst preheating

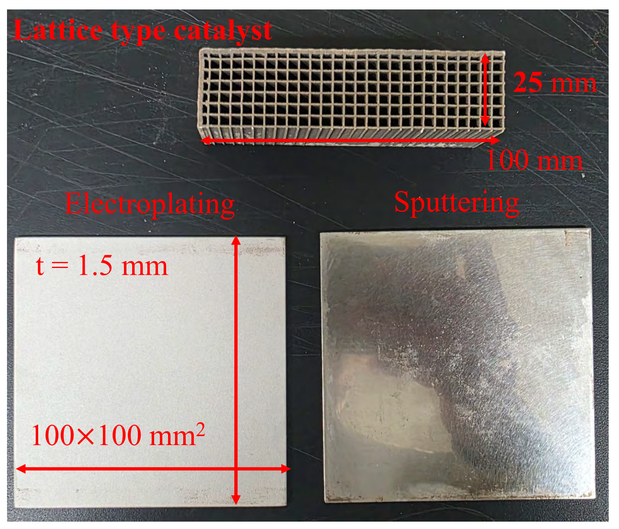

Test catalysts for reaction activation

► **Experimental Method**

- Hydrogen-air mixtures were supplied at hydrogen concentrations of **1~6 vol.%** and inlet velocities of **0.2~0.8 m/s** using MFCs.
- For the **lattice -type catalyst**, the hydrogen removal rate was evaluated by measuring the hydrogen concentrations at the catalyst inlet and outlet.
- For the plate type catalyst, the plates were preheated to **250~300°C** using a hot-air blower, followed by the injection of the hydrogen-air mixture.
- **Catalyst activation** was evaluated by measuring the increase in **plate surface temperature** caused by the **exothermal reaction between hydrogen and oxygen**.

► **Catalyst Specifications**

- Lattice Type Catalyst
  : KE-7580 from Heesung Catalysts Corp.
  : Hydraulic diameter of one cell: 3.04 mm, wall thickness: 0.7 mm
- Electroplated Catalyst : Pt electroplated on a titanium plate with a thickness of 0.5 μm
- Sputtered Catalyst : Ti and Pt deposited on an AISI 304 (EN 1.4301) plate with thicknesses of 20 nm and 100 nm, respectively.

3. RESULTS AND CONCLUSIONS

● Evaluation of catalyst activation according to the preheating temperature of plate type catalysts and the hydrogen removal rate of the lattice type catalyst according to inlet velocity and hydrogen concentration without preheating

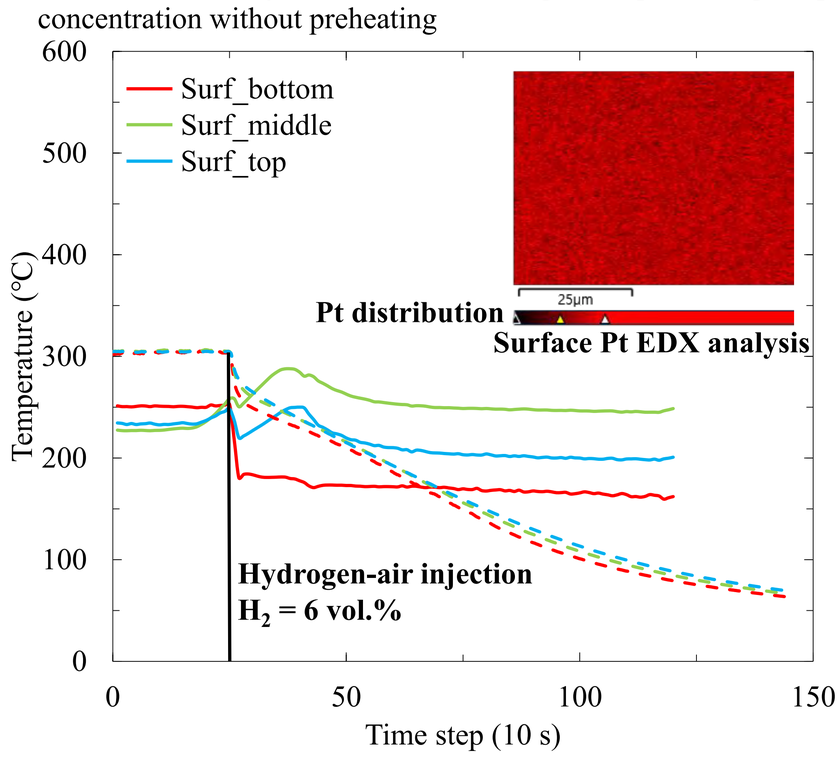

Surface temperature at the center of the plate when the hydrogen concentration is 6 vol.% after preheating the sputtering plate to 250, 300°C

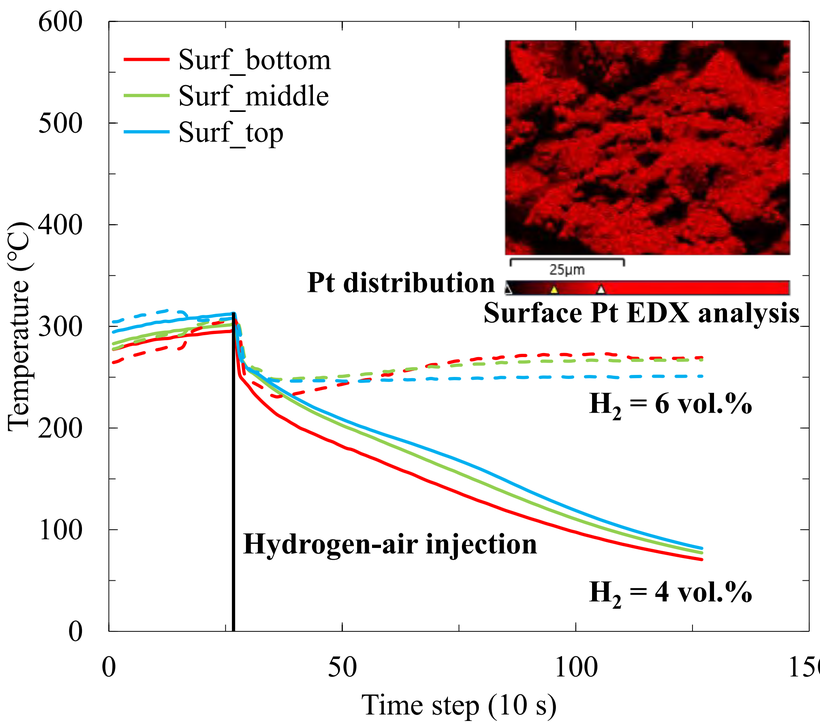

Surface temperature at the center of the plate when the hydrogen concentration is 4, 6 vol.% after preheating the electroplated plate to over 300°C

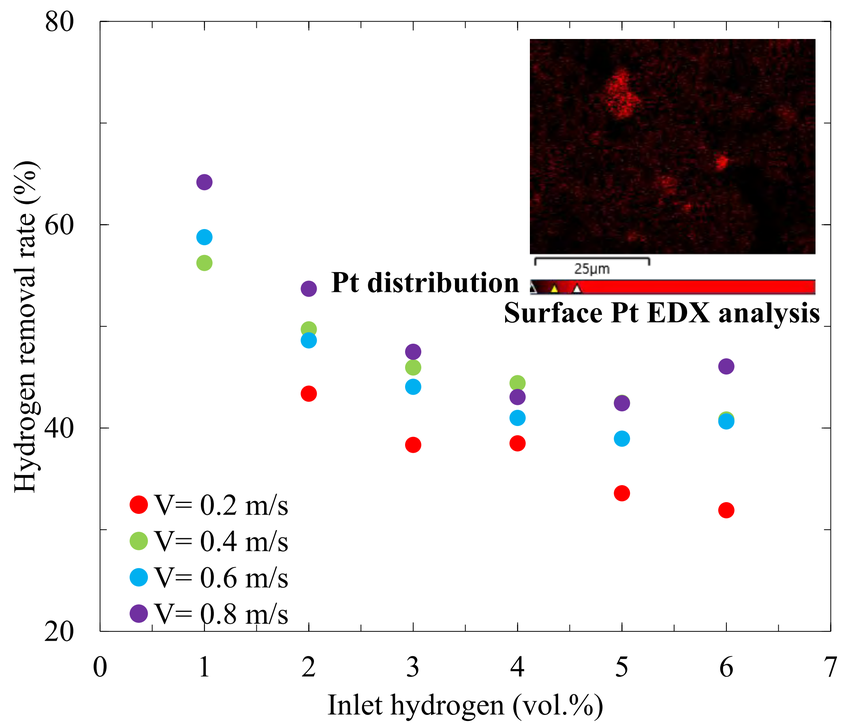

Hydrogen removal rate according to inlet velocitye and hydrogen concentration without preheating of honeycomb catalyst

- The **sputtered and electroplated Pt-coated plate** type catalysts were **not activated** under ambient-temperature and low-concentration hydrogen conditions, but **catalytic activation occurred and the surface temperature increased** when the catalysts were **preheated to 250~300°C** and supplied with hydrogen-air mixtures containing **6 vol.% hydrogen**
- The **lattice type catalyst** had Pt particles distributed on its porous surface, and **catalytic reaction activation occurred under ambient-temperature and low-concentration hydrogen conditions**, with the **hydrogen removal rate decreasing as the hydrogen concentration increased or the inlet velocity decreased**
- The **sputtered** catalyst plate had a **Pt thin-film structure** with few pores, and the **electroplated** catalyst plate had an **aggregated Pt structure**, resulting in a **limited active Pt surface area compared with the lattice type catalyst**
- Therefore, **porous gas diffusion pathways** and **a large active Pt surface area** are considered important for **activating Pt-catalyzed reactions** under ambient-temperature and low-concentration hydrogen conditions

Study of prototypical corium at solid state containing fission products: crystallographic and microstructural analysis, impact on weathering and leaching mechanisms

Mourier Timothé (1), Menut Denis (2), Domenger Renaud (1), Brackx Emmanuelle (1), Caprani Rafael (1), Jegou Christophe (3), Delacroix Jules (4), Piluso Pascal (4), Guinebretière René (5)

(1) CEA, DES, ISEC, DMRC, SASP, LMAT, (2) Synchrotron SOLEIL, Ligne MARS, (3) CEA, DES, ISEC, DPME, SEME, LMPA, (4) CEA, DES, IRESNE, DTN, SMTA, LEAG, (5) Université de Limoges, IRCER, UMR CNRS 7315

Type of abstract: Poster
Subject area: Ex-vessel corium interactions and coolability
Keywords: - prototypical corium - corium crystallographic structure - microstructure - fission products

In a water-cooled nuclear reactor, a loss of cooling systems can lead to core meltdown. This magma, formed at very high temperatures (T>2000K), is called corium and can pierce the reactor vessel to interact with the containment. Molten Core-Concrete Interaction (MCCI) occurred in three reactors at Fukushima-Daiichi in 2011 and in Chernobyl in 1986.

Tackling safety issues is crucial for nuclear energy. In this context, analysing the microstructure of coriums provides a better understanding of the environment in which this kind of specific material is formed to implement accident prevention and mitigation strategies. The dismantling of the Fukushima-Daiichi site raises scientific issues related to corium solid state knowledge. First, dismantling the damaged core is a long-term task, allowing time for the material to interact with environment through leaching process. Studying the final microstructural state of the corium provides informations on the material's ability to keep some non-volatile fission products. Secondly, the need to develop safe decommissioning strategies requires a prior knowledge of the main characteristics of the material.

For studying the mechanisms of formation and alteration of corium formed through MCCI, prototypical coriums are synthesised on the PLINIUS platform (CEA Cadarache). The synthesis used to simulate corium obtained by MCCI involves, beside oxygen, around twenty elements, the main ones being aluminium, silicon, calcium, chromium, iron, zirconium and uranium, and the minor ones being non-volatile fission products surrogates. The synthesis consists in melting at high temperature a mix of oxide powders. The crucible is then cut into slices to be analysed by energy-dispersive x-ray spectroscopy, electron backscatter diffraction and high-resolution x-ray diffraction. A quantitative analyse was performed on the x-ray diffraction diagrams with the Rietveld method implemented on the MAUD software.

These analyses show a complex material with $U_xZr_{1-x}O_2$ solid solutions, $Fe_{1-x}Cr_{2+x}O_4$ solid solutions and silicate phases.

12th CONFERENCE ON
SEVERE ACCIDENTS RESEARCH
May 18-22, 2026 - Madrid, Spain
ERMSAR 2026

Study of prototypical corium at solid state containing fission products: crystallographic and microstructural analysis, impact on weathering and leaching mechanisms

T. Mourier[1,2], D. Menut[3], R. Domenger[2], E. Brackx[2], R. Caprani[2], C. Jegou[4], J. Delacroix[5], P. Piluso[5], R. Guinebretière[1]

[1] Université de Limoges, IRCER, UMR CNRS 7315, 12 Rue Atlantis, 87068, Limoges, France
[2] CEA, DES, ISEC, DMRC, Université de Montpellier, 30200, Marcoule, France
[3] Synchrotron SOLEIL, Ligne MARS, route départementale 128, 91190, Saint-Aubin, France
[4] CEA, DES, ISEC, DPME, Université de Montpellier, 30200, Marcoule, France
[5] CEA, DES, IRESNE, DTN, SMTA, LEAG, 13108, Cadarache, France

Context

- Corium is a liquid magma formed at hight temperature by the melting of a nuclear reactor core [1].
- Corium's composition depend on the reactor conception (type of fuel, type of concrete…) and the accident scenario (temperature, pressure, atmosphere…) [2] [3].

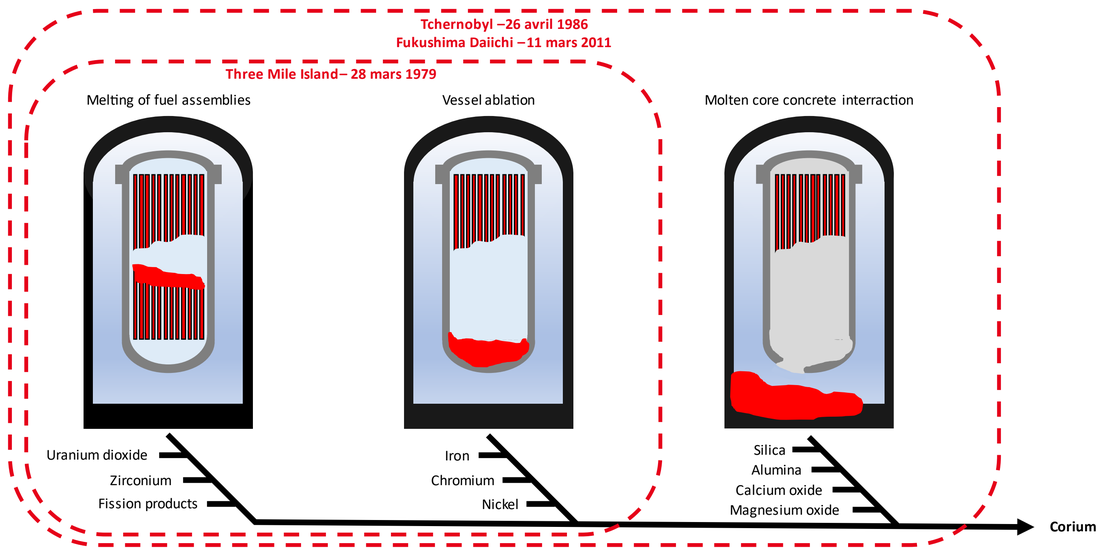

Schematic corium enrichment through nuclear incident

Theoretical composition of the prototypical corium

- The prototypical corium is made by melting at hight temperature a mix of powders representing the elements involved in the accident and their quantity

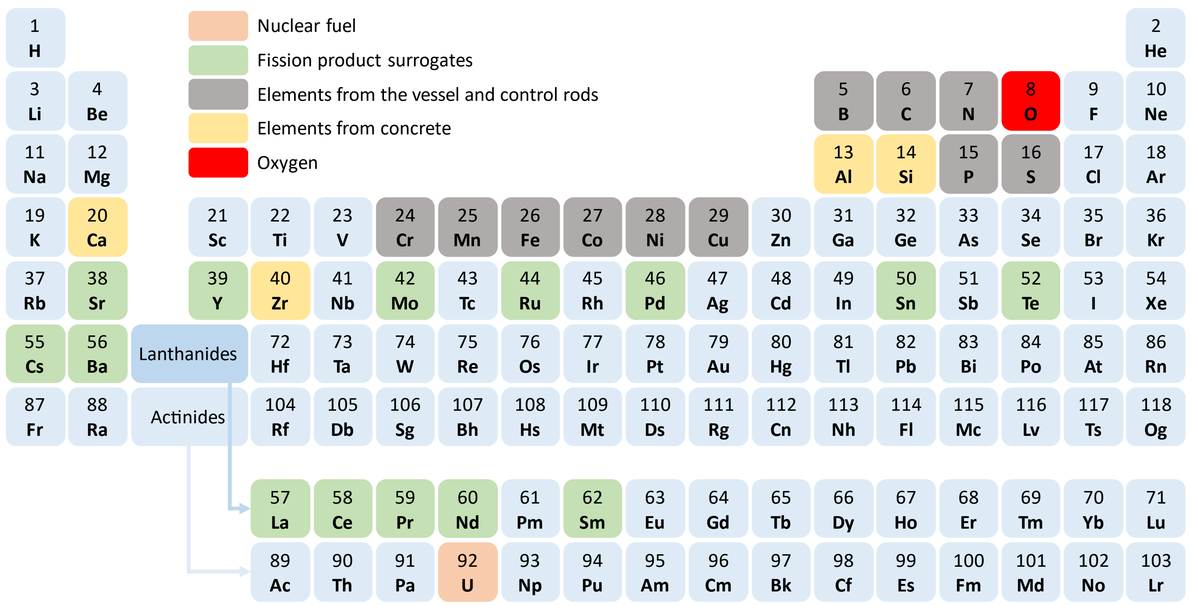

Example of the composition of a MCCI prototypical corium illustrated on the Mendeleyev Table (adapted from [4])

Structural and chemical heterogeneity

List of phases identified in a prototypical corium using a combination of EDS and EBSD analyses

Name	Chemical formula	Space group
U-Zr-O solid solution	$U_{1-x}Zr_xO_{2\pm y}$	$Fm\bar{3}m$
Zirconia	ZrO_2	$P2_1/c$
Chromium-aluminium solid solution	$FeCr_{2-y}Al_yO_4$	$Fd\bar{3}m$
Zircon	$ZrSiO_4$	$I4_1/amd$
Anorthite	$CaSi_2Al_2O_8$	$P\bar{1}$
Hedenbergite	$CaFeSi_2O_6$	$C2/c$
Quartz	SiO_2	$P3_221$
Corundum	Al_2O_3	$R\bar{3}c$
Fayalite	Fe_2SiO_4	$Pbmn$
Jadeite	$CaAl_2Si_2O_6$	$C2/c$
Fer	$Fe_{(metal)}$	$Im\bar{3}m$

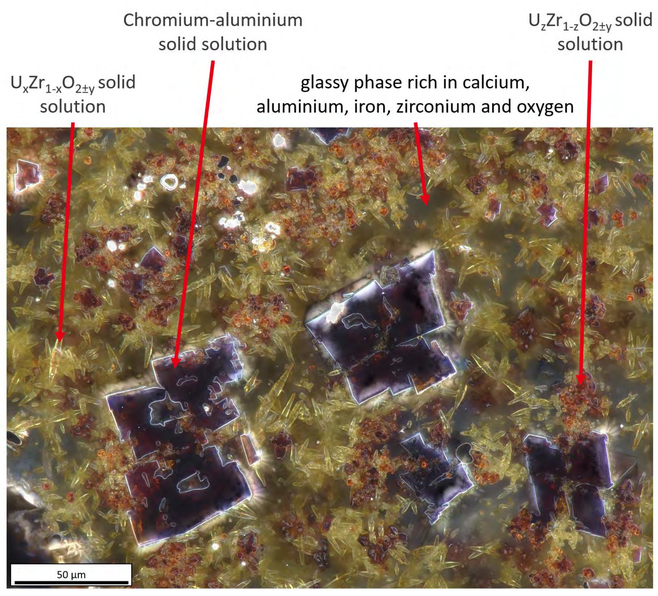

Optical micrograph of a prototypical corium

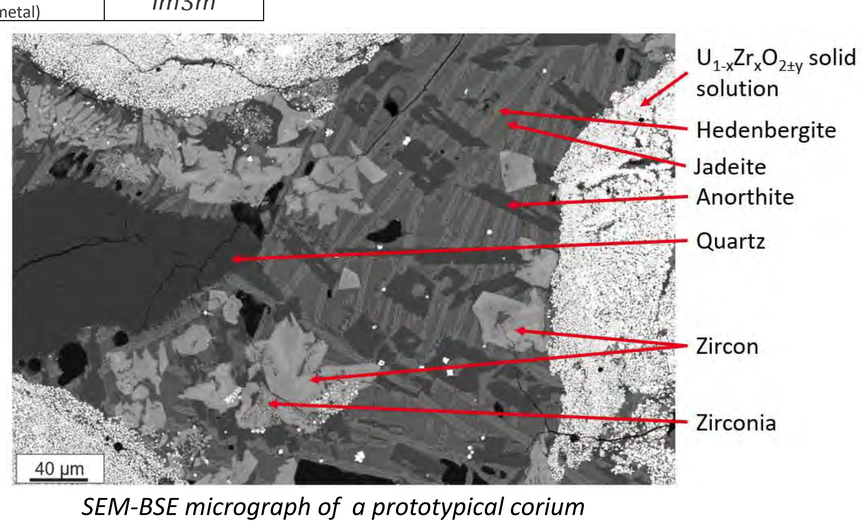

SEM-BSE micrograph of a prototypical corium

Solid solution : the $U_{1-x}Zr_xO_{2\pm y}$ case

- X-ray diffraction measurements are carried out at the CX2 station on the MARS beamline at the SOLEIL synchrotron, using:
  - an incident beam energy of 17 keV;
  - an incident beam size of 0.45 mm × 1 mm;
  - a flat and rotating sample.

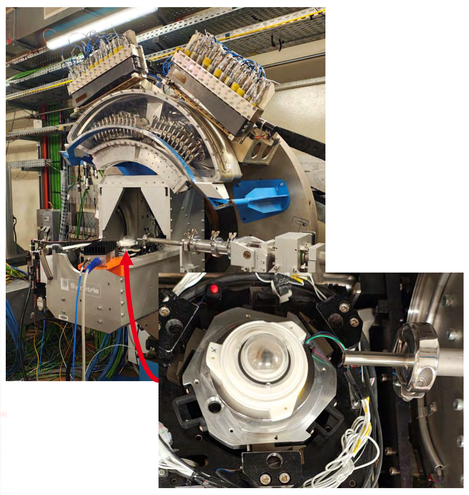

CX2 measurement station on MARS beamline, SOLEIL synchrotron [6]

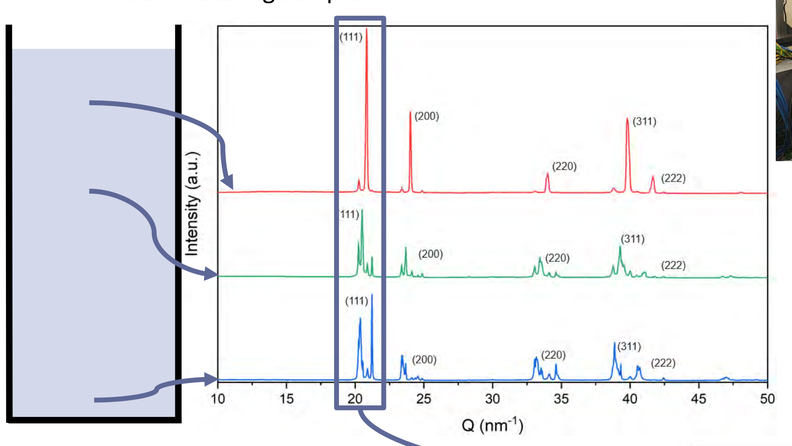

X-ray diffractograms of samples taken from three different heights within the synthesis crucible

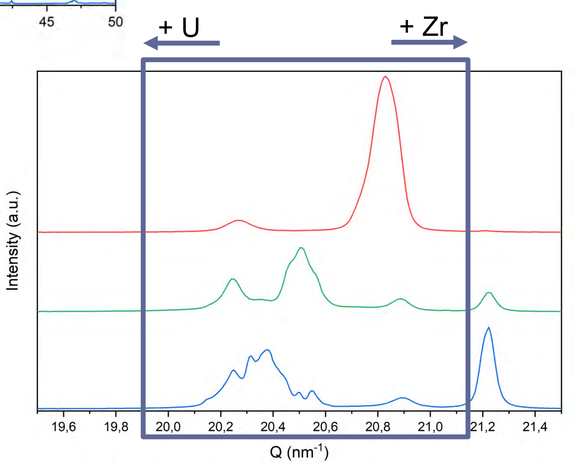

X-ray diffractograms of samples taken from three different heights within the synthesis crucible (plane family with Miller index (111) of the $U_xZr_{1-x}O_2$ solid solution)

- The elemental composition of the U-Zr-O solid solution varies with the height within the crucible used for the synthesis.
- **Assumption 1:** the O/M ratio is 2.00.
- The lattice parameter can be related to the zirconium content for the solid solution $U_xZr_{1-x}O_2$ by Végard's law [5]:

$$\mathbf{a = 5,468 - 0,3296\ x}$$

- **Assumption 2:** the crystals are micrometre-sized (verified by electron diffraction).
- Rietveld method: quantification of phases by refining a theoretical diffraction pattern (MAUD software) [6].
  - Using synchrotron radiation to achieve sufficient angular resolution
- Houska's method [2]: discretisation of the broadened peaks into a series of N elementary peaks, the parameters of which are obtained from a LaB6 standard. This method allows the continuous variation in the compositions of the solid solution $U_xZr_{1-x}O_2$ to be simulated

$$\mathbf{N = \frac{full\ width\ of\ U_xZr_{1-x}O_2\ peak}{mid-height\ width\ of\ LaB_6\ peak}}$$

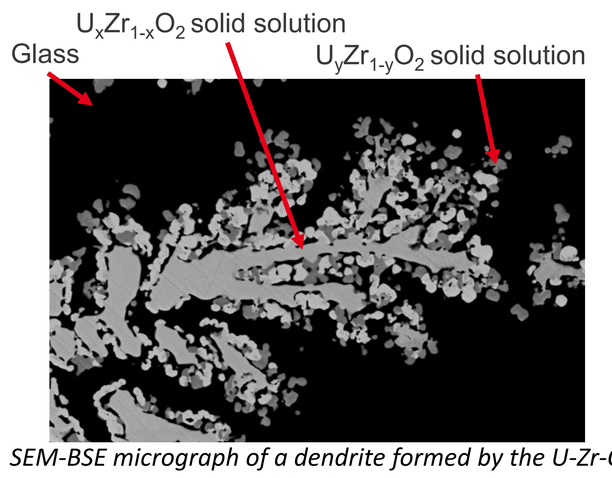

SEM-BSE micrograph of a prototypical corium solid solution

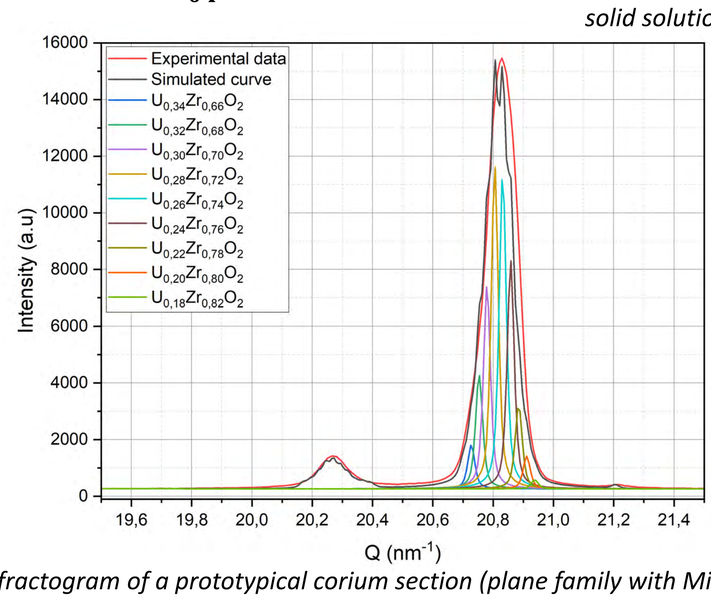

X-ray diffractogram of a prototypical corium section (plane family with Miller index (111) of the $U_xZr_{1-x}O_2$ solid solution) and distribution of 9 elemental compositions

Conclusion and outlook

- A combined analysis using SEM-EDS, EBSD and high-resolution X-ray diffraction allows to identify the microstructures of corium
- The addition of other methods, such as X-ray fluorescence spectroscopy (micro-XRF) and X-ray microdiffraction, should enable the localisation of fission products within the material
  - MARS beamline , NANOSCOPIUM beamline, (SOLEIL synchrotron facility)
- The collected data will be used to link the microstructure of the corium, the location of the fission product and the leaching behaviour.

Références

[1] M. Sanchez-Brusset, « Mécanismes d'oxydation de l'acier liquide lors de l'interaction Corium-béton à haute température en cas d'accident grave de réacteur nucléaire ». Thèse, Université de Perpignan; Via Domitia, 2015.
[2] M. Jizzini, « Etudes des phases métastables et stables de corium issues de trempe par approche multi échelle, étude d'un chemin réactionnel». Thèse, Université de Limoges, 2022.
[3] M. Jizzini, E. Brackx, P. Piluso, D. Menut, R. Guinebretiere, « Cationic local composition fluctuations in rapidely cooled nuclear fuel melts », Nuclear Materials Energy 31 (2022) 101183.
[4] C. Journeau, D. Molina, E. Brackx, R. Berlemont, Y. Tsubota, « Experiences from the cutting of metallic blocks from simulant Fukushima Daiichi fuel debris », Journal of Nuclear Science and Technology 61 (2024).
[5] P. Piluso, G. Trillon, C. Journeau, « The UO_2-ZrO_2 system at high temperature (T>2000K): importance of the meta-stable phases under severe accident conditions », Journal of Nuclear Materials, 344 (2005) 259-264.
[6] L. Lutterotti, « Total pattern fitting for the combined size-strain-stress-texture determination in thin film diffraction», Nuclear Instrumentation Methods Phys. Res. B 268 (2010) 334–340.

Acknowledgements: The VF-U3 sample fabrication has been carried out within the scope of contributions to the Japanese governmental subsidy program "Project of Decommissioning and Contaminated Water Management (Development of Analysis and Estimation Technology for Characterization of Fuel Debris)" funded at the Japan Atomic Energy Agency (JAEA) by the Japanese Ministry of Economy, Trade and Industry (METI) and organized by the International Research Institute for Nuclear Decommissioning (IRID).

COMPUTATIONAL THERMODYNAMIC STUDY OF THE EFFECT OF REACTED SACRIFICIAL MATERIAL AMOUNT ON EX-VESSEL MOLTEN CORIUM DENSITY IN A VVER-1000 REACTOR CORE CATCHER

Yuxuan Du, Andrei Komlev, Sevostian Bechta
Royal Institute of Technology (KTH)
Roslagstullsbacken 21, 10691 Stockholm, Sweden
yuxuand@kth.se; komlev@kth.se; bechta@safety.sci.kth.se

ABSTRACT

In a postulated severe accident (SA) in a nuclear power plant, one of the applied SA management strategies is core melt retention in ex-vessel core catcher (CC). For VVER-1000 and VVER-1200 reactors, this strategy is implemented by installing a crucible-type CC beneath the reactor vessel to accommodate the relocated corium. Sacrificial materials (SM), consisting of sacrificial steel and oxidic components, are incorporated into the CC to regulate the melt composition and thermophysical properties in a manner that promotes melt coolability and retention within the CC, suppresses fission product release, reduces hydrogen generation, and prevents corium re-criticality. One of the functional requirements for the SM is to lower the oxidic melt density below that of the metallic melt, thereby promoting the inversion of the oxidic and metallic layers and the formation of a molten corium pool with an oxidic top layer. The focusing effect of top metal layer is prevented in this configuration, and the risk of steam explosion or energetic interaction during top flooding of the molten pool is reduced compared to the state before layer inversion. In this study, a computational thermodynamic approach based on the NUCLEA-20 database is employed to investigate the influence of the reacted SM fractions on the compositions of oxidic and metallic layers in the stratified corium pool within the CC. The densities of the immiscible oxidic and metallic melts are evaluated to estimate conditions of layer inversion. Furthermore, the variations in phase composition underlying the layer inversion phenomenon are analysed from a thermodynamic perspective.

KEYWORDS
Severe accident, Ex-vessel melt retention, Sacrificial material, Thermodynamics

1. INTRODUCTION

The VVER-1000 design employs a crucible-type CC installed beneath the RPV to implement the EVR strategy. The CC is partially filled with sacrificial material (SM), which interacts with the relocated corium, promoting its cooling and stabilization [1,2]. Specifically, SM is employed to promote the inversion between the oxidic and metallic layers in the molten corium. This layer inversion is critical for the successful implementation of the EVR strategy, as it eliminates the focusing effect that locally increases heat flux to the cooling water at the surface of the molten metallic layer, mitigating steam explosions and reducing hydrogen generation during corium top flooding [3]. The present study employs a computational thermodynamics approach to investigate how varying fractions of reacted SM influences melt properties and molten pool behavior during ex-vessel melt stabilization, with particular emphasis on the possible inversion between the two immiscible oxidic and metallic layers.

2. METHODOLOGY

Thermodynamic modeling to obtain phase composition at equilibrium state is performed using the NUCLEA-20 thermodynamic database, which is specially developed for thermodynamic assessment of corium compositions in LWR SAs [4], in combination with the Thermo-Calc software [5], which employs Gibbs energy minimization. The calculation procedure and the computational tools employed in this study are illustrated in Fig. 1. To estimate the phase density, the model for ideal mixture of molar volumes was adopted [6].

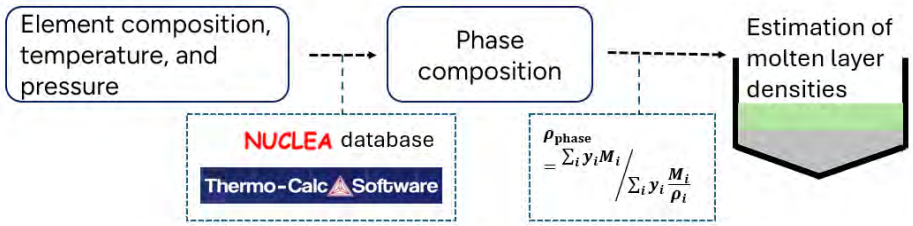

Figure 1. Calculation process and computational tools.

3. CASE STUDY

The input data for thermodynamic analysis consisting of masses and compositions of SM and relocated corium for specific VVER-1000 SA scenario was taken from Khabensky et al. [7]. Initial system for thermodynamic modeling includes 90 tons of SM and 117 tons of relocated corium (first and second release of corium from reference scenario [7]) with detailed composition presented in Table I.

Table I. Masses of SM and relocated corium components used in thermodynamic modeling

Material	Mass (t)	Composition
SM	27.6	Fe_2O_3
	11.6	Al_2O_3
	0.8	SiO_2
	50	Steel (71 wt.% Fe, 19 wt.% Cr, 10 wt.% Ni)
Relocated corium	33.5	UO_2
	4.5	ZrO_2
	9.5	Zr
	69.5	Steel (71 wt.% Fe, 19 wt.% Cr, 10 wt.% Ni)

To apply the thermal equilibrium condition, the temperature used for thermodynamic modelling of the molten pool in the core catcher was assumed to be the liquidus temperature of the corium, with a fraction of SM reacting with the corium and dissolving into both the oxidic and metallic melts, despite the significant temperature difference between metallic and oxidic liquids in reference data [7].

4. MODELLING RESULTS

The thermodynamic modeling results show that the immiscible oxidic and metallic liquid phases coexist in the corium prior to interaction with the SM, as illustrated in Fig. 2. The predicted presence of these two immiscible liquid phases is in good agreement with the modeling results reported by Khabensky et al. [7].

The density variation of the two distinct liquid phases with increasing SM participation is illustrated in Fig. 3. Under the SA scenario and assuming the system temperature equals to the liquidus temperature, when 36 wt.% of SM has reacted with the relocated corium, the metallic melt density becomes lower than that of the oxidic melt. With a further increase in the reacted SM fraction, a layer inversion is therefore expected.

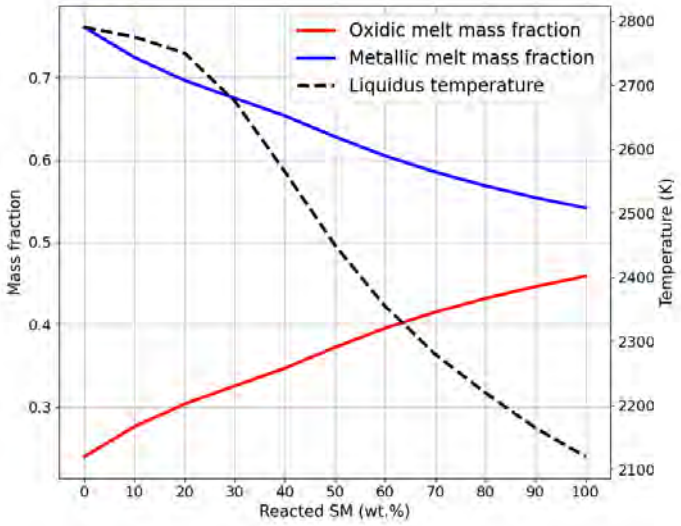

Figure 2. Mass fraction evolution of the two immiscible liquid phases and the system liquidus temperature with increasing fraction of reacted SM.

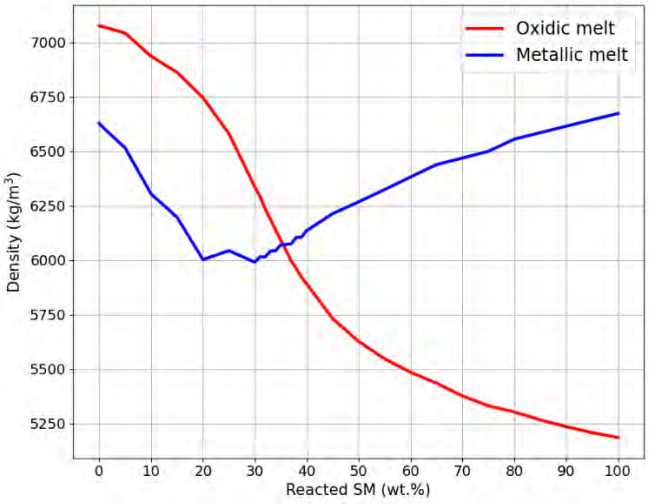

Figure 3. Density evolution of two immiscible liquid phases with increasing fraction of reacted SM.

As shown in Fig. 4(a), when approximately 20 wt.% of the SM has reacted, U and Zr become fully oxidized and no longer remain in the metallic melt, leading to a decrease in the metallic melt density. With further SM participation, the composition changes in the metallic melt occur mainly between Fe and Cr, whose densities are very similar. Therefore, the subsequent increase in density should be attributed to SM interaction with and dissolution in the metallic and oxidic melts, system oxidation, repartition of elements, and decrease in liquidus temperature of the system. As shown in Fig. 4(b), the mass fractions of the lighter oxides in oxidic melt, primarily Al_2O_3, increase, while those of the heavier oxides, primarily UO_2, decrease correspondingly.

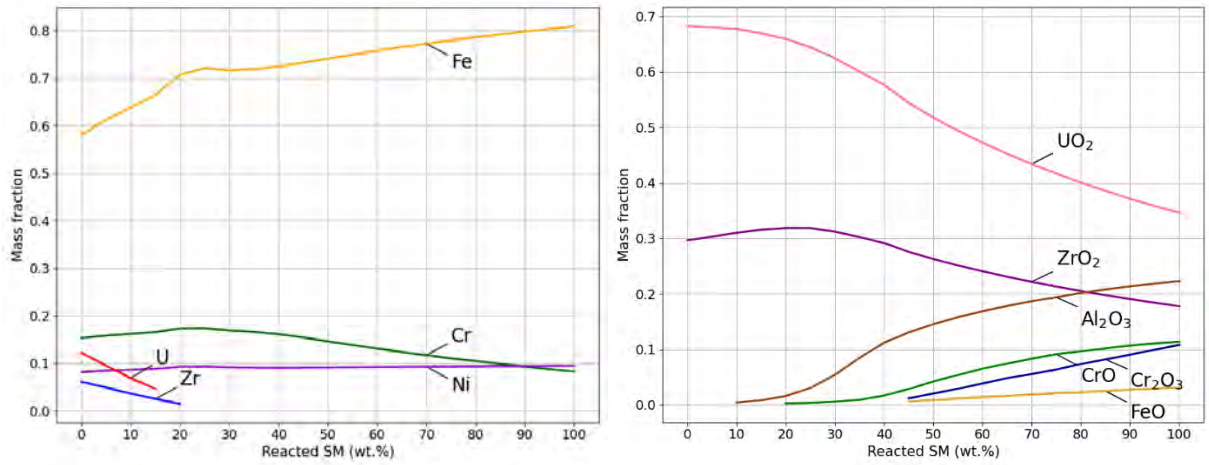

(a) (b)

Figure 4. Composition evolution of two immiscible liquid phases with increasing fraction of reacted SM: (a) Metallic liquid phase; (b) Oxidic liquid phase.

5. CONCLUSIONS

The main conclusions are as follows:

- With increasing SM fraction reacted and dissolved in the corium system, the liquidus temperature continuously decreases from 2790 K for the initial corium to almost 2100 K (Fig. 2).
- Inversion of originally top metallic and bottom oxidic layers happens after reaction and dissolution of approximately 36 wt.% of SM (Fig. 3).
- Due to the effective dissolution of low-density oxides, primarily Al_2O_3, in corium oxidic melt, its density continuously and effectively reduces from approximately 7100 to 5200 kg/m^3.
- Decrease of metal melt density before 20 wt.% of reacted SM can be explained by uranium oxidation and repartitioning into oxidic melt. Visible increase of metal melt density after 30 wt.% obviously follows its liquidus temperature decrease.

ACKNOWLEDGMENTS

This study was made possible by the supports of research projects from SSM (Swedish Radiation Safety Authority) and NEA (Nuclear Energy Agency).

REFERENCES

1. V.G. Asmolov, S.V. Bechta, V.M. Berkovich, V.V. Bezlepkin, V.S. Granovsky, V.V. Gusarov, V.B. Khabensky, A.E. Kisselev, I.V. Kukhtevich b, A.S. Sidorov g, V.F. Strizhov f, S.V. Svetlov, and V.N. Zagryazkin, "Crucible-type core catcher for VVER-1000 reactor," *Proceedings of ICAPP'05*, Seoul, 15–19 May 2005, Vol. 2, pp. 1221–1227 (2005).
2. A.A. Sulatsky, S.V. Bechta, V.S. Granovsky, V.B. Khabensky, E.V. Krushinov, S.A. Vitol, V.V. Gusarov, V.I. Almjashev, and P.V. Bezlepkin, "Molten corium interaction with oxidic sacrificial material of WER core catcher," *Proceedings of ICAPP'05*, Seoul, 15–19 May 2005, Vol. 2, pp. 1238–1246 (2005).
3. V. G. Asmolov, A. A. Sulatskii, S. V. Beshta, V. S. Granovskii, V. B. Khabenskii, E. V. Krushinov, S. A. Vitol, V. I. Al'myashev, V. V. Gusarov, and V. F. Strizhov, "The interaction of nuclear reactor core melt with oxide sacrificial material of localization device for a nuclear power plant with water-moderated water-cooled power reactor," *High Temp*, **45**, pp. 22–31 (2007).

4. S. Bakardjieva, M. Barrachin, S. Bechta, D. Bottomley, L. Brissoneau, B. Cheynet, E. Fischer, C. Journeau, M. Kiselova, L. Mezentseva, P. Piluso, T. Wiss, "Improvement of the European thermodynamic database NUCLEA," *Progress in Nuclear Energy*, **52**, pp. 84–96(2010).
5. J.O. Andersson, T. Helander, L. Höglund, P.F. Shi, and B. Sundman, "Thermo-Calc and DICTRA, Computational tools for materials science," *Calphad*, **26**, pp. 273–312 (2002).
6. X. Chen, L. Zhang, N. Li, and Y. Yuan, "A thermodynamic study of molten pool stratification morphology," *Proceedings of ERMSAR 2024*, Stockholm,May 13-16 2024.
7. A. Khabensky,V. S. Granovsky, S. Bechta, and V. V. Gusarov, "Severe accident management concept of the VVER-1000 and the justification of corium retention in a crucible-type core catcher," *Nuclear Engineering and Technology*, 41(5), pp. 561–574 (2009).

12th CONFERENCE ON
SEVERE ACCIDENTS RESEARCH
May 18-22, 2026 - Madrid, Spain
ERMSAR 2026

COMPUTATIONAL THERMODYNAMIC STUDY OF THE EFFECT OF REACTED SACRIFICIAL MATERIAL AMOUNT ON EX-VESSEL MOLTEN CORIUM DENSITY IN A VVER-1000 REACTOR CORE CATCHER

Yuxuan Du, Andrei Komlev and Sevostian Bechta
Royal Institute of Technology (KTH)
Roslagstullsbacken 21, 10691 Stockholm, Sweden

INTRODUCTION

The VVER-1000 design employs a crucible-type core catcher (CC) installed beneath the RPV to implement the ex-vessel retention (EVR) strategy for severe accident (SA) management. The CC is partially filled with sacrificial material (SM), which interacts with the relocated corium, promoting its cooling and stabilization [1,2].

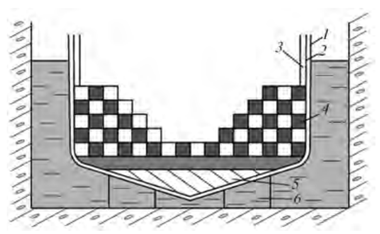

1. shell, 2. bin,
3. thermal protection shield,
4. SM, 5. concrete, 6.support.

Fig.1. The scheme of CC for VVER-1000 reactor [8].

Specifically, SM is employed to promote the **inversion between the immiscible oxidic and metallic layers in the molten corium.**

This layer inversion is critical for the successful implementation of the EVR strategy as it [3]:
- o eliminate the focusing effect that locally increases heat flux at the surface of the molten metallic layer,
- o mitigate steam explosions and reduce hydrogen generation during corium top water flooding.

The present study employs a computational thermodynamics approach to investigate how varying fractions of reacted SM influence melt properties and molten pool behavior during ex-vessel melt stabilization, with particular emphasis on the melt densities and the layer inversion.

METHODOLOGY

Thermodynamic modeling to obtain phase composition at equilibrium state is performed.

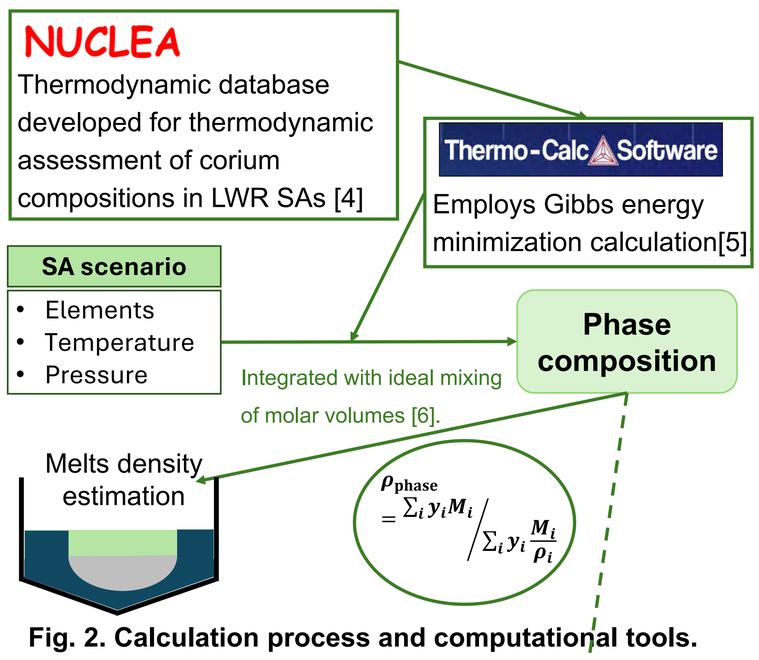

Fig. 2. Calculation process and computational tools.

By integrating additional physical properties into corium systems under diverse SA scenarios, this methodology has the potential to investigate a wide range of phenomena.

CASE STUDY

Table I. The initial system composition

	Mass	Composition
Sacrificial material	27.6 t	Fe_2O_3
	11.6 t	Al_2O_3
	0.8 t	SiO_2
	50 t	Carbon steel (Fe: 99.5 wt.%, C: 0.2 wt.%, Si: 0.3 wt.%)
Relocated corium	Oxidic melt: 28.1 t	UO_2: 68.3 wt.%, ZrO_2: 29.6 wt.%, Zr: 0.8 wt.%, U: 0.9 wt.%, Cr: 0.4 wt.%.
	Metallic melt: 88.9 t	Fe: 57.3 wt.%, Cr: 15.1 wt.%, U: 12 wt.%, Ni: 8.1 wt.%, Zr: 6.0 wt.%, ZrO_2: 1.5 wt.%.

The input data for thermodynamic analysis reflecting masses and compositions of SM and relocated corium for specific VVER-1000 SA scenario are taken from Khabensky et al. [7].

To apply the thermal equilibrium condition, the temperature used for thermodynamic modelling of the molten pool in the core catcher was assumed to be the liquidus temperature of the corium composition containing a fraction of reacted SM and dissolved in the melt.

MODELLING RESULTS

The predicted presence of these **two immiscible liquid phases** is in good agreement with the modeling results reported by Khabensky et al. [7].

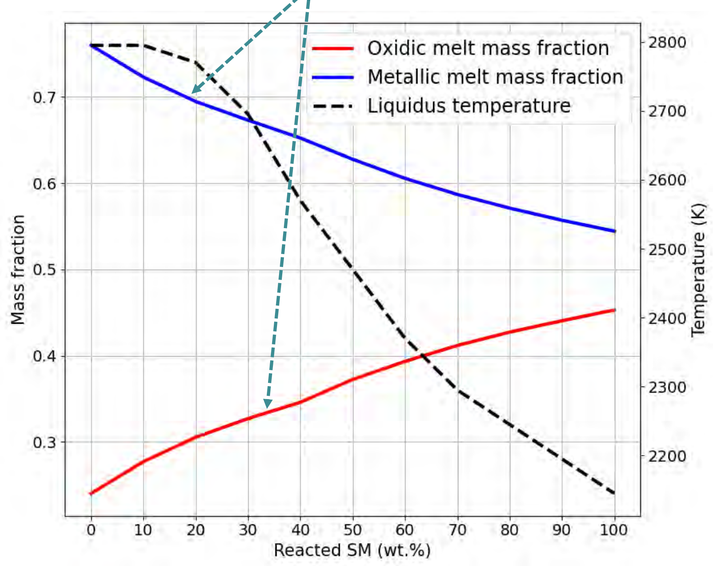

Fig. 3. Mass fractions of oxidic/metallic melts and system liquidus temperature vs. reacted SM fraction.

In the range of **30 wt.% to 40 wt.% of SM has reacted** with the relocated corium, the oxidic melt density becomes lower than that of the metallic melt.

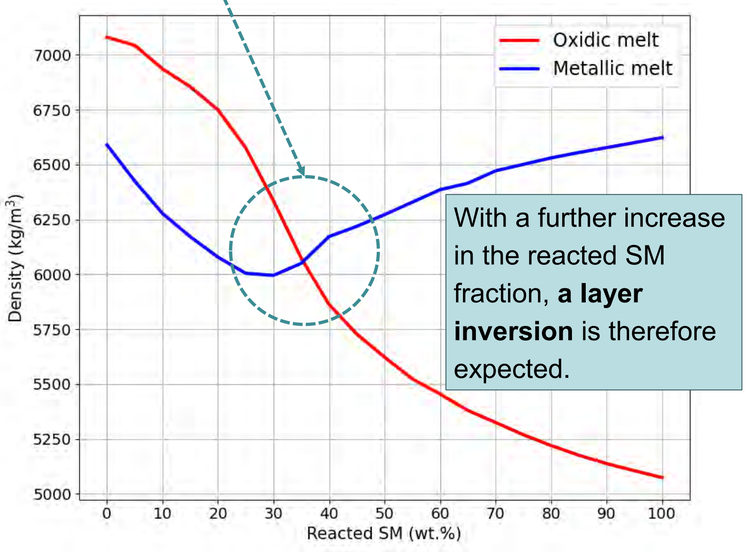

Fig. 4. Density evolution of oxidic/metallic melts vs. reacted SM fraction.

The mechanism of density variation is analyzed from the perspective of phase composition, as depicted in Fig. 5.

When approximately 20 wt.% of the SM has reacted, **U and Zr become fully oxidized** and no longer remain in the metallic melt, leading to a decrease in the metallic melt density.

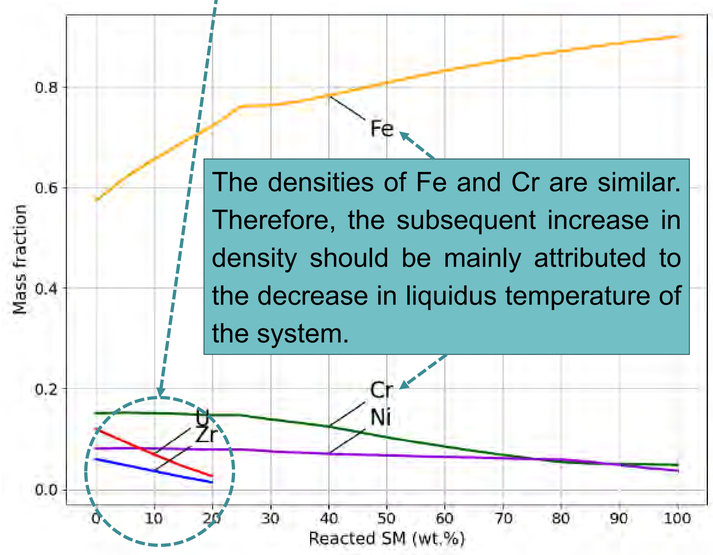

(a)

The mass fractions of the low-density oxides in oxidic melt, **primarily Al_2O_3, increase**, while those of the denser oxides, primarily UO_2, decrease correspondingly.

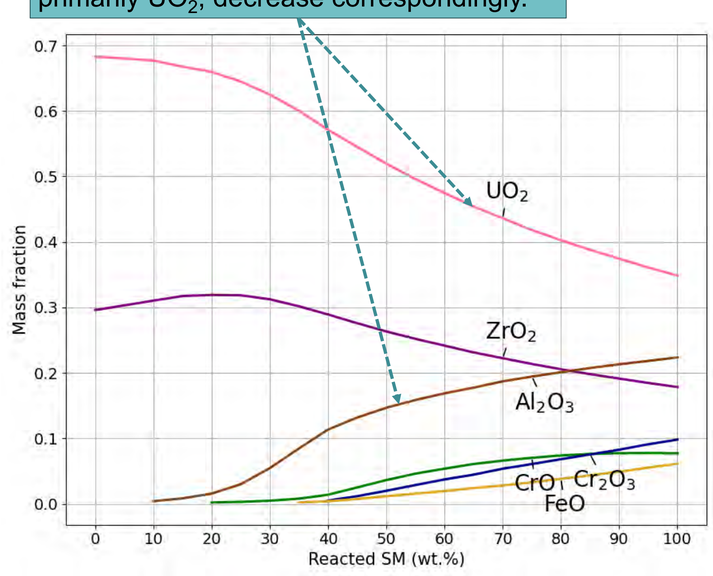

(b)

Fig. 5. Compositions of metallic (a) and oxidic melts (b) at different fractions of reacted SM.

CONCLUSIONS

The main conclusions are as follows:

- o With increasing SM fraction reacted and dissolved in the corium system, the liquidus temperature continuously and considerably decreases from 2795 K for the initial corium to almost 2145 K (Fig. 2).
- o Inversion of originally top metallic and bottom oxidic layers happens after reaction and dissolution of approximately 35 wt.% of SM (Fig. 3).
- o Due to the effective dissolution of low-density oxides, primarily Al_2O_3, in corium oxidic melt, its density continuously and effectively reduces from approximately 7100 to 5100 kg/m^3 (Fig. 3).
- o Decrease of metallic melt density before 20 wt.% of reacted SM can be explained by uranium oxidation and repartitioning into oxidic melt. Visible increase of metallic melt density after 30 wt.% obviously follows its liquidus temperature decrease (Fig. 4).

REFERENCES

[1] V.G. Asmolov, S.V. Bechta, V.M. Berkovich, V.V. Bezlepkin, V.S. Granovsky, V.V. Gusarov, V.B. Khabensky, A.E. Kisselev, I.V. Kukhtevich b, A.S. Sidorov g, V.F. Strizhov f, S.V. Svetlov, and V.N. Zagryazkin, "Crucible-type core catcher for VVER-1000 reactor," Proceedings of ICAPP'05, Seoul, 15–19 May 2005, Vol. 2, pp. 1221–1227 (2005).
[2] A.A. Sulatsky, S.V. Bechta, V.S. Granovsky, V.B. Khabensky, E.V. Krushinov, S.A. Vitol, V.V. Gusarov, V.I. Almjashev, and P.V. Bezlepkin, "Molten corium interaction with oxidic sacrificial material of WER core catcher," Proceedings of ICAPP'05, Seoul, 15–19 May 2005, Vol. 2, pp. 1238–1246 (2005).
[3] V. G. Asmolov, A. A. Sulatskii, S. V. Beshta, V. S. Granovskii, V. B. Khabenskii, E. V. Krushinov, S. A. Vitol, V. I. Al'myashev, V. V. Gusarov, and V. F. Strizhov, "The interaction of nuclear reactor core melt with oxide sacrificial material of localization device for a nuclear power plant with water-moderated water-cooled power reactor," High Temp, 45, pp. 22–31 (2007).
[4] S. Bakardjieva, M. Barrachin, S. Bechta, D. Bottomley, L. Brissoneau, B. Cheynet, E. Fischer, C. Journeau, M. Kiselova, L. Mezentseva, P. Piluso, T. Wiss, "Improvement of the European thermodynamic database NUCLEA," Progress in Nuclear Energy, 52, pp. 84–96(2010).
[5] J.O. Andersson, T. Helander, L. Höglund, P.F. Shi, and B. Sundman, "Thermo-Calc and DICTRA, Computational tools for materials science," Calphad, 26, pp. 273–312 (2002).
[6] X. Chen, L. Zhang, N. Li, and Y. Yuan, "A thermodynamic study of molten pool stratification morphology," Proceedings of ERMSAR 2024, Stockholm,May 13-16 2024.
[7] A. Khabensky,V. S. Granovsky, S. Bechta, and V. V. Gusarov, "Severe accident management concept of the VVER-1000 and the justification of corium retention in a crucible-type core catcher," Nuclear Engineering and Technology, 41(5), pp. 561–574 (2009).
[8] S. V. Beshta et al., "Formation of a nuclear reactor's molten core bath in a crucible-type corium catcher for a nuclear power station equipped with VVER reactors," Thermal engineering, vol. 58, no. 5, pp. 424–428, 2011.

ACKNOWLEDGMENTS

This study was made possible by the supports of research projects from SSM (Swedish Radiation Safety Authority) and NEA (Nuclear Energy Agency). The mobility action for presenting this work was partially supported by the ENEN2plus project (HORIZON-EURATOM-2021-NRT-01-13, Grant No. 101061677), funded by the European Union.

Contact
yuxuand@kth.se (Y. Du)

Evaluation of accident tolerant fuel using MELCOR2.2 on representative accident sequences in typical Japanese PWR

Sekine Masashi (1), Kaneko Junichi, Kikuchi Wataru, Kojo Retsu

(1) NRA

Type of abstract: Poster
Subject area: Other applications (fusion reactors, interim SNF storage, Accident Tolerant Fuels (ATFs), etc
Keywords: ATF, Severe accident, PWR, MELCOR2.2

Accident Tolerant Fuel (ATF) has been proposed as a safety enhancement for existing nuclear reactors. ATF is expected to mitigate metal-water reactions, reduce hydrogen generation during accidents, and extend the time available for accident management before core degradation occurs. However, its influence on the progression of severe accidents has not been sufficiently investigated.

This study evaluates the effects of different cladding materials, including Zircaloy, Cr-coated Zircaloy, FeCrAl, and SiC, on cladding temperature, hydrogen generation, and the timing of lower reactor vessel head failure during representative accident sequences such as Station Blackout and Loss of Coolant Accident in a typical Japanese Pressurized Water Reactor, using MELCOR 2.2. The analysis shows that when cladding temperature remains below 1200°C, which is the criterion for a design basis accident, both cladding temperature and hydrogen generation follow the oxidation reaction rate equation. As temperature increases and the accident progresses, however, hydrogen generation from ATF cladding can become comparable to or even exceed that from Zircaloy cladding, depending on the ATF type and accident sequence. These results suggest that during severe accident progression, hydrogen generation is influenced by factors such as accident sequence and cladding melting point than oxidation kinetics alone. The study showed that differences in cladding materials affect the timing of molten core release following reactor vessel failure.

12th CONFERENCE ON
SEVERE ACCIDENTS RESEARCH
May 18-22, 2026 - Madrid, Spain
ERMSAR 2026

Evaluation of Accident Tolerant Fuel using MELCOR2.2 on Representative Accident Sequences in Typical Japanese PWR

NRA, **Masashi SEKINE**, Junichi KANEKO, Wataru KIKUCHI, Retsu KOJO

1. Background & Objective

Background

- Accident Tolerant Fuel (ATF) has been proposed as a safety enhancement for existing nuclear reactors. ATF is expected to mitigate metal-water reactions, reduce hydrogen generation during accidents, and extend the time available for accident management before core degradation occurs.
- However, its influence on the progression of severe accidents has not been sufficiently investigated.

Objective

- ✓ This study investigates the impact of ATF cladding materials on cladding temperature, hydrogen generation, and reactor vessel lower head failure timing in Japanese PWR accident sequences using MELCOR 2.2.

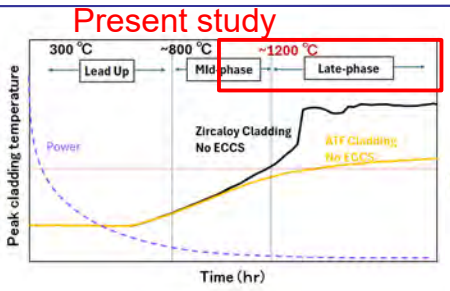

Fig. 1 Overview of cladding temperature progression under coolant-limited conditions in an LWR core.

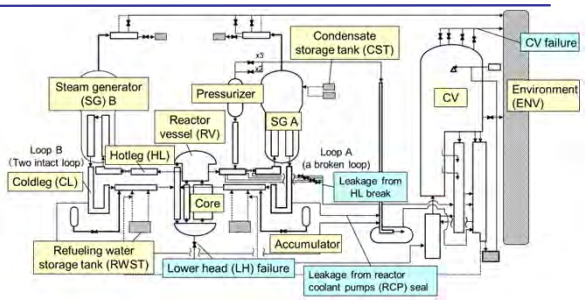

Fig. 2 MELCOR evaluation model of a typical three-loop PWR.

2. Modeling of ATF using MELCOR

	Zircaloy	Cr-coating [1, 2]	FeCrAl-ORNL [2, 3]	FeCrAl-MIT [2, 4]	SiC [5, 6]
Oxidation kinetics	MELCOR Default Model (Urbanic-Heidrick). Above 1,873 K, the oxidation model transitions to the high-temperature regime.	<1,600 K: Cr oxidation only; >1,600 K:, Zr oxidation only.	The oxidation model is based on the ORNL-developed B136Y model. Two models are considered to assess the impact of the transition temperature for iron-dominated oxidation: 1,648 K (MIT model) and 1,703 K (ORNL model).		Although both oxidation and oxide decomposition reactions can occur simultaneously for SiC, only the oxidation reaction is considered.
Melting temperature (K)	2,098 (Zr) 2,990 (Oxides)		1,773 (FeCrAl) 1,901 (Oxides)		1,804 (SiC) 2,900 (Oxides)
Failure temperature (K)	2,500		1,804	2,800	2,000
Cladding Modeling	Gap, Zircaloy, Pellet, Radius	Cr-coating +15μm, Pellet, Zircaloy	FeCrAl, Pellet		SiC, Pellet

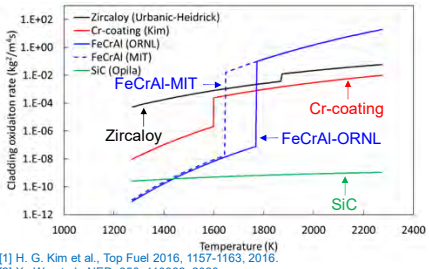

[1] H. G. Kim et al., Top Fuel 2016, 1157-1163, 2016.
[2] X. Wu et al., NED, 356, 110362, 2020.
[3] K. R. Robb et al., ORNL/SPR 2017/373, 2017.
[4] A. Gurgen et al., NED, 337, 38-50, 2018.
[5] E. J. Opila, Journal of American Ceramic Society, 86(8), 1238-1248, 2003.
[6] H. Ebrahimgo et al., ANE, 152, 107961, 2021.

3. Progression of Events in Representative Accident Sequences

SBO

SBO	Zircaloy case
0 hr	▼RCP seals leakage 1.5m³/h FW stops
1.1 hr	▼Opening of the PRZ-PORV
1.7 hr	▼ACC
2.0 hr	▼ Core damage
2.5 hr	▼CV spray; alternative low-pressure pump
4.7 hr	▼ Support plate failure
6.5 hr	▼ Lower head failure
24 hr ~	▼CV recirculation unit

Before lower head failure

▼Main event
▼Successful

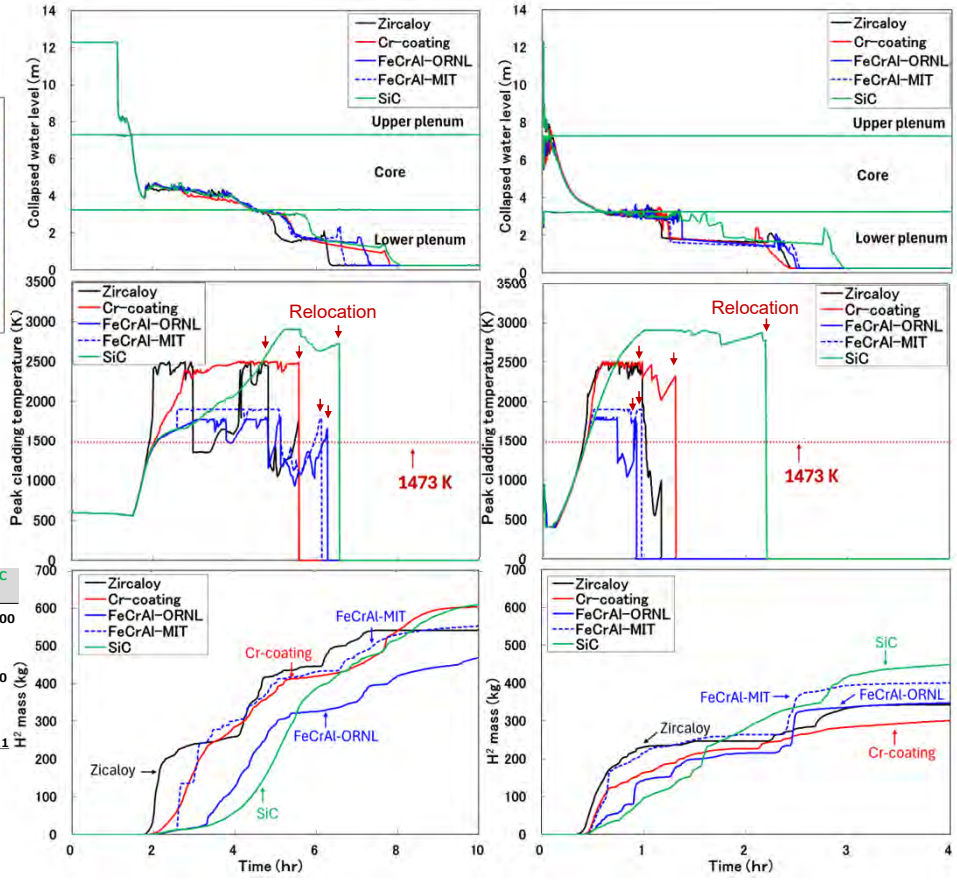

SBO	Zircaloy	Cr-coating	FeCrAl-ORNL	FeCrAl-MIT	SiC
PCT [K]	2,497	2,499	1,804	1,901	2,900
Lower head failure timing [hr]	6.5	7.8	7.4	7.0	8.0
H² mass [kg]	541	603	490	558	611

LOCA

LOCA	Zircaloy case
0 hr	▼Hot leg large break LOCA
	▼ACC
0.4 hr	▼ Core damage
0.9 hr	▼ Support plate failure
	▼CV spray; alternative low-pressure pump
2.5 hr	▼ Lower head failure
24 hr ~	▼CV recirculation unit

Before lower head failure

▼Main event
▼Successful

LOCA	Zircaloy	Cr-coating	FeCrAl-ORNL	FeCrAl-MIT	SiC
PCT [K]	2,497	2,499	1,804	1,901	2,900
Lower head failure timing [hr]	2.5	2.5	2.6	2.6	3.0
H² mass [kg]	343	301	347	400	450

4. Conclusion

- Analyses using MELCOR 2.2, reflecting differences in cladding materials, resulted in differences in PCT, hydrogen generation, and reactor lower head failure timing.
- These differences are mainly attributed to variations in the specified oxidation kinetics models, melting temperature, and failure temperature.
- Although cladding oxidation increases the melting temperature, severe oxidation can cause cladding failure and relocation below the melting point.
- In DBA (mid-phase) conditions, hydrogen generation from ATF is lower than that from conventional fuel. In contrast, it increases with accident progression in SA (late-phase) conditions.

QUENCH-19: Bundle Experiment on ATF FeCrAl Claddings under Severe Accident Conditions

Bachurina Diana (1), Schaefer Daniel Auri (1), Große Mirco (1), Steinbrück Martin (1), Stuckert Juri (1)

(1) Karlsruhe Institute of Technology

Type of abstract: Poster
Subject area: Other applications (fusion reactors, interim SNF storage, Accident Tolerant Fuels (ATFs), etc
Keywords: QUENCH; ATF; FeCrAl cladding

The QUENCH-19 experiment was the worldwide first bundle test to simulate severe accident conditions with accident-tolerant fuel (ATF) cladding materials. The test featured 24 FeCrAl cladding tubes developed and provided by Oak Ridge National Laboratory, along with FeCrAl Kanthal spacer grids, corner rods, and a shroud. The objective was to compare the behavior of FeCrAl cladding with conventional ZIRLO, previously tested in the QUENCH-15 experiment. The experiment was executed in four distinct stages: pre-oxidation (~6000s), transient heating (~1130s), extended constant-power heating (~1970s at 18.32kW), and termination by water flooding at a rate of 48g/s at peak cladding temperatures of ~1800K. During the test, a thin, 2–3µm protective aluminum oxide layer formed on the cladding at the highest temperature region. However, this layer was destroyed in some places, especially on the inner bundle rods, leading to complete cladding oxidation. Cladding failure occurred due to several mechanisms, including circumferential cracking from internal stresses induced by thermal expansion, eutectic interaction with thermocouples, the formation of molten FeO, and the relocation of FeCrAl melt into the gap between the ZrO_2 pellets and the cladding. Despite a longer high-power exposure (~2000s), the FeCrAl bundle produced significantly less hydrogen than the ZIRLO bundle (9.2g vs. 47.6g, respectively). The main source was the loss of the protective aluminum oxide layer and the melting of the claddings of the inner rods. The maximum hydrogen release rate reached during reflood was 280mg/s, which was considerably lower than the 1830mg/s measured in QUENCH-15. The results highlight both the advantages and challenges of FeCrAl alloys as ATF cladding materials. The key advantages are reduced hydrogen production and extended coping time, while the main challenges are their susceptibility to melt-induced degradation and oxide scale breakdown at high temperatures.

12th CONFERENCE ON
SEVERE ACCIDENTS RESEARCH
May 18-22, 2026 - Madrid, Spain
ERMSAR 2026

QUENCH-19: Bundle Experiment On ATF FeCrAl Claddings Under Severe Accident Conditions

Diana Bachurina, **Daniel Auri Schaefer**, Mirco Große, Martin Steinbrück, Juri Stuckert

Introduction

After Fukushima accident, focus shifted to Accident Tolerant Fuel (ATF) research.
Current goal: evaluate new materials behavior.

QUENCH-19 experiment: first bundle test with FeCrAl claddings **[1-2]**.
Serves as a benchmark to improve accident simulation codes (IAEA-ATF-TS project).

Experimental setup

Bundle Composition:

- 24 Cladding Tubes: B136Y ($Fe_{bal}Cr_{13}Al_{6.2}Y_{0.03}C_{0.01}$).
- Spacer Grids: 4 Kanthal AF.
- Corner Rods & Shroud: 7 Kanthal APM and Shroud.

Test Procedure (4 Stages):

- Stages 1 & 2: Pre-oxidation (~6000 s) and transient heating (~1130 s). Reference: Electrical power supply identical to test QUENCH-15 (ZIRLO).
- Stage 3: Constant power of 18.32 kW for ≈1970 s until expected local melting.
- Termination: Quenching at 1728 K (peak cladding temperature) via water flooding at 48 g/s.

Simulation Benchmark:

- **Collaboration**: Study involving 7 organizations.
- **Scope**: Simulation of temperature history (17 assembly elevations) and total H_2 release.

Results

The QUENCH-19 experiment resulted in a lower amount of hydrogen release (totally **9.2 g** with **1.2 g** during quench), even with longer time (**≈1970 s**) at highest temperature, compared to the **47.6 g** totally (**7 g** during quench) of the reference test (QUENCH-15).

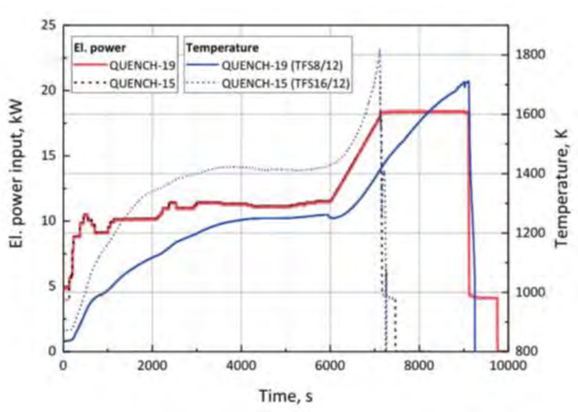

Fig. 1. Electric power input and bundle temperature in the hot zone for QUENCH-19 (FeCrAl) and reference test QUENCH-15.

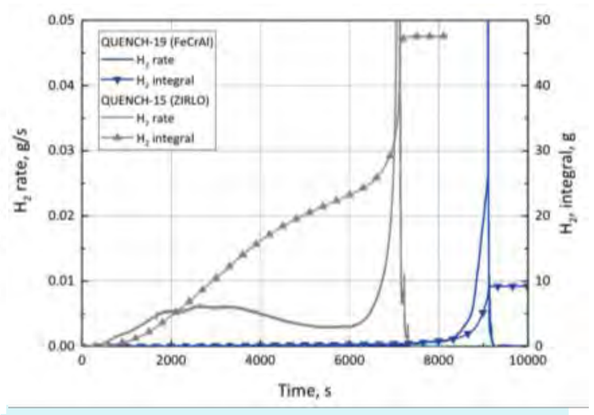

Fig. 2. Hydrogen release (total and rate) during the QUENCH-19 (FeCrAl) and reference test QUENCH-15.

Protective Layer: Generation of a thin Al_2O_3 layer (**2-3 µm**) on the outer cladding surface.

Local Failure: Destruction of the protective Al_2O_3 layer in inner rods, leading to complete cladding oxidation.

Melt Formation: Melting of FeO oxide at T>1650 K with subsequent relocation into the pellet-cladding gap and penetration between pellet grains, resulting in pellet destruction.

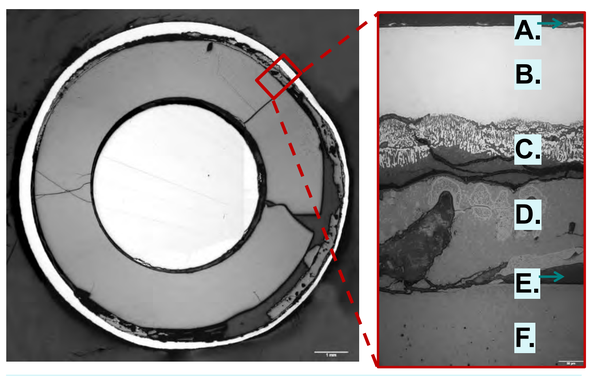

A. 2-3 µm Al_2O_3 layer;
B. residual metal cladding;
C. two layers of oxidized inner surface of cladding;
D. FeO melt with (FeCrAl)Ox precipitates;
E. FeO melt;
F. porous part of the pellet.

Fig. 3. rod 1 at 750 mm: melt interaction with cladding, depicting the residual cladding, the melt relocation.

Cladding Rupture: Observed failure of the cladding tubes following the quenching process.

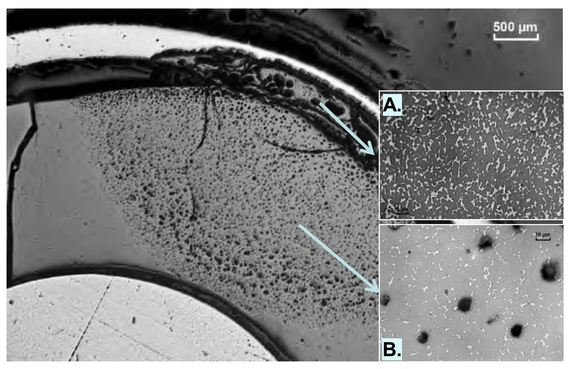

Fig. 4. rod 4 at 850 mm: interaction of melt with pellet and cladding thinning. **A.** oxidized FeCrAl precipitates (dark) in frozen FeO melt (light); and **B.** FeO melt (light) penetrated between the grains of ZrO_2 pellet.

Root Cause:

Higher thermal expansion coefficients compared to traditional Zr-based alloys.

Fig. 5. bundle side view: axial rupture of many claddings during quenching due to high thermal expansion coefficient.

Simulation Benchmark

➢ ***Temperature distributions***:

- Axial temperature: Most codes accurately predicted the position of maximum temperature at the 950 mm elevation.
- At 950 mm bundle elevation: Generally overestimated by all codes throughout the experiment.
  - **Internal Rods**: Results were considered satisfactory.
  - **Shroud**: Values were significantly overestimated.

➢ ***Hydrogen (H_2) Release*:**

- **Methodology**: All codes applied oxidation kinetic correlations from existing literature [**3 - 4**].
- Three codes achieved very good predictions for total H_2 mass, driven by accurate bundle temperature calculations.

Prediction Deviations

- **Overprediction of H_2** : Resulted from increased calculated temperatures.
- **Underprediction of H_2**: Resulted from individual modifications to the oxidation correlation for iron.

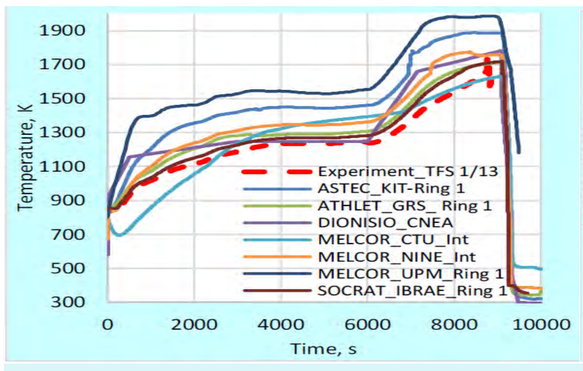

Fig. 6. Simulation for temperature progress for internal rods of the QUENCH-19 bundle. All codes overestimated the temperatures for the internal rods, but with satisfactory results.

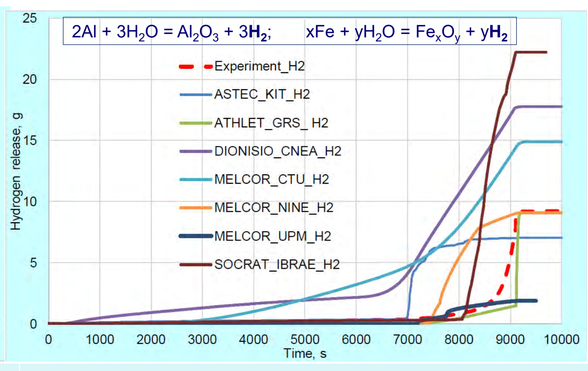

Fig. 7. Simulation results for hydrogen release during the QUENCH-19 bundle test. Good agreement with the experimental data for three codes.

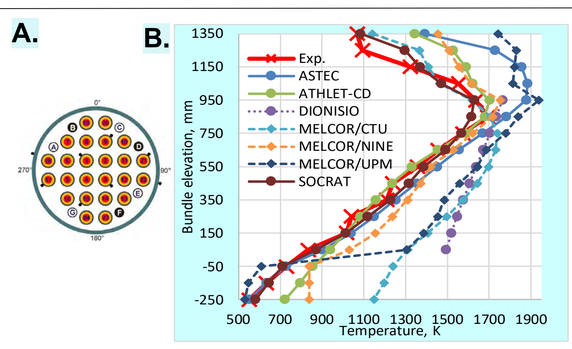

Fig. 8. A. Thermocouple disposition at bundle elevation 950 mm. B. Simulation for axial temperature distribution of the QUENCH-19 bundle for the measured values at a time 300 s before reflood.

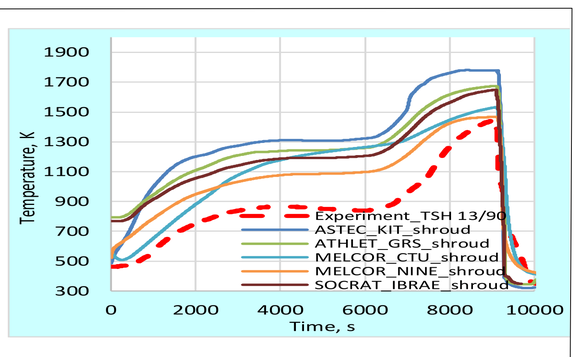

Fig. 9. Simulation for temperature progress for internal rods of the QUENCH-19 bundle. All codes significantly overestimated the temperatures for the shroud.

Conclusions

- ➢ Reduced hydrogen release for QUENCH-19 (9.2 g compared to 47.6 g in QUENCH-15).
- ➢ "Qualitative" Coping time: ≈ 2000 s for the FeCrAl claddings
- ➢ Oxidation of iron → lower melting temperature than the traditional Zry alloys.
- ➢ Higher thermal expansions coefficient of the FeCrAl alloy → failures of the cladding tubes during the quenching stage.
- ➢ Benchmark for simulating the bundle experiment: solid basis for adapting the simulation codes to new ATF materials.
- ➢ Good agreement with measured temperatures and hydrogen release achieved for some codes.

References

1 - J. Stuckert et al. 2022, https://doi.org/10.5445/IR/1000148370

2 - P. Doyle et al., 2023, https://doi.org/10.1016/j.jnucmat.2023.154433

3 - Kim et al. 2022 , https://doi.org/10.1016/j.jnucmat.2022.153696

4 - Field et al. 2018 https://doi.org/10.2172/1474581

Karlsruhe Institute of Technology

daniel.schaefer2@kit.edu

Institute of Applied Materials
Applied Materials Physics

Experimental investigation of top-flooding of corium in the MERELAVA facility

Sébastien Renaudière de Vaux (1), Viviane Bouyer (1), Christophe Journeau (1), Arthur Denoix (1)

(1) CEA, IRESNE, DTN, SMTA, LEAG, Cadarache, F-13108 Saint-Paul-Lez-Durance, France

Type of abstract: Poster
Subject area: Ex-vessel corium interactions and coolability
Keywords: Ex-vessel coolability, corium concrete interaction, water ingression, experimental facility

In a severe nuclear accident scenario, the reactor core melts and mixes with other materials, forming a substance called corium. This molten mass can breach the reactor vessel, spill out below it, and interact with the concrete structure (Corium-concrete interaction). Stopping the spread of corium in this situation is critical, and this configuration is known as ex-vessel retention. A key strategy for ex-vessel corium cooling involves top-flooding, whereby a solidified crust forms atop the corium and subsequently fractures. This process enables water to penetrate the crust's pores, enhancing heat extraction through boiling and latent heat mechanisms. This phenomenon is known as water ingression. Studied for over two decades, this mechanism remains a critical focus of nuclear safety research, as it is not fully understood to this day.

To further investigate water ingression, the MERELAVA facility was designed and built at CEA Cadarache. One of MERELAVA's key advantages is its ability to include a concrete layer beneath the corium, which allows to explore how water ingression behaves when corium interacts with concrete. Additionally, following the in-situ thermite reaction to generate up to 80 kg of corium, some trials employed an electromagnetic inductor to simulate decay heat, providing deeper insights into cooling dynamics under realistic conditions, in order to highlight steady-state coolability.

The unique features of the MERELAVA facility enable to investigate the water ingression mechanism in depth. The facility's instrumentation and capabilities provide a foundation for future experiments.

12th CONFERENCE ON
SEVERE ACCIDENTS RESEARCH
May 18-22, 2026 - Madrid, Spain
ERMSAR 2026

EXPERIMENTAL INVESTIGATION OF TOP-FLOODING OF CORIUM IN THE MERELAVA FACILITY

Sébastien RENAUDIÈRE DE VAUX, Viviane BOUYER, Christophe JOURNEAU, Arthur DENOIX

Energy Division – Severe accident experimental laboratory – Cadarache Center

Funding partners: anr© INVESTIR L'AVENIR EDF framatome

I - THE MERELAVA FACILITY: STUDY OF WATER INGRESSION

Top flooding of corium with water is a key strategy for severe accident mitigation, in the ex-vessel phase. The extracted heat flux is higher than the classical view of the conductive heat flux, thanks to the **water ingression phenomenon**.

Understanding how this phenomenon impacts the **sacrificial concrete ablation rate** is crucial for nuclear power plant safety. In the **CEA center of Cadarache**, the **MERELAVA facility** (Fig. 1) was built to study in depth the mechanisms at play, and the effect of the melt composition.

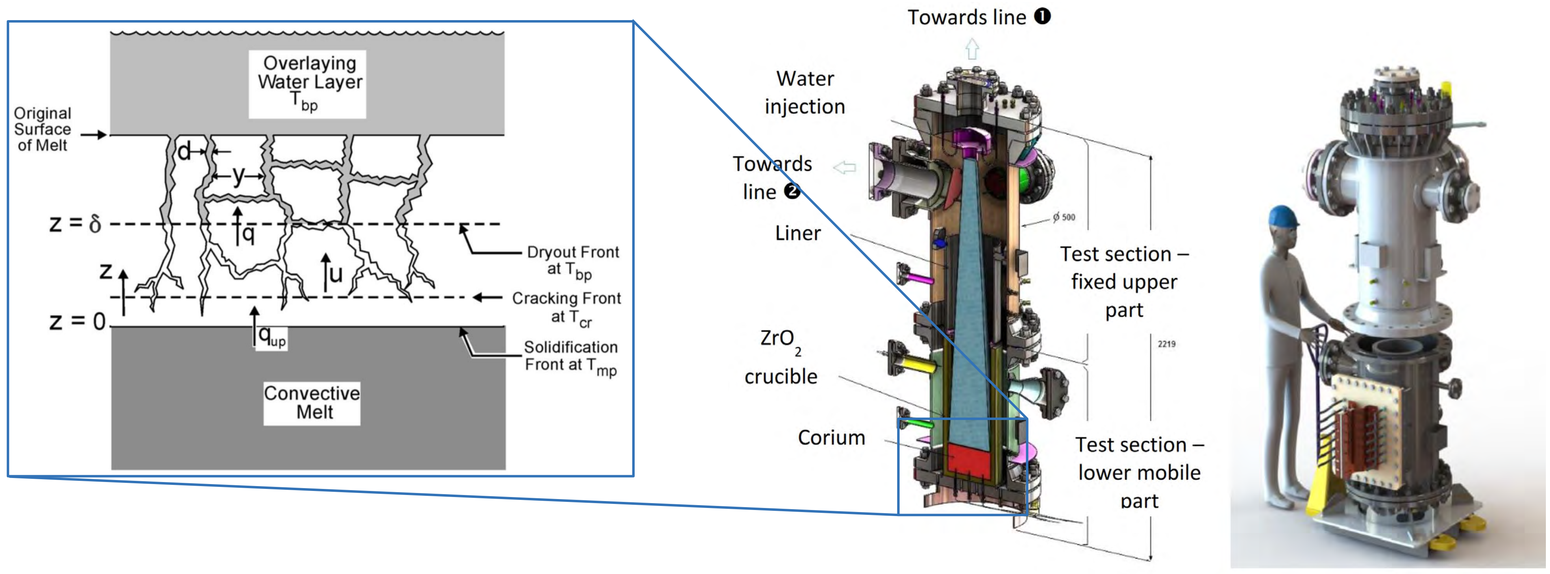

Fig 1. Water ingression mechanism [1] and sketch of the MERELAVA test-section [2] with and without induction heating.

II - TEST CONDITIONS AND SETUP

Possibility to use induction heating to mimic decay heat
→ tests ME-U4 and ME-U5;
→ concrete ablation.

The main parameters of the five tests presented are summarized in this Table.

	ME-U1	ME-U2	ME-U3	ME-U4	ME-U5
Initial melt composition (mass %)	UO_2/ZrO_2/Concrete/Cr: 64/26/4/6 (sand/lime)	UO_2/ZrO_2/Concrete/Steel: 54,4/23,3/8/14,3 Siliceous	UO_2/ZrO_2/Concrete/Steel: 49,9/21,4/13,6/15,1 Siliceous	UO_2/ZrO_2/Concrete/Steel: 54,4/23,3/8/14,3 Same as ME-U2, Siliceous	UO_2/ZrO_2/Zr/Steel/FP simulants: 37/25/25/9/3
Liquidus temperature	1797°C	2329°C	2202°C	2329°C	2353°C
Induction heating and concrete ablation	✗ No induction	✗ No induction	✗ No induction	✓ Induction heating during the whole trial / several cm of concrete ablation	✓ Induction heating only during the initial instants→ only ~ 1 – 2 cm ablation
Volume of water injected	91L in 13 injections of ~7L each/ average flowrate 8.4L/min	~74L in 9 injections of ~8.2 L each/ average flowrate 8L/min	~72.8L in 9 injections of ~8.5±0,9L each / average flowrate 8.8L/min	~74L in 9 injections of ~8.2L each average flowrate 8.8L/min	~74L in 9 injections of ~8.2L average flowrate 8.8L/min (same as ME-U4)

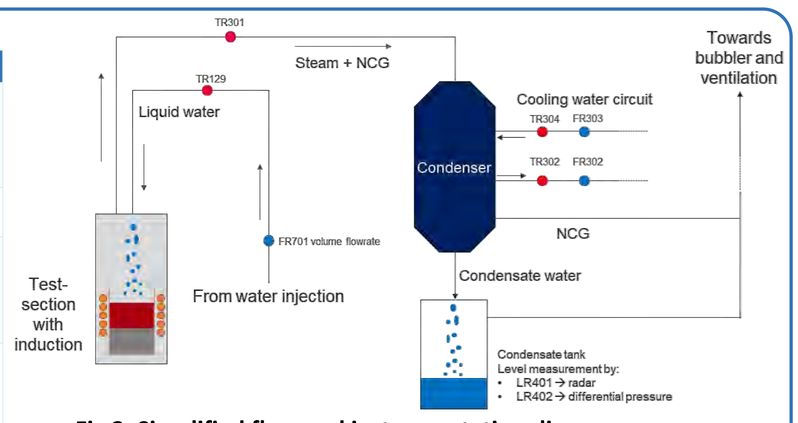

Fig 2. Simplified flow and instrumentation diagram.

III - FOCUS ON THE FIRST TEST WITH INDUCTION HEATING: ME-U4

A - WATER INJECTION SEQUENCE AND VOLUME HEATING

Electromagnetic power is started at the end of the thermitic reaction [3], and is gradually increased until coupling with the melt is ensured. After, power is reduced and varied manually during the test.

Water is injected by successive sequences of ~8 to ~9 liters, for safety reasons.

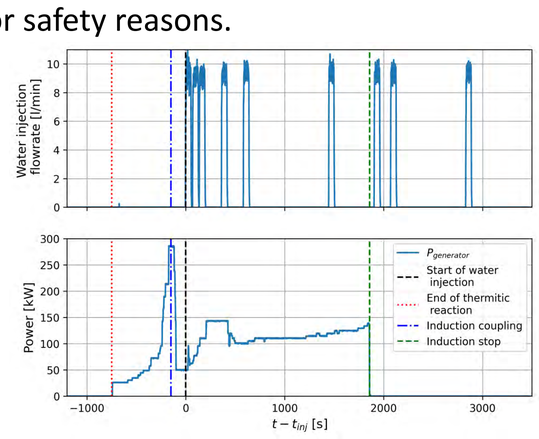

Fig 2. Water injection sequence and power injected during the trial.

B - HEAT FLUX ESTIMATES IN ME-U4

Two methods are used to measure the condensate flowrate:

1. Direct measurement of water level in the condensate tank (CT) by radar sensor (LR401): strongly perturbed by surface waves;
2. Measurement of differential pressure between the top and bottom of the tank (LR402). Assuming that the water is at rest, the flowrate is:

$$\dot{m}_{cond} = \frac{\pi R_{tank}^2}{g} \times \frac{d\Delta P_{LR402}}{dt} = \rho \pi R_{tank}^2 \times \frac{dz_{tank}}{dt}.$$

Both methods show similar tendencies, but due to the high noise level on the radar sensor, the differential pressure is selected for further analysis.

Then, two methods can be used to estimate the heat flux density in this configuration:

1. Injection temperature is close to saturation:

$$q'' \approx \dot{m}_{cond} h_{lv} / S_{pool}$$

with $\dot{m}_{cond}$ the condensate flowrate (LR402) in the condensate tank (CT) and h_{lv} the latent heat of vaporization.

2. Direct measurement from the heat exchanger (HX) as:

$$q'' = \dot{m}_{HX} c_p \Delta T_{HX} / S_{pool}$$

with $\dot{m}_{HX}$ and ΔT_{HX} the mass flowrate and temperature difference on the secondary side of the HX.

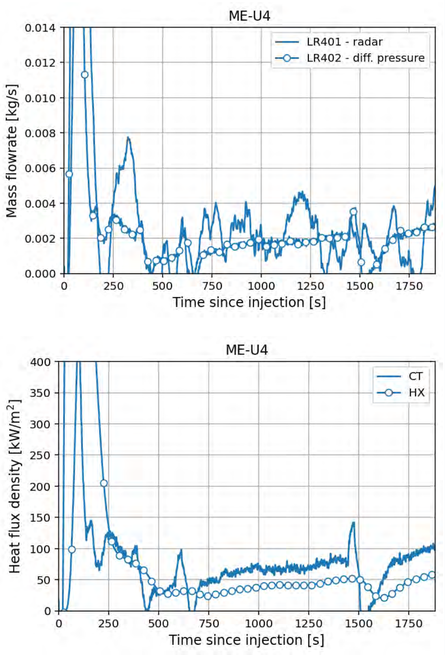

Fig 3. Steam (condensate) mass flowrates and heat flux density estimates.

C - MATERIAL REPARTITION IN ME-U4

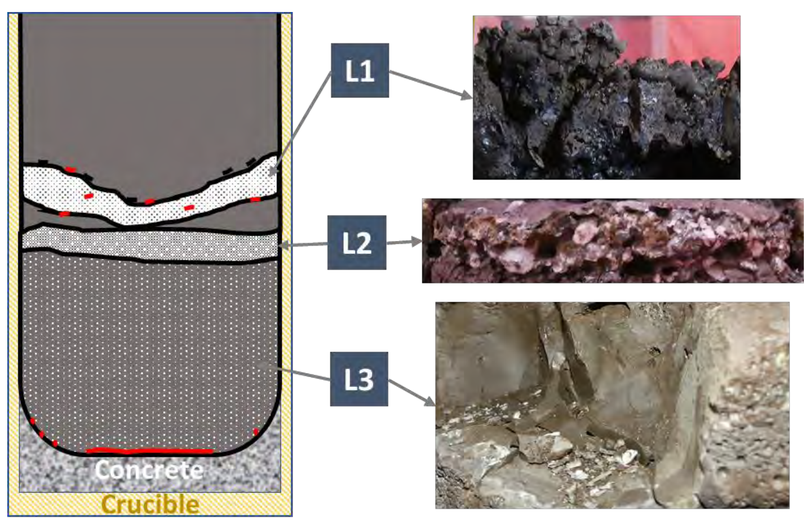

Fig 4. Material repartition in the ME-U4 test after cooling.

Main observations:

- Layered configuration in ME-U4
- Fractured layer (L1) on top of the block
- Concrete agregates in the upper part of the melt (L2)
- Compact corium layer (L3)

III - CONCLUSIONS

- **ME-U4 is the first test** carried out in the MERELAVA facility **with induction heating and concrete ablation.**
- Two methods for **heat flux estimates** are used and show consistent results.
- Results are **consistent with previous findings** of experimental programs. Analysis of melt after cooling reveals a **layered configuration** in the ME-U4 test.
- Future work will focus on data interpretation and in the experimental setup improvement.

REFERENCES

[1] Epstein, M. (2006). Dryout heat flux during penetration of water into solidifying rock. Journal of heat transfer, 128(8), 847-850.
[2] Journeau, C., Bouyer, V., Denoix, A., & Sauvecane, P. (2020). The new MERELAVA facility for ex-vessel corium flooding. In Proc. NENE2020, 29th Int. Conf. Nuclear Energy New Europe, Portorož, Slovenia.
[3] Denoix, A., Bouyer, V., Journeau, C., & Balland-Longeau, A. (2026). Production of prototypic corium in the VULCANO facility using uranothermite and induction heating. Annals of Nuclear Energy, 227, 111970.

ACKNOWLEDGMENT: Authors are grateful to the technical teams involved in the maintenance of the setup and in the realization of the trials.

MELCOR ANALYSIS OF THE NORDIC BWR PRESSURE SUPPRESSION POOL DURING SBO ACCIDENT

Govatsa Acharya, Dmitry Grishchenko, and Pavel Kudinov
KTH Royal Institute of Technology, Division of Nuclear Science and Engineering,
Albanova University Center, 10691 Stockholm, Sweden.
govatsa@kth.se; dmitrygr@kth.se; pkudinov@kth.se

ABSTRACT

Wetwell or pressure suppression pool in Boiling Water Reactors plays a vital role in severe accident mitigation by acting as a heat sink for escaping steam from the reactor primary system, a source of water for the emergency core cooling system, containment spray system and flooding of the cavity for debris cooling and retaining fission products released to the containment. During a station blackout accident (SBO) large amount of steam is discharged into the wetwell upon activation of the Automatic Depressurization System spargers. MELCOR is used in this study to simulate SBO in a Nordic BWR to characterize the conditions of steam and gases entering the pool, and retention of the fission products in the pool. The thermal hydraulic behaviour of the pool is also analyzed. The effects of MELCOR modelling parameters on the mass of fission products, mainly cesium and iodine mass fractions, in the pool are determined by sensitivity analysis performed in combination with DAKOTA. Correlation measures and Morris global sensitivity metrics for the modelling parameters are determined. It is observed that, unlike as in LOCAs, the mode of melt ejection from the vessel is not one of the major sources of uncertainty in SBOs. It is seen that aerosol agglomeration, CORSOR-Booth diffusion, and vapour diffusivity models are the most significant to the uncertainty in mass of fission products retained in the pool.

KEYWORDS
MELCOR, Nordic BWR, wetwell, fission product behaviour, severe accidents, DAKOTA

1. INTRODUCTION

Pressure suppression pool (PSP), or the wetwell (WW), is a defining safety feature of Boiling Water Reactor (BWR) containments. During loss of coolant accident (LOCA), steam is directed via blowdown (BD) pipes into the submerged pool where it condenses. This process simultaneously scrubs the fission products (FPs) – both aerosols particles and vapours – from the gas stream as bubbles rise through the water, thereby performing a critical function of radioactive source term reduction. As a consequence, during possible ex-vessel phase of the accident, the pool may boil by the decay heat of the ejected debris leading to remobilization of FPs. Post Fukushima Daiichi accident of 2011, research has intensified focus on this scrubbing phenomenon under extended severe accident sequences like station blackout (SBO), where pool dynamics are paramount [1]. A significant finding across studies is the large uncertainty in accident progression analysis, often due to incomplete knowledge of system states and complex, coupled phenomena. Reducing these uncertainties, especially regarding FP retention and source term release, is essential for reliable risk assessment and is fundamentally tied to the thermal-hydraulic behaviour of the WW [2][3][4][5].

The containment's pressure response depends on the WW's suppression function. Impairments such as thermal stratification can degrade condensation efficiency, potentially leading to sharp pressure spikes as witnessed at Fukushima [1]. The WW's performance is governed by competing processes: stratification

induced by steam injection into subcooled water, and mixing driven by pool convection or operator actions like spray initiation. These conditions create a dynamic environment that can either enhance scrubbing or lead to the re-release of deposited FPs [18]. Analytical tools for FP scrubbing include dedicated pool scrubbing codes like SPARC-90 [6], SUPRA [8] and BUSCA [7], which are implemented and validated within integrated severe accident codes such as MELCOR [9] and ASTEC [10]. Experimental programs like EPRI/BCL [11], POSEIDON [12], LACE-España [13], and the more recent OECD/NEA IPRESCA project [14] provide data on decontamination factors and hydrodynamics under prototypic pool conditions.

In the context of Nordic BWR, uncertainties relating to source term in Nordic BWRs are being assessed at KTH under the Risk Oriented Accident Assessment Methodology+ (ROAAM+) with the aim of improving current methodology for addressing safety issues [19][20][21][22][23][24][25]. The thermal-hydraulic performance of the WW during severe accidents is being studied in [15][16][17][18]. The present work extends the MELCOR analysis performed earlier in [24][25][32], to the uncertainties in the Nordic BWR WW response to SBO, and its effect on FP retention within the WW.

2. APPROACH AND METHODOLOGY

2.1. Nordic BWR Model Description

In continuation with the previous work performed to analyze LOCA, the input deck developed for the Oskarshamn Unit 3 with MELCOR v1.8.5 and subsequently upgraded to v2.2.18019 and maintained at KTH, was used in this study. Briefly, the reactor of study – as shown in Figure 1 is described here and for complete details can be found in the literature [23][25][26]. The model comprises of reactor pressure vessel (RPV) and the containment (CNT) represented by 27 control volumes (CVs), connected with 45 flow paths (FLs) and 73 heat structures (HSs). The vessel is represented by 6 rings and 19 axial levels, with the first 10 axial levels representing the lower plenum (LP); the 11th level represents the core support plate; 12th and 19th represent the core inlet and outlet regions; and levels 13-18 represent the active core region. The core is represented by 5 radial rings and the 6th ring represents the downcomer region.

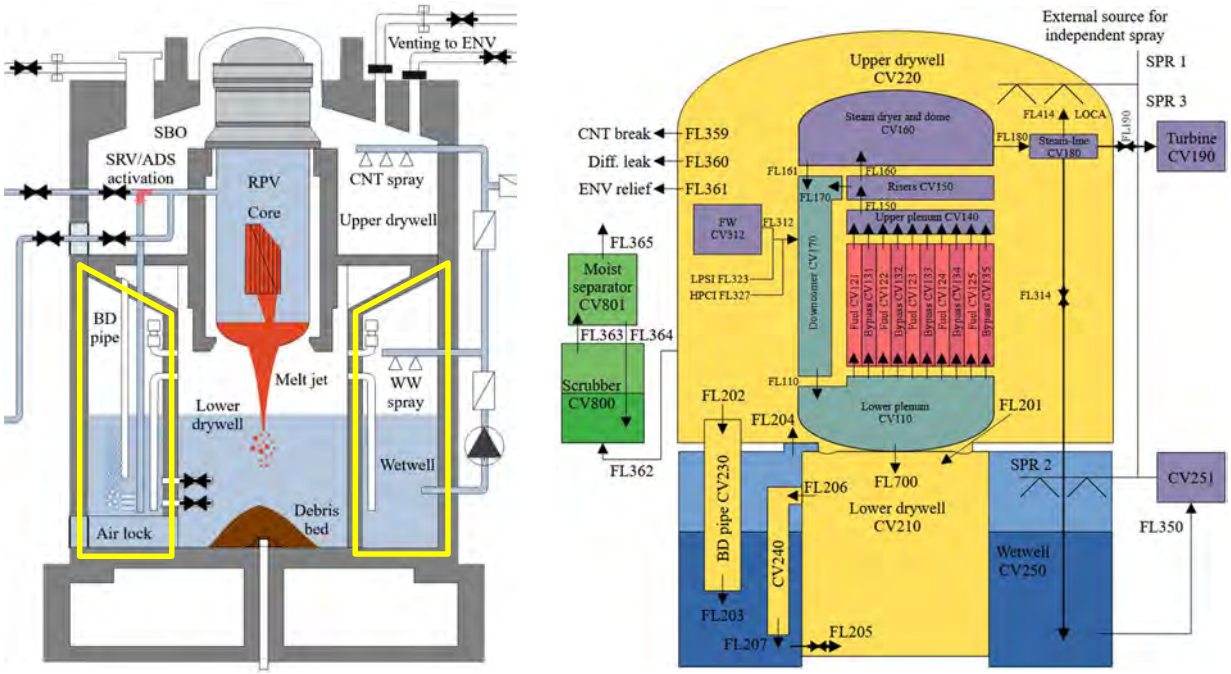

(a) Generic design. (b) MELCOR nodalization.

Figure 1. Nordic BWR model nodalization.

2.2. SBO Accident Description

For the Nordic BWR Level 2 PSA, of the 6 main release categories, RC4 containment bypass scenarios – transients like SBO or LOCA – majorly contribute to unacceptable release frequency and large early release frequency. Since the Fukushima accident, SBO has been a focus of many studies with modern computational tools. Here, the reactor experiences a simultaneous loss of the offsite power (LOOP) and diesel backup generators, which leads to complete loss of safety systems – high pressure and low pressure injection and spray systems – eventually causing core damage. The only systems available in the RPV for the removal of decay heat are the safety relief valves (SRVs) that are installed on the main steam lines, shown in the figure above as System 314 (FL314), to protect against over-pressure and operate as automatic depressurization system (ADS) that allow for coolant injection to the RPV (here unavailable). The other system available as a heat sink is the WW.

Once the turbine valves close and is isolated with no steam dump, the system 314 valves controls the pressure at 7MPa, maximum 7.05MPs. From the 4 main steam lines 64 blowdown pipes end in the WW pool which comprise the spargers discharging steam. Initially this performs a safety relief function. Upon sensing low downcomer level (L6 - 1m below top of active fuel (TAF)), ADS is initiated with all valves fully open. This action, while reducing primary pressure, also causes rapid loss of coolant and core uncovery. The steam from the blowdown heats the drywell, gradually increasing the pressure of the CNT. Uncovery of the core oxidizes the cladding, overheats the fuel elements and leads to their failure. Hydrogen released as a result also discharges along with steam into the WW space. FP aerosols and vapours released as cladding fails are forced in through the steam lines into the WW, where they are largely scrubbed at the vent exit. The debris so formed slumps to the core support plate, which fails leading to debris pool formation in the lowerhead (LH). With quenching of the slumped debris, water from the lower plenum (LP) now as superheated steam exits the RPV into the WW thereby rapidly increasing containment pressure. Though the peak pressure observed during this instance does not exceed the filtered containment venting (FCVS) limit (5.5bar), it is high at 2bar. The LH walls and control rod/instrumentation penetrations then fail under thermal stress or over-temperature, thereby ejecting debris and molten material to the cavity.

Timing of the above events as calculated by MELCOR for a reference case of SBO are presented in Table I. As a severe accident management (SAM) strategy cavity flooding is employed in Nordic BWRs for debris cooling during the ex-vessel phase. On detecting low downcomer level (L4 - 0.5m above TAF) water from the WW floods the lower drywell (LDW) cavity with a 600s delay, in preparation to arrest further progression of the debris. Upon ejection from the RPV the debris quenches and forms a cooled bed with negligible attack on the concrete floor, if any. In its absence, an uncoolable debris bed causes basemat failure by molten core concrete interaction (MCCI) or failure of the cable penetrations in the floor. However with this strategy there is a larger risk of energetic fuel coolant interaction (FCI), like a steam explosion (SE), that can compromise the containment integrity. An assumption is made for this RC4 accident that upon RPV failure, coincidentally the containment fails due to ex-vessel phenomenon, with a pathway for FPs opening to the environment. This is modelled as a $2m^2$ flowpath from the upper drywell (UDW). This effectively voids activating FCVS as the CNT is instantly depressurized.

Table I. Key events and timing during SBO.

Key event	Time [h]
L4 level	0.2
Uncovery of core	0.23
L6 level	0.31
Gap release	0.56
Particulate debris formation	0.62
Relocation to lowerhead	2.01
Core plate failure	2.01
RPV failure	2.73
LDW boiling	2.73
WW boiling	20

Mode of debris ejection to the cavity (parameter IDEJ in MELCOR, 0 (default) for both solid + molten, and 1 for molten) is a significant factor affecting uncertainties in FP release and behaviour during the ex-vessel

phase of the accident [25]. In the default case, when both solid and molten debris are ejected, all the mass and associated decay heat transfers to the cavity almost in short span (large release) or in small quantities (dripping mode), leaving no significant quantities of debris to remelt and eject later on. Whereas in IDEJ1, Hence, 2 splinter scenarios SBO-IDEJ0 and SBO-IDEJ1 are considered for study here.

2.3. Uncertainty Analysis using DAKOTA

MELCOR models are sensitive to input parameters, some more significant than others. Relying on a single calculation is therefore unreasonable, and quantification of sensitivities and uncertainties is necessary in safety evaluation. Firstly, based on literature, significant phenomena and 50 underlying uncertain parameters were listed. Then, an initial screening for sensitivity was performed if the selected figures-of-merit (FOMs) were greater or lesser than 50% of the reference case values. Subsequently, a calculation matrix with the 18 screened parameters was developed using DAKOTA [30] to perform Morris global sensitivity analysis [28] for each (IDEJ0 and IDEJ1) accident scenario and identify the most significant parameters to the respective FOMs. Here, with 5 level input space and trajectory of length 20, 380 samples were generated per splinter. Following Morris sensitivity analysis, uncertainty quantification is performed with 160 code runs for each of the splinter scenario with cases generated using Latin Hypercube Sampling (LHS) method. This sample number can yield good results with 95% confidence for one sided bound [29]. A MATLAB simulation platform couples DAKOTA and MELCOR input/output files to generate input, run simulations, and post-process the results. It automatically handles cases that crash by restarting them with time-step refinement. It should however be noted that time step itself is a parameter of significance, as accident progression varies for different time-step description [21].

For the application in this study cesium mass fraction and iodine mass fraction are selected as FOMs. More details of the methodology can be found in [23][24]. A total of 50 parameters were selected and 18 of them were screened for SBO. The list of uncertain parameters and their ranges considered is presented in APPENDIX A. For SBO, aerosol agglomeration shape factor (GAMMA), critical breach temperature in oxide shells (SC11312), activation energy in the CORSOR-Booth model (SC710641) and multiplication constant in the inertial impaction DF correlation for large Stokes number (SC71555) were found to be most significant for cesium and iodine (mainly as CsI) release in the source term [23][24]. The effect of these parameters, that are significant to source term, in modelling pool behaviour and retention is addressed.

3. MELCOR PHENOMENA MODELLING

MELCOR is a fully integrated, engineering computer code that comprises of several modules or packages that calculates equations concerning different phenomena occurring in a typical accident, core degradation, thermal-hydraulics, radionuclide (RN) release, transport and behaviour, structures oxidation, corium concrete interactions, to name a few. While MELCOR tries to mimic the complex nature of severe accidents, it is in some aspects limited by the nature of the code itself and the underlying assumptions. Specific to FP retention in the WW are the phenomena of instantaneous steam condensation upon exit from the sparger vents of the ADS valves, overestimation of water mass for decontamination, insufficient consideration of inertial impaction, and overestimation of the bubble breakup with submergence [27]. As the WW here is assumed to be a single CV, all the thermal-hydraulic properties are lumped together with no higher spatial resolution, in particular for thermal stratification and associated behaviour. Below, a brief description of choices made for important MELCOR RN release and transport models is provided [32].

3.1. Fission Product Release from the Core and Transport

The present study employs the revised CORSOR-Booth model (ICRLSE = -5 parameter in MELCOR) to simulate fission product release from high-burnup fuel. This formulation accounts for mass transport limitations by utilizing the Booth diffusion model alongside empirical correlations for cesium release, with

release fractions of other radionuclide classes scaled relative to the cesium release rates. The model was updated to reflect findings from the Phebus FPT1 experiments, that revealed cesium release speciation deviated from earlier assumptions. Specifically, the release was reformulated to consider cesium transport not only as cesium hydroxide (CsOH) but also as cesium molybdate (Cs_2MoO_4). Accordingly, radionuclides are grouped into 17 classes, with cesium represented in three distinct classes: CsOH (Class 2), CsI (Class 16), and Cs_2MoO_4 (Class 17). All vapour-phase iodine (Class 4) is assumed to combine with cesium to form CsI – a simplification, as the present MELCOR model does not treat detailed iodine pool chemistry. Initial FP inventory in the core is shown in Table II. Volatile fission products may be released at moderate temperatures, even prior to significant core degradation. Once released from the fuel, fission products may exist as vapours or aerosols depending on their class-specific vapour pressure and local temperature. Condensed particles are transported by bulk fluid flow as aerosols. These particles are also subject to Brownian diffusion and gravitational settling. Aerosols are tracked across discrete size sections with varying chemical compositions. Their distributions evolve due to five primary processes: (i) condensation and evaporation of water and fission products, (ii) particle agglomeration, (iii) deposition onto surfaces, (iv) advection between control volumes, and (v) engineered removal via filters, sprays, and pool scrubbing. While deposited aerosols can typically be resuspended and revapourized, resuspension was deactivated in this study, though all deposition models remained active.

Table II. Initial inventory of the first 12 RN classes in the core [kg].

XE	CS	BA	I_2	TE	RU	MO	CE	LA	UO_2 [ton]	CD	AG
505.4	292.5	226.2	22.8	44.5	334.6	382.2	647.3	622.4	12.6	1.5	9.4

3.2. Pool Scrubbing

Steam, gases and aerosols exiting a submerged vent into a pool are modelled to form large unstable globules that breakup into smaller bubble swarm that saturates with local conditions, rises upwards at a constant velocity and eventually break at the surface. Gases, such as hydrogen (non-condensable gases (NCGs)) instantly form thermal equilibrium with the pool. Absence of NCGs lead to condensation of a fraction of vapour (steam) in the bubbles that increases pool mass while remaining is transferred to the atmosphere. These processes ultimately remove FP aerosols and vapours from the injection material into the pool. This is quantified using the decontamination factor (DF), defined as the ratio of the mass of a radioactive material entering the pool to its mass leaving the pool.

The DF is calculated as the product of contributions from three successive regions: (i) Injection zone – at the vent exit, removal occurs due to: (a) Stefan flow from steam condensation, (b) inertial impaction and interception, especially for high-velocity jet regimes, and (c) centrifugal, diffusional, and gravitational deposition, particularly for multi-hole vents; (ii) Bubble swarm rise zone – during ascent, hydrodynamic interactions cause bubbles to coalesce and redisperse. Aerosol removal within each bubble continues via centrifugal, diffusional, and gravitational deposition. Particle size may also change due to steam absorption or evaporation, while vapours are removed primarily by diffusion; (iii) Pool surface zone – when bubbles break at the surface, droplet entrainment may carry fission products upward, with some droplets settling back by gravity. The efficiency of scrubbing depends on several factors, including vent submergence, pool subcooling, inlet velocity, particle size, and gas composition (steam and NCG content) [27]. In this study, all applicable scrubbing models are activated for the vent of interest, the ADS valves and BD exit, and not elsewhere (e.g., overflow pipe exit) to maximize decontamination.

4. RESULTS AND DISCUSSION

Results of MELCOR simulations for the reference SBO cases, sensitivity and uncertainty analysis are provided here. Of the few code crashes observed (<10%), all were successfully completed after a restart.

4.1. Wetwell Thermal-hydraulics

The wetwell behaviour in the reference MELCOR SBO case is provided here, for both IDEJ0 and IDEJ1 scenarios. All calculations have been run for 72h. The pressure in the RPV and the WW is shown in Figure 2(a) and (b). Following activation of the ADS at 0.34h, primary pressure rapidly reduces until active core is almost uncovered and cladding starts to melt. By then, most of the coolant inventory has transferred to WW. Subsequently, during the core degradation phase the pressure in the RPV increases gradually, as well as the pressure in the WW. Once debris slumps to the LP and is quenched, a small pressure spike is observed in the RPV. Following failure of the LH (LHF), the RPV is almost at the environment pressure (due to CNT failure at RPV). The flow rate of steam and hydrogen through the ADS valves is shown in Figure 2(c). The steam flux corresponding to the 2 functions of the ADS is shown in Figure 3(c).

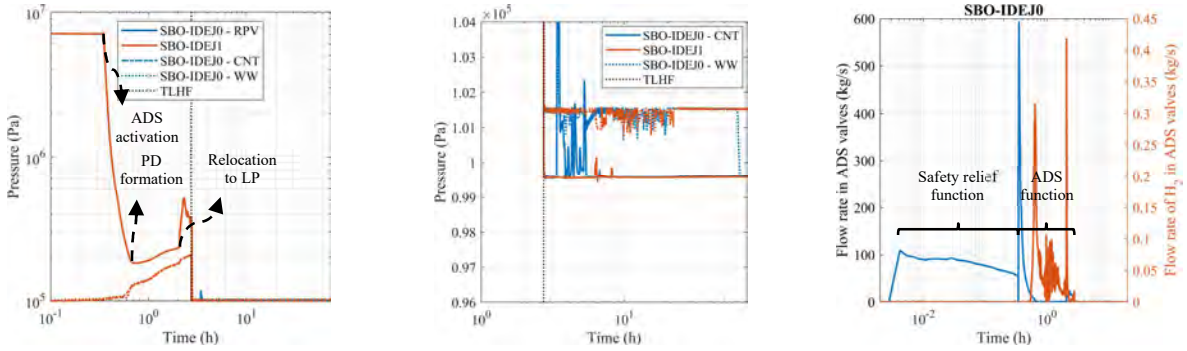

(a) Pressure in the RPV, CNT and WW.

(b) Pressure in CNT and WW (enlarged).

(c) Flow rate (of steam and H_2) in the ADS valves (FL314).

Figure 2. Time evolution of parameters in the reactor.

During the safety relief function to control the RPV pressure at ~7MPa, steam flux through the ADS valves is about 25-45kg/m^2-s. This roughly corresponds to condensation oscillation regime [31], where steam inflow rate is smaller than steam condensation rate, at relatively low pool bulk temperature. During ADS function, where steam flux reaches a maximum of 300kg/m^2-s, it forms a jet – the jetting regime – that holds its shape for some time as the steam condenses and other vapours and FPs are scrubbed. Following this, the steam flux gradually reduces as it bubbles through the valves, corresponding to slightly higher pool temperatures. During the peak pressure induced by quenching, a flux of about 10kg/m^2-s is observed. Hydrogen generated as a result of oxidation of the core is shown in Figure 3(b).

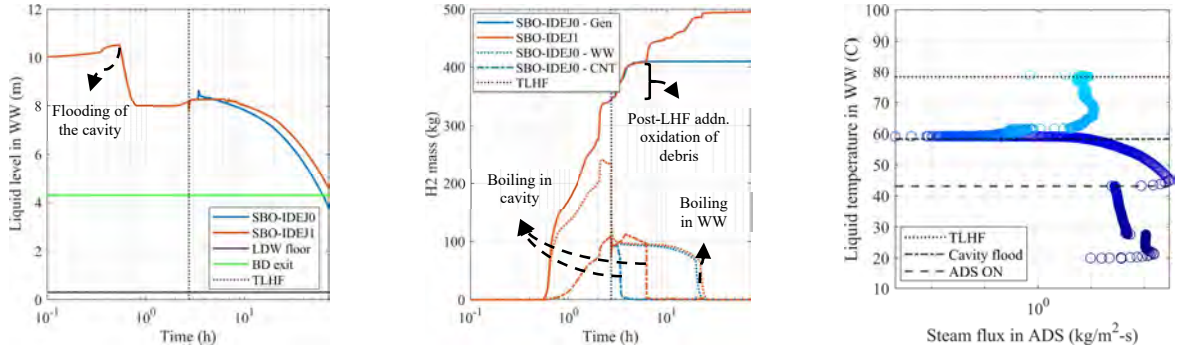

(a) Collapsed liquid level in the WW.

(b) Hydrogen generation and accumulation.

(c) Steam flux of the ADS against pool temperature.

Figure 3. Time evolution of parameters in the reactor.

Along with steam, a major fraction of H_2 is transferred to WW with almost 230kg at the time of LHF accumulated in the WW. A smaller fraction of H_2 generated, about 100kg at LHF, is transferred also the CNT through the vacuum breakers, which are activated when the WW has a greater pressure than the CNT.

Roughly 130kg of H_2 from the WW flows to the CNT and eventually to the environment when the RPV and the CNT fails at 2.73h. Subsequently when the cavity starts to boil producing large amounts of steam in the CNT, all H_2 from the CNT is expelled. Similarly, when the WW starts to boil, roughly at 20-25h depending on the scenario, all H_2 from the WW is also displaced. The liquid level in the WW is shown in Figure 3(a). As the WW is the source for the cavity flooding SAM strategy, at 0.54h liquid level falls by 2m, and once the RPV fails and boils away the water in the cavity, WW continuously replenishes it. Thereby, gradually the WW pool temperature, see Figure 4(a), increases while the liquid level reduces until it starts to boil.

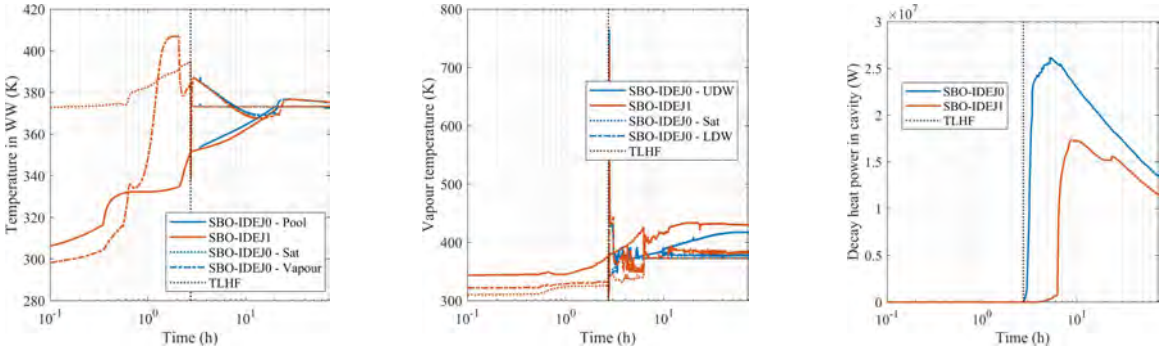

(a) Temperature in the WW. (b) Temperature in the CNT. (c) Decay power in the cavity.

Figure 4. Time evolution of parameters in the reactor.

By the end of 72h, WW liquid level has fallen to less than 4m, about 0.2m below exit of the BD pipes in the case of IDEJ0 and about 0.2m above exit of BD pipes in the case of IDEJ1. Differences between the two scenarios arise due to magnitude of decay power that is ejected to the cavity, shown in Figure 4(c). In the case of IDEJ1, large mass of molten debris is ejected at 6.5h instead of ~3h in case of IDEJ0. The final magnitude of debris ejected is slightly lesser in IDEJ1 than IDEJ0 as well. In IDEJ1, the remaining solid debris in the RPV, combined with molten debris being cooled in the cavity water, leads to higher vapour temperature (430K v/s 415K) in the UDW, shown in Figure 4(b). Post-LHF the damaged core in the RPV also leads to generation of ~95kg more H_2 in IDEJ1 than in IDEJ0, especially once cavity pool boils generating steam that flows in to the RPV through the breach in the LH.

4.2. Fission Product Behaviour

As mentioned earlier, FOMs considered in this study include cesium (CsOH, CsI and Cs_2MoO_4) and iodine (I_2 and CsI). The relative masses of these species in the WW during SBO-IDEJ0 and IDEJ1 and the absolute masses are shown in Figure 5(a), (b) and (c). Unlike in the case of LOCA where the maximum mass fraction of CS and I2 is about 0.23 and 0.25 [32], here during SBO the maximum mass fractions are more than twice, about 0.5 and 0.6 respectively. One can observe from Figure 5(a) and (b) that majority of CS and I2 in the WW is retained in the pool phase (>90%).

From the onset of gap release from the fuel matrix up to ~1.1h, FPs in the atmosphere phase of the WW control volume are negligible. Once the steam injected comprises large amounts of NCGs and is at temperatures greater than the saturation temperature, FP retention in the pool appears to reduce and RN mass in the atmosphere phase can be observed. Around 0.02 and 0.03 atmosphere mass fractions, and 0.01 and 0.02 deposited mass fractions of CS and I2 respectively are accumulated in the WW at time of LHF. During the ex-vessel phase the retained CS and I2 masses in the WW gradually reduce as a consequence of, (i) the WW inventory refilling the cavity and (ii) the WW pool boiling itself that re-entrains soluble FPs (particularly CsI) and vapours, seen as gradual reduction of CsI and CsM post LHF in Figure 5(c). The SPARC-90 model, and its implementation in MELCOR, generally assumes high retention when the pool is subcooled. When boiling occurs, the assumptions that lead to high retention (like efficient aerosol deposition in bubbles) are severely challenged, reducing the overall fission product scrubbing efficiency [33][9]. In the

case of IDEJ0, where the water in the WW is lost to the environment faster than in IDEJ1, by ~60h the liquid level falls below BD exit. Until then, the only meaningful pathway for the FPs to the CNT was through the pool along the valve connecting WW to cavity. However, after uncovery of the BD exit, all airborne aerosols and vapours have a direct course to the UDW, which is seen a rapid fall in CS and I2 fractions retained in the WW after ~60h. Looking closer at Figure 2(b), the pressure in the WW finally equalizes with the CNT at ~60h for this reason.

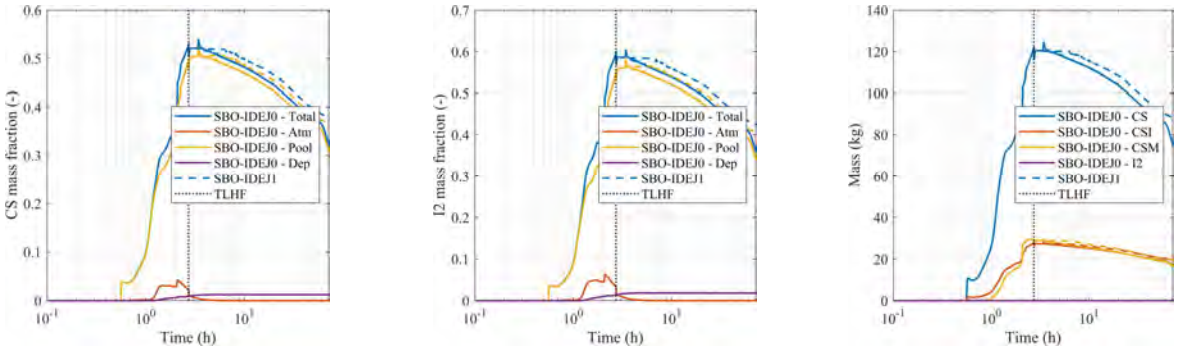

(a) Cesium mass fraction. (b) Iodine mass fraction. (c) Absolute mass of species.

Figure 5. Time evolution of FPs in the WW.

The decontamination factors at the ADS valves and the mass median diameters (MMD) of the airborne aerosols in the UDW, RPV and WW for the two accident scenarios are shown in Figure 6. Here, the MMD for RPV is from the steamdome that is at the top of RPV, just before steam lines, and is assumed to be the inlet CV for the ADS flowpath. From the time of PD formation the MMD in the RPV increases to ~5μm roughly corresponding water level in the RPV falling to LP.

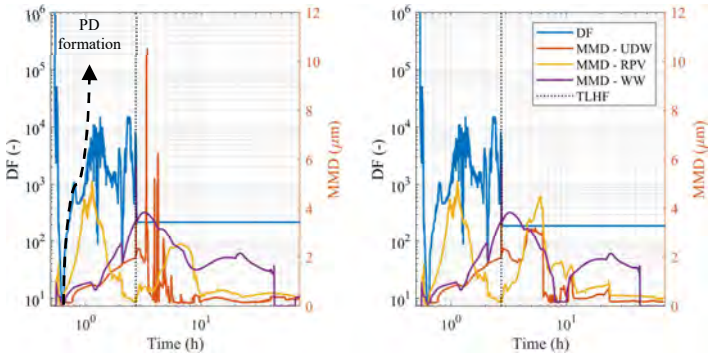

Figure 6. DF and size of particles during IDEJ0 (left) and IDEJ0 (right).

While dependence of DF on particle size cannot be strictly determined based on experimental results, analytical linear dependence can be determined [34]. Subsequently, as the pressure in the RPV starts to increase at ~1.1h when large degradation occurs and small sized aerosols are released from the core (also see [25] for more information on core degradation process during SBO-IDEJ0 and IDEJ1), the MMD reduces. When the size of aerosols entering the ADS valves (from the RPV steamdome) reduces, the amount of small sized aerosols (1μm) retained by scrubbing processes in the WW pool seems to also reduce, leading to these particles rising with the bubbles and entering the atmosphere phase of the WW – seen as the accumulation of CS and I2 in Figure 5(a) and (b) at ~1.1h. This and the effect of large presence of NCGs in the inlet reduces steam condensation and therefore pool scrubbing. The decontamination factor in the ADS valves is also observed to correspondingly rise to the order of 10^4 at ~1.1h and then reduce to ~10^3 by 2h, when core support plate fails, leading to quenching of hot debris and possible energetic remobilization of smaller aerosols. This is seen as a drop in MMD and coincidentally in the DF and the atmosphere mass fraction of FPs in Figure 5(c). Following LHF and energetic ejection of all debris, the MMD in the UDW is

below 1µm until end of the simulation. In the case of IDEJ1, it is observed that until that large mass ejection at ~6h, the MMD in the RPV rises once again to >4µm and this time, because there is an established pathway directly from RPV to the CNT along the breach, the MMD in the UDW also follows suit, increasing to ~3.5µm. While it is expected that the thermal-hydraulic behaviour of the WW should affect the FP scrubbing and behaviour, it is observed that at ~40h MMD sees an unexplained drop (and recovers at ~60h in the case of IDEJ0 likely due to transfer of some aerosols from the UDW to the WW via now uncovered BD pipes) without no other observable changes in other parameters in the WW. This may be due to complete flushing of all the airborne particles from the WW once the pool starts to boil off at ~20h. Further analysis is needed to properly ascertain the reason for this behaviour.

4.3. Initial Screening of Uncertain Parameters

About 73 different cases per splinter (IDEJ0 and IDEJ1) were run – from the initial 50 uncertain parameters for some parameters both upper and lower limit cases were included. Cases that resulted in more than 50% variation in the FOMs (cesium and iodine releases) from the reference case were selected for further sensitivity and uncertainty analysis. Unlike in the case of LOCA [] where bifurcations were observed in the thermal-hydraulic parameters of the plant due to FCVS being activated or not, here during SBO accident, FCVS driven grouping of accident progression are not observed. However in the case of SBO-IDEJ1, post LHF and massive ejection of molten debris to the cavity, leftover solid debris in the RPV leads to superheating the vapour in the atmosphere. The evolution of important plant parameters during SBO-IDEJ1 are presented in Figure 7 and Figure 8. As can be seen, those cases which result in larger debris to remain (and consequently smaller mass being ejected to the cavity) the decay heat in the core remaining after the RPV failure is larger. Because vapour can flow in through the breach it gets heated to a higher degree, almost 50°C more. This does not reflect in fission product retention in the WW.

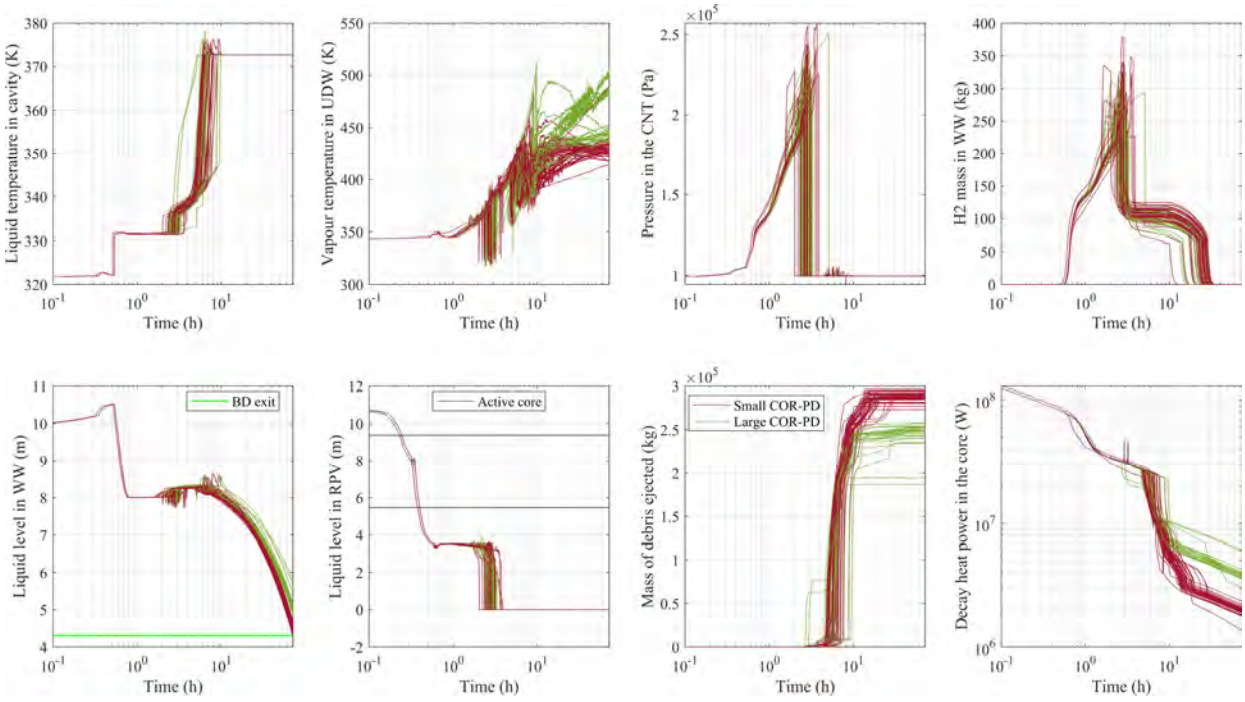

Figure 7. Time evolution of T/H parameters during SBO-IDEJ1.

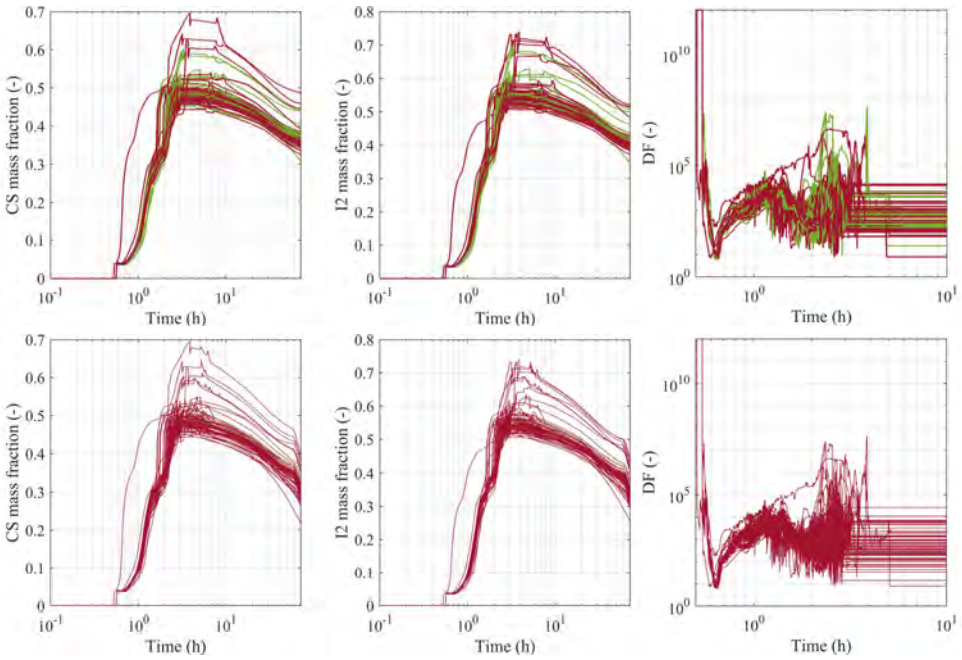

Figure 8. Time evolution of FPs during SBO-IDEJ1 (1st row) and SBO-IDEJ0 (2nd row).

Similar trends are observed for DF in the two scenarios, as most of the scrubbing occurs before LHF and the effect of mode of debris ejection is seen after LHF. Largely similar trends are observed in cesium and iodine mass fractions, except in the case of IDEJ0 where WW pool boils off below BD exit beyond ~60h when loss of FPs is increased.

4.4. Sensitivity and Uncertainty Analysis

For the 18 screened parameters Morris global sensitivity study was performed using samples generated using DAKOTA. The Morris index μ^* gives the significance of a parameter while Morris index σ gives the potential interaction with other parameters and non-linear input behaviour of the parameter. The Morris diagrams for CS and I2 mass fractions in the WW during SBO-IDEJ0 and IDEJ1 are presented in Figure 9 and Figure 10 respectively. The traditional correlation (Pearson and Spearman coefficients) plots for the same FOMs are presented in Figure 11 and Figure 12. The aerosol agglomeration shape factor (GAMMA) is the most significant factor in the amount of CS and I2 retained in the WW. This factor also has the largest linear correlation coefficients, indicating that increasing irregularity in aerosols increases the retention of FPs in the WW, mainly by gravitational settling and deposition. This is true in the case of both cesium and iodine irrespective of mode of debris ejection.

(a)

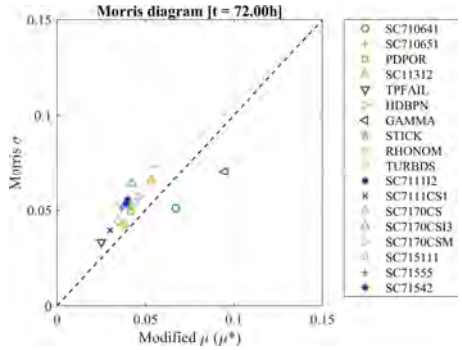

(b)

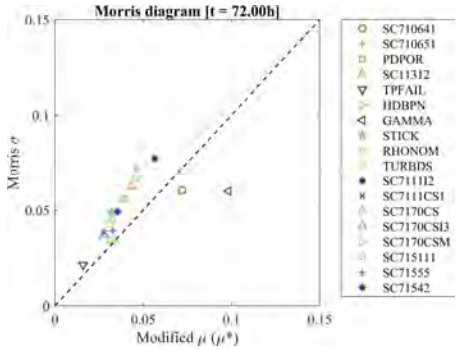

Figure 9. Morris diagrams for CS mass fraction in (a) SBO-IDEJ0 and (b) SBO-IDEJ1.

(a) (b)

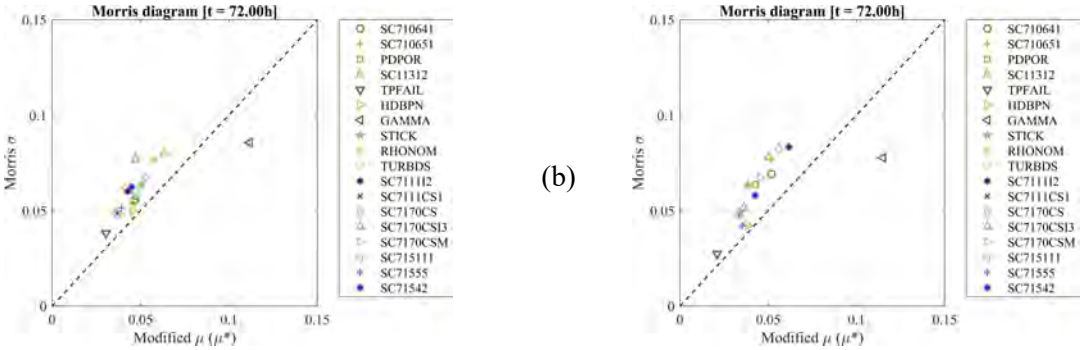

Figure 10. Morris diagrams for I2 mass fraction in (a) SBO-IDEJ0 and (b) SBO-IDEJ1.

(a) (b)

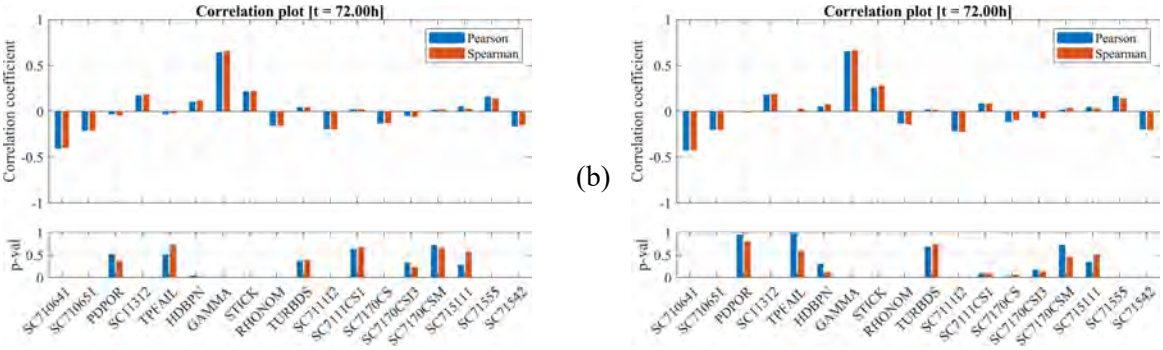

Figure 11. Correlation coefficients for CS mass fraction in (a) SBO-IDEJ0 and (b) SBO-IDEJ1.

(a) (b)

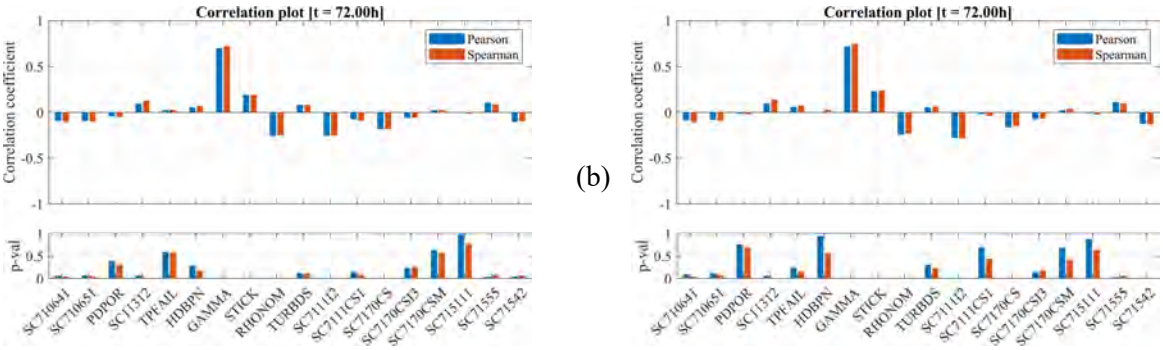

Figure 12. Correlation coefficients for I2 mass fraction in (a) SBO-IDEJ0 and (b) SBO-IDEJ1.

Next to GAMMA, the Activation energy in CORSOR-Booth release model (SC710641) is the most significant and negatively correlated to CS mass fraction. This is especially when one considers the most significant phenomenon that affects WW FP is the release of FPs from the fuel right after ADS is activated, so that any FP transfer to WW is affected by the release model. This is not however significant to I2, indicating most of the impact is towards species not containing CsI aerosols. SC11312 and SC7111I2, the critical temperature when molten material is released from oxide shells and vapour diffusivity constant for iodine RN class respectively, are significant parameters for iodine mass in WW during SBO-IDE0 and SBO-IDEJ1. SC1112 also affects debris relocation in the core which can be assumed to impact whether or not debris remains after LHF. These parameters are important due to their interaction and non-linear behaviour after the debris has been ejected to the cavity, and until just few hours after LHF it is only SC710641 which is the most significant parameter, indicating any future model development for analysis of WW FP retention should focus on advancing study of FP release models in the fuel.

(a) (b)

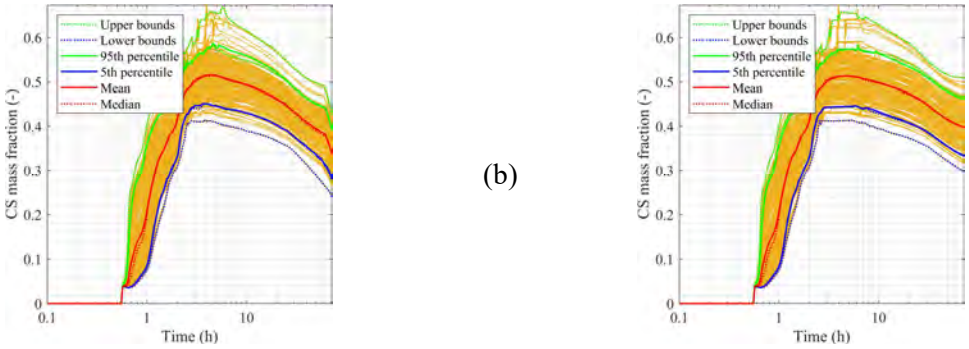

Figure 13. Uncertainty distributions in CS mass fraction in (a) SBO-IDEJ0 and (b) SBO-IDEJ1.

(a) (b)

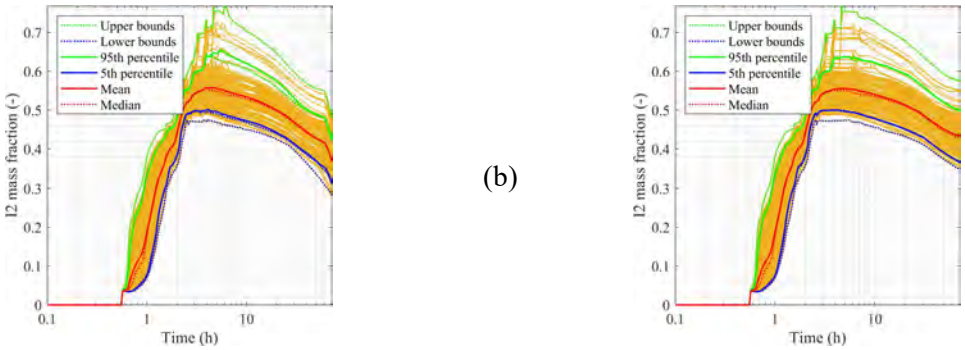

Figure 14. Uncertainty distributions in I2 mass fraction in (a) SBO-IDEJ0 and (b) SBO-IDEJ1.

Following the sensitivity analysis, the same 18 screened parameters were used to generate 160 samples with LHS in DAKOTA. The distributions of the FOMs in the WW are presented in Figure 13 and Figure 14. It is seen that 95th percentile of CS mass fraction in the IDEJ0 scenario lies around 0.39 and in the case of IDEJ1 around 0.46. From the peak mean retention of 0.5 at around LHF, due to evaporation and revapourization of aerosols, CS fraction reduces by 30% in IDEJ0 and 20% in IDEJ1. For the I2 mass fraction in the WW, the 95th percentile in IDEJ0 is around 0.47 and in IDEJ1 around 0.5. Consequently from the peak I2 retention of 0.55 at LHF, IDEJ0 sees around 32% and IDEJ1 around 15% by the end of 72h.

5. CONCLUSIONS

This paper analyzed the behaviour of the WW during an unmitigated SBO accident in Nordic BWR using MELCOR. Initially a reference accident case was analyzed to understand the thermal-hydraulics and fission product transport from the time of release in the RPV to the end of simulation at 72h for 2 splinter modes of debris ejection. It has to be kept in mind that all the analysis performed was with a single CV representing the WW without any axial distributions or natural circulation in the pool. As expected, it was observed that WW accumulates majority of the FPs such as cesium and iodine fractions in its pool phase. Presence of NCGs along with steam in the inlet of the ADS is seen to reduce scrubbing of the aerosols that are then transferred to the gas space. Differences in FPs retained based on mode of debris ejection was not as predominant as in LOCA, mainly because all the FPs released from the fuel have accumulated in the WW than elsewhere in the reactor (such as in CNT), where the mode of debris ejected can play a role. Based on the sensitivity analysis performed with 18 screened uncertain parameters, it was observed that SC710641 of the CORSOR-Booth release model and GAMMA of the aerosol dynamics model are the most significant parameters in the mass accumulated in the WW respectively before and after massive debris ejection to the cavity. From the magnitude of FPs in the WW itself, there appears to be no large impact of mode of debris ejection (IDEJ) during SBO on mass of FP retention in the WW. While effect of particle size, pool bulk temperature and NCGs on the DF was observed, effect of other variables such as nodalization and submergence of ADS valves needs to be assessed in the future.

ACKNOWLEDGMENTS

This work is supported by the Nordic Nuclear Safety Research (NKS), under the NKS-R STATUS activity (Contract: AFT/NKS-R(21)133/5) and by the SSM ROAAM+ project at the Royal Institute of Technology (KTH), Stockholm, Sweden.

REFERENCES

1. NEA, The Fukushima Daiichi Nuclear Power Plant Accident: OECD/NEA Nuclear Safety Response and Lessons Learnt, OECD Publishing, Paris, 2013.
2. R. Gauntt, et al., Fukushima Daiichi Accident Study (Status as of April 2012). SAND2012-6173, Sandia National Laboratories, Albuquerque, New Mexico, 2012.
3. M. Pellegrini, et al., Main findings, remaining uncertainties and lessons learned from the OECD/NEA BSAF project. NURETH18, August 18–22, Chicago, USA, 2019.
4. T. Lind, et al., Overview and outcomes of the OECD/NEA benchmark study of the accident at the Fukushima Daiichi NPS (BSAF), Phase 2 – results of severe accident analyses for unit 3. Nuclear Engineering and Design, 376, pp. 111138, 2021.
5. L.E. Herranz., et al., Lessons learned from the Fukushima analysis: The modeling of severe accidents in nuclear power plants. NURETH16, August 20–Sept. 4, Chicago, USA, 2015.
6. P.C. Owczarski,K. W. Burk, SPARC-90: A code for calculating fission product capture in suppression pools. NUREG/CR--5765, 1991.
7. S.A. Ramsdale, et al., BUSCA-JUN91 reference manual. PSI--95-05, 1995.
8. A.T. Wassel, et al., SUPRA: A Code for Simulating Removal of Radionuclides by Water Pools Under Severe Accident Conditions. EPRI/NP-3886-CCMP, 1985.
9. L.L. Humphries, et al., MELCOR Computer Code Manuals Vol. 1: Primer and Users' Guide Version 2.2.19018. SAND2021-0252 O, Sandia National Laboratories, Albuquerque, New Mexico, USA, 2021.
10. P. Chatelard, et al., ASTEC V2 severe accident integral code main features, current V2.0 modelling status, perspectives. Nuclear Engineering and Design, 272, pp. 119-135, 2014.
11. M. Kuhlman, et al., Scrubbing of fission product aerosols in LWR water pools under severe accident conditions. IAEA conference on Source Term Evaluation for Accident Conditions, pp. 633-648, 1985.
12. A. Dehbi, et al., Aerosol retention in low-subcooling pools under realistic accident conditions. Nuclear Engineering and Design, 203(2–3), pp. 229-241, 2001.
13. M. Marcos-Crespo, et al., LACE-España Experimental Programme on the Retention of Aerosols in Submerged Beds. CIEMAT, ITN/TS-08/DP-93, 1993.
14. L.S. Lebel, et al., Aerosol Experiments and Measurement Techniques on Pool Scrubbing-Related Source Term Issues. NURETH19, March 6-11, The Square, Brussels, Belgium, 2022.
15. H. Li, P. Kudinov, An approach toward simulation and analysis of thermal stratification and mixing in a pressure suppression pool. NUTHOS7, October 9, Seoul, Korea, Paper 243, 2008.
16. I. Gallego-Marcos, et al., Modelling of pool stratification and mixing induced by steam injection through blowdown pipes. Annals of Nuclear Energy, 112, pp. 624-639, 2018.
17. S. Estévez-Albuja, et al., Modelling of a Nordic BWR containment and suppression pool behavior during a LOCA with Gothic 8.1. Annals of Nuclear Energy, 136, pp. 107027, 2020.
18. X. Wang, et al., Simulation of jets induced by steam injection through multi-hole sparger using effective heat and momentum models. Nuclear Engineering and Design, 405, pp. 112222, 2023.
19. P. Kudinov, et al., A Framework for Assessment of Severe Accident Management Effectiveness in Nordic BWR Plants. Probabilistic Safety Assessment and Management PSAM12, June 22–27, Honolulu, Hawaii 2014.
20. S. Galushin, et al., Implementation of framework for assessment of severe accident management effectiveness in Nordic BWR. Reliability Engineering and System Safety, 203, pp. 107049, 2020.
21. D. Grishchenko, et al., Risk of containment failure due to ex-vessel steam explosion for Nordic BWRs. NURETH18, August 18-23, Portland, OR, 2019.
22. S. Galushin, et al., Analysis of the Effect of Vessel Failure and Melt Release on Risk of Containment Failure Due to Ex-Vessel Steam Explosion in Nordic Boiling Water Reactor Using ROAAM+ Framework. Nuclear Engineering and Radiation Science, 6(4), pp. 041113, 2020.
23. S. Galushin, et al., Source Term and Timing Uncertainty in Severe Accidents NKS-STATUS Phase 3 report. NKS-487, 2024.

24. G. Acharya, et al., Source Term Uncertainty Analysis of Severe Accidents in Nordic BWRs. NURETH20, August 20–25, Washington D.C., USA, 2023.
25. G. Acharya, et al., Effect of Debris Ejection Mode on the Accident Progression and Source Term in Nordic BWRs. ICONE32, June 22-26, Shandong, China, 2025.
26. L. Nilsson, Development of an Input Model to MELCOR 1.8.5 for Oskarshamn 3 BWR. SKI Report 2007:05, 2006.
27. L.E. Herranz, et al., Mitigation of source term in suppression pools: Large uncertainties in predictability. Annals of Nuclear Energy, 120, pp. 509-515, 2018.
28. F. Campolongo, et al., An effective screening design for sensitivity analysis of large models. Environment Modelling and Software, 22(10), pp. 1509-1518, 2007.
29. N.W. Porter, Wilks' Formula Applied to Computational Tools: A Practical Discussion and Verification. SAND2019-1901J, Sandia National Laboratories, Albuquerque, New Mexico, 2019.
30. K.R. Dalbey, et al., Dakota, A Multilevel Parallel Object-Oriented Framework for Design Optimization, Parameter Estimation, Uncertainty Quantification, and Sensitivity Analysis: Version 6.12 Theory Manual. SAND2020-4987, Sandia National Laboratories, Albuquerque, New Mexico, 2020.
31. A. Petrovic de With, et al., Three-dimensional condensation regime diagram for direct contact condensation of steam injected into water. International Journal of Heat and Mass Transfer, 50(9-10), pp. 1762-1770, 2007.
32. G. Acharya, et al., MELCOR Analysis of the Nordic BWR Pressure Suppression Pool During LOCA. ICAPP 2025, September 17–19, Juan-les-Pins, France, 2025.
33. A. Rýdl, et al., Modeling of Aerosol Fission Product Scrubbing in Experiments and in Integral Severe Accident Scenarios. Nuclear Technology, 205(5), pp. 655-670, 2018.
34. L.E. Herranz, et al., New pool scrubbing correlations based on reliable data. Annals of Nuclear Energy, 183, pp. 109639, 2023.

APPENDIX A

No	Parameter	Description	Range	Units
1	SC710641	Activation energy in Booth release model	241000 - 381400	J/kg-mole
2	SC710651	Equivalent sphere radius of fuel grain in Booth release model	0.000006 - 0.00001	m
3	PDPOR	Porosity of particulate debris	0.3 - 0.5	
4	SC11312	Critical breach temperature at which molten materials are released from an oxide shell or local blockage (crust)	2100 - 2500	K
5	TPFAIL	Failure temperature of the penetrations or the LH	1273 - 1600	K
6	HDBPN	Heat transfer coefficient between particulate debris and LH penetration	100 - 1000	W/m^2-K
7	GAMMA	Aerosol agglomeration shape factor	1 - 3	
8	STICK	Particle sticking coefficient	0.5 - 1	
9	RHONOM	Nominal aerosol density in gravitational deposition	1000 - 4900	kg/m^3
10	TURBDS	Turbulence energy dissipation rate	0.00075 - 0.00125	m^2/s^3
11	SC7111I2	Vapour diffusivity constant (characteristic energy of interaction between the molecules divided by the Boltzmann constant) for the FP vapours in the bulk gas (class 4)	467.5 - 632.5	K
12	SC7111CS1	Vapour diffusivity constant (characteristic diameter of the molecule) for the fission product vapours in the bulk gas (class 2)	3.0745 - 401595	A
13	SC7170CS	Saturation solubility at low and high temperature reference for Cs	3.3575 - 4.5425	kg/kg H_2O
14	SC7170CSI3	Saturation solubility at low temperature reference for CsI	0.374 - 0.506	kg/kg H_2O
15	SC7170CSM	Saturation solubility at low and high temperature reference for CsM	0.5695 - 0.7705	kg/kg H_2O
16	SC715111	Weber number multiplier used in the equation for the initial diameter of the gas globule for a sparger-type vent	2.9325 - 3.9675	
17	SC71555	Multiplication constant in the DF factor correlations for large Stokes number	0.9681 - 1.3098	
18	SC71542	Constant in the swarm velocity correlation	0.0025593 - 0.0034626	$I-s/cm^2$

12th CONFERENCE ON
SEVERE ACCIDENTS RESEARCH
May 18-22, 2026 - Madrid, Spain
ERMSAR 2026

MELCOR ANALYSIS OF THE NORDIC BWR PRESSURE SUPPRESSION POOL DURING SBO ACCIDENT

Govatsa Acharya*, Dmitry Grishchenko, Pavel Kudinov
KTH Royal Institute of Technology, Division of Nuclear Science and Engineering,
Albanova University Center, 10691 Stockholm, Sweden.

*govatsa@kth.se
dmitrygr@kth.se
pkudinov@kth.se

1. INTRODUCTION

Pressure suppression pool (PSP), or the wetwell (WW), is a defining safety feature of Boiling Water Reactor(BWR) containments. During loss of coolant accident (LOCA), steam is directed via blowdown (BD) pipes into the submerged pool where it condenses. This process simultaneously scrubs the fission products (FPs) – both aerosols and vapours – from the gas stream as bubbles rise through the water, performing a critical function of radioactive source term reduction.

Post Fukushima Daiichi accident of 2011, research has intensified focus on this scrubbing phenomenon under extended severe accident sequences like station blackout (SBO), where pool dynamics are paramount. A significant finding across studies is the large uncertainty in accident progression analysis, often due to incomplete knowledge of system states and complex, coupled phenomena. Reducing these uncertainties, especially regarding FP retention and source term release, is essential for risk assessment.

In the context of Nordic BWR, uncertainties relating to source term in Nordic BWRs are being assessed at KTH under Risk Oriented Accident Assessment Methodology+ (ROAAM+) with the aim of improving current methodology for addressing safety issues. The present work extends the MELCOR analysis performed earlier to the uncertainties in the WW response to SBO, and its effect on FP retention.

2. METHODOLOGY

A reference unmitigated SBO scenario was initially run with MELCOR v2.2.18019 to set the baseline calculation. (i) Based on literature, significant phenomena and 50 underlying uncertain parameters were listed. (ii) An initial screening for sensitivity was performed for the selected figures-of-merit (FOMs) (> 50% variation from the reference). (iii) A calculation matrix with the 18 screened parameters was developed using DAKOTA to perform Morris OAT global sensitivity analysis and identify the most significant parameters. For Morris analysis, 5 level input space and trajectory of length 20, 380 samples were generated. (iv) Uncertainty quantification was performed with 160 code runs (2nd order Wilks' 95/95 estimates) with cases generated using LHS. Cesium and Iodine mass fractions in WW were considered for the FOMs.

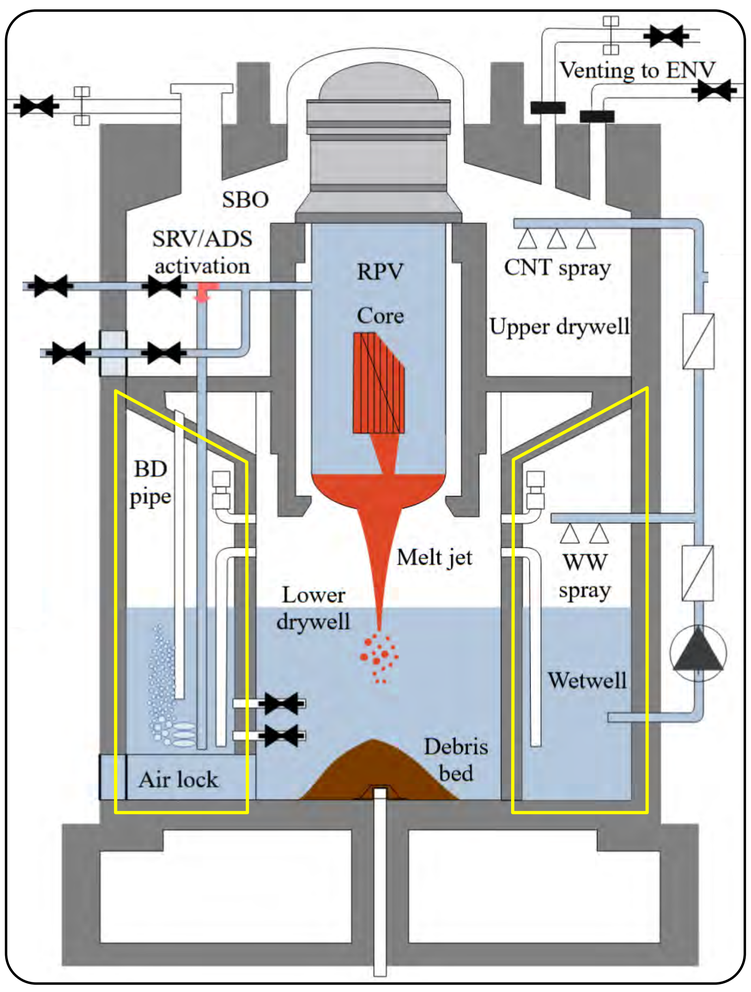

Screened uncertain input parameters.

No	Parameter	Description
1	SC710641	Activation energy in Booth release model
2	SC710651	Equivalent sphere radius of fuel grain
3	PDPOR	Porosity of particulate debris
4	SC11312	Critical breach temperature for release from an oxide shell or local blockage (crust)
5	TPFAIL	Failure temperature of the penetrations
6	HDBPN	Heat transfer coefficient between particulate debris and LH penetration
7	GAMMA	Aerosol agglomeration shape factor
8	STICK	Particle sticking coefficient
9	RHONOM	Nominal aerosol density
10	TURBDS	Turbulence energy dissipation rate
11	SC7111I2	Vapour diffusivity constant (characteristic energy of interaction by Boltzmann constant)
12	SC7111CS1	Vapour diffusivity constant (characteristic diameter of the molecule)
13	SC7170CS	Saturation solubility for Cs
14	SC7170CSI3	Saturation solubility for CsI
15	SC7170CSM	Saturation solubility for CsM
16	SC715111	Weber number multiplier in the initial diameter of the gas globule for a sparger-type vent
17	SC71555	Multiplication constant in the DF factor correlations for large Stokes number
18	SC71542	Constant in the swarm velocity correlation

3. RESULTS

Cesium fraction includes,
RN Class 2 – CsOH.
RN Class 16 – CsI.
RN Class 17 – CsM.
Iodine fraction includes,
RN Class 4 – I2.
RN Class 16 – CsI.

Key events and timing during SBO.

Key event	Time [h]
L4 level	0.2
Uncovery of core	0.23
L6 level	0.31
Gap release	0.56
Particulate debris formation	0.62
Relocation to lowerhead	2.01
Core plate failure	2.01
RPV failure	2.73
LDW boiling	2.73
WW boiling	20

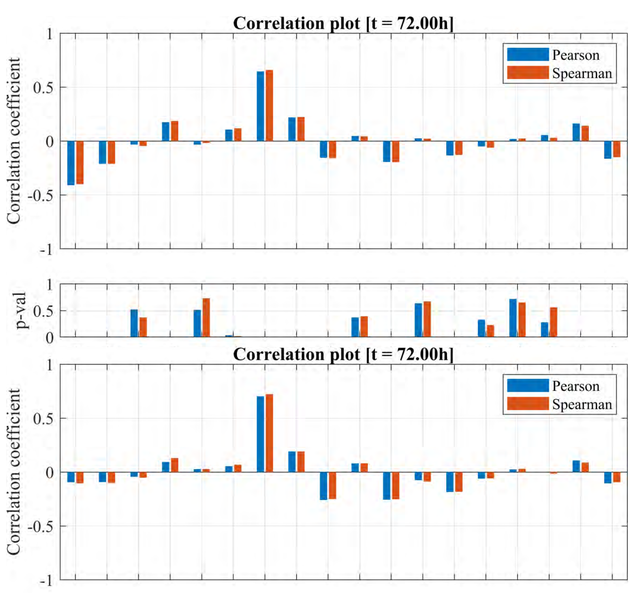

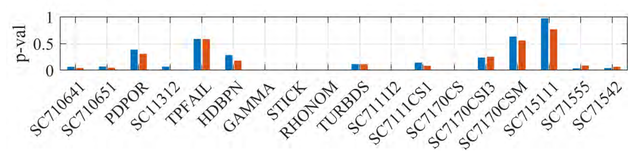

Correlation coefficients of CS and I2 mass fraction in the WW for SBO-IDEJ0.

Morris diagrams of CS and I2 mass fraction in the WW for SBO-IDEJ0.

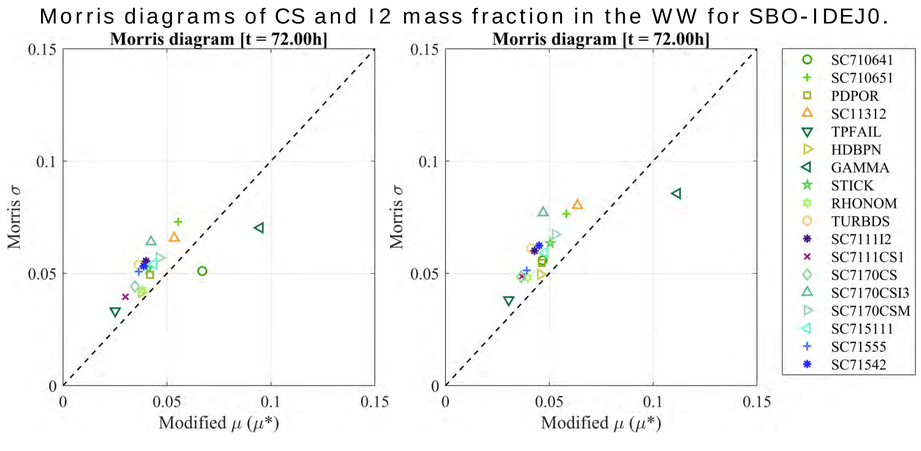

T/H parameters of the plant during SBO-IDEJ0.

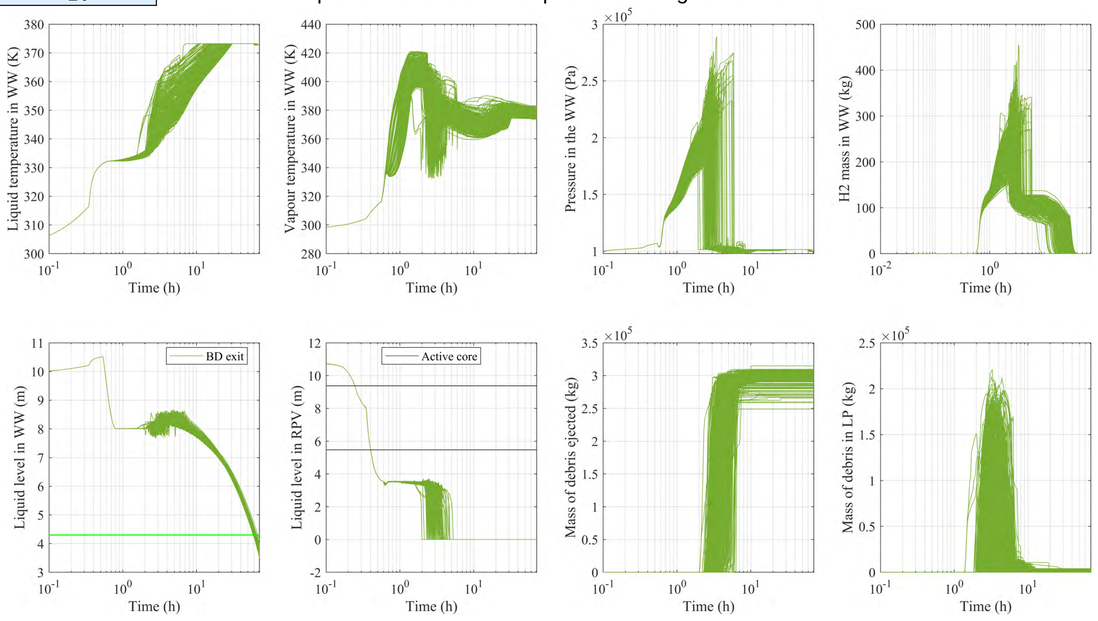

All deposition models and hygroscopic model turned ON, while resuspension model was turned OFF. Scrubbing was active only at the exit of BD pipes and ADS valves. 2 splinter scenarios – MELCOR parameter IDEJ0 and IDEJ1 – with and w/o solid debris ejection mode were tested. A MATLAB driver handles simulation crashes and restarts with automatic time-step refinement. All cases run for 72h.

Decontamination factor (DF) in the ADS valves for SBO-IDEJ0 and SBO-IDEJ1.

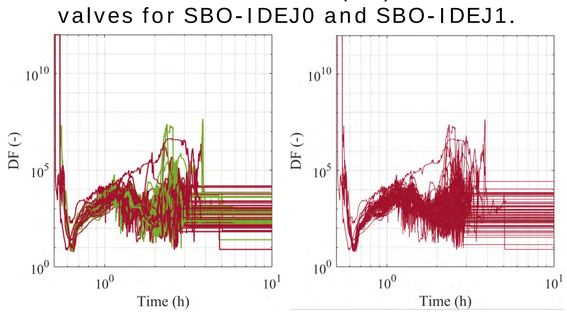

Uncertainty distributions of CS and I2 mass fraction in the WW for SBO-IDEJ0.

Uncertainty distributions of CS and I2 mass fraction in the WW for SBO-IDEJ1.

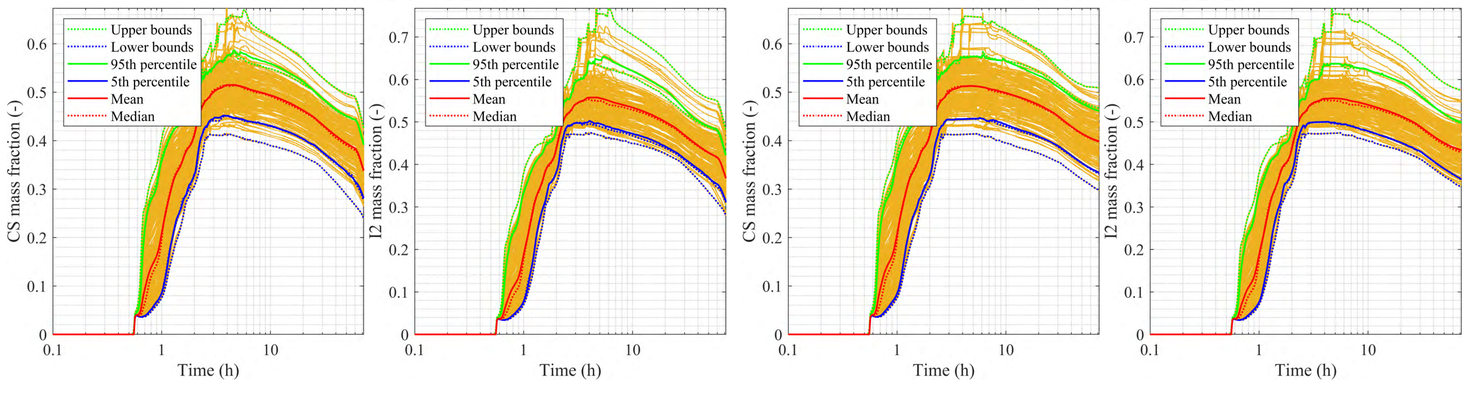

4. CONCLUSIONS

(i) WW accumulates majority of the FPs such as cesium and iodine fractions in its pool phase.
(ii) Effect of mode of debris ejection (IDEJ) was not as predominant as in LOCA, mainly because all the FPs released from the fuel have accumulated in the WW than elsewhere in the reactor (such as in CNT), where the mode of debris ejected can play a role.
(iii) SC710641 of the CORSOR-Booth release model and GAMMA of the aerosol dynamics model are the most important parameters in the mass accumulated in the WW.
(iv) While effect of particle size, pool bulk temperature and non-condensable gases on the DF was observed, effect of WW nodalization and submergence of ADS valves needs to be assessed in the future. It would also be interesting to study the effect of pool thermal stratification on the FP retention capabilities and its behaviour.

ACKNOWLEDGMENTS

This work is supported by the Nordic Nuclear Safety Research (NKS), under the NKS-R STATUS activity (Contract: AFT/NKS-R(21)133/5) and by the SSM ROAAM+ project at the Royal Institute of Technology (KTH), Stockholm, Sweden.

WW: wetwell, SRV: safety relief valve, ADS: automatic depressurization system, RPV: reactor pressure vessel, CNT: containment, BD: blowdown, DF: decontamination factor.

Assessing the Capabilities of MELCOR V2.2 against the QUENCH-19 Bundle Test with FeCrAl Cladding

Rosi Francesco (1), Cazado Mauricio Exequiel (2), Angelucci Michela (3), Paci Sandro (3), Gabrielli Fabrizio (2), Sánchez-Espinoza Victor Hugo (2)

(1) Karlsruhe Institute of Technology / University of Pisa, (2) Kalrsruhe Institute of Technology, (3) University of Pisa

Type of abstract: Poster
Subject area: Other applications (fusion reactors, interim SNF storage, Accident Tolerant Fuels (ATFs), etc
Keywords: QUENCH-19 FeCrAl alloy Hydrogen Generation MELCOR

Advanced Technology Fuel (ATF) concepts have been under development for over a decade, with a significant acceleration in recent years. The aim of these advanced materials is to enhance the safety margins of nuclear reactors in the event of a severe accident (SA) by limiting the hydrogen generation and preserving cladding integrity at high temperatures. Among the proposed ATF candidates, FeCrAl alloys have emerged as a promising option due to their excellent high-temperature oxidation resistance and their ability to reduce hydrogen release compared to conventional Zr-based claddings.

To evaluate the capability of integral SA codes to model innovative materials, this study compares the simulation performance of MELCOR V2.2 against the QUENCH-19 bundle test, which was conducted at the QUENCH large scale facility of the Karlsruhe Institute of Technology (KIT) in 2018. This experiment examined the thermal response, oxidation behaviour and hydrogen release of FeCrAl cladding rods in a bundle configuration under conditions representative of a severe accident. A MELCOR input model was developed to reproduce the experimental configuration and the results were compared with the measured temperatures and hydrogen generation data. Despite some deviations, the comparison shows a satisfactory agreement with the experimental data, highlighting the capability of MELCOR V2.2 to simulate SA scenarios involving ATF claddings such as FeCrAl.

ACKNOWLEDGEMENT: The work has been performed in the framework of the mobility program of the EU SEAKNOT project, which has received funding under the Grant Agreement No. 101060327. The content of this work reflects only the authors' view. The European Commission is not responsible for any use that may be made of the information it contains.

12th CONFERENCE ON
SEVERE ACCIDENTS RESEARCH
May 18-22, 2026 - Madrid, Spain
ERMSAR 2026

ASSESSING THE CAPABILITIES OF MELCOR V2.2 AGAINST THE QUENCH-19 BUNDLE TEST WITH FECRAL CLADDING

F. Rosi[1,2], M. E. Cazado[1], M. Angelucci[2], S. Paci[2], F. Gabrielli[1], V. H. Sánchez-Espinoza[1]

[1]Institute for Neutron Physics and Reactor Technology, Karlsruhe Institute of Technology (KIT), Germany
[2]Department of Civil and Industrial Engineering, University of Pisa (UNIPI), Italy.

1. Introduction & Motivation

- ATF concepts aim to improve reactor safety margins by **reducing hydrogen generation and extending coping** time under off-normal and accident conditions.
- FeCrAl alloys are particularly promising due to their **superior oxidation resistance** in high-temperature steam environments, compared to conventional Zr-based claddings.
- To evaluate the capability of **MELCOR V2.2** to model innovative cladding materials, this study compares simulation results against the **QUENCH-19 bundle test**, conducted at KIT's QUENCH large-scale facility in 2018, focusing on thermal response and hydrogen generation under representative severe accident conditions.

2. FeCrAl Cladding Concept

- Nuclear-grade FeCrAl typically contains ~10-13 wt% Cr and ~5-6 wt% Al. Mo/Y additives enhance oxidation and mechanical performance
- A protective Al_2O_3 layer provides strong oxidation resistance below ~1300 °C, above ~1400 °C Fe-oxide kinetics become dominant.
- **Main advantages**: reduced steam reaction kinetics and lower hydrogen generation.
- **Main challenges**: higher neutron absorption than Zircaloy, tritium permeability, and UO_2-FeO eutectic interactions at ~ 1335 °C.

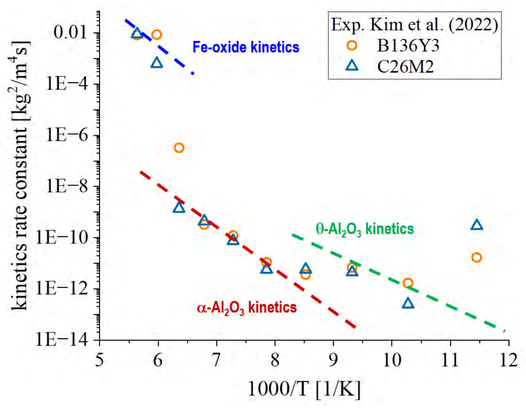

Fig. 1 - Parabolic rate constants of B136Y3 and C26M2 alloys with the parabolic constants of Fe-oxide, α-alumina and θ-alumina [1].

3. QUENCH-19 Bundle Test Modelling with MELCOR

QUENCH-19: first integral ATF bundle test worldwide, performed at KIT in 2018 with FeCrAl (B136Y3) rods.

It assessed the thermal response, oxidation behaviour, and hydrogen release of FeCrAl cladding under severe accident conditions.

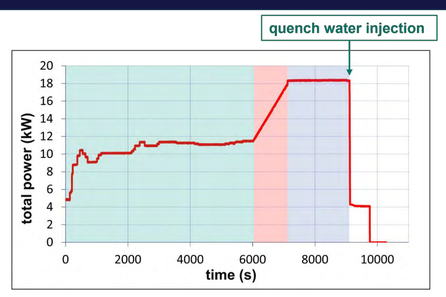

Fig. 2 – QUENCH-19 Electric power [2]

Key experimental findings

✓ No early temperature runaway relative to ZIRLO reference exp (QUENCH-15).
✓ Max. temperature ~200 K lower in the pre-oxidation phase.
✓ Strong H_2 reduction: 9.2 g vs 47.6 g (QUENCH-15).

MELCOR Modelling

CVH Nodalization

- **Test section** divided in **9 Control Volumes** (CVs).
- Additional CVs included for lower plenum, off-gas collector, argon insulation and auxiliary regions.

COR Radial Nodalization

- Test section divided in **three radial rings**.
- Ring 1 and 2 represent the heated region: 12 rods each.
- Ring 3 contains 7 corner rods (unheated) and shroud.

Core Components

- **B136Y3** material defined as the oxidizable user material. Properties obtained from literature and KIT data [3, 4] Claddings, corner rods, shroud, and spacer grids are represented with this user-defined material.
- **B136Y3OX oxide** material represented using MELCOR default properties.
- **W**, **Mo**, and **Cu** (heater/electrode) properties defined through the MP package.
- **ZrO_2 pellets** modelled via UO_2 as a placeholder material with ZrO_2 properties.

FeCrAl Oxidation Model

- Oxidation implemented via a user-defined **GOX model**.
- Ox. kinetics adapted from KIT separate-effect tests (SETs).
- Transition from α-Al_2O_3 to Fe-oxide kinetics at 1400 °C.

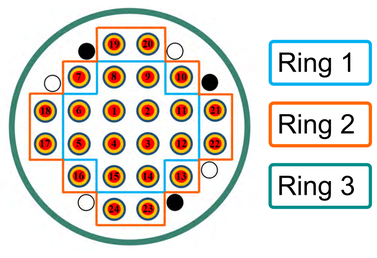

Fig. 3 – Radial Nodalization

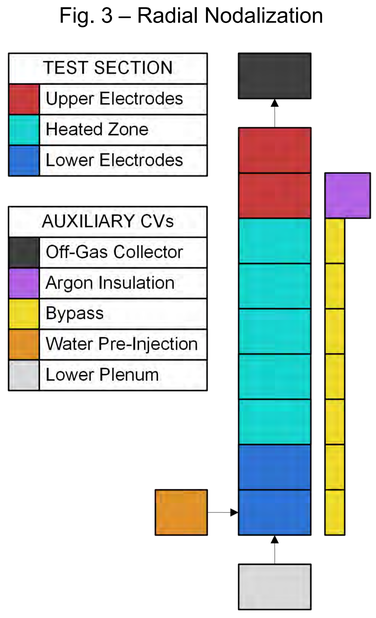

Fig. 4 – CVH Nodalization

4. Simulation Results

A. Cladding Temperature Evolution

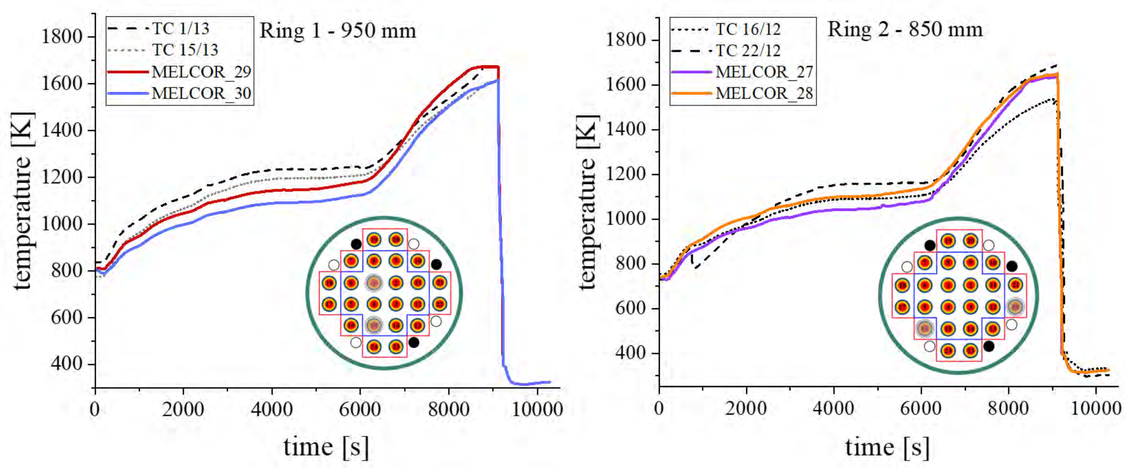

Fig. 5 – Cladding temperature comparison between the experimental data [2] and simulated results at 950 mm elevation in Ring 1 (left) and at 850 mm in Ring 2 (right). The dotted and dashed curves correspond to the experimental thermocouple data: the associated rod positions are highlighted in grey in the test cross-sections.

B. Hydrogen Generation

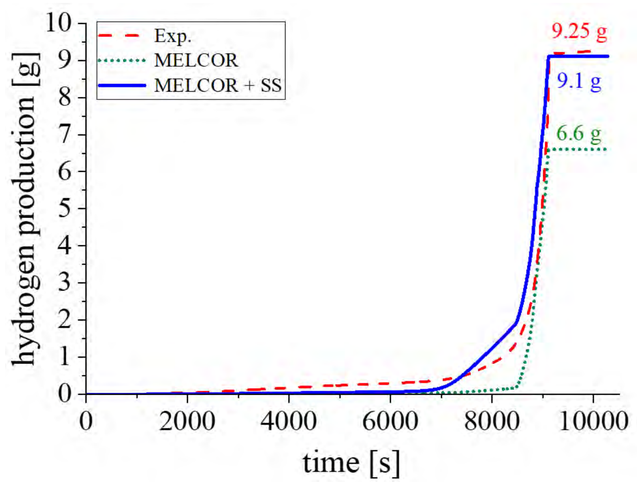

Fig. 6 – Cumulative hydrogen production comparison between the experimental data [2] and MELCOR results. The dotted line shows the MELCOR simulation that considers only the H_2 generated by the FeCrAl material. In contrast, the solid blue line includes the contribution of the oxidation of the stainless steel thermocouple sheaths.

- It is estimated that ~2 g of the experimental H_2 production originates from the **oxidation of stainless-steel thermocouple sheaths**, accounting for ~ 22% of the total measured H_2.
- As these components are not modelled explicitly in MELCOR, their contribution was estimated separately using simulated temperatures and the area of the exposed sheaths.

5. Conclusions

- A MELCOR input deck for QUENCH-19 was developed based on KIT report specifications and FeCrAl oxidation data obtained from KIT SETs.
- Despite some deviations, mainly attributed to core nodalization constraints, **MELCOR shows good agreement with QUENCH-19 data** for temperature evolution and cumulative hydrogen generation.
- **FeCrAl** cladding **significantly mitigates hydrogen generation below ~1400 °C** compared with equivalent tests using Zr-based alloys.
- Oxidation of stainless-steel thermocouple sheaths can provide a relevant additional hydrogen source in ATF experiments and should be considered in the interpretation of the results.

Acknowledgements

The work has been performed in the framework of the mobility program of the EU SEAKNOT project, which has received funding under the Grant Agreement No. 101060327. The content of this work reflects only the authors' view. The European Commission is not responsible for any use that may be made of the information it contains.

References

[1] C. Kim, et al., "Oxidation mechanism and kinetics of nuclear-grade FeCrAl alloys in the temperature range of 500-1500 °C in steam," *Journal of Nuclear Materials*, vol. 564, p. 153696, 2022.

[2] J. Stuckert, et al., "Results of the bundle test QUENCH-19 with FeCrAl claddings," *KIT Scientific Report NUSAFE-3575*, 2022.

[3] P. Aragon, et al., "Modelling FeCrAl cladding thermo-mechanical performance. Part I: Steady-state conditions," *Progress in Nuclear Energy*, vol. 153, 2022.

[4] K.G. Field, et al., "Handbook on the Material Properties of FeCrAl Alloys for Nuclear Power Production Applications (FY18 Version: Revision 1)," ORNL, 20218.

Reactor Physics and Dynamic

Contact: mauricio.cazado@kit.edu

The PIANOFORTE CATAPULT Project: Comprehensive Assessment and Preparedness for Emerging Nuclear Technologies

Gabrielli Fabrizio (1), Cazado M. E. (1), S. S. Ottenburger (1), M. Simon Cornu (2), T. Perko (3), J. Camps (3), G. De With (4), P. Roivainen (5), M. Martell Lamolla (6), D Diaconu (7), R. Gaspar (8)

(1) Karlsruhe Institute of Technology, (2) ASNR, (3) SCK CEN, (4) NRG Pallas, (5) STUK, (6) Merience SCP, (7) RATEN, (8) COFAC - Lusófona University

Type of abstract: Poster
Keywords: Preparedness, Radiological impact, Risk communication, AMRs, Urban siting

The PIANOFORTE CATAPULT project, coordinated by KIT (Germany) and launched in 2025, aims to build comprehensive guidance for Environmental Impact Assessment (EIA) and Emergency Preparedness and Response (EP&R) applied to small (water-cooled) and advanced modular reactors (gas- and lead-cooled), with strong integration of technical and social aspects.

The current knowledge supporting EIA and EP&R, regulatory approaches, and risk communication is mainly based on large water-cooled reactors. Nevertheless, SMRs and AMRs pose several challenges regarding i) limited state-of-art modelling for EIA and EP&R for near field, ii) the need to address the Euratom Basic Safety Standards for modular reactors' deployment, and iii) public concerns about new nuclear technologies, for which communication and community engagement must rely on trust and transparency.

Since EIA is not independent of public concerns and broader risks (and vice versa), a comprehensive approach to address these challenges is studied in CATAPULT. To this end, a highly interdisciplinary consortium (ASNR, COFAC - Lusófona University, KIT, Merience, NRG Pallas, RATEN, SCK CEN, STUK) has been established, combining a broad range of disciplines in radiation protection.

The project is structured around three scientific pillars: 1) Environmental and dose modelling, developing framework of computational methodologies for dose impact and environmental transport analyses tailored to EIA and EP&R for modular reactors; 2) Science-based regulatory compliance, providing recommendations to authorities, operators, and licensees to ensure scientifically credible demonstrations of radiation protection for the public, workers, and environment; and 3) Community Engagement & Risk communication, establishing a community-driven participatory framework by engaging general public, stakeholders, and communities to increase trust, transparency and co-decisions, while delivering evidence-based guidelines and materials for communicating EIA results and informing the public about modular reactor development and implementation.

This work presents CATAPULT's objectives, the strategy adopted to achieve them, and preliminary results.

12th CONFERENCE ON
SEVERE ACCIDENTS RESEARCH
May 18-22, 2026 - Madrid, Spain
ERMSAR 2026

The PIANOFORTE CATAPULT Project: Comprehensive Assessment and Preparedness for Emerging Nuclear Technologies

F. Gabrielli, M. E. Cazado

Karlsruhe Institute of Technology (KIT), Germany

Motivation

- The current knowledge supporting Environmental Impact Assessment (EIA) and Emergency Preparedness and Response (EP&R), regulatory approaches, and risk communication is mainly based on large water-cooled reactors
- SMRs and AMRs pose several challenges regarding
  - **limited state-of-art modelling for EIA and EP&R for near field**
  - need to address the **Euratom Basic Safety Standards** for deployment
  - the public concerns about new nuclear technologies, for which **communication and community engagement must rely on trust and transparency**
- **EIA not independent from the public concerns and wider risks at stake and vice versa**
- Further isolated research in the modelling, compliance, and communication areas will not deliver on practical solutions to the existing challenges

The CATAPULT Project

- **CATAPULT aims at building a comprehensive guidance for EIA and EP&R applied to Small (water-cooled) and Advanced Modular Reactors (Gas- and Lead-cooled) with tight cross-links between technical and social aspects**
- Highly interdisciplinary team (research centers, TSO, universities)
- PIANOFORTE Call 2, Topic 2, duration: 3 years (01.02.2025-31.01.2028)

Pillars, Scope, and Main Goals

- **Environmental and dose modelling**
  - **Improving/adapting the dose** impact and the environmental **transport models**
  - Delivering an **analysis framework tailored to the needs of modular reactors and their typical site locations** to guide end-users in EIA and EP&R modelling
- **Science-based regulatory compliance**
  - **Delivering a comprehensive set of recommendations to authorities, operators, and licensees** to ensure the scientific credibility of the demonstration of radiation protection of the public, including workers from nearby industries, and the environment
- **Community Engagement & Risk communication**
  - **Community-driven participatory framework**, to engage general public, relevant stakeholders, and communities to increase trust, transparency and co-decisions, towards a more holistic EIA
  - **Providing evidence-based, co-designed communication tools that clearly present EIA results and inform the public about modular reactors**

Work Plan and Methodology

- Cross-fertilization of research disciplines tailored to develop a fit-for purpose framework on EIA modelling, regulatory compliance, and engagement with the community

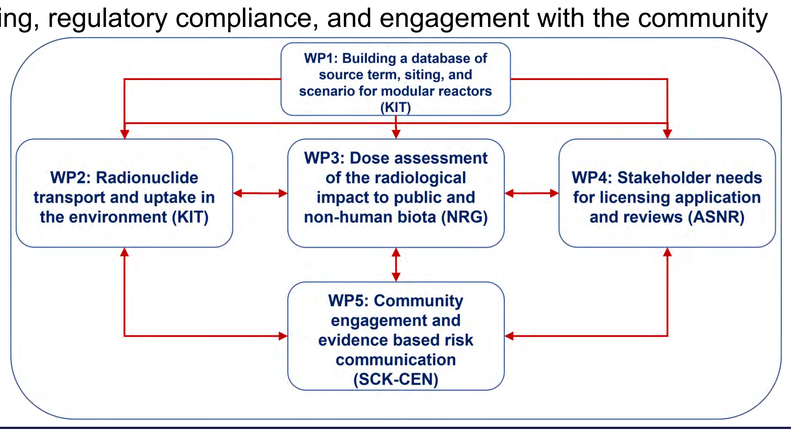

WP1 – Building a database of source term, siting, and scenario for modular reactors (KIT, RATEN, STUK)

- **Source terms database (nominal and accident conditions, atmospheric and effluent)**
  - Water-cooled SMR (submerged containment, 60 Mwe)
  - Lead-cooled ALFRED-like (125 MWe)
  - Gas-cooled HTR-like (200 MWth)
- **Extensive database of the siting (websites, maps, tables)**
  - **Industrial site** next to heavy/chemical industry (Stein, Limburg, Netherlands)
  - **Urbanized site** - close to urban and industrial zones (Arnhem, Gelderland, Netherlands)
  - **Natura2000 site** - Petten (Netherlands)
  - **Urbanized site for district heating** (Helsinki, Finland)

WP2 – Radionuclide transport and uptake in the environment (KIT, ASNR, NRG, SCK-CEN, STUK)

- **Adaptation and enhancement of state-of-the-art atmospheric and aquatic radionuclide transport and dispersion** as well as food chain models
- Improving the atmospheric transport and dispersion models for small-scale and urban conditions (LASAIR + JRODOS, FLEXPART + AROME)
- Aquatic transport and dispersion models (3D hydrological/compartment, high-resolution 2D-3D hydrological modelling of radionuclide pollutants, freshwater and low-flow rivers)
- Food chain models (e.g., JRODOS, SYMBIOSE, D-DAT)

WP3 – Dose assessment of the radiological impact to public and non-human biota (NRG, ASNR, SCK CEN, STUK)

- **Review and analysis of present models and selection of exposure conditions** for members of the public including workers from nearby industries and for non-human biota **based on stakeholder needs**
  - Dose calculations and a sensitivity analysis on the variations in exposure conditions to establish variations in dose for the (critical) reference person and wildlife
  - Identify deficiencies providing input for a work plan on future development
- **Prioritisation of features** that are important in the assessment (interaction with WP4)

WP4 – Stakeholder needs for licensing application and reviews (ASNR, NRG, RATEN, STUK)

- **Development of regulatory guidance** based on
  - **case studies** (WP1, WP2, WP3)
  - **round-tables with experts** from authorities and TSO involved in the reviewing of applications from prospective licensees
  - **feedback from a wider audience**, including developers of modular reactors, their subcontractors and representatives of public engagement and risk communication (WP5)

WP5 – Community engagement and evidence based risk communication (SCK CEN, COFAC-UL, MERIENCE)

- **Develop a two-stage Community-Driven approach** to enhance public perception and address public mistrust, mitigating “not in my backyard” (NIMBY) responses
- **Develop citizen-centred and evidence-based risk communication strategy and materials** related to EIA by providing transparent, accurate and comprehensible information from the other WPs (**Design Thinking Approach**)
- The **Delphi method** will be used to provide implementation guidance for effective and evidence-based risk communication by leveraging a panel of communication experts

Summary

- CATAPULT is tailored at the **specific needs of modular reactors** in assessing their radiological risks to the environment during routine and accidental operation
- CATAPULT uses **cutting-edge modelling**, **novel communication science**, and **broad stakeholder co-design** to deliver transparent, evidence-based EIAs
- With a **multi-disciplinary team**, CATAPULT aims at delivering **essential guidance** to authorities, TSOs, operators, and licensees, advancing a standardized, **fit-for-purpose EIA and EP&R approach**

Acknowledgements

This research is conducted in the context of the CATAPULT Project which received funding from the European Partnership for Radiation Protection Research PIANOFORTE Horizon Euratom Research (101061037) under the PIANOFORTE Funding Agreement Ref. ASNR 2025-0018

O. Murat, S. S. Ottenburger, D. Trybushnyi, W. Raskob, M. Simon-Cornu, N. S. Abdul Rashid, M. Roulier, N. Didelot, G. Mathieu, A. Mathieu, M. Martell Lamolla, G. De With, B. Mayer, A. Tacu, T. Van Dijk, D. Diaconu, M. Nitoi, M. Constantin, C. Dulama, T. Perko, J. Camps, J. Vives i Battle, T. Al Malhaini, A. Nagy, P. De Meutter, P. Roivainen, T. Routamo, T. Peltonen, M. Voutilainen, E. Hiittenkivi, J. Mannonen, R. Gaspar, S. Domingos, A. R. Farias, J. Reese

PIANOFORTE CATAPULT

Co-funded by the European Union

Contact: Fabrizio.gabrielli@kit.edu

https://pianoforte-partnership.eu/catapult

https://www.linkedin.com/company/pianoforte-partnership/

12th CONFERENCE ON
SEVERE ACCIDENTS RESEARCH
May 18-22, 2026 - Madrid, Spain
ERMSAR 2026

ASSAS project: Creating Infrastructure and Training Database for Surrogate Models for a Severe Accident Simulator

Anastasia Stakhanova, Fabrizio Gabrielli, Jonas Dressner, Markus Götz, Charlotte Debus - Karlsruhe Institute of Technology (KIT), Germany; Ivo Kljenak, Saso Dzeroski - Jožef Stefan Institute (JSI), Slovenia; Joan Fontanet Sáez - Unidad de Seguridad Nuclear (CIEMAT), Spain; Alessandro Longhi - Delft University of Technology, Netherlands; Marcello Savini - Alma Mater Studiorum University of Bologna, Italy; Christophe Jean Lino D'Alessandro - Paul Scherrer Institute (PSI), Switzerland; Gaëtan Blondet - PHIMECA ENGINEERING, France; Bastien Poubeau - Autorité de sûreté nucléaire et de radioprotection (ASNR), France

ASSAS - **A**rtificial Intelligence for the **S**imulation of **S**evere **A**ccident**S**

- Euratom project (Nov-22 to Oct-26)
- 14 partners - €3.7 million budget
- Coordinator: Bastien Poubeau (ASNR) (till March 2026), Ricaud Jean Marc (ASNR) - currently

Create a prototype simulator for a Western-type PWR

Severe accident code ASTEC (Accident Source Term Evaluation Code) developed by ASNR

+

Commercial simulation environment TEAM_SUITE® developed by Tecnatom

Speed-up severe accident simulations with:

- Input deck simplification
- Parallelization and code optimization
- Substitute parts of the code with surrogate models

Database for surrogate model training:

- Station blackout and medium break loss-of-coolant scenarios
- 10 operator actions as uncertain input parameters. Other model parameters fixed at their best estimate values.
- More than 1000 simulations performed
- Outputs: Scalar, 1D and 2D time dependent variables
- High saving frequency: all timesteps (1-10s)

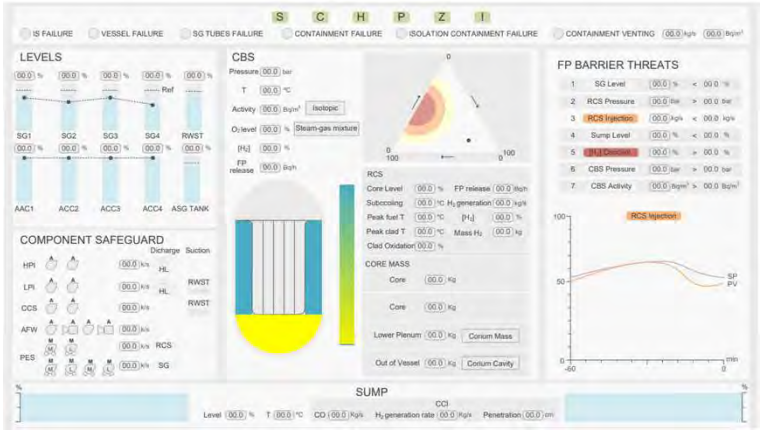

Simulator interface – Severe accident dashboard

DataHub

- Developed by SCC KIT
- Data stored at the Large Scale Data Facility (LSDF)
- Based on FAIR principles – Findable, Accessible, Interoperable, Reusable
- ASSAS partners can upload, download and explore data
- Potentially reusable for future collaborations beyond ASSAS

70-100 Gb binary ASTEC file (one sequence)

↓

1-2 Gb HDF5 file

By identifying the variables relevant for surrogate models training

17	1102	76.56 TB	2.3 TB	204
Registered users	Available Datasets	Binary storage size	HDF5 storage size	ASTEC variables per dataset
Researches with platform access	ASTEC simulation datasets	Binary simulation data	Hierarchical data format	Typical number of variables per dataset

Platform Statistics & Capabilities

ASNR · BEL V · ES GROUP · Ciemat · ENEA · ENERGORISK · Jožef Stefan Institute · ivs · KIT Karlsruhe Institute of Technology · KTH · PHIMECA L'ingénierie responsable · PAUL SCHERRER INSTITUT PSI · TU Delft · tecnatom

Project partners

assas

Artificial intelligence for Simulation of Severe Accidents
http://assas-horizon-euratom.eu
info@assas-horizon-euratom.eu

Karlsruher Institut für Technologie

3D Estimation Diagrams of Units 1–3 at the Fukushima Daiichi Nuclear Power Station Updated in 2025

Yamashita Takuya (1), Shimomura Kenta Shimomura, Nagai Eiichi, Yasumatsu Tomohiro, Nakashima Satoru, Ogino Shoya, Mizokami Shinya

(1) JAEA

Type of abstract: Poster
Subject area: Other applications (fusion reactors, interim SNF storage, Accident Tolerant Fuels (ATFs), etc
Keywords: Fukushima Daiichi Nuclear Power Station, 3D estimation diagrams

Internal investigations at the Fukushima Daiichi Nuclear Power Station (1F) have gradually clarified the plant conditions. Trial debris retrieval has provided additional insights, but individual datasets alone are insufficient to fully understand accident progression and overall plant status. Previously, two-dimensional estimation diagrams were developed to support visualization and comprehension of reactor conditions; however, these diagrams were limited in conveying spatial relationships and detailed information.

To enhance visualization and support decommissioning activities, three-dimensional estimation diagrams (3D estimation diagrams) have been developed by constructing a 3D model of the entire plant based on internal investigation results, design information, and estimates from analyses and simulated test results. The 3D diagrams enable interactive visualization from any viewpoint, allowing users to examine complex structures, assess debris locations, and interpret accident progression more intuitively.

By integrating data from multiple sources and presenting them in a spatially coherent 3D format, these diagrams facilitate better understanding of plant conditions, support planning of decommissioning operations, and improve communication among engineers and stakeholders.

The updated 3D estimation diagrams for Units 1–3, developed through 2025, are described, highlighting their role in enhancing comprehension of accident progression and contributing to more effective and efficient decommissioning strategies.

12th CONFERENCE ON
SEVERE ACCIDENTS RESEARCH
May 18-22, 2026 - Madrid, Spain
ERMSAR 2026

3D Estimation Diagrams of Units 1–3 at the Fukushima Daiichi Nuclear Power Station Updated in 2025

Takuya Yamashita, Kenta Shimomura (JAEA), Eiichi Nagai (Prometech), Tomohiro Yasumatsu (NDD), Satoru Nakashima, Shoya Ogino, Shinya Mizokami (TEPCO)

Abstract

Internal investigations at the Fukushima Daiichi Nuclear Power Station (1F) have gradually clarified the plant conditions. Trial debris retrieval has provided additional insights, but individual datasets alone are insufficient to fully understand accident progression and overall plant status. Previously, two-dimensional estimation diagrams were developed to support visualization and comprehension of reactor conditions; however, these diagrams were limited in conveying spatial relationships and detailed information. To enhance visualization and support decommissioning activities, three-dimensional estimation diagrams (3D estimation diagrams) have been developed by constructing a 3D model of the entire plant based on internal investigation results, design information, and estimates from analyses and simulated test results. The 3D diagrams enable interactive visualization from any viewpoint, allowing users to examine complex structures, assess debris locations, and interpret accident progression more intuitively.

By integrating data from multiple sources and presenting them in a spatially coherent 3D format, these diagrams facilitate better understanding of plant conditions, support planning of decommissioning operations, and improve communication among engineers and stakeholders. The updated 3D estimation diagrams for Units 1–3, developed through 2025, are described, highlighting their role in enhancing comprehension of accident progression and contributing to more effective and efficient decommissioning strategies.

Unit 1

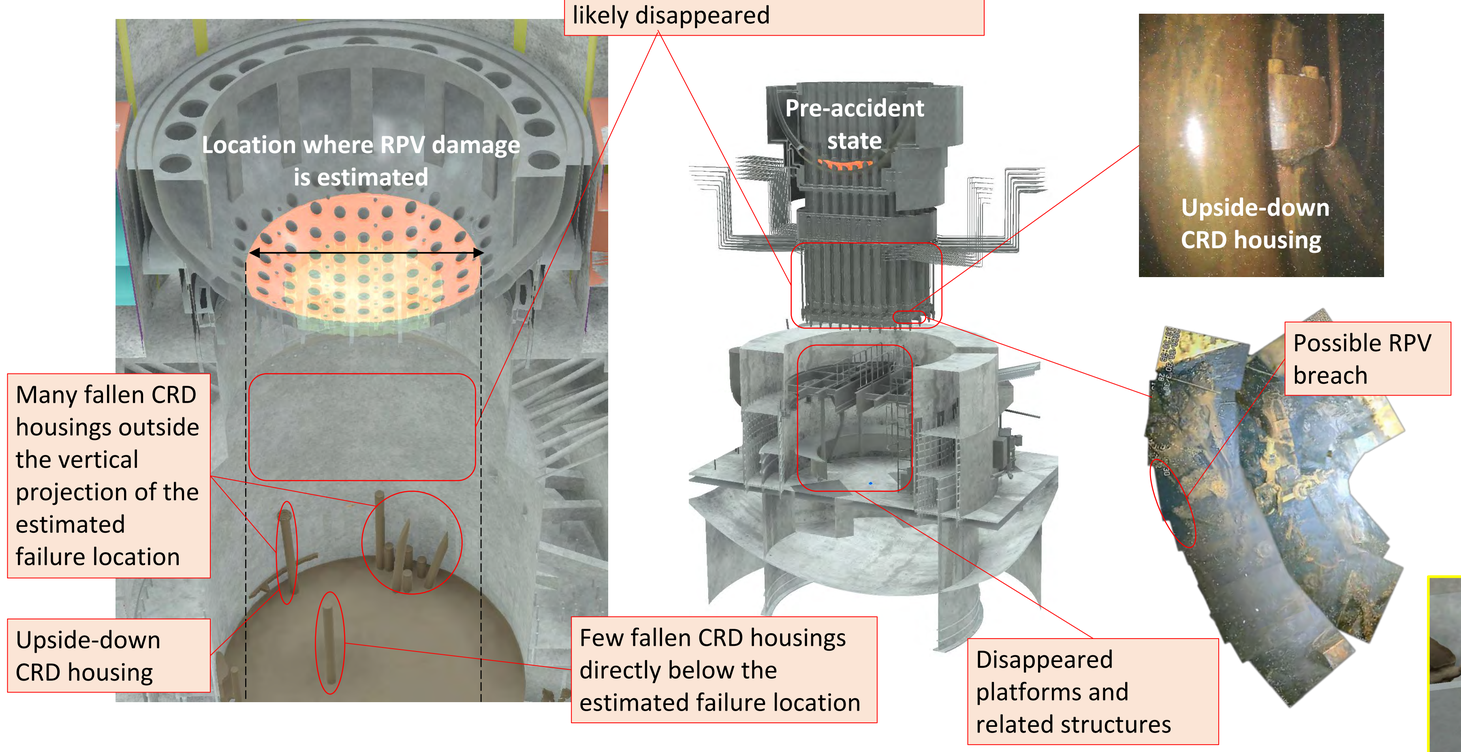

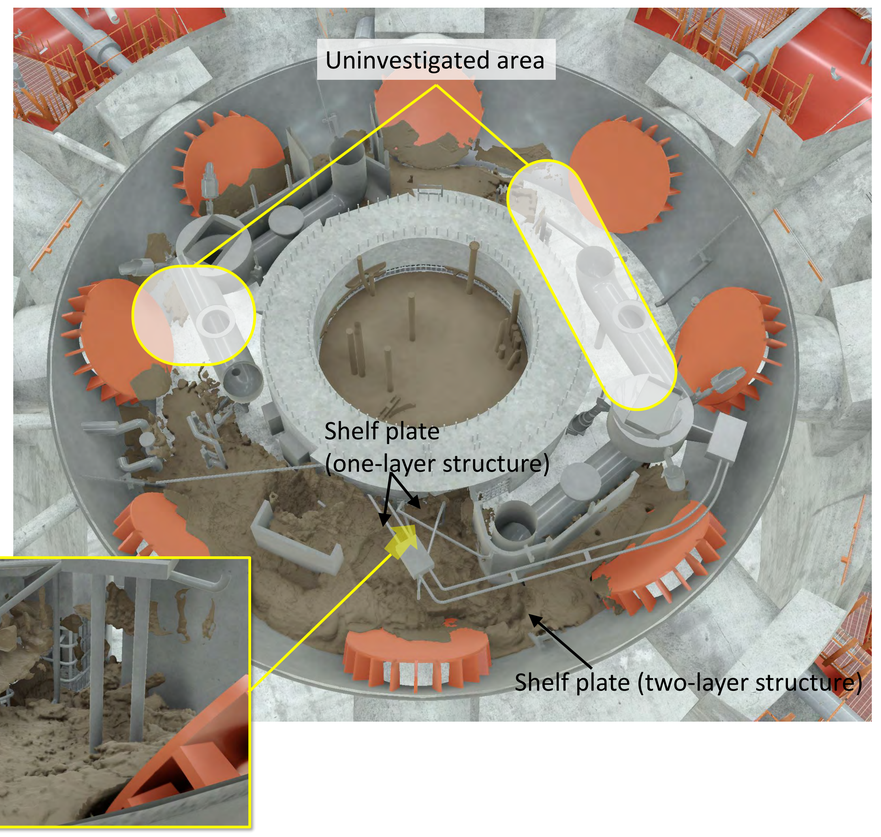

Unit 2

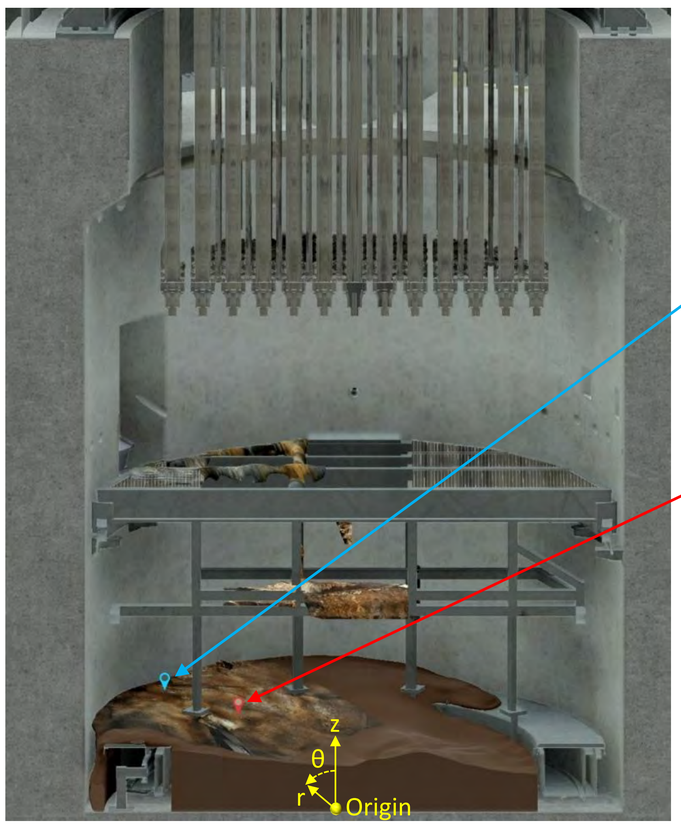

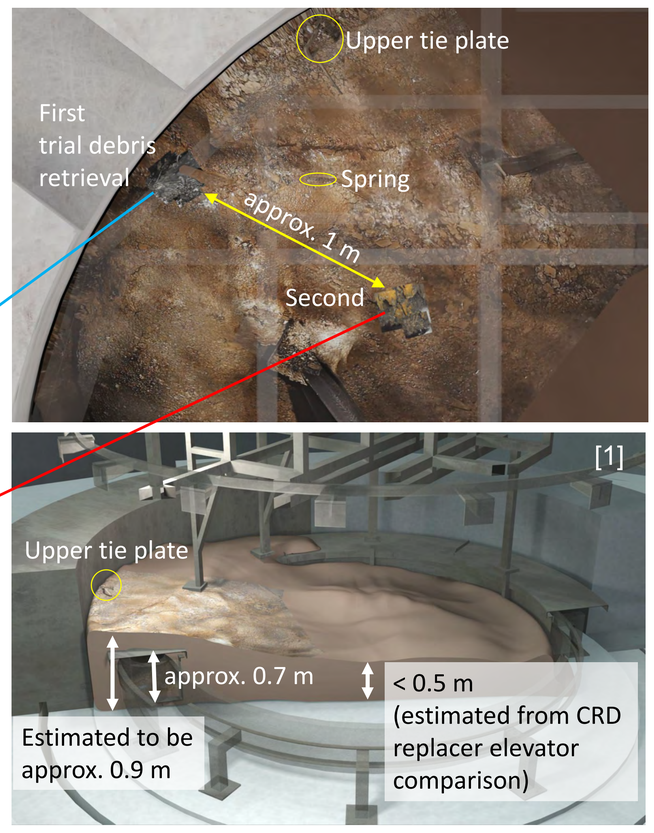

Estimated sampling locations

	Radial distance (r)	Angle from north (θ)	Height from floor (z)
First trial debris retrieval	approx. 2.4 m	approx. 54°	approx. 0.9 m
Second trial debris retrieval	approx. 1.4 m	approx. 42°	approx. 0.8 m

- Shown in a cylindrical coordinate system with origin at the pedestal floor center.
- Fuel debris height is estimated from platform leg coverage and is not directly measured; thus, it is a reference value.

Unit 3

In March 2026, the RPV lower head above this location was internally investigated using a micro-drone [2]. This will be reflected in the 3D estimation diagram in the near future.

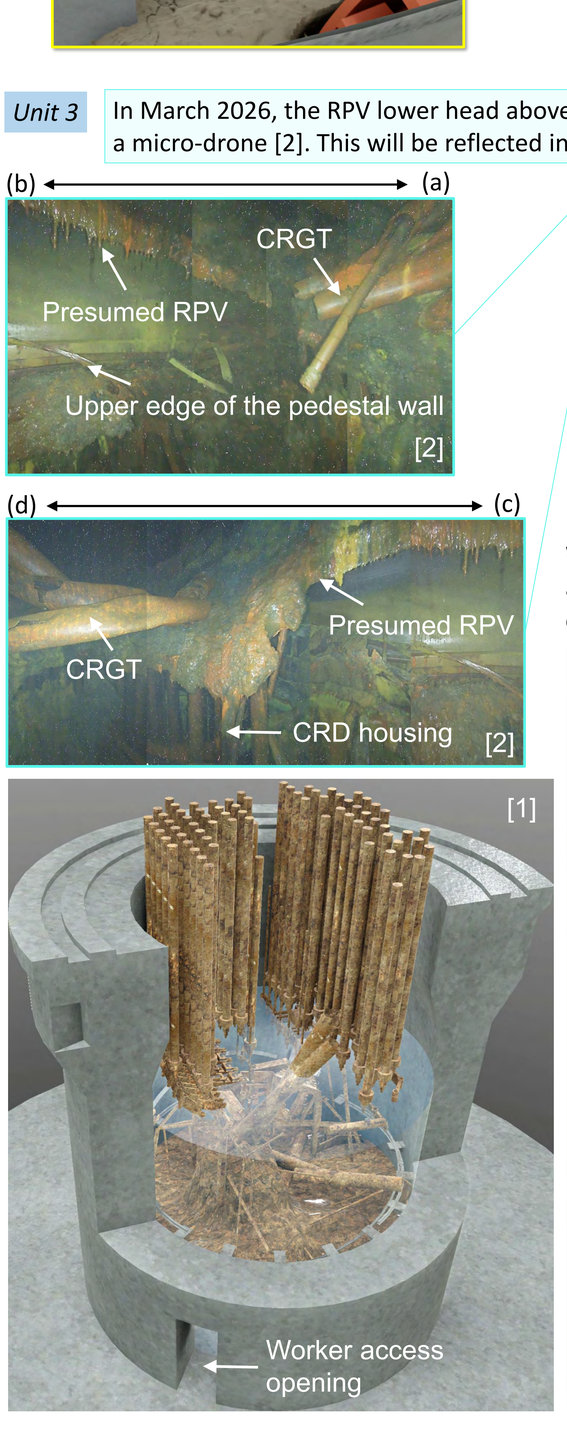

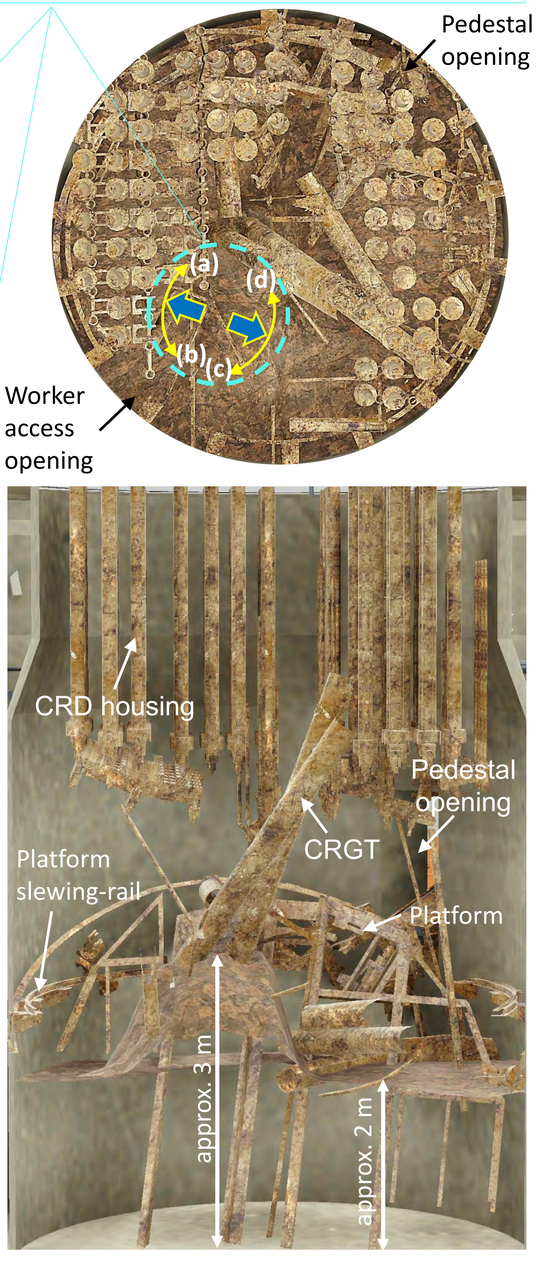

Reference

[1] Takuya.Y et al., “Development of 3D view application debrisEye for decommissioning of Fukushima Daiichi Nuclear Power Plant,” Proceedings of 11th European Review Meeting on Severe Accident Research Conference (ERMSAR 2024) (Internet), https://doi.org/10.5445/IR/1000174165/v2

[2] TEPCO, Completion of the in-air investigation inside the PCV of Unit 3 at Fukushima Daiichi Nuclear Power Station (micro-drone investigation) (in Japanese), March 19, 2026. https://www.tepco.co.jp/decommission/information/newsrelease/reference/pdf/2026/1h/rf_20260319_1.pdf (accessed April 23, 2026).

Acknowledgement

This study has been partly performed by the funds from the Japanese Ministry of Economy, Trade and Industry, Japan as The Subsidy Program “Project of Decommissioning, Contaminated Water and Treated Water Management (Development of Analysis and Estimation Technologies for Characterization of Fuel Debris） starting FY2025".

SOCRATES Horizon Euratom project on liquid source term

Kärkelä Teemu, Herranz Luis Enrique, Gregoire Anne Cécile, Lind Terttaliisa, Foreman Mark, Souvi Sidi, Komlev Andrei

Type of abstract: Poster
Subject area: Source term issues
Keywords: severe accident, source term, liquid phase chemistry, leaching, innovative

The SOCRATES Horizon Euratom project is joining 17 European and international organizations to advance nuclear safety. SOCRATES is dedicated to tackling the risks associated with the release of radioactive materials in liquid form during severe accident in nuclear power plant. At first, the project conducts an in-depth review of current knowledge on liquid source term, also focusing on how existing severe accident analysis codes can predict the chemical forms of radionuclides in liquid phase. This ensures that new findings are built on a well-established scientific baseline.

Experimental part of the SOCRATES project includes real/simulant corium leaching studies by combining water with representative severe accident chemistry conditions to better assess release kinetics of key radionuclides. Long term behaviour of water chemistry involving debris from concrete, paint and structural materials will be scrutinized with particular attention on cesium and strontium fate. SOCRATES will establish a robust experimental database allowing to refine computer models that predict radionuclides releases and reactivity in aqueous media. SOCRATES develops advanced computer models to simulate a range of liquid release scenarios, some of which might be integrated into European SA analysis codes, like ASTEC and AC^2.

From the innovative point of view, and recognizing the urgent need for effective clean-up, the project is also identifying and evaluating innovative absorbent materials (e.g. zeolites, clays, MOFs, and silicas). These new materials are being synthesized and tested for their potential to capture and remove radionuclides from water. To further support the timely actions and effectiveness of accident management responses, SOCRATES is developing an innovative miniaturized radiochemical laboratory to enable rapid on-site measurement of critical radionuclides like cesium and strontium in liquid phase.

SOCRATES will engage young researchers and students via visits to SOCRATES partner organizations and hands-on tasks in experiments, modelling and education.

12th CONFERENCE ON
SEVERE ACCIDENTS RESEARCH
May 18-22, 2026 - Madrid, Spain
ERMSAR 2026

ASSESSMENT OF LIQUID SOURCE TERM FOR ACCIDENTAL POST MANAGEMENT PHASE (EURATOM SOCRATES)

Teemu Kärkelä (VTT), Luis Herranz (CIEMAT), Anne Cécile Grégoire (ASNR), Terttaliisa Lind (PSI), Mark Foreman (CHALMERS), Sidi Souvi (ASNR), Andrei Komlev (KTH)

Objectives

- The EURATOM SOCRATES project addresses critical gaps in our understanding of the liquid source term during severe nuclear accidents and offers innovative solutions to mitigate and monitor the release of radionuclides into the environment.
- The project contributes to the mid-to-long-term management of nuclear power plants after a severe accident by enhancing safety, environmental protection, safe waste management and public well-being.

Key numbers

- Project duration from October 2024 to September 2028 with a total budget of €5.5 million.
- Involvement of 16 partners in the initiative.

Expected Impact

- **Comprehensive State-of-the-Art Report.** SOCRATES will review the current understanding of the liquid source term in SA, with emphasis on evaluating the capabilities of existing accident analysis codes.
- **Experimental database**. SOCRATES is building a database on water chemistry during nuclear accidents. Experiments will place major emphasis in investigating: specific fission products behavior in water; fuel debris leaching, including tests with real corium samples.
- **New computer code models**. SOCRATES will develop computer code models capable of predicting and managing the potential release of radioactive materials in liquid form during severe nuclear power plant accidents.
- **Innovative Absorbent Materials**. Promising absorbents for mitigating the release of radioactive materials in liquid form are being identified, and performance to demonstrated, including their own synthesis in SOCRATES.
- **Innovative Miniature Size Radiochemical Laboratory**. A novel miniature size radiochemical laboratory is being developed in SOCRATES to allow the early measurement of radionuclides of interest.

Partners

VTT (Finland), ASNR (France), CEA (France), Chalmers (Sweden), CIEMAT (Spain), EDF (France), ETH (Switzerland), Framatome (Germany), GRS (Germany), JRC (EU), KTH (Sweden), NUVIA (France), PSI (Switzerland), RUB PSS (Germany), SSTC NRS (Ukraine), UL (France)

Follow up the SOCRATES project:
https://socrates-euratom.eu/

SOCRATES

Project funded by
Schweizerische Eidgenossenschaft
Confédération suisse
Confederazione Svizzera
Confederaziun svizra
Swiss Confederation
Federal Department of Economic Affairs, Education and Research EAER
State Secretariat for Education, Research and Innovation SERI
The Associated Partner PSI is funded by the Swiss State Secretariat for Education, Research and Innovation (SERI).

This project has received funding from Horizon Europe – Euratom programme under grant agreement No 101163745 .

COMPARISON OF MONTE CARLO AND WILKS' METHODS FOR UNCERTAINTY QUANTIFICATION OF A SEVERE ACCIDENT IN A PWR

Piotr Darnowski[1,2]
[1]Institute of Heat Engineering, Warsaw University of Technology
Nowowiejska 21/25, 00-665, Warsaw, Poland
[2]National Atomic Energy Agency, Poland
piotr.darnowski@pw.edu.pl

ABSTRACT

The paper presents selected outcomes of an uncertainty quantification (UQ) study for a Generation-III pressurized water reactor (PWR, 4500 MWth) subjected to an unmitigated large-break loss-of-coolant (LB-LOCA) leading to core melt. Two approaches were compared: (i) a Wilks'-theorem-based method using small samples to estimate a 95/95 tolerance interval, and (ii) Monte Carlo with a large sample to estimate the percentile intervals via the empirical cumulative distribution function (eCDF). Severe-accident behavior was modeled with MELCOR 2.2 within the EU Horizon 2020 NARSIS project. The figure of merit was total hydrogen generation during the in-vessel phase. Additionally, the impact of the sampling strategy on Monte Carlo results was compared for Simple Random Sampling (SRS) and Latin Hypercube Sampling (LHS). The results confirm that the Wilks approach yields conservative tolerance interval estimates, as expected. For Monte Carlo, differences between SRS and LHS were minimal, but some were observed.

KEYWORDS
Uncertainty quantification; PWR; MELCOR; large-break LOCA; hydrogen

1. INTRODUCTION

Uncertainty quantification (UQ) for severe accidents has become a popular topic not only for academia but also for industry and regulators. In the past, quantifying uncertainty in severe accidents was quite challenging, as it often required advanced tools and a large number of calculations, which were limited by resource constraints. Nowadays, it has become easier, and this is one of the reasons for the development we observe in the field. Severe accidents are characterized by complex phenomena with multi-physics and multi-scale features, with the propagation of uncertainties and interdependencies. At some point, it becomes clear that uncertainties must be studied for proper safety assessment. Within the field of traditional design-basis analysis, UQ is well established, at least for some applications. [1]. Nevertheless, in severe accident-related fields, it remains a novel topic.

It is worth mentioning that IAEA SSG-2 recommends uncertainty assessment for severe accidents [2]. An important example from the author's perspective is that the Polish regulatory framework requires uncertainty assessment in severe accident analysis within Deterministic Safety Analysis [3]. It is not specified how to perform it. Still, one possible approach is to apply modern methods with statistical assessment of uncertainty, such as the GRS method with the Wilks approach. It is a demanding but provides more informed answers than simple parametric sensitivity studies.

Some research projects were conducted, some are ongoing, or planned – e.g., the recognized H2020 EU-MUSA (2019-2023), which focused entirely on the quantification of severe accident uncertainty. [4], [5], [6]. Another example is the H2020 NARSIS project (2017-2022), where one of the small tasks within the safety analysis work package was to explore S&UA for severe accidents (see [7], [8], [9]). This paper aims to share selected outcomes of the NARSIS with the community.

This paper presents an exercise comparing the popular Wilks/GRS approach. [10], with a limited number of samples (N=93), and Monte Carlo-type calculations with a larger sample (N=400). The motivation was to test these two approaches with a practical case and eventually observe the kinds of differences in results that are possible. Especially to observe if Wilks provides a conservative estimate of the tolerance interval. Additionally, results obtained with Monte Carlo Simple Random Sampling (SRS) and Latin Hypercube Sampling (LHS) are compared. The motivation is that many references use LHS (e.g., SOARCA report [11]), and the author used it in [7]. However, discussions can be found that claim this is not an appropriate approach. [12]. It is argued that Wilks' method requires an entirely random sample and that LHS is not recommended for tolerance limit estimation. The authors wanted to investigate possible effects in a practical case. These exercises were prepared within the NARSIS project, activities are ongoing to extend this work and this paper is part of it. A detailed report related to this work is in the NARSIS WP4 Deliverable 4.5 [8].

2. METHODS

2.1. Plant model and studied scenario

In the NARSIS project, a definition for a generic Gen-III 1600 MWe PWR plant was developed [13]. The computational model was prepared for the MELCOR2.2.18 computer code [14], [15]. This model was studied in [7] and also used in this work. It has a typical core model with a simplified RPV TH model (see Figure 1 (Right)) and a relatively simple RCS model (see Figure 1(Left)). It has simple single-node containment, which was added to reduce computational effort. Despite being simple, it is considered enough for a low-pressure large LOCA-type scenario and in-vessel phenomena. The scenario considered in this paper is LB-LOCA with a double-ended break of the hot leg (HL). The break is located on the loop with the pressurizer, with all active safety injections unavailable.

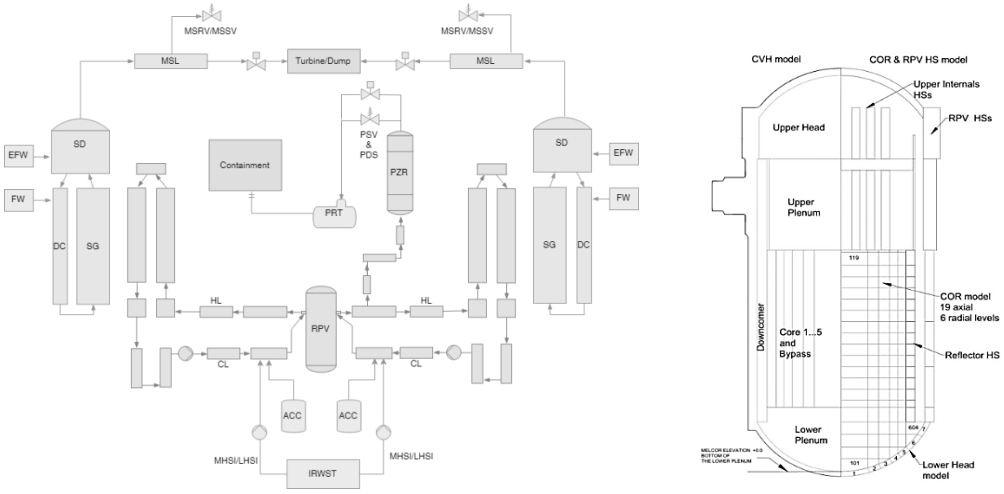

Figure 1. Left – RCS model. Right – RPV model. Based on [8] and [7].

2.2. Uncertainty methods

The in-house open-source tool dedicated to S&UA, the MelSUA, was applied [9]. The code version used to produce the results in this work is available on GitLab [16]. The tool was developed for the NARSIS project and was also applied in the report [8] and paper [7].
In this paper, results based on best estimate distributions are presented. Table I shows the MELCOR uncertainty parameters and their distribution data. Discussion and motivation behind using each parameter are available in [7]. The study is limited to the impact of different MELCOR-specific modelling parameters.

Table I. Uncertainty parameters and distributions selected for the study.

No	MELCOR Field Name	Description	Unit	Type	Best Est.	Distribution	Dist. parameters	Dist. Param. Values	Truncation
1	SC1131(2)	Zircalloy Melt Breakout Temp.	[K]	Continuous	2400	Triangular	a, b, c	[2100.0,2400.0,2550.0]	No
2	SC1132(1)	Fuel Rod Collapse Temperature	[K]	Continuous	2500	Normal	μ, σ	[2479.0, 83.0]	No
3	FUOZR	Fract. Dissolution of Uranium in Molten Zirconium	[-]	Continuous	0.2	Normal	μ, σ	[0.2, 0.09]	[0.0, 0.5]
4	HFRZZR	Candling/Refreezing HTC for Zirconium	[W/m^2-K]	Continuous	7500	Lognormal	μ, σ	[8.9227, 0.55962] [ln(7500), ln(1.75)]	[2000,22000]
5	DHYPD	Debris Diameter in Core Region	[m]	Continuous	0.01	Lognormal	μ, σ	[-4.4228, 0.69315] [ln(0.012), ln(2.0)]	[0.002, 0.05]
6	DHYPDLP	Debris Diameter in Lower Plenum	[m]	Continuous	0.002	Lognormal	μ, σ	[-5.2983, 1.0986] [ln(0.005), ln(3)]	[0.0020,0.060]
7	PORDP	Debris Porosity	[-]	Continuous	0.4	Normal	μ, σ	[0.38, 0.1]	[0.10,0.50]
8	FCELR	Radiation Exchange Factors – Radial	[-]	Continuous	0.1	Normal	μ, σ	[0.1, 0.035]	[0.020,0.30]
9	FCELA for PWR	Radiation Exchange Factors – Axial	[-]	Continuous	0.1	Normal	μ, σ	[0.1, 0.035]	[0.02,0.3]
10	HDBH2O	In-Vessel Falling Debris HTC	[W/m^2-K]	Continuous	100	Triangular	a, b, c	[100.0, 250.0, 2000.0]	No
11	SC1001	Zircaloy–Steam Oxidation Correlation	[-]	Discrete	1.0	Discrete Unifrom	1,2,3,4,5	[0.2 0.2 0.2 0.2 0.2] Details of models available in [7]	No
12	IRODDAMAGE	Time-at-Temperature Model	[-]	Discrete	1.0	Discrete Non-uniform	1,2,3	[0.8 0.1 0.1] Details of models available in [7]	No
13	TMLT	Interactive Model Melting/Eutectic Temp.	[K]	Equal	2500	Normal	Same as 2	Same as 2	Same as 2
14	HFRZSS	Candling/Refreezing HTC for Steel	[W/m^2-K]	Continuous	2500	Lognormal	μ, σ	[7.824, 0.40547] [ln(2500), ln(1.5)]	[1000,5000]
15	FSXSS	Fractional Dissolution of Steel Oxide in Molten Stainless Steel	[-]	Continuous	1.0	Normal	μ, σ	[1.0, 0.2]	[0.6,1]
16	SC1141(2)	Maximum Melt Flow Rate after Breakthrough	[kg/m-s]	Continuous	1.0	Triangular	a, b, c	[0.1, 1.0, 2.0]	No

2.3. Studied cases and sampling

The first case compares the Monte Carlo calculation with N=400 samples and the Wilks with N=93 samples, necessary to achieve a two-sided non-parametric 95/95 tolerance interval. For Monte Carlo, it is assumed that samples are enough to find a reasonable empirical Cumulative Distribution Function (eCDF) for FoM and estimate percentiles. However, 400 samples still can be considered a relatively low value, but much larger than the typical Wilks sample. Both cases were sampled using the Simple Random Sampling (SRS). In the second case, a Monte Carlo calculation via SRS is compared with a similar calculation using LHS sampling.

3. RESULTS AND DISCUSSION

3.1. Monte Carlo vs Wilks

In this section, results for the Wilks and Monte Carlo-based methods are compared. The hydrogen mass as a function of time for the Wilks dataset is presented in Figure 2 (Left), and the Monte Carlo in Figure 2 (Right). The black line presents the calculation with Best Estimate parameters. Fully completed MELCOR runs are presented as grey lines (Success), and partially successful cases are presented by red lines (Partial). Partially successful cases that converged after the time limit – the 2500s, which is the expected time when most hydrogen will be generated in most cases – have a small impact on the final FoM value, even when calculations fail. The mean value evolution is shown as a dark blue line, and is based on the interpolation

and extrapolation for both fully and partially successful cases. A box chart is presented, with the central bar representing the median value for the final FoM, the lower and upper quartiles shown as boxes, the minimum and maximum values that are not outliers (black whiskers), and outliers shown as blue circles. Table II presents numerical values for the final FoM.

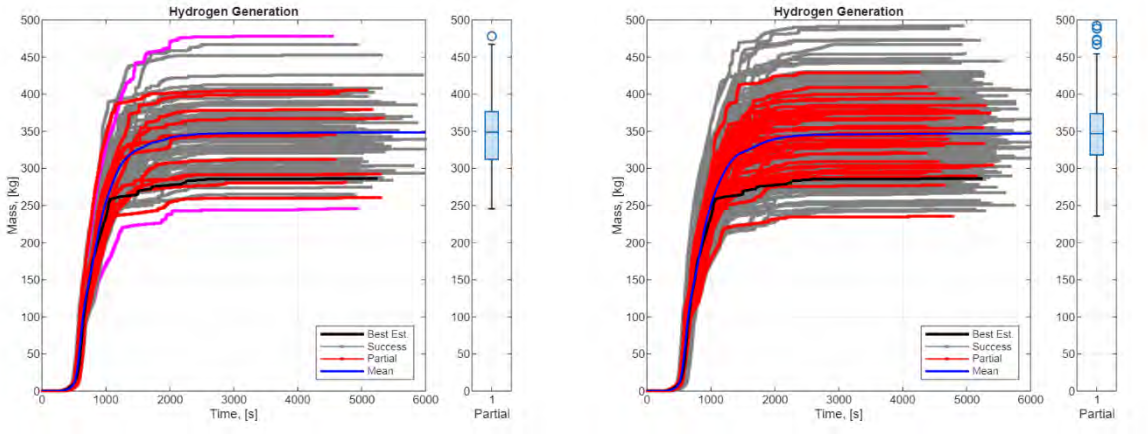

Figure 2. H2 mass vs time. Left – Wilks N=93 (min/max magenta). Right – Monte Carlo with SRS N=400.

It can be observed (see Figure 2 and Table II) that there are some differences between Wilks and MC. First of all, in MC, there are more upper outliers (Figure 2); the maximum/minimum values are larger/smaller than in Wilks (Table II). A larger sample has a solution covering a larger output space. For Wilks, the mean and median are slightly higher than for MC, and the central two quartiles interval (25 and 75) and percentile intervals (2.5, 5, 95, 97.5) have a larger spread (Table II). It is worth noting that the best estimate of FoM is substantially below the Median or Mean for both cases.

Table II. Selected metrics for final FoM (H2 [kg]) for Wilks and Monte Carlo (BE case excluded).

Final time FoM	Wilks 93	Monte Carlo SRS 400
Mean	348.3	346.6
Median	349.1	346.9
Standard Deviation	46.1	43.6
Quartile 25	312.8	317.6
Quartile 75	377.0	373.6
5/95 percentile	275.4 / 412.5	279.6 / 421.8
2.5/97.5 percentile	262.0 / 455.4	266.8 / 436.4
Min	**245.6**	235.8
Max	**478.3**	492.0
Best Estimate	286.6	286.6

Figure 3 (Left) presents Monte Carlo-based central intervals covering 50% (dark blue), 90% (medium blue), and 95% (light blue) of the sample, and compared with the Wilks minimum and maximum curves (magenta), indicating a 95/95 tolerance interval. The blue curve is the median from the Monte Carlo simulation. Data for MC presented in Figure 3 (Left) were processed, interpolated, and extrapolated to yield both successful and partially successful results. Figure 3 (Right) presents a comparison of the final time-step FoM empirical CDFs for Wilks and MC. Bounding curves for Wilks results representing 95/95 two-sided tolerance intervals can be compared with the 2.5-97.5 central interval represented by corresponding percentiles for MC. Where MC is single sample estimates of the percentiles, and Wilks provides a tolerance interval with

given confidence (95%) and coverage (95%). Importantly, Wilks' method does not estimate percentiles in the usual sense, and it does not guarantee that the resulting tolerance interval is central. Remembering about differences, we can, for comparison, estimate margins for FoM. For top/bottom bounds, Wilks predicted 478.3 kg and 245.6 kg, and for MC, 97.5% and 2.5% percentiles are 436.4 kg and 266.8 kg (see Table II). It gives margins equal to 41.9 kg and 21.2 kg, respectively.

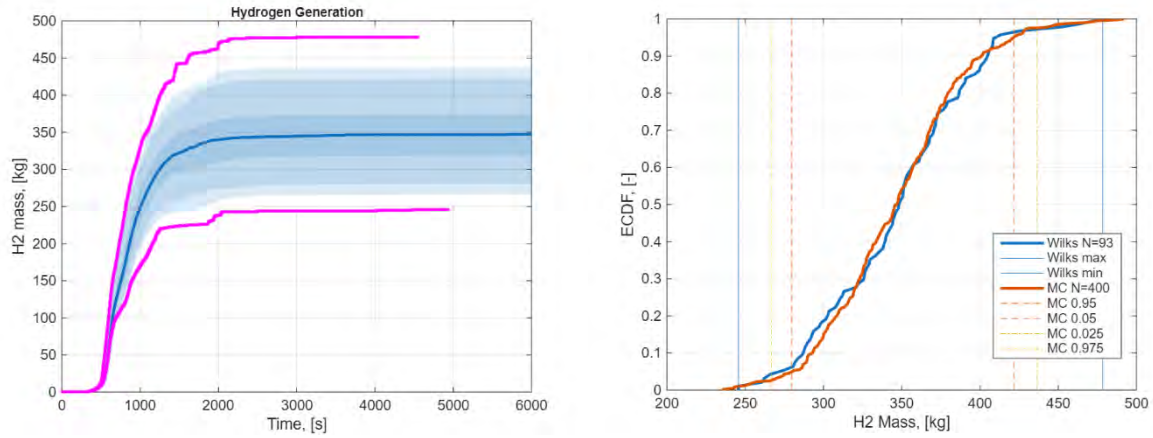

Figure 3. Left – Hydrogen mass (FoM) vs time with 50%, 90% and 95% central intervals for Monte Carlo and Wilks two-sided 95/95 tolerance intervals (magenta). Right – empirical CDFs for final FoM for Wilks and Monte Carlo with 2.5/97.5 and 5/95 percentiles (vertical lines).

From Figure 3, we observe that both the top and bottom limits are larger/lower than both 90% and 95% percentile regions for the Monte Carlo. It is the case for the whole transient. It was expected that the two-sided Wilks approach should conservatively bound the 2.5% and 97.5% percentile curves. Hence, it works as expected for this exercise. Empirical CDFs are slightly different for both Monte Carlo and Wilks (see Figure 3 (Right)). The MC curve is much smoother, which is due to the larger sample.

3.2. SRS vs LHS for Monte Carlo

Results for Monte Carlo with LHS are presented in Figure 4. The comparison of SRS and LHS is shown in Figure 5 and Table III. Hydrogen mass as a function of time in Figure 5 (Left) with SRS (blue) and LHS (red), where the plot covers the median curve, and central intervals with 50% (dark), 90% (medium shade), and 95% (light blue/red). Figure 5 (Right) presents the eCDFs for the final hydrogen mass. Numerical data for the final time FoM are presented in Table III.

Studying Figure 5, it can be observed that there is a small difference between the SRS and LHS results. There is a minimal downward shift of the 95% region for LHS – the top and bottom tails are shifted, and the distribution is shifted. It is also visible when studying percentiles in Table III. In the central 50% region, there is a minor effect. There is a substantial difference in the minimum value and a small difference in the maximum values (Table III). There are more outliers for LHS (see Figure 4 and Figure 2), as indicated by the max/min values (Table III). It is possible, as LHS should cover the input space more evenly, and it can produce more extreme outputs, but it can also be a random effect. LHS eCDF is smoother, a result of the even distribution of input parameters in the input phase space.

Table III. Selected final FoM (H2 [kg]) for Monte Carlo with SRS and LHS (BE case excluded).

Final time FoM	Monte Carlo LHS 400	Monte Carlo SRS 400
Mean	347.6	346.6
Median	346.1	346.9
Standard Deviation	42.8	43.6
Quartile 25	318.8	317.6
Quartile 75	373.8	373.6
5/95 percentile	277.4 / 419.5	279.6 / 421.8
2.5/97.5 percentile	263.9 / 429.5	266.8 / 436.4
Min	220.3	235.8
Max	495.5	492.0
Best Estimate	286.6	286.6

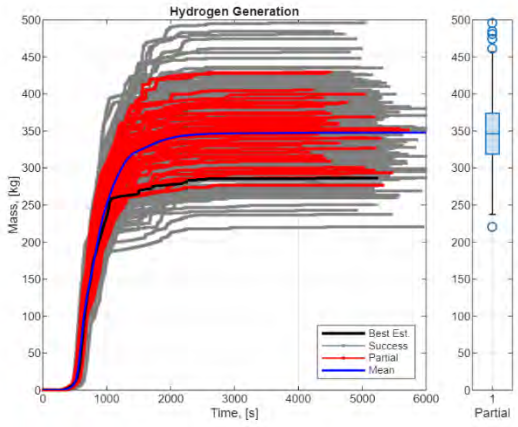

Figure 4. H2 mass vs time for MC with LHS.

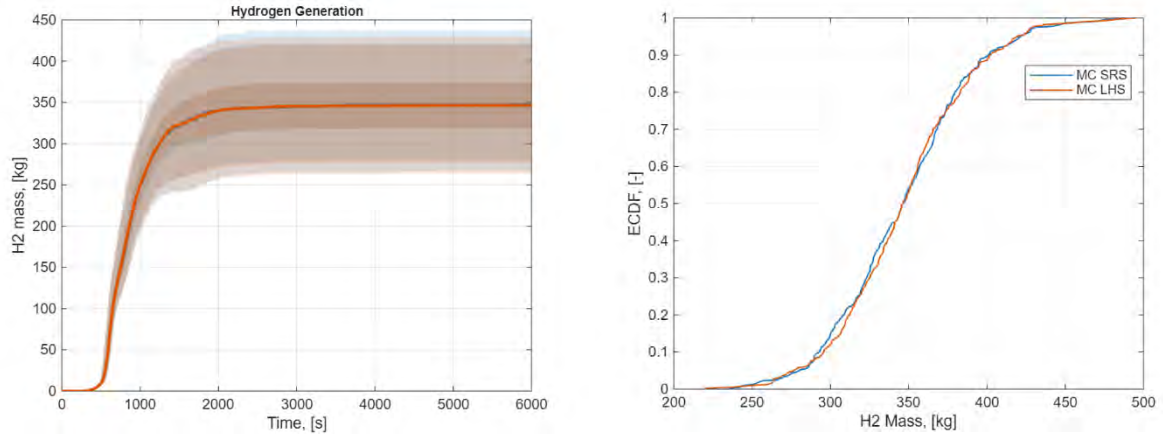

Figure 5. Left – Hydrogen mass (FoM) vs time with 50%, 90%, 95% central intervals for MC LHS (red) and SRS (blue). Right – empirical CDFs for final FoM for LHS (red) and SRS (blue).

3.3. Run statistics

A list of computed cases and statistics of success, partial success, and failed cases is presented in Table IV. Failed cases and partially failed cases introduce bias into the statistics of the obtained results. It is still a common issue in severe accident S&UA. The best approach would be to correct all failed cases, but it is a

challenging task when a dozen failures occur. In the case of Wilks, the results of the initial two instances failed before the partial success limit. Still, they were corrected successfully, and, as a result, all instances converged above the partial success limit of 2500 seconds. The authors were not able to correct failed cases in the Monte Carlo datasets.

Table IV. List of calculated cases/datasets and statistics. Additional case (+1) is the BE run.

Name	Sampling Method	No. of runs	Success/ Partial Success/Failed	Success / Partial Success Percentage
MC SRS	SRS (N=400)	400+1	353/397/3	88.2%/99.3%
MC LHS	LHS (N=400)	400+1	350/395/5	87.5%/98.5%
Wilks 93	SRS Wilks (N=93)	93+1	82/93/0	88.2%/100%

4. CONCLUSIONS

In the comparison between Wilks (N=93) and Monte Carlo (N=400), the practical test case illustrates that the Wilks yields a two-sided 95/95 nonparametric tolerance interval. In this particular case, the Wilks min–max envelopes the MC central 95% interval (2.5^{th}–97.5^{th} percentiles). In principle, it is not guaranteed, since Wilks provides a tolerance interval (coverage/confidence) rather than a central percentile interval. The observed differences in the figure of merit (FoM) between the MC bands and the Wilks bounds were relatively large, which is consistent with the conservative character of the Wilks approach. The final hydrogen mass (FoM) prediction margin, for top and bottom bounding values, was 41 kg and 21 kg, respectively between Wilks and MC percentiles (2.5^{th} –97.5^{th}).

Comparing Monte Carlo LHS and SRS, we did not observe a substantial difference in the overall results or in the cumulative distribution function of the final FoM. The main difference was the outliers for LHS. These are likely due to LHS's greater ability to reach the parameter space, leading to outliers. However, it is inconclusive because it could also be a random effect rather than a sampling method. Still, the difference due to outliers can be considered as not very significant, at least considering the studied FoM.

What is also essential is that some failed cases were observed, which is why the reader should have a proper margin of confidence. In the next step, it is possible to produce a larger sample (e.g., 900), use a set of independent samples (e.g., 3x300), or other approaches, to increase confidence in Monte Carlo outcomes. Other approach is to test various Wilks samples and study the impact of repeatability.

ACKNOWLEDGMENTS

Large portion of the work was prepared within NARSIS project. Activities beyond NARSIS were prepared without funding. NARSIS research project has received funding from the Euratom research and training programme 2014-2018 under Grant Agreement No. 755439—project Horizon 2020 NARSIS (New Approach to Reactor Safety Improvements). Warsaw University of Technology was a participant of the project.

REFERENCES

[1] R. P. Martin and C. Frepoli, *Design-Basis Accident Analysis Methods for Light-Water Nuclear Power Plants*, vol. 03. in Modern Nuclear Energy Analysis Methods, vol. 03. WORLD SCIENTIFIC, 2019. doi: 10.1142/11139.

[2] IAEA, 'Deterministic Safety Analysis for Nuclear Power Plants - IAEA SSG-2 Revision 1', 978–92–0–113309–0, 2019.

[3] Rada Ministrów, 'ROZPORZĄDZENIE RADY MINISTRÓW z z dnia 31 sierpnia 2012 r. Poz. 1043 w sprawie zakresu i sposobu przeprowadzania analiz bezpieczeństwa przeprowadzanych przed wystąpieniem z wnioskiem o wydanie zezwolenia na budowę obiektu jądrowego, oraz zakresu wstępnego', no. 130, 2012.

[4] L. E. Herranz *et al.*, 'The EC MUSA Project on Management and Uncertainty of Severe Accidents: Main Pillars and Status', *Energies*, vol. 14, no. 15, pp. 4473–4473, 2021, doi: 10.3390/en14154473.

[5] S. Brumm *et al.*, 'Uncertainty quantification for severe-accident reactor modelling: Results and conclusions of the MUSA reactor applications work package', *Annals of Nuclear Energy*, vol. 211, Oct. 2024, doi: 10.1016/j.anucene.2024.110962.

[6] S. Brumm *et al.*, 'Uncertainty quantification for severe-accident reactor modelling: Set-up and first results of the Horizon-2020 project MUSA', *Annals of Nuclear Energy*, vol. 191, p. 109919, Oct. 2023, doi: 10.1016/j.anucene.2023.109919.

[7] P. Darnowski, P. Mazgaj, and M. Włostowski, 'Uncertainty and Sensitivity Analysis of the In-Vessel Hydrogen Generation for Gen-III PWR and Phebus FPT-1 with MELCOR 2.2', *Energies*, vol. 14, no. 16, p. 4884, Aug. 2021, doi: 10.3390/en14164884.

[8] P. Darnowski *et al.*, 'D4.5 - Reactor safety analysis results useful for severe accident analysis, considering deterministic and probabilistic approaches', DOI: 10.3030/755439, NARSIS WP4 D4.5, 2023. [Online]. Available: https://ec.europa.eu/research/participants/documents/downloadPublic?documentIds=080166e5e6cc30e1&appId=PPGMS

[9] P. Darnowski and P. Mazgaj, 'MelSUA – An Open-Source MATLAB Toolbox for Sensitivity and Uncertainty Analysis with MELCOR Code', in *HND2022 Conference Proceedings*, Zadar, Croatia, 2022, p. 10. [Online]. Available: https://nuclear-option.org/wp-content/uploads/2022/11/S6-156.pdf

[10] H. Glaeser, 'GRS Method for Uncertainty and Sensitivity Evaluation of Code Results and Applications', *Science and Technology of Nuclear Installations Volume 2008, Article ID 798901,7pages doi:10.1155/2008/798901*, 2008.

[11] R. O. R. O. Gauntt, N. E. Bixler, and K. C. Wagner, 'An Uncertainty Analysis of the Hydrogen Source Term for a Station Blackout Accident in Sequoyah Using MELCOR 1.8.5', 2014.

[12] 'OECD/CSNI Workshop on Best Estimate Methods and Uncertainty Evaluations, 16-18 November 2011, Spain'. Accessed: Jan. 30, 2026. [Online]. Available: https://www.oecd-nea.org/upload/docs/application/pdf/2021-02/csni-r2013-8-part2.pdf

[13] H. Bruneliere *et al.*, 'D4.1 - Definition of a simplified theoretical NPP representative of the European fleet', NARSIS project report - non-public, 2018.

[14] L. L. Humphries, R. K. Cole, D. L. Louie, V. G. Figueroa, and M. F. Young, 'MELCOR 2.2 Computer Code Manual - Volume 1 - Primer and Users' Guide', 2017.

[15] L. L. Humphries, R. K. Cole, D. L. Louie, V. G. Figueroa, and M. F. Young, 'MELCOR 2.2 Computer Code Manual - Volume 2 - Reference Manual', 2017.

[16] P. Darnowski, 'MelSUA - MELCOR Sensitivity and Uncertainty Toolbox', GitLab Repository, 2021. [Online]. Available: https://gitlab.com/darczu/x-core/-/tree/master/Modules/MLC_package/SenstivityUncertanityAnalysis

12th CONFERENCE ON
SEVERE ACCIDENTS RESEARCH
May 18-22, 2026 - Madrid, Spain
ERMSAR 2026

COMPARISON OF MONTE CARLO AND WILKS' METHODS FOR UNCERTAINTY QUANTIFICATION OF A SEVERE ACCIDENT IN A PWR

Piotr Darnowski, Institute of Heat Engineering, Warsaw University of Technology, Nowowiejska 21/25, 00-665, Warsaw, Poland, piotr.darnowski@pw.edu.pl, **Paper 158**

Abstract The paper presents selected outcomes of an uncertainty quantification (UQ) study for a Generation-III pressurized water reactor (PWR, 4500 MWth) subjected to an unmitigated large-break loss-of-coolant (LB-LOCA) leading to core melt. Two approaches were compared: (i) a Wilks'-theorem-based method using small samples to estimate a 95/95 tolerance interval, and (ii) Monte Carlo (MC) with a large sample to estimate the percentile intervals via the empirical cumulative distribution function (eCDF). Severe-accident behavior was modeled with MELCOR 2.2 within the EU Horizon 2020 NARSIS project. The figure of merit was total hydrogen generation during the in-vessel phase. Additionally, the impact of the sampling strategy on Monte Carlo results was compared for Simple Random Sampling (SRS) and Latin Hypercube Sampling (LHS). The results confirm that the Wilks approach yields conservative tolerance interval estimates, as expected. For Monte Carlo, differences between SRS and LHS were minimal, but some were observed.

Motivation The exercise compares Wilks/GRS approach [10], with a limited number of samples (N=93), and MC calculations with a larger sample (N=400). The motivation was to test these two approaches with a practical case and eventually observe the kinds of differences in results that are possible. Especially to observe if Wilks provides a conservative estimate of the tolerance interval. Additionally, results obtained with MC SRS and LHS are compared. The motivation is that many references use LHS (e.g. [11]), and the author used it in [7]. However, discussions can be found that it is not an appropriate approach [12]. The authors wanted to investigate possible effects in a practical case. A detailed report related to this work is in the NARSIS D4.5 [8].

Plant model and studied scenario In the NARSIS, a definition for a generic Gen-III 1600 MWe PWR plant was developed [13]. The model was prepared for the MELCOR2.2.18 computer code [14], [15]. The scenario considered is LB-LOCA with a double-ended break of the hot leg (HL). The break is located on the loop with the pressurizer, with all active safety injections unavailable.

Uncertainty methods The in-house open-source tool dedicated to S&UA, the MelSUA, was applied [9]. The code is available on GitLab [16]. The tool was developed for the NARSIS project and was also applied in the report [8] and paper [7]. In this paper, results based on best estimate distributions are presented. Table I shows the uncertainty parameters.

Studied cases and sampling The first case compares the MC with N=400 samples and the Wilks with N=93 samples, necessary to achieve a two-sided non-parametric 95/95 tolerance interval. For MC, it is assumed that samples are enough to find a reasonable empirical Cumulative Distribution Function (eCDF) for FoM and estimate percentiles. However, N=400 still can be considered a relatively low value, but much larger than the typical Wilks sample. Both cases were sampled using the SRS. In the second case, a MC calculation was performed using LHS sampling with N=400.

Table I. Uncertainty parameters and distributions selected for the study.

No	MELCOR Field Name	Description	Unit	Type	Best Est.	Distribution	Dist. parameters	Dist. Param. Values	Truncation
1	SC1131(2)	Zircalloy Melt Breakout Temp.	[K]	Continuous	2400	Triangular	a, b, c	[2100.0,2400.0,2550.0]	No
2	SC1132(1)	Fuel Rod Collapse Temperature	[K]	Continuous	2500	Normal	m, s	[2479.0, 83.0]	No
3	FUOZR	Fract. Dissolution of Uranium in Molten Zirconium	[-]	Continuous	0.2	Normal	m, s	[0.2, 0.09]	[0.0, 0.5]
4	HFRZZR	Candling/Refreezing HTC for Zirconium	[W/m^2-K]	Continuous	7500	Lognormal	m, s	[8.9227, 0.55962] [ln(7500), ln(1.75)]	[2000,22000]
5	DHYPD	Debris Diameter in Core Region	[m]	Continuous	0.01	Lognormal	m, s	[-4.4228, 0.69315] [ln(0.012), ln(2.0)]	[0.002, 0.05]
6	DHYPDLP	Debris Diameter in Lower Plenum	[m]	Continuous	0.002	Lognormal	m, s	[-5.2983, 1.0986] [ln(0.005), ln(3)]	[0.0020,0.060]
7	PORDP	Debris Porosity	[-]	Continuous	0.4	Normal	m, s	[0.38, 0.1]	[0.10,0.50]
8	FCELR	Radiation Exchange Factors – Radial	[-]	Continuous	0.1	Normal	m, s	[0.1, 0.035]	[0.020,0.30]
9	FCELA for PWR	Radiation Exchange Factors – Axial	[-]	Continuous	0.1	Normal	m, s	[0.1, 0.035]	[0.02,0.3]
10	HDBH2O	In-Vessel Falling Debris HTC	[W/m^2-K]	Continuous	100	Triangular	a, b, c	[100.0, 250.0, 2000.0]	No
11	SC1001	Zircaloy–Steam Oxidation Correlation	[-]	Discrete	1.0	Discrete Unifrom	1,2,3,4,5	[0.2 0.2 0.2 0.2 0.2] Details of models available in [7]	No
12	IRODDAMAGE	Time-at-Temperature Model	[-]	Discrete	1.0	Discrete Non-uniform	1,2,3	[0.8 0.1 0.1] Details of models available in [7]	No
13	TMLT	Interactive Model Melting/Eutectic Temp.	[K]	Equal	2500	Normal	Same as 2	Same as 2	Same as 2
14	HFRZSS	Candling/Refreezing HTC for Steel	[W/m^2-K]	Continuous	2500	Lognormal	m, s	[7.824, 0.40547] [ln(2500), ln(1.5)]	[1000,5000]
15	FSXSS	Fractional Dissolution of Steel Oxide in Molten Stainless Steel	[-]	Continuous	1.0	Normal	m, s	[1.0, 0.2]	[0.6,1]
16	SC1141(2)	Maximum Melt Flow Rate after Breakthrough	[kg/m-s]	Continuous	1.0	Triangular	a, b, c	[0.1, 1.0, 2.0]	No

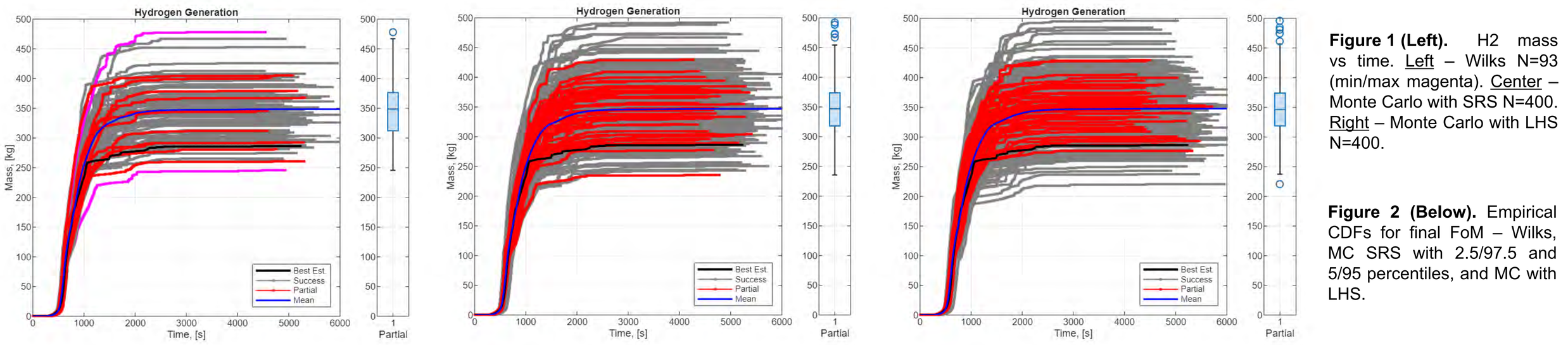

Figure 1 (Left). H2 mass vs time. Left – Wilks N=93 (min/max magenta). Center – Monte Carlo with SRS N=400. Right – Monte Carlo with LHS N=400.

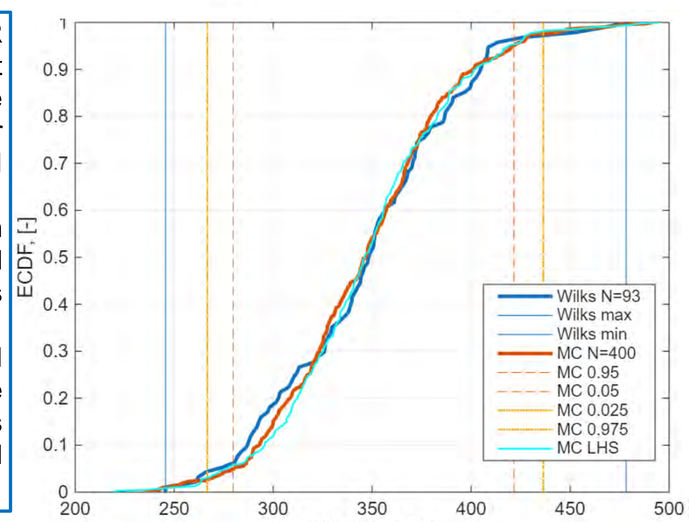

Figure 2 (Below). Empirical CDFs for final FoM – Wilks, MC SRS with 2.5/97.5 and 5/95 percentiles, and MC with LHS.

Results Monte Carlo vs Wilks The Wilks and MC SRS are compared in Figure 1. The black line presents the BE result. Fully completed MELCOR runs are presented as grey lines (Success), and partially successful cases are presented by red lines (Partial). Partially successful cases that converged after the time limit – the 2500s, which is the expected time when most hydrogen will be generated in most cases. The mean value evolution is shown as a dark blue line. A box chart, with the central bar is representing the median value for the final FoM, the lower and upper quartiles shown as boxes, the minimum and maximum values that are not outliers (black whiskers), and outliers shown as blue circles. Table II presents numerical values for the final FoM.

There are some differences between Wilks and MC. In MC, there are more upper outliers (Figure 1); the max/min values are larger/smaller than in Wilks (Table II). A larger sample has a solution covering a larger output space. For Wilks, the mean and median are slightly higher than for MC, and the central two quartiles interval (25 and 75) and percentile intervals (2.5, 5, 95, 97.5) have a larger spread (Table II). The best estimate FoM is substantially below the Median or Mean for both cases.

Figure 2 presents the eCDFs. Min/max curves for Wilks representing 95/95 two-sided tolerance intervals can be compared with the 2.5-97.5 central interval represented by corresponding percentiles for MC. Where MC is single sample estimates of the percentiles, and Wilks provides a tolerance interval with given confidence (95%) and coverage (95%). Importantly, Wilks' method does not estimate percentiles in the usual sense, and it does not guarantee that the resulting tolerance interval is central. We can estimate margins for FoM. For top/bottom bounds, Wilks predicted 478.3 kg and 245.6 kg, and for MC, 97.5% and 2.5% percentiles are 436.4 kg and 266.8 kg (Table II).

Results SRS vs LHS Results for MC with LHS are presented in Figure 1 (Right) and eCDFs in Figure 2. Data for the final time FoM are presented in Table II. It can be observed that there is a small difference between the SRS and LHS results. There is a minimal downward shift of the 95% region for LHS – the top and bottom tails are shifted, and the distribution is shifted. It is also visible when studying percentiles in Table II. In the central 50% region, there is a minor effect. There is a substantial difference in the minimum value and a small difference in the maximum values (Table II). There are more outliers for LHS (see Figure 1), as indicated by the max/min values (Table II). It is possible, as LHS should cover the input space more evenly, and it can produce more extreme outputs, but it can also be a random effect. LHS eCDF is smoother, a result of the even distribution of input parameters in the input phase space.

Conclusions In the comparison between Wilks and MC, the practical test case illustrates that the Wilks yields a two-sided 95/95 nonparametric tolerance interval. In this particular case, the Wilks min–max envelopes the MC central 95% interval (2.5th–97.5th percentiles). In principle, it is not guaranteed, since Wilks provides a tolerance interval rather than a central percentile interval. The observed differences in the FoM between the MC bands and the Wilks bounds were relatively large, which is consistent with the conservative character of the Wilks approach.

Comparing Monte Carlo LHS and SRS, we did not observe a substantial difference in the overall results or in the cumulative distribution function of the final FoM. The main difference was the outliers for LHS. These are likely due to LHS's greater ability to reach the parameter space, leading to outliers. However, it is inconclusive because it could also be a random effect rather than a sampling method. Still, the difference due to outliers can be considered as not very significant, at least considering the FoM.

What is also essential is that some failed cases were observed, which is why the reader should have a proper margin of confidence.

Table II. Selected metrics for (H2 [kg]) for Wilks and MC with SRS and LHS).

Final time FoM	Wilks N=93	Monte Carlo SRS N=400	Monte Carlo LHS N=400
Mean	348.3	346.6	347.6
Median	349.1	346.9	346.1
Standard Deviation	46.1	43.6	42.8
Quartile 25	312.8	317.6	318.8
Quartile 75	377.0	373.6	373.8
5/95 percentile	275.4 / 412.5	279.6 / 421.8	277.4 / 419.5
2.5/97.5 percentile	262.0 / 455.4	266.8 / 436.4	263.9 / 429.5
Min	245.6	235.8	220.3
Max	478.3	492.0	495.5
Best Estimate	286.6	286.6	286.6

References (all in full-paper)

[7] P. Darnowski, P. Mazgaj, and M. Włostowski, 'Uncertainty and Sensitivity Analysis of the In-Vessel Hydrogen Generation for Gen-III PWR and Phebus FPT-1 with MELCOR 2.2', Energies, vol. 14, no. 16, p. 4884, Aug. 2021, doi: 10.3390/en14164884.

[8] P. Darnowski et al., 'D4.5 - Reactor safety analysis results useful for severe accident analysis, considering deterministic and probabilistic approaches', DOI: 10.3030/755439, NARSIS WP4 D4.5, 2023. Available: https://ec.europa.eu/research/participants/documents/downloadPublic?documentIds=080166e5e6cc30e1&appId=PPGMS

[9] P. Darnowski and P. Mazgaj, 'MelSUA – An Open-Source MATLAB Toolbox for Sensitivity and Uncertainty Analysis with MELCOR Code', in HND2022 Conference Proceedings, Zadar, Croatia, 2022, p. 10. Available: https://nuclear-option.org/wp-content/uploads/2022/11/S6-156.pdf

[10] H. Glaeser, 'GRS Method for Uncertainty and Sensitivity Evaluation of Code Results and Applications', Science and Technology of Nuclear Installations Volume 2008, Article ID 798901,7 pages doi:10.1155/2008/798901, 2008.

[11] R. O. Gauntt, N. E. Bixler, and K. C. Wagner, 'An Uncertainty Analysis of the Hydrogen Source Term for a Station Blackout Accident in Sequoyah Using MELCOR 1.8.5', 2014.

[12] 'OECD/CSNI Workshop on Best Estimate Methods and Uncertainty Evaluations, 16-18 November 2011, Spain'. Available: https://www.oecd-nea.org/upload/docs/application/pdf/2021-02/csni-r2013-8-part2.pdf

[13] H. Bruneliere et al., 'D4.1 - Definition of a simplified theoretical NPP representative of the European fleet', NARSIS project report - non-public, 2018.

[14] L. L. Humphries, R. K. Cole, D. L. Louie, V. G. Figueroa, and M. F. Young, 'MELCOR 2.2 Computer Code Manual - Volume 1 - Primer and Users' Guide', 2017.

[15] L. L. Humphries, R. K. Cole, D. L. Louie, V. G. Figueroa, and M. F. Young, 'MELCOR 2.2 Computer Code Manual - Volume 2 - Reference Manual', 2017.

[16] P. Darnowski, 'MelSUA - MELCOR Sensitivity and Uncertainty Toolbox', GitLab Repository, 2021. Available: https://gitlab.com/darczu/x-core/-/tree/master/Modules/MLC_package/SenstivityUncertanityAnalysis

Acknowledgments The NARSIS project has received funding from the Euratom research and training programme 2014-2018 under Grant Agreement No. 755439—project Horizon 2020 NARSIS (New Approach to Reactor Safety Improvements).

Faculty of Power and Aeronautical Engineering
Warsaw University of Technology
ITC

Development of the SAFARI Code for Comprehensive Severe Accident Analysis in Nuclear Reactors: Containment Thermal-Hydraulics Analysis Module

Kum Ho Han, Jehee Lee, and Yeon-Jun Choo*
FNC Technology
Corresponding Address
khhan0529@fnctech.com; capable91@fnctech.com; yjchoo@fnctech.com

ABSTRACT

This paper describes the development and assessment of the SAVANNAH (Severe Accident Vessel-exterior Analysis of Non-equilibrium Nodal thermAl Hydraulics) module, a component of the SAFARI code designed for integrated severe accident analysis in nuclear reactors. The SAVANNAH module evaluates containment thermal-hydraulic behavior by modeling compartments as 'CELL' nodes and inter-compartment flows as 'FLOP' paths. The module utilizes discretized conservation equations for mass, energy, and momentum, which are solved via an iterative numerical scheme to account for the strong coupling between thermodynamic states and fluid velocities. Various constitutive models, including wall heat transfer and friction, are implemented to capture complex physical phenomena. The module was verified using conceptual problems—such as adiabatic hydrogen expansion and 1-D flow with minor losses —and validated against the HDR V44 large-scale containment experiment. Assessment results indicate that SAVANNAH accurately predicts analytical solutions and demonstrates good agreement with experimental data, particularly in long-term containment pressure and temperature trends.

KEYWORDS
SAFARI, SAVANNAH, Containment, Thermal-hydraulics

1. INTRODUCTION

The accurate prediction of containment thermal-hydraulic responses during a severe accident is fundamental to ensuring reactor safety and evaluating the efficacy of mitigation strategies. In South Korea, severe accident management and regulatory compliance have predominantly relied on international computational tools such as MELCOR [1], developed under the support of the U.S. Nuclear Regulatory Commission (NRC). However, recent restrictions on source code access imposed by the NRC have created significant hurdles for domestic researchers and regulators in adapting these codes to address South Korea's specific safety requirements and unique regulatory needs. Consequently, there is a pressing and urgent need to develop an independent, domestic analysis code tailored to Korea's severe accident management landscape.

To address this need, the SAFARI code is being developed as an integrated platform for comprehensive severe accident analysis, with the SAVANNAH (Severe Accident Vessel-exterior Analysis of Non-equilibrium Nodal thermAl Hydraulics) module specifically dedicated to simulating ex-vessel containment behavior. As the final barrier against radioactive release, the containment's integrity depends

* Footnote, if necessary, in Times New Roman font and font size 10

on complex interactions between coolant, non-condensable gases, and corium-related thermal loads. The SAVANNAH module employs a lumped-parameter approach, modeling the containment environment using distinct regions: a water pool and an atmospheric phase. Its numerical framework is strategically designed to align with proven methodologies used in MELCOR to ensure reliability while providing the necessary flexibility for local adaptation and source-level modifications.

This paper introduces the theoretical framework of the SAVANNAH module, including its governing equations, constitutive models, and numerical solution schemes. Furthermore, the module's performance is evaluated through verification against conceptual benchmarks and validation using the HDR V44 large-scale containment experiment.

2. CONCEPT OF SAVANNAH MODULE

The SAVANNAH (Severe Accident Vessel-exterior Analysis of Non-equilibrium Nodal thermAl Hydraulics) module within the SAFARI code is responsible for analyzing the thermal-hydraulic behavior inside the containment. This module models each compartment within the containment as a single numerical node, while the fluid flow between compartments is simulated as flow paths. In the SAVANNAH module, these nodes are called 'CELL,' and the flow paths are called 'FLOP.' Each CELL consists of a pool and an atmosphere, which can have different thermodynamic states. The pool is composed solely of water in liquid and vapor phases, without considering dissolved non-condensable gases. The atmosphere consists of water vapor and non-condensable gases.

During severe accidents, SAVANNAH tracks the mass of molten core (CORIUM) and radioactive substances released into the containment. While phenomena like FCI and MCCI are handled by specific SAFARI submodules, SAVANNAH integrates their effects by accounting for decay heat and the generation of non-condensable gases like hydrogen and carbon dioxide.

3. MODELS OF SAVANNAH MODULE

3.1. Discretized Governing Equations

3.1.1. Discretized mass conversion equation

Equation (1) represents the discretized mass conservation equations for each material within compartment i. Here, i denotes the compartment index, m the material index (1 for pool water, 2 for water vapor in the atmosphere, and 3 and above for non-condensable gases), Φ the phase (pool or atmosphere), and j the flow path index. The superscript d indicates the upstream (donor) compartment value, n the current time step, and o the previous time step. The variable $M_{i,m}$ denotes the mass of material m in compartment i, $\delta M_{i,m}$ represents the external mass source, and σ_{ij} describes the connectivity between compartment i and flow path j. The value of σ_{ij} is –1 if compartment i is connected as the 'from' node of flow path j, 1 if connected as the 'to' node, and 0 if no connection exists. The primary unknowns in this discretized mass conservation equation are the mass of each material ($M_{i,m}^{n}$) and the velocity of each phase within the flow path ($v_{j,\phi}^{n}$).

$$M_{i,m}^{n} - M_{i,m}^{n} = \sum_j \sigma_{ij} \alpha_{j,\phi}^{n} \rho_{j,m}^{d} v_{j,\phi}^{n} A_j \Delta t + \delta M_{i,m} \quad (1)$$

3.1.2. Discretized energy conversion equation

Equation (2) expresses the discretized energy conservation equations for each phase within compartment i. Here, $E_{i,\phi}$ represents the total internal energy of phase Φ in compartment i, and $\delta E_{i,\phi}$ denotes the external energy source. The primary unknowns in this discretized energy conservation equation are the internal energy of each phase ($E^n_{i,\phi}$), and the velocity of each phase in the flow path ($v^n_{j,\phi}$).

$$E^n_{i,\phi} - E^n_{i,\phi} = \sum_j \sigma_{ij}\alpha^n_{j,\phi}(\rho^d_{j,m}h^d_{j,m})v^n_{j,\phi}A_j\Delta t + \delta E_{i,\phi} \quad (2)$$

3.1.3. Discretized momentum conservation equation

Equation (3) describes the discretized momentum conservation equation for each phase in flow path j, where the momentum is influenced by the pressures of adjacent compartments i and k ($P_i^{\tilde{n}}$, $P_k^{\tilde{n}}$). In this equation, ΔP_{pp} represents the pressure change due to the pump, f is the friction coefficient, and K is the minor loss coefficient.

The momentum change in the flow path is governed by the pressure (including local head) of adjacent compartments, while the pressure and water level in each compartment are affected by the velocity along the flow path. Therefore, the momentum of the flow path is closely coupled with the mass and energy of the compartments, requiring iterative calculations. Variables with superscript d vary due to convection terms; for example, $P_i^{\tilde{n}}$ represents the pressure updated by considering pressure changes due to mass and energy transfer through the flow path based on the previous pressure value.

$$v^n_{j,\phi} = v^o_{j,\phi} + \frac{\Delta t}{\rho_{j,\phi}L_j}\left[P_i^{\tilde{n}} + \Delta P_{pp} - P_k^{\tilde{n}} + (\rho g \Delta z)^{\tilde{n}}_{j,\phi} - \left(f\frac{L_j}{D} + \sum K\right)\frac{\rho_{j,\phi}}{2}\left(|v^{n-1}_{j,\phi} + v^{n-2}_{j,\phi}|v^n_{j,\phi} - |v^{n-2}_{j,\phi}|v^{n-1}_{j,\phi}\right)\right] \quad (3)$$

3.2. Heat Structure Model

The heat structure model analyzes heat transfer inside and between compartments due to solids such as concrete or steel plates within the containment. The SAVANNAH heat structure model simulates heat conduction in solids using the one-dimensional heat conduction equation as shown in Equation (4).

$$\frac{\partial}{\partial t}\left(\rho C_p T\right) = \nabla \cdot (k\nabla T) + \dot{q} \quad (4)$$

Here, ρ, C_p, k, T, and $\dot{q}$ represent density, specific heat at constant pressure, thermal conductivity, temperature, and volumetric heat source, respectively.

3.3. Constitutive Equations

The constitutive equations in SAVANNAH include wall heat transfer models, wall friction models, and interfacial heat and mass transfer models between the pool and atmosphere. Representative constitutive equations implemented in SAVANNAH are summarized in Table I.

Wall heat transfer models include convection, condensation, and boiling, while radiation heat transfer is not yet implemented. Walls exchange heat with either the pool or the atmosphere within a CELL. The heat transfer area with each phase is determined by the wall geometry and the submersion ratio.

The wall friction model is divided into three regions based on Reynolds number (Re): laminar, turbulent, and transitional, with criteria as follows:

- Laminar: Re < 2200

- Turbulent: Re > 3000
- Transitional: 2200 ≤ Re ≤ 3000

When water and gas flow simultaneously through a flow path, horizontal stratified flow is assumed, and wall friction for two-phase flow is considered by adding interfacial friction to wall friction for each phase.

The interfacial heat and mass transfer model addresses heat and mass transfer across the pool-atmosphere interface within compartments, implemented based on heat and mass transfer analogy.

Table I. Constitutive equations of the SAVANNAH module

Type		Models	References
Natural Convection	**Larminar**	$Nu = 0.59Ra^{1/4}$	[2]
	Turbulent	$Nu = 0.13Ra^{1/3}$	[2]
Forced Convection		$Nu = 0.023Re^{0.8}Pr^{n}$	[3]
Condensation		HMTA, $\Gamma'' = \frac{M_s Sh D_{sg} \bar{c}}{D_h} ln\left(\frac{P_{tot} - P_{s,i}}{P_{tot} - P_{s,b}}\right)$	[4]
Boiling		$q'' = F \cdot h_{cv}(T_w - T_p) + S \cdot h_{npb}(T_w - T_{sat})$	[5]
Wall Friction (Darcy)	**Larminar**	$f_\phi = \frac{64}{Re}$	[6]
	Turbulent	$\frac{1}{\sqrt{f_\phi}} = -2\log_{10}\left[\frac{1}{3.7}\frac{\varepsilon}{d} + \frac{2.51}{Re}\left\{1.14 - 2\log_{10}\left(\frac{\varepsilon}{d} + \frac{21.5}{Re^{0.9}}\right)\right\}\right]$	[6]
	Transient	$f_\phi = \left(3.75 - \frac{8250}{Re}\right)\left(f_{\phi,Re=3000} - f_{\phi,Re=2200}\right) + f_{\phi,Re=2200}$	[6]
Interfacial Friction		$f_i = 900\left[\alpha\sqrt{\rho_g} + (1-\alpha)\sqrt{\rho_l}\right]$	[1]
Interfacial Heat & Mass Transfer		HMTA, $\Gamma'' = \frac{M_s Sh D_{sg} \bar{c}}{D_h} ln\left(\frac{P_{tot} - P_{s,i}}{P_{tot} - P_{s,b}}\right)$	[4]

4. NUMERICAL SOLUTION SCHEME

4.1. Iterative Scheme

Equations (1)–(3) represent the discretized mass conservation, energy conservation, and momentum conservation equations, respectively. To solve the mass and energy conservation equations, the convective terms in the flow paths must be determined. These convective terms are calculated through the momentum conservation equation. However, since the convective terms depend on the pressures of adjacent compartments, mass and energy information must be known beforehand. Because mass, energy, and momentum are closely interrelated, iterative calculations are required.

Figure 1 shows the flowchart for solving the governing equations in the SAVANNAH module. The 'Update Pressure Equation' step converts the pressures of adjacent compartments into velocity-related expressions, reformulating Equation (3) as a function of velocity. This allows the configuration and solution of a matrix for velocity calculation, yielding velocities of each phase within the flow paths. After velocity calculation, the mass and energy conservation equations are solved to determine the mass and energy of all compartments. Subsequently, the thermodynamic states of the pool and atmosphere consistent with the compartment mass and energy are found. The iteration continues until the difference

between the compartment pressure and the pressure from the previous iteration falls below a specified tolerance. Primary and secondary unknowns of this numerical method are summarized in Table II.

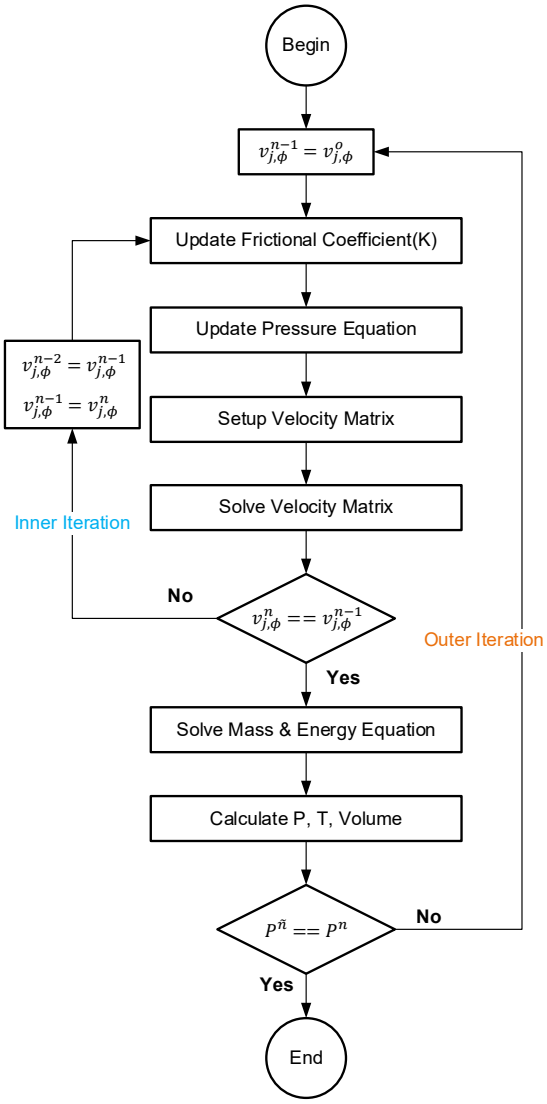

Figure 1. Flowchart for solving the governing equations

Table II. Unknown variables of the SAVANNAH module

Type	Variables	Unit
Primary Unknown	Material Mass	kg
	Phase Internal Energy	J
	Phase Velocity	m/s
Secondary Unknown	Pressure	Pa
	Phase Temperature	K
	Phase Volume	m^3

4.2. Equation of State (EOS)

Water properties are calculated based on IFC67 [7], while properties of non-condensable gases are computed according to McBride [8, 9].

Figure 2 illustrates the flowchart for determining the thermodynamic states of the pool and atmosphere consistent with the compartment mass and energy. Subscripts p and a denote the pool and atmosphere, respectively. As described previously, the compartment mass and energy are obtained by solving the mass and energy conservation equations. Since the volumes of each phase are initially unknown, the thermodynamic state of the pool is estimated using its specific internal energy and an assumed pressure. Next, the pool volume is calculated by multiplying the pool mass by its specific volume. Using the total compartment volume minus the pool volume, the atmosphere volume is determined. With the atmosphere volume known, the densities of its constituent gases can be calculated. Then, the thermodynamic state of the atmosphere is found based on its internal energy and constituent densities. Finally, the pressure difference between the assumed pressure and the calculated atmospheric pressure is evaluated. This entire process is repeated iteratively until the pressure difference falls below a predefined tolerance, confirming consistent thermodynamic states for both phases.

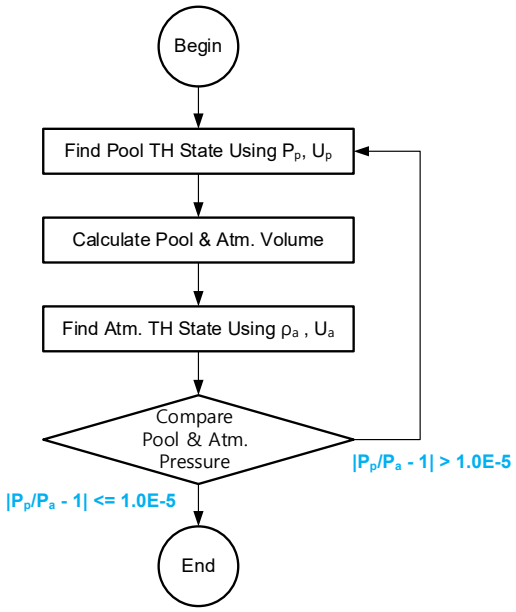

Figure 2. Flowchart for finding thermal-hydraulic states

5. ASSESSMENT

The assessment of the SAVANNAH module utilizes a V&V matrix consistent with those used for the V&V of the MELCOR and CAP codes. This assessment is categorized into conceptual problem assessments and experimental assessments. The conceptual problems consist of simplified scenarios with analytical solutions, serving as a verification phase to ensure that the fundamental functions and physical models of the code are correctly implemented. The experimental assessments represent the validation phase, where the module's performance is evaluated by simulating a containment test and comparing the results with experimental data. This paper presents a selected set of these assessment results.

5.1. Conceptual Problem Assessment

5.1.1. Adiabatic expansion of hydrogen

This conceptual problem evaluates pressure and temperature changes driven by the adiabatic expansion of hydrogen, a scenario previously utilized for MELCOR verification. The nodalization for this problem

consists of two control volumes (CELLs) and one flow path (FLOP). The test conditions for the control volumes and flow path are summarized in Table III.

Figure 3 illustrates a comparison between the analytical solution and the SAVANNAH calculation results for the pressure and temperature in Case 1. In these figures, the x-axis represents the mass of the donor cell (Cell #1), and the y-axis indicates the pressure or temperature. The results demonstrate that SAVANNAH accurately predicts the pressure and temperature behavior during hydrogen expansion. While not detailed in this paper, SAVANNAH also exhibited highly consistent results with the solutions in the remaining test cases.

Table III. Test condition for adiabatic expansion of hydrogen

Case	Cell #1			Cell #2			Flop	
	Volume [m^3]	P [bar]	T [K]	Volume [m^3]	P [bar]	T [K]	Area [m^2]	Minor loss [-]
1	1000	2.0	300	1000	1.0	300	0.05	2
2	1000	5.0	300	1000	1.0	300	0.05	2
3	100	2.0	300	1000	1.0	300	0.05	2
4	10000	2.0	300	1000	1.0	300	0.05	2
5	1000	2.0	300	1000	1.0	300	50.0	2
6	1000	2.0	300	1000	1.0	300	0.05	0.1

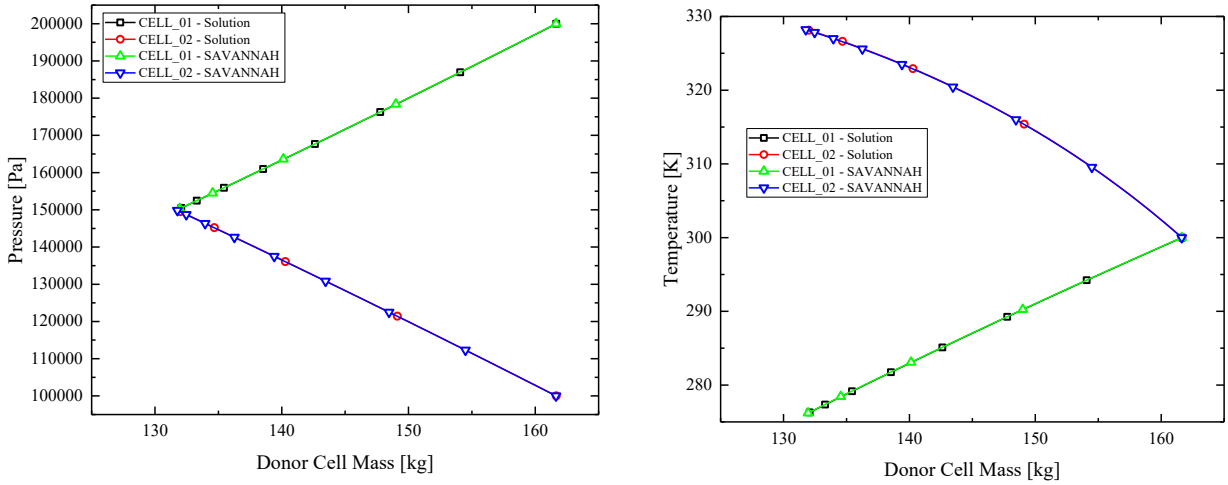

(a) Pressure (b) Temperature

Figure 3. Adiabatic expansion of hydrogen assessment results – Case 1

5.1.2. Semi-Infinite Solid Heat Structure

This problem is designed to verify whether the Heat Structure package accurately calculates the internal temperature distribution of a solid, a test case also adopted in MELCOR verification. The structure has a thickness of 10.0 m and a heat transfer coefficient of 10.0 W/m²-K between the wall and fluid. Other test conditions are provided in Table IV. Figure 4 compares the time-series temperature distribution within the structure between the analytical solution and the SAVANNAH calculation. The results confirm that the Heat Structure package in SAVANNAH appropriately predicts the temperature profile within the solid.

Table IV. Test condition for Semi-Infinite Solid Heat Structure

Case	Initial Temp. [K]	Bulk Temp. [K]	Material	Density [kg/m^3]	Heat Capacity [J/kg-K]	Conductivity [W/m-K]
1	300.0	450.0	Concrete	2300.0	650.0	1.6
2	300.0	450.0	Steel	7850.0	500.0	47.0
3	300.0	600.0	Concrete	2300.0	650.0	1.6

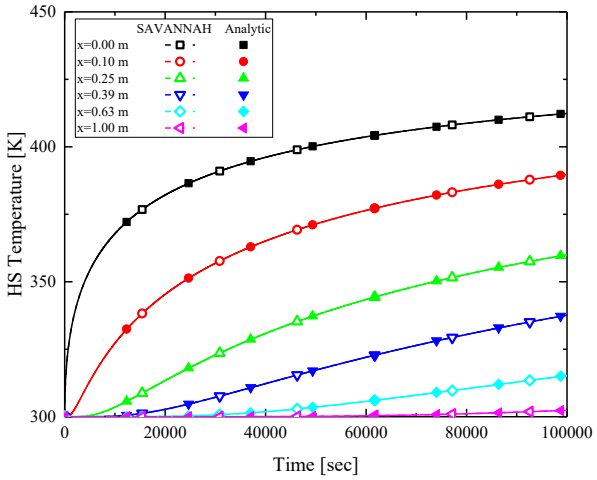

(a) Case #1

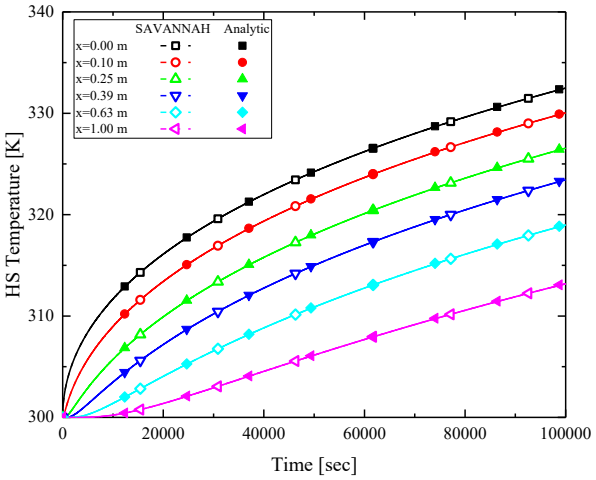

(b) Case #2

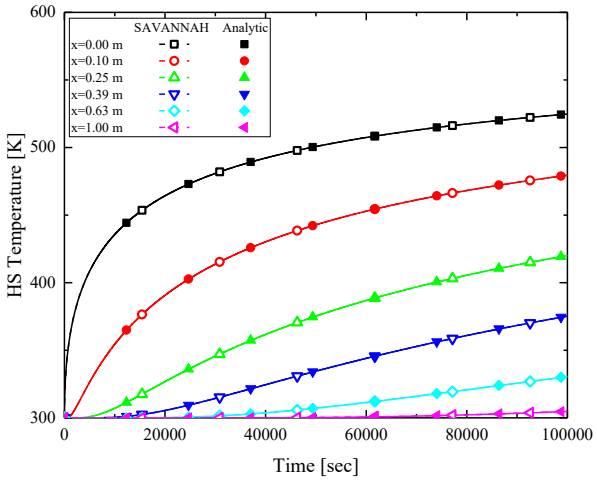

(c) Case #3

Figure 4. Semi-Infinite solid heat structure assessment results

5.1.3. 1-D flow with minor loss

Figure 5 defines this conceptual problem, which involves two sufficiently large control volumes connected by a single flow path. The flow path incorporates various components that induce minor losses and includes an elevation change. The flow path is characterized by a length of 160 m, a diameter of 0.2 m, and a surface roughness of 0.046 mm, with a total elevation change of 20 m. The total minor loss coefficient is 12.2, accounting for a sharp entrance (0.5), an open globe valve (6.9), a 12-inch bend (0.15), a regular 90° elbow (0.95), a half-closed gate valve (2.7), and a sharp exit (1.0). Figure 6 shows that the SAVANNAH calculation results are in good agreement with the analytical solution, demonstrating the module's capability to accurately simulate flow behavior in paths with significant minor losses.

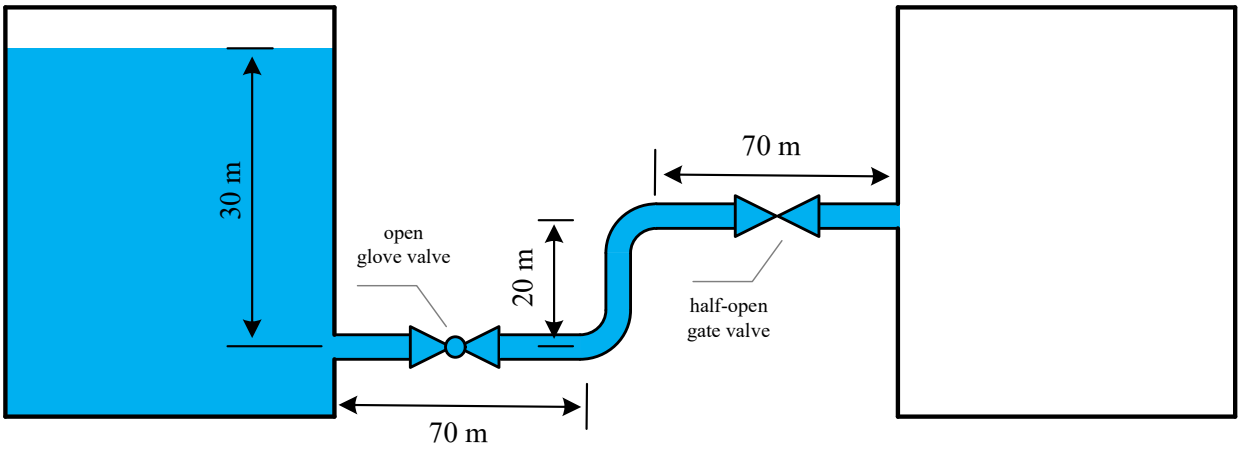

Figure 5. Conceptual problem: 1-D flow with minor loss

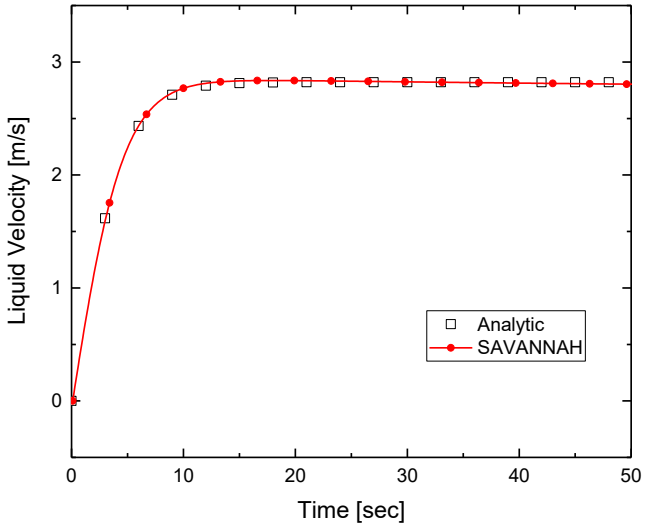

Figure 6. 1-D flow with minor loss assessment results

5.2. Experiment Assessment

5.2.1. HDR V44

Heissdampfreaktor (HDR) is a German superheated steam reactor, which was decommissioned. Through the experiments conducted in this facility, documents that describe the thermohydraulic behavior within a full-scale containment during a blowdown of water or steam/water in the reactor vessel of the containment [10, 11].

Main equipments of the experimental facility is a pressure vessel and a containment building. The indoor pressure vessel has a diameter of 3 m and a height of 11 m. Before a blowdown experiment, most structures inside the pressure vessel are removed to maximize the blowdown flow rate, and the free volume of the vessel is equal to 75 m3. The diameter, height, and total free volume of the containment are 20 m, 60 m, and 11,300 m3, respectively.

The blowdown experiments conducted in the HDR are sorted into several groups depending on their characteristics. Test V44 has a break in the compartment 1603, and the initial pressure of the compartment is 100 kPa. Moreover, the initial temperature of the compartment is generally about 25 ℃, and there is a minor stratification from the bottom to the top of the containment. The initial temperature is about 60 ℃ in a circular crack around the pressure vessel. Initial pressure and temperature of the pressure vessel are 11.1 MPa and 318 ℃, respectively. Finally, the water level of the pressure vessel is approximately 9.2 m.

The input information related to the Test V44 is written based on the reference [11]. Figure 7 illustrates the nodalization, which consists of five lumped volumes connected by junctions. Among the 41 thermal conductors modeled, three structures consist of steel-lined concrete. One side of each conductor is coupled to the lumped volumes, while the other side is assumed to be insulated.

Figure 8 compares the experimental data with the SAVANNAH calculation results for the states in the upper rooms. While SAVANNAH slightly overestimates both pressure and temperature in the early stages of the blowdown, the long-term results (after approximately 200 seconds) show a high degree of similarity to the experimental measurements.

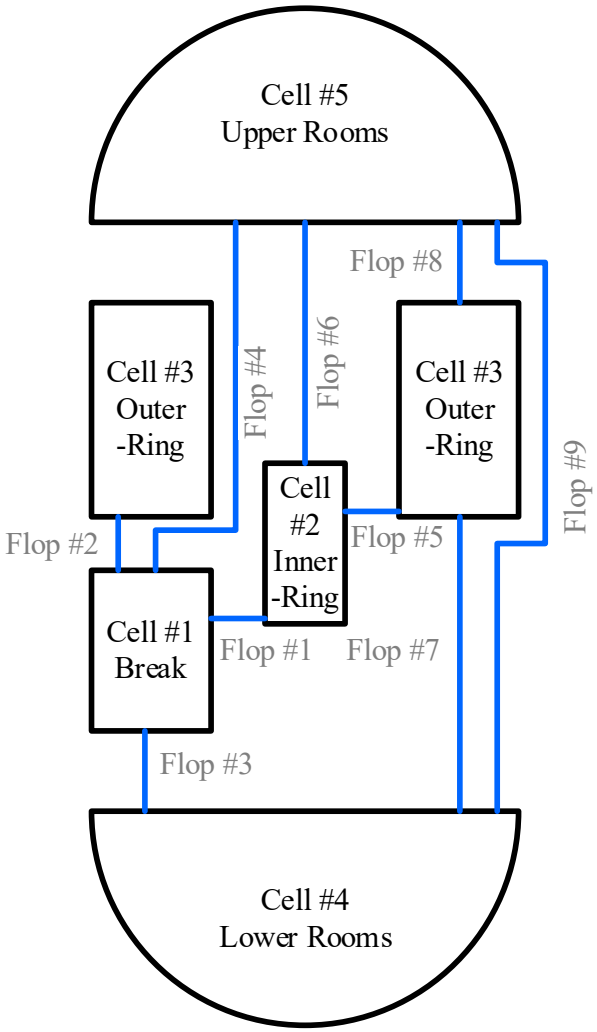

Figure 7. SAVANNAH nodalization: HDR Test V44

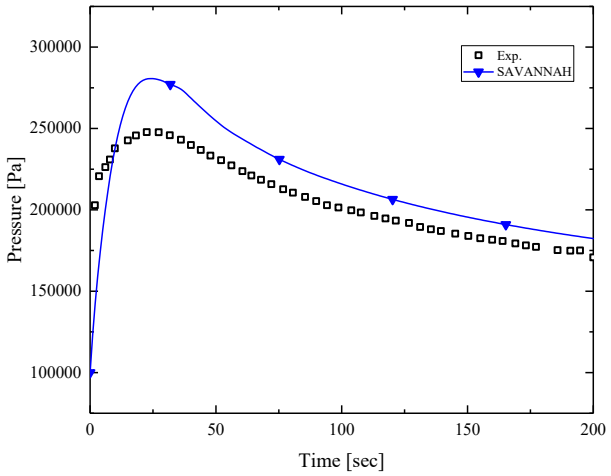

(a) Short-term results: Pressure

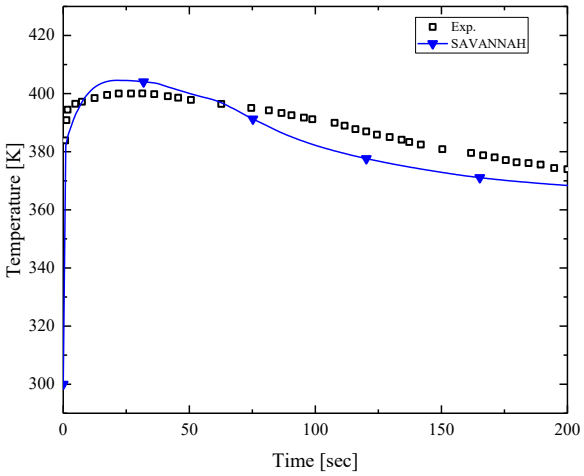

(b) Short-term results: Temperature

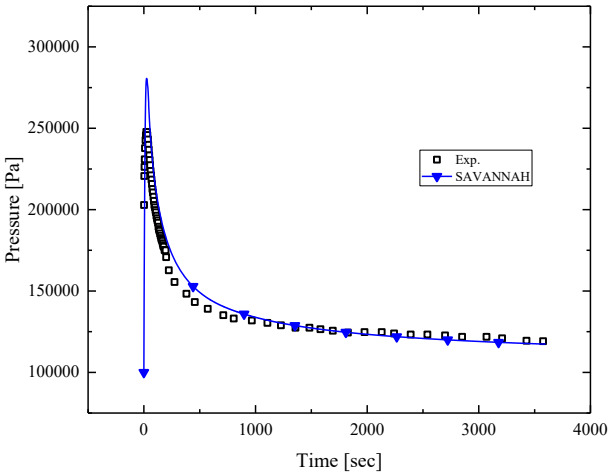

(c) Long-term results: Pressure

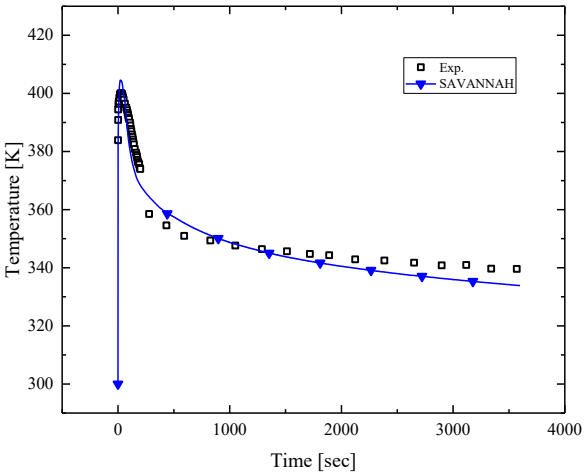

(d) Long-term results: Temperature

Figure 8. Assessment results of HDR V44

6. CONCLUSIONS

The SAVANNAH module has been developed to simulate containment thermal-hydraulic behavior during severe accidents within the SAFARI code framework. By employing a nodal approach and an iterative numerical scheme, the module effectively couples mass, energy, and momentum conservation equations. Verification against conceptual problems confirmed the correct implementation of fundamental physical models, while validation using the HDR V44 experiment demonstrated the module's capability to predict large-scale containment transients. Although slight overestimation occurred in the early blowdown phase of the HDR experiment, long-term trends showed high consistency with experimental data.

ACKNOWLEDGMENTS

This work was supported by the Nuclear Safety Research Program through the Korea Foundation Of Nuclear Safety(KoFONS) using the financial resources granted by the Nuclear Safety and Security Commission(NSSC) of the Republic of Korea. (No. 2106032)

REFERENCES

1. L.L. Humphries, B.A. Beeny, F. Gelbard, D.L. Louie, and J. Phillips, *MELCOR Computer Code Manuals Vol. 2: Reference Manual*, Sandia National Laboratories, SAND2017-0876, (2017).
2. W. H. McAdams, *Heat transmission*, Vol. 3, New York, McGraw-Hill (1954).
3. F. W. Dittus, and L. M. K. Boelter, *Heat transfer in automobile radiators of the tubular type,* International Communications in Heat and Mass Transfer, **12**(1), pp. 3-22 (1985).
4. R. B. Bird, W. E. Stewai, and E. N. Lightfoot, *Transport Phenomena*, Second Edition. (2002)
5. J. C. Chen, *Correlation for boiling heat transfer to saturated fluids in convective flow*, Industrial & engineering chemistry process design and development, **5**(3), pp. 322-329 (1966).
6. C. F. Colebrook, *Turbulent Flow in Pipes with Particular Reference to the Transition Region Between Smooth and Rough Pipe Laws,* Journal of Institution Civil Engineers, **11,** pp. 133-156 (1939).
7. International Formulation Committee of the 6th International Conference on the Properties of Steam, 1967, The 1967 IFC Formulation for Industrial Use, Verein Deustscher Ingenieure, Dusseldorf.
8. B. J. McBride et al., *Coefficients for Calculating Thermodynamic and Transport Properties of Individual Species*, NASA TM 4513, NASA, October (1993).
9. B. J. McBride et al., *NASA Glenn Coefficients for Calculating Thermodynamic Properties of Individual Species*, NASA/TP-2002-211556, NASA, September (2002).
10. M. Firnhaber, *International Standard Problem ISP 16: Rupture of a Steam Line within the HDR-Containment Leading to an Early Two-Phase Flow, Results of Post-Test Analyses*, Final Comparison Report, CNSI Report No. 112. (1985).
11. C.D. Leigh, *MELCOR Validation and Verification*, NUREG/CR-4830, SAND86-2689, U.S. Nuclear Regulatory Commission (1992)

Impact of FeCrAl Cladding Material on the Progression of a Severe Accident in a Generic BWR Mark-I NPP: analysis of a SBO Scenario with the ASTEC Code

Gazzola Eddy (1), Murat Onur (2), Cazado Mauricio Exequiel (2), Angelucci Michela (1), Paci Sandro (1), Gabrielli Fabrizio (2), Sánchez-Espinoza Victor Hugo (2)

(1) Department of Civil and Industrial Engineering, University of Pisa (UNIPI), 56122 Pisa, Italy, (2) Institute for Neutron Physics and Reactor Technology, Karlsruhe Institute of Technology (KIT), Hermann-von-Helmholtz-Platz, 1,76344 Eggenstein-Leopoldshafen, Germany

Type of abstract: Poster
Subject area: Other applications (fusion reactors, interim SNF storage, Accident Tolerant Fuels (ATFs), etc
Keywords: Severe Accident, FeCrAl alloy, BWR, Hydrogen Generation, ASTEC

FeCrAl alloys have gained significant attention as Advanced Technology Fuel (ATF) materials due to their superior high-temperature oxidation resistance compared to the conventional Zr-based alloys, and they are expected to mitigate hydrogen generation during Severe Accident (SA) transients. Furthermore, also motivated by the lessons learned from the Fukushima Daiichi accident, efforts have been undertaken at ASNR to extend the range of application of the ASTEC code to the analysis of SA scenarios in Boiling Water Reactors (BWRs). In particular, models of BWR-specific components have been developed and implemented in ASTEC.

The present work evaluates the performance of the ASTEC code by analyzing a short-term Station Black Out (SBO) sequence in a generic BWR4 Mark I reactor. The analysis, which did not account for the implementation of any emergency core cooling system, follows the relatively fast transient. Impact of adopting FeCrAl as ATF cladding material is assessed by using an oxidation correlation derived from separate effect test measurements conducted using the QUENCH facility at the Karlsruhe Institute of Technology (KIT) and thermophysical properties obtained from open literature sources, complemented by expert assessment at KIT.

The results demonstrate that the application of ATF cladding material led to a delay in the degradation of the fuel cladding and kept cladding material's integrity over an extended period of time due to a slower heat up in the core. Additionally, the ASTEC simulations indicated a decrease in the overall production of hydrogen gas. These findings contribute to the ongoing evaluation of ATF concepts within integral systems codes by establishing the advantages of such advanced materials and identifying the challenges in modelling their behavior across different accident phases.

ACKNOWLEDGEMENT

The work has been performed in the framework of the mobility program of the EU SEAKNOT project, which has received funding under the Grant Agreement No. 101060327.

12th CONFERENCE ON
SEVERE ACCIDENTS RESEARCH
May 18-22, 2026 - Madrid, Spain
ERMSAR 2026

IMPACT OF FeCrAl CLADDING MATERIAL ON THE PROGRESSION OF A SEVERE ACCIDENT IN A GENERIC BWR4 MARK-1 NPP: ANALYSIS OF A SBO SCENARIO WITH THE ASTEC CODE

Onur Murat[1], Eddy Gazzola[1,2], Mauricio Exequiel Cazado[1], Michela Angelucci[2], Sandro Paci[2], Fabrizio Gabrielli[1], Victor Hugo Sánchez-Espinoza[1]

[1]Karlsruhe Institute of Technology (KIT), Institute for Neutron Physics and Reactor Technology, Germany
[2]University of Pisa (UNIPI), Department of Civil and Industrial Engineering, Italy

1. MOTIVATION

- A **Station Blackout** (SBO) event can lead to severe accident if electrical power is not restored within the coping time.
- Conventional **Zr-based alloys** cladding has limitations under severe accident (SA) conditions, specifically rapid oxidation and massive hydrogen release.
- This study uses the ASTEC code to assess the potential of **Advanced Technology Fuels** (ATF) concepts. Particularly, **FeCrAl** cladding, to mitigate or limit the accident progression.

2. ASTEC MODEL AND ATF IMPLEMENTATION

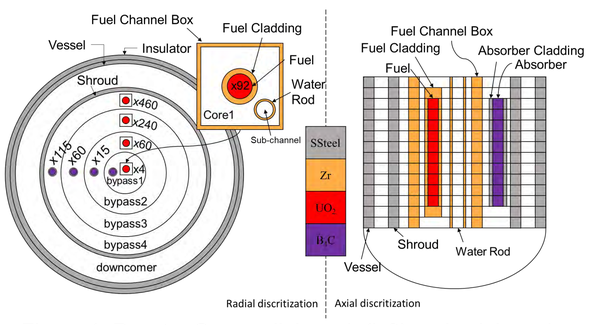

Figure 1. Reactor Core radial mesh (left) and axial mesh (right) loaded with GE14 10x10 fuel assembly [1]

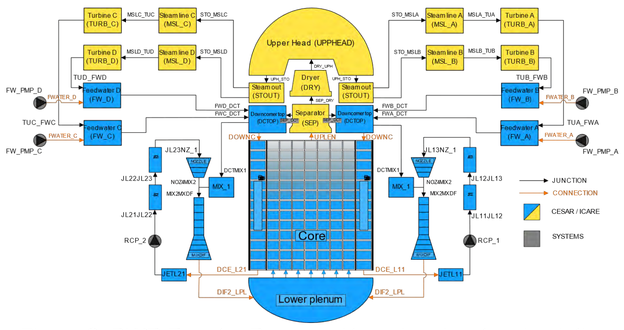

Figure 2. BWR Reactor Pressure Vessel and water circulation system [1]

- The reactor concept analyzed is [1] is a generic BWR-4 Mark-I with loaded 764 GE10x10 fuel assemblies.
- The active core discritized radially into 5 rings and axially 10 uniform meshes.

FeCrAl Implementation

- FeCrAl thermal properties were assess and defined for both solid and liquid phases.
- These properties are critical for accurately calculating the core's heat capacity and thermal response during the SBO transient.
- The oxidation model follows a Parabolic Rate Law where the oxygen mass gain:

$$\frac{dm_{O_2}^2}{dt} = K_P$$

$$K_P = A_{Gain} \cdot \left(e^{-\frac{B_{Gain}}{R \cdot T}}\right) \left[\frac{Kg^2}{m^4\, s}\right]$$

Temperature [K]	A_{Gain} $\left[\frac{Kg^2}{m^4\, s}\right]$	B_{Gain} $\left[\frac{J}{mol}\right]$	Comments
873 ≤ **T** < 1173	$5.376 \cdot 10^{-3}$	$1.847 \cdot 10^{5}$	θ-alumina
1173 ≤ **T** < 1273	$4.692 \cdot 10^{-12}$	0.0	-
1273 ≤ **T** <1648	5.018	$2.877 \cdot 10^{5}$	α-alumina
T ≥ 1648	$2.4 \cdot 10^{8}$	$3.527 \cdot 10^{5}$	Fe-oxide

- Strong oxidation rate occur at 1648 K from α-Al2O3 to Fe-oxide formation.

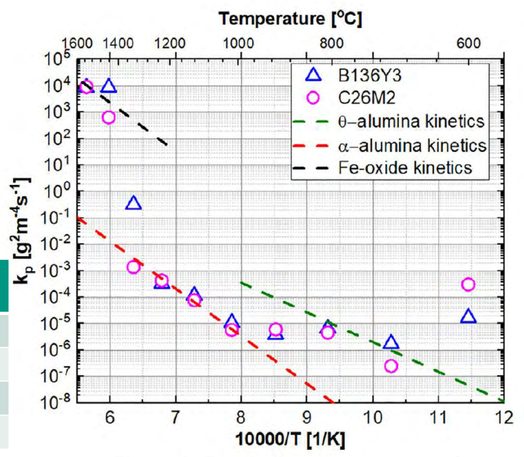

Figure 3. Parabolic rate constants of B136Y3 and C26M2 as a function of the temperature with the parabolic constants of Fe-oxide, θ-alumina and α-alumina [2]

3. BEST ESTIMATE CASE RESULTS

- Simulations indicate that substituting Zircaloy with FeCrAl significantly delays cladding failure and temperature escalation.
- FeCrAl cladding demonstrates a strong reduction in oxidation rates, leading to a significant decrease in total hydrogen production, in particular before the cladding failure.
- After extensive cladding failure and core degradation, the late-phase models still rely on Zr-based assumptions; therefore, late in-vessel results should be interpreted with caution.

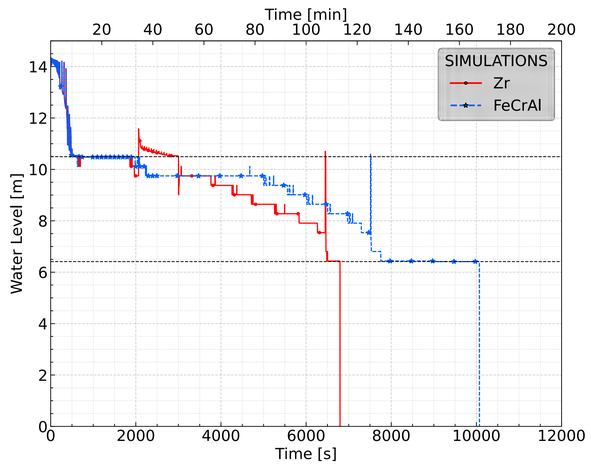

Figure 4. Water level in the vessel during accident progression

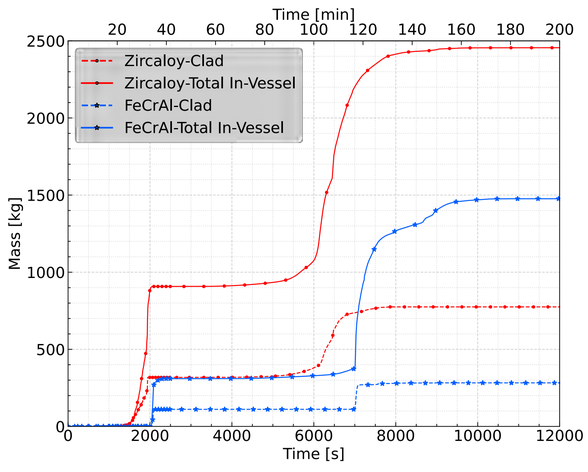

Figure 5. Hydrogen production resulted by the oxidation reaction

4. UNCERTAINTY AND SENSITIVITY ANALYSIS

- An Uncertainty and Sensitivity Analysis (U&SA) was conducted using the KIT in-house **KATUSA** tool [3]. Flow chart of the tool for uncertainty analysis is given below:

Sampling → Simulations → Identify failed simulations → Collect data from non-failed simulations → Adjust time grid and interpolate data → U&SA

- The analysis quantified the impact of uncertain inputs on Figures of Merit, specifically the cumulative hydrogen mass and total activity in containment.
- Two primary parameters were evaluated: an absolute temperature shift (T_{usa} between -50 and +50) and a kinetic multiplier (A_{usa} between 0.85 and 1.15).

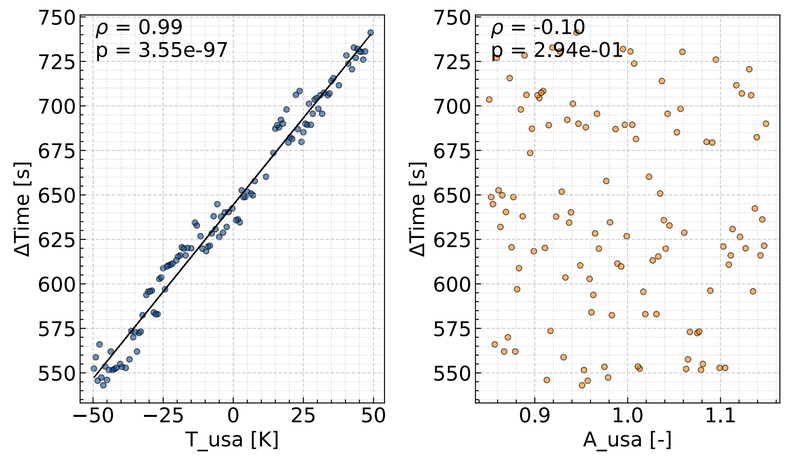

Figure 6. Spearman correlation analysis for hydrogen production delay

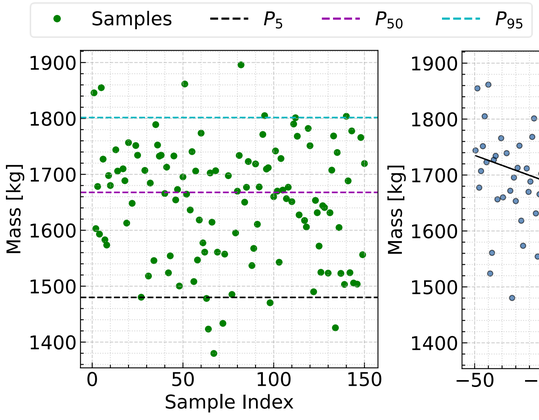

Figure 7. Uncertainty distribution and sensitivity of total RPV hydrogen generation to transition temperature T_{usa}

The very high Spearman correlation coefficient (ρ = 0.99) and negligible p-value (3.55e-97) indicate an almost perfect linear relationship between the temperature shift and the timing of hydrogen production.

Time delay is directly proportional to how long the protective α-alumina layer remains stable.

Even with uncertainties, the maximum hydrogen produced in the vessel (~1900 kg) is still significantly lower than the Zircaloy baseline (~2460 kg), confirming benefit of the FeCrAl material in terms of reactor safety.

The spearman coefficient indicate a moderate negative relationship between switching temperature and produces total hydrogen mass.

Increasing the transition temperature keeps the material in the α-alumina regime (slow oxidation) for a longer duration. Consequently, the core spends less time in the Fe-oxide regime (rapid oxidation) before the simulation ends or the geometry fails, leading to less hydrogen production.

5. CONCLUSION

- In an unmitigated SBO scenario, a generic BWR-4 Mark-I experiences rapid core degradation when utilizing standard Zircaloy cladding.
- The implementation of **FeCrAl ATF concepts successfully delays** the accident progression and massively decreases hydrogen generation.
- While oxidation kinetics strongly drive the accident progression, dedicated model for FeCrAl are still required to assess late-phase phenomena.

ACKNOWLEDGEMENTS

The work has been performed in the framework of the mobility program of the EU SEAKNOT project, which has received funding under the Grant Agreement No. 101060327. The content of this work reflects only the authors' view. The European Commission is not responsible for any use that may be made of the information it contains.

The authors gratefully acknowledge Dr. –Ing. Anastasia Stakhanova for her continuous support and expert feedback during the uncertainty analysis with the KATUSA tool.

REFERENCES

[1] Murat, O., Sanchez-Espinoza, V., Gabrielli, Wang, S., F., Stieglitz, R., and Queral, C., “Improved Analysis of the Short-Term Station Blackout Accidents of the Peach Bottom Unit-2 Reactor with ASTEC Including Radiological Impact and Statistical Analysis with JRODOS”, Nuclear Engineering and Design, Vol. 420, pages 113012, 2024. DOI: 10.1016/j.nucengdes.2024.113012

[2] C. Kim, et al., "Oxidation mechanism and kinetics of nuclear-grade FeCrAl alloys in the temperature range of 500-1500°C in steam," Journal of Nuclear Materials, vol. 564, p. 153696, 2022.

[3] Stakhanova, A., Gabrielli, F., Sanchez-Espinoza, V. H., Hoefer, A., & Pauli, E. M. (2023). Uncertainty and sensitivity analysis of the ASTEC simulations results of a MBLOCA scenario in a generic KONVOI plant using the FSTC tool. Annals of Nuclear Energy, 192, 109964. https://doi.org/10.1016/j.anucene.2023.109964

Reactor Physics and Dynamic

onur.murat@kit.edu
mauricio.cazado@kit.edu

STUDY OF THE IMPACT OF POLYDISPERSE DROPLET DISTRIBUTION IN THE SPRAY SYSTEM USING GOTHIC-3D

Gabicagogeascoa Carlota (1), Arfinengo-del-Carpio Sofía (1), Jiménez Gonzalo (1), Vázquez-Rodríguez Carlos (2), Martín-Valdepeñas Juan Manuel (3)

(1) Universidad Politécnica de Madrid UPM, (2) Forschungszentrum Jülich GmbH, (3) Consejo de Seguridad Nuclear (CSN)

Type of abstract: Poster
Subject area: Containment behavior incl. H2 explosion risk
Keywords: GOTHIC, THERMAL HYDRAULICS, SPRAY SYSTEM

During a severe accident in a Pressurized Water Reactor, a significant amount of hydrogen could be generated and released into the containment building. Hydrogen, when combined with steam and air has the potential to create a local gas mixture that could be flammable or even detonable. In this context, the activation of the containment building spray system may hinder hydrogen risk, as gas mixing is enhanced. However, condensation driven by the spray system could lead to a reduction of steam, potentially promoting the formation of a local combustible mixture. Therefore, the study of the spray system performance is essential for evaluating hydrogen combustion risk in the containment building.

The simulation of the spray system efficiency can significantly depend on the size distribution of the injected droplets. It can be treated by two different approaches: using a single characteristic droplet size (monodispersed) or considering a polydisperse distribution of droplet diameters classified into sections by size. The definition of different droplet size sections is essential to precisely capture their respective effects. However, due to the demanding computational requirements, the three-dimensional analyses often combine simpler approaches, using coarse meshes and monodisperse droplet populations.

In the framework of the GO-MERES 2 project, a collaborative agreement between the CSN and the Spanish Regulatory Council (CSN), the GOTHIC 8.3(QA) code is used to carry out an analysis of the spray actuation system using a polydisperse distribution in a 3D model. This has been accomplished through the simulation of H2P5 experimental series carried out at the PANDA facility in the OCDE/NEA HYMERES 2 project. The study presents a direct comparison between monodisperse and polydisperse distributions, analyzing the main thermal-hydraulic variables of interest.

12th CONFERENCE ON
SEVERE ACCIDENTS RESEARCH
May 18-22, 2026 - Madrid, Spain
ERMSAR 2026

H2P5 - GOTHIC analysis - Polydisperse droplet size implementation

CARLOTA GABICAGOGEASCOA CUESTA

In collaboration with: Sofía Arfinengo del Carpio (ETSII UPM), Gonzalo Jiménez (ETSII UPM), Carlos Vázquez-Rodríguez (Forschungszentrum Jülich GmbH), Juan Manuel Martín Valdepeñas (CSN)

INTRODUCTION

INFLUENCE OF CONTAINMENT SPRAYS – During Severe Accident (SA)

The main purpose of containment sprays is to decrease the containment pressure by causing steam condensation on spray droplets

The mechanisms of condensation and entrainment have the opposite consequences on hydrogen combustion

The atmosphere mixing due to the entrainment by falling droplets causes **a more uniform hydrogen concentration in the containment**

Steam condensation on droplets causes **a decrease of steam concentration** in the atmosphere and a corresponding **increase of hydrogen concentration**

DROPLET SIZE affects both the condensation rate and droplet velocity, which in turn influences entrainment

- The **H2P5 series** expanded the PANDA sprays test database by comparing a spray ring to a single nozzle configuration, proposing a scenario more representative of conditions expected in a nuclear power plant. Both configurations were tested under a stratified atmosphere formed by steam, air and helium
- This experiment was previously analyzed with the GOTHIC code using a monodisperse droplet size distribution (using the average drop diameter) and the simulations calculated a faster depressurization. One of the authors' main recommendations was considering the implementation of a polydisperse droplet size distribution as it has never been done before with the GOTHIC code

GOTHIC treats droplets as a distinct phase, separated from the continous liquid and vapor phases.

This enables defining various droplet sizes via the drop-field menu, allowing the model to simulate and independently track droplets of different sizes.

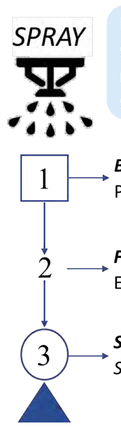

In GOTHIC, defining a spray nozzle as a source of mass, energy, and momentum requires three separate steps.

Boundary condition (BC)
Pressure, temperature, Flow rate

Flow Path (FP)
Elevation, hydraulic diameter, area

Spray component (SC)
SMD, GSD, cone angle

When multiple droplet sizes are injected, each size requires its own BC, FP, and SC. To ensure they all represent a single physical nozzle, all FP must be located in the same computational cell.

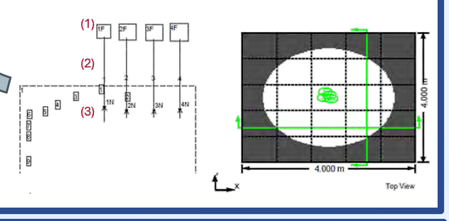

For this analysis only the **one nozzle configuration** was simulated

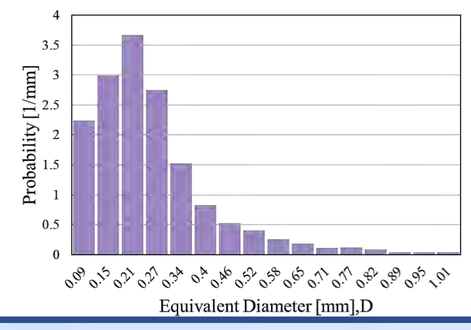

The 16 droplet sizes obtained from the spray probability density function were combined into four groups for computational efficiency.

	SMD (cm)
GROUP 1	0.018
GROUP 2	0.03229192
GROUP 3	0.05115525
GROUP 4	0.08533074

RESULTS

PRESSURE

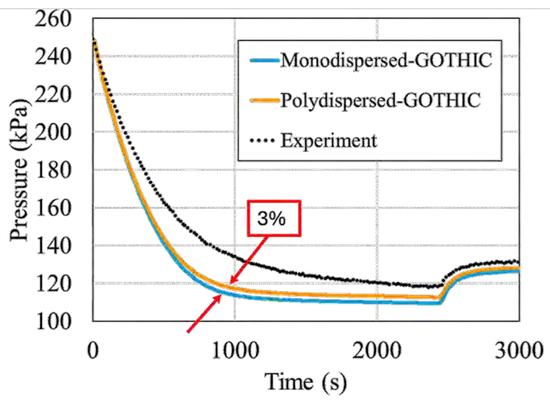

MONODISPERSE POLYDISPERSE

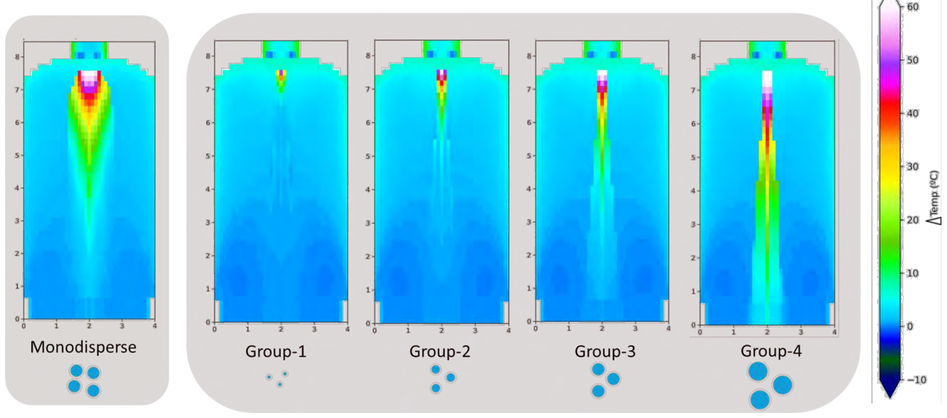

2D MAP illustrating the droplet–air thermal equilibrium at 250 s.

- In the monodisperse configuration, all droplets reach thermal equilibrium before arriving at the bottom (artificially maximizing the amount of energy they are able to extract.)
- Within the polydisperse spray, small droplets equilibrate rapidly owing to their higher surface-to-volume ratio, whereas larger droplets require significantly more time to heat up. As a result, the larger droplets reach the bottom of the vessel without attaining thermal equilibrium, thereby extracting less energy than their theoretical potential.

GAS TEMPERATURE

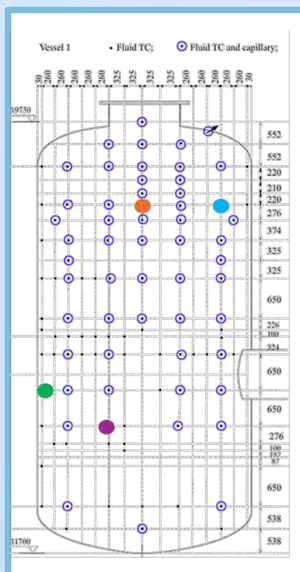

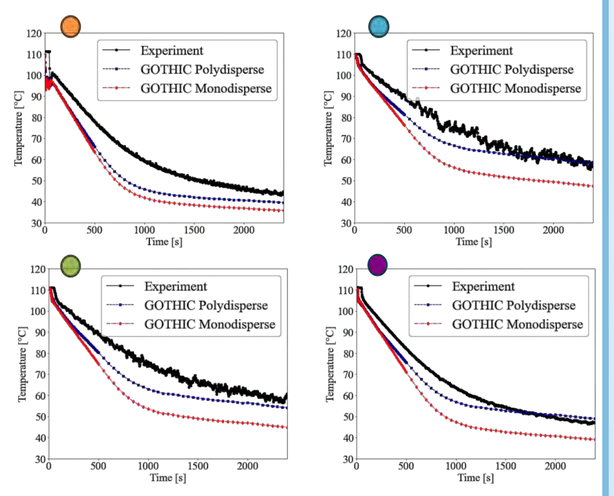

Improvement in the cooling trend when using the polydisperse model, which is now able to replicate the experimental values toward the end of the spray phase. This improvement is particularly evident near the walls and in the lower regions of the vessel.

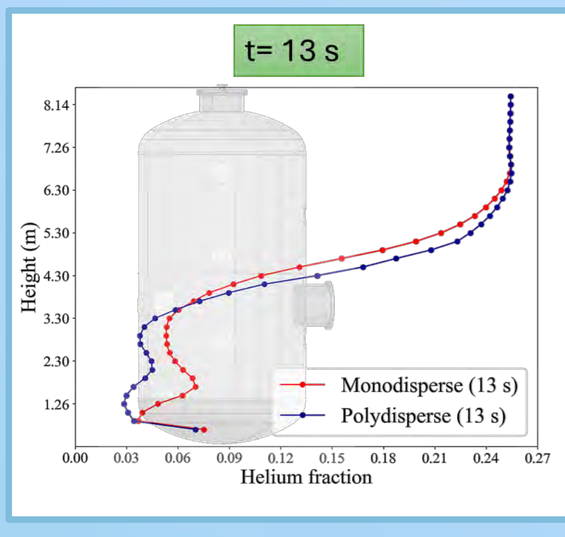

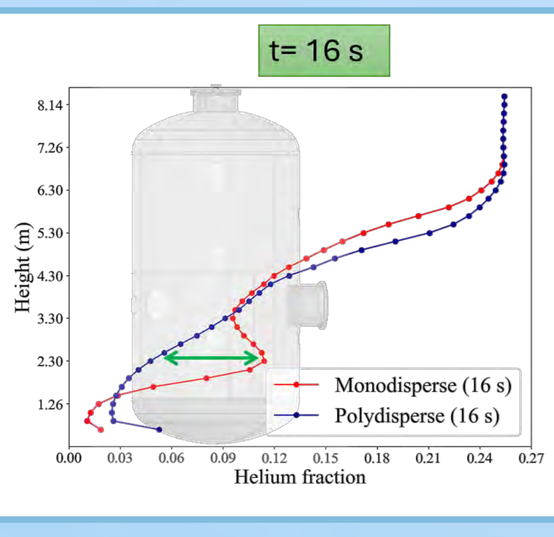

HELIUM FRACTION

HELIUM FRACTION 6% HIGHER IN THE MONODISPERSE CASE

This behavior can be driven by the gas-phase velocity field induced by droplet momentum transfer.

GAS VELOCITY

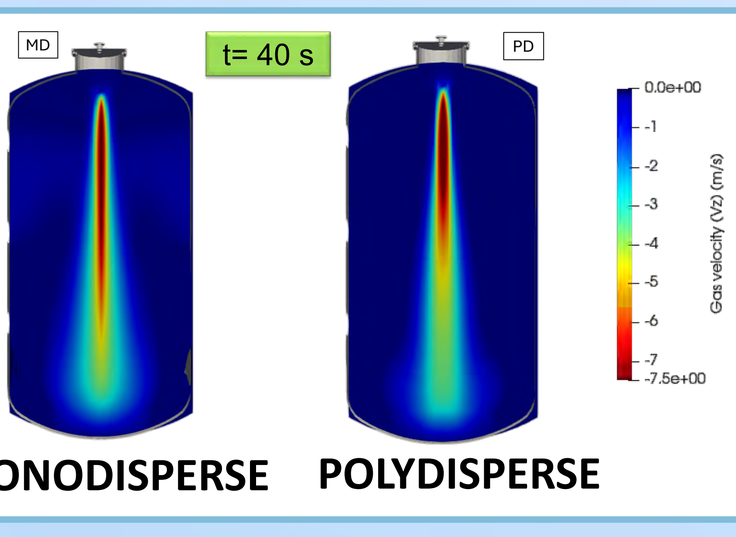

MONODISPERSE **POLYDISPERSE**

CONCLUSIONS

- While both approaches show similar overall trends, important local differences were identified in terms of heat and mass transfer, especially regarding vapor cooling and mixing patterns.
- The polydisperse model provided a more realistic representation of droplet behavior, revealing complex interactions between droplet size, temperature, and residence time. These findings suggest that droplet size distribution plays a significant role in the thermal-hydraulic response of spray systems and it's impact should be investigated at plant scale

GOTHIC™ incorporates technology developed for the electric power industry under the sponsorship of EPRI, the Electric Power Research Institute. This work was completed using a GOTHIC license for educational purposes provided by Numerical Advisory Solutions, LLC.

References

- Vázquez-Rodríguez C, Andreani M, Jiménez G, Kapulla R, Paranjape S, Manuel Martín-Valdepeñas J, Paladino D (2023a) Assessment of the depressurisation and mixing effects of two spray systems in the PANDA facility, part II – Simulations using GOTHIC8.3(QA). Nuclear Engineering and Design 403: 112120. https://doi.org/10.1016/j.nucengdes.2022.112120

Carlota Gabicagogeascoa
PhD candidate in Nuclear Engineering

ETSII UPM; José Gutiérrez Abascal, 2, 28006 Madrid, Spain

Tel: +34 910677153

Email: c.gcuest@upm.es

INVESTIGATING SEVERE ACCIDENT SCENARIOS FOR NOVEL NUCLEAR REACTORS: DEVELOPING THE GIROSCOPE METHODOLOGICAL FRAMEWORK FOR EMERGENCY PREPAREDNESS AND RESPONSE

Anna Wawrzynczak[1], Violeta Hansen[2], Erik Bergbäck Knudsen[2], Luke Lebel[3], Garik Patterson[3], Maciej Skrzypek[1], Piotr Kopka[1], Mats Isaksson[2]

[1] National Centre for Nuclear Research, Otwock-Świerk, Poland

[2] University of Gothenburg, Sahlgrenska Academy, Göteborg, Sweden

[3] Canadian Nuclear Laboratories (CNL), Chalk River, Canada

ABSTRACT

Novel nuclear reactors (NNRs) challenge generic source-term assumptions used in emergency planning. This work presents the GIROSCOPE framework, coupling mechanistic source-term modelling with consequence assessment to support risk-informed Emergency Preparedness and Response (EP&R). Reactor-specific releases are derived for representative high-temperature gas-cooled reactors (HTGRs), light-water small modular reactors (SLWRs), and compact molten salt reactors (CMSRs) under beyond-design-basis conditions. Results indicate that HTGR air ingress scenarios yield release fractions orders of magnitude lower than those assumed for large light-water reactors, while SLWR releases are highly sensitive to passive safety systems and natural retention mechanisms. No single accident sequence is universally bounding, motivating representative accident spectra for proportionate Emergency Planning Zone (EPZ) definition. GIROSCOPE provides a technical basis for tailoring EP&R to NNR risk profiles.

KEYWORDS

Mechanistic source term; Advanced reactors; Severe accidents; EP&R; EPZ

1. INTRODUCTION

NNRs, including small modular reactors and Generation IV concepts, differ fundamentally from conventional large light-water reactors in fuel forms, coolant systems, containment configurations, and passive safety features, challenging established approaches to radiological source-term estimation based on generic conservative assumptions. Their potential deployment in diverse environments further increases the importance of proportionate and technology-specific EP&R.

A central question for regulators and emergency planners is how severe accident source terms and off-site consequences for NNRs compare with those of conventional reactors, and how these differences should be reflected in EPZ definition. To address this need, the GIROSCOPE project develops an integrated framework for the mechanistic characterisation of radionuclide releases and their propagation to consequence assessment. This paper presents the GIROSCOPE methodology and its application to

representative advanced reactor concepts, focusing on severe-accident source terms and implications for EP&R.

2. GIROSCOPE FRAMEWORK AND METHODOLOGY

GIROSCOPE applies a Mechanistic Source Term (MST) approach, replacing generic conservative source terms with reactor-specific, physically based assessments of fission product generation, transport, retention, and release (Figure 1). Initial radionuclide inventories are derived from neutronic and depletion calculations and propagated through coupled fuel performance and integrated severe accident analyses to simulate accident progression and release pathways. Key phenomena include fuel degradation, aerosol formation and deposition, pool scrubbing, and containment retention. For compact light-water SLWR designs, natural retention mechanisms such as gravitational settling and diffusiophoresis are particularly influential due to high surface-area-to-volume ratios.

Time-dependent source terms from system-level severe accident modelling are propagated to consequence assessment tools and/or model chains to estimate dose, dispersion, and longer-term contamination relevant for emergency planning [1]. For emerging reactor technologies, probabilistic safety assessment data are often limited; representative accident scenarios are therefore defined using available design information and phenomenological understanding, supplemented where necessary by conservative assumptions [2,3]. Rather than relying on a single bounding sequence, GIROSCOPE adopts a spectrum-based approach, analysing multiple credible severe accident scenarios to support proportionate EPZ development.

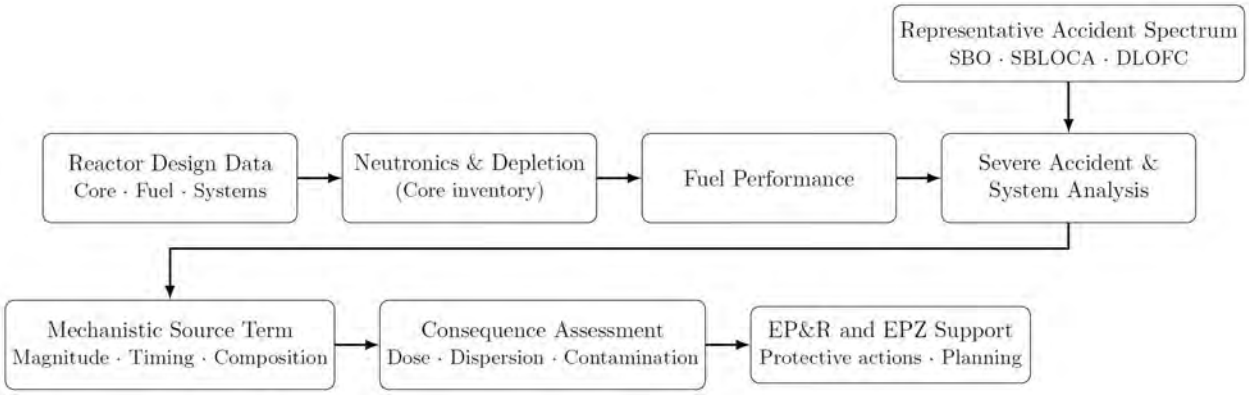

Figure 1. GIROSCOPE workflow coupling mechanistic source-term modelling with consequence assessment to support EP&R and spectrum-based EPZ definition.

3. REPRESENTATIVE CASE STUDIES AND ACCIDENT SCENARIOS

The GIROSCOPE framework was applied to representative HTGR, SLWR, iPWR, and CMSR concepts (Table I), including pebble-bed (Canada) and prismatic (Poland) HTGRs and BWR-type (Canada), PWR-type (Sweden) SLWRs, and a fluoride-salt CMSR (Denmark), enabling assessment of how core configuration, fuel form, containment layout, and passive safety features influence radionuclide release behaviour.

For HTGRs, depressurised loss-of-forced-cooling (DLOFC), or severe air ingress, was analysed to evaluate natural circulation onset, graphite oxidation, fuel temperature evolution, and radionuclide transport [4]. Both configurations employ TRISO fuel [5], providing micro-containment of fission products. Predicted release fractions for pebble-bed HTGRs were orders of magnitude lower than those typically reported for light-water reactors, even under severe air ingress. These source terms were incorporated into consequence studies that demonstrated reduced early-phase doses and indicated potential longer-term contaminated areas exceeding protective action guidelines (Figure 2) [6].

Figure 2 presents Total Effective Dose Equivalent (TEDE), consistent with the legacy framework implemented in NRC tools such as RASCAL. European emergency reference levels are defined in terms of effective dose within the ICRP 103 system adopted in the IAEA Basic Safety Standards [7,8]. Although numerical differences between TEDE and effective dose are expected to be small, the underlying conceptual distinction should be acknowledged.

SLWR analyses focused on station blackout (SBO) and small-break loss-of-coolant accidents (SBLOCA) [9]. Accident progression is governed by passive decay heat removal and containment thermal-hydraulics. In BWR designs, isolation-condenser operation may create containment bypass pathways, while pool scrubbing dominates caesium retention. PWR-type SLWRs similarly show strong sensitivity to passive coolant flow and containment retention.

For iPWRs, SBO scenarios with varying decay heat removal impairment were analysed alongside additional failures to develop source-term spectra for EPZ studies [3]. No single accident sequence is universally bounding, motivating the use of representative accident spectra. CMSR analyses are ongoing, focusing on radionuclide inventories and release behaviour in liquid-fuel systems.

Table I. Representative reactor concepts considered in GIROSCOPE

Reactor concept	Core config.	Coolant	Fuel	Power (MWth)	Key passive / retention feature	Representative severe accident
HTGR – Pola	Prismatic	Helium	TRISO	~30	TRISO fuel, graphite core, RCCS	DLOFC (air ingress)
HTGR – Canada	Pebble-bed	Helium	TRISO	~200	TRISO fuel, graphite core, RCCS	DLOFC (air ingress)
SLWR – Canada	BWR lattice	Light water	UO_2	~870	Pool scrubbing, passive containment cooling	SBO, SBLOCA
SLWR – Sweden	PWR lattice	Light water	UO_2	~1358	Passive coolant flow, containment retention	SBO, SBLOCA
iPWR – Canada	PWR lattice	Light water	UO_2	~160	Passive decay heat removal	SBO
CMSR	Liquid-fuel MSR	Molten salt	Liquid fuel	~30	Low-pressure system, online retention	Under definition

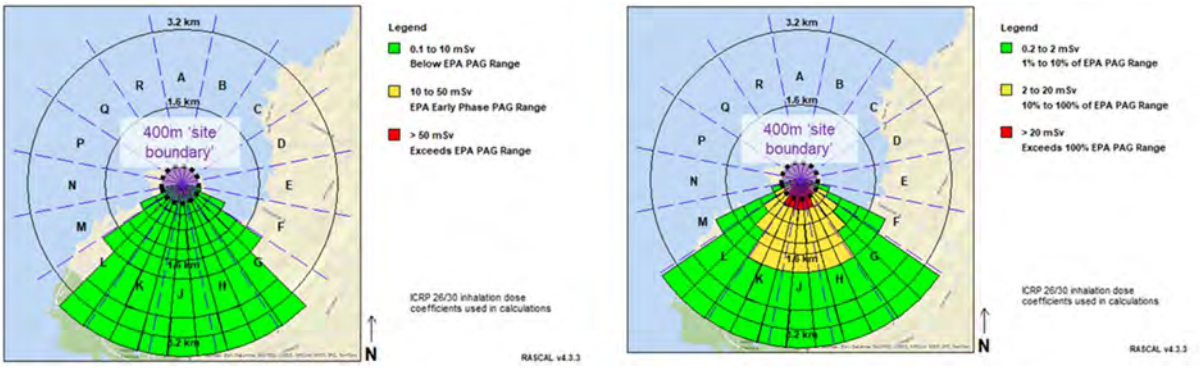

Figure 2. Representative TEDE predictions for an HTGR DLOFC accident (early phase left, one year right), adapted from Lebel et al. [6]. TEDE follows the ICRP 26 framework; comparison with European effective dose criteria is indicative.

4. IMPLICATIONS FOR EP&R AND CONCLUSIONS

The case studies demonstrate that radionuclide release characteristics for novel reactors strongly depend on reactor concept, containment configuration, and accident progression. HTGR analyses indicate substantially lower early-phase doses than conventional reactors, although longer-term contamination may still require protective actions [6]. For SLWRs, releases are highly sensitive to passive safety performance and natural retention mechanisms, including pool scrubbing and aerosol deposition.

Across all concepts, no single accident sequence is universally bounding, supporting representative accident spectra for proportionate, technology-specific EPZs. Overall, GIROSCOPE demonstrates the value of mechanistic source term methodologies for evidence-based EP&R, providing a technical basis for risk-informed emergency planning and regulatory safety cases for advanced nuclear reactor technologies.

ACKNOWLEDGMENTS

This work was funded by the GIROSCOPE project within the PIANOFORTE partnership under the European Union's Euratom Research and Innovation Programme, Grant Agreement No. 101061037.

REFERENCES

[1] P. Kopka, M. Spirzewski, and P. Darnowski, “Probabilistic Model Chain Methodology for Evaluating Radiological Consequences of Accidents in High-Temperature Gas-Cooled Reactors,” *Nuclear Engineering and Technology*, 57, 103779 (2025).

[2] M. Malicki and T. Lind, “MELCOR 2.2 iPWR LOCA Type Accident Analysis, Part II: Beyond Design Basis Accidents,” *Nuclear Engineering and Design, 430*, 113667 (2024).

[3] J. Cui, L. Lebel, A. Morreale, and D. Hummel, “MELCOR Model of iPWR and Application to Emergency Planning Zone Study,” *Nuclear Engineering and Design*, **442**, 114226 (2025). https://doi.org/10.1016/j.nucengdes.2025.114226

[4] F. Zhou, L. Lebel, D.W. Hummel, A.C. Morreale, D. Wojtaszek, and J. Cui, “Simulation of DLOFC Accident in a Generic Pebble Bed High-Temperature Gas-Cooled Reactor Using MELCOR,” Proceedings of the 5th Generation IV and Small Reactor Technology Division (G4SR) Conference, Ottawa, Canada, Oct. 1–4 (2024).

[5] M. Skrzypek, E. Skrzypek, and D. Muszyński, “Thermal-Hydraulic and Neutronic Deterministic Safety Analysis for the HTGR SMR Research Demonstrator for Poland,” *Nuclear Technology*, pp. 1–11 (2026). https://doi.org/10.1080/00295450.2025.2582290

[6] L. Lebel, F. Zhou, and D. Hummel, “Beyond EPZs: Nuclear Emergency Management Frameworks Using Site Boundary Emergency Planning Zones, with a Case Study on High-Temperature Gas Reactors,” *Annals of Nuclear Energy, 226*, 111808 (2026). https://doi.org/10.1016/j.anucene.2025.111808

[7] International Commission on Radiological Protection (ICRP), *The 2007 Recommendations of the International Commission on Radiological Protection*, ICRP Publication 103, *Annals of the ICRP* , 37(2–4) (2007).

[8] International Atomic Energy Agency (IAEA), *Radiation Protection and Safety of Radiation Sources: International Basic Safety Standards*, General Safety Requirements Part 3 (GSR Part 3), Vienna (2014).

[9] F. Zhou, A.C. Morreale, L. Lebel, J. Cui, and G. Patterson, “Severe Accident Analysis of a Generic Small Boiling Water Reactor,” Proceedings of the 14th International Topical Meeting on Nuclear Reactor Thermal-Hydraulics, Operation and Safety (NUTHOS-14), Vancouver, Canada, Aug. 25–28 (2024).

12th CONFERENCE ON
SEVERE ACCIDENTS RESEARCH
May 18-22, 2026 - Madrid, Spain
ERMSAR 2026

Severe Accident Source Terms for Novel Nuclear Reactors

The GIROSCOPE Methodological Framework for EP&R

A. Wawrzynczak[1], V. Hansen[2], E. Bergbäck Knudsen[2], L. Lebel[3], G. Patterson[3], M. Skrzypek[1], P. Kopka[1], M. Isaksson[2]
[1] National Centre for Nuclear Research, Poland; [2] University of Gothenburg, Sahlgrenska Academy, Göteborg, Sweden;
[3] Canadian Nuclear Laboratories, Chalk River, Canada
contact e-mail: anna.wawrzynczak-szaban@ncbj.gov.pl

Motivation and GIROSCOPE Methodological Framework

- Generic LWR source term assumptions are not directly transferable to novel nuclear reactors (NNRs).
- Severe accident releases may be strongly reactor and scenario specific.
- EP&R and EPZ arrangements should be based on traceable, technology specific source terms.
- GIROSCOPE WP2 develops a structured methodology for severe accident source term assessment.
- The source term describes release magnitude, isotopic composition, physical and chemical form, timing, duration, height, and dominant retention or bypass pathways.
- The resulting source terms provide inputs for consequence assessment and EP&R studies in WP3/WP4.

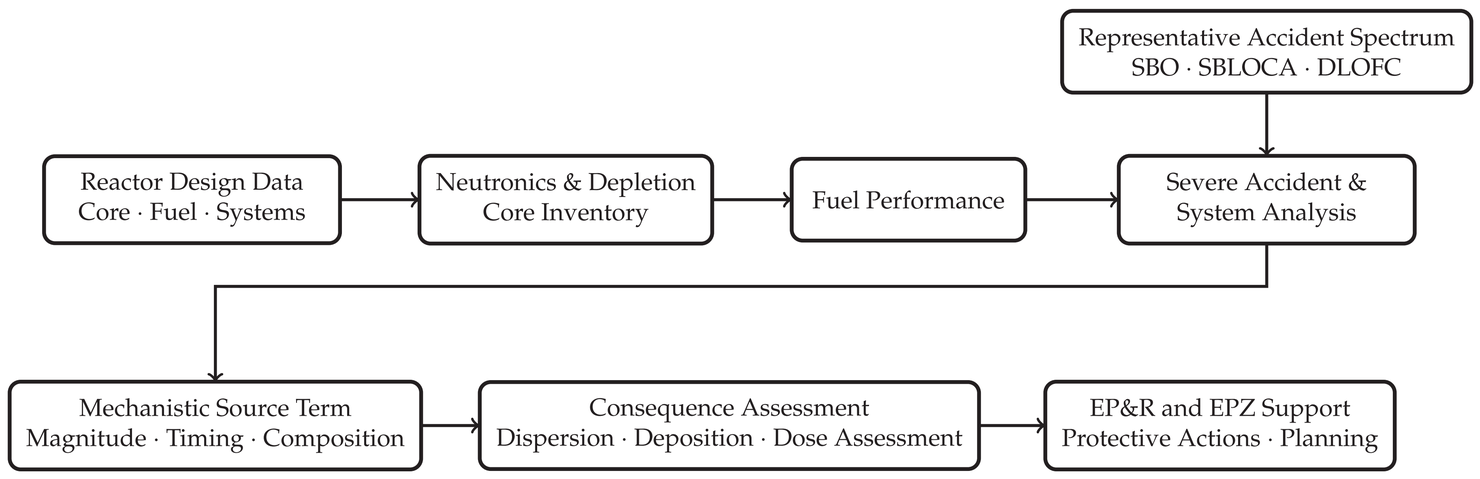

Fig. 1. GIROSCOPE workflow linking reactor design data, core inventory, accident progression, mechanistic source-term assessment, consequence assessment, and EP&R/EPZ support.

Key Findings from Case Studies

- **HTGR-POLA:** Severe accident source term estimated by using MELCOR/SERPENT inputs, STACY release calculations, and plant-level attenuation factors.
- **HTGRs:** TRISO fuel and graphite structures provide strong retention; DLOFC/air ingress cases indicate reduced early release potential.
- **SLWRs/iPWRs:** Releases are sensitive to passive safety performance, pool scrubbing, aerosol deposition, bypass pathways, and accident progression.
- **CMSR:** Source term assessment requires treatment of liquid-fuel inventory, salt chemistry, off-gas, tritium, and radionuclide partitioning.

Conclusions

- GIROSCOPE develops a structured and traceable methodology for severe accident source-term assessment in selected NNR concepts.
- Source terms for NNRs require technology-specific treatment of inventories, fuel forms, barriers, retention mechanisms, release pathways, timing, duration, height, and chemical/physical form.
- HTGR, SLWR, iPWR, and CMSR case studies show that release behaviour is strongly dependent on reactor concept, passive safety performance, containment or confinement design, and accident progression.
- Representative accident spectra provide a stronger technical basis for EP&R and EPZ studies than reliance on a single bounding sequence.
- Mechanistic Source Term methods provide traceable inputs for consequence assessment and support proportionate, risk-informed emergency planning.

Acknowledgements

This work was funded by the GIROSCOPE project within the PIANOFORTE partnership under the European Union's Euratom Research and Innovation Programme, Grant Agreement No. 101061037.

PIANOFORTE EUROPEAN PARTNERSHIP FOR RADIATION PROTECTION RESEARCH
GIROSCOPE
Co-funded by the European Union

Representative Reactor Concepts and Accident Scenarios

Concept	Key features	Representative scenarios	EP&R relevance
HTGR-POLA	Prismatic core, TRISO fuel, graphite moderator, RCCS	DLOFC, PLOFC	Source-term assessment for the Polish HTGR case
HTGR Canada	Pebble-bed TRISO fuel, helium coolant, RCCS	DLOFC / severe air ingress	Reduced early-release potential; long-term contamination still relevant
SLWR Canada	BWR-type design, pool scrubbing, ICS/PCCS	SBO, SBLOCA, ICS/PCCS impairment cases	Sensitivity to passive safety performance and pool scrubbing
iPWR Canada	Integral PWR, passive decay heat removal, compact containment	SBO spectrum, OP and CV break cases	Passive system degradation and bypass scenarios
RR-SLWR Sweden	PWR-type SMR, active/passive decay heat removal, LUHS	Core melt/RPV failure, LBLOCA, IBLOCA, SBO, MSLB, LoSHS; maximum credible multi-failure scenario	Severe multi-failure progression and source-term derivation
CMSR	Liquid fuel, molten salt, off-gas system, low-pressure operation	Fuel-salt leak and severe rupture scenarios	Salt chemistry, off-gas, tritium, and partitioning pathways

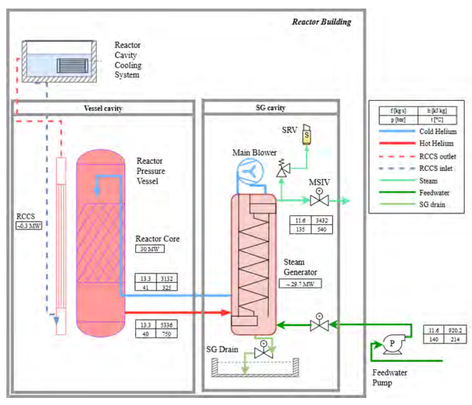

Fig. 2a. Simplified diagram of the HTGR-POLA Nuclear Steam Supply System.

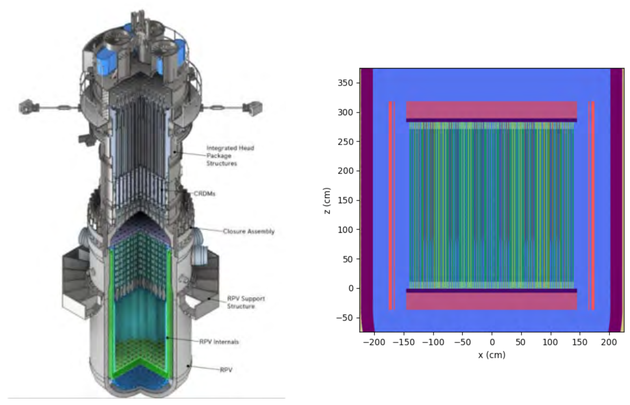

Fig. 2b. Rolls-Royce SLWR core model [Rolls Royce SRM Public Document Repository, 2025 https://gda.rolls-royce-smr.com/documents],and Xz cut through the neutronics model

Consequence Assessment and EPZ Implications

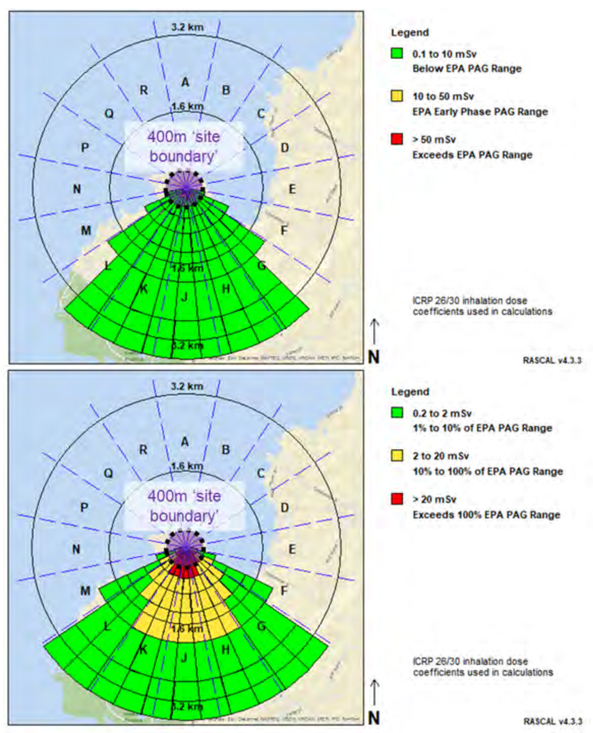

Fig. 3. Representative Total Effective Dose Equivalent predictions for an HTGR DLOFC accident: early phase, top; one-year impact, bottom. [Adapted from Lebel et al. 2026,DOI:10.1016/j.anucene.2025.111808].

- Reactor-specific, time-dependent source terms are propagated to consequence assessment tools.
- Outputs support assessment of dose, plume dispersion, deposition, and long-term contamination.
- Example HTGR calculations indicate limited early-phase doses for selected DLOFC cases, while longer-term contamination may still require protective actions.
- EPZ sizing should be supported by representative accident spectra rather than a single bounding sequence.

3D SIMULATION OF DEBRIS BED QUENCHING WITH TOP-FLOODING FOR FLOAT EXPEIMENTS

Anej Kukovič, Janez Kokalj and Mitja Uršič
Jožef Stefan Institute
Jamova cesta 39, 1000 Ljubljana, Slovenia
ak5994@student.uni-lj.si, janez.kokalj@ijs.si, mitja.ursic@ijs.si

Joerg Starflinger
University of Stuttgart
Pfaffenwaldring 31, 70569 Stuttgart, Germany
joerg.starflinger@ike.uni-stuttgart.de

Renaud Meignen
ASNR
Cadarache BP3, 13115 Saint-Paul-Lez-Durance, France
renaud.meignen@asnr.fr

ABSTRACT

In hypothetical severe nuclear accidents, the coolability of a debris bed formed after core meltdown is essential. Insufficient cooling can compromise containment integrity. Failure to ensure effective cooling can lead to further structural damage and the release of radioactive materials, posing a risk to the environment. To analyse this process, experiments were conducted at the FLOAT test facility of IKE, University of Stuttgart, Germany, focusing on the investigation of debris bed quenching under top-flooding conditions. The experimental configuration consisted of a cylindrical test section filled with approximately 44 kg of stainless-steel spheres, having a porosity of about 0.4, which was used as a physical model of a debris bed. Experiments were conducted at various initial temperatures, with and without counter-current gas injection, to reproduce the non-condensable gases released during molten corium–concrete interaction (MCCI).
Numerical simulations were performed using the MC3D computer code. The code was applied in 3D geometry to replicate the FLOAT experiments. With a sufficiently refined computational grid and by considering heterogeneous temperature and porosity distributions, the simulations captured three-dimensional effects observed experimentally, such as asymmetric front propagation and front instabilities. This work demonstrates the occurrence of 3D phenomena in the quenching process. It also estimates the code's ability to reproduce these effects and provides a direct comparison between simulated and measured data.

KEYWORDS
Nuclear safety, severe accidents, reflooding of debris bed.

1. INTRODUCTION

In a nuclear reactor, insufficient cooling can lead to fuel overheating, melting, and its relocation to the bottom of the reactor pressure vessel, where interaction with water forms porous debris [1]. The decay heat must still be removed to prevent remelting and further structural degradation. If the corium melts through the reactor pressure vessel, it can form debris in the reactor cavity, where interactions with water and concrete produce gases that may obstruct cooling [2].
To better understand debris-bed quenching phenomena, several experiments have investigated reflooding behaviour under different conditions. The FLOAT facility is designed to study debris-bed quenching under a range of initial conditions. The setup consisted of a cylindrical test section filled with stainless-steel spheres modelling the debris bed, with a layer of ceramic spheres placed underneath for support. Tests were performed at different initial temperatures and with or without bottom gas injection to mimic non-condensable gas release during MCCI (Molten-Core-Concrete-Interaction) [3].
The experimental results show that top-flooding quenching proceeds in two distinct stages. Initially, water infiltrates the bed along the wall due to lower porosity and reduced temperature. Once the lowest part of the debris bed is quenched, a water pool forms at the bottom, fed by the preferential water channels formed during the first cooling phase. The continued inflow raises the water level within the test section [4]. Once the front reaches the bottom and a stable water pool forms beneath the bed, overall cooling accelerates. The rising pool uniformly quenches the remaining hot spheres. Gas injection was found to hinder downward water penetration and increase the total quench time [4].
In this work, we develop a three-dimensional numerical model of debris-bed quenching using the MC3D code and compare the results with the FLOAT experimental data, with a focus on three-dimensional effects observed under varying initial configurations.

2. COMPUTATIONAL MODEL

To reproduce the experimental conditions, several grid configurations and initial setups were used. The main simulation domain consisted of three regions: a supporting layer composed of ceramic spheres, a debris-bed region formed by stainless-steel spheres with an average porosity of 0.4, and an upper zone in which the water pool above the debris bed could develop. The inflow of water was modelled at the top of the computational domain. Heterogeneities in debris bed temperature and reduced porosity near the wall were considered. To account for MCCI-driven gas release in some cases, upward gas injection was introduced at the bottom of the supporting structure.
The computational grid was cylindrical, with 91 cells in the axial direction and 12 cells in the radial direction. Two circumferential configurations were examined: one with six angular zones (6,480 total cells) and another with twelve angular zones (12,960 total cells). For comparison, a two-dimensional case with a 12 × 91 mesh was also evaluated.

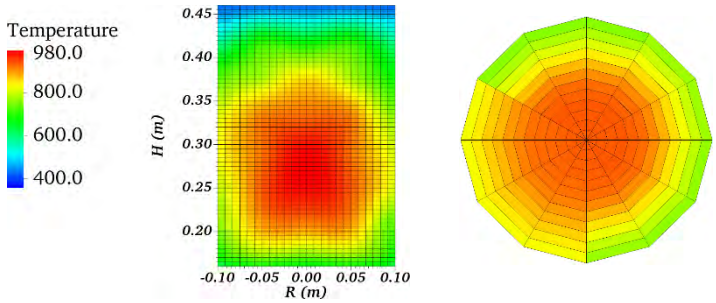

Figure 1: Simulated temperature profile of debris bed at cross-section 0°-180° (left) and temperature profile at height = 0.33 m (right).

The initial conditions were based on experiment F.33, which featured a maximum debris-bed temperature of 700 °C and its total mass of 44.1 kg. Using the thermocouple measurements, the temperature distribution across the entire debris bed was extrapolated.

3. SIMULATION RESULTS

The circumferential mesh resolution was evaluated by gradually increasing the number of partitions. With fewer than ten divisions, no significant asymmetries were observed, and the results remained consistent with the reference 2D simulation. Using twelve angular divisions, however, showed asymmetries that are qualitatively similar to those observed experimentally. It should be noted that the limited number of thermocouples in the experiment prevents a precise description of three-dimensional effects.
Figure 1 shows the comparison between the 2D simulation, the 3D case with six angular divisions, and the 3D case with twelve angular divisions.

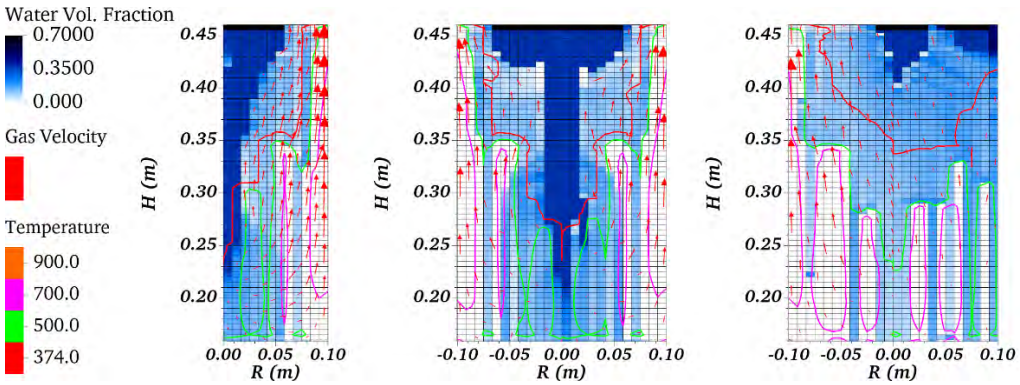

Figure 1: Comparison between the 2D simulation, the 3D case with six angular divisions, and the 3D case with twelve angular divisions at time = 120s

Quenching times, defined as the moment when a thermocouple reaches the water saturation temperature of 100 °C, were compared between the experiment and the simulation. In the experiment, the thermocouples located near the bed centre quenched first, along with some sensors at radial positions R = 50 mm and R = 90 mm. During the second phase, the remaining thermocouples indicate a more uniform quenching front propagation [5].
The simulations showed the onset of quenching approximately 30s later than observed experimentally, which seems to be the consequence of the finite thermal capacity of the stainless-steel particles modelled in the simulation, in comparison to the more immediate temperature drop registered by thermocouples in the experiment. All thermocouples located near the bed centre quenched during the first phase. Most sensors at a radius of 90 mm quenched uniformly during the second phase as the water pool advanced upward, with the exception of locations where downward-spreading flow channels caused earlier quenching. In this phase, a localized hot pocket formed at a radius of 50 mm in certain angular sections, causing the delay of thermocouples quenching. As shown in **Error! Reference source not found.**, the simulated thermocouples at 50 mm radius quenched later than those at 90 mm at the same height.
In the simulation with twelve circumferential divisions, the quench front initially formed near the bed centre, where preferential channels also began to develop at mid-radius. After approximately 40s, the main flow shifted locally toward the wall in certain angular sectors, while in other regions it remained centred but less intense and more dispersed. The second phase started once the water pool formed at the bottom of the supporting structure reached the lowest region of the debris bed. The water pool then rose to the top, completing the quench.

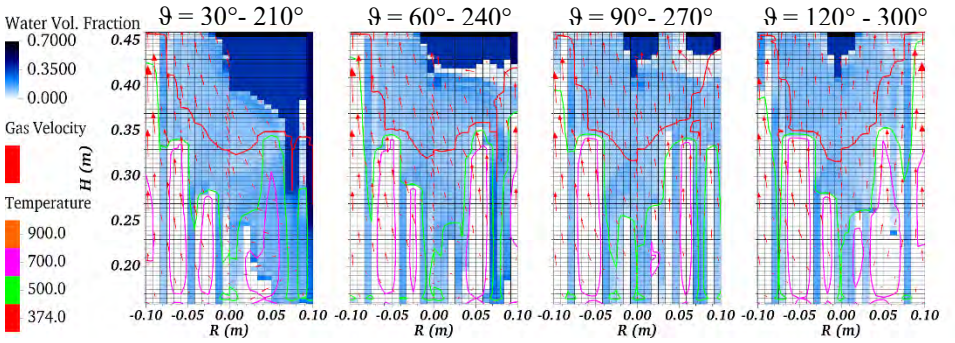

Figure 2: Results of simulation showing different angular partition at time 130s

To examine ex-vessel debris–concrete interaction (MCCI), additional experiments were performed with gas injection from the bottom. In this simulation, data from experiment F.32 are considered, which used initial conditions similar to those of F.33 but included bottom gas injection. The simulations with additional gas injection exhibited longer quenching times, while the quenching process remained generally unchanged.

4. CONCLUSIONS

The advantage of using a three-dimensional mesh with fine enough circumferential refinement is the ability to capture more detailed quenching processes and cooling asymmetries within the debris bed. The results demonstrate three-dimensional effects consistent with the experimental observations. At the onset of quenching, flow instabilities and water fingers develop, leading to partial cooling of the debris. When temperature and porosity heterogeneities are included, water flow in the near-wall region becomes apparent, further indicating that a 3D modelling represents the progression of quenching more accurately than a 2D model. During the first phase, water fingers and near-wall flow quench approximately 60% of the debris. Strong steam generation in regions not reached by the downward flow, together with the faster upward water penetration along the higher porosity region near the wall, restricts cooling in the mid-radius zone and leads to the formation of hot pockets. Such hot pockets pose a risk of local remelting of debris bed during the severe accident and complicate the overall quenching process. Consistent with experimental findings, additional non-condensable gases increase the quenching time. Overall, the simulations confirm that debris-bed quenching under top-flooding conditions is a complex process and that three-dimensional effects must be considered.

REFERENCES

1. A.V. Larraui “Analysis and modeling od ex-vessel underwater cooling processes of debris bed and molten corium pool in interaction with concrete.” Doctoral dissertation, Universite de Lorraine (2020).
2. M. Petroff, R. Kulenovic and J. Starflinger, “Experimental Investigation on Debris Bed Quenching with Additional Non-Condesnable Gas Injection,” *Journal of Nuclear Engineering and Radiation Science,* **8**(4), p.041702 (2022).
3. B.R. Shegal, *Nuclear safety in light water reactors: severe accident phenomenology,* pp. 91-120, Academic Press, Waltham, Massachusetts, USA (2011).
4. M.petroff, M. Schütz, J. Joshi-Thompson, R. Kulenovic, M. Buck and J. Starflinger, “Experimental and numerical investigation on debris bed quenching and development of an artificial neural network for quick quenching estimation,” *Nuclear Engineering and Design,* **441**, pp. 3-6 (2025).
5. T. Kelher, M. Petroff, J. Kokalj, M. Uršič, R. Kulenovic, L. Cizelj and J. Starflinger “Analyitical Model of Debris Quenching with Top-Flooding Configuration and Additional Gas Injection for FLOAT Experiments,” *Proceedings of the International Conference Nuclear Energy for New Europe*, Bled, Slovenia, September 6-9, 2021 pp. 1-5, (2021)

12th CONFERENCE ON
SEVERE ACCIDENTS RESEARCH
May 18-22, 2026 - Madrid, Spain
ERMSAR 2026

3D SIMULATION OF DEBRIS BED QUENCHING WITH TOP-FLOODING FOR FLOAT EXPERIMENTS

Anej Kukovič[1], Janez Kokalj[1], Mitja Uršič[1], Joerg Starflinger[2], Renaud Meignen[3]

Motivation

In hypothetical severe accidents, failure to ensure effective debris bed cooling can lead to further structural damage and the release of radioactive materials.

To analyse this process, simulation analysis of the experiments at the FLOAT test facility of IKE, University of Stuttgart, Germany, was performed. A 3D geometry was used to investigate more detailed local phenomena.

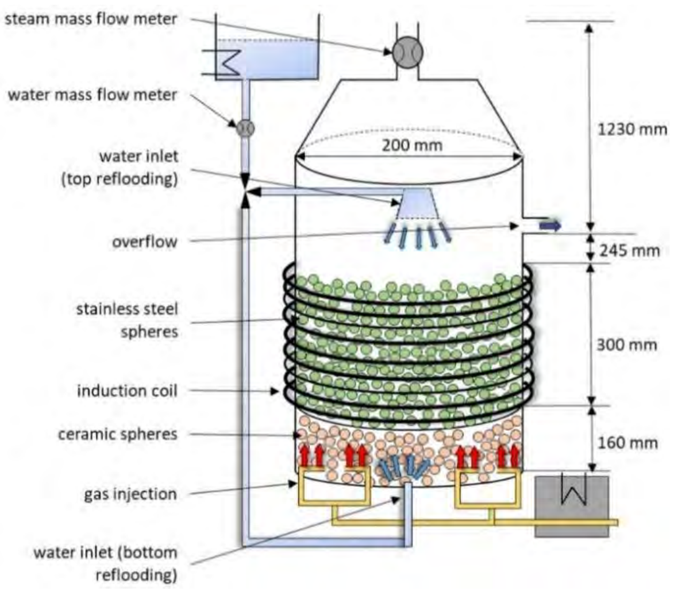

Figure 1: Design of FLOAT facility (IKE, University of Stuttgart, Germany).

Simulation Approach

Fuel-coolant interaction code MC3D (IRSN, France) was used. Main simulation characteristics:

- The main simulation domain regions are support zone with ceramic spheres, debris bed zone formed by stainless-steel spheres, and top zone filled with air.
- The temperature across the debris bed was extrapolated using the thermocouple measurements.

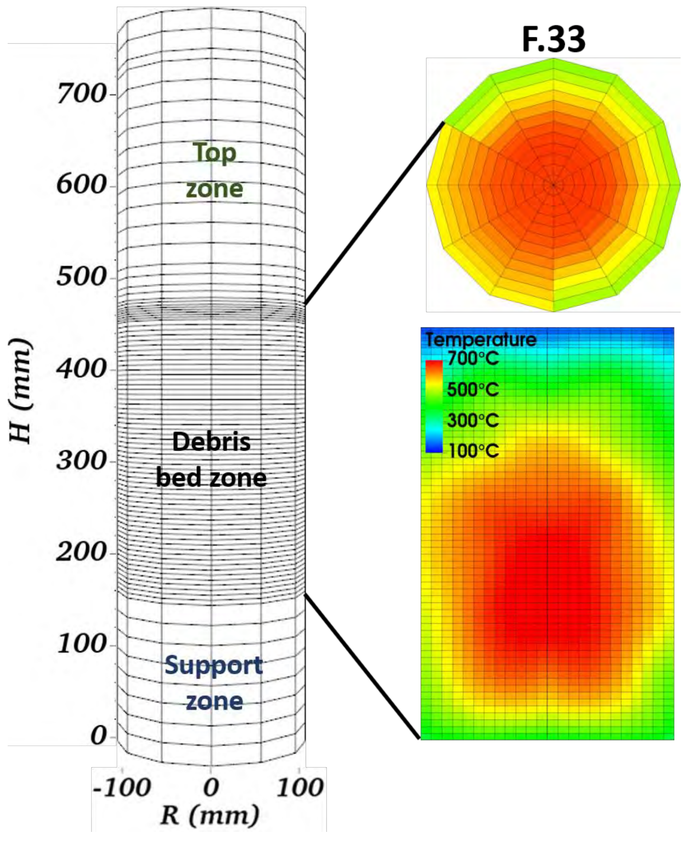

Figure 2: Simulation setup. Cylindrical computational grid with 91 cells in the axial direction, 12 in the radial direction, and 12 angular zones (12,960 total cells).

Simulation Results and Interpretation

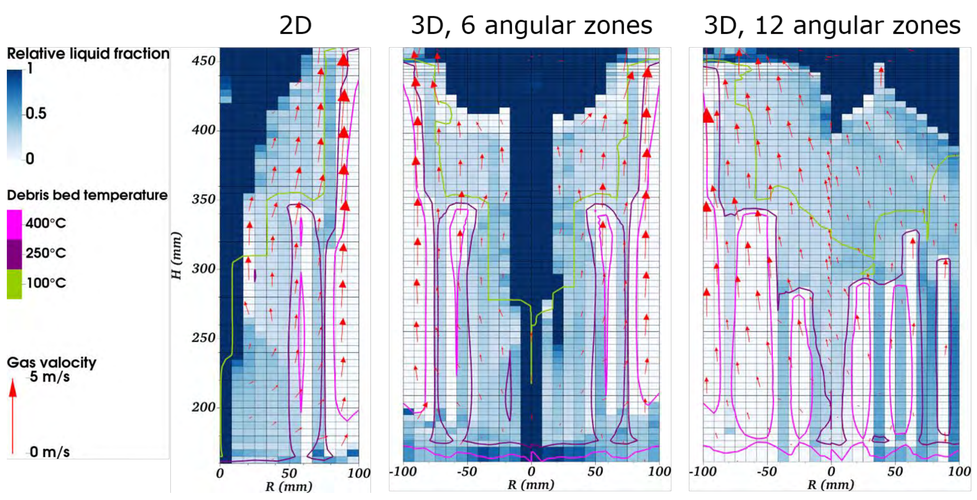

Simulation based on case F.33 with T_{AVG} = 524°C, without counter-current gas injection.

Figure 3: Comparison of 2D and 3D simulations with 6 and 12 angular divisions, at t = 130s.

Fine angular refinement allows us to observe 3D effect.

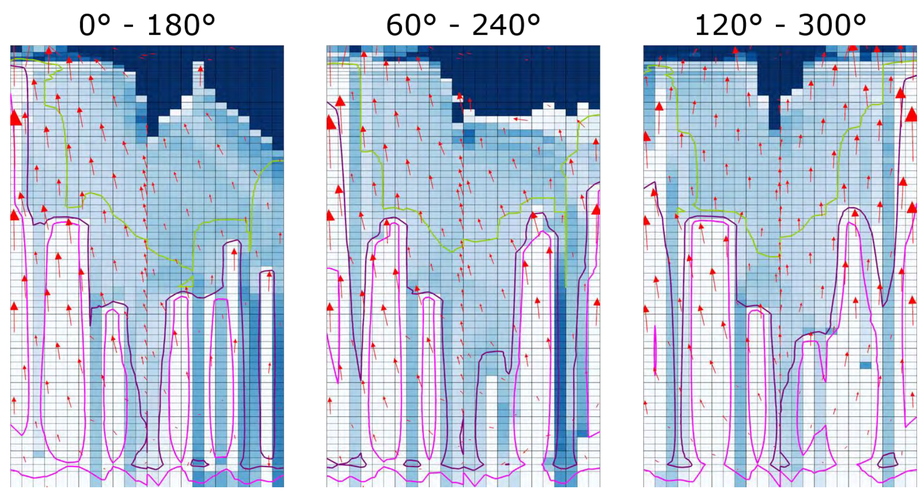

Figure 4: Results of 3D simulation with 12 angular divisions at angles 0° - 180° (left), 60° - 240° (middle), 120° - 300° (right), at t = 130 s.

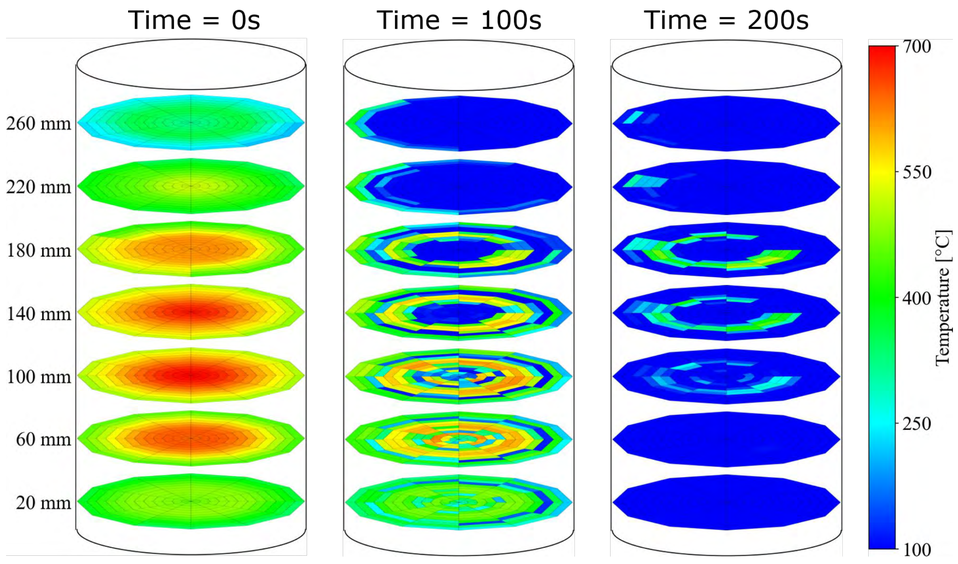

The quenching pattern shows preferential water penetration in the centre and partial penetration along the edge.

Figure 5: Cross-sectional views of the debris-bed temperature during quenching.

Delay in the beginning can be related to the heat capacity of stainless-steel spheres.

Quenching velocity is comparable to the experiment.

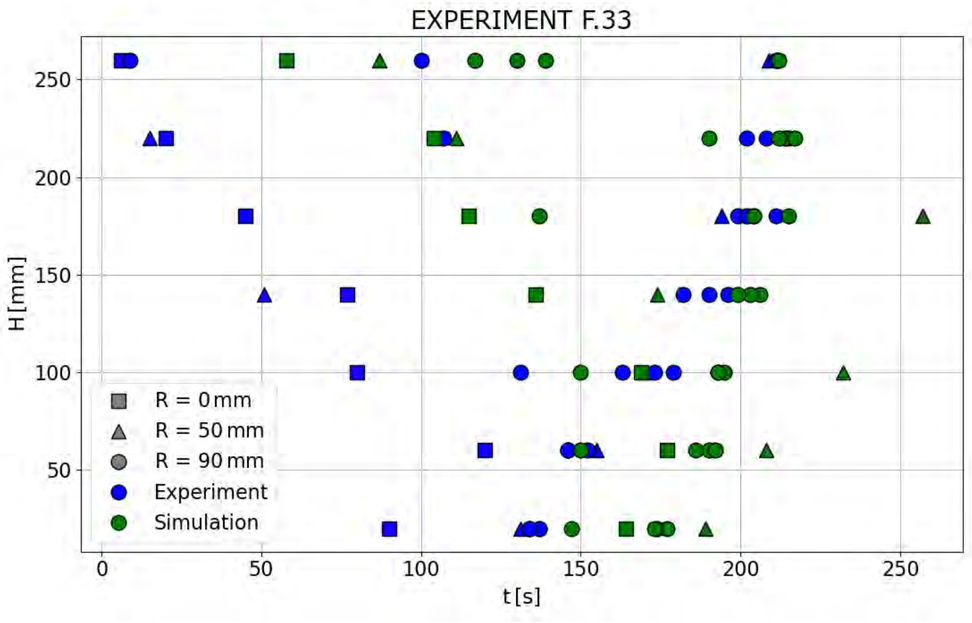

Figure 6: Comparison of debris bed quenching in simulation and experiment.

Discussion and Conclusions

- The advantage of using a three-dimensional mesh with fine enough circumferential refinement is the ability to capture more detailed quenching processes and cooling asymmetries within the debris bed.
- At the onset of quenching, flow instabilities and water fingers develop, leading to partial cooling of the debris. During the first phase, water fingers and near-wall flow quench approximately 60% of the debris.
- Strong steam generation in regions not reached by the downward flow, together with the faster upward water penetration along the higher porosity region near the wall, restricts cooling in the mid-radius zone and leads to the formation of hot pockets.

1 Jožef Stefan Institute, Reactor Engineering Division, Ljubljana, Slovenia; ak5994@student.uni-lj.si, janez.kokalj@ijs.si, mitja.ursic@ijs.si | r4.ijs.si
2 University of Stuttgart, Institute of Nuclear Technology and Energy Systems, Stuttgart, Germany; joerg.starflinger@ike.uni-Stuttgart.de | ike.uni-stuttgart.de
3 Nuclear Safety and Radiation Protection, Reactor Safety Division, Saint-Paul-Lez-Durance, France; renaud.meignen@asnr.fr | asnr.fr

MELCOR Severe Accident Analysis in LDR-lite: a District Heating Reactor

Marcello Principato (1)

(1) Sapienza University of Rome

Type of abstract: Poster
Subject area: Severe accidents in innovative reactor concepts such as Gen IV and Small Modular Reactors (SMRs)
Keywords: SANE, MELCOR, Design Extended Condition, Mitigation strategies.

In the recent years a district heating reactor has been developed at the VTT Research Centre of Finland. In this context, the Horizon Euratom Project SANE aims to explore the adapted reactor's design, as well as other non-electric nuclear applications. This work regards MELCOR simulations in the LDR-lite reactor, a small 50 MWth PWR. The MELCOR input deck is comprehensive of the overall design, from the primary system to the containment vessel, cavity pool and reactor hall, where other three operational units are located, simulated as heat losses to their corresponding pools. The results show the progression of the overall accidental sequence, from the initiating event to meltdown, and propose a preliminary evaluation of mitigation strategies related to LDR-lite.

12th CONFERENCE ON
SEVERE ACCIDENTS RESEARCH
May 18-22, 2026 - Madrid, Spain
ERMSAR 2026

MELCOR Severe accident analysis in LDR-lite: a District Heating Reactor

M.Principato [1], M. Malicki [1], T. Lind [1], T. Sevón [2]
[1] Paul Scherrer Institut - Center for Nuclear Engineering and Science, Switzerland [2] VTT Technical Research Centre of Finland

SANE EU project

Safety Assessment of Non-Electric uses of nuclear energy

Explore the non-electric uses of nuclear power, such as district heating , hydrogen production and desalination

Task 2.3: Severe accident analyses on LDR-lite

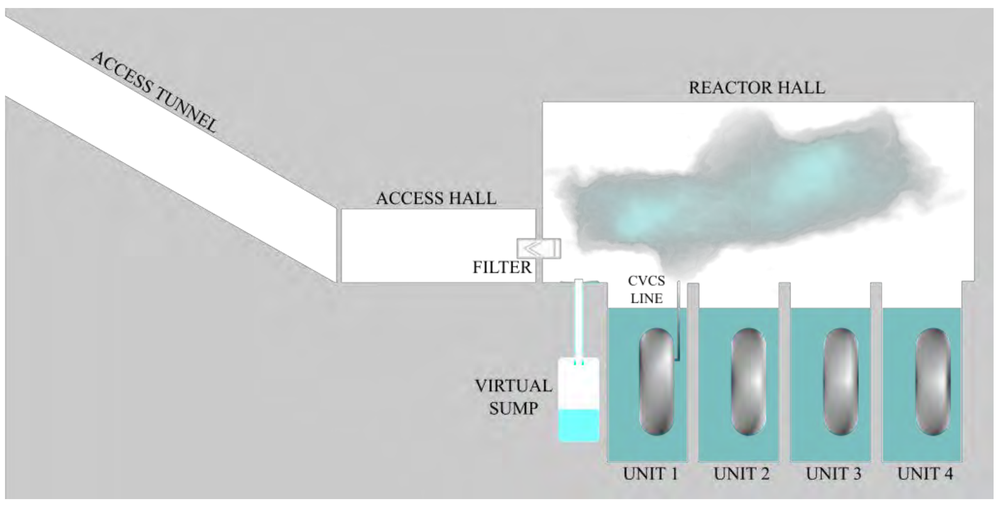

SA Scenario

Initiating event: CVCS line rupture + SBO
Simulation time: 21 days (~500 h)
Computational time: 5-10 days

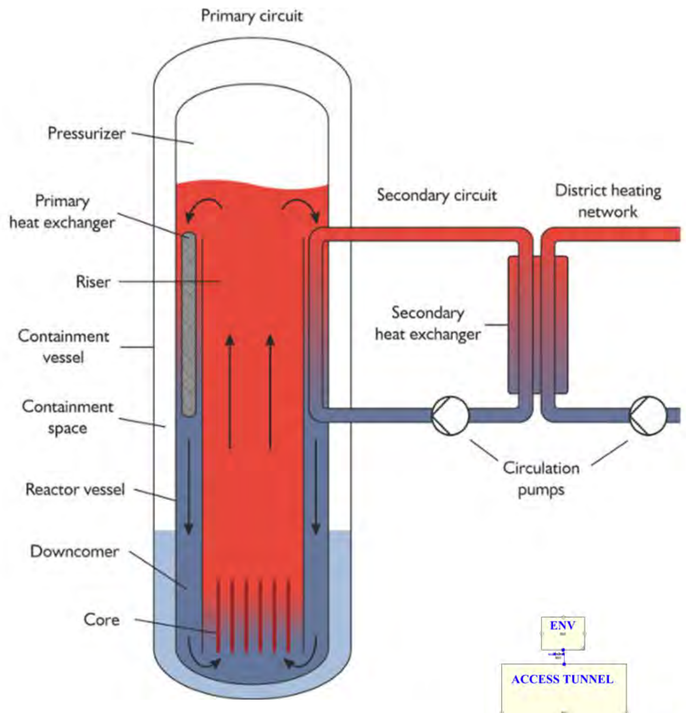

LDR-lite

Benchmark version of LDR-50 : district heating reactor by Steady Energy

Key features: normal operation primary circulation, N_2 bubble pressurizer, boron-free operation, passive heat removal, short reactor core

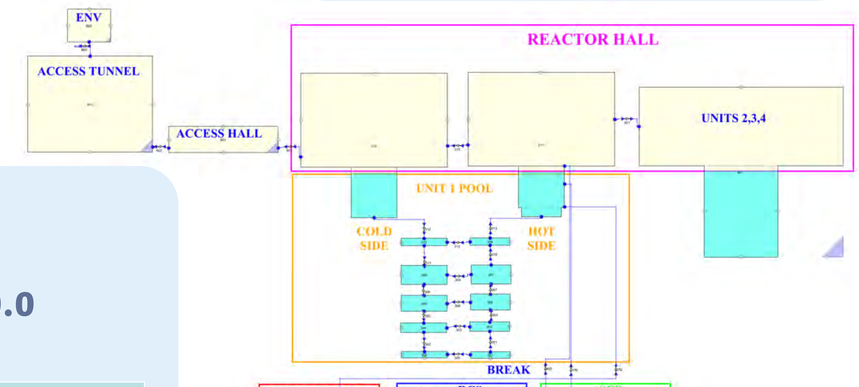

MELCOR

Code version: v2025.0.0
4 input versions:

NAME	Reactor Hall CVH	Reactor Hall HSs thickness	U1 pool HSs thickness
V0	3	1 m	None
V1	3	5 m	1 m
V2	3	5m	5 m floor 1 m wall
V3	31	5m	5 m floor 1 m wall

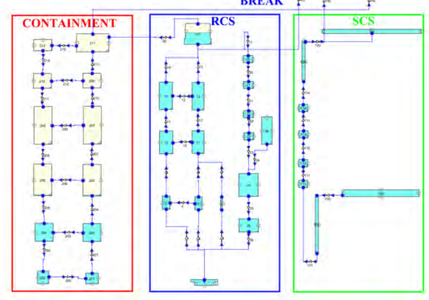

Vessel Water Level (m)

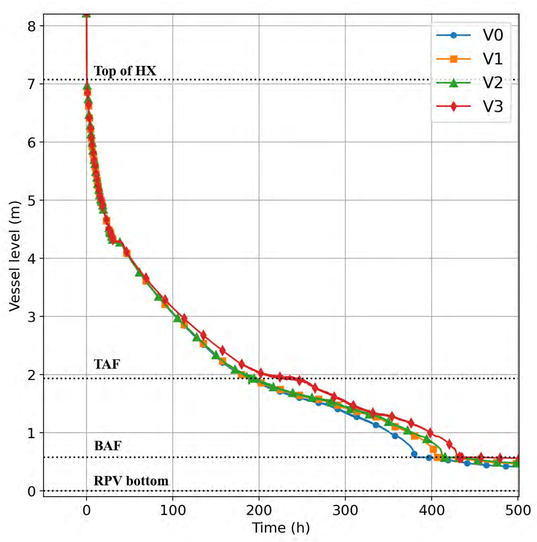

Peak Cladding Temperature (K)

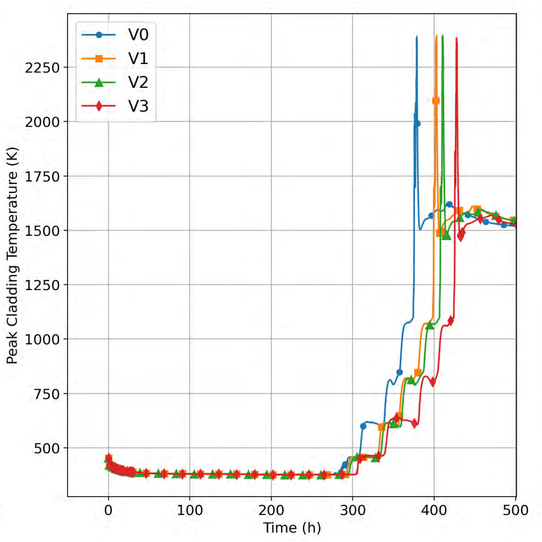

RH pressure (bar)

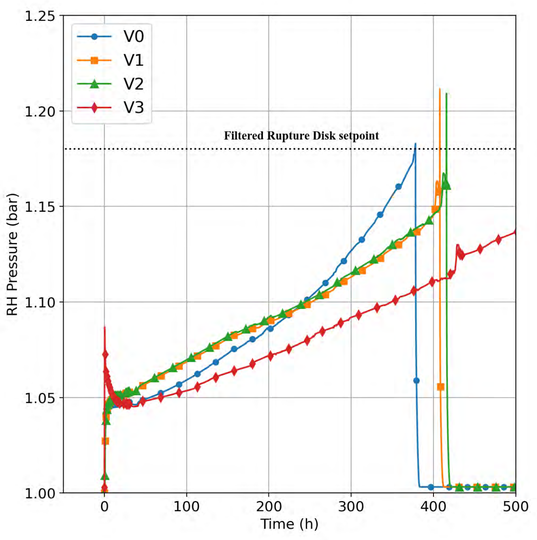

Results

Sequence:

- Primary water is discharged in the RH at 15 m (1m above the water pool).
- The RPV water level decreases slowly, and in turn the RH pressure increases.
- Minor Core damage is registered, resulting in a gap release.
- Core cooling is ensured by steam recirculation once the water level is below the core support plate (Decay heat is low).
- RH is equipped with a rupture disk that is opened at 0.18 bar_{gauge}. Releases dynamics will be investigated with an uncertainty and sensitivity analysis (the deposition time between the gap release and the rupture disk opening is a key parameter).

Conclusions

RH thermal inertia delays significantly the accident's sequence, granting substantial grace time.

No Unit 1 pool thermal stratification observed (high recirculation).

Core damage is limited to the upper portion of cladding (gap release).

Releases are very limited due to the filter's presence. Aerosol – borne classes are also mitigated by deposition on RH structures.

Future development

A sensitivity and uncertainty analysis will be carried out to explore the output realm in terms of RN releases and Core damage.

H_2 risk will be investigated with a high-fidelity code (containmentFOAM), to capture hydrogen dynamics in the Reactor Hall.

Noble gases behavior at the instant of release will also be investigated with containmentFOAM (low pressure difference, fast equalization)

Project funded by
Schweizerische Eidgenossenschaft
Confédération suisse
Confederazione Svizzera
Confederaziun svizra
Swiss Confederation
Federal Department of Economic Affairs, Education and Research EAER
State Secretariat for Education, Research and Innovation SERI

The Associated Partner PSI is funded by the Swiss State Secretariat for Education, Research and Innovation (SERI).

Funded by the European Union. Views and opinions expressed are however those of the author(s) only and do not necessarily reflect those of the European Union or European Atomic Energy Community (Euratom). Neither the European Union nor Euratom can be held responsible for them.

Funded by the European Union

ANALYSIS OF IVMR THROUGH ERVC FOR i-SMR USING CINEMA COMPUTER CODE

Rae-Joon Park, Seokgyu Jeong, Jaehyun Ham, Donggun Son, Sang Ho Kim
Korea Atomic Energy Research Institute
1045 Daedeok-daero, Yuseong-Gu, Daejeon, Korea
rjpark@kaeri.re.kr; jsk1201@kaeri.re.kr; jhham@kaeri.re.kr; donggunson@kaeri.re.kr;
sangho@kaeri.re.kr

ABSTRACT

Analysis on the IVMR(In-Vessel Melt Retention) through ERVC (External Reactor Vessel Cooling) for the i-SMR (innovative Small Modular Reactor) using CINEMA computer code has been performed. Best estimate calculations from the initiating event of the SBLOCA of 2-inch equivalent diameter at inside containment has been performed to evaluate the maintenance possibility of the reactor vessel integrity by the ERVC for 96 hours. In this sequence, one EDV (Emergency Depressurization Valve) and one ERV (Emergency Recirculation Valve) were opened by low pressurizer level signal, which resulted in the ERVC condition. A steady state calculation was performed in order to verify the input nodalization of CINEMA for the i-SMR. The steady state results for a selected set of parameters were in very good agreement with the operating conditions of the i-SMR. At the end of calculation, the masses of oxide corium and metallic corium are 24.9 ton and 24.8 ton, respectively. The reactor vessel did not fail by the ERVC in spite of some melting of the reactor vessel. The reactor vessel was melted to 60 % of the initial thickness of 0.182m. Maximum heat flux from the outer reactor vessel wall to the water inside containment is approximately 0.4 MW/m^2.

KEYWORDS
Small Modular Reactor, IVMR, ERVC, CINEMA Computer Code, SBLOCA

1. INTRODUCTION

As an integrated severe accident computer code development in Korea, CINEMA (Code for INtegrated severe accidEnt Management Analysis) has been developed for a stand-alone severe accident analysis [1]. The basic goal of this code development is to design a severe accident analysis code package by exploiting the existing domestic DBA (Design Basis Analysis) code system for the severe accident analysis. The CINEMA computer code is composed of CSPACE [2], SACAP (Severe Accident Containment Analysis Package) [3], and SIRIUS (SImulation of Radioactive nuclide Interaction Under Severe accident) [4], which are capable of core melt progression with thermal hydraulic analysis of the RCS (Reactor Coolant System), severe accident analysis of the containment, and fission product analysis, respectively. The CSPACE is the result of merging the COMPASS (COre Meltdown Progression Accident Simulation Software) and SPACE (Safety and Performance Analysis CodE for nuclear power plants) models [5], which is designed to calculate the severe accident situations of an overall RCS thermal-hydraulic response in SPACE modules and a core damage progression in COMPASS modules.
The i-SMR (innovative Small Modular Reactor) has been developing in Korea. The design and safety concepts were explained in reference [6]. This small reactor adopted the IVMR (In-Vessel Melt Retention) through ERVC (External Reactor Vessel Cooling) as a severe accident mitigation measure to prevent reactor vessel failure. This study is focused on a preliminary analysis on IVR-ERVC for the i-SMR using CINEMA

computer code. Best estimate calculations from the initiating events of the SBLOCA (Small Break LOCA) of 2-inch equivalent diameter at outside containment in the i-SMR has been performed to evaluate the maintenance possibility of the reactor vessel integrity by ERVC

2. CSPACE INPUT MODEL

The input model for the CINEMA calculation of the i-SMR was a combination of the SPACE and COMPASS input models. Heat structures for the fuel rods and the lower part of the reactor vessel in the SPACE input model were replaced by the COMPASS input models. In the SPACE model, the reactor core was simulated as five channels to evaluate the thermal-hydraulic behavior in detail, and each channel was composed of five axial volumes. In the COMPASS input model of this analysis, the component numbers for the fuel and control rods were five and five, respectively. The total masses of fuel and cladding are 21.4 ton and 6.4 ton, respectively. As shown in Fig.1, one SPACE volume is modelled for ERVC analysis. The lower reactor vessel is divided into 5 radial and 10 axial nodes. Lower vessel thickness is 0.182m. A steady state calculation was performed in order to verify the input nodalization of CINEMA for the i-SMR. The steady state results for a selected set of parameters were in very good agreement with the operating conditions of the i-SMR. The steady state conditions obtained from the simulation were used as initial conditions for the transient calculation.

3. RESULTS AND DISCUSSION

A best estimate calculation from the initiating event of the SBLOCA at outside containment was performed using the CINEMA computer code for 96 hours(4 days, 345,600 sec). In this sequence, one EDV (Emergency Depressurization Valve) and one ERV (Emergency Recirculation Valve) were opened by low pressurizer level signal, which resulted in the ERVC condition. Table I shows CINEMA results on the major events. When the cladding surface temperature reached 1,700 K, oxidation of the zircaloy was accelerated as the steam was supplied from the bottom of the reactor vessel. The bottom of the core dried out at 26,600 sec. At about 2,100K of the cladding surface temperature, the zircaloy inside the oxide shell began to liquefy and the outer portion of the fuel pellets was dissolved. The relatively thin ZrO_2 shell ruptured at about 2,390 K because the shell strength decreased with the temperature increase at 32,900 sec . The debris formed at the bottom of the fuel rods, where the liquefied mixture had resolidified. The melting temperature of the zirconium dioxide is 2,390 K, and that of the uranium dioxide is 2,400 K in these calculations. The melted core material had relocated to the lower plenum of the reactor vessel at 128,000 sec. In this calculation, the reactor vessel did not fail by ERVC. The total hydrogen generation mass was estimated as 233.2 kg.

Table I. CINEMA results on the major events.

Major Events	SBLOCA (sec)
Transient Initiated	0
Core Dryout	26,600
Fuel Melting and Relocation	32,970
Corium Relocation into Lower Head	128,000
Reactor Vessel Failure	No Failure
Total Hydrogen Generation Mass	233.2 kg

Fig. 1 shows CINEMA results on corium mass and height lower plenum. At the end of calculation, the masses of oxide corium and metallic corium are 24.9 ton and 24.8 ton, respectively. The mass of oxide

corium is equivalent to the metallic corium, which is different from the general PWR (Pressurized Water Reactor). Mass of metallic corium is higher than that of general PWR, because of higher initial mass. At the initial stage, all height was water. After the corium in the core initially relocates to the lower plenum at 128,000 sec, corium heights of oxide and metallic and debris increases, but the water height rapidly decreases. The two-phase mixture level is not zero, because of the condensed water injection through the ERV from the PCCS (Passive Containment Cooling System).

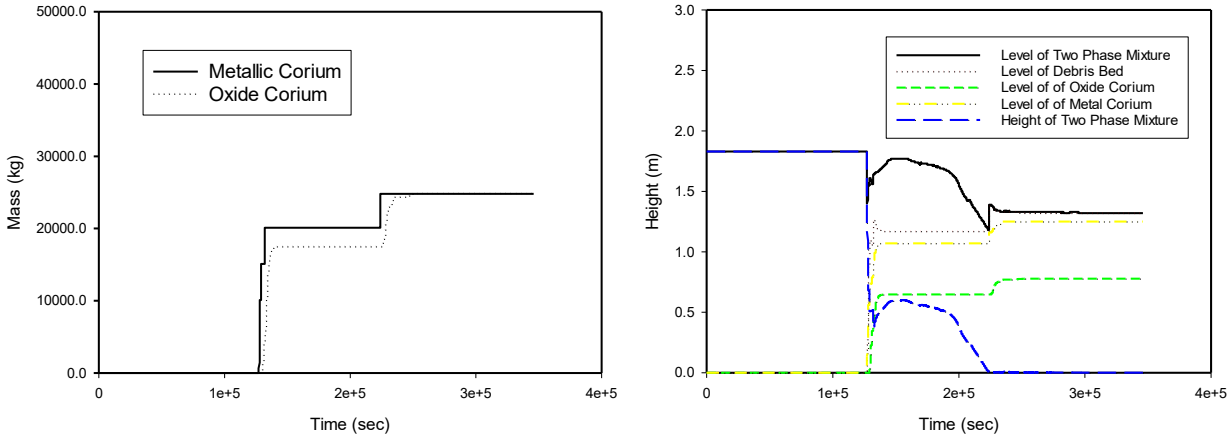

Figure 1. CSPACE Results on Corium Mass and Height in Lower Plenum.

Fig. 2 shows CINEMA results on heat flux from the outer vessel wall to water inside containment and reactor vessel thickness. Maximum heat flux is approximately 0.4 MW/m^2., which was based on El-Genk and Z. Guo correlation [7]. The initial reactor vessel thickness is 0.182 m. The reactor vessel did not fail by ERVC. However, the reactor vessel was melted to 60 % of the initial thickness. Fig. 3 shows CINEMA results on reactor vessel temperature. Node 1 and Node 10 are inside and outside reactor vessel, respectively. Maximum temperatures of Nodes 1 to 6 are melting temperature, which means the melting of reactor vessel inside.

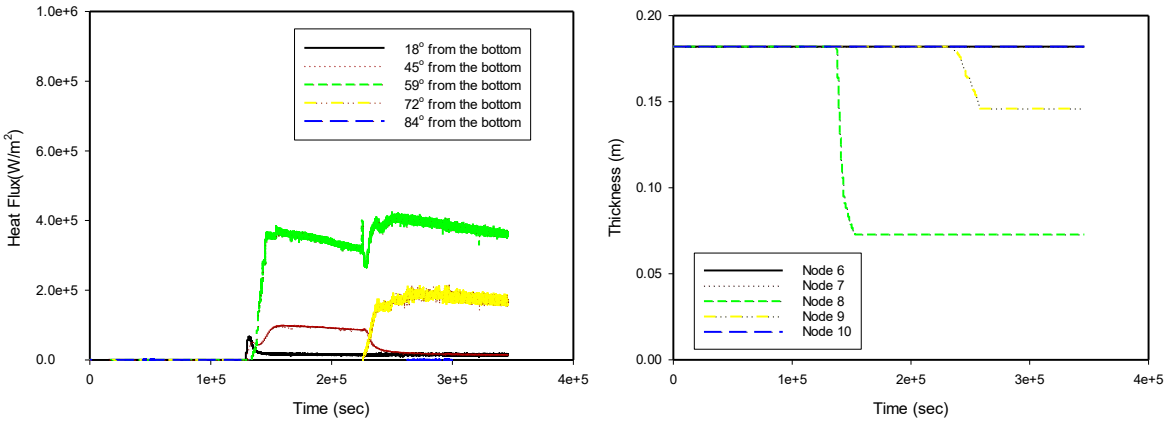

Figure 2 CINEMA Results on Heat Flux from the Vessel Wall to Water and Vessel Thickness.

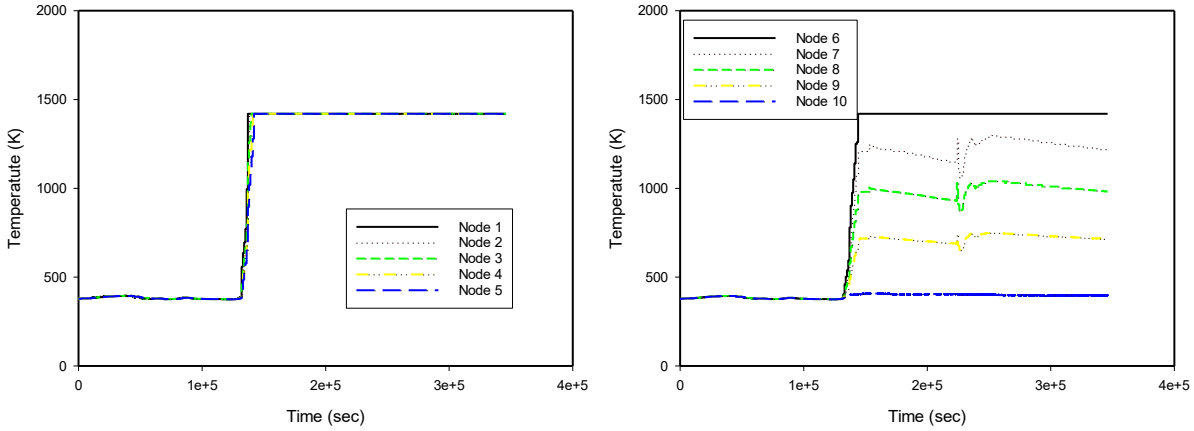

Figure 3. CINEMA Results on Reactor Vessel Temperature.

4. CONCLUSIONS

An analysis on the IVMR through the ERVC for the i-SMR using the CINEMA computer code. Best estimate calculations from the initiating event of the SBLOCA of 2-inch equivalent diameter at outside containment has been performed to evaluate the maintenance possibility of the reactor vessel integrity by the ERVC. The reactor vessel did not fail by the ERVC in spite of some melting of the reactor vessel. The reactor vessel was melted to 60 % of the initial thickness of 0.182m. Maximum heat flux from the outer reactor vessel wall to the water inside containment is approximately 0.4 MW/m^2. More detailed analysis of the ERVC for the i-SMR is necessary to evaluate the IVMR through the ERVC.

ACKNOWLEDGMENTS

This work was supported by the Innovative Small Modular Reactor Development Agency grant funded by the Korea Government(MSIT) (No. RS-2023-00259516).

REFERENCES

1. KHNP, KAERI, FNC, KEPCO E&C, "*CINEMA User Manual*," S11NJ16-2-E-TR-7.4, Rev. 0 (2018).
2. J.H. Song, D.G. Son, J.H. Bae, S.W. Bae, K.S. Ha, Chung, B.D., Choi, Y.J., "CSPACE for a Simulation of Core Damage Progression during Severe Accidents," *Nuclear Engineering and Technology*, **53** (2021).
3. FNC, "*SACAP User Manual*," S11NJ16-2-E-TR-7.4, Rev. 0. (2017).
4. K.S. Ha, S.I. Kim, H.S. Kang, D.H. Kim, "SIRIUS: a Code on Fission Product Behavior under Severe Accident," *Transactions of the Korean Nuclear Society Spring Meeting*, Jeju, Korea (2017).
5. S.J. Ha, "Development of the SPACE Code for Nuclear Power Plants," *Nuclear Engineering and Technology*, **43**(2011).
6. J.H. Ham, S.H. Kim, S.K. Jeong, "Preliminary severe accident analysis of INCV-LOCA in i-SMR using CINEMA code," *Trans. of KNS Spring Meeting*, Jeju Korea, Mar 9-10 (2024).
7. M. S. El-Genk and Z. Guo, "Transient Critical Heat Flux for Inclined and Downward Facing Flat Surfaces," *National Heat Transfer Conference*, San Diego USA, August 9-12 (1992).

12th CONFERENCE ON
SEVERE ACCIDENTS RESEARCH
May 18-22, 2026 - Madrid, Spain
ERMSAR 2026

ANALYSIS OF IVMR THROUGH ERVC FOR i-SMR USING CINEMA COMPUTER CODE

Rae-Joon Park, Seokgyu Jeong, Jaehyun Ham, Donggun Son, Sang Ho Kim (Korea Atomic Energy Research Institute)

KAERI Korea Atomic Energy Research Institute

1. Introduction

As an integrated severe accident computer code development in Korea, CINEMA (Code for INtegrated severe accidEnt Management Analysis) has been developed for a stand-alone severe accident analysis. The basic goal of this code development is to design a severe accident analysis code package by exploiting the existing domestic DBA (Design Basis Analysis) code system for the severe accident analysis. The CINEMA computer code are composed of CSPACE, SACAP (Severe Accident Containment Analysis Package), and SIRIUS (SImulation of Radioactive nuclide Interaction Under Severe accident), which are capable of core melt progression with thermal hydraulic analysis of the RCS (Reactor Coolant System), severe accident analysis of the containment, and fission product analysis, respectively, as shown in Fig. 1.

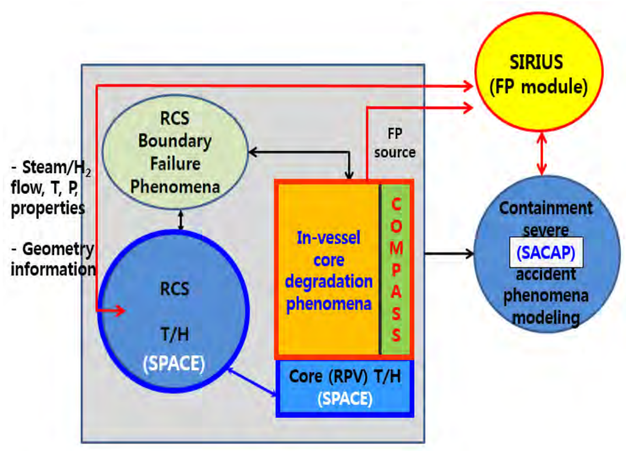

Fig. 1. CINEMA code structure.

Small reactor of i-SMR (innovative Small Modular Reactor) was adopted the IVR-ERVC (In-Vessel corium Retention through External Reactor Vessel Cooling) as a severe accident mitigation measure to prevent reactor vessel failure. This study is focused on an analysis on IVR-ERVC for the i-SMR using CINEMA computer code. Best estimate calculations from the initiating events of the SBLOCA (Small Break LOCA) of 2-inch equivalent diameter at outside containment in the i-SMR has been performed to evaluate the maintenance possibility of the reactor vessel integrity by ERVC.

2. CINEMA Input Model for i-SMR

Fig. 2 shows the CINEMA input model for i-SMR. In the COMPASS input model of this analysis, the component numbers for the fuel and control rods were five and five, respectively. The total masses of fuel and cladding are 21.4 ton and 6.4 ton, respectively. One SPACE volume is modelled for ERVC analysis. The lower reactor vessel is divided into 5 radial and 10 axial nodes. A steady state calculation was performed in order to verify the input nodalization. The steady state results for a selected set of parameters were in very good agreement with the operating conditions of the i-SMR. The steady state conditions obtained from the simulation were used as initial conditions for the transient calculation. Best estimate calculations from the initiating event of the SBLOCA at outside containment was performed using the CINEMA computer code for 96 hours(4 days, 345,600 sec). In this sequence, one EDV (Emergency Depressurization Valve) and one ERV (Emergency Recirculation Valve) were opened by low pressurizer level signal, which resulted in the ERVC condition.

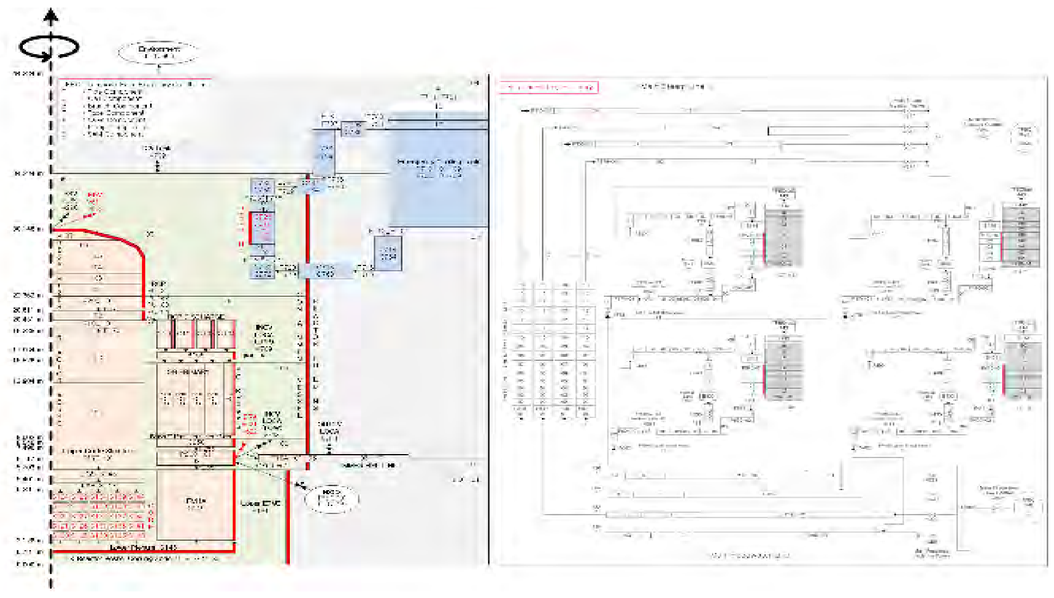

Fig. 2. CINEMA input nodalization for i-SMR.

3. Results and Discussion

Table 1. CINEMA results on major events.

Major Events	SBLOCA (sec)
Transient Initiated	0
Core Dryout	26,600
Fuel Melting and Relocation	32,970
Corium Relocation into Lower Head	128,000
Reactor Vessel Failure	No Failure
Total Hydrogen Generation Mass	233.2 kg

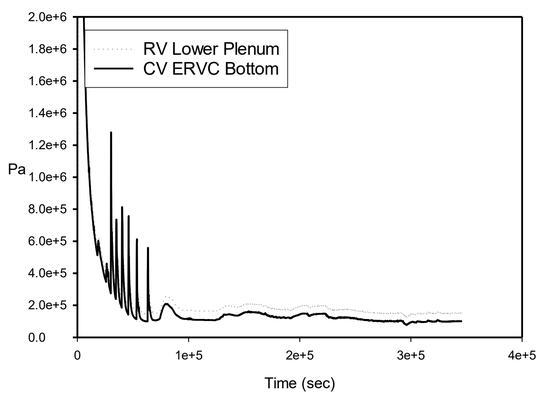

Pressure History

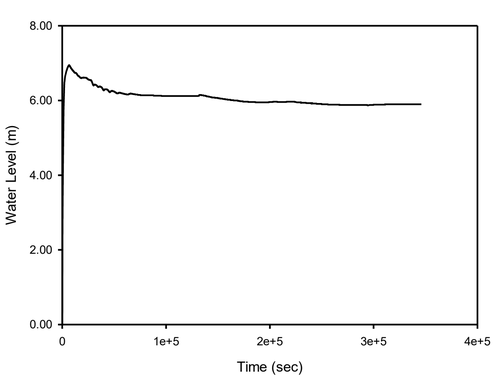

Water Level in Containment

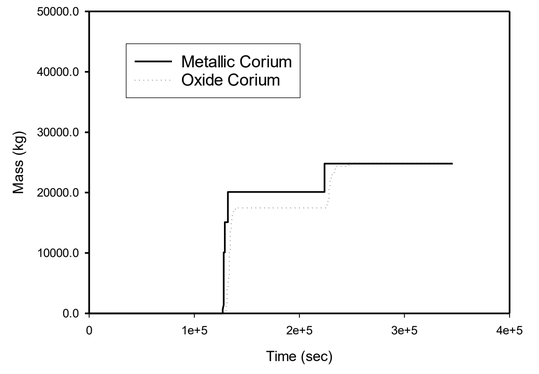

Corium Mass in Lower Plenum

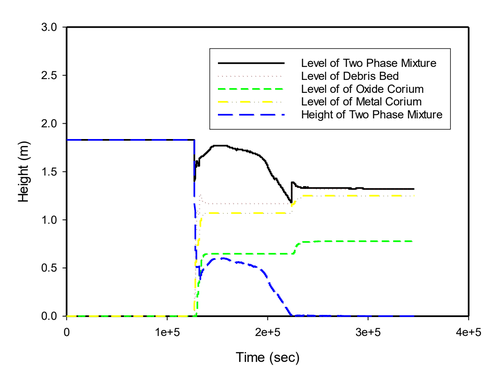

Corium Layer Height in Lower Plenum

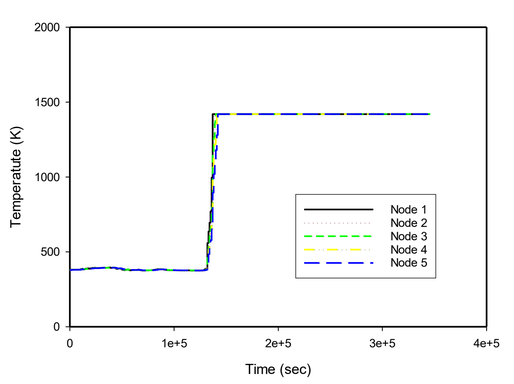

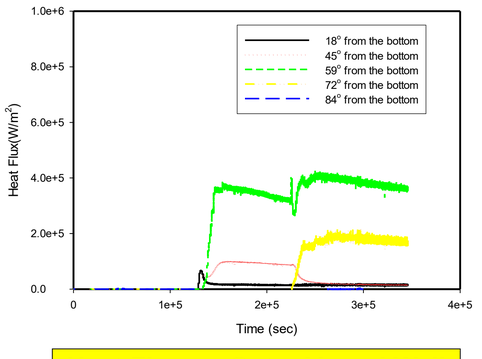

Heat Flux on Outer Vessel Wall

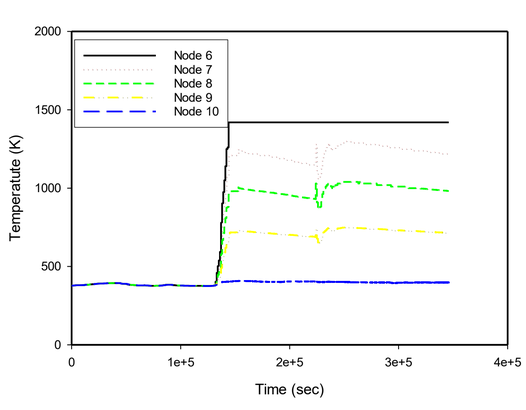

Reactor Vessel Temperature

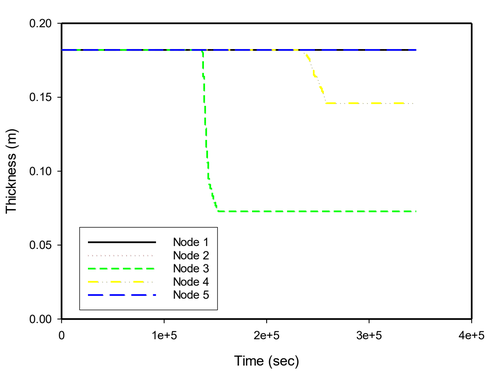

Reactor Vessel Thickness

Fig. 3 CINEMA results on SBLOCA in i-SMR.

4. Conclusions

The reactor vessel did not fail by the ERVC in spite of some melting of the reactor vessel. The reactor vessel was melted to 60 % of the initial thickness. Maximum heat flux from the outer reactor vessel wall to the water inside containment is approximately 0.4 MW/m^2. More detailed analysis of the ERVC for the i-SMR is necessary to evaluate the IVR-ERVC.

ANALYSIS OF SPREADING DISTANCE IN SPILL OUT ACCIDENT OF MOLTEN SALT REACTOR

Rae-Joon Park, Sang Mo An, Jun Ho Bae, SungIl Kim
Korea Atomic Energy Research Institute
1045 Daedeok-daero, Yuseong-Gu, Daejeon, Korea
rjpark@kaeri.re.kr; sangmoan@kaeri.re.kr; bjh@kaeri.re.kr; sikim@kaeri.re.kr

ABSTRACT

As a part of small reactor developments for the GEN-IV (Generation IV) reactors, a MSR (Molten Salt Reactor) is selected for reactor technology and safety aspects worldwide. The spreading and heat transfer behavior of radionuclide-bearing molten salt directly and indirectly affect the distribution of radionuclides during and after a salt spill accident. For this reason, the spreading and cooling process of the spill molten salt is very important for MSR safety. Analysis on spreading distance for the spill molten salt of KCl-NaCl-UCl_3 or KCl-UCl_3 in MSR has been performed using the ANSYS-Fluent computer code. The spreading distance of spill molten salt of KCl-NaCl-UCl_3 estimates as approximately 12.9 cm for 20 sec in condition with the mass flow rate of the spill molten salt of 0.1 kg/s for 20 sec and initial salt temperature of 923 K. The spreading distance of spill molten salt is 17.7 cm at 120 sec. The spreading distance of KCl-NaCl-UCl_3 is longer that of KCl-UCl_3, because the solidification temperature of KCl-UCl_3 is higher than that of KCl-NaCl-UCl_3. The spreading distance of 0.1 kg/s for 120 sec is longer that of 0.1 kg/s for 20 sec, because the spill molten salt is larger. An increase in the spill mass flow rate leads to increase in spreading distance, but it is not in proportion.

KEYWORDS
molten salt reactor, spill out accident, spreading distance, CFD, ANSYS-Fluent

1. INTRODUCTION

As a part of small reactor developments for the GEN-IV (Generation IV) reactors, a MSR (Molten Salt Reactor) is selected for reactor technology and safety aspects worldwide. In the MSRs, the molten liquid salt is the fuel and the cooling liquid at the same time. The first MSR was developed in the USA from 1,960 till 1,970 years, which was thermal-neutron-spectrum graphite moderated concepts [1]. Since 2005, European R&D (Research and Development) interest has focused on fast neutron MSR (MSFR) as a long-term alternative to solid-fueled fast neutrons reactors [2]. The general characteristics of MSR is molten fluorides or chloride salt as fuel fluid and low-pressure, high boiling-point coolant. In a safety of the MSR, the most important thing is a loss of the molten fuel salt with the coolant in the primary system. The spreading and heat transfer behavior of radionuclide-bearing molten salt directly and indirectly affect the distribution of radionuclides during and after a salt spill accident. For this reason, the spreading and cooling process of the spill molten salt is very important for MSR safety. Fig. 1 shows spreading and cooling concept of the spill molten salt in an environment condition.
Test and analysis on the spreading and cooling of the spill molten salt was performed in the SNL (Sandia National Laboratory) recently [3, 4]. Tests were conducted using a chloride salt composition representative of fast spectrum MSRs (eutectic NaCl-UCl_3) to highlight individual processes expected to affect the fate of

spill molten fuel salt and the radionuclides within during a salt spill accident. Spreading and cooling of the spill molten salt were analyzed using the MELTSPREAD computer code [5] for a scenario of molten FLiNaK spilling onto a flat stainless-steel substrate.

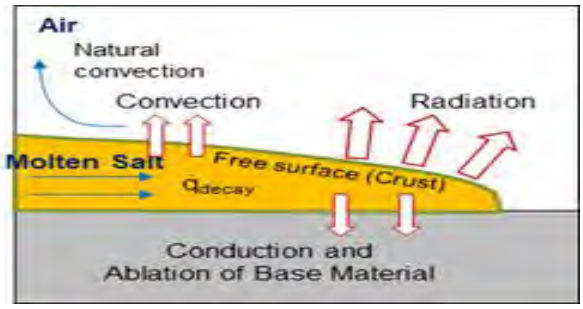

Figure 1 Spreading and Cooling Concept of the Spill Molten Salt.

Analysis on spreading and cooling in PWR was widely studied for severe accident mitigation. The developed methodology for corium spreading may be used for spreading of the molten salt for the MSR. Analysis on spreading distance of the spill molten salt as salt composition of KCl-NaCl-UCl_3 for marine MSR or KCl-UCl_3 for very small MSR has been performed using the ANSYS-Fluent computer code of CFD (Computational Fluid Dynamics) tool.

2. INPUT FOR ANSYS-FLUENT ANALYSIS

Input model for ANSYS-Fluent analysis on spreading and cooling of the spill molten salt was developed. Fig. 1 shows ANSYS-Fluent input model and mesh for spreading analysis of the spill molten salt.

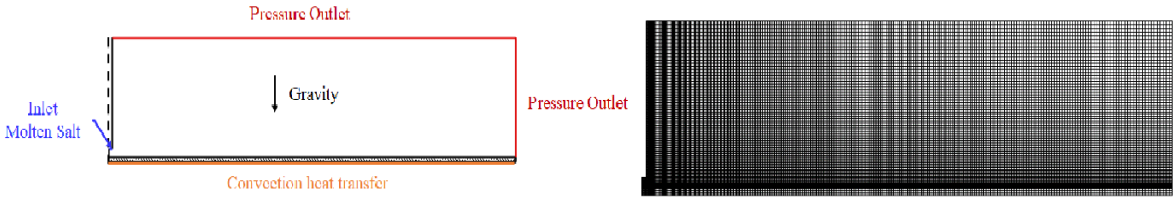

Figure 2 ANSYS-Fluent input model and mesh for spreading analysis of the spill molten salt.

In this study, the following conditions are used.

- Spill molten salt: KCl-NaCl-UCl_3(20.3-42.9-36.8 mol%) or KCl-UCl_3(47-53 mol%)
- Mass flow rate of spill molten salt: 0.1 kg/s to 20 kg/s for 20 sec, 0.1 kg/s for 120 sec
- Initial salt temperature: 923 K
- Solidification temperature: 743 K of KCl-NaCl-UCl_3 or 809 K of KCl-UCl_3
- Temperature of flat floor, atmosphere, and surrounding structures: 630 K
- Geometry: length 60 cm, height 15 cm, Bottom plate thickness: 6.35 mm
- Number of mesh: 32,000, Time step: 0.01 sec, Calculation time: 120 sec
- Analysis method: two-dimensional Axisymmetric
- Bottom condition: hear transfer coefficient input of 10 $W/m^2.K$

Table I shows material properties of spill molten salt of KCl-NaCl-UCl_3 and KCl-UCl_3 in ANSYS-Fluent analysis. In general, solidification temperatures and latent heat of fusion are very effective on the spreading distance of the spill molten salt. The Solidification temperature of KCl-NaCl-UCl_3 is higher than that of KCl-UCl_3, but the latent heat of fusion of KCl-NaCl-UCl_3 is less that of KCl-UCl_3.

Table I. Material properties of spill molten salt in ANSYS-Fluent analysis.

	KCl-NaCl-UCl_3	KCl-UCl_3
Composition (%)	20.3-42.9-36.8	47-53
Solidification Temperature (K)	743	809
Density (kg/m^3)	3,282	3,654
Specific Heat (J/kg.K)	570	475
Thermal Conductivity (W/m.K)	0.38	0.283
Dynamic Viscosity (m^2/s)	7.23 x 10^{-7}	7.86 x 10^{-7}
Latent Heat of Fusion (J/kg)	144,657	68,000

3. RESULTS AND DISCUSSION

Fig. 3 shows ANSYS-Fluent results on spreading distance of the spill molten salt (0.1 kg/s for 20 sec, 0.1 kg/s for 120 sec) with time increases as salt composition of KCl-UCl_3 or KCl-NaCl-UCl_3 in MSR. The spreading distance of spill molten salt of KCl-NaCl-UCl_3 estimates as approximately 15.0 cm for 20 sec in condition with the mass flow rate of the spill molten salt of 0.1 kg/s for 20 sec and initial salt temperature of 923 K. After this time, the spreading distance increases gradually to 120 sec, because the spill out of the molten salt was stopped at 20 sec. Finally, the spreading distance of spill molten salt is 17.7 cm at 120 sec. The spreading distance of KCl-NaCl-UCl_3 is longer that of KCl-UCl_3, because the solidification temperature of KCl-UCl_3 is higher than that of KCl-NaCl-UCl_3. The superheat of spill molten salt is effective on the spreading distance. The spreading distance of 0.1 kg/s for 120 sec is longer that of 0.1 kg/s for 20 sec, because the spill molten salt is larger. Fig. 4 shows ANSYS-Fluent results on spreading distance of the spill molten salt with time and spill mass flow rate as salt composition of KCl-NaCl-UCl_3. The spreading distance of the spill molten salt rapidly increases for initial 20 sec. After this time, the spreading distance increases gradually to 120 sec, because the spill out of the molten salt was stopped at 20 sec. An increase in the spill mass flow rate leads to increase in spreading distance, but it is not in proportion.

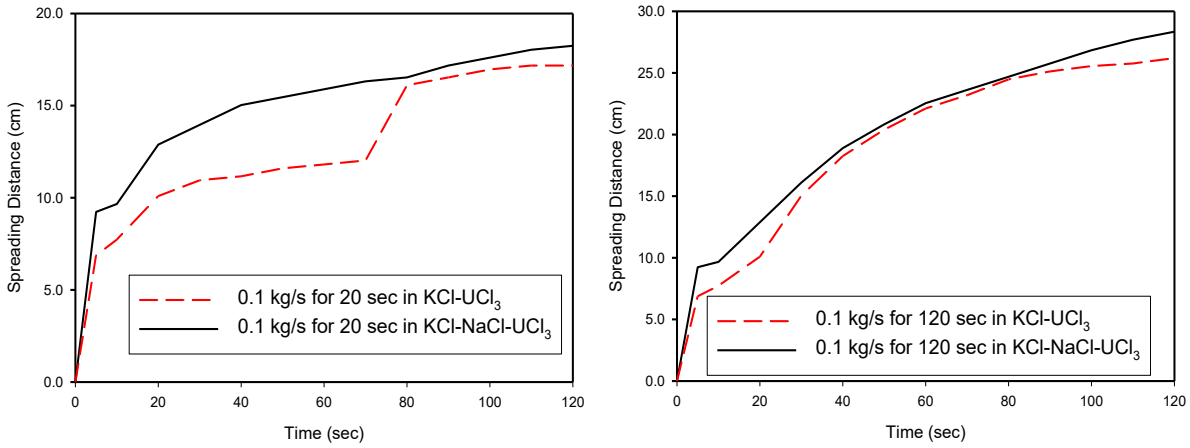

Figure 3 ANSYS-Fluent results on spreading distance

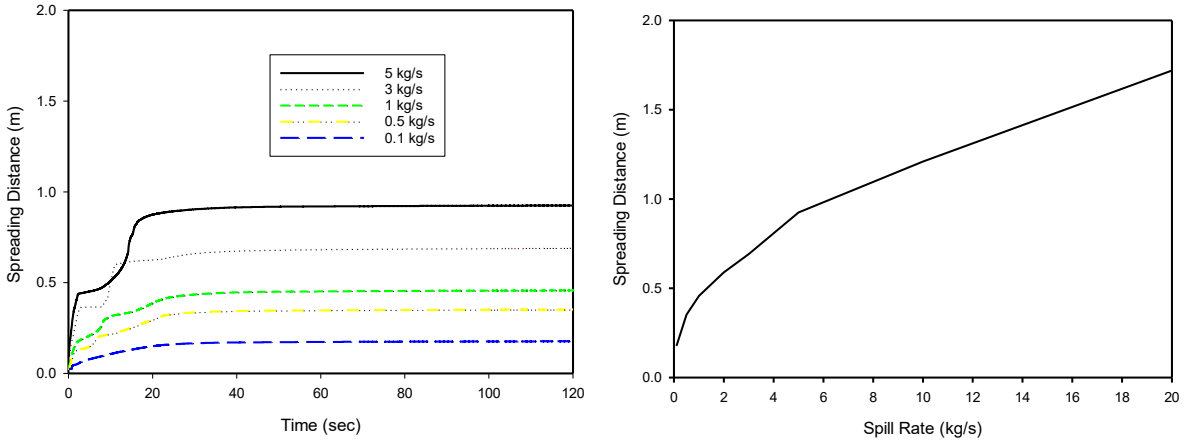

Figure 4 ANSYS-Fluent results on spreading distance

4. CONCLUSIONS

An analysis on spreading distance of the spill molten salt of KCl-NaCl-UCl_3 or KCl-UCl_3 in MSR has been performed using the ANSYS-Fluent computer code of CFD tool. The spreading distance of spill molten salt of KCl-NaCl-UCl_3 estimates as approximately 12.9 cm for 20 sec in condition with the mass flow rate of the spill molten salt of 0.1 kg/s for 20 sec and initial salt temperature of 923 K. After this time, the spreading distance increases gradually to 120 sec, because the spill out of the molten salt was stopped at 20 s. Finally, the spreading distance of spill molten salt is 17.7 cm at 120 sec. The spreading distance of KCl-NaCl-UCl_3 is longer that of KCl-UCl_3, because the solidification temperature of KCl-UCl_3 is higher than that of KCl-NaCl-UCl_3. The spreading distance of 0.1 kg/s for 120 sec is longer that of 0.1 kg/s for 20 sec, because the spill molten salt is larger. An increase in the spill mass flow rate leads to increase in spreading distance, but it is not in proportion. More calculations for the spill molten salt are necessary to estimate effect of the main parameters, such as material properties, released time and spreading channel width.

ACKNOWLEDGMENTS

"This work was supported by the National Research Foundation of Korea(NRF) grant funded by the Korea government(MSIT) (RS-2023-00261295)."

REFERENCES

1. S.J. Kim, S.H. Yun, "*Study of Development Direction for Molten Salt Reactor*," KAERI/RR-4532/2019 (2019).
2. Delphine et al., "A Methodology for the Identification of the Postulated Initiating Events of the Molten Salt Fast Reactor," *Nuclear Engineering and Technology,* **51**, p. 1024 (2019).
3. Sara Thomass, Josh Jackson, "*Modelling Molten Salt Spreading and Heat Transfer using MELTSPREAD-Model Development Updates*", ANL/CFCT-22/15 (2022).
4. Sara Thomass, Josh Jackson, "*MSR Salt Spill Accident Testing Using Eutectic NaCl-UCl_3*," ANL/CFCT-22/32, 2022.
5. M. Farmer, "*The MELTSPREAD Code for Modeling of Ex-Vessel Core Debris Spreading Behavior. Code Manual - Version3.0*," ANL Report. ANL-18/30 (2018).

12th CONFERENCE ON
SEVERE ACCIDENTS RESEARCH
May 18-22, 2026 - Madrid, Spain
ERMSAR 2026

ANALYSIS OF SPREADING DISTANCE IN SPILL OUT ACCIDENT OF MOLTEN SALT REACTOR

Rae-Joon Park, Sang Mo An, Jun-young Kang, Jun Ho Bae, Sungll Kim (Korea Atomic Energy Research Institute)

KAERI Korea Atomic Energy Research Institute

1. Introduction

In a severe safety of the MSR, the most important thing is a loss of the molten fuel salt with the coolant in the primary system. The spreading and heat transfer behavior of radionuclide-bearing molten salt directly and indirectly affect the distribution of radionuclides during and after a salt spill accident. For this reason, the spreading and cooling process of the spill molten fuel salt is very important for MSR safety. Fig. 1 shows spreading and cooling concept of the spill molten salt in an environment condition.

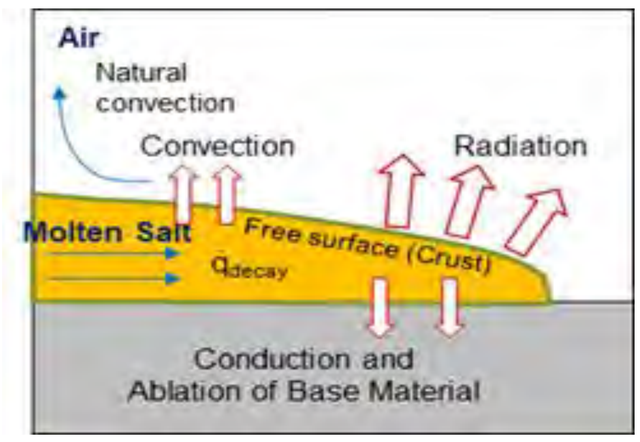

Fig. 1. Spreading and cooling concept of the spill molten salt.

Analysis on spreading and cooling in PWR was widely studied for severe accident mitigation. The developed methodology for corium spreading may be used for spreading of the molten salt for the MSR. Analysis on spreading distance of the spill molten salt as salt composition of KCl-NaCl-UCl_3 for marine MSR or KCl-UCl_3 for very small MSR has been performed using the ANSYS-Fluent computer code of CFD.

2. Input Model

In this study, the following conditions are used.

- Spill molten salt: KCl-NaCl-UCl_3(20.3-42.9-36.8 mol%) or KCl-UCl_3(47-53 mol%)
- Mass flow rate of spill molten salt: 0.1 kg/s or 0.5 kg/s for 20 sec or 120 sec
- Initial salt temperature: 923 K
- Solidification temperature: 743 K of KCl-NaCl-UCl_3 or 809 K of KCl-UCl_3
- Temperature of flat floor, atmosphere, and surrounding structures: 630 K
- Geometry: length 100 cm, height 15 cm
- Bottom plate thickness: 6.35 mm, Number of mesh: 32,000
- Time step: 0.0002 sec. Calculation time: 120 sec
- Analysis method: two-dimensional
- Bottom condition: hear transfer coefficient input of 10 W/m^2.K

The following models are used.

- Multiphase model: VOF (Volume Of Fluid)
- Viscous Model: K-epsilon, Realizable
- Mushy Zone Parameter on Solidification & Melting Model: 1e+5

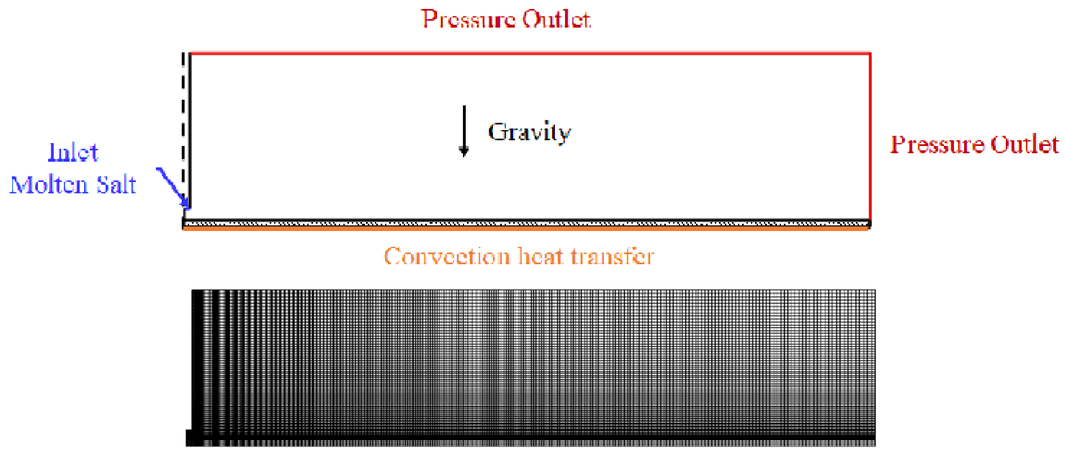

Fig. 2. Fluent input model and mesh generation.

Table 1 Material properties

	KCl-NaCl-UCl_3	KCl-UCl_3
Composition (%)	20.3-42.9-36.8	47-53
Solidification Temperature (K)	743	809
Density (kg/m^3)	3,282	3,654
Specific Heat (J/kg.K)	570	475
Thermal Conductivity (W/m.K)	0.38	0.283
Dynamic Viscosity (m^2/s)	7.23 x 10^{-7}	7.86 x 10^{-7}
Latent Heat of Fusion (J/kg)	144,657	68,000

3. Results and Discussion

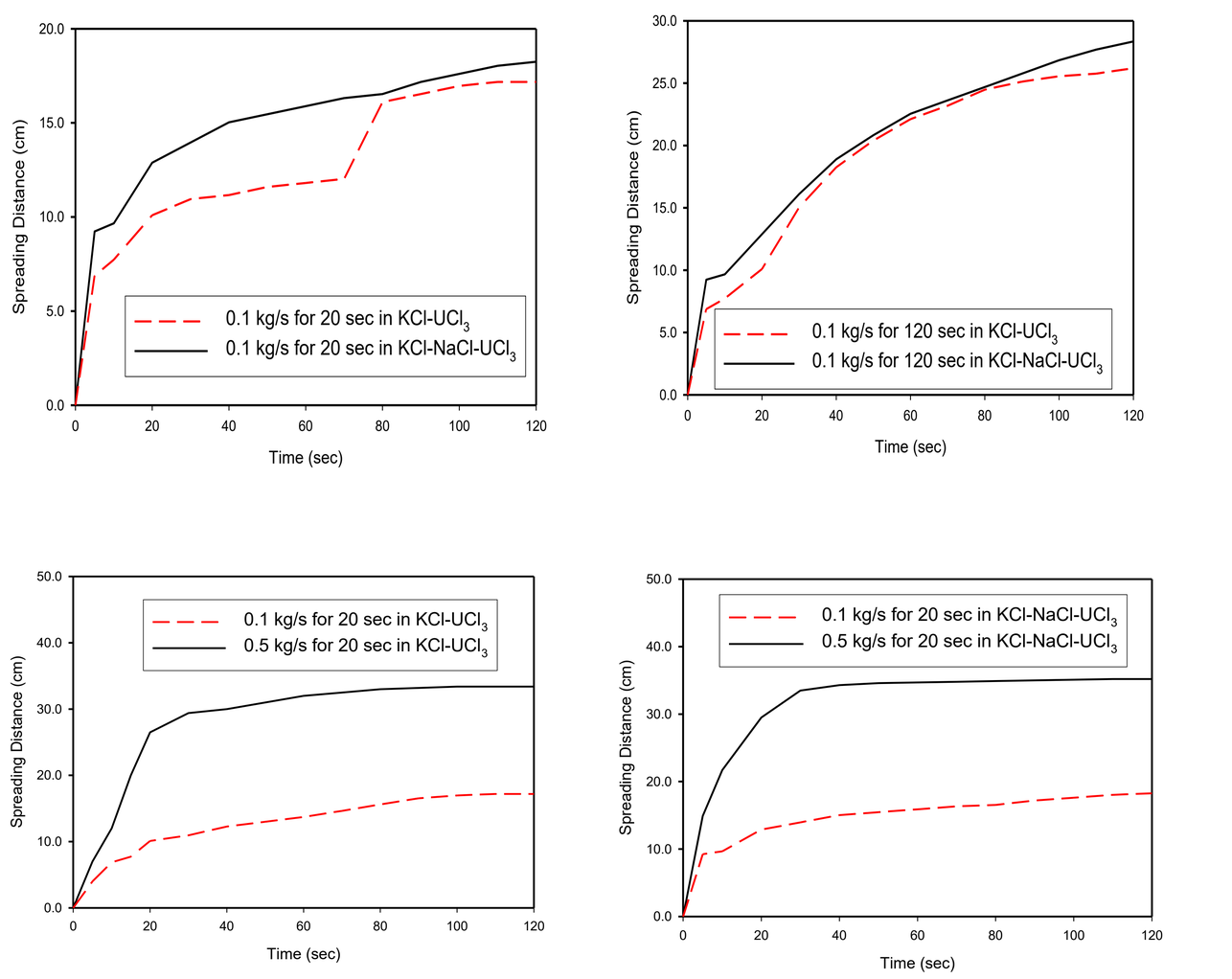

Fig. 3 Fluent results on spreading distance.

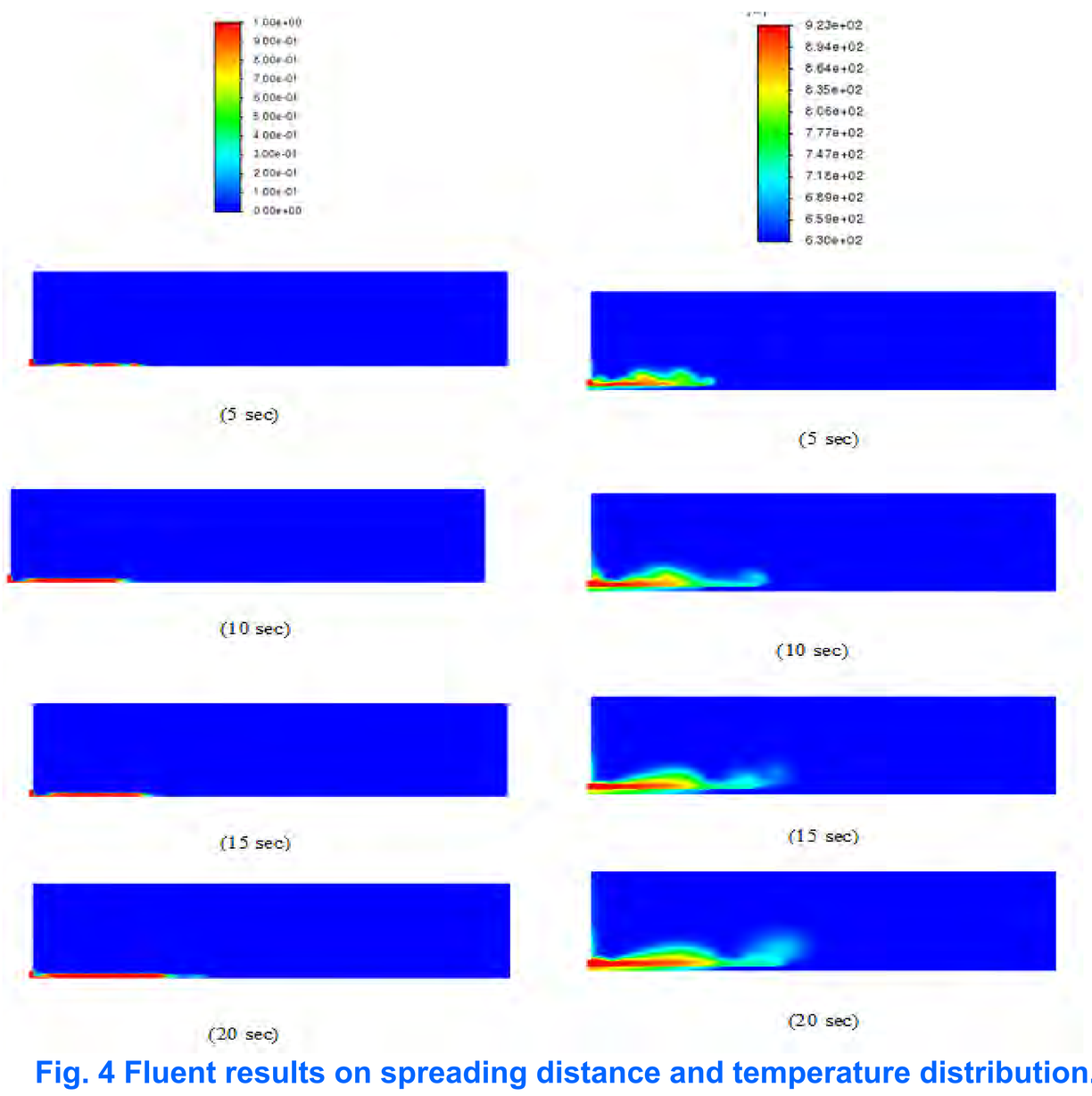

Fig. 4 Fluent results on spreading distance and temperature distribution.

4. Summary

The spreading distance of spill molten salt of KCl-NaCl-UCl_3 estimates as approximately 12.9 cm for 20 sec in condition with the mass flow rate of the spill molten salt of 0.1 kg/s for 20 sec and initial salt temperature of 923 K. After this time, the spreading distance increases gradually to 120 sec, because the spill out of the molten salt was stopped at 20 s. Finally, the spreading distance of spill molten salt is 17.7 cm at 120 sec. The spreading distance of KCl-NaCl-UCl_3 is longer that of KCl-UCl_3, because the solidification temperature of KCl-UCl_3 is higher than that of KCl-NaCl-UCl_3. The spreading distance of 0.1 kg/s for 120 sec is longer that of 0.1 kg/s for 20 sec, because the spill molten salt is larger.

DEVELOPMENT OF A FISSION PRODUCT MITIGATION SYSTEM FOR SEVERE ACCDIENT CONDITIONS IN SMALL MODULAR REACTORS

Jaehoon Jung*
Korea Atomic Energy Research Institute
111 Daedeok-daero 989beon-gil, Yuseong-Gu, Daejeon *34057, Republic of Korea*
Jaehoon Jung@kaeri.re.kr

WooYong Jung
Institute of Future Energy Technology, FNC
46, Tapsil-ro, Giheung-gu, Yongin-si, Gyeonggi-do, 17084, *Republic of Korea*
wyj@fnctech.com

Kaphyun Yoo, Jungsoo Oh
Century Corporation
86 Magokjungang-ro, Gangseo-gu, Seoul, Republic of Korea
kaphyoo@century.co.kr, jungsoh@century.co.kr

ABSTRACT

Small Modular Reactors (SMRs) and advanced reactors feature enhanced inherent and passive safety, resulting in very low probabilities of severe accidents. Nevertheless, additional engineered measures can further reduce potential radioactive releases under beyond design basis conditions. This paper presents the development of a compact fission product mitigation system for SMR applications, designed to remove airborne radioactive aerosols within the reactor protection building using a multi-stage, metal-fiber-based filtration concept. The current system focuses on aerosol mitigation, while allowing optional integration of iodine removal filters if required. Experimental evaluations confirm stable and high aerosol removal performance under representative severe-accident conditions, demonstrating the applicability of the proposed system as a building-integrated mitigation option for next-generation reactors.

KEYWORDS
Severe Accident, fission product, mitigation system, small modular reactors

1. INTRODUCTION

Small Modular Reactors (SMRs) and advanced nuclear reactor designs have gained significant attention as low-carbon energy sources capable of supporting global decarbonization goals. Compared with conventional large-scale nuclear power plants, SMRs feature lower core power, simplified system layouts, and extensive use of passive safety systems, which significantly reduce both the frequency and consequences of severe accidents. As a result, many SMR designs target core damage frequencies and large release frequencies several orders of magnitude lower than those of existing reactors. For example, the Korean innovative Small Modular Reactor(i-SMR), currently under development in Korea, is designed to

achieve an extremely low Core Damage Frequency (CDF) and Large Release Frequency (LRF) of 1×10^{-9} and 1×10^{-10} per reactor year, respectively [1].
Despite these favorable safety characteristics, the potential deployment of SMRs in proximity to population centers motivates the consideration of additional engineered measures to further limit radioactive material release under extremely unlikely severe accident scenarios. In particular, mitigation of airborne fission products within the reactor protection building can provide an effective means of reducing off-site radiological consequences and supporting emergency planning zone.
This paper introduces a compact fission product mitigation system currently under development for SMR and advanced reactor applications. The proposed system is designed to operate within the reactor protection building and focuses on the removal of airborne radioactive materials generated during severe accidents. Unlike conventional filtered containment venting systems used in large reactors, the proposed system operates in a closed-loop, recirculating mode to continuously reduce aerosol concentration within the building. It is further designed to achieve a reduction in airborne aerosol concentration by at least one order of magnitude during severe accident progression, depending on building design and system capacity. The system is compact, modular, and intended to be integrated into the building layout, making it compatible with the spatial and economic constraints of SMRs.

2. DESIGN CONCEPT OF THE FISSION PRODUCT MITIGATION SYSTEM

2.1. System overview

A collaborative effort between KAERI, FNC, and CENTURY is underway to develop a Radioactive Material Reduction System (RMRS) designed to reduce airborne radioactive material concentrations within the reactor protection building during severe accidents. The RMRS adopts a fan-driven forced ventilation approach to actively withdraw contaminated gas from the reactor protection building and deliver it to the filtration unit.
Once processed through the filtration unit, the decontaminated gas is returned to the building volume. This recirculating configuration minimizes direct environmental releases while progressively reducing in-building radioactive source terms. The modular design allows multiple RMRS units to be deployed depending on building volume and specific plant requirements. The concept is applicable to SMRs as well as other advanced reactor types.
Unlike passive safety systems, this approach enables stable and controllable flow rates independent of natural convection or pressure-driven leakage, which can be highly uncertain under transient severe accident conditions. It should be emphasized that the RMRS is not intended to replace inherent or passive safety features of SMR designs, but rather to serve as a complementary mitigation measure under beyond design basis accident scenarios when active system operation is available.
The current concept assumes powered operation of the system. While a detailed strategy for ensuring power availability under severe accident conditions is part of the overall accident management framework, it is beyond the scope of this study and may vary depending on plant specific accident management strategies. In practical applications, plant specific provisions, such as battery backed systems or dedicated emergency power supplies, may be incorporated to enhance system operability during station blackout (SBO) scenarios. Even in SBO scenarios, delayed or intermittent operation of the RMRS can still provide meaningful source term reduction, since aerosol concentrations typically evolve over extended time scales during severe accident progression.

2.2. Multi-Stage Filtration Configuration

The mitigation system employs a hierarchical, multi-stage filtration configuration optimized for severe accident environments:

1. Demister stage: Removes moisture droplets and large particles entrained in the gas stream.

2. Pre-filter stage: Captures micron-scale aerosol particles and reduces the loading on the downstream main filter.
3. Main filter stage: Utilizes a metal-fiber filter element designed to remove aerosol particles with high efficiency under elevated temperature and humidity conditions.

Metal-fiber filter materials fabricated from stainless steel or high-temperature alloys are adopted to ensure thermal resistance, mechanical robustness, and chemical stability under severe accident conditions [2,3]. Compared with conventional glass fiber HEPA filters, metal fiber filters provide superior durability and are less susceptible to thermal degradation, fire, and mechanical failure.

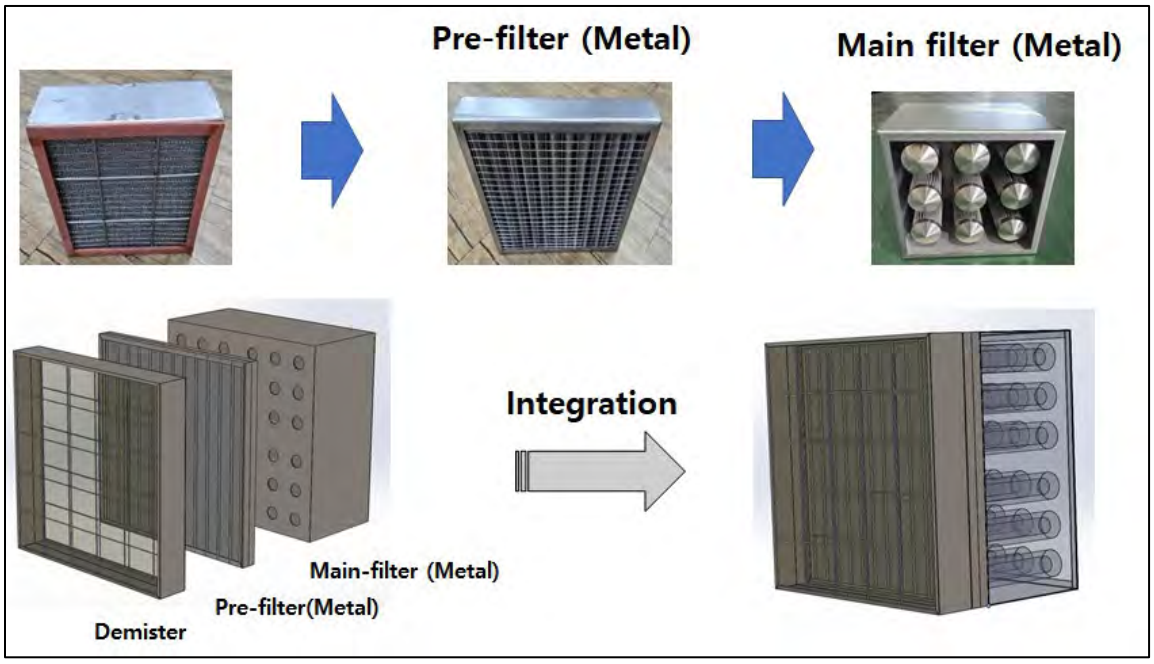

Figure 1. Conceptual images of multiple filtration system in RMRS [2]

3. OPERATING PRINCIPLE AND FUNCTIONAL SCOPE

3.1. Aerosol-Focused Mitigation Strategy

The current development phase of the mitigation system focuses on the removal of aerosolized fission products, which are known to contribute significantly to radiological source terms during severe accidents. Aerosol particles can be efficiently captured through filtration mechanisms such as interception, inertial impaction, diffusion, and thermophoresis, particularly when high-temperature-resistant filter media are employed.

To evaluate filtration performance under representative conditions, in the experiment reported in Ref. [4], solid spherical aerosol particles with a physical diameter of 0.3 μm were used as test particles. The particles were dispersed in ethanol and injected into the test section using a two-fluid nozzle. Experimental evaluations show that the metal-fiber filter achieves the targeted decontamination factor (DF) for aerosol removal of 100 under representative face velocities (0.047 ~0.06 m/s) and temperature conditions (30~90 ℃) relevant to reactor protection building environments during accident scenarios.

At the system level, the RMRS is designed with a target space decontamination capacity corresponding to a nominal flow rate 8 m3/min, which has been successfully achieved in the current system configuration.

3.2. Optional Iodine Removal Capability

While the baseline system configuration is optimized for aerosol removal, the overall design allows for the optional integration of iodine-specific removal components when required by plant safety objectives or regulatory requirements. Such components may include iodine adsorption filters based on silver-impregnated materials or other advanced sorbents. The target DF for iodine removal is approximately 50.
This flexible design approach allows the mitigation system to be adapted to various reactor designs and source term characteristics while maintaining the compactness and operational simplicity of the baseline configuration.

4. DEVELOPMENT STATUS AND APPLICABILITY TO ADVANCED REACTORS

A prototype-scale mitigation system has been developed and subjected to experimental performance testing using representative aerosol conditions. The tests demonstrate stable filtration performance across a range of temperatures and flow conditions, confirming the suitability of metal-fiber filters for severe accident environments.
The system is currently being developed for application in Korean i-SMR concepts; however, its design philosophy and operating principles are directly applicable to a wide range of advanced reactors, including integral pressurized water reactors and other compact reactor concepts. By providing an additional layer of in-building source-term reduction, the mitigation system can complement inherent and passive safety features and contribute to enhanced defense-in-depth.

5. CONCLUSIONS

This paper presented the concept and development status of a compact fission product mitigation system intended for severe accident conditions in Small Modular Reactors and advanced nuclear reactors. The system employs a multi-stage, metal-fiber-based filtration configuration to remove airborne radioactive aerosols within the reactor protection building.
The current design prioritizes aerosol fission product mitigation while allowing optional integration of iodine removal filters if required. Experimental evaluations confirm high filtration efficiency and robust performance under representative thermal–hydraulic conditions. The proposed system offers a practical and scalable option for enhancing source-term mitigation and strengthening safety margins in next-generation nuclear reactor designs.

ACKNOWLEDGMENTS

This work was supported by the Innovative Small Modular Reactor Development Agency grant funded by the Korea Government (MCEE) (No.RS-2023-00257695).

REFERENCES

1. S.G. Lim, H.S. Nam, D.H.Lee, and S.W.Lee, *"Design characteristics of nuclear steam supply system and passive safety system for Innovative Small Modular Reactor (i-SMR)"*, NET, 57, 2025, 103697
2. OECD/NEA, "*Filtered Containment Venting System (FCVS)-Status Report"*, 2024.
3. IAEA, *"Severe Accident Management Programmes for Nuclear Power Plant"*, Safety Reports Series No. 32, Vienna, 2012.
4. W.Y. Jung, J.H. Kang, K.W. Jang, J. Jung, and K. Yoo, *"Performance Evaluation of Aerosol Filtration for HEPA Level Metal Fiber Filter"*, Trans. Of KNS, Oct. 2025.

12th CONFERENCE ON
SEVERE ACCIDENTS RESEARCH
May 18-22, 2026 - Madrid, Spain
ERMSAR 2026

DEVELOPMENT OF A FISSION PRODUCT MITIGATION SYSTEM FOR SEVERE ACCDIENT CONDITIONS IN SMALL MODULAR REACTORS

Jaehoon Jung[a]*, WooYong Jung[b], Kaphyun Yoo[c], and Jungsoo Oh[c]
[a]Korea Atomic Energy Research Institute, Yuseong-gu, Daejeon, Korea
[b]Institute of Future Energy Technology, FNC, Giheung-gu, Yongin-si, Gyeonggi-do, Korea
[c]Century Corporation, Gangseo-gu, Seoul, Korea
*Corresponding author: jhjung@kaeri.re.kr

Introduction

1. Introduction

- Small Modular Reactors (SMRs) and advanced nuclear reactor designs have gained significant attention as low-carbon energy sources capable of supporting global decarbonization goals. SMRs feature lower core power, simplified system layouts, and extensive use of passive safety systems, which significantly reduce both the frequency and consequences of severe accidents. For example, the Korean innovative Small Modular Reactor(i-SMR), currently under development in Korea, is designed to achieve an extremely low Core Damage Frequency (CDF) and Large Release Frequency (LRF) of 1×10^{-9} and 1×10^{-10} per reactor year, respectively [1].
- Despite these favorable safety characteristics, the potential deployment of SMRs in proximity to population centers motivates the consideration of additional engineered measures to further limit radioactive material release under extremely unlikely severe accident scenarios.
- This study introduces a compact fission product mitigation system currently under development for SMR and advanced reactor applications. The proposed system is designed to operate within the reactor protection building and focuses on the removal of airborne radioactive materials generated during severe accidents.

[1] S.G. Lim, H.S. Nam, D.H.Lee, and S.W.Lee, "Design characteristics of nuclear steam supply system and passive safety system for Innovative Small Modular Reactor (i-SMR)", NET, 57, 2025, 103697

DESIGN CONCEPT OF THE FISSION PRODUCT MITIGATION SYSTEM

2. DESIGN CONCEPT OF THE FISSION PRODUCT MITIGATION SYSTEM

System overview

- A collaborative effort between KAERI, FNC, and CENTURY is underway to develop a Radioactive Material Reduction System (RMRS) designed to reduce airborne radioactive material concentrations within the reactor protection building during severe accidents.
- The RMRS adopts a fan-driven forced ventilation approach to actively withdraw contaminated gas from the reactor protection building and deliver it to the filtration unit.
- RMRS is not intended to replace inherent or passive safety features of SMR designs, but rather to serve as a complementary mitigation measure under beyond design basis accident scenarios when active system operation is available.
- Once processed through the filtration unit, the decontaminated gas is returned to the building volume. This recirculating configuration minimizes direct environmental releases while progressively reducing in-building radioactive source terms.
- The modular design allows multiple RMRS units to be deployed depending on building volume and specific plant requirements.

Multi-Stage Filtration Configuration

- The mitigation system employs a hierarchical, multi-stage filtration configuration optimized for severe accident environments.
  1. Demister stage: Removes moisture droplets and large particles entrained in the gas stream.
  2. Pre-filter stage: Captures micron-scale aerosol particles and reduces the loading on the downstream main filter.
  3. Main filter stage: Utilizes a metal-fiber filter element designed to remove aerosol particles with high efficiency under elevated temperature and humidity conditions.

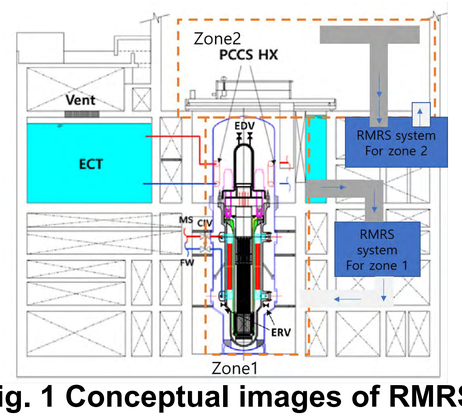

Fig. 1 Conceptual images of RMRS

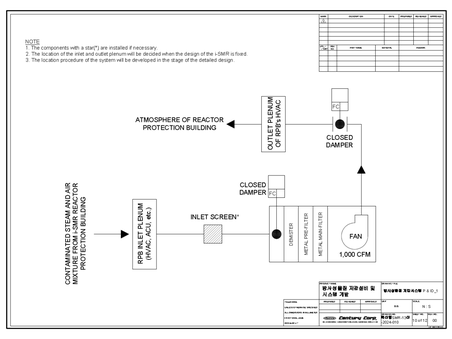

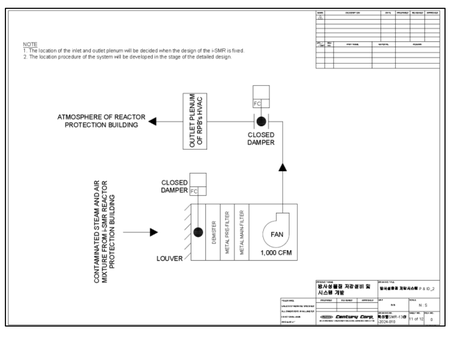

Fig. 2 RMRS application approach in SMR

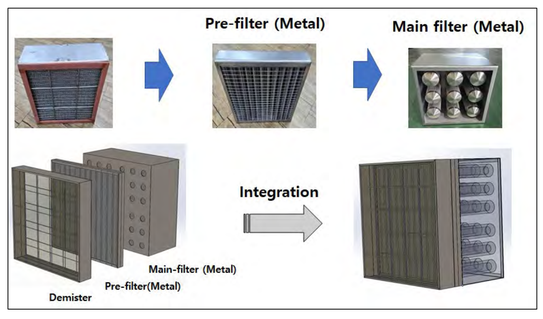

Fig. 3 Conceptual images of multiple filtration system in

FUNCTIONAL SCOPE & DEVELOPMENT STATUS

3. FUNCTIONAL SCOPE & DEVELOPMENT STATUS

Aerosol-Focused Mitigation Strategy

- The current development phase of the mitigation system focuses on the removal of aerosolized fission products.
- Experimental evaluations show that the metal-fiber filter achieves the targeted decontamination factor (DF) for aerosol removal of 100 under representative face velocities (0.047 ~0.06 m/s) and temperature conditions (30~90 ℃) relevant to reactor protection building environments during accident scenarios. In the experiment, solid spherical aerosol particles with a physical diameter of 0.3 μm were used as test particles.
- At the system level, the RMRS is designed with a target space decontamination capacity corresponding to a nominal flow rate 8 m3/min, which has been successfully achieved in the current system configuration.

Optional Iodine Removal Capability

- The overall design allows for the optional integration of iodine-specific removal components when required by plant safety objectives or regulatory requirements. Such components may include iodine adsorption filters based on silver-impregnated materials or other advanced sorbents. The target DF for iodine removal is approximately 50.
- This flexible design approach allows the mitigation system to be adapted to various reactor designs and source term characteristics

Development Status

- A prototype-scale mitigation system has been developed and subjected to experimental performance testing using representative aerosol conditions. The tests demonstrate stable filtration performance across a range of temperatures and flow conditions, confirming the suitability of metal-fiber filters for severe accident environments.
- The system is currently being developed for application in Korean i-SMR concepts; however, its design philosophy and operating principles are directly applicable to a wide range of advanced reactors, including integral pressurized water reactors and other compact reactor concepts.
- By providing an additional layer of in-building source-term reduction, the mitigation system can complement inherent and passive safety features and contribute to enhanced defense-in-depth.

Acknowledgements

This work was supported by the Innovative Small Modular Reactor Development Agency grant funded by the Korea Government (MCEE) (No.RS-2023-00257695).

The 12th European Review Meeting on Severe Accidents Research

May 18-22, 2026, Universidad Carlos III de Madrid, Madrid, Spain

TECHNICAL SESSION 1.3: SEVERE ACCIDENT SCENARIOS - UNCERTAINTY AND SENSITIVITY ANALYSES

Chairs: M. Angelucci (University of Pisa), L. E. Herranz (CIEMAT)

ID156	**Uncertainty quantification and sensitivity analysis of phenomenological uncertainty in the MAAP model for a severe accident loss of secondary heat sink** C. Marshall (Frazer-Nash Consultancy)	Paper Presentation
ID188	**Severe Accident analysis in a generic iPWR and uncertainty quantification of the results** F. Mascari (ENEA)	Paper Presentation
ID155	**Stepwise Uncertainty Analysis Methodology: First insights** R. Bocanegra Melian (ENSO)	Paper Presentation

UNCERTAINTY QUANTIFICATION AND SENSITIVITY ANALYSIS OF PHENOMENOLOGICAL UNCERTAINTY IN THE MAAP MODEL FOR A SEVERE ACCIDENT LOSS OF SECONDARY HEAT SINK

Claire Marshall, Jonathan Fowles
Frazer-Nash Consultancy, Rolls-Royce SMR
c.marshall@fnc.co.uk; jonathan.fowles@rolls-royce-smr.com

ABSTRACT

This paper presents uncertainty quantification and sensitivity analysis of severe accident progression for the Rolls-Royce Small Modular Reactor (SMR) using the MAAP code. The study focuses on phenomenological uncertainty and its impact on reactor pressure vessel and containment integrity during a loss of secondary heat sink fault. Key Figures of Merit (FoMs) analysed are peak containment pressure, primary circuit depressurisation timing, total hydrogen generation, time of first core relocation, and peak nodal heat transfer at the lower head.

A global probabilistic approach was applied, varying a wide range of phenomenological input parameters based on best-estimate probability distributions. Analysis using 2000 Latin Hypercube-sampled cases showed the base case is representative of the broader population, with narrow confidence intervals indicating robust sampling.

Correlation coefficients and linear regression identified correlated input parameters for each FoM. Most FoMs were found to be correlated to only a small subset of parameters, particularly those related to heat removal, core oxidation, and melt behaviour highlighting where improved input characterisation could reduce uncertainty.

A separate analysis with very small input variation was performed to attempt to isolate numerical uncertainty. Some FoMs showed highly condensed ranges, confirming that their uncertainty is largely driven by input variation and is reducible. Others retained significant spread, indicating numerical instability within the MAAP model contributes to residual uncertainty.

Overall, the results show that phenomenological uncertainty in MAAP severe accident modelling is dominated by a limited number of physical processes and model parameters. This analysis supports targeted model improvements, and enhances confidence in current MAAP-based severe accident analyses.

KEYWORDS
Uncertainty Quantification, MAAP, sensitivity analysis, SMR

1. INTRODUCTION

Severe accident analysis includes representation of many physical processes that are not fully understood and are represented in MAAP using empirical parameters whose values are not precisely known. These include parameters affecting heat transfer, oxidation behaviour, melt progression, natural circulation, etc. This complexity makes uncertainty quantification essential for demonstrating robustness of safety conclusions and for prioritising model and data improvements.

Public – Not Listed – Not Subject to Export Controls

To understand the impact of input parameter uncertainty on results and to identify input parameters which have a large impact on output uncertainty, global probabilistic uncertainty and sensitivity analysis has been performed.

In this paper a global, probabilistic Uncertainty Quantification (UQ) and Sensitivity Analysis (SA) framework is applied to the Rolls-Royce SMR MAAP model to assess key safety-relevant metrics for Reactor Pressure Vessel (RPV) and containment integrity in a Loss of Secondary Heat Sink (LoSHS) sequence.

2. METHODOLOGY

2.1. Overview

Five Figures of Merit (FoMs) relating to RPV and containment vessel integrity were analysed: (1) peak containment pressure, (2) time to primary circuit depressurisation, (3) total hydrogen generated in the core, (4) time of first core relocation, and (5) peak nodal heat transfer to the lower head. This paper pays particular attention to the results of peak nodal heat transfer to the lower head and total hydrogen generated in the core. Peak nodal heat transfer to the lower head is a key parameter linked to RPV integrity and total hydrogen generated in the core is linked to the potential for hydrogen deflagration and containment integrity.

RPV and containment vessel integrity are key to severe accident management, and it is important to understand whether the results from deterministic analyses are subject to high uncertainty and whether there is a risk of cliff edge effects. This analysis explores how uncertain modelling assumptions and inputs influence key output metrics and should identify areas where small changes in input parameters may lead to abrupt changes in system behaviour.

Once the FoMs were defined, an appropriate fault sequence was selected to effectively challenge and assess these metrics. The selected scenario is a LoSHS, this event initiates with a complete break of the main feedline to one steam generator, this is followed by failure of automatic depressurisation systems, mitigated by operator depressurisation of the primary circuit after the core exit temperature reaches a key threshold. Severe accident mitigative safety measures are assumed to function as intended. This sequence was selected as it is sufficient to test all of the chosen figures of merit while being similar in fault evolution to a number of other severe accident scenarios so that results from this work have wide applicability.

Latin Hypercube Sampling (LHS) was used to generate input samples, it is a type of stratified sampling. The range of each variable is divided into equally probable intervals, and an equal number of samples are taken from each interval for each variable.

Using LHS rather than simple random sampling gives improved coverage over the more probable areas of parameter space and lower coverage over the highly unlikely areas of parameter space. This improves sampling efficiency and therefore a reduced number of simulations is required to give adequate coverage.

For the baseline analysis 2000 cases were analysed, this was judged to be an appropriate balance between computational effort and the increased certainty gained from larger sample sizes.

2.1. Parameter Selection and Characterisation

Public – Not Listed – Not Subject to Export Controls

In this analysis, only continuous input parameters have been varied. Discrete parameters, such as binary switches, introduce abrupt changes in model behaviour that are not easily captured by the statistical methods chosen and would require a much larger set of analysis cases.

The set of input parameters included in the analysis was derived from the following sources:

- Variables highlighted in the Rolls-Royce SMR Severe Accident Test & Assessment Matrix.
- Variables used in prior targeted Rolls-Royce SMR sensitivity studies.
- Expert judgement on high-uncertainty phenomena for the chosen FoMs.
- Best practise from published UQ&SA MAAP studies for large PWRs [1] and [2].

Ranges and probability distributions for each input parameter prioritised physical plausibility, previous EPRI work [2] and MAAP parameter-file guidance. Probability distributions were uniform where knowledge was sparse, triangular or histogram bin captured skewness where evidence supported it, log-uniform was used where orders of magnitude were important.

2.2. Campaigns

This paper covers three coordinated UQ&SA campaigns:

- Baseline campaign: 2000 cases, sampling all 162 continuous phenomenological parameters, looking at uncertainty quantification and correlation coefficients.
- High-correlation campaign: 500 cases varying only the 20 parameters which showed the strongest correlations to any FoM based on correlation coefficients in the baseline campaign. This was used to perform a linear regression only.
- Small-range campaign: 500 cases with all parameters varied based on a uniform distribution, contracted to 1/100th of the original ranges. This was used to attempt to isolate residual numerical/model noise from input-driven variability. If a FoM's distribution remained wide under near-fixed inputs, this was interpreted as numerical sensitivity.

All calculations used MAAPv5.06 with the Rolls-Royce SMR MAAP model.

2.3. Error Catching

Identifying any cases which fail in any way which means the results are not reliable and deciding whether to exclude their results from the statistical analyses was done in two ways: looking at calculation failure times for those cases which terminated before the mission time and looking at mass and energy errors in the primary circuit and containment.

Rules have been developed which are specific for each FoM ensuring peaks or event times were achieved without unreasonable error values in order to use the result. Analysis case outputs judged to be unsuitable have been excluded from all statistical analysis and plots for that FoM.

Of the 2000 MAAP cases which were run in the baseline campaign, 26 of them failed less than 40 hours into the transient, a failure rate of 1.3%, and up to a maximum of 82 cases were excluded in total from one FoM, a maximum exclusion rate of 4.1%.

2.4. Uncertainty and Sensitivity analysis methods

Uncertainty quantification methods used included:

Public – Not Listed – Not Subject to Export Controls

- Calculation of the mean, standard deviation, coefficients of variation.
- 95% percentile tolerance intervals on data spread.
- 95% confidence intervals on the mean and standard deviations derived via the central limit theorem.

Sensitivity analysis methods used included:

- Partial Spearman rank correlations. Correlation coefficients are used to assess the strength and direction of association between each input variable and each output variable. The Spearman correlation assesses monotonic relationships in ordinal or non-normally distributed data and is robust to outliers. The partial spearman correlation evaluated the relationship between two variables while controlling for the influence of other variables.
- Stepwise linear regressions are used to develop best-fit models for each output metric based on the input parameters. By systematically relating variations in input parameters to changes in output FoMs, regression provides a quantitative means to identify which inputs are most influential and to what extent the model's behaviour can be predicted from its inputs

3. RESULTS

3.1. Baseline and high correlation campaign

The 2000 case baseline campaign shows narrow confidence intervals on the means and standard deviations for all FoMs, indicating that sufficient samples have been analysed to give statistically reliable characterisation of each FoM's distribution, with sampling error small relative to the observed variability. Additionally, the deterministic results obtained using best-estimate values for all input variables lie close to the mean and median across the FoMs. This indicates that the deterministic outputs are representative and not outliers and reflect high-probability behaviour for this scenario.

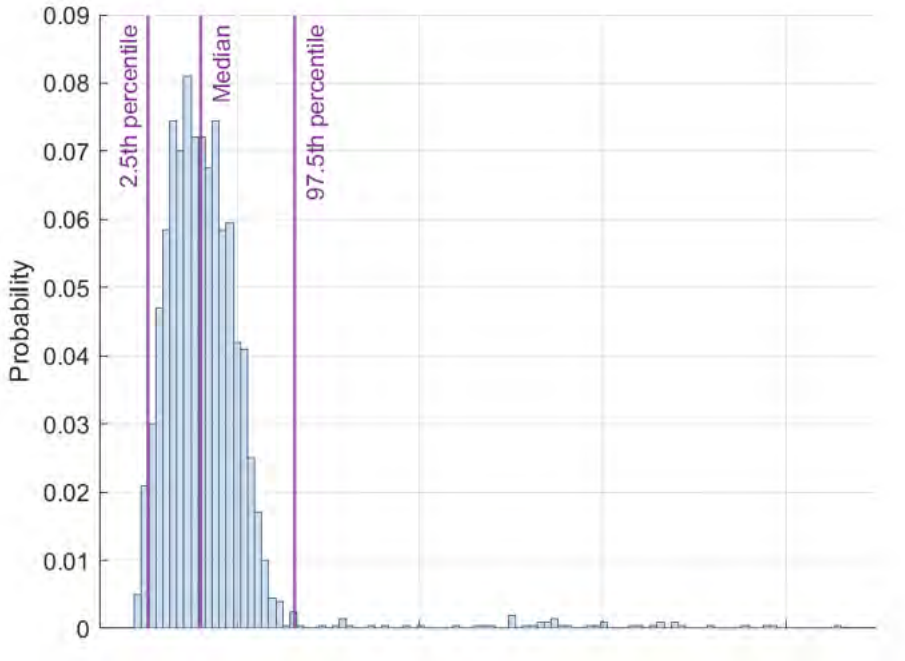

Figure 1 - Probability histogram for Peak Nodal heat transfer at the lower head

The coefficient of variation of a dataset is the ratio of the standard deviation to the mean, it gives a dimensionless way to compare the magnitude of variation between different FoMs. Peak nodal heat transfer at the lower head has a coefficient of variation of 0.41, meaning that the standard deviation is 41%

Public – Not Listed – Not Subject to Export Controls

of the mean, this indicates a high degree of variation. Figure 1 shows a probability histogram for the results from peak nodal heat transfer at the lower head, this shows a highly skewed distribution with a pronounced tail toward higher heat transfer.

This FoM is critical for assessing in vessel retention viability. The presence of high heat transfer outliers indicates that while most cases remain within acceptable bounds, the current assumptions on input parameter uncertainty suggest a small risk of very high heat transfer at the lower head. However it should be noted that Monte Carlo sampling will produce some input datasets which are highly improbable, and therefore the existence of a case that results in an increased risk of lower head failure would not indicate that this is a realistic outcome.

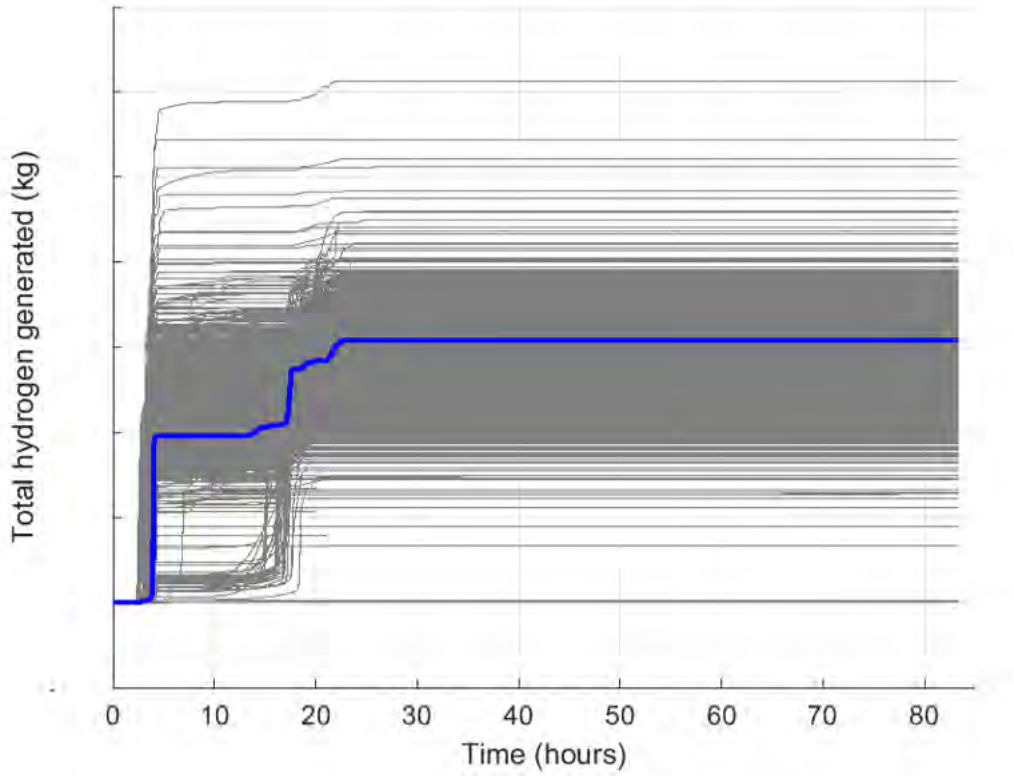

Figure 2 - Dispersion plot of cumulative total hydrogen generated in the core, MAAP variable MH2GEN1

Figure 2 shows the dispersion plot of total hydrogen generated in the core for all cases run, the base case deterministic analysis result is shown in blue. This shows a wide range of total amount of hydrogen produced with the timing of hydrogen production and the shape of the profile being similar in most cases. The deterministic case is shown to be around the middle of the results, in the area of high probability.

Figure 3 shows the probability histogram for total hydrogen production in the core. The population results appear to be close to a normal distribution and therefore the 95% tolerance intervals marked on the histogram, from the 2.5th percentile to the 97.5th percentile are very close to the tolerance interval calculated using the empirical rule.

Public – Not Listed – Not Subject to Export Controls

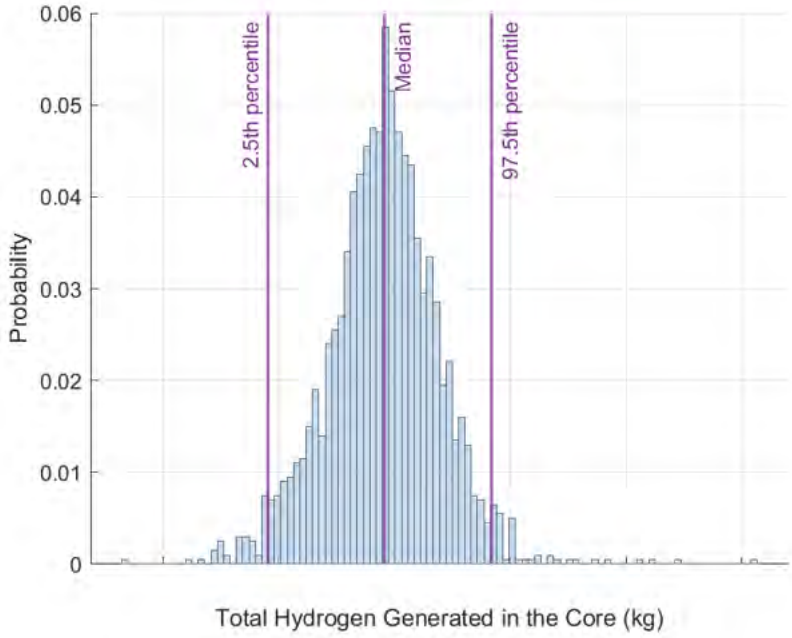

Figure 3 - Probability histogram for total hydrogen generated in the core

Figure 4 and 5 show the results of calculating the partial spearman correlation coefficient, with bars for the top 5 highest correlated parameters.

All high correlation coefficient input parameters have understandable physical reasons why they may be correlated with the FoM of interest. The amount of hydrogen generated in the core is linked to core temperature and how quickly the core melts, and the five highest correlated parameters are all related to this. The top three are VFCRCO, which is the porosity of a collapsed core region, FGBYPA which diverts gas flows in the core to the bypass channel when an entire axial row in the core is completely blocked and FVISC which is the multiplier for material viscosity used in the candling calculation. The highest correlation coefficient for total hydrogen generated in the core is only 0.3 which is a weak correlation.

A stepwise linear regression performed on the high correlation parameters campaign for total hydrogen generated in the core had an R-squared value of 0.46, indicating that 46% of the variability in the data could be explained by the regression. Four of the top five parameters with the highest correlation coefficients were also found to be significant in the regression, supporting the finding of a strong link between variation in these input parameters and variation in predictions of total hydrogen generated in the core.

In addition to those parameters defined above, EPSCUT and EPSCU2 which are related to the cutoff porosity which determine when the MAAP model moves between different fuel melt phases were also in the top 5 highest correlation coefficients and were found to be significant in the regression, and TCLMAX, the temperature that will lead to rupture if the cladding is at this temperature for 36 seconds was found to be significant in the regression.

Public – Not Listed – Not Subject to Export Controls

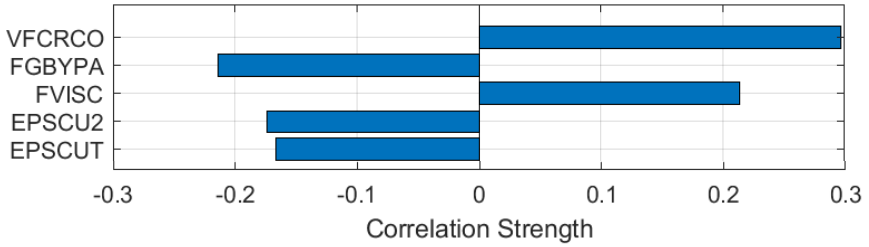

Figure 4 - Partial Spearman Correlation Coefficients, between mass of hydrogen generated in the core and the top 20 input variables

Peak heat transfer on the lower head shows much stronger correlation coefficients in comparison with total hydrogen generated in the core, up to a maximum of 0.67. All three parameters are related to heat transfer in the corium pool in the lower head. EMETALAYER is the emissivity of the light metal layer, FHDNA is the multiplier to the heat transfer coefficient to the lower crust in the corium molten pool and FHUPA is the multiplier to the heat transfer coefficient to the upper crust in the corium molten pool.

When a linear stepwise regression was attempted on the peak heat transfer on the lower head the regression was found to have a low explanatory power with an r-squared value of 0.24. This is likely to be because the long tail towards higher heat transfer suggests nonlinear behaviour.

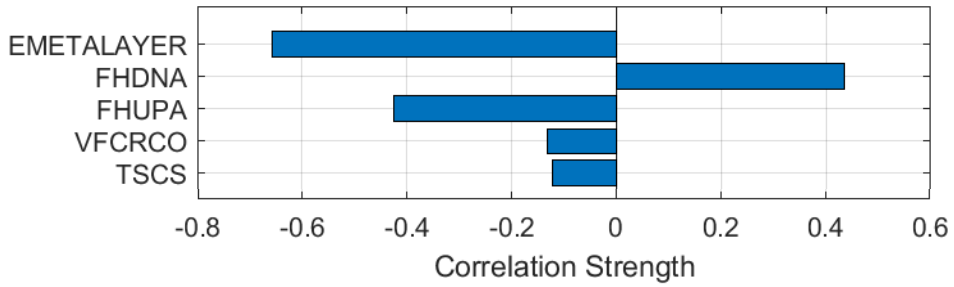

Figure 5 - Partial Spearman Correlation Coefficients, between peak nodal heat transfer at the lower head and the top 20 input variables

3.2. Small input range campaign

Table 1 compares coefficients of variation from the baseline and small input range campaign and describes the visible change in the probability histograms for each FoM.

FoM	Baseline coefficient of variation	Small-Range coefficient of variation	Qualitative Change
Peak Containment Pressure	0.07	0.02	Strong contraction; very narrow 95% tolerance interval range but small tail remains
Timing of RCS Depressurisation	0.04	0.02	Strong contraction, very narrow distribution remains
Peak heat transfer at lower head	0.41	0.17	More than 50% reduction; right tail significantly reduced but still present

Public – Not Listed – Not Subject to Export Controls

Total Hydrogen Generated in the Core	0.17	0.10	Partial reduction; residual spread significant
Time of first core relocation	0.27	0.05	Strong contraction; long tail to early relocation times significantly reduced

Peak heat transfer at the lower head shows a strong contraction in total distribution and a significant reduction in the length and density of the high heat transfer tail. This suggests that the majority of variation in this FoM is driven by input variation uncertainty, however the coefficient of variation is still the highest amount from the FoMs studied. Most other FoMs also show a strong contraction in distribution and a limited amount of remaining variation. This indicates that the majority of uncertainty in these FoMs can be explained by input variation.

On the other hand, for hydrogen generated in the core the coefficient of variation reduces by only around 41% and a broad distribution remains. This indicates that a large amount of uncertainty in hydrogen generated in the core cannot be removed by better understanding of input parameters and may be due to numerical instability.

4. CONCLUSIONS

Overall this analysis shows that out of the 162 MAAP input parameters whose impact on output uncertainty has been assessed, only a small number show any trends with the output FoMs for the accident scenario of interest. This suggests that for a LoSHS case, improvements to uncertainty levels on RPV and containment vessel integrity may be achieved by improving understanding of input uncertainty on a small number of input parameters.

However, the severe accident predictions have also been shown to have a large amount of noise and numerical uncertainty. Analysis of uncertainty with very small input ranges indicated that even if all input parameters are extremely well understood there will still be uncertainty in the output, potentially due to numerical uncertainty in the code.

This work has supported a number of Rolls-Royce SMR severe accident analysis team workstreams including:

- Updates to the Test Assessment Matrix (TAM), to highlight which variables had been found to be influential on phenomena of interest and which had not been found to be influential for this fault sequence.
- Quantifying uncertainty in predictions of FoMs in comparison to margin to safety acceptance criteria. For example showing that the margin to safety acceptance criteria is unlikely to be challenged by phenomenology uncertainty in the results of deterministic analysis.
- Identifying conservative assumptions for methodologies to ensure appropriate assessments when considering relative uncertainty.
- Sensitivity analysis results are used to prioritise areas of the MAAP model and parameters for improvement, by highlighting where input parameter improvement can have the greatest impact. However the small-range study demonstrates that for hydrogen generated in the core, variance in results are unlikely to be significantly reduced by input data improvements alone and bounding conservative assumptions are used.

Together these activities strengthen and help to substantiate a robust analysis method. This analysis method, in turn, provides evidence which supports key safety case claims and contributes to the probabilistic safety assessment.

Public – Not Listed – Not Subject to Export Controls

5. References

[1] K.-I. A. a. S.-Y. Park, "Best-practice severe accident uncertainty and sensitivity analysis for a short-term SBO sequence of a reference PWR using MAAP5," *Annals of Nuclear Energy,* 2022.

[2] EPRI, Severe Accident Uncertainty Quantification and Analysis Using the Modular Accident Analysis Program, EPRI Report 3002020762, 2021.

Public – Not Listed – Not Subject to Export Controls

UNCERTAINTY QUANTIFICATION AND SENSITIVITY ANALYSIS OF PHENOMENOLOGICAL UNCERTAINTY IN THE MAAP MODEL FOR A SEVERE ACCIDENT LOSS OF SECONDARY HEAT SINK

Claire Marshall

Frazer-Nash Consultancy

 © 2026 Rolls-Royce SMR Limited.

Public – Not Listed – Not Subject to Export Controls

PROJECT AIMS

Rolls-Royce SMR Severe Accident team's first look at overall MAAP model sensitivity and uncertainty.

The Plan

- Develop sensitivity analysis and uncertainty quantification analysis route.
- First use of route to test uncertainty in reactor pressure vessel and containment vessel integrity predictions.
- Investigate phenomenological and modelling uncertainty only.

Expected Outcomes

- Quantify level of uncertainty in chosen Figures of Merit (FoMs).
- Investigate how much of observed uncertainty may be attributable to irreducible numerical uncertainty in the model rather than reducible phenomenological uncertainty
- Identify input parameters whose uncertainty has a large impact on output uncertainty in the FoMs.

Public – Not Listed – Not Subject to Export Controls

METHODOLOGY - OVERVIEW

1. Select Figures of Merit (FoM)
2. Select accident scenario which will test the selected FoMs
3. Identify input parameters which may influence FoMs
4. Input parameter characterisation
5. Input parameter sampling
6. MAAP calculations
7. Process outputs and identify and remove failed runs
8. Uncertainty analysis
9. Sensitivity analysis

Public – Not Listed – Not Subject to Export Controls

METHODOLOGY – INITIAL DECISIONS

1. Select Figures of Merit (FoM)
   - Peak containment pressure (bara)
   - Timing of Reactor Coolant System (RCS) depressurisation (minutes)
   - Total hydrogen generated in the core (kg)
   - Time of first core relocation (minutes)
   - Peak heat transfer at the lower head (W)
2. Select accident scenario
   - Loss of Secondary Heat Sink (LoSHS) with no high pressure (HP) or low pressure (LP) blowdown via the Automatic Depressurisation System (ADS) and delayed blowdown via the Severe Accident Depressurisation Valve (SADV).
3. Identify input parameters
   - Continuous parameters only in this analysis
   - 162 identified from TAM, EPRI work, literature review and par file review
4. Input parameter characterisation
   - Triangular, uniform, normal or using histogram bins
5. Input parameter sampling
   - Latin Hypercube Sampling

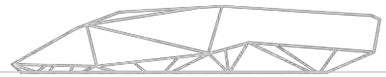

Public – Not Listed – Not Subject to Export Controls

METHODOLOGY – ANALYSIS METHODS

Sensitivity Analysis

- Correlation coefficients
  - Pearson and Spearman, rank and partial
- Linear stepwise regressions
- Pair plots used to visually display and identify relationships

Uncertainty Quantification

- Mean, range, standard deviation, coefficient of variation, 95% tolerance intervals on each output FoM
- 95% confidence intervals on the mean and standard deviation
- Histograms and overlay time series plots used to visually display spread of each FoM

Public – Not Listed – Not Subject to Export Controls

ANALYSIS – 3 SETS COMPLETED

1. Main analysis - *for overall uncertainty quantification*
   - 2000 LHS cases varying all 162 input parameters with best estimate probability distributions.

2. High correlation analysis - *for noise reduction and linear regression analysis*
   - 500 cases, varying only the 20 parameters with the highest correlations from the main analysis with best estimate probability distributions.

3. Very small input variations – *to isolate numerical uncertainty*
   - Attempts to remove any uncertainty driven by real changes in phenomena and isolate numerical uncertainty
   - 500 cases, varying all 162 input parameters with very small uniform distributions
   - Output FoM ranges compared with main analysis

Public – Not Listed – Not Subject to Export Controls

ANALYSIS – ERROR CATCHING

Two-stage error screening, FoM dependent:

1. Runtime-based screening. This excludes up to 1.3% of cases which fail before 40 hours.
2. Mass and energy balance screening, high mass errors in primary circuit allowable when primary circuit is almost empty.

Stage two is subjective, thresholds set for error inclusion limits and primary circuit emptiness criteria do change results, especially for outliers showing high heat transfer on the lower head.

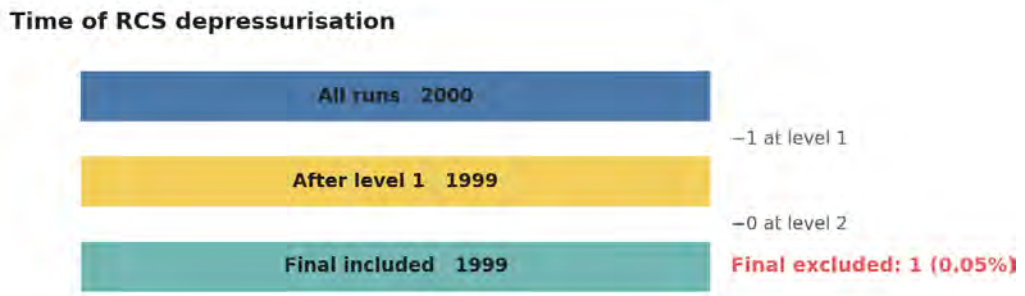

Public – Not Listed – Not Subject to Export Controls

RESULTS UNCERTAINTY QUANTIFICATION
PEAK HEAT TRANSFER AT THE LOWER HEAD (W)

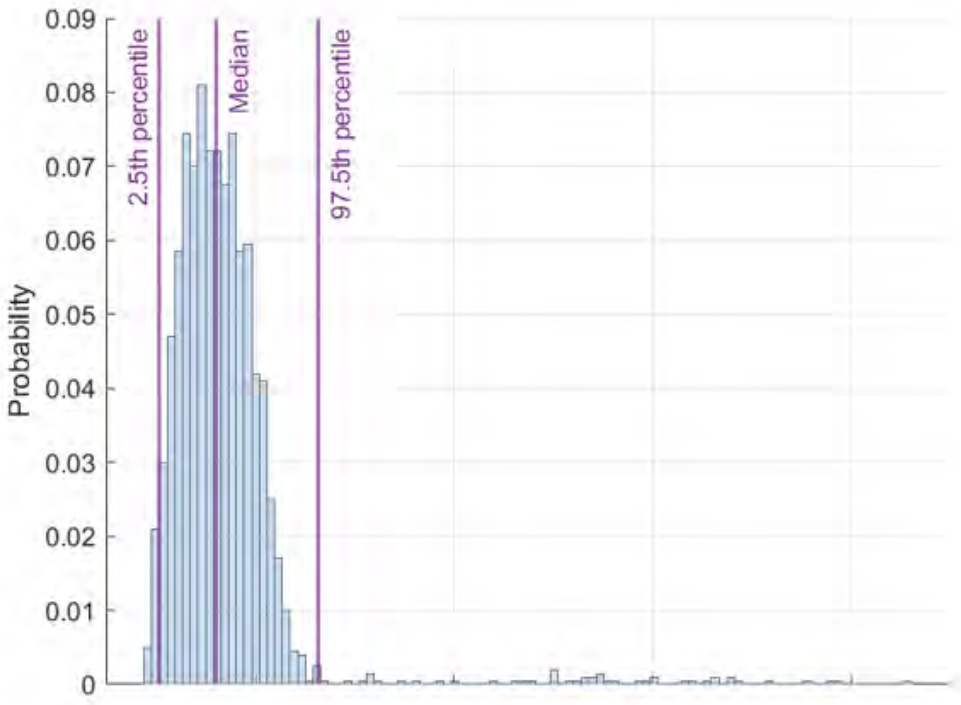

- 95% confidence intervals on the mean and standard deviation are small indicating a sufficient number of cases have been analysed.
- Lower-head heat transfer shows the largest relative uncertainty of all five FoMs. Coefficient of variation of 0.41.
- High heat transfer outliers drive this uncertainty.
- Right-skewed distribution with long upper tail
- Base case is near mean and median

Public – Not Listed – Not Subject to Export Controls

RESULTS SENSITIVITY ANALYSIS

PEAK HEAT TRANSFER AT THE LOWER HEAD (W)

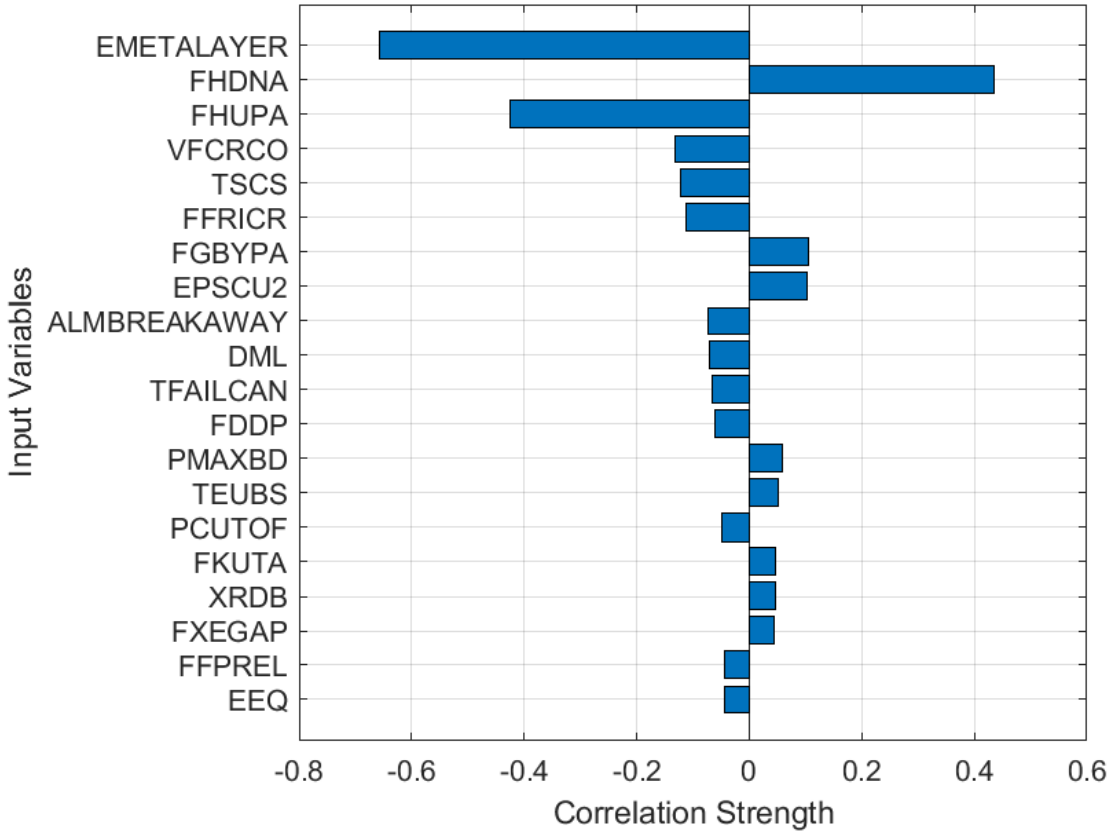

Uncertainty in lower head heat transfer uncertainty is driven by parameters which affect heat transfer within the molten corium

- EMETALAYER - the emissivity of the metal layer
- FHDNA - multiplier to the heat transfer coefficient to the lower crust in the corium molten pool
- FHUPA - multiplier to the heat transfer coefficient to the upper crust in the corium molten pool

Public – Not Listed – Not Subject to Export Controls

RESULTS UNCERTAINTY QUANTIFICATION
TOTAL HYDROGEN GENERATED IN THE CORE (KG)

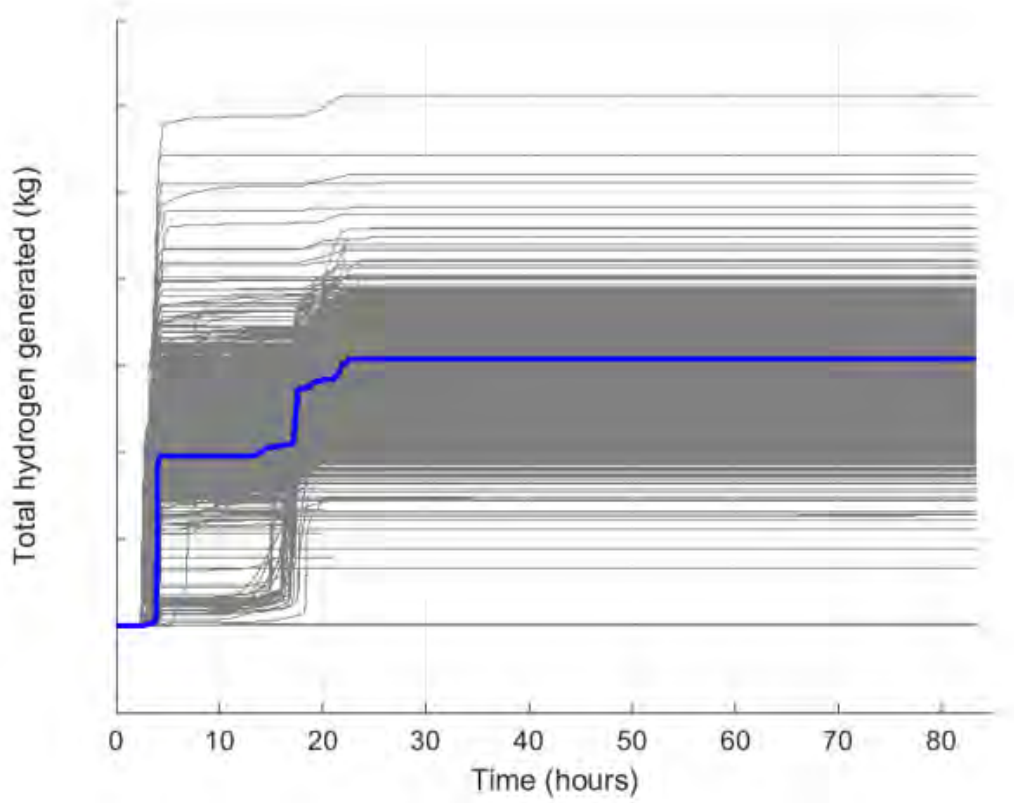

- Large absolute variation in total mass of hydrogen generated
- Significant proportion of the cases generate all their hydrogen very rapidly all at once, unlike the base case.
- Absolute base case result close to mean and median values

Public – Not Listed – Not Subject to Export Controls

RESULTS UNCERTAINTY QUANTIFICATION
TOTAL HYDROGEN GENERATED IN THE CORE (KG)

- 95% confidence intervals on the mean and standard deviation are small indicating a sufficient number of cases have been analysed.
- Distribution of results is close to a normal distribution.
- Coefficient of variation is 0.17, lower than for heat transfer at the lower head but still significant.

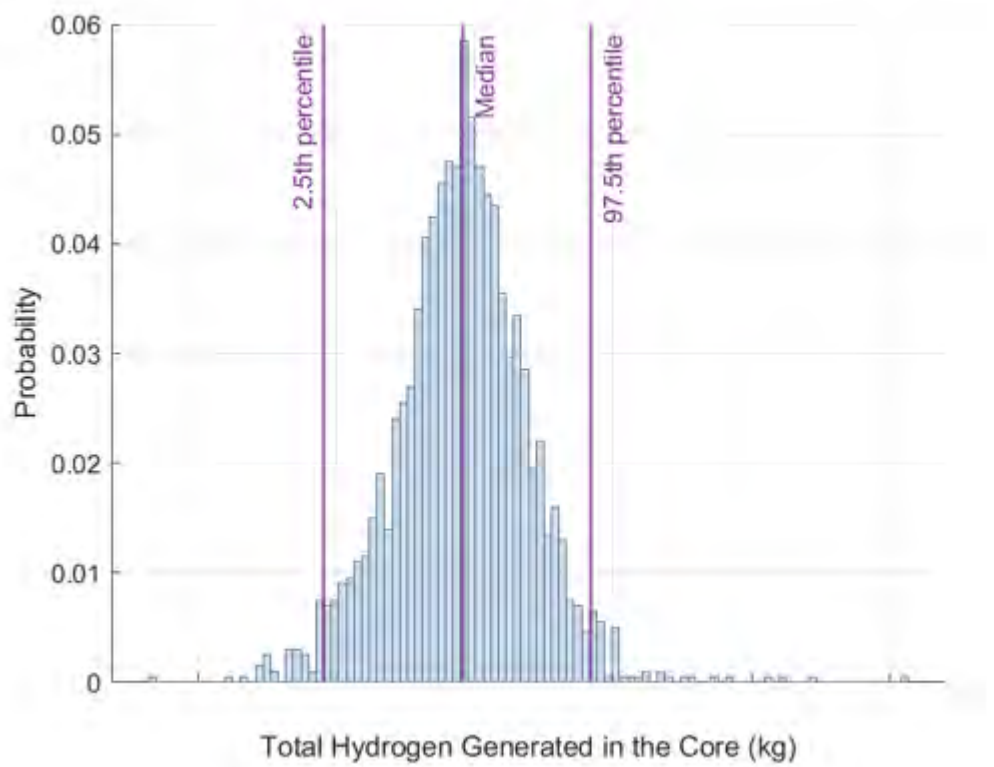

Public – Not Listed – Not Subject to Export Controls

RESULTS SENSITIVITY ANALYSIS

TOTAL HYDROGEN GENERATED IN THE CORE (KG)

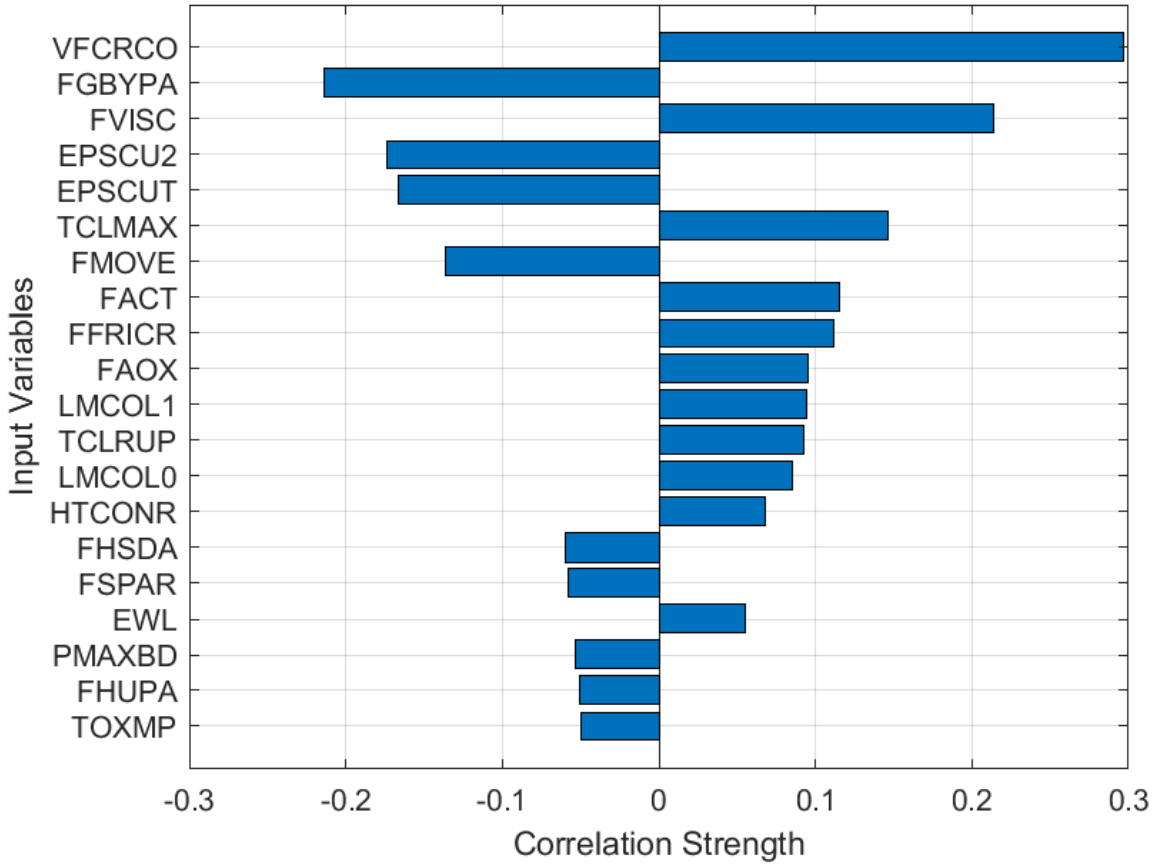

Uncertainty in hydrogen generation from the core is dominated by variables affecting core melt.

- VFCRCO – the porosity of a collapsed core region
- FGBYPA - diverts gas flows in the core to the bypass channel when an entire axial row in the core is completely blocked
- FVISC - multiplier for material viscosity used in the candling calculations

Public – Not Listed – Not Subject to Export Controls

RESULTS – SMALL INPUT VARIATION ANALYSIS
PEAK HEAT TRANSFER AT THE LOWER HEAD (W)

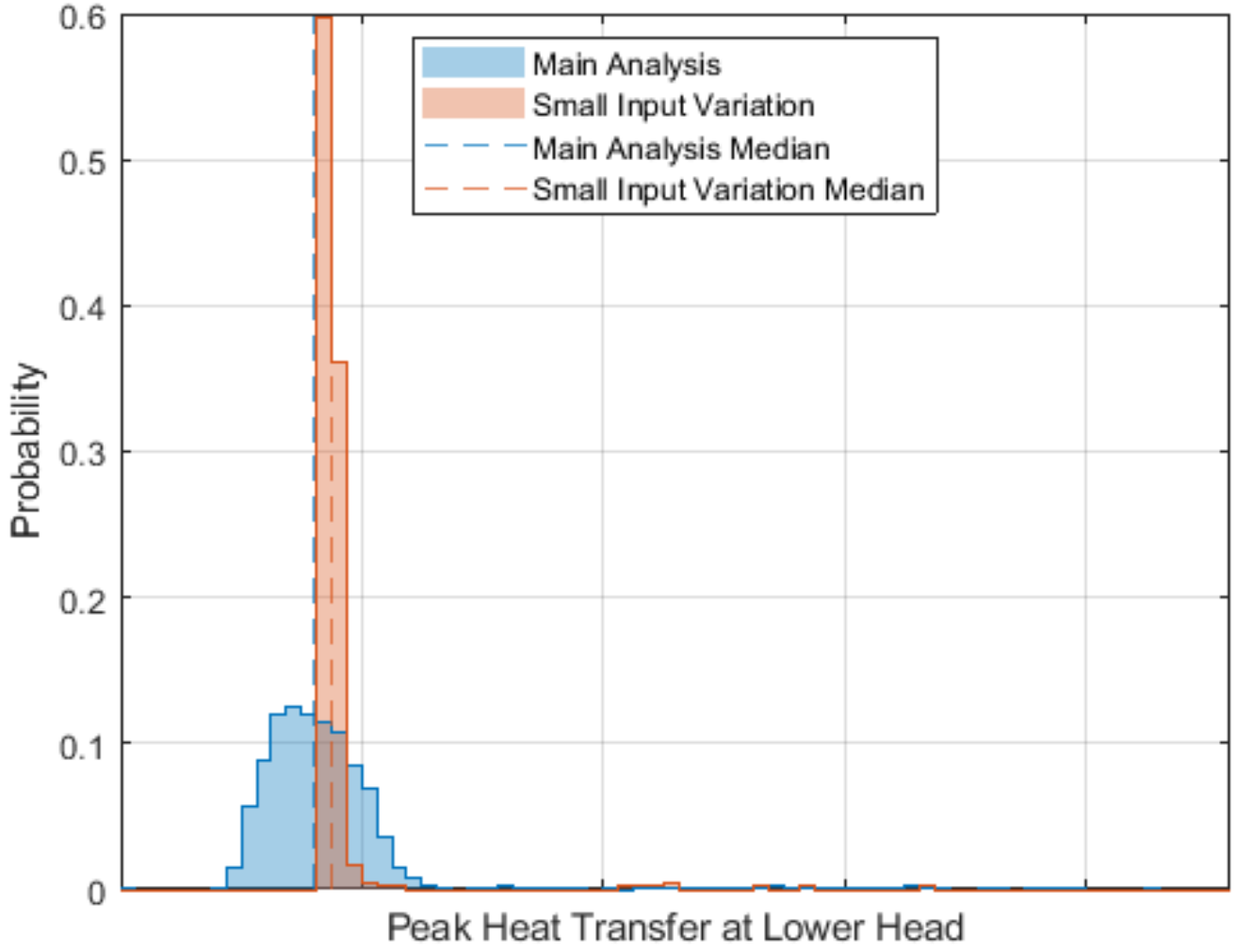

	Main Analysis	Small input variation analysis
Coefficient of variation	0.41	0.17

Public – Not Listed – Not Subject to Export Controls

RESULTS – SMALL INPUT VARIATION ANALYSIS
PEAK HEAT TRANSFER AT THE LOWER HEAD (W)

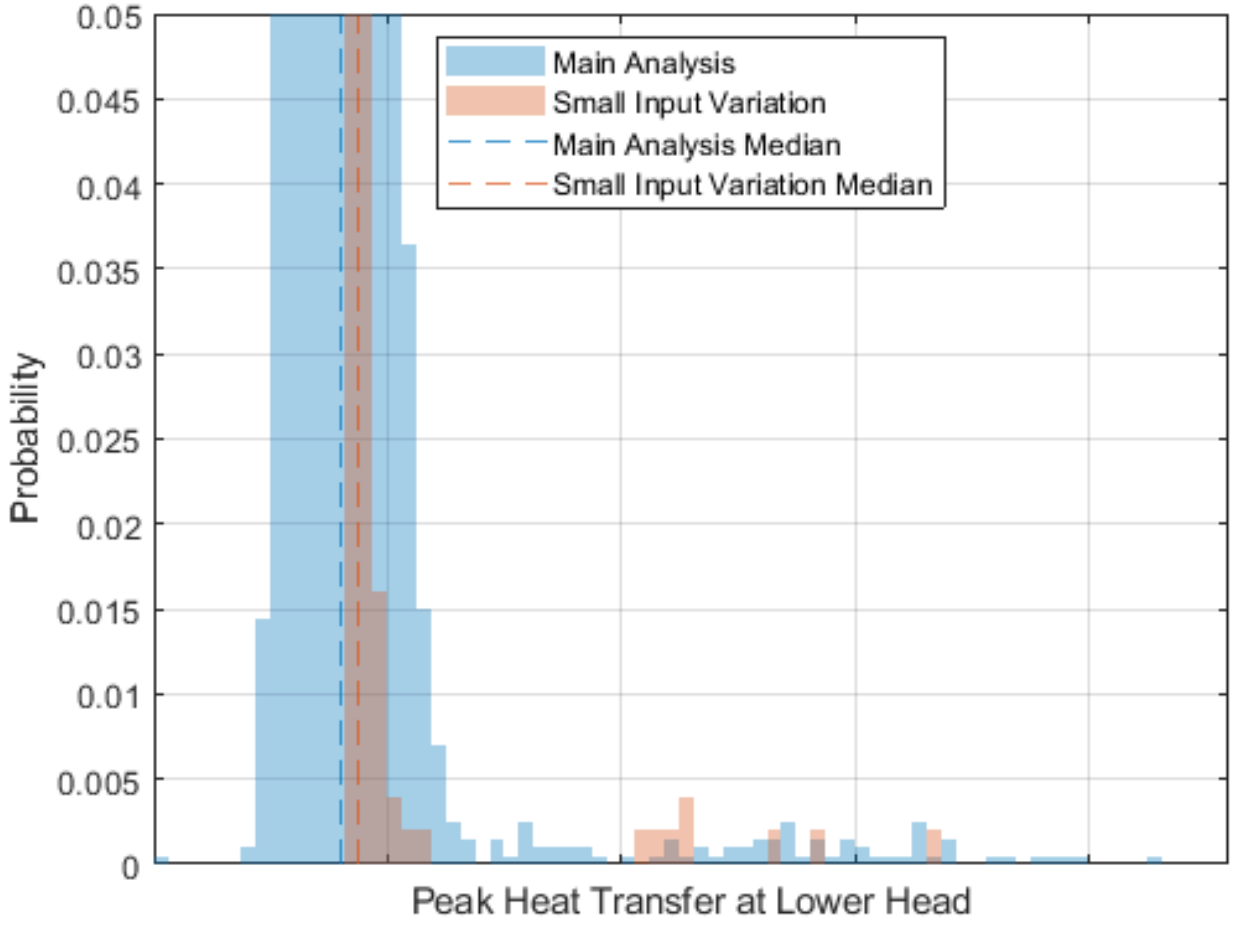

	Main Analysis	Small input variation analysis
Coefficient of variation	0.41	0.17

Public – Not Listed – Not Subject to Export Controls

RESULTS – SMALL INPUT VARIATION ANALYSIS
TOTAL HYDROGEN GENERATED IN THE CORE (KG)

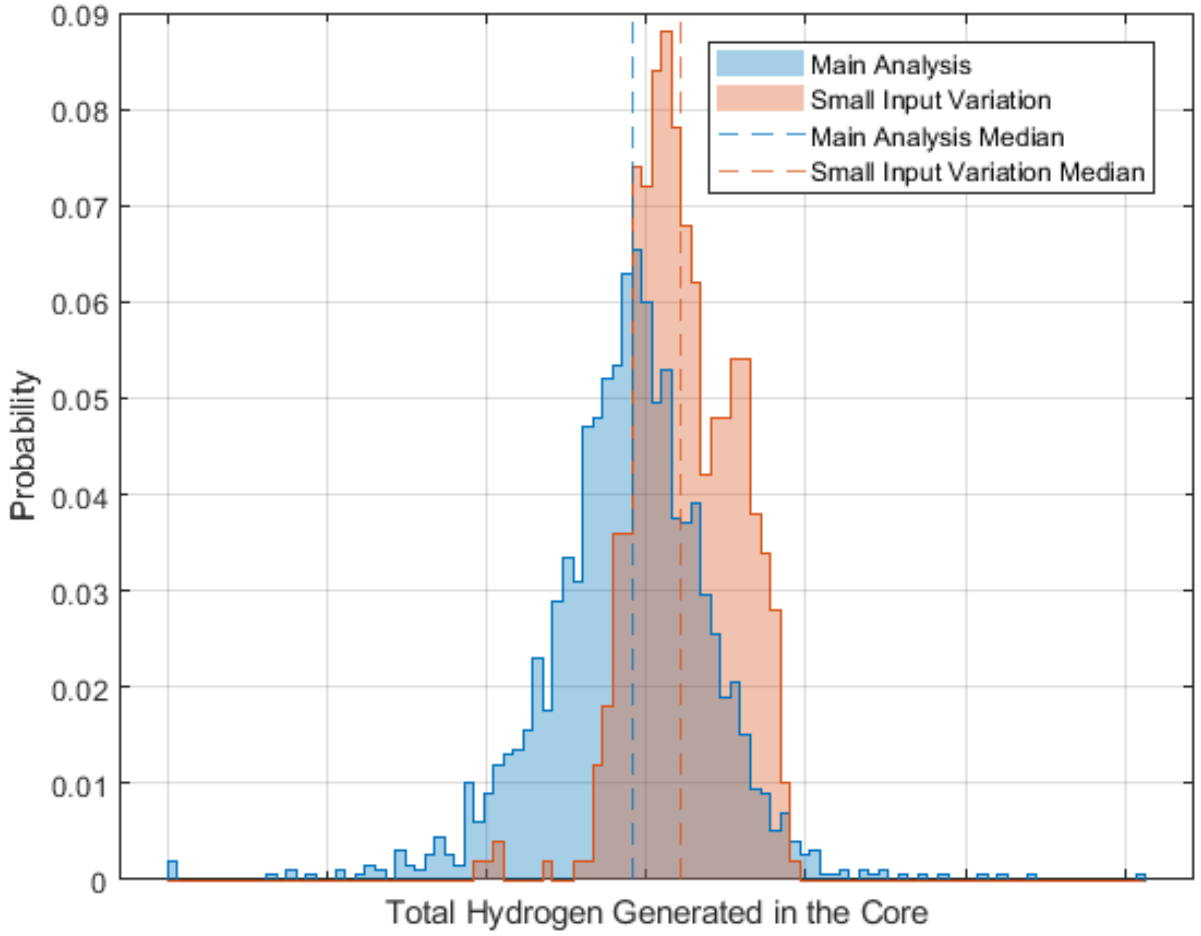

	Main Analysis	Small input variation analysis
Coefficient of variation	0.17	0.1

Public – Not Listed – Not Subject to Export Controls

RESULTS SUMMARY

- Peak lower-head heat transfer showed the largest relative uncertainty, with a right-skewed distribution and a small number of high-flux outliers driving the upper tail.
- Uncertainty in peak lower head heat transfer appeared to be driven mainly by corium heat transfer related parameters. Its uncertainty reduced substantially when the input ranges were narrowed. However, a residual upper tail remained, indicating that some uncertainty is still linked to numerical uncertainty in MAAP.
- Total hydrogen generation showed a broad, nearly normal distribution.
- Even with very small input ranges, hydrogen uncertainty remained significant: the 95% tolerance interval reduced by 43%, showing that a substantial part of the remaining uncertainty is not reducible through better parameter characterisation alone.

Public – Not Listed – Not Subject to Export Controls

USES

- Uses of the work to date:
  - Informed update to the Rolls-Royce SMR MAAP TAM
  - Part of justification that uncertainty is not greater than margin for IVR
  - Used to support hydrogen methodology development by showing irreducible modelling uncertainty in predicting hydrogen generation
  - Supports PSA level 2 development
- Potential future uses
  - Targeted uncertainty reduction by better understanding the most important input parameters

Public – Not Listed – Not Subject to Export Controls

POTENTIAL FUTURE WORK

1. **Investigation of outliers which show high heat flux at the lower head.**
2. **Inclusion of discrete parameters in the methodology, use of nested continuous parameter sampling within each sampled discrete parameter scenario.**
3. **Repeat the same methodology for a different fault sequence with same FoMs.**
4. **Improving parameter characterisation for the input parameters found to be most influential.**
5. Look at different figures of merit, potentially radiological consequences.
6. Additional more complex sensitivity analysis such as Sobol indices and physically based or machine learning regressions.

Public – Not Listed – Not Subject to Export Controls

Questions?

Public – Not Listed – Not Subject to Export Controls

ROLLS ROYCE SMR

BE SAFE. BE BOLD. BE INCLUSIVE. BE IMPACTFUL. BE CREATIVE. BE ENGAGED

Public – Not Listed – Not Subject to Export Controls

SEVERE ACCIDENT ANALYSIS IN A GENERIC iPWR AND UNCERTAINTY QUANTIFICATION OF THE RESULTS

G. Agnello
ENEA, C.R. Bologna, NUC-ENER-SIC
Via dei Mille 21, 40121, Bologna, Italy
giuseppe.agnello@enea.it

G. Grippo
University of Bologna
Department of Industrial Engineering (DIN), Viale del Risorgimento 2, 40136, Bologna, Italy
gianmarco.grippo2@unibo.it

E. Cilia
University of Bologna
Department of Industrial Engineering (DIN), Viale del Risorgimento 2, 40136, Bologna, Italy
erik.cilia@unibo.it

F. Mascari
ENEA, C.R. Bologna, NUC-ENER-SIC
Via dei Mille 21, 40121, Bologna, Italy
fulvio.mascari@enea.it

ABSTRACT

In view of the ongoing licensing process of Small Modular Reactors (SMRs) in Europe, increasing attention is devoted to assessing the capability of Severe Accident (SA) codes, such as MELCOR and ASTEC, to simulate SMR-specific phenomena under postulated transients. Among SMR concepts, integral Pressurized Water Reactors (iPWRs) represent a promising solution since they are based on the well proven technology and operational experience of large Light Water Reactors (LWRs). Within this framework, the present work, carried out in the context of the Horizon Euratom project "Safety Analysis of SMR with Passive Mitigation strategies – Severe Accident" (SASPAM-SA) coordinated by ENEA (Italy), investigates the application of the integral SA code MELCOR to the simulation of a SA scenario in a generic iPWR design. The analyzed sequence consists of a Loss of Coolant Accident (LOCA) initiated by the double-ended guillotine break of a Direct Vessel Injection (DVI) line, combined with the postulated failure of all passive safety systems. The present analysis focuses on the assessment of the main thermal-hydraulic and core degradation phenomena, with particular focus on production of hydrogen by oxidation of Zircaloy in the core. A Best Estimate Plus Uncertainty (BEPU) approach has been adopted to quantify the impact of uncertainties associated with key input parameters governing Zircaloy oxidation kinetics and core material behaviour. The results show a total hydrogen production from Zircaloy oxidation of about 400 kg, with an uncertainty band of 160 kg and a coefficient of variation of about 10%. The statistical analysis highlights the dominant role of oxidation kinetics parameters and eutectic temperature of the ZrO_2/UO_2 mixture in driving hydrogen generation. Finally, the study demonstrates the feasibility of applying BEPU methodologies to SA analysis in iPWR designs and provides preliminary insights into the uncertainty affecting hydrogen production predictions, supporting ongoing efforts in SMR safety assessment and licensing.

KEYWORDS
SASPAM-SA, SMR, MELCOR, BEPU

1. INTRODUCTION

In view of the ongoing licensing process for Small Modular Reactors (SMRs) in Europe, increasing attention is devoted to assessing the capability of computational integral Severe Accident (SA) codes to simulate SMR-specific phenomena under postulated accident scenarios. Codes such as MELCOR [1] [2] and ASTEC [3], originally developed for large Light Water Reactors (LWRs), are currently being applied to simulate advanced reactor concepts, including integral Pressurized Water Reactors (iPWRs). They are based on the well-established technology and operational experience of LWRs and are characterized by the integration of the main components of the Reactor Cooling System (RCS) within the Reactor Pressure Vessel (RPV) as well as the extensive use of passive safety systems. In view of their licensing process, state-of-the-art SA codes should be capable of simulating their advanced features and related phenomenology[1].
Within this framework, the Horizon Euratom SASPAM-SA project [4] [5], coordinated by ENEA (Italy), aims at assessing the capability of internationally recognized European and Non-European computational tools (largely used in Europe)[2] to simulate SA scenarios in iPWRs and to evaluate the associated radiological consequences. Previous activities have mainly focused on thermal-hydraulic analyses under Design Basis Accident (DBA) conditions, including uncertainty quantification using Best Estimate Plus Uncertainty (BEPU) methodologies, providing insights into key system responses during mitigated transients [6]. In line with the previous work, the aim of this paper is to apply the uncertainty methodology in the SA domain in a generic iPWR design and to give preliminary insights into the uncertainty of the code on the total production of hydrogen, representing a key Figure Of Merit (FOM) for nuclear safety. The analyzed sequence is a Loss of Coolant Accident (LOCA) with the postulated failure of all passive systems. Uncertain input parameters related to the main processes leading to hydrogen production during an SA sequence in LWR described in [7] [8] have been selected.

[1] Advanced designs, as iPWRs, are in general characterized by common features with the current operating large-LWR and by other specific features typical of their evolutionary designs, providing safety advantages that reinforce the first three levels of the Defence in Depth (DiD) principle. However, even if a plant is designed with advanced inherent features (through the reinforcement of the DiD levels 1, 2 and 3) allowing a reduction of the Core Damage Frequency (CDF), independent features for preventing and mitigating a severe accident sequence have to be included in its design (DiD level 4) together with the offsite emergency response (DiD level 5). Therefore, some scenarios that could lead to SAs need to be postulated and deterministically studied. Therefore, it is necessary to assess the capability of internationally recognized SA code to describe the behaviour of the most promising iPWR designs during SA scenarios and to predict the resulting radiological impact on-site and off-site.

[2] In order to maximize the knowledge transferability and impacts of the project two generic design-concepts, characterized by different design innovations in comparison with larger operating reactors, have been selected for the analyses: a) iPWR characterized by a submerged containment and electric power of about 60 MWe, called Design-1; b) iPWR characterized by the use of several passive systems, a dry containment and an electric power of about 300 MWe, called Design-2. These two generic reactor concepts include the main iPWR design features, considered in the most promising designs ready to go on the European market, allowing to assess in a wider way the capability of codes (SA and CFD) to simulate the SA phenomena typical of iPWR. It is not the project's objective to assess the generic reactor designs selected but, based on the project findings, to allow a more general statement on the code's applicability to currently favored designs under postulated SA condition. No Probabilistic Safety Assessment (PSA) considerations will be done in the project due to the generic nature of the reactor concept considered, then the scenarios identified will be characterized in terms of severity but not in terms of probability.

2. DESCRIPTION OF THE GENERIC IPWR DESIGN

The reference reactor considered in this work is a generic iPWR with a nominal power of 1000 MWth and an electrical output of 300 MWe [9] [10]. The design adopts an integral configuration in which all the main components of the Reactor Cooling System (RCS), including the core, Pressurizer (PRZ), Steam Generators (SGs) and Reactor Coolant Pumps (RCPs), are located inside the Reactor Pressure Vessel (RPV), as presented in Figure 1. The primary coolant flows upward through the core and riser region, then is directed radially into the upper annular plenum and circulated through compact helical-coil SGs by means of RCPs. After heat exchange in the SGs, the coolant flows downward through the downcomer and returns to the Lower Plenum (LP), closing the primary loop. As presented in Figure 2, the RPV is enclosed within a dry containment divided into two main regions: the Drywell (DW) and the Reactor Cavity (RC). This configuration plays a key role during potential accident conditions since the RPV-Containment coupling governs pressure evolution and heat transfer.

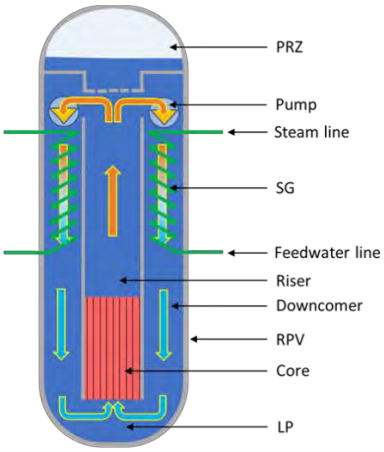

Figure 1. View of the RPV.

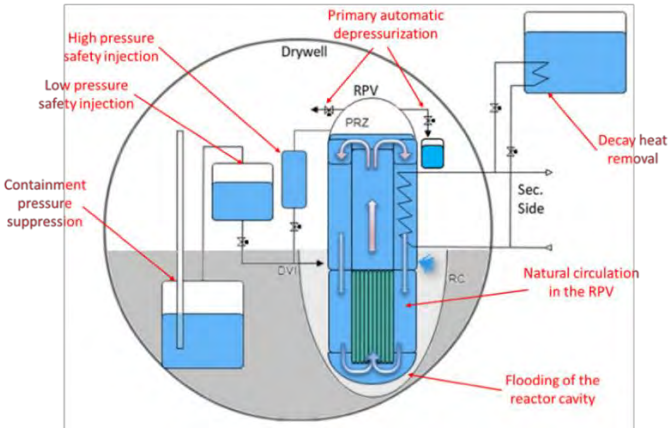

Figure 2. Layout of the RPV, containment and passive safety systems configuration.

The safety strategy of the iPWR fully relies on the use of passive safety systems, designed to enable natural circulation within the RPV via Riser-Downcomer (RI-DC) valves, passive decay heat removal (Emergency Heat Removal System, EHRS), primary automatic depressurization (Automatic Depressurization System, ADS), passive high-pressure safety injection (Emergency Boration Tanks, EBTs), passive low-pressure safety injection (Long-term Gravity Make-up System, LGMS), passive containment pressure suppression (Pressure Suppression System, PSS), passive flooding of the RC. Except for the heat sink of the decay heat removal system, these systems are largely located within the containment.

3. DESCRIPTION OF THE IPWR MELCOR NODALIZATION

The present SA analysis has been performed using the fully integrated SA code MELCOR [1] [2], able to simulate the thermal-hydraulic phenomena in steady-state and transient conditions and the main SA phenomena characterizing the RPV, the RC, the containment, and the confinement buildings typical of LWRs. More specifically, the MELCOR code v2023 has been used for the calculation reported in the present manuscript. A MELCOR nodalization of the generic iPWR design [11], based on a generic International Reactor Innovative and Secure (IRIS) [12] design, has been developed within the SASPAM-SA project based on publicly available data, scaling the available data of the SPES-3 experimental facility [13] [14] as well as by engineering evaluation from public general data available. The model, shown in Figure 3 in the SNAP view [15], combines a trade-off between the computational time and a detailed prediction capability of the transient thermal-hydraulic and core degradation phenomenology.

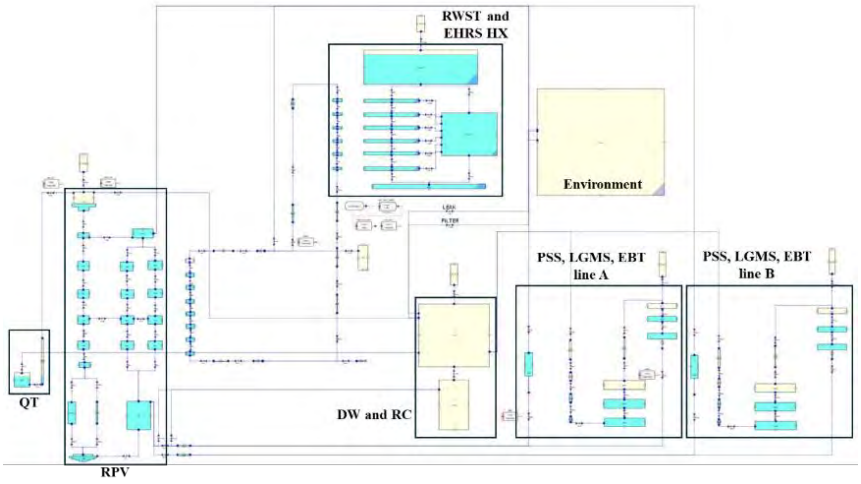

Figure 3. SNAP view of the MELCOR nodalization.

The RPV is modelled using multiple Control Volumes (CVs) representing the LP, core region, riser, Upper Plenum (UP), SGs, and downcomer. Furthermore, the core is modelled by the dedicated COR package to simulate the main core degradation phenomena. To simplify the model, the eight SGs have been modelled as an equivalent one, with four CVs on the primary side and eight CVs on the secondary side. The containment is modelled by two main CVs corresponding to the DW and the RC. The DW is thermally coupled with the environment through heat structures, while the RC is coupled with the MELCOR cavity model to simulate corium relocation and cavity flooding. The film tracking model has been implemented in the DW Heat Structures (HSs) to track the water film draining from the HS surfaces. No other models are considered. In order to prevent the DW rupture reaching the project pressure of 23 bar [10], leakage to the environment and fission vapors and aerosol filters have been considered. The filters and the leakage have been modelled as two flow path junctions, allowing communication between the DW and the environment (modelled as a single CV). In particular, the junction simulating the filter has been coupled with the aerosol and fission product filter models, and it operates when the DW pressure is between 8 and 16 bar. The leakage has been modeled considering 0.1% containment gas volume leaked per day at design pressure. Passive safety systems are present in the design with two parallel Direct Vessel Injection (DVI) lines. In this model, these lines have been modelled separately, including the EBT, the PSS, the PSS-vent and the LGMS. The EHRS has been modelled with a set of CVs hydraulically connected to the secondary side of the SGs. The loop is connected thermally with the Refueling Water Storage Tank (RWST), which represents the ultimate heat sink connected to the environment. In this regard, the equivalent EHRS Heat Exchanger has been modelled with six CVs thermally coupled with six CVs of the RWST. In total, nine CVs have been considered to model the RWST. The double-ended guillotine break of one DVI line is simulated by dynamically modifying the junction connections between the injection line and the primary system. At the Start Of the Transient (SOT) the junction connecting the injection systems to the RPV is closed, while junctions towards the control volume simulating the RC are opened, allowing the discharge of coolant into the containment. This modelling approach allows the representation of mass and energy release into the containment following the break, preserving the asymmetric behavior between the intact and broken passive safety system trains.

4. ANALYSIS OF THE REFERENCE CASE

The reference scenario is a LOCA initiated by the double-ended guillotine break of one of the two DVI lines [13] [16] [17] [18]. The DVI lines connect the two passive systems trains to the RPV, at an elevation located below the SGs outlet in the primary side. Considering the design layout, the selected LOCA is the worst accidental scenario since it occurs at the lowest possible elevation on the RPV. In this work, the postulated

failure of all the passive safety systems as well as the failure of ADS Stage-1 and ADS Stage-2 have been considered. Therefore, the transient can be divided into the following Phenomenological Windows (PhWs):

I. **Thermal-Hydraulic phase – PhW 1**: it evolves from the SOT to the core heat-up, identified when the cladding temperature reaches 1473 K. It includes the reactor SCRAM, the pumps coast-down, the Top Of Active Fuel (TAF) uncover, the Primary Coolant System (PCS) depressurization and containment pressurization.
II. **Early phase – PhW 2**: it starts with the fuel heat-up and ends with the start of loss of geometry of the core and its relocation into the LP (slumping). It is characterized by the Bottom of Active Fuel (BAF) uncover, onset of Zircaloy oxidation reactions, the runaway of Zircaloy oxidation reactions, the massive in-vessel hydrogen production.
III. **Late phase – PhW 3**: it starts when the corium is entirely relocated into the LP and includes the rest of the transient.

Following the break, the transient is driven by the blowdown of the RPV. Due to the loss of coolant from the PCS, the DW pressure increases and, at about 18 seconds after the SOT, the high containment pressure set-point triggers the S-signal, causing the transition from fission power to decay heat. After the S-signal, the Secondary Coolant System (SCS) pressure increases. The code predicts a pressure peak of about 120 bar. Figure 4 shows the PCS, SCS and containment pressure evolution. Due to the blowdown, the inventory of primary coolant decreases as well as the collapsed coolant level in the core region. As shown in Figure 5, the code predicts the uncover of the TAF at about 618 seconds after the SOT.

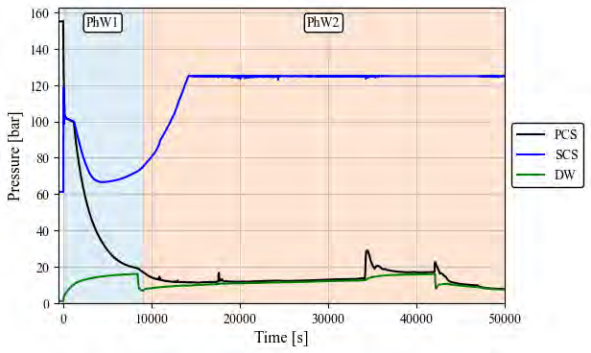

Figure 4. PCS, SCS and containment pressure.

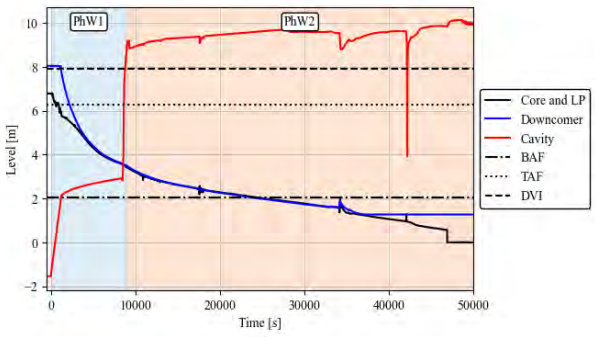

Figure 5. Core, downcomer and cavity collapsed coolant level.

During PhW 1, the PCS pressure follows the SCS pressure at about 100 bar. At about 3000 seconds after the SOT, the collapsed coolant level in the downcomer reaches the DVI elevation. The steam inside the RPV is vented into the containment, and the PCS pressure drops rapidly, followed by the decrease of the SCS pressure. At about 7300 seconds after the SOT, the DW pressure reaches the leak opening set-point. This causes a rapid depressurization of the containment to the atmospheric pressure, shown in Figure 4. Due to the fast depressurization of the DW, the code predicts the rapid rise of water level inside the PSSs through the PSS vent pipes and the injection into the DW. This causes a rapid increase in the collapsed coolant level in the RC, as observed in Figure 5. Although the collapsed level of coolant in the cavity reaches a level higher than the DVI level, no coolant is injected into the RPV because the primary pressure at this stage is still higher than the pressure prevailing in the DW. At this stage of the transient, the core is uncovered, and the collapsed level continues to decrease. The SCS pressure starts to increase again because heat removal through the SGs is no longer sufficient to balance the energy transferred from the PCS. The pressure rise is

eventually limited by the onset of SGs safety-valve cycling, as shown in Figure 4. The core uncover causes the fuel heat-up and the increase of the cladding temperature as shown in Figure 6.

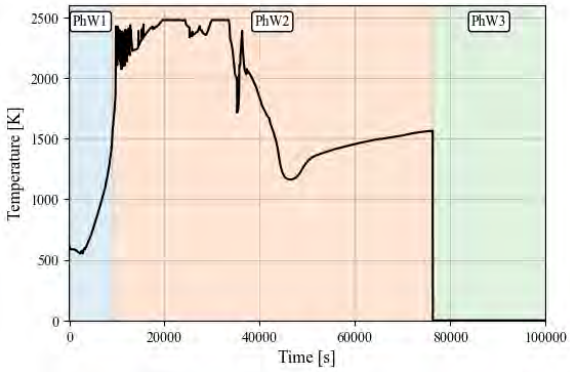

Figure 6. Maximum cladding temperature.

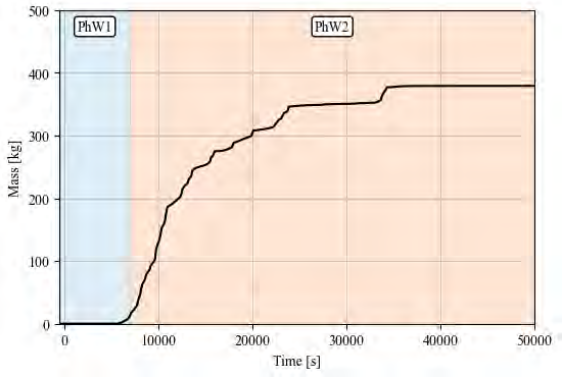

Figure 7. Cumulative hydrogen production.

During PhW 2, at about 8980 seconds after the SOT, the cladding temperature reaches the onset value for the Zircaloy oxidation reaction and the beginning of hydrogen generation. The cumulative hydrogen production predicted by the code is presented in Figure 7. At about 23000 seconds after the SOT, the collapsed level in the RPV reaches the BAF, leaving the core uncovered. Then, the core degradation mechanisms continue, and the corium relocation begins at about 35000 seconds, as highlighted in Figure 4 by the primary pressure peaks. In Table 1 the main events characterizing the SA sequence are reported.

Table 1. Main events of the SA reference case.

Event	Time [s]
Break	0
High Containment pressure signal (SCRAM, isolation SGs)	18
Low PRZ water level signal (Pumps coast-down and RI-DC valves opening)	70
Low PRZ pressure signal	92
TAF uncovered	618
Containment leak opening	7300
Start of H2 generation	8980
Start of the core relocation	35000
End of core relocation	76320

5. HYPOTHESES OF THE UNCERTAINTY ANALYSIS

The following uncertainty analysis has been conducted adopting the BEPU approach, in particular the probabilistic method to propagate input uncertainty [19]. The present uncertainty methodology has been used in several works in the thermal-hydraulics field [20] [21] [22] [23] and in the SA domain [24] [25] [26] [27] [28] [29]. It is generally based on statistical approaches to propagate input uncertainty, characterized by uncertain input parameters, to output uncertainty, expressed as the uncertainty in selected FOMs. Each uncertain input parameter is identified by a Probability Density Function (PDF), usually selected based on previous analyses, available experimental data, and engineering judgment [30]. Furthermore, a statistical correlation analysis involving FOMs and the uncertain input parameters is generally carried out. According to past activities developed in the framework of uncertainty quantification in Deterministic Safety Analysis [20] [22] [26], the simple and simple rank correlation coefficient are computed [31] [32]. For the present analysis, the simple rank correlation coefficient has been considered, and it has been calculated by using the

Spearman's correlation. It is representative of the degree of monotonous correlation between an uncertain input parameter and the FOM. As indicated in [32], the statistical correlation is significant if the coefficient is greater than 0.5 (or less than -0.5) or moderate if it is between 0.2 and 0.5 (or -0.2 and -0.5). Then, if the coefficient is between 0 and 0.2 (or between 0 and -0.2) the correlation is low. The Uncertainty Tool (UT) used in this uncertainty application has been developed by ENEA in collaboration with University of Palermo in the framework of the H2020 MUSA project, coordinated by CIEMAT (Spain) [26] [33] [34], and finalized in the framework of the International Atomic Energy Agency (IAEA) Coordinated Research Program (CRP) [27] [35] [36]. The goal of this uncertainty analysis is to apply the following uncertainty methodology to a postulated SA sequence in an advanced reactor design, such as the iPWR design. Furthermore, a key point is to investigate and characterize the uncertainties of the code about the production of hydrogen from Zircaloy oxidation. Thus, the FOM considered for the present uncertainty application is the total cumulative hydrogen production by Zircaloy oxidation the in core.
Seven of the main uncertain input parameters influencing the production of hydrogen in LWRs have been considered [7] [8]:

- **Zircaloy oxidation reaction kinetics - k_i**: kinetics parameters related to Zircaloy oxidation reaction. These coefficients are used to calculate the rate constant for Zircaloy oxidation following parabolic kinetics [1]. The rate constant R, expressed in $kg^2/m^4 \cdot s^{-1}$ as a function of temperature T(K) is calculated for Zircaloy by the following relations:

$$R(T) = \begin{cases} k_1 e^{-\frac{k_2}{T}}, & T \leq 1853\ K \\ k_3 e^{-\frac{k_4}{T}}, & T \geq 1873\ K \end{cases} \quad (1)$$

  The code uses an interpolated value in the temperature range between 1853 K and 1873 K. In the MELCOR oxidation model, these parameters can be edited as sensitivity coefficients.
- **Zircaloy Melt Breakout Temperature – Zr_Melt**: the oxidation of the fuel cladding forms a shell of ZrO_2 which can contain molten clad materials until the thickness of ZrO_2 or the temperature limit is crossed. For this reason, the molten mass candles and relocates. This parameter influences flow obstructions, steam interaction with zirconium and, consequently, hydrogen generation. In the MELCOR oxidation model, the breakout temperature for the cladding component is editable as a sensitivity coefficient.
- **Debris Porosity**: the porosity of core debris has an impact on oxidation processes because it influences heat transfer and surface area.
- **Eutectic temperature of ZrO_2/UO_2 mixture**: the melting point of the binary eutectic mixture of ZrO2 and UO_2 can affect the dynamics of blockage by candling materials and, consequently, oxidation processes. In MELCOR, this parameter has been modified by adjusting the value of the melting temperature of ZrO_2 and UO_2 and by varying the core component failure parameter.

Table 2 shows the uncertain input parameter with their distribution type and range of variation. Following Wilks' formula [37] [38] for the one-sided tolerance interval, at 95% probability content and 95% confidence level, a total of 59 runs are needed.

6. RESULTS

The uncertainty band of the FOM has been estimated as well as the mean, median and standard deviation. The statistical parameters of the FOM are reported in Table 3. The estimated uncertainty band is about 162.87 kg and the mean and median values are 401.44 and 414.45 kg respectively. Figure 8 shows the estimated PDF compared with the reference case, mean, median and upper and lower bounds. The simple rank correlation coefficients are shown in Figure 9. The statistical coefficients highlight a significant negative statistical correlation with the k_2 oxidation parameter and a significant positive statistical

correlation with the eutectic temperature of ZrO_2/UO_2 mixture. This behavior reflects the strong dependence of hydrogen production on oxidation kinetics and core degradation progression: higher oxidation rates enhance early hydrogen generation, while higher eutectic temperatures delay material relocation, prolonging high-temperature oxidation conditions. The uncertainty band of the hydrogen cumulative production from Zircaloy oxidation in the core during the entire SA sequence has been analyzed and presented in Figure 10. The uncertainty band increases after the Zircaloy oxidation runaway, reaching a value of about 160 kg at the slumping, consistently with the final uncertainty band. This trend indicates that most of the uncertainty is accumulated during the high-temperature oxidation phase preceding core relocation.

Table 2 Uncertain input parameters [7]**.**

Parameter	Unit	PDF	Reference value	Lower and upper bound		Reference
k_1	[$kg^2/m^4 \cdot s^{-1}$]	Uniform	29.6	Min	26.64	Engineering Judgment
				Max	32.56	
k_2	[$kg^2/m^4 \cdot s^{-1}$]	Uniform	16820	Min	15979	Engineering Judgment
				Max	17661	
k_3	[$kg^2/m^4 \cdot s^{-1}$]	Uniform	87.9	Min	43.95	Engineering Judgment
				Max	109.88	
k_4	[$kg^2/m^4 \cdot s^{-1}$]	Uniform	16610	Min	15448	Engineering Judgment
				Max	17773	
Zr_Melt	[K]	Normal	2400	Min	2250	[7]
				Max	2550	
PORDP	[-]	Normal (truncated)	0.38	Min	0.1	[8]
				Max	0.5	
EUT_T	[K]	Normal	2479	Min	2230	[39]
				Max	2728	

Table 3 Statistical parameters of the FOM.

Statistical Parameter	Unit	Value
Mean	[kg]	401.44
Median	[kg]	414.45
Lower bound	[kg]	307.09
Upper bound	[kg]	469.96
Standard deviation	[kg]	40.70
Coefficient of variation	[-]	0.10

By calculating the simple rank correlation coefficient, it is possible to investigate along the entire sequence how the uncertain input parameters affect the production of hydrogen from Zircaloy oxidation in core from a statistical correlation point of view. In Figure 11 the time trend of the correlation coefficient has been represented. Before the slumping of the molten core into the LP (35000 s after the SOT), cumulative hydrogen production presents a significant negative correlation with the parameter k_2, confirming the dominant role of oxidation kinetics during the early phase. Then, during the late phase of the transient, the EUT_T and k_2 parameters present a significant positive and negative statistical correlation with the hydrogen cumulative production from Zircaloy oxidation, respectively. This indicates a transition from kinetics-controlled to relocation-influenced behavior in hydrogen generation.

7. CONCLUSIONS

This work presents the application of the MELCOR code to the analysis of a SA scenario in a generic iPWR using the BEPU approach to quantify uncertainties affecting SA progression. The analysed scenario consists of a LOCA initiated by the double-ended guillotine break of one DVI line combined with the failure of all passive systems, leading to an early core uncover and core degradation conditions, promoting Zircaloy oxidation and significant hydrogen generation during the early phase of the transient. The reference calculation predicts a total hydrogen production from Zircaloy oxidation in the core of about 400 kg. The uncertainty analysis shows an uncertainty band of approximately 160 kg, with a coefficient of variation of 10%. The statistical correlation analysis highlights the dominant role of the Zircaloy oxidation kinetics parameters and the eutectic temperature of the ZrO_2/UO_2 mixture. In particular, the k2 parameter exhibits a significant negative correlation with hydrogen production, while the eutectic temperature shows a positive significant correlation, reflecting their influence on oxidation rates and core degradation mechanisms.

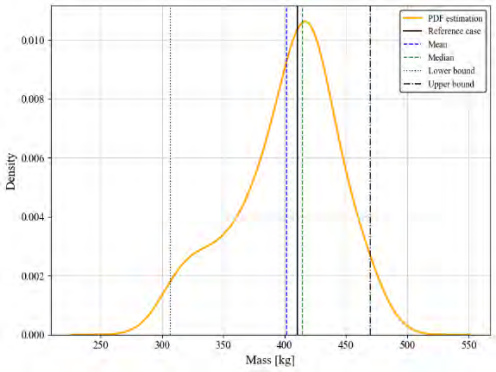

Figure 8 Estimation of the PDF of the FOM.

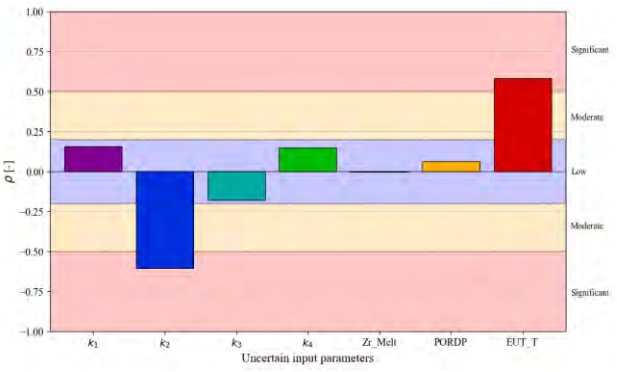

Figure 9 Simple rank correlation coefficients.

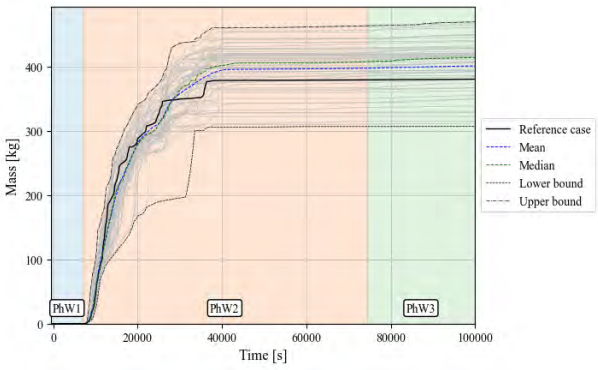

Figure 10 Hydrogen cumulative mass uncertainty band.

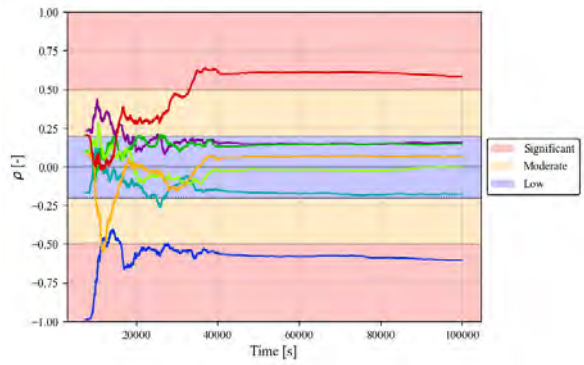

Figure 11 Simple rank correlation coefficient calculated along the transient.

The time-dependent analysis of correlation coefficients indicates that the afore mentioned parameters affect the early phase of the transient, before core relocation into the LP, while their influence tends to be stable during the late phase of the transient. Finally, the results demonstrate the feasibility of applying BEPU methodology to SA analysis in iPWR designs and provide preliminary insights into the uncertainty analysis associated with hydrogen production assessment. These findings contribute to ongoing efforts aimed at supporting the safety assessment and licensing of SMRs. Future work will extend the uncertainty analysis to additional FOMs, including fission products release and containment behavior, and to a set of different SA scenarios with different postulated failure of passive safety systems.

NOMENCLATURE

ADS: Automatic Depressurization System; **BEPU**: Best Estimate Plus Uncertainty; **DBA**: Design Basis Accident; **DiD**: Defence in Depth; **DVI**: Direct Vessel Injection; **DW**: Drywell; **EBT**: Emergency Boration Tank; **EHRS**; Emergency Heat Removal System; **EPZ**: Emergency Planning Zone; **FOM**: Figure Of Merit; **HX**: Heat eXchanger; **IAEA**: International Atomic Energy Agency**; iPWR**: Integral Pressurized Water Reactor; **IRIS**: International Reactor Innovative and Secure; **LGMS**: Long Term Gravity Make-up System; **LOCA**: Loss Of Coolant Accident; **LP**: Lower Plenum; **LWR**: Light Water Reactor; **PDF**: Probability Density Function; **PRZ**: Pressurizer; **PSA**: Probabilistic Safety Assessment; **PSS**: Pressure Suppression System; **QT**: Quench Tank; **RC**: Reactor Cavity; **RCP**: Reactor Coolant Pump; **RCS**: Reactor Coolant System; **RPV**: Reactor Pressure Vessel; **RWST**: Refueling Water Storage Tank; **SA**: Severe Accident; **SG**: Steam Generator; **SMR**: Small Modular Reactor; **SNAP**: Symbolic Nuclear Analysis Package; **SOT**: Start Of the Transient; **UP**: Upper Plenum; **UT**: Uncertainty Tool**.**

ACKNOWLEDGMENTS & DISCLAIMER

Funded by the European Union. Views and opinions expressed are however those of the author(s) only and do not necessarily reflect those of the European Union or European Commission-Euratom. Neither the European Union nor the granting authority can be held responsible for them.

ENEA carried out the research activity with MELCOR code and SNAP, obtained in the framework of the ENEA-ISIN agreement signed on March 23rd, 2020, as part of the General Arrangement between the United States Nuclear Regulatory Commission (US-NRC) and the Italian National Inspectorate for Nuclear Safety and Radiation Protection (ISIN).

REFERENCES

[1] L.L. Humphries, B.A. Beeny, F. Gelbard, T. Haskin, J. Phillips, J. Reynolds, R.C. Schmidt, «MELCOR Computer Code Manuals: Vol. 1: Primer and User's Guide Version 2.2 r2023.0,» Sandia National Laboratories, Albuquerque (USA), 2023.

[2] L.L. Humphries, B.A. Beeny, F. Gelbard, T. Haskin, D. Louie, J. Phillips, J. Reynolds, R.C. Schimidt, «MELCOR Computer Code Manuals: Vol. 2: Reference Manual Version 2.2 r2023.0,» Sandia National Laboratories, Albuquerque (USA), 2023.

[3] P. Chatelard e L. Laborde, «ASTEC V2.2 code validation: Illustrative results and main outcomes,» *Nuclear Engineering and Design,* vol. 413, 2023.

[4] SAFETY ANALYSIS OF SMR WITH PASSIVE MITIGATION STRATEGIES - SEVERE ACCIDENT (SASPAM-SA), [Online]. Available: https://www.saspam-sa.eu/.

[5] European Commission, SASPAM-SA, [Online]. Available: https://cordis.europa.eu/project/id/101059853.

[6] G. Agnello, G. Grippo, A. Bersano, F. Mascari, «Application of the probabilistic method to propagate input uncertainty on a DBA sequence in a generic iPWR,» in *Proceedings of the 11th European Review Meeting on Severe Accidents Research (ERMSAR2024)*, KTH Royal Institute of Technology, Stockholm, Sweden, May 13-16, 2024.

[7] R.O. Gauntt, N.E. Bixler, K. Wagner, «An Uncertainty Analysis of the Hydrogen Source Term for a Station Blackout Accident in Sequoyah Using MELCOR 1.8.5,» SAND2014-2210, Albuquerque, New Mexico, 2003.

[8] R.O. Gauntt, «Uncertainty Analyses Using the MELCOR Severe Accident Analysis Code,» *CSNI Workshop on the Evaluation of Uncertainties in Relation to Severe Accidents and Level 2 Probabilistic Safety Analysis,* 2005.

[9] M. Principato, F. Giannetti, M. Imperatori, M. D'Onorio, M. Garcia, L.E. Herranz, A. Bersano, F. Mascari, «Analyses of the MELCOR capability to simulate integral PWR using passive systems in a DBA scenario,» *Nuclear Engineering and Design,* vol. 437, n. 114004, 2025.

[10] SASPAM-SA, «Deliverable 2.2: iPWR input-deck and scenarios analyses,» 2024.

[11] F. Gabrielli, M. Di Giuli, M. Malicki, A. Bersano, P. Maccari, F. Giannetti, «Generic Data on Design 1 and Design 2,» SASPAM-SA, Milestone Version 0.3 (DRAFT), 2024.

[12] «INTERNATIONAL REACTOR INNOVATIVE AND SECURE, IRIS Plant Overview,» October 2002.

[13] M. Carrelli, L. Conway, M. Dzodzo, A. Maioli, L. Oriani, G. Storrick, B. Petrovic, A. Achilli, G. Cattadori, C. Congiu, R. Ferri, M. Ricotti, D. Papini, F. Bianchi, P. Meloni, S. Monti, F. Berra, D. Grgic, G. Yoder, A. Alamberti, «The SPES3 experimental facility design for the IRIS reactor simulation,» *Science and Technology of Nuclear installations,* vol. vol2009, n. 579430, 2009.

[14] R. Ferri, C. Congiu, «Conceptual design of SPES3-IRIS facility,» SIET 01 334 RT 07 Rev.1, Piacenza (Italy), 2008.

[15] Applied Programming Technology Inc., «Symbolic Nuclear Analysis Package (SNAP) User's Manual,» 2021.

[16] P. Maccari, F. Mascari, S. Ederli, P. Meloni, S. Manservisi, «ASTEC code DBA analysis of passive mitigation strategy on a generic IRIS SMR,» *Annals of Nuclear Energy,* vol. 156, n. 108194, 2021.

[17] R. Ferri, «SPES3-IRIS facility RELAP5 sensitivity analyses on the containment system for design review,» no. SIET 01 526 RT 09 Rev.0, 2010.

[18] A. Achilli, C. Congiu, R. Ferri, F. Bianchi, P. Meloni, D. Grgić, M. Dzodzo, «Integral Test Facilities and Thermal-Hydraulic System Codes in Nuclear Safety Analysis,» *Science and Technology of Nuclear Installation,* vol. Vol. 2012, n. 173637, 2012.

[19] H. Glaeser, «GRS Method for Uncertainty and Sensitivity Evaluation of Code Results and Applications,» *Science and Technology of Nuclear Installations,* vol. Volume 2008, n. 798901, 2008.

[20] A. Bersano, F. Mascari, M.T. Porfiri, P. Maccari, C. Bertani, «Ingress of Coolant Event simulation with TRACE code with accuracy evaluation and coupled DAKOTA Uncertainty Analysis,» *Fusion Engineering and Design,* vol. 159, n. 111944, 2020.

[21] F. Alcaro, A. Bersano, C. Bertani, F. Mascari, «BEPU analysis of a passive decay heat removal system with RELAP5/MOD3.3 and RELAP5-3D,» *Progress in Nuclear Energy,* vol. 136, n. 103724, 2021.

[22] G. Agnello, P.A. Di Maio, A. Bersano, F. Mascari, «Cold Leg LBLOCA uncertainty analysis using TRACE/DAKOTA coupling,» *Journal of Physics: Conference Series,* vol. 2177, n. 012023, 2022.

[23] A. Bersano, G. Agnello, P.A. Di Maio, G. Grippo, F. Mascari, «BEPU analysis of an Upgraded ICE facility test by TRACE/DAKOTA coupling,» *Journal of Physics: Conference Series,* vol. 2685, n. 012055, 2024.

[24] F. Mascari et al., «Main outcomes of the Phebus FPT1 uncertainty and sensitivity analysis in the EU-MUSA project,» *Annals of Nuclear Energy,* vol. 196, n. 110205, 2024.

[25] S. Brumm et al., «Uncertainty quantification for severe-accident reactor modelling: Results and conclusions of the MUSA reactor applications work package,» *Annals of Nuclear Energy,* vol. 211, n. 110962, 2025.

[26] G. Agnello, M. Massone, F. Mascari, «Uncertainty quantification application on the Phebus FPT1 using the coupling of MELCOR and DAKOTA in a Python environment/architecture,» *Nuclear Engineering and Design,* vol. 441, n. 114135, 2025.

[27] M. Garbarini, G. Agnello, A. Bersano, F. Gabrielli, L. Luzzi, F. Mascari, «Simulation of QUENCH-06 Experiment by MELCOR v2.2 with Uncertainty Analysis,» *Nuclear Technology,* pp. 1-20.

[28] P. Maccari, A. Bersano, S. Ederli, F. Gabrielli, F. Mascari, «Validation and uncertainty analysis of ASTEC in early degradation phase against QUENCH-06 experiment,» *Nuclear Engineering and Design,* vol. 414, n. 112600, 2023.

[29] O. Coindreau et al., «Uncertainty quantification for a severe accident sequence in a SFP in the frame of the H-2020 project MUSA: First outcomes,» *Annals of Nuclear Energy,* vol. 188, n. 109796, 2023.

[30] M.E. Stephens, B.W. Goodwin, T.H. Andres, «Deriving parameter probability density funtions,» *Reliability Engineering and System Safety,* vol. 42, pp. 271-291, 1993.

[31] K.A. Gamble, L.P. Swiler, «Uncertainty Quantification and Sensitivity Analysis Applications to Fuel Performance Modeling,» SAND2016-4597C, 2016.

[32] J.L. Rodgers, A. Nicewander, «Thirteen Ways to Look at the Correlation Coefficient,» *The American Statician,* vol. 42, pp. 59-66, 1987.

[33] L.E. Herranz, S. Beck, V.H. Sánchez-Espinoza, F. Mascari, S. Brumm, O. Coindreau, S. Paci, «The EC MUSA Project on Management and Uncertainty of Severe Accidents: Main Pillars and Status,» *Energies,* vol. 14(15), n. 4473, 2021.

[34] L.E. Herranz, S. Beck, V.H. Sánchez-Espinoza, F. Mascari, S. Brumm, O. Coindreau, S. Paci, «Major Achievements of the EC MUSA Project,» *Nuclear Technology,* pp. 1-11, 2025.

[35] IAEA, «Advancing the State of the Practice in Uncertainty and Sensitivity Methodologies for Severe Accident Analysis in Water Cooled Reactors in the QUENCH-06 Experiment,» IAEA-TECDOC-2045, 2024.

[36] IAEA, [Online]. Available: https://www.iaea.org/projects/crp/i31033.

[37] S.S. Wilks, «Determination of sample size for setting tolerance limits,» *The Annals of Mathematical Statistics,* vol. 12, pp. 91-96, 1941.

[38] S.S. Wilks, «Statistical prediction with special reference to the problem of tolerance limits,» *The Annals of Mathematical Statistics,* vol. 13, pp. 400-409, 1942.

[39] United States Nuclear Regulatory Commission, State-of-the-Art Reactor Consequence Analyses Project, «Uncertainty Analysis of the Unmitigated Short-Term Station Blackout of the Surry Power Station,» NUREG/CR-7262, 2022.

AGENZIA NAZIONALE PER LE NUOVE TECNOLOGIE, L'ENERGIA E LO SVILUPPO ECONOMICO SOSTENIBILE

SEVERE ACCIDENT ANALYSIS IN A GENERIC IPWR AND UNCERTAINTY QUANTIFICATION OF THE RESULTS

The 12h European Review Meeting on Severe Accident Research (ERMSAR2026), Madrid, Spain, May 18-22, 2026

G. Agnello[1], G. Grippo[2], E. Cilia[2], F. Mascari[1]

[1] ENEA, NUC-ENER-SIC, Bologna Research Center, Via dei Mille 21, 40121, Bologna, Italy.
[2] Department of Industrial Engineering (DIN), University of Bologna, Viale del Risorgimento 2, 40136, Bologna, Italy.

CONTENT

- INTRODUCTION
- DESCRIPTION OF THE GENERIC IPWR DESIGN AND MELCOR NODALIZATION
- ANALYSIS OF THE REFERENCE CASE
- HYPOTHESIS OF THE UNCERTAINTY ANALYSIS
- RESULTS
- CONCLUSIONS

INTRODUCTION

- In view of the ongoing licensing process for **Small Modular Reactors** (SMRs) in Europe, increasing attention is devoted to assessing the capability of computational integral **Severe Accident** (SA) codes to simulate SMR-specific phenomena under postulated accident scenarios.
- Within this framework, the Horizon Euratom **SASPAM-SA** project, coordinated by ENEA (Italy), aims at assessing the capability of internationally recognized **European and Non-European computational tools** (largely used in Europe) to simulate SA scenarios in integral PWRs (iPWRs) and to evaluate the associated radiological consequences.
- The aim of this activity is to apply the **probabilistic method to propagate input uncertainty** in the SA domain in a generic iPWR design and to give preliminary insights into the uncertainty of the code on the **hydrogen production** from zircalloy oxidation, representing a key Figure Of Merit (FOM) for nuclear safety.

CONTENT

- INTRODUCTION
- DESCRIPTION OF THE GENERIC IPWR DESIGN AND MELCOR NODALIZATION
- ANALYSIS OF THE REFERENCE CASE
- HYPOTHESIS OF THE UNCERTAINTY ANALYSIS
- RESULTS
- CONCLUSIONS

DESCRIPTION OF THE GENERIC IPWR DESIGN AND MELCOR NODALIZATION

- The reference reactor considered in this work is a **generic iPWR** with a nominal power of 1000 MW_{th}.
- The design adopt an **integral configuration** in which all the main components of the Reactor Cooling System (RCS) are located inside the Reactor Pressure Vessel (RPV), enclosed within a dry containment.
- The safety strategy of the iPWR fully relies on the **use of passive safety systems** such as Riser-Downcomer valves (RI-DC), Emergency Heat Removal System (EHRS), Emergency Boration Tanks (EBTs), Long-term Gravity Make-up System (LGMS) and Passive Suppression System (PSS).

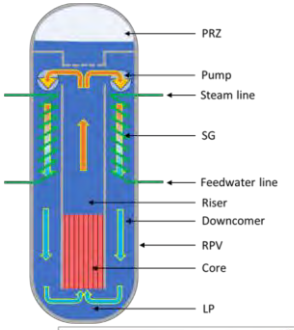

Integral RPV configuration

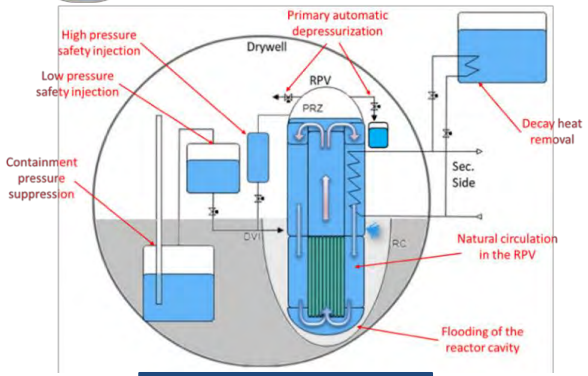

Containment configuration

DESCRIPTION OF THE GENERIC IPWR DESIGN AND MELCOR NODALIZATION

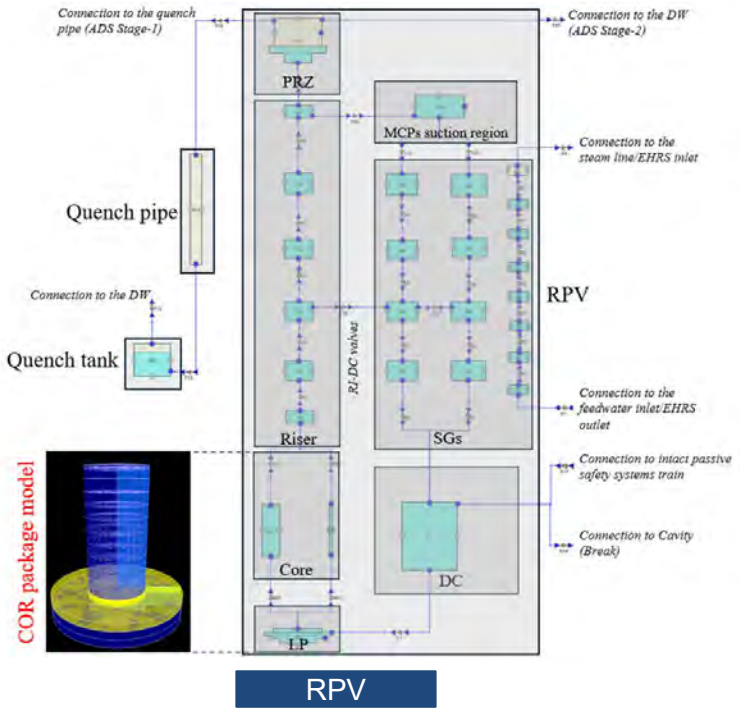

RPV

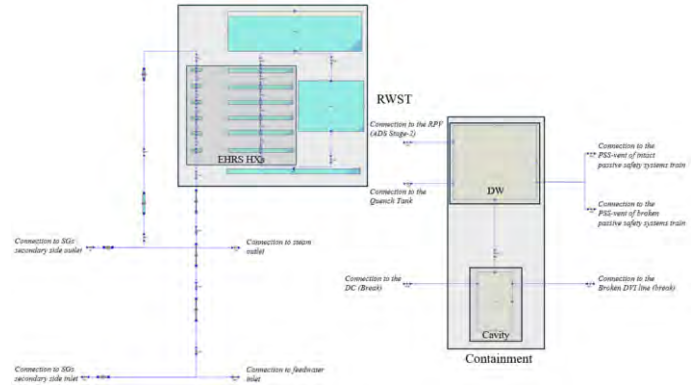

EHRS system and Containment

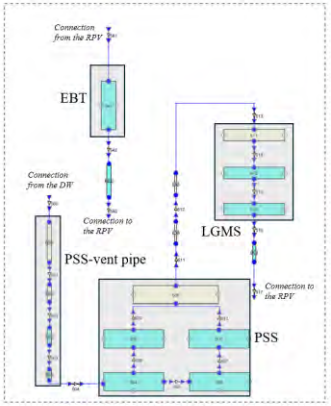

Intact passive safety systems train

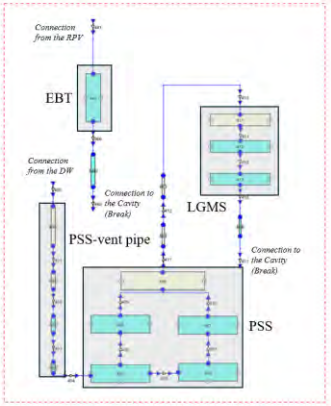

Broken passive safety systems train

PSS, EBT and LGMS trains

CONTENT

- INTRODUCTION
- DESCRIPTION OF THE GENERIC IPWR DESIGN AND MELCOR NODALIZATION
- ANALYSIS OF THE REFERENCE CASE
- HYPOTHESIS OF THE UNCERTAINTY ANALYSIS
- RESULTS
- CONCLUSIONS

ANALYSIS OF THE REFERENCE CASE

- The reference scenario is a **Loss Of Coolant Accident** (LOCA) initiated by the double-ended guillotine break of one of the two DVI lines.
- The **failure of all passive safety systems** has been postulated.
- The transient can be divided into **three Phenomenological Windows** (PhWs).

N.	PhW	Phenomena involved
1	*Thermal-hydraulic phase*	SCRAM, pumps coast-down, TAF uncover, Primary Coolant System depressurization, containment pressurization.
2	*Early phase*	BAF uncover, onset of Zircalloy oxidation reactions, runaway of Zircalloy oxidation reactions, massive in-vessel hydrogen production.
3	*Late phase*	Relocation of corium into the Lower Plenum (LP) and Lower Head (LH) heating.

ANALYSIS OF THE REFERENCE CASE

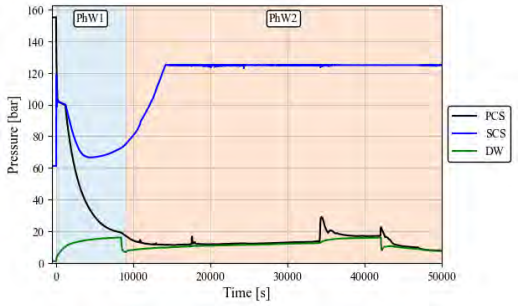

Pressure

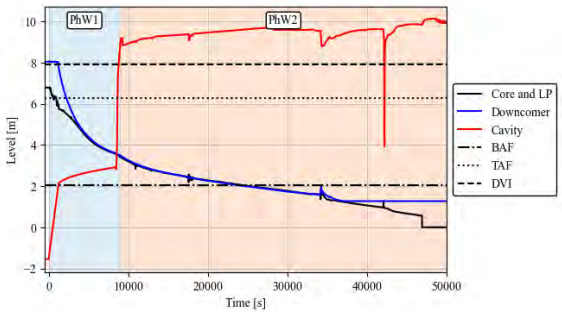

Collapsed Level

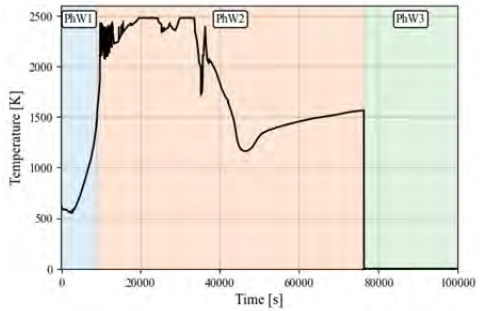

Cladding Temperature

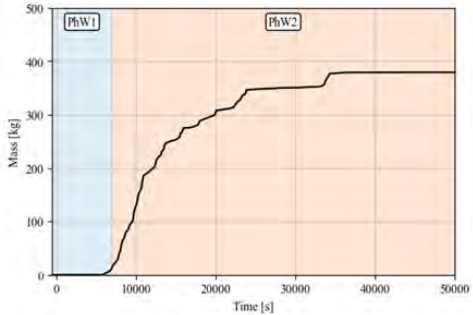

Hydrogen production

Event	Time [s]
Break	*0*
High containment pressure signal	*18*
Low PRZ water level signal	*70*
Low PRZ pressure signal	*92*
TAF uncovered	*618*
Containment leak opening	*7300*
Start of H2 generation	*8980*
Start of core relocation	*35000*
End of core relocation	*76320*

Table of the main events

CONTENT

- INTRODUCTION
- DESCRIPTION OF THE GENERIC IPWR DESIGN AND MELCOR NODALIZATION
- ANALYSIS OF THE REFERENCE CASE
- HYPOTHESIS OF THE UNCERTAINTY ANALYSIS
- RESULTS
- CONCLUSIONS

HYPOTHESES OF THE UNCERTAINTY ANALYSIS

- The **BEPU approach** has been used, adopting the probabilistic method to propagate input uncertainty.
- Key point is to investigate and characterize the **uncertainties** of the code about the **production of hydrogen from Zircaloy oxidation**. Thus, the FOM considered for the present uncertainty application is the **total cumulative hydrogen production by Zircaloy oxidation** the in core.
- Seven of the main uncertain input parameters influencing the production of hydrogen in LWRs have been considered.

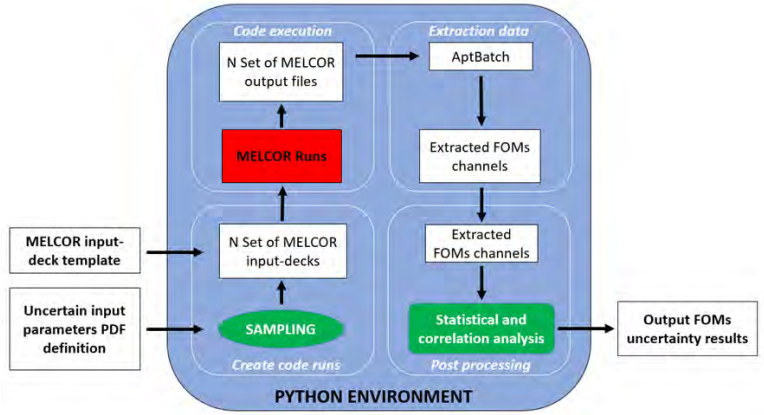

HYPOTHESES OF THE UNCERTAINTY ANALYSIS

Parameter	Unit	PDF	Reference value	Lower and Upper Bound	
k_1	[$kg^2/m^4 \cdot s^{-1}$]	Uniform	29.6	Min	26.64
				Max	32.56
k_2	[$kg^2/m^4 \cdot s^{-1}$]	Uniform	16820	Min	15979
				Max	17661
k_3	[$kg^2/m^4 \cdot s^{-1}$]	Uniform	87.9	Min	43.95
				Max	109.88
k_4	[$kg^2/m^4 \cdot s^{-1}$]	Uniform	16610	Min	15448
				Max	17773
Zr_Melt	[K]	Normal	2400	Min	2250
				Max	2550
PORDP	[-]	Normal (truncated)	0.38	Min	0.1
				Max	0.5
EUT_T	[K]	Normal	2479	Min	2230
				Max	2728

CONTENT

- INTRODUCTION
- DESCRIPTION OF THE GENERIC IPWR DESIGN AND MELCOR NODALIZATION
- ANALYSIS OF THE REFERENCE CASE
- HYPOTHESIS OF THE UNCERTAINTY ANALYSIS
- RESULTS
- CONCLUSIONS

RESULTS

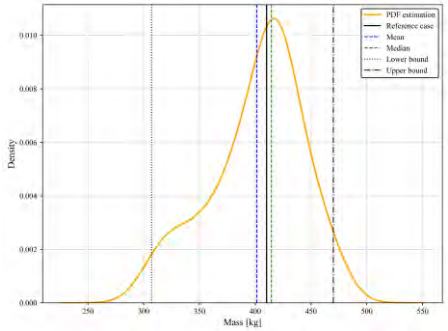

PDF of the FOM

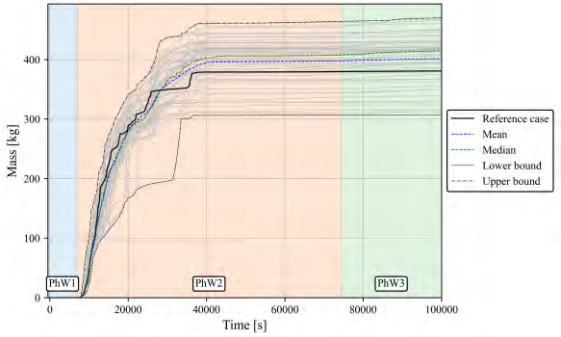

Uncertainty band

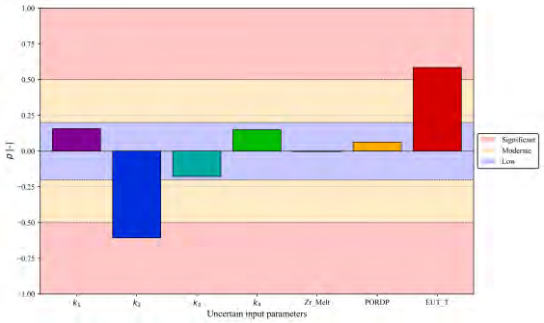

Simple rank correlation coefficients

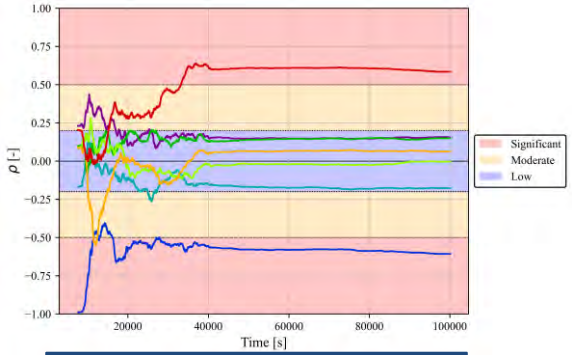

Simple rank correlation coefficientalong transient

Statistical Parameter	Unit	Value
Mean	[kg]	401.44
Median	[kg]	414.45
Lower bound	[kg]	307.09
Upper bound	[kg]	469.96
Standard deviation	[kg]	40.70
Coefficient of variation	[kg]	0.10

Statistical parameters of the FOM

CONTENT

- INTRODUCTION
- DESCRIPTION OF THE GENERIC IPWR DESIGN AND MELCOR NODALIZATION
- ANALYSIS OF THE REFERENCE CASE
- HYPOTHESIS OF THE UNCERTAINTY ANALYSIS
- RESULTS
- CONCLUSIONS

CONCLUSIONS

- The Horizon Euratom SASPAM-SA project, coordinated by ENEA (Italy), aims at assessing the capability of internationally recognized European and Non-European computational tools (largely used in Europe) to simulate SA scenarios in integral PWRs (iPWRs) and to evaluate the associated radiological consequences.
- Goal of the analysis is the application of the MELCOR code to the analysis of a SA scenario in a generic iPWR using the BEPU approach to quantify uncertainties affecting SA progression.
- The uncertainty analysis shows an uncertainty band of approximately 160 kg, with a coefficient of variation of 10%. The statistical correlation analysis highlights the dominant role of the Zircaloy oxidation kinetics parameters and the eutectic temperature of the ZrO_2/UO_2 mixture.
- Future work will extend the uncertainty analysis to additional FOMs, including fission products release and containment behavior, and to a set of different SA scenarios with different postulated failure of passive safety systems.

THANKS FOR YOUR ATTENTION!

Funded by the European Union

Funded by the European Union. Views and opinions expressed are however those of the author(s) only and do not necessarily reflect those of the European Union or European Commission-Euratom.
Neither the European Union nor the granting authority can be held responsible for them.

ENEA carried out the research activity with MELCOR code and SNAP, obtained in the framework of the ENEA-ISIN agreement signed on March 23rd 2020 as part of the General Arrangement between the United States Nuclear Regulatory Commission (US-NRC) and the Italian National Inspectorate for Nuclear Safety and Radiation Protection (ISIN).

F. Mascari, G. Agnello
fulvio.mascari@enea.it
giuseppe.agnello@enea.it

STEPWISE UNCERTAINTY ANALYSIS METHODOLOGY: FIRST INSIGHTS

Rafael Bocanegra, Victor Martinez-Quiroga, Marina Perez-Ferragut*
Energy Software Ltd. (ENSO)
rafael.bocanegra@ensobcn.com, victor.martinez@ensobcn.com, marina.pf@ensobcn.com

ABSTRACT

Energy Software S.L. (ENSO) has undertaken an innovative project to address the inherent uncertainties present in severe-accident analysis codes used in nuclear safety assessments. Building on the outcomes of two major international initiatives—IAEA CRP I31033 and the HORIZON-2020 MUSA project—ENSO has established a solid foundation for identifying and quantifying the main sources of uncertainty in severe-accident simulations. These initiatives also revealed key limitations, such as excessive computational time, frequent simulation failures, and truncation effects.

The proposed approach follows a stepwise structure, applying the Wilks methodology in two consecutive phases:

- In-vessel phase, focused on accident progression up to reactor pressure vessel failure, and
- Ex-vessel phase, analyzing the subsequent phenomena occurring within the containment.

This stepwise strategy enables the identification and quantification of uncertainty sources at different stages of the accident, providing essential insights for emergency decision making and supporting the design of future research in the field.

To validate the methodology, ENSO has developed an evaluation model of a Generation II four loop Westinghouse PWR reactor subjected to a low-pressure station blackout (SBO) scenario. The RELAP/SCDAPSIM code has been used for the in-vessel phase, while MELCOR has been employed for the ex-vessel containment analysis. An uncertainty analysis has been performed, and early results indicate both the robustness of the proposed methodology and its benefits in terms of computational efficiency and improved calculation stability.

However, several challenges have emerged during the long-term Molten Core Concrete Interaction (MCCI) phase, highlighting the need for further development and refinement.

KEYWORDS
Severe Accident, PWR, RELAP5, SCDAP, MELCOR, Uncertainty Analysis

1. INTRODUCTION

Following the Fukushima nuclear accident in 2011, nuclear regulatory authorities intensified efforts to study emergency procedures associated with Beyond Design Basis Accident (BDBA) scenarios [1][2]. As noted by the IAEA [3], analyzing BDBAs helps enhance the safety of Nuclear Power Plants (NPPs) by considering additional failures beyond those in Design Basis Accidents (DBAs). In Europe, comprehensive “stress tests” were conducted to evaluate reactor performance under Fukushima-like Severe Accident (SA) conditions, leading to safety improvements and reinforcing the need for deterministic analyses in BDBA studies.

A key challenge in deterministic methodologies lies in the uncertainties associated with physical models, correlations, and nodalization—such as initial/boundary conditions, discretization, and user effect. Over the last two decades, OECD/NEA initiatives have advanced Uncertainty Analysis (UA) using Best Estimate

* Footnote, if necessary, in Times New Roman font and font size 10

codes (BEPU), focusing on thermal-hydraulic, neutronic, and thermomechanical tools (UAM [4][5], EGUAM [6], WPRS [7]) and, especially, thermal-hydraulic codes (BEMUSE [8], PREMIUM [9], SAPIUM [10], ATRIUM [11]). BEPU methodologies based on Wilks/Wald formulations are now widely accepted. In Spain, CSN-funded projects have significantly expanded the related bibliography [12-29].

For BDBA scenarios involving core damage, Severe Accident (SA) codes such as MELCOR, MAAP, ASTEC, and RELAP/SCDAPSIM are required. However, only limited UA applications exist for these tools. In 2010, the USNRC performed a MELCOR-based UA within the SOARCA project [30] for Station Blackout (SBO) scenarios at Peach Bottom [31] and Sequoyah [32]. Additional UAs with ASTEC [33] and MAAP [34] in 2013 assessed uncertainties in source term and hydrogen generation, respectively.

More recently, two major projects have extended UA methodologies to SA conditions: the IAEA CRP I31033 [35][36] and the HORIZON-2020 MUSA project [37-42]. The IAEA initiative, involving CIEMAT and ENSO, examined the use of UAs across multiple reactor designs. MUSA, coordinated by CIEMAT with ENSO participation, identified key uncertainty sources in SA codes and tested multiple UA approaches for both reactors [38] and spent fuel pools [44]. MUSA also established comprehensive input-parameter lists with associated uncertainty ranges and PDFs for MELCOR, MAAP, ASTEC, and RELAP/SCDAPSIM, as well as detailed figures of merit (FOMs) for different scenarios.

Analyses of integral plant and containment models revealed that:

- Full-containment simulations are computationally demanding.
- Applying wide uncertainty ranges often caused simulation failures, hindering Wilks-based evaluations.
- SA scenarios require simultaneous estimation of multiple FOMs, necessitating the Wald methodology and more code runs.
- Bifurcations and cliff-edge effects were frequent, especially in the in-vessel phase, strongly influenced by fuel damage and molten-material accumulation, which affect vessel-failure timing and release magnitudes.

To address these challenges, ENSO is developing the Stepwise Uncertainty Analysis Methodology (SUAM) for source-term calculations in SA scenarios. Section 2 of this work describes the methodology, while Section 3 applies SUAM to a PWR SBO sequence. The final section summarizes the main insights and outcomes.

2. STEPWISE UNCERTAINTY ANALYSIS METHODOLOGY (SUAM)

The Stepwise Uncertainty Analysis Methodology (SUAM) provides a structured framework to independently and sequentially quantify uncertainties associated with the in-vessel and ex-vessel phases of a Severe Accident (SA). In this approach, tolerance limits obtained from the in-vessel analysis (up to reactor pressure vessel failure) are transferred as boundary conditions (BCs) to the ex-vessel containment calculations (see Figure 1). Each phase is modeled using its own dedicated nodalization, and, when appropriate, different computational codes may be employed to further isolate uncertainty sources and improve numerical robustness.

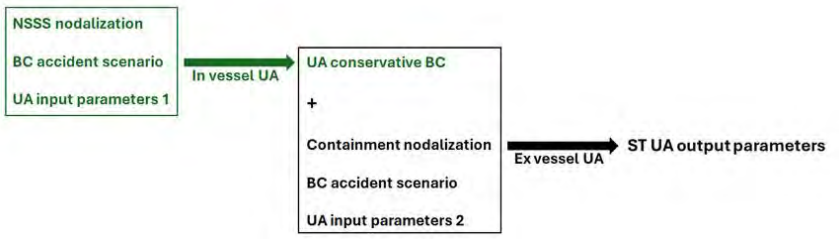

Figure 1: Stepwise Uncertainty Analysis Methodology for source term estimation

The methodology relies on two fundamental premises:

1. independent nodalization for the containment and the nuclear steam supply system (NSSS), and
2. ex-vessel boundary conditions derived directly from the in-vessel tolerance limits.

These principles were adopted to address limitations identified during ENSO's participation in the IAEA CRP I31033 [36] and HORIZON-2020 MUSA [37-42] projects. In those studies, large output variability in the in-vessel phase (driven by cliff-edge behavior and bifurcation phenomena) led to an unrealistic propagation of uncertainty into the source-term predictions. Additionally, uncertainty analyses requiring large sample sizes resulted in frequent simulation failures and prohibitive computational times. Segregating the NSSS and containment models improves numerical stability and significantly reduces the computational burden of large-scale UA campaigns.

SUAM follows the GRS uncertainty-evaluation framework [12], implementing the Wald's tolerance-limit formulation [33][34][45]. This approach determines the minimum sample size required to derive statistically consistent tolerance limits for multiple figures of merit (FOMs) simultaneously—an essential requirement for SA analysis, where numerous interdependent outputs must be treated collectively. A one-sided 95/95 statistical criterion is applied, selecting the most limiting value of the tolerance bound. This choice minimizes the required number of simulations—higher-order Wald formulations would increase the sample size—and reduces the sensitivity of the ex-vessel uncertainty quantification to cliff-edge or bifurcation effects occurring in the in-vessel phase.

3. APPLICATION OF SUAM TO A LONG-TERM SBO IN A PWR

The selected scenario is the long-term Station Black Out (SBO) in a Gen-II PWR. The reactor is a generic 4-loop Westinghouse design with a thermal power of 3400 MW and 17X17 fuel assemblies.

The specific requirements of the SUAM methodology for the simulation of the selected scenario are:

1. SA code for simulating the NSSS for the in-vessel phase: RELAP/SCDAPSIM.
2. SA code capable of simulating the containment during ex-vessel phase: MELCOR.
3. Independent nodalization for the NSSS and the containment.
4. In-vessel phase FOMs for obtaining the coupling BCs:
   a. Hydrogen released from the core into the containment.
   b. Noble gases (NG) released into the containment through Pressurizer (PZR) Power
   c. Operated Relief Valve (PORV) (He, Xe, Kr)
   d. Fission product (FP) released into the containment through PZR PORV (CsI, CsOH, Te, Sn, Cd)
   e. Debris released into the containment (Ag, Zr, UO2, ZrO2)
   f. Debris decay power.
   g. Time of Creep rupture.
   h. Coolant mass and energy released to containment.
5. Ex-vessel phase FOMs:
   a. Max. containment pressure.
   b. Max. containment Temperature.
   c. FP concentration and distribution into the containment.

d. FP leaked to environment

3.1. NSSS Evaluation Model

The NPP nodalization is derived from the RELAP/SCDAPSIM MOD3.4 (RS3.4) model developed by ENSO within the framework of its contribution to the MUSA WP5 project [38].

The in-vessel uncertainty analysis was carried out using the upgraded uncertainty analysis module (IUA2) implemented in RELAP/SCDAPSIM MOD3.4 [46]. The main features of this module include an automated procedure for performing Wilks/Wald-based uncertainty analyses, encompassing the determination of the required sample size, random sampling of input parameters from probability density functions (PDFs), and access to built-in code correlations for the perturbation of selected coefficients.

As indicated in Section 2, the uncertainty analysis was conducted using the multivariate formulation of the Wilks' equation developed by Wald. The Wald approach was selected because the output of the in-vessel analysis requires the statistical coverage of the tolerance limits for each figure of merit (FOM) to be ensured simultaneously. In the present study, five groups of independent FOMs were considered, as listed below:

- Maximum mass of H2 at the time of creep rupture.
- Maximum mass of NG released to the containment through PZR at the time of creep rupture (He, Xe, Kr)
- Maximum mass of FP released to the containment through PZR at the time of creep rupture (CsI, CsOH, Te, Sn, Cd)
- Maximum mass of Debris (UO2, ZrO2, Zr, Ag), maximum debris decay power and minimum time for the time creep rupture.
- Maximum inventory of water leaked into the containment and maximum enthalpy of water at the time of creep rupture

According to Wald's equation, the minimum number of runs required to estimate the 95/95 (or 5/95) tolerance limits for five output variables is 181 (see Table 1.1 in [47]).

In addition to the determination of the tolerance limits, the output data were used to assess potential correlations between input and output variables by calculating the Pearson, Spearman, and Kendall correlation coefficients. The selection of these coefficients allows for the identification of linear and monotonic relationships. The statistical significance of each coefficient was evaluated under the null hypothesis by computing the corresponding p-value, which represents the probability of observing a correlation by chance, and comparing it with the conventional threshold value of 0.05.

Table 1 presents the selected input parameters, which are associated with heat transfer, critical heat flux, interphase heat transfer, material properties, cladding behavior, radiation, core power, safety systems, and natural circulation. The table also specifies the corresponding probability density functions (PDFs) and the affected components.

Table 1: List of uncertain parameters for the in-vessel BEPU analysis

#	Phenomenon	Parameter [1]		PDF[2]	Components	Ref [3]
1	Heat transfer across solid surfaces	Film boiling HTC to liquid	HT-1	U [0.74; 1.29]	RELAP heat structures (heat transfer to the secondary) and SCDAP components (core)	[44]
2		Film boiling HTC to vapor	HT-2	U [0.49; 3.43]		[44]
3		Nucleate boiling HTC - subcooled	HT-3	T [0.76; 0.86; 1.19; 1.43]		[45]
4		Nucleate boiling HTC - saturated	HT-4	U [0.35; 2.5]		[44]
5		Vapor single phase HTC	HT-5	N [1., 0.2]		EJ
6	Interphase	Friction	IPH-1	U [0.75, 1.29]	Water fluid	[44]
7		Heat transfer global	IPH-2	U [0.27, 1.94]		[44]
8	Cladding behaviour under severe accident conditions	Zr oxidation rate and thickness	OXI	N [1,0., 075]	SCDAP fuel components	EJ
9		Rupture strain	SA-1	BE = 0.2, N [1., 0.1]		Code ranges
10		Temperature for failure of oxide shell	SA-2	BE=2500K, N [1, 0.1]		Code ranges
11	UO_2 properties	UO_2 thermal conductivity	MP-1	N/A		Code built-in
12		UO_2 heat capacity for T> 2830K	MP-2	N/A		Code built-in
13	Zr properties	Zr heat capacity	MP-3	N/A		Code built-in
14	Radiation	shroud thickness	SA-3	BE = 1.75 cm U [1.58, 1.92] cm	SCDAP shroud component	EJ [46]
15		shroud perimeter	SA-4	BE = 11.81 m U [10.63,12.99] cm		EJ [46]
16	Safety systems	ACC injection trip (pressure set point)	BC-1	N [1,0.024] sigma = 2.24%	ACC	[44]
17		ACC temperature	BC-2	N [1, 0.03] ºC		EJ, See Note (1)
18	Primary to secondary heat removal	SGs level	BC-3	N [1, 0.05]	SG	EJ, See Note (2)
19	Reactor power	Decay power factor (ANS79-3)	DP	N [1, 0.0408]	Core power table	[47]

[1] HT: heat transfer; HTC: heart transfer coefficient; CHF: critical heat flux; IPH: interphase phenomena SA: severe accident; BC: boundary condition; MP: material property; DP: decay power; OXI: oxidation
[2] BE = Best estimate, LN/N/U = Log normal/normal/uniform, T = Trapezoidal
[3] EJ = Expert judgment
Note (1) Estimated delta temperature due to season change
Note (2) Estimated uncertainty from design (ENSO)

3.2. Containment Evaluation Model

For the ex-vessel phase, the MELCOR code was employed. The verification of the coupling between RELAP/SCDAPSIM and MELCOR was performed using the results obtained from the in-vessel calculations carried out with the RELAP/SCDAPSIM code within the framework of the MUSA project [37]. In the subsequent phases of the present project, the results of the in-vessel uncertainty analysis presented in Section 3.1 will be used to perform both the base case simulation and the ex-vessel uncertainty analysis.

The containment nodalization is based on the information provided in [48]. It consists of 16 control volumes (CVs), which are used to represent the main compartments, including the steam generator cages, reactor

cavity, containment dome, lower compartments, among others. One of these control volumes is used to represent the boundary conditions of the environment.

The hydraulic connections between the containment compartments are modeled using 29 flow paths (FLs), while the containment heat sinks are represented by 39 heat structures (HSs). The COR and DCH packages are disabled, as the present analysis is a stand-alone containment calculation. However, the RN and CAV packages are kept active in order to capture fission product transport and corium–concrete interaction phenomena.

The mass and energy sources released into the containment are introduced through boundary conditions. The coolant mass and energy discharged into the containment through the pressurizer (PZR) power-operated relief valves (PORVs), together with the hydrogen generated by zirconium oxidation, are directly introduced into control volume CV 206 (lower compartments) using the "external source" option in MELCOR. The debris mass ejected from the reactor vessel is introduced into the reactor cavity (CV 101) by means of the Fuel Dispersal Interaction Package, which allows data to be extracted from an external data file, processed, and subsequently introduced into the CAV package. In a similar manner, fission product masses are introduced into the "Lower Compartments" control volume (CV 206) using the Radionuclide Package option "aerosol and vapor source," since it is assumed that all fission products are released through the PZR.

The uncertainty analysis was conducted using the two-sided Wilks' formulation of tolerance intervals rather than the Wald approach, since all figures of merit associated with the ex-vessel phase were considered to be independent of one another. Under this assumption, the required number of calculation cases was determined to be 93.

The input variables considered uncertain are listed in Table 2, together with the type of probability density function and their main parameters.

Table 2: List of uncertain parameters for the ex-vessel BEPU analysis

№	Parameter	Type	PDF	PDF parameters
1	RN_chi	Scalar	Beta	α:1.0 β:5.0 (1.0, 5.0)
2	RN_fslip	Scalar	Beta	α:4.0 β:4.0 (1.141, 1.277)
3	RN_ftherm	Scalar	Triangular	a:1.0 m:2.18 b:3.0
4	RN_gamma	Scalar	Uniform	a:1.0 b:3.0
5	RN_stick	Scalar	Beta	α:2.5 β:1.0 (0.2, 1.0)
6	RN_turbds	Scalar	Uniform	a:0.0 b:0.03
7	RN_tkgop	Scalar	Triangular	a:0.05 m:0.5 b:1.0
8	RN_deldif	Scalar	Uniform	a:1.0E-5 b:8.0E-3
9	FAIL_opA	Factor	Triangular	a:0.1 m:1.0 b:10.0
10	FAIL_mult_leakA	Factor	Triangular	a:0.1 m:1.0 b:10.0
11	FAIL_op_press	Scalar	Triangular	a:7.58E5 m:9.24E5 b:1.2E6
12	CAV_conc_rho	Factor	Uniform	a:0.95 b:1.02
13	CAV_Conc_STemp	Factor	Uniform	a:0.9 b:1.0
14	CAV_Conc_LTemp	Factor	Uniform	a:0.9 b:1.0
15	CAV_Conc_ATemp	Factor	Uniform	a:0.9 b:1.0
16	CAV_Ox_Emiss	Scalar	Uniform	a:0.5 b:1.0
17	CAV_Met_Emiss	Scalar	Uniform	a:0.5 b:1.0
18	CAV_Surr_Emiss	Scalar	Uniform	a:0.5 b:1.0
19	CAV_B_HTC	Factor	Uniform	a:0.97 b:1.03
20	CAV_R_HTC	Factor	Uniform	a:0.97 b:1.03
21	CAV_Ox_K	Factor	Uniform	a:0.97 b:1.03
22	CAV_Met_K	Factor	Uniform	a:0.97 b:1.03
23	HS_Conv_Lam	Scalar	Uniform	a:0.45 b:2.6
24	HS_Conv_Turb	Scalar	Uniform	a:0.45 b:2.6
25	INP_H2O_Mass	Factor	Uniform	a:0.95 b:1.05
26	INP_H2_Mass	Factor	Uniform	a:0.95 b:1.05
27	INP_DCH	Factor	Normal	μ:1.0 σ:0.0408 [0.92, 1.08]
28	INP_H2O_Pow	Factor	Normal	μ:1.0 σ:0.0408 [0.92, 1.08]

The pre-processing stage is performed using the uncertainty analysis tool integrated into the SNAP software, which is based on DAKOTA. The recommendations provided in NUREG/IA-0532 have been followed. This process significantly simplifies the inclusion and generation of the set of calculation cases required to obtain an adequate sample for the estimation of uncertainty in the figures of merit.

Regarding post-processing, a dedicated Python-based tool has been developed to read each of the output files generated by MELCOR for the full set of calculation cases. These outputs are processed to determine the uncertainty ranges and correlation coefficients for each figure of merit. Subsequently, all the information is exported to an automatically generated Excel file, which also includes the necessary plots to enable a comprehensive analysis by the analyst.

3.3. Accident sequence, results and discussion

3.3.1. In-Vessel phase

The accident sequence begins with reactor shutdown and isolation of the secondary system. As a result, the pressure in the secondary system increases above 7 MPa, leading to the automatic actuation of the steam generator (SG) relief valves. During this initial stage of the transient, decay heat is efficiently removed through heat transfer from the primary to the secondary system. Approximately 2 hours later, since the Auxiliary Feedwater System is not available, the SGs are depleted and the pressure in the primary system begins to rise, inducing liquid expansion in the pressurizer (PZR). About 10 minutes later, the setpoint of the PZR power-operated relief valve (PORV) is reached (16.2 MPa), initiating PZR relief action and resulting in a reduction of the primary system liquid inventory. Subsequently, approximately 2.5 hours after the onset of the transient, the first core uncover occurs, and an operator action (full opening of the PZR PORV) is performed when the core exit thermocouple (CET) temperature reaches approximately 623 K. This action causes a rapid depressurization of the primary system, which triggers accumulator (ACC) injection and core cooling. Figure 2 shows the water discharged through the PZR PORV during the different phases described above.

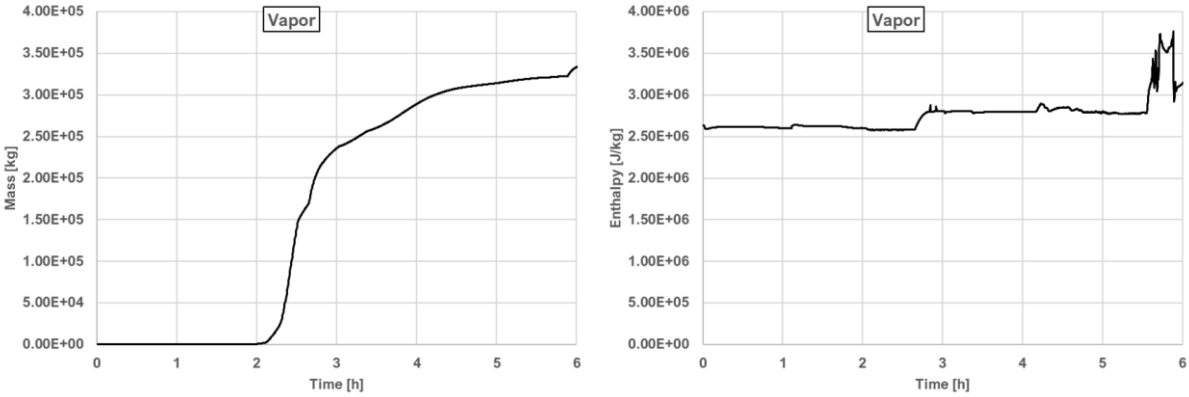

Figure 2: Mass and energy of the coolant released into the containment

Cladding oxidation begins at 1200 K, leading to an increase in heat generation within the fuel elements. As a consequence, core surface temperatures rise to approximately 2400 K, causing cladding expansion (ballooning), fuel rod rupture, and the release of volatile and soluble fission products, as well as hydrogen generated by the H_2O–Zr interaction. A fraction of these fission products, together with the generated hydrogen, are subsequently released into the containment through the pressurizer PORV, as shown in Figure 3.

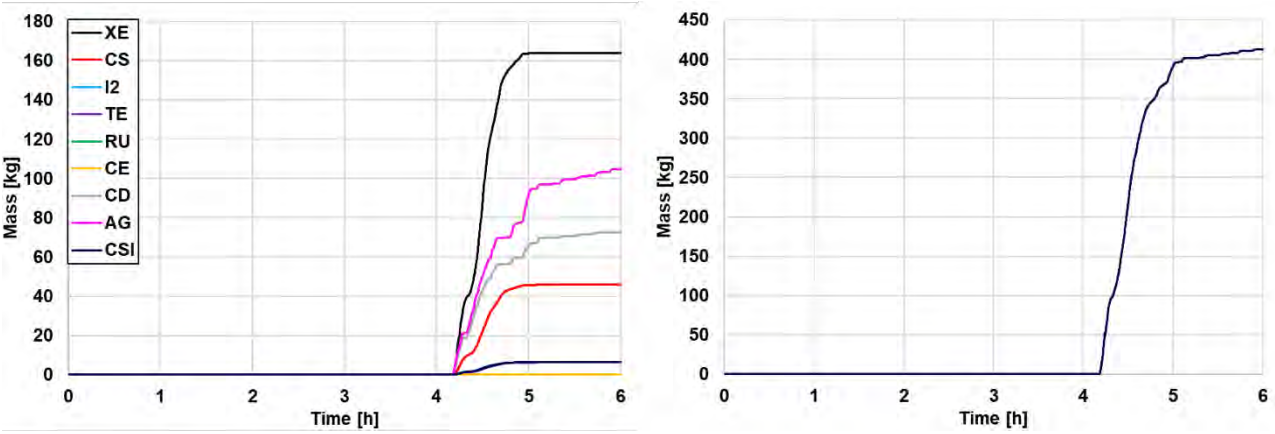

Figure 3: Mass of fission products (left) and hydrogen (right) released into the containment through the PZR.

Approximately 4.2 hours after the beginning of the transient, when the core surface temperature reaches 2873 K, oxide (U–Zr–O) formation and the development of a molten material pool occur. The molten material accumulates in the lower part of the core at around 5.65 hours, when core collapse takes place. Subsequently, structural materials accumulate in the lower plenum, leading to an increase in the reactor pressure vessel (RPV) wall temperature until creep rupture occurs (6.2 hours after the onset of the transient), resulting in the release of corium into the cavity (see Figure 4). At this point, the calculation is terminated.

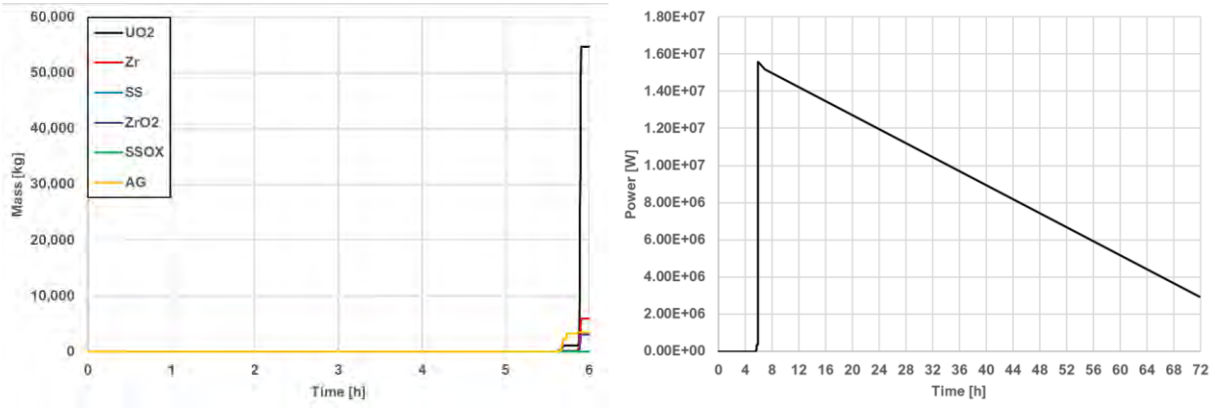

Figure 4: Mass of materials ejected through the RPV (left) and corresponding energy (right).

The results of the uncertainty analysis (UA) are presented in Table 3.

Table III. Tolerance limits for in-vessel FOMs

TAG	Units	Type	Base case	Tolerance limit 181
tPCT	hours	MIN	3.1	**2.7**
tFRUP	seconds	MIN	35.4	**20.8**
tDEB	minutes	MIN	33.2	**19.8**
tSLUMP	hours	MIN	1.7	**0.8**
tCREEP	**hours**	**MIN**	**2.2**	**1.3**
cumH2	**kg**	**MAX**	**262.1**	**420.9**
cumFPNC	kg	MAX	163.9	**225.0**
cumXe	**kg**	**MAX**	**147.3**	**202.2**

cumKr	**kg**	**MAX**	**16.6**	**22.8**
cumHe	**kg**	**MAX**	**4.7**	**6.2**
cumFPS	kg	MAX	111.1	**153.1**
contAg	**kg**	**MAX**	**107.4**	**945.5**
contCd	**kg**	**MAX**	**72.8**	**524.3**
contCsI	**kg**	**MAX**	**6.4**	**13.7**
contCsOH	**kg**	**MAX**	**45.9**	**102.0**
contSn	**kg**	**MAX**	**1.8**	**47.2**
contTe	**kg**	**MAX**	**6.2**	**15.4**
debAg	**tons**	**MAX**	**3.4**	**3.4**

The results show large deviations in the aerosols released from the control rods (contAg, contCd, and contSn in Table 3), with the base case value lying far from the tolerance limits.

3.3.2. Ex-Vessel phase

During the first 2 hours of the transient, pressure and temperature in the containment remain constant, as no releases occur either from the core or from the Reactor Coolant System (RCS). Shortly thereafter, pressurizer (PZR) relief operation begins and, when the pressurizer PORV fully opens, a rapid discharge of the RCS inventory results in a sharp increase in containment pressure (see Figure 5). The pressure evolution is practically uniform throughout all compartments, exceeding the pressure beyond which containment failure due to overpressure is assumed in most of the cases, leading to the release of inventory to the environment. Containment failure due to overpressure occurs over a wide time range, from approximately 19 to 65 hours, with a clear bifurcation in the scenario, as some cases do not exhibit overpressure failure. The dotted line represents the containment failure time in the base case calculation. A thorough analysis is required to determine which parameter needs to be truncated to avoid this bifurcation, as otherwise it would invalidate the determination of uncertainty ranges for this figure of merit.

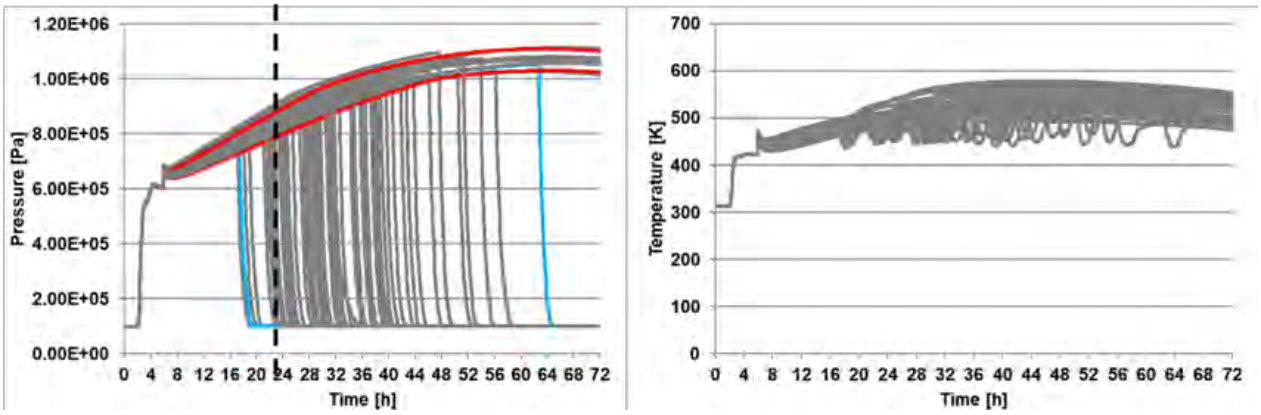

Figure 5: Containment dome pressure and temperature

Temperature also increases; however, unlike pressure, its evolution is heterogeneous. The highest temperature peak is reached in the reactor cavity when corium is ejected from the core. In the remainder of the containment, temperatures in some compartments slightly exceed 420 K approx. until containment failure occurs, at which point a slight cooling takes place due to the release of inventory to the environment. Subsequently, temperatures increase significantly, reaching up to 1070 K in the reactor cavity and between 620 - 820 K in the other compartments. This behavior is driven, among other phenomena, by forced convection induced by the chimney effect within the containment, which enhances heat removal from the corium in the cavity.

With regard to radionuclide (RN) release, Figure 6 shows the release of radionuclides to the environment. On the one hand, the release of nearly the entire vapor inventory can be observed, represented in this case by halogens (I_2 class). A clear bifurcation of the scenario is evident, showing that in cases where containment failure does not occur, the release of I_2 is limited and is solely due to containment leakage. Conversely, in cases where containment fails due to overpressure, the variability in the magnitude of the released mass is minimal, as nearly the entire inventory is released. Dispersion is observed only in the timing of the release, which is influenced by the containment rupture threshold.

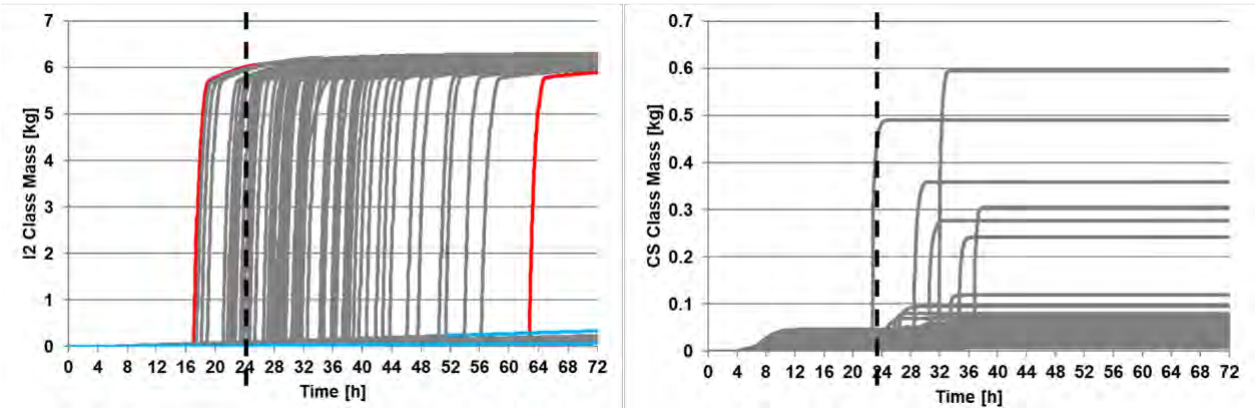

Figure 6: Halogens (left) and alkali metals (right) masses released to environment.

4. CONCLUSIONS

This work presents a first uncertainty analysis (UA) framework for severe accident (SA) calculations, addressing separately both the in-vessel and ex-vessel phases while explicitly accounting for key practical limitations typically encountered when applying integral SA codes within UA studies.

For the in-vessel phase analysis, a total of 208 simulations were performed, with 0 failed cases. The overall computation time was approximately 32 hours on an Intel i7-8700 (12 cores) platform, indicating that the in-vessel UA can be executed with robust numerical performance under the adopted setup.

For the ex-vessel phase analysis, a base case was first computed to verify the adequacy of the coupling between the NSSS and containment calculations. The coupling was found to operate correctly and produced reasonable results. The computational cost of the base case (corresponding to 72 hours of simulation time) was approximately 13.68 minutes on an Intel i7-12700H. A preliminary UQ was then carried out with 93 cases, requiring approximately 6.2 hours using 8 cores on the same platform. No failed cases were observed for $t < 24$ h, whereas 23 run cases (24%) failed for $t > 48$ h, which points to the relevance of the long-term MCCI phase and supports the need for further investigation on modeling the long-term MCCI scenarios with MELCOR.

Overall, the results confirm the feasibility of the proposed staged UA strategy and highlight long-term ex-vessel phenomena, particularly MCCI, as a key driver for late failures and a priority topic for continued methodological refinement.

5. ACKNOWLEDGEMENTS

The authors want to acknowledge the Spanish Nuclear Council for its support to this project under the framework of the CSN program of R&D.

REFERENCES.

1. CNSC, “Design Extension Conditions for Nuclear Power Plants”, Otawa: Canadian Nuclear Safety Commission, c2014.
2. Kral, P.; “Analyses of DEC for NPP’s in the Czech Republic and their implementation into SAR”, NURETH-18, Portland, 2019.

3. IAEA, “Deterministic Safety Analyses of Nuclear Power Plants”. IAEA Safety Standards Series No. SSG-2 (Rev.1), 2019.
4. IAEA, “Benchmarks for Uncertainty Analysis in Modelling (UAM) for the Design, Operation and Safety Analysis of LWRs. Volume I: Specification and Support Data for Neutronic Cases (Phase I)”. NEA/NSC/DOC (2013)7. 2013.
5. IAEA, “Benchmarks for Uncertainty Analysis in Modelling (UAM) for the Design, Operation and Safety Analysis of LWRs. Volume I: Specification and Support Data for the Core Cases (Phase II)”. NEA/NSC/DOC (2012)11. 2012.
6. https://www.oecd-nea.org/jcms/c_12861/expert-group-on-uncertainty-analysis-in-modellinge guam
7. https://www.oecd-nea.org/jcms/c_12832/working-party-on-scientific-issues-and-uncertaintyanalysis-of-reactor-systems-wprs
8. Perez-Ferragut M., Reventos F., et al. (1/24) “Uncertainty and sensitivity analysis of a LBLOCA in a PWR Nuclear Power Plant: Results of the Phase V of the BEMUSE programme”. Nuclear Engineering and Design 241 Issue 10 (2011) pages 4206-4222.
9. Skorek, T.; de Crécy, A.; Kovtonyuk, A.; et al; Pautz, A.; Mendizábal, R.; Freixa, J. et al. (8/31) 2019. “Quantification of the uncertainty of the physical models in the system thermal-hydraulic codes – PREMIUM benchmark”. Nuclear Engineering and Design. ISSN 00295493.
10. Baccou, et al., “SAPIUM: A Generic Framework for a Practical and Transparent Quantification of Thermal-Hydraulic Code Model Input Uncertainty”. Nucl. Sci. Eng. 194, 721–736. 2020.
11. Ghione, A., et al. “Application of SAPIUM guidelines to Input Uncertainty Quantification: the ATRIUM project”, in: ANS(Ed.), NURETH-20. Washington DC, USA. 2023.
12. H. Glaeser, “GRS Method for Uncertainty and Sensitivity Evaluation of Code Results and Applications”, Science and Technology of Nuclear Installations, 2008 (2008), pp. 1-7.
13. J.L. Munoz-Cobo, A. Escrivá, R. Mendizabal, F. Pelayo, J. Melara. “CSAU methodology and results for an ATWS event in a BWR using information theory methods.” Nuclear Engineering and Design 278 (2014) 445–464. http://dx.doi.org/10.1016/j.nucengdes.2014.07.036.
14. Duran-Vinuesa, L., Cuervo, D., 2021. “Uncertainty quantification and propagation with probability boxes”. Nuclear Engineering and Technology 53, 2523–2533.
15. Castro E., Ahnert C., Buss O., García-Herranz N., Hoefer A., Porsch D., “Improving PWR core simulations by Monte Carlo uncertainty analysis and Bayesian inference”, Annals of Nuclear Energy 95: 148-156, 2016.
16. Castro, E., Cuervo, D., García-Herranz, N. & Avramova, M., 2016. “Thermal-hydraulic uncertainty propagation in a Main Steam Line Breal scenario”. Sun Valley, Idaho, American Nuclear Society.
17. Castro, E., 2018. “Methodologies for sensitivity/uncertainty analysis using reactor core simulators with application to Pressurized Water Reactors”. Madrid: Universidad Politécnica de Madrid.
18. Castro, E., Sánchez-Cervera, S., García-Herranz, N. & Cuervo, D., 2018. “Impact of the homogenization level, nodal or pin-by-pin, on the uncertainty quantification with core simulators”. Progress in Nuclear Energy, Volume 104, pp. 218-228.
19. Bocanegra, R., 2019. “Towards a BEPU Methodology for Containment Safety Analyses”. Universidad Politécnica de Madrid, Madrid, Spain.
20. Freixa, J., Mendizábal, R., Martínez-quiroga, V., Casamor, M., Reventós, F., Sánchez-Perea, M., 2021. “On the validation of BEPU methodologies through the simulation of integral experiments: Application to the PKL test facility”. Nucl. Eng. Des. 379.
21. Freixa, J., Martínez-Quiroga, V., Casamor, M., Reventós, F., Mendizábal, R., 2019. “Validation of a BEPU methodology through a blind benchmark activity at the PKL test facility”, in: 18th International Topical Meeting on Nuclear Reactor Thermal Hydraulics, NURETH 2019.
22. Freixa, J., Martínez-Quiroga, V., Perret, G., 2023. “Assessment of the Choked Flow Model of RELAP5 for the Application of Inverse Quantification Methods”, in: ANS (Ed.), NURETH-20. Washington DC, USA.
23. Freixa, J., Martinez-Quiroga, V., Mendizabal, R., Sanchez-Perea, M., Ramón, F.J., 2022. "Validation of physical model uncertainties derived through the inverse method", in: NURETH19. pp. 1–16.

24. Reventos, F., et al., "BEMUSE Phase IV Report: Simulation of a LB-LOCA in ZION Nuclear Power PLant" NEA/CSNI/R(2008)6/VOL1,VOL2,VOL3.
25. Perez-Ferragut, et al., "Main Results of Phase IV BEMUSE Project: Simulation of a LB-LOCA in an NPP" Science and Technology of Nuclear Installations (2010), Volume 2010, Article ID 219294, doi:10.1155/2010/219294.
26. Reventos, F., "BEMUSE Phase V Report: Uncertainty and Sensitivity Analysis of a LB-LOCA in ZION Nuclear Power PLant" NEA/CSNI/R(2009)13.
27. Perez-Ferragut, M., Martínez-Quiroga, V., Casamor, M., Freixa, J., 2022. "Methodology for phenomenological code assessment with integral test data" Nuclear Engineering and Design 387 (111608).
28. Pericas R.; Ivanov K.; Reventós F.; Batet Ll "Comparison of Best Estimate Plus Uncertainties and Conservative Methodologies for a PWR MSLB Analysis Using Coupled 3D Neutron Kinetics/Thermal-Hydraulic Code" Journal paper. UNCT Nuclear Technology, Pages 193-201 | Received 11 Oct 2016, Accepted 20 Feb 2017, Published online: 04 May 2017
29. Freixa, J., Alfonso, Elsa De, Reventós, F., de Alfonso, E., 2016. "Testing methodologies for quantifying physical model uncertainties. A comparative exercise using CIRCE and IPREM (FFTBM)". Nucl. Eng. Des. 305, 653–665. https://doi.org/10.1016/j.nucengdes.2016.05.037
30. SNL, "State-of-the-Art Reactor Consequence Analyses (SOARCA) Project: Uncertainty Anlaysis Plan Recommended by Sandia Technical Staff", Draft-Document, 2010.
31. USNRC, "State-of-the-Art Reactor Consequence Analyses Project: Uncertainty Anlaysis of the Unmitigated Long-Term Station Blackout of the Peach Bottom Atomic Power Station". NUREG/CR-7155, SAND2012-10702P. 2016.
32. SNL, "An Uncertainty Analysis of the Hydrogen Source Term for a Station Blackout Accident in Sequoyah Using MELCOR 1.8.5". Letter Report SAND2014-2210. 2014.
33. K. Chevalier, et al., "Source term assessment with ASTEC and associated uncertainty analysis using SUNSET tool". Nuclear Engineering and Design 272 (2014) 207-218. 2013.
34. K. Roberts and R. Sanders, "Application of Uncertainty Analysis to MAAP4 analyses for level 2 PRA parameter importance determination". Nuclear Engineering and Technology. Vol. 45 No. 6. Nov. 2013.
35. Ahn, K. I., Mezio, F., Ali, S., Cao, X., Cho, Y. J., Khuwaileh, B., … Jevremovic, T. (2024). Uncertainty and Sensitivity Analyses for Postulated Severe Accidents of Reference PWRs and SMRs in the Frame of the IAEA CRP and Relevant Insights. Nuclear Technology, 1–27. https://doi.org/10.1080/00295450.2024.2422260
36. K.I. Ahn, et al., "Uncertainty and sensitivity analysis of the PWR and SMR by means of Severe Accident codes in the framework of the IAEA CRP I31033". International Conference on Topical Issues in Nuclear Installation Safety: Strengthening Safety of Evolutionary and Innovative Reactor Designs, 18-21 October 2022, Vienna, Austria
37. Herranz, L. E., Beck, S., Sánchez-Espinoza, V. H., Mascari, F., Brumm, S., Coindreau, O., & Paci, S. (2021). The EC MUSA Project on Management and Uncertainty of Severe Accidents: Main Pillars and Status. Energies, 14(15), 4473. https://doi.org/10.3390/en14154473
38. S. Brumm, F. Gabrielli, V. Sanchez-Espinoza, A. Stakhanova, M. Nudi, P. Groudev, P. Ou, L.E. Herranz, Uncertainty quantification for severe-accident reactor modelling: Set-up and first results of the Horizon-2020 project MUSA, Annals of Nuclear Energy, Volume 191, 2023, 109919, ISSN 0306-4549, https://doi.org/10.1016/j.anucene.2023.109919.
39. F. Mascari, et al., Main outcomes of the Phebus FPT1 uncertainty and sensitivity analysis in the EU-MUSA project, Annals of Nuclear Energy, Volume 196, 2024, 110205, ISSN 0306-4549, https://doi.org/10.1016/j.anucene.2023.110205.
40. S. Brumm, et al., Uncertainty quantification for severe-accident reactor modelling: Results and conclusions of the MUSA reactor applications work package, Annals of Nuclear Energy, Volume 211, 2025, 110962, ISSN 0306-4549, https://doi.org/10.1016/j.anucene.2024.110962.

41. Herranz, L. E., Beck, S., Sánchez-Espinoza, V. H., Mascari, F., Brumm, S., Coindreau, O., & Paci, S. (2025). Major Achievements of the EC MUSA Project. Nuclear Technology, 1–11. https://doi.org/10.1080/00295450.2024.2444081
42. Herranz, L., Gabrielli, F., Tiborcz, L., Mascari, F., Groudev, P., Pavel, G., & Paci, S. (2025). UaSA Application in Severe Accident Analysis: Challenges and Path Forward. Nuclear Technology, 211(12), 2903–2910. https://doi.org/10.1080/00295450.2025.2511536
43. Martinez-Quiroga, et al. (1/5), "Assessment of an SBO Fukushima likewise scenario for an iPWR design with RELAP5mod33 and RELAP/SCDAPSIMMOD3.5 codes", NURETH-19, 2022.
44. O. Coindreau, et al., "Uncertainty quantification for a severe accident sequence in a SFP in the frame of the H-2020 project MUSA: First outcomes". Annals of Nuclear Energy. Volume 188, March 2023.
45. A. Wald, "An extension of Wilks' method for setting tolerance limits". The Annals of Mathematical Statistics. Volume 14, 1943.
46. V. Martinez-Quiroga, M. Perez-Ferragut, 2025. "Enso contribution to the HORIZON 2020 MUSA project: In-Vessel Uncertainty Analysis with RELAP/SCDAPSIM/MOD3.4 and IUA2.0 of a long-term SBO scenario in a Gen-II PWR", in: NURETH-21, under review. 2025.
47. Mendizabal, R. "Contribución al estudio de las metodologías de cálculo realista con incertidumbre ("BEPU"), dentro del análisis determinista de seguridad de plantas nucleares" Dissertation presented at the Universidad Politécnica de Madrid (2016)
48. US NRC. Indian Point Unit 3 Updated Final Safety Analysis Report (UFSAR). 2011.

Stepwise **U**ncertainty **A**nalysis **M**ethodology in a PWR SBO and Its Impact on Source Term Analysis

Rafael Bocanegra

Víctor Martínez Quiroga

Marina Pérez Ferragut

Outline

- Introduction
- Stepwise Uncertainty Analysis Method
- In-Vessel Phase Calculation
- Ex-Vessel Phase Calculation
- Main Remarks
- Future Works

Introduction

Recent international initiatives related to Uncertainty Analysis:

- TH ➔ BEMUSE, PREMIUM, SAPIUM, ATRIUM
- SA ➔ MUSA, IAEA-CRP I31033

Observations made when using integral SA models:

- Computationally intensive
- Many input param. variations ➔ calculation instabilities
- Scenario bifurcations and/or cliff-edge effects

Objective:

- Develop a method to deal with (or avoid) the above-mentioned points

Stepwise Uncertainty Analysis Method (SUAM)

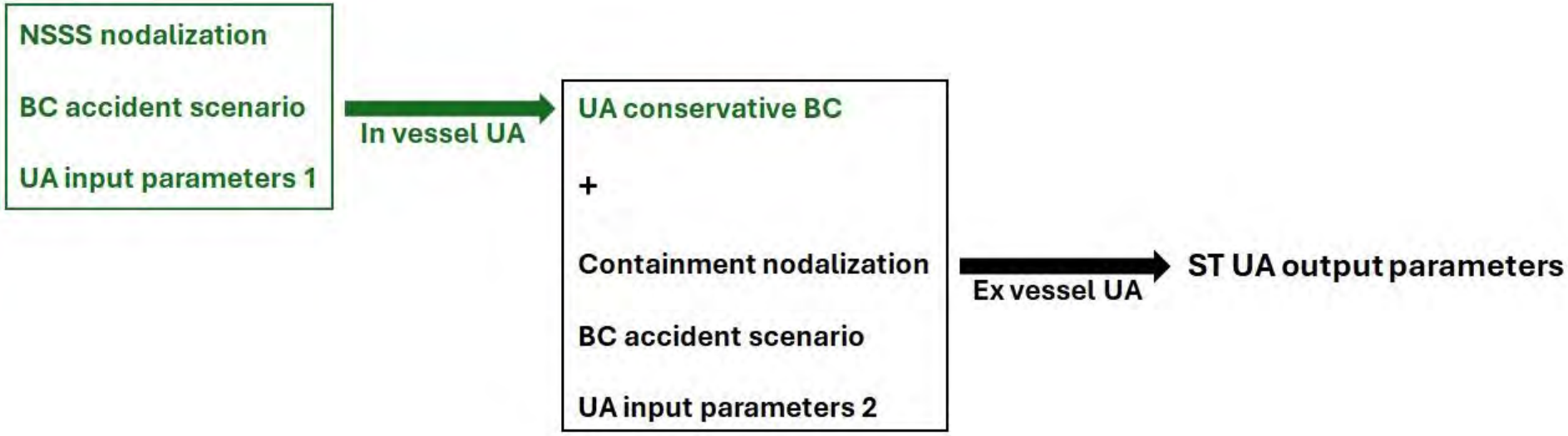

- **In-** and **Ex-**vessel phases computed separately
- Lesser input param. variations ➔ calculations more stable
- Increased control over the identification bifurcations and/or cliff-edge effects

In-vessel Phase Analysis

- NPP design: **Generic 4-Loop PWR**
- Code: **RELAP/SCADPSIM mod3.4**
- Scenario: **SBO with no mitigation**
- Systems available: **ACCs & RPV PORVs**
- Duration: **until RPV creep rupture**
- Number of simulations: **208** ➔ 6º order Wald (one-sided)

In-vessel Phase Analysis

Figures Of Merit ➔ Input for the containment evaluation model

- H_2 from core
- FP released
- FP decay heat
- Debris ejected
- Debris heat
- Coolant M&E released

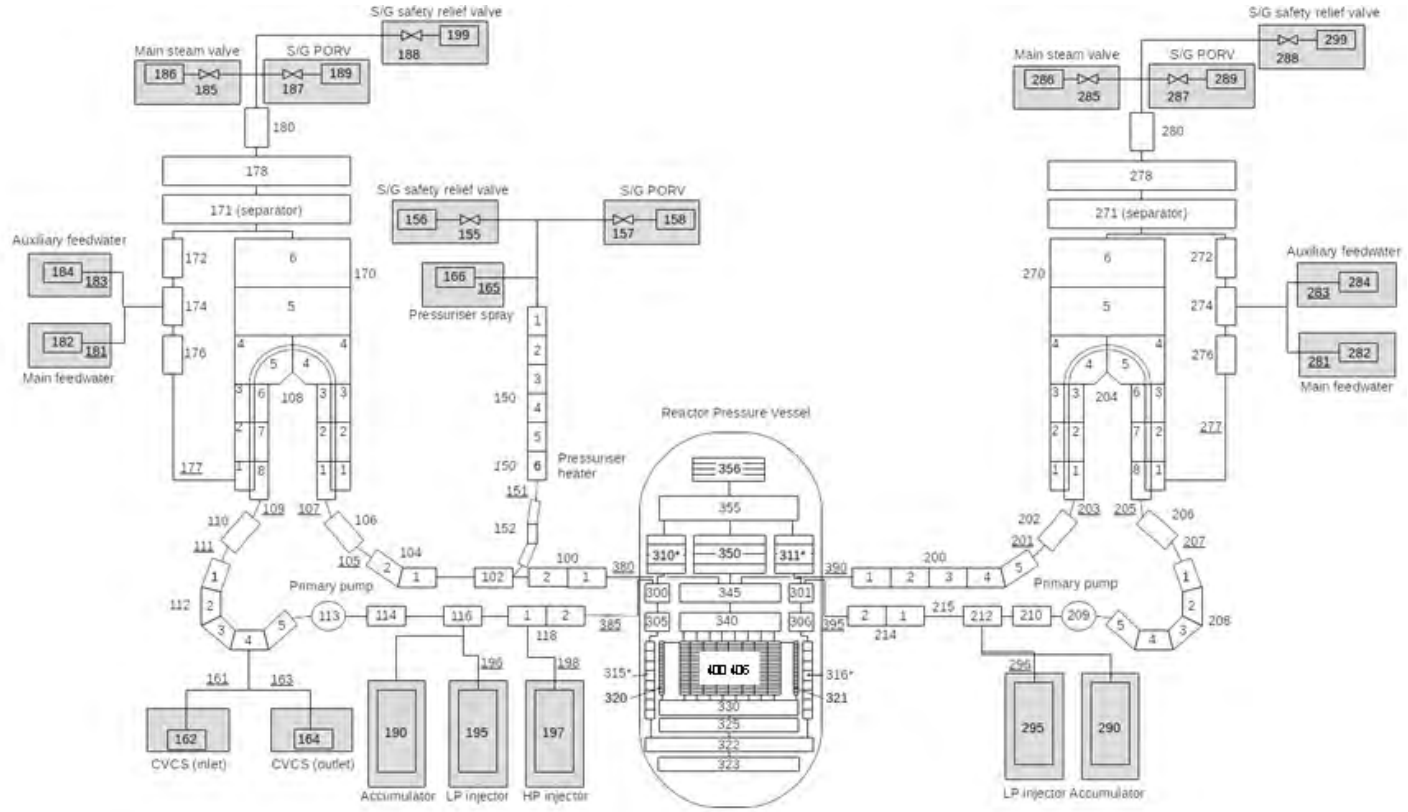

12th CONFERENCE ON SEVERE ACCIDENTS RESEARCH May 18-22, 2026 - Madrid, Spain ERMSAR 2026

In-vessel Phase Analysis

Figures of Merit ➔ Input for the containment evaluation model

- Coolant M&E released to the containment

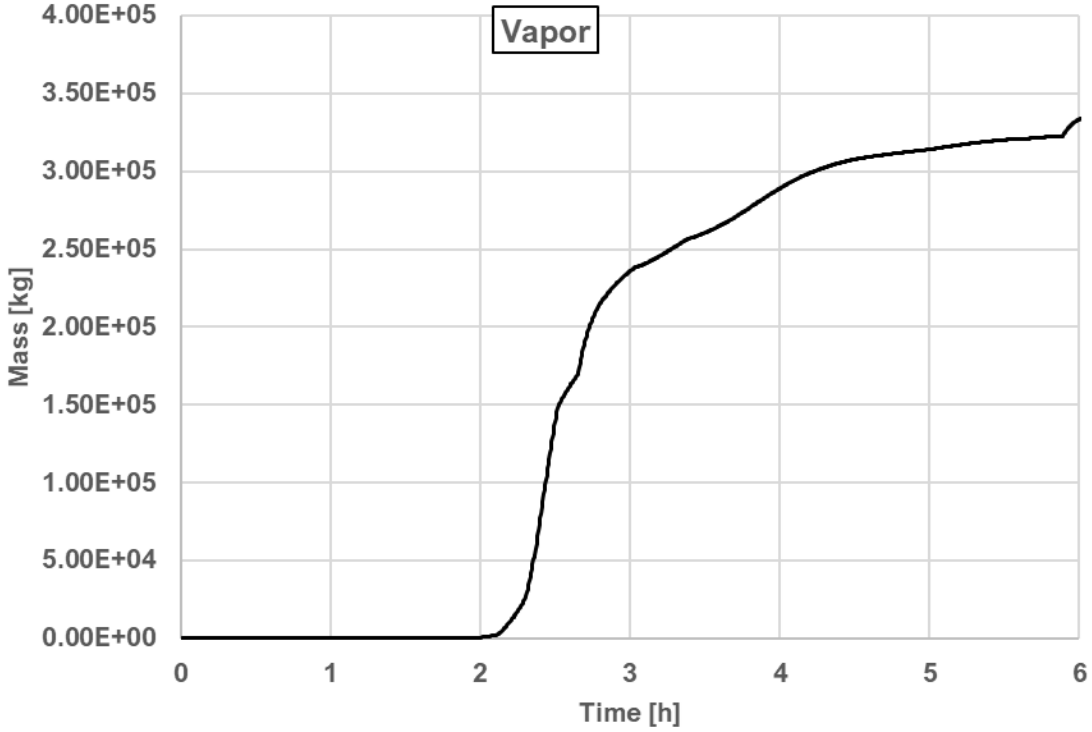

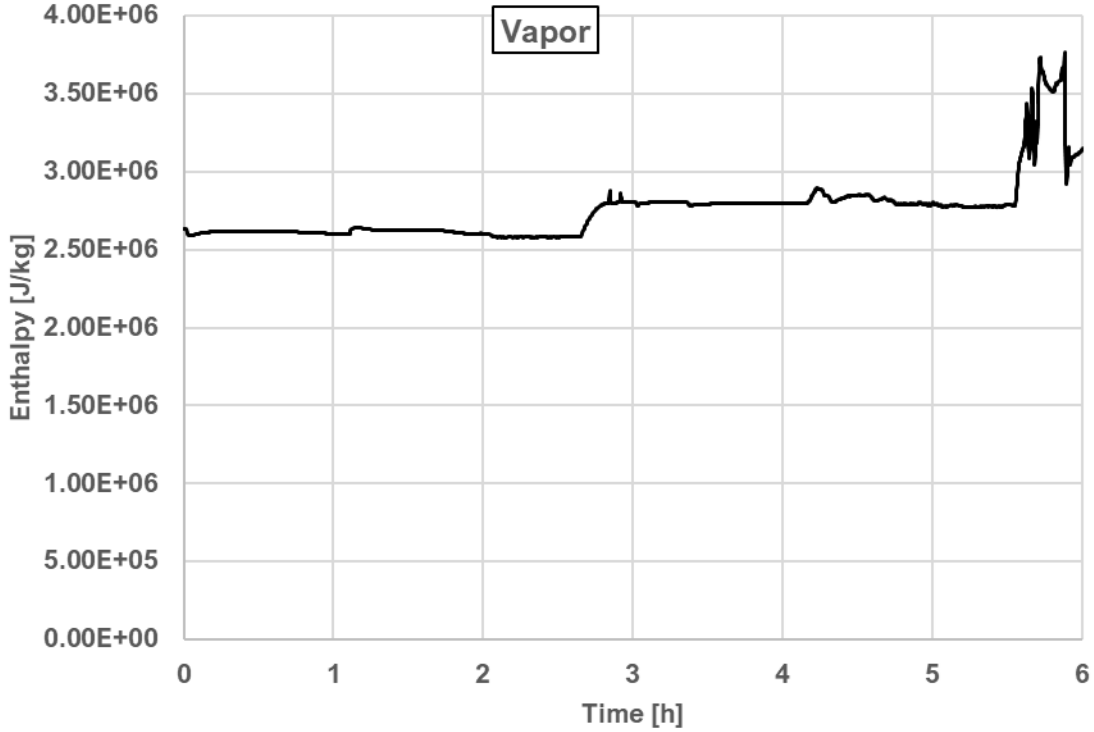

12th CONFERENCE ON SEVERE ACCIDENTS RESEARCH
May 18-22, 2026 - Madrid, Spain
ERMSAR 2026

In-vessel Phase Analysis

Figures of Merit ➔ Input for the containment evaluation model

- Fission Product and H_2 released to containment

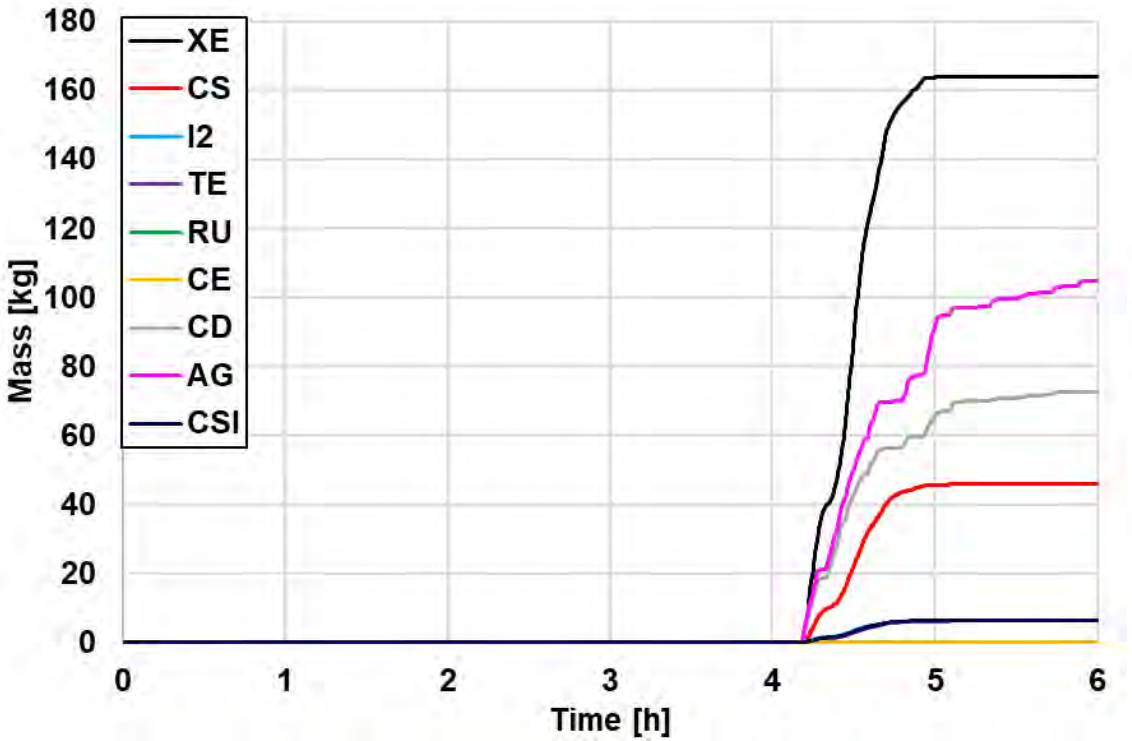

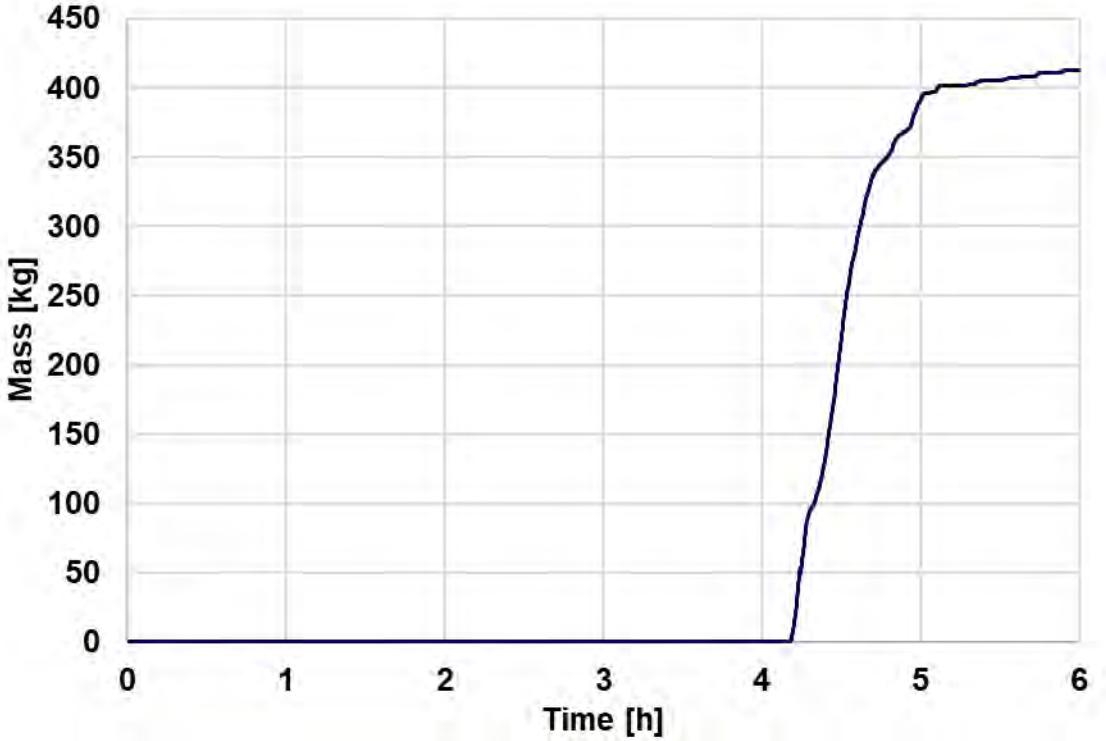

12th CONFERENCE ON SEVERE ACCIDENTS RESEARCH May 18-22, 2026 - Madrid, Spain ERMSAR 2026

In-vessel Phase Analysis

Figures of Merit ➔ Input for the containment evaluation model

- Debris M&E released to the reactor cavity

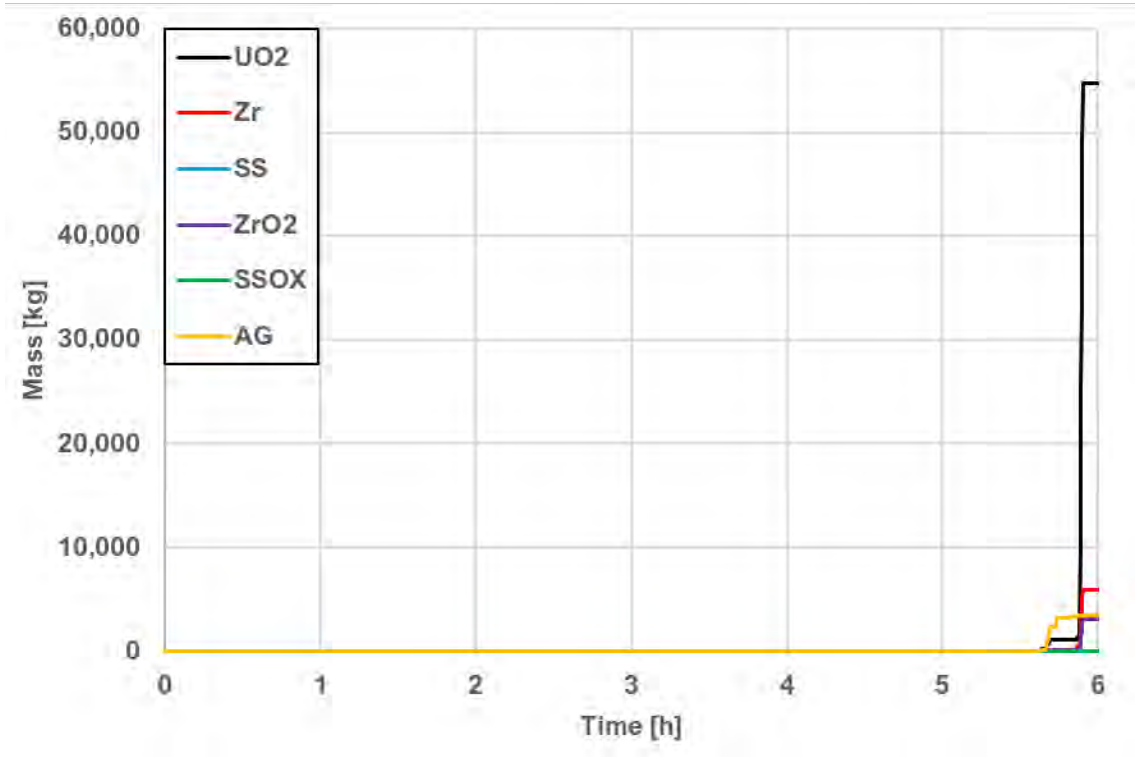

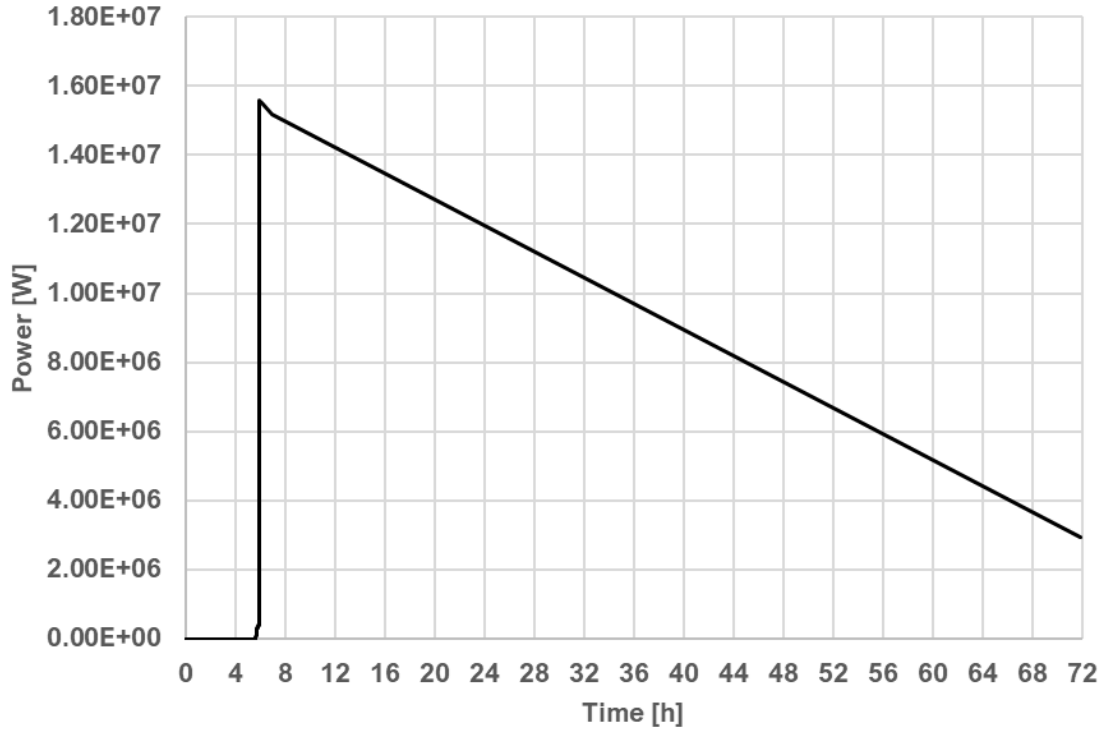

12th CONFERENCE ON SEVERE ACCIDENTS RESEARCH May 18-22, 2026 - Madrid, Spain ERMSAR 2026

Ex-vessel Phase Analysis

- NPP design: **Generic 4-Loop PWR**
- Code: **MELCOR 2.2 R2024**
- Scenario: **SBO with no mitigation**
- Systems available: **none**
- Duration: **72 hours**
- Number of cases: **1 (Base Case) + 93 (Preliminary UQ analysis)**

Ex-vessel Phase Analysis

- Nodes: **17 CVs**
- Flow paths: **27 FLs**
- Heat Structures : **49 HSs**
- Packages: **CVH, RN, CAV, FDI**
- Failure modes:
  - Containment Leak: **Pressure > 3.5 bar**
  - Overpressure Failure: **Pressure > 8.0 bar**

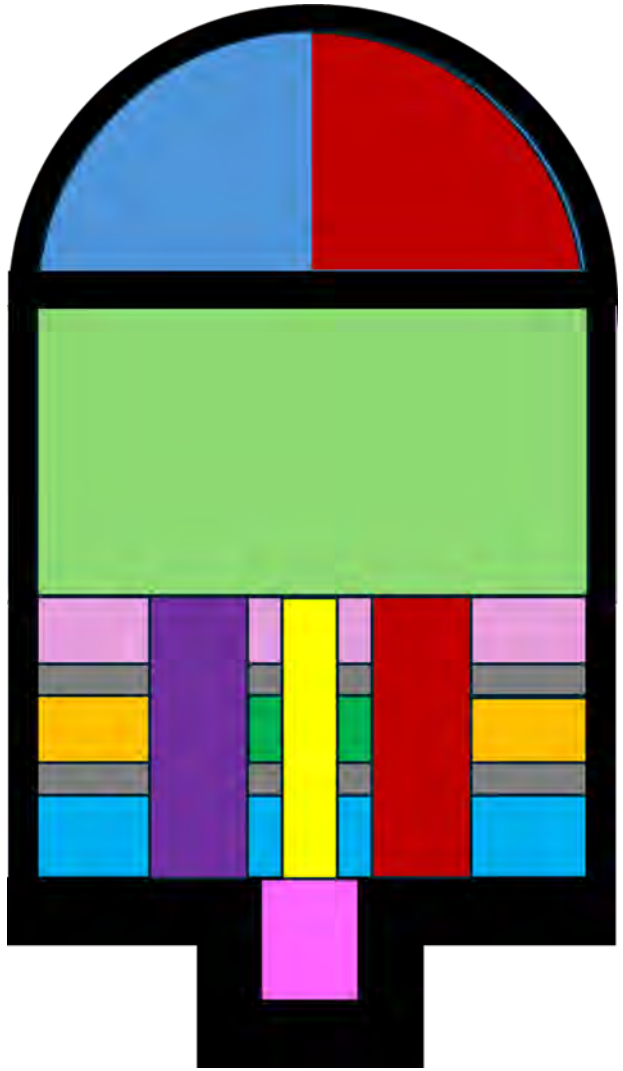

Ex-vessel Phase Analysis

- Nodes: **17 CVs**
- Flow paths: **27 FLs**
- Heat Structures : **49 HSs**
- Packages: **CVH, RN, CAV, FDI**
- **Figures of Merit**:
  - **Containment Pressure**
  - **Containment Temperature**
  - **FP released to environment**

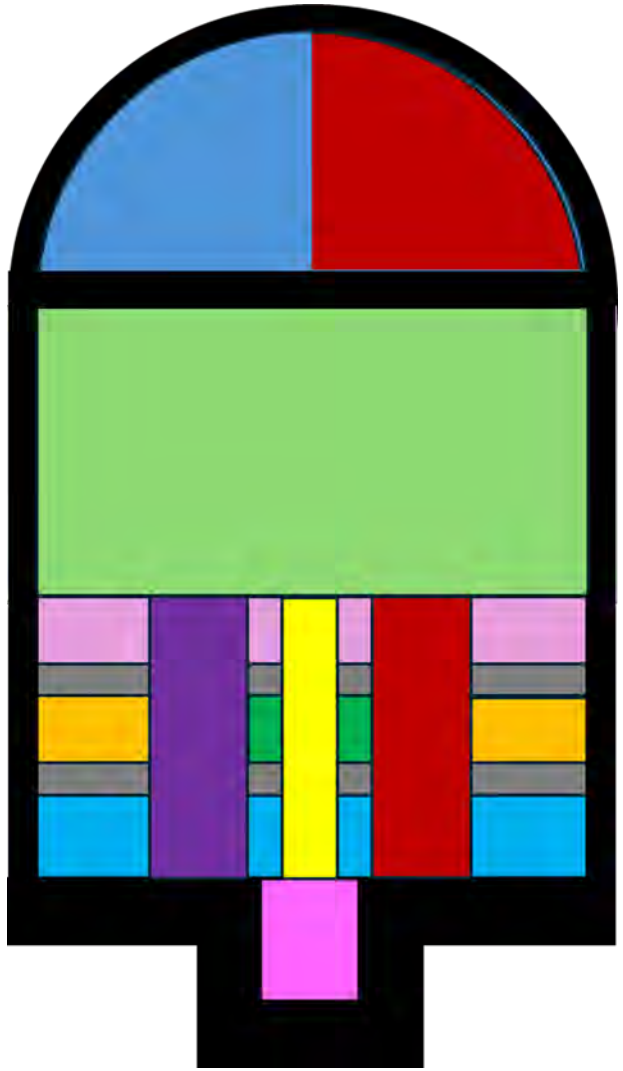

Ex-vessel Phase Analysis

- Containment Pressure and Vap. Phase Temp. (**Base Case**)

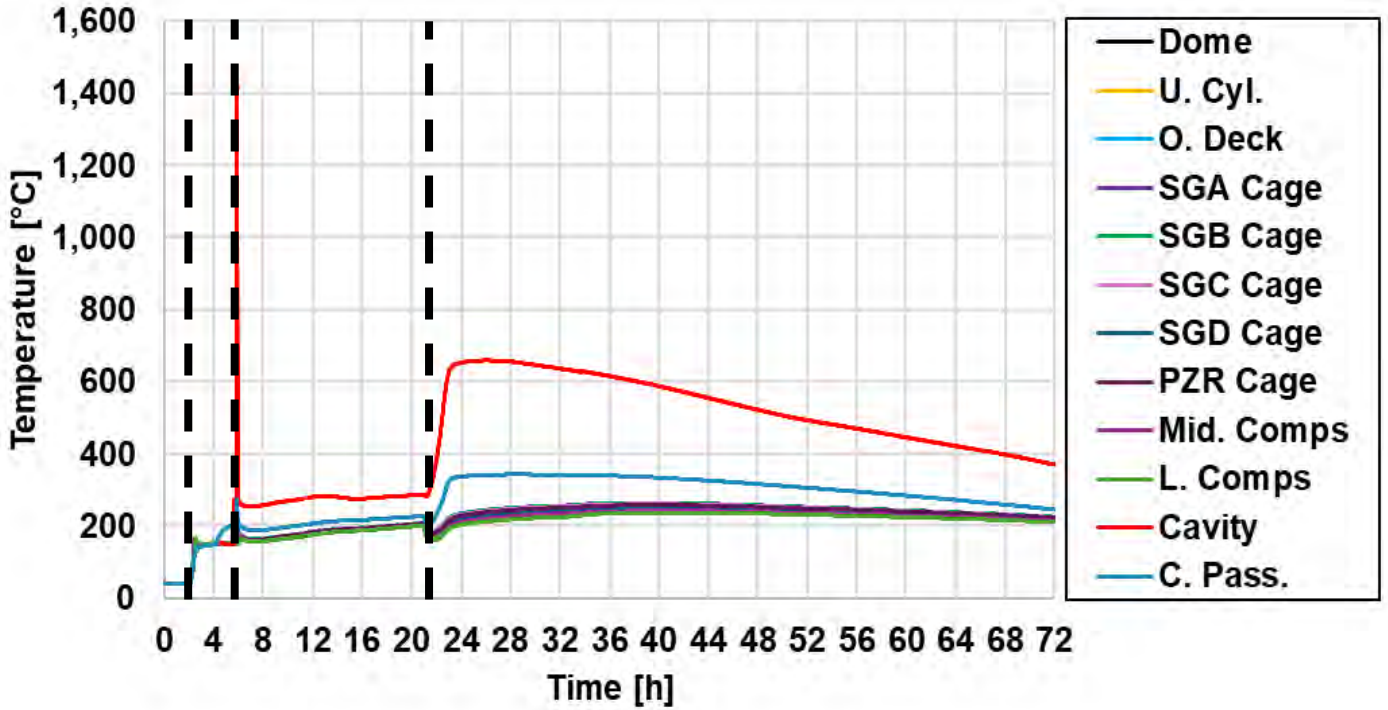

12th CONFERENCE ON SEVERE ACCIDENTS RESEARCH
May 18-22, 2026 - Madrid, Spain
ERMSAR 2026

Ex-vessel Phase Analysis

- Cyl. Surf. Temperature and Vap. Phase Temp. (**Base Case**)

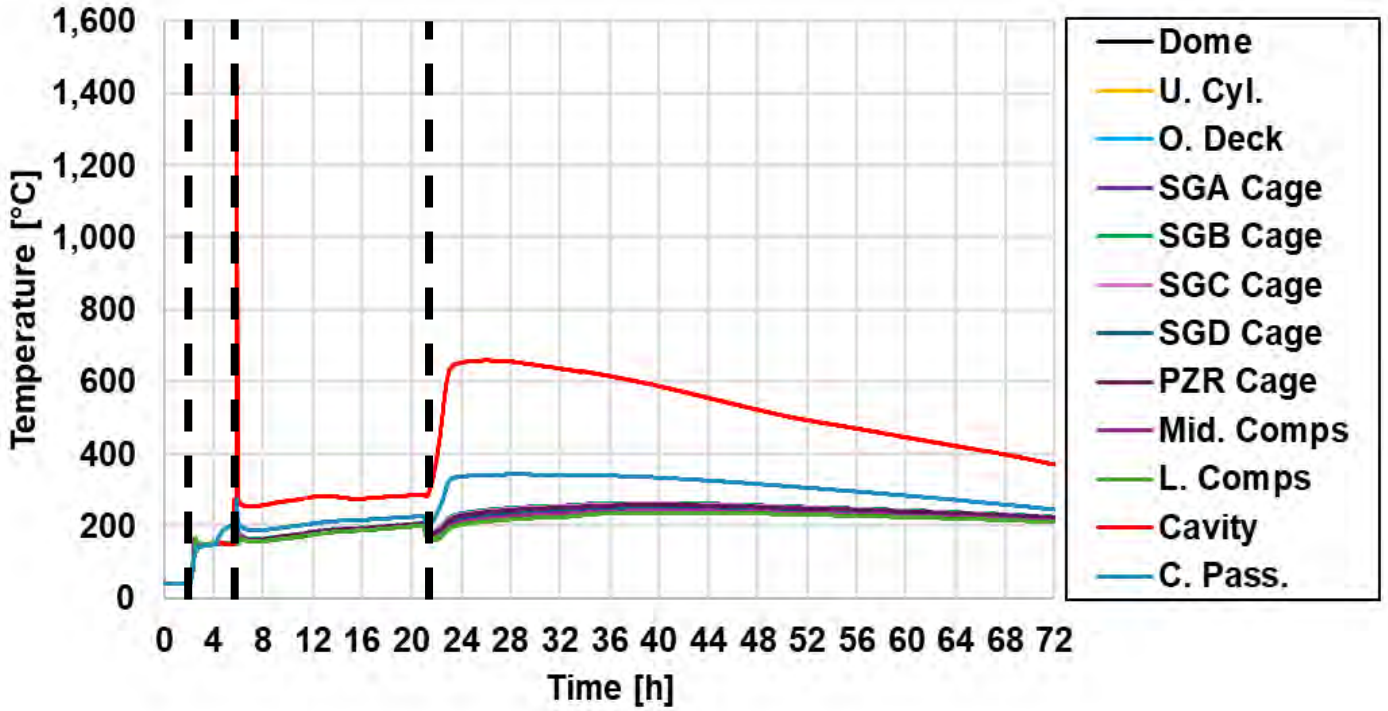

12th CONFERENCE ON SEVERE ACCIDENTS RESEARCH
May 18-22, 2026 - Madrid, Spain
ERMSAR 2026

Ex-vessel Phase Analysis

- Ex-vessel hydrogen and cavity ablation (**Base Case**)

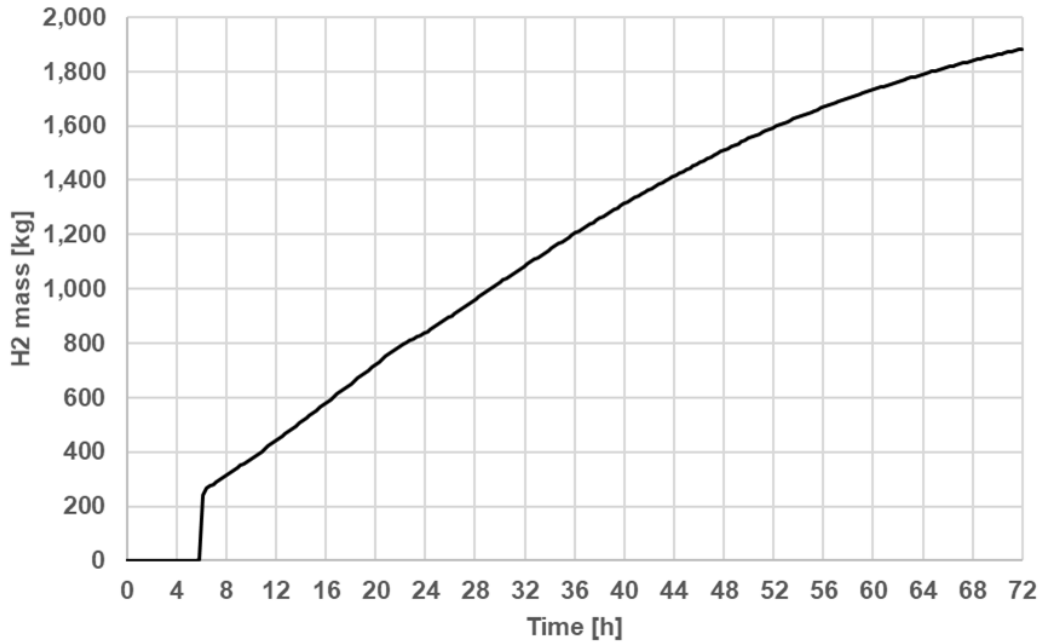

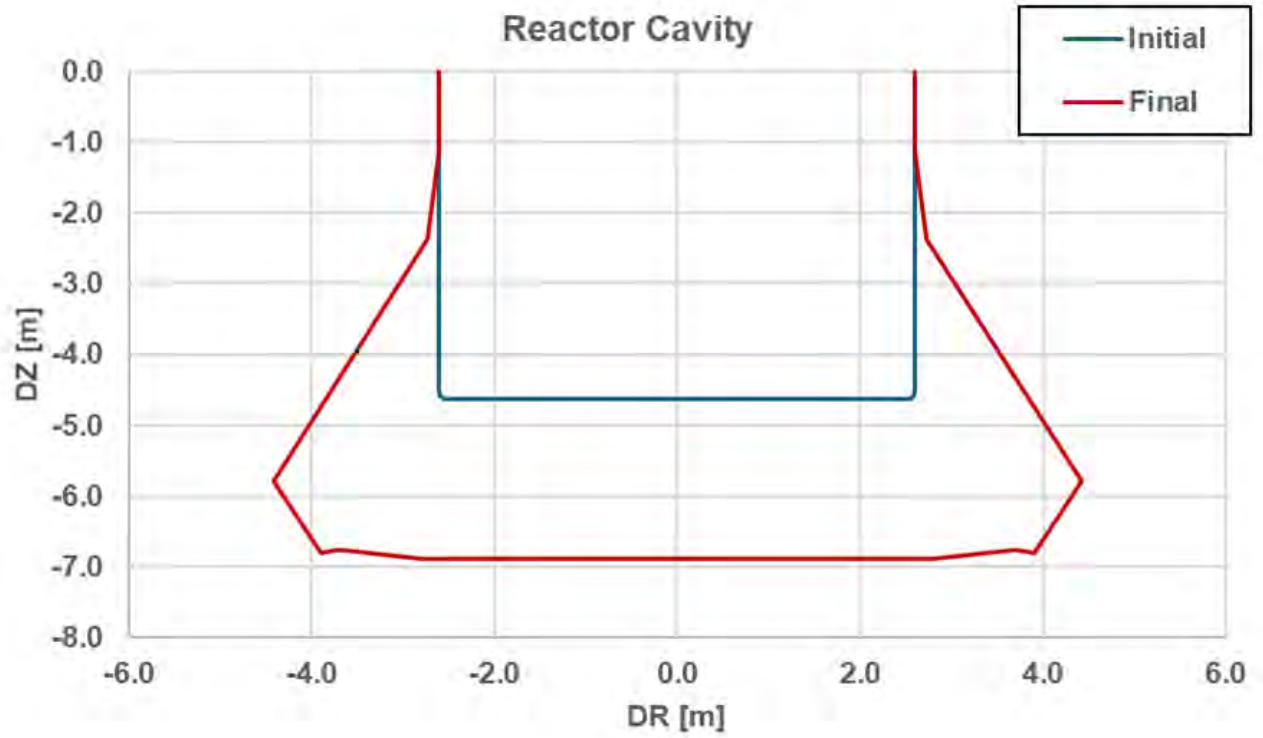

12th CONFERENCE ON SEVERE ACCIDENTS RESEARCH
May 18-22, 2026 - Madrid, Spain
ERMSAR 2026

Ex-vessel Phase Analysis

- FP relative concentration (**BASE CASE**)

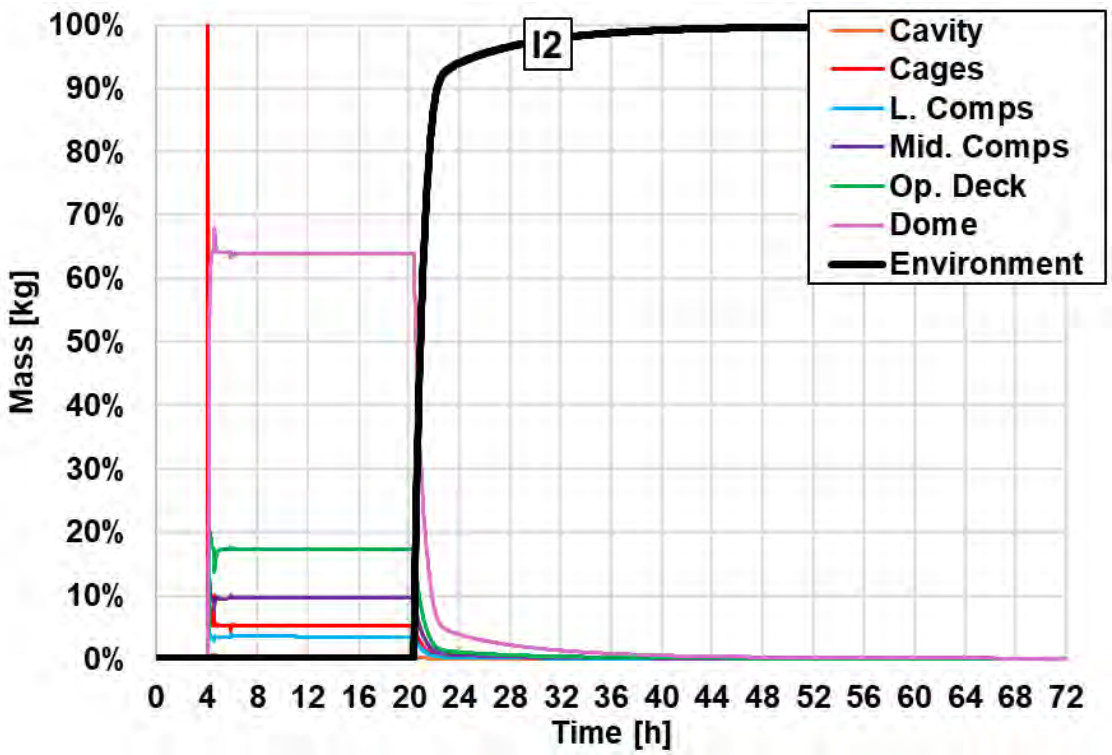

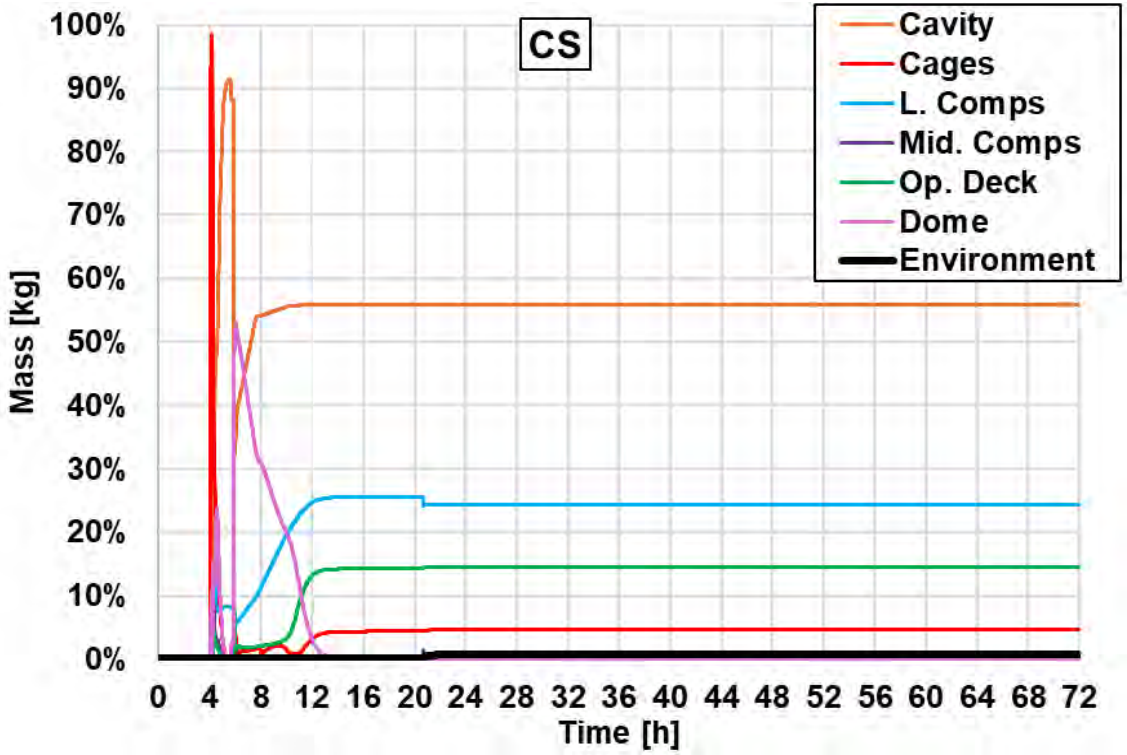

12th CONFERENCE ON SEVERE ACCIDENTS RESEARCH May 18-22, 2026 - Madrid, Spain ERMSAR 2026

UQ – Preliminary Analysis

- Nodes: **17 CVs**
- Flow paths: **27 FLs**
- Heat Structures : **49 HSs**
- Packages: **CVH, RN, CAV, FDI**
- Cases: **93 (Wilks 2-sided TLs)**
- **Figures of Merit**:
  - **Containment Pressure**
  - **Containment Temperature**
  - **FP released to environment**

№	Parameter	Type	PDF	PDF parameters
1	RN_chi	Scalar	Beta	α:1.0 β:5.0 (1.0, 5.0)
2	RN_fslip	Scalar	Beta	α:4.0 β:4.0 (1.141, 1.277)
3	RN_ftherm	Scalar	Triangular	a:1.0 m:2.18 b:3.0
4	RN_gamma	Scalar	Uniform	a:1.0 b:3.0
5	RN_stick	Scalar	Beta	α:2.5 β:1.0 (0.2, 1.0)
6	RN_turbds	Scalar	Uniform	a:0.0 b:0.03
7	RN_tkgop	Scalar	Triangular	a:0.05 m:0.5 b:1.0
8	RN_deldif	Scalar	Uniform	a:1.0E-5 b:8.0E-3
9	FAIL_opA	Factor	Triangular	a:0.1 m:1.0 b:10.0
10	FAIL_mult_leakA	Factor	Triangular	a:0.1 m:1.0 b:10.0
11	FAIL_op_press	Scalar	Triangular	a:7.58E5 m:9.24E5 b:1.2E6
12	CAV_conc_rho	Factor	Uniform	a:0.95 b:1.02
13	CAV_Conc_STemp	Factor	Uniform	a:0.9 b:1.0
14	CAV_Conc_LTemp	Factor	Uniform	a:0.9 b:1.0
15	CAV_Conc_ATemp	Factor	Uniform	a:0.9 b:1.0
16	CAV_Ox_Emiss	Scalar	Uniform	a:0.5 b:1.0
17	CAV_Met_Emiss	Scalar	Uniform	a:0.5 b:1.0
18	CAV_Surr_Emiss	Scalar	Uniform	a:0.5 b:1.0
19	CAV_B_HTC	Factor	Uniform	a:0.97 b:1.03
20	CAV_R_HTC	Factor	Uniform	a:0.97 b:1.03
21	CAV_Ox_K	Factor	Uniform	a:0.97 b:1.03
22	CAV_Met_K	Factor	Uniform	a:0.97 b:1.03
23	HS_Conv_Lam	Scalar	Uniform	a:0.45 b:2.6
24	HS_Conv_Turb	Scalar	Uniform	a:0.45 b:2.6
25	INP_H2O_Mass	Factor	Uniform	a:0.95 b:1.05
26	INP_H2_Mass	Factor	Uniform	a:0.95 b:1.05
27	INP_DCH	Factor	Normal	μ:1.0 σ:0.0408 [0.92, 1.08]
28	INP_H2O_Pow	Factor	Normal	μ:1.0 σ:0.0408 [0.92, 1.08]

Ex-vessel Phase Analysis

- Containment Pressure and Temperature (Preliminary **UQ**)

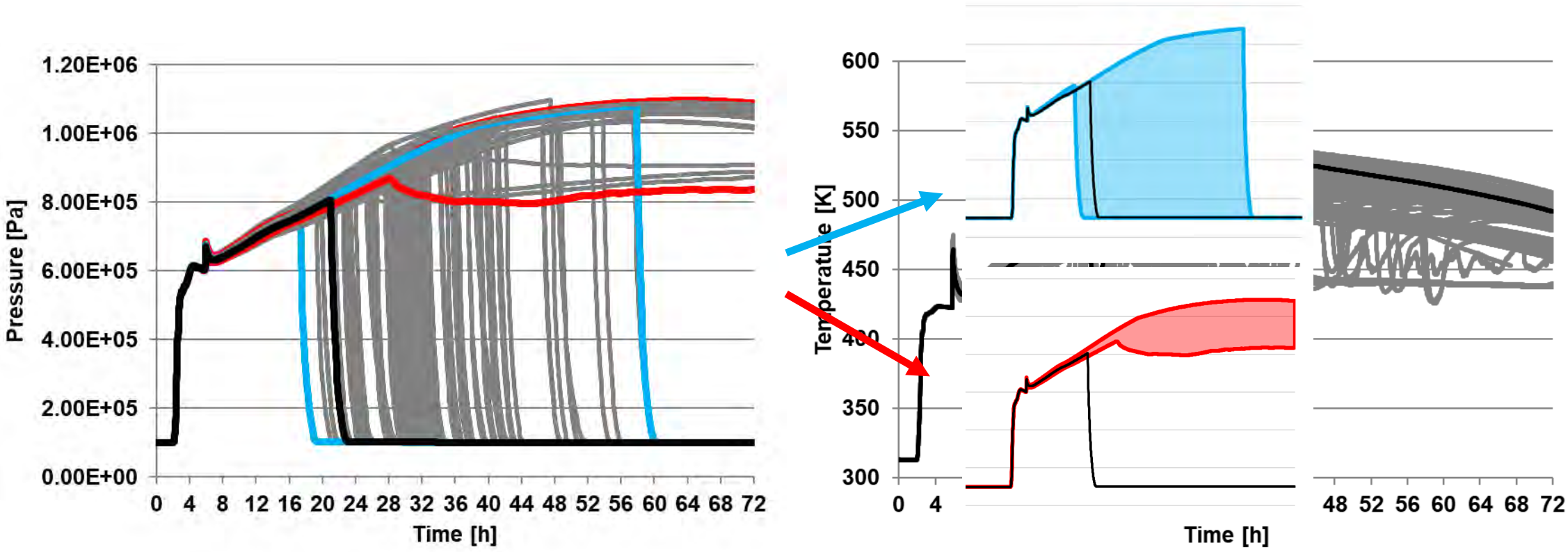

12th CONFERENCE ON SEVERE ACCIDENTS RESEARCH
May 18-22, 2026 - Madrid, Spain
ERMSAR 2026

Ex-vessel Phase Analysis

- Containment Pressure and Temperature (Preliminary **UQ**)

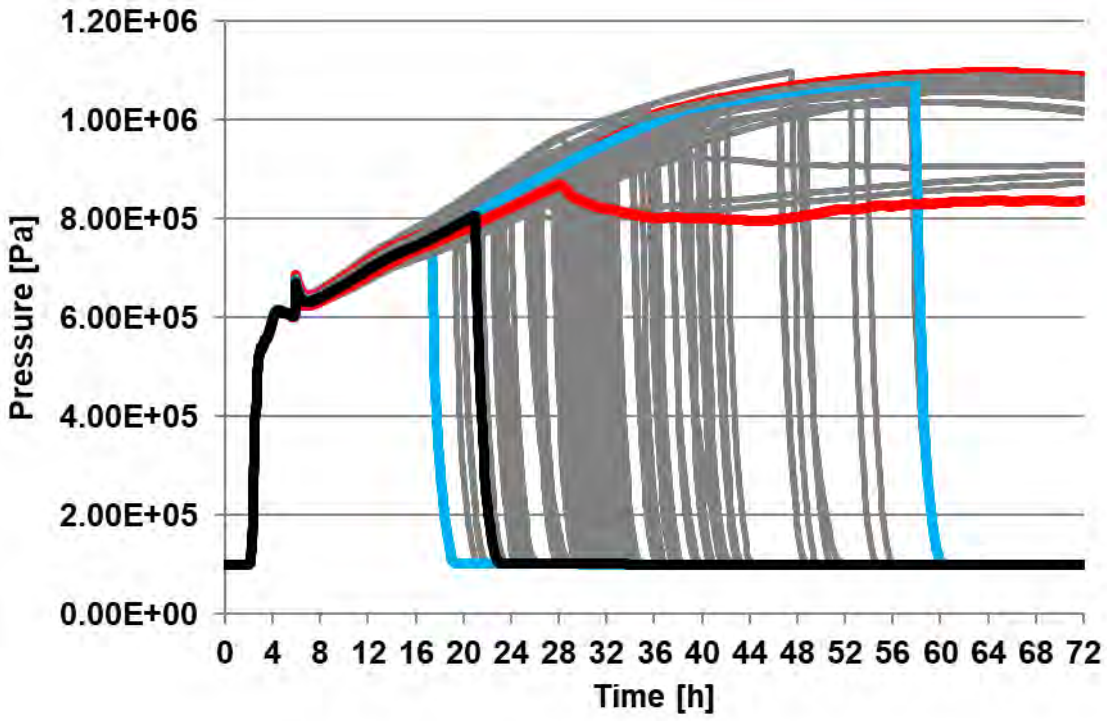

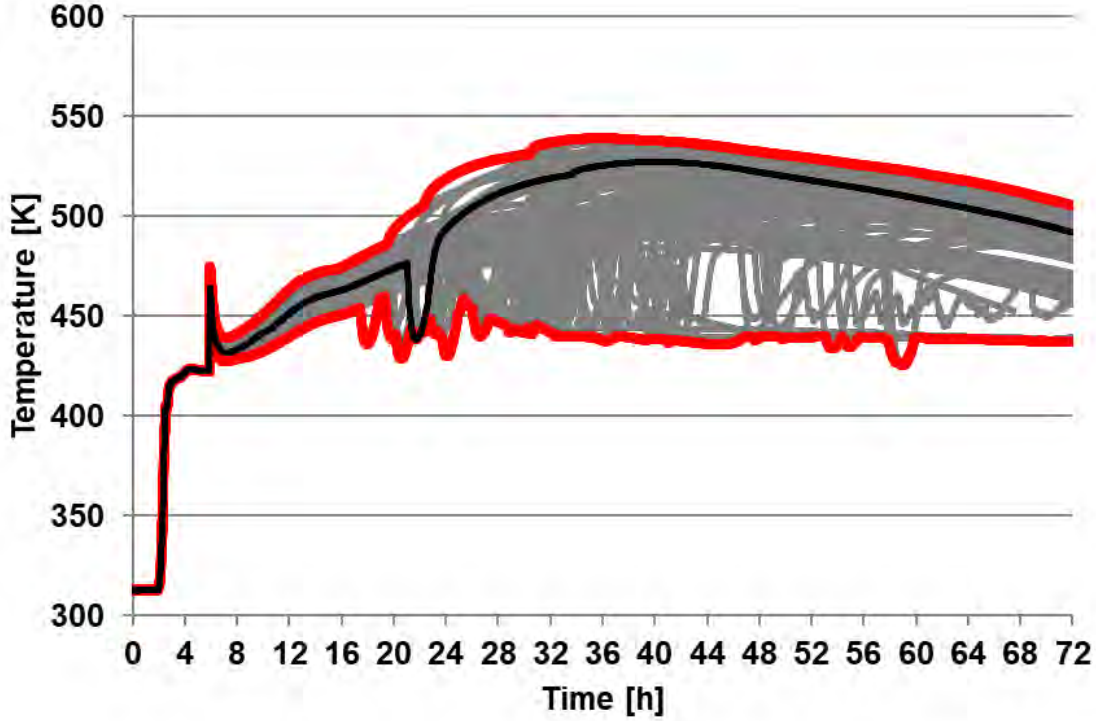

12th CONFERENCE ON SEVERE ACCIDENTS RESEARCH May 18-22, 2026 - Madrid, Spain ERMSAR 2026

Ex-vessel Phase Analysis

- Containment Pressure and Temperature (Preliminary **UQ**)

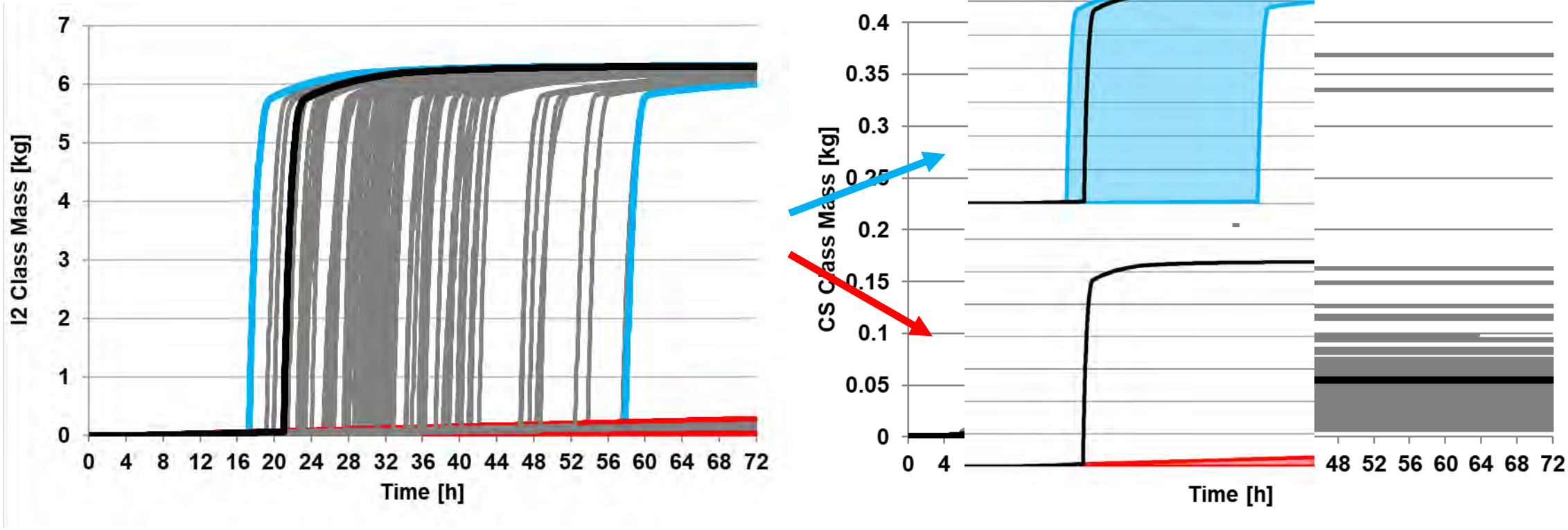

12th CONFERENCE ON SEVERE ACCIDENTS RESEARCH
May 18-22, 2026 - Madrid, Spain
ERMSAR 2026

Ex-vessel Phase Analysis

- Containment Pressure and Temperature (Preliminary **UQ**)

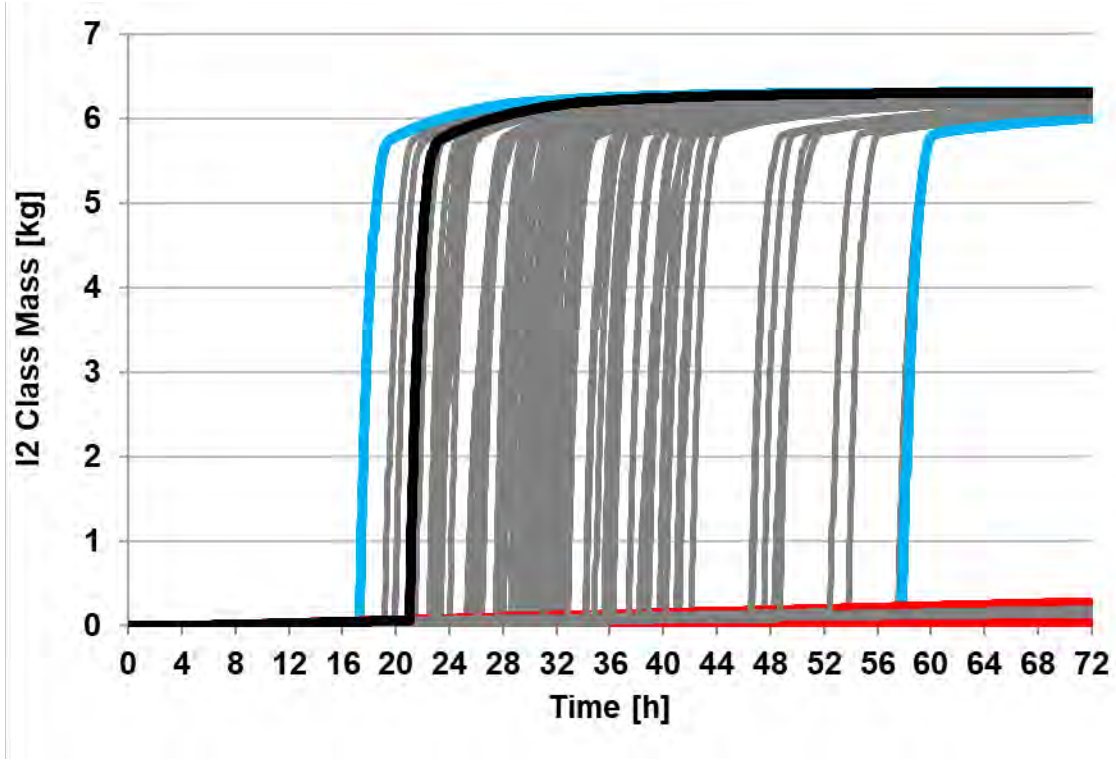

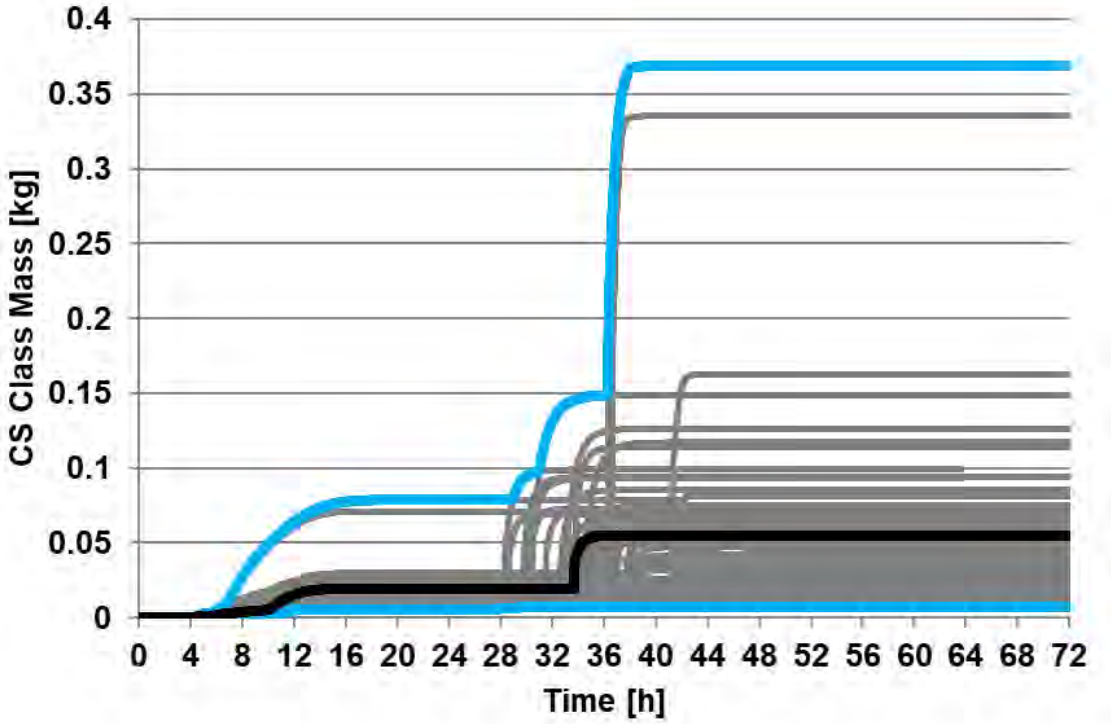

12th CONFERENCE ON SEVERE ACCIDENTS RESEARCH
May 18-22, 2026 - Madrid, Spain
ERMSAR 2026

Main Remarks

Observations made when using integral SA models in UA:

- Computationally intensive
- Many input param. variations ➔ calculation instabilities
- Scenario bifurcations and/or cliff-edge effects

Objective: Develop a method to deal with (or avoid) the above-mentioned points

- **In-** and **Ex-**vessel phases computed separately
- Lesser input param. variations ➔ calculations more stable
- Increased control over the identification bifurcations and/or cliff-edge effects
- Selection of an adequate containment code ➔ e.g. Hydrogen distribution

Main Remarks

In-Vessel Phase Analysis:

- Number of simulations: **208**
- Failed cases: **0**
- Computation time: **~ 32 hours (i7-8700 12 cores)**

Main Remarks

Ex-Vessel Phase Analysis:

- Base case to test the adequacy of coupling NSSS and cont. calculations.
- Reasonable results
- Base Case comp. time (72 hours simulation): **~ 13.68 min (i7-12700H)**
- Preliminary UQ (93 cases): **~ 6.2 hours (i7-12700H 12-cores)**
- Failed cases (< 48 h): **0**
- Failed cases (> 48 h): **6 (6.5%) ➔ Long-term MCCI phase**

Future Works

- Refine the ex-vessel phase evaluation model
  - Check CAV Package configuration ➔ Long-term MCCI calculation
  - Include the containment filtered venting system
- Complete the UQ using the input parameters derived from MUSA project.
- Employ an adequate code for H_2 distribution ➔ e.g. GOTHIC

Acknowledgements

The authors want to acknowledge the technical and financial support granted by the Spanish Nuclear Regulatory Body (CSN)

Thank you for your attention!

The 12th European Review Meeting on Severe Accidents Research

May 18-22, 2026, Universidad Carlos III de Madrid, Madrid, Spain

TECHNICAL SESSION 2.3: IN-VESSEL CORIUM AND DEBRIS COOLABILITY

Chairs: M. E. Cazado (KIT), M. Malicki (PSI)

ID147	**W-STORM sensitivity and uncertainty analysis for In Vessel Retention in integral Pressurized Water Reactors** M. Principato (PSI)	Paper Presentation
ID114	**Experimental Study on the Naturally Stratified Melt Pool Based on High-Temperature Chloride Salts and Mg–Al Alloys** F. Quan (China Nuclear Power Engineering Co., Ltd)	Paper Presentation
ID159	**Stand-alone analysis and evaluation of uncertainties of IVMR in SMR using AC2 code** M. Valincius (LEI)	Paper Presentation

W-STORM SENSITIVITY AND UNCERTAINTY ANALYSIS FOR IN VESSEL RETENTION IN INTEGRAL PRESSURIZED WATER REACTORS

M. Principato*, C. Ciurluini, and F. Giannetti
Sapienza University of Rome, Department of Electrical and Energy Engineering DIEE – Nuclear section
Corso Vittorio Emanuele II, 244, 00186 Rome, Italy
marcello.principato@uniroma1.it ; cristiano.ciurluini@uniroma1.it; fabio.giannetti@uniroma1.it

L. Carénini, F. Fichot
ASNR Autorité de Sûreté Nucléaire et de Radioprotection
Cadarache research centre, 13115 Saint-Paul-Lez-Durance, France
laure.carenini@asnr.fr; florian.fichot@asnr.fr

ABSTRACT

Within the framework of the Euratom project SASPAM-SA Work package 4, a 0D model for In Vessel Melt Retention has been developed by the University of Rome Nuclear Engineering Research Group (NERG) in collaboration with ASNR. The python tool called W-STORM already identified specificities in integral Pressurized Water Reactors (iPWR) with respect to Light Water reactors (LWR), highlighting needed adaptations in the integral Severe Accident (SA) codes models. A validation with respect to MASCA experimental results has been carried out to further strengthen W-STORM prediction of the thermochemical equilibrium established in the two pool scenario considered. Furthermore, a sensitivity and uncertainty analysis has been performed for the two different generic iPWR designs studied in SASPAM-SA project. The uncertainties associated with material properties, corium characteristics in the lower plenum and top boundary condition were selected from the literature and from SASPAM-SA WP2 activities dedicated to integral SA simulations in these designs. To perform the numerous calculations needed for the analysis, the python module Monaco has been used, which focuses on forward uncertainty propagation with basic Monte Carlo sampling. This analysis allows to cover a large scope of configurations for the study of In Vessel Retention. It also further quantifies the need for modelling improvements. The consideration of steady state configurations only is not sufficient when stratification inversion occurs and associated probability of forming a heavy metal layer is evaluated to be greater than 50% in both reactor designs. In addition, steady state configurations with light metal layer leading to significantly higher heat fluxes and vessel ablation, compared to the reference case were identified (average heat flux multiplied by a factor 2.7-2.8). Analysis performed showed that such configurations are due to the use of a simplified model for the radiative heat transfer at the top of the corium associated with high uncertainties. This highlights the benefits of improving radiation heat transfer models at the top of the pool, particularly for iPWR applications, where residual power losses due to radiation heat transfer play a major role, which is not the case for high-power PWRs.

KEYWORDS
SASPAM-SA, W-STORM, In Vessel Retention, Severe Accident, Steady-state analysis.

1 INTRODUCTION

In recent years, an increasing interest in studying Small Modular Reactors (SMR) has sparked throughout the nuclear community. Indeed, their deployment would tackle important aspects such as decarbonization, resilient electricity systems, and post-Fukushima regulatory expectations on accident prevention and mitigation [1]. In this framework, the paper is addressed towards integral Pressurized Water Reactors (iPWR), the type of SMRs which are the most easily deployable due to the know-how inherited from reactors of previous generations. In this context, a Horizon Euratom funded project, named SASPAM- SA, aims to investigate the applicability and transferability of the large operating experience associated with Light Water Reactors (LWR) to the near-term deployment of iPWRs, in view of Severe Accident (SA) and Emergency Planning Zone and European licensing needs. More information about the project can be found in [2].

Regarding iPWR, many of the numerous available reactor designs employ In Vessel Melt Retention (IVMR) as their mitigation strategy in case of SA [3][4][5][6]. This is a further common design feature that iPWRs share with some LWRs, such as the AP1000 [7] and HPR1000 [8]. The IVMR strategy aim is to retain corium in the Reactor Pressure Vessel (RPV), thanks to external vessel cooling. In most papers in literature, corium stratification is supposed to be a two-layered structure, with molten oxidic materials at the bottom, and molten metallic materials on top of it. This approach is indeed possible, but a three-layered configuration (light metal on top, oxidic pool in the middle, heavy metal at the bottom), also has been deemed possible by experimental data [9][10]. This configuration is characterized by transient behavior [11], and its imposed heat flux to the vessel might be even higher [10][12]. To preliminarily characterize IVMR in iPWRs, in the framework of SASPAM-SA, a Water cooled Small modular reacTors 0D in-vessel melt Retention Model (W-STORM) has been developed at the University of Rome, in collaboration with ASNR. The model's main purpose was to identify specificities in IVMR modelling in these reactors, to furnish partners with a tool that could give the magnitude of expected results and to be used as a teaching tool. W-STORM does not employ new heat transfer models with respect to other 0D models in the literature, but implements a thermochemical module, which was a valuable addition in terms of representativeness. Also, the model has been developed to be adaptable to many iPWR designs, with a flexible structure that can adapt to different iPWRs and their specific features (i.e. low volume of fuel and low volume of molten steel with respect to the lower plenum). In previous analyses [13], the model highlighted key features of iPWRs in IVMR, and suggested model improvements or implementation in current Severe Accident (SA) codes. Indeed, the code highlights that a larger quota of power from the oxide is transferred to the metal pool, due to the low aspect ratio of the former. Also, a thick oxide crust is registered (often neglected in LWRs, since its thickness is of some millimeters), and the occurrence of very thin metal layers is shown, leading to high radiation losses, whose models need to be refined in SA codes due to their impact. Also, it has been preliminarily evaluated that the occurrence of a metallic phase heavier than the oxide leading to stratification inversion would appear in iPWRs (mainly due to a small value of mass of steel with respect to the fuel mass). It could be even possible to have mixed pools, a situation for which there is no heat transfer model in literature. Some of the model issues mentioned above are being addressed in SASPAM-SA.

In this paper, a W-STORM validation for the thermochemical model is performed, together with a sensitivity and uncertainty analysis, with the Python tool Monaco [14]. Parameters' distributions and uncertainties come from literature, from SASPAM-SA data, or from engineering judgement. The main aim of this work is to further strengthen the conclusions from [13], supporting them with a broader set of input data. The paper starts with a brief description of W-STORM and its validation against MASCA experiments and a code benchmark on material properties. Then the sensitivity and uncertainty analysis framework is described, starting with a brief description of the Python package Monaco. A complete description of the

input distributions used in the calculations is provided, and the results, for three calculations applied to the two SASPAM-SA iPWR generic designs, are outlined.

2 W-STORM DESCRIPTION

In case of SA, core degradation can lead to relocation of RPV internals in the Lower Plenum (LP). Such events, in the absence of water reflooding, should lead to complete melting of the relocated material [15]. Since no deterministic models for Corium progress in the LP are yet available, in the early 2000s [16] the problem was addressed with conservative plausible scenarios. The developed Python tool represents indeed a steady state configuration of corium in the LP. A simple schematic of the configuration is displayed in Figure 1. Molten core materials (i.e. ZrO_2, UO_2, Stainless Steel (SS), Zr, U) are repartitioned in two pools, one made of oxides, and one made of metals. Fission products are neglected in this model, and decay heat is estimated based on the repartition of uranium content in the two pools. W-STORM employs three main models in its architecture: thermochemical, geometrical and heat transfer. For the first one, the model from [17] has been employed, whose results are discussed in the next section. The geometrical model is described in [13], and consists in the geometrical evaluation of molten pools' heights and surfaces, starting from the molten masses of their constituents. Regarding heat transfer, W-STORM's model is derived starting from the indications in [16], but employs spherical coordinates for the conduction problem and includes additional features, as widely discussed in [13].

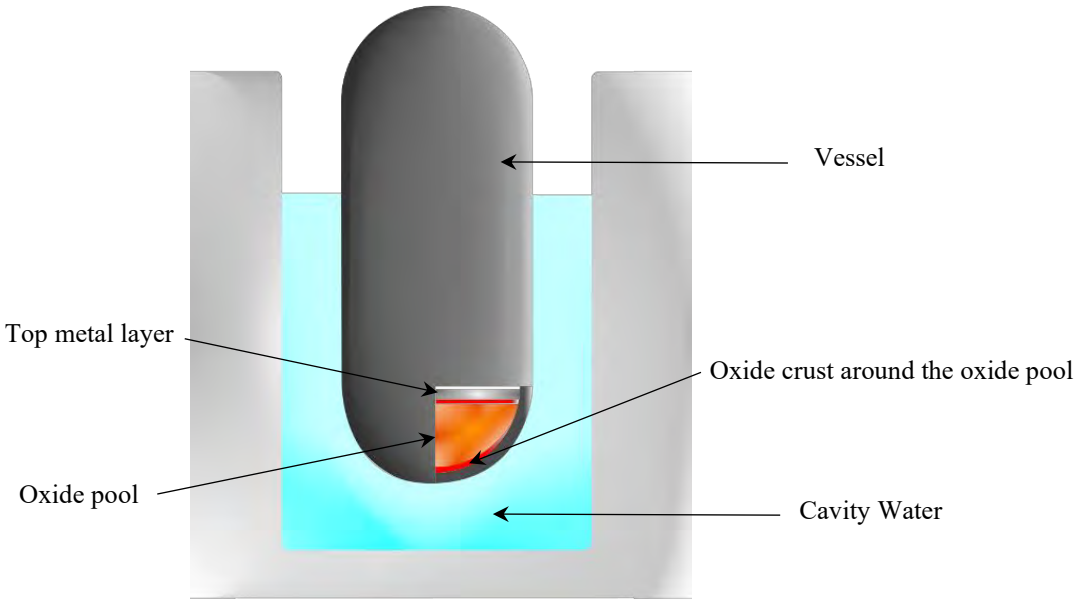

Figure 1: IVMR light metal configuration

W-STORM's computational sequence is briefly recalled, but a more detailed description can be found in [13]. The code's workflow starts with inputting the molten masses of Zr, UO_2 and SS, the Zr Degree of oxidation (C_{ox}), the decay power, LP geometrical characteristics, radiative heat transfer parameters, cavity atmosphere pressure and liquid level. Firstly, the thermochemical equilibrium is computed, defining the molar fraction of each element per phase. Both pools' thermophysical properties are then evaluated, following indications from [16]. If the metal phase obtained is able to stay on the top of the oxide pool (density threshold, cf. part 3), the model moves on to compute the system's geometrical characteristics. Once the geometries are defined, the heat transfer problem can be solved, starting with the oxidic pool's bulk temperature. Its evaluation is followed by the determination of heat fluxes in the downwards and upwards directions, with appropriate experimental correlations for the Nusselt numbers. The thermal field inside the vessel, the downwards crust thickness and the Critical Heat Flux are then evaluated at each polar

mesh. Lastly the heat transfer problem in the metal layer is solved, estimating the inner temperature of the vessel at Liquid Metal (LM) height. The heat transfer problem is then repeated until the generated power in the crusts converges. As an outer loop, the code checks if the vessel's inner temperature is higher than its melting point. If it is, the vessel's thickness is reduced and the corresponding mass is added to the SS mass, repeating the described cycle.

3 THERMOCHEMICAL MODEL COMPARISON WITH MASCA EXPERIMENTS

The oxide and liquid metal pools relative position strongly affects the IVMR heat transfer problem. Indeed, the occurring corium stratification in the LP drives what will be the heat load on the vessel. If the only configuration that can be treated by W-STORM heat transfer module is the two-phase pool with the oxidic pool on the bottom and the metallic one on top, thanks to the thermochemical model, W-STORM can predict also the configurations where the metal phase is heavier than the oxide (but not the associated thermal load on the vessel). The Iso-Density curves (lines representing where the oxide density is equal to the LM density) in the C_{ox} vs SS to UO_2 mass ratio are presented in Figure 2. A similar evaluation was conducted in [13], but in this instance the iso-density curves are compared against MASCA experimental results [18]. This kind of analysis is generic in nature, since the two generic SASPAM-SA designs are considered, as well as a generic PWR described in the IVMR EU funded project, named High Power Reactor (HPR) in this paper [19]. When a configuration lies above these curves, the code predicts a light metal stratification (i.e. LM on top, oxide at the bottom). On the other hand, if it is below the curves, the heavy metal layer configuration is predicted. In W-STORM, a 5% threshold is considered before the density inversion occurs (i.e. the metal layer is considered to be a "heavy metal" only when its density is 5% larger than the oxidic one). Indeed, a minimum mass density difference is necessary for triggering Rayleigh-Taylor instabilities leading to stratification inversion. In addition, intermediate configurations with close densities between oxide and metal phases and thus no clear stratification (as observed experimentally in the case of the MASCA MA-2 test) are also possible. As a consequence, the corium stratification evaluated by the code is determined in Figure 2 for each reactor considering the dashed line with the corresponding color. The MASCA experimental values are displayed as dots: the red experiments (MA-1, MA-3, MA-4, MA-5, MA-5b) indicate that the resulting experimental configuration is a heavy metal one, the green experiment (MA-6) refers to a light metal configuration, while the orange experiment (MA-2) exhibits no clear stratification.

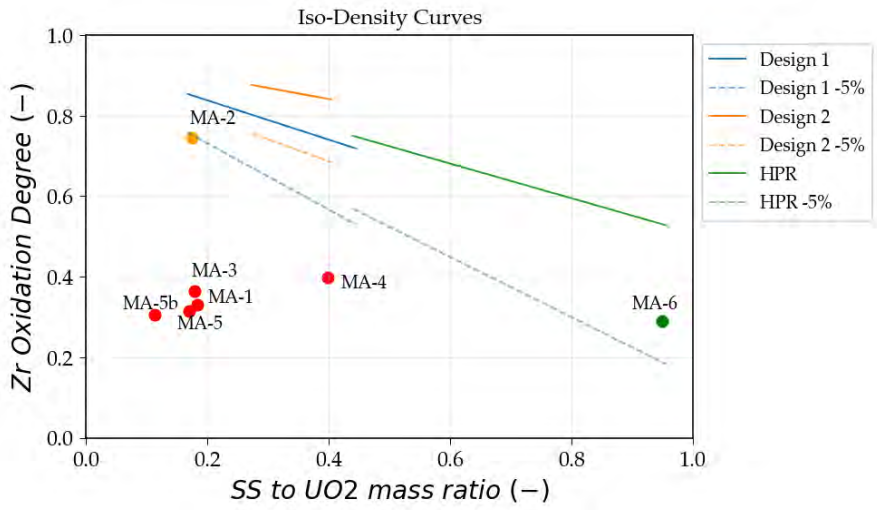

Figure 2: Iso-density curves for SASPAM-SA Design 1, Design 2, HPR and MASCA experimental results

For the 7 MA tests considered, W-STORM can predict experimental stratification configurations when the densities of the two phases is not too close as in MA-2 and MA- 4 tests, as synthetized in Table 1 and Table 2. It is important to highlight that this result depends on both thermochemical model and on the correlations used for the calculation of the densities of the phases.

Table 1: W-STORM comparison of predicted corium stratification with respect to MASCA experimental results

	Experimental Result	W-STORM (densities difference $\frac{oxide-metal}{oxide}$ in %)
MA-1	Heavy metal	Heavy metal (-6.7%)
MA-2	No clear stratification	Light metal (6.7%)
MA-3	Heavy metal	Heavy metal (-9.1%)
MA-4	Heavy metal	Light metal but less than 5% density difference (1.6%)
MA-5	Heavy metal	Heavy metal (-14.0%)
MA-5b	Heavy metal	Heavy metal (-18.7%)
MA-6	Light metal	Light metal (7.9%)

Table 2: W-STORM comparison of predicted mass fractions with respect to MASCA experimental values - oxide mass fraction w_{oxy} (i.e. mass of oxidic layer divided by the total mass), uranium mass fraction in the LM layer $w_{u,met}$ (i.e. mass of uranium in the LM pool divided by the total mass of the LM pool) and Zr mass fraction in the metal $w_{Zr,met}$

	Experimental Data			W-STORM			% Error		
	w_{oxy}	$w_{u,met}$	$w_{Zr,met}$	w_{oxy}	$w_{u,met}$	$w_{Zr,met}$	w_{oxy}	$w_{u,met}$	$w_{Zr,met}$
MA-1	0.781	0.425	0.103	0.718	0.440	0.116	8.08%	-3.42%	-12.8%
MA-2	0.878	0.201	0.055	0.832	0.242	0.073	5.19%	-20.5%	-31.9%
MA-3	0.726	0.43	0.173	0.725	0.432	0.145	0.17%	-0.53%	16.00%
MA-4	0.639	0.322	0.158	0.619	0.301	0.099	3.20%	6.47%	37.6%
MA-5	0.754	0.374	0.256	0.707	0.449	0.193	6.19%	-19.9%	24.5%
MA-5b	0.799	0.428	0.274	0.750	0.499	0.212	6.08%	-16.5%	22.5%
MA-6	0.565	0.215	0.142	0.428	0.204	0.069	24.2%	5.13%	51.7%

Results of W-STORM were also further compared to the results of other thermochemical models and codes based on the results of the benchmark published in [20]. Details of the results are presented in Appendix A. W-STORM agrees with the results from the other codes and as expected, is closer to the ones obtained with other codes based on the same Nandan Fichot thermochemical model [17]. The absence of consideration of limited Stainless Steel solubility in the oxidic phase, compared to the other codes, is also identified and proved to be limited.

This analysis highlights the appropriateness of W-STORM thermochemical model, that can predict the stratification configurations highlighted in MASCA (at least when densities of the two phases are not too close) and estimate the phases density similarly to other integral codes, while weakly underestimating the oxide layer density. This should slightly affect the occurrence of heavy metal cases in the analyses shown in the next sections.

4 SENSITIVITY AND UNCERTAINTY ANALYSIS

4.1 Monaco Python package and Input distributions

The python package Monaco [14] has been used to perform the sensitivity and uncertainty analysis. In general, Monaco requires the user to build three functions: preprocess(), run() and postprocess(). The preprocess function allows the user to define the simulation's input variables and their distributions, which will be sampled. The run function is essentially the user's model, in this case W-STORM, which returns the output variables. The postprocess method lets the user define the output variables, which are stored in the simulation's object. Once the three methods are defined, the user must initiate the simulation's object, in which the number of cases, sampling method, seed and the three pre-defined functions are passed. The simulation is then run, and the results can be collected. Monaco offers different postprocessing functions to plot the results, but custom ones were developed for W-STORM to depict the results more accurately.
The Monaco implemented sampling methods have been tested, and the Latin Hypercube method was selected. In [14], it is stated that the number of cases to run to get representativeness of the input hyperspace should be $n \geq 2^k$, where k is the number of inputs, and n the number of cases to run. Since the inputs are numerous (up to 34 for the cases with all uncertain parameters), this criterion would be infeasible in terms of CPU time. However, based on the Wilks formula [21] a relatively small number (around 100) are sufficient to get the statistical shape of the results and identify the most influential parameters[1]. Since W-STORM simulations are fast, a larger number of 2000 cases have been considered as a reasonable choice.
Three studies will be discussed in this paper. The first one is based on the SASPAM-SA Design 1 configuration and uncertainties associated with material properties are considered. Uncertain coefficients have been added in the material properties laws, following the approach developed by Rempe et al. [22] . The input distributions and the thermophysical properties considered are synthetized in Appendix B. Then, in the following studies, the main uncertain parameters identified for the corium characteristics in the LP and its top boundary condition have been considered in addition to the ones associated with the material properties. The input distributions considered for these additional uncertainty parameters are based on the results of integral SA simulations done in the scope of the SASPAM-SA project for different scenarios and for the two iPWR designs studied (Design 1 and Design 2). They are reported in Table 3. It should be noted that uncertainty associated with the modelling parameter used for the density inversion threshold is also considered.

Table 3: Main Input parameters distributions data

Symbol	Description	Unit	Distr. type	Min (Uniform)		Max (Uniform)	
				Design 1	Design 2	Design 1	Design 2
C	Oxide htc correlation index	-	Integer uniform	0	0	5	5
mFe	Mass of Stainless Steel	kg	Uniform	1500	15000	4500	22000
mUO_2	Mass of fuel	kg	Uniform	6000	40000	9000	55000
C_{ox}	Zr degree of oxidation	-	Uniform	0.3	0.3	0.7	0.7
ε	Metal Layer emissivity	-	Uniform	0.2	0.2	0.4	0.4

[1] $\gamma = 1 - \beta^N$, with N the number of calculations, γ the percentage of the results distribution covered, and β the confidence level. 99% of the results are thus covered with a confidence of 99% with around 500 simulations.

Ts	Average structures' temperature	K	Uniform	500	500	1500	1500
thresh	Inversion threshold	-	Uniform	0.0	0.0	0.1	0.1
P_m	Specific residual power	W/kg	Uniform	178	75	200	120

4.2 Results: Variation of material properties on Design 1

As a first analysis, only the parameters associated with the material properties have been used as input for W-STORM. Constant values were used for parameters in Table 3. They were chosen equal to the ones already adopted in [13]. For sake of brevity, only the parameters influencing materials density are reported in Figure 3. Two kinds of distributions per parameter are presented: the initial distribution (in blue) and the actual distribution (in orange). Indeed, some configurations cannot be evaluated by W-STORM. As already discussed, it is the case of configurations where LM is more than 5% denser than oxidic layer (Heavy Metal category). In addition, the code cannot deal with configuration with no ablation on the lower head and possible LM partial or complete solidification (low Focusing Effect, FE, category). On the other hand, an ablated thickness higher than 90% of the nominal thickness is also out of the scope of the code due to a possible mechanical failure (High FE category). Finally, numerical issues may also happen, but their general occurrence in these analyses is negligible. For this study the distribution of the "failed" calculations is given in Table 4. It is worth noting that, considering only uncertainties associated with material properties, about 50% of the calculations lead to the formation of a heavy metal layer. The results in Figure 3 identify the influence of the densities of UO_2 (a_1), ZrO_2 (a_3) and SS (a_6) on stratification inversion. Indeed, their actual distribution average value is shifted to values avoiding heavy metal occurrence with respect to initial input distributions. In the next section this occurrence is compared to the complete uncertainty calculations.

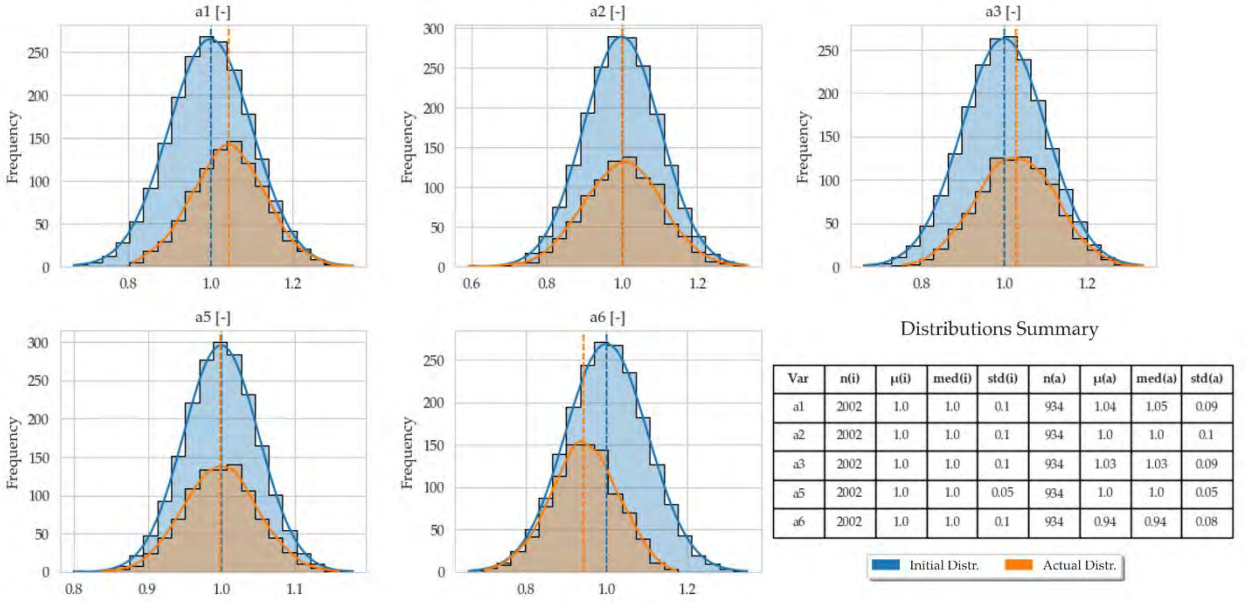

Var	n(i)	μ(i)	med(i)	std(i)	n(a)	μ(a)	med(a)	std(a)
a1	2002	1.0	1.0	0.1	934	1.04	1.05	0.09
a2	2002	1.0	1.0	0.1	934	1.0	1.0	0.1
a3	2002	1.0	1.0	0.1	934	1.03	1.03	0.09
a5	2002	1.0	1.0	0.05	934	1.0	1.0	0.05
a6	2002	1.0	1.0	0.1	934	0.94	0.94	0.08

Figure 3: Initial and Actual distribution of materials density multipliers[2] and distribution data (i subscript for initial, a for actual): n represents the number of cases, μ the mean value, med the median value and std the standard deviation

[2] The a_4 parameter is a dummy one and is not included in the graph.

In Figure 4, the distributions of main interesting output parameters are presented: the vessel residual thickness δ_v, the density difference between oxide and metal phases divided by the oxide density $\Delta\rho$, the power fraction dissipated by radiative heat flux in the metal layer RadF, the power fraction transmitted to the metal layer by the oxide Xup, the aspect ratio of the oxide HRox, the aspect ratio of the metal HRmet, the average downwards crust thickness δc and the FE heat flux (in front of the top metal layer) qf.

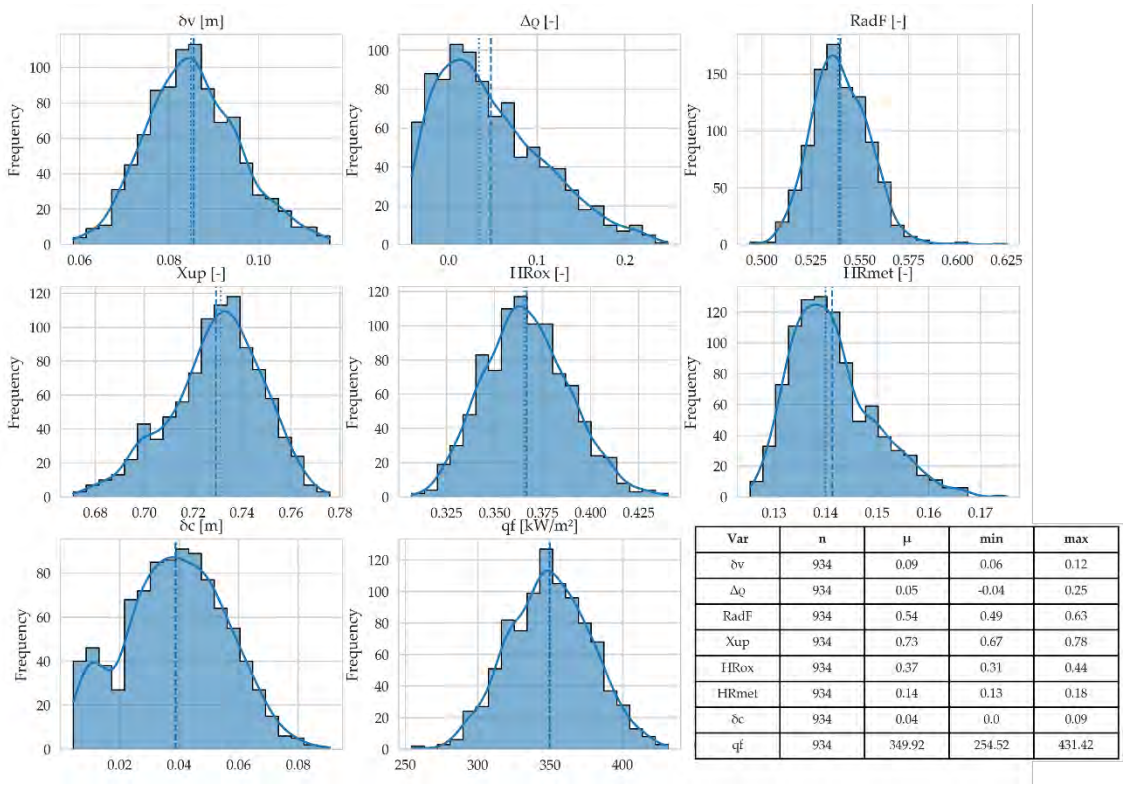

Var	n	μ	min	max
δv	934	0.09	0.06	0.12
ΔQ	934	0.05	-0.04	0.25
RadF	934	0.54	0.49	0.63
Xup	934	0.73	0.67	0.78
HRox	934	0.37	0.31	0.44
HRmet	934	0.14	0.13	0.18
δc	934	0.04	0.0	0.09
qf	934	349.92	254.52	431.42

Figure 4: Properties only calculation output distributions.

These results further consolidate the specificities of iPWR IVMR configurations compared to HPR identified in [13]: thick bottom oxide crust (a 4 cm mean value, one order of magnitude higher with respect to HPR), relatively high fraction of radiative power, lower aspect ratios in both oxide and metal, which respectively produce a high fraction of power transferred from the oxide to the LM, and a limited FE. The variation of the maximum heat flux around its average value remains limited when considering uncertainties associated with material properties (below +/-30% considering the minimum and maximum values). In accordance, comparable behaviour is obtained for the minimum vessel thickness.

4.3 Results: Complete input space variation on Design 1 and Design 2

In this last analysis, both the inputs from Table 3 and Appendix B are being sampled and fed to W-STORM. As in the previous section, the initial input distributions are modified into the ones corresponding to successful calculations (results are available in Appendix C). In these complete calculations, the success rate is quite low (12.9% in Design 1, 5.3% in Design 2), due to high occurrences of Heavy Metal and Low FE cases (cf. Table 4). However, the success cases correspond respectively to 257 and 105 calculations which allow performing a statistical analysis of these results.

Table 4: Occurrence frequency of W-STORM outcomes

Case	Success	Heavy Metal	High FE	Low FE	No Convergence
Design 1 Properties only	46.7%	50.2%	0.0%	1.6%	1.5%
Design 1 Complete	12.9%	55.7%	0.0%	30.4%	1.1%
Design 2 Complete	5.3%	64.7%	0.0%	29.8%	0.4%

As already hinted in Figure 2 and [13], for the analyzed iPWRs, there is a very high occurrence of stratification inversion cases. This result highlights the need for heat transfer models and experimental data in the case of stratification inversion, as their occurrence in iPWRs in IVMR conditions is rather high. Also, non-negligible occurrence of the low FE cases is registered, which are not a safety concern for the lower head, since their imposed heat flux on the vessel would be lower compared to other situations. Nevertheless, this highlights the impact of radiative heat transfer, which as depicted in Figure 5 and Figure 6, is of major importance in this heat transfer problem. In fact, the predicted average radiative fractions from the LM for both designs are higher with respect to HPR (20-30%) [19], and can go up to 80% (49% average for Design 1, 56% for Design 2). Since the radiative fractions are high, particular attention must be given to the radiative heat transfer modelling. In W-STORM case, the predicted fractions of radiated power might be the result of oversimplified modelling and the frequency of occurrencies of Low FE in Table 4 carry that uncertainty. In severe accident codes, it would be preferable to have more complex models that consider view factors and emissivity of the different surfaces.

The output distributions of main interesting parameters are reported in Figure 5 and Figure 6 respectively for Design 1 and Design 2. Regarding the average values obtained, an expected picture is depicted, as already stated in the previous section: high average downwards crust thickness, low oxide and LM aspect ratios, high radiative fractions, high fractions of power from the oxide to the LM and limited focusing effect, with respect to HPR. However, looking at extreme values, a maximum heat flux close to 1MW/m² is reached for Design 1 and 680kW/m² for Design 2. This is a significant increase compared to the average value of respectively 362kW/m² and 255kW/m² (multiplying factor of about 2.8 and 2.7). For such situations, the analysis shows that it corresponds to high mass of UO_2, low mass of steel, high residual power and low radiative heat transfer (high temperature for surrounding structures and low emissivity)[3]. This result is straightforward considering the focusing effect phenomenology (residual power concentration in front of the metal layer), but it allows quantifying the combined impact of these parameters. It is worth noting that in this analysis, considering a simplified modelling of radiative heat transfer at the top of the corium pool with significant uncertainties has a significant impact and it would be beneficial for further studies to improve this modelling as previously discussed for the occurrence of configurations with low heat flux.

It is worth noting that for such studies, the standard correlation coefficients like Pearson (based on assumption of a linear trend) or Spearman (based on ranking) are not informative. Indeed, the values obtained are either too low for allowing a robust analysis (typically below 0.3) or the relationships are obvious (for example, the value considered for the steel mass directly impacts the aspect ratio of the LM). Regarding the maximum heat flux output, the variables with the highest (in absolute terms) Spearman coefficients are around 0.3 and correspond to the mass of steel, the mass of fuel and the emissivity of the metal layer.

[3] For Design1, maximum heat flux is evaluated for mFe=1788kg, mUO2=8765kg, Pm=195W/kg, ε=0.25, Ts=1480K
For Design2, maximum heat flux is evaluated for mFe=15672kg, mUO2=53436kg, Pm=110W/kg, ε=0.25, Ts=1480K

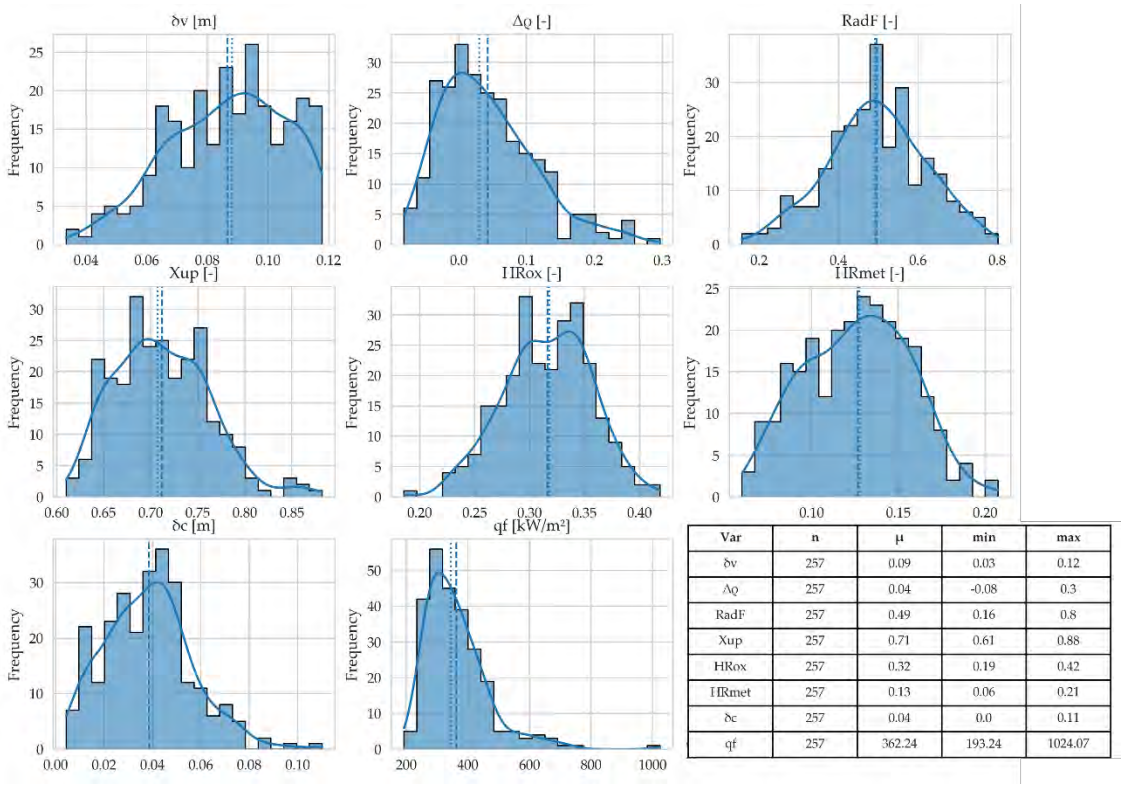

Var	n	μ	min	max
δv	257	0.09	0.03	0.12
ΔQ	257	0.04	-0.08	0.3
RadF	257	0.49	0.16	0.8
Xup	257	0.71	0.61	0.88
HRox	257	0.32	0.19	0.42
HRmet	257	0.13	0.06	0.21
δc	257	0.04	0.0	0.11
qf	257	362.24	193.24	1024.07

Figure 5: Design 1 output distributions

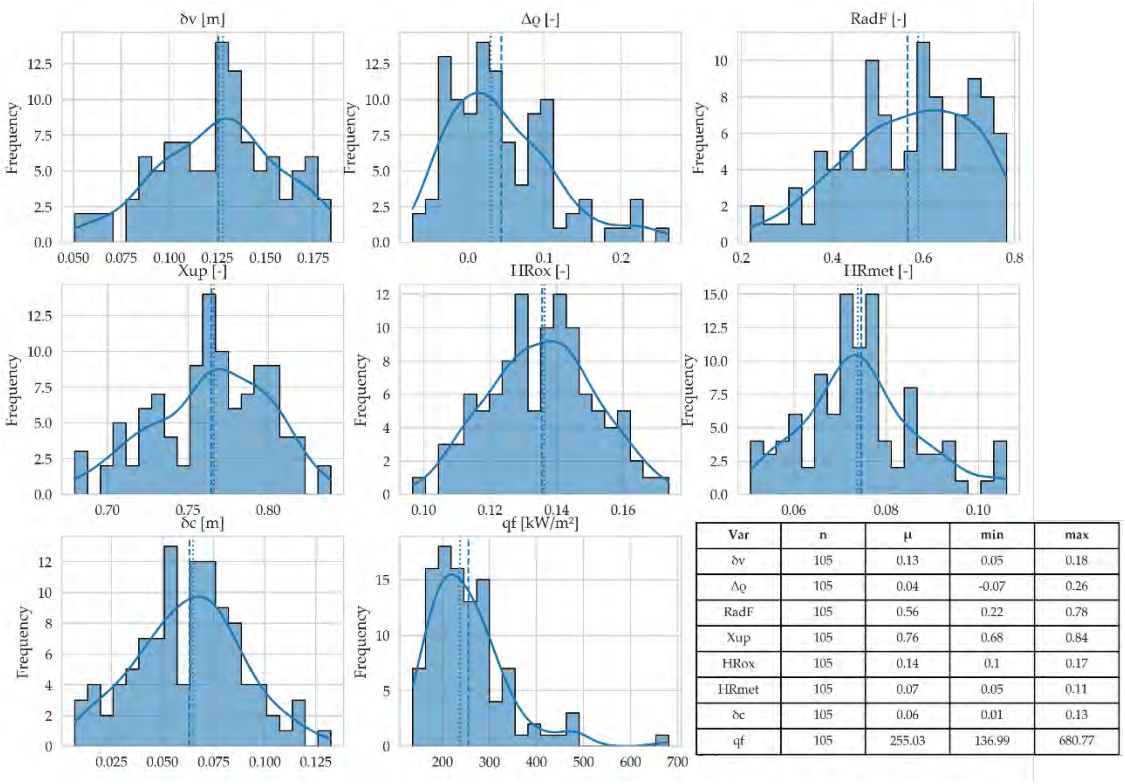

Var	n	μ	min	max
δv	105	0.13	0.05	0.18
ΔQ	105	0.04	-0.07	0.26
RadF	105	0.56	0.22	0.78
Xup	105	0.76	0.68	0.84
HRox	105	0.14	0.1	0.17
HRmet	105	0.07	0.05	0.11
δc	105	0.06	0.01	0.13
qf	105	255.03	136.99	680.77

Figure 6: Design 2 output distributions

5 CONCLUSIONS

The present paper describes the sensitivity and uncertainty analysis on W-STORM, a simple python IVMR 0D model developed in the framework of the SASPAM-SA project. W-STORM thermochemistry model was furtherly validated with respect to MASCA experiment, and its predicted properties were also compared to a code benchmark. W-STORM can predict MASCA experimental stratification configurations when the two phases' densities are sufficiently distanced. Furthermore, its prediction of corium composition as well as phases' density are included in the benchmark predicted ranges presented in [20]. The SAPSAM-SA two generic reactor concepts were analyzed in an IVMR state, and three main calculations were shown: a complete calculation varying all the presented input data (Reactor parameters + physical properties) for both designs, and a calculation with just varying physical properties. The reactor parameters input data were gathered in the SASPAM-SA project, while the physical properties data were extrapolated from literature. The Monaco python package was exploited to carry out sampling and running. The main data coming from the analysis of output variables depicts an expected picture: iPWRs are characterized by thick oxide crusts, low aspect ratios of LM and oxide, high radiative heat transfer, high power transferred from the oxide to the LM and limited FE. All parameters exhibit average values comparable to W-STORM previous work. The distribution limits associated with the maximum heat flux were identified and are inferred mainly from the radiative heat transfer model parameters.
Results further stress that in iPWRs there could be a high occurrence of Heavy Metal cases, due to a low steel to fuel mass ratio. Heat transfer models and experimental data are needed for this kind of configuration. It could even be possible that in some cases, the metallic and oxidic phases exhibit comparable densities, which would favor mixing instead of stratification. Also, the frequency of occurrence of partial/ complete solidification cases of the LM (low FE), with no ablation on the lower head was evaluated. However, the confidence in the low FE frequency is limited, since the radiative heat transfer model in W-STORM is rather simple. Indeed, more accurate radiative heat transfer models should be implemented in severe accident codes, since radiative heat transfer can play a major role in the system's dynamics.

6 REFERENCES

[1] IAEA, *Safety of Nuclear Power Plants: Design*, IAEA Safety Standards, Specific Safety Requirements No. SSR-2/1 (Rev. 1) (2016).
[2] Principato M. et al., "Analyses of the MELCOR capability to simulate integral PWR using passive systems in a DBA scenario", *Nuclear Engineering and Design*, **437**, 114004 (2025).
[3] NuScale Power LLC, "Introduction and General Description of the Plant, Final Safety Analysis Report". https://www.nrc.gov/docs/ML2330/ML23304A318.pdf (2023).
[4] Kang O.H., Lee B.J., Lim S.G., "Light water SMR development status in Korea", *Nuclear Engineering and Design*, **419**, 112966 (2024.)
[5] Yu H. et al., "Assessment of Severe Accident Management for Small iPWR under an ESBO Scenario", *Science and Technology of Nuclear Installations*, 1-10 (2019).
[6] Xiang Q. et al., "Research on debris in-vessel cooling and retention behavior for the small modular reactor ACP100", *Progress in Nuclear Energy*, **134**, 103641 (2021).
[7] Esmaili H., Khatib-Rhabar M, "Analysis of in-vessel retention and ex-vessel fuel coolant interaction for AP-1000", NUREG/CR-6849, ERI/NRC 04-201 (2004).
[8] Xing, J., Song, D., Wu, Y., "HPR1000: advanced pressurized water reactor with active and passive safety", *Engineering*, **2**(1), pp. 79–87 (2016).
[9] Asmolov V.G., et al., "The thermodynamics of U-Zr-Fe-O melts", *Thermophysical Properties of Materials*, **45**, pp. 305-312 (2007).

[10] S.V. Bechta, "Corium phase equilibria based on MASCA, METCOR and CORPHAD results", *Nuclear Engineering and Design*, **238**, pp. 2761-2771 (2008).
[11] Fichot F., Carénini L., "Some consequences of Material Interactions for In-Vessel Melt Retention", Proceedings of ICAPP 2015, Nice (France) (2015).
[12] Carénini L., Fichot F., Seignour N., "Modelling issues related to molten pool behaviour in case of In-Vessel Retention strategy", *Annals of Nuclear Energy*, **118** (2018).
[13] Principato M. et al., "In Vessel Melt Retention 0D model for integral Pressurized Water Reactors", The 11th European Review Meeting on Severe Accident Research (ERMSAR 2024), KTH Stockholm, Sweden, May 13-16 (2024).
[14] Shambaugh W.S., Monaco: A Monte Carlo Library for Performing Uncertainty and Sensitivity Analysis, SciPy Proceedings (2022).
[15] Bal Raj Sehgal et al., *Nuclear Safety in Light Water Reactors, Severe Accident Phenomenology*, Elsevier, Waltham, MA, USA (2012).
[16] Theofanous, T.G., Liu, C., Addition, S., Angelini, S., Kymälainen, O., Salmassi, T," In-vessel coolability and retention of core melt", *Nuclear Engineering and Design*, **169** (1997).
[17] Nandan S., Fichot F., Piar B., "A simplified model for the quaternary U-Zr-Fe-O system in the miscibility gap", *Nuclear Engineering and Design*, **364**, 110608 (2020).
[18] Tsurikov D. F. et al., "Main Results of the MASCA1 and 2 Projects", Kurchatov Institute, Integrated Report OECD MASCA Project (2007).
[19] Carénini L. et al., Main outcomes from the IVR code benchmark performed in the European IVMR project, *Annals of Nuclear Energy*, **146**, 107612 (2020).
[20] Le Tellier R. et al., "Main results of an in-vessel corium thermochemistry benchmark based on MASCA and CORDEB2 experimental data", *Annals of Nuclear Energy*, **220**, 111514 (2025).
[21] S. Wilks, "Determination of Sample Sizes for Setting Tolerance Limits," Ann. Math. Stat., 12, 1, 91 (1941); https://doi.org/10.1214/aoms/1177731788.
[22] Rempe J.L. et al., Potential for AP600 In-Vessel Retention through Ex-Vessel Flooding, Idaho National Laboratory, INEEL/EXT-97-0079, 1997.

APPENDIX A: W-STORM stratification model evaluation with respect to Benchmark [20]

The predicted density difference (calculated as LM density minus the oxide density) with respect to different codes as done in [20] were investigated. The results are collected in Table 5, and they highlight that the range of variability between codes is large, and W-STORM is close or inside the predicted ranges of other codes.

Table 5: Benchmark [20] and W-STORM comparison of the density difference between phases (metal – oxide) in kg/m³

	NRC KI - TSAR	IRSN - ASTEC	INRNE-BAS - ASTEC	IBRAE - HEFEST_URAN	CEA - PROCOR - S&F, M1	CEA - PROCOR - S&F, M2	W-STORM
MA-1	305.6	-35.3	-91.4	-342.9	245.3	42.8	516.6
MA-2	-717.3	-771.1	-785.6	-1075.9	-559.3	-763.2	-503.2
MA-3	543.6	315.4	316.1	-68.3	503.3	316.1	680.8
MA-4	64.8	-4.5	-50.5	-489.1	183.6	-7.6	-118.3
MA-5	794	712.7	721	542.4	907.3	740.9	1013.3
MA-5b	955.1	927	936.2	984.1	1100.8	937.7	1350.5
MA-6	-454.4	-271.1	-296.8	-809.3	-207.4	-334.4	-582.8

Furthermore, the density of each phase was tested against the results from other codes, by varying the considered mass of steel. The results are displayed from Figure 7 to Figure 14. The first noticeable difference is in the W-STORM oxide phase density variability with respect to the other codes (Figure 8 and Figure 12). These densities are indeed independent from the mass of steel, since one of the assumptions of [17] is the non-solubility of Stainless Steel in the oxidic phase. On the other hand, in Figure 7 and Figure 11 it is noticeable that the other codes implement this solubility. W-STORM indeed cannot predict the oxide density decrease and slightly underestimates the oxide density. For the LM layer, W-STORM agrees with the results from the other codes, finding itself between the curves values in Figure 9 and Figure 13.

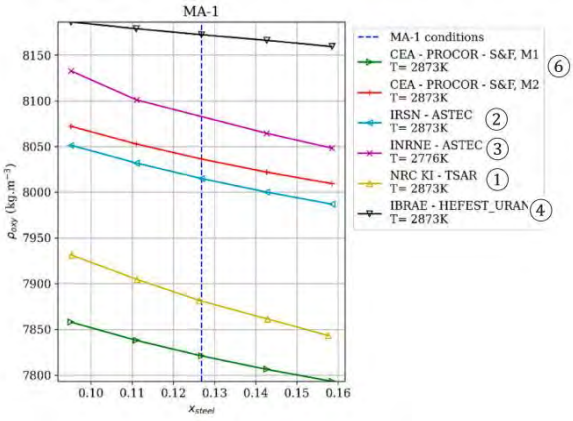

Figure 7: MA-1 test oxide density variability between codes [20]

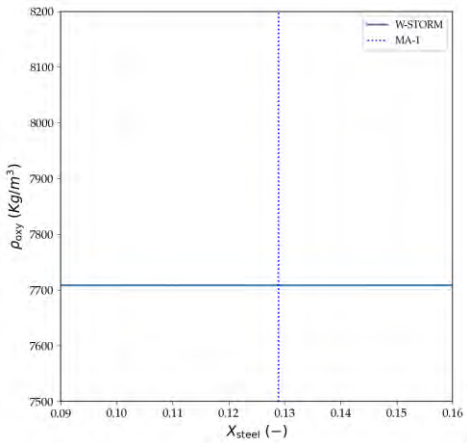

Figure 8: W-STORM oxide density prediction in MA-1 conditions

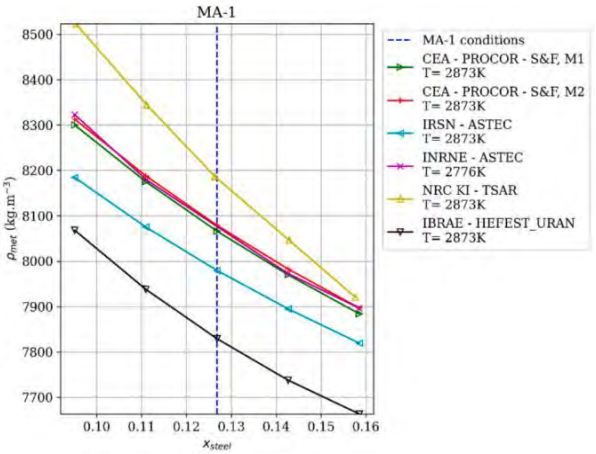

Figure 9: MA-1 test LM density variability between codes [20]

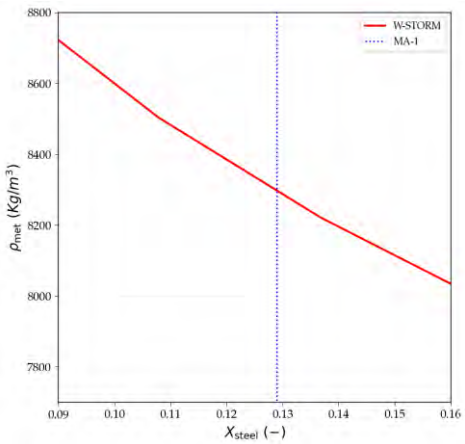

Figure 10: W-STORM metal density prediction in MA-1 conditions

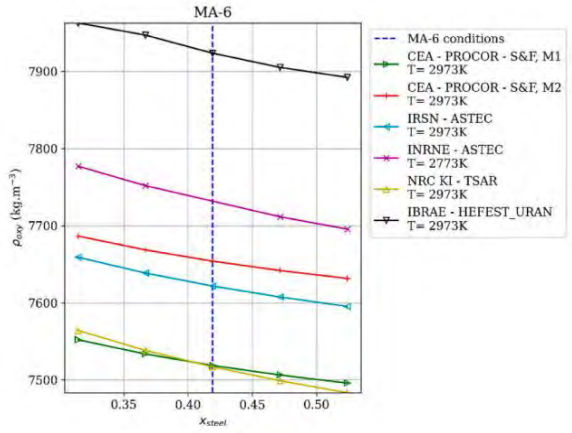

Figure 11: MA-6 test oxide density variability between codes [20]

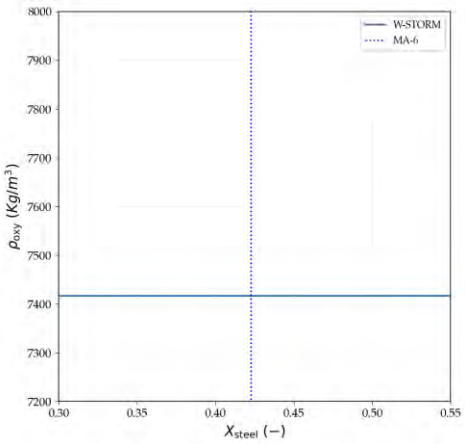

Figure 12: W-STORM oxide density prediction in MA-6 conditions

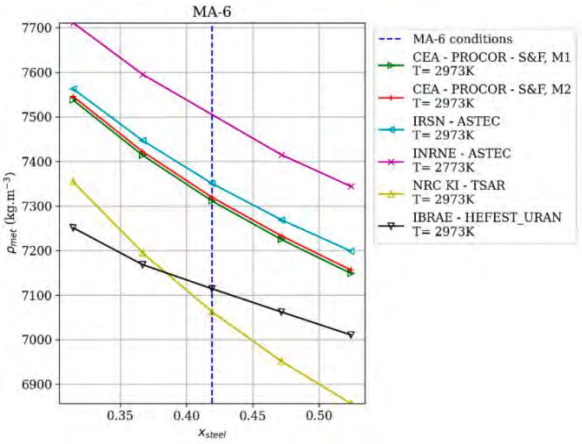

Figure 13: MA-6 test LM density variability between codes [20]

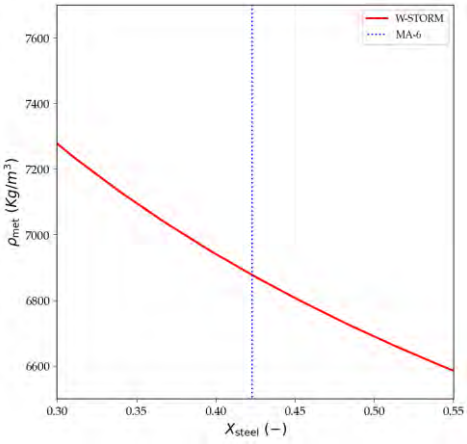

Figure 14: W-STORM metal density prediction in MA-6 conditions

APPENDIX B: Thermophysical properties input distributions

Table 6: Sampled parameters for thermophysical properties

Symbol	Description	Distr. type	Mean	Std
a_1	Multiplier of fuel density	Normal	1.0	0.1
a_2	Factor for U density	Normal	1.0	0.1
a_3	Multiplier of ZrO_2 density	Normal	1.0	0.1
a_5	Multiplier of Zr density	Normal	1.0	0.05
a_6	Multiplier of SS density	Normal	1.0	0.1
a_7	Multiplier of liquid fuel thermal conductivity	Normal	1.0	0.4
a_8	Multiplier of solid fuel thermal conductivity	Normal	1.0	0.01
a_9	Multiplier of ZrO_2 thermal conductivity	Truncated Normal	1.0	0.5692
a_{10}	Multiplier of Zr thermal conductivity	Normal	1.0	0.042
a_{11}	Multiplier of SS thermal conductivity	Normal	1.0	0.059
a_{12}	Multiplier of fuel specific heat capacity	Normal	1.0	0.1
a_{13}	Multiplier of U specific heat capacity	Normal	1.0	0.1
a_{14}	Multiplier of ZrO_2 specific heat capacity	Normal	1.0	0.015
a_{15}	Factor for Zr specific heat capacity	Normal	0.0	7.6
a_{16}	Multiplier of SS specific heat capacity	Normal	1.0	0.0765
a_{17}	Density averaging factor for oxide	Normal	0.0	0.02
a_{18}	Thermal conductivity averaging factor for oxide	Normal	0.0	0.05
a_{19}	Specific heat capacity averaging factor for oxide	Normal	0.0	0.1
a_{20}	Thermal expansion coefficient averaging factor for oxide	Normal	0.0	0.02
a_{21}	Multiplier for oxide viscosity	Normal	1.0	0.1
a_{22}	Multiplier for vessel thermal conductivity	Normal	1.0	0.1
a_{23}	Density averaging factor for LM	Normal	0.0	0.02
a_{24}	Thermal conductivity averaging factor for LM	Normal	0.0	0.05
a_{25}	Specific heat capacity averaging factor for LM	Normal	0.0	0.1
a_{26}	Thermal expansion coefficient averaging factor for LM	Normal	0.0	0.02
a_{27}	Multiplier for metal viscosity	Normal	1.0	0.1

APPENDIX C: Initial and actual input distributions obtained for complete analysis of Design 1 and Design2

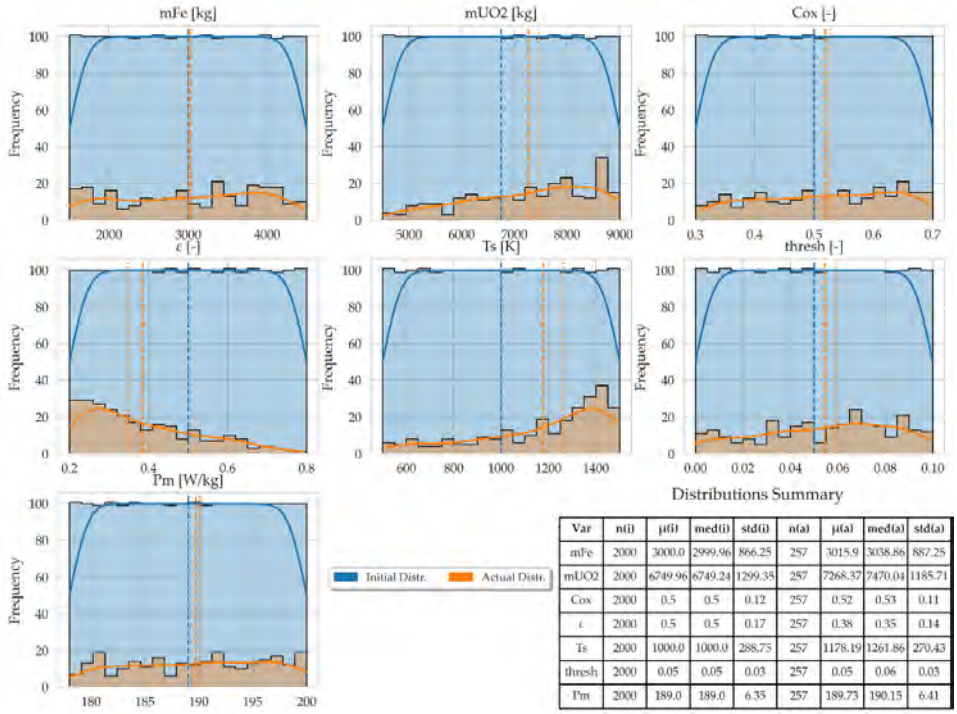

Var	n(i)	μ(i)	med(i)	std(i)	n(a)	μ(a)	med(a)	std(a)
mFe	2000	3000.0	2999.96	866.25	257	3015.9	3038.86	887.25
mUO2	2000	6749.96	6749.24	1299.35	257	7268.37	7470.04	1185.71
Cox	2000	0.5	0.5	0.12	257	0.52	0.53	0.11
ε	2000	0.5	0.5	0.17	257	0.38	0.35	0.14
Ts	2000	1000.0	1000.0	288.75	257	1178.19	1261.86	270.43
thresh	2000	0.05	0.05	0.03	257	0.05	0.06	0.03
Pm	2000	189.0	189.0	6.35	257	189.73	190.15	6.41

Figure 15: Design 1 Initial and Actual input distributions

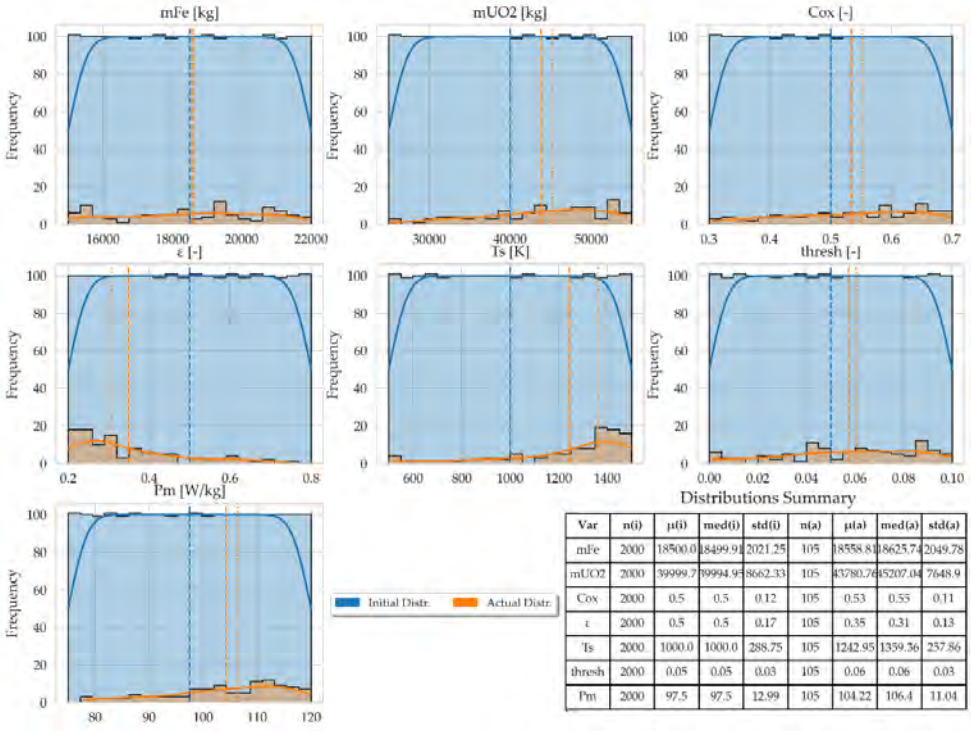

Var	n(i)	μ(i)	med(i)	std(i)	n(a)	μ(a)	med(a)	std(a)
mFe	2000	18500.0	18499.91	2021.25	105	18558.81	18625.74	2049.78
mUO2	2000	39999.7	39994.95	8662.33	105	43780.76	45207.04	7648.9
Cox	2000	0.5	0.5	0.12	105	0.53	0.55	0.11
ε	2000	0.5	0.5	0.17	105	0.35	0.31	0.13
Ts	2000	1000.0	1000.0	288.75	105	1242.95	1359.36	257.86
thresh	2000	0.05	0.05	0.03	105	0.06	0.06	0.03
Pm	2000	97.5	97.5	12.99	105	104.22	106.4	11.04

Figure 16: Design 2 Initial and Actual input distributions

W-STORM Sensitivity and Uncertainty analysis for In Vessel Retention in integral Pressurized Water Reactors

ERMSAR 2026

- **M. Principato** (Sapienza, now PSI), C. Ciurluini (Sapienza), F. Giannetti (Sapienza) , L. Carénini (ASNR), F. Fichot (ASNR)

- Madrid, 19th May 2026

W-STORM *(Water cooled Small modular reacTors 0D in-vessel melt Retention Model)*

Simple Python code developed in EU project SASPAM-SA

Model Aim:

- Fast running tool to provide SASPAM partners a magnitude of expected results
- Identify specificities of iPWRs in IVMR modelling

Key features:

- Written in Python, object based
- Adaptable to any iPWR

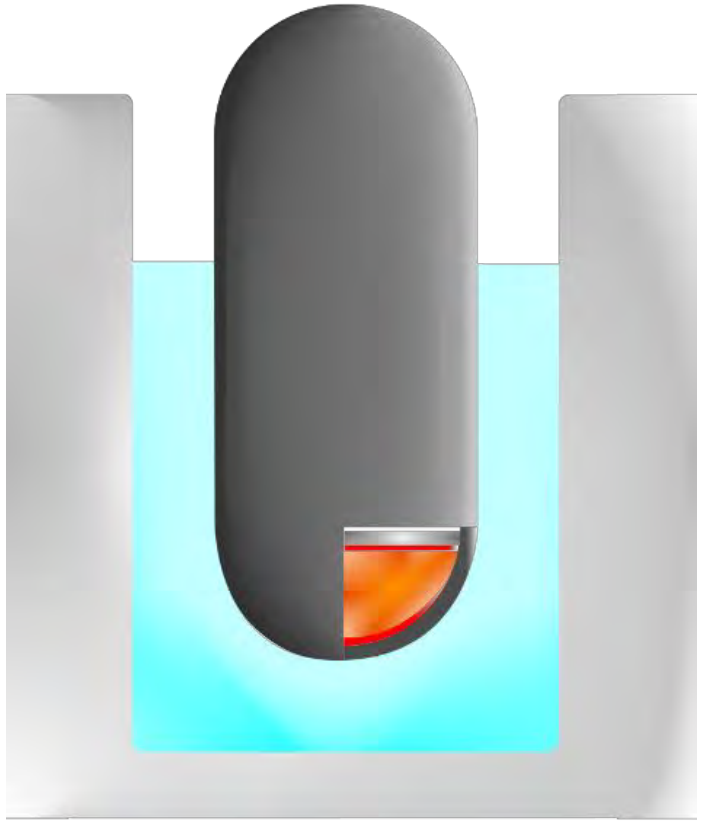

Workflow

Input data (Masses, Geometry, Cavity, Oxidation, Iter)

Thermochemical model ***(Nandan et al.)***

Composition and properties

Geometrical model

Heights and surfaces

Heat transfer model

Refine Vessel thickness

Results

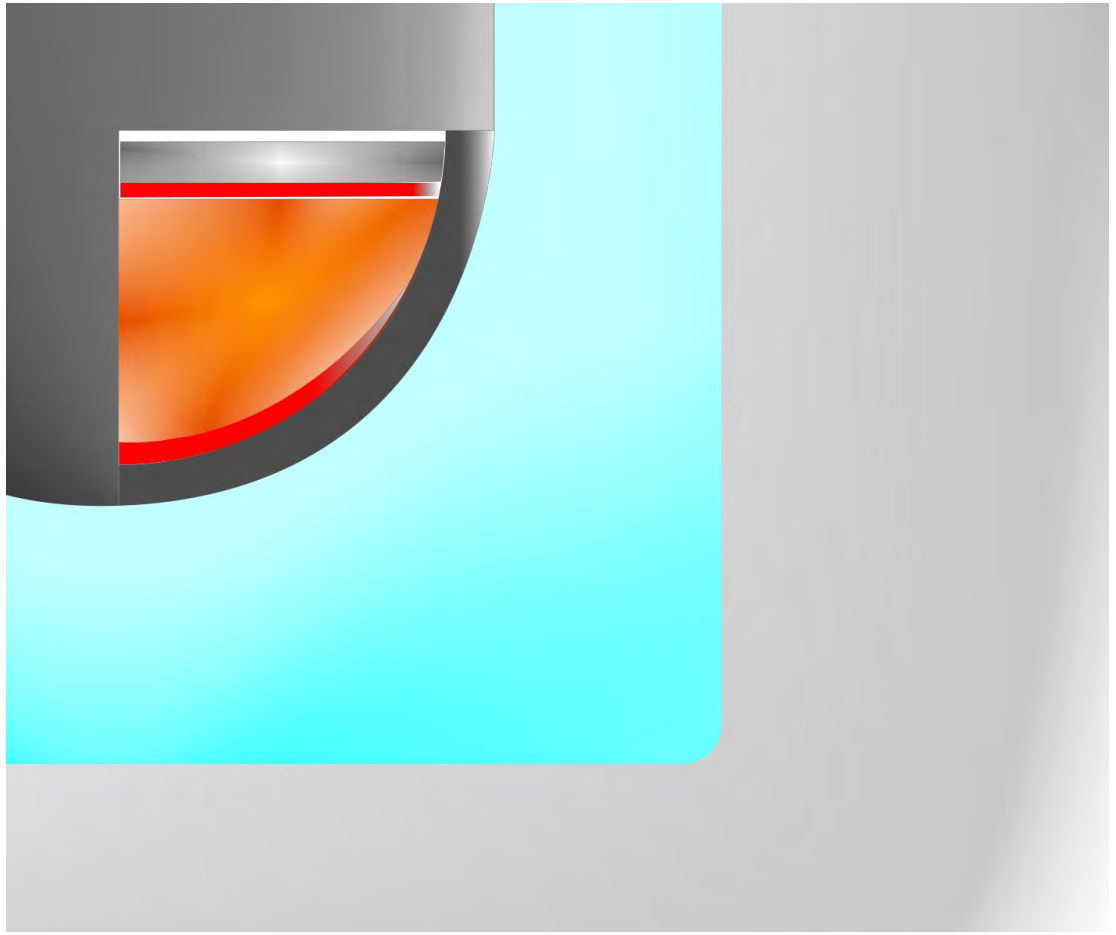

MASCA experiments comparison

- Since an uncertainty and sensitivity analysis is to be performed, the **Thermochemical model** (Nandan Fichot) was beforehand compared to Masca experiments
- **5%** threshold for inversion (Rayleigh-Taylor instabilities)
- Experimental stratification reproduced when the densities aren't too close

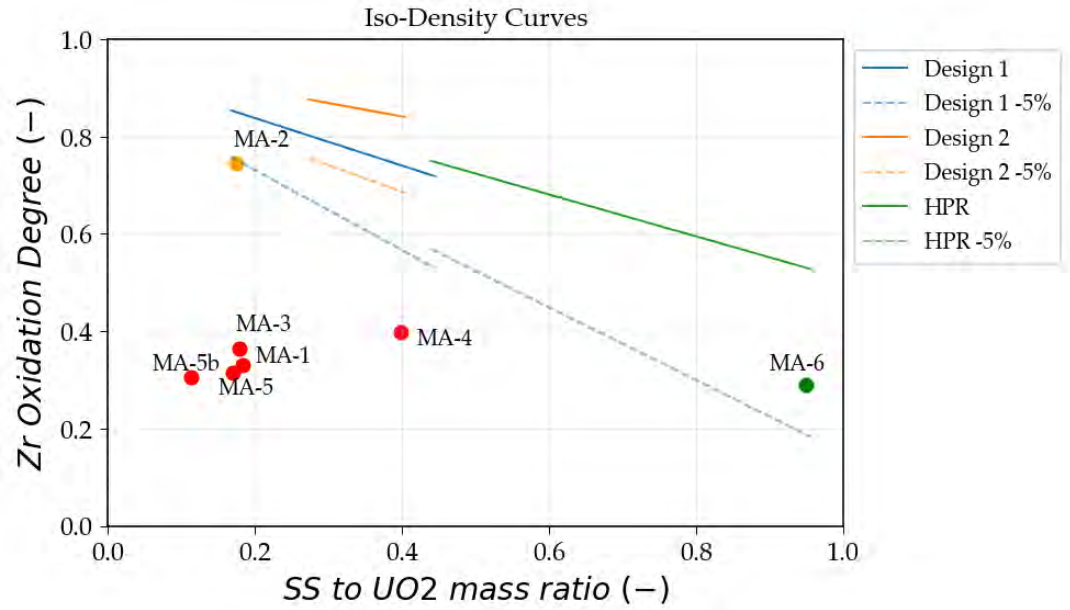

	Experimental Result	W-STORM (densities difference $\frac{\text{oxide}-\text{metal}}{\text{oxide}}$ in %)
MA-1	Heavy metal	Heavy metal (-6.7%)
MA-2	No clear stratification	Light metal (6.7%)
MA-3	Heavy metal	Heavy metal (-9.1%)
MA-4	Heavy metal	Light metal but less than 5% density difference (1.6%)
MA-5	Heavy metal	Heavy metal (-14.0%)
MA-5b	Heavy metal	Heavy metal (-18.7%)
MA-6	Light metal	Light metal (7.9%)

MASCA experiments comparison

Parameters:

- Mass fraction of oxide w_{oxy}
- Mass fraction of U in metal $w_{U,met}$
- Mass fraction of Zr in metal $w_{Zr,met}$

➢ MA-1, MA-2 and MA-3 are better reproduced overall, wrt to 4,5,5b and 6.

➢ Results for these parameters were also compared to a code Benchmark **(Le Tellier et al. 2025)**, and they are consistent with other codes using the same TC model (Nandan Fichot)

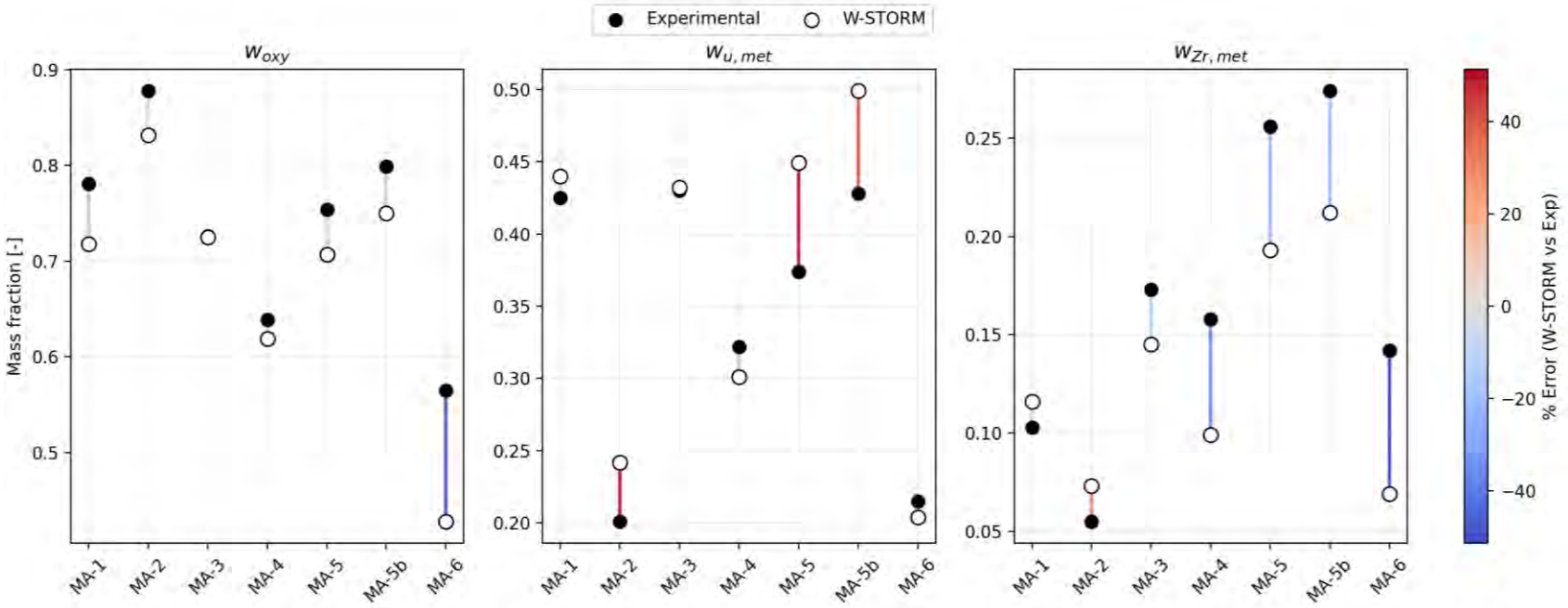

Benchmark comparison

Parameter:

- **Metal – Oxide density difference**

Results:

- Large range of variability between codes, W-STORM is close or inside the predicted range from other codes.

- Results depend on chosen correlations for materials density (which were not highlighted in the benchmark paper), and on the predicted mass fractions (TC model)

- Variability of phase density with mass of steel was also investigated. W-STORM underestimates oxide density slightly but well represents metal density.

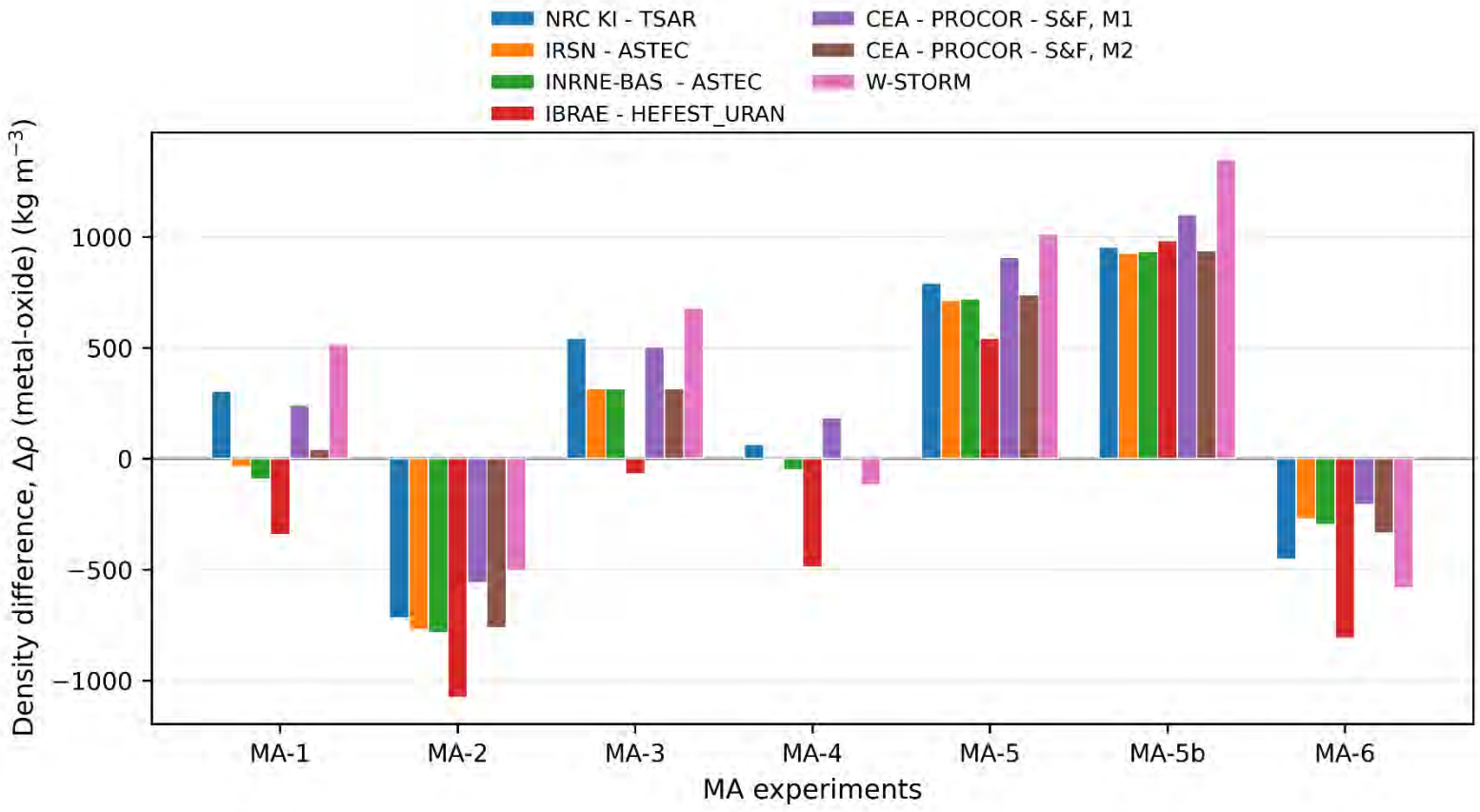

Sensitivity and Uncertainty analysis

➢ **Monaco Python package used to perform the analyses**

Simulations:

- Design 1 Variating only properties
- Design 1 Complete
- Design 2 Complete

- Number of cases per sim: ~2000

Parameters:

- **26 total parameters** for thermophysical properties (Density, Thermal conductivity, heat capacity, viscosity for each material)
- **7 reactor specific parameters**

- **Data from Literature and from SASPAM-SA**

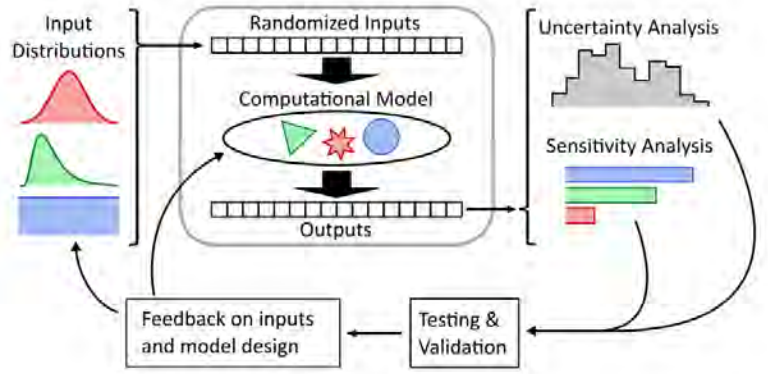

Symbol	Description	Unit	Distr. type	Min (Uniform)		Max (Uniform)	
				Design 1	Design 2	Design 1	Design 2
C	Oxide htc correlation index	-	Integer uniform	0	0	5	5
mFe	Mass of Stainless Steel	kg	Uniform	1500	15000	4500	22000
mUO_2	Mass of fuel	kg	Uniform	6000	40000	9000	55000
C_{ox}	Zr degree of oxidation	-	Uniform	0.3	0.3	0.7	0.7
ε	Metal Layer emissivity	-	Uniform	0.2	0.2	0.4	0.4
Ts	Average structures' temperature	K	Uniform	500	500	1500	1500
thresh	Inversion threshold	-	Uniform	0.0	0.0	0.1	0.1
P_m	Specific residual power	W/kg	Uniform	178	75	200	120

Cases handling

W-STORM cannot evaluate any IVMR configuration, only the "Classical" one. W-STORM output can be of many different types:

- Classic output (partial ablation): W-STORM success, outputting the overall results (heat fluxes, temperatures etc.)
- If there is no ablation (LM solidification): low FE
- If there is vessel failure (ablated thickness>90% nominal thickness): high FE
- If the metal layer is 5% heavier than the oxide: Heavy metal
- Numerical issues (rare)

Except for the Classic output, no results are printed for other cases, since they are out of the physical realm of the code

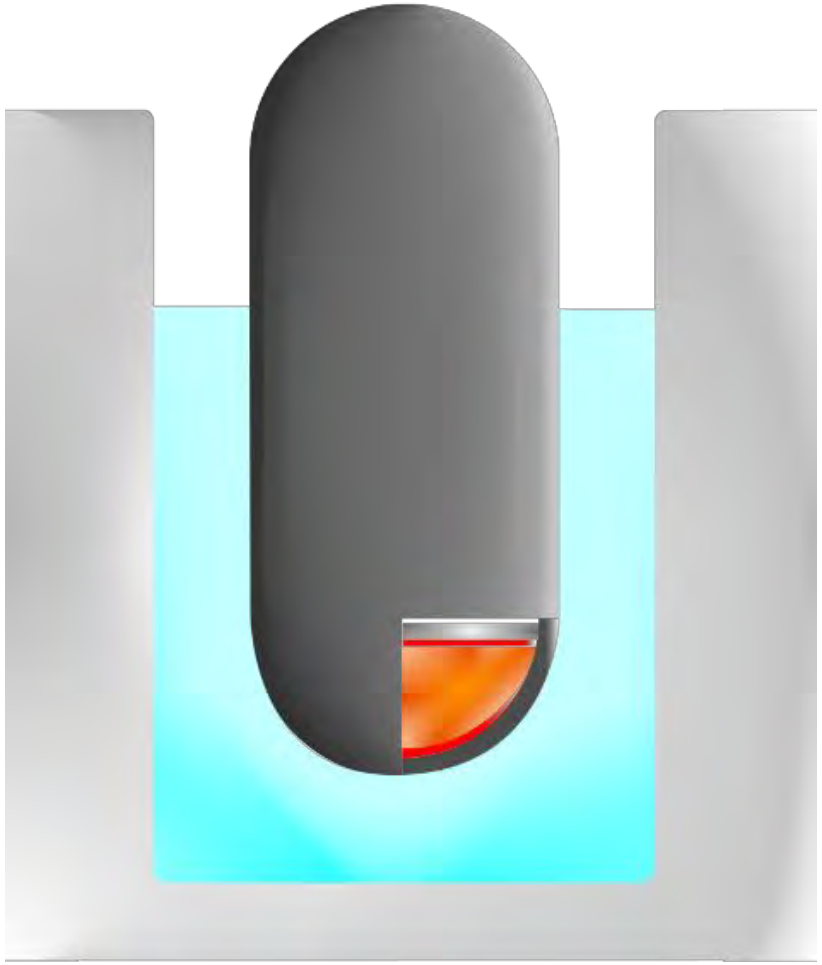

Design 1 properties only

- a1: UO_2 density multiplier
- a2: Factor for metallic U density
- a3: ZrO_2 density multiplier
- a5: Zr density multiplier
- a6: SS density multiplier

Initial distribution: given distribution by the user
Actual distribution: distribution filtered by W-STORM

~50% of cases lead to the formation of a heavy metal!

Actual distributions are shifted towards values that avoid heavy metal occurrence (i.e. , the low values for UO_2 density get filtered)

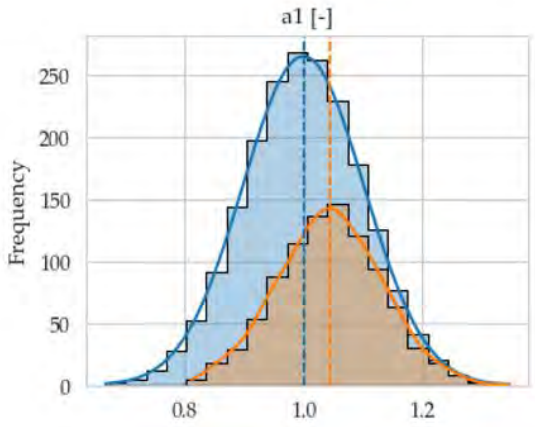

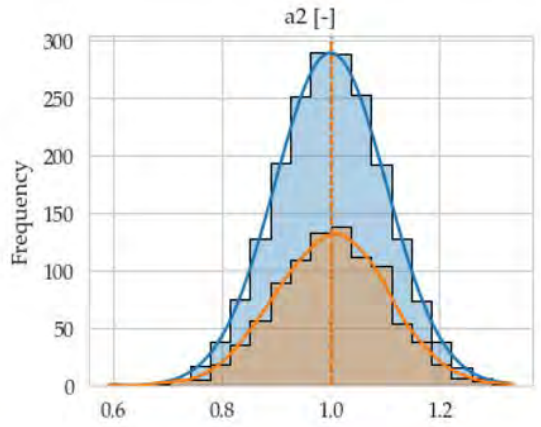

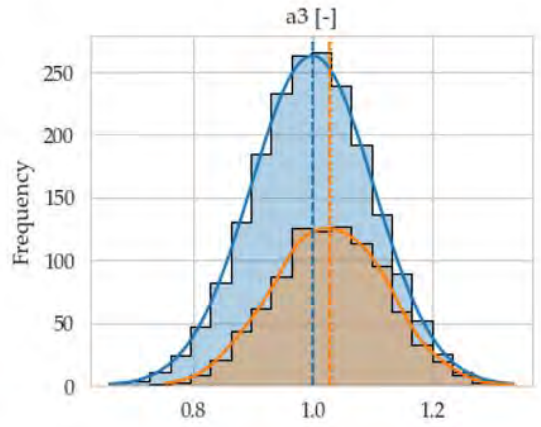

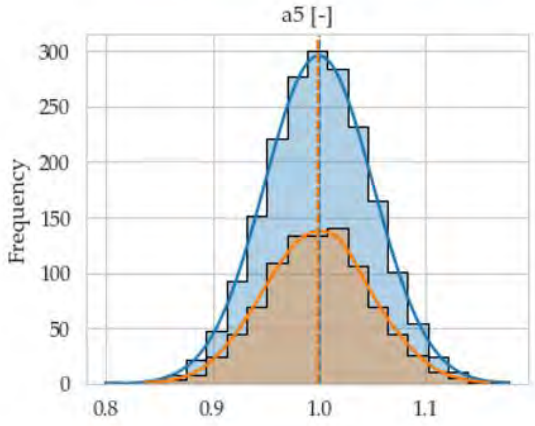

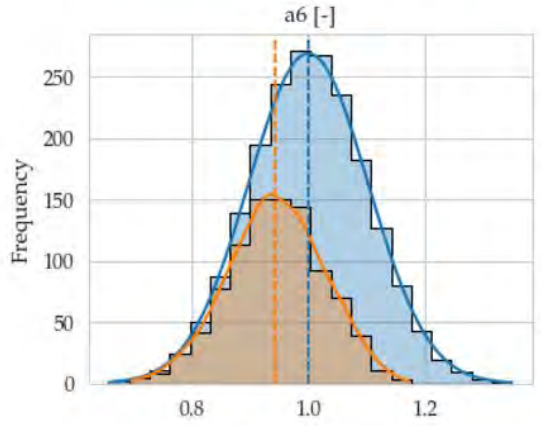

Distributions Summary

Var	n(i)	μ(i)	med(i)	std(i)	n(a)	μ(a)	med(a)	std(a)
a1	2002	1.0	1.0	0.1	934	1.04	1.05	0.09
a2	2002	1.0	1.0	0.1	934	1.0	1.0	0.1
a3	2002	1.0	1.0	0.1	934	1.03	1.03	0.09
a5	2002	1.0	1.0	0.05	934	1.0	1.0	0.05
a6	2002	1.0	1.0	0.1	934	0.94	0.94	0.08

Design 1 properties only

Outputs:

- Residual vessel thickness
- Oxide – metal relative density difference
- Metal radiative fraction
- Fraction of power transmitted to the top by the oxide
- Oxide and metal aspect ratios
- Crust average thickness
- Focusing effect heat flux

Expected and confirmed specificities: thick crust (4cm avg), high radiative fraction, low aspect ratios, high power from oxide to metal, and limited focusing effect.

Variation of maximum heat flux remains limited (below +-30% considering minimum and maximum)

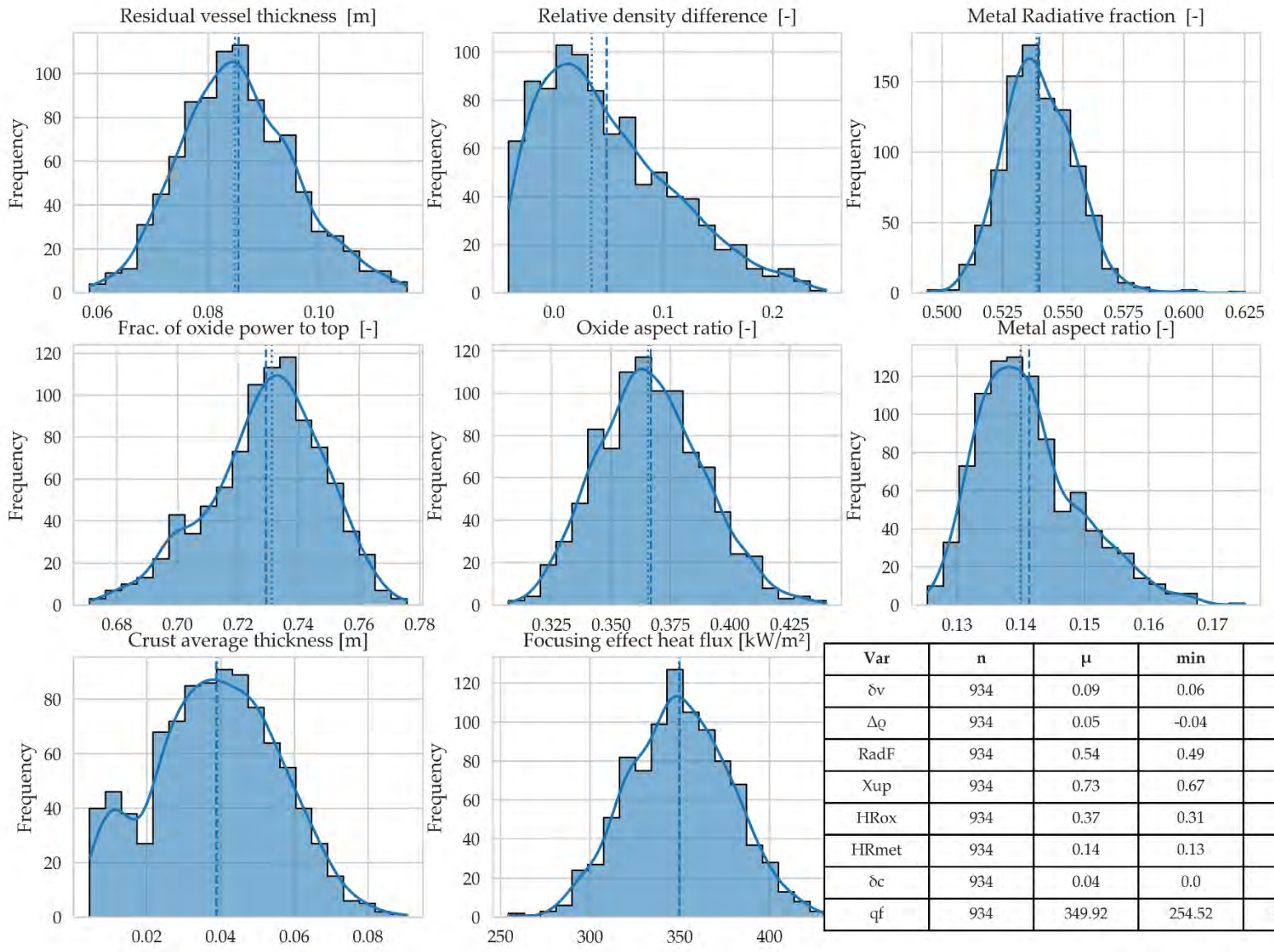

Var	n	μ	min	max
δv	934	0.09	0.06	0.12
Δϱ	934	0.05	-0.04	0.25
RadF	934	0.54	0.49	0.63
Xup	934	0.73	0.67	0.78
HRox	934	0.37	0.31	0.44
HRmet	934	0.14	0.13	0.18
δc	934	0.04	0.0	0.09
qf	934	349.92	254.52	431.42

Design 1 and Design 2 complete analysis

Case	Success	Heavy Metal	High FE	Low FE	No Convergence
Design 1 Properties only	46.7%	50.2%	0.0%	1.6%	1.5%
Design 1 Complete	12.9%	55.7%	0.0%	30.4%	1.1%
Design 2 Complete	5.3%	64.7%	0.0%	29.8%	0.4%

Low occurrence of "classical" stratified pool

High HM occurrence!

No predicted vessel failure

High solidification cases occurrence!

Need for heat transfer models and experimental data

Major importance of radiative heat transfer: more detailed models considering view factors and emissivity of different surfaces are needed

Design 1 and Design 2 complete analysis

Design 1

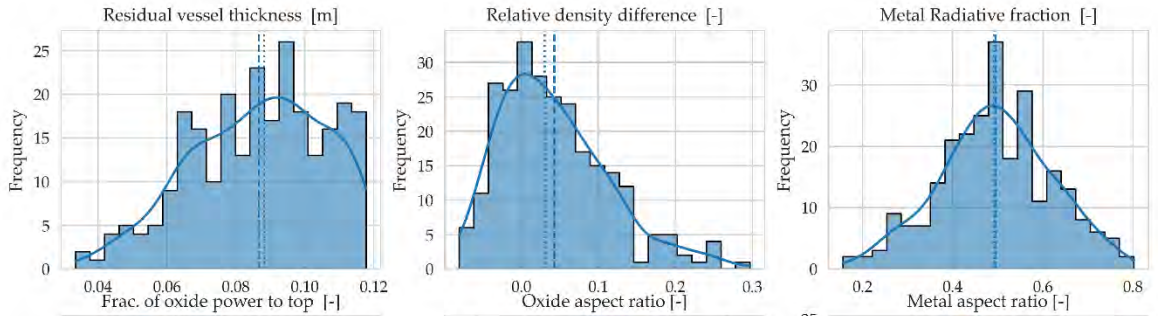

Var	n	μ	min	max
δv	257	0.09	0.03	0.12
ΔQ	257	0.04	-0.08	0.3
RadF	257	0.49	0.16	0.8
Xup	257	0.71	0.61	0.88
HRox	257	0.32	0.19	0.42
HRmet	257	0.13	0.06	0.21
δc	257	0.04	0.0	0.11
qf	257	362.24	193.24	1024.07

Design 2

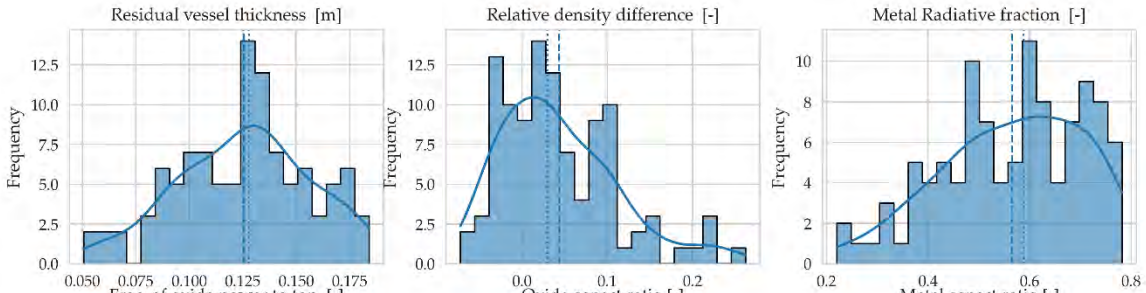

Var	n	μ	min	max
δv	105	0.13	0.05	0.18
ΔQ	105	0.04	-0.07	0.26
RadF	105	0.56	0.22	0.78
Xup	105	0.76	0.68	0.84
HRox	105	0.14	0.1	0.17
HRmet	105	0.07	0.05	0.11
δc	105	0.06	0.01	0.13
qf	105	255.03	136.99	680.77

Regarding average values, an expected picture is depicted just like the only properties calculation

Conclusions

- A W-STORM uncertainty and sensitivity analysis was carried out on SASPAM-SA designs through Monaco
- Reactor parameters and physical properties distribution were extrapolated from literature and from SASPAM-SA
- Spearman and Pearson coefficients for successful calculations are not informative (obvious relationships)
- Output parameters show an **expected picture** in IVMR in iPWR: thick dn crust, high radiative fraction, low aspect ratios, high power from oxide to metal, and limited focusing effect.
- Results further stress that in iPWRs there could be a high occurrence of Heavy Metal cases, due to a low steel to fuel mass ratio, **experimental data and heat transfer models are needed for this kind of configuration.**
- Frequency of occurrence of partial/ complete solidification cases (low FE) is significant. The confidence in this frequency is **limited**, due to the simple nature of the radiative heat transfer model in W-STORM. More **accurate radiative heat transfer models** should be implemented in SA codes, since radiative heat transfer can play a major role in the system's dynamics

Thank you for listening!

SAPIENZA
UNIVERSITÀ DI ROMA

- **M. Principato** (Sapienza, now PSI), C. Ciurluini (Sapienza), F. Giannetti (Sapienza) , L. Carénini (ASNR), F. Fichot (ASNR)

- Madrid, 19th May 2026

Experimental Study on the Naturally Stratified Melt Pool Based on High-Temperature Chloride Salts and Mg–Al Alloys

Fengyang QUAN, Ningxi JIA, Mengyi WANG
China Nuclear Power Engineering CO., LTD
Corresponding Address
quanfengyang@aliyun.com; jnx0913@sina.com; mengyiwxj@163.com

Jie PEI, Wei LI and Yidan YUAN*
China Nuclear Power Engineering CO., LTD
Corresponding Address
peijiepku@163.com; liweinml1983@aliyun.com; yidanyuan2010@aliyun.com

ABSTRACT

The effectiveness of In-vessel Retention (IVR) strategy is critically governed by the ability of the external cooling to envelop the heat flux distribution imposed on the reactor pressure vessel (RPV) inner wall by the melt pool (i.e., the core melt relocated to the lower head of the RPV). The stratification behavior of the melt pool—particularly the separation of the light metallic layer from the oxide layer—significantly influences the heat flux profile along the RPV inner wall. Owing to its high thermal conductivity and small thickness, the upper light metallic layer may lead to a pronounced “hot-spot” (known as the “focusing effect”), which represents a critical factor threatening the integrity of the RPV.

To investigate the heat transfer mechanisms in stratified melt pools, this study employed the SAMPO test facility, which utilizes a 2D slice structure scaled 1:4 to the prototype RPV lower head as the test section. Chloride salts and Mg–Al alloy were used as simulants for the oxide and metallic layers, respectively. To reproduce the core melt relocation process in the RPV lower head, block-shaped Mg–Al alloy were first distributed inside the test section, after which prepared high-temperature molten chloride salt (600℃) was poured in. Then, the Mg–Al alloy was melted by the salt and naturally stratified with it, successfully forming a two-layer melt pool with a new stratification pattern.

KEYWORDS
In-Vessel Retention, SAMPO, Stratified molten pool

1. INTRODUCTION

Nuclear power is widely recognized as an important clean energy source for humanity. Despite its distinctive characteristics and advantages as a clean energy, the massive public impact and huge socio-economic losses caused by severe accidents exert a profound influence on the global development of the nuclear industry. Historically, the Three Mile Island accident, the Chernobyl accident and the Fukushima nuclear accident [1] all triggered upheavals in the industry. To eliminate the risk of large-scale radioactive release, the third-generation nuclear power technology has developed In-Vessel Retention (IVR) and Ex-Vessel Retention (EVR) technologies respectively to respond to severe accidents. Among them, the IVR technology has been

* Footnote, if necessary, in Times New Roman font and font size 10

applied in both AP1000 and HPR1000, while the EVR technology has been adopted in EPR. This paper focuses on the heat transfer behavior of the in-vessel molten pool, a key phenomenon in the IVR technology.

Following a severe accident, the decay heat of core materials cannot be effectively dissipated, leading to core degradation. The resulting molten material migrates downward into the lower head of the reactor pressure vessel (RPV), forming a debris bed and potentially evolving into a molten pool. In the IVR scheme, to ensure the integrity of the RPV and mitigate the risk of large-scale radioactive release, the design incorporates External Reactor Vessel Cooling (ERVC)—whereby cooling water is supplied to the ex-vessel of the RPV lower head—to achieve effective cooling of the lower head. A critical challenge in this scheme is ensuring that the difference between the heat flux imposed on the inner wall of the lower head by the internal molten material and the cooling capacity of the external cooling water meets engineering threshold requirements. This ensures the lower head does not suffer melt-through or creep failure due to the decay heat of the internal molten corium.

In the early days, research on molten pool issues focused primarily on homogeneous molten pools, including experimental studies such as BALI, ACOPO and COPO, which yielded comprehensive findings on heat transfer in homogeneous molten pools [2-5].

However, with advances in materials science and the observation of metal phase separation during the MASCA project [6], the structural morphology of molten pools has evolved from homogeneous to double-layer or multi-layer configurations. Among these, the double-layer molten pool, featuring a light metal layer atop an oxide layer, has exerted a significant impact on existing IVR safety analyses. Due to its high thermal conductivity, the top metal layer induces a pronounced thermal focusing effect when it reaches a certain thickness, thereby challenging the feasibility of the IVR scheme.

International research on stratified molten pools has primarily centered on experimental facilities such as SIMECO and LIVE2D [7-8], yielding partial research data. Notably, the LIVE facility successfully achieved naturally stratified double-layer molten pools and verified the influence of the interphase shell on the thermal focusing effect. Nevertheless, molten pool experiments (including LIVE) are constrained by the temperature limits of simulant materials, preventing the simulation of heat transfer issues associated with low Prandtl (Pr) number metal layers. Consequently, uncertainties persist regarding the thermal focusing effect of metal layers in IVR applications.

To address molten pool problems involving low Pr number metal simulants, KTH Royal Institute of Technology in Sweden has developed chloride salt and low Pr alloy materials as simulants [9]. It plans to conduct experiments on heat transfer in stratified molten pools with a molten alloy top layer in the subsequent SIMECO-II experiment, aiming to supplement experimental data on heat transfer in low Pr number stratified molten pools.

To further advance experimental research on stratified molten pools, China Nuclear Power Engineering C O., Ltd. has constructed the SAMPO experimental facility [10], capable of conducting high-temperature (6 00°C) stratified molten pool experiments using chloride salt and magnesium-aluminum alloy as simulants. The first set of experiments focusing on stratified molten pools with ultra-thin metal layers has been compl eted.

2. Experimental Setup

2.1. SAMPO System

The SAMPO experimental facility adopts a two-dimensional 180° sliced configuration, with its geometric dimensions scaled at a 1:4 ratio relative to the lower head of China's HPR1000 reactor. The inner diameter

of the SAMPO test section is 1100 mm, and the slice thickness is 120 mm. The curved sidewall is made of stainless steel with a thickness of 30 mm, and a cooling water channel is designed outside the curved section to provide a constant-temperature cooling condition. The upper surface of the molten pool is a free liquid surface, and cooling water is contained in the top cover of the test section to ensure a constant temperature of the top structure. The front side adopts a double-layer glass structure: the inner layer is quartz, and the outer layer is high-temperature-resistant glass. The perimeter of the double-layer structure is equipped with a thermal insulation and sealing structure, which can effectively reduce heat loss through thermal convection. Through the visual surface, the molten pool morphology can be directly observed during the experiment.

The decay heat of the molten pool is simulated by heating with uniformly distributed heating rods. The molten material for the SAMPO experiment is prepared using the same smelting system, with the inner liner replaced according to the simulant materials at different temperatures. After the experiment, the simulant materials are recycled separately through recovery pipelines for reuse in subsequent experiments. The SAMPO system layout is shown in the Figure 1.

The molten salt furnace features an inner vessel constructed from commercially pure nickel. This material selection effectively mitigates the corrosive effects of chloride salts, ensuring structural integrity for up to 72 hours at 600 °C without severe corrosion failure. Consequently, this approach minimizes contamination of the molten salt by structural materials, thereby preserving its chemical purity.

Furthermore, in the SAMPO experimental system, an inert atmosphere is provided by argon gas from the protective gas system. Prior to the experiment, the protective gas system purges and maintains an inert atmosphere in all equipment of the experimental system. Before the injection of molten materials, the protective gas system is used to pressurize and control the system pressure, thereby facilitating the smooth injection of molten materials.

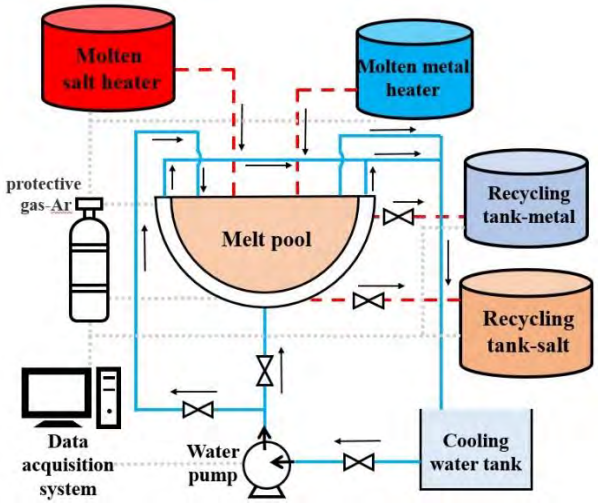

Figure 1. SAMPO System Scheme.

2.2. Simulant Materials

In the experiment, a ternary chloride mixed salt is used to simulate the lower oxide molten material, and a magnesium-aluminum alloy is used to simulate the upper metal molten material. The selected simulant materials meet the requirements for natural stratification in terms of density. Under experimental conditions, the density difference causes the magnesium-aluminum alloy to float above the molten salt layer, thereby achieving a double-layer molten pool structure similar to that of a prototype molten pool. Additionally, the Prandtl (Pr) number of the magnesium-aluminum alloy is close to that of the prototype metal layer material, enabling more accurate simulation of the molten pool heat transfer conditions. In this study, the purity of all

chloride salts employed exceeded 99%, while the magnesium-aluminum alloys were utilized in ingot form with impurity fractions below 1 wt%.

2.3. Instrumentation

The main measured data in this experiment are temperature signals, which are categorized by measurement area as follows: temperature inside the oxide layer molten pool, temperature inside the metal layer molten pool, inner wall temperature for heat flux measurement, outer wall temperature for heat flux measurement, and cooling water temperature. The scheme of the test section is presented in Figure 2.

- Thermocouples in the oxide layer molten pool: Arranged in layers at heights of 88 mm, 176 mm, 264 mm, and 352 mm respectively.
- Thermocouples in the metal layer molten pool: Start at a height of 440 mm, with a total of four layers spaced 44 mm apart.
- Thermocouple pairs for sidewall heat flux measurement: Divided into two regions, with the bottom of the test section as the 0° angle. One pair of thermocouples is installed every 5° from 0° to 65°, and another pair is installed every 2.33° above 65°. The thermocouples are perpendicular to the front surface of the curved section, and the measurement position is at the exact center of the curved section. The spacing between adjacent thermocouple pairs is 26 mm.
- The morphology of the crust layer is captured by a 4K high-definition camera. Flow meters are installed in each branch of the cooling channel of the test section to obtain actual cooling water flow rate data.

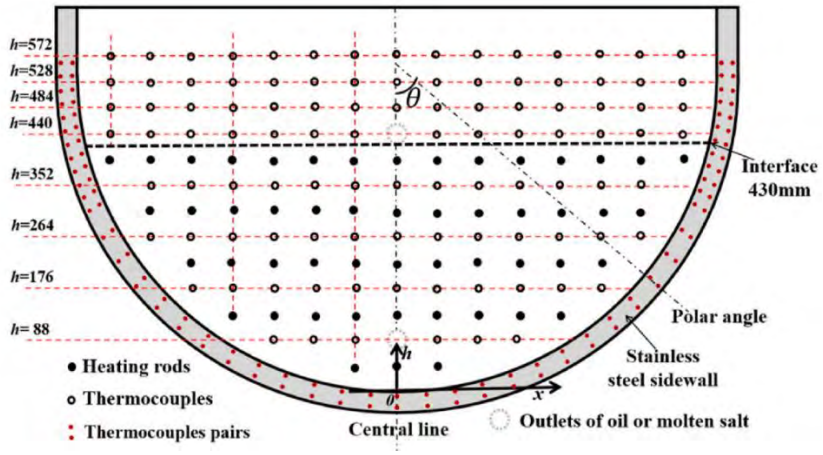

Figure 2. Distribution of TCs and Heating rods in SAMPO test section.

2.4. Experiment Matrix

To simulate the initial process of reactor core degradation and account for the threat of ultra-thin metal layers to IVR, fragmented oxide simulants and ingot-shaped metal simulants are pre-installed in the test section prior to the experiment. During the experimental preparation phase, molten chloride salt is prepared at 700℃ using a smelting furnace. After completing all preparation work, the molten chloride salt is injected into the test section via the injection system, and the heating power is gradually increased. Once the predetermined experimental operating conditions are reached, the cooling power and heating power are maintained to stabilize the system, thereby obtaining steady-state experimental data.

In this experiment, the theoretical injection level of the chloride salt reaches 430 mm, corresponding to a height angle of 77.4° for the curved section. The pre-installed magnesium-aluminum alloy in the test section melts to form a metal layer with a theoretical thickness of 40 mm. After injection, the molten salt is naturally melted by heat and forms a stratified structure. The decay heat power in this experiment is controlled at 10.8

kW. Basic experimental data of the high-temperature stratified molten pool are obtained through the establishment of a steady state. The experimental matrix is shown in Table 1.

Table I. Test Matrix

Oxide layer simulant	Height (mm)	Metallic layer simulant	Thickness (mm)	Heating Power (kW)
CsCl-KCl-LiCl	430	Mg-Al	40	10.8

3. Result

3.1. Stratification Process

After the injection of chloride salt, the gradual suspension and melting of magnesium-aluminum alloy ingots can be observed through the quartz glass. Due to their immiscible nature, obvious upward flow of molten metal droplets and aggregation at the top can be seen. However, a complete two-phase stratified state was not observed during the experiment: the formed metal layer only partially contacted the front glass surface, while most of it was encapsulated by the molten chloride salt. The entire process is shown in Figure 3.

Since aluminum in the magnesium-aluminum alloy reacts with quartz at high temperatures, the visualization process could only be maintained briefly during the high-temperature experiment. After the initial injection, as the reaction proceeded, the surface of the quartz observation window was gradually covered by reaction products. Only the gradual growth of the crust layer and the changes in crust thickness with variations in power could be observed.

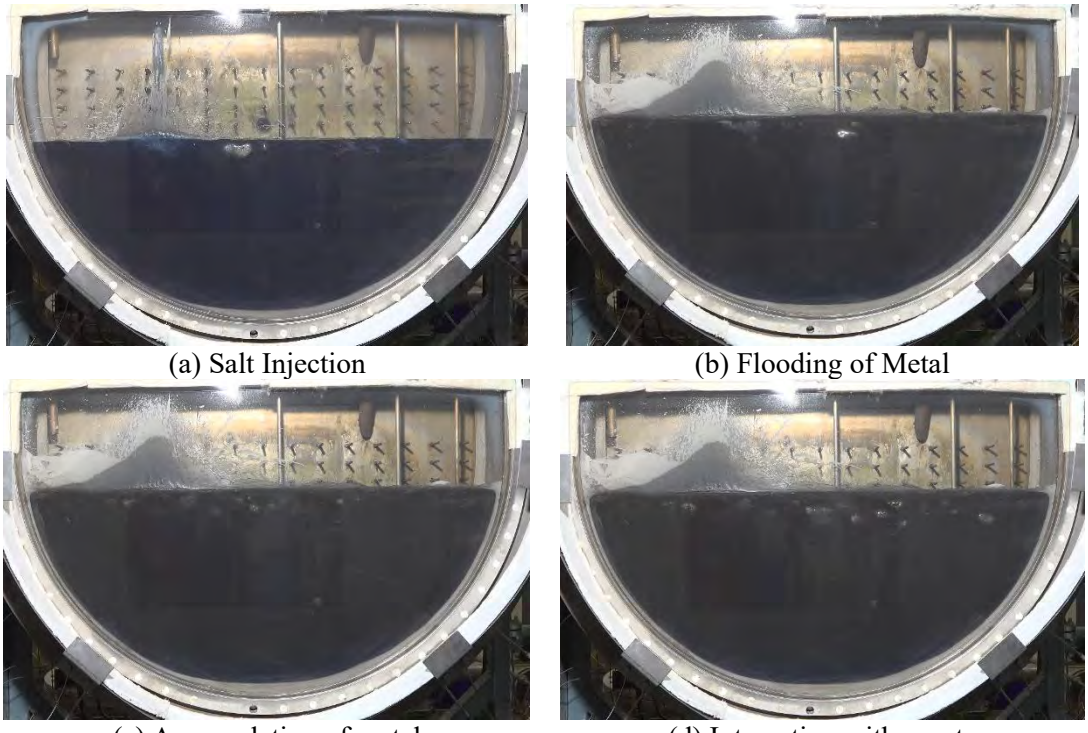

(a) Salt Injection (b) Flooding of Metal

(c) Accumulation of metal (d) Interaction with quartz

Figure 3. Injection process

3.2. Temperature distribution

The temperature distribution along the centerline is shown in Figure 4. Based on the calculated volume of the molten material, the theoretical position of the phase interface should be at 430 mm, with a metal layer thickness of approximately 40 mm. Temperature signals of the metal layer near the phase interface can be obtained through the thermocouples arranged in the molten pool. The temperature signal at the centerline (0 mm horizontal position) is provided by the inner thermocouple of the 0° angle heat flux thermocouple pair. It can be observed that the temperature along the molten pool centerline increases with height, reaches the maximum below the phase interface, and the corresponding maximum centerline temperature is 518℃. Additionally, the temperature in the molten pool becomes basically uniform when the height exceeds 200 mm.

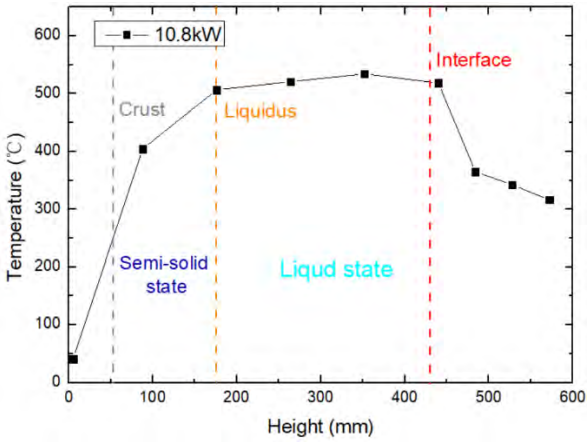

Figure 4. Centerline Temperature

For the steady-state results, a molten pool temperature contour map was generated using the thermocouples arranged inside the molten pool, and the result is shown in Figure 5. As can be seen from the contour map, the approximate distribution structure of the crust layer is presented, where the blue dashed line marks the theoretical phase interface. Nevertheless, it can be observed that above the phase interface, the temperatures on both sides of the metal layer are relatively low, showing a temperature distribution similar to that of the shell layer. A distinct local hot spot appears near the left shell layer inside the molten pool. The visualization results show that the overall morphology of the molten pool crust layer is highly consistent with the trend of the contour map. The molten pool is completely enclosed by the shell, and no obvious metal phase interface is observed. The solidus and liquidus temperatures were superimposed on the temperature contour plots to visualize the temperature distribution within the molten pool under steady-state conditions.

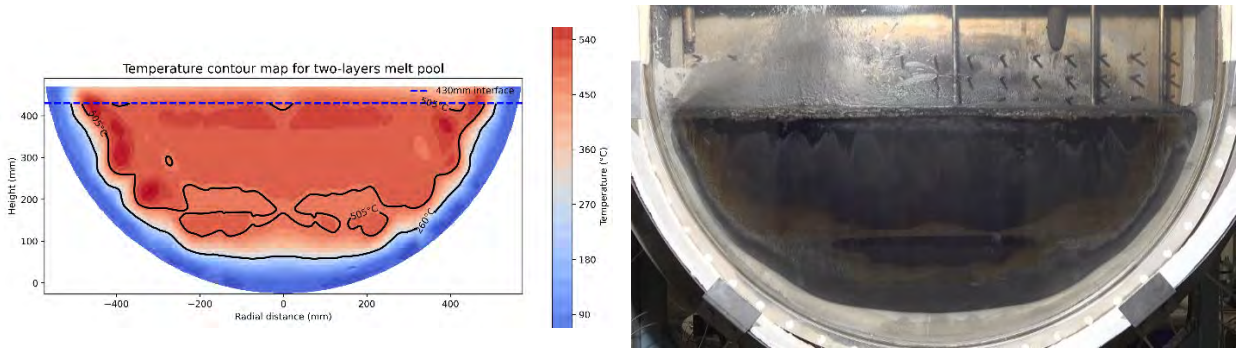

(a) Temperature Contour Map (b) Visualize results

Figure 5. Result of Temperature Contour Map

Figure 5 presents the theoretical solidus and liquidus temperatures of the chloride salt analogue, denoted by the 260 °C and 505 °C isotherms, respectively. By measuring the radial distance between these isotherms

and the arc-shaped boundary of the molten pool, the corresponding crust thickness was determined. These results were subsequently compared with the steady-state crust morphology obtained via HD camera visualization, as illustrated in Figure 6.

The comparison reveals distinct trends across different circumferential angles. In the range of 0° to 45°, the crust thickness derived from HD visualization is greater than that obtained from the thermal contour analysis. Conversely, above 45°, the crust thickness calculated from the temperature field is larger. This discrepancy is attributed to the interpolation methodology applied to generate the temperature contours.

Specifically, the temperature field reconstruction utilized thermocouple readings from the sidewall heat flux sensors and internal probes as input data. Due to the non-uniform spatial distribution of measurement points—with local refinement near the wall at approximately ±65° while maintaining a constant density in the bulk melt—the cubic spline interpolation yielded a non-uniform nodal support domain. In regions with excessive near-wall point density, the interpolation function tends to pull isothermal surfaces toward the dense nodes, artificially smoothing the actual radial temperature gradient. This results in a slightly overestimated solidified crust thickness in these areas. Conversely, in the bottom region (0° ± 50°), where the mesh is relatively sparse and curvature is high, the interpolation locally amplifies the radial gradient, leading to a slight underestimation of the crust thickness. Nevertheless, the overall trend of crust distribution at the bottom remains consistent with the visual observations.

Finally, it was observed that the cooling water temperature exhibited minor sinusoidal fluctuations (amplitude: ±1 °C, period: ~5 min) during the entire steady-state process. However, no corresponding fluctuations in crust morphology were detected experimentally, likely due to the limited resolution of the optical imaging system.

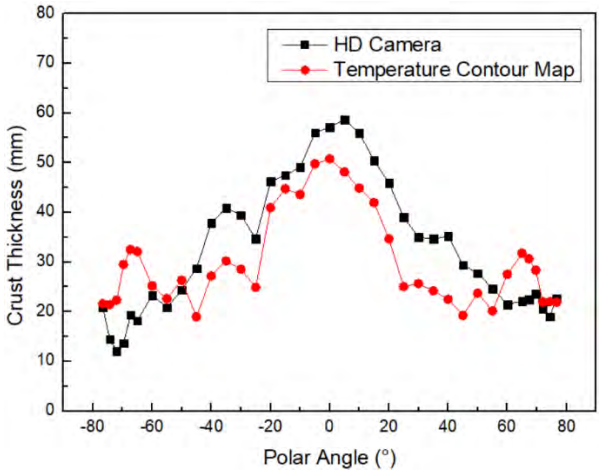

Figure 6. Crust thickness comparation between HD Camera and TC Map

3.3. Heat Flux distribution

The local heat flux was calculated using the temperature difference measured by the thermocouple pairs arranged on the sidewall and Fourier's Law of Heat Conduction:

$$q_w(\theta) = \lambda_{ss} \cdot \frac{T_{in}(\theta) - T_{out}(\theta)}{\mathrm{d}} \quad (1)$$

where $T_{in}(\theta)$ and $T_{out}(\theta)$ are the temperatures measured by the inner and outer thermocouples of the sidewall heat flux thermocouple pairs, respectively; d is the spacing between the two thermocouples, which is designed as 26 mm in this test facility; λ_{ss} is the thermal conductivity determined by the structural material. Since the test facility is made of stainless steel, the heat flux at the corresponding angle can be directly calculated using the above formula.

The distribution of heat flux on the left and right sides under the experimental operating condition is shown in the Figure 7. It can be found from the figure that the high-temperature region observed in the experimental contour map basically corresponds to the heat flux distribution. In this experiment, the theoretical phase interface position at 430 mm corresponds to a central angle of approximately 77°, a heat flux peak is observed in the heat flux distribution diagram around 70°. The theoretical maximum submergence height of the metal layer corresponds to a central angle of 81°; after the heat flux peak, a sharp decrease in heat flux is observed. However, no thermal focusing effect was observed during the entire experiment.

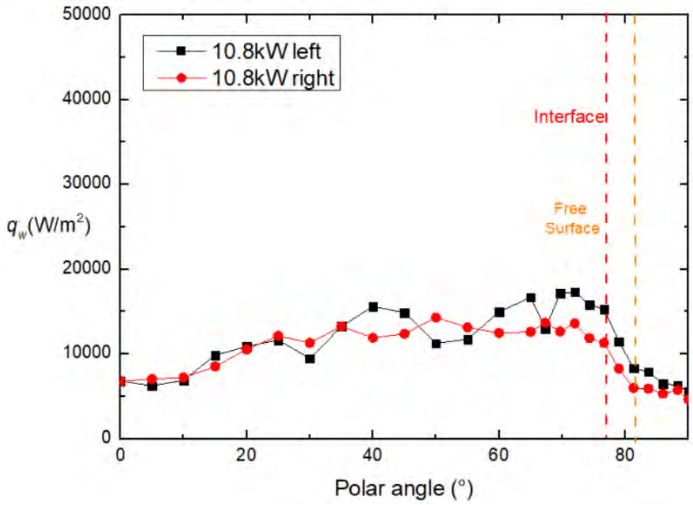

Figure 7. Heat Flux Distribution

Based on the heat flux distribution, the inner wall temperature $T_i(\theta)$ at corresponding angles can be calculated using Equation (2). Subsequently, the local solidified crust thickness and the average crust thickness are determined via Equations (3) and (4), respectively.

$$T_i(\theta) = T_{in}(\theta) + \frac{q_w(\theta) \cdot d}{\lambda_{ss}} \tag{2}$$

$$\delta_{calc}(\theta) = \lambda_{crust} \cdot \frac{T_{solid} - T_i(\theta)}{q_w(\theta)} \tag{3}$$

$$\overline{\delta_{calc}} = \frac{\sum \delta_{calc}(\theta) \cdot A(\theta)}{A_{tot}} \tag{4}$$

In Equation (2), d denotes the distance from the inner thermocouple of the pair to the inner wall surface. In Equation (3), T_{solid} represents the solidus temperature; for the data analysis in this study, the theoretical value of 260 °C was adopted. Here, $\delta_{calc}(\theta)$ corresponds to the solidified shell thickness at a given central angle. In Equation (4), $A(\theta)$ is the heat transfer area corresponding to the specific central angle, while A_{tot} refers to the total heat transfer area. A comparison of the normalized crust thickness is presented in Figure 7.

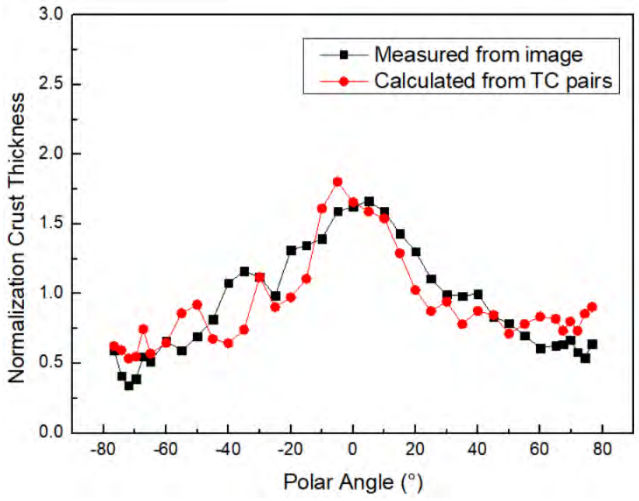

Figure 7. Comparison of normalized crust thickness between TC pairs calculation and HD visualization.

As shown in the figure, the crust thickness derived from the heat flux density exhibits a high degree of consistency with the image analysis results regarding the overall distribution trend. However, local deviations occur in the range of 40° to 60°. This anomaly is attributed to the configuration of the immersion heaters within the molten pool. The presence of the heater rods at these specific angles distorts the local heat flux measurements.

3.4. Cold-State Results

After the experiment, the system was naturally cooled while maintaining a constant-temperature boundary, and the internal state of the molten pool was observed. Upon opening the test section, the overall state of the molten pool is shown in Figure 8. A distinct gap is visible in the middle of the molten pool, which is consistent with the circumferential cooling process—since the central region cools last, a porous or vacuum structure is formed. This structure indicates that the solidification of the salt layer proceeds gradually inward from the curved section and the contact area with the top metal layer, thereby generating a local gap structure in the middle. In addition, as shown in the top view of the front side of the metal layer (Figure 9.), white chloride salt is present between the back plate and the metal layer. Combined with the observations from the front view, it is inferred that an ultra-thin contact may have formed between the metal layer and the back plate in practice.

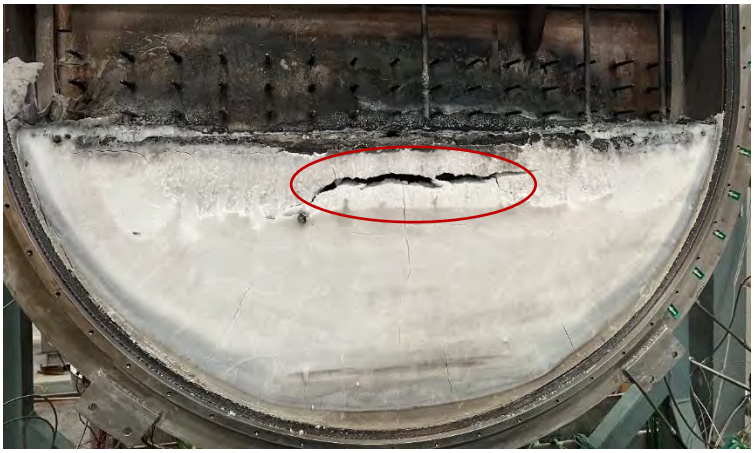

Figure 8. Solidified Molten Pool.

Figure 9. Solidified Molten Pool (Top View).

Further disassembly results are shown in Figure 10. After removing the salt layers on both sides, it was found that the metal layer was not in direct contact with the cooling sidewall. The bottom morphology of the metal layer is generally wavy, and the overall structure is thicker in the middle and thinner at both ends. This formed molten pool structure directly explains why no thermal focusing effect was observed in the sidewall heat flux results. Moreover, during the experiment, the volume of the metal layer caused direct displacement, leading to partial contact between the bottom of the metal layer and the heating rods. Consequently, in the temperature measurement data from the centerline thermocouples, the temperature inside the metal layer is close to the maximum temperature of the oxide layer. No temperature gradient resulting from a regular phase interface transition, such as those observed in water-oil or nitrate-heat transfer oil [10] operating conditions, was observed.

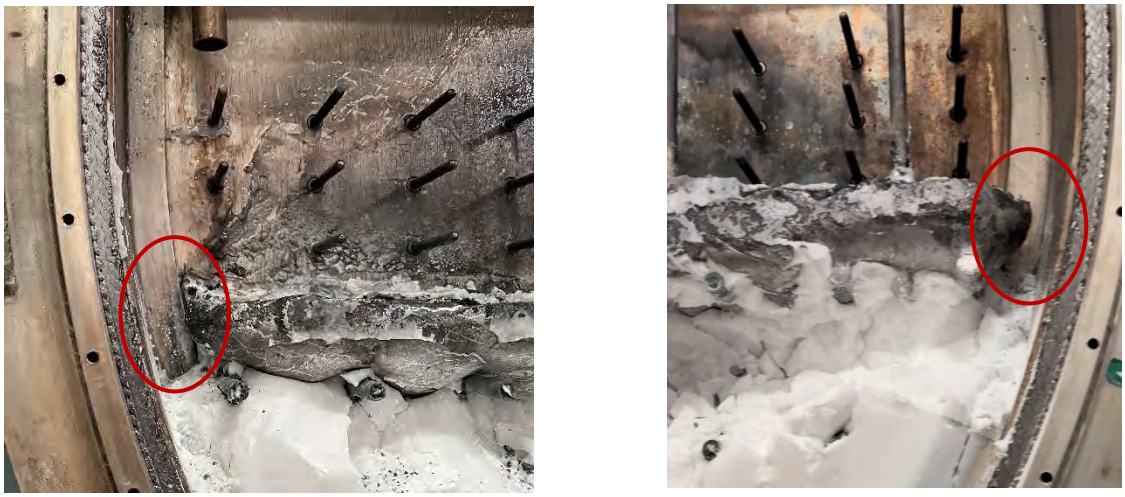

(a) Left Side (b) Right Side

Figure 10. Salt removed for Left side and right side.

4. CONCLUSIONS

The SAMPO experimental system is designed for conducting high-temperature molten pool experiments at 700℃. In this study, a naturally stratified molten pool experiment with a top metal layer having a Prandtl (Pr) number close to that of the prototype was successfully achieved. The experiment simulated the ultra-thin metal layer operating condition, and analyses were performed on the molten pool temperature

distribution, heat flux distribution, and cold-state structural morphology under high-temperature conditions. Based on the experiment, the key conclusions are summarized as follows:

- In the ultra-thin metal layer experiment, the temperature distribution along the centerline is consistent with the results of classical molten pool experiments. The centerline temperature in the molten pool first rises sharply with increasing height and then tends to stabilize. The temperature at the center and top of the molten pool is the highest and remains basically uniform.

- Affected by the morphology of the liquid metal, the top metal layer did not come into direct contact with the cooling sidewall during the actual experiment; instead, it formed an encapsulated morphology. This resulted in an overall sidewall heat flux trend similar to that of a homogeneous molten pool: the heat flux peak appears near a central angle of 70°, and the maximum submergence height angle of the molten material is approximately 82°, which is consistent with the heat flux distribution in homogeneous molten pools.

- The crust distribution trend derived from the heat flux density profile aligns closely with that obtained via visual observation. However, deviations arise primarily due to compositional changes in the chloride salt. The inherent corrosivity of high-temperature chlorides leads to metallic ion dissolution during both crucible preparation and experimental operation. Furthermore, impurities are introduced through chemical reactions between the magnesium-aluminum alloy and the quartz substrate. Since the current crust thickness calculations are predicated on the thermophysical properties of theoretically pure chloride salts, these alterations in composition inevitably result in discrepancies when comparing simulated results with visual data.

- This newly observed metal layer morphology differs from the commonly recognized stratified molten pool structure. Its formation may be attributed to the metal being pre-placed in the test section rather than injected from the top. However, due to the complexity of the actual conditions inside the reactor lower head, similar phenomena are likely to occur during core degradation. This phenomenon introduces new uncertainties: if chloride salt consistently forms an encapsulating layer on the sidewall as the metal layer thickness increases, the heat transfer characteristics of the molten pool under such conditions will be similar to those of a homogeneous molten pool, posing no threat to the existing IVR technology. Nevertheless, based on the currently observed metal layer structure, another possibility cannot be ignored: as the metal layer thickness increases, contact with the cooling sidewall may occur at a certain thickness. If this process is extremely slow, it may lead to prolonged excessively high local heat flux, thereby endangering the safety of IVR.

Therefore, as the first experiment in the series of high-temperature molten pool experiments, this study has gained valuable experimental experience. Meanwhile, the metal layer morphology observed in this experiment requires further comparison through subsequent experiments to verify and confirm the authenticity of such a morphology.

REFERENCES

1. Bal Raj Sehgal, *Nuclear Safety in Light Water Reactors - Severe Accident Phenomenology*, Chapter 1, Academic Press, Amsterdam, Netherlands.
2. Bonnet, J., Seiler, J., “Thermal hydraulic phenomena in corium pools: the BALI experiment.” *In: 7th ICONE*, 1999.Tokyo Japan.
3. T.G. Theofanous, M. Maguire, S. Angelini, T. Salmassi, “The first results from the ACOPO experiment”, *Nuclear Engineering and Design*, Volume 169, Issues 1–3, Pages 49-57 (1997).

4. Maria Helle, Olli KymaHiinen and Harri Tuomisto, “EXPERIMENTAL DATA ON HEAT FLUX DISTRIBUTION FROM A VOLUMETRICALL Y HEATED POOL WITH FROZEN BOUNDARIES”, Imatran Voima Oy Process Laboratory, DLV1-G380-0377.
5. T.G. Theofanous, “In-vessel coolability and retention of a core melt”, *Nuclear Engineering and Design*, 169, 1-48 (1997).
6. Asmolov, V., Bechta, S., Khabensky, V., Gusarov, V., Vishnevsky, V., “2004. Partitioning of U, Zr and FP between molten oxidic and metallic corium. In: MASCA Project (2000-2003)/Vol.1”. Proc. of the MASCA Seminar, 10–11 June 2004, Aix-en-Provence, France.
7. A. A. Gubaidullin, B. R. Sehgal, “SIMECO Tests in a Melt Stratified Pool”, *In: 10th ICONE*, 2002. Virginia, USA.
8. X. Gaus-Liu, Th. Cron, B. Fluhrer, Th. Wenz, “Experimental study and analytical analysis on the global heat transfer of stratified corium in LWR lower head”, *Nuclear Engineering and Design*, 372 (2021).
9. Peng Yu, Anderi Komlev, Walter Villanueva, Yichuan Li, Weimin Ma, Sevostian Bechta, “Pre-Test Simulations of SIMECO-2 Experiments on Stratified Melt Pool Heat Transfer”, *NUTHOS-11: The 11th International Topical Meeting on Nuclear Reactor Thermal Hydraulics, Operation and Safety*, 2016, Gyeongju, Korea.
10. Jie Pei, Mengyi Wang, Wei Li, Fengyang Quan, Qiang Guo, Yidan Yuan, Weimin Ma, “An experimental study on heat transfer in naturally stratified two-layer melt pools”, *Progress in Nuclear Energy*, 188 (2025).

Experimental Study on the Naturally Stratified Melt Pool Based on High-Temperature Chloride Salts and Mg–Al Alloys

Fengyang QUAN, Ningxi JIA, Mengyi WANG,
Jie PEI, Wei LI, Yidan YUAN
China Nuclear Power Engineering CO., LTD

19th May 2026

CONTENT

01 Introduction

02 Experimental Setup

03 Results

04 Conclusion

01

Introduction

I. Introduction

- Nuclear Power Industry development and Severe Accident
  - Severe Accident in History：TMI、Chernobyl 、Fukushima Daiichi
  - Severe accident management
- IVR and EVR Strategy
  - ✓ ERVC (AP1000, HPR1000, CAP 1400, etc.)
  - ✓ Core Catcher (EPR, VVER)

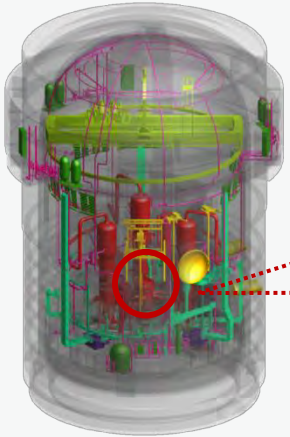

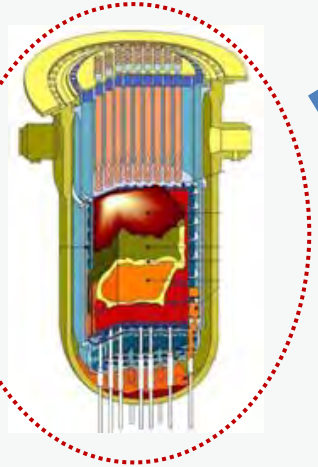

IVR

EVR

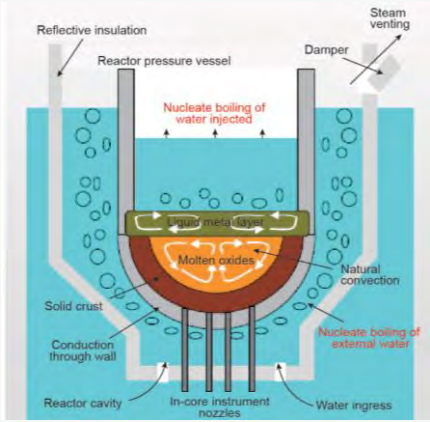

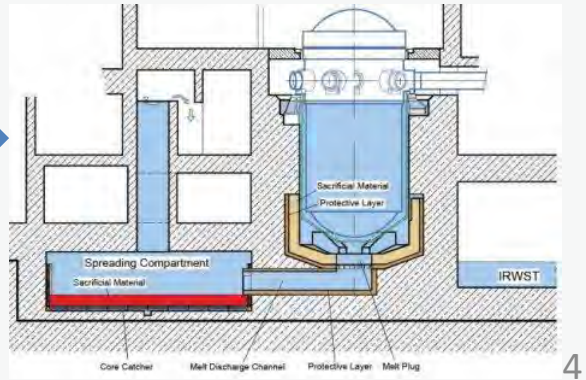

I. Introduction

- Melt pool heat transfer
  - Comprehensive findings on heat transfer in homogeneous molten pools, BALI, COPO, ACOPO etc.
  - Uncertainty exist in prototype molten pool's behavior with MASCA project's results.
  - Limited results with Stratified molten pool's research
    - Limited data for naturally stratified molten pool. (LIVE-2D, SIMECO)
    - Limited metallic layer simulant. (Low Pr)

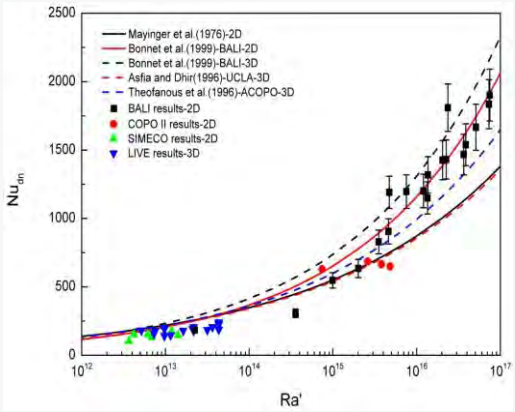

Ra'-Nu_{dn}

MASCA Results

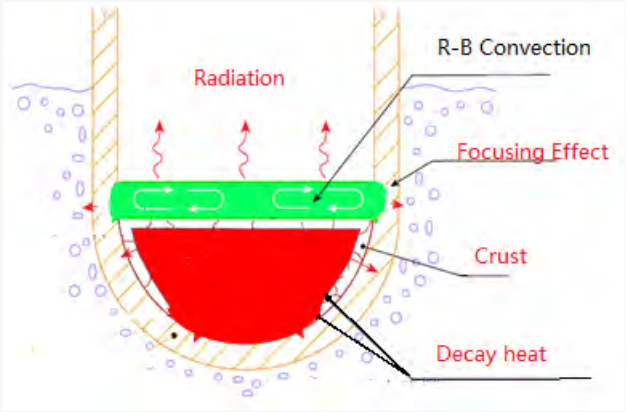

Scheme of stratified pool

I. Introduction

- SAMPO test facility
  - Conduct up to 600°C high temperature experiment
  - Conduct Low Pr number metallic simulant stratified molten pool experiment
  - Achieve Visibly, Naturally stratified molten pool
  - Refinement of the heat transfer correlation for the stratified molten pool module in the PISAA code

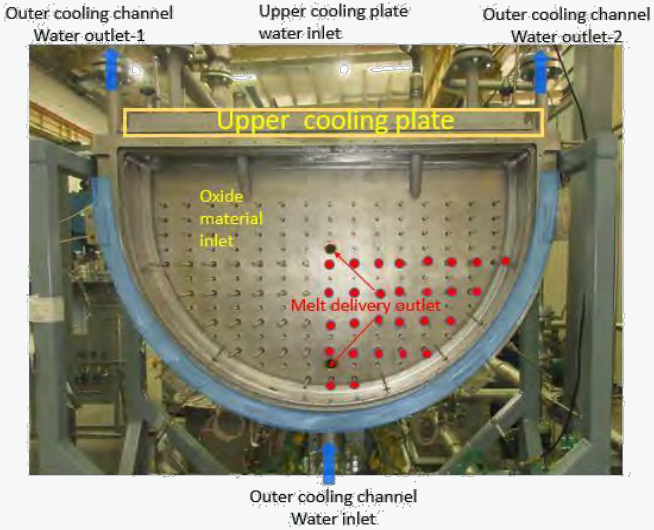

02

Experimental Setup

II. Experimental Setup

SAMPO | Simulant | Instrumentation | Test condition

SAMPO System Introduction

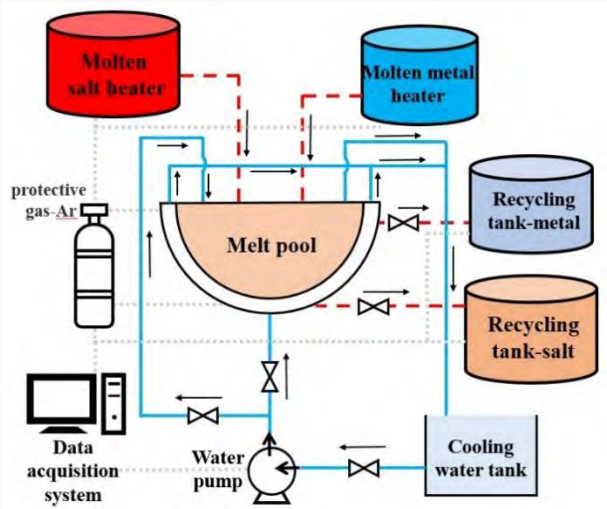

- Melt Pool Test Vessel
  - 1:4 Scale 180° 2D Slice facility
  - 120 mm Thickness
  - 30 mm thick vessel wall in ss
  - Decay heat power: up to 35 kW
- Ar-Gas protective system
- Corium preparation and recycle system
- Cooling System

II. Experimental Setup

Simulant

- Oxide simulant: CsCl-KCl-LiCl (Purity ≥ 99%)
  - Stable at 600℃
  - Larger density
- Metallic simulant： Mg-Al (Ingot)
  - Melting point at 437℃
  - Low Pr (~0.01)
  - Low density

II. Experimental Setup

SAMPO | Simulant | Instrumentation | Test condition

Instrumentation

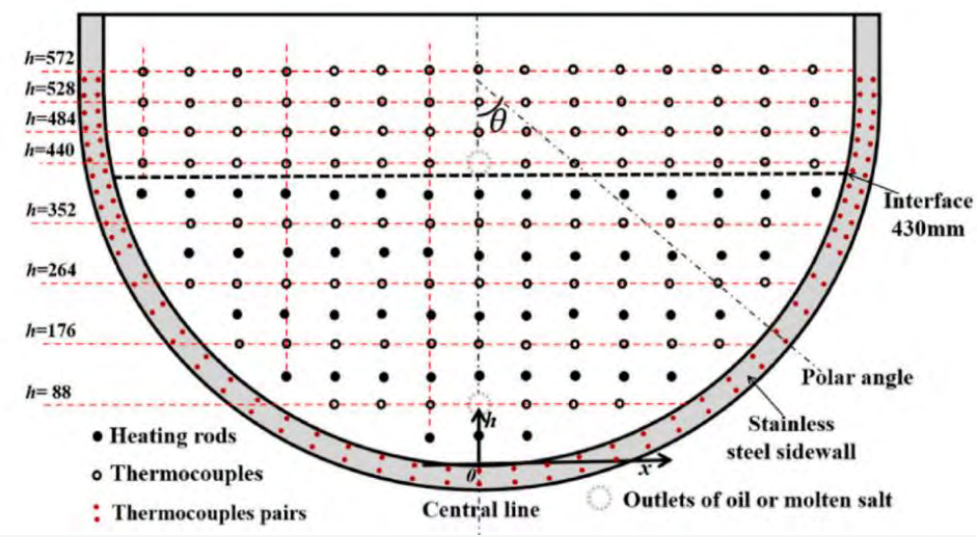

- Molten pool TC
  - Oxide layer：88 mm. 176 mm. 264 mm. 352 mm
  - Metallic layer： 440 mm, spaced at 44 mm, 4 layers in total
- Side wall TC pairs: Distance between: 26 mm
  - 0~65° ： Every 5°
  - 65~90° ： Every 2.33°
- 4K High-Definition Camera

II. Experimental Setup

SAMPO | Simulant | Instrumentation | Test condition

Test condition

- Simulate the initial process of reactor core degradation and account for the threat of ultra-thin metal layers
- Oxide layer height (theoretically): 430 mm
- Metallic layer height (theoretically): 40 mm

Oxide Simulant	Height(mm)	Metallic simulant	Height(mm)	Power(kW)
CsCl-KCl-LiCl	430	Mg-Al	40	10.8

03

Results

III. Results

中核集团 CNNC 中核工程 CNPE

Stratification process | Temperature Distribution | Heat Flux Distribution | Cold-State Results

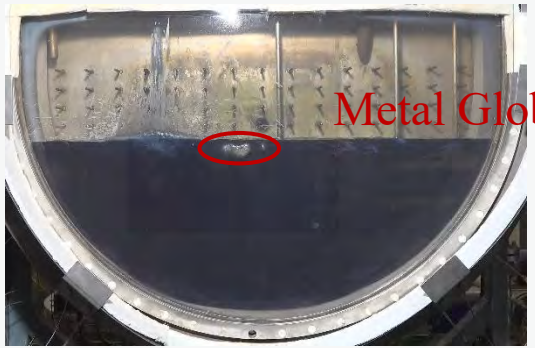

Injection of Molten Salt

- During injection, the metal ingot melts and levitates upward.
- The magnesium-aluminum alloy melts upon heating and forms molten metal globules.

III. Results

中核集团 CNNC 中核工程 CNPE

Stratification process | Temperature Distribution | Heat Flux Distribution | Cold-State Results

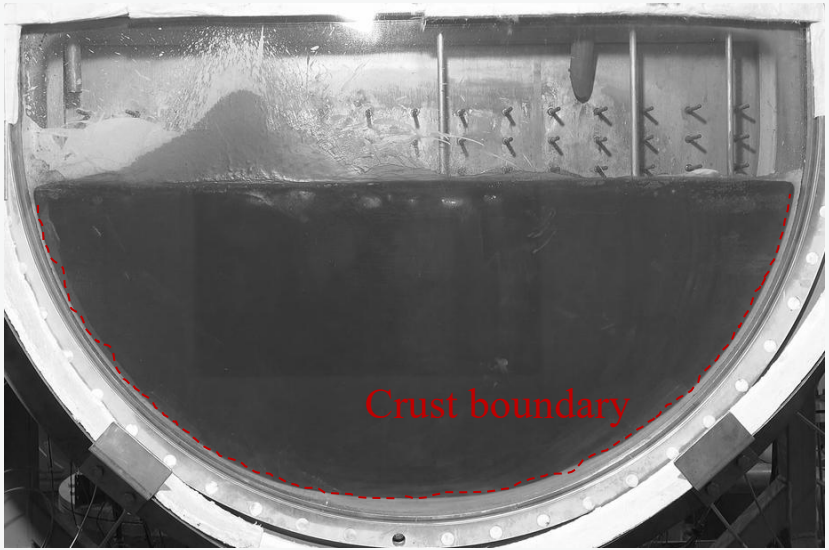

Molten metal aggregation

- Molten metal accumulates at the top of the melt pool.
- No obvious stratification was observed.
- As the reaction between quartz glass and metal progresses, observation of the metal layer morphology becomes increasingly difficult.
- The morphology of the crust layer can still be observed.

III. Results

Stratification process | Temperature Distribution | Heat Flux Distribution | Cold-State Results

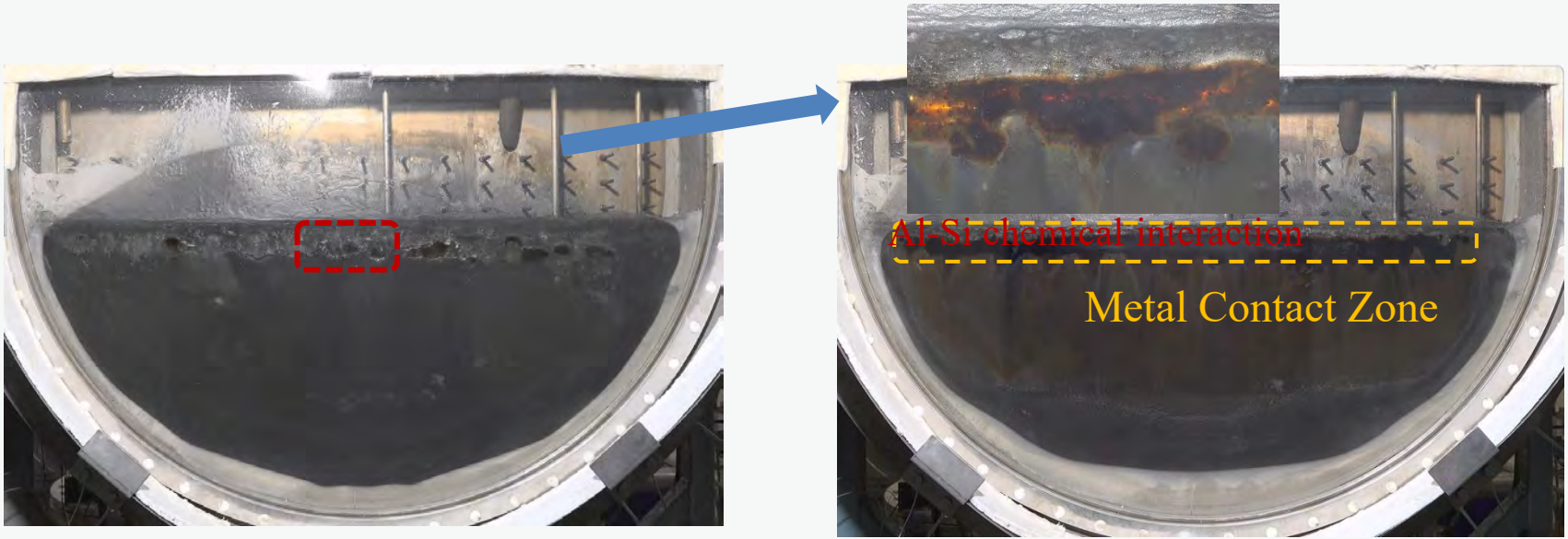

Reaction between metal and quartz glass

III. Results

Stratification process | Temperature Distribution | Heat Flux Distribution | Cold-State Results

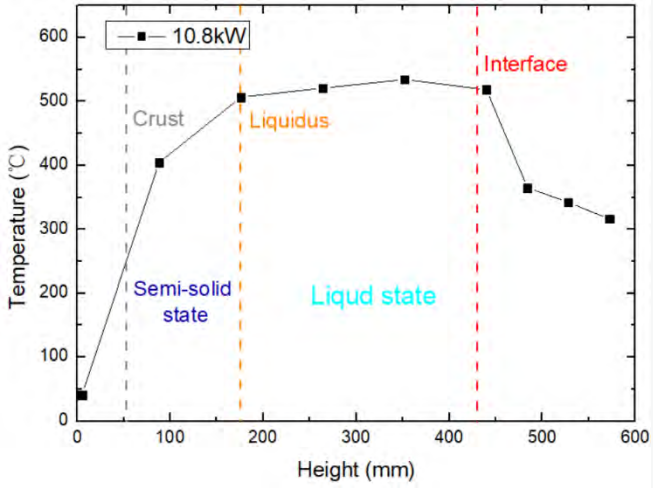

Temperature distribution along the centerline

- At the 0 mm position, the centerline temperature is provided by the thermocouple pair measuring heat flux at 0° , on the inner side of the corresponding thermocouple.
- The centerline temperature increases with the height of the melt pool.
- The maximum temperature below the phase interface is 518 ℃
- Above 200 mm, the melt pool temperature is essentially uniform.

III. Results

Stratification process | Temperature Distribution | Heat Flux Distribution | Cold-State Results

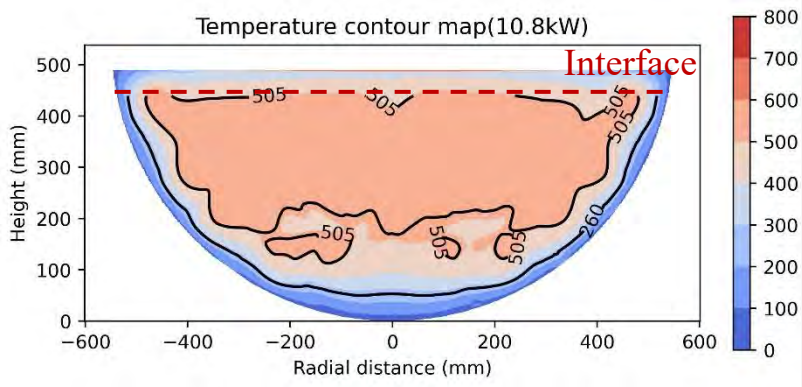

Temperature Contour Map

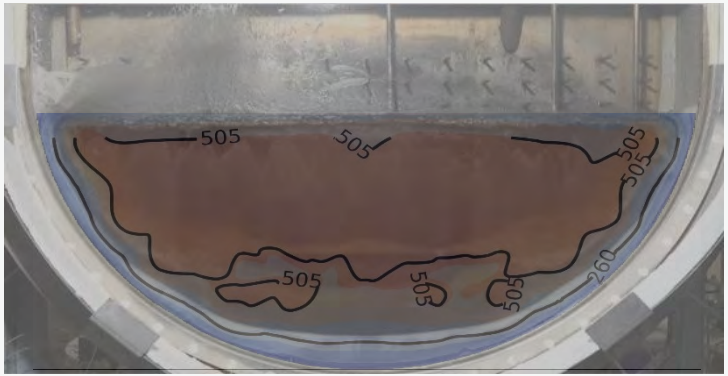

Visualize results for steady state

- On both sides of the metal layer above the interface, temperatures are lower, exhibiting temperature distribution characteristics similar to those of a shell layer.
- Localized hot spots appear clearly within the melt pool relates to the heater.
- The visualization results agree well with the contour plots, no distinct interface is observed.

III. Results

$$q_w(\theta) = \lambda \cdot \frac{T_{in}(\theta) - T_{out}(\theta)}{\mathrm{d}}$$

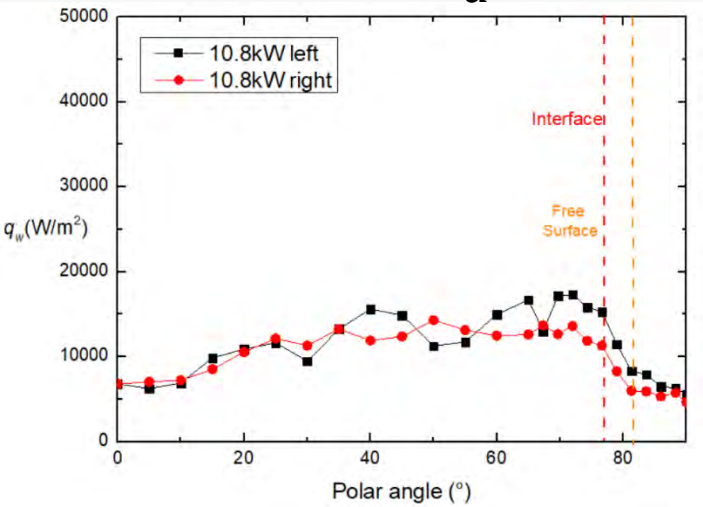

Side wall heat flux distribution

- The high-temperature regions in the experimental contour plot generally correspond to the heat flux distribution.
- At 430 mm, the theoretical phase interface is located at a center angle of 77°, while the heat flux peaks near 70°.
- The theoretical maximum liquid level is at 81°, and the heat flux drops sharply around this angle.
- No focusing effect was observed during the experiment.

III. Results

- Visible gaps appear in the solidified pool, which is consistent with the circumferential cooling process. Since the central region cools last, a porous or void structure is formed.
- White chloride salts are presented between the backplate and the metal layer; in the actual experiment, a relatively thin contact formed between the metal layer and the backplate.

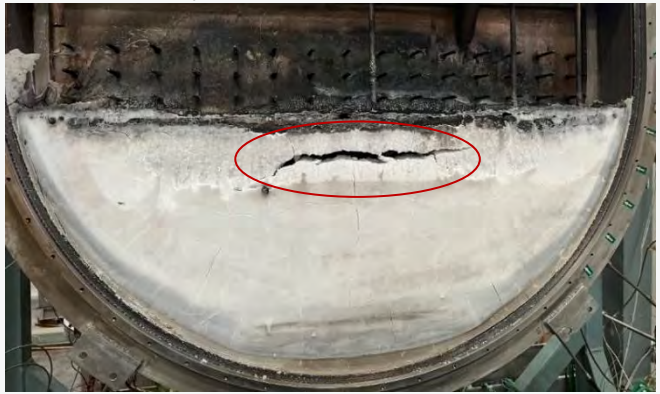

Solidified Pool (Removed the quartz front)

III. Results

- The metal layer is not in contact with either side.
- Metal layer bottom shows a wavy profile: thick in the middle, thin at the ends. This melt pool structure explains why no thermal focusing effect is observed in sidewall heat flux.
- No Temperature gradient from regular phase interface transition is observed.

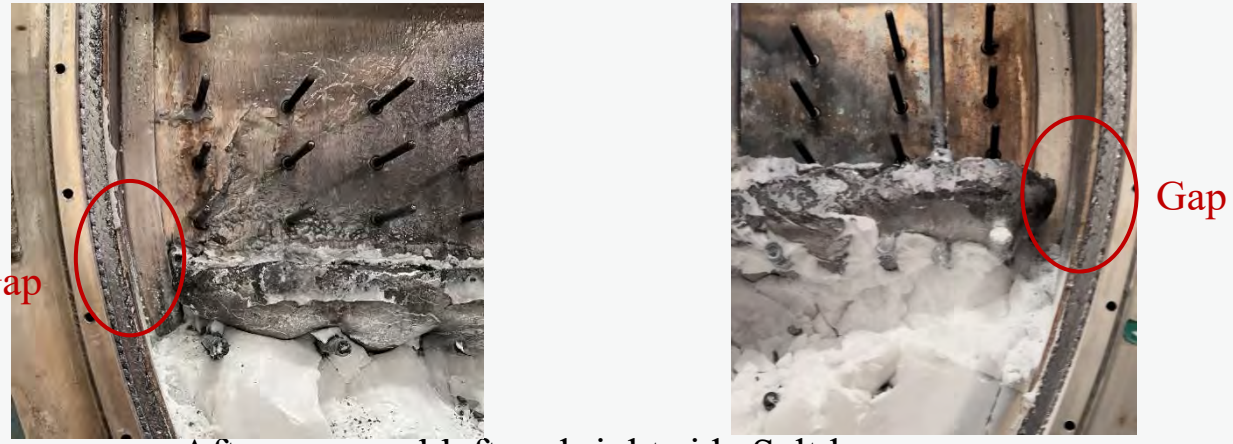

After removed left and right side Salt layer

04

Conclusion

IV. Conclusion

- In this thin metal layer experiments, the centerline temperature distribution agrees well with classical molten pool results. The centerline temperature initially rises sharply with height, then levels off. Temperatures at the pool center and top remain highest and essentially uniform.

- Due to the morphology of the molten metal, the top metal layer does not directly contact the cooled sidewall in the actual experiment, instead forming an encapsulated configuration. Consequently, the overall trend of sidewall heat flux resembles that of a homogeneous molten pool: the heat flux peaks near a center angle of 70°, and the maximum submergence angle of the molten material is approximately 81°, which is consistent with the heat flux distribution in a homogeneous molten pool.

IV. Conclusion

Newly observed metal morphology deviates from classic stratified pool, possibly due to pre-placed vs. injected metal. Yet, given lower head complexities, similar behavior is plausible during meltdown, introducing new uncertainties:

- If chloride salt maintains sidewall encapsulation with increasing metal thickness, pool heat transfer mimics homogeneous case, posing no risk to current IVR.
- With increasing metal layer thickness, sidewall contact may occur. If too slow, prolonged high local heat flux could compromise IVR safety.

中核集团 CNNC

中核工程 CNPE

Thank You for your attention!

STAND-ALONE ANALYSIS AND EVALUATION OF UNCERTAINTIES OF IVMR IN SMR USING AC² CODE

Mindaugas Valinčius*
Lithuanian Energy Institute
Breslaujos str. 3, 44403 Kaunas, Lithuania
Mindaugas.Valincius@lei.lt

L. Lovasz, P. Pandazis
Gesellschaft für Anlagen- und Reaktorsicherheit (GRS) gGmbH
Boltzmannstraße 14, 85748 Garching, Germany
Liviusz.Lovasz@grs.de; Peter.Pandazis@grs.de

ABSTRACT

In recent years, small and modular reactors (SMRs) have gained increasing attention in the nuclear energy sector. The SASPAM-SA project addresses, among other topics, severe accident strategies such as in-vessel melt retention (IVMR) in SMRs. Within this project, the IVMR strategy for a specific SMR design has been investigated by the Lithuanian Energy Institute (LEI) in cooperation with GRS, using the AC^2 system code (GRS, version 2023.4). This paper presents the main results of these analyses. The investigated reactor design is an integrated PWR with a classical type of spherical containment. The containment has a concrete floor and a cavity for reactor pressure vessel (RPV), which can be flooded in case of IVMR.
Using the stand-alone lower plenum module of AC^2, simulations were performed to assess the thermal response of the RPV under severe accident conditions. A comprehensive uncertainty and sensitivity analysis was performed, focusing on the uncertain parameters defining configuration and properties of molten materials (fuel mass, power density, etc.). The results show that even under conservative assumptions, the IVMR strategy is effective: the maximum outer heat flux (~259 kW/m²) remains well below critical heat flux thresholds, and the minimum residual vessel wall thickness exceeds 15 cm in all cases. The observation of focusing effect was limited, as the heat flux from the oxidic layer exceeded heat flux from the metallic layer. The analysis confirms that IVMR strategy is expected to be successful for investigated design, provided the cavity remains flooded. The findings support the applicability of AC^2 for IVMR evaluation in SMRs and highlight the importance of model assumptions and parameter uncertainties in safety margin assessments.

KEYWORDS
SMR; In-Vessel Melt Retention; Severe Accident; AC^2; Uncertainty Analysis

1. INTRODUCTION

Small Modular Reactors (SMRs) are increasingly regarded as a promising for deploying future nuclear reactor technologies. Their design focuses on achieving higher levels of safety and improving economic

performance, largely by reducing upfront investment costs and shortening construction time as a mass production.

In the range of SMRs, integral Pressurized Water Reactors (iPWRs) are considered as promising, since they are based on the previous generation Light Water Reactor (LWR) technology, but at the same time, introducing several advancements. Their inherent features are lower power output, an integrated design of Reactor Pressure Vessel (RPV) and safety ensured mainly by passive safety systems.

Even though SMR is a smaller reactor, it is nonetheless a nuclear installation, and safety is top priority. It must be demonstrated via safety analyses that the plant can operate safely. These analyses include design basis accidents (DBA), as well as design extension conditions (DEC). When it comes to severe accident (SA) management with significant core damage (DEC-B), the majority of currently developed SMR designs [1] rely on In Vessel Melt Retention (IVMR) as a severe accident management strategy (SAMS), to mitigate the consequences of SA.

In-vessel melt retention (IVMR) has been extensively investigated for High-Power Reactors (HPRs). Several modern reactor concepts, such as the AP1000 [2] and HPR1000 [3] incorporate this approach in their designs. The same strategy shows strong potential for integral pressurized water reactors (iPWRs) as well, and dedicated studies are being conducted within the Horizon Europe–Euratom project SASPAM-SA (Safety Analysis of SMR with Passive Mitigation Strategies – Severe Accident) [4], led by ENEA - a scientific research organization in Italy.

One of the key objectives of the SASPAM-SA project is to establish credible severe accident scenarios for iPWRs, assess how well existing experimental data apply to these reactor types, and identify the knowledge gaps that will require new experimental investigations. The project considers two generic iPWR designs for its analyses, named Design 1 and Design 2. Both SASPAM-SA designs share similar layouts within the RPV and SA mitigation, based on IVMR strategy.

This paper presents the work performed by the Lithuanian Energy Institute (LEI) in cooperation with GRS for Design 2 (**Figure 1**), which features several passive systems, a dry containment, and an electric power output of around 300 MWe. The analysis was performed using the AC² system code (GRS, version 2023.4), focusing on stand-alone lower plenum calculations with comprehensive uncertainty and sensitivity analysis. The uncertainty and sensitivity analysis was performed using the SUSA 4.2 software (GRS).

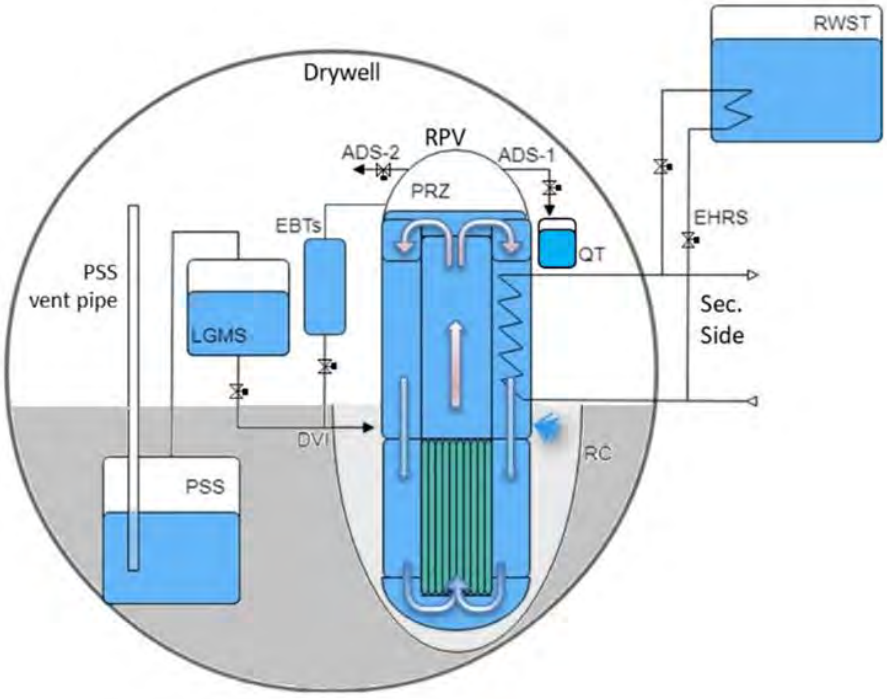

Figure 1. Design 2 layout.

2. AC² CODE AND MODELING APPROACH

2.1. AC² Code System

The code system AC² is the collection of GRS system codes ATHLET, ATHLET-CD and COCOSYS for the simulation of normal operation, transients, accidents up to severe accidents with radioactive release at the site boundary. ATHLET (Analyse der THermohydraulik von LEcks und Transienten) simulates the thermohydraulic behaviour in the reactor. ATHLET-CD (Core Degradation) extends these thermohydraulic modules with models for severe accident phenomena. The most important modules of ATHLET-CD include ECORE for core heat-up and degradation, FIPREM for fission product release, SAFT for transport and deposition, and AIDA/LHEAD for lower plenum processes and ex-vessel cooling.

2.2. AIDA Module for Lower Plenum Analysis

The AIDA module of ATHLET-CD is intended for simulation of late accident phenomena in the lower plenum. The module is an integral part of ATHLET-CD, and it also provides possibility of stand-alone simulation. It is equipped with a two-layer corium model (metal layer over the oxide layer), as illustrated in **Figure 2**. AIDA solves a 0-dimensional heat balance equation for each of the two layers and the interlayer crust. The crust formation between the wall and the oxide layer and between the oxide and metal layer is calculated with a 2-dimensional scheme.

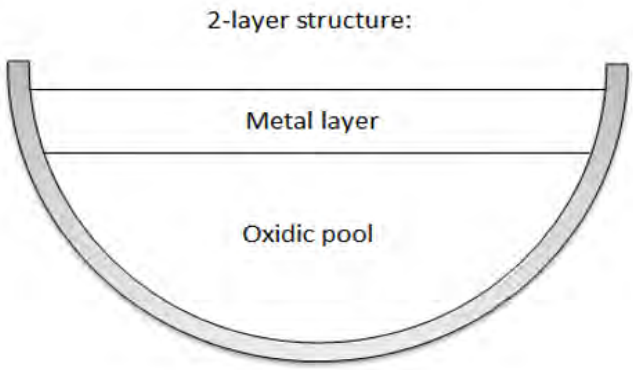

Figure 2. Two-layer corium configuration in AIDA module - metal layer above oxidic pool.

The current version of AIDA is able to simulate hemispherical, elliptical, trunked elliptical and trunked hemi-spherical lower plenum shapes together with the lower cylindrical part of the RPV. The wall ablation as well as the crust along the ablated wall are modelled.

2.3. Modelling Configuration for Design 2

For the Design 2 analysis, a stand-alone AIDA model was developed with detailed nodalization of the lower head geometry. The lower head nodalization (**Figure 3**) consists of 50 axial nodes for the hemispherical section and 27 axial nodes in the cylindrical part, with 20 radial rings providing sufficient spatial resolution for accurate heat transfer calculations.

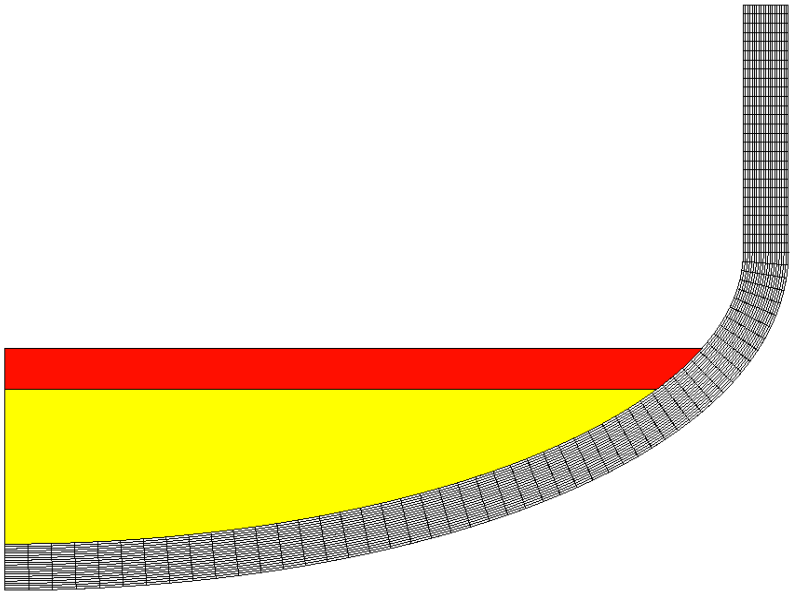

Figure 3. Lower head nodalization in AIDA showing 50 axial nodes in hemisphere and 27 nodes in cylindrical part with 20 radial rings.

A two-layer configuration is considered with the metal layer on top of the oxidic layer. Since AC² does not take into account thermochemistry, the configuration is the same during the entire simulation. For heat transfer from oxidic melt to upper crust, the Kelkar correlation was used. For heat transfer from oxidic melt to lower crust, the Asfia-Dhir correlation was used (**Figure 4**). These correlations were selected basing on AC^2 manual, where the code developers suggest using Kelkar(4)/Asfia-Dhir(7) or Bonnet-Seiler(6)/ Bonnet-Seiler(8) for upward/sideward heat transfer in real reactor simulations. However, Bonnet-Seiler correlations have a specified validity range of $10^{13}<Ra<10^{17}$, and since in current scenarios Ra is expected to be in ~10^{10} range, the Kelkar/Asfia Dhir correlations were selected. In all calculations it was assumed that 10% of the decay heat is present in the metallic layer, and 90% in the oxidic layer.
Since radiation from the metallic layer is modelled, the internal RPV structures are assumed to be at a constant 1100 K temperature as a boundary condition.

Nr.	Correlation for upward heat transfer (NCOUP)		Validity range
1	Kulacki-Emara (experimental)	$Nu = 0.34\ Ra^{0.226}$	
2	Mayinger (experimental)	$Nu = 0.345\ Ra^{0.233}$	
3	Mayinger (numerical sim.)	$Nu = 0.4\ Ra^{0.2}$	
4	Kelkar (numerical sim.)	$Nu = 0.18\ Ra^{0.237}$	
5	Reineke (numerical sim.)	$Nu = 0.49\ Ra^{0.18}\left(\frac{h}{R}\right)^{0.29}$	
6	Bonnet-Seiler (Exp. COPO-BALI)	$Nu = 0.381\ Ra^{0.234}$	$10^{13} < Ra < 10^{17}$
	Correlation for sideward heat transfer (NCODN)		
1	Mayinger (numerical sim.)	$Nu = 0.55\ Ra^{0.2}$	7 $10^{6} < Ra < 5$ 10^{14}
2	Kelkar (numerical sim.)	$Nu = 0.1\ Ra^{0.25}$	$Ra < 10^{16}$
3	Mini-ACOPO (experimental)	$Nu = 0.2\ Ra^{0.3}$	$10^{12} < Ra < 7$ 10^{14}
4	Jahn-Reineke (experimental)	$Nu = 0.54\ Ra^{0.18}\left(\frac{h}{R}\right)^{0.26}$	4 $10^{12} < Ra < 1.8\ 10^{13}$
5	Reineke (numerical sim.)	$Nu = 0.49\ Ra^{0.18}\left(\frac{h}{R}\right)^{0.29}$	
6	Reineke (numerical sim.)	$Nu = 0.64\ Ra^{0.18}\left(\frac{h}{R}\right)^{0.29}$	
7	Asfia-Dhir (experimental)	$Nu = 0.54\ Ra^{0.2}\left(\frac{h}{R}\right)^{0.25}$	
8	Bonnet-Seiler (Exp. COPO-BALI)	$Nu = 0.131\ Ra^{0.25}\left(\frac{h}{R}\right)^{0.19}$	$10^{13} < Ra < 10^{17}$

Figure 4. Available and selected correlations for heat transfer in the oxidic layer in AC² code (Kelkar for upward and Asfia-Dhir for sideward heat transfer).

The RPV surroundings (ex-vessel) temperature was set to 373 K, and heat transfer coefficient from external RPV surface to the surroundings was set to 10,000 W/m²K. The cavity is considered as always full of water, representing continuous external cooling conditions. These boundary conditions represent a bounding assumption for forced convective external cooling with the reactor cavity permanently flooded, consistent with IVMR success criteria. In this paper the focus is on in-vessel corium behavior and the resulting heat fluxes. For the actual IVMR evaluation and safety demonstration, the external reactor vessel cooling topic should be investigated separately.

3. INPUT DATA AND UNCERTAIN PARAMETERS

The input data for the Design 2 stand-alone calculations were consolidated from integral calculations results within the SASPAM-SA project. The reference design has a thermal power of 1000 MWth with a total UO_2 mass of 58 tonnes and Zr mass of 19.5 tonnes. The lower plenum internal radius is of 3.1 m for the lower head with a semi-elliptical shape and a height of 1.2 m. The vessel wall thickness is 19 cm in the reference case.

For the uncertainty analysis, ten key parameters were identified as having significant influence on IVMR performance. These parameters were varied within specified ranges. The parameters were selected based on integral simulations of SA scenarios, performed within SASPAM-SA project in a separate work package. These analyses showed the variation of material masses, proportions slumped in the lower head and other parameters, depending on the scenario, code used and applied assumptions. A uniform distribution was

assumed for all uncertain parameters in uncertainty analysis, and full dependence was considered between UO_2 mass and Zr mass. A total of 100 cases were generated to provide good coverage of the parameter space while maintaining computational efficiency. Each case was run to steady-state conditions to evaluate the corium thermal-hydraulic behavior and structural response of the vessel. The uncertain parameters and their ranges are presented in **Table I**.
The reference case was assumed to be the "expected worst case" scenario, where the entire fuel inventory slumps into the lower head with the highest power density. However, the uncertainty analysis should provide insights into whether there are some combinations, where, e.g., metal layer thickness or other parameters lead to even higher heat fluxes, despite fuel mass of power density are not at maximum.

Table I. Uncertain parameters reference values and uncertainty ranges

ID	Parameter	Reference	Minimum	Maximum
	Geometry of LP			
Par. 1	**Thickness of vessel (cm)**	**0.19**	**0.17**	**0.21**
	Degradation			
Par. 2	**Mass of UO2 in LP (t)**	**58.**	**25.**	**58.**
Par. 3	**Mass of Zr in LP (t)**	**19.5**	**8.5**	**19.5**
Par. 4	**Zr fraction oxidized in LP**	**0.5**	**0.3**	**0.7**
Par. 5	**Mass of Steel (t) in LP**	**15.**	**15.**	**22.**
Par. 6	**Power per unit mass of UO2 (W/kg)**	**120.**	**75.**	**120.**
	Material properties			
Par. 7	**Oxide conductivity (W/K/m)**	**2**	**1**	**3**
Par. 8	**Molten steel conductivity (W/K/m)**	**20**	**20**	**40**
Par. 9	**Vessel conductivity (W/K/m)**	**30**	**25**	**35**
Par. 10	**Metal emissivity (-)**	**0.5**	**0.2**	**0.8**

4. RESULTS AND DISCUSSION

4.1. Reference Case Results

The reference case calculation demonstrates successful IVMR with a stable two-layer configuration. **Figure 5** shows the final steady state temperature distribution and corium layer configuration. The oxide layer settles at the bottom of the lower plenum (HPOOL=0.79 m) with the metallic layer on top (HML=0.17 m). The average temperature in the metallic layer is 1524 K, while the oxide pool reaches 3729 K. A solid crust forms at the interfaces between the molten pool and the vessel wall. The 1524 K temperature of the metallic layer is rather low, which indicates that there is a fraction of solidified light metal, since liquidus temperature of the metallic layer is set to 1600 K. Unfortunately, there is no possibility to present the metallic layer crust thickness or solidified mass, because AC^2 version 2023.1, which was used for these calculations, does not provide such quantities. Newest AC^2 version 2025.0 was updated accordingly and is now able to output these quantities.

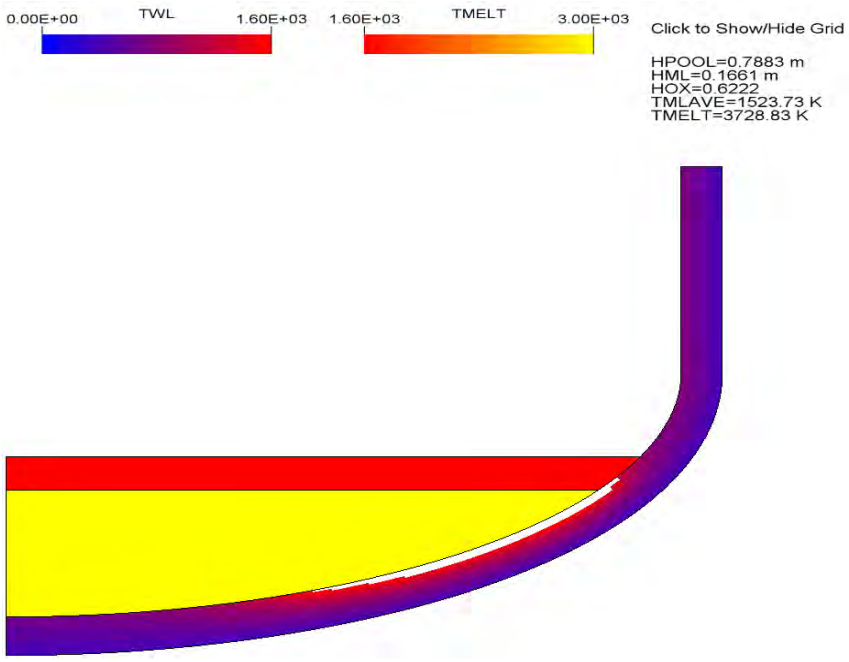

Figure 5. Final steady state of reference case showing wall temperature (TWL) and melt temperature (TMELT) distributions with layer heights.

4.2. Uncertainty Analysis Results

The uncertainty analysis performed by running 100 cases shows that IVMR is expected to be successful within the parameters range. The maximum outer heat flux is estimated from approximately 104 kW/m² to 259 kW/m² considering all cases (**Figure 6**). The minimum residual vessel wall thickness shows variation from approximately 15 cm to 21 cm (**Figure 7**). Notably, even in the worst case, the residual thickness exceeds 15 cm, well above the minimum structural requirement, which is usually assumed around 3 cm [6]. The main results of reference case and the extremes are presented in Table II.

Table II. Main results

Results	Reference	Minimum	Maximum
Min. residual vessel thickness (cm)	15.2	15.2	20.9
Max. local outer HF (kW/m²) at steady-state	259.1	104.8	259.1
Focusing factor	0.85	0.84	0.98
Thickness of top metal layer (m)	0.166	0.123	0.199
Thickness of oxide layer (m)	0.622	0.414	0.666
Lower crust thickness max. (cm)	4.7	4.7	6.7
Top crust thickness (cm)	2.9	2.8	5.6
Power lost by radiative HF / Total power	0.22	0.13	0.26

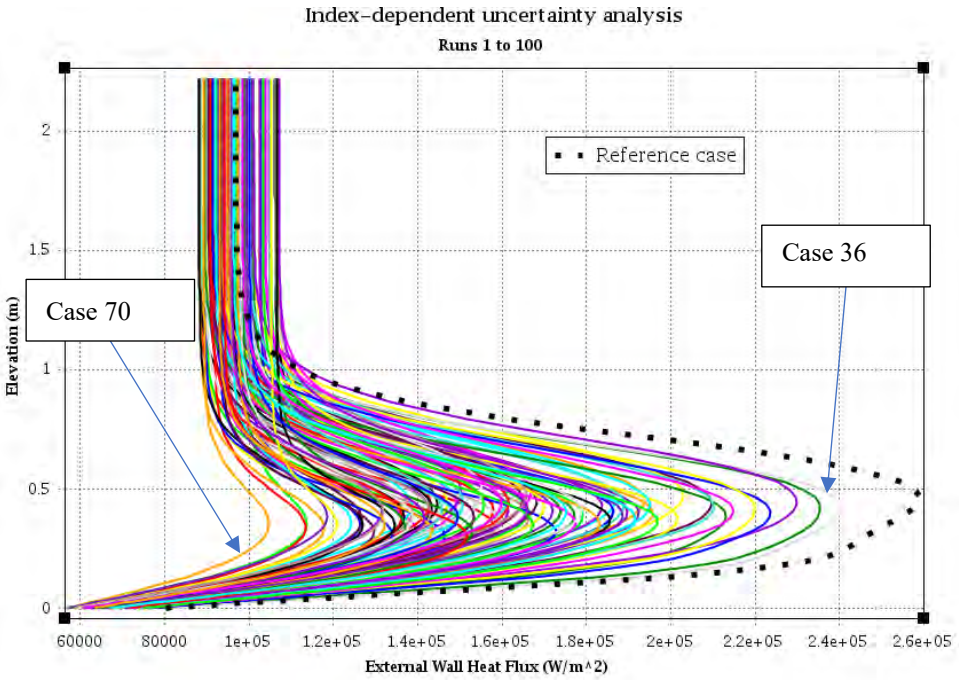

Figure 6. Uncertainty Analysis – axial Heat Flux profile (W/m²K) for all 100 cases.

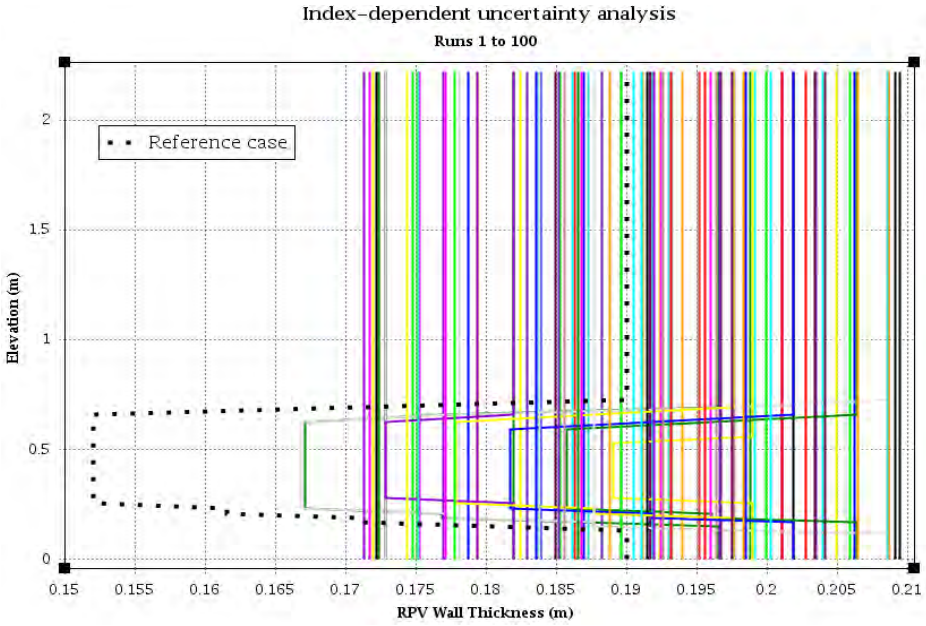

Figure 7. Axial wall thickness profiles for all 100 cases showing variation from 0.15 to 0.21 m. Reference case shown as dashed line.

The focusing factor (ratio of maximum outer heat flux in the top metal layer to maximum outer heat flux in the oxide layer) ranges from 0.84 to 0.98 across all cases. All values are less than 1.0, indicating that the oxide layer heat flux exceeds the metallic layer heat flux in all cases. This demonstrates that the focusing effect is not observed in Design 2, which is beneficial for IVMR success. However, the power split between layers is highly dependent on correlations used, so this is potentially a subject of code and user effect.

4.3. Comparison With CHF and Safety Margins

A critical aspect of IVMR evaluation is comparison of the calculated heat flux with the critical heat flux (CHF) threshold. For the external cooling configuration of Design 2, CHF findings by different experimental programs, (e.g. ULPU [5]), suggest values in the range of 1.0-1.5 MW/m² for the lower head region depending on wall inclination angle. Design 2 features a semi-elliptical lower head; the maximum heat flux of 259 kW/m² occurs at approximately 30-60° inclination from vertical, where available CHF data suggest local values in the range cited. The comparison is indicative of the safety margin; a geometry-specific CHF correlation would be required for design qualification.
The maximum heat flux calculated across all 100 uncertainty cases is approximately 259 kW/m². This represents only 17-26% of the CHF threshold, providing a safety margin of 74-83%. Even considering uncertainties in the CHF correlations themselves, the margin remains substantial.
No predicted melt-through is observed. The minimum residual wall thickness of 15 cm in the worst case significantly exceeds the typical minimum structural reference of approximately 3 cm [6], indicating that gross vessel perforation is not expected. Note that AC² does not model detailed mechanical response of the vessel; the residual wall thickness criterion is used as a surrogate indicator for melt-through prevention, not a full thermo-mechanical integrity assessment.

4.4. Sensitivity Analysis Results

The sensitivity analysis using Spearman's rank correlation coefficient identifies the most influential parameters affecting IVMR performance. **Figure 8** shows the sensitivity results for maximum heat flux, revealing that power per unit mass of UO_2 (Par. 6, gray) has the strongest positive correlation. Corium inventory parameters (UO_2 and Zr mass, Par. 2 and Par. 3, full dependence) also show significant influence, and are even more pronounced in the highest heat flux area, while thermal conductivities have moderate effects. The effect of Par. 6 having most influence at the bottom of the LP is the fact that other parameters are of the lowest impact, so this results in relatively larger impact. Moreover, if we look at **Figure 6**, we can see that the min and max difference in lowest part is significantly less than in upper LH regions in contact with corium.

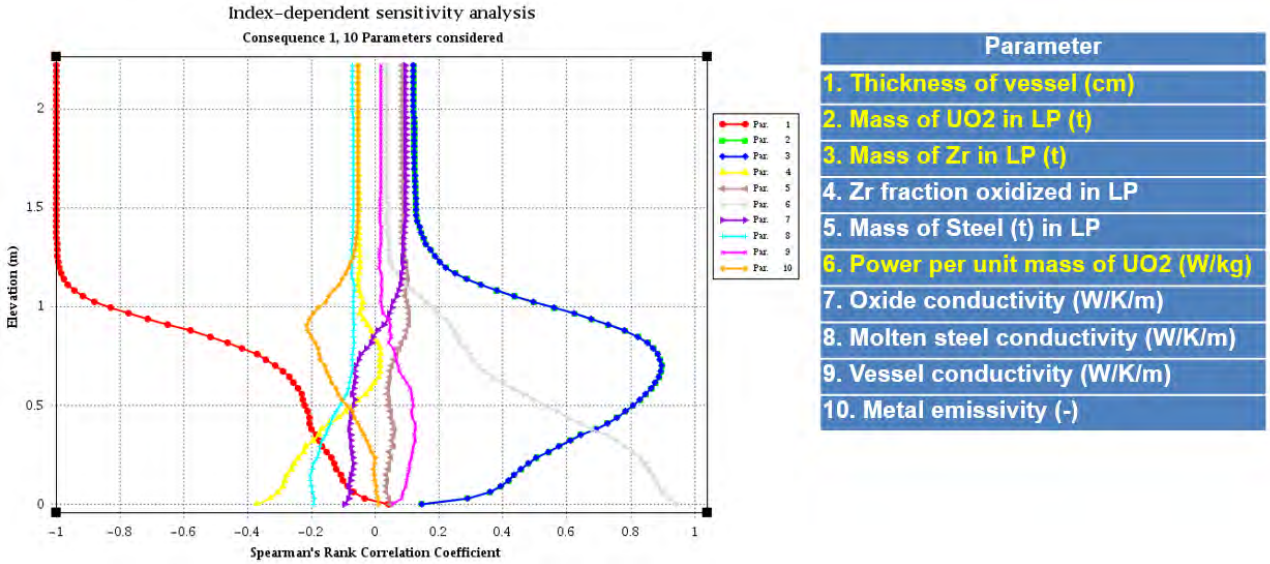

Figure 8. Sensitivity Analysis – parameters influence on axial Heat Flux profile.

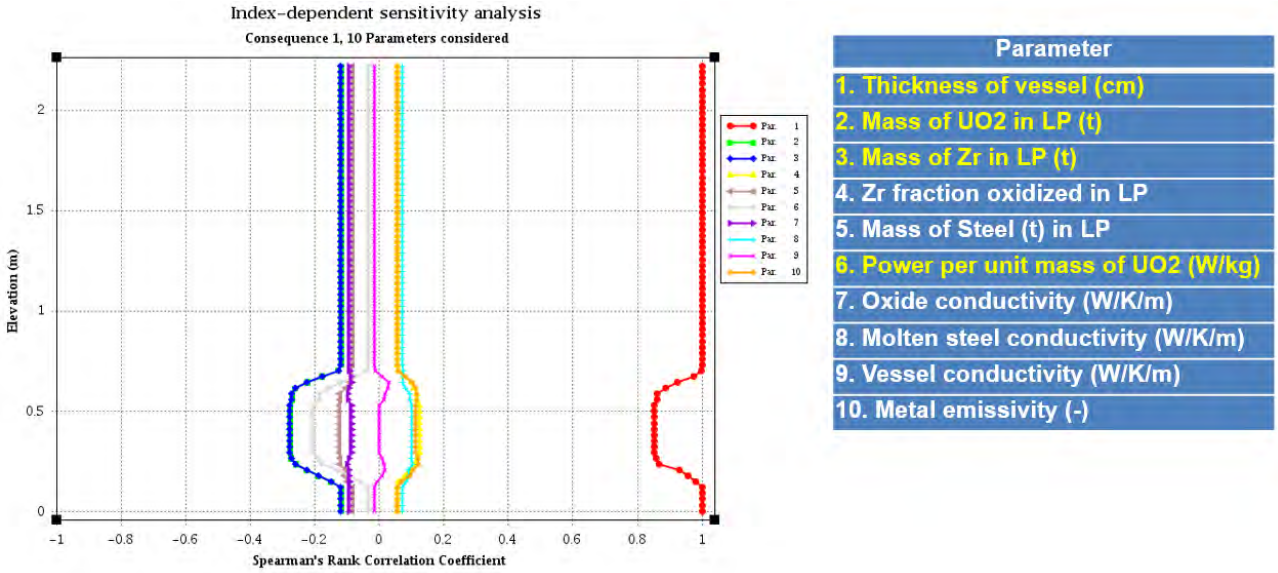

Figure 9. Sensitivity Analysis – parameters influence on axial Wall Thickness profile.

For minimum residual vessel wall thickness (**Figure 9**), the initial vessel wall thickness shows strong positive correlation - thicker initial wall provides more margin against ablation. Power parameters show negative correlation as higher power leads to more ablation and reduced residual thickness. Material thermal properties affect the thermal gradient through the vessel wall and ablation rate.

5. CONCLUSIONS

The AC² code system, particularly the AIDA module, demonstrates good applicability for IVMR analysis in SMR configurations. The stand-alone lower plenum calculations provide efficient evaluation of corium thermal-hydraulic behavior and structural response. However, several important limitations apply: (1) the 0-dimensional modelling approach and the neglect of thermochemical interactions may not capture all aspects of circulation, mixing, and layer composition evolution; (2) the stand-alone approach does not capture transient melt relocation timing or evolving decay heat distributions; (3)layer stratification is fixed throughout the simulation; and (4) model-form uncertainties from correlation selection are not included in the uncertainty quantification.. All these simplifications may lead to miss some specific cases, where transient processes causes higher heat fluxes and result in greater RPV wall ablation.
The uncertainty and sensitivity analysis highlights the importance of accurate characterization of decay heat and corium inventory. Material thermal properties show moderate influence, reflecting uncertainty in corium composition at prototypic conditions. The limited focusing effect observed is favorable and can be attributed to the relatively large lower plenum geometry, thin metallic layer, effective radiative heat transfer, and substantial oxide layer heat generation.
Compared to large reactor IVMR analyses, Design 2 benefits from lower absolute power, favorable surface-to-volume ratio, lower power density, and thicker vessel walls relative to thermal loads. These inherent advantages suggest that IVMR is more readily achievable in SMR designs, though proper external cooling system design remains essential.

After performing a comprehensive analysis of in-vessel melt retention for a generic SMR Design 2 using the AC² system code, the main conclusions are:

1. The IVMR strategy is effective for the investigated SMR design. The maximum outer heat flux (~259 kW/m²) remains well below critical heat flux thresholds (1.0-1.5 MW/m²).

2. The minimum residual vessel wall thickness exceeds 15 cm in all 100 uncertainty cases, demonstrating no predicted melt-through. Note that a full thermo-mechanical integrity assessment (creep rupture, plastic instability) is outside the scope of the AC² model and is recommended for future work.
3. The focusing effect is not observed. The heat flux from the oxidic layer equals or exceeds the metallic layer heat flux in all 100 investigated cases.
4. Sensitivity analysis identifies decay power, per unit mass (Par. 6) and corium inventory (UO_2 and Zr mass, Par. 2 and 3) as the primary parameters governing maximum heat flux. Initial vessel wall thickness (Par. 1) is the most important parameter for residual wall thickness, since with no ablation, initial wall thickness becomes the residual wall thickness. Material thermal conductivities show moderate to negligible sensitivity in the studied parameter ranges
5. The AC² code system demonstrates good applicability for IVMR evaluation in SMR configurations with efficient stand-alone analysis capabilities.
6. The findings support the viability of IVMR as a severe accident mitigation strategy for SMRs, provided the reactor cavity remains flooded.

ACKNOWLEDGMENTS

Funded by the European Union

Funded by the European Union. Views and opinions expressed are, however, those of the author(s) only and do not necessarily reflect those of the European Union or European Commission - Euratom. Neither the European Union nor the granting authority can be held responsible for them.

REFERENCES

1. IAEA, "Advances in small modular reactor technology developments", 2022 Edition, in IAEA advanced reactor information system (ARIS), Vienna (2022).
2. H. Esmaili and M. Khatib-Rhabar, "Analysis of in-vessel retention and ex-vessel fuel coolant interaction for AP-1000", NUREG/CR-6849, ERI/NRC 04-201 (2004).
3. J. Xing, D. Song, and Y. Wu, "HPR1000: advanced pressurized water reactor with active and passive safety", Engineering, 2(1), pp. 79-87 (2016).
4. European Commission, Safety Analysis of SMR with PAssive Mitigation strategies - Severe Accident - SASPAM-SA Project, (2023), available online on https://cordis.europa.eu/project/id/101059853.
5. T. G. Theofanous, J.P. Tu, T. Salmassi, et al. Quantification of Limit to Coolability in ULPU-2000 Configuration IV. Center for Risk Studies and Safety. 2002 May, CRSS Technical Report 02.05.
6. S. Brumm, M. Sangiorgi, F. Fichot, L. Carenini. Synthesis report about the updated methodology for demonstration of In-Vessel melt retention, EUR 30056 EN, Publications Office of the European Union, Luxembourg. doi:10.2760/56153, JRC119020. (2021)

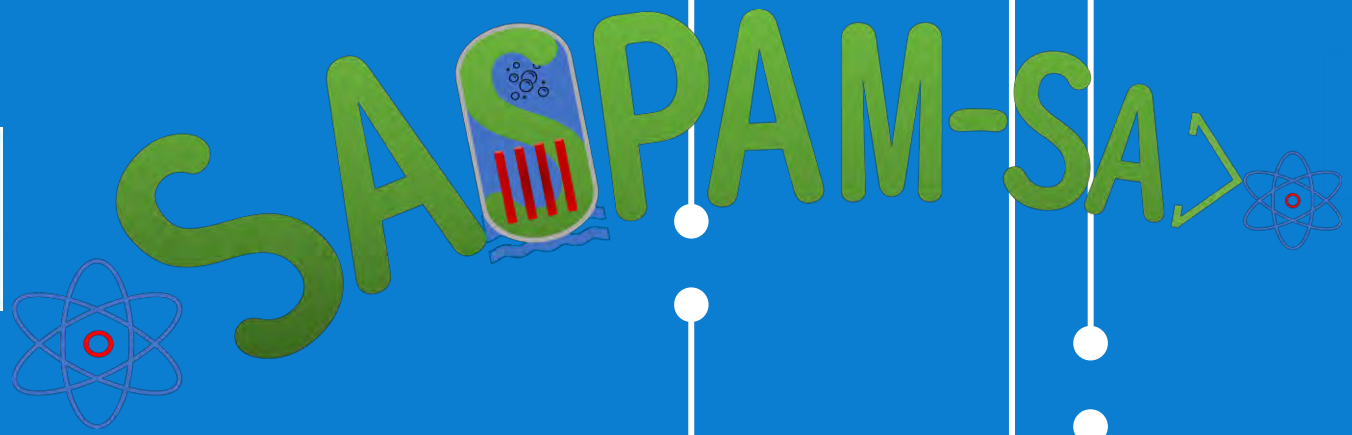

Stand-alone analysis and evaluation of uncertainties of IVMR in SMR using AC^2 code

M. Valinčius
Lithuanian Energy Institute

L. Lovasz, P. Pandazis
Gesellschaft für Anlagen- und Reaktorsicherheit (GRS) gGmbH

ERMSAR 2026

Madrid, Spain

18 – 22 May 2026

Content

- Introduction and frame of SASPAM-SA project
- Design
- Model and code specifics
- Analysis and Results
- Conclusions

SASPAM-SA overview

- Funded by the European Union – Horizon Europe–Euratom programme, led by ENEA (Italy)
- Aim – investigate the applicability and transfer of the operating large-LWR reactor knowledge and know-how to the near-term deployment of integral PWR (iPWR), in the view of Severe Accident (SA) and Emergency Planning Zone (EPZ) European licensing analyses needs.
- Progress – Two generic iPWR designs (Design 1 and Design 2) analysed by project partners, extended with Design 3 (BWR type) during the project
- LEI + GRS cooperation in Design 2 integral model development, modelling scenarios, including IVMR stand-alone calculations using AC^2 code and Uncertainty and Sensitivity analysis using SUSA code. As a part of benchmark exercise in SASPAM-SA project WP4 (led by ASNR).

“Design-2”

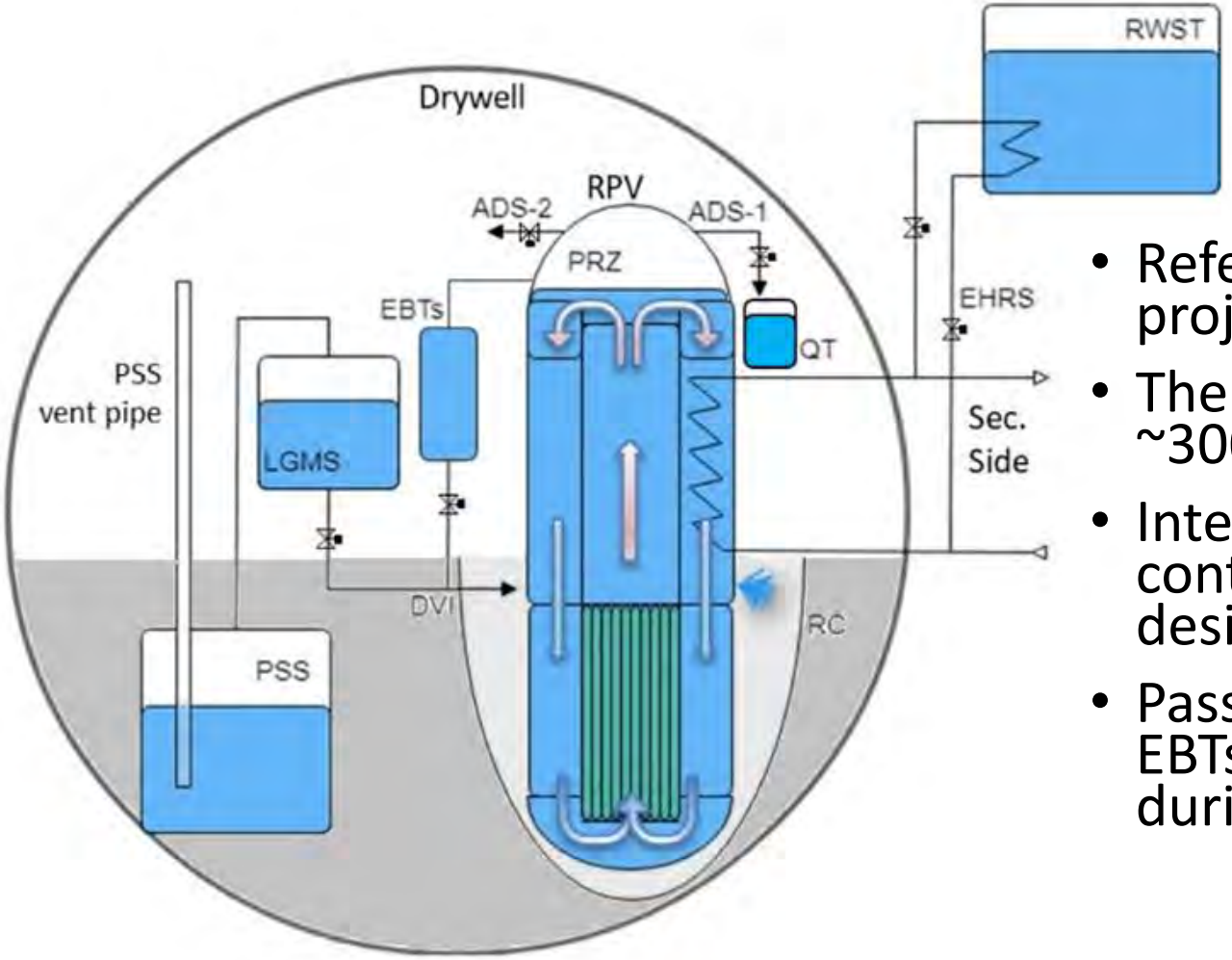

- Referenced as “Design 2” in SASPAM-SA project and related publications
- Thermal power: 1000 MWth; Electric output: ~300 MWe
- Integral PWR with classical spherical containment; concrete floor with RPV cavity designed for flooding in IVMR scenarios
- Passive safety systems (ADS, EHRS, LGMS, PSS, EBTs) ensure cooling without operator action during severe accident

AC² code overview

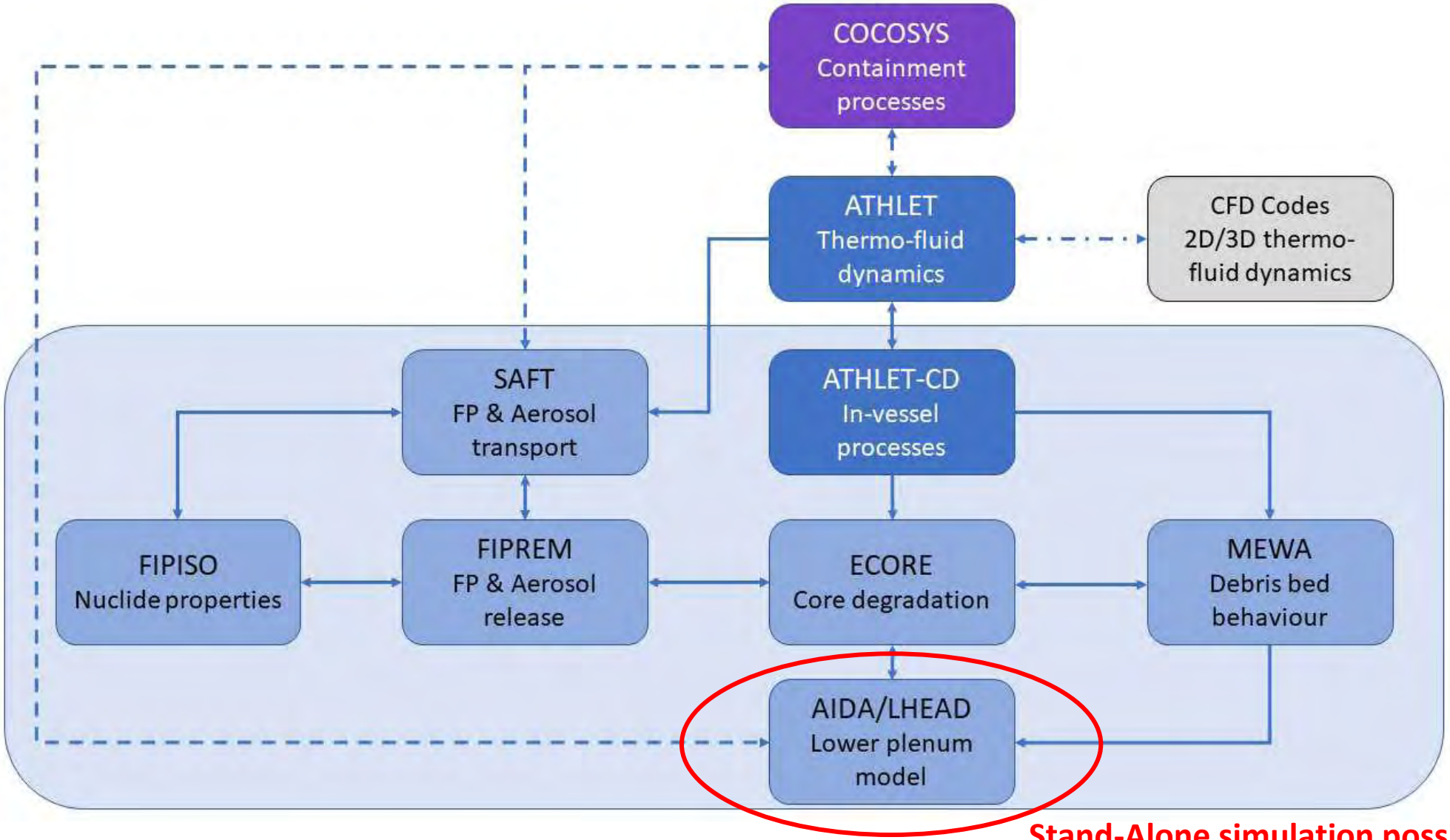

Stand-Alone simulation possible

LP simulation module AIDA in AC²

- *Trunked-elliptical*: RARPV > RIRPV and RARPV > RCRPV

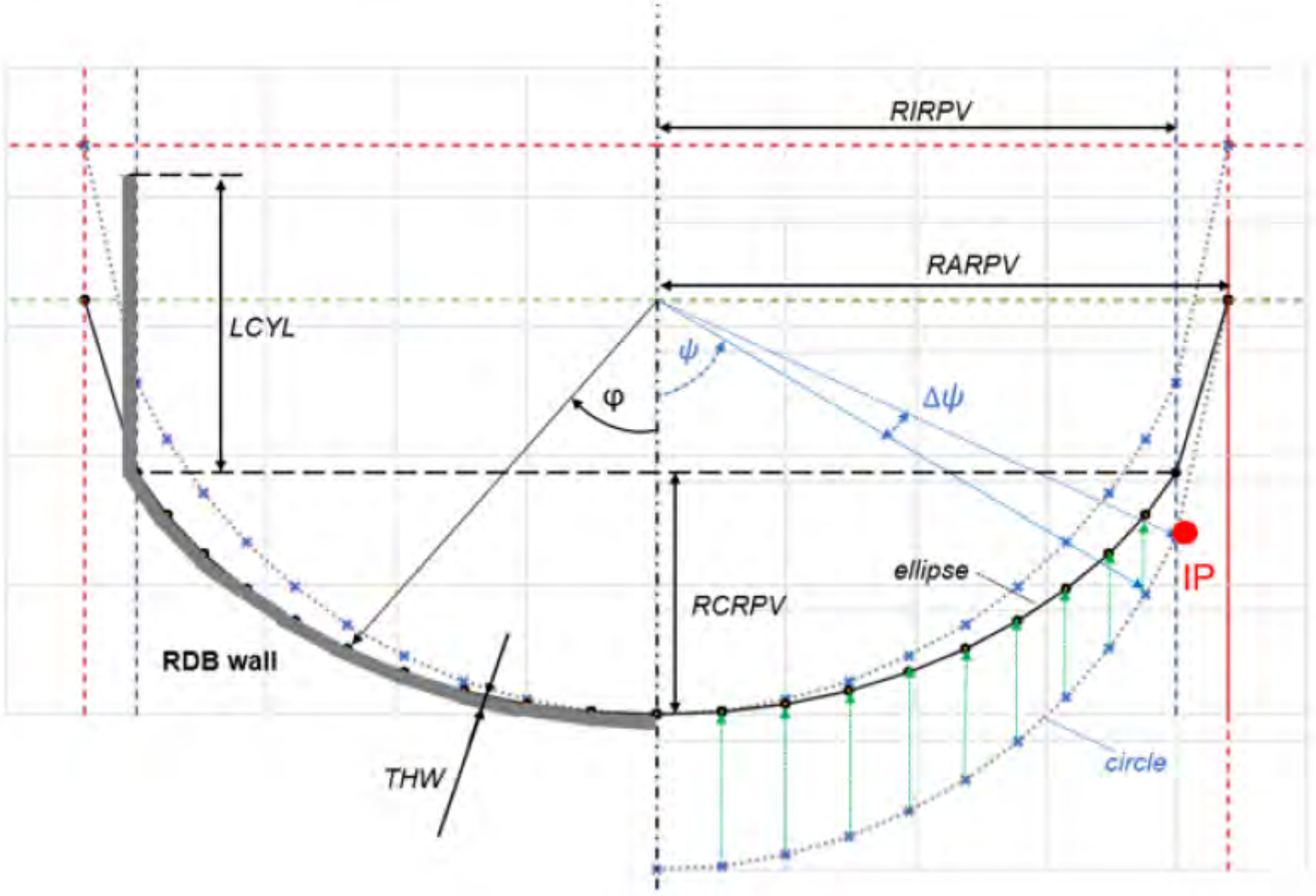

LP simulation module AIDA in AC²

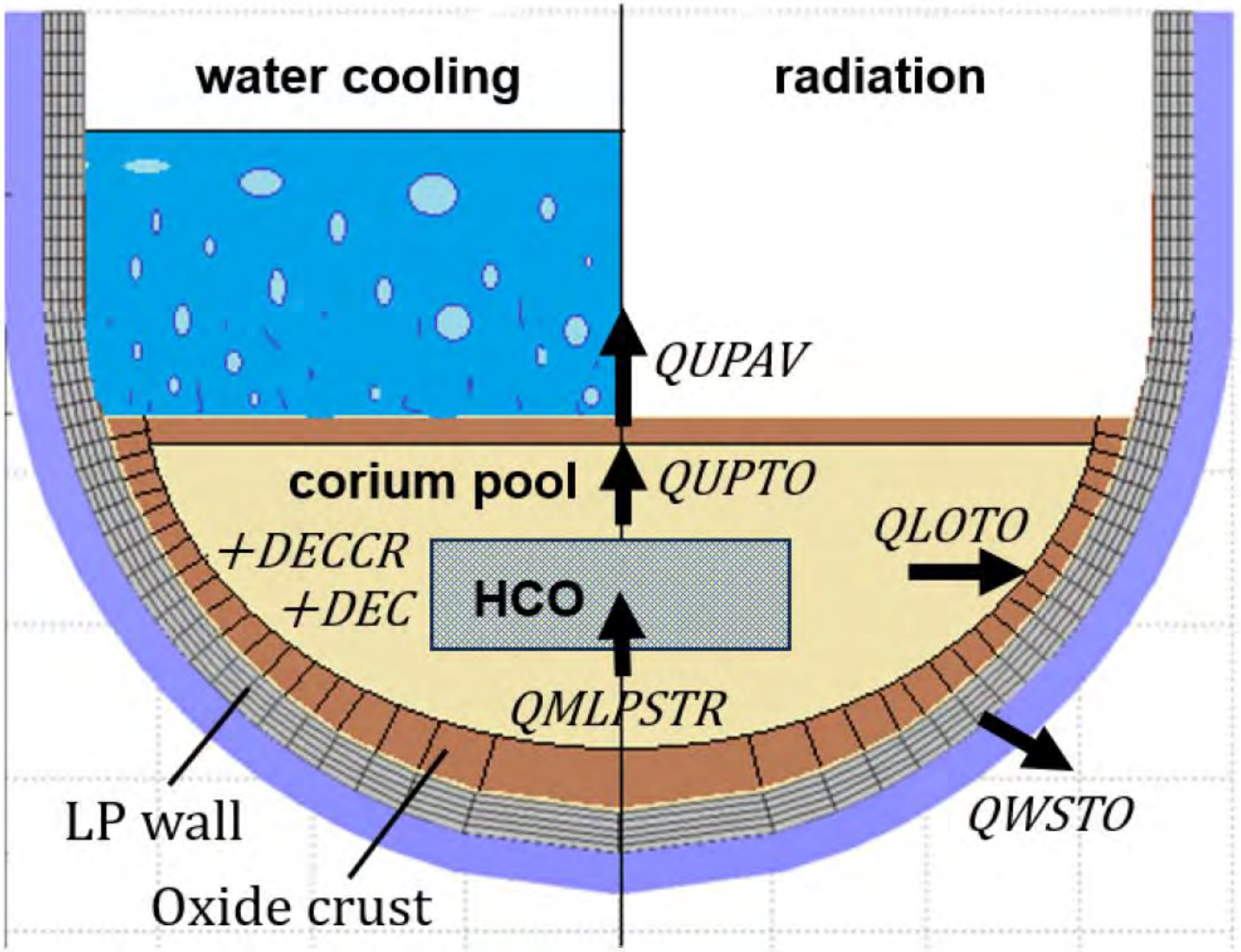

LP simulation module AIDA in AC²

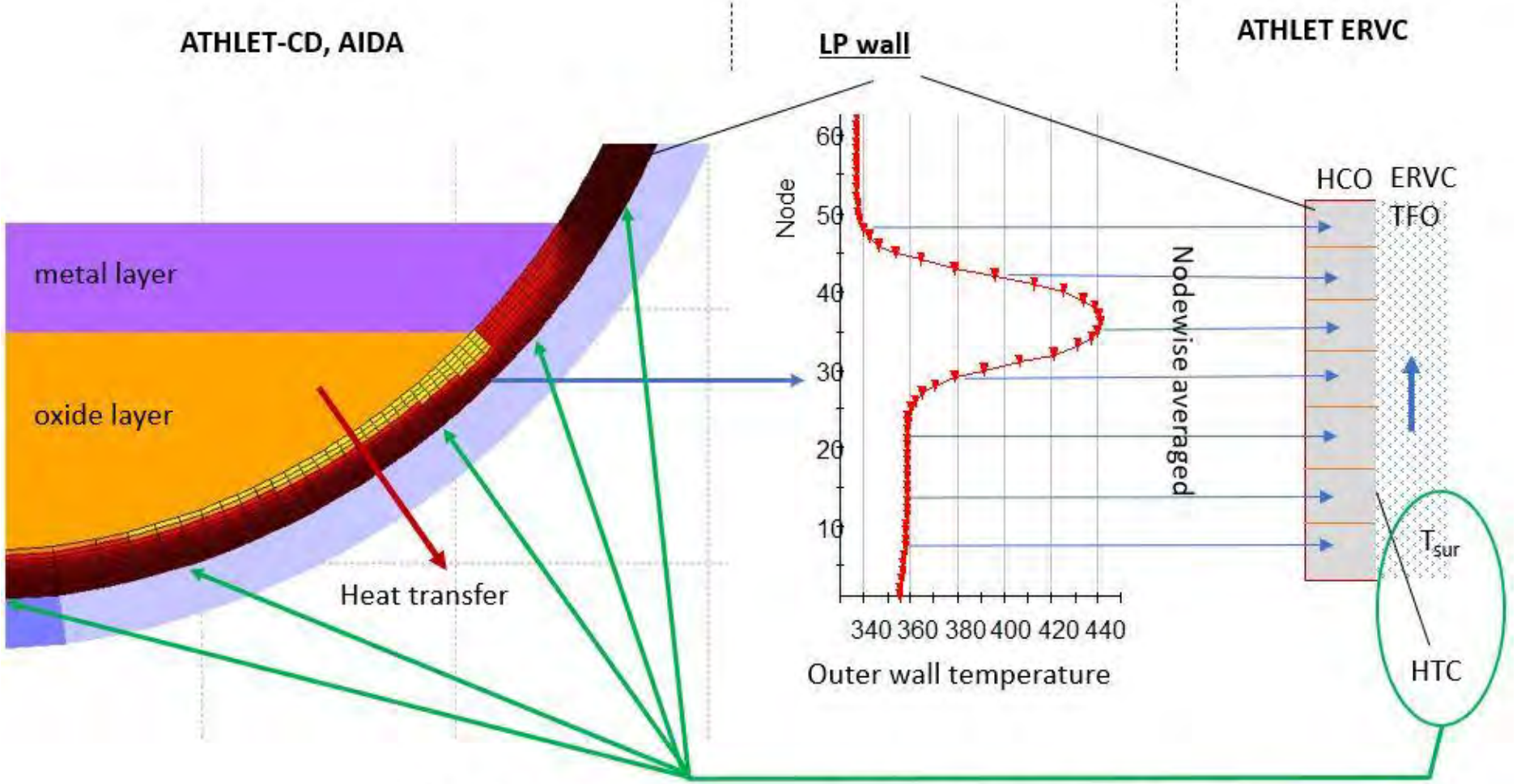

LP model in AIDA

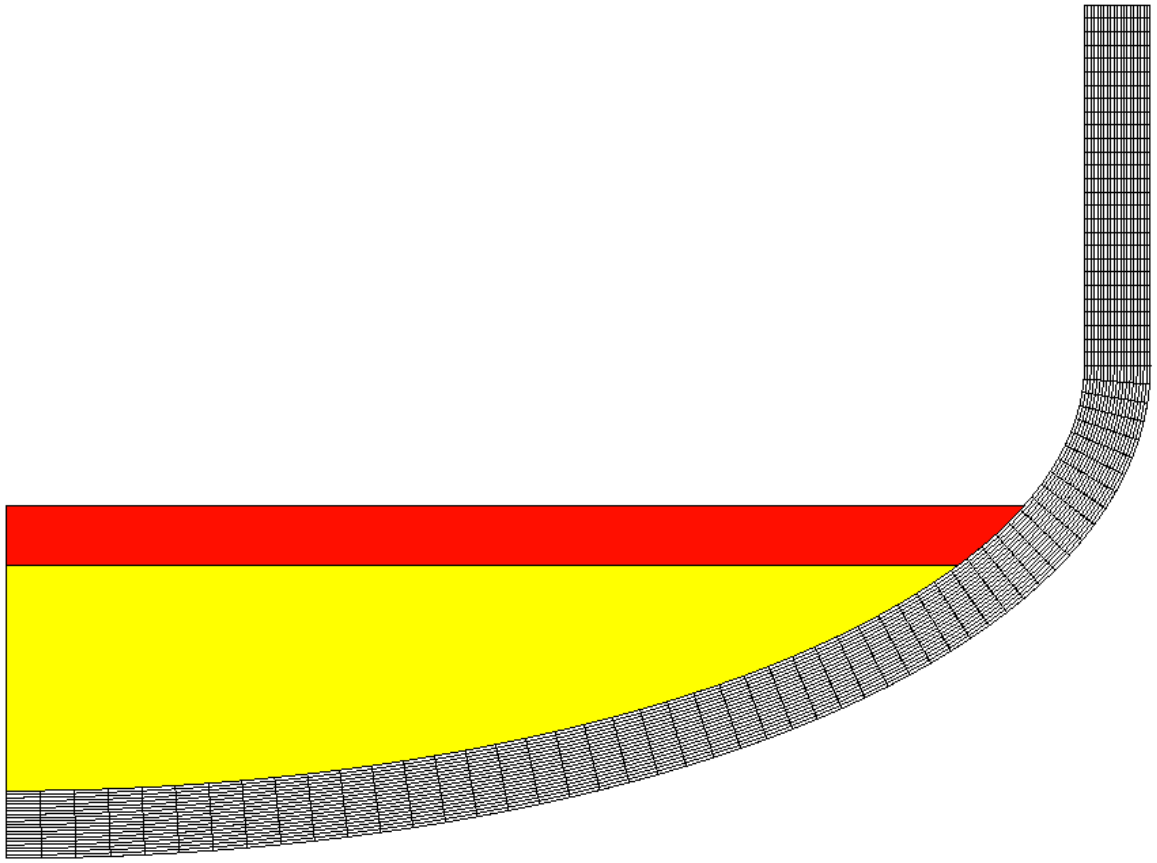

- Lower plenum wall nodalization in AIDA showing 50 axial nodes in hemisphere and 27 nodes in cylindrical part with 20 radial rings.
- Oxidic and metal layer are modelled in 0D

Investigated uncertain parameters, reference case and ranges

ID	Parameter	Reference	Minimum	Maximum
	Geometry of LP			
Par. 1	Thickness of vessel (cm)	0.19	0.17	0.21
	Degradation			
Par. 2	Mass of UO_2 in LP (t)	58.	25.	58.
Par. 3	Mass of Zr in LP (t)	19.5	8.5	19.5
Par. 4	Zr fraction oxidized in LP	0.5	0.3	0.7
Par. 5	Mass of Steel (t) in LP	15.	15.	22.
Par. 6	Power per unit mass of UO_2 (W/kg)	120.	75.	120.
	Material properties			
Par. 7	Oxide conductivity (W/K/m)	2	1	3
Par. 8	Molten steel conductivity (W/K/m)	20	20	40
Par. 9	Vessel conductivity (W/K/m)	30	25	35
Par. 10	Metal emissivity (-)	0.5	0.2	0.8

Input Data – Sources and Uncertainty Method

- **Data source:** Input data consolidated from integral SA scenario calculations within SASPAM-SA (separate work package), as a part of SASPAM-SA stand-alone benchmark type exercise. Scenarios showed variation in material masses, proportions slumped into the LP, and other parameters depending on scenario, code, and assumptions.
- **Uncertainty method:** SUSA software (GRS); Simple Random Sampling; 100 samples generated to give good parameter-space coverage while maintaining computational efficiency.
- **Distributions:** Uniform distribution assumed for all 10 parameters; full dependence applied between related parameters – UO_2 mass and Zr mass.
- **Run strategy:** Each of the 100 cases run to steady-state to evaluate thermal-hydraulic behaviour and structural integrity of the RPV lower head under the sampled parameter combinations.
- **Fixed assumptions:** Two-layer configuration constant throughout (no thermochemistry); 10% decay heat in metallic layer, 90% in oxidic layer; cavity always flooded (continuous external cooling).

Results

Results	Reference	Minimum	Maximum
Min. residual vessel thickness (cm)	15.2	15.2	20.9
Max. local outer HF (kW/m^2) at steady-state	259.1	104.8	259.1
Focusing factor	0.85	0.84	0.98
Thickness of top metal layer (m)	0.166	0.123	0.199
Thickness of oxide layer (m)	0.622	0.414	0.666
Lower crust thickness max. (cm)	4.7	4.7	6.7
Top crust thickness (cm)	2.9	2.8	5.6

Results

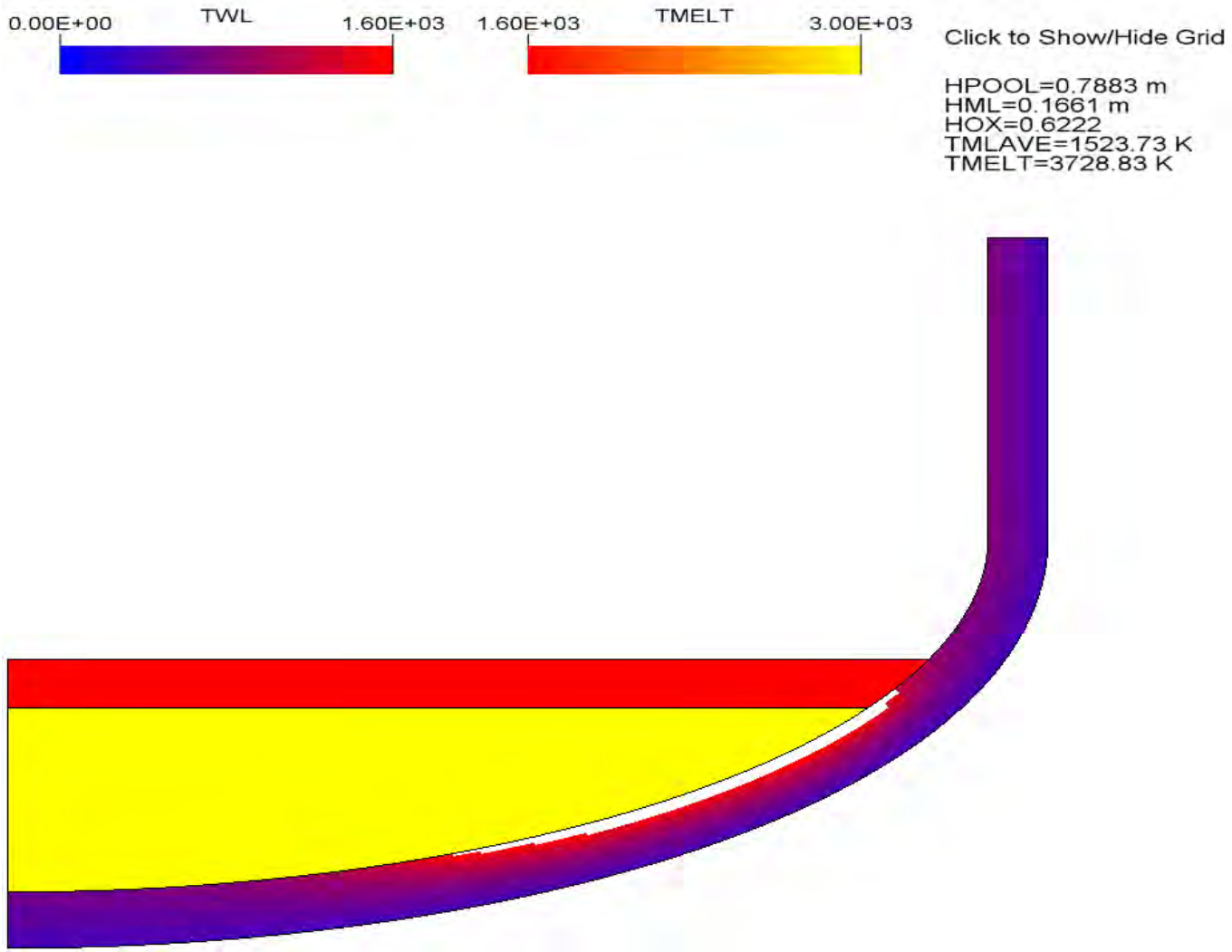

- Final steady state of reference case showing wall temperature (TWL) and melt temperature (TMELT) distributions with layer heights.

Uncertainty Analysis - Wall Heat Flux

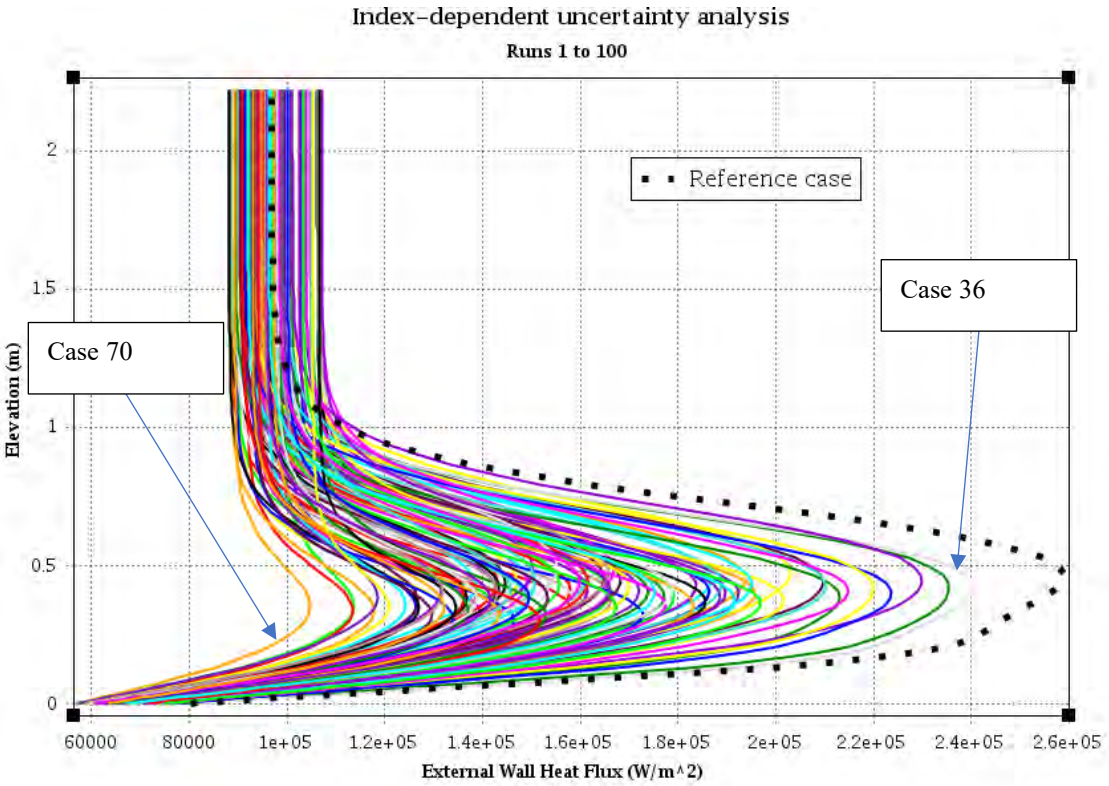

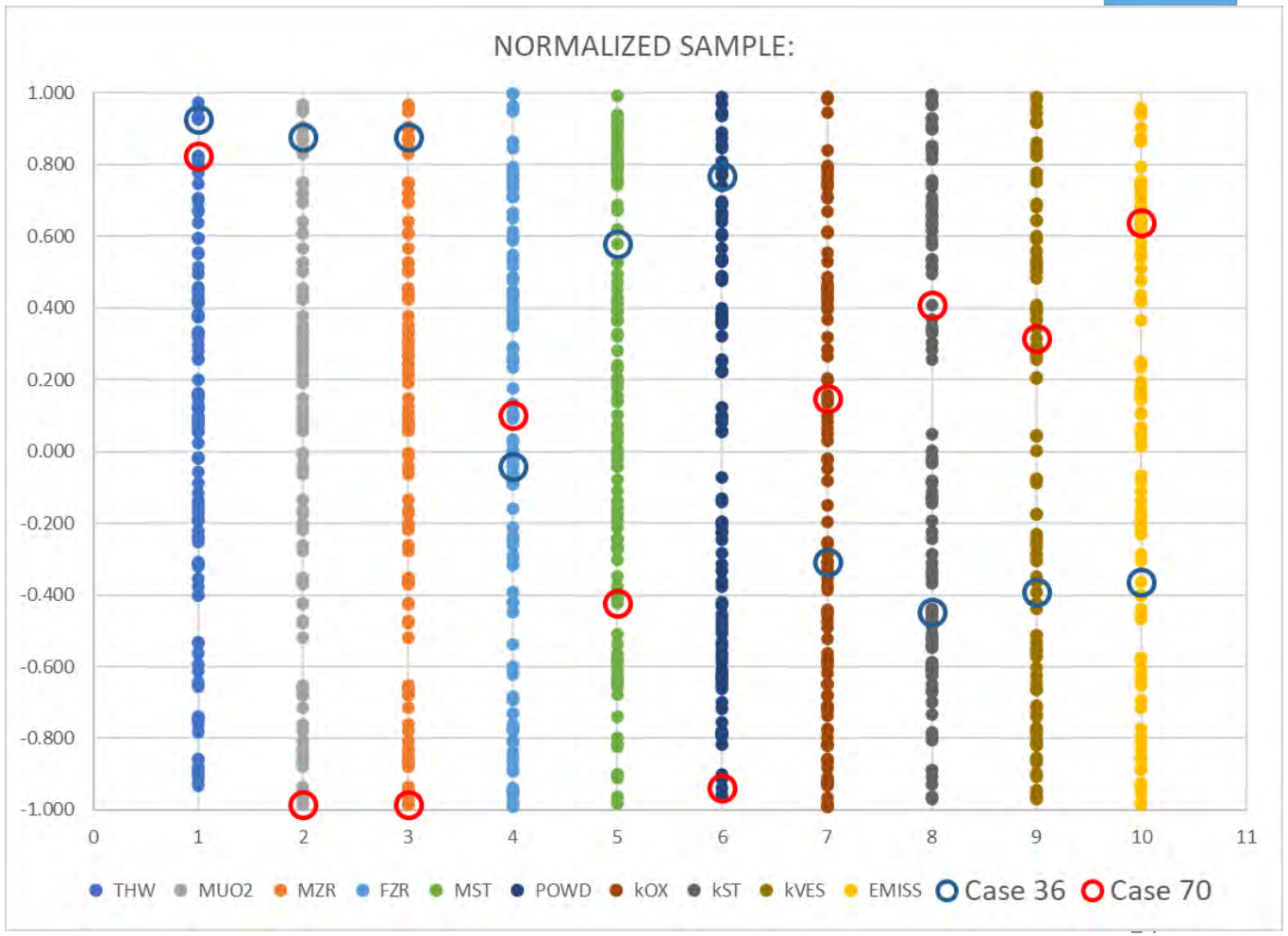

- Range 104 – 259 kW/m^2
- Reference case -> MAX heat flux

Safety Margins – Comparison with Critical Heat Flux

- **Maximum calculated heat flux:** ~259 kW/m² (Reference case, max of all cases) at the outer RPV wall in the upper debris region (~0.5–0.7 m elevation)
- **Critical Heat Flux (CHF):** Experimental programmes (e.g. ULPU-2000) suggest CHF in the range 1.0–1.5 MW/m² for the external cooling
- **Safety margin:** 259 kW/m² represents only a fraction of the CHF range, giving a large safety margin.
- **Focusing effect across all 100 cases:** Focusing factor (HF_metal / HF_oxide) ranges from 0.84 to 0.98. All values < 1.0, confirming that oxide layer HF exceeds metallic layer HF in every case – focusing effect NOT observed
- **Note on focusing:** Power split between layers depends on correlations and code assumptions – this is a subject of ongoing code and user-effect studies; AC² does not model thermochemistry, so the two-layer configuration is fixed

RPV Wall Ablation

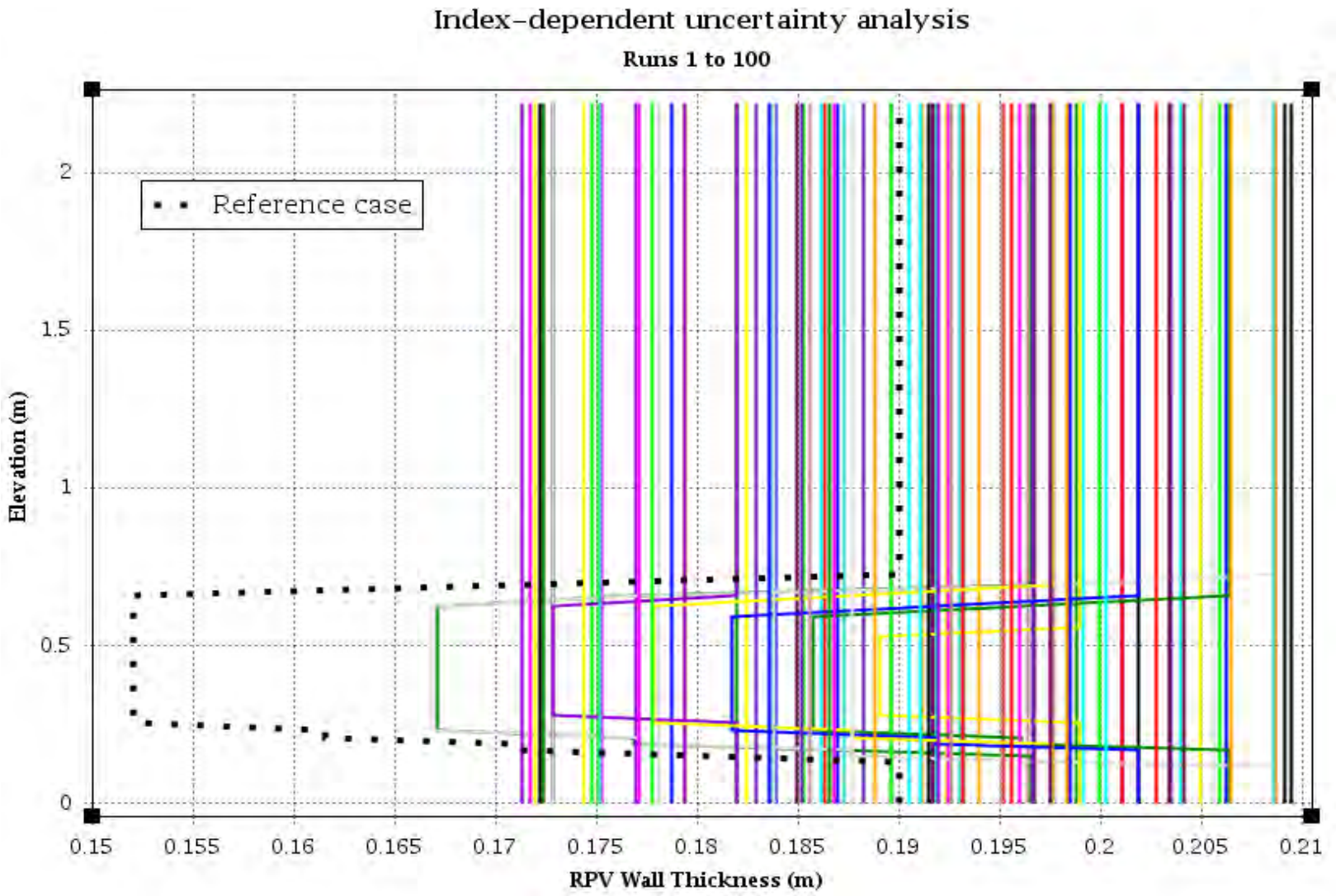

- RPV wall thickness as a function of elevation
- Wall ablation observed only in a few cases
- Reference case -> MAX heat flux, MAX ablation

Sensitivity analysis results

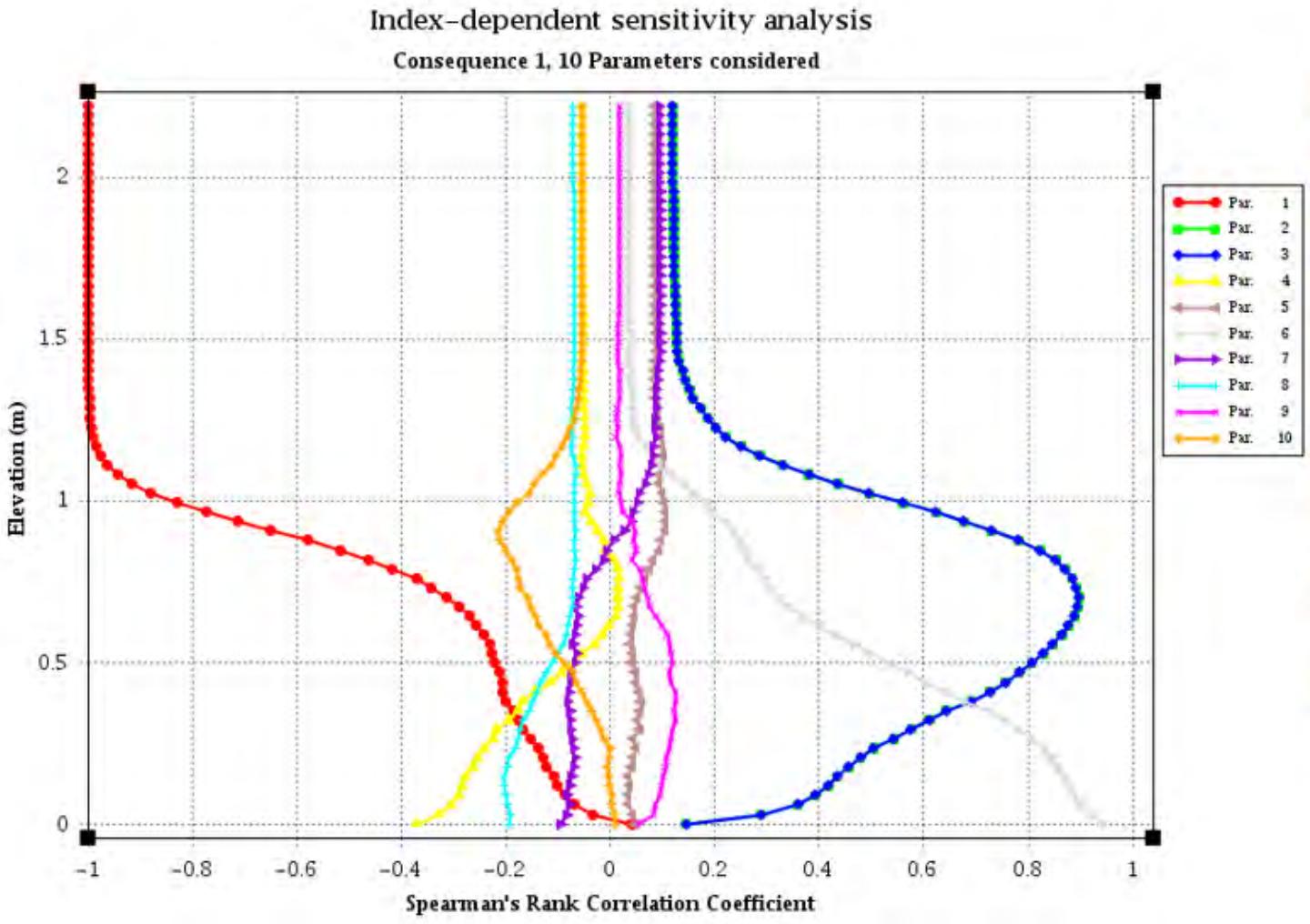

Parameter
1. Thickness of vessel (cm)
2. Mass of UO2 in LP (t)
3. Mass of Zr in LP (t)
4. Zr fraction oxidized in LP
5. Mass of Steel (t) in LP
6. Power per unit mass of UO2 (W/kg)
7. Oxide conductivity (W/K/m)
8. Molten steel conductivity (W/K/m)
9. Vessel conductivity (W/K/m)
10. Metal emissivity (-)

Sensitivity Analysis - Residual Wall Thickness

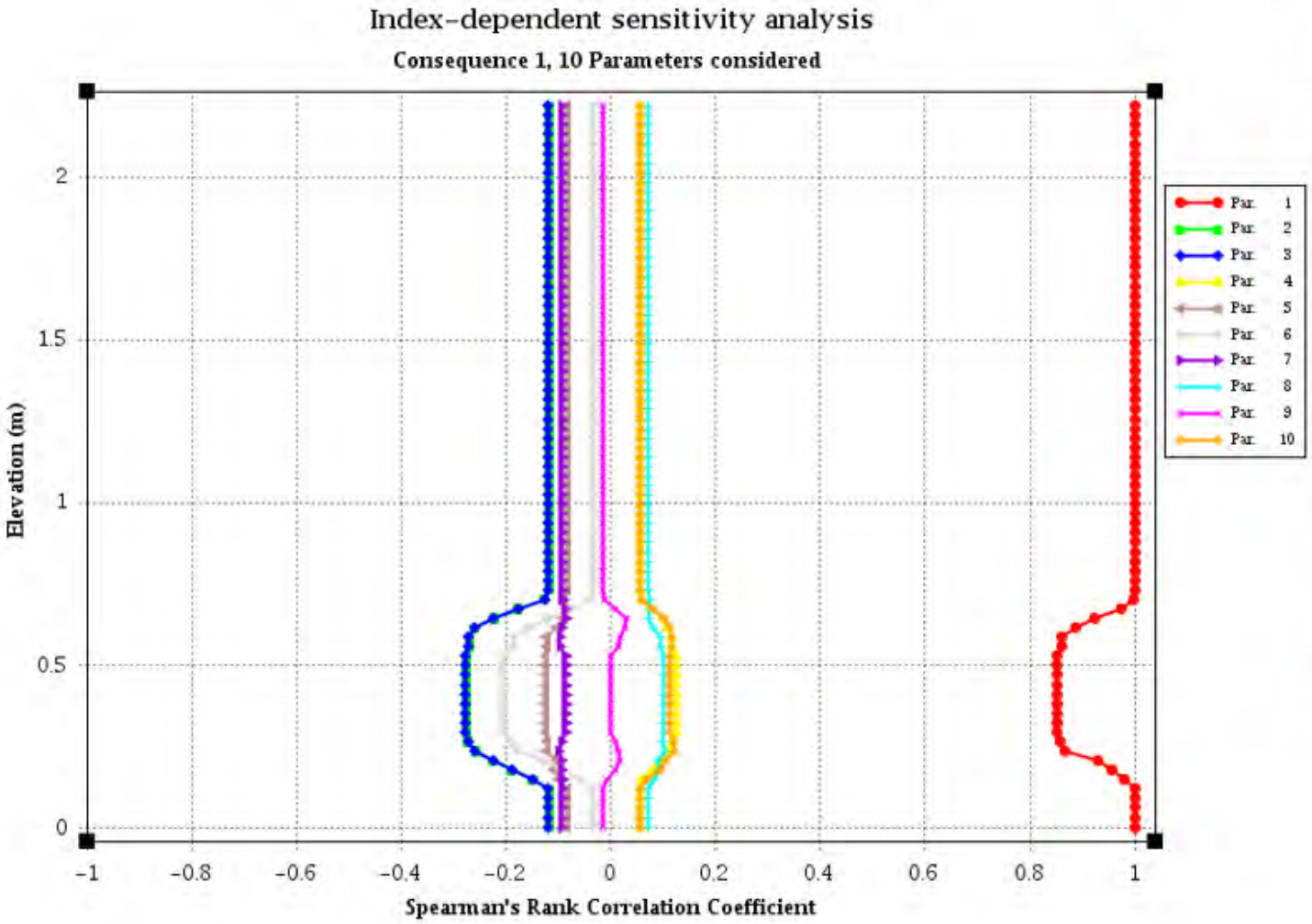

Parameter
1. Thickness of vessel (cm)
2. Mass of UO2 in LP (t)
3. Mass of Zr in LP (t)
4. Zr fraction oxidized in LP
5. Mass of Steel (t) in LP
6. Power per unit mass of UO2 (W/kg)
7. Oxide conductivity (W/K/m)
8. Molten steel conductivity (W/K/m)
9. Vessel conductivity (W/K/m)
10. Metal emissivity (-)

Conclusions

- The IVMR strategy is effective for the investigated SMR design. The maximum outer heat flux (~259 kW/m²) remains well below critical heat flux thresholds (1.0-1.5 MW/m²), providing a safety margin of 74-83%
- The minimum residual vessel wall thickness exceeds 15 cm in all 100 uncertainty cases + reference case, demonstrating robust structural integrity
- The focusing effect is limited. The heat flux from the oxidic layer equals or exceeds the metallic layer heat flux
- Sensitivity analysis identifies decay power, corium inventory, and thermal conductivity as key parameters. Careful characterization is needed for design-specific analyses
- The AC² code system demonstrates good applicability for IVMR evaluation in SMR configurations with efficient stand-alone analysis capabilities
- The findings support the viability of IVMR as a severe accident mitigation strategy for SMRs, provided the reactor cavity remains flooded

Acknowledgement/Disclaimer

SAFETY ANALYSIS OF SMR WITH PASSIVE MITIGATION STRATEGIES - SEVERE ACCIDENT

Funded by the European Union

Funded by the European Union. Views and opinions expressed are however those of the author(s) only and do not necessarily reflect those of the European Union or European Commission-Euratom.
Neither the European Union nor the granting authority can be held responsible for them.

The 12th European Review Meeting on Severe Accidents Research

May 18-22, 2026, Universidad Carlos III de Madrid, Madrid, Spain

TECHNICAL SESSION 4.2: EX-VESSEL CORIUM AND DEBRIS COOLABILITY

Chairs: F. Giannetti (University of Rome 'La Sapienza'), C. Journeau (CEA)

ID022	**Geometrical prerequisites for ex-vessel recriticality in flooded cavity containments** B. Engström (KTH)	Paper Presentation
ID153	**Performance of innovative sacrificial materials for PWR retrofitting - a reactor case study** P. Vacha (UJV)	Paper Presentation
ID136	**Development of the SAFARI Code for Comprehensive Severe Accident Analysis in Nuclear Reactors: Molten Corium-Concrete Interaction Analysis Module** J. Sung Choi (Seoul National University)	Paper Presentation

GEOMETRICAL PREREQUISITES FOR EX-VESSEL RECRITICALITY IN FLOODED CAVITY CONTAINMENTS

Björn Engström, Weimin Ma
Royal Institute of Technology (KTH)
Roslagstullsbacken 21, 10691 Stockholm, Sweden
bjorengs@kth.se, weimin@kth.se

ABSTRACT

The flooded cavity has many advantages in terms of corium coolability and prevention of basemat melt-through and therefore has been adopted as a severe accident management strategy (SAMS) in several reactor designs such as Nordic boiling water reactors. However, the risk of steam explosion in the wet cavity should be addressed. In addition, the molten fuel-coolant interactions (FCI) in the cavity water pool may create conditions for recriticality when the resulting debris particles are either dispersed in neutron moderating water or settled on the water pool bottom. Few studies have been conducted on recriticality of infinite debris beds, but little work is attributed to finite debris beds and the dispersal phase. Given the infinite multiplication factors greater than one from the previous studies, the present study proposes an approach to estimate the reactivity loss due to neutron leakage in a finite debris-water system and obtain the geometrical conditions for ex-vessel recriticality in both dispersal and settled phases of debris particles. The geometrical parameters include the melt jet breakup length and the lateral debris dispersal distance of the dispersed particles, as well as the height, the base diameter and the angle of repose of the debris bed.

KEYWORDS
Severe accident, ex-vessel corium, recriticality, flooded cavity, melt fragmentation

1. INTRODUCTION

The Nordic boiling water reactor (BWR) severe accident management (SAM) strategy of flooding the cavity below the reactor pressure vessel (RPV) with water has advantages in cooling of ex-vessel corium and possible prevention of basemat melt-through. However, the SAM strategy has the disadvantage of increasing steam explosion risk. Moreover, it may also create recriticality conditions for the quenched debris particles either dispersed in the neutron moderating water or settled on the cavity pool bottom (i.e. forming a debris bed).

The present knowledge of in-vessel severe accident phenomena suggests that the molten corium may be axially separated into two layers of melt in the RPV lower head: a metallic layer atop an oxidic layer, and ejected sequentially in time. The oxidic melt primarily consists of uranium-oxide fuel and the low-neutron-absorbing zirconium-oxide while the metallic melt contains primarily zircalloy and stainless steel, including melted control rods. Highly neutron-absorbing boron from melted control rods in the corium could reduce the risk of recriticality, and even the key elements of stainless steel (iron, nickel and chromium) have a relatively high absorption cross-section compared to zirconium. If the boron is retained in the metallic melt, the strong neutron-absorber will be absent when the oxidic melt is ejected into the flooded cavity, possibly creating recriticality conditions. A recriticality may deteriorate the debris coolability and ultimately threaten the containment integrity if it does occur and escalate.

Motivated by the interest in the risk of ex-vessel corium recriticality, few studies have been conducted on the potential of ex-vessel recriticality with the focus on the debris beds [1–3]. To our knowledge, no one has addressed the recriticality of ex-vessel corium during its dispersal phase, i.e. when debris

particles are dispersed in the water pool after melt ejection and fragmentation. Neutronics studies performed by Freiría López et al. [2–3], indicated infinite multiplication factors, k_{inf}, of debris-water systems can easily exceed 1.1 for a large range of configurations, provided that the reactor poison presence is low. Given the infinite multiplication factor is greater than unity, the shape and size of the debris-water system, which determine the reactivity loss due to neutron leakage, will dictate the conditions for recriticality. Thus, the prerequisites for recriticality can be estimated based on predetermined k_{inf} calculations and geometric data obtained from experiments or simulations such as molten corium jet breakup length, lateral debris dispersal distance, debris bed height, base diameter, and angle of repose.

In the present work, the geometrical prerequisites are calculated and applied to ex-vessel debris settling characteristics from experiments and simulations. Although the knowledge on characteristics of molten corium jet fragmentation and debris settling, temporal separation of materials during melt ejection and late in-vessel chemistry of reactor poisons is still developing, such estimates are essential in the first step toward understanding of ex-vessel recriticality risks.

2. RECRITICALITY OF DISPERSED DEPBRIS PARTICLES

The conditions for recriticality of ex-vessel corium can be semi-quantitatively approximated according to modified one-group diffusion theory which has been applied for criticality safety estimates [4] and historically in survey calculations, e.g. [5]. Because the neutron velocity is much greater than the debris particle velocity in water and because the contribution from delayed neutrons is very small in this context, we can assume steady-state conditions. Under steady-state critical conditions, the effective multiplication factor of a quasi-homogenous system, k_{eff}, equals unity according to

$$k_{\text{eff}} = 1 = k_{\text{inf}} \frac{1}{1 + M^2 B^2} \tag{1}$$

where the k_{inf} is the infinite multiplication factor required for criticality, M^2 is the migration area and B^2 is the geometrical buckling [4, 6]. The parameters k_{inf} and M^2 can be obtained from e.g. Monte Carlo simulations while B^2 is determined by the geometrical conditions of the system. B^2 is the eigenvalue of the Helmholtz equation and represents the neutron flux distribution and neutron leakage, independent of the system composition [6]. In this study we calculate B^2 for different geometries to determine what values of M^2 and k_{inf} are required for recriticality according to Eq. (1).

2.1. Recriticality of debris particles falling in water

A molten corium jet leaving the RPV lower head cannot be critical due to its limited size and lack of moderation, but moderating conditions may occur after the jet breaks up into debris particles which are subsequently quenched and dispersed in the water. The dispersed particles form a quasi-homogenous debris-water system, suspended in the water pool before it settles on the containment floor. The geometrical size of this system dictates the loss of reactivity due to neutron leakage according to Eq. (1).

If we assume radially symmetric jet fragmentation, the debris-water system can be described with cylindrical coordinates with axial height, L_{system}, and radial diameter, D_{system}, as illustrated in Fig 1. If we neglect air resistance when the melt falls from the vessel into the pool water, the system diameter can be described by

$$D_{\text{system}} = (\alpha + 1)\, D_{\text{jet}} = (\alpha + 1) \sqrt{\frac{4}{\pi} \dot{V}_{jet} \frac{1}{\sqrt{2gH}}} \tag{2}$$

if the volumetric flow rate of corium in the jet $\dot{V}_{jet}$, corium density, ρ_{corium}, fall height, H, gravitational constant, g, and the water-to-corium volume ratio of the dispersed particle system, α, are known

(cf. Fig. 1). Assuming a continuous corium jet and dispersion of debris particles, the axial height of the system equals the elevation difference between the pool depth L_{pool} and the jet breakup length, $L_{breakup}$. The jet breakup length can be estimated by the following equation based on Saito et al. [7–8]:

$$L_{system} = L_{pool} - L_{break} = L_{pool} - 2.1\sqrt{\frac{\rho_{corium}}{\rho_{water}}\,2H\,D_{jet}} \tag{3}$$

where ρ_{corium} and ρ_{water} are the densities of corium and water, respectively and D_{jet} is the melt jet diameter from Eq. (2). The value of H depends on the water pool level and the vessel failure location. As debris particles settle on the containment floor, a debris bed will grow and may reduce the axial size of the falling-particle system or change the boundary conditions. The debris bed is, however, neglected in the further discussions of section 2.1.

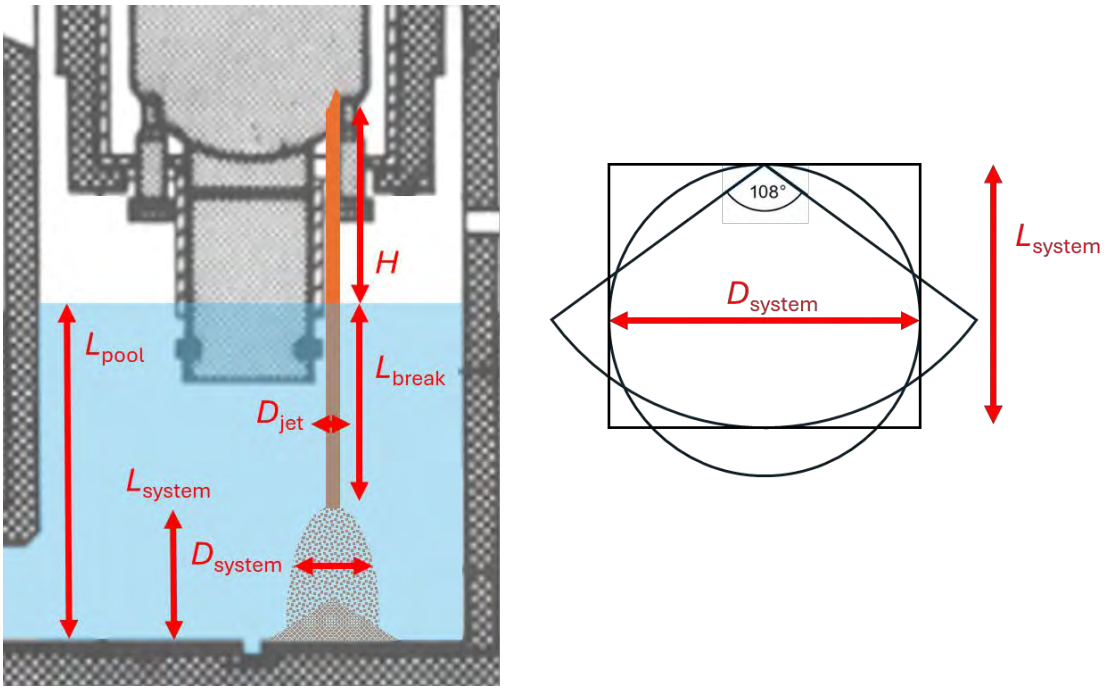

Fig. 1. Melt ejection, break-up and debris bed (left), and shapes for neutron buckling (right).

Geometrical buckling B^2 in Eq. (1) is determined by the system shape. Analytical solutions of B^2 exist for shapes that can be described in orthogonal coordinates [9]. For axially symmetrical shapes, radial diameter and axial height such as those described by Eq. (2) and Eq. (3) for a dispersed particles system can determine the buckling. For example, the following equations determine the buckling of a non-reflected system in the shape of a sphere, B^2_{sphere}, a spherical sector with aperture angle 108°, B^2_{sector}, and a cylinder, $B^2_{cylinder}$, described by

$$B^2_{sphere} = \left(\frac{3.1416}{R_{sphere}}\right)^2, \tag{4}$$

$$B^2_{sector} = \left(\frac{5.7635}{R_{sector}}\right)^2 \text{ and} \tag{5}$$

$$B^2_{cylinder} = \left(\frac{2.4048}{R_{cylinder}}\right)^2 + \left(\frac{3.1416}{L_{cylinder}}\right)^2, \tag{6}$$

respectively [4], [6], [9]. The radius and length of the dispersed particles system determine the buckling for each shape: The radius of the sphere shape R_{sphere}, is limited by half the system diameter, D_{system}, or half the system length, L_{system}. The radius of the spherical sector shape, R_{sector}, is limited by the system length, L_{system}. The radius of cylinder shape is limited by the by half the system diameter, D_{system}, and the length of the cylinder shape, $L_{cylinder}$ is limited by the system length, L_{system}.

The values of k_{inf} that are required for critical conditions, i.e. $k_{eff} = 1$, was obtained from Eq. (1) for a range of systems of debris particles dispersed in water based on corium ejected at an elevation of $H = 4.8$ m above a water pool of 8.5 m depth. The dispersion of debris particles is assumed to remain within a roughly cylindrical column, allowing the overall particle–water system to be described by Eq. (6) before the particles settle onto the containment floor. A migration area, M^2, of 50 cm^2, was chosen since the migration area for pure water and cold light water reactors is approximately 40 cm² and higher value increase leakage and decrease reactivity. Table I show the kinf required for critical conditions based on calculating B2 from Eq. (1–4), varying volumetric rates of corium ejection and water-to-corium volume ratios. Water-to-corium porosity corresponding to α are also shown for completeness (cf. [2], [3]). The cells with #### indicate large leakage with unrealistically high values of k_{inf}, i.e. greater than 2.00.

A high ejection rate produces greater system size, i.e. D_{system}. However, greater ejection rate also produces greater jet breakup-length, reducing the axial length of the system. The two counteracting effects produce a minimum required k_{inf} where the distance between the jet breakup point and the cavity floor equals the system diameter, D_{system}. If melt is slowed by structures below the vessel, the breakup length will decrease and the required k_{inf} will decrease further with ejection rates for all water-to-corium volume ratios.

Table I. Values of k_{inf} required for critical conditions with $M^2 = 50$ cm^2.

moderator/fuel	0.1	0.3	0.4	0.7	1.0	1.5	2.0	3.0	4.0	5.0	10	20	50	
porosity	0.10	0.20	0.30	0.40	0.50	0.60	0.67	0.75	0.80	0.83	0.91	0.95	0.98	
ejection rate [m^3/s]														axial size [m]
0.0001	#####	#####	#####	#####	#####	#####	#####	#####	#####	#####	#####	#####	1.21	7.5
0.0002	#####	#####	#####	#####	#####	#####	#####	#####	#####	#####	#####	1.63	1.11	7.4
0.0005	#####	#####	#####	#####	#####	#####	#####	#####	#####	#####	1.91	1.25	1.04	7.1
0.001	#####	#####	#####	#####	#####	#####	#####	#####	#####	#####	1.46	1.13	1.02	6.8
0.002	#####	#####	#####	#####	#####	#####	#####	#####	#####	1.77	1.23	1.06	1.01	6.5
0.005	#####	#####	#####	#####	#####	#####	#####	1.69	1.44	1.31	1.09	1.03	1.01	5.9
0.01	#####	#####	#####	#####	#####	1.88	1.61	1.35	1.22	1.15	1.05	1.01	1.00	5.5
0.02	#####	#####	#####	1.99	1.69	1.44	1.31	1.17	1.11	1.08	1.02	1.01	1.00	4.9
0.05	1.90	1.71	1.54	1.40	1.28	1.18	1.13	1.07	1.05	1.03	1.01	1.01	1.00	4.0
0.1	1.45	1.36	1.28	1.20	1.14	1.09	1.07	1.04	1.03	1.02	1.01	1.01	1.01	3.1
0.2	1.23	1.19	1.15	1.11	1.08	1.06	1.04	1.03	1.02	1.02	1.01	1.01	1.01	2.1
0.5	1.35	1.33	1.31	1.30	1.29	1.28	1.27	1.27	1.27	1.26	1.26	1.26	1.26	0.4
0.6	#####	#####	#####	#####	#####	#####	#####	#####	#####	#####	#####	#####	#####	0.1
2	#####	#####	#####	#####	#####	#####	#####	#####	#####	#####	#####	#####	#####	0.0

Monte Carlo calculations performed by Freiría López et al. in 2019 of water-immersed corium particles of variable size, including compositions comparable to the DEFOR and FARO experiments, suggest that k_{inf} of dispersed particles in water may be greater than unity for porosities of 0.3 to 0.9 [2–3]. Porosities greater than 0.9 were not simulated. Values of k_{inf} were found to be significantly greater than unity for porosities 0.7 to 0.8, up to 1.45 for fresh fuel [2] and up to 1.3 for uranium oxide of 12 GWd/t$_{HM}$ burnup [3]. The comparison of these results with the required k_{inf} of Table I suggests recriticality conditions in the ejection phase may be possible, depending on the melt ejection conditions, i.e. water-to-corium volume ratio, α, jet diameter, D_{jet} and volumetric flow, $\dot{V}_{jet}$.

It should be noted that additional conditions will of course influence reactivity. The assumptions made by Freiría Lopez et al. are conservative. Also, high melt temperatures will reduce reactivity slightly due to doppler broadening of ^{238}U. However, the impacts of particle temperature on k_{inf} and M^2 are expected to be small. Furthermore, the system may contain steam bubbles and steam film around debris particles which will affect the water-to-corium volume ratio in the k_{inf} calculations. The simulations in [2–3] show under-moderated conditions for porosities below 0.7–0.8, meaning the steam presence will *decrease* k_{inf} while porosities above 0.7–0.8 are over-moderated and steam will *increase* k_{inf}.

2.2. Recriticality in debris bed

When the debris particles have settled on the containment floor they will form a debris bed or pile. The geometrical prerequisites for the debris bed can be estimated analogously to the dispersal phase of debris particles. However, the shape is slightly different. As a first approximation, a spherical shape or a flat cylinder according to Eq. (4) or Eq. (6) may be appropriate. Experiments of jet fragmentation (e.g. [10]), suggest a debris bed will form a roughly conical geometry, for which no analytical solution to B^2 exist. However, B^2 estimates for arbitrary geometry can also be obtained by numerical solutions of the one-group diffusion eigenvalue equation

$$(M^2\nabla^2 + 1)\, \Phi(\bar{r}) = \frac{1}{k_{\text{eff}}}\, k_{\text{inf}}(\bar{r})\, \Phi(\bar{r}) \tag{7}$$

where $\Phi(\bar{r})$ and $k_{\text{inf}}(\bar{r})$ are the neutron flux and infinite multiplication at position given by position vector $\bar{r}$, respectively and M^2 is a position-independent migration area. By equating $k_{\text{inf}}(\bar{r})$ to unity for all positions within the desired shape and zero elsewhere, a k_{eff} value is obtained. The relationship between the k_{eff} and $k_{\text{inf}}(\bar{r}) = 1$ are related in Eq. (7) as k_{eff} and k_{inf} are related in Eq. (1). Thus, solving for B^2 in Eq. (1) with $k_{\text{inf}} = 1$ and k_{eff} obtained from Eq. (7) provides a method for obtaining an arbitrary geometric buckling estimate. Note that the buckling obtained by this method include neutrons reflected back into the system from the surrounding media whereas the analytical solutions in Eq. (4–6) does not.

Using this method, MATLAB calculations were performed in cylindrical coordinates to obtain B^2 and neutron flux distributions for three conical shapes with the angle of repose equal to 18°, 27° and 45°. Fig. 2 shows the neutron flux distribution for each case as a heat map, with brighter yellow regions indicating relatively high flux and darker blue regions indicating relatively low flux. Superimposed on the heat maps are red dots showing the conical debris geometry. As can be inferred from the flux distribution in Fig. 2, neutron flux is largely concentrated in a quasi-spherical region in the cone center, limited by cone height. From the numerical calculations, a correlation for B^2 in cm^{-2} was derived based on the angle of repose, θ and the base radius in cm, R given by

$$B^2_{\text{cone}} = 10(\tan\theta)^{-1.1}\, R^{-1.78}. \tag{8}$$

The correlation is valid to within 10% of the numerical results for θ = 18–45°, R = 60–300 cm and M^2 = 40–70 cm^2. The flux distribution in Fig. 2 and the correlation in Eq. (8) assumes complete or uniformly distributed water ingress. If void distribution inside the debris bed due to hindered water penetration or steam formation is known, the $k_{\text{inf}}(\bar{r})$ in Eq. (7) and the B^2 estimate could in principle be adjusted to account for this.

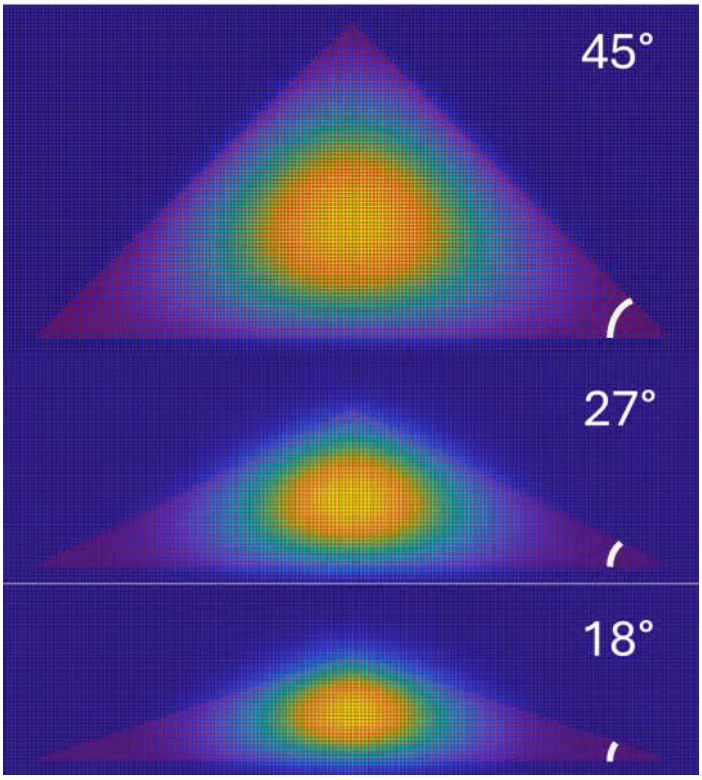

Figure 2. Neutron flux distribution and cone geometry for angles of repose of 18°, 27°, and 45°.

The migration area of the debris bed is harder to estimate than for the dispersed particles but could also be as low as 40 cm^2 or as high as 70 cm^2, roughly corresponding to a power reactor in cold and hot conditions, respectively. The correlation in Eq. (8) has been applied to plot the curves in Fig. 3, which shows the estimated bounding region of the values of k_{inf} required for critical conditions as a function of a conical debris bed radius. By comparing the region between the curves in Fig. 2 with the Monte Carlo simulations by Freiría López et al, A debris pile height exceeding 1 m would likely result in critical conditions, provided it consist of an isotropic uranium-dioxide porous bed without closed voids.

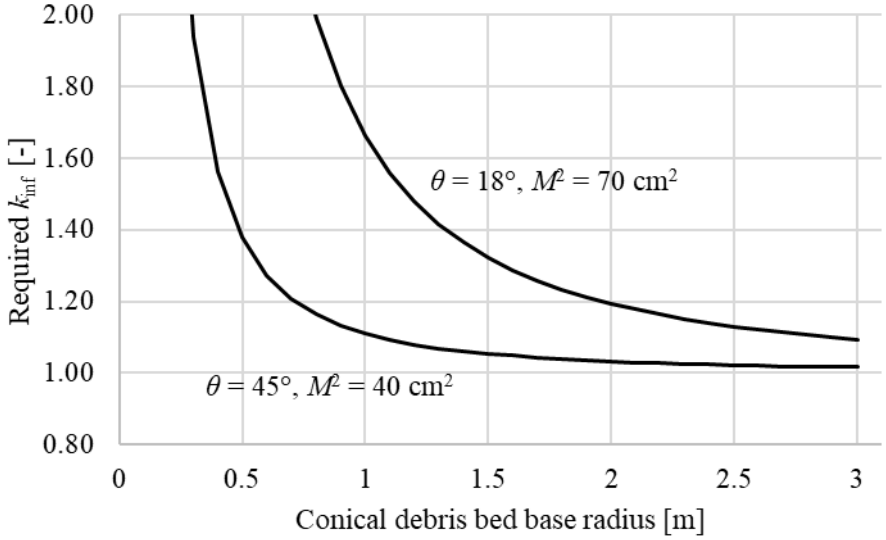

Figure 3. Required kinf for conical debris bed with angles of repose between 18° and 45°.

Consider the following illustrative example: Assume 50 tons of pure uranium oxide is ejected from a reactor vessel, forming a conical pile of porous debris with an angle of repose of 35° on a flooded containment floor. Further assume a debris bed porosity of 0.4 and a density of 8 tons/m^3 to obtain a base radius of 2.2 m and thereby a B^2 of 9.6×10^{-4} cm^{-2}. Fresh enriched uranium oxide, a particle size distribution comparable to that found in the DEFOR-A experiments and complete water ingression would yield a k_{inf} of 1.23 according to [2]. Eq. (1) and Eq. (8), together with the assumption of $M^2 = 40$ cm^2 would yield a k_{eff} of 1.18. The same example but instead assuming a porosity of 0.7 would yield a k_{eff} of 1.38. Both obtained values indicate significantly supercritical conditions.

3. CONCLUSION

The present work advances the previous studies of Freiría López et al. [2–3] on recriticality in infinite systems by also considering neutron leakage. The calculation results suggest recriticality is possible in both dispersal and settled phases of debris particles unless neutron absorbing materials (especially boron) are present. If no criticality occurs during the dispersal phase, critical conditions may occur later in a settled porous debris bed if there is sufficient water ingression and insufficient boron presence. The implication of the findings may be limited by the simple models which are incapable of coupling neutron kinetics with thermal-hydraulics in porous media, as well as incomplete knowledge of corium composition and ejection, fuel coolant interactions and resulting debris bed characteristics. Further progresses in these areas are needed to improve the understanding and assessment of ex-vessel recriticality risk. In particular, the results in this study suggest Monte Carlo simulations of k_{inf} and data of water-to-corium ratios, specifically addressing jet fragmentation and debris bed water ingress conditions, would make a significant contribution.

REFERENCES

1. Boulard, P., *Contribution to the multi-physical analysis of the risk of recriticality of corium during severe accident in a PWR reactor*, Université Paris-Saclay (2020).
2. M. Freiría López, M. Buck and J. Starflinger, "Neutronic modeling of debris beds for a criticality evaluation," *Annals of Nuclear Energy* **130**, pp. 164–172 (2019). https://doi.org/10.1016/j.anucene.2019.02.034
3. M. Freiría López, M. Buck and J. Starflinger, " Criticality Characteristics and Sensitivity Analysis of Fukushima Debris Beds Containing MCCI products", *Journal of Nuclear Engineering and Radiation Science* **6**(4) (2020). https://doi.org/10.1115/1.4047094
4. Bowen, Douglas & Busch, Robert, "Hand Calculation Methods for Nuclear Criticality Safety", https://doi.org/10.2172/1974330 (2023).
5. Hogerton, J.F. & Grass, R.C. eds. "The Reactor handbook vol. 1. Physics", pp 55–57, 462–463, https://doi.org/10.2172/4391168 (1953)
6. J. R. Lamarsh, *Introduction to Nuclear Reactor Theory,* pp 282–312, American Nuclear Society (Reprint), La Grange Park, Illinois 2002 (1966).
7. M. Saito, K. Sato and S. Imahori, "Experimental study on penetration behaviors of water jet into freon-11 and liquid nitrogen," *In: Proceedings of the ANS National Heat Transfer Conference*, Houston, USA, Vol. 3, pp 173–183 (1988)**.**
8. Yan Xiang Y. et al. "A numerical study on melt jet breakup in a water pool using coupled VOF and level set method", *Nuclear Engineering and Design* **426** (2024). https://doi.org/10.1016/j.nucengdes.2024.113363
9. Sjöstrand N.G., "Calculation of the Geometric Buckling for Reactors of Various Shapes", Aktiebolaget Atomenergi, Stockholm, Sweden (1958).
10. Karbojian, A., Kudinov, P., & Sehgal, B. R. (2009), "A scoping study of debris bed formation in the DEFOR test facility", *Nuclear Engineering and Design***, 239**(9), 1653–1659. https://doi.org/10.1016/j.nucengdes.2009.03.002

Geometrical Prerequisites for Ex-Vessel Recriticality in Flooded Cavity Containments

Björn Engström, Weimin Ma

Nuclear Power Safety group, Division of Nuclear Science and Engineering
Royal Institute of Technology, KTH

Introduction and Outline

Recriticality risk during melt ejection into **deep water pool**

- Fuel may be **separated** from neutron **absorbers** before/during melt ejection
- Dispersion in water create **moderating** conditions
- Monte-Carlo simulations by Freiría López et al. (2019, 2020) suggest fuel particles in water may yield **high k-inf values**

Recriticality **important** for fuel-coolant interactions and coolability

Neutron leakage calculations can provide insights

- **Complements k-inf** simulations by Freiría López et al.
- Neutron leakage determined by **geometrical conditions**
- Appropriate considering ex-vessel phenomena uncertainties

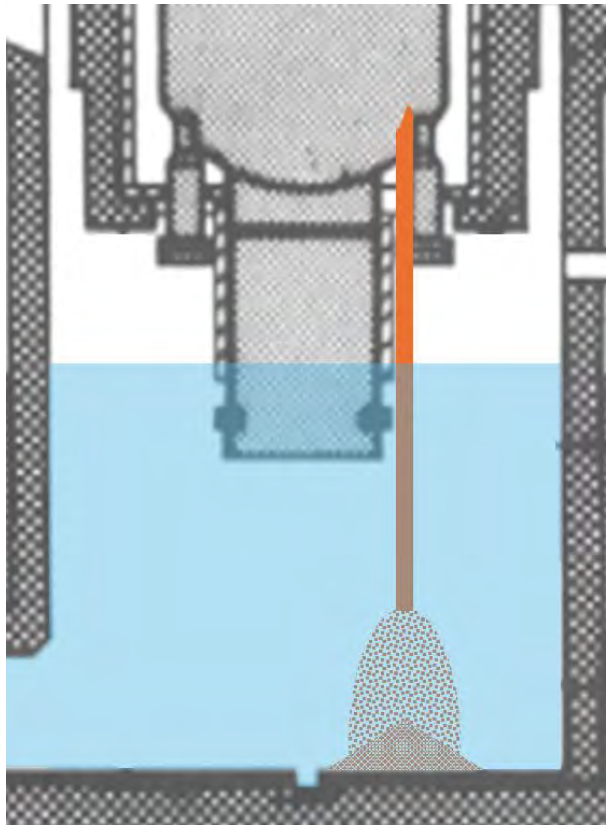

Theory - Neutronics

Neutron leakage

- based on geometrical buckling, B^2
- Radial coordinates (r, z)

Simplified neutronics sufficient for estimates

- Steady state (delayed neutron contribution negligible)
- One neutron energy group diffusion theory
- Quasi-homogenous system (uniform absorption/diffusion)
- Reasonable agreement with Monte Carlo, cf. Bowen & Busch (2023)

Some analytical solutions of B^2

$$B^2_{sphere} = \left(\frac{3.1416}{a}\right)^2$$

$$B^2_{108° sector} = \left(\frac{5.7635}{b}\right)^2$$

$$B^2_{cylinder} = \left(\frac{2.4048}{a}\right)^2 + \left(\frac{3.1416}{b}\right)^2$$

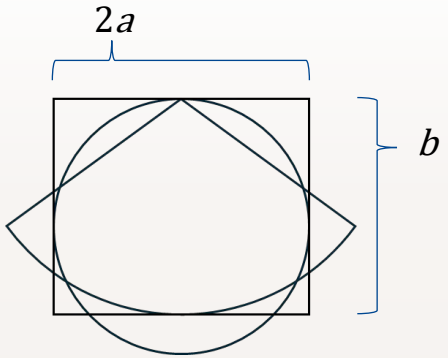

$$-\nabla \cdot D(r,z)\nabla\Psi(r,z) + \Sigma_a(r,z)\Psi(r,z) = \frac{1}{k_{\text{eff}}}\nu\Sigma_f(r,z)\Psi(r,z)$$

$$B^2M^2 + 1 = \frac{k_{\text{inf}}}{k_{\text{eff}}}$$

$\Psi(x)$	neutron flux
$D(x)$	neutron diffusion coefficient
Σ_a	condensed macroscopic absorption cross section
Σ_f	condensed macroscopic fission cross section
ν	fission neutron yield (prompt and delayed)
k_{eff}	effective multiplication factor (smallest eigenvalue)
k_{inf}	infinite multiplication factor $(\nu\Sigma_f/\Sigma_a)$
M^2	effective migration area (D/Σ_a)
B^2	Geometric buckling (helmholtz eigenvalue, $-\nabla^2\Psi/\Psi$)

Dispersed debris particles

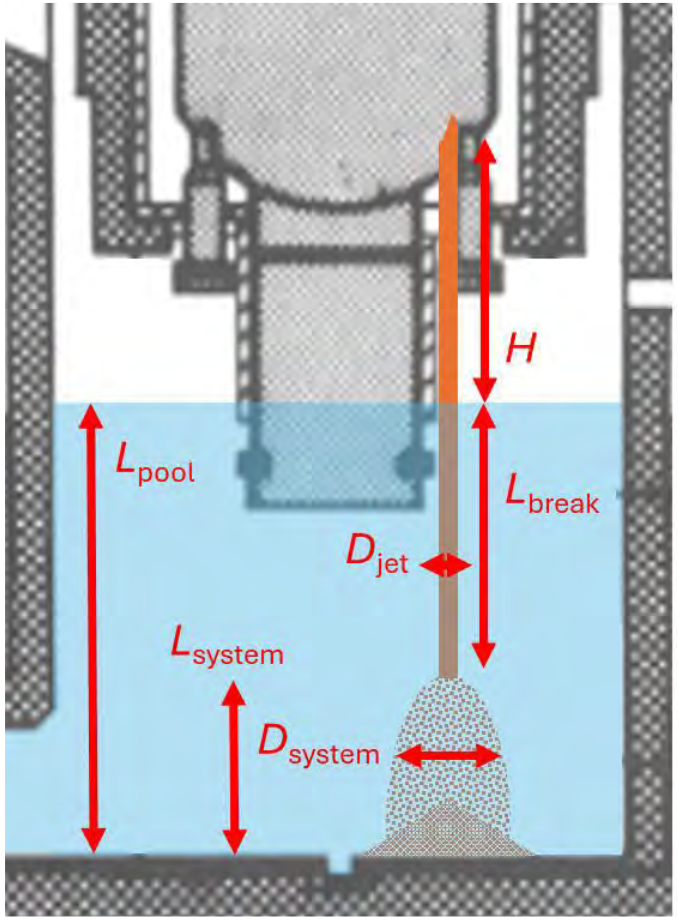

System Length based on break-up length (Saito, 1988):

$$L_{system} = L_{pool} - 2.1\sqrt{\frac{\rho_{corium}}{\rho_{water}} 2 H D_{jet}}$$

System Diameter based on free-fall and jet/water volume ratio:

$$D_{system} = (\alpha + 1) D_{jet}$$

$$D_{jet} = \sqrt{\frac{4}{\pi} \frac{\dot{m}_{corium}}{\rho_{corium}} \frac{1}{\sqrt{2gH}}}$$

H	height of vessel breach above water pool
L_{pool}	water pool depth
L_{break}	breakup length of corium jet
L_{system}	studied system height (axial length)
D_{system}	studied system diameter (radial length)
D_{jet}	corium jet diameter
ρ_{corium}	density of corium
ρ_{water}	density of water
α	water-to-corium volume ratio
$\dot{m}_{corium}$	mass flow of ejected corium from reactor vessel
g	gravitational acceleration

Dispersed debris particles cont.

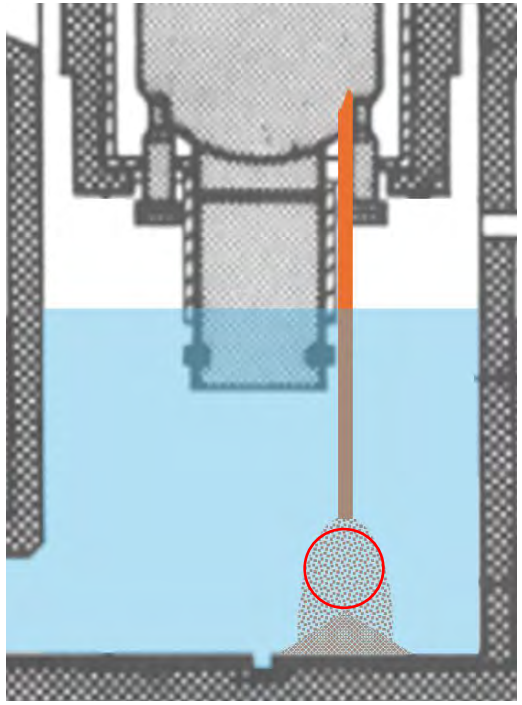

k-inf required for recriticality – M^2 = 50 cm^2

moderator/fuel	0.1	0.3	0.4	0.7	1.0	1.5	2.0	3.0	4.0	5.0	10	20	50	
porosity	0.10	0.20	0.30	0.40	0.50	0.60	0.67	0.75	0.80	0.83	0.91	0.95	0.98	
ejection rate [m^3/s]														axial size [m]
0.0001	#####	#####	#####	#####	#####	#####	#####	#####	#####	#####	#####	#####	1.21	7.5
0.0002	#####	#####	#####	#####	#####	#####	#####	#####	#####	#####	#####	1.63	1.11	7.4
0.0005	#####	#####	#####	#####	#####	#####	#####	#####	#####	#####	1.91	1.25	1.04	7.1
0.001	#####	#####	#####	#####	#####	#####	#####	#####	#####	#####	1.46	1.13	1.02	6.8
0.002	#####	#####	#####	#####	#####	#####	#####	#####	#####	1.77	1.23	1.06	1.01	6.5
0.005	#####	#####	#####	#####	#####	#####	#####	1.69	1.44	1.31	1.09	1.03	1.01	5.9
0.01	#####	#####	#####	#####	#####	1.88	1.61	1.35	1.22	1.15	1.05	1.01	1.00	5.5
0.02	#####	#####	#####	1.99	1.69	1.44	1.31	1.17	1.11	1.08	1.02	1.01	1.00	4.9
0.05	1.90	1.71	1.54	1.40	1.28	1.18	1.13	1.07	1.05	1.03	1.01	1.01	1.00	4.0
0.1	1.45	1.36	1.28	1.20	1.14	1.09	1.07	1.04	1.03	1.02	1.01	1.01	1.01	3.1
0.2	1.23	1.19	1.15	1.11	1.08	1.06	1.04	1.03	1.02	1.02	1.01	1.01	1.01	2.1
0.5	1.35	1.33	1.31	1.30	1.29	1.28	1.27	1.27	1.27	1.26	1.26	1.26	1.26	0.4
0.6	#####	#####	#####	#####	#####	#####	#####	#####	#####	#####	#####	#####	#####	0.1
2	#####	#####	#####	#####	#####	#####	#####	#####	#####	#####	#####	#####	#####	0.0

Work by Freiría López et al. suggest:

- k-inf > 1.0 for porosity 0.2-0.9 (uncertain beyond 0.9)
- k-inf 1.2-1.3 for porosity 0.7-0.8 (decreasing thereafter)

Debris bed

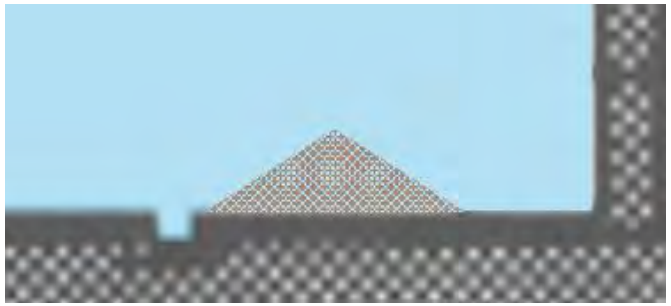

Numerical solution of cone

$$-M^2\nabla^2\Psi(r,z) + \Psi(r,z) = \frac{k_{\text{inf}}(r,z)}{k_{\text{eff}}}\Psi(r,z)$$

$$k_{\text{inf}}(r,z) = \begin{cases} 1, & r,z \in debris\ bed \\ 0, & r,z \notin debris\ bed \end{cases}$$

$$\downarrow$$

$$B^2_{cone} = \frac{1}{M^2}\left(\frac{1}{k_{\text{eff}}} - 1\right)$$

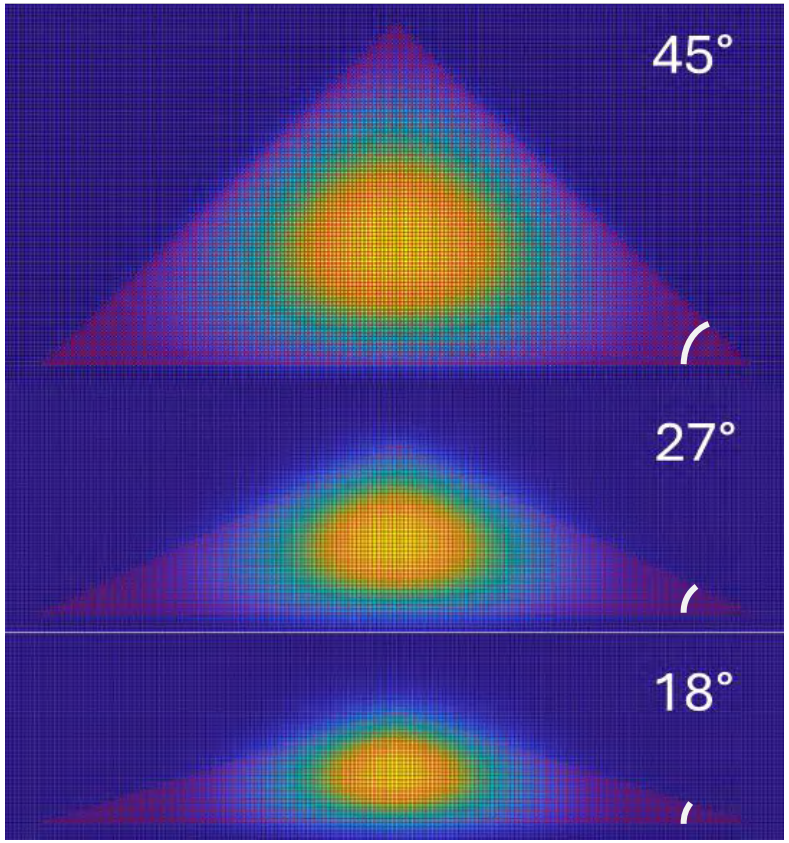

Neutron leakage predominantly determined by cone height.

Recriticality if axial size above ~1 m

- Water ingression
- Absorber presence (e.g. boron)

Correlation based on calculations

$$B^2_{cone} \approx 10\tan(\theta)^{-1.1}\,R^{-1.78}$$

accurate within 10% for:

- angle of repose, $\theta \in [18°,45°]$
- migration area, $M^2 \in [40\ cm^2, 70\ cm^2]$
- base radii, $R \in [60\ cm, 300\ cm]$.

Conclusions

- Study extends the work on k-inf by Freiría López et al. (2019, 2020) with **neutron leakage effects**.
- Results indicate **recriticality possible** for particles
  - **dispersed in a deep-water pool**
  - after **settling on the pool floor**

Additional considerations required for criticality

- sufficient **dispersion** of particles after jet break-up
- sufficient **water ingression** in debris bed
- no or weak **neutron absorbers** presence (e.g. boron)
- **steam** presence may limit moderation

- Further research required to improve **ex-vessel recriticality** analysis
  - Jet break-up and fragmentation
  - Particle dispersal, suspension & settling
  - Debris-bed composition & water ingression

Current findings are **limited** by:

- simplified modeling assumptions
- **uncertainty** in **corium ejection**, **fuel-coolant interactions** and **debris characteristics**

References

- M. Freiría López, M. Buck and J. Starflinger, "Neutronic modeling of debris beds for a criticality evaluation," *Annals of Nuclear Energy* **130**, pp. 164-172 (2019). https://doi.org/10.1016/j.anucene.2019.02.034
- M. Freiría López, M. Buck and J. Starflinger, "Criticality Characteristics and Sensitivity Analysis of Fukushima Debris Beds Containing MCCI products", *Journal of Nuclear Engineering and Radiation Science* **6**(4) (2020). https://doi.org/10.1115/1.4047094
- Bowen, D. G., & Busch, R. D. (2023). "Hand Calculation Methods for Nuclear Criticality Safety" https://doi.org/10.2172/1974330
- M. Saito, K. Sato and S. Imahori, "Experimental study on penetration behaviors of water jet into freon-11 and liquid nitrogen" *In: Proceedings of the ANS National Heat Transfer Conference*, Houston, USA, Vol. 3, pp 173-183 (1988).

KTH
VETENSKAP
OCH KONST

PERFORMANCE OF INNOVATIVE SACRIFICIAL MATERIALS FOR PWR RETROFFITING - A REACTOR CASE STUDY

Petr Vacha, Jan Komrska, Jirina Hejclova, Vaclav Tyrpekl
ÚJV Řež, a. s.
Hlavni 130, Husinec-Rez, 250 68, Czechia
petr.vacha@ujv.cz; jan.komrska@ujv.cz; jirina.hejclova@ujv.cz

ABSTRACT

Severe accidents in pressurized water reactors may result in reactor pressure vessel failure, ex-vessel corium relocation, and subsequent molten core–concrete interactions (MCCI). For the VVER-1000 design, preservation of containment integrity after MCCI constitutes the ultimate barrier against fission product release. While in-vessel retention and ex-vessel cooling strategies have been extensively investigated since the Fukushima Daiichi nuclear disaster, retrofit solutions for plants under operation remain constrained by geometry and system limitations. In particular, delayed water injection may lead to prolonged dry MCCI, increasing the risk of basemat ablation and challenge containment integrity. This study proposes and evaluates a combined ex-vessel stabilization concept tailored to VVER-1000 units. The strategy integrates (i) corium spreading to a predefined area, (ii) a refractory protective layer, (iii) a geopolymer-based sacrificial layer for chemical moderation, and (iv) delayed top flooding to establish long-term cooling through water ingression and melt eruptions phenomena. Spreading behavior was assessed using MELTSPREAD in previous work, while corium–material interactions and basemat ablation were analyzed with CORQUENCH under conservative assumptions in this work. Comparative simulations between limestone common sand concrete and geopolymer sacrificial materials indicate that the geopolymer significantly reduces hydrogen generation, further lowers the fraction of unoxidized metallic species in the melt, and decreases the solidus temperature by approximately 100 K, thereby enhancing coolability. Conservative modeling suggests 0.5 m geopolymer sacrificial layer can delay basemat attack for several hours without flooding. With top flooding initiated approximately 12 hours after accident onset, total concrete ablation remains limited. The results demonstrate that the proposed layered stabilization approach can maintain thermo-mechanical containment integrity with an adequate safety margin under delayed flooding conditions.

KEYWORDS
Ex-vessel stabilization, Sacrificial materials, VVER-1000

1. INTRODUCTION

Severe accidents involving core degradation and reactor pressure vessel (RPV) failure may lead to ex-vessel corium relocation and molten core–concrete interaction (MCCI). In pressurized water reactors, including the VVER-1000 design, preservation of containment integrity represents the ultimate barrier against fission product release. After the Fukushima Daiichi nuclear disaster, intensified research focused on both in-vessel retention (IVR) and ex-vessel corium cooling (ExVC) strategies worldwide.

Corium is a complex multiphase mixture of oxidic and metallic components (UO_2–ZrO_2–Zr–Fe–steel constituents) with strong temperature-dependent viscosity and internal heat generation due to decay heat.

During spreading, its rheology evolves rapidly as solid fraction increases near the solidus temperature. In the ex-vessel phase, cooling mechanisms include top flooding, water ingression (WI), and melt eruptions (ME), which significantly enhance heat transfer compared to pure conductive cooling through a crust layer. Experimental programs such as MACE and OECD-MCCI have demonstrated that WI and ME can increase heat flux to several hundred $kW \cdot m^{-2}$ under favorable conditions [1].

However, effective cooling requires timely water delivery. In retrofit scenarios for operating plants, immediate flooding cannot always be guaranteed due to geometric and system constraints. Delayed flooding may result in prolonged dry MCCI, threatening the structural integrity of the containment basemat.

The objective of this study is to investigate measures that can ensure short-term thermal protection of the basemat before active flooding begins, and facilitate long-term stabilization once water top-cooling is established. The ultimate goal is to showcase that the thermo-mechanical integrity of the containment structure can be maintained with a sufficient margin.

Spreading is assumed successful based on prior mechanistic analyses with MELTSPREAD. The present work concentrates on post-spreading thermal protection and chemical stabilization.

2. VVER-1000 SPECIFICS RELEVANT TO THE PRESENTED STUDY

The VVER-1000 containment features a rather complex geometry between the reactor cavity and designated spreading compartments. According to feasibility analyses for VVER-1000/V320 units, corium spreading would proceed from the RPV lower plenum into the reactor cavity and subsequently through a corridor into an adjacent spreading room prepared for top flooding. [2]

Unlike some Western PWR designs, the VVER-1000 reactor cavity concrete bottom is lined with steel layers serving as thermal shielding. This configuration complicates structural modifications in the cavity region. Additionally, inspection equipment pathways and the presence of the recirculation sump at the lowest elevation introduce further constraints for implementing IVR or extensive cavity redesign.

Experimental investigations with prototypic corium compositions have shown limited penetration into these layered steel systems, with rapid crust formation at the interface. This supports the feasibility of allowing corium to spread toward a prepared ex-vessel area rather than penetrating deeply into the shaft structures.

The spreading area typically includes approximately 25 m^2 in the reactor cavity and 60 m^2 in an adjacent compartment. Successful spreading requires sufficient corium fluidity at RPV failure. MELCOR-based analyses indicate volumetric solid fractions on the order of 10–15% at vessel breach, allowing spreading under most scenarios. Sensitivity analyses highlight the influence of:

- Solid fraction–temperature relations (U–Zr–Fe–O quaternary system),
- Pour rate through the rupture opening,
- Sequence of metallic versus oxidic phase relocation.

If no mitigation is applied and corium remains dry on concrete for extended periods, MCCI may lead to substantial basemat ablation, hydrogen production, and possible containment failure due to thermos-mechanical stress.

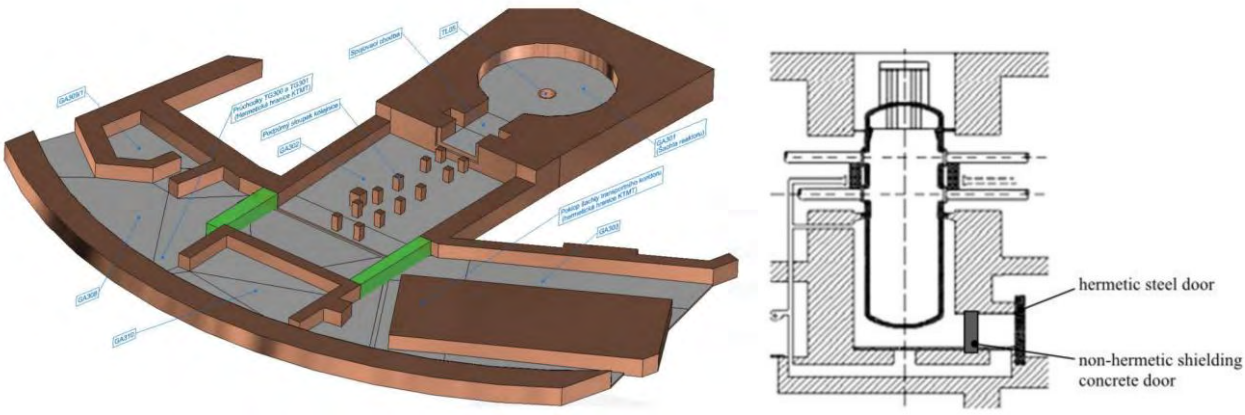

Figure 1. VVER-1000 reactor cavity and adjacent compartments. [2]

2.1. Delayed water inlet and basemat protection

Although top flooding is recognized as an effective long-term cooling strategy, its effectiveness can be significantly reduced when implemented after a substantial delay. In such cases, several adverse phenomena may occur prior to coolant injection. First, a thick and mechanically robust crust layer may form on the corium surface, impeding subsequent heat removal. Second, dense crust structures can substantially limit water ingression, thereby reducing cooling efficiency. Third, prolonged exposure to elevated temperatures may lead to progressive weakening and degradation of the underlying concrete before active cooling is initiated.

These limitations highlight the need for a passive mitigation measure capable of withstanding direct corium contact and delaying the onset of concrete damage. An effective protective system should possess a high melting temperature to ensure structural integrity under severe thermal loads, exhibit low chemical reactivity with corium to minimize detrimental interactions, and maintain mechanical stability under rapid thermal transients. Furthermore, the material should degrade in a controlled and gradual manner, avoiding abrupt or catastrophic failure that could compromise the cooling process.

3. STUDIED SOLUTION

In the light of the previous information, a combined ex-vessel corium stabilization strategy consisting of 5 steps is applied by the authors:

1. Spreading over a predefined area (assumed successful).
2. Primary thermal protection using refractory layer.
3. Chemical moderation of corium via geopolymer sacrificial layer.
4. Delayed top flooding with external water supply.
5. Enhanced cooling through WI and ME phenomena..

Short-term protection is therefore provided by refractory and insulating properties of the thermal protection layer. Long-term stabilization relies on water top flooding and reduced MCCI aggressiveness due to sacrificial material interaction.

3.1. Protective layer

A candidate protective layer material to avoid excessive basemat ablation is zirconia, used in various core catcher solutions such as EPR. Zirconia is a widely used material with melting temperatures above 2700 K. Its chemical stability against oxidic melts and corrosion resistance at high temperatures make it suitable for extreme applications such as protective layer in a core catcher. [3]

Zirconia's low thermal conductivity (2–3 $W \cdot m^{-1} \cdot K^{-1}$ at high temperature) provides significant thermal insulation, reducing heat flux to underlying concrete.

High-temperature corrosion studies [1][3] indicate that ZrO_2 exhibits limited dissolution in oxidic corium; dissolution kinetics depend on oxygen potential and interaction with metallic Zr and UO_2. Diffusion-controlled dissolution models suggest that reduction reactions are constrained by limited mass transport within the melt, particularly under stratified configurations.

Failure modes include:
- Thermochemical dissolution into oxidic corium,
- Reduction by metallic zirconium,
- Mechanical cracking due to thermal shock,
- Spallation from rapid temperature gradients.

However, ensuring complete integrity of the protective layer is not required for the studied solution. The design objective is only time delay — postponing concrete ablation for several hours until active cooling is established is deemed a success, even though the protective layer is severely damaged or completely destroyed in the process.

3.2. Sacrificial materials

Parallel research efforts have led to the development of geopolymer-based sacrificial liners intended for ex-vessel applications in severe accident scenarios. These materials are designed to replace conventional concrete in designated corium spreading areas. In contrast to ordinary siliceous or limestone concrete, geopolymers contain only minimal amounts of chemically bound water, thereby limiting steam generation during high-

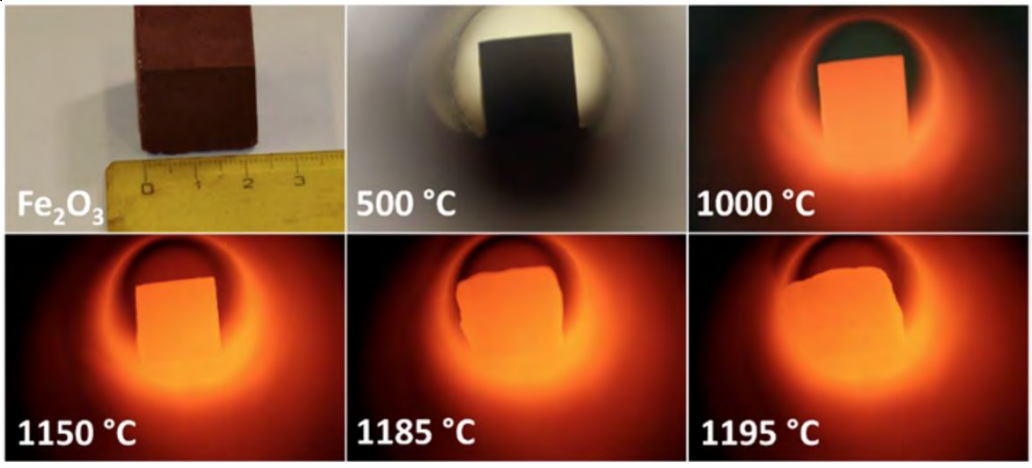

Figure 2. Geopolymer sacrificial material cube thermal resistance test.

temperature interaction. They retain their mechanical properties at temperatures up to approximately 500°C for short durations and remain stable below approximately 200°C under long-term conditions. In addition, these materials demonstrate resistance to gamma radiation, supporting their applicability in high-radiation environments.

During interaction with corium, geopolymer materials are engineered to produce significant quantities of carbon dioxide while generating only limited amounts of hydrogen. This behaviour reduces the overall production of flammable gases compared to conventional siliceous concrete. The release of gas promotes crust cracking, which may enhance heat transfer and coolability. Furthermore, chemical interactions between the geopolymer and corium can modify the oxidation state of the melt, leading to a reduction in the metallic fraction.

Comparative analyses performed using the CORQUENCH code indicate substantially lower hydrogen production and significant carbon dioxide release when geopolymer materials are used instead of conventional VVER-1000 concrete. This chemical buffering effect reduces exothermic metal oxidation reactions and mitigates the risk of containment pressurization.

The incorporation of geopolymer sacrificial layers over the zirconia protection may therefore contribute to oxidation of residual metallic zirconium, reduction of the initial corium temperature through endothermic reactions, and improved long-term coolability following flooding.

More information on the sacrificial materials chosen for this study can be found in [4] and [5].

4. ANALYSIS OF THE SACRIFICIAL MATERIAL PERFORMANCE

The studied accident scenario is a LB-LOCA, with conservative assumptions on timing of RPV failure (~4 hours). Corium spreading was analysed using the MELTSPREAD 3.0 code. More information on the scenario and the analyses of in-vessel phase and corium spreading can be found in [2].

The main aim of this study, the performance of the sacrificial material in comparison to LCS-type concrete, was studied using CORQUENCH 4.1 code. A layer of 0,5 m of sacrificial material was put on top of, with the containment basemat located underneath the protective layer. The results of interest are following:

- Chemical composition of the melt (to assess the potential of the melt to attack the protective layer)
- Amount and composition of non-condensable gases produced from the corium-sacrificial material interaction (to assess effects on containment integrity)
- Temperature of solidus and liquidus of the melt (to assess effects on corium coolability)

4.1. Modeling Considerations and CORQUENCH Conservatism

System codes such as CORQUENCH assume homogenized melt composition and do not resolve spatial distribution of species in sublayers [6]. This may lead to conservative predictions of zirconia ablation.

An illustrative example concerns CO_2 reduction to CO in contact with metallic layers. CORQUENCH predicts near-complete conversion, whereas experimental data show that approximately 90% of generated CO_2 may escape without reduction due to limited residence time. Consequently, predicted chemical aggressiveness toward refractory materials can be overstated.

To address unrealistic low-temperature ablation rates (mm·h⁻¹ below 1700 K), a cutoff bulk temperature of 2000 K was adopted in sensitivity analyses. Considering the thermal gradient across the zirconia layer, the interface temperature is significantly lower than bulk melt temperature, further supporting this assumption.

4.2. Corium properties after sacrificial material incorporation

A 500 mm-thick layer of sacrificial material was modelled in direct contact with corium immediately following completion of the spreading phase. Two candidate materials were considered: a conventional limestone common sand concrete (LCSC) and an innovative geopolymer-based formulation. The interaction between corium and the sacrificial layer was simulated using CORQUENCH. A one-dimensional (1D) modelling approach was adopted, and no top flooding with water was assumed. Each simulation was terminated once the entire sacrificial layer had been fully incorporated into the molten pool.

The calculated post-interaction melt compositions indicate that, in both cases, the overall chemical composition of the resulting melt is broadly comparable, as can be seen in Table I. However, the geopolymer scenario exhibits a lower fraction of unoxidized metallic species relative to the LCSC case. This difference is particularly relevant for zirconium-bearing phases, as the presence of unoxidized metals—especially Zr—can substantially accelerate degradation of protective layers through enhanced chemical reactivity and heat generation. The reduced content of unoxidized metals in the geopolymer case is therefore considered favourable from the standpoint of long-term melt stabilization and structural integrity.

Table I. Melt chemical composition (constituents below 1 % neglected)

	concrete	geopolymer
CONSTITUENT	**Mass fraction [-]**	**Mass fraction [-]**
UO2	0.37	0.38
ZRO2	0.17	0.16
CR2O3	0	0
NIO	0	0
B2O3	0.01	0
FE	0.03	0
CR	0	0
NI	0	0
ZR	0.01	0
U	0	0
B4C	0.01	0.02
SI	0	0
SIO2	0.03	0.09
CAO	0.16	0.06
MGO	0.02	0.04
AL2O3	0.01	0.14
FEO	0.12	0.05
FE2O3	0.03	0.03
FE3O4	0.03	0.03

Significant differences were observed in both the quantity and composition of non-condensable gases generated during corium–material interaction, see Table II. As anticipated, the geopolymer material produces relatively low amounts of hydrogen while generating predominantly carbon dioxide and limited quantities of carbon monoxide. In contrast, decomposition of the limestone concrete results in substantial hydrogen production. This distinction has important safety implications. The lower yield of flammable gases—particularly hydrogen—in the geopolymer case reduces the potential for deflagration or detonation compromising structural integrity of the containment.

Table II. Amount of NCGs produced by interaction with sacrificial material

	H_2	CO	CO_2	Total	
	mass (kg)	mass (kg)	mass(kg)	mass (kg)	amount of substance (kmol)
Concrete	1448	147	2311	3906	782
Geopolymer	202	503	7885	8590	298

With respect to thermophysical properties, the calculated solidus and liquidus temperatures of the resulting melts are similar for both materials, with one notable difference: incorporation of the geopolymer leads to a reduction in solidus temperature on the order of approximately 100 K, while the liquidus temperature remains essentially unchanged, see Table III. The lower solidus temperature implies that the melt remains fully or partially liquid over a broader temperature range during cooling. This behaviour may enhance the melt's effective cooling capability by delaying solidification and promoting improved heat transfer via convection prior to complete freezing of the melt.

Table II. Solidus and liquidus temperatures of the melt after incorporation of sacrificial materials

	Solidus T (K)	Liquidus T (K)
concrete	1508.7	2525.9
geopolymer	1403.0	2493.3

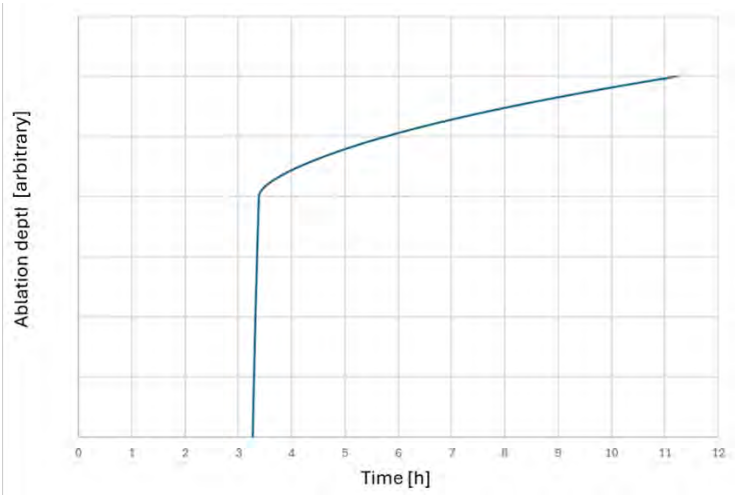

Figure 3. Rate of consumption of the sacrificial material and subsequent damage of the protective layer.

Overall, the simulations indicate that geopolymer-based sacrificial material offers several potential advantages over conventional limestone concrete, including reduced concentrations of unoxidized metals in the melt, significantly lower hydrogen production, and moderately improved thermophysical characteristics relevant to cooling performance.

4.3. Function of the protective layer

Following the incorporation of the sacrificial material, a subsequent analysis was performed using CORQUENCH to evaluate the rate of degradation of the protective layer under the assumption that no top flooding of the melt occurs. In this phase of the study, only geopolymer-based sacrificial materials were considered, as their performance was shown in the previous section to be superior to that of conventional concrete.

The primary objective of this analysis was to determine the duration for which the protective layer can maintain its integrity in the absence of top cooling by water. The results indicate that the selected refractory material can conservatively withstand thermal and chemical attack for approximately 8 hours before being fully consumed, as seen in the graph in Figure 3.

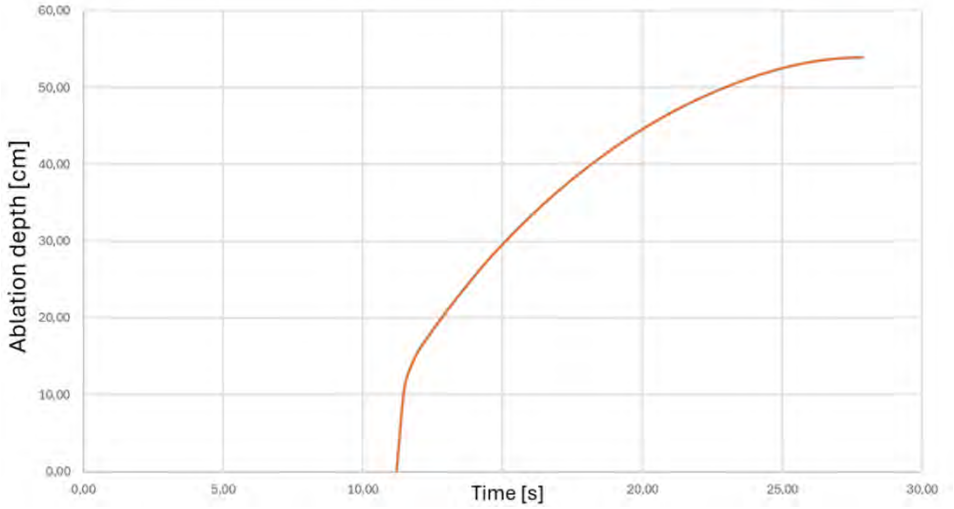

Figure 4. Rate of concrete ablation after failure of the protective layer (with top-flooded melt).

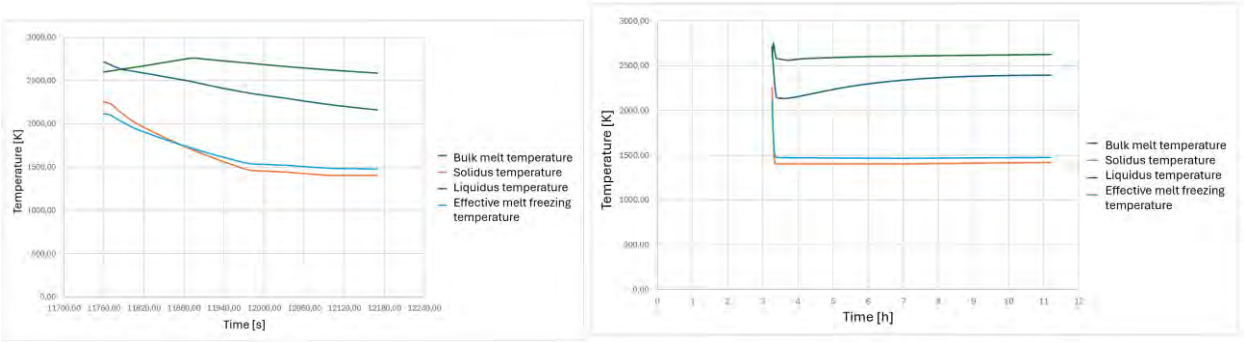

Figure 5. Temperatures in the melt during the consumption of the sacrificial material (left) and long-term during damage of the protective layer (right)

A subsequent scenario was then evaluated in which water is introduced onto the top surface of the corium after this period, corresponding to roughly 12 hours after the onset of the accident. The analysis shows that, under these conditions, the total ablation depth of the basemat concrete is limited to approximately 0.5 m, see Figure 4.

The results further demonstrate that, although the incorporation of the sacrificial material initially reduces the melt temperature due to dilution and endothermic interactions, the residual decay heat within the corium eventually offsets this cooling effect. As a result, the melt temperature begins to rise again after the initial decrease, see Figure 5.

5. CONCLUSIONS

The present study investigated a layered ex-vessel corium stabilization concept for VVER-1000 reactors under severe accident conditions with delayed water injection. The proposed approach combines refractory thermal protection, chemically engineered sacrificial materials, and subsequent top flooding to ensure both short-term basemat protection and long-term coolability.

The analyses indicate that stabilized zirconia provides effective short-term thermal insulation and chemical resistance, primarily serving as a time-delay barrier rather than a permanent containment solution. The incorporation of a geopolymer-based sacrificial layer beneath the corium significantly modifies melt chemistry compared with conventional limestone concrete. In particular, reduced hydrogen generation and lower concentrations of unoxidized metallic zirconium decrease both combustion risk and chemical aggressiveness toward protective structures. The moderate reduction in solidus temperature further supports improved cooling behaviour once flooding is established.

Conservative CORQUENCH simulations show that the combined layered system can withstand several hours of dry interaction and, with delayed top flooding, limit basemat erosion to manageable levels. Although residual decay heat eventually offsets the initial temperature reduction caused by sacrificial material incorporation, the transition to water-enhanced cooling mechanisms stabilizes the melt and prevents uncontrolled concrete attack.

Overall, the results support the technical feasibility of implementing a retrofit-oriented, layered ex-vessel stabilization system for VVER-1000 units. The concept offers a robust margin for containment integrity even in scenarios involving delayed flooding and represents a viable complementary strategy to existing severe accident management measures.

REFERENCES

1. OECD/NEA (2017). *State-of-the-Art Report on Molten Corium Concrete Interaction and Ex-Vessel Molten Core Coolability*. NEA/CSNI/R(2016)15.
2. M. Kotouč, et al.: “Assessment of Ex-Vessel Corium Coolability in the Containment of the VVER-1000 Reactor as a Measure of Severe Accident Mitigation,” *Proceedings of the 2022 10th European Review Meeting on Severe Accident Research*, Karlsruhe, Germany, May 16-19, 2022
3. Chevalier, J., Gremillard, L., & Virkar, A. V. (2009). The tetragonal–monoclinic transformation in zirconia: lessons learned and future trends. *Journal of the American Ceramic Society*, 92(9), 1901–1920.

4. Vácha, P., Kotouč, M. and Komrska, J. „Severe accident R&D in UJV Group“, *Proceedings of the 2024 11th European Review Meeting on Severe Accident Research,* Stockholm, Sweden*,* 13-16 May, 2024
5. V. Tyrpekl et al.: “Development of geopolymer based sacrificial materials for GENIV severe accident mitigation*”, Journal of Nuclear Materials* 553, (2021)
6. Farmer, M. T. (2018). *The CORQUENCH Code Manual*. Argonne National Laboratory.

Performance of innovative sacrificial materials for PWR retrofitting – a reactor case study

Petr Vácha, Jan Komrska, Václav Tyrpekl, Jiřina Hejčlová (ÚJV Řež)

12th Conference on Severe Accidents Research ERMSAR 2026, May 18-22, 2026, Madrid, Spain

Skupina ÚJV
LIDÉ | INOVACE | TECHNOLOGIE

SKUPINA ČEZ

OUTLINE

- **Background – VVER 1000 ex-vessel corium stabilization**
- **Innovative sacrificial materials based on Geopolymers**
- **Reactor case study – description**
- **Reactor case study – results**
- **Conclusions**

Background – VVER 1000 ex-vessel corium stabilization

BACKGROUND – VVER 1000 MELT STABILIZATION (1)

- **Melt stabilization in VVER-1000:**
- IVMR – theoretically possible, retrofitting would be challenging - > not yet used in any NPP
- EVMR – theoretically possible, retrofitting a little less challenging -> studied in various countries, not yet used in any NPP
  - Challenges to be solved – allowing spreading, limiting MCCI to retain basemat structural integrity, enabling timely top-flooding with water
- **In this study:**
- A possible approach to EVMR strategy in VVER-1000 using corium spreading and sacrificial materials studied
- Emphasis on the effect of sacrifical materials effects on the melt stabilization progression

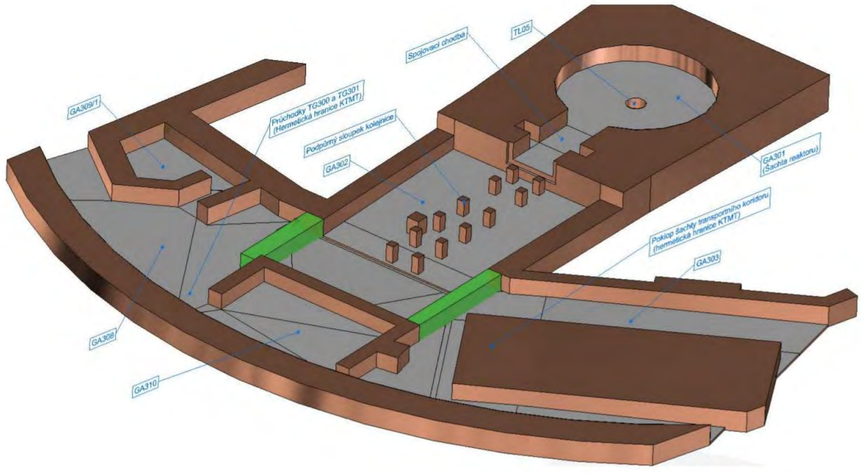

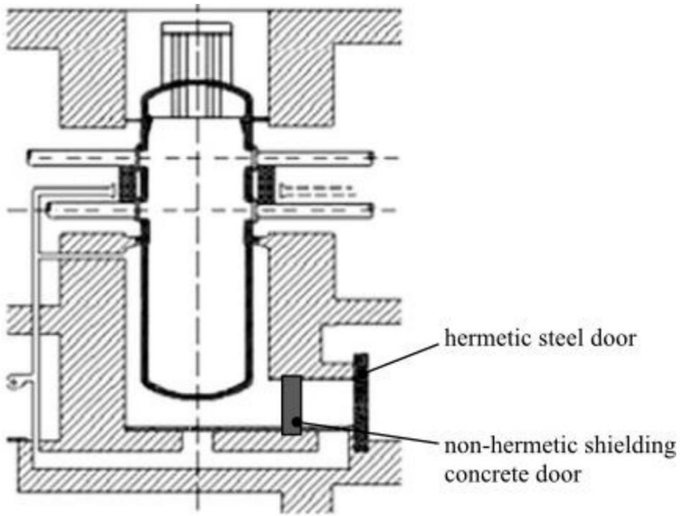

M. Kotouč, et al.: "Assessment of Ex-Vessel Corium Coolability in the Containment of the VVER-1000 Reactor as a Measure of Severe Accident Mitigation," *Proceedings of the 2022 10th European Review Meeting on Severe Accident Research*, Karlsruhe, Germany, May 16-19, 2022

BACKGROUND – VVER 1000 MELT STABILIZATION (2)

- **EVMR approach used in the study based on:**
- 1) RPV breach and corium ejection into dry cavity <- Initial conditions for the study, data taken from MELCOR/ASTEC simulation
- 2) Corium spreading to adjacent compartment – Assumed in the study, not modelled in detail (extensive R&D on this subject already done)
- 3) Corium-SM interaction – Compartment floor lined with a refractory layer and a sacrificial layer
- 4) Top-flooding with water, cooling – maximum delay of start of water inlet can be derived from the results of the study

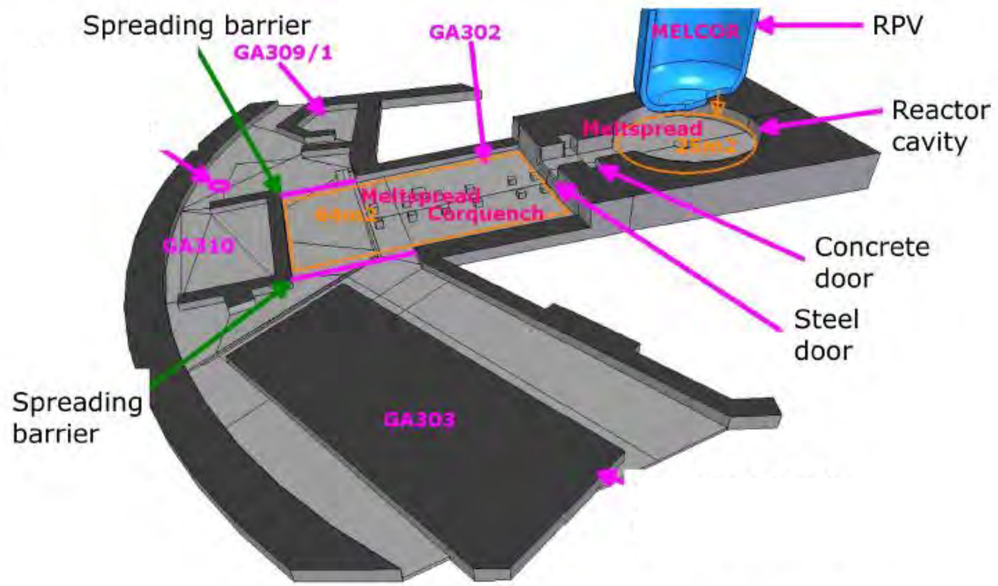

M. Kotouč, et al.: "Assessment of Ex-Vessel Corium Coolability in the Containment of the VVER-1000 Reactor as a Measure of Severe Accident Mitigation," *Proceedings of the 2022 10th European Review Meeting on Severe Accident Research*, Karlsruhe, Germany, May 16-19, 2022

Innovative Sacrificial Materials Based on Geopolymers

GEOPOLYMERS AS SACRIFICIAL MATERIALS (1)

- **Geopolymers:**
- A group of inorganic polymer materials resembling concrete, based on alumino-silicates
- Coarse matrix capable of incorporating huge amounts of filler materials (up to 90 Wt.%)
- Filler materials influence properties of the geopolymer to big extent
- Modern waste immobilization candidate materials in the context of nuclear energy
- **Several key advantages compared to concrete in SA:**
- Minimum of water in the material – way below 1 Wt. % (usually around 0,1 – 0,2 %) while exhibiting similar structural properties as concrete
- The coarse geopolymer matrix can be filled with functional materials – from „simple“ oxidizers to complex compounds changing the properties of the melt

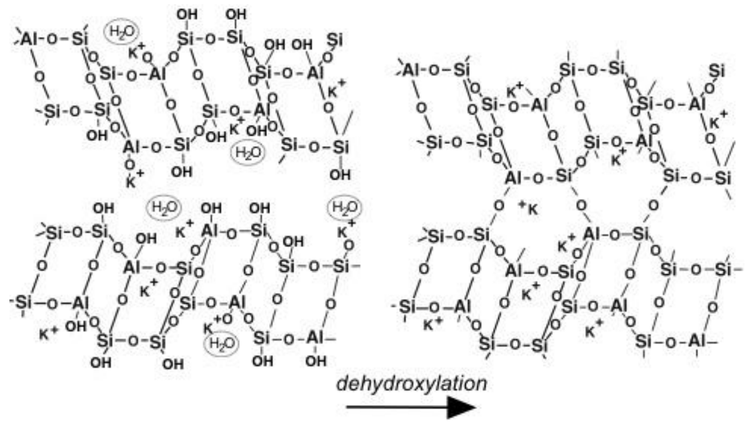

GEOPOLYMERS AS SACRIFICIAL MATERIALS (2)

- **Materials studied (experimentally and computationally) as fillers for the matrices so far:**
- $CaCO_3$ – Limestone, extensive gas production to enhance cooling via melt eruptions
- Al_2O_3 and Mg0 – refractory materials for the long-term exposure to corium
- Gd_2O_3 – neutron absorber
- Fe_2O_3 – dilution of oxide phase, functional material
- $Ca_3(PO_4)_2$ – functional material
- **All the materials very well characterized and important properties measured with excellent results:**
- Solidus and liquidus temperature (alone and in mixture with prototypical corium), thermal conductivity and specific heat capacity, thermogravimetry, mechanical strength, gamma radiation exposure, boric acid exposure
- Extensive R&D program under national and international collaborative programs

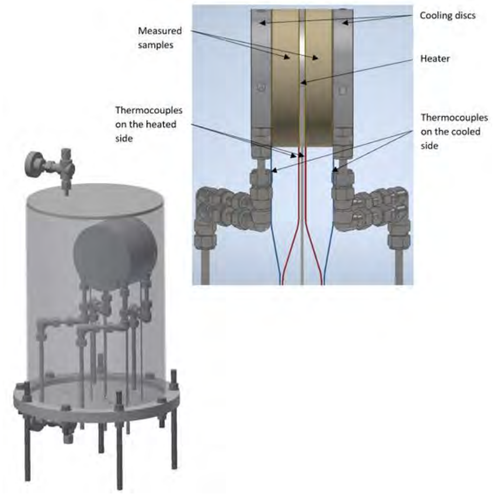

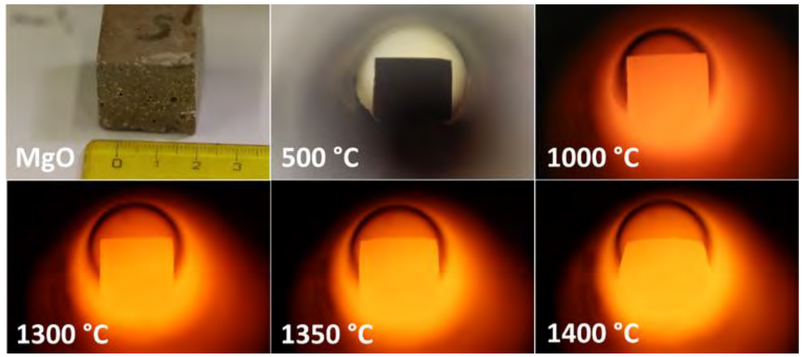

Reactor Case Study - Description

REACTOR CASE STUDY – CODES AND MODELS

- **Codes used:**
- ASTEC – in-vessel phase modelling (LB-LOCA), source of initial conditions (amount of corium, composition, properties) for the study
- (MELTSPREAD/CFD – not used in this study, but based on previous results, spreading and change in corium properties after spreading was assumed)
- CORQUENCH 4.1 – 2D modelling, 3 step approach used (separate calculations with data transfer):
    1) Sacrificial material incorporation into the corium
    2) Refractory layer attack
    3) MCCI and Top-flooding with water and cooling (top-flooding assumed at the time of protective layer failure)

- **Problem configuration:**
- Initial state: slab geometry, corium on top of 500 mm layer of sacrificial material, refractory layer underneath, basemat concrete under the refractory layer
- Materials and compositions:
    - Corium: from ASTEC calculation (see next slide)
    - Sacrificial material: limestone-geopolymer (see next slide)
    - Refractory layer: zirconia

REACTOR CASE STUDY – COMPOSITIONS

- **Initial material compositions:**
  - **Sacrificial material:**

Constituent	Wt. %
Matrix – $Na_2O \cdot SiO_2 + Al_2O_3$	8,14
Fire Clay A111 – (Mix of $Al_2O_3 + SiO_2$)	25,73
Filler – Calcite (CaCO3)	66,13

Corium:

Scenario	LB LOCA				
RPV failure instant [s]	12105				
Layer	*Heavy metals*	*Oxides*	*Light metals*		
Mass [kg]	6061	66116	48223		
Temperature [K]	1811	2749	1994		
Viscosity [Pa.s]	1.211E-02	9.099E-03	1.241E-02		
Density [kg/m3]	8078	7783	7720		
Material	*Mass [kg]*	*Mass [kg]*	*Mass [kg]*	*Total [kg]*	*Total [kg]*
B_4C	12	2	56	**70**	**70**
Cr	823	127	5753	**6703**	**6703**
Cr_2FeO_4	4	0	20	**24**	**24**
Fe	2804	432	19593	**22830**	**22830**
Ni	494	76	3452	**4022**	**4022**
NiO	1	0	8	**10**	**10**
U	1305	2668	8685	**12658**	**12658**
UO_2	138	44919	1443	**46500**	**46500**
Zr	426	844	2746	**4016**	**4016**
ZrO_2	54	16912	543	**17510**	**17510**
15Ch2NMFA	0	136	5922	**6057**	**6057**
	6061	**66117**	**48222**	**120401**	**120401**

J. Hrbek, et al.: "Investigation of prototypical corium interaction with samples of VVER-1000 in-vessel and ex-vessel structure," *Nuclear Engineering and Design (418), 2024*

REACTOR CASE STUDY – TROUBLESHOOTING

- **Gases produced from sacrificial material decomposition:**
- Codes such as CORQUENCH do not account for reaction kinetics – as long as any reactants are present in the system, they will react completely
- CO2 produced from the SM decomposition is all instantly reduced to CO <- large source term of CO in the initial phase of corium-SM interaction
- Simple experiment performed – two layers of metallic foils (Zr and steel) on top of SM sample (thicknesses proportionally the same as in the reactor case scenario), heat-up to decomposition temperature, measurement of CO2/CO ratio
- Findings – 90 % of gas produced from the reaction is CO2, 9 % CO, 1 % other

- **Zirconia attack**
- Similar story – as long as any potentially damaging constituent is present in the problem, the zirconia layer will be attacked by it <- overestimation of attack rate (but OK, we are conservative and we do not include mechanical problems such as cracking)
- However - zirconia layer never stopped disappearing in the calculation – test case over 100h with „infinite“ layer of zirconia, rate was slower but zirconia layer was decreasing even under 1500 K
  - Based on extensive literature research – manual cutoff of further zirconia layer attack at 2000 K melt temperature.

Reactor Case Study - Results

REACTOR CASE STUDY – SM VS. CONCRETE

- **Comparison between geopolymer-based SM and LCS-type concrete sacrificial layer**

Table I. Melt chemical composition (constituents below 1 % neglected)

	concrete	geopolymer
CONSTITUENT	Mass fraction [-]	Mass fraction [-]
UO2	0.37	0.38
ZRO2	0.17	0.16
CR2O3	0	0
NIO	0	0
B2O3	0.01	0
FE	0.03	0
CR	0	0
NI	0	0
ZR	0.01	0
U	0	0
B4C	0.01	0.02
SI	0	0
SIO2	0.03	0.09
CAO	0.16	0.06
MGO	0.02	0.04
AL2O3	0.01	0.14
FEO	0.12	0.05
FE2O3	0.03	0.03
FE3O4	0.03	0.03

Table II. Amount of NCGs produced by interaction with sacrificial material

	H_2	CO	CO_2	Total	
	mass (kg)	mass (kg)	mass(kg)	mass (kg)	amount of substance (kmol)
Concrete	1448	147	2311	3906	782
Geopolymer	202	503	7885	8590	298

Table II. Solidus and liquidus temperatures of the melt after incorporation of sacrificial materials

	Solidus T (K)	Liquidus T (K)
concrete	1508.7	2525.9
geopolymer	1403.0	2493.3

REACTOR CASE STUDY – SM PERFORMANCE

- **Results of CORQUENCH analysis:**
- SM is consumed relatively quickly (approx. 20 minutes)
- Refractory layer ablation rate stabilizes after 3 hours
- Without top-flooding, the temperatures of the system stay high-enough to consume the whole refractory layer

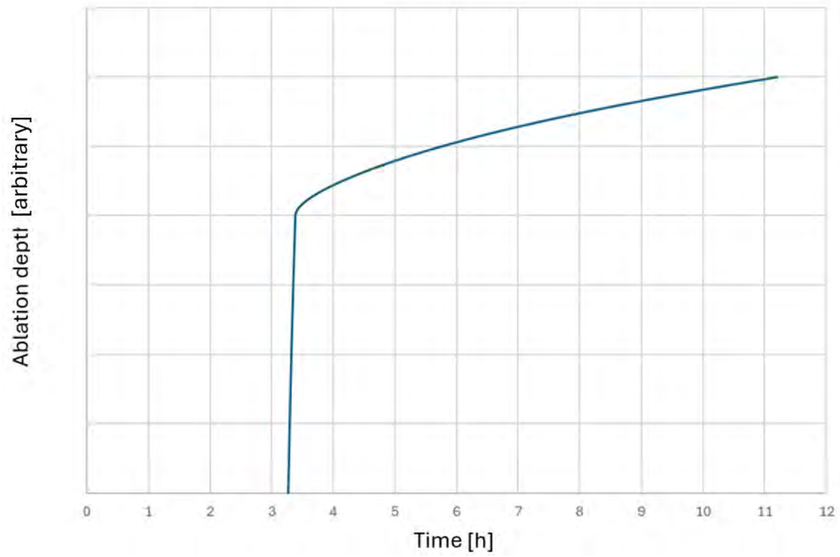

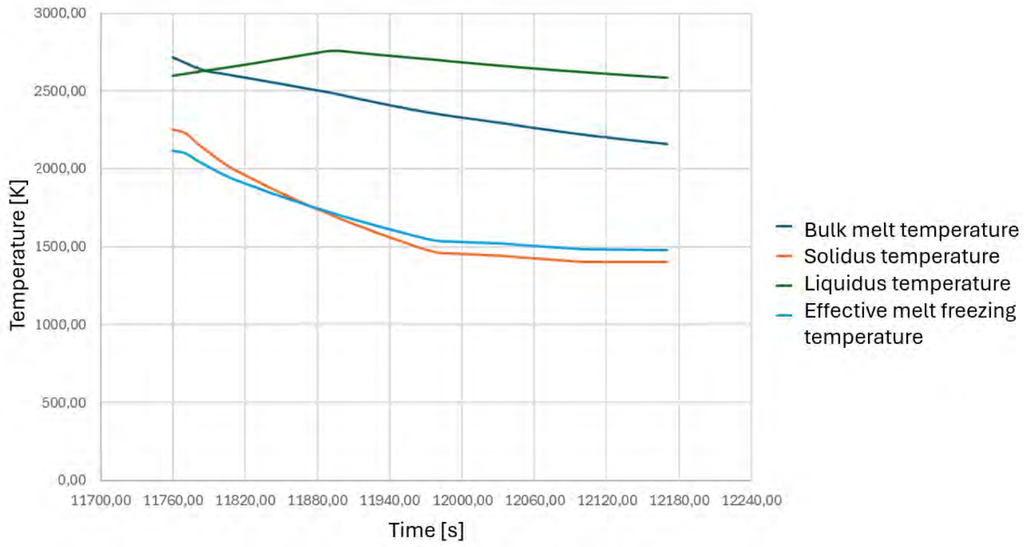

REACTOR CASE STUDY – STABILIZATION

- **Results of CORQUENCH analysis:**
- After consuming the refractory layer, a water-layer is assumed at the top of the corium
- Concrete ablation rate is steadily decreasing, reaching maximum depth at around 25 h mark
- Maximum ablation depth is relatively low, basemat retains its mechanical strength over majority of the cross-section

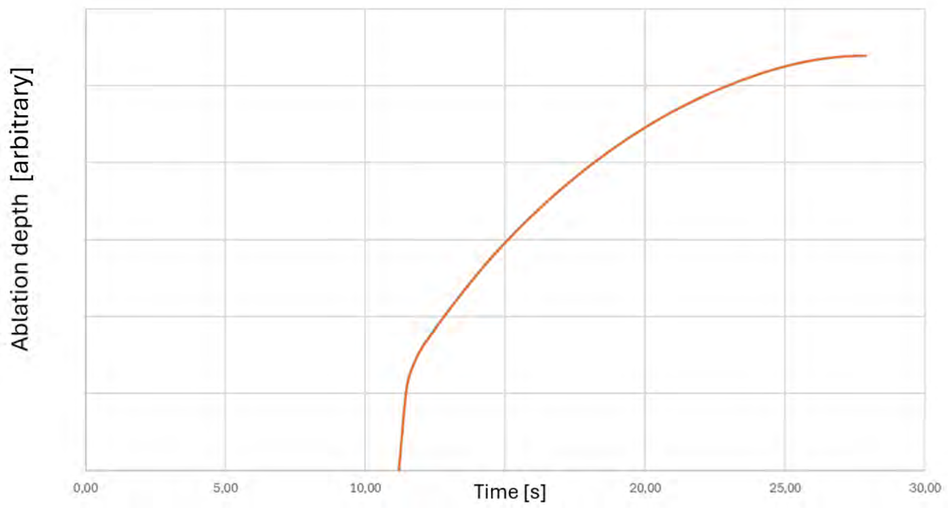

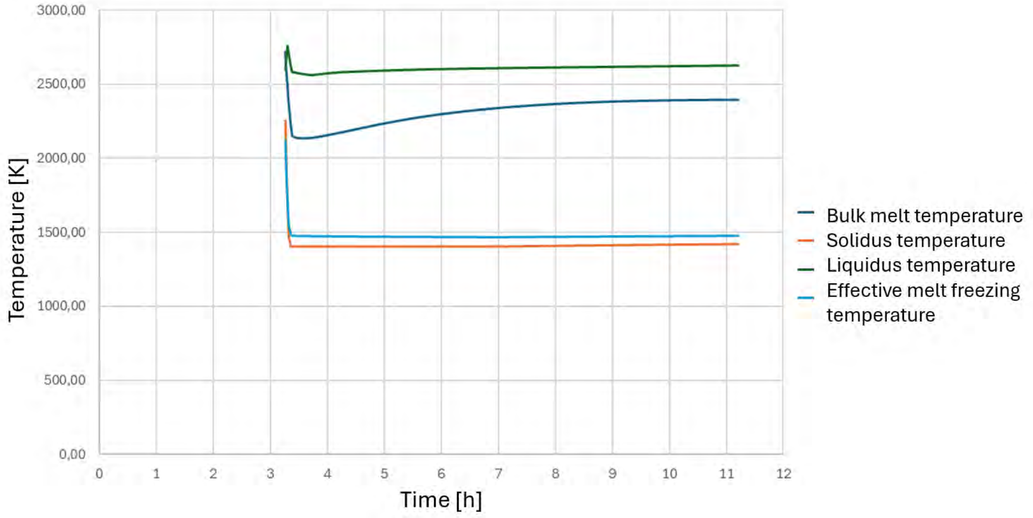

CONCLUSIONS

VVER-1000 ex-vessel melt stabilization

- Challenging, but possible as a retrofit
- Innovative approach in this study using the sacrificial geopolymers and refractory layer

Geopolymers

- Excellent sacrificial materials – low water content, up to 90 Wt.% of fillers to adjust corium parameters

Reactor case study

- VVER-1000 reactor, spreading assumed, focused on corium - sacrificial material interactions

Reactor case study

Promising, extensive amount of CO2 produced from geopolymer decomposition, melt temporarily stabilized (not attacking concrete) for up to 10 hours without top-flooding under the assumed conditions.

Děkuji za pozornost / Thanks for your attention!

(petr.vacha@ujv.cz)

Skupina ÚJV, člen Skupiny ČEZ

Skupina ÚJV
LIDÉ | INOVACE | TECHNOLOGIE

SKUPINA ČEZ

Development of the SAFARI Code for Comprehensive Severe Accident Analysis in Nuclear Reactors: Molten Core-Concrete Interaction Analysis Module

Jun Sung Choi[a], Tae Hwan Kim[a], Jin-Woo Kim[a], Eung Soo Kim[a*], Hyun Sun Park[a,b],**
[a]*Department of Nuclear Engineering, Seoul National University, 1 Gwanak-ro, Gwanak-gu, Seoul, Korea, Republic of*
[b]*Nuclear Research Institute for Future Technology and Policy, Seoul National University, 1 Gwanak-ro, Gwanak-gu, Seoul, Korea, Republic of*

Corresponding Address
*kes7741@snu.ac.kr; **hejsunny@snu.ac.kr

ABSTRACT

This study presents the development and validation of a Molten Core–Concrete Interaction (MCCI) analysis module within the SAFARI (Safety Analysis Code for Severe Accident Risk Identification) code, which is under development in South Korea as a regulatory-grade severe accident analysis tool. SAFARI is intended to support Severe Accident Management (SAM) strategies, and the implementation of a reliable MCCI module is a critical step in achieving this goal, as MCCI strongly influences the progression and consequences of ex-vessel severe accidents.

The MCCI module has been developed using a Python-based computational framework specifically tailored for MCCI calculations. It incorporates multi-physics models that represent the essential processes associated with corium–concrete interactions, including heat transfer, ablation, gas release, and corium pool configurations. To demonstrate its predictive capability, the module was evaluated against multiple benchmark experiments such as ACE-L2, SURC-2, CCI-2, and MOCKA 3.1. These validation cases cover a broad spectrum of conditions, including differences in corium states, concrete types, cavity geometry, and cavity boundary conditions. The results exhibited good agreement with experimental observations, capturing both thermal responses and ablation trends.

In addition, comparative studies with existing severe accident codes confirmed that the developed module provides comparable performance, reinforcing its applicability for regulatory safety evaluations. Overall, the study demonstrates that the SAFARI MCCI module offers a robust and versatile framework for analyzing ex-vessel accident progression and contributes to the broader goal of establishing an integrated severe accident analysis capability in South Korea.

KEYWORDS
MCCI, SAFARI, Severe accident, Corium, SAM

1. INTRODUCTION

When severe accident scenarios lead to core damage in a nuclear power plant, the nuclear fuel may melt and form molten fuel, commonly referred to as corium. If the accident progresses beyond reactor vessel failure, corium can be released into the reactor cavity, initiating ex-vessel severe accident phenomena that have a direct impact on containment integrity. To mitigate and terminate such accidents, various Severe Accident Management (SAM) actions are implemented, including cavity flooding and containment spray. The development and assessment of SAM strategies therefore require computational tools capable of consistently simulating a wide range of severe accident scenarios.

Integrated severe accident analysis codes have been widely used for this purpose, with representative examples including MELCOR, MAAP, ASTEC, and SAMPSON. While these codes provide comprehensive frameworks for severe accident analysis, there remains a need for analysis tools tailored to domestic reactor designs and regulatory requirements in South Korea. To address this need, the SAFARI (Safety Analysis Code For Severe Accident Risk Identification) code [1] has been under development as an integrated severe accident analysis tool for regulatory applications. SAFARI is designed to simulate accident progression from reactor vessel failure through ex-vessel phenomena, including corium coolability, molten core–concrete interaction (MCCI), and containment pressurization. The present study focuses specifically on the MCCI module within the SAFARI code.

When corium comes into contact with the concrete in the reactor cavity, MCCI occurs as a result of intense thermal and chemical interactions. Due to the high temperature of corium, typically exceeding 2000 K, substantial heat transfer to the concrete leads to concrete ablation and the formation of a molten concrete slag layer. This process progressively enlarges the cavity and generates gaseous decomposition products such as CO_2, H_2O, CO, and H_2, which can enhance convective heat transfer within the corium pool. Meanwhile, decay heat and oxidation reactions continue to supply energy to the corium, while cooling at the interfaces may result in the formation of solid crust layers. Heat removal from the corium upper surface strongly depends on cavity conditions, such as dry or flooded configurations, and significantly influences the long-term evolution of MCCI. In addition, corium stratification into oxide and metal layers may occur depending on material composition and accident conditions, further affecting heat transfer and concrete ablation behavior.

To analyze these complex phenomena, a number of MCCI analysis codes have been developed, including CORCON, COSACO, MEDICIS, CORQUENCH, and WECHSL. Among these, CORQUENCH, developed at Argonne National Laboratory, has been widely used due to its detailed treatment of key MCCI mechanisms and has served as a reference in the development of the SAFARI MCCI module. In parallel, numerous experimental programs have been conducted to investigate MCCI phenomena and provide data for code assessment. These include early metal-based experiments such as SWISS and SURC, as well as large-scale experiments using oxidic corium simulants, notably the CCI series, which provide valuable measurements of corium temperature and concrete ablation during the long-term MCCI phase.

In this study, the MCCI module of the SAFARI code is described and assessed using representative experimental data. The module has been developed to account for key factors influencing MCCI behavior, including cavity geometry, concrete type, and cavity cooling conditions. Validation calculations are performed using selected experiments, including ACE-L2, SURC-2, CCI-2 and MOCKA 3.1, which collectively cover a range of MCCI-relevant phenomena. Comparisons with experimental measurements and results from other MCCI analysis codes are presented to demonstrate the capability and performance of the SAFARI MCCI module. This paper presents an overall description of the Molten Core–Concrete Interaction (MCCI) module, referred to as MAMBA (MCCI Analysis Model with Basemat Ablation), implemented in the SAFARI code and assesses its performance using representative MCCI experimental data.

2. DESCRIPTION OF THE MAMBA MODULE

2.1. Module Overview

The MAMBA module is based on a lumped parameter method (LPM) framework and was developed with reference to the CORQUENCH code [2]. The MCCI domain is discretized into a limited number of nodes representing the corium, crust layers at the top, bottom, and side, and the underlying concrete. Governing mass and energy conservation equations are solved for each node. The module is implemented using a Python-based computational structure and evaluates a set of 10 state variables (X) that characterize the

MCCI process. These include the masses of corium and crust layers, concrete ablation depths in the axial and radial directions, crust thicknesses, and corium enthalpy

Figure 1. illustrates the calculation flow chart of the MAMBA module, in which tracking 10 state variables constitutes the core of the analysis. At the beginning of the calculation, the state variables are initialized. At each time step, the state of the corium pool is then identified as either homogeneous or stratified. Depending on the identified mode, secondary variables and surface-related quantities in each direction are evaluated. Based on these quantities, the governing equations are solved, and the resulting increments of the state variables (dX) are used to update the state variables at each time step, advancing the calculation.

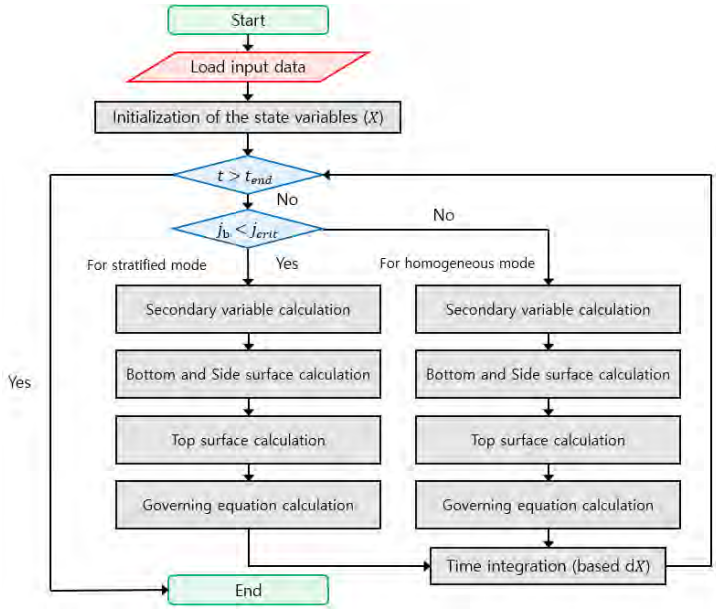

Figure 1. Calculation flow chart for the MAMBA module

2.2. Corium Configuration

The MAMBA module supports two analysis modes depending on the corium configuration: a homogeneous mode and a stratified mode. In the homogeneous mode, the corium is assumed to remain fully mixed throughout the calculation, whereas the stratified mode allows a transition from an initially homogeneous state to a layered configuration. This section describes the modeling approach adopted for the stratified configuration.

Although a stratified corium configuration with a denser oxidic layer beneath a metallic layer may exist initially, intense gas generation due to rapid concrete ablation during the early phase of MCCI promotes strong mixing, rendering the initial stratification short-lived. Accordingly, the MCCI code assumes a homogeneous corium state at the onset of the calculation and permits stratification only after gas-induced mixing subsides. The transition between the two modes is determined by the superficial gas velocity generated by bottom concrete ablation. When the gas velocity (j – Eq.1) calculated under the homogeneous assumption decreases below a critical threshold velocity (j_{crit} – Eq.2), the oxidic layer, having incorporated sufficient concrete, relocates to the upper region and the calculation proceeds in the stratified mode.

In this formulation, the stratification criterion is evaluated solely based on gas generation at the bottom concrete surface. Gas produced along the sidewalls is assumed to rise directly upward and therefore to have a negligible effect on the stratification interface. The critical gas velocity is defined using a density-based correlation derived from the BALISE experiments [3], with a constant value of C_{crit} = 0.054. In addition,

stratification is permitted only when the thickness of the metal layer exceeds 3 cm, ensuring sufficient thermal and mechanical stability of the layered configuration.

$$j = \frac{\dot{m}''_{b,gas}}{\rho_g} \tag{1}$$

$$j_{crit} = C_{crit}\frac{\rho_{met} - \rho_{ox}}{\rho_{ox}} \tag{2}$$

2.3. Governing Equations

The MAMBA module solves mass and energy conservation equations as its governing equations. Mass conservation is applied to the corium and crust nodes, while energy conservation is solved only for the corium. The concrete node does not have independent governing equations and is treated as an infinite mass reservoir that acts as a source or sink of mass and energy.

The formulation of the governing equations depends on the corium configuration. Differences in mass and energy exchange between nodes are accounted for by distinguishing between the homogeneous and stratified modes. Figure 2.3 schematically illustrates the mass and energy transfer paths among the nodes for each configuration. In the homogeneous mode, the corium interacts separately with the bottom and side concrete, whereas in the stratified mode, interactions with the side concrete are evaluated independently for the oxide and metal layers.

Accordingly, the governing equations are formulated to evaluate the time derivatives of the state variables associated with each mode. In the homogeneous mode, 5 state variable derivatives are computed, while in the stratified mode, 8 state variable derivatives are evaluated to account for the layered structure. The detailed formulations of the mass and energy conservation equations are presented in Sections 2.3.1 and 2.3.2, respectively.

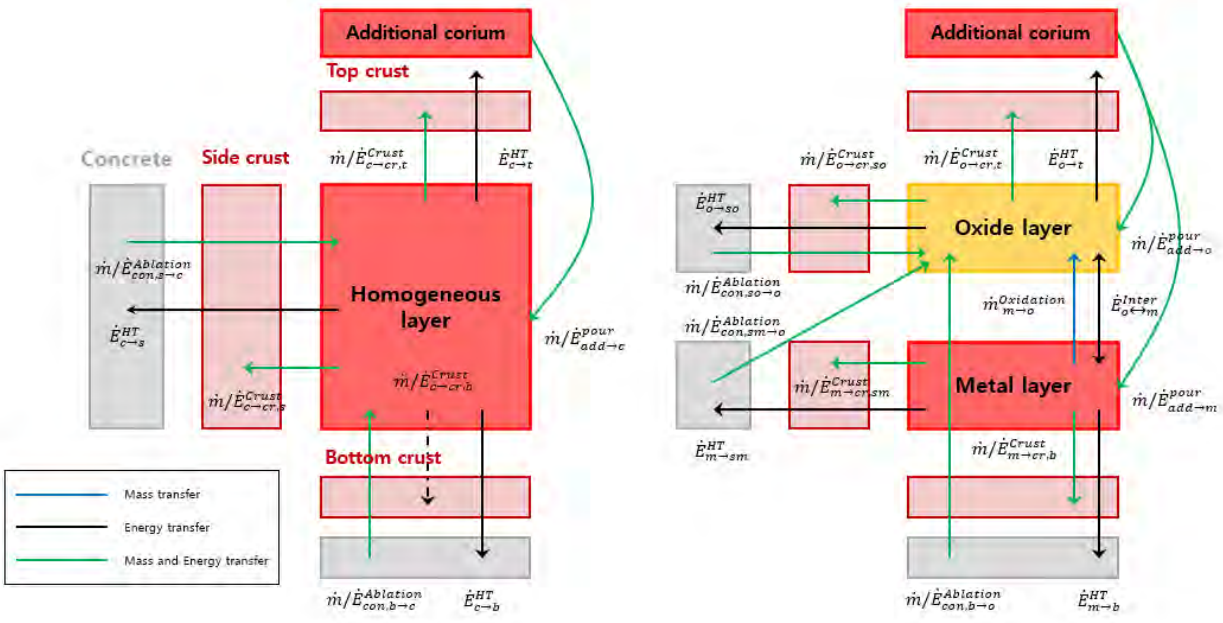

Figure 2. Calculation flow chart for the MAMBA module

2.3.1. Mass conservation equation

The mass conservation equations are formulated to evaluate the time derivatives of the corium mass in both homogeneous and stratified configurations. (Eq. 3 - 5) In the homogeneous mode, a single mass conservation equation is applied to the corium, whereas in the stratified mode, separate equations are solved for the oxide and metal layers. These equations account for the mass variations of the state variables resulting from the dominant physical processes considered in the module.

Mass changes in the crust nodes arise exclusively from crust formation at the corium boundaries. Accordingly, the mass loss associated with crust formation in the corium mass balance directly corresponds to the mass gain in the top, bottom, and side crust nodes. The crust mass evolution is evaluated based on the time derivatives of crust thickness obtained from the heat transfer model, including the effect of crust re-melting.

When stratification occurs, molten concrete generated by concrete ablation is treated as oxidic material and is added solely to the oxide layer in the mass balance. In addition, corium poured into the cavity is partitioned between the oxide and metal layers according to its composition, with oxidic components added to the oxide layer and metallic components added to the metal layer.

[Homogeneous layer]

$$\dot{m}_{c,i} = \dot{m}_{c\to c}^{Oxidation} - \dot{m}_{c\to cr,t,b,s}^{Crust} + \dot{m}_{con,b,s\to c}^{Ablation} + \dot{m}_{add\to c}^{Pour} \tag{3}$$

[Oxide layer]

$$\dot{m}_{ox,i} = \dot{m}_{met\to ox}^{Oxidation} - \dot{m}_{ox\to cr,t,so}^{Crust} + \dot{m}_{con,sm,so,b\to ox}^{Ablation} + \dot{m}_{add\to ox}^{Pour} \tag{4}$$

[Metal layer]

$$\dot{m}_{met,i} = -\dot{m}_{met\to ox}^{Oxidation} - \dot{m}_{met\to cr,b,sm}^{Crust} + \dot{m}_{add\to met}^{Pour} \tag{5}$$

2.3.2. Energy conservation equation

The energy conservation equation in the MAMBA module is solved only for the corium and is formulated to evaluate the time derivative of corium enthalpy. The enthalpy evolution is obtained by differentiating the total energy (E_c) of the corium and accounting for the dominant energy sources and sinks considered in the model. (Eq. 6)

$$\dot{E}_c = \frac{dE_c}{dt} = \dot{m}_c e + m_c \dot{e} \tag{6}$$

Depending on the corium configuration, separate energy conservation equations are applied in the homogeneous and stratified modes. (Eq. 7 - 9) The energy balance includes contributions from decay heat, heat transfer at the top, bottom, and side boundaries, and interlayer heat transfer in the stratified configuration. Decay heat is specified as a user input, while interlayer heat transfer between the oxide and

metal layers is evaluated as a function of the temperature difference between the layers using an established correlation [4].

For corium additionally poured into the cavity, the associated enthalpy is calculated based on its temperature and composition, and the distribution of this energy between the oxide and metal layers is prescribed by user input. When oxidic components are present in the incoming corium, oxidation reactions may occur due to gas generated from concrete ablation. Under the stratified configuration, oxidation is assumed to occur primarily in the upper oxide layer, with any remaining reactive species potentially continuing to react in the metal layer. Owing to the absence of a detailed physical model describing the residence time of incoming corium within the oxide layer, the partitioning of oxidation-related energy between the two layers is also treated as a user-defined parameter.

[Homogeneous layer]

$$\dot{E}_c = \dot{E}_{c\to c}^{Decay} - \dot{E}_{c\to t,b,s}^{HT} + \dot{E}_{con,b,s\to c}^{Ablation} - \dot{E}_{c\to cr,t,b,s}^{Crust} + \dot{E}_{c\to c}^{Oxidation} + \dot{E}_{add\to c}^{Pour} \quad (7)$$

[Oxide layer]

$$\dot{E}_{ox} = \dot{E}_{ox\to ox}^{Decay} - \dot{E}_{ox\to t,so}^{HT} + \dot{E}_{con,b,so,sm\to ox}^{Ablation} - \dot{E}_{ox\to cr,t,so}^{Crust} + \dot{E}_{met\to ox}^{Inter} + \dot{E}_{add\to ox}^{Pour} \quad (8)$$

[Metal layer]

$$\dot{E}_{met} = -\dot{E}_{met\to b,sm}^{HT} - \dot{E}_{met\to cr,b,sm}^{Crust} + \dot{E}_{met\to met}^{Oxidation} - \dot{E}_{ox\to met}^{Inter} + \dot{E}_{add\to met}^{Pour} \quad (9)$$

2.4. Heat Transfer Modeling

Effective cooling of the corium is one of the key factors governing the progression of MCCI phenomena. Accordingly, the MAMBA module explicitly models heat transfer in each direction relative to the corium geometry. The top heat transfer is primarily influenced by the cavity conditions, particularly the presence or absence of water, whereas heat transfer at the bottom and side surfaces is directly coupled to concrete ablation processes.

These directional heat transfer models constitute a core component of the MAMBA module, as they determine the temporal evolution of crust growth and concrete ablation. Depending on the corium configuration, the heat transfer calculations are formulated to evaluate the time derivatives of the relevant state variables associated with crust thickness and ablation depth in both homogeneous and stratified modes.

2.4.1. Top heat transfer modeling

The top heat transfer of the corium is developed to account for both dry and wet cavity conditions. The primary objective of the top heat transfer modeling is to evaluate the corium upper boundary temperature ($T_{t,I}$) and the rate of change of the top crust thickness ($\dot{\delta}_t$). Eq. 10 represents the balance equation used to determine the corium top boundary temperature, which accounts for the convective heat transfer from the corium interior and the heat transfer to the surrounding environment under dry or wet conditions.

The convective heat transfer from the corium to the top boundary is evaluated using a correlation [5] that accounts for gas generation during MCCI. For dry cavity conditions, heat removal from the top surface is

calculated based on thermal radiation, whereas for wet cavity conditions, it is evaluated using a heat transfer coefficient derived from the boiling curve of the coolant.

$$h_{r/wat}\left(T_{t,I} - T_{at/wat}\right) = h_t\left(T_c - T_{t,I}\right) \tag{10}$$

Eq.11 describes the evolution of the top crust thickness. The rate of crust growth is determined from an energy balance that considers the energy required for crust formation, heat conduction through the crust, and the convective heat transfer from the corium to the top boundary.

$$\rho_{cr}\Delta e_{cr}\dot{\delta}_t = -k_{cr}\frac{dT_{cr,t}}{dx} - h_t\left(T_c - T_{frz}\right) \tag{11}$$

2.4.2. Side and bottom heat transfer modeling

Since the side and bottom surfaces of the corium are in direct contact with the concrete, the corresponding heat transfer modeling is inherently coupled with concrete ablation. In the MAMBA module, the side and bottom heat transfer models are designed to evaluate the rate of change of concrete ablation depth ($\dot{\eta}$) as well as the evolution of crust thickness ($\dot{\delta}$). Two modeling approaches are implemented: a no-crust model and a crust-including model.

Eq. 12 represents the no-crust model used to evaluate the rate of concrete ablation. In this model, the ablation rate is determined from an energy balance between the energy required for concrete ablation and the heat transferred from the corium. The side and bottom heat transfer coefficients are evaluated by scaling the top heat transfer coefficient using a slag coefficient. [6]

$$\dot{\eta}_{b/s(so,sm)}\rho_{con}e_{dec,con} = h_{b/s(so,sm)}(T_c - T_{dc}) \tag{12}$$

Eq. 13 describes the concrete ablation rate in the crust-including model, where the energy balance accounts for the energy required for ablation, heat conduction through the crust, and heat conduction within the concrete. In addition, Eq. 14 evaluates the rate of change of crust thickness in the crust model, which is formulated in a manner analogous to the upper heat transfer modeling.

$$\rho_{con}\Delta e_{con}\dot{\eta}_{b/s(so,sm)} = -k_{cr}\frac{dT_{cr,b/s(so,sm)}}{dx} + k_{con}\frac{dT_{con}}{dx} \tag{13}$$

$$\rho_{cr}\Delta e_{cr}\dot{\delta}_{b/s(so,sm)} = -k_{cr}\frac{dT_{cr,b/s(so,sm)}}{dx} - h_{b/s(so,sm)}\left(T_c - T_{frz}\right) \tag{14}$$

3. VALIDATION AGREEMENT EXPERIMENTAL DATA

3.1. Validation Overview

To establish the reliability of the MAMBA module, several MCCI experiments were selected and used for validation. Table I. summarizes the validation experiments considered in this study. The validation was conducted using both one-dimensional (1-D) and two-dimensional (2-D) MCCI experiments. The 1-D

experiments focus exclusively on downward concrete ablation, whereas the 2-D experiments account for both downward and lateral ablation.

A total of 4 experiments were selected for validation. These experiments were chosen to represent a wide range of MCCI characteristics in terms of geometry, corium and concrete composition, and cavity conditions. By considering validation cases with diverse features, the robustness of the MAMBA module in analyzing MCCI phenomena is demonstrated.

Table I. Validation experiments for MAMBA module

	Experiment	MCCI geometry	Corium type	Concrete type	Cavity situation
1-D MCCI (Axial)	SURC-2	Cylindrical	Homogeneous	Basaltic	Dry
	ACE-L2	Rectangular	Homogeneous	Siliceous	Dry
2-D MCCI (Axial/Radial)	CCI-2	Rectangular	Homogeneous	LCS	Dry + Wet
	MOCKA 3.1	Cylindrical	Stratified	Siliceous	Dry

3.2. Validation Against 1-D MCCI Experiment

The validation of the MAMBA module against 1-D MCCI experiments was performed using the SURC-2 and ACE-L2 experiments. Figure 2 presents the validation results for the SURC-2 experiment, where the calculated corium temperature evolution and concrete ablation behavior are compared with experimental data. The results indicate that the overall experimental trends are reasonably reproduced by the MAMBA module.

In addition, to provide a reference comparison with existing severe accident analysis tools, the calculated results were compared with those obtained from MELCOR. [7] The comparison shows that the MAMBA predictions are comparable to those of MELCOR for the considered cases.

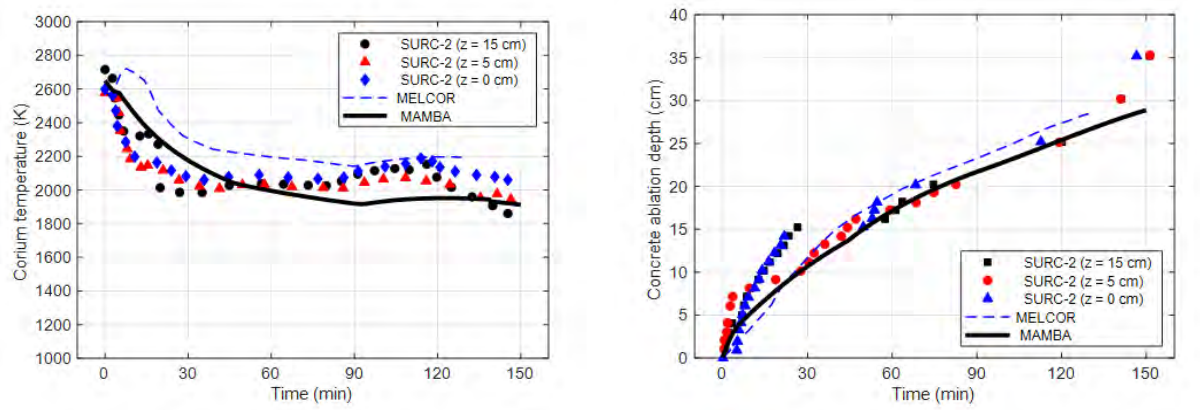

Figure 2. Validation results for SURC-2 (left: corium temperature; right: concrete ablation depth)

Figure 3 presents the validation results for the ACE-L2 experiment. The results obtained using the MAMBA module show overall agreement with the experimental data in terms of observed trends and are also comparable to those predicted by the MAAP code [8].

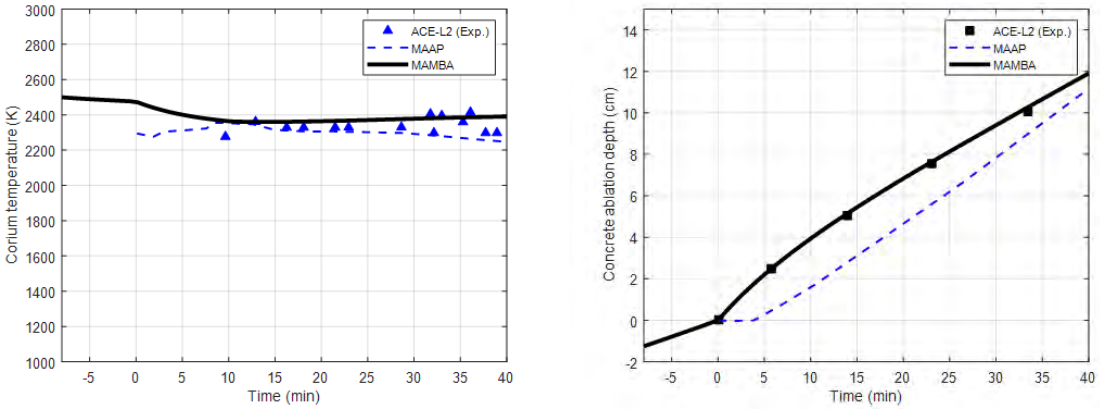

Figure 3. Validation results for ACE-L2 (left: corium temperature; right: concrete ablation depth)

3.3. Validation Against 2-D MCCI Experiment

The MAMBA module was also validated against 2-D MCCI experiments, namely the CCI-2 and MOCKA 3.1 tests. Figure 4 presents the validation results for the CCI-2 experiment. Overall, the calculated results show reasonable agreement with the experimental data in terms of observed trends and exhibit performance comparable to that of MELCOR [9].

It should be noted, however, that in the CCI-2 experiment, post-flooding is introduced after approximately 300 minutes, resulting in a transition to wet cavity conditions. While the concrete ablation behavior is reasonably reproduced under these conditions, the corium temperature tends to be underpredicted. This discrepancy is expected to be addressed through future improvements of the modeling approach.

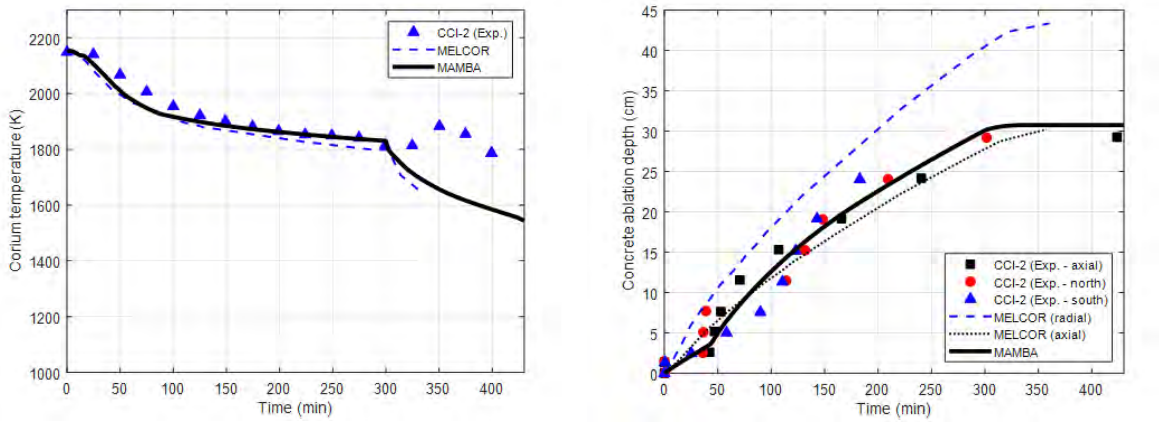

Figure 4. Validation results for CCI-2 (left: corium temperature; right: concrete ablation depth)

The MOCKA 3.1 experiment was designed to simulate MCCI conditions under corium pool stratification and was therefore selected to validate the stratified analysis mode of the MAMBA module. Figure 5 presents the validation results for the MOCKA 3.1 experiment. For this case, experimental data were available only for concrete ablation depth, and the comparison was performed accordingly.

Since validation results obtained using other MCCI codes for the MOCKA 3.1 experiment are not available, no code-to-code comparison could be performed. A key feature of the results is the transition from a homogeneous to a stratified corium configuration at approximately 3 minutes, when the stratification criterion implemented in the MAMBA module is satisfied. Following this transition, the results branch into two distinct layers, and the predicted ablation behavior for each layer shows overall agreement with the experimental measurements.

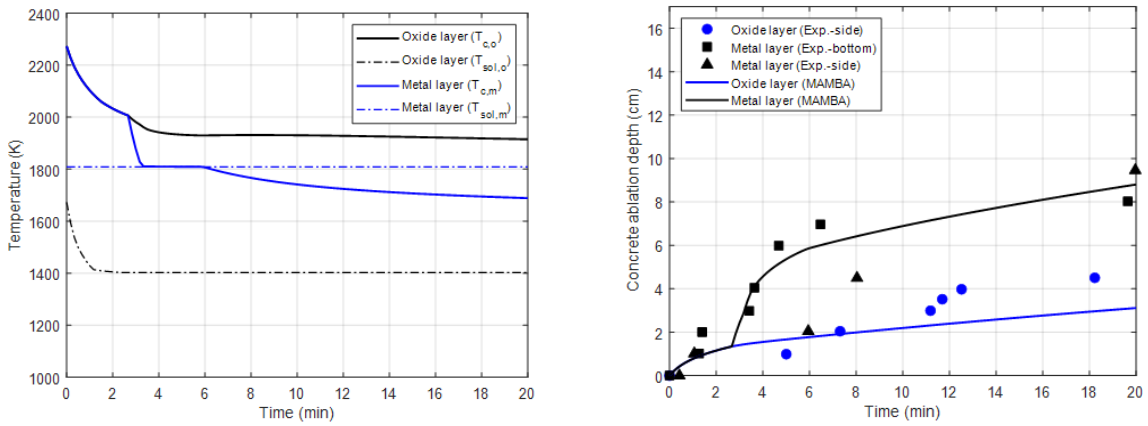

Figure 5. Validation results for MOCKA 3.1 (left: corium temperature; right: concrete ablation depth)

4. CONCLUSIONS

This paper presented the development and validation of the MCCI analysis module implemented in the SAFARI integrated severe accident analysis code. The module was developed to represent key physical processes governing corium–concrete interactions under ex-vessel accident conditions, including directional heat transfer, concrete ablation, crust formation, and corium pool configurations.

The modeling framework supports both homogeneous and stratified corium configurations and accounts for dry and wet cavity conditions through dedicated heat transfer models. The predictive capability of the module was evaluated using representative 1-D and 2-D MCCI experiments, and the results showed reasonable agreement with experimental trends across different geometries, material compositions, and boundary conditions. In addition, comparisons with existing severe accident analysis codes indicated comparable performance.

Overall, the results suggest that the developed MCCI module provides a consistent and practical analysis capability for ex-vessel severe accident scenarios within the SAFARI code and can support integrated severe accident evaluations related to SAM strategies.

ACKNOWLEDGMENTS

This work was supported by the Nuclear Safety Research Program through the Korea Foundation of Nuclear Safety (KoFONS) using the financial resource granted by the Nuclear Safety and Security Commission (NSSC) of the Republic of Korea (RS-2021-KN057910).

REFERENCES

1. Park, H. S., Chu, Y. J., Kim, E. H., Cho, Y. J., Lim, K., Lee, Y., ... Choi, J. S., ... Jeon, J. (2026). Development of the SAFARI Code for Comprehensive Severe Accident Analysis in Nuclear Reactors: Framework and Methodology. ERMSAR 2026, Madrid, Spain, May 18–22. (In-progress)
2. Farmer, M. (2010). The CORQUENCH Code for Modeling of Ex-Vessel Corium Coolability Under Top Flooding Conditions, Code Manual–Version 3.03. Argonne National Lab.(ANL), Argonne, IL (United States).
3. Tourniaire, B., & Bonnet, J. M. (2003). Study of the mixing of immiscible liquids by sparging gas-results of the BALISE experiments.
4. Greene, G. A., & Irvine Jr, T. F. (1988). Heat transfer between stratified immiscible liquid layers driven by gas bubbling across the interface (No. BNL-NUREG-41750; CONF-880724-26). Brookhaven National Lab., Upton, NY (USA).
5. Kutateladze, S. S., & Malenkov, I. G. (1978). Boiling and bubbling heat transfer under the conditions of free and forced convection. In International Heat Transfer Conference Digital Library. Begel House Inc.
6. Bradley, D. R. (1988, July). Modeling of heat transfer between core debris and concrete. In ANS Proceedings of the 1988 National Heat Transfer Conference, Houston (pp. 37-49).
7. Strizhov, V., Kanukova, V., Vinogradova, T., Askenov, E., & Nikulshin, V. (1996). An assessment of the CORCON-MOD3 code. Part 1: Thermal-hydraulic calculations (No. NUREG/IA-0129-Pt. 1). US Nuclear Regulatory Commission (NRC), Washington, DC (United States). Office of Nuclear Regulatory Research.
8. Alsmeyer, H. (1992). Second OECD (NEA) CSNI specialist meeting on molten core debris-concrete interactions. Proceedings.
9. Jung, W. H., Hwang, B., Park, S. H., & Moriyama, K. (2018, October). Simulation of CCI experiments for the sensitivity analysis with MELCOR 2.2. In Transactions of the Korean Nuclear Society Autumn Meeting. Yeosu, Korea.

Development of the SAFARI Code for Comprehensive Severe Accident Analysis in Nuclear Reactors: Molten Core-Concrete Interaction Analysis Module

Jun Sung Choi

Speaker: Tae Hwan Kim

Energy System Laboratory
Department of Nuclear Engineering
Seoul National University

ERMSAR 2026
May 19 2026

NUCLEAR ENERGY SYSTEM LAB

Contents

01 Introduction

02 Description of the MAMBA module

03 Validation agreement experimental data

04 Conclusions

1. Introduction

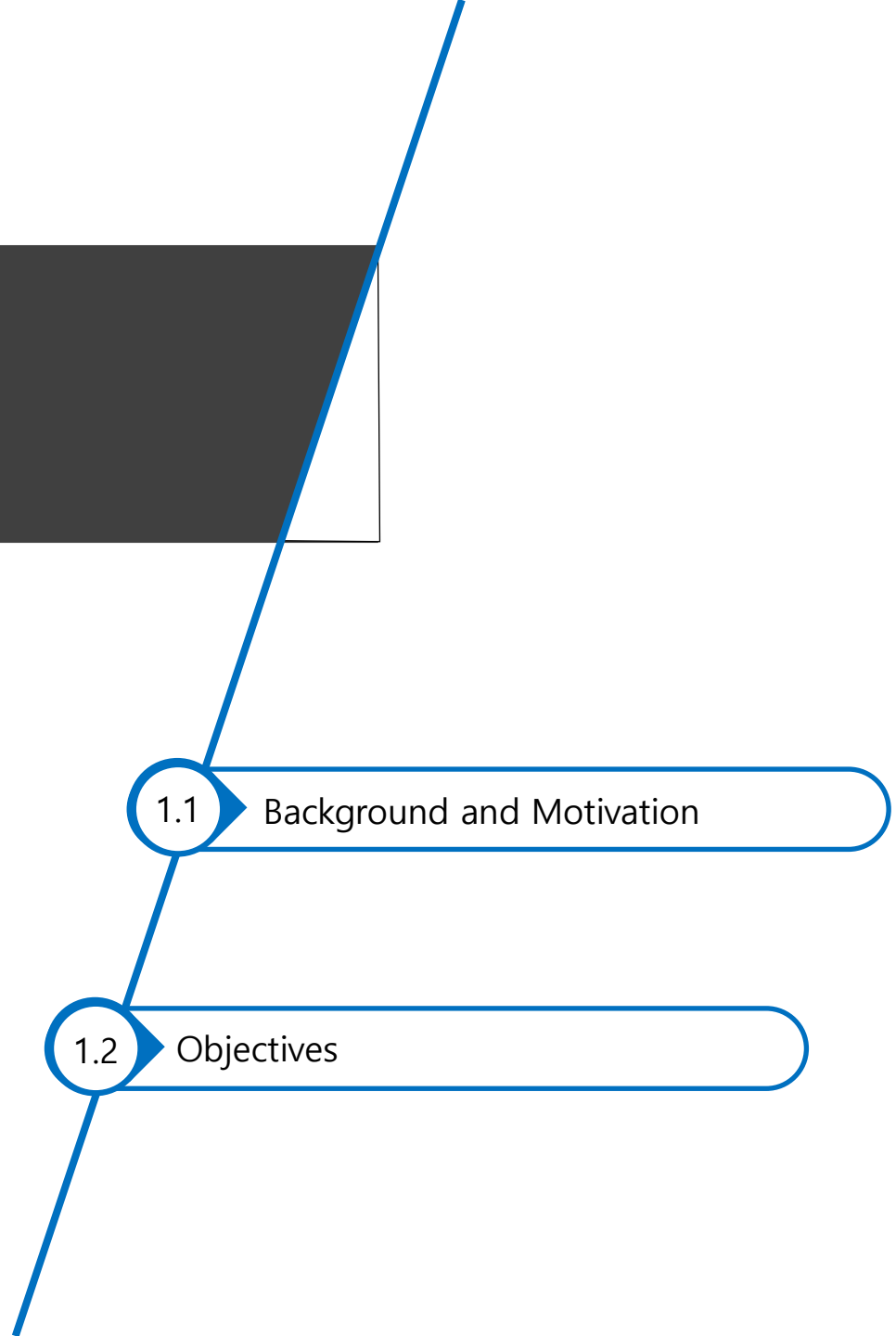

Introduction

1.1 Background and Motivation

- Nuclear fuel failure ($T_{cladding} > 1204℃$) leads to a nuclear severe accident.
- There are four steps in the Ex-vessel severe accident phenomena.
- Among them, the main phenomenon covered by this presentation is the Molten Core-Concrete Interaction (MCCI).

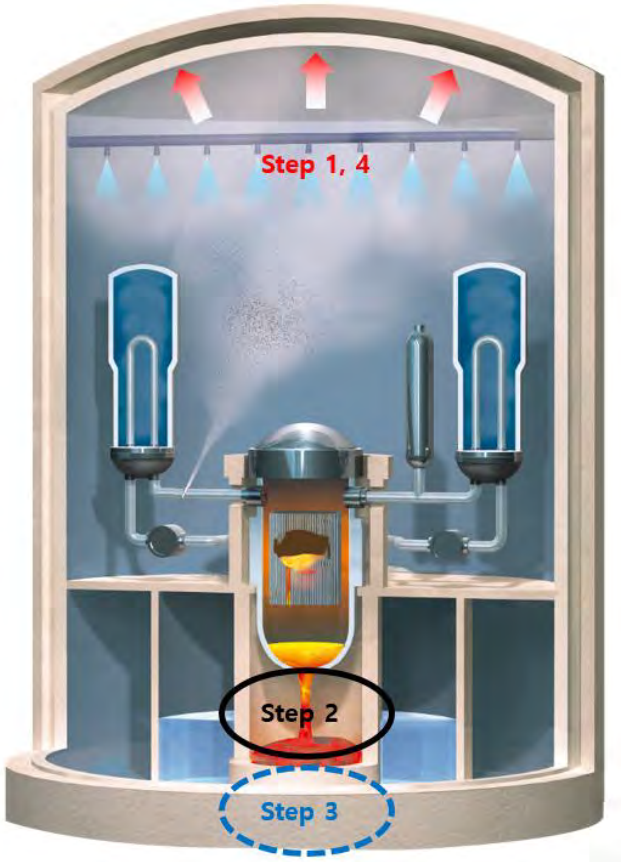

<Sequence of ex-vessel severe accident phenomena>

Step 1: Direct Containment Heating (DCH)

Step 2: Fuel-Coolant Interaction (FCI) & Steam Explosion (SE)

Step 3: Molten Core-Concrete Interaction (MCCI)

The key phenomenon in this study

Step 4: Hydrogen Explosion

Chatelard, P., Reinke, N., Arndt, S., Belon, S., Cantrel, L., Carenini, L., ... & Piar, L. (2014). ASTEC V2 severe accident integral code main features, current V2. 0 modelling status, perspectives. *Nuclear Engineering and Design*, *272*, 119-135.

Introduction

- MCCI phenomena occurs when hot corium meets cold concrete.
- In this reaction, the purpose is to maintain the integrity of the containment until the moment when non-condensable gas and decay heat no longer occur.
- Many complex physical phenomena occur simultaneously when MCCI occurs.

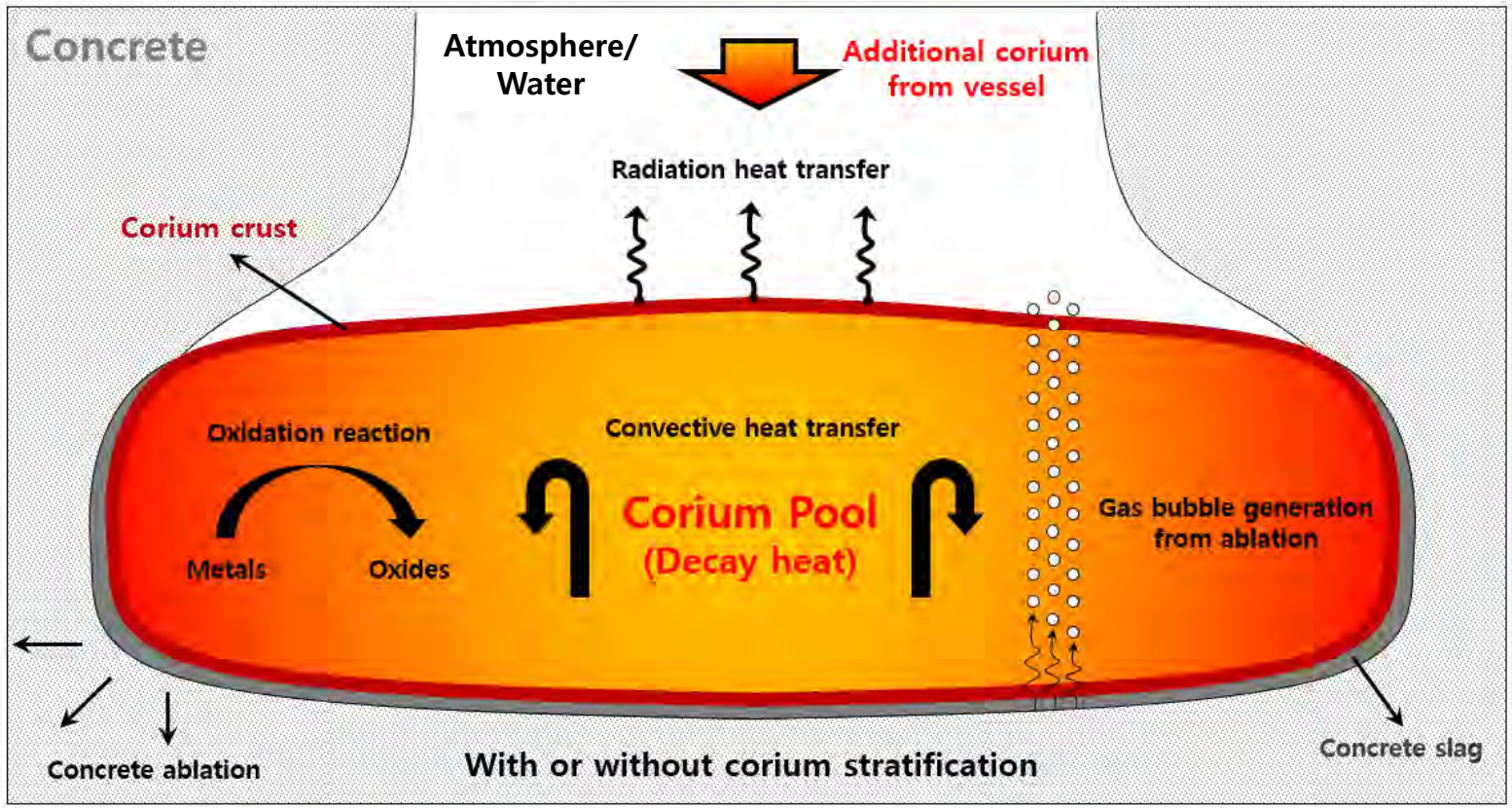

Introduction

- The SAFARI code is currently being developed as an integrated severe accident analysis code for domestic regulatory use in Korea, and performing a pre-flooding scenario analysis requires coupling between the MCCI and FCI codes developed within the same project.

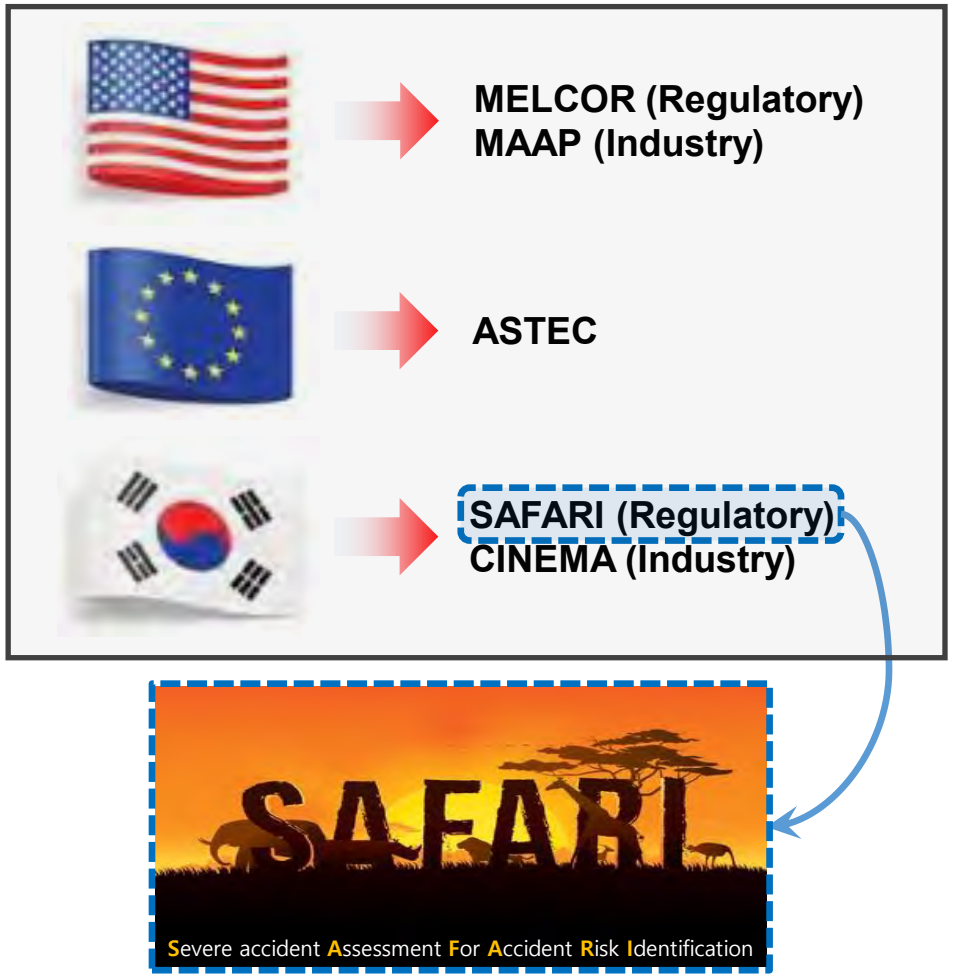

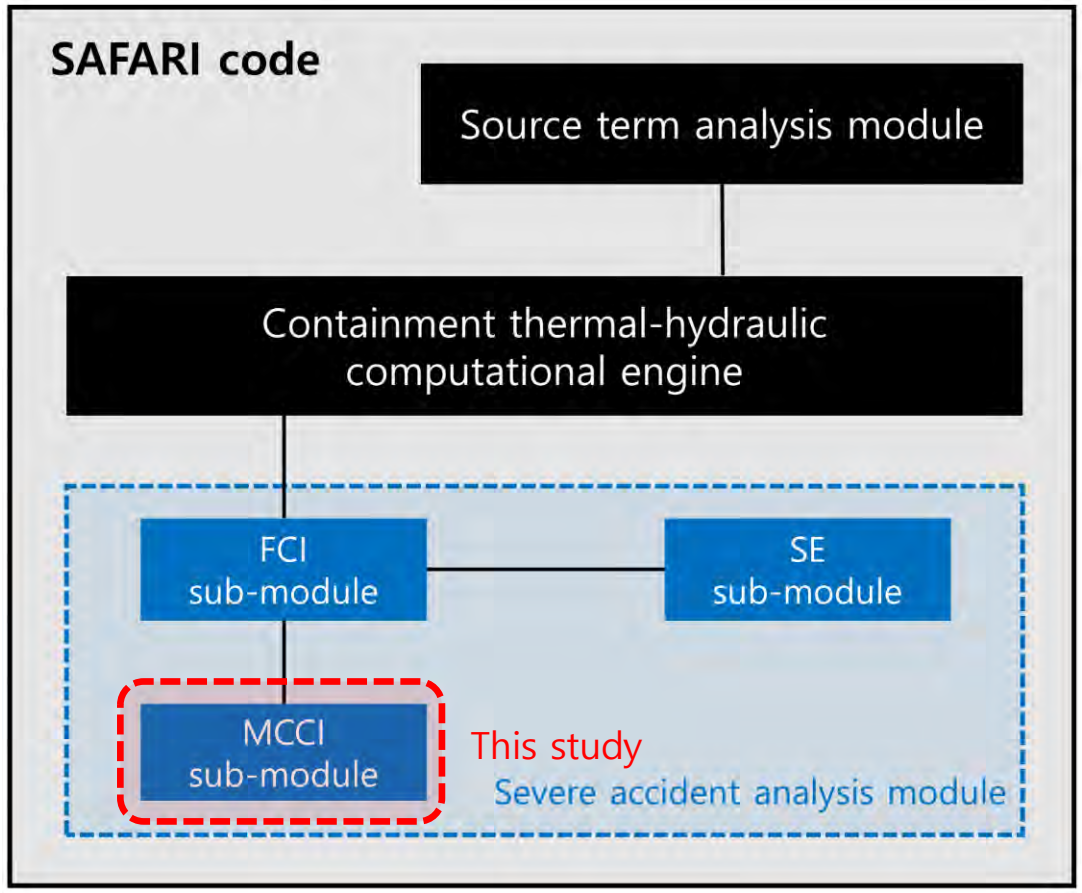

MAMBA (MCCI Analysis Model with Basemat Ablation) module

[https://www.shutterstock.com/ko/image-vector/vector-illustration-safari-text-design-on-471359051]

1.2 Objectives

- The objective of this study is to develop the MCCI module within the SAFARI code and to establish its reliability through validation of the developed module.

[Development of the MCCI module and Validation using MCCI experiment]

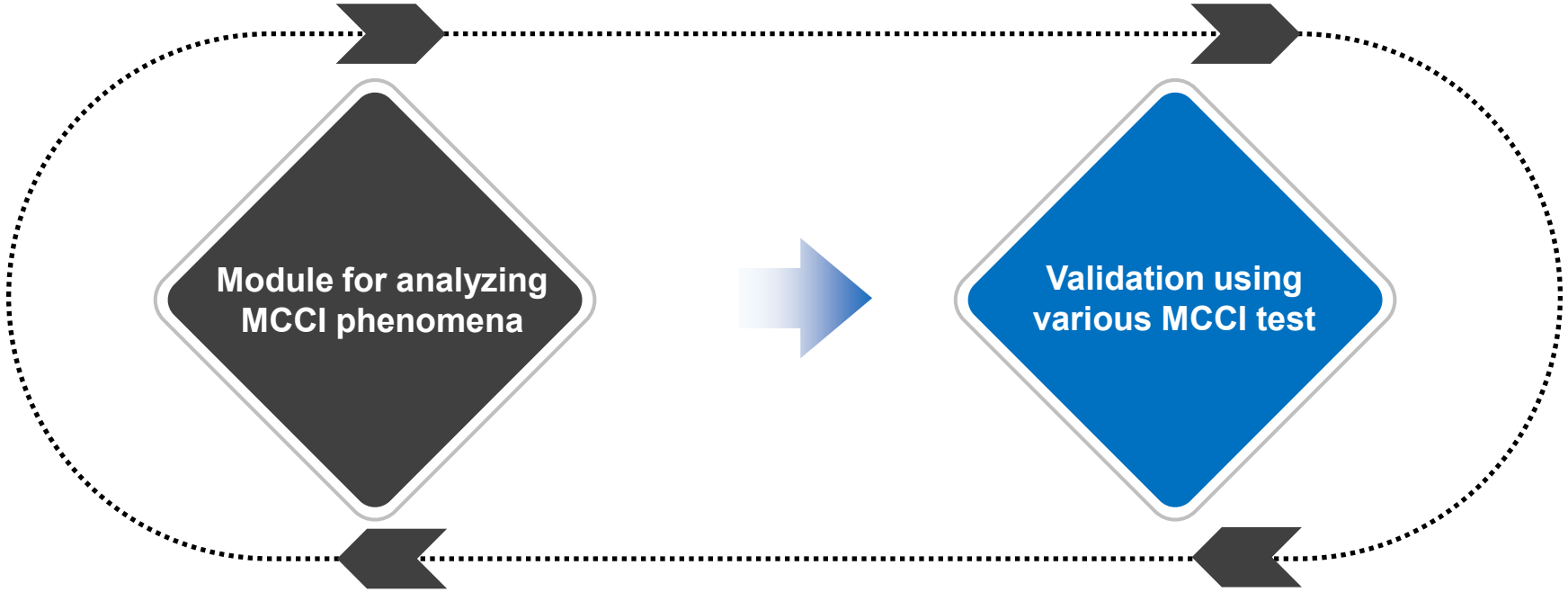

2. Description of the MAMBA module

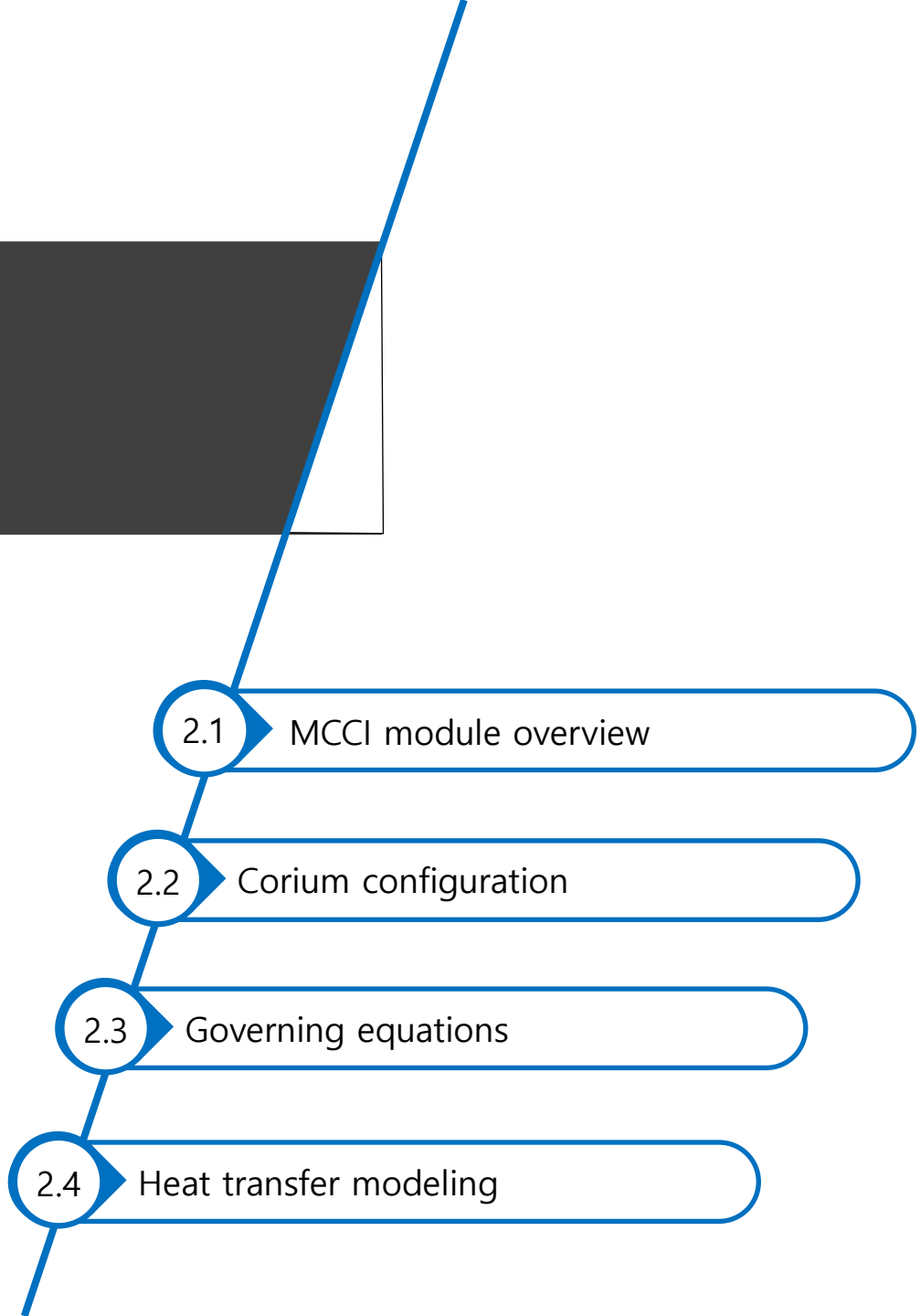

Description of the MAMBA module

2.1. MCCI module overview

Category	Details
Reference code	CORQUENCH code (ANL)
Analysis type	Lumped Parameter Method (LPM)
Language	Python
Geometry	✓ Cylindrical ✓ Rectangular
Geometry node	✓ Corium (Homogeneous and Stratified) ✓ Top crust ✓ Side crust ✓ Bottom crust ✓ Concrete
Governing equation	✓ Mass conservation equation (for each node except concrete) ✓ Energy conservation equation (for corium node)
Top heat transfer model	✓ Dry cavity model ✓ Wet cavity model
Concrete ablation model	✓ No-crust/Crust model
Material property model	✓ Corium property model ✓ Concrete property model ✓ Gas & Coolant property model

[Appendix 1]

Corium temperature **Concrete ablation depth**

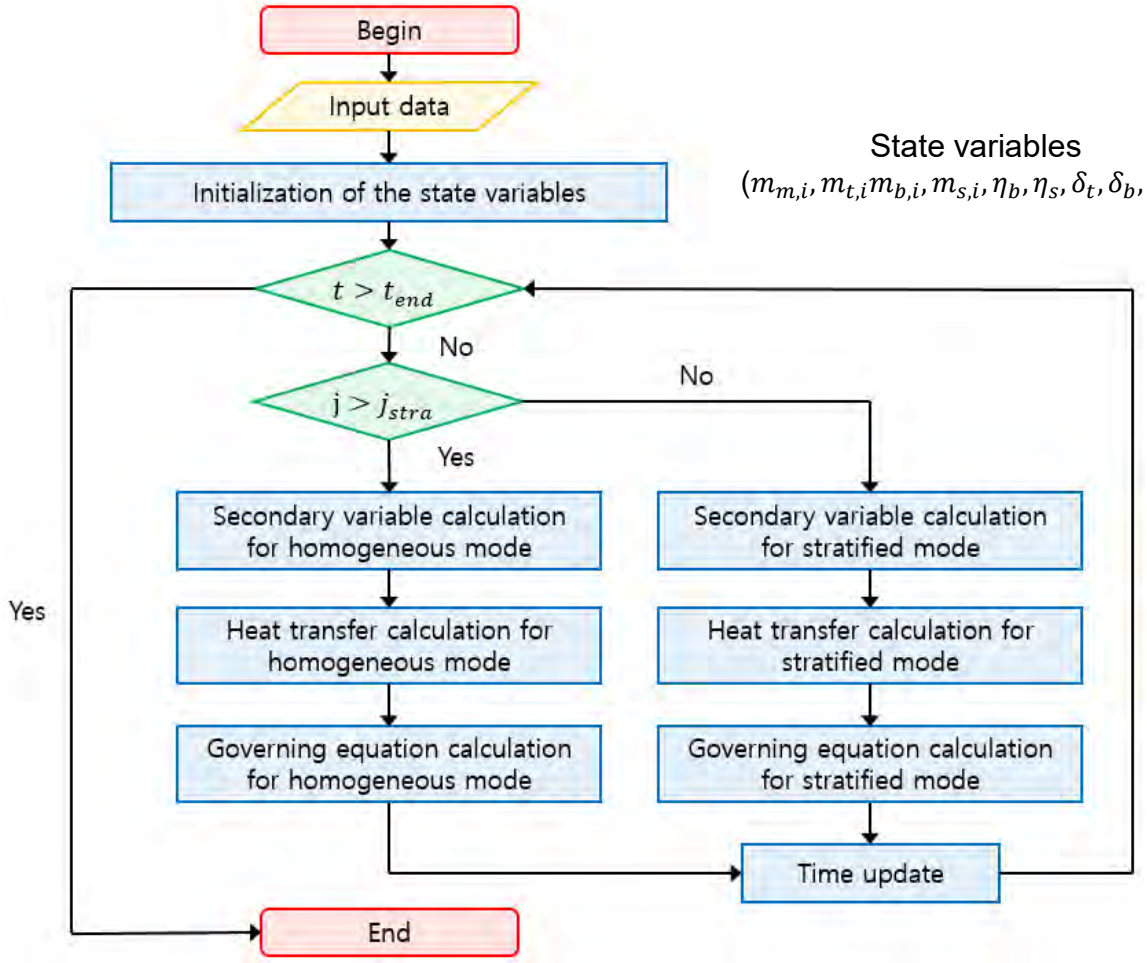

State variables
$(m_{m,i}, m_{t,i} m_{b,i}, m_{s,i}, \eta_b, \eta_s, \delta_t, \delta_b, \delta_s, e)$

<Flow chart of the MCCI code>

2.2. Corium configuration

- The MCCI process can involve corium stratification.
- Stratification may progress through three stages: initial stratification, homogenization, and re-stratification.
- In late phase of MCCI, re-stratification can occur, potentially leading to different thermal and physical characteristics between layers.

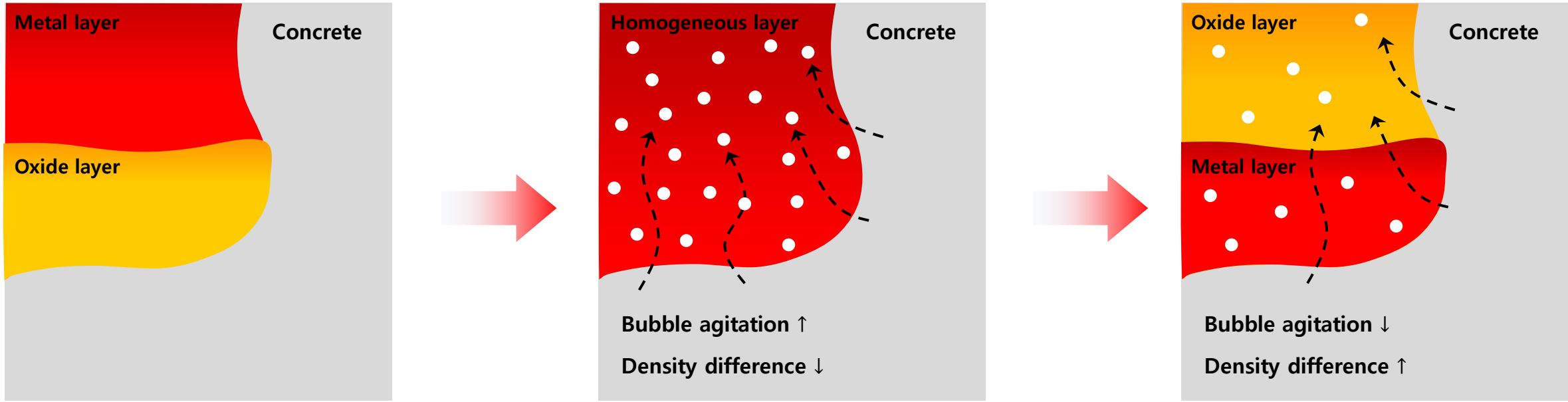

<Initial stratification> <homogenization> <Re-stratification>

Description of the MAMBA module

- In the early phase of MCCI, strong gas generation quickly disrupts the initial stratification, leading to a homogeneous state.
- Therefore, the proposed MCCI module begins with homogeneous corium. When the gas velocity criterion is satisfied, the code transitions to the re-stratification stage and continues the calculation.

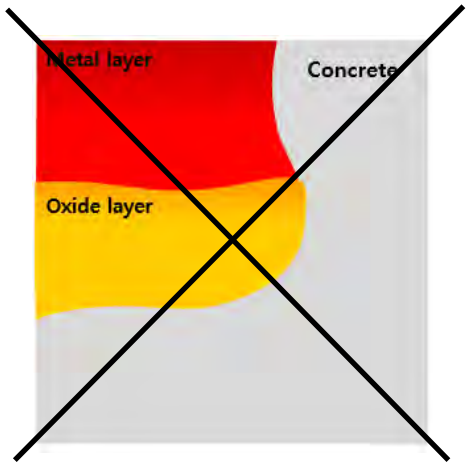

<Initial stratification – durability ↓>

Assumption

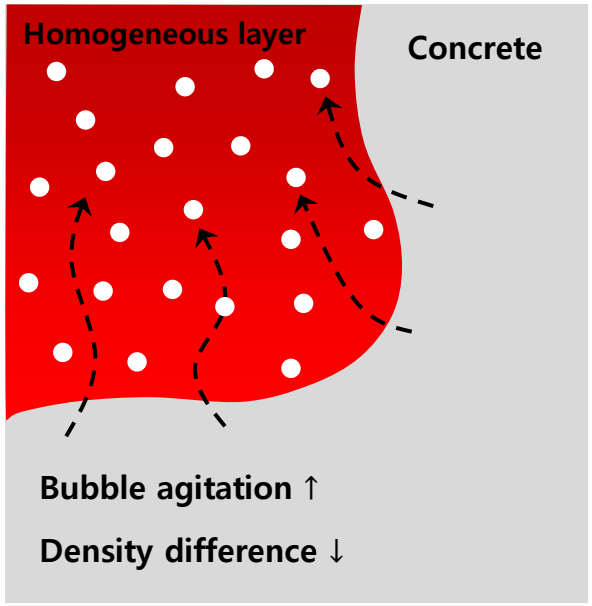

<Homogenous mode>

Mode change

$j_b < j_{crit}$

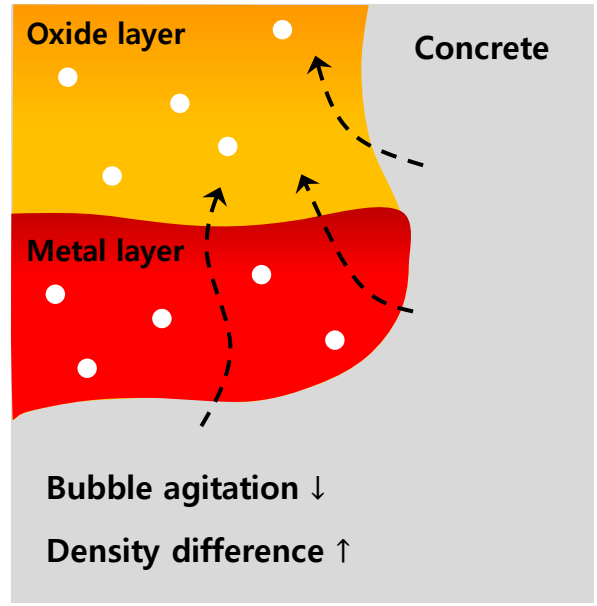

<Stratified mode>

$$j_{crit} = C_{stra}\frac{\rho_m - \rho_o}{\rho_o} \qquad C_{stra} = 0.054$$ (From BALISE exp.)

[Appendix 1]

Description of the MAMBA module

2.3. Governing equations

- The governing equations consist of the mass and energy conservation equations for each mode, with each term representing various phenomena occurring in the MCCI process.

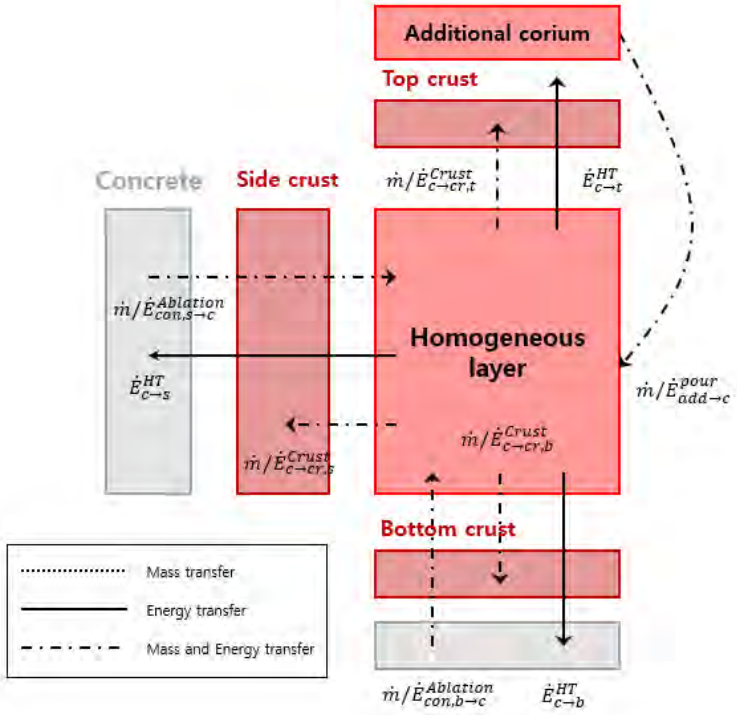

<Homogenous mode>

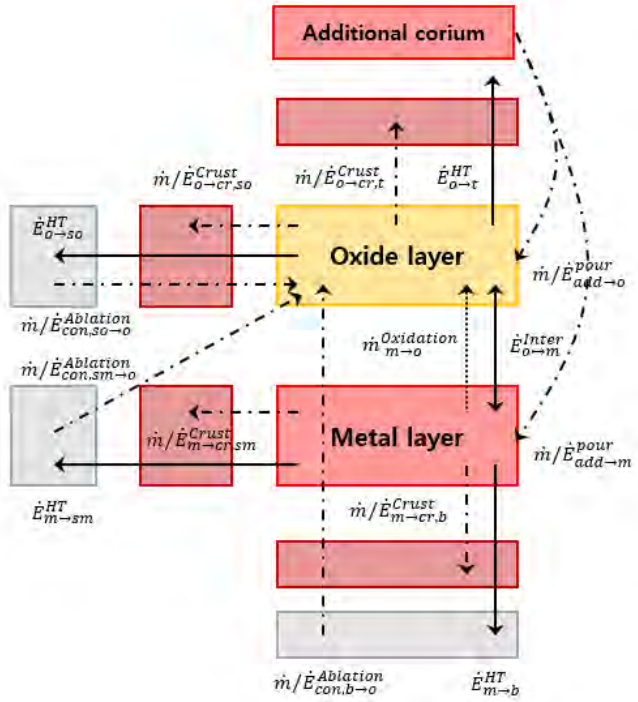

<Stratified mode>

[Homogeneous layer] $(+: source \ / \ -: sink)$

$$\dot{m}_{c,i} = \dot{m}^{Oxidation}_{cor\to cor} + \dot{m}^{Ablation}_{con,b,s\to cor} + \dot{m}^{Pour}_{add\to cor} - \dot{m}^{Crust}_{cor\to cr,t,b,s}$$

$$\dot{E} = \frac{dE}{dt} = \dot{m}e + m\dot{e}$$

$$\dot{E}_c = \dot{E}^{Decay}_{cor\to cor} + \dot{E}^{Ablation}_{con,b,s\to cor} + \dot{E}^{Oxidation}_{cor\to cor} + \dot{E}^{Pour}_{add\to cor} - \dot{E}^{Crust}_{cor\to cr,t,b,s} - \dot{E}^{HT}_{cor\to t,b,s}$$

[Oxide layer]

$$\dot{m}_{o,i} = \dot{m}^{Oxidation}_{m\to o} + \dot{m}^{Ablation}_{con,sm,so,b\to ox} + \dot{m}^{Pour}_{add\to o} - \dot{m}^{Crust}_{o\to cr,t,so}$$

$$\dot{E}_o = \dot{E}^{Decay}_{o\to o} + \dot{E}^{Ablation}_{con,b,so,sm\to o} + \dot{E}^{Inter}_{m\to o} + \dot{E}^{Pour}_{add\to o} - \dot{E}^{Crust}_{o\to cr,t,so} - \dot{E}^{HT}_{o\to t,so}$$

[Metal layer]

$$\dot{m}_{m,i} = \dot{m}^{Pour}_{add\to o} - \dot{m}^{Oxidation}_{m\to o} - \dot{m}^{Crust}_{m\to cr,b,sm}$$

$$\dot{E}_m = \dot{E}^{Decay}_{m\to m} + \dot{E}^{Oxidation}_{m\to m} + \dot{E}^{Inter}_{o\to m} + \dot{E}^{Pour}_{add\to m} - \dot{E}^{Crust}_{m\to cr,b,sm} - \dot{E}^{HT}_{m\to b,sm}$$

Description of the MAMBA module

2.4. Heat transfer modeling

2.4.1. Top heat transfer model

- In the proposed MCCI module, the top heat transfer model differs depending on whether the cavity is dry or wet, with the primary objective being the calculation of the top boundary temperature ($T_{t,I}$) and crust thickness derivative ($\dot{\delta}_t$).

[Dry cavity model]

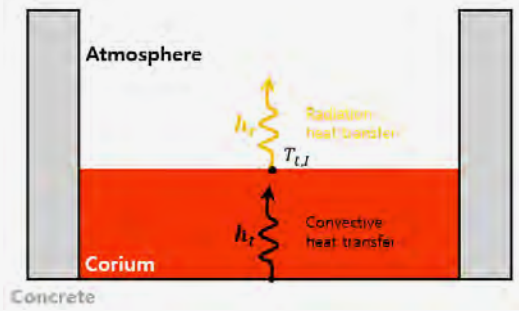

<No-crust>

✓ $\mathrm{h}_r(\mathrm{T}_{t,I} - \mathrm{T}_{at}) = \mathrm{h}_t(T_c - T_{t,I})$

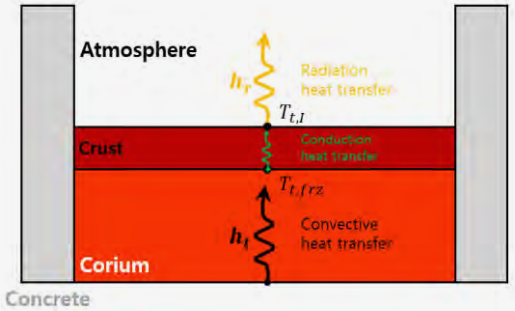

<Stable crust>

✓ $\mathrm{h}_r(\mathrm{T}_{t,I} - \mathrm{T}_{at}) = -\mathrm{k}_{t,c}\left.\frac{dT}{dx}\right|_{x=\delta_t}$

✓ $\rho_{t,c}\Delta e_{t,c}\dot{\delta}_t = -\mathrm{k}_{t,c}\left.\frac{dT}{dx}\right|_{x=0} - \mathrm{h}_t(\mathrm{T}_c - \mathrm{T}_{t,frz})$

[Wet cavity model]

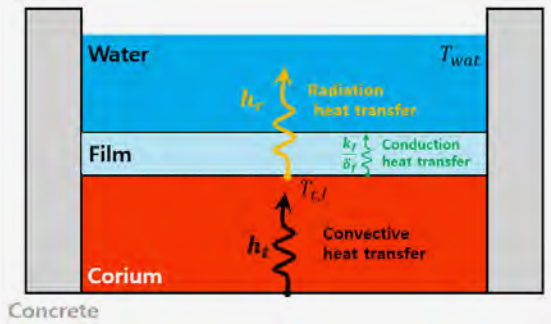

<No-crust>

✓ $\mathrm{h}_{wat}(\mathrm{T}_{t,I} - \mathrm{T}_{wat}) = \mathrm{h}_t(T_c - T_{t,I})$

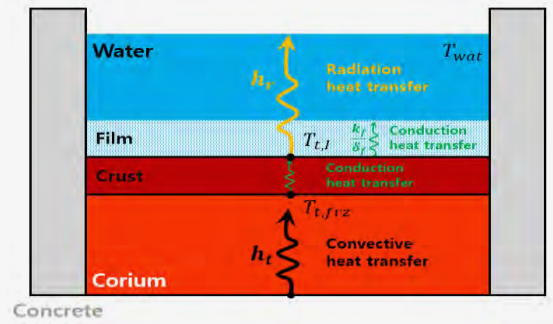

<Stable crust>

✓ $\mathrm{h}_{wat}(\mathrm{T}_{t,I} - \mathrm{T}_{wat}) = -\mathrm{k}_{t,c}\left.\frac{dT}{dx}\right|_{x=\delta_t}$

✓ $\rho_{t,c}\Delta e_{t,c}\dot{\delta}_t = -\mathrm{k}_{t,c}\left.\frac{dT}{dx}\right|_{x=0} - \mathrm{h}_t(\mathrm{T}_c - \mathrm{T}_{t,frz})$

[Temperature profile in crust]

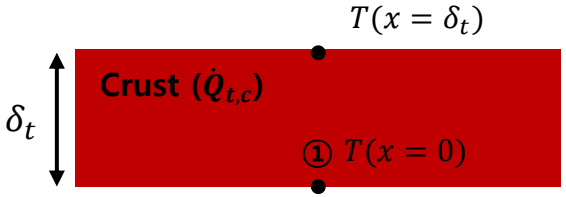

② $\mathrm{k}_{t,c}\frac{d^2T}{dx^2} = -\dot{Q}_{t,c}$ *(Heat equation in crust)*

③ $-\mathrm{k}_{t,c}\left.\frac{dT}{dx}\right|_{x=\delta_t} = \mathrm{h}_r(\mathrm{T}(\mathrm{x} = \delta_t) - \mathrm{T}_{at})$

➡ *Calculation of* $T(x)$

[Heat transfer coefficient for water]

$h_{wat} = \frac{k_f}{\delta_f} + h_r \quad or \quad (from\ Boiling\ curve)$

Based Berenson's correlation

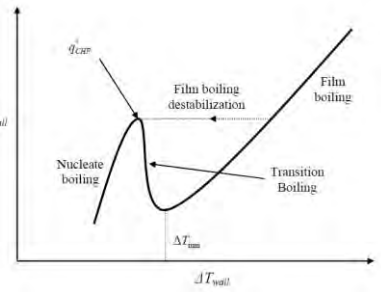

Description of the MAMBA module

2.4.2. Concrete ablation model

- In the proposed MCCI module, both a concrete ablation model that considers crust formation and a model that does not can be used.
- The objective of these models is to calculate the concrete ablation depth rate ($\dot{\eta}_{b,s}$) as well as the thickness rate of crust ($\dot{\delta}_{b,s}$).

[No-crust model]

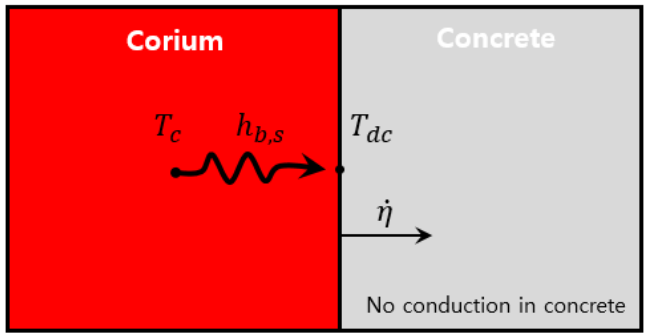

$$\rho_{con} e_{con,d} \dot{\eta}_s = h_s (T_c - T_{dc})$$

[Crust model]

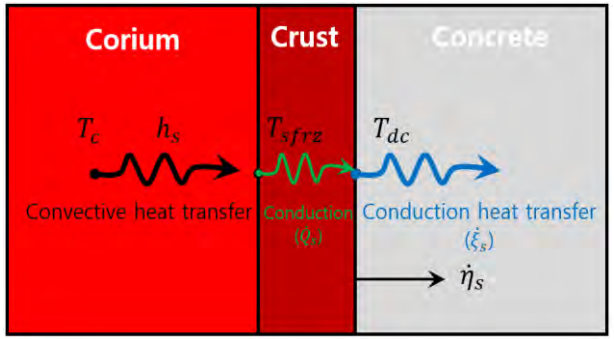

$$\rho_{s,c} \Delta e_{s,c} \dot{\delta}_s = -k_{t,c} \left. \frac{dT}{dx} \right|_{x=-\delta_s} - h_s (T_c - T_{s,frz})$$

$$\rho_{con} \Delta e_{con} \dot{\eta}_s - k_{con} \left. \frac{dT'}{dx} \right|_{x=\eta_s} = -k_{t,c} \left. \frac{dT}{dx} \right|_{x=0}$$

[Phase of crust model]

Phase 1 – Initial contact with crust growth

Phase 2 – Crust growth and re-melting with ablation

Phase 3 – No crust calculation after crust failure

[Appendix 2]

3. Validation agreement experimental data

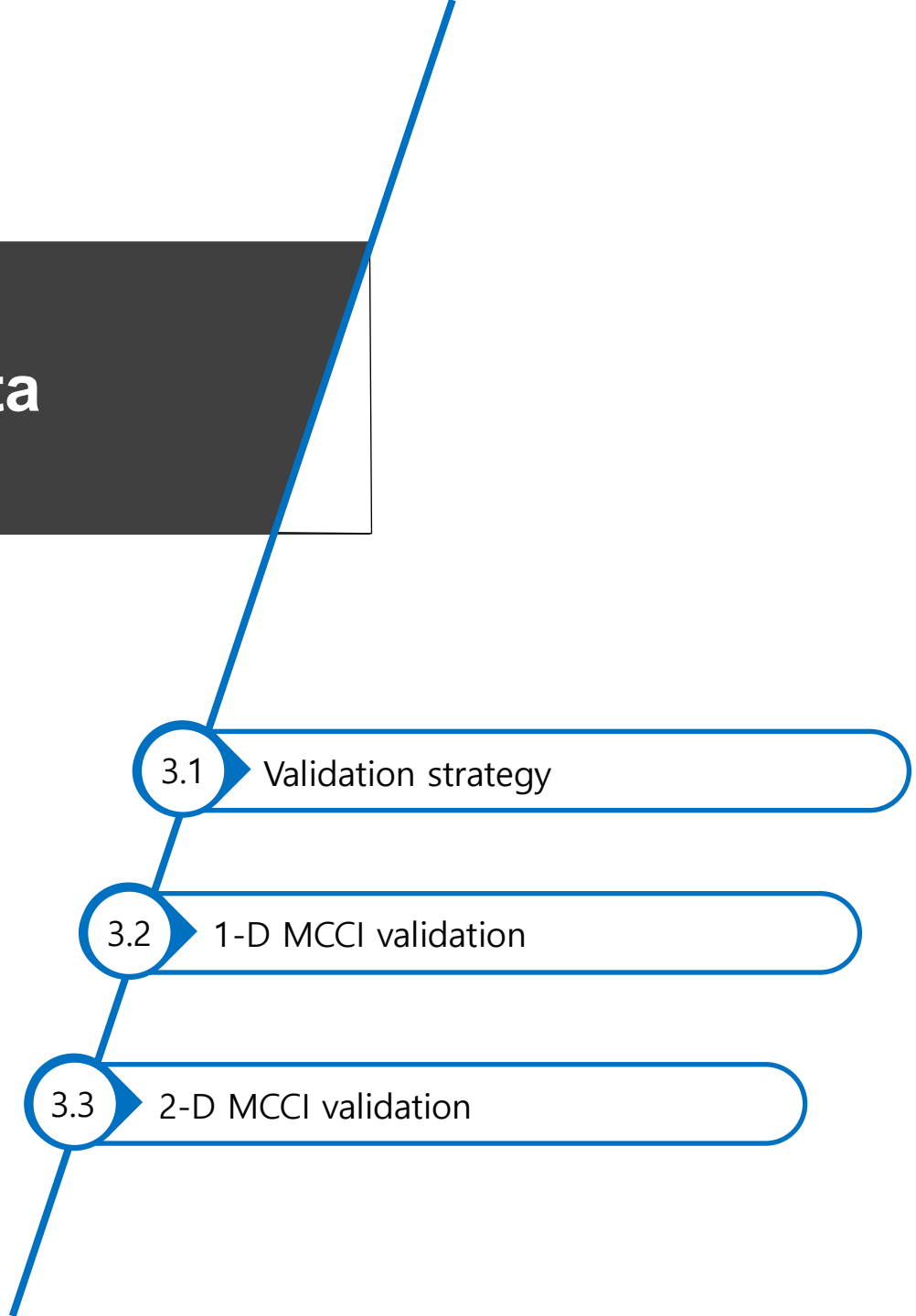

Validation agreement experimental data

3.1. Validation strategy

- The validation of the proposed MCCI module was conducted using selected experiments that account for a wide range of corium, concrete, and coolant.

	Experiment	MCCI geometry	Corium type	Concrete type	Cavity situation
1-D MCCI (Axial)	SURC-2	Cylindrical	Homogeneous	Basaltic	Dry
	ACE-L2	Rectangular	Homogeneous (*Concrete-metal inserts)	Siliceous	Dry
2-D MCCI (Axial/Radial)	CCI-2	Rectangular	Homogeneous	LCS	Dry + Wet
	MOCKA 3.1	Cylindrical	Stratified	Siliceous	Dry

Corium temperature

Concrete ablation depth

Validation agreement experimental data

3.2. 1-D MCCI validation

- The validation of the 1-D MCCI experiment was conducted using the SURC-2 and ACE-L2 experiments.

Conditions	SURC-2	ACE-L2
Geometry	1-D cylindrical	1-D Rectangular
Initial size of cavity	0.2 m (radius)	0.5×0.5 m^2
Initial corium mass $[kg]$	200	300
Initial corium temperature $[K]$	2,720	2,500
Corium composition	UO_2/ZrO_2 based corium	
Atmosphere pressure $[MPa]$	0.1	
Decay heat [kW]	10~35	97.2
Ablation model	Crust model	No-crust model
Boundary temperature $[K]$	1600	1700
Analysis mode	Only Homogeneous mode	
Time step $[s]$	0.5	
Total time $[s]$	9,000	2,700

[Appendix 3]

[Analysis geometry for SURC-2 and ACE-L2]

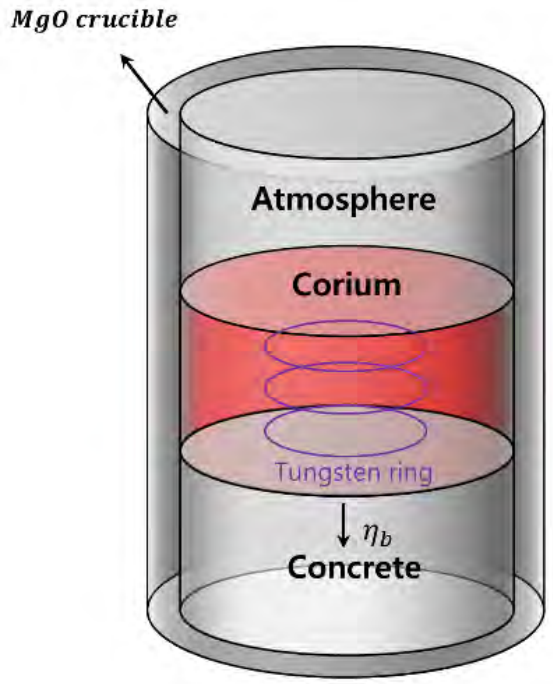

<SURC-2>

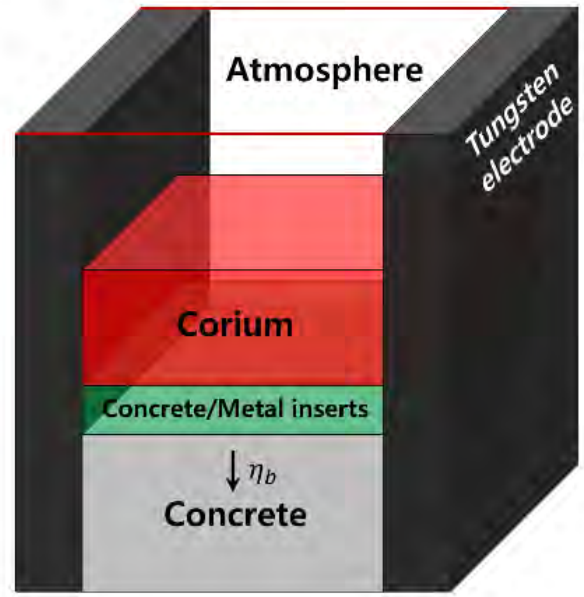

<ACE-L2>

Validation agreement experimental data

Corium temperature

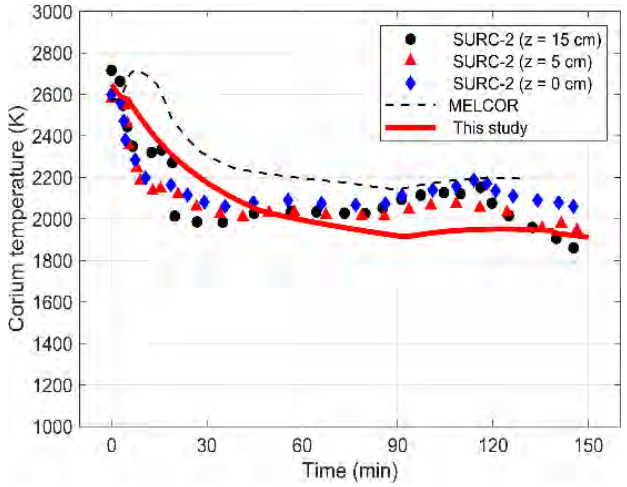

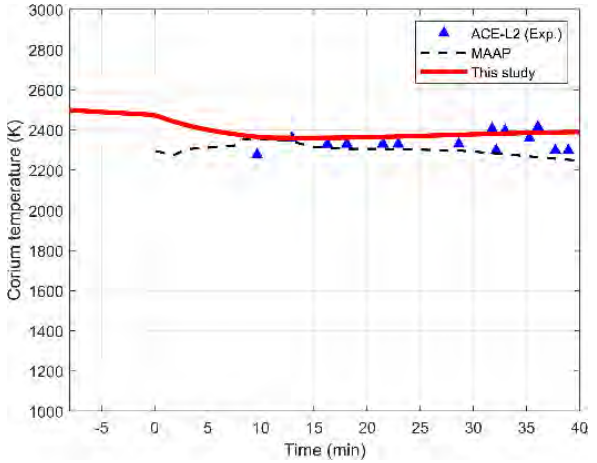

Concrete ablation depth

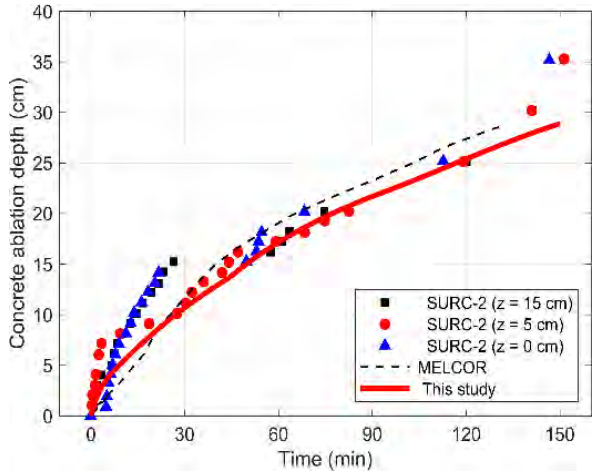

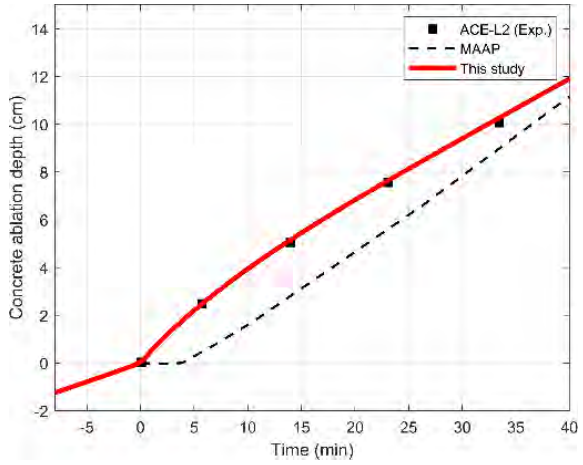

<SURC-2> **<ACE-L2>**

Validation agreement experimental data

3.3. 2-D MCCI validation

- The CCI-2 experiment is widely used for MCCI validation, maintaining a dry cavity condition for the first 300 minutes, followed by a wet cavity condition through post-flooding.

Conditions	Value
Geometry	2-D Rectangular
Initial size of cavity (L,W)	0.5×0.5 m^2
Initial corium mass $[kg]$	400
Initial corium temp. $[K]$	2,150
Corium composition	UO_2/ZrO_2 based corium
Atm. pressure $[MPa]$	0.1
Cavity condition	Dry(~18,000s) +Wet (18,000s~)
Decay heat [kW]	102
Boundary temp. $[K]$	1,350
Water temp. [K]	417
Ablation model	Crust model
Analysis mode	Only Homogeneous mode
Time step $[s]$	0.5
Total time $[s]$	27,000

[Appendix 3]

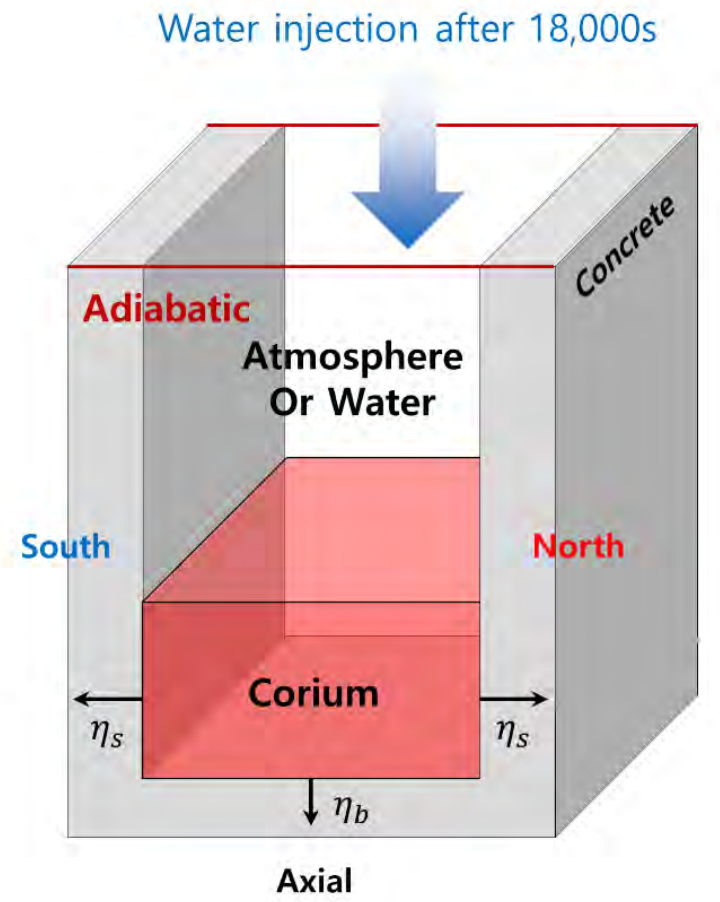

<Analysis geometry for CCI-2>

Validation agreement experimental data

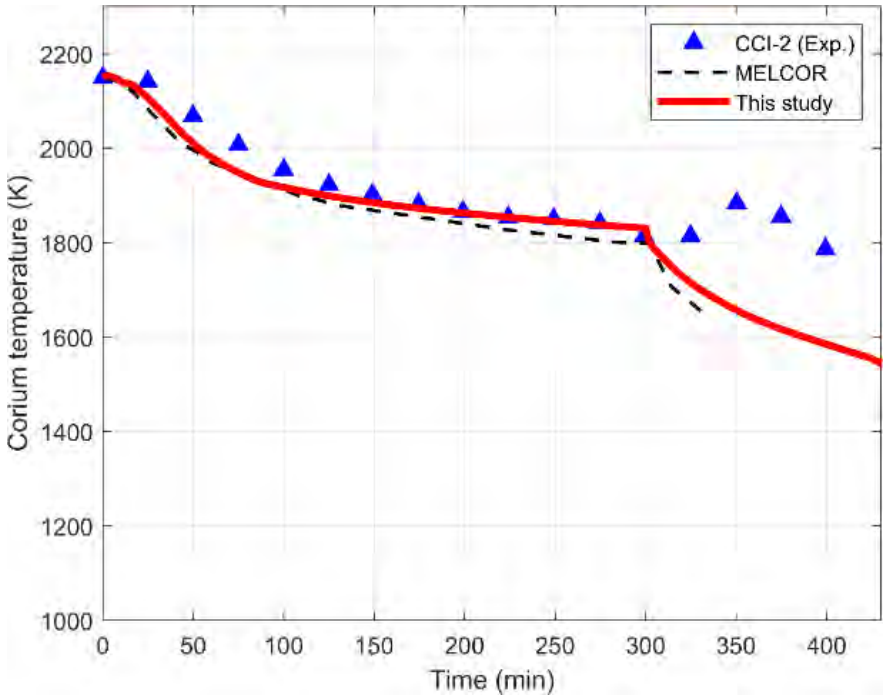

<Corium temperature>

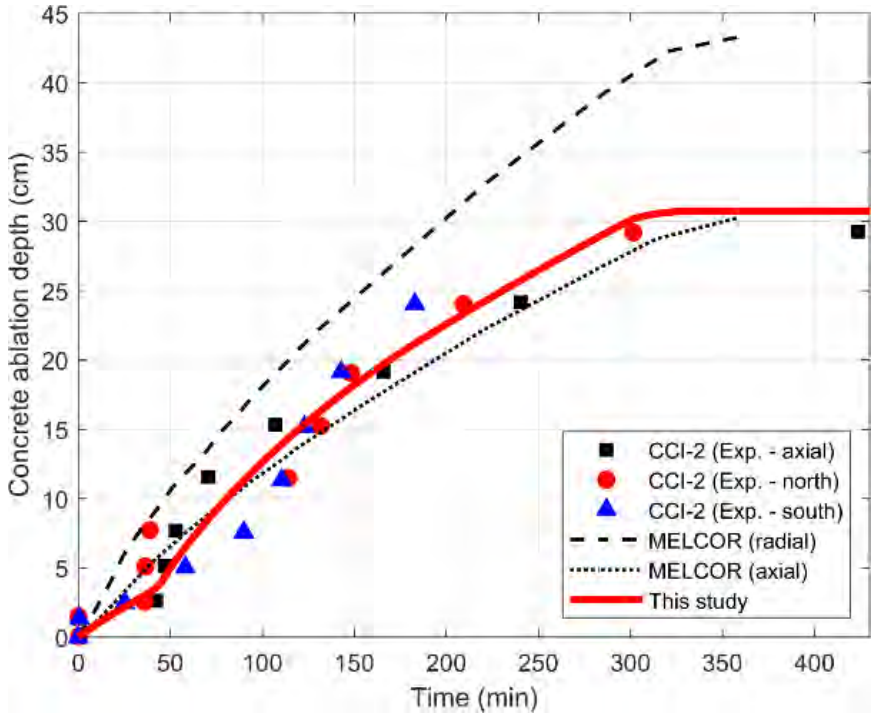

<Concrete ablation depth>

Validation agreement experimental data

- The MOCKA 3.1 experiment primarily generates corium using an alumina thermite reaction and is conducted with a light oxide layer, mainly composed of concrete constituents, and a metal layer consisting of Fe and Zr, leading to stratification.

Input data	Value
Geometry	2-D cylindrical
Initial width R $[m]$	0.125
Corium type	Alumina based
Corium mass $[kg]$	114 (initial) + 209 (additional)
Initial corium temperature $[K]$	2,273
Boundary temperature $[K]$	1,350
Cavity condition	Dry condition
Decay heat [KW]	0
Ablation modeling	No-crust model
Analysis mode	Transition to Stratified mode
Heat transfer coefficient model	Developed model
Solidus/Liquidus temp. model	$Al_2O_3 - CaO$ based model
Time step $[s]$	0.5
Total time $[s]$	1,200

[Appendix 4]

Additional corium injection

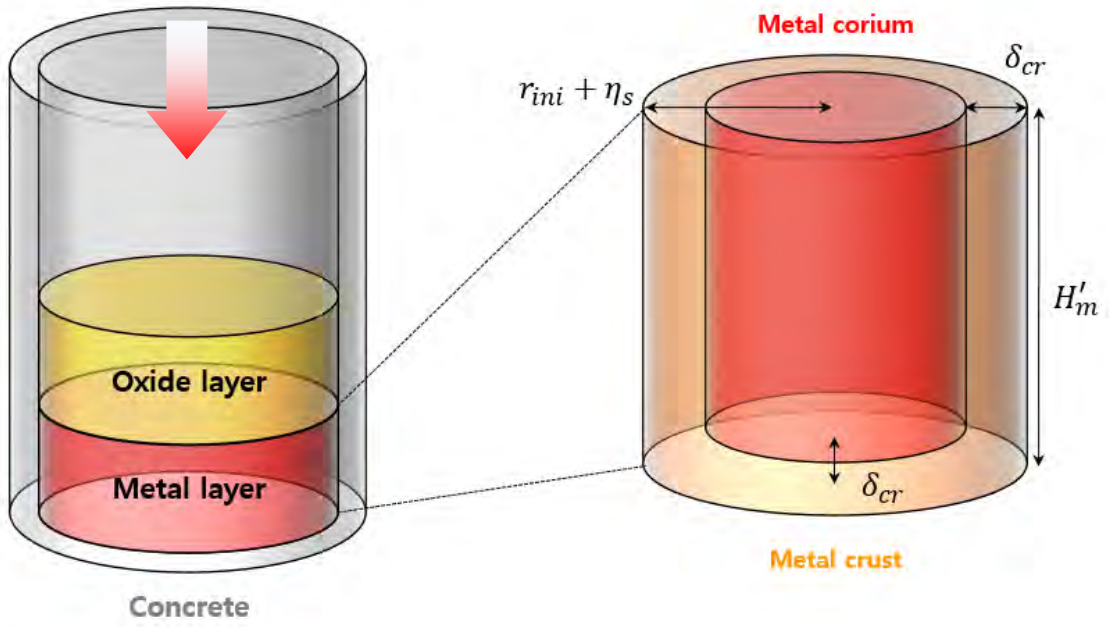

$Fe_2O_3 + 2Al \rightarrow 2Fe + Al_2O_3$
$(Alumina\ thermite\ reaction)$

<Experiment schematic>

<Ablation modeling approach>

[Appendix 4]

Validation agreement experimental data

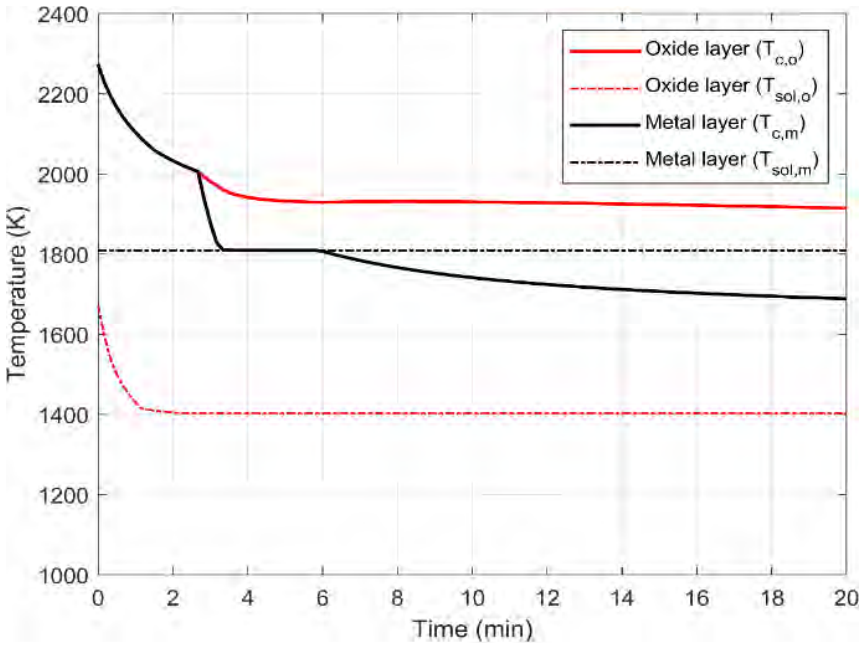

<Corium temperature>

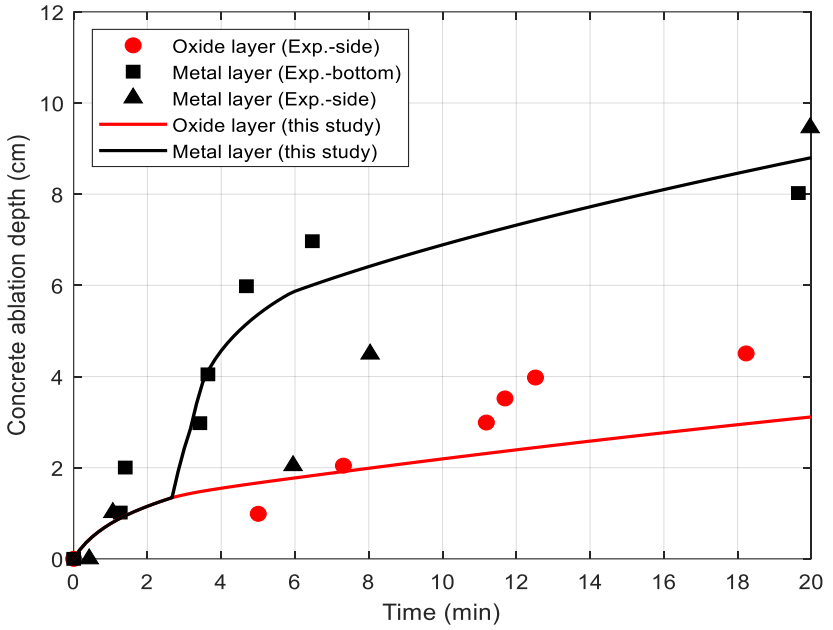

<Concrete ablation depth>

4. Conclusions

Conclusions

Development and Validation of the MAMBA module for MCCI Analysis within the SAFARI Code

- Development of an MCCI analysis module capable of detailed simulation of various phenomena accompanying MCCI
- Validation of the MCCI module against various MCCI experiments to establish its reliability

Development of a reliable MCCI analysis module for severe accident scenario analysis

THANK YOU!

cjs8088@snu.ac.kr

Appendix

◆ BALIS experiment

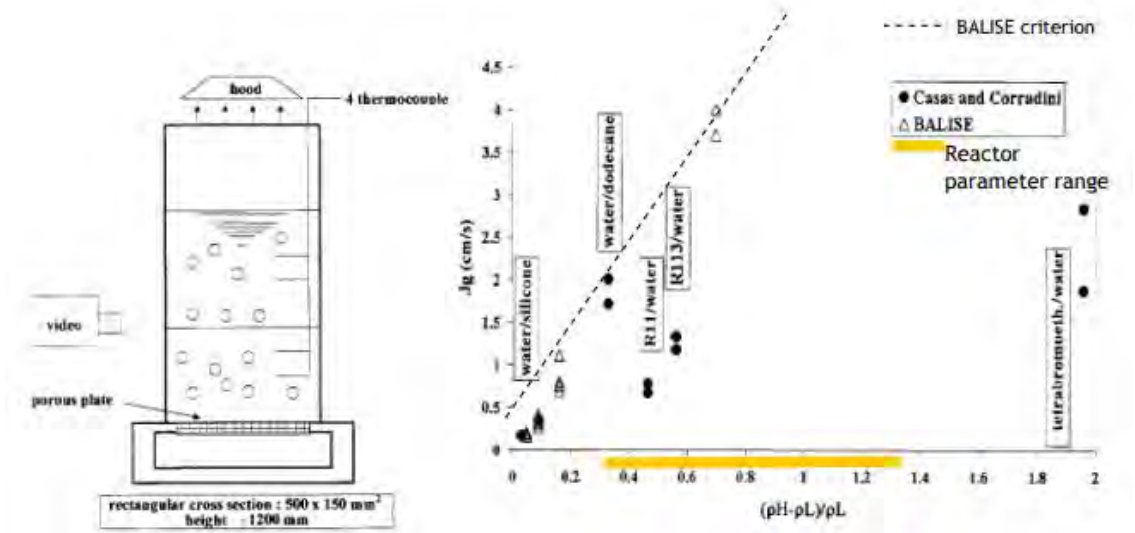

<BALISE experiment & data>

$$J_{fm} = 0.054\frac{(\rho_H - \rho_L)}{\rho_L}$$

<BALISE correlation>

◆ Additional MCCI modeling

[Top heat transfer coefficient (h_t)]

$$h_t = \begin{cases} 1.5\cdot 10^{-3}\left(\dfrac{c_m P j}{k_m g}\right)^{2/3}\dfrac{k_m}{L_\lambda}; & j < j_{tr} \\ 1.5\cdot 10^{-3}\left(\dfrac{c_m P j}{k_m g}\right)^{2/3}\left(\dfrac{j_{tr}}{j}\right)^{1/2}\dfrac{k_m}{L_\lambda}; & j \geq j_{tr} \end{cases}$$

[Bottom/side heat transfer coefficient ($h_{b,s}$)]

$$h_{b,s} = C_{slag} h_t$$

[Decay heat]

$$P = P_0 \times 0.1250 t^{-0.2752}$$

$$\dot{q}_{dec} = \frac{P}{m_{core}}$$

$$\dot{E}^{Decay} = \chi_{UO_2} m_c \dot{q}_{dec}$$

[Oxidation reaction]

$$Zr + 2H_2O \rightarrow ZrO_2 + 2H_2 + 6.5MJ/kg\ Zr$$

$$Zr + 2CO_2 \rightarrow ZrO_2 + 2CO + 6MJ/kg\ Zr$$

$$2Cr + 3H_2O \rightarrow Cr_2O_3 + 3H_2 + 2.6MJ/kg\ Cr$$

$$2Cr + 3CO_2 \rightarrow Cr_2O_3 + 3CO + 1.9MJ/kg\ Cr$$

$$Fe + H_2O \rightarrow FeO + H_2 + 60KJ/kg\ Fe$$

$$Fe + CO_2 \rightarrow FeO + CO - 0.4MJ/kg\ Fe$$

$$Si + 2H_2O \rightarrow SiO_2 + 2H_2 + 60KJ/kg\ Si$$

$$Si + 2CO_2 \rightarrow SiO_2 + 2CO - 0.4MJ/kg\ Si$$

Zr → Cr → Fe

Appendix 2

◆ Concrete ablation model for phase

- The concrete ablation model for each phase is calculated using the heat transfer equation.

[Phase 1]

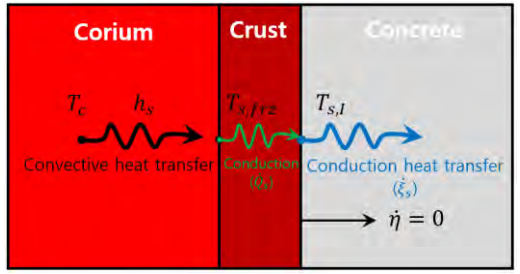

[Phase 2]

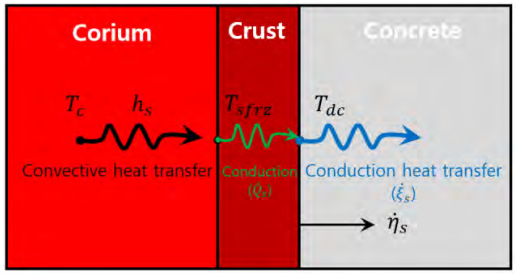

[Phase 3]

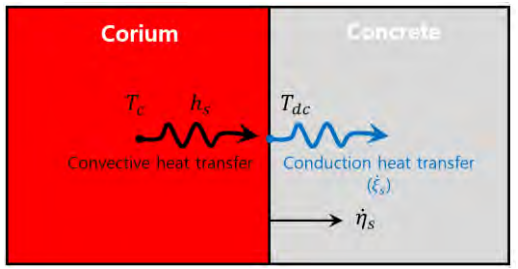

<Calculation $\dot{\delta}_s$, $\dot{\eta}_s$>

$$\rho_{s,c}\Delta e_{s,c}\dot{\delta}_s = -\mathrm{k}_{t,c}\left.\frac{dT}{dx}\right|_{x=-\delta_s} - \mathrm{h}_s(\mathrm{T}_c - \mathrm{T}_{s,frz})$$

$$\dot{\eta}_s = 0$$

$$\rho_{s,c}\Delta e_{s,c}\dot{\delta}_s = -\mathrm{k}_{t,c}\left.\frac{dT}{dx}\right|_{x=-\delta_s} - \mathrm{h}_s(\mathrm{T}_c - \mathrm{T}_{s,frz})$$

$$\rho_{con}\Delta e_{con}\dot{\eta}_s = -\mathrm{k}_{t,c}\left.\frac{dT}{dx}\right|_{x=0} + \mathrm{k}_{con}\left.\frac{dT'}{dx}\right|_{x=\eta_s}$$

$$\rho_{con}\Delta e_{con}\dot{\eta}_s = \mathrm{k}_{con}\left.\frac{dT'}{dx}\right|_{x=\eta_s} + h_s(T_c - T_{dc})$$

$$\dot{\delta}_s = 0$$

<Calculation $\dot{\xi}_s$>

$$\rho_{con}c_{con}\frac{dT}{dt} = k_{con}\frac{d^2T}{dx^2} + \dot{\eta}\frac{dT}{dx}$$

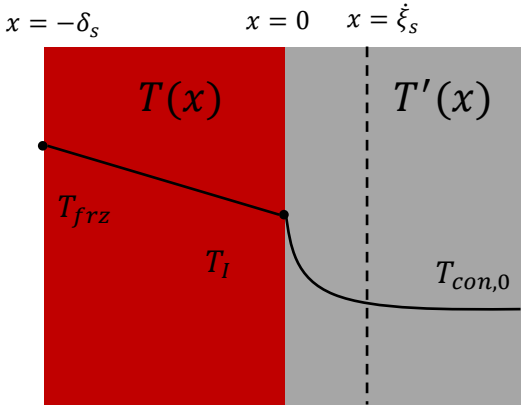

① $\mathrm{k}_s\frac{d^2T}{dx^2} = -\dot{Q}_s$

② $T(x=0) = T_{s,I}$ *or* T_{dc}

③ $T(x=-\delta_s) = T_{frz}$

➡ *Calculation of crust* $T(x)$

① $-\mathrm{k}_{t,c}\left.\frac{dT'}{dx}\right|_{x=0} = -\mathrm{k}_{con}\left.\frac{dT}{dx}\right|_{x=0}$

② $T'(x=\xi_s) = T_{con,0}$

③ $\left.\frac{dT'}{dx}\right|_{x=\xi_s} = 0$

➡ *Calculation of concrete* $T'(x)$

Appendix 3

◆ Detailed of validation

Parameter	ACE-L2	SURC-2	CCI-2
Corium composition	UO_2/ZrO_2 based (Table 2.3)	UO_2/ZrO_2 based (Table 2.3)	UO_2/ZrO_2 based (Table 2.3)
Concrete type	Siliceous (Table 2.4)	Basaltic (Table 2.4)	LCS (Table 2.4)
Concrete decomposition temperature [K]	1,450	1,470	1,500
Concrete solidus temperature [K]	1,403	1,350	1,393
Concrete liquidus temperature [K]	1,523	1,650	1,568
Initial corium temperature [K]	2,500	2,650	2,150
Atmosphere pressure [MPa]		0.1	
MCCI geometry	1D rectangular	1D cylindrical	2D rectangular
Bottom size [m]	0.5 (Width, Length)	0.4 (Diameter)	0.5 (Width, Length)
Top surface model (cavity conditions)	Dry cavity model		Dry + Wet cavity model
Bottom and Side surface model	No-crust model		Crust model
Total calculation time [s]	2,700 (step – 0.5)	9,000 (step – 0.5)	24,000 (step-0.5)

<Simulation conditions for validation>

	ACE-L2 (kg)	SURC-2 (kg)	CCI-2 (kg)
UO_2	216	140.9	242.5
ZrO_2	42.5	46.1	99.6
SiO_2	20.9	0	13.6
Al_2O_3	0	0	1.6
MgO	0	0	4.6
CaO	3	0	12.5
Zr	5.5	16.9	0
Cr	0	0	25.6
Fe	0	0	0
Total	287.9	203.9	400

<Corium composition for validation>

Appendix 3

◆ Detailed of validation

	ACE-L2 (Insert, Wt%)	ACE-L2 (Concrete, Wt%)	SURC-2 (Concrete, Wt%)	CCI-2 (Concrete, Wt%)
CO_2	0.6	1.7	1.5	30.4
H_2O	2.2	6.2	5	4.5
K_2O	0.5	1.4	3.8	0.6
Na_2O	0.3	0.7	1.4	0.3
TiO_2	0.3	0.8	0.8	0.1
SiO_2	24.8	69.7	57.9	22
CaO	4.8	13.6	13.8	26.4
MgO	0.25	0.7	4	11.7
Al_2O_3	1.5	4.2	7.3	2.5
Fe_2O_3	0.35	1	4.5	1.5
Fe	0	0	0	0
Cr	0	0	0	0
Ni	0	0	0	0
Zr	64.4	0	0	0

<Concrete composition for validation>

Parameter	Specification
Initial corium composition	• 68 kg (Al_2O_3 - 56 wt.%, CaO – 44 wt.%) • 42 kg (Fe) • 4 kg (Zr)
Additional corium composition (~ 21 min)	• 155 kg (Thermite) • 54 kg (Zr)
Concrete composition (main component – Siliceous type)	• 1 wt.% (CO_2) • 6.7 wt.% (H_2O) • 69.7 wt.% (SiO_2) • 13.7 wt.% (CaO)
Concrete decomposition temperature (T_{dc})	1430 K
Concrete solidus temperature ($T_{sol,con}$)	1403 K
Concrete liquidus temperature ($T_{liq,con}$)	1523 K
Initial corium temperature (T_c)	2273 K
Ambient temperature (T_{at})	850 K
Ambient pressure (P)	0.1 MPa
Simulation time (t_{end})	1,200 s (time step – 0.5 s)
Ratio of heat input from additional corium	0.75 (oxide layer) : 0.25 (metal layer)
Ratio of heat input from oxidation reactions	1 (oxide layer) : 0 (metal layer)

<Simulation conditions for MOCKA 3.1>

Appendix 4

◆ MOCKA 3.1 experiment

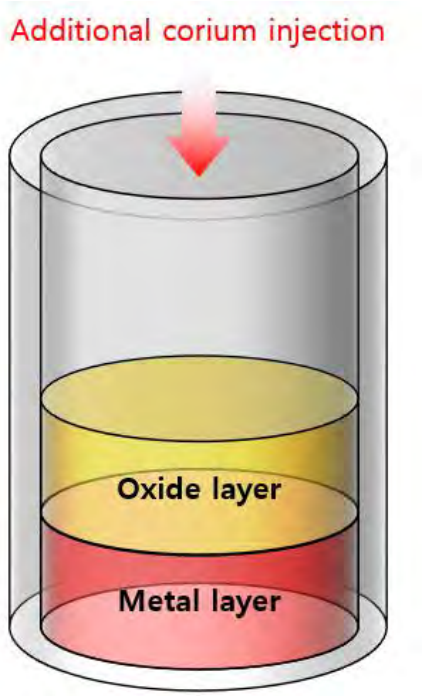

$Fe_2O_3 + 2Al \rightarrow 2Fe + Al_2O_3$
$(Alumina\ thermite\ reaction)$

[Initial corium composition]

	Al_2O_3	CaO	Fe	Zr	$Total$
Mass [kg]	38.1	29.9	42	4	114

[Additional corium composition – during 21min]

	Al_2O_3	Fe	Zr	$Total$
Mass [kg]	73.9	81.1	54	209

[Heat deposit in stratified layer]

	Additional corium heat	Oxidation reaction heat
Oxide layer	75%	100%
Metal layer	25%	0%

[Corium heat]
The energy possessed by the additional corium is divided between the oxide and metal layers, with 75% being applied to the oxide layer physically located above (utilizing the numerical values from the paper).

[Oxidation reaction heat]
It is assumed that the Zr contained in the additional corium undergoes oxidation as it passes through the upper oxide layer, and that all oxidation reaction heat is applied to the oxide layer (referenced from the paper).

Appendix 4

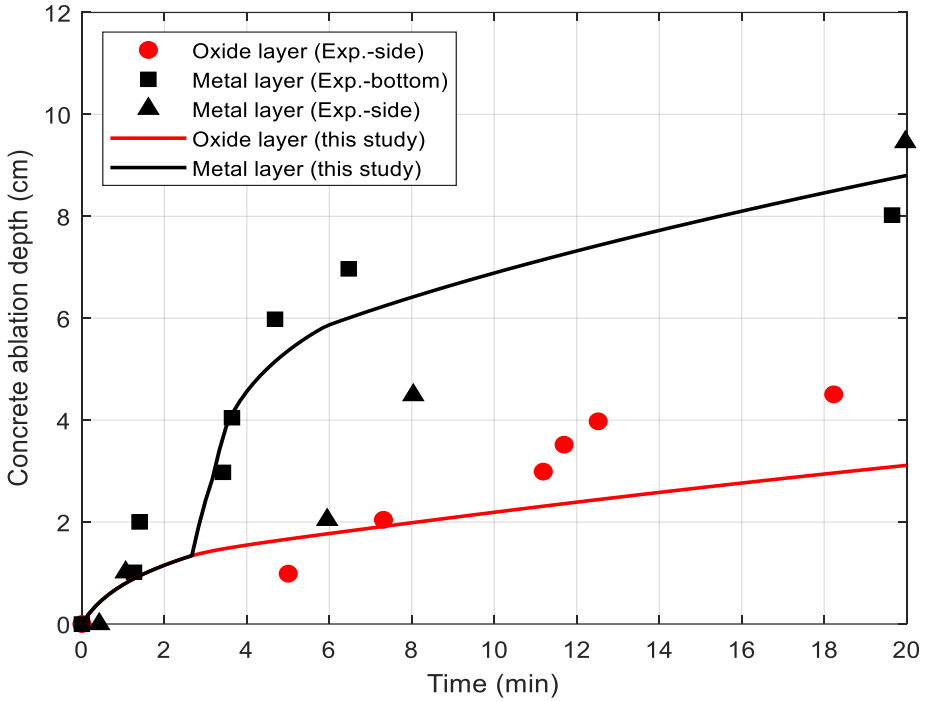

[Mention in the paper]

✓ Approximately 400 seconds after the start of the experiment, a crust forms on the metal layer.

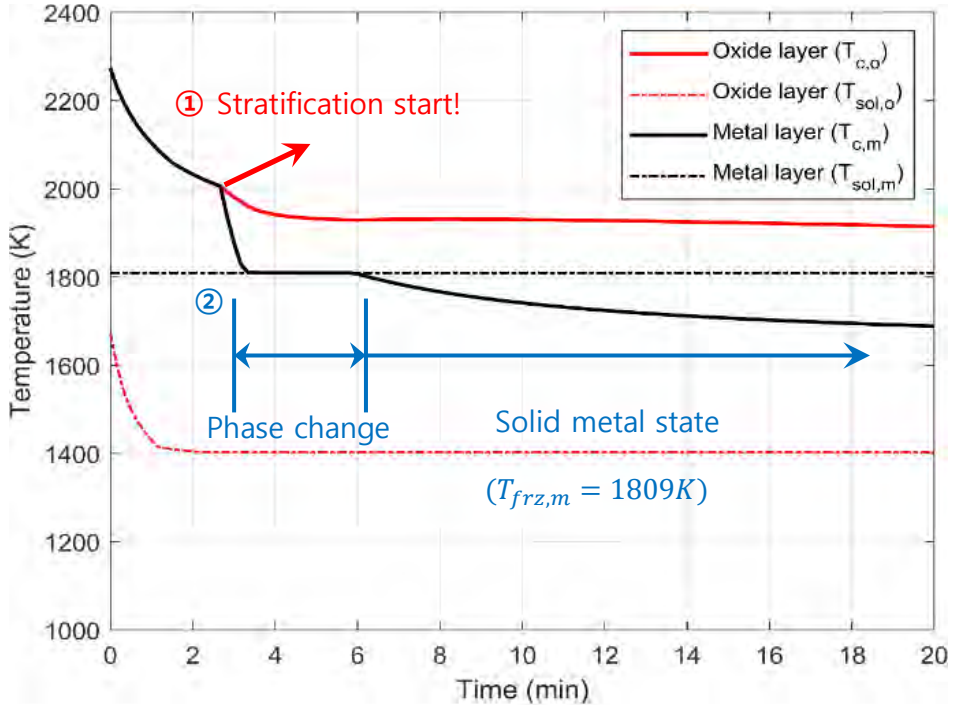

[Key aspects of the MOCKA 3.1 experiment]

✓ Transition to stratified mode

✓ Phase change of metal layer

◆ Metal layer crust modeling

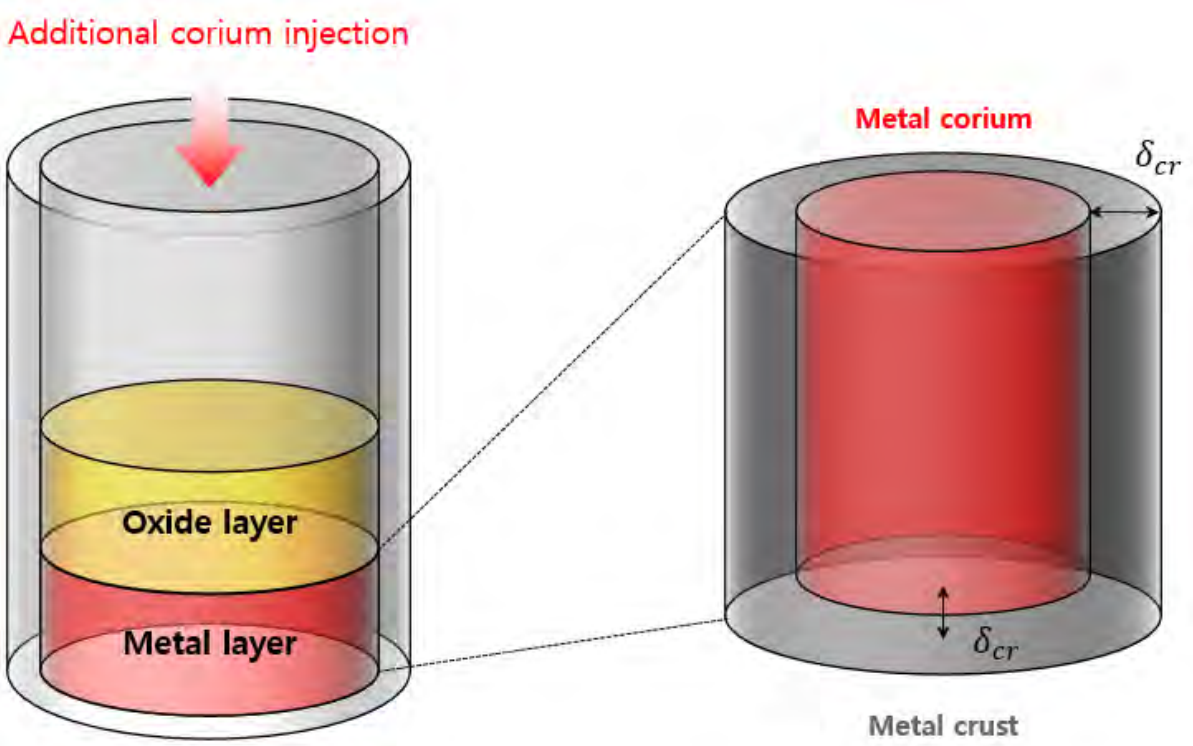

$$\rho_{con} e_{con,d} \dot{\eta}_s = h_s (T_c - T_{dc})$$

[Metal solid fraction in mushy zone]

$$solf_m = \frac{T_{liq,m} - T_{c,m}}{T_{liq,m} - T_{sol,m}}$$

[Mass of metal crust]

$$m_{cr} = solf_m * m_{c,m}$$

[Total crust volume & depth]

$$V_{cr} \;\&\; \delta_{cr}$$

[Initial crust depth]

$$\dot{\delta}_{cr} \rho_s \Delta e_s = \frac{k_{cr}}{\delta_{cr}} (T_{frz} - T_{dc})$$

[Heat transfer coefficient - mushy]

$$h_s' = \frac{k_{cr}}{\delta_{cr}} \qquad (T_{c,m} < T_{liq,m})$$

$$h_s' = \frac{k_{cr}}{0.5 \times H_{c,m}} \qquad (T_{c,m} < T_{sol,m})$$

◆ Metal layer crust volume and thickness

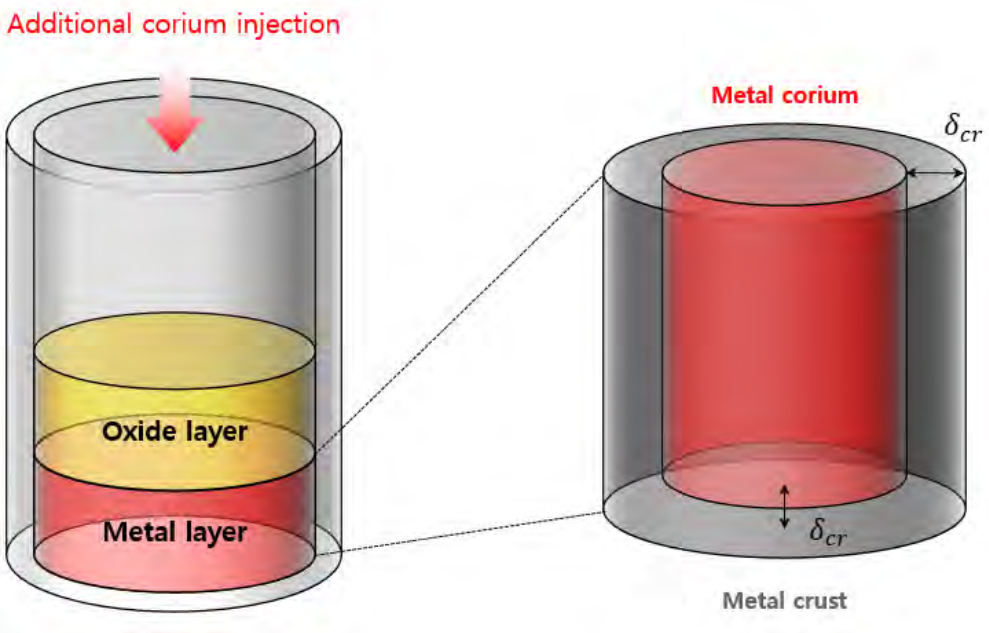

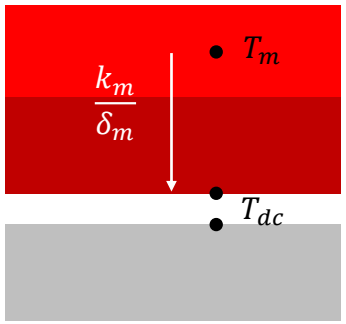

[Crust volume - no bubble in crust assumption]

$$V_{cr,sol} = m_{cr}/\rho_{cr}$$

$$V_{corium} = (m_{total} - m_{cr})/(\rho_m * (1-\alpha))$$

$$V_{all} = V_{corium} + V_{cr} \Rightarrow H'_m = \frac{V_{all}}{A_b}$$

[Crust volume by geometry – boundary crust assumption]

$$V_{outer} = \pi(r_{ini} + \eta_{side})^2 H'_m$$

$$V_{inner} = \pi(r_{ini} + \eta_{side} - \delta_{cr})^2 (H'_m - \delta_{cr})$$

$$V_{cr,geo} = V_{outer} - V_{inner}$$

[Crust volume by solid fraction & void fraction]

$$V_{cr,sol} = V_{cr,geo}$$

$$\pi(r_{ini} + \eta_{side})^2 H'_m - \pi(r_{ini} + \eta_{side} - \delta_{cr})^2 (H'_m - \delta_{cr}) = m_{cr}/\rho_{cr}$$

◆ Solidus and Liquidus temperature model

T_i

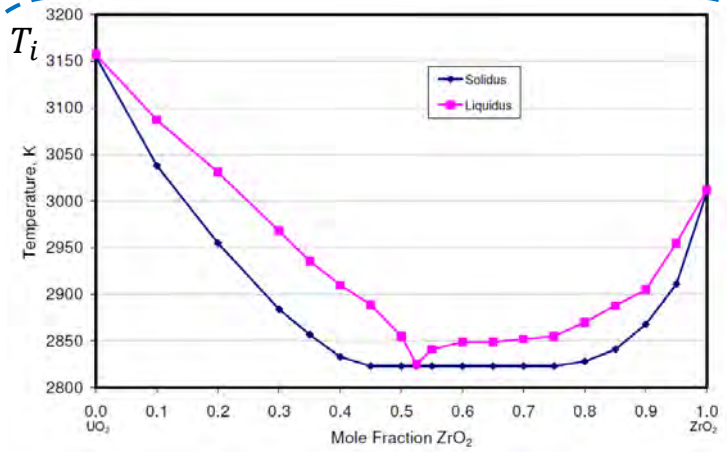

<$UO_2 - ZrO_2$ phase diagram >

Target value

$$F_{sol} = \frac{T_{sol,i} - T_{sol,o}}{T_{sol,i,} - T_{sol,con}}$$

$$F_{liq} = \frac{T_{liq,i} - T_{liq,o}}{T_{liq,i} - T_{liq,con}}$$

F_{sol}

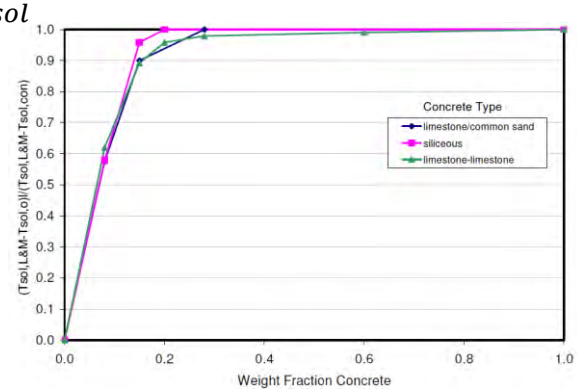

F_{liq}

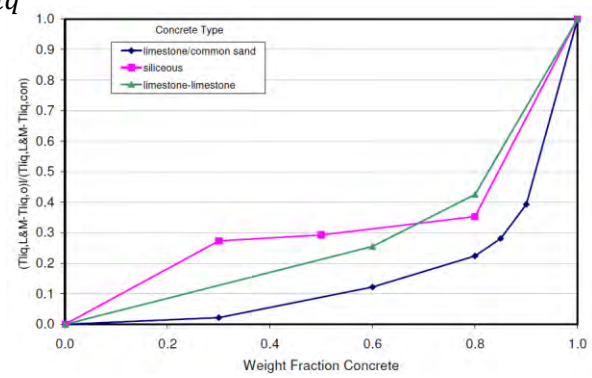

<Factor for core-concrete mixtures – left: solidus/ right: liquidus>

T_i

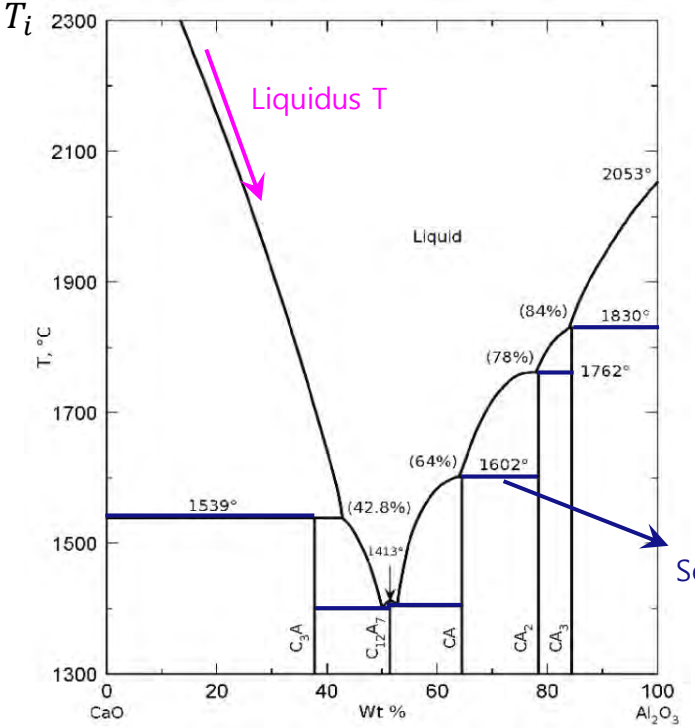

<$CaO - Al_2O_3$ phase diagram >

The 12th European Review Meeting on Severe Accidents Research

May 18-22, 2026, Universidad Carlos III de Madrid, Madrid, Spain

PLENARY SESSION: R&D INTERNATIONAL FRAMEWORKS: NEW PROJECT PLATFORMS AND DATABASES FOR SA (ROUND TABLE)

Chair: F. Rocchi (ENEA)

Euratom Research activities on Severe Accidents

A. Iorizzo (European Commission)

Recent IAEA Activities Related to Severe Accidents

A. Miassoedov (International Atomic Energy Agency)

Enabling Nuclear Safety Research: NEA Frameworks and Databases

M. Adorni (OECD Nuclear Energy Agency)

The 12th European Review Meeting on Severe Accidents Research

May 18-22, 2026
Universidad Carlos III de Madrid
Puerta de Toledo Campus

Euratom Research activities on Severe Accidents

Angelgiorgio IORIZZO
Unit C.4–Euratom Research
DG RTD Research & Innovation
European Commission

Outline

1. EC Policy Context on Nuclear Energy
2. The Euratom research and training programme
3. The Euratom Work programme 2026-2027
4. The next Euratom Research and Training Programme 2028-2032

EC Policy Context on Nuclear Energy

Speech by President von der Leyen at the Nuclear Energy Summit, Paris, 10.03.2026

"After years of declining investment, we need more to turn the tide. [...] We want this new technology [SMRs] to be operational in Europe by the early 2030s, so that it can play a key role alongside traditional nuclear reactors, in a flexible, safe, and efficient energy system."

Commissioner Zaharieva -Startups, Research and Innovation-, on the adoption of the Euratom WP 2026-27, Brussels, 19.03.2026

"The EU wants to lead the world in innovative nuclear technologies, which will be key to securing our energy independence, competitiveness and decarbonisation."

The Euratom research and training programme

- The Euratom Research and Training Programme is a complementary funding programme to Horizon Europe which covers nuclear research and innovation.
- The programme is planned in five-year cycles, with an extension for another two years in order to align with the Multiannual Financial Framework, the EU's seven-year budget cycle.
- It funds direct actions, which are research activities undertaken by the Commission's Joint Research Centre, and indirect actions - research activities undertaken by multi-partner consortia. The indirect actions are coordinated by the Directorate-General for Research and Innovation of the European Commission.

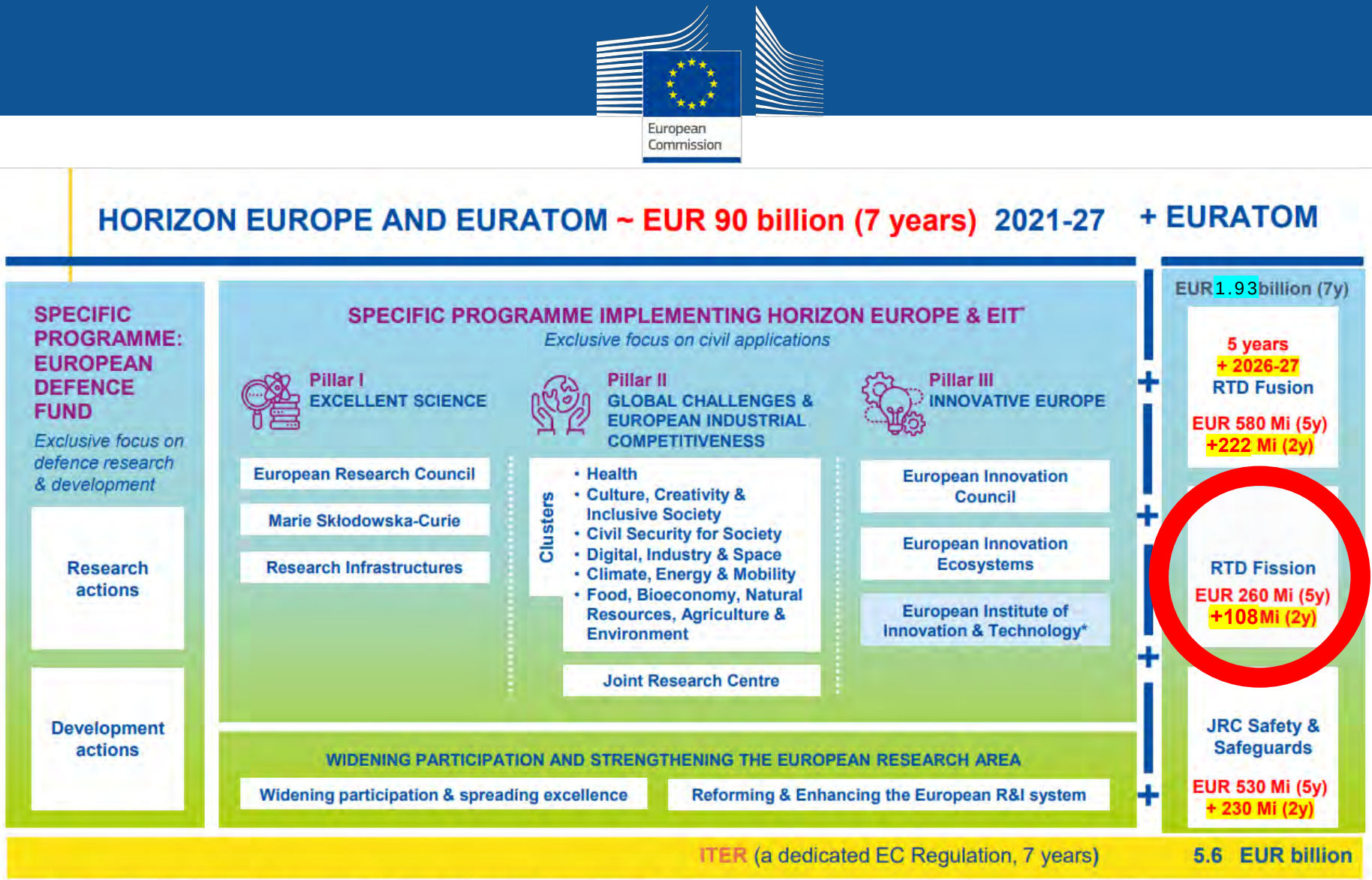

https://research-and-innovation.ec.europa.eu/index_en and Euratom https://research-and-innovation.ec.europa.eu/funding/funding-opportunities/funding-programmes-and-open-calls/horizon-europe/euratom-research-and-training-programme_en

→ Council Regulation (Euratom) 2025/1304 of 23 June 2025 https://eur-lex.europa.eu/eli/reg/2025/1304/oj/eng

The Euratom Work programme 2026-2027

- The 2026-2027 Euratom work programme for research is extending the 2021-2025 programme. It has a budget of €330 million:
  - €222 million for indirect actions in fusion research and development
  - **€108 million for indirect actions in nuclear fission,** safety and radiation protection

Euratom Research WP 2026-27

OPERATION:

- *The EC-DG RTD representing Euratom drafts the Euratom Research and Training WP containing topics of research*
- *Potential beneficiaries apply with proposals for research Projects*
- *These research Projects are evaluated by independent Experts panels*

TIMING:

- Adoption of the WP 2026-27 on 19 of March 2026, publication on 24 March 2026
- Deadline for application by 15 September 2026
- Evaluation October- November 2026
- Results of the evaluation by January 2027
- Indicative signature of the research projects by May 2027
- Projects to start from June 2027 on.

Euratom Research WP 2026-27 adopted on 19.03.2026

Safety of operating nuclear power plants and research reactors

HORIZON-EURATOM-2026-01-01 | Calls for proposals

Opening date: **23 April 2026** | Deadline date: **15 September 2026** | Single-stage

Open For Submission

Programme: **Euratom Research and Training Programme (EURATOM)** | Type of action: **EURATOM Research and Innovation Actions**

Safety of SMRs, advanced and innovative nuclear reactors and fuels

HORIZON-EURATOM-2026-01-02 | Calls for proposals

Opening date: **23 April 2026** | Deadline date: **15 September 2026** | Single-stage

Open For Submission

Programme: **Euratom Research and Training Programme (EURATOM)** | Type of action: **EURATOM Innovation Actions**

European Partnership for research in radiation protection and detection of ionisin...

HORIZON-EURATOM-2026-01-09 | Calls for proposals

Opening date: **23 April 2026** | Deadline date: **15 September 2026** | Single-stage

Open For Submission

Programme: **Euratom Research and Training Programme (EURATOM)** | Type of action: **EURATOM Cofund Actions**

Severe Accidents: vision beyond the WP 2026-27

- The Euratom Research mandate is to fund research on the safety of nuclear installations, the existing ones and the ones to come
- Severe Accidents consideration is crucial part of the safety assessment, this especially in the EU considering MS' nuclear regulations
- We note the need to continue funding research on SA for the existing NPPs and for the expected new designs: LW large-size, LW-SMRs, AMRs GEN-IV.

  - For the established technologies experimental data preservation should be considered
  - For the incoming new technologies experimental activity and code validation should be considered

The next Euratom Research and Training Programme 2028-2032

Proposal for a COUNCIL REGULATION
establishing the research and training programme of the European Atomic Energy Community for the period 2028-2032, complementing Horizon Europe, the Framework Programme for **Research and Innovation, and providing for the Community's** contribution to the ITER project, and repealing Regulation (Euratom) 2025/1304

- For the next MFF 2028-34 the EC proposed to double the Euratom Research budget from EUR 2 billion to EUR 4 billion for fusion and fission research.

Thank you for your attention!

Euratom research multilateral cooperation with international organizations IAEA and NEA-OECD

- IAEA Technical Working Group on Small and Medium Sized Modular Reactors (TWG-SMR)
  - Second Steering Committee Meeting of the International Network for Experiment and Code Validation Sharing – NEXSHARE 10-12 November 2025, IAEA, Vienna

- NEA-OECD Expert Group on Small Modular Reactors (EGSMR)
  - NEA-OECD EGSMR Workshop "SMR Safety Assessment: from Challenges to Achievements" 20-21 November 2025 NEA – Boulogne Billancourt (France)

Recent IAEA Activities Related to Severe Accidents

Presented by Alexei Miassoedov (IAEA/NENP/NPTDS)

The 12th European Review Meeting on Severe Accidents Research
May 18-22, 2026
Madrid, Spain

Outline

- Coordinated Research Projects (CRPs)
- Platforms, databases, publications
- Technical meetings
- AI for Nuclear

Division of Nuclear Power

Nuclear Power Engineering Section

The Section supports countries operating nuclear power plants or expanding their existing programmes to improve engineering, performance, management systems, human resource management, stakeholder involvement and technical infrastructure. It shares best engineering practices and innovations consistent with the global objectives of nuclear safety, security and non-proliferation. Read more →

Nuclear Power Technology Development Section

Fostering information exchange and collaborative research and development for advanced nuclear reactor technologies, this Section provides information to the IAEA's Member States on technology status and development trends for advanced reactor systems and their applications. Read more →

Nuclear Infrastructure Development Section

This Section is responsible for coordinating IAEA assistance to Member States considering or embarking on nuclear power programmes. It supports capacity-building, conducts review missions and offers guidelines, standards and workshops on developing the infrastructure for a safe, secure and sustainable nuclear power programme. Read more →

International Project on Innovative Nuclear Reactors and Fuel Cycles Section

The Section coordinates the activities of the membership-based International Project on Innovative Nuclear Reactors and Fuel Cycles (INPRO) to increase international cooperation on global nuclear energy sustainability, long term strategies and institutional and technical innovations for nuclear energy development and deployment. Read more →

Division Of Nuclear Installation Safety (NSNI)

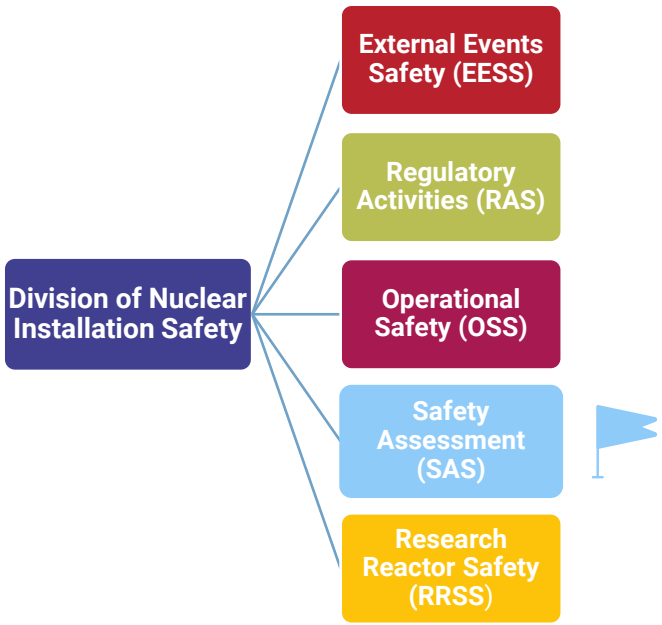

Three key missions:

- Development of **safety standards** for nuclear installations, and supporting publications
- Provision of **safety reviews and advisory services** to support the effective application of the safety standards
- Support to Member States in building and sustaining **capability and capacity** in nuclear safety

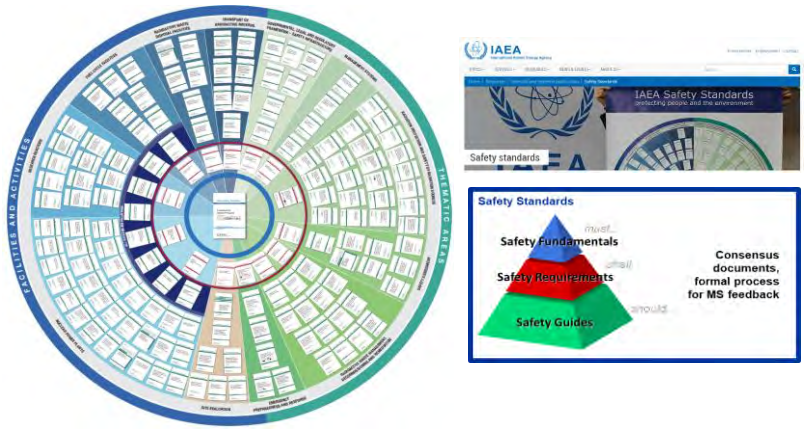

https://www.iaea.org/resources/safety-standards

A **new cycle of revision of the safety standards** under SAS responsibilities **has started** to cover:

- **All technologies of reactor designs** (water-cooled, non water-cooled, SMRs, microreactors, land-based or not, transportable reactors)
- **New applications used for civil purposes** (e.g. other than only electrical generation, as process heat, desalination, marine propulsion)
- **Interfaces between safety** and **security**, and safety and **safeguards**

Coordinated Research Activities

- Provide opportunities to engineers and scientists in developing and developed Member States to ***collaborate on research topics of common interest***
- ***Results of research activities supported by the Agency are disseminated to all Member States*** through national, international and IAEA scientific and technical publications, and other communications media
- ***118 active CRPs***

http://cra.iaea.org/cra/index.html

Completed in 2025: CRP on Developing a Phenomena Identification and Ranking Table (PIRT) and a Validation Matrix, and Performing a Benchmark For In-Vessel Melt Retention

CRP outputs:

- **TECDOC** aimed to harmonize the international understanding of scientific and technological bases underpinning crucial parts of the **safety demonstration of IVMR** (2026)
- **Technical Meeting** on the *Development of a Phenomena Identification and Ranking Table and a Validation Matrix, and Performing a Benchmark for In-Vessel Melt Retention* organised on **16–20 June 2025** to disseminate the outcomes

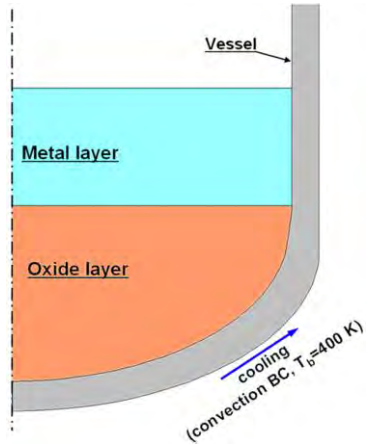

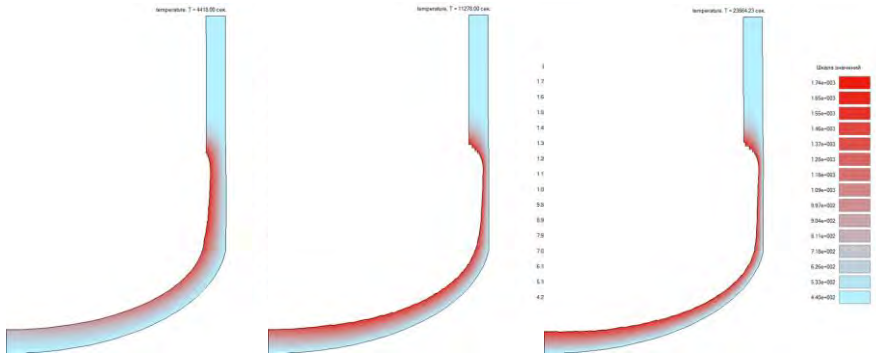

t = 200 s *t* =4 400 s *t* =23 500 s
Sequential states of heated/ablated vessel (start of loading from *t* =0)

CRP on IVMR: Key Messages, Conclusions, Future Work

- Significant progress achieved in the **harmonization of IVMR understanding, modelling, and validation**
- Strong integration of PIRT, VM, code benchmarking and reactor simulations
- Reactor design strongly impacts IVMR behaviour
  - Geometry, power level, and internal structures change dominant phenomena
- Current SA/CFD/FE codes show **good maturity for "standard" stratification cases**
- Uncertainty Propagation proved **highly valuable** and led to the concept of **Sensitive PIRT (SPIRT)** for quantitative ranking of phenomena
- Priority R&D needs:
  - Oxide–metal interaction kinetics during stratification inversion
  - Mechanical strength of ablated vessel wall under external cooling
- Additional model improvements needed:
  - Corium thermochemistry
  - Focusing effect in thin metal layers
  - Heat transfer in flat oxide pools
  - Radiative heat transfer modelling
  - Corium oxidation & steel corrosion
  - Debris bed melting / molten pool formation

New CRP on Ex-Vessel Corium Behaviour and Cooling (2026–2030)

- **Characterize state-of-the-art knowledge:** to assess key phenomena in EVCC, evaluate the robustness of current understanding for ex-vessel mitigation strategies, and identify R&D priorities to address uncertainties in initial and boundary conditions
- **Review experimental data:** assess available experimental data for model validation and identify gaps, including recent findings post-Fukushima Daiichi accident
- **Benchmark exercices:** comparing experimental data to models, focusing on key phenomena to identify deviations. The two-step approach involves:
  - Analysing open results under Fukushima-specific conditions to optimize parameters
  - Applying those parameters in a Fukushima-based scenario with spreading and MCCI phases, followed by sensitivity analyses
- **Organise training course:** develop a training course on applying severe accident codes to ex-vessel accident scenarios
- **Call for proposals open.** First RCM meeting planned on 3–6 November 2026.

CRP Expected Outcomes

1. **Harmonised understanding** of EVCC phenomena through a consensus-based PIRT.
2. **Consolidated experimental and plant data** for model validation and identification of remaining gaps.
3. **Improved modelling and simulation capabilities** and shared methodologies among Member States.
4. **Coordinated benchmark exercises**, including scenarios with accident management measures and a Fukushima-type accident case.
5. **Training and capacity-building materials** to support Member State application of severe accident codes to ex-vessel scenarios.

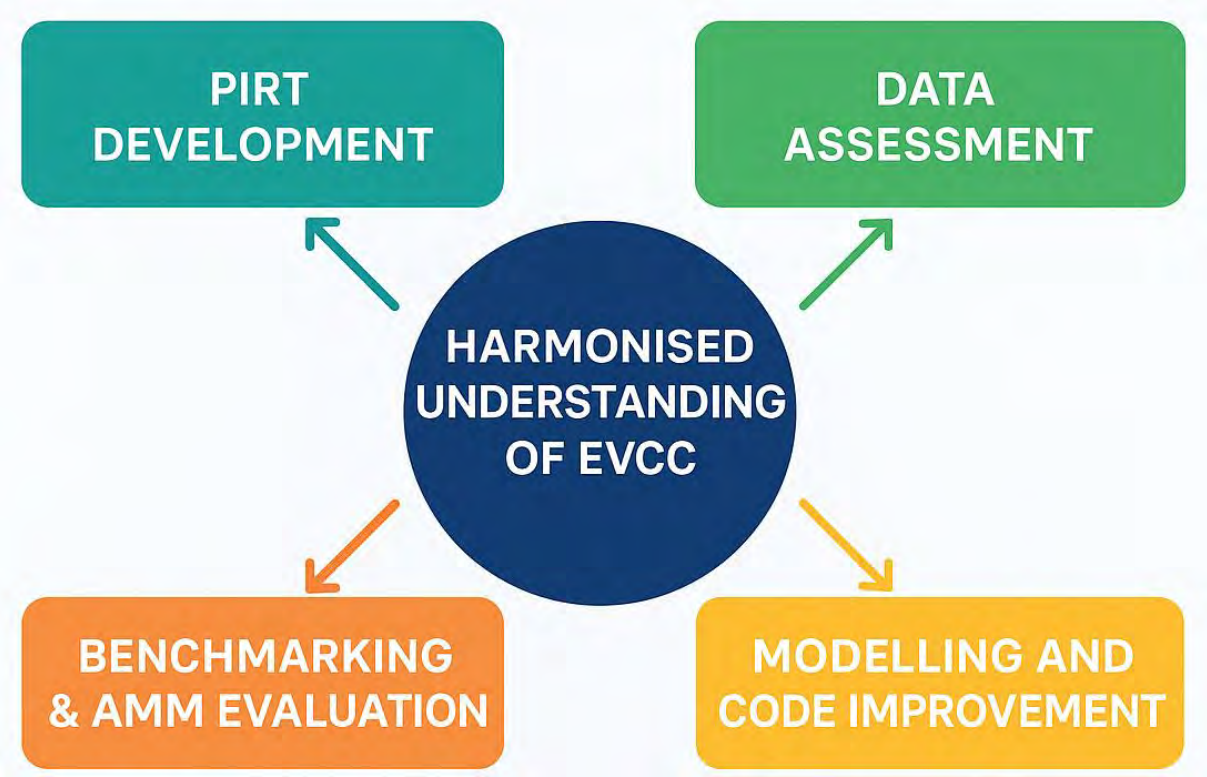

Background: Nuclear Harmonization and Standardization Initiative (NHSI)

Effective Global Deployment of **Safe and Secure** Advanced Nuclear Reactors

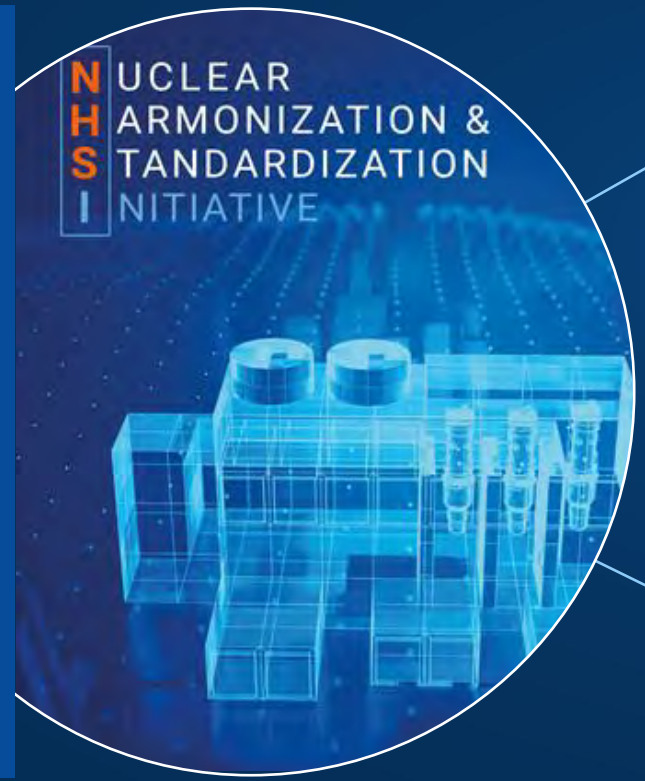

Harmonization of Regulatory Approaches Track

Advance the development of a Global Framework for Advanced Reactors Reviews (GFARR)

[Nuclear Harmonization and Standardization Initiative (NHSI)]

Harmonization and **S**tandardization of Industrial Approaches Track

Develop more standardized industrial approaches for SMR manufacturing, construction and operations to reduce licensing efforts, costs and deployment timelines.

- Regulators
- Governments
- Technology Holders
- Operators and other end-users
- International Organisations and Associations

Experimental Testing and Validation for Design and Safety Analysis Computer Codes - NEXSHARE Network

SMRs may require extending the validated boundaries of existing codes or include physical phenomena for which the experimental data lacks. The significant resources for validation or experimentation is a challenge to a safe and secure timely deployment of SMRs.

To address these challenges, the IAEA established **NEXSHARE**, a technical forum for global cooperation and resource sharing for experiments and code validation.

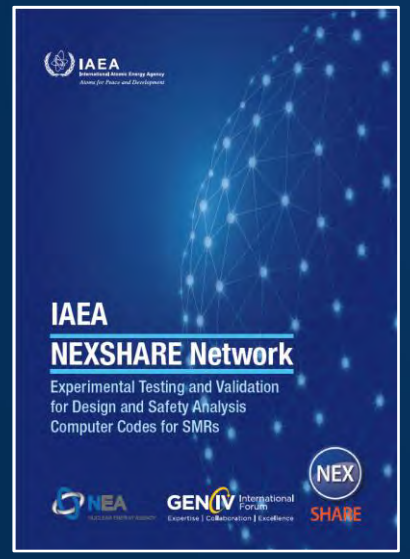

The Network is a collaboration with the **NEA**, the **Gen-IV Forum** and the **European Commission**.

- ✓ **Members**: Vendors, Experimental Facilities, TSO, International Organizations.
- ✓ **Events**: Workshops, webinars, SC meetings and Focus-Groups meetings.
- ✓ **Web interface**: Information on the topic, opportunity for collaborations, **Experimental Facility Catalogue.**
- ✓ **Focus Groups**: Work specific to a reactor family.

IAEA NEA NUCLEAR ENERGY AGENCY GEN IV International Forum European Commission

NEXSHARE's Mission and Objectives:

- Information Sharing on Experimental Facilities and Programmes.
- Enhance utilization of existing experimental facilities.
- Resources optimization for SMR code validation and experiments.
- Greater confidence on data and codes used in safety cases.

Experimental Facility Catalogue & Focus Groups

Experimental Facility Catalogue: Through filtering and search, members can find facilities that can be contacted to access existing data or generate new data needed for code validation of SMRs and Advanced Reactors.

Focus: Thermalhydraulics (separate & integral effects), neutronics, component/feature, severe accident & containment

LW-SMR

HTGR

LMFR

MSR

Integration of SANIS in NEXSHARE and Collaboration with SEAKNOT:

- In order to ensure maintenance and upgrade, it has been decided to integrate the SANIS database in NEXSHARE.
- Facilities will have to provide concurrence and additional information.
- In parallel, SEAKNOT is updating its Severe Accident Facility Catalogue.
- To avoid duplication of effort and requests to facilities, collaboration between SEAKNOT and NEXSHARE is ongoing for EU facilities.

IAEA NEXSHARE Network

Experimental Testing and Validation for Design and Safety Analysis Computer Codes for SMRs

EXPLORE THE EXPERIMENTAL FACILITIES >

Welcome to the IAEA NEXSHARE

Copyright © 2026 International Atomic Energy Agency (IAEA). All rights reserved.

IAEA SAMG-D toolkit

SAMG-D
Severe Accident Management Guideline Development toolkit

- **Module 1** Fundamentals of reactor safety
- **Module 2** Severe accident challenges and mitigation strategies
- **Module 3** Severe accident management guidelines
- **Module 4** Implementation, requirements and infrastructure

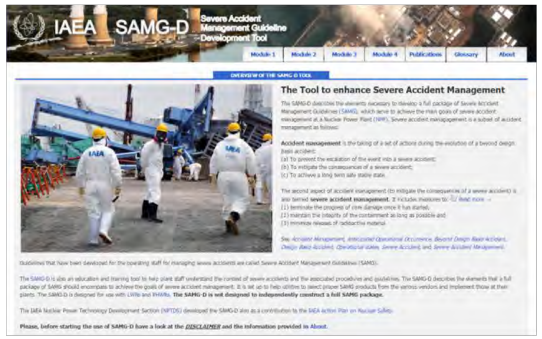

Nine Training Workshops

Toolkit revision planned in 2026-2027 (jointly with NSNI)

- Ensuring coherency with IAEA Specific Safety Guide SSG 54
- Information for BWRs, including practical examples of SAMG for BWRs
- Include additions or changes regarding CANDU reactors
- Review and update the sections focusing on computer codes used for the accident analysis
- Update the toolkit based on advances in the state-of-the-art revision of the list of references

10th SAMG-D Toolkit training workshop: 30 November – 4 December 2026, IAEA (in-person)

Publications

- Analysis and Modelling of Severe Accidents for Liquid Metal Fast Reactors, IAEA-TECDOC-2079 (2025)
- Progress in the Performance Assessment and Regulation of Passive Systems in Advanced Nuclear Power Plant Designs, TECDOC, jointly with NSNI (2026)
- Ex-vessel Phase of Severe Accidents in Water Cooled Reactors, TECDOC (2026)
- Artificial Intelligence Methods and Research Needs for the Design and Qualification of Advanced Reactors, TECDOC (2027)

TECDOC Ex-Vessel Phase of Severe Accidents in Water-Cooled Reactors

Publication and scope

- Comprehensive IAEA reference on ex-vessel severe accident phenomena in water-cooled reactors (PWR, BWR, CANDU).
- Covers accident progression after RPV failure, corium behaviour, containment challenges and mitigation strategies.
- Integrates experimental evidence, modelling tools, plant applications and lessons from Chernobyl and Fukushima.

Main objectives

- Consolidate current state of knowledge on ex-vessel corium behaviour.
- Review analytical codes, experiments and validation approaches.
- Support severe accident management and containment protection strategies.
- Identify remaining uncertainties and R&D priorities.

Structure

- Severe accident progression and transition to ex-vessel phase
- Forensic insights from Chernobyl and Fukushima accidents
- Key phenomena: melt release, FCI, debris beds, spreading, MCCI, FP behaviour
- Experimental programmes and large-scale testing databases
- Numerical tools and integrated severe accident codes
- Plant implementation examples and SAM measures
- Remaining issues, modelling gaps and future research needs

Some key messages from conclusions

- Fukushima investigations continue to reveal new issues and improve understanding of ex-vessel corium behaviour.
- Further coordinated international R&D, experiments and model validation are required to reduce uncertainties in corium cooling and containment protection.

Planned Schedule

The safety standards → below will incorporate a **new definition of severe accidents** (DEC-B), that will apply to all technology designs (w/o impact for WCRs)

Requirements and Safety guides	2025				2026				2027				2028				2029				2030				2031				2032				2033				2034				2035			
	Q1	Q2	Q3	Q4	Q1	Q2	Q3	Q4	Q1	Q2	Q3	Q4	Q1	Q2	Q3	Q4	Q1	Q2	Q3	Q4	Q1	Q2	Q3	Q4	Q1	Q2	Q3	Q4	Q1	Q2	Q3	Q4	Q1	Q2	Q3	Q4	Q1	Q2	Q3	Q4	Q1	Q2	Q3	Q4
SSR-2/1 (Rev.1) Design requirements	1	2	3		4	4	5	5	5	5	5	5	5	6	7	7	8	8	8	8	9, 10	11	12	12	13	14																		
SSG-30 Safety Classification of SSCs					1	2	3		4	4	5	5	5	5	5	6	7	7	8	8	9, 10	11	12	12	14																		
SSG-34 Electrical systems								1	2	3	4	4	5	5	5	5	5	6	7	7	8	8	9, 10	11	12	12	14																		
SSG-38 Construction of Nuclear Installations										1	2	3	4	4	5	5	5	5	5	6	7	7	8	8	9, 10	11	12	12	14																
SSG-39 Instrumentation and control								1	2	3	4	4	5	5	5	5	5	5	5	6	7	7	8	8	9, 10	11	12	12	14																
SSG-51 Human Factors Engineering												1	2	3	4	4	5	5	5	5	5	5	5	6	7	7	8	8	9, 10	11	12	12	14										
SSG-52 Reactor core design					1	2	3		4	4	5	5	5	5	5	5	5	6	7	7	8	8	9, 10	11	12	12	14																		
SSG-53 Reactor containment					1	2	3		4	4	5	5	5	5	5	5	5	6	7	7	8	8	9, 10	11	12	12	14																		
SSG-56 Reactor coolant					1	2	3		4	4	5	5	5	5	5	5	5	6	7	7	8	8	9, 10	11	12	12	14																		
SSG-62 Auxiliary systems														1	2	3	4	4	5	5	5	5	5	5	5	6	7	7	8	8	9, 10	11	12	12	14								
SSG-63 Fuel handling and storage								1	2	3	4	4	5	5	5	5	5	6	7	7	8	8	9, 10	11	12	12	14																		
SSG-64 Internal hazards														1	2	3	4	4	5	5	5	5	5	6	7	7	8	8	9, 10	11	12	12	14										
SSG-69 Equipment qualification																		1	2	3	4	4	5	5	5	5	5	6	7	7	8	8	9, 10	11	12	12	14						
SSG-88 Practical elimination																						1	2	3	4	4	5	5	5	5	5	6	7	7	8	8	9, 10	11	12	12	14		
SSG-90 Radiation protection																		1	2	3	4	4	5	5	5	5	5	6	7	7	8	8	9, 10	11	12	12	14						
SSG-61 Safety Analysis report																		1	2	3	4	4	5	5	5	5	5	6	7	7	8	8	9, 10	11	12	12	14						
SSG-XX Transportable NPPs: Design																1	2	3	4	4	5	5	5	5	5	6	7	7	8	8	9, 10	11	12	12	14								
GSR Part 4 (Rev.1) Safety assessment					1	2	3		4	4	5	5	5	5	5	6	7	7	8	8	9, 10	11	12	12	13	14																		
SSG-2 (Rev.1) Deterministic safety analysis												1	2	3	4	4	5	5	5	5	5	6	7	7	8	8	9, 10	11	12	12	14												
SSG-3 (Rev.1) Level 1 PSA																																											
SSG-4 (Rev.1) Level 2 PSA	12	12	14																													1	2	3	4	4	5	5	5	5	5	6	7	7
SSG-X (L3PSA) Level 3 PSA	2	3	4	4	5	5	5	5	5	6	7	7	8	8	9, 10	11	12	12	14																								
SSG-X (DS537) Safety demonstration	7	8	9, 10	9, 10	11	12	14																																				
SSG-25 (Rev.1) Periodic safety review	7	7	8	9, 10	9, 10	11	11	12	12	14																																	
SSG-54 Accident management												1	2	3	4	4	5	5	5	5	5	6	7	7	8	8	9, 10	11	12	12	14												
SSR-XX (New safety requirements Fusion)												1	2	3	4	4	5	5	5	5	5	6	7	7	8	8	9, 10	11	12	12	13	14											

Revision of SAFETY REPORTS SERIES No. 32 (2004) (in pre-print)

Revision 1, entitled "**Development and Implementation of Severe Accident Management Programmes for NPPs**":

- **Integrates lessons learned from Fukushima Daiichi accidents** (external events and common cause failures, review training and continuous improvement, multi-units and SFP, containment integrity, H2 management, I&C systems, heat removal and power supply systems)
- Safety Standards used as inputs for revising the report: **SSR-2/1 (Rev.1)**, **SSR-2/2 (Rev.1)**, **SSG-54** and **Member States enhanced AMPs**
- **Significant enhancements** in the report:
  - Consideration of multi-unit sites and spent fuel pool, inclusion of non-permanent equipment
  - Equipment and instrumentation reliability for accident conditions
  - Guidelines for transition between EOPs and SAMGs
  - Periodic Review and revision of Accident Management Programme
  - Rules for usage of SAMGs
  - Role of Regulatory Body in the development and implementation of SAMGs

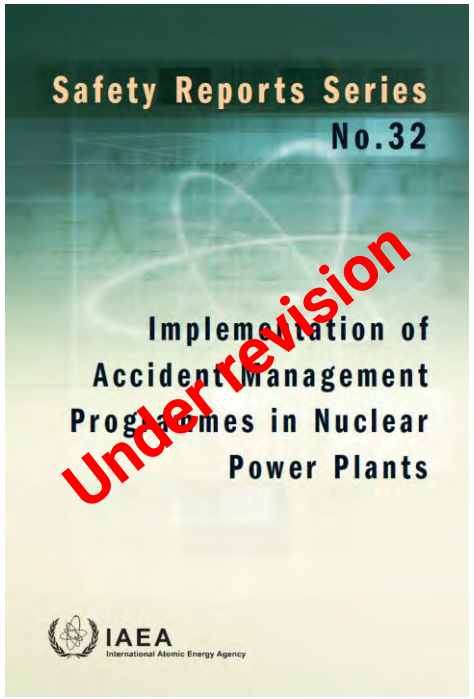

2024–2025 Technical Meetings

- Technical Meeting on Capitalizing on Artificial Intelligence Analysis to Accelerate the Technological Development of Evolutionary and Innovative Reactor Designs (4–7 November 2024)
  - 107 registered participants from 46 Member States, 33 technical presentations
- Technical Meeting on Progress in the Performance Assessment and Regulation of Passive Safety Systems in Advanced Nuclear Power Plant Designs (10-14 March 2025)
- Technical Meeting on Advancements and New Developments in Water Cooled Reactor Designs (6–9 May 2025)
- Technical Meeting on the Development of a Phenomena Identification and Ranking Table and a Validation Matrix, and Performing a Benchmark for In-Vessel Melt Retention (16–20 June 2025) to disseminate the outcomes of a CRP

2026–2027 Technical Meetings

- Technical Meeting on Policies and Strategies for the Long-Term Operation of Nuclear Power Plants, NPES (IAEA, 16–18 June 2026)
- Technical Meeting on Considerations for the Deployment of AI, NPES (IAEA, 27–31 July 2026)
- Technical Meeting on Artificial Intelligence Integration in Nuclear Operations: Bridging Intelligence and Operations for a Safe, Secure, and Resilient Nuclear Power Industry, NPES (IAEA, 5 Nov–4 Dec 2026)
- Technical Meeting on Application of Advanced Computational Methods and Codes for Design and Analysis of Advanced WCRs (IAEA, Q2/2027)
  - To share advances in computational methods (high-fidelity simulations, reduced-order models, system-CFD coupling, AI tools) for analysing and optimizing advanced WCRs, with emphasis on validation, integration, and experimental support.

IAEA Collaborating Centre on AI (CSOI, Purdue University, USA) 2023-2027

Facilitate programmatic activities and knowledge sharing in AI for nuclear power (AI4NP) to advance reactor designs and support industrial deployment of AI solutions at operating NPPs

Develop validation approaches for AI concepts in reactor technology, real-time operation, maintenance, design optimization, safety analysis, and accident management

Support human capacity building with training and educational courses on AI basics, opportunities, challenges, and applications for nuclear power software development, safety analysis and accident management

Joint IAEA-ICTP Workshop on Artificial Intelligence and Machine Learning in Advancing Nuclear Engineering and Technology: from Theory to Practice

- Comprehensive understanding of AI and ML concepts and applications in nuclear engineering
- Knowledge-based and data-based AI, ML paradigms, and decision support for optimal design, operation, maintenance, safety analysis, and risk assessment in nuclear technology
- Various ML approaches, including decision trees, tree ensembles, artificial neural networks, and data analytics
- Hands-on exercises with datasets to apply AI and ML in nuclear engineering problems
- 10–14 March 2025, ICTP, Trieste, Italy
- Planned in 2027

TECDOC Artificial Intelligence Methods and Research Needs for the Design and Qualification of Advanced Reactors

Objective:

- Identify key R&D areas where AI can accelerate advanced and FOAK reactor design
- Define technical gaps in modelling, validation, and data
- Propose benchmarking, uncertainty, and evidence-building approaches
- Provide a roadmap to support Member States in prioritizing AI integration

Scope:

- How AI R&D outputs should be structured to enable subsequent deployment work (deployment considerations covered in the NES No. NR-T-1.26)
- Targets the upstream technical R&D required for reactor design
- Education and capacity building
- Will provide the essential technical basis that directly enables and complements the downstream deployment guidance

Structure (Preliminary Table of Contents):

- Introduction (background, objectives, scope)
- Overview of AI methods for advanced reactor R&D
- Modelling and simulation (complexity reduction, multi-scale coupling)
- Inference and uncertainty quantification for FOAK validation
- Digital twin and document intelligence (use cases, limitations)
- Design optimization and automation
- Materials and fuel reload/management applications
- Data governance for R&D workflows
- Benchmarking and community exercises
- Education and training needs
- Recommendations and roadmap
- Conclusions

Resolutions Adopted at the 69th IAEA General Conference (2025)

Page 8, Point (s): Stressing the importance of…strengthening long-term research **programmes to learn about severe accidents**…

Page 13, Point (i): … activities for enhancing Member State capabilities in modelling, predicting and improving the **understanding of the behaviour of current and advanced nuclear fuel in normal operation and under accident conditions**.

P.14, Point 73: Encourages the Agency to facilitate the **exchange of results of research and development on severe accident management strategies** for nuclear power plants

P.14, Point 75: Encourages Member States to develop as necessary and implement **severe accident management guidelines** taking into account, inter alia, lessons learned from the Fukushima Daiichi nuclear power plant accident, and **requests the Secretariat to support their efforts through training workshops.**

1. **New CRP** on Ex-Vessel Corium Behaviour and Cooling.

2. **Yearly training workshops with the IAEA SAMG-D toolkit** are being organised by the IAEA to facilitate the development of severe accident management guidelines in Member States accounting lessons learned from Fukushima accident.

TOPICS

- Making the most of past experience
- Driving safety forward and reassessing safety concepts
- Using innovative technologies to enhance safety
- Taking international cooperation to the next level

https://www.iaea.org/events/tic2026

Acknowledgments

This presentation includes information kindly provided by colleagues from the IAEA Division of Nuclear Power and Division of Nuclear Installation Safety.

Their support is gratefully appreciated!

Thank you!

DISCLAIMER

This is not an official IAEA publication. The material has not undergone an official review by the IAEA. The views expressed do not necessarily reflect those of the International Atomic Energy Agency or its Member States and remain the responsibility of the author.

Although great care has been taken to maintain the accuracy of information contained in this presentation, neither the IAEA nor its Member States assume any responsibility for consequences which may arise from its use.

The use of particular designations of countries or territories does not imply any judgement by the IAEA as to the legal status of such countries or territories, of their authorities and institutions or of the delimitation of their boundaries.

The mention of names of specific companies or products (whether or not indicated as registered) does not imply any intention to infringe proprietary rights, nor should it be construed as an endorsement or recommendation on the part of the IAEA.

NEA
NUCLEAR ENERGY AGENCY

Enabling Nuclear Safety Research

NEA Frameworks and Databases

Martina ADORNI, Markus BEILMANN, Ahmed BENTAIB,

Nuclear Safety Technology and Regulation
OECD Nuclear Energy Agency (NEA)

© 2026 OECD / NEA

The Agency at-a-glance: premier international platform co-ordinating nuclear technology, policy, regulation, research and education

34

NEA member countries

82%

The world's installed nuclear capacity represented in the NEA

3500+

Global experts participating in NEA activities on a regular basis

Argentina
Australia
Austria
Belgium
Bulgaria
Canada
(Chile)
(Colombia)
(Costa Rica)
Czechia
Denmark
(Estonia)
Finland
France
Germany
Greece
Hungary
Iceland
Ireland
(Israel)
Italy
Japan
Korea
(Latvia)
(Lithuania)
Luxembourg
Mexico
Netherlands
(New Zealand)
Norway
Poland
Portugal
Romania
Russia (suspended)
Slovak Republic
Slovenia
Spain
Sweden
Switzerland
Türkiye
United Kingdom
United States

30 members both OECD and NEA members
4 NEA-only members
8 OECD-only members, not NEA

Non-member Partners: (May be invited to attend meetings of NEA bodies) :

Brazil
China
Ghana
India
Indonesia
Kenya
Peru
Philippines
Singapore
South Africa
Ukraine
United Arab Emirates
Viet Nam

Chinese Taipei

© 2026 OECD / NEA

Addressing technical safety assessment challenges: CSNI main focus

Expertise building mechanism for trust

Committee on the Safety of Nuclear Installations (CSNI)

- CSNI Progamme Review Group (CSNI PRG)
- Working Group on Risk Assessment (WGRISK)
- Working Group on Analysis and Management of Accidents (WGAMA)
- Working Group on Integrity and Ageing of Components and Structures (WGIAGE)
- Working Group on Human and Organisational Factors (WGHOF)
- Working Group on Fuel Safety (WGFS)
- Working Group on Fuel Cycle Safety (WGFCS)
- Working Group on External Events (WGEV)
- Working Group on Electrical Power Systems (WGELEC)
- Expert Group on Small Modular Reactors (EGSMR)

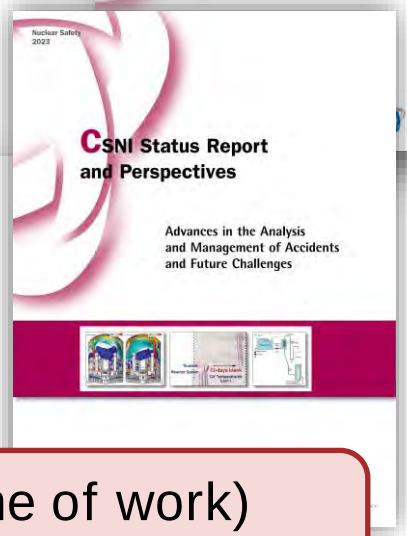

Long-Term Operation of Nuclear Power Plants

Small Modular Reactors

Safety assessment approaches and analyses of accidents: technical bases methodologies and tools

Bases to engage modernisation of regulatory approaches

Human aspects of nuclear safety

Code Validation Matrix update

CONTRIBUTORS to POW (programme of work) and BENEFICIARIES of its results

Challenges ahead which need CSNI experts' support

- Support future research frameworks.
- Data preservation and maintaining and dissemination of technical knowledge.
- Safety applications and safety assessment for Disruptive, Innovative and Emerging Technology.

Enabling conditions for safety assessment: a strong Policy of Excellence in Research

© 2026 OECD / NEA

1. Which data do we need - and for what purpose?

©2026 OECD/NEA

Indispensable, while great difficulties in investigation due to harsh conditions

Major Activities for Reactor Severe Accident Safety

Specialist Meetings and Workshops	International Standard Problems (ISPs) and Benchmarks	CSNI Code Validation Matrices (CCVMs)	Accident Management (AM)	Long-term Management
In-depth discussion = Brain-Storming on Phenomena	Investigation of Code and User Capabilities	Confirmation of Code & Model Capability against Experiment Data	Confirmation of Effectiveness of Reactor Countermeasures	Confirmation of Effectiveness of Reactor Countermeasures

Common to three areas

© 2026 OECD / NEA

CSNI Code Validation Matrix (CCVM)

Update & Extension need resources

Before **CCVM** and **STRESA**, there was no coordinated effort to preserve severe accident datasets.

Assess the adequacy, quality and completeness of the experimental database to properly characterise the behaviour of new advanced designs and to validate simulation tools

Current SET:
185 test facilities
1094 tests identified
67 thermal-hydraulic phenomena, now 116

1994

2022

Perspectives

- Established in 1987 for integral effect tests (ITF) and separate effects tests (SET) on LWR accidents
- Supplemented later for severe accident phenomena (in-vessel and containment), and VVER

- Necessary UPDATE for existing nuclear reactors and related technologies
- Necessary EXTENSION to emerging challenges of evolutionary and innovative reactor designs and nuclear technologies, including SMRs
- **Cooperation with IAEA NHSI NEXSHARE** collaborative network, workshops
- **Cooperation with EC SEAKNOT**

NEX SHARE

Data Preservation and Knowledge Transfer

Safe operation of nuclear power plants is supported with Safety Analyses based on a large volume of experimental data.

Task group *Harmonization of Methodologies for Thermal-Hydraulics Experimental Meta-Data Preservation, Collection and Qualification (THEMPo), to develop* High Level Guidance to be developed for practical applications

Call for ACTION: We are looking for new Leader(s) for THEMPO

THICKET to transfer implicit, explicit and tacit thermal-hydraulic and severe accident knowledge, competence and experience acquired through CSNI activities

Covers safety-relevant fields
of T/H, CFD, SA, fuel safety, PSA (Probabilistic Safety Assessment) and NEA JPs (Joint Projects) including 1F-related ones

Recommendations from the CSNI/SEGPD regarding preservation of key experimental data sets

© 2025 OECD/NEA

2. Data needs to be generated

©2026 OECD / NEA

NEA Joint Nuclear Safety Research Projects

While already addressed in recent and ongoing projects, future projects place ***greater emphasis on SMR designs and passive safety system innovations.***

Status in 2026

60 projects completed. Over **65 years** of collaborative nuclear safety research. **400 years** of cumulative experimental data and expertise. **81 projects** completed or active.

Nuclear Safety Joint Projects Count

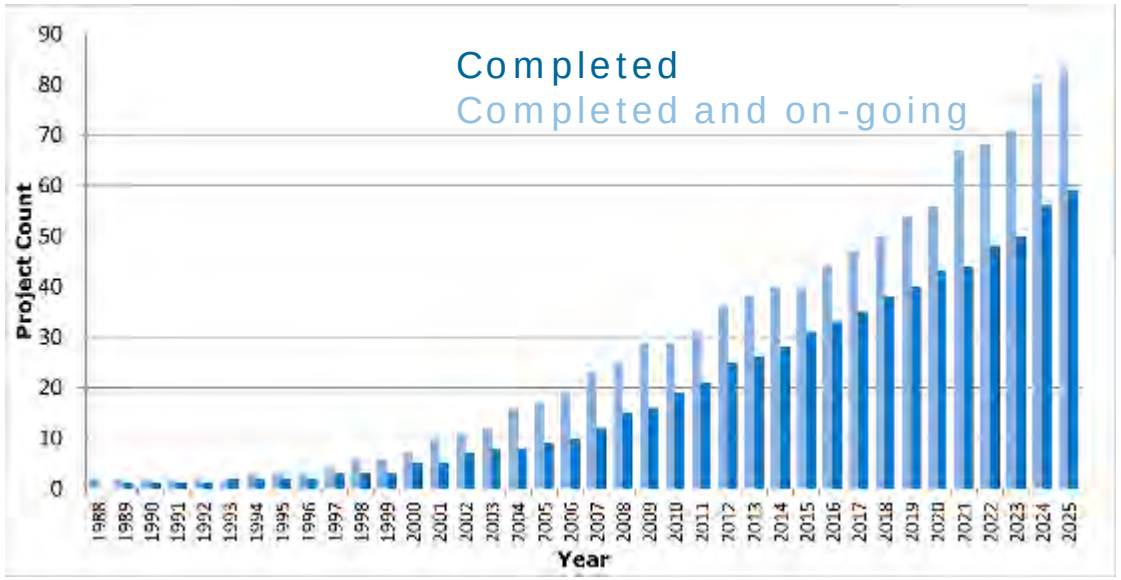

Nuclear Safety Joint Projects, Count per Technical Areas

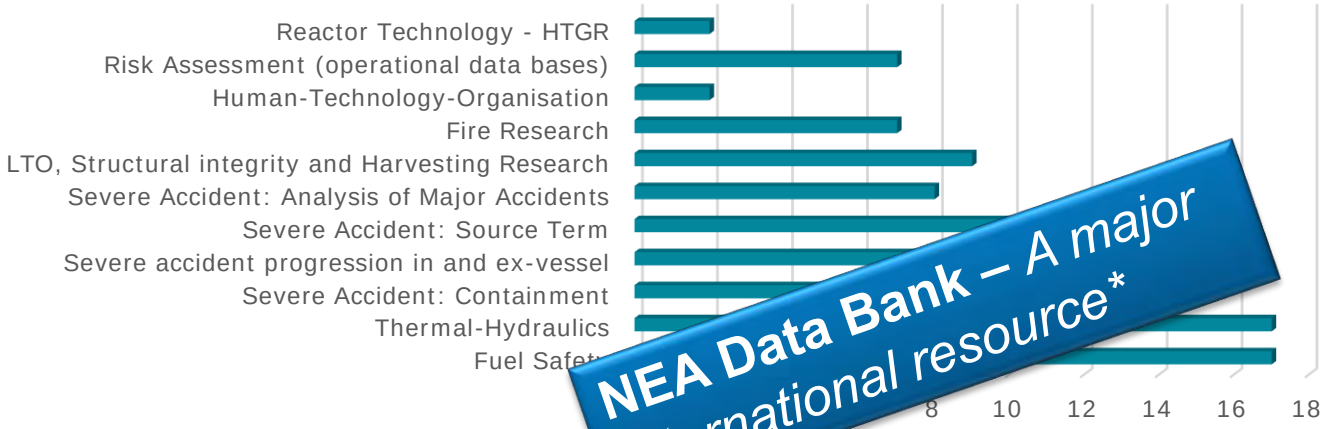

NEA Data Bank – A major international resource*

Advancing Nuclear Safety

NEA joint projects accelerate consensus on key safety challenges through shared expertise and cost-effective research

Urgent actions needed in nuclear safety research to enable safe deployment of nuclear reactors

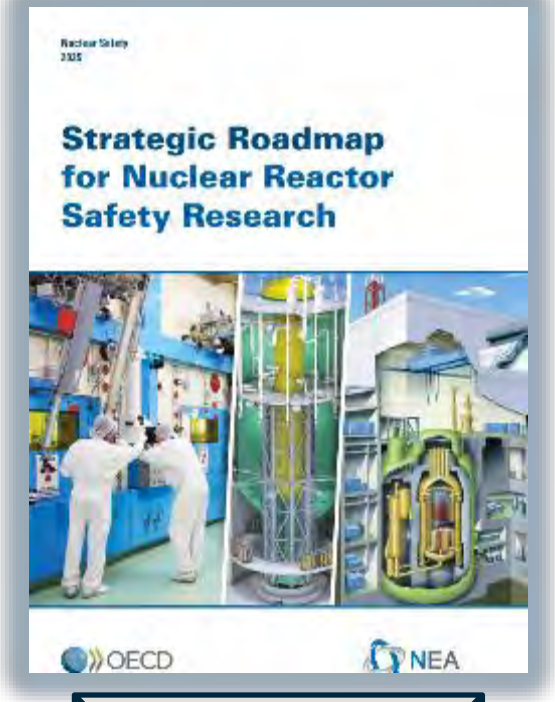

Download here

To mitigate loss of critical research capabilities: a strategic investment in public safety, environmental protection and long-term energy security

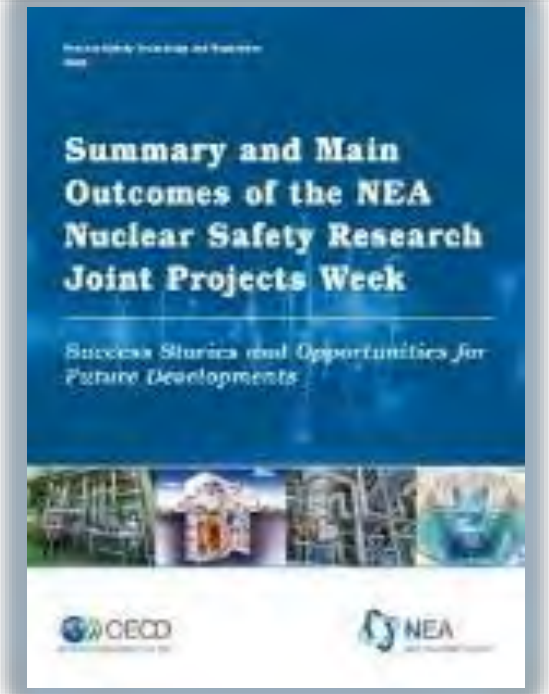

Download here

To advance nuclear safety through global cooperation: need for integrated frameworks in key areas, e.g. TH, SA

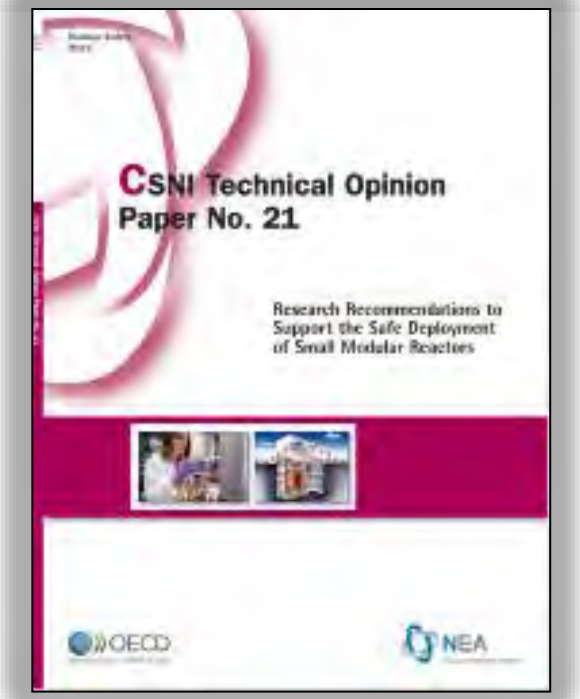

Download here

To assess sufficiency of technical bases for SMR safety evaluations: develop cured/validated data ecosystems for V&V of advanced models (e.g. CFD)

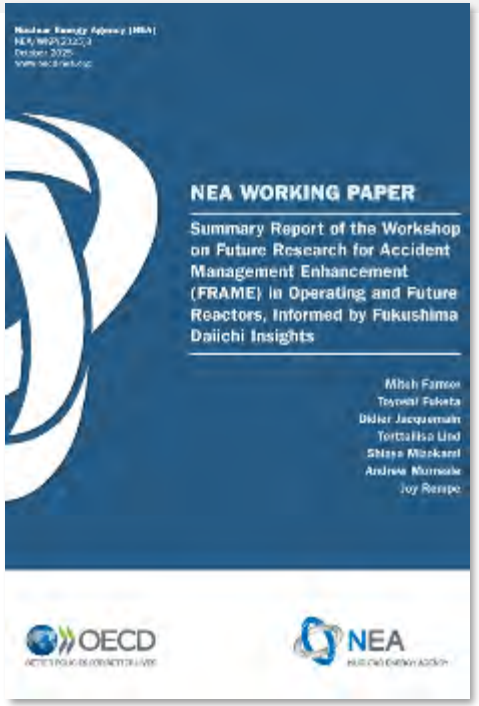

Download here

To expand research capabilities for SMRs: adapt existing capabilities and integrate new capabilities in collaborative frameworks

© 2025 OECD/NEA

Targets & Recommendations Severe Accidents Management

- Assess the efficiency and reliability of SA prevention and mitigation for LTO
- Study practical elimination of loss of containment for SMRs and advanced reactors

Analyses to be conducted and shared

including risk and uncertainty analyses, to identify and characterise plausible accident scenarios which can threaten the containment of radioactivity in advanced reactors (different containment concepts, new safety systems, including passive ones, and components with no or limited operating experience)

NEA to develop a framework

to coordinate experimental projects, support code development and validation, provide training, and preserve critical data for long-term use

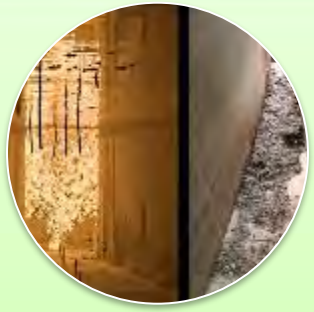

Stakeholders to support maintaining, modernising research facilities and integrating new ones

within a collaborative framework tailored for the safety demonstration of advanced reactor designs and systems and with integrating insights from the Fukushima-Daiichi accident

Include dedicated severe accident experiments as an integral part of pre-deployment testing of advanced fuels, claddings, and materials,

modelling of core degradation, fission product behaviour, and source term estimation

© 2025 OECD/NEA

Strategic Pathways for Inclusive, Globally Aligned Research in Key Nuclear Safety Research Areas

involving

Ongoing discussions and development of new networks and platforms

TH network and platform ATHENA

Harvesting components

NEA / ATHENA

- Global platform for nuclear TH safety research.
- Focus: water-cooled reactors, SMRs, advanced designs.
- Goals: sustain facilities, validate codes, share data.
- Add-ons: training, data preservation, new applications.
- Impact: safe, efficient, innovative nuclear expansion.

WORKSHOP Building the ATHENA Framework, 10 - 11 September 2026 at NEA https://www.oecd-nea.org/jcms/pl_116224/

3. Data needs to be used

©2026 OECD / NEA

International Standard Problems (ISPs) and Benchmarks

- Ongoing
  - ISP-54 on In Vessel Melt Retention (CNPE) – under preparation
  - ISP-53 based on the IRSN reflooding COAL experiments (IRSN)
  - ISP-52 on PKL experiment on Multiple SG U-tube rupture related to DEC-A scenario that may occur in the hypothetical scenario of a combined MSLB and MSGTR (ENEA, Framatome)
  - ISP-51 on ACME experiment on advanced core cooling mechanisms (HUST University)
  - ATRIUM = Application Tests for Realisation of Inverse Uncertainty quantification and validation Methodologies in thermal-hydraulics (T/H) (CEA)
  - Thermal mixing and fatigue in a T-junction connected dead-end leg – benchmarking and experimental validation of CFD (Vattenfall, ETZH, PSI)
- Completed recently
  - Fluid-structure interaction (FSI) benchmark to validate coupled CFD & CSD calculations based on OKBM experiments (OKBM)
  - PERSEO benchmark – as one of passive system (ENEA)
  - Cold Leg Mixing CFD – Uncertainty Quantification (UQ) (Texas A&M)
  - GEMIX mixing layer test for CFD prediction and UQ (PSI)
  - PREMIUM Post-BEMUSE Reflood Model Input Uncertainty Methods Benchmark (CEA, CSN, GRS, IRSN, UPC, UNIPI)

An ideal platform for developing and disseminating best modelling practices!

Conclusive remarks

- A unique non-political, member/expert-driven forum
  - A programme of work carried out by its members
  - Contribute, not just participate — and benefit

- From data to safety: an integrated approach
  - PRESERVE and qualify legacy and future data, and avoid loss of unique severe accident experimental capabilities
  - GENERATE new data through Joint Projects and improve coordination with new experimental frameworks
  - USE the data, strengthen code validation, uncertainty quantification and safety demonstration, enhance knowledge transfer for the next generation
- Engage actively in in NEA activities: CCVM, benchmarks, technical reports, workshops, joint projects and frameworks

Nuclear Safety Research is a Long-Term Challenge

© 2025 OECD/NEA

Acknowledgments

The NEA would like to express its sincere appreciation for the exceptional contributions of individuals who played key roles in the execution and success of the research activities outlined in this presentation.

Special recognition is given to the bureau members including past chairs, task leaders, contributors and members, project operating agents (OAs), program review group (PRG) chairs, management board (MB) chairs, benchmark coordinators, joint analytical workshop chairs and participants for their dedicated efforts and invaluable support throughout the process.

© 2026 OECD / NEA

Thank you for your attention!

Martina ADORNI

Nuclear Safety Technology and Regulation Division

OECD Nuclear Energy Agency

martina.adorni@oecd-nea.org

On behalf of those individuals who had a key role in the conduct and success of the activities described in this presentation.

© 2026 OECD / NEA

The 12th European Review Meeting on Severe Accidents Research

May 18-22, 2026, Universidad Carlos III de Madrid, Madrid, Spain

TECHNICAL SESSION 2.4: IN-VESSEL CORIUM AND DEBRIS COOLABILITY

Chairs: N. Seiler (CEA), A. Miassoedov (IAEA)

ID067	**A path forward to improve corium thermodynamic assessment by using surface tension data: results for the U-O binary system** R. Le Tellier (CEA)	Paper Presentation
ID109	**Estimation of the cooling rate of U-Zr-Fe-Cr-O sample which underwent melting** Y. Endo (Nippon Nuclear Fuel Development co., Ltd.)	Paper Presentation
ID059	**Critical Heat Flux in Pool boiling configuration for In-Vessel Melt Retention: literature review and recents experiments in THS-15 facility** K. At Khen (EDF)	Paper Presentation
ID145	**BWR RPV Lower Head Penetration Failure Caused by Eutectic Reactions with Zr-Rich Simulated Metal: ELSA-3 Test** K. Shimomura (JAEA)	Paper Presentation
ID102	**Investigation on In-Vessel Phase of BDB-LOCA of Supercritical Water-cooled Fast Reactor** Y. Kobayashi (Waseda University)	Paper Presentation

A PATH FORWARD TO IMPROVE CORIUM THERMODYNAMIC ASSESSMENT BY USING SURFACE TENSION DATA: RESULTS FOR THE U-O BINARY SYSTEM

A. Tourneix, Y. Miot, R. Le Tellier,
CEA, DES, IRESNE, DTN, SMTA, LMAG, Cadarache
F-13108 Saint Paul-lez-Durance, France
arthur.touneix@cea.fr, yanis.miot@cea.fr, romain.le-tellier@cea.fr

C. De Saint Jean
CEA, DAM, DIF
F-91297 Arpajon, France
cyrille.de-saint-jean@cea.fr

P. Piluso, J. Delacroix
CEA, DES, IRESNE, DTN, SMTA, LEAG, Cadarache
F-13108 Saint Paul-lez-Durance, France
pascal.piluso@cea.fr, jules.delacroix@cea.fr

ABSTRACT

CALPHAD-based corium thermodynamic modelling is impaired by the lack of activity or calorimetric experimental measurements for such liquids at very high temperatures. It relies almost exclusively on phase equilibrium data. As such, when the associated thermodynamic databases (e.g. NUCLEA, TAF-ID) are used to evaluate the liquid properties (e.g. chemical potential) out of equilibrium, their values come with a very large (and unquantified) uncertainty. This was clearly highlighted in recent thermodynamic evaluations (based on the Butler equation) of the interfacial tension between the oxide and metal liquid phases of the U-O-Zr-Fe system under equilibrium conditions. In particular, a strong sensitivity to the chemical potentials evaluated at the interface composition (that differs from the bulk liquids' compositions) was noticed. Indeed, for such out-of-equilibrium conditions, NUCLEA and TAF-ID predictions significantly differ while they are in rather good agreement at the bulk phases' equilibrium compositions. Based on this observation, a proof of concept was recently made regarding the use of gas/liquid surface tension data in the CALPHAD assimilation process (in the framework of Bayesian inference). Indeed, for such interfaces, some experimental data are available, even for high-temperature corium. It was shown on the well-assessed Cu-Mg system that gas/liquid surface tension data can effectively replace activity data for the assessment. These results are summarized in this paper where this proof of concept is extended to the binary U-O system and a path forward for the actual re-assessment of the liquid phase corium thermodynamic models is discussed.

KEYWORDS

liquid thermodynamic modelling, surface tension, corium, U-O, CALPHAD, Butler equation

1. INTRODUCTION

When considering multicomponent materials at very high temperatures (typically above 2700K), the knowledge of thermodynamic properties is very often impaired by the lack of calorimetric or activity experimental measurements for such liquids. As a consequence, when the associated thermodynamic databases are used to evaluate the liquid properties (e.g. enthalpy, chemical potential) out of equilibrium, the values of these properties come with a very large (and unquantified) uncertainty. Hence, numerical simulations of the behaviour of systems involving such liquids (e.g. multiphase thermalhydraulics) cannot be fully predictive. This is particularly true in the area of severe nuclear reactor accidents where such experimental data for liquids associated with the reactor core meltdown are almost non-existent. Considering the two main databases internationally used for corium systems, namely NUCLEA [1, 2, 3] and TAF-ID (Thermodynamics of Advanced Fuels-International Database) [4], this trend was highlighted in [5] where a renovated Butler equation-based model [6, 7] was used to evaluate the interfacial energy between the two liquids at equilibrium in the miscibility gap of the binary U-O and quaternary U-O-Zr-Fe systems. It was shown that the large differences in interfacial tension predictions depending on the database are to be attributed to the extrapolation of the chemical potentials out of global equilibrium conditions. For the sake of illustration, Figure 1 depicts the behaviour of the Uranium and Oxygen chemical potentials as a function of composition for the binary U-O system in the liquid miscibility gap range at $T = 2800$K. It can be observed that the two liquid phases predicted at equilibrium (in terms of compositions and chemical potentials) by the two databases are in good agreement but that the amplitude of the variations of the chemical potentials w.r.t. the equilibrium values is significantly larger with TAF-ID when compared with NUCLEA. Such differences are consistent with the fact that only one tie-line has been measured in the U-O miscibility gap region [8] and highlights the large uncertainty that is associated with the liquid phase Gibbs energy model calibration in these databases. It also points out that interfacial energies, as modelled through a Butler approach, are very sensitive to the Gibbs energy model extrapolation at the interface composition (that differs from the bulk phases compositions).

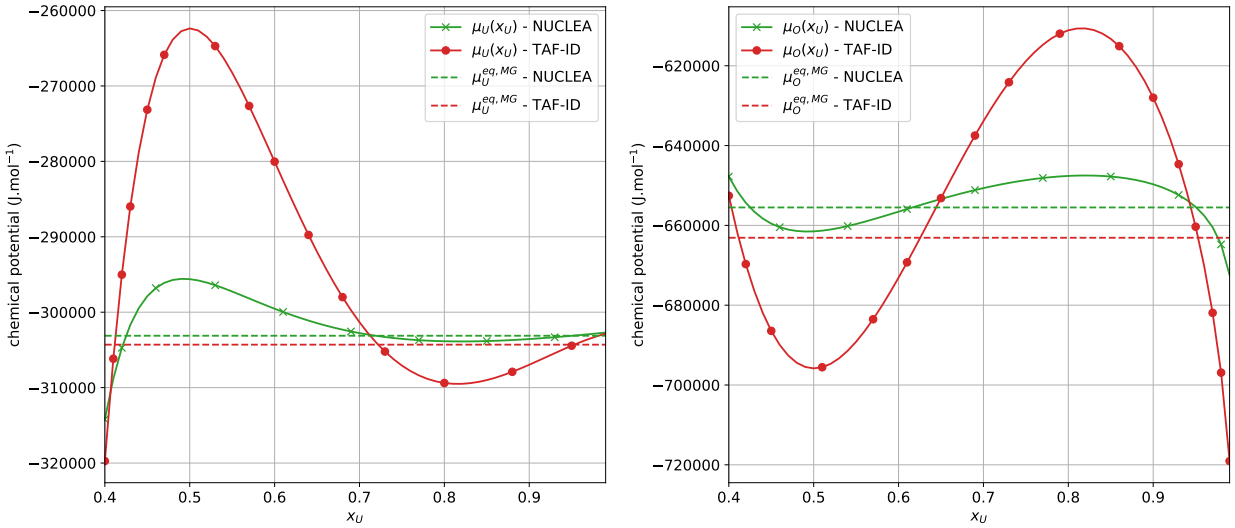

Figure 1. Liquid phase chemical potential (μ_U on the left and μ_O on the right) vs. x_U (molar fraction of Uranium) for the U-O system at $T = 2800$K as evaluated using the NUCLEA version 19.1 and TAF-ID version 10 databases – Equilibrium values in the miscibility gap are plotted in dashed lines – Figure reproduced from [5].

These databases are constructed using the CALPHAD method [9]. In this framework, improving the Gibbs energy model calibration for the liquid corium phase requires new data in the sub-stoichiometric range of composition but acquiring such data is very challenging. On the one hand, developing new experimental capabilities for calorimetric measurements at high temperature is a research avenue with many technical challenges to be tackled [10]. On the other hand, very good results have been obtained using classical molecular dynamics simulations for the properties of stoichiometric liquid (U,Zr)O_2 oxides [11] and metallic (U,Zr) melts [12] but accurate evaluation of sub-stoichiometric melts properties with such an approach is still an open issue.[1]

In this context, considering the fact that measuring surface tension between molten corium and an inert atmosphere is an existing experimental capability in the frame of the VITI facility at CEA Cadarache [14], a third way to improve the liquid corium phase Gibbs energy model has been recently investigated.[2] The idea pursued in the A. Tourneix Ph.D. thesis [15] consists in introducing liquid-gas surface tension data in the CALPHAD assessment process to improve the liquid phase model calibration. To this end, two questions have to be successively addressed. First, a thermodynamic model of surface tension was chosen and tested for its compatibility with the CALPHAD representation of the liquid phase and its *a priori* relevance. Following the work reported in [5] for liquid-liquid interfaces, a model based on different formulations of the Butler equation was considered and tested [16]. Its sensitivity to the underlying CALPHAD model was demonstrated and its predictions compared to experimental measurements of liquid-gas surface tension for the U-O-Zr system [17]. From there, a proof of concept on the binary Cu-Mg system was established for the integration of these data, through the Butler model, into the CALPHAD data assimilation process. In this paper, the main results of this proof of concept are presented and discussed with some additional results regarding the application of such an approach to the binary U-O system.

The paper is structured as follows. Section 2 introduces the Gibbs energy models for the liquid phase of both Cu-Mg and U-O systems along with the Butler-based surface tension model. The numerical method and associated tools considered for the data assimilation are summarized in Section 3. Numerical results are then presented and discussed in Section 4. Section 5 finally draws conclusions and presents perspectives of this work.

2. MODELS

2.1. Liquid phase Gibbs free energy model

For the thermodynamic modelling of the liquid phase, a non-ideal associate model, typically used in the NUCLEA database, is considered in the present work. Such a model is a special case of the general Compound Energy Formalism (CEF) where only one sublattice is considered and where, consequently, constituents and endmembers (in this case, the stoichiometric compounds) are one and the same. A full description of the different models describing the Gibbs energy in the CALPHAD framework is given in [9].

In order to present this model, the following notations are first introduced:

- $\underline{x}_{\mathcal{E}} = \{x_i\}_{i\in\mathcal{E}}$ are the component molar fractions and $\mathcal{E}$ the set of components;
- $\underline{y}_{\mathcal{S}} = \{y_j\}_{j\in\mathcal{S}}$ are the constituent molar fractions and $\mathcal{S}$ the set of constituents;
- T is the temperature.

[1] In this context, if *ab initio* molecular dynamics simulations are very promising, their application to non-stoichiometric composition is not trivial [13].

[2] It should be noted that an ambitious 5-year OECD/NEA project (Properties for reactor Simulation and uncertainties – COPS) has started in April 2024 and will largely increase the amount of surface tension data for corium mixtures.

The following transformation from $\underline{y}_{\mathcal{S}}$ to $\underline{x}_{\mathcal{E}}$ is then defined:

$$\mathtt{C} : \underline{y}_{\mathcal{S}} \longmapsto \left\{ x_i = \frac{\sum\limits_j b_{ij} y_j}{\sum\limits_k \sum\limits_j b_{kj} y_j} \right\}_{i \in \mathcal{E}} \tag{1}$$

where b_{ij} is the stoichiometric factor of component i in constituent j.

The non-ideal associated model represents the Gibbs energy per mole of constituents [J·mol^{-1}] according to the following decomposition:

$$\mathcal{G}_M : T, \underline{y}_{\mathcal{S}} \longmapsto \sum_{j \in \mathcal{S}} y_j \, {}^0\mathcal{G}_j(T) + RT \sum_{j \in \mathcal{S}} y_j \ln y_j + {}^E\mathcal{G}_M\left(T, \underline{y}_{\mathcal{S}}\right) \tag{2}$$

where ${}^0\mathcal{G}_j$ is the molar Gibbs energy of formation for pure constituent j [J·mol^{-1}], R is the universal gas constant [J·mol^{-1}·K^{-1}] and ${}^E\mathcal{G}_M$ is the excess contribution, the key ingredient of such model that takes into account the departure from ideality (the second term in Eq. 2 being associated with the ideal entropy of mixing). Considering the Redlich–Kister binary excess model, it is written as:

$${}^E\mathcal{G}_M : T, \underline{y}_{\mathcal{S}} \longmapsto \sum_{j \in \mathcal{S}} \sum_{l \in \mathcal{S} | l > j} y_j y_l \sum_{k=0}^{K_{j,l}} {}^kL_{j,l}(T) \left(y_j - y_l\right)^k \tag{3}$$

with $K_{j,l}$ the expansion order and ${}^kL_{j,l}(T)$ the interaction parameter, a function of temperature. From there, the Gibbs energy per mole of components can be obtained as:

$$\mathcal{G}_m : T, \underline{y}_{\mathcal{S}} \longmapsto \frac{\mathcal{G}_M\left(T, \underline{y}_{\mathcal{S}}\right)}{\mathcal{N}\left(\underline{y}_{\mathcal{S}}\right)} \tag{4}$$

where $\mathcal{N}$ is the total amount of components per mole of constituents *i.e.* $\mathcal{N}\left(\underline{y}_{\mathcal{S}}\right) = \sum\limits_k \sum\limits_j b_{kj} y_j$.

On one hand, in the general case, $\mathtt{C}$ is not invertible (in other words, $\mathrm{card}\,\underline{y}_{\mathcal{S}} > \mathrm{card}\,\underline{x}_{\mathcal{E}}$)) and, to make the link with measurable thermodynamic quantities for the modeled phase, it is needed to introduce the following Gibbs energy per mole of components:

$$\tilde{\mathcal{G}}_m : T, \underline{x}_{\mathcal{E}} \longmapsto \min_{\underline{y}_{\mathcal{S}} \,|\, \mathtt{C}\left(\underline{y}_{\mathcal{S}}\right) = \underline{x}_{\mathcal{E}}} \left(\mathcal{G}_m\left(T, \underline{y}_{\mathcal{S}}\right)\right) \tag{5}$$

that represent the "local" minimization of $\mathcal{G}_m$ for a given component composition $\underline{x}_{\mathcal{E}}$. For instance, the chemical potential of component k is obtained from $\tilde{\mathcal{G}}_m$ by $\mu_k = \frac{\partial \tilde{\mathcal{G}}_m}{\partial x_k}(T, \underline{x}_{\mathcal{E}})$. On the other hand, in the special case where $\mathcal{S} = \mathcal{E}$, this model is simplified into the substitutional model and the component chemical potentials can be evaluated analytically without any numerical minimization.

The activity of component k is defined by

$$a_k = \exp\left(\frac{\mu_k - \mu_k^\star}{RT}\right) \tag{6}$$

where $\mu_k^\star$ is the reference chemical potential of pure component k under the same p and T conditions.

We now restrict our presentation to the liquid phase of two binary systems: U-O and Cu-Mg. More precisely, we consider the non-ideal associated model for U-O of the NUCLEA database and the substitutional model for Cu-Mg considered in [18]. Focusing on the interaction parameters only, the parametrization of both databases is summarized in Table I. In both cases, four parameters associated with the description of the binary excess terms are considered in the assessment process for this work.[3]

[3]Note that the order of these expansions has not been questioned in this work; the interested reader is referred to [15] for further discussion concerning the Cu-Mg system.

Table I. Description of the interaction terms parametrization for the two binary systems.

System	$\mathcal{E}$	$\mathcal{S}$	Interaction terms' expansions
U-O	$\{U,O\}$	$\{UO_2,U,O\}$	${}^0L_{UO_2,U}(T) = {}^0c_0 + {}^0c_1T$
			${}^1L_{UO_2,U}(T) = {}^1c_0$
			${}^2L_{UO_2,U}(T) = {}^2c_0$
Cu-Mg	$\{Cu,Mg\}$	$\{Cu,Mg\}$	${}^0L_{Cu,Mg}(T) = {}^0c_0 + {}^0c_1T$
			${}^1L_{Cu,Mg}(T) = {}^1c_0 + {}^1c_1T$

2.2. Liquid/gas surface tension model

For modelling the surface tension between a liquid phase and a gas phase, a Butler-based model is considered. In this sharp interface framework, the zero-volume surface Γ at the interface between the liquid and gas phases is treated as an additional phase fully characterized by its component chemical potentials $\mu_k^\Gamma\left(T^\Gamma,\underline{x}_\mathcal{E}^\Gamma\right), \forall k \in \mathcal{E}$ as a function of its average temperature T^Γ and composition $\underline{x}_\mathcal{E}^\Gamma$. The chemical potential of component k is expressed as follows:

$$\mu_k^\Gamma : T^\Gamma, \underline{x}_\mathcal{E}^\Gamma \longmapsto \bar{\mu}_{k,\Gamma} - \sigma_\Gamma \omega_{k,\Gamma} \tag{7}$$

where σ_Γ is the surface tension, $\omega_{k,\Gamma}$ the partial molar surface associated with component k and $\bar{\mu}_{k,\Gamma}$ is the reduced chemical potential. Considering a planar surface under equilibrium conditions (uniform temperature T in particular), the general form of the Butler equation is then obtained from the uniformity of the chemical potentials over the system as follows: $\forall k \in \mathcal{E}$,

$$\sigma_\Gamma = \frac{\bar{\mu}_{k,\Gamma} - \mu_k}{\omega_{k,\Gamma}} \tag{8}$$

where μ_k is, in particular, the value of the chemical potential of component k in the liquid phase.

From there, if both the liquid and surface chemical potentials are decomposed, in analogy with a substitutional model of the Gibbs energy (see Eq. 2), by distinguishing a pure component term, a configurational entropy term and an excess term, one obtains the Butler equation under its classical form: $\forall k \in \mathcal{E}$,

$$\sigma_\Gamma = \sigma_{k,\Gamma}^\star \frac{\omega_{k,\Gamma}^\star}{\omega_{k,\Gamma}} + \frac{RT}{\omega_{k,\Gamma}} \ln\left(\frac{x_{k,\Gamma}}{x_k}\right) + \frac{{}^E\mu_{k,\Gamma}\left(T,\underline{x}_\mathcal{E}^\Gamma\right) - {}^E\mu_k\left(T,\underline{x}_\mathcal{E}\right)}{\omega_{k,\Gamma}} \tag{9}$$

where $\sigma_{k,\Gamma}^\star$ is the surface tension of pure component k, $\omega_{k,\Gamma}^\star$ the associated partial molar surface and ${}^E\mu_{k,\Gamma}\left(T,\underline{x}_\mathcal{E}^\Gamma\right)$ (resp. ${}^E\mu_k\left(T,\underline{x}_\mathcal{E}\right)$) the excess term for the surface (resp. the liquid phase).

While all the different terms associated with the liquid phase can readily be obtained from a CALPHAD-based Gibbs energy model (as introduced in the previous section), additional closures are needed for the surface terms. The surface tension of pure components are taken from the literature and are summarized in Table II.

Table II. Pure component surface tension laws as a function of temperature under the form $\sigma(T) = a - b\,(T - T_0)$ – For the Oxygen, in the temperature range of interest, it is supposed to be null.

Component	a [J.m^{-2}]	b [J.m^{-2}.K^{-1}]	T_0 [K]	Reference
U	1.675	$3.4 \cdot 10^{-4}$	1405.45	[19]
Cu	1.303	$2.3 \cdot 10^{-4}$	1356.0	[20]
Mg	0.559	$3.5 \cdot 10^{-4}$	924.0	[20]

Regarding the excess energy term, the standard assumption that it can readily be obtained from the liquid

model considering a proportionality relationship is made *i.e.*

$$^{E}\mu_{k,\Gamma}\left(T,\underline{x}_{\mathcal{E}}^{\Gamma}\right) = k_{\Gamma}\,{}^{E}\mu_{k}\left(T,\underline{x}_{\mathcal{E}}^{\Gamma}\right) \tag{10}$$

where the coordination number ratio k_{Γ} is introduced (see for instance [21]).

From there, Eq. 9 represents a non-linear set of equations whose unknown is the interface composition $\underline{x}_{\mathcal{E}}^{\Gamma}$.

3. NUMERICAL METHODS AND TOOLS

Regarding surface tension modelling, the Butler equation is solved using the in-house pyButler python module that is based on the OpenCalphad software [22] to handle the CALPHAD databases and perform Gibbs energy minimization. This module uses the same numerical approach as discussed in [5] and implements different forms of the Butler equation for both liquid/liquid and liquid/gas interfaces (see [16] for more details).

For the CALPHAD parameter calibration, a Bayesian inference framework was considered for this proof of concept in order to correctly treat uncertainty. To do so, the ESPEI software was used as a starting point [18]. It makes use of an affine-invariant ensemble sampler for Markov chain Monte Carlo (MCMC) [23] as implemented in the emcee python module [24]. Such a method was considered in this work for two main reasons. First of all, it makes no assumption on the dependency between the input parameters (from the CALPHAD model in the present case) and the output quantities (that can be obtained from the CALPHAD model and compared with available data) in the data assimilation process (in contrast with a linear model for instance [25]). Secondly, it is readily possible with such a method to marginalize over nuisance parameters. A nuisance parameter is a parameter that, in addition to the input parameters, is required in order to evaluate an output quantity and compare it with the corresponding data, but is otherwise of little interest. In other words, considering the set of input (resp. nuisance) parameters $\mathbf{c}$ (resp. $\mathbf{n}$) and the set of data $\mathbf{d}$, the probability density function (pdf) of interest is $p(\mathbf{c}|\mathbf{d})$ that is formally given by:

$$p(\mathbf{c}|\mathbf{d}) = \int p(\mathbf{c},\mathbf{n}|\mathbf{d})\, p(\mathbf{n})\, d\mathbf{n} \tag{11}$$

In practice, MCMC-generated sampling of values $(\mathbf{c}_t,\mathbf{n}_t)$ for the input and nuisance parameters from the joint distribution $p(\mathbf{c},\mathbf{n}|\mathbf{d})$ automatically provides a sampling of values $\mathbf{c}_t$ from the marginalized pdf $p(\mathbf{c}|\mathbf{d})$.

To draw samples $(\mathbf{c}_t,\mathbf{n}_t)$ from the posterior pdf $p(\mathbf{c},\mathbf{n}|\mathbf{d})$, an MCMC algorithm makes use of the Bayes' theorem:

$$p(\mathbf{c},\mathbf{n}|\mathbf{d}) = \frac{p(\mathbf{d}|\mathbf{c},\mathbf{n})\, p(\mathbf{c},\mathbf{n})}{Z} \tag{12}$$

where $p(\mathbf{d}|\mathbf{c},\mathbf{n})$ is the so-called likelihood pdf, $p(\mathbf{c},\mathbf{n})$ the prior distribution and $Z = p(\mathbf{d})$ the normalization independent of $\mathbf{c}$ and $\mathbf{n}$ (that is not evaluated). It consists in an iterative procedure based on Markov chains that converges to a stationary set of samples from the posterior distribution. The inverse convergence rate can be estimated by the integrated autocorrelation time that estimates the number of steps needed in the chain in order to draw independent samples from the target density. The affine-invariant ensemble sampler of the MCMC method implemented in emcee has been devised to reduce this time especially for strongly anisotropic distributions.

Within this framework, assuming that all data are independent, the likelihood pdf is decomposed as:

$$p(\mathbf{d}|\mathbf{c},\mathbf{n}) = \prod_{d_i \in \mathbf{d}} p(d_i|\mathbf{c},\mathbf{n}) \tag{13}$$

and, for each likelihood contribution $p(d_i|\mathbf{c},\mathbf{n})$, a maximum likelihood estimation strategy is followed assuming that the residuals are normally distributed and centered on zero *i.e.*

$$p(d_i|\mathbf{c},\mathbf{n}) = p_{\mathcal{N}_{0,\sigma_i}}(r_i) \tag{14}$$

where $p_{\mathcal{N}_{0,\sigma_i}}$ is the normal distribution centered on zero with standard deviation σ_i and $r_i = \tilde{d}_i(\mathbf{c},\mathbf{n}) - d_i$ is the residual associated with the estimation $\tilde{d}_i(\mathbf{c},\mathbf{n})$ of d_i. The ESPEI software was extended in such a way that, through an interface with the pyButler module, surface tension data predicted by the Butler model of Eq. 9 can be considered in $\mathbf{d}$ in addition to activities, mixing enthalpies and so on.

In the remainder, $\mathbf{c}$ will be the set of interaction parameters for the liquid phase model *i.e.* $\left\{{}^{i}c_{j}\right\}_{i,j}$ (see Table I) while $\mathbf{n}$ will be either $\{k_\Gamma\}$ or $\emptyset$ depending if k_Γ is calibrated and marginalized or not. This aspect will be further discussed in Section 4.

4. NUMERICAL RESULTS

4.1. Proof of concept on the Cu-Mg system

This section summarizes and illustrates the main results obtained in [15] where the introduction of surface tension data in the CALPHAD assimilation process was tested on the liquid phase of the Cu-Mg system.

The starting point of this incremental proof of concept was to create a reference assessment of the liquid Cu-Mg phase from Mg activity, enthalpy of mixing and liquidus data. From [26], 34 mixing enthalpies, more than 200 liquidus temperatures and 95 Mg activities were considered for the re-assessment of the liquid phase only.[4] In any case, a relative uncertainty $2\sigma_i/d_i$ of 15% was considered along with an improper prior (in such a way that the posterior is informed entirely by the data). 900 iterations with 40 chains have been performed as illustrated in Figure 2a in terms of the evolution of $-\ln\left(p\left(\mathbf{d}|\mathbf{c},\mathbf{n}\right)p\left(\mathbf{c},\mathbf{n}\right)\right)$ for the different chains. Accordingly, discarding the 200 first iterations (so-called burn-in), the maximum likelihood estimate of the parameters $\bar{\mathbf{c}}$ along with ± 1.94 standard deviation is shown in Table III while their distributions are illustrated in the corner plot of Figure 2b that displays the marginalized univariate distributions along the diagonal and the covariance between pairs of parameters below the diagonal.

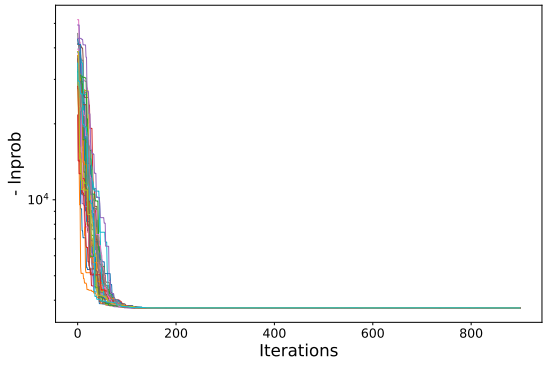

(a) Opposite of $\ln\left(p\left(\mathbf{d}|\mathbf{c},\mathbf{n}\right)p\left(\mathbf{c},\mathbf{n}\right)\right)$. Each line corresponds to the log probability of the accepted parameters for a single chain.

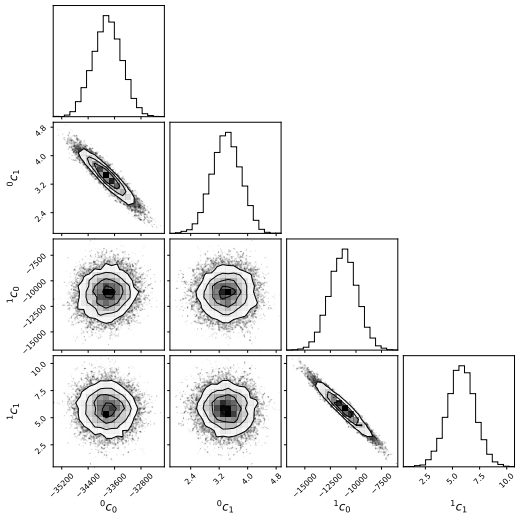

(b) Corner plot of the sampled posterior parameter distributions.

Figure 2. Reference assessment of the liquid Cu-Mg phase considering liquidus temperature, mixing enthalpy and Mg activity data – 900 iterations with 40 chains – $2\sigma_i/d_i = 15\%$ and improper prior.

[4] For the different solid phases in equilibrium with the liquid one depending on the composition, the original ESPEI assessment [18] was used.

Table III. Assessed parameters of the liquid Cu-Mg phase – maximum likelihood estimate ± 1.94 standard deviation.

	${}^0c_0$	${}^0c_1$	${}^1c_0$	${}^1c_1$
this work	$(-3.38 \pm 0.09) \cdot 10^4$	3.4 ± 0.9	$(-1.1 \pm 0.3) \cdot 10^4$	6 ± 3
[18]	$(-3.46 \pm 0.09) \cdot 10^4$	3 ± 6	$(-1.1 \pm 0.3) \cdot 10^4$	5 ± 9

In Table III, the results of the assessment performed in [18] are also presented for the sake of comparison. Both assessments well agree with a noticeable reduction of the uncertainty on ${}^0c_1$ and ${}^1c_1$ in our case that is attributed to the fact that activity data were not considered in [18].

From there, activity and surface tension were compared in terms of the information they give on parameters **c**. To do so, for a same composition and temperature grid, data were generated for both types of physical quantities considering the previously calibrated liquid phase model and a given value of k_Γ of 0.83 (the value estimated in [21] for metallic systems). These data are given in Tables IV and V for surface tensions and Cu activities respectively while the different datasets constructed from these data are summarized in Table VI. These datasets were used for performing assessments of parameters **c** for various values of the data relative standard deviation σ_i/d_i. In any case, for each parameter, the prior distribution was arbitrarily taken as a normal law of unit relative standard deviation with following mean values: $-8 \cdot 10^4$ for ${}^0c_0$, $-3 \cdot 10^1$ for ${}^0c_1$, $1.5 \cdot 10^4$ for ${}^1c_0$ and $6 \cdot 10^2$ for ${}^1c_1$.

Table IV. Generated surface tension data (J.m^{-2}) – Cu-Mg liquid phase.

	10%Cu	30%Cu	50%Cu	70%Cu	90%Cu
1100K	0.5199	0.5929	0.7254	0.9141	1.1492
1200K	0.4863	0.5615	0.6940	0.8822	1.1210
1300K	0.4526	0.5299	0.6623	0.8503	1.0926
1400K	0.4188	0.4979	0.6304	0.8182	1.0641

Table V. Generated Cu activity data – Cu-Mg liquid phase.

	10%Cu	30%Cu	50%Cu	70%Cu	90%Cu
1100K	0.0124	0.0584	0.1791	0.4515	0.8507
1200K	0.0152	0.0688	0.1991	0.4727	0.8558
1300K	0.0180	0.0791	0.2178	0.4915	0.8601
1400K	0.0209	0.0892	0.2351	0.5081	0.8638

Table VI. Sets of generated data used in the different assessments – Cu-Mg liquid phase.

	surface tension (Table IV)	Cu activity (Table V)
20 ST	all data	–
4 ST	data in red and blue	–
20 a_{Cu}	–	all data
4 a_{Cu}	–	data in red and blue
2 ST + 2 a_{Cu}	data in blue	data in blue
5 ST	data in red, blue and green	

In a first batch of assessments, the parameter k_Γ was not calibrated and was kept constant at its reference value. The results of these assessments are summarized in Figure 3 where the relative standard deviation of

the parameters posterior distribution is depicted as a function of σ_i/d_i. In Figure 3a, the different datasets are compared focusing on parameter ${}^0c_0$. Below a threshold σ_i/d_i value of about 10^{-1}, all assessments are successful and ${}^0c_0$ relative standard deviation decreases when σ_i/d_i decreases following a linear law (in all cases, the fit of a power-law $a \times (\sigma_i/d_i)^b$ gives $b \approx 1$). Because of the first-order dependency in both temperature and composition of the Gibbs energy model (see Table I), two temperature points along with two composition points are required when surface tension data or activity data are considered separately. In such "minimal" configurations, it can be seen that the assessments with surface tensions and activities (datasets (4 ST) and (4 a_{Cu}) respectively) gives similar results. Interestingly, because the surface tension through the Butler equation depends on both the bulk liquid composition and the interface composition, surface tension data and activity data at a same unique composition point can be combined to ensure a successful assessment. This is illustrated with the (2 ST + 2 a_{Cu}) dataset calculation in Figure 3a. As expected, when the number of data points is increased (datasets (20 ST) and (20 a_{Cu}) respectively), the parameter relative standard deviation is decreased; while this decrease is limited for surface tension data (a factor of 2 approximately), for activity data, it is more pronounced (a factor of 100 approximately). The same trends are exhibited for all **c** parameters as illustrated by Figure 3b that depicts the relative standard deviation convergence for the four parameters ${}^ic_j$ for dataset (4 ST).

On the overall, these numerical results demonstrate that surface tension data, as modelled through the Butler equation, play a very similar role to activity data in the calibration process of the Cu-Mg liquid phase Gibbs energy model.

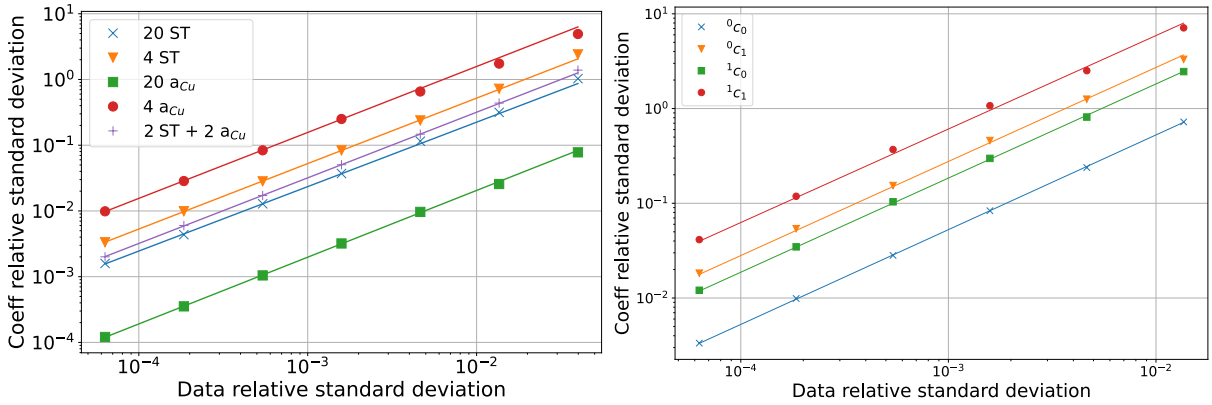

(a) Comparison of various datasets **d** for parameter ${}^0c_0$.

(b) Comparison of the four parameters ${}^ic_j$ for dataset (4 ST).

Figure 3. Evolution of the relative standard deviation of $p\left({}^ic_j|\mathbf{d}\right)$ as a function of σ_i/d_i considering various datasets (see Table VI) – Cu-Mg liquid phase.

However, the Butler equation introduces additional parameters that, in principle, should be considered as uncertain. In particular, different values of the coordination number ratio k_Γ can be found in the literature depending on the system under consideration and surface tension as evaluated through Eq. 9 is very sensitive to this parameter.[5] Accordingly, in the remainder of this proof of concept, this parameter has been considered as a nuisance parameter and was calibrated and marginalized. Doing so, the minimum number of data points for a proper MCMC convergence is increased by one. The successful assessment with dataset (5 ST), constructed from dataset (4 ST) by adding a single surface tension value, is illustrated in the corner plot of Figure 4a where, in particular, it can be seen that the marginalized univariate distribution of k_Γ

[5]The reader is refered to [16] for more details. The other parameters of Eq. 9 could also considered but, because of their uncertainty and/or the associated sensitivity of surface tension, their impact is more limited.

follows a Gaussian law centered on its reference value.[6] In Figure 4b, the relative standard deviation of the parameters posterior distribution is depicted as a function of σ_i/d_i. The same trends as with dataset (4 ST) and k_Γ kept constant (see Figure 3b) are observed with, in particular, a linear dependency of the relative standard deviation of $p\left({}^{i}c_j|\mathbf{d}\right)$ below a threshold σ_i/d_i value. It can be noted that this threshold value is decreased to about 10^{-3} while, in the asymptotic linear region, introducing k_Γ in the calibration process leads to a very limited increase of the **c** relative standard deviation (by a factor lower than 2).

Taking into account the uncertainty of the interface parameter k_Γ in the assimilation process (by adjusting and marginalising it) does not call into question the results obtained previously without taking this uncertainty into account. The information that surface tension data can provide on the liquid phase Gibbs energy is confirmed. In A. Tourneix Ph.D. thesis [15], this analysis on the Cu-Mg system with generated data was followed by assessments considering actual experimental measurements (including surface tension data measured in the VITI facility) that have confirmed their similar role and the complementarity of surface tension and activity data in calibrating the liquid phase model. For the sake of conciseness, they are not presented here.

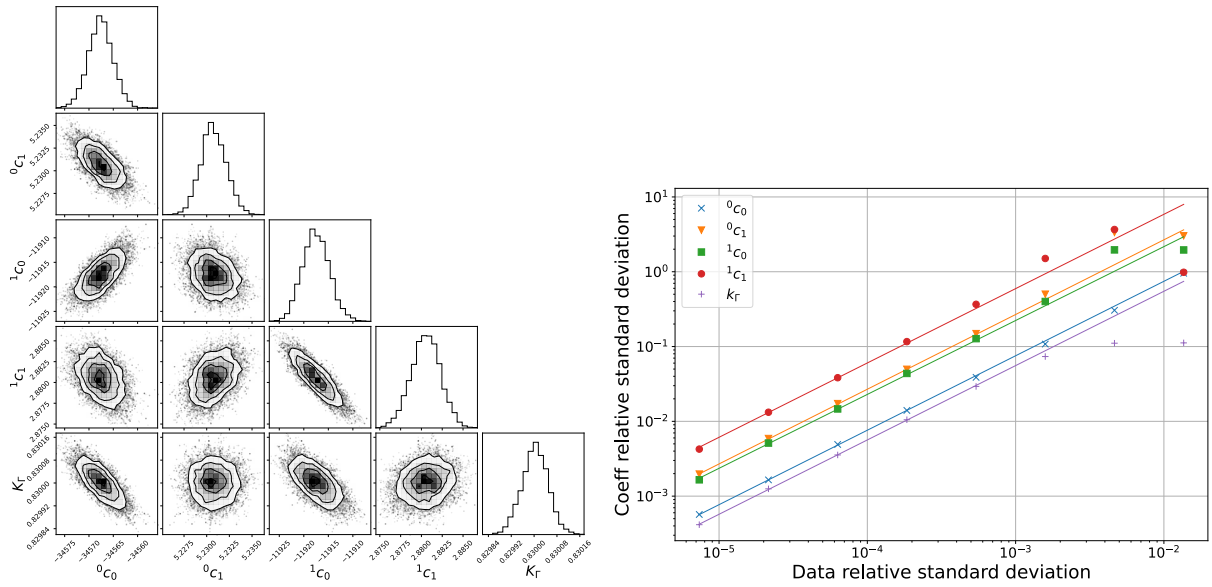

(a) Corner plot of the sampled posterior parameter distributions – $\sigma_i/d_i = 10^{-6}$ case.

(b) Evolution of the relative standard deviation of $p\left({}^{i}c_j|\mathbf{d}\right)$ and $p\left(k_\Gamma|\mathbf{d}\right)$ as a function of σ_i/d_i.

Figure 4. Assessment considering the calibration and marginalization of parameter k_Γ for dataset (5 ST) (see Table VI) – Cu-Mg liquid phase.

4.2. First results for the U-O system and the possible path forward

Considering the positive outcome of the proof of concept on the Cu-Mg system, tentative simulations were made on the U-O system. Following the same approach as for Cu-Mg, surface tension data were generated considering a k_Γ value of 0.94 (the value estimated in [21] for oxidic systems) and **c** values extracted from the NUCLEA database: $6.2 \cdot 10^4$ for ${}^0c_0$, $-1.1 \cdot 10^1$ for ${}^0c_1$, $-6.1 \cdot 10^4$ for ${}^1c_0$ and $-2.1 \cdot 10^4$ for ${}^2c_0$. These data are given in Table VII. An important difference w.r.t. the Cu-Mg system is that the U-O system exhibits

[6] The prior distribution for k_Γ was arbitrarily taken as a $[0,1]$-truncated normal law of 10% relative standard deviation with 0.8 mean value.

a liquid miscibility gap over an extended composition and temperature range. Accordingly, the composition points considered in Table VII were selected out of the miscibility gap region *i.e.* in conditions where the equilibrium between a unique liquid and an inert gaseous atmosphere is possible. This dataset was then used for performing an assessment of parameters $\mathbf{c}$ for various values of the data relative standard deviation σ_i/d_i. In any case, for each parameter, the prior distribution was arbitrarily taken as a normal law of unit relative standard deviation with following mean values: $-3.2 \cdot 10^4$ for ${}^0c_0$, $-7.1 \cdot 10^1$ for ${}^0c_1$, $1.1 \cdot 10^4$ for ${}^1c_0$ and $2.1 \cdot 10^4$ for ${}^2c_0$. The results in terms of relative standard deviation evolution are depicted in Figure 5a while Figure 5b shows the corner plot for the assessment with $\sigma_i/d_i = 10^{-4}$. On the overall, the same trends as for the Cu-Mg system are observed with an asymptotic linear regime below a below a threshold σ_i/d_i value. Additional assessments with k_Γ calibration (not shown) were also performed: the impact of this additional nuisance parameter was found similar as in the Cu-Mg case.

Considering these positive results, carrying out actual surface tension measurements of a sub-stoichiometric U-O melt (out of the miscibility gap range) could be a short-term way to improve the CALPHAD assessment of the associated liquid phase.

Table VII. Generated surface tension data (J.m^{-2}) – U-O liquid phase.

	34%U	40%U	43%U	93%U
3150K	0.8384	0.8667	0.8773	0.9019
3325K	0.8017	0.8268	0.8368	0.8918
3500K	0.7657	0.7872	0.7964	0.8781

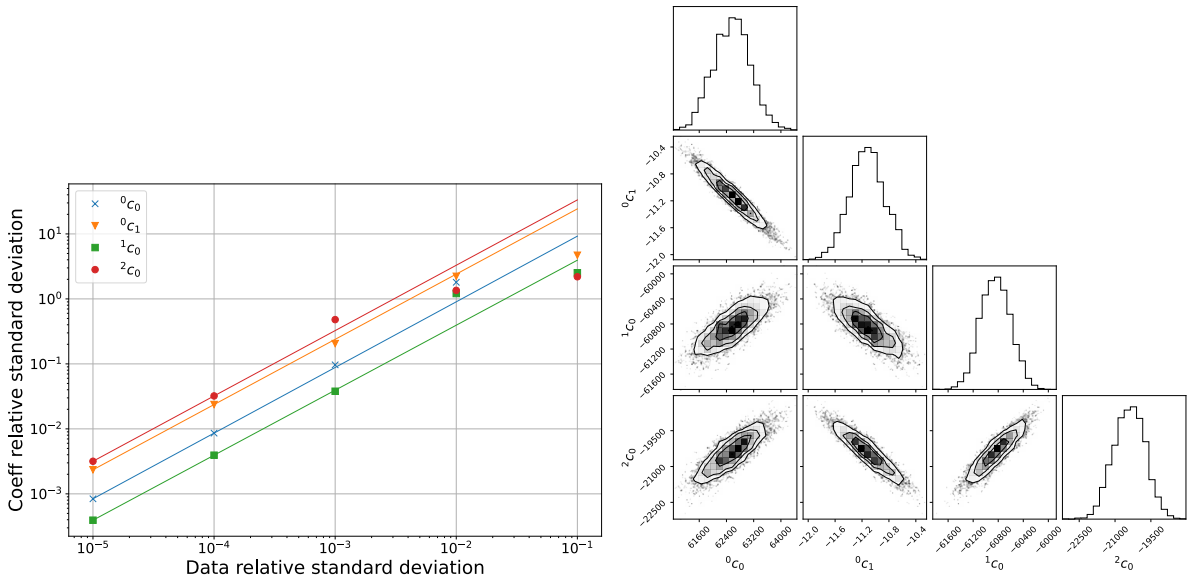

(a) Evolution of the relative standard deviation of $p\left({}^ic_j|\mathbf{d}\right)$ as a function of σ_i/d_i.

(b) Corner plot of the sampled posterior parameter distributions – $\sigma_i/d_i = 10^{-4}$ case.

Figure 5. Assessment for Table VII dataset – U-O liquid phase.

5. CONCLUSIONS AND PERSPECTIVES

In this paper, we have presented the positive outcomes of a proof of concept regarding the use of surface tension data to improve a liquid phase thermodynamic modelling in the frame of the CALPHAD method.

To do so, surface tension was modeled through the Butler equation and parameter calibration was made in the frame of Bayesian inference (with an MCMC approach) for an adequate uncertainty treatment. It was shown, through a detailed analysis with generated data on the well-assessed Cu-Mg system, that surface tension plays a role very similar to activities in the assessment process. Calibration and marginalization of the coordination number ratio, an additional uncertain parameter introduced in the Butler equation, was also carried out without impairing the CALPHAD assessment. Additional results on the U-O system were provided to confirm that this approach could be a viable short-term approach to improve the liquid phase description for corium systems for which data are very scarce.

Pursuing this research direction, the next steps would be the following. Carrying out surface tension measurements of sub-stoichiometric U-O melts (for compositions out of the miscibility gap range) in the VITI facility would provide data in such a way that the approach promoted here could be actually tested to improve the CALPHAD assessment of the associated liquid phase. To do such an assessment, while the Bayesian inference framework should be kept, the results of this paper suggest that the costly MCMC method could be replaced by a simpler (and approximate) linear model (as used in the CALPHAD assessment framework in [25]).

REFERENCES

[1] B. Cheynet, P. Chevalier, and E. Fischer, "Thermosuite," *Calphad*, vol. 26, no. 2, pp. 167–174, 2002.

[2] S. Bakardjieva, M. Barrachin, S. Bechta, D. Bottomley, L. Brissoneau, B. Cheynet, E. Fischer, C. Journeau, M. Kiselova, L. Mezentseva, P. Piluso, and T. Wiss, "Improvement of the european thermodynamic database NUCLEA," *Progress in Nuclear Energy*, vol. 52, no. 1, pp. 84–96, 2010.

[3] M. Barrachin, "Corium Experimental Thermodynamics: A Review and Some Perspectives," *Thermo*, vol. 1, no. 2, pp. 179–204, Sep. 2021, number: 2 Publisher: Multidisciplinary Digital Publishing Institute.

[4] C. Guéneau, N. Dupin, L. Kjellqvist, E. Geiger, M. Kurata, S. Gossé, E. Corcoran, A. Quaini, R. Hania, A. L. Smith, M. H. A. Piro, T. Besmann, P. E. A. Turchi, J. C. Dumas, M. J. Welland, T. Ogata, B. O. Lee, J. R. Kennedy, C. Adkins, M. Bankhead, and D. Costa, "TAF-ID: An international thermodynamic database for nuclear fuels applications," *Calphad*, vol. 72, p. 102212, Mar. 2021.

[5] K. Gajavalli and R. Le Tellier, "Butler-based thermodynamic modeling of interfacial energies for in-vessel corium systems," *Journal of Nuclear Materials*, vol. 569, p. 153935, Oct. 2022.

[6] J. A. V. Butler, "The Thermodynamics of the Surfaces of Solutions," *Proceedings of the Royal Society of London. Series A, Containing Papers of a Mathematical and Physical Character*, vol. 135, no. 827, pp. 348–375, 1932, publisher: The Royal Society.

[7] G. Kaptay, "A coherent set of model equations for various surface and interface energies in systems with liquid and solid metals and alloys," *Advances in Colloid and Interface Science*, vol. 283, p. 102212, Sep. 2020.

[8] C. Guéneau, M. Baichi, D. Labroche, C. Chatillon, and B. Sundman, "Thermodynamic assessment of the uranium-oxygen system," *Journal of Nuclear Materials*, vol. 304, no. 2–3, pp. 161 – 175, 2002.

[9] H. Lukas, S. G. Fries, and B. Sundman, *Computational Thermodynamics: The Calphad Method*. Cambridge University Press, 2007.

[10] A. Crochetet, "Mesure de propriétés thermo-physiques du corium en température," Ph.D. thesis under preparation, Orléans, 2022.

[11] T. Beigbeder, E. Bourasseau, and M. Rushton, "Thermophysical properties of liquid (U, Zr)O_2 by molecular dynamics," *Molecular Simulation*, vol. 47, no. 18, pp. 1502–1508, Dec. 2021, publisher: Taylor & Francis _eprint: https://doi.org/10.1080/08927022.2021.1987429.

[12] J. Tranchida, F. Nicaud, B. W. Beeler, and E. Bourasseau, "Thermophysical properties and unexpected

viscosity of liquid (U, Zr): An atomistic investigation," *The Journal of Chemical Physics*, vol. 160, no. 21, p. 214507, Jun. 2024.

[13] J.-P. Crocombette, O. Barbour, and F. Bruneval, "Structural and electronic properties of U_4O_9 from ab initio and empirical potential calculations," *Physical Review Materials*, vol. 7, no. 6, p. 063602, Jun. 2023, publisher: American Physical Society.

[14] J. Delacroix, P. Piluso, N. Chikhi, O. Asserin, D. Borel, A. Brosse, and S. Cadiou, "Measurements of Liquid AISI 304L Steel Density and Surface Tension, and Influence of Surface-Active Elements at High Temperatures," *steel research international*, vol. 93, no. 6, p. 2100624, 2022, _eprint: https://onlinelibrary.wiley.com/doi/pdf/10.1002/srin.202100624.

[15] A. Tourneix, "Amélioration de la modélisation thermodynamique de liquides multicomposants à haute température par assimilation de données de tension de surface," Ph.D. dissertation, 2025.

[16] A. Tourneix, C. Denier, R. Le Tellier, P. Piluso, and J. Delacroix, "Thermodynamic evaluation of liquid-gas surface tension for U-O-Zr mixtures using the Butler equation," in *Proc. of the 11th European Review Meeting on Severe Accident Research ERMSAR2024*, Stockholm, May 2024.

[17] C. Denier, A. Tourneix, J. Delacroix, R. Le Tellier, P. Piluso, and E. de Bilbao, "Density and surface tension of $U_{1-x}Zr_xO_{2-y}$ with different oxidation state: measurement and modelling at high temperature for nuclear severe accident applications," *Journal of Nuclear Materials*, vol. 615, p. 155928, Sep. 2025.

[18] B. Bocklund, R. Otis, A. Egorov, A. Obaied, I. Roslyakova, and Z.-K. Liu, "ESPEI for efficient thermodynamic database development, modification, and uncertainty quantification: application to Cu–Mg," *MRS Communications*, vol. 9, no. 2, pp. 618–627, Jun. 2019.

[19] E. E. Shpil'rain, V. A. Fomin, and V. V. Kachalov, "Density and surface tension of molten uranium," *High Temp. (Engl. Transl.); (United States)*, vol. 26:5, Sep. 1988.

[20] W. F. Gale and T. C. Totemeier, *Smithells Metals Reference Book*, 8th ed. Elsevier, Dec. 2003, google-Books-ID: zweHvqOdcs0C.

[21] T. Tanaka, K. Hack, T. Iida, and S. Hara, "Application of thermodynamic databases to the evaluation of surface tensions of molten alloys, salt mixtures and oxide mixtures," *International Journal of Materials Research*, vol. 87, no. 5, pp. 380–389, May 1996, publisher: De Gruyter.

[22] B. Sundman, U. R. Kattner, M. Palumbo, and S. G. Fries, "OpenCalphad - a free thermodynamic software," *Integrating Materials and Manufacturing Innovation*, vol. 4, no. 1, 2015.

[23] J. Goodman and J. Weare, "Ensemble samplers with affine invariance," *Communications in Applied Mathematics and Computational Science*, vol. 5, no. 1, pp. 65–80, Jan. 2010, publisher: Mathematical Sciences Publishers.

[24] D. Foreman-Mackey, W. M. Farr, M. Sinha, A. M. Archibald, D. W. Hogg, J. S. Sanders, J. Zuntz, P. K. g. Williams, A. R. j. Nelson, M. d. Val-Borro, T. Erhardt, I. Pashchenko, and O. A. Pla, "emcee v3: A Python ensemble sampling toolkit for affine-invariant MCMC," *Journal of Open Source Software*, vol. 4, no. 43, p. 1864, Nov. 2019.

[25] E. Lawrence, "Reconstruction fonctionnelle et analyse d'incertitudes dans le cadre d'un problème inverse de thermodynamique," phdthesis, Toulouse 3, Dec. 2020.

[26] C. A. Coughanowr, I. Ansara, R. Luoma, M. Hämäläinen, and H. L. Lukas, "Assessment of the Cu-Mg System / Optimierung des Systems Cu-Mg," *International Journal of Materials Research*, vol. 82, no. 7, pp. 574–581, Jul. 1991, publisher: De Gruyter.

A path forward to improve corium thermodynamic assessment by using surface tension data: results for the U-O binary system

The 12th European Review Meeting on Severe Accidents Research (ERMSAR2026), Madrid, Spain, May 18–22, 2026

A. Tourneix [1] Y. Miot [1] R. Le Tellier [1] (romain.le-tellier@cea.fr) C. De Saint Jean [2]
P. Piluso [1] J. Delacroix [1]
[1] CEA, DES, IRESNE, DTN, CADARACHE
[2] CEA, DAM, DIF, BRUYÈRES-LE-CHÂTEL

Outline

Introduction

Problem Statement

Models & methods

Proof of concept on the Cu-Mg system

Possible path forward with U-O system

Conclusions & Perspectives

1. Introduction

Context and problem statement

Context

Thermodynamic properties of corium phases

- Associated knowledge under the form of databases constructed by the CALPHAD method, in particular: NUCLEA [Bar21], TAF-ID [GDK+21]
- Algebraic models for the Gibbs energy of the different phases calibrated on experimental and atomistic simulation data
- These databases: very useful for constructing closure laws for the models describing corium associated phenomena in SA codes

The CALPHAD method goes beyond (global) equilibrium calculations

> *"These [Gibbs energy] functions can be extrapolated also outside the equilibrium state and thus, when they are included in a simulation model, provide information about values and gradients of the thermodynamic properties in space and time outside the range of stability of a phase."*
>
> *(H. Lukas, S. G. Fries, and B. Sundman, [LFS07], pp. 2)*

But "high-fidelity" databases are required to do so

Context

Status of corium databases through the example of the U-O binary system

- From OECD/NEA project TCOFF-2 System Identification and Ranking Table:
  "A system like (O,Zr,U) has now a good knowledge (average marks of 3.3 and 3.5) due to the considerable work that have been conducted in the past years on this system."
  (C. Journeau et al., [JBK+24])

- **Is it so?**

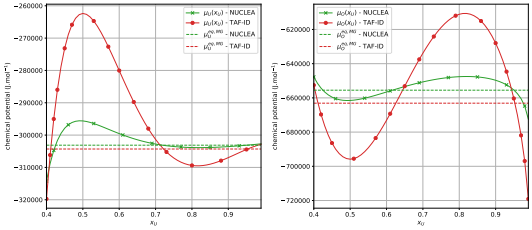

FIGURE 1: Liquid phase chemical potential (μ_U on the left and μ_O on the right) vs. x_U (molar fraction of Uranium) for the U-O system at $T = 2800$K – Equilibrium values in dashed lines

- Comparison of NUCLEA version 19.1 and TAF-ID version 10 in the liquid miscibility gap region:
  - Fairly good agreement at global equilibrium points
  - Large difference in the chemical potentials away from these equilibrium points
  - E.g. leads a factor 6 on the interfacial energy (at T_{liq}) as evaluated by the Butler equation [GLT22]

How can we move forward?

Problem Statement

Acquiring thermodynamic data for sub-stoichiometric melts is a challenge

- Developing experimental capabilities for calorimetric measurements at high temperature
  → many technical challenges to be tackled [Cro22]
- Good results obtained with classical molecular dynamics simulations for the properties of stoichiometric liquid $(U,Zr)O_2$ oxides [BBR21] and metallic (U,Zr) melts [TNBB24]
  → evaluation of sub-stoichiometric melts properties is an open issue
- *Ab initio* molecular dynamics simulations are very promising
  → their application to non-stoichiometric composition is an open issue [CBB23]

Measuring surface tension data for such melts is ongoing

- In particular in the VITI facility at CEA Cadarache [DPC$^+$22, DTD$^+$25]
- *cf.* ongoing OECD/NEA COPS project

Can we use surface tension data for improving the corium liquid Gibbs energy model?

This work

Proof of concept (PoC) regarding the use of liquid-gas surface tension data in the CALPHAD assessment of the liquid phase model

1. Choose a thermodynamic model of surface tension compatible with the CALPHAD representation of the liquid phase
   - ✓ Different formulations of the Butler equation tested [TDLT+24] on U-O-Zr system with comparison to experimental measurements [DTD+25]
     → Sensitivity to the underlying CALPHAD model and predictive capability demonstrated
2. Perform comparative assessments introducing liquid-gas surface tension data
   1. Choose a simple binary system → Cu-Mg system
   2. Assess how much information surface tension data can bring → comparison with activity data
   3. Correctly take into account uncertainty → Bayesian inference framework
   4. Start with “generated” data to put aside the issue of data-model adequacy
   5. Continue with actual experimental data

   - ✓ Done in the frame of A. Tourneix Ph.D. thesis [Tou25]

This presentation: analysis with “generated” data on Cu-Mg and U-O

2. Models & methods

Models - Liquid phase Gibbs free energy model

- Non-ideal associated model for U-O (as in NUCLEA)
- Substitutional model for Cu-Mg [CAL$^+$91, BOE$^+$19]
  - Gibbs energy per mole of constituents $\mathcal{G}_M : T, \underline{y}_{\mathcal{S}} \longmapsto \sum_{j\in\mathcal{S}} y_j \, {}^0\mathcal{G}_j(T) + RT \sum_{j\in\mathcal{S}} y_j \ln y_j + {}^E\mathcal{G}_M\left(T, \underline{y}_{\mathcal{S}}\right)$
  - Redlich–Kister binary excess model ${}^E\mathcal{G}_M : T, \underline{y}_{\mathcal{S}} \longmapsto \sum_{j\in\mathcal{S}} \sum_{l\in\mathcal{S}|l>j} y_j y_l \sum_{k=0}^{K_{j,l}} {}^k L_{j,l}(T) \left(y_j - y_l\right)^k$

System	$\mathcal{S}$	Interaction terms' expansions		
U-O	$\{UO_2, U, O\}$	${}^0L_{UO_2,U}(T)$	$=$	${}^0c_0 + {}^0c_1 T$
		${}^1L_{UO_2,U}(T)$	$=$	${}^1c_0$
		${}^2L_{UO_2,U}(T)$	$=$	${}^2c_0$
Cu-Mg	$\{Cu, Mg\}$	${}^0L_{Cu,Mg}(T)$	$=$	${}^0c_0 + {}^0c_1 T$
		${}^1L_{Cu,Mg}(T)$	$=$	${}^1c_0 + {}^1c_1 T$

- Gibbs energy per mole of components

$$\mathcal{G}_m : T, \underline{y}_{\mathcal{S}} \longmapsto \mathcal{G}_M\left(T, \underline{y}_{\mathcal{S}}\right) / \mathcal{N}\left(\underline{y}_{\mathcal{S}}\right)$$

$$\tilde{\mathcal{G}}_m : T, \underline{x}_{\mathcal{E}} \longmapsto \min_{\underline{y}_{\mathcal{S}} \mid \mathfrak{C}\left(\underline{y}_{\mathcal{S}}\right) = \underline{x}_{\mathcal{E}}} \left(\mathcal{G}_m\left(T, \underline{y}_{\mathcal{S}}\right)\right)$$

  - Chemical potential of components $\mu_k = \frac{\partial \tilde{\mathcal{G}}_m}{\partial x_k}(T, \underline{x}_{\mathcal{E}})$ and activity $a_k = \exp\left(\frac{\mu_k - \mu_k^\star}{RT}\right)$
- **Four parameters to be calibrated in both cases**

Models - Liquid/gas surface tension model: Butler equation

- Interface Γ separating two phases = an additional phase $(T^\Gamma, \underline{x}^\Gamma_{\mathcal{E}})$
  - Chemical potentials $\mu^\Gamma_k : T^\Gamma, \underline{x}^\Gamma_{\mathcal{E}} \longmapsto \bar{\mu}_{k,\Gamma} - \sigma_\Gamma \omega_{k,\Gamma}$
  - Reduced chemical potentials $\bar{\mu}_{k,\Gamma}$, surface tension σ_Γ and partial molar surfaces $\omega_{k,\Gamma}$
- Equilibrium conditions for a planar interface: $\forall k \in \mathcal{E}$

$$\sigma_\Gamma = \frac{\bar{\mu}_{k,\Gamma} - \mu_k}{\omega_{k,\Gamma}} \text{ with } \mu_k \text{ the chemical potentials in both phases}$$

  $\rightarrow$ Non-linear equation system (size = $\mathrm{card}\,(\mathcal{E}) - 1$) for unknown $\underline{x}^\Gamma_{\mathcal{E}}$
- Adapted formulation for a liquid/gas interface
  - CALPHAD-like decomposition of $\bar{\mu}_{k,\Gamma}$ and introduction of the pure component surface tensions $\sigma^\star_{k,\Gamma}$

$$\sigma_\Gamma = \sigma^\star_{k,\Gamma} \frac{\omega^\star_{k,\Gamma}}{\omega_{k,\Gamma}} + \frac{RT}{\omega_{k,\Gamma}} \ln\left(\frac{x_{k,\Gamma}}{x_k}\right) + \frac{{}^E\mu_{k,\Gamma}\left(T, \underline{x}^\Gamma_{\mathcal{E}}\right) - {}^E\mu_k\left(T, \underline{x}_{\mathcal{E}}\right)}{\omega_{k,\Gamma}}$$

  - Closure by standard assumption ${}^E\mu_{k,\Gamma}\left(T, \underline{x}^\Gamma_{\mathcal{E}}\right) = k_\Gamma \, {}^E\mu_k\left(T, \underline{x}^\Gamma_{\mathcal{E}}\right)$ with coordination number ratio k_Γ
  - ${}^E\mu_k$ function obtained from μ_k (CALPHAD liquid model)

Methods and codes

Butler equation

- in-house pyButler python module [TDLT$^+$24]
- OpenCalphad [SKPF15] for CALPHAD databases and Gibbs energy minimization

CALPHAD parameter calibration

- Bayesian inference framework (input parameters **c**, nuisance parameters **n** and data **d**)
  - Posterior pdf $p(\mathbf{c}, \mathbf{n}|\mathbf{d})$ using Bayes' theorem: $p(\mathbf{c}, \mathbf{n}|\mathbf{d}) \propto p(\mathbf{d}|\mathbf{c}, \mathbf{n})\, p(\mathbf{c}, \mathbf{n})$
  - Maximum likelihood (with $\tilde{d}_i(\mathbf{c}, \mathbf{n})$ estimation of d_i): $p(\mathbf{d}|\mathbf{c}, \mathbf{n}) = \prod_{d_i \in \mathbf{d}} p_{\mathcal{N}_{0,\sigma_i}}\left(\tilde{d}_i(\mathbf{c}, \mathbf{n}) - d_i\right)$
  - Markov chain Monte Carlo (MCMC) sampling: no assumption on the dependency between the input and output, straightforward marginalization over nuisance parameters (e.g. k_Γ)
- ESPEI software [BOE$^+$19] extended to consider surface tension data in **d** (in addition to activities...) by an interface with pyButler

3. Proof of concept

The Cu-Mg system

Starting point: reference assessment for the liquid phase

- 34 mixing enthalpies, more than 200 liquidus and **95 Mg activities** from [CAL+91]
- $2\sigma_i/d_i = 15\%$ and improper prior – 900 iterations with 40 chains
- Discarding the 200 first iterations (so-called burn-in), maximum likelihood estimate of $\bar{\mathbf{c}}$ along with ± 1.96 standard deviation:

	${}^0c_0$	${}^0c_1$	${}^1c_0$	${}^1c_1$
this work	$(-3.38 \pm 0.09) \cdot 10^4$	3.4 ± 0.9	$(-1.1 \pm 0.3) \cdot 10^4$	6 ± 3
[BOE+19]	$(-3.46 \pm 0.09) \cdot 10^4$	3 ± 6	$(-1.1 \pm 0.3) \cdot 10^4$	5 ± 9

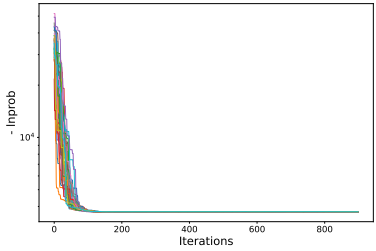

FIGURE 2: Opposite of $\ln\left(p\left(\mathbf{d}|\mathbf{c},\mathbf{n}\right)p\left(\mathbf{c},\mathbf{n}\right)\right)$. Each line corresponds to the log probability of the accepted parameters for a single chain.

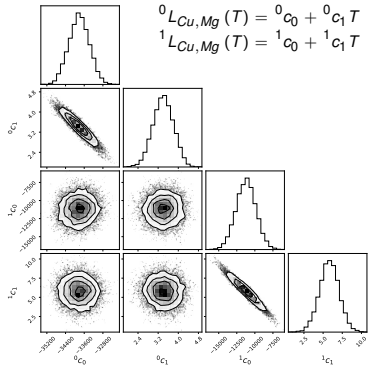

FIGURE 3: Corner plot of the sampled posterior parameter distributions.

Comparing activity and surface tension based assessments

Generated data from the reference assessment

- $k_\Gamma = 0.83$ ([THIH96], metallic systems)
- Datasets for comparing different assessments:

	surface tension	Cu activity
20 ST	all data	–
4 ST	data in red and blue	–
20 a_{Cu}	–	all data
4 a_{Cu}	–	data in red and blue
2 ST + 2 a_{Cu}	data in blue	data in blue
5 ST	data in red, blue and green	–

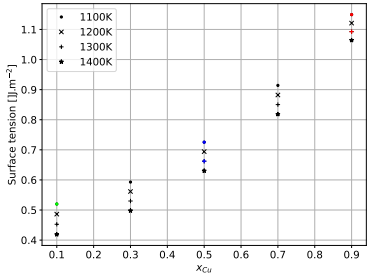

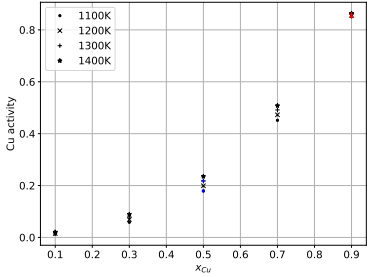

→ **compare activity and surface tension in terms of the information they give on parameters c**

Comparing activity and surface tension based assessments

Assessments with different datasets

- Varying the data relative std σ_i / d_i

N.B. Prior distribution arbitrarily taken as a normal law with mean values very far from the actual $\bar{\mathbf{c}}$ and unit relative std

Key observations

- All assessments are successful for $\sigma_i / d_i < 10^{-1}$
- Relative std of $p\left({}^{i}c_j | \mathbf{d}\right) \propto \left(\sigma_i / d_i\right)$
- Activity (or surface tension) data alone: two temperature points with two composition points needed because of first-order dependency of $\mathcal{G}_M$ in both T and composition
- Surface tension data play a very similar role to activity data
- Surface tension data combined with activity data: a single composition point is sufficient (*cf.* Butler equation)

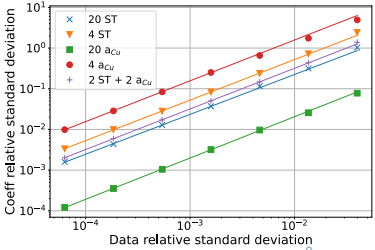

(A) Various datasets $\mathbf{d}$ for parameter ${}^{0}c_0$.

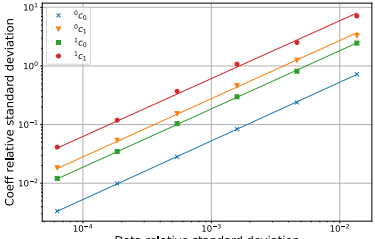

(B) Four parameters ${}^{i}c_j$ for dataset (4 ST).

Comparing activity and surface tension based assessments

About k_Γ in Butler equation

- An "uncertain" parameter (different values found in the literature, surface tension evaluation very sensitive to it)
- $\mathbf{n} = \{k_\Gamma\}$ so that k_Γ calibrated and marginalized

N.B. Prior distribution of k_Γ arbitrarily taken as a $[0, 1]$-truncated normal law of 10% relative std with 0.8 mean value

Key observations

- Minimum number of data points for a proper MCMC convergence increased by one $\rightarrow$ (5 ST) dataset
- Same trends as with dataset (4 ST) and k_Γ constant with:
  - Convergence threshold value σ_i/d_i decreased to about 10^{-3}
  - In the linear region, very limited increase of the **c** relative std

Positive outcome of the PoC on Cu-Mg

(incl. assessments with actual experimental data [Tou25])

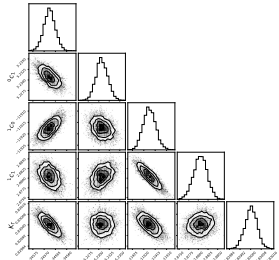

(A) Corner plot – $\sigma_i/d_i = 10^{-6}$ case.

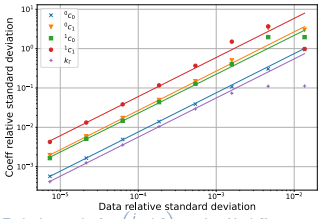

(B) Relative std of $p\left({}^{l}c_j|\mathbf{d}\right)$ and $p\left(k_\Gamma|\mathbf{d}\right)$ vs. σ_i/d_i.

3. Possible path forward

First results on U-O

First results for the U-O system

- Same approach as for Cu-Mg with “generated” data
- k_Γ value of 0.94 – *cf.* [THIH96] for oxidic systems – and **c** values from the NUCLEA
- Main difference: liquid miscibility gap over extended composition and T range
  $\rightarrow$ composition points such that equilibrium between a unique liquid and an inert gaseous atmosphere is possible
- e.g. results with 3 temperatures points and 4 composition points

Key observations

- Same trends as for Cu-Mg system
- Incl. k_Γ marginalization (not shown)

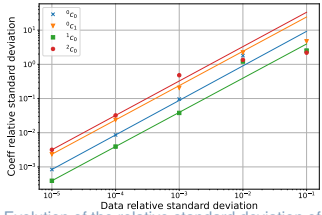

(A) Evolution of the relative standard deviation of $p\left({}^{i}c_j|\mathbf{d}\right)$ as a function of σ_i/d_i.

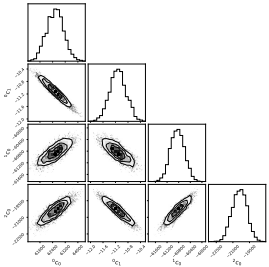

(B) Corner plot of the sampled posterior parameter distributions – $\sigma_i/d_i = 10^{-4}$ case.

Conclusions & perspectives

- Proof of concept about the use of surface tension data to improve liquid phase thermodynamic model in the frame of CALPHAD
- Key points:
  - Analysis carried out in the frame of Bayesian inference in order to adequately treat uncertainties
  - Butler-based modelling of surface tension
  - Detailed analysis with generated data on the well-assessed Cu-Mg system
  - Additional results on the U-O system to strengthen the analysis
- Main findings:
  - Surface tension data can advantageously replace or supplement activity data
  - k_Γ in Butler equation can be calibrated and marginalized without impairing the assessment
- Perspectives:
  - Measure surface tension of sub-stoichiometric U-O melts (out of the miscibility gap range) and revise the U-O liquid phase assessment with such data
  - Replace MCMC method by a simpler (and approximate) linear model (as used in the CALPHAD assessment framework in [Law20])

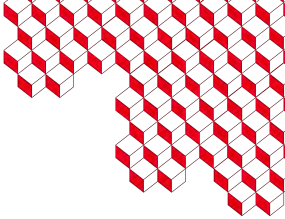

Thanks! Any questions?

References I

[Bar21] Marc Barrachin. Corium Experimental Thermodynamics: A Review and Some Perspectives. *Thermo*, 1(2):179–204, September 2021. Number: 2 Publisher: Multidisciplinary Digital Publishing Institute.

[BBR21] Théo Beigbeder, Emeric Bourasseau, and Michael Rushton. Thermophysical properties of liquid (U, Zr)O_2 by molecular dynamics. *Molecular Simulation*, 47(18):1502–1508, December 2021. Publisher: Taylor & Francis _eprint: https://doi.org/10.1080/08927022.2021.1987429.

[BOE+19] Brandon Bocklund, Richard Otis, Aleksei Egorov, Abdulmonem Obaied, Irina Roslyakova, and Zi-Kui Liu. ESPEI for efficient thermodynamic database development, modification, and uncertainty quantification: application to Cu–Mg. *MRS Communications*, 9(2):618–627, June 2019.

[CAL+91] Corinne A. Coughanowr, Ibrahim Ansara, Rauno Luoma, Marko Hämäläinen, and Hans Leo Lukas. Assessment of the Cu-Mg System / Optimierung des Systems Cu-Mg. *International Journal of Materials Research*, 82(7):574–581, July 1991. Publisher: De Gruyter.

References II

[CBB23] Jean-Paul Crocombette, Orane Barbour, and Fabien Bruneval. Structural and electronic properties of U_4O_9 from ab initio and empirical potential calculations. *Physical Review Materials*, 7(6):063602, June 2023. Publisher: American Physical Society.

[Cro22] Adrien Crochetet. *Mesure de propriétés thermo-physiques du corium en température*. Ph.d. thesis under preparation, Orléans, 2022.

[DPC+22] Jules Delacroix, Pascal Piluso, Nourdine Chikhi, Olivier Asserin, Damien Borel, Alexandre Brosse, and Stephen Cadiou. Measurements of Liquid AISI 304L Steel Density and Surface Tension, and Influence of Surface-Active Elements at High Temperatures. *steel research international*, 93(6):2100624, 2022. _eprint: https://onlinelibrary.wiley.com/doi/pdf/10.1002/srin.202100624.

[DTD+25] Caroline Denier, Arthur Tourneix, Jules Delacroix, Romain Le Tellier, Pascal Piluso, and Emmanuel de Bilbao. Density and surface tension of $U_{1-x}Zr_xO_{2-y}$ with different oxidation state: measurement and modelling at high temperature for nuclear severe accident applications. *Journal of Nuclear Materials*, 615:155928, September 2025.

References III

[GDK+21] C. Guéneau, N. Dupin, L. Kjellqvist, E. Geiger, M. Kurata, S. Gossé, E. Corcoran, A. Quaini, R. Hania, A. L. Smith, M. H. A. Piro, T. Besmann, P. E. A. Turchi, J. C. Dumas, M. J. Welland, T. Ogata, B. O. Lee, J. R. Kennedy, C. Adkins, M. Bankhead, and D. Costa. TAF-ID: An international thermodynamic database for nuclear fuels applications. *Calphad*, 72:102212, March 2021.

[GLT22] Kasi Gajavalli and Romain Le Tellier. Butler-based thermodynamic modeling of interfacial energies for in-vessel corium systems. *Journal of Nuclear Materials*, 569:153935, October 2022.

[JBK+24] C. Journeau, S. Bechta, A. Komlev, M. Kurata, T. Ohgi, T. Matsumoto, M. Afiqa, M. Barrachin, A. Quaini, C. Guéneau, D. Bottomley, A. Itoh, K. Nakamura, and M. Steinbrück. System Identification and Ranking Table (SIRT) for Chemical Thermodynamics of Severe Accidents. In *Proc. of the 11th European Review Meeting on Severe Accident Research (ERMSAR2024)*, Stockholm, Sweden, 2024.

[Law20] Eva Lawrence. *Reconstruction fonctionnelle et analyse d'incertitudes dans le cadre d'un problème inverse de thermodynamique*. phdthesis, Toulouse 3, December 2020.

References IV

[LFS07] H. Lukas, S. G. Fries, and B. Sundman. *Computational Thermodynamics: The Calphad Method*. Cambridge University Press, 2007.

[SKPF15] Bo Sundman, Ursula R Kattner, Mauro Palumbo, and Suzana G Fries. OpenCalphad - a free thermodynamic software. *Integrating Materials and Manufacturing Innovation*, 4(1), 2015.

[TDLT+24] Arthur Tourneix, Caroline Denier, Romain Le Tellier, Pascal Piluso, and Jules Delacroix. Thermodynamic evaluation of liquid-gas surface tension for U-O-Zr mixtures using the Butler equation. In *Proc. of the 11th European Review Meeting on Severe Accident Research ERMSAR2024*, Stockholm, May 2024.

[THIH96] Toshihiro Tanaka, Klaus Hack, Takamichi Iida, and Shigeta Hara. Application of thermodynamic databases to the evaluation of surface tensions of molten alloys, salt mixtures and oxide mixtures. *International Journal of Materials Research*, 87(5):380–389, May 1996. Publisher: De Gruyter.

References V

[TNBB24] J. Tranchida, F. Nicaud, B. W. Beeler, and E. Bourasseau. Thermophysical properties and unexpected viscosity of liquid (U, Zr): An atomistic investigation. *The Journal of Chemical Physics*, 160(21):214507, June 2024.

[Tou25] Arthur Tourneix. *Amélioration de la modélisation thermodynamique de liquides multicomposants à haute température par assimilation de données de tension de surface*. PhD thesis, 2025.

ESTIMATION OF THE COOLING RATE OF U-ZR-FE-CR-O SAMPLE WHICH UNDERWENT MELTING

Yoichi Endo, Kan Sakamoto, Atsushi Ouchi, and Hiroki Yokoyama
NIPPON NUCLEAR FUEL DEVELOPMENT CO., LTD.
2163 Narita-cho, Oarai-machi, Higashi-Ibaraki-gun, Ibaraki-ken, 311-1313, Japan
yoichi.endo@nfd.co.jp

Ryotaro Hagiwara, Masato Mizokami, and Mutsumi Hirai
Tokyo Electric Power Company Holdings, Inc.
1-1-3 Uchisaiwai-cho, Chiyoda-ku, Tokyo, 100-8560, Japan

ABSTRACT

Estimating the cooling rate of fuel debris formed during the accident at the Fukushima Daiichi Nuclear Power Station (FDNPS) is essential for understanding accident progression phenomena. In this study, we propose a method to estimate the cooling rate of U–Zr–Fe–Cr–O particles based on microstructural observations and a diffusion-based scaling model. Simulated U–Zr–Fe–Cr–O debris samples were fabricated under rapid- and slow-cooling conditions, and their phase-separated microstructures were characterized by scanning electron microscopy and transmission electron microscopy.
The results revealed that the phase-separation spacing of the interpenetrating microstructure varied with the cooling rate. By applying a diffusion-based scaling model to the measured spacing, the cooling rate of particles collected from the operating floor of Unit 2 at FDNPS was estimated to be on the order of 10^3 K/s. Furthermore, the feasibility of the estimated cooling rate was examined using a simplified heat-transfer model assuming a freely flying spherical molten droplet, demonstrating that the estimate is not thermally inconsistent. The relationship between cooling rate and equivalent droplet size was also evaluated.
This study provides a quantitative approach to infer the cooling conditions of U–Zr–Fe–Cr–O fuel-debris particles from phase-separated microstructures and is expected to contribute to a deeper understanding of accident progression behavior.

KEYWORDS
Accident Progression, Cooling rate, Phase separation

1. INTRODUCTION

At the Fukushima Daiichi Nuclear Power Station (FDNPS), an accident occurred in which cooling functions were lost due to the tsunami, leading to core melting. Deepening our understanding of accident progression is essential for safe decommissioning and for the design of nuclear reactors with improved safety; however, the situation remains highly uncertain. In this context, samples and debris collected from FDNPS are considered to contain information relevant to the formation processes of fuel debris. Accordingly, analyses of such samples and debris have been conducted to contribute to understanding accident progression. Previous analyses have reported particles containing high-temperature stable phases and particles exhibiting phase separation [1]. These particles are considered to retain the information on the fuel-debris formation process, including the cooling conditions during solidification. Specifically, the persistence of high-temperature stable phases suggests rapid cooling, whereas the observation of phase separation in systems with slow diffusion (e.g., in solids) implies slow cooling. However, these assessments remain qualitative and have not yielded numerical estimates of cooling rates.

Therefore, our research group has been exploring methods to infer formation-process information such as cooling rates from the information obtained through analyses of samples collected from FDNPS. We have previously investigated the relationships between cooling rate and the crystal structure and microstructure of $(U,Zr)O_2$ [2]. In the $(U,Zr)O_2$ system, cooling at rates on the order of 10 °C/min or lower results in phase separation and crystal-structure transformations, indicating sensitivity to slow cooling rates. In contrast, methods to infer higher cooling rates remain a challenge.

To address this, we focus not only on $(U,Zr)O_2$ but also on quinary U–Zr–Fe–Cr–O particles containing Fe and Cr [1, 3]. As shown in Fig. 1, particles collected from the operating floor of Unit 2 reactor building—specifically from the cover sheet (hereafter, the "2u OF particle")—and particles from a deposit fragment at the Unit 2 X-6 penetration (hereafter, the "2u X-6 PEN particle") consist of a U–Zr–O phase and a Cr–Fe–O phase. These particles are considered to have formed via phase separation of a U–Zr–Fe–Cr–O melt during cooling. Because such precipitation/phase-separated microstructures are presumed to arise via rapid diffusion in the liquid phase, they are expected to be sensitive to higher cooling rates, and the precipitate size may depend on cooling rate.

In this study, we perform microstructural observations of U–Zr–Fe–Cr–O simulated debris cooled at different cooling rates, and explore an approach to estimate the cooling rates of FDNPS samples.

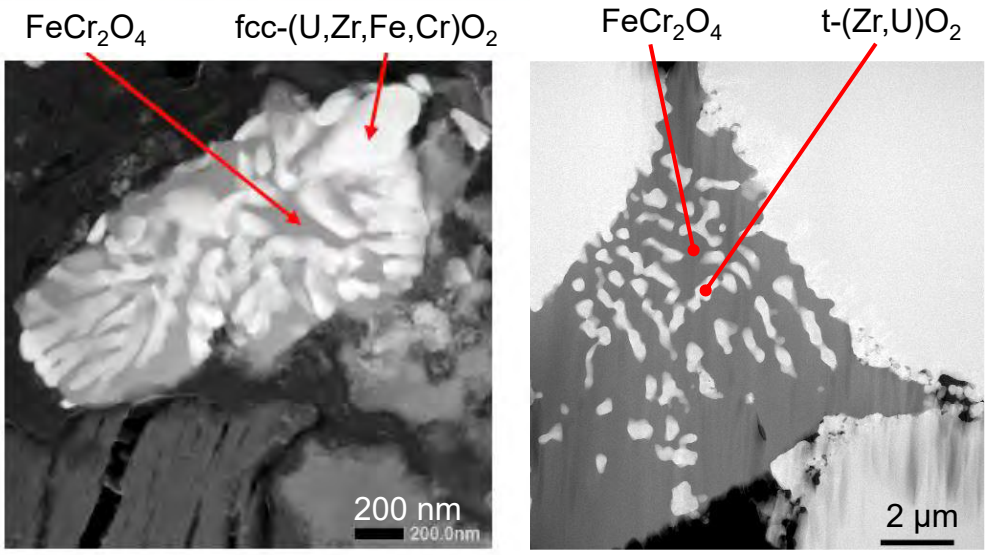

Figure 1. TEM images of 2u OF particle (left) [1] and 2u X-6 PEN particle (right) [3]

2. METHODS

2.1 Thermodynamic calculations for experimental condition design

To set the experimental conditions, thermodynamic calculations were performed using Thermo-Calc 2025b [4] with the Thermo-Calc Software IRSN Nuclear Alloys-Oxides Database v20 [5], assuming the approximate composition of the 2u OF particle. The metal-element ratio of the 2u OF particle was estimated from the compositions and area fractions of the $(U,Zr)O_2$ phase and the $FeCr_2O_4$ phase, yielding U:Zr:Fe:Cr = 20:15:25:40. The oxygen content was set by assuming that the analyzed products were oxides [1, 3] and that the atmosphere inside Unit 2 during the accident was not strongly oxidizing [6]. Accordingly, U and Zr were treated as dioxides, Fe as FeO, and Cr as $CrO_{1.5}$, corresponding to the oxide-component composition summarized in Table I. The results are shown in Fig. 2. The calculation indicated that the assumed composition becomes fully molten at slightly below 1900 °C, forming an oxide liquid phase.

Table I. Assumed oxide-component composition used for thermodynamic calculation and powder mixing

Component	UO_2	ZrO_2	FeO	$CrO_{1.5}$
Amount (mol%)	20	15	25	40

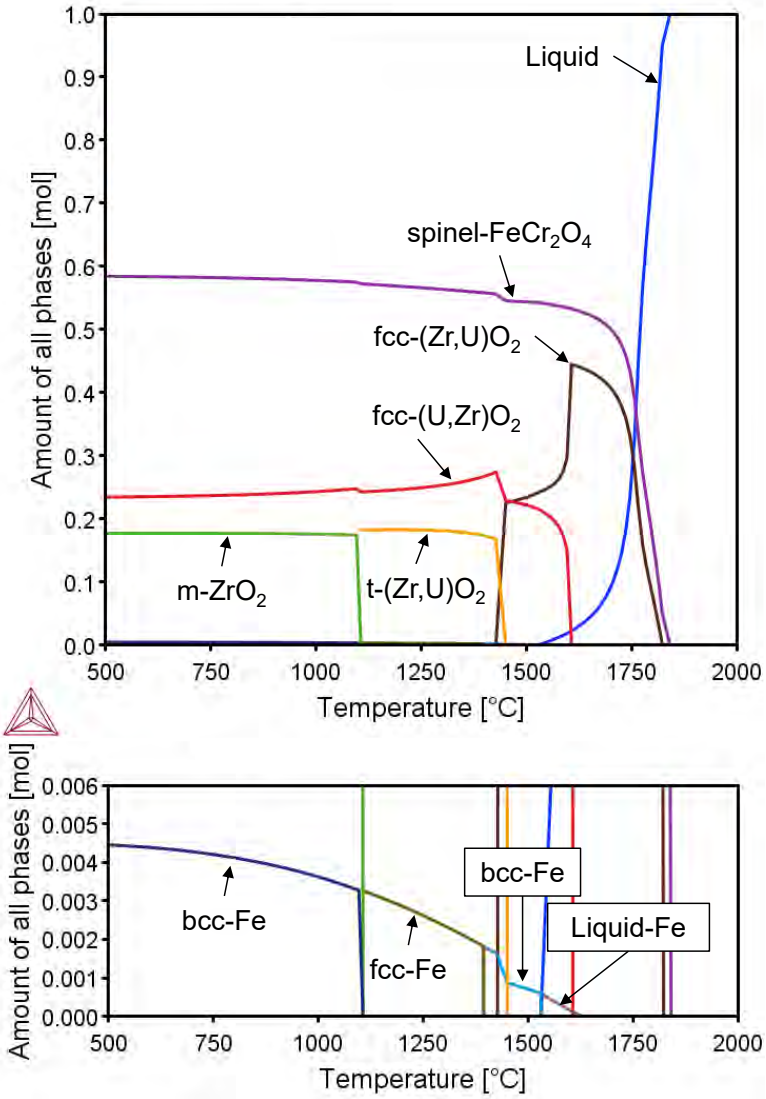

Figure 2. Thermodynamic calculation results with the approximate composition of the 2u OF particle. The lower panel shows an enlarged view of the vertical-axis range near 0–0.006.

2.2 Solidification experiments under different cooling rates

To examine the effect of cooling rate on the solidified microstructure, powders of UO_2, ZrO_2 (purity 98%, Kojundo Chemical Lab. Co., Ltd.), FeO (purity 99.5%, Kojundo Chemical Lab. Co., Ltd.), and Cr_2O_3 (purity 99.9%, Kojundo Chemical Lab. Co., Ltd.) were mixed to match the oxide-component composition shown in Table I. The mixture was heated at 1900 °C for 10 min in a yttria-stabilized zirconia (YSZ) crucible under an Ar (G2) flow. The Ar gas was passed through an oxygen-removal purifier before introduction into the furnace. The sample was then subjected to either rapid cooling (cooling rate: approximately 700 °C/min from 1900 to 1200 °C) or slow cooling (cooling rate: 5 °C/min). The measured temperature in this test was the value recorded by a radiation thermometer directed at the

bottom surface of the tungsten crucible containing the YSZ crucible and sample. The indicated temperature was calibrated using the melting points of pure metals, such as Pt and Rh, under the same optical configuration. A simplified one-dimensional heat-conduction calculation was then performed to estimate the thermal lag from the tungsten crucible to the U–Zr–Fe–Cr–O melt. The calculation indicated that the cooling of the melt center was delayed relative to that at the bottom surface of the tungsten crucible. Nevertheless, the cooling rate of the melt center around 1600–1500 °C, where the phase-separated microstructure is considered to have formed, was estimated to be approximately 600–800 °C/min, which is of the same order as the above cooling rate of 700 °C/min.

The obtained samples were mounted in resin, sectioned, and polished. The polished surfaces were then examined by scanning electron microscopy - energy dispersive X-ray spectroscopy (SEM-EDS) and transmission electron microscopy (TEM)-EDS, and electron diffraction.

3. RESULTS AND DISCUSSION

3.1 Results

Fig. 3 shows SEM (backscattered electron, BSE) images for the slowly cooled and rapidly cooled specimens. Phase-separated microstructures were observed in both specimens. No clear macroscopic stratification into oxide-rich and metal-rich layers was observed in the polished cross sections examined by SEM-EDS. In the slowly cooled specimen, the phase-separated microstructure was coarser than that in the rapidly cooled specimen.

Fig. 4 shows enlarged SEM-EDS maps of the rapidly cooled specimen. The bright regions in the SEM (BSE) image clearly coincided with U- and Zr-rich regions. Regions with lower U and Zr were Cr-rich. The dark regions in the SEM (BSE) image corresponded to Cr-rich regions. The Cr-rich regions could be further classified into Fe-rich areas and areas with low Fe. Oxygen was distributed throughout the specimen. Therefore, the presence of U–Zr–O, Cr–O, and Cr–Fe–O phases is suggested. The interpenetrating microstructure of the U–Zr–O phase and the Cr–Fe–O phase was similar to that observed in the 2u OF particle. The phase-separation spacing between U–Zr–O phase regions within this interpenetrating microstructure was on the order of 1 μm.

Fig. 5 shows an SEM (BSE) image of the slowly cooled specimen. Similar to the rapidly cooled specimen, it consisted of dark and bright regions. Interpenetrating microstructures were also observed; however, the phase-separation spacing was on the order of 10 μm, i.e., approximately one order of magnitude larger than that in the rapidly cooled specimen.

Fig. 6 shows TEM images of the rapidly cooled specimen (left) and the slowly cooled specimen (right). Based on TEM-EDS point analyses and electron diffraction, the rapidly cooled specimen contained fcc-$(U,Zr)O_2$ and spinel-$FeCr_2O_4$, while the slowly cooled specimen additionally contained bcc-(Fe,Cr). Table II summarizes a comparison among the 2u OF particle, the rapidly cooled specimen, and the slowly cooled specimen, including TEM results. For compositional data, multiple TEM-EDS point analyses were performed for each phase and averaged. For the U–Zr–O phase, all specimens exhibited an fcc structure, and the U:Zr ratio was approximately 6:4; thus, the simulated debris specimens were consistent with the 2u OF particle. TEM-EDS point analyses did not indicate significant Fe dissolution in the fcc-$(U,Zr)O_2$ phase within the resolution and quantification limits of the present analysis. For the Fe–Cr–O phase, the crystal structure was consistent (spinel), whereas the composition showed some deviation between the simulated debris and the 2u OF particle. However, thermodynamic calculations at 1500 °C (immediately after completion of solidification) for the (Fe,Cr):O = 3:4 system, using Cr/(Cr+Fe) as a parameter, indicate that the dominant phase remains spinel over a wide range of Cr/(Cr+Fe) = 0–0.77; therefore, such compositional differences are plausible. Notably, the Cr fraction in the Fe–Cr–O phase of the simulated debris approached the upper bound of this range.

Table II also lists the phase-separation spacing of the phase-separated interpenetrating region obtained from SEM observations. The spacing was approximately 1 μm for the rapidly cooled specimen and approximately 10 μm for the slowly cooled specimen. These spacings are larger than that of the 2u OF particle (approximately 0.1 μm). The experimentally identified solid phases were compared with the thermodynamic calculation shown in Fig. 2. The calculation predicted that fcc-$(U,Zr)O_2$ and spinel-$FeCr_2O_4$ phases remain stable down to lower temperatures after solidification, which is broadly consistent with the TEM results. The bcc-(Fe,Cr) phase observed in the slowly cooled specimen is also qualitatively consistent with the calculated appearance of a bcc Fe-rich phase at lower temperatures. However, the experimentally observed bcc phase contained both Fe and Cr, whereas the calculation assumes global equilibrium. In addition, the Fe content in the fcc-$(U,Zr)O_2$ phase may depend on the oxygen potential assumed in the thermodynamic calculation. Therefore, the comparison between the calculated and observed phase compositions should be regarded as qualitative.

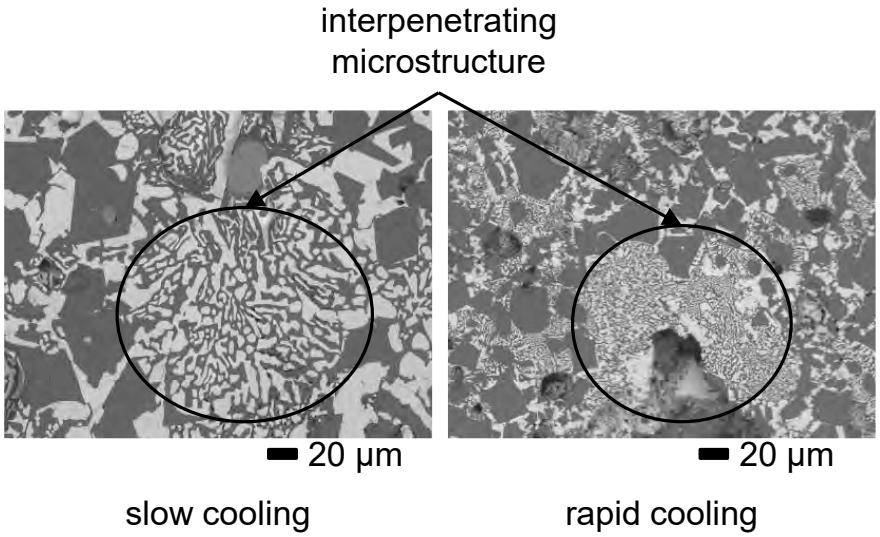

Figure 3. SEM images of slowly and rapidly cooled simulated fuel debris

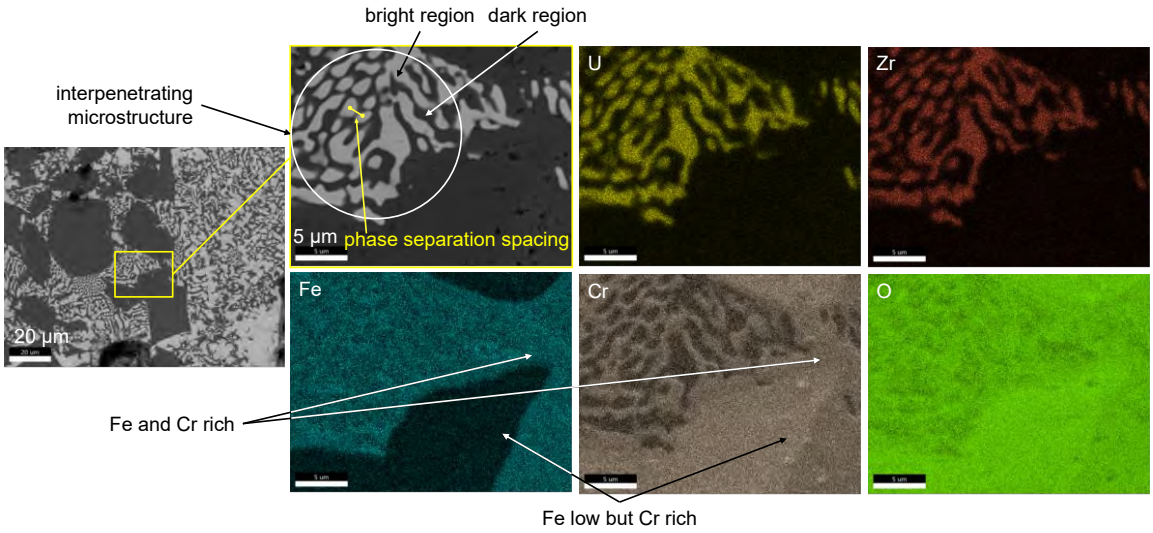

Figure 4. SEM-EDS maps of rapidly cooled simulated fuel debris

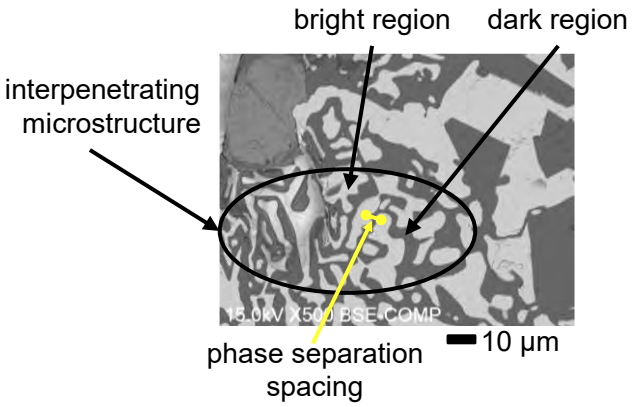

Figure 5. SEM image of slowly cooled simulated fuel debris

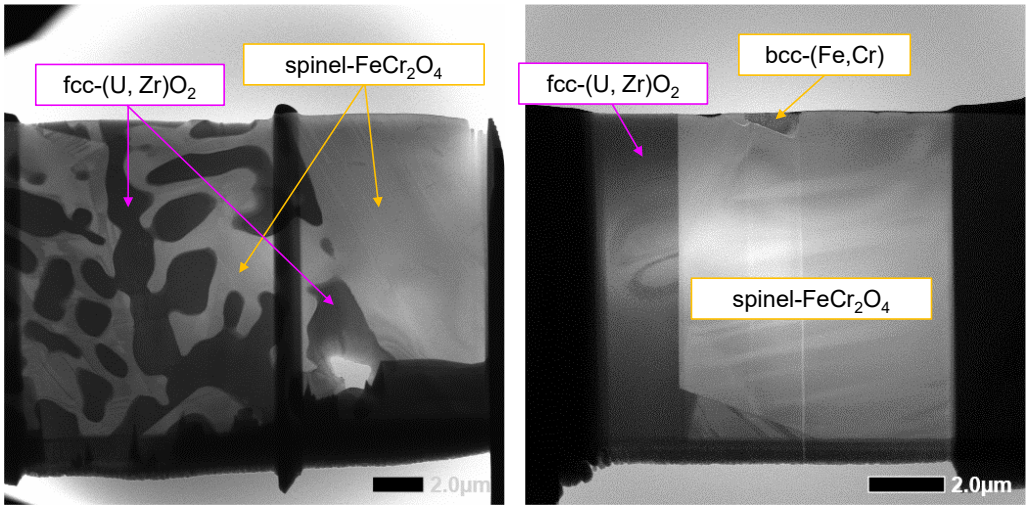

Figure 6. TEM images of rapidly (left) and slowly (right) cooled simulated fuel debris

Table II. Comparison among the 2u OF particle and the rapidly and slowly cooled simulated fuel debris specimens

Sample	Phase	Crystal structure	Composition (at%)	Phase-separation spacing
2u OF particle	U-Zr-O	fcc	U/(U+Zr)≈60	0.1 μm
	Fe-Cr-O	spinel	Cr/(Cr+Fe)≈60	
Rapid cooling	U-Zr-O	fcc	U/(U+Zr)≈64	1 μm
	Fe-Cr-O	spinel	Cr/(Cr+Fe)≈73	
Slow cooling	U-Zr-O	fcc	U/(U+Zr)≈53	10 μm
	Fe-Cr-O	spinel	Cr/(Cr+Fe)≈77	

3.2 Estimation of the cooling rate of the FDNPS particles

Using the phase-separation spacing in the interpenetrating region of the simulated debris microstructure as shown in the schematic image of Fig. 7, we attempted to estimate the cooling rate during formation of an FDNPS particle. Let the phase-separation spacing between adjacent bright regions in the interpenetrating phase-separated microstructure be L (cm), the characteristic formation time of this region be t (s), and the apparent diffusion parameter be D (cm^2/s). Assuming that diffusion follows Fick's law, the relationship can be expressed as:

$$L = \sqrt{Dt} \tag{1}$$

Let the temperature drop during formation of the interpenetrating region be ΔT (K) and the cooling rate be v (K/s). Because t=$\Delta T/v$, substitution yields:

$$D = \frac{vL^2}{\Delta T} \tag{2}$$

According to the thermodynamic calculation results in Fig. 2, the U–Zr–Fe–Cr–O melt is fully molten above approximately 1900 °C (oxide liquid phase). Upon cooling, crystallization of $(U,Zr)O_2$ and $FeCr_2O_4$ begins at slightly above 1800 °C and ends at approximately 1500 °C. Here, D should be regarded as an apparent diffusion parameter representing the characteristic mass transport associated with the formation of the interpenetrating phase-separated microstructure. It is not a tracer diffusion coefficient of a specific element. In this study, D was treated as constant over the temperature interval in which the interpenetrating microstructure formed. Although the absolute value of this apparent parameter depends on the assumed temperature interval ΔT, ΔT cancels out in the derivation of Eq. (3). Therefore, the present analysis does not require assigning a literature diffusion coefficient to a specific element.

Using the average apparent diffusion parameter $\overline{D}$ obtained from the rapidly cooled and slowly cooled specimens, the cooling rate v (K/s) for an FDNPS particle can be expressed as:

$$v_{\mathrm{p}} = \frac{\overline{D}\Delta T}{{L_{\mathrm{p}}}^2} = \frac{v_{\mathrm{R}}{L_{\mathrm{R}}}^2 + v_{\mathrm{S}}{L_{\mathrm{S}}}^2}{2\Delta T} \cdot \frac{\Delta T}{{L_{\mathrm{p}}}^2} = \frac{v_{\mathrm{R}}{L_{\mathrm{R}}}^2 + v_{\mathrm{S}}{L_{\mathrm{S}}}^2}{2{L_{\mathrm{p}}}^2} \tag{3}$$

where subscripts p, R, and S denote an FDNPS particle, the rapidly cooled specimen, and the slowly cooled specimen, respectively.

Fig. 7 plots the relationship between the cooling rate and the spacing of the interpenetrating microstructure. The region between the rapidly cooled and slowly cooled data points corresponds to interpolation and is shown by a solid line, whereas extrapolated regions are shown by dashed lines. The phase-separation spacing in the interpenetrating region is approximately 0.1 μm for the 2u OF particle and approximately 1 μm for the 2u X-6 PEN particle. The corresponding cooling rates are estimated to be on the order of 10^3 K/s and approximately 10 K/s, respectively. Because the present model is intended for order-of-magnitude estimation, the estimated cooling rates should be interpreted as order-of-magnitude values rather than precise numerical values.

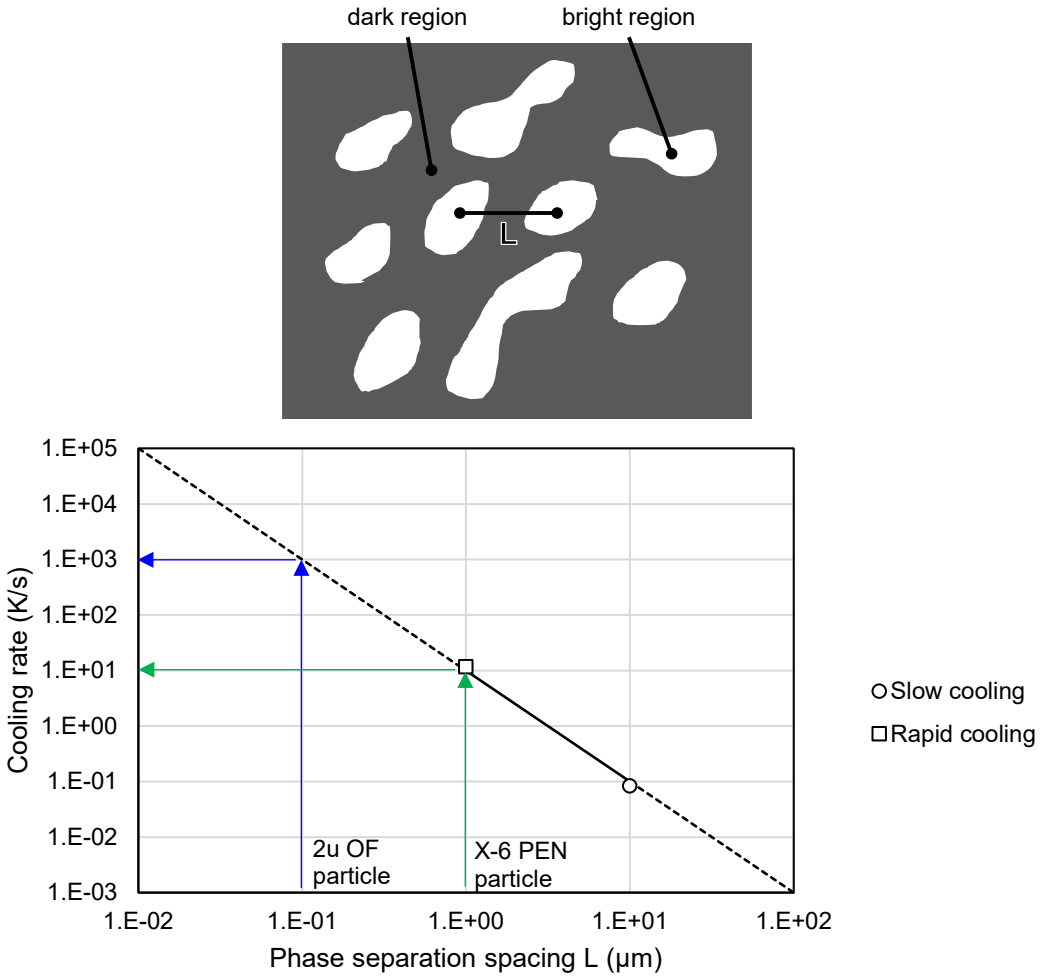

Figure 7. Schematic illustration of the phase-separation spacing L (upper panel) and relationship between phase-separation spacing and cooling rate (lower panel).

3.3 Estimation of the solidification scale from the estimated cooling rate of U–Zr–Fe–Cr–O melt droplets

The energy balance of a droplet can be expressed based on Newton's law of cooling [7] as:

$$\rho V c \frac{\mathrm{d}T}{\mathrm{d}t} = -A[h(T - T_\infty) + \varepsilon\sigma(T^4 - {T_\infty}^4)] \tag{4}$$

where ρ and c are the density and specific heat of the droplet, respectively; V is the volume; A is the surface area; T is the droplet temperature; T_∞ is the ambient temperature; h is the convective heat transfer coefficient; ε is the emissivity; and σ is the Stefan–Boltzmann constant.
For a spherical droplet with radius r,

$$\frac{A}{V} = \frac{3}{r} \tag{5}$$

therefore, the cooling rate is:

$$\frac{\mathrm{d}T}{\mathrm{d}t} = -\frac{3}{\rho c r}[h(T - T_\infty) + \varepsilon\sigma(T^4 - {T_\infty}^4)] \tag{6}$$

This equation allows estimation of the solidification scale (r) from the cooling rate (dT/dt) estimated by the diffusion model.

Because physical properties (ρ, c) of U–Zr–Fe–Cr–O melt droplets and parameters (h, ε) for the relevant system have not been reported, they were set as follows. The density ρ was calculated as a weighted average based on the densities of the input oxides: UO_2 (10.97), ZrO_2 (5.68), FeO (6.0), and Cr_2O_3 (5.22) [8], yielding $\rho=8\times10^3$ kg/m^3. This value is a weighted average of solid densities. Although density generally decreases in the liquid phase compared to the solid phase, the reduction is typically on the order of several tens of percent; thus, the order of magnitude remains unchanged. Because the purpose here is an order-of-magnitude evaluation, the weighted average of literature solid densities was used. If a lower melt density were assumed, the estimated solidification scale would become larger.

The specific heat c was set based on reported values for molten UO_2 and molten ZrO_2, approximately 380 J/kg/K and 815 J/kg/K, respectively [9]. In addition, based on NIST-JANAF data [10], the specific heats of molten FeO and molten Cr_2O_3 are approximately 949 J/kg/K and 1032 J/kg/K, respectively. Although the oxides other than FeO are not molten at the test temperature (1900 °C) as pure substances, the temperature dependence of specific heat in the molten state is small; therefore, these values were adopted. A weighted average yields $c=7\times10^2$ J/kg/K.

For h, it is known that the convective heat transfer coefficient for spherical droplets moving in a gas phase is on the order of $h\sim10^2$ W/m^2/K for mm-scale particles [7]; therefore, $h=100$ W/m^2/K was used. For emissivity ε, uranium oxides exhibit values of 0.70–0.90 [11], and emissivity of molten slag during steelmaking is reported as 0.75–0.87 [12]; therefore, $\varepsilon=0.8$ was assumed.

Using these values, and back-calculating the radius required to satisfy the cooling rate of 10^3 K/s estimated for the 2u OF particle, the radius is approximately 0.6 mm under $T=2000$ °C and $T_\infty=1000$ °C. Considering that the 2u OF particle was collected from the operating floor above the primary containment vessel, it may have solidified at a size range that could be released into the atmosphere, and the present model is not inconsistent with such a scenario. In contrast, the observed size of the 2u OF particle is less than approximately 1 μm, which is markedly smaller than the back-calculated droplet radius (0.6 mm). It is possible that a sub-millimeter droplet, once released into the atmosphere and solidified, was subsequently fragmented during processes prior to sampling.

Thus, this formulation enables estimation of the droplet size at solidification from a cooling rate estimated by the diffusion model. Fig. 8 shows the relationship between the cooling rate and droplet size. In the above equation, ρ and c contribute inversely (power of −1) to the cooling rate, while h and ε contribute linearly; in contrast, T and T_∞ contribute through the fourth-power radiation term, indicating high sensitivity to T and T_∞. Therefore, using $T=2000$ °C and $T_\infty=1000$ °C as a benchmark, cases of $T=2400$ °C and 1600 °C and cases of $T_\infty=1500$ °C and 500 °C are also shown. For the same droplet radius, the influence of droplet temperature is larger than that of ambient temperature.

From the cooling rate–size relationship, the 2u OF particle with an estimated cooling rate of 10^3 K/s corresponds to a droplet radius of approximately 0.3–1.5 mm, whereas the 2u X-6 PEN particle with an estimated cooling rate of 10 K/s corresponds to a droplet radius of approximately 30–150 mm. Considering that the 2u X-6 PEN particle was a particle in a deposit collected during hatch opening at the X-6 penetration, it is unlikely that it solidified as a droplet of such a large size. In this model, the internal temperature of the droplet is assumed uniform when estimating the solidification scale. In practice, the thermal conductivity of oxide melts is low; therefore, particularly for large particles, a temperature gradient between the surface and the interior is expected. If internal temperature distribution is considered, the surface temperature may decrease faster than predicted by this model, while the interior temperature may decrease more slowly. Such effects due to low thermal conductivity may contribute to uncertainty in estimating the solidification scale of the 2u X-6 PEN particle. This case is intentionally shown here to indicate the limitation of applicability. Defining the applicable range of the present model remains a subject for future work.

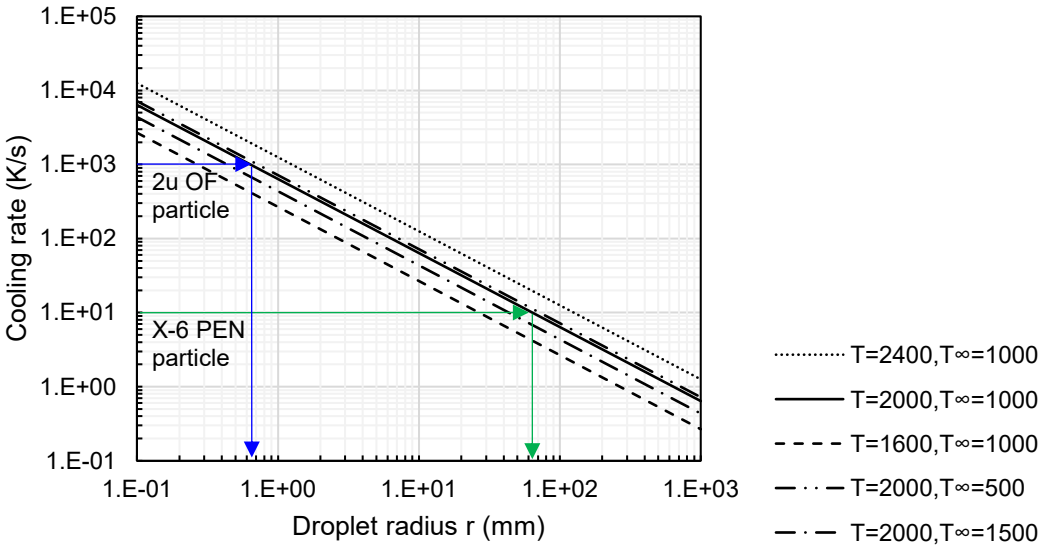

Figure 8. Relationship between droplet radius and cooling rate

4. CONCLUSIONS

In this study, we attempted to estimate the cooling rate of U–Zr–Fe–Cr–O system samples collected from FDNPS. Two types of U–Zr–Fe–Cr–O simulated debris specimens were fabricated under different cooling rates. A finely phase-separated microstructure consisting of fcc-$(U,Zr)O_2$ and spinel-$FeCr_2O_4$, similar to that observed in the FDNPS sample, was successfully obtained.

Using the phase-separation spacing in the finely phase-separated interpenetrating region of the simulated debris, the cooling rate of the 2u OF particle was estimated by a diffusion-based scaling model to be on the order of 10^3 K/s. This estimated cooling rate is not inconsistent from the viewpoint of heat transfer. Thus, this study demonstrates a method to estimate cooling conditions quantitatively from phase-separation spacing.

In addition, we proposed a heat-transfer-based model to estimate the droplet size at solidification from the estimated cooling rate. However, further investigation is required to define the range of applicability of this model. Overall, this study provides a framework for quantitatively estimating cooling conditions from phase-separated microstructures and is expected to contribute to reducing uncertainty in inferring the formation processes of fuel debris.

REFERENCES

1. TEPCO, “The 6th Progress Report on the Investigation and Examination of Unconfirmed and Unsolved Issues on the Development Mechanism of the Fukushima Daiichi Nuclear Accident”, Nov. 10th 2022, https://www.tepco.co.jp/en/hd/decommission/information/accident_unconfirmed/pdf/20221110-e.pdf
2. Endo et al., “RELATION OF COOLING RATE TO CRYSTAL STRUCTURE AND MICROSTRUCTURE OF (U, ZR)O_2”, *Proceedings of FDR2024 International Topical Workshop on Fukushima Decommissioning Research,* Fukushima, Japan, Oct 10th -13th, 2024, FDR2024-1013 (2024).
3. TEPCO, “Analysis of the sample collected from X-6 penetration for the Unit 2 (Translated from Japanese.)”, Feb. 27th 2025, https://www.tepco.co.jp/decommission/information/committee/roadmap_progress/pdf/2025/d250227_28-j.pdf
4. Andersson J.O., Helander T., Höglund L., Shi P.F., and Sundman B., “Thermo-Calc and DICTRA,

Computational tools for materials science." *Calphad*, **26**, pp. 273-312 (2002).
5. Thermo-Calc Software IRSN Nuclear Alloys-Oxides Database v20
6. Itoh, A. et al. "Early-phase core degradation interpretation by interaction between fuel cladding and fuel components in Fukushima Daiichi nuclear power plant Unit 2", *Journal of Nuclear Science and Technology*, **61**(11), pp. 1453–1469 (2024)
7. T. L. Bergman et al., *INTRODUCTION TO HEAT TRANSFER*, 8th ed., Wiley. (2011)
8. William M., *CRC handbook of chemistry and physics*. CRC press, (2016)
9. Woong Kee Kim et al., "Thermophysical properties of liquid UO_2, ZrO_2 and corium by molecular dynamics and predictive models", *Journal of Nuclear Materials* **491** pp. 126-137 (2017)
10. Chase, M.W., Jr., "NIST-JANAF Thermochemical Tables, Fourth Edition," *J. Phys. Chem. Ref. Data,* Monograph 9, pp. 1-1951. (1998)
11. Held, Peter C., and D. R. Wilder. "High‐Temperature Hemispherical Spectral Emittance of Uranium Oxides at 0.65 and 0.70 μm."*Journal of the American Ceramic Society* **52**(4) pp. 182-185 (1969)
12. Rangavittal, B. V., Köchner, H., and Glaser, B. "Experimental Determination of Slag Emissivities for Enhanced Slag Control by Infrared‐Based Systems," *Steel Research International*. **96**, 2400277 (2025)

Estimation of the Cooling Rate of U-Zr-Fe-Cr-O Sample Which Underwent Melting

Y. Endo[1], K. Sakamoto[1], H. Yokoyama[1], A. Ouchi[1],
R. Hagiwara[2], M. Mizokami[2], M. Hirai[2]
[1]NFD, [2]TEPCO HD

Copyright© NIPPON NUCLEAR FUEL DEVELOPMENT Co., Ltd. 2026. All rights reserved.

Motivation: Convert FDNPS* fuel debris observations into accident-progression information

Power the Future

Accident progression

Molten fuel debris formation → Cooling & solidification → Debris observation → Cooling rate inference

FDNPS fuel debris

https://fukushima.jaea.go.jp/debris/images/pict-20250529_4.png

Proposing estimation framework

- **Fuel debris can retain information on accident progression.**
- **Debris microstructures can record cooling and solidification histories.**
- **However, current interpretations are often qualitative.**

Purpose

- **Estimate the cooling rate of FDNPS fuel-debris particles from phase-separation spacing and check its thermal plausibility.**

* FDNPS: Fukushima Daiichi Nuclear Power Station

Copyright© NIPPON NUCLEAR FUEL DEVELOPMENT Co., Ltd. 2026. All rights reserved.

Target FDNPS particles: Fine U–Zr–O / Fe–Cr–O phase-separated microstructures

The target particles show sub-micron to micron-scale phase separation that may reflect cooling history.

Particle from operating floor of unit 2 (2u OF particle)

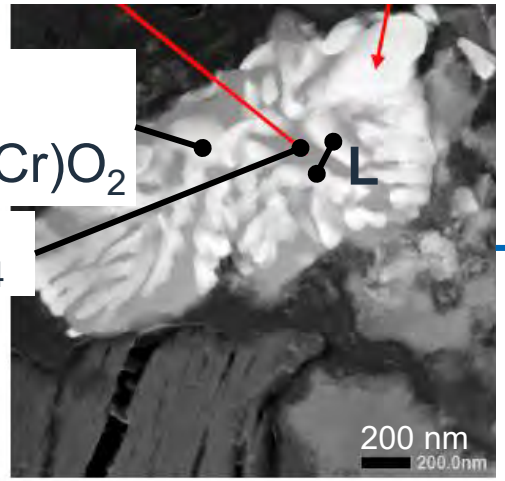

phase-separation spacing
L : ~0.1 μm

https://www.tepco.co.jp/en/hd/decommission/information/accident_unconfirmed/pdf/20221110-e.pdf

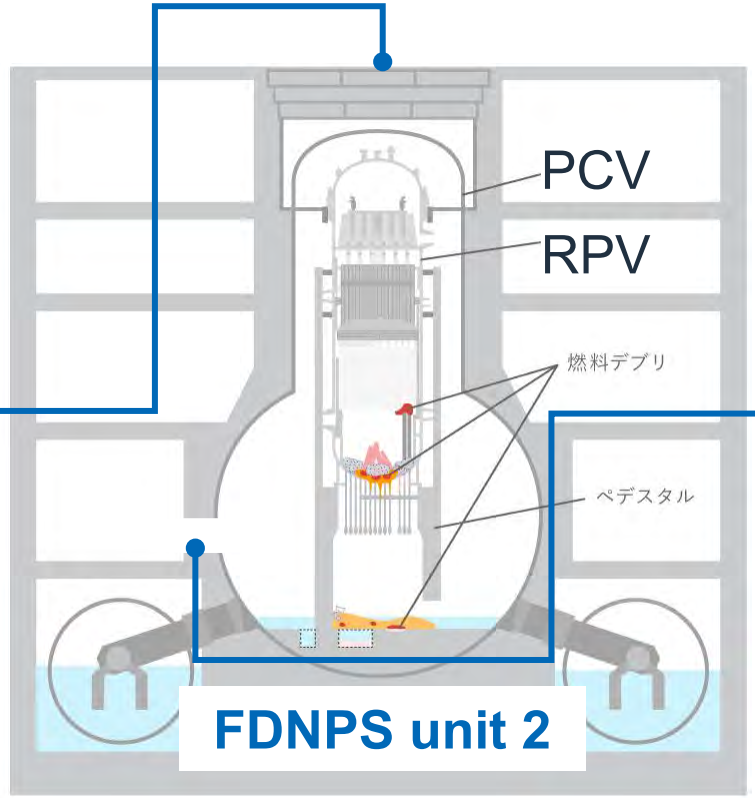

https://www.tepco.co.jp/decommission/common/images/progress/retrieval/unit2_img_index-j_01.png

Particle from X-6 penetration of unit 2 (2u X-6 PEN particle)

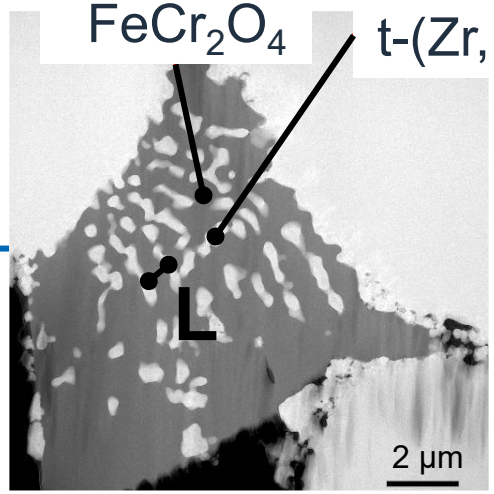

phase-separation spacing
L : ~1 μm

https://www.tepco.co.jp/decommission/information/committee/roadmap_progress/pdf/2025/d250227_28-j.pdf

Copyright© NIPPON NUCLEAR FUEL DEVELOPMENT Co., Ltd. 2026. All rights reserved.

Research question and strategy

Can phase-separation spacing (L) be calibrated against cooling rate (v) and applied to FDNPS particles?

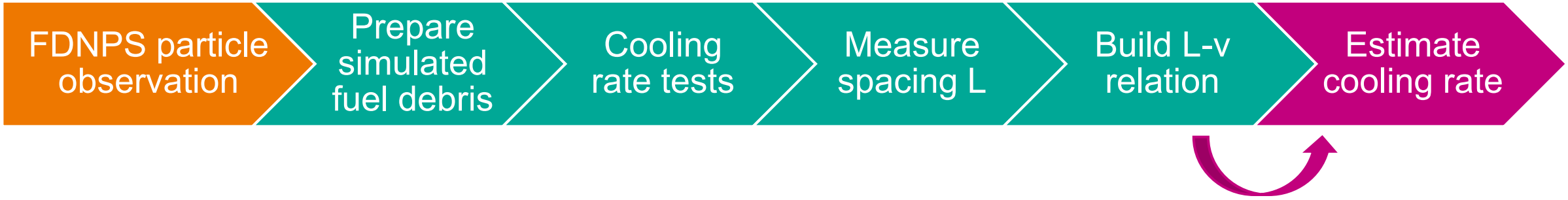

Simulated debris is not expected to match the FDNPS particle's spacing exactly; the spacing difference is used as the signal.
The model is deliberately presented as an order-of-magnitude cooling-rate estimate.

Copyright© NIPPON NUCLEAR FUEL DEVELOPMENT Co., Ltd. 2026. All rights reserved.

Experimental condition design: Ensure a molten U–Zr–Fe–Cr–O starting state

Thermodynamic calculation indicates that solidification starts from an oxide liquid between 1800 and 1900 °C for the approximate 2u OF composition.

Calculated phase amounts

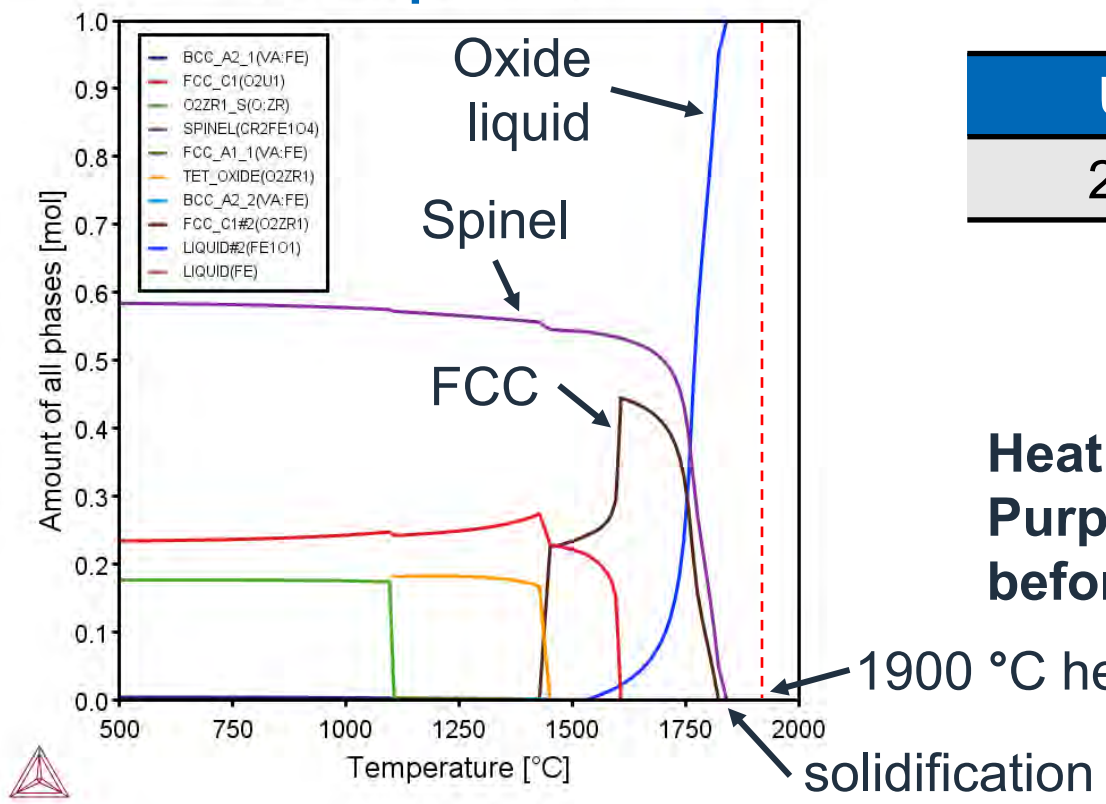

Approximate metal ratio

U	Zr	Fe	Cr
20	15	25	40

(at% of metal elements)

Heating condition: 1900 °C for 10 min in Ar.
Purpose: Start from a common molten state before rapid/slow cooling.

Copyright© NIPPON NUCLEAR FUEL DEVELOPMENT Co., Ltd. 2026. All rights reserved.

Experimental procedure

Two specimens were prepared from the same nominal melt and cooled at different rates.

UO_2+ZrO_2+ FeO+Cr_2O_3 → Mixing & compacting → 1900 °C, 10 min in Ar → Rapid: ~700 °C/min Slow: 5 °C/min → SEM-EDS / TEM-EDS electron diffraction

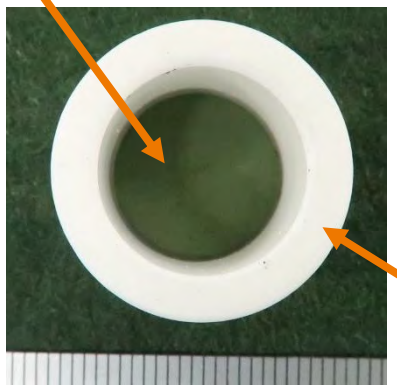

Top side

yttria-stabilized zirconia crucible

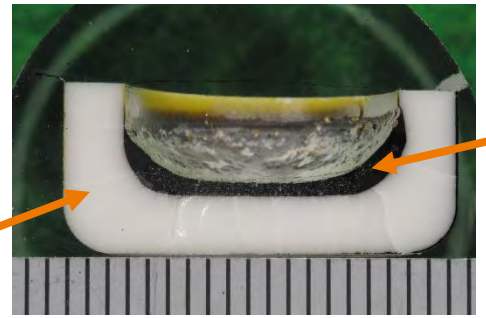

Cross section

melted & solidified sample

Note: Cooling rates were defined based on the temperature measured at the bottom of the tungsten crucible for both cooling tests.

Copyright© NIPPON NUCLEAR FUEL DEVELOPMENT Co., Ltd. 2026. All rights reserved.

Cooling-rate effect on microstructure: Rapid cooling gives finer spacing

The interpenetrating phase-separated region becomes approximately one order of magnitude finer under rapid cooling.

Rapid cooling

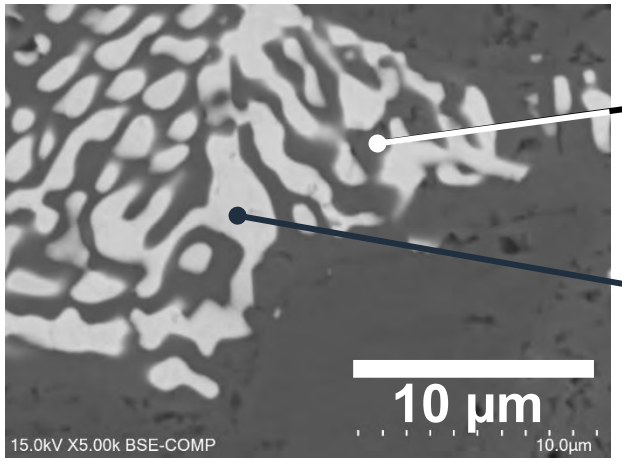

dark region

bright region

Slow cooling

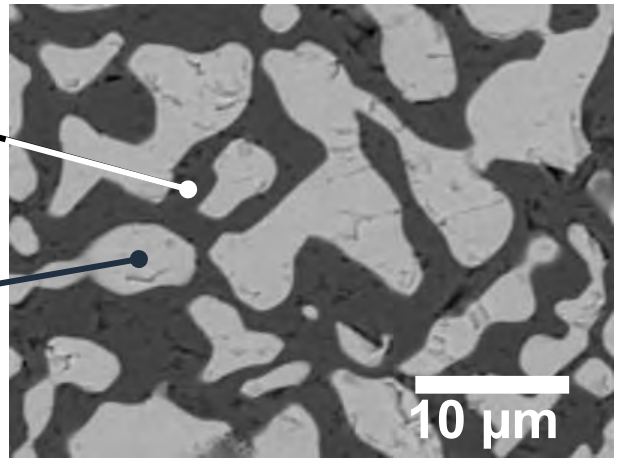

Images are shown at different magnifications to highlight the characteristic spacing.

finer spacing

phase-separation spacing L : ~ 1 μm

coarser spacing

phase-separation spacing L : ~ 10 μm

Copyright© NIPPON NUCLEAR FUEL DEVELOPMENT Co., Ltd. 2026. All rights reserved.

SEM-EDS confirms chemical partitioning in the interpenetrating region

BSE contrast corresponds to U–Zr–O-rich and Fe–Cr–O-rich regions.

interpenetrating phase-separated region

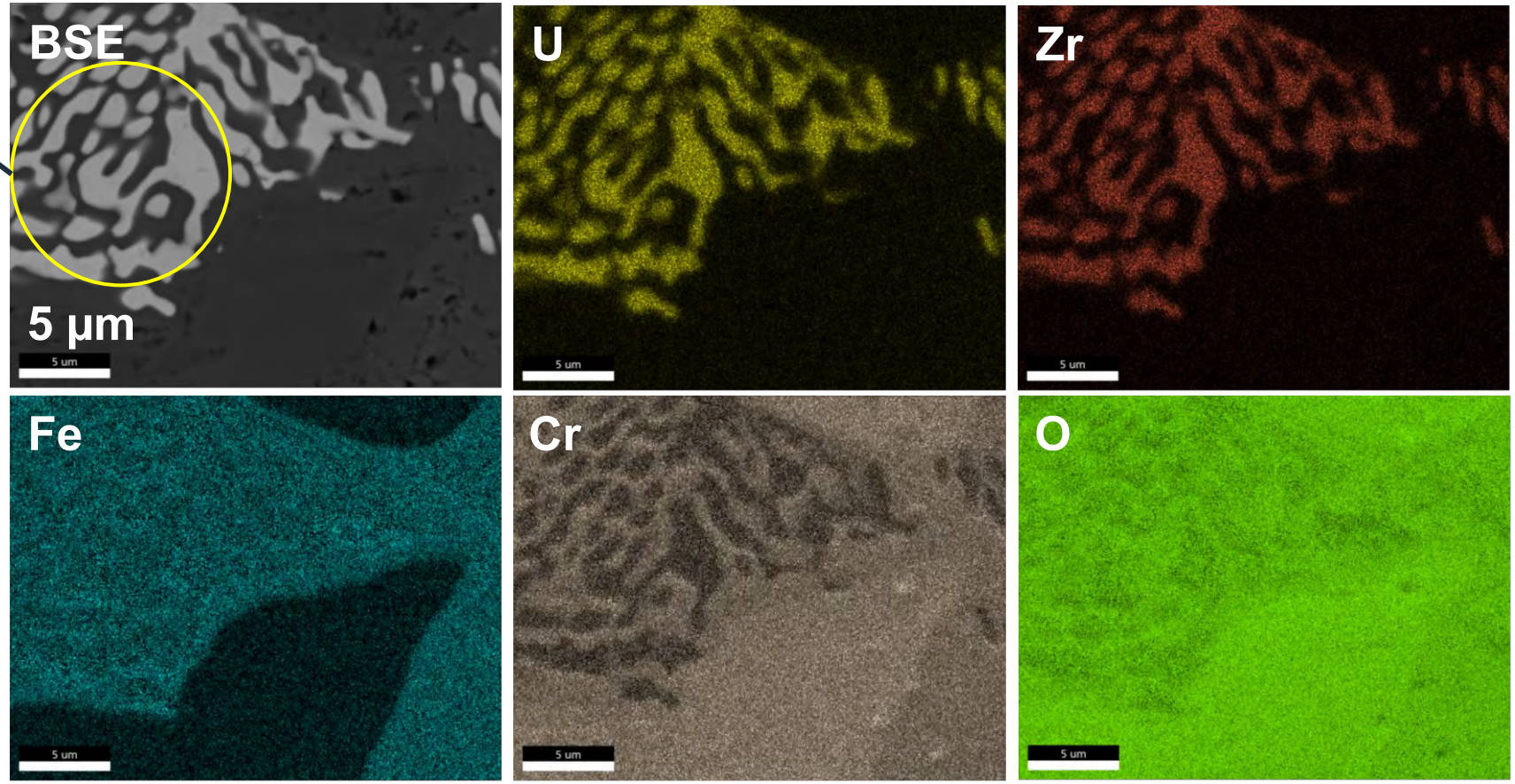

bright → U-Zr-O-rich
dark → Fe-Cr-O-rich

Copyright© NIPPON NUCLEAR FUEL DEVELOPMENT Co., Ltd. 2026. All rights reserved.

TEM phase identification: Major phases are consistent with those in the FDNPS particles

Power the Future

Major phases are fcc-$(U,Zr)O_2$ and spinel-$FeCr_2O_4$; slow cooling additionally shows bcc-(Fe,Cr).

Rapid cooling

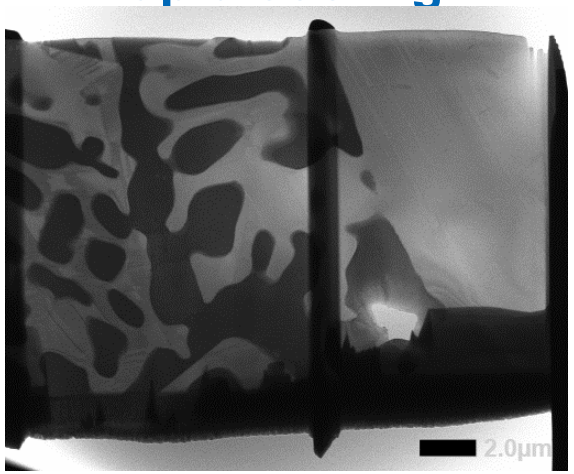

fcc-$(U,Zr)O_2$ and spinel-$FeCr_2O_4$

Slow cooling

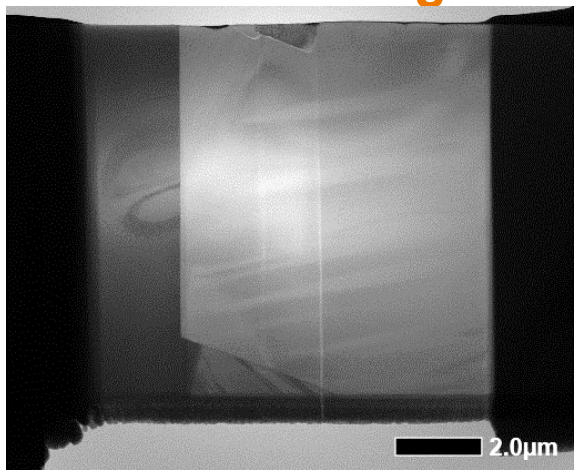

fcc + spinel + bcc-(Fe,Cr)

Interpretation

The simulated specimens are compositionally and crystallographically close enough to support a first-order cooling-rate calibration, although spacing differs from the FDNPS particle.

Copyright© NIPPON NUCLEAR FUEL DEVELOPMENT Co., Ltd. 2026. All rights reserved.

Diffusion-based model: Translate spacing into cooling rate

Assuming diffusion-controlled growth/coarsening, smaller spacing corresponds to shorter time and faster cooling.

Characteristic spacing

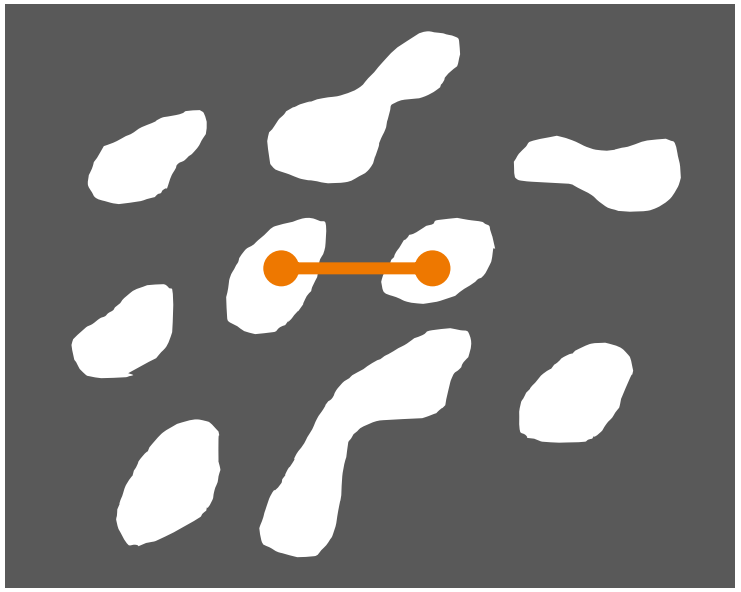

Same-phase spacing in the interpenetrating U–Zr–O / Fe–Cr–O microstructure.

Order-of-magnitude relation

$$L = \sqrt{(Dt)}$$

$$D = \frac{vL^2}{\Delta T}$$

$$v_p = \frac{v_R {L_R}^2 + v_S {L_S}^2}{2{L_p}^2}$$

L: characteristic phase-separation spacing
t: formation time of the interpenetrating region
D: effective diffusion coefficient
ΔT: temperature interval for formation
v: cooling rate
p, R, S: FDNPS particle, rapid cooling, slow cooling

Copyright© NIPPON NUCLEAR FUEL DEVELOPMENT Co., Ltd. 2026. All rights reserved.

Estimated cooling rates of FDNPS particles

Applying the spacing–cooling-rate trend gives ~10^3 K/s for the 2u OF particle and ~10 K/s for the X-6 PEN particle.

Calibration and extrapolation

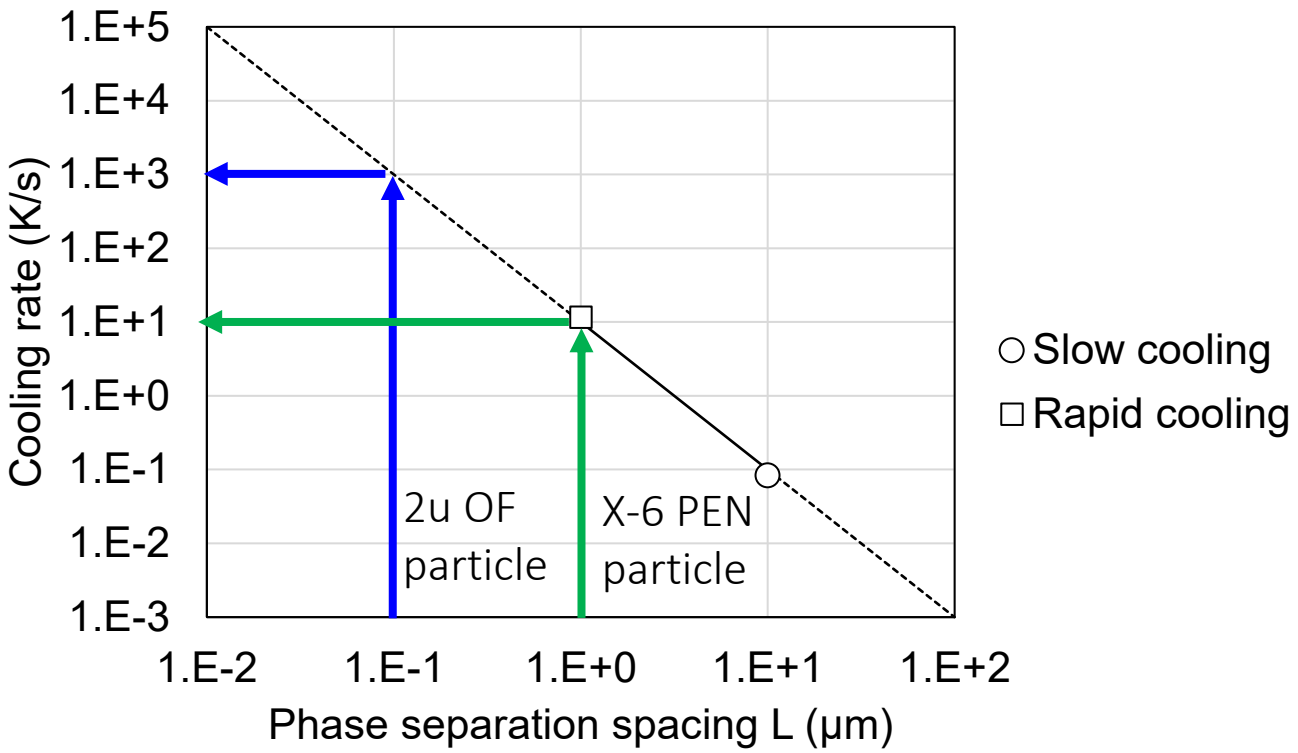

Key readout

- **Rapid cooling specimen: L ~ 1 μm**
- **Slow cooling specimen: L ~ 10 μm**
- **2u OF particle: L ~ 0.1 μm**
  → order of 10^3 K/s
- **X-6 PEN particle: L ~ 1 μm**
  → order of 10^1 K/s

Copyright© NIPPON NUCLEAR FUEL DEVELOPMENT Co., Ltd. 2026. All rights reserved.

Heat-transfer consistency check: Model

A simplified flying-droplet cooling model was used to check the plausibility of the microstructure-based cooling-rate estimate.

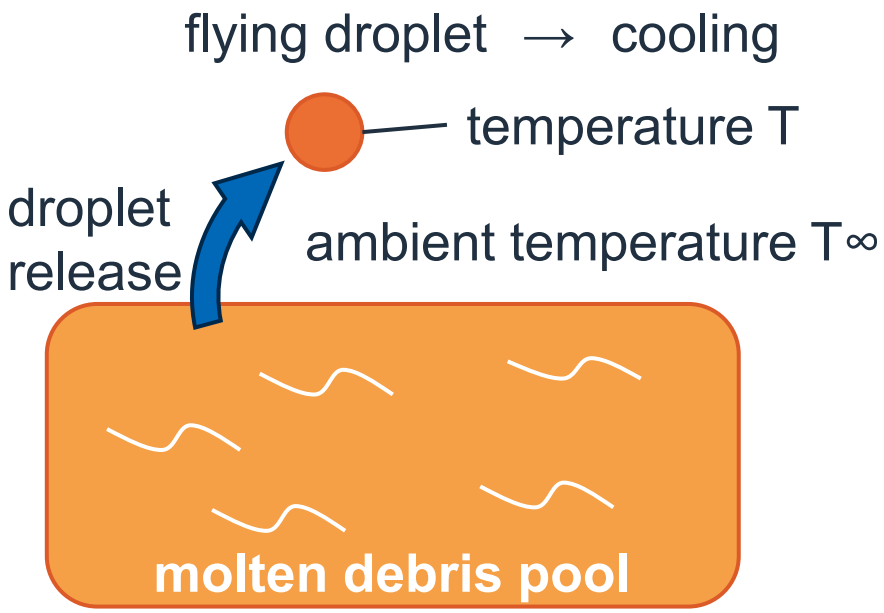

Simplified flying-droplet model

- **spherical molten droplet**
- **radius r**
- **temperature T**
- **ambient temperature T∞**
- **heat loss by convection and radiation**

$$\rho V c \frac{dT}{dt} = -A\left[h(T - T_\infty) + \varepsilon\sigma(T^4 - T_\infty^4) \right]$$

$$A/V = 3/r$$

smaller r → larger A/V → faster cooling

(ρ: density, c: specific heat, V: volume, A: surface area, h: convective heat-transfer coefficient, ε: emissivity, σ: Stefan–Boltzmann constant)

This model does not independently determine the cooling rate; it evaluates whether the microstructure-based cooling-rate estimate is physically plausible from a heat-transfer viewpoint.

Copyright© NIPPON NUCLEAR FUEL DEVELOPMENT Co., Ltd. 2026. All rights reserved.

Heat-transfer consistency check: Result

The 2u OF estimate corresponds to a sub-mm to mm-scale equivalent droplet, supporting the plausibility of the microstructure-based cooling-rate estimate.

Droplet cooling model

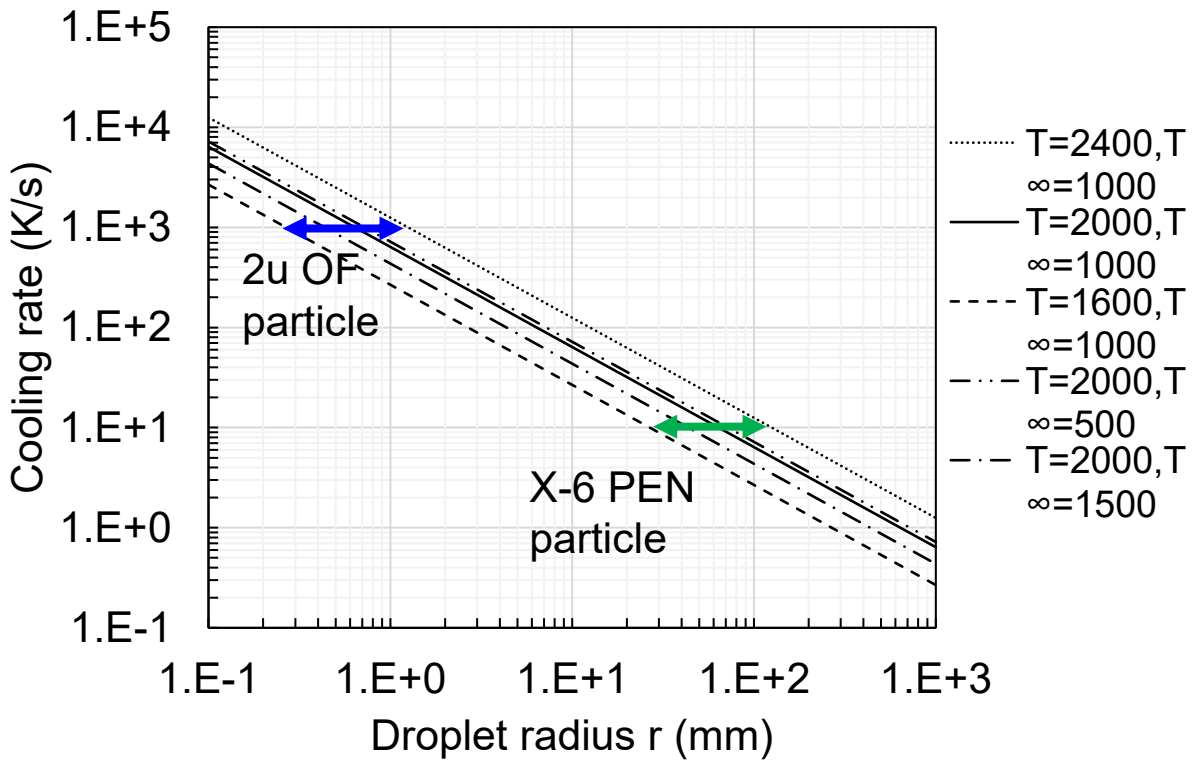

Key readout

- **2u OF particle:**
  Cooling rate estimated from microstructure:
  ~ 10^3 K/s
  - → **equivalent droplet radius: sub-mm to mm scale**
  - → **not thermally inconsistent with a flying-droplet scenario**
- **X-6 PEN particle:**
  Cooling rate estimated from microstructure:
  ~ 10^1 K/s
  - → **much larger equivalent droplet radius**
  - → **likely beyond the simple flying-droplet assumption**

Copyright© NIPPON NUCLEAR FUEL DEVELOPMENT Co., Ltd. 2026. All rights reserved.

Conclusions / Outlook

Conclusions

- Simulated U–Zr–Fe–Cr–O debris reproduced the major phases of the target FDNPS particles.
- Phase-separation spacing decreased with increasing cooling rate.
- A first-order framework was proposed to estimate cooling rate from phase-separation spacing.
- The 2u OF particle was estimated to have cooled on the order of 10^3 K/s.
- The heat-transfer check supports that this estimate is not thermally inconsistent.

Outlook

Future work will refine spacing statistics, sample temperature-history evaluation, and the applicability limits of the diffusion-based and heat-transfer models.

Copyright© NIPPON NUCLEAR FUEL DEVELOPMENT Co., Ltd. 2026. All rights reserved.

supplemental

Copyright© NIPPON NUCLEAR FUEL DEVELOPMENT Co., Ltd. 2026. All rights reserved.

Effect of thermal lag on the cooling-rate calibration

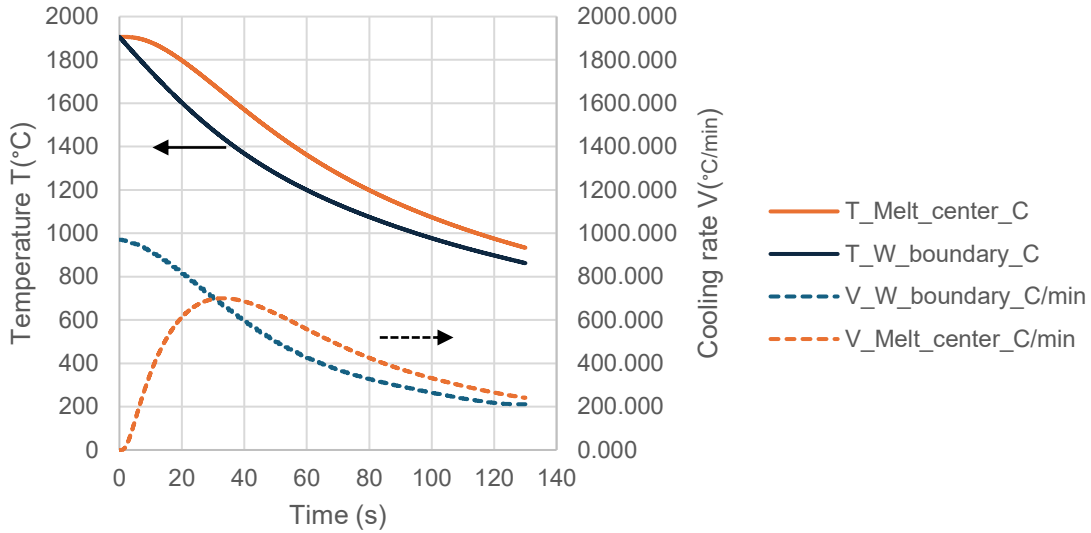

- The cooling-rate calibration was based on the measured temperature history at the bottom of the W crucible.
- Strictly, the relevant cooling rate for phase separation is the local cooling rate inside the oxide melt.
- A simplified 1D heat-conduction calculation was therefore performed to estimate the thermal lag between the W crucible bottom and the melt center.
- The melt-center cooling rate shows a delayed response and reaches a peak at around 35 s.
- This thermal lag represents a possible uncertainty when using the W crucible temperature as a proxy for the melt temperature.

Copyright© NIPPON NUCLEAR FUEL DEVELOPMENT Co., Ltd. 2026. All rights reserved.

Critical Heat Flux in Pool boiling configuration for In-Vessel Melt Retention: literature review and recents experiments in THS-15 facility

K. At Khen[1], D. Batek[2], S. Pujet[1], J. Zdarek[2], V. Krhounek[2]
[1] EDF R&D, [2] UJV
Corresponding Address
kresna.at-khen@edf.fr; david.batek@ujv.cz

ABSTRACT

In-Vessel Melt Retention (IVMR) is a strategy employed in several design of new nuclear reactors (e.g., AP1000, HPR1000, APR1400, CAP1400 …), and is also considered by some utilities to support lifetime extension of existing operating reactors. A prerequisite for the successful implementation of this strategy is that, at any time and location, the maximum heat flux at the outer surface of the reactor vessel wall remains below the critical heat flux (CHF). For medium- and high-power reactors (>1 GWe), the efficiency of external heat removal is generally enhanced through passive flow circulation, which increases CHF by raising the superficial velocity. This requires optimization of the flow path between the outer vessel wall and the thermal insulator acting as a liner, to maximize superficial velocity at critical locations. In contrast, for low-power reactors, heat removal can be achieved under pool boiling conditions, which do not require flow channel optimization. This article presents a comprehensive literature review of CHF experiments in pool boiling conditions applicable to external reactor vessel cooling (ERVC), primarily involving 'smooth' outer vessel walls (e.g., copper, stainless steel, or aluminum). In addition, it discusses the latest CHF measurements obtained on the THS-15 facility, which features an oxidized RPV steel outer vessel wall. These recent tests were conducted within the framework of the EU-funded EASI-SMR project, which addresses safety issues related to light water small modular reactor (LW-SMR) technology to support its deployment.

KEYWORDS
In-Vessel Retention, External Reactor Vessel Cooling, Pool boiling, Critical Heat Flux

NOMENCLATURE

16/18MND5	Low-alloy vessel steel in French nomenclature (~ SA508/SA533 in U.S. standards)
CHF	Critical Heat Flux
EDF	Electricité de France (Electricity of France)
DI	De-ionized water
ERVC	External Reactor Vessel Cooling
HF, HFF, HFP	Heat Flux, Heat Flux Factor, Heat Flux Profile
IRSN	Institute for Radiological Protection and Nuclear Safety, now ASNR
MIT	Massachusetts Institute of Technology
PSU	Penn State University
RPV	Reactor Pressure Vessel
STB	Sodium TetraBorate (buffering agents)
TSP	Trisodium phosphate (buffering agents)
UCSB	University of Santa Barbara California
UJV	Ústav Jaderného Výzkumu (Nuclear Research Institute)

1. INTRODUCTION

The Critical Heat Flux (CHF) is defined as the maximum heat flux that can be transferred from a specified region of the reactor vessel's external surface to the water surrounding the RPV, beyond which the onset of a boiling crisis occurs. The boiling crisis corresponds to the formation of a continuous vapor film on the heated surface, which drastically reduces the heat transfer coefficient between the vessel wall and the coolant. This phenomenon inhibits the removal of thermal energy generated by the corium pools inside the vessel, leading to progressive wall overheating and ultimately structural failure. On a local scale, CHF increases with water subcooling, RPV wall inclination (0° at the vessel bottom of the RPV and 90° at the cylindrical part), superficial velocity of the water (in $kg/m^2/s$), and hydrostatic pressure. Also, at low pressure —typical of reactor building pressure during a severe accident— CHF increases with roughness and wettability of the material. Using RPV steel increases CHF compared to stainless steel or copper commonly used in experimental setups.
For low-power reactors (< ~ 500 MWe), the necessity of vessel cooling by circulating water can be questioned, since the thermal loads from the corium pools to the vessel and their impact on the heat flux from the vessel to the surrounding water remain limited. Moreover, pool boiling cooling is simpler to implement than thermosiphon cooling, as it does not require optimized insulation to maximize superficial velocity. Under pool boiling conditions, the superficial velocity is virtually zero.

The objective of this article is to conduct a literature review on critical heat flux (CHF) values under pool boiling conditions and to fill existing data gaps in order to establish, to the extent possible, bounding CHF values that can be applied for any type of LWR design.

2. LITERATURE SURVEY OF CRITICAL HEAT FLUXES IN POOL BOILING SITUATIONS FOR ERVC APPLICATIONS

2.1. In-Vessel Retention in nuclear industry

Demonstrations of IVR feasibility for commercial reactors have primarily focused on low and medium-power units (VVER-440 at Lovisaa, AP600), and were extended to mid-size units (AP1000, HPR1000) and high-power units (APR1440, CAP1400) when a water circulation is implemented to enhance critical heat flux. However, due to the limited water volume available to flood the reactor cavity and establish a closed-loop circulation, some VVER-440 reactors (such as Paks NPP) do not employ water circulation but rely solely on pool boiling. While numerous references exist on CHF studies under natural or forced circulation conditions, literature on pool boiling scenarios is much scarcer and mainly relates to the early stages of IVR research.

To detect experimentally the CHF, a reference heat flux profile is progressively scaled until boiling crisis occurs, which is detected by a monotonic increase in wall temperature above the saturation point. Heat flux profiles were initially derived from corium pool experiments using simulant materials intended to cover all reasonable scenarios and provide a realistic bounding case with respect to thermal loading. In current practice, heat flux profiles applied in CHF test loops are generated by lumped parameter code calculations (MAAP, ASTEC, …) that rely on heat transfer correlations derived from such experiments. Corium-to-vessel wall heat flux increases monotonically with inclination and peaks in the upper region, generally where the metallic layer above the oxide pool induces a focusing effect (~90° inclination). Maximum residual power occurs under large-break loss of coolant accident (LOCA) scenarios, which generally yield the highest heat flux. In cases of partial vessel bottom filling, stratified corium pools and focusing effect may occur at less favorable inclination for steam removal (lower CHF). But generally, smaller corium oxyde pools have smaller residual power, reducing heat transfer to vessel wall.

2.2. Main CHF experiments in pool boiling

In pool boiling situation, full-scale height experiments which are reviewed here and discussed in the next chapter are CYBL facility [1], ULPU (configuration I) facility [2], and THS-15 facility [3]. The SBLB facility from Penn State University (PSU) is also discussed (3D vessel geometry, 1/8th) [1]: For reduced-scale 2D or 3D vessel geometries, caution is required due to distortion between hydrostatic pressure and inclination of the RPV wall. However, the same basic principle remains: as the focusing effect is in the upper region, maintaining residual power in the lower region consistent with the studied geometry allows CHF studies at the top of the corium pool.

2.3.1. CYBL (Cylindrical Boiling) facility

The CYBL facility is the forerunner of all In-Vessel Retention (IVR) experimental loops. It was constructed in the United States at Sandia National Laboratories to investigate originally the feasibility of an external RPV cooling in the 1990s. In particular, the program aimed to assess whether steam generated in the area near the 0° inclination (i.e., at the bottom head of the vessel) could be passively removed under pool-boiling conditions, and in the absence of any natural-circulation driving head. The test vessel used in CYBL is a full-scale (1:1) three-dimensional representation of a reactor pressure vessel. The only significant deviation from an actual RPV concerns the use of stainless steel for the mock-up, instead of RPV steel.

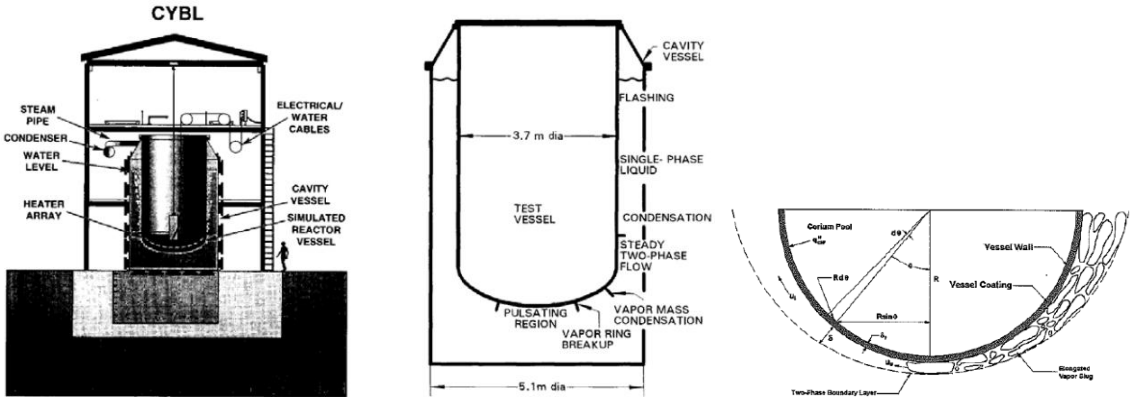

Figure 1. CYBL facility and 3D flow patterns

The thermal power of 6 MW was sufficient to reach the critical heat flux at very low inclination. For the experimenters, the observation of rapid, periodic, and asymmetric bubble bursts provided clear evidence that the local critical heat flux was not as low as initially expected. Indeed, the measured critical heat flux at 0° inclination, under saturated water conditions (i.e., without subcooling), was 500 kW/m², which remains a significant value. The horizontal gap between the vessel wall and the cavity wall was 70 cm [4].

2.3.2 ULPU facility (configuration I)

The ULPU facility was hosted at the University of California, Santa Barbara (UCSB) to support the certification of the AP600 and AP1000 reactors. The present discussion focuses on Configuration I, for which a series of experiments was conducted under pool-boiling conditions. This configuration is a 2D slice at 1:1 scale in height, and the SF-1 test series used copper heating blocks that could be positioned either

between 0° and 30°, or between 60° and 90°. In the reference [2], there is no data on the gap thickness. However, based on the schematics provided in the document, this gap appears to range between approximately 15 cm and 22 cm.

With "no" water height above the measurement location (i.e., saturation temperature which is a bounding condition with respect to CHF), the CHF values increase quasi-linearly with the inclination (in degrees, over the 0–30° range), rising from approximately 0.3 MW/m² to 0.69 MW/m², with very good reproducibility. A CHF value at 0° is observed to be lower (~ 0.32 MW/ m²) than the 0.5 MW/m² measured in CYBL. This can be explained by the greater difficulty for steam to escape in the more constrained 2D geometry of ULPU, compared with the 3D geometry of CYBL. Between 60° and 90° inclination, the CHF values obtained under pool-boiling and saturation conditions are around 1.1 MW/m².

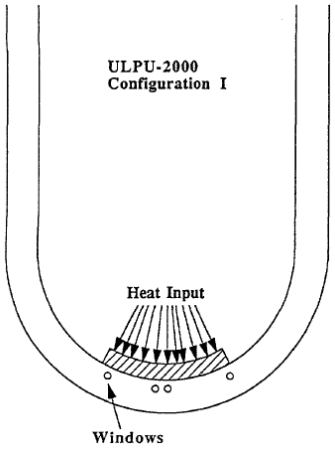

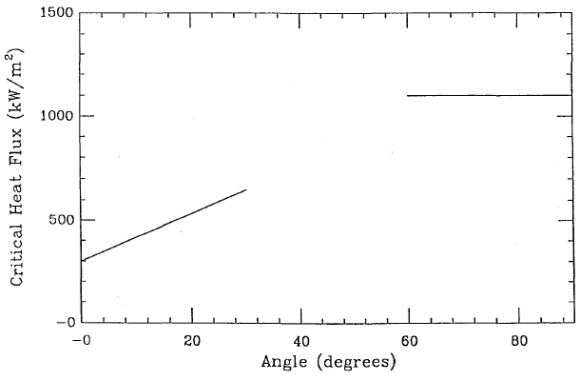

Figre 3.2. Critical heat flux as function of position on the lower head; from ULPU, in pool boiling.

Figure 2. CHF values measured in ULPU I (pool boiling, DI water at saturation, copper wall) [2]

2.3.3. THS-15 facility

In 2015, construction of the large-scale experimental facility THS-15 (Thermo-Hydraulic Stand 2015) was initiated at UJV. The facility is designed to assess the limits of coolability of a VVER-1000 RPV with respect to full length of the flow path (gravity head), using reactor axisymmetric geometry. As for ULPU experiments, it uses a a slice geometry (1/95th). The heat flux generated within the RPV by molten corium during a severe accident is simulated using electrically heated copper elements, with a maximum applied heat flux of 2.3 MW·m^{-2}. However, the cooled copper segments are coated with a 3-mm-thick V354 steel layer (which chemical composition is intented to be representative of VVER RPV steel) in order to provide surface conditions more representative for CHF measurements.

Figure 3. THS-15 facility

UJV performed some a series of tests for the Czech State Office for Nuclear Safety (SÚJB) in the frame of a Czech national project [3]. The thermal loading from the corium pools to the RPV wall was calculated using ASTEC code in Temelin VVER 1000/320 conditions. The CHF were measured with different surface treatments. Without any treatment (ie. RPV steel naturally oxidized), the obtained values are summarized in the table below, with a water gap of 50 cm and about 3 m of water height above the semi-ellipsoidical and cylindrical junction of the vessel. These values are compared with ULPU and CYBL CHF values (thought with different HFF, lower head RPV shape and water level).

	CHF [MW/m2] for 1:1 scale in height experiments		
RPV inclination	THS-15 (2D, RPV steel)	CYBL (3D, stainless steel)	ULPU I (2D, copper)
[0-10°]	0.42	~ 0,5	~ 0.3
15°	0.53	No data	~ 0,5
25°	0.65	No data	~ 0.6
45°	1	No data	No data
70°	1.35	No data	1.1
90°	1.92	No data	1.1

Table 1. Comparison of CHF values between THS-15, ULPU and CYBL experiments in pool boiling conditions at saturation temperature (with differents HF profiles) and atmospheric pressure

2.4. SBLB experiment

This facility was built at Pennsylvania State University (PSU) in the United States. It consists of a pressurizable water tank filled with DI water, equipped with a condenser, and capable of accommodating a reduced-scale (1/8th) 3D RPV mock-up built either in aluminium or stainless steel. The heat-flux distribution is defined according to five vertical zones. The observation of the different flow regimes was possible through an optical viewing window. The critical heat-flux (CHF) measurements obtained in pool boiling configuration are summarized in the following table and compared with the CYBL and ULPU data under saturated conditions. PSU provides an interpolation correlation for CHF values as a function of subcooling between 0 and 10 K and inclination between 0° and 90°.

Table 3 Comparison of the Local Critical Heat Fluxes Measured at Various Test Facilities Under Saturated and Subcooled Boiling Conditions

Local Angle of Inclination* θ	Local Critical Heat Flux, MW/m²				
	SBLB at PSU		CYBL at SNL	ULPU at UCSB	
	Saturated Boiling	Subcooled Boiling**	Saturated Boiling+	Saturated Boiling	Subcooled Boiling++
0°	0.40	0.59	0.50	0.28	0.50
30°	0.61	0.86	--	0.65	0.89
60°	0.85	1.05	--	--	1.18
90°	(1.00)	(1.35)	--	--	1.50

* θ = 0° corresponding to the bottom center and θ = 90° corresponding to the upper edge of the test vessel
** Pool boiling with a subcooling of 10 °C
\+ Based largely on small-scale quenching data
++ Natural convection boiling with a subcooling of 14 °C at the bottom center

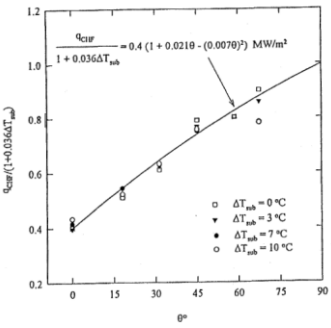

Table 2. Comparative table of CHF values measured in CYBL, SBLB, and ULPU – from [1]

In loops representing the vessel at reduced height, a geometric distortion occurs: the hydrostatic head (water height above the measurement point) does not vary with inclination in the same manner as for a given water level in the actual vessel. However, this effect results only in a few degrees of subcooling within the ranges covered by SBLB and ULPU I. Similar CHF values are observed in the 0–30° inclination sector for both SBLB (3D, 1/8th scale) and ULPU (2D, full height). No comparison is possible between 30° and 60° due to the absence of ULPU measurements.

3. SCALING FOR REACTOR APPLICATION

3.1. Effect of the RPV shape

When determining the critical heat flux (CHF), it seems logical to consider the influence of flow history: A CHF value recorded at an inclination of 90° is theorically affected by the cumulative energy absorbed by the fluid throughout the entire hemispherical—or semi-ellipsoidal—portion of the vessel. The HF profile is intended to represent the net thermal loading on the vessel wall from corium pools, after accounting for conduction through the vessel thickness. In practical, the CHF values obtained with different HF profiles or even at reduced scale are not significantly different in pool boiling situation, when considering only smooth surfaces (cleansed copper, stainless steel). PSU proposed an upscaling law, which it validated on ULPU over the 0–30° and 60–90° ranges.

3.2. Effect of gap size

The annular gap is defined as the distance between the vessel and the insulation (or liner) and is filled with water. From an industrial standpoint, the larger the annular gap, the greater the water inventory shall be to fill the reactor cavity.
From a phenomenological standpoint, experiments using inclinable test sections under forced-flow conditions (for thermosiphon applications) have shown either a weak influence of the gap size [5] and a very limited two-phase boundary-layer development [6]. In addition, the capillary length below which the gap width would start to perturb boiling is only on the order of ~2.5 mm. Therefore, a gap of 10 cm, 15 cm, or 20 cm should not to disturb the escape of bubbles. Recent experiments carried out by KAERI and Seoul National University [7] investigated the influence of gap size under pool-boiling conditions in the 1-10 mm range and in a “no-gap” (meaning “infinite gap” actually) configuration. Under saturation conditions, with a gap of 1 cm, the measured CHF was between 1 MW/ m² (@45° inclination) and 1.2 MW/m² (@90° inclination). Without any gap, these values increases up to 1.2 MW/ m² (@45° inclination) and 1.3 MW/m2

@90° inclination). Interestingly, the CHF values obtained for very small gaps (< 1 cm) are higher than those measured for a 10 mm gap. According to the authors, this effect is associated with flow induced by bubble detachment, leading to a local enhancement of heat transfer. However, such small gaps are not encountered in ERVC for commercial reactors.

Regardless of the size of the vapor bubbles and how they escape from the gap, the gap width may also influence the flow induced by natural convection. For sufficiently large gaps (on the order of several tens of centimeters), a convection loop may develop, generating a significant near-wall superficial velocity and thereby enhancing heat removal. Consequently, for gap sizes typical of commercial reactors (15 cm and above) under pool boiling conditions, it remains difficult to draw firm conclusions regarding the impact of the gap size on the critical heat flux (CHF) based on the currently available data.

3.3. Effect of surface material

At low pressure, surface effects of the heated wall have a significant influence on the critical heat flux (CHF). The MIT/EDF experiments quantified these surface effects under water circulation (350 to 1000 kg/m^2/s), as a high wettability is correlated to a high CHF. Experimental measurements conducted on oxidized 18MND5 samples indicate a superhydrophilic surface behavior, which leads to a ~ ×1.5 increase in the CHF relative to stainless steel under water circulation conditions [6]. Applying the CHF correlation to the local thermohydraulic conditions computed with Neptune_CFD for the ULPU IV loop (which uses copper heating blocks) reproduced the CHF values defended by Westinghouse [8]. Unfortunately, this correlation cannot be applied to pool-boiling situations, where the superficial velocity is virtually zero.

In an “upward-facing” pool-boiling configuration (ie. stagnant fluid above the heated wall), the use of oxidized RPV steel in the BETA experiment at UCSB [9] led to a gain of approximately ×1.7 in CHF[1] compared with cleansed copper.
A comparison between the ULPU-I and THS-15 results presented in the previous chapter (without any consideration of the applied HF profile) also shows an increase in the CHF (~ ×1.5 in the range 70°-90°).

Regarding the VVER V354 steel which is used to cover the THS-15 heater blocks (and intented to be similar to VVER RPV steel), no specific data on wettability are available. Given the similar chemical compositions of 16MND5 and V354 steels, comparable surface oxidation behavior is expected. Owing to its slightly higher chromium content, V354 steel may exhibit increased corrosion resistance, making the associated CHF results possibly bounding[2] with respect to PWR vessel steels.

	Typical Chemical Composition (wt.%)			
Element	**16MND5 (PWR RPV steel)**	**V354 (THS-15)**	**15Kh2NMFA (VVER RPV steel)**	**Stainless steel (304L)**
Carbon (C)	0.16 – 0.20	0.12 – 0.18	0.12 – 0.18	≤ 0.03
Manganese (Mn)	1.20 – 1.60	0.80 – 1.10	0.30 – 0.60	≤ 2.00
Silicon (Si)	0.15 – 0.35	≤ 0.20	0.17 – 0.37	≤ 1.00
Nickel (Ni)	0.40 – 1.00	—	1.00 – 1.50	8.0 – 12.0
Molybdenum (Mo)	0.45 – 0.60	0.80 – 1.00	0.40 – 0.70	—

[1] “Effect of surface material and aging by exposure to air and to boiling (…) leads to an increase of the CHF (typically from ~750kW/m^2 to over ~1300kW/m^2 in pool boiling configuration)” [9]

[2] The potential improvement in critical heat flux (CHF) would most likely be masked by the inherent uncertainties associated with CHF measurement.

Chromium (Cr)	≤ 0.30	1.25 – 1.50	1.80 – 2.30	18.0 – 20.0
Vanadium (V)	—	0.20 – 0.30	0.10 – 0.30	—
Copper (Cu)	≤ 0.25	—	≤ 0.10	—
Phosphorus (P)	≤ 0.020	≤ 0.020	≤ 0.015	≤ 0.045
Sulfur (S)	≤ 0.010 – 0.020	≤ 0.015	≤ 0.015	≤ 0.030
Iron (Fe)	Balance	Balance	Balance	Balance

Table 3. Typical chemical composition (in wt.%) of 16MND5, 15Kh2NMFA,V354 and stainless steels

3.4. Effect of water chemistry

The water chemistry (presence of dissolved boron or buffering agents) may also influence the critical heat flux (CHF), although its effect is less significant than that of the wall material surface, and experimental trends have not been clearly established.
In the BETA facility (pool-boiling in an up-facing configuration) [9], the use of TSP appears to decrease the CHF on SA508, although UCSB considers that the available data are insufficient to draw a definitive conclusion. However, the CHF obtained with SA508 and TSP nevertheless remains far higher than the CHF obtained with copper in demineralized water or with TSP. The impact of adding boric acid alone did not allow clear trends to be established. No tests were performed with the combination of boric acid and TSP.
Under thermosiphon-representative conditions with 18MND5 samples [6], the impact of boron and STB on the CHF measured with demineralized water only were also unclear, but overall, the discrepency was at max < 14% (superficial velocity of 500 and 1000 kg/m2/s ; inclination of 45° and 90°).

3.5. In summary

The vessel size does not appear to have a significant effect on the critical heat flux, provided that the system remains in a pool-boiling configuration. In contrast, the natural oxidation that develops on the external surface of the vessel has a pronounced impact on the critical heat flux, both under thermosiphon and pool-boiling in an up-facing conditions. The CHF values measured on copper (ULPU) or stainless steel (SBLB) surfaces are considered bounding, since under identical conditions, a CHF measured on oxidized RPV steel would be higher. This chapter also highlighted a lack of experimental data, particularly for covering the full range of inclinations relevant to IVR applications.

4. DEFINITION OF A CHF METHODOLOGY IN POOL BOILING SITUATION INDEPENDENT OF THE THERMAL HEAT FLUX PROFILE

4.1. Objectives

In this context, an experimental program has been proposed within the EASI SMR European Project to establish a pool-boiling CHF correlation representative of naturally oxidized RPV steel, making use of the existing THS-15 facility operated at UJV. The resulting correlation is intended to remain broadly applicable—independent of reactor design—and robust even in situations where the detailed thermal loading imposed by corium pools on the vessel wall is not precisely known.

4.2. Heat flux profile

4.2.1. “Bounding” HF profile

In general, thermal-flux distribution profiles may be taken directly from simulant-corium experiments (e.g., COPO or ACOPO), which provide the heat flux imposed on the inner vessel wall by molten corium pools. However, the preferred approach is to apply the heat-flux profile from the vessel toward the coolant, as this inherently accounts for thermal diffusivity through the vessel wall thickness.
That said, when the various scenarios of corium relocation into the lower head are insufficiently characterized, a bounding thermal-flux profile can be employed to encompass the full spectrum of plausible thermal loadings. This approach enables the determination of an envelope critical heat-flux curve. This is the methodology we propose to discuss here.

Corium pools configuration

In PWRs, the upper metallic layer above the oxidic pool (containing ~90% of the decay heat) is responsible for dissipating the highest heat fluxes, leading to the so-called “focusing effect.” In contrast, VVER reactors, which contain a relatively larger in-vessel metallic inventory, may exhibit maximum heat fluxes localized in the upper region of the oxide layer[3]. In certain transient configurations, a three-layer stratification can develop. From bottom to top, this configuration consists of a heavy metallic pool, an oxide pool, and a light metallic pool. However, reactor calculations performed using severe accident codes such as ASTEC or MAAP have not identified situations leading to higher thermal loads than those associated with a two-layer configuration (e.g., a top light metallic layer over a heavy oxidic layer). The oxide pool is dominated by natural-convection phenomena, and the overall angular distribution of the thermal load as a function of the inclination is well established. The overlying metallic layer generates a localized peak in the heat flux along the inclination corresponding to its position. Representing the whole system using a linearized envelope profile provides a conservative estimate of the heat transferred to the coolant, as illustrated in the schematic figures below. Thus, the critical heat fluxes determined using this envelope loading remain valid for any realistic pool configuration.

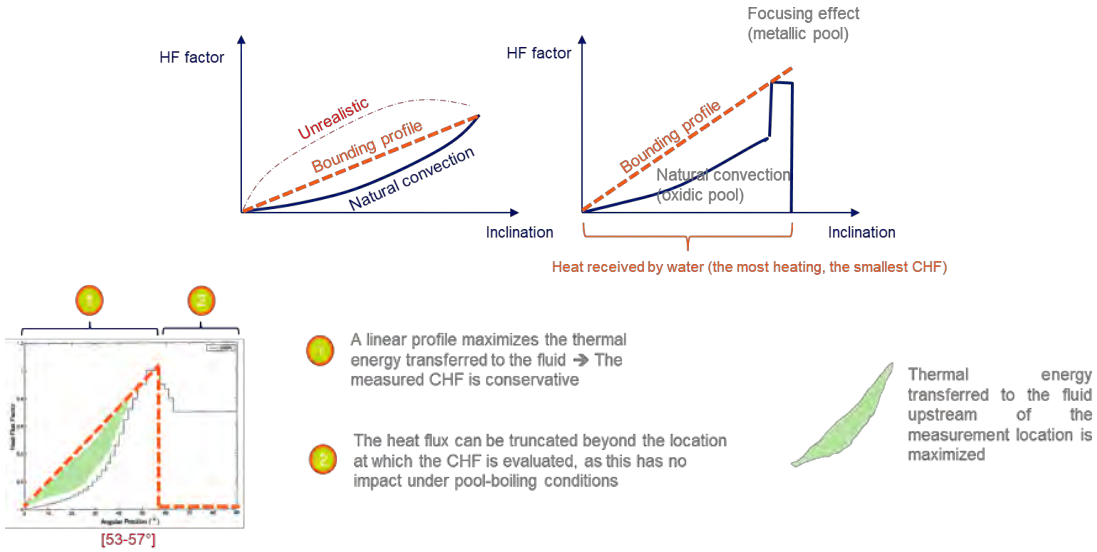

Figure 4. Simplified and bounding heat flux profile (in orange)

[3] The peak heat flux is dissipated in the upper region of the oxide layer as a result of natural convection. Thanks to the thickness of the overlying metallic layer due to the relatively high in-vessel metal inventory, this peak heat flux is not necessarily located within the metallic phase, in contrast to typical PWR configurations

4.2.2. "ELSMOR" HF profile

As a sensitivity heat-flux profile, the following ASTECv3 results from IRSN are proposed. These results were generated for an SMR design as part of a benchmark exercise involving the MAAP and ASTEC codes within the ELSMOR European Project [10] for an station blackout (SBO) scenario.

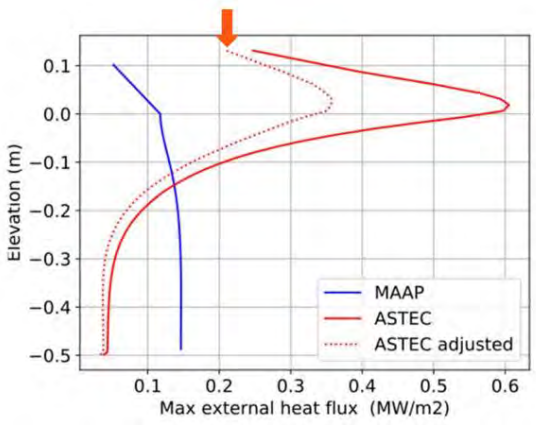

Figure 5. ELSMOR profile ("ASTEC adjusted") used as a sensitivity HF profile (from [10])

4.4. Experimental procedure applied to THS-15

To determine the CHF, the slope of the heat flux profile is increased incrementally until critical boiling conditions are reached. The retained value is the heat flux corresponding to the increment immediately preceding the onset of boiling crisis. The same procedure is applied for all inclinations of the test matrix.

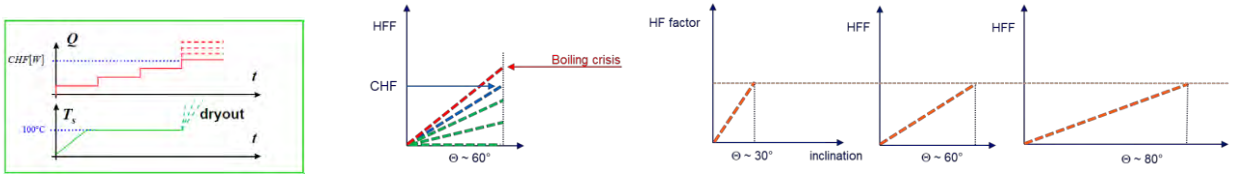

Figure 6. CHF detection for linear HFP (left: standard protocol to detect CHF ; center: protocol applied for 60° of inclination; right: HFF applied at each inclination if interest). The same protocol is applied for ELSMOR profile.

The following power shaping correction proposed by Theofanous et al. [2] is applied for the heat-flux profiles used on THS-15 experiment in order to account for the specificity of slice configuration (singularity at 0° inclination) vs sector configuration (reactor case):

$$HFF_{Slice}(\theta) = HFF_{prototypical} \times \frac{\sin\theta}{sin\theta_m} \text{ for } \theta < \theta_m$$

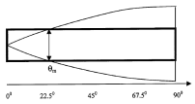

where θ_m is the location under consideration for CHF measurement.

4.5. Experimental matrix

In order to fulfil the objective of defining bounding critical-heat-flux data capable of covering a broad spectrum of scenarios and designs, the parameters listed below are hereby designated as reference:

- Ambient pressure : atmospheric (bounding)
- Water temperature and chemistry : saturated (bounding), DI water
- Water submergence : as low as reasonnably possible (bounding) – a sensitivity is done to check and quantify in pool boiling the increase of CHF with water height (hydrostatic pressure) ;
- Coating: as it is (naturally oxidized RPV steel)
- Gap size: 50 cm

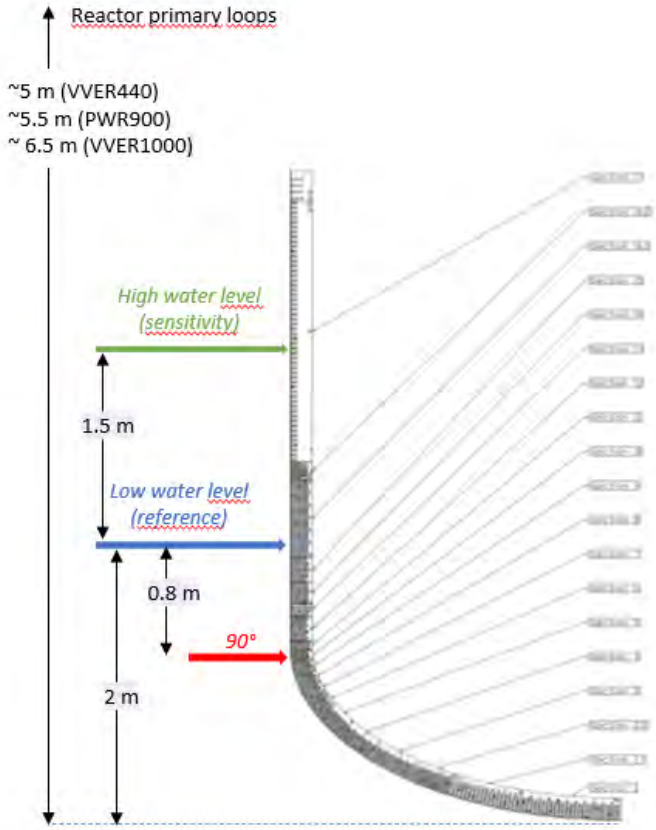

Figure 7. Water levels

4.6. Thermal losses

During the tests, it was important to maintain saturated water conditions in the region close to the RPV surface (approximately 0–15 cm from the RPV wall). Eight temperature measurement points are installed inside the cavity to monitor the thermal conditions, as shown in the figure below.

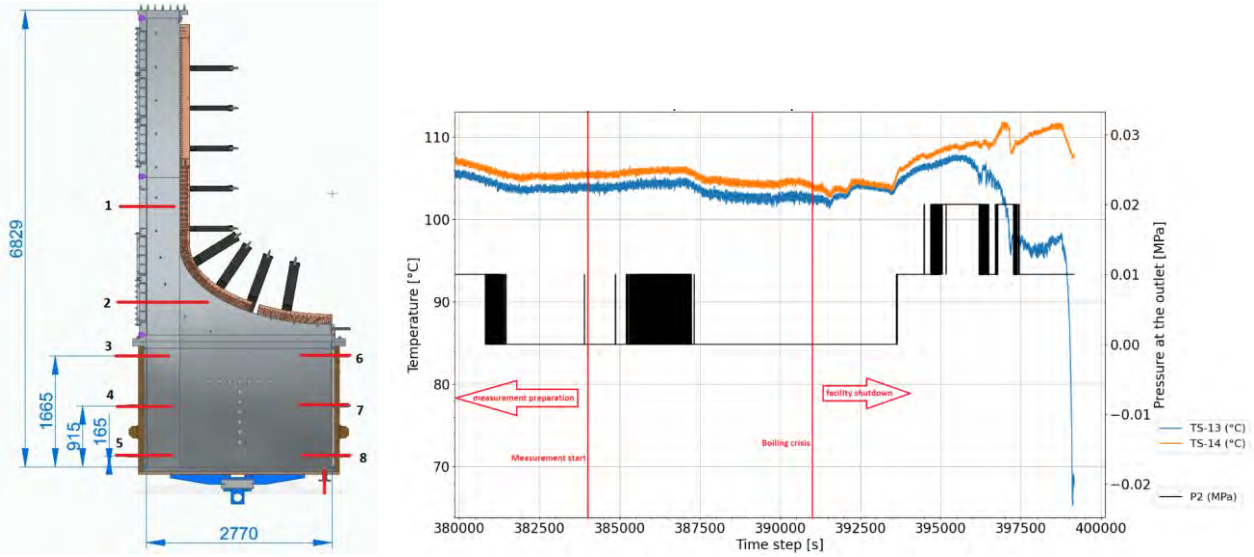

Figure 8. Location of the 8 thermocouples in the flooded cavity and example of water temperature

Thermocouples labeled 1 in fig. 8 (“TS-13” on the graph) and 2 in fig. 8 (“TS-14”) reach saturation temperature when heat flux is generated from the RPV (see examples in the graph on Fig. 8). The other thermocouples (labeled 3 to 8) are generally not at saturation level during the tests due to thermal stratification of the water. In this case, the water volume in the lower part of the cavity does not significantly contribute to heat transfer.

4.7. Results of CHF tests on THS-15 facility

At 90°, the degradation of the heaters on THS-15 facility limits the maximum achievable heat flux to approximately 1.7 MW/m², whereas at 80° the heaters are still intact. Therefore, the maximum inclination where CHF is recorded is 80°. All CHF measurements are duplicated.

Linear (bounding) HF profile (50 cm gap)				
RPV inclination	Low water level		High water level (+ 1.5 m)	
	1st Measurement [MW/m^2]	2nd Measurement [MW/m^2]	1st Measurement [MW/m^2]	2nd Measurement [MW/m^2]
30°	0.82	0.82	0.87	0.92
45°	1.05	1.09	1.37	1.22
60°	1.26	n/a		
80°	1.67	1.71		
90° (limited power)	> 1.76 (maximum heat flux)	> 1.58 (maximum heat flux)	> 1.71 (maximum heat flux)	> 1.63 (maximum heat flux)

Table 4. CHF values for bounding linear HF profile, 50 cm gap

e-SMR HF profile (50 cm gap)				
RPV inclination	Low water level		High water level (+ 1.5 m)	
	1st Measurement [MW/m^2]	2nd Measurement [MW/m^2]	1st Measurement [MW/m^2]	2nd Measurement [MW/m^2]
30°	0.97	0.92	0.97	0.97
45°	1.17	1.07	1.27	1.17
60°	1.31	n/a		
80°	1.8	1.76		
90° (limited power)	> 1.71 (maximum heat flux)			

Table 5. CHF values for ELSMOR e-SMR HF profile, 50 cm gap

4.8. Discussion

The measured critical heat flux values are generally consistent with those reported in the literature, and the observed trends are in line with the understanding of boiling crisis phenomena regarding surface properties of the wall. Surprisingly, the thermal flux profile has only a low influence on the critical heat flux values. The application of a maximized thermal loading, intended as an envelope for any possible thermal configuration, did not lead to a collapse of the critical heat flux values; on the contrary, these values remain high in absolute terms. This indicates that comparing CHF value between 2 facilities with different applied HFF makes sense. As anticipated, the use of reactor vessel steel, rather than a copper wall, results in an increase in critical heat flux across all tested inclinations (30° to 80°).

	Effect of HF profile (RPV steel				Effect of material surface		
RPV inclination [degree]	Linear (bounding)	ELSMOR	Δ%		Copper (ULPU)	RPV Steel	Δ%
	Mean CHF [MW/m^2]	Mean CHF [MW/m^2]			Mean CHF [MW/m^2]	Mean CHF [MW/m^2]	
30°	0.82	0.95	+16%		0.67	0.82	+22%
45°	1.07	1.12	+4%		-	-	-
60°	1.26	1.31	+4%		1.1	1.26	+14%
80°	1.69	1.78	+5%		1.1	1,69	+53%

Table 6. Effect of Heat Flux Profile and surface material on the CHF

As expected, increasing the water level leads to a higher CHF (+20% at a 45° inclination). In a real NPP, the water level typically reaches the elevation of the primary circuit loops, which is significantly higher than in the experimental configuration. This would further increase the CHF.

4.9. Correlation

For gap size of 50 cm, the following empirical bounding correlation is proposed:

$$CHF\ (MW/m2) = 0{,}0156.\theta + 0{,}3694$$

where θ is the angular position expressed in degrees (0° corresponding to the bottom of the vessel).

The validity range is proposed for this bounding correlation:

- RPV vessel steel (15Kh2NMFA or 16MND5) as it is (naturally oxidized);
- Gap size : 50 cm;
- Water level: higher than ~ 250 cm above the height of bottom of the vessel;
- Water chemistry and water temperature: DI water, saturated;
- Thermal heat profile from corium pool: any realistic profile.

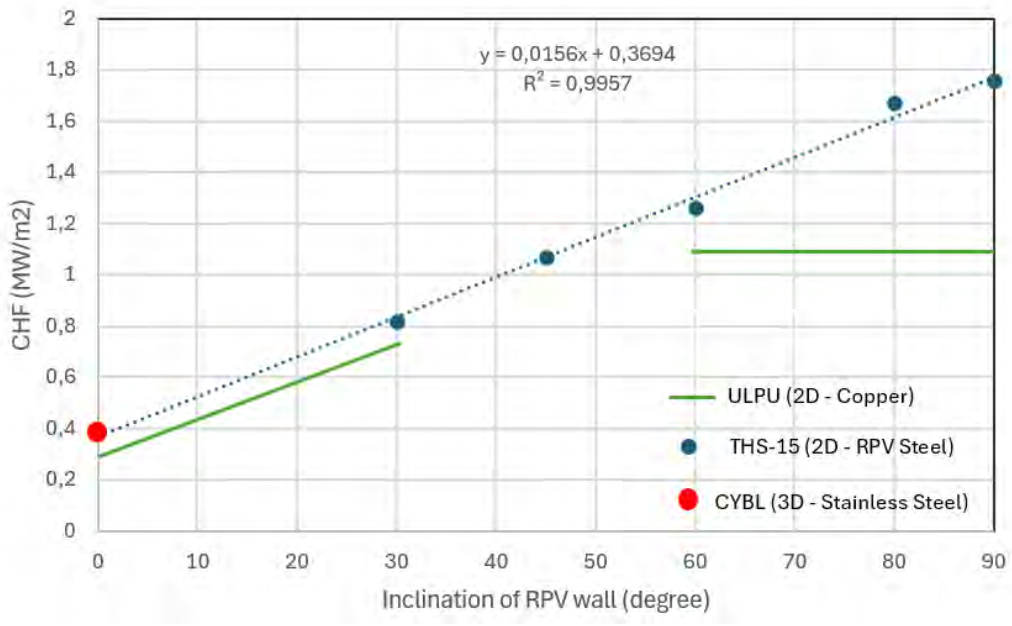

Figure 9. THS-15 results using bounding HFF profile (compared to ULPU-1 and CYBL data)

5. CONCLUSIONS AND PERSPECTIVES

A correlation for the Critical Heat Flux (CHF) under pool boiling conditions has been developed in the context of studies supporting the In-Vessel Retention (IVR) strategy. The correlation is intended to provide pragmatic and bounding CHF values that may be applicable to a range of Light Water Reactor (LWR) designs, without requiring detailed prior knowledge of the external heat flux distribution along the reactor pressure vessel (RPV) wall. The associated experimental programme was designed using a bounding heat flux profile, together with conservative assumptions regarding water height in the cavity, water temperature and ambiant pressure, consistent with severe accident conditions.

The proposed correlation contributes to the existing CHF database for pool boiling on RPV-like geometries, which remains limited. In particular, it complements previous full-scale CYBL and full-height ULPU-I experimental programmes by considering a more representative RPV surface material and by extending the available data over a broad range of wall inclinations relevant to IVR applications.

The relatively high measured values of CHF are mainly attributed to the use of RPV steel, which exhibits enhanced wetting properties compared with copper or stainless steel surfaces commonly used in full-scale in height IVR loop. This effect has been previously observed in earlier dedicated separate-effects experiments.

The influence of water chemistry (e.g. demineralized water with buffering agents and/or boric acid) was not addressed in the present study. From a safety assessment perspective, such effects may warrant further consideration if the coolability margins for a specific reactor design are found to be limited. Where sufficiently large margins are demonstrated, additional investigations of water chemistry effects are not expected to be a priority.

As a next step, the impact of the RPV–insulation annular gap will be examined by reducing the gap width from 50 cm to 15 cm. In the current configuration, a gap of 50 cm may allow the development of a natural convection cell in the THS-15 facility, potentially leading to a non-zero local superficial velocity at the RPV wall. Such effects could influence the measured CHF and should be quantified to confirm the conservatism and applicability of the proposed correlation.

AKNOWLEDGEMENT

The tests whose results are presented in Tables 4 and 5 were financially supported by the European Commission within the framework of the EASI-SMR project.

REFERENCES

[1] Cheung et al., « Critical Heat Flux (CHF) Phenomenon on a Downward Facing Curved Surface », NUREG/CR-6507 - PSU/ME- 97-7321

[2] T.G. Theofanous et al., "IN-VESSEL COOLABILITY AND RETENTION OF A CORE MELT", DOE/ID-10460, VOLUME 1, October 1996

[3] D. Batek et al., "THS-15 Experimental facility: Effect of Surface Roughness on CHF Values". The 11 European Review Meeting on Severe Accident Research (ERMSAR2024), KTH, Stockholm, Sweden, May 13-16, 2024

[4] T. Y. Chu et al. "Large-Scale Boiling Experiments of the Flooded Cavity Concept for In-Vessel Core Retention", OECD/CSNI/NEA Workshop on Large Molten Pool Heat Transfer, Nuclear Research Centre Grenoble, France, 9th-11th March 1994

[5] S. Rouge, I. et al., "Reactor vessel external cooling for corium retention SULTAN experimental program and modeling with CATHARE code," Workshop on In-Vessel Core Debris Retention and Coolability, Garching, Germany, March 3-6., 1998.

[6] M. Trojer et al. "A margin missed: The effect of surface oxidation on CHF enhancement in IVR accident scenarios". Nuclear Engineering and Design, 335, 140-150, 2018

[7] Sang W. Noh et al., "Critical heat flux in various inclined rectangular straight surface channels", Experimental Thermal and Fluid Science 52 (2014) 1–11

[8] K. Atkhen, "CHF experiments for external reactor vessel cooling Possible use of CHF correlations for reactor applications", International Seminar IVMR-2020 –Juan-les-Pins, January 21-23, 2020

[9] Dinh, T.-N., Tu, J.P., Salmassi, T., Theofanous, T.G., 2003, "Limits of coolability in the AP1000 related ULPU-2400 configuration V facility". University of California, Santa Barbara, CRSS-03/06. https://www.nrc.gov/docs/ML0319/ML031920123.pdf)

[10] J. Bittan et al., "Comparison between EDF MAAP5.04 and ASTECv3 codes on an hypothetical Severe Accident on the ELSMOR project NUWARD-Like SMR Design", The 11 European Review Meeting on Severe Accident Research (ERMSAR2024), KTH, Stockholm, Sweden, May 13-16, 2024

Critical Heat Flux in Pool boiling configuration for In-Vessel Melt Retention: literature review and recent experiments in THS-15 facility

K. At Khen[1], D. Batek[2], S. Pujet[1], J. Zdarek[2], V. Krhounek[2]

[1] EDF R&D

[2] UJV

Corresponding author : kresna.at-khen@edf.fr

12th CONFERENCE ON
SEVERE ACCIDENTS RESEARCH
May 18-22, 2026 - Madrid, Spain
ERMSAR 2026

1. Introduction
2. Literature Survey
3. Experimental parameters
4. CHF results
5. Conclusions and perspectives

Introduction

- In the framework of the In-Vessel corium Retention (IVR) strategy for commercial nuclear reactor, two external cooling modes are considered
  - Pool boiling configuration
  - Water circulation around the vessel
    - ✓ Either by natural circulation (thermosiphon loop) or forced circulation (pumps)

- For low power reactor (typically < ~500 MWe), pool boiling configuration may have the following advantages
  - Robustness (no need to optimize the gap geometry)
  - Stable flow (not concerned by hydraulic instabilities, or flow oscillations)
  - Simpler than thermosiphon and probably more forgiving in degraded situation (do not depend on the baffle behavior …)

- Objective of this work
  - To attempt to determine a bounding critical heat flux correlation for pool boiling conditions in PWRs, applicable regardless of design-specific parameters such as thermal loading from the corium pools to the vessel wall
  - May be useful-during pre-conceptual design phase to evaluate margins for vessel coolability when IVR strategy is considered

Literature survey

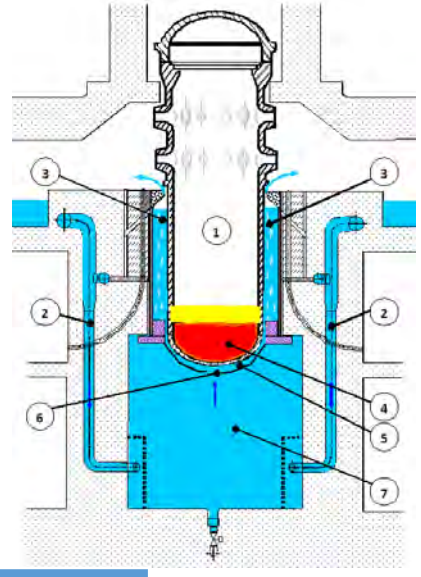

- Few commercial reactors use pool boiling to remove decay heat
  - Example : Paks VVER-440 units (implemented as a post-design modification)
- Few experiments were done in pool boiling configuration for severe accident applications. Experimental facilities and programs examined in this study are:

	CYBL (Cylindrical BoiLing facility- Sandia National Lab)	ULPU I (UCSB)	SBLB (Penn State Univ.)
Scale	3D, 1:1	2D slice, 1:1 in height	3D, 1:8
Vessel shape	Semi-ellipsoidal	Hemispherical (slice)	Hemispherical
Material	Stainless steel	Copper	Stainless steel or aluminium

- None of these facilities use reactor vessel steel (low-alloy ferritic steel)
  - Past separate effect tests have shown that roughness and wettability is enhanced when using vessel steel (e.g. 16/18/20MND5 or SA508/SA533), then increasing critical heat flux

Literature survey: CHF values

- CYBL (saturated water data)
  - 400 kW/m^2 obtained at low inclination (~ 0°)
  - ☹ No data for other inclinations (power limitation)

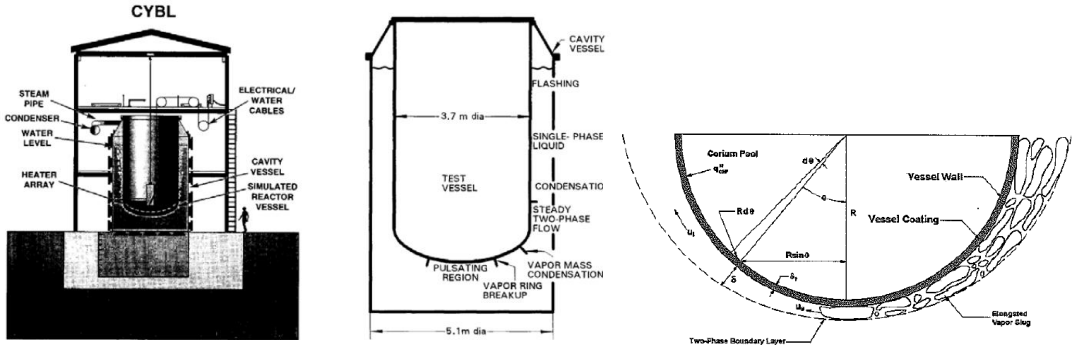

From [Chu, 1994]

- ULPU I (saturated water data)
  - 0°-30° of inclination: CHF linearly raises from 320 to 670 kW/m^2
  - 60°-90° : CHF ~ 1.1 MW/m^2 (no detailed data published)
  - ☹ No data in the range 30°-60°

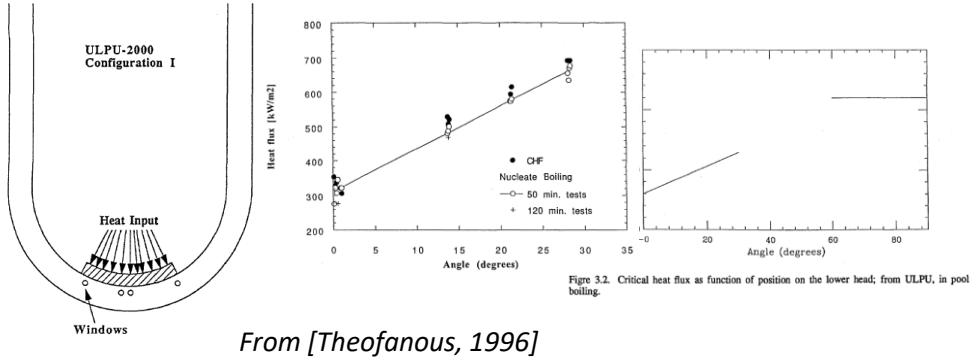

Figre 3.2. Critical heat flux as function of position on the lower head; from ULPU, in pool boiling.

From [Theofanous, 1996]

- SBLB (saturated water data)
  - CHF increases constantly from 0.5 MW/m^2 (@20°) to 0.9 MW/m^2 (@70°)
  - PSU proposed a scaling law for full-size vessel applications

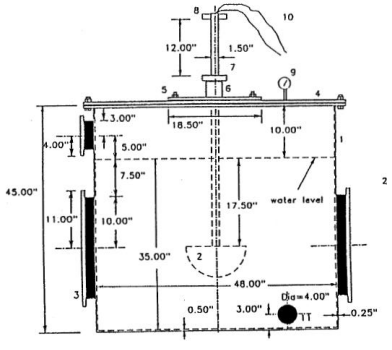

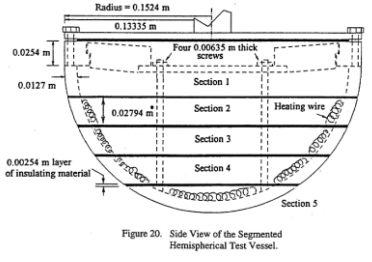

Figure 20. Side View of the Segmented Hemispherical Test Vessel.

From [Cheung, 1997]

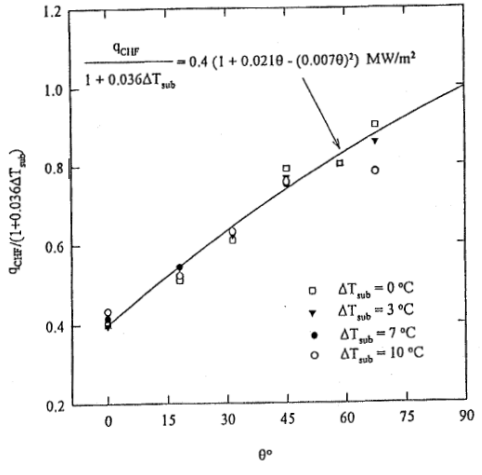

Literature survey: Key findings

- Typical values at saturated water
  - 0.3-0.4 MW/m^2 @0°
  - 0.6 – 0.65 MW/m^2 @30°
  - 0.85 – 1.1 MW/m^2 @60°

- These values were obtained for different heat flux profiles, but sensitivity to these profiles has not been investigated

- Questions that arise:
  - Which CHF in the range 30° to 90° ?
  - What if using vessel (i.e. low-alloy ferritic) steel ?
  - How significantly does the HFF impact the CHF ?

Table 3 Comparison of the Local Critical Heat Fluxes Measured at Various Test Facilities Under Saturated and Subcooled Boiling Conditions

Local Angle of Inclination* θ	Local Critical Heat Flux, MW/m^2				
	SBLB at PSU		CYBL at SNL	ULPU at UCSB	
	Saturated Boiling	Subcooled Boiling**	Saturated Boiling+	Saturated Boiling	Subcooled Boiling++
0°	0.40	0.59	0.50	0.28	0.50
30°	0.61	0.86	--	0.65	0.89
60°	0.85	1.05	--	--	1.18
90°	(1.00)	(1.35)	--	--	1.50

* θ = 0° corresponding to the bottom center and θ = 90° corresponding to the upper edge of the test vessel
** Pool boiling with a subcooling of 10 °C
\+ Based largely on small-scale quenching data
++ Natural convection boiling with a subcooling of 14 °C at the bottom center

From [Cheung, 1997]

Effect of surface material

- Experimental evidence of an increase of CHF at low pressure, when using vessel steel instead of copper / stainless steel
  - Pool boiling on an upward-facing heated surface: BETA Experiment
    - **0.75 → 1.3 MW/m²** when switching from cleansed copper to oxidized steel
  - Under circulating flow: for example, EDF/MIT tests
    - **1,6 →2.3 MW/m²** @500 kg.m^{2}.s^{-1}, 90° inclination, and ~ 12 K subcooling
  - ➢ No clear physical explanation, but measurements indicate increased surface roughness and wettability when using vessel steel

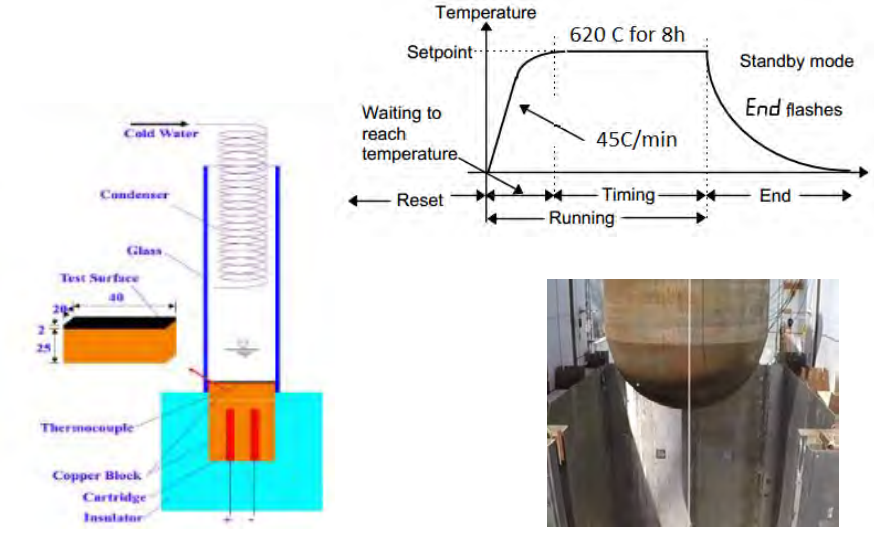

BETA (UCSB) from [Dinh 2003]

Vogtle AP1000 plant (courtesy of Bechtel)

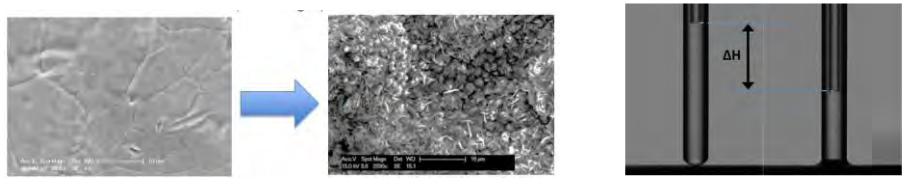

Increase of roughness and porosity – Wickability tests (MIT/EDF program, from [Trojer 2018])

2024 : Opportunity through EASI-SMR project to perform some CHF test in pool boiling situation on THS-15 facility at UJV using vessel steel

THS-15 facility at UJV

- Main characteristics
  - 2D-slide, 1:1 in height (VVER1000 geometry)
  - Naturally oxidized vessel steel covering the heaters
  - Can be configurated for pool boiling situation

THS-15 facility - from [Batek, 2024]

- Heater surface material : V354

	Typical Chemical Composition (wt.%)			
Element	16MND5 (PWR RPV steel)	V354 (THS-15)	15Kh2NMFA (VVER RPV steel)	Stainless steel (304L)
Carbon (C)	0.16 – 0.20	0.12 – 0.18	0.12 – 0.18	≤ 0.03
Manganese (Mn)	1.20 – 1.60	0.80 – 1.10	0.30 – 0.60	≤ 2.00
Silicon (Si)	0.15 – 0.35	≤ 0.20	0.17 – 0.37	≤ 1.00
Nickel (Ni)	0.40 – 1.00	—	1.00 – 1.50	8.0 – 12.0
Molybdenum (Mo)	0.45 – 0.60	0.80 – 1.00	0.40 – 0.70	—
Chromium (Cr)	≤ 0.30	1.25 – 1.50	1.80 – 2.30	**18.0 – 20.0**
Vanadium (V)	—	0.20 – 0.30	0.10 – 0.30	—
Copper (Cu)	≤ 0.25	—	≤ 0.10	—
Phosphorus (P)	≤ 0.020	≤ 0.020	≤ 0.015	≤ 0.045
Sulfur (S)	≤ 0.010 – 0.020	≤ 0.015	≤ 0.015	≤ 0.030
Iron (Fe)	Balance	Balance	Balance	Balance

Objective of the experimental program / test parameters

- Choice of bounding parameters
  - Ambient pressure: atmospheric
  - Water level: as low as possible (low submergence)
  - Water temperature: at saturation
  - Coating: as it is (no treatment)
- Gap size
  - “No gap” (~ 50 cm)
- Water chemistry
  - None (De-Ionized water)

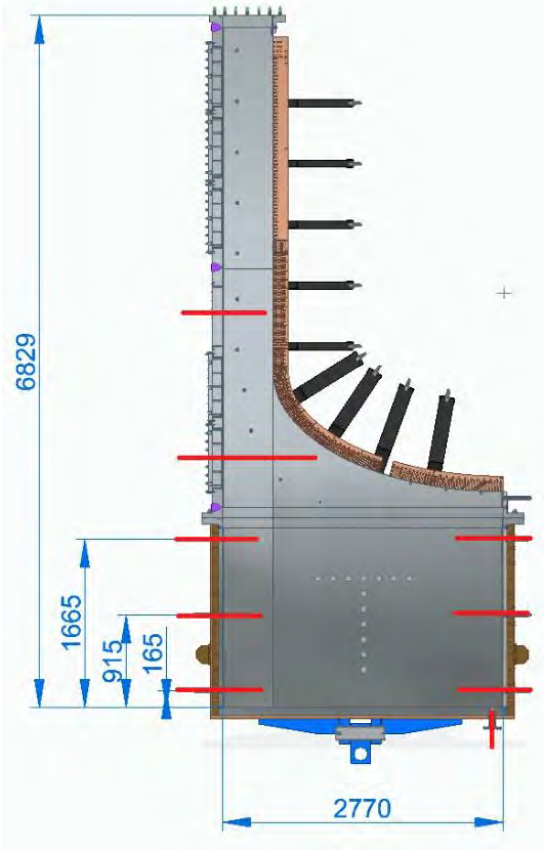

Test parameters (con't)

- Heat Flux Profile
  - **"Linear":** for a given inclination, bounding profile can be set so that the amount of energy that heats the water before CHF location is maximized

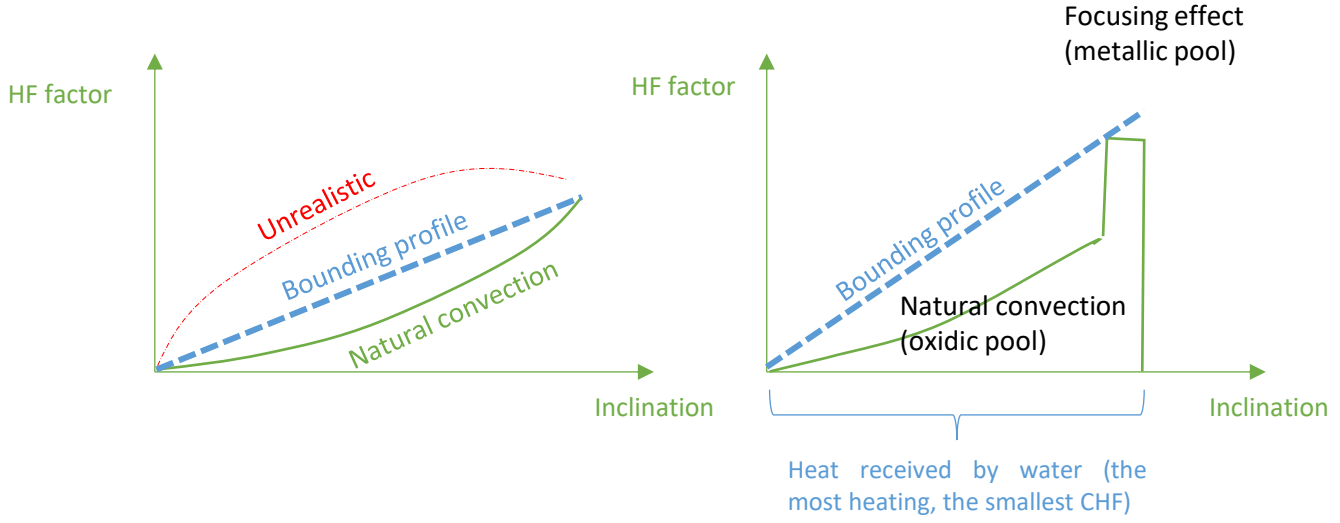

✓ *Example on a ULPU HFP*

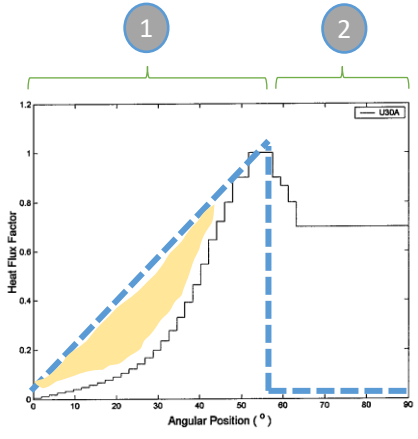

[53-57°]

1 *A linear profile maximizes the thermal energy transferred to the fluid ➔ The measured CHF is conservative*

2 *The heat flux can be truncated beyond the location at which the CHF is evaluated, as this has no impact under pool-boiling conditions*

Thermal energy transferred to the fluid upstream of the measurement location is maximized

Test parameters (con't)

- Inclinations
  - 30°, 45°, 50°, 60°, 80°, 90°
    - ✓ depending on the condition of the heating cartridges
- Methodology for CHF measurement
  - For each inclination of the test matrix, HFF is set linear
  - Theofanous' correction [Theofanous, 1996] is then applied to take into account slice geometry

$$HFF_{Slice}(\theta) = HFF_{prototypical} \times \frac{\sin\theta}{sin\theta_m} \text{ for } \theta < \theta_m$$

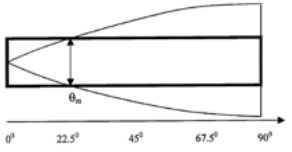

  - To detect the CHF, the HF slope is increased until a rapid increase in temperature is detected by the thermocouples located near the surface of the heaters

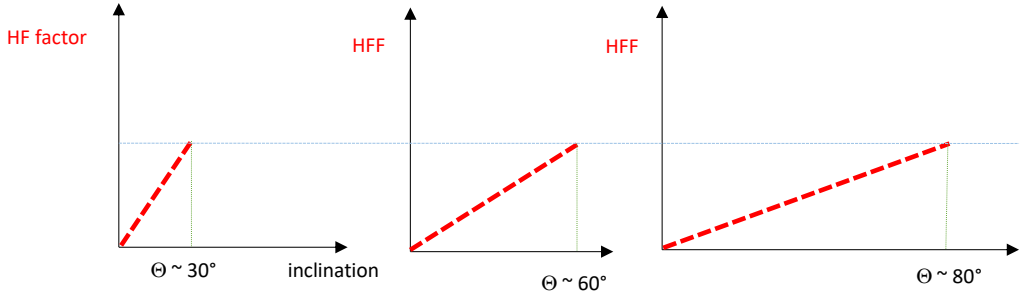

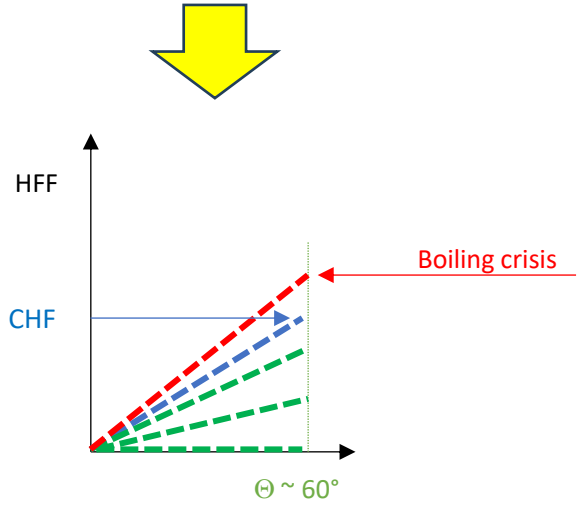

Test parameters (con't) - Sensitivity

- Sensitivity studies
  - On water level
    - ✓ Reference level is set at low level
    - ✓ Sentivity : higher water level (+ 1.5 m)
    - ✓ In reactor situation, the water level would reach the primary loop
  - On the heat flux profile
    - ✓ a HFF from ASTEC calculation on E-SMR design (from ELSMOR European Project) is used

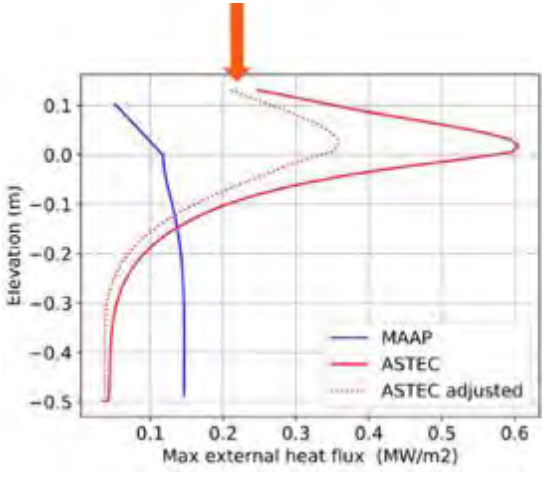

from [Bittan, 2024]

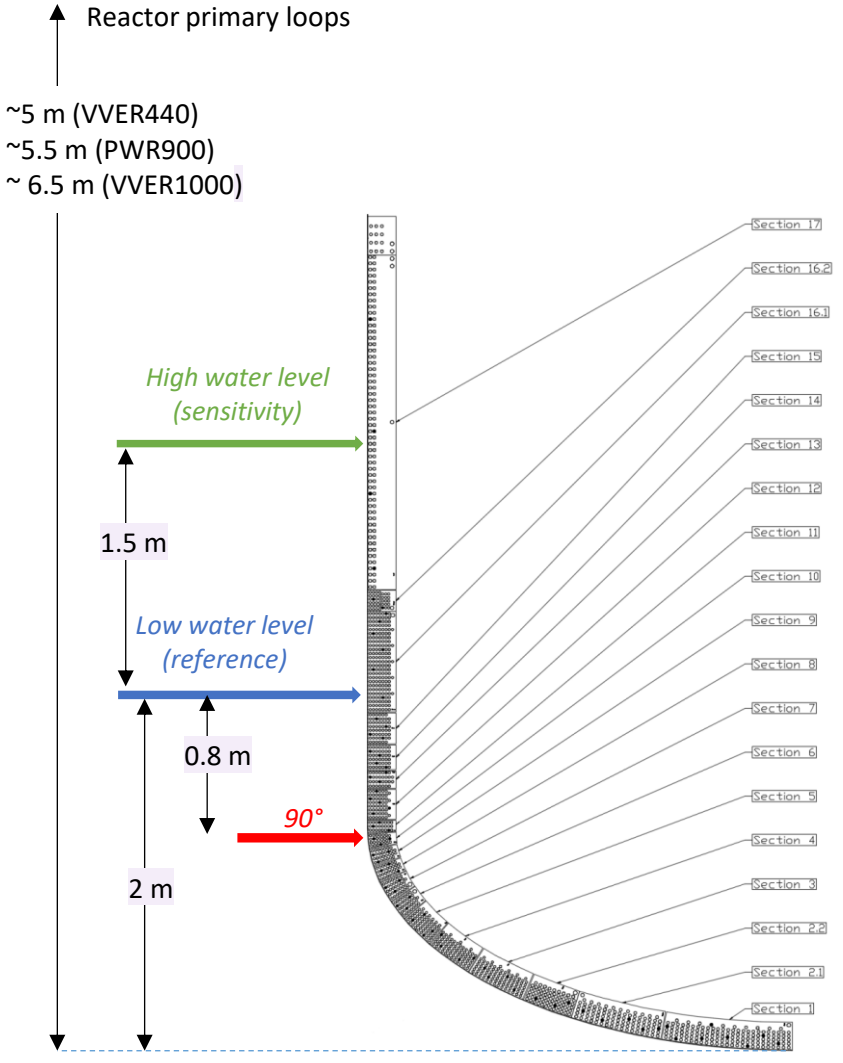

CHF results

- Reference parameters (linear HFF)
  - At ~90° inclination, the heating cartridges did not dissipate enough heat to reach critical heat flux

Linear (bounding) HF profile		
RPV inclination	Low water level	
	1st Measurement [MW/m²]	2nd Measurement [MW/m²]
30°	0.82	0.82
45°	1.05	1.09
60°	1.26	n/a
80°	1.67	1.71
90° (limited power)	> 1.76 (maximum heat flux)	> 1.58 (maximum heat flux)

- Comparison with literature
  - Heat Flux Factor used for CHF detection are different
    - ✓ bounding (“linear”) for THS-15 (hemi-ellipsoidal)
    - ✓ depending on the reactor design considered for ULPU (hemispherical)
  - ✓ Bounding curve may be approached by *CHF (MW/m²) = 0.0156Θ (degree) + 0.3694*

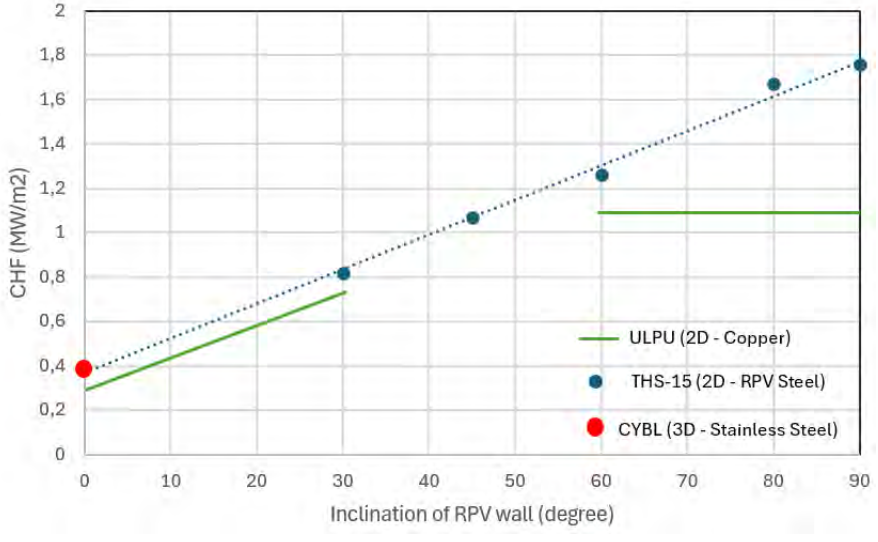

CHF results (sensitivity)

- Effect of Heat Flux Factor profile and effect of surface material

	Effect of HFF profile (RPV steel)		
RPV inclination [degree]	Linear (bounding) Mean CHF [MW/m²]	ELSMOR Mean CHF [MW/m²]	Δ%
30°	0.82	0.95	+16%
45°	1.07	1.12	+4%
60°	1.26	1.31	+4%
80°	1.69	1.78	+5%

	Effect of surface material		
RPV inclination [degree]	Copper (ULPU) Mean CHF [MW/m²]	RPV Steel Mean CHF [MW/m²]	Δ%
30°	0.67	0.82	+22%
45°	-	-	-
60°	1.1	1.26	+14%
80°	1.1	1,69	+53%

  - o "Realistic" HFF logically provides slightly higher CHF than the bounding HFF, though not significantly
  - o Effect of surface material has a more significant impact on CHF

- Effect of water level
  - o Higher water level increases logically the CHF
  - ✓ Higher CHF are expected if the cavity is flooded until the primary loops

Effect of water level					
RPV inclination	Low water level Mean CHF (linear) [MW/m²]	Low water level Mean CHF (ELSMOR) [MW/m²]	"High" water level (+ 1.5 m) 1st Measurement [MW/m²]	"High" water level (+ 1.5 m) 2nd Measurement [MW/m²]	Δ%
30°	0.82	0.95	0.90	0.97	+10% ; + 5%
45°	1.07	1.12	1.30	1.32	+21% ; +17%
60°	1.26	1.31			
80°	1.69	1.78			

Conclusion

- Main insights
  - CHF values with bounding assumptions are provided for ERVC under and IVR strategy when pool boiling is considered, especially considering bounding heat flux profile and very low water submergence compared to reactor situation
  - The study addresses a gap in the literature by providing critical heat flux data
    - ✓ for inclinations between 30° and 60°
    - ✓ specifically for reactor vessel steel
  - These values are significant, with heat fluxes reaching at least 1 MW/m² at 45° and about 1.7 MW/m² at 80° inclination for a 50 cm gap size.
  - These values can be used to assess reactor vessel coolability margins when the design is not well defined (e.g., safety system architecture and corium loading)
- Perspectives
  - The effect of the gap still needs to be assessed. A narrower gap is advantageous for designers, as it reduces the water volume needed to initially flood the reactor cavity
  - The effect of vessel shape (semi-ellipsoidal or hemi-spherical) has also to be assessed

NB : effect of water chemistry cannot be assessed in THS-15 facility. Past studies ([Dinh, 2003], [Trojer, 2018]) did not show a clear tendency of the impact of boron and/or alkaline buffering agent on the CHF, either under pool boiling or circulating flow.

Thank you
Any question ?

References

- [Batek, 2024] Batek D., Zdarek, J., Kotouc M., et al."THS-15 Experimental facility: Effect of Surface Roughness on CHF Values", 11th Conference on SEVERE ACCIDENTS RESEARCH May 13-16, 2024 – Stockholm, Sweden
- [Bittan, 2024] Bittan J., Bakouta N., Zambaux J.-A., Carénini L., “Comparison between EDF MAAP5.04 and ASTECv3 codes on an hypothetical Severe Accident on the ELSMOR project NUWARD-Like SMR Design”, The 11 European Review Meeting on Severe Accident Research (ERMSAR2024), KTH, Stockholm, Sweden, May 13-16, 2024
- [Cheung, 1997] « Critical Heat Flux (CHF) Phenomenon on a Downward Facing Curved Surface », Cheung et al., NUREG/CR-6507 - PSU/ME- 97-7321
- [Chu, 1994] « Large-Scale Boiling Experiments of the Flooded Cavity Concept for In-Vessel Core Retention », OECD/CSNI/NEA Workshop on large molten pool heat transfert, Grenoble, France, 1994
- [Dinh, 2003] Dinh.-T.N., Tu, J.P., Salmassi, T., Theofanous, T.G., 2003, “Limits of coolability in the AP1000 related ULPU-2400 configuration V facility”. University of California, Santa Barbara, CRSS-03/06. https://www.nrc.gov/docs/ML0319/ML031920123.pdf)
- [Theofanous, 1996] « IN-VESSEL COOLABILITY AND RETENTION OF A CORE MELT», DOE/ID-10460, VOLUME 1, October 1996
- [Trojer, 2018] Trojer M., Azizian R., Paras J., Mckrell T., Atkhen, K., Bucci M., Buongiorno J., “A margin missed: The effect of surface oxidation on CHF enhancement in IVR accident scenarios”. Nuclear Engineering and Design, 335, 140-150, 2018

BWR RPV Lower Head Penetration Failure Caused by Eutectic Reactions with Zr-Rich Simulated Metal: ELSA-3 Test

Kenta Shimomura[1], Takuya Yamashita[1] *
1. Japan Atomic Energy Agency (JAEA)
2-4, Tokai-mura, Ibaraki, Japan
shimomura.kenta@jaea.go.jp, yamashita.takuya38@jaea.go.jp

ABSTRACT

Internal investigations at the Fukushima Daiichi Nuclear Power Station (1F) have been conducted by Tokyo Electric Power Company Holdings (TEPCO HD); however, the condition of the reactor pressure vessel (RPV) has not yet been confirmed. To clarify the RPV damage progression during the accident, a simulation test (ELSA-3) was conducted using the LEISAN test facility owned by JAEA, focusing on the interaction between a zirconium-containing liquid metal (304SS-83wt% Zr alloy) that discharged to the bottom of the RPV lower head and the lower head structural components, forming a liquid metal pool and potentially causing failure through eutectic reactions.

The test results showed that at the lower head penetration region, the eutectic reaction (approximately 1250°C) between the simulated metal debris and the lower structural components (CRD housings and CRD stub tubes) caused melting of the structural components, allowing the simulated metal debris to flow into the CRD housings. This eutectic reaction temperature is below the melting point of the individual structural materials, indicating that failure can occur due to inter-material eutectic reactions even without reaching the melting point. These results suggest that for Zr-rich molten materials, damage may occur through eutectic reactions between materials even below their melting points.

KEYWORDS
Reactor Pressure Vessel, Eutectic reaction, CRD

1. INTRODUCTION

Internal investigations of the Fukushima Daiichi Nuclear Power Station (1F) are being conducted by Tokyo Electric Power Company Holdings (TEPCO HD); however, the condition of the reactor pressure vessel (RPV) has not yet been sufficiently confirmed.

To clarify the damage status of the RPV associated with accident progression, a simulated experiment (ELSA-3: Experiment on Late In-vessel Severe Accident Phenomena) was conducted, focusing on failure caused by material interactions (eutectic reactions) between the lower structural components of the RPV and a molten metal pool formed at the bottom of the lower head, resulting from the relocation of zirconium-containing liquid metal. In the previous ELSA series, the ELSA-1[1] teste focused on the local failure behavior of the RPV structure caused by zirconium (Zr)-rich simulated metal debris. Conversely, the ELSA-2[2][3] test was conducted under conditions with high stainless steel content, which provided the insight that failure remains limited under such compositions.

2. FAILURE MODES OF THE LOWER HEAD

When the reactor pressure vessel (RPV) is not under high-pressure conditions, failure of the lower head (LH) during a severe accident (SA) in a boiling water reactor (BWR) occurs as a result of molten core

materials relocating to the lower plenum. LH failure is caused by mechanical factors, thermal factors, and eutectic melting that depends on the composition of the molten pool.
Examples of mechanical factors include plastic deformation, creep damage, and buckling. Thermal failure occurs when LH structural materials are heated beyond their melting points. When eutectic melting occurs between the LH structural materials and the relocated core materials, failure can take place at temperatures lower than the melting point of the LH materials.
The dominant failure mechanism of the LH depends on the condition of the core during slumping. If most of the core fuel is molten during the slumping process, thermal damage caused by high-temperature molten oxide fuel becomes dominant. In contrast, if a large portion of the fuel remains unmelted, mechanical damage or eutectic melting-induced failure is more likely to occur.
In addition to fuel materials, metallic core components such as fuel cladding, control rods, and channel boxes undergo eutectic melting and relocate to the lower plenum. In BWRs, Ni/Zr, Fe/Zr, UO_2/Zry, and Fe/B systems are among the first materials to relocate. The molten metals initially solidify in the lower plenum, but are subsequently reheated by falling solid fuel fragments, forming a molten metal pool.
In mechanically dominated failure, heating due to the amount and height of accumulated debris within the RPV leads to vessel deformation and eventual rupture. When eutectic melting is dominant, partial liquefaction of LH structural materials occurs due to eutectic reactions between the molten metal pool and the LH structures, resulting in damage. Because the LH consists of structural components and welds made of stainless steel and nickel-based alloys, eutectic interactions between these materials and the molten metal pool can cause damage at the boundary regions.
Furthermore, the LH of a BWR contains many components such as control rod drive (CRD) housings, which are thinner than the RPV shell and therefore more susceptible to eutectic melting-induced failure. The material configuration around the CRD housing is shown in Figure 1. As shown in the Figure 2, when the weld between the CRD housing and the CRD stub tube is lost, the CRD housing is designed to rest on the grid clamp.

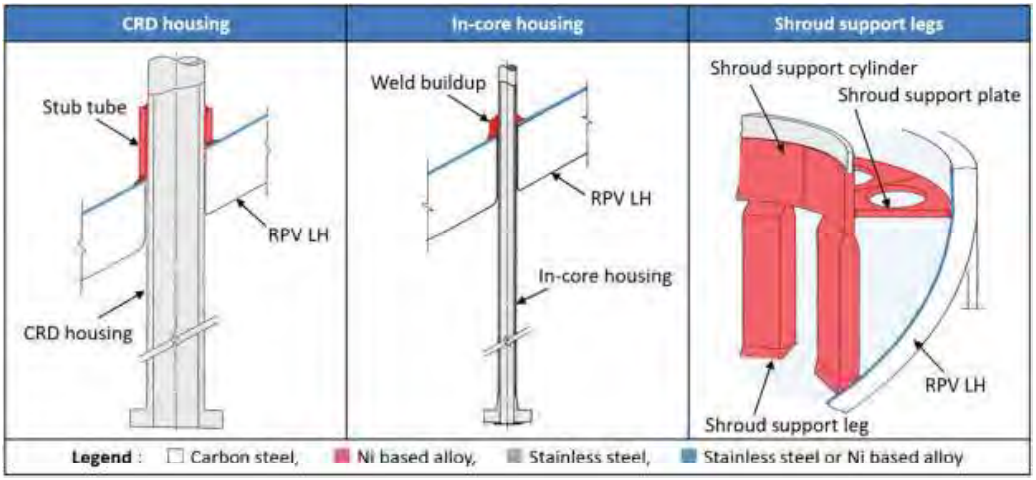

Figure 1 Material composition around the CRD housing [1]

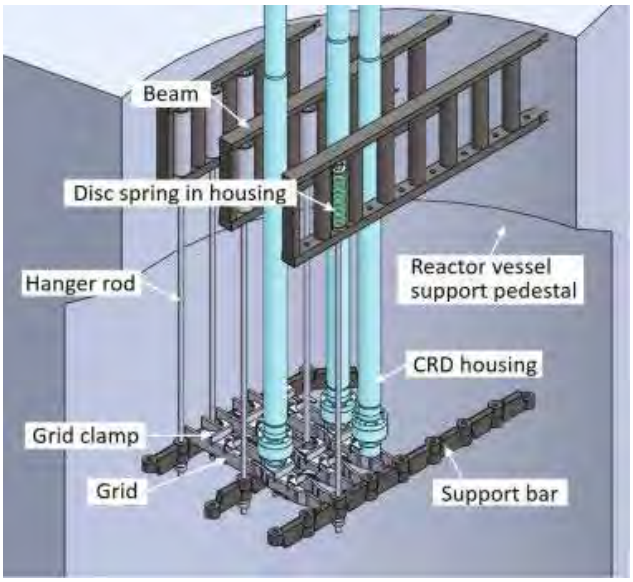

Figure 2 Structural layout around the grid clamp [1]

3. EXPERIMENT

3.1. EXPERIMENTAL OVERVIEW

This experiment was conducted using a test specimen that simulates the lower head of the reactor pressure vessel (RPV) and the control rod drive (CRD) system of Unit 2 at the Fukushima Daiichi Nuclear Power Station (1F2).

To simulate metallic debris relocating from the reactor core to the lower head during a severe accident, surrogate metal debris composed of SUS304–83 wt.% Zr was loaded into the specimen. This composition was selected based on a pseudo-binary phase diagram, as it becomes liquid at a relatively low temperature of approximately 1080°C. The selected ratio was determined with reference to the results of the CMMR tests [4], which simulated fuel melting behavior during slumping in Unit 1F2.

After the surrogate metal debris flowed into and blocked the CRD housings, the liquid level was set to allow observation of interactions between the remaining molten metal debris at the bottom of the RPV lower head and the lower head structural materials (Figure 3). The test was performed using the large-scale experimental facility LEISAN (Large-scale Equipment for Investigation of Severe Accidents in Nuclear Reactors) owned by JAEA/CLADS (Collaborative Laboratories for Advanced Decommissioning Science). The debris was heated and melted to form a molten metal pool, and failure caused by eutectic reactions with the CRD housings and CRD stub tubes in the lower plenum was investigated.

It should be noted that uranium was not used in this experiment because the facility was not designed for hot testing. The external views of the test apparatus and specimen are shown in Figure 4.

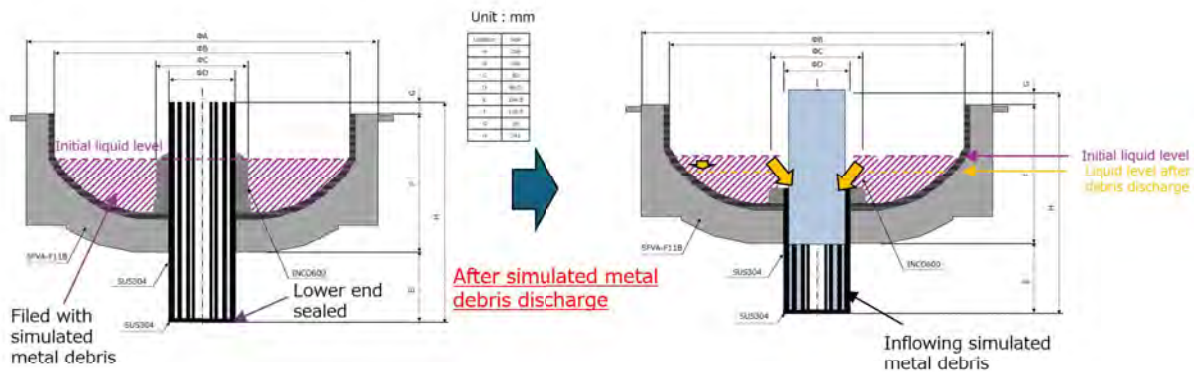

Figure 3 Liquid level setting

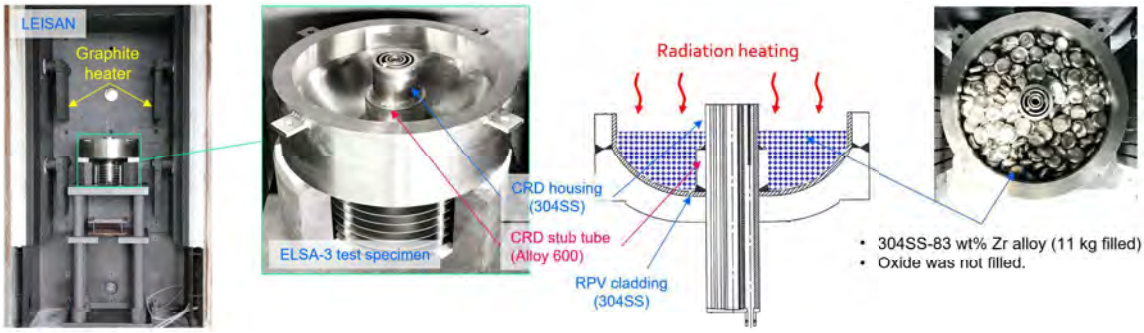

Figure 4 The ELSA-3 test apparatus and specimen

3.2. ACCIDENT PROGRESSION OF UNIT 2

Figure 5 presents an overview of the accident progression in Unit 2[1]. Immediately before failure of the lower head (LH), a decrease in RPV pressure was observed at 4:10 on March 15, accompanied by a reduction in steam generation within the RPV. This behavior suggests that the depletion of liquid water in the lower plenum led to a decline in steam production.

In Unit 2 (1F2), the formation of a large molten fuel pool was limited; therefore, the fuel debris that relocated to the lower plenum was likely in particulate form. In this situation, metallic debris that fell during the early stage of core damage was reheated and remelted by heat from the oxide fuel particles. The remelted metallic debris is considered to have formed a molten metal pool by filling the voids between the solid particulate oxide fuel.

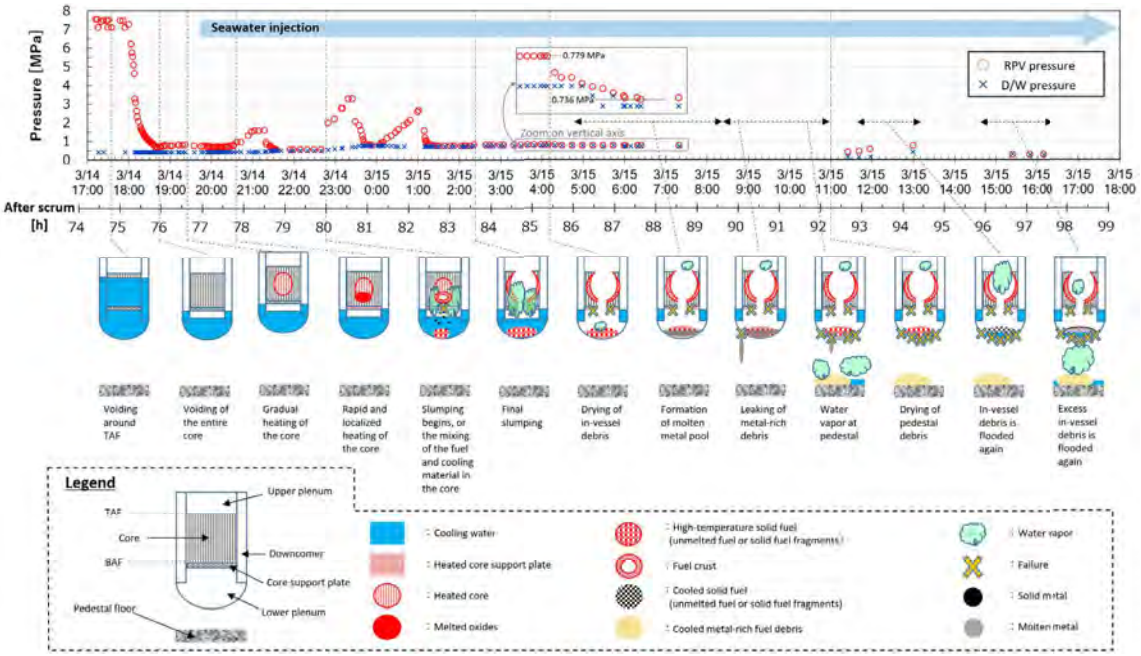

Figure 5 1F2 accident progression (2011) [1]

3.3. EXPERIMENTAL CONDITIONS

The experimental conditions were established based on the accident progression analyses and evaluations described above. The objective of this experiment was to clarify the failure behavior inside the CRD housings when debris accumulated in the lower plenum melts under steam-starved conditions.

In an actual reactor, a molten metal pool is formed through heating by oxide fuel; however, this process cannot be directly reproduced in the LEISAN facility. Therefore, surrogate debris was melted using radiative heat transfer from graphite heaters.

The test atmosphere consisted of argon gas with a purity of 99.99%. The test temperature was controlled by adjusting the output of the graphite heaters so that the temperature history of the specimen met the prescribed conditions, based on the results of thermal-hydraulic analyses from the RPV PJ [5]. During the test, temperatures were measured using thermocouples installed at various locations, and the behavior was observed using cameras mounted on the experimental apparatus.

3.4. EXPERIMENTAL RESULTS

The experimental results confirmed that eutectic reactions between the surrogate metal debris and the lower structural components—namely the CRD housings and CRD stub tubes—caused damage to these components at the lower head penetrations. The temperature history during the test is shown in Figure 6. The temperatures of the CRD housings and stub tubes at the time of failure were approximately 1300°C. Figures 7 and 8 present the pseudo-binary phase diagrams for the stainless steel (74%Fe–18%Cr–8%Ni)–zirconium system and the stainless steel (74%Fe–18%Cr–8%Ni)–zirconium–Alloy 600 (74%Ni–16%Cr–10%Fe) system, respectively. In this study, tungsten-rhenium thermocouples were employed to accommodate temperature measurements in the high-temperature range exceeding 1300°C. The measurement uncertainty is based on the ASTM E230/E230M-17 standard. At the failure temperature observed in this test (approximately 1300°C), the measurement error of the thermocouples is evaluated to be ±13°C.

From these phase diagrams, the eutectic reaction temperature between the 304SS–83 wt.% Zr alloy and the CRD housings and stub tubes is approximately 1250°C. The observed failure temperature in this experiment closely corresponds to this eutectic temperature, indicating that the structural components failed at temperatures below their respective melting points.

Because no external loads or constraints were applied to the specimen, mechanical effects can be neglected. After the failure of the CRD housings and stub tubes, the inflow of surrogate metal debris into the CRD housings was also observed.

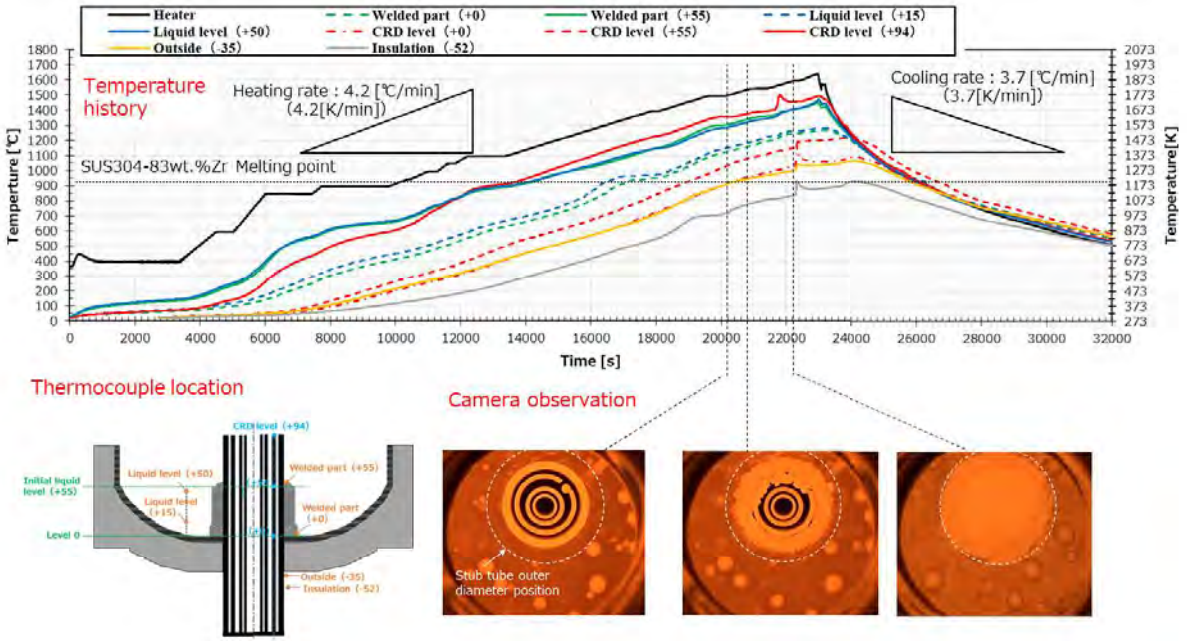

Figure 6 The temperature history during the test

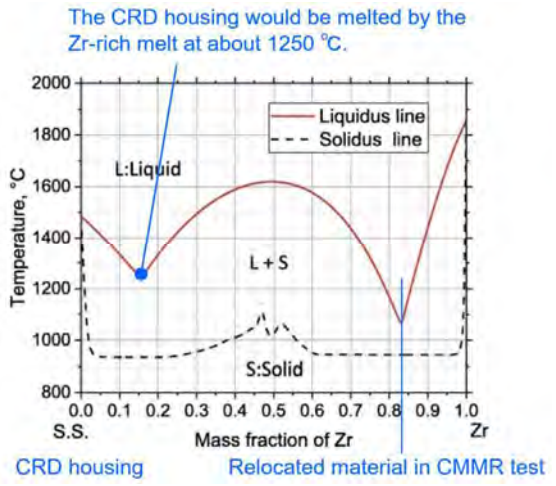

Figure 7 Quasi-binary phase diagram of stainless steel (74%Fe-18%Cr-8%Ni)-Zirconium–

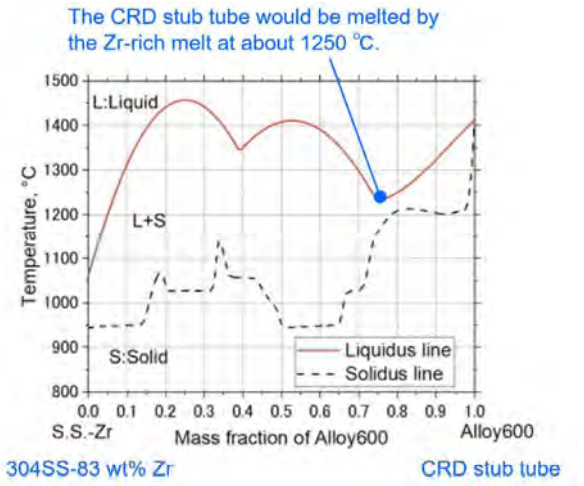

Figure 8 Quasi-binary phase diagram of stainless steel (74%Fe-18%Cr-8%Ni) – Zirconium-Alloy600 (74%Ni-16%Cr-10%Fe) [1]

3.5. POST-TEST OBSERVATIONS

Figure 9 shows the cutting position of the specimen, and Figure 10 shows the cross-sections of the specimen after cutting. EPMA analyses targeting Fe, Ni, O, and Zr were conducted in the region indicated by the blue box in the figure, and the results are presented in Figure 11. The specimens were mounted in epoxy resin alongside standard samples (Inconel, SUS304, SUS310S, SFVA, and Fe-Zr pellets) and

mirror-polished prior to analysis. The Ni distribution confirms that the upper portion of the CRD stub tube had disappeared, which is attributed to the diffusion of Ni into the molten surrogate debris.
The Zr distribution further indicates that Zr-rich material, namely the surrogate debris, flowed into the region where the stub tube had been lost. Furthermore, the molten metallic debris that rose along the CRD housing nearly obstructs the upper opening. However, the formation of a Laves phase at this opening restricts the amount of material flowing into the CRD housing.
The molten material was observed to have flowed out from the locations where the CRD housing and stub tube had melted. These results demonstrate that the Zr-rich molten material was capable of melting the CRD housing and stub tube at approximately 1300°C.
Based on the test results, the experiment is considered to have progressed through the following behaviors (Figure 12).

Step 1 First, the test specimen was filled with simulated metallic debris, and heating was initiated using a heater based on radiative heat transfer.

Step 2 Due to radiative heating from the heater, the surface began to melt, with nickel from the stub tube diffusing into the molten metal, while iron from the CRD housing surface diffused into the molten metal.

Step 3 Subsequently, a phenomenon in which the molten metal climbed up along the CRD housing occurred.

Step 4 The surface of the CRD housing became covered, and a thin oxide layer and the Laves phase were formed. Part of the molten metal that climbed up flowed into the interior of the CRD housing.

Step 5 Due to the formation of the oxide layer, dripping was limited. The upper part of the stub tube disappeared owing to eutectic reactions, eroding the CRD housing, and molten metal flowed into the interior of the CRD housing from the side of the stub tube.

Step 6 Similarly to the climbing behavior along the side of the CRD housing, molten metal also climbed up outside the test specimen and flowed out of the vessel, with dripping still being limited, as described in Step 5.

Figure 9 Cutting position

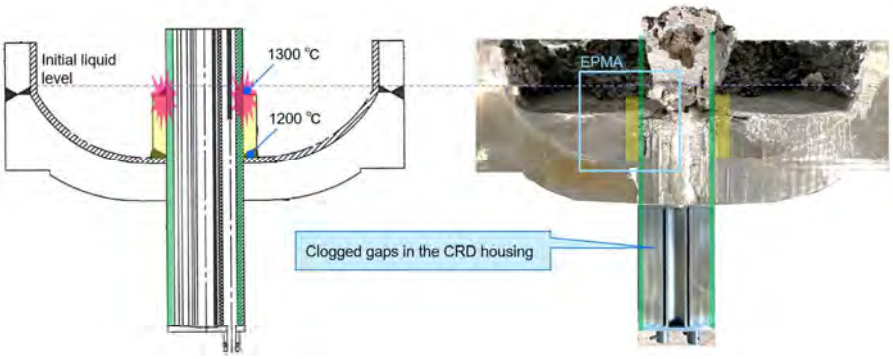

Figure 10 The cross-section of the post-test specimen

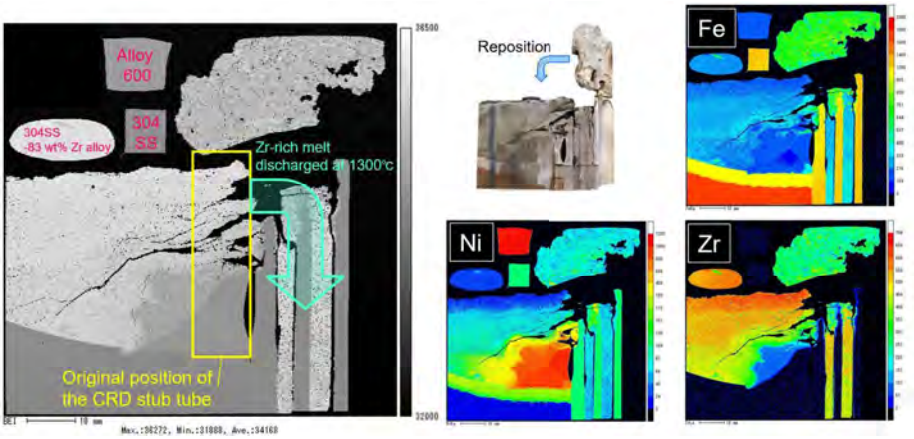

Figure 11 EPMA analysis

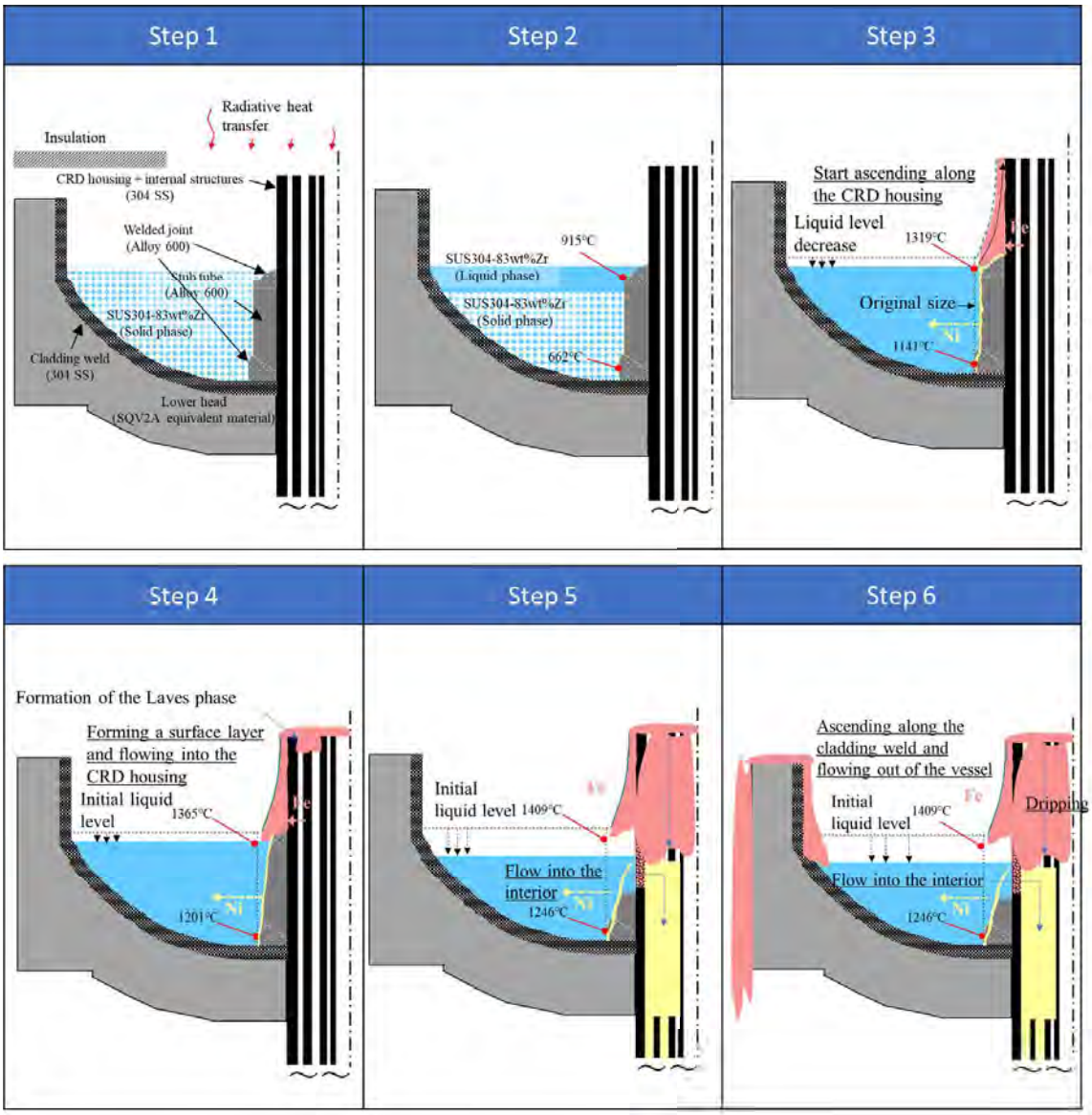

Figure 12 Schematic illustration of the test progression

4. ANALYSIS OF THE RESULTS

Based on the results of the ELSA-3 experiment, the failure of the CRD housings and stub tubes in Unit 2 (1F2) is estimated to have progressed through the following Steps 1 to 4. The conditions at each step are illustrated in Figure 13.

1. Zr-rich molten material relocated to the lower plenum and was reheated by fuel debris.
2. Some CRD housings and stub tubes failed due to eutectic reactions at temperatures below their respective melting points.
3. The molten material flowed into the CRD housings through the damaged regions.
4. As the stub tubes melted, the load previously supported by the weld joints between the CRD housings and stub tubes was transferred to the support bars.

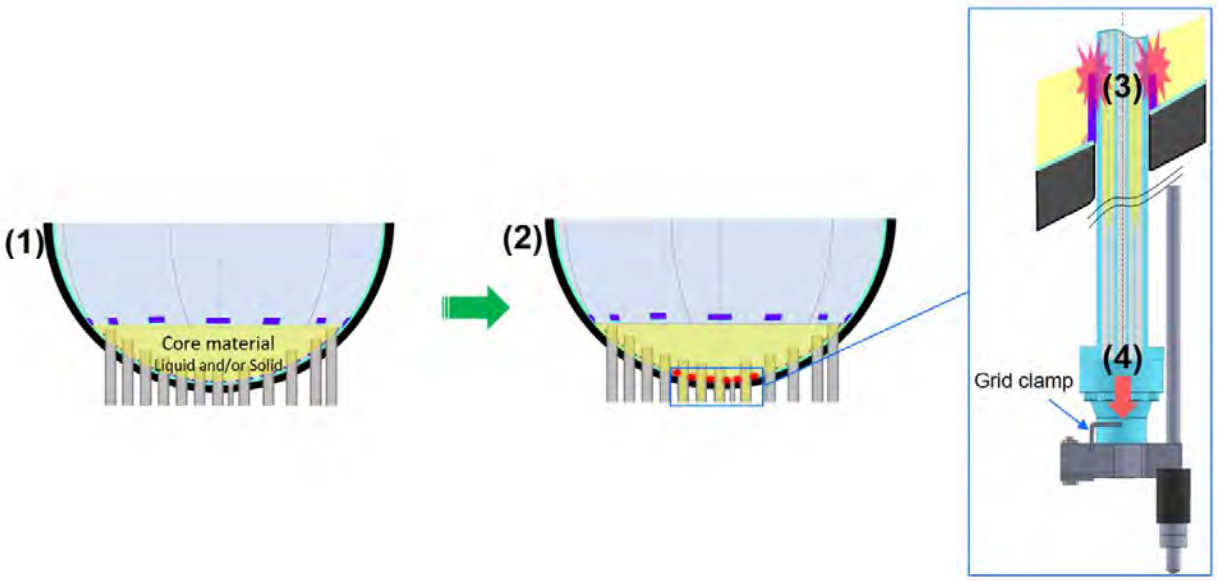

Figure 13 Estimation of the 1F2 accident progress

5. Conclusions

To clarify the accident progression at Unit 2 of the Fukushima Daiichi Nuclear Power Station, tests were conducted focusing on eutectic melting as part of the investigation into failure behaviors at the bottom of the Reactor Pressure Vessel (RPV).To understand the failure mechanisms caused by the eutectic reaction between the zirconium (Zr)-rich molten metallic debris accumulated in the lower plenum and lower internal structures (such as Control Rod Drive (CRD) housings), simulated metallic debris (SUS304-83wt.%Zr) was radiatively heated using graphite heaters in an argon atmosphere within the large-scale test facility LEISAN. The test results demonstrated that the CRD housing and stub tubes failed at approximately 1300°C, a temperature significantly lower than the melting points of the individual materials. Consequently, it is estimated that many of the CRD stub tubes in the actual reactor have melted, and the CRD housings are likely seated on and supported by the CRD housing support components.

ACKNOWLEDGMENTS

- This study has been performed by the funds from Ministry of Economy, Trade and Industry, Japan as The Subsidy Program “Project of Decommissioning, Contaminated Water and Treated Water Management (Development of Analysis and Estimation Technologies for Characterization of Fuel Debris (Development of Estimation Technologies of RPV Damaged Condition, etc.)" which started in 2022.

REFERENCES

1. T.Ymashita et al., “BWR lower head penetration failure test focusing on eutectic melting”, Annals of Nuclear Energy Volume 173, August 2022, 109129, https://doi.org/10.1016/j.anucene.2022.109129
2. Japan Atomic Energy Agency, “Clarification of Debris Formation Conditions on the Basis of the Sampling Data and Experimental Study Using Simulated Fuel Debris and Reinforcement of the Analytical Results of Severe Accident Scenario (Contract Research) -FY2022 Nuclear Energy Science & Technology and Human Resource Development Project”, JAEA-Review 2024-014, August 2024, DOI:10.11484/jaea-review-2024-014
3. Japan Atomic Energy Agency, “Clarification of Debris Formation Conditions on the Basis of the Sampling Data and Experimental Study Using Simulated Fuel Debris and Reinforcement of the Analytical Results of Severe Accident Scenario (Contract Research) – FY2023 Nuclear Energy Science

& Technology and Human Resource Development Project –“, JAEA-Review 2025-007, September 2025, DOI:10.11484/jaea-review-2025-007
4. T.Yamashita et al., “Post-test Analyses of the CMMR-4 Test”, NERS-21-1055, ASME J of Nuclear Rad Sci. Apr 2022, https://doi.org/10.1115/1.4051443
5. Japan Atomic Energy Agency, “Development of Analysis and Estimation Technologies for Characterization of Fuel Debris (Development of Estimation Technologies of RPV Damaged Condition, etc.)”, Project of Decommissioning, Contaminated Water and Treated Water Management, October 25, 2023, https://en.dccc-program.jp/5373

The 12th European Review Meeting on Severe Accident Research (ERMSAR2026)
Madrid, Spain

BWR RPV Lower Head Penetration Failure Caused by Eutectic Reactions with Zr-Rich Simulated Metal: ELSA-3 Test

May 18-22, 2026

*Kenta Shimomura, Takuya Yamashita

Japan Atomic Energy Agency (JAEA)

This study has been performed by the funds from Ministry of Economy, Trade and Industry, Japan as The Subsidy Program “Project of Decommissioning, Contaminated Water and Treated Water Management (Development of Analysis and Estimation Technologies for Characterization of Fuel Debris (Development of Estimation Technologies of RPV Damaged Condition, etc.)" which started in 2022.

Outline

1. **Introduction**

2. **Failure modes of the lower head/About the Control Rod Drive (CRD)**

3. **Experiment**
   - 3.1 Experimental overview
   - 3.2 Experimental conditions
   - 3.3 Experimental results
   - 3.4 Post test observations

4. **Analysis of the results**

5. **Conclusions**

6. **Latest topics**

1. Introduction

- Estimated Diagrams of Internal Conditions of Units 1–3 at Fukushima Daiichi Nuclear Power Station (1F)

- Based on past evaluations, it is estimated that the Reactor Pressure Vessel (RPV) has been breached (holes have formed).

- Current focus is placed on damage caused by material interaction (eutectic reaction) among various RPV failure modes

  - Damage due to material interaction (eutectic reaction) between liquid metallic core materials (Zr) and lower structural components at the RPV lower head.

To investigate the damage status of the RPV bottom and the inflow of molten material into the Control Rod Drive (CRD) housings under conditions where metallic debris is present at the bottom of the RPV, tests are conducted using specimens simulating the RPV lower head section (ELSA: Experiment on Late In-vessel Severe Accident phenomena). These tests demonstrate the possibility of damage resulting from material interactions (eutectic reactions) between the RPV lower head components and the metallic debris.

Estimated Diagram of Internal Conditions of Unit 1*

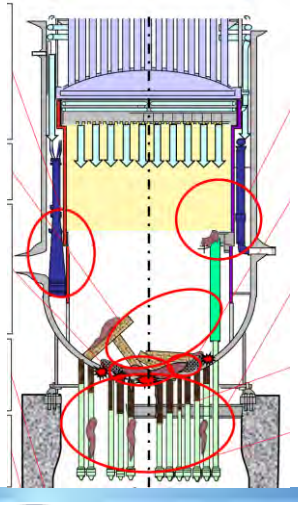

Estimated Diagram of Internal Conditions of Unit 2*

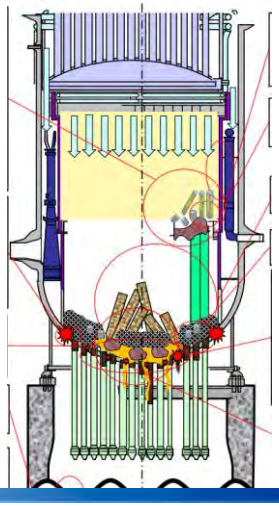

Estimated Diagram of Interna Conditions of Unit 3*

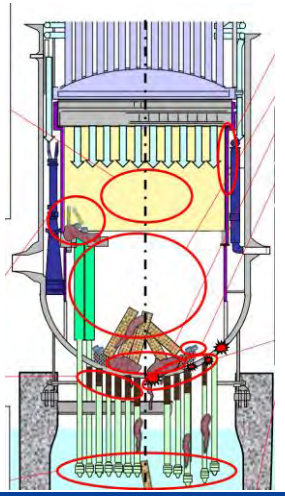

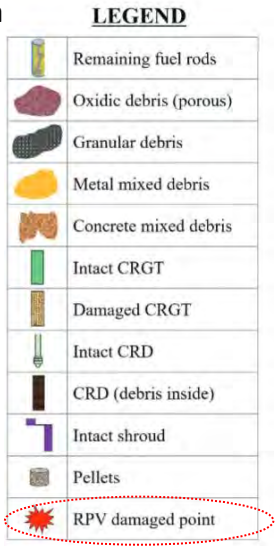

※ debriswiki
https://fdada-plus.info/wiki/index.php?title=%E7%82%89%E5%86%85%E7%8A%B6%E6%B3%81%E6%8E%A8%E5%AE%9A%E5%9B%B3#.E3.83.87.E3.83.96.E3.83.AA.E5.88.86.E5.B8.83.E3.83.BBRPV.E3.83.BBPCV.E7.8A.B6.E6.85.8B.E3.81.AE.E6.8E.A8.E5.AE.9A.E5.9B.B3

2. Failure modes of the lower head

2. Failure modes of the lower head

Failure Modes at the RPV Lower Head
- Thermal failure
- Mechanical failure
- Failure due to material interaction

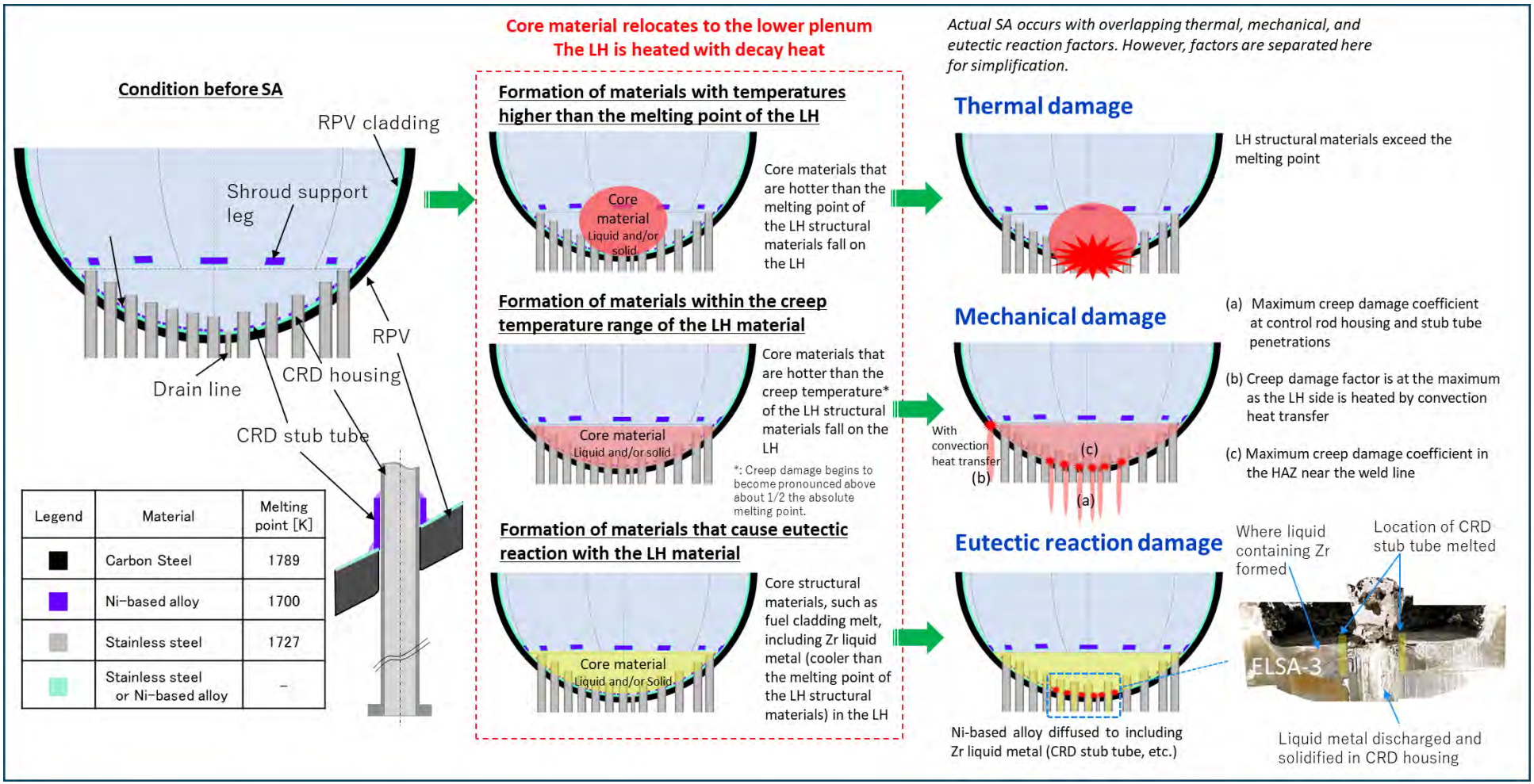

2. About the Control Rod Drive (CRD)

- Within the Control Rod Drive (CRD) mechanism, the CRD housing is only welded to the CRD stub tube, which in turn is welded to the RPV weld cladding.
- The structure is designed such that if the weld between the CRD housing and the CRD stub tube is lost, the CRD housing will seat on the grid clamp.

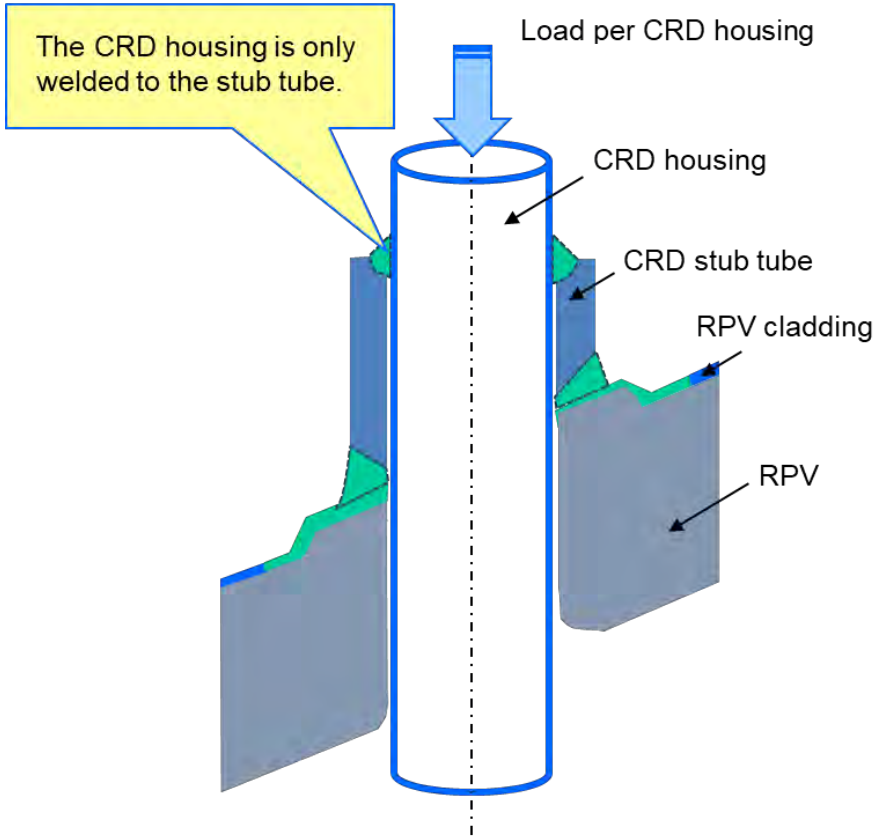

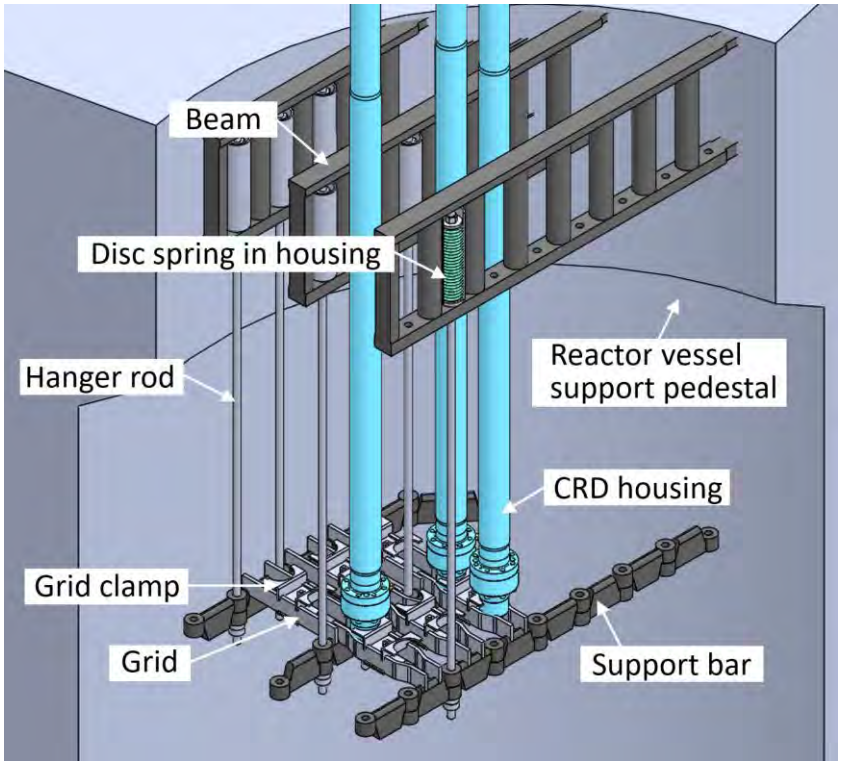

■ : Stainless steel, ■ : Ni based alloy, ■: Carbon steel

3. Experiment

3.1 Experimental overview

- Test specimens simulating the RPV lower head (including weld cladding), CRD housings, and CRD stub tubes were fabricated.
- "SUS304-83wt.%Zr" was selected as the simulated metallic debris to be filled into the specimens. This composition was chosen based on the SUS304-Zr pseudo-binary phase diagram as a Zr-rich ratio that liquifies at low temperatures, reflecting CMMR (Core Material Melting and Relocation) test results where Zr-rich materials were found to melt preferentially.

External view of the test specimen

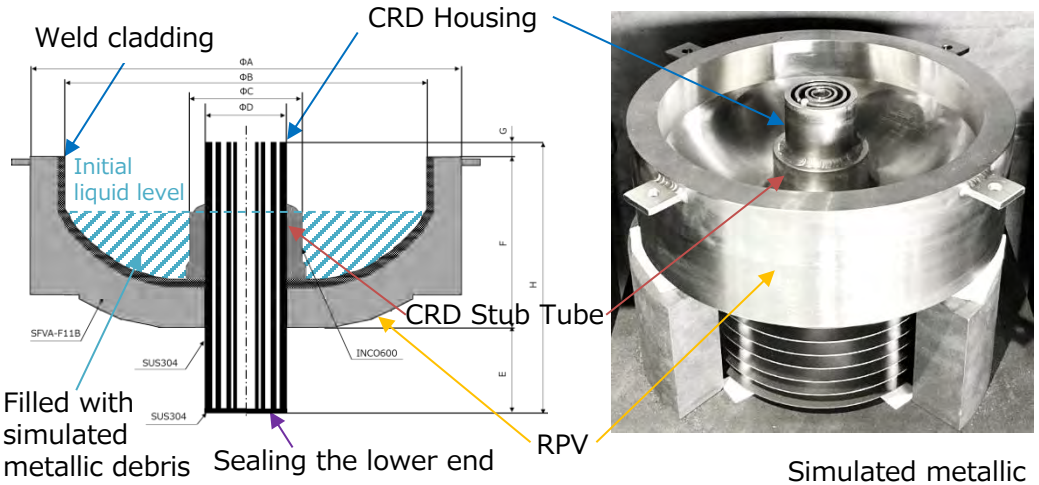

Unit : mm

Part	Dimensions
A	316
B	226
C	82
D	60.5
E	104.5
F	126.5
G	10
H	241

Component	Material
CRD Housing	Stainless steel
CRD Stub Tube	Nickel alloy
RPV	Low-alloy steel
Weld cladding	Stainless steel
Simulated metallic debris	SUS304-83wt.%Zr

※ : T. Yamashita、et al.、"BWR lower head penetration failure test focusing on eutectic melting"、Annals of Nuclear Energy 173 (2022) 109129.
https://www.sciencedirect.com/science/article/pii/S0306454922001645

Simulated metallic debris
Density : 6770kg/m^3
Amount used:11kg

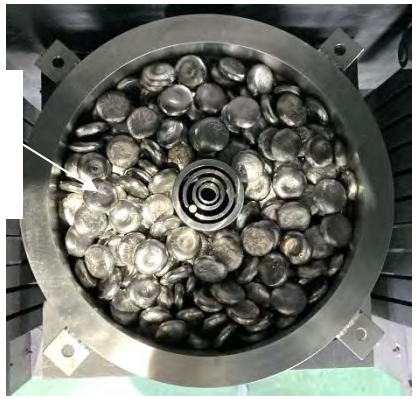

Pseudo-binary phase diagram of SUS304-Zr※

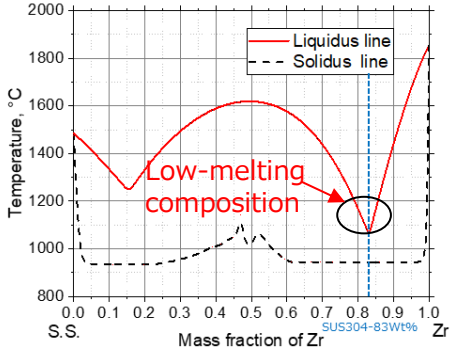

※ : T. Yamashita、et al.、"BWR lower head penetration failure test focusing on eutectic melting"、Annals of Nuclear Energy 173 (2022) 109129.
https://www.sciencedirect.com/science/article/pii/S0306454922001645

CMMR test※

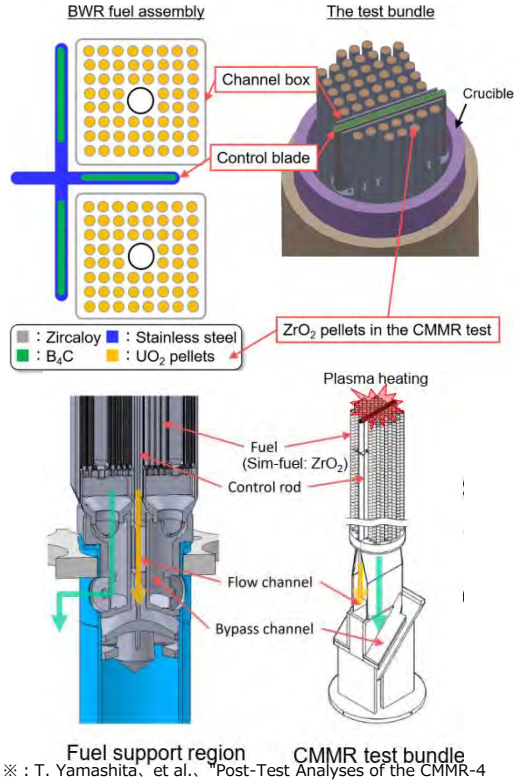

※ : T. Yamashita、et al.、"Post-Test Analyses of the CMMR-4 Test"、Journal of Nuclear Engineering and Radiation Science APRIL 2022, Vol.8 / 021701-1
https://asmedigitalcollection.asme.org/nuclearengineering/article/8/2/021701/1111101/Post-Test-Analyses-of-the-CMMR-4-Test

3.2 Experimental conditions

- To observe the reaction between the simulated metallic debris and the lower head structural components after the debris has flowed into and blocked the CRD housing, the liquid level height was established to ensure that the debris remaining in the lower head would react with those lower head components .
- Using the large-scale test facility (LEISAN facility) owned by JAEA/CLADS, the materials were heated and melted with graphite heaters to form a liquid pool. Damage caused by eutectic reactions with the CRD housing and CRD stub tubes was then observed. Following the test, the specimen was cut for cross-sectional observation and analysis.

Liquid level height setting

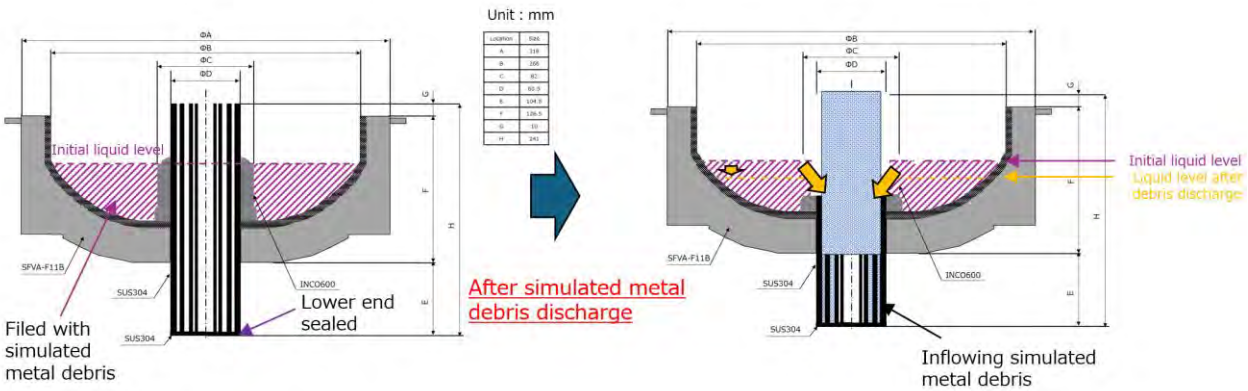

LEISAN Facility

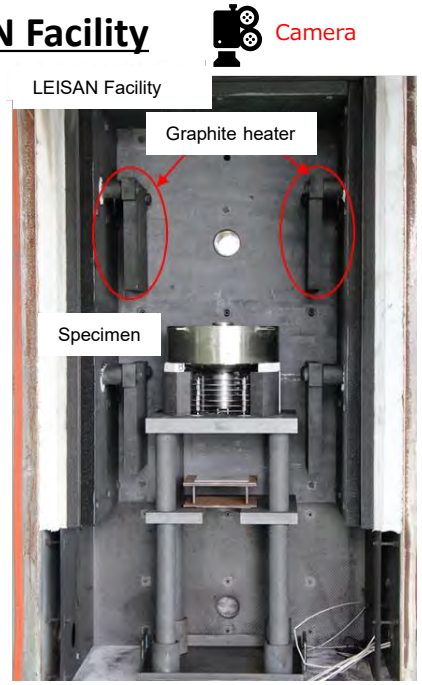

※：LEISAN Facility
（Large-scale Equipment for Investigation of Severe Accidents in Nuclear reactors）、Installed at JAEA/CLADS（Tomika）

3.3 Experimental results

- During the test, temperature measurements were conducted using thermocouples installed at various locations, and observations were made using cameras installed in the test apparatus.
- The heating rate was established based on the temperature history obtained from a thermal-hydraulic analysis* of the actual reactor (Unit 2). The heating rate was set to 4.2° C/min. During the cooling phase, the temperature was reduced with a target rate of 3.7° C/min, considering the constraints of the test apparatus.

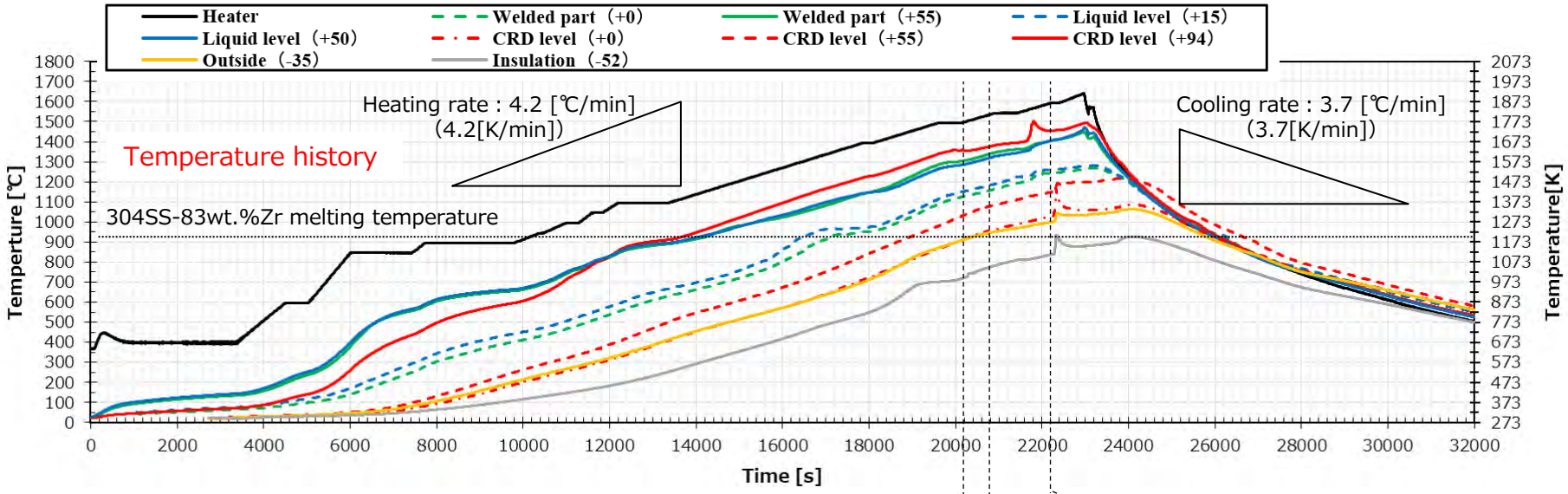

Thermocouple locations

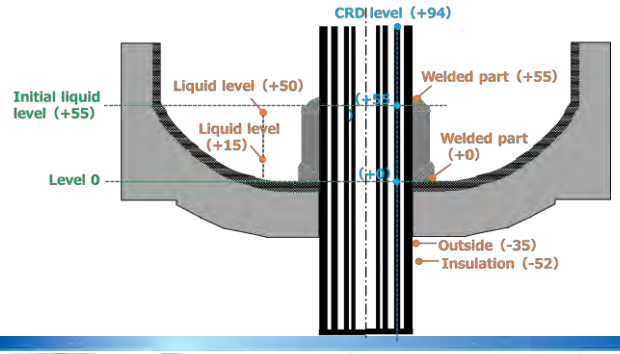

Camera observation

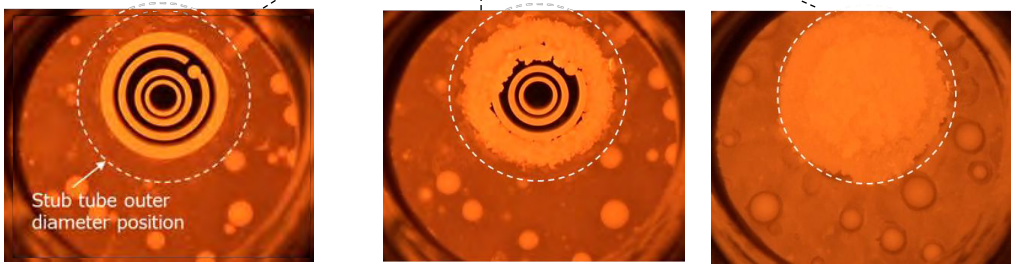

*https://en.dccc-program.jp/6928, JAEA, Development of Analysis and Estimation Technology for Characterization of Fuel Debris "3. Development of Estimation Technologies of RPV Damaged Condition and Fuel Debris Migration Behavior in PCV, etc.", October 30, 2025

3.4 Post test observations

- The specimen was sectioned after the test, and the cross-sections were observed. The loss (disappearance) of the CRD stub tubes and the inflow of molten metallic debris into the CRD housings were confirmed. Additionally, it was observed that the molten metallic debris climbed the sides of the CRD housings and the specimen walls, resulting in inflow into the CRD housings and outflow from the vessel.
- The total amount of simulated metallic debris filled into the specimen was 11 kg. Based on the amount found inside the CRD housings (approx. 1.7 kg [upper part: ~0.8 kg, lower part: ~0.9 kg]) and the residual amount remaining in the vessel (approx. 4.3 kg), the amount that adhered to the vessel sides or flowed out of the vessel was approximately 5 kg.

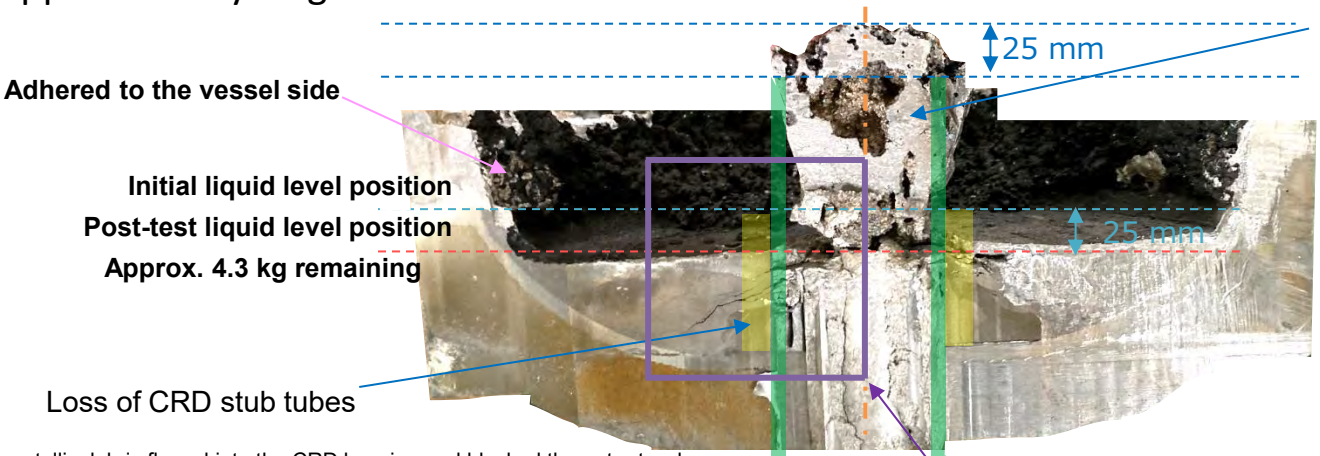

Molten metallic debris climbed the side of the CRD housing and flowed into it. (Upper part: Approx. 0.8 kg of molten metallic debris flowed in.)

Cutting position

・Molten metallic debris flowed into the CRD housing and blocked the outer two layers. (Approximately 0.9 kg of molten metallic debris flowed into the lower part.)
・The temperature of the molten metallic debris at the time of outflow (thermocouple: Welded part (+55)) was approximately 1300° C (1573.15K).
・The temperature of the CRD housing (thermocouple: CRD level (+0)) was approximately 930° C (1203.15K), which is comparable to the melting temperature of the simulated metallic debris.

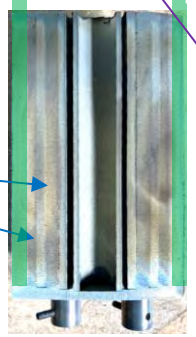

- Analysis was conducted over an 8 cm × 8 cm area (refer to the next page for analysis results).The upper part of the CRD housing was analyzed in a horizontal position (laid on its side) due to the constraints of the analytical equipment.

Upper part of the CRD housing

Horizontal position

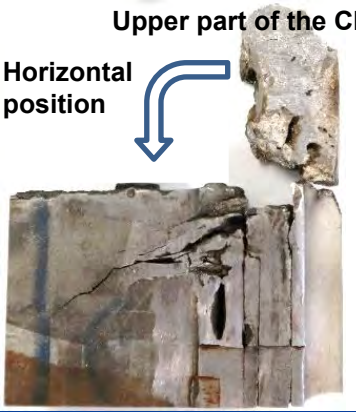

3.4 Post test observations

- EPMA analysis (target elements: Fe, Ni, O, and Zr) was performed on an 8 cm × 8 cm area of the specimen cross-section. Following the EPMA analysis, XRD analysis was conducted on the same cross-section.
- The molten metallic debris that crept up the CRD housing blocked most of the upper opening; however, the inflow from the upper opening into the CRD housing was limited due to the formation of the Laves phase at the opening.
- The upper part of the CRD stub tube melted through reaction with the molten metallic debris, leading to the migration of the molten metallic debris from the melted section.

EPMA analysis

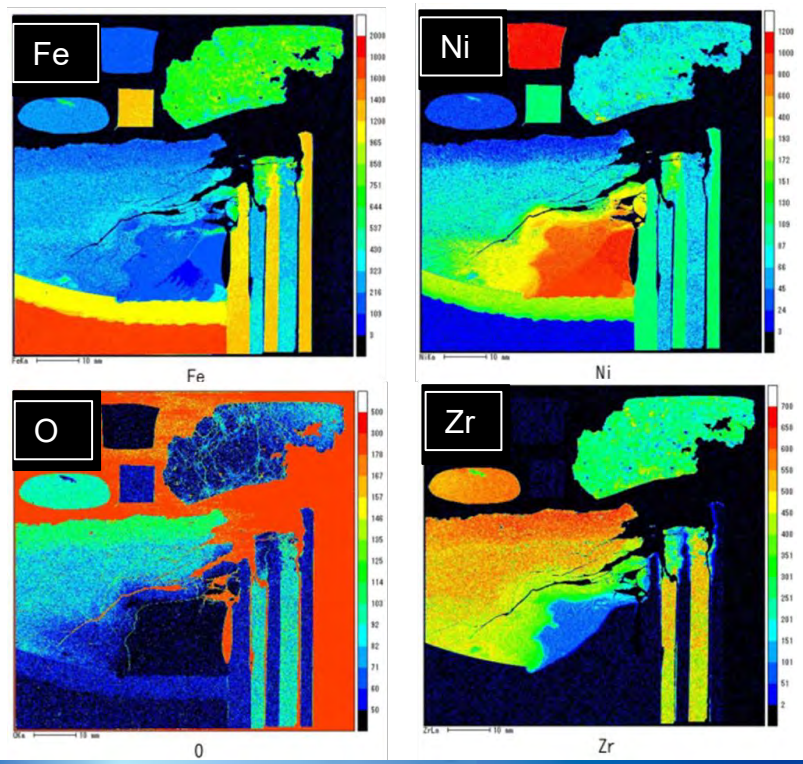

XRD analysis

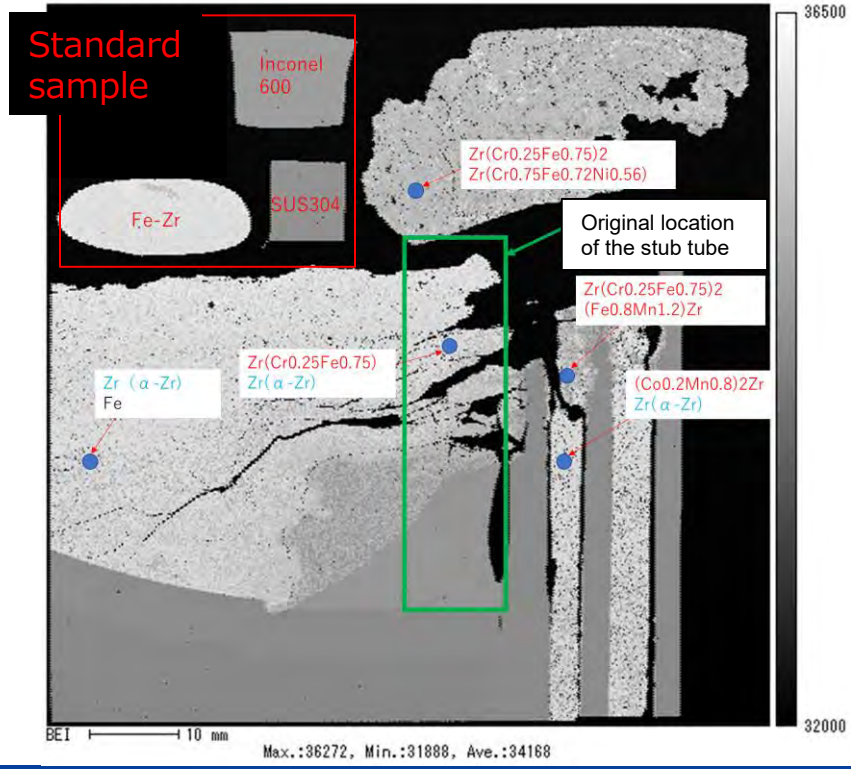

4. Analysis of the results

4 Analysis of the results

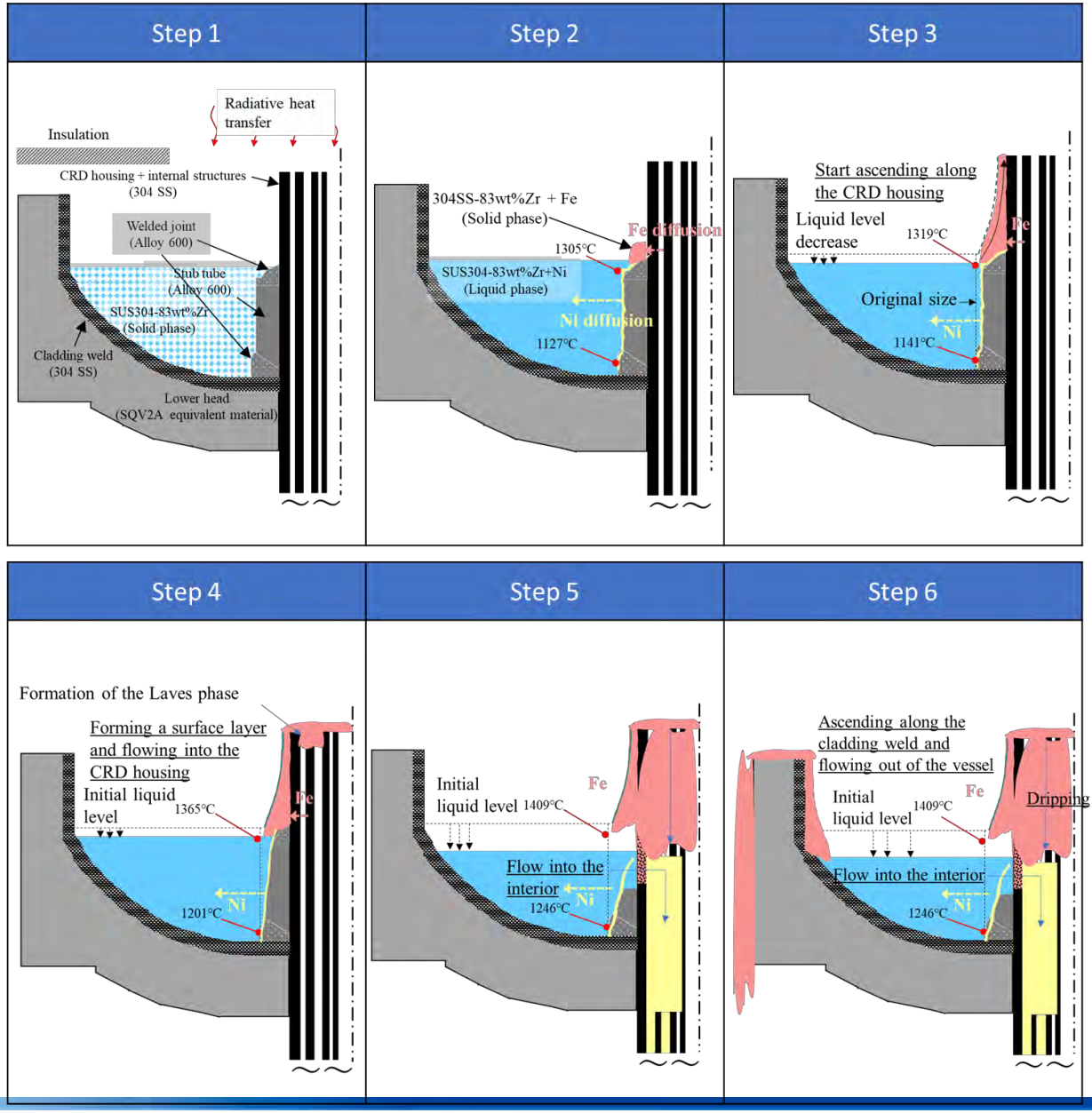

5. Conclusions

Conclusions

In addition to RPV failure modes caused by temperatures exceeding the melting point and creep rupture, it was found that the melting of internal structures at lower temperatures can lead to an RPV boundary breach.

5 Conclusions

Estimation of 1F Accident Progression

1. Zr-rich molten material relocated to the lower plenum and was reheated by fuel debris.
2. Some CRD housings and stub tubes were severely damaged due to eutectic reactions at temperatures below their respective melting points.
3. The molten material flowed into the CRD housings through the breached regions.
4. As the stub tubes melted, the load previously supported by the weld joints between the CRD housings and stub tubes was transferred to the support bars.

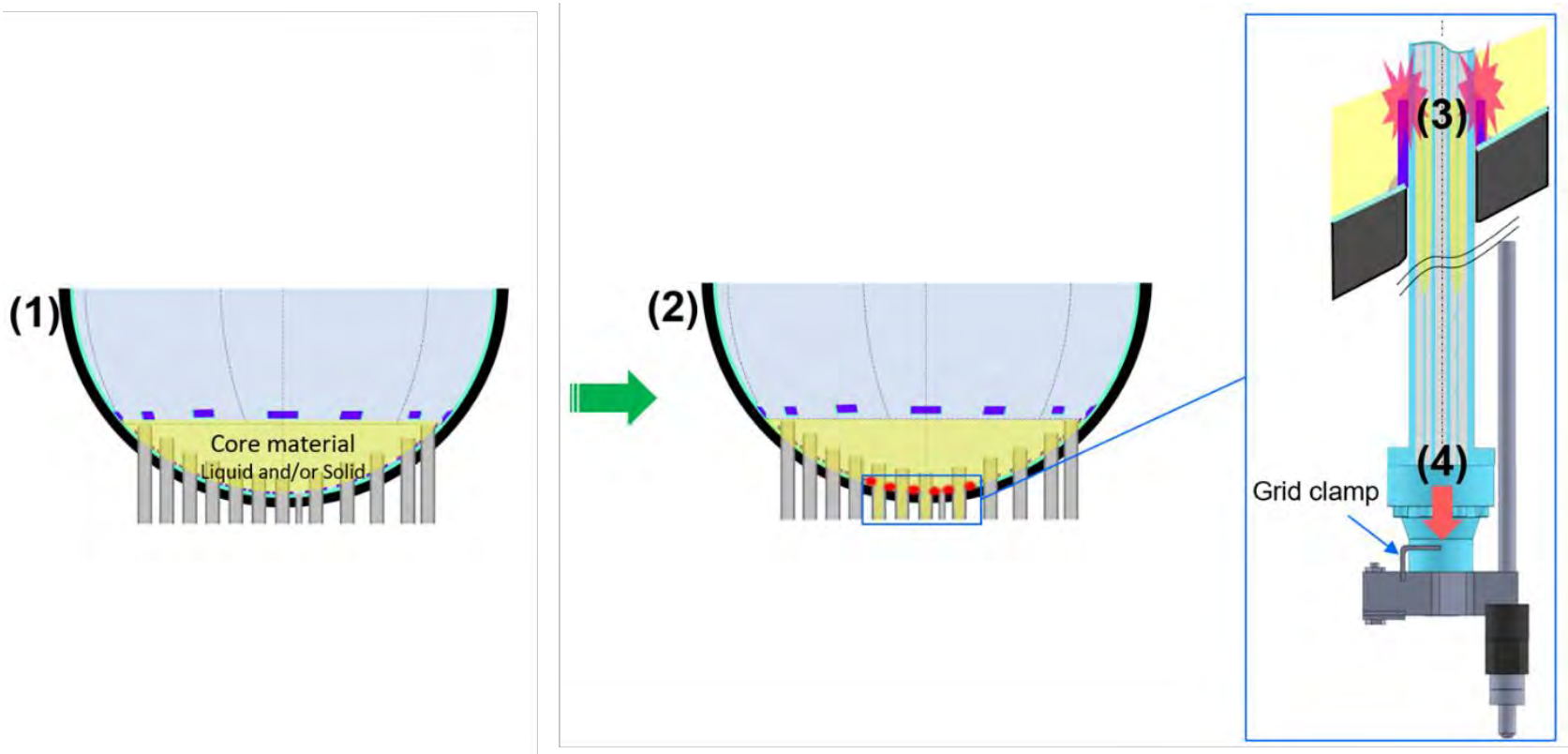

6. Latest topics

The internal drone investigation of Unit 3 confirmed a breach of the RPV. At the breached bottom part of the RPV, the CRD stub tubes had disappeared, and the CRD housings were found to have cleanly detached. This is considered to be due to a phenomenon similar to that observed in the ELSA-3 test.

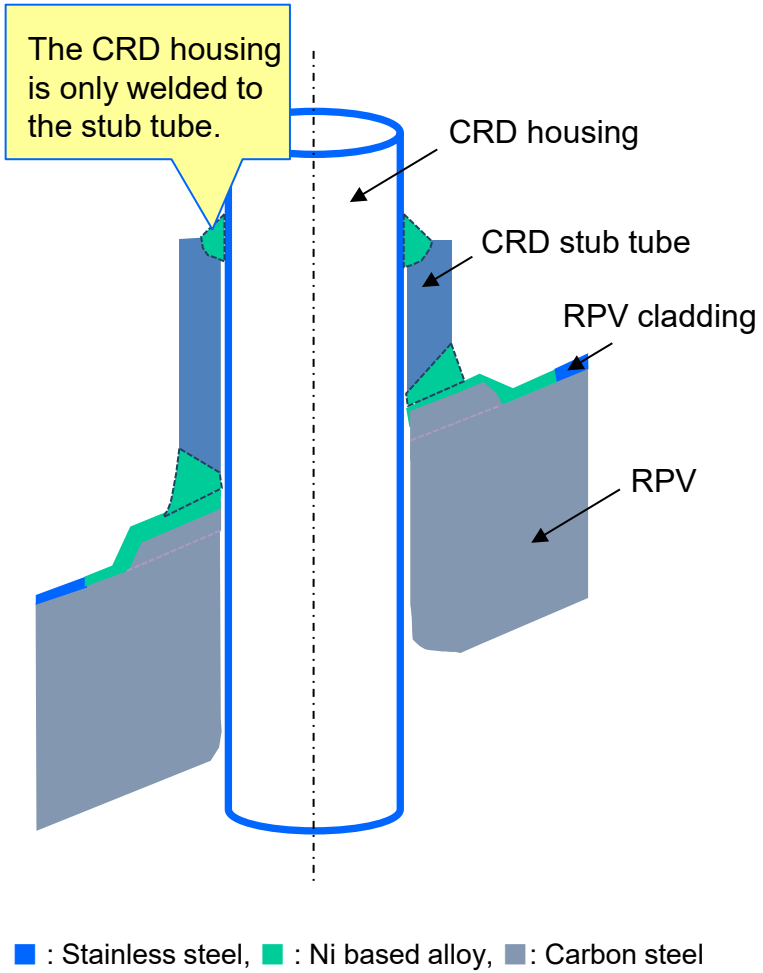

*

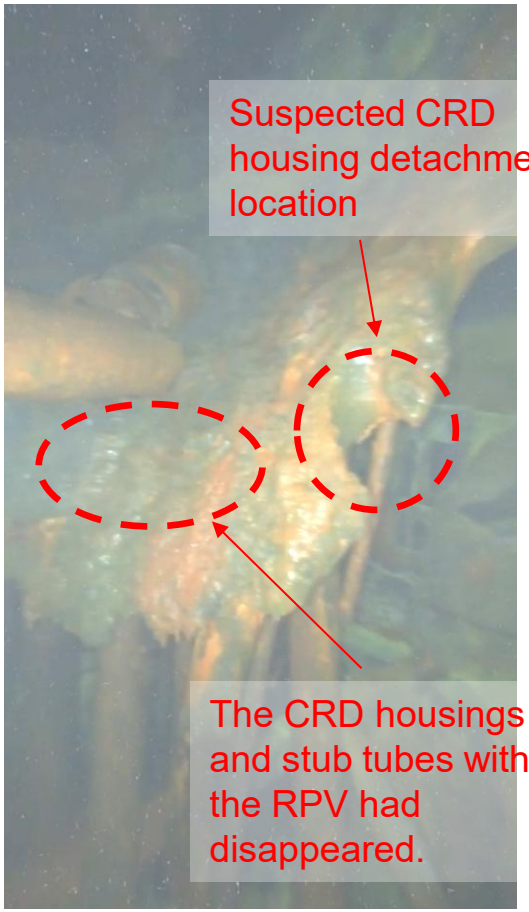

*TEPCO, 動画アーカイブ, 2026/3/19(木) 3号機マイクロドローン調査（原子炉圧力容器底部付近）
https://www.tepco.co.jp/library/movie/detail-j.html?catid=107299&video_uuid=15805

<Video×740>

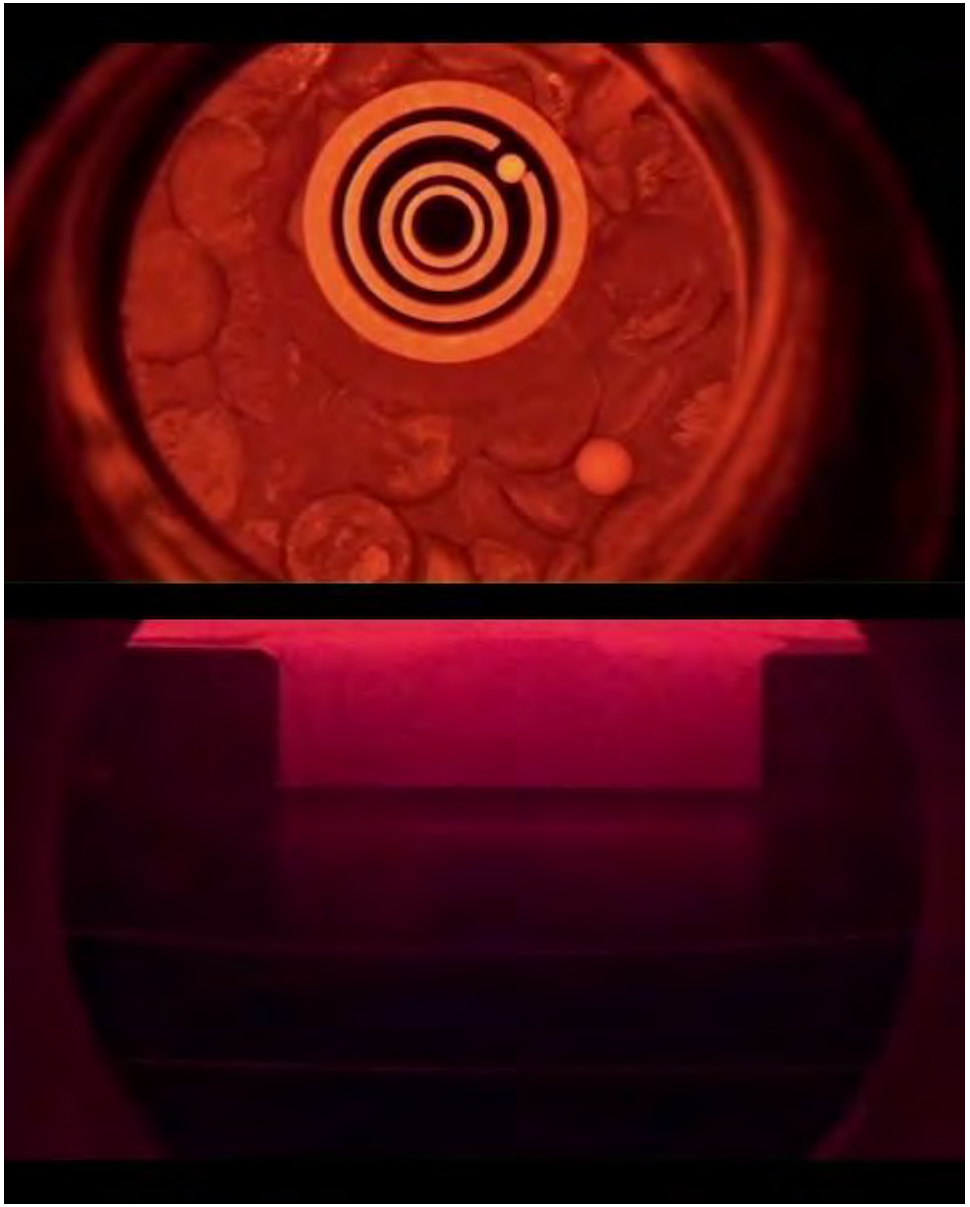

Investigation on In-Vessel Phase of BDB-LOCA of Supercritical Water-cooled Fast Reactor

Yuma Kobayashi[1], Akifumi Yamaji[2]
[1] Cooperative Major in Nuclear Energy
Waseda University
3-4-1 Okubo, Shinjuku-Ku, Tokyo 169-8555, Japan
58_yuma42168w@toki.waseda.jp

[2] Cooperative Major in Nuclear Energy
Waseda University
3-4-1 Okubo, Shinjuku-Ku, Tokyo 169-8555, Japan
akifumi.yamaji@waseda.jp

ABSTRACT

Supercritical Water-cooled Reactor (SCWR) is the Generation IV water-cooled reactor, which adopts unique once-through direct cycle plant system. Namely, the core is cooled with once-through coolant flow as in PWR and the entire core coolant is directly fed to the turbine as in BWR, because the coolant does not exhibit liquid / gas phase change. The Reactor Pressure Vessel (RPV) is like that of PWR with no flow bypasses in the upper core and the Primary Containment Vessel (PCV) is like that of BWR with suppression chamber (S/C). Stainless-steel or other advanced materials are being considered for the fuel cladding, channel boxes. This study addresses the fast reactor concept (Super FR), which has minimal coolant inventory in RPV.

The basic safety principle of the once-through direct cycle system is that the core cooling is ensured by keeping the core flow rate at supercritical pressure and the core is effectively cooled by depressurizing RPV in managing design basis accidents (DBAs) including the Loss-of-Coolant Accident (LOCA). However, the plant concept has not been established for managing Beyond-Design Basis (BDB) accidents, such as BDB-LOCA, where all means of water injections are assumed to fail.

This study investigates the in-vessel phase of the plant behavior of Super FR during BDB-LOCAs. Following a single line break, the initial blowdown phase from supercritical pressure (25 MPa) to subcritical pressure is analyzed with ASYST code based on point kinetics and node-junction models. Then, the plant parameters were transferred to MELCOR code for the subsequent core heat-up, oxidation, degradation, slumping, up to the moment of RPV failure. Different scenarios are analyzed with focus on managing non-condensable hydrogen gas generation and PCV pressurization.

KEYWORDS
SCWR, BDB-LOCA, Severe Accident, once-through direct cycle plant system, MELCOR

1. INTRODUCTION

As the main contribution of cost of fossil fueled fire power plants is the fuel cost, coal-fired power plants have evolved to operate at higher pressure and temperature above the critical point of water (22.1 MPa and 374℃) to improve the thermal efficiency and compensate for the large fuel cost since the 1970s. In contrast, the main contribution of cost of nuclear power is the costs of construction, operation and maintenance. Hence, the main benefit of operating water-cooled reactors at supercritical pressure is reducing such costs by simplifying and downsizing the plant system. More specifically, the nature that supercritical water does not exhibit phase change (i.e., boiling) enables elimination of all systems and components associated with separation of steam from water [1] [2].

Supercritical Water-cooled Reactors (SCWRs) are being researched and developed in Japan, the EU, Canada, China, and Russia including small modular reactor scale designs [3]. The Canadian designs adopt the pressure-tube type designs like CANDU reactors [4] while most other designs adopt the pressure-vessel type designs like BWR / PWR. Both the thermal neutron spectrum reactor and fast reactor concepts are being developed [5] [6]. The average core outlet coolant temperatures range from 400°C [7] to over 600℃ [4]. Advanced stainless steel, Oxide Dispersion Strengthened (ODS) steel, and nickel-based alloys and other high temperature alloys and corrosion resistant materials are considered as candidate materials for core structures such as fuel cladding [8].

The Balance Of Plant (BOP) of SCWR is basically the same as that of the existing supercritical coal fired power plant and the basic design concepts have been developed including startup, control, stability, transient management, Design Basis Accident (DBA) management (including Loss Of Coolant Accident (LOCA)), and Anticipated Transient Without Scram (ATWS)[1] [2]. The design concepts with passive safety systems have also been developed [9]. The Primary Containment Vessel (PCV) and Emergency Core Cooling System (ECCS) are like those in BWRs while many designs adopt PWR-like Reactor Pressure Vessel (RPV) and control rod designs [10].

Since SCWR is a pressurized system, LOCA is defined as DBA and the system must prevent large-scale core degradation and maintain a coolable core geometry during such events [10]. The key characteristics of LOCA of SCWR arise from the nature of supercritical water-cooling that water / steam separation is not needed and the system becomes once-through direct cycle, where the entire core coolant is fed directly to the turbine. As the result, there is no core bypass of coolant and large coolant flow is induced through the core in LOCA, leading to no / minimal core heat-up during the blowdown phase. Subsequently, the core is reflooded without large-scale damage when ECCS operation is assumed [11] [12].

However, studies on Beyond Design Basis LOCA (BDB-LOCA), assuming failures of all means of water injections, are limited. The preceding study on BDB-LOCA with total core meltdown developed the concept of In-Vessel Retention (IVR) of the fuel debris by flooding the RPV bottom exterior [13]. The key identified issue was managing the PCV pressure by efficient condensation of excess steam by the suppression chamber (S/C). More specifically, the key issues were reducing and evaluating the in-vessel non-condensable hydrogen gas generation due to oxidation of the core structure materials (e.g., stainless-steel fuel cladding) by steam at elevated temperature [13]. However, the preceding study mainly focused on the long-term plant behavior and did not investigate the blowdown phase and the differences between the hot-leg and cold-leg breaks.

Hence, this study aims to clarify the key characteristics and potential issues of in-vessel phase of a BDB-LOCA for a supercritical water-cooled fast reactor (Super FR). More specifically, the differences in the blowdown phase for different break locations (hot-leg break and cold-leg break) with respect to in-vessel hydrogen generation and the PCV pressure history are investigated. The ASYST code [14] was utilized to analyze the blowdown phase from the supercritical pressure to subcritical pressure. Moreover, the plant

parameters at the end-of-calculations by ASYST were transferred to MELCOR [15] code analysis to evaluate the post blowdown core heat-up phase.

2. DESIGN FEATURES AND ANALYSIS MODELS AND SCENARIOS

2.1 Core and Plant Design Features and Specifications

Super FR with operating pressure of 25 MPa and core thermal power of 2867 MWth [16] was selected as the reference design. The in-vessel design specifications were determined by referring to the earlier core design study [16] as summarized in **Table Ⅰ**. The core consists of 349 fuel assemblies with 631 fuel rods arranged in hexagonal lattice. The fuel mass and the structure (stainless-steel) mass were estimated from the available information in reference [16]. **Figure 1** describes the reactor system configurations. The compact PCV is equipped with S/C. During RPV depressurization, steam is discharged into the water of the suppression chamber (S/C) via safety relief valve (SRV) lines for condensation. The volume ratio between the drywell (D/W) and the suppression chamber (S/C) is about the same as that of ABWR [13].

Table Ⅰ. Specifications of the plant (RPV and PCV)

In-vessel design parameters [16]	
Pressure [MPa] / power [MWth] / core flow rate [kg/s]	25 / 2867 / 1906
Core inlet / outlet temperatures [°C]	295 / 433
Active height[mm]/equivalent diameter [mm]	1400 / 4840
Fuel rod diameter [mm] / gap [mm] / lattice	9.05 / 0.50 / hexagonal
In-vessel structure material / mass [kg]	Stainless steel (SS) / 21256
Doppler reactivity [10^{-4}%Δk/k/K] / coolant density [%Δk/k/(g/cc)]	-0.11 / 6.20
Other design parameters	
Line cross-section area (cold-leg / hot-leg) [m^2]	0.092 [13] / 0.27 [13]
PCV total volume / D/W volume / S/C volume [m^3]	7900 [1] / 2530 [13]/ 5370 [13]

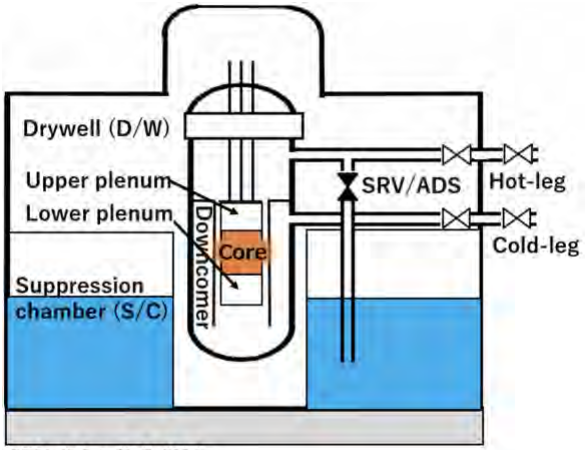

Figure 1. Configurations of the reactor system.

2.2 ASYST Analysis Models

The LOCA blowdown phase of Super FR from supercritical pressure was analyzed with ASYST code to evaluate the reactor pressure, flow rate, temperature, and power. ASYST [14] is a thermal-hydraulic analysis code based on point kinetics approximation and the node-junction method, primarily for in-vessel phase of the accident. **Figure 2** describes the in-vessel node and junctions for Super FR, where PCV is represented by a single large volume.

The critical flow from the break was evaluated using the standard Ransom-Trapp model based on the non-equilibrium gas-liquid two-fluid model [17] to consider the choking phenomena as the supercritical fluid rapidly expands and transitions into a subcritical two-phase flow at the break. In the meantime, the Dittus-Boelter correlation for single-phase forced convection heat transfer was utilized to evaluate the fuel cladding temperature at supercritical pressure and different correlations were applied under subcritical pressure depending on different heat transfer regimes, such as nucleate boiling, transition boiling, and film boiling, based on the boiling curve of the ASYST/RELAP5 code [17].

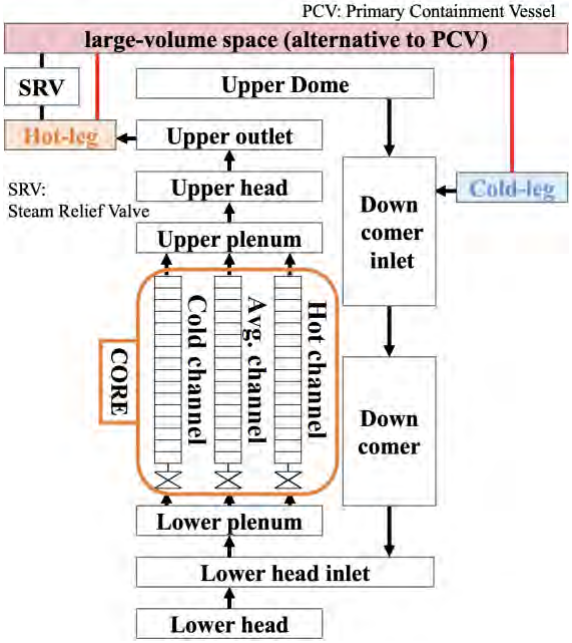

Figure 2: In-vessel node junction model (ASYST).

2.3 MELCOR Analysis Models

The thermal responses within RPV and PCV during the post blowdown phase was analyzed using the severe accident analysis code MELCOR-2.2 (Version 9541) [15]. The initial conditions for the MELCOR analysis were prepared by transferring the end of blowdown phase in-vessel thermal parameters calculated by ASYST code. Specifically, these parameters included core power, RPV pressure, fuel cladding temperature distributions, reactor water level, and reactor water temperature.

Figure 3 illustrates control volumes (CVs), flow paths (FLs) of PCV and RPV, and cell divisions of RPV used in the analysis. The active fuel length of the core was divided into 7 axial cells and 4 radial rings and one bypass ring. The lower plenum was also divided into cells as shown in **Figure 3**.

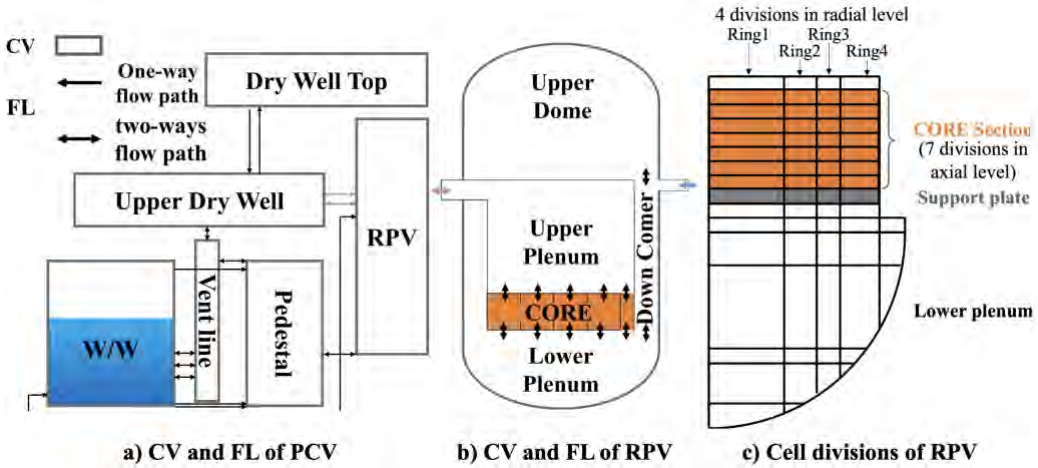

Figure 3: CV, FL and Cell divisions of PCV and RPV (MELCOR).

The oxidation reaction between stainless steel and steam during core heat-up was considered with the standard Arrhenius type rate constant above temperature (T) 1100 K as shown below.

$$K(T) = 2.42 \cdot 10^9 \exp\left(-\frac{42400}{T}\right) \quad (1700\ K > T > 1100\ K) \tag{1}$$

Then, due to lack of sufficient evidence to define specific failure conditions of the stainless steel cladded core, the default MELCOR core collapse models for stainless steel cladded fuel were adapted [15]. Namely, the intact fuel was converted to particulate debris when:
(a) the unoxidized cladding metal wall thickness reduced to the minimum threshold of 0.1 mm, or:
(b) the fuel temperature exceeded the maximum threshold of 1700 K.

Similarly, the core support plate was assumed to fail at the default MELCOR setting temperature of 1273 K [15], which would determine the moment of the slumping of the core ring being supported by the corresponding ring of the core support plate. The influences of changing failure criteria of the core and core slumping on the PCV pressure and temperature management of Super FR may be considered in future studies.

Following the core slumping, the default MELCOR quench model was applied. In this study, the hydraulic diameter of particulate debris was set to the default value of 2 mm. In the default settings, the quench heat transfer coefficient is 2000 W/m²/K until the leading edge of the falling debris reached the bottom of the lower plenum. For stationary particulate debris beds in the plenum water pool, the Lipinski zero-dimensional correlation was applied with the dry out heat flux, q_d given by the following relationships:

$$q_d = 0.756 h_{lv} \left[\frac{\rho_v(\rho_l - \rho_v) g d \varepsilon^3 (1 + \lambda_c/L)}{(1-\varepsilon)[1 + (\rho_v/\rho_l)^{1/4}]^4}\right]^{\frac{1}{2}} \tag{2}$$

where, h_{lv} is the latent heat of water, ρ_l is the water density, ρ_v is the vapor density, g is the gravitational acceleration, d is the debris particle diameter, ε is the debris bed porosity, L is the total debris bed depth, and $\lambda_c$is the liquid capillary head in the debris bed.

3. PLANT BEHAVIOR OF SUPER FR DURING BDB-LOCA

In this study, a 100% large break in the hot-leg (0.27 m²) and the cold-leg (0.0916 m²) were assumed as the two representative initiating events. Following the actuation logics of the safety systems adopted by preceding studies [18], the reactor scram signal was assumed by either flow rate low level-1 (90%) or pressure low level-1 (24.0 MPa). The signal to actuation delay of 0.55 s was assumed and scram was assumed to complete by 2.8 s after the initial break. In LOCA, the reactor scram is governed by the pressure low criterion. Then, the reactor is further depressurized by actuation of the Automatic Depressurization System (ADS), which opens all the Steam Relief Valves (SRVs) with total opening area of 0.27 m^2 when the reactor pressure has decreased to 23.5 MPa. In the standard design basis LOCA, high pressure and low-pressure injection systems are actuated with flow rate low level-2 (20%) and flow rate low level-3 (6%) or pressure level low level-2 (23.5 MPa). However, in this study, all means of water injection were assumed to fail to evaluate BDB-LOCA.

3.1. Hot-Leg / Cold-Leg Breaks

3.1.1 Blowdown Phase (ASYST)

The blowdown phase analysis results with ASYST are presented in this section. The simulation covered the period from the initial break through the reactor scram, the RPV depressurization to the subcritical pressure until 7 seconds after the break as the changes of the plant thermal parameters (power, pressure, coolant flow rate and reactor water level) with time became moderate. More specifically, the transfer timing had to have sufficient delay after the initial break so that the pressure had fallen below the critical pressure (22.1 MPa) and rapid power fluctuations due to void and Doppler effects were no more significant, because MELCOR could not treat such short-term reactivity feedbacks. By referring to the pressure and power histories shown in **Figure 4**, it seemed that the transfer timing had to be later than 3 seconds after the initial break. In this study, some extra margin was considered to wait for the plant thermal parameters to stabilize until 7 seconds after the break.

Figure 4 shows the histories of the reactor power, the RPV pressure, the reactor water level, and the core flow rate for the hot-leg and cold-leg break scenarios. Although the break area of the hot-leg was approximately three times larger than that of the cold-leg, the coolant density in the hot-leg was about one-sixth that of the cold-leg. Consequently, the results indicate that the cold-leg break leads to faster depressurization and a more rapid decrease in the reactor water level than the hot-leg break for the initial short period (less than one second) after the break.

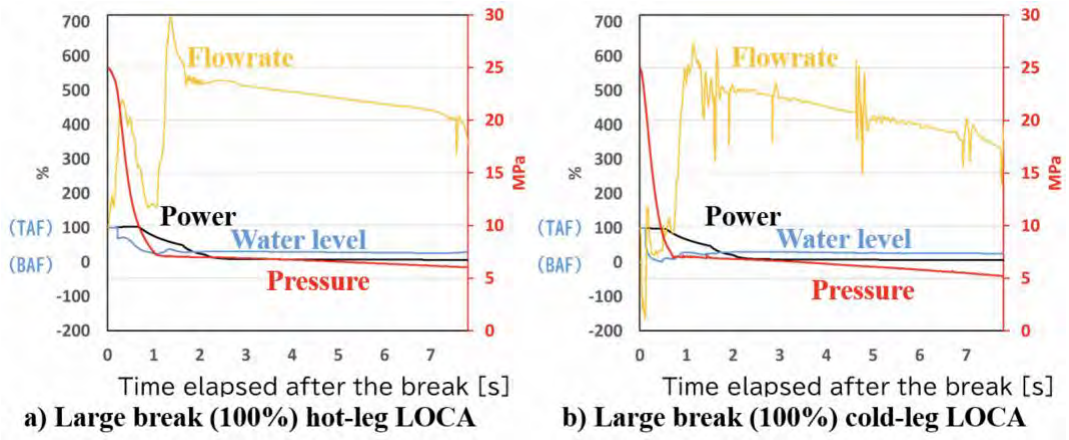

Figure 4: Core power, pressure, collapsed water level, and flow rate histories (blowdown phase).

Figure 5 shows the peak temperature histories (temperature of the 10th axial segment out of 14 divisions) of the hot channel up to 7 seconds after the break. The reactor power changes immediately after the breaks were governed by the negative coolant void reactivity coefficient resulting from the decrease in the core water level and the negative fuel Doppler reactivity coefficient resulting from fuel temperature changes. In the hot-leg break, the coolant flowed towards the break point induced a significant core flow rate (466% as can be seen from **Figure 4**), which led to reduction of the fuel temperature. Consequently, positive reactivity was inserted by the negative Doppler effect, which dominated the effect of the negative reactivity insertion by the negative void reactivity effect. As a result, the reactor power increased temporarily to approximately 103% of the rated power. Conversely, in the cold-leg break, the coolant flow towards the break point led to temporal reverse flow and flow stagnation in the core as can be seen from **Figure 4**, which led to core heat-up. Consequently, the combined Doppler and void reactivity feedback led to moderate change in the reactor power until the reactor scram. Following the reactor scram, the core temperatures in both the hot-leg and cold-leg breaks continuously decreased as the core flow rate was kept high by the reactor depressurization.

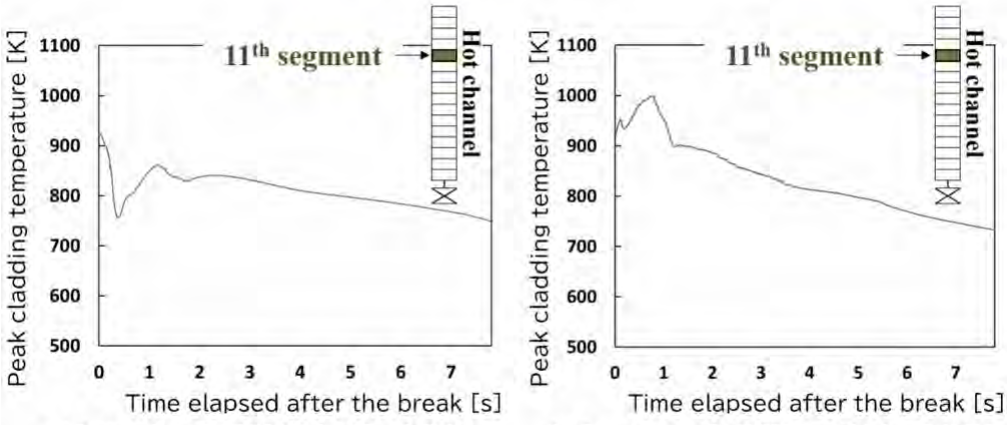

Figure 5: Fuel cladding peak temperature histories (blowdown phase).

Table Ⅱ summarizes the parameters relating ASYST results and MELCOR input at 7 s after the break. The in-vessel parameters, such as the core power, the RPV pressure, the fuel cladding temperatures, the core water level and the core water temperature were transferred from ASYST to MELCOR. However, ex-vessel

parameters, such as the energy and H_2O mass released from RPV to PCV during the 7 seconds and the initial D/W filler gas (N_2) mass swept from D/W to S/C could not be transferred or evaluated. The integrals of the in-vessel fuel decay power until the time of the RPV failures for the cold / hot-leg breaks (about 4.6 hours after the break) were about 433 / 439 GJ, while the corresponding energy transfers from RPV to PCV by MELCOR analyses were about 230 / 270 GJ. The ASYST analyses indicated that the energy released from RPV to PCV during the initial 7 seconds were about 36.0 GJ / 18.1 GJ for the cold / hot-leg breaks, respectively (corresponding to about 13.5% / 6.3% of the energy transferred from RPV to PCV from the initial line break to the RPV failure for the cold and hot leg-breaks, respectively).

Thus, the current study has obvious limitations regarding evaluation of the short-term PCV management. Namely, the current study cannot evaluate the rapid pressurization and heat-up of PCV immediately after the break. Moreover, the initial release of water / steam from the break is expected to sweep the initial D/W filler gas (N_2) to S/C. Consequently, accumulation of the non-condensable gas (N_2) is expected to reduce the S/C capability to manage PCV pressurization. The N_2 gas sweeping may be dependent on the break flow, which in tern may depend on the flow rate of the ADS line from RPV to S/C through SRVs. Since current ASYST code cannot model S/C and therefore cannot evaluate the flow rate splits between the break and the ADS line, evaluation of N_2 sweeping is not possible. Sensitivity analyses with different assumptions of post blowdown N_2 distributions among D/W and S/C may be a possible alternative evaluation for future study.

Table Ⅱ. Parameters relating ASYST results to MELCOR input (7 s after the break)

	Hot-leg break	Cold-leg break
Transferred from ASYST to MELCOR		
Core power [%]	6.71	6.67
RPV pressure [MPa]	6.18	5.51
Fuel cladding temperatures	As shown in Fig. 5(a)	As shown in Fig. 5(b)
Core water level [m]	BAF+1.16	BAF+1.20
In-vessel water temperature (saturated) [℃]	278.95	271.85
Not transferred from ASYST to MELCOR		
Energy released from RPV to PCV [GJ]	18.1	36.0
H_2O mass released from RPV to PCV [kg]	8,454	28,358
N_2 mass swept from D/W to S/C [kg]	Not evaluated	Not evaluated

3.1.2 Post Blowdown Phase without Water Injection (MELCOR)

This section presents the post blowdown phase analysis results by MELCOR using the initial parameters listed in **Table Ⅱ** (Section 3.1.1). **Figure 6** shows the core temperature histories for the hot-leg and cold-leg break scenarios at the core locations corresponding to those of the ASYST analyses (i.e., at the peak temperature elevation during the blowdown phase). As discussed in Section 3.1.1, during hot-leg break, the steam generated in the vessel flows through the core towards the break. In contrast, during cold-leg break, most of the steam generated in the vessel flows to the break without passing through the core. As the result, the post blowdown phase core heat-up rate of the cold-leg break was higher than that of the hot-leg break. Consequently, the core collapse of the cold-leg break was earlier than that of the hot-leg break.

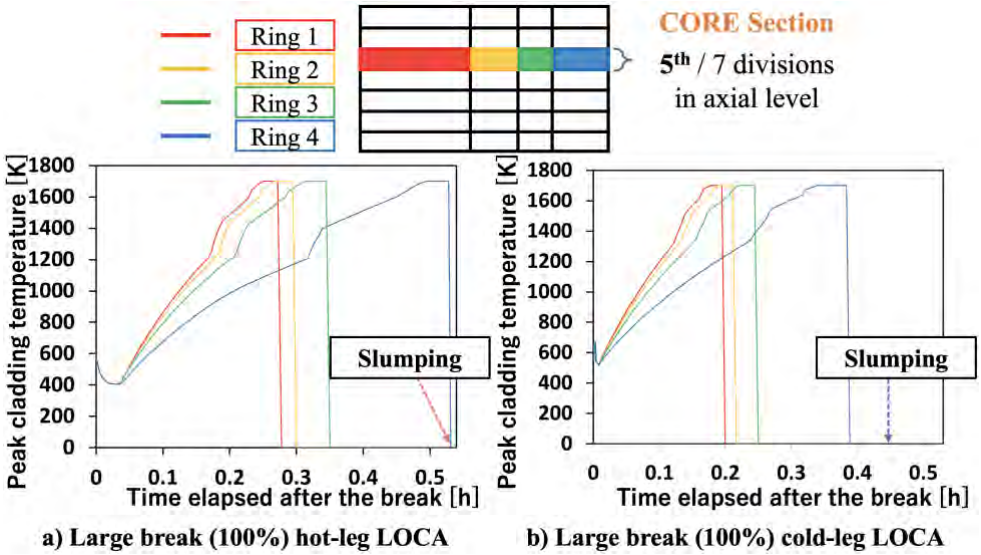

Figure 6: Fuel cladding temperature histories (post blowdown phase).

Figure 7 shows the changes in the drywell (D/W) pressure and hydrogen (H_2) partial pressure, as well as the suppression chamber (S/C) pressure and hydrogen partial pressure. As was discussed in Section 3.1.1, during the hot-leg break, the steam generated in the vessel flows through the core towards the break. Such high temperature steam flow through the core promoted oxidation of the metals (e.g., fuel cladding) within the core, increasing the H_2 partial pressure in D/W until the core slumping. Following the core slumping, large steam generation in the vessel swept H_2 from D/W to S/C. In contrast, during cold-leg break, most of the steam generated in the vessel flows through the break without passing through the core. As a result, H_2 generation before the core slumping was limited in the cold-leg break LOCA. However, following the core slumping, H_2 partial pressure in D/W increased significantly.

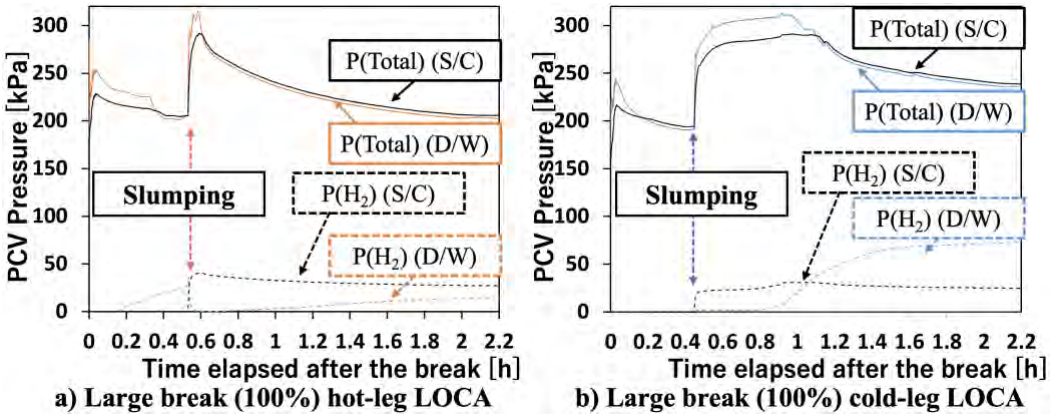

Figure 7: D/W and S/C pressures (post blowdown phase).

As shown in **Figure 8**, H_2 generation was limited after the core slumping in the hot-leg break, while significant H_2 generation is seen after the core slumping in the cold-leg break. The difference between the two cases can be understood from the histories of the H_2 generation (**Figure 8**) and the downcomer water volume (**Figure 9**). By correlating the two figures, it can be understood that in the cold-leg break, significant

amount of water is temporarily kept in the downcomer, which gradually flows down to the lower plenum, where hot fuel debris bed is oxidized between 0.45 h- 1.12 h.

The temporal reservation of the downcomer water and gradual flow down to the lower plenum may be understood from the major and minor flow paths during the cold-leg break LOCA as shown in **Figure 10**. As can be seen from Figure 10, the steam generated in the lower plenum by the core slumping has effectively no other alternatives but to flow through the downcomer, pushing the in-vessel residual water in the downcomer volume. As the lower plenum water is depleted and steam generation rate decreases, the water being pushed up in the downcomer volume may gradually flow back to the lower plenum, where hot fuel debris bed is available for water-metal oxidation reactions. Such hold-up of water inventory in the downcomer does not occur in the hot-leg break, because the steam generated in the lower plenum bypasses the downcomer to the break. Therefore, the prolonged H_2 generation after the core slumping is a unique feature of the cold-leg break LOCA of the once-through direct cycle plant system.

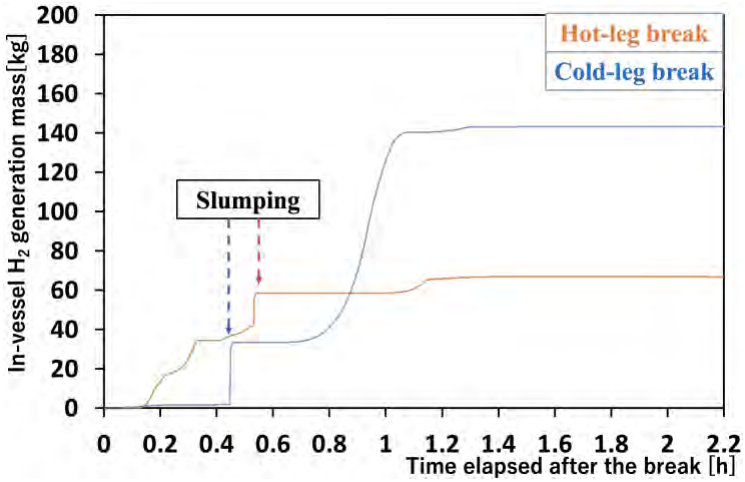

Figure 8: In-vessel H_2 generation (post blow down phase).

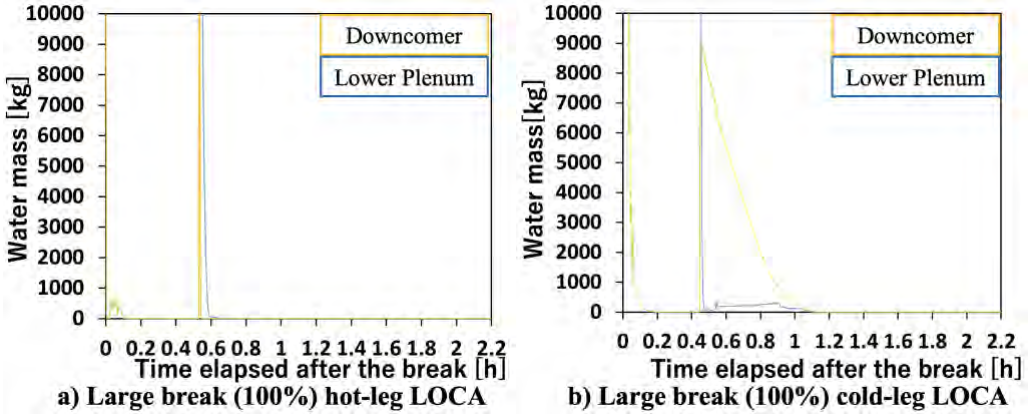

a) Large break (100%) hot-leg LOCA **b) Large break (100%) cold-leg LOCA**

Figure 9: Lower plenum and Downcomer water inventory (post blowdown phase).

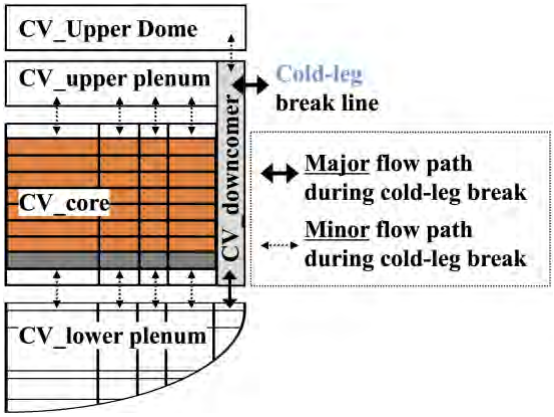

Figure 10: Major and minor flow paths during the cold-leg break LOCA.

4. CONCLUSIONS AND FUTURE WORKS

The in-vessel phase of BDB-LOCA plant behavior of Supercritical Water-cooled Fast Reactor (Super FR) was analyzed by dividing the accident to the blowdown phase from the supercritical to the subcritical pressure and the subsequent post blowdown phase, assuming failures of all means of water injections. ASYST code was utilized to analyze the blowdown phase and the plant parameters (core power, RPV pressure, fuel cladding temperature distributions, reactor water level, and reactor water temperature) at the end-of-calculations by ASYST were transferred to MELCOR code analysis to evaluate the post blowdown core heat-up phase. The blowdown phase analysis results confirmed the same features of the once-through direct cycle plant system as identified in the preceding studies. Namely, the hot-leg break was featured with rapid core cooling as strong core flow was induced by the coolant flow to the break point through the core. In contrast, the cold-leg break was featured with moderate core heat-up until the reactor scram as the flow to the break point did not induce such large core flow rate.

The following features of the once-through direct cycle plant system have been newly identified through post blowdown phase analyses of BDB-LOCA. In the hot-leg break, H_2 generation was mainly prior to the core slumping as the steam generated in the vessel passed through the core and oxidized the core structural materials. Such H_2 generation was terminated by the core slumping. In the cold-leg break, H_2 generation prior to the core slumping was limited as the steam generated in the vessel did not flow through the core. In the cold-leg break, H_2 generation was significant in the post-core slumping phase, as the lower plenum water was pushed and held-up in the downcomer by the steam flow from the lower plenum to the break point through the downcomer. Consequently, as the lower plenum water depleted and the steam generation rate decreased, the downcomer water flowed back to the lower plenum, leading to significant H_2 generation due to oxidation of the debris bed.

Future works include investigating the effects of accident scenarios, design parameters, and analytical models on the hydrogen generation history and long-term plant pressure management. For example, it is necessary to clarify how core slumping history, break size, rated thermal power, and critical flow models affect the break flow behavior and hydrogen generation characteristics in BDB-LOCA of the once-through direct cycle plant system.

REFERENCES

1. Y. Oka et al., *Super Light Water Reactors and Super Fast Reactors: Supercritical-Pressure Light Water Cooled Reactors*, Springer, New York, NY, USA (2010).
2. Y. Oka and H. Mori, *Supercritical-Pressure Light Water Cooled Reactors*, Springer (2014).

3. GenIV International Forum, "Super Critical Water Reactors (SCWR)," https://www.gen-4.org/generation-iv-criteria-and-technologies/super-critical-water-reactors-scwr.
4. J. Pencer and A. Colton, "Progression of the Physics Conceptual Design for the Canadian Supercritical Water Reactor," *Proceedings of the 34th Annual Conference of the Canadian Nuclear Society*, Toronto, Canada (2013).
5. T. Someya and A. Yamaji, "Core design of a high breeding fast reactor cooled by supercritical pressure light water," *Nuclear Engineering and Design*, pp. 30-37 (2016).
6. S. Noda, T. Someya, and A. Yamaji, "Flexible core design of Super FBR with multi-axial fuel shuffling," *Nuclear Engineering and Design* (2017).
7. J. Wu, N. Maekawa, and Y. Oka, "Single-Pass Core Design of a Low-Temperature Super LWR," *Journal of Nuclear Science and Technology* (2013).
8. D. Guzonas and R. Novotny, "Supercritical water-cooled reactor materials - Summary of research and open issues," *Progress in Nuclear Energy* (2014).
9. Sutanto and Y. Oka, "Passive safety system of a super fast reactor," *Nuclear Engineering and Design* (2015).
10. Y. Ishiwatari et al., "Safety of Super LWR, (I) Safety System Design," *Journal of Nuclear Science and Technology* (2005).
11. Y. Ishiwatari et al., "LOCA Analysis of Super LWR," *Journal of Nuclear Science and Technology* (2006).
12. Sutanto and Y. Oka, "Accidents and transients analyses of a super fast reactor with single flow pass core," *Nuclear Engineering and Design* (2014).
13. K. Funatsu and A. Yamaji, "Primary containment vessel management during severe accidents of the supercritical water-cooled fast reactor with in-vessel retention," *Annals of Nuclear Energy*, **218**, p. 111438 (2025).
14. Innovative Systems Software, *ASYST VER 4 User Reference Manual - Volume I: Advanced Fluid Systems Thermal Hydraulics Analysis* (2020).
15. L.L. Humphries et al., *MELCOR Computer Code Manuals, Vol. 2: Reference Manual, Version 2.2*, SAND2017-0443 O, Sandia National Laboratories, Albuquerque, NM, USA (2017).
16. S. Noda et al., "Core design study of Super FBR with multi-axial fuel shuffling and different coolant density," *Proceedings of 2018 26th International Conference on Nuclear Engineering (ICONE26)*, London, England, July 22–26, 2018 (2018).
17. Innovative Systems Software, *ASYST VER 4 User Reference Manual, Volume I: Advanced Fluid Systems Thermal Hydraulics Analysis*, Innovative Systems Software, LLC, Idaho Falls, ID, USA (2020).
18. S. Ikejiri, Y. Ishiwatari, and Y. Oka, "Safety analysis of a supercritical-pressure water-cooled fast reactor under supercritical pressure," *Nuclear Engineering and Design* (2010).
19. T. Shiraishi, "Design of the advanced accumulator for the pressurized water reactor," *Journal of Nuclear Engineering and Design*, pp. 3910-3912 (2011).
20. International Atomic Energy Agency (IAEA), "Heat Transfer Behaviour and Thermohydraulics Code Testing for Supercritical Water Cooled Reactors (SCWRs)," IAEA-TECDOC-1746 (2014).
21. The RELAP5 Development Team, *RELAP5/MOD3 Code Manual, Volume II: User's Guide and Input Requirements*, Idaho National Engineering Laboratory Lockheed-Martin Idaho Technologies Company (1995).
22. The Japan Society of Mechanical Engineers, *Steam Tables*, 5th ed., Maruzen, Tokyo, Japan (1999).

Investigation on In-Vessel Phase of BDB-LOCA of Supercritical Water-cooled Fast Reactor

Waseda University

Yuma KOBAYASHI, Akifumi YAMAJI

Supercritical Water-cooled Reactor (SCWR)

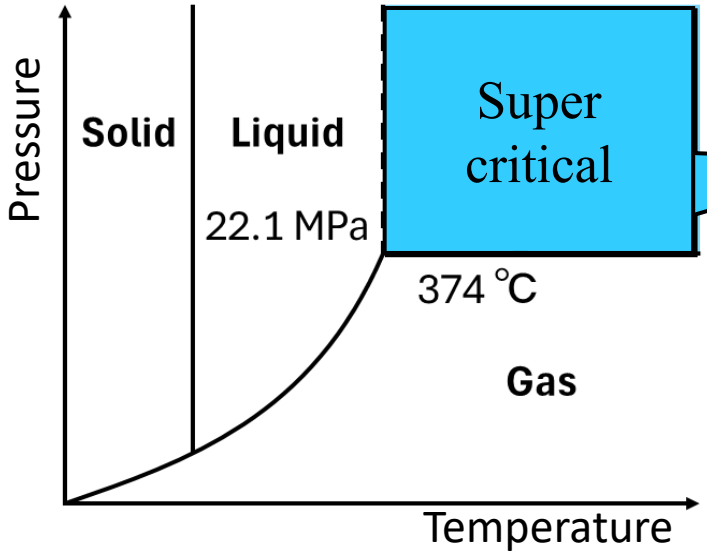

Outlet: 400℃ to over 600℃

Fuel cladding candidates:
Advanced stainless steel,
high temperature alloys

SCWR GEN IV

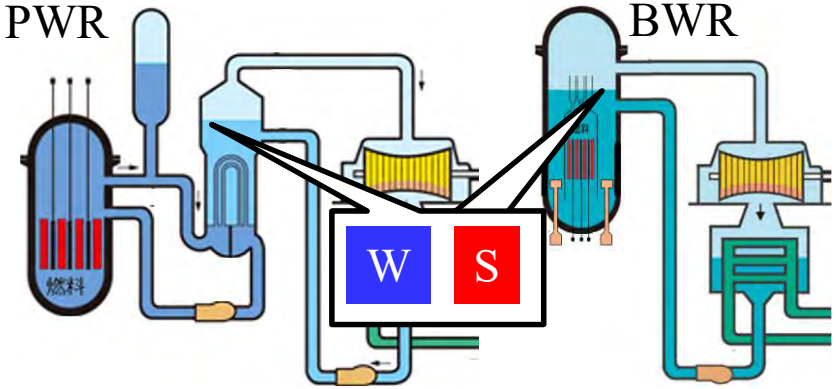

Pressure Vessel Type Pressure Tube Type

This study

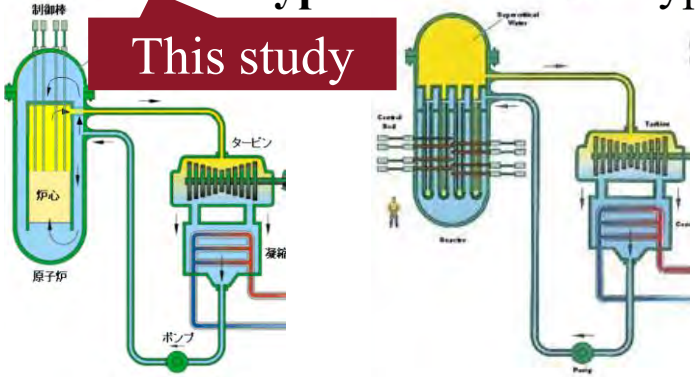

In-vessel Coolant flow

Once-through	recirculation	**Once-through** same as PWR

Entire flow to Turbine

Indirect cycle	**Direct cycle**	**Direct cycle** same as BWR

Key Focus: Once-through × Direct Cycle

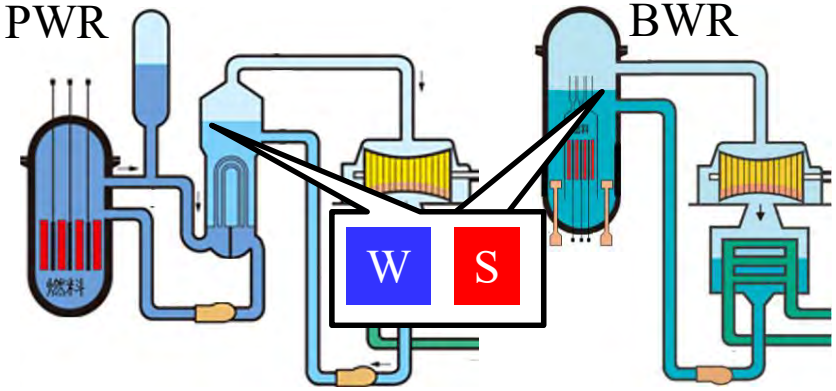

Pressure Vessel Type

This study

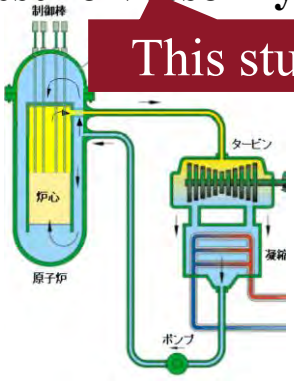

In-vessel Coolant flow

Once-through	recirculation	**Once-through** (same as PWR)

Entire flow to Turbine

Indirect cycle	**Direct cycle**	**Direct cycle** (same as BWR)

Confinement Boundary

Large D/W	Small D/W + S/C	Small D/W + S/C

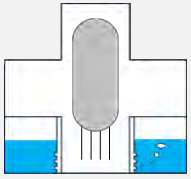

SCWR is unique due to Once-through + S/C combination strategy.

Feature of LOCA of Super FR[1]

Focus of **B**eyond **D**esign **B**asis **A**ccident (**BDBA**): **PCV management**

Blowdown Phase

- Reactor scram
- **Peak Cladding Temperature** (PCT) **～1000℃** reached in the first few seconds
- Core cooling recovered by **induced flow (～250 %) by depressurization**.
- **Depressurization completed in 30-40 s**

Reflooding Phase

- Low Pressure Core Injection (LPCI) activated.
- PCT never exceeds that of the blowdown phase.

Major core degradation is prevented, and the core cooling is maintained.

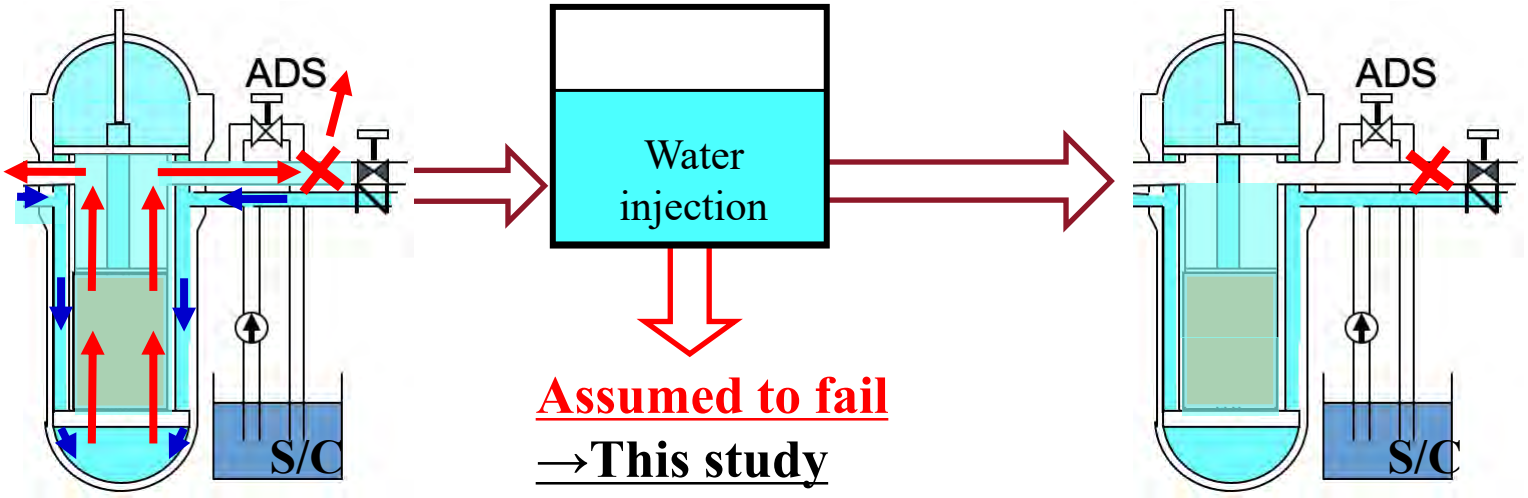

[1] Sutanto, Y. Oka, *Journal of Nuclear Engineering and Design*, (2014).

Differences from Previous Studies (What's NEW)

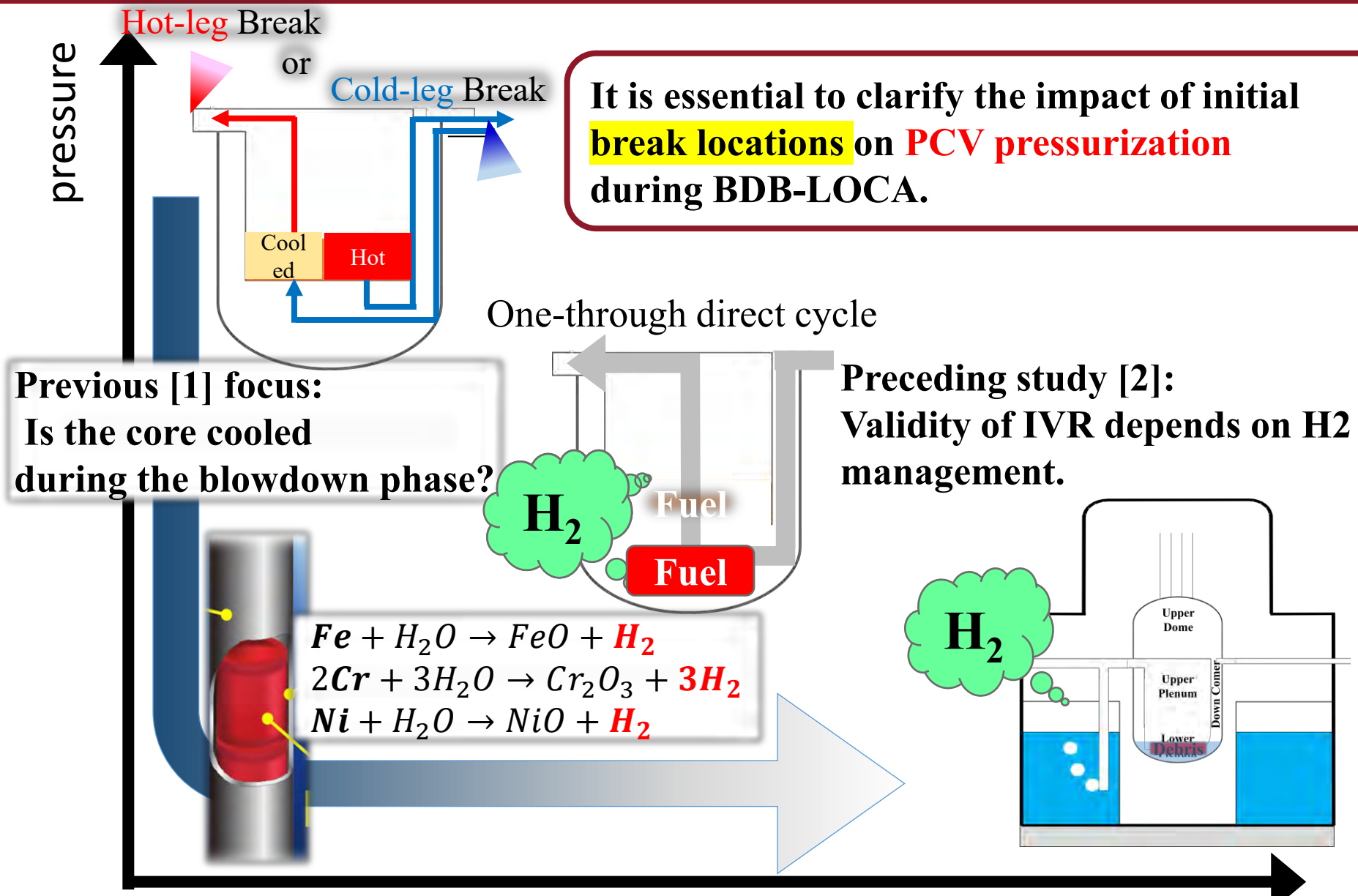

It is essential to clarify the impact of initial break locations on PCV pressurization during BDB-LOCA.

Previous [1] focus:
Is the core cooled during the blowdown phase?

Preceding study [2]:
Validity of IVR depends on H2 management.

[1] Sutanto, Y. Oka, *Jour. Nucl. Eng. and Design* (2014).
[2] K. Funatsu and A. Yamaji, Annals of Nuclear Energy, (2025).

Purpose

BDB ：Beyond Design Basis
LOCA ：Loss Of Coolant Accident

Purpose

This study aims to
clarify the effects of different break locations (Hot-leg / Cold-leg break) on the In-vessel hydrogen generation / PCV pressure history during BDB-LOCA.

How do the **Once-through direct cycle** affect plant pressure controllability?

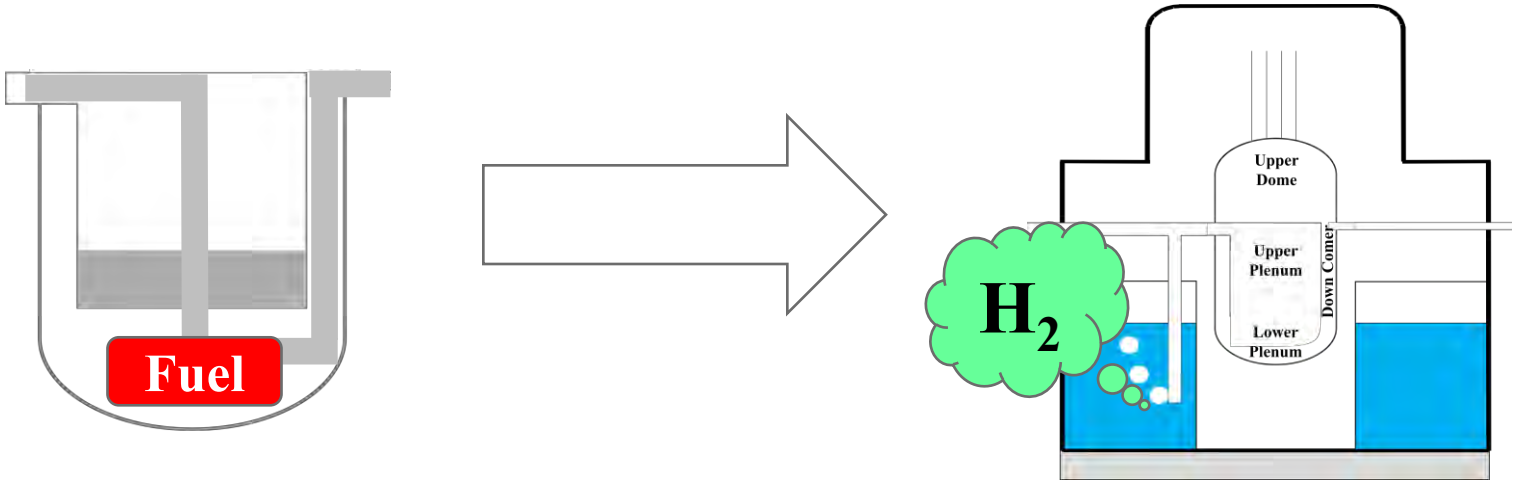

Sequential Analysis Approach

Scenarios：a 100% large break in the hot-leg and the cold-leg BDB-LOCA

operating → 100% large break → Reactor Scram → all means of water injection fails → BDB LOCA

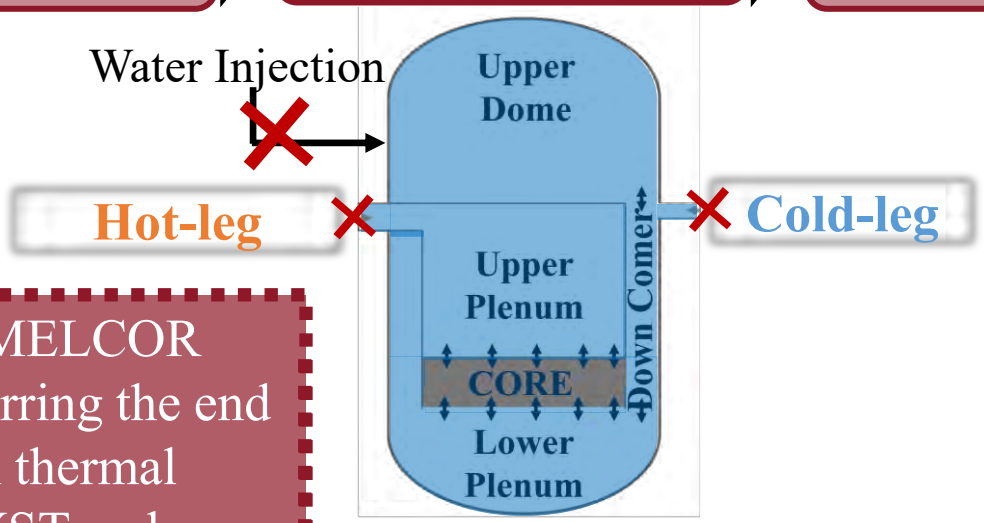

The initial conditions for the MELCOR analysis were prepared by transferring the end of blowdown phase in-vessel thermal parameters calculated by ASYST code.

ASYST（～7 sec）

The LOCA blowdown phase of Super FR from supercritical pressure.

MELCOR（～hours）

The thermal responses within RPV and PCV during the post blowdown phase.

Plant Design

DESIGN FEATURES : Super FR & The compact PCV is equipped with S/C.

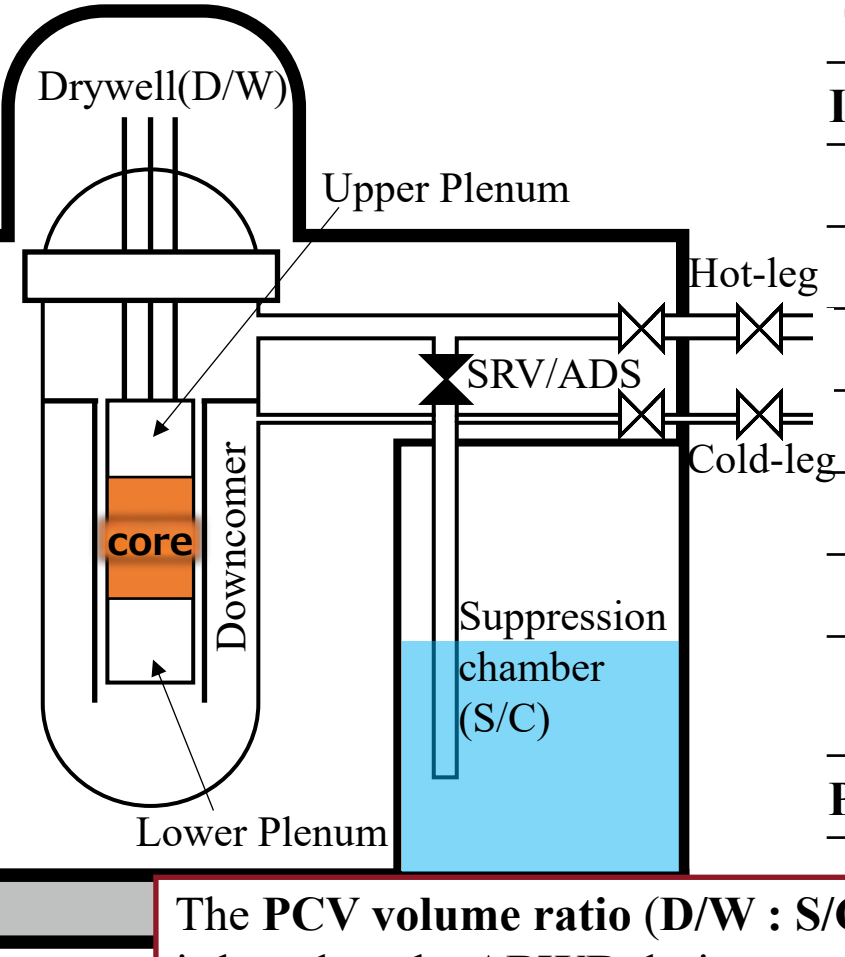

The **PCV volume ratio (D/W : S/C)** is based on the **ABWR** design

Table I: Specifications of the plant (RPV and PCV)

In-vessel design parameters [3]	
Pressure [MPa]	25
Power [MWth]	2867
Core inlet temperature [°C]	295
Core Outlet temperature [°C]	433
Active height [mm]	1400
equivalent diameter [mm]	4840
In-vessel structure material / mass [kg]	Stainless steel (SS) / 21256
PCV design parameters	
PCV total volume [m^3]	7900 [4]
D/W volume [m^3]	2530 [2]
S/C volume [m^3]	5370 [2]

[2] K.Funatsu, et al. Annals of Nuclear Energy (2025).
[3] S. Noda, Sukarman, et al. Proc. of ICONE26, 2018, July 22-26, London, England
[4] Y. Oka, S. Koshizuka, et al. Proc. of GENES4/ANP2003, 2003, Sep. 15-19, Kyoto, Japan, Paper No. 1168

ASYST Analysis Models

Analysis code
ASYST

1-D point reactor kinetics model
1-D thermal hydraulic model

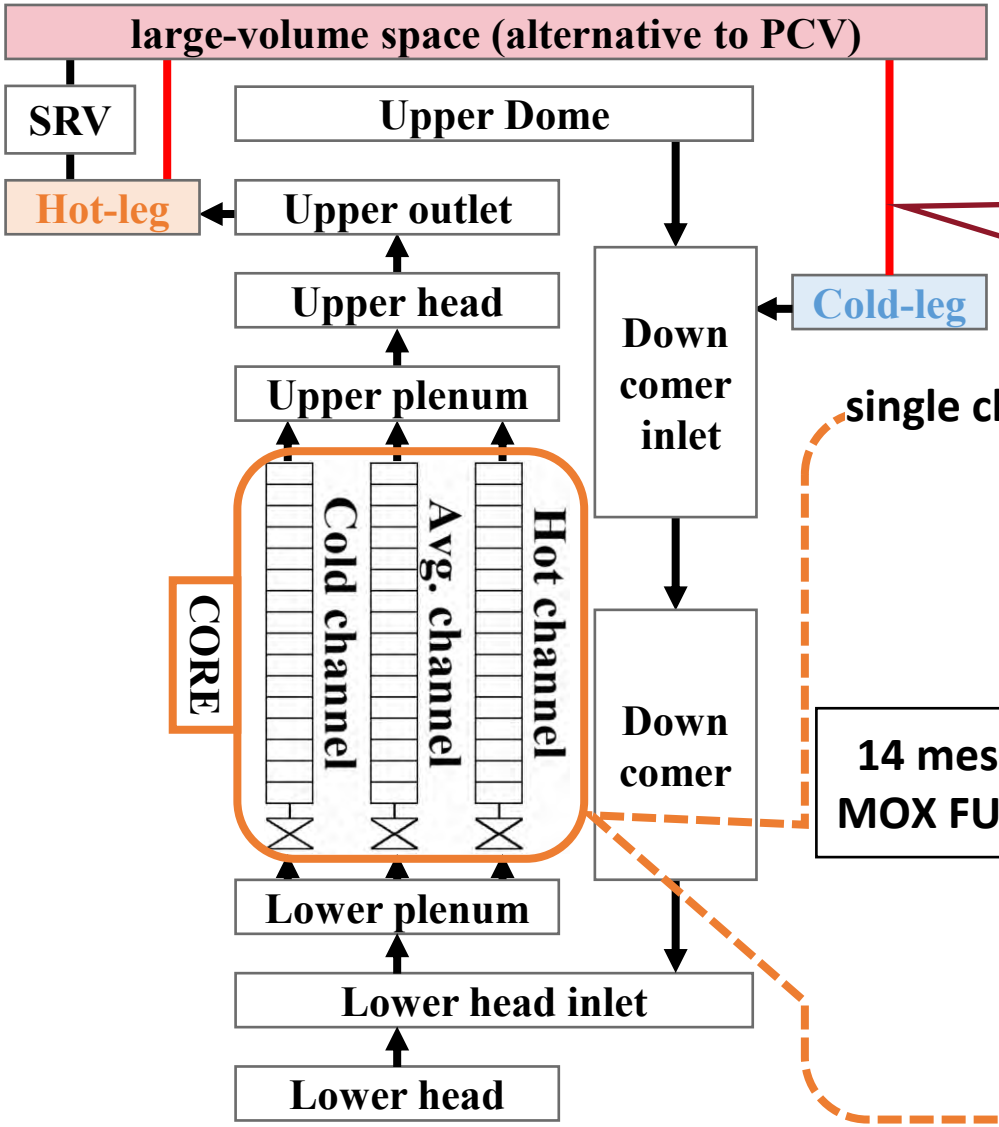

Critical flow (break flow)

Ransom-Trapp model based on the non-equilibrium gas-liquid two-fluid model

Heat transfer

Supercritical pressure

- Dittus-Boelter

Subcritical pressure (by boiling regimes):

- Nucleate: Chen's / Bromley's
- Superheated: Dittus-Boelter's

Super FR Plant Nodolization in MELCOR

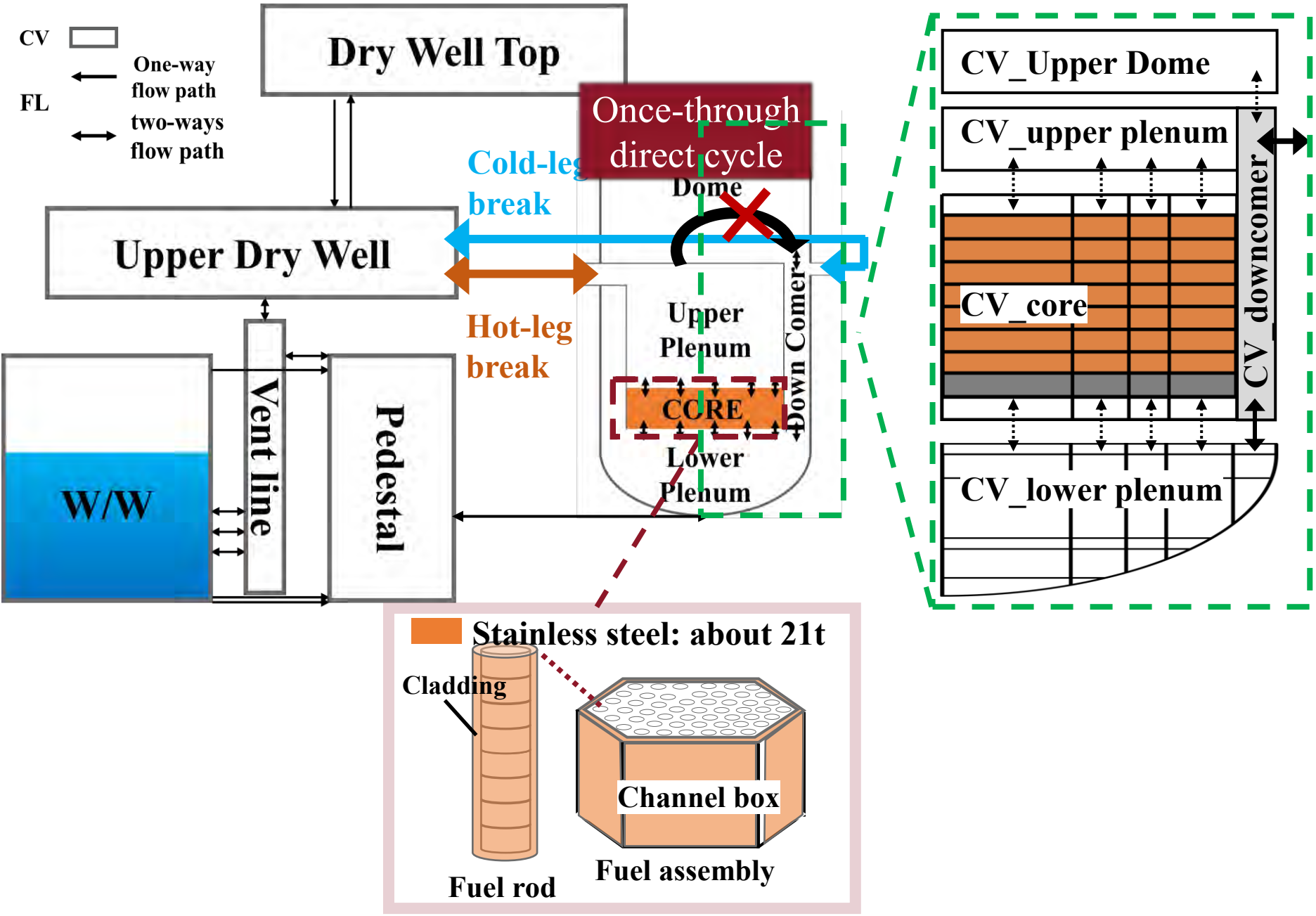

Core degradation model in MELCOR[5]

Core Collapse
(the default MELCOR core collapse models for stainless steel cladded fuel)

1. **Cladding Thickness:** Unoxidized metal wall < 0.1 mm
2. **Fuel Temperature:** >1700K

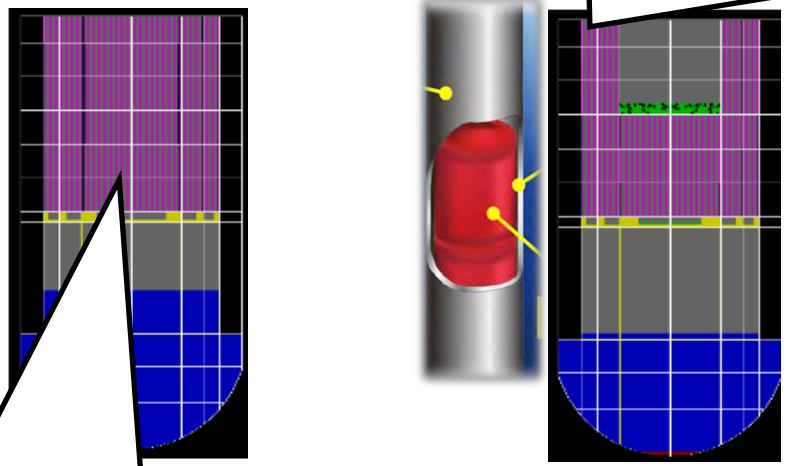

Oxidation rate of Claddings[4]
(Stainless steel) (**T≧1100 K**)

$$K(T) = 2.42 \cdot 10^{9} \exp\left(-\frac{42400}{T}\right)$$

(1700 K > T > 1100 K)

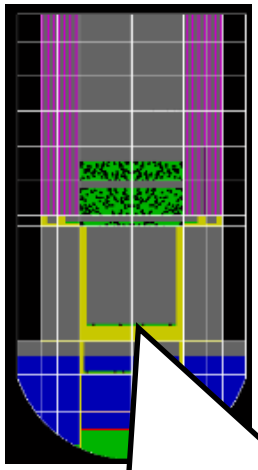

Core support plate failure
(MELCOR default)
(**T≧1273 K**)

[5] Sandia National Laboratories, MELCOR Computer Code Manuals Vol. 2: Reference Manual Version 2.2 r2023.0, 2023.

Blowdown Phase Results (ASYST code)

ASYST Analysis (Flow rate, Power, Pressure)

From the initial break to 7 seconds after the break

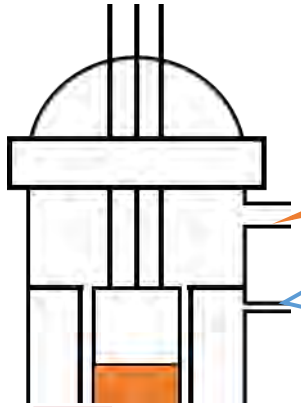

Hot-leg break: 120 kg/m^3, 0.27m^2
(433℃)

1/6 x3

Cold-leg break: 752 kg/m^3, 0.09m^2
(295℃)

Faster depressurization and water level reduction (～1s)

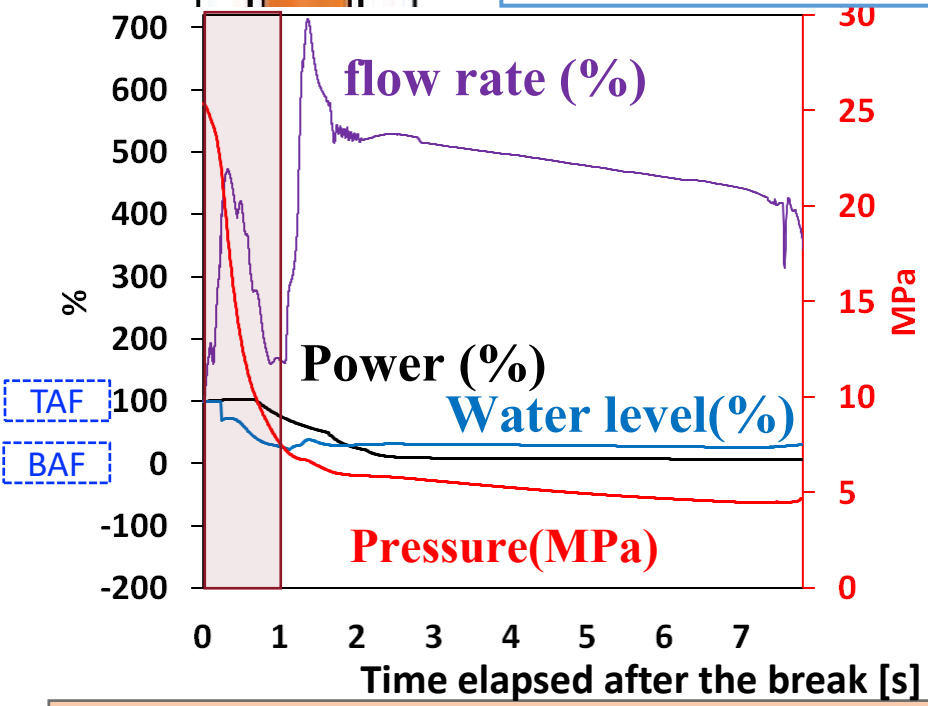

100% Hot-leg break

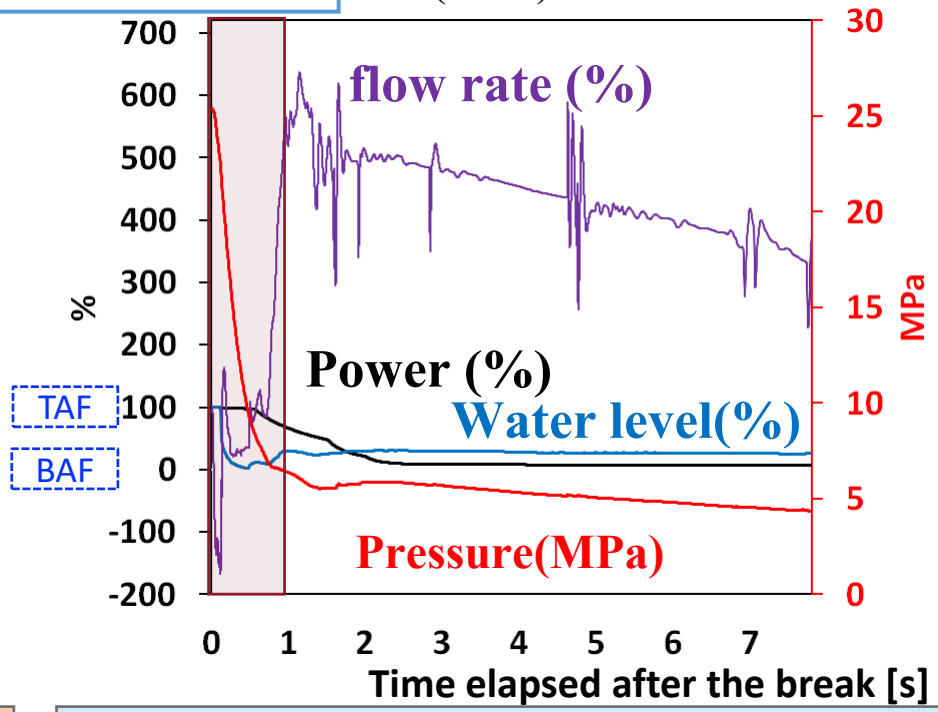

100% Cold-leg break

[6] NIST Chemistry WebBook: Thermophysical Properties of Fluid Systems.https://webbook.nist.gov/chemistry/fluid/

ASYST Analysis (Cladding temperature)

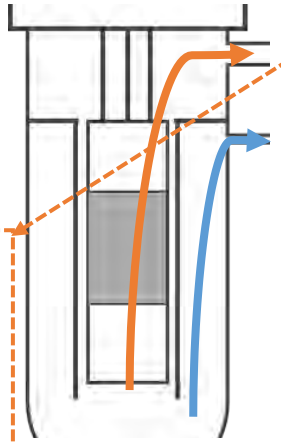

Hot-leg break **through the core**

Cold-leg break **NOT** through the core

Cooled by large coolant flow through the core

No large flow through the core, leading to core heat up.

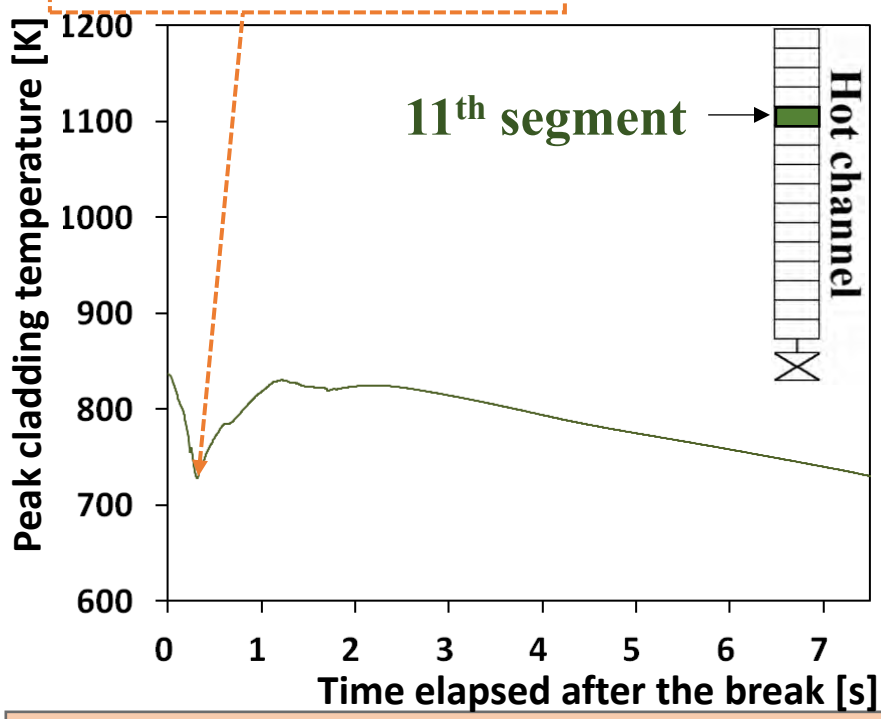

100% Hot-leg break

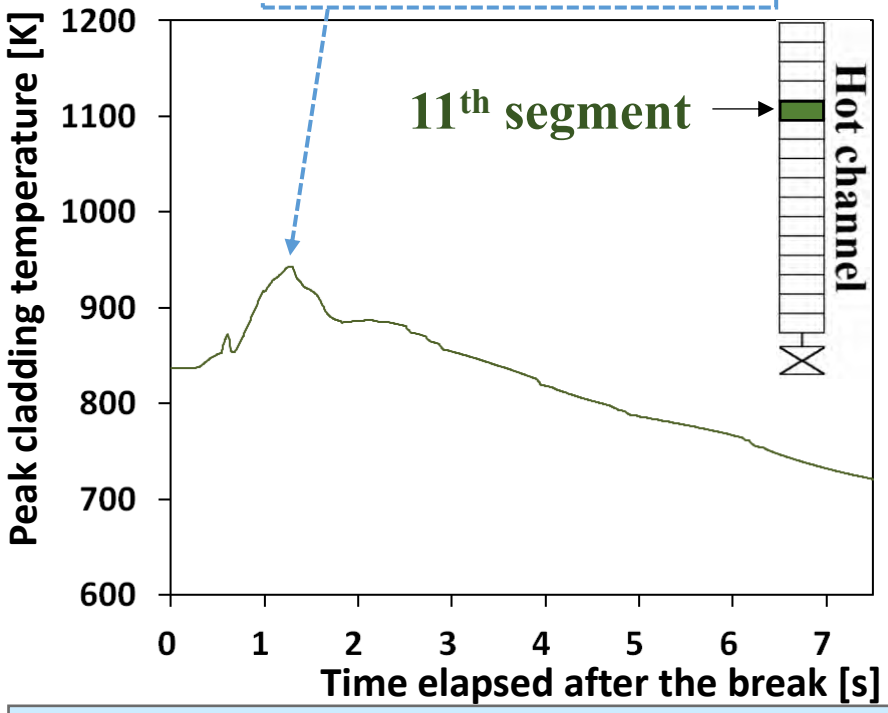

100% Cold-leg break

ASYST-to-MELCOR Parameter Transfer

NOT considered / transferred from ASYST to MELCOR

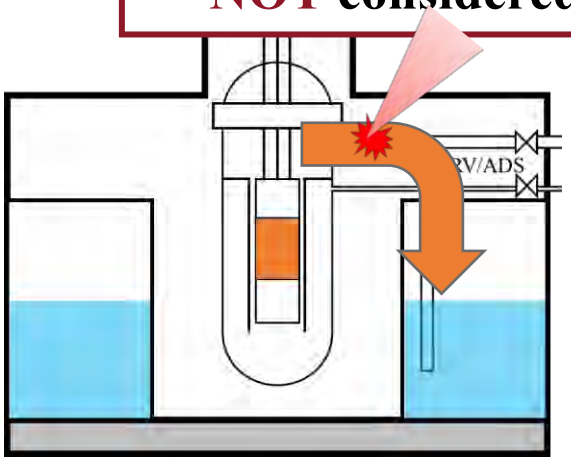

(1) Rapid heat-up & pressurization of PCV

(2) N_2 sweeping during blowdown

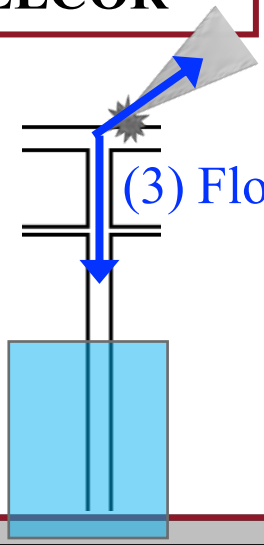

(3) Flow split

(4) Cumulative energy released from RPV to PCV in the first 7 seconds

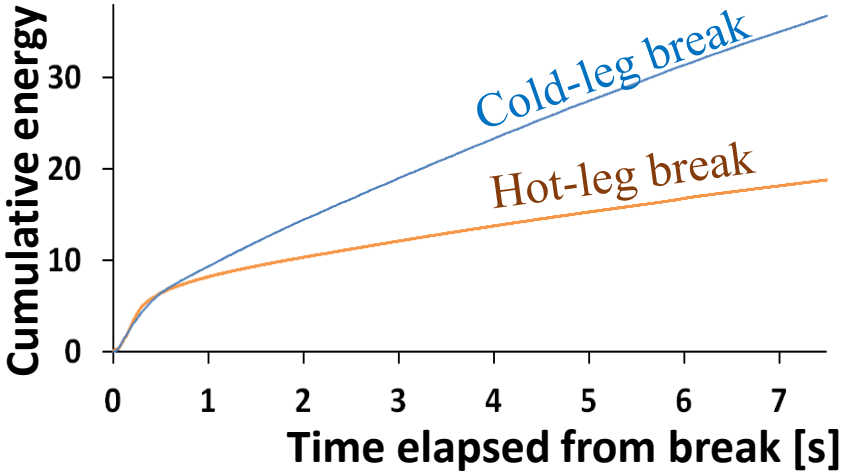

(*~RPV fails(4.6h):
Hot-leg break: 433GJ / Cold-leg break: 439 GJ)

Considered in this study

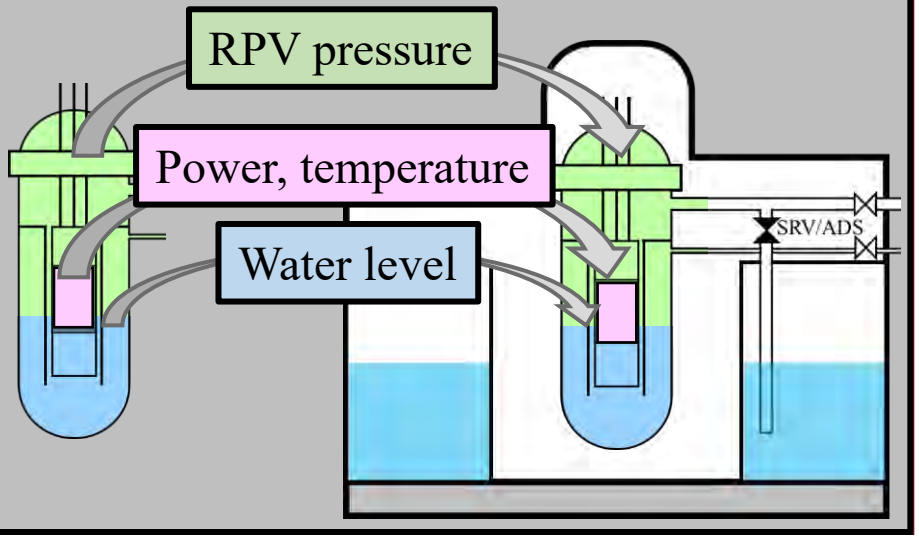

Post-blowdown Phase Results (MELCOR code)

MELCOR: D/W Pressure changes

From the line break to in-vessel dry out

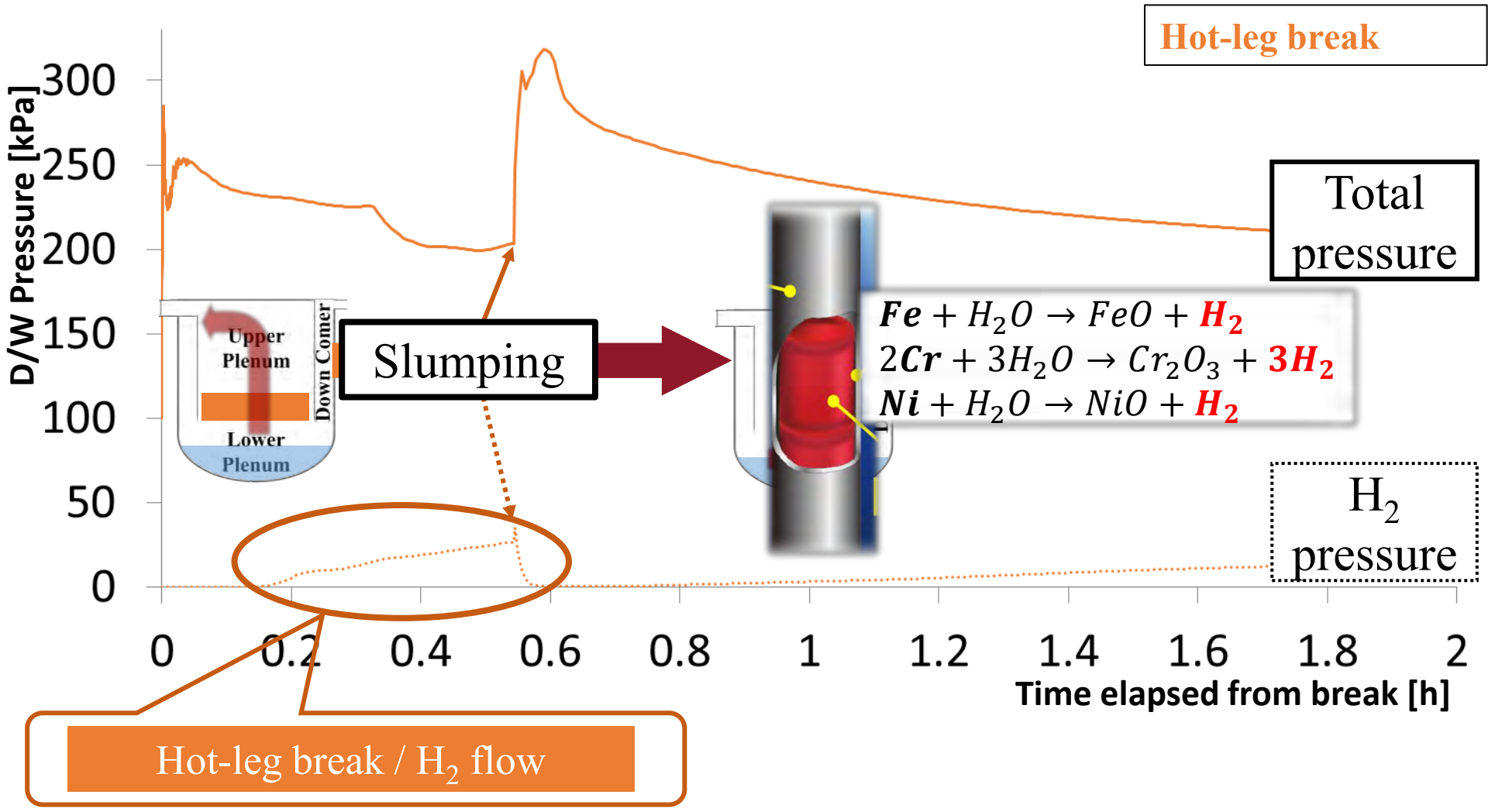

MELCOR: D/W pressure

From the line break to in-vessel dry out

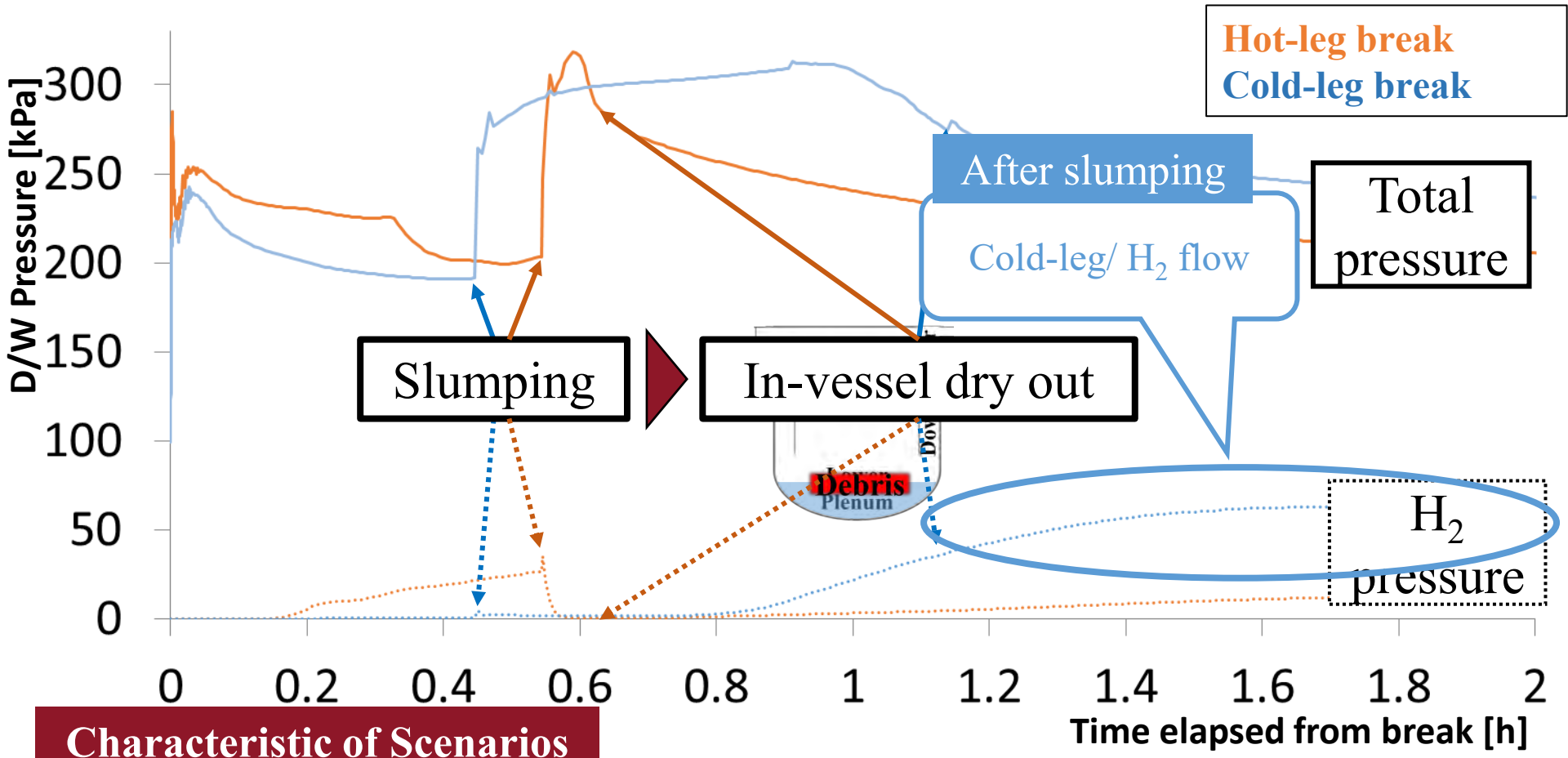

Characteristic of Scenarios

1. No significant difference before the core slumping between hot-leg / cold-leg break.
   →The short duration between the blowdown **phase** and the **core slumping**.
2. A significant difference occurred **after the core slumping**.
   →The large amount of H_2 generated in cold-leg break.

Mechanism of H_2 generation after core slumping[18]

Characteristics of the cold-leg break in the once-through direct cycle

The upward water movement in the downcomer arises from the steam flow moving toward the cold-leg break.

Steam generation decreases the upward flow weakens.
→the downcomer water flows in.

a part of the debris to become superheated steam.
→generated a large amount of hydrogen.

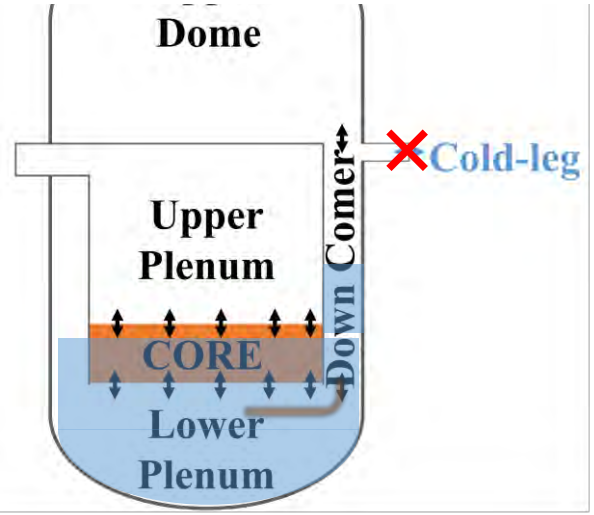

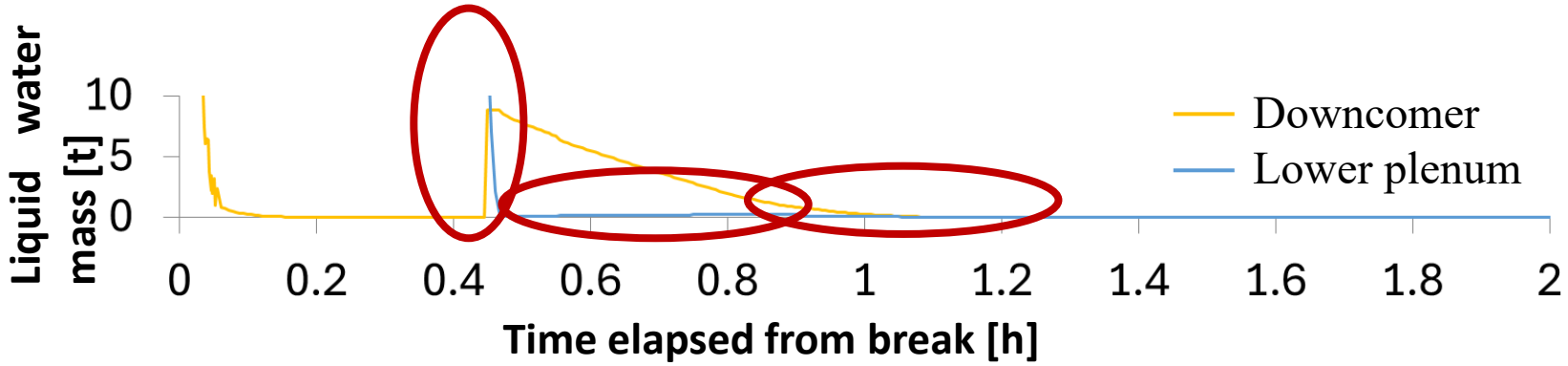

Conclusions

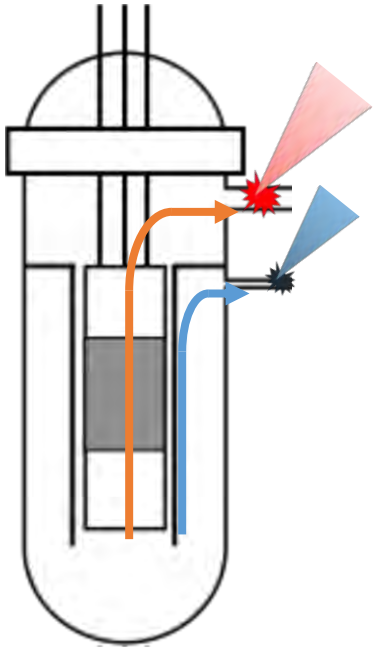

Once-through
(no re-circulations)

100% Hot-leg break

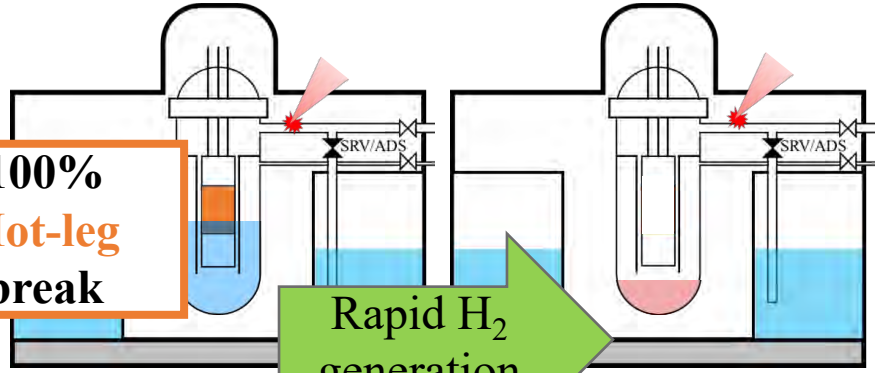

Rapid H_2 generation

100% Cold-leg break

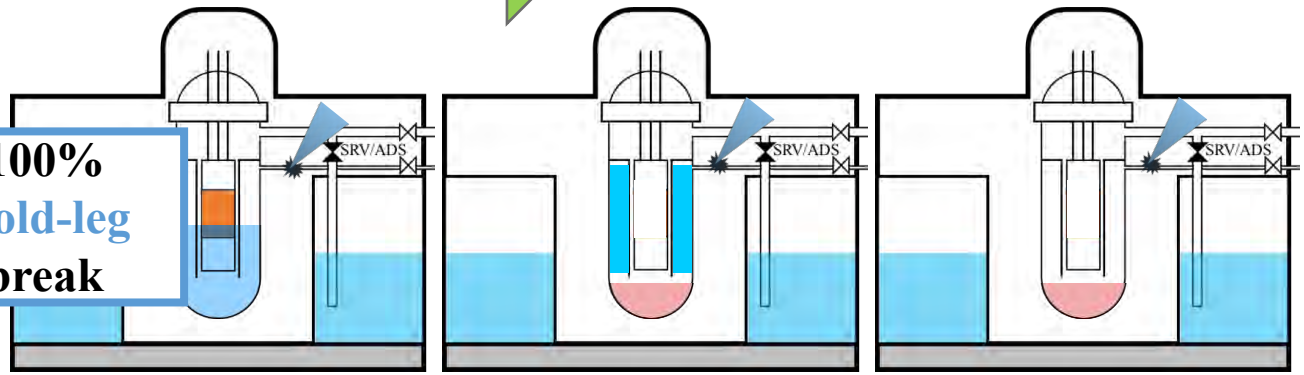

Prolonged H_2 generation

ASYST(～7s)

MELCOR (4.6 hours)

Future Works on blowdown phase

- Short term PCV management.
- Sweeping of N_2 from D/W to S/C.
- Flow split between break flow and ADS line.

The 12th European Review Meeting on Severe Accidents Research

May 18-22, 2026, Universidad Carlos III de Madrid, Madrid, Spain

TECHNICAL SESSION 1.4: SEVERE ACCIDENT SCENARIOS

Chairs: L. Carénini (ASNR), M. Braun (Framatome)

ID037	**Integral Phenomena Identification and Ranking Table on Severe Accidents: Methodology and Major Outcomes** L. E. Herranz (CIEMAT)	Paper Presentation
ID138	**More than two decades of activities on Severe Accident Management Guidelines (SAMG) in Tecnatom and Westinghouse** A. Tanarro Onrubia (Westinghouse)	Paper Presentation
ID150	**Simulating the asymmetrical behavior of TMI-2 accident with AC2/ATHLET-CD** L. Lovasz (GRS)	Paper Presentation
ID007	**ASSAS Simulator for Severe Accident analysis for educational purposes** M. Martin Garcia (Westinghouse)	Paper Presentation

INTEGRAL PHENOMENA IDENTIFICATION AND RANKING TABLE ON SEVERE ACCIDENTS: METHODOLOGY AND MAJOR OUTCOMES

L.E. Herranz[1]
[1]CIEMAT, Unit of Nuclear Safety Research, 28040 Madrid, Spain.
Luisen.herranz@ciemat.es

F. Gabrielli[2]
[2]KIT, Karlsruhe Institute of Technology, 76344 Eggenstein-Leopoldshafen, Germany
fabrizio.gabrielli@kit.edu

P. Piluso[3]
[3]CEA/IRESNE, Centre de Cadarache – Bât.219-D – 13108 St Paul Lez Durance cedex, France.
pascal.piluso@cea.fr

I. Kljenak[4]
[4]JSI, Jozef Stefan Institute, Ljubljana, Slovenia
ivo.kljenak@ijs.si

M Freitag[5]
[5]BT, Becker Technologies GmbH, 65239 Hochheim a. Main, Germany
freitag@becker-technologies.com

ABSTRACT

Major achievements have been made in severe accident (SA) research in the last decades. However, there is still a need for further research mainly driven by remaining gaps, new scenarios brought up by upcoming technologies (i.e., advanced technology fuels, ATF, and small modular reactors, SMR), more stringent safety requirements and optimization of SA management. At the same time, an efficient use of available resources (analytical/experimental knowhow, experimental facilities and advanced modeling approaches) should be pursued to make the most out of it. Under the frame of the EU SEAKNOT (Severe Accident research and KNOwledge ManagemenT for LWRs) project, the PIRT (Phenomena Identification and Ranking Table) methodology has been adapted to fit the full-scope SA field, based on a phenomenon pre-screening by domain (i.e., in-vessel, ex-vessel, containment and source term) sequentially coupled with a phase-PIRT process, both led by source term as top-level objective. Such an adaptation is described in this paper. From more than 400 phenomena initially, about 10% have been finally recommended as issues requiring further investigation based on their poor knowledge and their safety significance. Among them, issues related to Fukushima Daiichi accidents and associated to new upcoming technologies have been considered. This paper identifies and succinctly discusses the bases for their selection.

KEYWORDS
Severe Accidents; R&D priorities; PIRT; database and modelling.

1. INTRODUCTION

Severe accidents are known to dominate the risk associated to the commercial production of nuclear power. A vast amount of research has been done in this field after the TMI2 accident in 1979. Preservation of knowledge and know-how gathered, though, might be at stake at present because of the retirement of senior scientists and engineers and the loss of access to old archives. At the same time, innovation in nuclear technologies (i.e., SMRs and ATFs) and in severe accident analysis, i.e., Uncertainty and Sensitivity

Analysis (UaSA) and Artificial Intelligence (AI), might mean a change in the SA analysis paradigm. These factors, along with the progressive reduction of resources in SA, stand out the timeliness of critically reviewing the knowledge acquired to project a SA research roadmap that result in an enhanced understanding of accident unfolding and, consequently, an optimization of AM. A key element to achieve the goal is to involve and enable young scientists and engineers by conducting a proper transfer of both knowledge and knowhow. These are the major drivers underneath the EURATOM SEAKNOT project (GA 101060327 [1]), which is coordinated by CIEMAT and participated by a total of 16 European organizations plus 1 associated partner.

One of the instruments used to outline a SA research roadmap for the coming decade has been the PIRT methodology, which origin dates back to the times when the USNRC developed the Code Scaling, Applicability and Uncertainty (CSAU) evaluation methodology to support the application of the BEPU (Best Estimate Plus Uncertainty) methods in safety analyses of commercial Nuclear Power Plants (NPPs) (Boyack B., 1989). A PIRT is a table in which phenomena within a defined topic and scope are identified and ranked according to their importance. Soon, the PIRT proved to be useful in numerous applications (Wilson G.E., 1998), mostly within the domain of Design Basis Accidents (DBAs).

At the beginning of this century, the EU EURSAFE project (1998–2002) conducted the first-of-a-kind PIRT on SAs with a full scope. More than 1000 phenomena were identified, and a few more than 100 were considered worth of investigation, their safety significance being substantial and the knowledge about them lacking [4]. More recently, in 2015, a Source Term (ST) PIRT based on findings from the Fukushima Daiichi NPP accident identified almost 70 phenomena and ranked at the top the radionuclide release from molten fuel in the early phase of the accident and the Molten Core Concrete Interaction (MCCI) and iodine chemistry in the late phase [5]). Three years later, in 2018, the results of a PIRT dedicated to Spent Fuel Pool (SFP) related accidents were published; out of the eighteen phenomena highlighted as having priority for research, roughly half were related to fuel rod performance under SA conditions [6]. In 2020, the PIRT approach was employed to identify the relevant physical phenomena that computer codes should include for a proper representation of In-Vessel Retention (IVR) of corium during SAs [7]. The most recent research priority ranking conducted in Europe, with a marked qualitative nature, addressing the full SA domain dates back on 2019 [8]; nevertheless, this study cannot be considered a PIRT exercise.

The next sections describe the major outcomes of the PIRT application to the entire domain of SAs, including new technologies like Water-Cooled SMRs (WC-SMRs) and ATFs, under the frame of the SEAKNOT project. For a better contextualization, a synthesis of the methodology adaptation is given before presenting the results.

2. THE PIRT APPROACH

The PIRT is the backbone of SEAKNOT. Along with a database collection (WP2) and a European experimental infrastructure mapping and critical analysis, the PIRT is one of the essential ingredients to write up a research roadmap for the short- and mid-term (5-10 years) on SA. Generally speaking, the PIRT has been grounded on State Of the Art (SOAR) reports recently issued, previous global and partial PIRT exercises mentioned above, and the outcomes of open research projects since practically the beginning of this century (see the extensive list of references in this paper).

2.1. PIRT Adaptation

The first step when facing a PIRT on SA is to adapt the work initially proposed in the field of thermal-hydraulics and Design Basis Accidents (DBA) [2] to the SA domain. Even if a few applications in the SA domain have been already reported (as mentioned above), most of them were restricted to specific systems

and scenarios. The SEAKNOT PIRT extends over the entire SA domain, including in-vessel, ex-vessel, containment, and source term areas. Likewise, WC-SMRs and near-term ATFs are being also considered.

The specific problem this PIRT addresses is the identification of the SA issues which research would lead to better characterize and, if possible, reduce uncertainties, as well as to efficiently enhance mitigation of SA consequences. The focus is on the potential effect of the issues on source term (i.e., radiological releases from the Nuclear Power Plant, NPP). The specific variables monitoring such an effect are: onset time, rates and composition of the releases to the environment of a selection of radionuclides (I131; I132; Cs137; Ru106; Te132; Kr88; Xe133; Xe135). In other words, those variables for the given isotopes were the bases of the evaluation criteria.

The drastic difference expected in source term between the in-vessel and the ex-vessel phases recommends to split accident sequences accordingly. The PIRT was developed in two sequential steps: domain-PIRT and phase-PIRT. In the domain PIRT, the SA domain was split into sub-domains: in-vessel core degradation; ex-vessel corium behavior; containment and source term. The first task in each of them was the phenomenon identification, which on purpose was separated from the ranking process. Note that in the case of containment and source term, some phenomena were dealt with twice in case they played a role in both accident phases (i.e., in-vessel, in-V; and ex-vessel, ex-V). Once all the phenomena considered relevant were listed, the ranking stage was launched.

Ranking consisted in assessing the relative importance of phenomena (sometimes processes) with respect to the evaluation criteria noted above. The research priority was assessed based on existing knowledge and safety significance of each phenomenon; each of these concepts split into three levels (i.e., low, L; medium, M; high, H). Knowledge was weighed on data availability and representativeness, and modeling maturity; as in the case of priority, three levels were set to both data and models. Figure 1 shows how knowledge and safety significance were combined to define priority. It was high priority (H) whenever knowledge was poor (L) and safety significance was high. Low priority was attributed whenever safety significance was low and/or existing knowledge was high. The rest of cases (3) was given a medium ranking level but ordered by priority: the maximum (M1) given to high safety significance and the minimum (M3) to mid-impacting phenomena on which there was some knowledge.

		Safety Significance		
		Low	Medium	High
Knowledge	Low	L (Poor understanding; irrelevant)	M2 (Poor understanding; mild effect)	H (Poor understanding; impacting)
	Medium	L (Some understanding; irrelevant)	M3 (Some understanding; mild effect)	M1 (Some understanding; impacting)
	High	L (Sound understanding; irrelevant)	L (Sound understanding; mild effect)	L (Sound understanding; impacting)

Figure 1. PIRT ranking

In Figure 2 the structure of the table used to list and rank phenomena is displayed. Even if minor differences might exist between the four sub-domains, all of them included this minimum information: a reference number; a phenomenon name; a short description; its potential link to a system or a component; the accident phase, since some phenomena might be present only in one of the accident phases (i.e., in-V and ex-V) of the accident or even if they extend over both phases the boundary conditions might be notably different; the ranking boxes; and, very important, the references supporting the associated ranking.

					Knowledge		Safety Significance	Priority		
Ref. Number	Phenomenon	Short Description	Comp/ Sub-system	Accident Phase	Data	Model			Refs.	
C-1	Homogeneous steam condensation	Phase change of steam in a gas atmosphere driven by a local oversaturation	N.A.	In-v	H	M	L	L	D M	[1], [2] [3]
ST-1									D M	

C-Containment; ST- Source Term; In-v – In-vessel; Ex-v – Ex-vessel; N.A. – Not Applicable

Figure 2. Basic PIRT template

At the end of the domain-PIRT, the results coming from each specific sub-domain were merged into the accident phase perspective (the phase-PIRT stage). To do so, the ranking given in each sub-domain was reviewed to make sure each phenomena considered H-ranked, still kept that condition when examined from the accident phase perspective. This allowed cross-checking the previous rankings and gave the opportunity for a more uniform ranking over the different sub-domains. To practically articulate this phase-PIRT, the final ranking was done through a specific template which main inputs, once the phenomena shortly described, were: information still lacking; connection with source term; and, safety significance. Needless to say, for each of them credited references were requested.

Figure 3 displays the whole flowchart described in the previous paragraphs showing at the top the source term integral equation as the final objective of the SEAKNOT PIRT.

As a very last step, the final set of H-ranked phenomena were submitted to an external revision. The reviewer group consisted mostly of regulators and TSO (Technical Support Organization) experts on SA, but also representatives of international organizations, like NEA (Nuclear Energy Agency) and IAEA (International Atomic Energy Agency), with activities on SA and nuclear safety. They were supposed to raise criticism on each specific phenomenon they do not agree with for any reason, and were also requested to support their rationale with credited references.

2.2. PIRT limitations

The PIRT methodology is a structured way to identify and prioritize phenomena based on the existing knowledge and safety importance, which makes it a useful tool for the final purpose of the SEAKNOT project: to outline a SA research roadmap for the next 5-10 years. However, the best use of PIRT outcomes requires not just to know its potential but also to be aware of its limitations:

- Correctness of PIRT outcomes is conditioned by the field it is applied to. PIRT is heavily based on knowledge. While it is true that a vast knowledge has been grasped on SA since the first accident in a commercial NPP (TMI-2), it is not less true that SA scenarios are intrinsically uncertain and the more the scenario evolves the less known the NPP state. Therefore, the accuracy of PIRT outcomes in SAs are by far more questionable than those coming from other domains, like DBA. Awareness of this is indispensable for the right consideration of the SA PIRT results.
- Accuracy of PIRT outcomes decreases with extension of its scope. In other words, the more focused the PIRT on a specific scenario, the better assessment should be expected. However, at the same time, addressing “individual pieces of a puzzle” hinders a cross-comparison of phenomena importance among SA sub-domains, which is the purpose of this PIRT. Hence, one should be aware that a broad scope hinders an accurate assessment of the relative importance. In terms of scenario scope, SEAKNOT dig down to sub-domains, but not any deeper. This conditioned its accuracy.

- Expertise is not “a cheap commodity to get”. Expertise is the main working tool of a PIRT. Two key pillars of a PIRT are associated to it: knowledge level and perspective diversity. SEAKNOT paid attention to both from the very beginning. The level of expertise depended mostly on the project partners (17 organizations, all of them familiar with SA) and they were responsible for appointing individual experts of their staff to each specific sub-domain panel. Diversity was given a major importance since the project conception. Bringing entities with different perspectives and mind-sets (i.e., academia, research, industry, regulators, …) into the project and ensuring their involvement, were the ways devised to achieve a sound critical assessment, unbiased by the lack of sufficient background or by the “research inertia” of keeping “business-as-usual” (i.e., SA research).

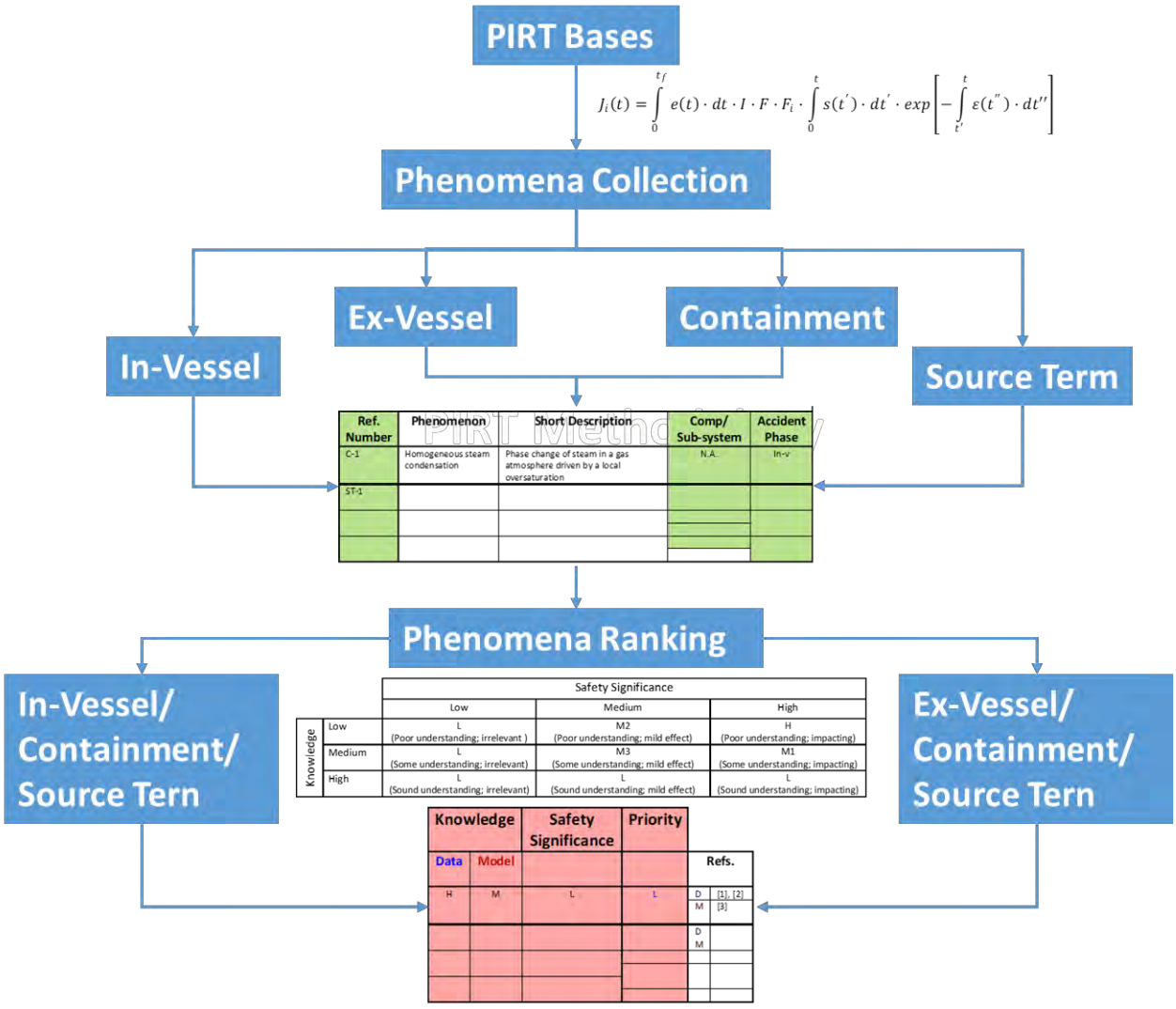

Figure 3. Flowchart of the SEAKNOT PIRT

- Practicalities in the application of the PIRT methodology adaptation. No matter how accurate and thoroughly described the methodology is, different interpretations in its application always come up whenever PIRT needs expert grouping. SEAKNOT suffered from this heterogeneity and that was one of the reasons behind the double review in the phase-ranking step. Nevertheless, some of that heterogeneity persisted to the end. Just an example, some sub-domains accepted new phenomena (coming with new technologies or recent observations from Fukushima) as a driver for investigation, even if there was not any proof of their potential impact. This was due to the misconception that anything outside the PIRT would be excluded from the final SA research roadmap.

In short, important limitations have been experienced when applying the PIRT methodology in SEAKNOT. Nevertheless, two main instruments have been used to deal with them: awareness, which did allow reducing their impact as much as feasible while developing the PIRT; and, flexibility in the PIRT reading, which will guide the integration of the outcomes in the final research roadmap to be produced within the SEAKNOT project.

3. PRELIMINARY OUTCOMES

According to the last phase of the PIRT process, the major outcomes will be split into in-vessel and ex-vessel phases. Whenever the same phenomena were selected in both phases, the new features will be highlighted in the ex-vessel section. Note that the word “preliminary” is added in the title of this section because at the time this paper is written the external review of the PIRT process is still pending.

3.1. In-Vessel phase

The In-Vessel phase aims at ranking the physical phenomena/processes mainly affecting source term occurring in the Reactor Pressure Vessel (RPV), containment, and source term domains’ path. As described in Chapter 2, just those phenomena/processes ranked high are described next.

3.1.1. In-Vessel domain

Initially, this sub-domain was divided to list the phenomena to consider into: core degradation, reflooding, corium behavior in RPV (Reactor Pressure Vessel) bottom head, RPV integrity and RIA (Reactor Initiated Accidents). A total of almost 200 phenomena were listed. By applying the PIRT methodology, as described in section 2, only 4 H-ranked phenomena were finally considered (Table I).

Table I. In-Vessel domain: High-ranked phenomena

#ID	In-vessel scenario	Phenomena
InV-1	Reflooding of a degraded core	Geometrical configuration of the degraded core (in between rod-like and molten pool)
InV-2	Lower head molten pool	Kinetics of segregation & stratification of materials
InV-3	Lower head molten pool	Crust thermal-mechanical behavior
InV-4	RPV failure under ERVC	Mechanical resistance of RPV wall

The beneficial impact of reflooding a massively degraded core might be compromised by channels blockage. Integral experiments to support thorough model validation are lacking, and scaling up from small tests to reactor cores is uneasy [9]. There are still discrepancies on some key phenomena for accident unfolding, like quenching efficiency [10-14]. In the same scenario, some codes predict a fast and complete quenching,

while others highlight the existence of non-coolable regions in the core. The effect on source term is associated with the extension and kinetics of metal oxidation [13,14], whose corresponding enthalpy release would entail higher in-core temperatures and a larger and faster fission product release from the core [9,15]. Additionally, from a safety perspective the amount and kinetics of hydrogen released and the entire in-core evolution (amount of molten corium reaching the lower head) might affect the containment and RPV bottom head integrity, respectively.

High temperature (over oxide melting temperature) molten pools in the RPV bottom head involve two immiscible liquid phases of oxides and metals. Their stratification is heavily impacted by the migration kinetics of the quaternary system U-O-Zr-Fe elements. Despite the analytical developments [16,17] and experimental work (e.g., MASCA [18], CORDEB [19], and CORDEB2 [20]), there is still a lack of high-temperature prototypical experimental data. Despite the indirect impact on source term, a more accurate description of these molten pools might largely affect the thermal-mechanical behavior of the integrity of the lower head (high safety relevance), affecting both the onset of the ex-vessel phase of the accident (if it happens) and the magnitude and kinetics of material downloaded in the reactor cavity, if RPV eventually fails.

The TMI-2 post-accident investigations revealed the significance of the crust thermal-mechanical behavior [21, 22]. Crust modelling is accounted for in mechanistic codes and in some LP integral codes like ASTEC and MELCOR [23, 24]. Nevertheless, crust effects on core degradation dynamics are not considered due to the lack of integral experimental data. A key issue is the molten steel relocation and the interaction of species through the oxide crust, which directly impact the maximum heat flux in transient situations in the lower plenum, so affecting the RPV wall degradation and the RPV integrity. The potential of a crust breach and a massive in-vessel corium relocation into the lower plenum would lead to a pressure peak, a sudden increase of hydrogen production and additional fission product release [25].

Behavior of thinned out RPV lower head walls under large temperature gradients (ex-vessel cooling, ECVR) is highly uncertain, as concluded in the H2020 IVMR project [10, 26] and the subsequent IAEA CRP J46002 one [27]. There is still a lack of integral experimental data and predictive modelling of partially ablated walls under ECVR conditions. The safety significance is related to the loss of RPV integrity and, as a consequence, the onset of the ex-vessel phase of the accident. In other words, any potential source term resulting from the ex-vessel phase of an accident would be prevented if the IVMR-ERVC strategy would support considering RPV failure practically eliminated in flooded cavity conditions.

3.1.2 Containment domain

The containment domain mostly deals with thermal-hydraulics, which is a field vastly addressed by investigation since the onset of nuclear power back in the 1960s. In other words, it is hard to find out issues where no experimentation or modeling have been attempted over the past decades. Given the condition for an H-rank knowledge (i.e., no “representative” data and no “capable” model available), that were apparently not considered as being fulfilled by the majority of the contributors, the phenomena considered here strictly correspond only to the M1 (“medium high”) classification (but are still referred as “high priority” compared to other phenomena). Thus, phenomena considered highly safety relevant with some necessary knowledge still missing have been brought up (Table II). Out of more than 50 phenomena, the ones considered worth for further investigation boiled down to 4.

Table II. Containment domain: Highly ranked physical phenomena

#ID	Accident phase	Physical phenomenon
Ct-1	In-Vessel, Ex-Vessel	Gas combustion
Ct-2	In-Vessel, Ex-Vessel	Spray mass and energy exchange
Ct-3	In-Vessel, Ex-Vessel	Buoyancy/heating from structures
Ct-4	In-Vessel	Filtered containment venting system dynamics

In-containment combustion of hydrogen [28] generated in the reactor core by oxidation of core materials (mostly Zr alloys) would increase pressure [29]. Under certain conditions (fast deflagrations and detonations), the resulting dynamic pressure loads may have the potential to damage safety systems or even containment structures. If pressure increases beyond the containment design threshold, containment integrity might be even compromised (loss of final barrier of the defense-in-depth concept). The direct effect on source term would be through the paths opened between containment atmosphere and environment, in case of loss of containment integrity; and, indirectly, if combustion affects the performance of some mitigation systems and vice versa within the containment. Experiments conducted so far were not as representative as needed: initial homogeneous atmospheres (not likely in severe accidents) and lack of systematic variation of conditions (hydrogen and steam concentration, atmosphere structure), except in the THAI programs [30]; very few tests explored the transition from deflagration to detonation (DDT) (the effect of realistic geometry characteristics on flame acceleration was only generically investigated) [31, 32]. Existing models provide satisfactory results in terms of pressure and temperature, but a poor characterization of spatial flame propagation. This is the main reason for the high-priority ranking of this process.

Even though, in-containment combustion might happen during in-vessel and ex-vessel phases, major differences do exist:

- Combustible gas generation rate (due mostly to molten core-concrete interaction - MCCI) during the ex-vessel phase is much slower, although it usually lasts much longer.
- In addition to hydrogen, carbon monoxide (CO), which is also a flammable gas, is being generated due to MCCI.
- In case of PARs installed within the containment, oxygen starvation might happen in the ex-vessel phase and prevent combustion from occurring.

Containment sprays are a source of coolant droplets, dispersed from a high elevation in the containment over the maximum possible fraction of the containment atmosphere and then freely falling down due to gravity [29]. Sprays might be actuated following discharge from the primary system to depressurize the atmosphere by steam condensation on droplets (mass exchange) and to cool the atmosphere (energy exchange). Momentum exchange also plays a role, as the downward motion of droplets causes mixing of the containment atmosphere. Finally, the washing down of aerosols from the containment atmosphere decreases the maximum amount that may eventually leave the containment, thus influencing the source term. On the other hand, condensation of steam caused by sprays may cause such a decrease in steam concentration in the containment that the atmosphere becomes flammable due to corresponding increase of hydrogen and air concentration. The reason for the high-priority ranking of this process is the deficient theoretical modelling [33-36] as perceived by the contributors, in spite of various performed experiments [36, 37]. Apparently, there is a lack of systematic experimental parametric studies within the same facilities, where the spray mass flow rate and the spray droplet parameters would be varied, and which would be suitable for further model development.

In the ex-vessel phase, sprays are more likely to be used, as a significant amount of fission products in the containment atmosphere is expected. However, as an excessive increase of flammable gas concentration may also occur due to intense steam condensation, such options should be studied individually case by case.

In any containment, there are some systems with relatively elevated temperature due to the operation of the plant, resulting in "hot" structures in contact with the atmosphere. This may heat the atmosphere locally, first inducing transport due to buoyancy and then circulation in the entire containment volume. Also, the containment atmosphere might become (locally or globally) superheated. In general, gas transport within the containment may mix the containment atmosphere and prevent the formation of regions with high concentrations of flammable gases (the opposite case, that is that gas transport within the containment could lead to formation of regions with high local hydrogen concentration, which increases the probability of combustion, is theoretically possible but not likely). Superheated gas may also cause degrading of in-containment sensors, cables and safety systems. The reason for the high-priority ranking of this process is that the agreement between experimental [38, 39] and theoretical (simulation) [40, 41] results is not as good as could have been expected (as buoyant flow is a basic phenomenon that has been modelled since the beginning of research in fluid mechanics). At present, the main reason seems to be the deficient modelling of turbulence. This phenomenon is expected to become gradually less significant during the ex-vessel phase due to the gradual cooling of structures.

Venting of the containment through the Filtered Containment Venting System (FCVS) causes an outbound flow from the containment, which in turn induces circulation of the containment atmosphere. Gas transport within the containment, induced by venting, may lead to mixing and prevention of the formation of regions with high local hydrogen concentration (as already stated before, the opposite effect is not likely). However, due to lack of specific experiments, flow dynamics induced by the venting are mostly speculations [42-44]. This, as well as the perceived lacking in theoretical modelling, are the reasons for this process to have been assigned a high priority. This priority was assigned in the in-vessel accident phase, probably as this is the phase during which the highest hydrogen concentration is expected, eventually leading to hydrogen combustion (as occurred in the Three Mile Island-2 accident in the USA in 1979), so that venting would be most beneficial in preventing hydrogen explosion (which is related to safety and source term as described earlier).

3.1.3. Source Term domain

Within the source term domain, a total list of 56 phenomena has been identified, most of which related to both the In-vessel and Ex-vessel phase. These phenomena link to the release of gaseous and particulate fission products from the intact and deteriorated fuel (in-vessel), their transport, chemical reactions and aerosol behavior within the RCS and the containment as well as their potential release via containment leaks and breaches. By applying the PIRT methodology, 2 H-ranked phenomena were considered (Table III).

Table III. Source Term domain: High-ranked phenomena

#ID	In-vessel scenario	Phenomena
ST-1	Full/partial core degradation	High-burnup and MOX FP release characteristic
ST-2	FP release by intact geometry	FP release from Fuel – ATF

High-burnup UO_2 and MOX fuels show significantly enhanced release of semi-volatile and low-volatile fission products compared to standard UO_2, as demonstrated by the VERCORS/VERDON programs [45,46,47]. Altered release kinetics have also been observed for volatile fission products, indicating a strong dependence on fuel composition during in-vessel severe accident conditions from early to late phases. Available data are scarce and limited to a few dedicated programs, many of which are not publicly

accessible. Current models are mainly developed and validated for standard UO_2 fuels and only poorly address MOX and high-burnup effects, resulting in notable uncertainties [48]. The phenomenon is relevant for both current and advanced reactor designs and may also indirectly affect residual decay heat through the release of specific fission products.

Fission product release from doped UO_2 accident-tolerant fuels (ATF) in intact geometry during the early in-vessel phase is of high safety relevance. While several dopants (e.g. Cr, Al, Si, Ti, Mo) are known to improve fuel performance, experimental data on FP release, speciation, and chemistry remain scarce, particularly under accidental conditions. Existing databases are limited, and most models are developed for standard UO_2 and are poorly validated for doped fuels [49,50]. OECD/NEA FORESEEN will focus on the Cr dopant behavior and might impact the PIRT rating in future [51]. Key knowledge gaps include the lack of systematic data on dopant effects on FP retention and release, limited understanding of FP–dopant chemical interactions, and insufficient coverage of normal and accident conditions. Chromium-doped fuels are a particular focus of ongoing and future OECD/NEA activities, but current experimental evidence on volatile FP behavior (e.g. Cs, I) is very limited. Indirect effects on the source term are expected through altered FP chemistry, aerosol formation, and transport, potentially affecting cesium and iodine behavior.

3.2. Ex-Vessel phase

As the previous chapter did with the In-Vesssel phase, this one aims at ranking phenomena heavily impacting source term once RPV integrity has been lost. Next, just the H-ranked phenomena are succinctly described along with the rationale supporting their consideration.

3.2.1. Ex-Vessel domain

A total of almost 48 phenomena were listed. By applying the PIRT methodology, as described in section 2, 5 H-ranked phenomena were considered (Table IV).

Table IV. Ex-Vessel domain: High ranked physical processes

#ID	Ex-Vessel scenario	Phenomena
ExV-1	"Wet" RPV failure location (bottom vs. side)	Fuel Coolant Interaction (FCI) and steam explosion: oxidation & solidification during corium premixing & fragmentation
ExV-2	"Wet" RPV failure (water in the reactor pit)	"Stratified" Steam Explosion (SSE)
ExV-3	Molten corium concrete interaction (MCCI)	MCCI at large scale (~5 m reactor pit)
ExV-4	Long term MCCI	Vertical/horizontal melt through (radiological consequences)
ExV-5	Degraded reactor pit after MCCI	Concrete disappearance (standing rebars)

During FCI, the premixing/jet fragmentation step remains partially known whereas it strongly impacts steam explosion energetics and even, in case of no steam explosion, corium debris bed formation and its coolability [52,53]. Oxygen sub-stoichiometric or metallic corium melt might strongly impact steam explosions energetics and corium debris bed formation and coolability [52,53,54], during the premixing and jet fragmentation phases of the Fuel Coolant Interaction (FCI). While their knowledge is incomplete, its effect on accident scenarios might be substantial, as it fosters oxidation and fast hydrogen generation and corium solidification [54,55,56]. From one hand, the impact on possible containment damage with a stronger steam explosion and from the

other hand the fission products release from the corium droplet during FCI in these conditions are today not well known.

Stratified Steam Explosion (SSE) can occur if a corium melt is released in a limited amount of water (i.e., in case of partially reflooded cavity or underwater corium spreading) [52,53]. Interaction dynamics between corium and water largely differs from that expected in case of a jet immersed in a large mass of deep water [57,58,59]. The high energetic interaction generates a shock wave pressurization and propagation. What is specifically missing is a pool of representative (i.e., prototypic corium composition) experimental data that enable both model development and validation. A possible consequence would be the motion/displacement of heavy components such as the vessel or the steam generator with possible consequences on containment and so possible fission products release outside of the containment.

MCCI [60,61] is a critical phenomenon that results in specific threats for containment integrity [21]: basemat penetration, over-pressure, combustible gas generation. Even though investigated over decades, there are still some key issues that are needed to investigate:

- The effect of scale in the MCCI phenomenology. MCCI is expected to occur in reactor pits (even 5-6 m diameter) in case of RPV failure or later in even larger spreading chambers for some reactor designs. Most experiments carried out so far have been conducted at a substantially smaller scale than the large dimensions of some reactor pits (MACE tests were done at a 1.2x1.2 scale [62], rather smaller yet [63]). Given that the dominant phenomena (thermochemistry, thermal-hydraulic, heat transfer, degassing, ablation, thermomechanical properties of degraded concrete) are strongly sensitive to scaling, large scale data would be of primary relevance to scale-up existing data and to support model validation. The absence of modelling to explain a more rapid ablation in vertical or horizontal directions according to the nature of the concrete implies uncertainties [63], especially for vertical ablation with risk for the ground waters. Both MCCI topics are crucial to assess reliably the delay of possible failure of the containment and so the possible release of radioactivity outside of the containment.
- Long term behaviour. Under the frame of OECD/NEA projects addressing Fukushima (i.e., BSAF, ARC-F and FACE) the MCCI-related observations in the long-run have brought up major discrepancies with the current MCCI understanding encapsulated in MCCI models. On one side, a large difference has been reported between models' predictions and data from the site after more than 5 days of the accident [64,65]. Even if some hypotheses have been formulated to explain them, still some long-term data would be needed to support variable settings, like concrete ablation temperature, or the effect of some processes, like through-concrete conduction. On the other, video recordings of pedestal vertical walls showing intact rebars with no concrete cover did strike all expectations. At present such concrete removal under the harsh prevailing conditions anticipated in the pit during the accident, cannot be plausibly explained.

3.2.2. Containment domain

As noted in section 3.2.1., the same containment phenomena, although under different prevailing conditions, were H-ranked for the ex-vessel phase, except for Ct#4 (gas dynamics induced by FCVS operation).

3.2.3. Source Term domain

The following phenomena in the source term domain are related to the Ex-Vessel domain, only. By applying the PIRT methodology, 5 H-ranked phenomena were considered (Table V).

Table V. Source Term domain: High-ranked phenomena

#ID	Ex-vessel scenario	Phenomena
ST-3	Steam condensation conditions	FP transport onto surfaces under condensing conditions (non-soluble)
ST-4	FP in sumps	Gaseous mass-transfer at gas/water surfaces and in liquid films
ST-5	FP in CNT with organics	Iodine reactions with organics other than paints
ST-6	FCVS operation	Gaseous and particulate FP retention by FCVS
ST-7	Non-hermetic CNT	Liquid release from containment via cracks and leakage paths

FPs transport onto surfaces due to steam condensation is significant, and an accurate quantification may reduce the uncertainties on the safety margins [66]. The published PIRT regarding the Fukushima Daiichi NPP accident [67] suggested also high importance of the phenomenon in the ST assessment. Validated models predicting aerosol behavior inside the CNT relate primarily to the gas phase [66,67,68] but not to the liquid phase. An adequate description of aerosol transport downwards the wall by the condensate is complex and corresponding validation data that include concentration and particle size data measurements are very rare [69]. Most of existing models do not allow FP product transport in any other component except the vapor phase [66,67].

Aqueous organic iodide production is one of the main sources for gaseous organic iodides inside the CNT which are strongly related to the potential source term to the environment due to corresponding high radiotoxicity [70,71,72]. The capture, transport and release of iodine species by the CNT sump water is still insufficient for a comprehensive understanding of chemistry and mass transfer kinetics [73]. Gaseous contaminants present in the CNT during an accident, e.g. nitric acid, may affect the pH of liquid water films which subsequently can affect the iodine release rate [71,74] and High Molecular Weight organic iodine compounds (HMWI) reactions owe very limited validation [74].

Iodine speciation in the CNT is of primary importance to assess radiological consequences in case of outside releases. Feedback on SA accident (TMI2, Fukushima) concerning iodine speciation of outside releases shows large uncertainties due to rapid decay heat and possible evolution in the atmosphere. Even if there are uncertainties, large presence of Org-I is still suspected [75], also supported by a less efficient trapping of FVCS in case of filtering releases [76]. The identification of potential sources of Org-I, in addition to epoxy paints, would directly impact the ST from the CNT. ESTER project data highlights that some other reactive pathways must be considered in SA simulations [77] and potential sources of Org-I must be experimentally evaluated to confirm these findings and validate improved models.

Particulate and gaseous retention by FCVS involves gaseous absorption, chemical reaction and physical separation of solid and aerosol-borne radioactive particles from a high-energy, steam-non-condensable gas mixture through a combination of thermodynamic, hydrodynamic, and filtration mechanisms. Even though knowledge is accessible via literature and FCVS vendor, sub-micron aerosol retention (e.g., <0.3 μm) is not consistently validated across systems including performance drops in some designs without deep-bed filtration [78,79]. Long-term retention stability under high radiation and thermal loads is insufficiently characterized and such conditions might include the risk of re-suspension or re-volatilization. Decay heat

impact on filter media and aerosol re-release is underexplored, especially for extended venting cycles [80]. There exists data related to adsorbents materials or compounds that may enhance the retention of FP and iodine in FCVS, such as, Ag in zeolites [81] or Na_2SO_3 in wet scrubbing systems [82]. However, a more exhaustive database is required to support the design of FCVS in terms of types of materials, operating conditions, mechanism of retention, and performance. New models are required to design FCVS systems with new material candidates [83,84], and a broader set of operating conditions needs to be included.

During Fukushima accident, direct discharge of water to the ocean has been observed, and radiological consequences evaluated [85] Contaminated water has also been found in the auxiliary building. This behaviour could have a very strong impact on the source term transferred to the environment. The EU project SOCRATES shall contribute to an enhanced understanding of liquid source term as well as corresponding model development [85].

4. KEY INSIGHTS

The material here presented will be used to build a roadmap on SA research which was conceived to efficiently articulate the available resources for the coming decade. The full-scope PIRT exercise conducted under the frame of the EC SEAKNOT project settled key insights that are worth highlighting:

- PIRT (Phenomena Identification and Ranking Table) is a systematic methodology that can guide a deep review of research needs in SA. Nonetheless, even if providing a sound basis, a SA research roadmap should go beyond the PIRT outcomes by accounting the drawbacks of the method and by adding other information sources, like new observations made in real SA transients.
- Out of roughly 400 phenomena/processes critically reviewed, about 20 remain seen most relevant investigating based on the poor knowledge existing and their potential safety impacts. However, contrary to knowledge level, which assessment was strongly supported, safety relevance was not so deeply and specifically done. It is likely that after feedback from expert external groups (AB and EUG) the final list of phenomena of interest might change.

ACKNOWLEDGMENTS

The work presented in this communication was done under the frame of the SEAKNOT project. This project has received funding from the Euratom Research and Training Programme 2021-2023 under grant agreement No 101060327. The content of this paper reflects only the authors' view. The European Commission is not responsible for any use that may be made of the information it contains.

REFERENCES

[1] https://cordis.europa.eu/project/id/101060327
[2] Wilson, G.E. and B.E. Boyack, 1989. CSAU (Code Scaling, Applicability and Uncertainty), a tool to prioritize advanced reactor research. Winter Meeting de la American Nuclear Society, San Francisco, 26-30 Noviembre 1989. Proceedings of the fifth nuclear thermal hydraulics, American Nuclear Society, 377-385. NUREG/CR-5249, CONF-891103.
[3] Wilson, G.E. and B.E. Boyack.¡, 1998. The role of the PIRT process in experiments, code development and code applications associated with reactor safety analysis. Nuclear Engineering and Design, 1998. 186: pp.23-27.

[4] Magallon, D., Mailliat, A., Seiler, J.-M., Atkhen, K., Sjövall, H., Dickinson, S., Jakab, J., Meyer, L., Buerger, M., Trambauer, K., Fickert, L., Sehgal, B.R., Hozer, Z., Bagues, J., Martin-Fuentes, F., Zeyen, R., Annunziato, A., El-Shanawany, M., Guentay, S., Tinkler, C., Turland, B., Puebla, L.E.H., 2005. European expert network for the reduction of uncertainties in severe accident safety issues (EURSAFE). Nuclear Engineering and Design 235, 309–346. https://doi.org/10.1016/j.nucengdes.2004.08.042.

[5] Suehiro S., Sugimoto J., Hidaka A., Okada H., Mizokami S., Okamoto K., 2015. Development of the source term PIRT based on findings during Fukushima Daiichi NPPs accident, Nuc. Eng. And Des. 286, 163-174, ISSN 0029-5493, https://doi.org/10.1016/j.nucengdes.2015.02.005.

[6] Martin J. Trégourès N., 2023. OECD/NEA R&D priorities for loss-of-cooling and loss-of-coolant accidents in Spent-Fuel-Pools. Nuclear Engineering and Design 410, 112380, https://doi.org/10.1016/j.nucengdes.2023.112380.

[7] F. Fichot et al., 2020. Elaboration of a Phenomena Identification Ranking Table (PIRT) for the modelling of In-Vessel Retention. Annals of Nuclear Energy 146, 107617.

[8] Manara D, Jacquemain D, Van Dorsselaere JP, Bottomley PD, Adorni M, Journeau C, Pontillon Y, Lind T, Herranz LE, Rocchi F, Schaffrath A, de la Rosa Blul JC, Bechta S, Duspiva J, Kljenak I & Dejardin P, 2019. Severe accident research priority ranking: a new assessment eight years after the Fukushima Daiichi accident. Proceedings of the 9th European Review Meeting on Severe Accident Research (ERMSAR 2019), Prague, Czech Republic, March 18-20, 2019.

[9] W. Hering, et al.: Degraded core reflood: Present understanding and impact on LWRs, Nuclear Engineering and Design 237, p. 2315-2321, 2007

[10] NEA (1991), TMI-2 Analysis Exercise Final Report, OECD Publishing, Paris

[11] G. Bandini, et al., OECD Benchmark Exercise on the TMI-2 Plant: Analysis of an Alternative Severe Accident Scenario, ERMSAR 2012, Cologne (Germany), March 21-23, 2012

[12] Chatterjee, B. et al. (2015). Ability of current advanced codes to predict in-vessel core melt progression and degraded core coolability. Benchmark exercise on the Three Mile Island-2 plant, NEA/CSNI/R(2015)3, OECD Publishing, Paris

[13] Luxat D., Hanophy J. & Kalinich D., Modular Accident Analysis Program (MAAP) - MELCOR Crosswalk Study Phase 1, EPRI Technical Report, Report 3002004449, 2014

[14] N. Andrews & al., MELCOR-ASTEC Crosswalk of the Accident at Fukushima-Daiichi Unit 1: Phase I Analysis (NUREG/IA-0510), USNRC, 2019

[15] M. Steinbrück, et al., Synopsis and outcome of the QUENCH experimental program, NED, 240, Issue 7, 2010, 1714-1727, https://doi.org/10.1016/j.nucengdes.2010.03.021.

[16] S. Nandan, et al., A simplified model for the quaternary U-Zr-Fe-O system in the miscibility gap, NED, 364, 2020

[17] F. Fichot and L. Carénini, In-Vessel Melt Retention Severe Accident Management Strategy for Existing and Future NPPs, Final Project report, November 2019.

[18] MASCA: NEA (2007), Main Results of the MASCA1 and 2 Projects: Integrated Report, OECD Publishing, Paris.

[19] CORDEB: F. Fichot, B. Michel, V. Almjashev, C. Le Guennic, N. Bakouta, R. Le Tellier, P. Piluso, T. Keim, Chemical Interactions of Molten Steel with (U-Zr-O) Corium: Main Outcomes of the CORDEB Program, NED, 388, 2022, https://doi.org/10.1016/j.nucengdes.2021.111588.

[20] Le Tellier, L. Carénini, F. Fichot, R. Gencheva, P. Groudev, I. Melnikov, M. Golubev, A. Filippov, Main results of an in-vessel corium thermochemistry benchmark based on MASCA and CORDEB2 experimental data, ANE, 220, 2025, https://doi.org/10.1016/j.anucene.2025.111514.

[21] B. R. Sehgal, Nuclear Safety in Light Water Reactors Severe Accident Phenomenology, Elsevier, 2012.

[22] J. Rempe, et al.: Revisiting Insights from Three Mile Island Unit 2 Postaccident Examinations and Evaluations in View of the Fukushima Daiichi Accident, NSE 172, 2012.

[23] IRSN, ASTEC: PHYSICAL MODELLING OF THE ICARE MODULE V3.1.2, THEORETICAL MANUAL, Cadarache, July 2024.

[24] L. L. Humphries, et al., MELCOR Computer Code Manuals, Vol. 2: Reference Manual, Version 2024.0, Sandia National Laboratories SAND2024-02104 O, March 2024
[25] NUREG/CR-6193, Primary System Fission Product | Release and Transport Please, see page 37 of the doc
[26] F. Fichot, et al., Methodology of safety evaluation of In-Vessel Retention, International Seminar "In-vessel retention: outcomes of IVMR project", Palais des Congrès, Juan-les-Pins, France, January 21-22, 2020.
[27] L. Carénini, et al., IVMR MODELLING WITH TRANSIENT EFFECTS DURING MOLTEN POOL FORMATION AND STABILIZATION – OUTCOMES FROM MODELS' COMPARISON PERFORMED IN THE IAEA CRP J46002, Proc. ERMSAR2024, https://doi.org/10.5445/IR/1000174165/v2.
[28] A.L. Sánchez, F.A. Williams, Recent advances in understanding of flammability characteristics of hydrogen, Prog. Energy Combust. Science 41, 1-55, 2014.
[29] I. Kljenak, A. Bentaib, T. Jordan, Hydrogen behavior and control in severe accidents. In: B.R. Sehgal (Ed.), Nuclear Safety in Light Water Reactors, Elsevier, 186–227, 2012.
[30] S. Gupta, M. Freitag, G. Poss, THAI experimental research on hydrogen risk and source term related safety systems, Front. Energy 15(4), 887–915, 2021. [31] A. Bentaib, A. Bleyer, H.G. Wilkening, D. Baraldi, E. Takasuo, R. Huhtanen, Hydrogen combustion with concentration gradients in experiments and simulations - Preliminary results of ENACCEF benchmark, Proc. European Review Meeting on Severe Accident Research, Karlsruhe, Germany, 2007.
[32] Ran Liu, Jingyi Yu, Xiaoming Yang, Yong Liu, Rubing Ma, Yidan Yuan, Study on hydrogen combustion flame acceleration mechanism and prediction method during severe accidents in nuclear power plants, Energies 18, 2150, 2025.
[33] M. Babić, I. Kljenak, B. Mavko, Simulations of TOSQAN containment spray tests with combined Eulerian CFD and droplet-tracking modelling, Nuclear Engng Design 239, 4, 708-721, 2009.
[34] J. Malet, L. Blumenfeld, S. Arndt, M. Babic, A. Bentaib, F. Dabbene, P. Kostka, S. Mimouni, M. Movahed, S. Paci, Z. Parduba, J. Travis, E. Urbonavicius, Sprays in containment: Final results of the SARNET spray benchmark, Nuclear Engng Design 241, 6, 2162–2171, 2011.
[35] C. Vázquez-Rodríguez, M. Andreani, G. Jiménez, R. Kapulla, S. Paranjape, J.M. Martín-Valdepeñas, D. Paladino, Assessment of the depressurisation and mixing effects of two spray systems in the PANDA facility, part II – Simulations using GOTHIC8.3(QA), Nuclear Engng Design 403, 112120, 2023.
[36] C. Loiseau, S. Mimouni, E. Studer, Numerical simulation of wall condensation and spray using the MISTRA experiments, Nuclear Engng Design, 402, 112111, 2023.
[37] C. Vazquez-Rodríguez, R. Kapulla, S. Paranjape, M. Andreani, G. Jimenez, J.M. Martín-Valdepenas, D. Paladino, Assessment of the depressurization and mixing effects of two spray systems in the PANDA facility, part I – Experimental results, Nuclear Engng Design 412, 112453, 2023.
[38] OECD/NEA, OECD/SETH-2 Project on PANDA and MISTRA experiments, Final summary report, NEA/CSNI/R (2012)5, 2012.
[39] OECD/NEA, Resolving complex safety relevant issues related to hydrogen release in nuclear power plant containments during a postulated severe accident, NEA/CSNI/R (2018)11, 2018.
[40] S. Kelm, J. Lehmkuhl, W. Jahn, H.-J. Allelein, A comparative assessment of different experiments on buoyancy driven mixing processes by means of CFD, Annals Nuclear Energy 93, 50–57, 2016.
[41] G. Vijaya Kumar, M. Kampili, S. Kelm, K. Arul Prakash, H.-J. Allelein, CFD modelling of buoyancy driven flows in enclosures with relevance to nuclear reactor safety, Nuclear Engng Design 365, 110682, 2020.
[42] L.S. Lebel, E. Lessard, K. Batten, T. Clouthier, Experimental evaluation of re-entrainment from wet scrubber filtered containment venting systems. Nuclear Engineering and Design, vol. 369, no. 13, 2020.

[43] J. Ahad, T. Rizwan, A. Farooq, K. Waheed et al., Study of hydrodynamics and iodine removal by self-priming venturi scrubber. Nuclear Engineering and Technology, 2022.
[44] J. Yang, D. Suckow, T. Lind, H.M. Prasser, Study of level swell for a Filtered Containment Venting System at the VEFITA facility. Progress in Nuclear Energy, vol. 113, pp. 7-17, 2019.
[45] Y. Pontillon et al., Nucl. Eng. Desgn., 2010, 240 / pages 1843 / 1853 / 18
[46] Y. Pontillon et al. J. Nucl. Mater., 495, 363-384, 2017.
[47] C. Le Gall et al., J. Nucl. Mater., 530, 151948, 2020.
[48] A Germain, et al., Nucl. Eng. Des., 111778, July 2022.
[49] I W. Ngarayana, et al., Exploring the effects of Al and Si dopants on the accident tolerant fuels of UO2 pellets for light water reactor, Nuclear Engineering and Design, Volume 418, 2024, 112902
[50] NUREG/CR-7283, "Phenomena Identification Ranking Tables for Accident Tolerant Fuel Designs Applicable to Severe Accident Conditions", 2021.
[51] OECD/NEA FORESEEN (FissiOn pRoducts bEhavior under SeverE accident with New fuel concepts) project proposal, 2025. Operating Agent is ASNR (France).
[52] P. Piluso et al., "Ex-Vessel Fuel Coolant Interaction - (EVFCI), recent analyses from OECD/NEA"-EVSE 2017.
[53] R. Meignen et al. (2014), "Status of steam explosion understanding and modelling", Annals of Nuclear Energy, 74, pp. 125-133.
[54] J. Delacroix, R. Le Tellier, P. Piluso, "Oxygen diffusion in liquid (over)stoichiometric corium", Nuclear Engineering and Design, Volume 337, October 2018, Pages 148-160.
[55] V. Khabensky et al. Modeling of Molten Corium Oxidation in the Presence of an Oxide Crust on the Melt Surface, Technical Physics 66(2):221-228, 10.1134/S1063784221020146.
[56] L. Manickam, An Experimental Study on Melt Fragmentation, "Oxidation and Steam Explosion during Fuel Coolant Interactions", PhD KTH 2018.
[57] H. Jo, J. Wang, M. Corradini. "Stratified steam explosion energetics". Nuclear Engineering and Technology 51 (2019) 95-103.
[58] A. Konovalenko, A. Karbojian, P. Kudinov, "Experimental results on pouring and underwater liquid melt spreading and energetic melt-coolant interaction", in: The 9th International Topical Meeting on Nuclear Thermal-Hydraulics, Operation and Safety (NUTHOS-9), Kaohsiung, Taiwan, September 9-13, American Nuclear Society, 2012.
[59] P. Kudinov et al. "Premixing and steam explosion phenomena in the tests with stratified melt-coolant configuration and binary oxidic melt simulant materials", Nuclear Engineering and Design 314 (2017) 182–197.
[60] "MCCI State of the Art Report OECD/NEA MCCI Phenomenology and Modeling", OECD/NEA/CSNI Report, 2016.
[61] M. Farmer, T. Lomperski, S.Basu, and M. Bucknor, "Core–concrete interaction experiments with reactor materials." Nuclear Engineering and Design, 236 (2006), pp. 177–196. DOI: 10.1016/j.nucengdes.2005.09.010.
[62] M. T. Farmer; W. Spencer; J. L. Binder; and D. J. Hill,"Status and Future Direction of the Melt Attack and Coolability Experiments (MACE) Program at Argonne National Laboratory", Paper ICONE-9697, Icone 9, Ninth International Conference On Nuclear Engineering, April 8-12, 2001, Nice, France.
[63] C. Journeau, P. Piluso, JF. Haquet, E. Boccaccio et al. "Two-dimensional interaction of oxidic corium with concretes: The VULCANO VB test series", Annals of Nuclear Energy 36 (2009) 1597–1613.
[64] M.Pellegrini et al. "Analysis of the Long-Term Interaction Between Molten Core and Dry Concrete at Fukushima Daiichi Unit 1", 24 Jul 2024, Nuclear Technology, DOI: 10.1080/00295450.2024.2371267.
[65] B. Grambow et al. (2022): Ten years after the NPP accident at Fukushima: review on fuel debris behavior in contact with water, Journal of Nuclear Science and Technology, 59(1): 1-24, DOI:10.1080/00223131.2021.1966347.

[66] NEA, “State of the art report on nuclear aerosols”, OECD Publishing, Paris, (2009).
[67] S. Suehiro, J. Sugimoto, A. Hidaka, H. Okada, S. Mizokami, K. Okamoto, “Development of the source term PIRT based on findings during Fukushima Daiichi NPPs accident”, Nuclear Eng. Design 286, 163-174 (2015). https://doi.org/10.1016/j.nucengdes.2015.02.005.
[68] NEA, “International Standard Problem ISP37: VANAM M3 – A multi compartment aerosol depletion test with hygroscopic aerosol material”, OECD Publishing, Paris, (1996).
[69] M. Freitag, S. Gupta, S. Beck, M. Sonnenkalb, “Experimental and Analytical Investigations of Aerosol Processes –Wash-Out and Wash-Down”, Nuclear Science and Engineering, 193 198-210 (2018). https://doi.org/10.1080/00295639.2018.1479091.
[70] B. Clement, L. Cantrel, G. Ducros, F. Funke, L. Herranz, A. Rydl, G. Weber, C. Wren; State of the art report on iodine chemistry; NEA/CSNI/R(2007)1.
[71] Proceedings of the Workshop on Source Term: A Report by the Committee on the Safety of Nuclear Installations Working Group on the Analysis and Management of Accidents, NEA/CSNI/R(2020); 4 April 2022.
[72] L.E. Herranz, D. Jaquemain; Research needs on Source Term: a CSNI/WGAMA perspective; Proceedings of the 10th European Review Meeting on Severe Accidents Research (ERMSAR2022); Karlsruhe; Germany, May 16-19 2022
[73] N. Girault, L. Bosland, S. Dickinson, F. Funke, S. Güntay, L.E. Herranz, D. Powers; LWR severe accident simulation: Iodine behaviour in FPT2 experiment and advances on containment iodine chemistry; Nuclear Engineering and Design 243 (2012) 371– 392
[74] J. Kalilainen, T. Lind; Uncertainty quantification study on gas phase iodine release from Fukushima Daiichi accident in unit 3; Annals of Nuclear Energy 166 (2022) 108740.
[75] Kataka et al., Detailed source term estimation of the atmospheric release for the Fukushima Daiichi Nuclear Power Station accident by coupling simulations of an atmospheric dispersion model with an improved deposition scheme and oceanic dispersion model. Atmos. Chem. Phys. 15, 1029–1070, 2015. doi:10.5194/acp-15-1029-2015
[76] Ahad, J. et al. Review of Filtered Containment Venting System (FCVS) Eleven Years After Fukushima Accident. Nuclear Technology 2024. DOI: 10.1080/00295450.2024.2302716
[77] ESTER OECD project, https://www.oecd-nea.org/jcms/pl_58926/experiments-on-source-term-for-delayed-releases-ester-project
[78] IAEA-TECDOC-1812, Severe Accident Mitigation through Improvements in Filtered Containment Vent Systems and Containment Cooling Strategies for Water Cooled Reactors, IAEA, 2017.
[79] NEA/CSNI/R(2009)5, State-of-the-Art Report on Nuclear Aerosols, Committee on the Safety of Nuclear Installations, 2009.
[80] NEA/CSNI/R(2014)7, OECD/NEA/CSNI Status Report on Filtered Containment Venting, Committee on the Safety of Nuclear Installations, 2014.
[81] Albiol T. et al., https://doi.org/10.1016/j.anucene.2018.02.024. 2018.
[82] Wen J. et al., https://doi.org/10.1016/j.ijheatmasstransfer.2017.07.023. 2017.
[83] Lind T.- et al., https://doi.org/10.3389/fnuen.2025.1567507. 2025.
[84] Solaija T.J. et al., https://doi.org/10.1109/PGSRET.2017.8251802. 2017.
[85] SOCRATES https://socrates-euratom.eu/

GOBIERNO DE ESPAÑA
MINISTERIO DE CIENCIA, INNOVACIÓN Y UNIVERSIDADES

Ciemat
Centro de Investigaciones Energéticas, Medioambientales y Tecnológicas

Integral Phenomena Identification & Ranking Table on Severe Accidents:

Methodology & Major Outcomes

L.E. Herranz*, F. Gabrielli (KIT), P. Piluso (CEA), I. Kljenak (JSI), M. Freitag (BT)

*luisen.herranz@ciemat.es
Unit of Nuclear Safety Reseach
Departament of Nuclear Fission
CIEMAT

Contents

01 Introduction

02 The PIRT Approach

03 Major Outcomes

04 Main Insights

GOBIERNO DE ESPAÑA
MINISTERIO DE CIENCIA, INNOVACIÓN Y UNIVERSIDADES

Ciemat
Centro de Investigaciones Energéticas, Medioambientales y Tecnológicas

01

Introduction

The SEAKNOT Crossroad

GOBIERNO DE ESPAÑA
MINISTERIO DE CIENCIA, INNOVACIÓN Y UNIVERSIDADES
Ciemat
Centro de Investigaciones Energéticas, Medioambientales y Tecnológicas

New technologies arrival
(SMRs; ATFs)

Loss of « intangible assets »
(senior's expertise & old archives)

A **roadmap**
(what, where & how)

Need of a capable «workforce »
(Knowledge & knowhow)

New methodologies
(UaSA; AI &ML)

The Pathway

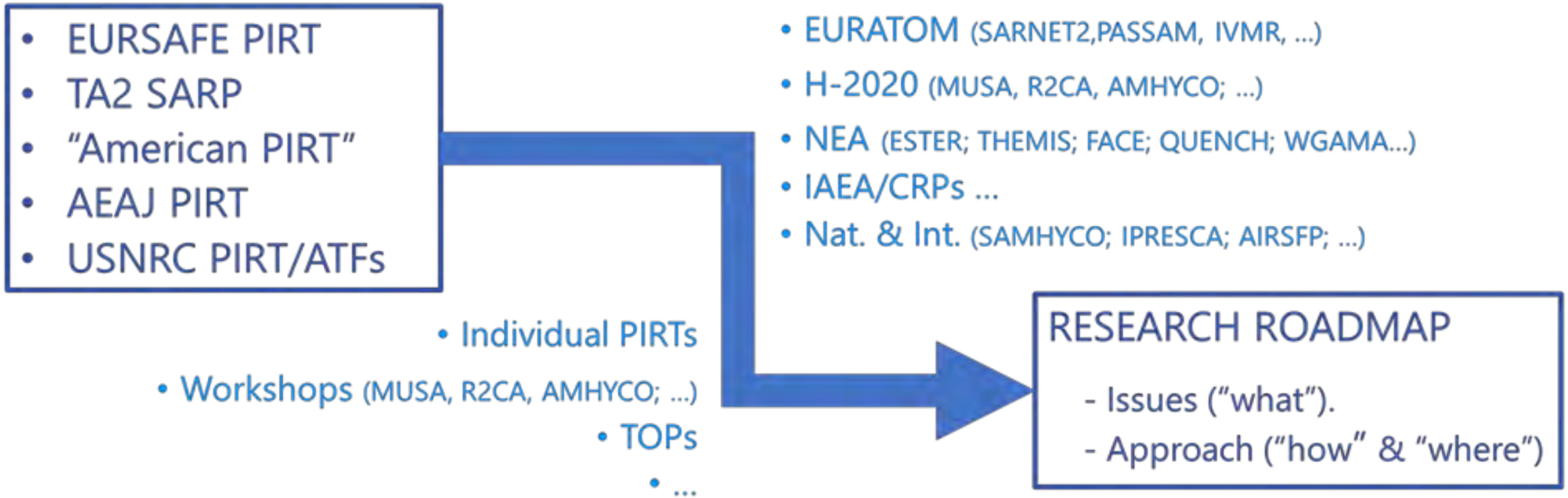
• EURSAFE PIRT
• TA2 SARP
• "American PIRT"
• AEAJ PIRT
• USNRC PIRT/ATFs
• Individual PIRTs
• Workshops (MUSA, R2CA, AMHYCO; ...)
• TOPs
• ...
• EURATOM (SARNET2,PASSAM, IVMR, ...)
• H-2020 (MUSA, R2CA, AMHYCO; ...)
• NEA (ESTER; THEMIS; FACE; QUENCH; WGAMA...)
• IAEA/CRPs ...
• Nat. & Int. (SAMHYCO; IPRESCA; AIRSFP; ...)
RESEARCH ROADMAP
- Issues ("what").
- Approach ("how" & "where")

Objective & Scope

- **Identify the major SA issues worth new R&D activities**

  Critically assess existing SA knowledge by

  - Identifying SA issues by sub-domains (In-V; Ex-V; Cont.; ST).
  - Assessing the knowledge gaps (data & models).
  - Evaluating their safety significance.

- **Focus on water-cooled reactors (LWRs +** WC-SMRs & ATFs)
- **5-10 years time horizon.**

02 The PIRT Approach

The PIRT Background

- PIRT: Step 3 in CSAU (Code Scaling, Applicability and Uncertainty) Method. (BEPU application in safety analysis; USNRC,1988).
- PIRT: A way to set technical basis for experimental programs.
- PIRT: A means to establish computer codes phenomenological requirements.
- PIRT: A methodology broadly used in SA (… but adaptation required!).
  - "Development of the source term PIRT based on findings during Fukushima-1 NPPs accident", 2015.
  - "PIRT: R&D Priorities for Loss-of-Cooling and Loss-of-Coolant Accidents in SNF Pools", 2018.
  - "Elaboration of a PIRT for the modelling of In-Vessel Retention", 2020.

The PIRT Structure

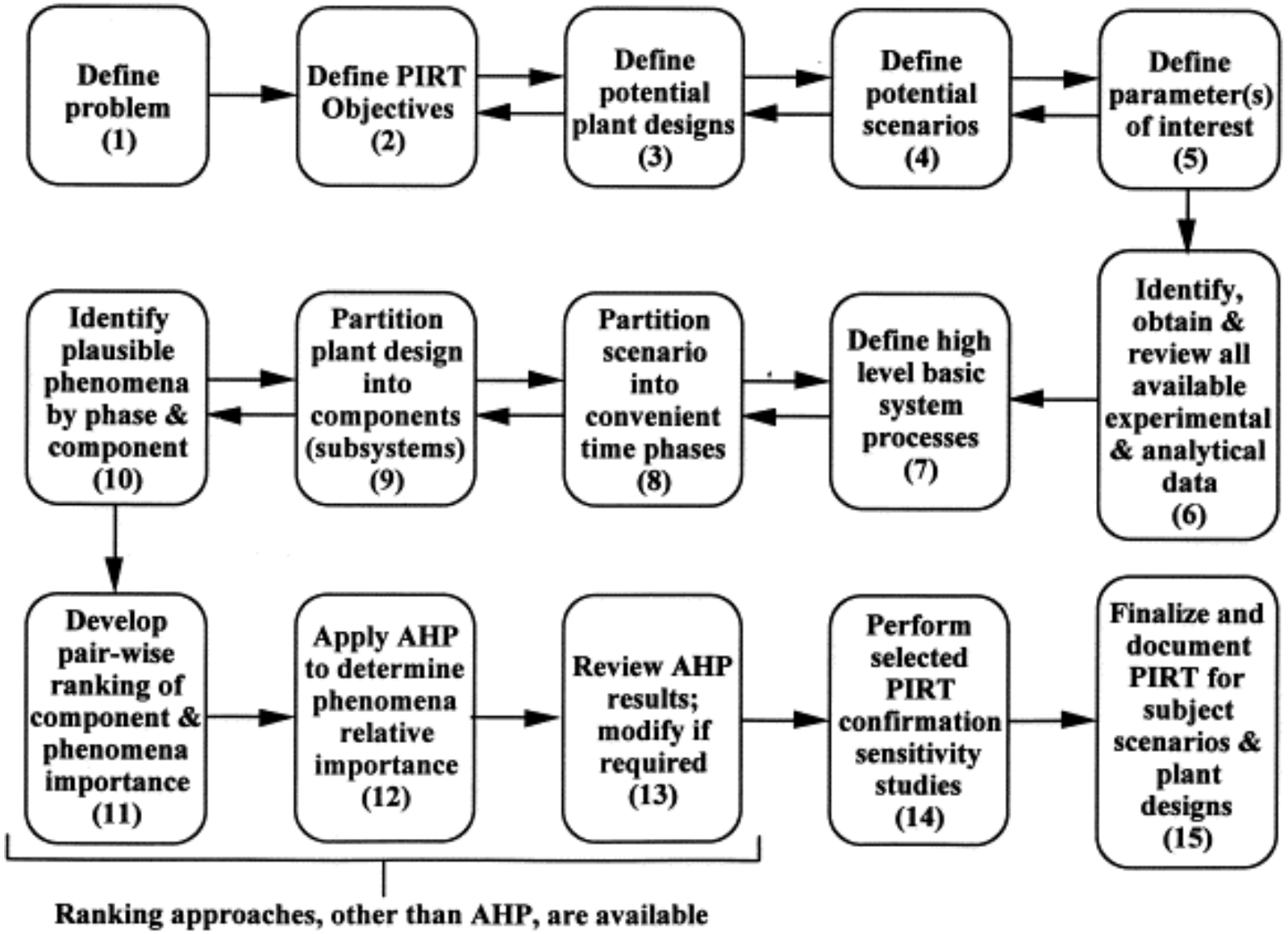

Wilson et al., 1998

The PIRT Essential Steps

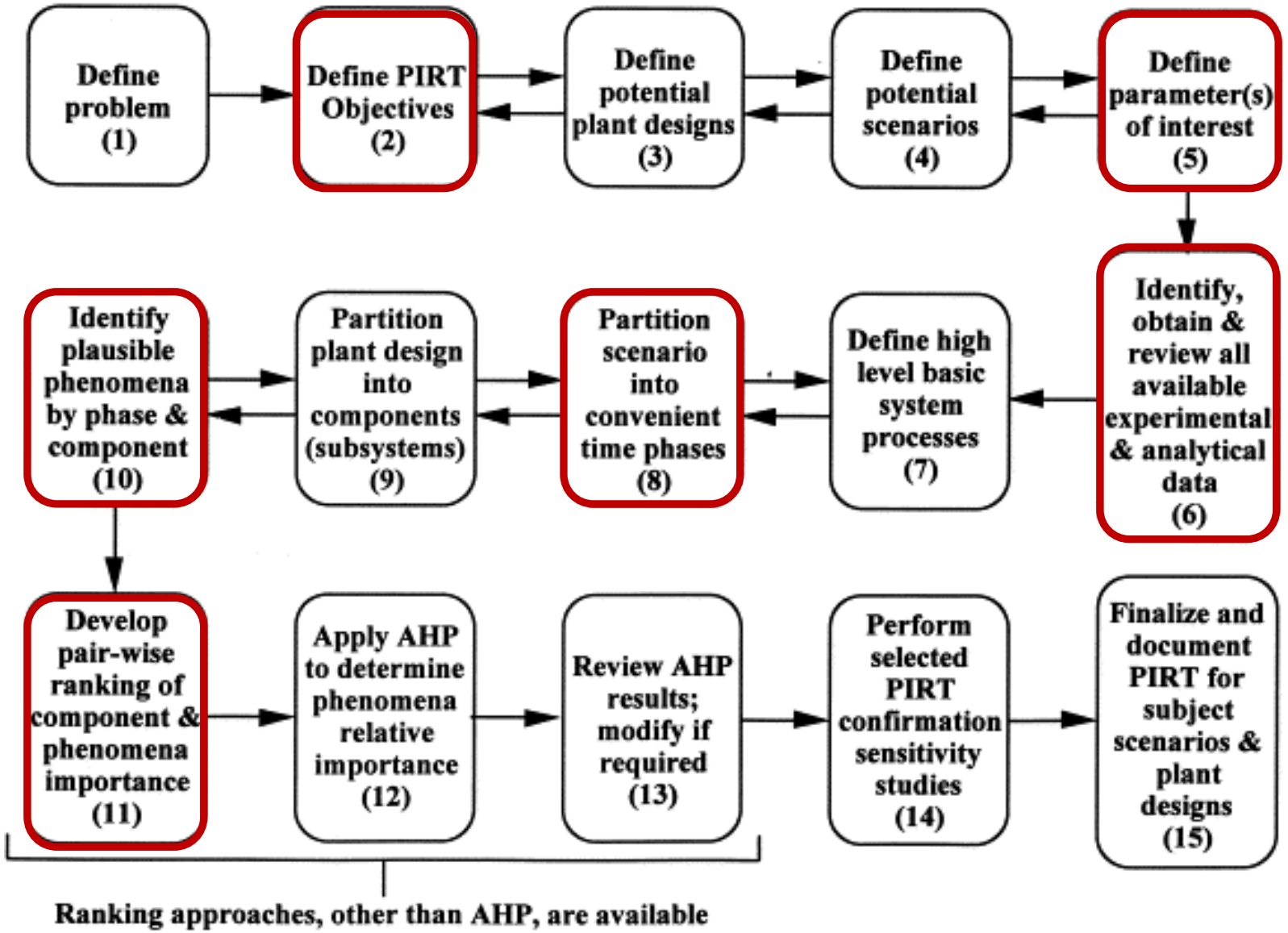

The PIRT Essential Steps

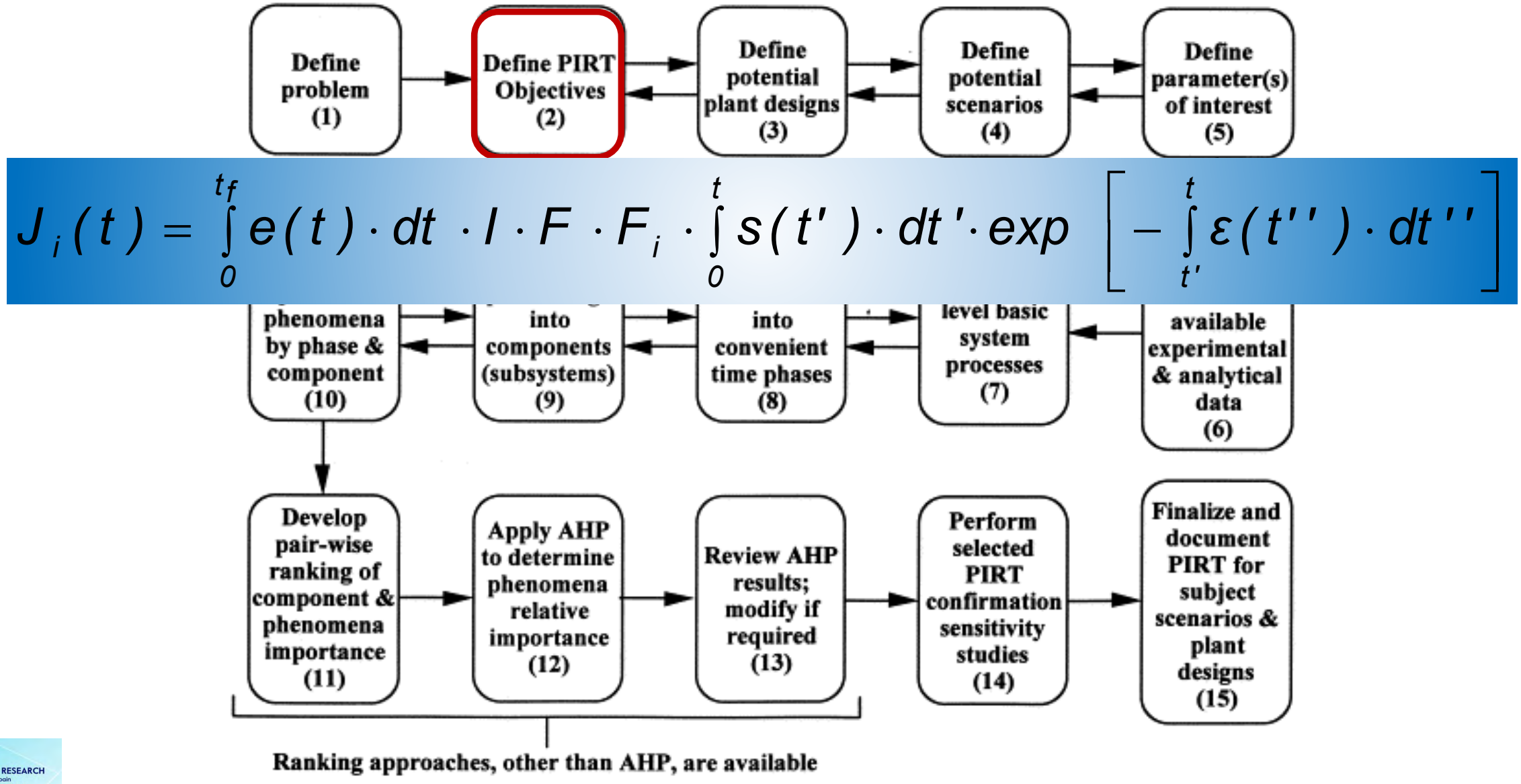

$$J_i(t) = \int_0^{t_f} e(t) \cdot dt \cdot I \cdot F \cdot F_i \cdot \int_0^{t} s(t') \cdot dt' \cdot \exp\left[-\int_{t'}^{t} \varepsilon(t'') \cdot dt'' \right]$$

The PIRT Essential Steps

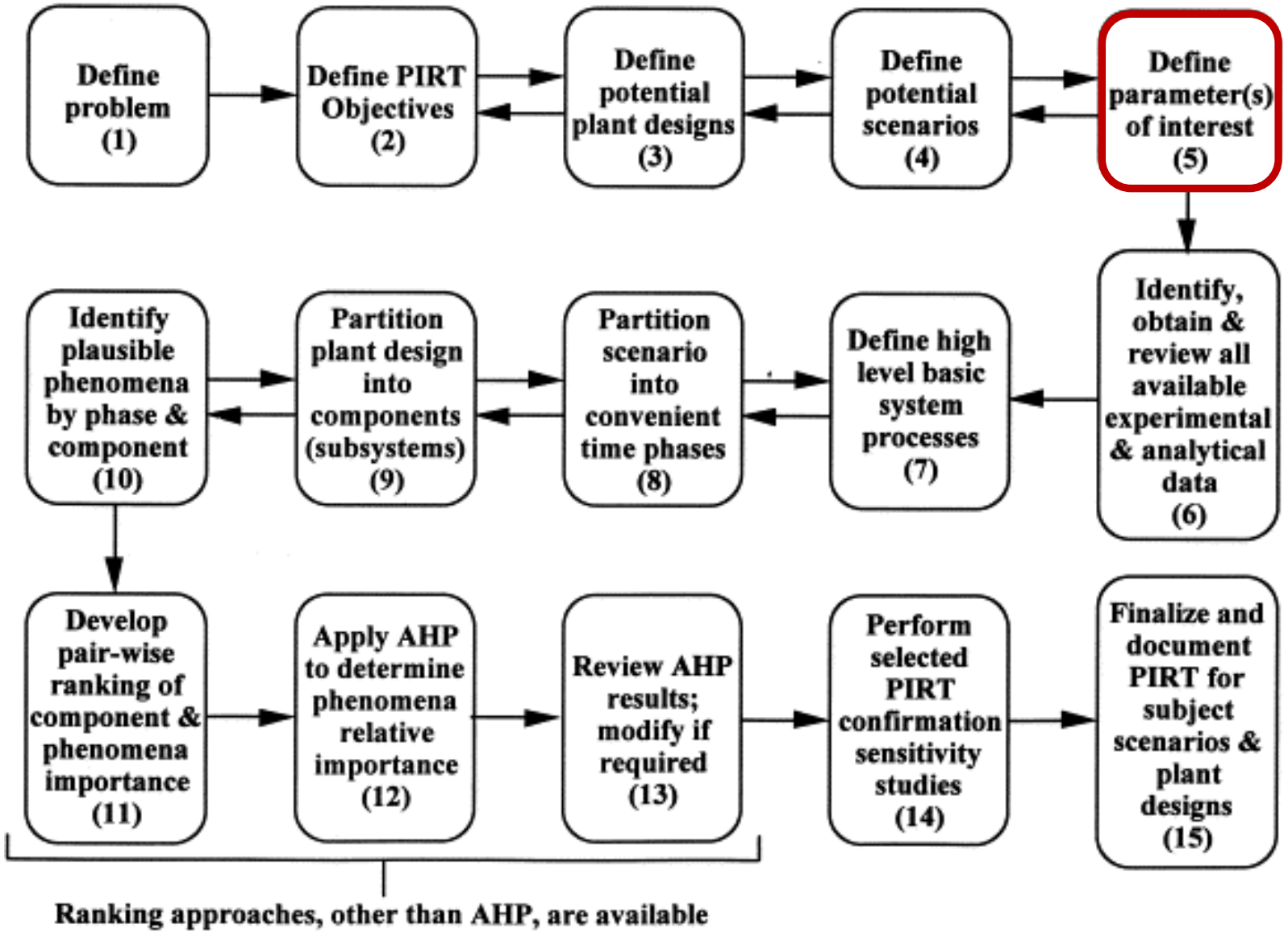

I; Cs; Te; Ru; Kr; Xe

- **Onset time**
- **Release rates**
- **Composition**

The PIRT Essential Steps

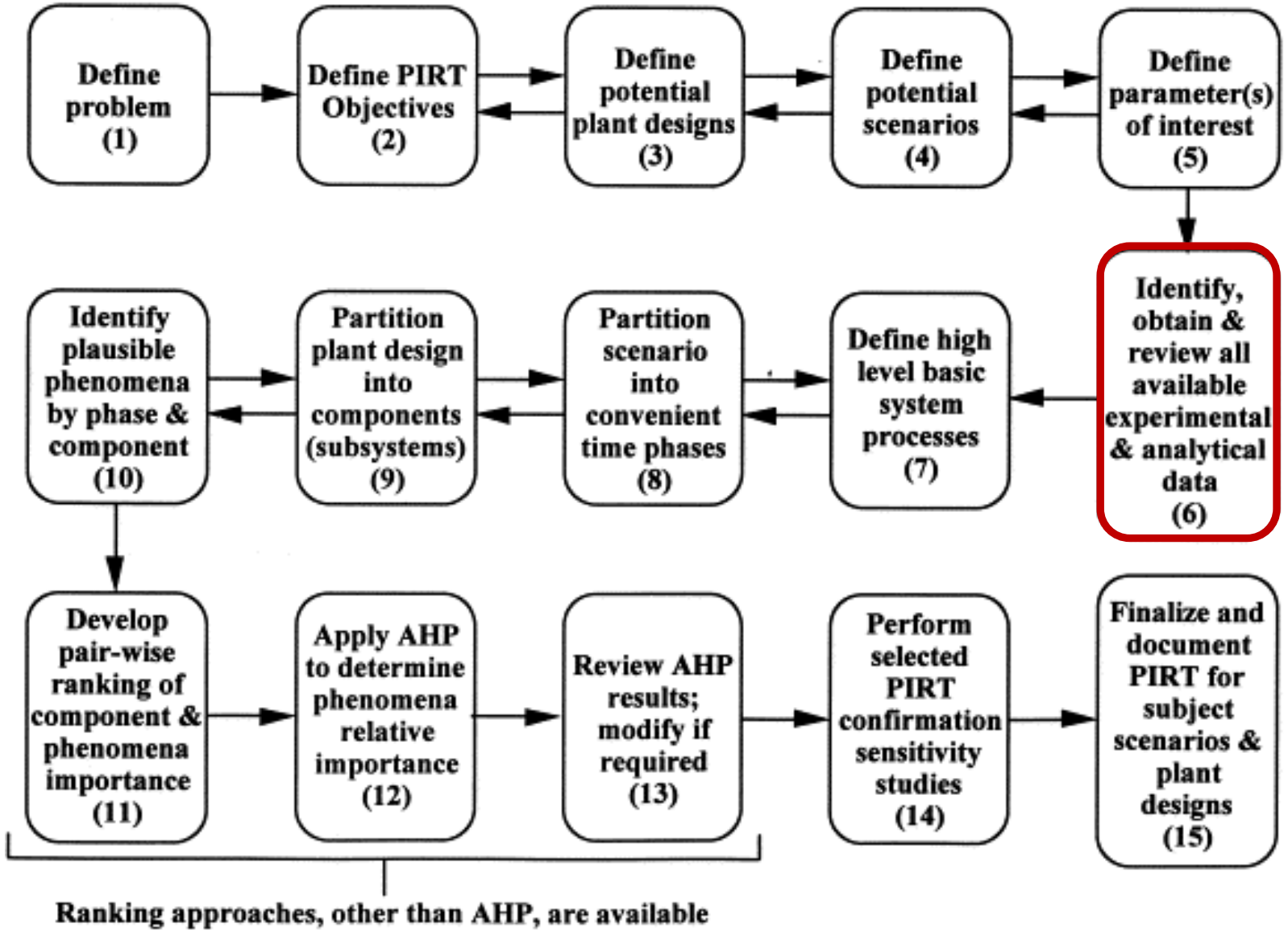

- **EURSAFE PIRT to SARP**.
- High-level American PIRT (SBO-focused).
- AEAJ PIRT on Source Term (Fukushima-based).
- USNRC PIRT on ATFs (NUREG/CR-7283).
- EURATOM (SARNET2, CESAM, ALISA, PASSAM, SAFEST, IVMR, …)
- HORIZON-2020 (MUSA, R2CA, AMHYCO; …)
- OECD/NEA (BIP; STEM; BSAF; ARCF; THAI; ESTER; THEMIS; FACE; QUENCH; …)
- IAEA/CRPs …
- Other nat. & int. projects (SAMHYCO; IPRESCA; AIRSFP; …)

The PIRT Essential Steps

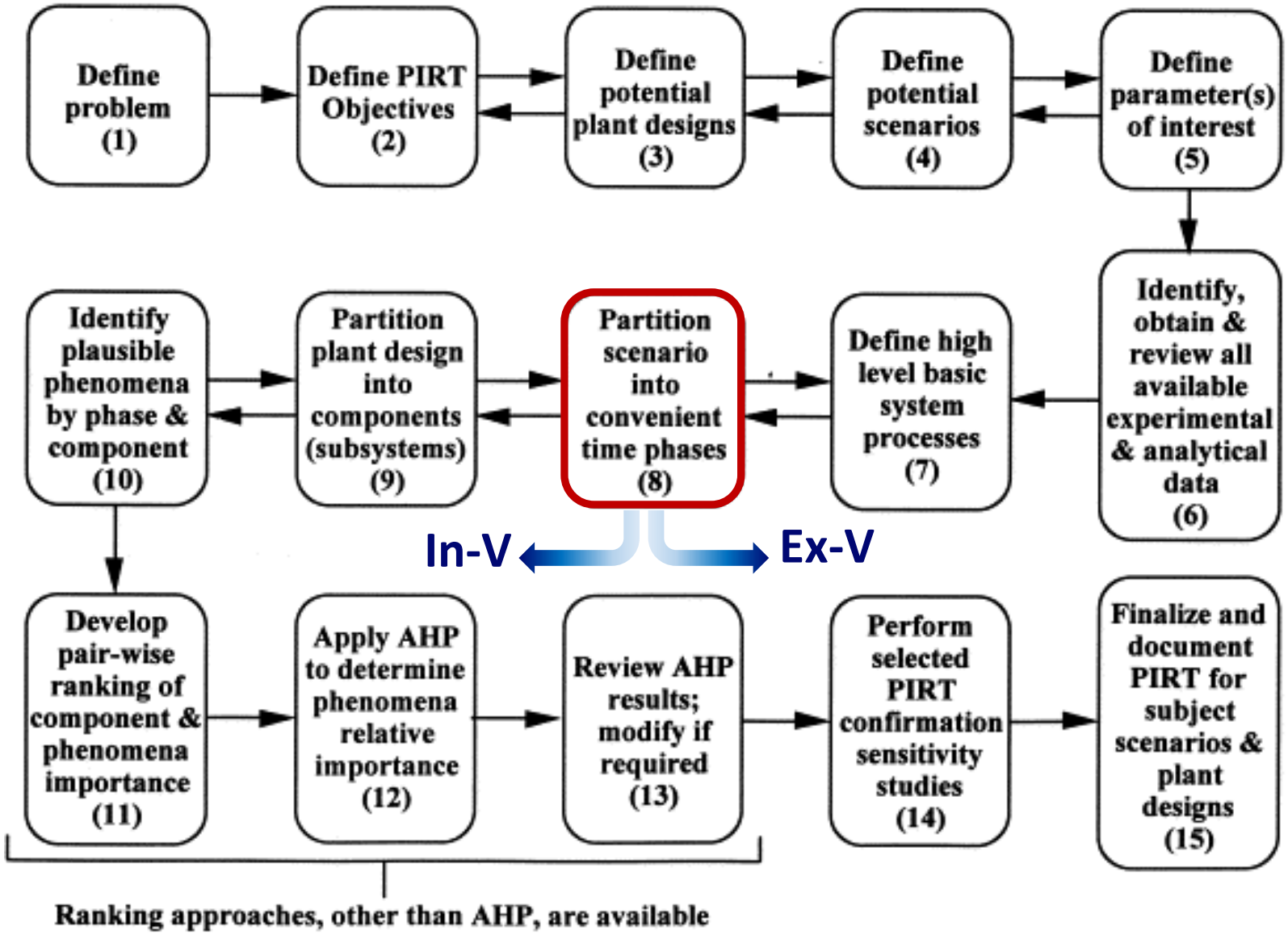

The PIRT Essential Steps

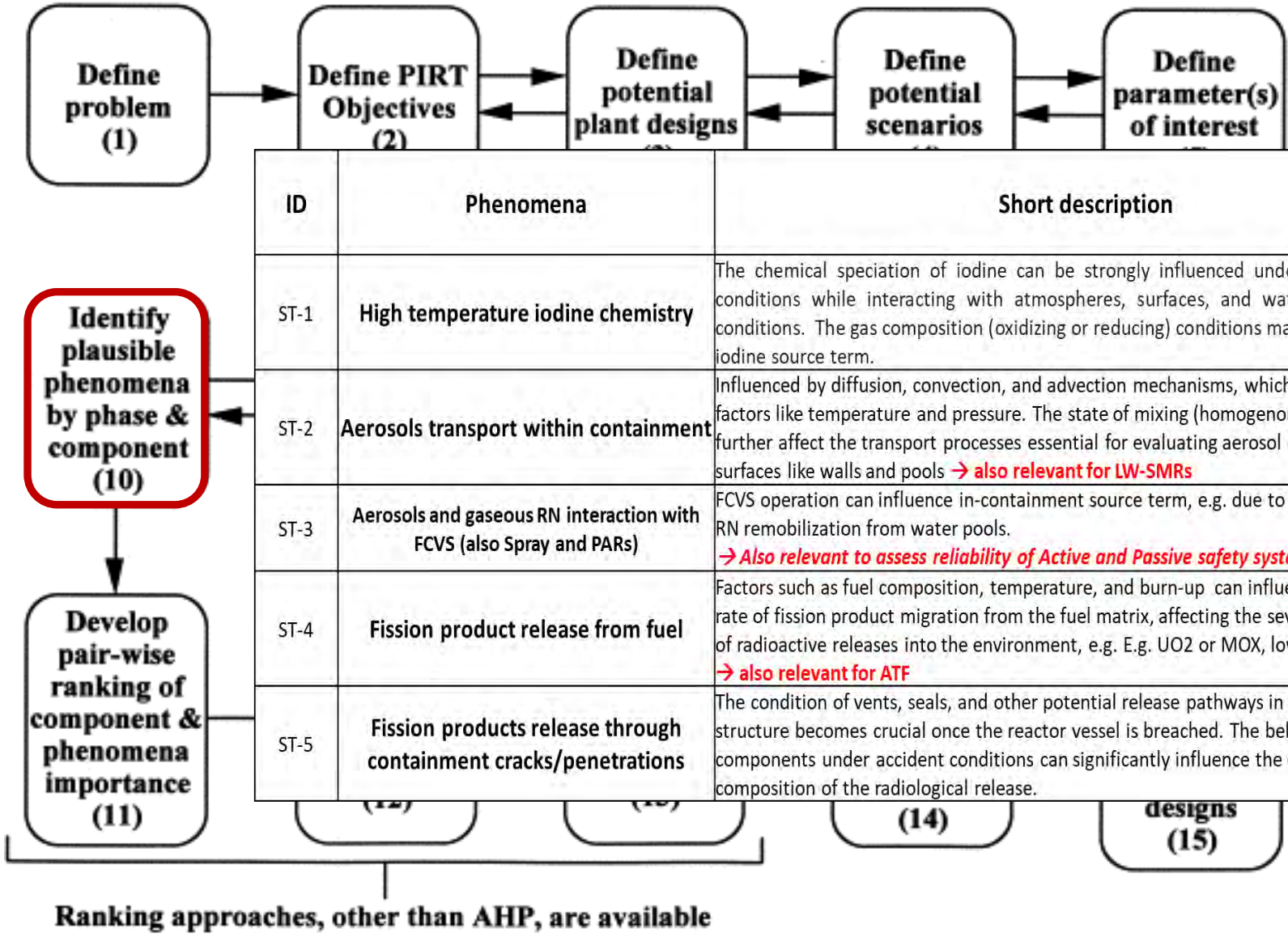

ID	Phenomena	Short description	Accident Phase (In-V, Ex-V)
ST-1	High temperature iodine chemistry	The chemical speciation of iodine can be strongly influenced under high-temperature conditions while interacting with atmospheres, surfaces, and water pools under SA conditions. The gas composition (oxidizing or reducing) conditions may further impact the iodine source term.	In-V
ST-2	Aerosols transport within containment	Influenced by diffusion, convection, and advection mechanisms, which are affected by factors like temperature and pressure. The state of mixing (homogenous or stratified) can further affect the transport processes essential for evaluating aerosol deposition on surfaces like walls and pools → also relevant for LW-SMRs	In-V, Ex-V
ST-3	Aerosols and gaseous RN interaction with FCVS (also Spray and PARs)	FCVS operation can influence in-containment source term, e.g. due to aerosols or gaseous RN remobilization from water pools. *→ Also relevant to assess reliability of Active and Passive safety systems*	In-V, Ex-V
ST-4	Fission product release from fuel	Factors such as fuel composition, temperature, and burn-up can influence the extent and rate of fission product migration from the fuel matrix, affecting the severity and duration of radioactive releases into the environment, e.g. E.g. UO2 or MOX, low or high burn-up → also relevant for ATF	In-V, Ex-V
ST-5	Fission products release through containment cracks/penetrations	The condition of vents, seals, and other potential release pathways in the containment structure becomes crucial once the reactor vessel is breached. The behavior of these components under accident conditions can significantly influence the extent and composition of the radiological release.	Ex-V

The PIRT Essential Steps

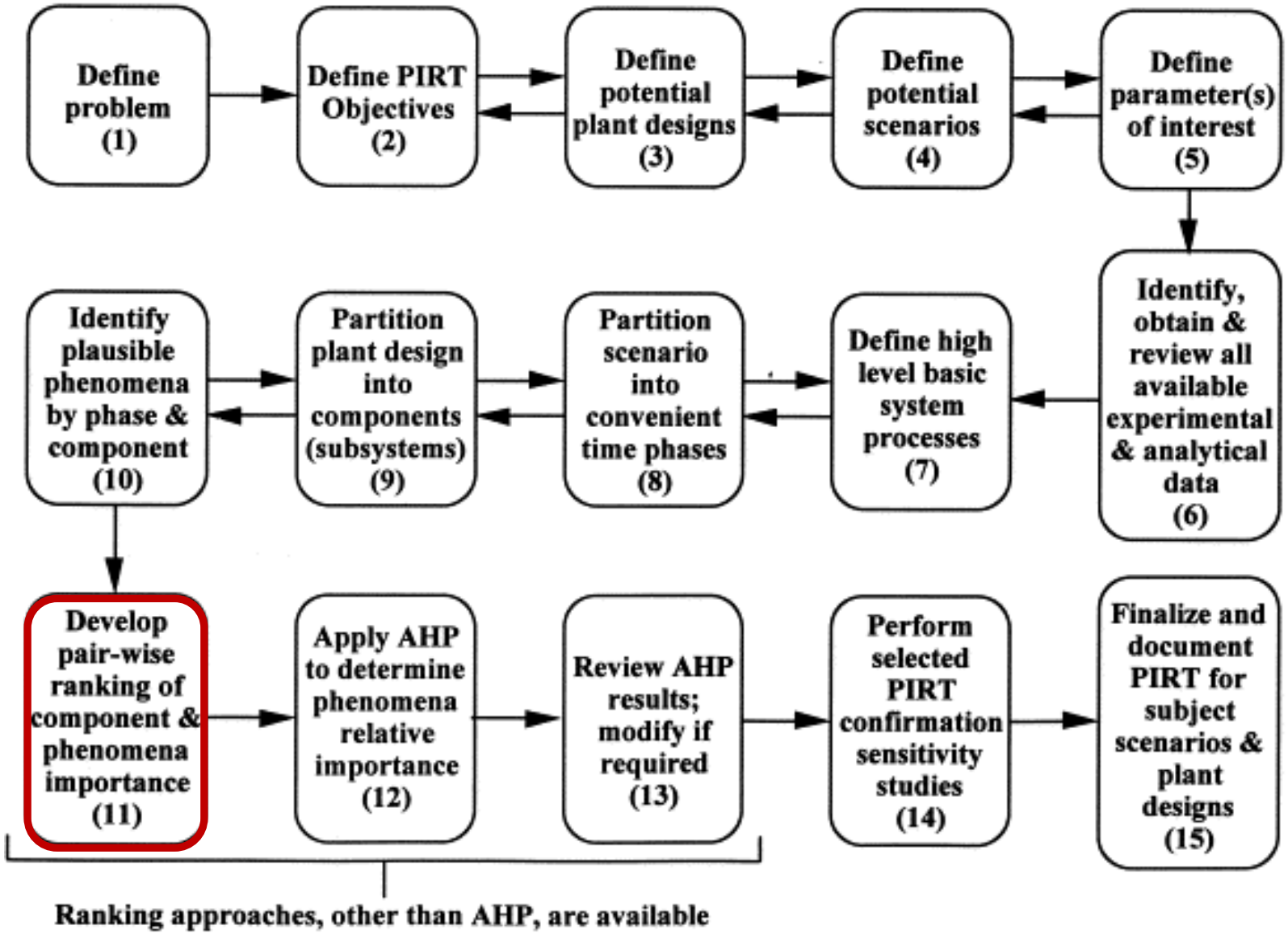

The PIRT Essential Steps

The Knowledge Ranking

	Low	Medium	High
Data	No data available	Data available, but not directly applicable	Data available & qualified for validation
Model	No model available	Model available but highly uncertain	Model validated & implemented in codes

		Data		
		Low	**Medium**	**High**
Model	**Low**	L (Unknown)	L (Qualitative understanding)	M (Bases for “known” set)
	Medium	L (Uncertain approximation)	M (Qualitatively assessed approximation)	M (Soundly assessed approximation)
	High	L (Uncertain model)	M (Qualitatively assessed model)	H (“Known”)

The PIRT Essential Steps

The Final Ranking

		Safety significance		
		Low	**Medium**	**High**
Knowledge	**Low**	L (Poor understanding; irrelevant)	M2 (Poor understanding; mild effect)	H (Poor understanding; high impact)
	Medium	L (Some understanding; irrelevant)	M3 (Some understanding; mild effect)	M1 (Some understanding; high impact)
	High	L (Sound understanding; irrelevant)	L (Sound understanding; mild effect)	L (Sound understanding; high impact)

The PIRT Essential Steps

PIRT "Flowchart"

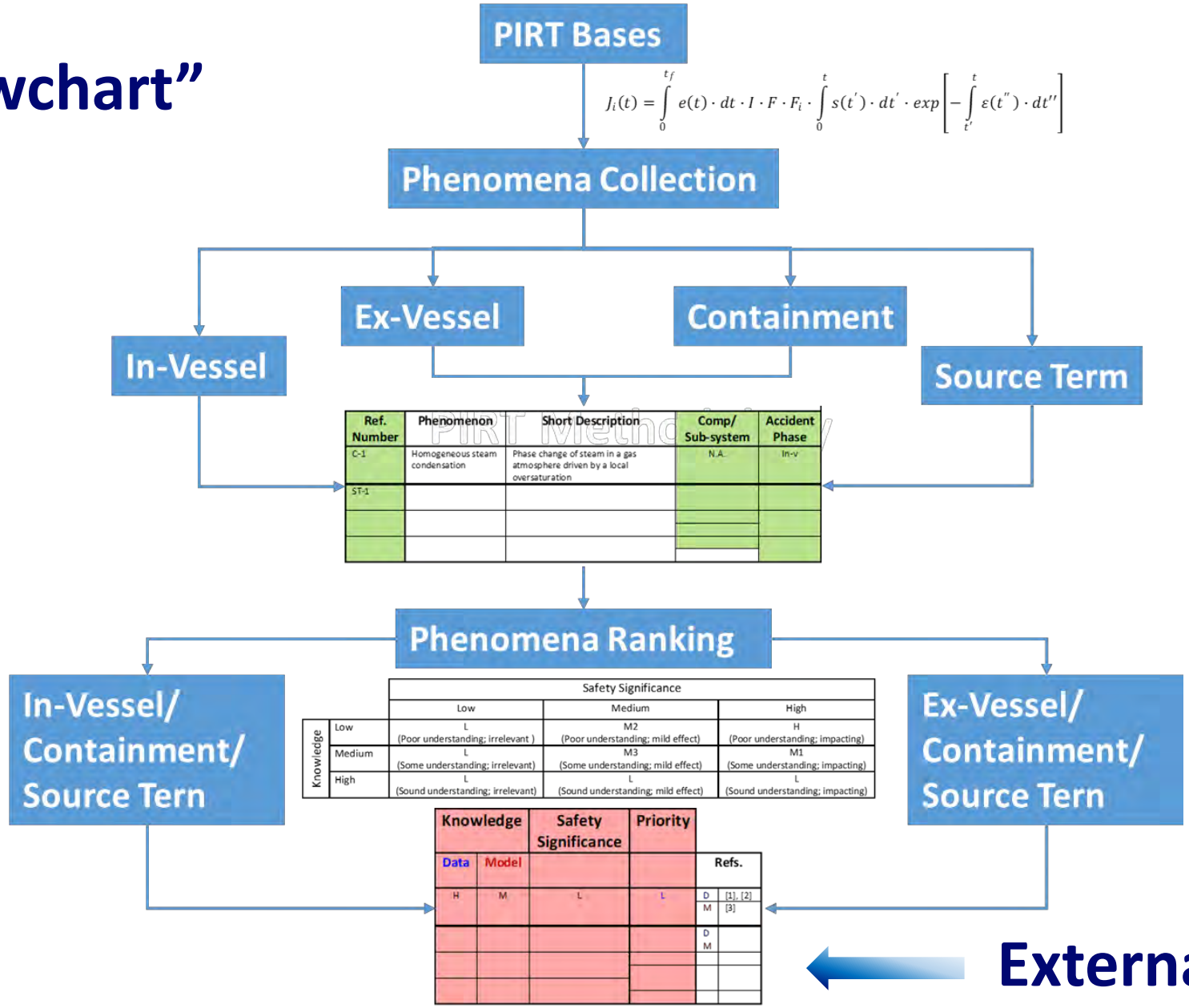

External review!

The PIRT Challenges

- PIRT is a knowledge-based method. SA are intrinsically uncertain.

  Awareness!

- The larger the PIRT scope, the less accurate outcomes.

  Awareness!

- Expertise (knowledge & perspective diversity) is the PIRT main asset.

  Partnership & diversity & External review groups (AB&EUG).

- Practicalities in the application of the PIRT methodology.

  Understanding & Phase PIRT.

The PIRT Practicalities

- To “adapt” the agreed **methodology.**
- To achieve **a uniform application of the methodology** in domains.
- To **integrate** the input from domains.

- To **stretch the boundaries** to WC-SMRs and ATFs (WP1.2-.5).
- To keep the **safety-focus** throughout the work.

Trade-off between resources and efforts!

03

Major Outcomes

Major Outcomes

In-Vessel Phase

GOBIERNO DE ESPAÑA
MINISTERIO DE CIENCIA, INNOVACIÓN Y UNIVERSIDADES
Ciemat
Centro de Investigaciones Energéticas, Medioambientales y Tecnológicas

In-RPV

#ID	In-vessel scenario	Phenomena
InV-1	Reflooding of a degraded core	Geometrical configuration of the degraded core (in between rod-like and molten pool)
InV-2	Lower head molten pool	Kinetics of segregation & stratification of materials
InV-3		Crust thermal-mechanical behavior
InV-4	RPV failure under ERVC	Mechanical resistance of RPV wall

In-Vessel Phase

Containment

#ID	Accident phase	Physical phenomenon
Ct-1	In-V, Ex-V	Gas combustion
Ct-2	In-V, Ex-V	Spray m & E exchange
Ct-3	In-V, Ex-V	Buoyancy/heating from structures
Ct-4	In-V	FCVS dynamics

Major Outcomes

In-Vessel Phase

GOBIERNO DE ESPAÑA
MINISTERIO DE CIENCIA, INNOVACIÓN Y UNIVERSIDADES
Ciemat
Centro de Investigaciones Energéticas, Medioambientales y Tecnológicas

Source Term

#ID	In-vessel scenario	Phenomena
ST-1	Full/partial core degradation	High-burnup and MOX FP release characteristics
ST-2	FP release from intact geometry	FP release from Fuel (ATF)

Ex-Vessel Phase

In-Cavity

#ID	Ex-Vessel scenario	Phenomena
ExV-1	"Wet" RPV failure location (bottom vs. side)	FCI & SE: oxidation & solidification during corium premixing & fragmentation
ExV-2	"Wet" RPV failure (water in the reactor pit)	"Stratified" Steam Explosion (SSE)
ExV-3	MCCI	MCCI at large scale (~5 m reactor pit)
ExV-4		LT Vertical/horizontal melt through (radiological consequences)
ExV-5		Concrete disappearance (standing rebars)

Ex-Vessel Phase

GOBIERNO DE ESPAÑA
MINISTERIO DE CIENCIA, INNOVACIÓN Y UNIVERSIDADES
Ciemat
Centro de Investigaciones Energéticas, Medioambientales y Tecnológicas

Source Term

#ID	Ex-vessel scenario	Phenomena
ST-3	Steam condensation conditions	FP transport onto surfaces under condensing conditions (non-soluble)
ST-4	FP in sumps	Gas mass-transfer at gas/water surfaces and in liquid films
ST-5	FP in CNT with organics	Iodine reactions with organics other than paints
ST-6	FCVS operation	Gaseous and particulate FP retention by FCVS
ST-7	Non-hermetic CNT	Liquid release via cracks and leakage paths

04

Main Insights

Main Insights

- 20 phenomena out of almost 400 identified, ranked high.
- PIRT is far from being an infallible tool in SA.
- Awareness of PIRT limitations, strengthens its usefulness.
- Next SEAKNOT step: **A SA research roadmap!**

Thank you for your attention!

Unit of Nuclear Safety Research
Department of Nuclear Fission
CIEMAT
luisen.herranz@ciemat.es

MORE THAN TWO DECADES OF ACTIVITIES ON SEVERE ACCIDENT MANAGEMENT GUIDELINES (SAMGs) IN TECNATOM AND WESTINGHOUSE

Tanarro Onrubia, Agustin
Tecnatom / Westinghouse
agustin.tanarroonrubia@westinghouse.com

Giner Gonzalez, Amparo
Westinghouse
amparo.ginergonzalez@westinghouse.com

ABSTRACT

The Severe Accident Management Guidelines (SAMGs) provide guidance to operators and designated support staff for use if accident conditions progress beyond the prevention capabilities described in Emergency Operating Procedures (EOPs).

SAMGs are designed to fill the void beyond the EOPs with respect to formalized guidance for responding to an accident which progresses beyond limited core or spent fuel overheating due to inadequate core cooling (i.e., a Severe Accident). These guidelines employ strategies intended to arrest the progression of fuel damage, maintain the capability of the containment as long as possible, and minimize radiological releases.

For more than two decades, Tecnatom, currently owned by Westinghouse, has continued to carry out different activities associated with SAMGs for the Spanish Westinghouse design Nuclear Power Plants (NPPs).

With the integration of Tecnatom into Westinghouse in November 2023, the merged company's capabilities and field of action have increased with the contribution of Westinghouse experts in the development and maintenance of the generic PWROG SAMGs and access to related projects in other countries.

This paper presents the above activities in Tecnatom and Westinghouse, with special attention to those associated with the development, validation and implementation of plant-specific SAMGs.

KEYWORDS

Severe Accident Management Guidelines, PWR

1. INTRODUCTION

Since 2001, in a close collaboration with the engineering and operation staff of Spanish Westinghouse design Almaraz, Ascó and Vandellós NPPs, Tecnatom has participated in the development and validation of the specific SAMGs for these plants, based on the generic guidelines of the owners' group of the technology supplier, Westinghouse Owners' Group (WOG), currently PWR Owners' Group, (PWROG).

Following the integration of Tecnatom into Westinghouse, the company scope of action in the SAMGs field has extended to other countries with the currently underway development of the plant specific SAMGs for Framatome design Koeberg NPP in South Africa.

Other activities associated with the Severe Accident Management (SAM) carried out at Tecnatom include:

- The design of training plans and delivery of courses on phenomenology and management of severe accidents for operation crews and Emergency Response Organization (ERO) personnel in Spanish NPPs and abroad (United Arab Emirates, China, etc.)
- The development of Technical Support Center (TSC) computer aiding tools for using SAMGs in real or simulated severe accident scenarios.
- The implementation of severe accident codes (MAAP) into Full Scope Replica Simulators (Laguna Verde NPP, Mexico) and Interactive Graphic Simulators (Almaraz NPP, Spain)
- The development of severe accident simulation tools based on IA surrogate models. The company is currently involved in the ASSAS (Artificial intelligence for Simulation of Severe Accidents) European Union project, which is presented in another paper within this meeting.

2. HISTORY OF THE DEVELOPMENT OF THE WOG/PWROG GENERIC SAMGs

The Three Mile Island accident in 1979 showed that, although highly unlikely, accidents seriously affecting the fuel in the core or Spent Fuel Pool of a NPP can have very serious consequences for the plant itself and its surroundings.

Consequently, the need arose to broaden the objectives of nuclear safety, which until then had been basically focused on preventing such accidents, to provide plants with the means to mitigate their consequences in the event of a severe accident, including equipment and organisational and procedural frameworks designed for this purpose.

As a result, the so-called Severe Accident Management Guidelines (SAMG) were developed to cover the void beyond the Emergency Operating Procedures (EOPs) for operating staffs by adopting the existing safety systems and technical support under severe accident conditions. It was expected that the SAMG can extend significantly the Defence in Depth (DiD) concept providing strategies to mitigate the consequences of severe accidents.

In 1992, the Electric Power Research Institute (EPRI) published the Severe Accident Management Guidance Technical Basis Report (TBR) (References 1 and 2) which included an extensive description of severe accident involved phenomena and identified Candidate High-Level Actions (CHLA) based on the analysis of accident scenarios.

These actions and technical information became the cornerstone of generic SAMGs for Light Water Reactors (LWRs). In line with the design features of the different LWRs owner groups, generic SAMGs were developed by the owner groups by adapting the suggested CHLAs in the EPRI TBR report. This set of generic guidelines were used afterwards by individual plants as the basis for their plant specific SAMGs.

The WOG SAMG is a well-known generic SAMGs set which, through their several revisions, has been widely applied to Westinghouse design PWRs, and adapted also to other PWR designs including VVER and CANDU reactors. It encompasses guidelines for operators in the Main Control Room (MCR), and diagnostic tools and guidelines for the Technical Support Center (TSC).

While the MCR is responsible for EOPs, the TSC would be in charge of identifying the plant damage states and direct actions to MCR staffs during SAM. This means that the operational authority shifts from MCR to TSC with the transition from EOPs to SAMGs.

The initial **WOG SAMG Revision 0** (Reference 3), published in 1994, was intended to provide an initial generic basis for individual Westinghouse PWR plant owners to develop a first guide specific to their plants, based on a structured decision-making process and use of stepwise structured guidelines and flowcharts. This approach minimised training requirements and provided a tool for mitigating the consequences of the severe accident under potentially high stress conditions

The components of the WOG SAMG Revision 0 are shown in Figure 1

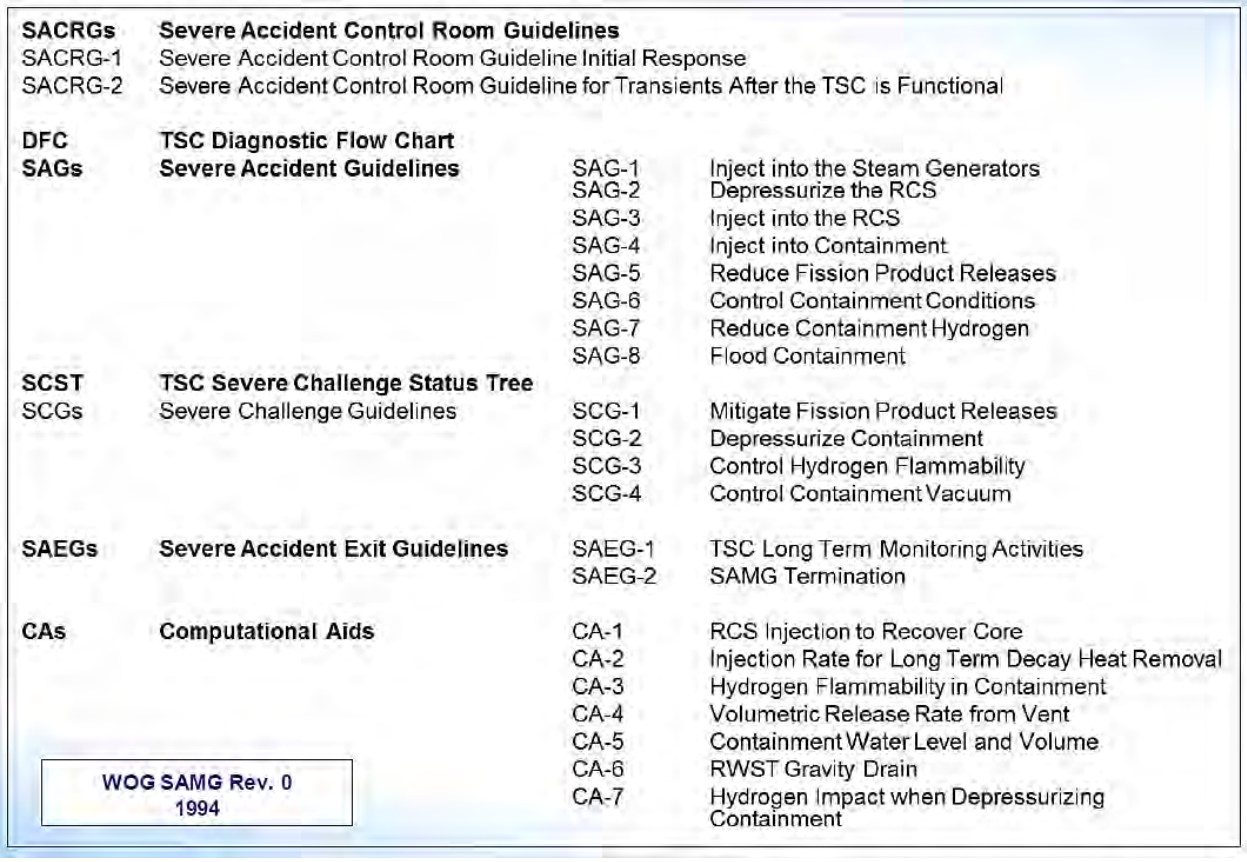

Figure 1: WOG SAMG Rev.0 Components

Revisions to the generic guidance were performed when improvements were made to the understanding of severe accident phenomena, plant modifications were introduced to facilitate mitigation of severe accidents, and lessons were learned from implementation and performance of drills and exercises.

In this way, the generic **WOG SAMG Revision 1** (Reference 4), published in 2001, incorporated significant improvements to the SAMGs, arising from several years of experience in training, validation and exercises on the specific guidelines of the different plants.

The Fukushima Daiichi Nuclear Power Plant (NPP) accident, that took place on 11 March 2011, initiated a significant number of activities at the international level to reassess the safety of existing NPPs, evaluate the sufficiency of technical means and administrative measures available for emergency response, and develop recommendations for increasing the robustness of NPPs to withstand extreme External Events (EE) and Beyond Design Basis Accidents (BDBA).

One of the lessons learned from the Fukushima Daiichi NPP accident was that the scope of SAM needed to be extended to consider important aspects as: plant shutdown conditions, multi-unit events, loss of instrumentation and control, long-duration events, accidents initiated in spent fuel pools, devastated site and surrounding conditions, harsh environments and widespread contamination.

In addition. critical for the successful implementation of the strategies during an emergency is to ensure appropriate training of responders on the procedures and guidelines to be followed.

The EPRI TBR report was also updated in 2012 (References 5 and 6), not only accounting for the initial lessons learned from the Fukushima accident, but also reflecting the enhanced understanding of severe accident behaviour gained from research and analyses conducted in the 20 years after the publication of the original report.

Generic **WOG SAMG Revision 2** (Reference 7) was issued for implementation in February 2013, following the Fukushima accident. This revision was intended to address short term post-Fukushima modifications to the SAMGs, addressing specific issues raised by the revised TBR.

In Europe and other countries outside the US, WOG type SAMGs have been used as the basis for plant specific SAMGs in many Westinghouse PWRs (eg Beznau, Ringhals, Asco, Vandellos, Almaraz, Tihange and others), at Framatome/AREVA plants (eg Koeberg), at Siemens/AREVA plants (eg Borssele) and in VVER reactors in Central Europe (Bohunice, Mochovce, Temelin, Dukovany).

However, the approach to systems upgrades for the mitigation of severe accidents has been different in the US and Europe (Reference 16), with European plants generally opting to backfit mitigation systems such as Hydrogen Passive Autocatalytic Recombiners (PAR) and Filtered Containment Venting Systems (FCVS). In addition, certain issues such as severe accidents occurring from shutdown initial condition have always received more attention in Europe than in the US. This has led to specific needs for international plants implementing SAMGs which were originally developed in the US.

To address some of these issues, in 2012-2013, a European PWROG project **PA-PSC-1081** (Reference 8) was performed This project addressed several issues and updates to guidance for the systems upgrades and backfits that were implemented across the industry to enhance severe accident mitigation capabilities. It also addressed severe accidents occurring from initial shutdown states. Main items accounted for by this project and addressed in several WENX documents (References 8.1 to 8.7). included:

- Passive Autocatalytic Recombiner (PAR) hydrogen control systems
- Filtered Containment Venting Systems (FCVS)
- Plants without containment hydrogen monitoring system,
- Guideline for a severe accident combined with loss of all DC power and instrumentation
- Shutdown initial plant condition
- Simultaneous severe accidents in multiple units at a single site

Other owners' groups of PWRs in the US have also developed generic SAMGs with considerations of their reactor designs, including the Combustion Engineering Owners' Group SAMG (CEOG SAMG), Babcock & Wilcox Owners' Group SAMG (B&WOG SAMG).

Since 2013 a consolidated PWROG SAMG project **PA-PSC-0932** was developed by combining the SAMG approaches with operating experiences of WOG, CEOG and B&WOG. The main framework of the consolidated PWROG SAMG was based on the WOG approach and enhanced and adapted to new insights, including lessons learned from the Fukushima accident, feedback from exercises/drills, human factors, and benefits from other SAMG approaches.

As a result, in February 2016 the official revision of the generic **PWROG-15015-P Revision 0** SAMGs (Reference 9), applicable to Westinghouse, Babcock & Wilcox and Combustion Engineering design PWRs, was issued. This revision included very significant changes in the structure and rules of use of the generic SAMGs, to the point of considering it the beginning of a new line of development of the guidelines and therefore designating it as Revision 0.

The basic structure and components of the PWROG consolidated SAMG are shown in Figure 2.

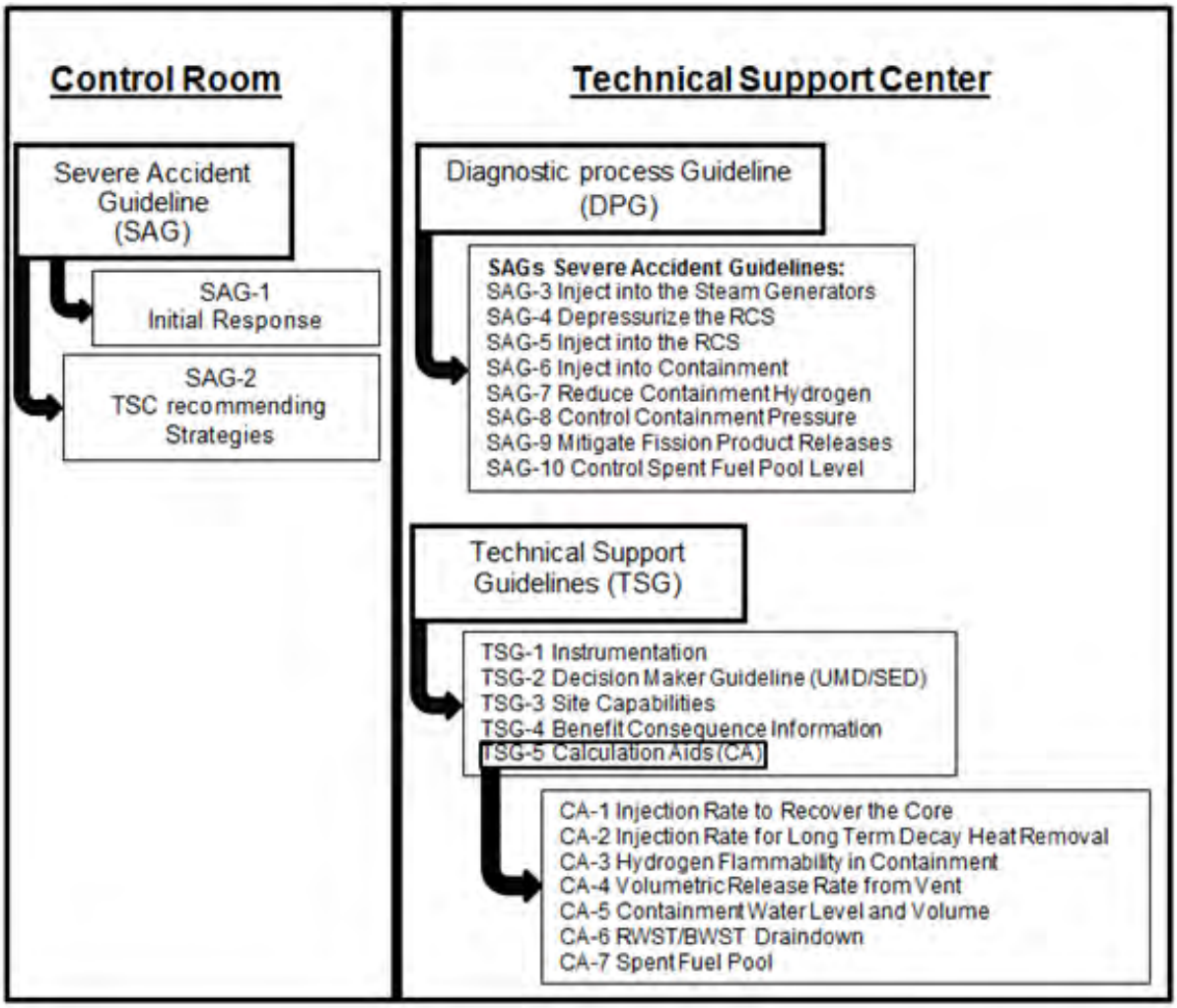

Figure 2: Main Components of the PWROG SAMG

The main new features of this review were

- New set of guidelines:
  - 2 Control Room Guides (SAG-1 and SAG-2) replace SACRG-1 and SACRG-2.
  - Diagnostic Process Guideline (DPG) replaces the DFC and SCST of previous versions and identify, by means of a colour code, the priority for the implementation of the guidelines based on two criteria: the severity of the threat to the specific barrier associated to each guide and the expected chronology of these threats.
  - 8 Technical Support Center guides (SAG-3 to SAG-10) replace previous versions of SAGs and SCGs.
  - 5 Technical Support Guides (TSGs).

- New structure of the TSC guidelines to increase the level of proceduralizing by means of a pre-established selection of the strategy to be implemented based on the existing conditions (positive and negative impacts associated with the existing conditions are implicitly considered in the guidelines). With this structure the TSC 'decision-making' burden associated to the assessment of positive and negative impacts is greatly reduced.
- Supplemental Base Information on Left Page (TSC guidelines).
- Introduction of 'Priority Actions' in Control Room SAG-1.
- Independent management for accidents affecting only fuel in the Spent Fuel Pool (SFP).

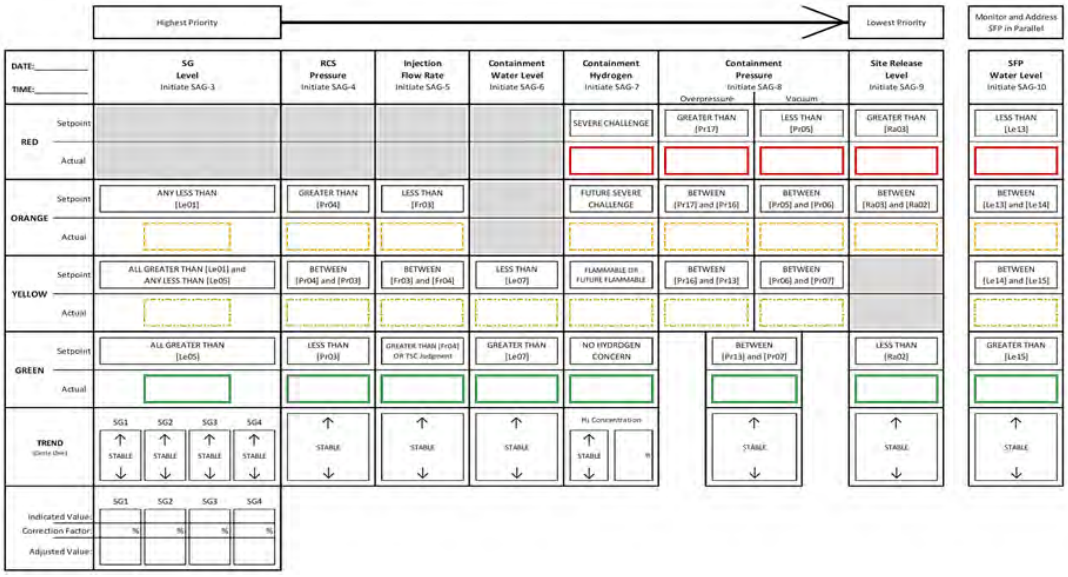

Figure 3 Diagnostic Process Guideline (DPG) Parameter Sheet

The differences between the US and European approaches can have a major impact on SAMGs and have meant that developing and maintaining plant specific SAMGs based on US generic reference guidelines has become more and more complex for European plants. While the international PWROG project PSC-1081 described above addressed many of these differences, it did not produce a new dedicated set of generic guidelines for plants with additional severe accident mitigation features.

To address this, in December 2016, under project **PSC-1413**, a new PWROG generic SAMGs **PWROG-16059-P, Revision 0** (Reference 9) was issued specifically for international plants, based on a reference plant design typical in Europe (with large dry containment, PARs, filtered vent, etc), and taking into account the Revision 1 and 2 changes to the initial WOG SAMG Revision 0, the changes from project PSC-1081, and also certain selected features of the revised consolidated PWROG-15015-P Revision 0 SAMGs developed for the US plants under project PSC-0932 (e.g., the Diagnostic Process Guideline, DPG).

However, to minimize changes and reduce training and SAMG writing burden, some aspects of the original WOG SAMG Revision 2 were retained, maintaining the content and format of the Severe Accident Guidelines (SAGs) and Severe Challenge Guidelines (SCGs) (though they will be called from the new DPG), Computational Aids (CAs) and Severe Accident Control Room Guidelines (SACRGs) (though modified) for control room use

Finally, in March 2021, under **PA-PSC-1844** project (Reference 9), the PWROG initiated an effort to integrate an International Reference Plant (IRP) design into the Generic PWROG-15015-P SAMGs for US

plants. The resulting generic SAMG revision will increase access to the latest PWROG SAMG features for additional PWROG member plant designs with PARs and FCVS and will address severe accidents arising from shutdown initial conditions.

Although several features from PWROG-15015-P such as the Diagnostic Process Guideline (DPG) were already added to PWROG-16059-P, some beneficial features were not added, including the new structure of the TSC guidelines to increase the level of proceduralizing by means of a pre-established selection of the strategy to be implemented based on the existing conditions.

Combining to a single PWROG SAMG volume, applicable to all members, will increase efficiencies in the generic SAMG maintenance program. Moving to a consistent format will also help with regulatory inquires or other questions related to SAMG differences between international member SAMGs and the generic PWROG SAMG. A multidisciplinary team undertook the effort to update and verify every PWROG SAMG guideline, basis document and computational aid impacted by the IRP addition.

A preliminary version of the PWROG-15015-P SAMGs with the changes approved prior to January 1, 2022 to integrate the IRP features has been developed in 2024 with the name **PWROG-15015-P Revision 0-Plus**. A validation of the SAMG changes for the IRP design was completed and is documented in PWROG-23003-P (Reference 13).

The official updated revision will be referred to as **PWROG SAMG Revision 1**, and is scheduled to be published in April 2028.

A general scheme of the WOG/PWROG SAMGs history is given in Figure 4

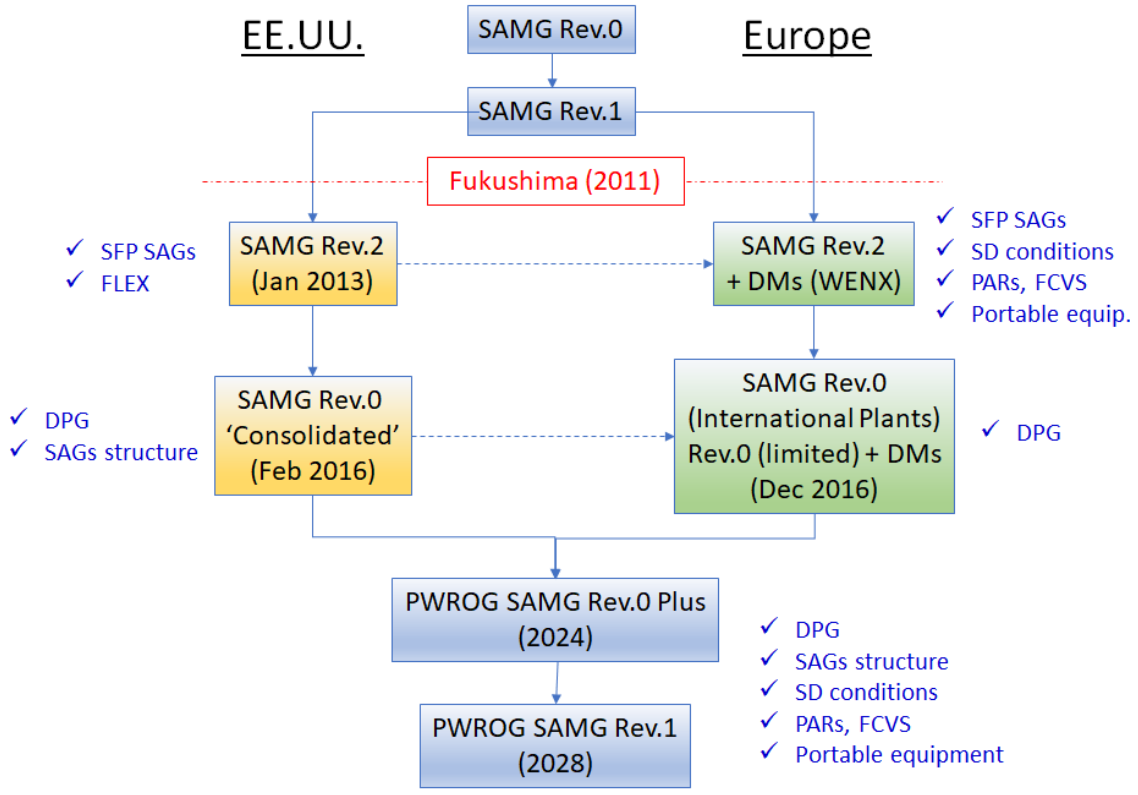

Figure 4 WOG/PWROG generic SAMGs history

3. SPANISH WESTINGHOUSE DESIGN NPPs SPECIFIC PLANT SAMGs DEVELOPMENT

Since 2001, in close collaboration with the engineering departments of the Spanish PWR Westinghouse design Almaraz, Ascó and Vandellós NPPs, Tecnatom has developed the successive revisions of the plant-specific SAMGs, with the generic guidelines of the owner groups (WOG/PWROG), as references. Tecnatom tasks in these developments also included the validation of the specific guidelines and the training of the involved plant personnel.

The initial development of the plant specific SAMGs of Almaraz, Ascó and Vandellós NPPs was developed in 2001, taking as a reference the generic WOG SAMGs Revision 0 (Reference 3). Therefore, the components and structure of these plant specific SAMGs are the same than that of the generic reference shown in Figure 1 above.

In 2011, Revision 1 of the plants-specific SAMGs was approved based on the generic WOG SAMG Revision 1 (Reference 4).

In 2016, Revision 2 of the plant-specific SAMGs, based on the generic WOG SAMG Revision 2 (Reference 7) was approved, which was a major update to the plant-specific SAMGs in the wake of the lessons learned from the Fukushima accident. Thus, the main modifications implemented were the introduction of strategies based on the use of portable equipment and the incorporation of two additional guidelines (SAG-9 and SCG-5) for the mitigation of accidents with damage to the fuel stored in spent fuel pools.

However, as noted, Revision 2 of the generic reference SAMGs did not consider the additional severe accident mitigation capabilities introduced in many plants outside the United States through certain design modifications, in particular:

- Hydrogen Passive Autocatalytic Recombiners (PAR).
- Filtered Containment Venting Systems (FCVS).
- Direct Reactor Cavity Injection capability (only implemented in Ascó and Vandellós NPPs).

Therefore, during 2015 and 2016, the Spanish Westinghouse design NPPs implemented strategies to take advantage of these capabilities in their plant specific guides by applying the basic generic guidelines generated in the European PWROG project PA-PSC-1081 (Reference 8), to extend the scope of the guides to accidents initiated at shutdown conditions and implement the post-Fukushima design modifications introduced in the plants, generating Revision 2A of the SAMGs.

Subsequently, Ascó and Vandellós NPPs plants contracted Tecnatom again to develop a new revision of their plant-specific SAMGs based on the generic PWROG-15015-P, Revision 0 for US plants (Reference 9). The components and structure of these plant specific SAMGs are the same than that of the generic reference shown in Figure 2 above.

Among the most relevant changes, the new Revision 0 includes a new TSC diagnostic tool, the Diagnostic Process Guideline (DPG), which replaces the diagnostic trees (Diagnostic Flowchart, DFC, and Severe Challenge Status Tree, SCST) of the previous revisions. The DPG introduces a new scheme to diagnose the level of threats to the different fission product barriers based on the ranges of selected basic parameters associated to these threats. Such ranges are represented by a colour code that allows to establish the priority of the guidelines to be implemented by the TSC at all times.

By replacing the DFC and SCST diagnostic trees from previous revisions, the two groups of TSC guidelines for potential damage (SAGs) or severe challenges (SCGs) to which diagnostic these trees directed have also been unified into a single group of Severe Accident Guides (SAG) to which the DPG directs.

In this latest revision, the structure of the TSC guidelines themselves was also substantially modified in order to increase their 'proceduralisation', reducing the demand for decision-making by the TSC to select the strategies to be implemented based on their positive effects and potential negative impacts. To this end, in the development of the guidelines, the positive and negative impacts of the available strategies based on the existing conditions were already implicitly considered, and based on this each guide leads directly to the strategy considered most appropriate for such conditions, exempting the TSC from the need to decide on the strategy to be implemented.

Another important new feature of Spanish W-PWR SAMGs Revision 0 was the incorporation of 5 Technical Support Guides (TSGs) with supporting information, including Calculation Aids to complement the information provided by the instrumentation, or alternative means of measurement in case of loss of instrumentation or uncertainties about the reliability of their readings.

As described in the previous section, the new generic PWROG SAMGs Revision 0 for US plants did not include the strategies associated with the design modifications introduced in European plants, and the PWROG-16059-P Revision 0 issued later for plants outside the US only partially implemented the changes in the structure of the guidelines to provide them with a greater proceduralization.

Consequently, the Spanish Westinghouse design NPPs decided to include into their plant specific SAMGs, currently in force, all the changes in the structure and use of the generic PWROG SAMGs Revision 0 for US plants, and to an undertake additional developments to introduce the strategies associated with the design modifications implemented in the plants. Asco and Vandellós plants once again entrusted this development to Tecnatom.

Figure 5 represents the development of the plant specific SAMGs for the Spanish Westinghouse design NPPs.

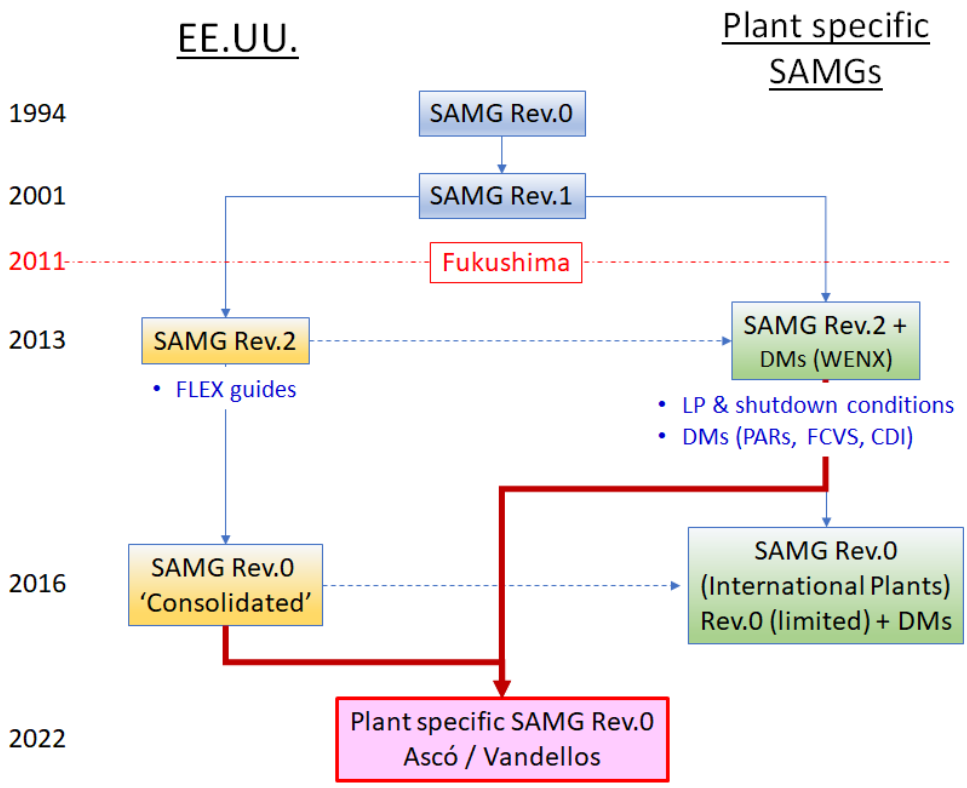

Figure 5 Spanish W-PWR plant specific SAMGs development

Prior to the approval and entry into force of the new plant specific SAMGs, training programs were carried out for all personnel involved in their use, both the MCR operation crews and all the TSC groups, including exercises on their use in postulated scenarios.

Finally, the approval and implementation of the new plant specific SAMGs required their prior verification and validation process, in accordance with the requirements of the IS-36 Safety Instruction of the Nuclear Safety Council (CSN, Spanish Regulatory Body) (Reference 15) and following the indications of the plants Severe Accident Management Guidelines (PG-SAMG) Generation Plans. The validation consisted of tabletop exercises on postulated severe accident scenarios in order to verify the ability for the correct use of the SAMGs by the personnel involved in the management of severe accidents in the plant, especially the TSC teams and MCR operation crews, evaluating the ease of reading, the consistency and homogeneity of the guides and the identification of the information.

4. KOEBERG NPP (SOUTH AFRICA) SPECIFIC PLANT SAMGs DEVELOPMENT

Subsequent to the Fukushima Daiichi NPP accident in 2011, the South African National Nuclear Regulator (NNR) directed Koeberg Nuclear Power Station (KNPS) to perform an External Events Safety Re-assessment to identify vulnerabilities and to devise likely modification measures, and technical features required to enable the plant to mitigate the consequences of an extreme External Event (EE).

To comply with NNR's requirements, Eskom (Koeberg NPP utility) developed an extensive review of the existing accident procedures, and identified plant vulnerabilities which were required to be addressed. These vulnerabilities included shortcomings in the existing KNPS procedures and guidance to cope with Beyond-Design Basis Accidents (BDBA) and External Events (EE).

In November 2024, Eskom and Westinghouse signed a contract for the development of a project to resolve the vulnerabilities detected in the Koeberg NPP procedures. The project scope covered a wide range of procedures enhancements to ensure that the plant is adequately covered to provide guidance on how to deal with an Extended Loss of Alternating Current Power (ELAP), respond in the event of an external hazard and manage severe accidents.

The project, currently under development, is divided into four Work Packages (WPs) that will cover the required procedures and document updates and developments. Westinghouse provides the qualified and competent resources to support the scope of all four WPs.

In particular, WP4, “Updates to the Severe Accident Management Guidelines (SAMGs)”, consists in the revision and adaptation of the SAMGs currently in force in Koeberg to the structure and contents of the generic PWROG-15015-P Revision 0-Plus SAMGs (Reference 12).

A post-Fukushima update of the generic WOG SAMG Revision 2 (Reference 7) on which the current Koeberg-specific SAMG are based, was released in 2013. This followed the 2012 revision of the EPRI Technical Basis Report (References 5 and 6), which forms the technical basis of the WOG/PWROG generic SAMGs.

Koeberg specific SAMGs were reviewed and updated against this released generic SAMGs, and related background documents were generated. The purpose of these updates was to keep the Koeberg SAMG aligned with international best practices. These updates are in addition to an earlier 2012 update of the Koeberg-specific SAMG that followed an internal Eskom post-Fukushima review.

The base scope of the ongoing project will develop an updated set of plant specific SAMGs in compliance with generic PWROG-15015-P Revision 0-Plus (Reference 12). As explained above, this update to the original PWROG-15015-P, Revision 0 (Reference 9) includes all the features of PWROG-16059-P, Revision 0 (Reference 10) which were developed for an “International Reference Plant”. It is now the single

reference PWROG generic SAMG and will become the PWROG supported version (for example for generic maintenance).

To develop the final plant-specific SAMGs for Koeberg Units 1 and 2, the first step was to collect the applicable plant data

- Current version of the Koeberg Plant-Specific SAMGs, Setpoints & CAs
- Plant Design features
- Instrumentation information
- Spent Fuel Pool characteristics
- Details of Instrumentation for Key SAMG Parameters
- Details of plant equipment and mitigating system resources

In parallel with these data package development a process to systematically identify plant changes has been required due to Koeberg specific design features.

In January 2026, the Revision 0-A draft of the new Koeberg specific guidelines has been delivered for Eskom comments and feedback. In Table I, the relation between current Koeberg and Rev 0-A SAMGs are shown.

Once Eskom's comments are analysed and discussed, the resulting modifications will be incorporated to generate Revision 0-B, which will also be sent to Eskom for further comments. The modifications resulting from the analysis of this new feedback will be incorporated into the Revision 0-B to generate the Revision 0-C on which the verification and validation processes will be carried out.

Finally, after implementing the modifications resulting from the validation, Revision 0 will be generated and must be approved by Eskom and the Regulatory Body.

Following the approval of the new Koeberg specific SAMGs Revision 0 and prior to their entry into force, Westinghouse will conduct an initial training process for personnel involved in their use, including MCR operation and TSC personnel.

The project is scheduled to close by the end of 2027.

Prior to this project, Westinghouse has participated in other development projects or post-Fukushima updating of plant specific SAMGs taking as reference the generic PWROG SAMGs in other plants, such as Ringhals (Sweden) or Sizewell B (UK) NPPs.

In addition, Westinghouse actively participates from its formation in PWROG activities for the development and maintenance of both the generic Emergency Response Guidelines (ERGs), basis of the plant-specific EOPs, and the generic SAMGs, reference of the plant-specific guidelines.

Table I: Current Koeberg and Rev 0-A specific SAMGs

PWROG 15015-P Rev.0 Plus SAMGs			Current Koeberg SAMGs		
TSC Diagnostic Tool	DPG	Diagnostic Process Guideline	DFC	Diagnostic Flow Chart	TSC Diagnostic Tools
			SCST	Severe Challenge Status Tree	
			SAEG-1	Long Term Monitoring	TSC Exit Guidelines
			SAEG-2	SAMG Termination	
MCR Guidelines	SAG-0	Loss of DC and/or Instrumentation			
	SAG-1	Initial Response	KWB-SACRP-1	Severe Accident Control Room Procedure - Initial Response	MCR Guidelines
			KWB-SACRP-3	Severe Accident Control Room Procedure - Initial Response for RRA aligned for service	
	SAG-2	TSC Recommending Strategies	KWB-SACRP-2	Severe Accident Control Room Procedure for Transients after TSC is Functional	
TSC Guidelines	SAG-3	Inject Into Steam Generators	SAG 1	Inject into the Steam Generators	TSC Guidelines • Severe Accident Guidelines (SAGs) • Severe Challenge Guidelines (SCGs)
	SAG-4	Depressurize RCS	SAG 2	Depressurize the RCP	
	SAG-5	Inject Into RCS	SAG 3	Inject into the RCP	
	SAG-6	Inject Into Containment	SAG 7	Inject into the Containment	
	SAG-7	Reduce Containment Hydrogen	SAG 6	Reduce Containment Hydrogen	
			SCG 3	Mitigate CCI Concerns	
	SAG-8	Control Containment Pressure	SAG 5	Control Containment Conditions	
			SCG 2	Depressurize Containment	
			SCG 4	Control Containment Vacuum	
	SAG-9	Mitigate Fission Product Release	SAG-4	Reduce Fission Product Releases	
			SCG 1	Mitigate Fission Product Releases	
	SAG-10	Control SFP Level	SAG 8	Mitigate Fuel Building Challenges	
TSC Technical Support Guidelines	TSG-1	Instrumentation			
	TSG-2	Ultimate Decision Maker			
	TSG-3	Site Capabilities			
	TSG-4	Benefit Consequence			
	TSG-5	Computational Aids			
	CA-1	Injection Rate To Recover the Core	CA-1	RCP injection to recover core	Computational Aids
	CA-2	Injection Rate for Long Term Decay Heat Removal	CA-2	Injection rate for long term Decay Heat Removal	
	CA-3	Hydrogen Flammability in Containment	CA-3	Hydrogen flammability in containment	
	CA-4	Volumetric Release Rate from Vent	CA-4	Volumetric release rate from vent	
	CA-5	Containment Water Level	CA-5	Containment water level and volume	
	CA-6	RWST Gravity Drain			
	CA-7	Spent Fuel Pool			
			CA-6	H2 impact on depressurising containment	
			CA-7	Radiation Level as a function of time after shutdown	

5. SEVERE ACCIDENT MANAGEMENT TRAINING ACTIVITIES

Tecnatom and Westinghouse develop training plans and material and teach courses with different scopes on phenomenology and management of severe accidents for, among others, the following objectives:

- Initial training for operation and TSC personnel prior to the entry into force of each revision of the plant-specific SAMGs, including follow-up exercises of the guidelines on predefined scenarios.
- Continuous retraining of operating personnel and TSCs involved in the use of SAMGs, including exercises to follow the guidelines.
- Training in severe accidents and SAMGs for all Emergency Response Organization (ERO) personnel.
- Preparation training for ROs and SROs license examination.
- Preparation of exercises and drills.

6. DEVELOPMENT OF SEVERE ACCIDENT MANAGEMENT AIDING TOOLS

The PROMOCAT application is a computer tool, developed by Tecnatom, and implemented since 2013 at the Vandellós and Ascó power plants, to support the TSC in the overall management of an emergency and provide training during the preparedness phase:

- following and evaluating plant parameters in real time
- allowing source term calculation
- including specific modules for all the different TSC and ERO groups, which incorporates all the necessary actions to be performed during the emergency

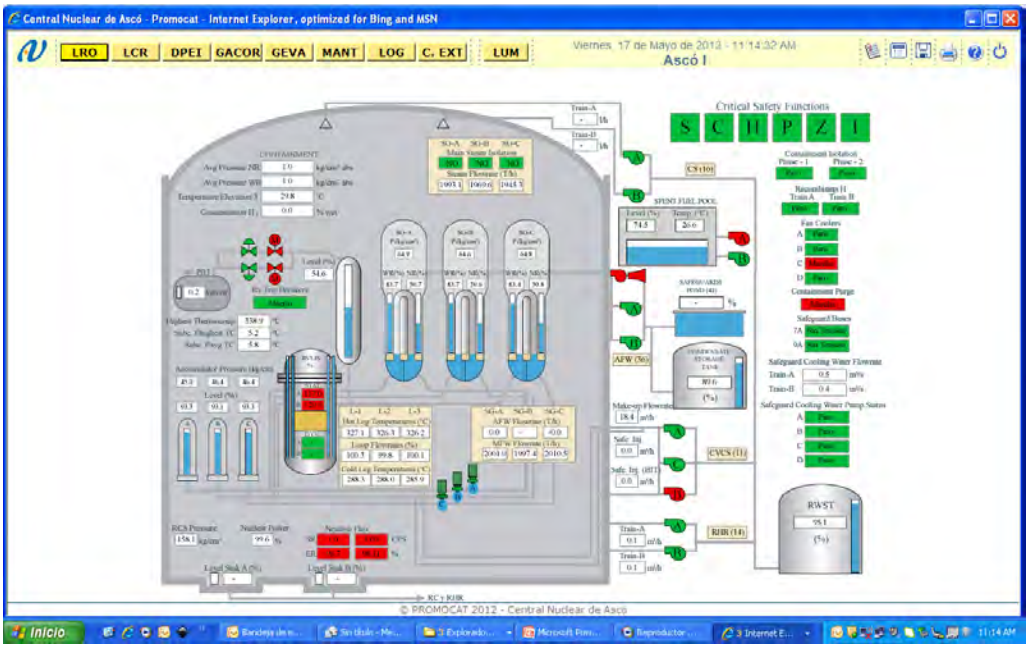

Figure 6. PROMOCAT Operation Screen.

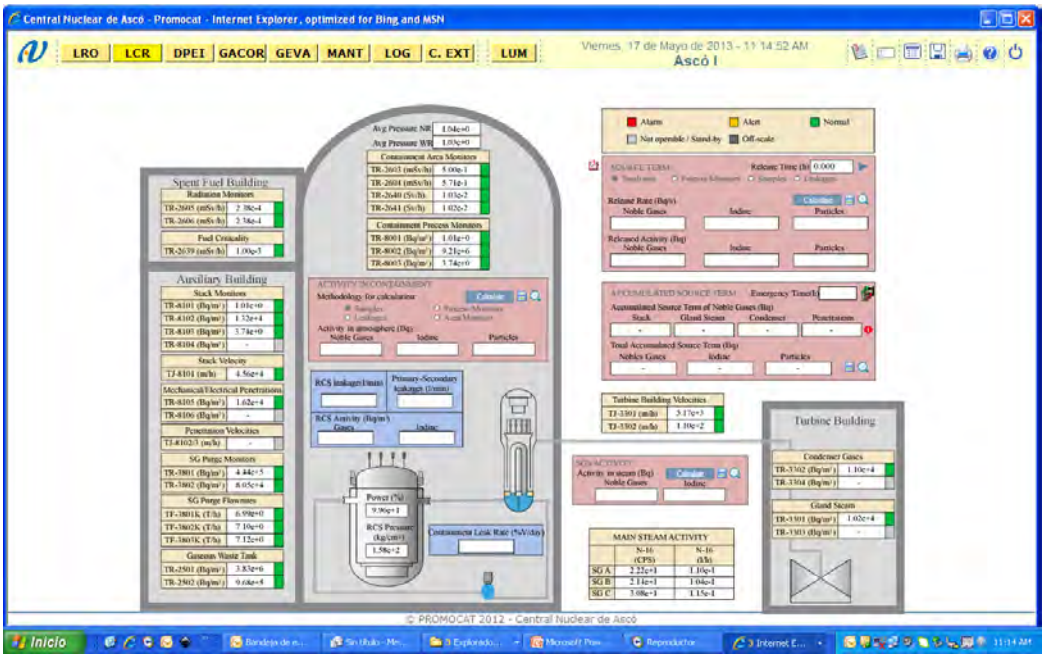

Figure 7. PROMOCAT Radiological Control Group Screen

To this end, it has different screens to help the different TSC groups in carrying out their functions, as well as facilitating the integration of these functions:

- Evaluation Group (Figure 6)
- Radiological Control Group (Figure 7)
- Emergency Director Guide
- Administration Module, that allows the management and administration of the different parameters and process of the Application.
- Historical Module, which gathers all the main actions performed during the Application session.
- Drill Module, that allows running a specific predefine simulation

The PROMOCAT application has two operating modes: REAL and DRILL. Once one of them has been chosen, the way of operation between the modules of the application will be the same, except for the origin of the parameters and variables data in the management of the emergency.

In this way, if the REAL mode is selected, the values of the monitored variables are obtained from the Safety Parameter Display System (SPDS), i.e. from the databank of the parameters measured in the plant. If the DRILL mode is selected, the data will be obtained from an Excel file containing the information of the variables and equipment for different times, which allows its use for exercises and drills.

After the implementation of Vandellós and Ascó specific SAMGs Revision 0, their new structure, based on the DPG made it necessary to modify the PROMOCAT SAMG module in depth.

First phase of the development of the new SAMG module, already implemented in the plants and used in the latest annual drills, provides access to the Revision 0 documents of the plant-specific SAMGs and facilitates the continuous and automatic acquisition of the values of the parameters required by the DPG to determine the level of threat to the barriers against the release of fission products, and consequently, select the priority guide to be implemented at all times depending on the conditions of the plant.

In addition, it provides an estimate of the trends of the values of these parameters, automatically selects the preferable instrumentation from which to obtain the data when there are alternative measurements, allows the automation of certain calculations such as those of correction factors of the levels of the steam generators, allows the manual entry of the values by the user when the instrumentation is lost or is not reliable, facilitates the monitoring of the accident through the ability to graph the parameters and activates the display of certain alarms.

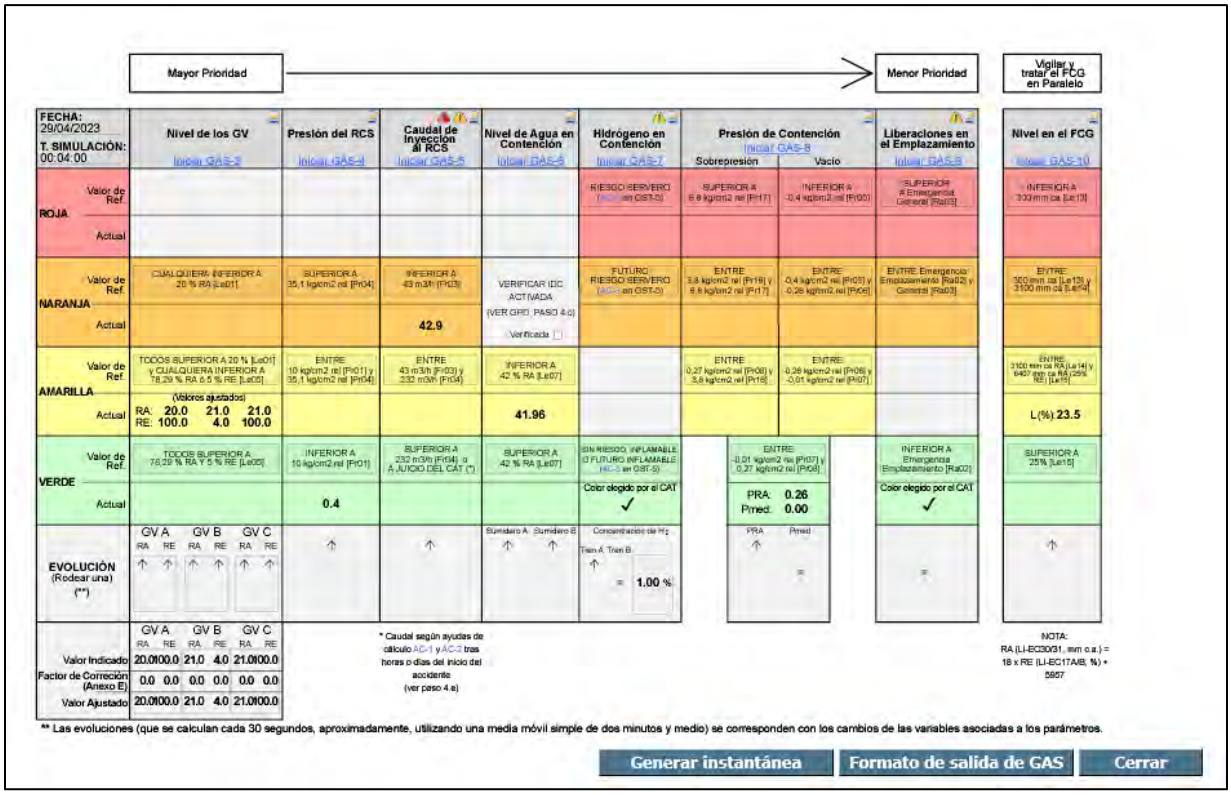

Figure 7. DPG Parameters Sheet screen

7. CONCLUSIONS

Tecnatom, currently integrated in Westinghouse, has played a leading role in the development, revision and updating of the Severe Accident Management Guidelines (SAMG) for the Spanish Nuclear Sector since 2001. In this way, it has accumulated extensive experience and knowledge in the field of phenomenology and management of this type of accidents which, in addition to promoting the continuous improvement of the capacities of the plants for the prevention and mitigation of these through the successive revisions of the specific guidelines, has contributed to advancing in other related developments and activities, such as the training of personnel involved in emergencies and the design and development of support systems for their management and SAMGs use.

Following the integration into Westinghouse, the activities described in relation to Severe Accident Management continue and are expanded internationally.

REFERENCES

1. Severe Accident Management Guidance Technical Basis Report (TBR) Volume 1: Candidate High-Level Actions and Their Effects. Electric Power Research Institute (EPRI), Palo Alto, CA: 1992. 101869.
2. Severe Accident Management Guidance Technical Basis Report (TBR) Volume 2: The Physics of Accident Progression. Electric Power Research Institute (EPRI), Palo Alto, CA: 1992. 101869.
3. WOG SAMG Revision 0, "*Severe Accident Management Guidance*", WOG Program MUHP 2310 (1994).
4. WOG SAMG Revision 1, "*Severe Accident Management Guidance*", WOG Shop Order MUHP 2315 (October 2001).
5. Severe Accident Management Guidance Technical Basis Report (TBR) Volume 1: "*Candidate High-Level Actions and Their Effects*". Electric Power Research Institute, Palo Alto, CA: October 2012. 1025295.
6. Severe Accident Management Guidance Technical Basis Report (TBR) Volume 2: "*The Physics of Accident Progression*". Electric Power Research Institute, Palo Alto, CA: October 2012. 1025295.
7. WOG SAMG Revision 2, "*Severe Accident Management Guidance*", SAMG 2nd Addendum, PWROG PA-PSC-0932 (February 2013)
8. SAMG Update for International Participants, PWROG Project PA-PSC-1081(2013)
    8.1. WENX-12-35, Task 1.1 -Modifications to SAMG for P ARs and Task 1.3 - Modifications to SAMG for Absence of Hydrogen Monitoring
    8.2. WENX-13-10, Task 1.2-Modifications to SAMG for Filtered Containment Vent
    8.3. WENX-13-26, Task 1.4 -Strategies for Loss of all D.C./Instrumentation
    8.4. WENX-13-36, Task 1.5 -Pre- and Post-Vessel Failure Strategies and Vessel Failure Detection Report
    8.5. WENX-13-31, Task 2.1 -SAM at Shutdown -Alternate Entry Condition
    8.6. WENX-13-30, Tasks 2.2 & 2.3 - SAM at Shutdown-Alternate/Additional Actions and Strategies -Generic Diagnostics and Guidelines
    8.7. WENX-13-53, Task 3 - Implications of Multi-Unit Severe Accidents for SAMG
9. PWROG-15015-P, Revision 0, "*PWROG Severe Accident Management Guidelines*", PWROG PA-PSC-0932 (February 2016)
10. PWROG-16059-P, Revision 0, "*Severe Accident Management Guidance for International Plants*". PWROG PA-PSC-1413 (December 2016)
11. PA-PSC-1844, "*Integration of International Reference Plant into Generic PWROG Severe Accident Management Guidelines (SAMG)*" (March 2021)
12. PWROG-15015-P Revision 0-Plus. "*PWROG Severe Accident Management Guidelines*", PWROG PA-PSC-1844 (Rev 0-Plus with SDW-20-007) (2024)
13. PWROG-23003-P, "*PWROG SAMG Validation Report – IRP Design*" (October 2023)
14. "*Accident Management Insights after the Fukushima Daiichi NPP Accident*". Report of the CNRA Task Group on Accident Management. NEA/CNRA/R(2014) (February 2014)

15. Nuclear Safety Council (Spanish Regulatory Body) Instruction IS-36 on emergency operating procedures and the management of severe accidents at nuclear power plants (January 2015)
16. Robert J. Lutz, Jr.; Robert P. Prior. "*Comparison of Fukushima response in the United States and Europe*" (24th International Conference on Nuclear Engineering ICONE24. June 26-30, 2016, Charlotte, North Carolina, USA)
17. Robert P. Prior; A. Henoch. "*PWR Severe Accident Management Guidelines and the Role of the Ultimate Decision Maker*" (October 2015)
18. Jack Stringfellow. "*The PWR Owners Group Role in Fukushima Response". IAEA Technical Meeting on Operational Experience with Implementation of Post-Fukushima Actions in Nuclear Power Plants*" (March 2017)
19. Robert P. Prior. "PWROG Severe Accident Management Guidelines – Development and Status". IAEA Technical Meeting on the Implementation and Integration of Accident Management and Response" (September 2017)
20. Guidelines and Interface with Emergency Preparedness and Response
21. Nan Zhao et al. "*A review of the assessment of severe accident management guidelines and actions through analytical simulations*". Annals of Nuclear Energy. Volume 180, January 2023

12h European Review Meeting on Severe Accident Research (ERMSAR2026)
Madrid, Spain, May 18-22, 2026

MORE THAN TWO DECADES OF ACTIVITIES ON SEVERE ACCIDENT MANAGEMENT GUIDELINES (SAMGs) IN TECNATOM AND WESTINGHOUSE

Agustin Tanarro (Westinghouse)
Amparo Giner (Westinghouse)

Westinghouse

tecnatom

Severe Accidents in NPPs Research and Application

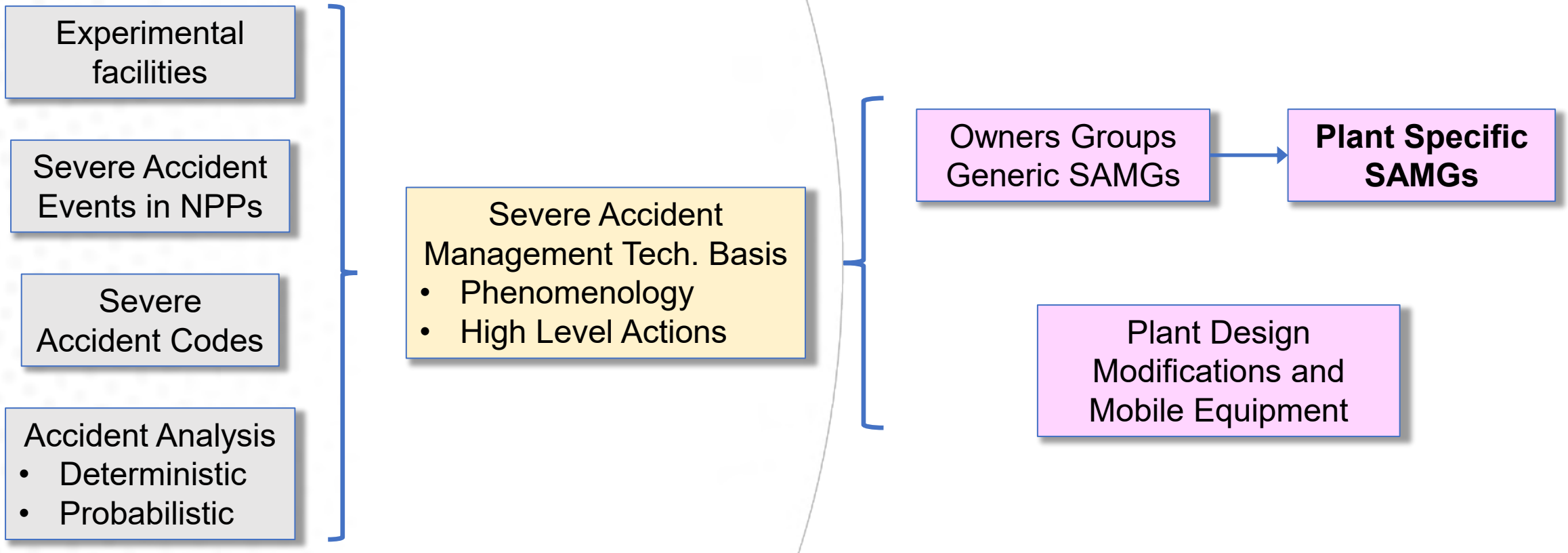

Severe Accident Management Guidelines (SAMGs)

Severe Accident specific (phenomenological / operational) conditions

Very different from those postulated in Design Basis Accidents (DBA) ⇒ analysis of severe accidents requires considering additional involved mechanisms and plant operability conditions:

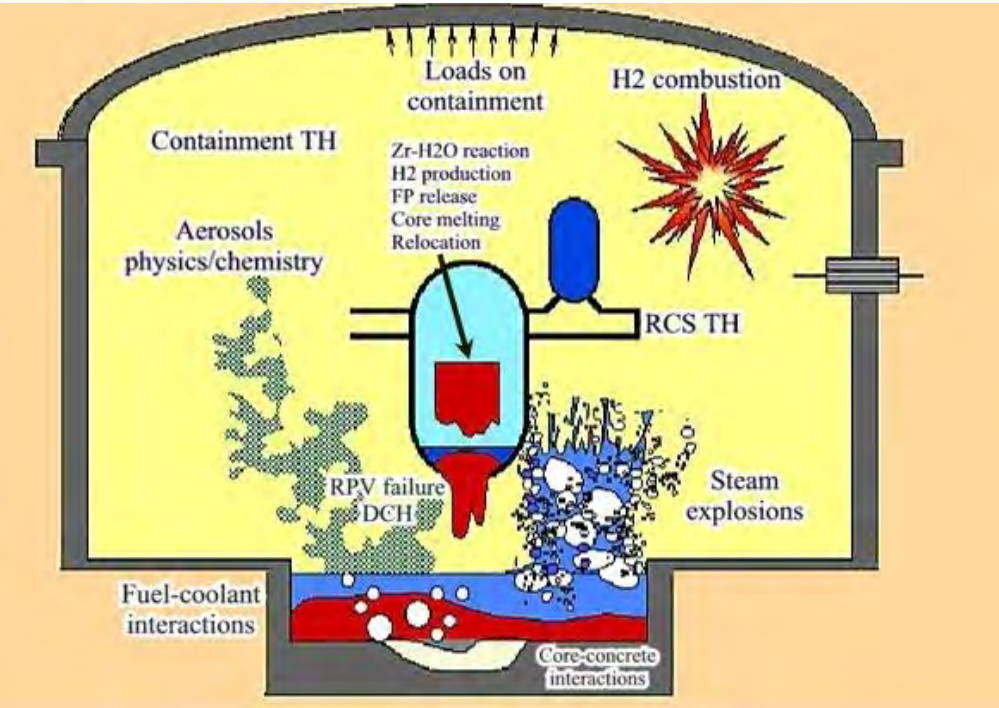

- ✓ chemical reactions at high temperatures
- ✓ additional heat sources
- ✓ geometry changes
- ✓ materials strength and interactions
- ✓ potential radioactive releases to the environment
- ✓ containment conditions and phenomena
- ✓ systems availability
- ✓ alternative systems
- ✓ ……

Severe Accident Management Guidelines (SAMGs)

Severe Accident Management Guidelines (SAMGs) provide guidance to operators and Emergency Response Organization staff for use if accident conditions progress beyond the prevention capabilities described in Emergency Operating Procedures (EOPs).

- SAMGs are needed because responding to a Severe Accident requires new strategies and priorities that are not adequately addressed by other operating procedures
- SAMGs are designed to fill the void beyond the EOPs and other accident response procedures for responding to an accident which progresses beyond limited core or spent fuel overheating due to inadequate core cooling (i.e., a Severe Accident).
- These guidelines employ strategies intended to
  - ✓ arrest the progression of fuel damage
  - ✓ maintain the capability of the containment as long as possible, and
  - ✓ minimize radiological releases

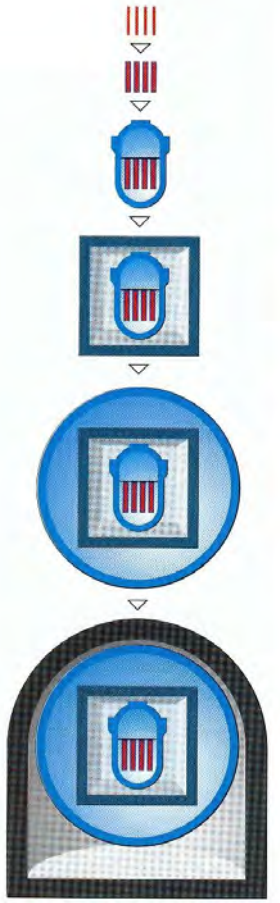

Severe Accident Management Guidelines (SAMGs)

Accident Management (AM) → encompasses those actions and strategies taken during the course of an accident aimed to :

1. Prevent or delay the escalation of the event (DBE) into a severe accident (core damage)	Emergency Operating Procedures (EOPs)
2. Mitigate Severe Accident consequences : • terminating the progress of core damage once it has started and retain the core within the reactor vessel • maintaining containment integrity as long as possible • minimizing on-site/off-site radioactive releases • achieving a long-term safe and stable condition	Severe Accident Management Guidelines (SAMGs)
3. Protect the safety and health of workers and general public	Emergency Plan (EP)

Severe Accident Management Guidelines (SAMGs)

EOPs	SAMGs
• Designed primarily for **Design Basis Accidents**	• Applied when core damage has occurred → provide management strategies for **Severe Accidents**
• Objective : core damage **PREVENTION**	• Objective : core damage consequences **MITIGATION** → to protect remaining fission product boundaries (RCS, containment), arrest severe damage progression and prevent / mitigate / delay radioactivity releases.
• Priority → **maintaining fuel integrity** and restoring core cooling	• Priority → **protecting fission product barriers** and minimizing releases
• Used by the **Control Room (CR) staff**	• Used by the **Control Room (CR) and Technical Support Center (TSC) staff**
• 'Rule based' procedures → no positive and negative effects balance evaluation; **verbatim compliance** required	• 'Knowledge-based' guidelines → identify potential strategies and associated positive/negative effects to support a **decision making process**
• Sympton based	• Sympton based

Development of the WOG/PWROG Generic SAMGs

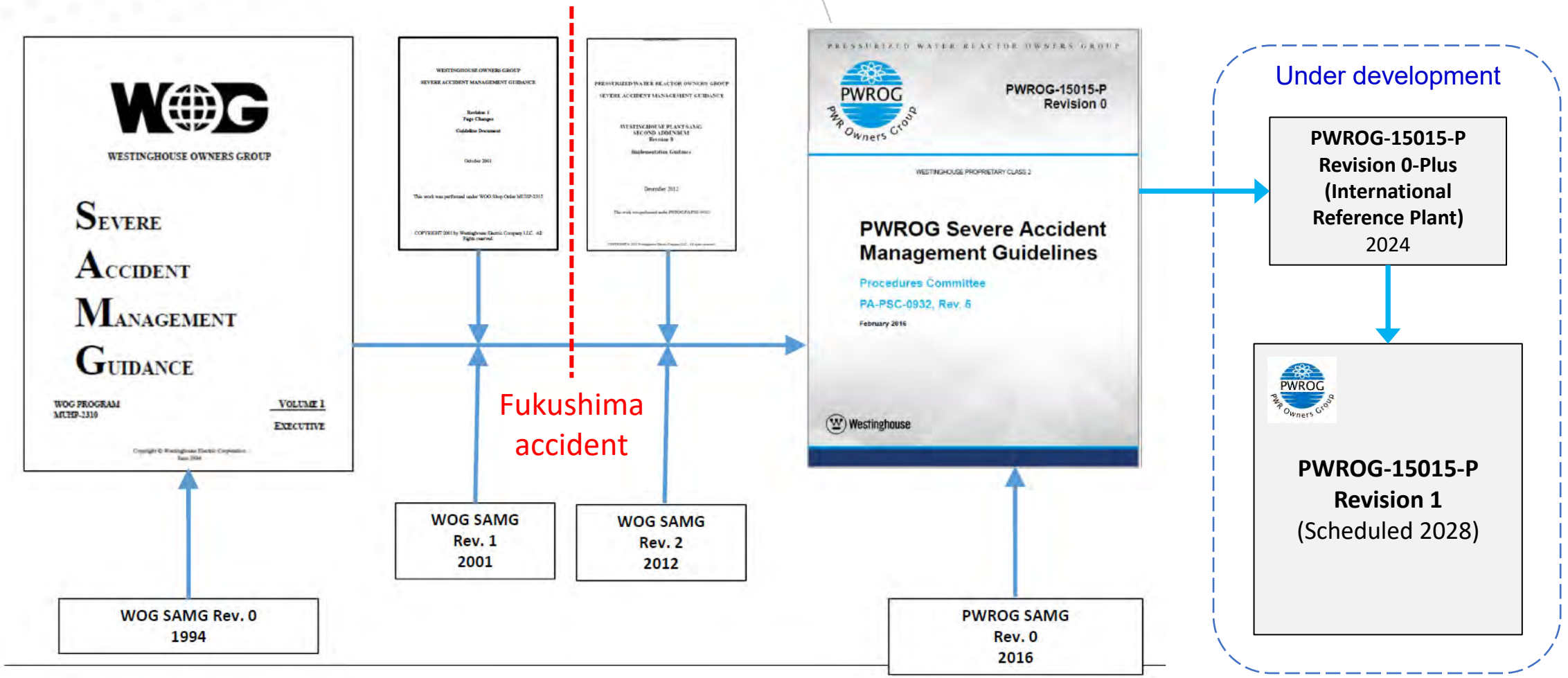

Development of the WOG/PWROG Generic SAMGs

- In March 2021, the PWROG initiated an effort to integrate an International Reference Plant (IRP) design into the generic PWROG-15015-P SAMGs for US plants. The resulting generic SAMGs revision will increase access to the latest PWROG SAMG features for additional PWROG member plant designs with Passive Autocatalytic Recombiners (PARs) and Filtered Containment Venting System (FCVS) and will address severe accidents arising from shutdown initial conditions.
- A preliminary version of the PWROG-15015-P SAMGs with the changes approved prior to January 1, 2022 to integrate the IRP features has been developed and validated in 2024 with the name PWROG-15015-P Revision 0-Plus.
- The official updated revision will be referred to as PWROG SAMG Revision 1 and is scheduled to be published in April 2028.

Development of the WOG/PWROG Generic SAMGs

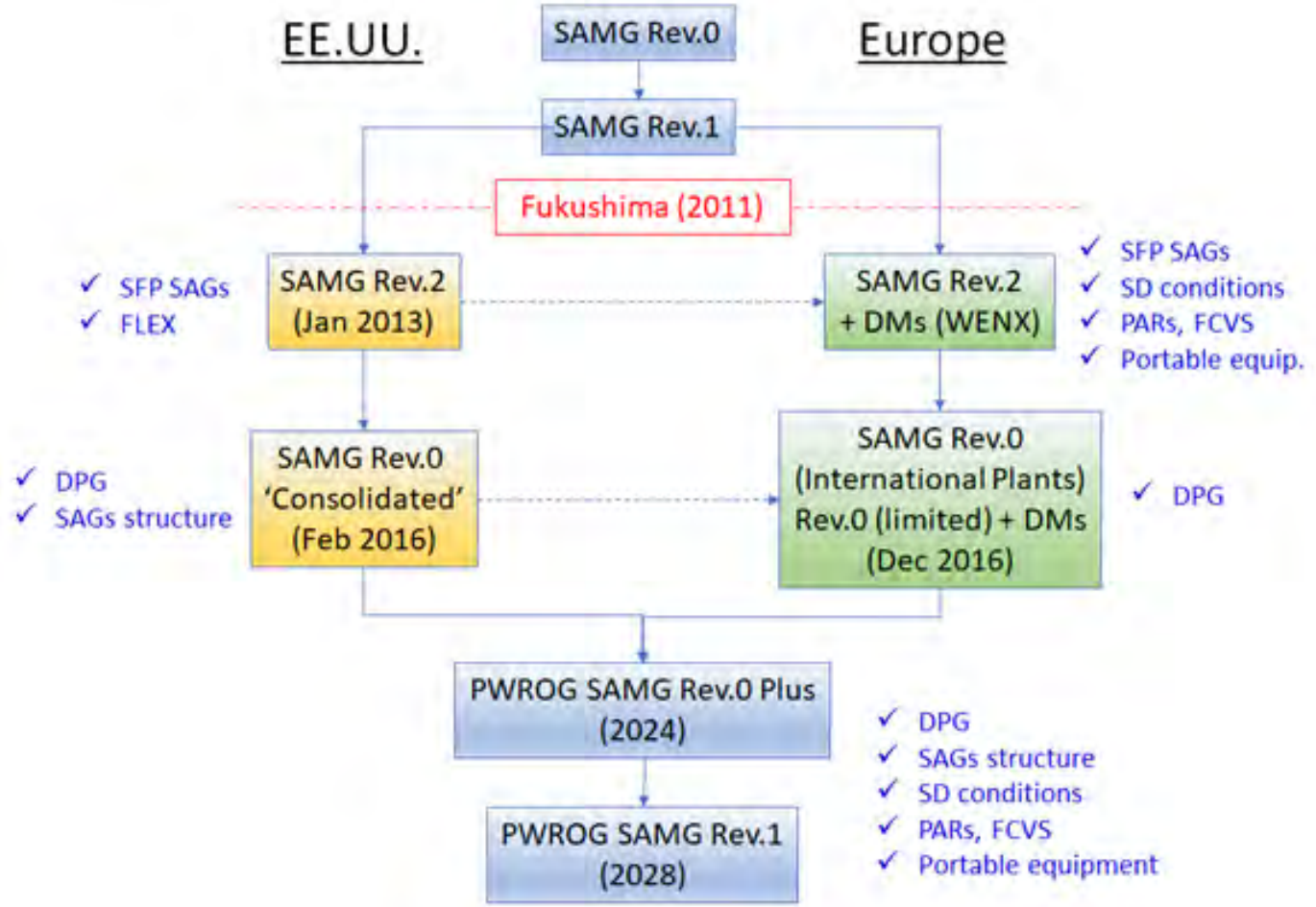

Development of Plant Specific SAMGs

Implementation of the Plant Specific SAMG Programs

- Applicability analysis of the WOG/PWROG generic guides, customization to the specific plant and reference documentation generation, including :
  - plant specific setpoints
  - specific computational aids
  - plant systems performance
  - equipment identification
  - specific alignments
  - instrumentation capacities
  - SAMGs interface with EOPs and E-Plan
- Organizational and procedural changes
- SAMGs Writing, according to “WOG/PWROG Writer Guide” and “EOP Writing Guidelines” and the specific methodology developed in the documentation process.
- SAMGs Verification and Validation → to evaluate standards and criteria to be accomplished. and check the SAMGs ease of use by CR and TSC staff

Tecnatom / Westinghouse activities in SAMGs

- Since 2001, Tecnatom has participated in the development and validation of the specific SAMGs for Almaraz, Ascó and Vandellós Westinghouse design NPPs, based on the different revisions of the generic guidelines of the Westinghouse Owners' Group (WOG), currently PWR Owners' Group, (PWROG).
- Following the integration of Tecnatom into Westinghouse, the scope of action in the SAMGs field has extended to other countries, as the currently underway development of the plant specific SAMGs for Framatome design Koeberg NPP in South Africa.
- Westinghouse has also participated in the development projects or post-Fukushima updating of Ringhals (Sweden) or Sizewell B (UK) specific SAMGs, using the generic PWROG SAMGs as reference,
- In addition, Westinghouse actively participates from its formation in PWROG activities for the development and maintenance of both the generic Emergency Response Guidelines (ERGs), reference of the plant-specific EOPs, and the generic SAMGs, reference of the plant-specific guidelines.

Tecnatom / Westinghouse activities in SAMGs

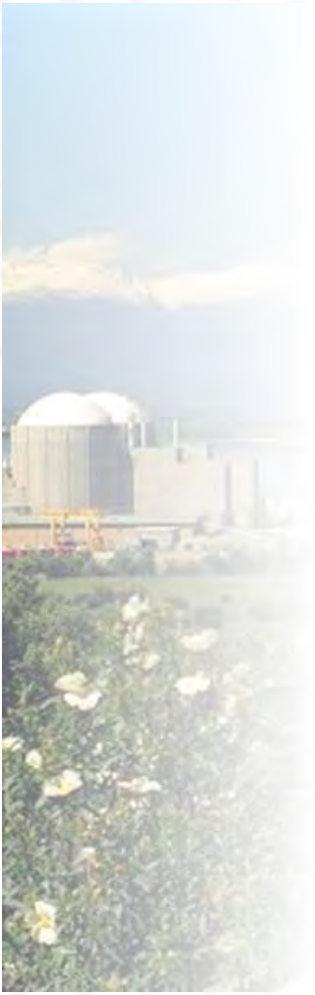

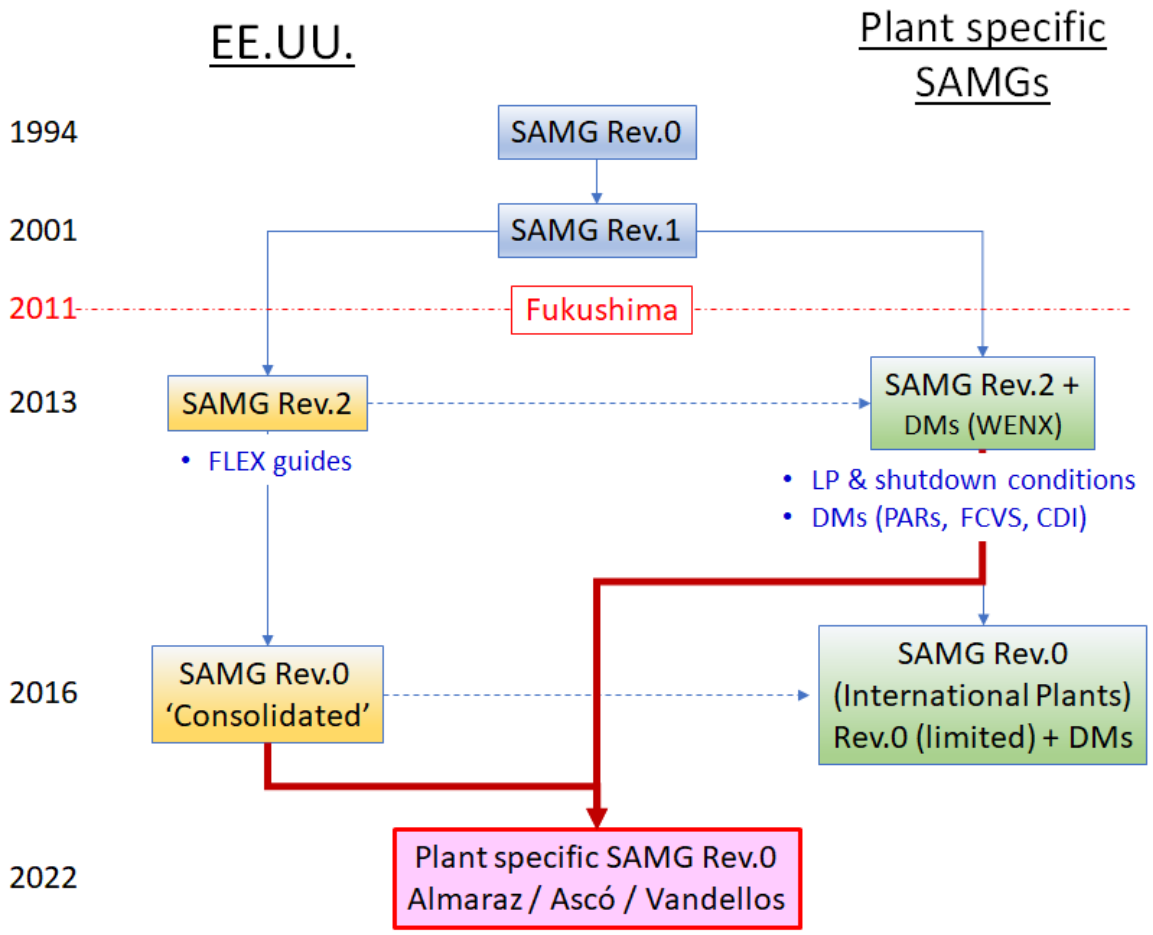

Tecnatom / Westinghouse activities in SAMGs

Koeberg NPP specific SAMGs update project

In November 2024, Eskom and Westinghouse signed a contract to enhance a wide range of Koeberg NPP procedures to deal with an Extended Loss of Alternating Current Power (ELAP) respond in the event of an external hazard and manage severe accidents.

The project, currently under development, is divided into four Work Packages (WPs) that will cover the required procedures and document updates and developments. Westinghouse provides the qualified and competent resources to support the scope of all four WPs.

WP4, “Updates to the Severe Accident Management Guidelines (SAMGs)”, consists in the revision and adaptation of the SAMGs currently in force in Koeberg to the structure and contents of the generic PWROG-15015-P Revision 0-Plus SAMGs

The base scope of the ongoing project will develop an updated set of plant specific SAMGs in compliance with generic PWROG-15015-P Revision 0-Plus.

Tecnatom / Westinghouse activities in SAMGs

Other activities associated with Severe Accident Management (SAM)

- Design of training plans and delivery of courses on phenomenology and management of severe accidents for operation crews and Emergency Response Organization (ERO) personnel in Spanish NPPs and abroad (United Arab Emirates, China, etc.)
- Development of Technical Support Center (TSC) computer aiding tools for using SAMGs in real or simulated severe accident scenarios.
- Implementation of severe accident codes (MAAP) into Full Scope Replica Simulators (Laguna Verde NPP, Mexico) and Interactive Graphic Simulators (Almaraz NPP, Spain)
- Development of severe accident simulation tools based on IA surrogate models. The company is currently involved in the ASSAS (Artificial intelligence for Simulation of Severe Accidents) European Union project, presented in another paper within this meeting and in the visit to Westinghouse headquarters in Madrid.

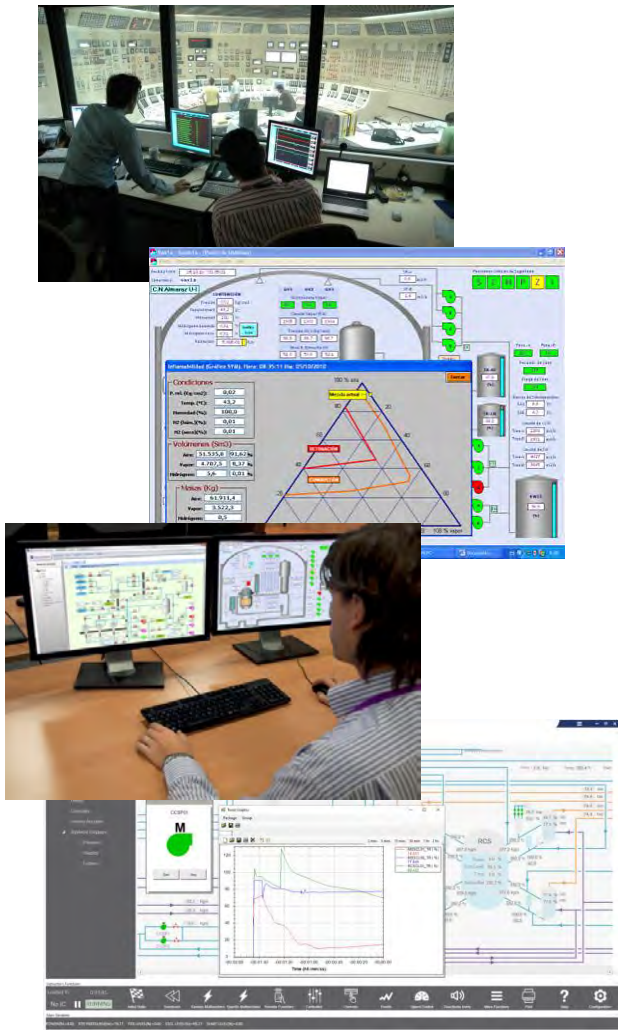

Thanks for your Attention. Any question?

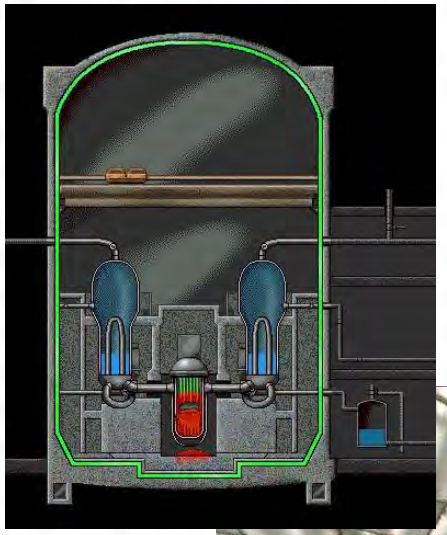

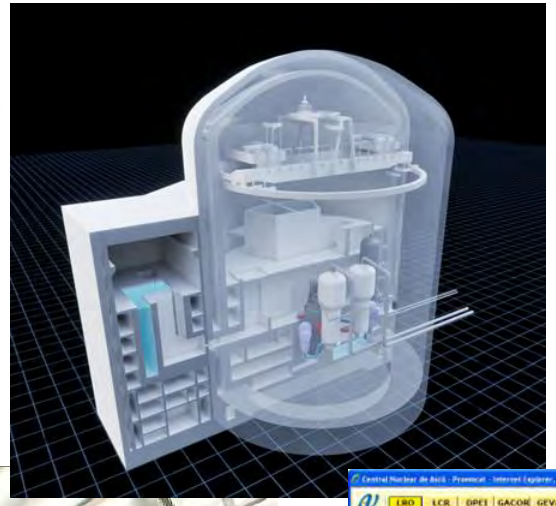

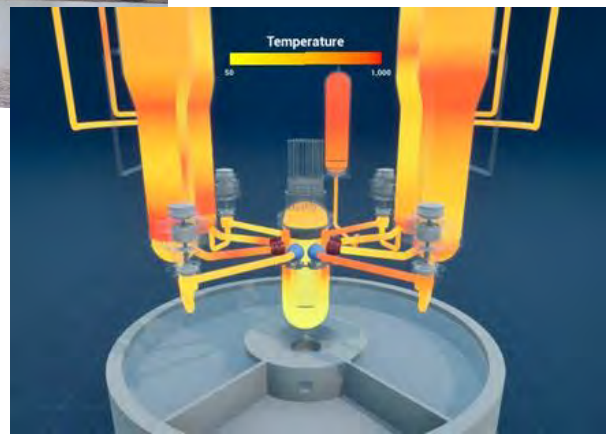

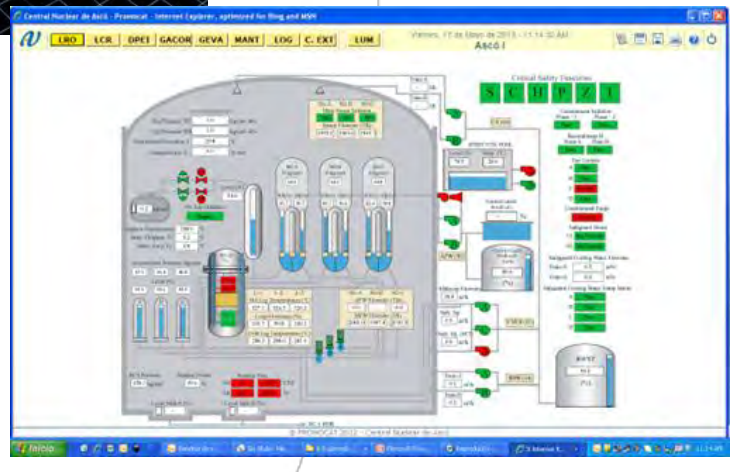

12h European Review Meeting on Severe Accident Research
(ERMSAR 2026)
Madrid, Spain, May 18-22, 2026

Simulating the asymmetrical behavior of TMI-2 accident with AC2/ATHLET-CD

Liviusz Lovász
GRS
Boltzmannstr. 14
85748, Garching, Germany
liviusz.lovasz@grs.de

Marco K. Koch
Ruhr-Universität Bochum (RUB), PSS
Universitätsstr. 150, 44801 Bochum, Germany
marco.koch@pss.ruhr-uni-bochum.de
ORCID-ID 0000-0001-7260-5250

ABSTRACT

The accident in Unit-2 of the nuclear power plant Three Mile Island has been extensively investigated in the scientific community for decades. The knowledge gathered from the accident investigations have been used for code developments and validations. TMI-2 accident simulation is also part of the validation matrix for the AC^2/ATHLET-CD system code. However, due to the internal structure of the code, it was not possible to reproduce the asymmetrical characteristics of the accident.

Recent improvements to the AC^2/ATHLET-CD system code have enabled azimuthal nodalization within the core region. This allows the adequate representation of local effects also during a severe accident.

Firstly, the paper presents briefly the necessary model developments to consider local conditions during a severe accident. Due to departing from the mandatory ring-shaped nodalization of the core region, models that took advantage of the classically cylindrical nodalization of the core region had to be refactored or developed anew. This applies in particular to the thermal radiation and to the horizontal melt relocation models.

Secondly, the new nodalization option including the newly developed models are used to reproduce the asymmetrical characteristics of the TMI-2 accident with AC^2/ATHLET-CD, and the reasons for this behaviour are discussed. The paper also provides an overview of the potential future applications of the non-ring-shaped nodalization option of AC^2/ATHLET-CD.

KEYWORDS
AC2, Severe Accident, TMI-2, Core Degradation

1. INTRODUCTION

In order to ensure and further improve the safety of existing and new-built nuclear reactors, computer codes have been developed that can simulate the response of the entire nuclear power plant to an initiating event. The simulations of potential scenarios have the capacity to identify vulnerabilities in the design of power

plants, thus enabling the implementation of countermeasures. Historically, the development and utilization of these system codes was primarily focused on the analysis of design basis accidents. However severe accidents like TMI-2, Chernobyl and Fukushima Daiichi highlighted the importance of the investigation of severe accidents. Existing codes were extended, and new codes were developed that could take into account the phenomena that predominantly or exclusively occur during a severe accident, including hydrogen production, melting processes, lower plenum phenomena and fission product release and transport.

In order to achieve the most accurate representation of the actual evolution of the accident, it would be ideal to investigate every structure within the cooling circuit and of the core separately. However, it is important to note that modelling and simulating each fuel pin individually would result in a substantial increase in the computational costs of the simulation. This is particularly relevant when considering that the development of the relevant codes (AC^2/ATHLET-CD, RELAD/SCADAP, MELCOR, etc.) [3, 8], [1] started multiple decades ago, at a time when the capabilities of computers were significantly more limited than they are today, but high-resolution reactor level analyses of a whole accident are still prohibitively numerically expensive and not suitable for uncertainty analyses as well.
The construction of reactors is such that the core parameters are as close to uniformity and symmetry as possible. This is done in order to ensure reliable, safe (with the greatest margin to safety criteria) and economic operation of the nuclear power plant. This reactor core characteristics led to one of the main assumptions of the most relevant severe accident codes: instead of modelling and nodalizing each fuel pin individually, they are grouped together horizontally in concentric rings and axially into multiple axial nodes. An example of a typical core nodalization is shown in Figure 1.

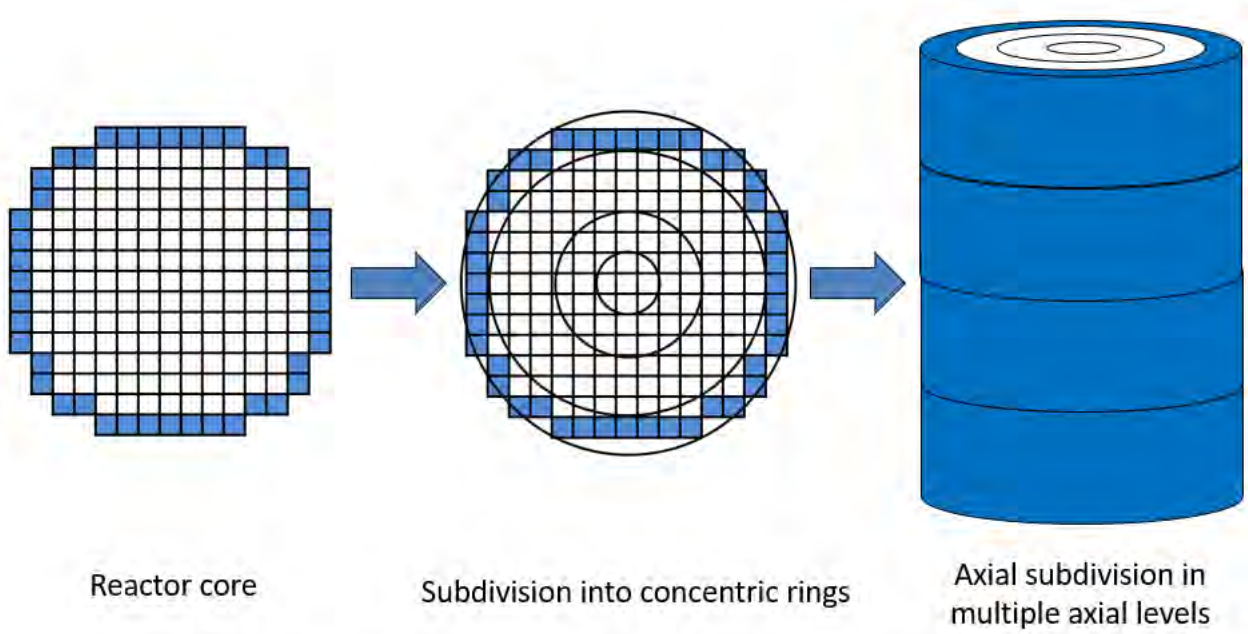

Figure 1. Example for a typical core nodalization in severe accident codes [7]

Each ring consist of multiple fuel rods (typically multiple thousands [6]). Ring shaped nodes are used and enforced, because it is assumed that the core configuration and the boundary conditions are cylindrically symmetrical. All the fuel rods defined within a ring are assumed to behave identically, meaning all the intensive parameters are the same, the extensive parameters are summed up within a ring. With this method, the required computational times for the simulations can be reduced significantly. Instead of simulating ~50000 fuel rods divided into multiple axial segments, these codes usually use 4-6 axially subdivided rings [10, 14].

The method briefly described above is widely used and accepted. It has some drawbacks, however. It adequately represents accidents with symmetrical initial and boundary conditions that progress symmetrically, but due to the enforced ring shaped nodalization, the simulations cannot differentiate azimuthal differences within the core region. If the accident has some local effects (local blockages, control rod ejection), asymmetrical characteristics (differently cooled core regions) or even minor deviances from an ideally symmetrical condition, then these asymmetrical effects can impact the accident evolution significantly. Such spontaneous symmetry breaking is expected in realistic scenarios. The analysis of such kinds of accidents is not adequately possible with the standard ring-shaped nodalization method. This created a motivation for model development in AC^2/ATHLET-CD.

In order to be able to simulate and analyse severe accidents with strongly asymmetrical characteristics, a new core nodalization method was implemented into AC^2/ATHLET-CD, that allows the azimuthal discretization of the ring-shaped nodes, allowing a more adequate consideration of local and asymmetrical effects during a severe accident. The departure from the obligatory ring-shaped nodalization inherently increases the required computational time for the analyses, but the increase is compensated for by the significant advancement of the IT capabilities. The new nodalization method required significant changes to the code, as the models that took advantage of the cylindrically symmetrical nodalization had to be either adjusted, refactored or newly developed.

This paper discusses the required model changes and demonstrates their usability on the TMI-2 accident, which had an asymmetrical characteristic. So far, the TMI-2 accident has mainly been analyzed under symmetrical conditions. This paper analyses the simulation of the accident by taking local effects also into account by using an azimuthally subdivided core. A potential explanation for the asymmetrical accident evolution is also provided.

2. REQUIRED MODEL DEVELOPMENTS TO ALLOW AZIMUTHAL NODALIZATION IN THE CORE REGION

The difficulty of considering local effects during an accident using a severe accident code can be summarized with the help of Figure 2. The upper part visualizes the issues mentioned in the introduction. The core has to be nodalized horizontally into concentric rings. If there is a local effect in the core (regardless of the origin of the local effect), its impact has to be averaged over the whole ring, as the main assumption of severe accident codes is that all the fuel rods within a core node behave identically. This leads to the redistribution of the local effect over the whole ring, thus losing its local impact. This generalization can impact the whole accident evolution. Let's assume a hypothetical scenario, where the cooling of a certain region in the core is limited, for example due to a local blockage.

- Real case: the local reduction of the cooling can lead to film boiling and local fuel degradation, eventually.
- Modelled case with the standard ring-shaped nodes: The impact of the cooling reduction has to be distributed along the whole ring, thus the cooling reduction per fuel rod is lower than if it were only considered locally. This could lead to a situation, where the reduced cooling is still sufficient to cool the core and prevent melting.

This hypothetical example shows that the evolution of the accident can strongly depend on the type of nodalization and highlights the potential drawbacks of using the mandatory, standard ring-shaped nodalization.

The solution to these issues is to allow the azimuthal discretization of the core rings. With this, a node can be defined around the local effect. The effect is still redistributed along the node, but as the node is smaller

and defined around the local effect, the impact of the redistribution is smaller. This is depicted in the bottom part of Figure 2.

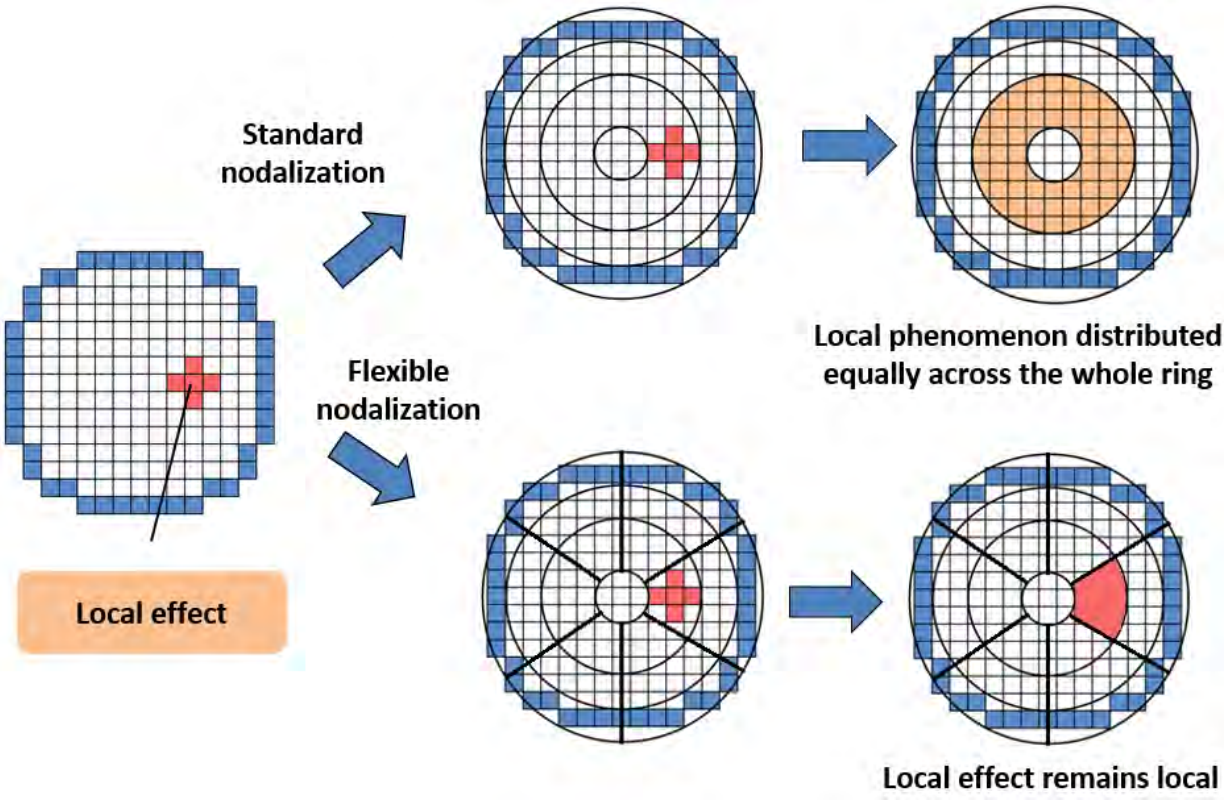

Figure 2. Consideration of local effects depending on the nodalization type [7]

As the ring-shaped nodalization was hardcoded into AC²/ATHLET-CD, internal changes to the code were necessary to allow a user-defined number of azimuthal sectors. This required model changes and their verification, validation. These are presented in the following chapters.

2.1. Model Developments

Due to the departure from the ring-shaped nodalization it had to be checked whether any of the existing models is impacted by this change and whether these models took advantage of the assumption that the boundary conditions are cylindrically symmetrical. After a detailed review of the code base, the following conclusions were made [13]:

- Most of the simulated phenomena are calculated for a single fuel pin (regardless of the node shape and size):
  - Heat generation, conduction, convection, oxidation, cladding failure, fission product release, axial melt relocation.
  - Results of the single rod calculation are multiplied by the number of rods in a node.
  - No model changes are needed.
- The modelling of fluid flow is already flexibly definable:
  - No model changes are needed.
- Heat radiation between nodes:
  - Model changes are needed, standard model is based on cylindrically symmetrical assumptions
- Radial relocation of melt:

- Model changes are needed, standard model is based on cylindrically symmetrical assumptions

The last two points will be introduced briefly below.
The change of the shape of the nodalization has no impact on the heat radiation processes within a cell. Changes had to be made in the modelling of heat radiation towards neighbouring cells. In the standard, ring-shaped nodalization scheme, horizontal heat radiation is only considered from a ring towards its inner and/or outer neighbour. If a neighbouring node is molten, then the next neighbouring node is taken. This is illustrated on the left side of Figure 3. The calculation of the required view factors between the ring shaped nodes is calculated via means of analytical correlations [9]. Importantly, due to the nature of the nodalization no shadowing effects can occur.
This is no longer true for the nodalization scheme where azimuthal discretization is made possible. During the core degradation process configurations can form, which create a total or partial shadowing effect between two free surfaces for heat radiation rays. Right side of Figure 3 shows a possible configuration with shadowing effects. Red areas indicate molten nodes. Heat radiation from side "2" towards side "5" is unblocked, but heat radiation rays from side "8" towards side "5" are partially blocked by the still intact surfaces of "6" and "7". This effect has to be taken into account in the adjusted heat radiation model. Unfortunately, due to shadowing effects, analytical solutions for the determination of view factors are not applicable.

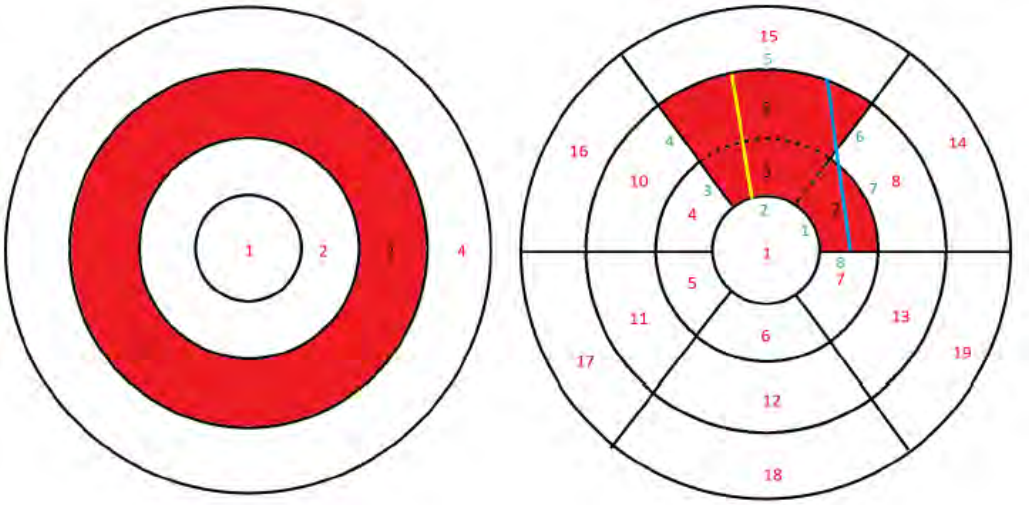

Figure 3. Left: no shadowing effects possible. Right: possible shadowing effects [7]

To solve the issues of the standard heat radiation model with the neighbour identification and shadowing effects, the following code changes were made:

- Creation of an algorithm that identifies the surfaces that exchange radiative heat with each other, both in intact and degraded states of the core.
- In the areas, where the core is intact, the old heat radiation model is used, however, it is modified, so that it is able to consider heat radiation also in azimuthal direction.
- For the areas, where core nodes have relocated and a cavity was formed, a numerical method was implemented to determine the required view factors for the heat radiation, including shadowing effects.

Due to length limitations, a detailed introduction to the developed model and its verification and validation is omitted here. It is described in detail, including its verification and validation in [7] and is summarized in [11, 12, 17].

The model developments for the consideration of the horizontal melt relocation also in an azimuthally subdivided core required less effort than the consideration of the heat radiation in a 3D cavity. The physical model was left unchanged, the relocating mass is still dependent on the melt height differences in the neighbouring nodes, as described in detail in [9]. The only adjustment to the model was the adequate identification of the target nodes for the horizontal melt relocation. In a ring-shaped nodalization, the melt could only relocate to an inner or outer neighbouring ring, while in a three-dimensionally nodalized core, the melt can also relocate azimuthally. The identification process for the correct neighbouring target node is the same as for the heat radiation between intact nodes.

3. TMI-2 ACCIDENT

The accident in the unit 2 of Three Mile Island nuclear power plant is one of the few, if not the only accident, that happened in a light water reactor, that is well documented, and where the accident progression has a definite asymmetrical characteristic. The accident started with the opening of the pilot operated relief valve (PORV) that stuck open, which remained undetected long enough and which caused significant loss of coolant. The ensuing core uncovery then led to fuel degradation, melt formation and relocation. The melt relocated to the lower plenum in one segment of the core, on the outer side. The accident is described in detail in numerous literature like [2, 15, 16] to name a few. The final state of the core is illustrated on the left side of Figure 4. The right side of the figure shows the assumed location of the relocation, which is close to loop-B.

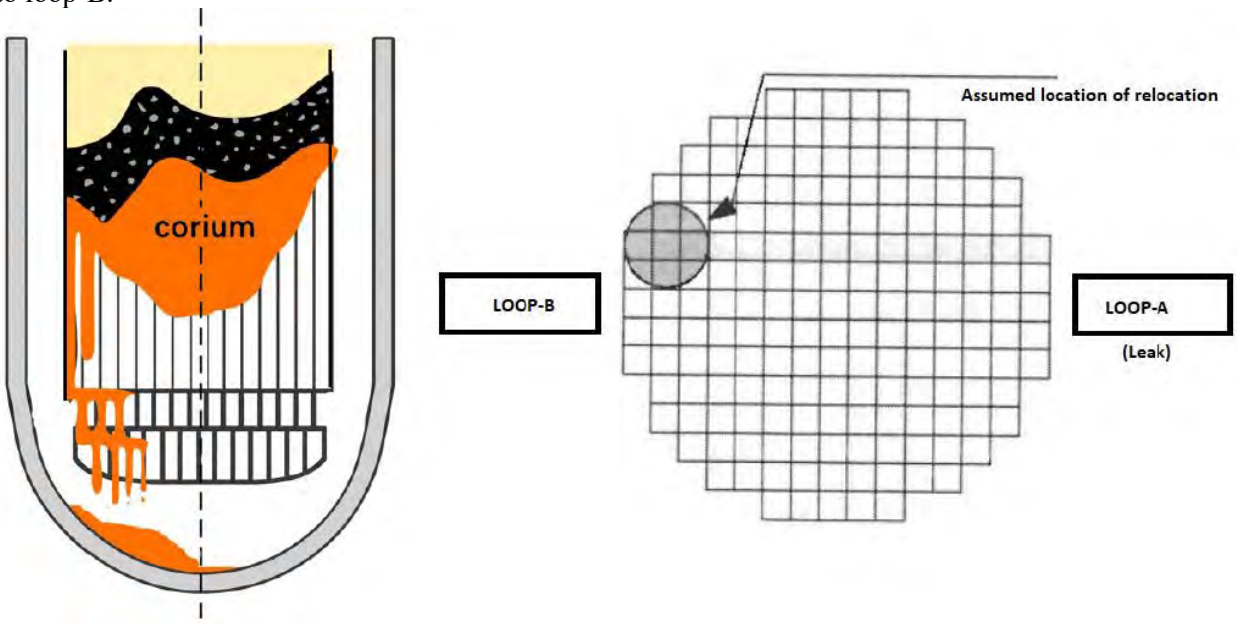

Figure 4. Left: Sideways relocation of melt (vertical cut), Right: assumed location of relocation (horizontal cut) [7]

The figure shows the clear asymmetrical characteristics of the accident, which for reasons described in the previous chapters, could not be adequately represented in severe accident codes using standard ring-shaped core nodes.
The following chapter will demonstrate that the newly developed nodalization method and models allow the consideration of the asymmetrical characteristics when the rings are subdivided azimuthally. The results are also used to partially validate the newly developed method and provides a possible explanation for the reason of the asymmetrical behaviour of the accident.

3.1. TMI-2 input decks

The TMI-2 accident has been used for validation of ATHLET-CD for many decades; therefore an input deck was already available. This input deck includes all the major components of the primary circuit and defines the actual events during the accident, like the timings of the operator actions, as boundary and initial conditions. This input deck nodalizes the core region axially into multiple levels and horizontally into concentric rings, therefore it cannot address the asymmetry of the accident leading to a one-sided melt relocation by definition. The core nodes are connected to one upper plenum volume that distributes the coolant into loop A and loop B. The two loops are modelled separately, including the steam generators, pumps and in loop A the pressurizer with the PORV. The two cold legs per loop enter a common ring-shaped downcomer node that leads the coolant to the lower plenum. From lower plenum volume, that is only axially subdivided, the fluid is distributed to the four core ring nodes and to the core bypass. A detailed description of the standard TMI-2 input deck can be found in [4].
This input deck was used as basis for the creation of the input deck with azimuthal nodalization. The azimuthal subdivision of the core into four sectors results in more cells, which leads to an increase in computational needs. The subdivision of the core region into four azimuthal segments was chosen to reflect the potential impact of the mass flows of the 2 hot legs and 4 cold legs. A higher number of subdivisions would have been possible, but to keep the increase in the computational time at a minimum, the subdivision was not increased above 4. Future investigations might repeat this analysis with higher subdivision. We know from the literature that the relocation of melt to the lower plenum happened closer to loop B (right side of Figure 4). By subdividing the rings into four azimuthal segments like shown in Figure 5, the local impact can be taken into account. The effect is still averaged over the node (right side of Figure 5) but allows the qualitative representation of the accident progression.

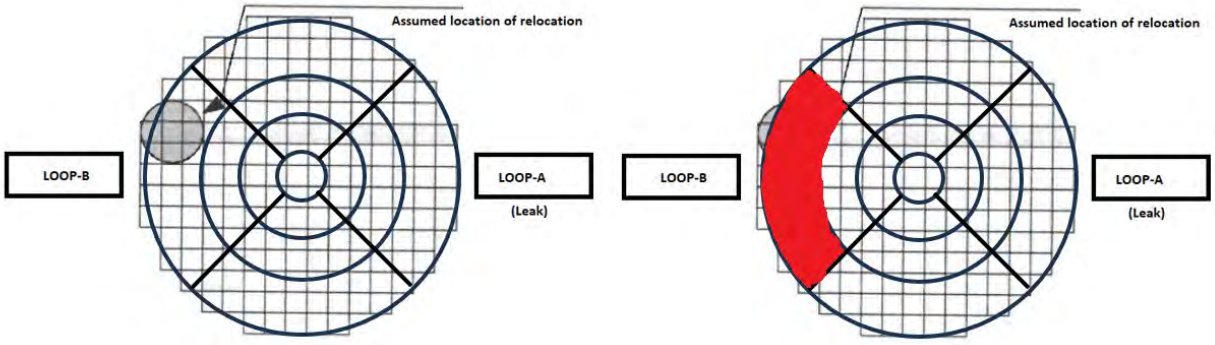

Figure 5. Left: Core nodalization to represent local effects during TMI-2 accident. Right: averaging effect of the azimuthal nodalization [7]

The azimuthal subdivision alone does not create an asymmetrical behaviour. In order to achieve an asymmetrical behaviour some kind of asymmetrical effect had to be implemented into the input deck. After literature review, the followings conclusions were made what effects could have influenced the accident asymmetrically:

- Besides minor differences in local parameters, the core can be considered as cylindrically symmetrical. Thus, the origin of the asymmetrical behaviour is from the outside of the core region. The core parameters were defined symmetrically.
- The leak through the PORV in the pressurizer was located in loop-A, which could have an asymmetrical impact on core cooling. Therefore, a thermohydraulical nodalization was implemented in the input deck that can reflect this behaviour.
- The heat removal from the two steam generators were different due to the different secondary side pressures and feedwater supply [2]. These could also asymmetrically influence the core cooling and requires the same type of nodalization to take into account as in the previous point.
- Different operation of the main coolant pumps in loop A and B.

Based on these findings, subdividing only the core region azimuthally should not lead to an asymmetrical accident evolution, besides smaller numerical effects [5], as all the core nodes receive symmetrical conditions, because the impacts of the two different loops are averaged out in the only axially subdivided upper and lower plenum volumes. To allow physical phenomena-based 3D effects to take place, the whole pressure vessel had to be subdivided azimuthally and had to be connected to each. This led to the final nodalization of the pressure vessel shown in Figure 6 as a cross-sectional cut from the top.

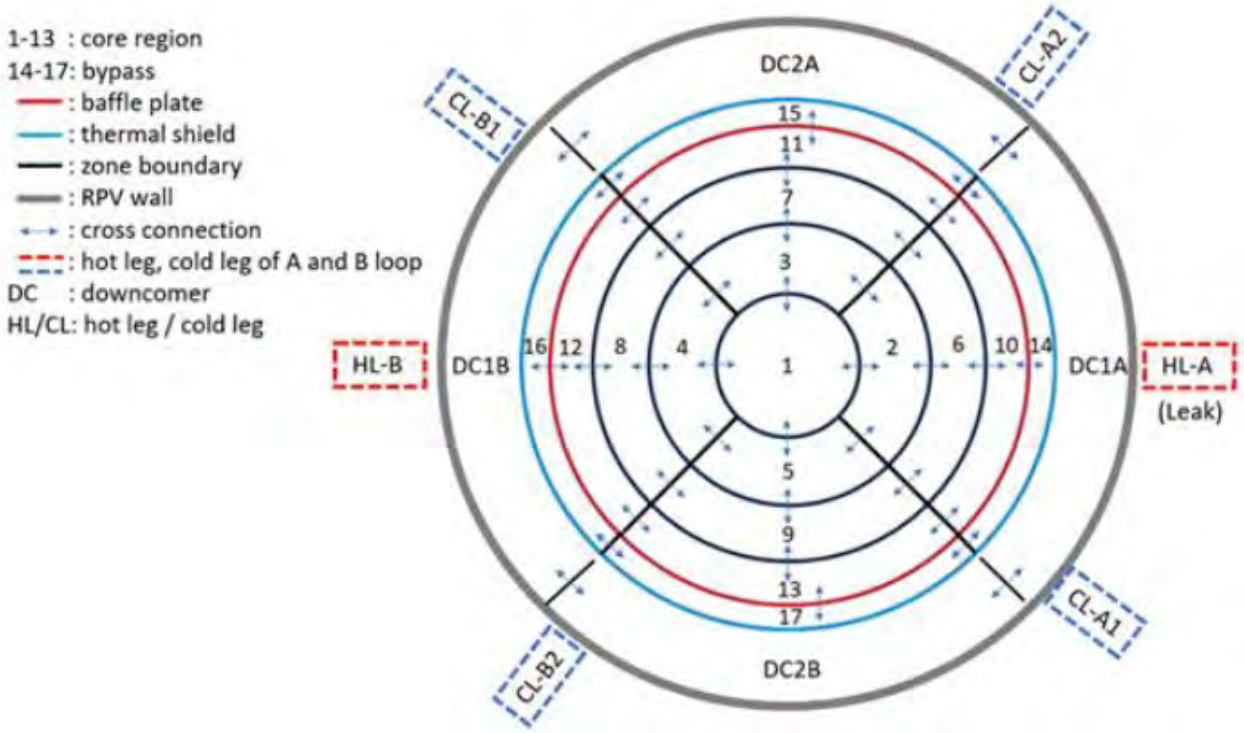

Figure 6. Top view of the 3D nodalization of the inside of the reactor pressure vessel [7]

The accident scenario of TMI-2 was simulated using an input deck with an azimuthally subdivided reactor pressure vessel. The goal of these calculations is to demonstrate the impact of the nodalization on the accident progression, partially verify/validate the new models using the available TMI-2 data and to explain the reason for the asymmetrical tendence observed during the accident. The main findings are presented and summarized in the following chapter.

3.2. Analysis of the simulation results using azimuthally subdivided core

It is well documented in [4] that using a ring-shaped nodalization for the core, AC^2/ATHLET-CD is capable, with some exceptions, of capturing the integral evolution of the accident. It is important that this is also true for the case where the core is azimuthally subdivided. Figure 7 is a useful indicator of whether this criterion is met. It shows the pressure evolution measured in TMI-2, as well as the results of simulations with ring-shaped and 3D core nodalization, starting 100 minutes after the accident sequence began. The first 100 minutes of the accident sequence is omitted, because there are no significant differences between the simulated and measured data. The first differences start to occur after the PORV is closed. The pressure starts to increase, however, in case of the 3D nodalization the pressure increases more rapidly, but the difference to the measured value is still not too large. The difference could be attributed to different temperature distributions in the core, which will be discussed later. Larger differences occur after the main coolant pump in loop B is activated, which delivers water into the already partially degraded core. This results in a large increase in pressure, but both simulations overestimate the pressure increase. It is a known

issue that AC²/ATHLET-CD can overestimate the heat transfer and thus the pressure increase in some cases during the quenching process. As both calculations show the same behaviour, it is not caused by the new model developments or by the azimuthal nodalization, therefore it is not discussed further in this paper. Both simulations fall back approximately to the measured pressure values after the peak, but keep increasing faster than in the real case, indicating again an overestimation of the heat transfer from the hot structures/melt to the water. The pressure evolution then follows the real trend, although the case with the 3D nodalization shows some delay. Larger qualitative difference occurs at around 224 minutes into the accident sequence. When the molten material from the core relocates to the lower plenum, it gets into contact with water and fragments. The resulting large surface area intensifies the heat transfer from the melt/debris to the water, leading to a pressure peak as visible in Figure 7. The relocation of the melt is initiated in the simulations also at T=224 minutes, but AC²/ATHLET-CD lacks fragmentation modelling. Therefore, it cannot reproduce the resulting pressure peak. This modelling gap is, however, not in connection with the topic of this paper.

Looking at the overall accident evolution based on the pressure data, we can conclude that both simulations can qualitatively describe the accident scenario. The larger differences can be explained by gaps in the AC²/ATHLET-CD modelling base, that is not the topic of this paper. Notably, the differences between measured and simulated values were slightly larger for the input deck with the detailed nodalization, for which some explanation is given below.

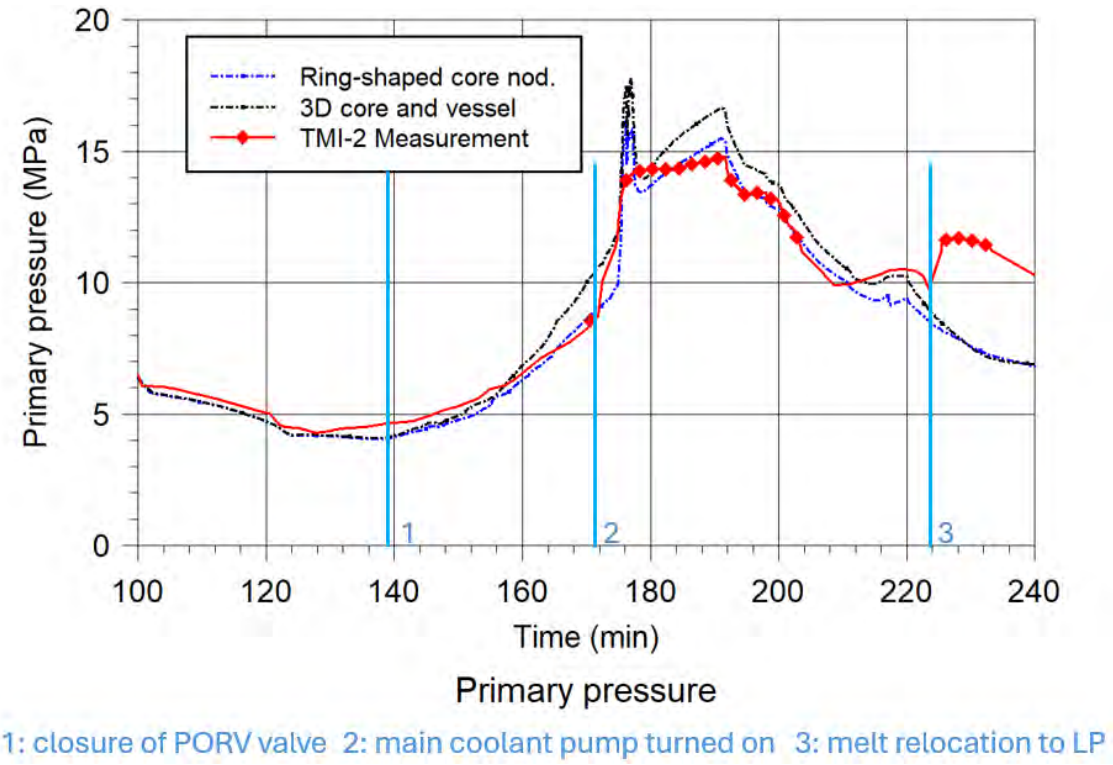

Figure 7. Evolution of the primary pressure during the accident in TMI-2. Simulated and measured values

Following the previous summary of the overall accident evolution, the objective of this paper is addressed. As already mentioned previously, the main goal of this paper is to demonstrate the capability of AC²/ATHLET-CD to reproduce the asymmetrical characteristics of the accident and give an explanation on the origin of the asymmetrical effect.

Figure 8 shows the side view of the state of the core at the end of the simulation. As the created nodalization is three-dimensional, a cross-sectional cut view from one direction is insufficient to represent the 3D state of the core. Consequently, the left and right sides of the figure show the same reactor at the same time, viewed from the direction indicated by the arrow in the graph. The figure depicts the reactor vessel, fuel and control rods, as well as the melt in the lower plenum. The colours of the structures indicate their temperatures. For easier orientation, the node numbers of Figure 6 are also shown in Figure 8.
It is clearly visible that a cavity was formed during the core degradation process. However, it is also apparent that the form of the created cavity is not cylindrically symmetrical. Segment "2" is not molten, which is located on the opposite side of the assumed location of the material relocation to the lower plenum (see Figure 4). Alternatively, this can be expressed as follows: the core is more degraded in the direction of loop-B. There are two important conclusions to be drawn from this fact. Firstly, the calculation managed to create a cylindrically asymmetrical core degradation. Secondly, the resulting asymmetrical core degradation is shifting in a direction closer to loop-B, like in the real accident. There is also a slight local effect in direction of loop-A in the segment “6”, where a node also melted. This can be attributed to the fact, that due to the creation of the cavity, segment “2” can radiate its energy (using the newly developed heat radiation model for the 3D cavity) to colder areas and more coolant can get to the hot surfaces of segment “2”, thus intensifying its cooling. Segment “6” doesn’t have this extra cooling effect, thus melts. The first objective of this analysis was reached, as it was demonstrated that with the 3D nodalization of the core, the asymmetrical characteristics of the accident could be reproduced on a qualitative level.

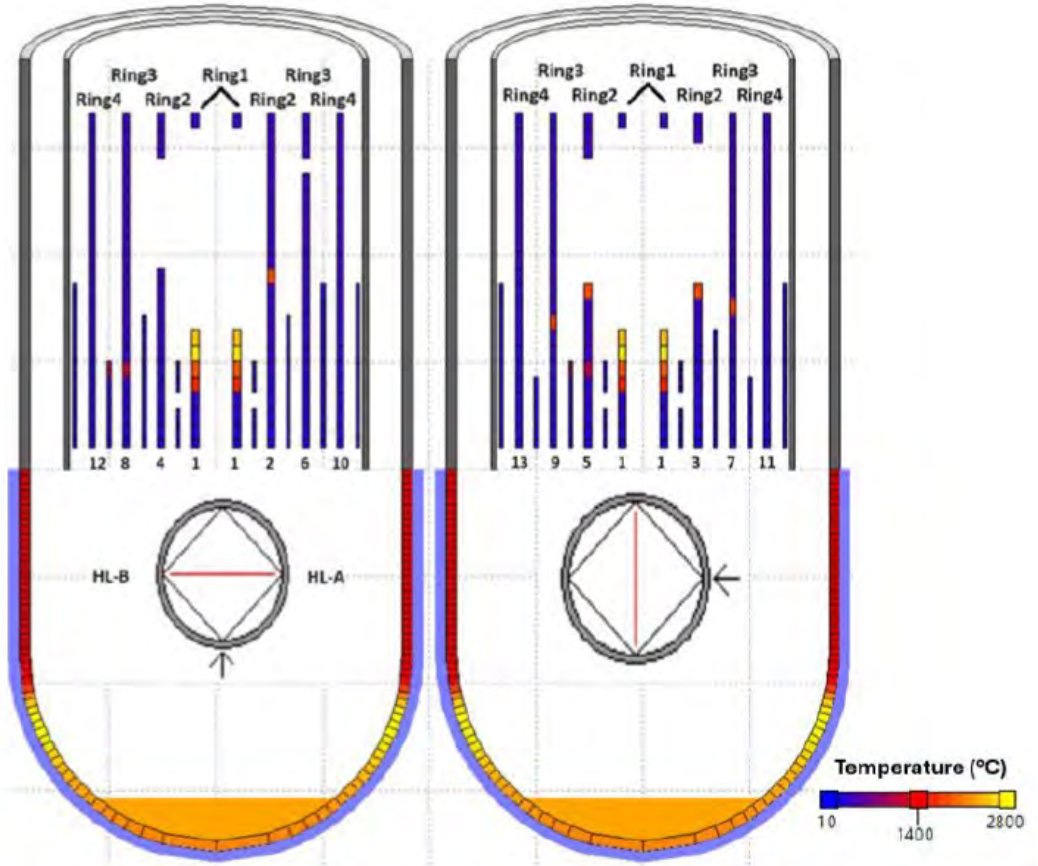

Figure 8. Cross sectional cut of the reactor vessel from the direction of the indicated arrow, using the detailed nodalization. [7]

The second objective of this analysis is to find an explanation for the reason of the asymmetrical accident evolution. For this a deeper and more local analysis is needed. We know based on Figure 8 that the side

closer to loop-B degraded more than the side of the reactor closer to loop-A. The temperature evolution of these two sides were compared, specifically the fuel temperatures at the axial elevation of 3.4 m (axial node 18) of rod group “12” and “10”. This is depicted in the top right corner of Figure 9. Up until the core is covered with water, i.e. up until around 6500 seconds after the start of the accident, the temperature differences between the two sides are negligible. They start to deviate from each other slightly, but a larger and significant difference occurs at around 7200 seconds, where the auxiliary feedwater injection into the steam generator in loop-A was increased, then shortly afterwards stopped. This results in a larger heat removal from loop-A, leading to an increased mass flow rate in loop-A that results in a short-term flow reversal in loop-B, too. This can be seen in the bottom graph of the right side of Figure 9. As a result of this flow reversal, colder fluid is falling onto the upper segments of rods closer to loop-B, which results in a temporary cooling of those fuel rods. After the feedwater injection to steam generator-A stopped, the mass flows returned to their previous directions. At this stage of the accident, contrary to the expected results, the region closer to loop-B is colder than the region of the core, that remained intact at the end of the accident.

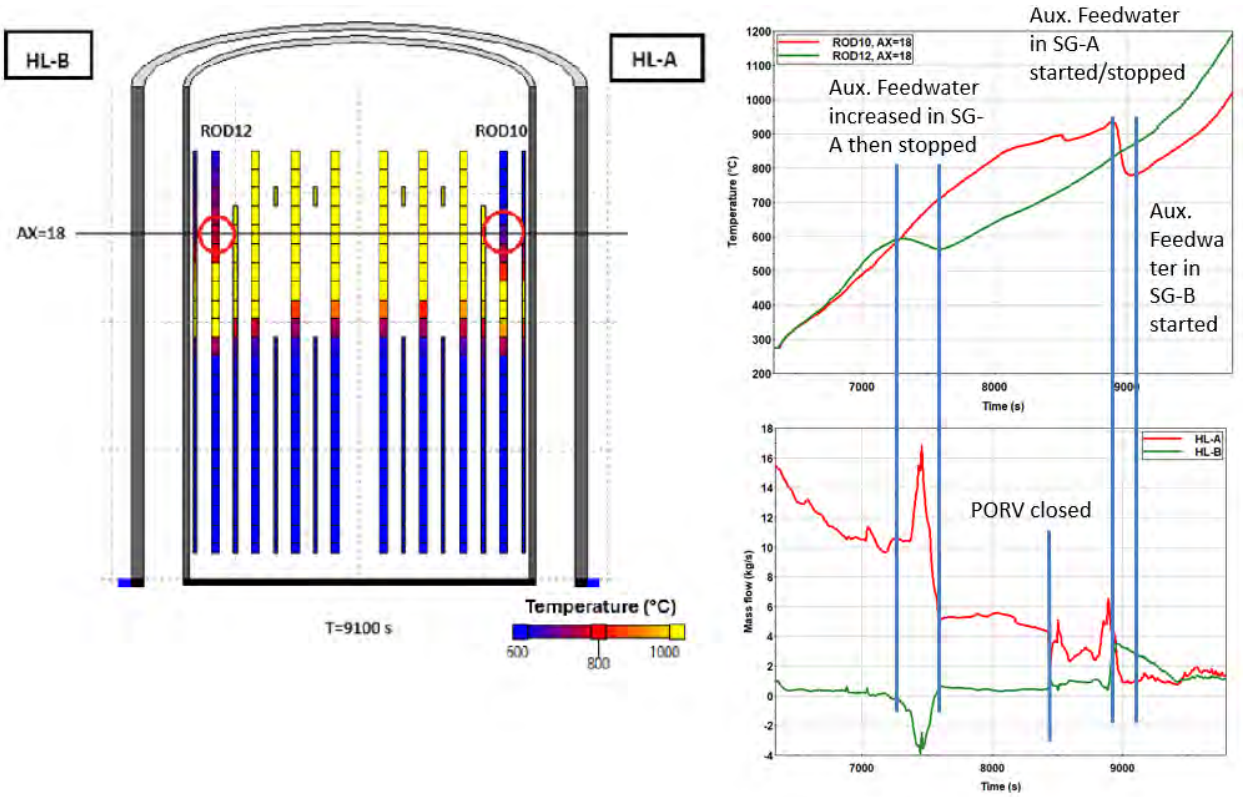

Figure 9. Evolution of fuel temperatures on two opposite sides of the core [7]

Rod group “12” remained colder for about 1500 seconds. The leak through the pressurizer was detected at approximately 8500 seconds into the accident and was closed. However, this had only a minor impact on the mass flows and thus on the temperature evolution of the investigated fuel rods, as can be seen in Figure 9. At around 9000 seconds, the operators started the feedwater injections in steam generators A and B, but then turned it off in loop A again, influencing the heat removal from the reactor. These actions caused large mass flow changes, again within the core as well. The local mass flow changes caused rod group “10” to cool down, as seen in the top right graph of Figure 9. From this time on, the side of the reactor closer to loop-A remained colder during the entire accident evolution, up until core reflooding. Left side of Figure 9 depicts at T=9100 seconds into the accident the location of the fuel rods that were compared and shows that the left side of the reactor is about 100 °C warmer than the right side. Thus this region reaches onset of the

extensive oxidation earlier, causing an earlier rapid heat-up and eventually an earlier core degradation, leading to the cavity formation as can be seen in Figure 8.

Using the azimuthally subdivided core nodalization it was possible with AC²/ATHLET-CD to reproduce qualitatively the asymmetrical core degradation of the TMI-2 accident and to give a hypothesis why the accident evolved non symmetrically. The location of the leak in only one of the loops appears to have exerted a minor asymmetrical effect on the accident evolution, contrary to the author's expectations. However, the different heat removal from the primary system through the steam generators impacted the accident scenario more significantly according to the presented AC²/ATHLET-CD simulation.
The simulation results are promising and plausible, but the asymmetrical tendency of the accident evolution is predominantly captured qualitatively, quantitative improvements are still possible. The lack of quantitative accuracy can be traced back to two things.
Firstly, the AC²/ATHLET-CD models lack some key phenomena (such as fuel fragmentation and relocation outside of the core) or consider them in a simplified way (e.g.: quenching process). These limitations are not associated with the newly developed models, but the finer nodalization enhances their impact on the overall calculation.
Secondly, the input deck parameters have a certain degree of uncertainty. Some of these uncertainties come from the accident itself, for example the exact temperature when the fuel started to relocate. Some of them are caused by the finer, azimuthal nodalization of the pressure vessel. The exact geometry gets a larger importance, if the nodalization is finer, and some of the form loss factors and exact dimensions were not known to the user at the time of the input deck creation. Changing these values can have a significant impact on the quantitative results of the simulation.
For these reasons, future works will focus on improving the model basis of AC²/ATHLET-CD and on further enhancing the TMI-2 input deck. Also uncertainty analyses are planned to identify the factors that influenced the accident the most. Related changes can allow the code to reproduce the real accident evolution more realistically and accurately.

4. SUMMARY AND OUTLOOK

This paper presents an option implemented in AC²/ATHLET-CD that allows users to depart from the mandatory ring-shaped core nodalization in most severe accident codes, thus enabling local effects to be taken into account. This required the refactoring or newly developing of the models that took advantage of the symmetrical boundary conditions of the mandatory ring-shaped nodalization. Most notably the models of heat radiation and horizontal melt relocation were refactored/newly developed. Using this new nodalization option, including the newly developed and refactored models, the TMI-2 accident was simulated. It was chosen to be analyzed because the accident evolution has a proven, well documented asymmetrical characteristic. This was reflected by creating an azimuthally subdivided core. The results obtained show the asymmetrical behaviour, although with some quantitative differences to the actual measurements. These differences and future improvement options were discussed. A possible explanation was also found and analysed why the accident evolved asymmetrically.

In the future, the departure from the mandatory ring-shaped nodalization allows the investigation of design extension condition scenarios, where a strong local impact is expected, like, for example, accident scenarios with control rod ejection or partial core reflooding from the top. The power distribution of spent fuel pools are usually not cylindrically symmetrical, this approach can be applied there, too, as was already demonstrated in [12]. It also allows to investigate if minor deviations from an ideally symmetrical condition can lead to a larger asymmetrical progression, which is not unlikely for such non-linear processes and the numerical schemes used in AC²/ATHLET-CD. This option does not make the standard ring-shaped nodalization obsolete but enables the future investigation of scenarios with strong local effects.

REFERENCES

[1] Brockmeier, U. 1996. *Modellbasis der Störfallanalyseprogramm ATHLET/CD, ICARE2, MELCOR und SCADAP/RELAP5*. Statusbericht EUR 16937.

[2] Electric Power Research Institute (EPRI). 1980. *Analysis of Three Mile Island-Unit 2 Accident* NSAC-80-1. DOI=10.2172/5598769.

[3] Gauntt, R. O., Cole, R. K., Erickson, C. M., Gido, R., Gasser, R. D., Rodriguez, S. B., and Young, M. F. 2000. *MELCOR Computer Code Manuals: Reference Manuals Version 1.8.5*. Techreport NUREG/CR-6119, Volume 2, Revision 2. Sandia National Laboratories.

[4] Hollands, T., Di Nora, V. A., Lovasz, L., Pandazis, P., Tiborcz, L., and Wielenberg, A. 2023. *ATHLET-CD 3.4.0 Validation* GRS-P-4/Vol. 3 Rev. 3.

[5] Hollands, T., Tiborcz, L., Skorek, T., Junk, M., and Wielenberg, A. 2024. *Improved methodology for the determination of model uncertainties using the example of ATHLET*. GRS- 785.

[6] Klein-Heßling, W. 2014. *Analyse kernzerstörungs- und quelltermrelevanter Prozesse mit ASTEC und ATHLET-CD/COCOSYS*. GRS-Bericht GRS-351. Gesellschaft für Anlagen- und Reaktorsicherheit (GRS) gGmbH, Köln, Garching b. München, Berlin, Braunschweig.

[7] Lovasz, L. 2026. *Further development of ATHLET-CD for simulations of accidents with asymmetrical characteristics*. *Dissertation - submitted*. PSS.

[8] Lovasz, L., Austregesilo, H., Bals, C., D'Alessandro, C., Hollands, T., Lu, C., Pandazis, P., Tiborcz, L., and Weber. 2025. *ATHLET-CD 3.5 User's Manual* GRS-P-4/Vol. 1 Rev. 10.

[9] Lovasz, L., Austregesilo, H., Bals, C., D'Alessandro, C., Hollands, T., Lu, C., Pandazis, P., Tiborcz, L., and Weber, S. 2025. *ATHLET-CD 3.5 Models and Methods* GRS-P-4/Vol. 2 Rev. 1.

[10] Lovasz, L. and Pandazis, P. 2023. Simulation of an SBO Accident in a PWR with AC2/ATHLET-CD with and without using ATF Cladding Material. In *32nd International Conference Nuclear Energy for New Europe* (Book of Abstracts).

[11] Lovasz, L., Weber, S., and Koch, M. K. 2018. Comparison of a Hypothetical Strongly Asymmetrical Severe Accident Using the Standard and the New Nodalization Method with the Code System AC2. In *27th International Conference Nuclear Energy for New Europe (NENE2018)*. *Book of Abstracts*.

[12] Lovasz, L., Weber, S., and Koch, M. K. 2018. New Approach for Severe Accident Simulations in Spent Fuel Pools Using the Code System AC². In *NUTHOS-12*. *12th International Topical Meeting on Nuclear Reactor Thermal-Hydraulics, Operation and Safety*.

[13] Lovasz, L., Weber, S., and Koch, M. K. 2018. Simulation of asymmetric severe accidents using the code system AC2. In *Annual Meeting on Nuclear Technology 2018*. *Proceedings*.

[14] Pandazis, P. and Weber, S. 2019. SIMULATION OF IN-VESSEL RETENTION SCENARIOS IN PWR WITH ATHLET-CD. In *Proceedings of the 18th International Topical Meeting on Nuclear Reactor Thermal Hydraulics 2019. NURETH 2019.*

[15] TMI-2 Analysis Exercise Task Group. 1988/1990. *TMI-2 Analysis Exercise*. *Final Report*.

[16] TMI-2 Analysis Exercise Task Group. 1992. *TMI-2 Analysis Exercise Final Report*.

[17] Weber, S., Austregesilo, H., Bals, C., Herb, J., Hollands, T., Langenfeld, A., Lovasz, L., Pandazis, P., Sarkadi, P., Schubert, J.-D., and Tiborcz, L. 2019. *Weiterentwicklung des Systemrechenprogramms ATHLET-CD zur Simulation von Unfällen im Primärkreislauf. Abschlussbericht*. GRS-Bericht GRS-535.

Simulating the asymmetric behavior of TMI-2 accident with AC2/ATHLET-CD

Liviusz Lovasz (GRS), Marco K. Koch (RUB)

ERMSAR 2026 - The 12th European Review Meeting on Severe Accidents Research, Madrid, Spain, 18-22.05.2026

What is AC²?

- **AC²**:
  - **A**THLET
  - ATHLET-**C**D
  - **C**OCOSYS
- Deterministic system code system for accident analysis
- Covers a wide spectrum of phenomena

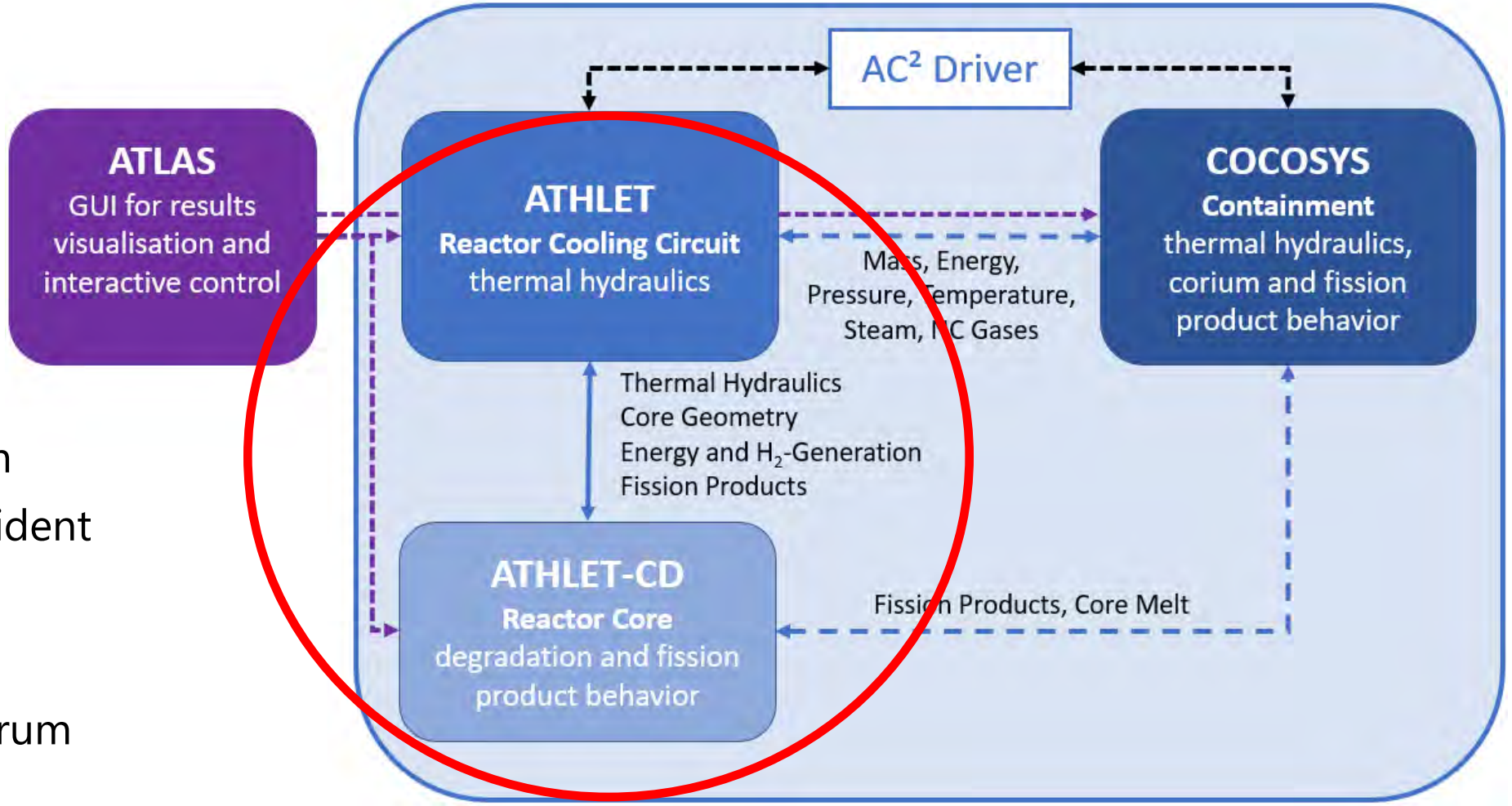

© Gesellschaft für Anlagen- und Reaktorsicherheit (GRS) gGmbH

Core representation

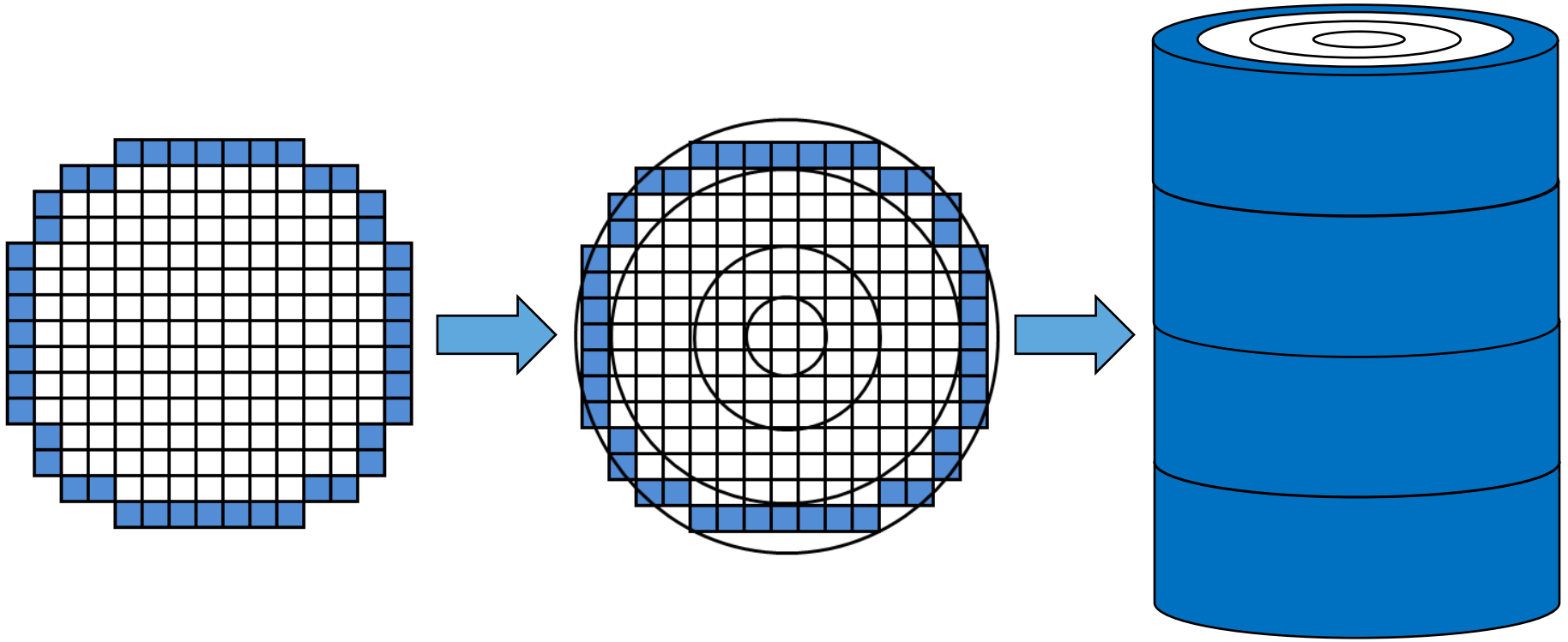

Source: Lovasz, L. 2026. *Further development of ATHLET-CD for simulations of accidents with asymmetrical characteristics. Dissertation - submitted.* PSS.

Reactor core

Subdivision into concentric rings

Axial subdivision in multiple axial levels

- All fuel rods/structures within an axially/radially defined node behave identically
- Good applicability in symmetric conditions

Accidents with asymmetrical characteristics

- Control rod ejection
- Asymmetric reflooding from above
- Non-uniform power distribution
- Small local deviations from ideally symmetric conditions can lead to extended asymmetric characteristics

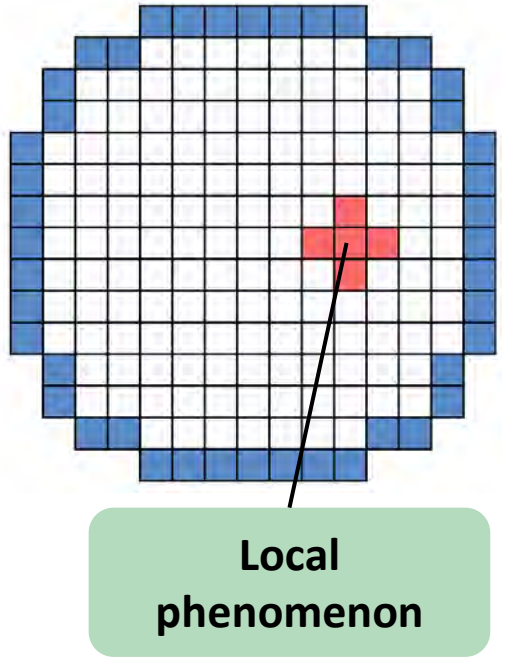

Source: Lovasz, L. 2026. *Further development of ATHLET-CD for simulations of accidents with asymmetrical characteristics. Dissertation - submitted.* PSS.

Ring nodalization vs local effects

- Ring-like nodalization might lead to incorrect and unrealistic results if there are azimuthally asymmetric effects

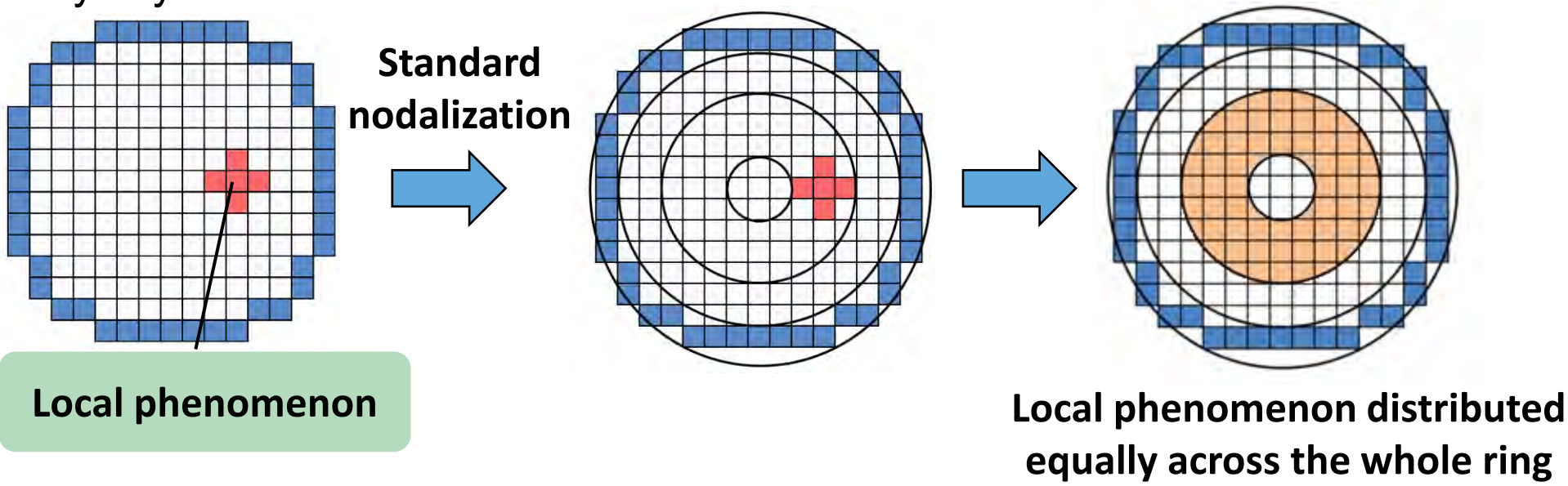

- Possible consequences (example):
  - Local power peak → enough to degrade and melt the core locally
  - Distributed, averaged power peak → not enough to degrade the core, all safety standards are met
- The nature of the core nodalization influences the simulation results

Source: Lovasz, L. 2026. *Further development of ATHLET-CD for simulations of accidents with asymmetrical characteristics. Dissertation - submitted.* PSS.

Real life example for asymmetric accident evolution

- TMI-2 accident
- Melt relocation to the lower plenum happened though one quadrant of the core
- Motivation:
  - Reproduce the asymmetric characteristics of the accident evolution

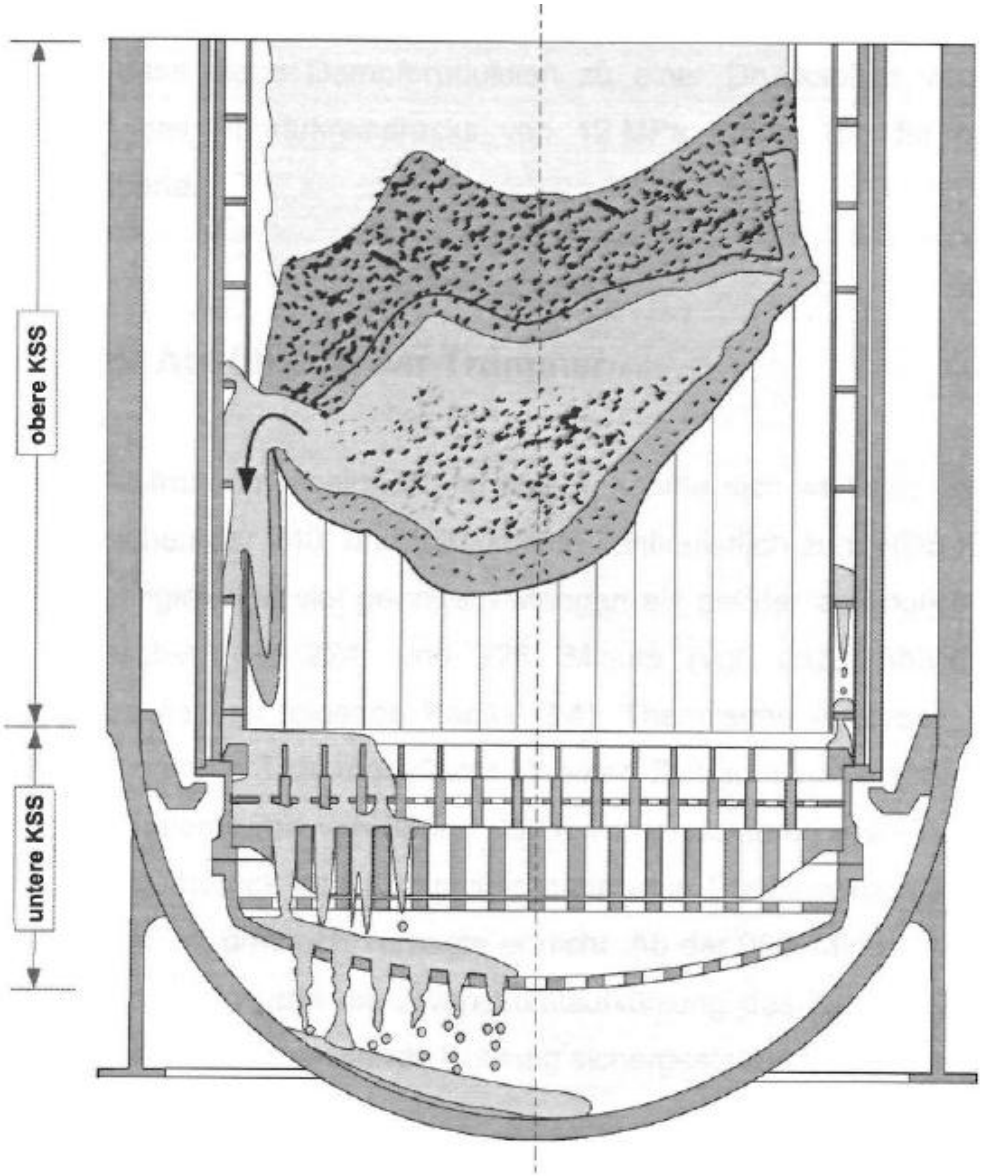

Source: T. Drath, et al.: Simulation des TMI-2 Unfalls mit dem Programmsystem ATHLET-CD (Teil 1), RUB-LEE, BMWi 150 1241, 12.2004

Flexible nodalization: think globally, nodalize locally

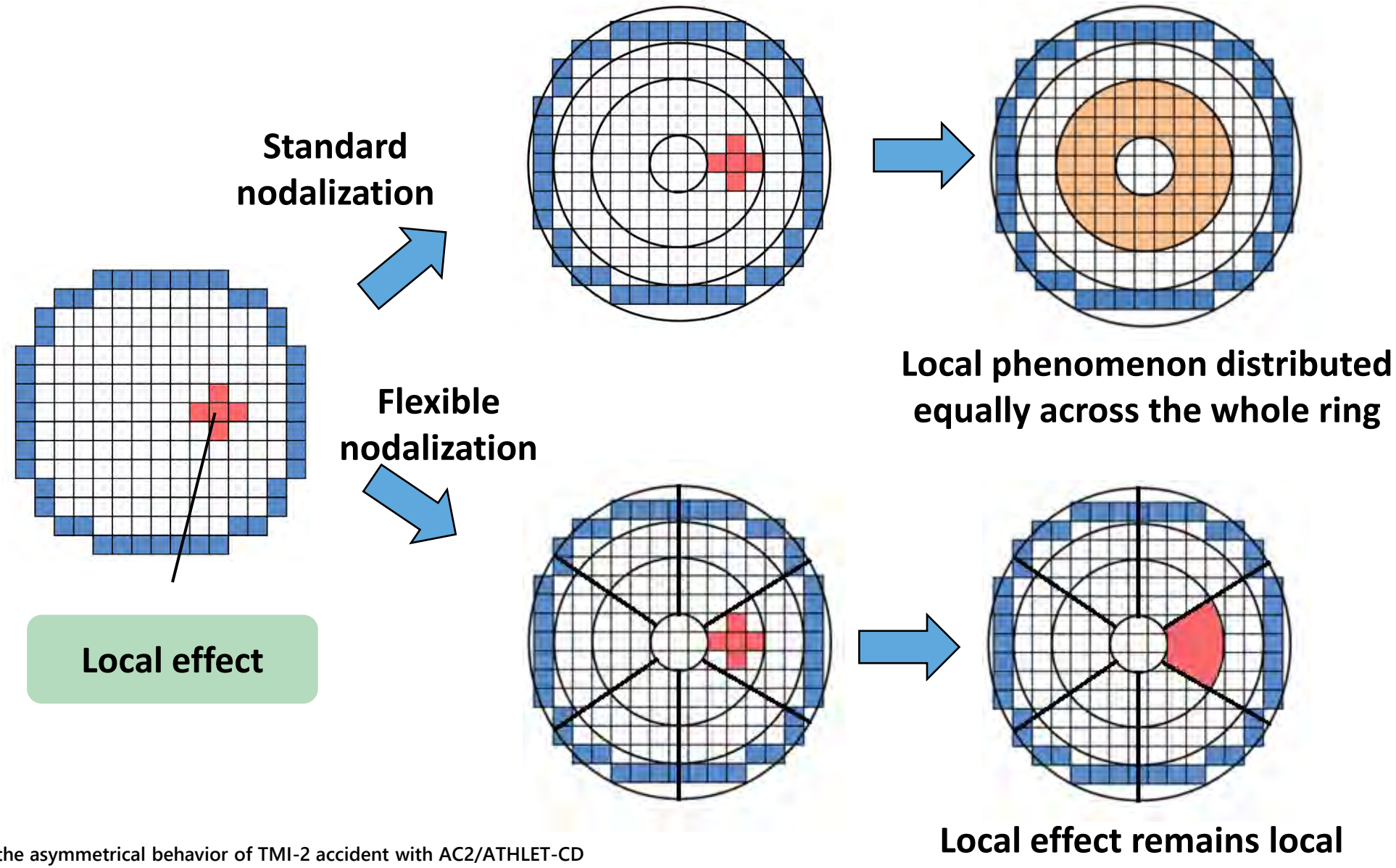

Source: Lovasz, L. 2026. *Further development of ATHLET-CD for simulations of accidents with asymmetrical characteristics. Dissertation - submitted.* PSS.

Change of mandatory nodalization

- Azimuthal subdivision of the rings
  - User-dependent amount of subdivision
  - Required data derived from other geometrical data
  - Innermost “ring” not subdivided
    - Avoid singularity problem

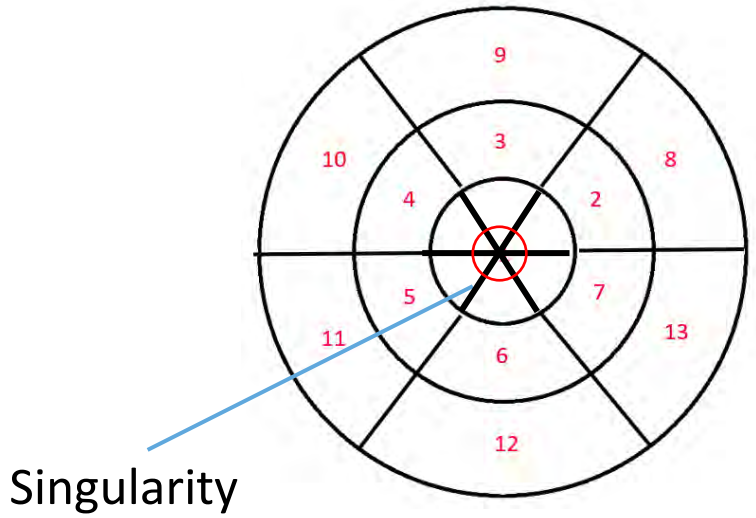

- Similar/same nodalization as in ATHLET for 3D core nodalization
    - Used for DBA

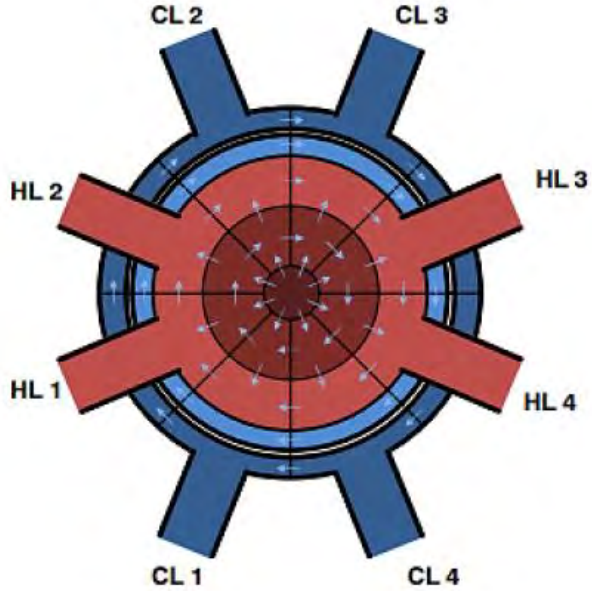

Source: P. Schöffel et. al.: ATHLET3.4.0 Users's Manual, nov. 2023

Required model changes due to nodalization change

- Most of the simulated phenomena are calculated for a single fuel pin (regardless of the node shape and size):
  - Results multiplied by the number of rods in a node
  - No model changes needed ✓

- Thermohydraulics (ATHLET) are flexibly definable
  - No model changes needed ✓

- Heat radiation between nodes, horizontal relocation of melt
  - Model changes needed, standard model is based on cylindrically symmetrical assumptions

- Additional model changes due to newly discovered bugs, minor, unrelated improvements

Heat radiation – degraded geometry (flexible nodalization)

- Identification of target areas complex
- Shadowing effects (3D)
- No cylinder-cylinder radiation

} Numerical determination of view factors

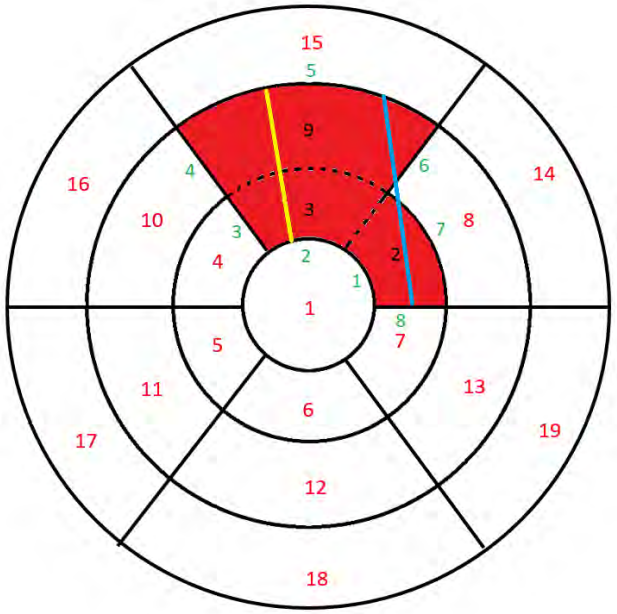

Cross section - reactor

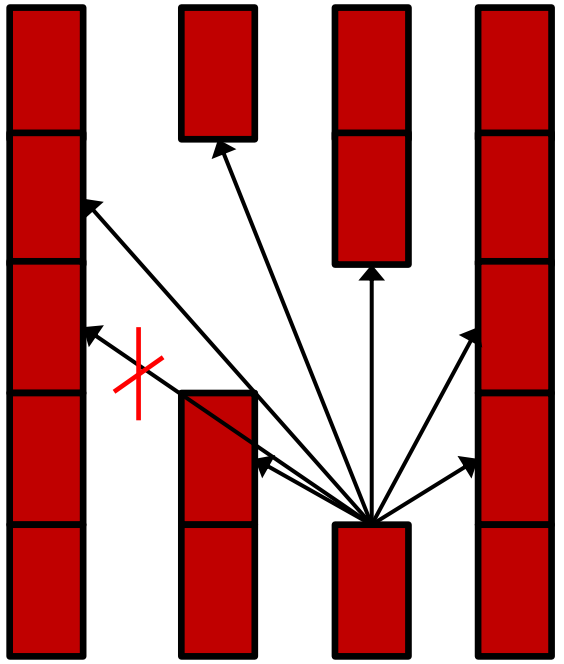

Longitudinal cut - reactor

Source: Lovasz, L. 2026. *Further development of ATHLET-CD for simulations of accidents with asymmetrical characteristics. Dissertation - submitted.* PSS.

Heat radiation – flexible nodalization - logic

- Old heat radiation model between neighbouring intact nodes
  - Slight adjustments regarding directions and partners
- After a cavity is created, free surfaces are formed
  - New view factors are calculated numerically between all the surfaces, including shadowing effects
- Heat exchanged via heat radiation calculated:
  - Pure axially
  - Pure horizontally
  - Diagonally
- View factors remain constant until further node melts
- Exchanged power added to energy equation of the structures

Application: TMI-2 accident

- 2 – loop PWR
- LOCA due to stuck open PORV valve
- Severe accident

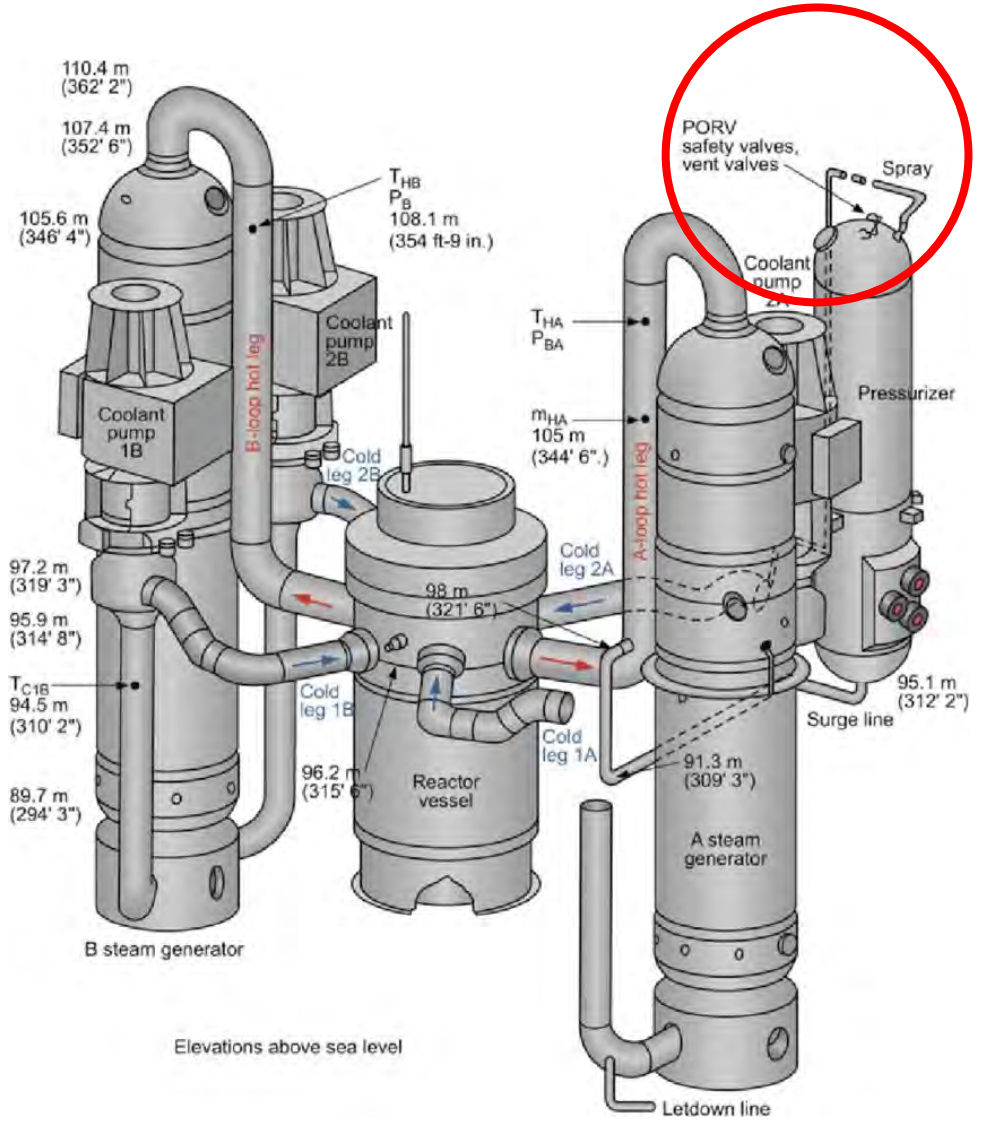

Source: TMI-2 - A Case Study for PWR Instrumentation Performance during a Severe Accident - Scientific Figure on ResearchGate. Available from: https://www.researchgate.net/figure/2-TMI-2-primary-system-layout_fig8_282614161 [accessed 16 Mar, 2022]

TMI-2 asymmetric behaviour

- Proven asymmetric behaviour

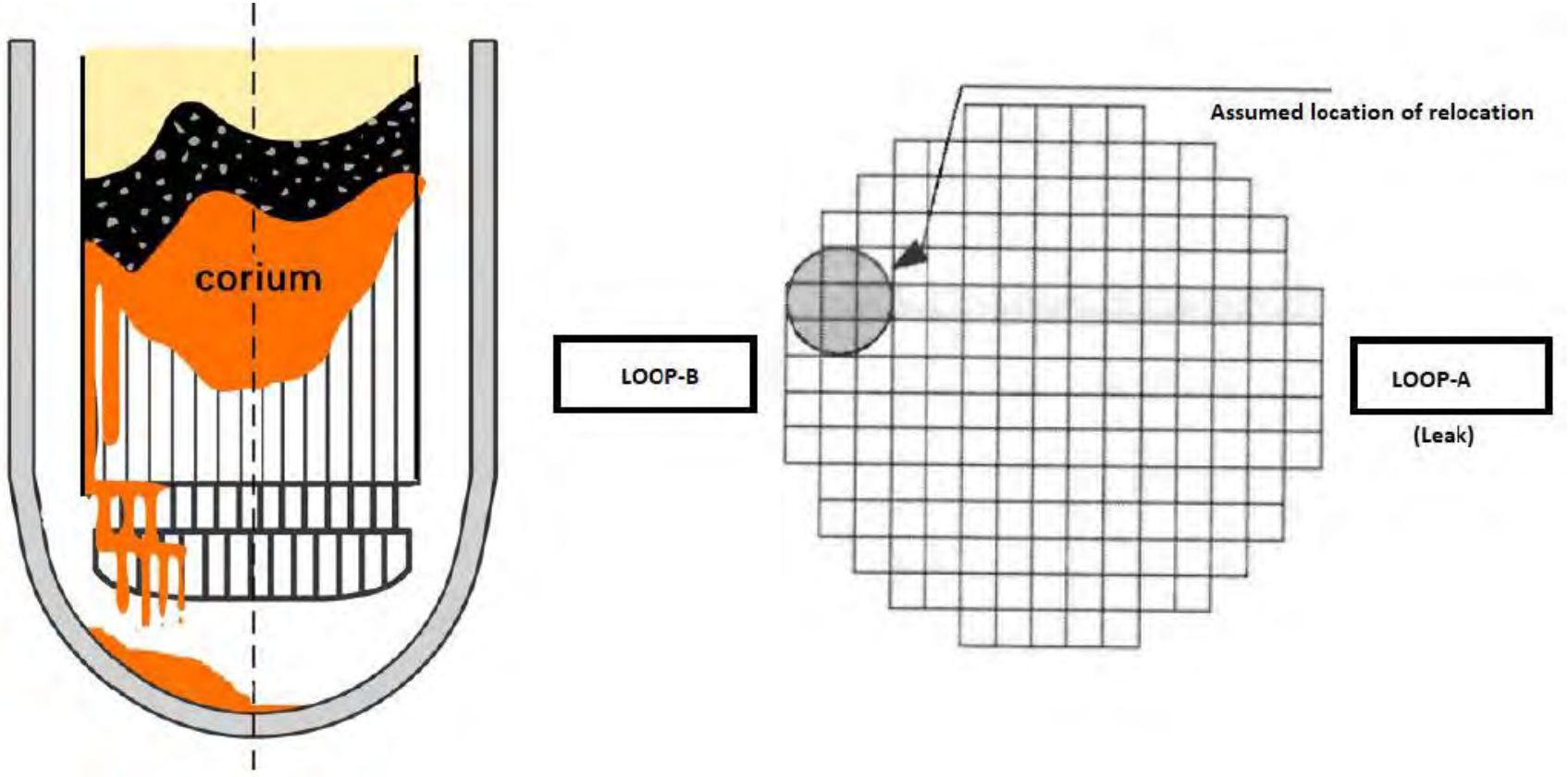

Source: Lovasz, L. 2026. *Further development of ATHLET-CD for simulations of accidents with asymmetrical characteristics*. *Dissertation - submitted*. PSS.

TMI-2 accident: old method

- Core nodalization
  - Rings

- Local impact can not be considered
  - Rings create an average

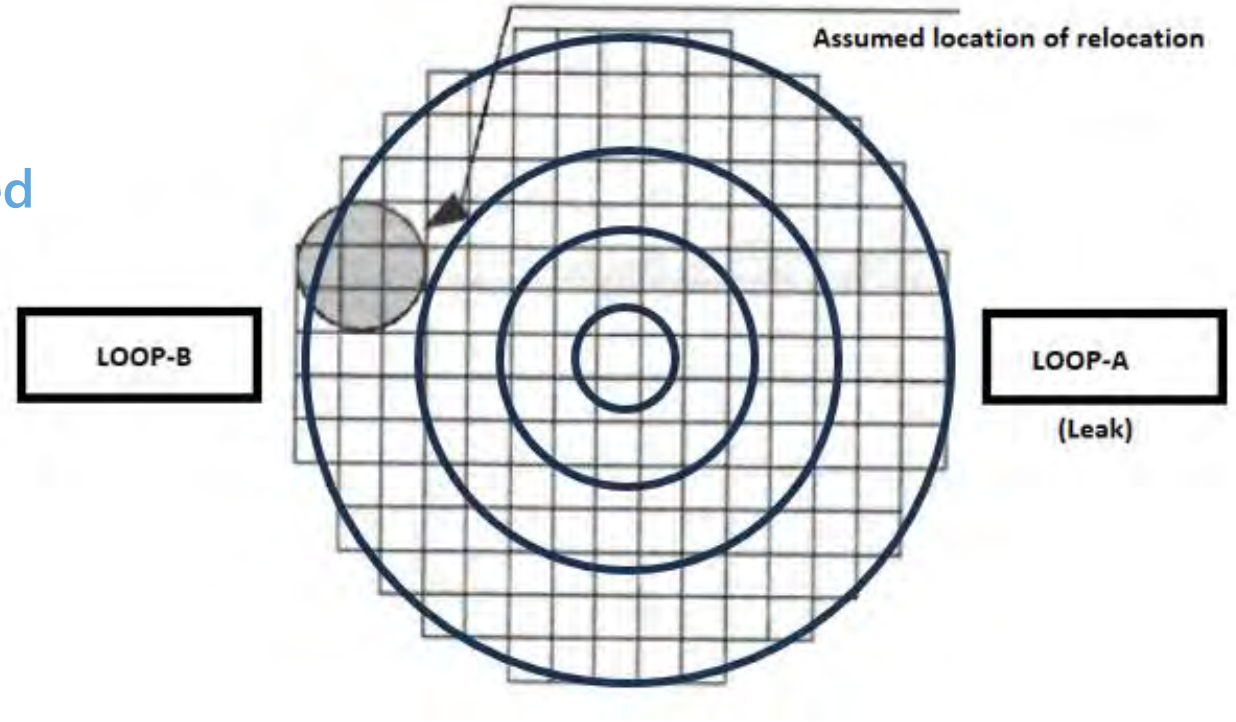

Source: T. Drath, et al.: Simulation des TMI-2 Unfalls mit dem Programmsystem ATHLET-CD (Teil 1), RUB-LEE, BMWi 150 1241, 12.2004

TMI-2 accident: new method

- Azimuthally subdivided core nodalization
  - Local impact remains local

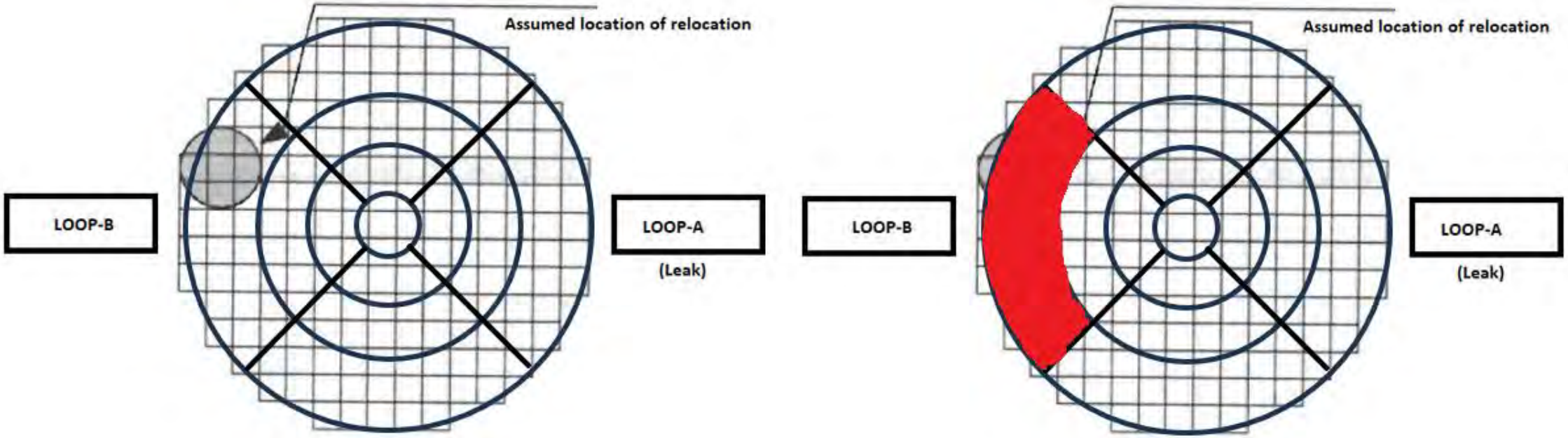

Source: Lovasz, L. 2026. *Further development of ATHLET-CD for simulations of accidents with asymmetrical characteristics. Dissertation - submitted.* PSS.

TMI-2 accident: new method

- Symmetrical boundaries → symmetrical simulation

- Asymmetric impacts had to be defined
  - Leak in one leg (hot leg A)
  - Different heat removal from steam generators due to different feedwater supply
  - Main coolant pumps operated differently

- Everything else → symmetrically defined

- Nodalization
  - Each element has its own structure, element, no artificial grouping and simplifications
  - Practically a 3-D nodalization of RPV, separate modelling of the loops

TMI-2 simulation: integral results

- **Evolution of pressure:**
  - Good indicator about the accident evolution
  - Similar progression
  - Small deviations from the real measurements
  - Qualitatively fairly good agreement for both calculations
  - Some missing models:
    - No fragmentation→ No pressure peak during melt relocation to LP

- **Overall accident evolution similar**

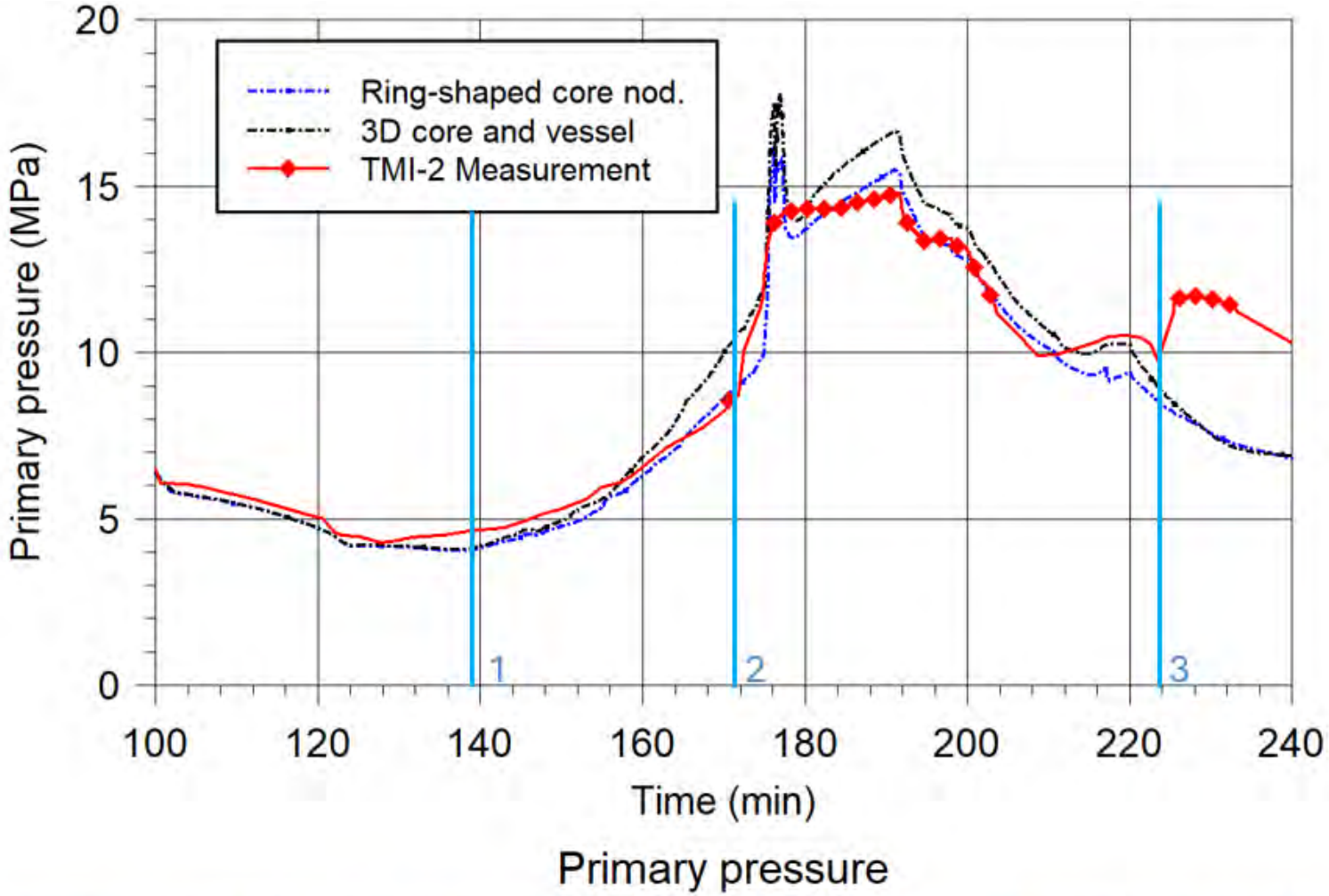

Primary pressure

1: closure of PORV valve 2: main coolant pump turned on 3: melt relocation to LP

TMI-2 simulation: local results

- Clearly asymmetric characteristics in RING 2

- Closer to HL-B
  - As expected
  - As in real plant

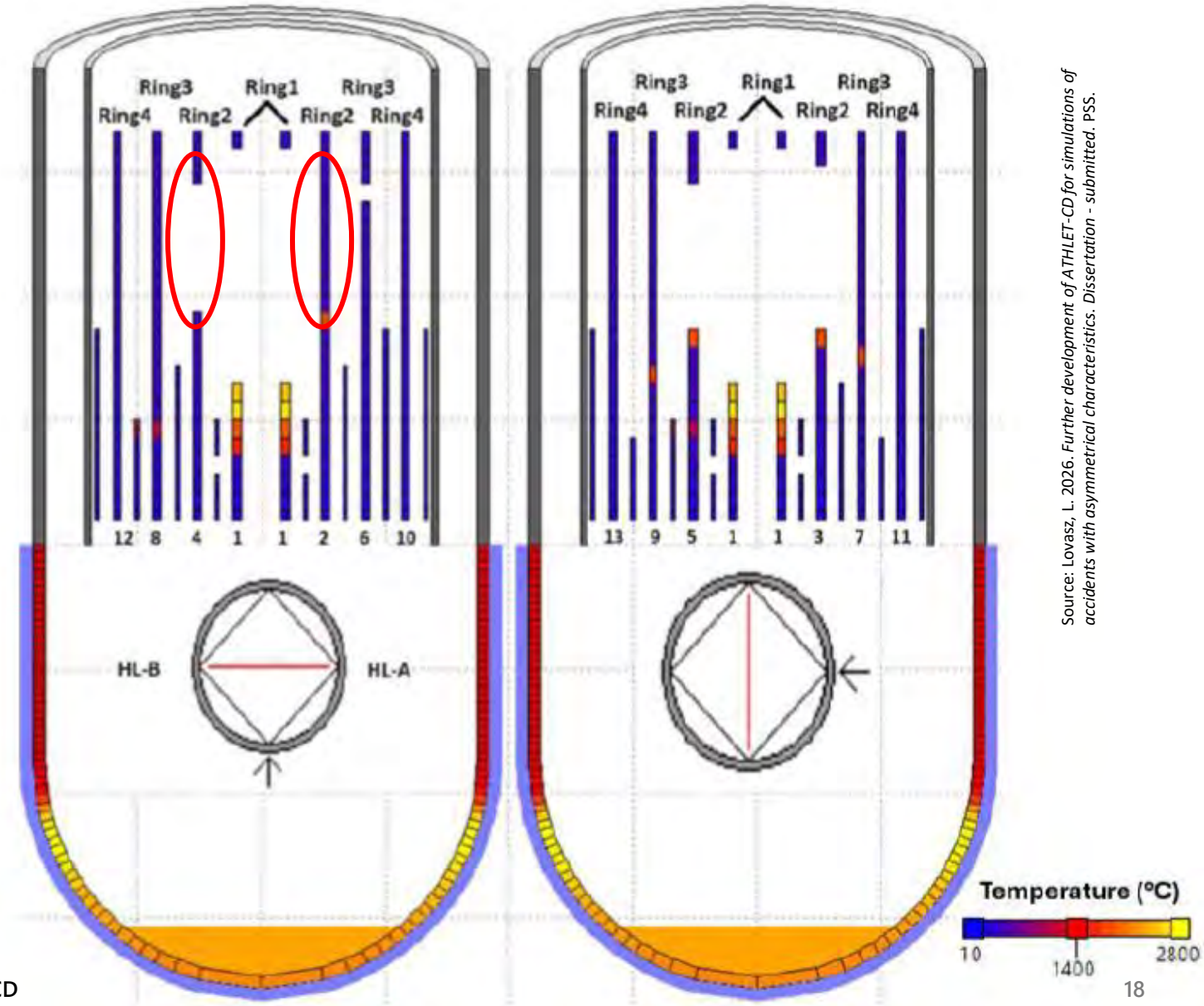

Source: Lovasz, L. 2026. *Further development of ATHLET-CD for simulations of accidents with asymmetrical characteristics. Dissertation - submitted.* PSS.

TMI-2 simulation: reason for asymmetry

- Different feedwater supply to SG-s
- One sided leak (PORV) minor impact

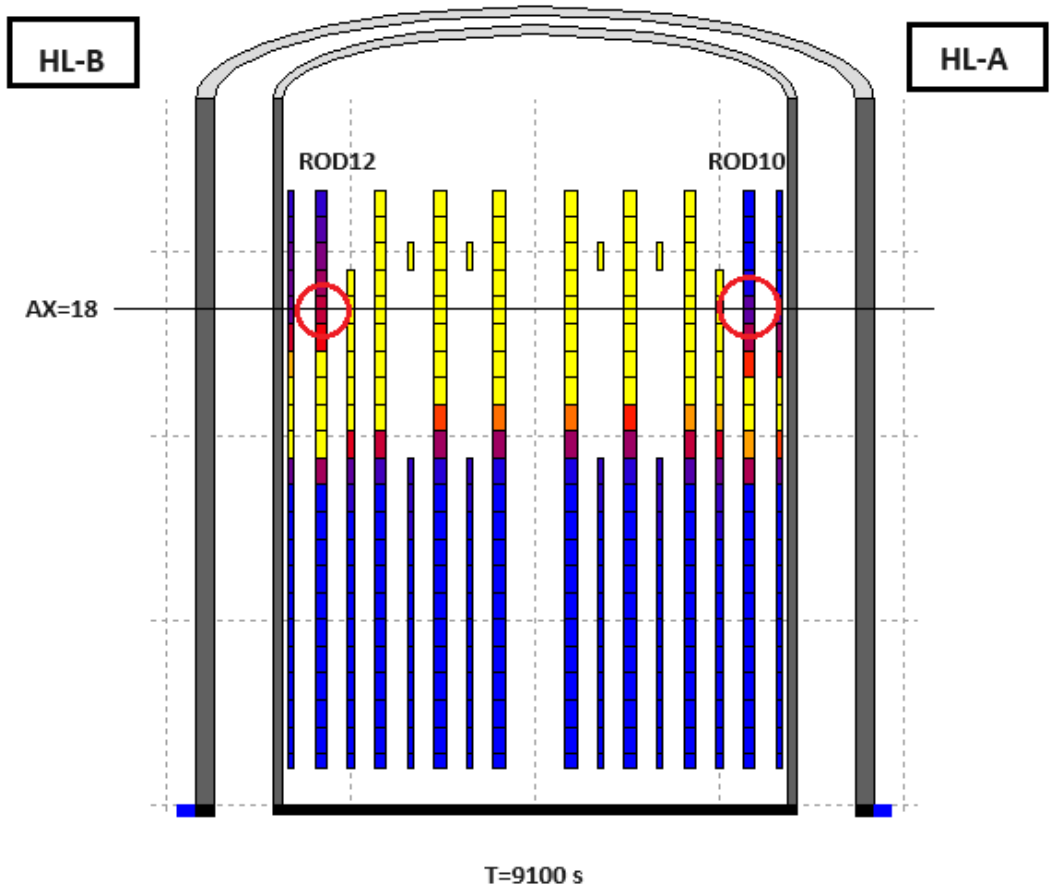

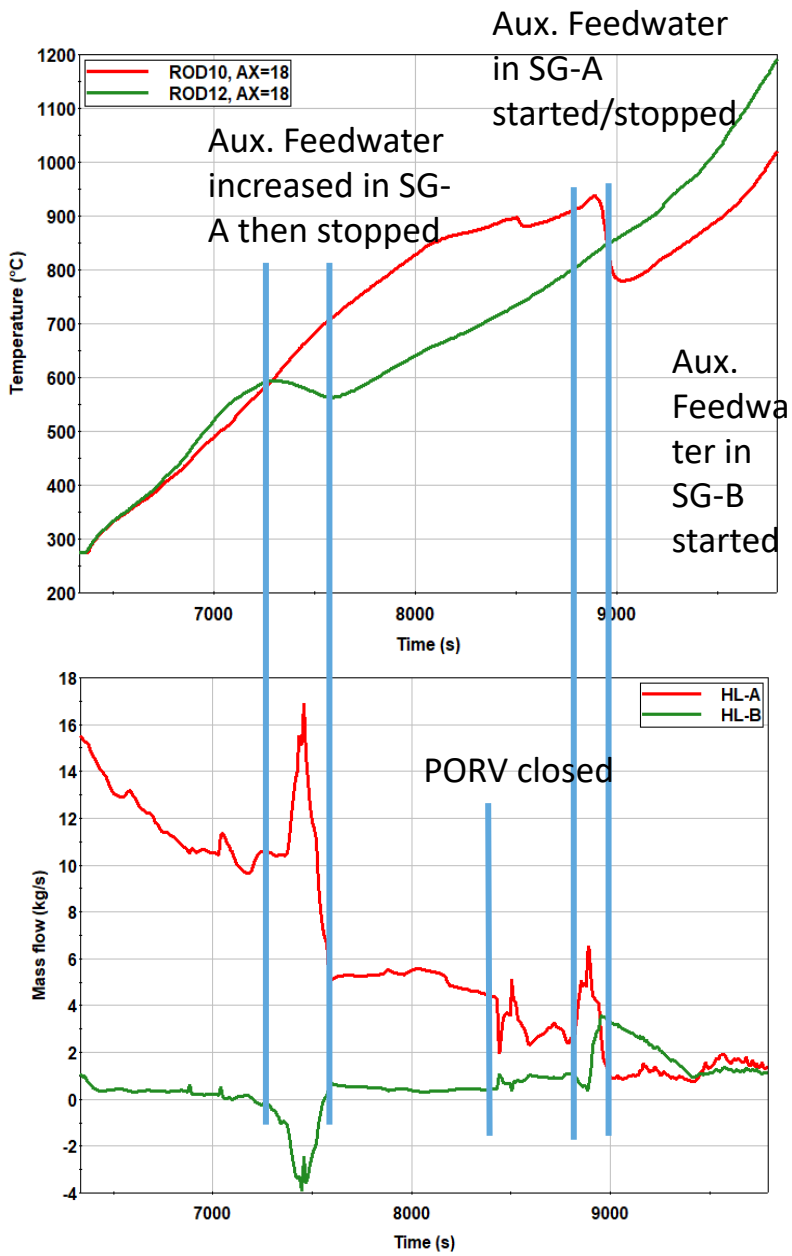

Source: Lovasz, L. 2026. *Further development of ATHLET-CD for simulations of accidents with asymmetrical characteristics. Dissertation - submitted*. PSS.

Conclusions and outlook

- ATHLET-CD core nodalization changed
  - Azimuthal subdivision possible
  - Models adjusted / newly developed

- TMI-2 was simulated using the new nodalization
  - Asymmetric behaviour reproduced
  - Possible explanation found

- Future improvements needed:
  - Input deck
  - Models: melt relocation, fragmentation, debris bed, etc.

- Theoretical option created to consider local effects during a severe accident

Thank you for your attention!

The work was carried out as part of a research project commissioned by the Federal Ministry for the Environment, Climate Action, Nature Conversvation and Nuclear Safety (BMUKN)

ENHANCING SEVERE ACCIDENT CODES WITH SIMULATION CAPABILITIES FOR NUCLEAR TRAINING APPLICATIONS

Mariano Martín and Isabel Parrado*
Westinghouse
Avenida Montes de Oca, 1
San Sebastian de los Reyes, Spain
mariano.martingarcia@westinghouse.com; isabel.parradorodriguez@westinghouse.com

Bastien Poubeau
Autorité de Radioprotection et de Sureté Nucléaire (ASNR)
PSN-RES
F-92260, Fontenay aux Roses, France
bastien.poubeau@asnr.fr

ABSTRACT

Simulators for Nuclear Power Plants are essential tools for training plant operators [1]. Nevertheless, most existing simulators worldwide are limited to Design Basis Accidents and do not address the management of Severe Accidents [2]. The importance of realistic training for such scenarios has grown significantly following the implementation of post-Fukushima safety enhancements, which introduced measures to better mitigate severe accident conditions [3].

The European project ASSAS (Artificial Intelligence for Simulation of Severe Accidents) seeks to bridge this gap by developing a proof-of-concept severe accident simulator. This prototype will incorporate a generic Pressurized Water Reactor based on fundamental principles, with its Graphical User Interface designed by Westinghouse.

Beyond serving as a demonstrator for future industrial-grade simulators, this basic-principles simulator is intended to support educational and training activities focused on severe accident phenomenology. Achieving this goal required balancing several challenges: representing the complexity of severe accidents without overwhelming users, covering a broad range of phenomena and operational situations with a limited set of systems and scenarios, and ensuring accurate real-time simulation performance.

This paper presents the work carried out by Westinghouse, in charge of the development of the simulator within the ASSAS project. It details the development of simulator specifications and interfaces, the selection of systems and scenarios, and the design of the Graphical User Interface, along with the main criteria adopted to meet the project objectives.

KEYWORDS
Simulator, Training, TEAMSUITE®, ASTEC, Graphical User Interface

1. INTRODUCTION

The European project **ASSAS (Artificial Intelligence for Simulation of Severe Accidents**) was initiated in 2022 with the objective of developing a proof-of-concept simulator for Nuclear Power Plant (NPP) Severe Accidents (SA), primarily for educational and training purposes. The simulator integrates the ASTEC (Accident Source Term Evaluation Code) [1], developed by ASNR (France), within a commercial simulation environment based on TEAM_SUITE®, Westinghouse's modeling and simulation platform.

The prototype aims to illustrate the key phenomena associated with severe accidents and to serve as a training tool for a broad audience, including students, nuclear professionals (operators, TSOs, regulators, emergency responders), and non-specialists such as decision-makers and civil society. To fulfill these objectives, the simulator incorporates:

- An intuitive graphical interface for scenario control and evolution.
- Clear visualization of critical severe accident phenomena.
- Real-time or accelerated execution without significant loss of accuracy.

To enable real-time operation, ASTEC has been adapted to maintain acceptable fidelity while ensuring seamless interaction with the industrial simulation environment TEAM_SUITE®. The prototype employs non-sensitive data from a generic 4-loop, 1,300 MWe PWR model, with scalability to other reactor designs, including BWRs. Ultimately, the project seeks to demonstrate the feasibility of integrating severe accident capabilities into full-scope simulators, which are currently limited to design-basis scenarios.

A distinctive feature of ASSAS is the investigation of Artificial Intelligence (AI) techniques to develop surrogate models for selected physical models or plant systems [2]. Users will have the option to select between native ASTEC physics-based models and data-driven surrogates. Machine learning approaches are being explored to create fast, efficient models that significantly enhance computational performance. Unlike first-principles models, AI-based models learn correlations from training data, offering substantial speed advantages. However, their complexity increases with the number of input/output variables—a challenge commonly referred to as the "curse of dimensionality." To mitigate this, the simulator limits the number of available actions while preserving sufficient flexibility to illustrate key severe accident phenomena. Adding new systems, actions, and malfunctions remains technically feasible when relying exclusively on physics-based ASTEC models.

This paper presents the design process of the simulator, including interface development, ASTEC integration, scenario selection, and validation methodology.

2. A GRAPHICAL USER INTERFACE (GUI) SERVING OUR PEDAGOGICAL OBJECTIVES

The data presented to the user is selected to support operation of the defined scenarios and to provide a clear understanding of severe accident behavior. The GUI design follows a minimalist philosophy aimed at decision-making in critical situations, emphasizing clarity and cognitive efficiency. Key principles include:

- **Reducing cognitive load:** Display only essential information to avoid overwhelming the user and enable focus on critical system states.
- **Visual hierarchy:** Highlight key parameters while relegating secondary data to less prominent levels or making them accessible on demand.
- **Context and clarity:** Ensure each data point serves a clear purpose in understanding accident progression and supporting safe, timely decisions.
- **Progressive interaction:** Allow deeper exploration of details only when necessary (for example through pop-up windows), preventing screen overload.

The selected data is categorized into three groups according to the accident phase: (i) typical instrumentation for nominal operation and transients, (ii) variables associated with Design Basis Accidents (DBA), and (iii) parameters and flags related to the severe accident phase.

To complement this approach, the interface includes a selector that enables users to switch between two visualization modes: one displaying all variables available in the Human-Machine Interface (HMI) and another limiting the view to those typically present in a real Main Control Room (MCR). For example, the concentration of combustible gases in the containment will be hidden in the MCR view. When a Station Blackout (SBO) malfunction is active, transmitters not battery-backed are lost. This feature combines flexibility for comprehensive analysis with operational realism for training and assessment.

1.1 Summarizing severe accident data efficiently

The simulator interface is structured as a hierarchical display tree, comprising five main views: Home display, Overview display, Systems display, Severe Accident display, Alarm display.

The Home display provides a comprehensive representation of the Nuclear Power Plant layout, enabling navigation to individual system views by selecting the corresponding system icons.

The second level, referred to as the Overview display, consolidates and presents the most critical parameters for each system in a single interface.

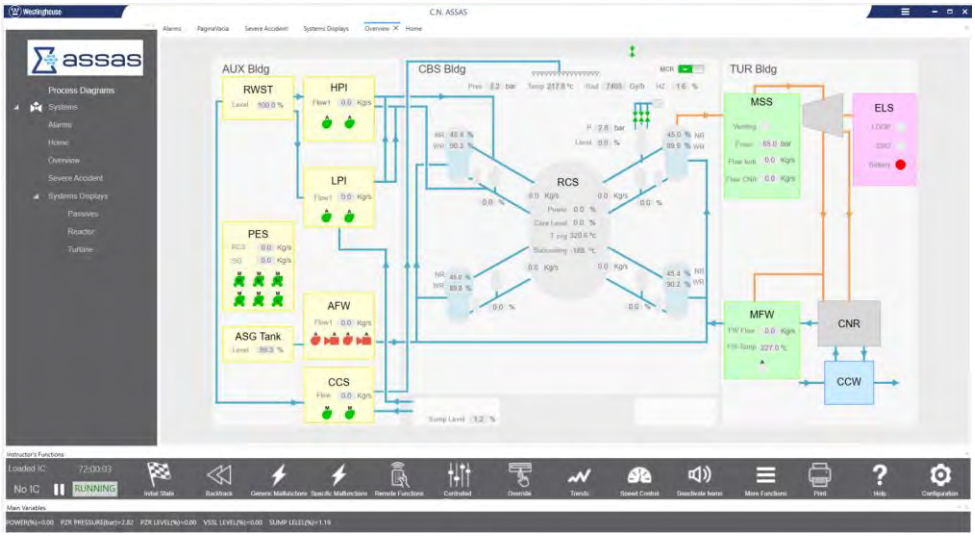

Figure 1. Overview Display.

The third level, the Systems display, offers an extensive view encompassing all plant systems. Users can explore this display through scrolling functionality. As the simulator is designed for conceptual understanding rather than operator training in a realistic environment, this structure facilitates a clearer comprehension of plant operations and system interdependencies.

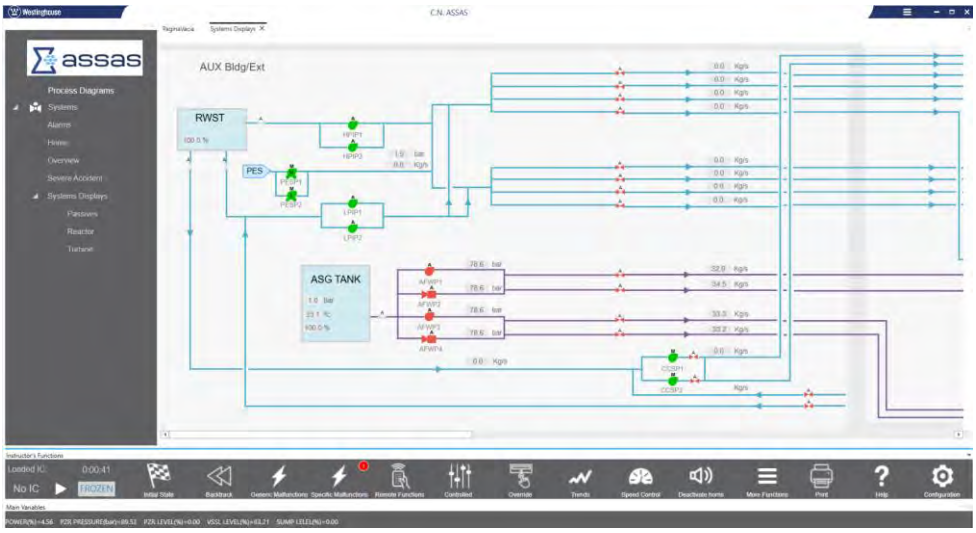

Figure 2 System Display 1

The alarm display shows, for each system, the alarms that appear during the scenario. For didactic purposes, these alarms have been grouped into three categories: (i) alarms associated with normal operation, (ii) alarms triggered by the progression of a Design Basis Accident (DBA), and (iii) alarms related to the severe accident phase.

The Severe Accident display provides advanced functionalities designed to support detailed monitoring and analysis during severe accident scenarios. Key features include:

- A Shapiro diagram illustrating hydrogen (H_2) and carbon monoxide (CO) flammability conditions, associated to a pop-up window giving the detailed steam-gas mixture composition inside the containment (hydrogen, carbon monoxide, steam, oxygen, carbon dioxide).
- Interactive buttons adjacent to activity indicators, enabling pop-up windows that display isotopic compositions within the containment and those released to the environment. These include specific radionuclides representative of a chemical family, to show their different behavior during the accident [6]:
    - Xe-133 (representing Noble gases)
    - I-131 and I132 separated in organic, inorganic, and aerosol forms (representative of Halogens)
    - Cs-134, 136 and 137 (representative of Alkali metals)
    - Te-132 (for the Tellurium group)
    - Sr-90 (representative of Barium and Strontium)
    - Ru-103 (representative of Noble metals)
    - La-140 and Cm-242 (for Lanthanides and Actinides)
    - Pu-241 (for the Cerium group)
    - Mo-99 (for Early transition elements)
    - Sb-127 (for Highly volatile metals)
- A summary of corium formation in the core region, the vessel lower plenum and the reactor pit, associated with a pop-up window giving the mass of magma and debris in 38 different meshes.
- In the safeguard component area, the current alignment of each safety system is clearly identified by highlighting in black the labels corresponding to its active suction source and discharge point.

The display also includes a **Fission Product Barrier Threats** table, which identifies potential challenges based on plant parameters exceeding predefined thresholds. This table supports decision-making regarding

applicable mitigation strategies and is complemented by a graph showing the time evolution of selected variables.

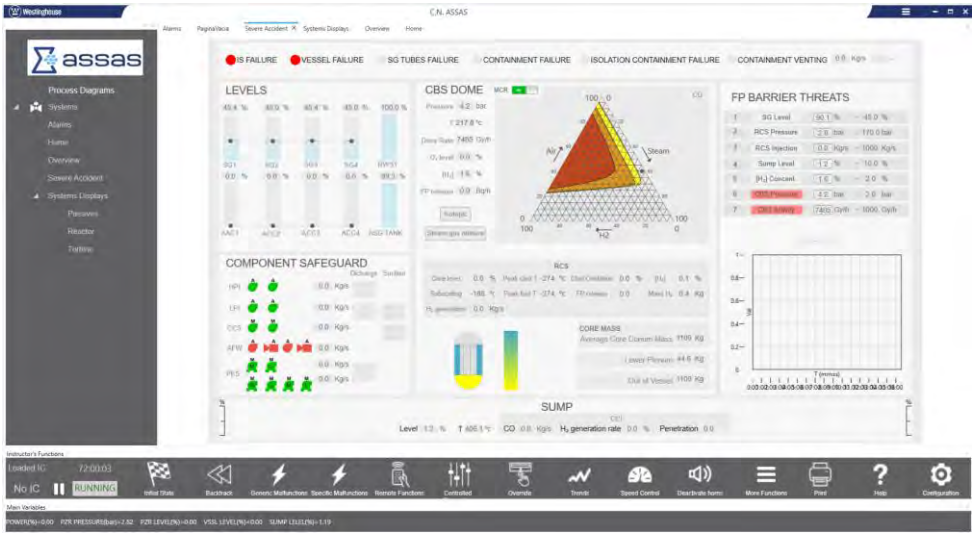

Figure 3 Severe Accident Display

1.2 An interactive tool

The Instructor Station (IS) is the application responsible for providing the instructor, or any other user of the Simulator, with the control and supervision capabilities of a simulation session of the ASSAS Simulator.

The Instructor Station (IS) provides the capability to reset the simulator to a selected initial condition, enabling the user to initiate the simulation from a steady-state configuration, immediately following the onset of an accident, or at any point within the accident sequence. Furthermore, the IS allows the recording of snapshots at any stage of the simulation for subsequent analysis. These snapshots include complete ASTEC savings with all physical variables used for computation.

An additional functionality of the Instructor Station is the ability to introduce predefined malfunctions during the simulation, such as Loss of Coolant Accident (LOCA), Station Blackout (SBO), or Steam Generator Tube Rupture (SGTR) with fixed rupture severities.

The Instructor Station provides real-time monitoring of simulation performance by displaying the current time-step value and CPU utilization. This functionality enables the identification of potential numerical convergence issues and deviations from real-time execution, ensuring the stability and reliability of the simulation process.

Interactive functionality allows users to operate components by selecting active elements such as valves and pumps. Additionally, any displayed variable can be plotted by clicking on its corresponding readout. Visual indicators are employed to denote component status: active pumps and open valves are displayed in red, whereas inactive components appear in green.

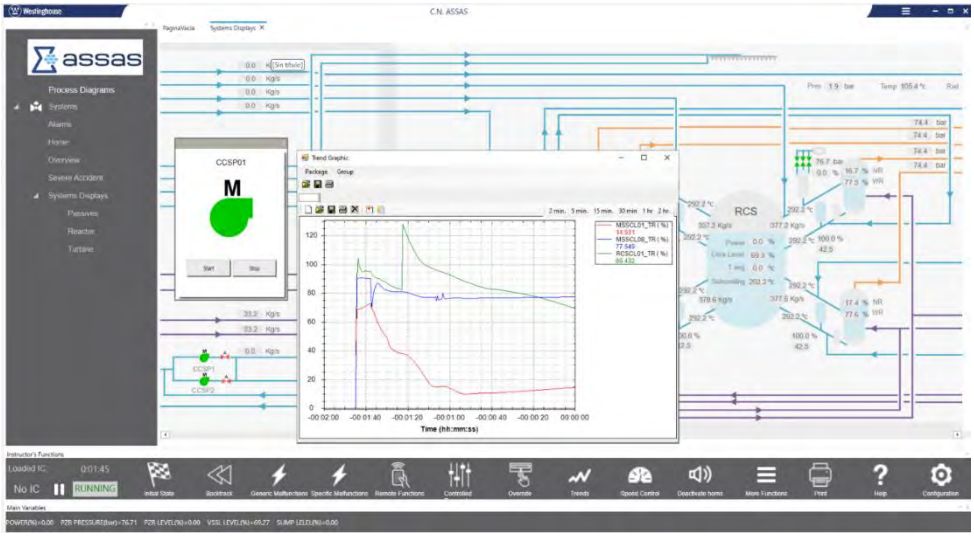

Figure 4 Plots and Controls

1.3 Virtual reality

The objective of this tool is to provide 3D animated and interactive visualizations of key components of a four-loop PWR nuclear power plant—such as the reactor core, vessel, coolant system, steam generators, and containment building—to offer users additional insight into system behavior during severe accident scenarios. Designed for didactic purposes, the interface aims to help users understand the progression of severe accidents in an integrated environment. It provides a qualitative rather than quantitative representation of plant conditions, since the physical phenomena are not known with the level of details presented in the display. A disclaimer will make it clear to the user.

The main functionalities include visualization through Virtual Reality (VR) images of critical physical parameters—such as temperature, void fraction, pressure, hydrogen concentration, core degradation, and water level—based on data provided by the Human-Machine Interface (HMI). The magnitude of the value will be indicated by a color scale in all components, interpolating from the value in each ASTEC control volume. These visualizations cover the containment area, the primary circuit, and different sections of the reactor core, enabling an immersive and intuitive understanding of accident evolution.

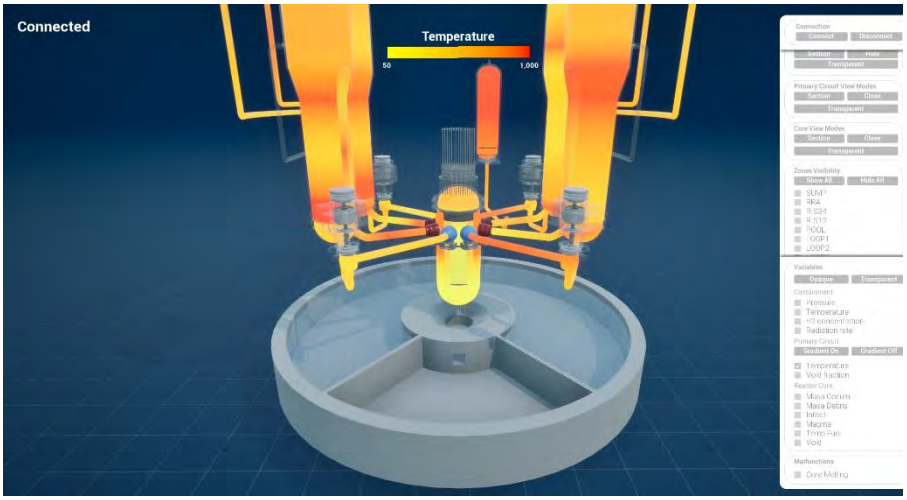

Figure 5 VR image

3. A REACTOR MODEL SHOWING THE MAIN PHENOMENA OF A SEVERE ACCIDENT

Two scenarios have been considered in the specifications of the simulator:
- SBO with Auxiliary Feedwater (AFW) Turbine Driven Pump (TDP) failure,
- LOCA with Safety injection and Containment spray systems failure.

These scenarios have been chosen, one with high pressure and the other with low pressure, to try to cover as much phenomenology as possible [7]. In real life, these are the scenarios that are used to validate the severe accident management guidelines because they go through most of the guideline strategies.

These scenarios define:
- The operator actions that must be modelled by ASTEC or the data-driven surrogate models.
- The transmitters that the final user must monitor at least.
- The involved phenomena.

The specific evolution will depend on the automatic actions, instructor and operator actions taken by the user. The simulator can be used in a discovery mode, for which all actions are allowed for the trainee. In the training mode, malfunctions are triggered by the instructor from his own station, limiting the possibilities for the trainee to operator actions. The additional malfunctions include the induced steam generator tube rupture and the delay to recover some active safety systems.

Due to the presence of Passive Autocatalytic Recombiners (PARs) and other modelling choices, calculation results show that combustion and explosion risks can be avoided. Therefore, the combustion model of ASTEC is not used.

3.1 Scope of the simulator

The ASSAS simulator scope covers just the Design Basis Accident (DBA) and the Severe Accident (SA), excluding the normal operation. So, Turbine, Condenser, Condensate, Circulating water, Reactor Heat Removal and Chemical and Volumetric control systems are out of scope.

The systems that are presented to be operated or monitored by the GUI are:
- Auxiliary Feedwater System (AFW).
- Reactor Coolant System (RCS) including PORVs (Pressure Operated Relief Valve), RCP (Reactor Coolant Pumps) and safety valves.
- Main Steam Supply System (MSS) including SGs.
- Containment Cooling Sprays (CCS). It is assumed to fail but it can be recovered in the LOCA sequence (instructor action).
- High- and Low-Pressure Injection System (HPI), assumed unavailable in both sequences
- Accumulator Injection System (ACI).
- Portable Equipment System (PES), with a deployment delay fixed by the instructor.
- Filtered Containment Venting System (FCVS), based on a sand bed filter.

AFW and PES have been removed from ASTEC input deck to be developed by Team_SUITE® tools (Team_Flow for thermohydraulics and Team_Logic for logics). The objective was to show the interoperability of both tools, illustrating how data could be imported from an existing DBA simulator to extend it to severe accidents.

3.1.1 Portable Equipment System (PES) scope

It has been decided to include PES in the simulator, to show the user important mitigation actions for the considered scenarios, in line with the strategy deployed by many operators. To show the effect of early and late involvement of PES, the instructor can impose a delay between 20 minutes and 24 hours to connect them. The PES consists of external pumps installed at certain plant locations to supply cold water, enabling the removal of accumulated latent heat from the coolant and structural materials, which results from residual heat generation after a reactor trip.

It is considered that the system has a limited number of portable pumps that can be used in the simulator: three medium-pressure (21bar) and three low-pressure (12bar) pumps. Each type of pump can be connected to a pair of Steam generators, or to the RCS. In this latter case, cold water is injected into the cold legs and hot legs simultaneously, through the safety injection lines. The volume injected in the RCS is limited to avoid an overfilling of the sumps and the flooding of the reactor cavity, in line with the ex-vessel melt retention strategy. In addition, the input deck used in the simulator does not include a model for the external cooling of the vessel and for the water-coolant interaction in case of vessel rupture with a flooded cavity. As far as the Steam generators are concerned, it is assumed that the PES will be regulated not to exceed 44% of the narrow range level, in line with the regulation of the AFW system.

These types of pumps comply with the requirements of the system in both situations: In the need of high-pressure water injection and in the other case where a high flow of water is needed to avoid an induced SGTR on hot and dry SGs.

3.1.2 Game Over Flags and simulation end

The simulator includes specific “game over” flags to indicate when the scenario exceeds its intended scope. They correspond to situations that are challenging or even impossible to model with ASTEC, and that relate to a failure of the severe accident mitigation strategy. These conditions are:

- **High-pressure vessel rupture (above 20 bar):** The simulator displays the message *“Simulator out of scope: high-pressure vessel rupture possibly leading to direct containment heating and containment threat.”* Such situations can be modelled by ASTEC, but with a high computational cost, probably not compatible with real-time execution. They were expected to be difficult to capture with machine learning models as well. So, they were excluded from the scope of the simulator for simplicity.
- **High-pressure containment failure (above 6 bar):** The message *“Simulator out of scope: probable containment failure due to overpressure”* is shown. Anyway, ASTEC does not include a mechanical model of the containment, making the modelling of such transient impossible with the current implementation of the simulator.
- **Basemat melt-through:** The message *“Simulator out of scope: containment failure due to basemat melt-through”* is displayed. ASTEC cannot model the evolution of the accident after the complete failure of the basemat.

The maximal simulation time is fixed at 5 days, considering that the emergency response would switch to a different organization and time scale after this duration, with more external support to the site. It is also considered that catastrophic containment failure is less likely after this delay.

3.2 Scenario 1: LOCA with Safety injection and Containment spray systems failure scenario

The phenomena considered in the simulation cover two main phases: the Design Basis Accident (DBA) phase and the Severe Accident phase.

During the DBA phase, the initiating event is a 6-inch cold leg LB-LOCA (Large Break LOCA) combined with the failure of the active Safety Injection (SI) systems (LPI and HPI) and containment spray systems. The CSS can be recovered during the simulation with a delay fixed by the instructor varying from 1 to 24 hours after the LOCA initiation. This leads to rapid RCS depressurization, reactor and turbine trip on low pressure, SI signal activation (with SI failure), and containment pressurization. Additional phenomena include extensive Departure from Nucleate Boiling (DNB), core blowdown, RCP coastdown, ineffective accumulator discharge due to core bypass, and loss of safeguard systems. Fuel overheating occurs, and fission products—mainly from the fuel gap—are released into the RCS. The user may have the possibility to inject water from the Portable Equipment System to mitigate the accident, with a delay fixed by the instructor.

The Severe Accident phase involves high cladding temperatures promoting oxidation, extensive cladding failures, and further fission product release into the RCS. Hot gas circulation within the RCS occurs, accompanied by hydrogen generation and discharge of steam and hydrogen into the containment through the broken leg. Autocatalytic recombiners are assumed available to mitigate hydrogen (and later CO) accumulation and prevent explosions.

As the accident progresses, increased fission product release to containment occurs, followed by core melting and relocation, corium slump into the reactor vessel lower plenum, and potential lower head failure according to ASTEC model criteria. Subsequent phenomena include corium discharge into containment, corium-concrete interaction, ex-vessel hydrogen and CO generation, recombination by autocatalytic devices, containment basemat ablation, and containment pressurization. Long-term risks include containment overpressure failure, and eventual filtered venting of fission products.

Several actions are proposed to the trainee to mitigate the accident progression. The PORVs of the pressurizer and the steam generators can be opened, with little expected effect due to the RCS depressurization. Since the AFW is assumed available, PES can only be used to inject water into the RCS. The CSS can be actuated manually once it has been recovered. The FCVS can be operated when the pressure exceeds 5bar, in line with typical depressurization strategies.

3.3 Scenario 2: SBO with AFW failure scenario

The simulated phenomena are divided into two main phases: the Design Basis Accident (DBA) phase and the Severe Accident phase.

In the DBA phase, the initiating event is a Station Blackout (SBO) combined with the failure of the Auxiliary Feedwater Turbine-Driven Pump (AFW-TDP). This leads to RCP coastdown, reactor trip, and unavailability of turbine bypass. Active safeguard systems fail, including HP and LP safety injection (except passive accumulators) and auxiliary feedwater. Steam generators dry out, degrading the RCS heat sink, while pressure rises until safety and relief valves cycle. The pressurizer PORV/SRV opens as RCS pressurization continues, subcooling is lost, and natural circulation is impaired due to AFW loss and steam presence in SG tubes. Ultimately, the core becomes uncovered and overheats.

The Severe Accident phase includes globally the same phenomena as the scenario 1 (the discharge of hot gases into the containment occurs through the pressurizer valves or an induced primary breach). In addition, the instructor can trigger a creep failure of SG tubes. The simulator also includes a possible creep failure of the primary circuit due to the circulation of superheated steam at high pressure, based on a physical model of ASTEC.

The actions proposed to the trainee to mitigate the accident slightly differ from the LOCA sequence. The PORVs of the pressurizer and the steam generators can be opened like in the LOCA sequence, thanks to their battery back-up. In this sequence, PES can only be connected both to the RCS and the Steam generators. They will start to operate when the concerned circuit's pressure will have decreased to their maximal counterpressure. The CSS is assumed unavailable during the whole sequence, due to the loss of electric power. The conditions for the opening of the FCVS are the same as for the LOCA sequence, since the main valve of the system is manual.

4. TECHNICAL CHALLENGES OF THE SIMULATOR DEVELOPMENT

4.1 Interface between the simulator and ASTEC

The integration of ASTEC within Westinghouse's Team-K environment has been made using a dll (dynamic link library) supplied by ASNR. This dll is loaded from an interface to parse the commands from Team-K to ASTEC, and also to connect Simulator's variables with the Odessa database (ASNR's proprietary hierarchical database format used by ASTEC), thus permitting writing and reading values in both directions.

The following image shows the top level ASSAS simulator Architecture, in which ASTEC is one of the possible simulation modules.

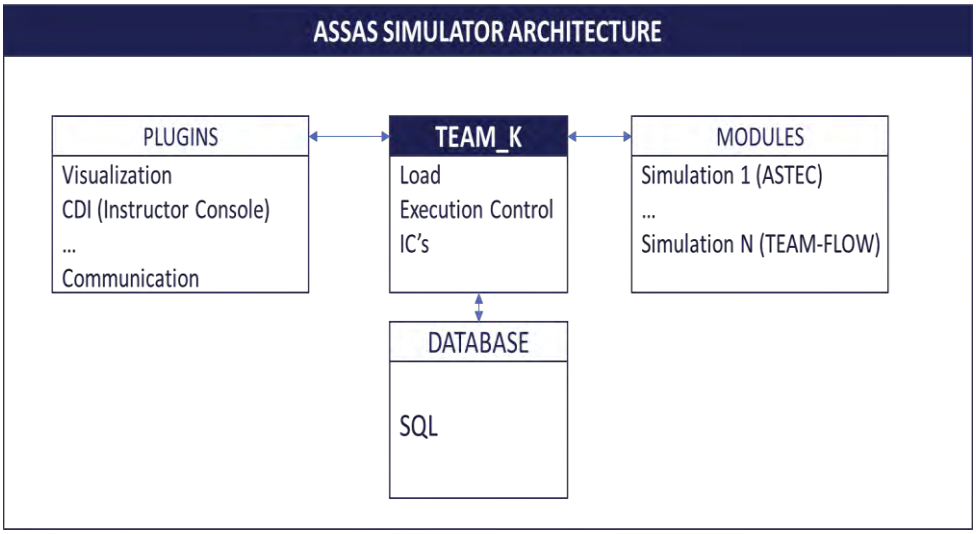

Figure 6 TEAM_K and ASTEC integration

After the integration, the resulting simulator supports the following functions:

- Start, Run, Pause, Stop from the GUI.
- Plot graphs of the calculated variables.
- Saving and Loading Initial Conditions.
- Interaction with ASTEC Simulation with GUI interactive commands.
- The integration of machine learning models is transparent for the simulator. The models can be called by ASTEC directly, or they will read and write in the Odessa database, through which they will interact with the simulator.
- Team-K can call other Team-Suite® models to include additional engineering systems, logic controllers, or a physical interface for example.

4.2 Performance tests

The results of the CPU-time consumption tests show that the simulator achieves expected performances. For the first 200 seconds of the simulation, ASTEC uses a reduced time step (0.1s) to limit calculation uncertainties. In this phase, the simulator is in average twice slower than real time. When the ASTEC time step reaches its nominal value of 1s, the simulator runs 2 to 3 times faster than real time, until it reaches the core degradation phase. For that complex phase of the accident, the acceleration factor is close to one. After the vessel rupture, the phenomena in the primary and secondary circuits are no longer computed, limiting the simulation to the containment models. This allows the simulator to run an order of magnitude faster than real time. The GUI and external models don't have significant impact on execution time.

4.3 Validation

The ASSAS project plans three distinct implementations of ASTEC:

1. The reference ASTEC version (physics-based model).
2. The reference ASTEC integrated with TEAM_SUITE®.
3. An optimized ASTEC version incorporating surrogate models (ASSAS version) integrated with TEAM_SUITE®.

The integration of ASTEC with TEAM_SUITE® is expected to introduce virtually no regression, as most physical models remain under ASTEC's control. Simulator performance will be assessed by comparing user-displayed data across the different ASTEC versions, using the reference model as the benchmark. Specific validation methods will be proposed for the integration of machine learning surrogate models.

5 CONCLUSION: SUMMARY OF THE ACHIEVEMENTS AND PERSPECTIVE ABOUT FUTURE TASKS

In the frame of ASSAS, the reference severe accident code ASTEC has been coupled with the commercial simulation platform TEAM_SUITE® to build a basic-principles severe accident simulator. This simulator benefits from the advanced functionalities offered by TEAM_SUITE®: ergonomic and customizable GUI, interactive simulation, easy data plotting and analysis, management of real time execution, easy navigation between various pre-saved initial conditions, etc. Improvements of ASTEC and of the reactor input deck made it possible to run the simulation in real time, offering realistic training conditions.

Efforts have been dedicated to the pedagogical relevance of the simulator. Severe accidents scenarios have been selected to show the main phenomena in various conditions and the effect of accident mitigation strategies. The interface was designed to be intuitive, attractive and synthetic, while offering the possibility to dive in specific details. This makes the simulator a powerful tool to spread severe accident knowledge to a broader audience.

Even if the simulator appears simple at first sight, with only a few operator actions, it can be adapted to industrial needs with limited efforts. New features can be added to the ASTEC input deck or directly in TEAM_SUITE®, thanks to the bidirectional interface between both systems. It can include additional accidental scenarios, more engineering systems, more automatisms, etc. The GUI can also be easily replaced by a full replica of a control room. The impact of such modifications on calculation time would probably be negligible.

The next step of ASSAS will consist in developing, interfacing and evaluating data-driven surrogate models, to check their impact on the accuracy and performance of calculations. Since machine learning models will

be trained on data generated with a specific design, their ability to generalize to new designs remains an open question.

ACKNOWLEDGMENTS

Funded by the European Union under the grant agreement no. 101059682. Views and opinions expressed are however those of the author(s) only and do not necessarily reflect those of the European Union or the European Commission-Euratom. Neither the European Union nor the granting authority can be held responsible for them.
Authors acknowledge the support of Alexei Miassoedev from the International Atomic Energy Agency for the development of the simulator specifications.

REFERENCES

1. *Application of simulation techniques for accident management training in nuclear power plants*, IAEA TECDOC SERIES, IAEA-TECDOC-1352 (May 2003).
2. Nuclear Energy Agency Committee on the Safety of Nuclear Installations, *Informing Severe Accident Management Guidance and Actions for Nuclear Power Plants through Analytical Simulation*, NEA/CSNI/R (2017)16 (2nd July 2018).
3. European Nuclear Safety Regulators Group, *Compilation of recommendations and suggestions – Peer review of stress tests performed on European nuclear power plants* (26th July 2012).
4. Lionel Chailan, Loic Bosland, Laure Carénini, Julien Chambarel, Frederic Cousin, *et al.*, "Overview of ASTEC integral code status and perspectives," 9th European Review Meeting on Severe Accident Research (ERMSAR2019), Prague, Czech Republic, March 2019, doi: ⟨irsn-04106726⟩
5. Bastien Poubeau, Yann Richet, Lionel Chailan, Fulvio Mascari, Mattia Massone, et al. "Horizon Euratom ASSAS project: can machine-learning make fast and accurate severe accident simulators a reality?" *Proceedings of the 11 th European Review Meeting on Severe Accident Research (ERMSAR2024)*, Kungliga Tekniska Högskolan, May 2024, Stockholm, Sweden. pp.1-12, ⟨10.5445/IR/1000174165⟩. ⟨irsn-04588965⟩
6. Rafael J. Caro, Isabel Parrado, "ASSAS project, Artificial intelligence for Simulation of Severe AccidentS; Simulator development and Isotopic Source Term proposals", *EPJ Nuclear Sci. Technol.* **11** 26 (2025), DOI: 10.1051/epjn/2025014
7. D. Jacquemain, *Nuclear Power Reactor Core Melt Accidents, Current State of knowledge*, EDP Sciences, France (2015)

assas

Artificial intelligence for
Simulation of Severe Accidents
http://assas-horizon-euratom.eu
info@assas-horizon-euratom.eu

ERMSAR 2026

Westinghouse

ASSAS SIMULATOR

Severe Accident analysis for educational purposes

Funded by the European Union. Views and opinions expressed are however those of the author(s) only and do not necessarily reflect those of the European Union or the European Commission-Euratom. Neither the European Union nor the granting authority can be held responsible for them.

Westinghouse Proprietary Class 2 | © 2022 Westinghouse Electric Company LLC. All Rights Reserved.

ERMSAR 2026.-ASSAS SIMULATOR

- Introduction
- Simulator Specification
- Simulator Architecture
- Challenges
- Demo

Westinghouse Proprietary Class 2 | © 2022 Westinghouse Electric Company LLC. All Rights Reserved.

ERMSAR 2026.-ASSAS SIMULATOR

INTRODUCTION

- ASSAS Project (2022-2026)
  - Integration of a Severe Accident Code: ASTEC, in a commercial simulation environment: TEAM_SUITE®
- Educational purposes
  - Reduce Cognitive Load: Display essential information
  - Visual hierarchy.
  - MCR-mode / Engineering
  - User interaction
- Limitations
  - Generic 4-loop 1300 Mwe PWR
  - Two DBA scenarios
  - Scope

Westinghouse Proprietary Class 2 | © 2022 Westinghouse Electric Company LLC. All Rights Reserved.

ERMSAR 2026.-ASSAS SIMULATOR

SIMULATOR SPECIFICATION

- ANSI/ANS 3.5 NPP Simulators for Training and Examination
  - 3.1 Simulator capabilities
    - 3.1.1 Real time and repeatability
    - 3.1.2 Limits of simulation
    - 3.1.3 Steady-state and normal evolutions
    - 3.1.4 Malfunctions
  - 3.2 Scope of simulation
    - 3.2.1 Physical fidelity and human factors
    - 3.2.2 Systems to be simulated and the degree of completeness
  - 3.3 Simulator instructor station capabilities
    - 3.3.1 Initial conditions and backtracks
    - 3.3.2 Malfunctions (Generic and Specific)
    - 3.3.3 Other features
    - 3.3.4 Local operator actions
    - 3.3.5 Data collection

Westinghouse Proprietary Class 2 | © 2022 Westinghouse Electric Company LLC. All Rights Reserved.

ERMSAR 2026.-ASSAS SIMULATOR

SIMULATOR SPECIFICATION

- Generic 4-loop 1300 PWR
- Two scenarios
  - SBO with Auxiliary Feedwater (AFW) Turbine Driven Pump (TDP) failure,
  - LOCA with Safety injection and Containment spray systems failure.
- Scope adapted to Design Base Accident (DBA) and Severe Accident (SA)
- Operator actions limited
  - SG's and PZR PORVS
  - AFW and PES
  - Containment spray and venting
- ASSAS Graphical User Interface (GUI)
  - Main Control Room / educational Modes
  - Consider battery backed equipment and instrumentation

Westinghouse Proprietary Class 2 | © 2022 Westinghouse Electric Company LLC. All Rights Reserved.

ERMSAR 2026.-ASSAS SIMULATOR

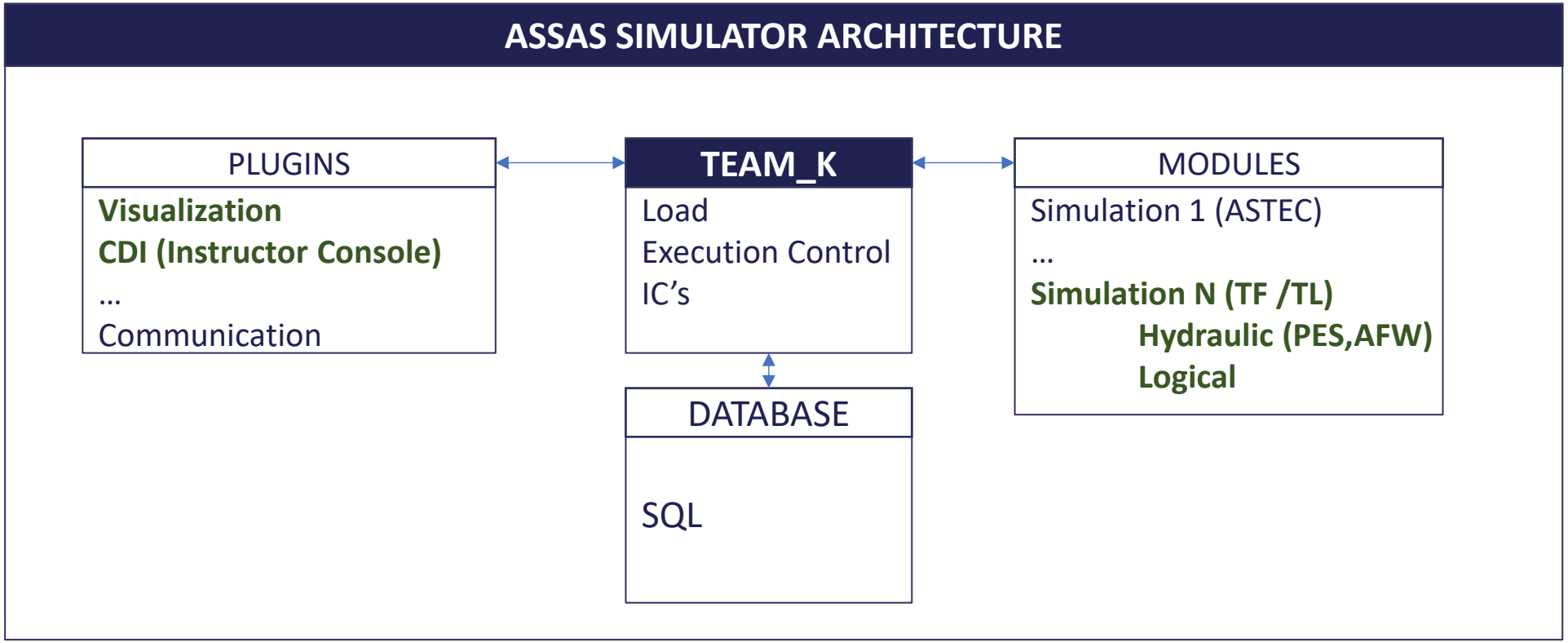

Westinghouse Proprietary Class 2 | © 2022 Westinghouse Electric Company LLC. All Rights Reserved.

ERMSAR 2026.-ASSAS SIMULATOR

ASSAS SIMULATOR ARCHITECTURE

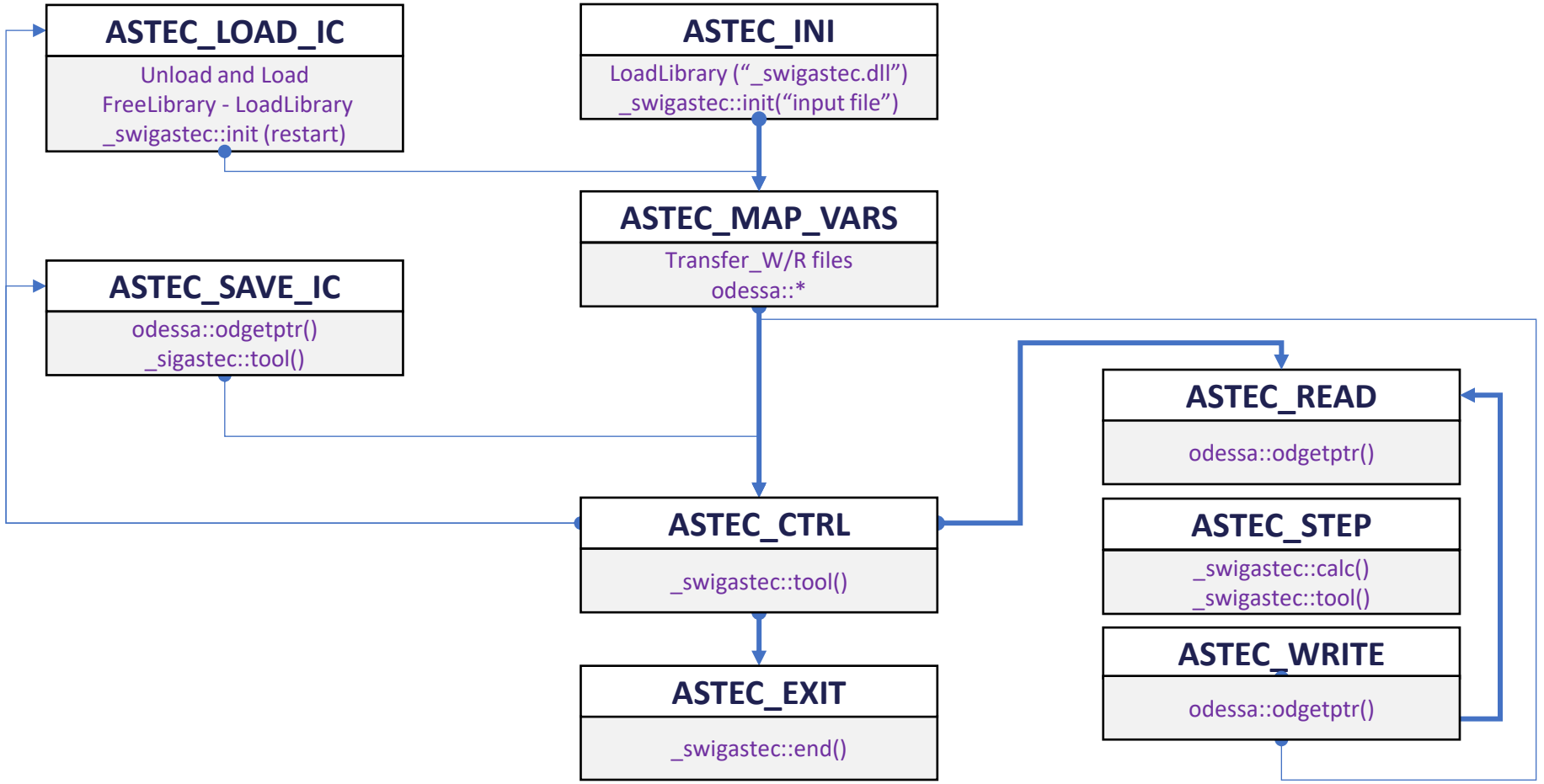

Westinghouse Proprietary Class 2 | © 2022 Westinghouse Electric Company LLC. All Rights Reserved.

ERMSAR 2026.-ASSAS SIMULATOR

CHALLENGES

- Integration of ASTEC in TEAM_K
  - **Synchronization (Solved)**
  - **Speed-up (Code and model optimization)**
  - **Memory Leaks when RESTART (Solved)**
  - **Check consistency when restart (Checked)**
- HMI & TEAM_SUITE models:
  - **Communicating variables, API**
  - **Input from ASTEC → TF and HMI**
  - **Input from TF -> ASTEC (Thermalhydraulics)**
  - **Input from HMI -> ASTEC (manual actuations)**
  - **Alarms Logic & Electrical Systems (TL)**
  - **Severe Accident Display**
  - **Simulator performance**
  - **Initial Conditions**
  - **Trigger initiators manually.**

Westinghouse Proprietary Class 2 | © 2022 Westinghouse Electric Company LLC. All Rights Reserved.

ERMSAR 2026.-ASSAS SIMULATOR

CHALLENGES

- Virtual Reality Module
  - Enables an immersive and intuitive understanding of accident evolution
  - Tuning: variables, scale ranges
- **VALIDATION**. Acceptance Test Procedures
  - Reference values from actual ASTEC version
  - Comparison with actual ASTEC version & TEAM_SUITE integration
  - Comparison with IA ASTEC version & TEAM_SUITE integration

Westinghouse Proprietary Class 2 | © 2022 Westinghouse Electric Company LLC. All Rights Reserved.

ERMSAR 2026.-ASSAS SIMULATOR

HMI

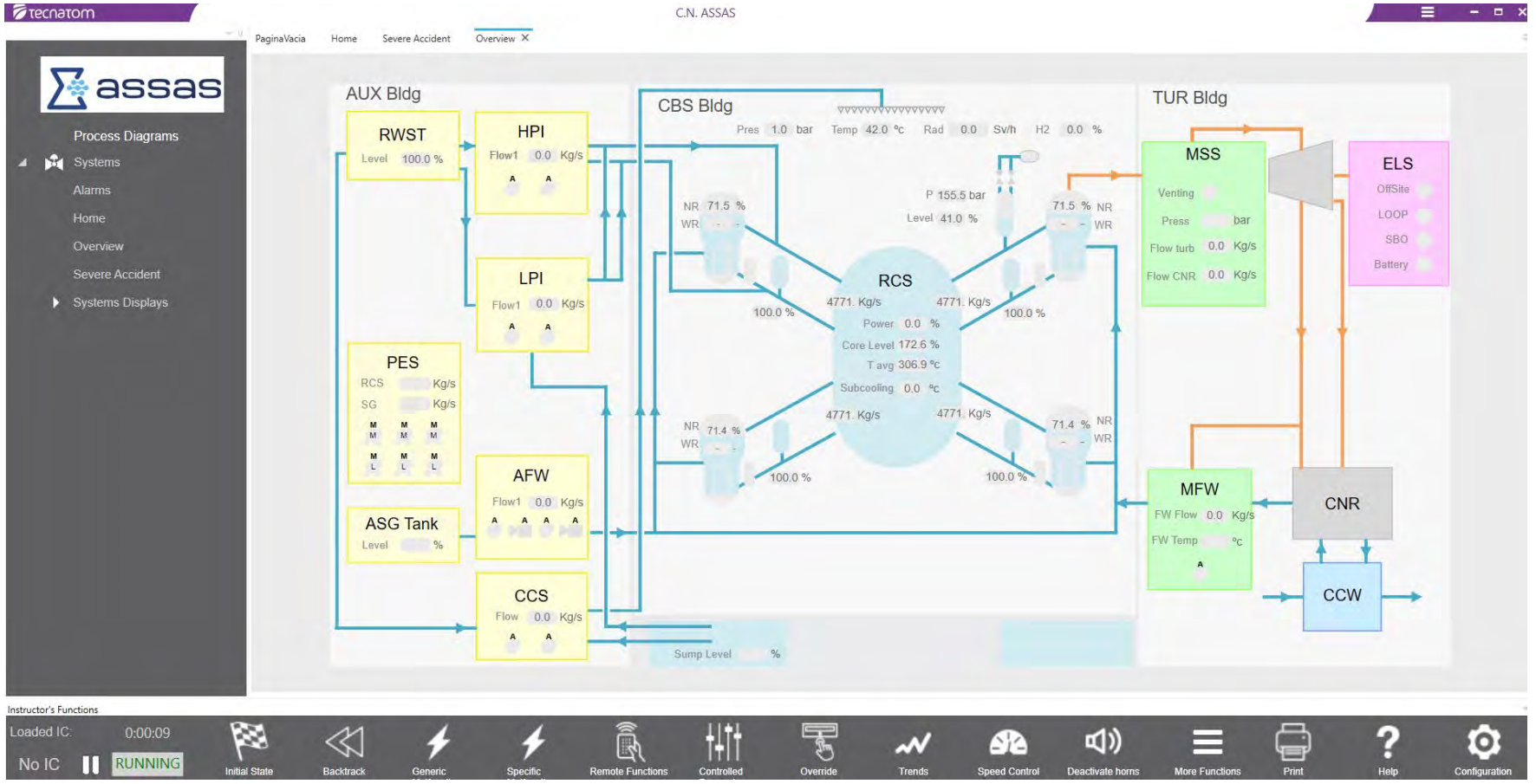

Westinghouse Proprietary Class 2 | © 2022 Westinghouse Electric Company LLC. All Rights Reserved.

ERMSAR 2026.-ASSAS SIMULATOR

HMI

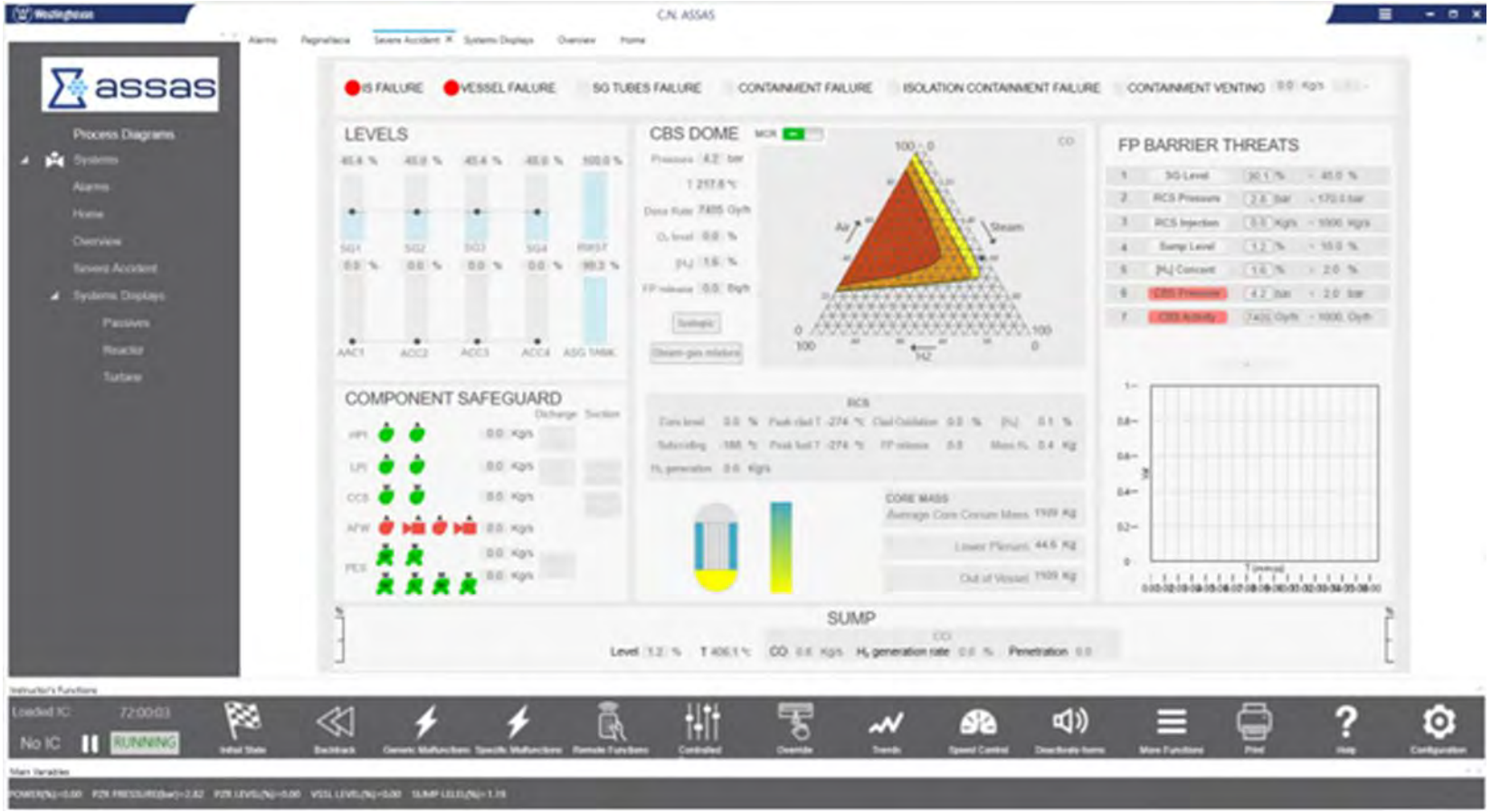

Westinghouse Proprietary Class 2 | © 2022 Westinghouse Electric Company LLC. All Rights Reserved.

ERMSAR 2026.-ASSAS SIMULATOR

VR

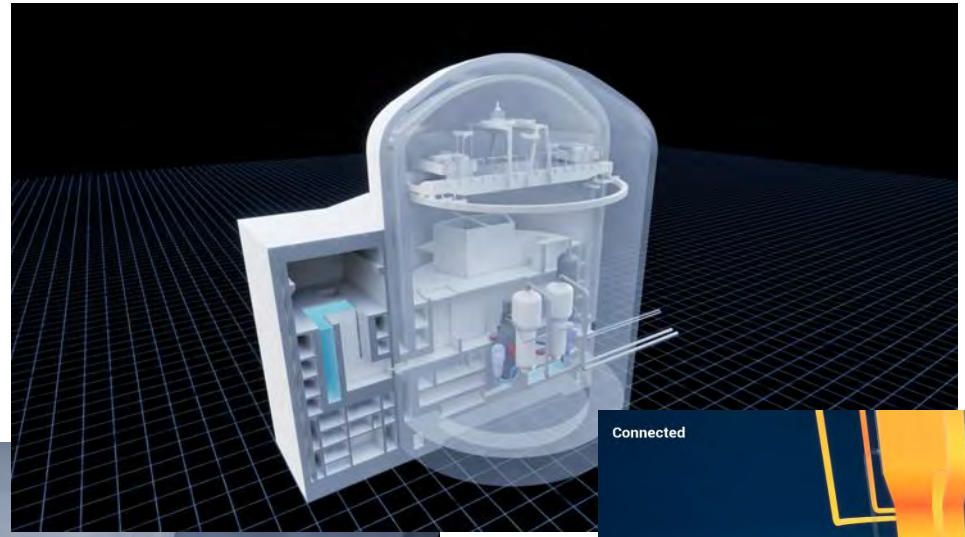

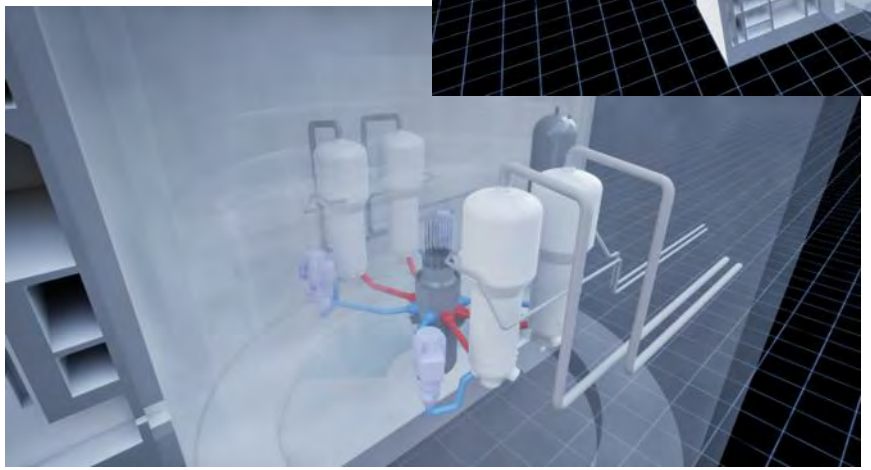

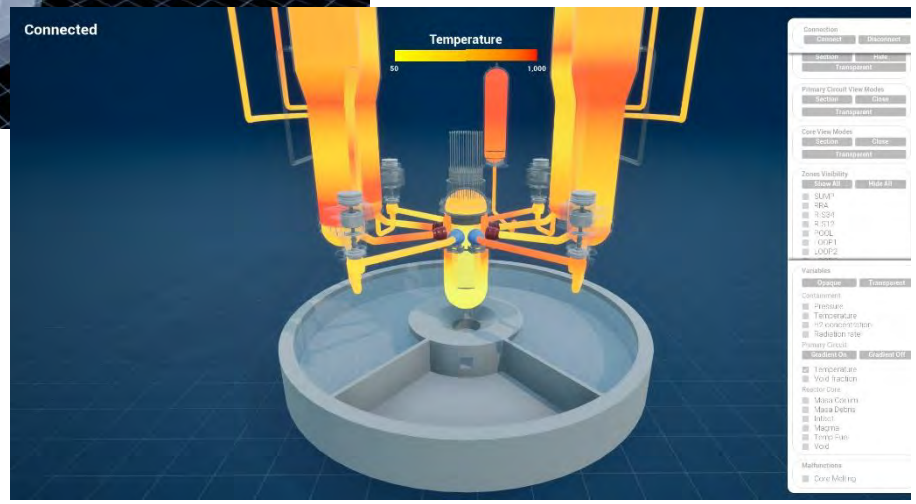

Westinghouse Proprietary Class 2 | © 2022 Westinghouse Electric Company LLC. All Rights Reserved.

ERMSAR 2026.-ASSAS SIMULATOR

DEMO

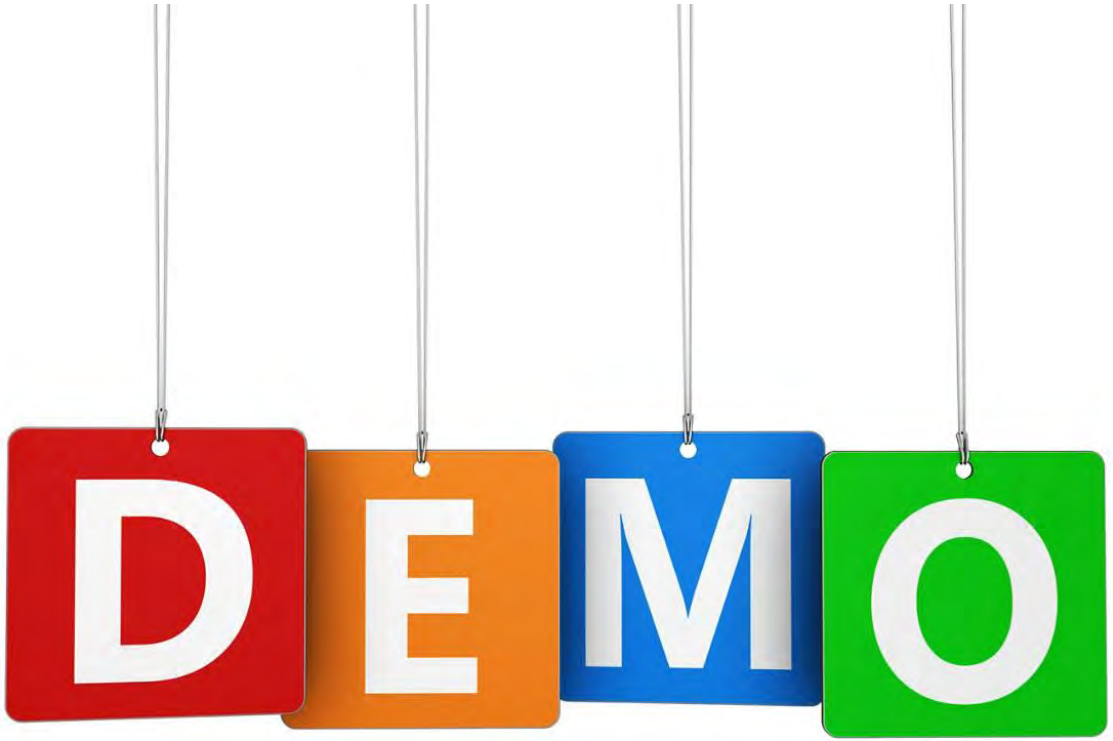

Westinghouse Proprietary Class 2 | © 2022 Westinghouse Electric Company LLC. All Rights Reserved.

The 12th European Review Meeting on Severe Accidents Research

May 18-22, 2026, Universidad Carlos III de Madrid, Madrid, Spain

TECHNICAL SESSION 4.3: EX-VESSEL CORIUM AND DEBRIS COOLABILITY

Chairs: S. Bechta (KTH), C. Journeau (CEA)

ID108	**Merging NUCLEA and Mephista databases: Over three decades of building a European Nuclear Thermodynamic Database for severe accident phenomenology.** B. Michel (ASNR)	Paper Presentation
ID057	**Simulation of Melt Debris Spreading Behavior in a Core Catcher Using THERMOS** W. Kikuchi (NRA)	Paper Presentation
ID076	**Experimental Study on the Interaction Between Molten Corium Simulant and Sacrificial Materials** N. Li (China Nuclear Power Engineering Co., Ltd)	Paper Presentation
ID083	**Advancing the Jet Breakup Length Model for Fuel-Coolant Interaction in Light Water Reactors** Kwang-Hyun Bang (Tetras Co.)	Paper Presentation
ID087	**Numerical Simulation of Melt Dry Spreading in CoSMUS Experiments** L. Zhao (KTH)	Paper Presentation

MERGING NUCLEA AND MEPHISTA DATABASES: OVER THREE DECADES OF BUILDING A EUROPEAN NUCLEAR THERMODYNAMIC DATABASE FOR SEVERE ACCIDENT PHENOMENOLOGY

Bénédicte Michel, Bruno Piar, and Marc Barrachin
Autorité de Sûreté Nucléaire et de Radioprotection (ASNR/PSN-RES/SAM)
CEN Cadarache, Saint Paul lez Durance, FRANCE
benedicte.michel@asnr.fr ; bruno.piar@asnr.fr ; marc.barrachin@asnr.fr

Evelyne Fischer
Université Grenoble Alpes, CNRS, SIMaP
Saint Martin d'Hères, FRANCE
evelyne.fischer@grenoble-inp.fr

ABSTRACT

In the 1990s, the importance of understanding the chemical phenomena that occur during a nuclear accident has been recognized. This led to the development of two non-ideal thermodynamic databases using CALPHAD method: NUCLEA is mainly devoted to the study of in and ex-vessel corium progression whereas Mephista is dedicated to fuel degradation and release of fission products. The NUCLEA database contains 20 atoms. U, O and Zr represent the corium, Fe, Ni and Cr describe the steel of the vessel and structures whereas Ag, In, B and C depict the control rods. It also contains the main non-volatile fission products: Ba, La, Ru and Sr as well as the main elements of concrete: Al, Ca, Mg and Si. Finally, Ar and H are considered in the gas phase. The Mephista database contains 16 atoms, 12 of which (U-Zr-O-Fe-Si-C-Ba-La-Ru-Sr-Ar-H) are shared with NUCLEA. It also includes Pu to account for MOX fuels, along with the following additional fission products: Cs, Mo, and Ce. The modeling of common systems is performed identically. The merging of these databases, which began in 2023, has just been completed. As a result, NUCLEA-26 is now able to address the issues of fuel degradation, fission product release as well as those of the overall corium progression. The database will continue to be improved by considering experimental and ab initio calculations-based data that will be produced. This article provides a general overview of the models used in the database and the different systems assessed. Finally, application cases involving multicomponent systems are considered in the context of corium–concrete interaction studies.

KEYWORDS
Corium, Thermodynamic Database, NUCLEA, Ex-Vessel

1. INTRODUCTION

In the field of nuclear safety, the importance of a good understanding of chemical phenomena that could occur during a possible severe accident in Light Water Reactors (LWR) was identified from the end of the 1980s. At the same time, the use of the CALPHAD method developed in 1970 [1] was increasing due to the improvement of computers capabilities. This method, which consists in a critical assessment of experimental data, a definition of a simple physical model for the Gibbs energy of the phase and an

optimization procedure to define the values of the model parameters, allows to use all available thermochemical and phase diagram data in a consistent way [2].

The main objective of the Euratom ENTHALPY project (European Nuclear Thermodynamic Database for in- and ex-vessel applications) (2000-2003) was to merge the 2 non-ideal corium-oriented thermodynamic databases existing in Europe, TDBCR and MTDATA respectively developed by THERMODATA and AEA-T, in one European commonly agreed database and to extend it to key in- and ex-vessel elements [3]. This project led to the first version of the NUCLEA database in 2003. Since then, this database was continuously improved by THERMODATA until 2014 and then by ASNR with the technical support of the CNRS SIMAP laboratory (Grenoble Alpes University) and the financial support of EDF and CEA [4], [5].

The NUCLEA-23 database, released in 2023, contained 20 atoms. U, O and Zr represent the corium, Fe, Ni and Cr describe the steel of the vessel and structures whereas Ag, In, B and C depict the control rods. It also contains the main non-volatile fission products: Ba, La, Ru and Sr as well as the main elements of concrete: Al, Ca, Mg and Si. Finally, Ar and H are considered in the gas phase.

In parallel, another database, the Mephista database also developed by THERMODATA and then ASNR, contained 16 atoms. 12 of which (U-Zr-O-Fe-Si-C-Ba-La-Ru-Sr-Ar-H) are shared with NUCLEA. It also includes Pu to account for MOX fuels, along with the following additional fission products: Cs, Mo, and Ce. The common systems were modeled identically, avoiding consistency issues between the two databases. As a result, merging them mainly consisted of modeling the many missing systems. This merger, which began in 2023, has just been completed. As a result, NUCLEA-26 is now able to address the issues of fuel degradation, fission product release, as well as those of the overall corium progression.

As it developed, the database was applied to multi-component systems representative of the reactor case. Calculations were performed and compared with experimental results in systems involving numerous chemical elements. They pointed out systems to be improved and sometimes lead to experimental programs dedicated to key systems. The experimental data produced in more than 30 years in the field of corium thermodynamics is reviewed in [6].

Thus, even if the number of atoms in the database should not change in the next future, the database will continue to be improved by considering experimental and theoretical chemistry-based data that will be produced or by modeling key ternary systems not yet modeled.
This article provides a general overview of the models used in the database and the different systems assessed. Finally, application cases involving multicomponent systems are considered in the context of corium–concrete interaction studies.

2. NUCLEA DATABASE DESCRIPTION AND ASSESSED SYSTEMS

The NUCLEA-26 database contains 24 elements:

- O, U, Pu, Zr (fuel modeling),
- Ag, In, B, C (control rods),
- Fe, Cr, Ni (vessel),
- Ba, Ce, Cs, La, Mo, Ru, Sr (fission products),
- Al, Ca, Mg, Si (concrete) and
- Ar, H (atmosphere, solely included in the gaseous phase).

The NUCLEA database is built with the compound energy formalism (CEF) [7], [8] which allows to describe the thermodynamic properties of phases with sublattices and the modeling use, in particular, the associated model [9] [A,A_aB_b,B] which is a special case of a CEF model with only one sublattice and three

constituents whose one, the associate, is a stoichiometric compound formed from the other two. A maximum of 3 sublattices is considered in the solutions modeling. The excess Gibbs energy terms are expressed with Redlich-Kister polynomials [10] and the extrapolation in the ternary is the Muggianu's extrapolation model [11]. All unaries data are taken from SGTE unary database[1] if they exist and updated according to SGTE unary database evolution. Few ternary interactions, almost all in the liquid phase, are assessed and no reciprocal interaction is considered. Magnetism is considered in magnetic species and in BCC_A2 (body-centered cubic phase) and FCC_A1 (face-centered cubic phase) solutions with few excess terms.

A pragmatic approach has been adopted to answer nuclear safety issues related to severe accident management and, if the thermodynamic database is defined in the 298.15-3500K temperature range, a more specific attention is paid to the 1200-3500K temperature range. Thus, all solutions are considered to be disordered (no short-range order in solution is modeled) and low non-stoichiometry of compounds are not considered (compounds are considered to be stoichiometric in this case). This simplification may reduce the accuracy of solid-phase modeling, particularly at low temperatures, but, we are particularly interested in the liquid phase and modeling non-stoichiometry and ordering requires adding parameters, and the more parameters there are, the more extrapolation problems can occur.

For corium applications in particular (e.g. in-vessel corium retention), NUCLEA must cover all compositions ranging from the metallic to the oxidic state. It is developed following the CALPHAD methodology and includes the modeling of all 231 binary systems, as well as all pseudo-binary systems. Pseudo-binary systems refer to binary systems involving two of the following oxides: Al_2O_3, B_2O_3, BaO, CaO, Ce_2O_3, CeO_2, Cr_2O_3, Cs_2O, CsO_2, FeO, Fe_2O_3, In_2O_3, La_2O_3, MgO, MoO_2, MoO_3, NiO, Pu_2O_3, PuO_2, SiO_2, SrO, UO_2, and ZrO_2. When no experimental data are available for a given system, the thermodynamic description is based on estimates. In addition, 44 ternary systems are fully modeled, and their list is presented in Table I. Furthermore, 27 sections derived from quaternary systems, listed in Table II, as well as the $BaMoO_3$-$BaUO_3$-$BaZrO_3$ section of the quinary Ba-Mo-O-U-Zr system, are also modeled.

Table I. Assessed ternary systems

Ag-Mo-O	B-C-Fe	B-C-U	B-C-Zr	B-Fe-U	B-Fe-Zr	C-Cr-Fe
C-Cr-Mo	C-Cr-Ni	C-Fe-Mo	C-Fe-Ni	C-O-Pu	C-O-U	C-O-Zr
C-Pu-U	C-U-Zr	Ca-Mo-O	Ce-Cs-O	Ce-Fe-O	Ce-O-Pu	Ce-O-U
Cr-Cs-O	Cr-Fe-O	Cr-Fe-Ni	Cr-Fe-Zr	Cr-Mo-O	Cr-Ni-O	Cr-Ni-Zr
Cr-O-Zr	Cs-Mo-O	Fe-Mo-O	Fe-Ni-O	Fe-Ni-Zr	Fe-O-Pu	Fe-O-U
Fe-O-Zr	Fe-Pu-U	Fe-Pu-Zr	Fe-U-Zr	Mo-O-U	O-Pu-U	O-Pu-Zr
O-U-Zr	Pu-U-Zr					

[1] Database initially based on Dinsdale's data [12] and still improved by the Scientific Group Thermodata Europe (SGTE)

Table II. Assessed sections in quaternary systems

Al-B-Ca-O	Al_2O_3 -B_2O_3 -CaO	Al-B-O-Si	Al_2O_3 -B_2O_3 -SiO_2
Al-B-O-Mg	Al_2O_3 -B_2O_3 -MgO	Al-Ca-Fe-O	Al_2O_3 -CaO-FeO-Fe_2O_3
Al-Ca-Mg-O	Al_2O_3 -CaO-MgO	Al-Ca-O-Si	Al_2O_3 -CaO-SiO_2
Al-Ca-O-Zr	Al_2O_3 -CaO-ZrO_2	Al-Ce-O-Si	Al_2O_3 -Ce_2O_3 -SiO_2
Al-Fe-O-Si	Al_2O_3 -FeO-Fe_2O_3 -SiO_2	Al-Mg-O-Si	Al_2O_3 -MgO-SiO_2
Al-O-Si-U	Al_2O_3 -SiO_2 -UO_2	Al-O-Si-Zr	Al_2O_3 -SiO_2 -ZrO_2
Al-O-U-Ar	Al_2O_3 -UO_2 -ZrO_2	B-Ca-Mg-O	B_2O_3 -CaO-MgO
B-Ca-O-Si	B_2O_3 -CaO-SiO_2	B-Mg-O-Si	B_2O_3 -MgO-SiO_2
Ba-Cs-Mo-O	$BaMoO_4$ -Cs_2MoO_4	Ca-Cr-O-Si	CaO-CrO-Cr_2O_3 -SiO_2
Ca-Fe-O-Si	CaO-FeO-Fe_2O_3 -SiO_2	Ca-Fe-O-U	CaO-FeO-UO_2
Ca-Mg-O-Si	CaO-MgO-SiO_2	Ca-Mg-O-Zr	CaO-MgO-ZrO_2
Ca-O-Si-U	CaO-SiO_2 -UO_2	Ca-O-Si-Zr	CaO-SiO_2 -ZrO_2
Fe-O-Si-U	FeO-SiO_2 -UO_2	Fe-O-Si-Zr	FeO-SiO_2 -ZrO_2
O-Si-U-Zr	SiO_2 -UO_2 -ZrO_2		

In NUCLEA-26, 710 solid stoichiometric phases, 31 liquid stoichiometric phases, 100 solid solution phases, one liquid solution phase and one gaseous phase (composed of 258 species) are modeled.

3. EXAMPLE OF VALIDATION OF NUCLEA DATABASE IN THE CONTEXT OF CORIUM-CONCRETE INTERACTIONS

In parallel with its development, the NUCLEA database was applied to various application cases. This made it possible to identify the systems to be improved and to validate the database. An example is presented to illustrate the capabilities of the database. Calculations performed with the NUCLEA-26 database and NucleaToolbox 4.6 [13] are compared with experimental results obtained in the Euratom ENTHALPY project [14] devoted to the investigation of corium-concrete chemistry.

3.1. Problem Statement

If the corium cannot be stabilized in the reactor vessel, the mixture of molten materials resulting from the fuel, cladding and structural elements degradation could melt through the reactor vessel and relocate on the concrete basemat of the reactor cavity. The concrete is mainly composed of SiO_2, $CaCO_3$ and H_2O and decomposes in presence of corium in condensed species (SiO_2 and CaO) and gaseous species (H_2O and CO_2). Thus, the core-concrete mixture is composed of heavy oxides (UO_2 and ZrO_2), light oxides (mainly SiO_2 and CaO), metals (Fe, Ni, Cr and Zr) and low volatile fission products stirred by gases generated from concrete decomposition. When oxides and metals species mix, oxidation reactions can occur and

generate gaseous species such as H_2, CO and SiO. The core-concrete mixture is a multi-component, multiphasic (gas, liquid, solid) melt whose composition changes progressively during the molten core concrete interaction (MCCI). MCCI is characterized by the coupling of several phenomena: high temperature concrete decomposition, bubbling corium pool thermohydraulics and physicochemistry of corium melts. Different modelings of MCCI exist but they generally rely on the liquidus and/or the solidus temperatures of the pool or a temperature based on a threshold in the volumetric liquid fraction of the pool.

During the Euratom ENTHALPY project, primarily dedicated to the creation of the NUCLEA database, ten liquidus and solidus temperatures of key subsystems of the overall system UO_2-ZrO_2-SiO_2-FeO_x-CaO-Al_2O_3-Cr_2O_3 relevant to severe accidents were measured [14]. They were first determined by Visual Polythermal Analysis (VPA) in an Induction Melting Cold Crucible (IMCC) furnace. The melt was superheated in order to homogenize it and melt down all the charge materials. A melt sample was taken at temperature for effective composition determination. The power introduced into the melt was decreased until films and crusts started appearing at the melt surface during the molten pool cooling. The melt surface temperature was measured by a spectral ratio pyrometer. The arithmetic mean between the maximum film and the minimum melt temperatures is assumed to be the liquidus temperature. In its turn, the solidus temperature is assumed to be the arithmetic mean between the maximum crust and the minimum film temperatures. Then, the solidified bulk was used for liquidus temperature determination by VPA in the Galakhov's microfurnace and for solidus temperature determination by Differential Thermal Analysis (DTA). In the Galakhov's microfurnace, the liquidus temperature is defined as the temperature at the moment the sample spreads across the tungsten holder surface. The solidus temperature is determined as the initiation of the endothermic effect at heating the sample and of the exothermic effect at its cooling. If these temperatures are different, the value obtained when heating the sample was regarded as the more credible one. All measurements were carried out under inert atmosphere. The determination of sample chemical composition and microstructure were determined by means of Scanning Electron Microscopy with Energy Dispersive X-ray spectroscopy (SEM/EDX). Based on these temperature measurements, performed using different experimental techniques and for compositions that may slightly vary, the authors recommend a solidus temperature and a liquidus temperature associated with a given composition. Compositions of urania-zirconia samples mixed with steel oxides without concrete (MC_WC series), limestone concrete (MC_LC series), limestone-common sand concrete (MC_LCSC), concrete and steel oxide (MC_CSO series) and a zirconia sample (without urania) mixed with concrete and steel oxides (MC_WU) as well as the recommended solidus and liquidus temperatures, if any, are presented in Table III.

Table III. Compositions, in weight-%, and measured solidus and liquidus temperatures, if any, of the ten ENTHALPY tests [14].

	UO_2	ZrO_2	FeO	Cr_2O_3	SiO_2	CaO	Al_2O_3	solidus (K)	liquidus (K)
MC_WC_1	41.7	16.4	41.5	0	0	0	0.4	1623	2073-2133
MC_WC_2	43.3	17.8	28.9	10.0	0	0	0	-	1983-2033
MC_LC_1	61.9	14.9	0	0	0	23.2	0	2133-2143	2163-2253
MC_LC_2	33.6	13.5	0	0	0	26.4	26.5	1613	2043
MC_LCSC	31.5	9.5	0	0	25.5	33.5	0	1733-1793	2073-2133

MC_CSO_1	33.8	14.5	30.1	7.5	14.1	0	0	1633-1673	1873-1913
MC_CSO_2	24.2	7.9	9.1	0	25.0	33.8	0	1513-1633	*2073-2153*[a]
MC_CSO_3	37.9	13.5	16.9	12.0	12.1	7.6	0	1663-1673	1933-1973
MC_CSO_4	41.4	15.5	12.0	4.2	13.6	6.3	7.0	1523	2073-2133
MC_WU	0.3	39.5	28.8	3.6	12.0	2.7	13.1	1593	2073-2153

[a] this recommended value seems erroneous because it is significantly higher than the values measured by the three methods.

3.2. Results and Discussion

The comparison between measured and computed solidus and liquidus temperatures for corium-concrete mixture is presented in Table IV.

Table IV. Comparison between measured and computed solidus and liquidus temperatures for corium-concrete mixture.

	solidus (K)			liquidus (K)		
	experimental	computed	ΔT	experimental	computed	ΔT
MC_WC_1	1623	1552.0	-71.0	2073-2133	2050.0	-23
MC_WC_2	-	1566.0	-	1983-2033	2090.0	57
MC_LC_1	2133-2143	2064.0	-69.0	2163-2253	2309.0	56
MC_LC_2	1613	1728.0	115.0	2043	1993.0	-50
MC_LCSC	1733-1793	1686.0	-47.0	2073-2133	2129.0	ok
MC_CSO_1	1633-1673	1443.0	-190.0	1873-1913	1981.0	68
MC_CSO_2	1513-1633	1486.0	-27.0	*2073-2153*	1954.0	*-119*
MC_CSO_3	1663-1673	1401.0	-262.0	1933-1973	2033.0	60
MC_CSO_4	1523	1349.0	-174.0	2073-2133	2151.0	18
MC_WU	1593	1340.0	-253.0	2073-2153	2197.0	44

ΔT is the difference between computed and experimental values. When the experimental temperature is given as an interval, and the calculated value lies outside this range, the difference is computed as the calculated temperature minus the closest bound of the experimental interval.
Liquidus temperatures are well reproduced: the difference does not exceed 70 K except for test MC_CSO_2 for which the reported recommended value seems to be wrong. Indeed, for this test, the liquidus temperature measured by VPA is 1882 ± 46 K in the IMCC furnace, 1684–1765 K in Galakhov's furnace, and 1823 K by DTA, whereas the recommended range is 2073–2153 K. If, as for the other tests,

the liquidus temperature recommended is assumed to be the one measured by VPA in IMCC furnace, the discrepancy is reduced to only 26 K.

Solidus temperatures are less accurately reproduced, with differences of up to 260 K. However, experimental results should be interpreted with caution. Except for MC_LC_2 test, the computed solidus temperature is always lower than the experimental one.

For this specific test, the evolution of the enthalpy derivative with respect to temperature (ΔH/ΔT) and the phase weight fractions are plotted as a function of temperature in Figure 1. Boettinger [15] has shown that when this apparent heat capacity curve is inverted and expanded along the horizontal axis, it provides an approximate representation of the shape of the DTA signal during melting. Calculated solidus and liquidus temperatures are plotted in black, while experimental ones are plotted in green and blue, respectively.

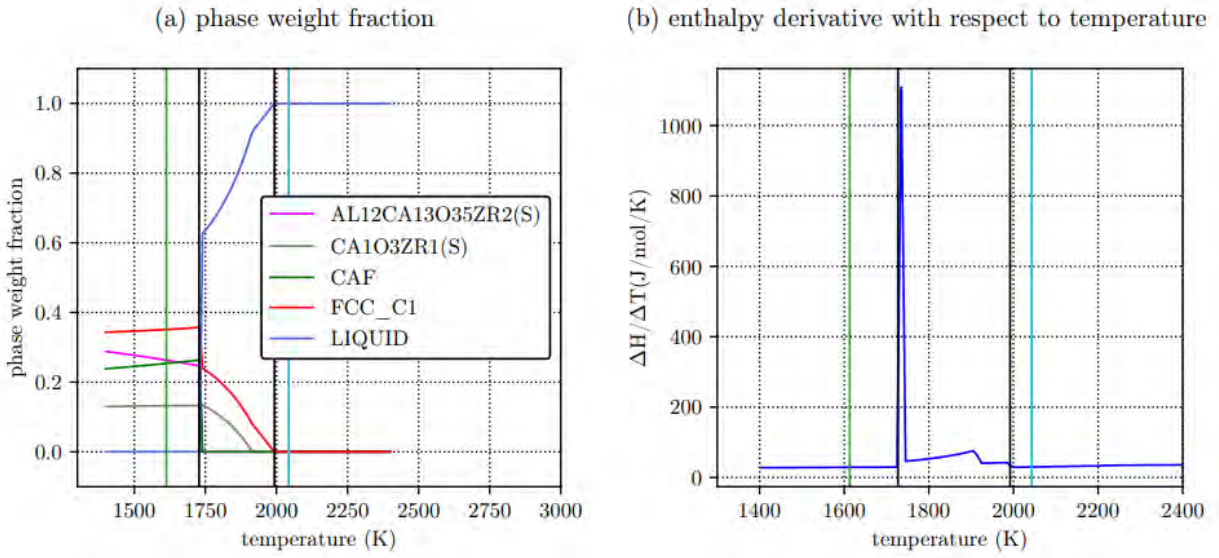

Figure 1. Evolution of the calculated phase weight fractions (a) and enthalpy derivative with respect to temperature (b) as a function of temperature for the MC_LC_2 test.

The solidus temperature calculated with NUCLEA corresponds to the solidification at 1728 K of the 62 w-% liquid phase into 26 w-% of the Al_2CaO_4 compound (the only compound in the CAF phase which is the solution due to the extension of this compound to $CaFe_2O_4$ in the Al-Ca-Fe-O system), 25 w-% of the $Al_{12}Ca_{13}Zr_2O_{35}$ compound, and an additional 11 w-% of the FCC_C_1 phase. It is important to note that the detection of such an invariant reaction during heating requires the presence of the quaternary compound in the initial sample. This compound may be challenging to form without subjecting the sample to annealing for a considerable duration before the DTA measurement at heating.

For the most frequent cases where the calculations do not match the experimental data, it should be kept in mind that peaks in the DTA signal may appear whenever a phase transformation occurs. As a result, the determination of the solidus temperature can be confused with another phase transformation (this misinterpretation is all the more common as the complexity of the system increases), even though a liquid phase is present. For instance, for the MC_CSO_3 test, the evolution of the enthalpy derivative with respect to temperature (ΔH/ΔT) and the phase weight fractions plotted as a function of temperature in Figure 2 indicate that the reported solidus temperature may actually correspond to the transformation of the TET_OXIDE phase (stable phase of ZrO_2 in which 20 w-% of UO_2 are dissolved) into an FCC_C1

phase (solution of fluorite structure rich in UO_2 and ZrO_2) rich in ZrO_2 in this case. Calculated solidus and liquidus temperatures are plotted in black, while the experimental solidus and liquidus temperature ranges are plotted in green and blue, respectively.

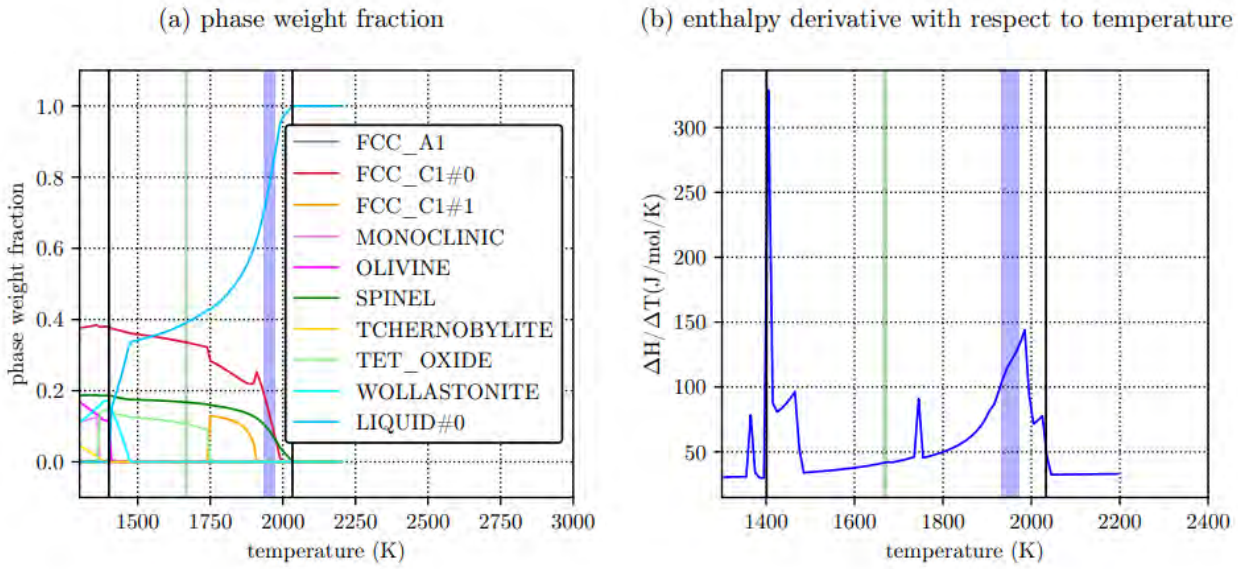

Figure 2. Evolution of the calculated phase weight fractions (a) and enthalpy derivative with respect to temperature (b) as a function of temperature for the MC_CSO_3 test.

4. CONCLUSIONS

The NUCLEA thermodynamic database, developed using the CALPHAD method, comprises 24 elements. It covers both metallic and oxide composition domains and enables the modeling of material evolution during a potential severe accident, from fuel degradation to in-vessel corium interactions and ex-vessel corium–concrete interactions.

The database validation example, chosen in the domain of corium-concrete interactions, highlights the difficulty of performing high-temperature experimental measurements in multiphase mixtures and, consequently, the limited amount of experimental data available to support the database assessment. Nevertheless, the NUCLEA results are satisfactory, particularly with respect to the calculation of the liquidus temperature.

The database will continue to be improved as new experimental data become available.

REFERENCES

[1] L. Kaufman and H. Bernstein, *Computer Calculation of Phase Diagram with Special Reference to Refractory Metals*, Academic Press, New York, USA (1970).

[2] H. Lukas, S. G. Fries, and B. Sundman, *Computational Thermodynamics: The Calphad Method*, Cambridge University Press (2007).

[3] A. Debremaecker, “European Nuclear Thermodynamic Database for In and Ex-vessel Applications (ENTHALPY)”, *FISA*, volume 1 (2003).

[4] S. Bakardjieva, M. Barrachin, S.V. Bechta, D. Bottomley, L. Brissonneau, B. Cheynet, E. Fischer, C. Journeau, M. Kiselova, L.P. Mezentseva, P. Piluso, and T. Wiss, "Improvement of the European thermodynamic database NUCLEA", *Progress in Nuclear Energy*, **52**(1), pp. 84–96 (2010).

[5] S. Bakardjieva, M. Barrachin, S.V. Bechta, P. Bezdicka, D. Bottomley, L. Brissonneau, B. Cheynet, O. Dugne, E. Fischer, M. Fischer, V.V. Gusarov, C. Journeau, V.B. Khabensky, M. Kiselova, D. Manara, P. Piluso, M. Sheindlin, V. Tyrpekl, and T. Wiss, "Quality improvements of thermodynamic data applied to corium interactions for severe accident modelling in SARNET2", *Annals of Nuclear Energy*, **74**, pp. 110–124 (2014).

[6] M. Barrachin, "Corium experimental thermodynamics: A review and some perspectives", *Thermo*, **1**(2), pp. 179–204 (2021).

[7] M. Hillert, "The Compound Energy Formalism", *Journal of Alloys and Compounds*, **320**, pp. 161–176 (2001).

[8] B. Sundman and J. Agren, "A regular solution model for phases with several components and sublattices, suitable for computer applications", *Journal of Physics and Chemistry of Solids*, **42**, pp. 297–301 (1981).

[9] F. Sommer, "Association model for the description of thermodynamic functions of liquid alloy. I basic concepts", *Z. Metallkde.*, **73**, pp. 72–76 (1982).

[10] O. Redlich and A.T. Kister, "Algebraic representation of thermodynamic properties and the classification of solutions", *Industrial and Engineering Chemistry*, **40**(2), pp. 345–348 (1948).

[11] Y.-M. Muggianu, M. Gambino, and J.-P. Bros, "Enthalpies de formation des alliages liquides Bismuth-Etain-Gallium à 723K. Choix d'une représentation analytique des grandeurs d'excès intégrales et partielles de mélange", *Journal de Chimie Physique*, **72**, pp. 83–88 (1975).

[12] A.T. Dinsdale, "SGTE Data For Pure Elements", *Calphad*, **15**(4), pp. 317–425 (1991).

[13] B. Piar, "NucleaToolbox 1.3 user's manual", Technical report SAG/2016-00135, IRSN/PSN-RES (2016).

[14] S. Hellmann, "Liquidus and solidus temperatures in the subsystem UO_2-ZrO_2-(SiO_2-FeO_x-CaO-Al_2O_3-Cr_2O_3)", Technical Report SAM-ENTHALPY(03)-D011, Framatome ANP (2003).

[15] W.J. Boettinger, U.R. Kattner, K.W. Moo, and J.H. Perepezko, *DTA and Heat-flux, DSC Measurements of Alloy Melting and Freezing*, NIST (2006).

ASNR Autorité de sûreté nucléaire et de radioprotection

NUCLEA database
a European Nuclear Thermodynamic Database for severe accident phenomenology

ERMSAR 2026 - 12th European Review Meeting on Severe Accident Research Conference

B. Michel, B. Piar, M. Barrachin, E. Fischer

May 18-22, 2026

NUCLEA: A thermodynamic database developed since the 1990s

Keys thermodynamic systems for severe accident applications

Keys systems for corium applications

- **for the fuel degradation**: O-U-Zr for UO_2 fuel and U-Pu-O-Zr for MOX fuel,
- **for in-vessel corium**: Fe-O-U-Zr for UO_2 fuel and Fe-U-Pu-O-Zr for MOX fuel,
- **for fissions products (FPs) contributing to residual power**: UO_2-FPs
- **for ex-vessel corium**: Fe-O-U-Zr + Ca and Si.

Impact of 'minor' elements

- **Ni and Cr**: for steels for in-vessel corium phenomenology,
- **B, C, Ag and In**: for the impact of control rods on the degradation,
- **Al and Mg**: for concretes for ex-vessel phenomenology.

Development of NUCLEA, a non-ideal solution database, by THERMODATA:

- first version released in 2003 as part of the EC ENTHALPY program,
- owned by ASNR since 2014,
- coupled with the ASNR ASTEC code.

NUCLEA database developed using the CALPHAD approach

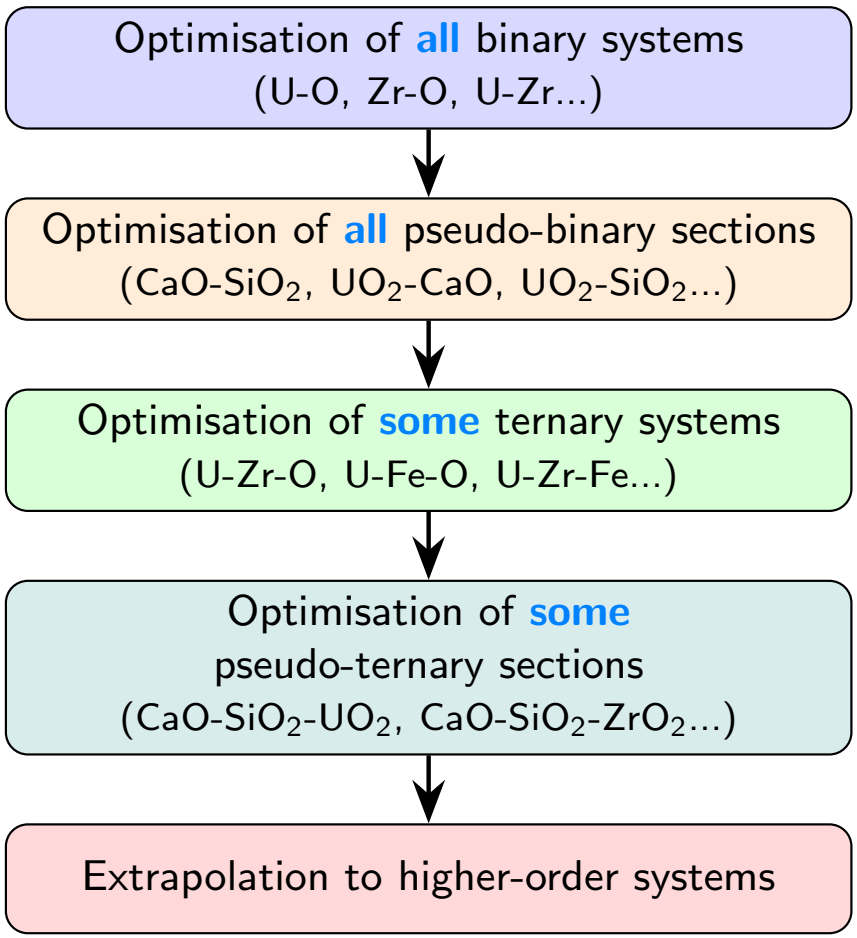

Database models for Gibbs energy

- Pure element Gibbs energy functions derived from the SGTE unary database.
- Solution modeling uses the compound energy formalism (CEF) (including the associated model)

Need for thermodynamic and phase diagram reliable data

- Few thousands publications analysed since 1990 to select data
- Dedicated projects to produce key data for corium and FPs applications
- Continuous work

The database covers all compositions ranging from the metallic to the oxidic state

NUCLEA database: the 2026 version

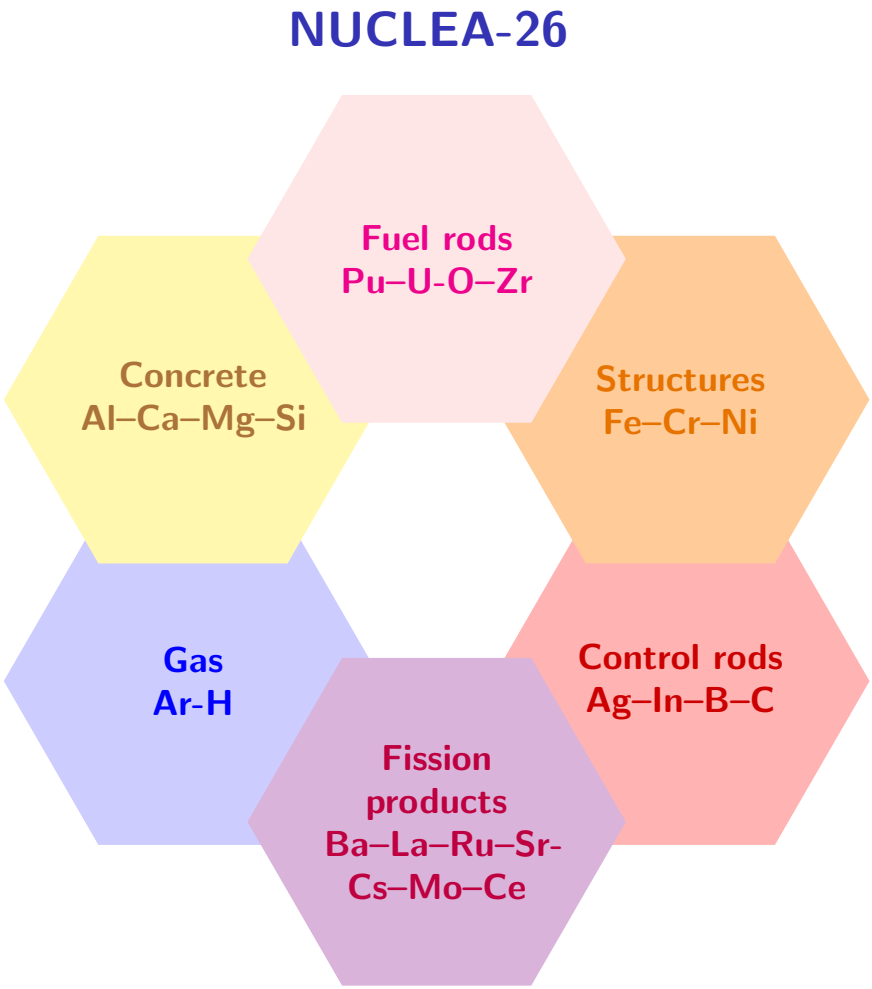

Since 2014:

- Development of an ASNR software, **NucleaToolbox**, to compute phase equilibria and manage the database development and analysis,
- Merger between NUCLEA and Mephista, an ASNR database dedicated to fuel degradation,
  ⇒ **adding of Cs, Ce, Mo and Pu to NUCLEA.**

The database contains 24 chemical elements and is now able to address the issues of fuel degradation, fission product release, and corium progression

NUCLEA database: the results of numerous research programs

Dedicated programs:

- either for obtaining data in certain binary or ternary systems in order to directly improve their modeling,
- or for obtaining data in systems involving numerous elements in order to qualify the database.

ASNR has been extensively involved in all these programs

Impact of these research programs on NUCLEA development

Acquisition of high-temperature thermodynamic data is challenging, particularly for uranium-containing samples, and few data are available.

$\Rightarrow$ acquisition of **thermodynamic** data in the following systems:

- U-O, U-O-Zr, U-O-Fe...
- UO_2-CaO, UO_2-SiO_2, UO_2-FeO...

Database development: U-Zr-O phase diagram

2600K

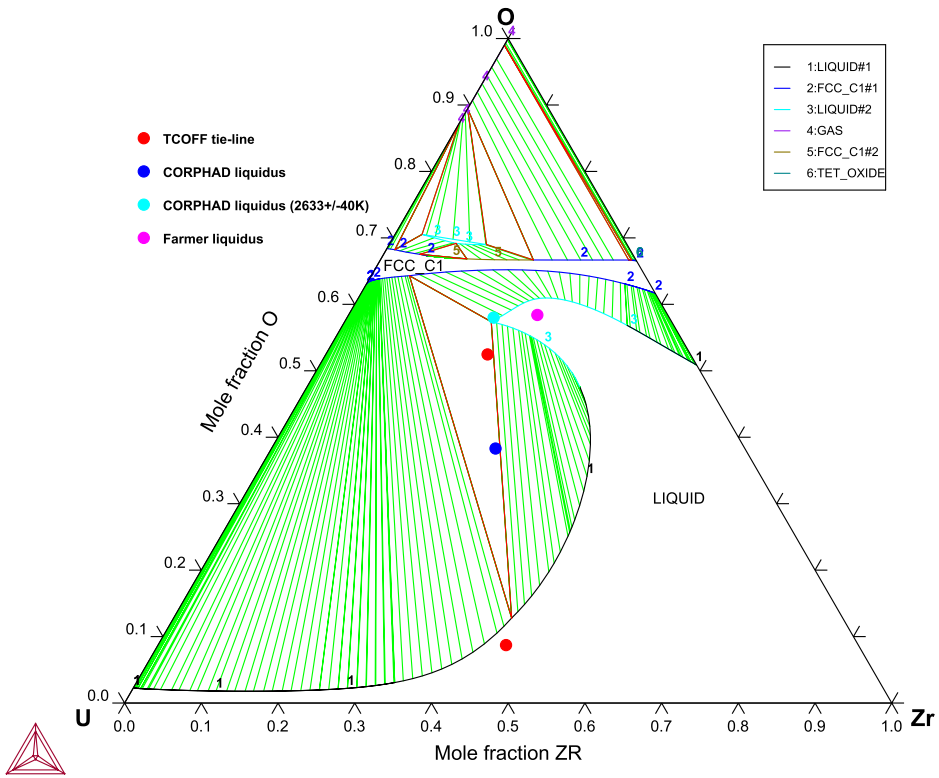

2950K

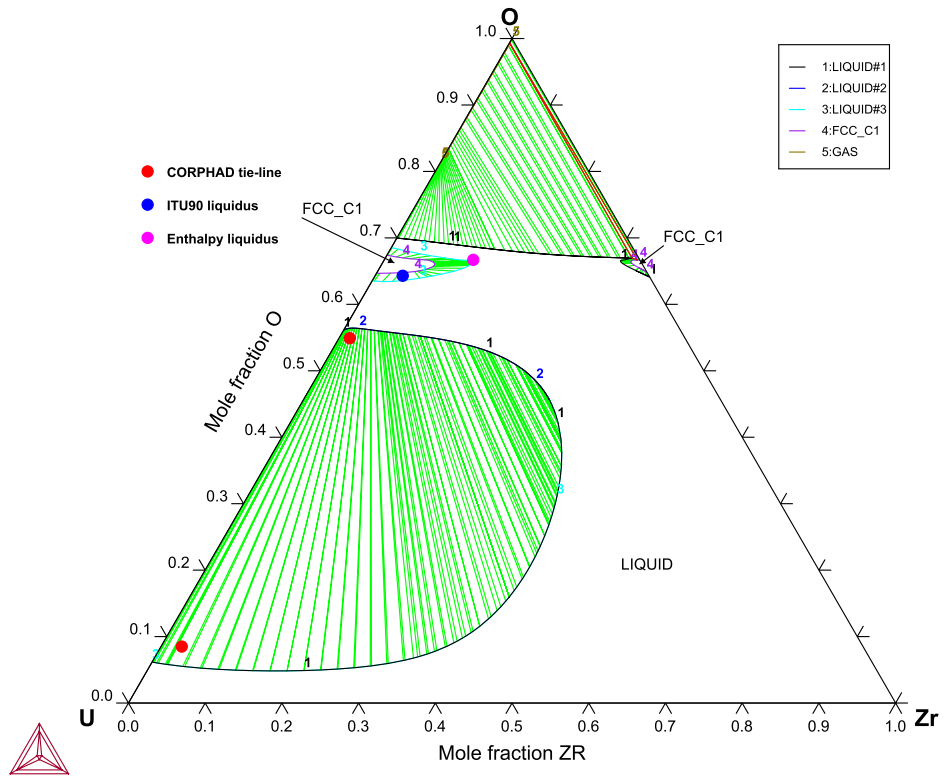

Good agreement but still few data at these temperatures

Database development: UO_2-CaO section

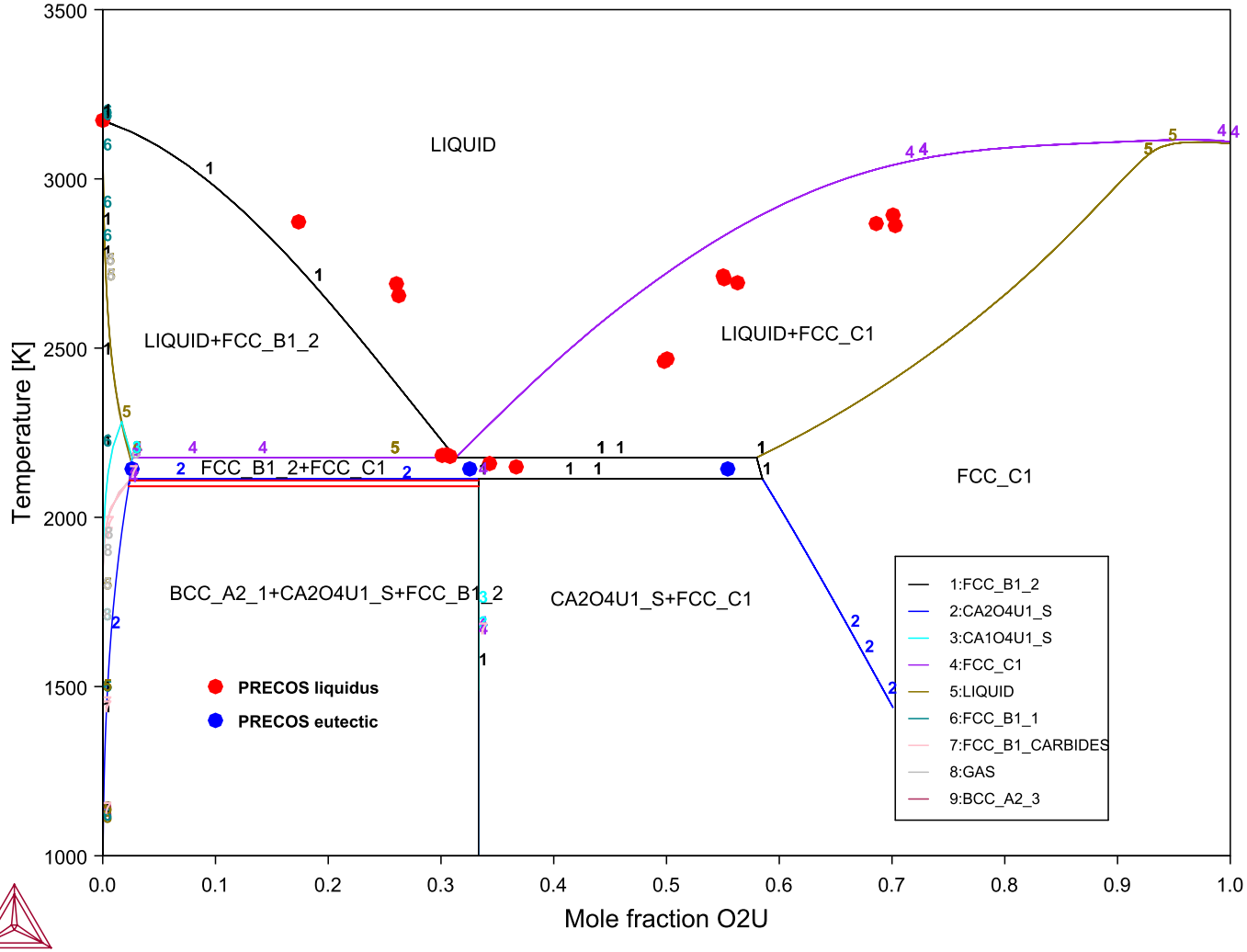

Good agreement for the eutectic but difficulties in reproducing the liquidus curves.

Impact of research programs for In-Vessel Issues

Due to the low solubility of the metal in the corium, 2 liquids of different density can form and the determination of the position and the thickness of the metallic layer is crucial for a possible focussing effect.

Keys parameters are:

- the zirconium oxidation degree of the corium, C_n,
- the U/Zr ratio,
- the metallic fraction in the melt.

$\Rightarrow$ 38 tests were carried out in MASCA and MASCA2 projects to deal with liquids demixing, 31 in a small device (STFM series) and 7 in a larger one (MA series)

In-Vessel Validation: Composition of the metallic ingot

Comparison betwwen experimental and calculated compositions of the metallic ingot versus metallic fraction in the melt for C_{32}, U/Zr = 1.2 at 2900K (18 tests)

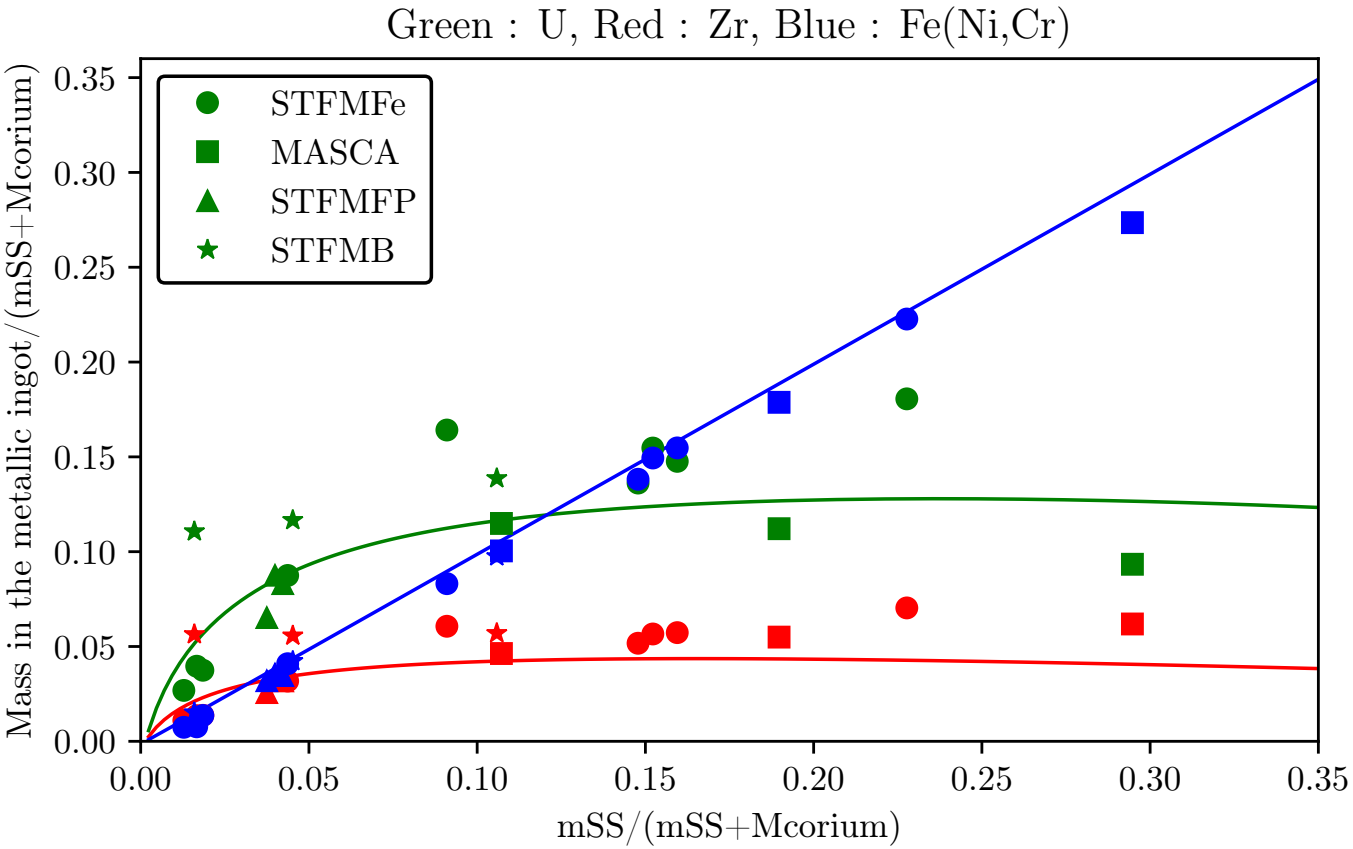

U increases in the metallic phase up to 10% and then remains constant.

⇒ Trends are satisfactorily reproduced.

In-Vessel Validation: Fission Products Partition

MASCA MA3 Test

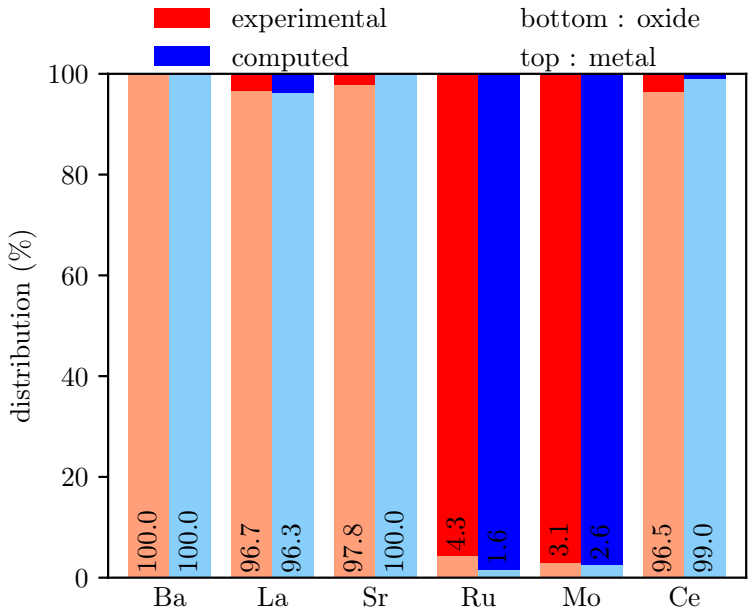

MASCA MA4 Test

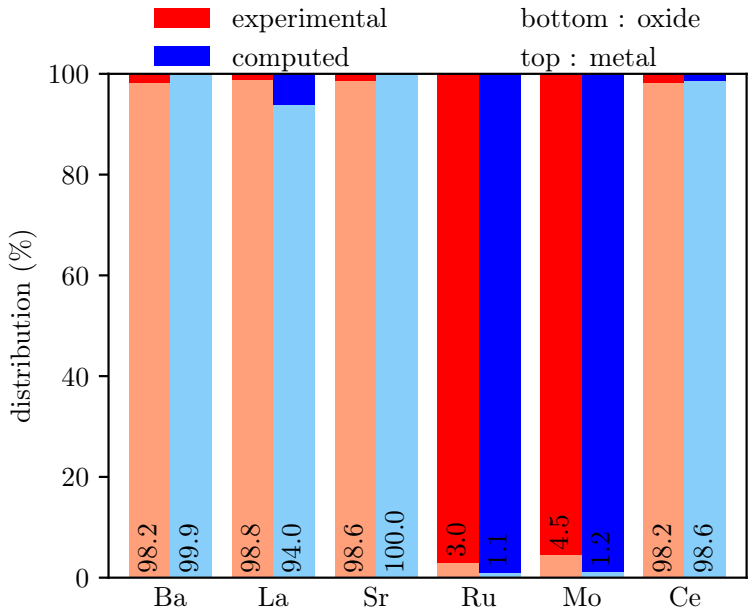

- Ba, La, Sr, and Ce $\Rightarrow$ oxide phase,
- Mo and Ru $\Rightarrow$ metallic phase.

Good agreement between the calculated and experimental FPs partitioning

Impact of research programs for Ex-Vessel Issues

Ex-vessel issues are an even greater challenge because the impact of the concrete components, CaO, SiO_2 (and MgO and Al_2O_3) must be included.
Modeling involves multiple temperatures (concrete ablation, pool solidification) and possibly the liquid fraction (xliq).

⇒ Databases are generally validated by comparing liquidus and solidus temperatures.

Remarks on solidus temperature determination

Most of these programs follow a three-stage experimental procedure:

- First, Visual Polythermal Analysis (VPA) in an Induction Melting Cold Crucible (IMCC) furnace measured the **liquidus temperature**, samples were taken from the molten pool.
- Then, melt samples were analysed to determine the **effective composition** of the molten pool (segregation due to temperature gradient).
- Finally, the **solidus temperature** was measured by Differential Thermal Analysis (DTA) by heating one of these samples.

⇒ Samples may not be in thermodynamic equilibrium (rapid cooling)

Ex-Vessel Validation: Solidus and Liquidus Determination

ENTHALPY Program

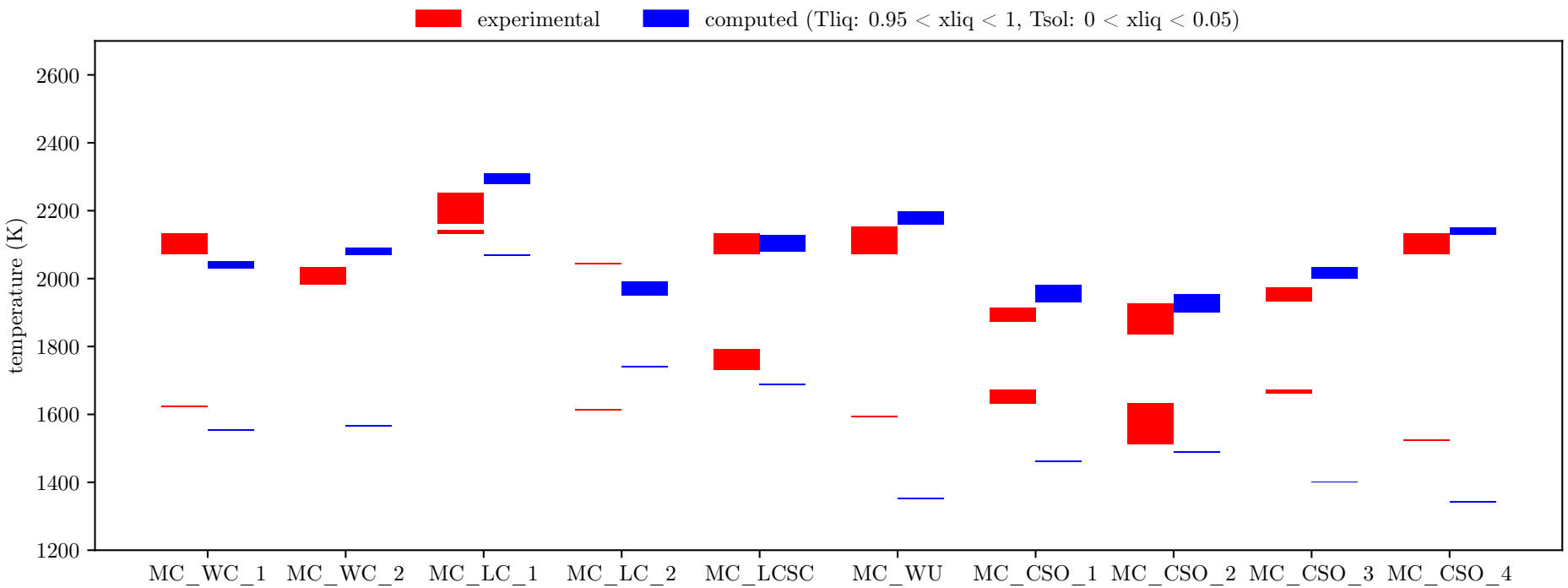

Liquidus temperatures: good agreement (<70K)

Solidus temperatures: poor agreement (up to 260K)

Issues in Solidus Determination 1/2

MC_LC_2	UO_2	ZrO_2	CaO	Al_2O_3
w-%	33.6	13.5	26.4	26.5

Phase weight fraction

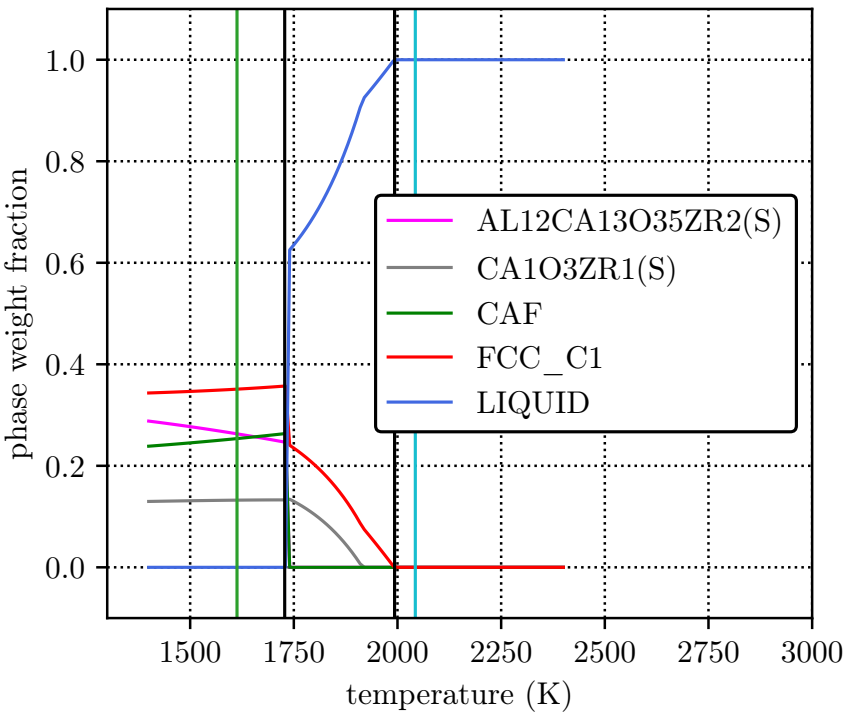

Derivative of enthalpy versus temperature

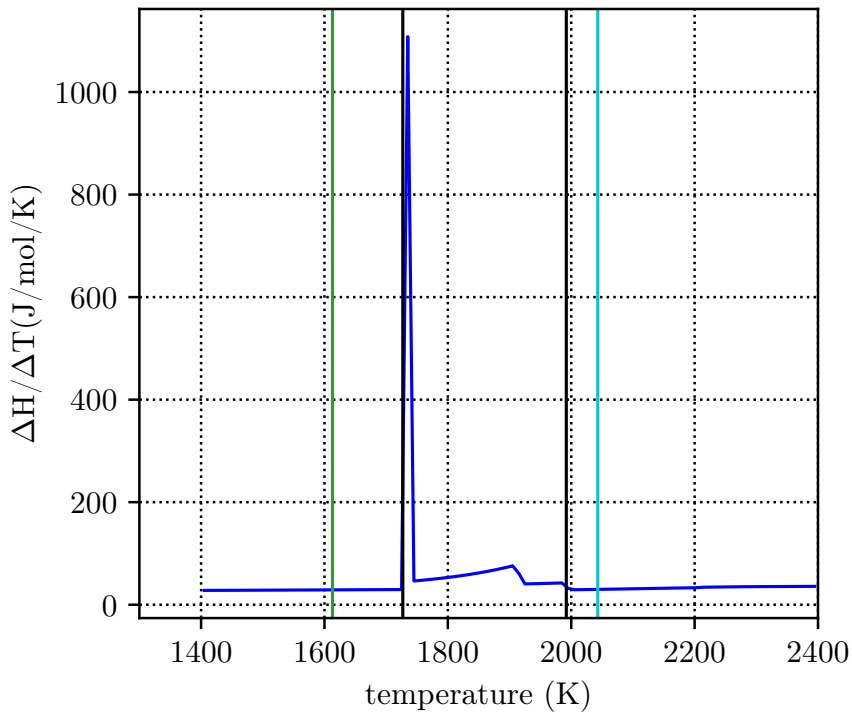

Quinary system ⇒ expected reliable extrapolation but Tsolidus overestimated by 110K
Tsolidus linked to the melting of $(Al_2O_3)_6(CaO)_{13}(ZrO_2)_2$ ⇒ possibly not formed during cooling

Issues in Solidus Determination 2/2

MC_CSO_3	UO_2	ZrO_2	FeO	Cr_2O_3	SiO_2	CaO
w-%	37.9	13.5	16.9	12	12.1	7.6

Phase weight fraction

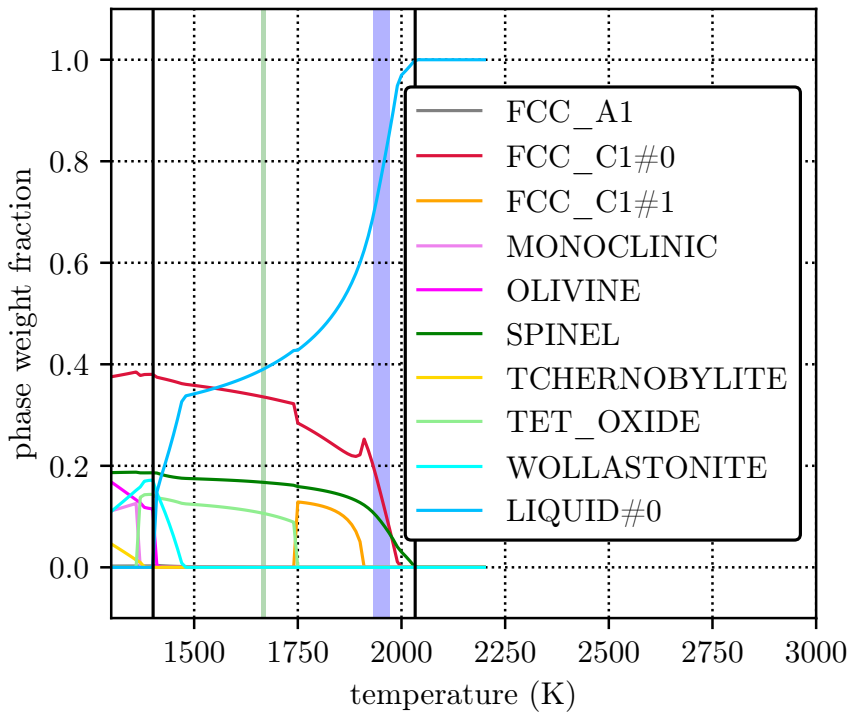

Derivative of enthalpy versus temperature

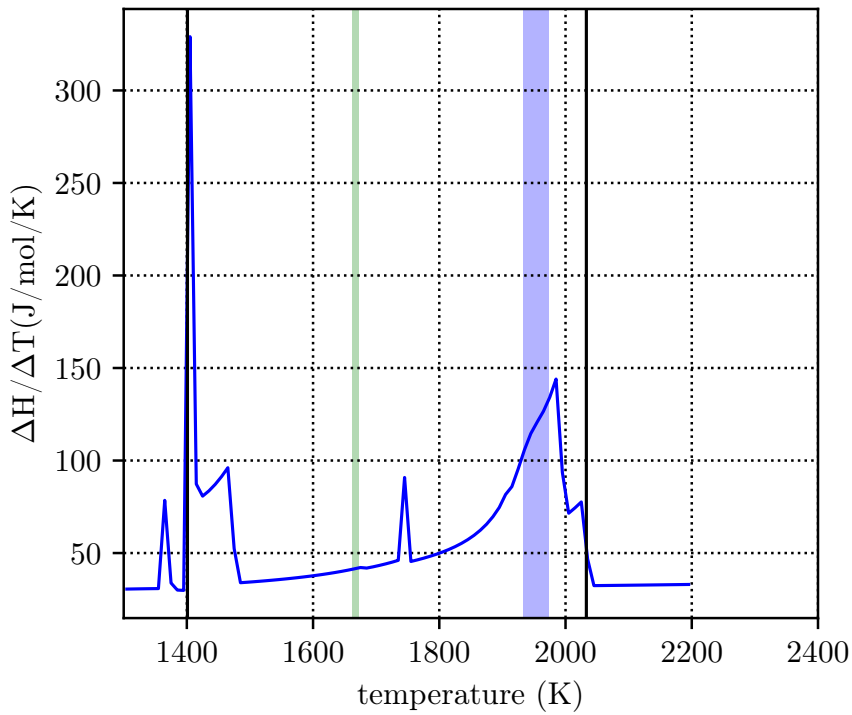

several thermal arrests in multi-component system ⇒ difficult to assign one to Tsolidus
Tsolidus linked to the melting of olivine, $(Ca,Fe)_2SiO_4$ ⇒ possibly not formed during cooling

Conclusion

- NUCLEA-26 database is able to address the issues of fuel degradation, fission product release, and corium progression.
- Validation of NUCLEA for in-vessel conditions: good agreement for U–Zr evolution in the metallic ingot and fission product partitioning between oxide and metal.
- For ex-vessel conditions: good agreement for the liquidus temperature, but determining the solidus temperature is more challenging.
- Coupling of NUCLEA with ASTEC/ICARE for IVR studies and with ASTEC/MEDICIS for ex-vessel applications.

Future developments

new data integration, possible ternary extensions, no additional elements planned

Publications

- article on NUCLEA validation recently submitted to Annals of Nuclear Energy (*NUCLEA: A thermodynamic database validated for severe accident codes*)
- article on NUCLEA modeling and NucleaToolbox software currently being written

SIMULATION OF MELT DEBRIS SPREADING BEHAVIOR IN A CORE CATCHER USING THERMOS

Wataru KIKUCHI, Masashi SEKINE, Retsu KOJO, and Junichi KANEKO
Nuclear Regulation Authority
Roppongi-First-Bldg. 1-9-9, Roppongi, Minato-ku, Tokyo, Japan
kikuchi_wataru_2p5@nra.go.jp; sekine_masashi_we6@nra.go.jp; kojo_retsu_px2@nra.go.jp; kaneko_junichi_hc6@nra.go.jp

Koetsu ITO, and Hidetoshi MORITA
Engineering department
FMIC R&D INC.
105, 2-7-13 Kyounanchou, Musashino City, Tokyo, Japan
ko-ito@fmic-rd.com; h-morita@fmic-rd.com

ABSTRACT

Stable corium cooling in ex-vessel regions is a critical issue during severe accidents in light water reactors. The dry cavity strategy is an effective mitigation approach that involves spreading molten debris in a core catcher before water injection. For this strategy to be effective, the molten debris must spread uniformly to ensure efficient cooling. Physical properties such as apparent viscosity, which evolves during solidification, play a crucial role in melt spreading. These properties are strongly influenced by the boundary conditions, particularly the initial temperature and mass flow rate of the molten debris released into a core catcher. This study used the THERMOS code system to simulate molten debris spreading behavior in an european pressure reactors type core catcher under dry cavity conditions. Sensitivity analyses were performed, focusing on molten debris temperature and mass flow rate. The results reveal that the shape and distribution of the debris bed vary significantly depending on these parameters. Differences in the release mass flow rate substantially affect the melt circulation and oxide distribution in the core catcher. At high mass flow rates, mixing between the low-temperature circulating melt and the high-temperature melt descending from the slope reduced the overall molten debris temperature. At low mass flow rates, weak circulation from low inertia led to early solidification and the formation of dams on the slope. These results indicate that thermal and hydrodynamic conditions govern spreading and highlight the need for accurate viscosity-evolution and oxide-effect models. The findings are applicable to the evaluation of the dry cavity strategy in severe accident management.

KEYWORDS
THERMOS, Debris bed, Melt spreading, Core catcher, Ex-vessel

1. INTRODUCTION

During severe accidents in light water reactors, failure of the lower head of the reactor pressure vessel (RPV) may result in molten debris migrating into the cavity (referred to as the pedestal in boiling water reactors, BWRs) within the containment vessel (CV) [1]. To mitigate molten corium-concrete interaction (MCCI) and prevent basemat failure, either a wet cavity strategy or dry cavity strategy is adopted to maintain the

debris bed within the cavity in a stable cooling state [2-5]. The wet cavity strategy involves preflooding the cavity before RPV failure, thereby promoting jet fragmentation and enhancing cooling effectiveness. Conversely, the dry cavity strategy involves the installation of a core catcher, etc., to effectively spread molten debris within the dry cavity, which is then stabilized using water injection or a cooling system. The dry cavity strategy has garnered considerable attention because of its advantages, such as a practical elimination of steam explosion risk, and has already been implemented in reactors such as european pressu re reactors (EPRs) [4],[5].

Regarding debris bed formation under dry conditions, data have been obtained from experimental programs, such as COMAS [6], RIT [7], KATS [8],[9], ECOKATS [10], and VULCANO [11]. Analysis results of debris bed formation behavior under dry conditions within the core catcher using CORFLOW code [12], THEMA code [13], and MPS code [14] were reported. However, these analyses did not account for the initial conditions of the released debris or the temporal evolution of high-resolution physical properties.

To reduce uncertainties in the molten debris spreading behavior, simulations were conducted using the THERMOS code system [15], considering high-resolution time-dependent variations in material properties. Stable molten debris cooling in the dry cavity strategy requires that the debris be widely spread within a core catcher. The objective of this study is to determine whether the THERMOS analysis method, previously applied in representative Japanese BWR analyses [15], can be extended to dry cavity strategies such as debris spreading within a core catcher. This paper presents the results of analyses conducted using THERMOS, focusing on the molten debris temperature and release mass flow rate.

2. OVERVIEW OF THERMOS CODE SYSTEM

THERMOS code system [15] comprises modules such as JBREAK [2], MSPREAD [18],[19], and THEMAT [15]. JBREAK [2] solves the hydrodynamics of molten jets, including release from the RPV, interaction with coolant, impingement on obstacles, and impact on the floor. JBREAK has been validated [2] based on the DEFOR-A experiments [16],[17], focusing on molten jet breakup and droplet behavior under wet conditions. MSPREAD models molten debris deformation and cooling after reaching the floor surface, specifically its spreading, solidification due to cooling, and transition into stationary debris as apparent viscosity increases [18],[19]. The floor-surface irregularities (e.g., sumps and weirs) is considered in the melt spreading process. MSPREAD has been validated [19],[20] using dry-condition melt spreading experiments (KATS-12 [9], ECOKATS-1 [10], and VULCANO-VEU7 [11]) and wet-condition experiments (PULiMS E10 [16]). THERMAT calculates physical properties based on the temperature of different material mixtures and the mass fraction of each component. The density of molten debris is evaluated as a mass-fraction-weighted average. The Da Andrade exponential function [21] is applied to compute the viscosity for each composition, and the apparent viscosity of molten debris is evaluated using the Ramacciotti model [22].

These modules interact through two-way interfaces at each time step and computational cell to handle complex molten debris behavior. Coupled analysis of ex-vessel molten debris behavior within the CV of a representative Japanese BWR has been conducted using the THERMOS – JBREAK / MSPREAD / THERMAT) system [15].

3. ANALYSIS CONDITIONS FOR DEBRIS BED FORMATION IN A CORE CATCHER

Figure 1 shows the core catcher geometry considered in this study. The dimensions (17.6-m wide and 11.0-m deep) are based on AREVA's EPR design [4],[5]. Molten debris released from the RPV falls as a molten jet onto a 7.2-m sloped surface inclined at 2°, subsequently spreading within the core catcher [4],[5].

The molten jet fall and floor impingement are calculated using JBREAK, whereas the melt spreading and cooling on the floor are computed using MSPREAD. The interface between JBREAK and MSPREAD employed the method described in the BWR analysis [15]. The computational mesh size is consistent with that employed in the VULCANO-VEU7 validation [19] and BWR analyses [15]. Based on these studies,

the contact thermal resistance between the floor and molten debris is set to 0.00012 $m^2 \cdot K/W$ and the Ramacciotti model's coefficient is set to 6.3.

This analysis focuses exclusively on metallic molten debris behavior within the core catcher, neglecting the effects of UO_2 and concrete. The composition of molten debris released from the RPV is derived from the s tation brack out (SBO) scenario of a representative Japanese BWR, as applied in previous THERMOS analyses [15]. The debris comprises Zr, Fe, Cr, Ni, Fe_2O_3, Cr_2O_3, and NiO, with a time-dependent release history [15]. This history indicated a consistently metal-rich composition across all time periods. Approximately 57 s after the molten debris was released, a small quantity of oxides appeared, constituting approximately 5% of the molten debris.

Eight cases were analyzed (Table I) to investigate the influence of release velocity and temperature. In an EPR, a holding zone (port) is located outside the RPV; a 0.36-m diameter (equivalent to 0.1 m^2) is employed in this study because the port failure area is typically ≥ 0.1 m^2. From this failure area, molten debris was released at either 1.52 m/s (corresponding to 1,000 kg/s) or 0.66 m/s (corresponding to 333 kg/s, respectively), with a total mass of up to 100 tons. The initial debris temperatures corresponding to the initial superheats of 11 K, 111 K, 511 K, and 911 K were 1,900 K, 2,000 K, 2,400 K, and 2,800 K, respectively. Concrete mixing within the port and core catcher was neglected, and static water injection into the core catcher was not considered.

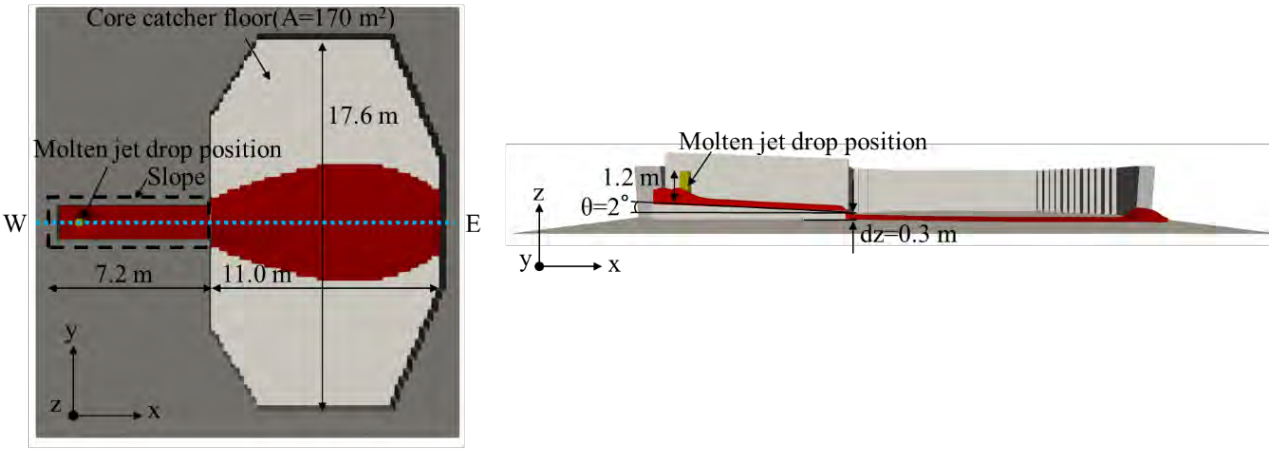

(a) Top view (b) Side view

Figure 1. Spatial Modeling of the EPR Core Catcher.

Table I. Analysis Conditions

	Molten jet diameter [m]	Initial release velocity [m/s] (release mass flow rate [kg/s])	Initial melt temperature [K] (initial superheat [K])
Case 1-L	0.36	0.60 (333)	1900 (11)
Case 2-L	0.36	0.60 (333)	2000 (111)
Case 3-L	0.36	0.60 (333)	2400 (511)
Case 4-L	0.36	0.60 (333)	2800 (911)
Case 1-H	0.36	1.52 (1000)	1900 (11)
Case 2-H	0.36	1.52 (1000)	2000 (111)
Case 3-H	0.36	1.52 (1000)	2400 (511)
Case 4-H	0.36	1.52 (1000)	2800 (911)

4. ANALYSIS OF RESULTS

4.1. Influence of Thermal and Hydrodynamic Conditions on Melt Spreading Behavior

Case 2-H represents a scenario with a high molten jet release velocity and a molten debris superheat of 111 K, indicating high fluidity. Figure 2 shows the molten jet in yellow and the spreading debris on the floor surface in red. After impinging on the sloped surface, the molten jet flows into the core catcher and subsequently spreads throughout the entire core catcher after colliding with the wall opposite the slope. These results demonstrate that the THERMOS analysis system can qualitatively capture high-resolution spreading behavior of molten debris within the core catcher.

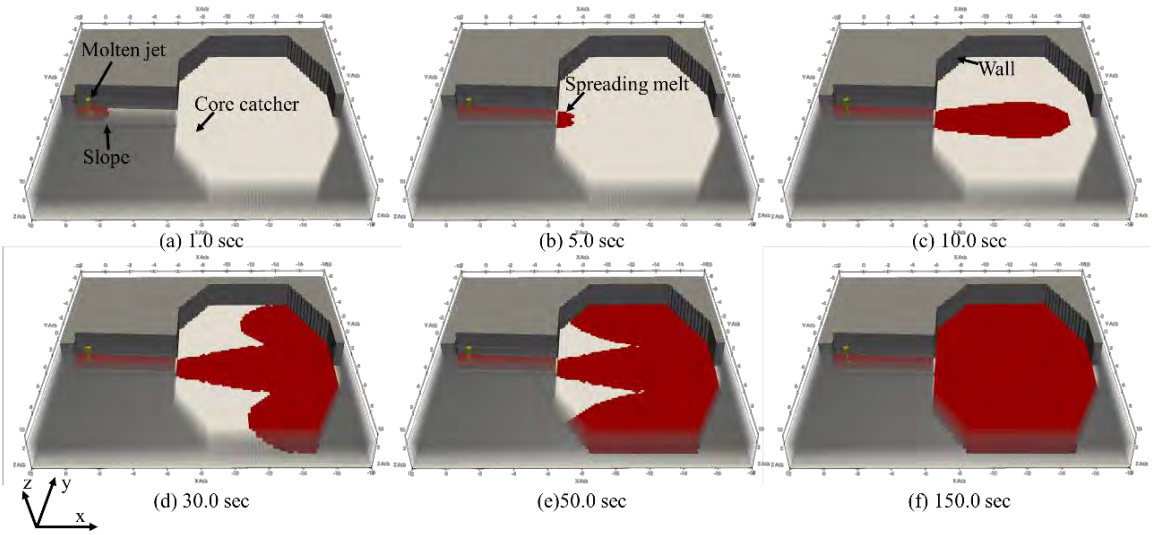

Figure 2. Spreading Behavior of Molten Debris within the Core Catcher for Case 2-H.

Figure 3 shows the time history of the molten debris spreading area for all analysis cases, divided into (a) t he initial short period (0–50 s) and (b) the extended period (0–350 s) until spreading cessation. Colored plo ts represent high-mass-flow-rate cases, whereas white plots indicate low-mass-flow-rate cases. Molten deb ris temperatures of 1900 K, 2000 K, 2400 K, and 2800 K are shown in blue, purple, green, and red, respect ively. As marked in Fig. 3(a), the spreading behavior exhibits three characteristic inflection points:

(I) molten debris flows from the sloped surface into the core catcher;
(II) molten debris impacts the core catcher wall and transitions to circulating flow; and
(III) molten debris spreads across the entire core catcher and terminates.

The results clearly indicate that spreading across the entire core catcher occurs more rapidly at higher molten jet mass flow rates or higher initial debris temperatures. As shown in Fig. 3(b), complete spreading is achieved within approximately 100 s for high-mass-flow-rate cases, regardless of temperature. Conversely, at low mass flow rates, complete spreading does not occur when the molten debris temperature is relatively low (e.g., 1900 K or 2000 K). These observations highlight the combined effect of thermal and hydrodynamic conditions on debris spreading behavior. Specifically, higher temperatures reduce apparent viscosity, promoting lateral flow, whereas higher mass flow rates increase momentum, accelerating melt spreading on the catcher floor. This interplay is critical for evaluating the effectiveness of the dry cavity strategy, as insufficient spreading may lead to localized overheating and structural failure. A more detailed quantitative analysis of these factors is provided in the following sections.

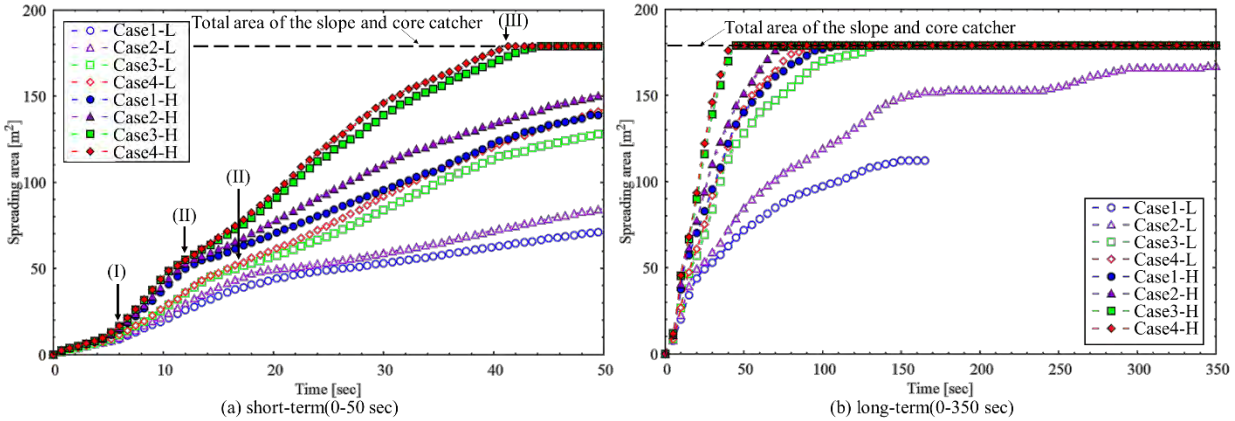

Figure 3. Time History of Molten Debris Spread Area for All Analysis Cases.

4.2. Detailed Analysis

4.2.1. Effect of the Released Molten Debris Temperature

Figure 4 shows apparent viscosity contours and the time evolution of velocity vectors during molten debris spreading for low-mass-flow-rate cases, focusing on the influence of initial debris temperature. Solidified melt is shown in gray. In all cases, the molten jet accelerates along the sloped surface before entering the core catcher and spreading across the floor. Subsequently, the flow impacts the wall opposite the slope exit and circulates along the core catcher wall. In cases with initial temperatures exceeding 2400 K (Figs. 4(c) and 4(d)), a stable circulation flow develops within the core catcher, indicating extremely high fluidity.

Figure 5 compares temperature, superheat, apparent viscosity, and spreading velocity along the E–W cross-section (Fig. 1) at 100 s and 150 s, where notable differences among cases are observed. As shown in Figs. 4(b-5), (c-4), and (d-4), the cooled circulating melt mixes with the incoming debris at the slope exit. Consequently, as shown in Figs. 5(a-1), (a-2), (b-1), and (b-2), a sharp decrease in melt temperature and superheat occurs at the slope exit after the circulating flow reaches this region (at 150 and 100 s for Cases 3-L and 4-L, respectively). Nevertheless, for high-superheat cases, such as Cases 3-L and 4-L, solidification does not occur because the superheat remains positive and no notable increase in apparent viscosity is observed (Figs. 5(a-3) and (b-3)). As a result, molten debris continues to spread rapidly within the core catcher, with only a slight reduction in velocity at the mixing point (Figs. 5(a-4) and (b-4)).

In contrast, in low-superheat cases (case 1-L and case 2-L; Figs. 4(a) and (b)), the initial apparent viscosity is high and solidification occurs during circulation. Insufficient circulation prevents complete spreading across the core catcher. At 150 s, the molten debris exhibits negative superheat and flows in a partially solidified, highly viscous state (Figs. 5(a-1), (a-2), (b-1), and (b-2)). Particularly, the temperature approaches the solidus (≈1895 K) in Case 1-L, resulting in extremely high apparent viscosity that halts spreading.

The above results demonstrate that high initial temperature promotes stable circulation flow and enhances fluidity, making temperature a dominant factor governing spreading behavior. This finding underscores the importance of accurately modeling thermal properties and apparent viscosity evolution when evaluating dry cavity strategies for severe accident mitigation.

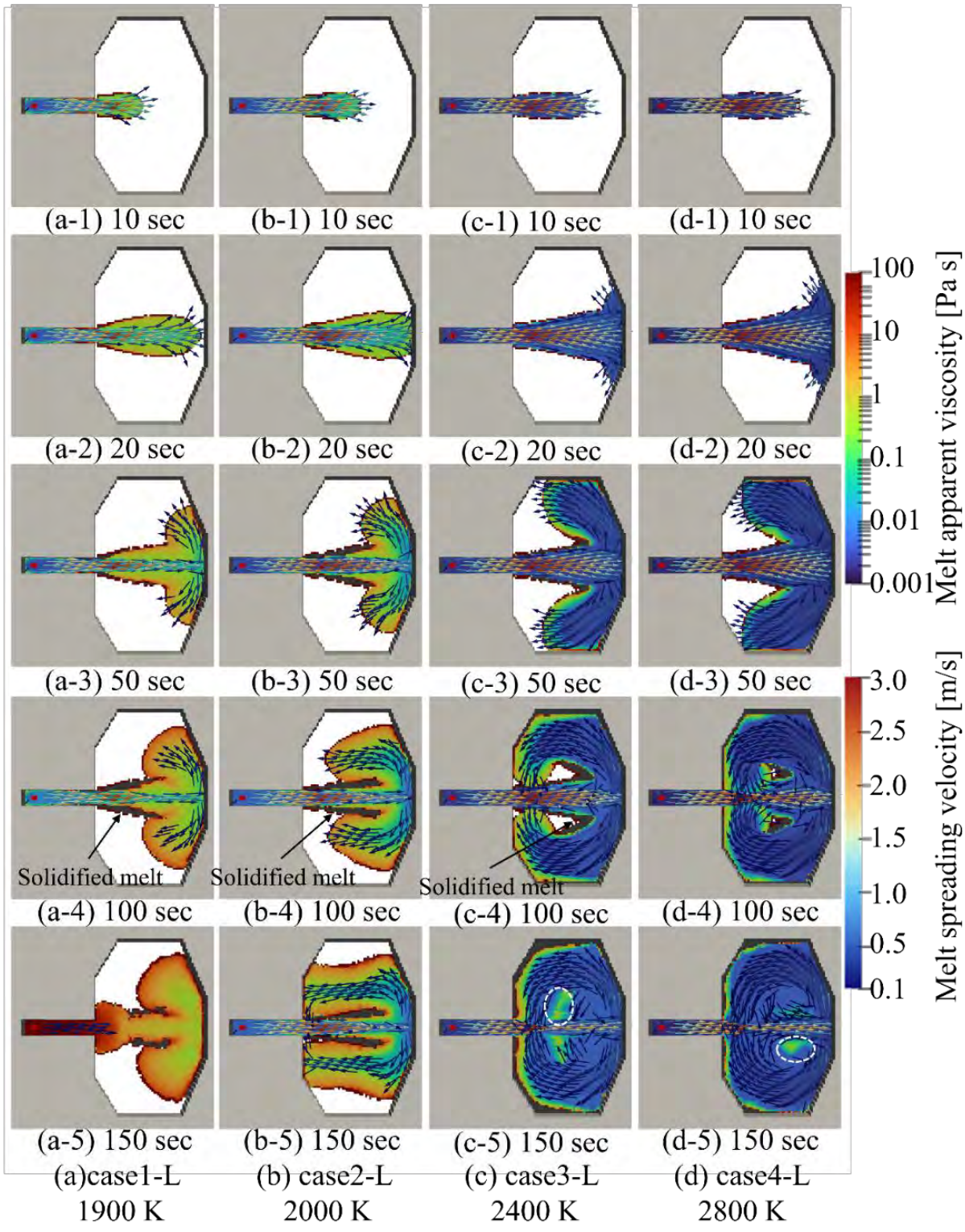

Figure 4. Time Progression of Apparent Viscosity Contours and Velocity Vector during Melt Spreading.

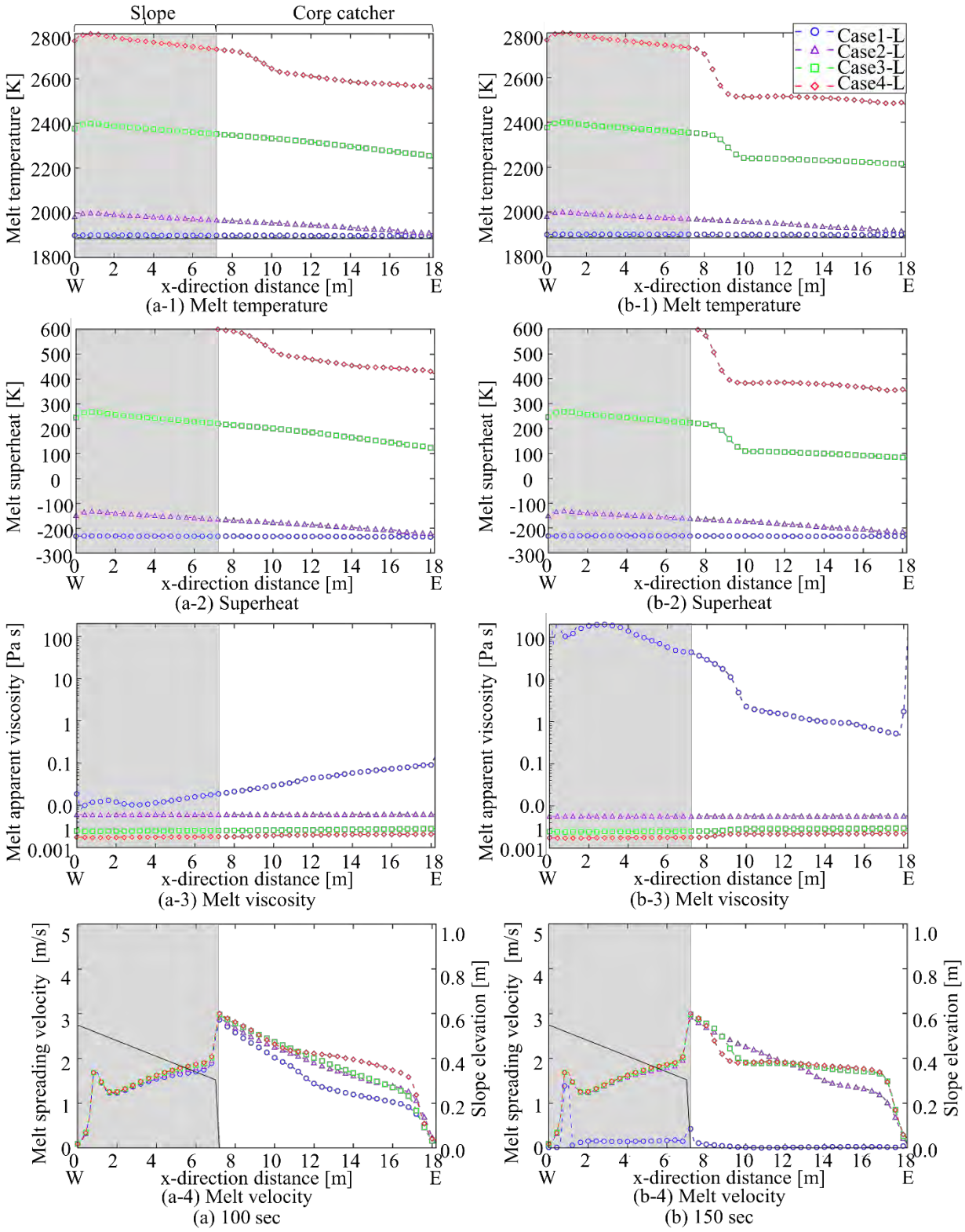

Figure 5. Comparison of Melt Temperature, Superheat, Apparent Viscosity, and Velocity Distribution in the E–W Cross-Section for Low-Mass-Flow-Rate Cases.

4.2.2. Effect of Released Mass Flow Rate Under Low-Temperature Conditions

As mentioned in Section 4.2.1, the melt spreading stopped midway in Case 1 at low mass flow rates and low temperature (1900 K). Meanwhile, as shown in Fig. 3, the melt spreading did not stop at high mass flow rates, even at low temperature (1900 K). Therefore, this section presents the analysis results focusing on the differences between the low- and high-mass-flow-rate cases at 1900 K.

Figure 6 shows the temporal evolution of apparent viscosity contours and velocity vectors during debris spreading for Case 1 at 1900 K, emphasizing the effect of release velocity. For high and low-mass-flow-rat e cases, the melt spreading across the floor-surface impinges on the wall opposite the slope exit, resulting in momentum loss after wall impingement towing to diminished inertial forces. For high-mass-flow-rate ca ses, the large inertial force of the molten debris generates a strong circulating flow even after wall impact, enabling the debris to spread across the entire core catcher. In contrast, the initial inertia is small for low-mass-flow-rate cases, and the momentum necessary to establish sufficient circulating flow is lost through wall impingement. Consequently, circulating flow fails to develop and melt spreading ceases.

Figure 7 shows the oxide-fraction distribution within the molten debris. The THERMOS analysis results apply the debris composition released during the SBO scenario of a representative Japanese BWR, as calculated by MELCOR. Oxides begin to appear approximately 50 s after release. Compared to the low-mass-flow-rate condition, the high-mass-flow-rate condition exhibits a higher oxide fraction over a wider area. The oxide fraction considerably influences the solidus/liquidus temperatures and, consequently, the physical properties of the molten debris.

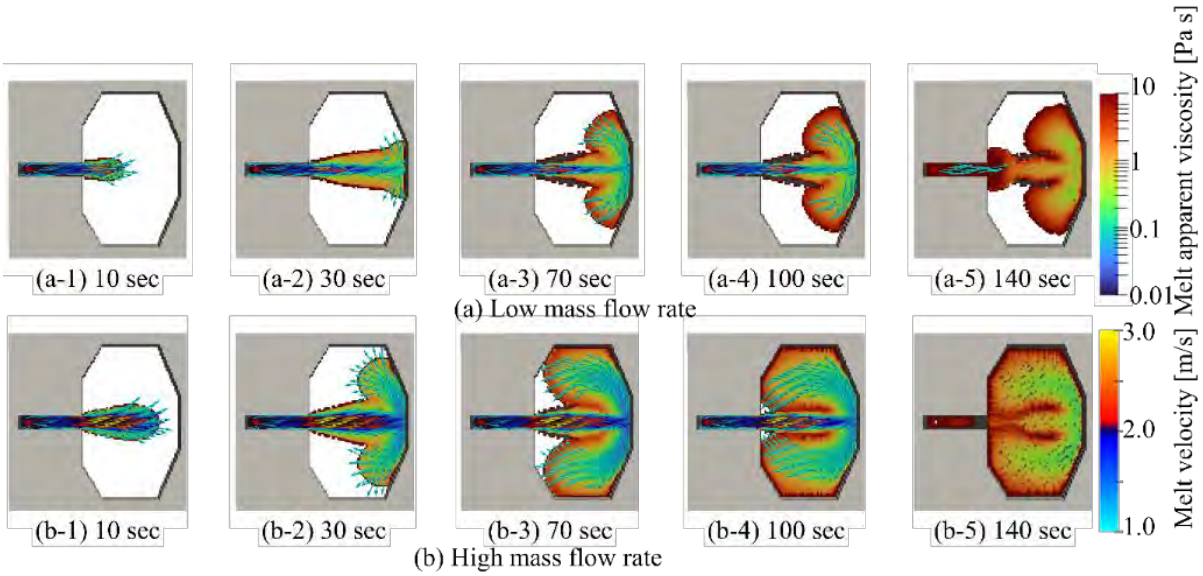

Figure 6. Progression of Debris Bed Apparent Viscosity and Velocity Distribution Based on Mass Release.

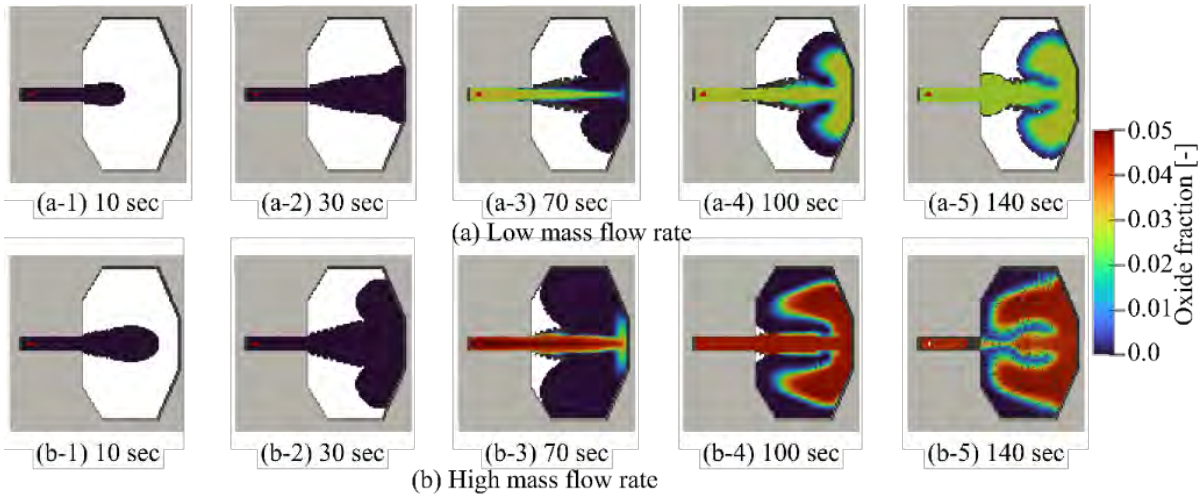

Figure 7. Progression of Oxide Mass Fraction in Debris Bed Due to Mass Release.

Figure 8 summarizes the distributions of molten debris temperature, superheat, spreading velocity, apparen t viscosity, and debris bed thickness along the E–W cross-section, divided into (a) short-term (10, 20, and 5 0 s) and (b) long-term (100, 120, and 140 s) intervals. Analysis results are shown with blue outlines and re d fills for low- and high-mass-flow-rate cases, respectively.

From the short-term perspective (10–50 s after release; Fig. 8(a-1)), the molten jet fell and spread along the slope, causing the melt temperature to decrease by approximately 10 K. As noted earlier, oxide-rich molte n debris began to appear around 50 s, raising the debris liquidus and solidus temperatures (Fig. 8(a-2)). Co nsequently, the melt superheat became negative by about 250 K and apparent viscosity increased over time (Fig. 8(a-3). Nevertheless, continuous jet release drove further molten debris spreading, resulting in debris beds of roughly uniform height under low- and high-mass-flow-rate conditions.

From the long-term perspective (100–140 s after release; Fig. 8(b-1)), sufficient circulation flow developed under high-mass-flow-rate conditions, promoting molten debris mixing at the slope exit and causing a temperature decrease. In contrast, circulation flow was absent at low mass flow rates, resulting in a nearly uniform temperature distribution. The molten debris solidus temperature increased after approximately 50 s due to oxide supply. Notably, the solidus temperature was only about 5 K lower for the high-mass-flow-rate cases than for the low-mass-flow-rate cases. Because these cases involved negative superheat, this slight difference in solidus temperature significantly affected the apparent viscosity. Although the melt temperature was lower at high mass flow rates, the oxide-mixing effect reduced the solidus temperature. Consequently, the apparent viscosity was lower at higher mass flow rates. As a result, the high-mass-flow-rate cases maintained higher momentum and achieved complete spreading across the core catcher. After 120 s, the spreading slowed dramatically in both cases and eventually ceased due to extremely high apparent viscosity. For the low-mass-flow-rate cases, jet discharge had stopped, causing debris to accumulate and form a slope-like dam (Fig. 8(b-5)).

The difference in discharge mass flow rate influenced the circulating melt flow formation within the core catcher and the oxidized material distribution within the molten debris. For the high-mass-flow-rate cases, the melt temperature decreased due to mixing between the circulating low-temperature melt and high-temperature melt from the slope exit. However, the oxide fraction lowered the solidus temperature, maintaining low-apparent viscosity and ensuring fluidity, which allowed the melt to spread throughout the entire core catcher. Meanwhile, for the low-mass-flow-rate cases, insufficient circulation developed due to low inertia, causing the melt to solidify before achieving full spreading. The released melt solidified on the slope, resulting in dam formation. These results demonstrate that the release velocity of molten debris strongly influences its spreading behavior within the core catcher.

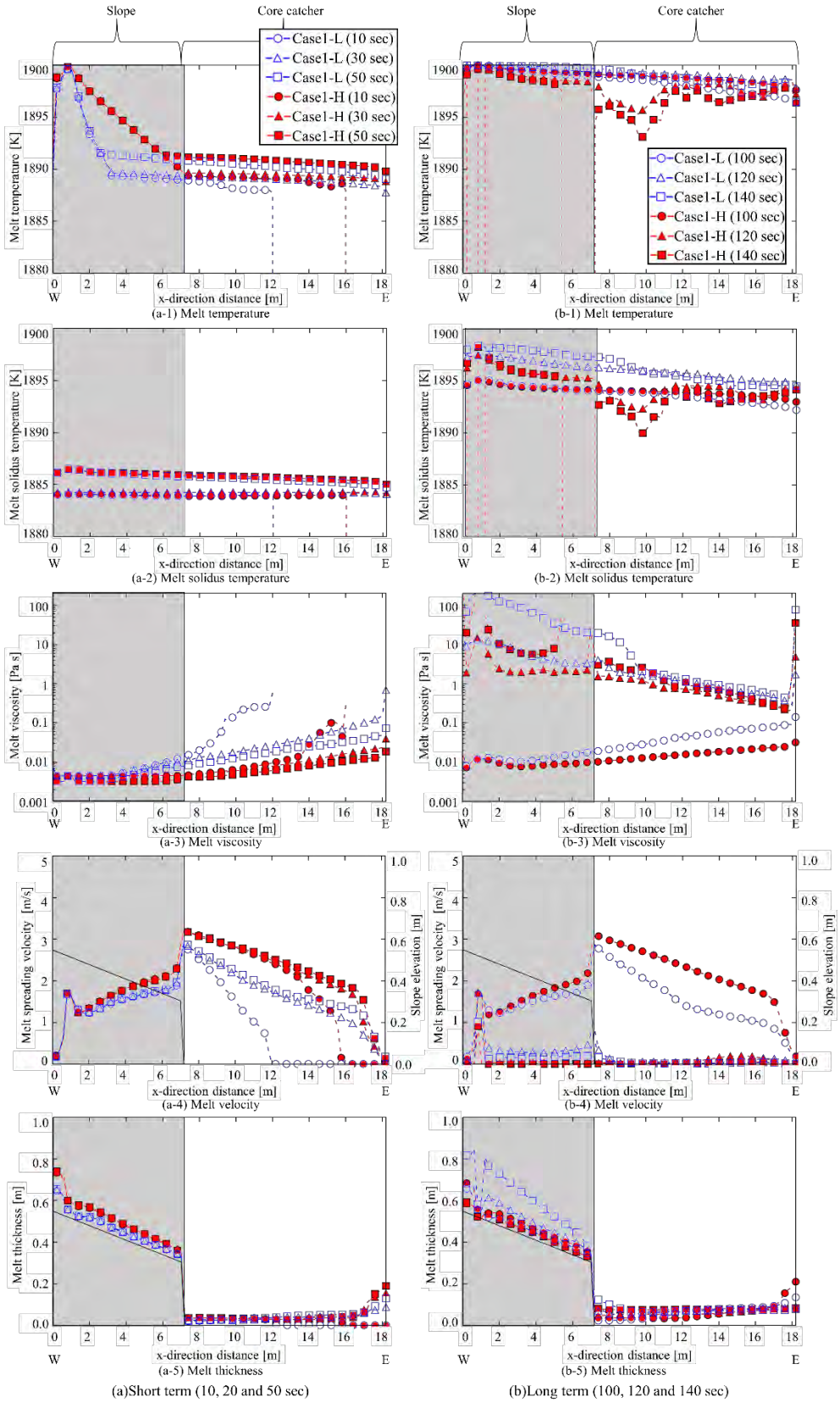

Figure 8. Effects of Mass Flow Rate on Various Parameters in the E–W Cross-Section.

5. CONCLUSIONS

The THERMOS analysis system was applied to a core catcher system representative of the dry cavity strategy. A sensitivity analysis focusing on the molten debris temperature and release rate was conducted to evaluate the debris bed formation process within an EPR-type core catcher under dry conditions. The THERMOS analysis system enabled high-resolution simulation of the apparent viscosity evolution during melt spreading and the convective behavior of molten debris within the core catcher.
The sensitivity analysis results indicated that the temperature of the released molten debris strongly influences its apparent viscosity, which governed fluidity, and was a dominant factor affecting spreading behavior within the core catcher. Furthermore, differences in the released mass considerably impacted the formation of melt circulation flow and the distribution of oxides within the core catcher. At high mass flow rates, the melt temperature decreased due to mixing between the circulating low-temperature melt and high-temperature melt flowing from the slope exit. However, the oxide fraction lowered the solidus temperature, thereby maintaining low-apparent viscosity and enabling complete spreading across the core catcher. Meanwhile, at low mass flow rates, insufficient circulation developed due to low inertia, causing the melt to solidify before full spreading occurred and resulting in the formation of a dam on the slope.
Debris bed formation is a complex, three-dimensional, transient phenomenon that cannot be accurately evaluated using simplified one-dimensional correlations. The THERMOS analysis system demonstrated its capability to address these complexities through coupled modeling of molten jet, melt spreading, and thermophysical property evolution. This study, based on MELCOR analysis results for a representative BWR SBO scenario, assumed a molten debris composition that was predominantly metal-rich with limited oxide content. Future work will include analyses considering the reduction of solidus temperature due to concrete incorporation under conditions dominated by UO_2-rich molten debris.

REFERENCES

1. Seghal, B.R, "*Nuclear safety in light water reactors: severe accident phenomenology,*" Elsevier Academic Press, Inc, USA.
2. W. Kikuchi, A. Hotta, K. Ito, M. Shimizu, "*Development of an evaluation method for debris bed formation behavior focusing on the agglomeration mechanism observed in the DEFOR-A test using THERMOS/JBREAK-DPCOOL-MSPREAD,*" Nuclear Engineering and Design 439, 114041 (2025).
3. N. Sahboun, T. Matsumoto, Y. Iwasawa, Z. Wang , T. Sugiyama, "*Development of a formulation to predict molten core spreading in an LWR severe accident,*" Annals of Nuclear Energy, Vol. 195, 110145 (2024).
4. M. Fischer, "T*he severe accident mitigation concept and the design measures for core melt retention of the European Pressurized Reactor (EPR),*" Nuclear Engineering and Design, Vol. 230 pp. 169-180 (2004).
5. M. Fischer, A. Henning, R. Surmann, "*Mitigation of severe accidents in AREVA's Gen 3+ nuclear power plants,*" Nuclear Engineering and Design, Vol. 269 pp. 323- 329 (2014).
6. W. Steinwarz, et al., "*Investigations on the Phenomenology of Ex-vessel Core Melt Behaviour. Final Report,*" EU 4th FWP, EXV-COMAS(99)-D27, (1999).
7. B.R. Sehgal, et al., "*Experimental Investigations on Melt Spreading in One and Two Dimensions. RIT/NPS Research Report,*" EU-KTH/NPS/CSC1-9812-SE, (1998).
8. B. Eppinger, G. Fieg, W. Schutz, and U., Stegmaier, "*KATS experiments to simulate corium spreading in the EPR core catcher concept,*" OECD workshop on ex-vessel debris coolability Proceedings, (2000).
9. B. Eppinger, G. Fieg, H. Massier, W. Schütz, U. Stegmaier and G. Stern, "*Simulations experimente zum Ausbreitungsverhalten von Kernschmelzen: KATS-8 bis KATS-17,*" FZKA-6589, 10.5445/IR/2700496, (2001).

10. H. Alsmeyer, T. Cron, J. J. Foit, G. Messemer, S. S. Schmidt, W. H. Häfner and H. Kriscio, "*Test report of the melt spreading tests ECOKATS-V1 and ECOKATS-1, ex-vessel core melt stabilization research,*" FZKA 7064 (2004).
11. C. Journeau, J. F. Haquet, B. Spindler, C. Spengler and J. Foit, "*The VULCANO VE- U7 corium spreading benchmark,*" Progress in Nuclear Energy. Vol. 48, Issue 3 pp. 215-234 (2006).
12. R. Wittmaack, "*Simulation of free-surface flows with heat transfer and phase transitions and application to corium spreading in the EPR,*" Nuclear Technology, Vol. 137 pp 194-212 (2002).
13. M. Eddi, G. Bandini, "*Preliminary Analysis on Corium Spreading in Reactor Core-catcher with THEMA Code,*" SAM-ECOSTAR-P07-17/01, (2002).
14. J. W. Kim, H. S. Yoo, T. H. Lee, Y. Ahn, M. C. Kwon, E. S. Kim, "*Numerical Investigation on the Structural Integrity of an Ex-vessel Core Catcher under Guillotine-type RPV Failure Using Smoothed Particle Hydrodynamics,*" 21st International Topical Meeting on Nuclear Reactor Thermal Hydraulics Proceedings, Busan Korea, August, (2025).
15. W. Kikuchi, A. Hotta, N. Adachi K. Ito and H. Yugo, "*Analysis of Ex-vessel Debris Bed Formation of Multi-material and Multiphase Composition Based on Coupled System of MELCOR2 and THERMOS-JBREAK/MSPREAD,*" Nuclear Engineering and Design., Vol. 414, 112569, (2023).
16. A. Konovalenko, W. Villanueva, T. Matsumoto, S. Bechta, et al., "*Investigation of cooling phenomena of high temperature molten core: Phase-4, Rmelting of multi-component debris (REMCOD), Debis Bed Formation (DEFOR) and Pouring and Underwater Liquid Melt Spreading (PULiMS),*" Division of Nuclear Power Safety Royal Institute of Technology. (2018).
17. A. Konovalenko, W. Villanueva, S. M. Hoseyni, S. Bechta., et al., "*Investigation of cooling phenomena of high temperature molten core: Phase-5, Modification of the facilities and third test series of separate effect studies,*" Division of Nuclear Power Safety Royal Institute of Technology. (2019).
18. A. Hotta, K. Hadachi, W. Kikuchi, M. Shimizu, "*Development of a horizontal two- dimensional melt spread analysis code, THERMOS-MSPREAD Part-1: Special models and validations based on dry spreading experiments using molten oxide mixtures and prototype corium,*" Nuclear Engineering and Design. Vol. 386, 111523. (2022).
19. A. Hotta, K. Hadachi, W. Kikuchi, M. Shimizu, "*Development of a horizontal two- dimensional melt spread analysis code, THERMOS-MSPREAD Part-2: Spreading models, numerical solution methods and verifications,*" Nuclear Engineering and Design. 386, 111523. (2022).
20. W. Kikuchi, A. Hotta, K. Ito, H. Yugo, M. Shimizu, "*Development of molten jet quench model for shallow pool based on PULiMS-E10 test,* " Mechanical Engineering Journal. Vol. 12 Issue 4, (2025).
21. Da, C., Andrade, E.N., "*LVIII. A theory of the viscosity of liquids*.—Part II," The London, Edinburgh, and Dublin Philosophical Magazine and Journal of Science, Series 7, 698-732. https://doi.org/10.1080/14786443409462427. (1934).
22. M. Ramacciotti, C. Journeau, F. Sudreau. and G. Cognet, "*Viscosity models for corium melts,*" Nuclear Engineering and Design.Vol. 204, 377-389.(2001).

Aula-1.A.01 #57

Nuclear Regulation Authority, Japan

Simulation of Melt Debris Spreading Behavior in a Core Catcher Using THERMOS

The 12th European Review Meeting on Severe Accident Research (ERMSAR2026)
May 18-22, 2026
Madrid, Spain

Wataru KIKUCHI, Masashi SEKINE, Retsu KOJO, and Junichi KANEKO
(Nuclear Regulation Authority)
Koetsu ITO, Hidetoshi MORITA (FMIC R&D INC.)

Contents

- ◆Background and objectives
- ◆Overview of THERMOS
- ◆EPR analysis condition
- ◆Analysis results
  - ✓2-D melt spreading behavior
  - ✓History of the molten debris spread area
  - ✓Effect of temperature on spreading behavior
  - ✓Effect of release flow rate on spreading behavior
  - ✓Re number evaluation
- ◆Conclusion

Contents

◆**Background and objectives**

◆Overview of THERMOS

◆EPR analysis condition

◆Analysis results

✓2-D melt spreading behavior

✓History of the molten debris spread area

✓Effect of temperature on spreading behavior

✓Effect of release flow rate on spreading behavior

✓Re number evaluation

◆Conclusion

Background and objectives

Background

- In Japan, the dry cavity strategy utilizing a core catcher is planned for the SRZ-1200 to prevent containment vessel failure caused by a molten core in the event of a severe accident.
- In France, the European Pressurized Reactor (EPR) has begun operation using a dry cavity strategy that incorporates a core catcher.

Objectives

- To investigate debris bed behavior in an EPR core catcher under dry cavity conditions using the **debris bed formation and cooling analysis code :THERMOS developed by the NRA** in Japan.

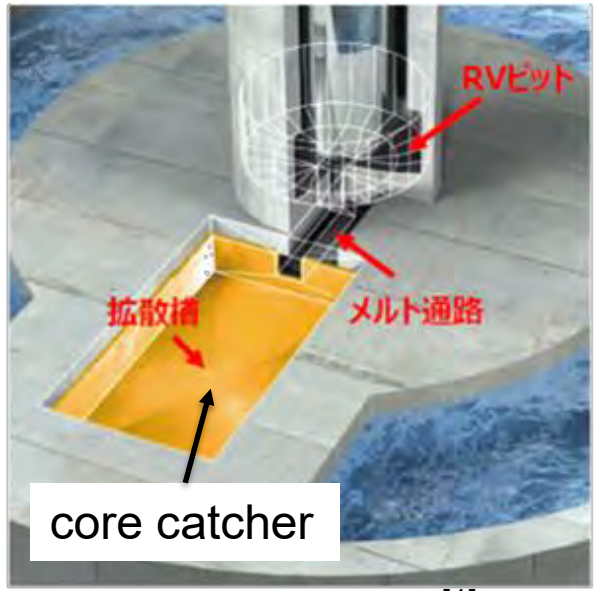

SRZ-1200 [1]

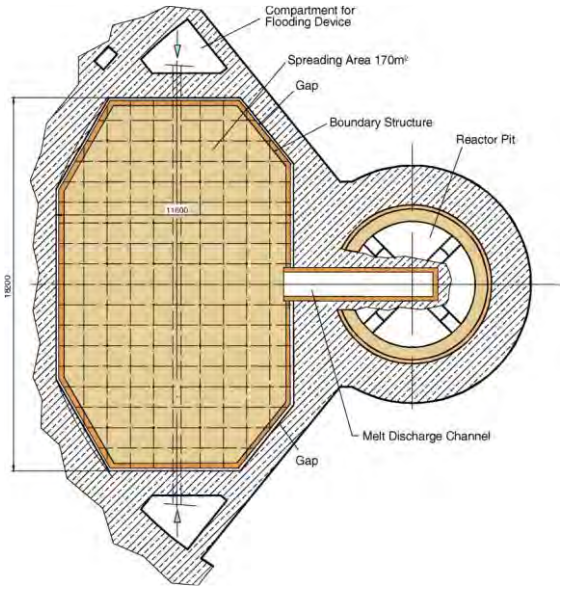

EPR [2]

[1] https://www.da.nra.go.jp/view/NRA100006848?contents=NRA100006848-002-004#pdf=NRA100006848-002-004

[2]M. Fischer, The severe accident mitigation concept and the design measures for core melt retention of the European Pressurized Reactor (EPR), NED 230, 169–180 (2004).

Contents

- ◆Background and objectives
- ◆**Overview of THERMOS**
- ◆EPR analysis condition
- ◆Analysis results
  - ✓2-D melt spreading behavior
  - ✓History of the molten debris spread area
  - ✓Effect of temperature on spreading behavior
  - ✓Effect of release flow rate on spreading behavior
  - ✓Re number evaluation
- ◆Conclusion

Overview of THERMOS

MELCOR2

● **Debris release history from the lower head.**

MELTHER

MELCOR2-THERMOS interface soft

- Mapping from the R-Z to the 3D cartesian coordinate system
- Conversion of the multi-phase & multi-material compositions in MELCOR2 to the molten and particle phases of metals and oxides in JBREAK.

Applied in this analysis

: THERMOS modules

THERMOS

THERMAT

Material libraries

JBREAK

Molten jet falling based on the 3D VOF and particle debris settlement based on Lagrangian method.

- Momentum & energy interaction with the ambient fluids based on the multi-fluid VOF method
- Jet impingement onto the floor considering liquid - solid phase separation
- Settlement in air/water : Particle debris based on the free fall algorithm

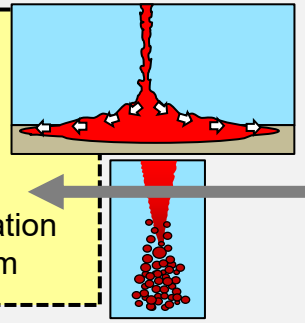

Two-way coupling

- Momentum and energy source terms.
- The flow field.

Filtration of the molten jet into the debris bed.

DPCOOL

Underwater debris bed cooling.

Local re-melting and solidification in the debris bed.

MSPREAD

Molten debris spreading behavior based on the horizontal 2D shallow water equation

- Molten debris spreading and **solidification** based on the multi-layer models
- Sump / Pedestal slit weir

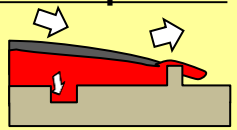

REMELT

Material interactions and liquid phase filtration in the particle bed.

Viscosity model for solidification melt

◆ **Viscosity of liquid phase**

✓ Averaged based on melt composition using Da Andrade model (If melts of UO_2, Zr, etc.)

$$\mu_{liq,m} = 6.12\times 10^{-5}\sqrt{T_{sol,m}}F_{\mu,c}(T)exp\left[\frac{1.8033T_{sol,m}^{1.348}}{R}\left(\frac{1}{T}-\frac{1}{T_{sol,m}}\right)\right]$$

$F_{\mu,c}$: Ratio of gram atomic weight 1/2 to molar volume 2/3
T : melt temp

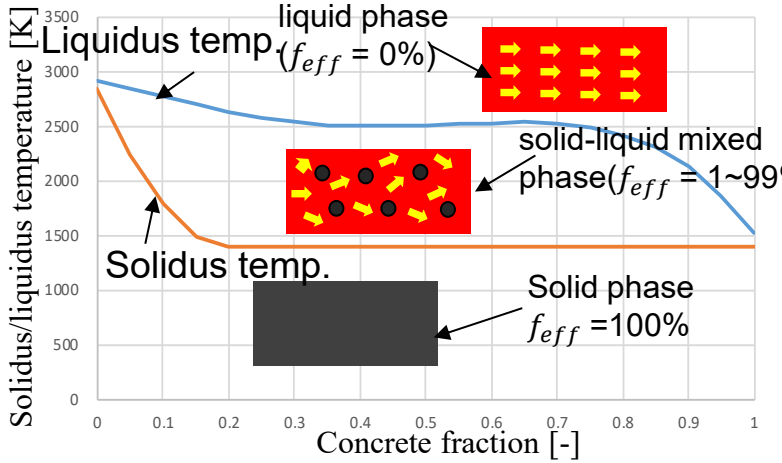

◆ **Debris apparent viscosity of solid-liquid mixed phase**

As the debris temperature decreases between the liquidus and solidus temperature, a partially solidified dispersed phase is formed and contributes to the increase in viscosity using Ramacciotti model.

✓ Debris apparent viscosity :μ_{eff}

Ramacciotti coefficient (Sensitivity parameters in this study)

Viscosity liquid phase

$$\mu_{eff} = \mu_{liq,ave}\cdot\exp\left(2.5\cdot C_R\cdot f_{eff}\right)$$

Volume ratio of solidified melt in melt

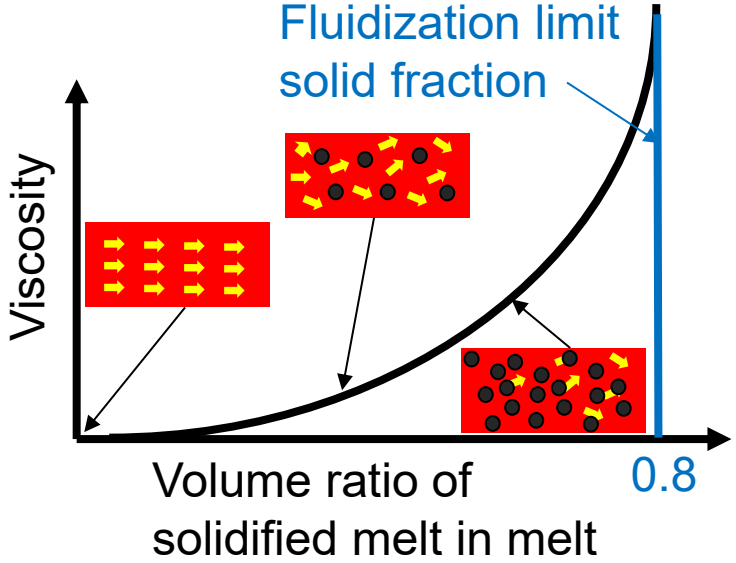

✓ **Melt spreading terminates** when the volume ratio of solidified melt exceeds Fluidization limit solid fraction (=0.8 in this study).

THERMOS validation results based on dry condition tests

THERMOS (MSPREAD) was in **good agreement with the melt spreading behavior** measured in the dry condition tests such as KATS-12,VULCANO-VEU7, ECOKATS-1 and ECOKATS-2.

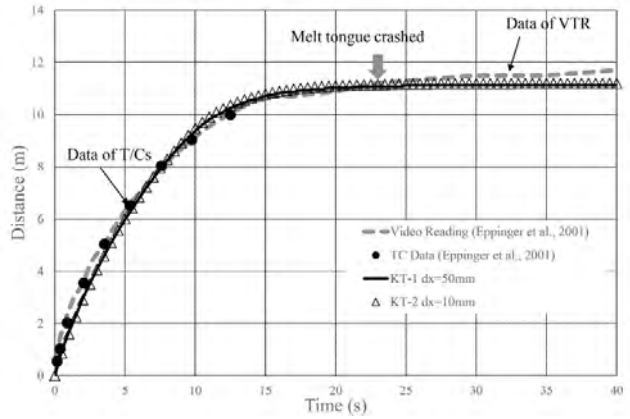

KATS-12 [3]

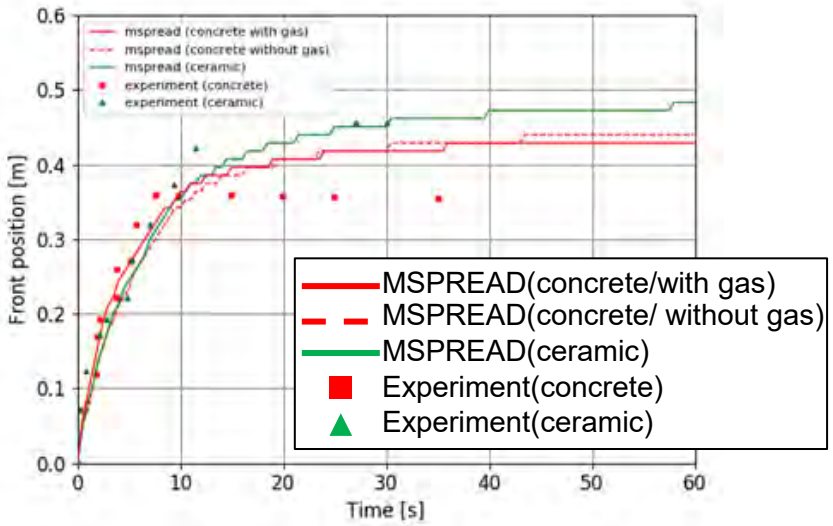

VULCANO-VEU7 [3]

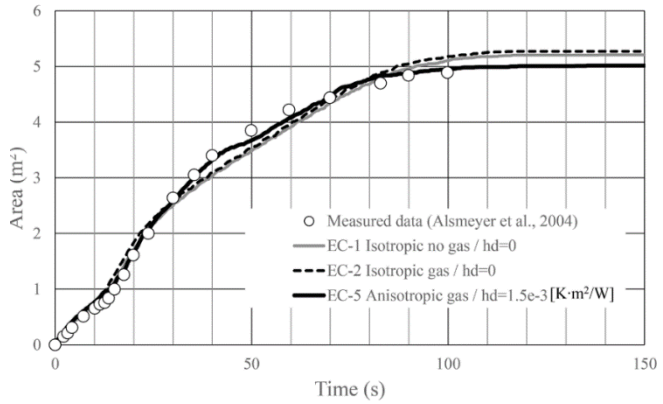

Experiment

THERMOS

ECOKATS-1 [3]

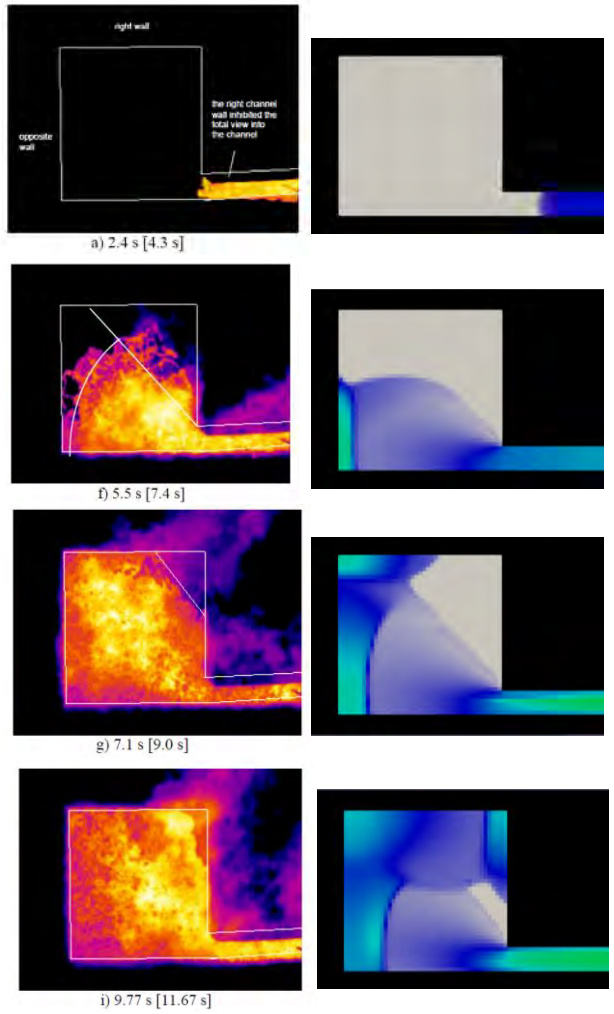

Experiment THERMOS

ECOKATS-2

[3]Hotta, A., et al., 2022a. Development of a horizontal two- dimensional melt spread analysis code, THERMOS-MSPREAD Part-2: Special models and validations based on dry spreading experiments using molten oxide mixtures and prototype corium. Nucl. Eng. Design. 387, 111598.

Analysis results for BWR Mark-I under dry condition

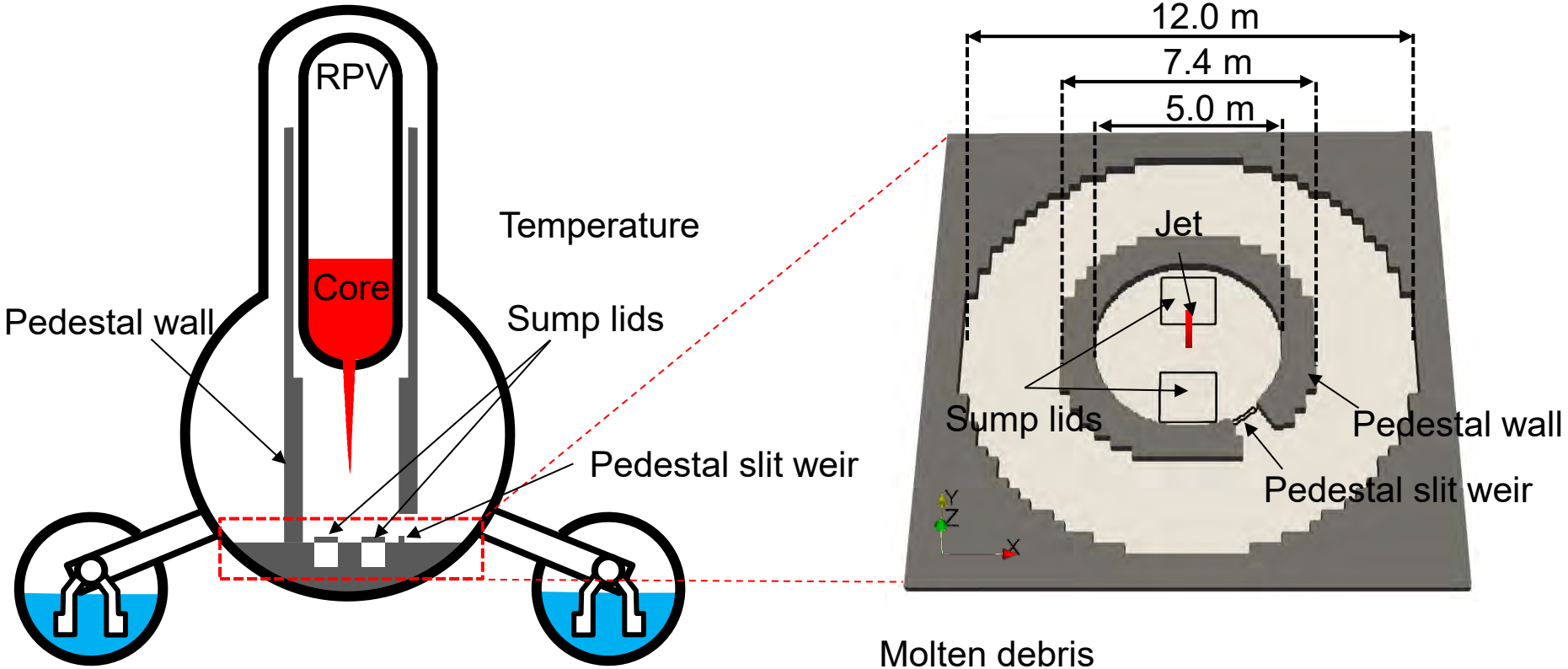

Molten debris temperature

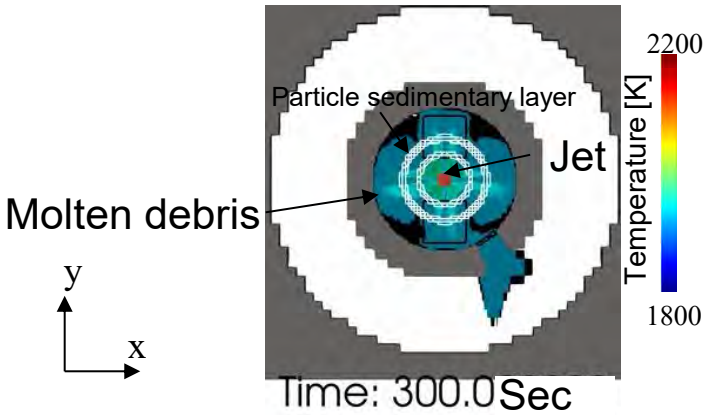

Molten debris solid fraction

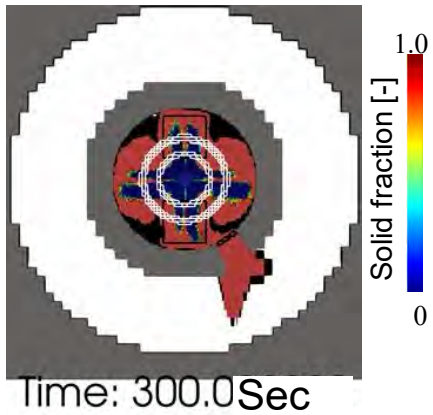

Molten debris apparent viscosity

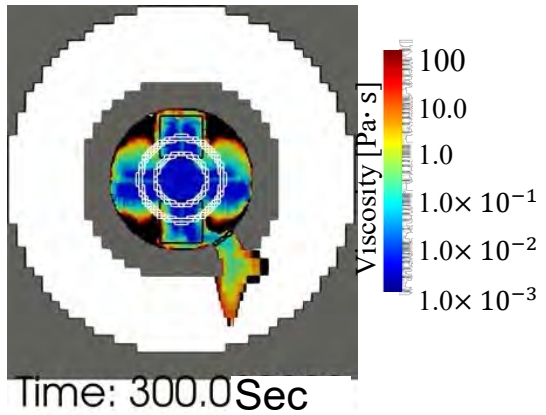

Molten debris thickness

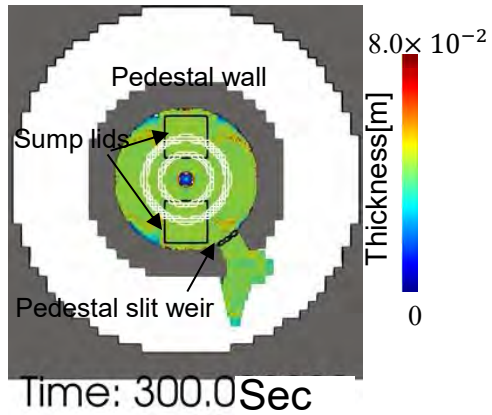

[4]Kikuchi, W., et. al., 2025, Development of an evaluation method for debris bed formation behavior focusing on the agglomeration mechanism observed in the DEFOR-A test using THERMOS/JBREAK–DPCOOL–MSPREAD, Nuclear Engineering and Design Volume 439, 114041

Contents

- ◆Background and objectives
- ◆Overview of THERMOS
- ◆**EPR analysis condition**
- ◆Analysis results
  - ✓2-D melt spreading behavior
  - ✓History of the molten debris spread area
  - ✓Effect of temperature on spreading behavior
  - ✓Effect of release flow rate on spreading behavior
  - ✓Re number evaluation
- ◆Conclusion

Analysis conditions for geometry

- The geometry for THERMOS was modeled based on the publicly available EPR geometry.
- The slope angle was set to 2 degrees.
- It was assumed that the melt jet freely falls the distance of 1.2 m between the melt plug and the slope.
- In these analyses, the sacrificial concrete placed in a core catcher was not considered.

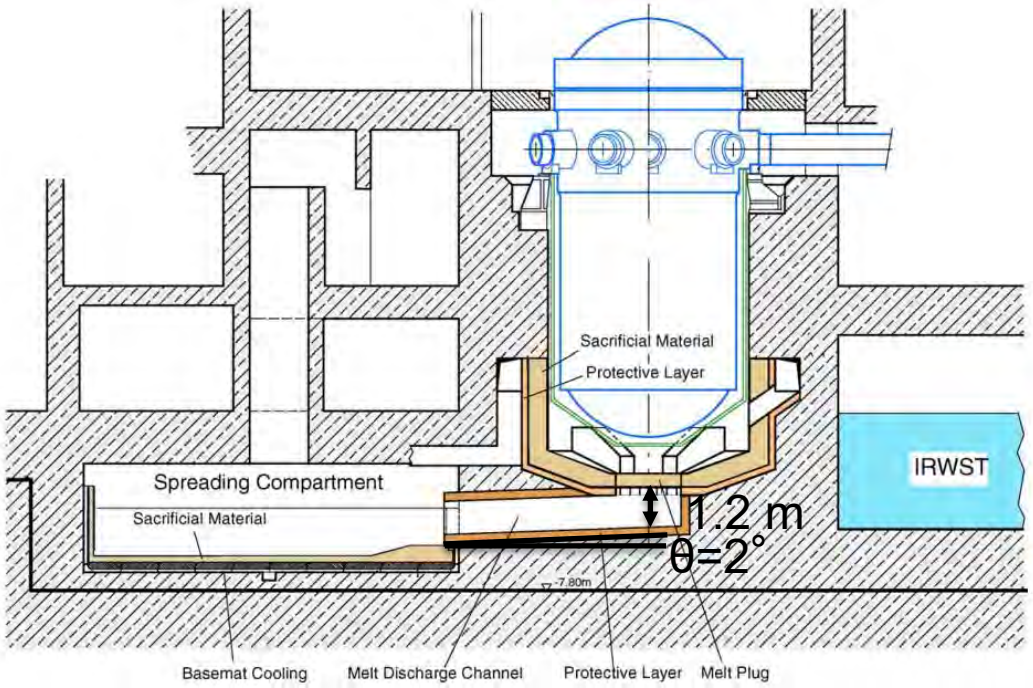

Publicly available EPR geometries[2]

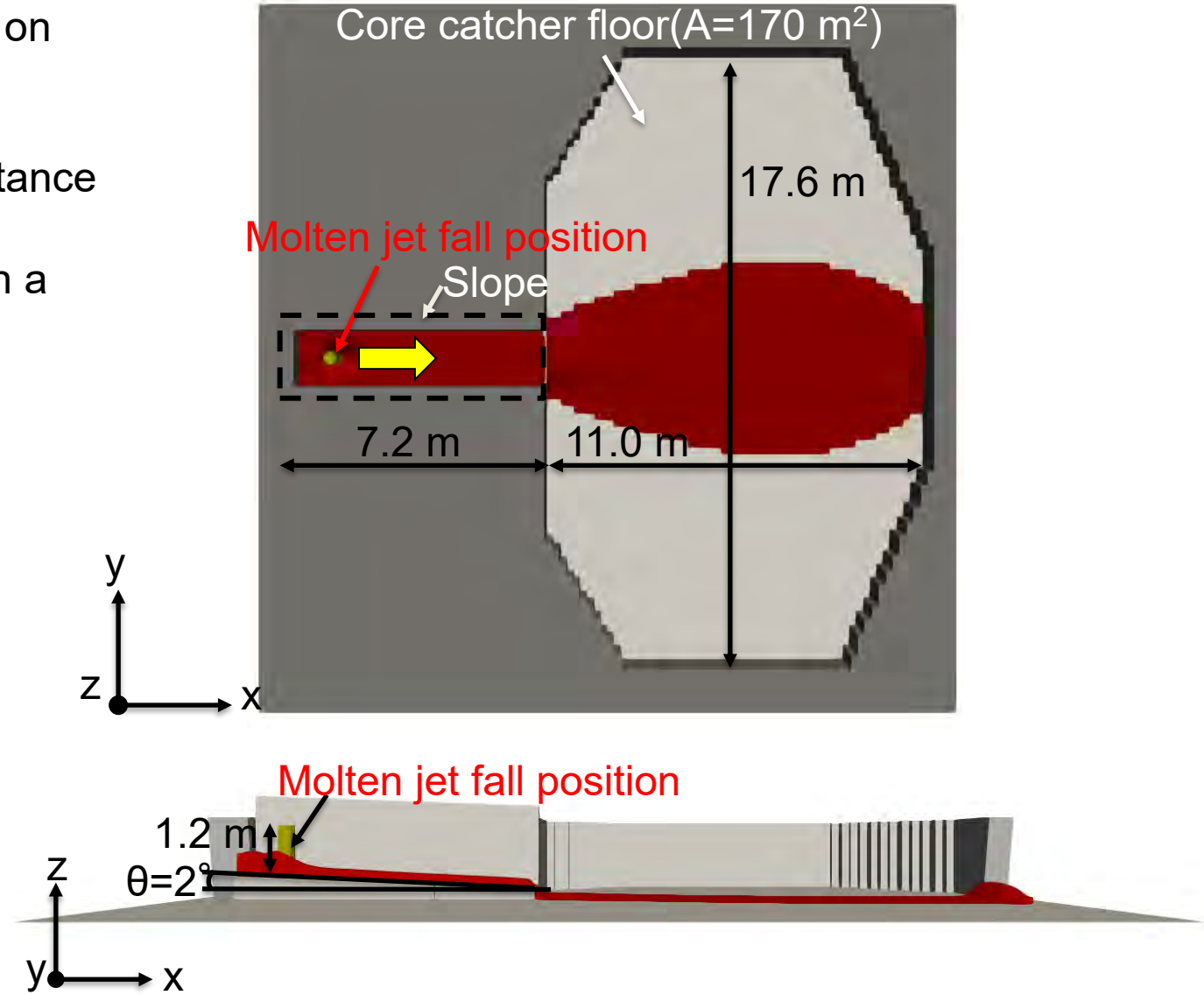

THERMOS analysis geometry

[2]M. Fischer, The severe accident mitigation concept and the design measures for core melt retention of the European Pressurized Reactor (EPR), NED 230, 169–180 (2004).

Analysis conditions for released molten debris

- The **release mass flow rate(low or high)** and **temperature (1900,2000,2400 or 2800)** of the molten debris were chosen as sensitivity parameters.
- The molten debris composition used in the analysis for the BWR Mark-I was also applied in this core catcher analysis.

Sensitivity analysis cases

	Release mass flow rate [kg/s] (Release velocity [m/s])	Temperature [K] (superheat* [K])
Case 1-L	333 (0.60)	1900 (11)
Case 2-L	333 (0.60)	2000 (111)
Case 3-L	333 (0.60)	2400 (511)
Case 4-L	333 (0.60)	2800 (911)
Case 1-H	1,000 (1.52)	1900 (11)
Case 2-H	1,000 (1.52)	2000 (111)
Case 3-H	1,000 (1.52)	2400 (511)
Case 4-H	1,000 (1.52)	2800 (911)

***Superheat**
= temperature-liquidus

Initial liquidus:1889 K
Initial solidus :1884 K

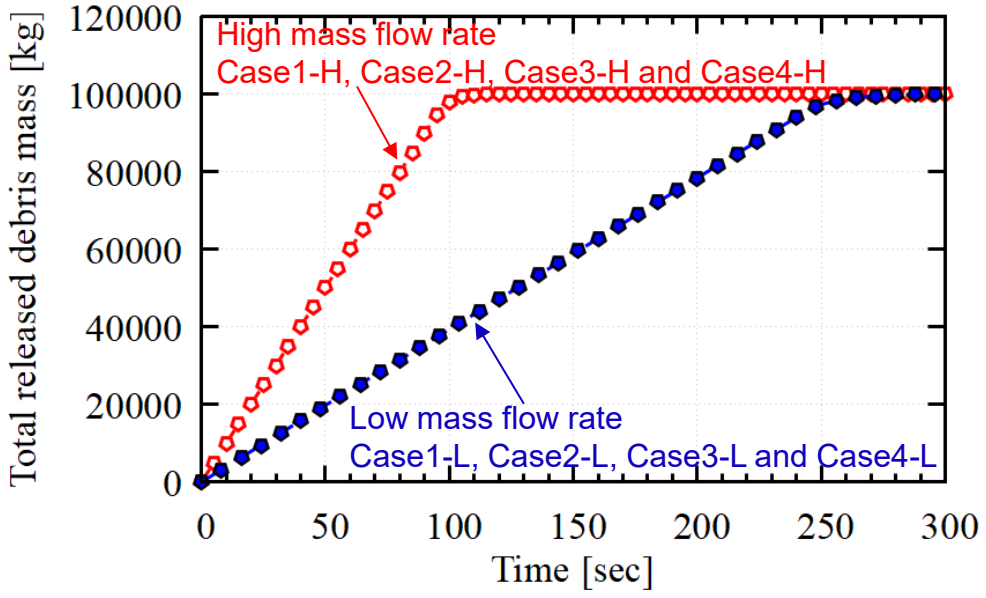

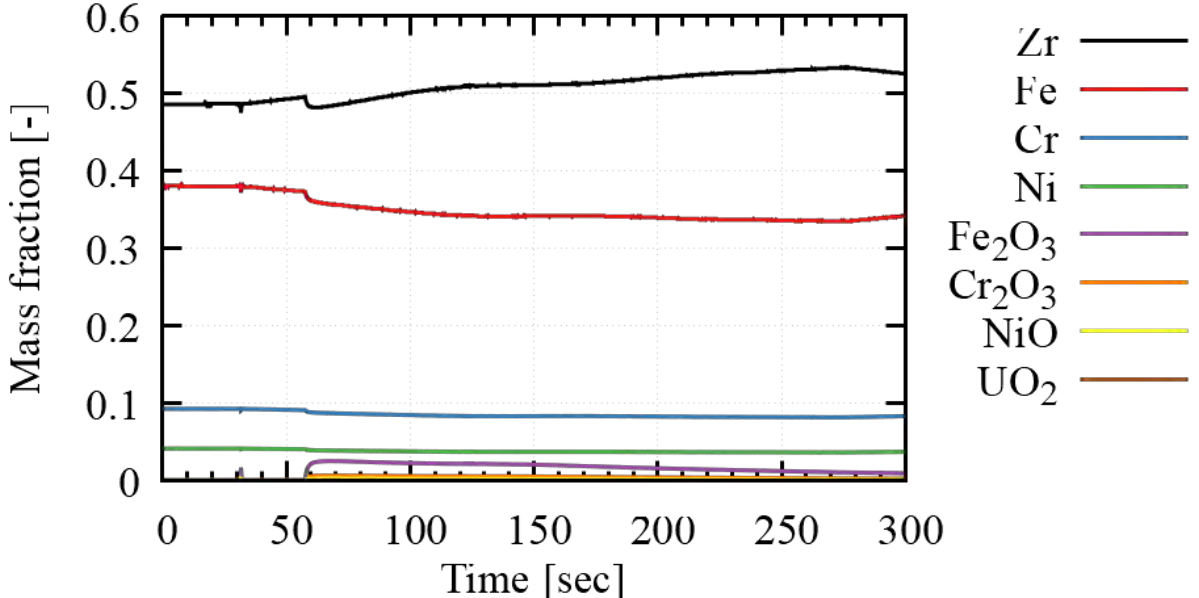

Contents

- ◆Background and objectives
- ◆Overview of THERMOS
- ◆EPR analysis condition
- **◆Analysis results**
- **✓2-D melt spreading behavior**
- ✓History of the molten debris spread area
- ✓Effect of temperature on spreading behavior
- ✓Effect of release flow rate on spreading behavior
- ✓Re number evaluation
- ◆Conclusion

2-D melt spreading behavior (melt thickness and spreading velocity)

- Compared to low flow rates, **high flow rates** caused the molten debris to **spread more rapidly** a core catcher.
- Under high flow rate conditions, the **molten debris circulated** in a core catcher.

Case4-H(velocity: **1.52 m/s**)

*Time [sec]

Case1-H(1900 K/ 11 K)

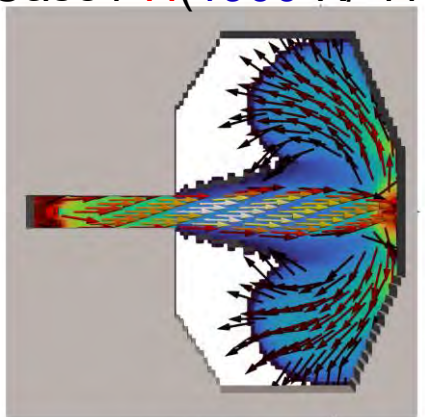

Case2-H(2000 K/ 111 K)

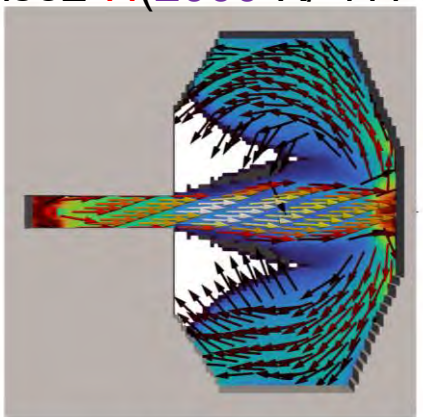

Case3-H(2400 K/ 511 K)

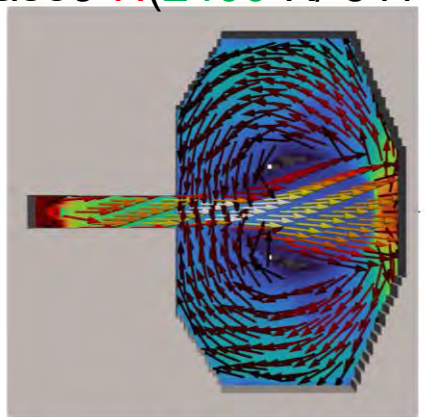

Case4-H(2800 K/ 911 K

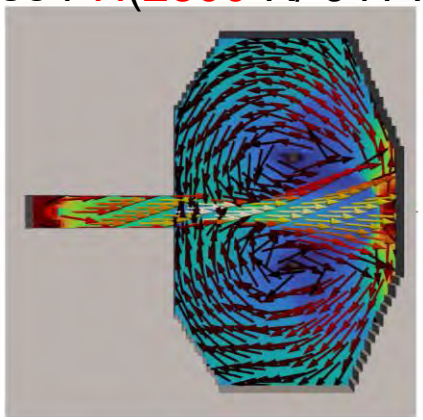

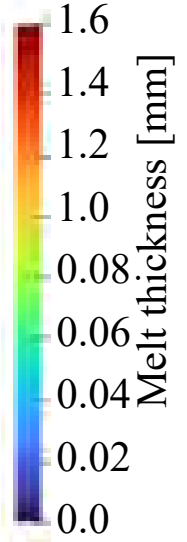

Case4-L(velocity: **0.60 m/s**)

Case1-L(1900 K/ 11 K)

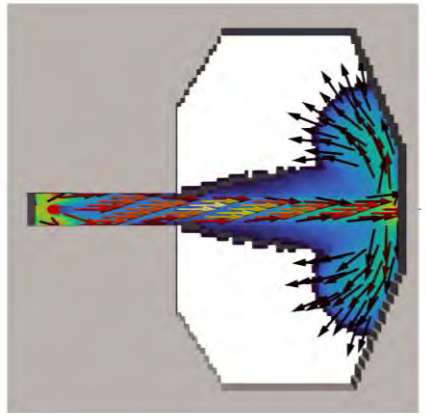

Case2-L(2000 K/ 111 K)

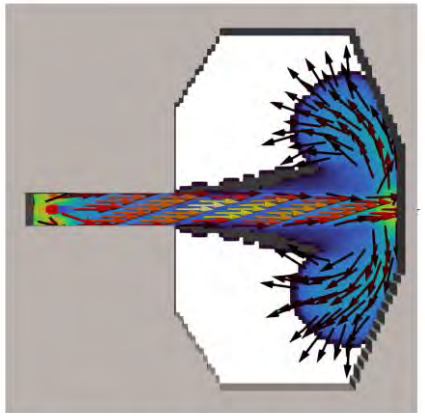

Case3-L(2400 K/ 511 K)

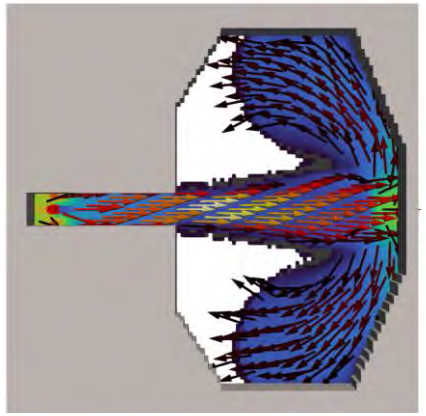

Case4-L(2800 K/ 911 K)

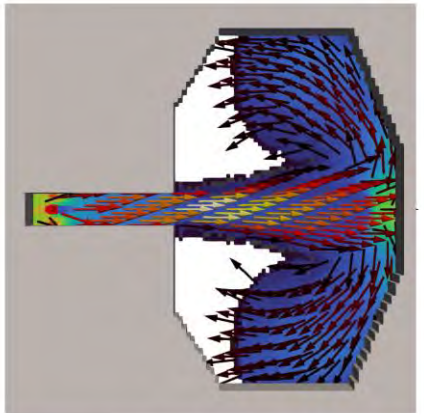

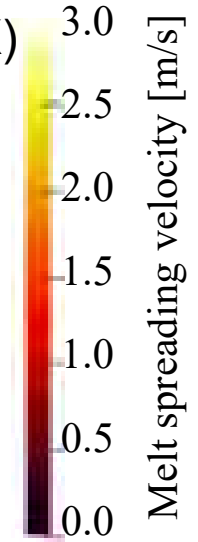

2-D melt spreading behavior (melt apparent viscosity)

◆ The lower the temperature of the released molten debris, the higher its apparent viscosity.

Case4-H(velocity: **1.52 m/s**)

*Time [sec]

Case1-H(1900 K/ 11 K)

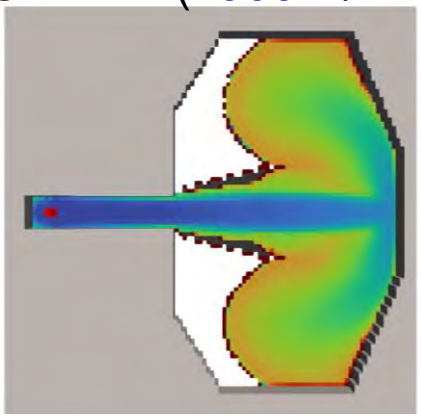

Time: 41.000000

Case2-H(2000 K/ 111 K)

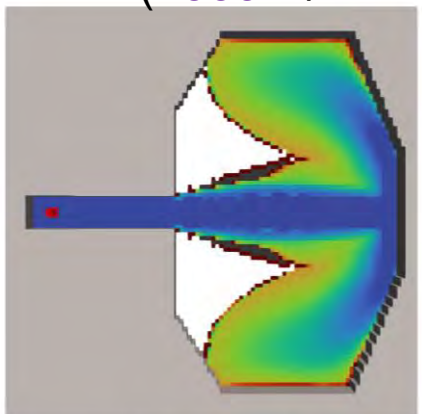

Time: 51.000000

Case3-H(2400 K/ 511 K)

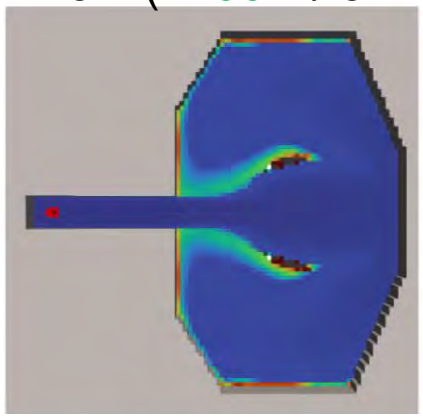

Time: 46.000000

Case4-H(2800 K/ 911 K)

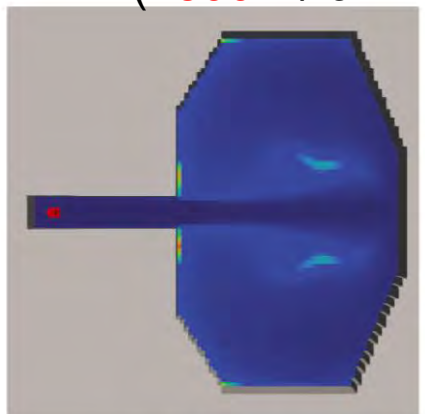

Time: 51.000000

Case4-L(velocity: **0.60 m/s**)

Case1-L(1900 K/ 11 K)

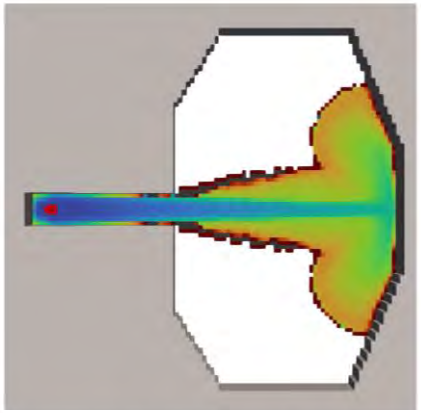

Time: 55.000000

Case2-L(2000 K/ 111 K)

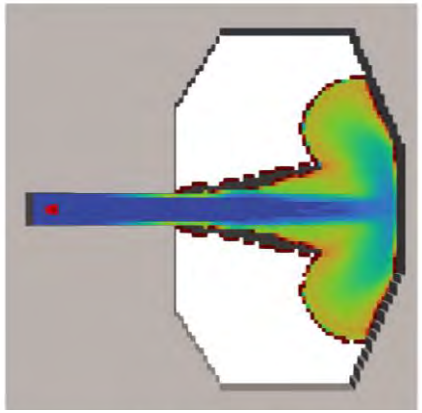

Time: 51.000000

Case3-L(2400 K/ 511 K)

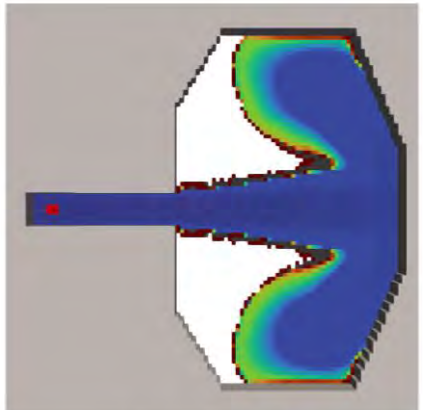

Time: 51.000000

Case4-L(2800 K/ 911 K)

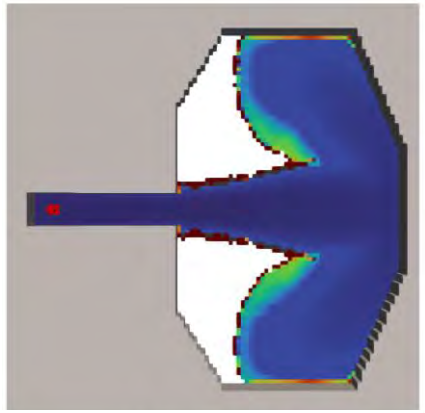

Time: 46.000000

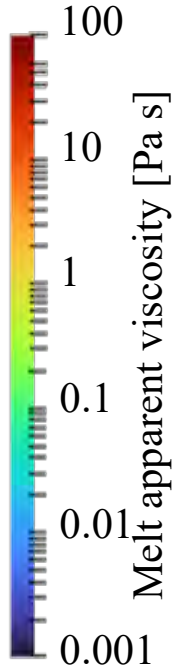

Contents

- ◆Background and objectives
- ◆Overview of THERMOS
- ◆EPR analysis condition
- ◆Analysis results
  - ✓2-D melt spreading behavior
  - ✓**History of the molten debris spread area**
  - ✓Effect of temperature on spreading behavior
  - ✓Effect of release flow rate on spreading behavior
  - ✓Re number evaluation
- ◆Conclusion

History of the molten debris spread area in a core catcher

Case1-H(**velocity:1.52 m/s**, melt temp.:**2800 K**/ superheat:**911 K**)

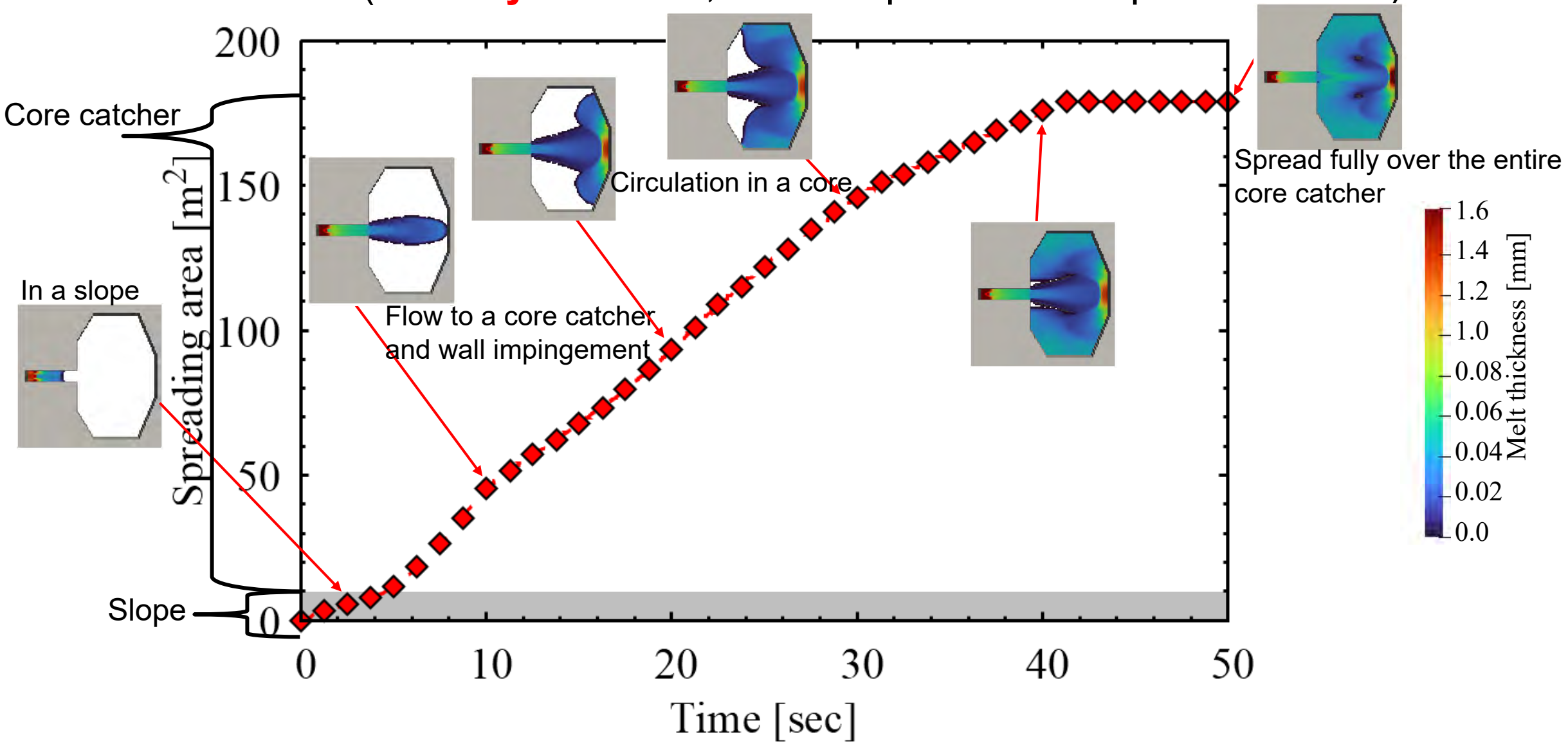

History of the molten debris spread area in a core catcher

Case2-H(**velocity:1.52 m/s**, melt temp.:**2400 K**/ superheat:**511 K**)

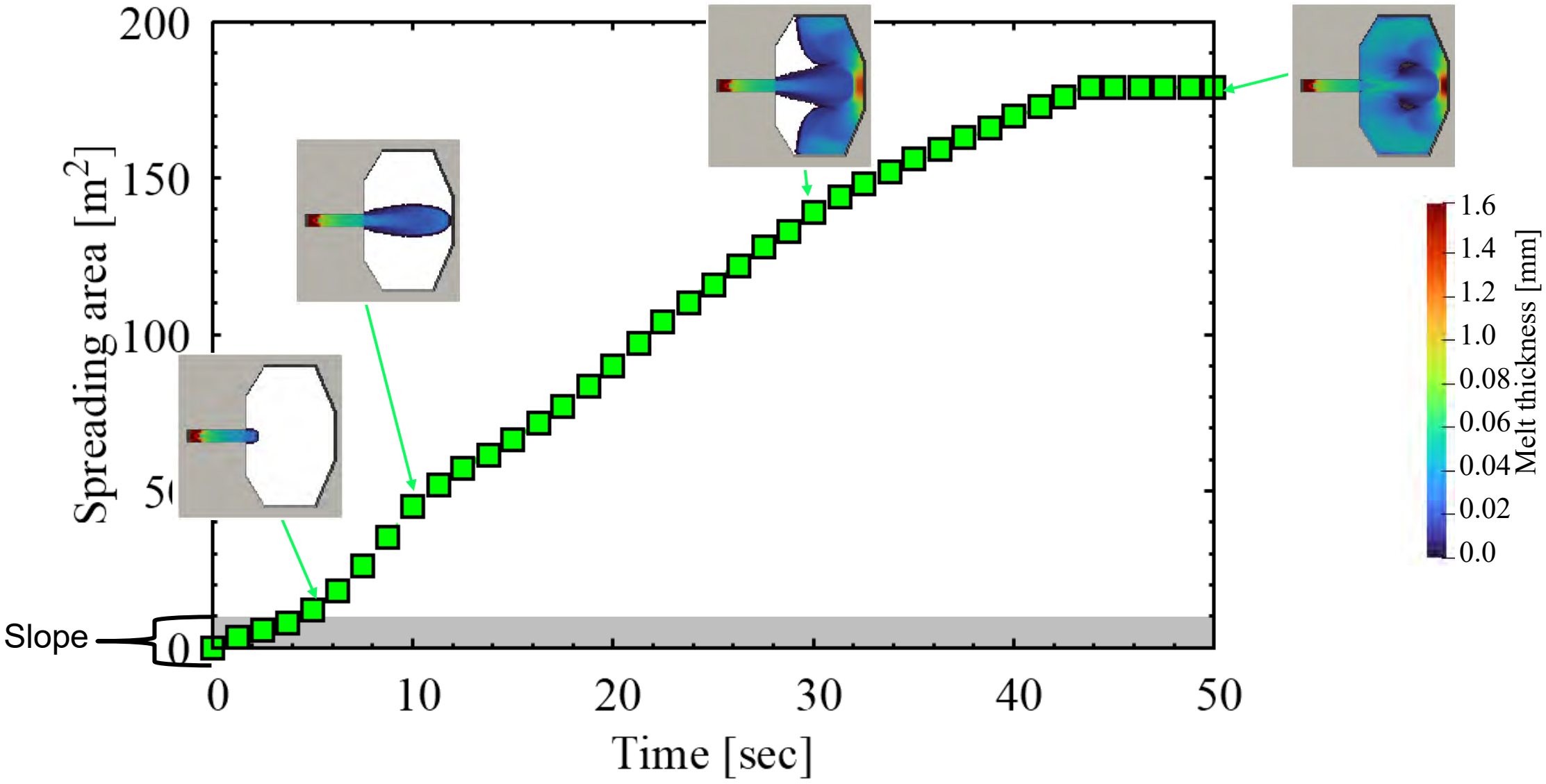

History of the molten debris spread area in a core catcher

Case3-H(**velocity:1.52 m/s**, melt temp.:**2000 K**/ superheat:**111 K**)

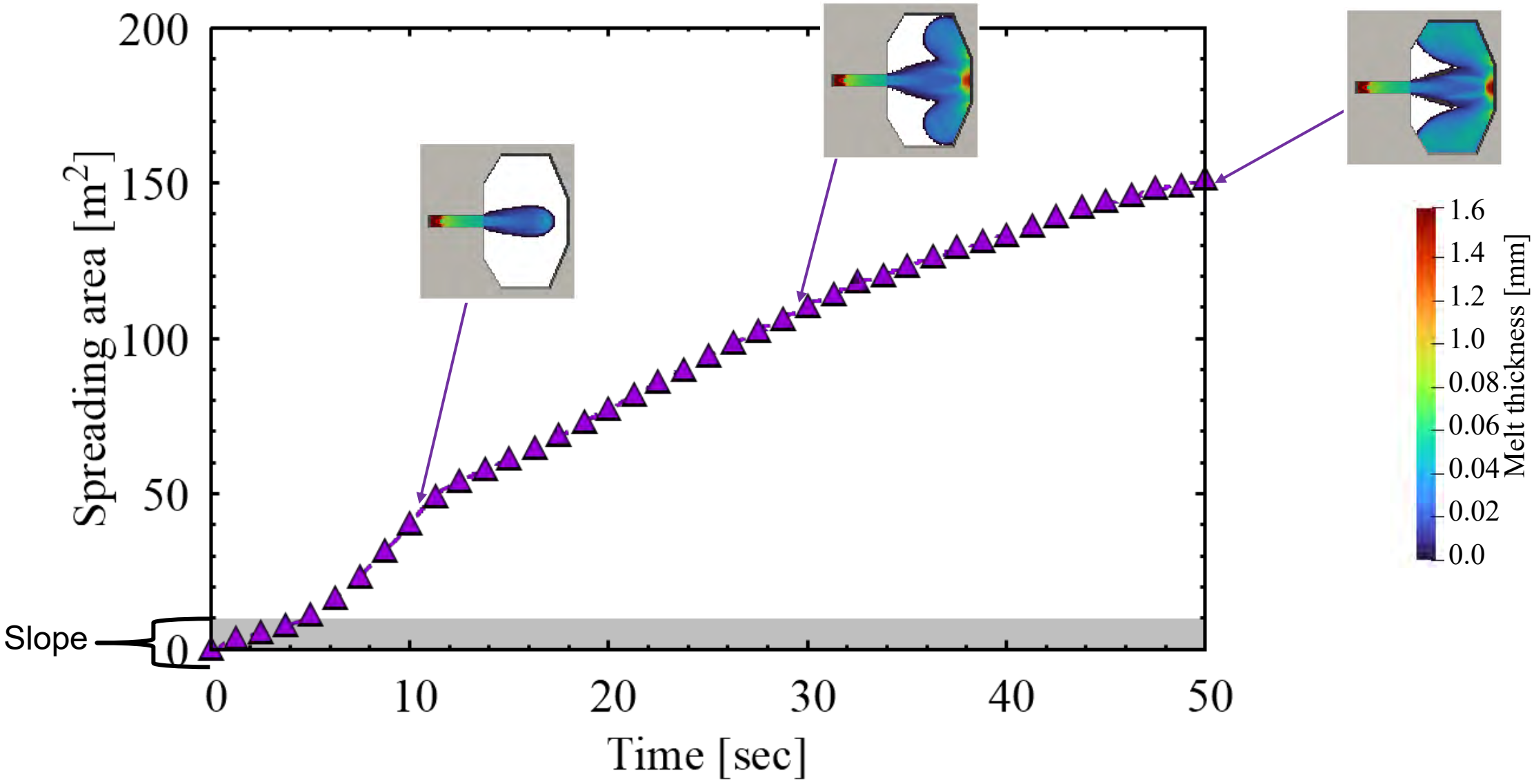

History of the molten debris spread area in a core catcher

Case4-H(**velocity:1.52 m/s**, melt temp.:**1900 K**/ superheat:**11 K**)

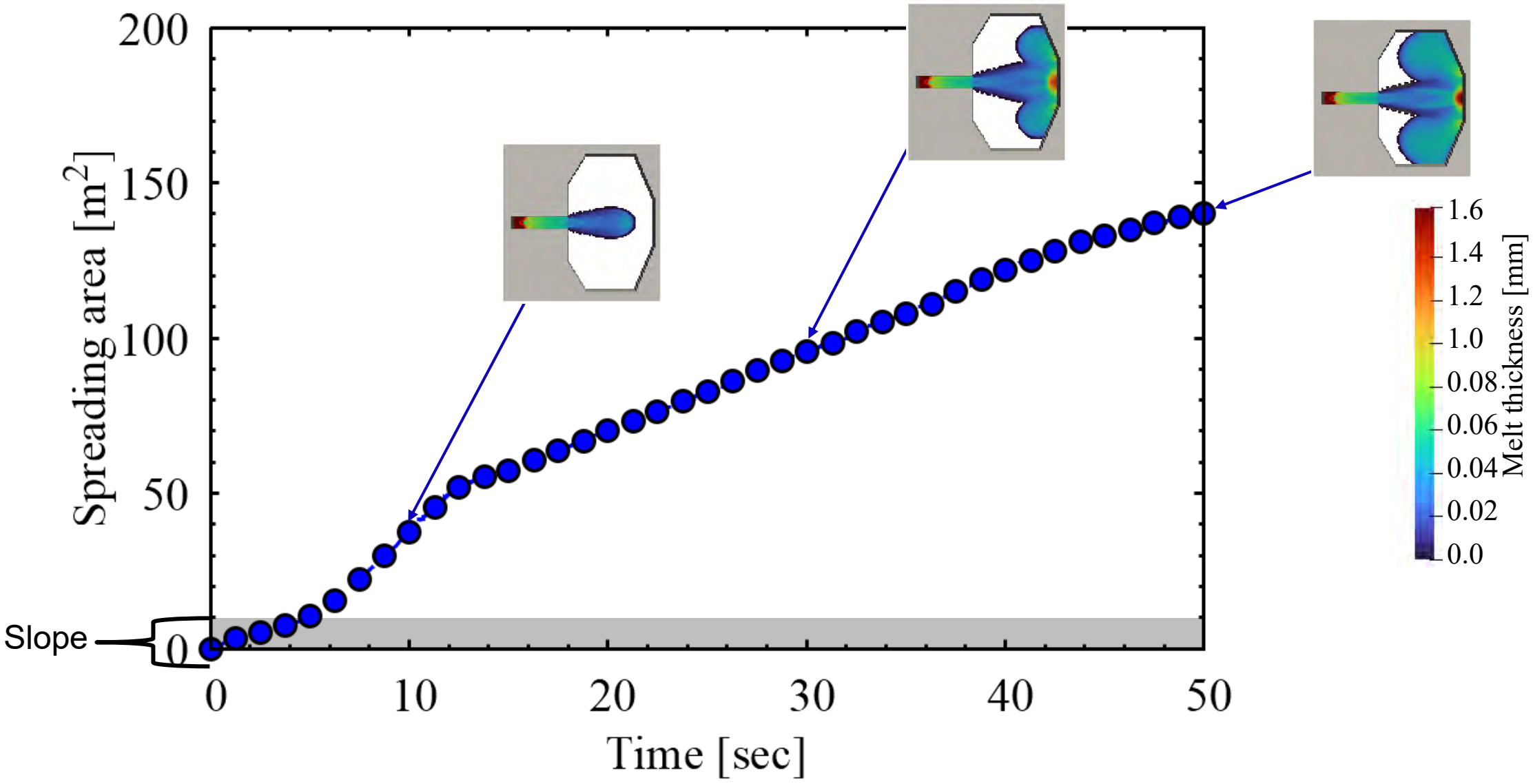

History of the molten debris spread area in a core catcher

Case1-L(**velocity:0.60 m/s**, melt temp.:**2800 K**/ superheat:**911 K**)

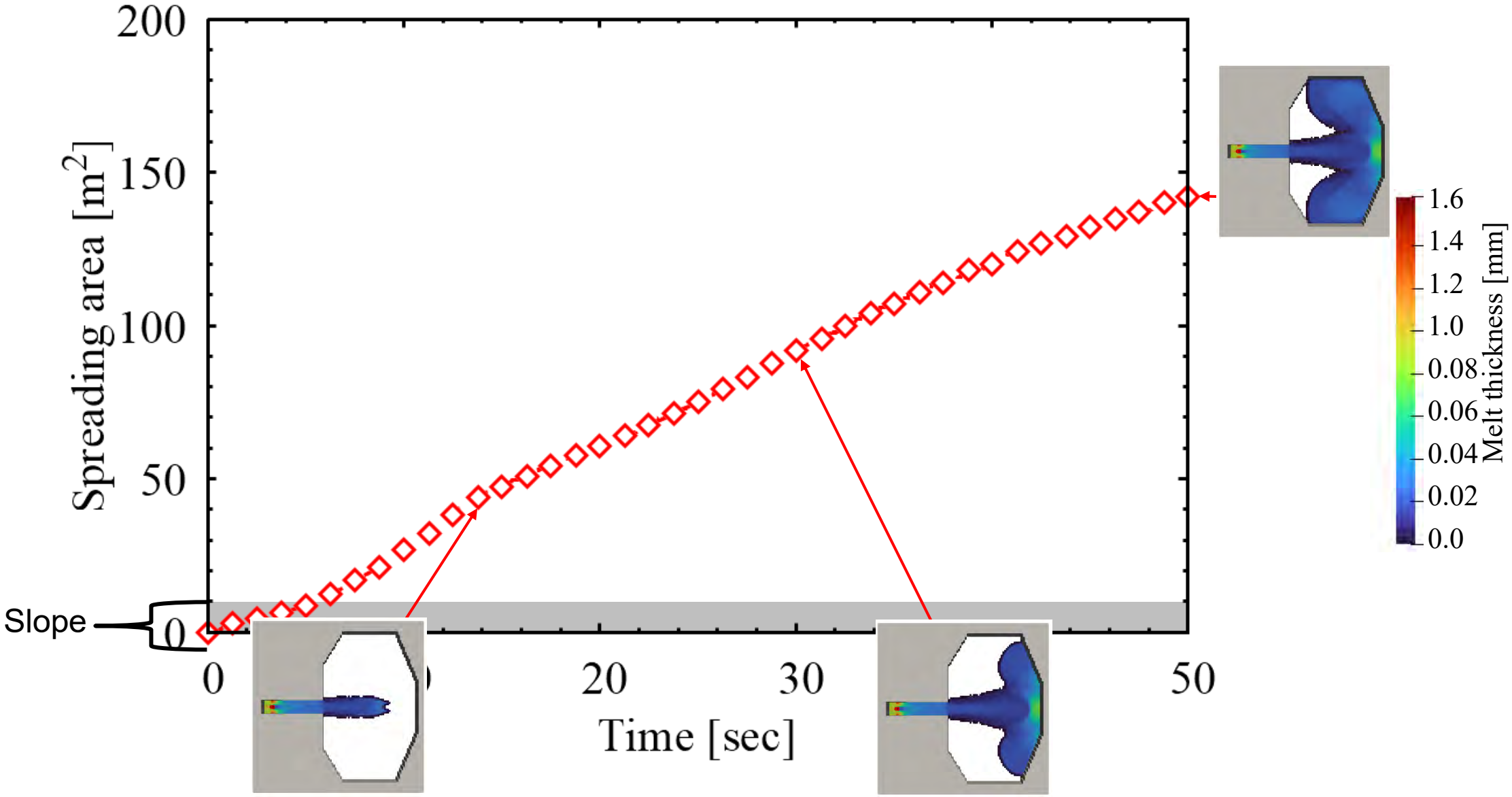

History of the molten debris spread area in a core catcher

Case1-L(**velocity: 0.60 m/s**, melt temp.:**2400 K**/ superheat: **511 K**)

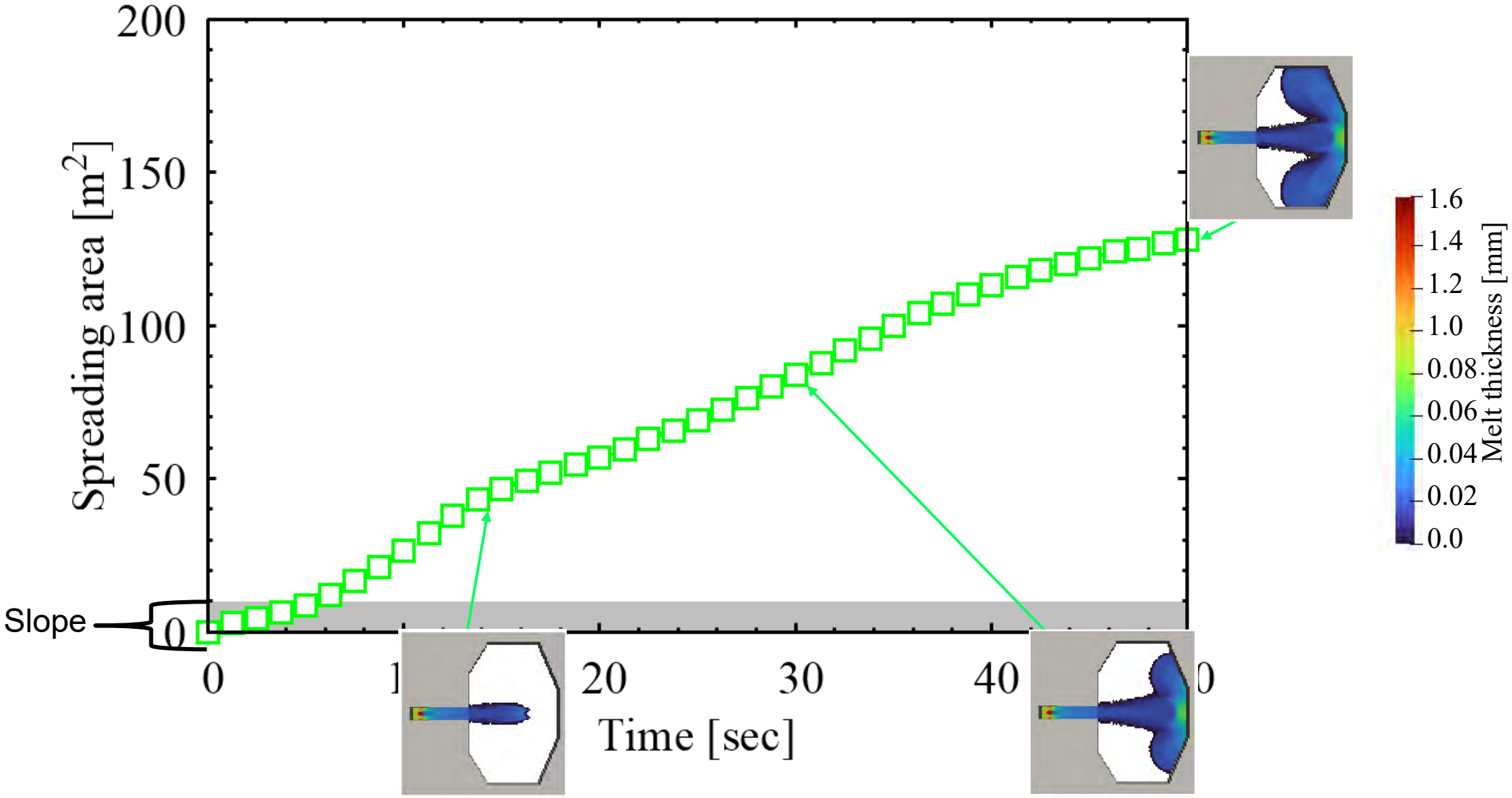

History of the molten debris spread area in a core catcher

Case3-L(**velocity: 0.60 m/s**, melt temp.:**2000 K**/ superheat:**111 K**)

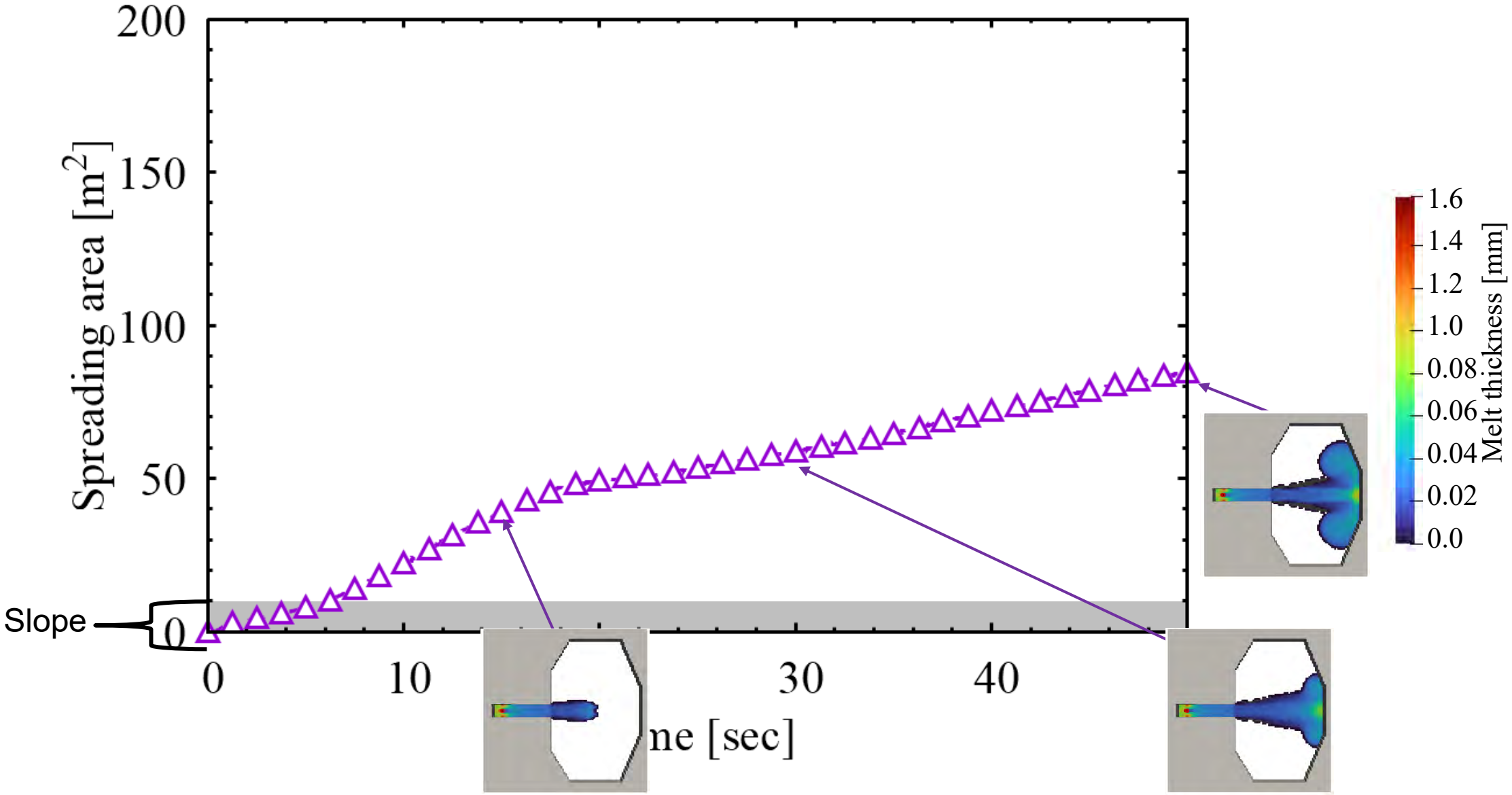

History of the molten debris spread area in a core catcher

Case4-L(**velocity: 0.60 m/s**, melt temp.:**1900 K**/ superheat:**11 K**)

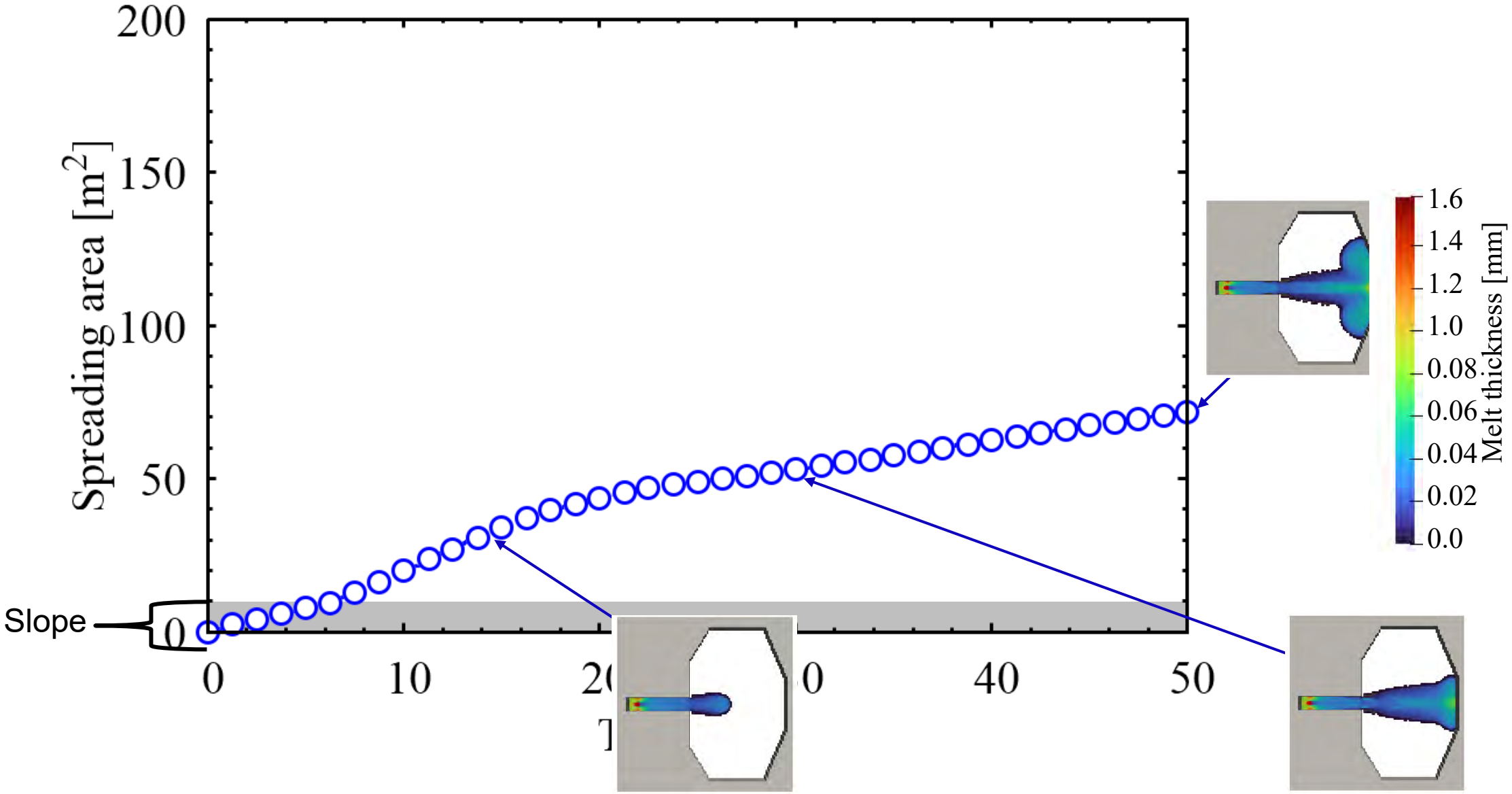

Summary of history of the molten debris spread area in a core catcher

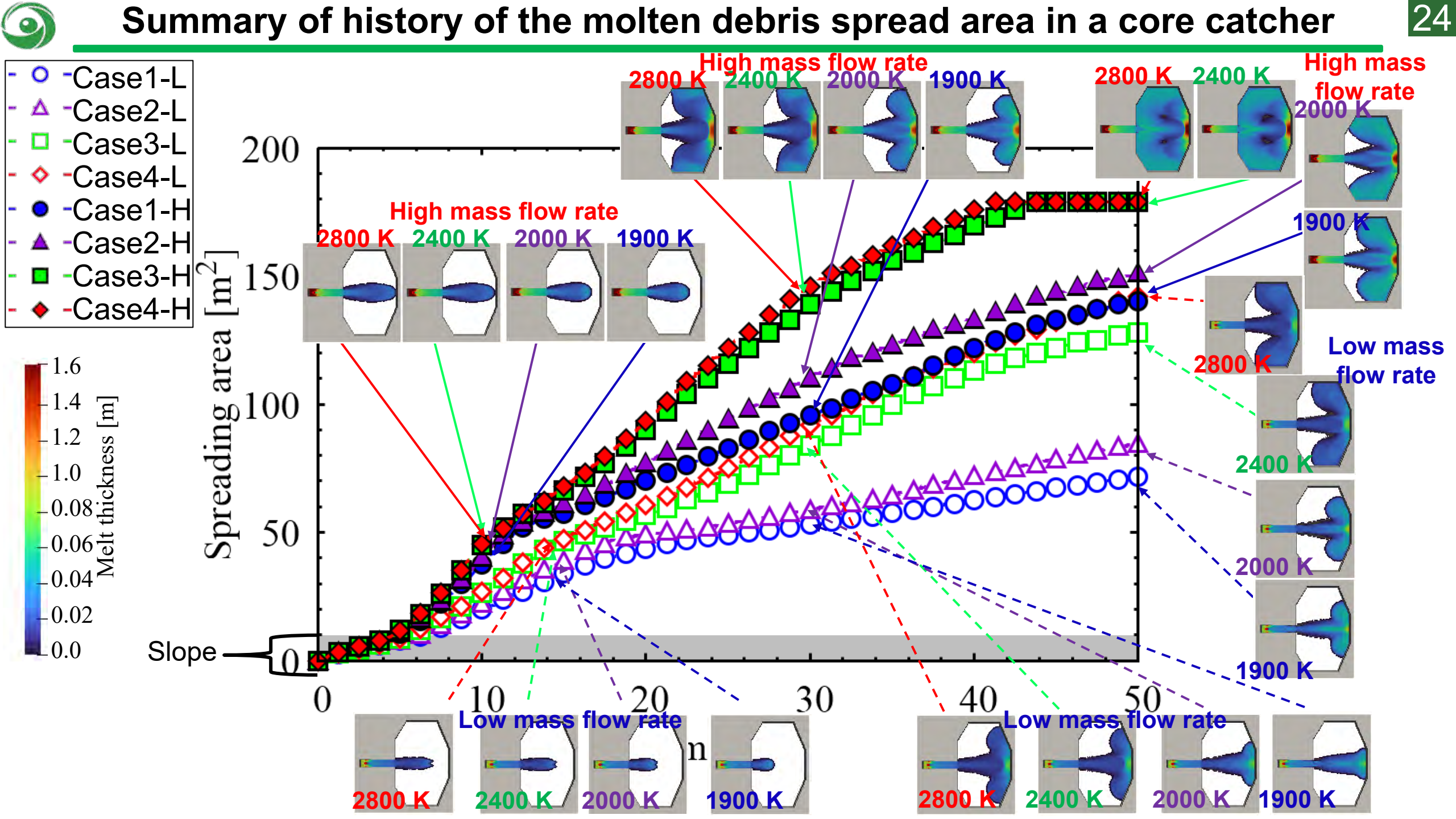

Summary of long history of the molten debris spread area in a core catcher

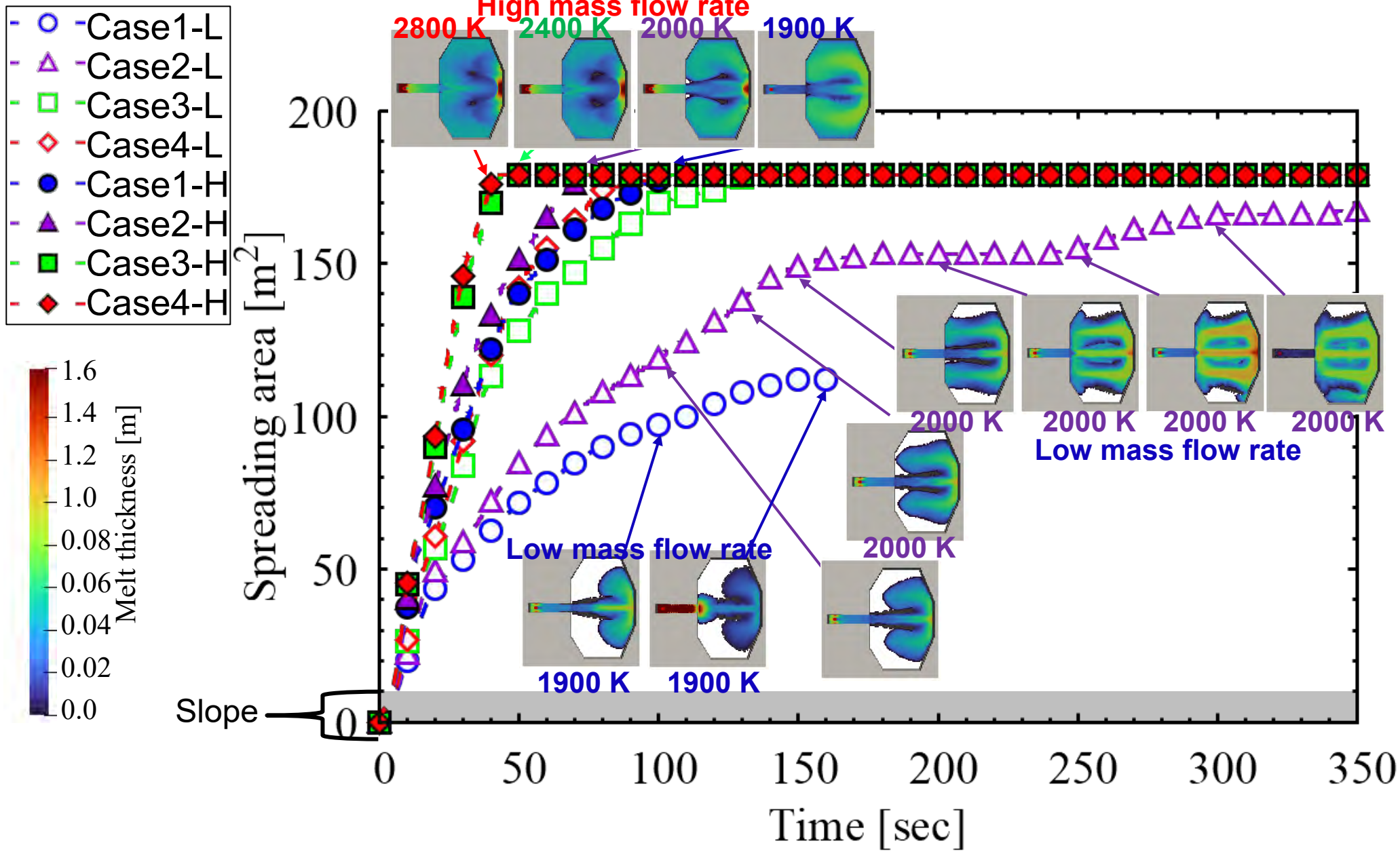

The mass flow rate and temperature affected the history of the molten debris spread area.

End time of spreading and associated spreading area

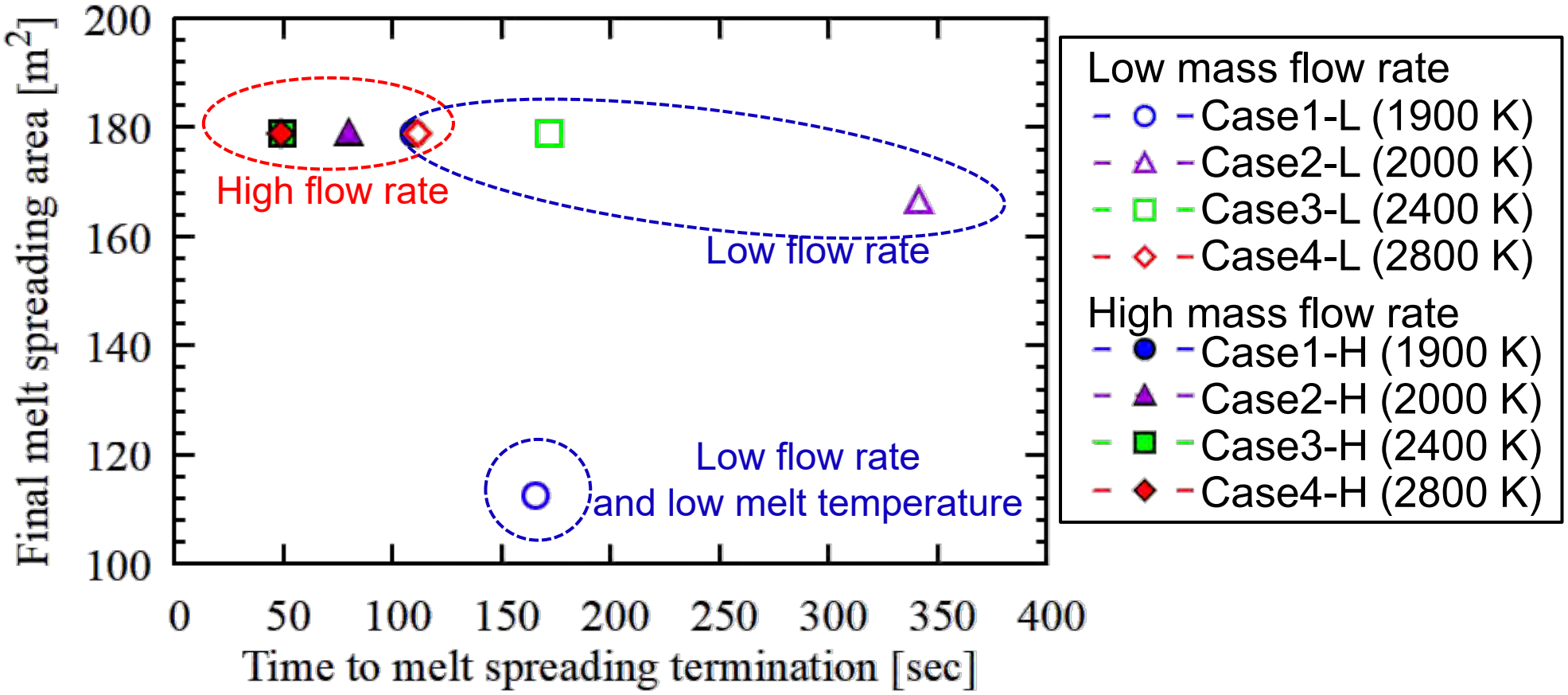

- **High flow rate**: **Molten debris fully spread over a core catcher.**
- **Low flow rate**: **The molten debris temperature affected the final spread area.**
  At lower molten debris temperatures, spreading stopped before the debris covered the entire core catcher.

⇨ **The mass flow rate and temperature affected the end time of spreading and associated spreading area.**

Contents

- ◆Background and objectives
- ◆Overview of THERMOS
- ◆EPR analysis condition
- ◆Analysis results
  - ✓2-D melt spreading behavior
  - ✓History of the molten debris spread area
  - ✓**Effect of temperature on spreading behavior**
  - ✓Effect of release flow rate on spreading behavior
  - ✓Re number evaluation
- ◆Conclusion

Effect of temperature on spreading behavior under low flow rate conditions

◆ **Low melt release** (velocity: 0.60 m/s) condition

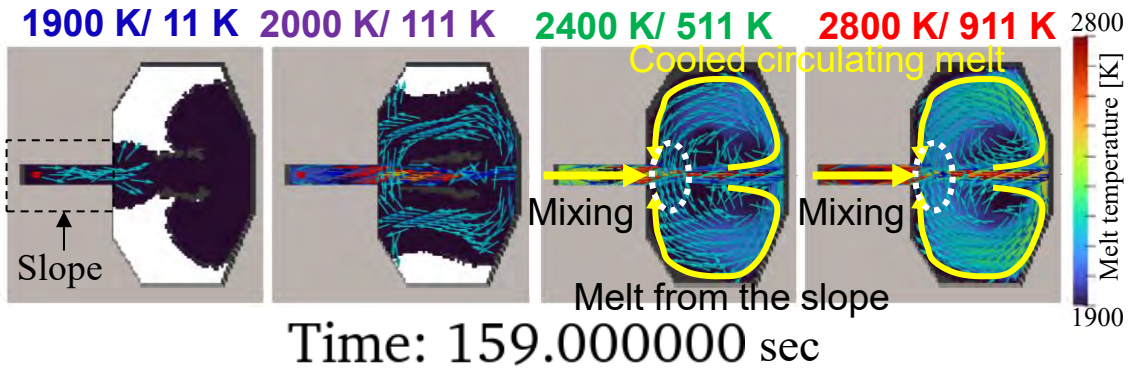

50 sec (**before** circulation) 150 sec (**after** circulation)

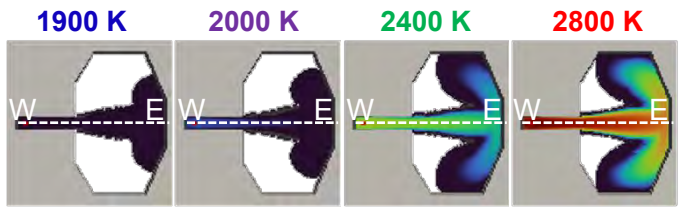

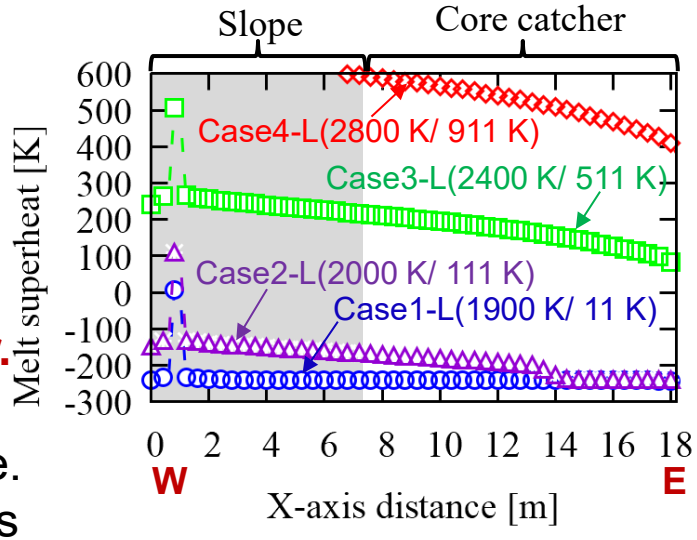

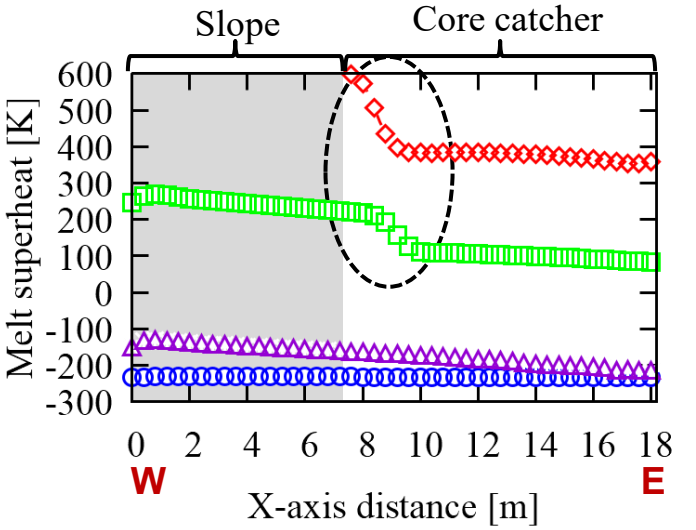

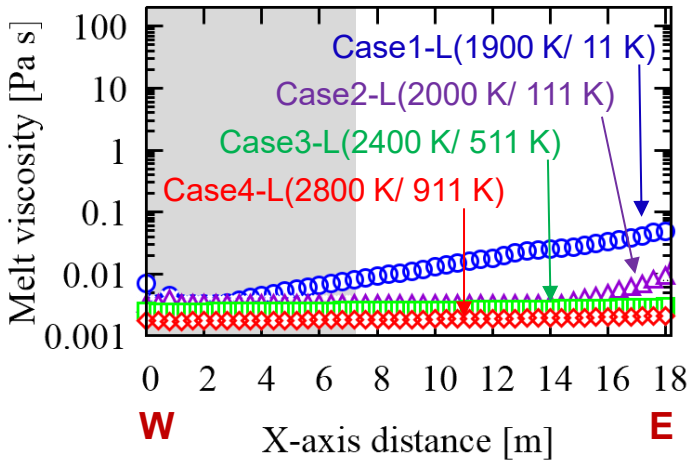

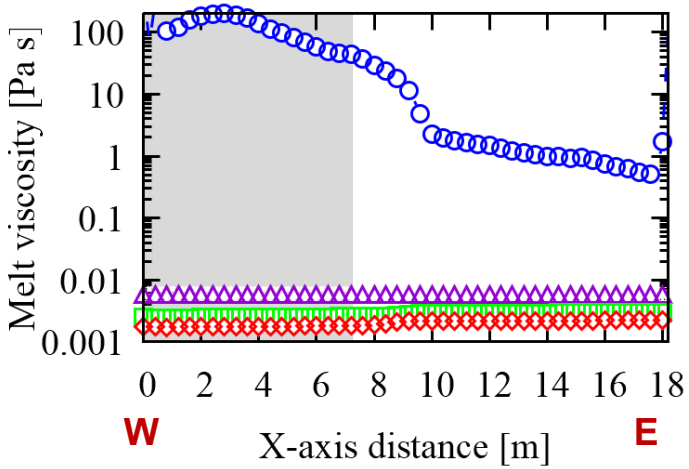

◆ **High-temperature conditions (2400,2800 K)**:

✓ The **circulation** occurred after about 100 sec.

✓ The **cooled circulating melt mixed with the melt flowing from the slope outlet into a core catcher.**

✓ The **melt temperature (superheat) decreased**.

✓ Despite the mixing, the superheat remained positive. **No significant increase in apparent viscosity** was observed.

✓ The molten debris **continued to spread rapidly** within a core catcher.

◆ **Lowest-temperature conditions (1900 K)** :

✓ The circulation **did not occur at any time**.

✓ Under 1900 K conditions, the molten debris showed high apparent viscosity at 150 sec, and its **spread terminated.**

Contents

- ◆Background and objectives
- ◆Overview of THERMOS
- ◆EPR analysis condition
- ◆Analysis results
  - ✓2-D melt spreading behavior
  - ✓History of the molten debris spread area
  - ✓Effect of temperature on spreading behavior
  - ✓**Effect of release flow rate on spreading behavior**
  - ✓Re number evaluation
- ◆Conclusion

Effect of release mass flow rate on spreading behavior under low-temp. conditions

- **At low mass flow rates, melt spreading terminated** under lowest-temperature conditions (1900 K/ 11 K).
- **At high mass flow rates, melt spreading continued** even under the same condition of lowest-temperature (1900 K/ 11 K).

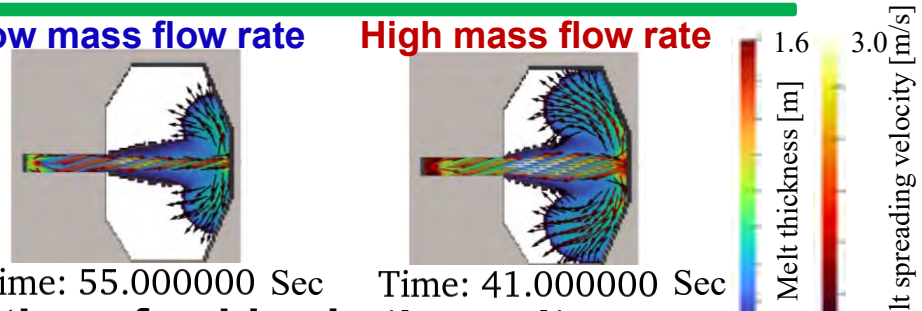

Apparent viscosity and spreading velocity

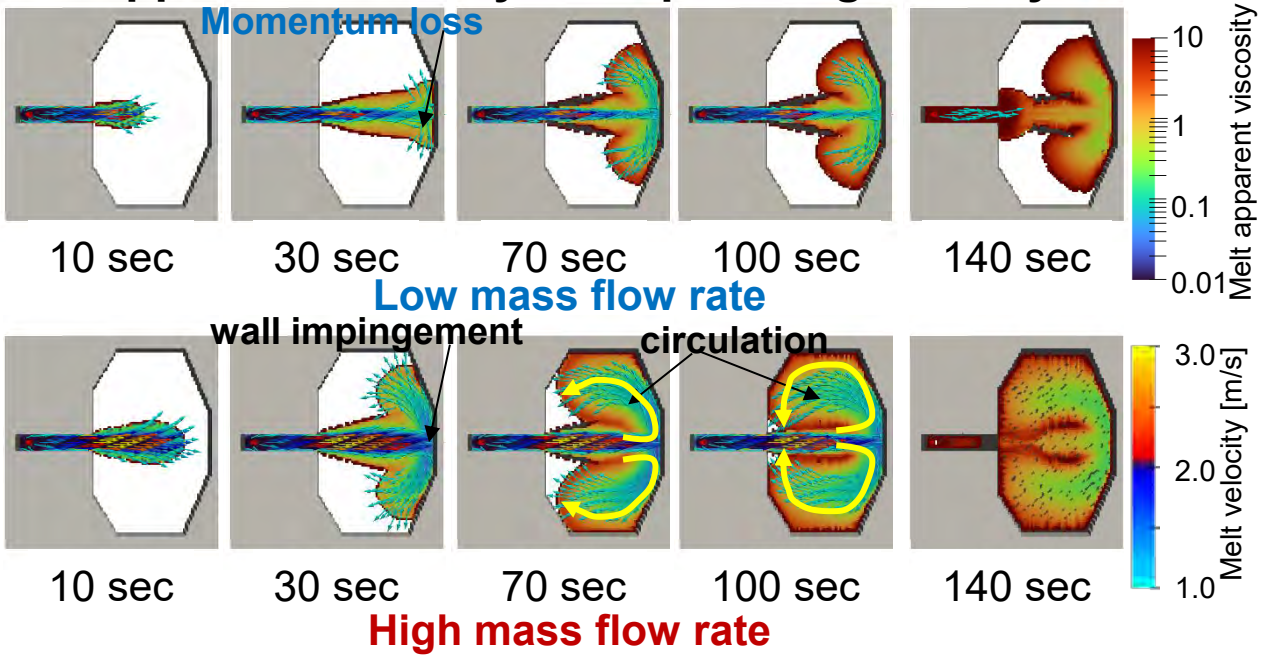

Mass fraction of oxides in the melt

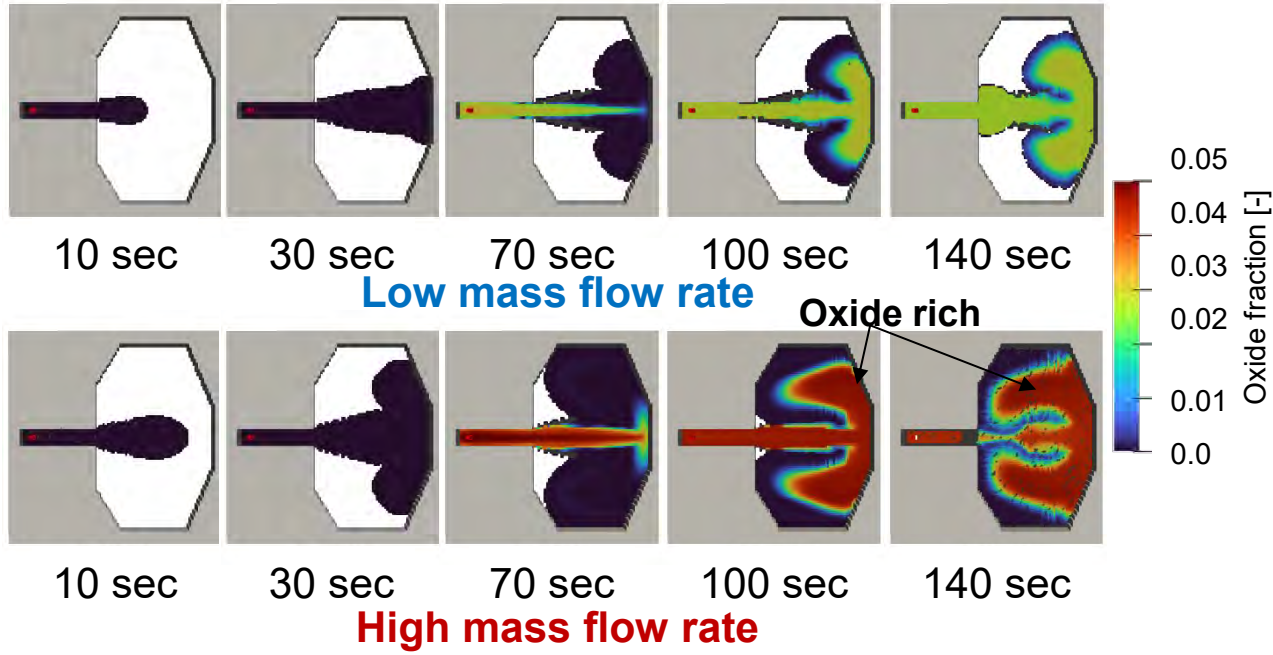

- **Low mass flow rates:** The combination of **insufficient inertia** and **momentum loss due to wall impingement** suppressed **circulation**, causing **spreading to terminate.**
- **High mass flow rates:** The **large inertia** of the molten debris generated **strong circulation** after wall impingement, enabling **spreading throughout a core catcher**.
  Debris composition also affected spreading: **oxides released after approximately 50 s** were distributed more widely and influenced the **solidus temperatures**.

Contents

- ◆Background and objectives
- ◆Overview of THERMOS
- ◆EPR analysis condition
- ◆Analysis results
  - ✓2-D melt spreading behavior
  - ✓History of the molten debris spread area
  - ✓Effect of temperature on spreading behavior
  - ✓Effect of release flow rate on spreading behavior
  - ✓**Re number evaluation**
- ◆Conclusion

Re number evaluation of molten debris spread behavior

- There are many key parameters that affect molten debris spreading.
- Among these, the **inertia** and **apparent viscosity of the molten debris** are important, so the Re number was applied.

$$Re = \frac{\rho_{melt} u_{melt} d}{\mu_{melt}}$$

ρ_{melt} : Debris density [kg/m3] u_{melt} :Spreading velocity [m/s]

d :Characteristic length (slope exit width: 1.6 m)

μ_{melt} : Apparent viscosity of debris [Pas]

- The Re number at the slope outlet can be correlated with the final spreading area.

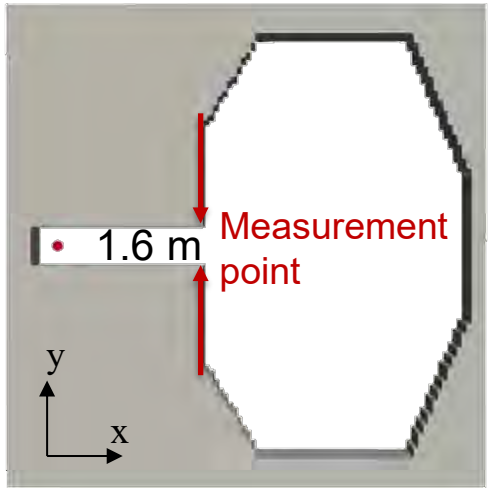

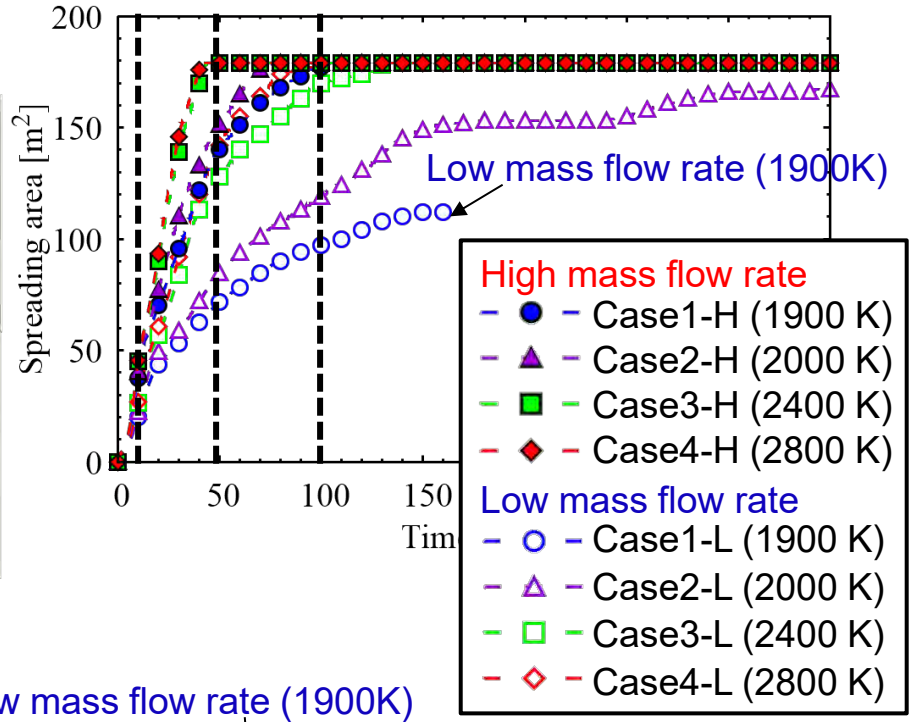

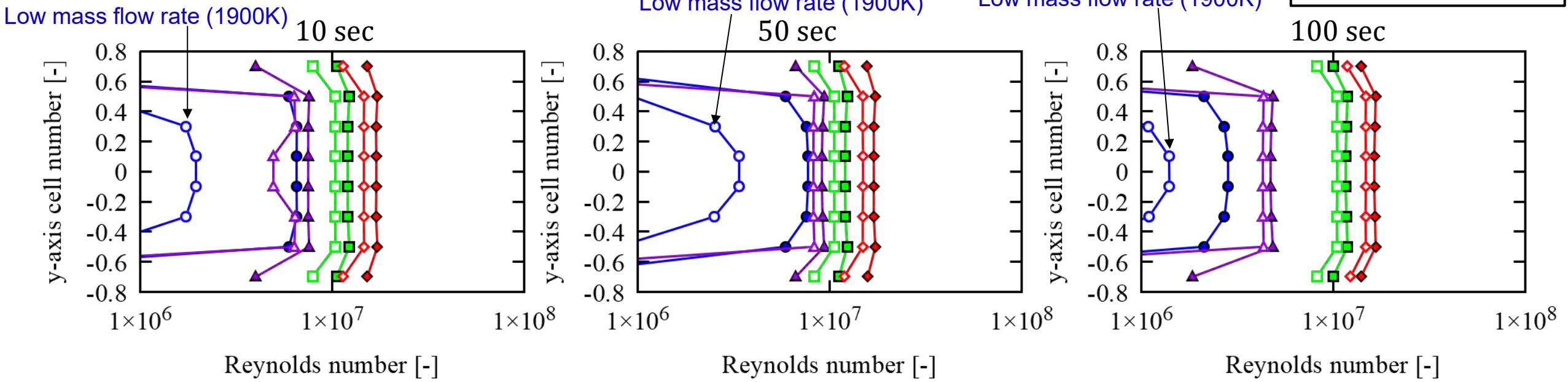

Contents

- ◆Background and objectives
- ◆Overview of THERMOS
- ◆EPR analysis condition
- ◆Analysis results
  - ✓2-D melt spreading behavior
  - ✓History of the molten debris spread area
  - ✓Effect of temperature on spreading behavior
  - ✓Effect of release flow rate on spreading behavior
  - ✓Re number evaluation
- **◆Conclusion**

Conclusion

◆ **2-D melt spreading behavior**

✓ Compared to low flow rates, **high flow rates** caused the **molten debris to spread more rapidly** a core catcher.

✓ **Under high flow rate conditions, the molten debris circulated** in a core catcher.

◆ **History of the molten debris spread area**

✓ The **mass flow rate** and **temperature** affected the **history of the molten debris spread area**.

◆ **Effect of temperature and mass flow rate on spreading behavior**

✓ The analysis showed that molten debris **temperature strongly controls apparent viscosity**.

✓ At low mass flow rates, insufficient inertia limited circulation, causing the molten debris to solidify and spreading to terminate.

◆ **Re number evaluation**

✓ The **Re number at the slope outlet was identified as a key parameter governing molten debris spreading** in a core catcher.

◆ **Future plans**

✓ Future work will focus on **UO_2 mixed with sacrificial concrete**, where a larger solidus–liquidus temperature gap is expected.

Thank you for your kind attention.

kikuchi_wataru_2p5@nra.go.jp

Experimental study on the interaction between molten corium simulant and Sacrificial Materials

Nan Li, Li Zhang, Erhui Chen, Hongliang Wang, Yidan Yuan*
CNNC Key Laboratory for Severe Accident Research in Nuclear Power Safety,china Nuclear Power Engineering Co., Ltd.
Beijing, 100048, China

ABSTRACT

The ex-vessel retention(EVR) strategy serves as a critical method for the safe containment of molten corium during severe nuclear accidents. Within core catchers, high-temperature molten corium are interacted with sacrificial material, thereby reducing its temperature while promoting the oxidation of reactive metals which helps suppress hydrogen gas generation. This interaction not only increases the overall volume of the molten mixture but also enhances the contact area with the catcher wall, which effectively reduce heat flux on the cooling surface. A new experiment platform called COLOR has been established to carry out experiments on the interaction of molten corium. Pre-experiments were carried out using Fe_2O_3-ZrO_2 mixture as molten corium. The erosion rate of Fe_2O_3-ZrO_2 system was 0.2mm/s which was the same in the ablation front. Furthermore, a simplified heat transfer model was established to evaluate the thermal flux and crust thickness at the crucible wall and the computational results show good agreement with the experimental observations.

KETWORDS

Ex-vessel Retention; Sacrificial materials; Interaction between sacrificial materials and melt

1. Introduction

Severe accident, also termed design-beyond-accident or design-extended accident, refers to a reactor experiencing large-scale melting[1]. To ensure nuclear power plant safety, the design incorporates a defense-in-depth system with three barriers against radioactive leakage: fuel elements, primary circuit pressure boundaries, and containment vessels. The occurrence of such an accident may cause failure of these barriers, leading to the release of molten materials and radioactive substances, which would have the most significant impact on the environment and public health. Therefore, appropriate measures must be implemented to prevent and mitigate such accidents.

The Ex-vessel melt Retention (EVR) Strategy is a critical measure to ensure the core melt is cooled and retained within the containment vessel, thereby maintaining its integrity and preventing the leakage of both the molten material and radioactive byproducts. Sacrificial materials are used in the design of Core Cather to cope with the various needs during melt relocation[2], such as: avoiding transient thermal shocks, lowering melt temperature, diluting volumetric power density, increasing melt mobility, and protecting the cooling channel. The selection of sacrificial materials and verification of their performance is one of the key technologies in the development of Core Catcher.

The selection of sacrificial materials is closely related to their function, which is to interact physicochemically and chemically with the core melt to change the melt pool characteristics and structure. Sacrificial materials include: Sacrificial Metal Sacrificial Material (SSM) and Oxide Sacrificial Material (OSM). The main function of SSM is to reduce the temperature of the mixed system. OSM is the main component of sacrificial materials, usually consisting of oxides of light metals, whose main function is: 1) to oxidize the active metals in the melt so as to minimize the production of hydrogen. 2) to reduce the density of the melt until inversion occurs (metal layer below, oxide above) to avoid thermal focusing effects. 3) to reduce the temperature of the melt and the liquid phase line temperature after mixing with it. 4) to minimize the production of the non-condensable gases 5) to prevent the re-criticality of the melt.[3-5]

During a typical severe accident of VVER[6], when the pressure vessel sidewall is broken, the molten corium fall into the CC, interacting with the sacrificial material. The oxides in the sacrificial material melt rapidly, increasing the volume of the melt and effectively reducing its heat release rate. Meanwhile，active metal in corium (such as Zr,Cr) are oxidized and rise to the surface of the melt to form solid crust. Through corium-sacrificial material interaction, the density of the oxide melt is reduced and finally lower than that of the metal. The inversion of the metallic layer and oxide layer occurs[7-8].

The interaction experiments between sacrificial materials and molten materials have been extensively researched[9-11]. The properties of mixtures of U-Zr-O-Fe have been studied and the phase diagram of mixture system has been redrawn by Bechta. S.M. An [12]conducted experiments to investigate the erosion characteristics of zirconia melt on various materials and derived the corresponding calculation formulas.A model of interaction has been developed based on the experiment SACR-8 and SACR-9[13]. This model assumes the chemical reaction and generation of heat happens in a reaction layer adjacent to the SM surface. In addition, according to the results of the experiments, the velocity of interaction front is approximately constant. It does not depend on the concentration of Zr if the

concentration of Zr is higher than 5 mass%. VESTA was used for the jet impingement experiments, which verify the convective heat transfer model that estimates the ablation rate of special concrete more reasonably even though some water content in the material may result in a radiation heat transfer through the suddenly created steam layer[14].KAERI also set up an experiment to research the ablation characteristics of the concrete[15].

In order to study the interaction process between the molten material and the sacrificial material, the interaction experimental platform—COLOR platform was built. The simulation experiments of the interaction between the molten material and the sacrificial material were carried out on the COLOR platform, and the molten erosion rate were obtained. Furthermore, a simplified heat transfer model was established to evaluate the thermal flux and crust thickness at the crucible wall and the computational results show good agreement with the experimental observations.

2. New experiment platform—COLOR

The platform can melt 20kg molten corium and conduct melt-sacrificial interaction test, molten pool temperature and ablation rate measurement. The schematic of experiment facility is shown in Figure 2.1. The platform consists of a furnace vessel, a cold crucible, a corium heating system including a high-frequency power supply, an induction coil and an inverter, a temperature measurement system, and a control system, a cooling system for removing the heat generated in the cold crucible, the induction coil, and the high-frequency power supply.

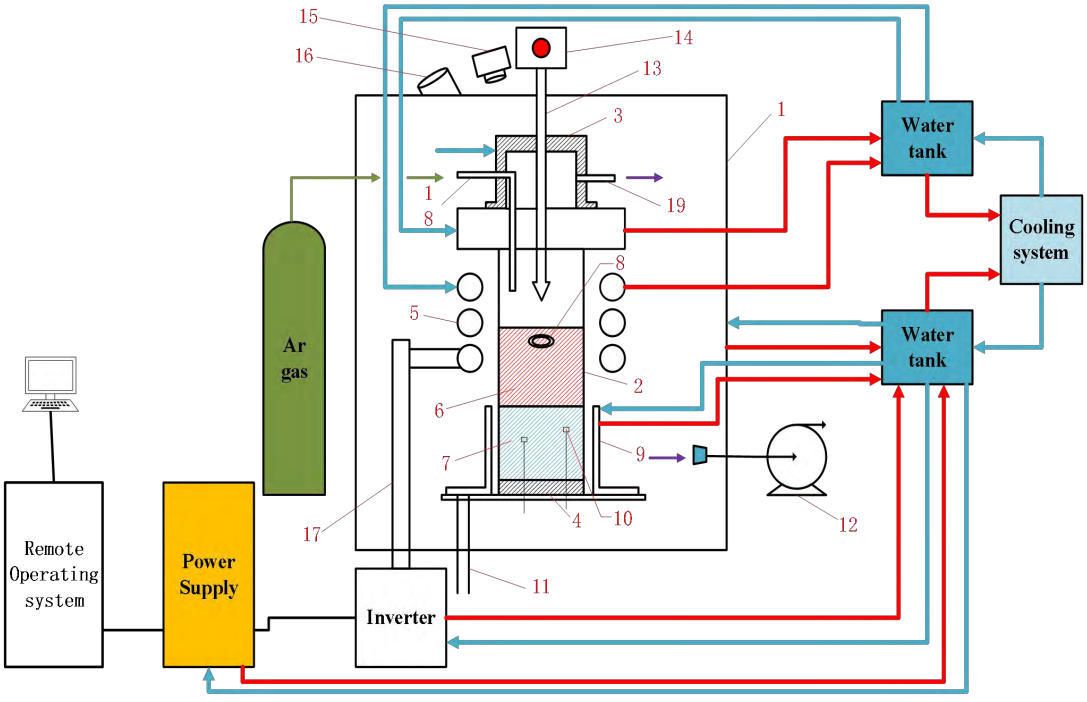

Figure 2.1 A schematic of COLOR facility.
1-furnace vessel; 2-cold crucible; 3-crucible lid; 4- water cooled bottom; 5-induction coil; 6-molten corium; 7-sacrificial material; 8-metal ring; 9-shielding; 10- thermocouples; 11-lifter; 12-vacuum pump; 13-thermometer tube; 14-infrared pyrometer; 15-camera; 16-window; 17-coaxial electrodes; 18-inlet; 19-outlet

The furnace vessel uses double-layer stainless steel structure with cooling water, which protect the cold crucible and guarantee high vacuum environment and structural stability. Observation windows and video cameras are provided to observe the situation in the cold crucible during the experiment. The cold crucible has dimensions of 160 mm in diameter and 600 mm in height, which is made by copper pipe (Figure 2.2). Cold water is allowed to flow into each tube to cool down the interface between the melt and tube to maintain a solid boundary surrounding the melt. The crucible wall can be divided into two half so that the material could be discharged easily after the test. Crucible water jacket collects the multi-channel cooling water of the crucible wall and connects to the cooling water system through the main channel.

The high-frequency power supply is designed to have a capacity of 200kW and 150kHz in frequency, melting temperature can reach more than 2800°C. Induction coil can move up and down to heat different areas, ensuring that the material is fully melted. The shielding device is located in the lower part of the crucible to prevent sacrificial materials from being heated by induction as well as electromagnetic interference to the thermocouples.

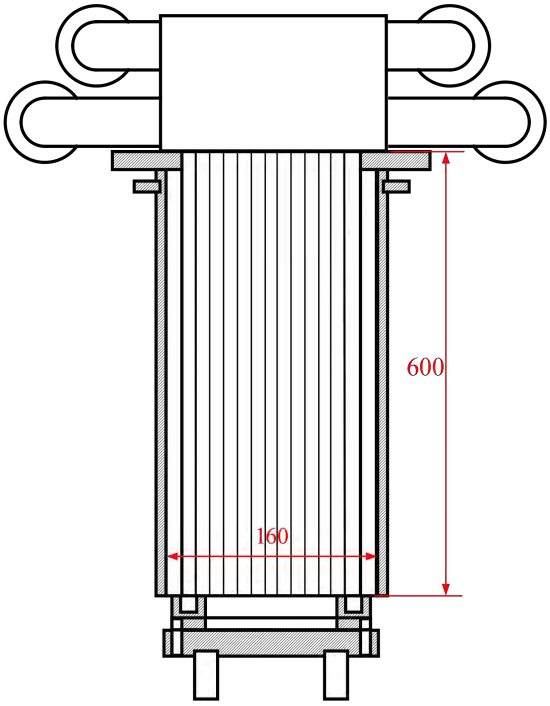

Figure 2.2 The structure of cold crucible

The melt temperature is monitored by infrared thermometer and it has a temperature range of 1000-3200 ℃ within ±0.5% error. A thermometer tube whose head is made by tungsten is arranged above the crucible and extends into the furnace through a vacuum seal to measure the temperature of the molten pool. Tungsten head is used to break up the hard shell that may exist on the surface of the molten material in order to measure the temperature of the molten pool. The velocity of ablation are obtained by thermocouples embedded in the SM[1,13]. The specific assumptions are as follows: firstly, set a point (x0,y0,z0) and a moment (t0) that the interaction begins,Secondly, record the position of the i-th thermocouple (xi, yi, zi) and the moment of corrosion(ti) when its temperature has a sharp increase.

The ablation rate W can be calculated using the following formula:

$$W = \frac{\sqrt{(x_i - x_0)^2 + (y_i - y_0)^2 + (z_i - z_0)^2}}{t_i - t_0} \quad (1)$$

The primary component of molten corium is ZrO_2. Since ZrO_2 is non-conductive at room temperature, electromagnetic induction heating is not feasible. Therefore, a conductive circuit is formed by embedding metal ring into ZrO_2. The metal is first heated by a high-frequency power source. At high temperatures, the oxidation of the metal generates heat, raising the temperature of the surrounding oxide to the conduction temperature.

3. Pre-experiment on the interaction between molten corium simulant and Sacrificial Materials

3.1 Pre-experiment of ZrO_2 -Fe_2O_3

The pre-experiment uses Fe_2O_3 powder as SM and ZrO_2 powder as the molten corium. Fe_2O_3 powder was loaded at a height of 22.5cm for the lower layer, while ZrO_2 was loaded in both lump and powder forms at a height of 20cm for the upper layer. The middle of the induction coil is arranged as high as the top surface of ZrO_2 and it was gradually moved down to heat up the ZrO_2.The initial position of shielding device is at the upper surface of Fe2O3 layer. In order to calculate the ablation rate, Type K thermocouples are arranged at different locations in the sacrificial material. The specific scheme is shown in Figure 3.1.

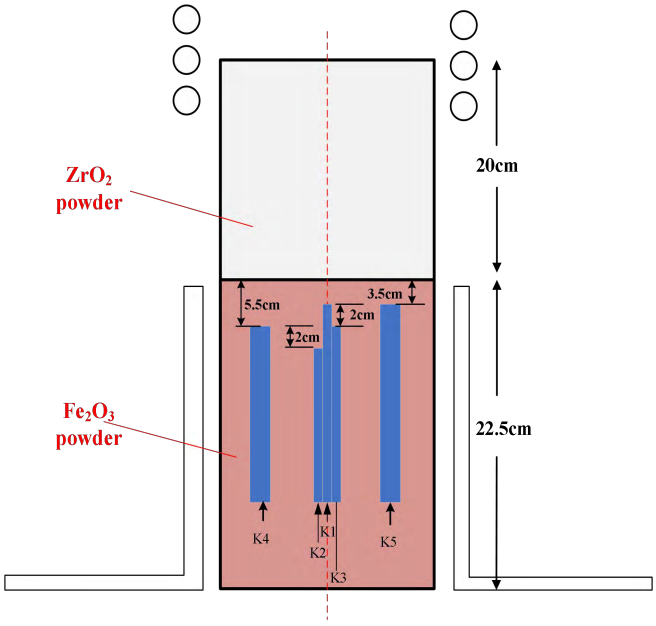

Figure 3.1 The distribution of material and facilities in the Preliminary experiments of ZrO_2 -Fe_2O_3

The experiment lasted approximately 30 minutes. Initially, the heating power was incrementally increased in a stepwise manner to monitor the melting process of the molten material. The coil is moved down by 4cm at 800s and 1160s; the shielding moves down and the ablation starts at 1600s.

After the experiment, open the crucible and analyse the ingot. The result are shown in Figure 3.2, which also gives the initial position of the Fe_2O_3 layer and the ZrO_2 layer. The corrosion depth of

Fe_2O_3 is 9cm and the ablation front is almost flat which proves the axial ablation rate is the same in the ablation front. Iron oxide powder remains unmelted at the bottom of the crucible. Figure 3.3 proposes the internal structure of the test section. A cavity is formed above the oxide ingot. Since ZrO_2 powder is used in the experiments, there are a large number of pores within the ZrO_2 layer. ZrO_2 increases in density during heating. Both of these points lead to the decrease in volume of the material. In addition, the ablation of ZrO_2 and Fe2O3 also leads to the decrease the volume of the material. So the large cavity is formed. In the melting process, the melt is cooled by the crucible sidewall and oxide crust is formed. The main components of oxide ingots are ZrO_2 and $Fe2O_3$. It indicates that ZrO_2 has been melted and has corroded with Fe_2O_3.

Figure 3.2 The results of Fe_2O_3-ZrO_2 test section
1-initial position of the top surface of ZrO_2 layer;2-initial position of the top surface of Fe_2O_3 layer;
3-ablation front; 4-unmelted Fe_2O_3

Figure 3.3 The internal structure of the test section
1-oxide crust; 2-cavity; 3-oxide ingot; 4-ablation front

Type K thermocouples are used in the experiment and the highest measured temperature are 1300°C which would be recorded as the arrival of the ablation. All thermocouples are damaged. The thermocouples readings during the experiment are shown in Figure 3.4. The temperature of thermocouples is about 100°C before shielding device is moved down. Correspondingly, the temperature of the thermocouples begin to rise until the thermocouples are damaged.

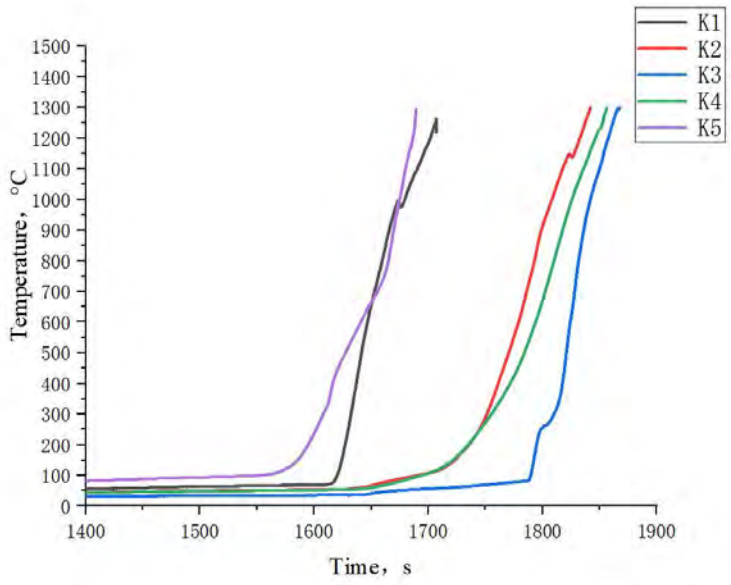

Figure 3.4 Temperatures measured by thermocouples during the pre-experiment

Damage time of the thermocouples are planned to calculate the ablation rate W. However different types of thermocouples have the different time for damage process, heat-up time which means the time when the thermocouples start to heat up are used to calculate the ablation rate W. All of them are shown in Table 1. The average ablation rate is 0.19mm/s

Table 1 Damage time and Heat-up time of the thermocouples

Thermocouples	Damage time /s	Time for Damage process /s	Heat-up time /s	Distance to the top of Fe_2O_3 layer /mm
K1	1707	87	1620	35
K2	1842	127	1715	55
K3	1867	80	1787	75
K4	1856	146	1710	55
K5	1689	111	1578	35

The changes of current and heat power in the test are shown in the Figure 3.5. At the start of the test, the power is increased in steps to 75kW. At 400~800s, the current drops which means the ZrO_2 powder begins to melt. Because the conductivity of the melt increases after melting, a magnetic field in the opposite direction of magnetic fields generated by high-frequency power sources is generated in the melt (Lenz's Law). Figure 3.6 shows the heat power and heat loss during the heating process over time. The total heat loss includes the heat loss from the crucible wall, crucible base, power supply, and coil.

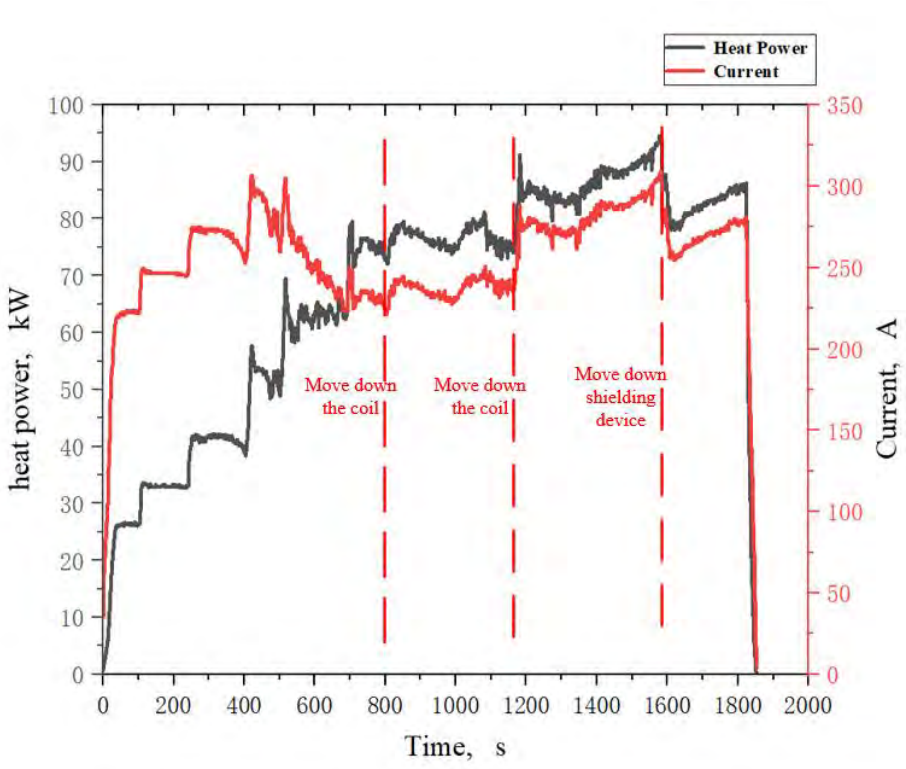

Figure 3.5 The profile of current and heat power during the heat process

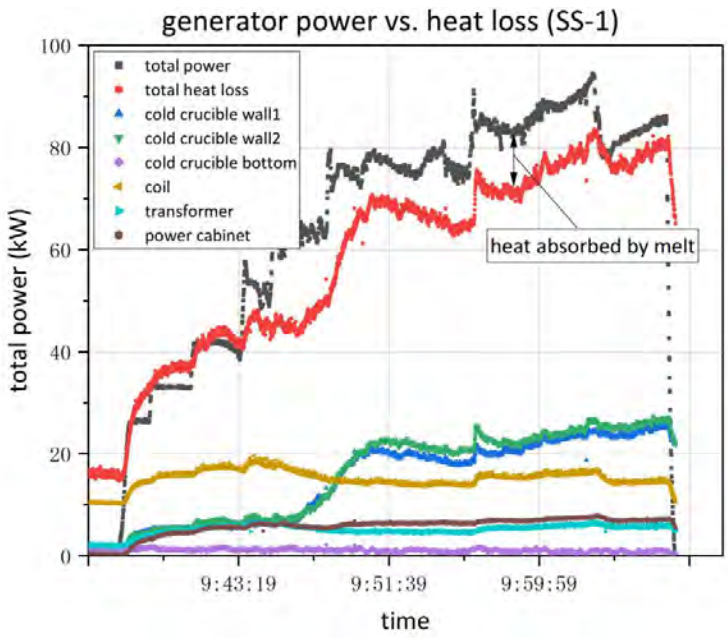

Figure 3.6 heat power and heat loss during the heating process

3.2 Pre-experiment of ZrO_2 and Sacrificial Materials

After completing the pre-experiment with Fe_2O_3 and ZrO_2, the experiments with ZrO_2 and sacrificial materials commenced. The composition of the sacrificial material placed in the lower layer is Fe_2O_3-Fe_3O_4-Al_2O_3. A layer of 3cm thick zirconia powder is laid on the bottom of the sacrificial material to prevent the molten material from flowing out of the crucible through the gap between the sacrificial material and the crucible. The upper layer is filled with 20cm high zirconia powder, and the total mass is 10.2 kg. The setting of material and facilities is shown in Figure 3.7.

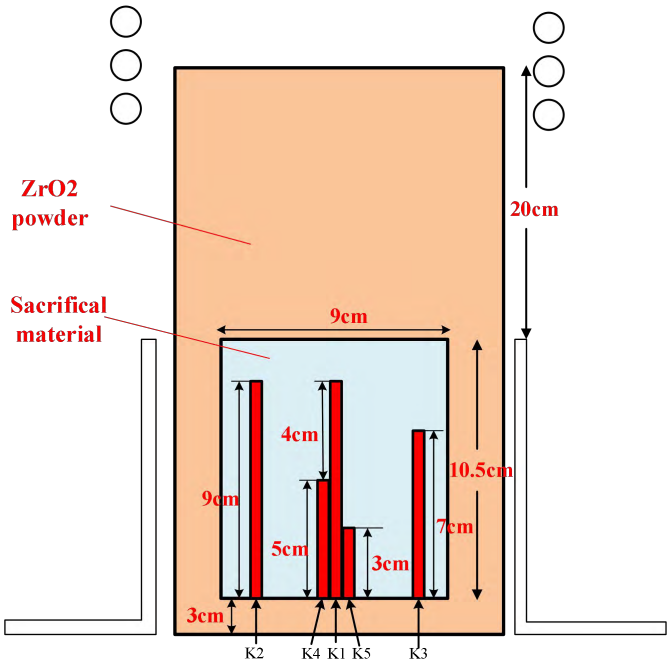

Figure 3.7 The setting of material and facilities in the pre-experiment of ZrO_2 and SM

The experiment results after disassembly and drying are shown in Figure 3.8. The erosion depth of ZrO_2 on the sacrificial material is 6 cm, the cavity is formed on the top of the ingot, and 2 cm crust is formed on the inner wall of the crucible.

Figure 3.8 Results of ZrO_2-sacrificial material experiment
1-initial height of ZrO_2 layer, 2-initial height of SM, 3-ablation front, 4-unmelted SM, 5-cavity, 6-crust

Based on experimental data, a simplified heat transfer model for the molten pool-crust-cooling water system was established (Figure 3.9), with the following assumptions:

1) The cooling water flow rate is the same for each copper tube.
2) Only the molten region is in contact with the external environment during the heating process.
3) The heat transfer between the crust and the cooling water is turbulent forced convection.

The thickness of the crust is calculated with formula (2),(3),(4). The thickness of the crust is 1.92cm, which is 4% different from the actual measurement.

$$q=h(T_w-T_0) \tag{2}$$

$$Nu=0.023Re^{0.8}Pr^{0.4} \tag{3}$$

$$q=k(T_m-T_w)/d \tag{4}$$

where q is the heat flux from the hard shell of crucible wall to coolant, h is the convective heat transfer coefficient, T_w is the temperature of the outer wall of hard shell, T_0 is the temperature of coolant, Nu is the Nusselt number, Re is the Reynolds number, Pr is the Prandtl number, k is the thermal conductivity of hard shell, d is the thickness of hard crust, T_m is the temperature of inner wall of hard crust.

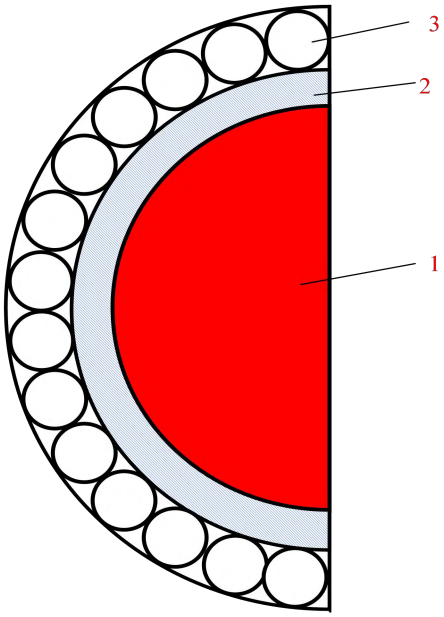

Figure 3.9 Heat transfer model for the molten pool-crust-cooling water system
1-molten pool, 2-crust, 3-water flow path

4.Conclusion

This paper introduces the new platform built COLOR for the melt interaction with sacrificial material.Two sets of preliminary experiments were completed on this experimental bench. The erosion rate of Fe_2O_3-ZrO_2 interaction was 0.2 mm/s. A simple heat transfer model of molten material, hard shell and cooling water was established, and the theoretical calculation value of the edge wall hard shell was obtained, which was 4% different from the experimental results.

Further experiments will be conducted to investigate the interaction between molten materials and sacrificial materials. Based on experimental data and conclusions, a model for molten-sacrificial material interactions will be developed. This model will be utilized in specialized analysis programs for severe accidents to simulate molten material behavior and the interaction processes within the core catcher.

Reference

[1] Sun Yang. Simulation study on the core meltdowns process of severe accident [D]. Harbin Engineering University, 2009.

[2] Fischer, Manfred, et al. "Core melt stabilization concepts for existing and future LWRs and associated research and development needs." Nuclear technology 196.3 (2016): 524-537.

[3] Gusarov, V. V., et al. "Physicochemical modeling and analysis of the interaction between a core melt of the nuclear reactor and a sacrificial material." *Glass Physics and Chemistry* 31 (2005): 53-66.

[4] Khabensky, Vladimir Benzianovich, et al. "Severe accident management concept of the VVER-1000 and the justification of corium retention in a crucible-type core catcher." *Nuclear Engineering and Technology* 41.5 (2009): 561-574.

[5] Granovsky, V. S., et al. "Modeling of melt retention in EU-APR1400 ex-vessel core catcher." *International Congress on Advances in Nuclear Power Plants*. Vol. 2012. 2012.

[6] Beshta, S. V., et al. "Formation of a nuclear reactor's molten core bath in a crucible-type corium catcher for a nuclear power station equipped with VVER reactors." *Thermal engineering* 58 (2011): 424-428.

[7] Fermi E, Von Neumann J. Taylor instability at the boundary of two incompressible liquids[J]. Collected Papers of Enrico Fermi, 1953: 821-824.

[8] Steinwarz W, Häfner W, Alkan Z, et al. COMAS: representative spreading experiments with view to core melt mitigation[J]. 2000.

[9] Gusarov, V. V., et al. "Interaction of a material based on aluminum and iron oxides with a metal melt." *Russian Journal of Applied Chemistry* 80 (2007): 528-535

[10] Bechta S V, Krushinov E V, Almjashev V I, et al. Phase diagram of the ZrO2–FeO system[J]. Journal of nuclear materials, 2006, 348(1-2): 114-121.

[11] Beshta, S. V., et al. "Phase transformation in the binary section of the UO 2-FeO-Fe system." *Radiochemistry* 49 (2007): 20-24.

[12] An S M, Ha K S, Min B T, et al. Ablation characteristics of special concrete due to an impinging zirconium-dioxide melt jet[J]. Nuclear Engineering and Design, 2015, 284: 10-18.

[13] Asmolov, Vladimir Grigor'evich, et al. "The interaction of nuclear reactor core melt with oxide sacrificial material of localization device for a nuclear power plant with water-moderated water-cooled

power reactor." *High Temperature* 45 (2007): 22-31.

[14] An, S. M., et al. "Ablation characteristics of special concrete due to an impinging zirconium-dioxide melt jet." *Nuclear Engineering and Design* 284 (2015): 10-18.

[15] .Kim, Hwan Yeol, et al. "Introduction of VESTA facility and melting test results." (2011).

Experimental study on the interaction between molten corium simulant and sacrificial material

Nan LI, Li ZHANG, Erhui CHEN,
Jie PEI, Hongliang WANG, Yidan YUAN

China Nuclear Power Engineering Co., Ltd.

CONTENTS

01 Background

02 COLOR facility

03 Pre-test

04 Conclusion and Future works

01

Background

1.Background

- Ex-vessel retention
  - Use core catcher (CC) to cool and retain core melt when the pressure vessel fails in a serious accident
- Sacrificial material (SM)
  - High-temperature (2800℃) core melt would cause threat to the CC and containment through MCCI
  - Arranged Sacrificial material to change status of the core melt to keep integrity of the CC
  - SM plays an important role in stabilization and long-term cooling of the core melt for the CC

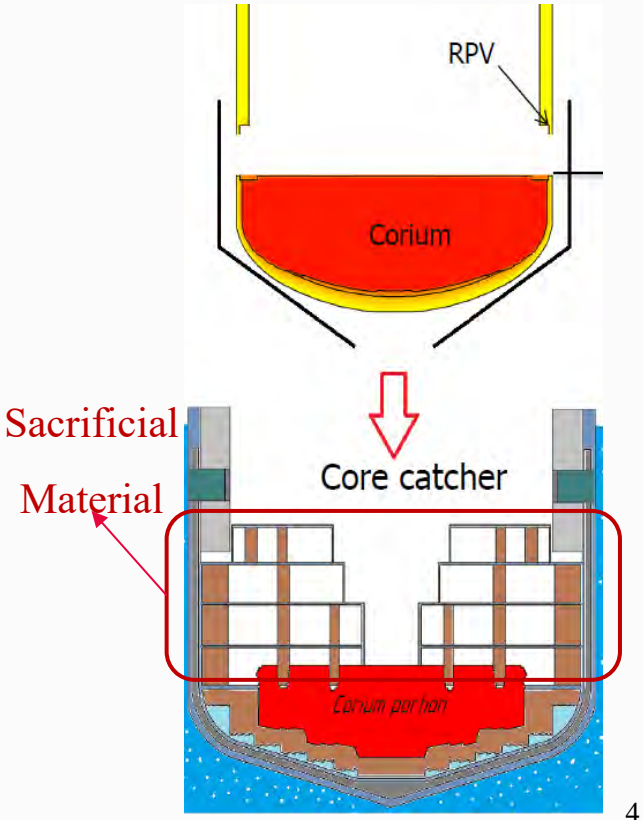

1.Background

Primary functions of SM

dilution of the core melt

- to decease the temperature and volumetric power density of the core melt

lower the liquidus temperature of the molten pool (melt-sacrificial material mixture)

- to ensure chemistry reaction and convection mobility

ensuring the metallic phase underneath the oxide

- to avoid heat flux focusing and hydrogen generation

oxidize as much active metals (U、Zr、Cr) as possible

- to prevent possible hydrogen generation when encountering with water

reducing concentration of fission products and ensuring subcritical of the melt

Objective

In order to test the properties of the Specifically designed sacrificial material and investigate interaction mechanisms between corium and sacrificial material.

Test ID	PT-1	PT-2	PT-3	PT-4	PT-5
Atmosphere	Air		Argon		
SM composition	Fe_2O_3	Fe_2O_3, Al_2O_3	Fe_2O_3, Al_2O_3	Fe_2O_3, CaO	Fe_2O_3, SrO
Melt composition	ZrO_2	ZrO_2	UO_2 ZrO_2 Zr	UO_2 ZrO_2 Zr	UO_2 ZrO_2 Zr
Melt mass	10kg	12.5kg	20kg	20kg	20kg

02

COLOR facility

2. COLOR facility

COLOR（COLd crucible for cOrium behavior Research）

Induction-melting facility for prototypic oxidic melts up to 2800° C

Examples of application

- Interaction of corium - concrete / sacrificial material
- Selection of concrete / sacrificial material
- Transient tests for metallic / oxidic melts

Principle

- Cold crucible, high frequency induction heating

Technical parameter

temperature:	up to 2800° C
melt mass:	1 - 20 kg
frequency range:	1 – 150kHz
maximum power:	200 kW

2. COLOR facility

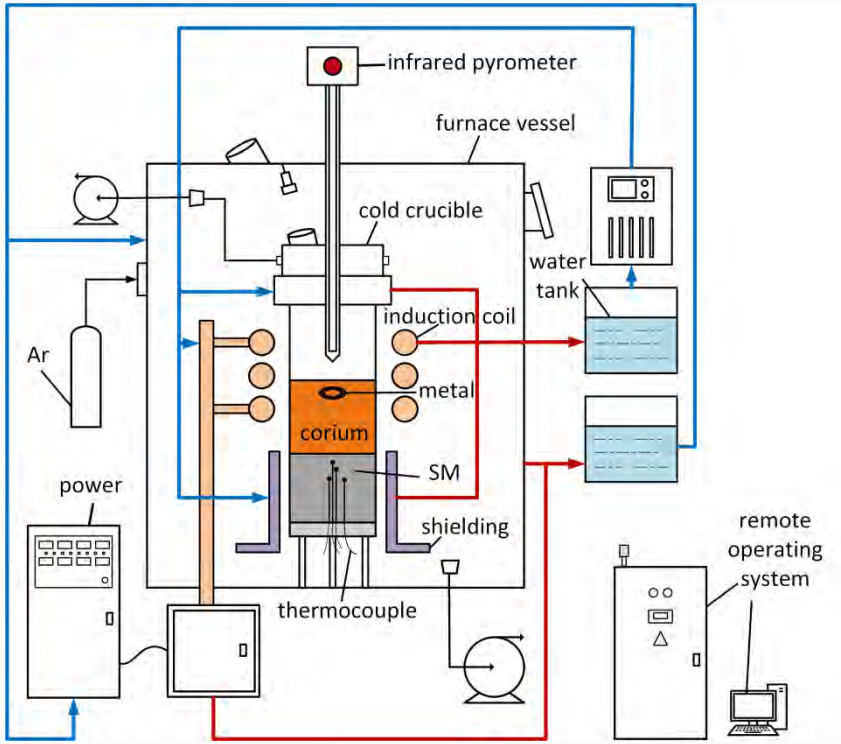

Main data
- **Temperature of melt**
- **Ablation rate**

1. vacuum chamber: provide environment

Vacuum chamber
Value
Observation window
camera

2. experiment materials

Corium
Sacrificial material
Metal for start melting

3. cold crucible: φ160mm, h600mm

Crucible wall
Crucible lid
Crucible bottom plate
Crucible holder

4. power and shielding system

Power cabinet
Inverter
Induction coil
shielding

➡ **h: 20cm, move vertically**
➡ **h: 30cm, move vertically, protect materials from electromagnetic**

5. temperature measurement system

Thermocouples
Infrared pyrometer

➡ **ablation rate**
➡ **internal temperature of melt**

6. gas control system

Vacuum pump
Argon
Extraction pump

7. water cooling system

Water tanks
Water cooler
Cooling circuit

8. Remote operating system

Remote operation system

03

Pre-test

3.1 Pre-test of ZrO_2 -Fe_2O_3 （PT-1）

Experiment Condition

SM simulant	Fe_2O_3
Corium simulant	ZrO_2
Height of SM	22.5cm
Height of corium	20cm
Frequency of power	150kHz
Atmosphere	air

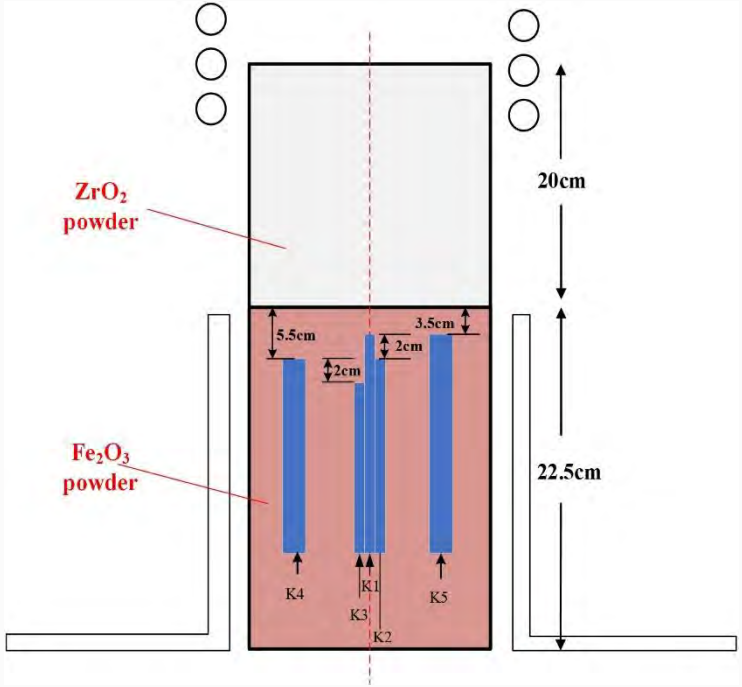

The distribution of material and facilities in the Preliminary experiments of ZrO_2 -Fe_2O_3

Test Operation Steps

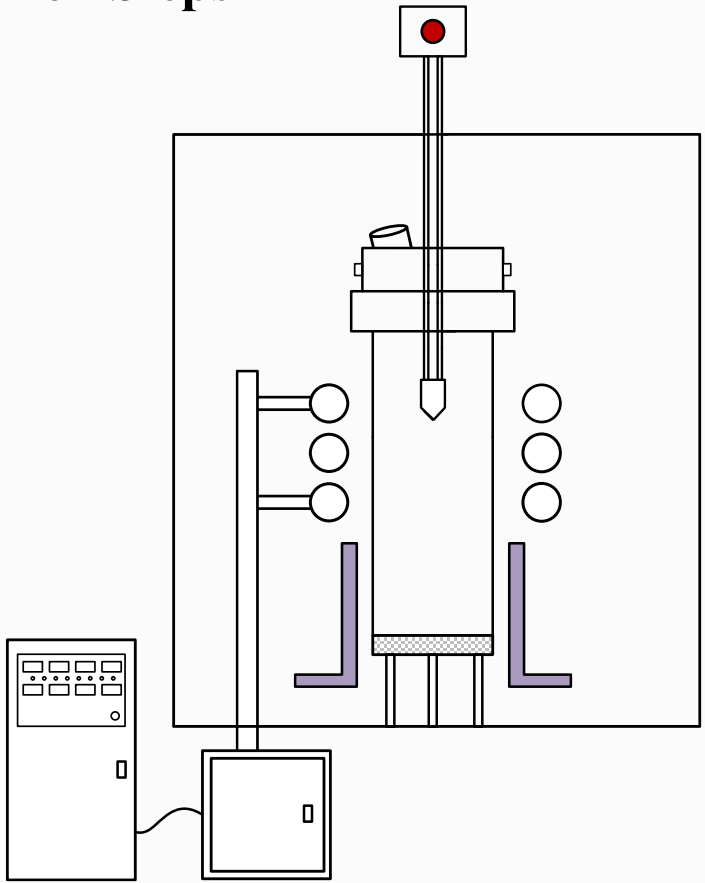

Test Operation Steps

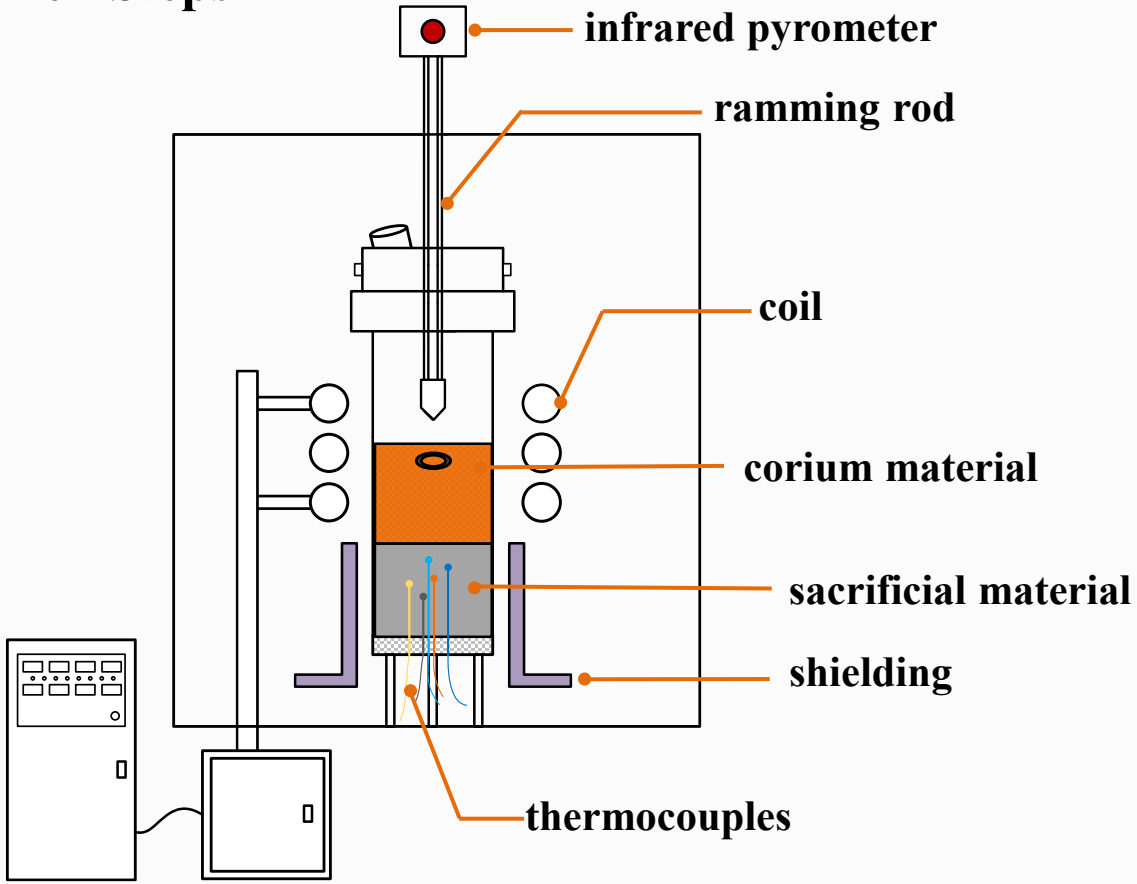

Test Operation Steps

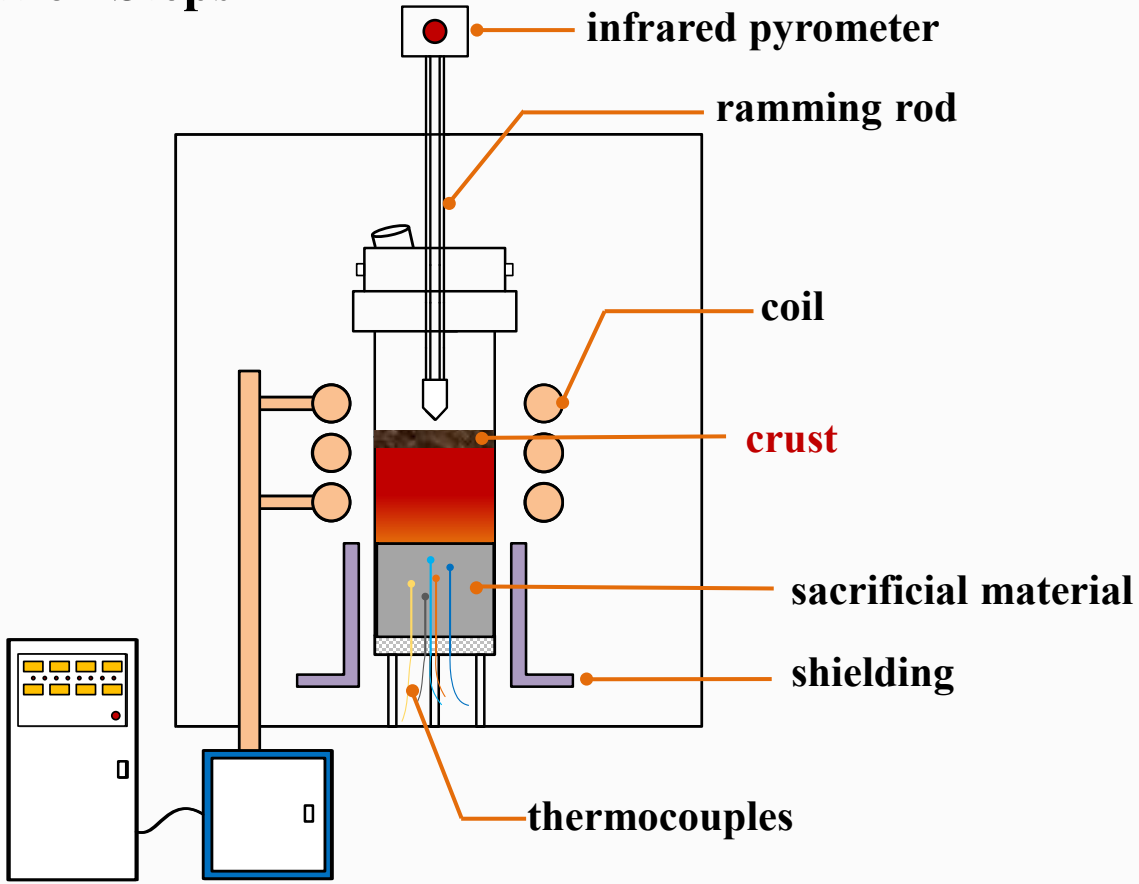

Test Operation Steps

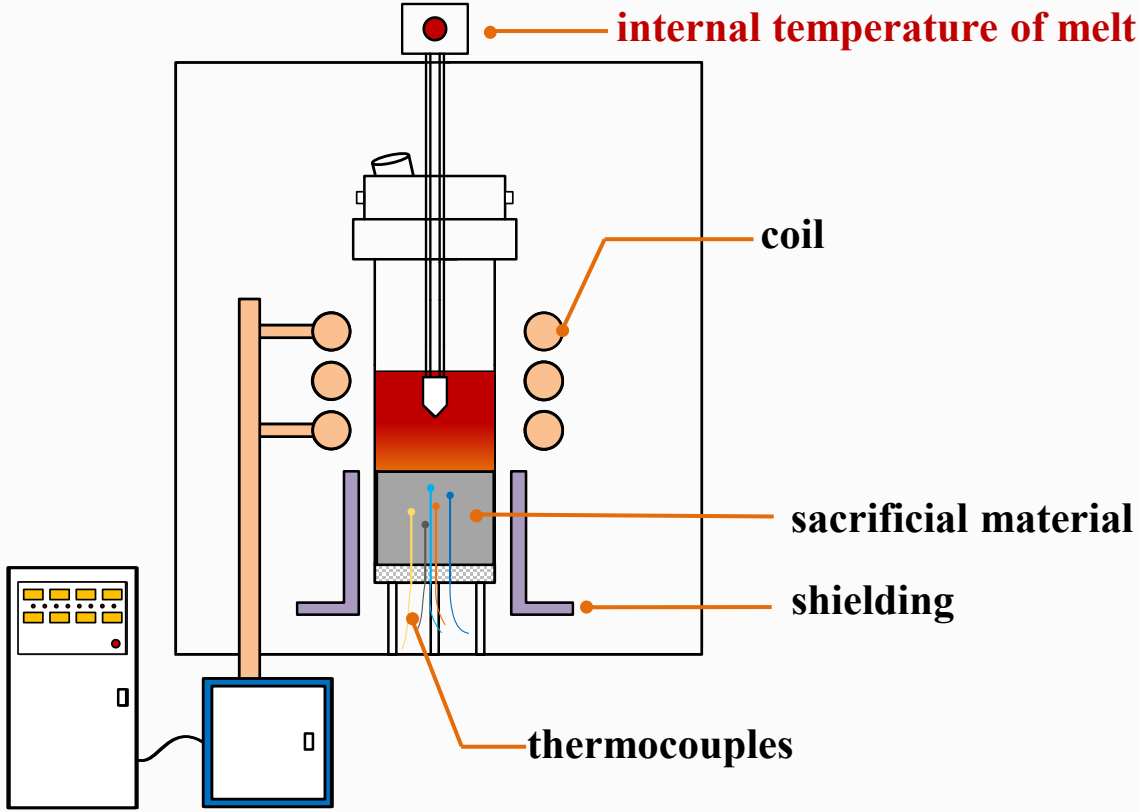

Test Operation Steps

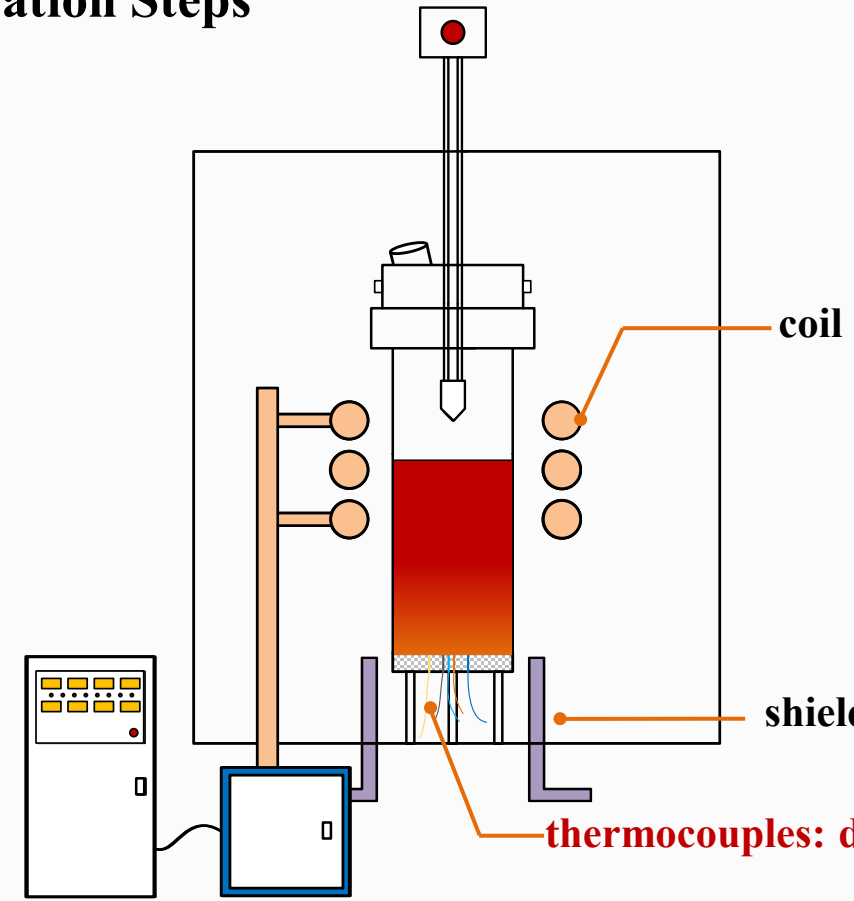

3.1 Pre-test of ZrO_2 -Fe_2O_3

The profile of current and heat power during the heat process

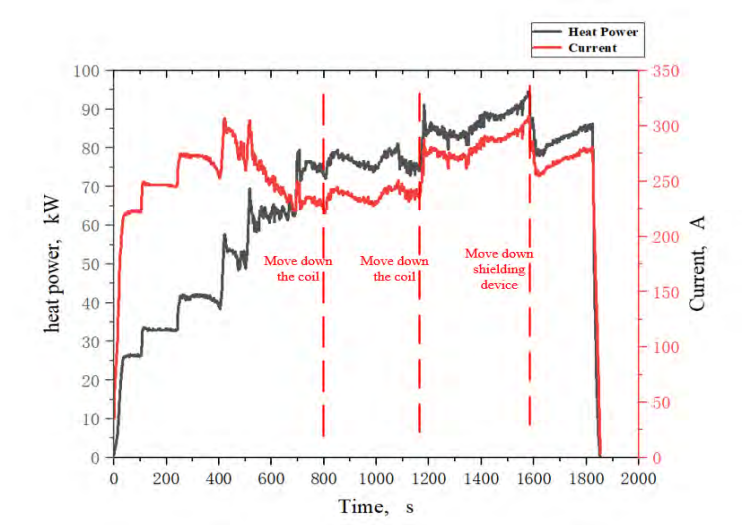

during melt generation the generator power was increased steadily to **70 kW**
current decreased as the corium starts melting, since the molten material began conducting electricity

Heat power and heat loss during the heating process

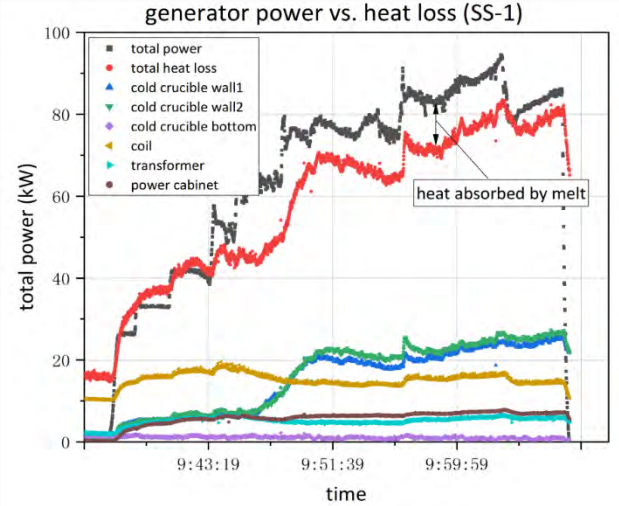

- heat absorbed by the melt: **15~20kW**

3.1 Pre-test of ZrO_2 -Fe_2O_3

Test Results

Surface of molenpool

The temperature of molten pool >2700° C

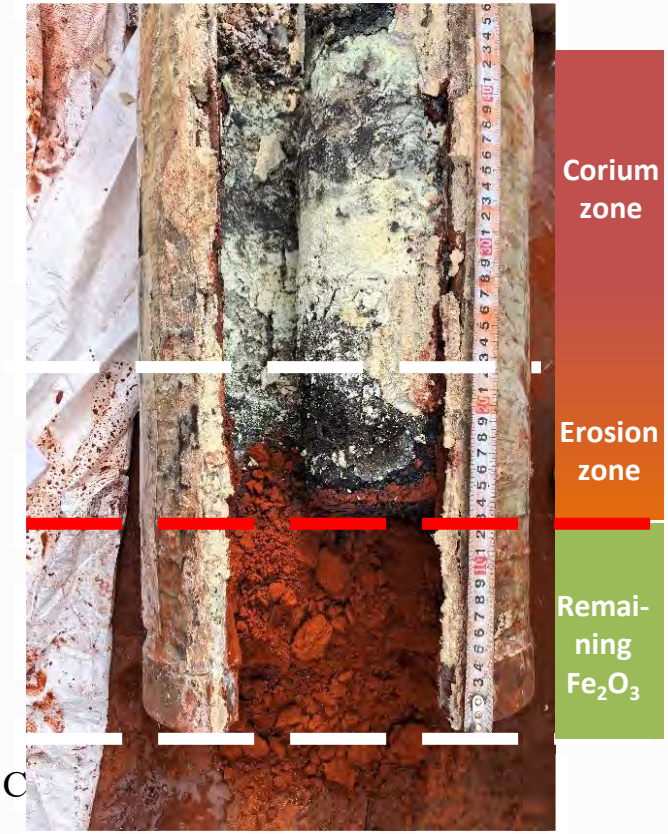

Ablation result

internal structure

1-oxide crust; 2-cavity; 3-oxide ingot; 4-ablation front

3.1 Pre-test of ZrO_2 -Fe_2O_3

Test Results

5 type-K thermocouples to detect ablation progress and provide ablation rate.

Thermocouples layout :

K1(-35mm, R~0) K5(-35mm, R~5mm)

K2(-55mm, R~0) K4(-55mm, R~5mm)

K3(-75mm, R~0)

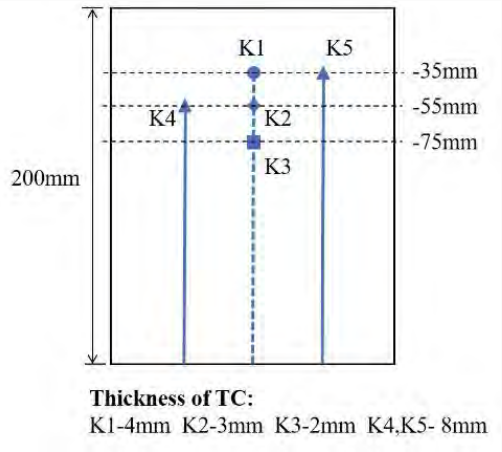

The average ablation rate is 0.19mm/s.

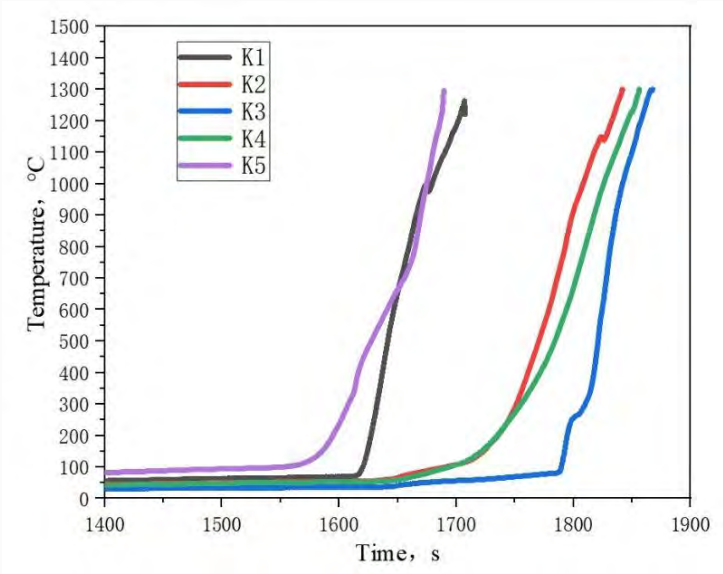

thermocouple data/ablation rate

3.1 Pre-test of ZrO_2 -Fe_2O_3

Test Results

The highest temperature measured by the infrared pyrometer is 2500℃ during the experiment , which is lower than the melting point of ZrO_2

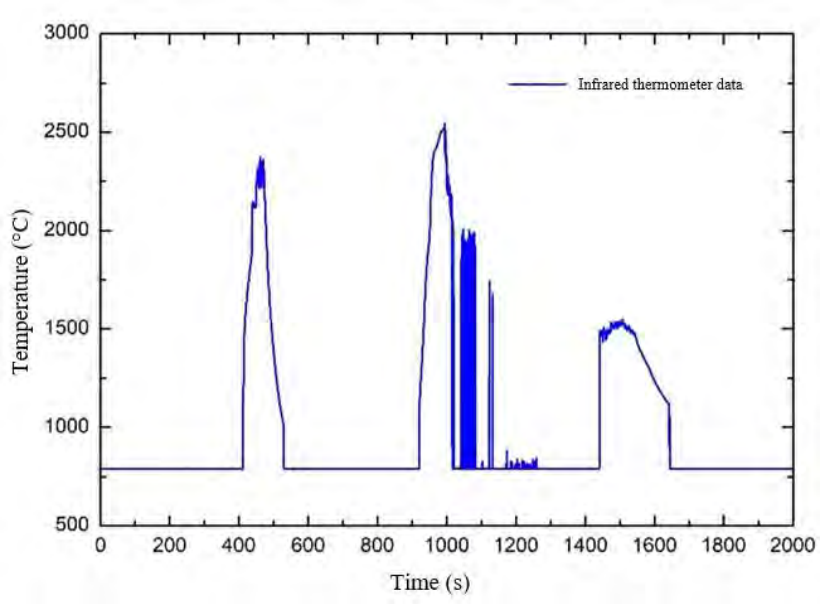

Reason:

- Crust on the surface
- Smoke/ aerosols

Tungsten head

3.1 Pre-test of ZrO_2 -Fe_2O_3

Analysis of sidewall crust

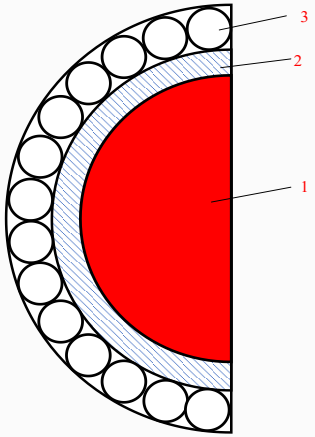

Heat transfer model for the molten pool-crust-cooling water system
1-molten pool, 2-crust, 3-water flow path

Crust thickness: ~2cm

symbol	explanation	value	unit
Q	cooling power of water	9.40	kW
D	diameter of corium	15	cm
H	height of corium	20	cm
d_0	diameter of water tube	20	cm
q	**heat flux from corium to water**	**199.47**	**kW/m^2**
T_0	temperature of the water	37	℃
λ	heat conductivity of water	0.63	W/(m·K)
Pr	Prandtl number	4.64	
υ	kinematic viscosity	$7.028_{7}\times10^{-}$	m^2/s
Re	Reynolds number	33914.84	
Nu	Nusselt number	177.36	
h	**convective heat transfer coefficient**	**5586.920**	**$W/(m^2\cdot K)$**
T_w	**temperature of the wall**	**72.7**	**℃**
k	heat conductivity of corium	1.4	W/(m·K)
T_m	melt point of corium	2800	℃
d	**crust thickness**	**1.92**	**cm**

3.2 Pre-test of ZrO_2 and Sacrificial Material （PT-2）

Test Results

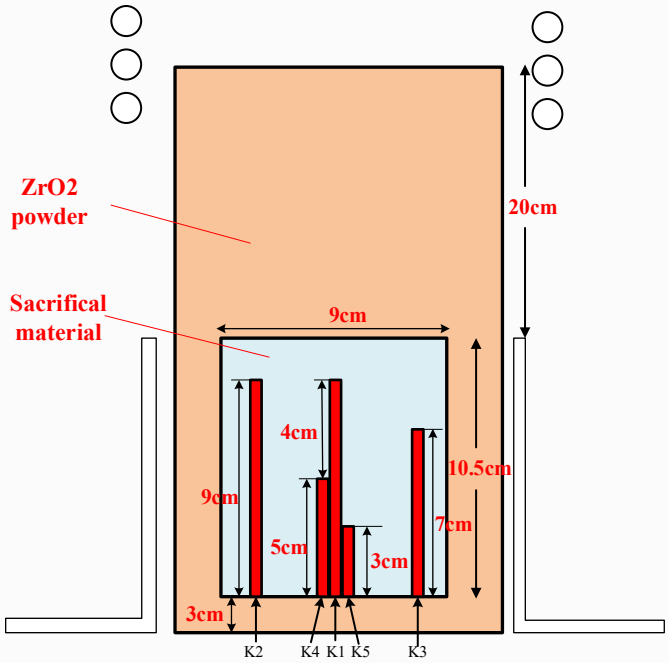

The distribution of material and facilities in the Pre-test of ZrO_2-SM

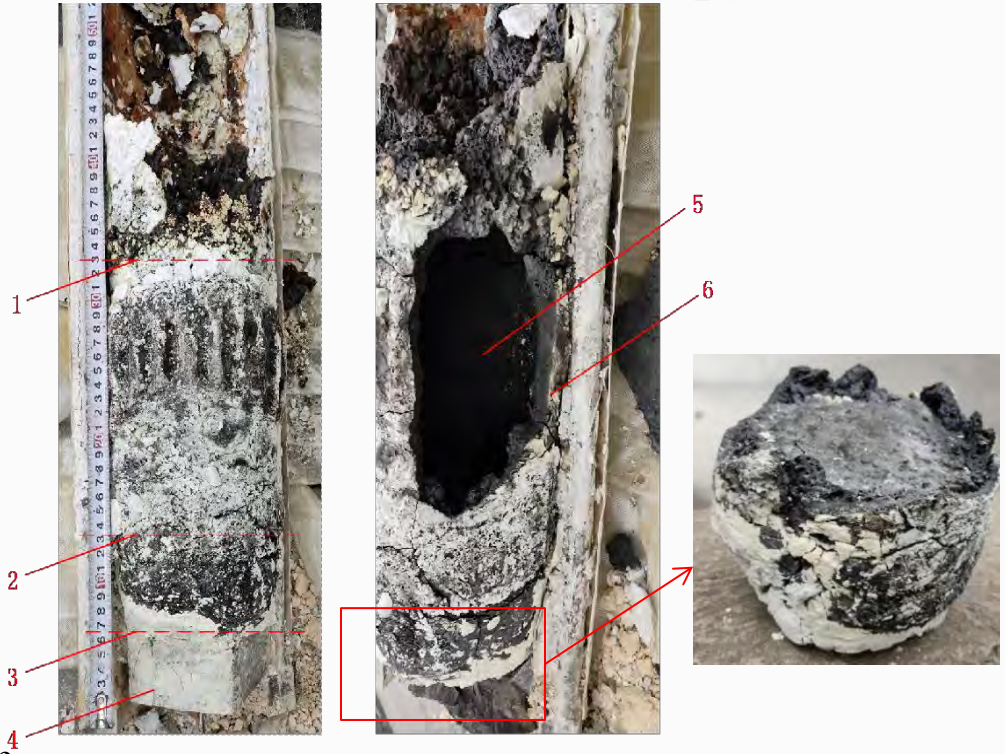

1-initial height of ZrO_2 layer, 2-initial height of SM, 3-ablation front, 4-unmelted SM, 5-cavity, 6-crust

04

Conclusion and Future works

4. Conclusion and Future works

- A platform COLOR has been built for studying the core melt behavior. It enables the melting of a 20 kg melt, with temperature over 2800° C.
- Pre-test on the interaction between simulant and Sacrificial Material have been completed and the ablation rate of PT-1 is 0.19 mm/s.。
- More experiments will be conducted to investigate the interaction between prototype melt and new sacrificial materials.

中核集团 CNNC

中核工程 CNPE

Thank you!

2026. 05. 20

ADVANCING THE JET BREAKUP LENGTH MODEL FOR FUEL-COOLANT INTERACTION IN LIGHT WATER REACTORS

Kwang-Hyun Bang*
Tetras Co.
Busan, Korea
khbang02@gmail.com

Eunho Kim
Korea Institute of Nuclear Safety
Daejon, Korea
eunhokim@kins.re.kr

ABSTRACT

The molten corium interaction with the coolant in the reactor cavity may produce a violent steam explosion thus this can be an additional risk of containment failure in pre-flooding strategy during a nuclear reactor severe accident. The amount of corium jet breakup in a pre-flooded reactor cavity is affected by the depth of water pool. As a correlation approach in estimating the amount of jet breakup, two jet breakup length models of Saito et al. and Epstein & Fauske were assessed for selected FARO test data and found that both models significantly overpredicted the debris mass. A new model for jet breakup length has been proposed based on the Kelvin-Helmholtz instability for melt-steam-water interfaces. The prediction of debris mass of FARO tests was significantly improved by the new model. From the analysis of pre-flooded PWR cavity using the new jet breakup length model, it was found that for 30 cm diameter jet, the fraction of debris mass was less than 40% in a 4 m deep pool. The rate of jet breakup and the particle size are greatly influenced by the vapor film thickness between the hot melt and the coolant water. An analytical model for estimating the vapor film thickness on vertical plate encompassing subcooled liquid has been developed based on the assumption of laminar boundary layer flow. The solution of the model revealed various film boiling parameters such vapor film thickness, vapor velocity profile and heat transfer rate from the hot surface as well as to the subcooled liquid. For high superheat of 2000 K case, the laminar assumption seemed not valid due to high vapor velocity. To overcome the shortcoming, a turbulent model is to be developed in the future.

KEYWORDS
Severe accident, Steam explosion, FCI, Jet breakup, Film boiling

1. INTRODUCTION

In light water reactors (LWRs) if the coolant supply in the reactor coolant system becomes insufficient or even stops, the reactor fuel overheats, melts, and then relocates into the lower plenum of reactor vessel. The molten core in the reactor vessel lower head may threaten the vessel integrity and when the vessel lower head fails the molten corium can be released and accumulated on the concrete floor of the reactor cavity. If the cavity is dry, the molten corium ablates the concrete floor, so-called an MCCI (Molten Core Concrete Interaction) occurs and there is a potential risk of concrete base mat penetration.

There has been a study that has proposed that water addition on the corium pool in the cavity can enhance the cooling of the corium, thus reduce the risk of MCCI significantly [1]. This post-flooding strategy, however, relies on the complex mechanism of water ingression through the cracks in the solidified crust, thus the success probability of corium cooling can be marginal.

One other option is to flood the reactor cavity before the reactor vessel fails. In this case, the released molten corium jet interacts with water coolant in the cavity and breaks up into small particles, then forms particle debris bed on the cavity floor. The risk of MCCI in this case is speculated lower than that of a dry cavity, although this cannot be completely assured due to remaining uncertainties in the ex-vessel FCI and debris bed coolability. Besides, the molten corium interaction with the coolant in the cavity may produce a violent steam explosion thus this can be an additional risk of containment failure in this pre-flooding strategy.

One of the important lessons learned from the past severe accidents (Fukushina-1, Chernobyl) is that the maintaining the reactor containment integrity is a crucial aim during a severe accident to protect the public from radiation hazard. Despite the MCCI can be a cause of containment failure in a long-term phase, the steam explosion can be a cause of early containment failure when the amount of fission product source term inside the containment is relatively high. This may imply that an early containment failure must be prevented and a severe accident management action should be focused on preventing the early containment failure. In this respect, the timing of water addition is important in the severe accident management perspective.

When the pre-flooding strategy is chosen for severe accident management action, the risk of an energetic Fuel-Coolant Interaction (FCI) should be assessed. An FCI is a highly complex, multi-physics process involving molten fuel jet and droplet breakup, as well as heat and mass transfer among the hot molten fuel, liquid coolant, and coolant vapor. It is sometimes referred to as a "thermal explosion," driven by the rapid transfer of thermal energy from the molten fuel to the coolant, leading to the instantaneous vaporization of the liquid coolant. The resulting high pressure propagates through fuel-coolant mixture, causing fine fragmentation of molten fuel droplets into particles smaller than 0.1 mm [2]. This drastic increase of heat transfer surface area is considered the primary driving force for explosion propagation through the fuel-coolant mixture. The elevated pressure then expands against surrounding structures, potentially causing damage depending on the explosion's intensity.

In the OECD/NEA international program SERENA, FCI has been studied with a particular focus on evaluating the capabilities of computational codes to predict FCI-induced dynamic loads on reactor structures. In the first phase of the SERENA project [3], predictions from various FCI codes were compared against experimental data. The comparison revealed that the codes were still unable to reproduce all observed attributes with the same level of accuracy and also that a large uncertainty exists in the prediction of coolant void fraction and corium jet breakup.

The prediction of melt jet breakup is important not only because the rate of jet breakup and resulting droplet size affect significantly the energetics of steam explosion, but also because the amount of fragmented melt mass and the drop size affect the coolability of debris bed on the concrete floor. The physical mechanisms of melt jet breakup include the Rayleigh-Taylor instability, boundary layer stripping, and the Kelvin-Helmholtz instability, as depicted in Fig. 1 [4]. It is noted that the left hand-sided figure for boundary layer stripping in Fig. 1 shows only the leading edge and broken drops of a cylindrical jet from the post-processing of a CFD result. Most FCI codes [5-8] have its own modeling approach on jet breakup, but those models tend to involve a complex numerical algorithm or to assume a continuous process for the cyclic nature of jet breakup process.

One of the simple, but semi-empirical models is called jet breakup length model. The distance of melt jet traveling to a point of complete breakup is called ‘jet breakup length’ and there have been a few studies on building a semi-empirical relation of the jet breakup length: Saito et al [9], Epstein and Fauske [10]. An

Figure 1. Illustration of jet breakup at leading edge by boundary layer stripping (left) and at lateral surface by Kelvin-Helmholtz instability (right)

experimental work by Bang et al. [11] using cold Woods metal reported that the Epstein and Fauske correlation is more suitable than Saito's for the high-temperature corium jet breakup.

In this paper, the level of accuracy of the existing jet breakup length models are evaluated for some selected FARO tests [12]. Also, an advanced, theoretically-based model for jet breakup length is proposed and evaluated using the experimental data. Based on the new jet breakup length model, the mixing limit of corium jet pouring into pre-flooded reactor cavity is discussed. Finally, a numerical model for predicting vapor film thickness is presented.

2. JET BREAKUP LENGTH

2.1. Evaluation of Existing Models for Jet Breakup Length

As introduced in the previous section, there are two major models for jet breakup length: Saito et al. [9] and Epstein & Fauske [10]. Saito et al. conducted experiments using 90°C water jet injected into Freon-11 pool at temperature ranging from 2 to 23.2 °C, or alternatively, a 10 to 19 °C water jet injected into a liquid-nitrogen pool at −195.8 °C. The water jet diameter was in the range of 5 to 40 mm and jet velocity was in the range of 2.5 to 15 m/s. They confirmed that instabilities were generated due to the vapor flow occurring between the jet and the cooling liquid. As a result, the jet was fragmented and the vapor-enshrouded jet penetrated further into the coolant. They observed that the jet penetration length increased with increasing jet velocity, jet diameter, and the density ratio between the jet and the coolant. Based on the energy balance between the two fluids, an experimental correlation for the jet penetration length was developed as a function of jet diameter, density ratio of jet and coolant, and Froude number of the jet.

$$\frac{L_{brk}}{D_j} = 2.1\left(\frac{\rho_j}{\rho_c}\right)^{0.5} Fr^{0.5},\ Fr = \frac{V_j^2}{gD_j} \tag{1}$$

Epstein and Fauske examined the mean entrainment velocity at the leading edge of a turbulent flow based on Taylor's earlier hydrodynamic study of a hot turbulent gas plume rising in air. Taylor assumed that the entrainment velocity is proportional to the time-averaged cross-sectional velocity of the turbulent flow. This proportionality constant was experimentally defined as the entrainment coefficient and was assumed to have a value of 0.1. Epstein and Fauske assumed that the amount of fragment stripped from the jet into the surrounding fluid along the jet side surface is constant, and they considered the rate of fragment mass reduction to be proportional to the difference between the velocity of the flow field and the instantaneous accelerated velocity of the fragments. Under this assumption, the jet breakup time can be derived from a

Table 1. Calculation of jet breakup for selected FARO tests [12]

	L-06	L-08	L-14	L-19	L-20	L-24	L-28	L-33
Pressure, MPa	5.0	5.8	5.0	5.0	2.0	0.5	0.5	0.4
Melt mass(1), kg	18	44	125	157	96	176	175	100
Melt temperature, K	2923	3023	3123	3073	3173	3023	3052	3070
Melt release dia., mm	100	100	100	100	100	100	50	50
Free fall distance, m	1.83	1.53	1.04	1.99	1.12	1.07	0.89	0.77
Water depth, m	0.87	1.00	2.05	1.10	1.97	2.02	1.44	1.60
Melt jet length(2), m	0.31	0.77	2.18	2.74	1.67	3.07	12.2	6.98
Water temperature, K	539	536	537	537	485	425	424	293
Cake mass, kg	6	14	20	80	21	27	77.4	8.8
Debris mass, kg	12	30	105	77	75	141	84	89
(% of total mass)	(67)	(68)	(84)	(51)	(78)	(84)	(52)	(92)
Ave. debris size, mm	4.5	3.8	4.8	3.7	4.4	2.6	3.0	2.6
Saito's prediction (%)								
void fraction = 0.0	87	94	100	96	100	100	100	100
void fraction = 0.3	79	86	100	90	100	100	100	100
Epstein's prediction (%)								
void fraction = 0.0	98	100	100	100	100	100	100	100
void fraction = 0.3	92	96	100	99	100	100	100	100

[Note] (1) Melt composition: UO_2+ZrO_2 (80%+20%), (2) Based on melt density=7300 kg/m^3

force balance between the kinetic energy of the fragments undergoing breakup and the kinetic energy of the surrounding fluid. Using this jet breakup time, the relationship of jet breakup length was developed.

$$\frac{L_{brk}}{D_j} = \frac{1}{2E_o}\left(\frac{\rho_j}{\rho_c}\right)^{0.5} \tag{2}$$

The constant ranging from 0.05 to 0.1 was recommended for E_o. It is noted that the Epstein & Fauske correlation is independent of jet velocity, but a function of density ratio of water and corium. This model is based on the entrainment concept caused by the Kelvin-Helmholtz instability and it does not account for the condition of hot melt undergoing film boiling at the melt-coolant interface.

In order to assess the validity of these two models for hot corium-water interactions, selected FARO test data [12] were applied to the correlations. The jet breakup process is assumed to have a conical shape, as shown in Fig. 2. If the water pool depth is smaller than the estimated jet breakup length, the fraction of melt that remains as an unbroken "cake" can be approximated as the ratio of the cross-sectional area of the unbroken portion of the jet to that of the initial jet at the cavity floor level. The relationship between the debris mass fraction, water pool depth, and jet breakup length is given in Fig. 2.

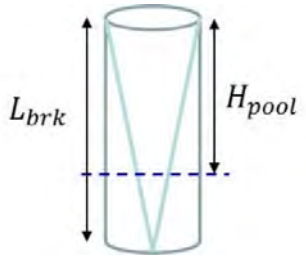

$$\alpha_{debris} = 1 - \left(\frac{D_o}{D_j}\right)^2 = 1 - \left(1 - \frac{H_{pool}}{L_{brk}}\right)^2$$

Figure 2. Relation for fraction of debris mass broken from conical jet

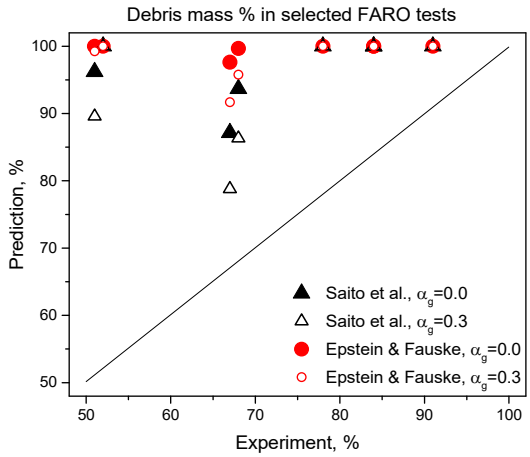

Figure 3. Comparison between the prediction of jet breakup length model and experimental data

The major experimental conditions and the calculation results of selected FARO tests are summarized in Table 1. The comparison of the prediction and the experimental data for the fraction of debris mass is shown in Fig. 3. In the FARO tests, the fraction of debris out of the total corium mass ranged from 51% to 92%. But, as shown in Fig. 3, both the two correlations of jet breakup length greatly overpredicted the debris mass and in more than half the test cases the predictions indicate 100% jet breakup.

The effect of void in coolant pool was also examined by assuming 30% void. This could be the case when melt pouring time was longer so that the melt jet continued to pour after the coolant became a two-phase pool by coolant boiling. As for the tests L-28 and L-33, larger mass of corium with smaller jet diameter results in melt jet length much longer than the coolant pool depth: 1.44 m coolant pool depth v.s. 12.2 m melt jet length in L-28 test. The estimated melt jet lengths are given in Table 1 for comparison purpose. The mean density of liquid and vapor was replaced for the coolant density and the results are listed in Table 1 and also marked by open symbols in Fig. 3. The void fraction of 30% can lower the coolant density to 70% of pure liquid and this level of reduction in liquid density does not alter the jet breakup length by a significant amount.

It is noted that the present estimation of debris mess using the jet breakup length model did not account for re-melting or agglomeration of particles. Re-melting of particles can occur if the solid particles are surrounded by highly superheated melt or the decay heat is higher than the heat loss rate from the particle. The later case of decay heat is not relevant in FARO tests, but the re-melting by contacting superheated melt could occur. Unfortunately, however, this can not be identified since only the posttest data are available.

2.2. Theory of Advanced Jet Breakup Length Model

Epstein and Fauske [13] also proposed a formulation of Kelvin-Helmholtz instability for melt-steam-water system which may represent the hot melt undergoing film boiling. However, the solution of the dispersion equation involves complex numbers so that an analytical expression of the fastest growing wave number could not be obtained. They were able to show only the two limiting cases where analytic solutions can be obtained; thin film and thick film. The fastest growing wave number and the associated maximum growth constant for these two limiting cases are:

For thin film:

$$k_{D,o} = \frac{2\,\rho_j\,\rho_l\,(V_l - V_j)^2}{3(\rho_j+\rho_l)(\sigma_j+\sigma_l)} \tag{3}$$

$$n_{D,o}^2 = \frac{\rho_j\,\rho_l k_{D,o}^2\,(V_l - V_j)^2}{(\rho_j+\rho_l)^2} - \frac{(\sigma_j+\sigma_l)k_{D,o}^3}{(\rho_j+\rho_l)} \tag{4}$$

For thick film:

$$k_{D,\infty} = \frac{2\,\rho_j\,\rho_g\,(V_g - V_j)^2}{3(\rho_j+\rho_g)\sigma_j} \tag{5}$$

$$n_{D,\infty}^2 = \frac{\rho_j\,\rho_g k_{D,\infty}^2\,(V_g - V_j)^2}{(\rho_j+\rho_g)^2} - \frac{\sigma_j k_{D,\infty}^3}{(\rho_j+\rho_g)} \tag{6}$$

Based on the formulation of Kelvin-Helmholtz instability for melt-steam-water system by Epstein & Fauske, Bang et al. [14] obtained a numerical solution of the complex-variable dispersion equation of the Kelvin-Helmholtz instability in melt-steam-water system for various relative velocity and film thickness. The solutions were then fitted into the correlations of the fastest growing wave number and the maximum growth constant as follow.

Fastest growing wave length:

$$\frac{k_D}{k_{D,\infty}} = 1 + \frac{1}{\frac{k_{D,\infty}}{k_{D,o}} + 25(V_g - V_j)^{1.5}\delta + (k_{D,\infty}\delta)^2} \tag{7}$$

Growth constant at k_D:

$$\frac{n_D}{n_{D,\infty}} = 1 + \frac{1}{\frac{n_{D,\infty}}{n_{D,o}} + 5(V_g - V_j)^{1.5}\delta + 100(n_{D,\infty}\delta)^2} \tag{8}$$

Now, following the entrainment concept proposed by Epstein and Fauske, the new formulation of the jet breakup length which accounts for film boiling has been developed. The jet breakup length can be ideally defined as the distance which the jet leading edge travels for the time period for which the entrainment front reaches the center of the jet from the jet surface, i.e., the completion of jet breakup. The entrainment velocity is formulated from the Kelvin-Helmholtz instability by Epstein and Fauske [10] as

$$v_{en} \sim \frac{\pi}{16}\left(\frac{\lambda_D}{\tau}\right) \tag{9}$$

where λ_D is the fastest growing wave length and τ is the time scale of the growth and is basically $1/n_D$. The jet breakup length is then the jet velocity multiplied by the time of jet breakup completion.

$$L_{brk} = V_j \cdot (\frac{D_j}{2})/v_{en} \tag{10}$$

Combining Eqs. (9) and (10) and adjusting the constant for the consistency between the KHI and the entrainment concept [10], the proposed jet breakup length is

$$\frac{L_{brk}}{D_j} = \frac{1}{2\sqrt{3}E_o} V_j \left(\frac{k_D}{n_D}\right) \tag{11}$$

The fastest growing wave number, k_D, and the maximum growth constant, n_D, are calculated using Eqs. (7) and (8). The recommended value for the constant Eo is 0.1.

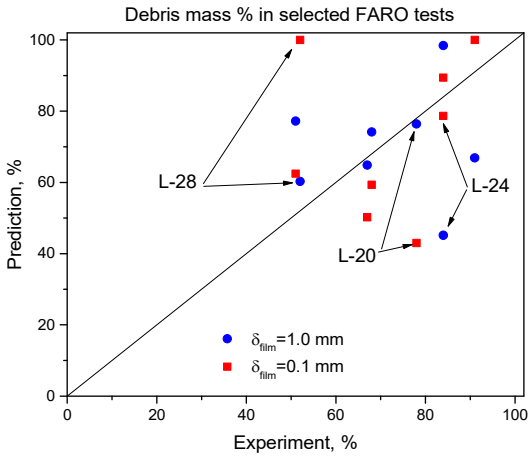

Figure 4. Comparison of debris mass between the prediction of the advanced jet breakup length model and experimental data

The proposed new jet breakup length correlation was assessed using the selected FARO tests and the results are shown in Fig. 4. In general, the debris mass prediction by the proposed jet breakup length model is greatly improved. The important shortcoming of the new model, however, is that the vapor film thickness is not known and be assumed. When thin vapor film of 0.1 mm is assumed, the test L-20 is underpredicted and the test L-28 is overpredicted by greater degree. But it is good to observe that when the vapor film of 1 mm thickness is assumed, the predictions of both L-20 and L-28 tests are greatly improved, as illustrated using arrows in Fig. 4. On the contrary, thinner vapor film of 0.1 mm gives better prediction that 1 mm vapor film in test L-24. Nonetheless, the vapor film thickness at the time of instability initiation must be known. There is no experimental data of vapor film thickness reported for such high temperature corium and water. An analytical modeling of film boiling can be an informative approach for finding the vapor film thickness. In the following section 3, laminar boundary layer modeling of film boiling on a vertical plate is presented.

2.3. Application of Advanced Jet Breakup Length Model to Reactor Conditions

The jet breakup length predicted by Eq. (11) for a typical PWR corium-water FCI condition is shown in Fig. 5. In case of no film boiling, the dimensionless jet breakup length is around 15 and independent of jet entry speed as same as Epstein-Fauske model. However, if there is vapor film between the melt and water, the dimensionless jet breakup length jumps to over 40 even though the vapor film thickness is assumed unpractically thin, 0.01 mm.

For pre-flooding strategy of a PWR cavity in which coolant is filled prior to the breach of reactor pressure vessel, the fraction of corium jet breakup into particle debris is an interesting subject. If the jet breakup length is shorter than the depth of coolant pool in the cavity, the corium is completely broken up and it forms a debris bed on the cavity floor. However, the jet breakup length is longer than the coolant pool depth, a fraction of corium remains as a cake (i.e., unbroken mass) on the cavity floor and the coolability remains as a concern depending on the size of such a cake.

The fraction of the debris mass (α_{debris}) can be estimated using the jet breakup length formulation of Eq. 11. For 30 cm diameter corium jet, the fraction of debris is calculated for the pool depth of 4 m and 7 m and shown in Fig. 5. If no vapor film (isothermal case), most of the jet is broken up since the jet breakup length is shorter than 4 m. However, in hot corium case in which vapor film exists, although the vapor film thickness is not known precisely, the jet breakup length becomes much longer, thus the fraction of debris

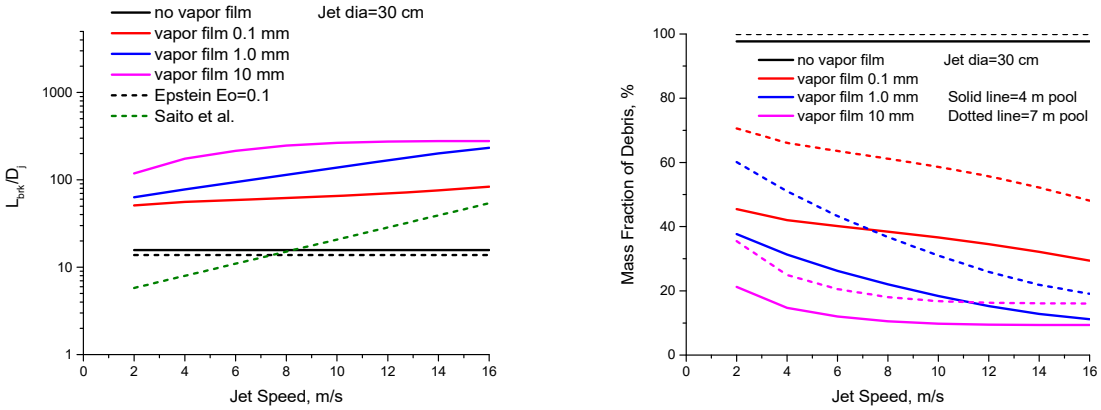

Figure 5. Jet breakup length (left) and mass fraction of debris (right) predicted by the proposed jet breakup length model

becomes smaller, less than 40% in 4 m deep pool. This implies that the coolant pool depth is an important parameter in the view of ex-vessel debris coolability. The experimental data of jet breakup length is scarce due to the explosive nature of FCI experiments as well as poor availability of good measurement technique. This makes it difficult to better validate the applicability of the proposed relation of jet breakup length.

3. ANALYTICAL MODELING OF FILM BOILING ON VERTICAL PLATE

It is observed that the proposed jet breakup length model is strongly influenced by the vapor film thickness. Although the film boiling is one of common boiling modes, the information on the vapor film thickness on vertical plate is scarce in the literature. Bromley [15] is the first who proposed film boiling model for vertical plate, but it is limited to saturated film boiling and the interfacial shear at the interface is not matched. Thus, in this study, an analytical film boiling model has been developed under the assumption of laminar boundary layer. Laminar boundary layer modeling for film boiling over a sphere was developed by Bang [16] and the present modeling is an extension to a vertical plate. Both velocity fields of vapor and liquid are computed and the energy equations of both vapor and liquid are also solved to include subcooled film boiling as shown in Fig. 6.

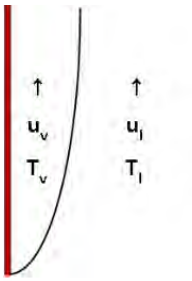

Figure 6. Film boiling on vertical plate

The boundary layer equations for vapor and liquid in film boiling on vertical plate can be written as below.

For vapor:

$$u\left(\frac{\partial u}{\partial x}\right)+v\left(\frac{\partial u}{\partial y}\right)=\nu_v\left(\frac{\partial^2 u}{\partial y^2}\right)+g_0\frac{\rho_l-\rho_v}{\rho_v} \quad (12)$$

$$u\left(\frac{\partial T}{\partial x}\right) + v\left(\frac{\partial T}{\partial y}\right) = \alpha_T\left(\frac{\partial^2 T}{\partial y^2}\right) \tag{13}$$

For liquid:

$$u\left(\frac{\partial u}{\partial x}\right) + v\left(\frac{\partial u}{\partial y}\right) = \nu_l\left(\frac{\partial^2 u}{\partial y^2}\right) \tag{14}$$

$$u\left(\frac{\partial T}{\partial x}\right) + v\left(\frac{\partial T}{\partial y}\right) = \alpha_T\left(\frac{\partial^2 T}{\partial y^2}\right) \tag{15}$$

These equations can be reduced to ordinary differential equations by similarity transformation.

For vapor:

$$f''' + \left[\frac{1}{2}\right] f f'' = \left[-\left(\frac{Gr_x}{Re_x^2}\right)_{vap}\right] \tag{16}$$

$$\theta'' + Pr_v\left[\left(\frac{1}{2}\right)\right] f\,\theta' = 0 \tag{17}$$

For liquid:

$$F''' + \left[\frac{1}{2}\right] F F'' = [0] \tag{18}$$

$$\Theta'' + Pr\left[[0] + \left[\left(\frac{1}{2}\right)\right] F\right]\Theta' = [0] \tag{19}$$

At the interface of vapor and liquid, the velocity and tangential shear must be matched and these interfacial relations are

$$F'(0) = f'(\eta_\delta) \tag{20}$$

$$F''(0) = \sqrt{\frac{\rho_v \mu_v}{\rho_l \mu_l}} f''(\eta_\delta) \tag{21}$$

$$F(0) = \sqrt{\frac{\rho_v \mu_v}{\rho_l \mu_l}} f(\eta_\delta) \tag{22}$$

The relation between the energy balance at the interface and the evaporation rate can be written as

$$\frac{Ja_v}{Pr_v}[-\theta'] - \frac{Ja_l}{Pr_l}[-\Theta']\sqrt{\left(\frac{\rho_l \mu_l}{\rho_v \mu_v}\right)} + \frac{[Nu_r]}{\sqrt{([Re_v])}}\left(\frac{Ja_v}{Pr_v}\right) = \left[x\frac{\partial \eta_\delta}{\partial x}\right] f' + \frac{1}{2} f \tag{23}$$

These set of equations with the boundary and interfacial conditions were numerically solved. The solution of the model revealed various film boiling parameters such vapor film thickness, vapor velocity profiles and heat transfer rate from the hot surface as well as to the subcooled liquid. First, a set of solutions obtained for a moderate wall temperature, the superheat temperature of 400 K in the atmospheric pressure. The water subcooling was varied from the saturation condition to 50 K subcooling. Fig. 7 shows the vapor film thickness for different liquid subcooling and it is observed the vapor film thickness can be smaller than 1 mm in high subcooling of water.

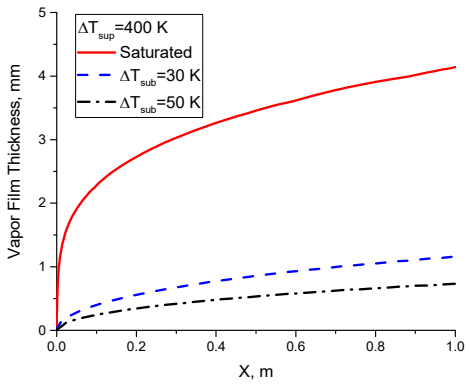

Figure 7. Effect of subcooling on film thickness (400 K superheat)

The calculated local heat transfer coefficient is compared with the Bromley model in Fig. 8 and it is found that the Bromley model seems to overpredict. The vapor velocity profiles in the film are illustrated in Fig. 9 and the ratio of the average vapor velocity to free stream liquid velocity is also given in Fig. 9. In saturated film boiling, the average vapor velocity is ten times as large as the free-stream liquid velocity.

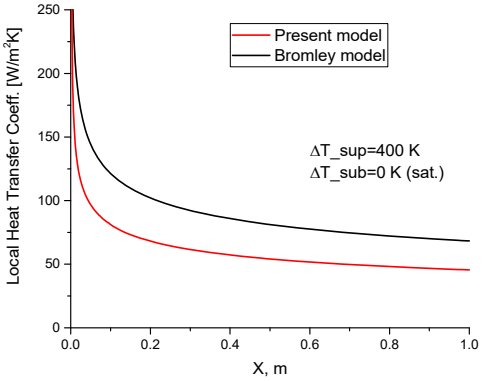

Figure 8. Comparison of heat transfer coefficient with Bromley model (400 K superheat)

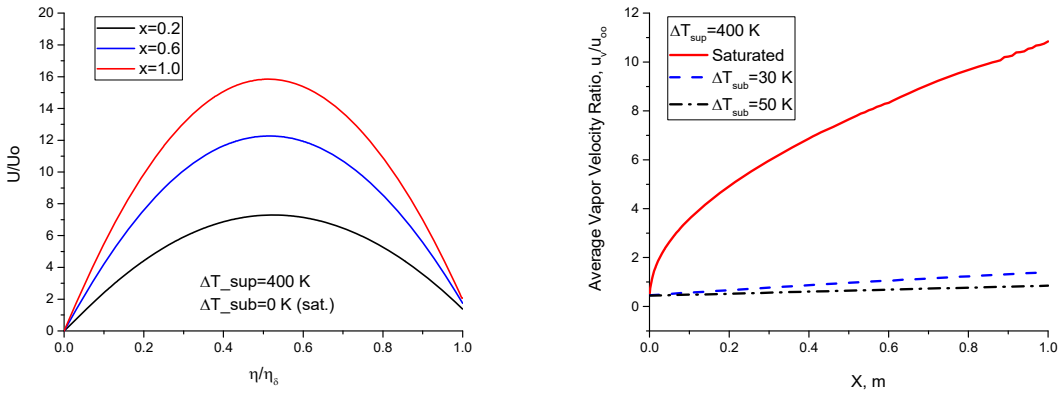

Figure 9. Vapor velocity profile (left) and average vapor velocity (right) for 400 K superheat

In fuel-coolant interaction during a severe accident, the molten fuel temperature is as high as 3000 K. Although the physical realm of the state in which water contacts such a high temperature surface can be very complex, it is assumed that film boiling develops between the hot surface and liquid. For superheat of 2000 K, the solution was hardly obtained except for the first few tens of centimeters. This problem could be caused by the assumption of laminar flow since the vapor flow becomes very high and the vapor film develops very thicker even for high subcooling of liquid. Fig. 10 shows the vapor film thickness and the average vapor velocity for 2000 K superheat. For better solutions for high temperature corium, turbulent model is to be developed in the future.

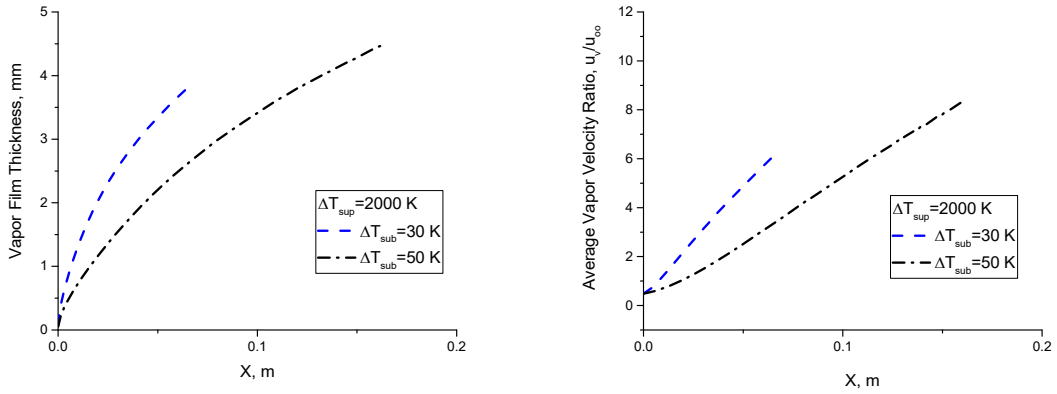

Figure 10. Vapor film thickness (left) and average vapor velocity (right) for 2000 K superheat

4. CONCLUSIONS

The molten corium interaction with the coolant in the cavity may produce a violent steam explosion thus this can be an additional risk of containment failure in pre-flooding strategy. The amount of corium jet breakup in a pre-flooded reactor cavity is affected by the depth of water pool. As a correlation approach in estimating the amount of jet breakup, two jet breakup length models of Saito et al. and Epstein & Fauske were assessed for selected FARO test data and found that both models significantly overpredicted the debris mass.

A new model for jet breakup length has been proposed based on the Kelvin-Helmholtz instability for melt-steam-water interfaces. The prediction of debris mass of FARO tests was significantly improved by the new model. From the analysis of pre-flooded PWR cavity using the new jet breakup length model, it was found that for 30 cm diameter jet, the fraction of debris mass was less than 40% in a 4 m deep pool.

It was found that the rate of jet breakup and the particle size are greatly influenced by the vapor film thickness between the hot melt and the coolant water. An analytical model for estimating the vapor film thickness on vertical plate encompassing subcooled liquid has been developed based on the assumption of laminar boundary layer flow. The solution of the model revealed various film boiling parameters such vapor film thickness, vapor velocity profiles and heat transfer rate from the hot surface as well as to the subcooled liquid. For high superheat of 2000 K case, the laminar assumption seemed not valid due to high vapor velocity. To overcome the shortcoming, a turbulent model is to be developed in the future.

NOMENCLATURE

D Diameter
Fr Froude number

Subscripts

g	Gravitational number
Gr	Grashof number
H	Depth
Ja	Jacob number
k	Wave number
L	Length
n	Growth constant
Nu	Nusselt number
Pr	Prandtl number
Re	Reynolds number
T	Temperature
u	Velocity
V, v	Velocity

brk	Breakup
c	Coolant
D	Fastest growing
g	Gas
j	Jet
l	Liquid
o	Thin vapor
pool	Coolant pool
v	Vapor
∞	Thick vapor

Greeks

α	Thermal diffusivity
δ	Film thickness
μ	Viscosity
σ	Surface tension
ρ	Density

λ	Wave length
τ	Time constant
θ	Dimensionless temperature
η	Similarity variable

ACKNOWLEDGMENTS

This work was supported by the Nuclear Safety Research Program through the Korea Foundation of Nuclear Safety (KoFONS) using the financial resource granted by the Nuclear Safety and Security Commission (NSSC) of the Republic of Korea (Contract No. RS-2021-KN063410).

REFERENCES

1. Lomperski, S., Farmer, M.T., Experimental evaluation of the water ingression mechanism for corium cooling, Nuclear Engineering and Design, 237, pp. 905-917 (2007).
2. Huhtiniemi, I., Magallon, D., Hohmann, H, Results of recent KROTOS FCI tests: alumina versus corium melts, Nuclear Engineering and Design, 189, 379-389 (1999).
3. OECD/NEA, SERENA Final Report, SERENA-Steam Explosion Resolution for Nuclear Applications, NEA/CSNI/R(2007)11 (2007).
4. Kim, M.S, Bang, K.H., CFD Simulation of Kelvin-Helmholtz Instability and Boundary Layer Stripping for Interpretation of Melt Jet Breakup Mechanisms, The 19th International Topical Meeting on Nuclear Reactor Thermal Hydraulics (NURETH-19), Brussels, Belgium, March 6-11 (2022).
5. Carachalios, C., Bürger, M., Unger, H., A transient two-phase model to describe thermal detonations based on hydrodynamics fragmentation, Proc. International Meeting on LWR Severe Accident Evaluation, Cambridge, MA, TS6.8 1–8 (1983).
6. Chu, C.C. and Corradini, M.L., One-Dimensional Transient Model for Fuel-Coolant Interaction Analysis, Nuclear Engineering and Design, 101, 48-71 (1989).
7. Meignen, R., Picchi, S., Lamome, J., Raverdy, B., Castrillon Escobar, S., Nicaise, G., The challenge of modeling fuel–coolant interaction: Part I. Premixing, Nuclear Engineering and Design, 280, 511–527 (2014).
8. Bang, K.H., Kim, M.S., Shin, D.J., Kim, D.H., Three-Dimensional Lagrangian-Eulerian Modeling and Analysis of Fuel-Coolant Interaction, Nuclear Engineering and Design, 444, 114408 (2025).

9. Saito, M., Sato, K., Imahori, S., Experimental study on penetration behaviors of water jet into freon-11 and liquid nitrogen, ANS Proceedings of National Heat Transfer Conference, vol. 3, Houston, U.S.A., pp. 173–183 (1988).
10. Epstein, M., Fauske, H.K., Applications of the Turbulent Entrainment Assumption to Immiscible Gas-Liquid and Liquid-Liquid Systems, Trans. Institute of Chemical Engineers, Vol. 79, Part A, pp. 453-462 (2001).
11. Bang, K.H., Kim, H.T., Tan, V.D, Experiment and Modeling of Jet Breakup in Fuel-Coolant Interactions, Annals of Nuclear Energy, 118, pp. 336-344 (2018).
12. Magallon, D., Characteristics of corium debris bed generated in large-scale fuel-coolant interaction experiments, Nuclear Engineering and Design, 236, 1998-2009 (2006).
13. Epstein, M., Fauske, H.K., Steam film instability and the mixing of core-melt jets and water. ANS Proc. National Heat Transfer Conf., Denver, pp. 277-284 (1985).
14. Bang, K.H., Kumar, R., Kim, H.T., Modeling corium jet breakup in water pool and application to ex-vessel fuel-coolant interaction analyses, Nuclear Engineering and Design, 276, pp. 153-161 (2014)
15. Bromley, L.A., Heat Transfer in Stable Film Boiling, Chem. Eng. Prog. Ser. 46, 221-227 (1950).
16. Bang, K.H., Numerical prediction of forced convection film boiling heat transfer from a sphere, Int. J. Heat Mass Transfer, 37, pp. 2415-2424 (1994).

Advancing the Jet Breakup Length Model for Fuel-Coolant Interactions in Light Water Reactors

Kwang-Hyun Bang[1)] and Eunho Kim[2)]

[1)]Tetras Co. & Korea Maritime and Ocean Univ.

[2)] Korea Institute of Nuclear Safety

The 12th Conference on Severe Accidents Research (ERMSAR 2026)

Madrid, Spain, May 18-22, 2026

Contents

- Introduction to ex-vessel coolability
- Review of Jet Breakup Length Models
- Advanced Jet Breakup Length Model
- Numerical Modeling of Film Boiling
- Conclusions

PWR Ex-Vessel Cooling Strategy

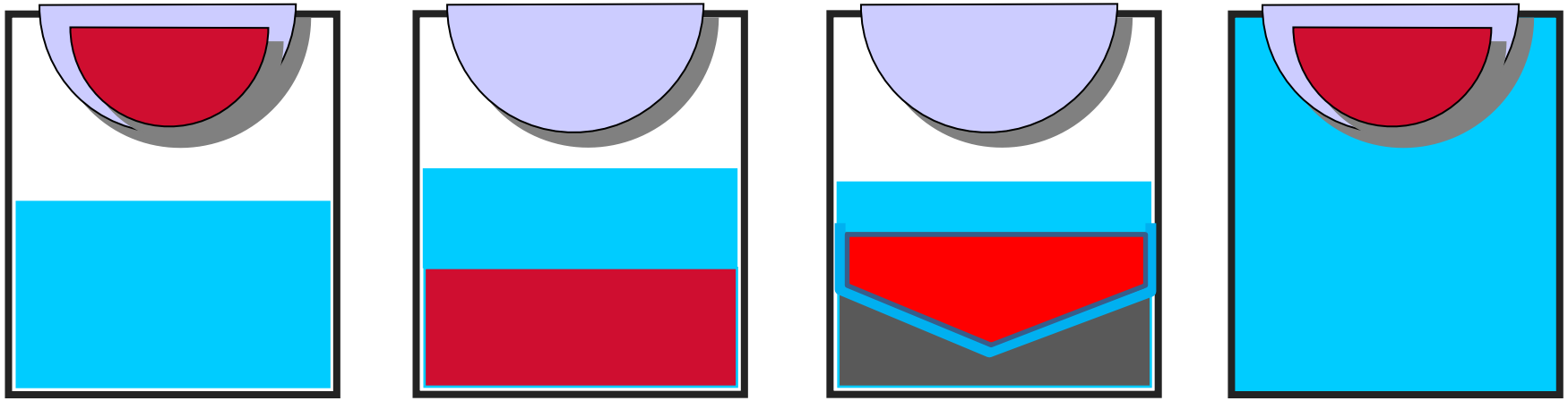

Pre-Flooding	Post-Flooding	Core Catcher	IVR-ERVC
System 80+	MACE/ACE	EPR	AP600
APR1400		EU-APR	(APR1400)
Debris bed	Less FCI risk	No MCCI	No E.V. risk
FCI risk	MCCI	High cost	Success?

Pre-Flooding & FCI

- Corium jet breaks up into particles in pre-flooded cavity.
- Debris bed of particles larger than 3 mm is likely coolable if the bed height is low (<~0.3 m).
- Steam explosion may occur,

  but the impulse must be low

  enough not to fail cavity.

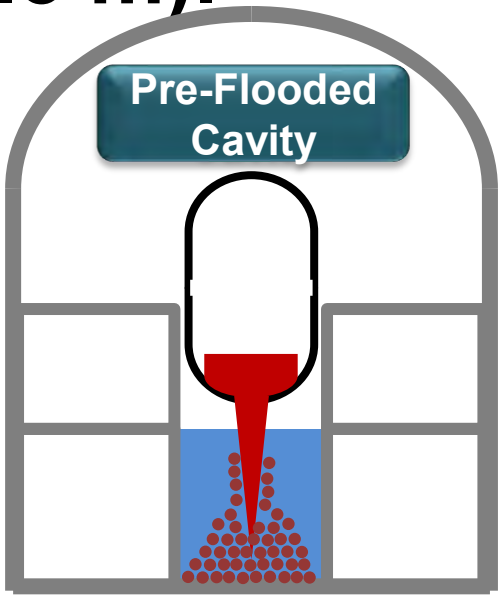

Ex-Vessel Corium Jet

- **Amount of corium jet breakup has been a key to ex-vessel coolability as well as steam explosion intensity.**
- **Spreading, particle size, and debris bed geometry are also concern.**

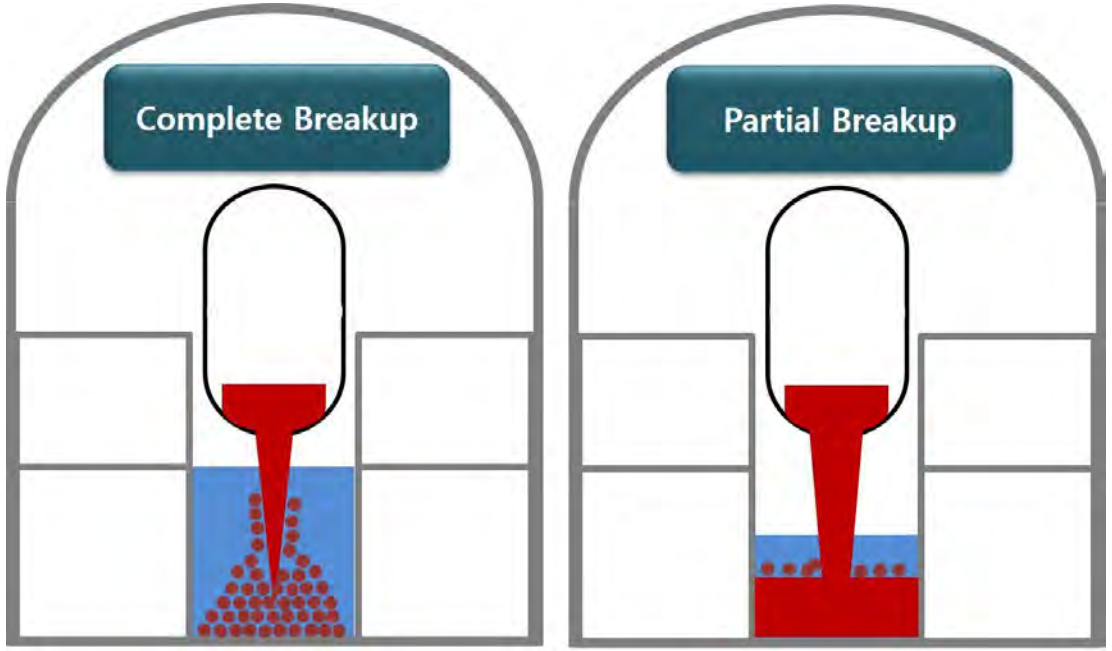

Research Objectives

- Evaluate the performance of jet breakup length models
- Develop a jet breakup length model with account of vapor film between melt and coolant
- Numerical calculation of vapor film thickness

Melt Jet Breakup Study

- **A number of experimental studies on melt jet breakup worldwide**

Corium, ~2900°C
(TROI, KAERI)

Oxides, ~1100°C
(DEFOR, KTH)

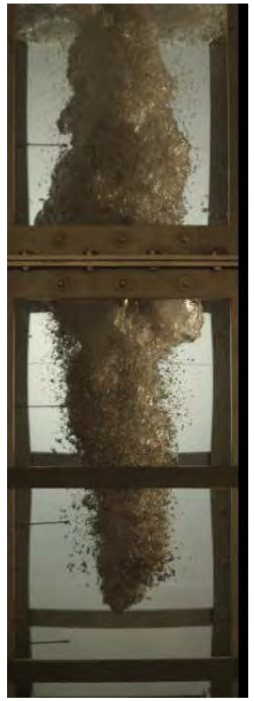

Sn-Bi, ~300°C
(MATE, POSTECH)

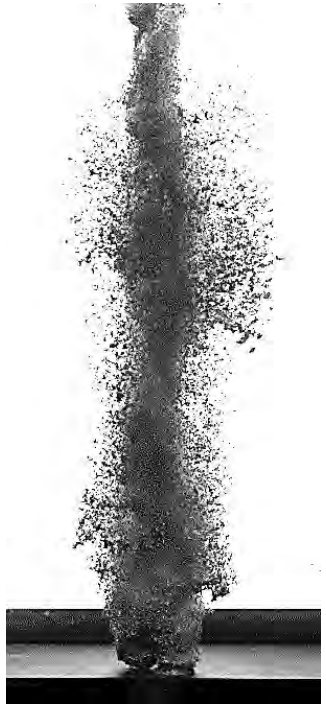

Woods metal, 85°C
(COLDJET, KMOU)

Jet Breakup Modeling

- Jet breakup length correlation
  - Saito et al.
  - Epstein and Fauske
  - Simple, but semi-empirical
- Physics-based modeling
  - Viscous stress induced: boundary layer stripping
  - Instability induced: Rayleigh-Taylor, Kelvin-Helmholtz
  - Inertia exchange: drop breakup
  - FCI codes have their own modeling approach
  - Complex transient phenomenon involving boiling

Saito et al. Model

- Study jet penetration for water/R-11 and water/LN2
- R-11: ρ~1476 kg/m^3, T_B=23.8°C, D_j=5~40 mm
- LN2: ρ~806 kg/m^3, T_B=-196°C, D_j=5 mm
- Propose a '**penetration length**' correlation

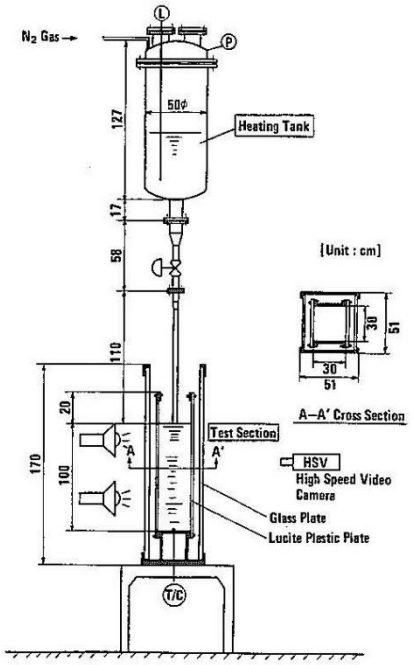

$$L_{brk}/D_j = 2.1\left(\frac{\rho_j}{\rho_\infty}\right)^{1/2}\frac{u_j}{\sqrt{gD_j}}$$

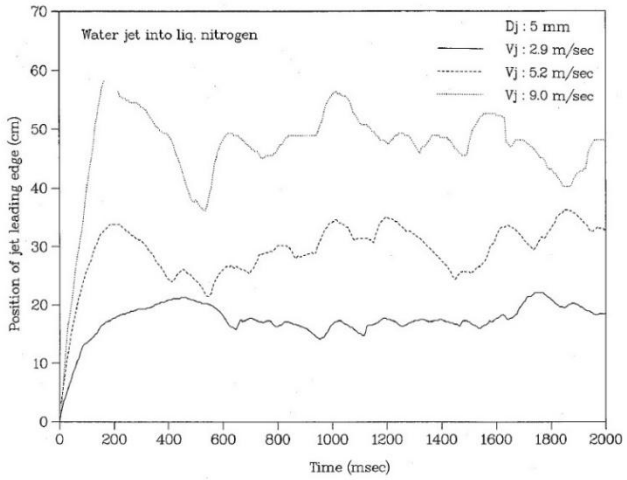

Epstein & Fauske Model

- Turbulent entrainment of hot gas in air (Taylor, 1945)
- Ricou & Spalding (1961) added density ratio.
- Kelvin-Helmholtz instability theory

$$v_{en} \sim \frac{\pi^2}{8\sqrt{3}} \left(\frac{\rho_\infty}{\rho_j}\right)^{1/2} u$$

- Tests of high speed (~100 m/s) water jet in air (1~40 bars) showed that jet velocity has little effect on jet breakup length.

$$L_{brk} = t_{brk} u = \frac{D_j/2}{v_{en}} u = \frac{D_j/2}{E_o \left(\frac{\rho_\infty}{\rho_j}\right)^{1/2} u} u = \frac{1}{2E_o} D_j \left(\frac{\rho_j}{\rho_\infty}\right)^{1/2}, E_o = 0.05\sim0.1 \; from \; data$$

Comparison of Two Models

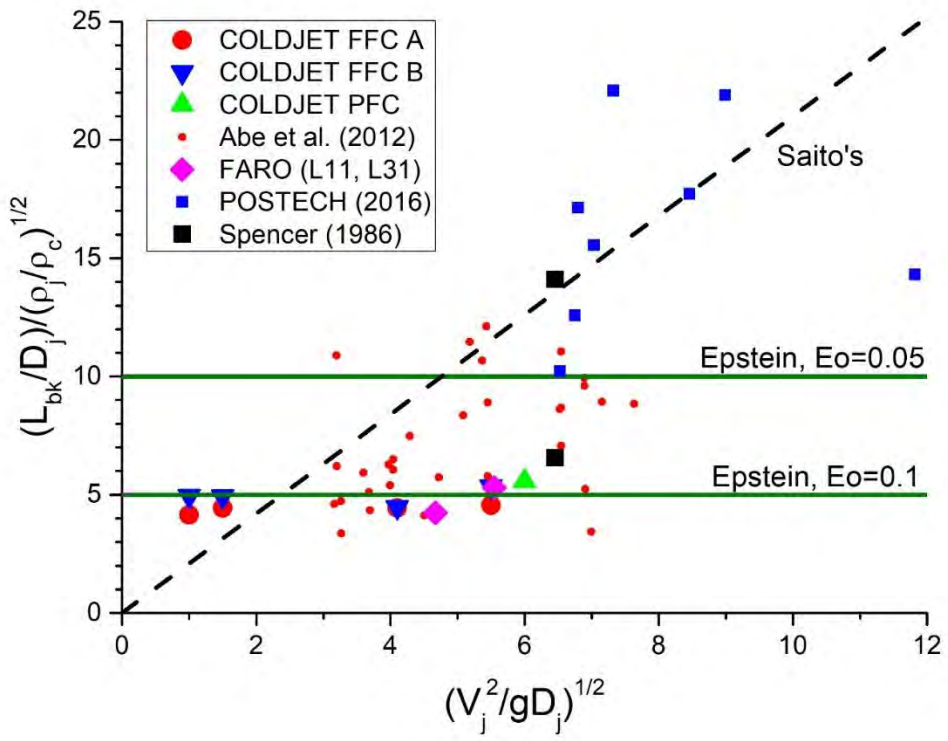

Saito's

$$\frac{L_{brk}}{D_j} = 2.1\left(\frac{\rho_j}{\rho_c}\right)^{1/2}\left(\frac{V_0}{gD_j}\right)^{1/2}$$

Epstein's

$$\frac{L_{brk}}{D_j} = \frac{1}{2E_0}\left(\frac{\rho_j}{\rho_c}\right)^{1/2}$$

- **It appears that Epstein model is good for high temperature corium (film boiling) or cold melt (no boiling), while Saito model is good for moderate temperature melts (probably nucleate boiling).**

Recent Work (KTH, 2022)

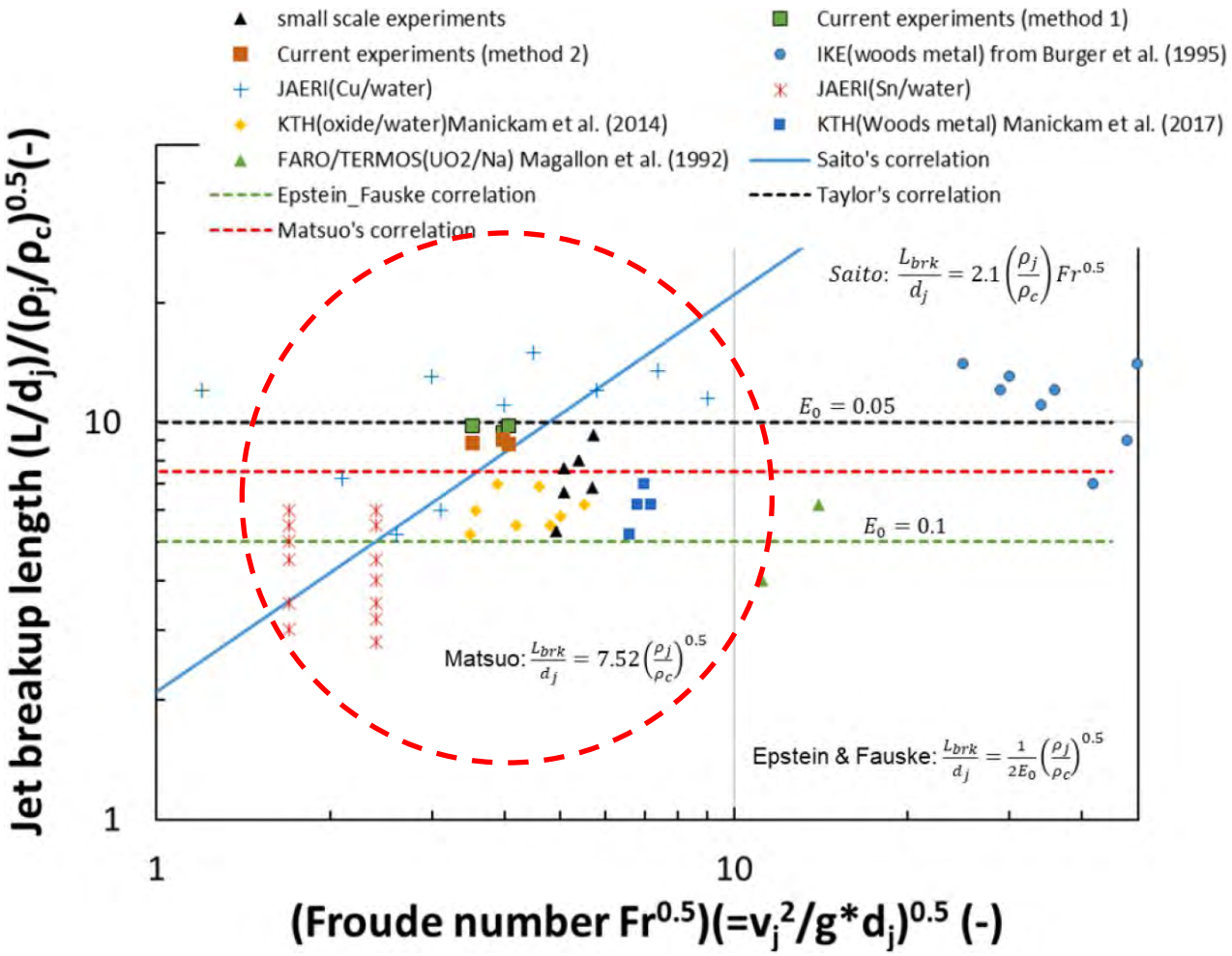

Prediction of FARO Data

	L-06	L-08	L-14	L-19	L-20	L-24	L-28	L-33
Pressure, MPa	5.0	5.8	5.0	5.0	2.0	0.5	0.5	0.4
Melt mass, kg	18	44	125	157	96	176	175	100
Melt temperature, K	2923	3023	3123	3073	3173	3023	3052	3070
Melt release dia., mm	100	100	100	100	100	100	50	50
Free fall distance, m	1.83	1.53	1.04	1.99	1.12	1.07	0.89	0.77
Water depth, m	0.87	1.00	2.05	1.10	1.97	2.02	1.44	1.60
Melt jet length, m	0.31	0.77	2.18	2.74	1.67	3.07	12.2	6.98
Water temperature, K	539	536	537	537	485	425	424	293
Cake mass, kg	6	14	20	80	21	27	77.4	8.8
Debris mass, kg	12	30	105	77	75	141	84	89
(% of total mass)	(67)	(68)	(84)	(51)	(78)	(84)	(52)	(92)
Ave. debris size, mm	4.5	3.8	4.8	3.7	4.4	2.6	3.0	2.6
Saito's prediction (%)								
void fraction = 0.0	87	94	100	96	100	100	100	100
void fraction = 0.3	79	86	100	90	100	100	100	100
Epstein's prediction (%)								
void fraction = 0.0	98	100	100	100	100	100	100	100
void fraction = 0.3	92	96	100	99	100	100	100	100

Note: Kudinov et al. (NED, 2013) considered "cake" as "agglomerated mass."

Pool Depth vs. Jet Length

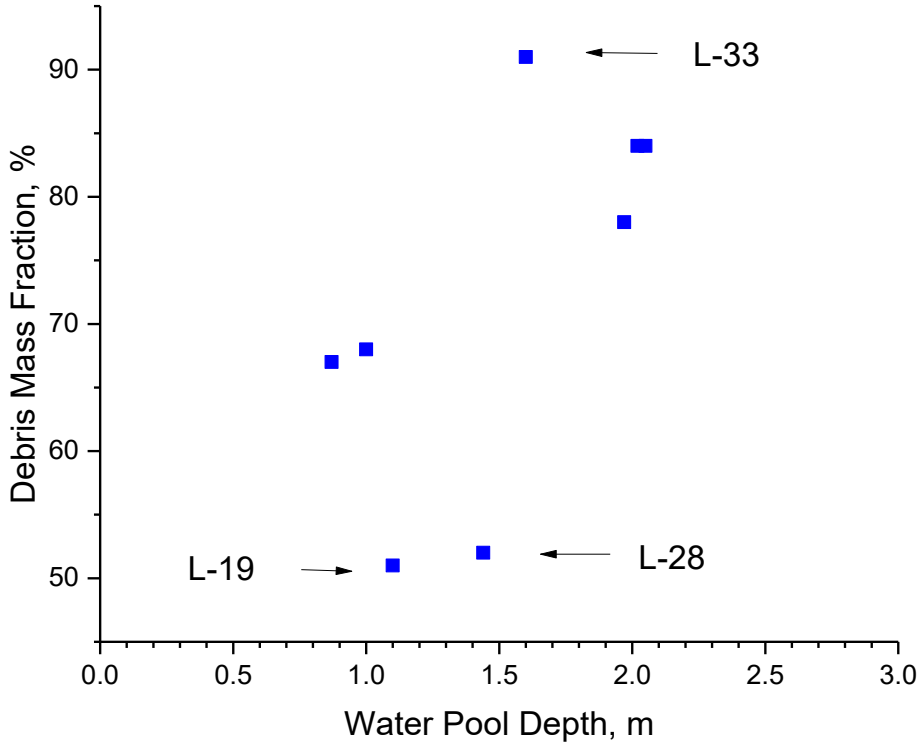

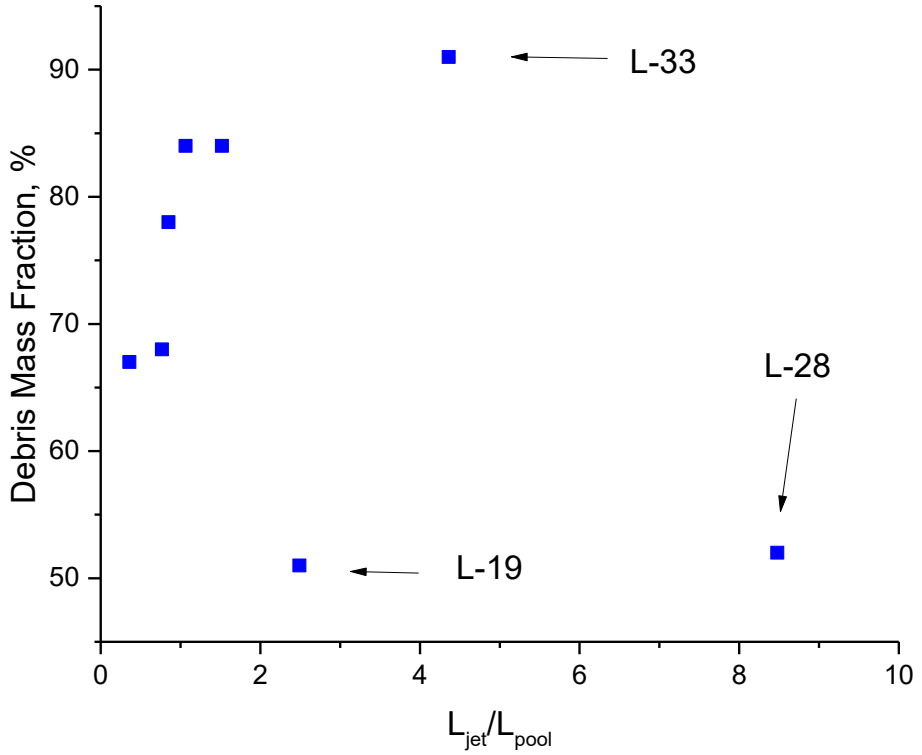

L-19: Longer free fall in low pool depth
L-28: Long melt pouring time (~5 s) by reduced jet diameter (10 cm → 5 cm)
L-33: Triggered explosion when 25% melt entered.

Prediction of FARO Debris Mass

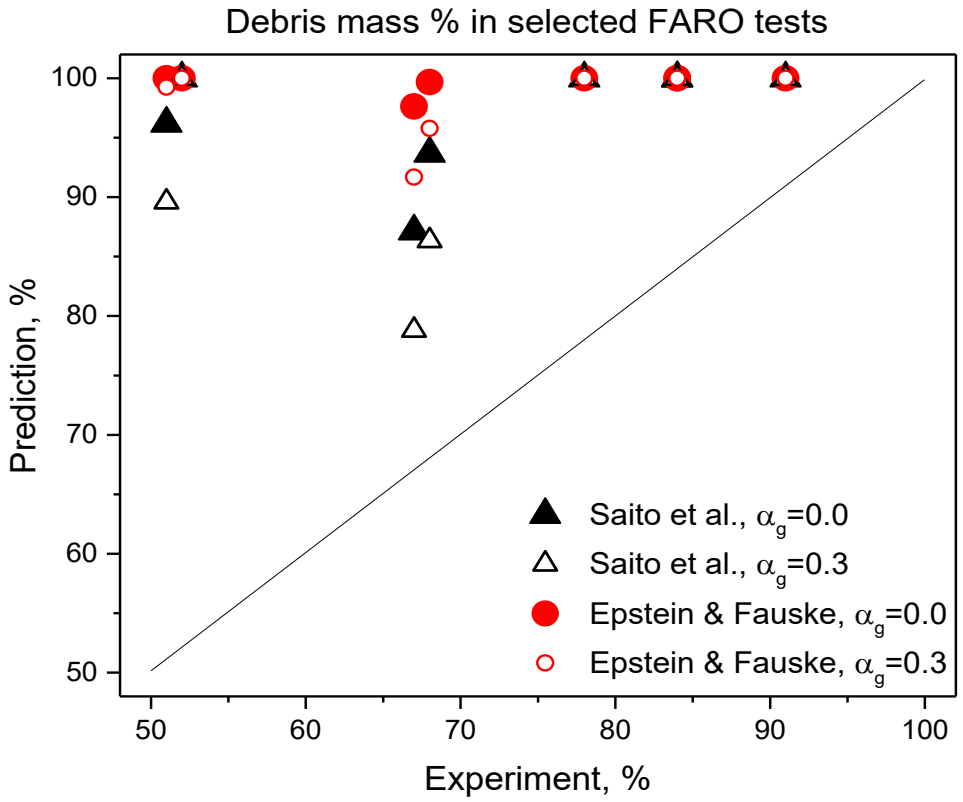

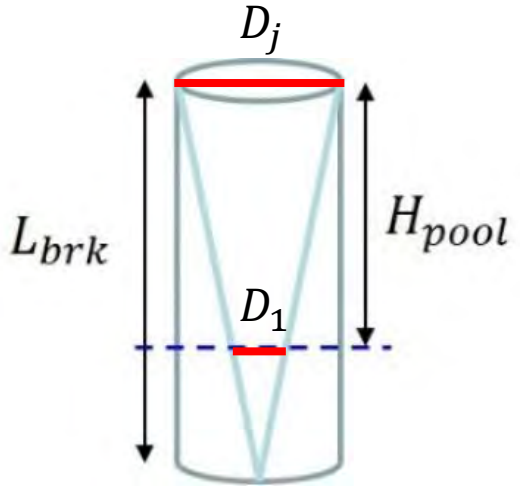

$$\alpha_{debris} = 1 - \left(\frac{D_1}{D_j}\right)^2 = 1 - \left(1 - \frac{H_{pool}}{L_{brk}}\right)^2$$

Note: re-melting or agglomeration could occur in FARO, but these are not accounted for in this analysis, nor clearly identified in FARO posttest debris.

Account of Vapor Film

- **Epstein & Fauske proposed melt-vapor-water KHI model (1985)**
- **Complex dispersion equation: unable to obtain analytic solution for k_D and n_D**

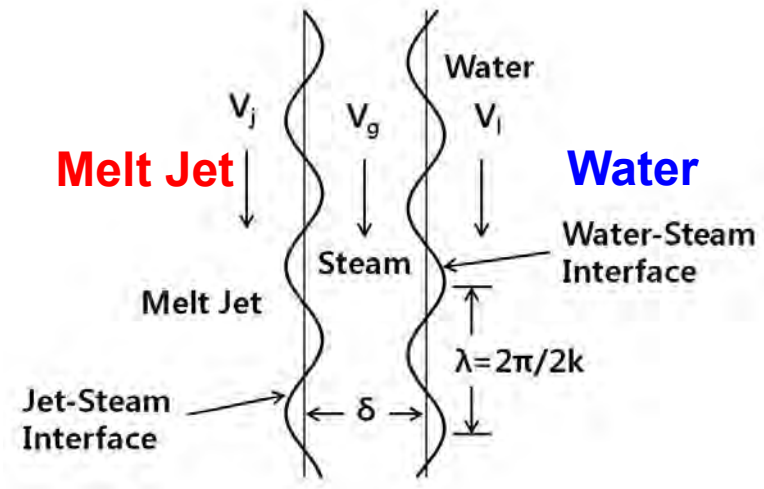

$$\eta \sim e^{ikx+nt}$$

$$[\rho_g(n+ikV_g)^2+\{\rho_l(n+ikV_l)^2+\sigma_l k^3\}$$
$$\cdot\tanh(k\delta)]\cdot[\rho_j(n+ikV_j)^2+\sigma_j k^3]$$
$$+\rho_g^2(n+ikV_g)^4\tanh(k\delta)$$
$$+\rho_g(n+ikV_g)^2[\rho_l(n+ikV_l)^2+\sigma_l k^3]=0$$

Numerical Solutions for k_D, n_D

k_D: Fastest growing wave number

n_D: Growth constant corresponding to k_D

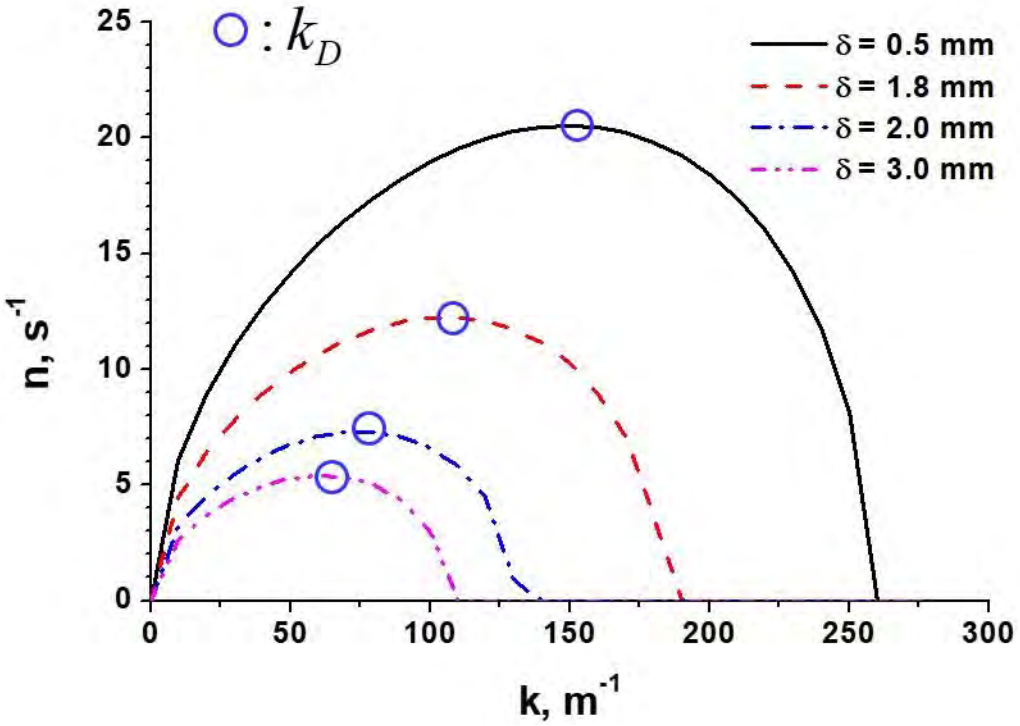

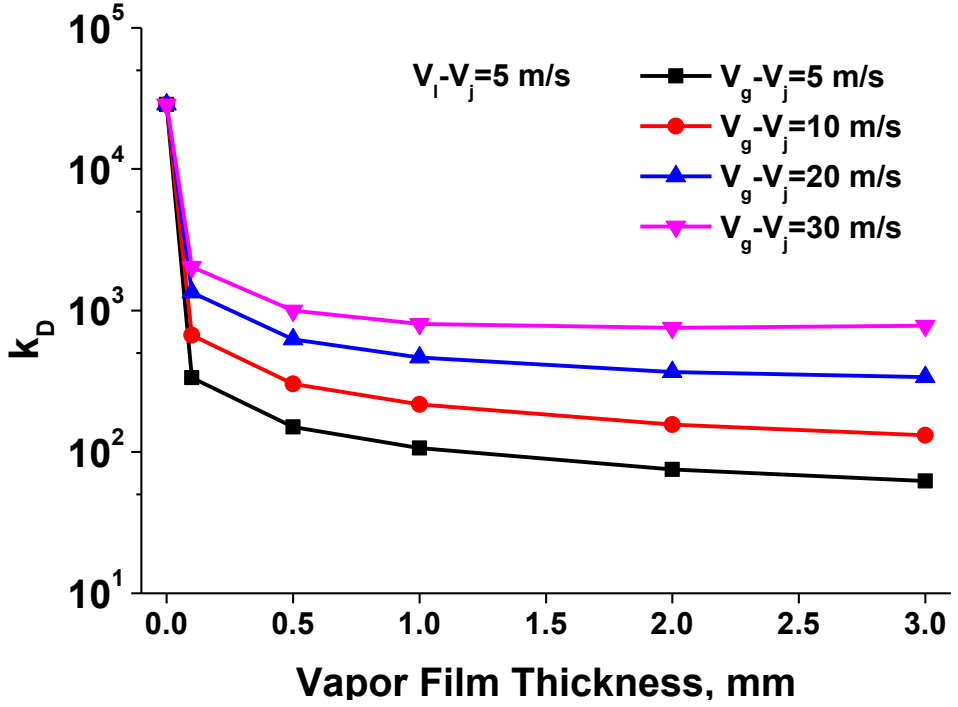

(Bang et al., NED, 2014)

Correlated Numerical Solutions

$$\frac{k_D}{k_{D,\infty}} = 1 + \frac{1}{\frac{k_{D,\infty}}{k_{D,o}} + 25\left(V_g - V_j\right)^{1.5}\delta + \left(k_{D,\infty}\delta\right)^2}$$

$$\frac{n_D}{n_{D,\infty}} = 1 + \frac{1}{\frac{n_{D,\infty}}{n_{D,o}} + 5\left(V_g - V_j\right)^{1.5}\delta + 100\left(n_{D,\infty}\delta\right)^2}$$

Thin vapor film: (kδ→0)

$$k_{D,o} = \frac{2\,\rho_j\,\rho_l\left(V_l - V_j\right)^2}{3\left(\rho_j + \rho_l\right)\left(\sigma_j + \sigma_l\right)}$$

$$n_{D,o}^2 = \frac{\rho_j\,\rho_l k_{D,o}^2\left(V_l - V_j\right)^2}{\left(\rho_j + \rho_l\right)^2} - \frac{\left(\sigma_j + \sigma_l\right)k_{D,o}^3}{\left(\rho_j + \rho_l\right)}$$

Thick vapor film: (kδ→∞)

$$k_{D,\infty} = \frac{2\,\rho_j\,\rho_g\left(V_g - V_j\right)^2}{3\left(\rho_j + \rho_g\right)\sigma_j}$$

$$n_{D,\infty}^2 = \frac{\rho_j\,\rho_g k_{D,\infty}^2\left(V_g - V_j\right)^2}{\left(\rho_j + \rho_g\right)^2} - \frac{\sigma_j k_{D,\infty}^3}{\left(\rho_j + \rho_g\right)}$$

Jet Breakup Length with δ_{film}

- **Beginning from Epstein & Fauske model, a new jet breakup length model has been developed with account of vapor film thickness.**
- **Yet, it requires the information on vapor film thickness.**

$$v_{en} \sim \frac{\pi}{16}\left(\frac{\lambda_D}{\tau}\right) \qquad \tau \sim \frac{1}{n_D} \qquad \lambda_D = \frac{2\pi}{k_D}$$

$$L_{brk} = V_j \cdot \left(\frac{D_j}{2}\right) / v_{en} \quad \rightarrow \quad \frac{L_{brk}}{D_j} = \frac{1}{2\sqrt{3}E_o} V_j \left(\frac{k_D}{n_D}\right)$$

Prediction of FARO Data

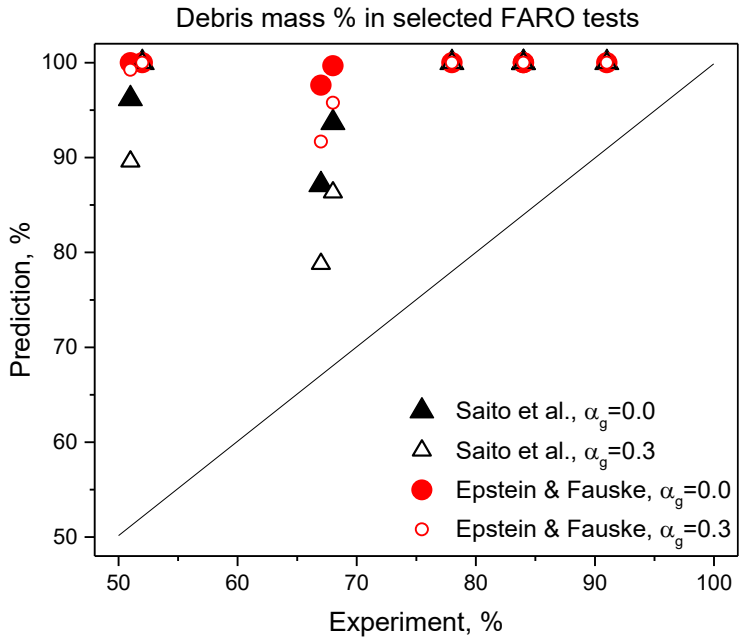

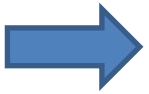

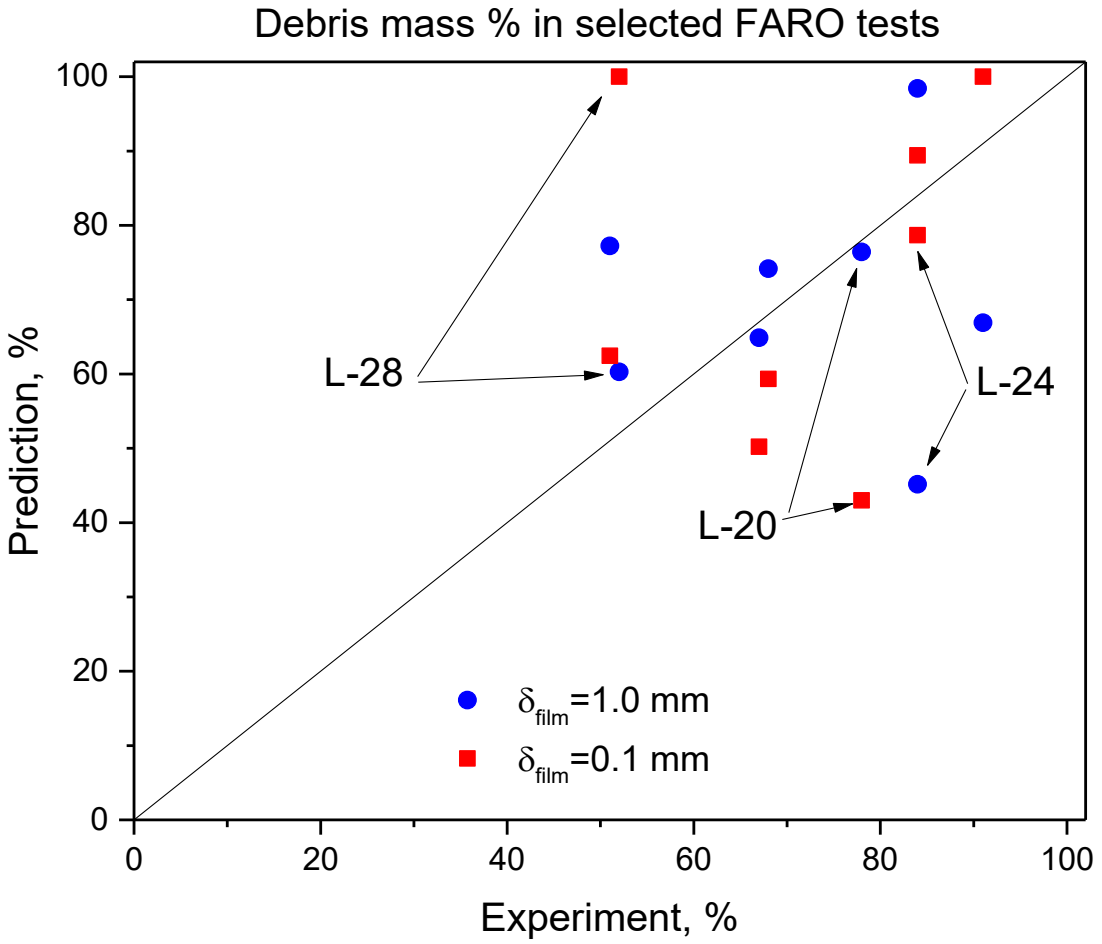

δ_{film} Effect

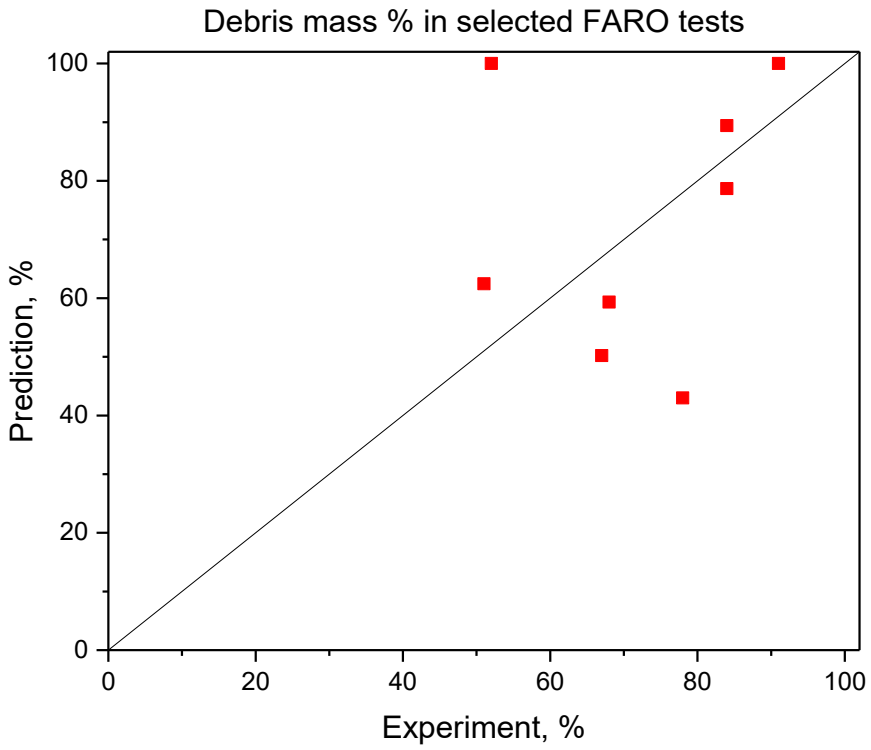

δ_{film}=0.1 mm

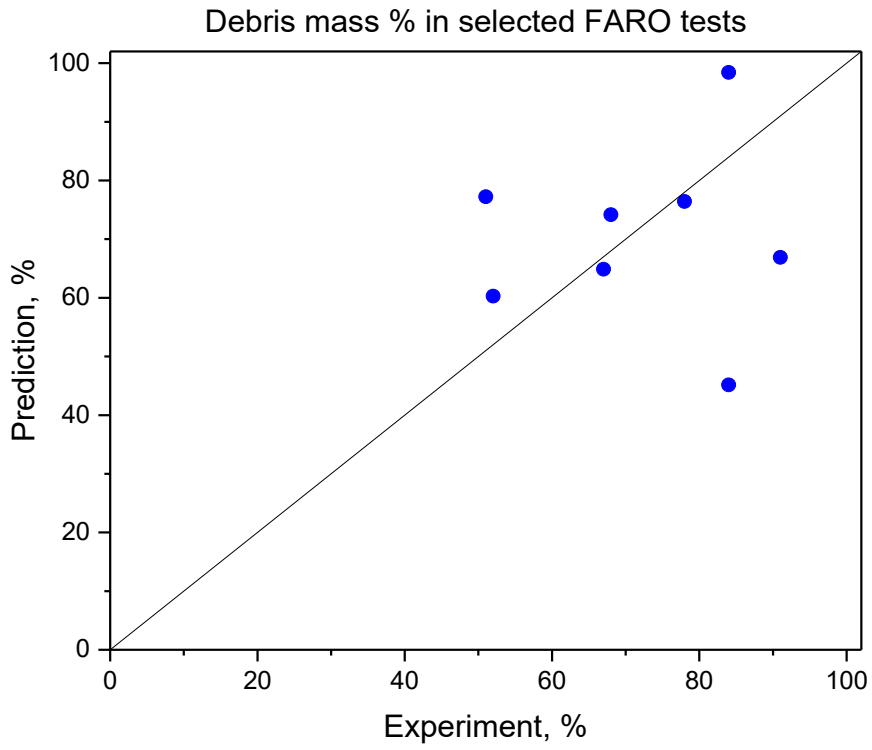

δ_{film}=1.0 mm

Estimation of Reactor Case

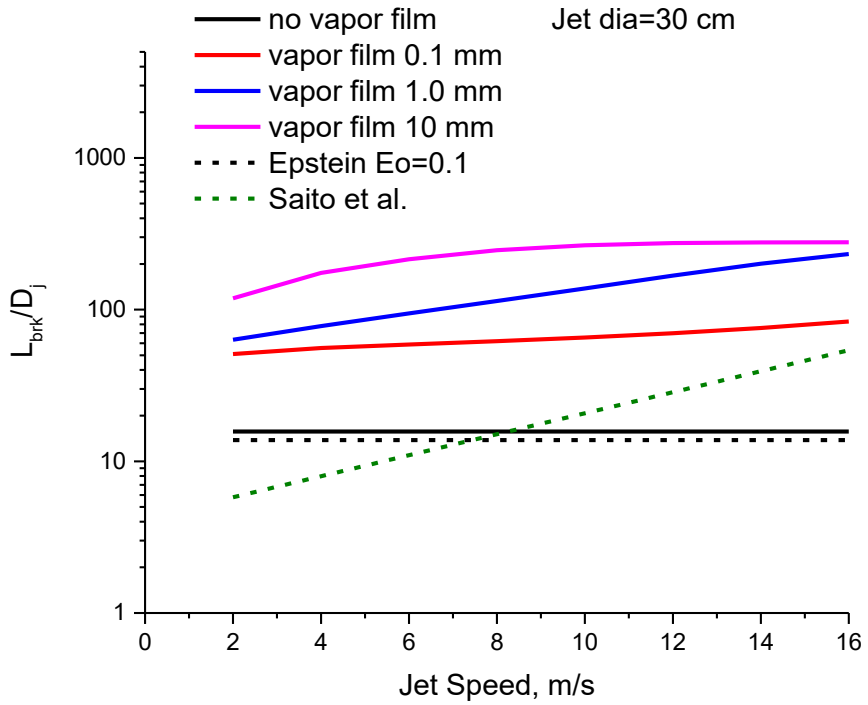

Jet Breakup Length

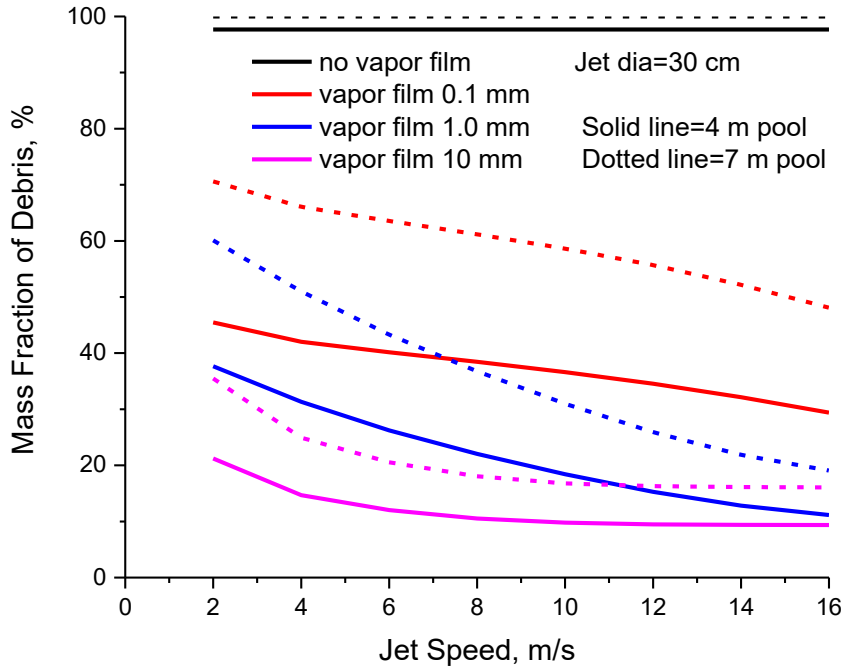

Debris Mass

With just 1.0 mm thick vapor film, the jet breakup length is longer than 50 times the jet diameter: 15 m for 0.3 m dia. Jet.

Vapor film thickness and vapor velocity are important parameters.

Film Boiling Model

- **Jet diameter >> vapor film thickness : vertical flat surface approx.**
- **Since Bromley analysis (1950) for saturated liquid, information on vapor film thickness is scares.**

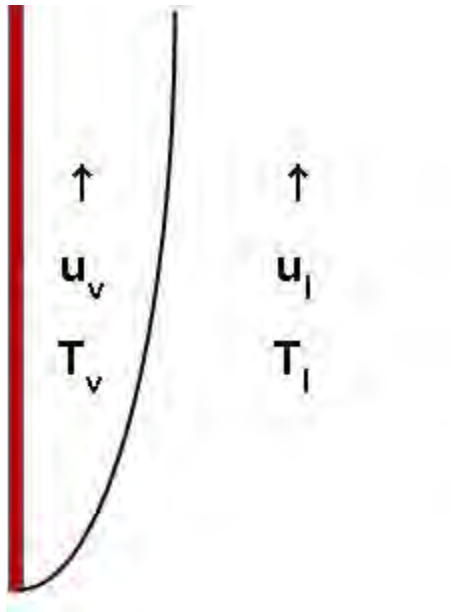

Vapor

$$u\left(\frac{\partial u}{\partial x}\right)+v\left(\frac{\partial u}{\partial y}\right)=\nu_v\left(\frac{\partial^2 u}{\partial y^2}\right)+g_0\frac{\rho_l-\rho_v}{\rho_v}$$

$$u\left(\frac{\partial T}{\partial x}\right)+v\left(\frac{\partial T}{\partial y}\right)=\alpha_T\left(\frac{\partial^2 T}{\partial y^2}\right)$$

Liquid

$$u\left(\frac{\partial u}{\partial x}\right)+v\left(\frac{\partial u}{\partial y}\right)=\nu_l\left(\frac{\partial^2 u}{\partial y^2}\right)$$

$$u\left(\frac{\partial T}{\partial x}\right)+v\left(\frac{\partial T}{\partial y}\right)=\alpha_T\left(\frac{\partial^2 T}{\partial y^2}\right)$$

Major assumptions:

- **Boundary layer flow**
- **Laminar flow**
- **Smooth interface**

Similarity Transformation

$$f''' + \left[\frac{1}{2}\right] f f'' = \left[-\left(\frac{Gr_x}{Re_x^2}\right)_{vap} \right]$$

$$\theta'' + Pr_v \left[\left(\frac{1}{2}\right)\right] f\ \theta' = 0$$

$$F''' + \left[\frac{1}{2}\right] F F'' = [0]$$

$$\Theta'' + Pr \left[[0] + \left[\left(\frac{1}{2}\right)\right] F \right] \Theta' = [0]$$

Interfacial Conditions

$$F'(0) = f'(\eta_\delta)$$

$$F''(0) = \sqrt{\frac{\rho_v \mu_v}{\rho_l \mu_l}}\, f''(\eta_\delta)$$

$$F(0) = \sqrt{\frac{\rho_v \mu_v}{\rho_l \mu_l}}\, f(\eta_\delta)$$

$$\frac{Ja_v}{Pr_v}[-\theta'] - \frac{Ja_l}{Pr_l}[-\Theta'] \sqrt{\left(\frac{\rho_l \mu_l}{\rho_v \mu_v}\right)} + \frac{[Nu_r]}{\sqrt{([Re_v])}} \left(\frac{Ja_v}{Pr_v}\right) = \left[x \frac{\partial \eta_\delta}{\partial x} \right] f' + \frac{1}{2} f$$

Solution for T_s=500°C, V_j=4 m/s

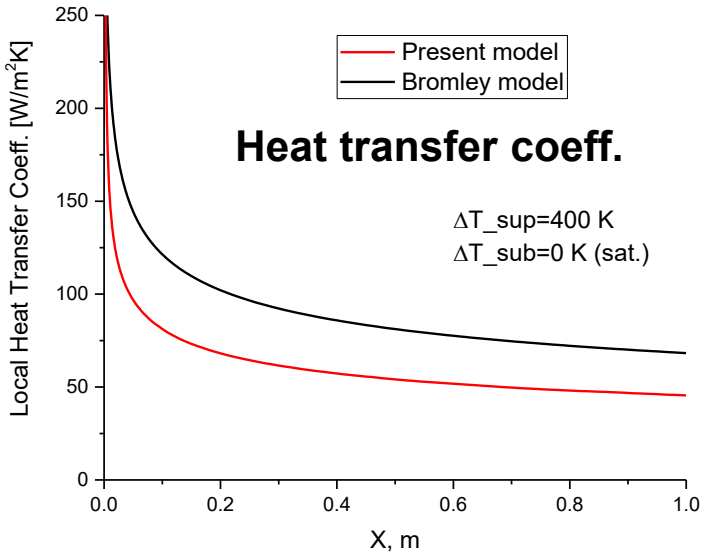

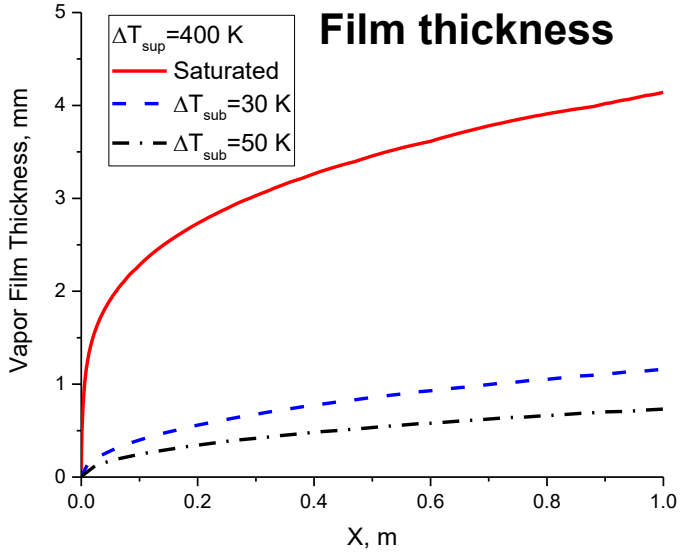

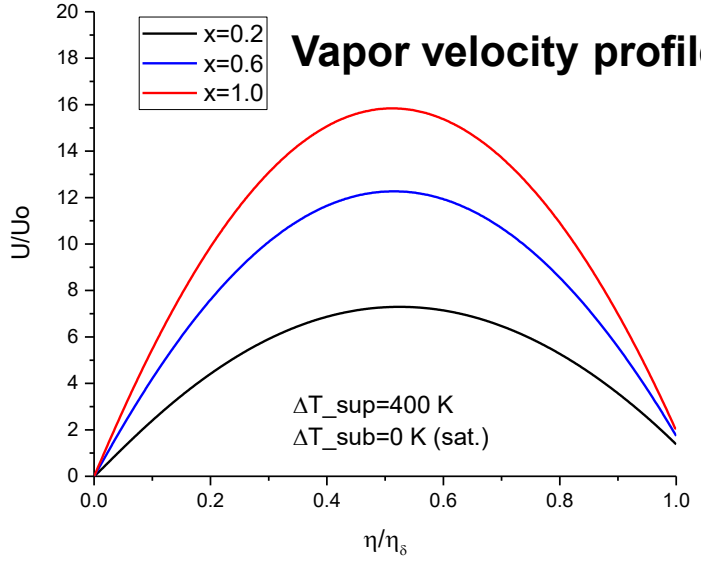

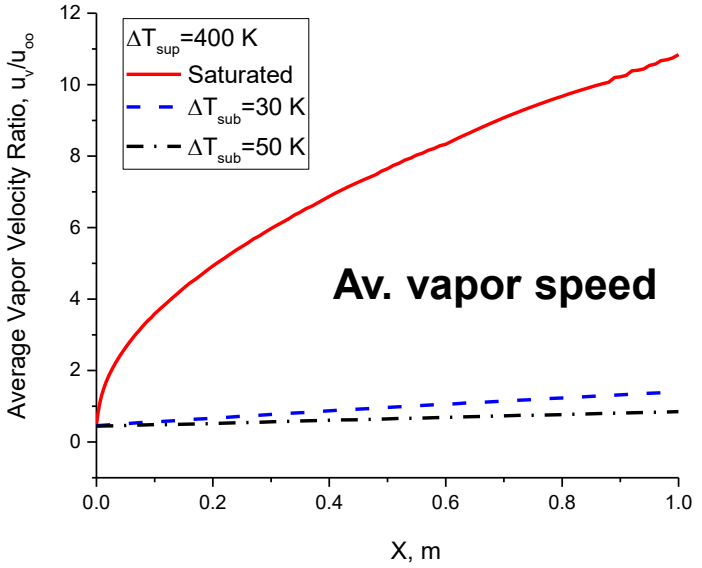

Solution for T_s=2100°C, V_j=4 m/s

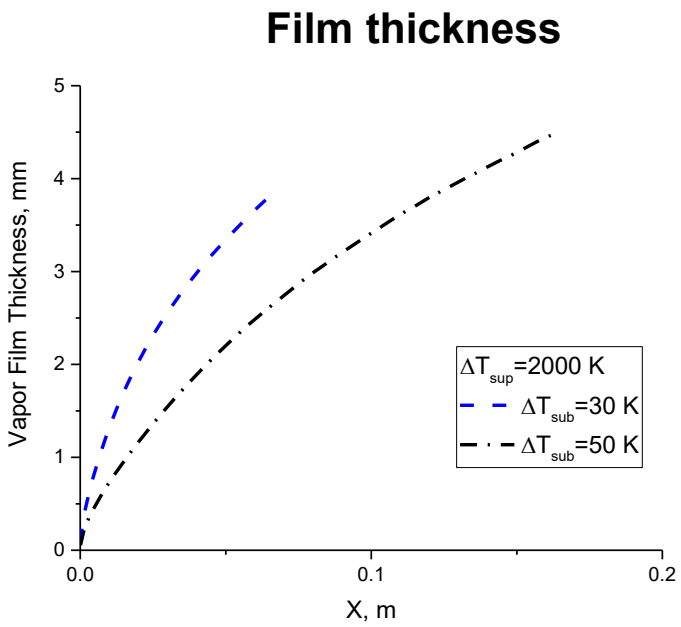

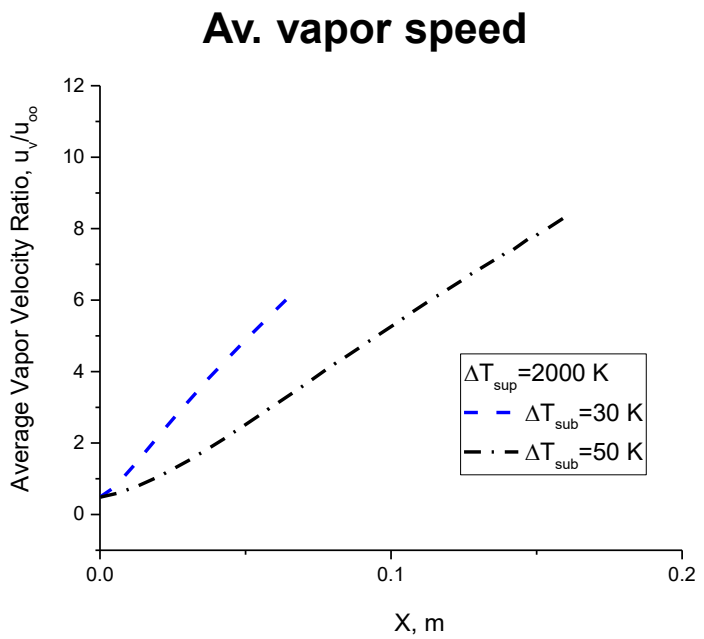

- For high temperature surface, vapor film grows much thicker and numerical convergence failed, possibly due to the assumption of laminar flow.
- If jet breakup discontinues vapor film flow, the vapor film thickness on the first short length (~0.1 m) would be relevant.

Conclusions

- Amount of corium jet breakup in ex-vessel is a key to corium coolability and MCCI as well as steam explosion intensity.
- Existing jet breakup length models tend to overpredict debris mass of FARO data.
- A new formulation of jet breakup length is proposed by taking account of vapor film.
- Existence of vapor film on the corium jet surface increases significantly the jet breakup length.
- Film boiling on vertical plate has been modeled and solved for vapor film thickness.

COCOSYS simulation of CsI decomposition under irradiation and the formation of organic iodide in the containment

Chuanhe Lu*, Holger Nowack
Gesellschaft für Anlagen- und Reaktorsicherheit (GRS)
D-50667 Cologne, Germany
chuanhe.lu@grs.de; holger.nowack@grs.de

ABSTRACT

Iodine is one of the most hazardous fission products (FP) released to the containment of a nuclear power plant during a severe accident. The metallic iodide aerosol CsI is one of the main airborne iodine species in the containment and the CsI decomposition with formation of gaseous iodine species is a primary concern in nuclear accident scenarios. The thermal and radiolytic decomposition of CsI generates molecular iodine, which can further react with organic compound and form the organic iodide. In this paper the AC^2/COCOSYS code is applied to simulate and analyze the CsI decomposition and related iodine aerosol transport in the containment of LOCOV tests. The LOCOV experiment in the French EPICUR facility studied the decomposition of deposited CsI aerosol and the reactivity of I_2(g) with methane to quantify the organic iodide formation rate in the presence of volatile organic compounds (VOC) [1]. The COCOSYS simulation investigates the decomposition of CsI aerosol, the organic iodide formation and the distribution of the different iodine species across the coupon, the atmosphere, the vessel walls and the filter. The simulation results of LOCOV model show that the thermal decomposition of CsI is very slow, but a fast decomposition of CsI is observed under irradiation. The injected methane reacts with I_2 and organic iodide is generated, while the oxidation of I_2 with ozone produces iodine oxide aerosol IO_x. The gas phase I_2 in vessel deposits on the surfaces of vessel wall. With the time going on, the deposited I_2 reacts with Fe. Higher dose rates caused higher CsI decomposition and RI generation rates. The comparisons between simulation results and measurements show the modelling capabilities of organic iodide formation with COCOSYS in two LOCOV tests.

KEYWORDS
CsI decomposition, organic iodide, aerosol, irradiation

1. INTRODUCTION

Iodine is one of the most hazardous fission products (FP) released to the containment during a severe nuclear reactor accident. The evolution of volatile iodine concentration is determined by a balance between formation and deposition processes [2-4]. Volatile molecular iodine (I_2) can be produced from the iodine deposited on painted surfaces or from suspended aerosols [2-5]. The organic iodide compounds (RI) can be produced from iodine deposited on painted surfaces or reaction between iodine and organic gas, like methane [1-12]. The low-molecular-weight RI is harder to trap for the filter, making it more likely to be released into the environment. It makes the studies of volatile molecular iodine release and RI formation very important in the severe accident management.

The metallic iodide aerosol CsI is one of the main airborne iodine species in the containment and the CsI decomposition with formation of gaseous iodine species is a primary concern in nuclear accident scenarios [1, 7, 13]. The CsI decomposition process can be affected by many parameters. The AER-CsI test series in

the STEM-EPICUR program studies the behavior of CsI aerosols deposited on different surfaces of the containment and the ability to produce volatile iodine species [1]. The effects of various experimental parameters on the iodine species releases were evaluated: initial CsI concentration on the coupon, relative humidity, temperature, dose rate and nature of the coupon surface (stainless steel, quartz or EPOXY paint). The extensive experiment program STEM-EPICUR has been performed to obtain data concerning iodine volatilizations.

STEM-EPICUR program also investigated the formation of organic iodide from the painted surface in the containment atmosphere under various conditions [4, 6]. The initial concentration of iodine deposited on the painted coupon and the relative humidity were found to have significant impacts on the volatilization of organic iodide [6]. The ESTER-EPICUR tests investigated the iodine chemistry within the containment, focusing on the RI formation pathways not involving paints [14]. Specifically, the LOCOV tests examined reactivity under gamma irradiation on metal surfaces, such as electropolished stainless and galvanized steel, within an oxygen-depleted atmosphere containing organic gases (CH_4). The effects of methane, ethylene, surface, species and dose rate are checked through different tests.

The advanced iodine model (AIM), part of the AFP2 module in the AC^2-COCOSYS containment code, was developed to simulate aerosols, fission products and iodine chemistry [15-17]. Within AFP2, the CsI decomposition rate is calculated based on the dose rate, available CsI mass and a 'damage term' that accumulates proportionally to radioactivity, and a model dependent recovery rate. The recovery rate serves to buffer both the acceleration and deceleration of the decomposition process. In this study, COCOSYS is utilized to simulate CsI decomposition, RI formation, and the resulting distribution of iodine species across the coupons, atmosphere, vessel walls, and filters as investigated in the LOCOV and LOCOV2 tests.

2. Model Setup

The LOCOV and LOCOV2 tests utilized steel coupons as substrates for CsI deposits within a containment vessel. While the LOCOV test employed electropolished stainless steel with an initial iodine concentration of 1.86×10^{-4} mol/m^2, the LOCOV2 test used galvanized steel with a concentration of 1.60×10^{-4} mol/m^2 (see Table 1).

Table I. Experimental setups of LOCOV and LOCOV2

Test	LOCOV	LOCOV2
Coupon	Electropolished stainless steel	Galvanized steel
Aerosol	CsI	CsI
CsI concentration (mol/m^2)	$1.86\text{x}10^{-4}$	$1.60\text{x}10^{-4}$
Temperature (°C)	120	120
Pressure (bars)	3.5	3.5
Pre-irradiation	1 hour with dry air	1 hour with dry air 3 hours with wet air 50% R.H.
Irradiation	43 hours with Air (3% O_2) + 2% CH_4 + 50% R.H.	
Post-irradiation	1 hour with dry air (3% O_2) + 2% CH_4	
Dose rate (kGy/h)	1.2	6.9

Compared with LOCOV test, LOCOV2 test was performed with higher dose rate. The experiment is performed with continuous air flow that is directed through the vessel and released over a filter line in which the released chemical iodine components are trapped and analyzed according to the chemical compositions

that are separated in the different stages of the used May-pack filters. The air temperature in vessel is 25 °C and the pressure is 3.5 bar; both stay constant during the experiments LOCOV and LOCOV2. There is 1-hour pre-irradiation sweeping phase and 1-hour post-irradiation sweeping phase with 8.72×10^{-6} kg/s dry air (3% O_2 + 2% CH_4) for LOCOV test. LOCOV2 has extra 3 hours of pre-irradiation wet air sweeping period after the one-hour dry air sweeping phase. The irradiation phase duration is about 44.3 hours with 50% R.H. air (3% O_2 + 2% CH_4), in which the air gas injection rate is 6.25×10^{-6} kg/s and water injection rate is 1.54×10^{-6} kg/s. The different volatile iodine species (I_2, IO_x, RI) released during the test are transferred to the May-pack device and trapped on the different filters. The conceptual setup of the tests is shown in Fig.1.

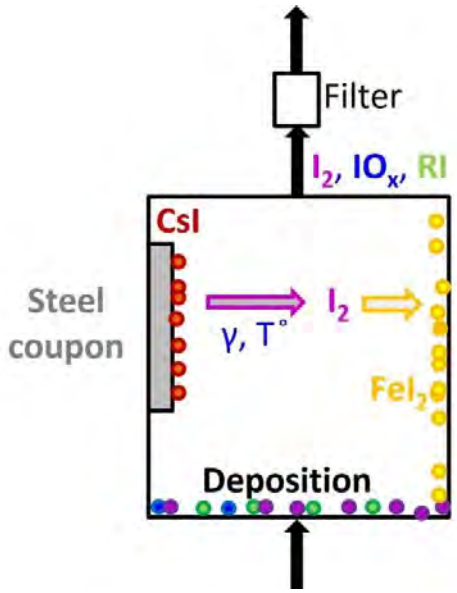

Figure 1. Conceptual model of LOCOV and LOCOV2 tests.

The principal reactions related to the CsI decomposition, RI formation and related iodine chemistry are shown in Fig. 2. In the iodine model AIM the decomposition of deposited CsI(dep) at the surface of coupon is simulated with two reactions that take place under irradiation: a faster reaction under irradiation with the production of I_2 and a slower reaction with the production of IO_x.

$$2\mathrm{CsI(dep)} + 2\mathrm{H_2O(g)} \xrightarrow{\gamma} \mathrm{I_2(g)} + 2\mathrm{CsOH(dep)} + 2\mathrm{H^+} \quad (1)$$

$$\mathrm{CsI(dep)} + \frac{1}{2}\mathrm{H_2O(g)} + \frac{x+0.5}{3}\mathrm{O_3(g)} \xrightarrow{\gamma} \mathrm{CsOH(dep)} + \mathrm{IO_x(g)} \quad (2)$$

A new conceptual model with a damage term is implemented for the CsI reaction under irradiation (Eq. 3). The idea behind the new model is to model the typical time dependent behavior of a delayed decomposition of CsI by introducing a damage term H (H for harm and to distinguish it from the dose D) in the reaction mechanism. The damage term accumulates proportional to the deposited mass, a model dependent recovery rate and the reaction rate of CsI:

$$\frac{dH}{dt} = m_{CsI} D_{gas} - H f_{rec} - \frac{\dot{r}}{m_{CsI}} H \quad (3)$$

The new CsI decomposition rate is then simply described as:

$$\frac{d[\mathrm{CsI}]}{dt} = -k_r^{\gamma} H \quad (4)$$

Where:

H	Damage term [kg·kGy/h]
m_{CsI}	Available CsI mass [kg]
D_{gas}	Dose rate [kGy/h]
f_{rec}	Recovery factor, which is a function of decomposition rate [1/s]
$\dot{r}$	Reaction rate of CsI [kg/s]
[CsI]	CsI concentration at the coupon surface [kg/ m^2]
k_r^{γ}	Radiolytic reaction coefficient [1/(m^2·kGy)]

Generally, the decomposition rate is high when there is more available CsI mass and the dose rate is high. At the beginning, there is more CsI available for reaction, so the decomposition rate will be high. As irradiation consumes more CsI, the amount available for reaction diminishes, leading to a decrease in the decomposition rate. However, the recovery factor f_{rec} also declines alongside the decomposition rate, effectively buffering the overall rate reduction.

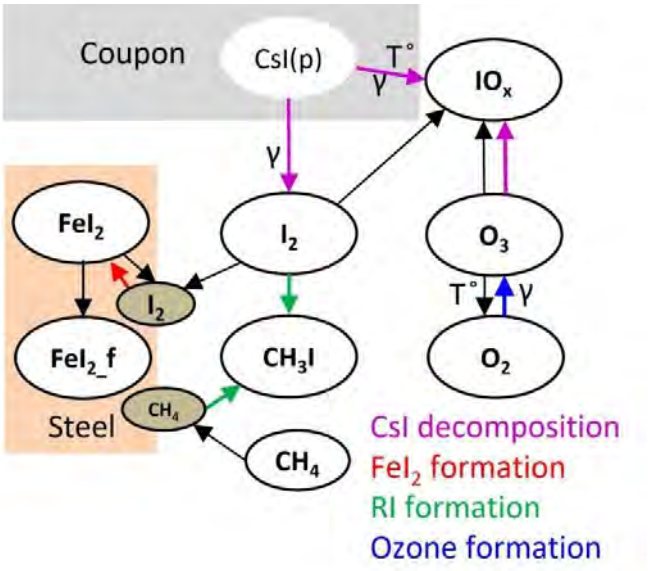

Figure 2. Schematic modelling of CsI destruction and RI formation.

Depending on the dose rate, ozone is formed from the oxygen in the air. Radiolytically produced ozone can react with gaseous I_2 to form IO_x aerosols, which exhibit distinct behavior compared to gaseous I_2. The backward conversion of IO_x to I_2 is also possible under accident typical gas temperatures. Deposition of I_2 onto steel surface and the subsequent chemical reaction with steel is an unwanted removal process for volatile iodine from the gas phase e.g. in iodine tests. The reaction of gaseous iodine (I_2) with dry stainless-steel surfaces can be described as the sequence of two processes: an initial, fast and reversible physisorption process, followed by a slower chemical reaction of the physical sorbed I_2 with the steel producing chemisorbed, non-volatile metal iodides (represented by FeI_2). FeI_2 can be further oxidized forming strongly bound iron-iodide-oxides FeI_2_f, which is a permanent iodine sink, and no iodine can be released from it into the gas phase again. Organic iodine formation occurs through a reaction of deposited methane with gaseous I_2, which was considered as the best model through comparing the different RI generation mechanisms models results with test measurements.

3. Simulation Results

3.1. LOCOV test simulation

The measurement showed that there is 30.7% missing mass balance at the end of LOCOV test [14]. Therefore, the LOCOV model simulated with COCOSYS focuses on the released iodine mass evolution in filter, the mismatch of iodine mass on coupon at the end is ignored.

Methane is injected into the vessel during the whole test process, so in the first 1 hour, the concentration of methane in the vessel increases quickly. When the irradiation starts, the radiolysis of the air/steam atmosphere produces ozone immediately (Fig. 3). The radioactive decomposition of CsI releases I_2. The oxidation of I_2 by ozone produces IO_x; simultaneously, the thermal production of IO_x also consumes ozone. Due to these ozone-consuming reactions, the ozone concentration decreases slightly and then maintains a constant level until the end of irradiation. Due to the extremely slow thermal decomposition of CsI, the IO_x concentration remains negligible and therefore omitted from the figure. Injected methane reacts with I_2 to generate organic iodine; however, the generation rate declines as the I_2 concentration is depleted. Once the irradiation stops, the production of both ozone and I_2 from CsI decomposition also ends. The remaining ozone and I_2 react rapidly, consuming both reactants in a short timeframe. Consequently, the concentration of methane begins to recover, while the concentration of organic iodine decreases sharply.

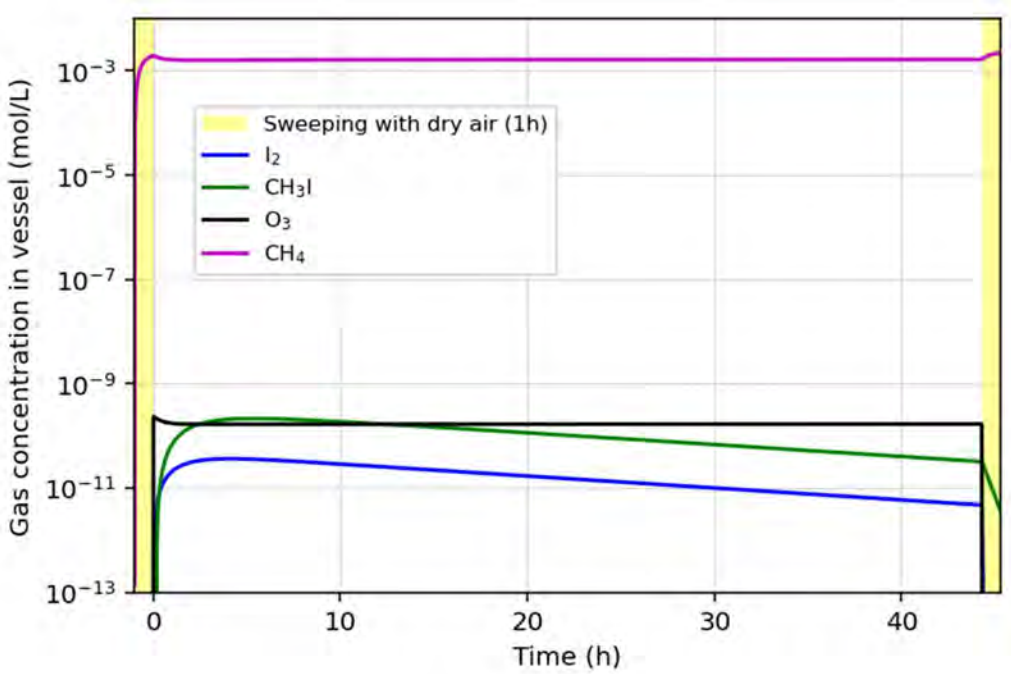

Figure 3. Evolution of gas phase species concentration in the containment for LOCOV model.

Fig. 4 illustrates the overall iodine balance across the hosts coupon, vessel atmosphere, vessel structures, and filter. At the end of simulation, there is totally 74.9% iodine deposited at the steel surface, 14.5% iodine in filter, 10.6% iodine on coupon. Due to the continuous flow design of the experiment, only a small fraction is present in the vessel atmosphere during the whole experimental sequence. The released gas phase I_2 from CsI decomposition in vessel deposits on the surfaces of the vessel walls. With the time going on, the deposited I_2 reacts with Fe and the FeI_2 is produced. FeI_2 can be further oxidized forming strongly bound iron-iodide-oxides, so the deposited iodine mass in form of FeI_2 continues increasing (Fig. 5). On the other hand, the deposited I_2 starts decreasing 10 hours after the irradiation. Because of the low concentration of

airborne IO_x, the deposited iodine in form of IO_x can be ignored. At the end of simulation, 95% of steel surface deposited iodine are FeI_2, only 5% are in form of I_2. Characterizing the spatial and chemical distribution of iodine is essential for understanding the system's behavior. This approach ensures the model can be accurately calibrated as more detailed experimental data becomes available.

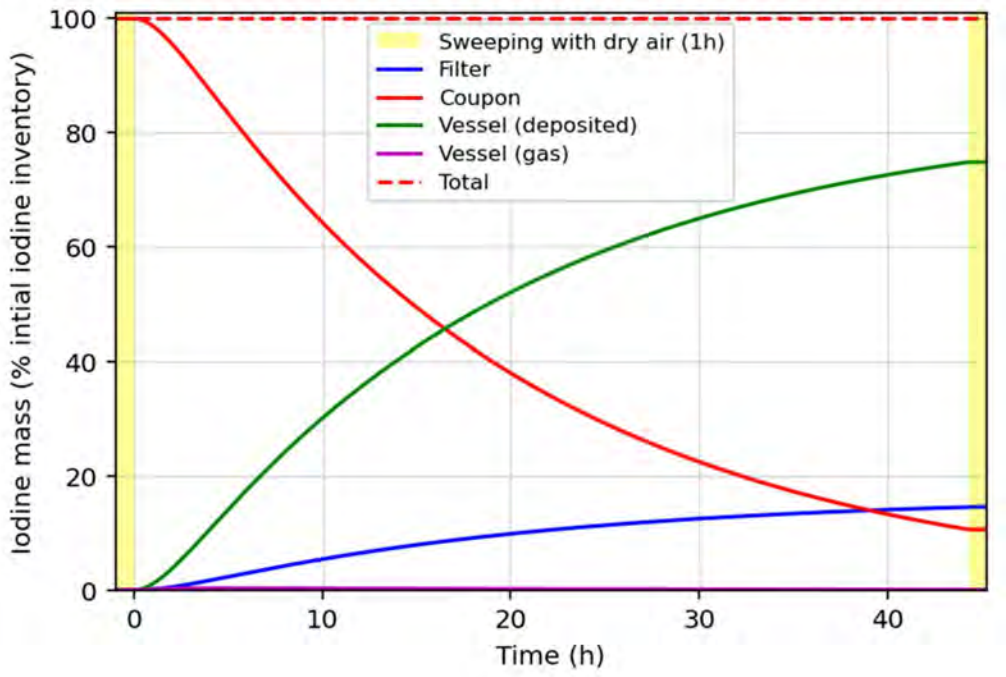

Figure 4. Evolution of iodine mass distribution for LOCOV model.

The simulated iodine mass in the filter is compared with experimental measurements from the LOCOV test in Fig. 6. The simulation indicates that the I_2 generation and subsequent organic iodine production rates are lower during the initial irradiation phase, resulting in a more gradual increase in the filter load. Generally, the simulation accurately captures the observed evolution of organic iodine. For the molecular iodine on the filter, there is 3.5% deposition at the end of simulation, which is a little bit lower than the measured data. The linear gradient trend in the measured data suggests a quasi-constant gas I_2 concentration within the vessel. However, during the final one-hour dry air weeping phase, after irradiation stopped, a sudden release of molecular iodine was detected on the filter. The mechanism behind this release remains unclear and requires more detailed observation. The simulation shows no more molecular iodine released from the system in the last hour. Same as the test observation, the concentration of IO_x is very low and can be ignored. The radioactive decomposition dominates the CsI release.

Within the COCOSYS calculation a large part of iodine is trapped on the steel walls of the vessel. This is a possible explanation for the large balance error observed in the experiment. However, the iodine-steel model of COCOSYS is derived from the specifics of the THAI vessel operated by Becker Technologies in Germany [18]. The steel inside the EPICUR facility is different and assumed to be inert to iodine deposition and reaction to a great extent. Therefore, the actual iodine sink remains unknown, though the piping utilized during the experiment may also account for the large balance error.

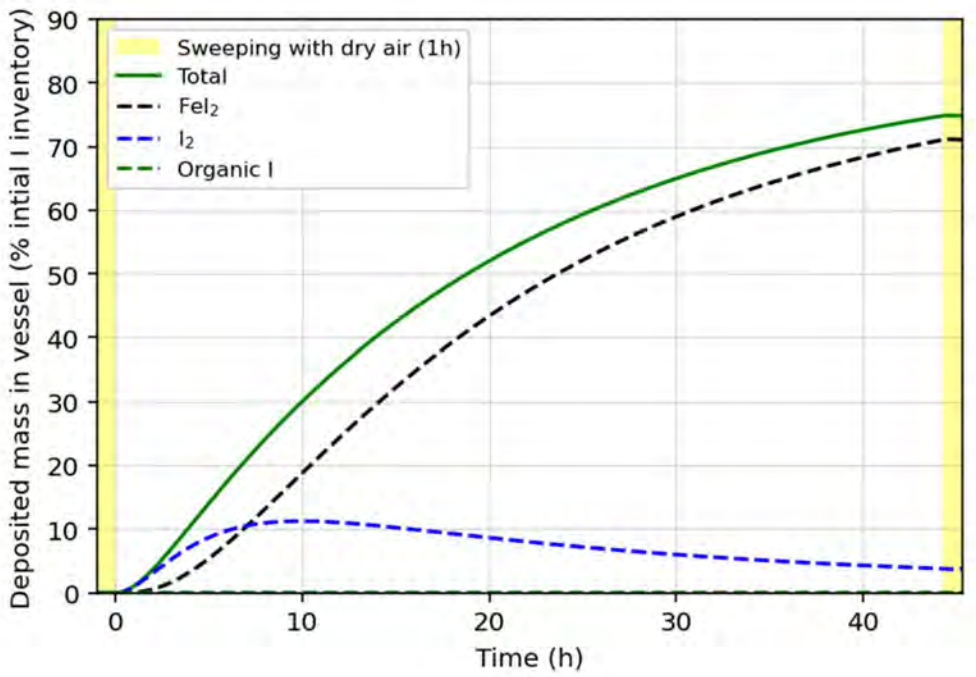

Figure 5. Evolution of deposited iodine at the steel surface for LOCOV model.

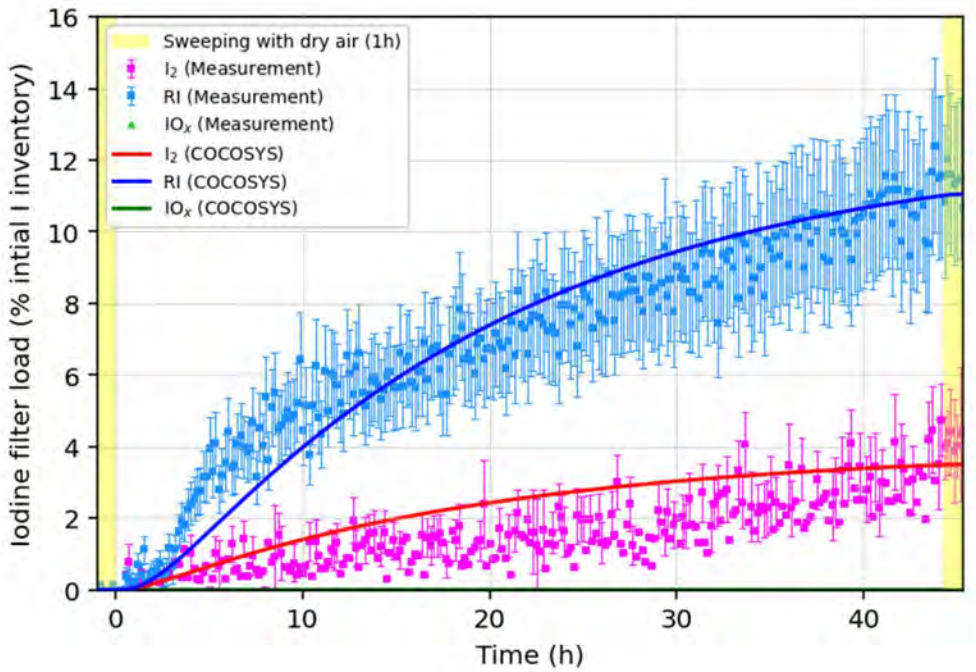

Figure 6. Comparison of measured and simulated iodine activity in filter for LOCOV test.

3.2. LOCOV2 test simulation

The chemical model implemented in COCOSYS as depicted in Fig.2 has been developed on LOCOV results. To estimate the general validity of this model and check the sensitivity of dose rate on CsI

decomposition and RI generation, also the experiment LOCOV2 has been simulated. Different from LOCOV test, LOCOV2 used galvanized steel as the coupon surface material and higher dose rate. Because of the higher dose rate in LOCOV2, which is 6.9 kGy/h compared to only 1.2 kGy/h in LOCOV test, the decomposition rate of CsI on coupon and the ozone generation rate are higher in LOCOV2 simulation. Therefore, the molecular iodine I_2 concentration in the containment increases quickly when the irradiation starts, and the concentration of ozone is much higher compared with LOCOV model (Fig. 7). Consequently, the generation rate of RI is higher, too. These higher concentrations of I_2 and RI cause more iodine mass transport out of the vessel and into the filter (Fig. 8). This fast mass flow-out limits the deposition of iodine on the steel wall surfaces. At the end of simulation, there is almost 54% iodine mass in the filter, and there is still 46% iodine mass on the coupon (Fig. 8). The iodine deposition at the containment wall surface can be ignored.

At the end of experiment LOCOV2 there is 0.3% IO_x, 29.1% I_2 and 23.0% RI deposition on the filters compared to the initial inventory. Compared to the LOCOV test, higher rates of CsI decomposition of RI formation resulted in a greater release of molecular and organic iodine. Generally, the simulated organic iodine on the filter shows good agreement with the measured RI evolution (Fig. 9). Regarding the molecular iodine on the filter, the simulation shows a slower release rate in the first 20 hours compared to experimental results. The damage term implemented in COCOSYS buffers the high CsI decomposition rate when both the dose rate and available CsI mass are elevated. This likely explains why the model underestimates the initial rapid release of molecular iodine; However, the simulation successfully captures the overall release trends.

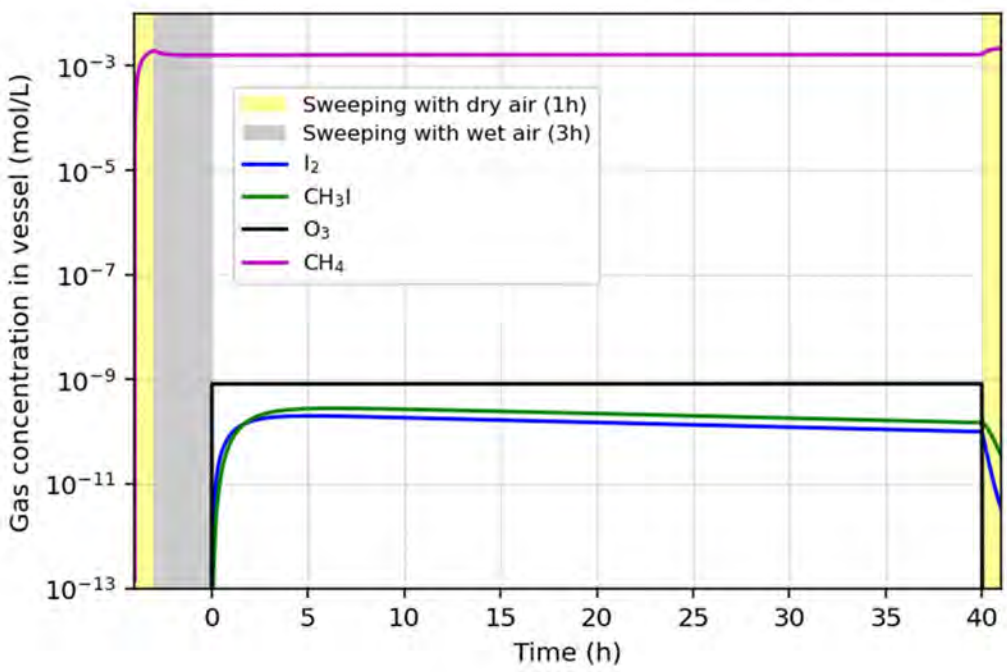

Figure 7. Evolution of gas phase species concentration in the containment for LOCOV2 model.

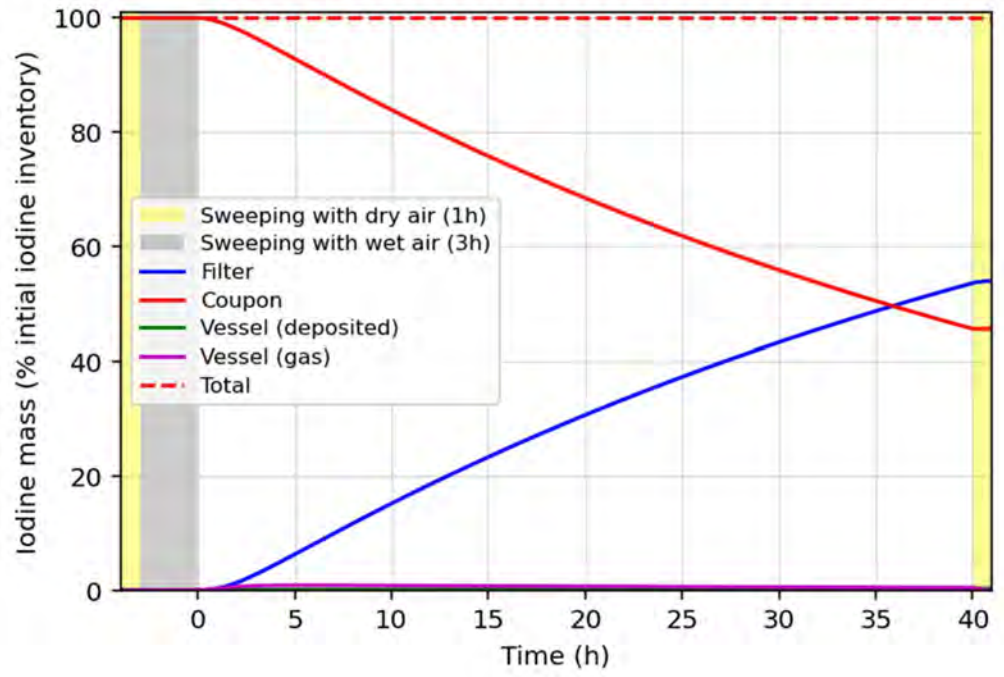

Figure 8. Evolution of iodine mass distribution for LOCOV2 model.

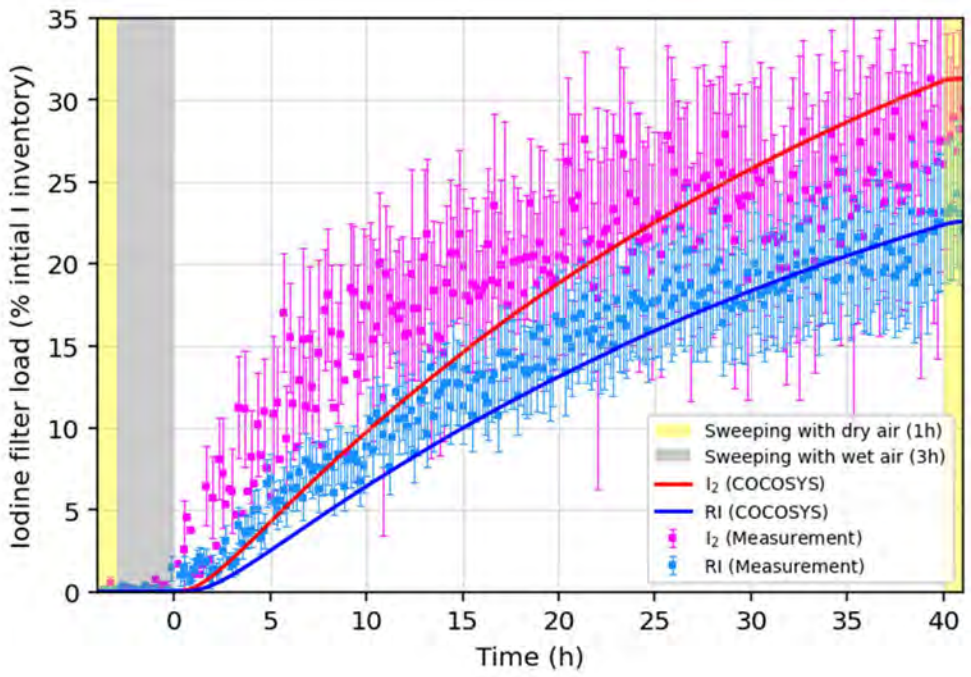

Figure 9. Comparison of measured and simulated iodine activity in filter for LOCOV2 test.

4. CONCLUSIONS

The LOCOV and LOCOV2 tests, which investigate CsI decomposition and RI generation, were simulated using the AFP2 module in COCOSYS. The models show that irradiation significantly accelerates CsI decomposition compared to thermal processes. Injected methane reacts with I_2 to generate organic iodine, while the oxidation of I_2 by ozone produces IO_x aerosols. Additionally, gaseous I_2 deposits onto the steel vessel walls, where the model predicts a subsequent reaction with iron to form FeI_2. While higher dose rates increased CsI decomposition, the lower I_2 deposition rate on the steel wall in LOCOV2 may be attributed to relatively high humidity, a phenomenon warranting further study. Overall, the agreement between simulation and experimental data demonstrates the robust capabilities of COCOSYS in modelling organic iodide formation.

In these experiments, a specific fraction of iodine reacts with volatile organic compounds (VOC). While these species may form directly at the steel surfaces, the underlying mechanisms remain unidentified. Additionally, mass balances are often incomplete across various tests. COCOSYS simulations indicate this may be due to the trapping of iodine species on the EPICUR vessel walls or within the external piping. To further clarify the generation processes of organic and molecular iodine, additional measurement data on the coupon and steel structure surfaces are required.

ACKNOWLEDGMENTS

The authors acknowledge the OECD ESTER project and the IRSN team (now ASNR) with respect to the experiment data and the related synthesis reports.

This paper reflects only the author's view, and the OECD NEA is not responsible for any use that may be made of the information it contains.

The development and the validation of AC^2 is sponsored by the German Federal Ministry for Environment, Climate Action, Nature Conservation and Nuclear Safety (BMUKN) based on decisions by the German Bundestag within several projects.

The authors are grateful to the anonymous reviewers for their thorough evaluation and valuable suggestions, which helped improve the clarity and impact of this paper.

REFERENCES

1. J. Colombani, C. Pascal, L. Martinet, C. Duffieus and O. Leroy, *AER-CsI STEM/EPICUR tests synthesis report: Formation and release of iodine volatile species from CsI aerosols under radiation,* IRSN, France, Rapport n° PLEIADE PSN-RES/SEREX/2015-00292, STEM n° 23 (2015).
2. J.C. WREN, J.M. Ball and G.A. Glowa, "Chemistry of iodine in containment," Nuclear technology, 129(3), pp. 297-325 (2000).
3. R. Zilliacus, P. Koukkar, T., Karjunen, H. Sjövall, *Formation and behaviour of organic iodine*, Nordic nuclear safety research, ISBN 87-7893-095-2, Finland (2002).
4. S. GUILBERT et al, "Radiolytic oxidation of iodine in the containment at high temperature and dose rate," *Proceedings of the Nuclear Energy for New Europe*, Portoroz, Slovenia, Sept 10-13 (2007).
5. L. Bosland, K. Chevalier-Jabet, *Main lessons learnt from 40 years of R&D on iodine source term prediction: Identification of the main parameters governing iodine volatility in PHEBUS FP tests*, Progress in Nuclear Energy 177, 105473, ISSN 0149-1970, https://doi.org/10.1016/j.pnucene.2024.105473 (2024).

6. J. Colombani, L. Bosland, C. Pascal, L. Martinet and C. Gomez, *Experimental study of organic iodide formation from painted surfaces in the containment atmosphere during a severe accident,* ICAPP 2011, Nice & Fréjus, France, May 2011. Irsn-04841918 (2011).
7. L. Bosland, O. Leroy, C. Alvarez, M. Chebbi, C.M. Louvet, S. Bourrous and K.C. Jabet, *Study of CsI and iodine oxides (IOx) aerosols and trapping efficiency of small aerosols on sand bed and metallic filters under irradiation*, Annals of Nuclear Energy, 142, pp.104013, 10.1016/j.anucene.2021.104013, hal-03409665 (2021).
8. L. Bosland, J. Colombani, *Study of iodine releases from epoxy and polyurethane paints under irradiation and development of a new model of iodine-Epoxy paint interactions for PHEBUS and PWR severe accident applications*, J Radioanal Nucl Chem, 314, 1121-1140, https://doi.org/10.1007/s10967-017-5458-9 (2017).
9. L. Bosland, S. Dickinson, G.A. Glowa, L.E. Herranz, H.C. Kim, D.A. Powers, M. Salay, S. Tietze, *Iodine–paint interactions during nuclear reactor severe accidents*, Annals of Nuclear Energy, 74, 184-199, https://doi.org/10.1016/j.anucene.2014.07.016 (2014).
10. S. Guilbert, L. Bosland, S. Fillet, D. Jacquemain, B. Clement, F. Andreo, G. Ducros, S. Dicknson, L. E. Herranz, J. Ball, *Formation of organic iodide in the containment in case of a severe accident,* 2008 Annual Meeting on American Nuclear Society, Anaheim (CA), United States, June 2008, pp.261-292, Irsn-04841909 (2008).
11. X. Gong, D. Qin, M. Zhong, H. Liu, H. Wu, M. Kang, *Kinetic study of diiodine adsorption behavior on the epoxy paint in PWRs*, J Radioanal Nucl Chem 334, 2891-2900, https://doi.org/10.1007/s10967-025-10050-0 (2025).
12. O. Leroy and L. Bosland, *Study of the stability of iodine oxides (IxOy) aerosols in severe accident conditions*, Annals of Nuclear Energy, 181, pp.109526, 10.1016/j.anucene.2022.109526, hal-03969323 (2023).
13. L. Bosland and J. Colombani, *Study of the radiolytic decomposition of CsI and CdI_2 aerosols deposited on stainless steel, quartz and Epoxy painted surfaces*, Annals of Nuclear Energy, 141, pp.107241, https://doi.org/10.1016/j.anucene.2019.107241 (2020).
14. O. Leroy, *ESTER-EPICUR synthesis experimental report*, ISRN, France, Report n° IRSN/2024-00170, ESTER n° 9 (2024).
15. J. Hoffrichter and M. K. Koch, *Simulation of LOCA-typical containment conditions with COCOSYS on the basis of THAI-test TH-29.3*, Kerntechnik, 84 (5), pp.434-440, https://doi.org/10.3139/124.190035 (2019).
16. L. Tiborcz and S. Beck, *Uncertainty and sensitivity analysis of the fission product behaviour in the Phébus FPT1 test with the system code AC2*, Nuclear Engineering and Design, 429, pp.113594, ISSN 0029-5493, https://doi.org/10.1016/j.nucengdes.2024.113594 (2019).
17. S. Arndt, S. Band, S. Beck, D. Eschricht, D. Iliev, H. Nowack, N. Reinke, C. Spengler, W. Klein-Heßling, M. Sonnenkalb, G. Weber, *COCOSYS 3.3.0 User Manual*, Gesellschaft für Anlagen- und Reaktorsicherheit (GRS) gGmbH, GRS-P-3/ Vol. 1 (2025).
18. S. Gupta, T. Kanzleiter, K. Fischer, G. Poss, *Reactor Safety Research Program at THAI Test Facility,* Proceedings of the 17th Pacific Basin Nuclear Conference, Cancun, Mexico, October 2010 (2010).

Simulation of melt spreading in CoSMUS experiments using the MPS method

Lu Zhao, Weimin Ma, Andrei Komlev, Sevostian Bechta

KTH Royal Institute of Technology
Stockholm, Sweden
20/05/2026

Outline

- Introduction
- Modelling approach
- Simulation of oxidic melt dry spreading
- Concluding remarks & Outlook

Introduction

❑ Significance

- ➢ Following vessel failure, corium (molten core material) will pour onto the containment floor and likely spread.
- ➢ Spreading extent influences melt coolability (i.e., deeper melt are difficult to cool).
- ➢ Spreading melt can lead to thermal attack on important structures (i.e., concrete) and threaten containment integrity.

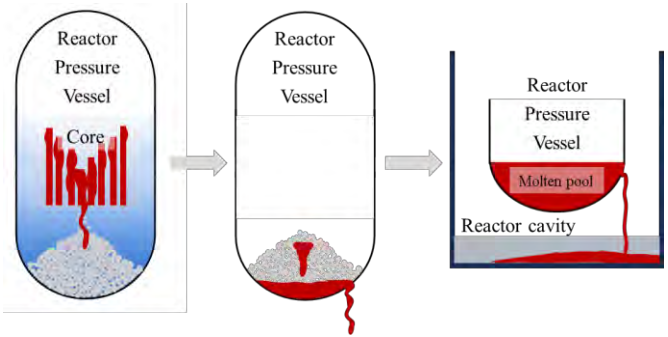

❑ Phenomenology

- ➢ Hydrodynamic motion: gravitational, viscous, inertial and surface forces
- ➢ Heat transfer with liquid-solid phase change
- ➢ Additional phenomena: concrete ablation, gas generation, melt eruption, etc.

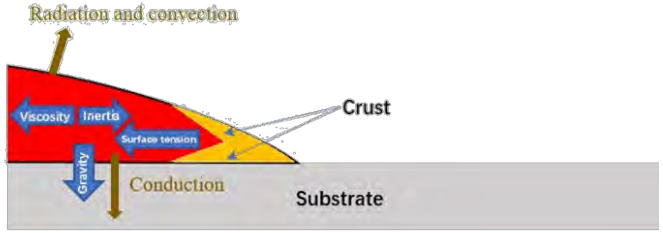

❑ Objectives

- ➢ Further validate the capability of MPS code for dry spreading analysis.
- ➢ Deepen the understanding of melt dry spreading mechanisms.

MPS modelling approach

- Moving particle semi-implicit (MPS) method is employed

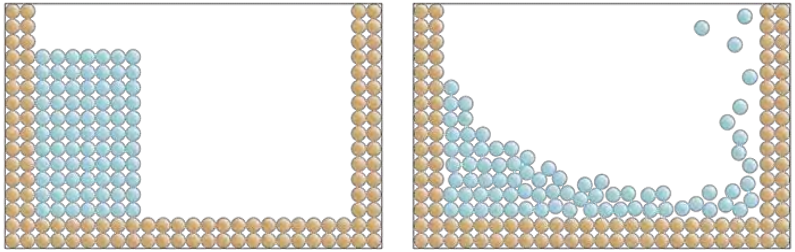

Example: water column collapse

- <u>What is MPS method?</u>

✓ Lagrangian approach for incompressible free surface flow.

✓ The computation domain is represented by particles.

✓ Pressure term is calculated implicitly.

- <u>Why choose MPS method here?</u>

✓ Allows large deformation of interfaces.

✓ No numerical diffusion.

✓ Easier to generate particle configuration.

Main equations

- **Mass conservation**

$$\frac{D\rho}{Dt} + \rho\nabla \cdot \mathbf{u} = 0$$

- **Momentum conservation**

$$\frac{D\boldsymbol{u}}{Dt} = -\frac{1}{\rho}\nabla P + \nu\nabla^2\mathbf{u} + \boldsymbol{g} + \frac{\boldsymbol{F}}{\rho}$$

Weight function

$$\omega(r) = \begin{cases} \frac{r_e}{r} - 1 & (0 < r < r_e) \\ 0 & (r_e \le r) \end{cases}$$

Particle number density

$$n_i = \sum_{j \neq i} \omega(|\boldsymbol{r}_j - \boldsymbol{r}_i|)$$

Free surface detection

$$\langle n \rangle_i^* < \beta n^0, \beta<1$$

Gradient discretization

$$\langle \nabla\phi \rangle_i = \frac{d}{n^0}\sum_{j \neq i}\left[\frac{\phi_j - \phi_i}{|\boldsymbol{r}_j - \boldsymbol{r}_i|^2}(\boldsymbol{r}_j - \boldsymbol{r}_i)\omega(|\boldsymbol{r}_j - \boldsymbol{r}_i|)\right]$$

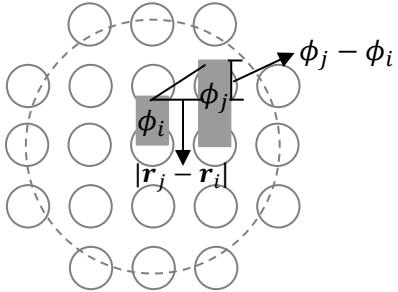

Laplacian discretization

$$\langle \nabla^2\phi \rangle_i = \frac{2d}{\lambda n^0}\sum_{j \neq i}\left[(\phi_j - \phi_i)\omega(|\boldsymbol{r}_j - \boldsymbol{r}_i|)\right]$$

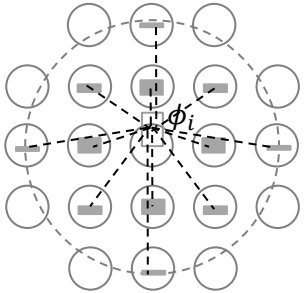

Additional models (1)

- **Heat transfer model**

$$\frac{DH}{Dt} = k\nabla^2 T + S_Q$$

$$H_i^{k+1} = H_i^k + k\Delta t \cdot \frac{2d}{\lambda n^0} \sum_{j \neq i} \left(T_j^k - T_i^k\right) \omega\left(\left|\boldsymbol{r_j} - \boldsymbol{r_i}\right|\right) + S_Q \Delta t$$

$$T = \begin{cases} T_s + \dfrac{H - H_s}{\rho C_{p,s}} & H < H_s \\ T_s + \dfrac{(H - H_s)(T_l - T_s)}{H_l - H_s} & H_s \leq H \leq H_l \\ T_l + \dfrac{H - H_l}{\rho C_{p,l}} & H > H_l \end{cases}$$

T_s and T_l are the solidus and liquidus temperature; H_s and H_l are the enthalpies at the liquid and solid state.

- **Phase change model**

$\gamma \geq \gamma_{threshold}$ *particle is solid*
$\gamma < \gamma_{threshold}$ *particle is liquid*

$$\gamma = \begin{cases} 1 & H < H_s \\ \dfrac{H_l - H}{H_l - H_s} & H_s \leq H \leq H_l \\ 0 & H > H_l \end{cases}$$

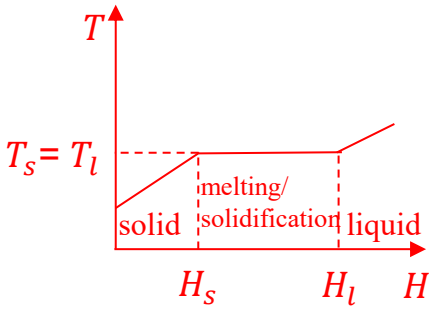

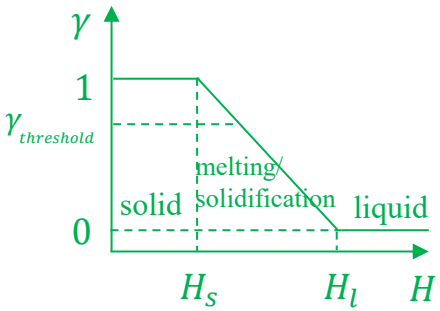

Additional models (2)

➢ Surface tension model

- Interparticle potential: $p(r) = \begin{cases} \frac{1}{3} C_f \left(r - \frac{3}{2} l_0 + \frac{1}{2} r_e\right)(r - r_e)^2 & r < r_e \\ 0 & r \geq r_e \end{cases}$

- Force: $\boldsymbol{F}_{st} = -\frac{\partial p(r)}{\partial \boldsymbol{r}} = -C(r - l_0)(r - r_e)\frac{\boldsymbol{r}}{r}$

  C_f: the potential force coefficient between fluid particles, $C_f = \frac{6\sigma l_0^2}{\sum\left(r - \frac{3}{2} l_0 + \frac{1}{2} r_e\right)(r - r_e)^2}$

➢ Wettability (contact angle)

- Based on contact angle: $C_{fs} = \frac{C_f}{2}(1 + \cos\theta)$

  C_{fs}: the potential force coefficient between fluid and solid particles

  θ: the contact angle

Description of CoSMUS experiment

- The "dam break" melt supply method is employed to eliminate jet-coolant interaction and fragmentation, while minimize heat loss and ensure symmetrical melt delivery.
- The facility is composed of melt delivery system, and the test section.

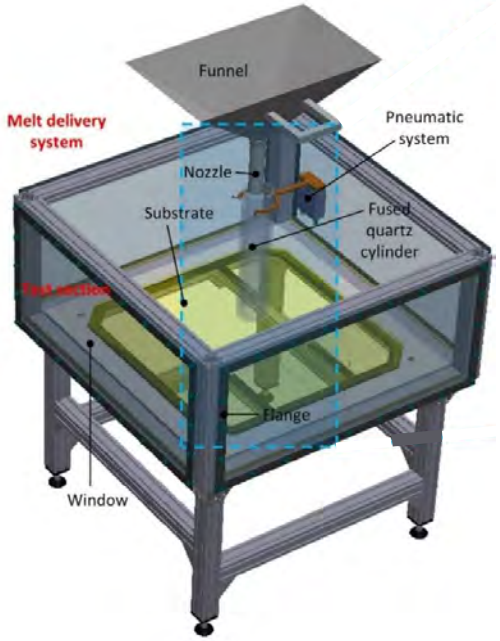

CoSMUS test matrix							
Expt.	**Melt type**	**Cavity condition**	**Composition**	**Melt volume (l)**	**Melt superheat (°C)**	**Water subcooling (°C)**	**Gap for melt flow (mm)**
CoSMUS 01a_DM	**Metal**	**Dry**	**Zn**	**0.81**	**11**	**-**	**10**
CoSMUS 01b_DM				**0.96**	**75**	**-**	**10**
CoSMUS 01c_DM				**0.97**	**90**	**-**	**10**
CoSMUS 02_WM		**Wet**		**0.99**	**71**	**4±1**	**10**
CoSMUS 03_DO	**Oxide**	**Dry**	**Eutectic Bi_2O_3-WO_3 mixture**	**0.82**	**66**	**-**	**10**
CoSMUS 04_WO		**Wet**		**0.86**	**36**	**5±1**	**10**
CoSMUS 05_WO				**0.75**	**10**	**4±1**	**60**

Simulation of oxidic melt dry spreading

- Using eutectic WO_3-Bi_2O_3 mixture as an oxidic corium simulant, the CoSMUS03_DO test was conducted with the superheat of 66 °C.
- A quarter-section of the test is simulated to reduce computational time as the high-speed camera indicates symmetrical spreading.

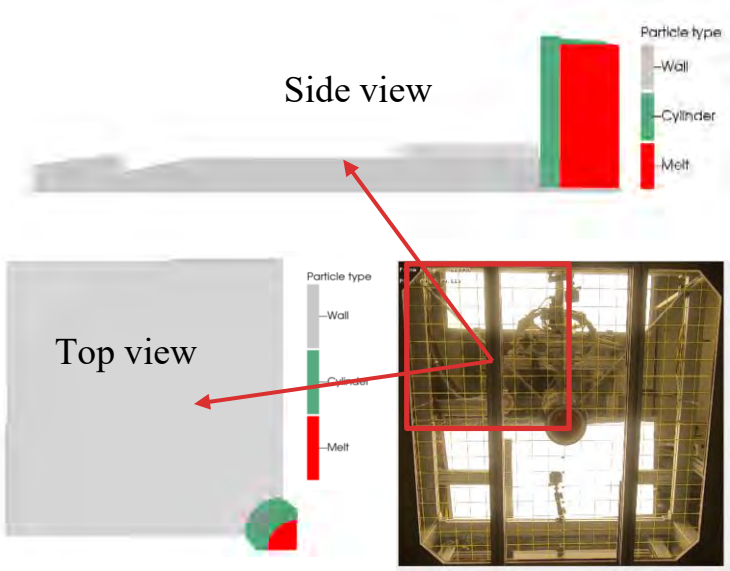

Thermophysical properties and initial conditions for CoSMUS03_DO

Parameter	Melt	Substrate
Material	Eutectic WO3-Bi2O3	Quartz
Density, kg/m^3	6724	2650
Specific heat, J/(kg·K)	501	690
Thermal conductivity, W/m/K	1.6	1.4
Emissivity	0.85	-
Viscosity, pa·s	0.003	-
Latent heat, kJ/kg	196.606	-
Surface tension, N/m	0.3-0.4	-
Melting point, K	1148	-
Initial temperature, K	1214	293

Results of CoSMUS03_DO test (1)

Melt spreading process

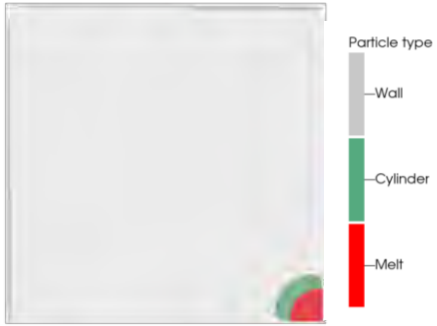

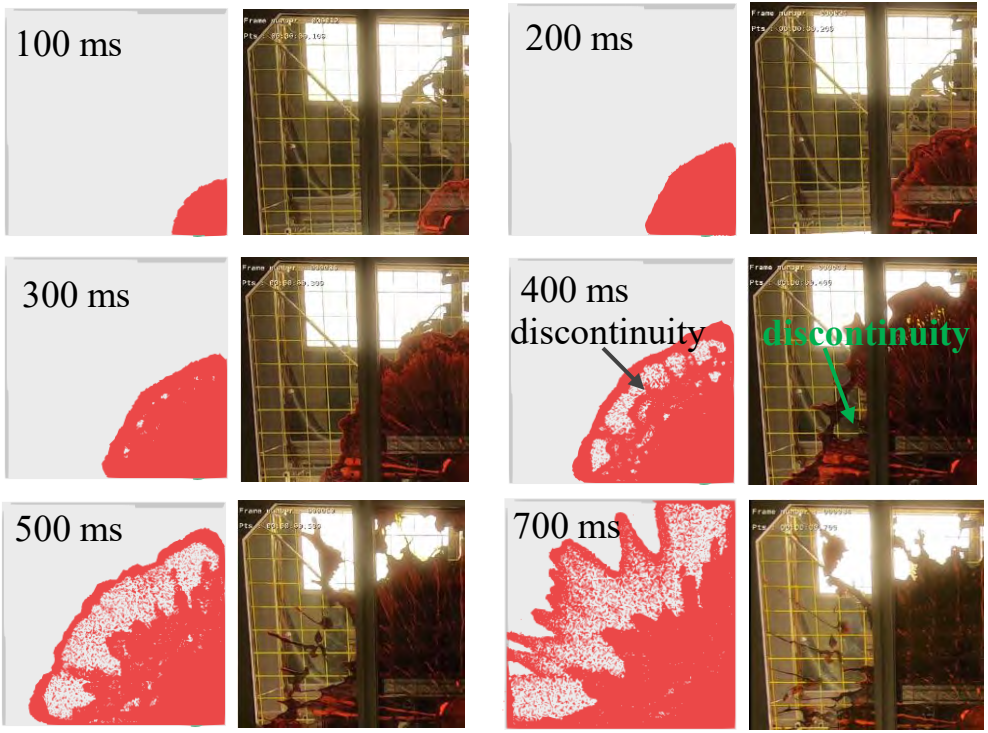

- Before 300 ms, both the experiment and simulation show a rapid spreading with a symmetrical shape and smooth edge.
- After 300 ms, melt discontinuity is observed at melt front due to low surface tension. As melt spreads further, the melt front becomes highly irregular, forming finger-like structures due to instabilities.
- Fingers appear earlier and are narrower in the experiment.

Results of CoSMUS03_DO test (2)

Evolution of melt leading edge

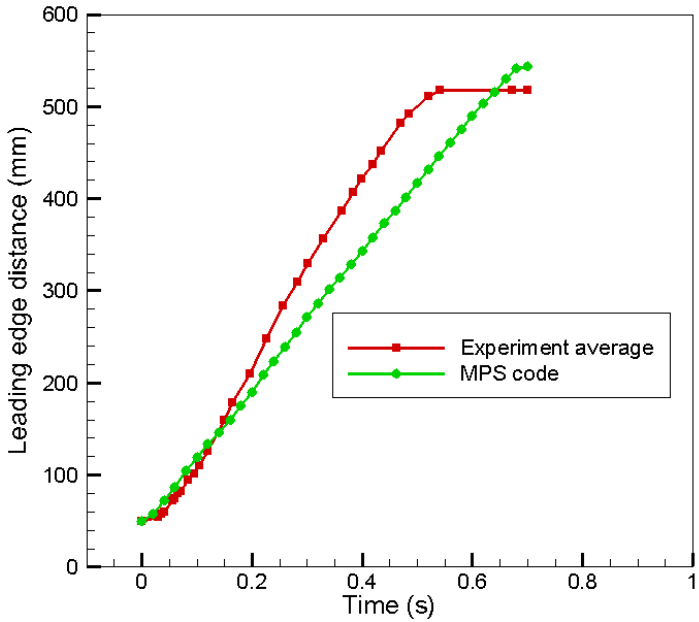

- Both the experimental and numerical data show a nearly constant velocity of melt leading edge over time, followed by a termination phase.
- The simulation predicts a lower spreading rate and larger edge distance. These discrepancies may arise from uncertainties in the estimation of key physical parameters (e.g., surface tension, wettability).

Results of CoSMUS03_DO test (3)

Melt top surface temperature field

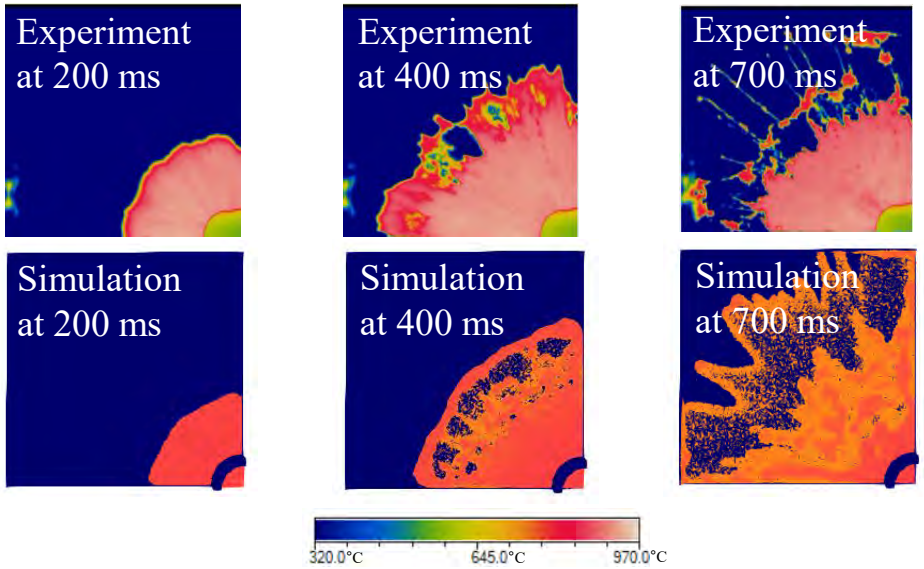

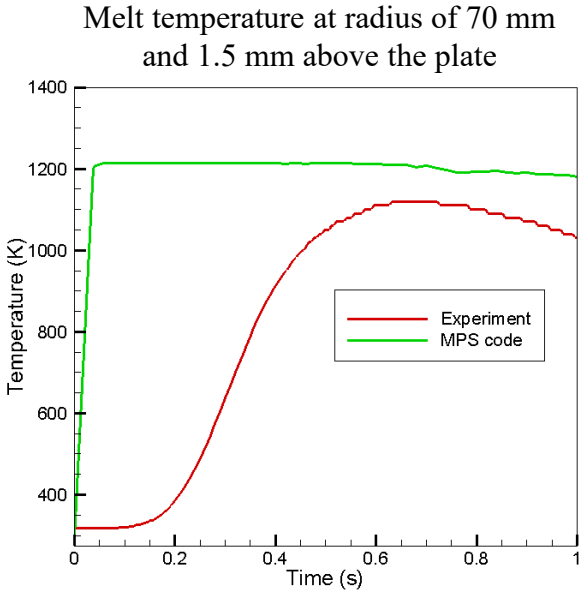

- With melt spreading further and reaching a large area, the temperature at the top of the melt decreases with time.
- Experiment shows a higher melt top surface temperature, which may be caused by the uncertainty in the IR camera emissivity setting.
- The simulation predicts a rapid temperature rise, while experimental data exhibit a more gradual temperature rise.
- After reaching the peak temperature, the experiment shows a gradual decline, likely due to the incomplete contact between thermocouples and the melt & the crust formation around TC junctions.

Concluding remarks & Outlook

Concluding remarks

- Melt discontinuity and fingers are observed from the periphery of oxidic melt.
- The simulation predicts a rapid temperature rise, while the experimental data shows a more gradual temperature increase at a given position.
- Uncertainties in the estimation of key physical parameters (surface tension, wettability) can cause discrepancies between the simulation and experimental results.

Outlook

- Sensitivity analysis of key parameters will be conducted to better quantify their influences.
- Apply the code in reactor-scale safety analysis.

Thank you

for your attention!

The 12th European Review Meeting on Severe Accidents Research

May 18-22, 2026, Universidad Carlos III de Madrid, Madrid, Spain

TECHNICAL SESSION 5.3: HYDROGEN RISK AND CONTAINMENT BEHAVIOR

Chairs: G. Jiménez (Universidad Politécnica de Madrid), E.-A. Reinecke (FZJ)

ID002	**Influence of Containment Pressurization Rates on the Assessment of Severe Accident Risk** Kwang-Il Ahn (KAERI)	Paper Presentation
ID045	**Benchmark on Counter Current Flow in Multi-Compartment Containment using THAI Test Data** J. Hermann (Becker Technologies GmbH)	Paper Presentation
ID068	**Systematic analysis of the influence of the spray actuation on the hydrogen risk using a 3D GOTHIC PWR-W model** C. Vázquez-Rodríguez (FZJ)	Paper Presentation
ID003	**Assessment and Applicability of a Stand-Alone Containment Methodology for Hydrogen and CO Risk Evaluation in Severe Accidents** J. Fontanet (CIEMAT)	Paper Presentation

INFLUENCE OF CONTAINMENT PRESSURIZATION RATES ON THE ASSESSMENT OF SEVERE ACCIDENT RISK

Kwang-Il Ahn
Korea Atomic Energy Research Institute
989-111 Daedeokdaero, Yuseong, Daejeon, 34057, Republic of Korea
kiahn@kaeri.re.kr

ABSTRACT

A realistic assessment of the probabilities of containment-failure modes (e.g., leaks and ruptures) is essential for improving the quality and credibility of Level 2 probabilistic safety assessments (PSAs) for nuclear power plants (NPPs). The paper presents the technical background on the impact of two representative scenarios—slow- and fast-pressurizations—characterized by different containment-pressurization rates and commonly used in severe-accident risk analyses and Level 2 PSAs. Both approaches fundamentally rely on probabilistic-fragility curves that are developed independently for two distinct failure modes—leaks and ruptures of predefined nominal size. In some cases, smaller leakage modes—below the nominal leak size—may be explicitly included to enable a more realistic evaluation of probabilistic-safety goals concerning a release of 100-TBq Cs-137. Findings from relevant case studies are presented together with key insights on their implications for Level 2 safety and performance goals, including Large Early Release Frequency (LERF) and the Cs-137 release risk.

KEYWORDS
Level 2 PSA, Containment Scenarios, Failure Modes & Probabilities, Severe Accident Risk Implications

1. INTRODUCTION

In nuclear power plants (NPPs), Level 2 Probabilistic Safety Assessment (PSA) evaluates containment performance and characterizes the associated severe-accident risk by considering a range of severe-accident progressions that arise from various core-damage sequences [1]. Many countries establish their own probabilistic safety goals for severe-accident risk [2]—for example, Large Early Release Frequency (LERF), Large Release Frequency (LRF) (defined in some jurisdictions as the 100-TBq Cs-137 release frequency), and Containment Failure Frequency (CFF), as shown in Table I. The LERF is employed as a surrogate risk indicator for severe accident-induced early fatalities, thereby embodying a quantitative health objective (QHO) [3, 4]. The LRF serves as a surrogate indicator for severe accident-induced long-term public health effects and land-contamination risk. By contrast, the frequency of 100-TBq Cs-137 releases specifically quantifies the severe accident-induced long-term land-contamination risk.

Various factors—modeling assumptions, data gaps, and scenario variability—introduce conservatism and uncertainty into the assessment of these Level 2 risk indicators. This paper concentrates on potential containment failure modes and their impact on the severe accident risk, emphasizing the need for a more robust technical basis to estimate the associated risk indicators.

Within the LERF assessment, many Level 2 PSAs evaluate the probabilities of two distinct containment failure modes—leak and rupture. Some Level 2 PSAs explicitly consider two pressure-load types that may be imposed on the containment during a severe-accident progression [5]: (a) slow pressure loads; (b) fast

pressure loads. The slow load denotes a pressure increase that is slower than the time required for a breach to depressurize the containment, typically arising from the gradual generation of steam and non-condensable gases. Although thermodynamically rapid, this load is slow relative to the structural response. The fast/rapid load, by contrast, describes a pressure rise that exceeds the depressurization time through a breach. Rapid pressure loads may arise from high-pressure melt ejection, detonation or deflagration of combustible gases, and steam spikes generated by ex-vessel fuel–coolant interactions. From this viewpoint, we first present case studies that examine how these two pressure-load types affect leak and rupture failure probabilities.

Certain cases require the explicit consideration of a leakage mode that is smaller than the conventional leak size, whose nominal size is typically equivalent to the containment-design leakage rate, in order to evaluate more accurately the potential release of Cs-137 to the environment, in addition to the conventionally applied leak and rupture modes. This is because such a small-leakage mode in a Level 2 PSA can alter both the amount and the rate of radioactive material released, and consequently the environmental impact. If the probabilities of the three failure modes (small-leakage, leak, and rupture) are not distinguished in the fission-product source-term evaluation, the Level 2-related risk and the resulting probabilistic consequence-analysis can be underestimated, potentially leading to inadequate emergency-response measures or off-site risk. In this context, an additional case study is presented to provide a technical basis for assessing how the inclusion of a small-leakage mode could affect a 100-TBq Cs-137 release risk.

This paper primarily focuses on structural failure or damage of the containment that may occur during severe accidents; bypass-containment events, although recognized as another contributors to Level 2 risk, are excluded from the analysis.

Table I. Level 1 and 2 related safety goals defined in several countries

Country	Level 1 risk	Level 2 risk	Objects/Remarks
Canada (Regulator)	CDF < 10^{-5} /ry	SRF (1000-TBq I-131) < 10^{-5} /ry LRF (100-TBq Cs-137) < 10^{-6} /ry	New plants
Czechia (Licensee)	CDF < 10^{-4} /ry CDF < 10^{-5} /ry	LERF (> 1 % Cs-137, up to 10 h from fuel damage) < 10^{-5} /ry LERF: practically eliminated	Existing plants (incl. SFP) New plants (incl. SFP)
Finland (Regulator)	CDF < 10^{-5} /ry	LRF (100-TBq Cs-137) < 5.0×10^{-7} /ry	All plants (incl. new)
France (Regulator)	CDF < 10^{-5} /ry CDF < 10^{-6} /ry	LRF: practically eliminated (not quantitatively specified)	New plants (all modes/hazards) New plants (internal events)
Hungary (Regulator)	CDF < 10^{-4} /ry CDF < 10^{-5} /ry	L(E)RF < 10^{-5} /ry L(E)RF < 10^{-6} /ry	Existing plants New plants
Japan (Regulator)	CDF < 10^{-4} /ry	CFF < 10^{-5} /ry 100-TBq Cs-137 < 10^{-6} /ry	All plants (incl. new)
R. Korea (Regulator)	CDF < 10^{-4} /ry CDF < 10^{-5} /ry	LERF < 10^{-5} /ry LERF < 10^{-6} /ry 100-TBq Cs-137 < 10^{-6} /ry	Existing plants APR1400 follow-up All plants (incl. new reactors)
Sweden (Licensee)	CDF > 10^{-5} /ry < 10^{-4} /ry	L(E)RF (> 0.1 % of core inventory) < 10^{-7} /ry	All plants
USA (Regulator)	CDF < 10^{-4} /ry CDF < 10^{-5} /ry	LERF < 10^{-5} /ry LERF < 10^{-6} /ry	Existing plants New plants
IAEA	CDF < 10^{-4} /ry CDF < 10^{-5} /ry	LERF < 10^{-5} /ry LERF < 10^{-6} /ry	Existing plants New plants

CDF = core damage frequency, SRF = small release frequency, SFP = spent fuel pool, ry = reactor year

2. DEFINITION OF THE PROBLEM AND RELEVANT CASE STUDIES

According to internationally recognized guidelines—e.g., NUREG-1150 [5] and the EPRI PSA Application Guide [6]—the two containment-failure modes employed in Level 2 PSA, leak and rupture are defined for a large, dry, pre-stressed, reinforced-concrete containment that has a cylindrical body with a hemispherical dome, as follows:

- Leak: *a containment breach that halts a gradual pressure buildup and requires 2 h or more to depressurize the large dry containment*. A typical example of this failure mode is the failure of the equipment hatch ring or the tearing of the containment liner plate, with nominal opening sizes ranging from 0.04 to 0.1 ft² (approximately 0.0037—0.0093 m²).
- Rupture: *a containment breach that depressurizes the containment within 2 h*. A typical example of this failure mode is hoop failure of the containment due to membrane stresses in the cylindrical wall. Such a rupture is typically characterized by a break greater than 1.0 ft², with nominal opening sizes ranging from 1.0 ft² (0.0929 m²) to 2.0 ft² (0.1858 m²).

As applied in the Level 2 PSA for the reference PWR [7], the probability density function (PDF) and the cumulative distribution function (CDF)—for the two failure modes are shown in Table II and Fig. 1. The modes are estimated independently for the cylindrical wall, each mode characterized by nominal break sizes of 0.1 ft² and 1.0 ft², respectively.

Table II. Containment fragility curves of the reference plant

Failure Modes	Lognormal PDF as a Function of Pressure Load (p)	Median Pressure (p_m, *psig*[1])	Logarithmic Standard Deviation (β)
Leak	$f(p) = \frac{1}{\beta\sqrt{2\pi}p}\exp\left[-\frac{(\ln(p)-\ln(p_m))^2}{2\beta}\right]$	162	0.14
Rupture		189	0.21

[1] 1 psig = 0.006894757 MPa

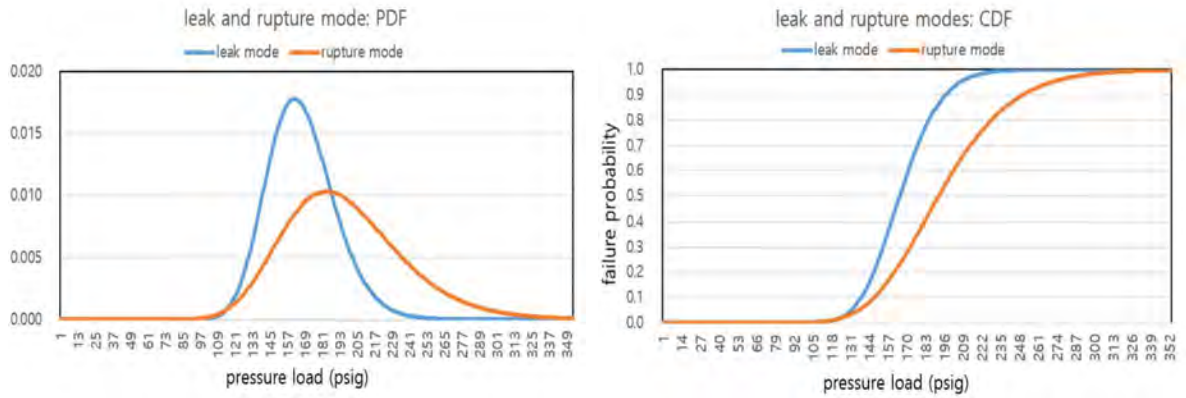

Figure 1. Containment fragility curves of the reference plant: PDF and CDF.

The Level 2 risk indicator, LERF (Large Early Release Frequency) is defined as the aggregate frequency of all accident scenarios that cause large, unmitigated releases from the containment to the environment prior to an effective evacuation of the surrounding population, thereby creating the potential for early health effects. The accident scenarios encompassed by LERF involve (a) unscrubbed, unfiltered releases of radioactive material resulting from containment isolation failures; (b) containment-bypass events such as interfacing-system loss-of-coolant accidents (ISLOCA) and induced-steam-generator tube ruptures (I-SGTR); and (c) any scenario that causes containment damage or failure that is equivalent to the "large" release defined above. These releases occur at, or shortly after, the reactor vessel breach—generally within 4 h of the breach in a pressurized-water reactor (PWR). As is the case in many countries, the Korean Level

2 PSAs also adopt the definition of LERF given above.

Regarding the 100-TBq Cs-137 release risk, some countries (e.g., Canada and Finland) embed this requirement in the Large Release Frequency (LRF) requirement, as shown in Table I. In the Level 2 context, LRF is defined as the aggregate frequency of all accident scenarios that could lead to any release to the environment (a) requiring long-term relocation of the population or (b) exceeding100-TBq Cs-137. In contrast, other countries—most notably Korea and Hungary—treat the criterion as a separate metric. The Korean Level 2 PSA defines the overall release frequency as the sum of the LERF and the Large Late Release Frequency (LLRF). LLRF represents a late-phase containment failure that is triggered by excessive pressurization and can release airborne fission products during the 72-h mission window assumed in a Level 2 PSA. Both LERF and LLRF are derived from Level 2 PSA Source Term Category (STC) event tree, as illustrated in Fig. 2.

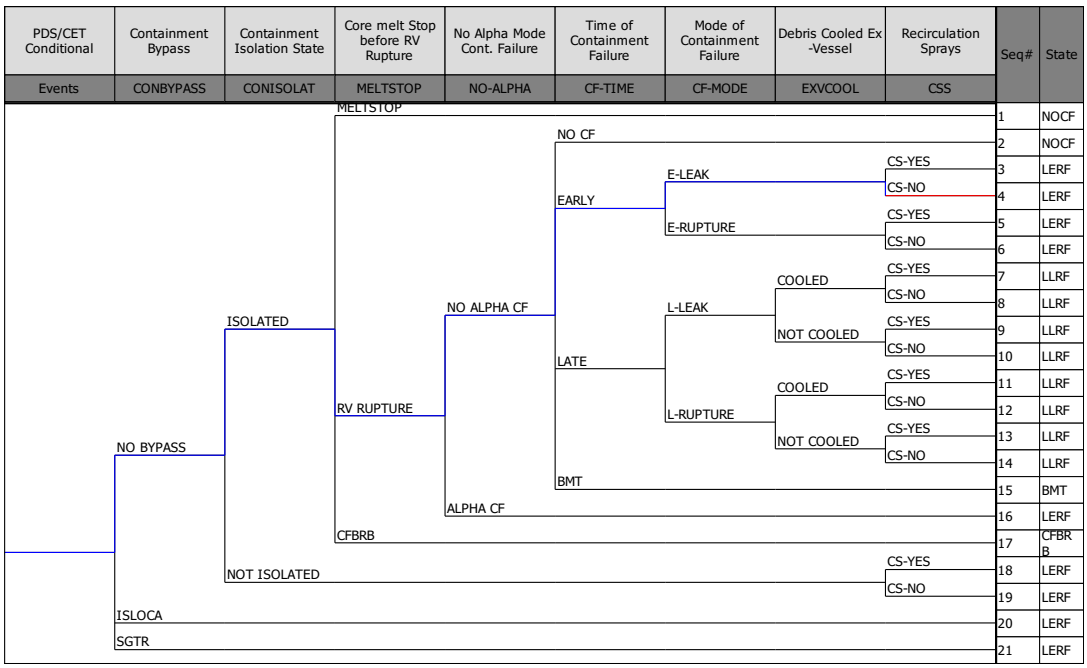

Figure 2. STC classification event tree of the reference plant.

The following sections illustrate how the two different containment pressurization scenarios—slow and fast—affect the relevant containment failure mode probabilities, the associated STC frequencies and LERF values, and the provisional impact of small leakage size on the assessment of a 100 TBq Cs-137 release risk.

2.1. Influence of containment pressurization scenarios to relevant failure probabilities

2.1.1. Case 1: scenarios involving slow pressurization

For slow pressurization, it is generally assumed that a leak occurs first at a given pressure, and rupture follows only in a subset of cases without considering a transition between leak and rupture [5, 8]. Under slow pressurization, we further assume that containment failure is governed by the failure mode that occurs at the lowest pressure, with each probability distribution estimated independently. In such case, both leak and rupture probabilities at a given pressure—$P_l(p)$ and $P_r(p)$, respectively—are evaluated using the following expressions:

$$P_l(p) = \int_0^p f_l\,(p')[1 - F_r(p')]dp' \quad (1a)$$
$$P_r(p) = \int_0^p f_r\,(p')[1 - F_l(p')]dp' \quad (1b)$$
$$P_{no}(p) = 1 - [P_l(p) + P_r(p)]dp' \quad (1c)$$

Where:
$f_l(p), f_r(p)$: PDFs of the leak and rupture, respectively, with respect to the pressure p,
$F_l(p), F_r(p)$: CDFs of the leak and rupture, respectively, with respect to the pressure p,
$P_l(p), P_r(p), P_{no}(p)$: Leak, rupture, and no failure probabilities at the pressure p, respectively.

According to Equation (1), the cumulative probabilities of a containment leak and rupture up to pressure p account for the conditional probabilities that leak and rupture have not occurred at or below that pressure, respectively. Based on the fragility curves shown in Table II, the leak and rupture probabilities evaluated for this case are presented in Fig. 3.

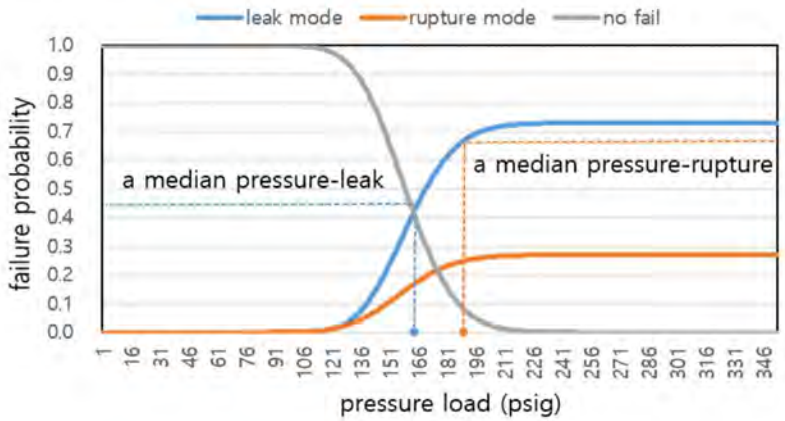

Figure. 3. Estimated probabilities for each failure mode: Case 1.

According to Fig. 3, up to approximately 75 psig, there is no difference between the rupture and leak probabilities, as both are nearly zero. However, from that point up to approximately 189 psig—where the rupture probability reaches its median—the probability of leak increases at a faster rate than that of rupture, resulting in a significantly higher leak probability. Beyond this point, the rate of increase for both probabilities declines markedly. For example, the probabilities of leak and rupture at the median pressure of the leak mode are 0.44050 and 0.17529, respectively, whereas they are 0.67868 and 0.25367 at the median pressure of the rupture mode. Unlike in Case 1, the leak probability does not decrease to zero but instead remains consistently near its maximum value of approximately 0.73. Similarly, the rupture probability does not increase to 1.0 but remains consistently at its maximum value of approximately 0.27.

2.1.2. Case 2: scenarios involving fast pressurization

In the presence of fast pressurization, the pressure will continue to rise if the failure mode is a leak, and thus a rupture failure may occur even though the initial failure at the pressure p was a leak [5, 8]. This is based on the belief that a leak does not arrest pressurization, and therefore, rupture following a leak remains possible. In this case, the leak probability is reduced by an amount proportional to the fraction of cases that transition to rupture. Then, under fast pressurization, both leak and rupture probabilities, $P_l(p)$ and $P_r(p)$, are expressed as follows [8–10]:

$$P_l(p) = F_l(p)[1 - F_r(p)] \quad (2a)$$
$$P_r(p) = \int_0^p f_r\,(p')dp' = F_r(p) \quad (2b)$$
$$P_{no}(p) = 1 - [P_l(p) + P_r(p)]dp' \quad (2c)$$

According to Equation (2a), the cumulative probability of a containment leak up to pressure p accounts for the conditional probability that rupture has not occurred at or below that pressure. Fig. 4 and Table III show the leak and rupture probabilities for Case 1, and their comparison with Case 2, respectively, evaluated using the fragility curves provided in Table II.

According to the figure and table, Cases 1 and 2 exhibit similar trends up to approximately 120 psig. However, beyond this point, Case 2 shows a much higher rupture probability than Case 1. For example, in Case 1, the probabilities of leak and rupture at the median pressure of the leak mode are 0.44050 and 0.17529, respectively, whereas in Case 2, they are 0.38427 and 0.23146. Similarly, at the median pressure of the rupture mode, the probabilities of leak and rupture are 0.67868 and 0.25367 in Case 1, and 0.43228 and 0.5 in Case 2, respectively. This difference can be attributed to a portion of the leak probability transitioning into rupture probability under fast pressurization as the pressure increases or a simultaneous occurre3nce of both failure modes. From this perspective, Case 2 represents a more conservative scenario than Case 2. Fig. 5 illustrates, for reference, how leak-induced rupture progressively influences the corresponding rupture probability as pressure increases, particularly when both leak and rupture occur concurrently.

Overall, Cases 1 and 2 demonstrate that, despite the two different pressurization scenarios employed, the sum of the leak and rupture probabilities at a given pressure load remains conserved and thus does not affect their contribution to the LERF (or LRF) under a given pressure.

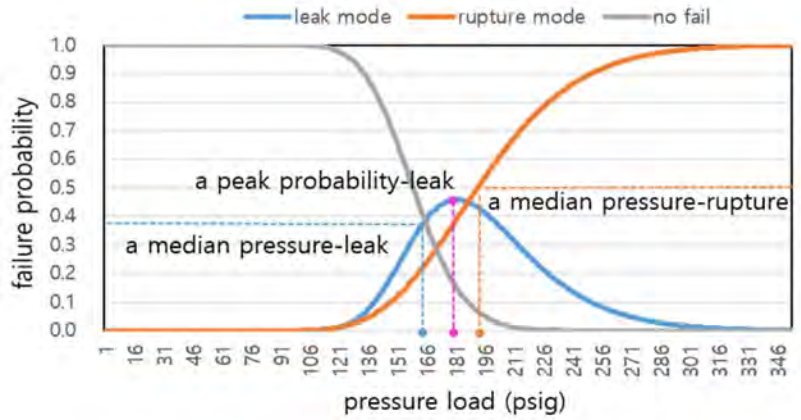

Figure 4. Estimated probabilities for each failure mode: Case 2.

Table III. Failure mode probabilities evaluated in Cases 1 and 2

Pressure (*p, psig*)	Cases	P_l	P_r	P_{no}
75	Case 1	0.0	0.00001	0.99999
	Case 2	0.0	0.00001	0.99999
100	Case 1	0.00038	0.00122	0.99850
	Case 2	0.00028	0.00122	0.99850
120	Case 1	0.01600	0.01518	0.96882
	Case 2	0.01579	0.01527	0.96895
162[1]	Case 1	**0.44050**	**0.17529**	**0.38421**
	Case 2	**0.38427**	**0.23146**	**0.38427**
178	Case 1	0.61419	0.23243	0.15338

	Case 2	0.45895	0.38762	0.15343
189[2]	Case 1	**0.67868**	**0.25367**	**0.06765**
	Case 2	**0.43228**	**0.5**	**0.06772**
200	Case 1	0.70995	0.26407	0.02597
	Case 2	0.36777	0.60618	0.02605
250	Case 1	0.72935	0.27065	0.00009
	Case 2	0.09135	0.90857	0.00009

[1] a median pressure of the leak mode ($p_{m,\,leak}$), [2] a median pressure of the rupture mode ($p_{m,\,rupt}$).

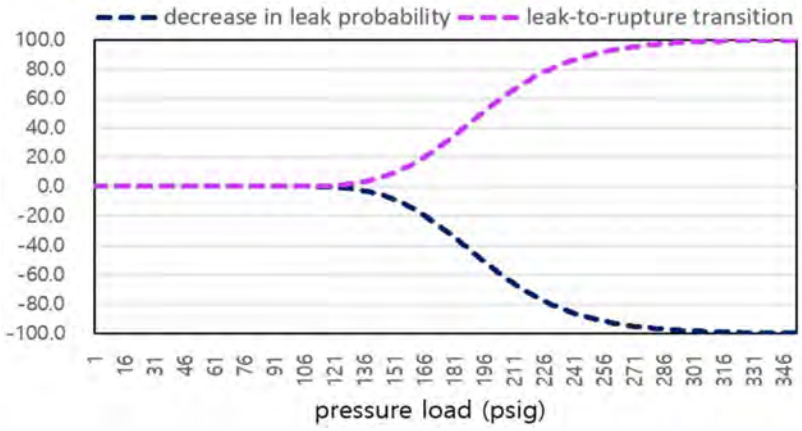

Transition probability (%) = $100 \times [F_l(p)F_r(p)]/[1 - P_{no}(p)]$

Figure 5. Transition in failure probability from leak to rupture: Case 2.

2.2. Case 3: Influence of small leakages on the 100-TBq Cs-137 risk indicator

As shown in Table I, several countries set a regulatory threshold of 100-TBq for the Cs-137 release. The corresponding mass of this radionuclide is derived as follows.

$$\mathrm{A} = \lambda \cdot \mathrm{N} = \lambda \cdot (\frac{\mathrm{m}}{\mathrm{M}})\mathrm{N}_A \tag{3a}$$

$$\mathrm{m} = \frac{\mathrm{A}\cdot\mathrm{M}}{\lambda\cdot\mathrm{N}_A} = 31.25\ \mathrm{g}\ /100\ TBq \tag{3b}$$

Here, A (activity in Bq) = 100 TBq = 1.0×10^{14} Bq, λ (decay constant) = $\ln 2/t_{1/2}$ = 0.693/ (30.17 y) = 7.28×10^{-10}/s, $t_{1/2}$ (half-life) = 30.17 y, M (molar mass) = 137 g/mol, and N_A (Avogadro constant) = 6.023×10^{23}/mol.

For the reference plant [11], the design requirement specifies that the leakage of radioactive material must not exceed 0.2 % (or, under the more stringent condition, 0.1%) of the free containment volume within the first 24 h at a design leakage pressure of 57 psig (≈0.49 MPa), and thereafter must be limited to ≤ 0.1 % of the containment volume per day. A conservative severe-accident analysis of the station-blackout (SBO) scenario [12] shows that, in the absence of any structural failure of the containment, up to 20 g of airborne Cs-137 can be released during the first 24 h (10 g if the 0.1 % leakage limit is applied). Within the 72-h mission window used for the Level 2 PSA, the cumulative release could reach 40 g (≈30 g for the 0.1 % limit). These releases exceed the Cs-137 release threshold of 100 TBq (≈31 g), except when the 0.1 % leakage limit is imposed, in that case the release remains below the threshold even though the containment has not suffered structural damage.

Other accident scenarios may exhibit trends comparable to those of the SBO case, yet the design-pressure threshold can still be exceeded under any of the following conditions: (a) the containment is pressurized beyond its design pressure without structural degradation; (b) minor structural degradation occurs as a result of the pressurization—although the degradation size is considerably smaller than that assumed for nominal leak modes typically considered in Level 2 PSA (e.g., a 0.1 ft² opening in the reference plant); or (c) relevant uncertainties are introduced into the analysis [13, 14].

Consequently, relying exclusively on the nominal leak and rupture failure modes used in Level 2 PSAs—traditionally the basis for estimating the Cs-137 release threshold of 100 TBq—may underestimate the total release potential, especially in multi-unit incidents where the cumulative effect of minor leaks from each unit can be substantial.

The minor leakage pathways described above—those that can exceed the Cs-137 release threshold of 100-TBq—are expected to lie just above the design containment-leakage limit but still below the nominal leak threshold. Under the newly introduced *small-leakage* mode, certain accident scenarios considered in Level 2 PSAs, in which fission products (including Cs-137) are released into the containment without producing a measurable leak or rupture, may be re-classified as surpassing the Cs-137 release limit of 100-TBq. In these cases the probabilities of leak and rupture are recalibrated by applying the transition probability from the no-containment-failure condition to the small-leakage mode.

Once the small leakage mode—capable of producing an environmental release of Cs-137 that exceeds 100-TBq—is identified and its probability distribution is characterized, the probability of this mode, together with the probabilities of the conventional leak and rupture modes, are re-evaluated by extending the formulations of Cases 1 and 2 to cover all three failure modes [8, 10].

2.2.1. Scenarios involving slow pressurization

$$P_1(p) = \int_0^p f_1(p')[1 - F_2(p')][1 - F_3(p')]dp' \quad (4a)$$
$$P_2(p) = \int_0^p f_2(p')[1 - F_1(p')][1 - F_3(p')]dp' \quad (4b)$$
$$P_3(p) = \int_0^p f_3(p')[1 - F_1(p')][1 - F_2(p')]dp' \quad (4c)$$
$$P_{no}(p) = 1 - \sum_1^3 P_i(p) = \prod_i^3 [1 - F_i(p)] \quad (4d)$$

Here, subscripts i = 1, 2, and 3 denote the small leakage, leak, and rupture modes, respectively, and $P_i(p)$ and $F_i(p)$ represent the corresponding failure probabilities and CDFs at the pressure p.

2.2.2. Scenarios involving fast pressurization

$$P_1(p) = F_1(p) \prod_{i=2}^3 [1 - F_i(p)] \quad (5a)$$
$$P_2(p) = \int_0^p f_2(p')[1 - F_3(p')]dp' \quad (5b)$$
$$P_3(p) = \int_0^p f_3(p')[1 - F_2(p')]dp' \quad (5c)$$
$$P_{no}(p) = 1 - \sum_1^3 P_i(p) = \prod_i^3 [1 - F_i(p)] \quad (5d)$$

3. CONCLUSIONS

In the first part of this paper, two case studies were performed to assess the impact of relevant pressurization scenarios on the leak- and rupture-probability estimates for Level 2 PSAs under slow and fast conditions. The second part emphasizes the need to consider small-leakage modes that can affect Cs-137 releases.

The following summarizes the key findings of these case studies.

(1) **Containment pressurization-condition effect on relevant risk indicators** – In the two case studies, Case 1 assumes a slow pressurization while Case 2 assumes a fast pressurization
- For a given pressure the combined leak- and rupture-probability is conserved; consequently the contribution of the combined probability to the LERF/LRF does not change.
- However, the individual leak- and rupture-probabilities differ between the two approaches. The fast-pressurization scenario (Case 2) yields higher individual probabilities than the slow-pressurization scenario (Case 1). From this viewpoint, Case 2 is the more conservative of the two.
- Implications for the downstream STC analysis – These pressurization-condition differences can temporarily affect the results of the subsequent STC scenario-based probabilistic consequence analysis. This is because the STC analysis explicitly uses the source-term results and the associated probabilities (or frequencies) for each leak and rupture mode; therefore any shift in the individual probabilities feeds through to the final consequence estimates.

(2) Provisional influence of small leakage modes on relevant risk indicator
- As highlighted in Case 3, restricting containment-failure modes to the conventional leak and rupture categories employed in traditional Level 2 PSAs may underestimate the potential release of Cs-137—particularly in multi-unit accident scenarios, where small-leakage modes could contribute substantially to the total release.
- Accordingly, both the nominal range of these small-leakage modes (which spans from slightly above the design leakage level to just below the nominal leak mode) and their impact on relevant risk indicator associated with the environmental release of 100-TBq Cs-137 must be systematically evaluated to enable a more realistic assessment.

ACKNOWLEDGMENTS

This work was supported by a National Research Foundation of Korea (NRF) grant, funded by the Korean government (MSIT: Ministry of Science and ICT) (No. RS-2022-00143695).

REFERENCES

1. USNRC, *PRA Procedure Guide: A Guide to the Performance of Probabilistic Risk Assessments for Nuclear Power Plants*, NUREG/CR-2300, United State Nuclear Regulatory Commission (U.S. NRC), Washington, DC, USA (1983).
2. OECD/NEA, *Use and Development of Probabilistic Safety Assessments at Nuclear Facilities*, NEA/CSNI/R(2019)10, Organization for Economic Cooperation and Development (OECD) Nuclear Energy Agency (NEA), Paris, France (2020).
3. USNRC, *An Approach for Using PRA in Risk-Informed Decision on Plant Specific Changes to the Licensing Basis*, Reg. Guide 1.174, United State Nuclear Regulatory Commission (U.S. NRC), Washington, DC, USA (1998).
4. M. Khatib-Rahbar, R. Karimi, "An Approach to Definition of Large Release," *7th International Conference on Probabilistic Safety Assessment and Management (PSAM 7)*, Berlin, Germany (June 2004).
5. USNRC, *Severe Accident Risks: An Assessment for Five US Nuclear Power Plants*, NUREG-1150, United State Nuclear Regulatory Commission (U.S. NRC), Washington, DC, USA (1990).
6. EPRI, *PSA Applications Guide*, EPRI TR-105396, Electric Power Research Institute (EPRI), Palo Alto, CA, USA (1995).
7. KHNP, *SKN Units 3&4 Level 2 PSA: Full-power and Internal Events*, Korea Hydro & Nuclear Power Co., Ltd, (KHNP), Daejeon, Korea (2015).

8. J.C. Helton, R.J. Breeding, S.C. Hora, "Probability of containment failure mode for fast pressure rise," *Reliability Engineering and System Safety*, **35**, pp.91–106 (1992).
9. K.I. Ahn et al., "On the plant-specific impact of different pressurization rates in the estimation of containment failure mode probabilities," *Reliability Engineering and System Safety*, **84**, pp.129–139 (2004).
10. K.I. Ahn et al., "Development of a computer code, CONPAS, for an integrated level 2 PSA," *Nuclear Engineering and Technology* (formerly known as Journal of the Korean Nuclear Society), **30**(1), pp.58–74 (1998).
11. KHNP, *Hanul Units 3&4 Level 2 PSA: Full-power and Internal Events*, Korea Hydro & Nuclear Power Co., Ltd, (KHNP), Daejeon, Korea (2015).
12. Y.J. Cho et al., "Uncertainty Analysis of Source Term for OPR1000 Station Blackout Accident," *Transactions of the Korean Nuclear Society Autumn Meeting*, Jeju, Korea (May 2025).
13. K.I. Ahn, S.Y. Park, "Best-practice Severe Accident Uncertainty and Sensitivity Analysis for a Short-term SBO Sequence of a Reference PWR using MAAP5," *Annals of Nuclear Energy*, **170** (108981) (2022).
14. W. Choi, K.I. Ahn, S.J. Kim, "Effect of Mitigation Strategies in the Severe Accident Uncertainty Analysis of the OPR1000 Short-term Station Blackout Accident," *Nuclear Engineering and Technology*, **54**(12), pp.4534-4550 (2022).

Influence of Containment Pressurization Rates on the Assessment of Severe Accident Risk (SAR)

Kwang-Il Ahn

KAERI, Rep. of Korea, kiahn@kaeri.re.kr

OUTLINE

- **Motivation**
- **Problem statement**
  - Containment pressurization-related issue
  - Large release of Cs-137 related problem
- **Relevant case studies**
- **Summary**

Level 2 PSA Studies in SARNET/ERMSAR

- **SARNET** (EURATOM FP7, '04.04 ~ '08.05; integrated into NUGENIA, mid 2013) **WP5:**
  - **WP5.1:** *comparison of Level 2 PSA approaches and identification of improvement needs*, including (1) accident progression event tree (APET, including systems behaviour, containment leakages and human reliability), (2) physical phenomena, (3) releases assessment, (4) uncertainties assessment methods.
  - **WP5.2:** *improvement of methodologies for the assessment of uncertainties*
  - **WP5.3:** *improving APET methodology using dynamic reliability techniques*.
- **Level 2 PSA in ERMSAR** (SARNET knowledge spreading)
  - **ERMSAR-2005 (1st ERMSAR)**, Aix-en-Provence, 14-16 Nov. 2005
    - *Overview of SARNET progress on PSA 2 topic*, B. Chaumont (IRSN)
    - *Comparison of approaches for physical phenomena assessment in Level 2 PSA*, J. Eyink (Framatome ANP) & H. Löffler (GRS)
  - **ERMSAR-2007 (2nd ERMSAR)**, FZK, Karlsruhe, 12-14, June 2007
    - *Level 2 PSA - Comparison between classical and dynamic reliability methods*, E. Raimond & T. Durin (IRSN)
    - *OECD CSNI WGRISK Activities in the L2 PSA Field: an International Point of View*, J-M. Lanore & E. Raimond (IRSN)
  - **ERMSAR-2008 (3rd ERMSAR)**, Nesseber, Bulgaria, 23-25 Sept. 2008
    - L2 PSA methods harmonization, B. Chaumont & E. Raimond (IRSN)
  - ….

1. Motivation & context

- **Level 2 PSA:** Evaluates containment performance and severe accident risk following core damage sequences, and relevant key risk indicators are characterized as LERF, LRF (100-TBq Cs-137), CFF.
  - **LERF** (Large Early Release Frequency) – a surrogate indicator of early fatalities, expected during the early stage of a severe accident or at the moment of a RPV breach.
  - **LRF** (Large Release Frequency) or **Cs-137 release limit** – an indicator of long-term health effects (latent-cancer fatality) and land contamination. Korea, Japan, Canada, Finland adopt a 100-TBq Cs-137 release threshold, limiting the combined frequency of the relevant scenarios to $< 1.0 \times 10^{-6}$/ry.
  - **CFF** (Containment Failure Frequency) – the frequency of structural damage to the containment building and of bypass events (e.g., ISLOCA, spontaneous/induced SGTR).
- **Underlying problem:** A realistic assessment of containment failure modes (leak and rupture) is essential for credible safety evaluations; however, modeling assumptions and scenario variations introduce uncertainties into Level 2–relevant risk indicators.
- **The present study:** Investigate the impact of pressurization rates (slow vs. fast) and the role of “minor leakage” modes in achieving Level 2–relevant safety goals.

1. Motivation & context

Level 2-relevant risk targets defined in several countries

Country	Level 1 risk	Level 2 risk	Remarks
Canada (Regulator)	CDF < 10^{-5} /ry	SRF (1000-TBq I-131) < 10^{-5} /ry LRF (100-TBq Cs-137) < 10^{-6} /ry	New plants
Czechia (Licensee)	CDF < 10^{-4} /ry CDF < 10^{-5} /ry	LERF (> 1 % Cs-137, up to 10 h from fuel damage) < 10^{-5} /ry LERF: practically eliminated	Existing plants (incl. SFP) New plants (incl. SFP)
Finland (Regulator)	CDF < 10^{-5} /ry	LRF (100-TBq Cs-137) < 5.0×10^{-7} /ry	All plants (incl. new)
France (Regulator)	CDF < 10^{-5} /ry CDF < 10^{-6} /ry	LRF: practically eliminated (not quantitatively specified)	New plants (all modes/hazards) New plants (internal events)
Hungary (Regulator)	CDF < 10^{-4} /ry CDF < 10^{-5} /ry	L(E)RF < 10^{-5} /ry L(E)RF < 10^{-6} /ry	Existing plants New plants
Japan (Regulator)	CDF < 10^{-4} /ry	CFF < 10^{-5} /ry; 100-TBq Cs-137 < 10^{-6} /ry	All plants (incl. new)
Korea (Regulator)	CDF < 10^{-4} /ry CDF < 10^{-5} /ry	LERF < 10^{-5} /ry LERF < 10^{-6} /ry 100-TBq Cs-137 < 10^{-6} /ry	Existing plants APR1400 follow-up All plants (incl. new reactors)
Sweden (Licensee)	CDF < 10^{-4} /ry	L(E)RF (> 0.1 % of core inventory) < 10^{-7} /ry	All plants
USA (Regulator)	CDF < 10^{-4} /ry CDF < 10^{-5} /ry	LERF < 10^{-5} /ry LERF < 10^{-6} /ry	Existing plants New plants
IAEA (Recommend)	CDF < 10^{-4} /ry CDF < 10^{-5} /ry	LERF < 10^{-5} /ry LERF < 10^{-6} /ry	Existing plants New plants

2. Problem statement

- **Influence of pressurization rate on leak & rupture probabilities**
  - Leak & rupture as the two dominant containment failure modes considered in Level 2 PSA.
  - Pressurization rate determining whether a leak can stop a further build-up of cont. pressure.
- **Containment failure modes** (structural), for a large/dry PWR (pre-stressed, reinforced-concrete containment having a cylindrical body with a hemispherical dome)**:**
  - **Leak**: A breach that halts gradual pressure buildup and requires ≥ 2 hours to depressurize.
    - Nominal size: 0.04–0.1 ft²
    - A typical failure mode: a failure of the equipment hatch ring or the tearing of the containment liner plate
  - **Rupture**: A breach that depressurizes the containment within 2 hours. Nominal size: > 1.0 ft².
  - Relevant fragility curves of the reference PWR: typically estimated using lognormal PDFs
    - Median Pressure : 162 psig for a leak mode; 189 psig for a rupture mode.

Failure Modes	Lognormal PDF as a Function of Pressure Load (p)	Median Pressure (p_m, psig)	Logarithmic Standard Deviation (β)
Leak	$f(p) = \frac{1}{\beta\sqrt{2\pi}p}\exp\left[-\frac{(\ln(p)-\ln(p_m))^2}{2\beta}\right]$	162	0.14
Rupture		189	0.21

2. Problem statement

(1) ST release sequences leading to LERF/LRF

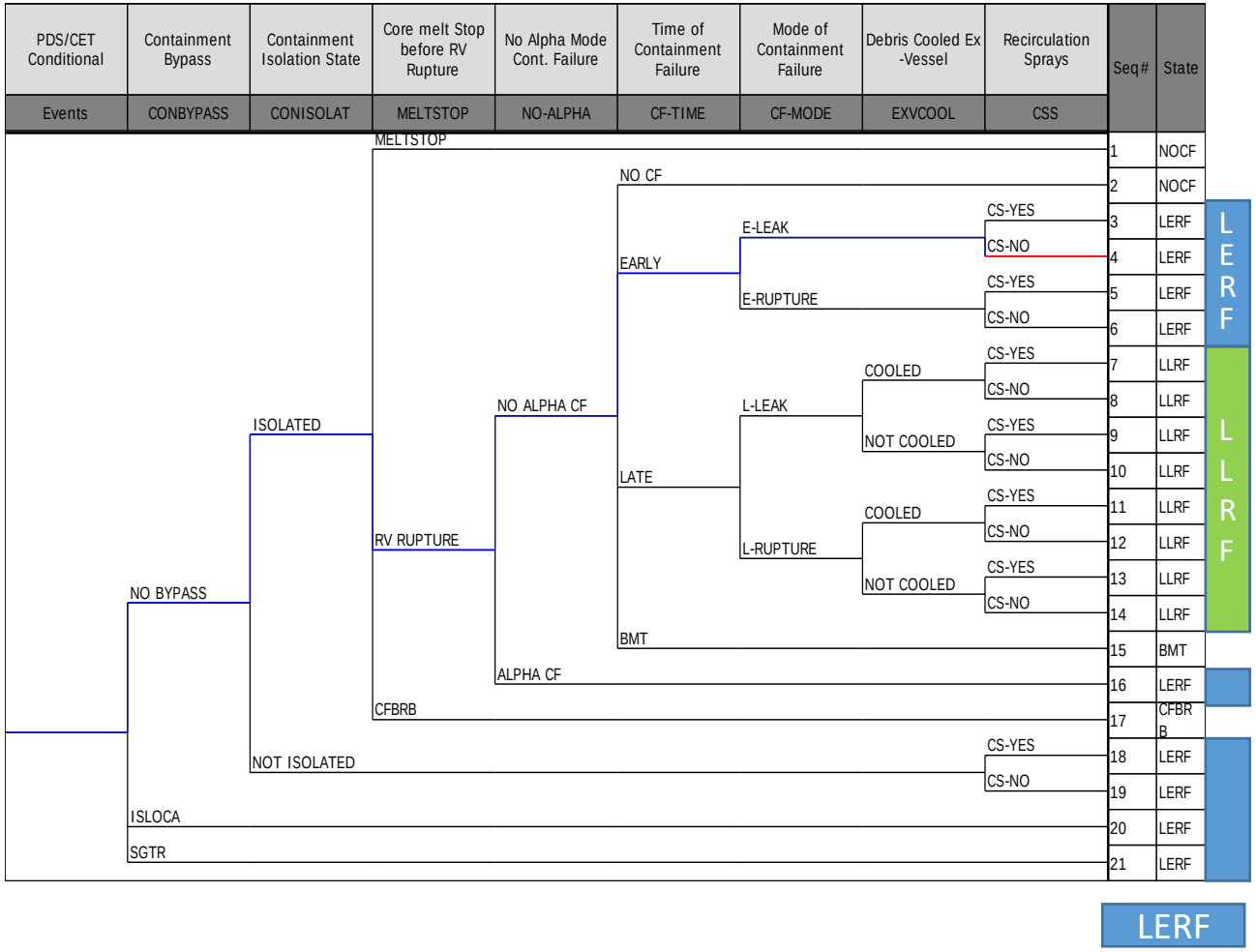

STC defined in the reference Level 2 PSA (derived from APET)

- **LERF**: the aggregate frequency of all accident scenarios, causing **large**, unmitigated releases **prior to** an effective evacuation of the surrounding population **(early)**.
  - Relevant accident scenarios: (a) unscrubbed releases of radioactive material resulting from cont. isolation failures; (b) cont.-bypass events such as ISLOCA & I-SGTR; and (c) any scenario causing cont. damage or failure that is equivalent to the above “large” release.
  - Relevant time window: at, or shortly after, the RPV breach—generally within 4 h of the breach in PWR.
- **LLRF** (Large Late Release Frequency): includes **late-phase** containment failure scenarios, causing **large**, unmitigated releases of airborne FPs during the **72-h mission time** assumed in a Level 2 PSA
- **LRF** (in the Korean Level 2 PSA)**: LERF + LLRF**;
  ***Cs-137 release limit** – an indicator for land contamination risk

2. Problem statement

(2) Fast/slow pressurization scenarios defined in the reference Level 2 PSA

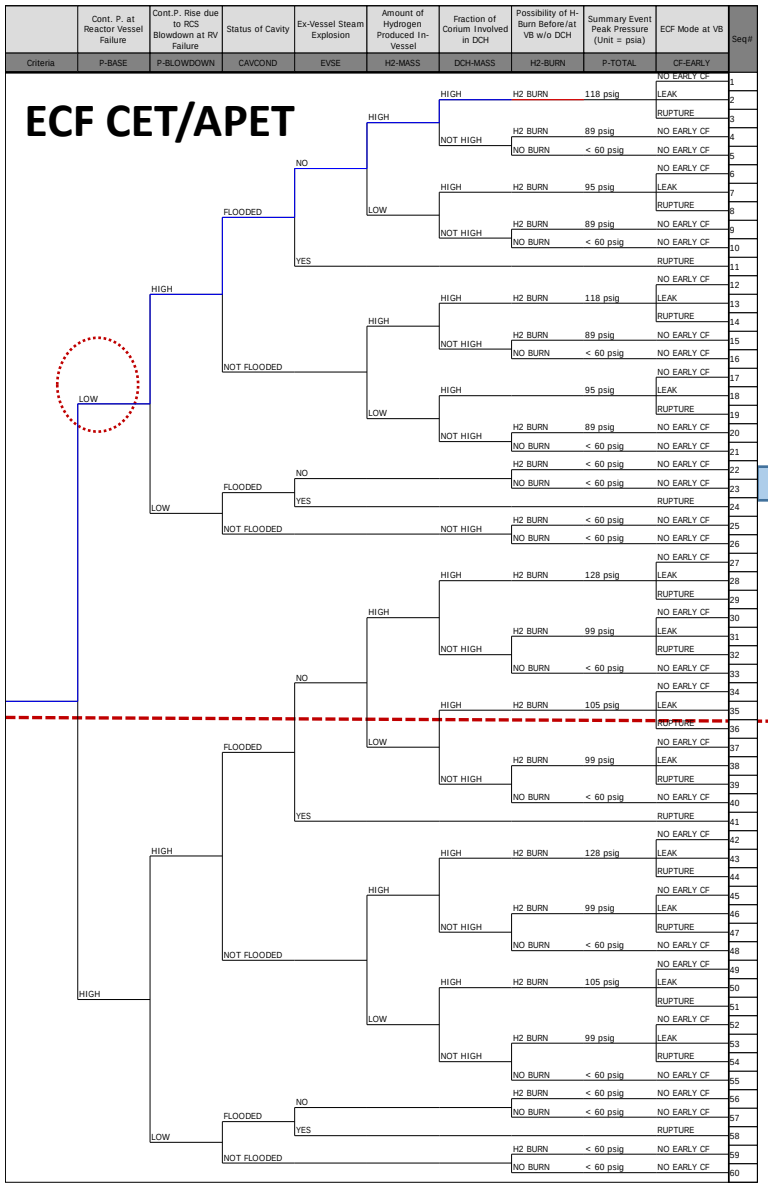

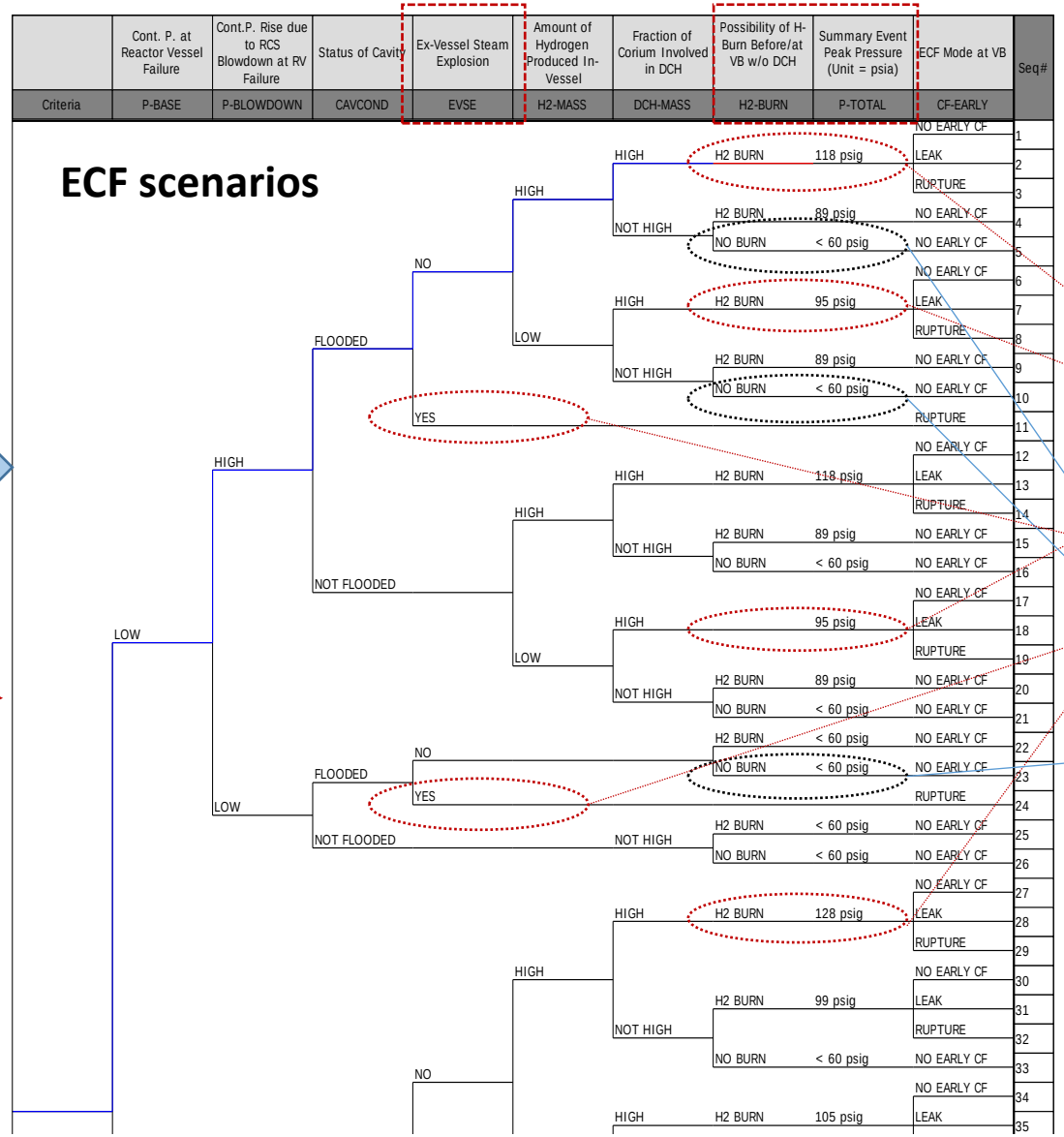

Classification of ECF scenarios

- Dynamic (H-Burn)
- Dynamic (Ex-S/E)
- Slow-p (No Burn)

3. Case studies (pressurization rate)

❑ Case 1 - Slow pressurization scenarios

- Pressure Dynamics: The pressure increase is slower than the **system's** depressurization capacity (e.g., gradual steam over-pressurization, non-condensable gas generation from MCCI).
- Failure Logic: The lowest-pressure failure mode governs the outcome; once a leak occurs, it relieves the pressure, preventing further buildup.
- **Failure-Path: Leak (**or **rupture) →** *(if pressure continues)* **→ Leak-only (**or **rupture–only) (no other failure mode)**

❑ Case 2 - Fast pressurization scenarios

- Pressure Dynamics: Pressure rise exceeds the depressurization capacity (HPME, Ex-S/E, H-combustion/detonation).
- Failure Logic: A leak does not arrest pressurization; Rupture can follow the leak, giving much higher rupture probabilities than in Case 1.
- **Failure-Path: Leak → *(if pressure continues)* → additional leak or rupture; Rupture terminates pressure rise → no further failures. If pressure stops after the first leak, the event ends as a *leak-only* failure.**

❑ Probabilistic formulation for failure modes (*f* = PDF, *F*=CDF, *p*= pressure load)

Case	Leak prob. (P_l)	Rupture prob. (P_r)	No Fail (P_{no})
Case 1 (slow-p)	$P_l(p) = \int_0^p f_l(p')[1 - F_r(p')]dp'$	$P_r(p) = \int_0^p f_r(p')[1 - F_l(p')]dp'$	$P_{no}(p) = 1 - [P_l(p) + P_r(p)]dp'$
Case 2 (fast-p)	$P_l(p) = F_l(p)[1 - F_r(p)]$	$P_r(p) = \int_0^p f_r(p')dp' = F_r(p)$	

3. Case studies (pressurization rate)

❑ Results for the reference plant:

- **Case 1 (slow)**
  - Up to approximately 189 psig—where the pressure reaches its median of the rupture mode, the leak probability increases at a faster rate than that of rupture, resulting in a significantly higher leak probability.
  - Beyond this point, the rate of increase for both probabilities declines markedly. Beyond 200 psig, the leak probability stabilizes at ~0.73, while the rupture probability stabilizes at ~0.27.
- **Case 2 (fast)**
  - At 181 psig, the leak probability reaches its maximum (~0.46), but the rupture probability continuously increases
  - For the fast case, rupture can follow the leak, thereby shifting a portion of the leak probability to rupture mode.

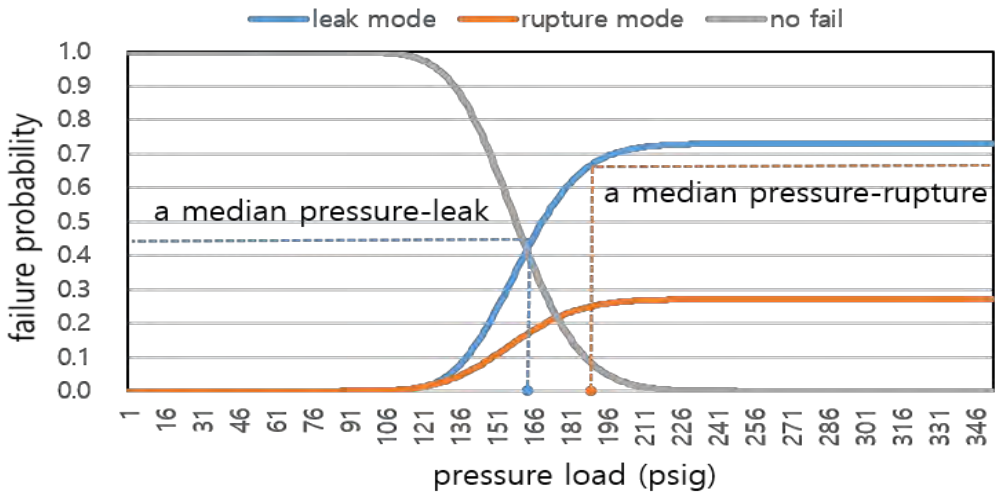

Case 1: Estimated probabilities for each failure mode

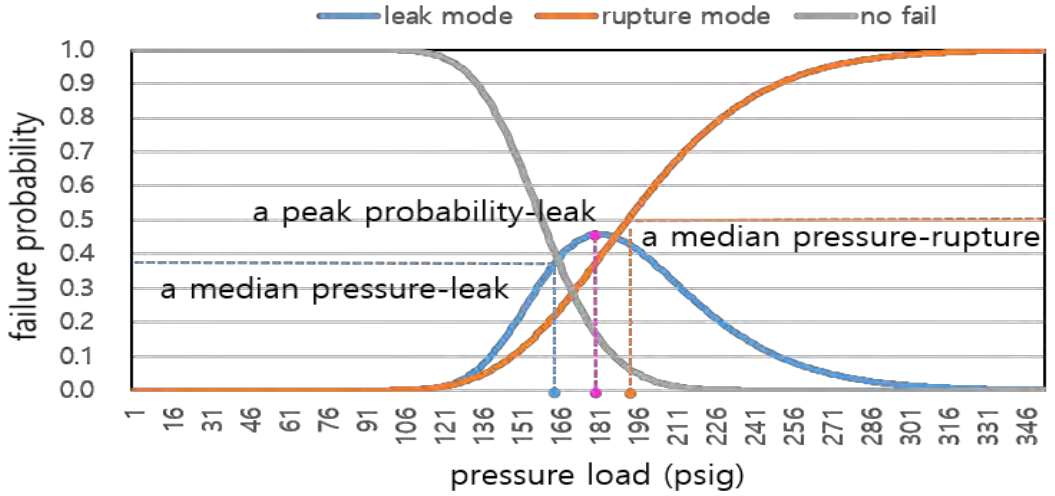

Case 2: Estimated probabilities for each failure mode

3. Case studies (pressurization rate)

❑ Comparison of pressurization influence:

- **The sum of leak and rupture probabilities remains conserved across both scenarios.**
  - For any pressure, P_{leak} + $P_{rupture}$ remains constant between Cases 1 & 2.
  - Consequently, the combined contribution to LERF/LRF does not change. Only the individual leak and rupture probabilities differ.
- **Changes in individual probabilities influence STC analysis because source-term calculations use separate leak and rupture frequencies.**
  - Shift in individual probabilities → temporary change in probabilistic consequence estimates.
  - Fast-pressurization scenario yields higher rupture frequencies → larger estimated consequences.

Case 2: Transition from leak to rupture mode

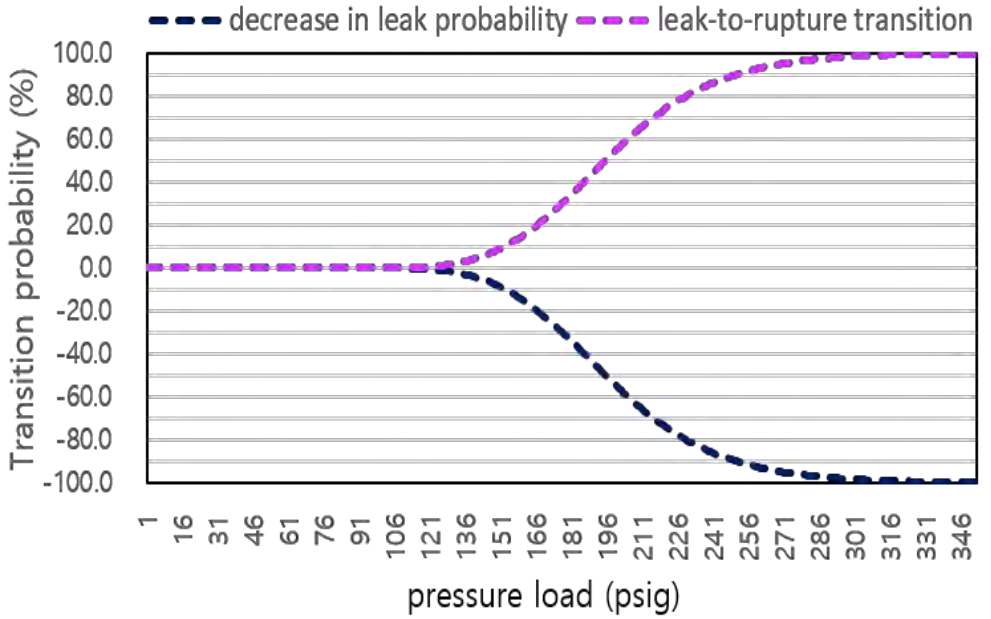

Transition probability (%) = $100 \times [F_l(p)F_r(p)]/[1 - P_{no}(p)]$

For fast pressure, leaks converted into additional leaks or *ruptures as the pressure continues to rise*

3. Case studies (pressurization rate)

- **Failure mode probabilities evaluated at specified pressures:**

Pressure (p, psig)	Cases	P_l	P_r	P_{no}
75	Case 1	0.0	0.00001	1.0
	Case 2	0.0	0.00001	
100	Case 1	0.00038	0.00122	0.999
	Case 2	0.00028	0.00122	
120	Case 1	0.01600	0.01518	0.969
	Case 2	0.01579	0.01527	
162[1]	Case 1	0.44050	0.17529	0.384
	Case 2	0.38427	0.23146	
178	Case 1	0.61419	0.23243	0.153
	Case 2	0.45895	0.38762	
189[2]	Case 1	0.67868	0.25367	0.068
	Case 2	0.43228	0.5	
200	Case 1	0.70995	0.26407	0.026
	Case 2	0.36777	0.60618	
250	Case 1	0.72935	0.27065	0.0
	Case 2	0.09135	0.90857	

[1] *a median pressure of the leak mode ($p_{m,\ leak}$),* [2] *a median pressure of the rupture mode ($p_{m,\ rupt}$).*

3. Case studies (minor leakage)

❑ Cs-137 risk relevant issue:

- Threshold for 100-TBq Cs-137: ≈ 31.25 g (achievable without structural failure of the containment).
  - Design leakage limit of reference plant: ≤ 0.2% (or stricter 0.1%) of containment free volume at 57 psig
  - Problem: For a SBO scenario analysis, the cumulative release could reach 40 g within 72 h mission time, exceeding the threshold even without structural failure unless the stricter 0.1% leakage limit is applied.
  - Risk impact: Relying solely on nominal leakage sizes may underestimate release potential, particularly in multi-unit incidents, where cumulative minor leaks can push the total release above the 100-TBq threshold.
  - Traditional Level-2 PSA (limiting to only leak + rupture) could underestimate total Cs-137 release.

❑ Re-evaluating the Cs-137 risk:

- Minor leakage definition: a leakage pathways or minor structural degradation exceeding the design leakage limits but remaining below the nominal leak threshold (e.g., 0.1 ft^2).
- Classification: Containment scenarios previously categorized as “no failure” may be reclassified as exceeding the 100-TBq release limit.
- Proposed approach: Extend the Cases 1 & 2 formulations to include a third failure mode (minor-leakage), enabling probability recalibration.

3. Case studies (minor leakage)

- **Probabilistic formulation of three failure modes** (*f* = PDF, *F*=CDF, *p*= pressure load)

Case	Minor leakage (P_1)	Leak (P_2)	Rupture (P_3)	No Fail (P_{no})
Slow-p	$P_1(p) = \int_0^p f_1(p')[1-F_2(p')][1-F_3(p')]dp'$	$P_2(p) = \int_0^p f_2(p')[1-F_1(p')][1-F_3(p')]dp'$	$P_3(p) = \int_0^p f_3(p')[1-F_1(p')][1-F_2(p')]dp'$	$P_{no}(p) = 1 - \sum_1^3 P_i(p) = \prod_i^3 [1-F_i(p)]$
Fast-p	$P_1(p) = F_1(p)\prod_{i=2}^3 [1-F_i(p)]$	$P_2(p) = \int_0^p f_2(p')[1-F_3(p')]dp'$	$P_3(p) = \int_0^p f_3(p')[1-F_2(p')]dp'$	

4. Summary & take-away

- **Pressurization influence on the Level 2-relevant risk:**
  - Combined (leak + rupture) probability is conserved for a given pressure → no change in overall LERF/LRF contribution.
  - Fast pressurization (Case 2) leads to higher rupture probabilities → more conservative one.
  - These differences can affect source-term and offsite consequence analyses.
- **Minor-leakage influence on the Cs-137 release risk:**
  - Excluding minor-leakage modes may underestimate Cs-137 release potential, especially in multi-unit scenarios.
  - Minor-leakage openings may lie between the design leakage limit and the nominal leak threshold.
  - Incorporating them provides a more realistic assessment of the 100-TBq Cs-137 risk indicator.
- **Moving forward:**
  - **Integrate the identified issues into the conventional Level-2 PSA framework**
  - **Feed the relevant results into downstream safety-critical STC & risk analyses**

Thank you for your attention

BENCHMARK ON COUNTER-CURRENT FLOW IN MULTI-COMPARTMENT CONTAINMENT USING THAI TEST DATA

J. Hermann, M. Freitag, E. Schmidt
Becker Technologies GmbH
Neckarstraße 12-14, 65239 Hochheim, Germany
hermann@becker-technologies.com; freitag@becker-technologies.com;
eike.schmidt@becker-technologies.com

S. Band, D. Iliev
Gesellschaft für Anlagen- und Reaktorsicherheit (GRS) gGmbH,
Schwertnergasse 1, 50667 Cologne, Germany
sebastian.band@grs.de; dimitar.iliev@grs.de

Z. Liang, A. John, M. Zanoni
Hydrogen Technologies Branch, Canadian Nuclear Laboratories,
286 Plant Rd, Chalk River, Ontario, K0J 1J0, Canada
zhe.liang@cnl.ca; aneesh.john@cnl.ca; marco.bazelattozanoni@cnl.ca

ABSTRACT

In large containments, atmospheric counter-current flows can occur during design-basis accidents (DBAs) and severe accidents, particularly within and between compartments and their openings (e.g. in the pressure reduction system of an RBMK 1000). These flows have been observed in containment test facilities, such as the THAI TH-27 benchmark, and predicted by computational fluid dynamics (CFD) codes, notably in analyses in the vicinity of the steam generators of the German KONVOI design. Studies have shown that strong shear flows and significant density differences in the gas could cause changes in the local flow direction, which could ultimately lead to counter-current flows. Experimental investigations of counter-current flows in liquids and two-phase mixtures in the primary circuit have also been used successfully to develop and validate models for accident analysis codes.

This work involved the validation and benchmarking of models that predict atmospheric counter-current flows based on experiments conducted in the THAI facility. The test configuration consisted of the THAI test vessel (TTV) without the inner cylinder and the parallel attachable drum (PAD). The TTV and the PAD were connected by the lower connecting pipe. Two tests, TH-35 and TH-36, were conducted to generate counter-current flow data across a range of Reynolds numbers, capturing the transition from laminar to turbulent flow regime. The counter-current flow was induced by injecting hot air and steam into the TTV and extracting gas from the top of the PAD. The difference in gas density between the two vessels caused the hot gases to flow into the PAD, where they descended as a plume. Simultaneously, colder air and steam flowed backwards from the PAD into the TTV, through the lower half of the connecting pipe. In both tests, three steady state subphases were defined, in which the gas injection mass flows were kept constant. Vessel pressure had to be regulated by injecting gas into the TTV and releasing gas from the PAD.

The test data was recorded with high spatial and temporal resolution for validating semi-empirical modeling approaches used in LP and CFD. This paper reports on the experimental findings and the results of the benchmark, which reveal the complexity of the flow phenomena and the necessity of making adequate assumptions about heat transfer and boundary conditions in the simulation models.

KEYWORDS
Severe Accident, Containment, Counter-current flows, THAI, Benchmark, Thermal hydraulics

1. INTRODUCTION

Atmospheric counter-current flows can occur in design-basis accidents (DBA) and severe accidents (SA) in large containments, especially in small compartments and in flow openings (e.g. in the pressure reduction system of an RBMK 1000) between individual compartments. Such flows have also been detected in containment test facilities, e.g. in the TH-27 benchmark **[Fre18]** and were predicted for containments by CFD analyses in the vicinity of the steam generators of German KONVOI plants **[Roy00]**, **[Rud15]**.

The Counter-current flow itself is represented by a special case of a strong shear flow, where the flow direction changes its flow direction locally due to density differences in the gas. Experimental investigations on counter-current flows in liquids and two-phase mixtures in the primary circuit **[Pra12]**, **[Ste92]** have already been successfully used to develop and validate suitable models in AC^2 (ATHLET) **[Ler19]**. For a correct prediction of atmospheric counter-current flows, a model extension based on a semi-empirical approach that accounts for turbulent effects has been implemented, e.g. in the COCOSYS module **[Ili19]**. The corresponding model parameters were calibrated using experimental data from the SETH project **[Set12]** and validated using the TH-35 benchmark.

The objective of test TH-35 and its benchmark was to investigate the strength and intensity of a counter-current flow in a range of Reynolds numbers, representing the transition between laminar and turbulent flows. The $THAI^+$ facility consisting of the THAI test vessel (TTV) without inner cylinder and the parallel attachable drum (PAD) connected by the lower connecting pipe was used in test TH-35. The counter-current flow was forced to occur by injecting hot gases into the TTV and removing a gas mixture from the top of the PAD. The different gas densities in the two vessels allowed for hot gases flowing to the cold PAD where the hot gas ascended as a plume. At the same time, cold fluid was flowing backwards from the colder PAD into the hotter TTV, along the lower half of the connecting pipe.

Three steady-state sub-phases were defined, in which the gas injections were kept constant. It was mandatory to regulate the vessel pressure in sliding pressure mode, by injecting gas into the larger TTV and releasing gas from the PAD. The test data allows for validating semi-empirical modelling approaches of LP codes and CFD models. Specific features of the test data which can be used for validation purposes are:

- stationary hot temperature inside a large volume
- steady-state vessel pressure regulation during the three gas injection phases
- several measurements capturing the flow distribution in the lower connecting pipe
- dense temperature measurements in both compartments connected to the lower connecting pipe
- record of the steam condensation rates in both large volumes.

1. TEST CONFIGURATION

The basic configuration of the $THAI^+$ facility and the most important dimensions, Figure 1, are given in **[Fre16]**. The $THAI^+$ configuration consists of the THAI test vessel (TTV) and the smaller parallel attachable drum (PAD) which are connected in test TH-35 by one pipe segment of DN 500 installed at the level of the sump compartments. It is to be noticed that for test TH-35 the inner cylinder and all condensate trays are removed from the THAI test vessel.

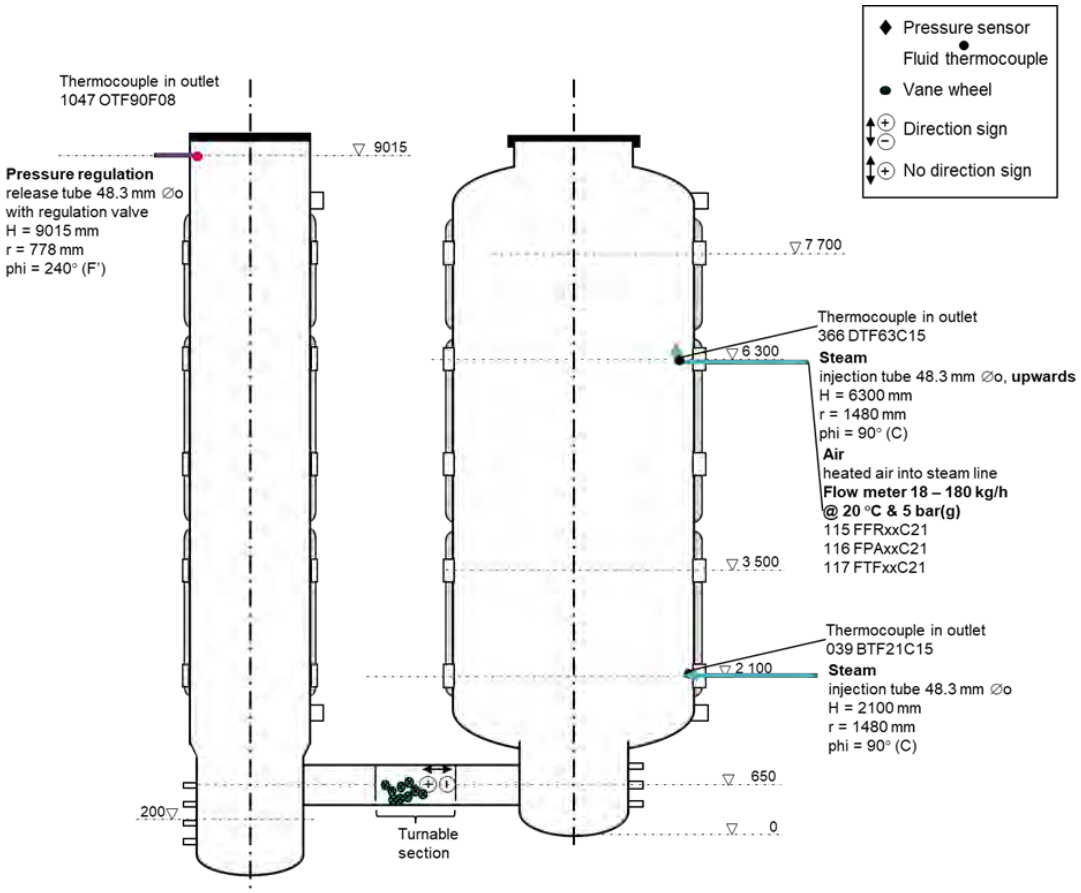

Figure 1. Configuration of the THAI+ vessels

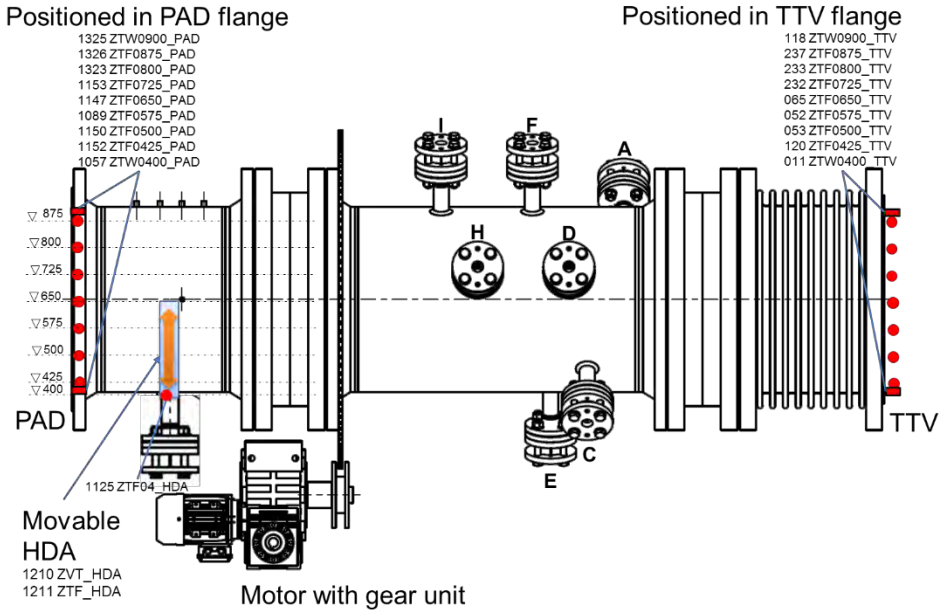

Figure 2. Lower connecting pipe including METUSA, HWA-probe and t/c installed at flanges to PAD and TTV sump compartment (gas and wall)

In contrast to the standard THAI$^+$ configuration, the METUSA flow measurement system was installed in the lower connecting pipe, see Figure 2. METUSA consists of two rotatable flanges which envelope an 885 mm long DN 500 pipe section into which 9 vane wheels were installed. Each of the 24 mm ∅ vane wheels was installed at a different pipe radius between centerline and outer wall surface. Additionally, 6 of the vane wheels had been installed at different angles and axially in distance of 50 or 100 mm in order to minimize the flow disturbance. By turning the pipe section by 360°, each of the vane wheels runs along a circular path. The summation of the six circular paths, each being 24 mm thick, allows to calculate the velocity distribution inside the pipe accurately. Negative velocity values indicate a flow direction from TTV to PAD vessel and positive vice versa. Beside the METUSA, a hot wire anemometer (HWA) probe was installed in the lower connecting pipe to record the backward flow along the pipe radius. Pre-heated air was injected vertically upwards at an elevation of 6.3 m, r = 1.48 m, angle C, injection tube (Figure 1) into the TTV using a pipe exit diameter of 43.1 mm $\varnothing_i$.

2. TEST PROCEDURE

The test transient for TH-35 consisted of a preconditioning phase followed by a main test phase, the latter subdivided into three quasi steady-state phases:

t = −74640 s	All three thermal oil mantels of TTV activated in heating mode, flow direction downwards, primary oil temperature set to 142 °C.
t = −74280 s	The TTV's lower and upper vessel shoulder and the vessel lid were heated electrically with target temperature of 140 °C. The TTV vessel columns were heated with target temperature of 140 °C. The TTV sump compartment was not heated.
t = 0 s	Start of pre-heated air flow injection with 10.1 g/s (temperature 91.8 °C) into TTV vessel at H = 6.3 m; stabilization of pressure by regulating PAD's uppermost exhaust valve at H = 9.015 m
t = 5 820 s	Increase of pre-heated air flow rate to 20 g/s (temperature 117.3 °C), and vessel pressure regulated
t = 11 760 s	Increase of pre-heated air flow rate to 29.9 g/s (temperature 124.3 °C), and vessel pressure regulated
t= 17520 s	Air injection stopped

The initial test conditions, measured at t= 0 as being the time of starting the air injection are listed in Table I. The temperature distribution of the vessel walls and the fluid temperature was provided with the resolution of Table II. To the benchmark participants. The fluid temperature distribution at t = 0 s still includes some temperature fluctuations, especially due to the very different wall temperatures inside the TTV and PAD sump. The pressure regulation was executed very precisely, i.e. pressure fluctuations occurred within less than 2 mbar during the test.

Table I. Measured initial test conditions for tests TH-35

Conditions	TH-35
Vessel total pressure (MPa)	0.1304
TTV wall temperatures (°C)	139
PAD wall temperatures (°C)	22.4
TTV steam concentration (%)	<0.5 vol%

Table II. Inside vessel wall and fluid temperatures before air injection at t = 0 s

Avg. wall temperatures	TTV wall temp >8.17 m	°C	140.5	Avg. fluid temperatures	TTV Section "D"	°C	136.1
	TTV oil mantles 1.82-8.17	°C	137.9		TTV Section "A+C"	°C	135.8
	TTV Lower Section 1.82- 1.2	°C	138.5		TTV Section "B"	°C	135.0
	TTV Sump <1.2 m	°C	73.9		TTV Sump	°C	53.7
	PAD wall temp >8.17 m	°C	22.1		PAD Section "O"	°C	24.8
	PAD oil mantles 1.82-8.17	°C	22.4		PAD Section "M"	°C	25.7
					PAD Section "L"	°C	25.5
	PAD Sump <1.1 m	°C	21.6		PAD Sump (gas)	°C	22.2
	Lower Pipe	°C	33.3		Lower Pipe	°C	36.1

Figure 3 depicts the air injection rate and the air injection temperature measured at the pipe exit. The air flow rate is stabilized within less than 2 min after starting or increasing the air injection mass flow. The temperature of the injected air did not reach equilibrium with the inner vessel temperature, but the injected air is easily heated up and mixed by the hot gas atmosphere inside the TTV.

The thermal oil mantles and the electrical heaters of the TTV were started at t = −74640 s and operated in heating mode until end of the test. The vessel temperatures have been stabilized long before starting the main phase of the experiment. The injected heating power beyond the initial heating phase balanced the thermal losses of the vessel's insulation. Averages of thermal oil and electrical heating power are given in Table III for the three phases.

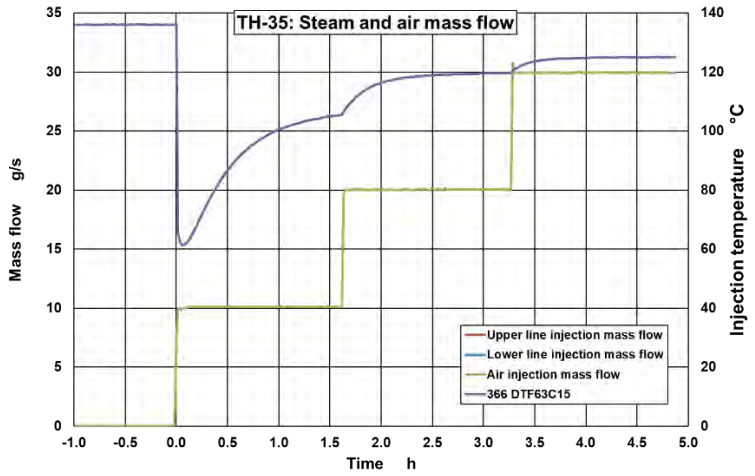

Figure 3. TH-35 air mass flow rate and temperature at air release location

Table III. Average of thermal oil and electrical heating power

	Phase 1	Phase2	Phase3
Start time (s)	0	5820	11760
End time (s)	5820	11760	17520
Upper mantle (kW)	2.20	2.22	2.17
Middle mantle (kW)	3.24	3.26	3.21
Lower mantle (kW)	3.59	3.59	3.55
Upper elect. heat (kW)	2.60	3.23	3.00
Lower elect. heat (kW)	1.74	1.59	1.57

3. TEST RESULTS

The temperature distribution at the vessels' sumps and the lower connecting pipe is depicted in Figure 4 for phase 1. The temperature data were taken from the temporal center of the phase and averaged over 10 minutes. The colour map reveals that hot gases are transported in a very small layer at the top of the pipe from TTV to PAD, while the gas temperature at the center of the pipe and at the lower half is much colder. The velocity measurement data of HWA and METUSA provide a velocity profile along the vertical axis of the pipe, Figure 5. The reverse flow is stable while the forward flow increases with increasing air injection rate. Comparison of the temperature distribution inside the lower connecting pipe (Figure 4) with the velocity profile shows that cold gases are transported backwards from PAD to TTV in the lower half of the pipe. The forward flow from TTV to PAD at the upper half of the pipe transports a small layer of hot gases at the upper pipe wall together with colder gas at pipe center. This indicates that the recirculated gases are mixed within the TTV sump compartment without ascending into the plenum of the TTV and transported back to the PAD immediately.

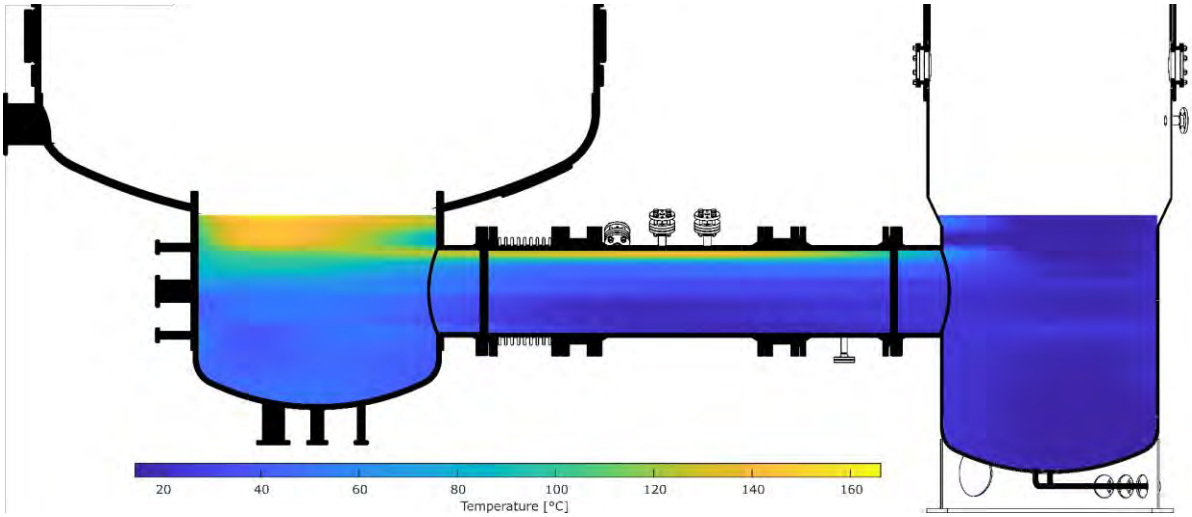

Figure 4. TH-35 gas temperature distribution at the vessels' sumps and the connecting pipe for phase 1, data averaged between t = 45 and 55 min

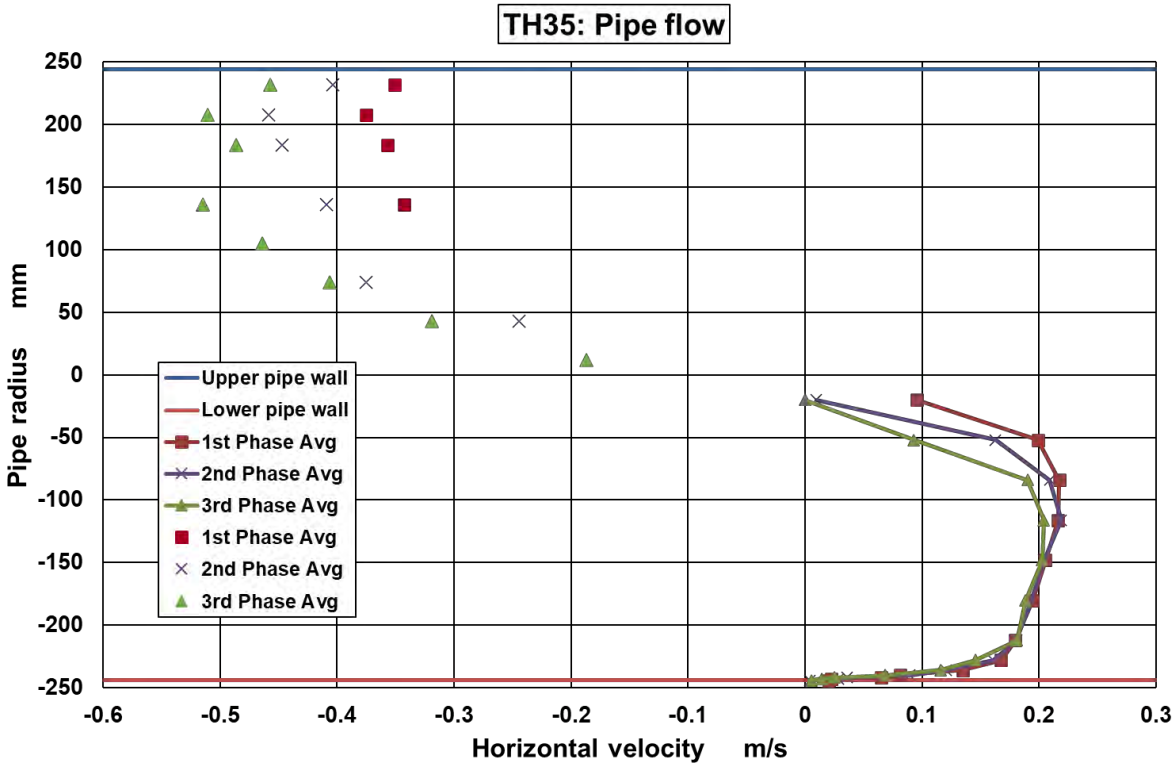

Figure 5. TH-35 averaged flow velocities along the vertical axis of the connection pipe, comparison of all three phases

4. SIMULATION MODELS

Benchmark simulations were performed by CNL using the CFD type GOTHIC code [Rah12] [Got18] and GRS submitted results using the lumped-parameter code COCOSYS (AC^2) [Kle17] [Arn21]. The following provide insights into the model set-ups.

GRS-COCOSYS-B

The nodalization used for the TH-35 benchmark is presented in Figure 6. The nodalization consists of 67 zones for the TTV, 66 zones for the PAD and 4 zones for the lower connecting pipe totalling 137 zones for the THAI$^+$ facility. In addition to those zones, 7 environmental zones and 3 heating mantle zones were used. The walls of the TTV, PAD and the connecting pipe were modelled with a total of 134 structures. A plume was used to model the rising of the hot air that was being injected during the experimental phases.

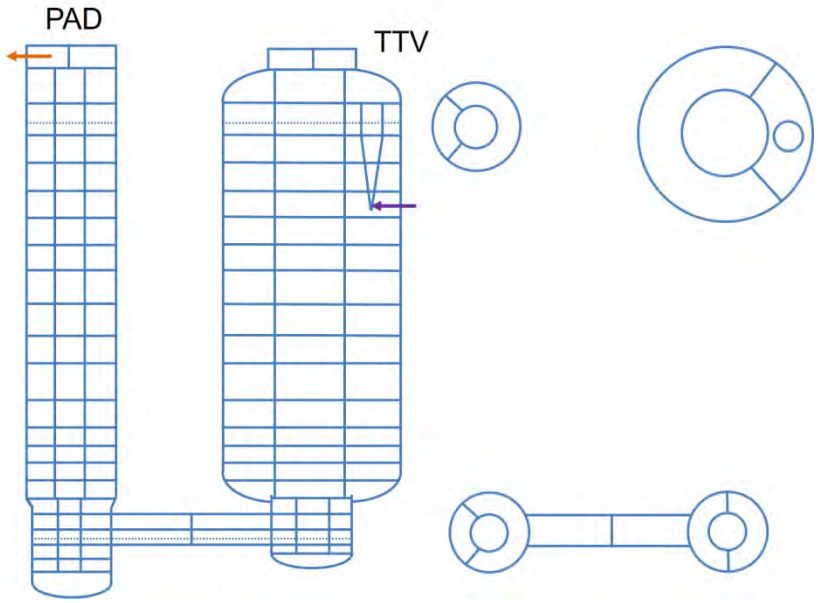

Figure 6. COCOSYS nodalization of the THAI+: side view (left) and cross-section view (right) at two levels

COCOSYS is a lumped parameter code and the mass flow in the junctions between zones are modelled according to [Arn21]. The modelling strategy representation of the counter current is documented in [Ili19]. A stepwise linear shape of the turbulence flow loss coefficient is assumed for Reynolds number in the transition regime. For TH-35 a maximal pressure loss coefficient of $\zeta_{max}^{turb} = 0.25$ was used. This value is based on previous numerical experiments comparing simulations performed with COCOSYS and simulations performed with the commercial CFD program ANSYS CFX [CFX16].

CNL-GOTHIC-B and CNL-GOTHIC-R

The GOTHIC model representation of the THAI$^+$ facility is shown in Figure 7. The test facility was represented by five GOTHIC control volumes (Vol. 1 for the TTV sump, Vol. 2 for the main region of the TTV, Vol. 3 for the PAD sump, Vol. 4 for the main region of the PAD, and Vol. 5 for the lower connection pipe). The control volumes were subdivided on a 3D Cartesian grid and connected to one another with 3D connectors. The average grid spacings in the nodalization of the control volumes are given in Table IV. The grid spacing was not always made uniform in the control volumes when aligning them with natural geometric features of the system was more practical. Only half of the facility was modeled because of the symmetrical geometry.

Table IV. GOTHIC model control volume nodalization

Control Volume	Average Grid Spacing			Number of Cells
	x	y	z	
1	0.228 m	0.228 m	0.285 m	72
2	0.263 m	0.263 m	0.620 m	936
3	0.259 m	0.259 m	0.295 m	108
4	0.259 m	0.259 m	0.612 m	234
5	0.354 m	0.244 m	0.244 m	16

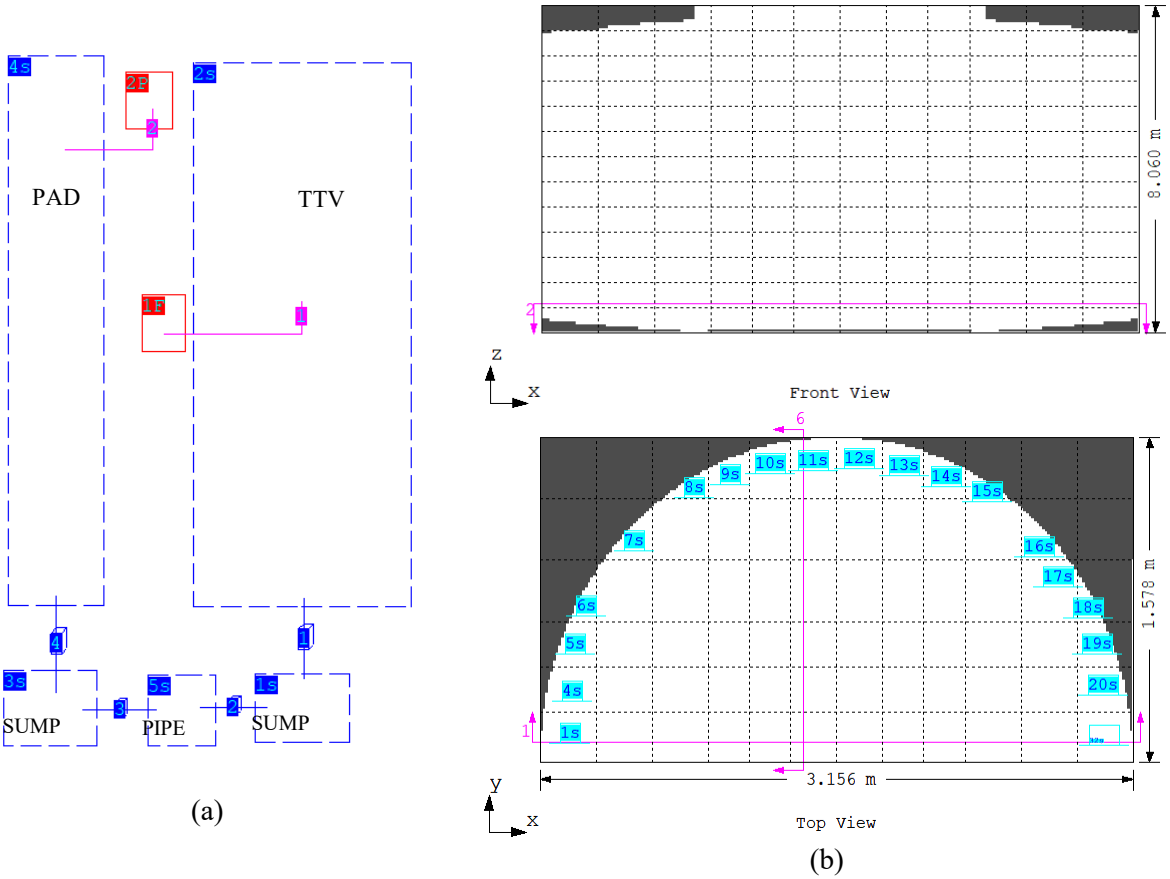

Figure 7. CNL-GOTHIC control volume layout (a) and 3D nodalization for TTV main vessel (b) for the blind simulation of TH-35

Thermal conductors were used to model heat transfer to internal structures. The conduction was modeled as 1D and perpendicular to the structure surface, and involved the combination of stainless steel, insulation, and aluminum. Only the stainless-steel vessel wall layer was modeled in the jacketed regions of the TTV and PAD, where an external temperature boundary condition corresponding to the mantle oil temperature (138 °C) was applied. The gas release through the PAD's relief valve was modelled by a pressure boundary (2P) to maintain the constant vessel pressure. Air injection was modelled by a flow boundary (1F).

5. SIMULATION EXERCISE

By heating the THAI vessel and injecting hot air into the TTV, gas is transferred to the PAD vessel through the DN500 connecting pipe at sump compartment level. The test facility was operated at constant pressure by removing gas mixture from the top of the second vessel (PAD). The different gas densities in the two vessels let hot gases flow to the cold PAD where the hot gas rose as a plume. At the same time, cold fluid was flowing backwards from the PAD into the hotter TTV, along the lower half of the connecting pipe. Velocity measurement data was evaluated along the vertical axis of the pipe circumferentially extrapolated, beyond availability of measurement data. This provided an estimate of the forward and backward volumetric flow in the pipe for the three test phases. The forward flow based on the interpreted test data would be 0.031 m^3/s in phase 1, 0.038 m^3/s in phase 2 and 0.046 m^3/s in phase 3, Figure 8. The forward flow in GRS-

COCOSYS-B agrees well with the test data. The backward flow based on the interpreted test data would be 0.023 m^3/s in phase 1, 0.022 m^3/s in phase 2 and 0.021 m^3/s in phase 3, Figure 9. The backward flow in the COSOSYS simulation is slightly below the test data.

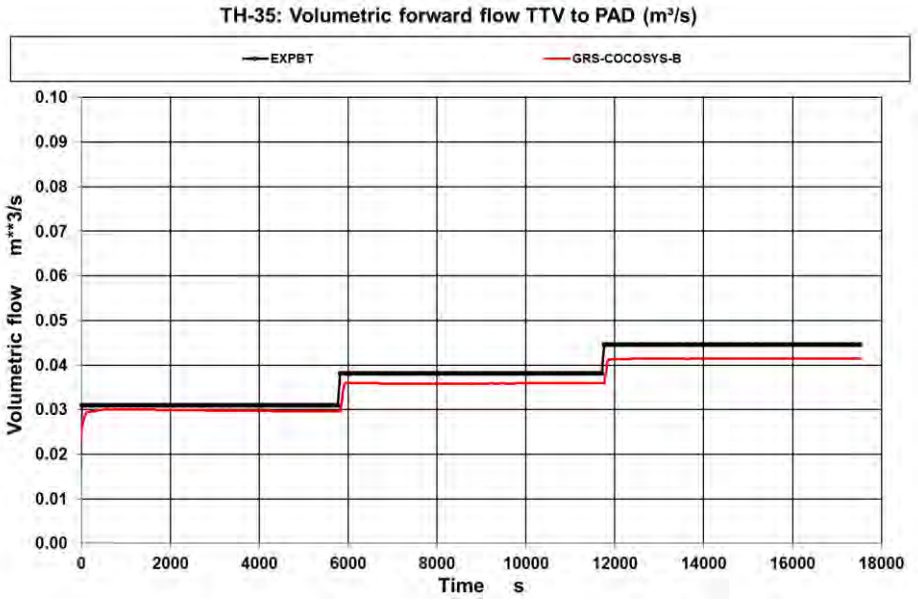

Figure 8. Gas flow through lower connection pipe in forward flow direction, i.e., TTV to PAD

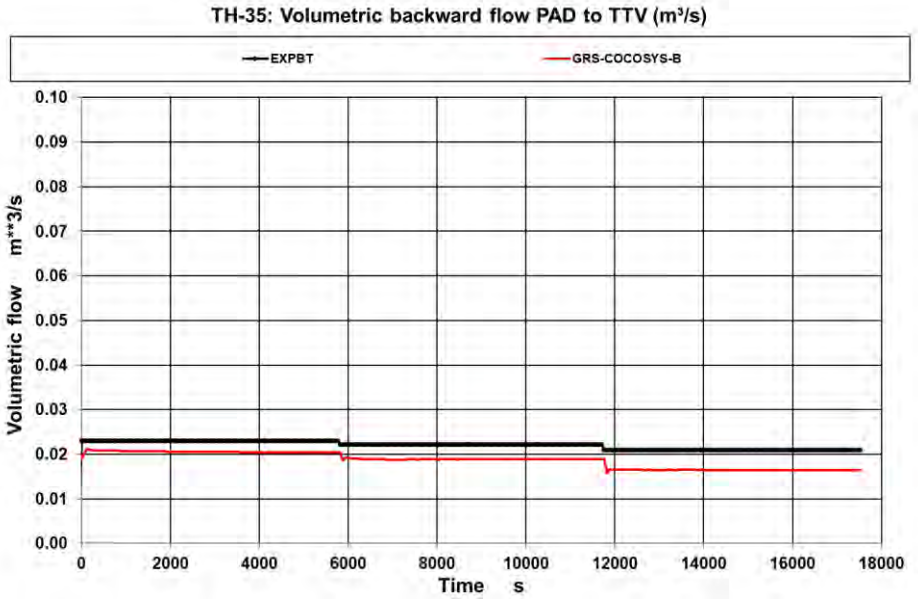

Figure 9. Gas flow through lower connection pipe in backward flow direction, i.e., PAD to TTV

6. SUMMARY

Two experiments investigating counter-current gas flows between two compartments were carried out at the THAI test facility. Data of test TH-35 were used for a simulation exercise. The simulations were conducted based on a specification report that provided participants with the geometric details as well as the initial and boundary conditions of test TH-35 but did not include the actual experimental results.

The forward and reverse flows in the connecting pipe were assessed using local velocity measurements. Overall, the comparison between simulation outcomes and experimental data is encouraging, particularly with respect to both flow directions, the net forward flow, and the ratio of forward to reverse flow.

In a second experiment, the heated TTV vessel was filled with an air–steam mixture, and additional steam and air were injected to initiate both flow and counter-current flow. The findings showed that steam entering the cooler PAD vessel caused rapid heating of its walls due to steam condensation. This heating effect decreased the temperature difference between the two vessels, thereby weakening the driving force for counter-current flow. As a result, forward flow velocities remained nearly constant throughout the three phases, while reverse flow velocities decreased significantly during the transient phase of the experiment.

ACKNOWLEDGMENTS

The project was supported with funds from the Federal Ministry for the Environment, Nature Conservation, Nuclear Safety and Consumer Protection (BMUV) under grant number 1501630.

The development and validation of COCOSYS are funded by the Federal Ministry for the Environment, Climate Action, Nature Conservation and Nuclear Safety (BMUKN).

REFERENCES

[Arn21] Arndt, S., Band, S., Beck, S., Eschricht, D., Iliev, D., Klein-Heßling, W., Nowack, H., Reinke, N., Sonnenkalb, M., Spengler, C., Weber, G.: COCOSYS 3.1 User Manual. Gesellschaft für Anlagen- und Reaktorsicherheit (GRS) gGmbH (GRS), GRS-P-3 / Vol. 1, 2021

[CFX16] CFX-16 User Manual

[Fre16] Freitag, M.; Kühnel, A.; Langer, G.: Extension of the THAI test facility by installation of the second vessel – PAD, Technical Report 150 1455 – THAIPLUS – TR, Becker Technologies, Eschborn, May 2016

[Fre18] M. Freitag, et al. „Benchmark exercise TH-27 on natural convection with steam injection and condensation inside the extended THAI facility“, Annals of Nuclear Energy, Volume 116, 2018, Pages 90-104, ISSN 0306-4549

[Got18] GOTHIC Thermal Hydraulic Analysis Package, Version 8.3(QA), November 2018

[Ili19] Iliev, D.: New developments in the thermal hydraulic module THY of the COCOSYS program, part of the AC 2 software package: turbulence in gaseous countercurrent flows. Kerntechnik, Bd. 84, Nr. 5, S. 453–466, DOI 10.3139/124.190078, 2019

[Kle17] Klein-Heßling, W.; Arndt, S.; Nowack, H.; Spengler, C.; Schwarz, S.; Eschricht, D.; Beck, S.; COCOSYS V2.4 - User's Manual, GRS – P – 3/1, Revision 1a, May 17, 2017

[Ler19] G. Lerchl, et al. ATHLET 3.2 Validation, February 2019, GRS – P – 1 /Vol. 3 Rev. 5

[Pra12] S. Prayitno, et al., Counter Current Flow Limitation of Gas-Liquid Two-Phase Flow in Nearly Horizontal Pipe, Science and Technology of Nuclear Installations, vol. 2012, Article ID 513809, 9 pages, 2012. https://doi.org/10.1155/2012/

[Rah12] Rahn, F; GOTHIC Thermal Hydraulic Analysis Package, Technical Manual Version 8.0. Palo Alto, USA: EPRI, 2012

[Roy00] Royl P. et al., GASFLOW Analysen zur Wirksamkeit eines Rekombinatorkonzepts bei einem postulierten Surge-Line LOCA im Kernkraftwerk Neckarwestheim-2, FZKA 6333, March 2000

[Rud15] L. Rudolph and Á. Pérez-Salado: Influence of the counter-current flow around the recombiners on their recombination rate, Fachgespräch zur Versuchsauslegung HR-43- HR-45, Eschborn, 02 Juli 2015

[Set12] OECD/SETH-2 PROJECT PANDA AND MISTRA EXPERIMENTSFINAL SUMMARY REPORT NEA/CSNI/R(2012)5, 06-Apr-2012

[Ste92] M. Stephan, F. Mayinger: Experimental and Analytical Study of Countercurrent Flow Limitation in Vertical Gas/Liquid Flows. Chem. Eng. Technol. 15 (1992) 51–62

BENCHMARK ON COUNTER-CURRENT FLOW IN MULTI-COMPARTMENT CONTAINMENT USING THAI TEST DATA

J. Hermann, M. Freitag, E. Schmidt
Becker Technologies GmbH

S. Band, D. Iliev
Gesellschaft für Anlagen- und Reaktorsicherheit (GRS) gGmbH,

Z. Liang, A. John, M. Zanoni
Hydrogen Technologies Branch, Canadian Nuclear Laboratories,

On behalf of:
Federal Ministry
for the Environment, Climate Action,
Nature Conservation and Nuclear Safety
of the Federal Republic of Germany

Outline

- Motivation
- THAI+ test setup and procedure
- Experimental Results
- Benchmark Setup and Results
- Conclusion

Motivation

Motivation

- Counter current flow phenomena are observed in experiments or can occur in multi-compartment containments
  - THAI TH-27 [Fre18]
  - CFD of KONVOI steam generator towers [Roy00]

- Governing physics:
  - Local differences in T and ρ
  - Reversal of flow direction
  - Strong shear and enhanced turbulence

- Simulation codes need high spatial nodalization or modelling to predict this behaviour
  - E.g. COCOSYS countercurrent flow model for gaseous flows based on TH-27 [Ili19]

- Benchmark initiated in THAI-research framework:
  - Provide high resolution experimental results of counter current flows (TH-35, TH-36)
  - Blind Benchmark with participation by CNL and GRS for code validation

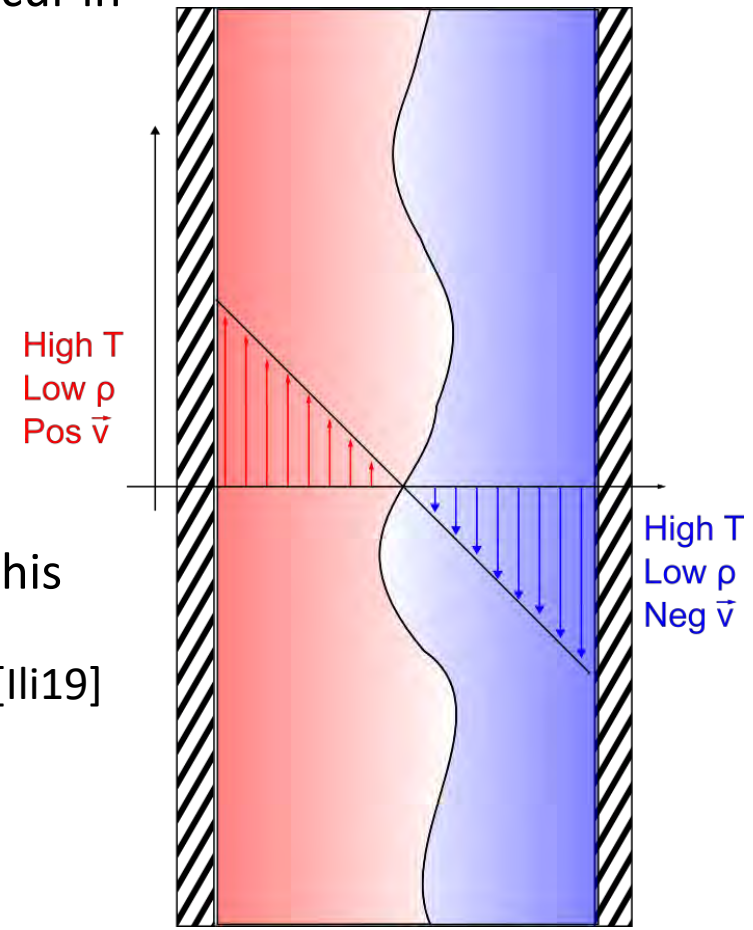

THAI+ test setup

THAI+ Facility

- THAI+: Multi-compartment Test facility for **T**hermal-hydraulics, **H**ydrogen, **A**erosols, **I**odine
- 2 vessel configuration (14 bar at 180 °C)
  - THAI test vessel (TTV)
  - Parallel Attachable Drum (PAD)
- System can be heated or cooled independently via three thermal oil mantles (accuracy +/- 1 °C)
- Access trough flanges for (optical) measurement systems
- Approved for H_2, CO and radiolabeled I_2 in combination with deflagrations

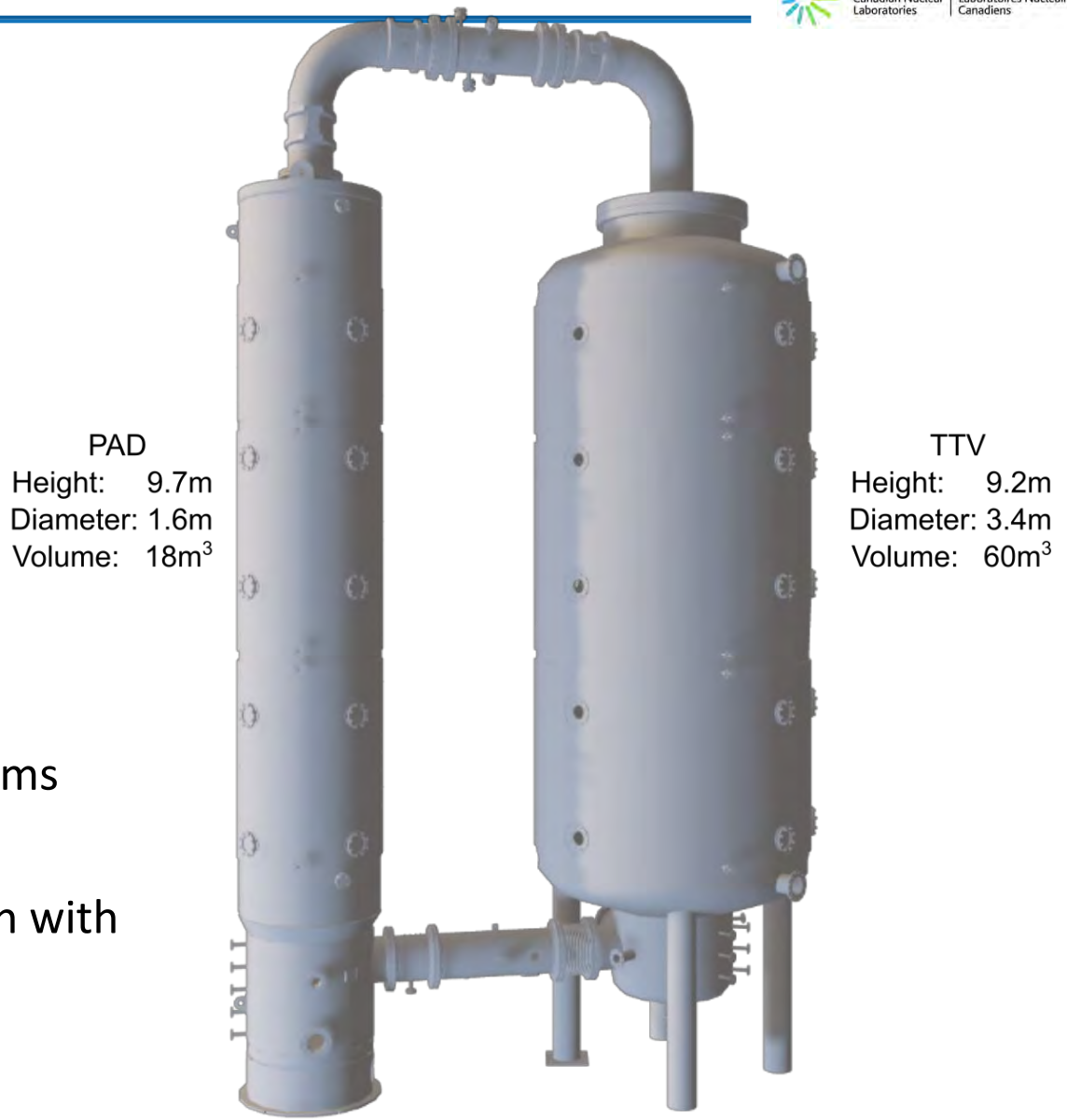

Test Setup

- Internal components removed
- Vessels connected at 0.65m with DN500 pipe.
  No top connection
- Injection of preheated air into TTV at 6.3m
- Venting of PAD vessel for pressure control at top lid
- Oil mantle heating for vessel preconditioning
  - TTV: Controlled heating
  - PAD: No active heating (Ambient Temperature)
- Electronic heating of lid and sump area for TTV

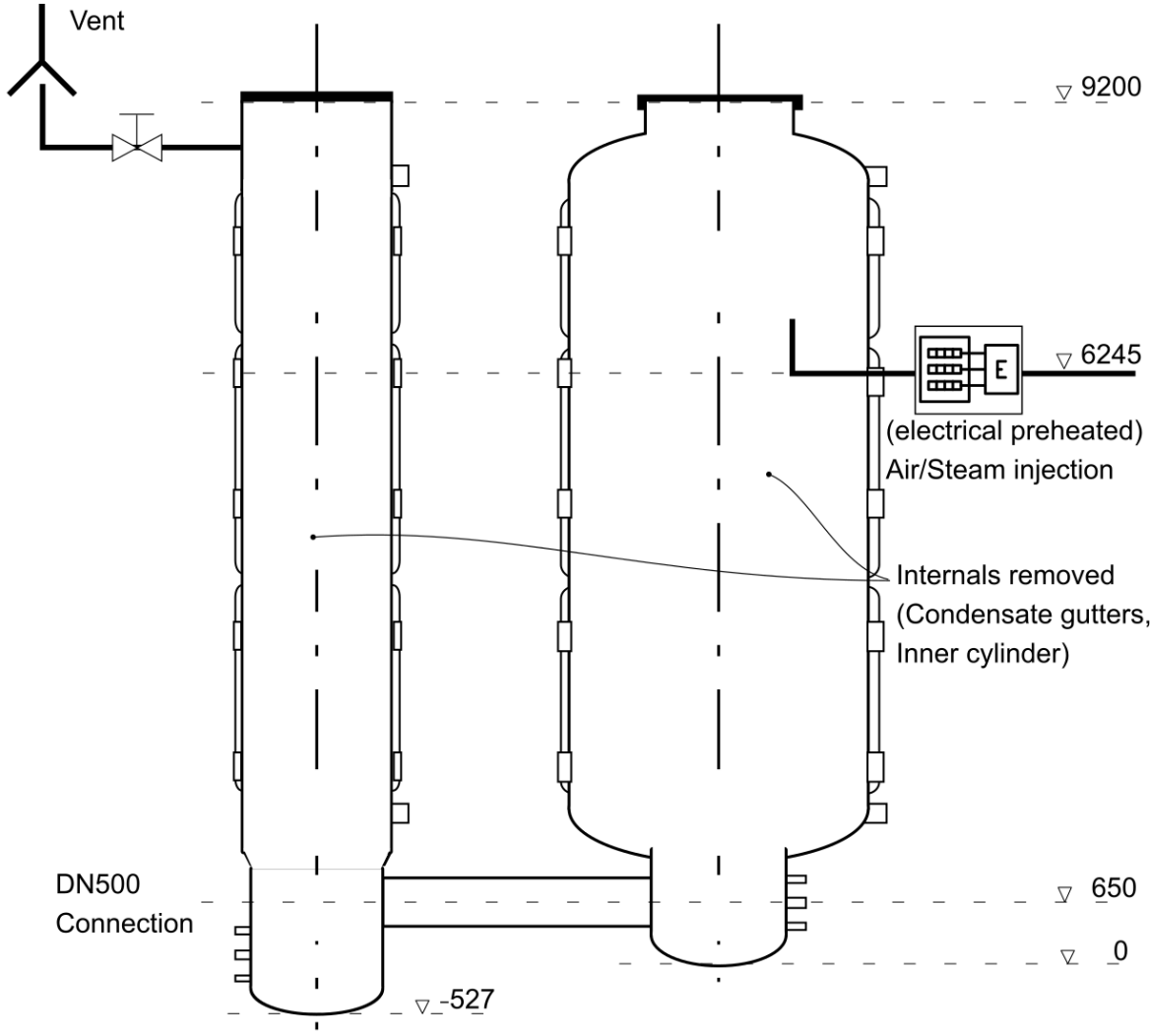

Test Setup

- Internal components removed
- Vessels connected at 0.65m with DN500 pipe.
  No top connection
- Injection of preheated air into TTV at 6.3m
- Venting of PAD vessel for pressure control at top lid
- Oil mantle heating for vessel preconditioning
  - TTV: Controlled heating
  - PAD: No active heating (Ambient Temperature)
- Electronic heating of lid and sump area for TTV

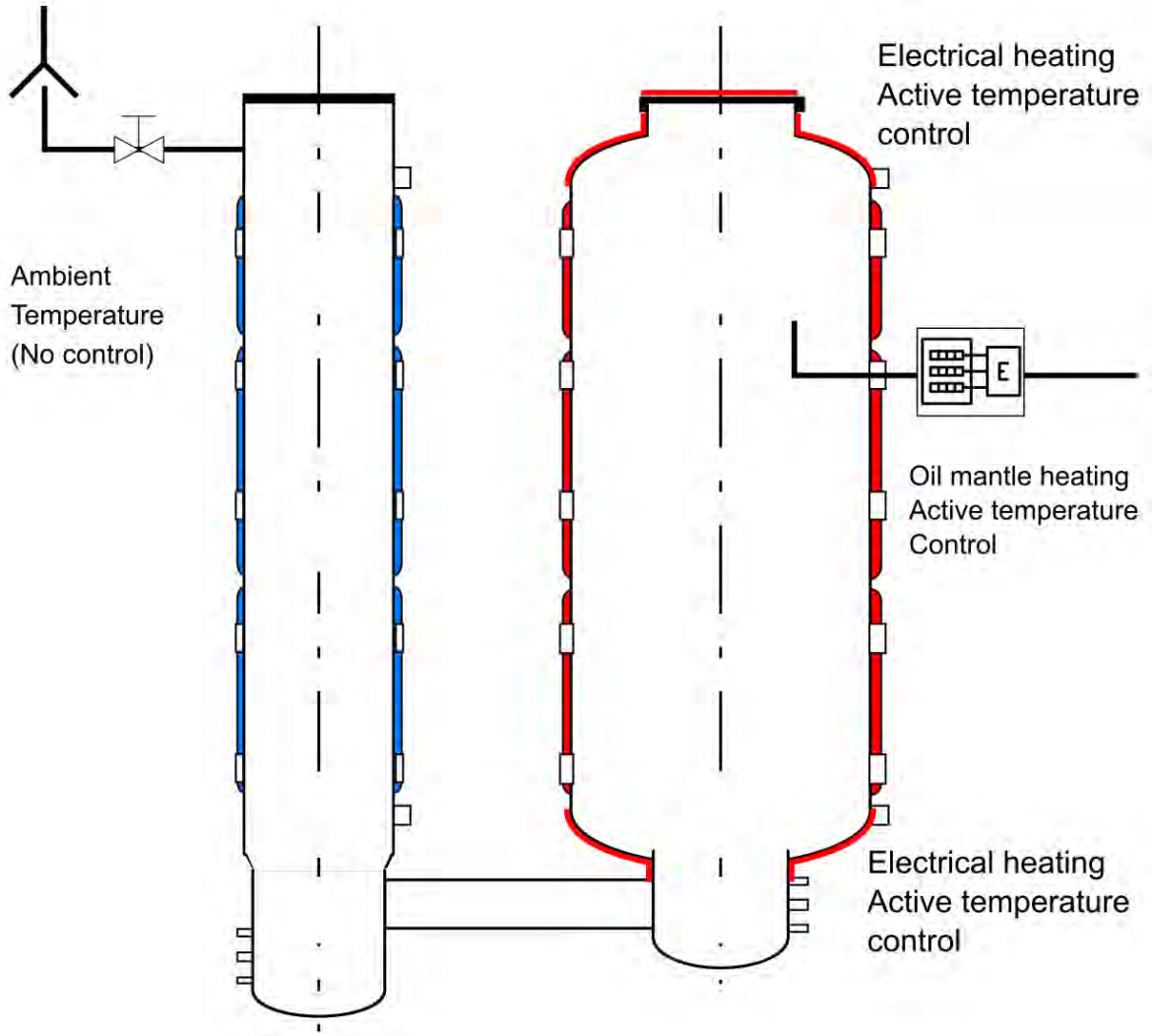

Test Instrumentation

- High resolution wall and fluid temperature instrumentation (Type- K thermocouples) in both vessels
- Piezo resistive pressure transducer for abs. and rel. vessel pressure (both)
- METUSA interconnection pipe
  - Fluid and wall temperature profile
  - Rotating vane wheel anemometer for volume flow rate
  - Traversable Hot-Wire-Anemometer for high-res velocity profile

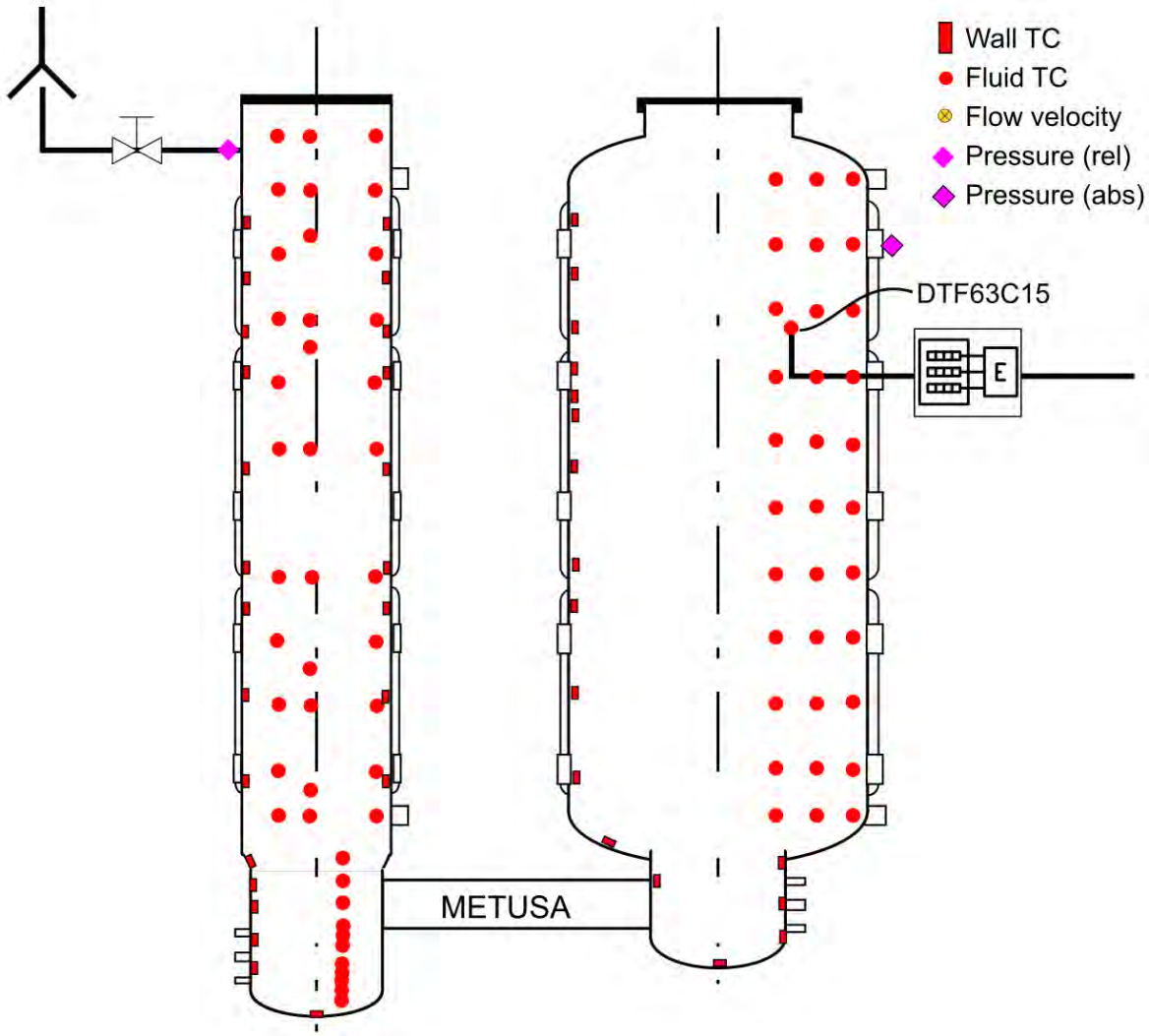

Test Instrumentation

- High resolution wall and fluid temperature Type- K Thermocouples in both vessels
- Piezo resistive pressure transducer for abs. and rel. vessel pressure (both)
- METUSA interconnection pipe
  - Fluid and wall temperature profile
  - Rotating vane wheel anemometer for volume flow rate
  - Traversable Hot-Wire-Anemometer for high-res velocity profile

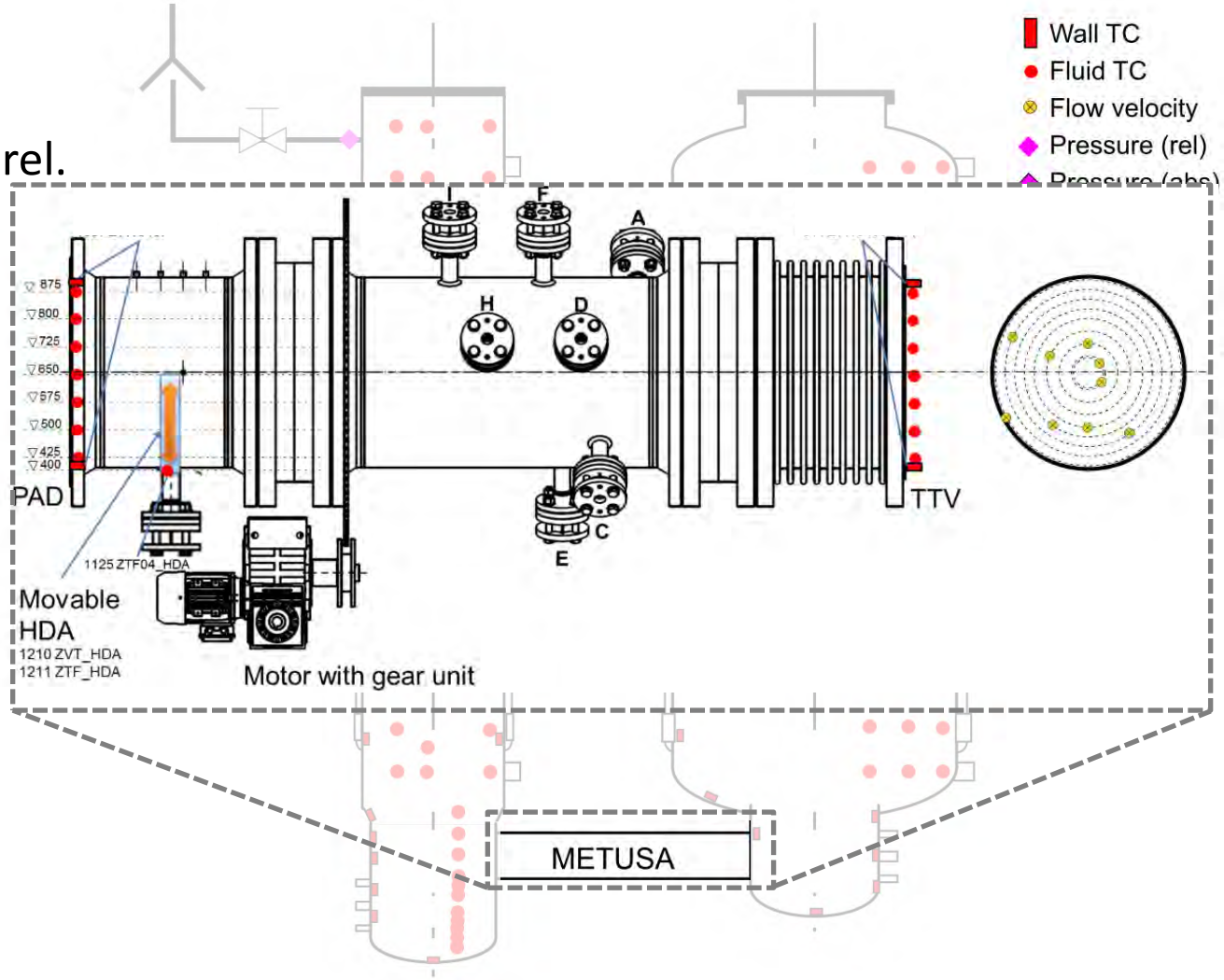

Test Procedere TH-35

- Preconditioning Phase (-21 h to T_0):
  - Initial atmosphere: Air, 1bar (a)
  - Heating up vessel from ambient conditions using oil mantel and electrical heating
    - TTV: 140°C
    - PAD: no heating, ~ 25°C
    - METUSA: no heating, but gas exchange due to therm expansion of the heated TTV gases
- 1st Test Phase (T_0)
  - Injection of preheated Air to TTV (10 g/s)
  - Hot Air will be forced through intersection pipe
  - Hot plumes ascend in PAD
  - Cold air descends in PAD
  - Counter-current flow develops in intersection
- 2nd Test Phase (T_0+1.5h)
  - Increase of air mass flow to 20 g/s
- 3rd Test Phase (T_0+3.0h)
  - Increase of air mass flow to 30 g/s

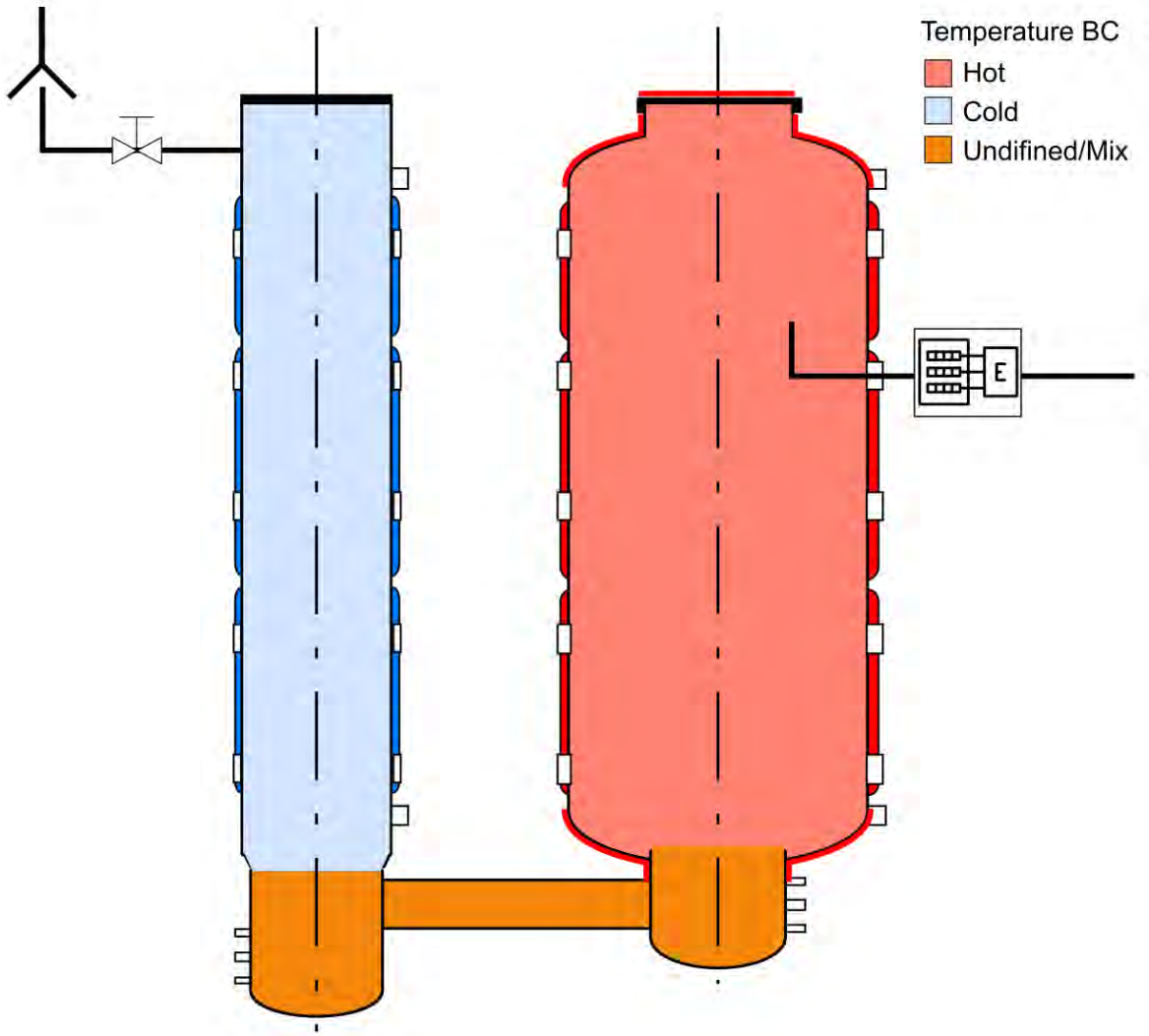

Test Procedere TH-35

- Preconditioning Phase (-21 h to T_0):
  - Initial atmosphere: Air, 1bar (a)
  - Heating up vessel from ambient conditions using oil mantel and electrical heating
    - TTV: 140°C
    - PAD: no heating, ~ 25°C
    - METUSA: no heating, but gas exchange due to therm expansion of the heated TTV gases
- 1st Test Phase (T_0)
  - Injection of preheated Air to TTV (10 g/s)
  - Hot Air will be forced through intersection pipe
  - Hot plumes ascend in PAD
  - Cold air descends in PAD
  - Counter-current flow develops in intersection
- 2nd Test Phase (T_0+1.5h)
  - Increase of air mass flow to 20 g/s
- 3rd Test Phase (T_0+3.0h)
  - Increase of air mass flow to 30 g/s

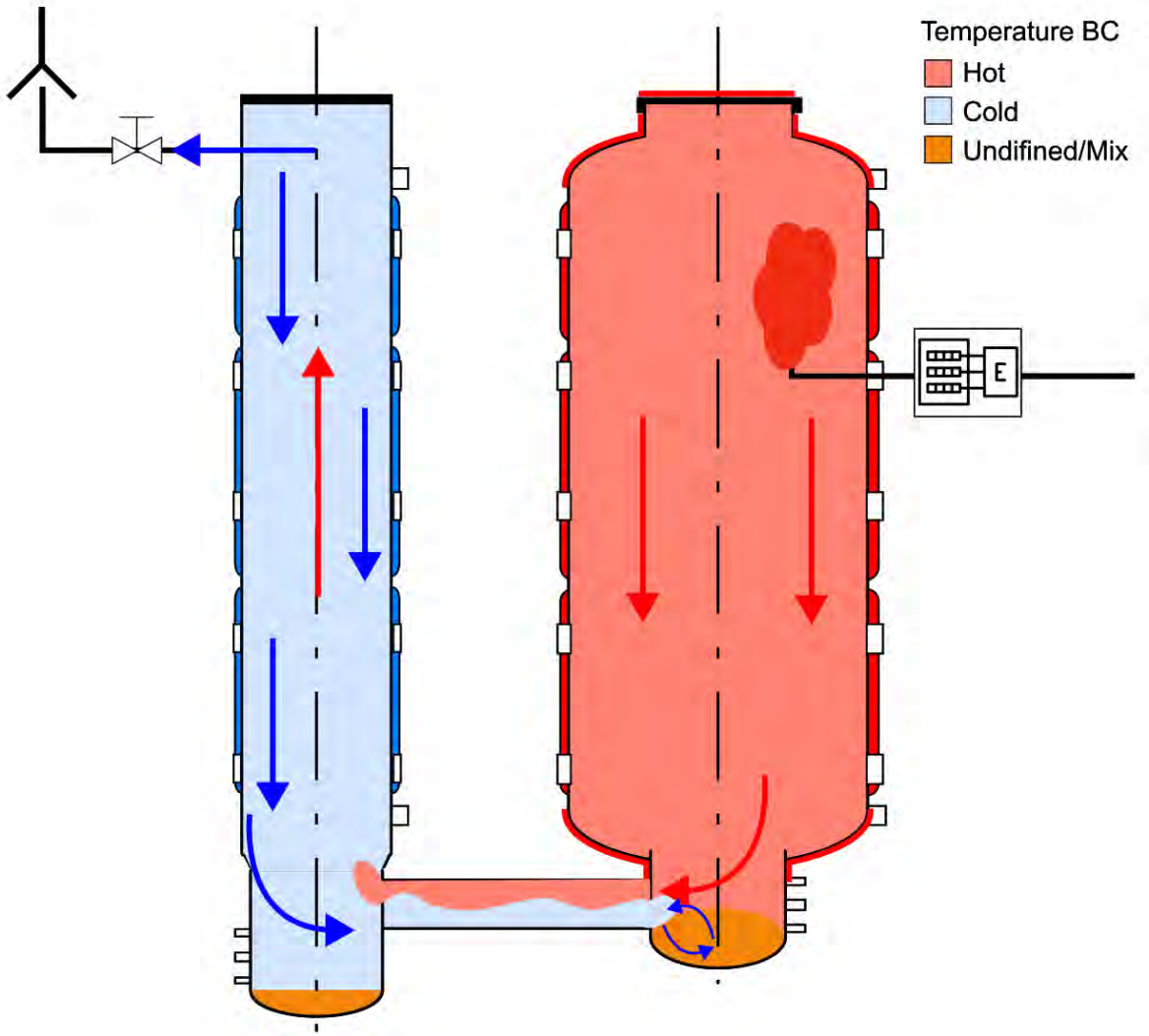

Experimental Results

Experimental Results

- Boundary conditions before test start (T_0 =0 h):
  - Heating started 21h prior to T_0
  - Stable conditions held for >1.5h
  - Target Temperature and humidity met at T_0

- 1st Test Phase (T_0)
  - Adjustment of target air flow <30s
  - Injected air temperature slightly below vessel fluid temp
  - No overall temperature decrease due to wall heating
  - Pressure regulation with fluctuation <2mbar during test

- 2nd and 3rd Test Phase:
  - Target mass flow rates reached within few seconds
  - Air temperature reaches steady state ~1h after change of injection rate

- No steam injection in TH-35 (Conducted in TH-36)

Avg. wall temperatures				Avg. fluid temperatures			
TTV wall temp >8.17 m	**°C**	**140.5**		**TTV Section "D"**	**°C**	**136.1**
TTV oil mantles 1.82-8.17	°C	137.9		TTV Section "A+C"	°C	135.8
TTV Lower Section 1.82- 1.2	°C	138.5		TTV Section "B"	°C	135.0
TTV Sump <1.2 m	°C	73.9		TTV Sump	°C	53.7
				PAD Section "O"	°C	24.8
PAD wall temp >8.17 m	°C	22.1		PAD Section "M"	°C	25.7
PAD oil mantles 1.82-8.17	°C	22.4		PAD Section "L"	°C	25.5
PAD Sump <1.1 m	°C	21.6		PAD Sump (gas)	°C	22.2
Lower Pipe	°C	33.3		Lower Pipe	°C	36.1

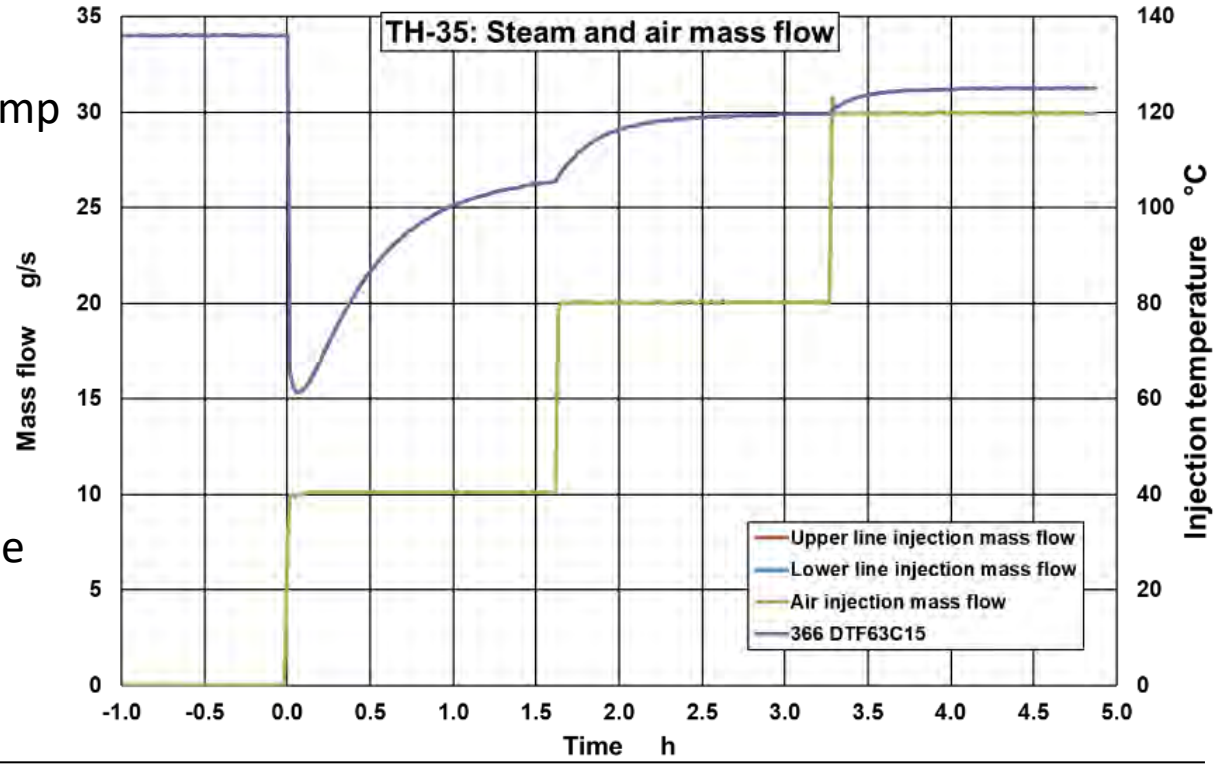

Experimental Results

- Expected temperature distribution in pipe section:
  - Temperature increase in upper part of pipe
  - Indication for mass transfer in upper segment
  - Steep temperature gradient 100°C / 200 mm
- Developed countercurrent flow established in intersection
  - Negative velocity: Flow from THAI to PAD
  - Pos. velocity: Flow from PAD to THAI
- 1st test phase:
  - Centreline velocity <0.1m/s (below vane wheel detection threshold)
  - Noticeable flow of “COLD” fluid from TTV sump compartment to PAD
- 2nd + 3rd test phase:
  - Magnitude and spatial dimension of neg. velocity (forward flow) increase with mass flow
  - No change in cold return flow at lower pipe wall

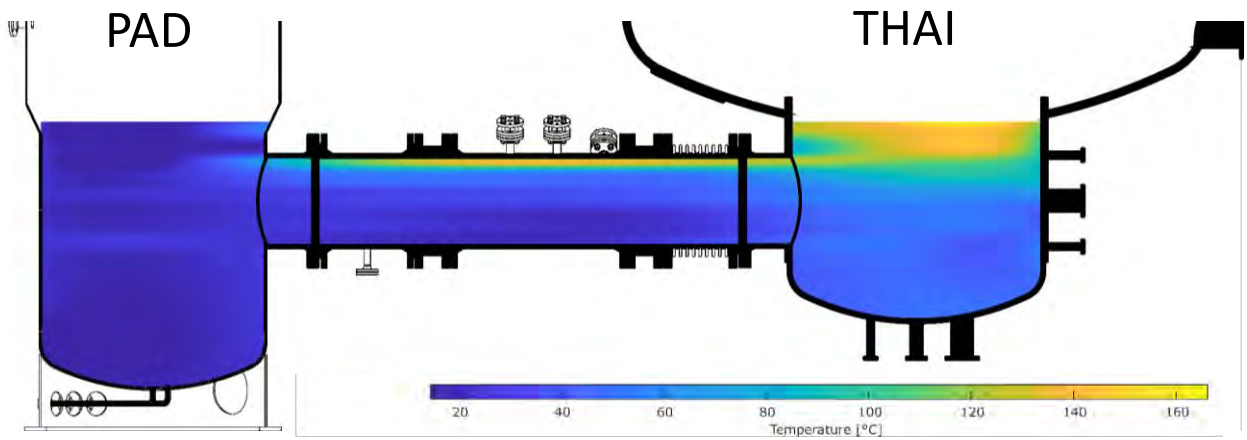

Averaged temperature distribution during 1st test phase between T0+0.75 h and 0.9 h

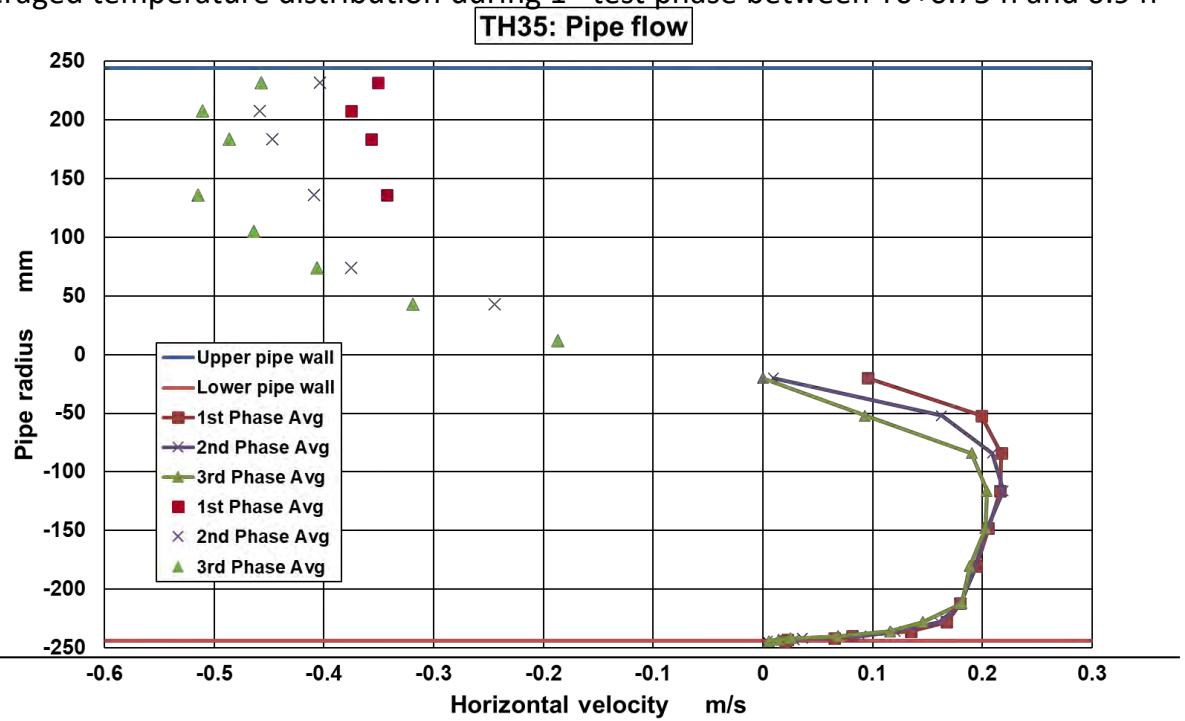

Benchmark Setup and Results

Numerical Setup

- GSR COCOSYS*

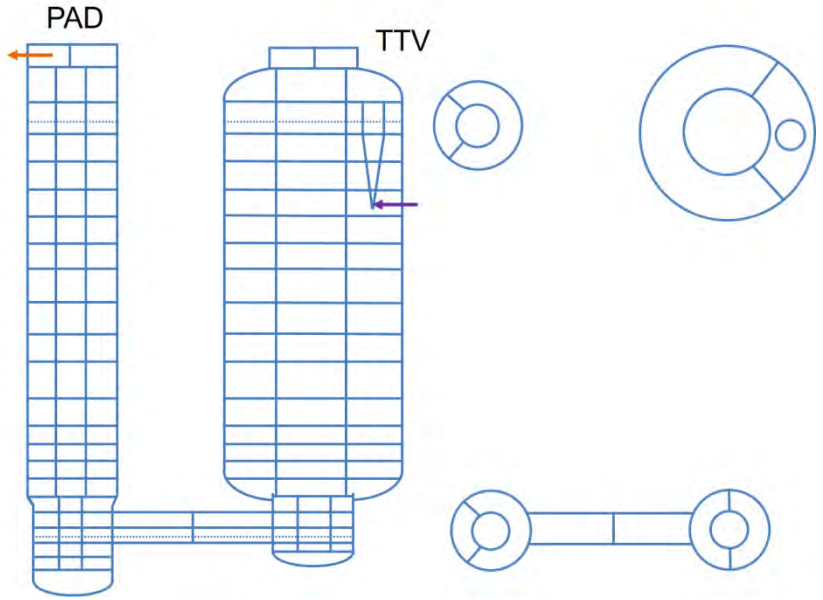

- 137 zones for vessel (67 TTV, 66 Pad, 4 Interconnection)
- Separate node for plume
- Turbulence flow loss coefficient is assumed for Reynolds number in the transition regime
- A maximal pressure loss coefficient of $\zeta_{max}^{turb} = 0.25$ was used

*Corresponding Author: **D. Iliev, GRS**

- CNL GOTHIC**

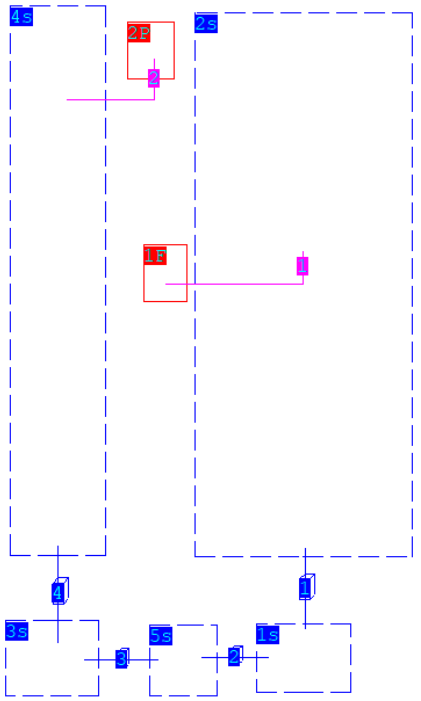

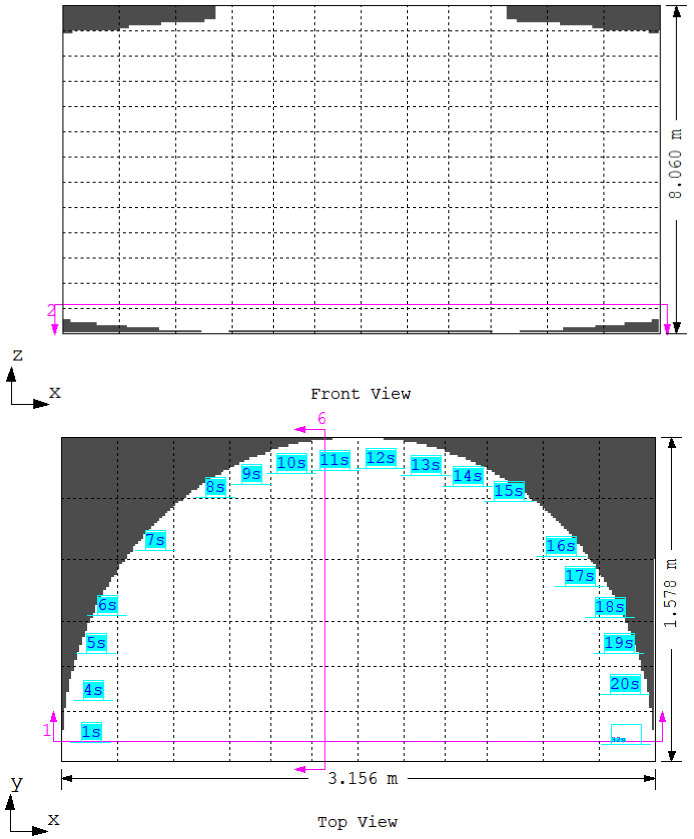

- Five control volumes (TTV, PAD, Pipe TTV Sump, PAD Sump)
- Each control volumes subdivided on a 3D Cartesian grid
- Use of symmetry boundary conditions
- Heat transfer to stainless steel liner modelled, const T in oil mantle as boundary conditions

** Corresponding Author: **Z. Liang, CNL**

Benchmark Results

- Evaluation method
  - Integration spatially resolved flow measurement from experiment
  - Comparison between exported volume flow from simulation
- Forward flow: From heated TTV to PAD
- Backward flow: From PAD to heated TTV

Backward Flow

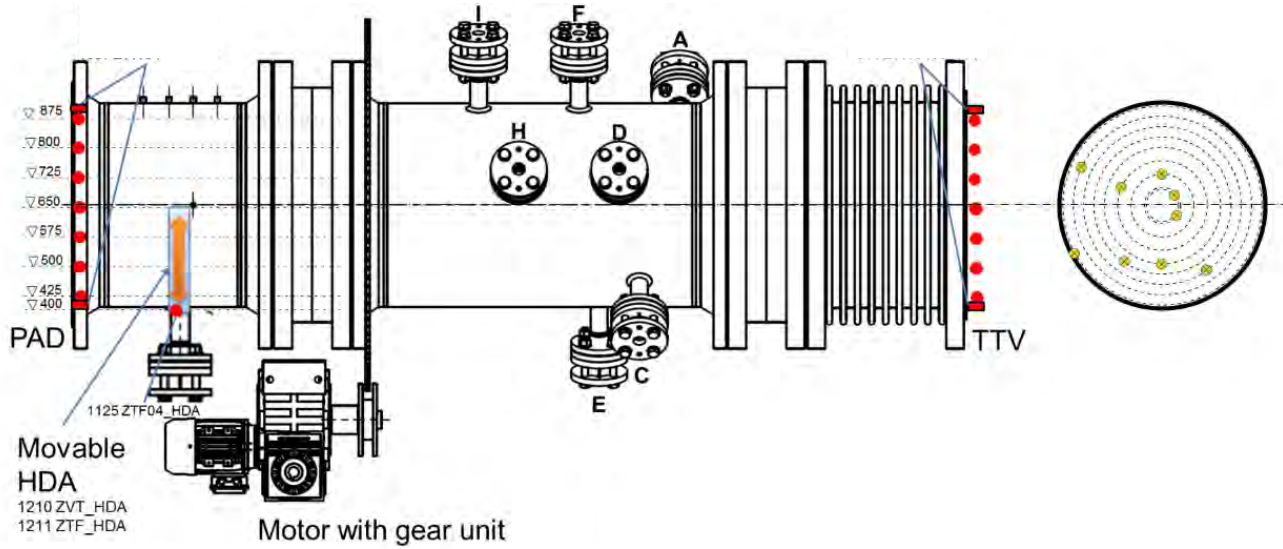

Forward Flow

Benchmark Results

- Comparison of exp. and simulation results

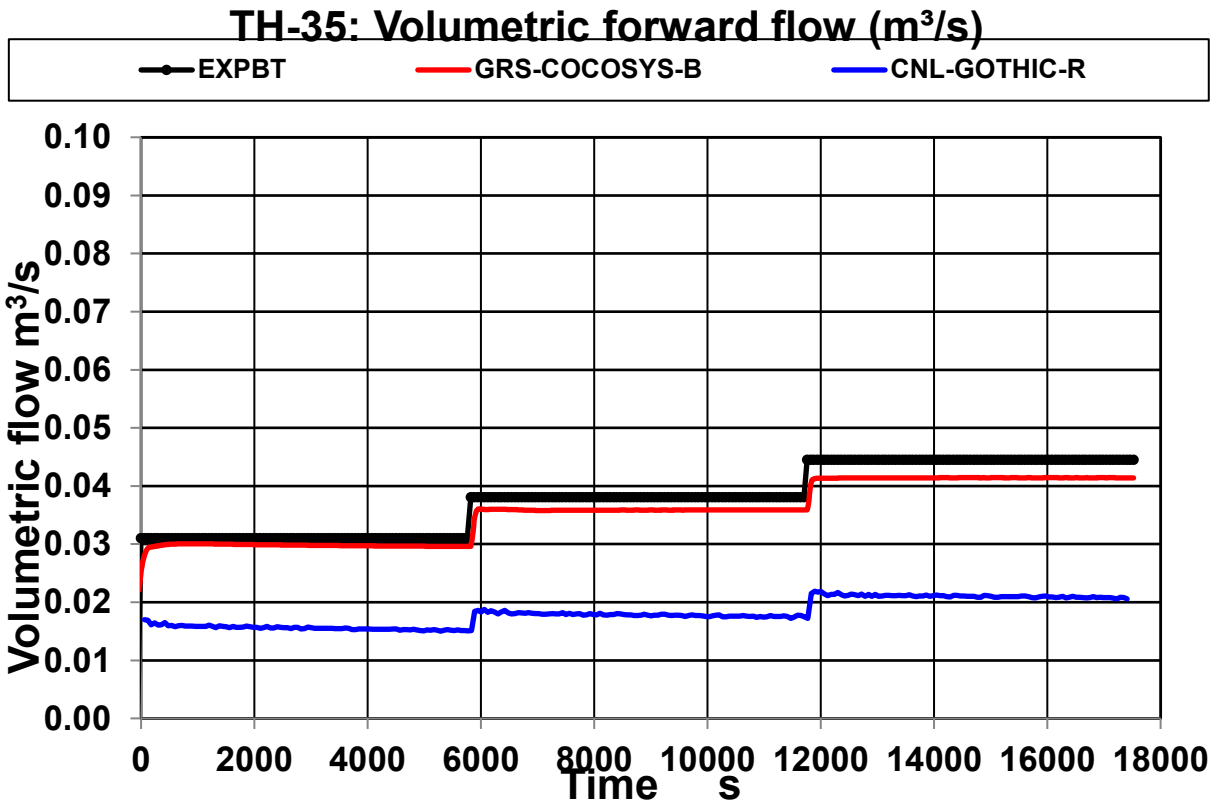

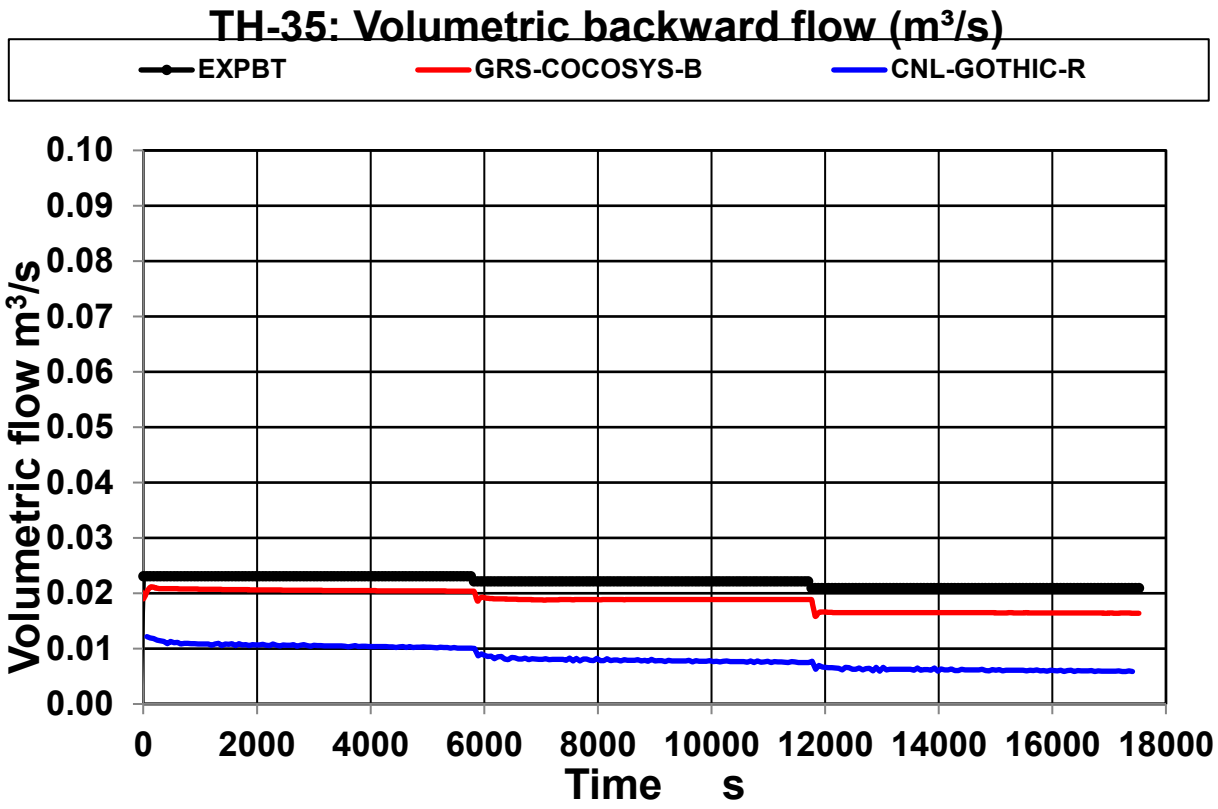

- Phenomenologically both codes capture countercurrent flow
- Prediction of COCOSYS in very good agreement
- Higher injection rates increase forward flow significantly, but backward flow only slightly

Summary and conclusions

Summary and conclusions

- THAI+ facility used for experimental investigation of countercurrent flows

- Successful test campaign with parametric studies on turbulence and gas composition
- Main findings:
  - Forward flow scales with mass injection rate
  - Forward flow is thermally stratified!
  - Backward flow is quasi constant if thermal gradient is steady-state
  - Mixing of backward flow within the TTV sump compartment, no ascend into TTV vessel
- Benchmark using simulation codes COCOSYS (GRS), GOTHIC (CNL)
  - Countercurrent flow captured by both tools
  - Prediction of COCOSYS in good accordance with experimental results

- High resolution data available for code benchmarking
  - TH35: Countercurrent Flows in Air Atmosphere
  - TH36: Countercurrent Flows in Steam-Air Atmosphere

Acknowledgements

The national THAI research program is carried out on behalf of the Federal Republic of Germany, represented by the
German Federal Ministry for the Environment, Climate Action, Nature Conservation and Nuclear Safety

On behalf of:

Federal Ministry
for the Environment, Climate Action,
Nature Conservation and Nuclear Safety

of the Federal Republic of Germany

Thank you for your attention!

Dr. Jens Hermann
Becker Technologies GmbH
Neckarstraße 12-14
65239 Hochheim
Germany
Phone: +49 6146-52897-15
Mail: hermann@becker-technologies.com

12.08.2025: THAI, PAD and Nu-eX stand firm

[Fre18] M. Freitag, et al. „Benchmark exercise TH-27 on natural convection with steam injection and condensation inside the extended THAI facility“, Annals of Nuclear Energy, Volume 116, 2018, Pages 90-104, ISSN 0306-4549

[Roy00] Royl P. et al., GASFLOW Analysen zur Wirksamkeit eines Rekombinatorkonzepts bei einem postulierten Surge-Line LOCA im Kernkraftwerk Neckarwestheim-2, FZKA 6333, March 2000

[Ili19] Iliev, D.: New developments in the thermal hydraulic module THY of the COCOSYS program, part of the AC 2 software package: turbulence in gaseous countercurrent flows. Kerntechnik, Bd. 84, Nr. 5, S. 453–466, DOI 10.3139/124.190078, 2019

Backup

Backup

1st digit: Location (TTV = THAI Test Vessel)

A **A**nnulus of TTV
B **B**ase zone of TTV
C **C**entral cylinder of TTV
D **D**ome of TTV
E external heat **E**xchangers
F steam + air **F**eed lines
G condensate **G**athering (collector) within PAD
H **H**e/H_2 feed & sampling lines
J heating/cooling **J**acket + insulation of TTV
K heating/cooling jac**K**et + insulation of PAD
L **L**ower zone of PAD
M **M**iddle section of PAD
O d**O**me of PAD
P auxiliary equi**P**ment PAD
Q auxiliary e**Q**uipment TTV
R test **R**oom (= environment of TTV and PAD)
S **S**ump zone of TTV
T sump/**T**rap zone of PAD
V steam (**V**apour) generator
W condensate (**W**ater) collector within TTV
X external heat e**X**changers of PAD
Z Connecting Pipe between TTV and PAD
(polar angle gives flange position at THAI, radius gives the position along the pipe axis)

2nd+ 3rd digit: Measured quantity, measuring system

F.. **F**low FI flow **I**ndicator, general
FR flow indicator, **R**otameter-type
FT flow indicator, **T**urbine flow meter
M.. **M**oisture (Humidity) MD relative humidity (**D**ew point method)
TD **D**ew point **T**emperature
P.. **P**ressure
PA **A**bsolute pressure
PD **D**ifferential pressure
PG **G**auge pressure
T.. **T**emperature
TC wall **C**ondensate temperature (thermocouple)
TD **D**ew point temperature (Pt-100)
TF **F**luid temperature (thermocouple)
TR fluid temp. (Pt-100 **R**esistance thermometer)
TW **W**all surface temperature (thermocouple)
V.. Flow **V**elocity
VL obtained from **L**aser Doppler velocimeter
VT measured by **T**urbine flow meters

4th + 5th digit: Elevation, in dm
6th digit: Key for polar angle
(rotational axis shifted translationally from THAI axis to PAD axis)
7th + 8th digit: Radial distance from vessel axis, in dm
9th digit: Supplement, if necessary

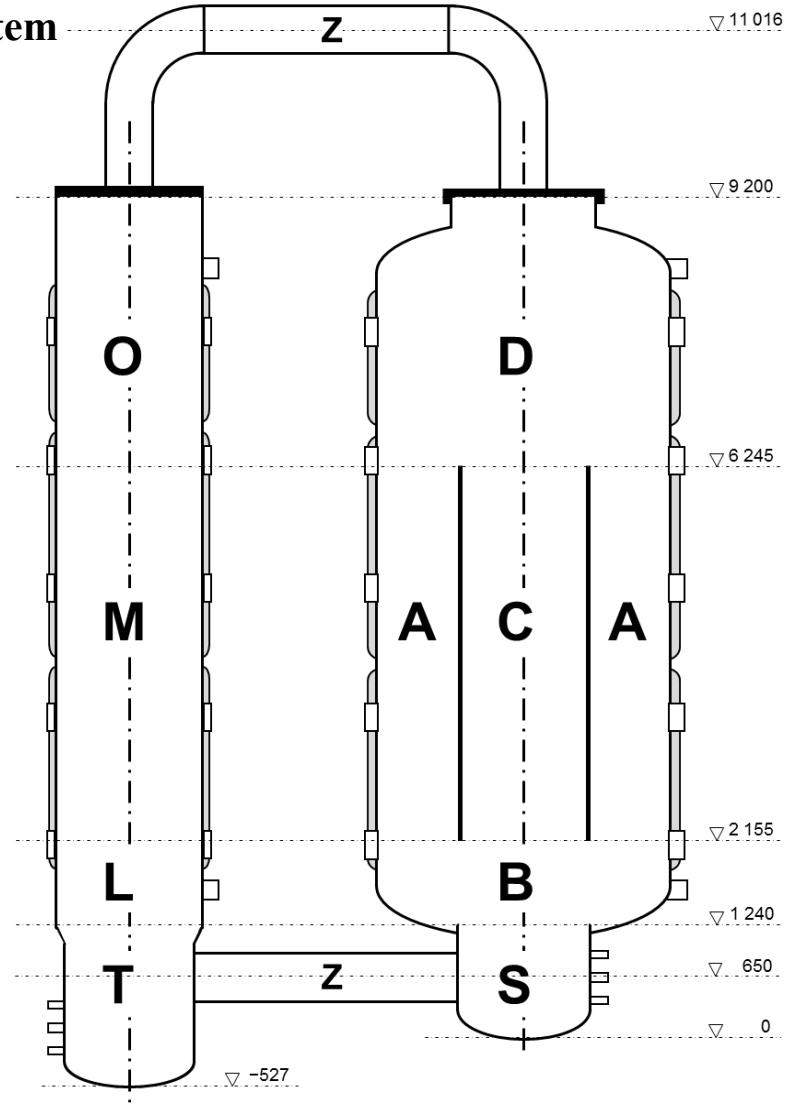

SYSTEMATIC ANALYSIS OF THE INFLUENCE OF THE SPRAY ACTUATION ON THE HYDROGEN RISK ACCIDENT USING A 3D GOTHIC PWR-W MODEL

Carlos Vázquez-Rodríguez [1,2*], Gonzalo Jiménez[1*], Juan Manuel Martín-Valdepeñas[3]
[1] Universidad Politécnica de Madrid (UPM), José Gutiérrez Abascal, 2, 28006 Madrid, Spain.
[2] Forschungszentrum Jülich GmbH, Wilhelm-Johnen-Straße, 52428 Jülich.
[3] Consejo de Seguridad Nuclear (CSN), Pedro Justo Dorado Dellmans, 11, 28040 Madrid, Spain).
c.vazquez-rodriguez@fz-juelich.de; gonzalo.jimenez@upm.es; jmmv@csn.es

ABSTRACT

The actuation of the spray safety system is known to have a significant impact on the evolution of the hydrogen combustion risk inside the containment building of PWR reactors. Its actuation decreases the quantity of steam in the containment, while its mixing effect homogenises the containment atmosphere, avoiding local accumulations of hydrogen that could otherwise be the main contribution to the hydrogen risk. While the steam content in the containment tends to a steady value that can be estimated by a simpler heat and mass balance, the local distribution of hydrogen depends on complex 3D flows. This works recognises the need of studying this issue using 3D models, addresses the complexities and numerical cost of its numerical modelling, and proposes a systematic evaluation of the positive/negative impact of the spray system actuation on the hydrogen risk.

The systematic analysis, performed under the CSN/UPM-GOMERES and UE-AMHYCO projects, includes the selection of a bounding sequence in terms of H2 risk, different postulations of the main safety system actuations (PAR and spray), and a postprocessing strategy to extract adequate safety relevant figures of merit to compare the cases. All the scenarios postulated in this work, based on a Station Black Out (SBO) accident releasing ~850 kg of hydrogen to the containment building, concluded that the cooling effect of the spray has a more significant impact than the mixing. Therefore, the late recovery of the spray induced more severe conditions. Last, since all the scenarios without PARs lead to non-acceptable hydrogen risks with the current postulations, an alternative strategy for the late recovery of the spray for designs without PARs is proposed.

KEYWORDS
Hydrogen, Containment, GOTHIC, Spray, PARs

1. INTRODUCTION

Containment spray systems are implemented in most containment designs [1] because they provide a highly effective means to cool down and depressurise the containment. Indeed, they were originally designed and sized against criteria dominated by pressure/temperature control and source-term reduction via the wash-down of aerosols [2]. Nevertheless, although the spray was not conceived as a hydrogen-mitigation device, its actuation can have a major impact on the severe-accident hydrogen risk by simultaneously (i) enforcing a strong cooling/condensation sink that removes steam; (ii) driving large-scale mixing that reshapes the 3D distribution of hydrogen and steam in the containment [3]. In the compartmentalised geometry of a containment the assessment of the spray mixing is not trivial, because the hydrogen risk characterisation (slow deflagrations versus mixtures with flame-acceleration potential) is governed by local heterogeneities rather than by a single global average [4]. Consequently, the fast-changing conditions induced by the spray

actuation and the complex flow structures of the containment make a 3D assessment with sufficient thermal-hydraulic resolution particularly necessary to evaluate the combustion risk.

The need to go beyond the well-established Lumped Parameter (LP) approach for topics such as hydrogen risk is aligned with the conclusions of the systematic review published by Zhao et al. [5], which concluded that the use of more detailed models is a central factor in improving the Severe Accident Management Guidelines (SAMGs). In this context, spray actuation and/or recovery are among the most complex SAMG decisions, because they couple multiple –and potentially competing– objectives (containment depressurisation, aerosol wash-down, and hydrogen risk management), for which the net effect may be beneficial or adverse depending on the scenario. Therefore, while analytical tools are essential to inform SAMGs in such conditions, any safety-relevant contribution must assess spray operation systematically across different postulations and quantify its interactions with other mitigation systems, such as Passive Autocatalytic Recombiners (PARs), ignitors, fan coolers, or Filtered Containment Venting Systems (FCVS)).

Following these two requirements –detailed 3D modelling and a systematic assessment of spray actuation across postulations– a search in the open literature yields only a small number of journal publications addressing hydrogen risk with 3D tools [6–11], summarised in Table I. The reduced size of the list is explained by the level of complexity of the issue –3D modelling of a multi-phase, multi-scale, multi-component fluid domain, with strong fluid-solid interactions, engineering systems, and long transients– and its associated computational cost. Furthermore, based on the authors' evaluation, none of the listed references meets the combined scope and depth needed to be labelled as a detailed and systematic 3D analysis of spray actuation, for the reasons highlighted in red in Table I. Therefore, this work intents to contribute to the state of the art by improving the scope –in terms of number of cases and the use of a systematic approach– and the thermal-hydraulic resolution –in terms of accuracy and number of cells– of the comparable studies available in the open literature. This objective can be achieved only by acknowledging that, in order to maintain affordable computational costs, selective simplifications of the physics of the problem must be implemented.

Table I. Scientific publications performing 3D evaluations of the spray influence on the H_2 risk

Reference	Code	Number of Cells	Advanced spray implementation*	Other Safety Systems	Number of Cases (Transient time)
(Mohaved et al., 2003)	GASFLOW	-	NO	NO	2 (2.8 h)
(Kim et al., 2006)	GASFLOW	66 960	NO	NO	2 (2.8 h)
(Xiong et al., 2009)	GASFLOW	54 000	NO	Spray recirculation	3 (1.9 h)
(Huang et al., 2011)	GASFLOW	60 480	NO	PARs, Ignitors	7 (1.9 h)
(Téchy et al., 2013)	GASFLOW	41 000	NO	NO	4 (20 h)
(Fernández-Cosials et al., 2017)	GOTHIC	1829	NO	FCVS	65 (5.6)
This work	GOTHIC	70 400	YES	PARs, Recirculation	24 (9 h)

*An advanced implementation requires: thermal & mechanical non-equilibrium when modelling gas and droplets interactions, evaporation of the liquid reaching the walls, and to use the real number of nozzles when modelling the spray safety system

To close the Introduction –and precisely in line with this balance between thermal-hydraulic resolution and computational affordability– all simulations have been performed with GOTHIC8.3(QA). The features of the code are extensively described in previous publications [12] but, in a few words, it could be described as a "Hybrid System Level and Coarse Grid CFD Tool [13]", meaning that the code allows combining the LP and CFD resolutions in the same model. Indeed, in the open spaces of the containment, GOTHIC solves the Reynolds-Average Navier Stokes equations in a similar fit as the commercial CFD codes, and close to the walls, it uses heat and mass transfer correlations like the nuclear legacy system codes. This hybrid approach enables the use of relatively coarse 3D meshes because the correlations close the equations without modelling the fluid boundary layer, saving tens of thousands of cells.

1. A SYSTEMATIC APPROACH TOWARDS COMBUSTION RISK EVALUATION

The systematic approach used to quantify the influence of the spray actuation on the hydrogen combustion risk, whose results are summarized in this work, are part of a PhD Thesis developed under the framework of CSN/UPM-GOMERES and UE-AMHYCO projects [4]. The blocks in Figure 1 summarise the different work lines deemed necessary to label the current research as a systematic evaluation. Nevertheless, for the sake of brevity, this section will simply provide a brief summary of some of the blocks with the necessary references to more detailed information. This paper will cover the blocks in different tones of blue in Figure 1, with subsections 2.1, 2.2, and 2.3 describing the sequence selection criteria, the figures of merit for the combustion risk evaluation, and the systematic exploration of different activation criteria for the spray. Later, section 3 will describe the results of the simulation with and without PARs.

The contribution to the state of the art ambitioned in Table I—including spray and other safety systems, with a 3D model at containment scale, for up to 24 distinct transients with 9 h of simulated time—can only be achieved by accepting, at every stage of the work, that affordable computational costs require selective simplifications of the underlying physics. This immediately rules out the most detailed gas-to-droplet interaction approaches, such as Euler–Lagrangian schemes, spray atomisation, internal droplet temperature gradients, and droplet–droplet interactions (break-up, coalescence, etc.) Alternatively, this work adopts a relatively coarse mesh and a monodispersed representation of the droplet field, accounts for thermal and mechanical non-equilibrium in the gas–droplet coupling, includes evaporation of the liquid reaching the walls, and preserves the real number of nozzles when representing the spray rings of a generic PWR-W.

To evaluate whether the proposed approach retains the critical physics needed to assess the *global* impact of spray operation in terms of containment cooling and hydrogen mixing, it has been validated against six PANDA experiments, selected to span a range of representative conditions and phenomena for the intended plant-scale application. Two of these experiments (one of them including a spray ring) were performed within the OECD/NEA HYMERES-2 Project and were comprehensively discussed in [14], while the corresponding results for the remaining four tests are available in [4]. Overall, the validation exercise showed a solid qualitative agreement with the experimental measurements for the six simulated experiments; in quantitative terms, however, the simulations exhibited a consistent overestimation of the spray cooling effect. Since such quantitative deviations observed at the PANDA scale may directly affect the quantification of the hydrogen risk when extrapolated to the containment analysis, the present systematic evaluation will include a set of parametric cases to consider the impact of equivalent deviations before extracting any safety-relevant conclusion.

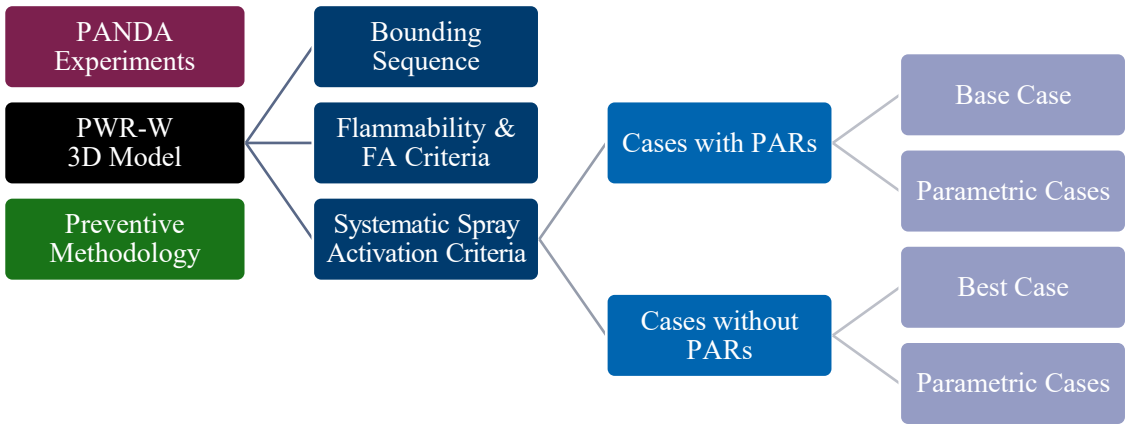

Figure 1. Flowchart of the systematic approach on evaluating the impact of the spray on the H_2 risk

In addition to the lessons learnt from the PANDA validation, the 3D PWR-W containment model used for the calculations was developed following the "Preventive Methodology" described in detail in [12], which provides a practical framework to optimise the computational cost of GOTHIC models through a geometry definition strategy tailored to the porous-media approach. This methodology introduces targeted geometric simplifications that remove the root causes of numerical issues associated with particular cell configurations —especially when targeting fine meshes on the order of 1 m³ per cell— observed in previous UPM GOTHIC models, which often led to unaffordable computational costs. As demonstrated in [12], the 3D PWR-W model used in this work achieved a reduction of the computational cost by a factor of about 40 when compared with models using an even coarser cells (1.5 m³ per cell vs. 1.95 m³ of the previous finest model).

1.1. Bounding Sequence Selection

The next step of the systematic approach to estimate the impact of the spray actuation on the hydrogen combustion risk was the selection of a bounding accident sequence combining: (i) severity in terms of combustion potential; and (ii) an a priori expectation of high sensitivity to spray operation. In this work, the transient was selected from the sequences made available within the EU AMHYCO Project [15], which were screened by the project partners to maximise the expected combustion risk based on expert judgement, rather than targeting the most probable sequences from a full Level 2 probabilistic risk assessment.

A detailed description of AMHYCO's selection criteria is provided in [15]. In brief, the screening using LP Severe Accident (SA) codes considered peak combustible gas molar fractions in the containment, total combustible gas mass, maximum release rates, and containment pressure levels, complemented by an overall qualitative assessment. In the present application, the selected sequence particularly prioritised the combination of a high total hydrogen mass and high containment pressures, since this pairing is expected to maximise the potential cooling effect of spray actuation (or recovery).

The transient selected in this work is a Station Black-Out (SBO) calculated by IRSN with ASTEC within AMHYCO [15], and implemented as time-dependent mass and energy sources for the containment model. Figure 2 summarises the releases: an initial two-phase intermittent discharge followed by steam releases, all originating from the Pressuriser Relief Tank (PRT). Later, once core degradation is ongoing, the pressurizer relief valves lock open progressively depressurising the primary circuit. The slow steam–core interaction yields up to 848 kg of hydrogen by the end of the in-vessel phase. These work simulations' are stopped at the time of the reactor vessel failure. The main milestones of the sequence are summarised in Table 2. In the absence of spray actuation, the containment pressure remains between 3.5 and 4.5 bar most of the transient, so any postulated spray recovery is expected to significantly affect the containment thermal-hydraulic conditions.

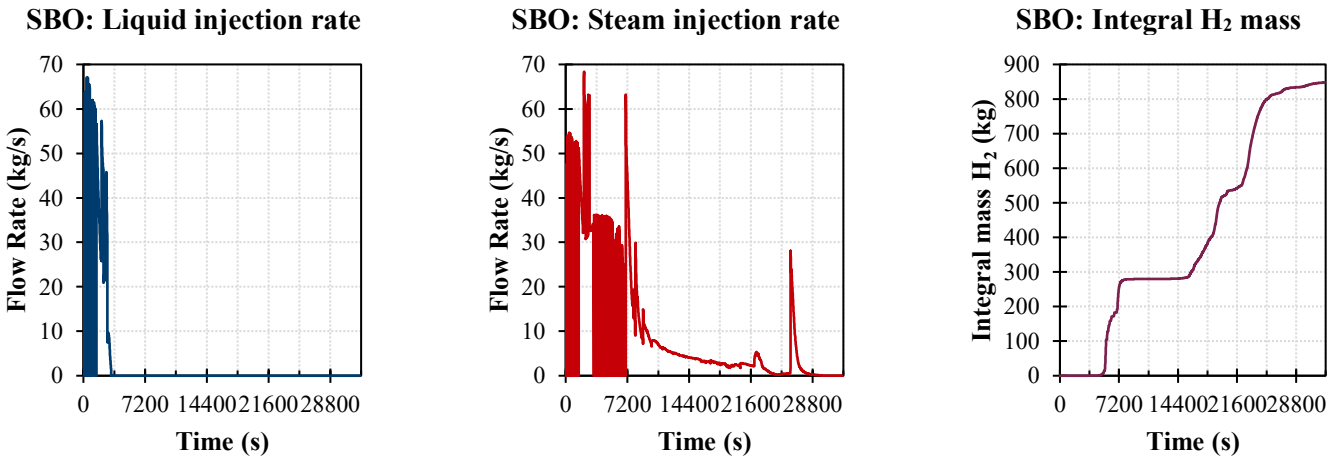

Figure 2. Boundary conditions for the containment analyses calculated by IRSN using ASTEC [15]

Table 2. On the left, main milestones of the simulated SBO. On the right, postulated spray recoveries

	Time in GOTHIC
Loss of all offsite power	- 2 h 37 min
Rupture of PRT (Pressure relief Tank) disks	-11 min
Pressuriser valves locked opened (SAMG action)	1 h 56 min
Accumulator tank discharge	2 h 9 min
RPV failure	8 h 58 min

Case IDs	Spray On	Spray Off
v010	**No Spray**	**No Spray**
v011	**7200 s**	**14400 s**
v012	**10800 s**	**18000 s**
v013	**14400 s**	**21600 s**
v014	**18000 s**	**25200 s**
v015	**21600 s**	**28800 s**
v016	**25200 s**	**32400 s**

1.2. Systematic Spray Activation Criteria

To label the assessment of spray operation as systematic, the analysis must postulate alternative recovery logics and timings rather than a single best-estimate actuation time. This is particularly relevant for the present SBO, in which sprays are unavailable by definition. Hence, the analysed cases represent postulated spray recoveries framed as candidate SAMG actions after core degradation has started. As summarised in Table 2, the time window for these recoveries happens just after the SAMG action of IRSN calculation, triggered by a high core-temperature signal and leading operators to keep the pressuriser valves open to depressurise the primary circuit, and avoid a potential early containment failure by direct containment heating.

On this basis, the spray "activation criteria" are defined as discrete recovery times starting after the SAMG entry, which occurs at approximately 2 h in the present GOTHIC calculations (Table 2). The spray is then recovered once per hour from 2 h to 7 h, including a reference case without spray, and each recovery is modelled as a 2 h direct spray phase. This duration is consistent with the assumed water availability, since the spray is postulated as the only system drawing from the Reactor Water Storage Tank and the available inventory supports approximately 2 h of direct injection at the nominal flow rate. Moreover, the transition to the recirculation phase is postulated as failed in the base cases, and is only explored within the parametric cases. These postulations are not intended to reproduce any plant-specific SAMG logic, but to illustrate how an analytical tool can screen candidate high-level mitigation actions by comparing alternative timings and boundary conditions. The same recovery windows are analysed with and without PARs, yielding 14 base cases, which are complemented by 10 parametric cases exploring spray actuation parameters, PAR efficiencies, recirculation availability, and selected material properties.

Finally, the boundary conditions associated with the spray safety system correspond to a generic PWR-W for which the spray is the only dedicated containment heat-removal system (i.e., no fan coolers are modelled). The nominal liquid flow rate is 208 kg/s per train, and the present work postulates the operation of a single train. The system consists of three spray rings (104, 64, and 48 nozzles), and each nozzle injects 1 kg/s of droplets with an SMD of 1000 μm, at 30 °C, and with a full cone angle of 60°.

1.3. Flammability and Flame Acceleration (FA) Criteria

A systematic analysis requires a well-defined figure of merit to enable consistent comparisons between cases. In the context of hydrogen combustion, previous methodologies [16,17] typically differentiate between slow deflagrations, conditions with the potential to promote Flame Acceleration (FA), or, in more extreme cases, a deflagration-to-detonation transition (DDT). While slow deflagration remains a relevant safety concern for the containment –since it may challenge systems and instrumentation needed for accident

management– the containment structure is generally expected to withstand such slow regimes, but not the much higher dynamic pressures associated with FA or DDT [3]. Moreover, hydrogen combustion cannot be halted once initiated. Thus, the emphasis of the present evaluation is placed on preventing conditions that could lead to FA. Accordingly, the primary safety criterion adopted in this work is to avert FA conditions, and whenever they are identified, the parametric analysis will explore mitigation alternatives.

The FA assessment is based on the σ criterion, which builds on the dimensionless analysis proposed by Dorofeev et al. [18] from a broad experimental database. The σ criterion evaluates the expansion ratio between burned and unburned mixtures and compares it to a critical value (σ_c) that depends on the initial conditions and mixture composition. In this work, the computation of the σ followed the guidelines given in [16]. Accordingly, the hydrogen risk is quantified here through a cell-by-cell post-processing of the 3D simulation results. Specifically, the computed pressure, temperature and gas composition of each cell. Each cell is first tested for flammability, and only flammable cells are subsequently evaluated for FA potential. The flammability limits account for the effect of mixture temperature and, in addition to the limits given in [16], implement a lower oxygen concentration threshold to account for hydrogen starvation conditions potentially induced by the PARs. For each flammable cell, σ is divided by the critical value σ_c to obtain the σ-index (σ_i), and cells with $\sigma_i \geq 0.92$ are labelled as FA-prone, where the threshold accounts for the ±8% uncertainty reported by [18]. The resulting σ field is retained cell-by-cell, both to compute the integral FA hydrogen mass and to enable 3D visualisations of FA potential in different containment regions.

Finally, the figure of merit to compare the different cases will be the temporal evolution of the total hydrogen mass in the containment with the potential to undergo FA, obtained by summing the hydrogen mass of all the cells where $\bar{\sigma} \geq 0.92$. It is important to note that combustion processes are out-of-scope of the present simulations. Therefore, hydrogen is accumulated inside the containment without considering partial combustions processes triggered by spurious ignition sources. Also, since the simulations are stopped before entering in the ex-vessel phase, CO is not included in these analyses.

2. SBO WITHOUT PARs AND SPRAY RECOVERY

This section will present the unmitigated cases, i.e., the different spray activation windows simulated in the model without PARs. Although these unmitigated SBO cases will also serve as a reference to quantify the role of PARs and their interaction with spray recovery, their relevance goes beyond a purely comparative purpose. For PWR-W containments in the United States, the need for PARs has been repeatedly discussed across licensing and post-event reviews (TMI-2, the AP600 design, and post-Fukushima), with the recurring conclusion that PAR installation is not required provided that pre-established hydrogen-control requirements are correctly implemented. Consequently, the "without PARs" configuration remains representative existing plant conditions and is therefore analysed here with an equivalent scope as the mitigated cases.

The unmitigated cases will be presented in two sub-sections. Section 3.1 presents selected results of the different spray recovery windows to: (i) understand the impact of spray recovery by comparing spray vs no-spray cases; and (ii) evaluate the relevance of local conditions on the global combustion risk metrics. Section 3.2 then summarises the parametric cases used to challenge the base-case conclusions, also showing a spray operation strategy aiming to reduce the combustion risk for PWR-W without PARs. All simulations were performed on a single desktop computer (Intel i7-8700, 3.2 GHz) using six MPI ranks: the reference case without spray required 91.3 h, whereas the corresponding case with spray required 118.9 h, with the increase attributed to the higher velocities induced by droplet injection.

2.1. Spray activation windows

The global evolution of the containment thermal hydraulics and the hydrogen combustion risk for the different spray recoveries are summarised in Figure 3 (containment pressure) and Figure 4 (total FA mass).

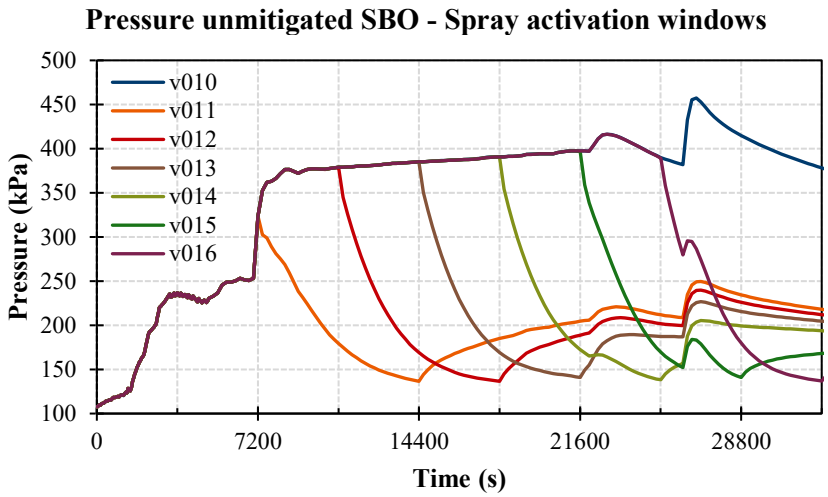

Figure 3. Unmitigated SBO containment pressure evolution for different spray activation windows

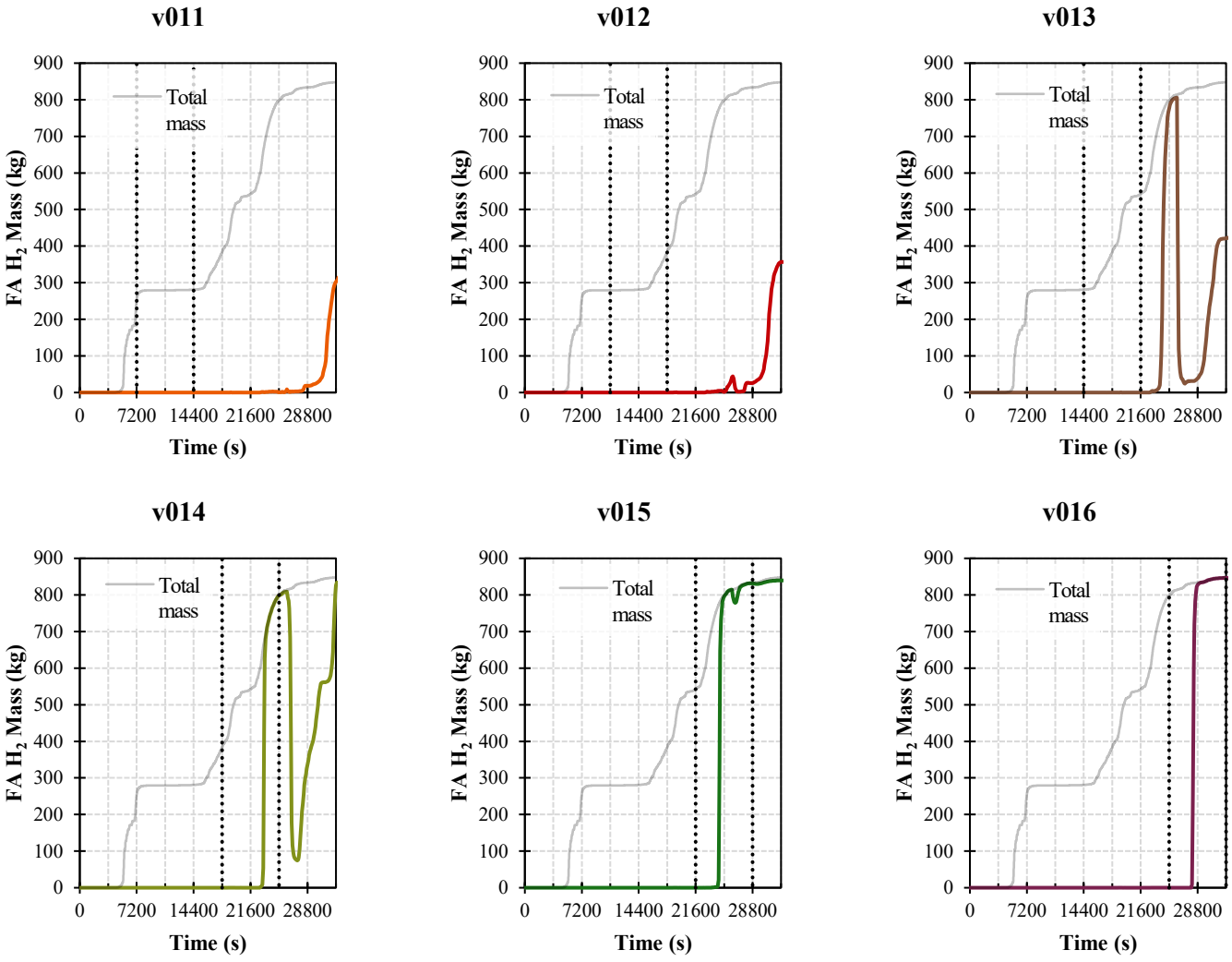

Figure 4. Mass of hydrogen with FA potential ($\sigma_i > 0.92$) for different spray activation windows
Each graph shows the evolution of the flammable H2 for the spray activation windows indicated with dotted lines. The thin grey line is used to guide the eye for comparing the FA mass with the total H_2 mass released to the containment

The containment pressure response in Figure 3 shows two radically different containment conditions in cases with and without spray recovery. Generally, the pressure increase is driven by the time-dependent mass and energy injections (see Figure 2), with intermittent releases during the early phase (before 7200 s) and, later, a sharp increase when the primary circuit is depressurized. In the case without spray, wall condensation partly mitigates the pressure rise but cannot compensate for the continuous steam and hydrogen inflows. By contrast, all spray-recovery cases exhibit the same characteristic response: the 2 h direct spray phase produces an abrupt pressure reduction, followed by a pressure rebound once droplet injection is stopped, as steam and hydrogen injections continue and the containment is warm-up again. The impact of the spray on pressure increases with later recoveries: for identical droplet flow rate and injection temperature, the pressure drop grows from about 190 kPa for activation at 2 h to about 250 kPa for activation at 7 h, consistent with the larger temperature difference between the droplets and the vapour phase at later times.

Figure 4 reports with colours matching the former pressure lines the figure of merit introduced in section 1.3, i.e., the total hydrogen mass with potential to produce a FA ($\sigma_i \geq 0.92$), for the different spray recovery windows (v010 is not included because the FA mass remains zero without spray). The grey line provides the total hydrogen injected to the containment to facilitate the interpretation of the results. The main trend is that later spray recoveries –linked with the lowest containment pressures and, therefore, steam concentrations– lead to higher FA masses as the atmosphere becomes less inerted. Indeed, in the latest recoveries (v015–v016), the FA mass matches the total injected hydrogen. In earlier recoveries, the FA curves frequently lie below the grey line, indicating phases in which only part of the hydrogen inventory is in FA conditions while the remainder is not. This behaviour already implies that local conditions, not only global averages, affect the integral FA mass.

The relevance of the local concentration of hydrogen is illustrated in Figure 5 (right). First, the figure on the left show that without spray the σ_i field remains well below the 0.92 threshold, consistent with the null FA mass in v010. When the spray is recovered, the FA condition may appear in regions with relatively small heterogeneities. Generally, the local H_2 maximums occur in the lower elevations of the containment rather than in the dome. This non-trivial phenomenon is explained by a complex combination of the hydrogen release point, the containment compartments, small density-driven flows, and the heterogeneous wall condensation, which once the spray has stopped, is concentrated in the concrete walls located at the lower elevations. Indeed, and as shown in Figure 5 (right), the mass of hydrogen with FA potential ($\sigma_i \geq 0.92$) in case v011is concentrated in the lower compartments. Since the local heterogeneities are driven by 3D flows, and even when the global thermohydraulic trends are well captured by LP codes, the identification of the worst combustion risk condition may require a 3D evaluation.

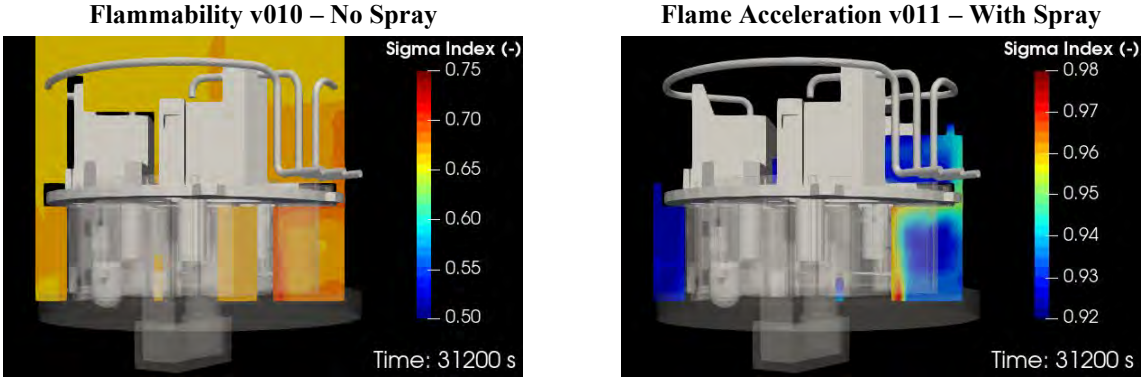

Figure 5. 2D slice of $\bar{\sigma}$ at the location of the hydrogen injection with thresholds for flammability and FA
On the left, all the cells within the flammability limits ($\bar{\sigma} > 0$) are coloured, and on the right the threshold value is $\bar{\sigma} > 0.92$ and therefore the coloured cells may have a FA regime

2.2. Parametric cases

The conclusions extracted from section 2.1 are systematically challenged with dedicated parametric cases, both to probe robustness and to cover known modelling uncertainties/inaccuracies linked to the necessary simplifications of the physics to perform these calculations with acceptable computational cost (see section 1). For the unmitigated SBO, the parametric cases included: (i) alternative hypotheses for spray recirculation availability, (ii) spray injection temperature, (iii) concrete thermal conductivity, and (iv) spray mass flow rate. For the sake of brevity, only one subset is illustrated here, with the remaining ones available in [4]. As an example of the "challenge" logic, the worst recovery window (v015) was repeated with a reduced spray flow rate (75% of nominal, based on the validation of our modelling approach) to obtain less severe (more steam-inerted) conditions. Since the total H_2 mass under FA conditions remained significant, it is re-stated that this scenario has the potential to induce non-acceptable combustion risks for PWR-W without PARs.

A second objective of the parametric analysis is to explore mitigation-oriented operating alternatives. The spray operation cannot always be treated as a discretionary hydrogen-mitigation action (it may be demanded for pressure control before SAMG actions). Therefore, rather than concluding that "spray recovery should be avoided", [4] evaluates whether modifying spray *operating conditions* can combine pressure control while retaining enough steam inertisation to suppress FA. In the most penalising window (v015), the direct spray phase is repeated with warmer droplets (80 °C, v015b). Instead of showing this case, which removed the FA risk, Figure 6 directly show the parametric case used to challenge its robustness. Specifically, v015c combined the warmer droplets with an increase of the concrete thermal conductivity up to 2.25 W/m·K.

Figure 6 shows that the postulated higher concrete conductivity reduces the pressure already before spray recovery (from ~400 kPa in v015 to ~300 kPa in v015c by the 6th hour), implying a lower steam content and, therefore, potentially worse hydrogen conditions. During spray operation, the hotter spray temperature limits the pressure drop (≈250 kPa in v015 and ≈70 kPa in v015c), i.e., it avoids excessive steam removal while still providing depressurisation. Consistently, Figure 6 (right) shows that FA conditions are suppressed in v015c (even though mixtures remain flammable), indicating that warmer spray injection – even when maximising the steam removed by wall condensation– provides a practical balance between containment pressure control and hydrogen-risk mitigation for PWR-W designs without PARs.

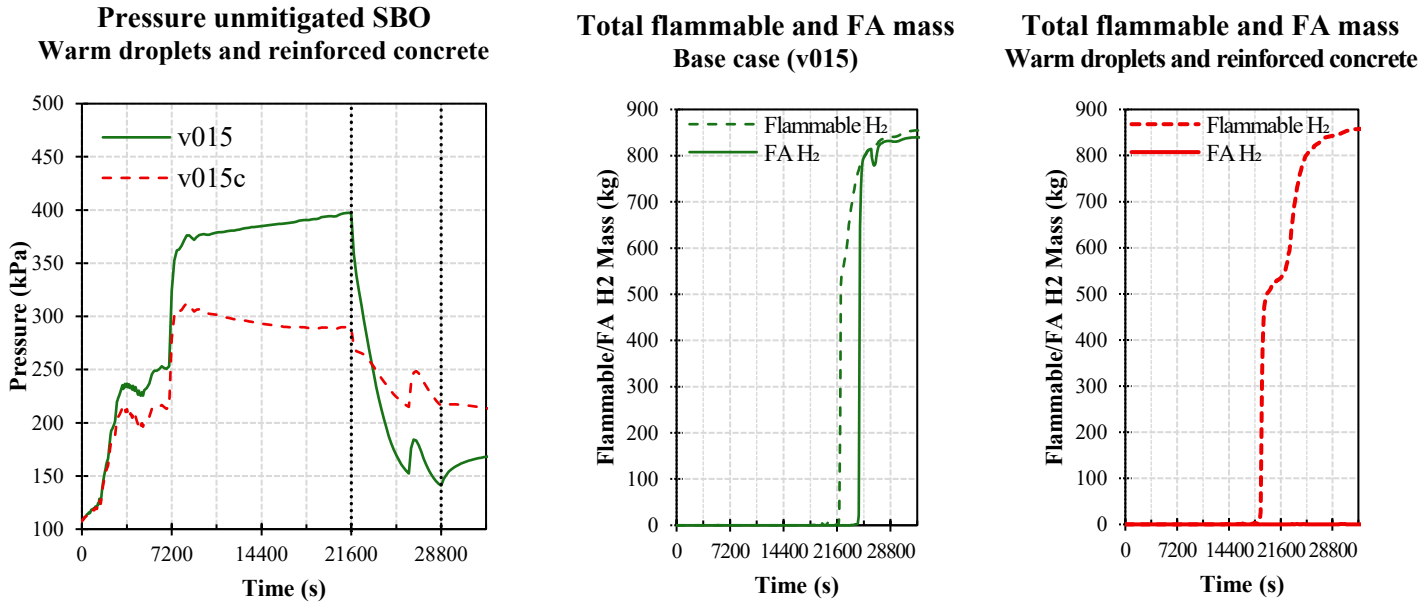

Figure 6. Illustration of the combustion risk limitation by increasing spray injection temperature

3. SBO WITH PARs AND SPRAY RECOVERY

PARs constitute the standard hydrogen control and mitigation system in the European Union, and the comparison in Figure 7 illustrates their effect under the present SBO conditions. The 'generic' PAR sizing and layout adopted in the present model are documented in [12]. Since all cases including PARs remain far from FA conditions, the results are discussed in terms of compartment-averaged H_2 volume fractions rather than the FA criterion. Each line in Figure 7 represents the volume average of a separated compartment, with the matching between lines and zones given in the caption. The comparison shows three representative spray windows for direct reference: "no spray", "early spray", and "late spray", shown without PARs in the top row (v010, v011, v015) and with PARs in the bottom row (v110, v111, v115). The results show that PAR actuation markedly reduces the containment-average H_2 levels across all spray timings: whereas the unmitigated cases reach room-averaged peaks of the order of 10.5–13.5%, the cases mitigated with PARs remain within roughly 4.5–6.5%. The dominant concentration peak is consistently associated with the main release phase between the 6th and 7th hour (see Figure 2), when PARs cannot fully offset the large injection rates.

As in the previous section, the conclusion that PARs suppress FA is challenged through parametric variations, including (i) reduced PAR recombination efficiency down to 40% of nominal, and (ii) an increased concrete thermal conductivity to intensify wall condensation and decrease steam inertisation. Even under these penalising assumptions, the predicted FA mass remains negligible and no significant FA conditions are obtained for any sequence mitigated with PARs.

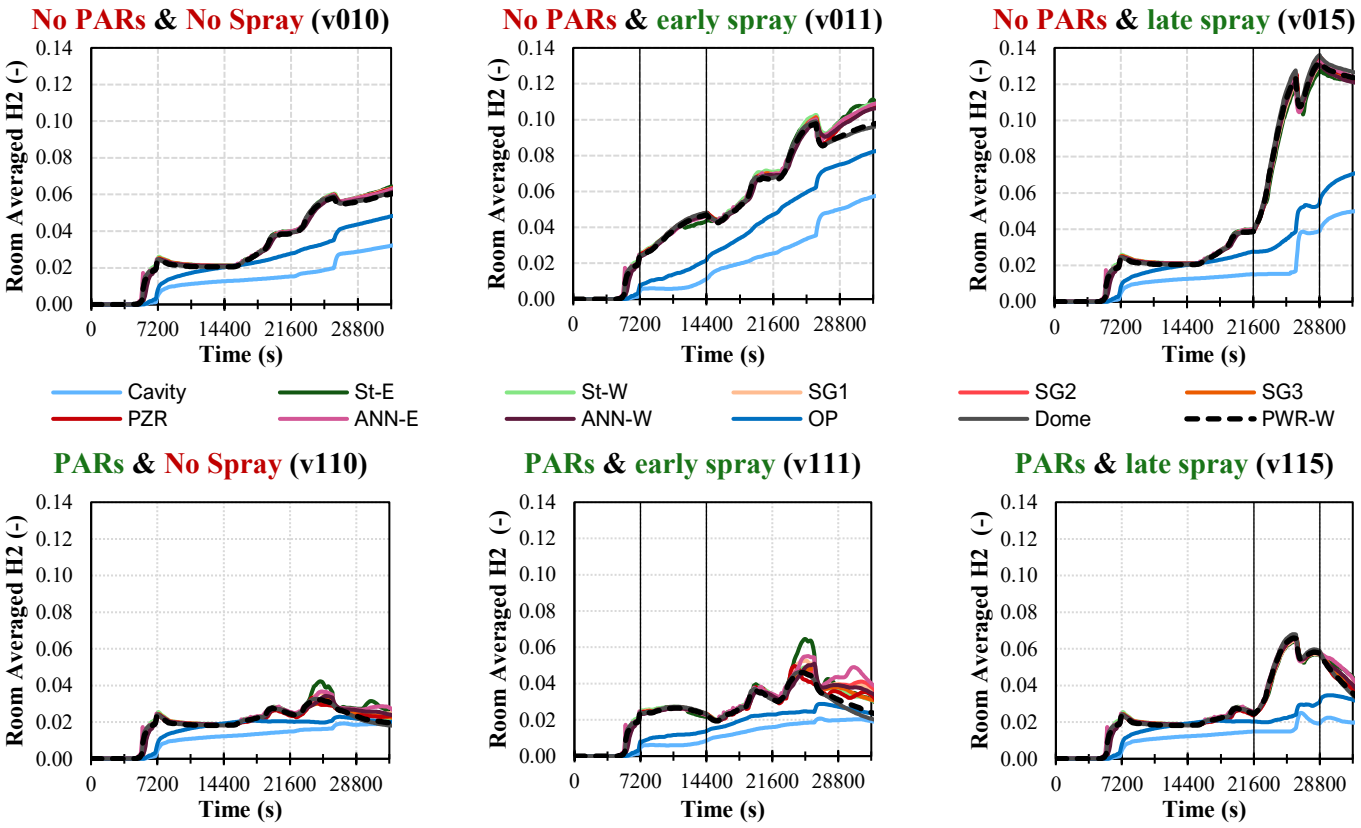

Figure 7. Averaged H2 fractions without (top) and with PARs (bottom) and different spray actuation
Each line of the graph represents an averaged volume fraction for different compartments of the containment. The dashed line "PWR-W" is an average for the full containment. The "SG" and "PZR" labels refer to the different steam generators and pressuriser compartments. "OP" is the outage pool, the "ANN" lines are the open spaces outside the secondary shielding, and St-E" and "St-W" stands for the closed spaces of the containment stairs

4. CONCLUSIONS

This work aimed to improve both the scope (systematic evaluation) and the thermal-hydraulic resolution (plant-scale 3D modelling) of the limited set of comparable studies in the open literature evaluating the influence of the spray activation on the hydrogen risk. Across all scenarios simulated in this research and in alignment with the findings from most prior studies in the open literature, the initiation of the spray system resulted in worsened conditions in relation to hydrogen risk. Research on the spray system in the nuclear industry used to open the articles discussing the "compensating effects" of the spray actuation, with steam removal as a negative factor and containment homogenisation as a positive factor. For the sequence simulated in this work –added to complementary calculations with other available transients– the role of steam removal is significantly more relevant. It should not be discarded that the spray activation may positively impact the hydrogen risk for very particular conditions with low steam release in the containment and a strong hydrogen stratification within the containment. Nevertheless, the simulations performed in this article suggest that steam removal must be the main issue to consider in the SAMGs before activating the spray during a severe accident.

A key element of the systematic approach is that safety-relevant statements are challenged with dedicated parametric cases . Indeed, the two main conclusions of this research, at the bullet points below, are challenged as follows:

- "All the spray activation windows for the sequences without PARs induced conditions with the potential to create fast hydrogen combustion". This statement is reinforced by a parametric case designed to create the conditions minimising the combustion risk (reduced spray flow rate, lower bound of concrete thermal conductivity, and tightened fast flame criteria). The identification of fast flame conditions in the enveloping case highlights the high risk associated with a late operation of the spray during a severe accident in designs without PARs.
- "The PARs system impeded the formation of mixture with potential to create fast hydrogen combustions". The conservativeness of this statement is proved by a parametric case designed to create the conditions maximising the combustion risk (up to a 60% decrease of the recombination efficiency and a lower bound of concrete thermal conductivity). There was no FA risk associated with the enveloping case, reinforcing the statement on the efficiency of PARs.

Lastly, this article has proposed an alternative to reduce the risk of flame acceleration in cases without PARs. Typically, the spray activation prioritises containment pressure signals –in several cases, it will be initiated before the hydrogen generation phase– so the recommendation cannot be limited to "do not activate the spray". Therefore, the alternative would be to make compatible the primary role of the spray, the cooling of the containment, while keeping enough steam in the containment to avoid the most severe hydrogen risk conditions. Specifically, it would consist of setting a higher injection temperature for the sprayed droplets for both the direct and recirculation phases of the spray injection.

These conclusions remain conditional on the adopted modelling scope: no explicit combustion modelling (such as PAR-induced ignitions) or simulations limited to the in-vessel phase. Future works could include: (i) extend the analysed sequences into the ex-vessel phase and asses more sequences; (ii) improve calculation of PARs efficiency and spray modelling; (iii) include additional safety devices as filtered venting or fan coolers; and (iv) evolve from selected parametric case to a comprehensive best-estimate-plus-uncertainty framework.

ACKNOWLEDGMENTS

This research been funded by the Spanish Nuclear Safety Regulator (Consejo de Seguridad Nuclear) through the GO-MERES Project. The AMHYCO project has received funding from the Euratom research and training programme 2019-2020 under Grant Agreement n°945057. The content of this paper reflects only the author's view. The European Commission is not responsible for any use that may be made of the

information it contains. This work was completed using a GOTHIC license for educational purposes provided by Numerical Advisory Solutions, LLC. The authors also wish to extend their appreciation to the personnel of EPRI and Numerical Advisory Solutions company.

REFERENCES

1. OECD/NEA, *Status Report on Hydrogen Management and Related Computer Codes*, NEA/CSNI/R(2014)8 (2014).
2. ANSI/ANS, *PWR and BWR Containment Spray System Design Criteria.Pdf* (1979).
3. IAEA, "Mitigation of Hydrogen Hazards in Nuclear Power Plants", *IAEA-TECDOC-1661*, Vienna, Autria (2011).
4. Vázquez-Rodríguez, C., "Advanced implementation of the spray safety system into a 3D-GOTHIC PWR-W containment model and its impact on the hydrogen combustion risk", Universidad Politécnica de Madrid (2023).
5. Zhao, N., Ma, W., and Bechta, S., "A review of the assessment of severe accident management guidelines and actions through analytical simulations", *Annals of Nuclear Energy*, **180**, p. 109448 (2023).
6. Mohaved, M. A., Eyink, J., and Travis, J. R., "Effect of spray activation on the reactivity of the hydrogen-air-steam mixture in the containment of the EPR" (2003).
7. Kim, J., Lee, U., Hong, S.-W., Kim, S.-B., and Kim, H.-D., "Spray effect on the behavior of hydrogen during severe accidents by a loss-of-coolant in the APR1400 containment", *International Communications in Heat and Mass Transfer*, **33**(10), pp. 1207–1216 (2006).
8. Xiong, J., Yang, Y., and Cheng, X., "CFD Application to Hydrogen Risk Analysis and PAR Qualification", *Science and Technology of Nuclear Installations*, **2009**, pp. 1–10 (2009).
9. Huang, X. G., Yang, Y. H., Cheng, X., Al-Hawshabi, N. H. A., and Casey, S. P., "Effect of spray on performance of the hydrogen mitigation system during LB-LOCA for CPR1000 NPP", *Annals of Nuclear Energy*, **38**(8), pp. 1743–1750 (2011).
10. Téchy, Z., Kostka, P., Lajtha, G., Elter, J., and Tóth, É., "Analysis of Severe Accident Hydrogen Management for Paks NPP", *NURETH-15*, Pisa, Italy (2013).
11. Fernández-Cosials, K., Jimenez, G., Bocanegra, R., and Queral, C., "Study of hydrogen risk in a PWR-W containment during a SBO scenario; Tau parameter definition and application on venting strategy analysis", *Nuclear Engineering and Design*, **325**(April), pp. 164–177 (2017).
12. Vázquez-Rodríguez, C., Jiménez, G., Arfinengo-del-Carpio, S., Bocanegra, R., Domínguez-Bugarín, A., Serra, L., Estévez-Albuja, S., and Fernández-Cosials, K., "The Preventive Methodology: A priori modification of the containment geometry to boost the computational efficiency of GOTHIC 3D models", *Nuclear Engineering and Design*, **432**, p. 113718 (2025).
13. Harvill, R. C., Lane, J. W., and George, T. L., "Hybrid System Level and Coarse Grid CFD Tool for Three-Dimensional Natural Circulation, Mixing, and Stratification Modeling", *Nuclear Technology*, **208**(1), pp. 1–26 (2022).
14. Vázquez-Rodríguez, C., Andreani, M., Jiménez, G., Kapulla, R., Paranjape, S., Manuel Martín-Valdepeñas, J., and Paladino, D., "Assessment of the depressurisation and mixing effects of two spray systems in the PANDA facility, part II – Simulations using GOTHIC8.3(QA)", *Nuclear Engineering and Design*, **403**, p. 112120 (2023).
15. Herranz, L. E., Fontanet, J., Braun, M., Bentaib, A., Bleyer, A., Maas, L., Kljenak, I., Leskovar, M., Hoffrichter, J., Koch, M. K., Müer, M., Iskra, A., and Cherednichenko, O., *AMHYCO D2.2 - Identification and Analysis of Accident Sequences with Posing High H2/CO Combustion Risk* (2023).
16. Martín-Valdepeñas, J. M., Jiménez, M. A., Martín-Fuertes, F., and Fernández, J. A., "Improvements in a CFD code for analysis of hydrogen behaviour within containments", *Nuclear Engineering and Design*, **237**(6), pp. 627–647 (2007).
17. Bentaib, A., Meynet, N., and Bleyer, A., "Overview on hydrogen risk research and development activities: Methodology and open issues", *Nuclear Engineering and Technology*, **47**(1), pp. 26–32 (2015).
18. Dorofeev, S. B., Kuznetsov, M. S., Alekseev, V. I., Efimenko, A. A., and Breitung, W., "Evaluation of limits for effective flame acceleration in hydrogen mixtures", *Journal of Loss Prevention in the Process Industries*, **14**(6), pp. 583–589 (2001).

Systematic analysis of the influence of the spray actuation on the hydrogen risk using a 3D GOTHIC PWR-W Model

Carlos Vázquez-Rodríguez[1,2], Gonzalo Jiménez[2], J.M Martín-Valdepeñas[3]

[1]FZJ, [2]UPM, [3]CSN

12h European Review Meeting on Severe Accident Research (ERMSAR2026) - Madrid, Spain, May 18-22, 2026

2. PANDA Spray Experiments

1. Introduction
2. Systematic Evaluation H_2 Risk
3. SBO and spray recovery: No PARs
4. SBO and spray recovery: with PARs
5. Conclusions

1. Introduction

- The **containment building** is the last physical barrier of the defence-in-depth principle. It must prevent the uncontrolled release of radioactive materials.

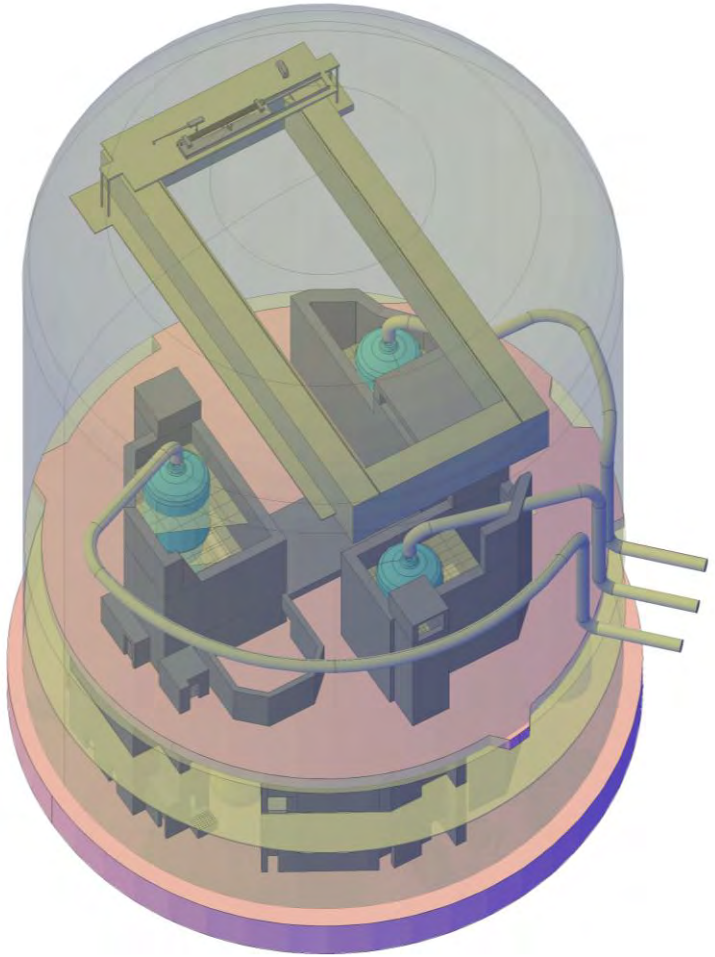

Main considerations for the containment design basis (from the 60s)

Cooling
(Pressure & Temperature)

Source Term
(Fission products removal)

After TMI-II accident (1979)

Hydrogen Risk

1. Introduction

- The **containment spray** is a relevant safety system for most designs of containment buildings. It was **designed** to **cool down** the containment and **remove soluble fission products**.

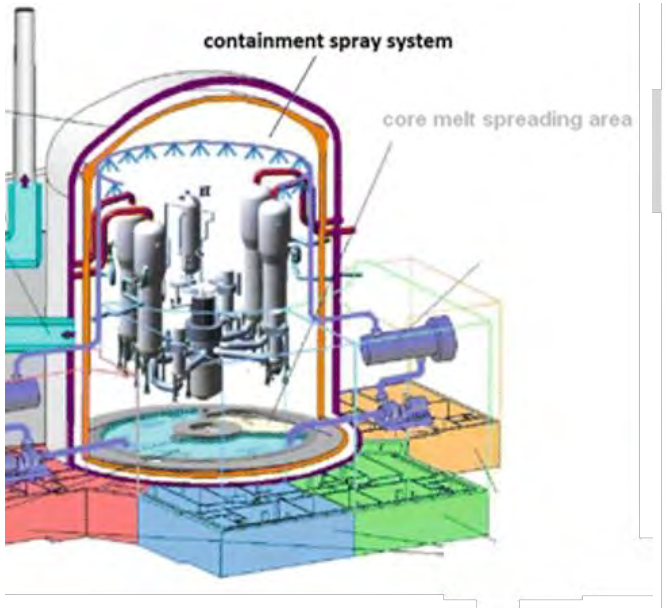

PWR - Large Dry

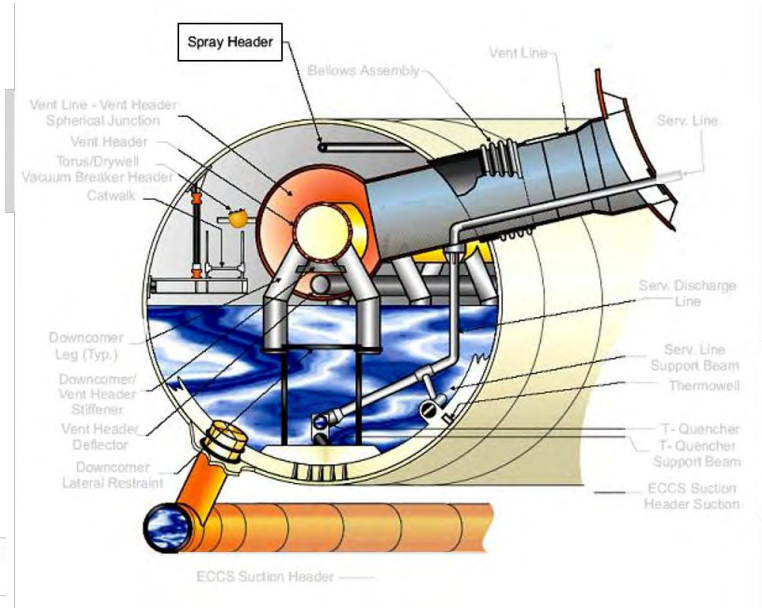

BWR - Mark I

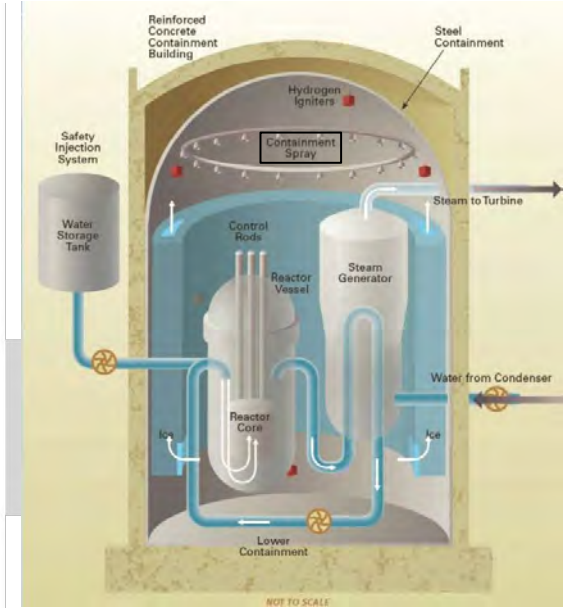

PWR - Ice Condenser

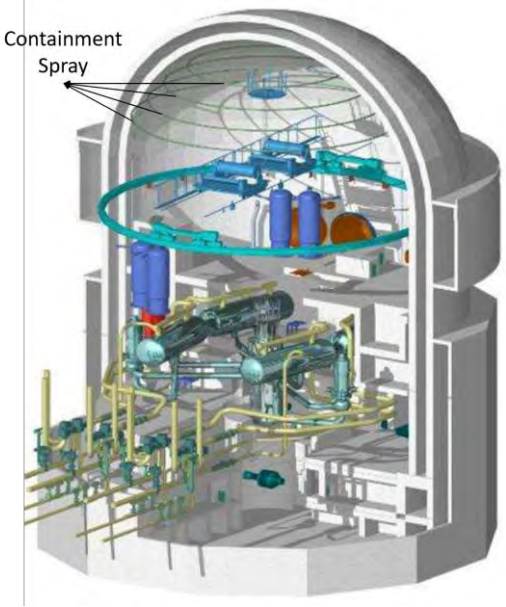

VVER - AES92

*These figures were adapted from public documents of NEA and NRC

1. Introduction

- Complex evaluation of the spray actuation in terms of H_2/CO combustion risk
  - ✓ (1 → 2) **Positive for H_2/CO risk:** Ability to mix stratified environments (hydrogen clouds)
  - ✓ (2 → 3) **Negative for H_2/CO risk:** Increases the hydrogen concentration by condensing steam

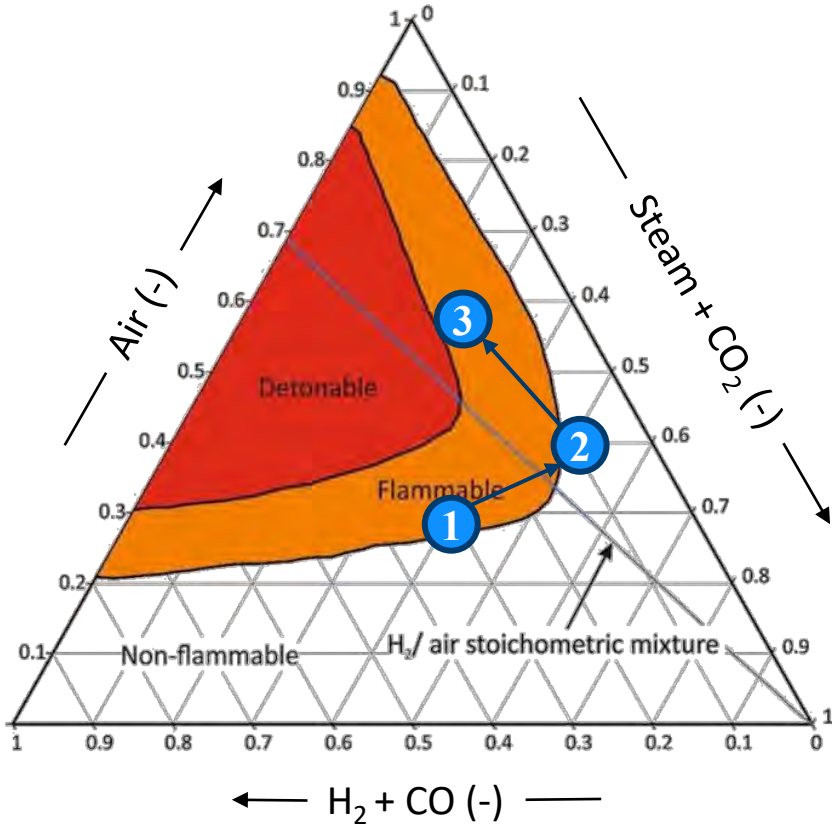

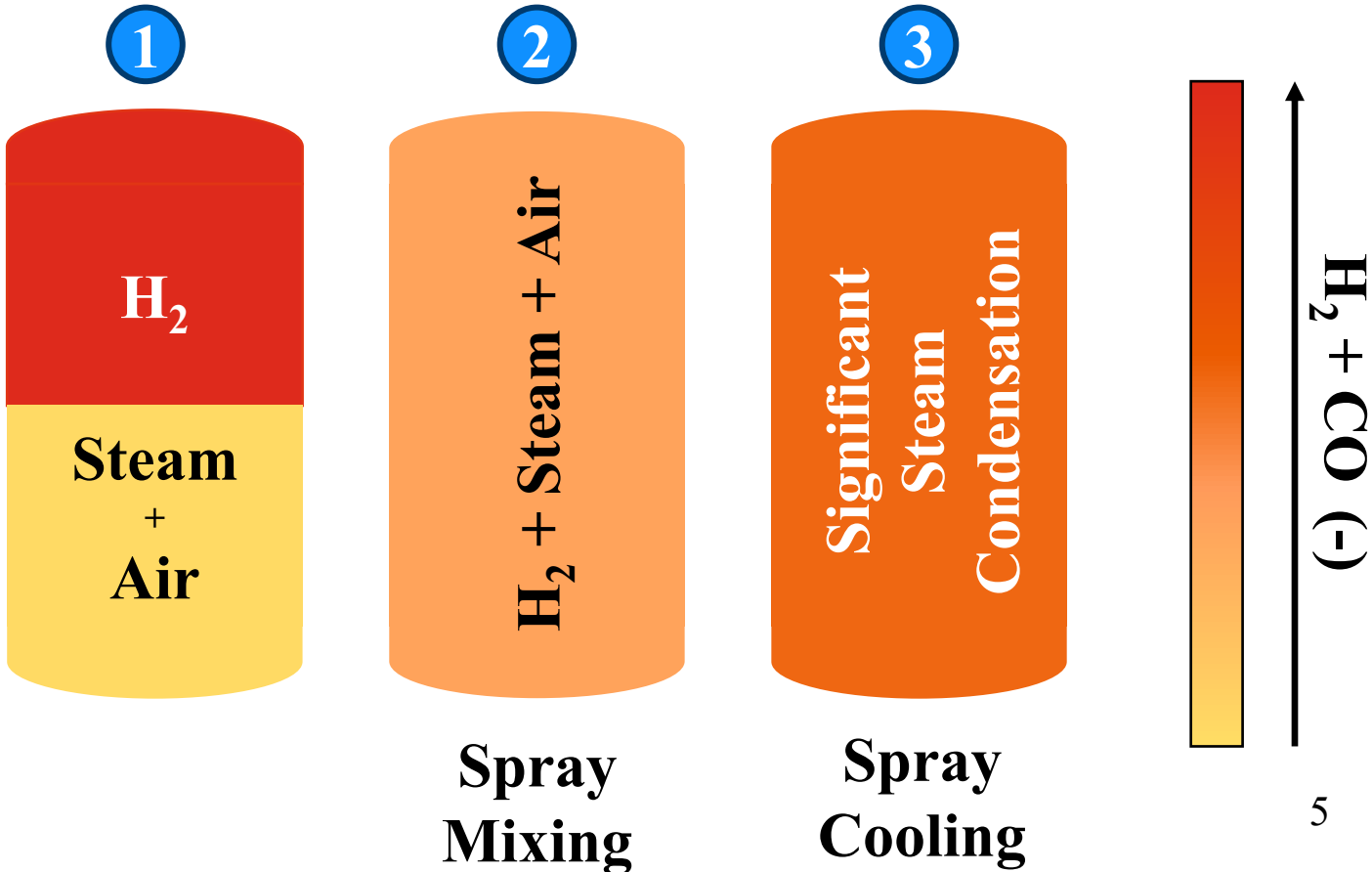

1. Introduction

- The level of **complexity** of the modelling issues is **reflected by the scarce number of works in the open literature** doing 3D NPP analyses of the hydrogen risk including the spray system

Reference	Code	Number of Cells	Advanced spray implementation*	Other Safety Systems	Number of Cases
(Mohaved et al., 2003)	GASFLOW	-	NO	NO	2
(Kim et al., 2006)	GASFLOW	66 960	NO	NO	2
(Xiong et al., 2009)	GASFLOW	54 000	NO	Spray recirculation	3
(Huang et al., 2011)	GASFLOW	60 480	NO	PARs, Ignitors	7
(Téchy et al., 2013)	GASFLOW	41 000	NO	NO	4
(Fernández-Cosials et al., 2017)	GOTHIC	1829	NO	FCVS	65

* An advanced implementation requires: thermal & mechanical non-equilibrium when modelling gas and droplets interactions, evaporation of the liquid reaching the walls, and to use the real number of nozzles when modelling the spray safety system

1. Introduction

- The level of **complexity** of the modelling issues is **reflected by the scarce number of works in the open literature** doing 3D NPP analyses of the hydrogen risk including the spray system

OBJECTIVE: Optimise the **physical modelling** and improve the **thermal-hydraulic resolution** of previous publications in the open literature to evaluate the impact of the spray actuation on the hydrogen risk:

Publication	Code	Number of Cells	Advanced spray implementation*	Other Safety Systems	Number of Cases
(Mohaved et al., 2008)	GASFLOW	-	NO	NO	2
(Kim et al., 2006)	GASFLOW	66 960	NO	NO	2
(Xiong et al., 2009)	GASFLOW	54 000	NO	Spray recirculation	3
(Huang et al., 2011)	GASFLOW	60 480	NO	PARs, Ignitors	7
(Téchy et al., 2013)	GASFLOW	41 000	NO	NO	4
(Fernández-Cosials et al., 2017)	GOTHIC	1829	NO	FCVS	65

* An advanced implementation requires: thermal & mechanical non-equilibrium when modelling gas and droplets interactions, evaporation of the liquid reaching the walls, and to use the real number of nozzles when modelling the spray safety system

2. Systematic Evaluation H_2 Risk

- Sequential steps towards the **use of GOTHIC8.3 to evaluate the impact of different alternatives of the spray actuation** on the hydrogen risk

Vázquez-Rodríguez, et al., 2023. Assessment of the depressurisation and mixing effects of two spray systems in the PANDA facility, part II – Simulations using GOTHIC8.3(QA). Nuclear Engineering and Design 403

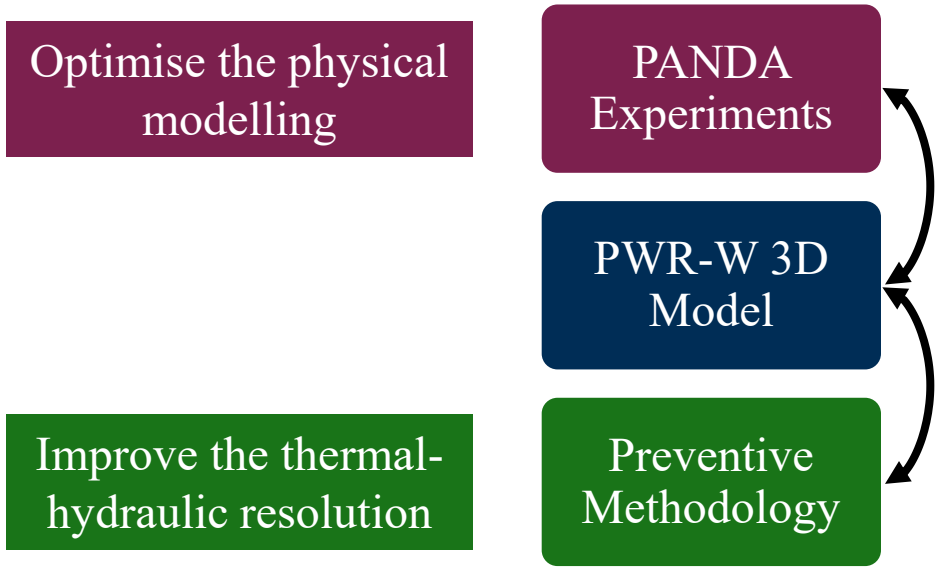

Vázquez-Rodríguez, C., et al., 2025. The Preventive Methodology: A priori modification of the containment geometry to boost the computational efficiency of GOTHIC 3D models. Nuclear Engineering and Design 432

NUCLEAR TECHNOLOGY
© 2021 The Author(s). Published with license by Taylor & Francis Group, LLC
DOI: https://doi.org/10.1080/00295450.2020.1870371
Check for updates

ANS

Hybrid System Level and Coarse Grid CFD Tool for Three-Dimensional Natural Circulation, Mixing, and Stratification Modeling

R. C. Harvill,[a] J. W. Lane,[a]* and T. L. George[b]
[a]Zachry Nuclear Engineering, Inc., 200 Regency Forest Drive, Suite 330, Cary, North Carolina 27518
[b]Zachry Nuclear Engineering, Inc., 1955 Jadwin Avenue, Suite 440, Richland, Washington 99354

Received August 26, 2020
Accepted for Publication December 23, 2020

The GOTHIC code

Similar to CFD in open spaces and similar to system codes close to the walls

2. Systematic Evaluation H_2 Risk

- Sequential steps towards the **use of GOTHIC8.3 to evaluate the impact of different alternatives of the spray actuation** on the hydrogen risk

Vázquez-Rodríguez, et al., 2023. Assessment of the depressurisation and mixing effects of two spray systems in the PANDA facility, part II – Simulations using GOTHIC8.3(QA). Nuclear Engineering and Design 403

Optimise the physical modelling

PANDA Experiments

Identification of the main droplet phenomena and understanding the impact of the coarse meshes and the simplifications needed to keep the affordability of the plant scale simulations

PWR-W 3D Model

Improve the thermal-hydraulic resolution

Preventive Methodology

Geometry simplifications at the 0.1 m scale giving a factor 40 acceleration of simulation time

Vázquez-Rodríguez, C., et al., 2025. The Preventive Methodology: A priori modification of the containment geometry to boost the computational efficiency of GOTHIC 3D models. Nuclear Engineering and Design 432

2. Systematic Evaluation H_2 Risk

- Sequential steps towards the **use of GOTHIC8.3 to evaluate the impact of different alternatives of the spray actuation** on the hydrogen risk

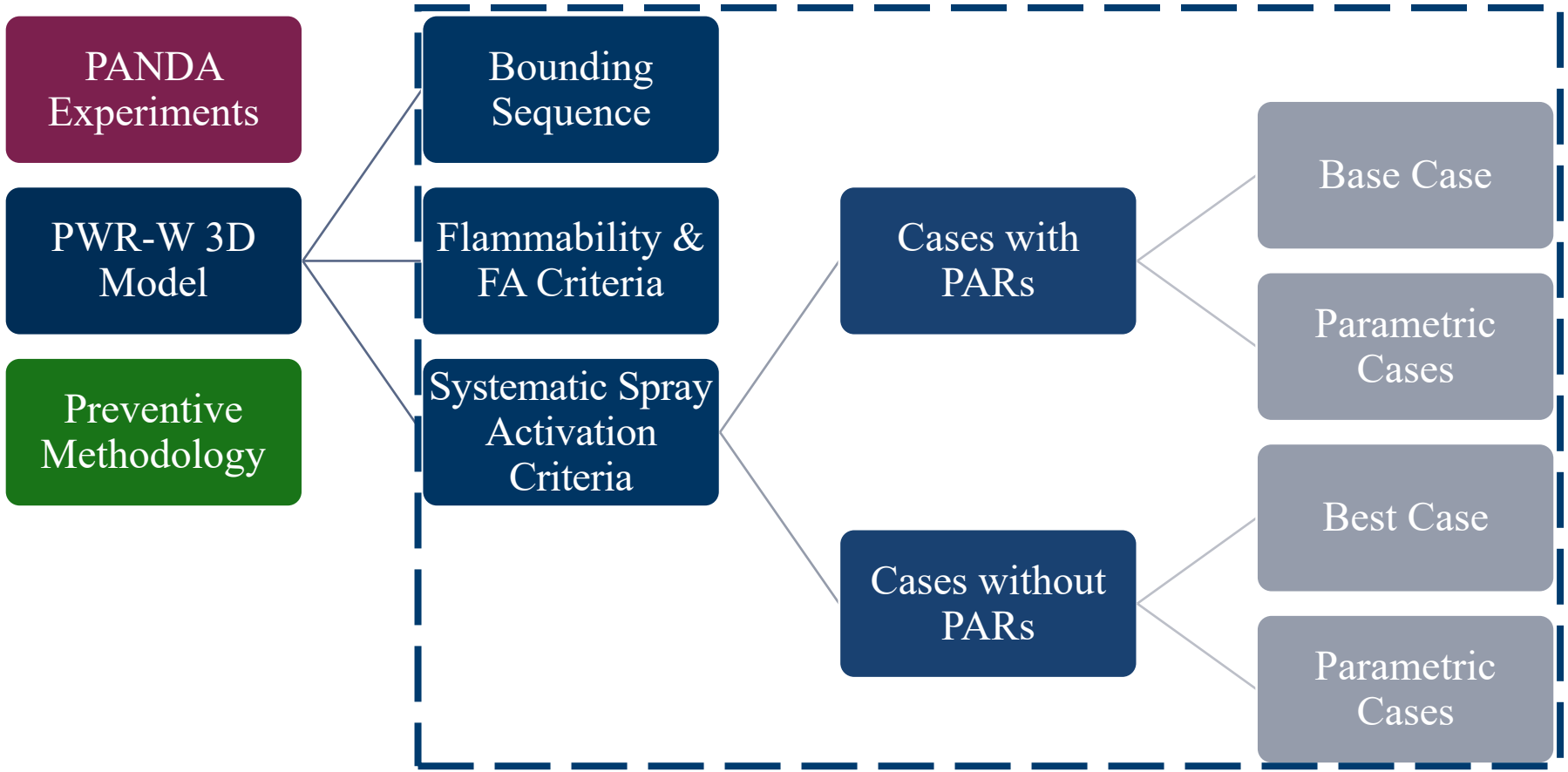

Out of Scope:

- Severe accident **sequence from IRSN** calculations
- Only **in-vessel** phase
- Hydrogen **cannot ignite** and accumulates in the containment

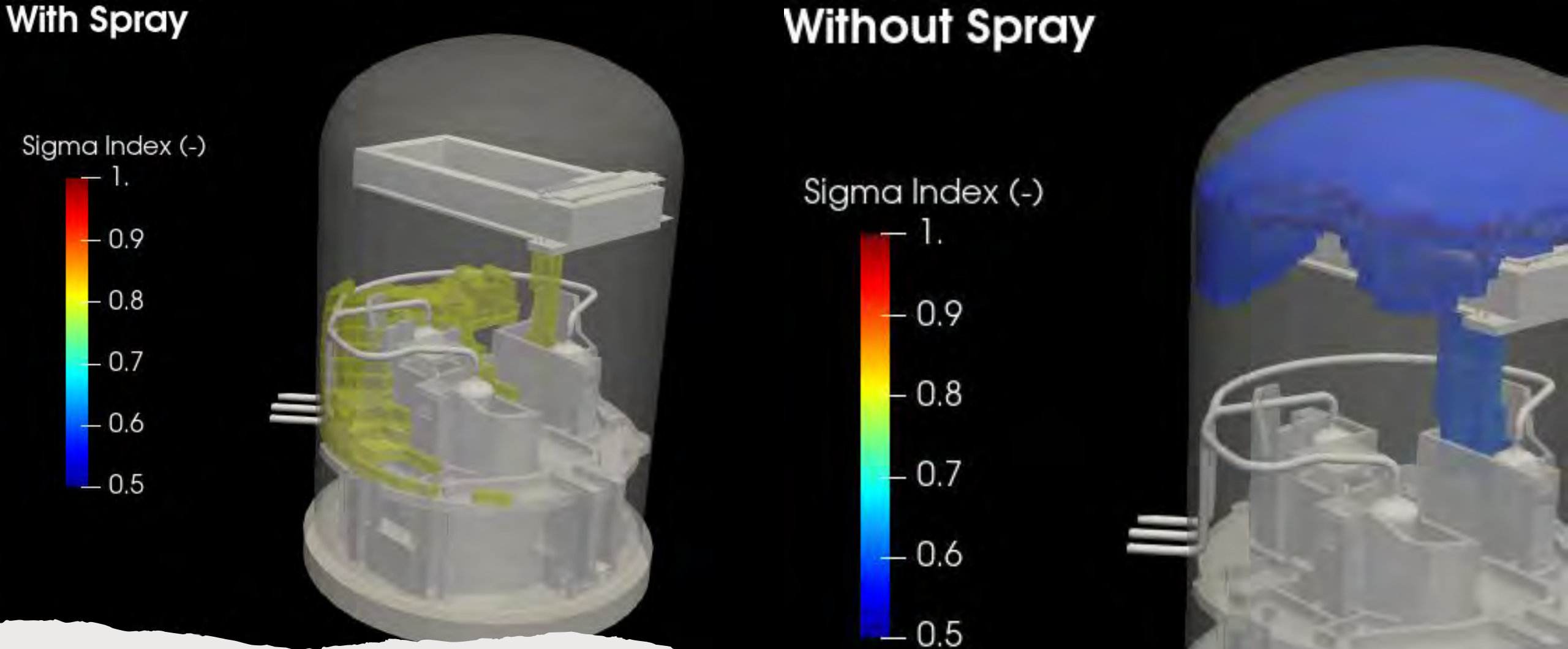

3. SBO and spray recovery: No PARs

A systematic evaluation of late recoveries of the spray safety system after an SBO

3. SBO and spray recovery: No PARs

- **Sequence selection**: High containment pressure to **maximise the impact of the spray + Upper bound of hydrogen generation +**

	Time ASTEC	Time GOTHIC
Loss of all offsite power	0 h	- 2 h 37 min
Rupture of PRT disks	2 h 26 min	-11 min
Pressuriser valves locked opened	4 h 33 min	1 h 56 min
Accumulator tank discharge	4 h 46 min	2 h 9 min
RPV failure	11 h 35 min	8 h 58 min

Reference Name	Spray On	Spray Off
No Spray	-	-
Spray Window 1	7200 s (2 h)	14400 s (4 h)
Spray Window 2	10800 s (3 h)	18000 s (5 h)
Spray Window 3	14400 s (4 h)	21600 s (6 h)
Spray Window 4	18000 s (5 h)	25200 s (7 h)
Spray Window 5	21600 s (6 h)	28800 s (8 h)
Spray Window 6	25200 s (7 h)	32400 s (9 h)

📖 AMHYCO D2.2 - Identification and analysis of accident sequences with posing high H2/CO combustion risk

Liquid Release Rate

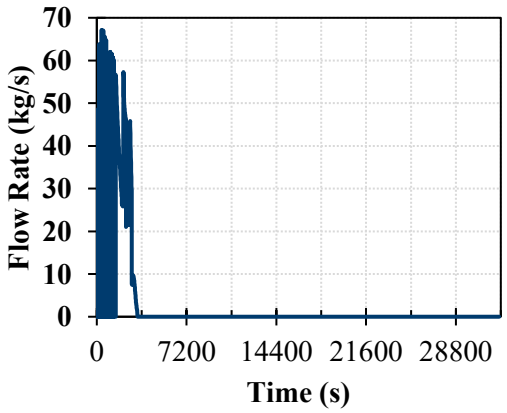

Steam Release Rate

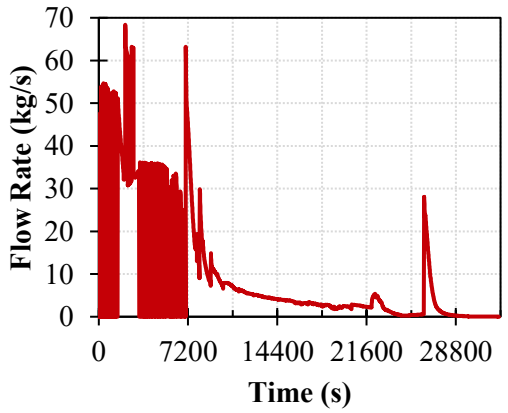

Hydrogen Release Rate

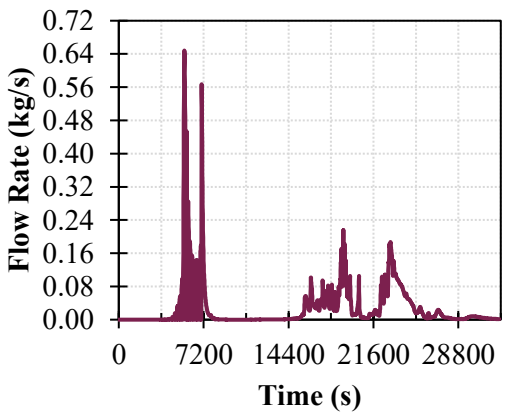

Hydrogen Integral Release

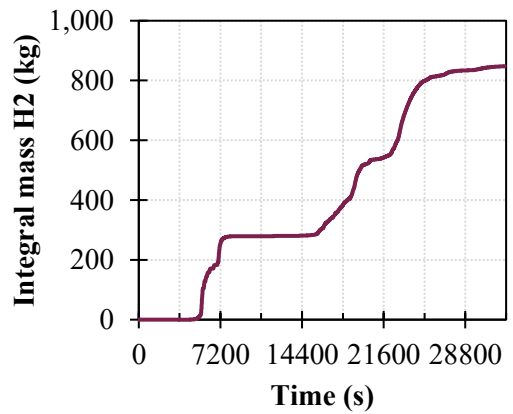

3. SBO and spray recovery: No PARs

- Flammability is evaluated based on mixture properties $(T, x_{H_2O}, x_{O_2}, x_{H_2}, x_{N_2})$
- The same mixture properties allows calculating the **σ criterion for Flame Acceleration** (FA). **The σ index is the safety criterion for our cases.**

Flammability Limits

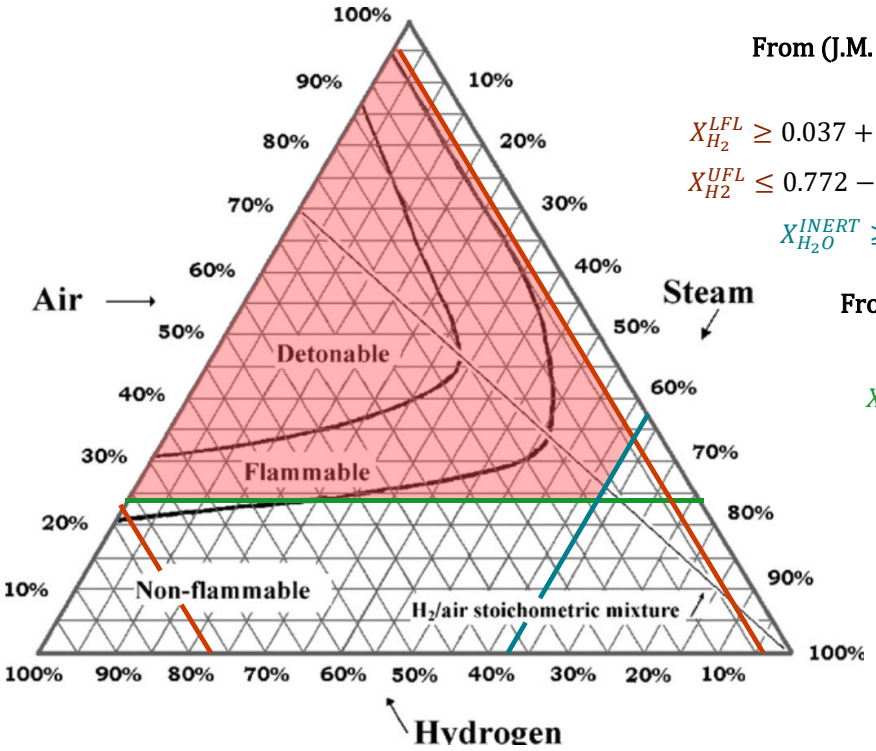

From (J.M. Martín-Valdepeñas et al., 2007)
NED 237, 627–647

$$X_{H_2}^{LFL} \geq 0.037 + 0.011 X_{H_2O} - 4.16 \cdot 10^{-5} \cdot (T - 373)$$

$$X_{H2}^{UFL} \leq 0.772 - 1.087 X_{H_2O} + 2.71 \cdot 10^{-4} \cdot (T - 373)$$

$$X_{H_2O}^{INERT} \geq 0.63 + 3 \cdot 10^{-4} \cdot (T - 373)$$

From MELCOR Analytical Package
(Humpries et al., 2017)

$$X_{Air} > 0.238 \rightarrow (X_{O_2} \geq 0.05)$$

Flammable Region for $T = 373\ K$

Flame Acceleration (FA)

based on σ criterion

Flame acceleration if $\rightarrow$ $\sigma_i = \frac{\sigma}{\sigma^*} \geq \mathbf{0.92}$

$$\sigma = \frac{\rho_{unburn}}{\rho_{AICC}}$$

$$\sigma^* = 0.9 \cdot 10^{-5} \left(\frac{E_a}{T_u}\right)^3 - 0.0019 \left(\frac{E_a}{T_u}\right)^2 + 0.1807 \left(\frac{E_a}{T_u}\right) + 0.2314$$

Dorofeev et al. / Journal of Loss Prevention in the Process Industries 14 (2001) 583–589
J.M. Martin-Valdepeñas et al. / Nuclear Engineering and Design 237 (2007) 627–647

3. SBO and spray recovery: No PARs

- **4-5 days of real time for a 9-hours sequence**. The fastest we could go with our finest model (70000 cells) for the ex-vessel phase is **7 seconds of CPU Time for each second of the transient**

Case IDs	Spray On	Spray Off	Recirculation Phase	PAR actuation
v010	No Spray	No Spray	No Spray	NO
v011	7200 s	14400 s	No Spray	NO

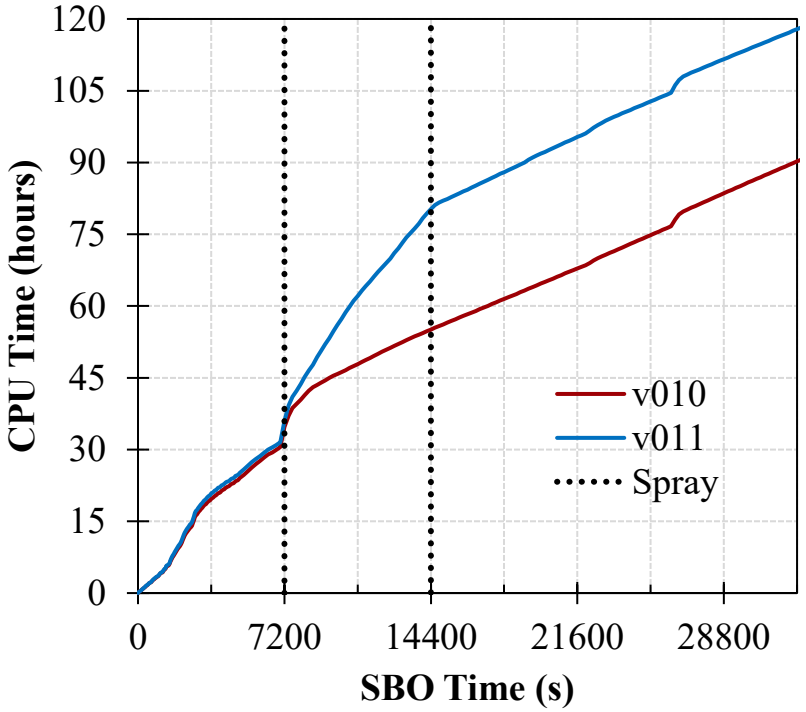

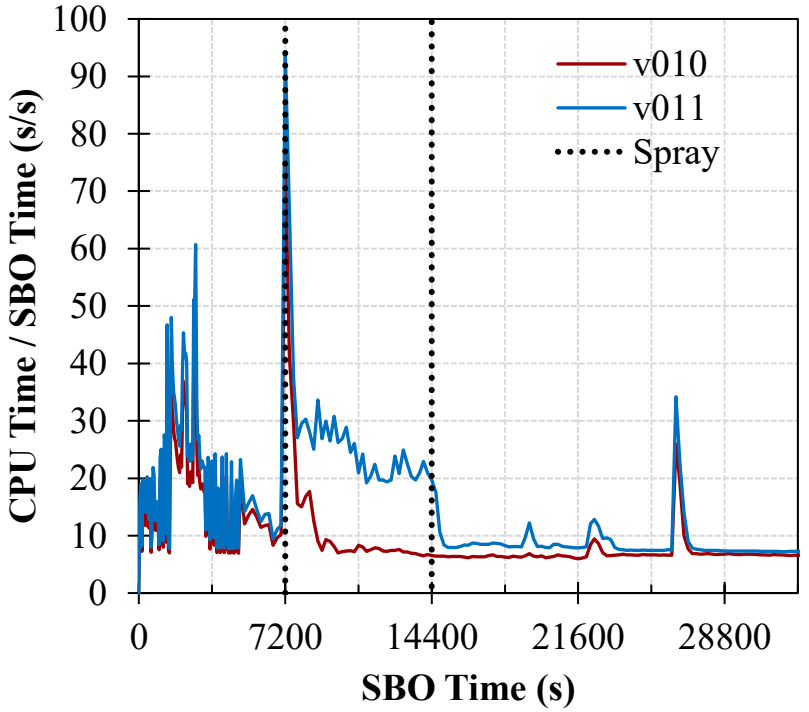

Spray vs. No Spray sequences

4.2 Cases without PARs

- Section oriented to **identify the additional insights offered by the 3D codes**

Case IDs	Spray On	Spray Off	Recirculation Phase	PAR actuation
v010	No Spray	No Spray	No Spray	NO
v011	7200 s	14400 s	No Spray	NO

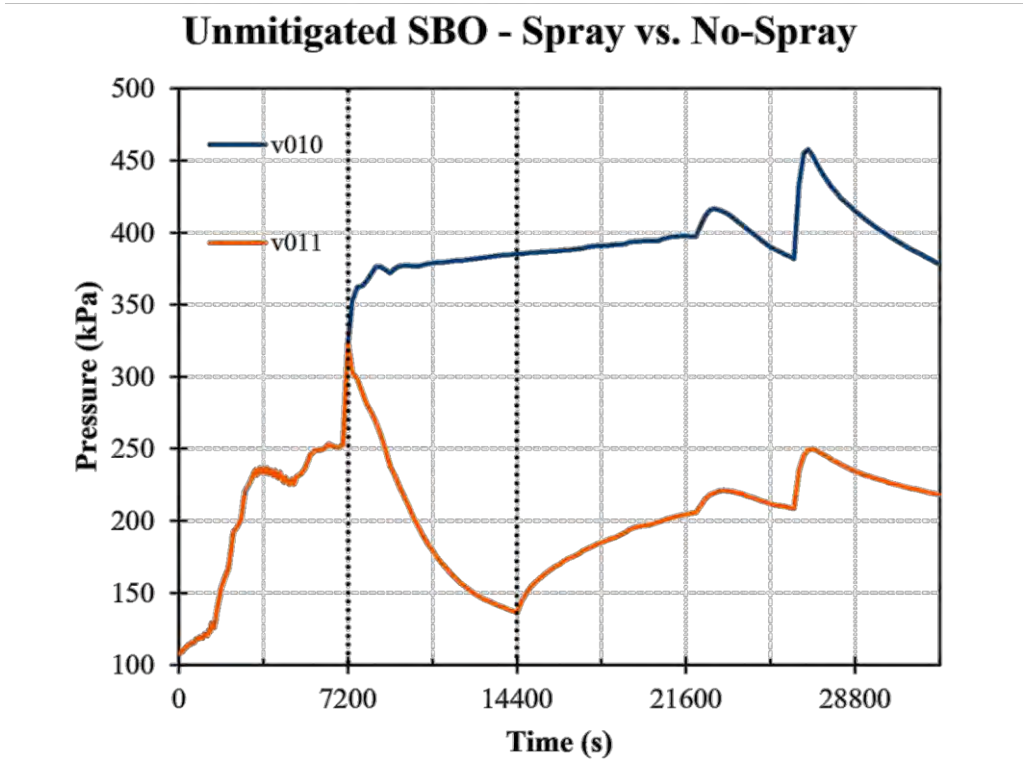

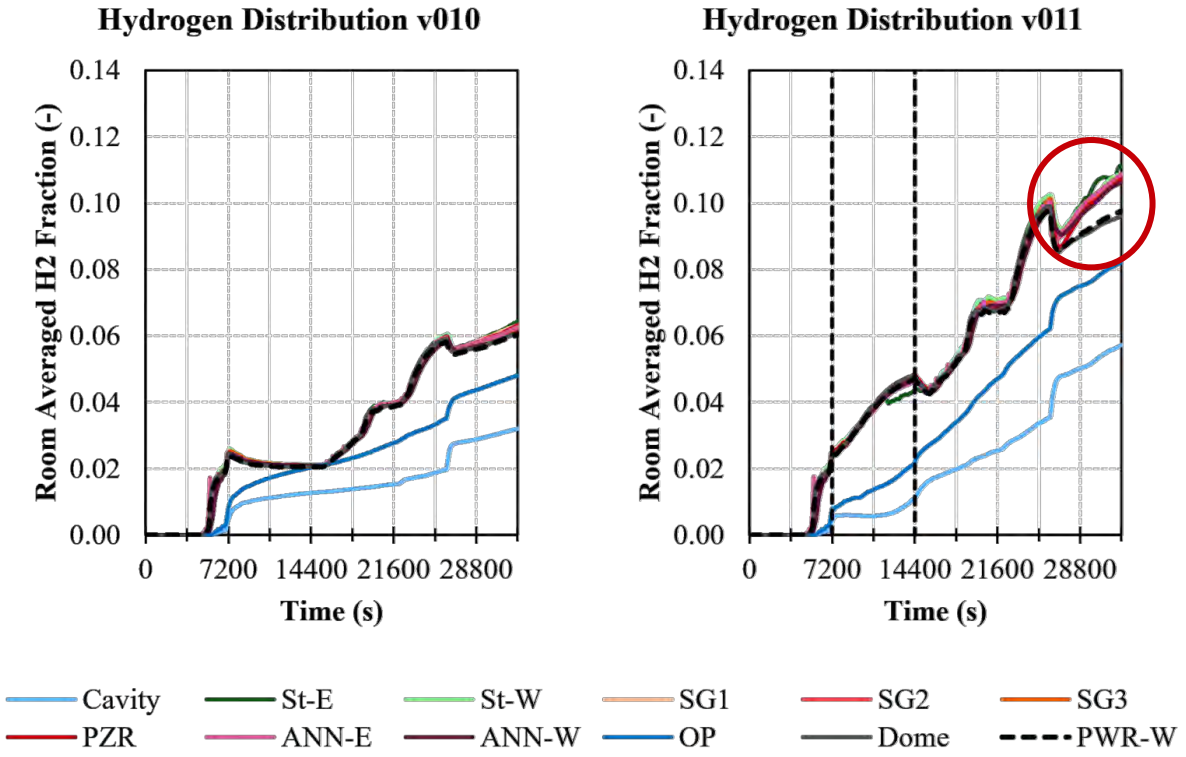

Spray vs. No Spray sequences

3. SBO and spray recovery: No PARs

- The **H_2 heterogeneities are relevant in terms of hydrogen risk quantification**

Case IDs	Spray On	Spray Off	Recirculation Phase	PAR actuation
v010	No Spray	No Spray	No Spray	NO
v011	7200 s	14400 s	No Spray	NO

Flammable and FA Mass – Spray vs. No Spray

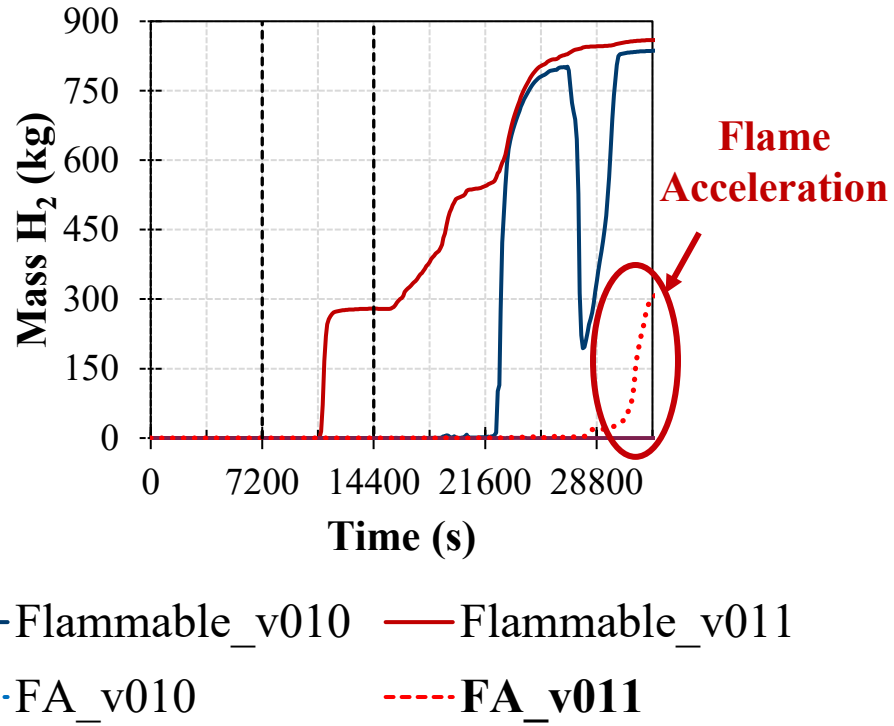

Sigma Index v011 – With Spray

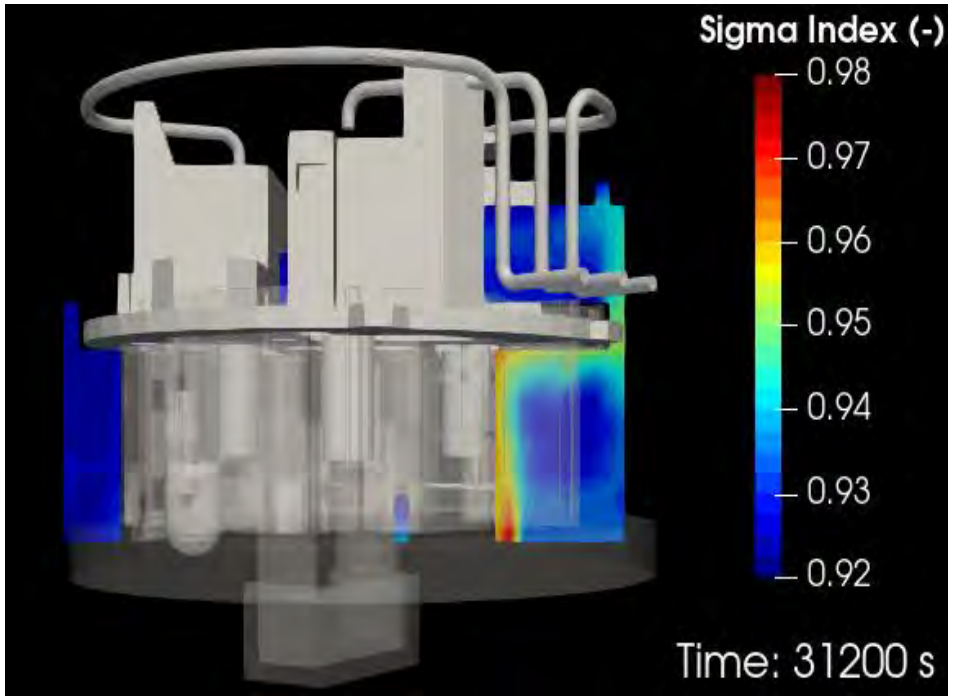

H_2 Heterogeneities and flame acceleration

3. SBO and spray recovery: No PARs

Pressure Unmitigated SBO – Spray Activation Windows

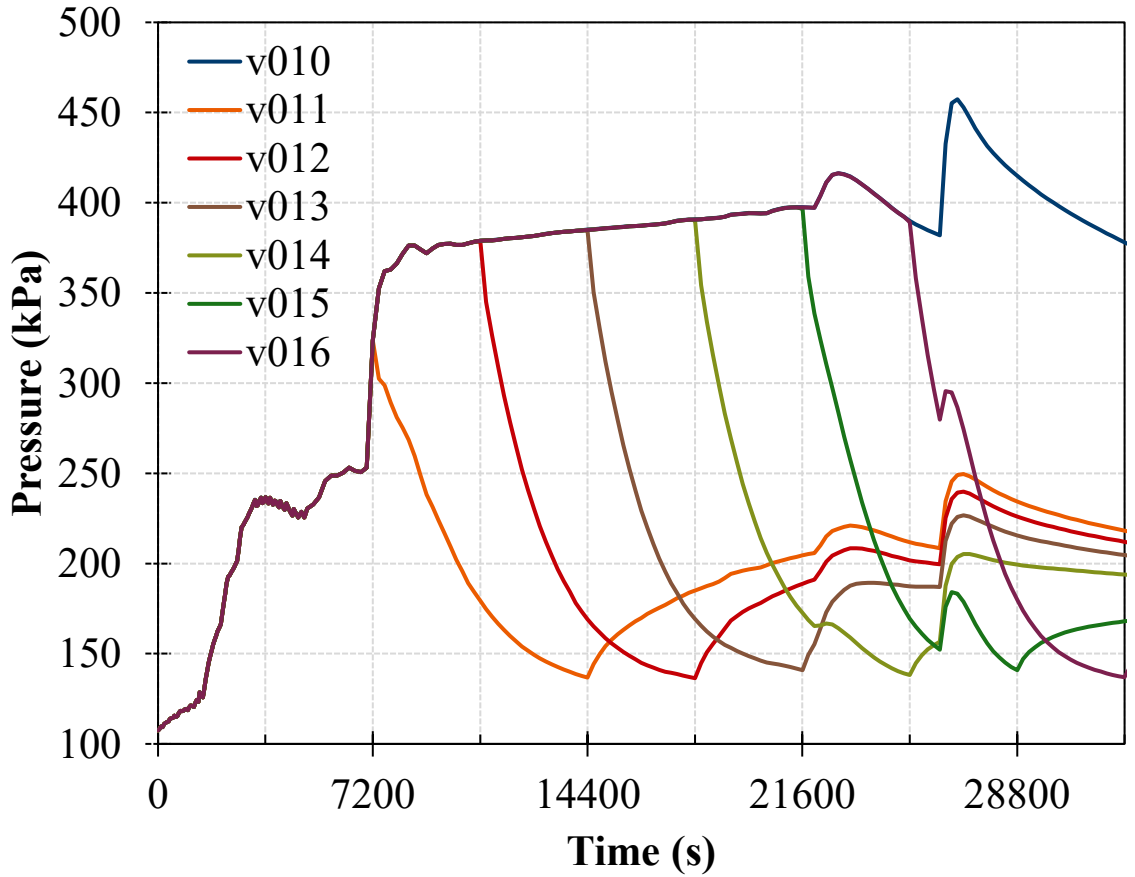

Case IDs	Spray On	Spray Off
v010	No Spray	No Spray
v011	7200 s	14400 s
v012	10800 s	18000 s
v013	14400 s	21600 s
v014	18000 s	25200 s
v015	21600 s	28800 s
v016	25200 s	32400 s

Evaluation of different timings for the spray recovery

3. SBO and spray recovery: No PARs

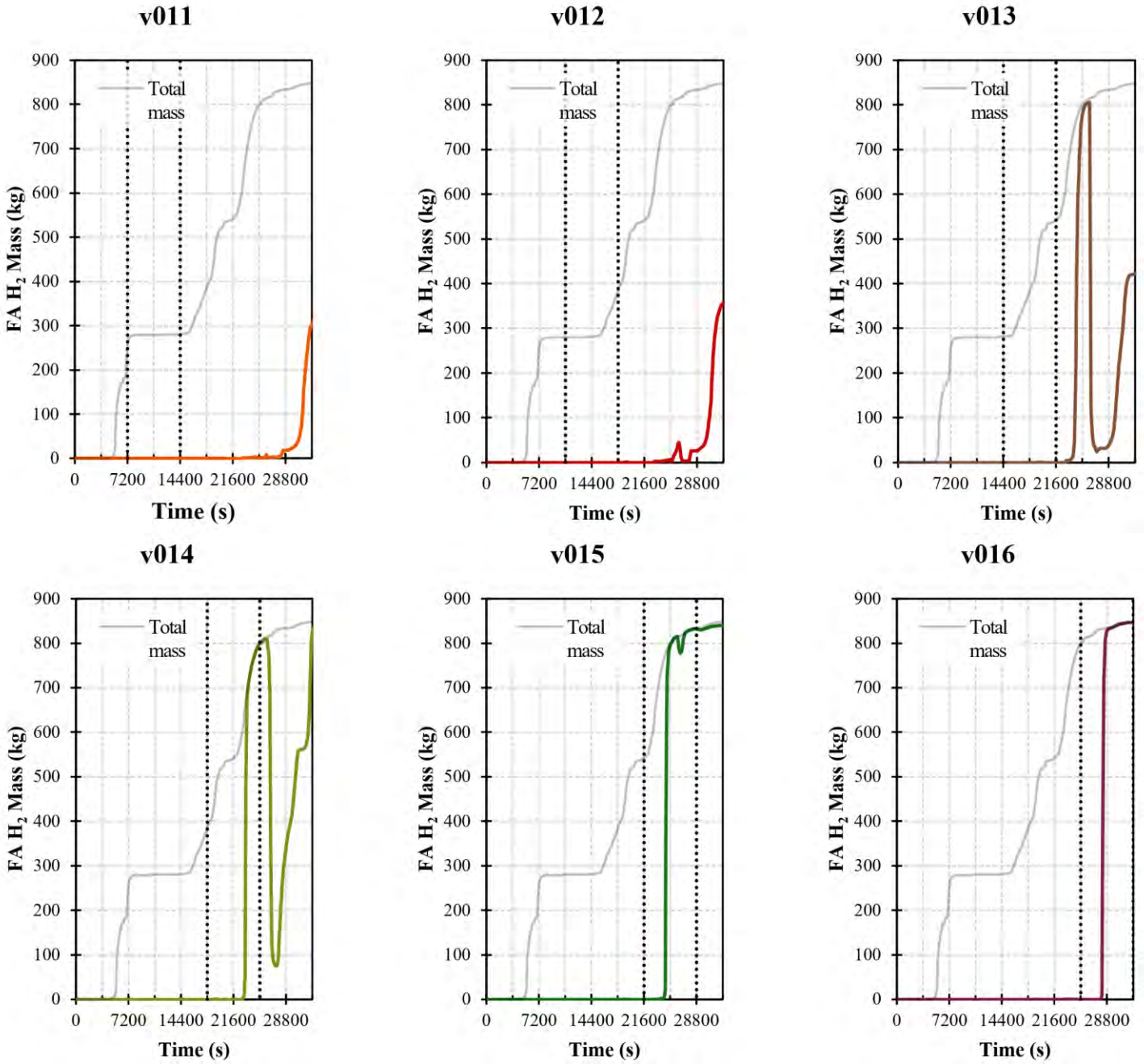

Case IDs	Spray On	Spray Off
v010	No Spray	No Spray
v011	7200 s	14400 s
v012	10800 s	18000 s
v013	14400 s	21600 s
v014	18000 s	25200 s
v015	21600 s	28800 s
v016	25200 s	32400 s

Cases without PARs: All the cases using the spray had a significant H_2 risk

3. SBO and spray recovery: No PARs

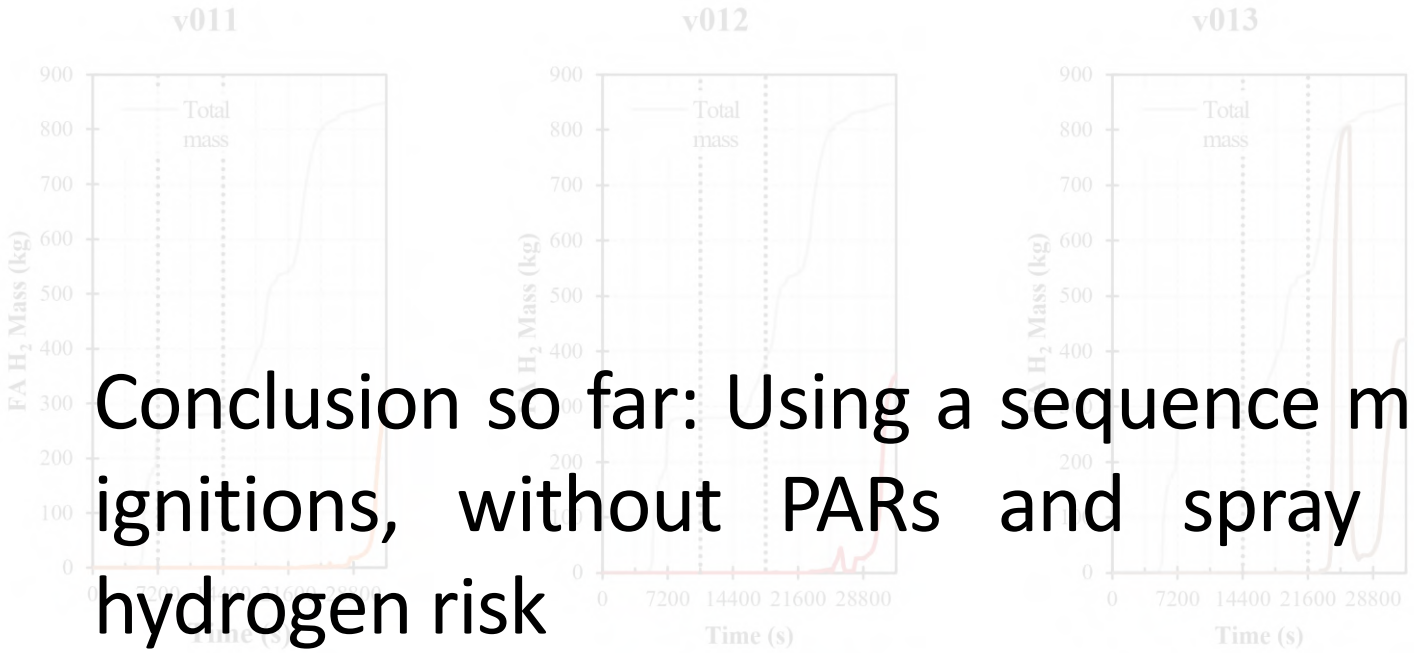

Conclusion so far: Using a sequence maximising H_2 generation, no ignitions, without PARs and spray recovery -> Unacceptable hydrogen risk

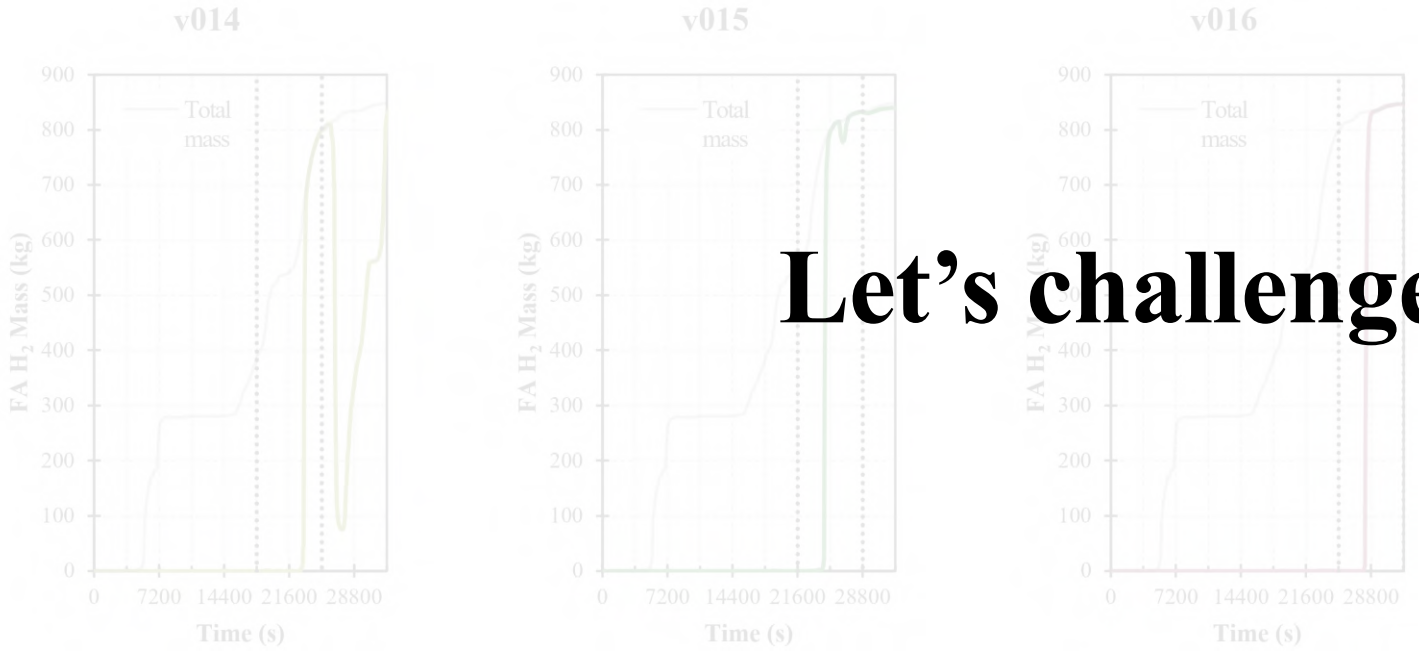

Let's challenge this!

Case IDs	Spray On	Spray Off
v010	No Spray	No Spray
v011	7200 s	14400 s
v012	10800 s	18000 s
v013	14400 s	21600 s
v014	18000 s	25200 s
v015	21600 s	28800 s
v016	25200 s	32400 s

Cases without PARs: All the cases using the spray had a significant H_2 risk

3. SBO and spray recovery: No PARs

- The first set of PCs aimed at **challenging the identified FA conditions**

Case IDs	Spray On	Spray Off	Spray Flow Rate	σ_i Threshold	Concrete conductivity
v015	21 600 s	28 800 s	**208 kg/s**	**0.92**	**0.9 W/m-K**
v015a	21 600 s	28 800 s	**156 kg/s**	**1**	**0.9 W/m-K**

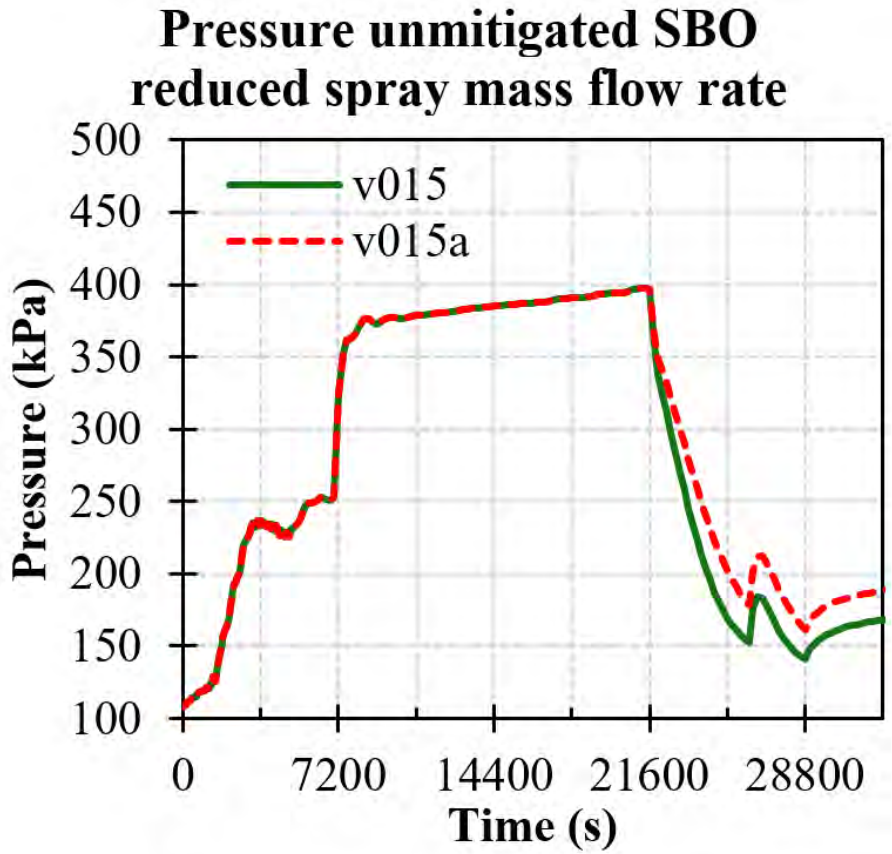

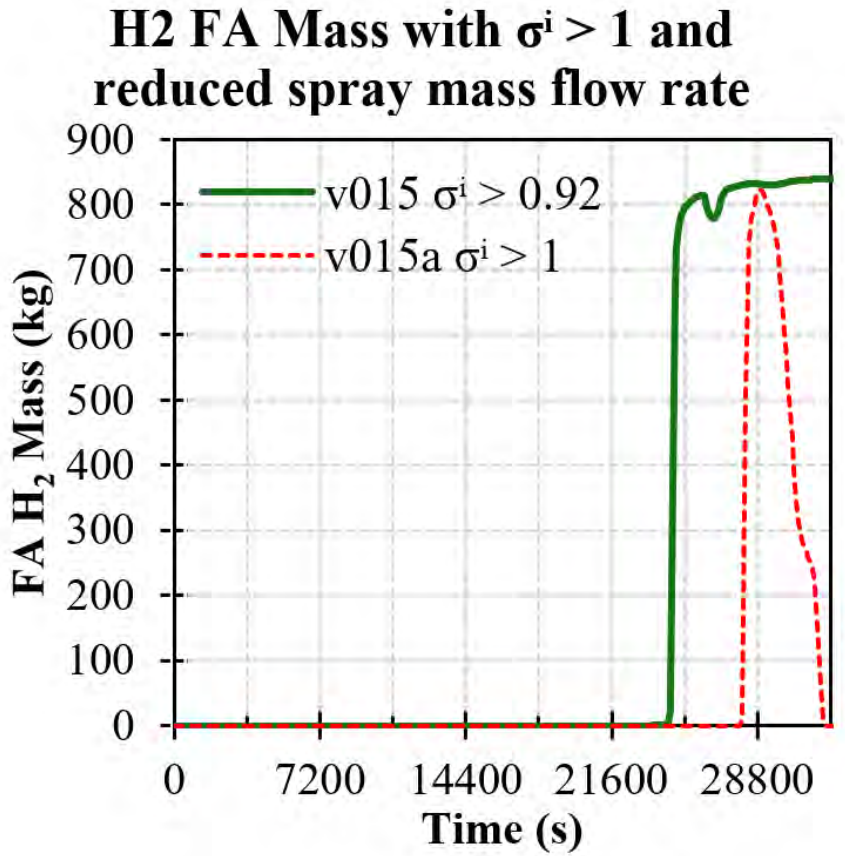

3. SBO and spray recovery: No PARs

- The second set of PCs aimed at **evaluating a strategy to avoid the FA conditions**

Case IDs	Spray On	Spray Off	Spray temperature	Concrete Conductivity
v015	21600 s	28800 s	**30 ºC**	**0.9 W / m-ºC**
v015b	21600 s	28800 s	**80 ºC**	**0.9 W / m-ºC**
v015c	21600 s	28800 s	**80 ºC**	**2.25 W / m-ºC**

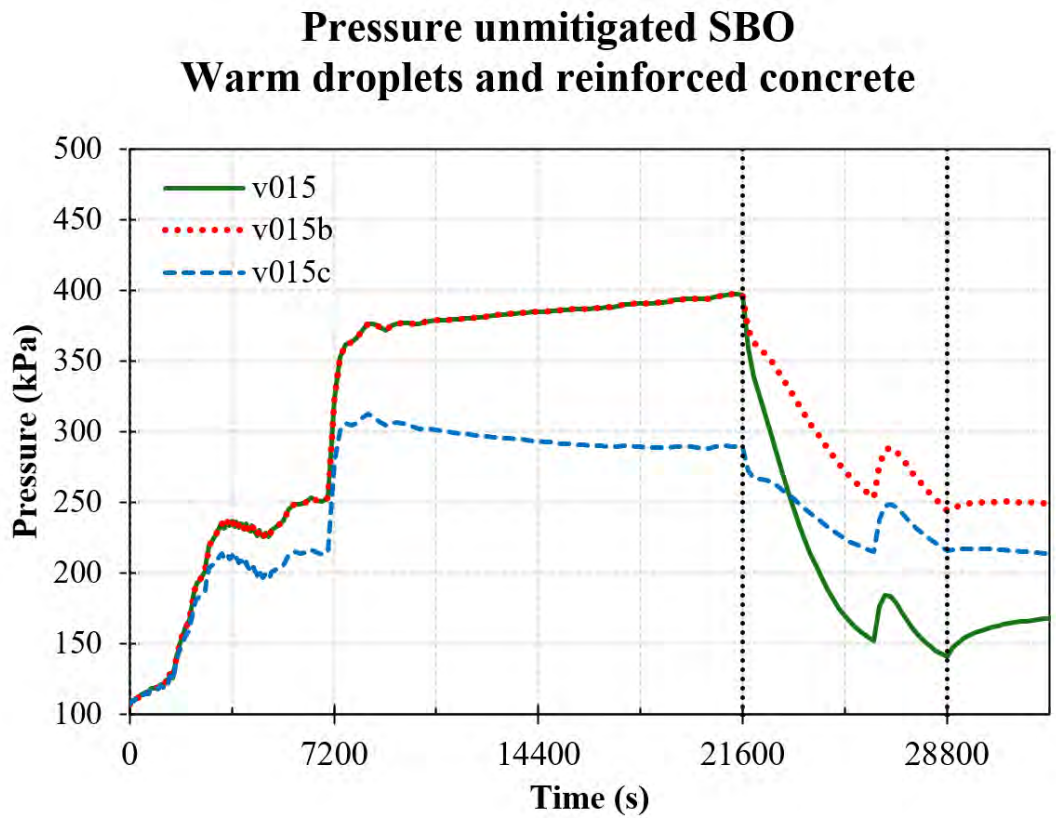

3. SBO and spray recovery: No PARs

- The second set of PCs aimed at **evaluating a strategy to avoid the FA conditions**

Case IDs	Spray On	Spray Off	Spray temperature	Concrete Conductivity
v015	21600 s	28800 s	**30 ºC**	**0.9 W / m-ºC**
v015b	21600 s	28800 s	**80 ºC**	**0.9 W / m-ºC**
v015c	21600 s	28800 s	**80 ºC**	**2.25 W / m-ºC**

v015

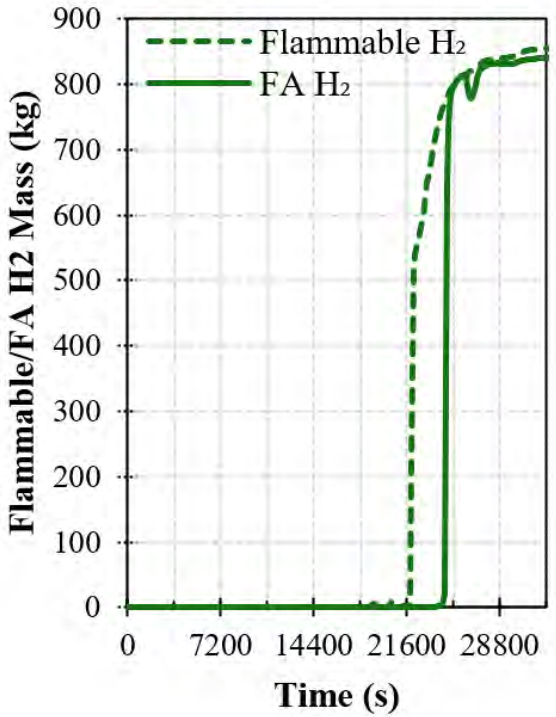

v015b

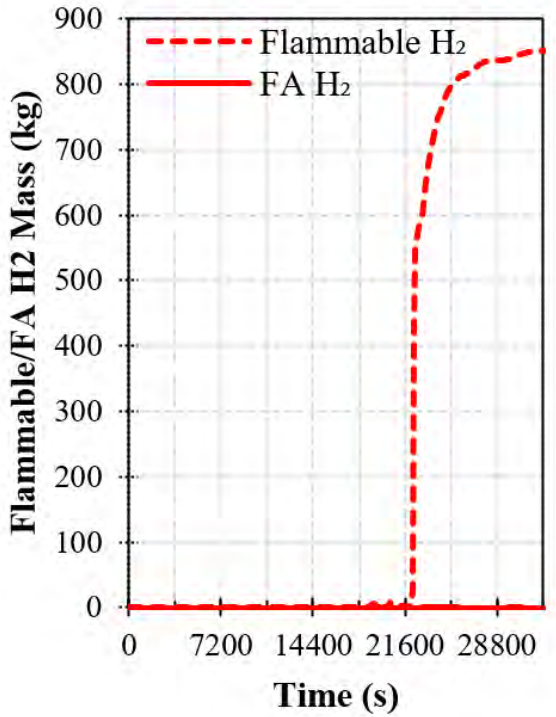

v015c

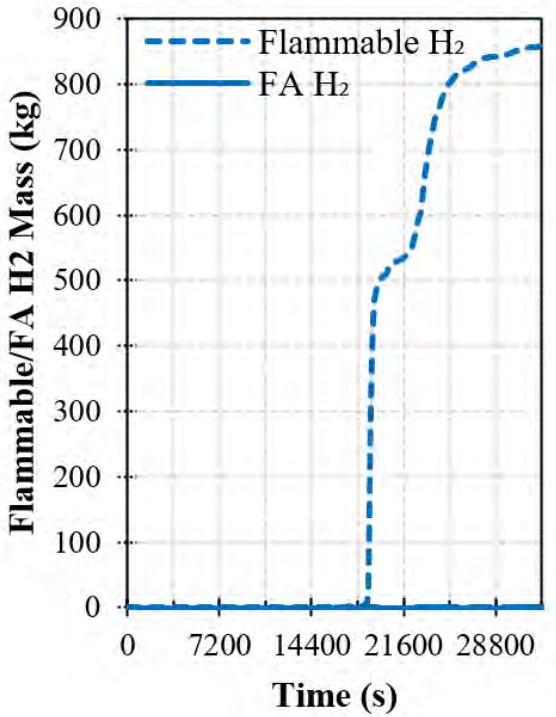

2. PANDA Spray Experiments

1. Introduction
2. Systematic Evaluation H_2 Risk
3. SBO and spray recovery: No PARs
4. **SBO and spray recovery: with PARs**
5. Conclusions

4. SBO and spray recovery: With PARs

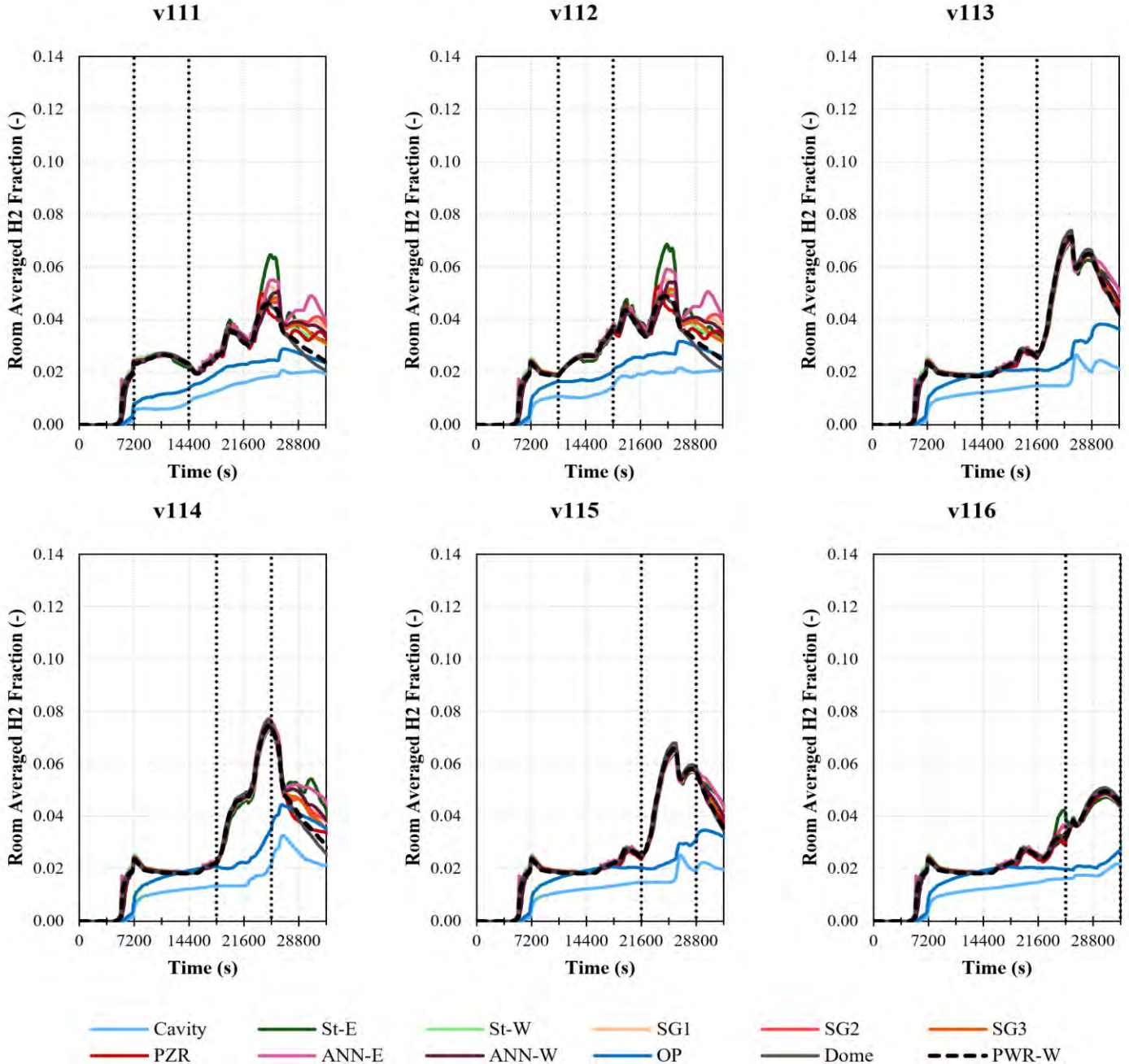

Case IDs	Spray On	Spray Off
v110	No Spray	No Spray
v111	7200 s	14400 s
v112	10800 s	18000 s
v113	14400 s	21600 s
v114	18000 s	25200 s
v115	21600 s	28800 s
v116	25200 s	32400 s

Evaluation of different timings for the spray recovery

4. SBO and spray recovery: With PARs

- Not relevant FA conditions for cases with PARs

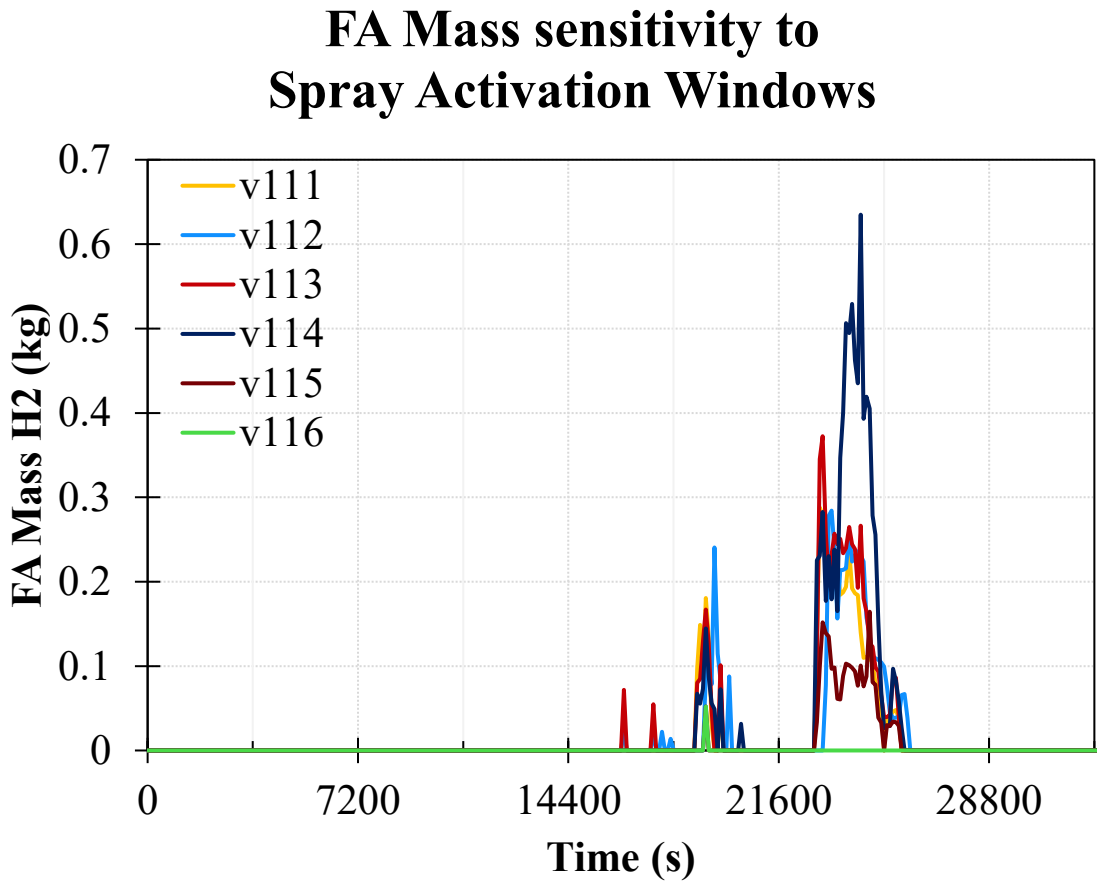

Case IDs	Spray On	Spray Off
v110	No Spray	No Spray
v111	7200 s	14400 s
v112	10800 s	18000 s
v113	14400 s	21600 s
v114	18000 s	25200 s
v115	21600 s	28800 s
v116	25200 s	32400 s

Evaluation of different timings for the spray recovery

4. SBO and spray recovery: With PARs

- PCs aimed at **challenging the mitigation of FA conditions by PARs**

Case IDs	PAR efficiency
v115	100 %
v115a	85 %
v115b	70 %
v115c	55 %
v115d	40 %

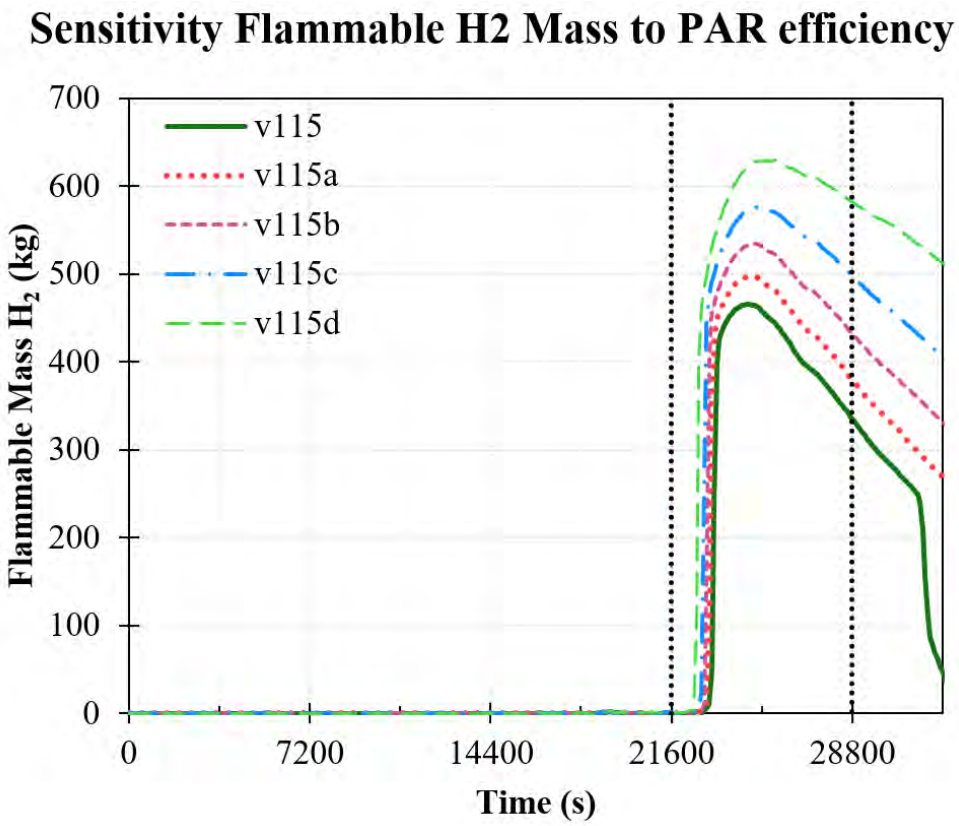

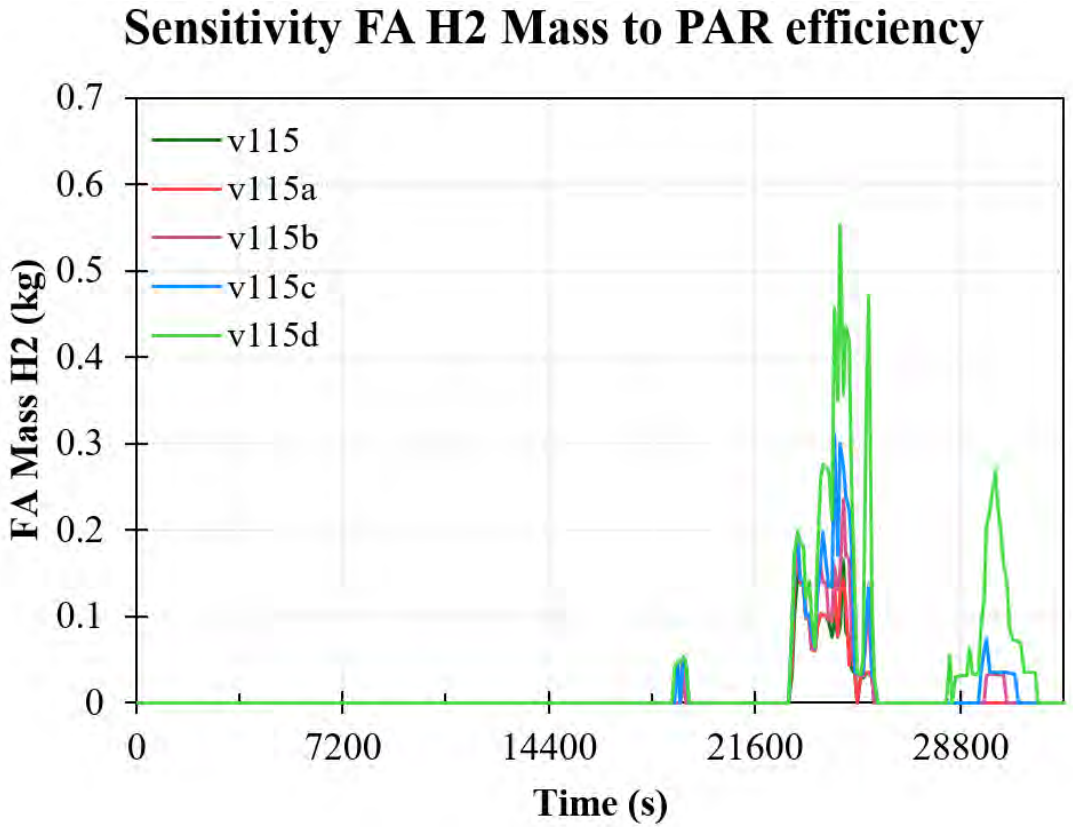

2. PANDA Spray Experiments

1. Introduction
2. Systematic Evaluation H_2 Risk
3. SBO and spray recovery: No PARs
4. SBO and spray recovery: with PARs
5. **Conclusions**

5. Conclusions

Reference	Code	Number of Cells	Advanced spray implementation*	Other Safety Systems	Number of Cases
(Mohaved et al., 2003)	GASFLOW	-	NO	NO	2
(Kim et al., 2006)	GASFLOW	66 960	NO	NO	2
(Xiong et al., 2009)	GASFLOW	54 000	NO	Spray recirculation	3
(Huang et al., 2011)	GASFLOW	60 480	NO	PARs, Ignitors	7
(Téchy et al., 2013)	GASFLOW	41 000	NO	NO	4
(Fernández-Cosials et al., 2017)	GOTHIC	1829	NO	FCVS	65
This work	GOTHIC	70 400	YES	PARs, Recirculation	24

* An advanced implementation requires: thermal & mechanical non-equilibrium when modelling gas and droplets interactions, evaporation of the liquid reaching the walls, and to use the real number of nozzles when modelling the spray safety system

5. Conclusions

- Our 3D modelling approach with **GOTHIC has proven its readiness to be applied in conjunction with LP codes** (offering additional insights) **and CFD codes** (identifying scenarios of interest) in an integral safety evaluation methodology
- For all the cases simulated with our PWR-W 3D Model the negative effect of the spray actuation (steam removal) is stronger than positive (gas mixing)
- Within the proposed systematic approach, the complementary **parametric cases reinforced the sensitive H_2 risk quantification conditioned by the uncertainty of the simulations**
- The proposal of **using higher droplet temperatures** for containments without PARs enables the **coexistence of the design functions of the spray safety system while keeping under control the hydrogen risk**

LOOKING FORWARD TO DISCUSSING YOUR QUESTIONS!

Carlos Vázquez-Rodríguez[1,2], Gonzalo Jiménez[2], J.M Martín-Valdepeñas[3]

[1]FZJ, [2]UPM, [3]CSN

12h European Review Meeting on Severe Accident Research (ERMSAR2026) - Madrid, Spain, May 18-22, 2026

ASSESSMENT AND APPLICABILITY OF A STAND-ALONE CONTAINMENT METHODOLOGY FOR HYDROGEN AND CARBON MONOXIDE RISK EVALUATION IN SEVERE ACCIDENTS

Joan Fontanet, Luis E. Herranz
Unit of Nuclear Safety Research (CIEMAT)
Av. Complutense 40, 28040 Madrid (Spain)
joan.fontanet@ciemat.es; luisen.herranz@ciemat.es

ABSTRACT

Combustible gases in light-water reactor containments is a central element of severe-accident management. Within the EU-AMHYCO project, the "generic containment" methodology, developed within the SARNET project, was adopted to enable consistent comparisons of mitigation strategies across organizations and codes by prescribing both boundary conditions and nodalization. This paper investigates key modelling options when applying such methodology by investigating their effect on the analysis of a large-break LOCA sequence in a 3-loop Westinghouse PWR containment with MELCOR 2.2. Through sensitivity studies, the results obtained highlight how relevant is making the right modelling decisions when setting the "generic containment" scenario. Otherwise, the methodology might mislead proper accident management decisions. A large-break LOCA sequence is simulated with MELCOR v2.2 using a full-plant model to generate time-dependent mass and energy releases into the containment. These releases are then imposed as external sources in the stand-alone containment model. The results support the use of the stand-alone generic containments for benchmarking and sensitivity studies, while highlighting the need for previous assessment steps.

KEYWORDS
Severe accidents; Containment; Combustible gases; Stand-alone model; MELCOR

1. INTRODUCTION

During a severe accident, steam reacts with hot claddings to produce hydrogen (H_2) and release thermal energy, the latter resulting in an even faster core degradation. Oxidation of other in-vessel metals, like steel, also contribute to H_2 generation, though to a lesser extent. Moreover, in case of Reactor Pressure Vessel (RPV) failure, the molten material falling into the cavity decomposes concrete and, eventually, result in further generation of H_2, but also large amounts of carbon monoxide (CO), which is also combustible. The resulting H_2/CO-air-steam mixture can form a flammable cloud that, if it ignites, might threaten the integrity of components and safety systems and even containment. Such energetic phenomena happened in the containment of TMI-2 [1] and in the reactor buildings of Units 1, 3 and 4 at the Fukushima-Daiichi Nuclear Power Plant [2]. The management of combustible gases in light-water reactor containments is a cornerstone of accident management.

The present paper is a sequel of some of the activities conducted within the EC AMHYCO project [3], funded by the European Union. Various mitigation strategies were explored using a generic stand-alone containment model [4]. CIEMAT focused on a 3-loop Westinghouse analysis undergoing a SBO and LB-LOCA accidents. This paper investigates the potential effect of some of the key hypotheses made when applying the generic-containment approach to gain insights into combustible gases management. To do so, MELCOR 2.2 has been used to simulate a LB-LOCA accident.

2. APPROACH AND METHODOLOGY

The European SARNET-II project (2009-2013) developed a methodology to define a "Generic-containment Model" for a German-KWU plant [5]. The reason for defining such a generic stand-alone containment model was to enable its use by all participants in a multi-step benchmark on containment thermal-hydraulics. Thereby, the nodalization effect and influences from other simulation domains were eliminated or at least minimized in the conclusions of the comparison results.

This methodology was further used in the NUGENIA-SAMHYCO-Net project (2017-2020) and, more recently, in the EU-AMHYCO project (2020-2025) [3], which extended it to Western PWR (PWR-W) and to VVER reactors. Figure 1 shows the different steps of the methodology, including results assessment. Since this paper's scope is limited to the PWR-W, the only model described below is this one. To meet the objectives of the AMHYCO project, the generic-containment model must be built up from publicly available data [6] and the boundary conditions and nodalization must be precisely determined.

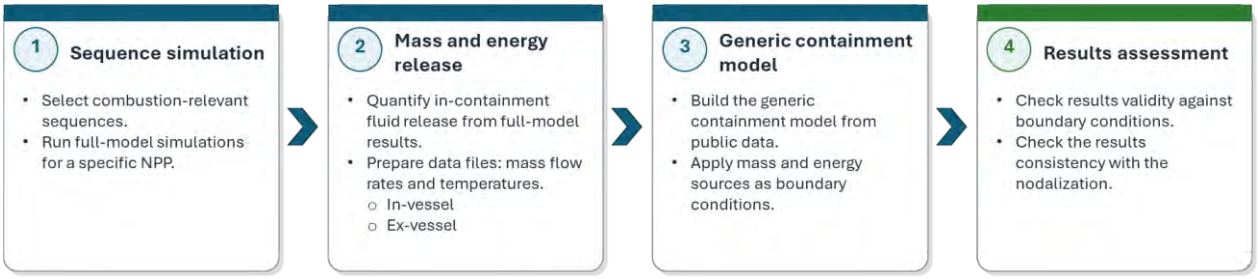

Figure 1. Flowchart with methodology steps.

2.1. Sequence and full-plant model

Among the sequences simulated in AMHYCO, a LBLOCA was selected to perform a detailed assessment as presented in this paper. This sequence is defined as a double-ended guillotine break in the hot leg in the pressurizer loop. This sequence is characterized by a rapid release of hot water into the containment and subsequent vaporization. The initial containment pressure rise is mitigated by the automatic activation of sprays at 2.6 bar setpoint, and when the Refueling Water Storage Tank (RWST) empties, the spray system changes to recirculation mode (i.e., pumping water from the containment sump). The LBLOCA evolves with a relatively low steam concentration in the containment and, consequently, the pressure is low, while the fraction of combustible gases is significant. Table I collects the main event chronology of the sequence.

Table I. Chronology of main events in the LBLOCA sequence

Event	Time
Fluid release	0.003 s
Sprays activation	4.1 s
First H2 release	0.32 h
Total core uncovering	1.2 h
Sprays on recirculation mode	2.1 h
RPV failure	2.4 h
Onset of MCCI gas generation	2.6 h

The MELCOR v2.2 code [7] is used to simulate the LBLOCA sequence in a 3-loop Westinghouse PWR 1000 MWe with a large and dry containment. All the systems and components of the plant: core, primary

circuit, steam generators and secondary circuits, cavity, and containment are modelled. The core and the Reactor Coolant System (RCS) are modelled in accordance with the recommendations of the SOARCA project [8]. Each loop is modelled individually with 29 control volumes (including the accumulators). The core consists of 5 channels in 5 axial nodes, plus the bypass. The vessel is completed with the downcomer, the lower plenum, and four nodes for the upper plenum. A total of 138 nodes defines the primary and the secondary circuits. In addition to the 82.6·tons of fuel (UO_2), in the core region, there are a total of 23.2 tons of zirconium in the fuel cladding and about 44.8 tons of stainless steel in other metallic structures, which are available for oxidizing with steam to generate hydrogen.

2.1.1. Approximations and hypotheses

Water injection safety systems in the primary system, other than hydro-accumulators, are assumed to be unavailable. Each accumulator injects 24.3 m^3 through a valve-controlled flow-path as primary pressure drops below 46 bar.

As for combustible gas modelling two major assumptions are made in the simulation:
- The BURN package of MELCOR, devoted to simulating the gases deflagrations, is not activated.
- PARs are not considered.

The reason underneath both assumptions is to maximize the combustible gas accumulation in containment as much as feasible.

The pedestal region plays a key role in the combustible gas generation ex-vessel. Modelling of the MCCI relies on two additional assumptions in CORCON-Mod3 module of MELCOR [7]:
- A single-cavity region.
- A single-layer approach for the molten pool. Namely, the materials in corium are fully mixed.

Interesting to note that a generic limestone concrete type has been selected for the concrete slab in the cavity [9], with no additional iron mass for the reinforcing bars (no specific data available).

The in-containment spray system model has been set according to plant specifications:
- Constant flowrate of 0.208 m3/s at 293.15 K (from the RWST), injected at the dome compartment.
- Activation setpoint 2.6 bar containment pressure.
- Once RWST empties, the water source is switched to the containment sump.

2.1.2. Containment nodalization

The containment model consists of 19 nodes connected by a flow path (Figure 2). The annular regions surrounding the SGs and PRZ compartments are physically divided into two levels by a slab. Therefore, two flow paths must be defined for those compartments to each of the annular compartment levels. Similarly, for the connections between the different SGs and PRZ compartments, the same division into levels has been kept. Some equipment compartments or stairwells also connect the different levels of the containment vertically.

A total of 41 flow paths are defined from center to center of the connected volumes, following the guidelines in MELCOR's [7]. Finally, the model accounts for 168 heat structures, including steel and/or concrete, providing surfaces for in-containment heat transfer and condensation.

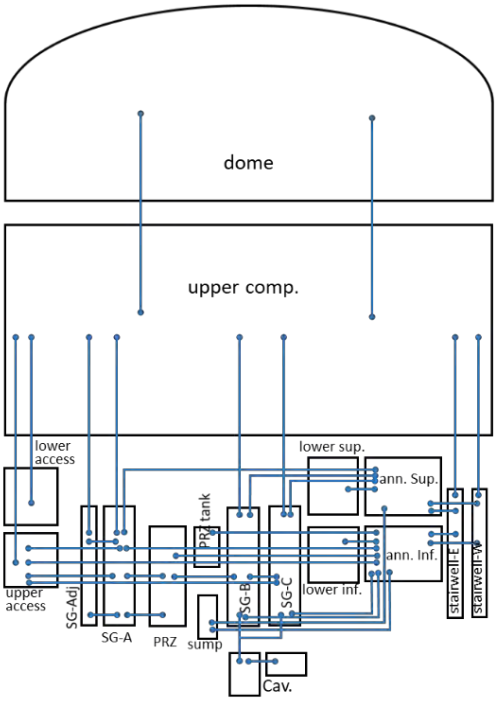

Figure 2. Containment nodalization scheme for the full model.

2.2. Stand-alone model

2.2.1. Boundary conditions

Based on the generic containment defined in the AMHYCO project [6], CIEMAT built up the input deck for MELCOR v2.2, in which mass and energy sources associated with gas releases from the primary circuit are derived from the previous full-model simulations (Figure 3) and given as external sources by *ad hoc* MELCOR control functions.

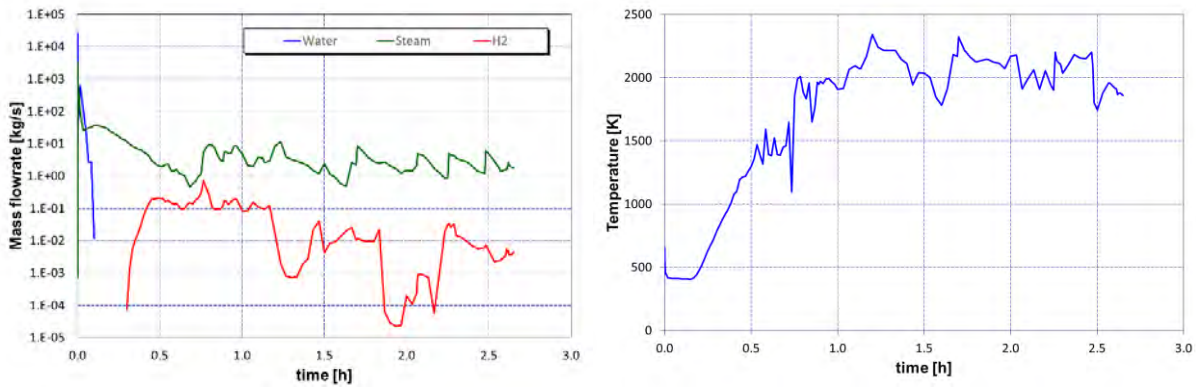

Figure 3. Fluid sources in the in-vessel phase: mass flow rates (left) and temperature (right).

A similar approach is used for the ex-vessel gas sources (Figure 4), although in this case gases are supposed to be released at thermal equilibrium with the corium in the cavity.

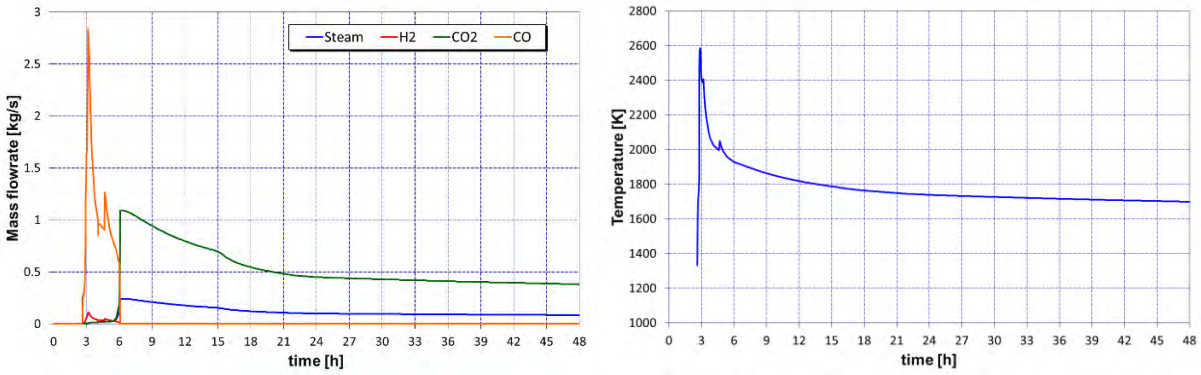

Figure 4. Fluid sources in the ex-vessel phase: mass flow rates (left) and temperature (right).

Two approaches are considered for modelling heat transfer from the molten corium in the cavity pit to the cavity atmosphere:

- A direct heat source in the cavity atmosphere of the stand-alone model. Convective and radiative losses from the corium surface, as estimated by MELCOR in the full-model calculation are included.
- A "fabricated" horizontal heat structure (HS) is set in the cavity with the full cavity cross-section as surface area. This HS is modelled with the bottom surface temperature set to the corium temperature from the full-model simulation, whereas the upper surface exchanges the heat to the atmosphere above it (a high thermal conductivity along with a very thin thickness guarantee the same temperature at both surfaces). Results of both approaches are compared in the sections below.

2.2.2. Containment nodalization

The total internal free volume is represented by 11 control volumes (Figure 5). A large dome volume is defined, covering the upper and dome compartments of the full model. In contrast with the full mode, the annular region is divided into two lateral volumes to capture possible asymmetries of the scenario. Table II summarizes the main characteristics of the containment model and compares the full and generic models.

A total of 32 flow paths are defined to model the gas flows between these volumes. Flow path lengths are defined as the center-to-center distances between volumes. Moreover, 71 heat structures provide the heat transfer and condensation areas for all concrete and steel containment surfaces.

The same safety system definition is used in the generic-containment model, so that no differences in simulation arise from modelling the safety systems within the containment.

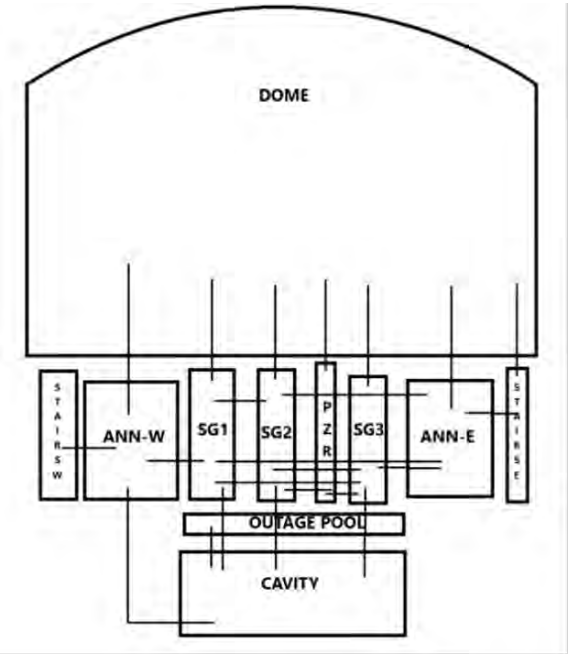

Figure 5. Containment nodalization scheme for the generic-containment model.

Table II. Main Characteristics of the containment models and correspondence between the full model and the generic model

Compartment (full model)	Volume (m^3)	Compartment (generic model)	Volume (m^3)
Cavity + adj. room	369	Cavity	775
SG-A	1207	SG-1	1469
SG-A (adj.)	132		
PRZ	581	PRZ	411
SG-B	1779	SG-2	1717
SG-C	1878	SG-3	1906
RPV access (inf)	207	Outage pool	1178
RPV access(sup)	1203		
PRZ tank	177	Annulus-east	3306
Lower comp. (inf)	470	Annulus-east/west	3306/ 3458
Annulus (inf)	3473		
Lower comp. (sup)	391		
Annulus (sup)	2942		
Cont. sump	269	Stairswell-east	218
Stairswell-A	97		
Stairswell-B	143	Stairswell-west	111
Upper	34965	Dome	46744
Dome	16755		

3. Methodology review

3.1. Fluid mass and energy sources into the containment

The main concern in applying the methodology is the correct definition of the fluid and energy sources to make sure the stand-alone model reproduces the full-model containment scenario along the entire sequence. Therefore, a first step is to confirm that fluids delivery (mass and energy associated) is properly captured in the tables set-up from the full-plant model (Figure 3 and Figure 4). To do so, the full-plant deck is simplified by removing all the MELCOR packages not directly involved in the containment simulation (i.e., core, primary and secondary loops, etc.) and leaving just those essential for containment and its associated safety systems. Note that setting all key flow paths (i.e., from the cavity to the SG room where the LOCA break is located) is essential and should be carefully conducted. In other words, no difference other than fluid sources set as boundary conditions of the stand-alone can feed any discrepancy between full and stand-alone models.

Two different approaches are considered:

a) Heat-source approach

Corium heat losses are directly modelled as a source in the cavity atmosphere. When doing so, the pressure shows a very similar evolution to that in the full-model approach, with negligible differences observed in the in-vessel phase (Figure 6). However, in the ex-vessel phase, the heat-source approach slightly overpredicts pressure, and the deviation grows until 21 h. This discrepancy is less than 8% at the end of the calculation, which is not a substantial difference but might anticipate the actuation of the FCVS in a few hours (~ 3 h) with respect to the full-model estimates. Given the limited effect of the thermal difference (< 2%), temperature differences can support just part of the pressure difference noted; in other words, such as approached more steam remains airborne in the stand-alone calculation (Figure 7). This might be associated to different reasons: slight differences in the sources due to the integration time steps, slightly higher water temperature that gets higher saturation pressure, and/or even to different inter-compartment flows that might yield less steam condensation. Confirming these edges is beyond the scope of this paper, given the size of the discrepancies found. However, it is worth noting how such differences might affect the gas cloud flammability (Figure 8). Although the deflagration potential of CO is known to be significantly lower than that of H_2, the concentrations of both gases are shown together in the figures below for simplicity. Interestingly, a slight overestimation of the steam molar fraction has a visible but not drastic consequence in the combustion risk.

b) Heat-structure (HS) approach

Using an HS to estimate the heat losses from the corium in the cavity yields a similar in-containment trend to that of the heat-source approach, although the pressure and temperature overestimation is even higher (Figure 6). This discrepancy between the two approaches is noticeable between 3 and ~21 h.

This study highlights that splitting the containment model and setting representative boundary conditions for the heat and mass transfer is not a straightforward task. The two approaches intended resulted in visible discrepancies with the full-scope model, the biggest ones reported when using the HS approach: between 15 and 25% overprediction during some time periods (4-9 h) in terms of pressure and a bit less than 10% underestimate in steam molar fraction (same time period). In other words, any of the approaches attempted, particularly the HS one, leads to more steam content in the cavity atmosphere and to lower combustion risk (Figure 7 and Figure 8).

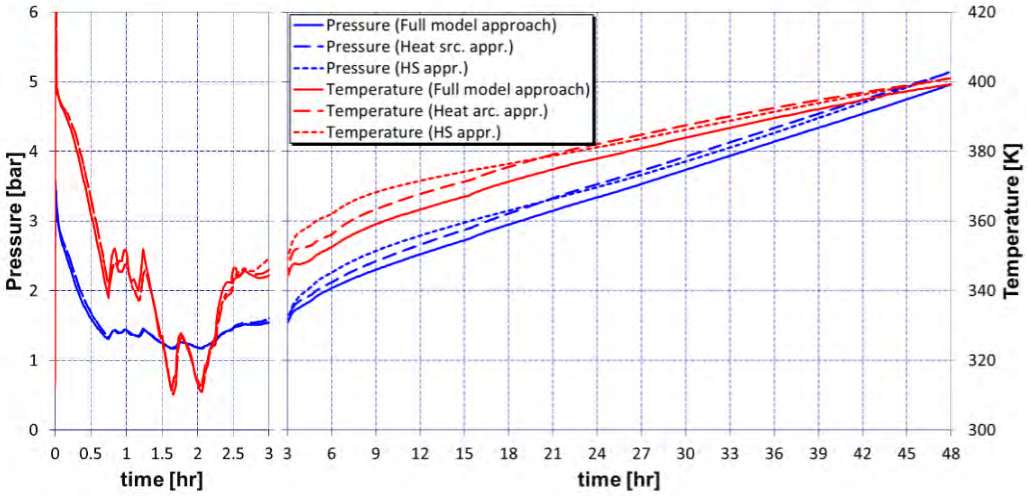

Figure 6. Evolution of pressure and temperature in the dome. Assessment of source definition.

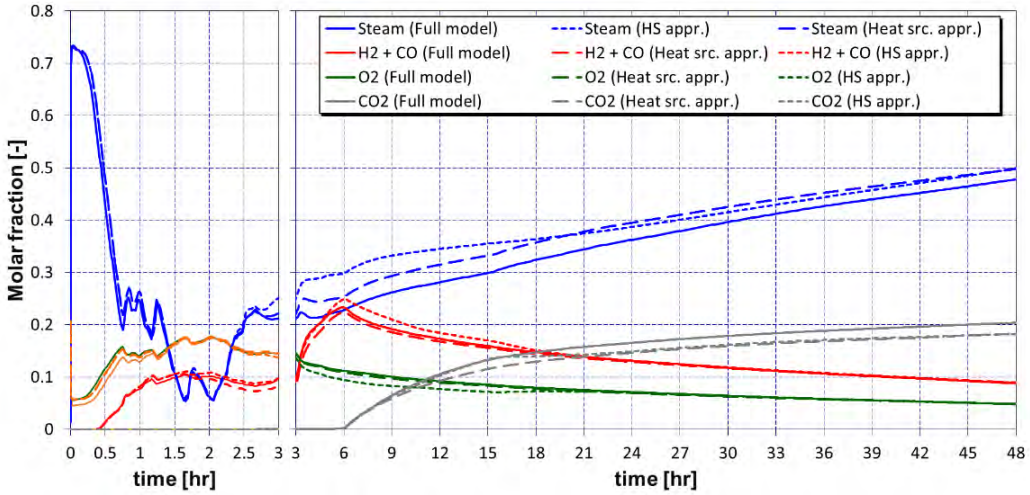

Figure 7. Atmosphere composition in the upper compartment. Assessment of source definition.

In summary, the verification of the stand-alone boundary conditions resulted in a negligible effect when sources and sprays are high (in-vessel phase). However, when mass flow and their momentum are low (ex-vessel phase), the stand-alone approach introduces significant deviations that are not straightforward to identify.

3.2. Nodalization effect

Defining compartments and their connections (flow paths) is a key task when building a simulation model with lumped-parameter codes. This is even further emphasized when the focus is on local gas composition. Therefore, when applying this methodology, which entails using a generic-containment nodalization, the effects must be checked and quantified. Thus, the results of the following simulations have been compared: The containment stand-alone model with the external sources. This model uses the same containment nodalization as the full model (Figure 2), with external sources and the heat source approach in the cavity. The generic-containment model as defined in AMHYCO (Figure 5) with the same external sources as the previous simulation.

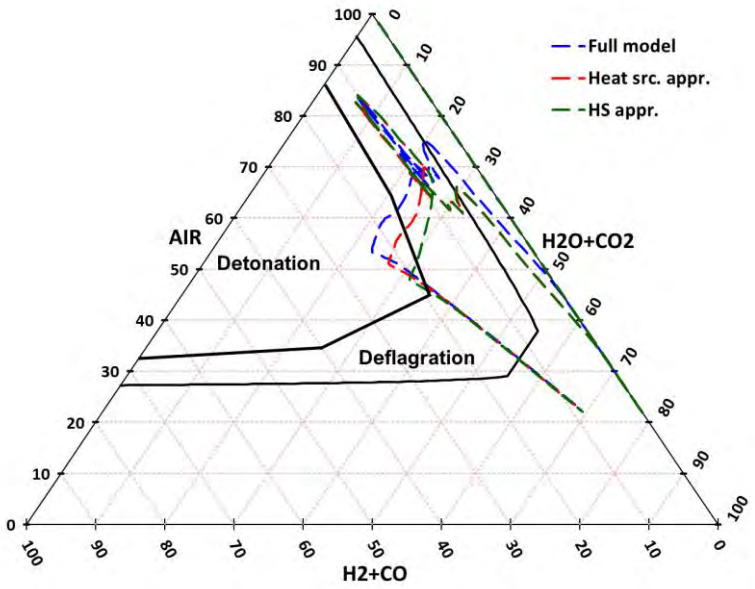

Figure 8. Shapiro diagram in the upper compartment. Assessment of source definition.

Figure 9 shows the comparison of the pressure and dome temperature evolution for simulations. The full-model approach is kept in figures for comparison. During the in-vessel phase, evolution is primarily governed by the intense mass source into the containment and by condensation on cold surfaces or on sprayed droplets. As a consequence, the effect of the containment nodalization is secondary in this phase of the accident. The effect is higher during the ex-vessel phase as gas sources momentum is smaller than during the in-vessel phase, and the distribution from the cavity to other compartments is more meshing-dependent. The generic-containment model notably underpredicts pressure (more than 12% with respect to the full-scope model). As observed, most of this difference does not come from the thermal discrepancy, but from the steam remaining airborne in the case of the generic containment. Given that the same mass and energy flows were set, the reason behind this difference should be evaporation/condensation in both models. Through Figure 10 and Figure 11, it is noted that despite the combustible gas compositions are not that different, when bringing them into the Shapiro diagram, there is a visible discrepancy in the flammability of both gas mixtures.

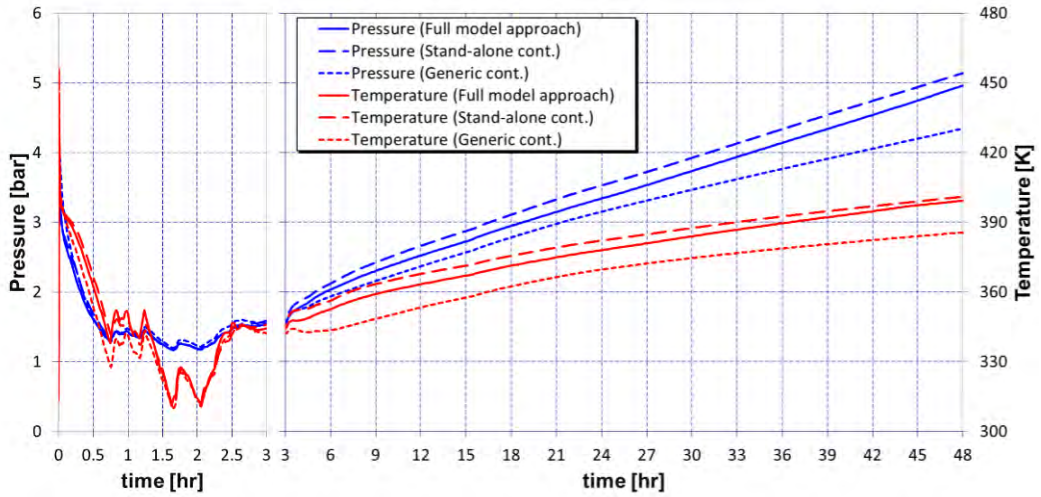

Figure 9. Evolution of pressure and dome temperature. Assessment of the nodalization effect.

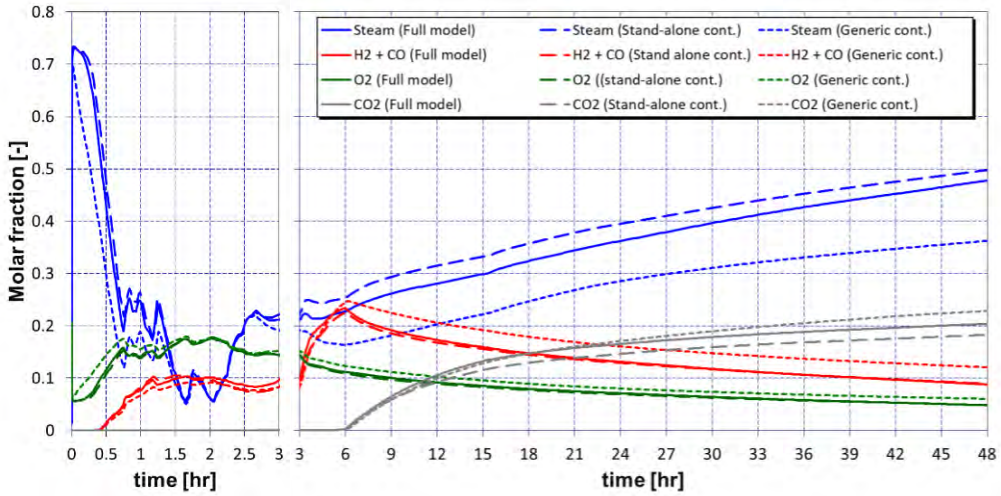

Figure 10. Atmosphere composition in the dome compartment. Assessment of the nodalization effect.

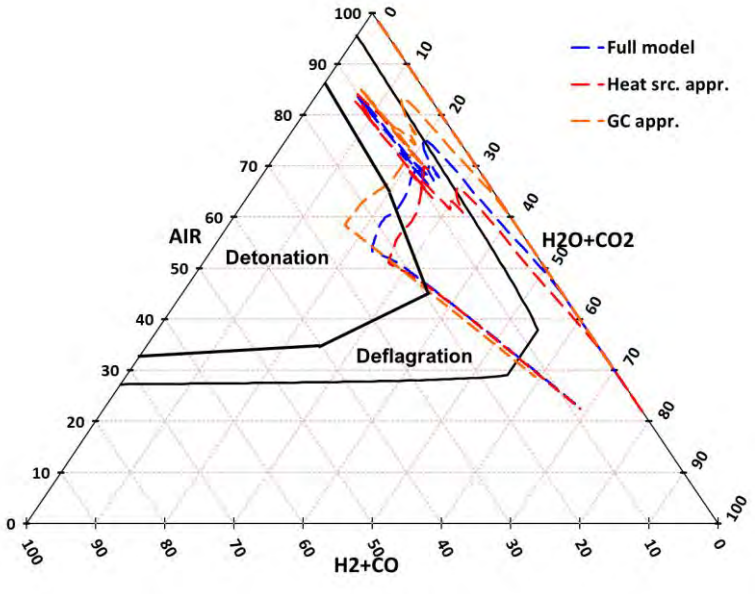

Figure 11. Shapiro diagram in the dome compartment. Assessment of the nodalization effect.

Again, in the in-vessel phase of the accident, the slight discrepancies introduced by the nodalization are attenuated as the accident progresses. During the ex-vessel phase, however, the energy distribution from the cavity to the other containment compartments is more mesh-dependent, leading to significant effects on the local evaporation–condensation balance and, consequently, on the containment pressure and atmospheric composition.

4. CONCLUSIONS

The generic stand-alone containment approach, as developed in SARNET and adopted in the AMHYCO project, is a valuable approach for comparing mitigation strategies, particularly for combustion risk. Nonetheless, its application should carefully consider three main aspects:

- Mass and heat sources definition. Translating the information resulting from the full-plant model, requires a thorough understanding of the mass and energy management in the code (MELCOR 2.2). The external boundary conditions set in the input deck should mimic such management as tight as possible, which given the huge complexity of SA codes, is far from being trivial.
- Ex-vessel onset. As a result of the RPV breach, major energy and mass transfer happen into the cavity and capturing them all is very challenging and is subject to approximations. The two more straightforward options tested in this work have been the direct injection of energy into the cavity atmosphere and the inclusion of an "fabricated" structure representing high-temperature corium. According to what observed in previous sections, a direct injection is preferable even if moderate deviations noted with respect to the full-scale model in the case of MELCOR 2.2.
- Nodalization effect. When changing containment meshing gas atmosphere flammability will likely change. Even if same sources used, the different compartment volumes and flow-paths result into changing balances like evaporation/condensation that eventually end up in different atmosphere compositions and, hence, gas mixture flammability. Such an effect is more pronounced during the ex-vessel phase.

The results shown in this work are specific for a LB-LOCA in a large Western PWR when using MELCOR 2.2. However, the conclusions withdrawn above do have a generic nature, except when referring to the code used.

ACKNOWLEDGMENTS

The AMHYCO project, coordinated by the UPM (Universidad Politécnica de Madrid) has received funding from the Euratom research and training programme 2019-2020 under Grant Agreement n°945057. The content of this paper reflects only the authors' view. The European Commission is not responsible for any use that may be made of the information it contains.

MELCOR is an integral severe accident code developed by Sandia National Laboratory (SNL). It is used at CIEMAT thanks to the CSARP agreement between SNL and the Spanish Regulatory Body (Consejo de Seguridad Nuclear – CSN).

REFERENCES

[1] B. R. Sehgal, Ed., 'Chapter 3 - Early Containment Failure', in *Nuclear Safety in Light Water Reactors*, Boston: Academic Press, 2012, pp. 185–306. doi: 10.1016/B978-0-12-388446-6.00003-4.
[2] TEPCO, 'Evaluation of the Situation of Cores and Containment Vessels of Fukushima Daiichi Nuclear Power Station Units-1 to 3 and Examination into Unsolved Issues in the Accident Progression. Progress Report No. 3', May 2015.
[3] G. Jiménez *et al.*, 'AMHYCO Project – Towards an Enhanced Accident Management of the H2/CO Combustion Risk', in *The 19th International Topical Meeting on Nuclear Reactor Thermal Hydraulics (NURETH-19)*, Brussels (Belgium), Mar. 2022.
[4] S. Kelm *et al.*, 'Detailed assessment of combustion risk and PAR efficiency in the late phase of a severe accident within the European AMHYCO project', *Nuclear Engineering and Design*, vol. 446, p. 114588, Jan. 2026, doi: 10.1016/j.nucengdes.2025.114588.
[5] St. Kelm *et al.*, 'Generic Containment: Detailed comparison of containment simulations performed on plant scale', *Annals of Nuclear Energy*, vol. 74, pp. 165–172, Dec. 2014, doi: 10.1016/j.anucene.2014.07.006.
[6] L. Serra, A. Domíngues-Bugarín, C. Vázquez-Rodríguez, and G. Jiménez, 'D2.1 – Data for the generic containment analysis (PWR-W, PWR-VVER, PWR-KWU)', UC-Euratom, AMHYCO D2.1, Mar. 2023.
[7] L. L. Humphries *et al.*, 'MELCOR Computer Code Manuals Vol. 2: Reference Manual Version 2.2.r2023', Sandia National Laboratories, Albuquerque, SAND2023-10994 O, Jan. 2023.

[8] K. Ross, J. Phillips, R. O. Gauntt, and K. C. Wagner, 'MELCOR Best Practices as Applied in the State-of-the-Art Reactor Consequence Analyses (SOARCA) Project', Sandia National Laboratories, NUREG/CR-7008, 2014.
[9] L. L. Humphries *et al.*, 'MELCOR Computer Code Manuals Vol. 1:Primer and User's Guide Version 2.2.r2023', Sandia National Laboratories, Albuquerque, SAND2023-10997 O, Jan. 2023.

Assessment and Applicability of a Stand-Alone Containment Methodology for Hydrogen and Carbon Monoxide Risk Evaluation in Severe Accidents

Joan Fontanet, Luis E. Herranz

**joan.fontanet@ciemat.es*
Unit of Nuclear Safety Research
Department of Nuclear Fission
CIEMAT

ERMSAR2026
Madrid (Spain) 18-22 May 2026

Contents:

01 Introduction

02 Approach and Methodology

03 Sequence and Plant Model

04 Methodology Assessment

05 Final Remarks

01

INTRODUCTION

Introduction

Essentials

- **Framework**

  H2020 EURATOM AMHYCO project (2020-2025).

  Extensive use of the “Generic Containment” approach to analyze containment thermal-hydraulics and H_2 and CO distribution.

- **Objective**

  Highlight the importance of verifying the hidden steps involved in the process from the full-plan model to the “Generic Containment” model.

  Evaluate the potential effects of key hypotheses and approaches underneath the "Generic Containment" approach.

- **Scope:**
  - PWR-W containment (1000 MWe).
  - LBLOCA.

- **Analytical tool:** MELCOR 2.2 r2023

02

APPROACH AND METHODOLOGY

The AMHYCO strategy

Generic Containment Approach

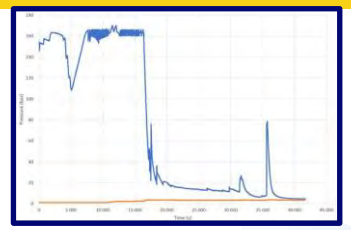

FULL-PLANT MODEL

Sequence analysis

Verification tests!

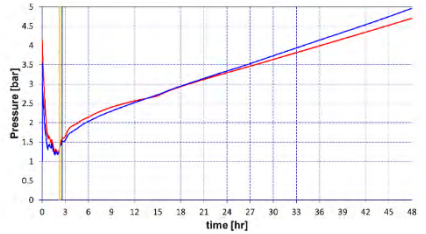

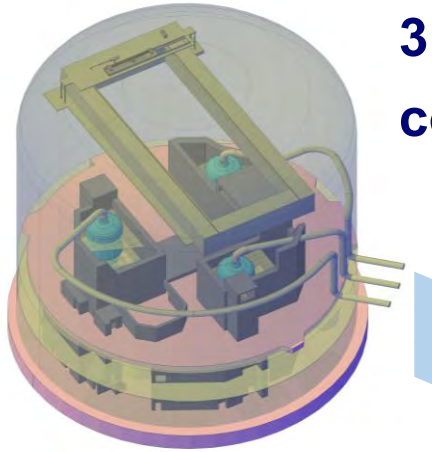

3D-CAD containment

Generic containment Analysis

Developed in SARNET-II (2009-2013)
Also used in SAMHYCO-Net (2017-2019)
Extended in AMHYCO (2020-2025)

CFD

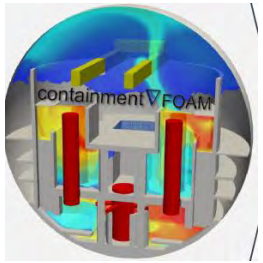

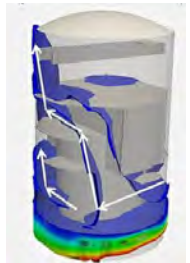

GOTHIC

LP

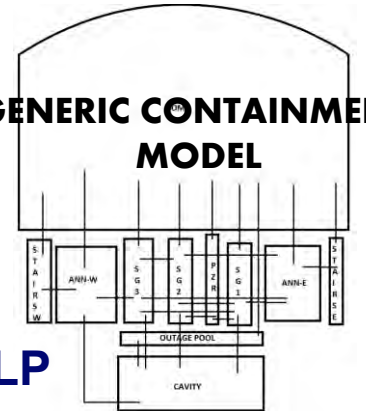

GC methodology

Methodology's steps

1 Sequence simulation

- Select combustion-relevant sequences.
- Run full-model simulations for a specific NPP.

2 Mass and energy release

- Quantify in-containment fluid release from full-model results.
- Prepare data files: mass flow rates and energy rates.
  - o In-vessel
  - o Ex-vessel

3 GC model

- Build the generic containment model from public data.
- **Propose a simplified nodalization.**
- **Apply mass and energy releases as boundary conditions (sources).**

4 Results assessment

- **Check results validity against boundary conditions.**
- **Check the results consistency with the nodalization.**

The "Generic Containment" harmonizes containment modeling and reduces simulation computation time while maintaining the representativeness of the scenario.

03

SEQUENCE AND PLANT MODEL

Sequence and plant

Model description

- **Westinghouse 3-loop PWR (1000 Mwe)**
  - Limestone-type concrete is assumed for MCCI
  - The cavity is modeled using the single-layer approach.
  - The BURN package of MELCOR (combustion) is not activated.
  - PARs are not modeled.

- **Double-ended guillotine break in the HL (PRZ loop)**
  - No safety systems are available in the RCS (except accumulators).
  - Sprays are available in the containment.

Event	Time
Initial event	0.0 s
Fluid release to the containment	0.0 s
Sprays activation (injection mode)	4.1 s
First H_2 release to the containment	0.3 h
Total core uncovering	1.2 h
Sprays switch to recirculation	2.1 h
Ex-vessel phase	2.6 h

Containment model

Full-model approach

- **Sprays characteristics:**

  Setpoint 2.6 bar

  Injection mode: 0.208 m^3/h at 293.15 K

  Recirculation mode: water intake from the sump

- **Low steam content & low pressure**

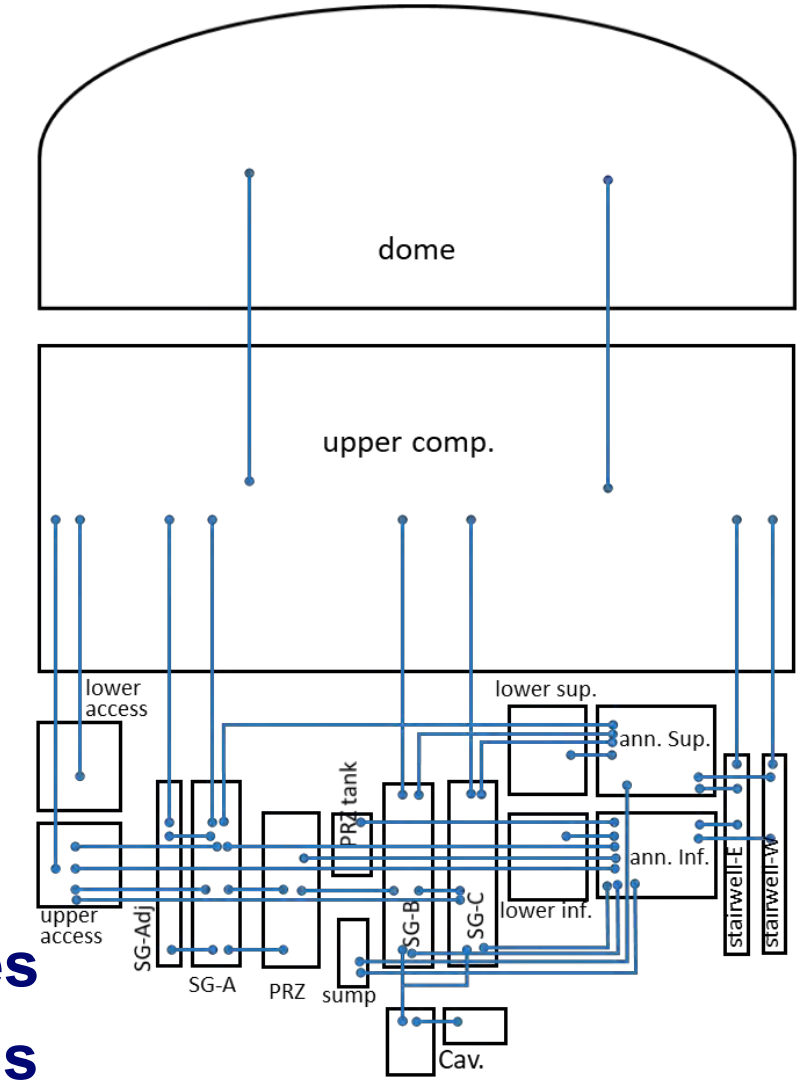

19 control volumes

42 flow paths

Containment model

Gas releases

In-Vessel phase

Mass flowrate

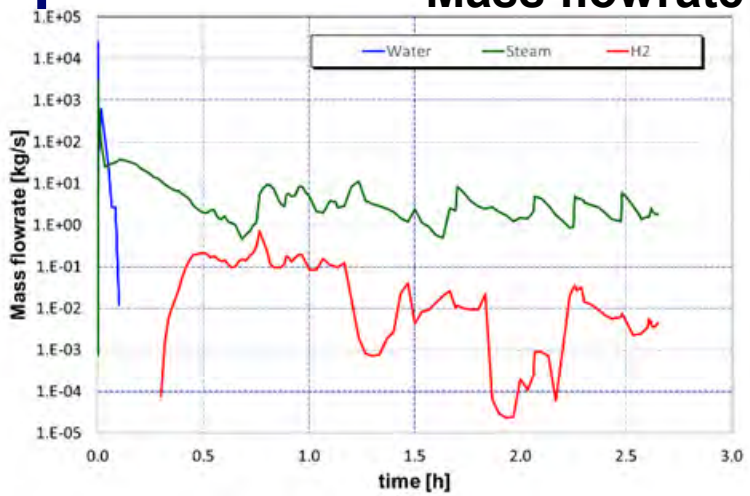

Temperature

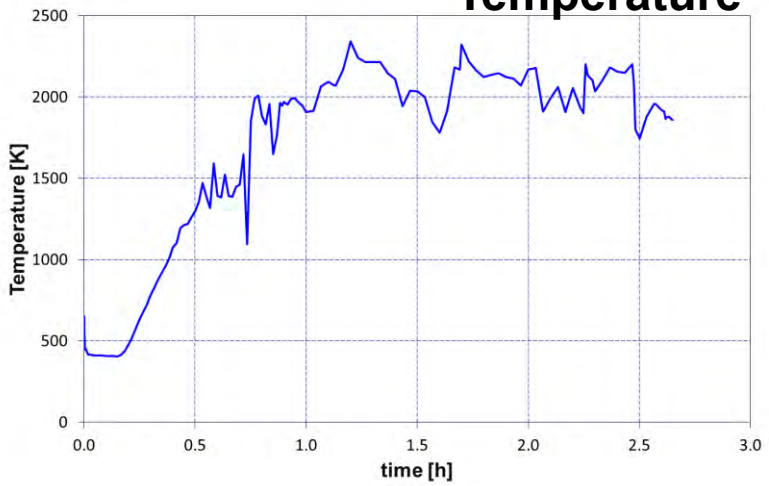

Ex-Vessel phase

Mass flowrate

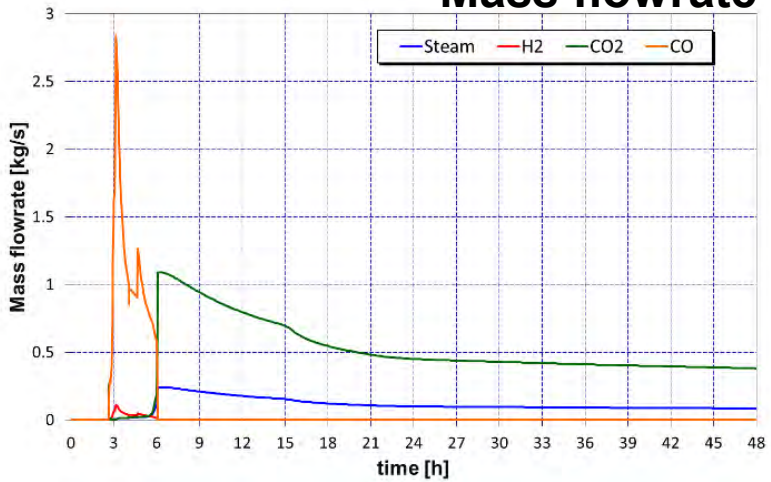

Temperature

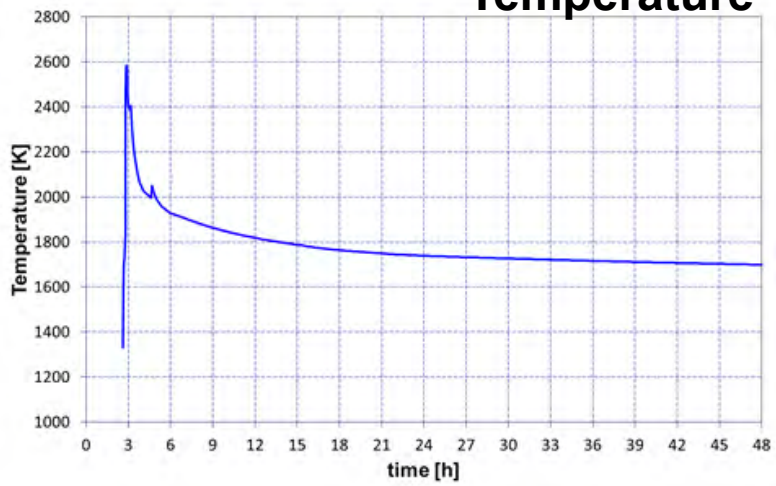

04

METHODOLOGY ASSESSMENT

Methodology assessmet

I. Sources (fluid and energy)

Full model

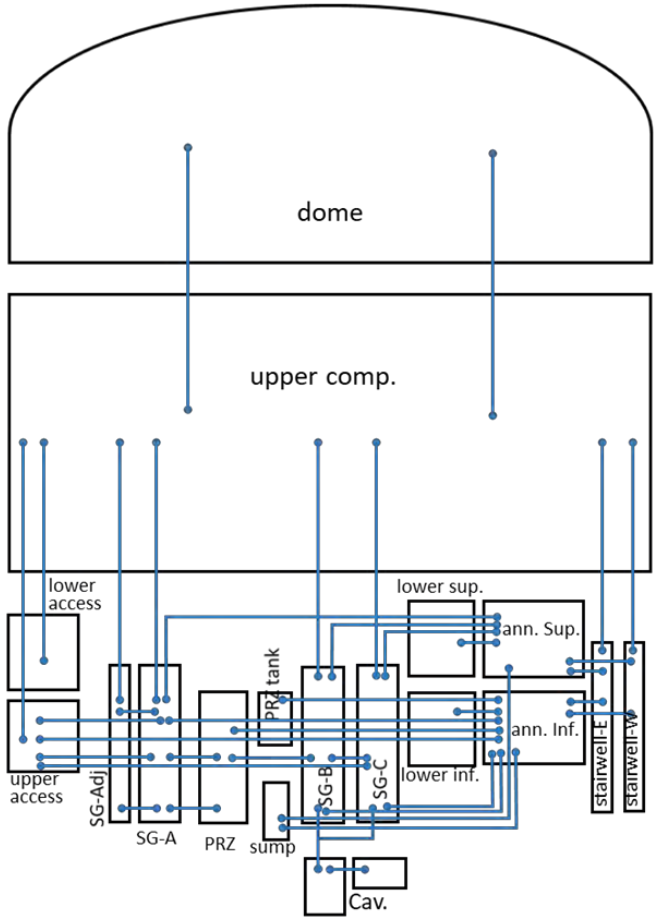

Fluid Source
Heat Sources (fluid)

Heat Sources
(hot corium in cavity)

- Direct heat (to atm.)
- Hot heat structure

Stand-alone model

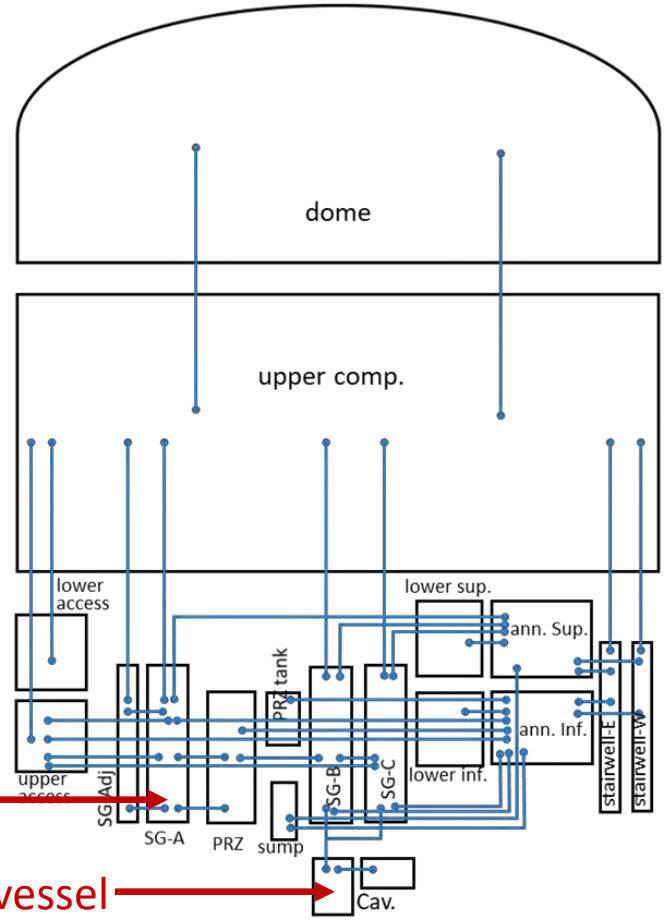

in-vessel
H_2, H_2O

ex-vessel
H_2, CO, H_2O, CO_2, heat

Source effect results

Pressure and temperature

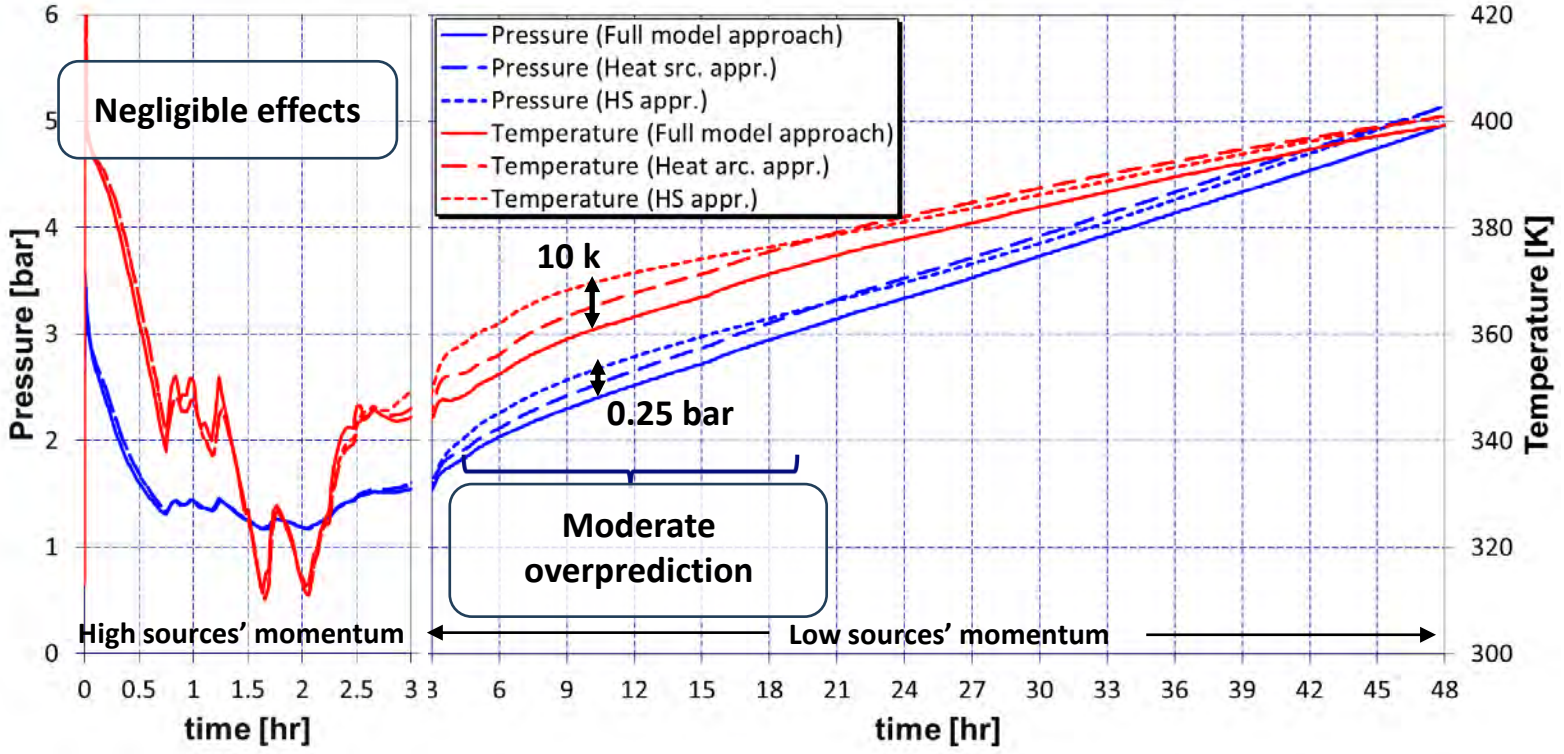

Stand-alone model:

- Limited effect of temperature discrepancies on the pressure overprediction.

  Definition of the **ex-vessel Boundary Conditions** is not a straightforward task.

Source effect results (2)

Atmosphere composition

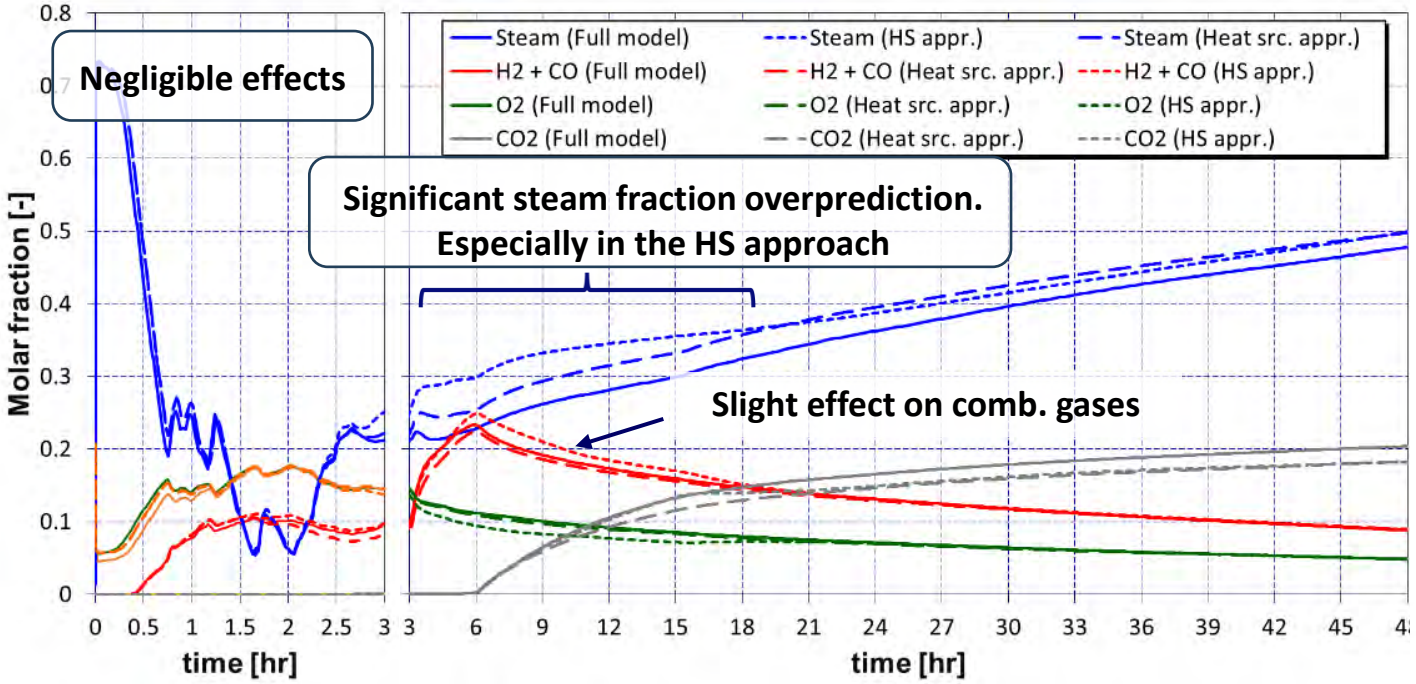

Shapiro diagram

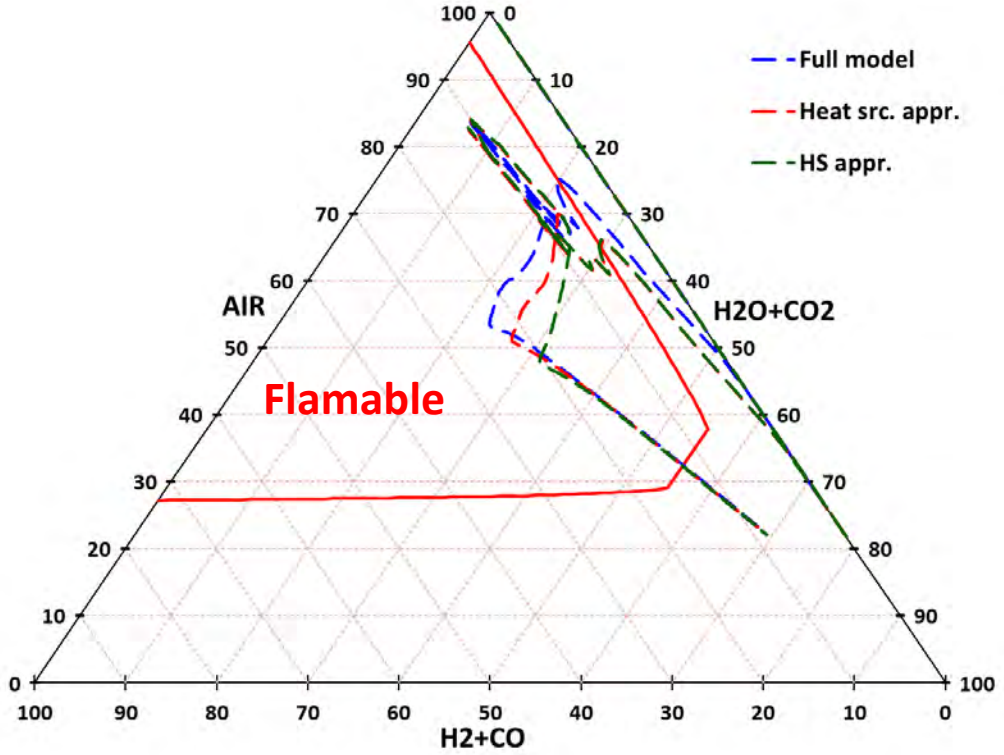

Overestimation of steam in the containment due to:
Higher T_{sat}, inter-compartment flow

Visible effect on the gas cloud flammability
(less conservative in the stand-alone model).

The “heat source” approach provides better results.

Methodology review (2)

GC Nodalization

Stand model

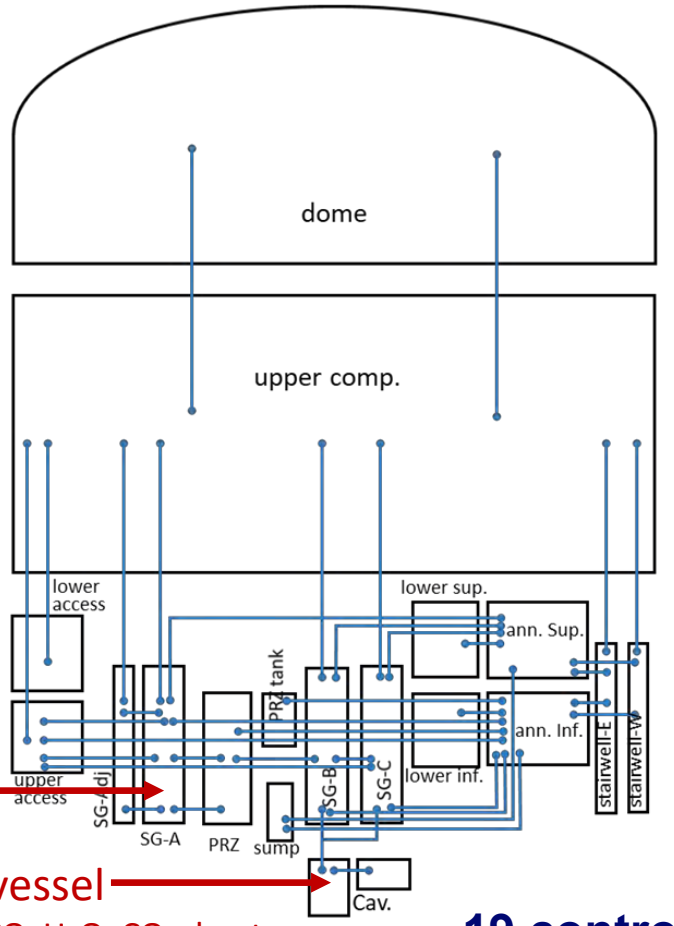

19 control volumes

42 flow paths

Contain. nodalization

(Heat Source approach)

Generic containment

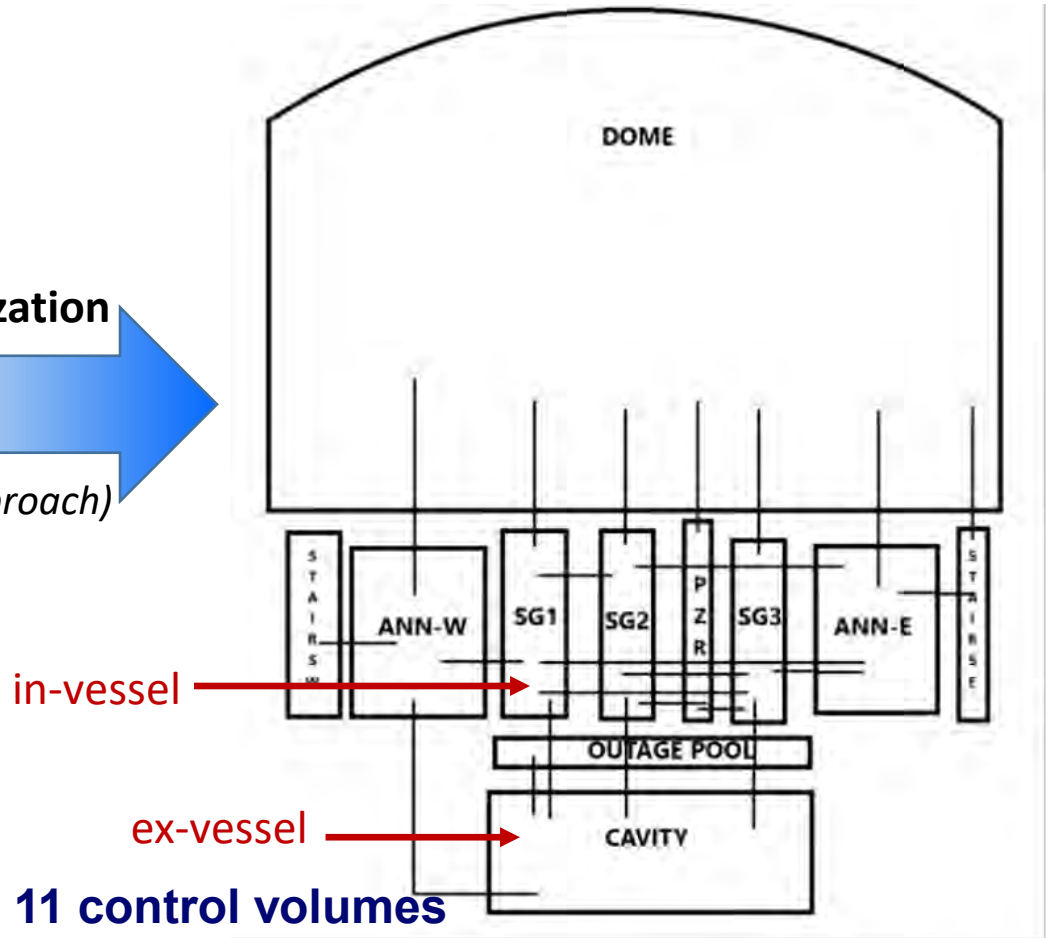

11 control volumes

32 flow paths

GC effect results

Pressure and temperature

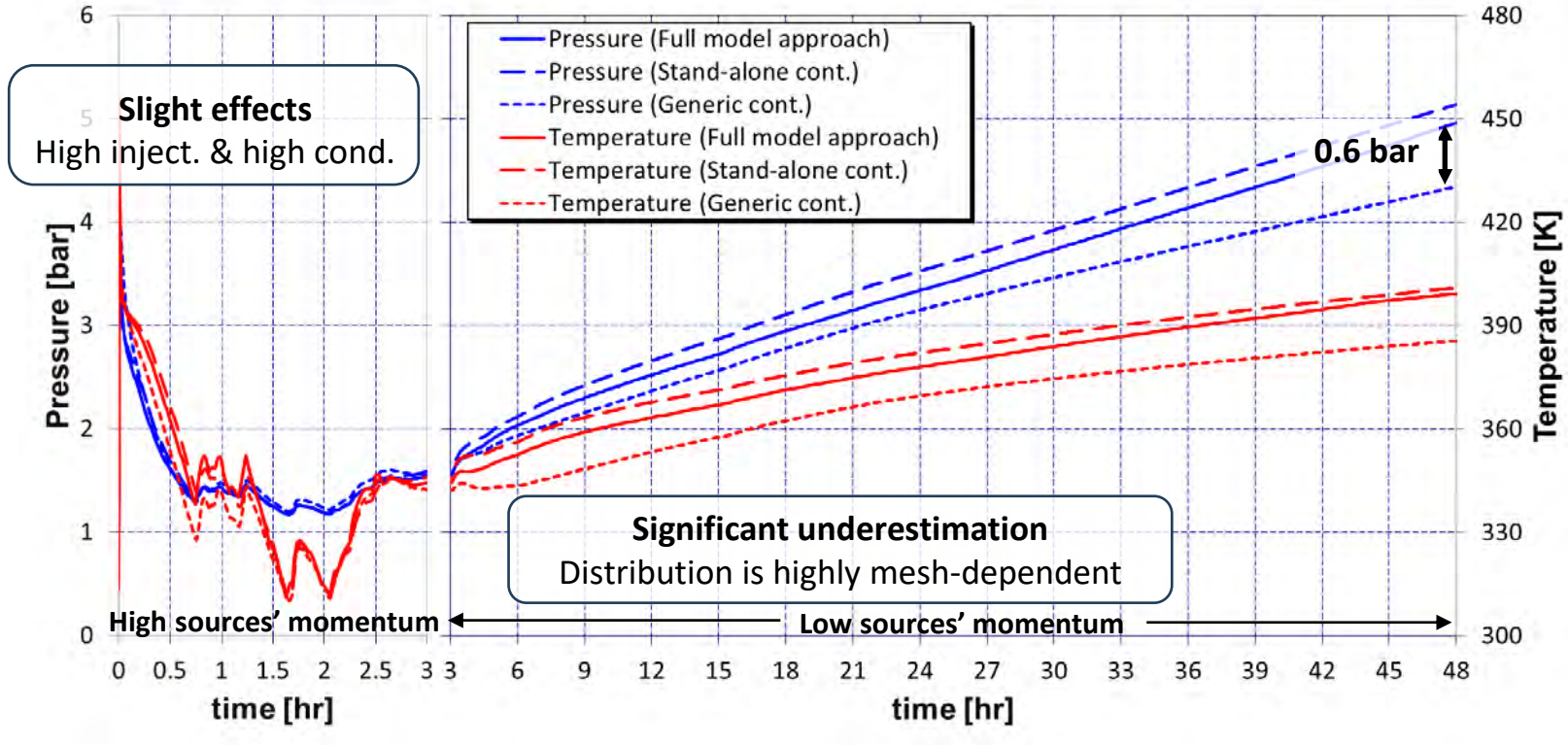

Generic model:

- Pressure difference does not come from thermal discrepancies **BUT** from the steam content in the containment atmosphere.

GC effect results (2)

Atmosphere composition

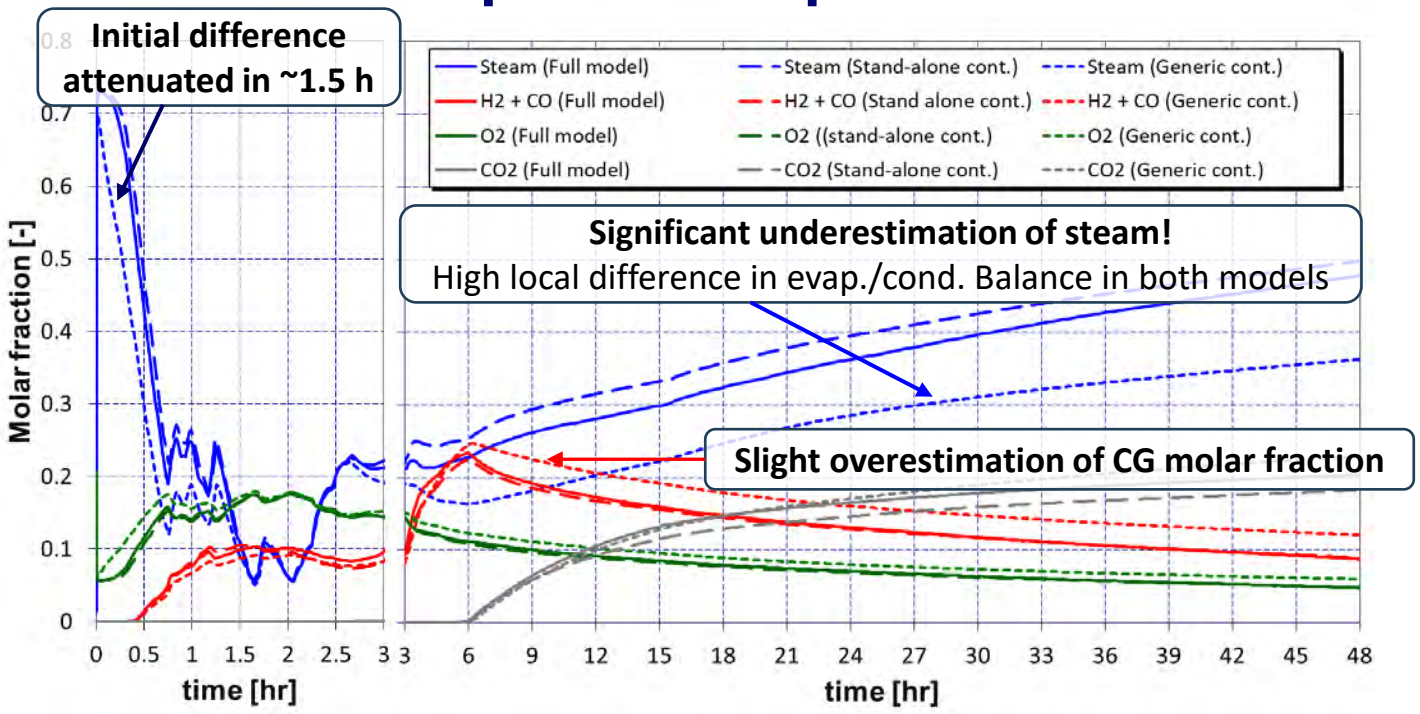

Temperature difference triggers the difference in local evaporation/condensation balance

Shapiro diagram

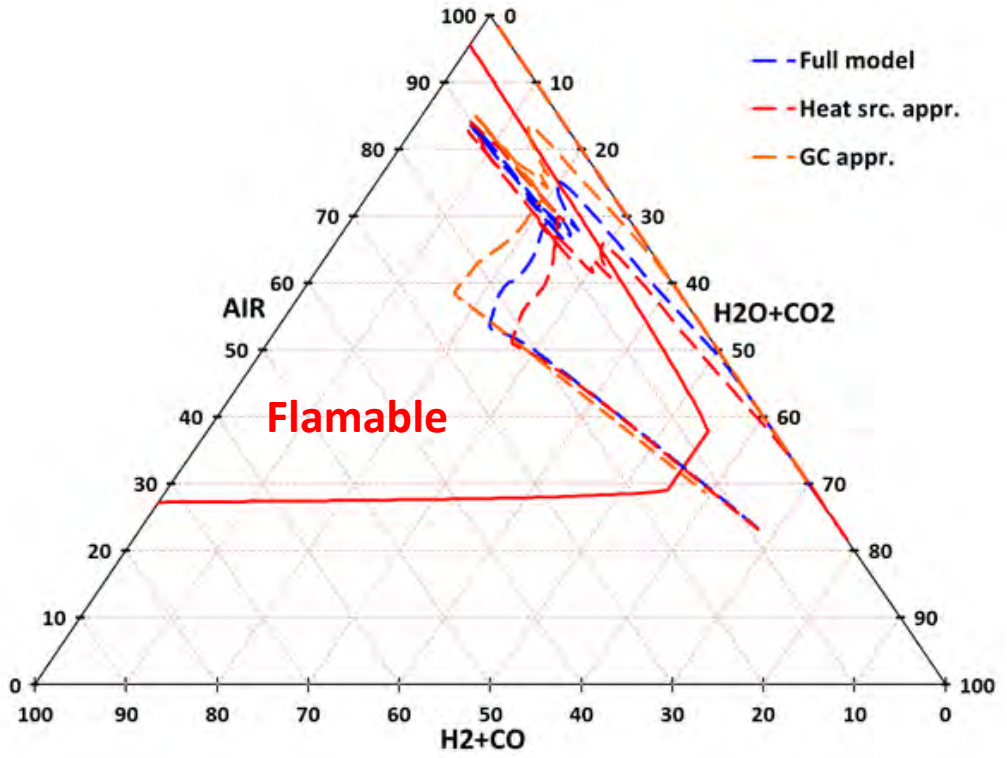

Significant effect on the gas cloud flammability (more conservative).

05

FINAL REMARKS

Final remarks

- **The “Generic Containment” methodology is a valuable approach for comparing mitigation strategies and combustion risk.**
- **Three main aspects must be carefully assessed when applying this methodology:**
  - Mass and energy sources definition is not a straightforward task and requires a thorough understanding of mass and energy management in the code. Boundary conditions must keep the representativeness of the full plant model.
  - **Ex-vessel onset** is a key event. Large energy and fluid sources and small momentum poses a challenge for the “Generic Containment” application in the ex-vessel phase.
  - Meshing is fundamental to the evaporization/condensation balance, and it might end up significantly affecting the flammability of the cloud.
- **Any discussion of the results of the “Generic Containment” application must take into account the deviations from the initial full model.**

This work is a sequel to the AMHYCO project.

This AMHYCO project has received funding from the European Union's **EURATOM Horizon 2020** research and innovation programme **grant number 945057**.

The content of this paper reflects only the authors' view. The European Commission is not responsible for any use that may be made of the information it contains.

SEAKNOT

12th CONFERENCE ON
SEVERE ACCIDENTS RESEARCH
May 18-22, 2026 - Madrid, Spain
ERMSAR 2026

Thank you for your attention!

Unit of Nuclear Safety Research
Department of Nuclear Fission
CIEMAT
email@ciemat.es

The 12th European Review Meeting on Severe Accidents Research

May 18-22, 2026, Universidad Carlos III de Madrid, Madrid, Spain

TECHNICAL SESSION 6.3: SOURCE TERM

Chairs: A.-C. Grégoire (ASNR)

ID129	**Investigation on Effect of Aerosol Generation Rates on Deposition on Obstacle Structure Surface under Venting Decontamination in the Decommissioning of Fukushima Daiichi Nuclear Power Plant after Severe Accident** R. Xu (University of Tokyo)	Paper Presentation
ID039	**Chemistry of Chromium in the Reactor Coolant System in severe accident conditions from an ATF type core** J. Bouchain (ASNR)	Paper Presentation
ID043	**Interfacial gas transfer in gas-liquid flows: a comparative study of advanced experimental and computational techniques** A. Ramos-Perez (PSI)	Paper Presentation
ID207	**Impact of ASTEC's Advanced Modeling in Gas and Adsorbed Phases Chemistry on the Source Term** S. M. O. Souvi (ASNR)	Paper Presentation

Investigation on Effect of Aerosol Generation Rates on Deposition on Obstacle Structure Surface under Venting Decontamination in the Decommissioning of Fukushima Daiichi Nuclear Power Plant after Severe Accident

Ruicong Xu*, Ravinder Kumar, Zeeshan Ahmed, Yosuke Nishimura
Nuclear Professional School, The University of Tokyo
2-22 Shirane-shirakata, Tokai-mura, Ibaraki, 319-1188, Japan
xurc@g.ecc.u-tokyo.ac.jp; ravinderkumar@g.ecc.u-tokyo.ac.jp; zeeshan@g.ecc.u-tokyo.ac.jp; nishimura-y@g.ecc.u-tokyo.ac.jp

Hanyu Wang
Department of Nuclear Engineering and Management, The University of Tokyo
7-3-1 Hongo, Bunkyo-ku, Tokyo, 113-8656, Japan
wang-hanyu@g.ecc.u-tokyo.ac.jp

Avadhesh Kumar Sharma
School of Mechanical Engineering (SMEC), Vellore Institute of Technology
Chennai, Tamil Nadu, 600127, India
avdhruva@gmail.com

Ryo Yokoyama, Shuichiro Miwa
Nuclear Professional School, The University of Tokyo
2-22 Shirane-shirakata, Tokai-mura, Ibaraki, 319-1188, Japan
yokoyamaryo395@g.ecc.u-tokyo.ac.jp; miwa@n.t.u-tokyo.ac.jp

Shunichi Suzuki
Institute of Engineering Innovation, The University of Tokyo
7-3-1 Hongo, Bunkyo-ku, Tokyo, 113-8656, Japan
s_suzuki@n.t.u-tokyo.ac.jp

Koji Okamoto
Nuclear Professional School, The University of Tokyo
2-22 Shirane-shirakata, Tokai-mura, Ibaraki, 319-1188, Japan
okamoto@n.t.u-tokyo.ac.jp

ABSTRACT

After suffering from a severe nuclear accident, lots of technical issues and engineering concerns were generated for the safe and effective decommissioning of Fukushima Daiichi nuclear power plant. During the decommissioning of the Fukushima Daiichi nuclear power plant, aerosols generated during fuel debris retrieval can accumulate on internal structures of the primary containment vessel and alter contamination pathways under ventilation. Understanding how aerosol generation intensity influences surface deposition under such low-velocity venting conditions is therefore important for radiological safety and decontamination planning. This study experimentally investigates aerosol deposition onto a cubic obstacle

* Corresponding and presenting author.

placed in a vertical ventilation column using zirconia aerosols as simulants. Aerosol injection rates from 0.24 to 1.8 g/h and deposition durations of 6 and 12 hours were examined in the UTAD[2] facility under laminar flow representative of PCV conditions. Deposited mass measurements were combined with surface morphology observations. Results show that both higher aerosol injection rates and longer exposure times lead to significantly increased surface deposition. The increase is not only due to greater particle supply but also to the progressive evolution of the deposited layer. Surface morphologies reveal a transition from discrete particles to dense agglomerated structures, which enhance the surface's ability to retain subsequent injecting aerosols. This behavior explains the strong dependence of contamination on aerosol generation rate. These findings provide insight for identifying hotspot contamination regions and for optimizing ventilation and operational strategies during Fukushima Daiichi decommissioning.

KEYWORDS

Aerosol deposition; Obstacle Structure; Venting decontamination; Fukushima Daiichi decommissioning

1. INTRODUCTION

Severe nuclear accidents can lead to extensive core damage and fuel debris formation, accompanied by the release of radioactive aerosols inside the primary containment vessel (PCV) [1–5]. During the ongoing decommissioning of the Fukushima Daiichi Nuclear Power Station (1F-NPP), aerosol generation, transport, and surface contamination have become major concerns for radiological protection and operational safety [6–8]. Many internal structures within the damaged PCV exhibit high radiation levels and require decontamination prior to debris retrieval, while fuel debris must often be segmented into smaller pieces using remote cutting technologies, which further promotes aerosol production [9–11].

High-power laser techniques have recently been proposed as effective tools for surface decontamination and debris cutting in such environments [9,12–16]. However, these processes are known to generate large quantities of submicron aerosols, particularly within the Greenfield gap size range (0.1–1 μm), which are difficult to remove using conventional spray systems due to low mechanical collection efficiencies [17–20]. To address this limitation, lots of recent studies focused on enhanced spray-based mitigation approaches, including pre-injection of water mist and electrically charged mist and spray droplets, which significantly improve aerosol capture through intensified agglomeration and electrostatic interactions [21–30].

Despite the demonstrated efficiency of these spray-based technologies in controlled experiments, their practical deployment inside the highly complex geometry of the damaged PCV remains challenging. Certain regions are inaccessible to sprays, and in such areas ventilation systems become an alternative means of aerosol control by maintaining negative pressure and directing airflow toward filtration units [31, 32]. However, ventilation itself may unintentionally promote aerosol dispersion and surface deposition on internal structures, resulting in secondary contamination and increased decontamination workload [33].

Aerosol deposition and transport have been extensively studied under turbulent flow conditions in environmental, industrial, and nuclear applications [34–36]. Within the nuclear field, large experimental programs (e.g., FALCON, MARVIKEN, PHEBUS) and severe accident analysis codes have provided substantial understanding of particle transport and surface contamination in turbulent regimes [7,37–39]. More recent studies also investigated aerosol generation and transport during cutting of debris simulants and activated materials [40–42]. However, predicting aerosol deposition remains difficult due to re-entrainment, surface conditions, and complex particle–flow interactions [43].

The ventilation conditions expected during 1F decommissioning differ fundamentally from these turbulent scenarios. Engineering assessments indicate that gas velocities inside the PCV drywell may be as low as 0.01–0.1 m/s, corresponding to laminar flow regimes under normal ventilation and thermal convection conditions [45]. Under laminar flow, deposition is governed primarily by gravitational settling and

Brownian diffusion rather than turbulence-induced impaction [46]. In addition, the presence of structural obstacles can locally disturb the flow field, creating stagnation zones and recirculation regions that strongly influence particle trajectories and deposition behavior. These effects remain insufficiently understood under decommissioning conditions.

Therefore, simplified and well-controlled experimental studies are essential to isolate the fundamental mechanisms governing aerosol deposition near obstacles. The present work conducts such an investigation using the UTAD^2 (the University of Tokyo, Aerosol Dispersion & Deposition) facility. It is noted that the aerosol generation rates may vary by using different laser operation conditions during decommissioning. Therefore, by introducing a representative cubic obstacle into a low-velocity venting flow with different aerosol feed rates, this study examines how effect of aerosol generation rates affects aerosol transport and surface contamination. The findings aim to improve the understanding of aerosol deposition under laminar ventilation, provide insight into potential contamination hotspots inside the PCV, and support the development of predictive tools and mitigation strategies for Fukushima Daiichi decommissioning.

2. EXPERIMENTAL FACILITY AND SETUP

2.1. Test section and obstacle configuration

Experiments were conducted in the UTAD^2 facility, consisting of a transparent vertical polycarbonate pipe 3.2 m in height and 11.4 cm in inner diameter. Figure 1 shows the experimental facility. A ventilation fan controlled by a variable frequency drive is installed at the top of the column, together with a high-efficiency filter to remove exhausted aerosols. During deposition experiments, the fan was operated at 2.0 Hz, generating a bulk flow velocity of approximately 0.08 m/s, representative of low-flow ventilation expected during 1F decommissioning. The lower end of the pipe serves as the air inlet. Aerosols are injected near the bottom of the test section and transported upward by the ventilation flow. A detachable 20-cm-high section is located at mid-height, where a cubic aluminum obstacle (6 cm side) is installed. Figure 2 illustrates the details of the obstacle. Aerosols transported by the flow interact with this obstacle and deposit on its surfaces. As shown in Figure 1, there are two locations, P1 and P2, which are considered for pressure, velocity and aerosol measurements.

2.2. Aerosol generation

Zirconium dioxide (ZrO_2) aerosol was used to simulate aerosols generated during debris cutting and laser processing. This material choice is based on previous studies showing similar particle characteristics during laser cutting of debris simulants [8, 16]. A Palas RBG-1000 powder disperser was employed to generate stable aerosol injection. The device uses a piston-brush feeding mechanism and compressed air dispersion to produce reproducible airborne particles. The generator was operated at different feed rates with a gas flow of 27–28 L/min for different experimental runs, producing the adjustable aerosol supply rate of 0.24–1.8 g/h.

Because particle agglomeration occurs during dispersion, the actual airborne size distribution inside the test section was measured independently, rather than assumed from powder properties. A Dekati HR-ELPI+ (High-Resolution Electrical Low-Pressure Impactor) was used to measure aerosol number concentration and size distribution at the upstream location (i.e., P1 shown in Figure 1). Aerosols were sampled through a sampling tube with 10 L/min flow rate. The HR-ELPI+ classifies particles by inertial impaction and measures concentration via electrical current after corona charging, allowing real-time size-resolved measurements from 6 nm to 10 μm. Figure 3 shows the aerosol concentration measurement results at the P1 location. As shown in Figure 2, the aerosol size distribution is larger than the manufacturer's data (a mass median diameter of 0.15 μm), indicating aerosol agglomeration during injection and dispersion.

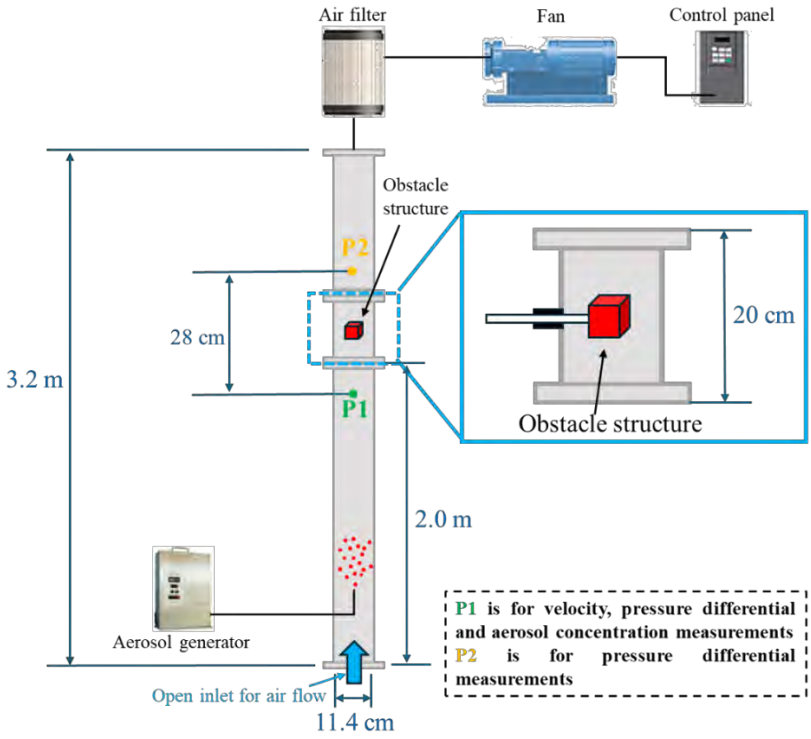

Figure 1. The UTAD[2] experimental facility.

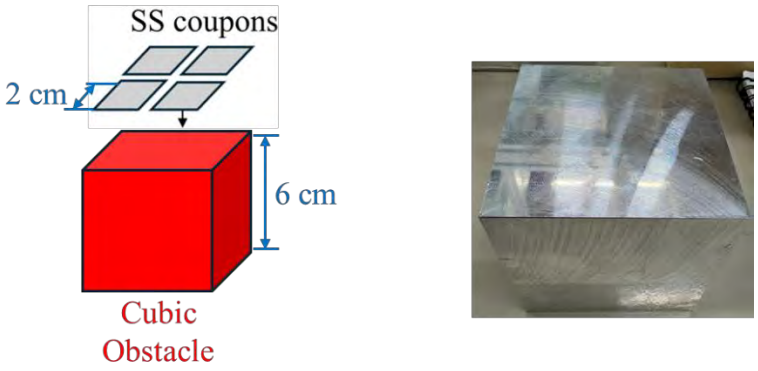

Figure 2. Illustration of the obstacle structure.

2.3. Deposition quantification

To quantify deposited mass, as shown in Figure 2, four stainless steel (SS) square coupons (≈2 cm) were attached to the top surface of the obstacle. These coupons represent typical reactor structural materials and allow high-precision weighing. Before and after each experiment, coupons were weighed using an A&D BM-22 microbalance with 1 μg resolution. Deposited mass was determined from the mass difference. The uncertainty of the gravimetric deposition measurement was mainly associated with the microbalance resolution, coupon handling, ambient humidity, and possible coupon-to-coupon variability. Although complete run-to-run repetition was limited due to the long duration of each deposition experiment, all coupons were weighed before and after the tests using the same microbalance, and the same cleaning, mounting, removal, and weighing procedures were applied to all cases. Surface morphology of deposited particles was examined using a Keyence VHX-X1 digital microscope with 2D/3D imaging capability and sub-micron resolution, enabling visualization of particle coverage and agglomeration.

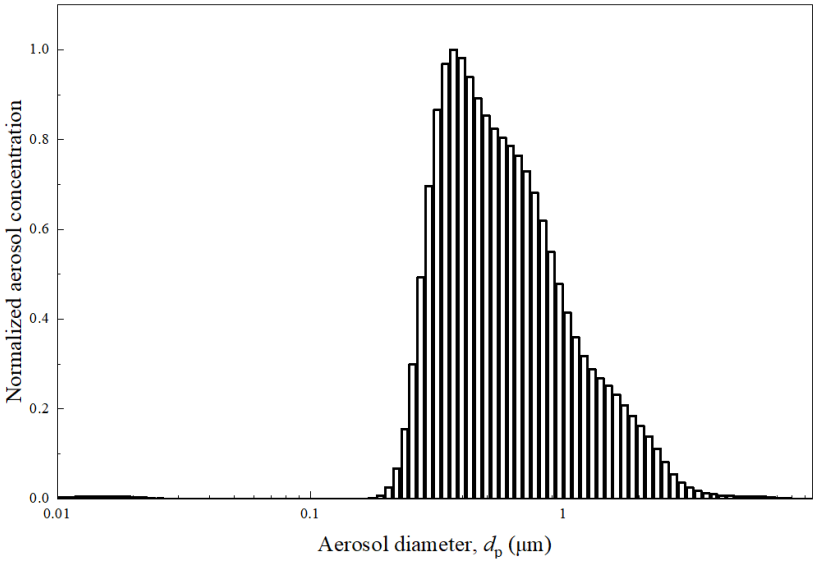

Figure 3. Aerosol size distribution.

2.4. Experimental procedures

Figure 4 shows the general experimental procedures. Prior to each run, the coupon was cleaned, weighed, and mounted on the obstacle. The obstacle was installed in the test section, followed by aerosol injection and simultaneous ventilation. Experiments were conducted under ambient laboratory conditions with continuous ventilation, preventing temperature gradients and minimizing thermophoretic effects. Deposition durations (t_{dep}) were fixed at 6 and 12 hours. After each test, the obstacle was removed, the coupons were re-weighed, and surface imaging was performed. All surfaces were cleaned before subsequent runs to ensure consistent initial conditions. Table I lists the conditions for experimental cases. To minimize possible disturbance of deposited aerosols during post-experimental handling, a fixed handling protocol was applied for all tests. After aerosol injection and ventilation were stopped, the detachable test section was carefully opened only after allowing the internal flow to fully cease. The obstacle was then removed slowly while maintaining its original orientation, and the coupons were not directly touched during transportation. The coupons were transferred to the balance using clean tweezers by gripping only the coupon edges. No brushing, wiping, or air blowing was applied before weighing. The transportation distance between the test section and the microbalance was kept short, and the post-test weighing was performed immediately after removal. Since the same procedure was applied to all experimental cases, possible handling-induced losses were minimized and treated as part of the measurement uncertainty. In addition, visual inspection before and after transportation did not show obvious particle detachment or redistribution on the coupon surfaces.

3. RESULTS AND DISCUSSION

3.1. Characterization of flow resistance

Before performing aerosol deposition experiments, it is necessary to understand the baseline ventilation behavior of the UTAD[2] facility and to quantify how the presence of the obstacle influences the flow field under different operating conditions. Such characterization ensures that the deposition experiments are conducted under well-defined and reproducible flow regimes and provides a physical basis for interpreting subsequent aerosol deposition behavior. To achieve this, flow velocity and pressure drop measurements were conducted in the absence of aerosol injection. This not only avoids contamination of the measuring probes but also allows an accurate assessment of the intrinsic ventilation characteristics of the system. The ventilation fan frequency varied over a wide range to examine both laminar and turbulent regimes.

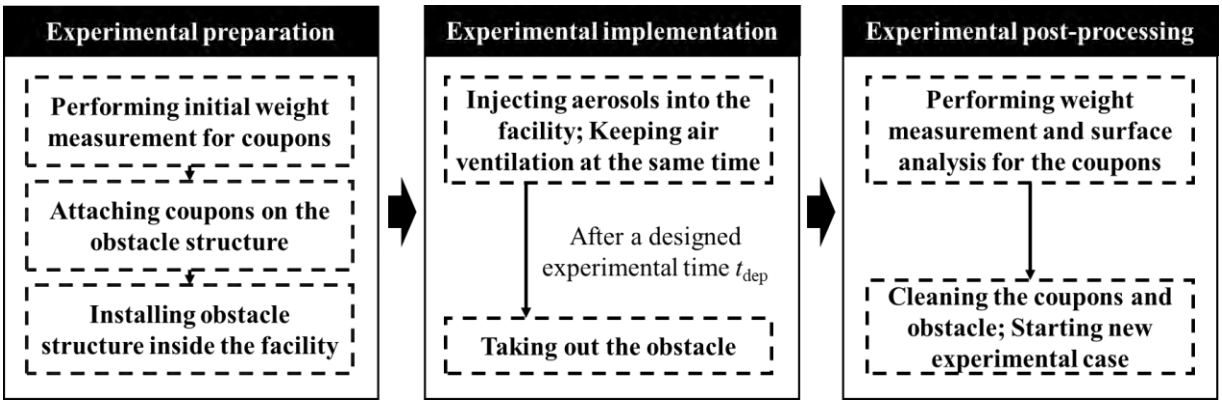

Figure. 4. Experimental procedures.

Table I. Experimental cases.

Case	Aerosol type	Deposition time, t_{dep} [h]	Aerosol injection rate, $\dot{m}_p$ [g/h]
1	ZrO_2	6	0.24
2	ZrO_2	6	0.60
3	ZrO_2	6	1.20
4	ZrO_2	6	1.80
5	ZrO_2	12	0.24
6	ZrO_2	12	0.60
7	ZrO_2	12	1.20
8	ZrO_2	12	1.80

The local flow velocity at the upstream measurement position (P1) was measured using a hot-wire anemometer, while the pressure difference between the upstream and downstream locations (P1 and P2) was recorded using a high-precision differential pressure transmitter. To quantitatively evaluate the effect of the obstacle, the dimensionless loss coefficient K was calculated:

$$K = \frac{2\Delta P}{\rho_{air} v_{flow}^2} \quad (1)$$

where ΔP indicates the pressure differences, ρ_{air} represents the air density, and v_{flow} is the flow velocity. The flow velocity used in Eq. (1) was measured at the pipe centerline at the upstream position P1. Therefore, the calculated K should be regarded as an apparent loss coefficient based on the local velocity rather than a strict cross-section-averaged value. Since the same measurement position and procedure were applied to both the obstacle and no-obstacle cases, the relative comparison of flow resistance remains meaningful, although the non-uniform laminar velocity profile may affect the absolute value of K.

Fig. 5 presents the variation of the loss coefficient as a function of Reynolds number $Re = \frac{\rho_{air} v_{flow} D}{\mu_{air}}$, where μ_{air} means the air viscosity and D denotes the inner diameter of the test section. A clear distinction between laminar and turbulent regimes can be observed. In the laminar region, the values of K for the cases with and without the obstacle remain nearly identical. This indicates that, under low Reynolds number conditions, the overall flow resistance is governed primarily by viscous shear along the pipe wall rather than by form drag induced by the obstacle. In contrast, as the Reynolds number increases and the flow approaches turbulent conditions, the loss coefficient for the obstacle case becomes significantly larger than that of the unobstructed pipe. This behavior reflects the increasing contribution of flow separation, vortex shedding, and form drag around the obstacle under turbulent conditions. These results have important implications for the deposition study. Under the lowest fan frequency used in the aerosol experiments that indicate lowest

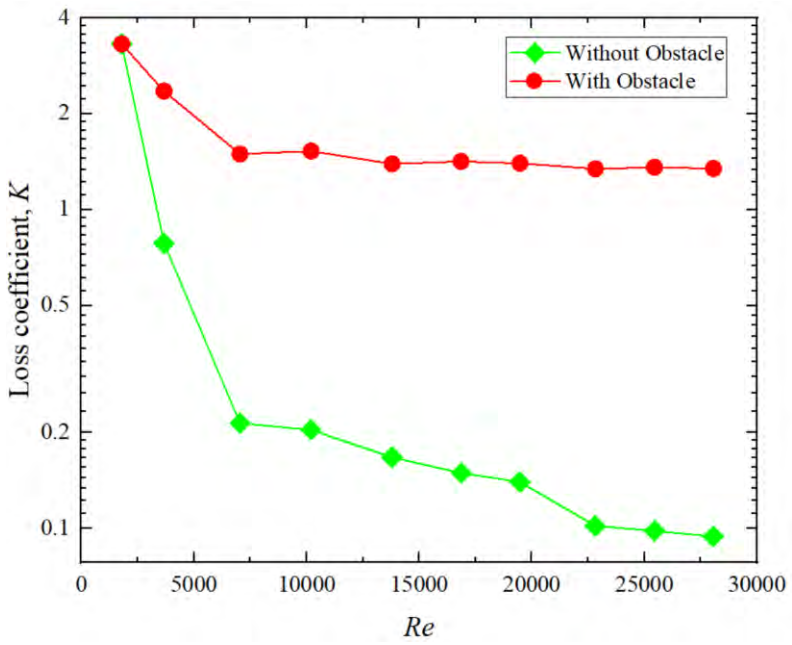

Figure 5. Variation of the loss coefficient under different Reynolds numbers.

flow velocity and lowest Reynolds number, the flow falls well within the laminar regime. Therefore, the obstacle has minimal influence on the global flow resistance but may still locally disturb the flow field, creating stagnation and recirculation regions without introducing turbulence, which is representative of the expected flow environment inside the Fukushima PCV during decommissioning operations.

3.2. Deposition mass variation

Figure 6 illustrates the evolution of aerosol deposition mass under different aerosol injection rates and deposition durations. Two clear trends can be identified. First, for a fixed deposition time, the deposited mass increases as the aerosol injection rate increases. Second, for a fixed injection rate, the deposited mass continuously increases with longer deposition time. These two tendencies suggest that surface contamination is affected by both particle supply and the evolution of surface condition during prolonged deposition, although the present gravimetric data alone cannot fully decouple these two effects. On the one hand, the influence of injection rate can be understood beyond a simple increase in particle supply. On the other hand, as demonstrated by the surface morphology observations in Figure 7, deposition initially occurs in the form of discrete particles, which gradually transform into clusters and interconnected agglomerated layers. When the injection rate is higher, this transformation takes place more rapidly. The surface therefore reaches a state characterized by significant roughness and three-dimensional particle accumulation at an earlier stage. Once such agglomerated structures are formed, the deposited layer itself acts as an efficient collector for incoming aerosols by providing numerous attachment sites and enhancing particle–particle interactions. Consequently, higher injection rates accelerate the transition of the surface into a condition that favors further particle retention. However, this effect is not expected to be pronounced at the early stage when the surface coverage is still limited. It becomes more evident after a sufficient deposited layer has formed, because the rough and agglomerated layer provides additional attachment sites for incoming aerosols.

The effect of deposition time shows a similar enhancing characteristic in Figure 6. At the shorter deposition (e.g., 6 hours), deposition is mainly controlled by the attachment of individual particles onto a relatively smooth surface. As time progresses, the continuous accumulation of particles modifies the surface morphology, increasing its effective roughness and its ability to trap additional aerosols. This explains why

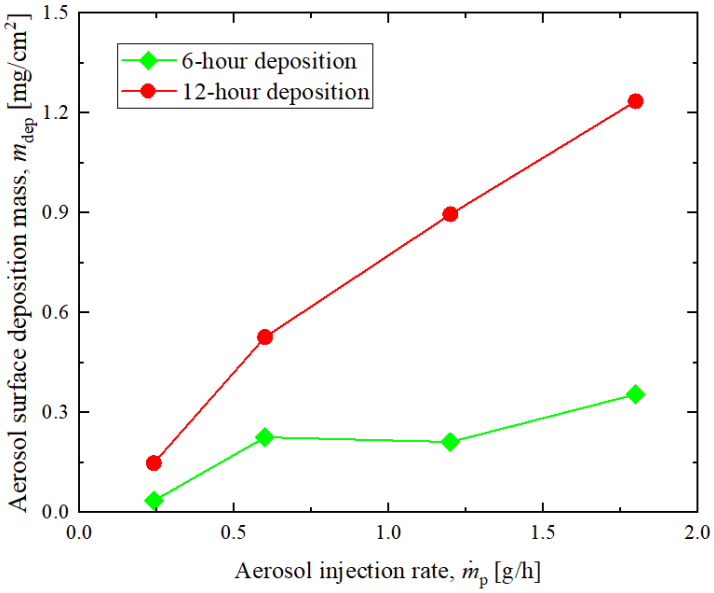

Figure 6. Variation of deposition mass with increase of aerosol injection rate.

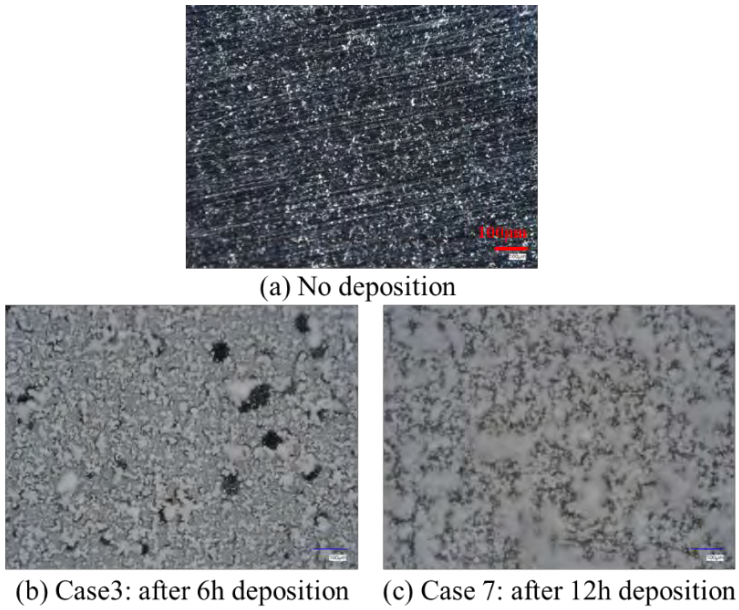

Figure 7. Aerosol deposition morphologies after different deposition times ($\dot{m}_p$=1.20 g/h).

the growth of deposited mass does not simply follow a constant rate, but becomes more evident at longer deposition times, as illuminated in Figure 6. The surface gradually evolves for receiving particles and promoting further accumulation. The combined influence of injection rate and deposition time indicates that aerosol surface deposition is strongly affected by the dynamic evolution of the deposited layer itself. A higher particle supply and longer deposition both contribute to faster development of agglomerated surface structures, which in turn enhance subsequent deposition. Therefore, the trends observed in Figure 6 reflect a progressive deposition process rather than a purely transport-limited phenomenon. In addition, a simple comparison between the 12 h and 6 h cases shown in Figure 6 further supports this interpretation. If deposition were controlled only by exposure time, the 12 h/6 h deposited-mass ratio would be expected to be approximately 2.0. The observed ratio becomes larger at higher aerosol injection rates, suggesting that the effect of prolonged exposure is strengthened when the particle supply is high. This behavior is consistent

with the formation of a rough and agglomerated deposited layer, which provides additional attachment sites for incoming aerosols.

From a practical engineering decommissioning viewpoint, these findings imply that during operations associated with high aerosol generation rates, such as debris cutting or surface decontamination, structural surfaces inside the containment environment may become rapidly contaminated if exposure is sustained. Controlling the instantaneous aerosol release rate and limiting prolonged exposure under such conditions can be effective strategies to mitigate progressive surface contamination during decommissioning activities. While it should be noted that the present measurements were limited to the top surface of the cubic obstacle. Therefore, the obtained deposition mass represents the local deposition behavior on the top-facing coupons rather than the complete spatial distribution over the whole obstacle. Since the front, side, top, and wake regions may experience different local flow conditions, face-resolved deposition measurements will be needed in future work to quantify the spatial variability around the obstacle. Furthermore, it should be noted that the present dataset is still limited to selected injection rates and deposition durations; therefore, additional intermediate data points and repeated tests will be required in future work to further confirm the quantitative trend.

4. CONCLUSION

This study experimentally investigated aerosol deposition onto a representative obstacle structure under low-velocity venting decontamination conditions relevant to the Fukushima Daiichi decommissioning scenarios. Using controlled zirconia aerosol injection in the UTAD[2] facility, the influence of aerosol generation rate and deposition duration on surface contamination behavior was systematically examined. The results demonstrate that surface deposition is not governed solely by particle supply, but strongly influenced by the dynamic evolution of the deposited layer itself. Higher aerosol injection rates and longer deposition times both accelerate the transformation of the surface from discrete particle coverage to agglomerated and interconnected structures. These morphological changes significantly enhance the surface's ability to retain subsequently arriving particles, leading to a progressive deposition process. The findings indicate that obstacle structural surfaces located within ventilation paths are particularly susceptible to rapid contamination when aerosol generation is sustained. From an engineering perspective, controlling instantaneous aerosol release rates and limiting prolonged exposure under high-generation conditions can be effective strategies to mitigate progressive surface contamination during debris retrieval and decommissioning operations. This work provides fundamental understanding and practical insight into aerosol deposition behavior under laminar venting conditions, contributing to the identification of contamination-prone regions and the optimization of decontamination and ventilation strategies inside the Fukushima Daiichi PCV.

ACKNOWLEDGMENTS

The authors acknowledge the financial support and valuable technical insights from Tokyo Electric Power Company (TEPCO) that are of great importance to the completeness of this study.

REFERENCES

1. R. Xu, S. Cheng, Y. Xu, Y. Tan, and H. Zhang, "Effect of coolant boiling induced by accumulated debris on flow-regime characteristics of debris bed formation behavior for sodium-cooled fast reactor: Experimental and modeling study with gas injection," *Progress in Nuclear Energy*, **166**, pp. 104963 (2023).
2. Z. Ahmed, R. Kumar, A.K. Sharma, R. Xu, R. Yokoyama, W. Villanueva, H. Yamano, M. Pellegrini, and K. Okamoto, "Characterization and visualization of eutectic melt in B4C powder and pellet-based/304 stainless steel composite control rods under radiative heating," *Journal of Nuclear Materials*, **617**, pp. 156120 (2025).

3. Z. Ahmed, R. Kumar, A.K. Sharma, R. Xu, R. Yokoyama, Y. Nishimura, W. Villanueva, H. Yamano, M. Pellegrini, and K. Okamoto, "Experimental and numerical analysis of boron diffusion in eutectic melt under uniform radiative heating of B4C-SS control rod composites," *International Communications in Heat and Mass Transfer*, **170**, pp. 110016 (2026).
4. R. Xu, X. Liu, and S. Cheng, "Numerical study of debris bed formation behavior for severe accident in sodium-cooled fast reactor by using least square MPS-DEM method," *Nuclear Engineering and Design*, **415**, pp. 112624 (2023).
5. R. Xu, S. Cheng, Y. Xu, Y. Tan, and H. Zhang, "Investigations on flow-regime characteristics during debris bed formation behavior in sodium-cooled fast reactor by releasing high-temperature particles," *Nuclear Engineering and Design*, **395**, pp. 111866 (2022).
6. A.K. Sharma, H. Liang, R. Xu, E. Ozdemir, S. Miwa, R. Terabayashi, S. Suzuki, M. Pellegrini, S. Hasegawa, and N. Erkan, "Radioactive aerosol control and decontamination in the decommissioning of the Fukushima Daiichi Nuclear Power Station," *Nuclear Technology*, **209**(12), pp. 2030–2043 (2023).
7. E. Ozdemir, S. Miwa, E. Porcheron, S. Suzuki, and K. Okamoto, "Aerosol deposition and dispersion during nuclear reactor decommissioning," *Nuclear Engineering and Design*, **414**, pp. 112623 (2023).
8. E. Porcheron, C. Dazon, T. Gelain, C. Chagnot, I. Doyen, C. Journeau, E. Excoffier, and D. Roulet, "Fukushima Daiichi fuel debris retrieval: results of aerosol characterization during laser cutting of non-radioactive corium simulants," *Journal of Nuclear Science and Technology*, **58**(1), pp. 87–99 (2021).
9. E. Porcheron, Y. Leblois, T. Gelain, C. Chagnot, C. Journeau, and D. Roulet, "Assessment of spray and pool scrubbing efficiencies for means of mitigation against aerosol dispersion in the context of fuel debris retrieval at Fukushima Daiichi: Part I," *Journal of Nuclear Engineering and Radiation Science*, **8**(3), pp. 031701 (2022).
10. E. Porcheron, Y. Leblois, T. Gelain, C. Chagnot, C. Journeau, and D. Roulet, "Assessment of spray and pool scrubbing efficiencies for means of mitigation against aerosol dispersion in the context of fuel debris retrieval at Fukushima Daiichi: Part II," *Journal of Nuclear Engineering and Radiation Science*, **8**(3), pp. 031702 (2022).
11. R. Xu, A.K. Sharma, R. Kumar, Z. Ahmed, R. Yokoyama, S. Miwa, S. Suzuki, and K. Okamoto, "Efficient radioactive aerosol removal with the development of water mist pre-injection methods and advanced spray charging system for safe Fukushima Daiichi decommissioning: insights from recent experimental studies in UTARTS facility," *Journal of Nuclear Science and Technology*, **62**(12), pp. 11 56–1179 (2025).
12. Q. Wang, F. Wang, C. Cai, H. Chen, F. Ji, C. Yong, and D. Liao, "Laser decontamination for radioactive contaminated metal surface: A review," *Nuclear Engineering and Technology*, **55**(1), pp. 12–24 (2023).
13. A.K. Sharma, R. Xu, Z. Ahmed, S. Miwa, B. Blaisot, S. Suzuki, H. Liang, and N. Erkan, "Scavenging of laser-generated aerosols with electrostatic-charged spray droplets," *Journal of Aerosol Science*, **174**, pp. 106254 (2023).
14. A.K. Sharma, R. Xu, Z. Ahmed, S. Miwa, S. Suzuki, and A. Kosuge, "Investigation of aerosol generation through laser cleaning of various surfaces and optimization of mist & spray scavenging," *Journal of Aerosol Science*, **177**, pp. 106329 (2024).
15. R. Xu, A.K. Sharma, E. Ozdemir, S. Miwa, and S. Suzuki, "Numerical investigation on improved spray system for efficient aerosol removal during the decommissioning of Fukushima Daiichi nuclear power plants," *Nuclear Engineering and Design*, **419**, pp. 112960 (2024).
16. A.K. Sharma, R. Xu, Z. Ahmed, R. Kumar, S. Miwa, and S. Suzuki, "Aerosol generation characteristics during laser cutting of carbon and stainless steel surfaces for nuclear power plant decommissioning," *Annals of Nuclear Energy*, **230**, pp. 112156 (2026).
17. E. Porcheron, P. Lemaitre, D. Marchand, W. Plumecocq, A. Nuboer, and J. Vendel, "Experimental and numerical approaches of aerosol removal in spray conditions for containment application," *Nuclear Engineering and Design*, **240**(2), pp. 336–343 (2010).

18. E. Porcheron, P. Lemaitre, A. Nuboer, V. Rochas, and J. Vendel, "Experimental investigation in the TOSQAN facility of heat and mass transfers in a spray for containment application," *Nuclear Engineering and Design*, **237**(15–17), pp. 1862–1871 (2007).
19. R. Xu, A.K. Sharma, E. Ozdemir, S. Miwa, S. Suzuki, and M. Pellegrini, "Investigation on aerosol spray scavenging by using a multi-hole nozzle with water mist for decommissioning of Fukushima Daiichi power plants," *Proceedings of the 30th International Conference on Nuclear Engineering (ICONE30)*, Kyoto, Japan, May 21–26, pp. 1304 (2023).
20. G. Cherrier, E. Belut, F. Gerardin, A. Tanière, and N. Rimbert, "Aerosol particles scavenging by a droplet: Microphysical modeling in the Greenfield gap," *Atmospheric Environment*, **166**, pp. 519–530 (2017).
21. H. Liang, Q. Zhou, N. Erkan, and S. Suzuki, "Improvement of aerosol spray scavenging efficiency with water mist," *Journal of Aerosol Science*, **153**, pp. 105697 (2021).
22. R. Xu, A.K. Sharma, E. Ozdemir, S. Miwa, and S. Suzuki, "Experimental investigation on effective aerosol scavenging using different spray configurations with pre-injection of water mist for Fukushima Daiichi decommissioning," *Nuclear Science and Techniques*, **35**, pp. 42 (2024).
23. R. Xu, A.K. Sharma, R. Kumar, Z. Ahmed, S. Miwa, and S. Suzuki, "Agglomeration-enhanced removal of Greenfield-gap aerosols by electrically charged water mist under varying water spray scrubbing conditions," *Separation and Purification Technology*, **397**, pp. 138103 (2026).
24. R. Xu, A.K. Sharma, S. Miwa, and S. Suzuki, "Improvement of aerosol spray scavenging efficiency by pre-injecting electrically charged water mist," *Journal of Environmental Chemical Engineering*, **12**(6), pp. 114608 (2024).
25. R. Xu, A.K. Sharma, S. Miwa, and S. Suzuki, "Development of improved spray system with effective electrical electrodes for aerosol removal: An experimental study in UTARTS facility," *Journal of Aerosol Science*, **181**, pp. 106431 (2024).
26. A. Guette, Z. Ahmed, R. Xu, A.K. Sharma, R. Kumar, R. Yokoyama, S. Miwa, S. Suzuki, and K. Okamoto, "An optimised current-controlled electrostatic charging water system for enhanced aerosol removal in Fukushima decommissioning," *Journal of Aerosol Science*, **190**, pp. 106671 (2025).
27. R. Xu, A.K. Sharma, R. Kumar, Z. Ahmed, H. Laffolley, R. Yokoyama, S. Miwa, and S. Suzuki, "Enhanced hazardous aerosol mitigation from laser-irradiated surfaces using an optimized electrically charged spray system," *Chemical Engineering Science*, **318**, pp. 122192 (2025).
28. Z. Ahmed, R. Kumar, A.K. Sharma, R. Xu, S. Miwa, K. Okamoto, and S. Suzuki, "Effect of wettability and particle size on aerosol removal efficiency in charged and neutral water spray systems," *Journal of Environmental Chemical Engineering*, **13**(2), pp. 115822 (2025).
29. R. Xu, A.K. Sharma, R. Kumar, Z. Ahmed, H. Laffolley, Y. Nishimura, S. Miwa, and S. Suzuki, "High-efficiency hazardous Greenfield gap aerosol removal in reactor decommissioning: Effect of spray configuration on performance of induction-charging spray systems," *Separation and Purification Technology*, **390**, pp. 136936 (2026).
30. R. Xu, A.K. Sharma, Z. Ahmed, R. Kumar, H. Laffolley, R. Yokoyama, S. Miwa, S. Suzuki, and A. Kosuge, "Efficient control and removal of laser-generated aerosol particles by combining water spray with pre-injection of electrical charged mist for nuclear reactor decommissioning," *Nuclear Science and Techniques*, **37**, pp. 12 (2026).
31. J. Yang, D.Y. Lee, S. Miwa, and S.-w. Chen, "Overview of filtered containment venting system in nuclear power plants in Asia," *Annals of Nuclear Energy*, **119**, pp. 87–97 (2018).
32. R. Kumar, Z. Ahmed, R. Xu, A.K. Sharma, R. Yokoyama, S. Miwa, S. Suzuki, and K. Okamoto, "Investigation of aerosol particle dispersion and removal via non-reacting gas for Fukushima Daiichi plant decommissioning," *Journal of Environmental Chemical Engineering*, **13**(4), pp. 117246 (2025).
33. E. Ozdemir, R. Xu, S. Miwa, S. Suzuki, and K. Okamoto, "Numerical and experimental approach for dust dispersion and deposition behavior for safe decommissioning activities," *Energy Sources, Part A: Recovery, Utilization, and Environmental Effects*, **46**(1), pp. 8070–8087 (2024).
34. N.A. Fuchs, R.E. Daisley, M. Fuchs, C.N. Davies, and M.E. Straumanis, "The mechanics of aerosols," *Physics Today*, **18**(4), pp. 73–73 (1965).

35. S.K. Friedlander and H.F. Johnstone, "Deposition of suspended particles from turbulent gas streams," *Industrial & Engineering Chemistry*, **49**(7), pp. 1151–1156 (1957).
36. D. Costa, J. Malet, and E. Géhin, "Dry aerosol particle deposition on indoor surfaces: Review of direct measurement techniques," *Aerosol Science and Technology*, **56**(3), pp. 261–280 (2022).
37. T.J. Heames, D.A. Williams, N.A. Johns, N.M. Chown, N.E. Bixler, A.J. Grimley, and C.J. Wheatley, *VICTORIA: A Mechanistic Model of Radionuclide Behavior in the Reactor Coolant System under Severe Accident Conditions*, Nuclear Regulatory Commission, Washington DC, USA (1990).
38. J. Ishikawa, T. Sugiyama, and Y. Maruyama, "Source term analysis considering B4C/steel interaction and oxidation during severe accidents," *Proceedings of the 25th International Conference on Nuclear Engineering (ICONE-25)*, Shanghai, China, July 2–6 (2017).
39. J. Malet, L. Alloul, N. Michielsen, D. Boulaud, and A. Renoux, "Deposition of nanosized particles in cylindrical tubes under laminar and turbulent flow conditions," *Journal of Aerosol Science*, **31**(3), pp. 335–348 (2000).
40. E. Porcheron, S. Peillon, T. Gelain, C. Chagnot, C. Journeau, and D. Roulet, "Analysis of aerosol emission and dispersion during the laser cutting of Fukushima fuel debris simulants," *Proceedings of the 26th International Conference on Nuclear Engineering (ICONE-26)*, London, UK (2018).
41. Z. Ma, T. Ma, B. Wang, D. Li, C. Su, L. Liu, P. Hu, Z. Li, L. Chen, and X. Tang, "Meso-scale numerical analysis for transport and deposition behaviors of radioactive aerosols under severe nuclear accident," *Progress in Nuclear Energy*, **150**, pp. 104314 (2022).
42. Q. Zhou, T. Saito, S. Suzuki, K. Yano, and S. Suzuki, "Microparticles with diverse sizes and morphologies from mechanical and laser cutting of fuel debris simulants and geopolymer as a covering material," *Journal of Nuclear Science and Technology*, **58**(4), pp. 461–472 (2021).
43. A. Dehbi, "A CFD model for particle dispersion in turbulent boundary layer flows," *Nuclear Engineering and Design*, **238**(3), pp. 707–715 (2008).
44. Nuclear Damage Compensation and Decommissioning Facilitation Corporation, *Technical Strategic Plan 2024 for Decommissioning of the Fukushima Daiichi Nuclear Power Station of Tokyo Electric Power Company Holdings, Inc.*, Tokyo Electric Power Company Holdings, Tokyo, Japan (2024).
45. Mitsubishi Heavy Industries Ltd., *Estimation of Gas Flow Velocity in the Fukushima Daiichi Dry Well*, Internal report in Mitsubishi Heavy Industries Ltd., Tokyo, Japan (2024).
46. A. Guha, "Transport and deposition of particles in turbulent and laminar flow," *Annual Review of Fluid Mechanics*, **40**, pp. 311–341 (2008).

東京大学 THE UNIVERSITY OF TOKYO

NPS 東京大学原子力専攻 Nuclear Professional School, The University of Tokyo

原子力国際専攻 Nuclear Engineering and Management

ERMSAR 2026

12th European review meeting on severe accident research conference

Investigation on Effect of Aerosol Generation Rates on Deposition on Obstacle Structure Surface under Venting Decontamination in the Decommissioning of Fukushima Daiichi Nuclear Power Plant after Severe Accident

Ruicong Xu, Ravinder Kumar, Zeeshan Ahmed, Yosuke Nishimura, Hanyu Wang,
Avadhesh Kumar Sharma, Ryo Yokoyama, Shuichiro Miwa, Shunichi Suzuki, Koji Okamoto

Outline

- Background
- Experimental condition
- Results and discussion
- Summary

1. Background

- **1F Primary Containment Vessel (PCV)**

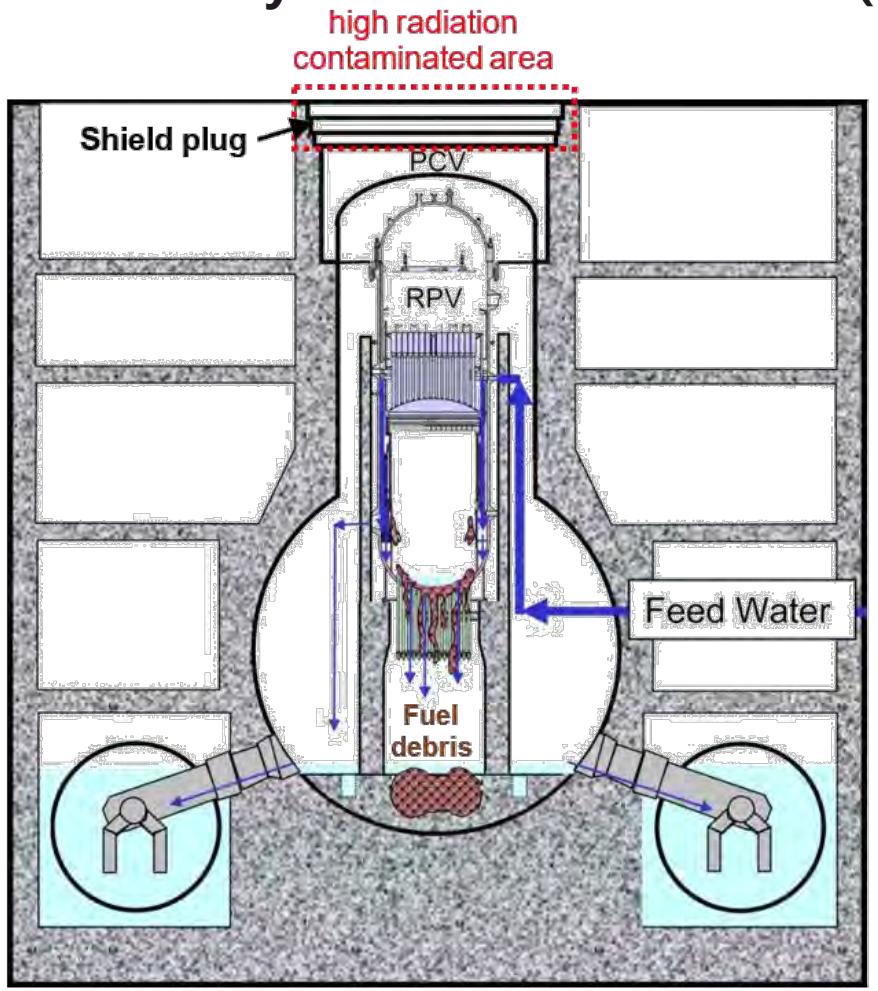

Retrieve Debris from Fukushima Daiichi NPP:
Decontaminate surface-fixed radioactive materials
(e.g., **surface cleaning**)
Cut re-solidified fuel debris into pieces for retrieval by robot
(e.g., **laser cutting, AWJ cutting**)

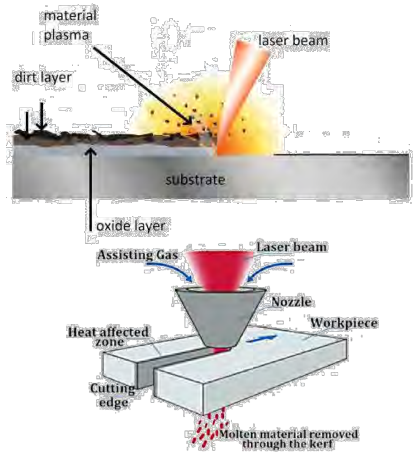

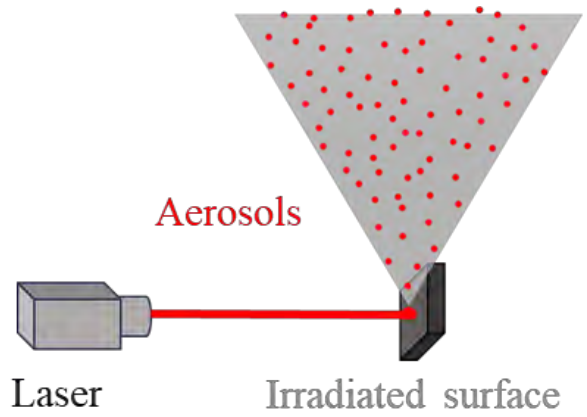

Generation of APs
APs escape through rising bubbles
APs attached on internal structures resuspend

Unknown consequences of internal
radiation exposure to workers and the public

[1] Journeau C., et al., J. Nucl. Sci. Technol., 2018 55(9):985–995
[2] Sharma A.K., et al., Nucl. Tech., 2023 DOI: 10.1080/00295450.2023.2186675
[3] Sharma A.K., et al., J. Aerosol Sci., 2023 174: 106254.

1. Background

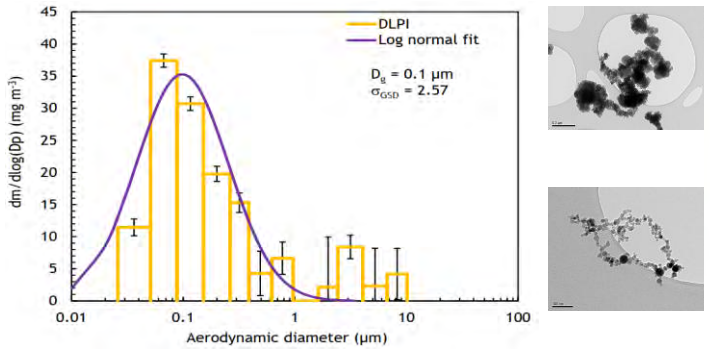

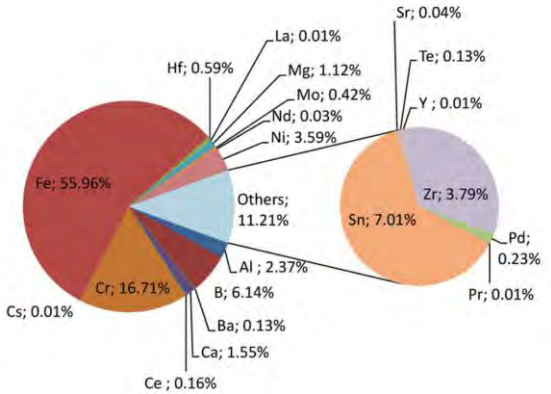

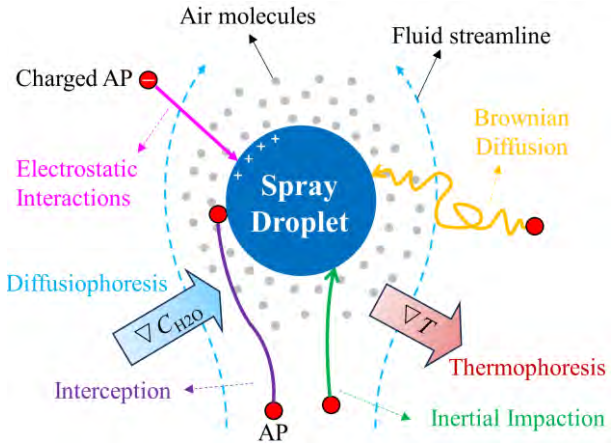

Mechanisms of aerosol removal by spray droplet

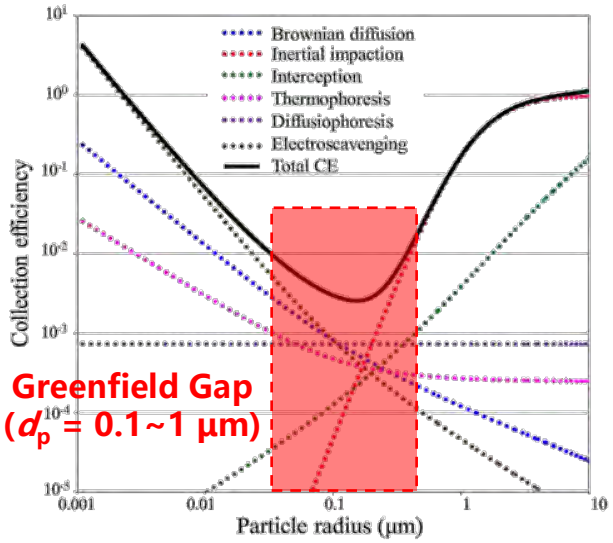

Our previous outcomes:

1. Source term analysis: Laser-Generated Aerosol Characteristics

2. Sink term enlargement: Development of Charged Spray-Mist System for Efficient Aerosol Scavenging

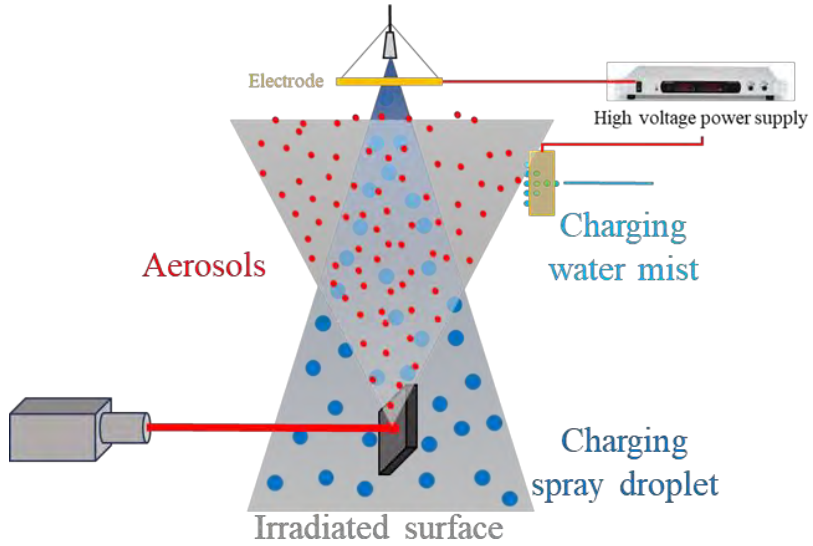

How are the aerosol dispersion & deposition behaviors?

1. Murata K.K., et al., NUREG/CR–6533, 1997
2. Ardon-Dryer et al., Atmos. Chem. Phys., 15: 9159–9171 (2015).

1. Background

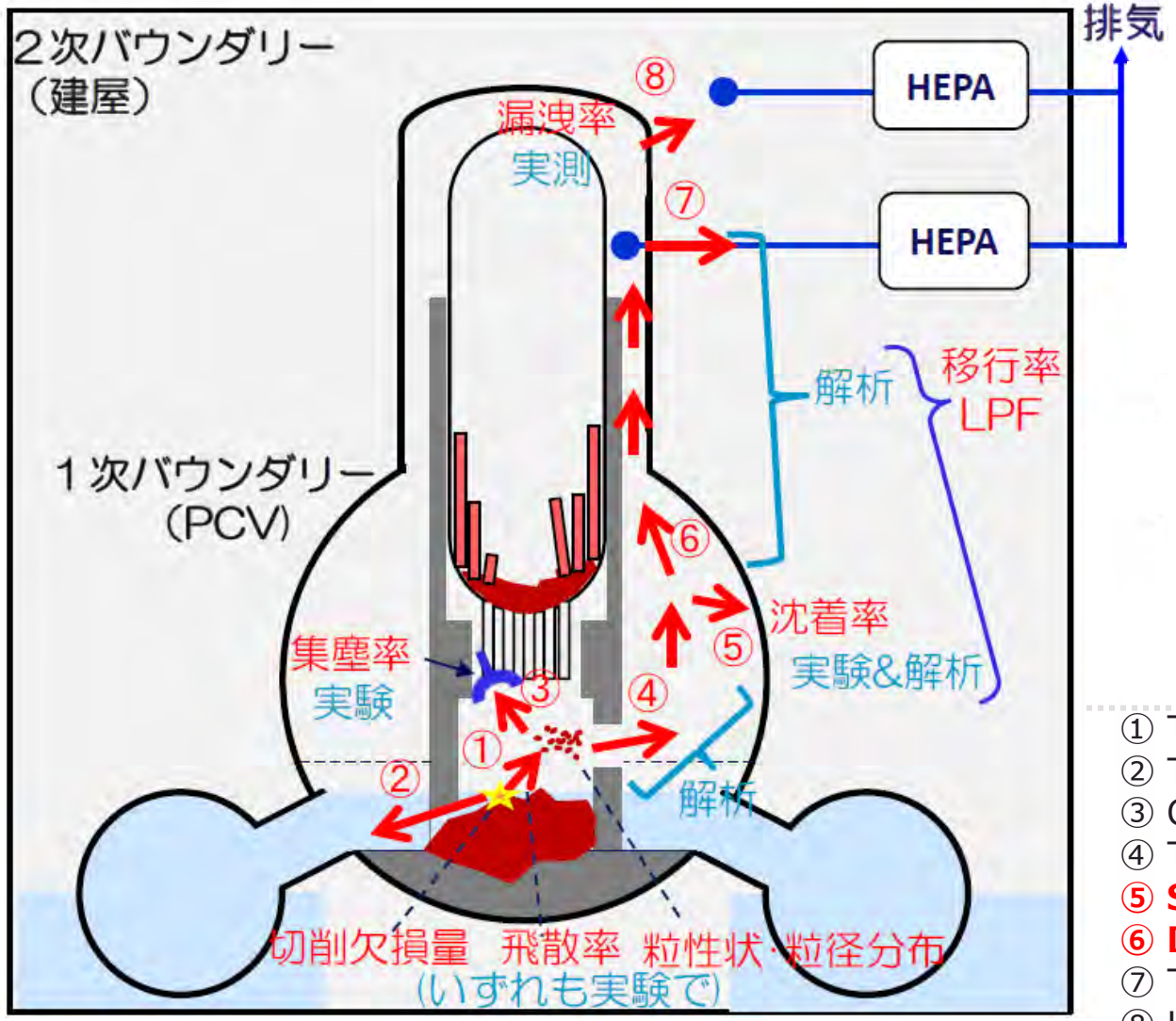

[1]電力中央研究所,安全システムの開発（ダスト飛散率データ取得）2022年度最終報告, 2023

Radioactivity Source Term (US DOE: DOE-HDBK-3010-94)

Source Term=MAR×DR×ARF×RF×LPF

- MAR (Material-at-Risk): The total quantity of radioactive material subjected to physical stress, measured in grams or curies.
- DR (Damage Ratio): The fraction of the MAR that is impacted by the accident conditions.
- ARF (Airborne Release Fraction): The proportion of radioactive material that becomes aerosolized and suspended in the air due to accident-induced stress.
- RF (Respirable Fraction): The fraction of airborne radioactive material that can be inhaled by humans.
- **LPF (Leak-Path Factor): The proportion of radioactive material that escapes after passing through various filtration or deposition mechanisms.**

① Transition of cutting aerosols to the gas phase
② Transition of cutting aerosols to the liquid phase
③ Collection by the local aerosol collection system
④ Transition from the pedestal to the PCV
⑤ Sedimentation and deposition inside the PCV/exhaust system
⑥ Dispersion & migration within the PCV
⑦ Transition to the PCV exhaust system
⑧ Leakage from the PCV to the building

1. Background

- It is considered that the PCV ventilation system flow rate will be a maximum of approximately 1000m^3/h.
- Based on rough estimation by considering the volume of gas/cross-sectional area of the drywell and the possible influence of debris decay heat and application of abrasive water jet, this may lead to approximate **0.01~0.1 m/s** gas velocity and an expected **laminar flow** inside the overall PCV.
- In laminar flows, **aerosol deposition** is governed by mechanisms such as gravitational settling, Brownian diffusion, thermophoresis and inertial impaction.
- However, **the presence of structural obstacles** and induced suction flows can introduce significant flow field perturbations, altering particle trajectories and deposition patterns in ways that are not yet well characterized.
- Understanding these effects is particularly relevant for the design of aerosol mitigation strategies inside the PCV and around debris retrieval points, where both physical obstructions and air extraction devices are routinely employed.

[1]MHI report

1. Background

Objective:

- Evaluating the LPF in 1F decommissioning by studying the aerosol deposition

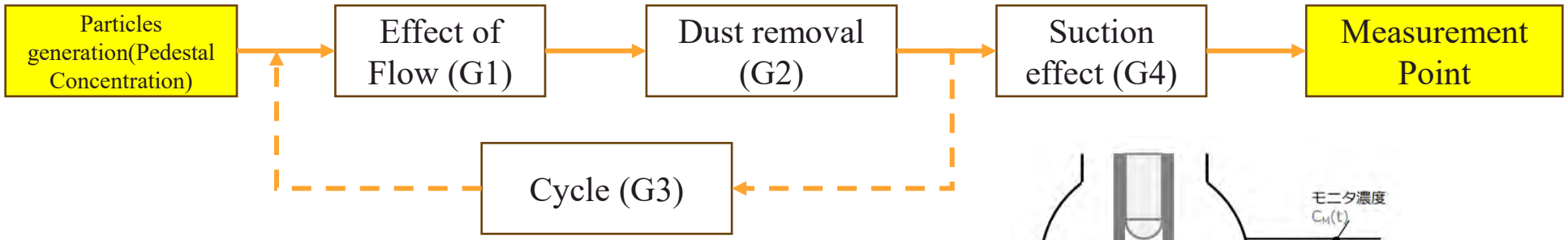

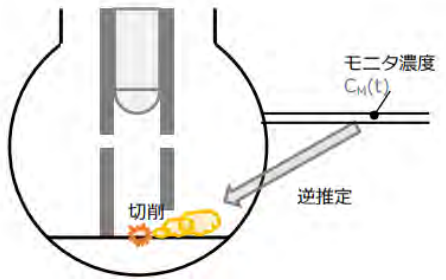

Study on the aerosol deposition behaviors

- To study flow resistance and dust adhesion behavior caused by equipment inside the PCV
- To support analysis of aerosol source & sink terms in 1F decommissioning

Outline

- Background
- Experimental condition
- Results and discussion
- Summary

2. Experimental condition

- **Experimental facility**

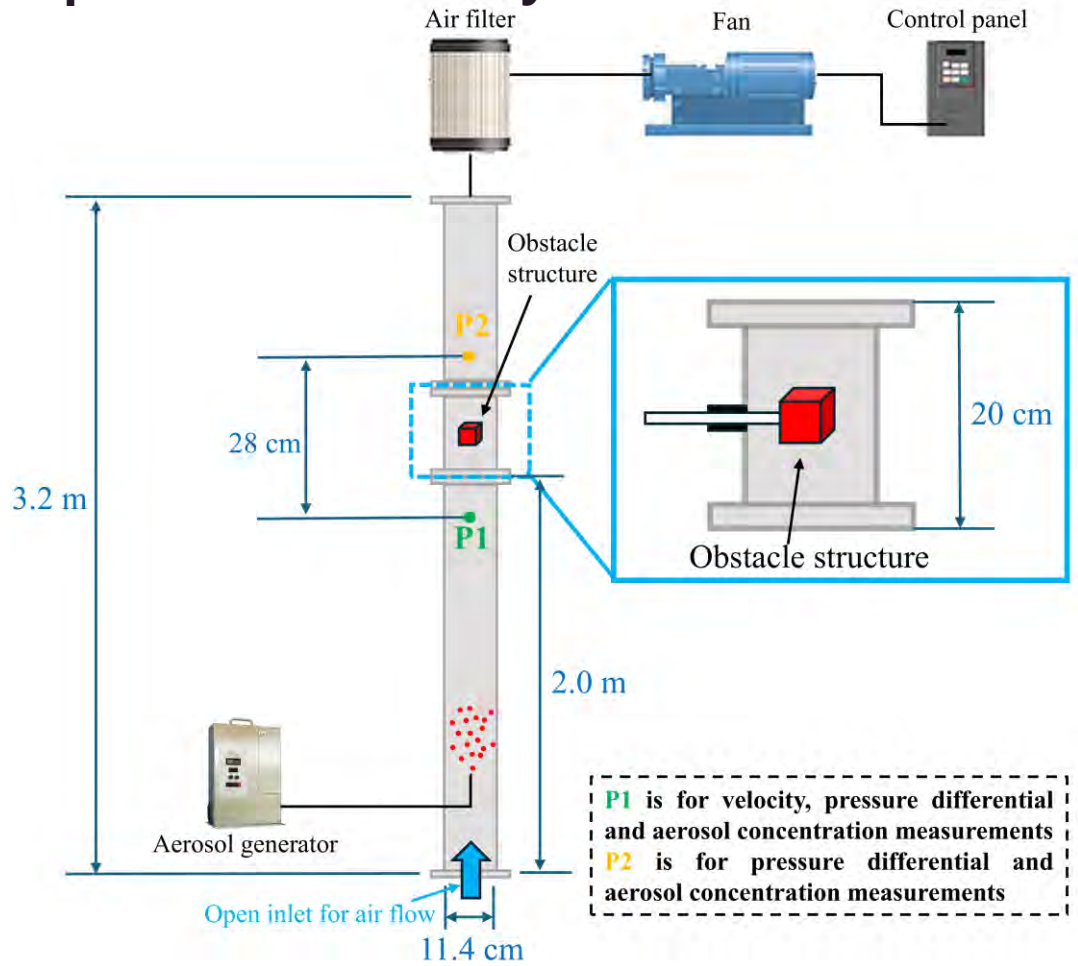

UTAD² (**A**erosol **D**ispersion & **D**eposition in a Long Pipe in The **U**niversity of **T**okyo) facility

2. Experimental condition

- **Aerosol generation**

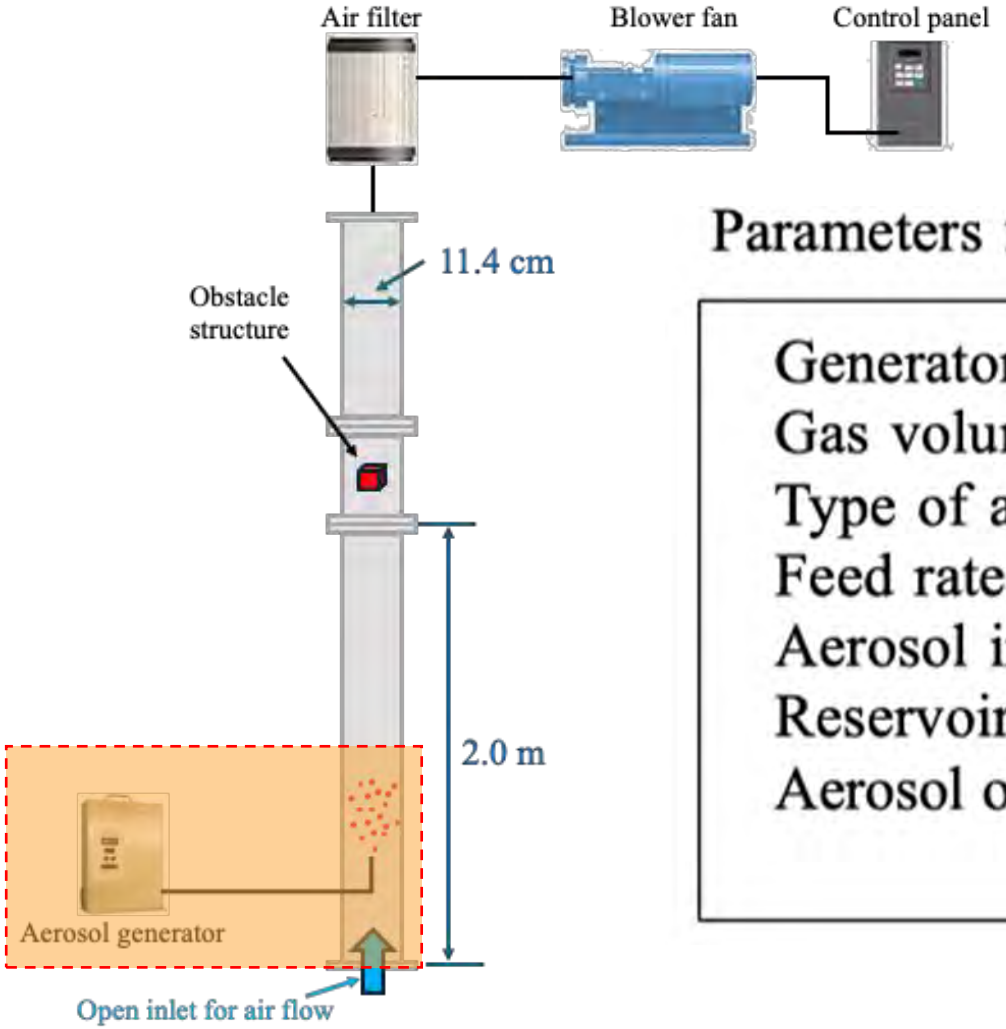

Parameters for Aerosol Injection by the RBG 1000 Generator

Generator model	RBG 1000
Gas volume flow (L/min)	27 to 28
Type of aerosol particles	ZrO_2
Feed rate (mm/h)	**2 to 15**
Aerosol injection mass rate (g/h)	**0.24 to 1.80**
Reservoir inner diameter (mm)	14
Aerosol outlet dispersion cover, Φ (mm)	$\Phi_{inside} = 3.6$; $\Phi_{outside} = 6.0$

2. Experimental condition

- **Aerosol generation**

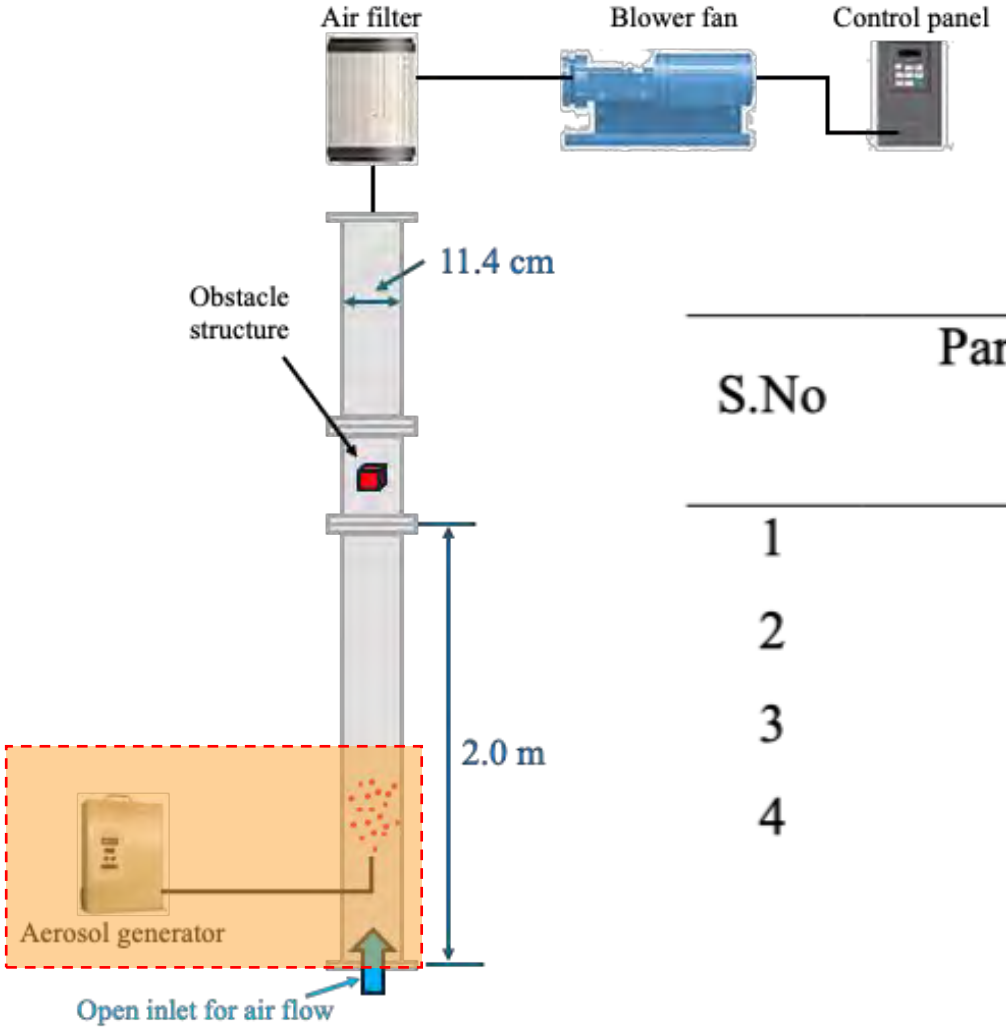

S.No	Particle feed rate (g/h)	Air velocity (m/s)	Concentration (P/cm^3)
1	0.24	0.09±0.01	45,000±2,000
2	0.60	0.09±0.01	1,20,000±5,000
3	1.20	0.09±0.01	3,50,000±10,000
4	1.80	0.09±0.01	6,20,000±7,000

2. Experimental condition

- **Aerosol generation**

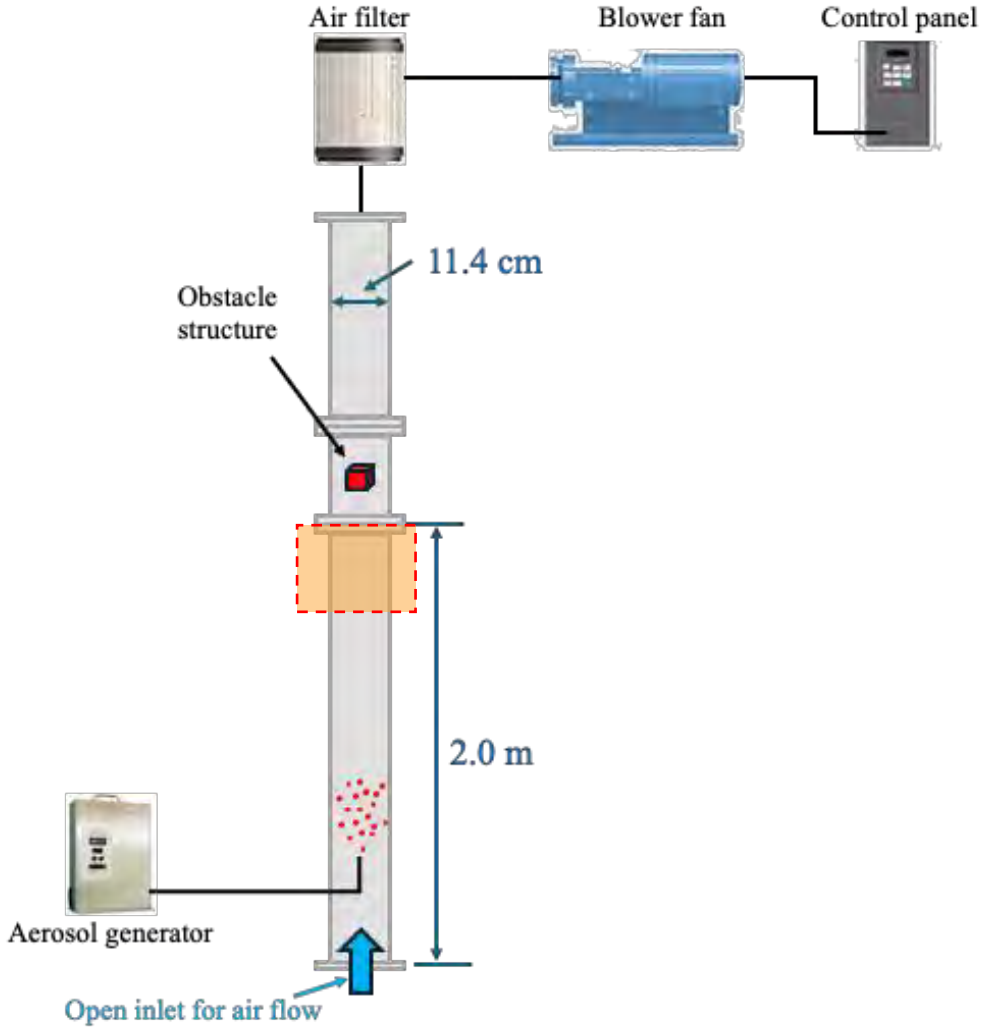

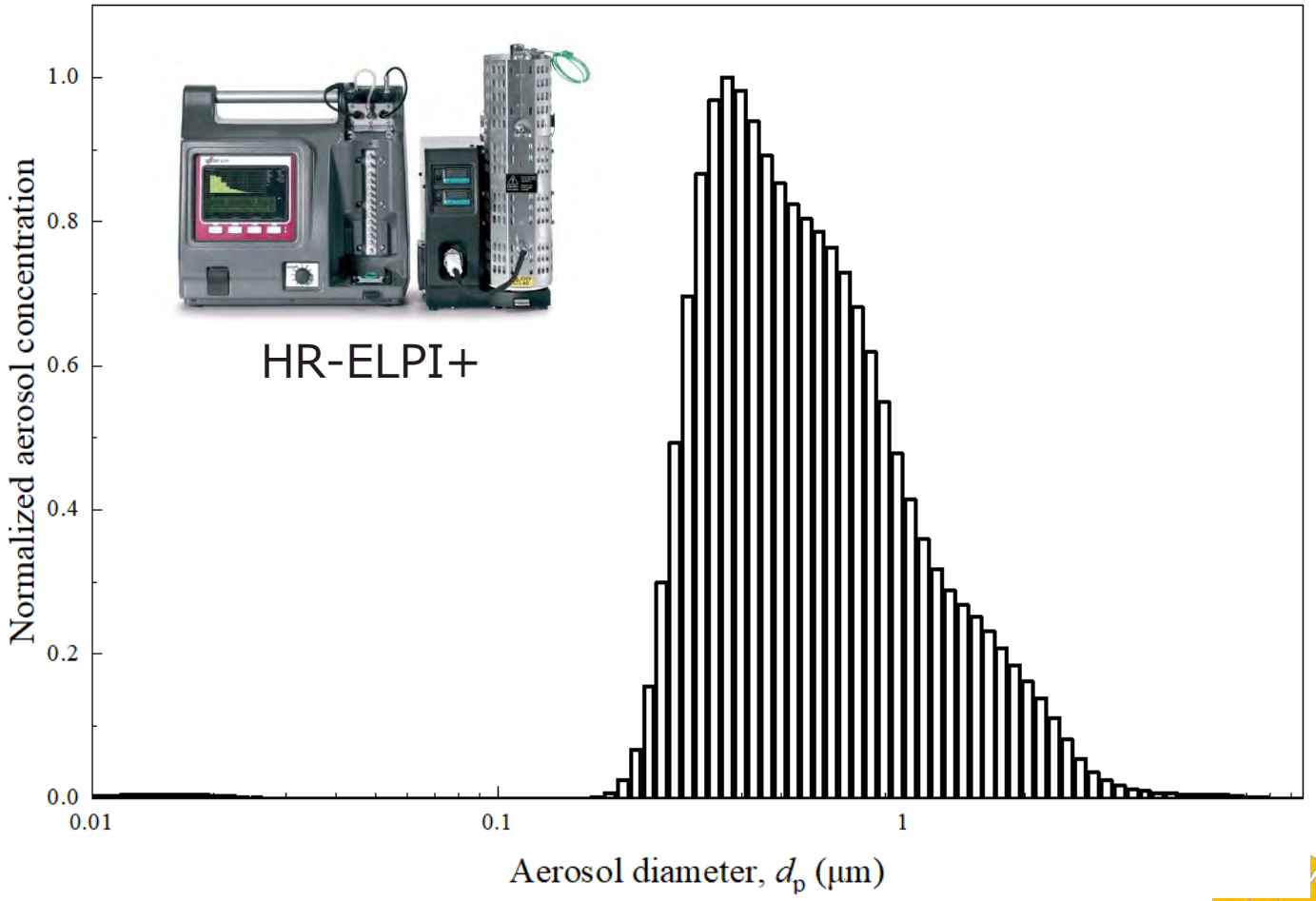

2. Experimental condition

- **Obstacle structure**

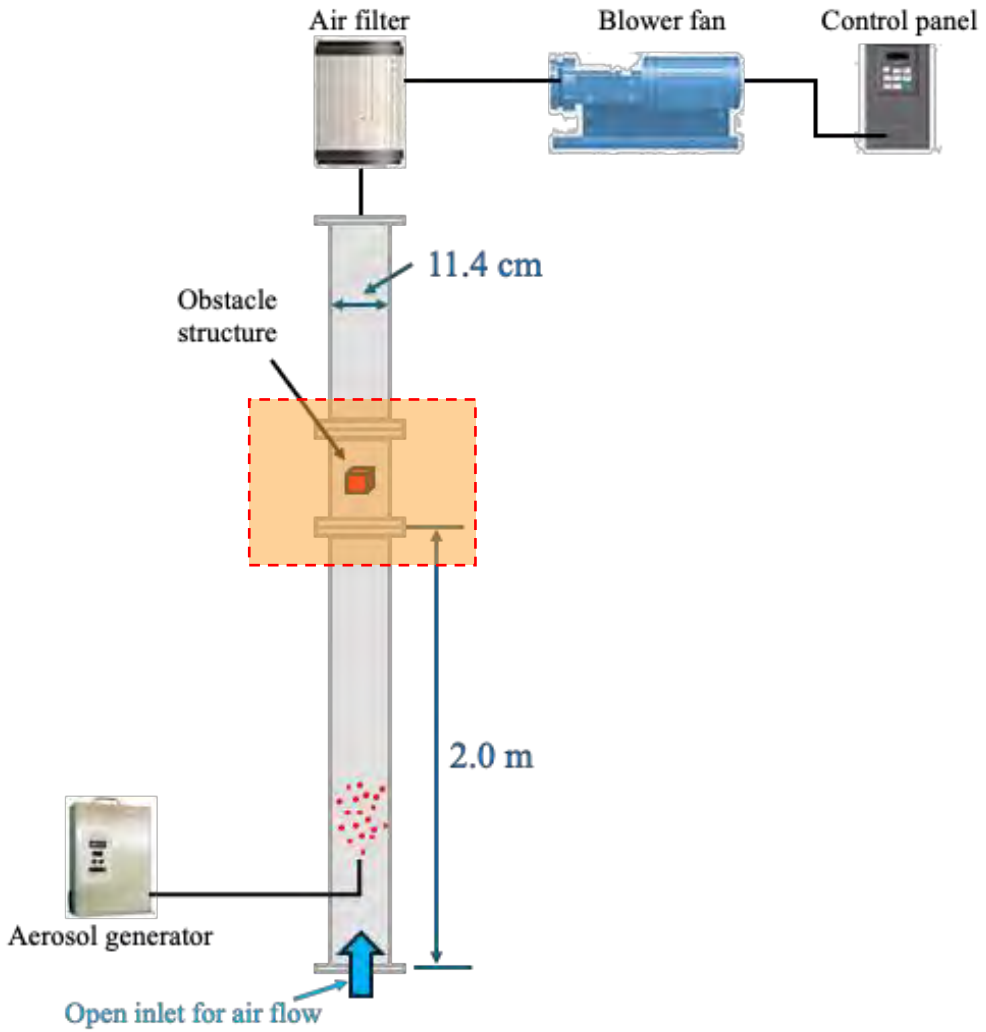

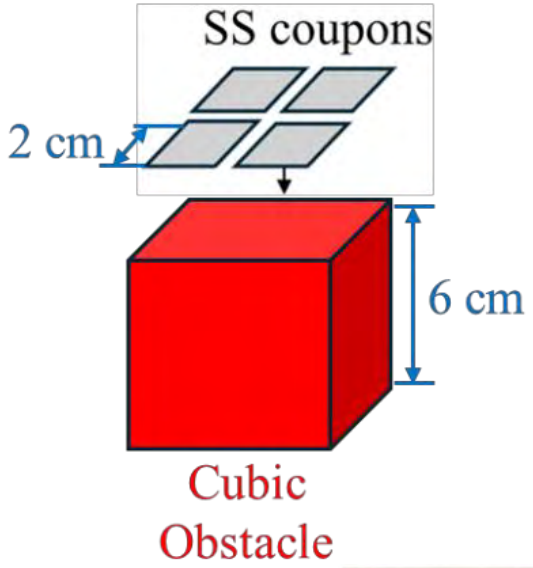

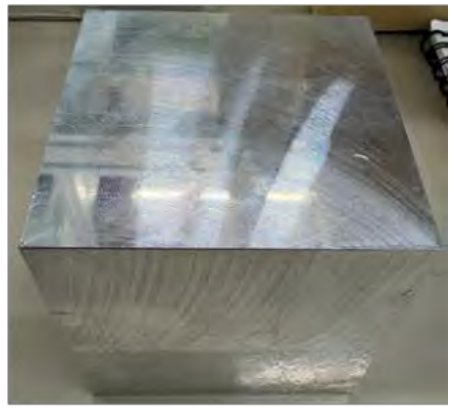

2. Experimental condition

- **Venting condition**

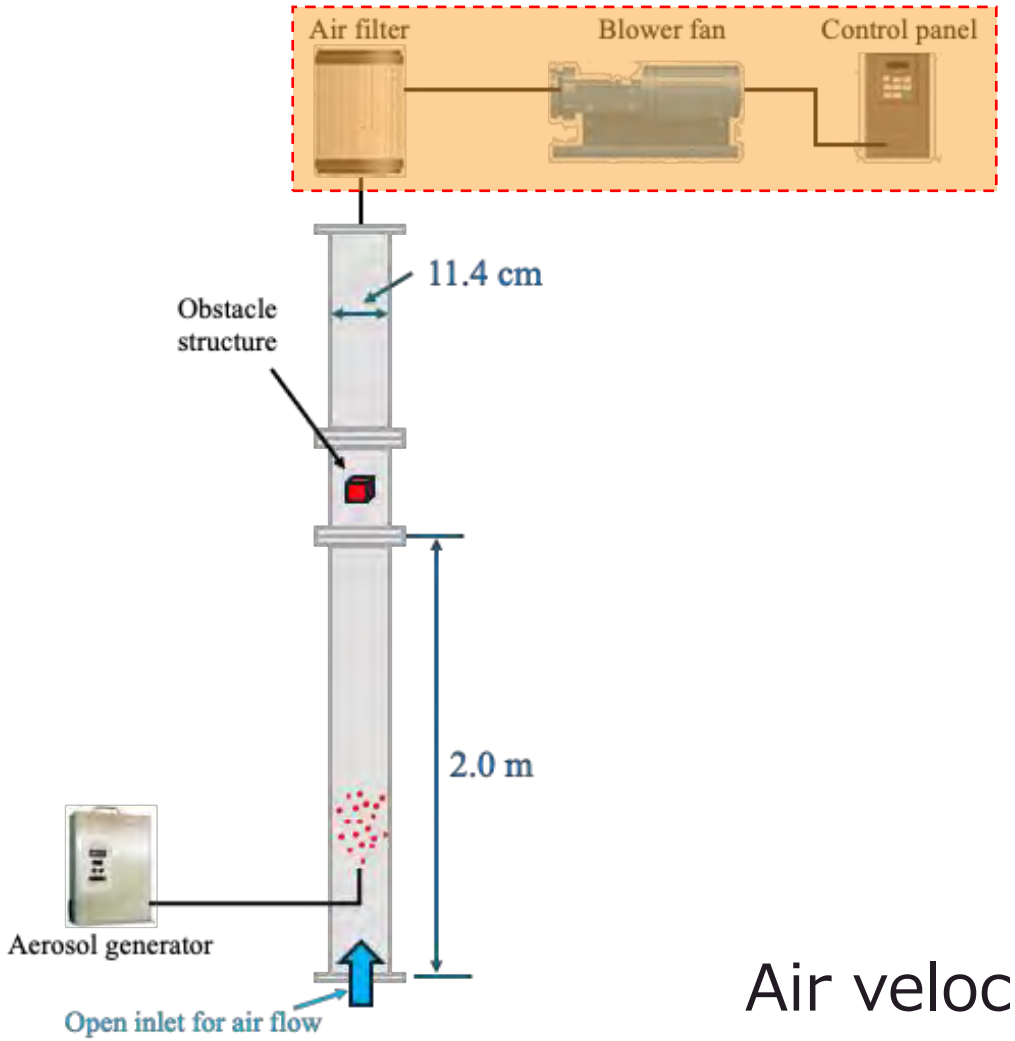

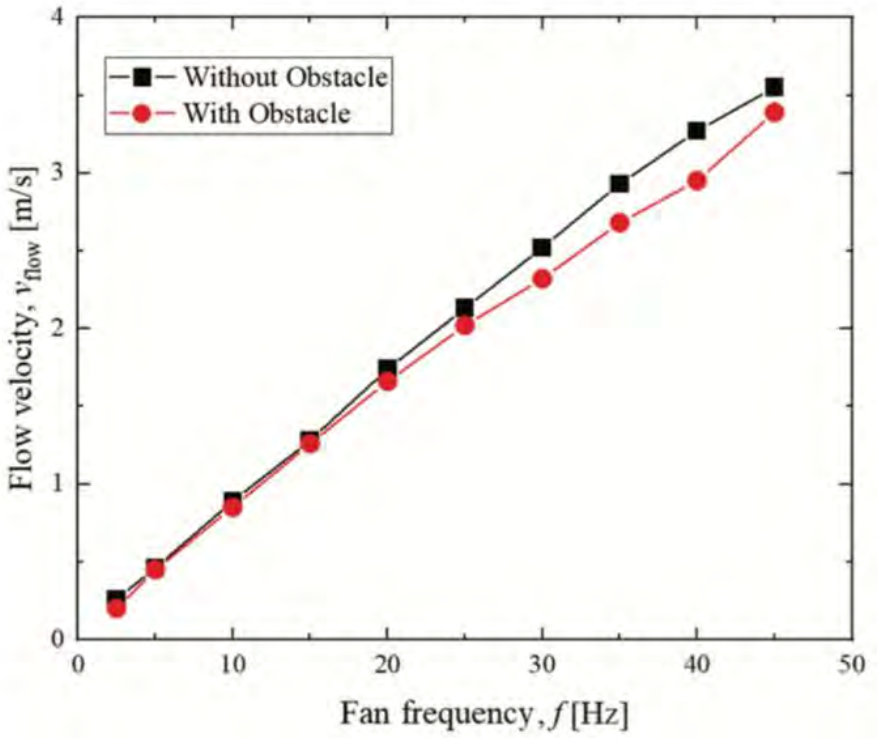

Blower frequency: **2Hz**

Air velocity inside the facility: **0.08～0.10m/s**

2. Experimental condition

- **Experimental procedure**

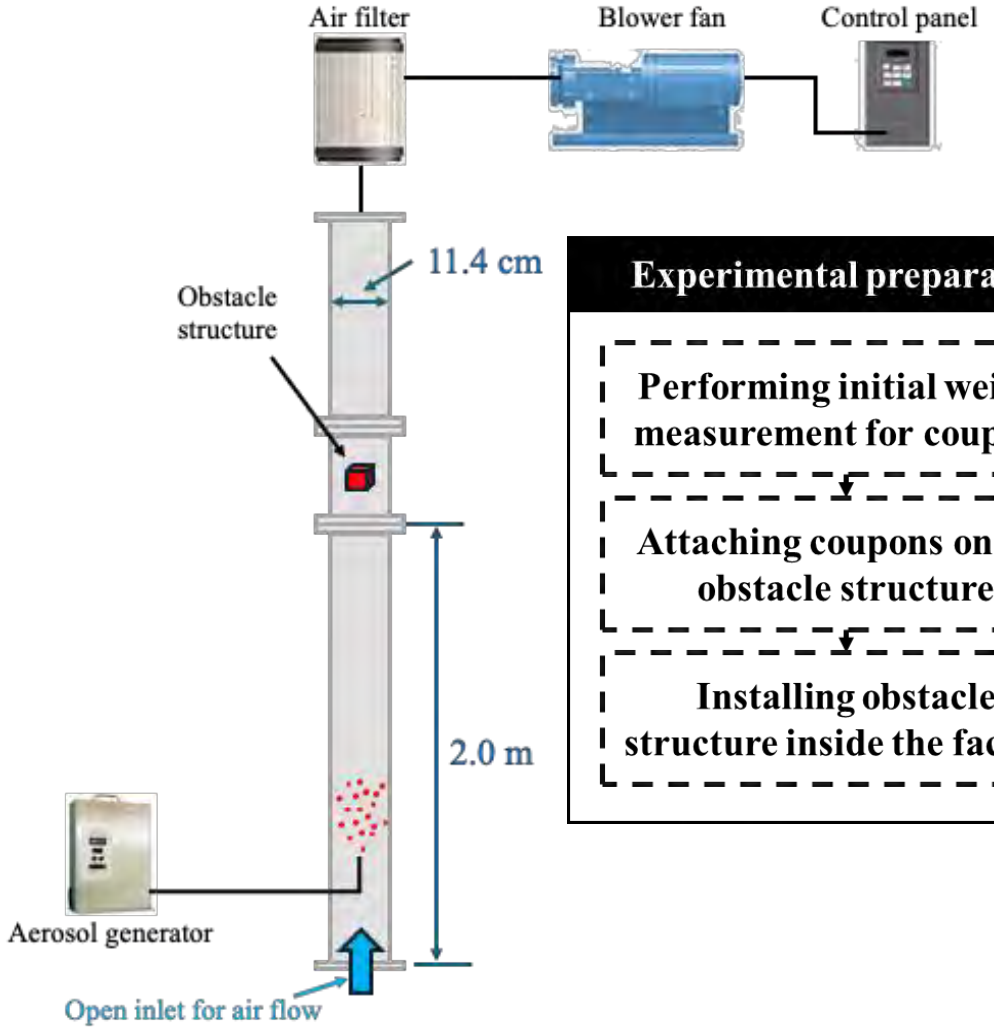

Experimental preparation

- Performing initial weight measurement for coupons
- Attaching coupons on the obstacle structure
- Installing obstacle structure inside the facility

Experimental implementation

- Injecting aerosols into the facility; Keeping air ventilation at the same time
- After a designed experimental time t_{dep}
- Taking out the obstacle

Experimental post-processing

- Performing weight measurement and surface analysis for the coupons
- Cleaning the coupons and obstacle; Starting new experimental case

2. Experimental condition

- **Experimental cases**

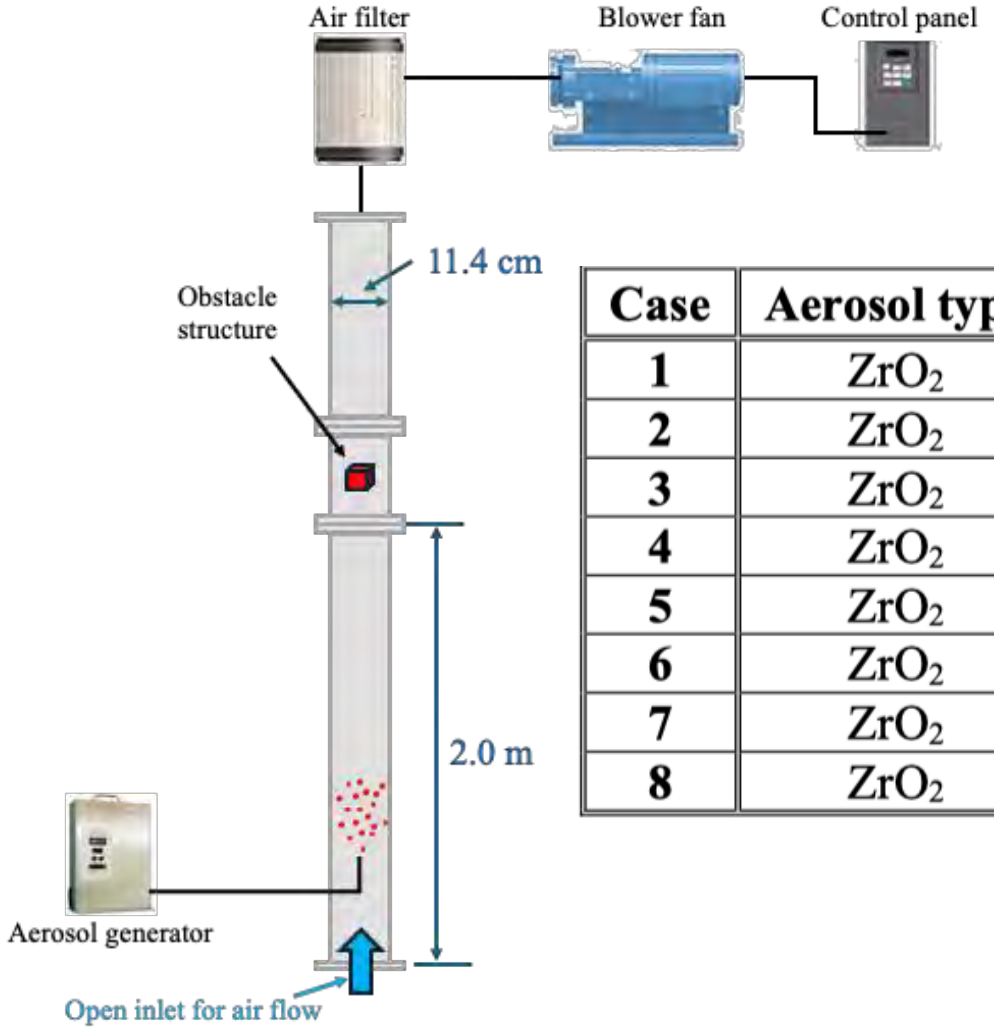

Case	Aerosol type	Deposition time, t_{dep} [h]	Aerosol injection rate, $\dot{m}_p$ [g/h]
1	ZrO_2	6	0.24
2	ZrO_2	6	0.60
3	ZrO_2	6	1.20
4	ZrO_2	6	1.80
5	ZrO_2	12	0.24
6	ZrO_2	12	0.60
7	ZrO_2	12	1.20
8	ZrO_2	12	1.80

Outline

- Background
- Experimental condition
- Results and discussion
- Summary

3. Results and discussion

- **Flow resistance evaluation for the obstacle**

Loss coefficient: $K = \frac{\Delta p}{\frac{1}{2}\rho V^2}$

- Under low Reynolds number conditions, the overall flow resistance is governed primarily by viscous shear along the pipe wall rather than by form drag induced by the obstacle.

- As the Reynolds number increases and the flow approaches turbulent conditions, the loss coefficient for the obstacle case becomes significantly larger than that of the unobstructed pipe, reflecting the increasing contribution of flow separation, vortex shedding, and form drag around the obstacle under turbulent conditions.

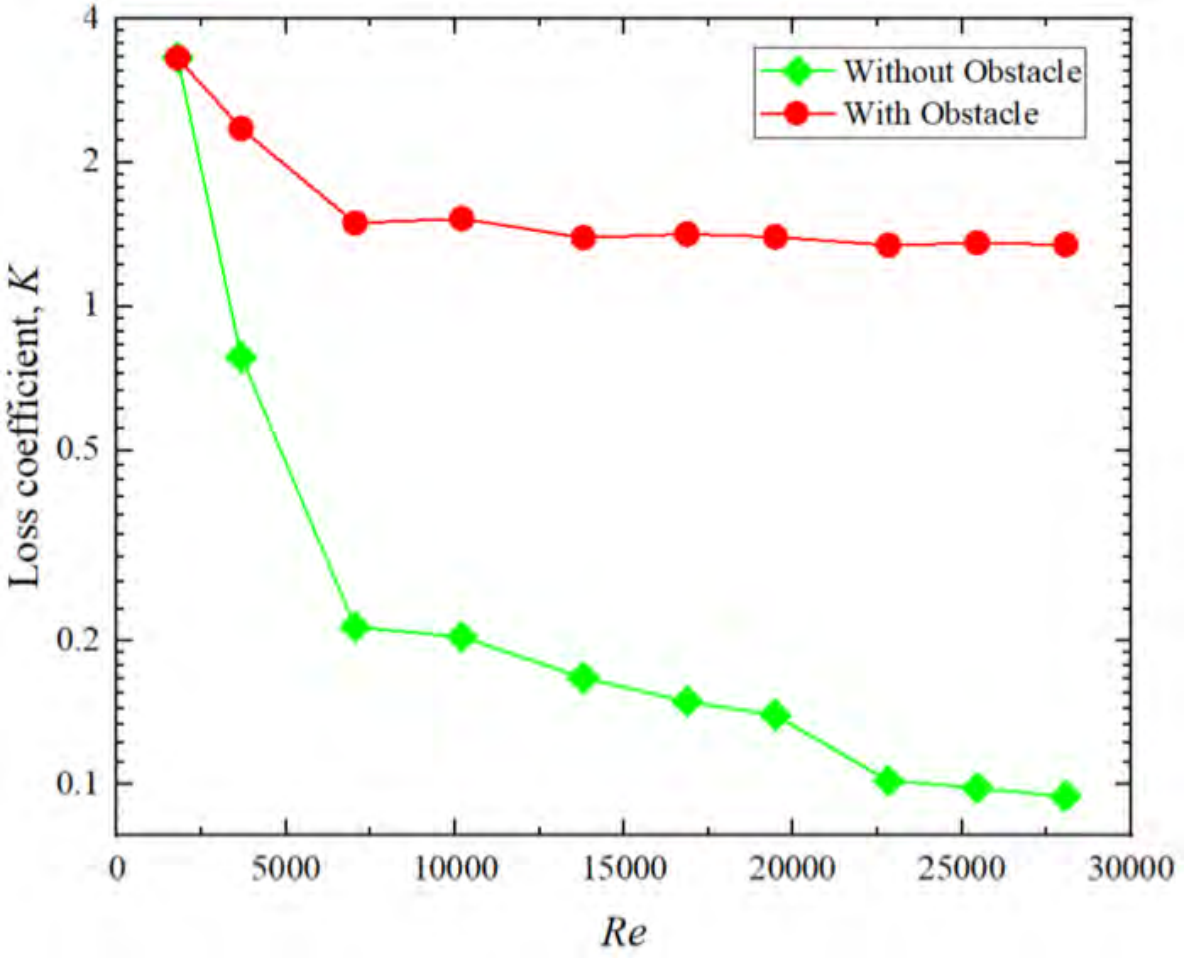

3. Results and discussion

- For a fixed deposition time, the deposited mass increases as the aerosol injection rate increases.
- For a fixed injection rate, the deposited mass continuously increases with longer deposition time.
- The mass gains from the later 6-hour deposition (↔) are generally higher than the first 6-hour deposition (↔).
- This may be caused by surface condition changes during the deposition procedures.

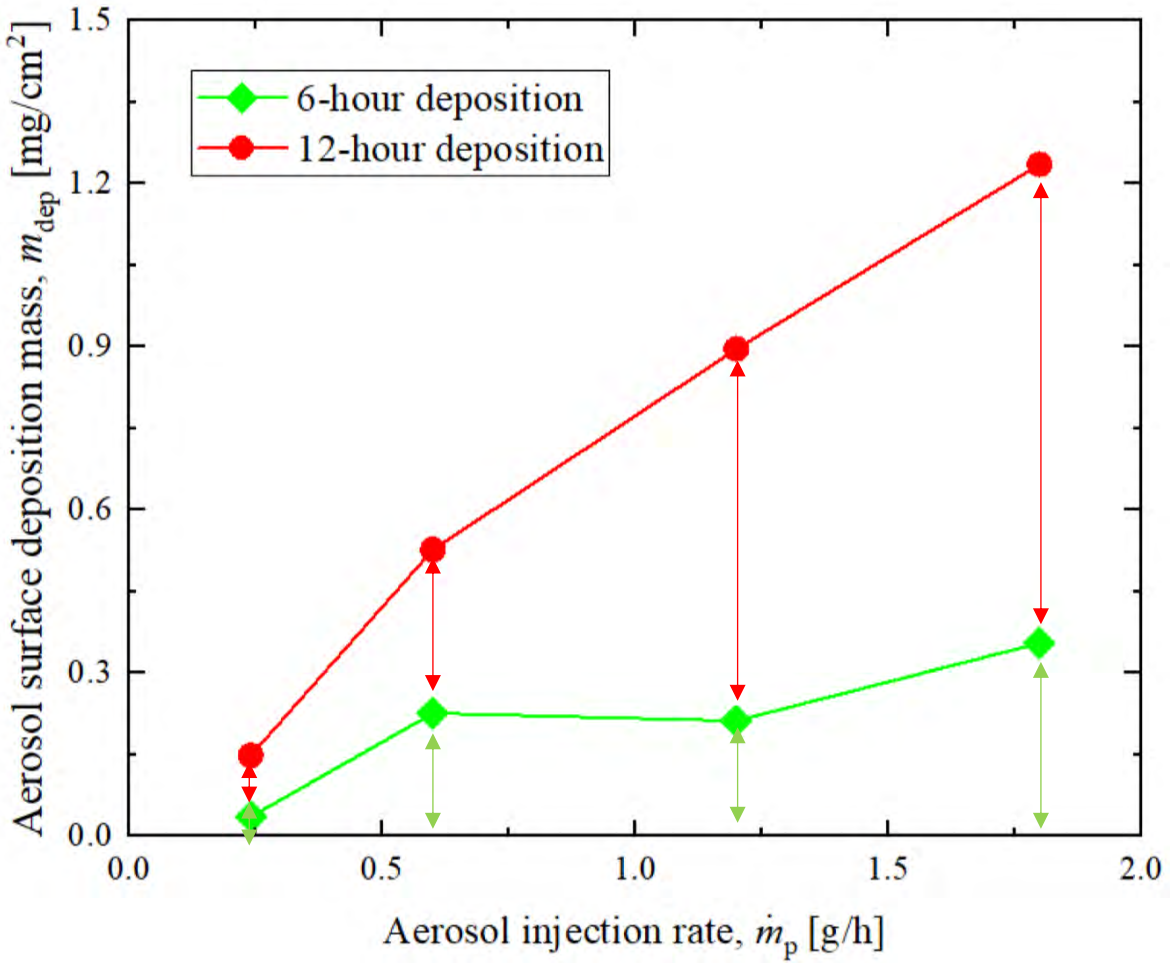

3. Results and discussion

(a) No deposition

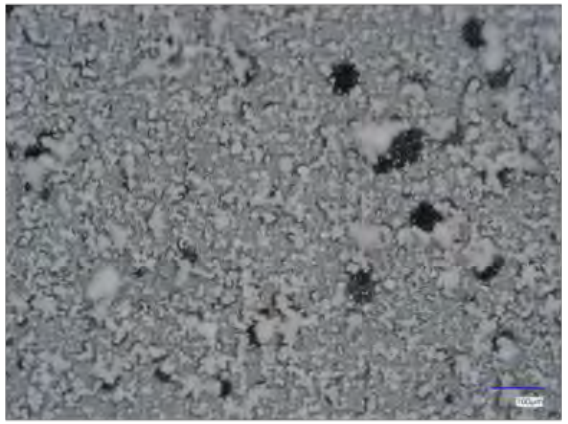

(b) Case3: after 6h deposition

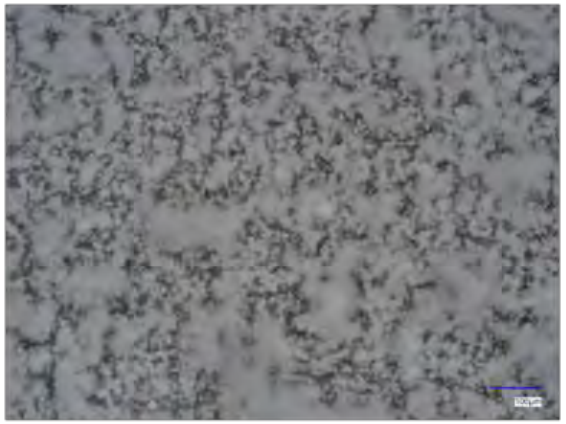

(c) Case 7: after 12h deposition

- **LIBS results show an increase in aerosol particle number density and agglomeration on both horizontal upward-facing and vertical surfaces.**

Net deposition → deposition + agglomeration

- During operations associated with high aerosol generation rates, structural surfaces inside the containment environment may become rapidly contaminated if exposure is sustained.
- Controlling the instantaneous aerosol release rate and limiting prolonged exposure under such conditions can be effective strategies to mitigate progressive surface contamination during decommissioning activities.

Outline

- Background
- Experimental condition
- Results and discussion
- Summary

4. Summary

- Investigated aerosol deposition onto a representative obstacle under low-velocity venting conditions relevant to Fukushima Daiichi decommissioning.
- Using ZrO_2 aerosol in the UTAD[2] facility, we examined how injection rate and deposition time affect surface contamination.
- Deposition is driven not only by particle supply, but also by the evolving morphology of the deposited layer itself.
- Higher injection rates and longer times shift the surface from discrete particles to agglomerated, interconnected structures, which capture incoming particles more efficiently and drive progressive deposition.
- Obstacle surfaces along ventilation paths are highly vulnerable to rapid contamination under sustained aerosol generation.
- Limiting peak release rates and prolonged exposure can effectively mitigate progressive contamination during debris retrieval and decommissioning.

Special Issue Opening for Submission

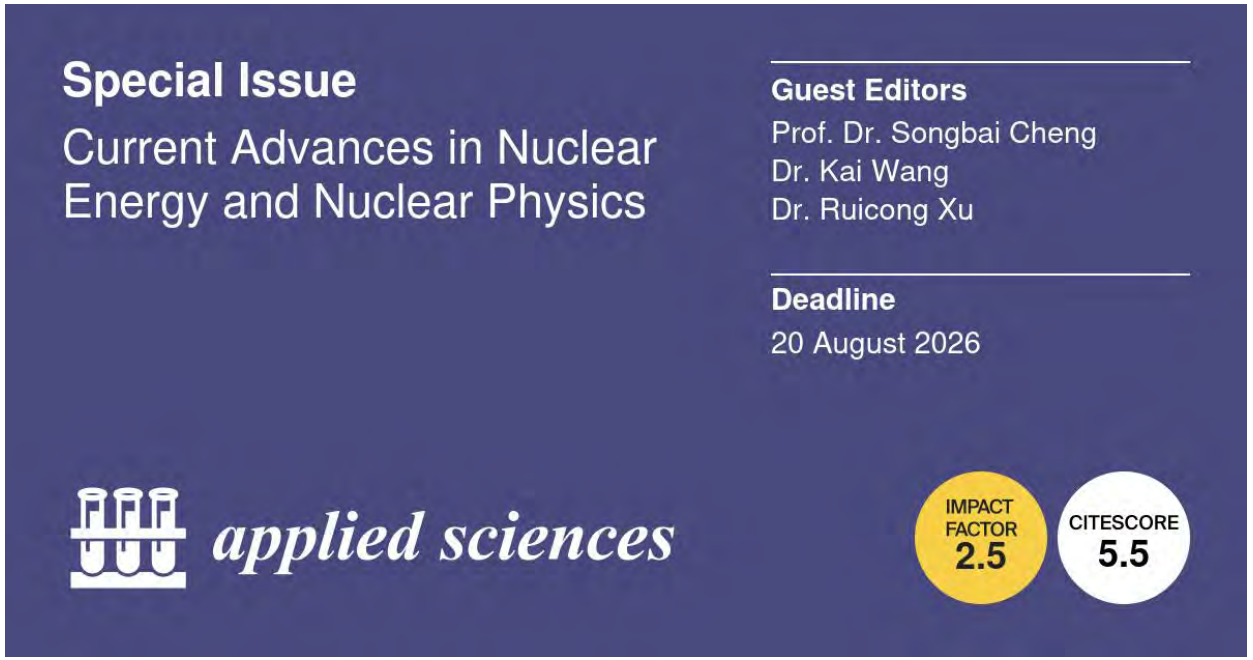

Special issues in *Materials* and *Applied Sciences* are opening for submission related to Nuclear Engineering & Energy

東京大学 THE UNIVERSITY OF TOKYO

原子力国際専攻 Nuclear Engineering and Management

NPS 東京大学原子力専攻 Nuclear Professional School, The University of Tokyo

ERMSAR 2026

Ruicong Xu, Ravinder Kumar, Zeeshan Ahmed, Yosuke Nishimura, Hanyu Wang,
Avadhesh Kumar Sharma, Ryo Yokoyama, Shuichiro Miwa, Shunichi Suzuki, Koji Okamoto

Q&A

Thank you very much for your attention.

xurc@g.ecc.u-tokyo.ac.jp

[Tokai Office]: 2-22 Shirane-shirakata, Tokai, Ibaraki, Japan

Chemistry of Chromium in the Reactor Coolant System in severe accident conditions from an ATF type core – Experiments and Modelling (ASTEC)

Joâo BOUCHAIN

Autorité de Radioprotection et de Sûreté Nucléaire (France)

Joao.bouchain@asnr.fr

AC. Grégoire, S. Souvi, J. Denis

Autorité de Sûreté Nucléaire et de Radioprotection (ASNR), PSN-RES, F-13115, Saint Paul-lez-Durance, France

anne-cecile.gregoire@asnr.fr; sidi.souvi@asnr.fr; jean.denis@asnr.fr

JF. Paul

Unité de Catalyse et de Chimie du Solide (UCCS), ModSpec, Université de Lille, 59655, Villeneuve d'Ascq

jean-francois.paul@univ-lille.fr

Following the Fukushima accident, enhancing the safety of existing nuclear facilities became essential to ensure adequate safety margins during incidental and accidental situations. Developing new accident-tolerant nuclear fuels should offer better performance during normal operation, transient conditions, and Design Basis Accident (DBA) scenarios than the current UO_2/Zr alloy. To this end, chromium-based Advanced Technical Fuel (ATF) concepts are being developed.

The most advanced concept is chromium coating of the fuel cladding which should limit hydrogen production and be beneficial for accident management. However, the impact of this type of fuel on the source term remains unknown. In case of severe accident, significant quantities of chromium could be released. The airborne chromium could then:

- i) be released in a toxic oxidation state (Cr^{VI}),
- ii) interact with other volatile fission products (Cs, I, Mo) and modify the source term.

To study these phenomena, an experimental line has been developed at ASNR[a]. This line enables $Cr_2O_{3(s)}$ to be heated to 1550°C, leading to the chromium vaporization with gaseous Mo and Cs species, in a controlled atmosphere (H_2O, O_2, N_2) to simulate primary circuit transport in severe accident conditions.

The various chromium species volatilized and redeposited are analysed by XRD, ICP-OES/MS, UV-Visible, IR and XPS. Cr^{VI} transport downstream of the bench has been observed. Some tests are ongoing to investigate experimental parameters.

The goal is to refine/validate the ASTEC (Accident Source Term Evaluation Code) simulation tool developed by ASNR, to assess potential outside releases mainly of Cs and Cr concerned by this kind of ATF fuel.

KEYWORDS: chromium, LOCA, ATF, transport, source term

1. Introduction

New concepts of advanced fuel design concepts (ATF) are currently in development phase [1]. The main purpose of these fuels is to get more robust fuel performance and economic benefits for Pressurized Water Reactor (PWR). The safety must be ensured in nominal conditions and in the case of accidental situation like Loss Of Coolant Accident (LOCA). This last situation is taken into account during the design of PWR reactors.

Various ATF-concepts are being developed to mitigate issues related to LOCA-type accidents. Three chromium containing ATF are being considered:

- Chromium coating of the fuel cladding [2-3]. The aim is to form a protective chromium oxide layer. This layer decreases the cladding oxidation by steam, thus reducing the formation of dihydrogen gas. This layer also improves the mechanical resistance of the cladding against swelling and therefore delays its rupture when the temperature rises. This concept is being studied as part of the OECD Quench ATF project.
- Incorporation of Cr_2O_3 into the fuel pellet [4-6] (ANR BENEFICIA). This method increases the size of the uranium dioxide grains. The enlargement of the grains increases the transfer time of fission products (FP) to the grain boundaries, lengthening the average travel distance. However, this approach also modifies the diffusion rate coefficient of the fission products.
- Incorporation of chromium inside the fuel cladding (Fe-Cr-Al alloys) [1].

The most advanced chromium containing ATF concept is the metal chromium coating on the fuel cladding [2-3]. This coating can decrease the kinetic of steam oxidation by two orders of magnitude in nominal or LOCA conditions [7] (Figure 1).

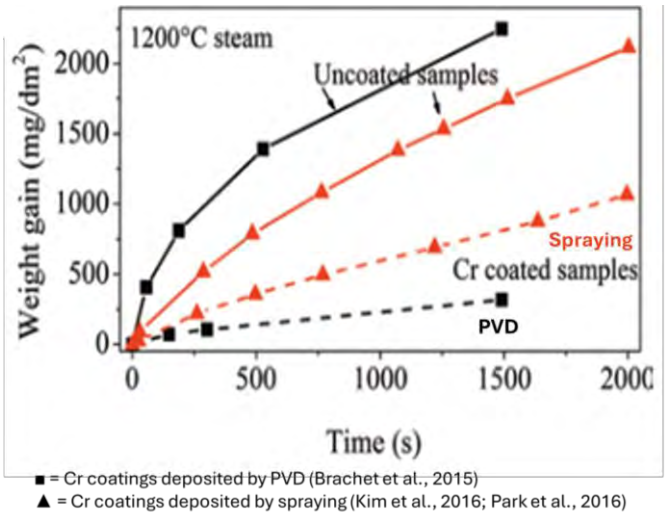

Figure 1 : Comparison of corrosion rate of uncoated and Cr-coated Zr-based alloys, fabricated by different processes (PVD and spraying), in a high-temperature steam atmosphere representative of LOCA conditions. [7]

Nevertheless, international assessments have identified significant knowledge gaps concerning the chromium behavior under severe accident conditions. The main purpose of the previously mentioned projects (BENEFICIA, Quench, FORESEEN) is to address these gaps and improve the understanding of chromium behavior. This PhD work also contributes to this objective.

The amount of chromium in an ATF core can be significant considering either the incorporation of chromium inside the pellet or as a coating. For PWR, it can represent up to several hundred kilograms of chromium [2-3; 7-8]. This large quantity of chromium can be volatilized in case of severe accident [9-10] in oxidizing conditions. Airborne chromium could then: i) be released in a toxic oxidation state (Cr^{VI}); ii) or interact with volatile fission products (Cs, I, Mo) that may also be released.

Chromium has a strong affinity for cesium (cesium chromites [11]) and molybdenum (chromium molybdates [12]). It is therefore necessary to study the behavior of chromium in interaction with these PFs under severe accident conditions to get a better assessment of potential releases. These elements are

vaporized at high temperature (≈ 1550°C) and transported in the primary circuit which has a decreasing thermal gradient (down to 150°C). The transporting atmosphere is mainly composed of steam. In such conditions, several physico-chemical processes may change species states and form. The vaporized species can then [8]: i) adsorb and condense on surfaces; ii) nucleate to form aerosols and agglomerates; iii) or remain in a gaseous state.

The transported species are referenced to the aerosols and gaseous species which could be released into the confinement vessel, or even into the environment depending on the severe accident scenario.

The goal of this study is then to get a better understanding of the transport of chromium in the primary circuit in such accidental conditions through experiments. Analyses will be carried out to identify the different species involving chromium deposited and transported. These experiments will enable the creation of an experimental database to validate the ASTEC calculation code [13]. SOPHAEROS module will be enhanced by the addition of chromium reactivity in accident situations.

The experimental procedure for chromium vaporization will be presented in the first chapter along with the analytical procedure. Modelling using SOPHAEROS will also be described in this chapter. The experimental results of chromium vaporization tests in an atmosphere mainly composed of steam will be presented in the second chapter. The third chapter will be dedicated to modelling results. A discussion based on the comparison of modeling and experiments, as well as improvements needed, will then be held. In conclusion, the different chromium reactions occurring in these accident scenarios will be summarized.

2. Materials and Methods

2.A. Experimental facility (ACCrAS)

The ACCrAS (Analysis of Chromium behavior in case of Severe Accidents) experimental bench simulates the chemical transport of chromium in a thermal gradient between 1550 and 150°C with controlled flow and atmosphere. As shown in Figure 2, the ACCrAS bench is divided into three parts:

- Main circuit: high-temperature tubular furnace capable of heating up to 1550°C. The chromium precursor ($Cr_2O_{3(s)}$) is deposited in an yttria-stabilized zirconia (Zr8Y) crucible (1 cm^2) inside of the alumina tube (ϕ = 30 mm, L = 1 m). Transport mainly takes place from the center of the furnace (1550°C) to the downstream filter (150°C). Linings (Zr8Y, ϕ = 30 mm, L = 10 cm) and coupons (Zr8Y, L = 5 cm, l = 1 cm) are used to recover the deposits.

- Upstream of the furnace: steam generation, injection of the incoming gas flow (atmosphere), and pressure monitoring.

- Downstream of the furnace: separation of the flow into different lines named “By-Pass”, “Main line” and “Kinetic line”. The main and bypass lines are designed to separate transported aerosols from the gas. The aerosols are recovered on a quartz filter, and condensable gases are recovered in acid bubblers. The kinetic line enables real-time measurements of the transported chromium (gas + aerosols).

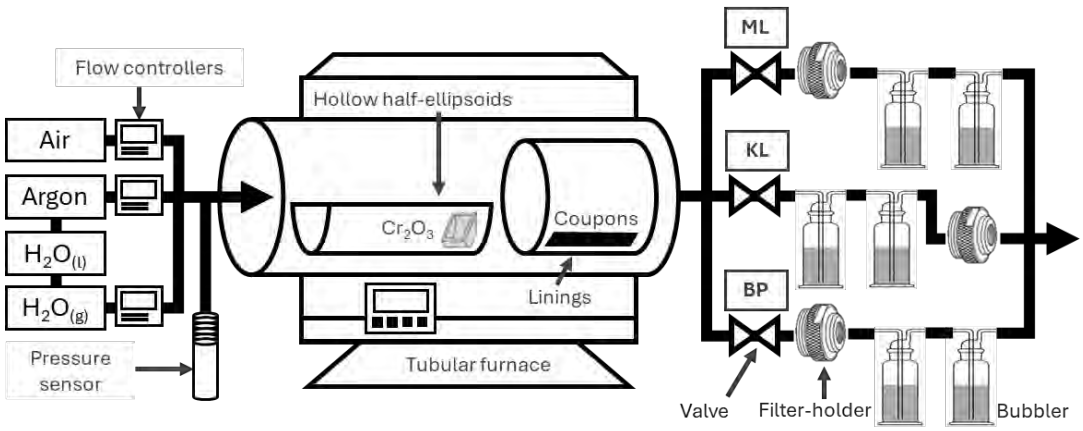

Figure 2 : Diagram of the ACCrAS experimental bench. ML = Main Line, KL = Kinetic Line, BP = By-Pass

Thermal maps (Figure 3) allow to define the collection temperature of the deposits by relating temperature and position in the ACCrAS bench. The impact of flow rate on temperature is negligible between 0.5 and 1.0 NL.min^{-1}. Downstream the vaporization zone (furnace's center), the ACCrAS bench shows a strong decreasing thermal gradient over the first 30 cm (-40°C.cm^{-1} on average).

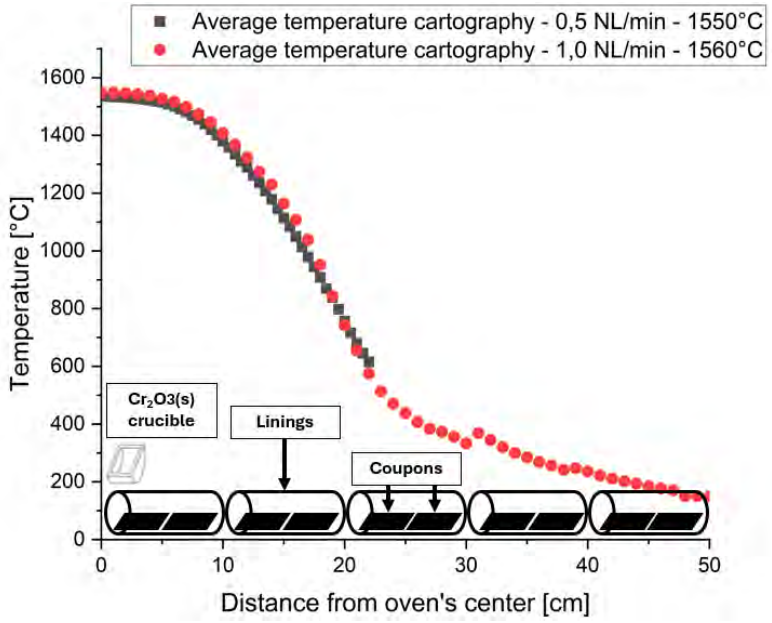

Figure 3 : Thermal maps carried out on the ACCrAS test bench taken at 1550°C for 0.5 NL.min^{-1} and 1560°C for 1.0 NL.min^{-1}. 0 cm = furnace's center, 50 cm = downstream flange.

A test consists of three distinct stages:

i) the heating ramp: the gas flow (0.1 NL.min^{-1} of argon) is directed downstream into the By-Pass line during this stage;
ii) the 4-hour temperature plateau at 1550°C: the gas flow is directed into the main line;
iii) and the cooling ramp: the gas flow (0.1 NL.min^{-1} of argon) is directed downstream into the By-Pass line.

During the temperature plateau, the gas flow is composed of 80% (v/v) water vapor and 20% (v/v) air. The experimental setup is maintained at 150°C outside the furnace using heating sleeves and coils to prevent condensation of water vapor.

A preliminary test has been conducted to determine the vaporized chromium quantity during heating and cooling ramp. Less than 6 µg of chromium were recovered into the bench. This mass is negligible compared to the one vaporized during ACCrAS tests.

Thermal maps can then discriminate a temperature area for each lining and coupon and are also useful to determine the residence time of the particles. The residence time is calculated over a distance (Δx) based on pressure (P), temperature (T), pipe volume (cross-section "S" and length "Δx"), and molar flow rate (N) according to Equation 1. For a total carrier gas flow rate of 0.5 NL.min^{-1} at atmospheric pressure: the residence time between the center of the furnace and the filter is 16 seconds.

Equation 1 : Residence time of a particle as a function of volume, pressure, temperature, volume, and flow rate.

$$Residence\ time\ (s) = \frac{P\ (Pa) \times S\ (m^2) \times\ \Delta x(m)}{R\ (J.K^{-1}.mol^{-1} \times N\ (mol.s^{-1}) \times T\ (K)}$$

2.B. Post-test analyses and characterization

Post-test analyses aim to determine the elementary distribution of chromium in the deposits, aerosols and gas, as well as the nature of the chemical species. The first step consists of performing non-destructive surface analyses on the coupons: XRD, FTIR, Raman, SEM, EDX, XPS and TOF-SIMS.

The second step is to wash every ACCrAS bench pieces (liners, cradles, filters, alumina tube, and PFA tubing) with nitric acid (0,15 M), to recover soluble chromium species, expected to be Cr^{VI} species.

It is then necessary to dissolve the refractory deposits of chromium-containing species that have formed on the coupons and linings, expected to be Cr^{III} species. The chromium (III) oxide is known to be highly resistant to dissolution [14-16]. Two dissolution procedures were specifically developed for this work.

The nitric acid solutions can be analyzed using UV-Visible spectroscopy to determine the presence of chromium (VI) which presents characteristic absorption bands at 278 and 350 nm [17]. This method is less sensitive (detection limit = 2,5 ppm) than ICP-OES. Finally, all dissolved samples can be analyzed by Inductively Coupled Plasma (ICP) techniques for the quantitative determination of chromium.

ICP-OES (Optical Emission Spectroscopy) method can quantify the chromium between 25 and 100 pbb at the 205.560 and 267.716 nm wavelengths in pure nitric matrix with an uncertainty of +/- 10% at 95% confidence level. Matrix effects related to the presence of diluted chlorine increased the uncertainty up to 40% in the worst case.

2.C. Modelling method (SOPHAEROS)

The ASTEC (Accident Source Term Evaluation Code) [13] software is developed to predict the source term in the event of an accident. The SOPHAEROS module can simulate the chemistry and transport of FPs and other elements in a primary circuit or in experimental benches. Input parameters are the chemical system (species and concentration), the geometrical description of the line (subdivided in volumes), thermal conditions, atmosphere composition and flow. The SOPHAEROS module determines the chemical speciation in each volume using predefined chemical paths (kinetically controlled).

The objective of the ACCrAS device is to provide validation data on the reactivity of chromium under accident conditions for comparison with SOPHAEROS software simulations. The ACCrAS test bench is modeled in SOPHAEROS with 36 volumes as shown in Figure 4. The temperature within each volume is assumed to be isothermal and is determined using a polynomial fit of the thermal maps shown previously. The pression is set at 1 atm in the modelling and the total flow is set at 0,4 $NL.min^{-1}$ of water and 0,1 $NL.min^{-1}$ of argon or N_2/O_2 mix (80%/20%).

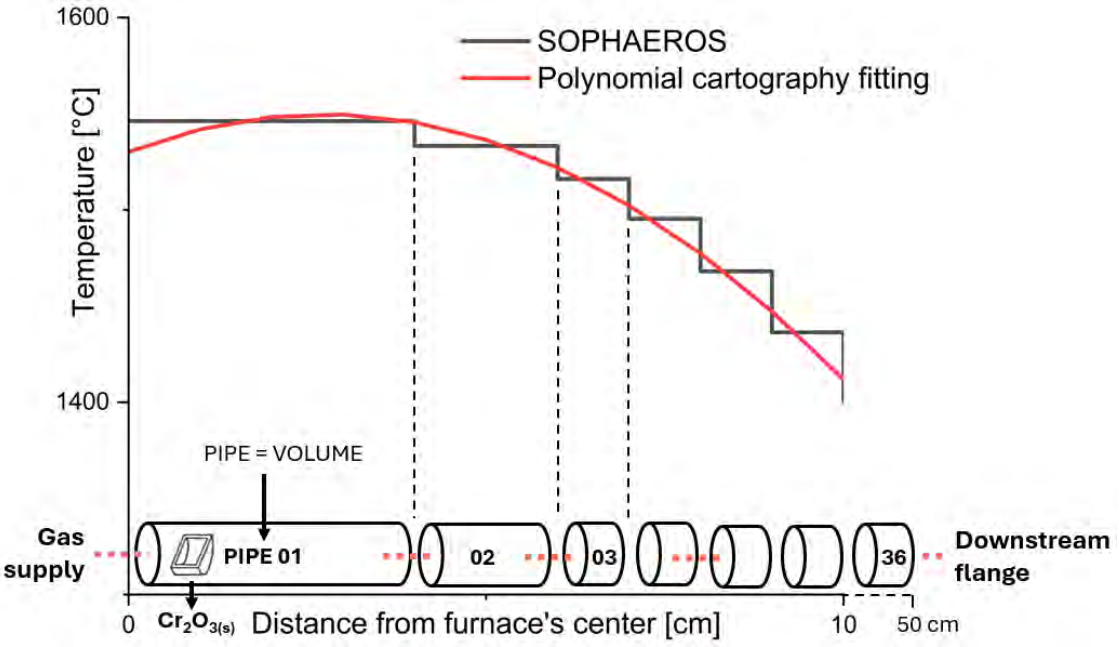

Figure 4 : Diagram showing how the SOPHAEROS module works and representing the 10 first centimeters of the ACCrAS bench in this module. The volumes represented in SOPHAEROS are isothermal and are compared with the polynomial fit of the thermal maps realized at 1 NL.min^{-1} and 1560 °C presented in Figure 3.

For each relevant species of severe accident situation, the MDB database [13] developed by ASNR provides a set of thermodynamic data (enthalpy, entropy, heat capacity, …) and physicochemical data

(particle size, density, conductivity, …). Chromium oxides and hydroxides are present in the SOPHAEROS database (MDB) but this one does not currently contain mixed species with chromium in interaction with cesium and molybdenum.

For chromium oxides, several types of chemical reactions are encoded: the volatilization/condensation reactions of Cr_2O_3(s) at different surface states, as well as chemical reactions in the gas phase. It is necessary to define the stability of the Cr_2O_3(s) surface according to its state in order to correctly formulate the condensation and vaporization reactions of Cr_2O_3(s). DFT calculations were performed [18] to determine the relative energy of the different surface states of $Cr_2O_{3(s)}$ and are summarized in Figure 5. Note that the surface area of a Cr_2O_3 unit cell is 21.23 Å^2 [18].

Termination	Stoichiometry	N[O_2]	ΔE (meV/Å^2)	
From Cr-O–Cr	Cr-O_3–Cr (*I*)	$Cr_{12}O_{18}$	0	00
	Cr-O_2–Cr (*V*)	$Cr_{12}O_{16}$	–1	202
	Cr-O_3–Cr-O_1 (*II*)	$Cr_{12}O_{20}$	1	–50
	Cr-O_3–Cr-O_2 (*III*)	$Cr_{12}O_{22}$	2	–27
	Cr-O_3–Cr-O_3 (*IV*)	$Cr_{12}O_{24}$	3	–32
	Cr-Cr-$O_{3/2}$ (*VI*)	$Cr_{12}O_{18}$	0	80
From Cr2-$O_{3/2}$	Cr-Cr *VII*)	$Cr_{12}O_{15}$	–3/2	321
	Cr-Cr-O_1 (*VIII*)	$Cr_{12}O_{17}$	–1/2	135
	Cr-Cr-O_2 (*IX*)	$Cr_{12}O_{19}$	1/2	21
	Cr-Cr-O_3 (*X*)	$Cr_{12}O_{21}$	3/2	–20

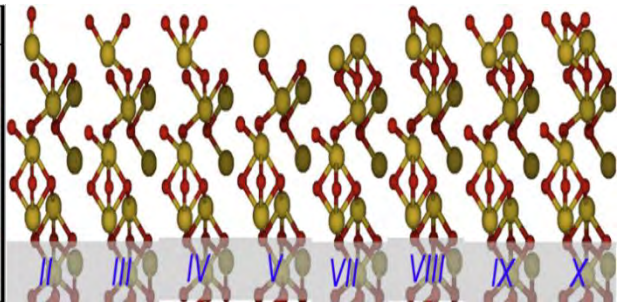

Figure 5 : Stoichiometry, energy and O_2 difference of different $Cr_2O_{3(s)}$) surfaces compared to a hexagonal lattice of surface (I) (left) and representation of the termination of these surfaces (right). Yellow : Cr, red : O. [18]

The different surface states of $Cr_2O_{3(s)}$ are labelled with roman numerals ranging from (I) to (X). The hydrogenated and hydrated surface states described in the publication of S. Souvi et Al. (2017) [18] have also been incorporated into the MDB database. It is then possible to define condensation and volatilization reactions.

The chromium condensation following the $CrO_{3(g)}$ deposit on the surface X can be schematized as in the Figure 6. This figure also represents the vaporization of $CrO_{3(g)}$ from $Cr_2O_{3(s)}$.

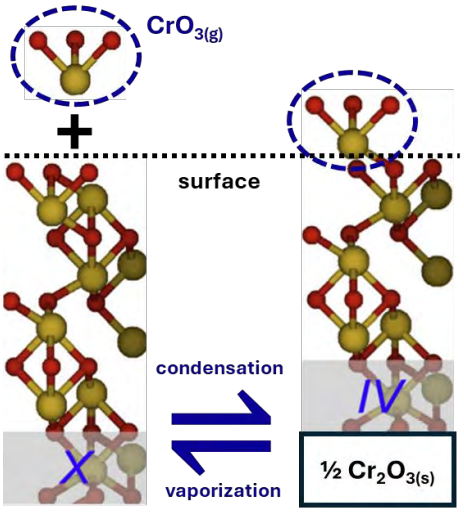

Figure 6 : Schematic representation of chromium condensation by deposition of $CrO_{3(g)}$ on mcrCrO_3 (X).

The condensation of a new layer of Cr_2O_3(s) after the deposition of CrO_3(g) as schematized previously is described following Equation 2.

Equation 2 : Condensation of chromium by deposition of $CrO_{3(g)}$ on Cr-Cr-O_3 surface, labelled X.

$$\frac{1}{2}Cr_{12}O_{21}(\mathrm{X}) + \mathrm{CrO_{3(g)}} \rightarrow \frac{1}{2}Cr_{12}O_{24}(\mathrm{IV}) + \frac{1}{2}\mathrm{Cr_2O_{3(s)}}$$

Following the previous equation and the ones described in the S. Souvi et Al. (2017) publication [18], the calculation of the free enthalpy of the reaction can then be written according to Equation 3:

Equation 3 : Free enthalpy of the chromium condensation reaction by deposition of $CrO_{3(g)}$ on surface X.

$$\Delta rG°(X \rightarrow IV, T) = \frac{1}{2} \times G°(Cr_2O_{3(s)}, T) - G°(CrO_{3(g)}, T) + 21,23\ [Å^2] \times \Delta E \left[\frac{J}{mol.Å^2}\right] + \frac{Nb(O_2)}{2} \times G°(O_{2(g)}, 0K)$$

All reactions leading to a change in the state of the $Cr_2O_{3(s)}$ surface from molecules comprising H, O, and Cr were added into the database. The surfaces "-Cr-O_3-H_x-Cr-O_y" are renamed "mcrH_xO_y" and the surfaces "-Cr-Cr-O_y-H_x" are renamed "mcrCrH_xO_y" in SOPHAEROS. Gas molecules considered in the simulation are $O_{[1-3]}$, $H_{[1-2]}$, $H_{[1-2]}O_{[1-2]}$, $Cr_{[1-2]}O_{[0-3]}$, $CrHO_{[1-3]}$, $CrH_2O_{[2-4]}$, $CrH_3O_{[3-4]}$ and $CrH_4O_{[4-5]}$.

The dimerization and decomposition reactions of atmospheric elements (O, O_2, H_2O, H_2O_2, HO_2, H) as well as the gas phase reactions of chromium-containing molecules are also taken into account. The SOPHAEROS module then allows the chemical speciation to be visualized for each moment (with a defined time step) of the simulation in the condensed, sorbed, gas, and aerosols phases.

3. Experimental results

Several chromium transport tests were carried out under various conditions in the experimental bench. The conditions that can vary include the atmosphere (water vapor, air, or argon) and the presence of cesium and molybdenum precursors. Only the tests involving the vaporization of chromium alone in air and steam will be presented (Table I) and discussed here.

Table I : Summary table of ACCrAS tests performed, objectives and specifications.

Test name	Objective	Note
ACCrAS-Cr-1	Transport test in steam and air atmosphere	Only 2h30 of steam during plateau Cracked and crumbled filter
ACCrAS-Cr-2	Kinetic of chromium transport (gas + aerosols) downstream at 150°C	No filter on the main line Bubbler not cooled
ACCrAS-Cr-3	Reproducibility test of ACCrAS-Cr-1	Only 2h30 of steam during plateau Slightly cracked filter

During these tests, 20 mg of $Cr_2O_{3(s)}$ (i.e., 263.2 µmol of Cr) are placed in a Zr8Y crucible in the center of the furnace. The chromium is vaporized under a flow of 0.4 NL.min^{-1} of $H_2O(g)$ and 0.1 NL.min^{-1} of synthetic air (80% $N_{2(g)}$ + 20% $O_{2(g)}$) during the 4-hour step period at 1550°C. Photographs of the collection coupons, filters and bubblers after these tests are shown in Figure 7.

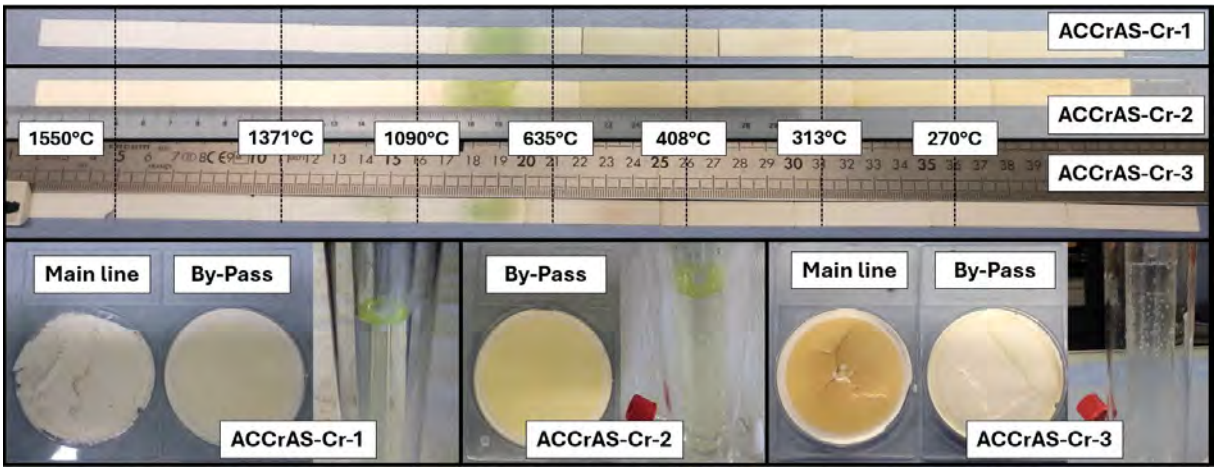

Figure 7 : Photographs of collected coupons, filters (main line and/or bypass) and bubblers (main line) from the ACCrAS-Cr-(1 to 3) tests.

A green deposit can be observed between 770°C and 1015°C on the coupons for all these tests. A second green deposit is also observable at around 1175°C only in the third test. Small brown deposits also appear at lower temperatures below 635°C. Even though the main line filter in the ACCrAS-Cr-3 test cracked

slightly, a yellowish deposit can be observed on it. Slight yellow deposits are also visible on the bypass filters in the ACCrAS-Cr-(1 and 2) tests. The main line bubblers show a yellowish coloration when the filter is crumbled (ACCrAS-Cr-1) or when there is no filter (ACCrAS-Cr-2).

Indeed, no further oxidation of the Cr_2O_3 precursor was observed after several hours under an oxidizing atmosphere (steam/air) at 1550 °C, as confirmed by XRD and IR characterization [19]. A quantitative dissolution of the remaining mass of Cr_2O_3 precursor is difficult to achieve due to grain growth. The amount of chromium vaporized is then determined by the difference in mass of the crucible containing the chromium (III) oxide before and after the test. Quantitative ICP-OES analyses were used to determine the distribution of chromium deposited throughout the experimental setup following dissolution of the deposits (Figure 8).

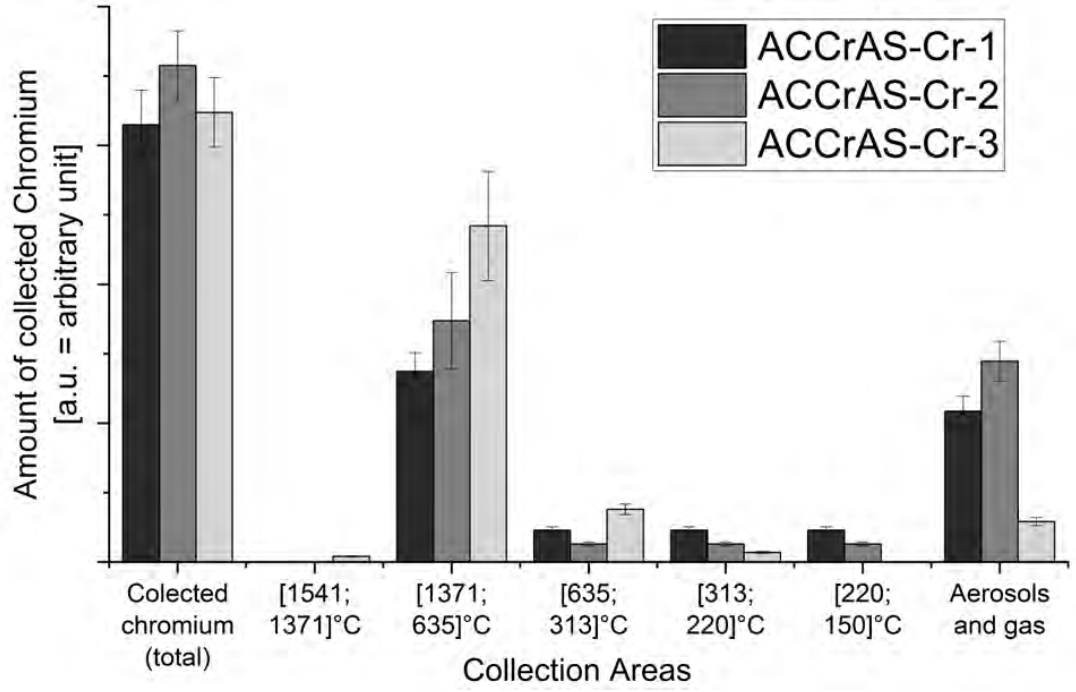

Figure 8 : Histogram showing the distribution of chromium in the ACCrAS-Cr-(1 to 3) tests. Chromium vaporization for 4 hours at 1550°C under 80% water vapor and 20% air. The y-axis shows the proportion of chromium recovered as a function of vaporized chromium amount during the test.

The fractions of chromium vaporized during these tests ranged from 15 to 20 %. The lower chromium vaporization level observed in the ACCrAS-Cr-(1 and 3) tests can be attributed to the shorter exposure to a steam-containing atmosphere during these tests. The most reliable value is that of the ACCrAS-Cr-2 test, since there were no malfunctions affecting the atmosphere during this test.

The chromium mass balance (first column in Figure 8) was calculated as the ratio between the mass of chromium collected and the mass loss of the Cr_2O_3 precursor from the crucible. The mass balance in these tests ranges from 60 to 70%, which is perfectible. Unrecovered fractions are attributed to the underestimation of the deposits with the experimental matrix in ICP-OES. Especially in the ACCrAS-Cr-3 test, despite its much more intense yellowish color, the mass of chromium measured on the filter of the main line of this test (2.4 µg Cr) is as low as that of the filter of the bypass line of the ACCrAS-Cr-2 test (2.6 µg Cr).

The amount of chromium deposited is between 60 and 65% of the mass vaporized during the ACCrAS-Cr-(1 and 2) tests. The green deposits were identified as Cr(III) species by Raman spectroscopy, XPS and XRD. The amount of chromium transported downstream of the bench therefore represents between 35 and 40% of that collected in these first two tests and are identified as Cr(VI) species.

These deposits on the filters appear to be Cr^{VI} aerosols, as they are both yellowish and highly soluble in nitric acid (0.7%). Unfortunately, the presence of Cr(VI) species could not be confirmed by UV-Visible

spectroscopy since these species appear to be unstable over time in nitric acid solution. The main hypothesis is the possible reduction of Cr^{VI} in nitric solution.

The amount of chromium dissolved in the bubblers is minor (< 10%) compared to that present on the filters in the ACCrAS-Cr-3 test. It is therefore possible to assume that chromium is mainly transported downstream of the bench as aerosols. The ACCrAS-Cr-2 test is used to determine the kinetics of chromium transported (aerosols + gas) to the downstream bubbler. In the first approach, chromium transport kinetic can be interpolated by a linear model (Figure 9) with a delay of approximately 40 minutes.

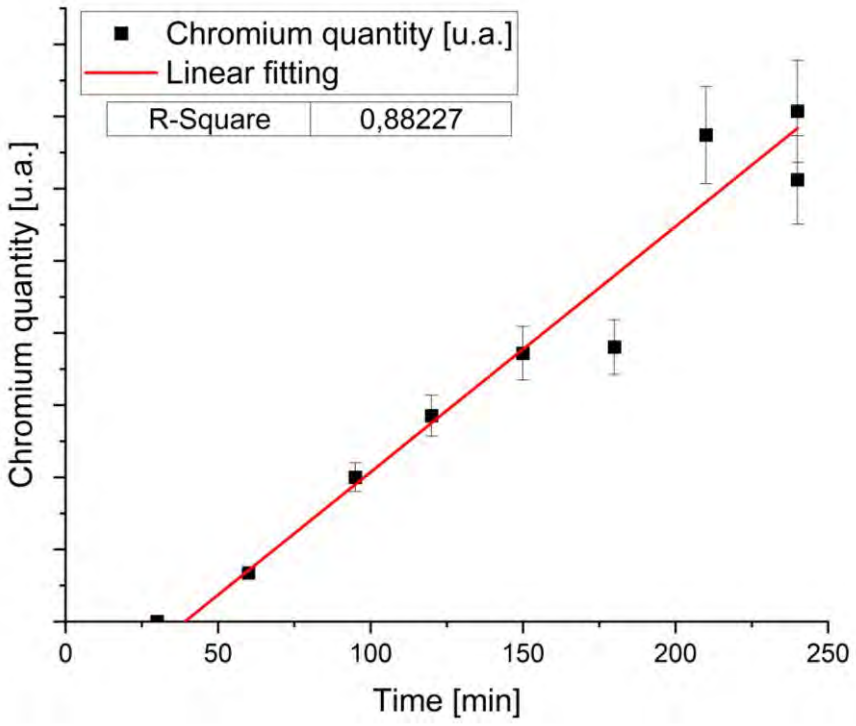

Figure 9 : Transport kinetics of chromium in terms of mass [µmol] as a function of time [minutes] from the start of the step at 1550°C during the ACCrAS-Cr-2 test.

The transport delay cannot be explained by the residence time (16 seconds) of the carrier gas down to the bubbler. Additional measurements should be performed at the early stage of chromium vaporization to enable further investigation. However, the most plausible explanation is that transport is initially limited due to preferential condensation on the bare surface but becomes more favorable in a second stage once chromium-containing sites are present.

4. Modeling results

SOPHAEROS model was used to simulate the distribution of different chromium species in gaseous, condensed, and sorbed phases in the ACCrAS experimental bench. It is then possible to compare the simulation results with the experimental tests based on the following information: i) the mass of vaporized chromium (III) oxide; ii) the mass distribution and speciation of deposited chromium as a function of temperature; iii) the quantity and oxidation state of chromium transported in aerosol form trapped on the filter; iv) As well as the amount and oxidation state of gaseous chromium transported and solubilized in the bubbler.

The input parameters of the experiment described in the code are as follows: 4-hour step at 1550°C with $Q(O_2)$ = 0.02 $NL.min^{-1}$, $Q(N_2)$ = 0.08 $NL.min^{-1}$ and $Q(H_2O)$ = 20 $g.h^{-1}$ under a pressure of 1 atm with initially 20 mg of $Cr_2O_{3(s)}$. To enable comparison between SOPHAEROS outputs and the experimental results, the powder specific surface area was adjusted in the simulation. The experimentally measured mass of vaporized chromium was then used as a reference.

The gaseous chromium simulation shows that $Cr^{III}_2O_{3(s)}$ vaporizes mainly into $Cr^{VI}O_{3(g)}$ and in a less extent $Cr^{IV}O_{2(g)}$, which quickly reach kinetic equilibrium with $Cr^{V}HO_3(g)$. From t = 5 seconds, and at around 770°C (20 cm), the formation of $Cr^{VI}H_2O_{4(g)}$ is calculated coming mainly from $Cr^{VI}O_{3(g)}$ as well as the formation of $Cr^{III}H_3O_{3(g)}$ from $Cr^{V}HO_{3(g)}$. A steady state appears to be reached as early as t = 75 seconds. Simulations (Figure 10) predict the deposition of $Cr^{III}_2O_{3(s)}$ at high temperatures between 875 and 1395°C (10.4 and 18.8 cm). This $Cr^{III}_2O_{3(s)}$ deposit represents 7% of the vaporized chromium. The chromium is transported downstream of the circuit mainly in the form of $Cr^{VI}H_2O_4(g)$ and $Cr^{III}H_3O_3(g)$ in low fraction. Adsorption (sorbed phase) of chromium at low temperature is also simulated.

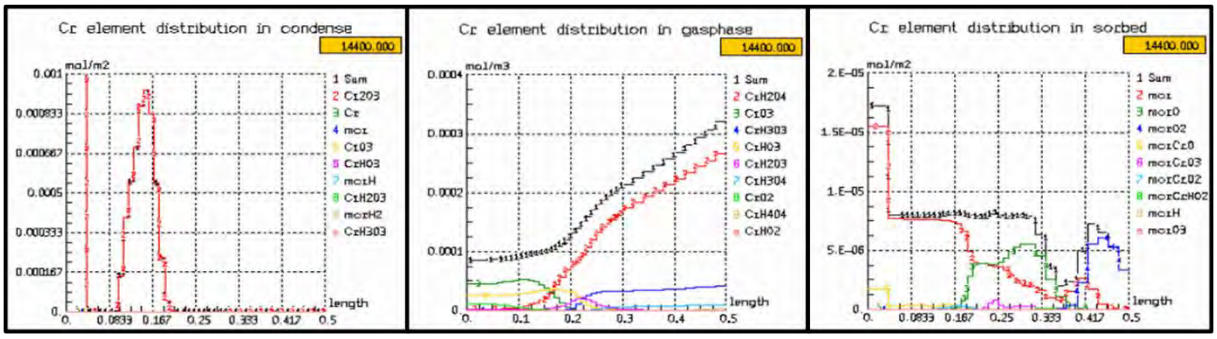

Figure 10 : SOPHAEROS simulation of chromium distribution (mol/m³ in volume or mol/m² on surfaces) at t_{final} = 4 h as a function of distance from the center of the furnace. Left) condensed phase; center) gas phase; right) sorbed surface states.

At 1550 °C, gaseous chromium species (Figure 10) are predominantly $CrO_{3(g)}$ (55 mol%), followed by $CrHO_{3(g)}$ (31 mol%) and $CrO_{2(g)}$ (14 mol%). Numerous reactional pathways lead to the deposition of $Cr_2O_{3(s)}$. The major part (> 99%) of these pathways involves reactions with $CrO_{3(g)}$ and $CrO_{2(g)}$.

Simulations show that $CrH_2O_{4(g)}$ comes from the decomposition of $CrO_{3(g)}$ and $CrHO_{3(g)}$ at high temperature. $CrH_2O_{4(g)}$ would then mainly come from the intermediate hydroxides $CrH_4O_{4(g)}$ and $CrH_4O_{5(g)}$ at low temperature. $CrHO_{3(g)}$ also leads to the formation of $CrH_3O_{3(g)}$ under 635°C.

5. Discussion

Despite the experimental difficulties encountered (loss of integrity of the downstream filter and the instability of Cr(VI) in solution), these experiments show good reproducibility in terms of chromium vaporized, deposited, and transported. The results of these experiments can then be compared with the SOPHAEROS modeling in Table II.

Table II : Comparative table between ACCrAS experiments and SOPHAEROS modeling. Chromium deposition and transport in a gradient temperature from 1550°C and 150°C after the vaporization of $Cr_2O_{3(s)}$ at 1550°C in an atmosphere composed of water (0.4 NL.min⁻¹) and air (0.1 NL.min⁻¹).

Areas of interest	ACCrAS experimental results	SOPHAEROS simulations
"High temperature" deposits	$Cr_2O_{3(s)}$ – [770 ; 1015]°C	$Cr_2O_{3(s)}$ – [875 ; 1395]°C strongly underestimated
"Low temperature" deposits	$Cr^{III}H_3O_{3(s)}$? - < 635°C	Condensation not calculated (surface adsorption observed)
Gas and Aerosols transported (150°C)	Cr^{VI} (Mainly aerosols)	$Cr^{VI}H_2O_{4(g)}$ + $Cr^{III}H_3O_{3(g)}$ strongly over estimated

This comparison shows similarities in position (+/- 5 cm) of high-temperature chromium deposits (> 635°C), as well as the transport of chromium (+VI) downstream of the bench. However, the fraction of chromium deposited is significantly underestimated by the model, even though the chemical form (Cr_2O_3) is similar.

Low-temperature deposits (< 635°C) are observable in experiments but are not predicted by the simulations. Raman analyses currently being processed suggest that these deposits may be amorphous chromium (III) hydroxide (CrH_3O_3). Deposition of chromium (III) hydroxide cannot be modeled because this species is not currently referenced in the SOPHAEROS thermodynamic databases in either crystalline or amorphous form. This may explain the discrepancy between modelling and experiments.

The proportion of gas and aerosols transported downstream of the bench is overestimated in the modeling compared to the experiments. Nevertheless, modelling predicts Cr transport in the Cr(VI) form ($CrH_2O_{4(g)}$) consistently with Cr(VI) mainly found at the experimental line outlet (very soluble and yellow aerosols).

Efforts must therefore be made in both experiments and modeling concerning the vaporization of chromium alone. The prospects for experimental improvements are to refine the thermal profile of the deposits using narrower parts and to verify the chemical structure of the deposits at low temperatures. The future works for computational improvements would then be: i) the addition of aerosol formation simulation; ii) the addition of thermodynamic data associated with the crystalline and amorphous states of $Cr(OH)_3$; iii) and the addition of condensation reactions with other solid species.

6. Conclusion

The results of experimental tests show that chromium (III) oxide vaporizes significantly at 1550°C in an atmosphere containing water vapor (0.4 $NL.min^{-1}$) and air (0.1 $NL.min^{-1}$). The vaporization rate of chromium under these conditions is around 800 $\mu g.h^{-1}$. Chromium vaporization in a pure argon atmosphere is three orders of magnitude lower than in an atmosphere containing water vapor.

Chromium deposition in the thermal gradient (1550-150°C) is reproducible in the tests conducted under these conditions. According to the experiments, most of the vaporized chromium is condensed in the form of $Cr_2O_{3(s)}$ between 770 and 1015°C on an yttria-stabilized zirconia surface. According to the modeling, only 7% of the vaporized chromium would be condensed in the form of chromium (III) oxide between 875 and 1395°C. Most of this $Cr_2O_{3(s)}$ deposit would result from reactions involving $CrO_{2(g)}$ and $CrO_{3(g)}$. According to experiments, chromium is then transported downstream of the bench at 150°C in the form of aerosols of Cr^{VI}, representing almost 40% of the amount of vaporized chromium. A linear kinetics of Cr^{VI} transport downstream is measured after a delay of several dozen minutes.

According to the model, 93% of the vaporized chromium is transported in the form of $Cr^{VI}O_2(OH)_{2(g)}$ (majority) and $Cr^{III}H_3O_{3(g)}$ (minority). The transported chromium $Cr^{VI}O_2(OH)_{2(g)}$ would come from the decomposition of $CrO_{3(g)}$ and $CrHO_{3(g)}$ at high temperature, then would mainly come from the intermediates $CrH_4O_{4(g)}$ and $CrH_4O_{5(g)}$ at low temperature. The transported chromium (III) hydroxide $CrH_3O_{3(g)}$ is thought to originate mainly from the decomposition of $CrHO_{3(g)}$ at high temperatures.

The modeling can be improved given the differences in transport/deposit proportions observed with experiments. However, the results are generally consistent regarding the species deposited and formed.

Tests on the vaporization of chromium in interaction with Cs and Mo fission products were also carried out later on in atmospheres composed of water vapor with argon or air.

Acknowledgement

Authors thank EDF for their financial support to this work and also OECD project FORESEEN partners.

7. Bibliography

[1] M. Khatib-Rahbar et Al., « Review of Accident Tolerant Fuel Concepts with Implications to Severe Accident Progression and Radiological Releases », NUREG/CR-7282 (2021), ERI/NRC 21-203

[2] H. G. Kim et Al., « Adhesion property and high-temperature oxidation behavior of Crcoated Zircaloy-4 cladding tube prepared by 3D laser coating », Journal of Nuclear Materials (2015), Volume 465, P531-539

[3] L. Bourgeois et Al., « Factors governing microstructure development of Cr203-doped UO2 during sintering », Journal of Nuclear Materials (2001), Volume 297, P313-326, http://dx.doi.org/10.1016/S0022-3115(01)00626-2

[4] L. A. Karpuyk et Al., « Accident tolerant fuel with chromium-coated fuel-rod cladding », Atomic Energy (2021), Volume 130, Issue 3, P149-155, http://dx.doi.org/10.1007/s10512-021-00786-9

[5] M. W. D. Cooper et Al., « Fission gas diffusion and release for Cr2O3-doped UO2: From the atomic to the engineering scale », Journal of Nuclear Materials (2021), Volume 545-152590, https://doi.org/10.1016/j.jnucmat.2020.152590

[6] V. Peres et Al., « High temperature chromium volatilization from Cr2O3 powder and Cr2O3-doped UO2 pellets in reducing atmospheres », Journal of Nuclear Materials (2012), Volume 423, P93-101, http://dx.doi.org/10.1016/j.jnucmat.2012.01.001

[7] C. Tang et Al., « Protective coatings on zirconium-based alloys as accident-tolerant fuel (ATF) claddings », Corrosion Review (2017), Volume 35, https://doi.org/10.1515/corrrev-2017-0010

[8] D. Jacquemain, « Nuclear Power Reactor Core Melt Accidents », ISBN: 978-2-7598-1835-8 (2015)

[9] G. Cénérino, « Accidents graves des réacteurs à eau de production d'électricité », Rapport IRSN-2008/98-FR (2008)

[10] B. B. Ebbinghaus, « Thermodynamics of Gas Phase Chromium Species: The Chromium Oxides, the Chromium Oxyhydroxides, and Volatility Calculations in Waste Incineration Processes », Combustion and flame (1993), vol 93 p 119-137, https://doi.org/10.1016/0010-2180(93)90087-J

[11] D. C. Fee et Al., « Phase Equilibria In The Cs-Cr-O System », Journal of Nuclear Materials (1979), Volume 84, P286-294, https://doi.org/10.1016/0022-3115(79)90169-7

[12] R. Buhler et Al., « Preparation and Characterization of a New TernaryChromium(III)–Molybdenum(VI) Oxide Cr2–2xMoxO3 », Journal of Solid State Chemistry (1998), Volume 140, P350-353, https://doi.org/10.1006/jssc.1998.7899

[13] P. Chatelard et Al., « ASTEC V2 severe accident integral code main features, current V2.0 modelling status, perspectives », Nuclear Engineering and Design (2014), Volume 272, P119-135, https://doi.org/10.1016/j.nucengdes.2013.06.040

[14] P. Chandramohan et Al., « Dissolution of Chromium Containing Oxides by Dissolved Ozone (DOz) coupled with Permanganate », Progress in Nuclear Chemistry (2023), https://doi.org/10.1016/j.pnucene.2023.104818

[15] V. Balaji et Al. « Studies on the Process Development for the Chemical Decontamination of Stainless-Steel Systems: Novel Observations », Industrial & Engineering Chemistry Research (2006), Volume 45, Issue 13, P4461-4470, https://pubs.acs.org/doi/10.1021/ie058013e

[16] V. Balaram, « Microwave dissolution techniques for the analysis of geological materials by ICP-MS », Current Science (1997), Volume 73, Issue 11, P1019-1023

[17] A. Sanchez-Hachair et Al., « Hexavalent chromium quantification in solution: Comparing direct UVevisible spectrometry with 1,5-diphenylcarbazide colorimetry », C. R. Chimie (2018), Volume 21, P890-896

[18] S. Souvi et Al., « Influence of water, dihydrogen and dioxygen on the stability of the Cr_2O_3 surface: A first-principles investigation », Surface Science (2017), Volume 666, P44-52

[19] A. S. O. Gomes et Al., « A micro-Raman spectroscopic study of Cr(OH)3 and Cr2O3 nanoparticles obtained by the hydrothermal method », J. Raman. Spectrosc. (2017), Volume 48, P1256-1263, DOI 10.1002/jrs.5198

CHEMISTRY OF CHROMIUM IN THE REACTOR COOLANT SYSTEM IN SEVERE ACCIDENT CONDITIONS FROM AN ATF TYPE CORE – EXPERIMENTS AND MODELING (ASTEC)

BOUCHAIN Joâo (ASNR)

GREGOIRE Anne-Cécile (ASNR)
PAUL Jean-François (UCCS)
DENIS Jean (ASNR)
SOUVI Sidi (ASNR)

• CHROMIUM BEHAVIOUR IN ACCIDENTAL CONDITIONS

↗ safety performance (PWR*)
Advanced Technical Fuel (ATF)

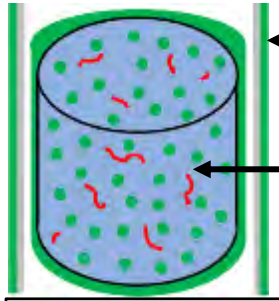

↘ fuel cladding oxidation
[M. Steinbruck (2021)]
↗ grain size
↘ FP* release from pellets
[T. Roubille (2024)]

Accident with ATF (cladding ≈ 1200°C)

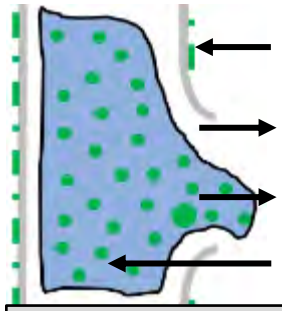

Oxidized and broken cladding
FP* release (radioactive)
Cr^{VI} release (toxic)
Fuel melting

SA* situation with ATF (core > 1400°C)

B. B. Ebbinghaus (1993)
Cr volatilization above **900°C** (H_2O)

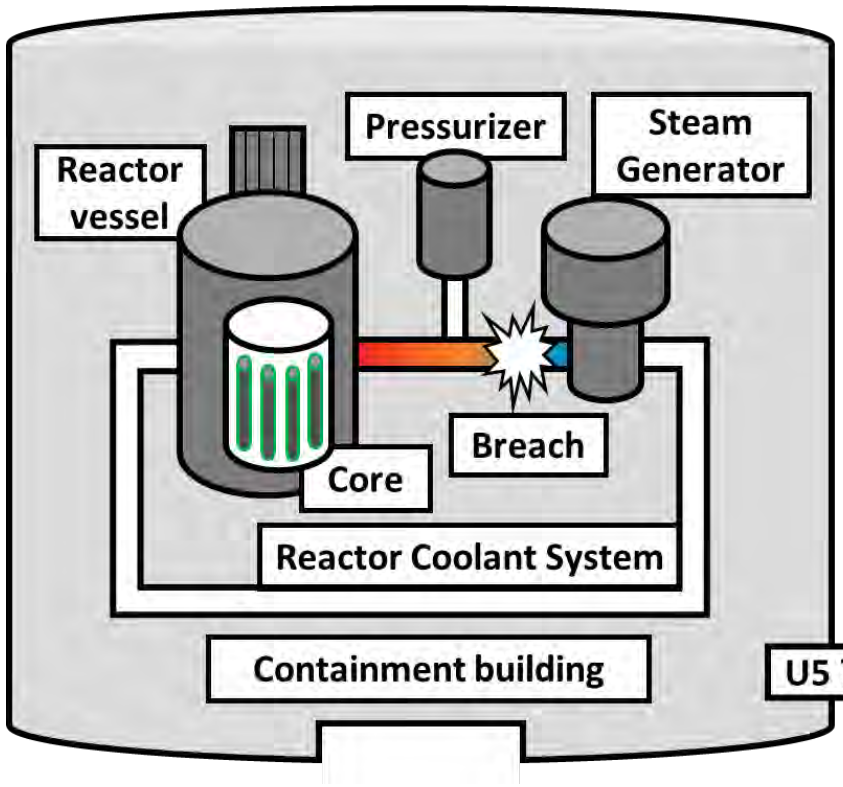

Cr^{VI} (carcinogenic)
Cr^{51} $T_{1/2}$ ≈ 28 days
^{137}Cs $T_{1/2}$ ≈ 30 years
^{131}I $T_{1/2}$ ≈ 8 days

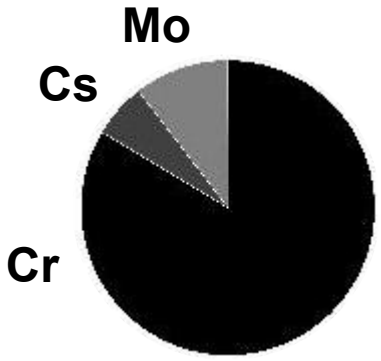

Orders of magnitude
m(Cr, PWR*) ≈ 1 ton
m(Cr) = **8** × m(**Mo**)
m(Cr) = **14** × m(**Cs**)

B. B. Ebbinghaus (1993), "Thermodynamics of Gas Phase Chromium Species: The Chromium Oxides, the Chromium Oxyhydroxides, and Volatility Calculations in Waste Incineration Processes*", Combustion and Flame, 93 : 119-137 (1993)
M. Steinbruck (2022), "High-temperature oxidation and quenching of chromium-coated zirconium alloy ATF cladding tubes with and w/o pre-damage", Journal of Nuclear Materials, 559 (2022) 153470
Théo Roubille (2024), "Etude théorique de la microstructure et du comportement des produits de fission dans le combustible d'oxyde d'uranium dopé à l'oxyde de chrome." Université Claude Bernard - Lyon I, ⟨NNT : 2024LYO10355⟩. ⟨tel-04966272⟩

• THESIS GOAL

D. Jacquemain (2015)

Process in the Primary Circuit determine FPs release

Deposition | **Transport**

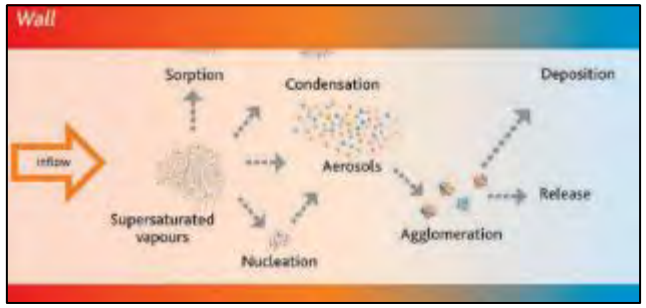

ACCrAS experimental bench

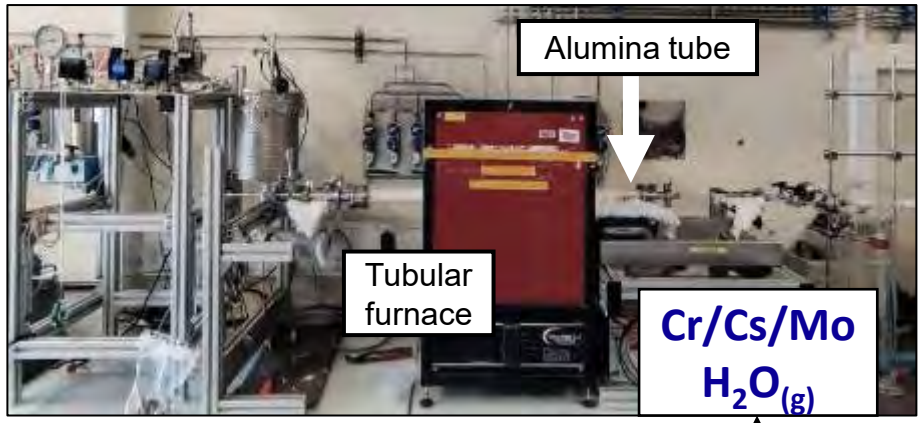

Cr/Cs/Mo
$H_2O_{(g)}$

Primary circuit severe accident simulation

SOPHAEROS

+ Cr

Thesis goal

Understand Physico-chemical phenomena including Cr
(deposition/transport)
inside Primary Circuit
governing source term

Experimental studies (Cr/Cs/Mo)

Modeling (ASTEC)
predict source term

D. Jacquemain (2015), "Nuclear power reactor core melt accidents: Current state of knowledge", IRSN / EDP Sciences

OUTLINES

01
MATERIALS AND METHODS

Experimental facility (ACCRAS)
Thermal maps + SOPHAEROS
SOPHAEROS : Cr vap/cond mechanisms

02
RESULTS (Cr)

Experimental results (80% H_2O / 20% Air)
Raman (Cr_2O_3) + UV-Visible (Cr^{VI})
Comparison of modeling and experiments

03
DISCUSSION

Conclusion and perspectives

01

MATERIALS AND METHODS

• ACCRAS FACILITY → Analysis of ChRomium behavior during a Severe Accident

Experimental bench simulating
Primary Circuit during **Severe Accident**
(1550°C - Cr_2O_3 - steam atmosphere)

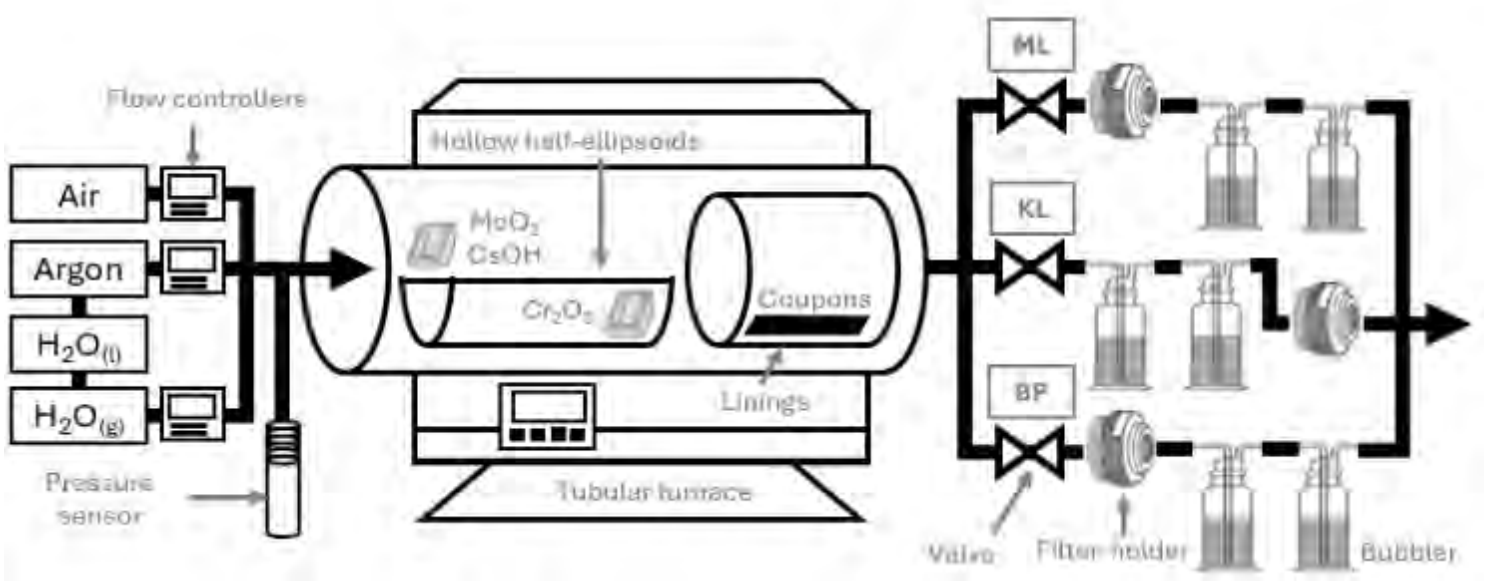

Crucible area = 1 cm^2

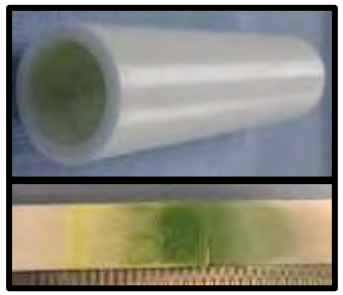

Qualitative analyses

Collection components :
Coupons/Linings → **Deposits**
Filters → **Aerosols**
Bubbler → **Gas**

Quantitative analyses in solution

Cr(III) **dissolution** methods developped :

Microwave assisted digestion
Nitric and Permanganic dissolution
(paper in preparation)

• THERMAL MAPS + SOPHAEROS MODELING

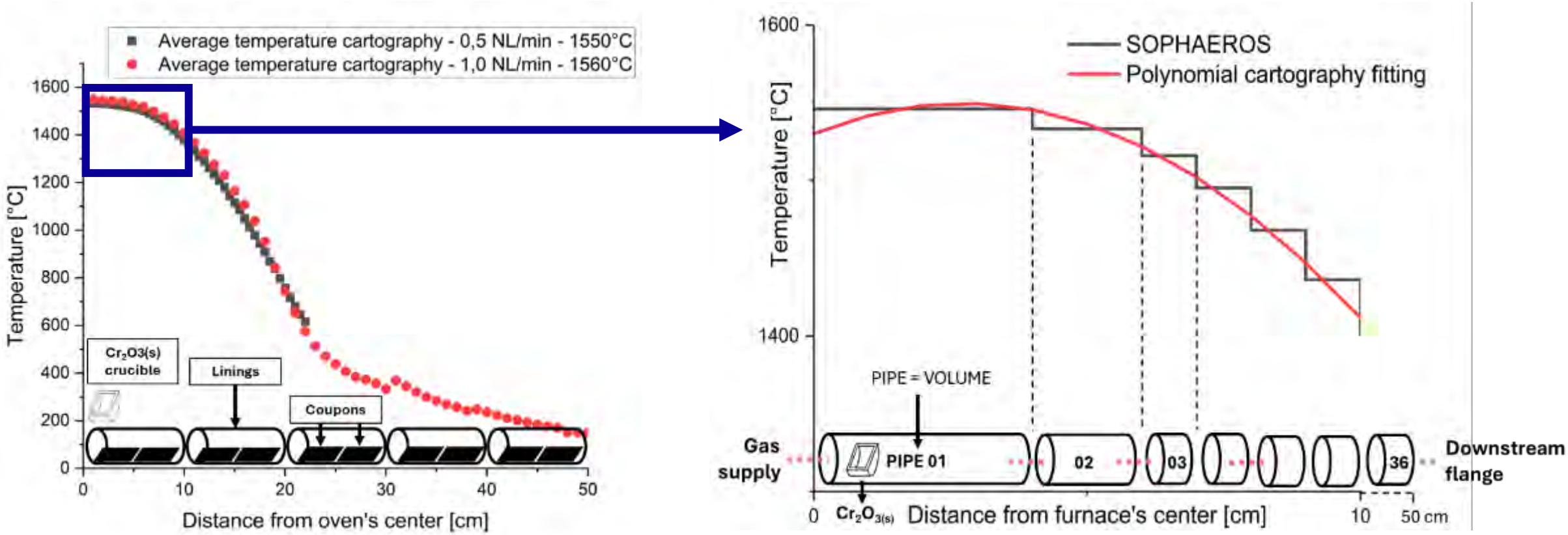

Thermal maps
Deposits temperature
Residence time determination
Modeling nodalization

Modeling (ASTEC/SOPHAEROS) :
Isothermal volumes
Thermodynamic (G°) parameters
MDB database

• SOPHAEROS : Cr_2O_3 CONDENSATION/VAPORIZATION MECHANISM

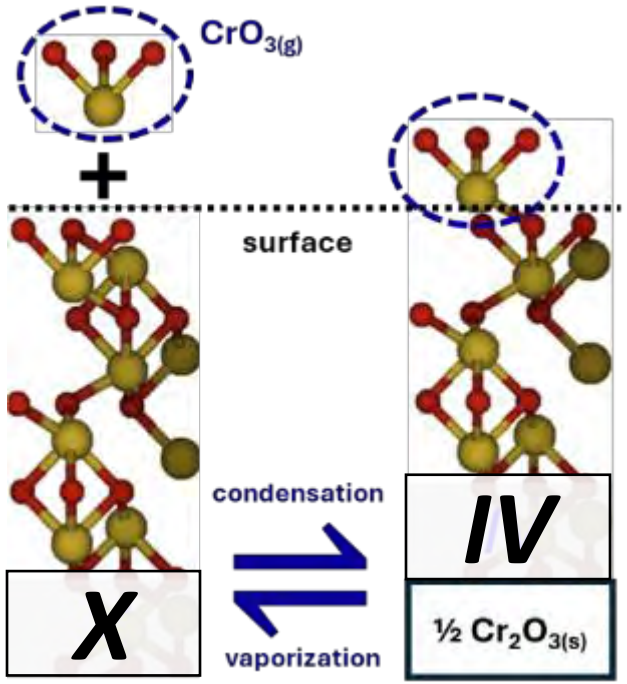

S. M. O. Souvi (2017) → **relative energy** of **surface states Cr_2O_3**

Chemical reaction pathways for
Condensation and **vaporization**
Surface states $Cr_2O_{3(s)} \rightleftharpoons Cr\text{-}O\text{-}H_{(g)}$

Example : $\frac{1}{2}Cr_{12}O_{21}(X) + CrO_{3(g)} \rightarrow \frac{1}{2}Cr_{12}O_{24}(IV) + \frac{1}{2}Cr_2O_{3(s)}$

$$\Delta rG°(X \rightarrow IV, T) = \frac{1}{2} \times G°(Cr_2O_{3(s)}, T) - G°(CrO_{3(g)}, T) + 21{,}23\ [Å^2] \times \Delta E_{(X \rightarrow IV)}\left[\frac{J}{mol.Å^2}\right] + \frac{\Delta_{X \rightarrow IV} Nb(O_2)}{2} \times G°(O_{2(g)}, 0K)$$

S. M. O. Souvi (2017)

Name	Stoichiometry	Termination	$Nb(O_2)$	$\Delta E_{(Y \rightarrow 0)}$ (meV/Å²)
X	$Cr_{12}O_{21}$	Cr-Cr-O_3	**3/2**	**-32**
IV	$Cr_{12}O_{24}$	Cr-O_3-Cr-O_3	**3**	**-20**

S. M. O. Souvi (2017), "Influence of water, dihydrogen and dioxygen on the stability of the Cr2O3 surface: A first-principles investigation", Surface Science, 666 (2017) 44-52

02

RESULTS

Name	Element	Atmosphere	Number of tests performed
H_2O/air	Cr	80% H_2O 20% air	5

*Gas flow rate = 0.5 NL/min
*Residence time (furnace center → filter) ≈ 15 sec
*Pressure = 1 atm
*Cr_2O_3 1550°C for 4 hours

• TRANSPORT EXPERIMENTS (Cr_2O_3 – 80% H_2O / 20% AIR)

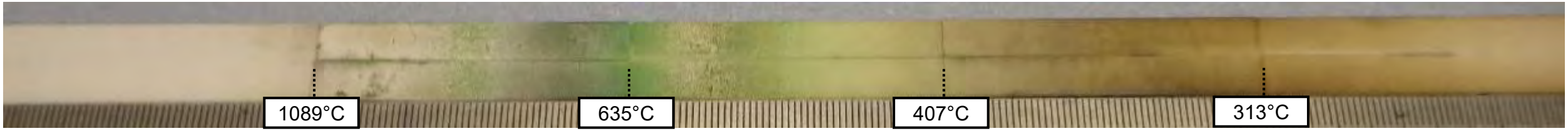

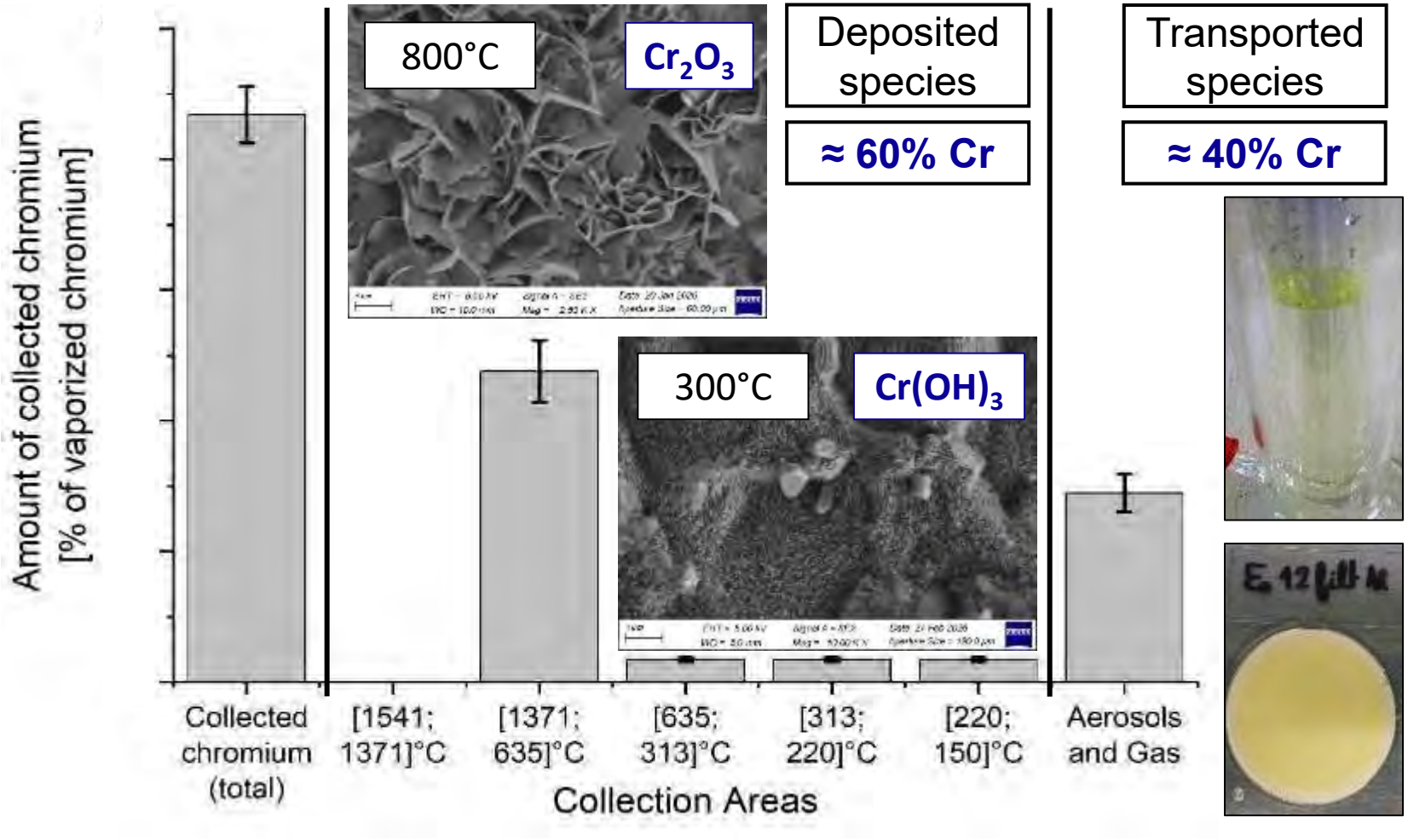

$Cr_{vaporized} \approx 800\ \mu g.h^{-1}$

Transport kinetic linear over time

Deposition

XPS, **Raman**, XRD → $\mathbf{Cr^{III}_2O_3}$
Green deposits > 600°C

XPS, Raman → $\mathbf{Cr^{III}(OH)_3}$
Brownish deposits < 600°C

Transport

UV-Visible, solubility → $\mathbf{Cr^{VI}}$
90% aerosols - 10% gas (yellow)

• DEPOSITS RAMAN (Cr_2O_3) AND TRANSPORT UV-VISIBLE (Cr^{VI})

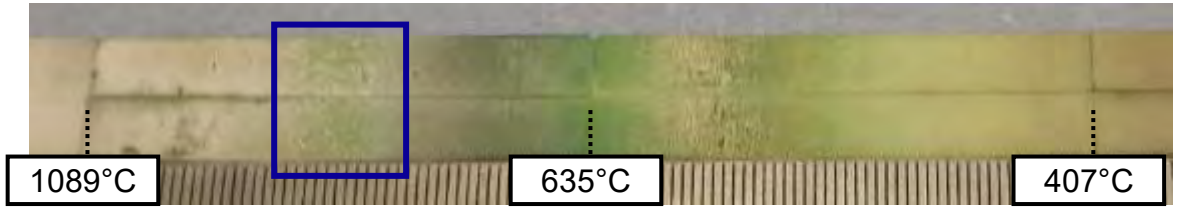

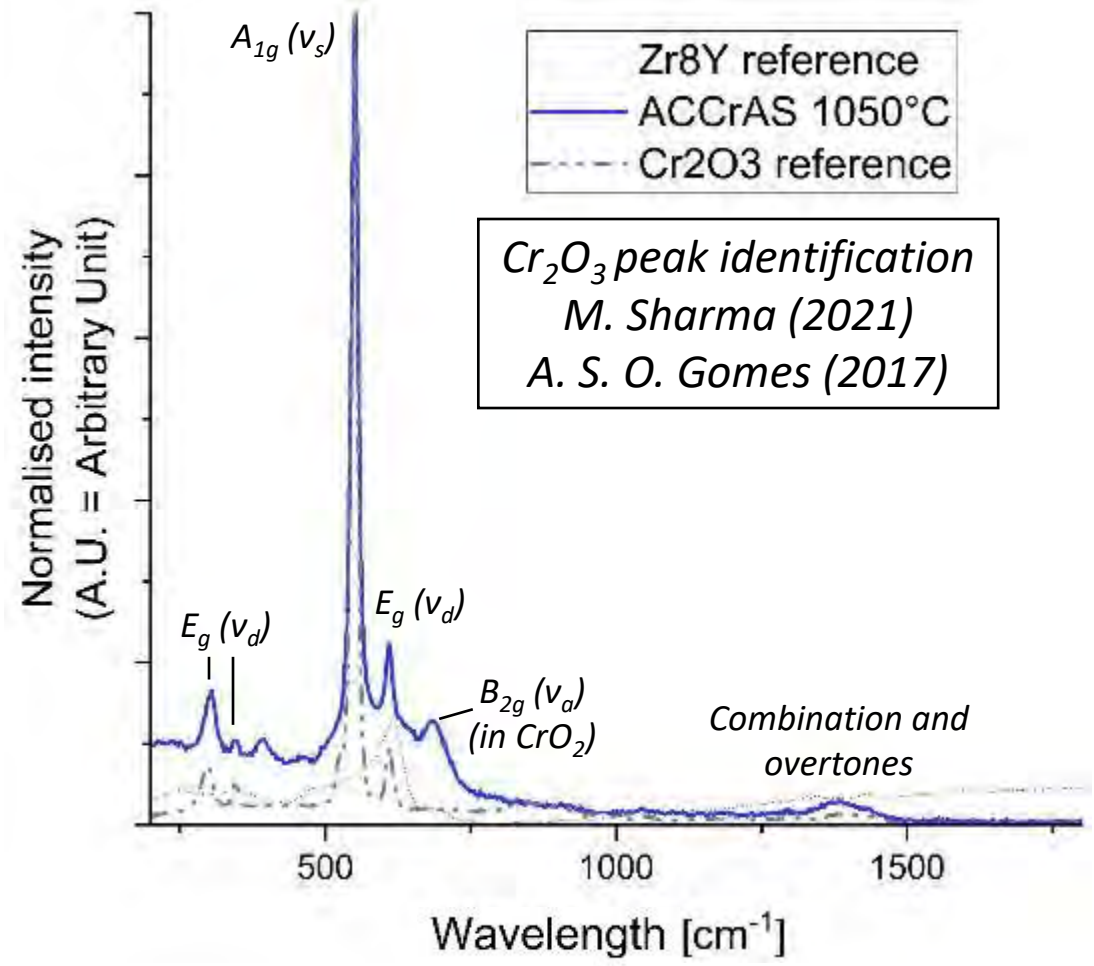

Cr_2O_3 peak identification
M. Sharma (2021)
A. S. O. Gomes (2017)

A. Sanchez-Hachair (2018)
pH < 5 → $HCrO_4^-$
λ_{max} = 350 nm

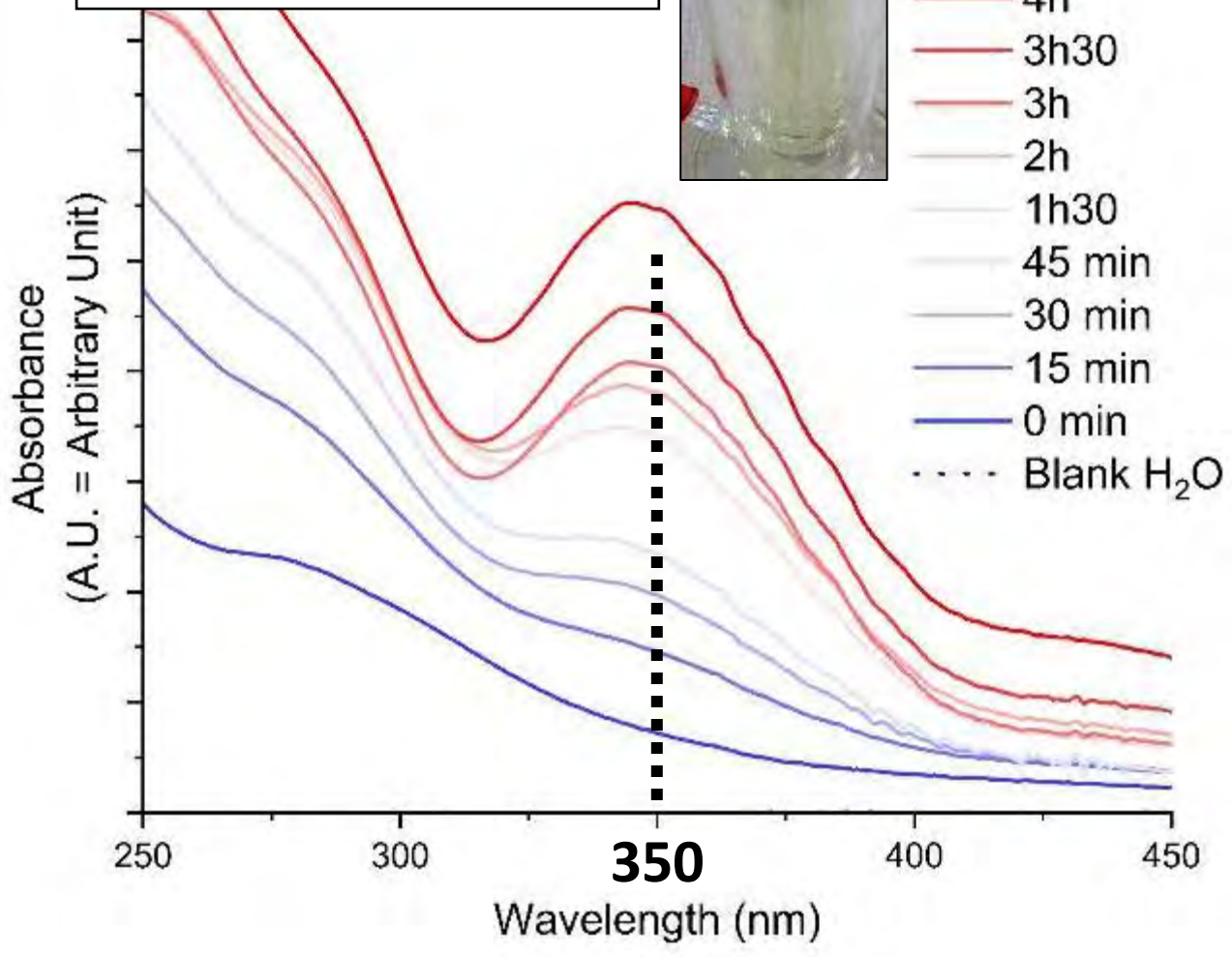

M. Sharma (2021), "Single step fabrication of nanostructured Cr2O3-MoO2 composite flexible electrode for top-notch asymmetric supercapacitor ", Applied Surface Science, 555(2021)149721
A. S. O. Gomes (2017), "A micro-Raman spectroscopic study of Cr(OH)3 and Cr2O3 nanoparticles obtained by the hydrothermal method", Journal of Raman Spectroscopy, 48 (2017) 1256-1263
A. Sanchez-Hachair (2018), "Hexavalent chromium quantification in solution: Comparing direct UV-visible spectrometry with 1,5-diphenylcarbazide colorimetry", Comptes Rendus Chimie, 21 (2018) 890-896

• SOPHAEROS : MODELING RESULTS AND COMPARISON (H_2O/AIR)

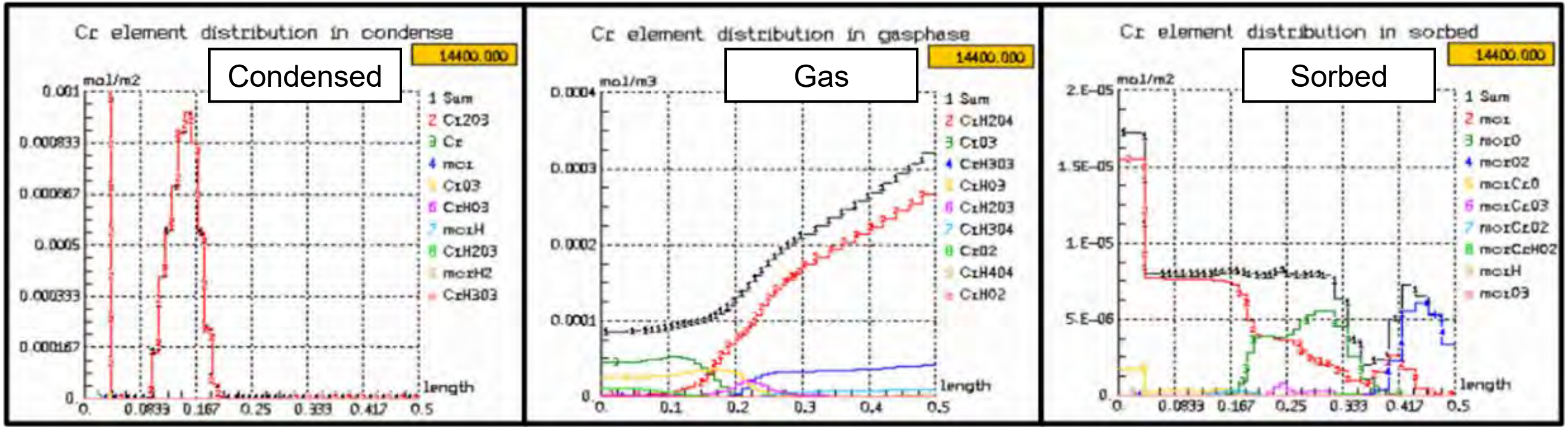

Areas of interest	ACCrAS experimental results	SOPHAEROS simulations
"High temperature" deposits	$Cr_2O_{3(s)}$ – [770 ; 1015]°C	$Cr_2O_{3(s)}$ – [875 ; 1395]°C strongly underestimated
"Low temperature" deposits	$Cr^{III}H_3O_{3(s)}$? - < 635°C	Condensation not calculated (surface adsorption observed)
Gas and Aerosols transported (150°C)	Cr^{VI} (Mainly aerosols)	$Cr^{VI}H_2O_{4(g)} + Cr^{III}H_3O_{3(g)}$ strongly over estimated

03

DISCUSSION

• CONCLUSION AND PERSPECTIVES

Cr_2O_3 vaporization experiments (80% H_2O + 20% Air or Argon)

$Cr^{III}_2O_{3(s)}$ deposition > 600°C + **$Cr^{III}(OH)_3$ deposition** < 600°C
Cr(VI) transport 150°C (Mainly aerosols)

Less oxydative atmosphere **(Air → Argon)**
↘ Cr_2O_3 **vaporization** and **transported proportion - similar chemical speciation**

Comparison experiments-modeling (SOPHAEROS)

Qualitative agreement (Cr^{III} deposition + Cr^{VI} transport)

Quantitative discordance (transport overestimated in simulations)

Perspectives

Cr/Cs/Mo experiments (H_2O/Air + H_2O/Argon) → In progress
SOPHAEROS Cr modeling → To be improved
Cr/Cs/Mo/I experiments (H_2O/H_2/B) → Future works (FORESEEN)
SOPHAEROS Cr/Cs/Mo/I modeling → Future works (FORESEEN)

ASNR Autorité de sûreté nucléaire et de radioprotection

THANK YOU FOR YOUR ATTENTION

DO YOU HAVE ANY QUESTIONS?

UCCS UNITÉ DE CATALYSE ET CHIMIE DU SOLIDE

Université de Lille

EDF

INTERFACIAL GAS TRANSFER IN GAS-LIQUID FLOWS: A COMPARATIVE STUDY OF ADVANCED EXPERIMENTAL AND COMPUTATIONAL TECHNIQUES

Alvaro Ramos Pérez*, Terttaliisa Lind, Yohei Sato, and Victor Petrov
PSI Center for Nuclear Engineering and Sciences, Paul Scherrer Institute
Forschungsstrasse 111, 5232 Villigen PSI, Switzerland
alvaro.ramos-perez@psi.ch; terttaliisa.lind@psi.ch; yohei.sato@psi.ch; victor.petrov@psi.ch

Yating Wang
Institute of Nuclear and New Energy Technology, Tsinghua University
Beijing 100084, China
wangyt20@mails.tsinghua.edu.cn

Annalisa Manera, Horst-Michael Prasser
Department of Mechanical and Process Engineering, ETH Zürich
Rämistrasse 101, 8092 Zürich, Switzerland
maneraa@ethz.ch; prasser@lke.mavt.ethz.ch

ABSTRACT

Interfacial gas mass transfer in two-phase gas-liquid flows plays a key role in the retention of radioactive gases in pool scrubbing. A comparative fundamental analysis is provided between high-resolution measurements with a Wire-mesh sensor and a Volume-of-Fluids Direct Numerical Simulation code for gas-liquid water co-current upward bubbly flow at atmospheric conditions with CO_2 injection as a gas simulant. The Wire-mesh sensor measurements provide 2D plane time-resolved visualizations and quantitative data on the void fraction and dissolved CO_2 concentration. The computational simulations include an irregular stencil formulation at the interface to compute the mass transfer. There is a good correlation between experiments and simulations in the evolution of the hydrodynamics and mass transfer in terms of the axial rising distance and gas flow rate. Discrepancies are observed in the bubble fragmentation due to unresolved interaction between the gas-liquid interface and turbulence in the simulations. The non-instantaneous dissociation of the dissolved CO_2 introduces a time delay in the experimental evaluation of the mass transfer. Such comparative studies among experimental and computational methods provide a valuable assessment of the capabilities of the state-of-the-art techniques and contribute to an improved understanding and further optimization of gas-liquid flow nuclear safety systems.

KEYWORDS
Mass transfer, Gas-liquid flows, WMS experiments, CFD simulations

* Corresponding author

1. INTRODUCTION

In a severe accident scenario in a nuclear power plant light-water reactor with core degradation, pool scrubbing is an essential process, among other retention strategies, to capture harmful radioactive particles and gaseous species [1]. Modelling and evaluation of pool scrubbing is performed analytically with the use of well-established lumped parameter codes such as SPARC-90 [2] and BUSCA [3] whose development and validation have been based on integral tests of radioactive species retention [4]. With the continuous development of computational capabilities, in addition to the existing lumped parameter codes, advanced analytical methods such as Computational Fluid Dynamics (CFD) have been acknowledged to play a more relevant role in the nuclear safety domain [5]. In the context of pool scrubbing, CFD activities have been developed in the IPRESCA [6] project to assess its use in the simulation of two-phase gas-liquid flows in reactor systems. Namely, the first attempts have performed code-to-code comparison of flow bubble hydrodynamics in low-momentum flows [7]. Volume-of-Fluids (VOF) [8] and Euler-Euler [9] methods have been used to reproduce higher gas injection flows in the liquid pool experiments from [10]. As pointed out in [8], variables such as time-averaged void fraction or gas velocity are available in the current experiments and can be captured with the current CFD methods. However, there is a larger uncertainty in pool scrubbing-related computational studies for evaluating local quantities, such as bubble sizes, shapes, or interfacial area density, for which more recent studies have performed dedicated investigations [11], [12]. These are fundamental to extending the use and validation of CFD codes for computing the end goal transport of species, whether particles or gases, through the gas-liquid interface.

This study aims to support the analysis of gas mass transfer in gas-liquid flows and the extension of CFD codes to more complex flow applications, such as chemical reactors or pool scrubbing processes, by a comparative analysis of high-resolution experiments and simulations of a dissolvable gas (CO_2)-liquid co-current upward bubbly flow under atmospheric conditions. The experimental data is obtained with a Wire-mesh sensor (WMS) based technique developed in [13] from which the hydrodynamics and mass transfer via the void fraction and concentration field of the dissolved gas can be fully resolved. Additionally, a quantitative evaluation of the bubble size, velocity, interfacial area density, and mass transfer fluxes is also provided. From the computational simulations side, the in-house DNS code PSI-BOIL [14] is employed to compute the gas-liquid co-current upward bubbly flow with mass transfer. This CFD code is based on a VOF method to capture the gas-liquid interface and uses the sharp-interface phase-change approach to compute the mass transfer. It has been recently adapted for the single bubble mass transfer of CO_2 [15]. During the experiments, HSC imaging will be used to provide additional qualitative information and validation on the gas-liquid flow dynamics.

This research is conceived as an evaluation study in which both WMS and CFD results will be compared at the same relevant flow scales and variables. The ultimate goal is to assess the current capabilities of two state-of-the-art experimental and computational techniques under non-ideal flow conditions and to provide further guidance for improving and extending the applications of these methods to flows of industrial interest, such as pool scrubbing.

2. INSTRUMENTATION AND METHODS

2.1. Experimental and computational models

The WMS measurements were presented in a previous study by the author's [13] whose simplified description, in consideration of the follow-up CFD parametric model, is included here. The experiments were conducted in a $l_{ch} = 50\,mm$ square cross-section, upward gas-liquid co-current flow channel at the ARAGO facility of the Paul Scherrer Institute (**Figure 1a**). The gas flow Q_g of 100% CO_2 was injected upwards via a $d_{inj} = 6\,mm$ inner and $d_{inj,out} = 8\,mm$ outer diameter orifice at an adjustable distance h from 42 to $540\,mm$ (every $50\,mm$) to the WMS measurement plane. Three gas flow rates were used,

leading to the following gas superficial velocities $j_g = 0.4 \cdot 10^{-2}, 1.4 \cdot 10^{-2}$, and $5.7 \cdot 10^{-2}\ m/s \pm 1\ \%$. The liquid flow to compensate for the WMS grid intrusiveness on the bubble gas motion was set to Q_l with a corresponding associated liquid superficial velocity $j_l = 0.39\ m/s \pm 5\ \%$. The three-layer WMS was installed at $M1$ and $M2$ axial locations, and results of the combination of two measurement planes, i.e., *Receiver 1-Transmitter* and *Receiver 2-Transmitter* with an axial resolution or pitch of $\Delta z = 1\ mm$. The radial pitch or distance between neighboring $0.05\ mm$ diameter wires in the measurement plane is $\Delta x = \Delta y = 1\ mm$, with an acquisition frequency of $f = 3200\ Hz$. Each experimental point has a measurement time of $t_{meas,WMS} = 10\ s$ which is repeated three times. The uncertainty in the WMS results indicates the standard deviation $\pm\sigma$ between test repetitions.

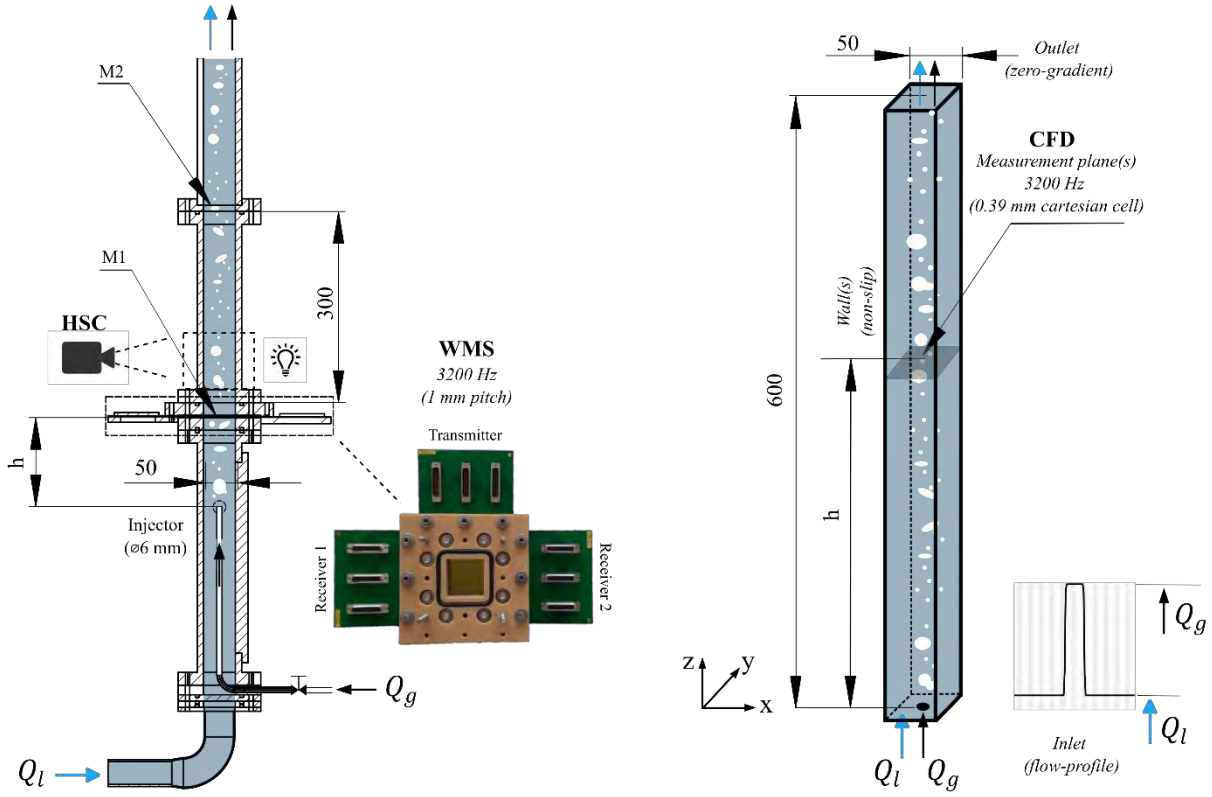

Figure 1. Scheme of the ARAGO set-up for the WMS and HSC experiments (a), and computational domain used for the CFD simulations (b).

The CFD model employed in the gas-liquid upward co-current flow mass transfer is a 3D DNS simulation with a Finite Volume Method (FVM) discretization, which uses the Volume-of-Fluids (VOF) approach to solve for the gas-liquid interface, and a sharp-interface phase-change model to account for the mass transfer of dissolved species at the interface. The models are integrated into the in-house open-source CFD code PSI-BOIL [14] and have been modified and applied by the authors to the modelling of the absorption of gas bubbles in a liquid [15]. The inlet velocity condition is a flat profile as a function of the flow rates Q_g (at the injector) and Q_l (in the liquid bulk) with a smooth transition between both regions (**Figure 1b**). The validity of such an imposed and assumed profile to capture the experimentally measured bubble formation and initial size distribution is discussed in the following Section 3.1. The computational domain of the gas-liquid mass transfer experiments in the column (**Figure 1b**) is discretized using a Cartesian mesh of resolution $\Delta x_{CFD} = 0.39\ mm$ in a cross-sectional size 50 x 50 mm (128 x 128 cells) with a total height of $H = 600\ mm$ (1536 cells) leading to a total number of $25 \cdot 10^6$ cells. The used spatial resolution is largely

limited by the computational cost of the simulations, which is 34 days at $j_g = 5.7 \cdot 10^{-2}\ m/s$ using 128 cores in the Merlin 6 cluster at the Paul Scherrer Institute, and it is acknowledged to be a relevant limitation of the CFD results. The effects of the mesh resolution in the CFD results for the different gas injection conditions are discussed in the following Section 3. For the sake of comparison with the WMS measurements, a series of axial planes are located at a distance h where the void fraction ε, the dissolved CO_2 concentration c_l, and the axial velocity w are recorded with a frequency f. The simulations were conducted for $t = 2.0\ s$ of physical time where only the range $t_{meas,CFD} = [1.0, 2.0]\ s$, under assumed steady-state conditions, is used for comparison with the WMS results.

2.2 Data post-processing methods

The development of the WMS for the study of gas-liquid flows in the last couple of decades has led to a wide set of methods and validation studies from which systematic review of the methodology can be found in [16]. The goal of the present study is not the further development of WMS post-processing techniques, but rather to provide a common framework for analyzing WMS and CFD data based on the author's previous work and methodologies for interfacial mass transfer in gas-liquid flows [13]. In this regard, and for the sake of the reader's understanding, the basis of the WMS and CFD post-processing framework are briefly described below.

The raw data WMS measurements of conductivity $u_{i,j,k}$ at the crossing point $[i, j]$, at location $[x, y]$ in the measurement plane, for the frame $[k]$ are calibrated to obtain the void fraction $\varepsilon_{i,j,k}$ and the concentration of dissolved CO_2 in the liquid $c_{l_{i.j.k}}$. For the void fraction $\varepsilon_{i,j,k}$, the so-called Maxwell expression is used in the regions where the gas is present, i.e., the normalized conductivity with respect to the single-liquid phase $g_{i,j,k} < 1.0$. In the liquid phase, i.e., wherever $g_{i,j,k} \geq 1.0$, the concentration $c_{l_{i.j.k}}$ is calculated [13]. For the CFD, the recorded void fraction at the grid nodes of the measurement planes $\varepsilon_{i,j,k}$ is a direct result; thus, no further processing is required. The liquid region where the CFD values of $c_{l_{i.j.k}}$ are calculated is defined as $\varepsilon_{i,j,k} < 0.5$. Respectively, for the gas region $\varepsilon_{i,j,k} \geq 0.5$. The three-layer WMS data of the void fraction and dissolved CO_2 in the liquid can be used to compute the average axial velocity of the gas $\langle w_g \rangle_{i,j}$ and liquid $\langle w_l \rangle_{i,j}$ phase respectively. This operation is performed through cross-correlation of the bottom and top WMS transmitter-receiver pairs planes, where a specific time delay, for a fixed known distance, is observed between the measurements [17]. Together with the time-averaged values of $\langle \varepsilon \rangle_{i,j}$ and $\langle c_l \rangle_{i.j}$, it is possible to estimate the time-averaged mass flux of dissolved species $\langle \dot{m}_l \rangle_{i,j}$ through the WMS plane:

$$\langle \dot{m}_l \rangle_{i,j} \cong \langle w_l \rangle_{i,j} \langle c_l \rangle_{i.j} (1 - \langle \varepsilon \rangle_{i,j}) \tag{1}$$

A similar operation can be performed with the CFD results, but in this case, both fluxes can be calculated instantaneously, as the axial velocity $w_{i,j,k}$ is resolved in time, and no prior time-averaging is required, so that:

$$\dot{m}_{l_{i,j,k}} = w_{i,j,k} c_{l_{i.j.k}} \tag{2}$$

A posteriori time-averaging is possible for (2), to obtain $\langle \dot{m}_l \rangle_{i,j}$, and evaluate the validity of the formulation used in (1). By integration on the cross-section of the total mass flux of dissolved species, $\langle \dot{M}_l \rangle$ can be obtained. The associated interfacial area density $a_{g_{i,j,k}}$ can be approximated from the norm of the gradient of the void fraction as formulated by [18]. Finally, both for the WMS and CFD data, the bubble sizes are characterized by identifying interconnected volumes where $\varepsilon_{i,j,k} \geq \varepsilon_{th} = 0.1$, and using the bubble velocity W_b as the average of the measured gas velocities w_g inside each identified bubble.

3. RESULTS AND DISCUSSION

3.1. Flow hydrodynamics

The flow hydrodynamics of the co-current gas-liquid flow in the column ranges from single individual ellipsoid bubbles rising at the channel center at $j_g = 0.4 \cdot 10^{-2}\ m/s$ to a complex heterogeneous distribution of bubble sizes covering the entire cross-section for $j_g = 5.7 \cdot 10^{-2}\ m/s$ (**Figure 2**).

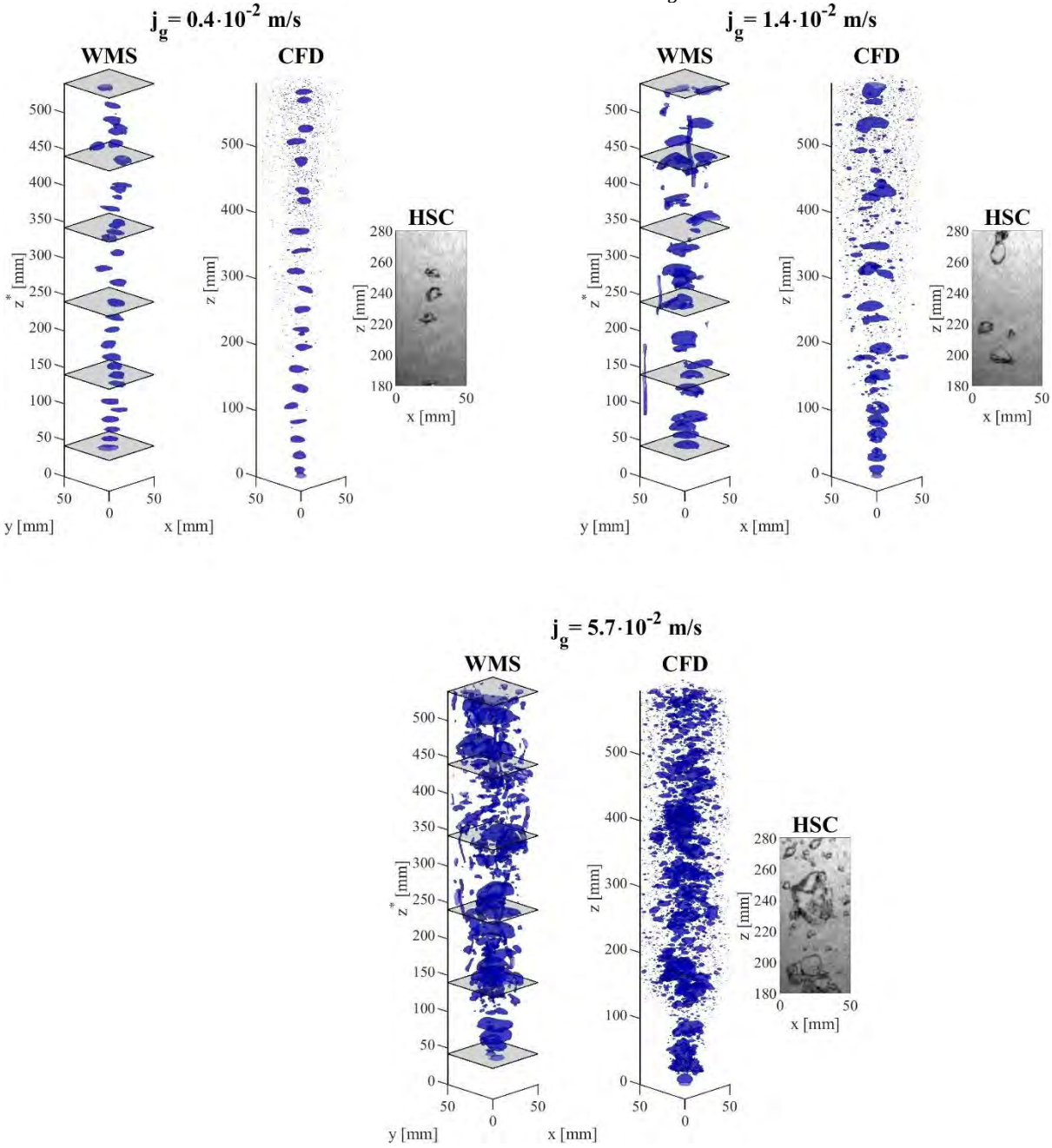

Figure 2. Void fraction contours at $\varepsilon = 0.1$ for the CFD and WMS for different gas superficial velocities j_g, where the WMS data is reconstructed from the plane measurements (gray planes) at $h = 42, 140, 240, 342, 440$ and $540\ mm$, and the vertical axis is converted from WMS time frames k to distance z^* using the average gas velocity W_g. The HSC shows the side imaging of the flow for the window $h = [180, 280]\ mm$.

In terms of the axial evolution from the injection to the top of the column, the bubble rising process is characterized by a radial dispersion of the gas flow and an enhanced interaction between neighboring bubbles. This interaction leads to the formation of larger caps or slugs, as well as the fragmentation into smaller spherical bubbles, which spreads the initial monodisperse bubble size into a broader and polydisperse distribution. As pointed out in the previous study by the authors [13], such dispersion and bubble interaction behavior is enhanced with the increase in the gas superficial velocity. It is also associated with higher turbulence, mixing levels, and shorter rising lengths from the initial injection to the fully developed gas-liquid flow conditions [19]. From a qualitative point of view in **Figure 2**, the WMS and CFD results, as well as the HSC data in the measurement window in the vicinity of the injector, show the described and similar bubble shape, size, and axial evolution.

At the highest gas superficial velocity $j_g = 5.7 \cdot 10^{-2}\ m/s$, the CFD results show a clear overprediction of the bubble fragmentation and do not reproduce the presence of the large slugs, which are instead captured both by the WMS and HSC measurements. It is hypothesized that the overprediction of the CFD bubble fragmentation is due to the unresolved interaction between the gas-liquid interface and the turbulence levels at the current mesh resolution. The imposed velocity profile at the inlet boundary condition, instead of the simulation of the flow process with the injector walls, can also contribute to the earlier fragmentation of the globules at the largest gas flow injection velocity. The presence of this artifact is also visible in the CFD results in the form of small spherical bubbles detaching from the ellipsoids at $j_g = 0.4 \cdot 10^{-2}$ and $1.4 \cdot 10^{-2}\ m/s$. However, over-fragmentation becomes more critical with the increase in gas flow, and thus in turbulence, and on the finer mesh requirements to capture the entire spectrum of turbulent scales.

The intrusiveness of the WMS in terms of the bubble velocity and fragmentation is a known limitation [20] of this experimental technique. Near the mesh grid, bubbles not only decelerate due to the inertial, buoyant, and surface tension forces balance, but can also experience shape deformation. While similar bubble volumes are observed between the WMS and CFD results at $j_g = 1.4 \cdot 10^{-2}\ m/s$, in the case of the WMS data, the ellipsoids are flattened and show a larger major axis length.

The volumetric bubble size distribution provides a quantitative evaluation of the hydrodynamics of the gas-liquid co-current flow (**Figure 3**). At the injector's vicinity ($h = 42\ mm$), the monodisperse peak at $d_b \approx 9.0\ mm$ for $j_g = 0.4 \cdot 10^{-2}\ m/s$ and at $d_b \approx 12.0\ mm$ for $j_g = 1.4 \cdot 10^{-2}\ m/s$ are in good agreement between the WMS and CFD results. This shows that the computational model and the used Inlet boundary condition can adequately characterize the injection and bubble formation process. The wider dispersion and higher values of the right distribution tail (larger bubble sizes) for $j_g = 5.7 \cdot 10^{-2}\ m/s$ shows that over-fragmentation at the largest gas velocity is already a computational issue at the injection location. The results close to the injection show that the computational model and the used Inlet boundary condition can adequately characterize the injection and bubble formation process for gas velocities up to $j_g = 1.4 \cdot 10^{-2}\ m/s$, whereas over-fragmentation appears at the injector for larger gas flow rates and more turbulent flows. The increase in the average bubble volume and the spreading of the calculated size distribution with the rising distance ($h = 540\ mm$) are also well captured by the CFD. The most remarkable discrepancies appear, as expected, at the highest superficial velocity $j_g = 5.4 \cdot 10^{-2}\ m/s$ where the overestimation of the bubble breakup and fragmentation leads to the formation of a smaller bubble size tail in the distribution, evident at $h = 540\ mm$.

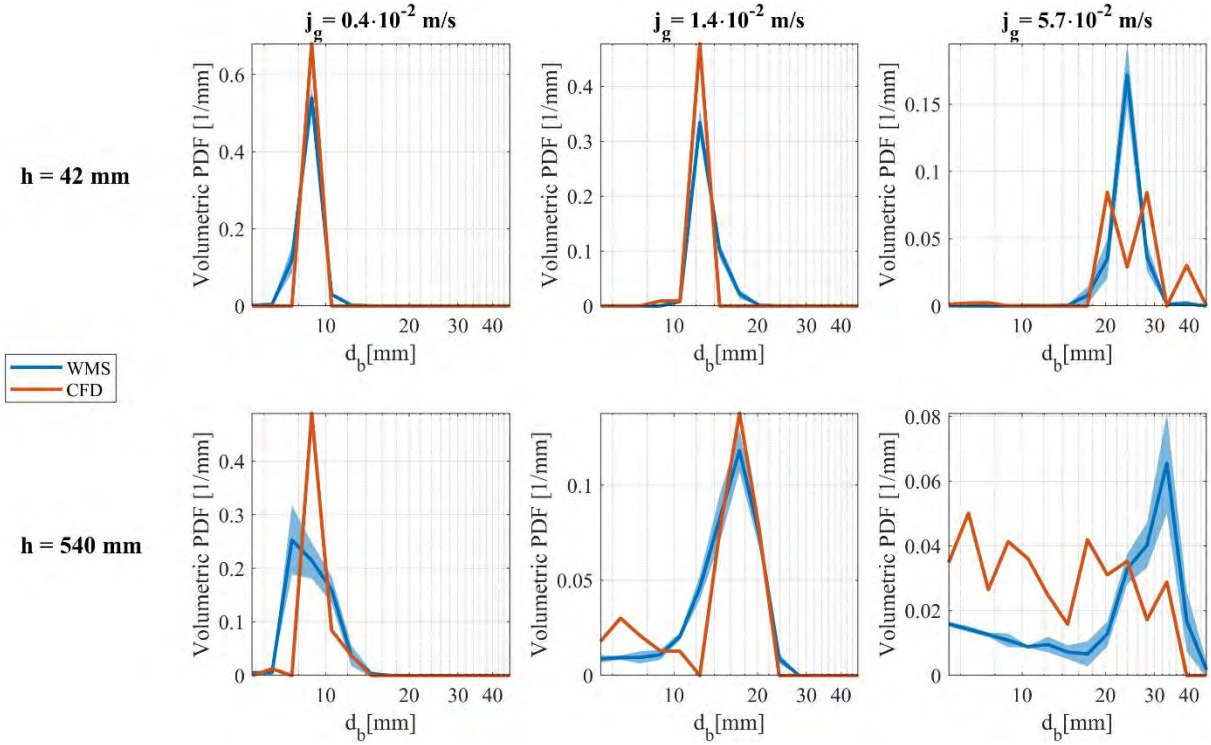

Figure 3. Volumetric Probability Density Function (PDF) of the bubble size d_b for the WMS and CFD as a function of the gas superficial velocity j_g, height $h = 42\ mm$ (top) and $h = 540\ mm$ (bottom). The *shaded* regions indicate the standard deviation $\pm\sigma$ between test repetitions.

In gas-liquid mass transfer processes, the liquid side mass transfer coefficient k_l and the interfacial area density a_g are the most relevant variables in the study of the mass transfer flux $\dot{m}_g$, whose standard formulation scales as $\dot{m}_g \propto k_l a_g$. According to the WMS results in **Figure 4**, for the gas superficial velocities $j_g = 0.4 \cdot 10^{-2}\ m/s$ and $j_g = 1.4 \cdot 10^{-2}\ m/s$, the integrated time-averaged value of the interfacial area density $\int \langle a_g \rangle dS_{ch}$ decreases in height. This is because of the observed coalescence in **Figure 3** which increases the average bubble volume and thus decreases the surface to volume ratio which scales as $\propto 1/d_b$.

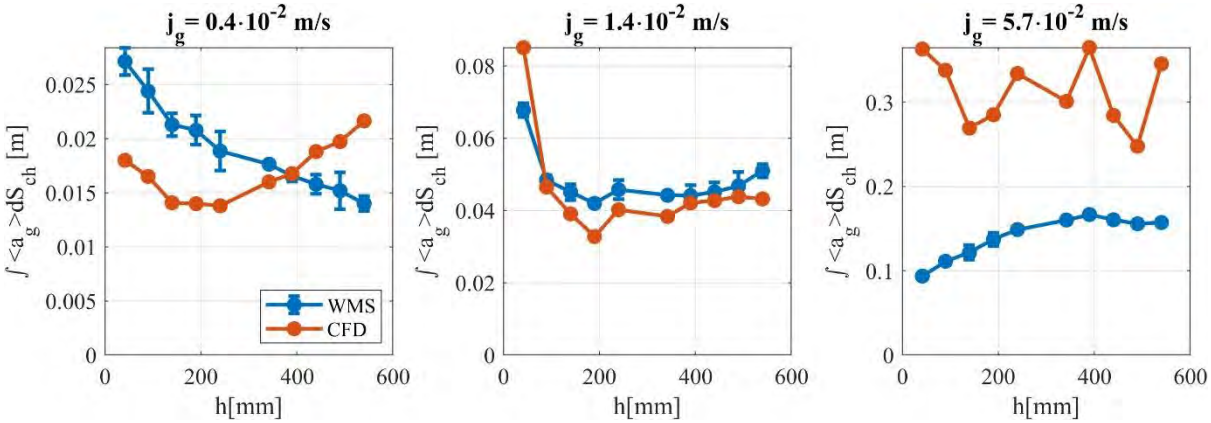

Figure 4. Integration of the time-average interfacial area density $\int \langle a_g \rangle dS_{ch}$ for the WMS and CFD as a function of the gas superficial velocity j_g and height h.

The CFD results in **Figure 4** effectively capture the mentioned evolution for $j_g = 1.4 \cdot 10^{-2}\ m/s$, while in the case of $j_g = 0.4 \cdot 10^{-2}\ m/s$, the increase of the predicted bubble fragmentation in height leads to a simultaneous increase in the interfacial area density, which is not observed in the experiments. As expected, the most significant discrepancy appears at $j_g = 5.7 \cdot 10^{-2}\ m/s$ where the over-fragmentation of bubbles in the CFD results due to the increase of turbulence levels leads to a value of the interfacial surface that doubles the value of the WMS measurements. The observed WMS and CFD differences in the interfacial area density are not the only, but one of the main reasons for subsequent discrepancies in the total mass transferred between the phases. The lack of extensive statistical data, i.e., physical simulation time under steady-state conditions, in the CFD results also leads to some oscillations of the interfacial area density values at the highest gas flow conditions of $j_g = 5.7 \cdot 10^{-2}\ m/s$.

3.2. Interfacial mass transfer

The flow hydrodynamics and mass concentration in the liquid field in **Figure 5** is based on the reconstructed plane results from the WMS and the fully resolved CFD. This visualization provides a comparison between experiments and simulations on the same scale for an entire complex flow process. In line with the aims of this work, it provides a more detailed insight into the mesoscale flow characteristics and CFD model validation. Both for the WMS and CFD results, the rising of the bubbles in the column leads to a cumulative increase in the dissolved concentration c_l in the liquid bulk. The mass transfer at the gas-liquid interface is governed, at these gas-liquid turbulent flow conditions (liquid flow associated Reynolds $Re_l \approx 10^4$) by the unsteady eddy renewal of the thin concentration layer on the liquid side of the gas-liquid interface [21]. Downstream of each bubble, a recirculation or wake region forms, where the advected high-concentration volume of dissolved species accumulates. This is particularly visible at the near-injector region of the CFD results. As the gas flow develops in height and dispersion and turbulence levels increase, the turbulent diffusive transport between the downstream wakes and the liquid bulk is enhanced, leading to more vigorous mixing and a homogeneous increase in the overall concentration of dissolved species in the liquid phase.

From a qualitative point of view, there is an overall agreement between the WMS and CFD on the axial evolution and radial dispersion of the concentration in the liquid (**Figure 5**). Still, remarkably larger concentration gradients are reported close to the injector in the CFD results. Given the low associated rising time at these axial locations, it is suggested that the discrepancy originates from the presence of a non-negligible dissociation time of CO_2 in the water [22]. Therefore, a time or rising distance delay appears between the absorption of $CO_2(aq)$ as modeled by the CFD, and the signal conductivity from the ions HCO_3^- and H^+as measured by the WMS from the equilibrium reactions $CO_2(aq) + H_2O \rightleftarrows H_2CO_3 \rightleftarrows HCO_3^- + H^+$. The time delay possibly resulting from the kinetic limitations of dissociation of CO_2 in the water and CFD outlines the importance of considering chemical kinetics in mass transfer processes in gas-liquid non-ideal flows, where the targeted time scales can be within the range of absorption and dissociation chemical reactions.

The gas-liquid mass transfer can be quantitatively evaluated from the mass flux of dissolved species $\dot{m}_l$, respectively $\langle \dot{M}_l \rangle$ when integrated in the cross-section plane. The mass flux of dissolved species represents the total dissolved CO_2 transported by the liquid, and thus the cumulative amount of mass transferred from the gas to the liquid at a certain rising distance h (**Figure 6**). From the CFD results, both the approximation $\langle \dot{m}_l \rangle \cong \langle w \rangle \langle c_l \rangle (1 - \langle \varepsilon \rangle)$ in (1) and the time-averaging of the instantaneous mass flux $\langle \dot{m}_l \rangle = \langle w c_l \rangle$ in (2) can be computed. The agreement between the two approaches, as shown in **Figure 6**, proves the validity of the approximation (1) to evaluate the total mass transfer, and to compare the CFD and WMS data.

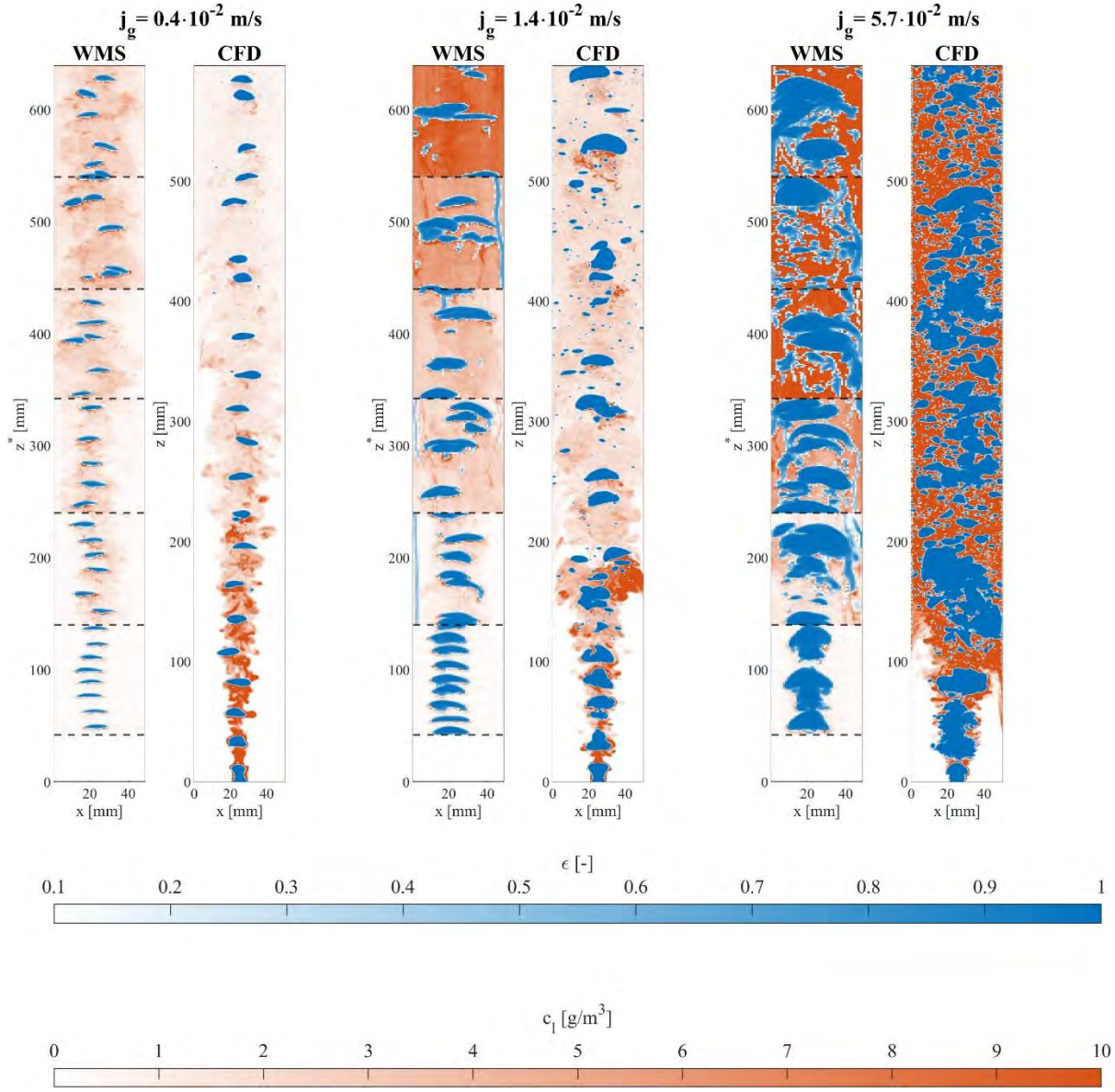

Figure 5. Concentration c_l and void fraction ε projection with threshold $\varepsilon_{th} = 0.1$ for the CFD and WMS for different gas superficial velocities j_g, where the WMS data is reconstructed from the plane measurements (dashed lines --) at $h = 42,\ 140, 240, 342, 440$ and $540\ mm$, and the vertical axis is converted from WMS time frames k to distance z^* using the average gas velocity W_g.

At the lowest and intermediate superficial velocities $j_g = 0.4 \cdot 10^{-2}\ m/s$ and $j_g = 1.4 \cdot 10^{-2}\ m/s$, the experimental and computational results show a similar evolution of the mass transfer flux in the studied height range of the column. This agreement is concurrent with the captured evolution of the interfacial area density, as shown in **Figure 4**. The underestimation of the expected high concentration gradients by the WMS close to the injector is reflected in **Figure 6** as a lower measured mass transfer by the WMS when $h < 240\ mm$. As the transferred and dissolved CO_2 dissociates into ions with the rising distance h, the concentration measured by the WMS increases, and thus the measured mass flux of dissolved species increases. At the highest measurement points, namely $h > 390\ mm$, the trend is inverted, and the CFD underestimates the mass transfer compared to the WMS results.

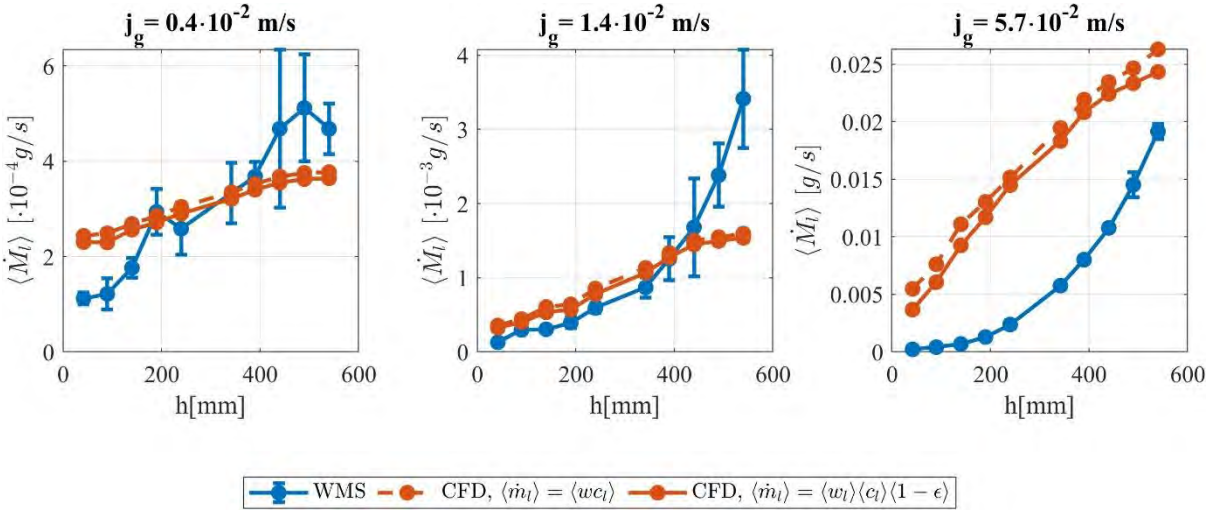

Figure 6. Total time-averaged mass flux of dissolved species $\langle \dot{M}_l \rangle$ for the WMS and CFD as a function of the gas superficial velocity j_g and height h.

In the current CFD model [15], the interfacial mass transfer, being computed as the gradient of the concentration in the liquid phase normal $\vec{n}$ to the gas-liquid surface $\dot{m}_g \propto D(\nabla c_l) \cdot \vec{n}$, is underestimated for coarse mesh sizes, as the resolution $\Delta x_{CFD} = 0.39\, mm$ is used in the current simulations. A convergence study of the model for a single bubble case [15] has reported that the mass transfer results do not lie in the convergence asymptotic regime for the current resolution, with a larger discrepancy in the mass transfer coefficient. In contrast, in our more practical application in this study, a reasonable agreement is found at the superficial velocities $j_g = 0.4 \cdot 10^{-2}\, m/s$ and $j_g = 1.4 \cdot 10^{-2}\, m/s$. While a further refinement and convergence analysis might be desirable, at the current computational cost, this is not feasible, and such systematic bias in the evaluation of the concentration gradient must be acknowledged.

For the largest superficial velocity of $j_g = 5.7 \cdot 10^{-2}\, m/s$, the discrepancy between the experimental and simulation results is primarily dominated by the previously discussed significant overestimation of the interfacial area density. The larger turbulence levels at these conditions lead to a wider range of turbulent scales to solve, and the finer mesh requirements not being fulfilled result in a more significant impact of the unresolved gas-liquid stresses at the interface, thus bubble fragmentation, interfacial area density overestimation, and the resulting mass transfer are also not being properly reproduced.

4. CONCLUSIONS

A fundamental comparative study of mass transfer in gas-liquid flows with a high-resolution WMS and the DNS CFD code PSI-BOIL for gas-liquid flows has been performed in this study. The primary objective was to cross-evaluate the current capabilities of state-of-the-art experimental and computational techniques for studying multiphase flow applications with mass transfer in nuclear safety, such as in pool scrubbing processes.

The first part of the evaluation considered the most relevant variables in the analysis of the gas-liquid flow hydrodynamics, namely the bubble size distribution, gas phase velocity, and interfacial area density. In this regard, there is a general agreement between the WMS and CFD results up to a gas superficial velocity of around $10^{-2}\, m/s$ with single point injection. Above this range, the increase in turbulence levels of the gas-liquid flow mixture leads to a significant over-fragmentation of the ellipsoid and cap bubbles in the

calculations. At the largest gas flow rate and turbulence levels, the initial bubble size formation and distribution are also affected by the over-fragmentation with the currently imposed inlet velocity profile. Measurements with an HSC support this observation. This over-fragmentation bias in the CFD results directly affects the calculation of the interfacial area density and, therefore, is reported to be the most relevant limitation that needs to be resolved in the CFD model to characterize the mass transfer for superficial velocities larger than $10^{-2}\,m/s$. A bubble deformation is also acknowledged in the WMS results. The following evaluation of the mass transfer has pointed out the limitations of the WMS and CFD mesoscale comparison of the concentration field of dissolved CO_2 when assuming chemical equilibrium conditions. For non-ideal flows, the chemical process and time scales of the hydration and dissociation of CO_2 should be taken into consideration for both CFD modelling and WMS post-processing, as they may fall within the range of the relevant turbulent time scales. Overall, the CFD predictions on mass transfer agree with the WMS experimental results for the superficial velocities below $10^{-2}\,m/s$. It is also acknowledged here that the employment of coarse structured meshes, restricted by the computational cost, is an important limitation of this study, which leads to a systematic underestimation of the fluxes as a function of the concentration gradients. Furthermore, as the gas flow rate and turbulence levels increase, so do the mesh refinement requirements to capture the entire range of turbulence scales and thus the reported issues of unresolved stresses at the gas-liquid interface. The extension of subgrid modelling and unstructured meshes in PSI-BOIL is considered in the future to solve the over-fragmentation and gradient underestimation in the CFD results.

ACKNOWLEDGMENTS

The support of this work by Swiss National Science Foundation (SNSF) under Doctoral Grant 200021_200734 (03/2022-12/2026) for the project *Simultaneous measurement of aerosol mass transfer and hydrodynamics in gas-liquid two-phase flow systems* is gratefully acknowledged.

BIBLIOGRAPHY

[1] I. A. E. Agency, Severe Accident Mitigation Through Improvements in Filtered Containment Vent Systems and Containment Cooling Strategies for Water Cooled Reactors: Proceedings of a Technical Meeting on Severe Accident Mitigation Through Improvements in Filtered Containment Venting for Water Cooled Reactors Held in Vienna, Austria, 31 August-3 September 2015. International Atomic Energy Agency, 2017.

[2] P. C. Owczarski and K. W. Burk, "SPARC-90: A code for calculating fission product capture in suppression pools," Nuclear Regulatory Commission, Washington, DC (United States). Div. of Regulatory Applications; Pacific Northwest Lab., Richland, WA (United States), NUREG/CR-5765; PNL-7723, Oct. 1991. doi: 10.2172/6120360.

[3] S. A. Ramsdale, S. Guentay, and H. G. Friederichs, "BUSCA-JUN91 Reference manual for the calculation of radionuclide scrubbing in water pools," Germany, 3-923875-66–5, 1995.

[4] D. D. Paul, L. J. Flanigan, J. C. Cunnane, R. A. Cudnik, R. P. Collier, and R. N. Oehlberg, "Radionuclide scrubbing in water pools," in Proceedings of the American Nuclear Society meeting on fission-product behaviour and source term research, 1985. Accessed: Apr. 14, 2025. [Online]. Available: https://inis.iaea.org/search/search.aspx?orig_q=RN:20072395

[5] NEA, "Requirements for CFD-Grade Experiments for Nuclear Reactor Thermal Hydraulics," Paris, 2022. Accessed: Sep. 12, 2025. [Online]. Available: https://oecd-nea.org/jcms/pl_65844/requirements-for-cfd-grade-experiments-for-nuclear-reactor-thermal-hydraulics?details=true

[6] S. Gupta et al., "Integration of pool scrubbing research to enhance Source-Term calculations (IPRESCA) project – Overview and first results," Nuclear Engineering and Design, **vol. 404**, p. 112189, Apr. 2023, doi: 10.1016/j.nucengdes.2023.112189.

[7] A. Dehbi, X. Cheng, Y. Liao, Y. Okagaki, and M. Pellegrini, "A comparative CFD exercise on bubble hydrodynamics using Euler-Euler and interface tracking approaches," in Proceedings of 19th International Topical Meeting on Nuclear Reactor Thermal Hydraulics (NURETH-19), Brussels, Mar. 2022.

[8] Y. Liao, J. Li, and D. Lucas, "Investigation on pool-scrubbing hydrodynamics with VOF interface-capturing method," Nuclear Engineering and Design, **vol. 390**, p. 111713, Apr. 2022, doi: 10.1016/j.nucengdes.2022.111713.

[9] S. Li, P. Apanasevich, D. Lucas, and Y. Liao, "Euler-Euler CFD simulation of high velocity gas injection at pool scrubbing conditions," Exp. Comput. Multiph. Flow, **vol. 5**, no. 4, pp. 365–380, Dec. 2023, doi: 10.1007/s42757-022-0149-3.

[10] Y. Abe, K. Fujiwara, S. Saito, T. Yuasa, and A. Kaneko, "Bubble dynamics with aerosol during pool scrubbing," Nuclear Engineering and Design, vol. 337, pp. 96–107, Oct. 2018, doi: 10.1016/j.nucengdes.2018.06.017.

[11] P. Papadopoulos, "Experimental Evaluation of Gas Retention in Two-Phase Flows relevant to Pool Scrubbing in FCVS," Doctoral Thesis, ETH Zurich, 2022. doi: 10.3929/ethz-b-000568575.

[12] T. Betschart, T. Lind, and H.-M. Prasser, "Investigation of two-phase flow hydrodynamics under SGTR severe accident conditions," Nuclear Engineering and Design, **vol. 366**, p. 110768, Sep. 2020, doi: 10.1016/j.nucengdes.2020.110768.

[13] A. R. Perez, T. Lind, V. Petrov, A. Manera, and H.-M. Prasser, "Visualization and quantification of gas–liquid mass transfer in a sparger flow using a wire-mesh sensor," Chemical Engineering Science, p. 122360, Aug. 2025, doi: 10.1016/j.ces.2025.122360.

[14] B. Niceno, Niceno/PSI-BOIL/https://github.com/Niceno/PSI-BOIL. (Jun. 10, 2025). C++. Accessed: Sep. 08, 2025. [Online]. Available: https://github.com/Niceno/PSI-BOIL

[15] Y. Wang and Y. Sato, "Direct numerical simulation of a rising CO2 bubble dissolving in quiescent water at high Schmidt number," International Journal of Multiphase Flow, p. 105566, Dec. 2025, doi: 10.1016/j.ijmultiphaseflow.2025.105566.

[16] C. Tompkins, H.-M. Prasser, and M. Corradini, "Wire-mesh sensors: A review of methods and uncertainty in multiphase flows relative to other measurement techniques," Nuclear Engineering and Design, **vol. 337**, pp. 205–220, Oct. 2018, doi: 10.1016/j.nucengdes.2018.06.005.

[17] A. Manera, H.-M. Prasser, D. Lucas, and T. H. J. J. Van Der Hagen, "Three-dimensional flow pattern visualization and bubble size distributions in stationary and transient upward flashing flow," International Journal of Multiphase Flow, **vol. 32**, no. 8, pp. 996–1016, Aug. 2006, doi: 10.1016/j.ijmultiphaseflow.2006.03.005.

[18] H.-M. Prasser, S. Stucki, T. Betschart, and J. Eisenberg, "Interfacial area density measurement using a three-layer wire-mesh sensor," in International Topical Meeting on Nuclear Reactor Thermal Hydraulics 2015 (NURETH-16): Chicago, Illinois, USA, 30 August - 4 September 2015, Curran, 2015, pp. 403–418. Accessed: Dec. 28, 2024. [Online]. Available: https://www.research-collection.ethz.ch/handle/20.500.11850/112522

[19] T. J. Liu, "Bubble size and entrance length effects on void development in a vertical channel," International Journal of Multiphase Flow, **vol. 19**, no. 1, pp. 99–113, Feb. 1993, doi: 10.1016/0301-9322(93)90026-Q.

[20] D. Ito, H.-M. Prasser, H. Kikura, and M. Aritomi, "Uncertainty and intrusiveness of three-layer wire-mesh sensor," Flow Measurement and Instrumentation, **vol. 22**, no. 4, pp. 249–256, Aug. 2011, doi: 10.1016/j.flowmeasinst.2011.03.002.

[21] P. V. Danckwerts, "Significance of Liquid-Film Coefficients in Gas Absorption," Ind. Eng. Chem., **vol. 43**, no. 6, pp. 1460–1467, Jun. 1951, doi: 10.1021/ie50498a055.

[22] W. Knoche, "Chemical Reactions of CO2 in Water," in Biophysics and Physiology of Carbon Dioxide, C. Bauer, G. Gros, and H. Bartels, Eds., Berlin, Heidelberg: Springer, 1980, pp. 3–11. doi: 10.1007/978-3-642-67572-0_1.

PSI Center for Nuclear Engineering and Sciences

Interfacial gas transfer in gas-liquid flows

A comparative study of advanced experimental and computational techniques

A. Ramos Perez, T. Lind, Y. Sato. V. Petrov[1]

A. Manera, H-M. Prasser[2]

Y. Wang[3]

ERMSAR2026-Madrid, 19th May 2026

[1]PSI, Centre for Nuclear Engineering and Sciences (Villigen, Switzerland)
[2]ETHZürich, Department of Mechanical and Process Engineering (Zürich, Switzerland)
[3]Tsinghua University, Institute of Nuclear and New Energy Technology, (Beijing, China)

Introduction: Pool scrubbing and *local* studies

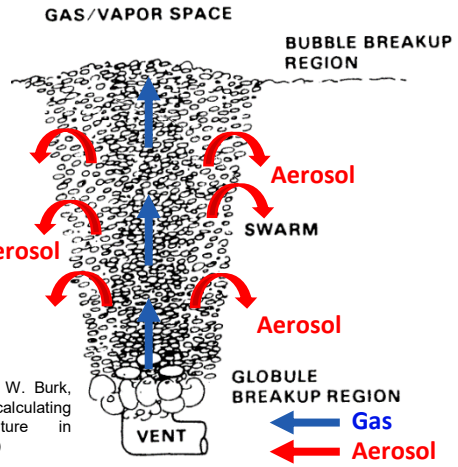

P. C. Owczarski and K. W. Burk, "SPARC-90: A code for calculating fission product capture in suppression pools" (1991)

Comparison at the ***integral*** *level*

MELCOR

AC² COCOSYS

Local measurements
(Hydrodynamics + Mass Transfer)

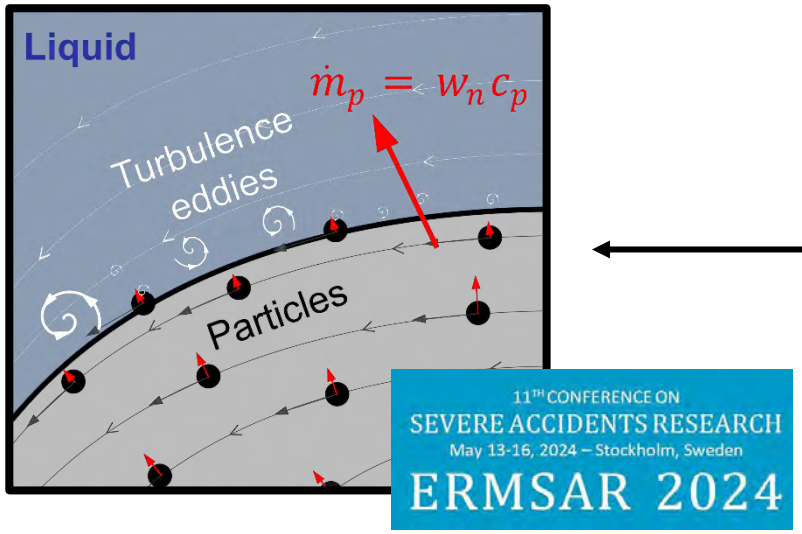

11TH CONFERENCE ON SEVERE ACCIDENTS RESEARCH
May 13-16, 2024 – Stockholm, Sweden
ERMSAR 2024

Comparison at the ***local*** *level*

Analytical models (CFD)
(Hydrodynamics + *Mass Transfer*)

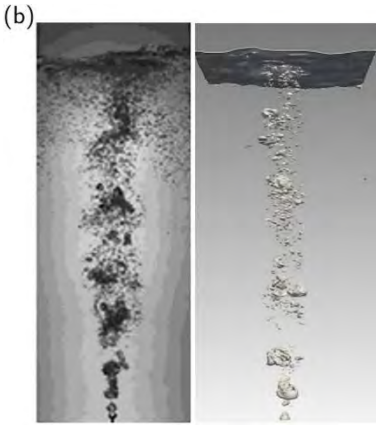

Yixiang Liao, Jiadong Li, Dirk Lucas, "Investigation on pool-scrubbing hydrodynamics with VOF interface-capturing method" (2022)

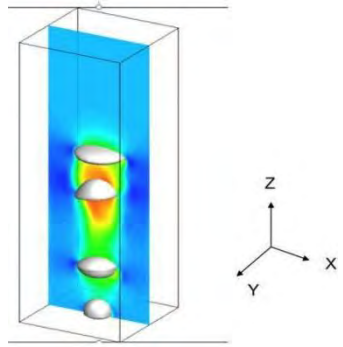

A. Dehbi, X. Cheng, Y. Liao, Y. Okagaki, M. P ellegrini. "A CompArAtive CFD Exercise on Bubble HydrodynAmics Using Euler-Euler and InterfAce TrAcking ApproAches" (2022)

Introduction: Pool scrubbing and *local* studies

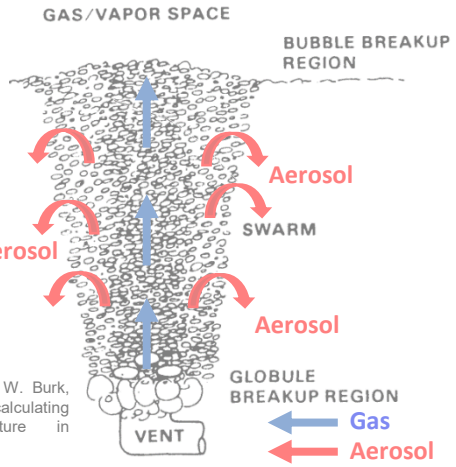

P. C. Owczarski and K. W. Burk, "SPARC-90: A code for calculating fission product capture in suppression pools" (1991)

Comparison at the ***integral*** *level*

MELCOR

AC² COCOSYS

Local measurements
(Hydrodynamics + Mass Transfer)

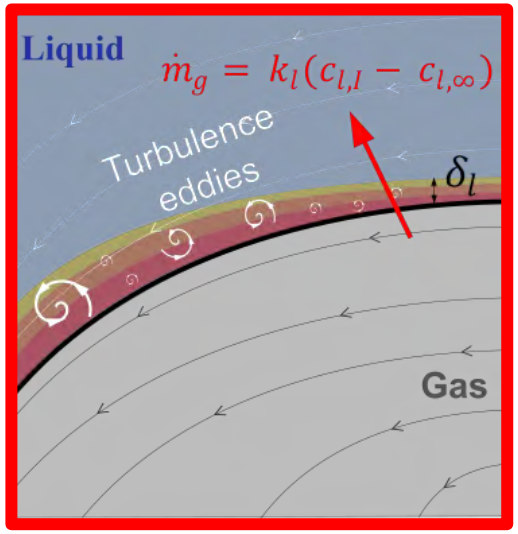

Comparison at the ***local*** *level*

Analytical models (CFD)
(Hydrodynamics + *Mass Transfer*)

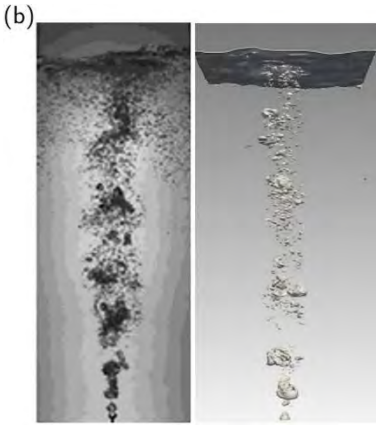

Yixiang Liao, Jiadong Li, Dirk Lucas, "Investigation on pool-scrubbing hydrodynamics with VOF interface-capturing method" (2022)

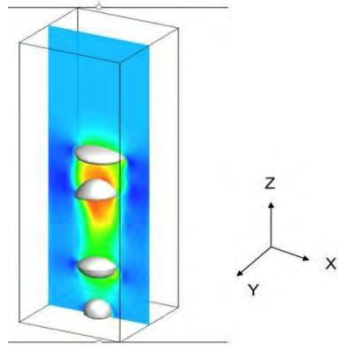

A. Dehbi, X. Cheng, Y. Liao, Y. Okagaki, M. P ellegrini. "A CompArAtive CFD Exercise on Bubble HydrodynAmics Using Euler-Euler and InterfAce TrAcking ApproAches" (2022)

Instrumentation and methods

WMS experiments

Two-phase, gas mass transfer	CO_2
3-layer WMS	$\Delta x = 1.0\ mm$
Bubbly flow regime	$j_g = 0.4 - 5.7 \cdot 10^{-2}\ m/s$
Optical imaging HSC	$h = [180, 280]\ mm$

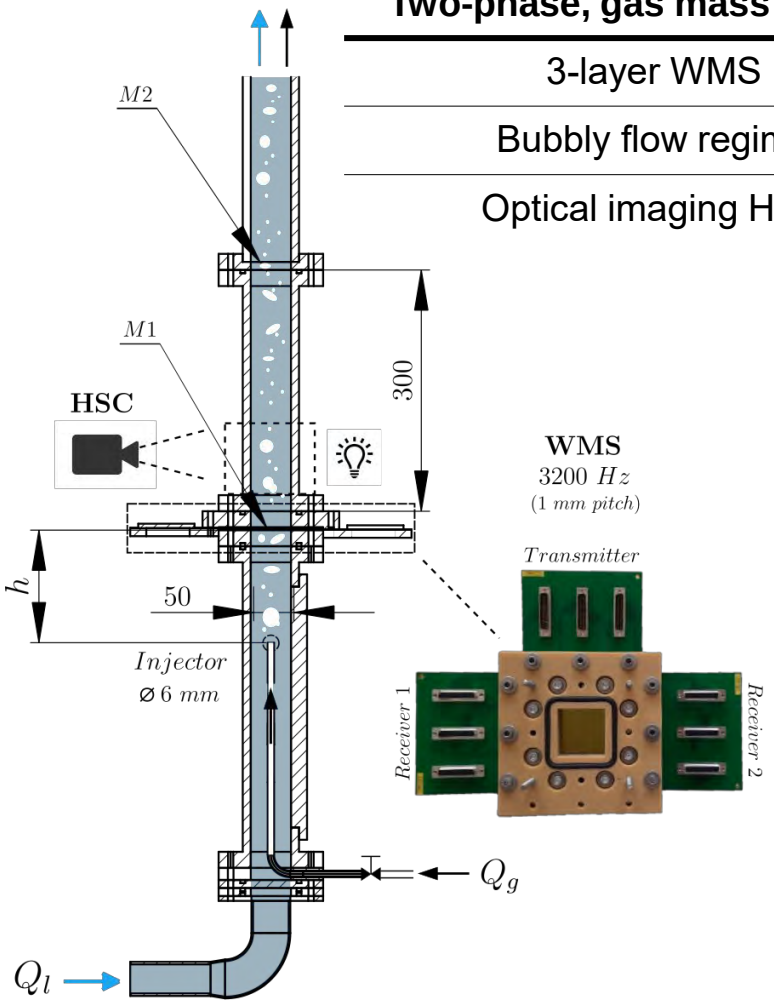

Instrumentation and methods

WMS experiments

Two-phase, gas mass transfer	CO_2
3-layer WMS	$\Delta x = 1.0\ mm$
Bubbly flow regime	$j_g = 0.4 - 5.7 \cdot 10^{-2}\ m/s$
Optical imaging HSC	$h = [180, 280]\ mm$

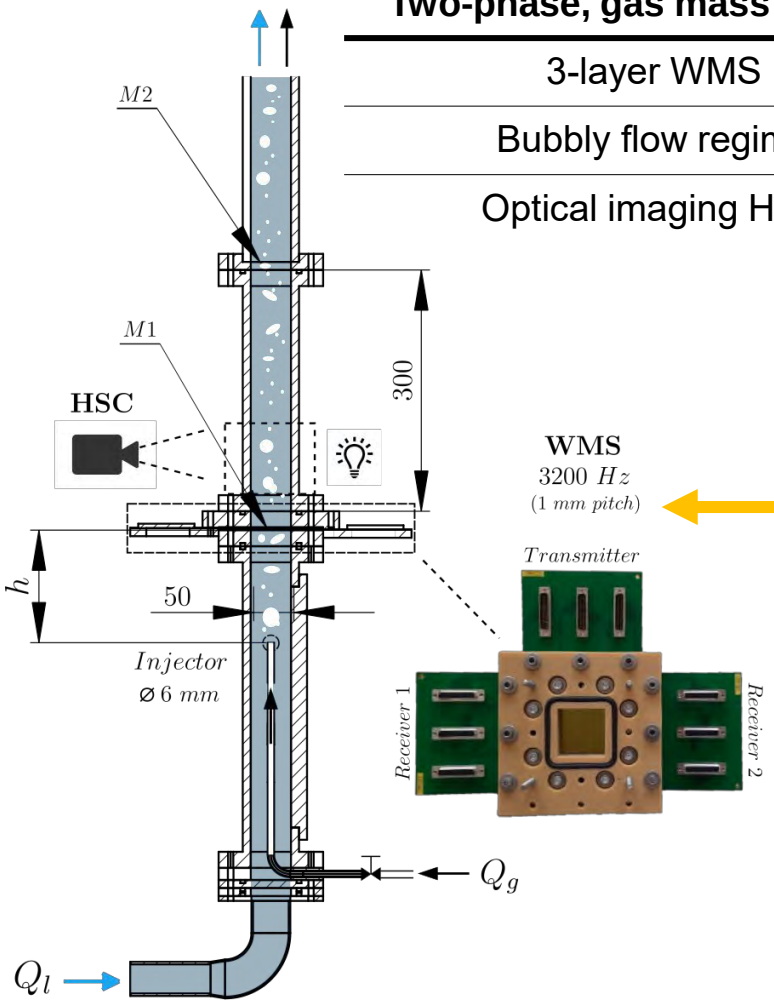

*(!) CFD **same** scale comparison*

Direct Numerical Simulation (DNS)	*Finite-Volume-Method*
Two-phase flow	*Volume-of-Fluids (VOF)*
Superficial mass flux	$\dot{m}_g = D(\nabla c_l)$
Interface treatment	*Sharp-interface phase-change*

CFD simulations

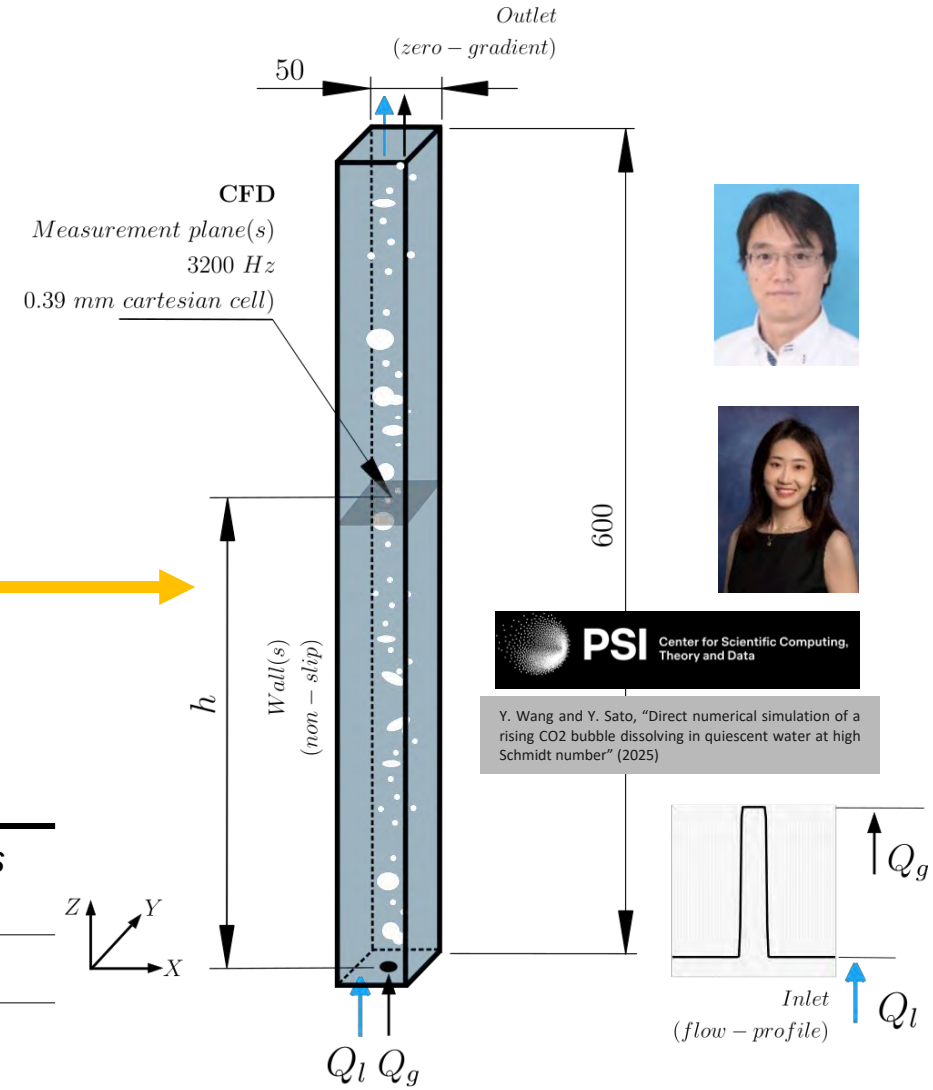

PSI Center for Scientific Computing, Theory and Data

Y. Wang and Y. Sato, "Direct numerical simulation of a rising CO2 bubble dissolving in quiescent water at high Schmidt number" (2025)

Instrumentation and methods

Data post-processing methods

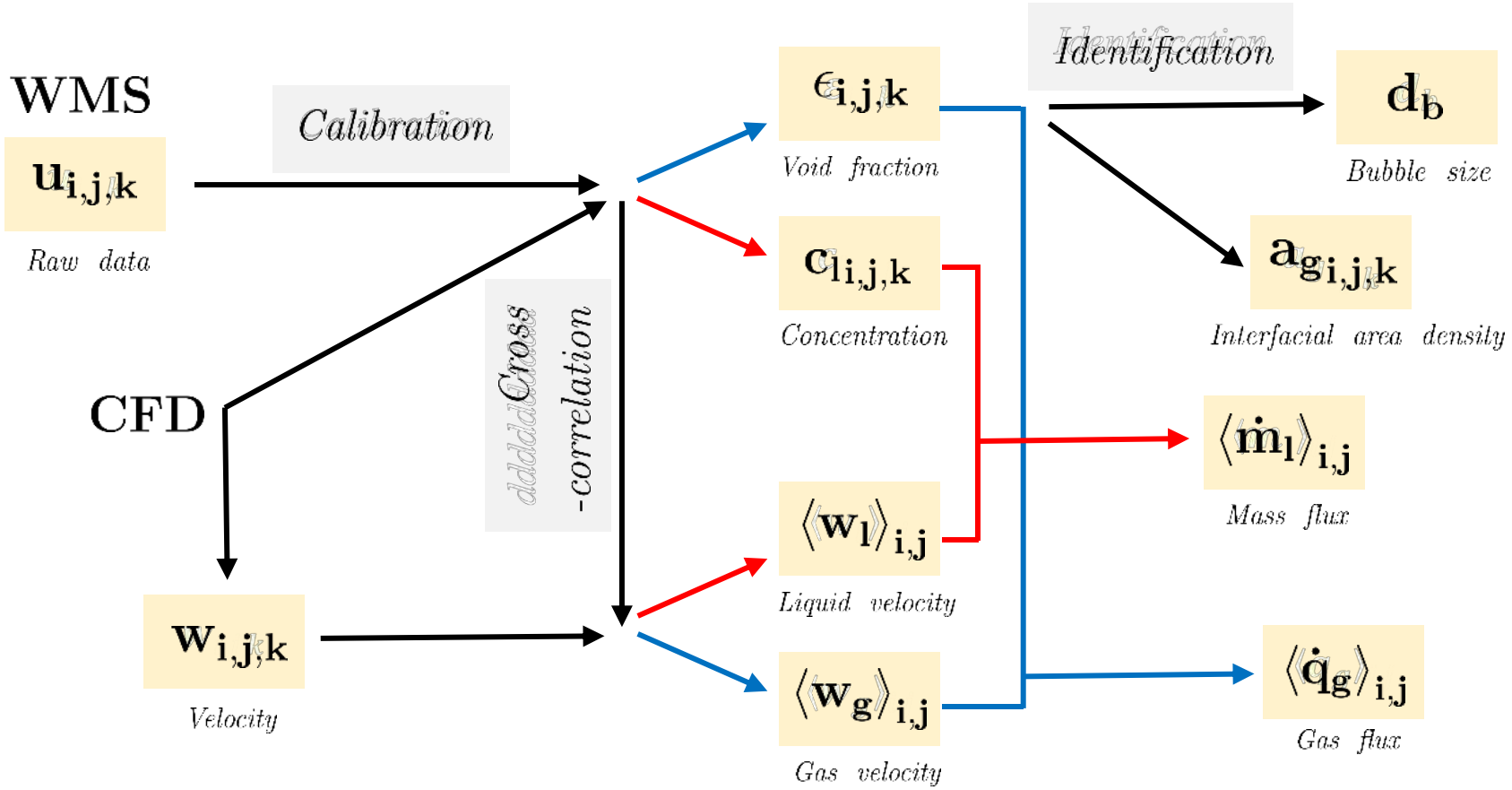

Results: flow hydrodynamics

Bubble rising process characterized by bubble interaction and axial dispersion → enhanced by gas superficial velocity leading to higher mixing levels (*turbulence*)

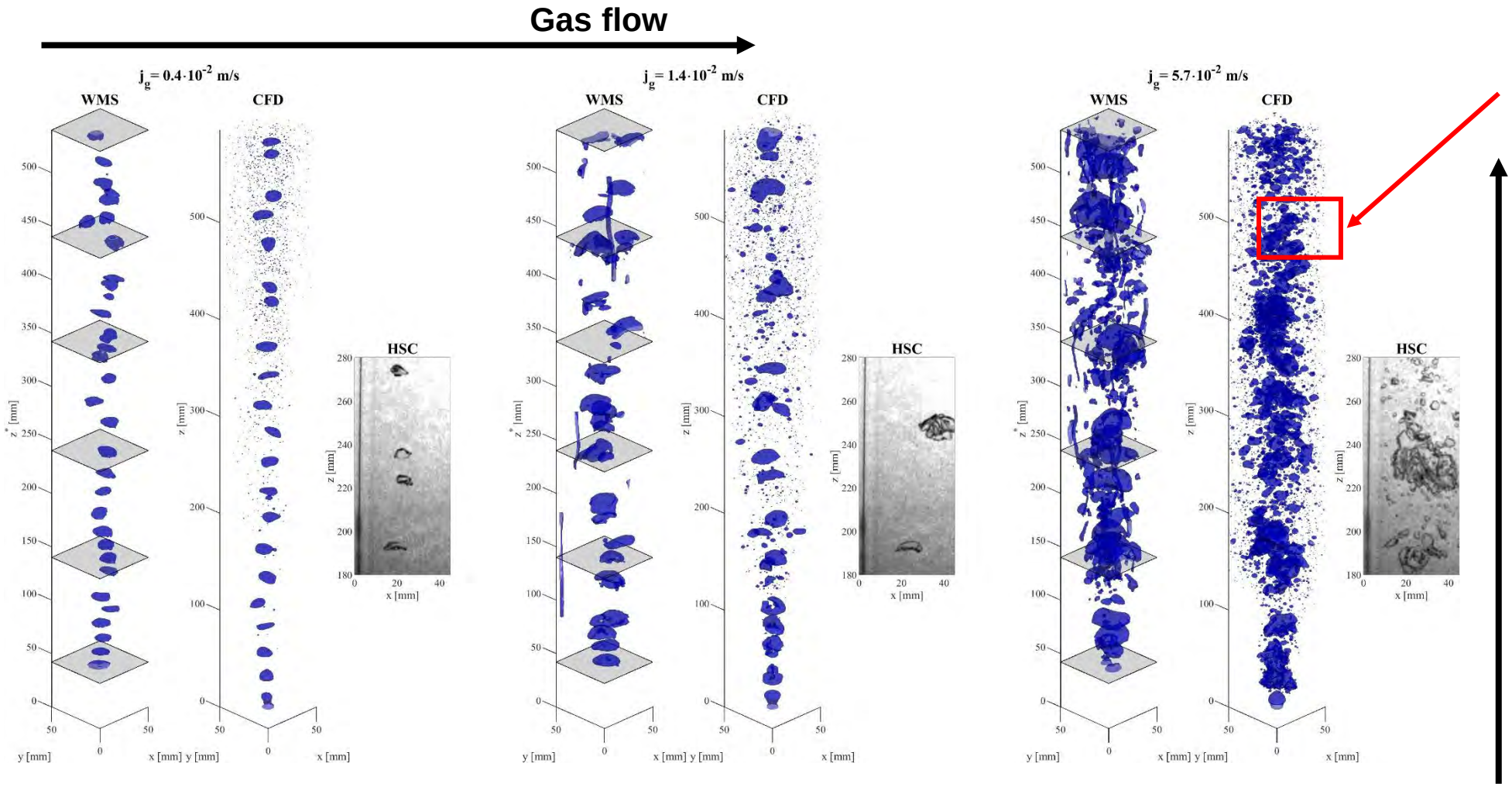

Overprediction of the bubble fragmentation (*unresolved turbulent interfacial stresses*)

* (3D) Contours for $\varepsilon = 0.1$

PSI Center for Nuclear Engineering and Sciences

A. Ramos Perez ETHZ/PSI

Results: flow hydrodynamics

- Well-captured monodisperse distribution at the near-injection region at low gas superficial velocities, wider distribution of sizes d_b from the CFD results

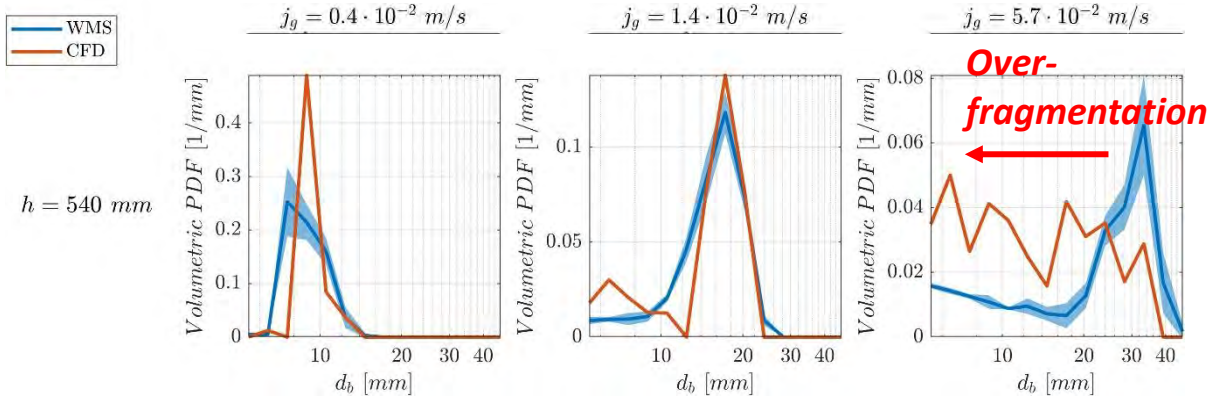

Gas flow

Interfacial area density → *Bubble size distribution*

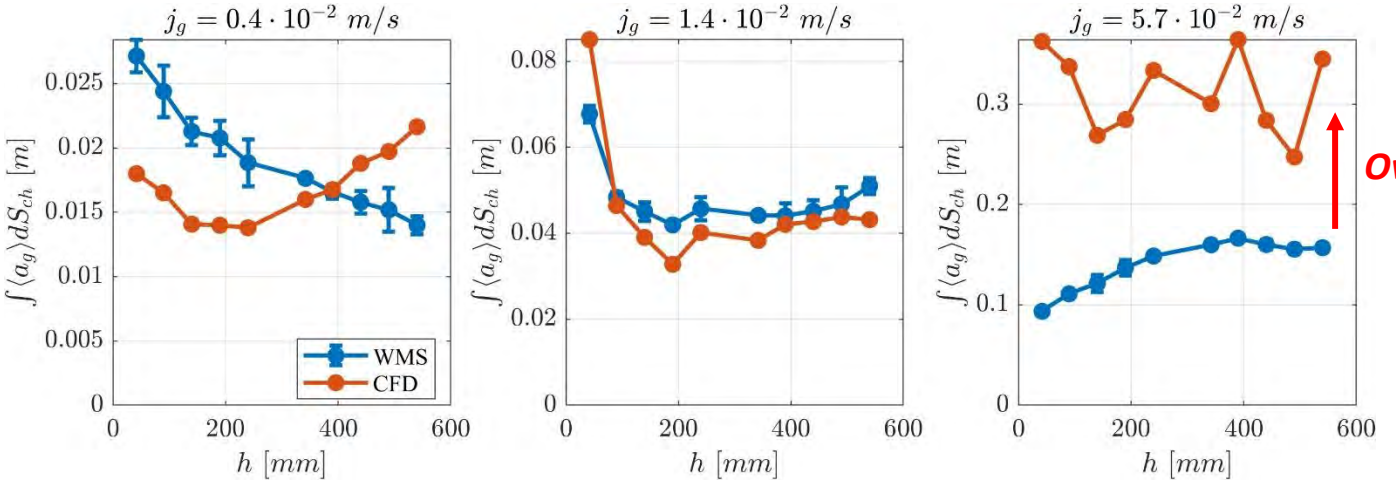

- The mass flux is linearly proportional to the key variable of the interfacial area density

Results: flow hydrodynamics

- Both WMS and CFD results are self-consistent in the conservation of the ***bubble volume***

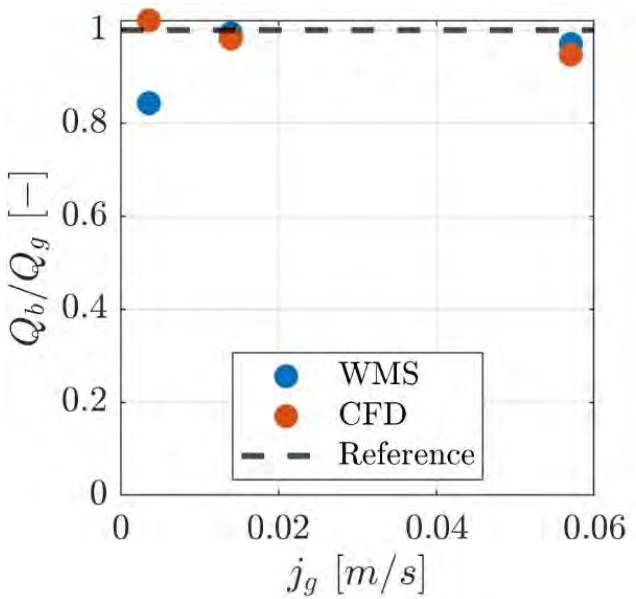

Interfacial area density — **Gas flow** → *Validation of the hydrodynamic results*

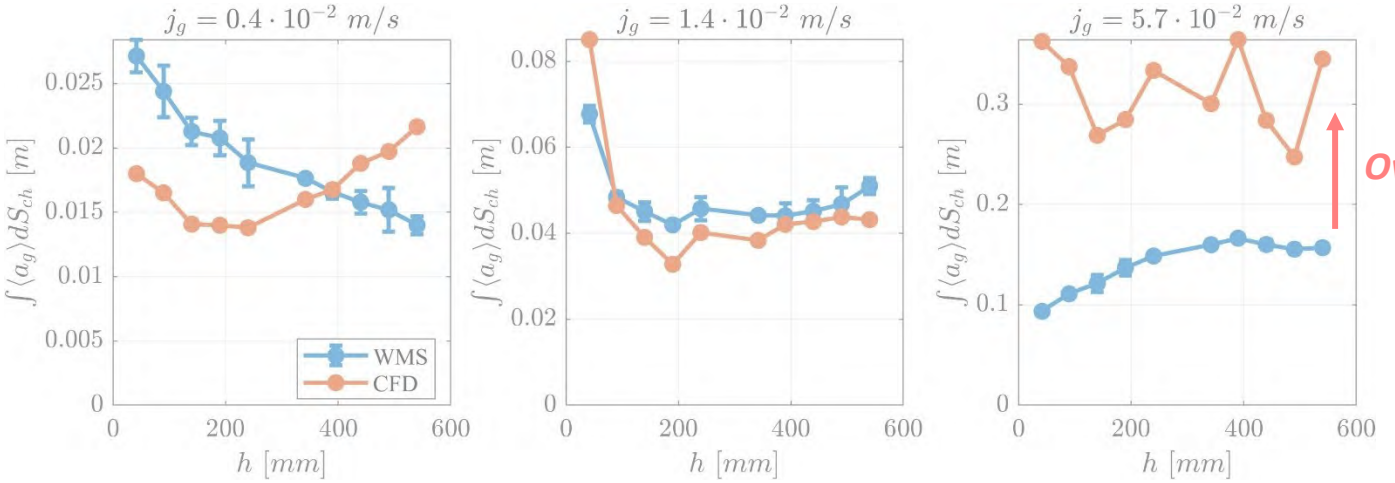

Over-fragmentation

- The mass flux is linearly proportional to the key variable of the interfacial area density

Results: interfacial mass transfer

- Mass transfer underestimation, slow dissociation of CO_2 into ions

Slow — Chemical equilibria

$$\boldsymbol{CO_2(aq)} + H_2O \rightleftarrows H_2CO_3 \rightleftarrows \boldsymbol{HCO_3^-} + H^+$$

Fast

Chemical kinetics

$$\frac{d[CO_2(aq)]}{dt} = k^*_{H_2CO_3}[H_2CO_3] - \boldsymbol{k^*_{CO_2}}[CO_2(aq)]$$

Integral mass flux $\rightarrow \langle \dot{m}_l \rangle \approx \langle w_l \rangle \cdot \langle c_l \rangle \langle 1 - \varepsilon \rangle$

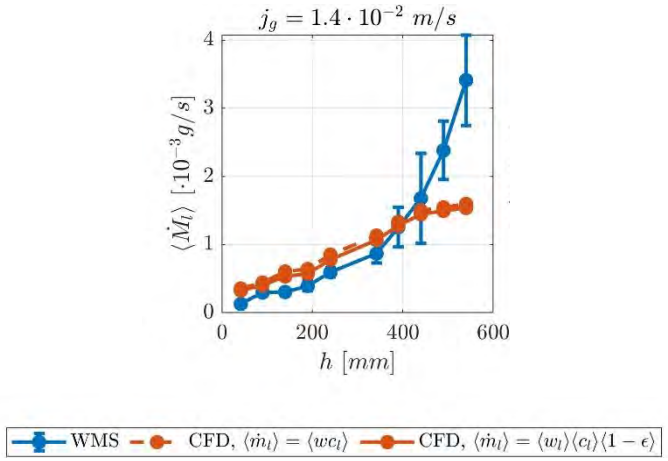

Gas flow

PSI

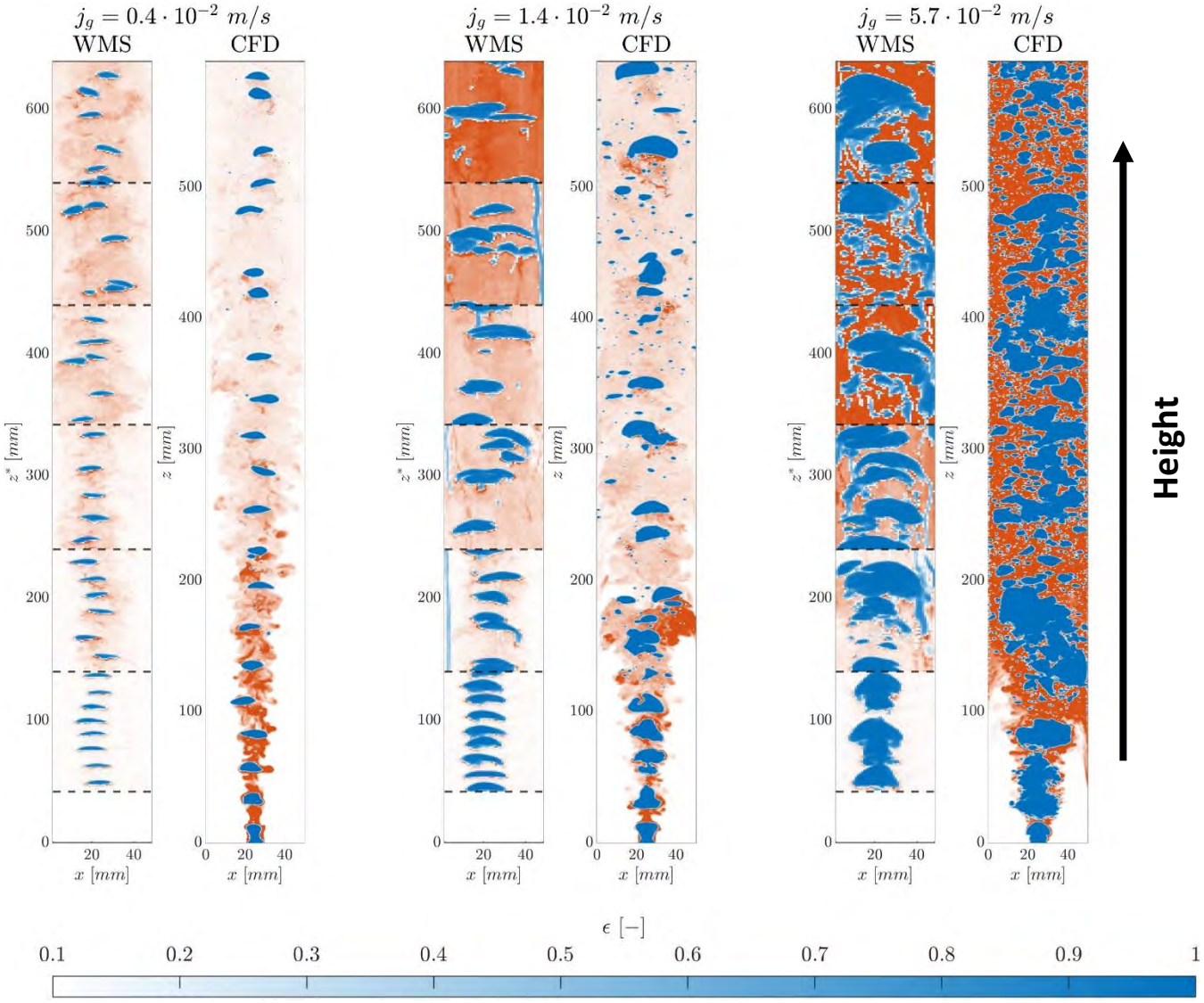

*(2D) Projections with threshold $\boldsymbol{\varepsilon_{th} = 0.1}$, for $\Delta z^* = 100\ mm$ *Frames* at axial position h

Conclusions

Asco Nuclear Power Plant (Spain) and Filtered Venting Containment System (AREVA)

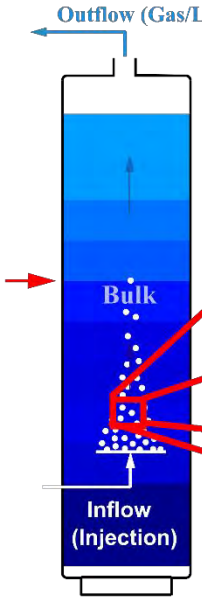

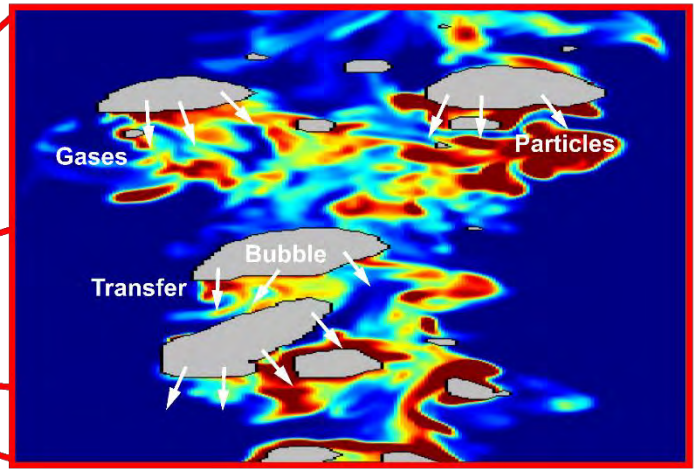

Gas-liquid bubbly flow transfer processes

Conclusions

Asco Nuclear Power Plant (Spain) and Filtered Venting Containment System (AREVA)

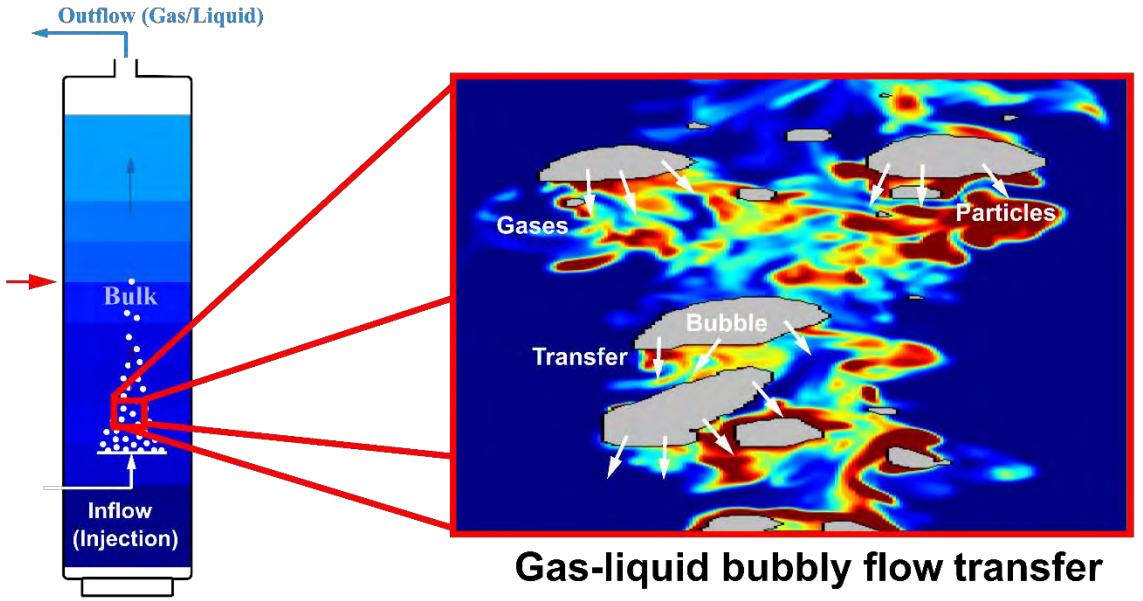

Gas-liquid bubbly flow transfer processes

Funding support:

Schweizerische Eidgenossenschaft
Confédération suisse
Confederazione Svizzera
Confederaziun svizra

Swiss National Science Foundation

Captured local gas-liquid flow hydrodynamics (bubble size, interfacial area) at low gas injection conditions ($< 10^{-2}\ m/s$)

Mass transfer local evaluation, signal delay due to chemical kinetics (**WMS**)

*(!) Local **same** scale comparison*

Unresolved turbulent stresses at the interface (**CFD**)

IMPACT OF ASTEC'S ADVANCED MODELING IN GAS AND ADSORBED PHASES CHEMISTRY ON THE SOURCE TERM

Guillaume Astier, Olivia Coindreau, Loris Gelin, and Sidi M. O. Souvi*
Autorité de Sûreté Nucléaire et de Radioprotection (ASNR)
PSN-RES/SAM/LETR
F-13115, Saint-Paul-lez-Durance, France
guillaume.astier@asnr.fr ; olivia.coindreau@asnr.fr ; loris.gelin@asnr.fr ; sidi.souvi@asnr.fr

ABSTRACT

In this work, we present the impact of the new chemical modelling, implemented in the ASTEC code, dedicated to the source term evaluation during a severe nuclear accident. This new modelling approach is based on three major developments: (i) The removal of the thermodynamic equilibrium assumption in the gas phase, replaced by a generalized chemical kinetics model, relying on the systematic generation of reaction pathways and the approximation of kinetic rate constants. (ii) The introduction of surface reactivity, including non-congruent condensation and evaporation processes, allowing a more accurate representation of the chemistry of previously challenging species, such as $CsHMoO_4$(g) and RuO_4(g). (iii)The enrichment of the thermodynamic database, with the inclusion of new species in the condensed, adsorbed, and gaseous phases. This paper details the scientific motivations and the physical foundations of these developments. Their impacts on source term evaluation will be illustrated through comparisons with experimental results from the GAEC, CHIP, and CHIP+ programs. A particular focus will be placed on the speciation of iodine at the outlet, in both gaseous (I_2, HI, IOH, …) and aerosol forms (CsI, AgI, CdI_2, …).

KEYWORDS
ASTEC, Source term, Surface chemistry,

1. INTRODUCTION

In the context of a severe accident (SA) in a nuclear power plant (NPP), the release of fission products (FPs) can result in extensive contamination, posing significant risks to both human health and to the environment. In case of atmospheric releases into the environment following early containment venting procedure or containment failure, iodine can account for a large part of the radiological consequences owing to its volatility and substantial radiotoxicity. The amount of iodine source term (ST) is strongly linked to the physico-chemical forms of the released radioisotopes, especially the fraction present in gaseous or aerosol form in the containment.

In the early 1990s, it was generally assumed that iodine enters the containment predominantly in aerosol form. Thus, NUREG/CR-5732 [1] stated -based on thermodynamic calculations- that the chemical forms of iodine entering the containment from the RCS can reasonably be characterized as at least 95% caesium iodide (CsI), with the remaining 5% present as gaseous I_2 and HI. For caesium, the main prevailing assumption was that the CsOH is in large excess [2]. However, it later became apparent that the situation is more complex. In particular, the large scale Phébus FP test series showed that several condensable iodide forms not associated to caesium may exist in the RCS [3]. Moreover, a significant amount of iodine under a gaseous form was found in the containment early during the bundle transient phase, implying that this gas originates from the circuit [4-6]. Both shortcomings in thermochemical properties and the equilibrium assumption in the circuit gas phase have been put forward to account for the differences between the theoretical and the experimental results [7-8; 3].

To enhance the understanding of the key chemical processes involving released FPs and control rod materials in the RCS during a severe accident, as well as to develop an experimental database, the ISTP-CHIP (2005–2012) and the follow-up CHIP+ (2012–2018) experimental programs were launched at IRSN [9]. Chemical systems involving iodine, main released FPs which can interfere with iodine (Cs and Mo) and control rod material (B, Cd, Ag and In) were considered. Experiments conducted on the I–O–H system revealed kinetic limitations in the reactivity of gas phase iodine [10]. In contrast, no significant kinetic limitations were observed when Cs is added in quite large excess relative to iodine, enabling the principal caesium species (CsI, CsOH) to be accurately described using the thermodynamic equilibrium assumption [11]. The formation of caesium molybdates can be clearly evidenced when both Mo and Cs are considered [11], whereas results obtained from the B-Cs-I-O-H system tend to show that the formation of caesium borates is less favourable [12]. Finally, when silver, indium, or cadmium (SIC) is introduced into the Mo-Cs-I-O-H chemical system, numerous metallic molybdates involving SIC components are formed [13]. These species compete with Cs-molybdate formation and may diminish the scavenging effect of Mo towards Cs.

At the same time, significant effort was devoted to developing a kinetic scheme for iodine transport through the RCS, with the objective of improving the ASTEC software (Accident Source Term Evaluation Code). A kinetic model for iodine, oxygen, and hydrogen, comprising 33 reactions was developed by Xerri et al. [14], building upon the scheme originally proposed in Wren's report [7]. This model was applied to re-interpret the FPT1 experimental data- with a notable improvement- although similar progress was not achieved for FPT3 [15]. The model was further applied to reproduce experimental observations for both the I–O–H system [10] and the Cs–Mo–I–O–H system [11]. The model provides a good reproduction of the experimental trends observed in the two CHIP PL tests involving Mo, Cs, I, O, and H under both oxidizing and reducing conditions. In particular, the formation of gaseous iodine (I_2) in oxidizing carrier gases, driven by the formation of Cs_2MoO_4, is well captured by the model—whether using the thermodynamic equilibrium assumption or incorporating iodine kinetic reactions. However, the caesium-molybdate deposition profile is not accurately captured, as the model overpredicts deposition in the high-temperature region of the tube.

To improve the agreement with the CHIP experimental results, especially the deposition profiles in the high- and low-temperature sections, several improvements have been implemented in ASTEC:

1. The kinetic model for the gas phase, initially developed for the I-O-H system (Xerri et al., 2012), is generalized to all elements. It relies on the systematic generation of reaction pathways and the approximation of kinetic rate constants. It thus eliminates the need for the thermodynamic equilibrium assumption in the gas phase.
2. The introduction of surface reactivity, including non-congruent condensation and evaporation processes, allowing a more accurate representation of the chemistry of previously challenging species, such as $CsHMoO_4$(g), H_2MoO_4(g) and RuO_4(g).
3. The enrichment of the thermodynamic database, with the inclusion of new species in the condensed, adsorbed, and gaseous phases.

This paper details in section 2 the improvements implemented in the ASTEC code. Experiments (GAEC IOH and CHIP PL tests) are then simulated and the capability of the code to reproduce the experimental data is discussed in Section 3.
In the following sections the different models are distinguished as follows:

- Th_Eq: Thermodynamic equilibrium.
- Kin_v0: I-O-H kinetic model used in publications [10], [11] and [15].
- Kin_v0-Eq: I-O-H kinetic model used in [10] with (H-O) subsystem at equilibrium
- Kin_v1: Generalized kinetic model with the enriched database described in this paper

2. NEW DEVELOPMENTS IN ASTEC

The French *Autorité de Sûreté Nucléaire et de Radioprotection* (ASNR) is developing the ASTEC code, which aims at simulating an entire SA sequence from the initiating event up to the release of radioactive elements in the environment. The SOPHAEROS module of ASTEC is responsible for the transport of FPs, the physics of aerosols and the chemistry of FPs and structural materials in both the primary circuit and the containment. Given the variety of chemical elements that may be involved (and consequently the large number of species to be considered), reliable modeling of this chemistry requires kinetic data covering several thousand reaction pathways (homogeneous and heterogeneous) over a wide temperature range, often exceeding 2000 °C.

2.1. Generalization of kinetic control

The kinetic data available in the database associated with ASTEC does not cover the chemistry of all species already identified from a thermodynamic standpoint. Moreover, databases continue to grow much faster in thermodynamic data than in kinetic data, mainly thanks to ab initio methods. It should be noted that it is far easier to compute the thermodynamic properties of a species than to evaluate the kinetics of its formation or destruction. This situation raises a fundamental question: how can one best model a system for which complete thermodynamic data are available but kinetic data are only partially known? In other words, how can the evolution of the kinetically controlled part of the system be combined with the spontaneous adaptation of the other part at thermodynamic equilibrium? To address this challenge, the simplest approach is to replace thermodynamic equilibrium—for the part of the system for which only thermodynamic data are available—with a fast kinetic process. This yields a system entirely governed by kinetics: one part following real reaction rates, the other governed by artificially accelerated rates. The question then shifts to the very definition of "fastness": how can one assign to each reaction pathway a rate constant that is both sufficiently high—not to impose an artificial dynamic constraint—and proportional to thermodynamic reality, i.e., to the relative stability of products and reactants? In other words, can we define a maximum or an upper bound for chemical rate constant?

The maximum rate constant has been evaluated for A+B→AB type reactions by adopting collision theory formalism, expressing the reaction rate as the product of a collision frequency, noted $Freq_{A\&B}$, and a reactivity probability P^{REACT}:

$$v_d = Freq_{\mathrm{A\&B}} \times P^{REACT} \tag{1}$$

Then, the reactivity probability has been evaluated at molecular energy states level, and the following upper bound expression has been determined:

$$v_d^{\mathrm{UB}} = K_d^{\mathrm{UP}}[A][B] \tag{2}$$

$$k_d^{\mathrm{UB}} = \sigma Av \sqrt{\left(\frac{8k_BT}{\pi\mu_{\mathrm{AB}}}\right)}\, Q\left(\frac{3}{2}(N_{\mathrm{AB}}-1), \frac{E_{EF}}{k_BT}\right)\frac{P}{P^{\circ}} exp\left(\frac{-\Delta_r G^o(T)}{RT}\right) \tag{3}$$

$$k_r^{\mathrm{UB}} = \sigma Av \sqrt{\left(\frac{8k_BT}{\pi\mu_{\mathrm{AB}}}\right)}\, Q\left(\frac{3}{2}(N_{\mathrm{AB}}-1), \frac{E_{EF}}{k_BT}\right)\frac{P}{RT} \tag{4}$$

where v_d^{UB}, k_d^{UB} and k_r^{UB} stand for upper bound for forward rate, forward rate constant and backward rate constant, respectively. σ is the collision cross section, μ_{AB} is the reduced mass of fragments A and B, Av is Avogadro number, k_B is Boltzmann constant, T is the temperature, P is the pressure, $P°$ is standard pressure, R is the perfect gas constant ($R = Av \times k_B$) and N_{AB} the number of atoms in the molecule AB. E_{EF} is efficient energy, defined as the larger of the dissociation energy at 0 K and the activation energy: $E_{EF} = \max(D_0, E_a)$.. Q is regularized upper incomplete gamma function:

$$Q(a,x) = \frac{\Gamma(a,x)}{\Gamma(a)} \tag{5}$$

Thus, if the activation energy E_a is not known, $E_{EF}$is assigned a default value equal to D_0, which ensures a physically meaningful limiting rate. The present work will highlight the impact of this generalized kinetic on the source term evaluation.

2.2. Surface reactivity

Unlike reactivity in the gas or condensed (homogeneous) phases, surface reactivity is inherently heterogeneous. It involves an adsorbed phase and enables mass transfer between two other phases through the interface. The first step in introducing surface reactivity into SOPHAEROS consisted in accounting for the adsorbed phase within the thermodynamic database associated with ASTEC. The main difficulty of this step lies in the lack of thermodynamic data related to the adsorbed phase, particularly the absence of standard Gibbs free energy of formation in this phase, i.e., no ΔG°f(ads). In contrast to the gas and condensed phases, for which ΔG°f(g) and ΔG°f(c) are intrinsic properties of each species, ΔG°f(ads) depends both on the species under consideration and on the nature of the adsorption sites (substrate), as well as on the state of coverage of adsorption sites, due to changes in the local environment of these sites during adsorption. As a result, at this stage, such reactivity can mainly be addressed for species (or systems) for which ΔG°f(ads) values have been evaluated using *ab initio* calculations. Examples include the adsorption and decomposition of **CsHMoO₄** and **H₂MoO₄** on **MoO₃** surface (non-congruent condensation) [19] and [20], the adsorption and decomposition of **RuO₄** on a **RuO₂** surface, as well as the impact of **NOx** on the non-congruent condensation of **RuO₄** [16] and [20]. Given the difficulty of performing such calculations for all systems of interest, generic approximations for these data are proposed. The details and the relevance of these approximations will be discussed in a dedicated paper. It was then necessary to introduce the concept of reactive sites, after which surface chemistry could be described through a set of elementary reactions of the type:

$$\mathrm{A(g) + site \rightarrow A(ads)} \quad \text{or} \quad \mathrm{A(g) + B(ads) \rightarrow AB(ads)} \tag{6}$$

The kinetic modeling must account for both transport effects, to properly describe the diffusion of species toward reactive sites (so-called “physical” limitations), and chemical effects that come into play once the species is in the vicinity of the reactive site (energy barriers associated with the formation or breaking of chemical bonds). Accordingly, the forward (K_d) rate constant can be expressed in the following form:

$$K_d = K^{phys.} K^{chim.} \tag{7}$$

Physical limitations ($K^{phys.}$) are evaluated using correlations that are widely accepted in the literature, such as the Chilton–Colburn analogy leading to:

$$K^{phys.} = \frac{\tau^A \sigma_A}{S_{TOT}} \tag{8}$$

Where τ^A the Chilton–Colburn analogy condensation/vaporization flux, S_{TOT} is the total surface area, and σ_A is the specific surface area of the adsorption sites.
As for chemical limitations ($K^{chim.}$), ab initio calculations remain the most appropriate approach to characterize them. The associated rate constant takes the following general form:

$$K^{chem.} = k_0(T)exp\left(\frac{E_a}{RT}\right) \quad (9)$$

However, these chemical limitations are expected to be less significant at high temperatures, as is the case in the primary circuit. Therefore, by default, the value of $K^{chem.}$ is assigned to one. To determine backward rate constant (K_r), we use the relation between equilibrium constant (K_c^{eq}) and kinetic constants:

$$K_r = \frac{K_d}{K_c^{eq}} \quad (10)$$

For a reaction such as A(g) + B(ads) → AB(ads):

$$K_c^{eq} = \frac{\theta_{AB}^{eq}}{[A]^{eq}\theta_B^{eq}} = \frac{RT}{P^\circ}exp\left(\frac{-\Delta_r G^\circ}{RT}\right) \quad (11)$$

And thus:

$$K_r = K_d\frac{P^\circ}{RT}exp\left(\frac{\Delta_r G}{RT}\right) \quad (12)$$

Where $[A]^{eq}$, θ_{AB}^{eq}, and θ_B^{eq}stand for the equilibrium gas concentration of A and the equilibrium surface fractions occupied by AB and B, respectively.

2.3. Enrichment of the thermodynamic database

In addition to the data related to the adsorbed phase required to address surface chemistry, particularly non-congruent condensation, the main effort was devoted to enriching the thermodynamic database with gaseous species. Indeed, extending the kinetic approach instead of relying on thermodynamic equilibrium requires the inclusion of specific intermediate species that ensure connectivity within reaction pathways. Most of these intermediates had no influence under thermodynamic equilibrium assumptions and were therefore not previously considered in the database. The list of the main species for which Gibbs free energies of formation have been calculated and incorporated into the database is given below:
Condensed phase: H_2MoO_4, Cs_2MoO_4, $Cs_2Mo_2O_7$
Adsorbed phase (MoO_3 surface): H_2MoO_4, Cs_2MoO_4, $Cs_2Mo_2O_7$
Adsorbed phase (RuO_2 surface): RuO_4, H_2O, O_2, NO, NO_2, HNO_3
Gas phase:
Ag–Mo–O system: $AgMoO_2$, Ag_2MoO_2, $AgMoO_3$, Ag_2MoO_3, $AgMoO_4$, $AgHMoO_4$, Ag_2MoO_4, $Ag_2Mo_2O_7$
Cs–Mo–O system: $CsMoO_3$, Cs_2MoO_3, $CsMoO_4$, $CsHMoO_4$, Cs_2MoO_4, $Cs_2Mo_2O_7$
Cd–Mo–O system: $CdMoO_3$, $CdMoO_4$, $CdMo_2O_7$

3. MODEL–EXPERIMENT COMPARISON

This section aims to highlight the improvements achieved by the new model in predicting iodine chemistry using data from two distinct experimental series. Thus, to validate the developments described in the preceding section, the following experimental tests have been simulated with the ASTEC/SOPHAEROS code:

- The first experimental series (IOH GAEC tests) consists of tests carried out in an open-flow reactor in which molecular iodine was injected at high temperature (>1440 K) under either reducing or oxidizing atmosphere. These tests were performed on a small-scale test facility initially developed by Lacoué-Nègre [17] and Gouello et al. [18] within the framework of the CHIP program. The objective of these experiments was to determine iodine gas-phase speciation at 423 K following recombination across a strong temperature gradient, under conditions representative of those encountered during severe accident (SA) scenarios. The main experimental parameters were the atmospheric composition and the iodine concentration. The tests used for the validation are the first two performed in reducing conditions (IOH-1 and IOH-2) and the two performed in oxidizing conditions (IOH-4 and IOH-5) [10]

- The second experimental series (CHIP PL tests) was conducted in the CHIP facility, which was designed to detect and quantify gaseous iodine at the circuit outlet as a function of several parameters, including residence time, temperature gradient, carrier gas composition ($H_2O/H_2/Ar$), and the nature and concentration of elements injected into the line. The separate injection of elements in the CHIP PL configuration makes it possible to achieve both an excess of Mo relative to Cs and an excess of Cs relative to I, as observed in the Phébus experiments. The tests used for the validation are those involving Mo, Cs, I, O, and H (PL_MoCsI_3 and PL_MoCsI_2 tests[11], and those involving Mo, Cs, I, O, H plus one element representative of the SIC control rod ([Cd + MoCsI] and [Ag + MoCsI] tests) [13].

3.1. Simulation of the IOH GAEC tests

The IOH GAEC experiments [10]were conducted in a high-temperature tubular furnace equipped with an alumina tube (30 mm inner diameter, 1 m in length). The carrier gas was supplied at the inlet of the test line and consisted of either a steam/argon mixture or a hydrogen/argon mixture (with H_2 concentrations up to 3 vol.%). Gaseous iodine was generated by sublimation of molecular iodine pellets and transported by a low argon flow before being directly injected into the high-temperature zone at 1810 K. The reactants were then cooled in the reaction zone, characterized by a strong temperature gradient (from 1810 K down to 423 K) and a residence time of a few seconds. Downstream of the reaction zone, the transport line ended in four independent sampling lines, each equipped with two gas scrubbers connected in series and an aerosol filter, enabling the collection and characterization of chemical species.

3.1.1. Reducing conditions

Table I. impact of model evolution on its ability to reproduce the measurements of iodin speciation (GAEC tests IOH-1 & IOH-2)

	IOH-1	IOH-2
Carrier Gas composition (v/v%)	Ar/H_2 (97.3/2.7)	Ar/H_2 (99/1)
Measured deposits in the main line (%)	35.6 ± 2.8	26 ± 1.8
Measured Iodine released at 423 K (%)	64.4 ± 3.5	74 ± 5.2
HI and HOI **(%)**		
Measurement	**85.9 ± 2**	**79.5 ± 1**
Th_Eq	100	100
Kin_v0	5.2	3.2
Kin_v0-Eq	90.5	78.4
Kin_v1	92	82

Under reducing conditions (absence of oxygen), ASTEC/SOPHAEROS calculations assuming thermodynamic equilibrium predict exclusively HI at the outlet, whereas a quantity of I_2 were observed

experimentally [10]. It puts in evidence that the {I, O, H} system undergoes some kinetic limitations in reducing conditions, for residence time of several seconds and for the H/I molar ratio used in these tests (9.9 10^3 for IOH-1 and 3.2 10^3 for IOH-2). The previous kinetic model (Kin_v0) predicts that a great amount of the iodine at the outlet (from approx. 75 to 90%) remains as I_2, in disagreement with the experimental data. In Kin_v0-Eq version, this discrepancy was addressed by assuming a partial thermodynamic equilibrium for {O, H} subsystem. Using the new modelling (Kin_v1) the agreement with the experimental measurements is satisfactory without any equilibrium assumption.

3.1.2. Oxidizing conditions

Under oxidizing conditions, the thermodynamic equilibrium assumption (Th_Eq) predict exclusively I_2 at the outlet, whereas measurable amounts of iodine were detected in the aqueous phase of scrubber (9.1±6% for the IOH-5 test and 3.8±1% for the IOH-4 test), attributed to HI [10].The previous modeling (Kin_v0) predicts that between 65% (IOH-4) and 80% (IOH-5) of iodine is released as molecular iodine, which is lower than the experimental values, see table II. Again, this discrepancy was addressed by assuming equilibrium for the subsystem (H-O). The generalized kinetic model (Kin_v1) yields values in good agreement with experimental measurements. At this stage, the primary strength of the new modelling (Kin_v1) lies in its improved internal consistency, as it can treat the full I–O–H chemical system, including the H-O sub-system, without relying on assumptions of partial thermodynamic equilibrium.

Table II. Impact of model evolution on its ability to reproduce the measurements of iodin speciation (GAEC tests IOH-4 & IOH-5)

	IOH-4	IOH-5
Carrier Gas composition (v/v%)	H_2O/Ar (50/50)	H_2O/Ar (50/50)
Measured deposits in the main line (%)	17.5 ± 1.4	33 ± 2.9
Measured Iodine released at 423 K (%)	82.5 ± 4.8	67 ± 4
I_2 (%)		
Measurement	**96.2 ± 1**	**90.9 ± 6**
Th_Eq	100	100
Kin_v0	65	80.1
Kin_v0-Eq	92.4	96.2
Kin_v1	96	98

3.2. Simulation of the CHIP PL tests

The CHIP PL experiments were conducted in the CHIP test line [11]. The test line (3.5 m in length and 60 mm in inner diameter) consists of two tubes connected by a specific junction: an alumina tube (2 m long) located in the high-temperature zone, and a stainless-steel tube (1.5 m long) forming the transport zone, which simulated the reactor coolant system (RCS) piping. The thermal profile along the test line is achieved using a high-temperature oven together with heated upstream and downstream sections. It consists of three zones: (i) a preheating zone extending from the inlet flange (800 °C) to the high-temperature oven; (ii) a high-temperature zone maintained at 1600 °C; and (iii) a “transport zone” in which the temperature decreases from 1600 °C to 150 °C, producing a steep temperature gradient. The steam/carrier gas mixture is directly supplied at the inlet of the high-temperature alumina tube. Except for silver (which is directly deposited in the main line as silver powder), the reagents of interest are vaporised in external generators connected to the main line. Gaseous iodine is obtained by sublimation of molecular iodine pellets. Caesium, molybdenum and cadmium vapours are produced by vaporization of respectively caesium hydroxide, molybdenum trioxide and metallic cadmium. The vaporised reagents (i.e. I2, CsOH, MoO3 and Cd) are then transported in separate lines with an increasing temperature gradient up to the HT zone where they are mixed. The residence time from the high-temperature zone to the outlet (10–11 s) is representative of a

severe accident scenario involving a break in the cold leg of the RCS. The test line terminates with an integral quartz aerosol filter followed by gas scrubbers filled with a sodium hydroxide solution to trap gaseous iodine species. Just upstream of this final filter is the connection to the sampling lines, which allow the measurement of iodine speciation between gaseous I_2 and other forms of Iodine, including aerosols.

3.2.1 PL_MoCsI_2 and PL_MoCsI_3 tests

The results are displayed in Table III. They show that the progression from full equilibrium model (Th_Eq) though the partially equilibrium based (Kin_v0-Eq) to the new modelling (Kin_v1) leads to a significant reduction in the discrepancy between calculations and measurements.

Table III. impact of model evolution on its ability to reproduce the measurements of iodine speciation (CHIP: PL_MoCsI_2 & PL_MoCsI_3)

		PL_MoCsI_2 - Ar / H_2O / H_2 = 94.8 / 2.4 / 2.8			
		Exp. (%)	Kin_v1 (%)	Kin_v0-Eq (%)	Th_Eq (%)
I	Total released	62.0±3.1	59.4	69.4	97.8
	I_2(g) ratio	1.0±1.0	0.0	3.4	97.8
	Total Deposited	38.0±3.1	40.6	30.6	0.2
	HT / LT ratio	1.5±0.1 / 36.5±3.0	1.1 / 39.5	n.a.	0.0 / 0.2
Cs	Total released	48.1±3.0	44.8	53.9	32.3
	Total Deposited	51.9±3.0	55.2	46.1	67.7
	HT / LT	34±2.7 / 18±1.5	29.4 / 25.7	n.a.	17.5 / 50.2
Mo	Total released	33.4±4.6	25.0	64.6	23.0
	Total Deposited	66.6±4.6	75.0	35.4	77.0
	HT / LT	57±4.5 / 9.6±0.8	52.0 / 23.0	n.a.	40.9 / 36.1
		PL_MoCsI_3 - H_2O / He / Ar = 50.8 / 44.1 / 5.1			
		Exp. (%)	Kin_v1 (%)	Kin_v0-Eq (%)	Th_Eq (%)
I	Total released	100	94.0	92.6	99.9
	I_2(g) ratio	88.3±6.4	82.0	76.3	99.9
	Total Deposited	0.0	6.0	7.4	0.1
	HT / LT	0.0 / 0.2±0.2	0.0 / 6.0	n.a.	0.0 / 0.1
Cs	Total released	73±1.6	68	43.4	30.8
	Total Deposited	27	32	56.6	69.2
	HT /LT	11±1 / 16±1.3	12.3 / 19.6	n.a.	13.5 / 55.7
Mo	Total released	75±1.7	68.0	54.1	30.7
	Total Deposited	25±2.0	32.0	45.9	69.3
	HT / LT	4±0.3 / 21±1.7	10.0 / 22.0	n.a	12.5 / 56.8

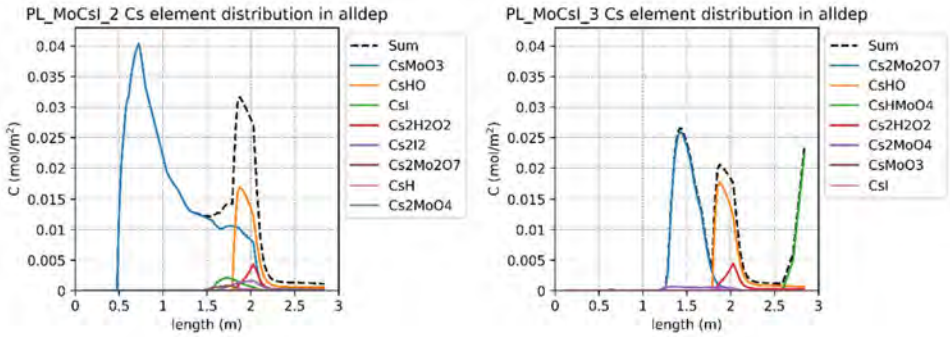

Figure 1. Deposition profiles of Cs species along the tube (PL_MoCsI_2 & PL_MoCsI_3)

For PL_MoCsI_2, the new modelling provides a very good estimate of the measured transport of iodine (60% vs 62±3.1% measured) as well as that of caesium (45% vs 48±3% measured). However, the transport of molybdenum remains slightly underestimated (25% calculated vs 33±5% measured). All transported iodine is predicted to be in aerosol form (CsI), see Table III, in good agreement with measurements. The new modelling reproduces the deposition profiles reasonably well, those of iodine, for which deposition on both tubes, alumina (high temperature) and steel (low temperature), is very well captured. It's worth highlighting the good agreement obtained for caesium and molybdenum deposition on both tubes. One can notice that the tendency of the new modelling to underestimate the transport is in conjunction with an overestimation of deposit at low temperature, zone where the deposit is more governed by aerosols deposition rather than gas condensation. In other words, chemistry modeling is not necessarily the one to blame for this difference. This overall improvement in deposition is mainly attributed to the introduction of new species containing reduced molybdenum Mo(V), such as $CsMoO_3$, Mo_2O_8, etc., see Figure 1. In addition, the formation of different oxidation states of molybdenum (IV, V, and VI) was experimentally evidenced in this test [18].
For PL_MoCsI_3, the new modelling reproduces the overall experimental trends and provides a satisfactory prediction of deposition and transport phenomena, including the gaseous iodine fraction (82% compared with 88.3±6.4% measured). It should be emphasized that, within the present modeling framework, only the main tube is considered; consequently, the calculated gaseous fraction corresponds to the iodine fraction at the outlet of this tube. The recent model developments have a limited impact on iodine transport, which is only slightly reduced. In contrast, they significantly affect the transport behavior of caesium (Cs) and molybdenum (Mo), leading to a markedly improved agreement between calculated results and experimental observations. This improvement mainly arises from the enrichment of the thermochemical database, particularly through the introduction of $CsHMoO_4$. This addition strongly limits the formation of Cs_2MoO_4 and, as a result, substantially reduces high-temperature deposition of both Cs and Mo. Under oxidizing conditions and at high temperatures, caesium is therefore predominantly distributed between two gaseous species: CsOH (the injected species) and $CsHMoO_4$. As temperature decreases, two additional gaseous species (CsI and Cs_2MoO_4) appear only in trace amounts at intermediate temperatures, at the expense of CsOH, which nevertheless remains present until aerosol formation occurs at low temperatures.

3.2.2 CHIP+: PL_MoCsI_Cd and PL_MoCsI_Ag tests

Since both experiments (Cd and Ag) were designed to address the same questions, namely whether these control-rod elements can form iodides (CdI or AgI) and molybdates ($CdMoO_4$ and $AgMoO_4$), a direct comparison of their main outcomes is proposed below.

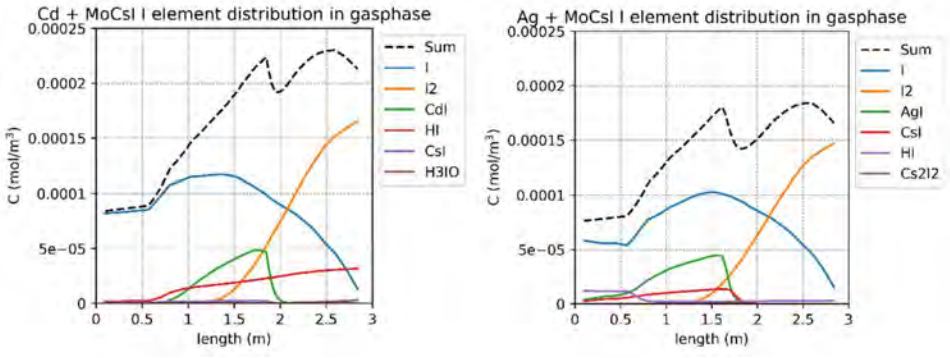

Figure 2: gaseous profiles of I along the tube for PL_MoCsI_Cd (left) & PL_MoCsI_Ag (right) tests

Although the modeling predicts quantitatively comparable results for the two experiments, few qualitative differences are observed particularly concerning gaseous iodine speciation (I_2/HI), aerosol speciation (AgI/CsI or CdI/CsI), Figure 2. At high temperature, iodine speciation is not similar in both experiments,

for *PL_MoCsI_Cd* , the atomic form of iodine is the only species present at the outlet of the furnace whereas, for the *PL_MoCsI_Ag* test, AgI, I, CsI and HI are formed in the very central part of the furnace. This difference highlights the impact of H_2 injected, in the Ag test, in stabilizing Cs atomic at high temperature, and consequently promoting the CsI formation, as observed previously in PL_MoCsI_2 test. On the other hand, CdI is formed further downstream, i.e., at a later stage, due to the thermodynamic stability of Cd atomic compared to silver.

Table IV. Impact of model evolution on its ability to reproduce the measurements of iodin speciation (CHIP+: PL_MoCsI_Cd & PL_MoCsI_Ag)

		PL_MoCsI_Cd H_2O / He / Ar = 49.4 / 42.8 / 7.8			**PL_MoCsI_Ag H_2O / Ar / H_2 = 49.6 / 48.6 / 1.8**		
		Exp.	Kin_v1	Th_Eq	Exp.	Kin_v1	Th_Eq
I	Released	87	80.3	45.9	~85	83.3	70
	I_2(g) ratio	28±6.5	23.7	0.3	2±1	18.6	0
	Deposited	13	19.7	54.1	15	16.7	24
	HT / LT	0 / 13±1.3	0.0 / 19.7	0.6 / 53.5	0 / 15±7	1.3 / 15.4	0.6 / 23.3
Cs	Released	74	72	37.98	80	79	61.43
	Deposited	26	28	62.02	20	21	38.58
	HT / LT	10±1 / 16±1.5	9 / 19	9.4 / 52.6	6±1 / 14±1	2 / 19	11.5 / 27
Mo	Released	59	53	25.09	43	54.5	30.65
	Deposited	41	47	74.91	57	45.5	69.36
	HT / LT	31±3 / 10±1	32.5 / 14.5	36.2 / 38.7	47±4 / 10±1	37.4 / 8.1	53.8 / 15.5
Cd or Ag	Released	56	66.7	42.09	37	41	32
	Deposited	44	33.3	57.91	63	59	68
	HT / LT	3±0.3 / 41±4	2.7 / 30.6	1.09 / 56.8	57±5 / 6±1	49 / 9	52 / 16

As regards the comparison with measurements, Table IV reveals that iodine (I), caesium (Cs), and molybdenum (Mo) exhibit the same trends as those observed in the previous tests, with a satisfactory agreement for both transport and deposition on the two tubes. The gaseous I_2 fraction is well predicted for the Cd test but is overestimated for the Ag test.

The reaction mechanisms of the I–Ag–Cs–O–H system are currently under re-evaluation in order to better assess transport phenomena, in particular through the reassessment of certain thermo-kinetic data. Nevertheless, it should be emphasized that the experiment involving silver (Ag) presented several challenges and unexpected behaviors from a data analysis perspective. Consequently, it cannot be excluded that the associated uncertainty margins are larger than those initially estimated.

At this stage, silver appears to exhibit a higher capacity to trap molybdenum than cadmium, as it forms two molybdenum-bearing compounds ($AgMoO_3$ and Ag_2MoO_4), whereas only one such compound is formed with cadmium ($CdMoO_4$; see Figure 3). In particular, $AgMoO_3$ plays a key role, since its formation from the injected species Ag and MoO_3 proceeds via a barrierless reaction. As a consequence, a smaller fraction of molybdenum remains available to react with caesium and form $CsMoO_3$, $CsHMoO_4$, or Cs_2MoO_4 in the silver experiment. This, in turn, increases the availability of caesium to form CsI, at the expense of AgI formation.

The injection of hydrogen in the Ag experiment, at a flow rate comparable to that of molybdenum, does not promote the formation of $CsMoO_3$, in contrast to what was observed for the PL_MoCsI_2 test under reducing conditions. Instead, its impact on molybdenum is primarily associated with the formation of Mo_3O_8 species.

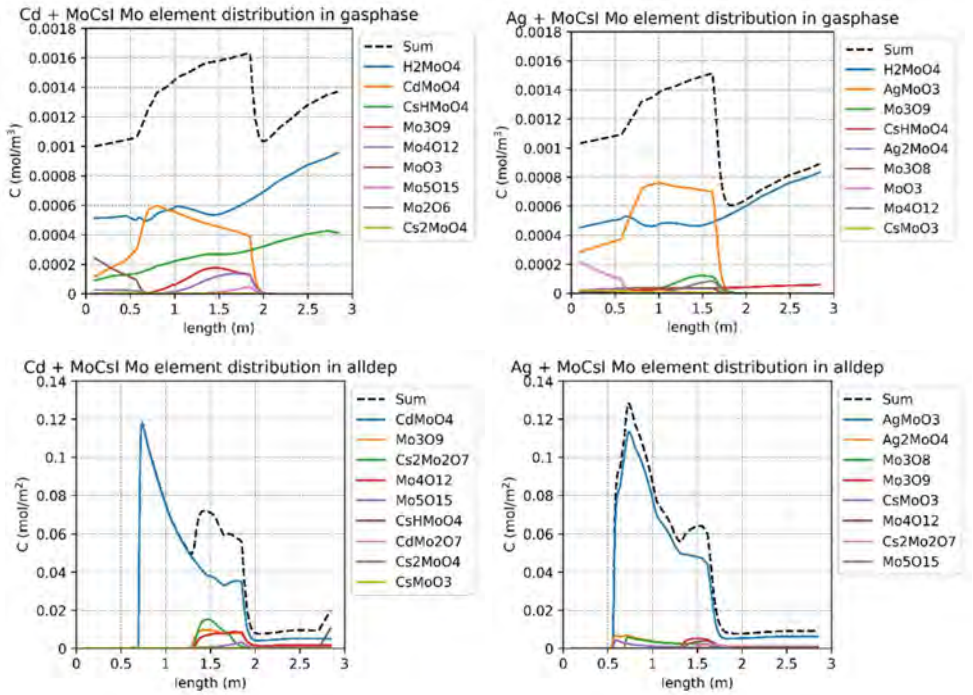

Figure 3: Gaseous (top) & Deposition (bottom) profiles of Mo along the tube : PL_MoCsI_Cd (left) & PL_MoCsI_Ag (right)

4. CONCLUSIONS

In this paper, we present an overview of the recent developments in chemistry modeling implemented in the ASTEC code. The main advances include the replacement of the thermodynamic equilibrium assumption with a generalized kinetically controlled model, the introduction of surface reactivity, and the enrichment of the thermokinetic database associated to ASTEC code. The improved capability of the code to predict experimental observations has been assessed on the GAEC, CHIP, and CHIP+ test series. For the GAEC experiments, we demonstrate that this new approach is more consistent, as it no longer requires assuming partial thermodynamic equilibrium for specific subsystems, as was the case in the previous version (where improved results were obtained when the H–O subsystem was assumed to be at equilibrium). The robustness of the model is further evaluated using the CHIP tests, for which the simulations reproduce the experimental measurements very well, including the transport of the different elements, the gaseous I_2 fraction, and the deposition profiles. Similar trends are also obtained for the CHIP+ experiments (MoCsI+Cd and MoCsI+Ag).

According to the results, both silver and cadmium exhibit a high reactivity toward molybdenum. This reactivity reduces the availability of molybdenum to interact with caesium, thereby increasing the capability of caesium to partially trap iodine. In addition, both elements are capable of directly trapping a fraction of iodine through the formation of AgI or CdI. Nevertheless, these effects remain partial, as a fraction of gaseous iodine is still measured in the sampling lines in both experiments, highlighting a chemistry governed by complex kinetic limitations that warrant further investigation. In particular, the differences observed in the transported I_2 fraction call for a reassessment of the thermokinetic behavior of silver system.

5. REFERENCES

1. E. C. Beahm et al., *Iodine Chemical Forms in LWR Severe Accidents*, NUREG/CR-5732, ORNL/TM-1186, Oak Ridge National Laboratory (1992).
2. D.A. William, *OECD International Standard Problem Number34 Falcon Code Comparison Report*, NEA/CNSI/R(94)27 (1994).
3. N. Girault, and F. Payot, "Insights into iodine behaviour and speciation in the Phébus primary circuit", *Ann. Nucl. Energy* **61**, pp. 143–156 (2013).
4. N. Girault, S. Dickinson, F. Funke, A. Auvinen, L. Herranz, and E. Krausmann, "Iodine behaviour under LWR accident conditions: Lessons learnt from analyses of the first two Phebus FP tests", *Nucl. Eng. Des.* **236**, pp. 1293-1308 (2006).
5. N. Girault, C. Fiche, A. Bujan, and J. Dienstbier, "Towards a better understanding of iodine chemistry in RCS of nuclear reactors", *Nucl. Eng. Des.* **239**, pp. 1162-1170 (2009).
6. B. Simondi-Teisseire, N. Girault, F. Payot, and B. Clément, "Iodine behaviour in the containment in Phébus FP tests", *Ann. Nucl. Energy* **61**, pp. 157-169 (2013).
7. D.J. Wren, AECL Report 7781 Atomic Energy of Canada Ltd., 1983.
8. L. Cantrel, and E. Krausmann, "Reaction Kinetics of a Fission-Product Mixture in a Steam-Hydrogen Carrier Gas in the Phebus Primary Circuit", *Nucl. Technol.* **144** (2003).
9. B. Clément, and R. Zeyen, "The Phébus Fission Product and Source Term International Programs", *Proc. Int. Conf. on Nuclear Energy for New Europe*, Bled, Slovenia, 5-8 September, Nuclear Society of Slovenia (2005).
10. A.C. Grégoire, Y. Délicat, C. Tornabene, F. Cousin, L. Gasnot, N. Lamoureux, and L. Cantrel, "Study of the iodine kinetics in thermal conditions of a RCS in nuclear severe accident", *Ann. Nucl. Energy* **101**, pp. 69–82 (2017).
11. A.C. Grégoire, J. Kalilainen, F. Cousin, H. Mutelle, L. Cantrel, A. Auvinen, T. Haste, and S. Sobanska, "Studies on the role of molybdenum on iodine transport in the RCS in nuclear severe accident conditions", *Ann. Nucl. Energy* **78**, pp. 117–129 (2015).
12. M. Gouello, "Chemistry of iodine and aerosol composition in the primary circuit of a nuclear plant in severe accident conditions", Ph.D. thesis, University J. Fourier, Grenoble (2012).
13. A.C. Grégoire, S. Sobanska, C. Tornabene, D. Talaga, A.S. Mamede, S. Morin, and L. Cantrel, "Influence of SIC control rod material on the iodine release in case of nuclear severe accident – Chemical reactivity with fission products in thermal conditions of RCS", *Ann. Nucl. Energy* **168** (2022).
14. B. Xerri, S. Canneaux, F. Louis, J. Trincal, F. Cousin, M. Badawi, and L. Cantrel, "Ab initio calculations and iodine kinetic modeling in the reactor coolant system of a pressurized water reactor in case of severe nuclear accident", *Computational and Theoretical Chemistry* **990**, pp. 194–208 (2012).
15. L. Cantrel, F. Louis, and F. Cousin, "Advances in mechanistic understanding of iodine behaviour in PHEBUS-FP tests with the help of ab initio calculations", *Ann. Nucl. Energy* **61**, pp. 170–178 (2013).
16. E.P. Hessou, F. Virot, M. Calatayud, and S.M.O Souvi, "Ab Initio Investigation of the Competitive Adsorption of RuO4 and NOX on a RuO2 Surface: Assessment of RuO4 Release in a Severe Nuclear Accident", *Journal of Physical Chemistry C* **129(23)**, pp. 10463 (2025).
17. M. Lacoué-Nègre, "Chimie de l'iode dans le circuit primaire d'un réacteur nucléaire en situation d'accident grave – Etude de mélanges CsI/MoO3 sous vapeur d'eau", Ph.D. thesis, Lille-1 University (2010).
18. M. Gouello, H. Mutelle, F. Cousin, S. Sobanska, and E. Blanquet, "Analysis of the iodine gas phase produced by interaction of CsI and MoO3 vapours in flowing steam", *Nucl. Eng. Des.* **263**, pp. 462–472 (2013).
19. M. Saab, S.M.O. Souvi, J. Denis, F. Virot, and M. Calatayud, "Ab Initio Insight into CsHMoO4 and H2MoO4 Complexes on MoO3 Surfaces", *Journal of Physical Chemistry C* **128(50)**, pp. 21447 (2024).
20. Jadon, A.; Girault, N.; Piar, B.; Petitprez, D.; Souvi, S. M. O. Analytical Ab Initio-Based Modeling of the Adsorption Isotherm. *J. Phys. Chem. C* **2018**, *122* (42)

Impact of ASTEC's Advanced Modeling in Gas and Adsorbed Phases Chemistry on the Source Term

Guillaume Astier, Olivia Coindreau, Loris Gelin, and **Sidi M. O. Souvi***

Autorité de Sûreté Nucléaire et de Radioprotection:
ASNR/PSN-RES/SAM/LETR

ERMSAR 2026 – Madrid, Spain

01

INTRODUCTION

LIMITS OF THERMODYNAMIC EQUILIBRIUM

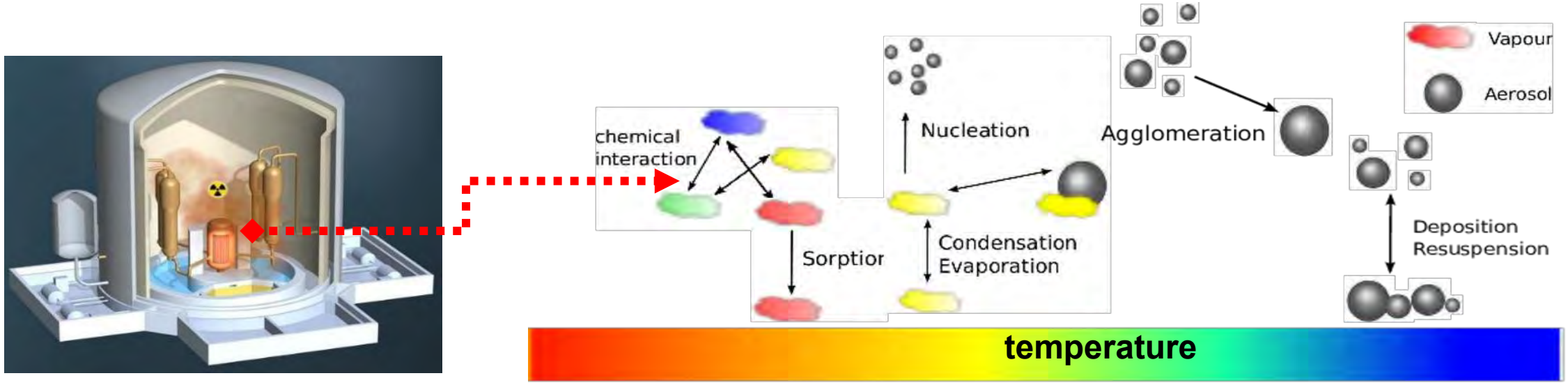

- **Previous assumption:** Thermodynamic equilibrium (Th. Eq.) for speciation in the gas phase**.**
- **Experimental feedback:** Th. Eq. does not hold (e.g., I–O–H system).
  - Need to generalize the **kinetic** & to consider the **surface chemistry**.
- **The Paradox:**
  - Thermodynamic data ($\Delta_f G$) are abundant and easy to compute (ab initio).
  - Kinetic data (E_a, rate constants) are scarce and complex to evaluate.
- **How can thermodynamic data be used to estimate missing kinetic parameters?**

02

GASEOUS PHASE: NEW KINETIC MODELING

FROM THERMODYNAMIC DATA TO KINETIC DATA

- **Molecules try to agglomerate!**
- **Temperature tends to separate them.**

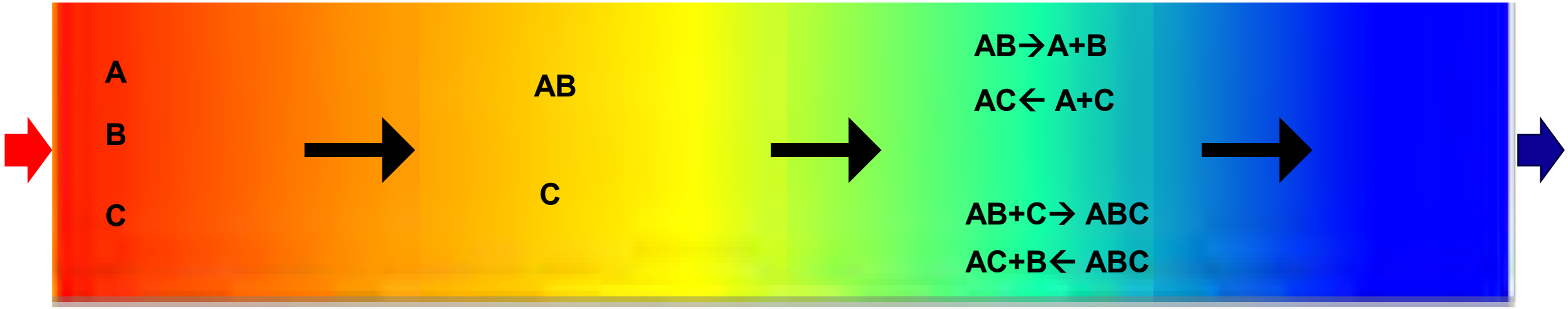

- **Objectif:** consider the impact of the unstable intermediate on the kinetics.

REHABILITATION OF COLLISION THEORY

- **Reaction rate expressed as a product:** $v_f = Freq_{A\&B} \times P^{REACT}$

- **Reactivity Probability (P^{REACT}):** Evaluated at the molecular energy states level:

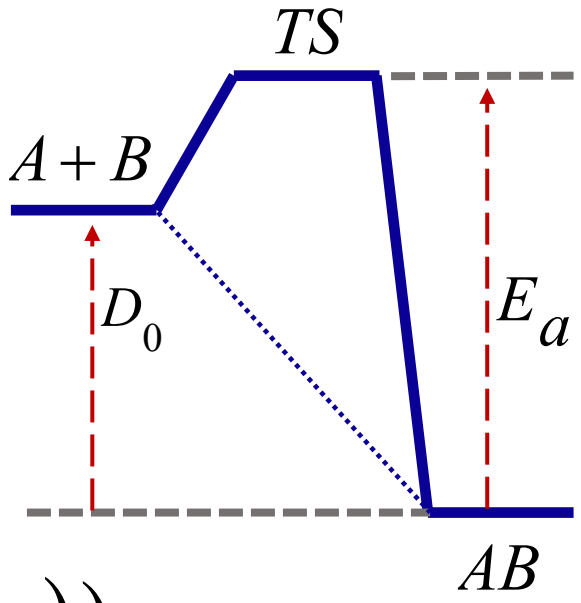

- **The Upper-Bound Formula:**
  - Relies strictly on macroscopic thermodynamic properties ($\Delta_r G°$).
  - Uses fundamental dissociation energy (D_0) at 0 K when activation energy (E_a) is unknown.

$$v_d^{\mathrm{UB}} = Freq_{A\&B} \times P_{A+B \mapsto AB}^{REACT}\left(\Delta_r G; \max\left(E_a, D_0\right)\right)$$

- **Result:** A physically meaningful maximum rate, proportional to the relative stability of products and reactants.

COMPARISON WITH LITERATURE DATA (NIST)

- **Barrierless reactions:** The approach perfectly reproduces experimental observations and temperature dependence.

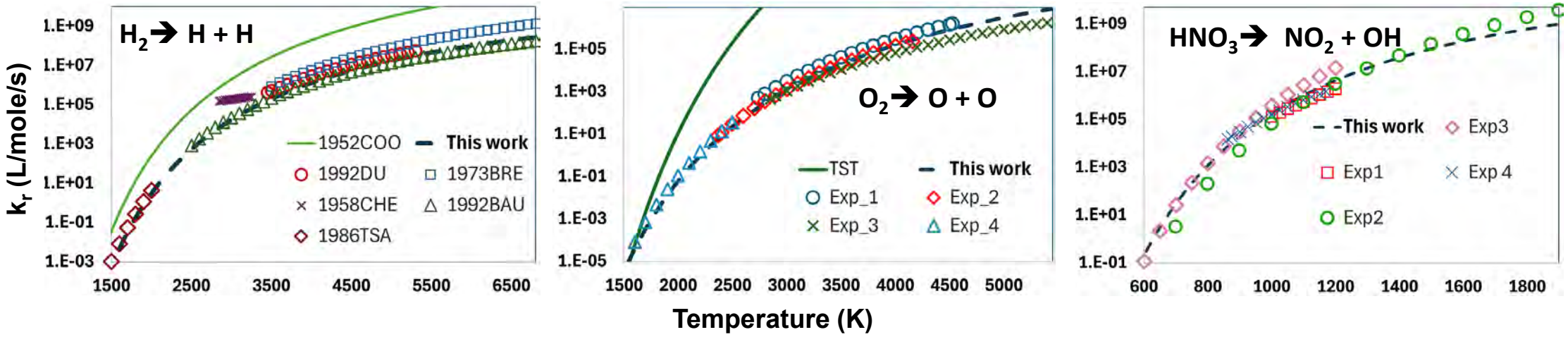

- **Reactions with energy barrier:** Replacing D_0 with an ab initio calculated E_a provides highly promising results.

- **Advantage:** Allows discrimination between different measured kinetics using only basic thermodynamic data.

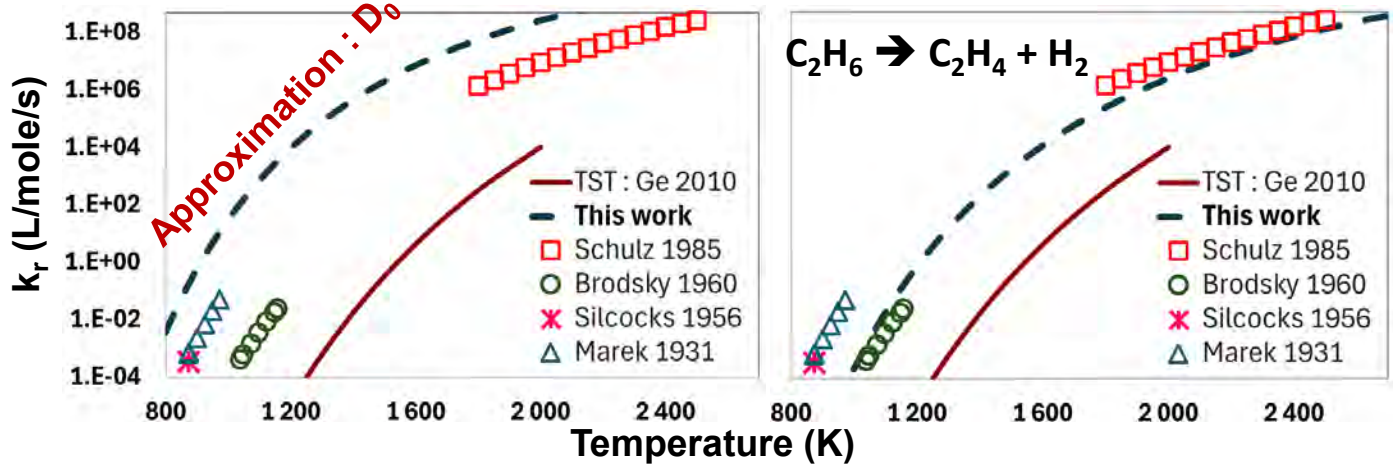

ANALYTICAL TESTS - CS-I-MO SYSTEM

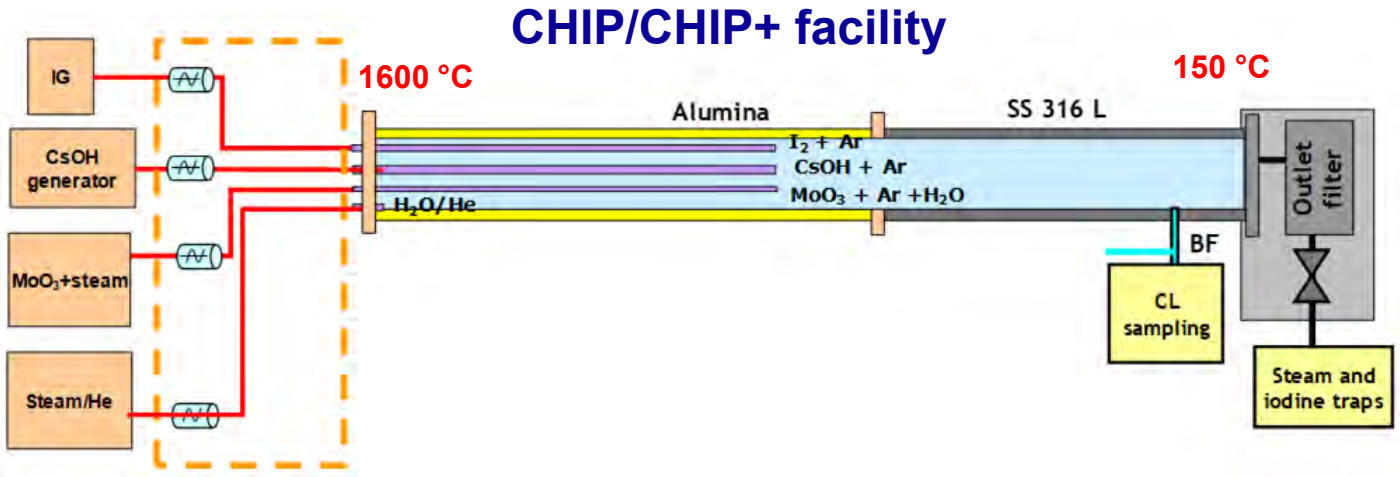

- 6 tests with different compositions.
- Both calculation, performed with :
  - Database enriched with data for Mo, Cs, Cd, and Ag.
  - Including surface decomposition of $CsHMoO_4$, H_2MoO_4.
- New model: upper bound of kinetics rates reproduces better the experimental transport.

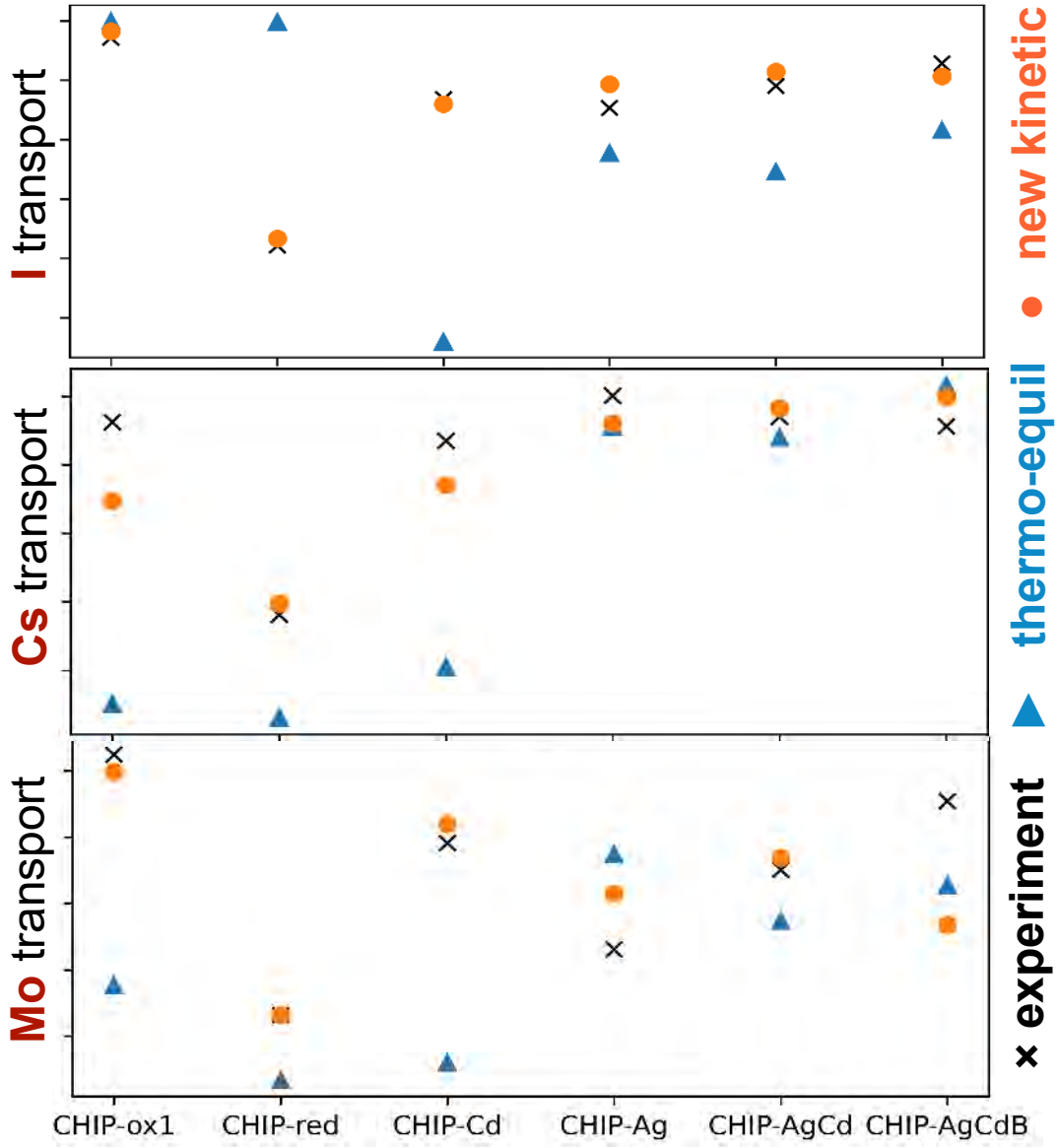

03

ADSORBED PHASE: SURFACE REACTIVITY

SURFACE REACTIVITY

- **Motivation:** the no-congruent evaporation/condensation of **RuO_3** and **RuO_4**

- **Full thermodynamic equilibrium**

➔No transport of Ru.

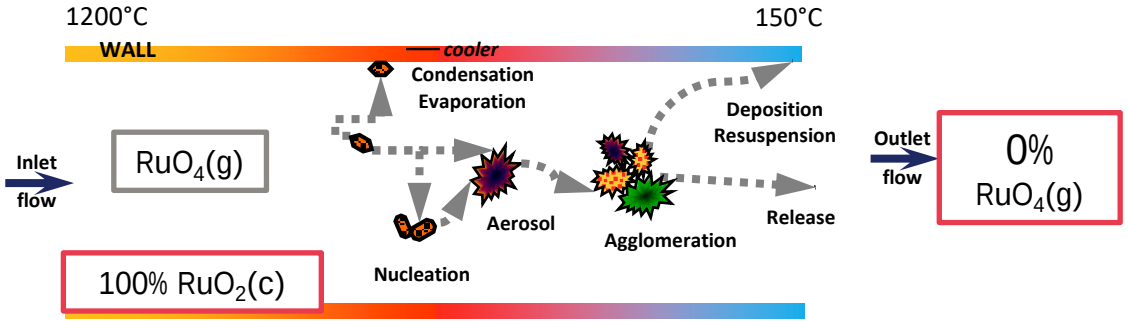

- **Thermodynamic equilibrium in gas phase + congruent condensation.**

➔Full transport of Ru.

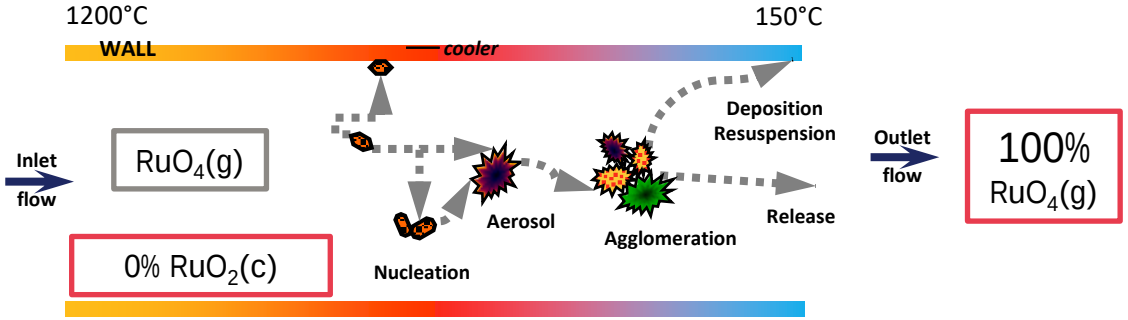

- **Experiments (ASNR facility)➔ transport : 1% to 50%.**

- **Surface decomposition of RuO_4 & RuO_3 must be considered.**

INTRODUCING SURFACE CHEMISTRY

Concept:

- Introduction of "**active sites**"

  Single adsorption: $A_g + S_0 \rightleftharpoons A_s$

  Multiple adsorption: $B_g + A_s \leftrightarrow AB_s$

- Considering **Adsorbed phase** in the MDB

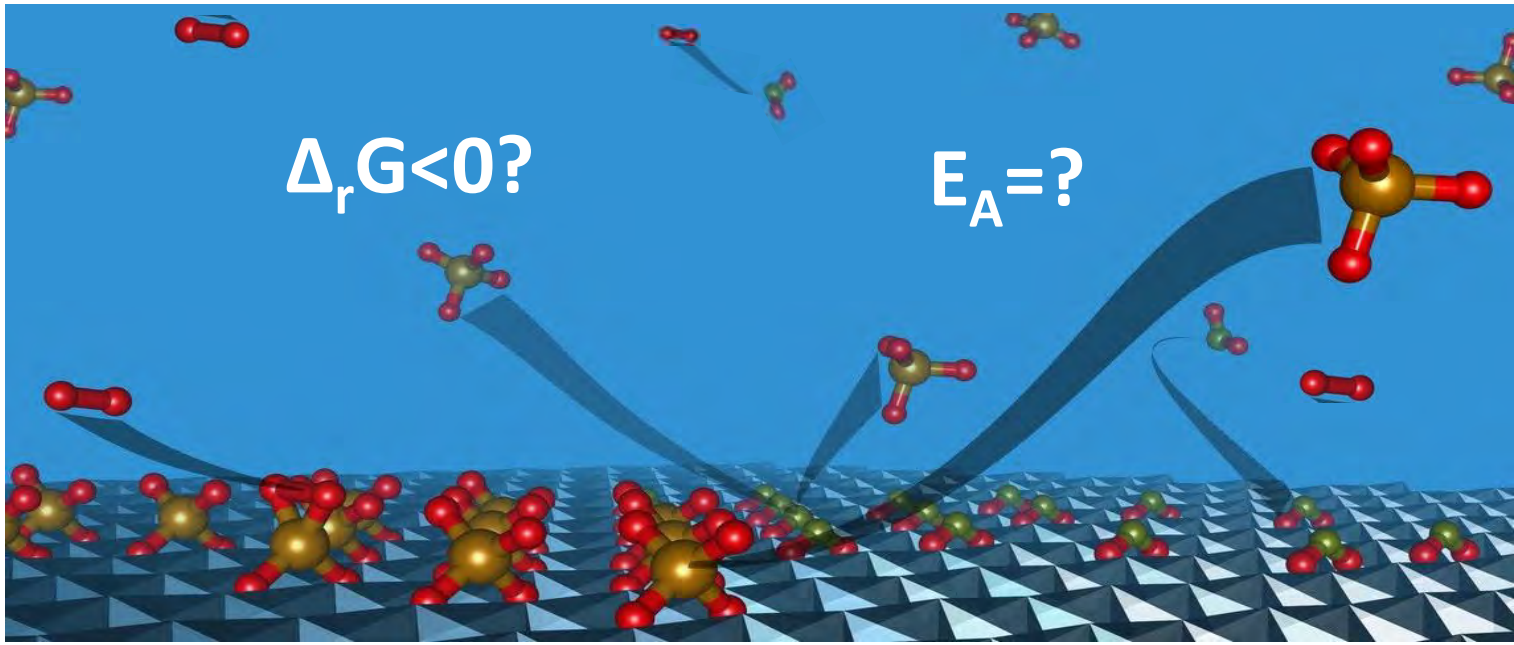

Data: Adsorption Gibbs energies

- Calculated via ab initio (e.g., RuO4, CsHMoO4).
- approximated generically from existing MDB

Kinetic Laws:

- Controlled by diffusion toward the surface (Physical limitation: Chilton-Colburn analogy).
- Controlled by adsorption/desorption energy barriers (Chemical limitation).

SURFACE REACTIVITY

- **Approximated data:** via Mean Field Approximation (MFA); boundary conditions are approximated

$G^{o}_{(ad)}(\theta,T)$ = $(1-\theta)\times G^{o}_{(ad)}(0,T)$ + $\theta\times G^{o}_{(ad)}(1,T)$

Intermediate coverage

Isolated adsorption

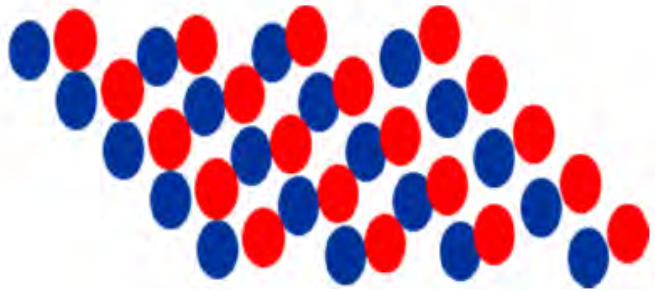

Full monolayer coverage

- **Generic approximations are made based on thermodynamic data of gaseous & condensed species (in MDB)**

ANALYTICAL TESTS – RU SYSTEM

- **Challenges:** the no-congruent evaporation/condensation of **RuO_3** and **RuO_4**

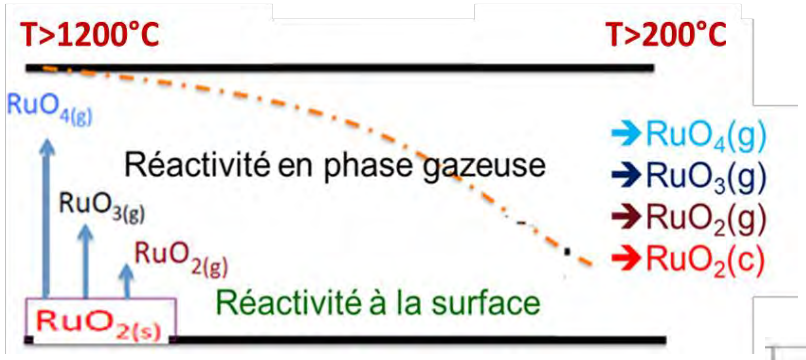

- RuO_4 (g) ↔ RuO_4 adsorb)
- RuO_4(adsorb) ↔ RuO_2(c) + O_2(g)

- RuO_3 (g) ↔ RuO_3 adsorb)
- RuO_3(adsorb) ↔ RuO_2(c) + O (g)
- 2xRuO_3(adsorb) ↔ 2xRuO_2(c) + O_2(g)

- **ASTEC vs experiment (START test :quartz tub and low flowrate)**

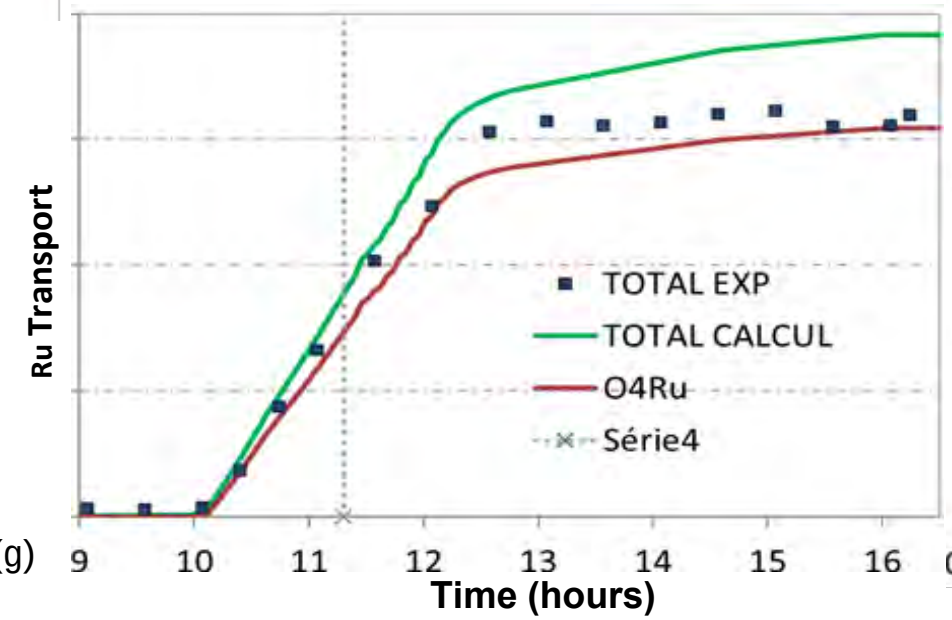

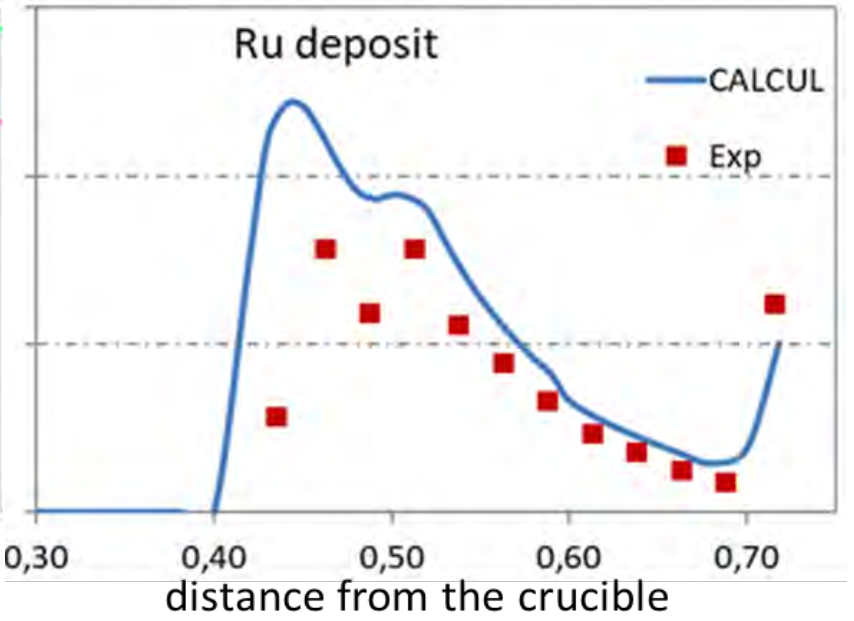

- **ASTEC reproduces the experimental observations**

INTEGRAL TEST – RU SYSTEM

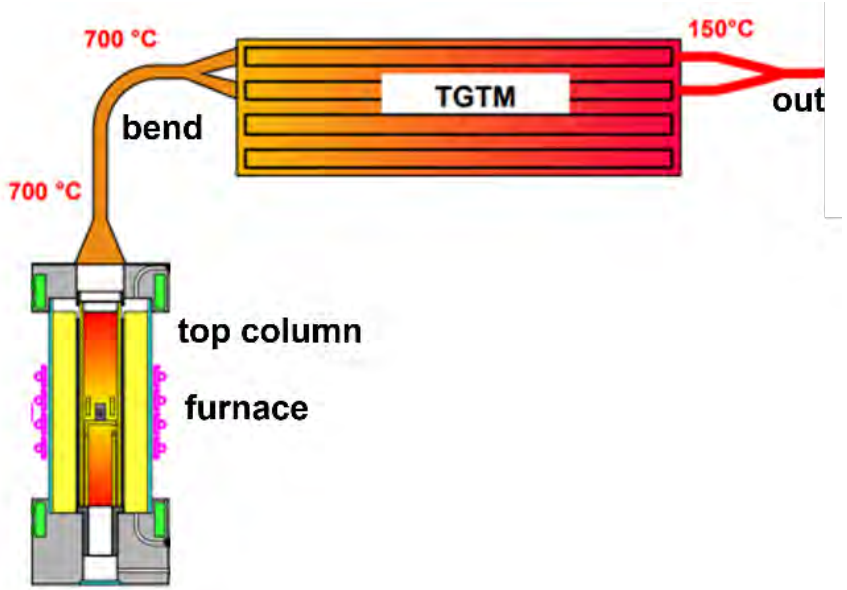

Ru	ASTEC	EXP
out	32.92%	30.81%
top column	44.18%	41.72%
bend	14.08%	17.80%
tube #1	0.08%	0.00%
tube #2	3.31%	3.85%
tube #3	4.33%	4.99%
tube #4	1.11%	0.82%

High T Ru deposit in top column

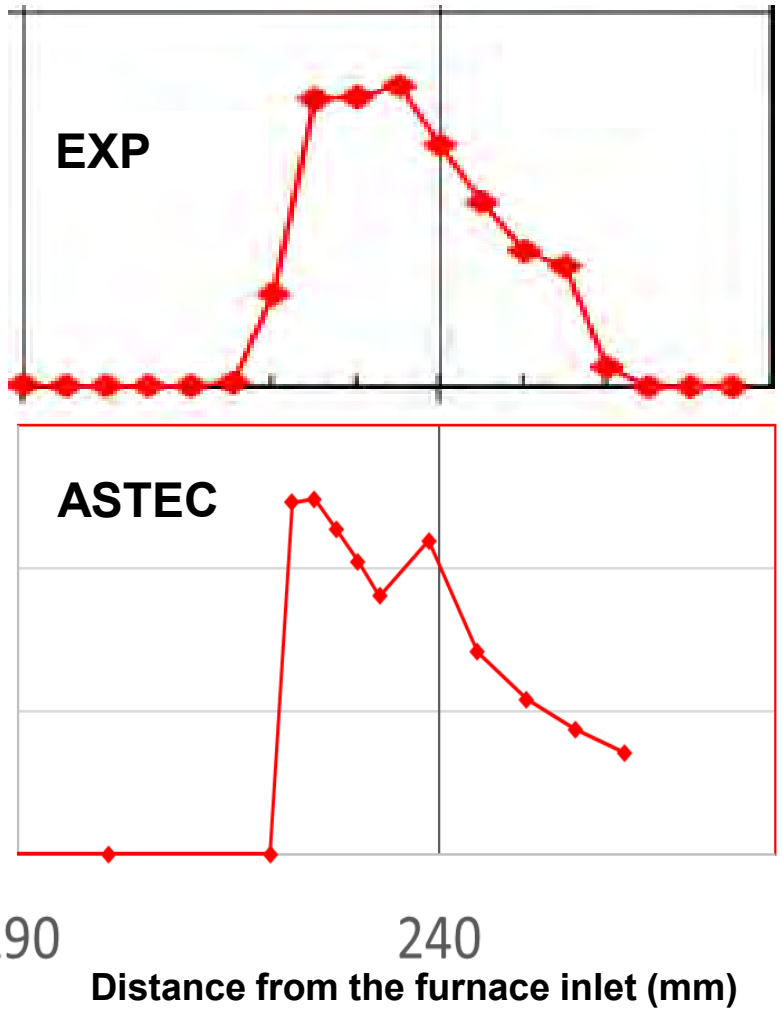

Ru deposit in TGTM

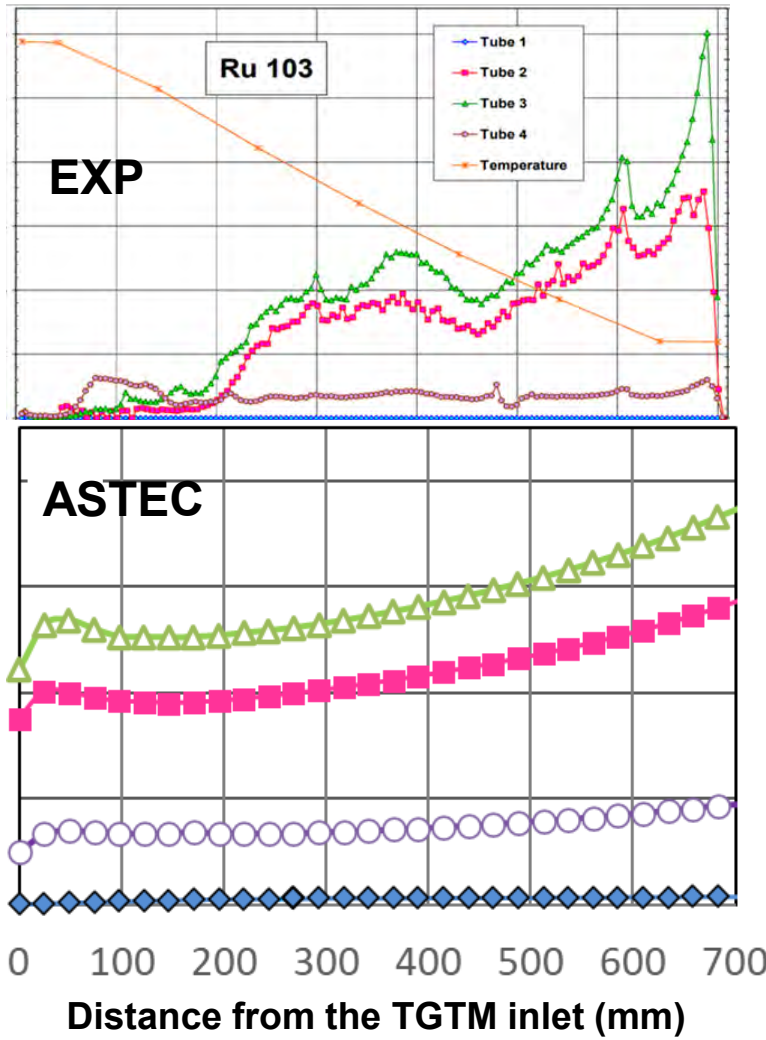

- ASTEC reproduces the observations for T ranging from 2200 °C down to 150 °C.

04

CONCLUSION

TAKE HOME MESSAGES

- **New trajectory for chemistry modeling is under implementation in the ASTEC/SOPHAEROS module.**
  - **Gas phase:** the thermodynamic assumption could be replaced by a generic chemical pathway.
  - **Surface reactivity** can now be considered.
  - All parameters (Gibbs energies of adsorption and rate constants) can be **generically approximated from the existing thermodynamic database (MDB)**.
- **Requirement:** Continue improving the MDB with **adsorption Gibbs energies** and accurate rate constants (including **activation energies**).
- **Surface reactivity** plays a key role in understanding and reproducing **Ruthenium**, **Cesium** and **Molybdenum** chemistry and transport.
- The **validity of these models holds for large temperature range** (from 2200 °C to 150 °C).

ACKNOWLEDGMENTS TO THE SOPHAEROS TEAM:

G. ASTIER

O. COINDREAU

M. JOBELIN

WITHOUT WHOM THIS WORK WOULD NOT HAVE BEEN POSSIBLE

THANK YOU FOR YOUR ATTENTION

ANALYTICAL TESTS – RU SYSTEM

Challenges : the no-congruent evaporation/condensation of RuO_3 and RuO_4

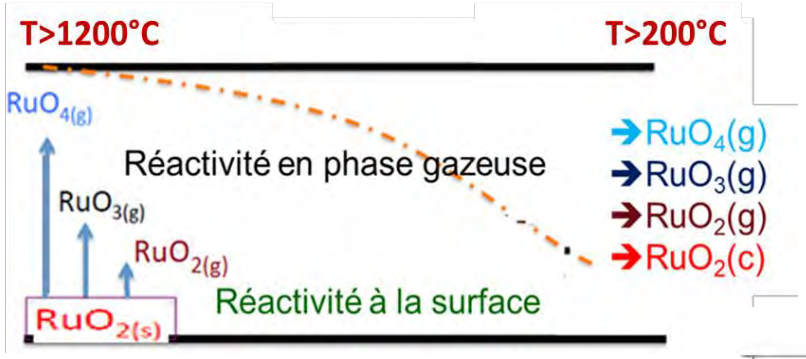

- RuO_4 (g) ↔ RuO_4 adsorb)
- RuO_4(adsorb) ↔ RuO_2(c) + O_2(g)
- RuO_3 (g) ↔ RuO_3 adsorb)
- RuO_3(adsorb) ↔ RuO_2(c) + O (g)
- RuO_3 (g) ↔ RuO_3 adsorb)
- 2xRuO_3(adsorb) ↔ 2xRuO_2(c) + O_2(g)

- **ASTEC vs experiment (START test stainless steel tube and low/high flow rates)**

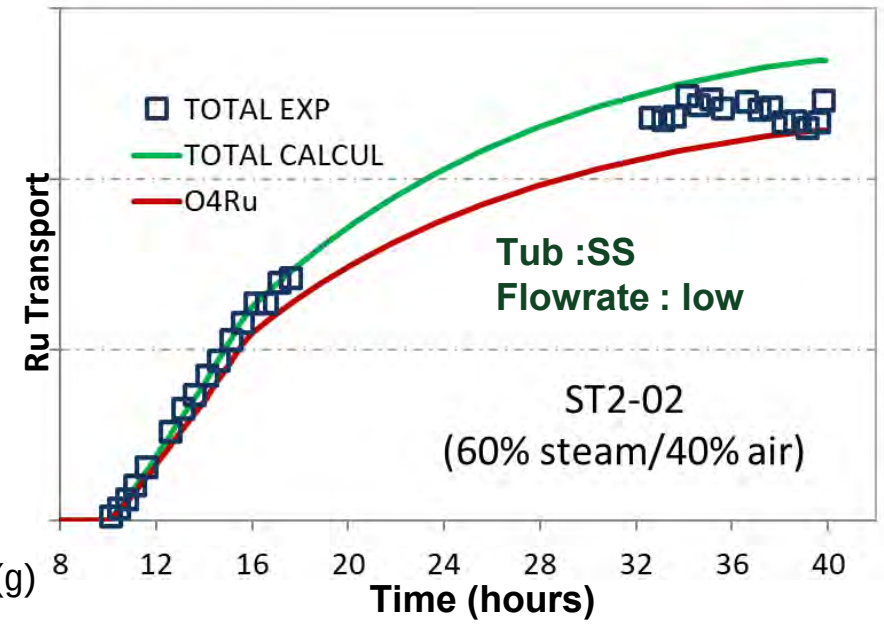

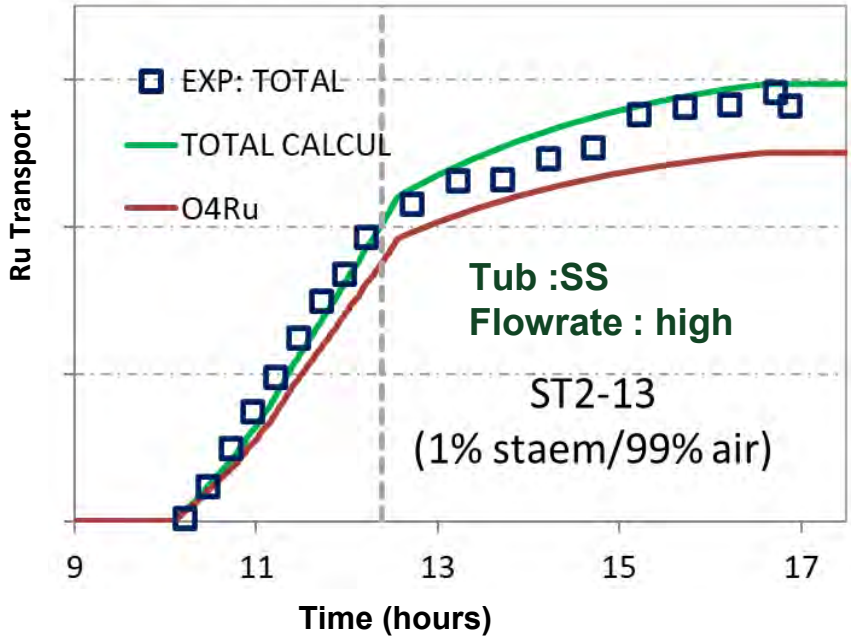

- **ASTEC reproduces the experimental observations**

UPPER-BOUND OF KINETIC RATES

$$\nu_d = Freq_{A\&B} \times \int \pi\left(\varepsilon^A\right) \times \pi\left(\varepsilon^B\right) \times P^{coll}_{\varepsilon^A + \varepsilon^B \mapsto \varepsilon^{AB}} d\left(\varepsilon^A\right) d\left(\varepsilon^B\right)$$

collision frequency between A and B

probability that A and B have the energies ε^A and ε^B

probability that the system ends up in the molecular form AB after the collision

$$A + B \leftrightarrow AB$$

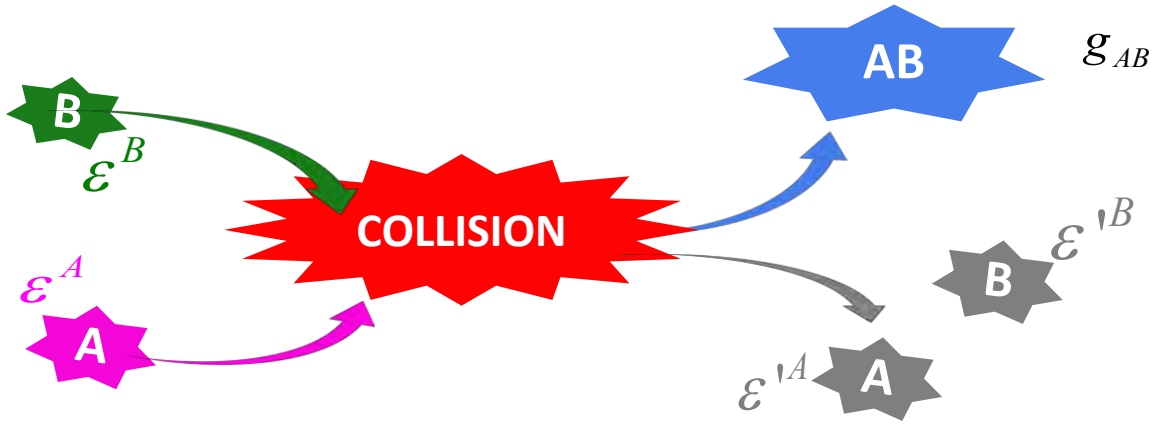

$$\left.\begin{aligned} & g_{AB}\left(\varepsilon^{AB} - \varepsilon_0^{AB}\right) \\ & + \\ & \int_{\varepsilon_0^A}^{\varepsilon^{AB} - \varepsilon_0^B} g_A\left(\varepsilon - \varepsilon_0^A\right) g_B\left(\varepsilon^{AB} - \varepsilon - \varepsilon_0^B\right) d\left(\varepsilon\right) \end{aligned}\right\} = \Omega\left(\varepsilon^{AB}\right) \qquad P^{coll}_{\varepsilon^A + \varepsilon^B \mapsto \varepsilon^{AB}} = \frac{g_{AB}\left(\varepsilon^{AB} - \varepsilon_0^{AB}\right)}{\Omega\left(\varepsilon^{AB}\right)}$$

UPPER-BOUND OF KINETIC RATES

$$\nu_d = Freq_{A\&B} \times \int \pi\left(\varepsilon^A\right) \times \pi\left(\varepsilon^B\right) \times P^{coll}_{\varepsilon^A + \varepsilon^B \mapsto \varepsilon^{AB}} d\left(\varepsilon^A\right) d\left(\varepsilon^B\right)$$

collision frequency between A and B

probability that A and B have the energies ε^A and ε^B

probability that the system ends up in the molecular form AB after the collision

$$k_d^{\max} = \sigma \sqrt{\left(\frac{8k_BT}{\pi\mu_{AB}}\right)} N_A Q\left(\frac{3}{2}\left(N_{AB}-1\right), \frac{D_0}{k_BT}\right) \frac{P}{P^\circ} \exp\left(\frac{-\Delta_r G^o(T)}{RT}\right)$$

$$k_r^{\max} = \sigma \sqrt{\left(\frac{8k_BT}{\pi\mu_{AB}}\right)} N_A Q\left(\frac{3}{2}\left(N_{AB}-1\right), \frac{D_0}{k_BT}\right) \exp\left(\frac{-D_0}{k_BT}\right) \frac{P}{RT}$$

σ: surface of collision

μ: reduced mass

N_A : Avogadro

D_0 : Disssociation energy (at 0 K)

$\Delta_r G^o(T)$: Gibbs energy of reaction

SURFACE REACTIVITY

Validation : ASTEC vs analytical expressions

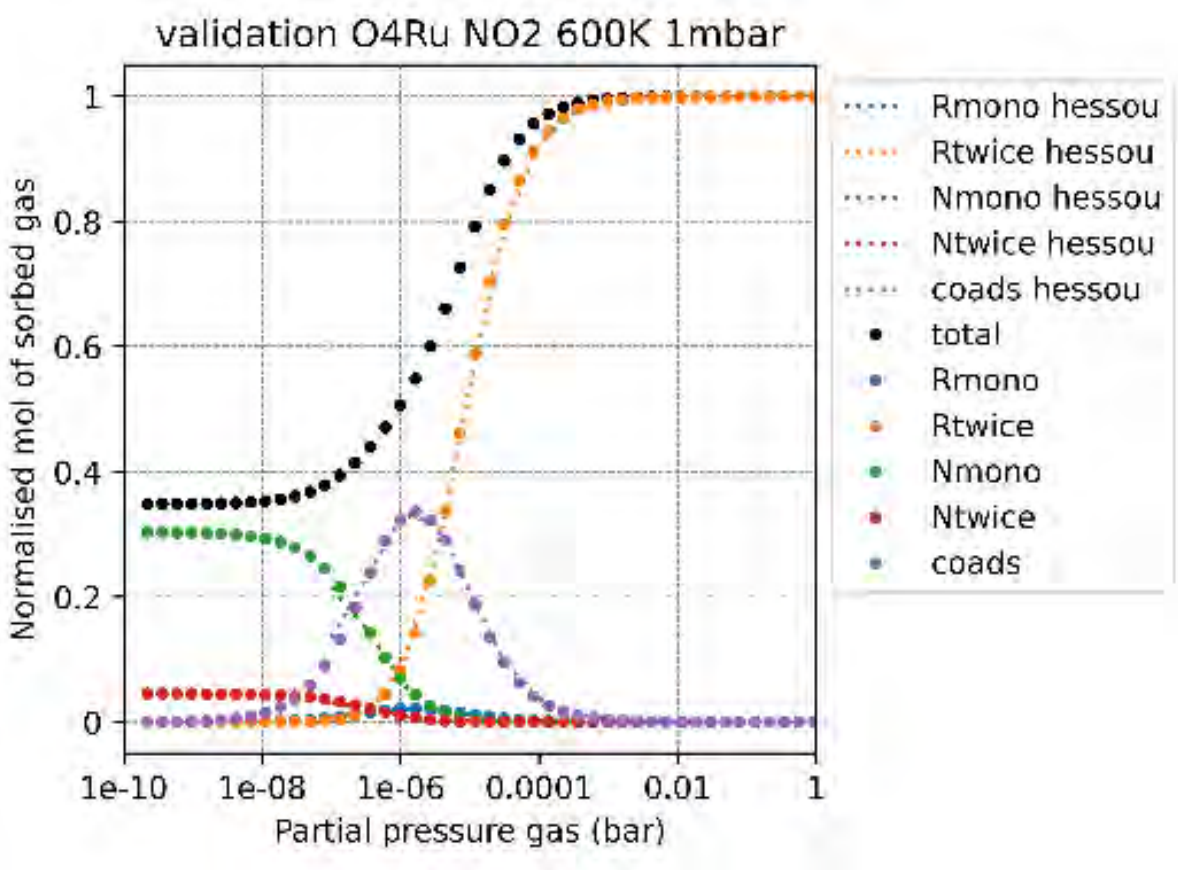

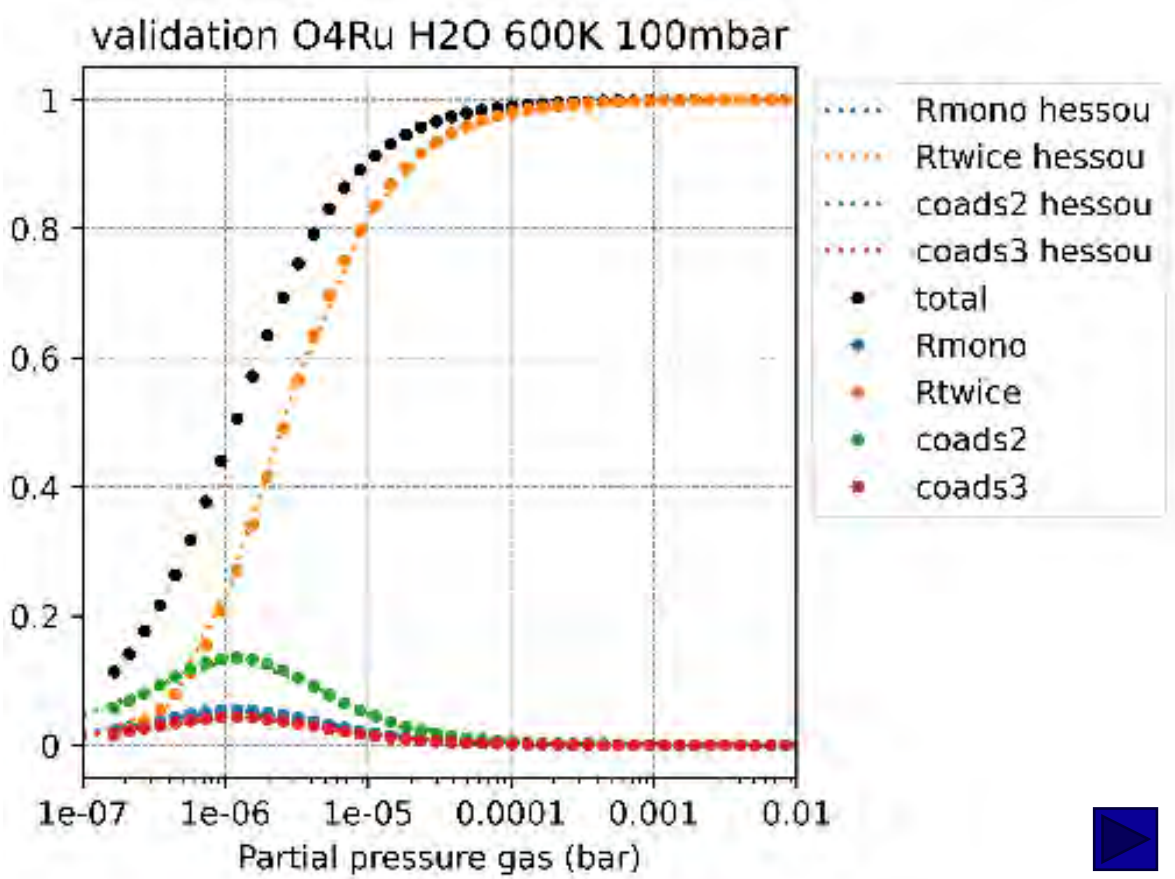

*E. **Hessou**, F. Virot, M. Calatayud, S. Souvi "Ab Initio Investigation of the Competitive Adsorption of RuO4 and NOx on a RuO2 Surface: Assessment of RuO4 Release in,a Severe Nuclear Accident" Journal of Physical Chemistry C, 2025, 129 (23)*

Jadon, A.; Girault, N.; Piar, B.; Petitprez, D.; Souvi, S. M. O. "Analytical Ab Initio-Based Modeling of the Adsorption Isotherm" J. Phys. Chem. C, 2018, 122 (42)

ARTICLE | September 24, 2018

Analytical ab initio-Based Modeling of the Adsorption Isotherm

Ankita Jadon, Nathalie Girault, Bruno Piar, Denis Petitprez, and Sidi M. O. Souvi*

Access Through Your Institution | Other Access Options | Supporting Information (1)

Abstract

An analytical ab initio-based model for adsorption isotherm is presented. As input data, this model takes the adsorption Gibbs free energies of different possible coverages within a reasonably large unit cell. In this way, the lateral interactions between adsorbates and their dependence on temperature are included. The self-dependence of surface coverage is taken into account via the introduction of heterogeneity of adsorption and the use of an appropriate configurational partition function. The model reproduces the isotherm and selectivity (for binary gas mixtures) of ab initio-based grand-canonical Monte Carlo simulations. The presented isotherm has a moderated dependence on the width of the chosen ab initio unit cell, particularly for high surface loading. This isotherm seems to be a very good approximation for the grand-canonical solution, depending on the accuracy and completeness of the ab initio data.

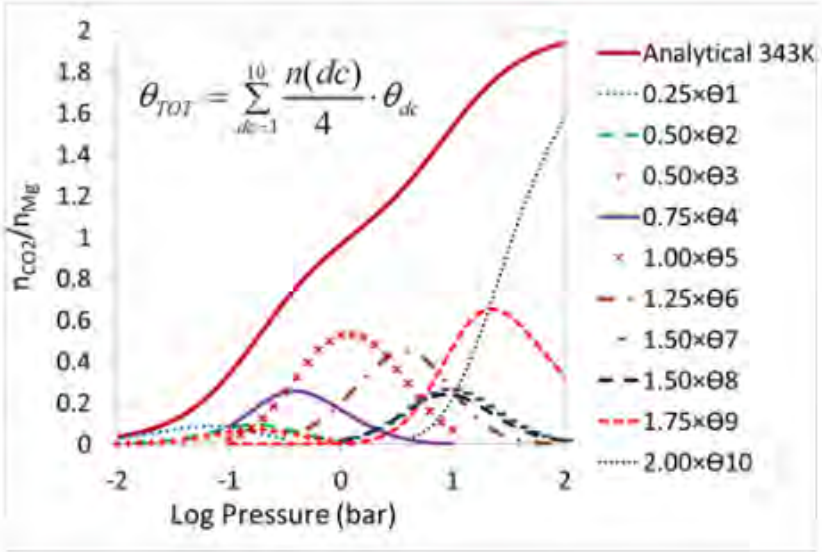

Copyright © 2018 American Chemical Society

The Journal of Physical Chemistry C > Vol 128/Issue 50 > Article

Cite Share Jump to Expand

C: CHEMICAL AND CATALYTIC REACTIVITY AT INTERFACES | December 11, 2024

Ab Initio Insight into $CsHMoO_4$ and H_2MoO_4 Complexes on MoO_3 Surfaces

Mariam Saab, Sidi M. O. Souvi*, Jean Denis, François Virot, and Monica Calatayud*

Access Through Your Institution | Other Access Options | Supporting Information (1)

Abstract

Solid surfaces play a crucial role in many processes, yet their impact on nuclear safety is not well understood. This study investigates how solid surfaces affect the behavior of radioactive gaseous species, focusing on the interaction of fission product complexes formed under nuclear accident conditions. Specifically, we examine the condensation and decomposition of Cs–Mo complexes, $CsHMoO_4$ and H_2MoO_4, when interacting with MoO_3 deposits in a reactor cooling system, considering two surface terminations: O and Mo. Using density functional theory (DFT), we calculate the Gibbs free energy for these reactions on MoO_3 surfaces at temperatures ranging from 300 to 1800 K. $CsHMoO_4$ condenses below 850 K and dissociates between 300 and 650 K on O-MoO_3 and 650–1250 K on Mo-MoO_3, forming Cs_2MoO_4 and MoO_3, along with steam release. H_2MoO_4 condenses below 500 K and decomposes between 600 and 800 K, but only on Mo-terminated surfaces. These findings improve the accuracy of nuclear simulations, helping to predict species composition and transport within the reactor cooling system during accidents.

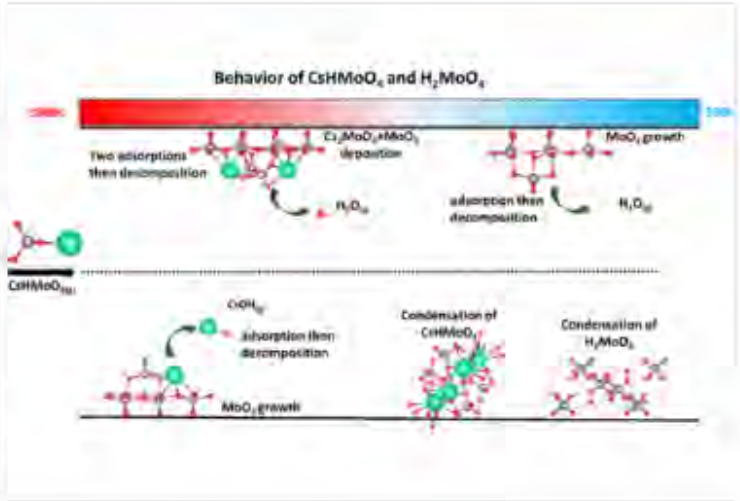

Copyright © 2024 American Chemical Society

The Journal of Physical Chemistry C > Vol 129/Issue 23 > Article

Cite Share Jump to Expand

C: CHEMICAL AND CATALYTIC REACTIVITY AT INTERFACES | May 29, 2025

Ab Initio Investigation of the Competitive Adsorption of RuO_4 and NO_X on a RuO_2 Surface: Assessment of RuO_4 Release in a Severe Nuclear Accident

Etienne P. Hessou, François Virot, Monica Calatayud*, and Sidi M. O. Souvi*

Access Through Your Institution | Other Access Options | Supporting Information (1)

Abstract

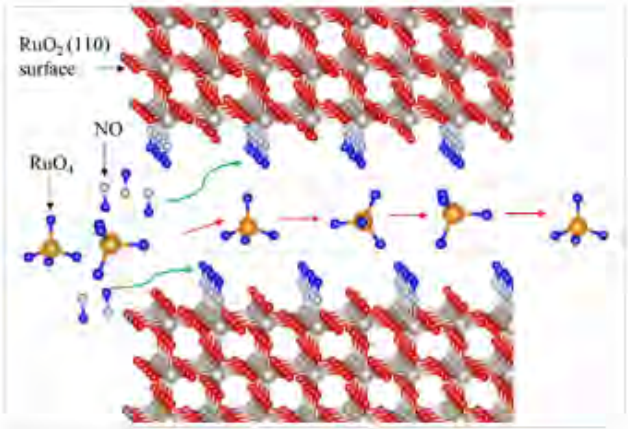

Nuclear safety has recently become a central issue in the context of the current energy and geopolitical crises. Accurate estimates of the nature and extent of radioactive species potentially released from nuclear facilities are essential for assessing and optimizing safety plans. Computational techniques appear as a powerful tool to understand the formation and transport of such species and to quantify their amount. This study focuses on the decomposition of gaseous ruthenium tetroxide (RuO_4), a fission product likely to be released into the emergency ventilation ducts in the event of an accident at a fuel reprocessing plant. RuO_4(g) is expected to decompose during its transport on the available surfaces into solid RuO_2 (c) and amorphous O_2(g). However, other species like NO_X present in the environment might interact with the surfaces of the growing deposit (RuO_2), poisoning the reactive sites vis-à-vis the RuO_4 adsorption/decomposition and favoring its transport in the gas phase to the environment. To understand this poisoning effect on RuO_2 surfaces, we carried out periodic density functional theory calculations at the PBE level. The impact of dispersion corrections (PBE+D level) is presented in the Supporting Information. RuO_4, NO, and NO_2 molecules at different coverages are computed on the RuO_2 (110) surface. We provide adsorption Gibbs free energies, isotherms, and the poisoning effect in the conditions of an accident. Our results show that the NO_X seems to have a noticeable poisoning impact on the RuO_2 (110) surface, reducing the adsorption of RuO_4(g), the first step of the condensation mechanism. Our calculations show that this impact increases with NO_X partial pressure and decreases with temperature. The results of the study will also be of interest in other fields like heterogeneous catalysis, where RuO_x surfaces are involved.

Copyright © 2025 American Chemical Society

The 12th European Review Meeting on Severe Accidents Research

May 18-22, 2026, Universidad Carlos III de Madrid, Madrid, Spain

TECHNICAL SESSION 4.4: EX-VESSEL CORIUM AND DEBRIS COOLABILITY

Chairs: P. Piluso (CEA), X. Gaus-Liu (KIT)

ID049	**Further development of a machine learning model for predicting the long-term coolability of debris beds** N. Richter (RUB)	Paper Presentation
ID121	**AI-Driven Estimation of Corium Thermophysical Properties for Ex-Vessel Corium Stabilization Simulations** R. Monod (ASNR)	Paper Presentation
ID130	**Investigation on the Melt Transport Behavior in the Drywell of Fukushima Daiichi Nuclear Power Plant Unit-1 with MPS Method** X. Li (JAEA)	Paper Presentation
ID139	**An advanced graph neural network application to highly viscous newtonian fluid flow towards the rapid corium spreading simulation** H. Asatsuma (University of Tokyo)	Paper Presentation

FURTHER DEVELOPMENT OF A MACHINE LEARNING MODEL FOR PREDICTING THE LONG-TERM COOLABILITY OF DEBRIS BEDS

Nicole Richter, Juliane Neuhaus and Marco K. Koch
Ruhr-Universität Bochum (RUB), Plant Simulation and Safety (PSS)
Universitätsstraße 150, 44801 Bochum, Germany
richter@pss.rub.de; neuhaus@pss.rub.de; koch@pss.rub.de
0009-0001-0952-4869, 0009-0004-3280-7930; 0000-0001-7260-5250

ABSTRACT

This paper outlines ongoing research activities in a national-funded joint project that uses machine learning (ML) methods to predict late-phase phenomena observed in severe accidents. The focus is on the long-term coolability of debris beds in the lower plenum, their melting and possible discharge into the cavity as a debris bed outside the reactor pressure vessel. Due to the complexity of the phenomena that can occur during this process, system codes may require high computing capacities.
The aim of the work described in this paper is to develop a ML model capable of quickly predicting the coolability of water-saturated debris beds, thereby significantly accelerating calculations within system codes. Therefore, a Gaussian Process Regression (GPR) combined with an artificial neural network (ANN) was developed, resulting in several advantages. Firstly, GPR models can extrapolate beyond the limits of the training data more effectively, since not all possible parameter combinations can be included in the training data. Secondly, they provide uncertainty in the prediction, which is important for the interpretability of the results. Combined with the ability of ANN to learn even complex relationships, this approach is well suited for the planned model development, as first results already confirm. The model is therefore able to predict the target variables with sufficient accuracy even under initial conditions that have not been trained previously.

KEYWORDS
Machine learning, artificial neural network, severe accident, coolability, debris bed

1. INTRODUCTION

The safety of nuclear reactors is a critical factor in preventing postulated accidents and minimizing their consequences. If a serious accident occur in which the fuel rods are damaged due to insufficient cooling, and a debris bed forms in the reactor pressure vessel (RPV), successful long-term cooling of the debris bed is essential to prevent remelting and impairment of the RPV's integrity. In the worst case, failure of the RPV can lead to the release of melt into the containment, and an ex-vessel debris bed might form that must also be cooled over the long term to prevent interactions between the debris-bed material and the reinforced concrete. It is essential to understand and predict the sequence of events in order to minimise the consequences. As part of international reactor safety research, extensive efforts are made [1, 2].
System codes are frequently used for this purpose, such as the AC² program package developed by the German Gesellschaft für Anlagen- und Reaktorsicherheit (GRS) gGmbH. This code enables the simulation of the reactor's thermohydraulic behavior during normal operation, disturbances, and accident scenarios [3]. To enhance the accuracy of these simulations, the underlying model basis is continuously improved. Because many phenomena during a severe accident are highly complex, realistic simulation requires

substantial numerical effort. Detail codes such as COCOMO (Corium Coolability Model) only focus therefore on the simulation of debris bed cooling using mechanistic models [4]. The coolability of the debris bed is a key aspect of accident mitigation and depends on many different parameters, e.g., particle size and shape as well as porosity and geometry. Over time, the structure can also change, and local melt pools or dryouts can form [5–7]. Because COCOMO performs detailed calculations for multi-flow phenomena, the results are very accurate, but the computation time exceeds real elapsed time during an accident. For the simulations used in this study, COCOMO required an average of one hour of processing time. If incorporated into a system code, the computation time would compound and thus be inefficient. To significantly reduce this computation time without losing too much information, a joint research project is pursuing an approach that involves the development of a machine learning (ML) model. For this purpose, COCOMO is used to generate training data, enabling a machine learning model to learn from the detailed simulations and replicate their behaviour. The aim is to develop a model that can capture the essential physical phenomena represented by COCOMO and integrate it into a PSS in-house version of the AC² system code. This would make a high level of detail available within a fast-running system code while significantly reducing computational effort. Over the course of the project, several ML model approaches have already been developed and investigated [8, 9], with a focus on the development of artificial neural networks.

Machine learning is a branch of artificial intelligence that enables software to learn from examples and experience without being explicitly programmed. There are three main learning mechanisms: supervised learning, unsupervised learning, and reinforcement learning. In supervised learning, which is of particular interest in this paper, labelled data are used to train ML models, where both input variables and desired outcomes are known [10-14]. Another approach to machine learning is artificial neural networks (ANNs), which consist of neurons connected by nodes, typically organized in layers. The input data are read in by the input layer and then passed to one or more hidden layers, where the information is processed. The output is finally generated in the output layer. The information from the individual nodes is multiplied by weights, which are adjusted during the training process. At the end of each layer, the information is summed up and passed on to an activation function, which influences its transfer to the next layer. The general structure of an ANN is shown in Figure 1. By using ML and ANNs, complex relationships between input and output data can be identified and corresponding rules can be derived. This enables the creation of powerful models that can learn from data and make predictions or decisions [15, 16].

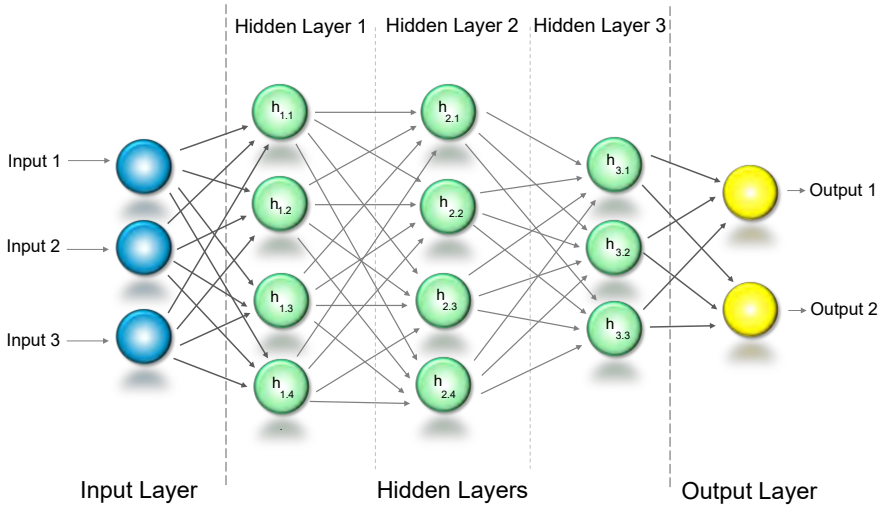

Figure 1: Generic artificial neural network.

In addition, a Gaussian Process Regression (GPR) model was developed [9]. GPR is a machine learning technique that employs a non-parametric approach to predict and model complex, non-linear data, typically assuming a zero-mean prior. The model generates a distribution over a large number of functions for the training data, which are considered a sample. This distribution is characterized by a mean function, representing the expected value, and a covariance function (kernel), representing the dependency between points. An example of a covariance function is the radial basis function [17, 18].

This paper describes the further development of an ANN that is enhanced through combination with a GPR model, a technique known as Deep Kernel Learning (DKL). This combination leverages the advantages of both structures to predict relevant parameters during the cooling of a debris bed in the containment within a very short time. The results of this work aim to reduce the computation time for simulating nuclear reactor accidents and to improve the safety of nuclear reactors.

2. TRAINING DATA

For the creation of the training data basis, the dryout experiments at the DEBRIS test facility [19] at IKE were used as a foundation. The system comprises a debris bed located in a pressure vessel, fully submerged in water, a water buffer tank to keep the water level constant, and the connecting piping. The test pressures were 1, 3, and 5 bar. Specifically, the debris bed is placed in a PTFE (polytetrafluoroethylene) crucible (height = 870 mm, internal diameter = 125 mm) inside a glass cylinder with an induction coil; a high-frequency generator inductively heats the particles as a substitute for decay heat. Above a ceramic base layer (~60 mm), the test particles consist of pre-oxidized steel spheres (2, 3, 6 mm) with a layer thickness of 640 mm. Water is supplied from the top (Top Flooding) or from the bottom (Bottom Flooding). [20]

The training dataset was generated using the detailed code COCOMO and originates from numerical simulations based on an input file provided by IKE and validated against the DEBRIS experiments described above, with a cylindrical, axisymmetric geometry and a mesh of 1,400 cells (see Figure 2). To generate as many input files as possible, the porosity, particle diameter, and the system pressure are varied and combined within physical limits. These parameters also serve as ML features, including the saturation temperature; the parameters used and their data ranges are shown in Table I. The target quantity is the dryout heating power. This is determined in COCOMO via interval nesting: first, a coarse search is performed in 100 W/kg steps between 200 and 2,200 W/kg, starting from the maximum value, with the dryout criterion checked to narrow the range. Subsequently, within the interval, the midpoint of the currently tightest bounding power pair is iteratively simulated until the interval width is below 1 W/kg. The reported mean yields the dryout heating power with an accuracy of ±0.5 W/kg; the simulation accuracy is not included.

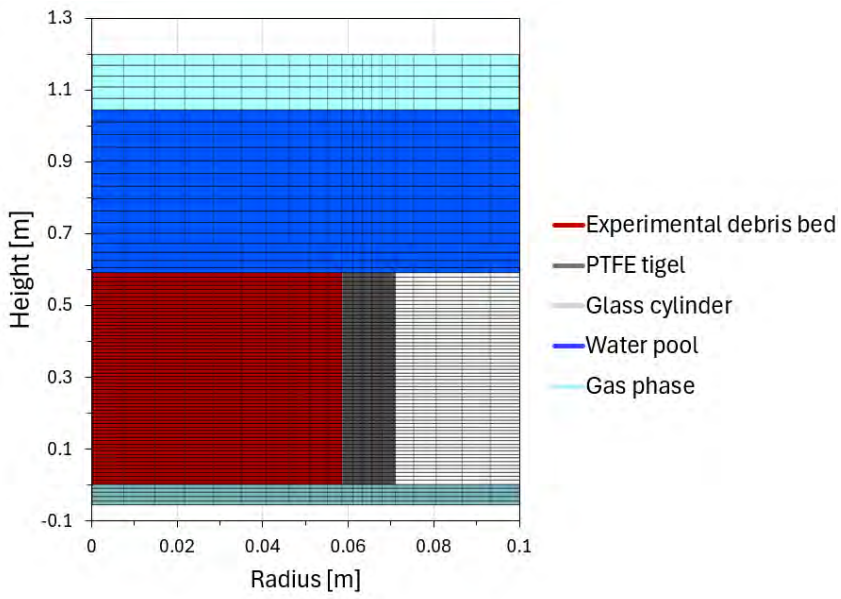

Figure 2: Geometry of the input files used for training data generation with COCOMO.

The dataset created using this method consists of a total of 250 data points. It is divided into training and test data, with 80% randomly selected for training. The remaining 20% serve as test data. Since the overarching aim of this project is to integrate the developed ML model into a severe accident code to significantly accelerate predictions, user influence is a non-negligible factor. Consequently, the model may be provided with parameter ranges and material compositions that were not covered in the training data. As it is not feasible to include the virtually infinite combinations in the training dataset, knowledge of the prediction deviation when the ML model is forced to extrapolate is indispensable. Recognizing that ML models achieve their best performance only within the bounds of the training data, an additional validation dataset of 100 data points was therefore generated, featuring a different material composition than the DEBRIS training data. In addition, the parameter ranges were slightly adjusted. The exact data domains are provided in Table I.

Table I. Varied parameters and data rooms

Parameter	Pressure [MPa]	Porosity [-]	Particle diameter [m]	Saturation temperature [K]	Dryout heating power [W/kg]
DEBRIS set	0.1 – 0.5	0.27 – 0.47	0.0025 – 0.0061	373 – 425	150 - 860
Validation set	0.1 – 0.5	0.37 – 0.51	0.0005 – 0.0040	373 – 425	220 - 2090

3. MODEL DEVELOPMENT

All models presented here were developed in Python using the PyTorch framework and trained via supervised learning. The dataset based on the DEBRIS experiments was divided into training data (80%) and test data (20%). In addition, a separate validation set was employed to assess the model configuration independently of the test data. As the initial model architecture, a multilayer neural network (NN) with four layers was chosen, consisting of an input layer, two hidden layers, and an output layer. The hidden layers

used the ReLU activation function to capture nonlinear relationships and improve training dynamics. To select the final model parameters and structure, a systematic hyperparameter analysis was conducted, in which different configurations were evaluated and compared based on their performance on the validation set. The final assessment of generalization capability was performed on the validation set.

A GPR with a special kernel is utilised. The kernel in the model is a combination of a constant kernel and a Radial Basis Function kernel. The constant kernel adds a constant component to the model, while the RBF kernel determines the smoothness of the predicted function. The initial values and ranges for both kernel components are specified to initialise and optimise the model parameters. The code initialises the GPR with the defined kernel and sets the noise level of the observations to 0.01. The noise level refers to the variance of the noise that is added to account for uncertainties such as measurement errors. The model is then trained with the training data. The next step is to predict the target values for the test dataset, also calculating the standard deviations to quantify the uncertainties of the predictions

To leverage the strengths of both previous models to improve the prediction of the validation data, Deep Kernel Learning is used. The GPR model is particularly well suited for data extrapolation, while the NN model can better capture complex relationships between variables. The DKL model is trained as follows: first, the training data are fed into an NN and the network is trained. Next, the outputs of the NN's last hidden layer are passed to an GPR model and used to train it. This is done because the GPR learns more effectively when it is provided with multiple data inputs. The NN consists of five layers and uses the activation functions ReLU, tanh, and sigmoid. The GPR model uses a Matérn kernel, scaled by an additional parameter. Through this combination of NN and GPR, the model can exploit the advantages of both approaches and thus, in principle, provide improved predictions on the validation data.

4. RESULTS AND METRICS

The evaluation of machine learning models is of critical importance, with the primary objective being to ensure robust and accurate predictions on previously unseen data, thereby validating the model's generalizability and the efficacy of the training process. In the context of supervised learning, the discrepancy between the prediction of the model and the actual value of the simulation in the entire data set is calculated. A significant discrepancy signifies inadequate performance of the machine learning model, while a negligible discrepancy indicates optimal performance. There exist numerous methods for calculating this discrepancy through the utilisation of so-called loss functions. One such approach involves the calculation of the mean absolute error (MAE). This approach is susceptible to outliers, which can be mitigated by employing as an alternative loss function. In this case, the mean value is calculated using the deviation between the predicted and actual values of the entire data set [21]. Another option is to use the R^2 value, which is a measure of the quality of the predictions of the ML model. The value can be between 0 and 1, where 1 corresponds to a prediction of 100% [22]. Another parameter of interest is the maximum error (MAX). These three metrics were selected as the evaluation guidelines for this work.

In relation to simulating real accidents or even generic scenarios with a system code, there is a nearly infinite number of parameter combinations, which can also change during the process. The influence of users should not be underestimated either. It is therefore possible that the models have to work with boundary conditions that were not covered by the training data. For this reason, the focus should be on a suitable selection of samples. Especially for different material compositions, as these can change during the process and are difficult to estimate in reality. For this reason, it is important to know where the limits of the models are and what the deviations are for data outside the trained parameter ranges in order to be able to interpret the results appropriately. Furthermore, the aim is of course to minimise these deviations. Therefore, all models were tested on two different data sets and the results were compared.

The results of the NN and the GPR model for the test data, based on the DEBRIS experiments, are shown in Figure 3. Here, the models' predictions are plotted against the actual simulation data. In the case of perfect agreement, the points lie on the trend line. Both models exhibit good performance, which is reflected not only in the graphical representations but also in the metrics. The R^2 scores of all models exceed 0.9, indicating strong predictive capability. The R^2 score refers to the 20% test data drawn from the DEBRIS dataset. In this comparison, the NN performs worst with 0.969, while the GPR model achieves the best score at 0.997. Considering the MAE and the maximum error as well, the GPR model (5.55 and 16.92 W/kg) delivers the best performance in predicting the dryout heating power for the test data. Conversely, the NN (19.09 and 79.19 W/kg) performs worst on these metrics. For test data that reflects the trained range, these two models are therefore very well suited for predicting dryout heating power.

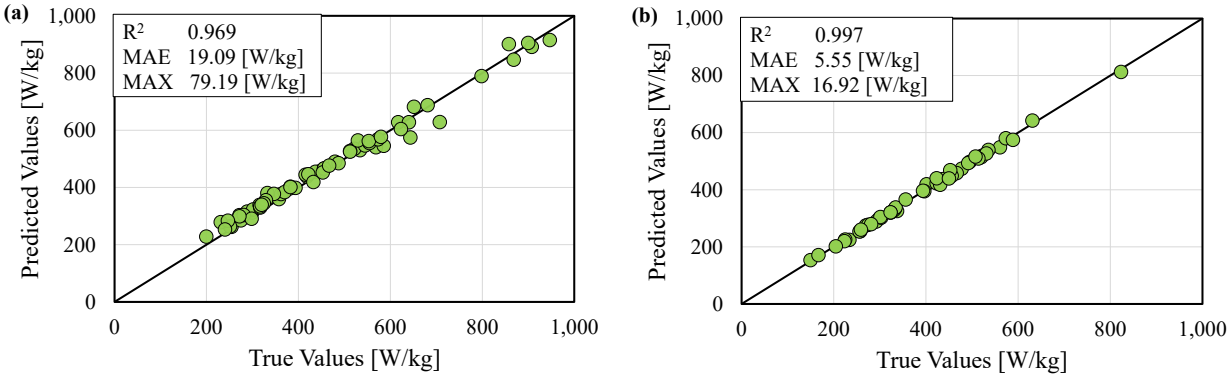

Figure 3. Prediction of NN (a) and GPR (b) for the DEBRIS test data.

When the models are provided with validation data featuring a different material composition, a very different picture emerges. Here, both models perform significantly worse. The MAE of the neural network and the GPR model are above 100 W/kg. Although the maximum error is considerably higher for the GPR model, at 505.20 W/kg, than for the NN (296.80 W/kg), the majority of its predictions are closer to the true value. Compared with GPR, the NN substantially underestimates most of the test data. Nevertheless, the predictions of both models are unsatisfactory when they are forced to extrapolate due to the different material composition and slightly differing parameter ranges. This outcome was to be expected; however, given the aim of integrating the ML model into a system code and the associated user influence, it cannot be guaranteed that only material and parameter combinations encountered during training will occur in practice, so at least an improvement of these validation results is required.

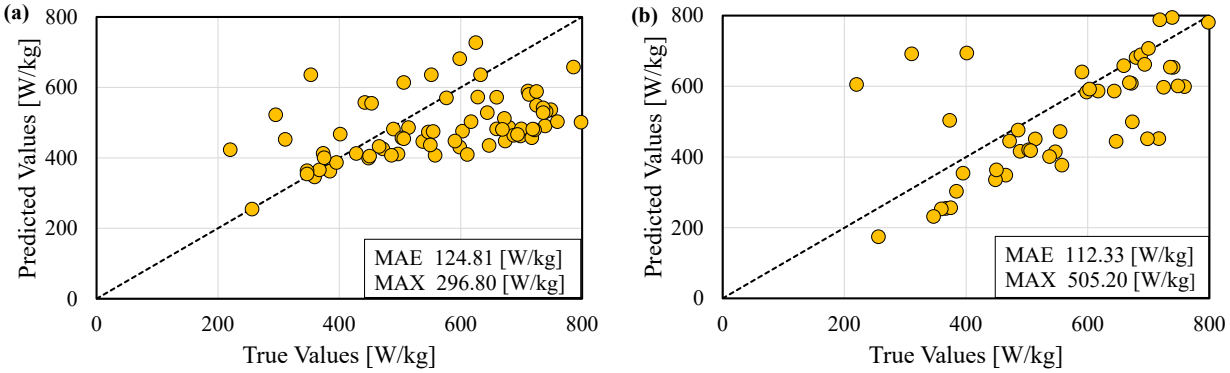

Figure 4. Prediction of NN (a) and GPR (b) for the validation data.

To combine the strengths of both ML models, the development of a combined model was pursued. The hypothesis is that a combined model will demonstrate excellent predictions for both the DEBRIS test data and the validation data, which differs from the training data. As illustrated in Figure 5, the outcomes for both data sets are presented, with the green dots representing the predictions for the DEBRIS data and the yellow dots denoting those for the validation data. Firstly, it is evident that the combined model exhibits inferior performance in comparison to NN and GPR on the DEBRIS test data. The R^2 score remains above 0.9, however, all three metrics have deteriorated. In the context of the problem under consideration and the training data employed, the combined model does not appear to be the optimal choice. However, given that the objective of this study is to enhance the prediction accuracy for entirely unseen validation data, the combined model is evaluated using precisely this data. As demonstrated in Figure 5, a substantial enhancement is observed in direct comparison with the other two models. Naturally, deviations from the true value are still observable, but the MAE is almost halved relative to the NN. The maximum error can also be improved somewhat. Moreover, the dryout heating power is no longer underestimated in most cases; instead, a distinctly more balanced picture emerges. In general, most predictions lie within the 20% margin. The hypothesis that predictions would improve for data deviating from the domain on which the model was trained has been confirmed.

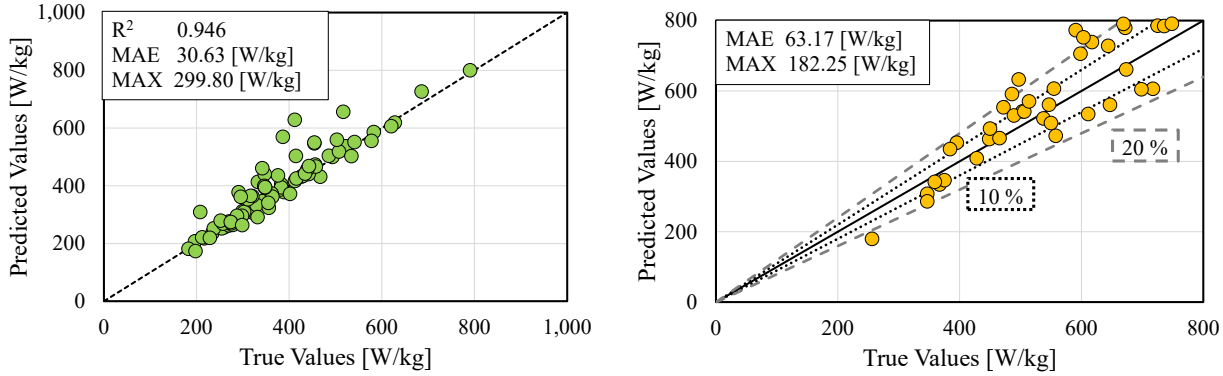

Figure 5. Prediction of the combined model for the DEBRIS test data (left) and the validation data (right).

5. CONCLUSIONS

In case of a postulated severe accident scenario involving ex-vessel debris bed formation, long-term cooling is a key factor in accident mitigation. The phenomena occurring during this process can be modelled with severe accident codes. Due to their complexity, however, these codes require substantial computational effort and long computing times. The work presented in this paper aims to significantly reduce these computation times using machine learning models, without losing too many details.

More specifically, this paper describes the further development of a machine learning model for predicting the dryout heating power of a debris bed. The initial model architecture was a multilayer neural network with four layers: an input layer, two hidden layers, and an output layer. The hidden layers used the ReLU activation function to capture nonlinear relationships and improve training dynamics. A systematic hyperparameter analysis was conducted to select the final model parameters and structure. A Gaussian Process Regressor with a special kernel was also used. The kernel in the model is a combination of a constant kernel and a radial basis function kernel. The third model is a hybrid version of an artificial neural network

and a Gaussian Process Regression model. The idea behind this combination is to leverage the strengths of both models to improve predictions for validation data that differ from the training data in terms of material composition. Since the ML model is to be integrated into a system code, it is not possible to cover all possible parameter combinations in the training data. The model is therefore forced to extrapolate. Even though the performance of an ML model degrades significantly under extrapolation, the predictions should remain within a reasonable range so as not to overly affect the subsequent calculations of the system code.

The R^2 value for the combined model is around 0.95, which is slightly lower than for the individual models but still very good. The results for the validation data show that the combined model provides improved predictions. The mean absolute error is reduced from over 100 W/kg to 63 W/kg, representing an improvement of about 40%. Most predictions fall within a 20% band, indicating a satisfactory agreement between predictions and actual values. The individual models tend to underestimate the validation data. In this regard, the combined model yields more balanced predictions. The results of the work thus confirm the assumption that combining the capabilities of neural networks and Gaussian process regression models improves predictions outside the trained range.

ACKNOWLEDGMENTS

With funding from the:
Federal Ministry of Research, Technology and Space

This project is funded by the Federal Ministry of Research, Technology and Space (BMFTR) under the funding code 02NUK078B.
The training data was determined using the IKE detail code COCOMO.

REFERENCES

1. Jacquemain, D. et al., *Nuclear power reactor core melt accidents. Current State of Knowledge,* EDP Sciences, Les Ulis, France (2015).
2. Buck, M., “Modelling of the Late Phase of Core Degradation in Light Water Reactors.” Dissertation, IKE 2-153, Institut für Kernenergetik und Energiesysteme, University of Stuttgart, Stuttgart (2007).
3. F. Weyermann et al., “AC² 2023 – User Manual”, GRS-P-15/Vol.1 Rev. 1 (2023).
4. Buck, M. and Pohlner, G., “Ex-Vessel Debris Bed Formation and Coolability – Challenges and Chances for Severe Accident Mitigation“, *Proceedings of 2016 International Congress on Advances in Nuclear Power Plants (ICAPP 2016)*, San Francisco, CA, April 17-20 (2016).
5. Leininger, S., “Experimentelle Untersuchungen der Kühlbarkeit prototypischer Schüttungskonfigurationen unter dem Aspekt der Reaktorsicherheit.” Dissertation, IKE 8-126, Institut für Kernenergetik und Energiesysteme, University of Stuttgart, Stuttgart (2017).
6. Buck, M. et al., “Modellentwicklung zu Schmelzeverhalten und Kühlbarkeit in Reaktordruckbehälter und Sicherheitsbehälter. Abschlussbericht zum Vorhaben BMWi 1501482,” IKE 2-171, Institut für Kernenergetik und Energiesysteme, University of Stuttgart, (2018).
7. Peschel, J., “Erweiterung der Spätphasen-Modellbais des Systemscodes AC2 zur Simulation von Schüttbetten“, Dissertation, AG Plant Simulation and Safety, University of Bochum, Bochum (2024).
8. Richter, N. and Koch, M.K., ”Development of a ML model to predict the long-term cooling of debris beds”, *Proceedings of KERNTECHNIK 2024*, Leipzig, June 11-13 (2024).
9. Richter, N.; Neuhaus, J. and Koch, M. K. “Development of a Machine Learning Model for Predicting the Long-term Coolability of Ex-vessel Debris Beds for Extension of Systemcode Modelling“, *Proceedings of NURETH-21, 21st International Topical Meeting on Nuclear Reactor Thermal Hydraulics*, Busan, 2025.

10. Döbel, I. et al., "Maschinelles Lernen: Eine Analyse zu Kompetenzen, Forschung und Anwendung. Fraunhofer-Gesellschaft,", Fraunhofer-Gesellschaft, München (2018)
11. Nasteski, V, "An overview of the supervised machine learning methods", *Horizons B*, **4**, pp. 51-62 (2017).
12. Jiang, T. et al., "Supervised Machine Learning: A Brief Primer," *Behaviour Therapy*, **51**, pp. 675-687 (2020).
13. Choo, K.; Greplova, E.; Fischer, M.H.; Neupert, T., *Machine Learning kompakt – Ein Einstieg für Studierende der Naturwissenschaften*, Chapter 3, Springer Verlag Zürich (2020).
14. Frick, D.; Gadatsch, A.; Kaufmann, J.; Lankes, B.; Quix, C.; Schmidt, A.; Schmitz, U. *Data Science – Konzepte, Erfahrungen, Fallstudien und Praxis*, pp. 225-239, Springer Verlag, Mönchengladbach, Germany (2021).
15. Basler, D., *Neuronale Netze mit C# programmieren – Mit praktischen Beispielen für Machine Learning im Unternehmenseinsatz*, Chapter 1 and 2.5, Hanser, München, Germany (2021).
16. Sandeep, P, "Thermo-hydraulic Analysis of Wall Bounded Flows with Supercritical Carbon Dioxide Using Direct Numerical Simulation." Dissertation, IKE 8-131, Institut für Kernenergetik und Energiesysteme, University of Stuttgart, (2018).
17. Schulz, E.; Speekenbrink, M.; Krause, A., "A tutorial on Gaussian process regression: Modelling, exploring, and exploiting functions", *Journal of Mathematical Psychology*, **85**, pp: 1-16 (2018).
18. Shi, J. Q. and Choi T., *Gaussian Process Regression Analysis for Functional Data, Chapman and Hall/CRC*, Chapter 2.1, New York, USA (2011).
19. Leininger, S. and Kulenovic, R., "Description of DEBRIS Experiments", Technical report, IKE 5-TB-5, Institut für Kernenergetik und Energiesysteme, University of Stuttgart, Stuttgart (2016).
20. Rashid, M. "Coolability of Volumetrically Heated Particle Beds", Dissertation, University of Stuttgart, Stuttgart, 2017.
21. Kotu, Vijay and Deshpande, Bala, *Data Science – Concepts and Practice*, Second Edition, Morgan Kaufmann, Elsevier, Chapter 12, pp: 395-445 (2019).
22. Han, J.-H. and Chi, S.-Y., "Consideration of Manufacturing Data to Apply Machine Learning Methods for Predictive Manufacturing", *Proceedings of Eighth International Conference on Ubiquitous and Future Networks (ICUFN)*, Vienna, July 06-08 (2016).

RUB

RUHR-UNIVERSITÄT BOCHUM

Further Development of a Machine Learning Model for Predicting the Long-term Coolability of Debris Beds

Nicole Richter, Juliane Neuhaus, Marco K. Koch

ERMSAR | Madrid, Spain | 20th May 2026

PSS Plant Simulation and Safety
Prof. Dr.-Ing. Marco K. Koch

INTRODUCTION

- In the case of a severe accident, debris beds may form as a result of insufficient cooling
- After successful quenching, long-term cooling is essential to prevent renewed melting of the debris bed
- Highly complex and numerically demanding processes
- In reactor safety research severe accident codes are used to simulate accident scenarios and therefore the coolability of debris beds

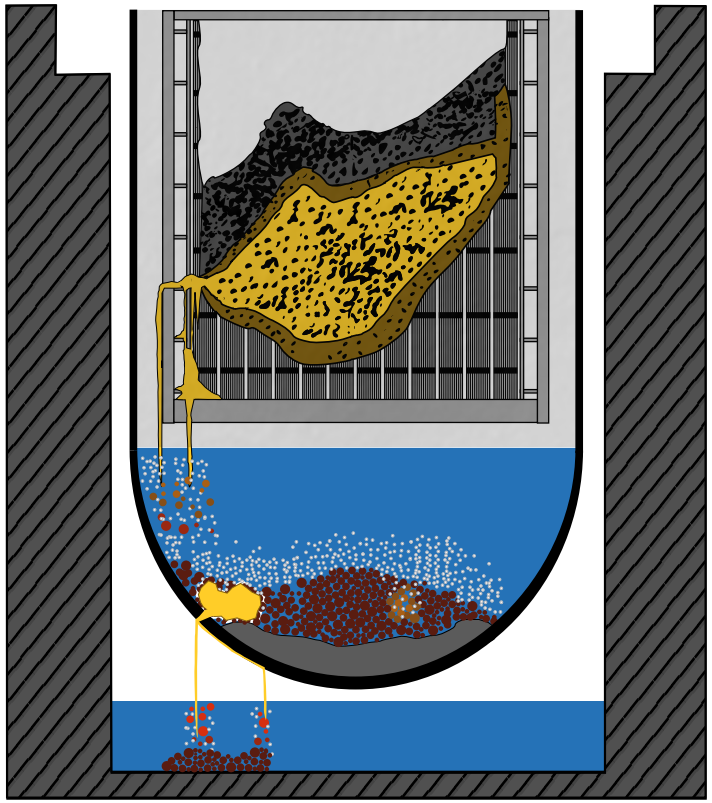

Figure: Peschel, 2024

INTRODUCTION

- Long-term cooling is critical for safety
  - Prevents remelting of debris bed due to decay heat
  - Maintains integrity of RPV and containment
  - Insufficient cooling leads to localised drying out
- Key parameter: Dryout heat flux
  - Determines maximum heat flux before dryout
  - Essential for predicting long-term cooling capability
- System codes accurate but computationally intensive

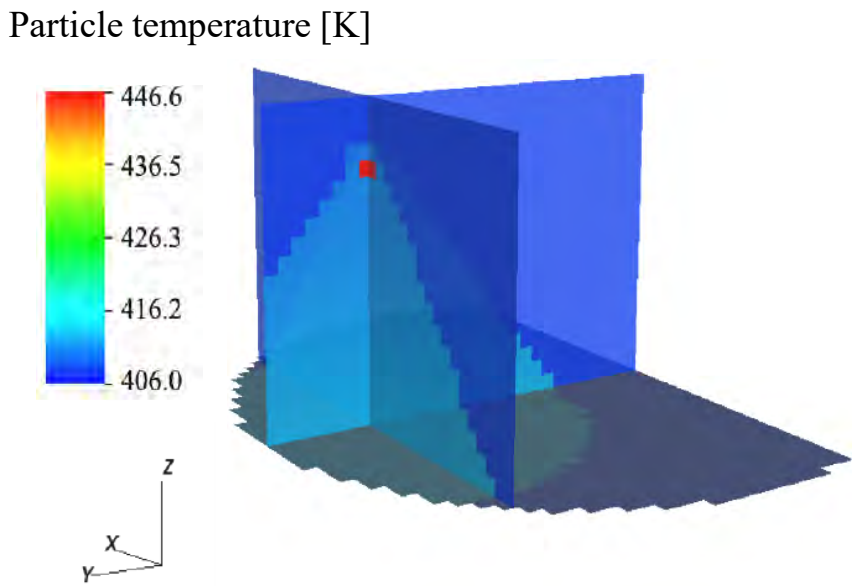

Figure: Hartmann, 2020

INTRODUCTION

Problem

- Due to the complexity of some phenomena
  - High numerical effort
  - Long computing times

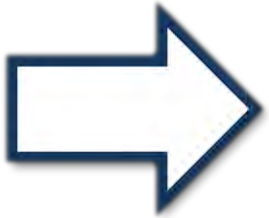

Aim

- Reduction of computing time
- Minimal loss of detail

Concept

Use of machine learning model to predict the coolability of debris beds

Integration into the severe accident code AC²

Basics of Machine learning

Artificial Intelligence

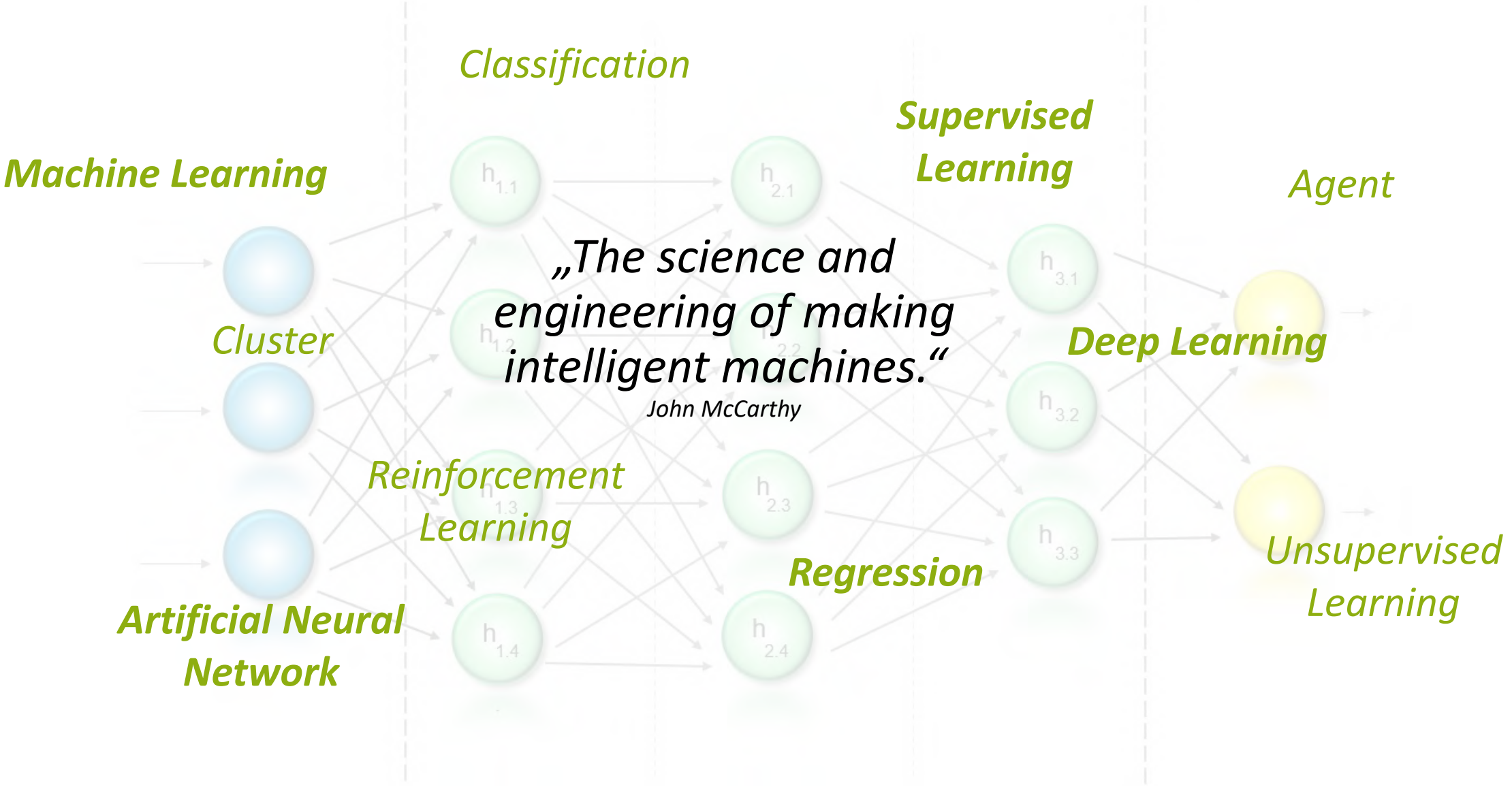

Basics of Machine learning

Artificial Intelligence

The purpose of machine learning models and algorithms is to identify meaningful correlations in input data and derive rules based on these correlations.

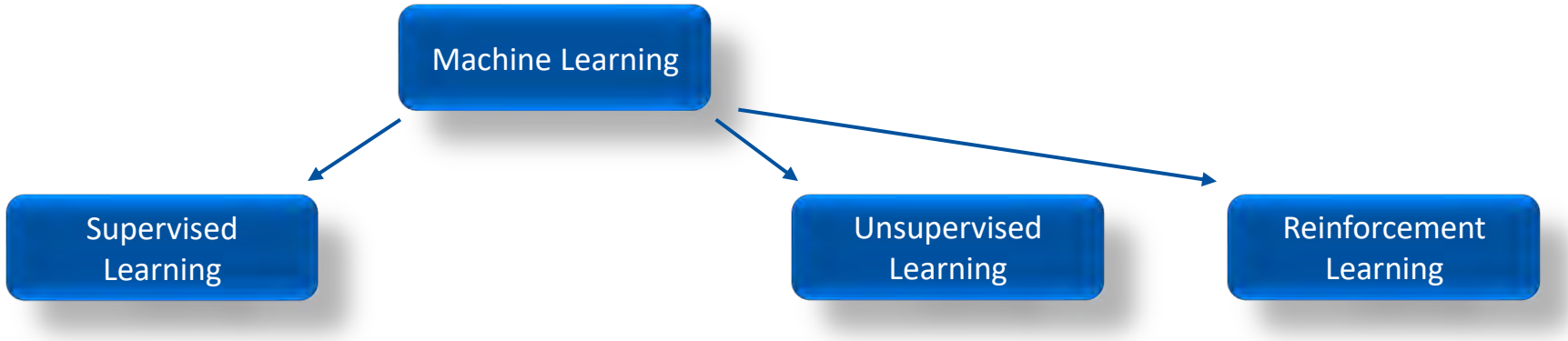

Basics of Machine learning

Artificial Intelligence

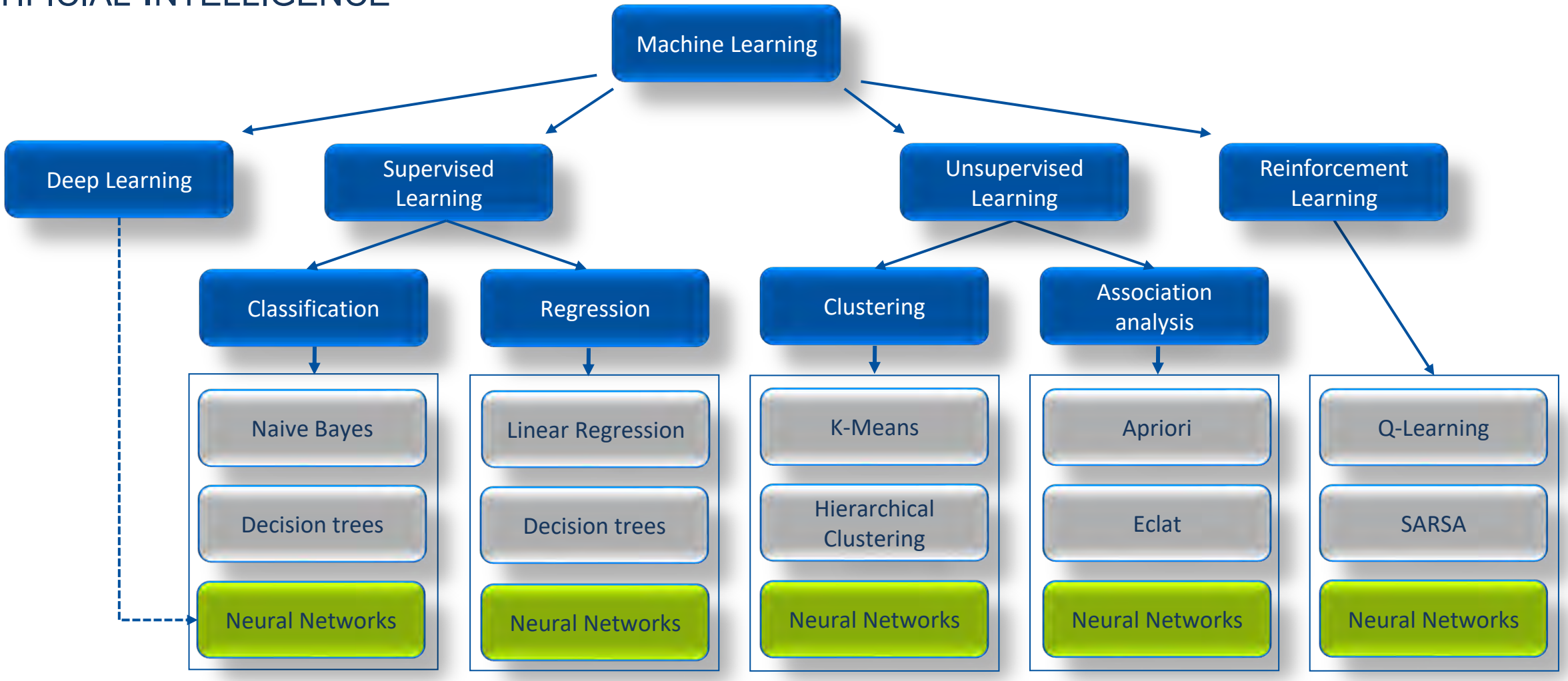

BASICS OF MACHINE LEARNING

ARTIFICIAL NEURAL NETWORKS

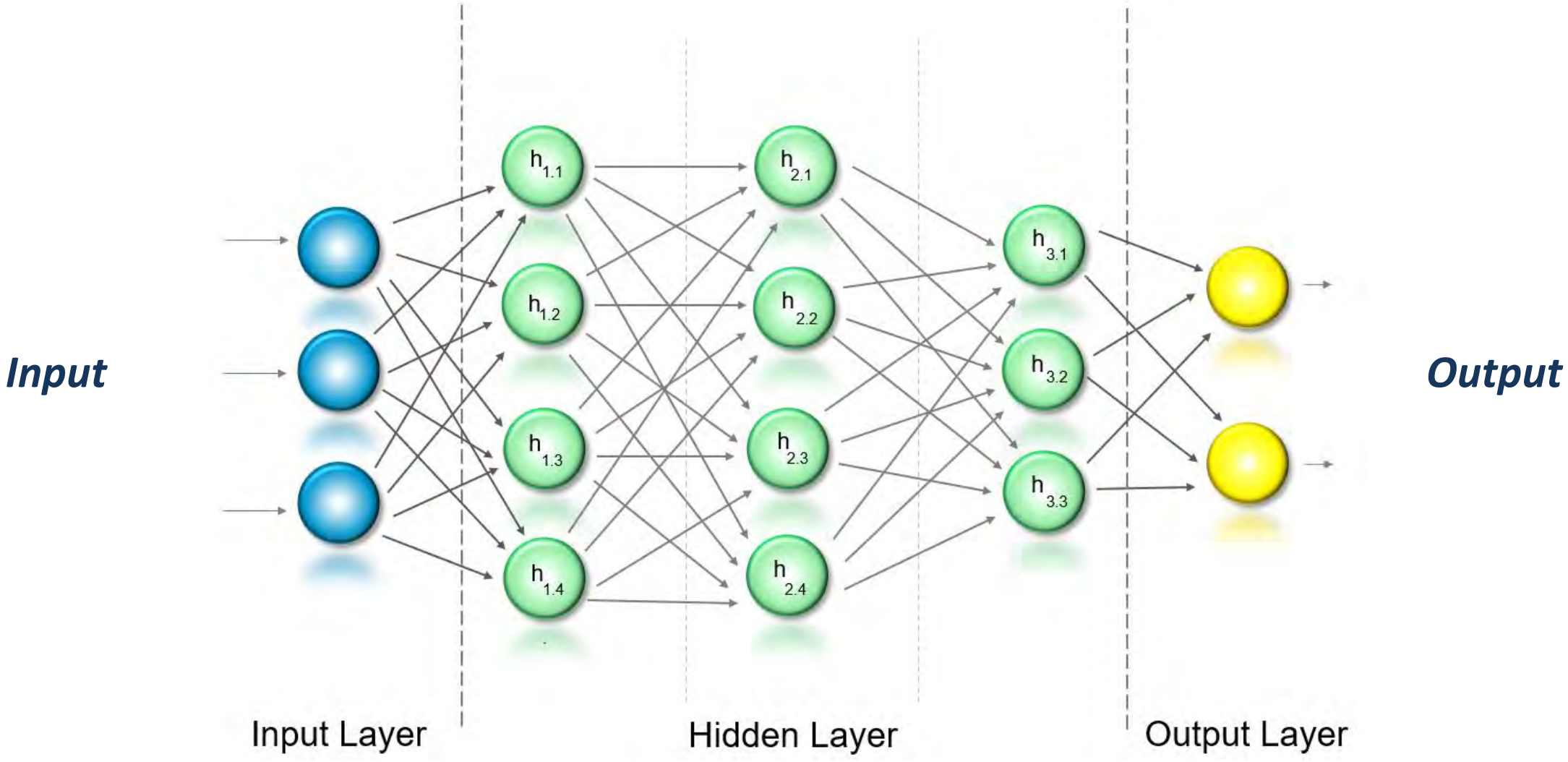

Basics of Machine learning

Gaussian Process Regression (GPR)

- Non-parametric method used to predict and model complex data.
  - Distribution of the training data across all possible functions that describe this data.
  - This distribution is characterised by a mean function and a covariance function, or `kernel´
  - In this model: Radial Basis Function
- Not only outputs individual data points, but also provides a probability distribution
- Training data is regarded as a „sample“

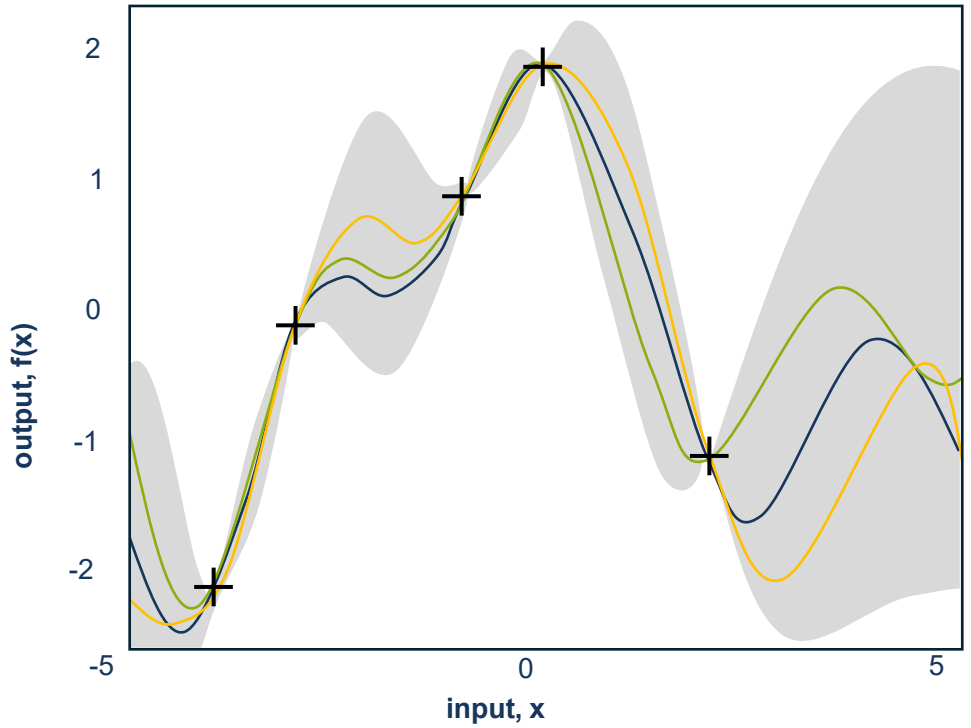

Training Data

- Creation of an initial database with the detail code COCOMO
- Basis: DEBRIS dryout tests of the IKE
- Parameter variation:
  - Input parameters: *system pressure, particle diameter, porosity, saturation temperature*
  - Output parameters: *dryout heating power*

	System Pressure [MPa]	Particle Diameter [m]	Porosity [-]	Saturation Temperature [K]
Range	**0.1 – 0.5**	**0.0024 – 0.006**	**0.27 – 0.46**	**373 - 425**

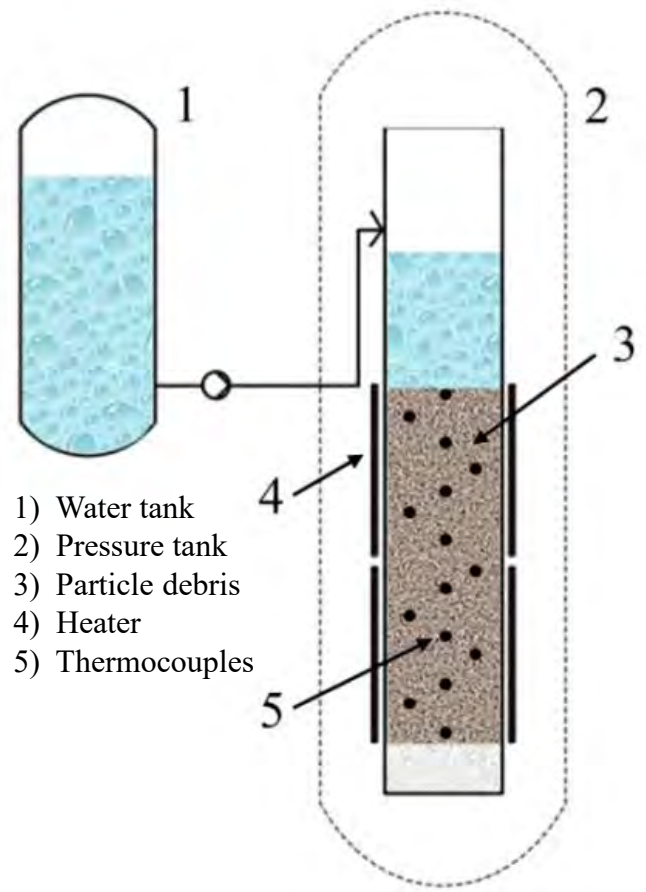

Figure: Schematic representation of the DEBRIS test facility
Source: Hartmann 2020, IKE

Training Data

Input data set

- System pressure 0.1 MPa – 0.5 MPa
- Inlet flow at the bottom constant
- Heated particles with increasing power
- Stop-condition: **liquid temperature → saturation temperature + 5K**
  - ↳ Dryout
- Data set is split into 80% training data and 20% test data

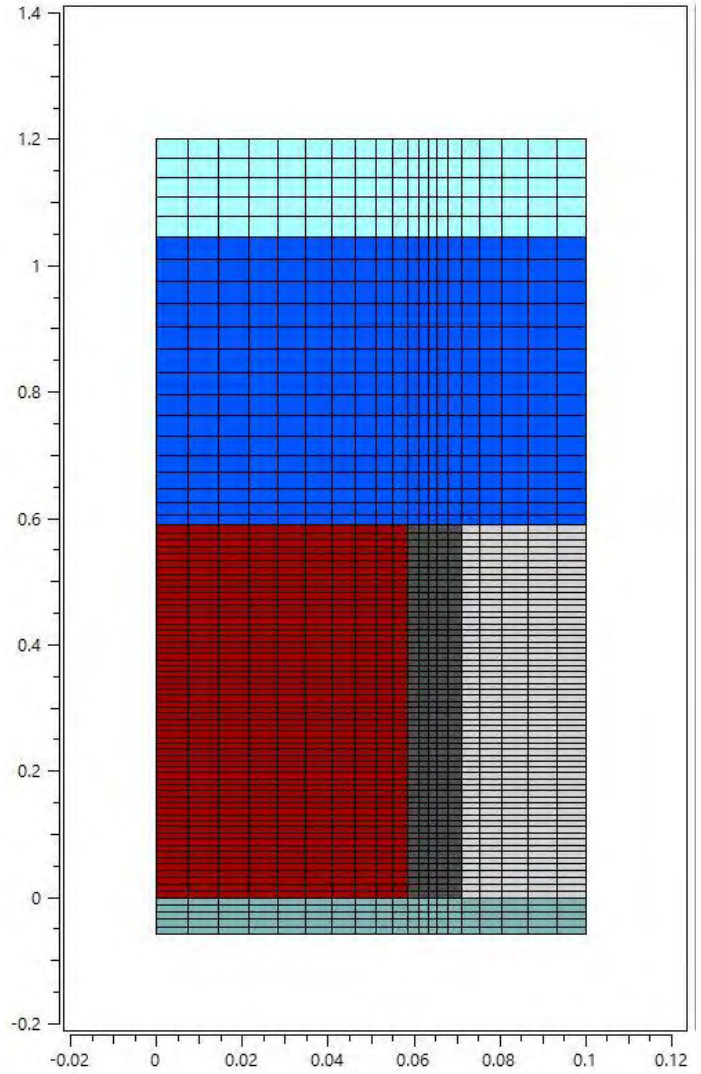

Figure: Nodalisation DEBRIS input deck; axes: length in metres; Source: COCOMO

Preliminary Results

Test data

Neural Network

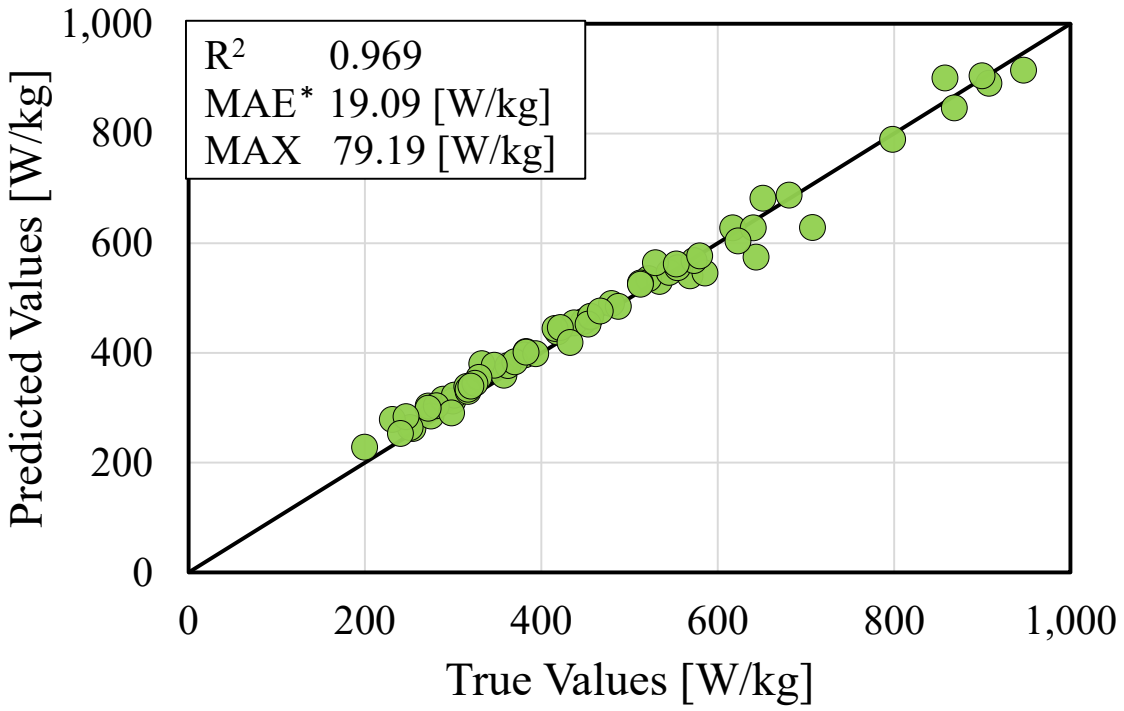

GPR model

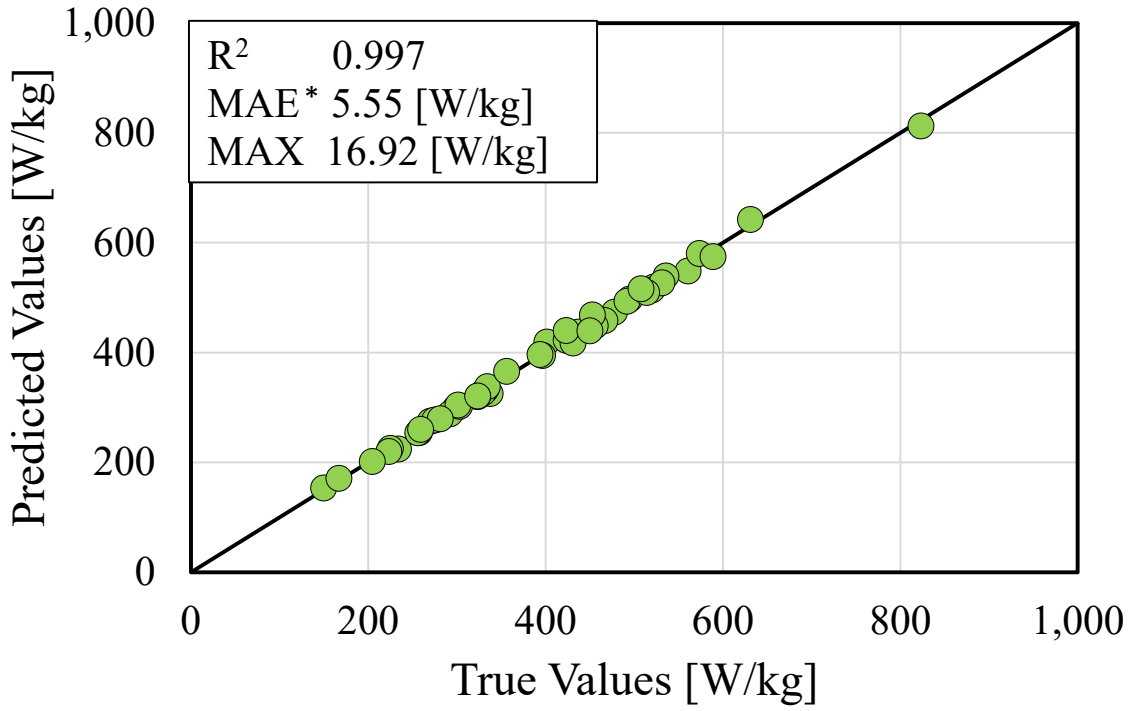

Model Speed:
Each result took half a milisecond

*Mean absolute Error

Validation Data Set

- Data set with different material data
- Hypothetical corium parameter outside the trained range
- COCOMO simulation data

- ‘Blind test’
- Investigate limits of the models
- Training set cannot cover all possible combinations

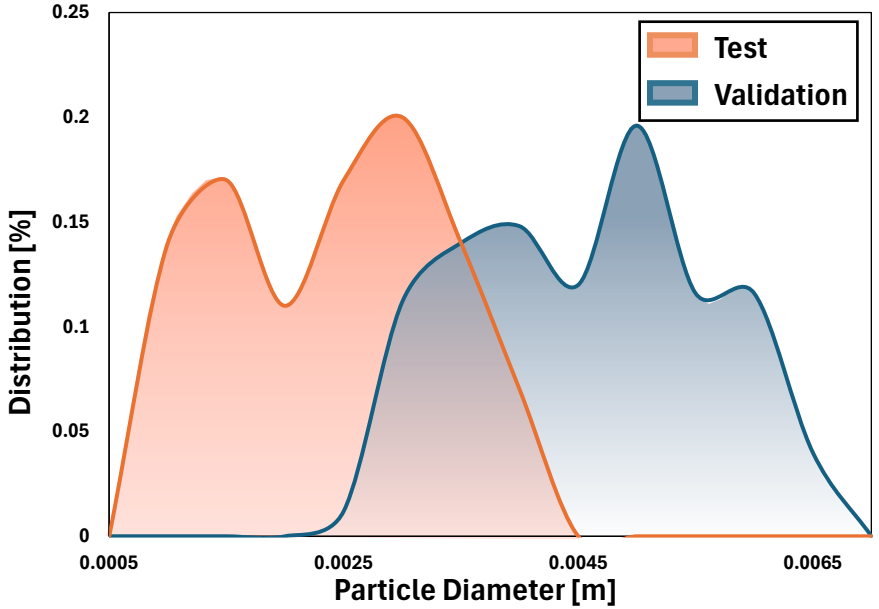

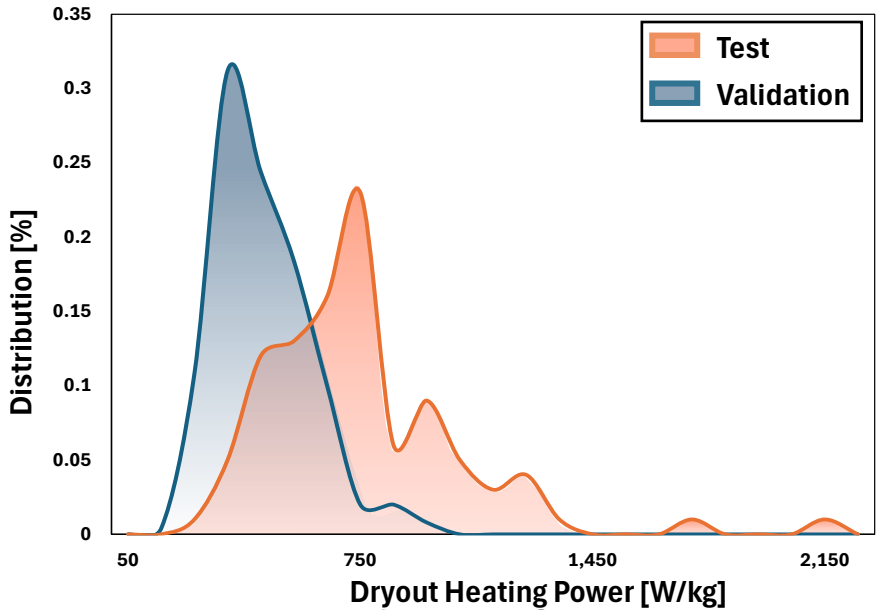

Preliminary Results

Validation Data

Neural Network

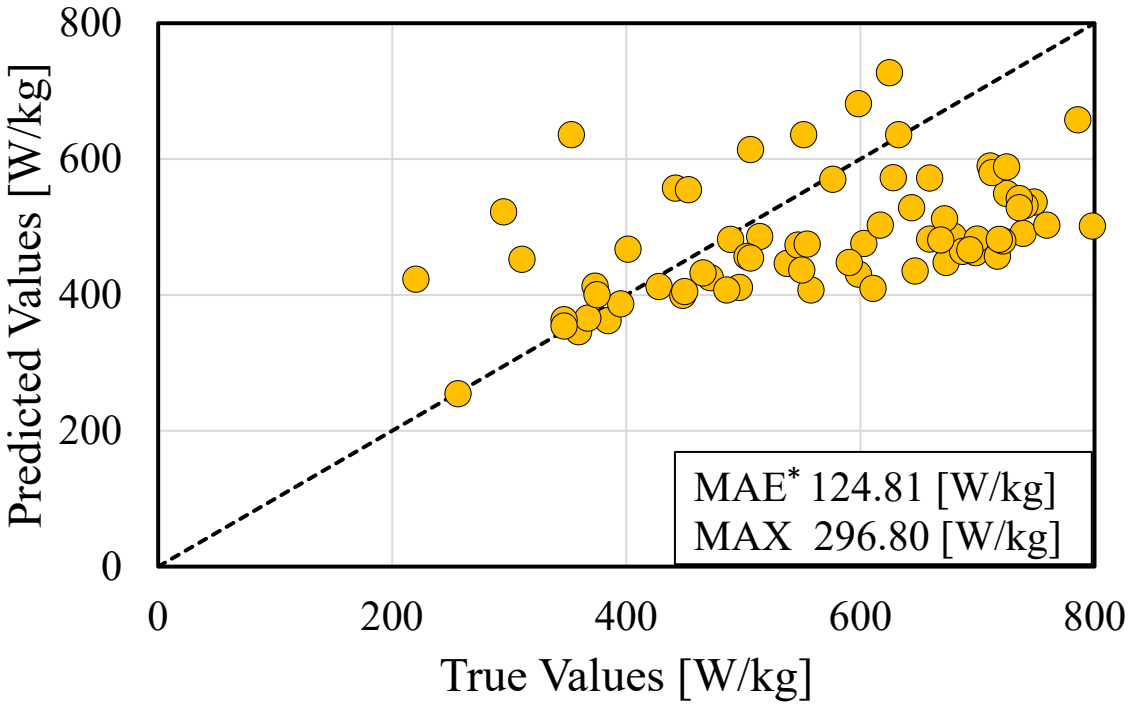

GPR model

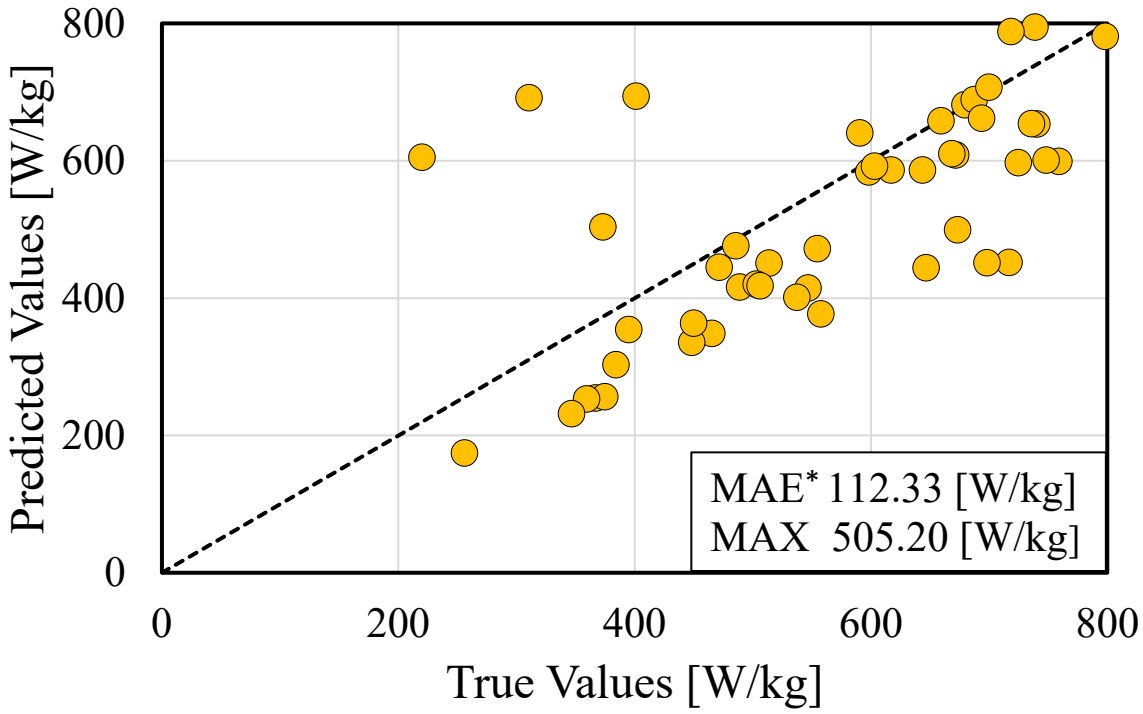

*Mean absolute Error

Coupling of Neural Network and GPR

- Idea: Coupling Neural Network and GPR to improve prediction of the validation data set
  - GPR is capable of better extrapolation
  - Neural Network performs better complex relationships
- Training data first read into Neural Network and trained, then results of the last hidden layer of the Neural Network passed on to GPR and trained with it
- Neural Network consists of 5 layers and uses ReLU, tanh and Sigmoid activation functions
- GPR has a Matern kernel, scaled with an additional parameter

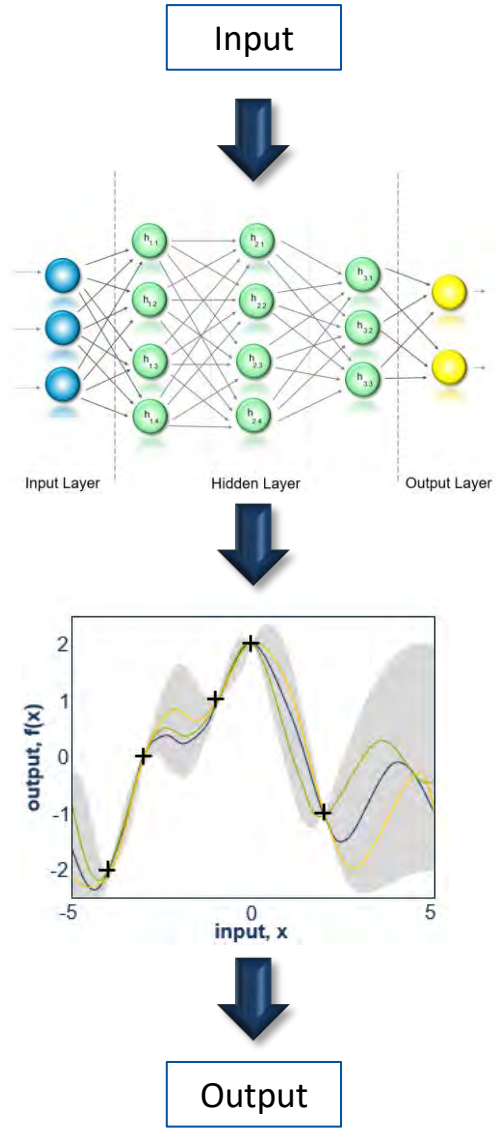

Preliminary Results

Coupling Model

Test data

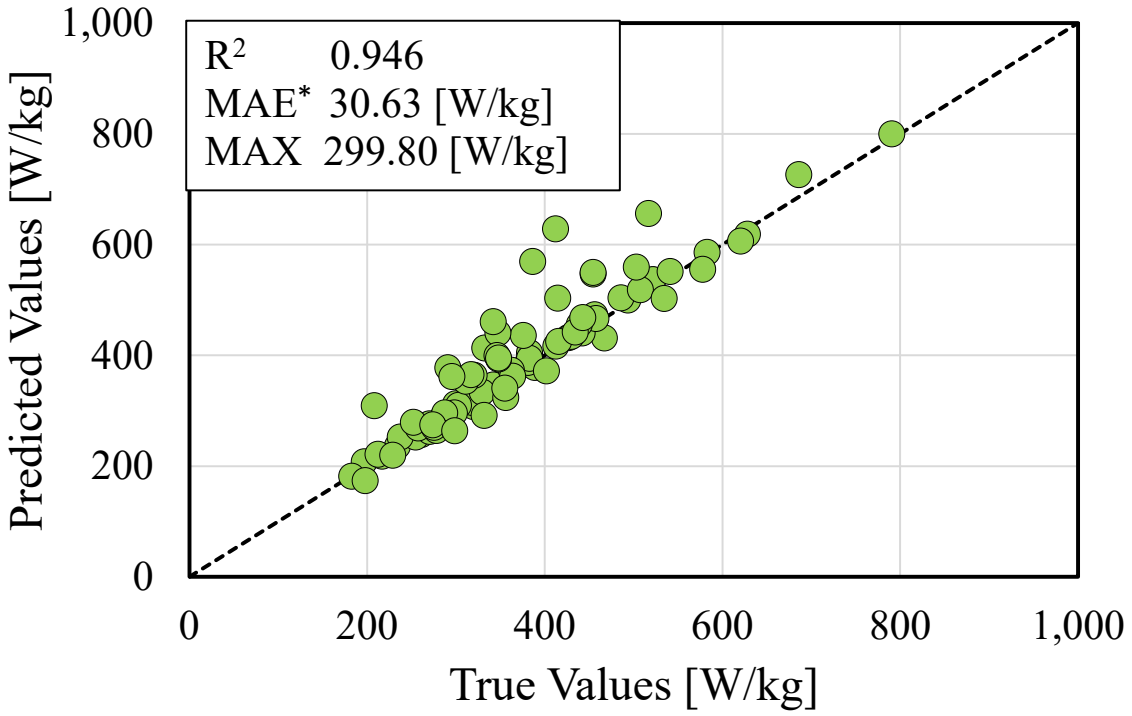

Validation data

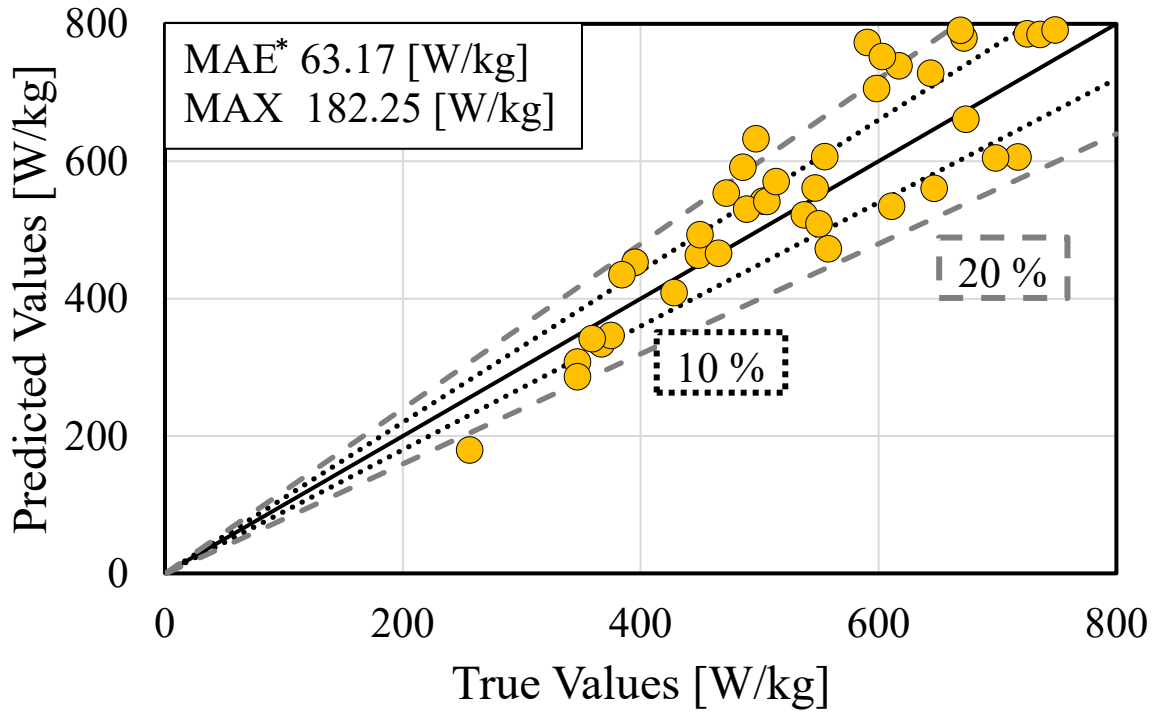

*Mean absolute Error

Preliminary Results

Validation Data

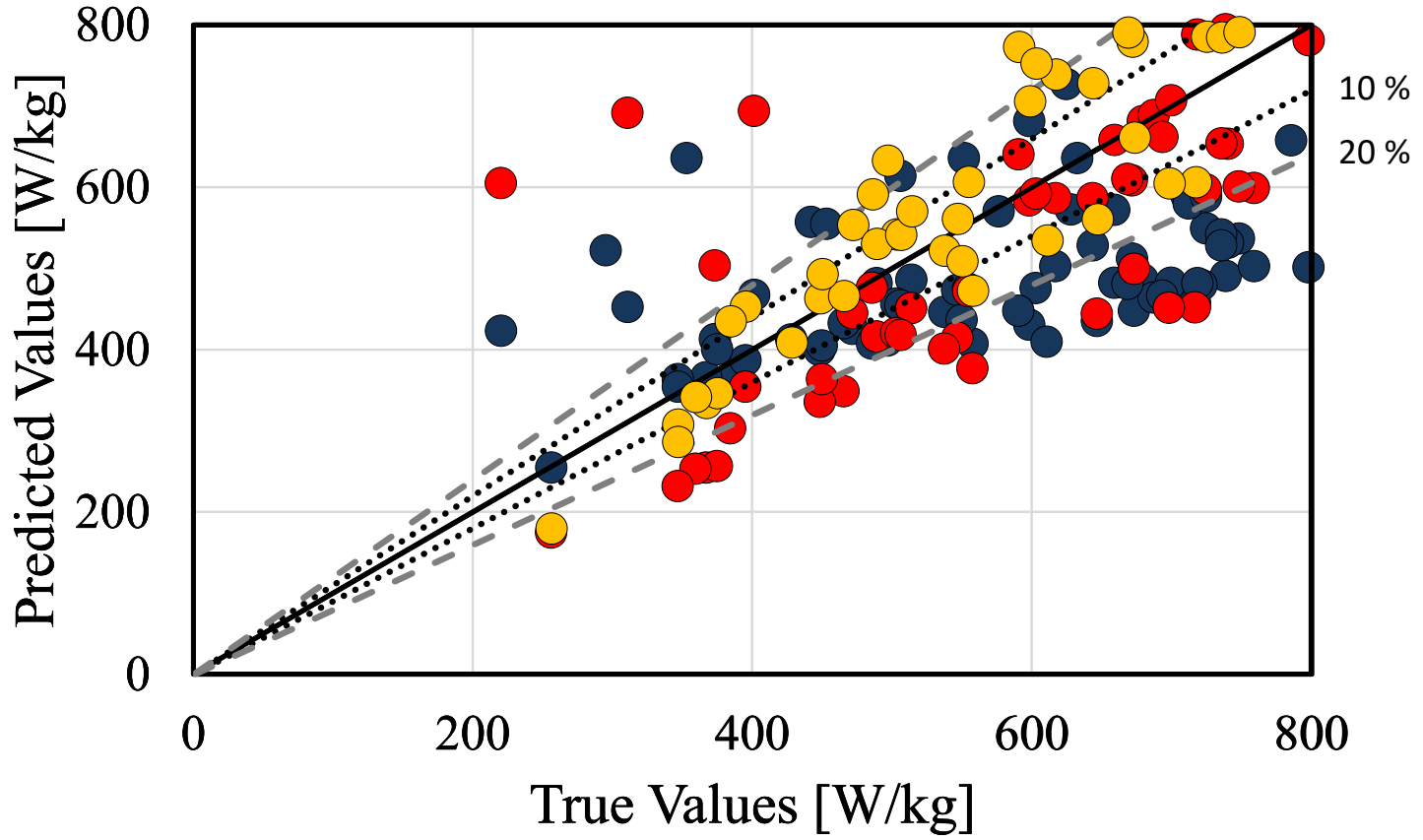

Conclusion

- Successful creation of an initial database
- Development of promising machine learning approaches
- Recognition of the limits
  - Very accurate predictions within the trained range
  - Significant deviations in predictions for data outside the valid range
- Development of initial Neural Network and GPR combining model

↳ Improved performance for data outside the defined limits (extrapolation)

Outlook

- Improve the quality of the networks / Modification
- Focus on coupling with AC²
  - Align models with the system code requirements
  - Time dependent
  - Adjustment of parameters

  ↳ Generate new datasets

- Integration into the AC² system code
- Application to power plants

ACKNOWLEDGEMENT

With funding from the:

This project is funded by the Federal Ministry of Research, Technology and Space (BMFTR) under the grant number 02NUK078B.

Thank you for your attention!

Nicole Richter
Nicole.Richter@pss.rub.de

Juliane Neuhaus
Juliane.Neuhaus@pss.rub.de

Prof. Marco K. Koch
Marco.Koch@pss.rub.de

RUHR-UNIVERSITÄT BOCHUM

PSS Plant Simulation and Safety
Prof. Dr.-Ing. Marco K. Koch

Universitätsstr. 150 | D-44801 Bochum

pss.rub.de

AI-DRIVEN ESTIMATION OF CORIUM THERMOPHYSICAL PROPERTIES FOR EX-VESSEL CORIUM STABILIZATION SIMULATIONS

Raphaël Monod, Charlaine Bouillet and Jean Baccou

Autorité de Sûreté Nucléaire et de Radioprotection (ASNR)
F–13115 Saint-Paul-lez-Durance, France
raphael.monod@asnr.fr; charlaine.bouillet@asnr.fr; jean.baccou@asnr.fr;

ABSTRACT

The management of severe accidents in some second- and third-generation reactors is based on stabilizing the corium outside the vessel by spreading and pouring water onto the upper crust. The coolability of the melt is estimated using different models, including water ingression, which depends on thermodynamic properties such as the mass liquid fraction or volumetric liquid fraction of corium. However, corium is a highly complex mixture that may contain a large number of chemical elements, and the accurate calculation of its properties is both difficult and computationally expensive.

In the ASTEC software, the traditional strategy relies on preliminary calculations performed with a thermodynamic equilibrium code. For a given corium composition at vessel failure and a given concrete composition, the properties are obtained by interpolating a two-dimensional table in temperature and composition derived from these preliminary calculations, allowing the evolution of the mixture during corium–concrete interaction to be tracked.

This approach is satisfactory when the corium composition evolves solely due to the addition of concrete of constant composition, but it loses validity in the presence of phenomena such as gas release, secondary flow of corium from the vessel to the cavity, or interaction with basemat made of concretes of different types.

To overcome these limitations, a new approach has been developed based on machine learning. Two neural networks were trained on Gibbs minimizer NucleaToolbox calculations with the NUCLEA thermodynamic database to directly estimate the mass liquid fraction and volumetric liquid fraction of corium from temperature and effective atomic compositions, regardless of the actual corium–concrete mixture composition.

The aim of the paper is first to present the methodology used to develop these neural networks, and then to highlight the impact of using them to account for the real composition of the corium–concrete mixture in a severe accident simulation code such as ASTEC.

KEYWORDS
Corium-concrete interaction; Thermophysical properties; Machine learning; ASTEC; NucleaToolbox

1. INTRODUCTION

In the event of a severe accident involving the core melt in a nuclear power plant, two management strategies can be considered. The first involves attempting to cool the reactor vessel from the outside to preserve its integrity and keep the corium inside the vessel. The second accepts a potential vessel failure and allows the corium to spread outside the vessel so that it can be cooled and stabilized. Whether the corium is retained in-vessel or ex-vessel, its physical and thermodynamic properties play a major role in the stabilization process. In the case of ex-vessel corium stabilization however, the corium composition is more complex and varies significantly with time due to its interaction with the basemat concrete.

The Accident Source Term Evaluation Code (ASTEC) is a software tool developed by ASNR [1] that allows the modelling of a nuclear accident from its initiation to the release of the source term into the environment; In particular, ASTEC has dedicated models to evaluate the two severe accident-management strategies: in-vessel corium retention [2] and ex-vessel corium retention [3]. This paper discusses new developments that have been carried out for ex-vessel retention strategy evaluation with the MEDICIS module of ASTEC that handles molten corium-concrete interaction (MCCI).

In MEDICIS, the corium may contain up to 12 elements after its interaction with the concrete: Al, C, Ca, Cr, Fe, H, Ni, Mg, O, Si, U, and Zr. The resulting mixture has complex thermodynamic properties. One of the most important properties, regarding the evaluation of the corium stabilization is its liquid fraction. In MEDICIS, the mass liquid fraction and the volumetric liquid fraction are particularly employed. Mass liquid fraction is defined as the total mass of the liquid phases divided by the total mass of all solid or liquid phases at thermodynamic equilibrium. Volumetric liquid fraction is defined as the total volume of the liquid phases divided by the total volume of all solid or liquid phases at thermodynamic equilibrium.

The computation time for a single equilibrium point of such a mixture using a Gibbs energy minimizer such as NucleaToolbox and the NUCLEA thermodynamic database, though relatively modest (typically a few seconds to a minute per calculation), is not compatible with a direct, on-the-fly call during an ASTEC run. Traditionally, ASTEC therefore relies on pre-computed tables for compositions that are approximately close to the actual mixture of the simulation. In the best-case scenario, when the vessel fails, the composition of the corium that falls into the cavity can be saved and the calculation can be halted. The tables are then generated for a range of mixing ratios between that corium and the concrete that forms the cavity. These calculations can be time-consuming, the operation is manual, and this approach does not fully account for all phenomena that might produce a corium-concrete mixture composition different from a simple mass-weighted average of the initial corium and the cavity concrete. Such phenomena include secondary pouring from the vessel with compositions differing from the first corium slump, gas emission, or compositions formed from multiple concrete sources.

To overcome this limitation, we propose in this work a new fast-to-evaluate surrogate model that can accurately predict the volumetric and mass liquid fractions of a mixture at a specified temperature. Pressure is not treated as a variable and is fixed at 1 bar. The difficulty in building this model stems from the nature of the data to be computed, which exhibit various behaviours depending on the mixture composition. Indeed, the disappearance or appearance of certain phases as a function of temperature can have a large impact on the simulated quantity, producing data with steep gradients or even discontinuities (Fig. 1, from [4]). Classical regression models consequently lose significant accuracy in these regions. To capture this specificity, the model construction relies on a machine-learning approach that employs a bagging ensemble of neural networks.

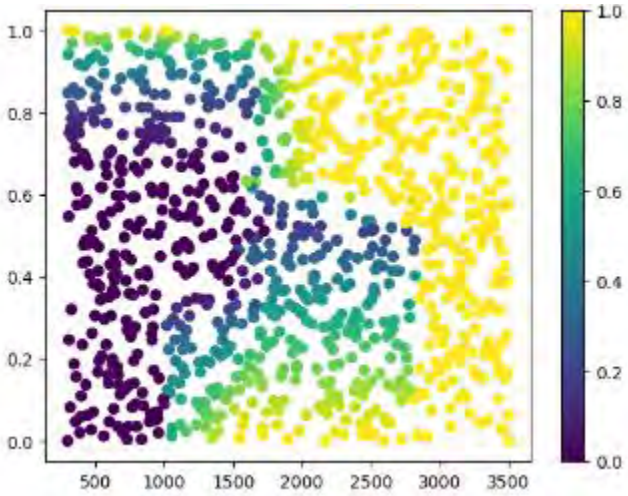

Figure 1. Mass liquid fraction of corium (colour) as a function of temperature (abscissa) and oxygen proportion (ordinate).

The paper is organized as follows. Section 2 presents the construction of the model. The model is then employed in the ASTEC Section 3, replacing the pre-computed tables, within the corium-concrete interaction module. Then the Section 4 is dedicated to the conclusion.

2. CONSTRUCTION OF THE SURROGATE MODEL

The construction of the model rests on two essential ingredients, which are detailed in the following three subsections. The first ingredient is the generation of a representative database for the problem of interest, which will be used for training, validation, and testing of the model. A key aspect of this generation is the removal of potentially aberrant simulated values caused by incorrect thermodynamic equilibria. The second ingredient is the choice of the modelling family that will be used to represent the model.

2.1. Generation of the Training Database

The training database was assembled by blending standard corium with the various concretes used in French nuclear power plants, in several different proportions. Each of these mixtures was partitioned into three phases: an oxidized phase, a metallic phase, and a gaseous phase, using an extremely simple atom-recombination algorithm based on an empirical affinity of atoms to assemble into molecules. From these three phases, four distinct compositional mixtures were constructed: the oxidized composition, the metallic composition, the fully purified gas composition, and the total composition. All molar fractions were subsequently rounded to the nearest multiple of 1/256, to limit the over-representation of certain regions and to guarantee a bijective mapping between the ASCII values of the data sets and the binary values used by the codes, thereby simplifying the construction of the calculation database.
In total, 6129 different compositions were generated. For each of these compositions, a temperature-dependent table of length 225 was produced, yielding 1379025 thermodynamic equilibrium calculations. Of these, 472 failed to converge and were therefore excluded from the training database.

2.1.1. Deleting of non-global equilibria

It can happen that an energy-minimisation software converges to a local, rather than the global, minimum. In such cases the Gibbs free energy G(T) may exhibit discontinuities, as can the mass or volumetric liquid

fractions as functions of temperature. Because these solutions are not the ones sought and they lead to discontinuities, it is essential to detect and exclude them from the training database.

For a homogeneous phase (i.e., with a fixed number of moles n) and at a fixed pressure P, the constant-pressure heat capacity is

$$C_p = -T \left.\frac{\partial^2 G}{\partial T^2}\right|_{n,P} \tag{1}$$

At the temperatures considered (above 500 K), where quantum effects are negligible, the system is in equilibrium and the pressure is atmospheric, we can assume that heat capacities are strictly positive, i.e.

$$-T \left.\frac{\partial^2 G}{\partial T^2}\right|_{n,P} > 0 \tag{2}$$

Because of linearity, for several homogeneous phases whose individual compositions remain fixed, the average heat capacity is simply the mass-weighted mean of the elemental heat capacities. Consequently, the above relation remains valid for any collection of homogeneous phases with fixed individual compositions. Now let us consider a region where the individual phase compositions change (appearance, disappearance, or evolution). Take three temperatures $T_1 < T_2 < T_3$ that are infinitesimally close to each other. If the phase compositions did not evolve, and letting $G_k = G(n, T_k, P)$, we would have

$$-T \left.\frac{\partial^2 G}{\partial T^2}\right|_{n,P} = -T_2 \frac{2}{T_3 - T_1}\left(\frac{G_3 - G_2}{T_3 - T_2} - \frac{G_2 - G_1}{T_2 - T_1}\right) \tag{3}$$

Suppose now that at T_3, a change in composition occurs because a more stable equilibrium exists. Denote by $G'_3 = G'(n,T_3,P)$ the new Gibbs-energy value. The more stable equilibrium satisfies $G'_3(n,T_3,P) < G3(n,T_3,P)$. Hence

$$\frac{G'_3 - G_2}{T_3 - T_2} - \frac{G_2 - G_1}{T_2 - T_1} < \frac{G_3 - G_2}{T_3 - T_2} - \frac{G_2 - G_1}{T_2 - T_1} \tag{4}$$

and therefore

$$-T_2 \frac{2}{T_3 - T_1}\left(\frac{G'_3 - G_2}{T_3 - T_2} - \frac{G_2 - G_1}{T_2 - T_1}\right) > -T_2 \frac{2}{T_3 - T_1}\left(\frac{G_3 - G_2}{T_3 - T_2} - \frac{G_2 - G_1}{T_2 - T_1}\right) > 0 \tag{5}$$

Thus, for the global Gibbs energy G_{global} of the system, which can switch from one phase arrangement to another as a function of temperature, we obtain

$$-T_2 \frac{2}{T_3 - T_1}\left(\frac{G_{global3} - G_{global2}}{T_3 - T_2} - \frac{G_{global2} - G_{global1}}{T_2 - T_1}\right) > 0 \tag{6}$$

So

$$\frac{2}{T_3 - T_1}\left(\frac{G_{global3} - G_{global2}}{T_3 - T_2} - \frac{G_{global2} - G_{global1}}{T_2 - T_1}\right) < 0 \tag{7}$$

In other words, whether the individual phase compositions remain fixed or change with temperature, the global Gibbs-energy function is concave. Any point where it would be convex would imply that the equilibrium calculated at T_1 or T_3 is not the global minimum (obtaining a more stable equilibrium at T_2 would not alter the concavity). In such cases, the arbitrary choice is to exclude from the training database the point between T_1 and T_3 that exhibits the lowest second derivative.

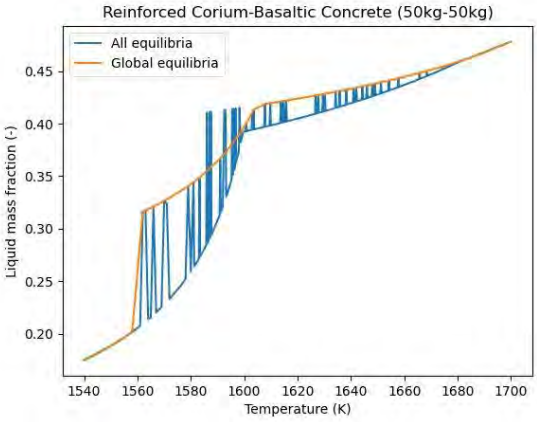

Figure 2. Liquid mass fraction as a function of temperature. The blue curve represents all points, while the yellow curve has been filtered to remove points that lie on non-global equilibrium.

Fig. 2 shows the volumetric liquid fraction in a region that is particularly problematic because of the high concentration of non-global equilibria. It is evident that removing the points with the algorithm described above produces a far smoother, more regular curve.

2.1.2. Final training database

From the algorithm outlined in section 2.1, we obtained 1378553 converged calculations. Among them, 14121 were detected as non-global equilibria, which accounts for about 1 % of the calculations, and were removed from the training database. Consequently, 1364432 points could be used.

2.2. Choice of the Modelling Family

A preliminary study [4] was conducted using a reduced database that consisted of mixtures with a small set of elements (Fe, O, U, Zr). The goal was to compare different model families – namely k-nearest neighbours, random forests, and multi-layer perceptrons. For the first two families the hyper-parameters (6 neighbours, 400 trees) were tuned by cross-validation. The architecture of the multi-layer perceptron was also optimized via grid search and comprises: an input layer of 5 neurons (temperature plus the 4 atomic fractions), three fully-connected hidden layers with 100 neurons each, using ReLU activation, a single-output neuron with a sigmoid activation.
Choosing the model type and its hyper-parameters is beyond the scope of this paper; all details can be found in [4]. Only a few results are shown here because they guided the choice of model structure for the study that follows, which uses the 12-element database described earlier. The models' performance for the mass liquid fraction and for the volumetric liquid fraction is comparable. Consequently, only the results for the mass liquid fraction are presented in the following.

Fig. 3 illustrates the performance of the three modelling families by plotting the predicted mass-liquid fraction against the exact values over the test set (25 % of the database). The mean-squared error (MSE) is also reported.

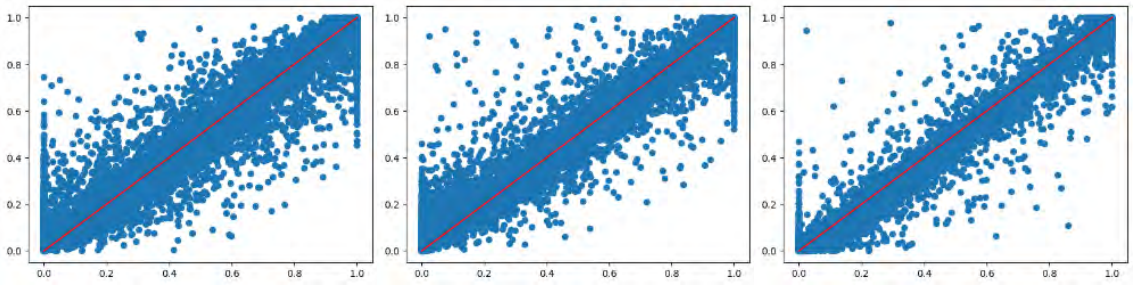

a) (b) (c)

Figure 3. Prediction of the mass liquid fraction. Predicted values as a function of true values for the k-nearest neighbors (a), random forests (b), and multilayer perceptron (c) models.

The multi-layer perceptron modelling produced the most accurate predictions, and therefore it was selected for the subsequent study. To increase stability and precision—particularly in regions with discontinuities—a bagging ensemble of ten multilayer perceptrons was employed. In this approach, several perceptrons sharing the same architecture as the one described earlier were trained, each using a bootstrap sample drawn from the entire training set. The final model's prediction is the average of the ten individual predictions. This ensemble method yields better results than a single perceptron (see Fig. 4).

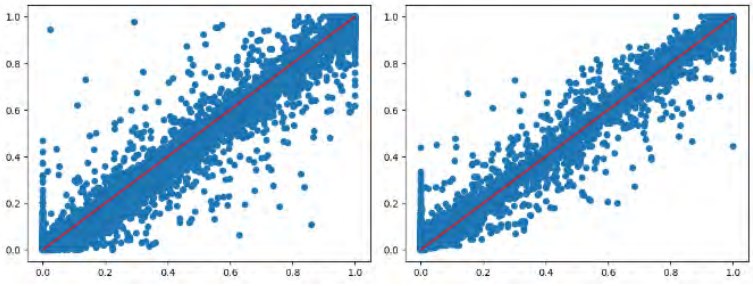

(a) MSE=0.54e-3 **(b) MSE=0.37e-3**

Figure 4. Prediction of the mass liquid fraction. Predicted values as a function of true values for the multilayer perceptron (a) and the bagging ensemble of 10 multilayer perceptrons (b) models.

2.3. Retain Model For 12 Atoms Compositions

For the main study presented in this paper, we adopt a bagging ensemble of ten multilayer perceptrons. Each perceptron shares the same architecture as described earlier, except that the input layer now contains 13 neurons (temperature plus the 12 atomic fractions). Thus, each network consists of an input layer with 13 neurons (temperature + 12 compositional components), three fully-connected hidden layers of 100 neurons each, using ReLU activation, a single-output neuron with a sigmoid activation.

With the inclusion of biases, each perceptron has 21 701 trainable parameters. These parameters are learned from the detailed database described in Section 2.1. It is worth noting that, in addition to improving predictive accuracy, the bagging procedure yields a standard deviation associated with the predictions, providing an estimate of the uncertainty in the predicted quantity. This uncertainty information can be leveraged to add new simulations (active learning), as explained in [4]. Figure 5 displays the performance of the bagging model on a test set drawn from the database. The root-mean-square error (RMSE) is 0.014, and the correlation coefficient exceeds 0.99.

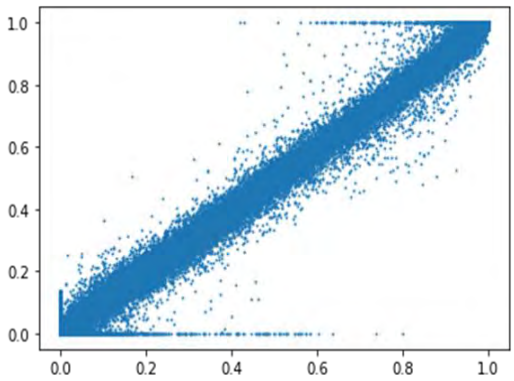

Figure 5. Predicted values of the liquid mass fraction as a function of true values using the bagging ensemble of 10 multilayer perceptrons in the case of 12 atoms.

For use of this model in ASTEC studies, additional non-trainable layers are added upstream of the network to convert the inputs into mole fractions and to handle the nondimensionalisation used during training. This makes the model easier to use by the client code and, more importantly, ensures that its inputs and outputs match those of the legacy models.

3. RESULTS

3.1. Models applied to specific compositions

The models were used to compare corium–concrete mixing results for a typical corium and three typical concretes of empirical composition that were not used to build the training dataset. These three concretes are of different types: siliceous concrete, limestone concrete, and basaltic concrete. The mass compositions of the corium are given in Table I, and the mass compositions of the concretes are given in Table II. Note that the concrete compositions include reinforcing steel.

Table I. Typical corium composition

Species	Mass fraction (%)
UO2	52
ZrO2	13
Zr	2

Fe	22
Cr	7
Ni	4

Table II. Typical concretes compositions

Species	Reinforced siliceous concrete mass fraction (%)	Reinforced limestone concrete mass fraction (%)	Reinforced basaltic concrete mass fraction (%)
Al2O3	2.5	2	14
CO2	0.5	24	-
CaO	12	35	12
Fe	5	9	4
H2O	5	5	4
SiO2	75	24	60
MgO	-	1	-
Fe2O3	-	-	6

For each concrete, a composition consisting of 50 kg of corium and 50 kg of concrete is considered. After rounding to 1/256 quanta, the compositions of the resulting mixtures are given in Table III.

Table III. Composition of three typical mixtures

Species	Reinforced siliceous concrete mole fraction (/256)	Reinforced limestone concrete mole fraction (/256)	Reinforced basaltic concrete mole fraction (/256)
Al	2	1	11
C	0	21	0
Ca	8	24	8
Cr	5	5	5
Fe	18	21	21
H	21	21	17
Ni	2	2	2
Mg	0	1	0
O	141	133	140
Si	47	15	39
U	7	7	8
Zr	5	5	5

For each of these compositions, the surrogate model results for the mass liquid fraction are compared with those provided by the minimization code. Fig. 6a shows the results for the mixture using siliceous concrete, Fig. 6b for the mixture using limestone concrete, and Fig. 6c for the mixture using basaltic concrete. In each case, the results obtained with the surrogate model are compared with those obtained using the NucleaToolbox thermodynamic minimizer. We observe that, for all three concrete families, the results provided by the surrogate model are in good agreement with the reference results.

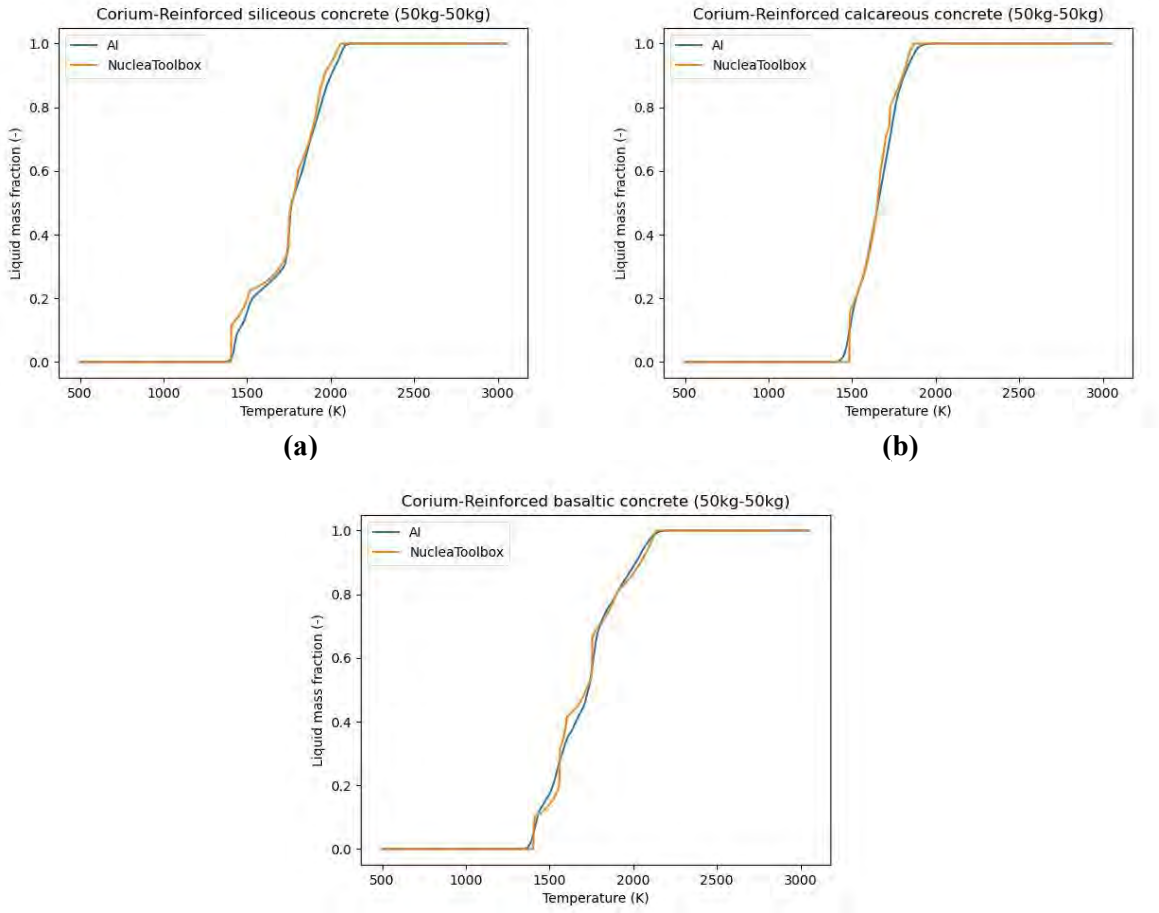

Figure 6. Mass liquid fraction as a function of temperature computed by AI (in blue) and by NucleaToolbox (in yellow) for mixture with 50% in mass of siliceous concrete (a), limestone concrete (b) and basaltic concrete (c).

3.2. Usage in an ASTEC computation

In this paragraph, calculations are performed with the MEDICS module of the ASTEC code and correspond to a reactor case. For the comparison with the surrogate model, it is assumed that all the corium is relocated at the reactor vessel failure, with the spreading of the corium in the reactor cavity. There is no secondary flow of corium from the reactor vessel to the reactor cavity after the reactor vessel rupture. The basemat is made of a single concrete.

The initial corium mass corresponds to the melting of the entire core and of the lower plenum hemisphere, the lower plenum internals, and the baffle. The initial temperature of the corium is taken equal to 3000 K. Two types of concrete are used for the comparison, a Limestone/Common Sand (LCS) concrete and a siliceous concrete, which both are part of the model's learning base.

It is assumed that the reactor vessel failure is supposed to occur three hours after the automatic shutdown of the reactor. The residual power is calculated by the ISODOP module of ASTEC, based on an isotopic inventory. The corium reflooding starts at the beginning of the MCCI.

For each type of concrete, two calculations are performed:

- In the first case, the evolution of the mass liquid fraction and the volumetric liquid fraction of the corium versus temperature are evaluated according to the quantity of concrete incorporated in the corium by using pre-calculated tables from NucleaToolbox Gibbs minimizer and NUCLEA database developed at ASNR;
- In the second case, the evolution of the mass liquid mass fraction and the volumetric liquid fraction of the corium versus temperature are evaluated during the calculation according to the composition of the corium by using the surrogate model.

The solidification temperature is another material parameter used by the MEDICIS models. It is evaluated from the volumetric liquid fraction. Fig. 7 shows a comparison of the solidification temperature evolution according to the concrete mass incorporated in the corium during the calculations. For each type of concrete, the values provided by the substitution model are very similar to those calculated by NucleaToolbox.

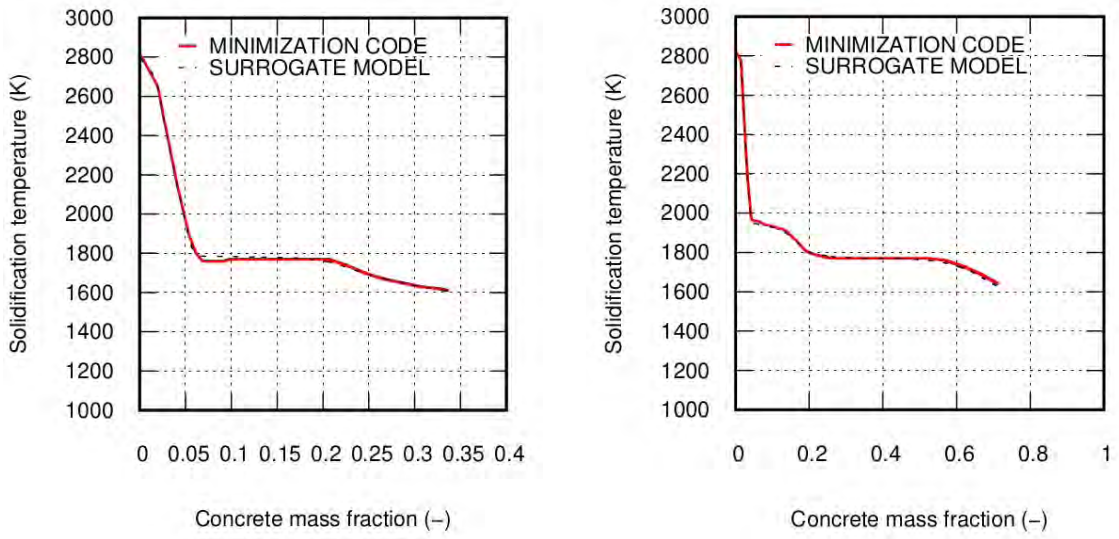

LCS concrete *siliceous concrete*

Figure 7. Evolution of the solidification temperature versus concrete mass fraction.

The evolution of the corium temperature versus time is presented in Fig. 8. The figure shows that using the surrogate model provides the same results as using pre-calculated tables from NucleaToolbox. The same holds for the other characteristic quantities of the calculations, including the ablation profiles.

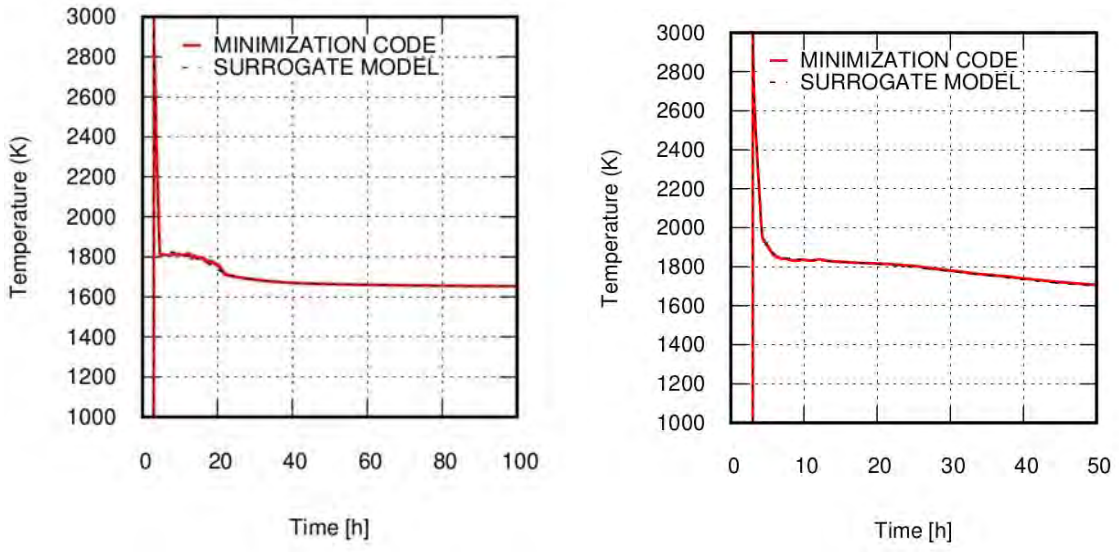

LCS concrete *siliceous concrete*

Figure 8. Evolution of the corium temperature versus time.

4. CONCLUSIONS

Surrogate models for the computation of the mass liquid fraction and the volumetric liquid fraction were developed using neural networks, based on a bagging ensemble of multilayer perceptrons. These models yield good results, both on standalone test cases and when integrated into a more complex code such as ASTEC. Although these models have not yet been optimized, they presently add a CPU overhead that makes an ASTEC run roughly 20–25 times slower when it relies solely on MEDICIS. Up to this point, we have considered only the physical outcome, and no optimization—trivial or otherwise—has been implemented. Profiling is underway, and we are exploring further optimisations, including the possibility of delegating network inference to a GPU.

The main difficulty lies in building a training dataset that covers a domain as wide as possible without over-representation, while keeping its size reasonable. A reduction method was tested and proved to be effective. Further works deal with improvement of the database using dataset enrichment strategies that refer to the large literature of active learning. Moreover, the work presented here was applied to ex-vessel compositions and could be extended to in-vessel compositions.

REFERENCES

1. P. Drai et al., “ASTEC V3: A comprehensive Integral Code for Nuclear Safety Analysis and Research”, *Proceedings of NURETH conference*, Busan, Korea (2025).
2. L. Carénini et al. “IVMR modelling with transient effects during molten pool formation and stabilization – Outcomes from models’ comparison performed in the IAEA CRP J46002”, *Annual of Nuclear Energy,* **218** (2025).
3. C. Bouillet, “Analysis of Corium Coolability in MCCI Conditions for two Types of Concrete, using ASTEC Calculations”, *Proceedings of NURETH conference*, Washington D.C., USA (2023).
4. A. Roblin, “Deep learning metamodeling of a numerical simulator with discontinuous outputs”, Aix-Marseille University, Internship report, (2023).

ASNR Autorité de sûreté nucléaire et de radioprotection

MAY 18-22TH 2026

Raphael Monod – Jean Baccou – Charlaine Bouillet
Contact: raphael.monod@asnr.fr

ERMSAR 2026

AI-DRIVEN ESTIMATION OF CORIUM THERMOPHYSICAL PROPERTIES FOR EX-VESSEL CORIUM STABILIZATION SIMULATIONS

INTRODUCTION AND CONTEXT

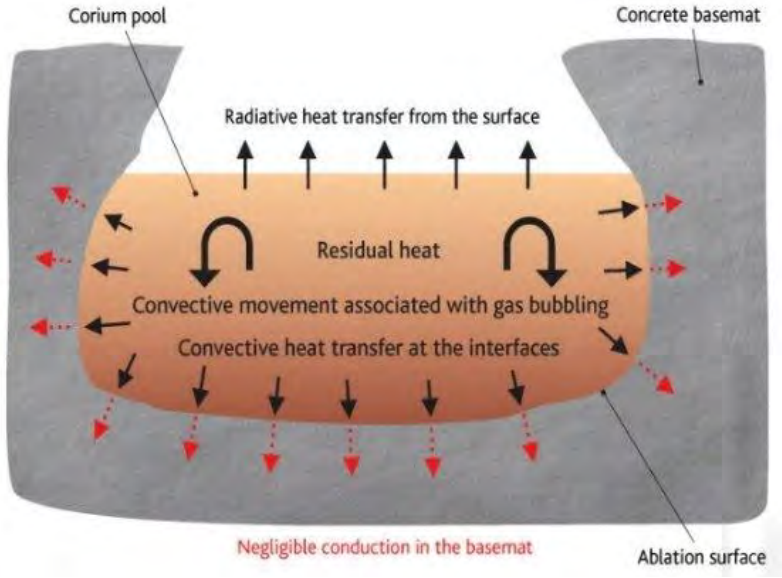

- Obtaining better estimates of material properties contributes to more relevant simulation results for nuclear transient accidents.

- One step of an accident can be the Molten Corium Concrete Interaction (MCCI). In simulations, the mixture can be typically composed of 12 atoms (Al, C, Ca, Cr, Fe, H, Ni, Mg, O, Si, U, Zr)

- For an accurate simulation of corium ex-vessel stabilization, codes like ASTEC (Accident Source Term Evaluation Code) require the following properties of the corium–concrete mixture:
  - o the mass liquid fraction (as a function of temperature),
  - o the volumetric liquid fraction (as a function of temperature),
  - o the solidus temperature (the temperature at which the volumetric liquid fraction is 1%),
  - o the solidification temperature (the temperature at which the volumetric liquid fraction is 50%, for example),
  - o the liquidus temperature (the temperature at which the volumetric liquid fraction is 99%).

- These properties are partly obtained using a thermochemical code capable of calculating the different phases of a complex mixture. The present work is based on NucleaToolbox, developed by ASNR.

SURROGATE MODEL OBJECTIVES

- Drawbacks of a direct link with a thermochemical code:
  - What should be done in **case of non-convergence**?
  - How can we detect points that have converged to a local **(non-global) minimum**, and how should they be handled?
  - The **CPU cost** of a call to a thermochemical software can be high, even prohibitive, especially if it must be used to invert a function within an iterative algorithm (for instance, finding the temperature corresponding to a given liquid fraction).
  - **Access** to a thermochemical software and material databases is required

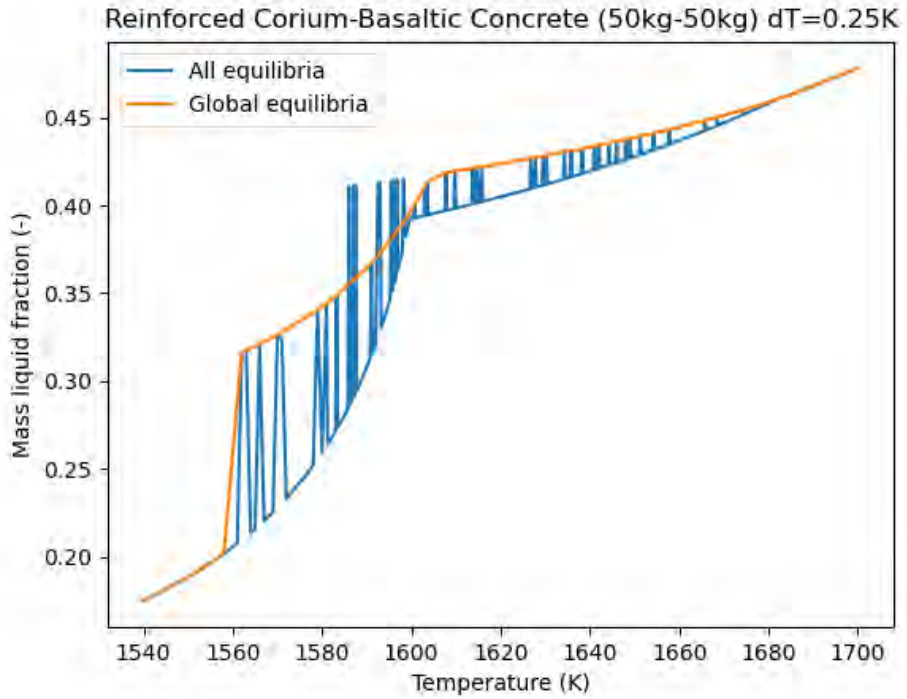

- Solution: Create a surrogate model of the thermochemical code.

[Mass/Volumetric]LiquidFraction = f(Temperature,Composition)

- Main difficulty: Presence of high gradients and discontinuities

SPECIFICATION OF THE SURROGATE MODEL

[Mass/Volumetric]LiquidFraction = f(Temperature,Composition)

- 13 inputs (1 temperature and 12 atomic molar compositions whose sum equals one)
  - Temperature: float between 500.K and 3050.K, multiple of 1/64=0.015625
  - Compositions: float between 0. and 1., multiple of 1/256=0.00390625
- 1 output (mass liquid fraction or volumetric liquid fraction)
  - Float between 0. and 1.
- Training dataset cardinality
  - 1.127.772 entries before cleaning
  - 1.119.732 entries after cleaning (after removing non global equilibria)

DETECTING AND REMOVING NON GLOBAL EQUILIBRIA (1/3)

- Minimizer looks for a minimum value of the Gibbs energy G

- The second derivative of G versus T (at phases composition and pressure fixed) is linked to the thermal capacity, which is positive

$$C_p = -T \left.\frac{\partial^2 G}{\partial T^2}\right|_{PhasesComposition,P} > 0$$

$$-T_2 \frac{(G_1 - 2G_2 + G_3)}{T_3 - T1} > 0$$

$$G_3' < G_3$$

$$-T_2 \frac{(G_1 - 2G_2 + G_3')}{T_3 - T1} > -T_2 \frac{(G_1 - 2G_2 + G_3)}{T_3 - T1} = C_p > 0$$

$$\frac{\partial^2 G}{\partial T^2} < 0$$

- But... it may be necessary to have a sufficiently fine temperature resolution to obtain enough good points...

DETECTING AND REMOVING NON GLOBAL EQUILIBRIA (2/3)

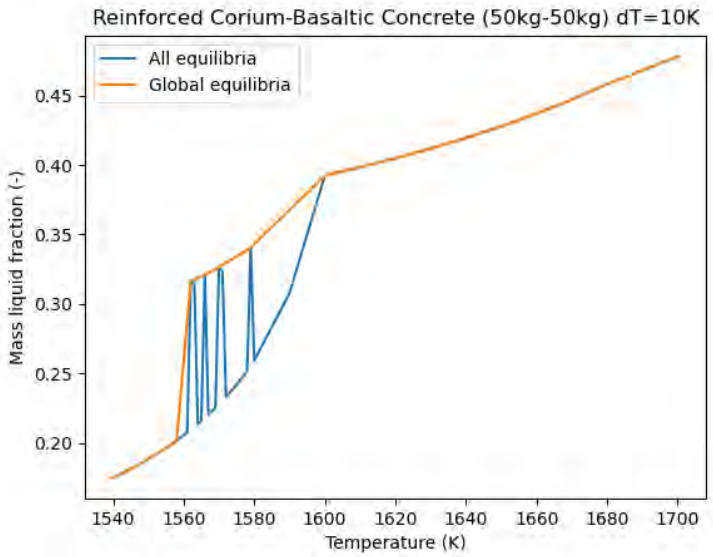

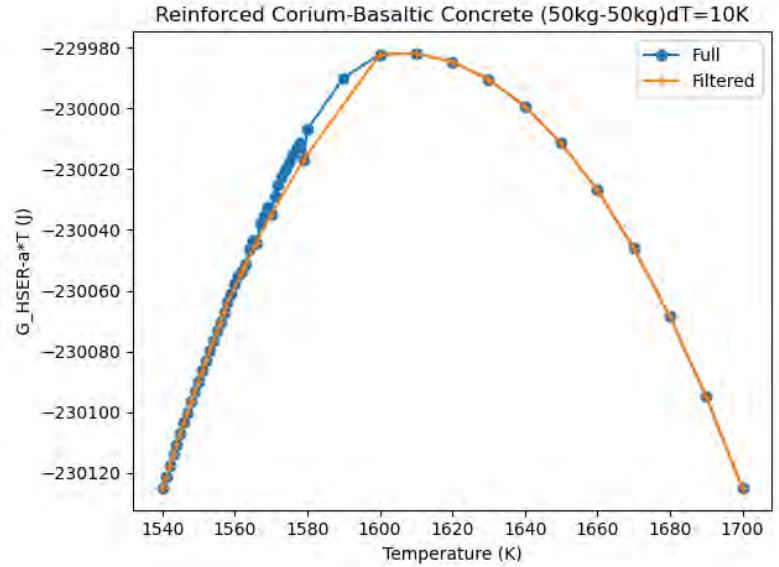

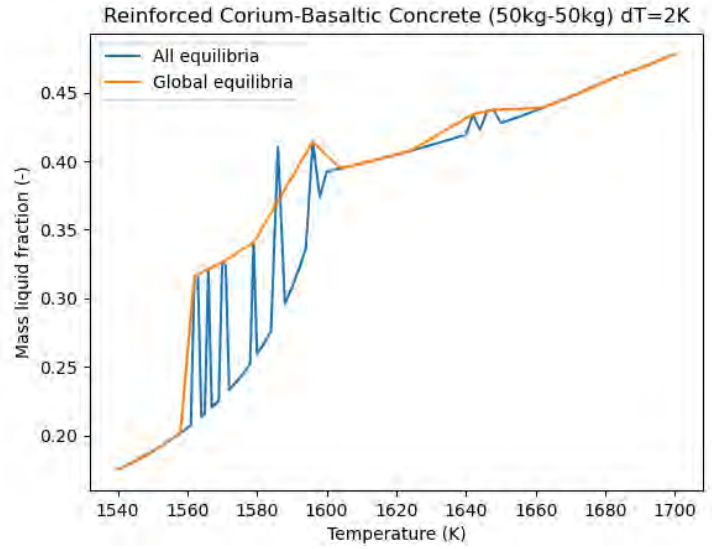

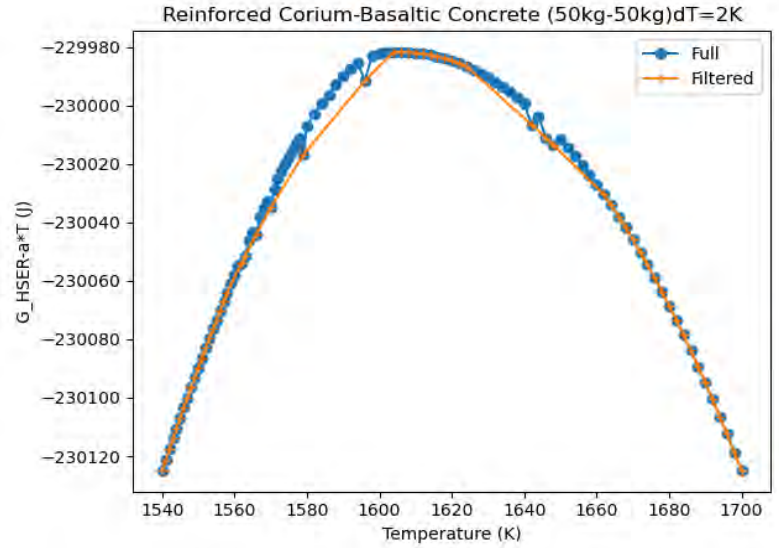

DETECTING AND REMOVING NON GLOBAL EQUILIBRIA (3/3)

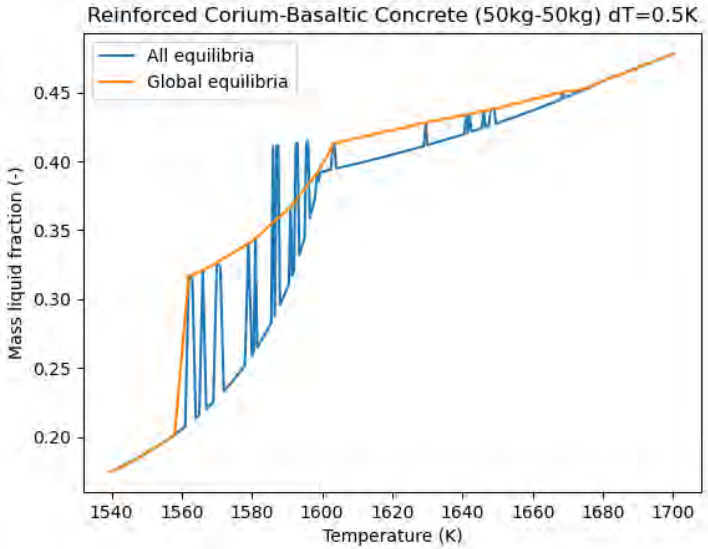

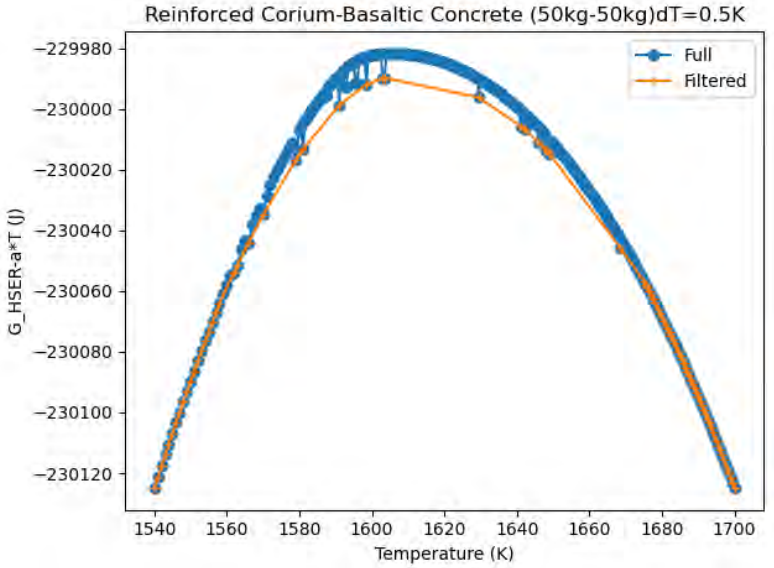

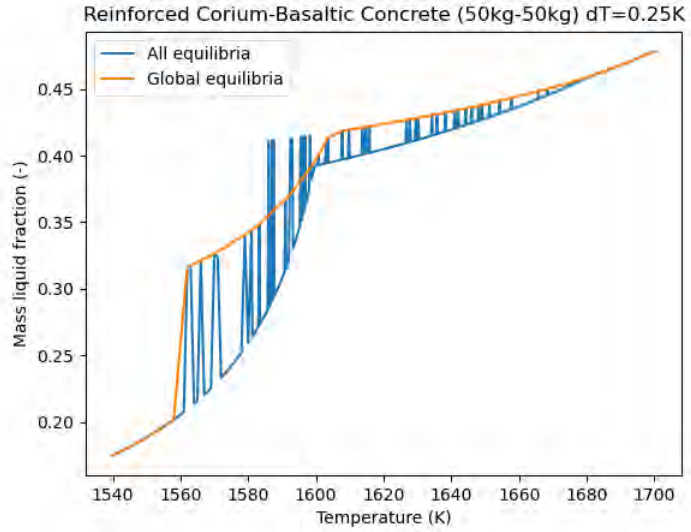

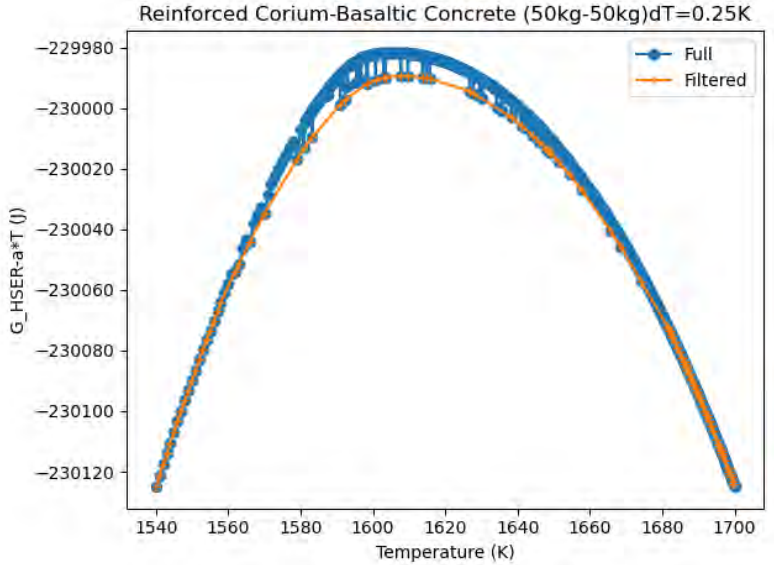

TESTED MODELS

- First work had objective to compare different models (KNN, Random Forest, Gaussian Process, Multi Layers Perceptron, Baggings of MLP, etc.) and hyper parameters

- Bagging of 10 MLP retained:
  - 3 hidden layers with RELU
  - 1 output layer with sigmoid
  - 21701 parameters
  - Additional non-trained layer placed right after the input layer to manage the scaling

- Thanks to bagging:
  - Better accuracy using the mean over networks
  - Error estimation using the standard deviation over networks
  - Estimator to add new entries in the training database (Query by bagging)
  - How removing entries ?

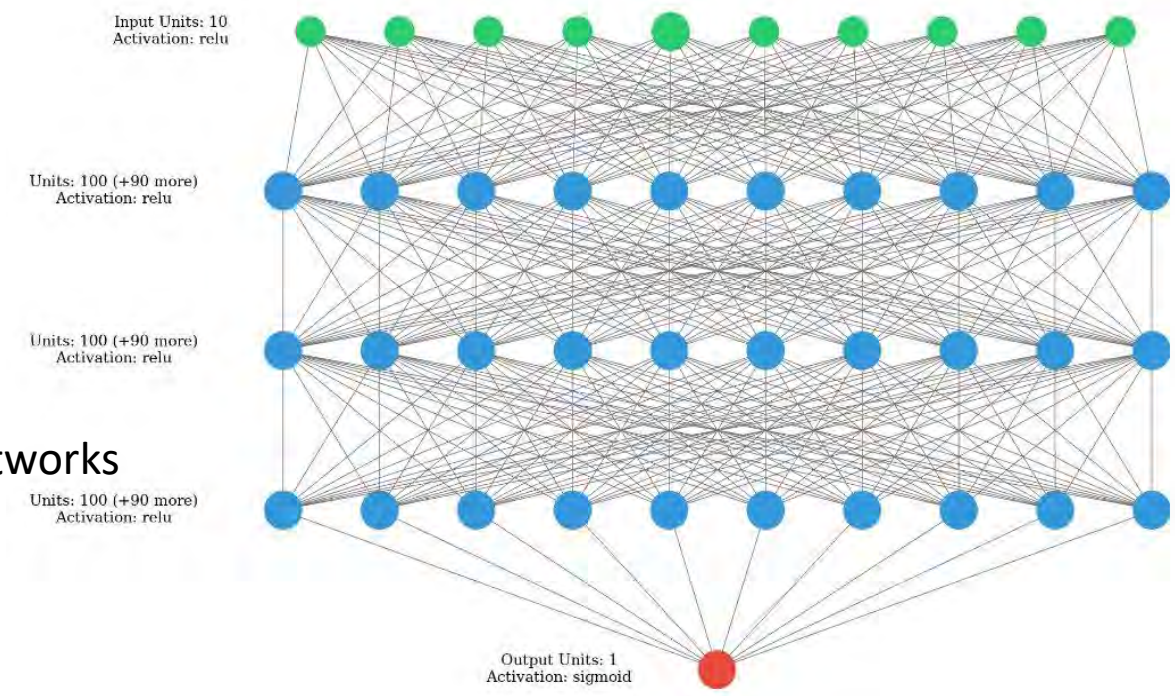

FINAL MODEL STATISTICS

- Split 50% train / 50% test
- Bagging of 10 MLP
- RMSE (Root Mean Square Error): 0.014
- Correlation coefficient: 0.99

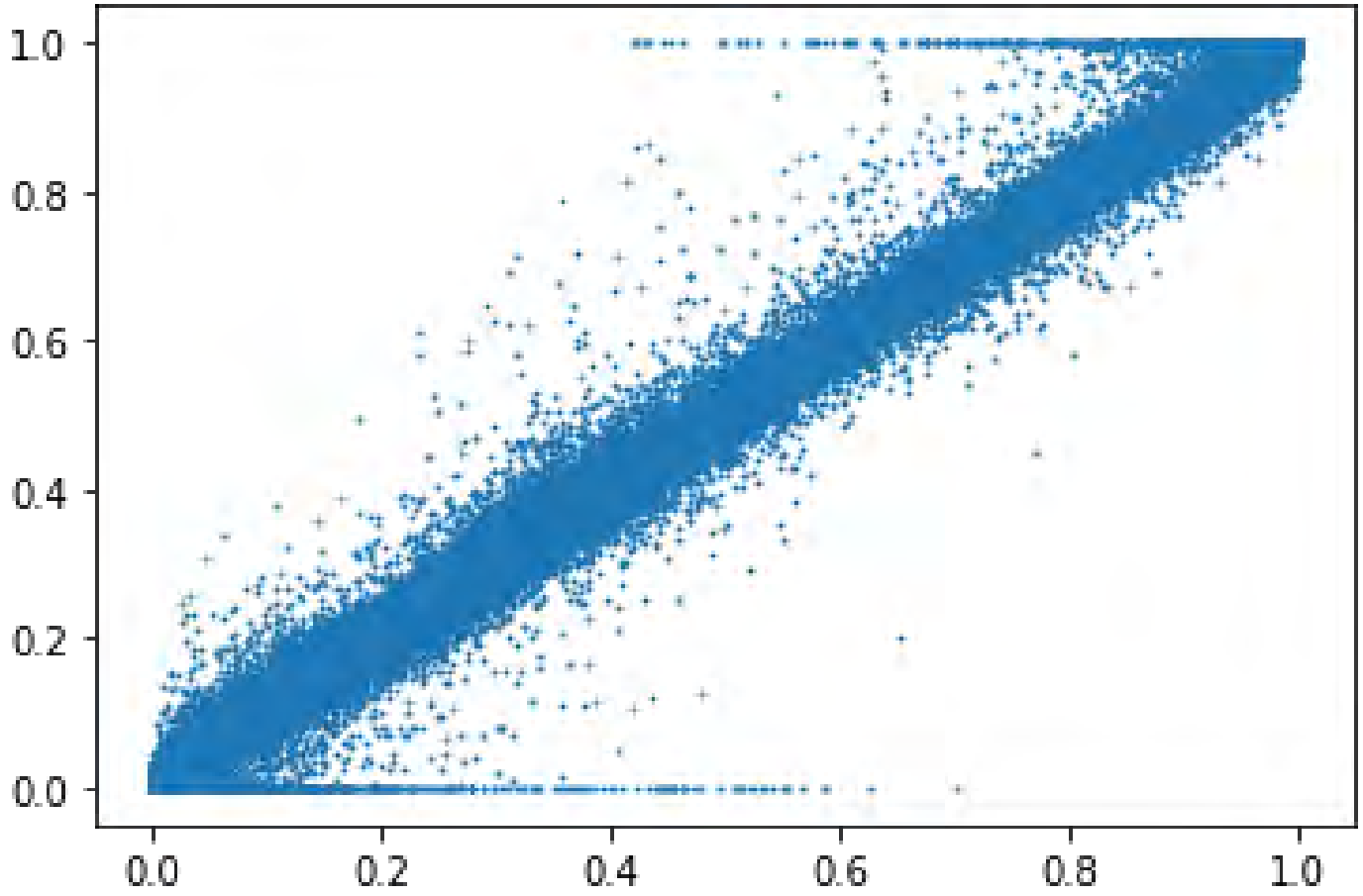

Predicted values versus exact values for test points

EXAMPLES

- A typical corium

Species (Corium)	Masses fraction (%)
UO2	52.3
ZrO2	13.2
Zr	02.4
Fe	22.2
Cr	06.4
Ni	03.5

- Three typical reinforced concretes: a siliceous concrete, a limestone concrete, and a basaltic concrete.

Species	Reinforced siliceous concrete masses fraction (%)	Reinforced limestone concrete masses fraction (%)	Reinforced basaltic concrete masses fraction (%)
Al2O3	2.5	2	14
CO2	0.5	24	-
CaO	12	35	12
Fe	5	9	4
H2O	5	5	4
SiO2	75	24	60
MgO	-	1	-
Fe2O3	-	-	6

EXAMPLES

- For each concrete, we study the liquid mass fraction of a mixture consisting of 50 kg of corium and 50 kg of concrete.

Species	Corium - Reinforced siliceous concrete mol fraction (/256)	Corium - Reinforced limestone concrete mol fraction (/256)	Corium - Reinforced basaltic concrete mol fraction (/256)
Al	2	1	11
C	0	21	0
Ca	8	24	8
Cr	5	5	5
Fe	18	21	21
H	21	21	17
Ni	2	2	2
Mg	0	1	0
O	141	133	140
Si	47	15	39
U	7	7	8
Zr	5	5	5

RESULTS (SILICEOUS VS LIMESTONE VS BASALTIC)

- Mass liquid fraction for the three mixtures as a function of temperature.

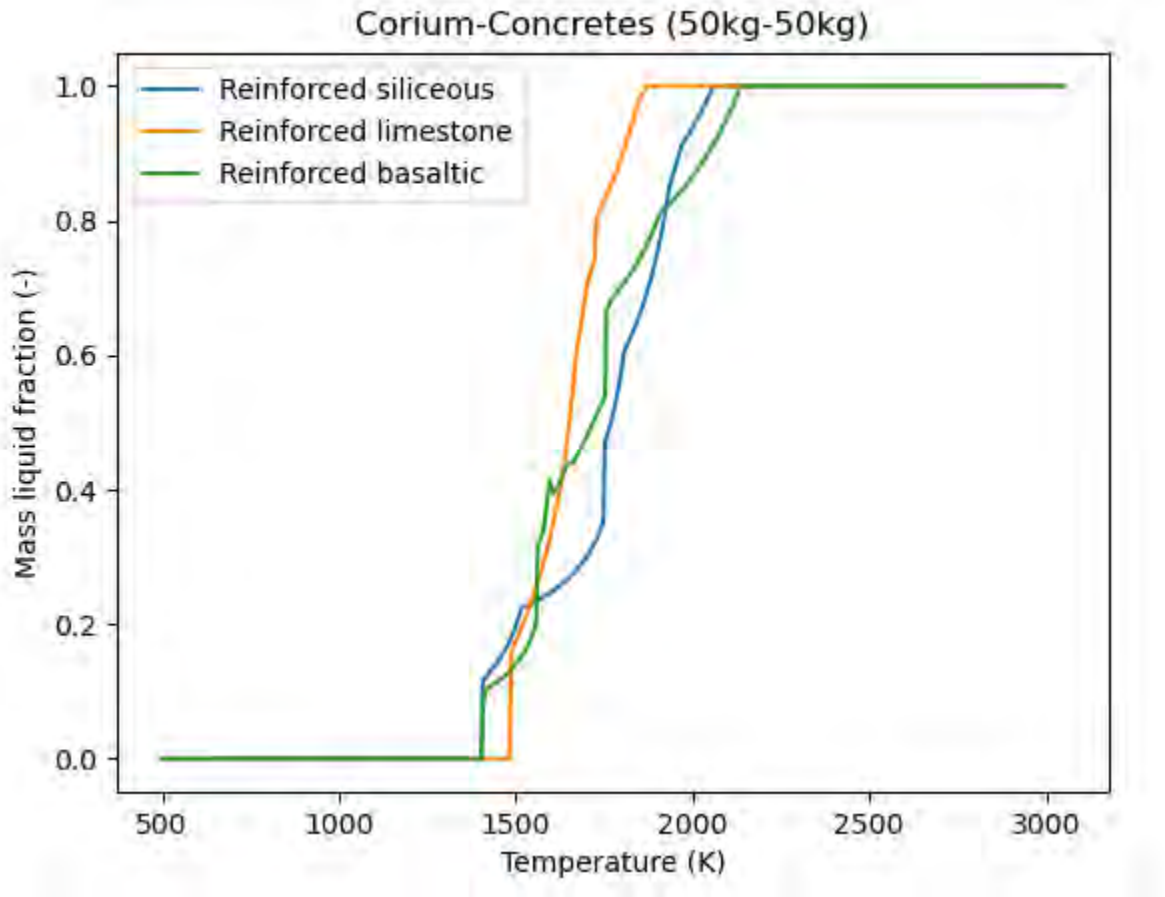

RESULTS (SILICEOUS CASE)

- Mass liquid fraction for corium-reinforced siliceous concrete, NucleaToolbox vs surrogate model

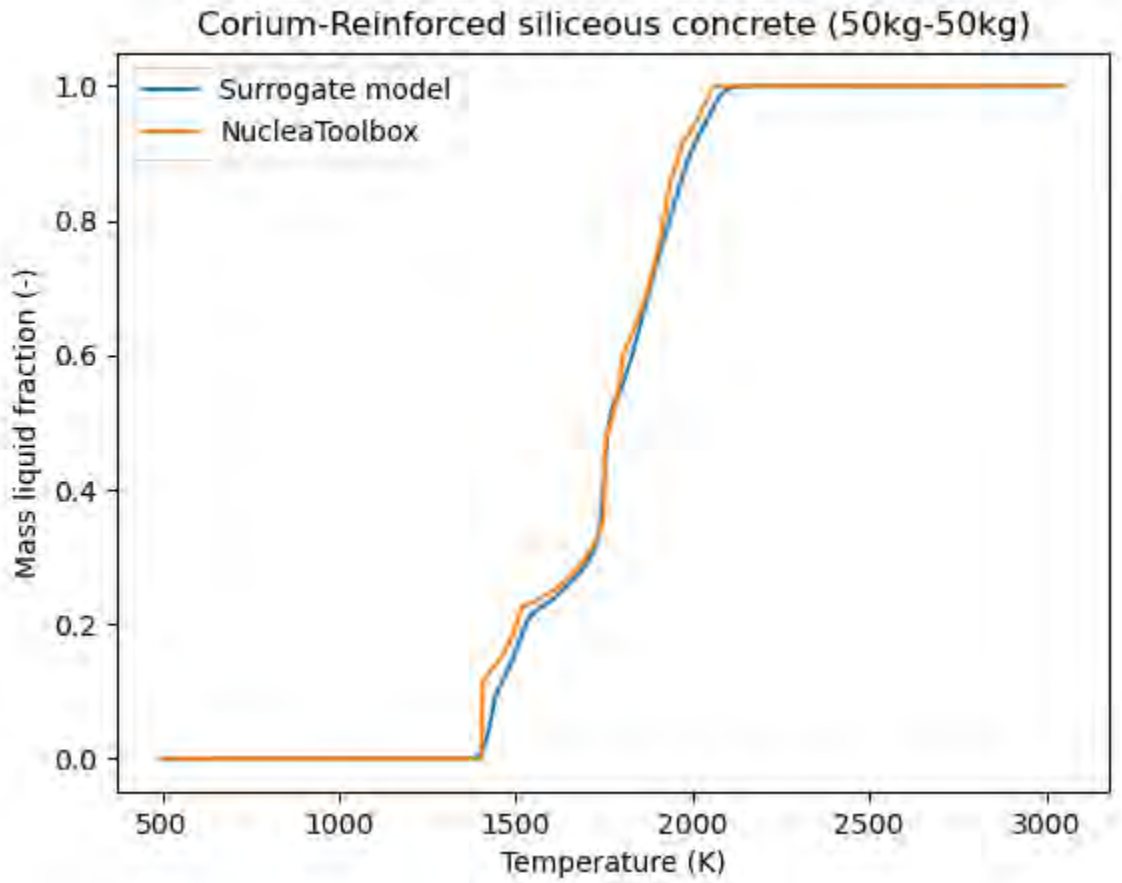

RESULTS (LIMESTONE CASE)

- Mass liquid fraction for corium-reinforced limestone concrete, NucleaToolbox vs surrogate model

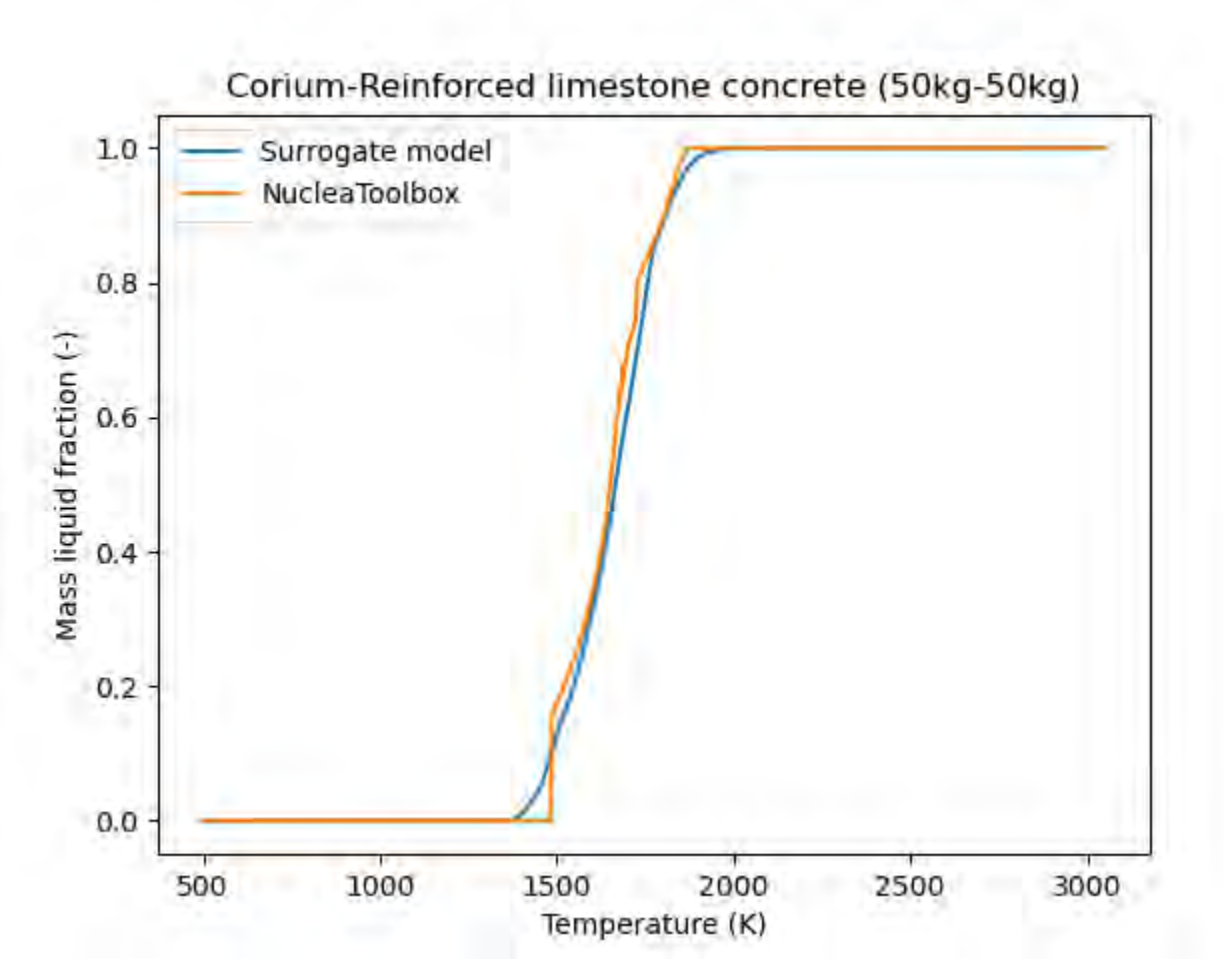

RESULTS (BASALTIC CASE)

- Mass liquid fraction for corium-reinforced basaltic concrete, NucleaToolbox vs surrogate model (with different discretizations to remove local equilibria pointed on the figures)

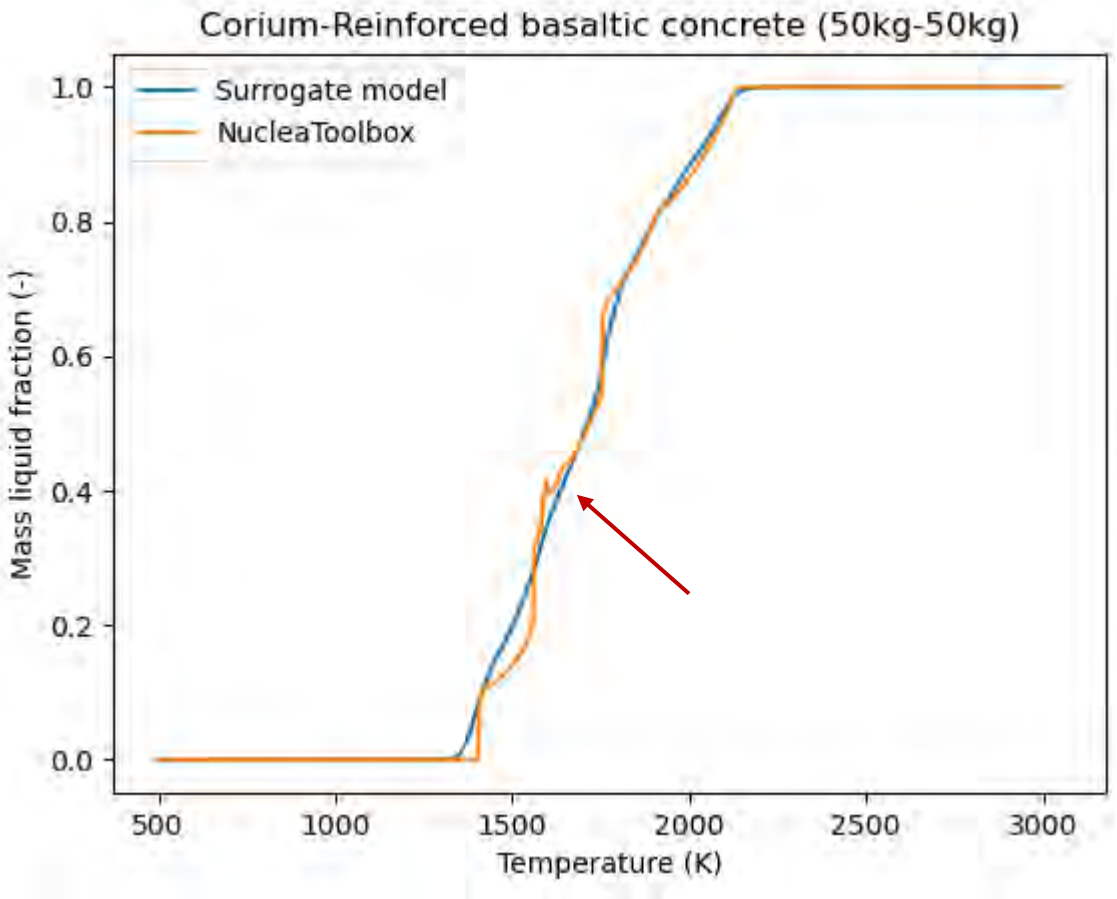

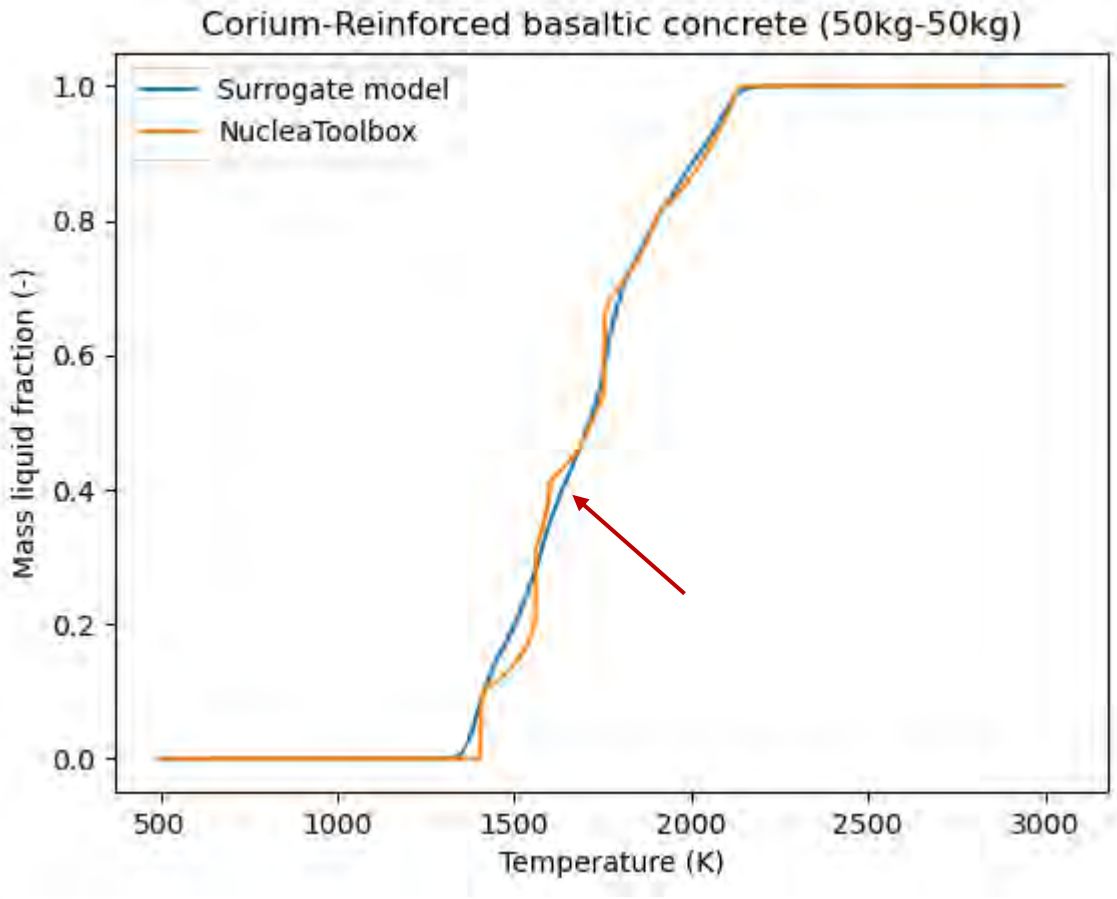

APPLICATION TO ASTEC

- Remember of used properties:
  - the mass liquid fraction => [Bagging of 10] Neural Network[s]
  - the volumetric liquid fraction => [Bagging of 10] Neural Network[s]
  - the solidus temperature => inversion of volumetric liquid fraction with a Brent algorithm
  - the solidification temperature => inversion of volumetric liquid fraction with a Brent algorithm
  - the liquidus temperature => inversion of volumetric liquid fraction with a Brent algorithm

APPLICATION TO ASTEC, SINGLE CONCRETE CASE

Axial Erosion vs Time

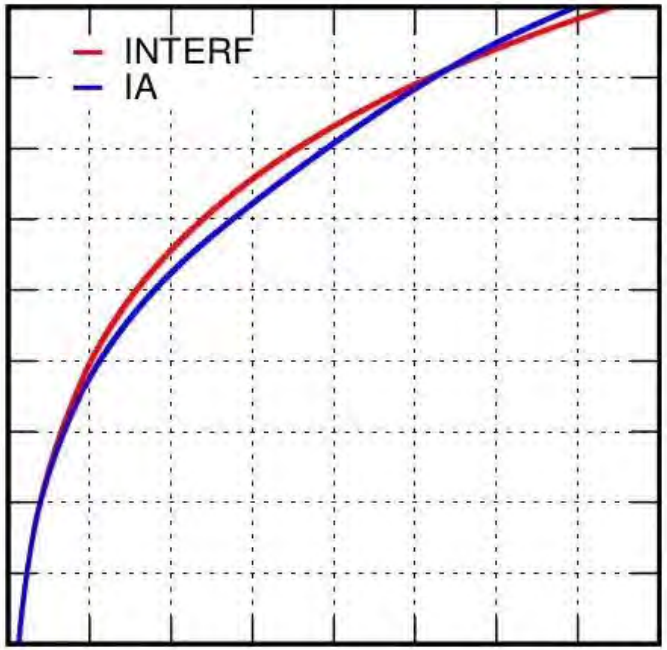

Thermal flux to concrete vs Time

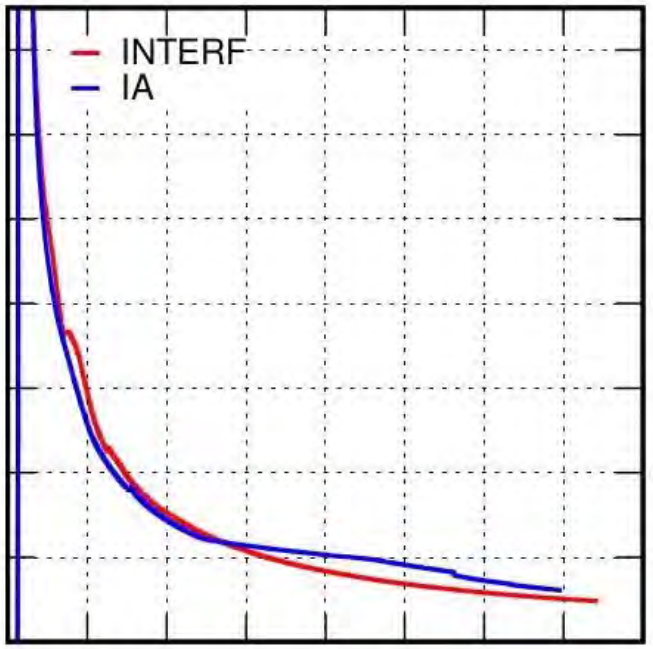

Note: INTERF is the current tool used by ASNR to compute mass and volumetric liquid fractions.

APPLICATION TO ASTEC, SINGLE CONCRETE CASE

Oxide layer temperature vs Time

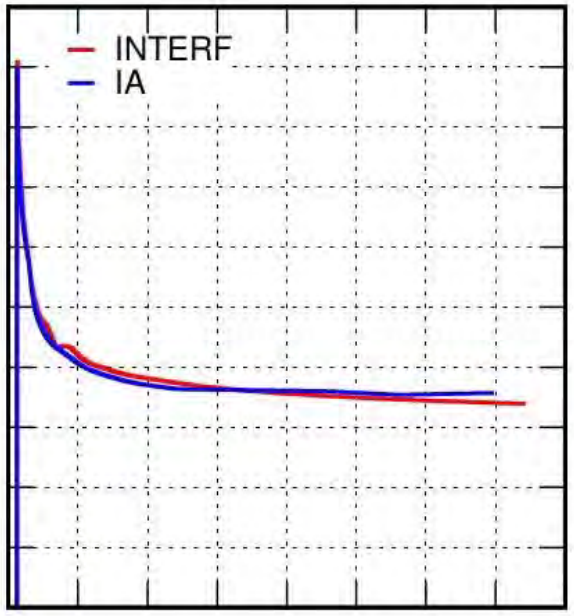

Corium mass fraction versus time

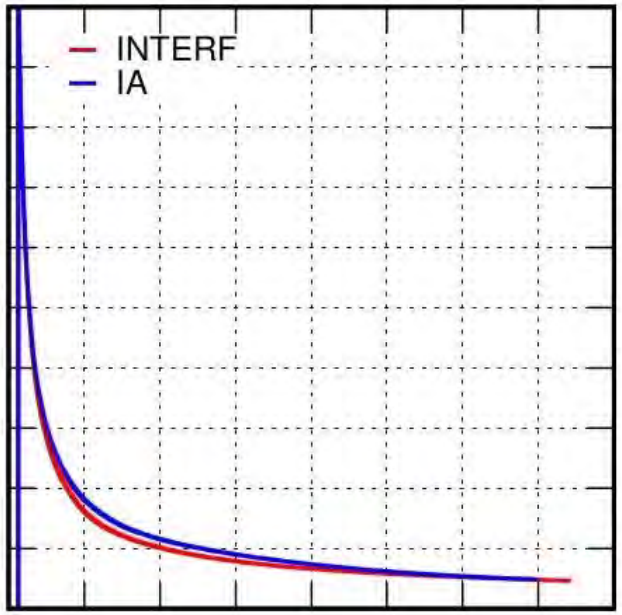

Solidification temperature versus corium mass fraction

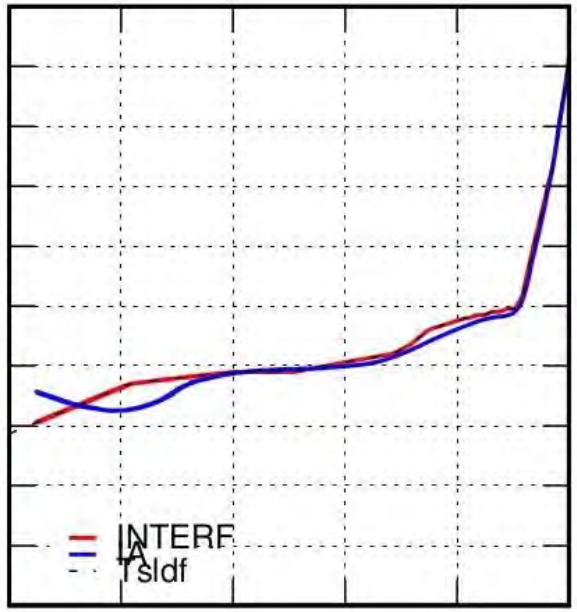

APPLICATION TO ASTEC, TWO CONCRETES CASE

- For nuclear power plants whose basemat concrete is highly siliceous, EDF is considering thickening the basemat with a sacrificial concrete layer.
- This two-layer configuration with different concrete types is not handled well by ASTEC.
- Estimating the corium-concrete mixture properties using those of the highly siliceous concrete is overly conservative, while using the properties of the sacrificial concrete is not bounding.
- The AI model is particularly useful in this case. It was compared against NucleaToolbox calculations at several operating points.
- Note: XHO is an estimator of the corium fraction in the mixture.

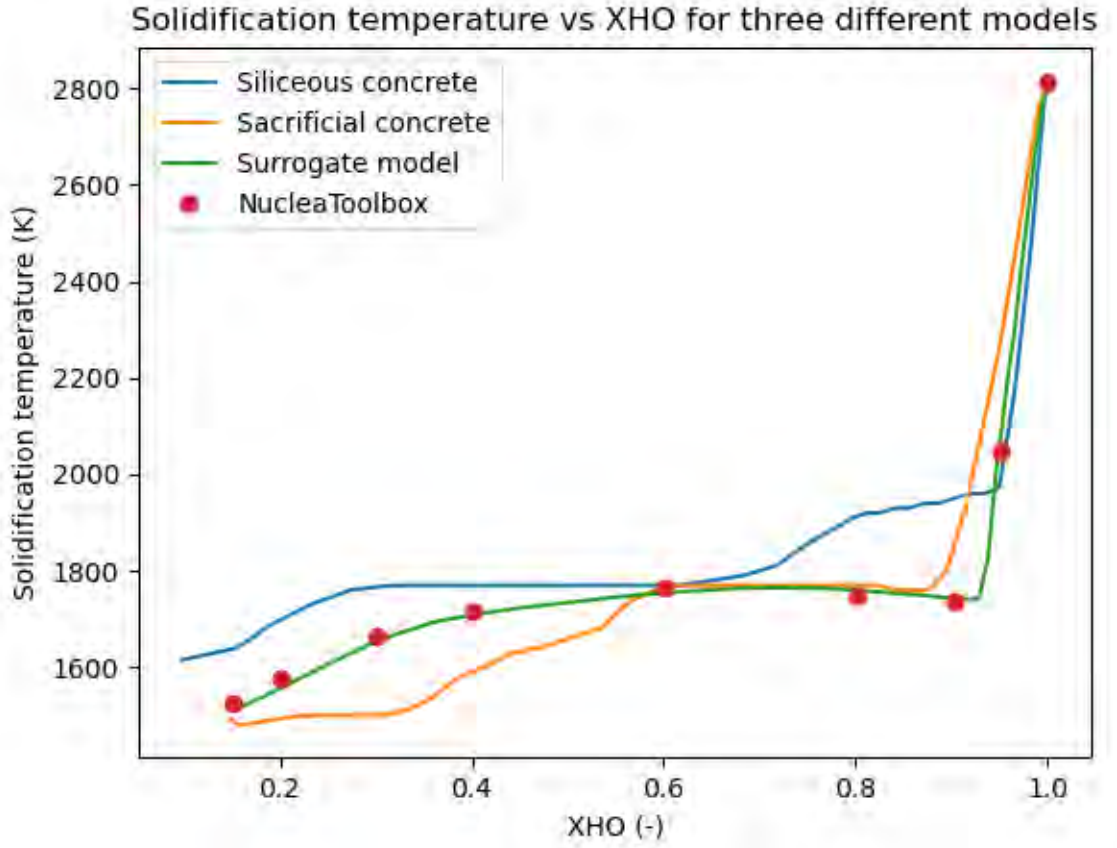

BEFORE CONCLUSION, TRY TO REDUCE TRAINING DATABASE

- Remove point if liquid mass fraction is inside a segment of 0 or 1
- 421.198 entries instead of 1.119.732 (37.6%)
- Bagging of 10 MLP
- RMSE (Root Mean Square Error): 0.015 (instead of 0.014)
- Correlation coefficient: 0.99 (not changed)

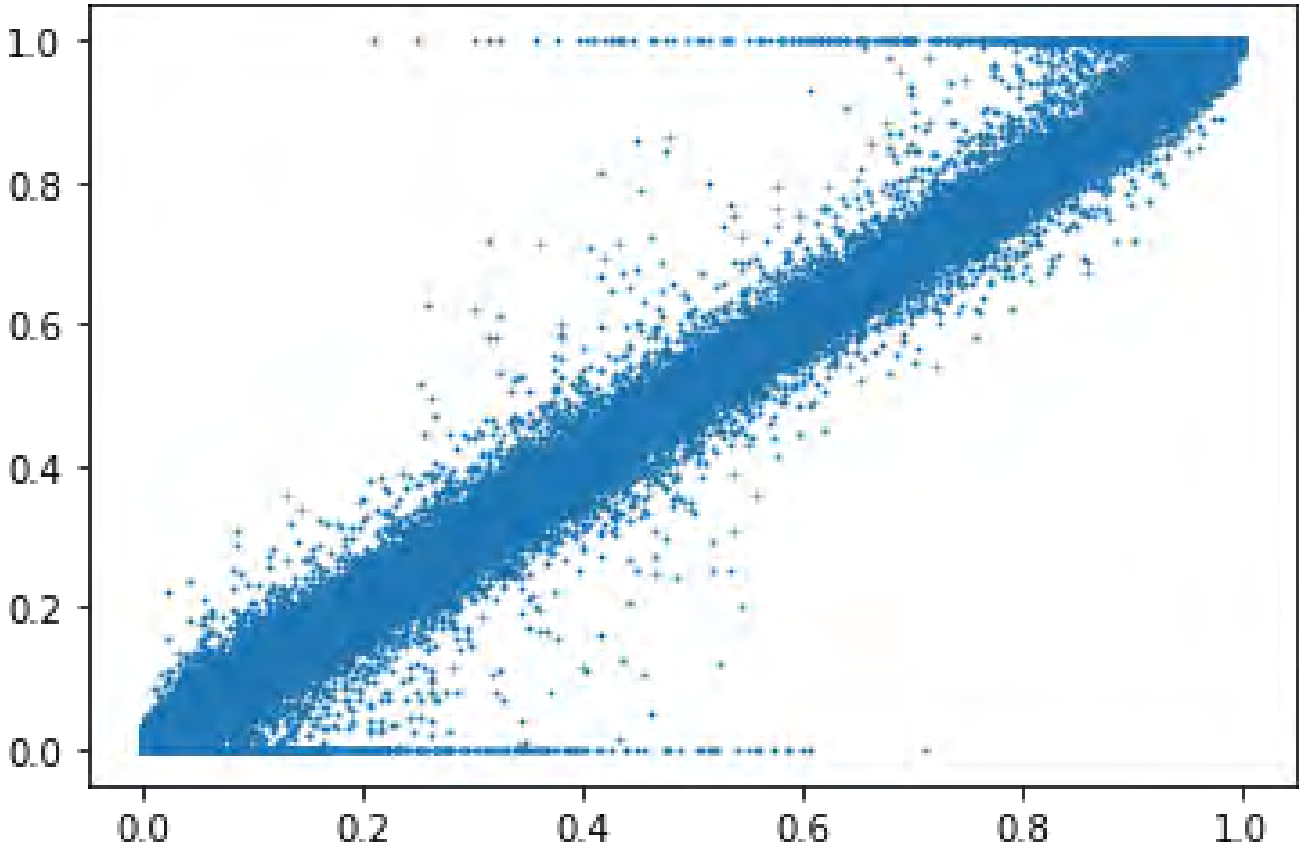

Predicted values versus exact values for test points

CONCLUSION AND PERSPECTIVES

- Goods result of the AI model in test examples
- Goods results applied to ASTEC computation
- Optimization is coming to reduce CPU time cost
- The biggest difficulty is to have a learning database covering all cases
- Some solutions to expand the training dataset have been investigated (but not here)
- A first solution to reduce the training dataset has also been investigated

THANK YOU FOR YOUR ATTENTION

INVESTIGATION ON THE MELT TRANSPORT BEHAVIOR IN THE DRYWELL OF FUKUSHIMA DAIICHI NUCLEAR POWER STATION UNIT-1 WITH MPS METHOD

Xin Li[1], Akifumi Yamaji[2], Ikken Sato[3], Takuya Yamashita[4]

[1] Japan Atomic Energy Agency
790-1 Otsuka, Motooka, Tomioka-machi,
Futaba-gun, Fukushima 979-1151, Japan
li.xin@jaea.go.jp

[2] Graduate School of Advanced Science and Engineering
Waseda University
3-4-1 Okubo, Shinjuku-Ku, Tokyo 169-8555, Japan
akifumi.yamaji@waseda.jp

[3] Waseda Research Institute for Science and Engineering
Waseda University
3-4-1 Okubo, Shinjuku-Ku, Tokyo 169-8555, Japan
kenichivich@aoni.waseda.jp

[4] Japan Atomic Energy Agency
2-4 Shirakata, Tokai-mura, Naka-gun,
Ibaraki 319-1195, Japan
yamashita.takuya38@jaea.go.jp

ABSTRACT

Internal investigations of the Fukushima Daiichi Unit-1 Primary Containment Vessel (PCV) revealed distinct debris signatures including a shelf-like deposit inside the pedestal above intact exposed rebars, and extensive spreading in the Drywell annulus without thermal damage to metallic structures. These observations suggest that concrete ablation and melt transport occurred at moderate temperatures, contrasting with the high-temperature conditions (>1500 °C) typical of classic MCCI experiments.

These features may be explained by a hypothesized melt spreading scenario where the initial high-temperature corium interacts with concrete and structural materials within the pedestal, generating a subsequent melt that later relocates or redistributes in the PCV, herein termed a "MCCI-derived secondary product".

This paper numerically investigates the spreading behavior of such a MCCI-derived secondary product. A two-dimensional geometry was established with scaled inflow conditions based on an estimate of 1F Unit-1. Using the Lagrangian Moving Particle Semi-implicit (MPS) method, the melt spreading dynamics and associated crust formation behavior were analyzed to identify the potential rheological properties and solidification criteria of the melt that can explain the observed deposit distribution and morphology in the D/W annulus of Unit-1. The results provide plausible insights into the late-phase accident progression and melt transport behavior of Unit-1.

KEYWORDS

Fukushima Daiichi Nuclear Power Plant Unit-1, melt spreading, severe accident, MPS method

1. INTRODUCTION

The decommissioning of the Fukushima Daiichi Nuclear Power Station requires improved understanding of fuel debris relocation and deposition inside the Primary Containment Vessel (PCV) to facilitate retrieval planning and operations. Recent internal investigations of the Unit-1 PCV have revealed widespread deposits in the Drywell (D/W) annulus. A distinct feature of these deposits is their non-uniform morphology characterized by a pronounced gradient in deposit height above the floor, decreasing with distance from the pedestal opening [1,2]. A schematic summary of the key Unit-1 observations motivating this study is

provided in Figure 1, including the widespread D/W deposits, the decreasing deposit-height trend from the pedestal opening, and the exposed standing rebars near the pedestal opening.

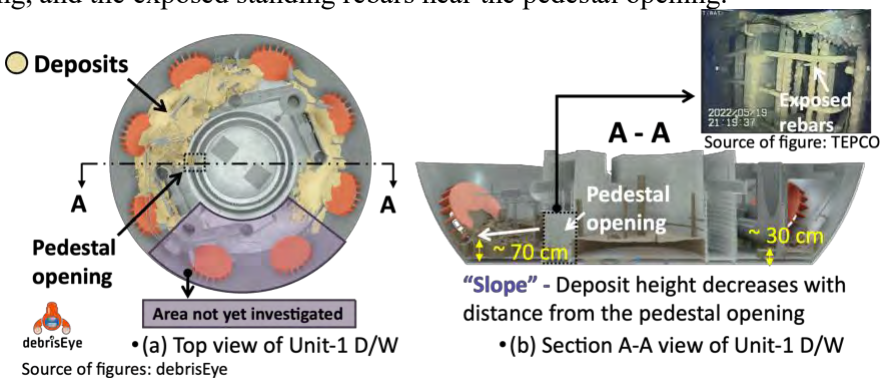

Figure 1. Schematic of key observations from Unit-1 PCV internal investigation

These observations, especially the absence of clear high-temperature melt traces on jet deflectors and metallic structures, are not readily explained by direct relocation of high-temperature corium alone. One plausible interpretation is that the initial high-temperature corium was largely retained inside the pedestal by crust formation, local debris-bed blockage, or limited discharge pathways, while prolonged concrete ablation under decay heat later generated a more concrete-rich, lower-temperature melt capable of relocating into the D/W through locally reopened or overflowed pathways. This subsequent material is herein termed a "MCCI-derived secondary product (MCCI-DSP)", defined as an MCCI-originated product that subsequently relocates, redistributes, or forms away from the primary reaction zone. For Unit-1, the MCCI-DSP is assumed to be a concrete-rich melt with possible Fe-bearing oxide contributions. Existing deposit analyses indicate that the U content is less than 1 wt% in the sampled deposits from the Unit-1 D/W annulus, suggesting that fuel-bearing components could be minor [3]. However, limited entrainment of such species cannot be excluded.

The Unit-1 observations motivate renewed attention to cooling-controlled spreading, where free surface heat loss and crust formation can strongly influence both spreading kinetics and final deposit morphology. However, the severe accident database for ex-vessel spreading has largely been built around single-release experiments where spreading and freezing occur over relatively short durations (typically in the order of tens of seconds), such as VULCANO and ECOKATS series [4,5]. These experiments generally represent gravity–viscous spreading regimes and target the maximum spreading distance governed by gravity-driven flow, viscous resistance, and bulk solidification. Although dedicated spreading codes such as MELTSPREAD and THEMA have been benchmarked against the extensive database of spreading experiments, they are based on the shallow-water approximation which does not explicitly resolve vertical variations in velocity, temperature, and phase [6–8]. Additionally, they are primarily only validated against spreading length for short durations. Consequently, the spreading dynamics under conditions of continued inflow and extended timescales, with a focus on the spreading morphology associated with the front / leading-edge crust behavior, remain insufficiently understood in the nuclear severe accident field.

To address this gap, this study utilizes the Moving Particle Semi-implicit (MPS) method [9,10], a Lagrangian particle framework suited for capturing free surface topological changes accompanied by phase changes. Building upon past successful applications of MPS method to melt spreading analyses [11–13], this study aims to clarify the mechanisms of (i) wide-area spreading under continuous inflow and (ii) sustained slope formation consistent with the Unit-1 deposits. A two-dimensional simulation geometry was established to simulate the spreading of MCCI-derived secondary product melt in a representative circumferential slice of the Unit-1 D/W annulus. Radiative / convective cooling from the free surface is considered and a temperature-dependent viscosity model for the mushy zone, with a high viscosity assigned

to near-solid material (crust) was employed. The roles of bulk viscosity and crust rigidity were discussed with sensitivity cases.

2. NUMERICAL METHOD

2.1. Governing Equations and Discretization of MPS Method

The governing equations of the MPS method for incompressible flows are described as conservation of mass, momentum, and energy as follows:

$$\frac{D\rho}{Dt} = -\rho\nabla.\mathbf{u} = 0 \tag{1}$$

$$\frac{D\mathbf{u}}{Dt} = -\frac{1}{\rho}\nabla P + \frac{1}{\rho}\nabla\cdot(\mu\nabla\mathbf{u}) + \mathbf{g} + \frac{\mathbf{F_s}}{\rho} \tag{2}$$

$$\rho\frac{Dh}{Dt} = k\nabla^2 T + Q \tag{3}$$

where ρ is the density, $\mathbf{u}$ is the velocity, P is the pressure, μ is the dynamic viscosity, $\mathbf{g}$ is the gravitational acceleration, $\mathbf{F_s}$ represents external forces except gravity, such as surface tension. h is the specific enthalpy, T is the temperature, k is the thermal conductivity, and Q is the external volumetric heat source or sink.

In order to reduce the discretization error and improve the numerical accuracy, the original particle interaction models have been modified using the second-order corrective matrix developed by Duan et al. [9,10]. The discretization models for the gradient, divergence, and Laplacian operators are shown in Eqs. (4) – (6):

$$\langle\nabla\phi\rangle_i = \frac{1}{n_0}\sum_{j\neq i}\left\{w_{ij}\frac{\phi_j-\phi_i}{r_{ij}}\left(\begin{bmatrix}\mathbf{C}_1\\ \mathbf{C}_2\\ \mathbf{C}_3\end{bmatrix}P\right)\right\} \tag{4}$$

$$\langle\nabla\cdot\mathbf{u}\rangle_i = \frac{1}{n_0}\sum_{j\neq i}\left\{w_{ij}\frac{\mathbf{u}_j-\mathbf{u}_i}{r_{ij}}\left(\begin{bmatrix}\mathbf{C}_1\\ \mathbf{C}_2\\ \mathbf{C}_3\end{bmatrix}P\right)\right\} \tag{5}$$

$$\langle\nabla^2\phi\rangle_i = \frac{1}{n_0}\sum_{j\neq i}\left\{w_{ij}(\phi_j-\phi_i)\frac{[\mathbf{C}_4+\mathbf{C}_5+\mathbf{C}_6]P}{l_0 r_{ij}}\right\} \tag{6}$$

where ϕ is a scalar variable; $\mathbf{C}_1$ to $\mathbf{C}_6$ are the first to sixth rows of the corrective matrix $\mathbf{C}$ defined in [10], respectively; r_{ij} is the distance between particle i and particle j; l_0 is the constant initial particle size.

The weight function (between the reference particle i and its neighbor particle j) w_{ij} and particle number density n_i are defined as:

$$w(r) = \begin{cases}\left(\frac{r_{ij}}{r_e}-1\right)^2, & 0\le r_{ij} < r_e\\ 0, & r_e \le r_{ij}\end{cases} \tag{7}$$

$$n_i = \sum_{j\neq i} w(|\mathbf{r_i}-\mathbf{r_j}|) \tag{8}$$

The particle shifting technique is implemented by relocating the particles from the particle-dense region to the particle-dilute region. The particles in a particle-dense region are moved by the position vector as:

$$\delta\mathbf{r_i} = -\frac{l_0\Delta r_i}{n_0}\sum_{j\neq i}\frac{w_{ij}}{r_{ij}^2}\mathbf{r_{ij}} \tag{9}$$

More details on the particle shifting technique for the internal and surface particles can be found in [14].

2.2. Temperature, Phase Change, and Viscosity Models

The following specific enthalpy - temperature relationship is adopted in the current MPS method to evaluate the thermal state and phase change of each particle, and the temperature is updated through the enthalpy-based energy equation.

$$h(T) = \begin{cases} C_{p,s}T, & T \le T_s \\ h_s + (h_l - h_s)\frac{T-T_s}{T_l-T_s}, & T_s < T < T_l \\ C_{p,l}T + L, & T \ge T_l \end{cases} \quad (10)$$

$$h_s = C_{p,s}T_s \quad (11)$$

$$h_l = C_{p,l}T_l + L \quad (12)$$

where $C_{p,s}$, $C_{p,l}$ are specific heat of the material for its solid and liquid state, respectively; T_s is the solidus temperature; T_l is the liquidus temperature; h_s and h_l are the specific enthalpies at the solidus and liquidus temperature, respectively; L is latent heat. Note that a single, constant latent heat (L) is assigned to the MCCI-DSP melt as an effective property. This is a simplified treatment of a multicomponent melt. Species-dependent latent heats and detailed solidification sequences, as may occur for example in corium–concrete mixtures, are not explicitly resolved.

The viscosity model utilized in the current MPS method is temperature-dependent and is associated with the solid fraction γ of the melt:

$$\mu = \begin{cases} \mu_l, & \gamma = 0 \\ \mu_l exp(2.5C\gamma), & 0 < \gamma < \gamma_{th} \\ \mu_{solid}, & \gamma \ge \gamma_{th} \end{cases} \quad (13)$$

The solid fraction γ is defined to change linearly between solidus T_s and liquidus temperature T_l as:

$$\gamma = \begin{cases} 0, & T \ge T_l \\ \dfrac{T_l - T}{T_l - T_s} & T_s < T < T_l \\ 1 & T \le T_s \end{cases} \quad (14)$$

where C is an empirical parameter between 4 and 8, and the current study uses 6, μ_l is the liquid viscosity of the melt at the liquidus temperature. Similarly, Eq. (14) approximates the solid fraction as a linear function of temperature over the solidification range. This treatment assumes an effective mixture behavior and does not explicitly account for species-dependent phase fractions, densities, or latent heats. The viscosity remains as the liquid viscosity of the melt at the liquidus temperature when $\gamma = 0$. The viscosity changes exponentially with solid fraction between 0 and a defined threshold solid fraction γ_{th}, following the correlation developed by Ramacciotti et al. [15]. When the solid fraction of a melt particle increased beyond γ_{th}, it is deemed as solidified (namely, a crust particle) and its viscosity is increased to the solid viscosity μ_{solid}, which is set as 10^5 Pa·s in the current study.

2.3. Radiative heat loss and convective cooling from the free surface

In the present MPS framework, heat transfer within the condensed phases is explicitly resolved by heat conduction via the particle interaction model, while convection is naturally captured by the Lagrangian motion of particles. However, since the ambient gas phase is not explicitly modeled, simplified heat transfer models are adopted to define the boundary cooling conditions at the free surface. Specifically, both the radiative and convective heat loss from the free surface is considered as heat sink of a particle represented by Q in Eq. (3). The radiative heat flux $q_{radiative}$ removed from the free surface is evaluated based on Stefan-Boltzmann law as:

$$q_{radiative} = \sigma\varepsilon(T^4 - T_{background}^4) \quad (15)$$

where σ is Stefan-Boltzmann constant, ε is the emissivity, and $T_{background}$ is the background temperature for the thermal radiation.

Similarly, the convective heat flux $q_{convective}$ removed from the free surface is evaluated using Newton's cooling law as:

$$q_{convective} = h_c(T - T_{envioronment}) \quad (16)$$

where h_c is the convective heat transfer coefficient and $T_{envioroment}$ is the environment temperature.

Additionally, once the melt spreads onto the concrete substrate, heat transfer at the melt–concrete interface is resolved by conductive heat transfer between neighboring particles. Subscale heat-transfer processes at the interface are not explicitly modeled, and no additional thermal contact resistance is imposed in the present model, such as that inferred in the VULCANO tests [4]. Therefore, the interface treatment corresponds to ideal thermal contact and may overestimate heat loss to the substrate if an effective contact resistance develops.

3. SIMULATION GEOMETRY, CONDITIONS, AND THERMO-PHYSICAL PROPERTIES

The simulation geometry is depicted in Figure 2. The current two-dimensional MPS simulation represents a circumferential slice of the Unit-1 D/W annulus. A buffer pool is arranged beneath the injection inlet to mitigate potential numerical instabilities that may arise from melt impingement on the floor and subsequently affect the spreading process. The concrete substrate connected to the buffer pool is 2.0 m long with a thickness of 0.06 m. A constant-velocity inflow boundary on the left side supplies the MCCI-derived secondary product melt (hereafter referred to as "the melt") at 0.016 m/s, corresponding to a mass flow rate of 2 kg/s for the modeled half D/W annulus (i.e., 4 kg/s for the full annulus). This rate is a scaling estimate derived from an equilibrium energy balance that the decay power is depleted by the generation of the melt, using an early high decay-power level (roughly 7 MW) and an assumed concrete decomposition enthalpy (1779 kJ/kg **[16]**). While subject to uncertainties, this value is adopted as an order-of-magnitude boundary condition to characterize the hydrodynamics of the active spreading phase of the melt in the D/W annulus.

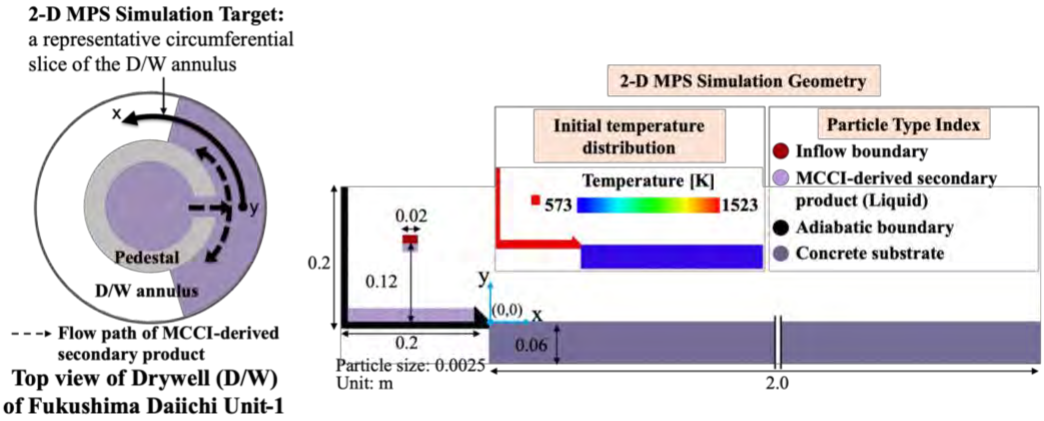

Figure 2. MPS simulation target and geometry

Regarding the boundary conditions, the melt within the buffer pool boundary is treated as adiabatic. Once the melt spreads onto the concrete substrate, heat transfer is considered, including the conductive heat loss to the concrete substrate and convective and radiative heat loss to the atmosphere (see Eq. (15) and (16)). In the current study, h_c is set as 10 W/m^2/K, which is in the order of general natural convection of gas. $T_{background}$ and $T_{envioronment}$ are both set as a constant 573 K. The feedback on the environment temperature and background temperature due to the radiative and convective heat loss from the melt is neglected.

The thermophysical properties used in this study are listed in Table I. The thermophysical properties of the MCCI-derived secondary product are primarily taken from those of basaltic concrete [17]. Regarding the phase change temperatures, recent heating tests on Unit-1 aggregate surrogates (basalt, andesite, and sandstone) confirmed that all aggregate types are fully melted by 1473 K [18]. Since the specific phase change behavior of the secondary product is not uniquely constrained, the liquidus temperature is set to 1523 K as a representative value that is modestly above the beforementioned fully melted temperature 1473

K. Solidification of MCCI-derived secondary product melt is modeled in terms of solid fraction γ that increases from 0 to 1 between the liquidus (1523 K) and solidus temperature (1350 K) (see Eq. 14). The transition to the solid viscosity μ_{solid} is fundamentally defined by the immobilization temperature of 1473 K. For implementation in the Ramacciotti viscosity model, this temperature is converted to the corresponding solid fraction, γ_{th} (0.289). This value is lower than the solid fractions of approximately 50 vol% often associated with spreading termination in corium experiments, such as VULCANO VE-U7 [19], because it is not used here as a universal rheological immobilization criterion. Instead, it is a phenomenological, temperature-based threshold for the onset of effectively rigid crust formation for the Unit-1 MCCI-DSP.

Table I. Thermo-physical properties used in the current study

Thermo-physical properties	MCCI-derived secondary product	Basaltic concrete
Density (kg/m^3)	2240.0	2240.0
Specific heat (J/kg/K)	1250.0	1250.0
Heat conductivity (W/m/K)	2.5	2.5
Viscosity at liquidus temperature (Pa·s)	Low viscosity case: 5.00×10^{-3}	2.70 x10^{-3}
	High viscosity case: 22.36	
Solidus temperature (K)	1350	1350
Liquidus temperature (K)	1523	1650
Fusion heat (kJ/kg)	442.5	442.5

Two reference liquid viscosities are considered, i.e., a low-viscosity case with $\mu_l = 5.00\times10^{-3}$ Pa·s and a high-viscosity case with $\mu_l = 22.36$ Pa·s, which is the viscosity of basalt. These two bounding viscosities are intended to examine bulk melts with initially high and low contrast with respect to the crust viscosity μ_{solid}, respectively. In addition to the temperature-dependent viscosity increase associated with solidification (see Eq. (13) and (14)), an optional freezing criterion is introduced to represent an effectively rigid crust at the leading edge. Specifically, when a crust particle (i.e. the temperature drops below the immobilization temperature of 1473 K) and its velocity magnitude falls below 10^{-4} m/s, the particle coordinates are fixed in space until remelting. In the present model, mechanical failure (e.g., cracking or fracture-driven breaching) is not considered.

To investigate the respective influences of bulk viscosity and effectively rigid crust on slope formation and persistence, three sensitivity cases are considered as listed in Table II.

Table II. Sensitivity case conditions

Case ID		μ_l(Pa·s)	Freezing criterion
1	**Low Viscosity - Freezing (LV-F)**	5.00×10^{-3}	On
2	**Low Viscosity - No Freezing (LV-NF)**	5.00×10^{-3}	Off
3	**High Viscosity - Freezing (HV-F)**	22.36	On

4. RESULTS AND DISCUSSION

4.1. Overview of Spreading Length and Behavior

The spreading length histories of the MPS simulation cases are depicted in Figure 3. The two low-viscosity cases show intermittent spreading advances characterized by “stop-and-go” cycles and stagnation plateaus, while the high-viscosity case exhibits continuous advance.

In the early phase (time < 50 s), the two low-viscosity curves almost overlap despite the short plateaus, which indicates temporary stagnation of the melt front advance due to crust formation. As spreading progressed, the effect of cooling became more prominent, leading to more significant crust formation, especially at the melt front. As a result, the spreading length and behavior start to diverge. In the current study, such front crust behavior dominates not only the spreading behavior, i.e., "stop-and-go" or continuous creeping, but also the melt deposit morphology, which will be detailed in the following sections.

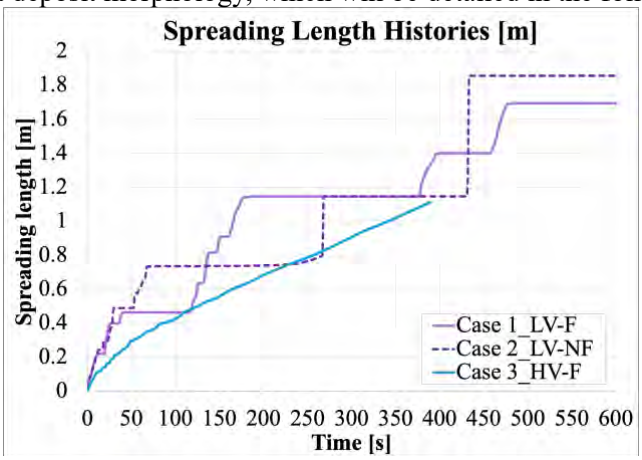

Figure 3. Spreading length histories of MPS simulation cases

4.2. Spreading behavior of Low-viscosity cases: morphology evolution and slope formation

4.2.1. Phase I: early rapid advance with transient crust effects

Figure 3 summarizes the early spreading behavior of the low-viscosity cases with (LV-F) and without (LV-NF) the freezing criterion. Up to approximately 12 s, the two cases exhibit nearly identical spreading length histories and a relatively thin layer of melt with nearly uniform thickness along the spreading direction, indicating that the initial advance is governed primarily by viscous-gravity spreading under continuous inflow and that the effect of crust treatment remains insignificant at this stage.

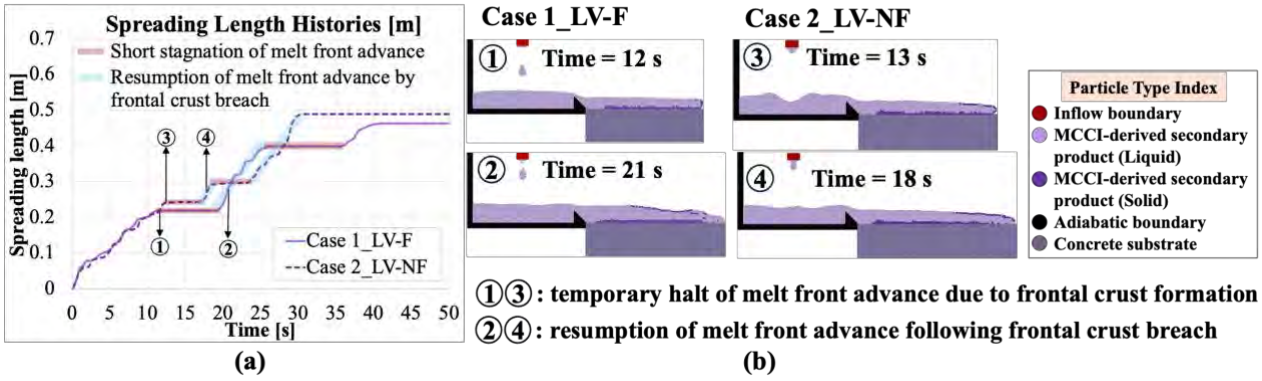

Figure 4. (a) Spreading length history for Phase I (b) Snapshots of representative moments of MPS simulations in LV-F and LV-NF cases (Phase I)

After 12 s, both curves start to exhibit short plateaus resulting in intermittent increases of spreading length. These short stagnations are highlighted in .
Figure **4** (a) and are interpreted as temporary halts of melt front advance induced by frontal crust formation, which was later breached (thermally but not mechanically) to allow for resumption of melt front advance. Such transient behavior of crust breach and resumption of melt advance is detailed in the Snapshots 1 to 4 in .
Figure **4** (b), and the corresponding temperature / solid fraction distribution of melt are shown in Figure 5.

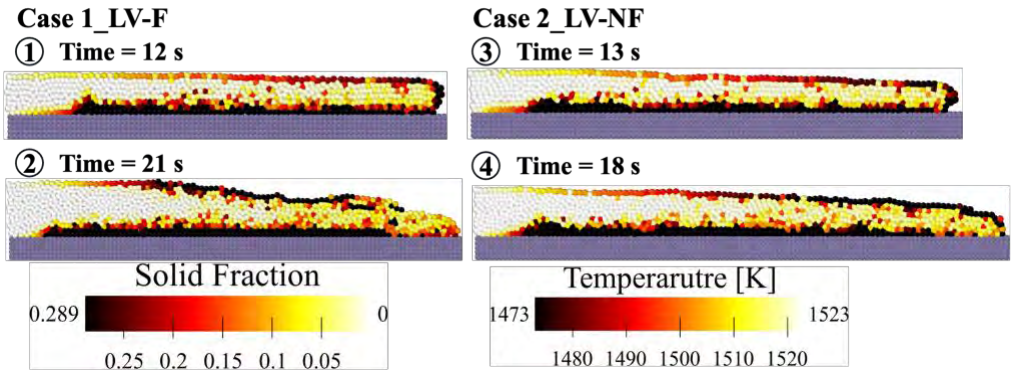

Figure 5 Temperature / solid fraction distribution of melt for representative moments of MPS simulations in LV-F and LV-NF cases

Snapshots 1 and 3 correspond to the onset of such short plateaus for the LV-F (t =12 s) and LV-NF (t = 13 s) cases, respectively. In both cases, a high-solid-fraction thin layer developed near the free surface and concentrated at the melt front due to radiative and convective heat loss to the environment. Through the viscosity model dependent on solid fraction, the frontal crust locally increased the effective viscosity and reduced the front mobility, leading to an apparent halt of the melt front advance, producing the short plateaus in the spreading length histories shown in Figure 4 (a).

Snapshots 2 (LV-F, t = 21 s) and 4 (LV-NF, t = 18 s) illustrate the subsequent resumption of melt front advance. As the inflow continued, the melt from the hot interior reached the front and led to the frontal crust breach. It should be noted that, in the present modeling, "crust breach" refers to recover of advance through either (i) thermal remelting of immobilized crust or (ii) hydrostatically driven viscous creep / advection of the highly viscous crust. When the freezing criterion is activated and crust particles are fixed in space, mechanism (ii) is no longer available. Thus, in the LV-F case a crust fixed in space can be "breached" only by thermal remelting. While in LV–NF, crust particles are not artificially fixed in space, so both (i) and (ii) can apply, allowing for front advance even when crust remains at the melt front. This can explain why some crust particles can still be observed at the melt front when melt front advance resumed in Snapshot 4 for the LV-NF case, while the melt front appears completely crust free in Snapshot 2 for the LV-F case.

Overall, Phase I shows that while global spreading histories remain comparable, frontal crust formation already strongly affects the instantaneous advance of the melt front. High bulk thermal energy prevents the crust from becoming a durable barrier, allowing repeated breaches through remelting (LV-F) or viscous deformation (LV-NF). Consequently, both cases exhibit "stop-and-go" cycles driven by the competition between rapid surface cooling and advective heat supply from the hot interior. Notably, the dynamics observed in most spreading experiments generally correspond to this phase. These short stagnations foreshadow the Phase II divergence, where crust persistence ultimately controls the transition to sustained crust anchoring and slope formation.

4.2.2 Phase II: Long stagnation

Following the initial "stop and go" cycles of Phase I, both cases transition into Phase II characterized by extended plateaus ("long stagnation") in the spreading length (e.g., t≈ 42–114 s for LV-F and t≈ 68 – 225 s for LV-NF in Figure 6 (a)), despite the continuous inflow. This indicates that the global kinematics in Phase II are no longer controlled by the supply rate alone, but by the frontal crust development under cooling. Considering mass conservation, because the spreading length remains unchanged while inflow persists, the injected melt mass must be accommodated by an increase in the melt thickness in 2-D. The key difference between LV–F and LV–NF is how this melt thickening is redistributed along the spreading direction.

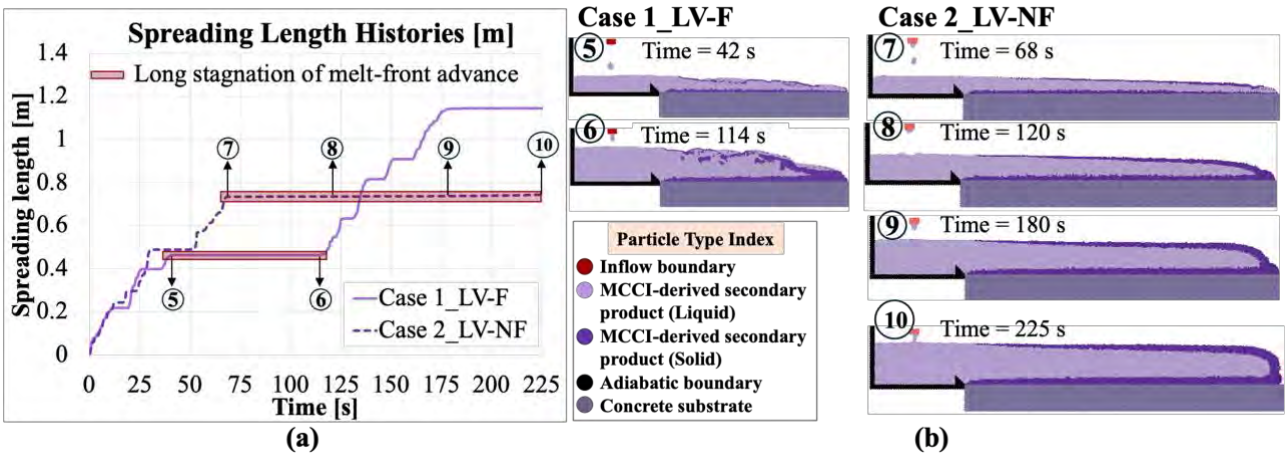

Figure 6 (a) spreading length histories with Phase II highlighted (b) Snapshots of representative moments of MPS simulations in LV-F and LV-NF cases (Phase II)

In the LV-F case, once the freezing criterion immobilizes the crust particles and fixes them in space, the frontal crust behaves as an effectively rigid obstruction at the melt front. Forward melt transport through the front is strongly suppressed, and continued inflow produces damming and upstream accumulation, generating a pronounced thickness gradient ("slope") behind the stalled front (see Snapshots 5-6 in Figure 6(b)). In other words, during Phase II the LV–F system converts sustained inflow into a vertical thickening pool against a fixed rigid front, establishing a persistent slope in the subsequent evolution. This process suggests the kinematic anchoring of the crust could be the direct origin of the persistent slope observed in the Fukushima Unit-1 deposits.

In contrast, the LV-NF case maintains a relatively uniform thickness, characterized instead by pronounced morphological evolution of the "nose". Because the frontal crust remains by assumption a mobile Newtonian fluid, hydrostatic pressure gradients drive slow viscous creep, progressively transforming the front from a sharp wedge into a rounded "bullet-nose" (Snapshots 7 – 10). This reshaping reflects the fundamental tendency of viscous gravity currents to level out to minimize potential energy. Although high viscosity of the frontal region suppresses rapid extension, internal viscous relaxation continues to smooth sharp thickness gradients.

The comparison between LV-F and LV-NF cases reveals that macroscopic stagnation arises from two fundamentally different physical states. In LV-F, long stagnation is due to the effectively rigid frontal crust working as a rigid dam to support a persistent slope. In LV-NF, stagnation is a state of creep-limited flow, where the crust resists rapid extension but continues to viscously relax and flatten under hydrostatic load. This contrast is essential for the subsequent interpretation of slope persistence, namely the frontal crust needs to sustain a hydrostatic head without creeping (LV-F) so that a thickness gradient in the deposited profile can be produced and sustained. It should also be noted that sustained slopes may be produced by other rheological mechanisms, such as non-Newtonian or yield-stress behavior. In the present study, the freezing criterion is used as a simplified kinematic representation of an effectively load-bearing frontal crust, rather than as the only possible physical mechanism for slope preservation [20].

4.2.3 Phase III: Resumption of melt front advance by overriding

Figure 7 compares the late stage spreading length histories following the Phase II stagnation. Both cases exhibit intermittent resumption of melt front advance, manifested as stepwise increases in the spreading lengths, herein defined as Phase III. These stepwise increases in spreading length occur at t ≈ 118, 375, 450 s for LV-F and t≈ 260, 430 s for LV-NF. Such spreading length increases are driven by overriding, where

a new flow path bypasses the previously stagnated front. However, the significantly higher spreading rate observed in the LV-NF events reflects a fundamental mechanism divergence between the two cases.

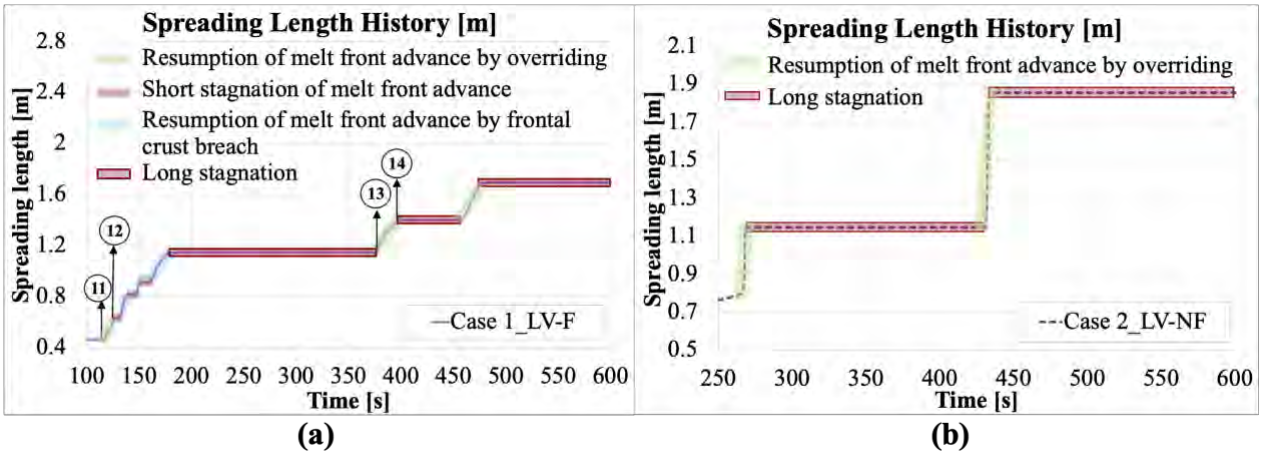

Figure 7 (a) Spreading length histories of LV-F case (b) Spreading length histories of LV-NF case

I. LV–F: overriding via hot-melt bypass over an immobilized frontal crust

Figure 8 (a) shows representative snapshots illustrating the overriding mechanisms in the LV–F case. During the preceding stagnation, the frontal crust developed into an effectively rigid barrier. Continuous inflow led to the accumulation of upstream melt until a preferential flow path was established that overrode this barrier. These overriding events are illustrated by Snapshots 11 (t = 118 s) and 13 (t = 378 s) in Figure 8 (a), where a thin, rapidly advancing interior melt layer overrode the immobilized nose (arrows indicate the dominant melt flow paths). Because the newly advancing layer was thin, it was cooled efficiently and rapidly developed a new frontal crust which temporarily halted the renewed advance until it locally remelted again (see Snapshots 12 (t = 126 s) and 14 (t = 395 s) in Figure 8(a)). These short "stop-and-go" episodes similar to those in Phase I are visible in the late-time spreading history (e.g., t≈126–175 s in Figure 7 (a)), indicating that overriding events can be followed by rapid re-establishment of frontal crust and short stagnations.

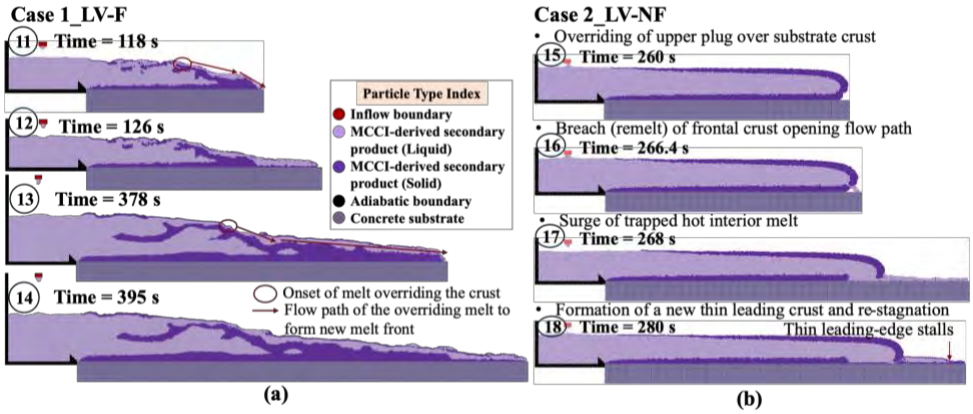

Figure 8 Snapshots of representative moments of MPS simulations for (a) LV-F and (b) LV-NF cases (Phase III)

II. LV–NF: overriding initiated by plug creep triggering interior melt discharge

In LV-NF, the frontal region remained a highly viscous but mobile Newtonian plug. Phase III occurred when this slow evolution enabled the bulk melt to override the cooled substrate / basal crust and open a flow

path for the hot interior melt. As shown in Figure 8 (b), the plug crept forward under hydrostatic load until the frontal crust confinement breached (Snapshot 16). Once breached, the low-viscosity interior discharged rapidly, surging along the floor as a thin melt layer (Snapshots 17-18). Unlike the controlled bypass over the readily formed crust structure in LV-F, such discharge dispersed the accumulated potential energy of melt in a sudden surge, producing a sharp step increase in spreading length in Figure 7 (b).

Overall, Phase III in LV-F can be interpreted as a thermal bypass of the frontal crust region, rather than remobilizing the originally anchored front through remelting, while in LV–NF the overriding event can be interpreted as a two-stage process: (i) gradual plug reconfiguration by viscous creep / advection, followed by (ii) rapid discharge and spreading of hot interior melt once the constraining crust is sufficiently weakened. In both cases, Phase III can be short-lived, and the spreading kinetics quickly transitioned back to intermittent advance punctuated by short stagnations as in Phase I or long stagnations in Phase II.

4.3 High-viscosity case (HV–F): continuous advance and uniform deposition tendency

Figure 9 presents the spreading behavior for the high-viscosity case (HV-F). In contrast to the intermittent "stop-and-go" dynamics of the low-viscosity cases, the HV-F case exhibits continuous advancement characterized by a rounded nose (Snapshots 19-20). This behavior stems from the high viscosity of the bulk melt, which facilitates efficient momentum diffusion from the interior to the leading edge.

As shown by the solid fraction and velocity distribution in Figure 9 (b), the viscous interior physically dragged the developing crust forward, maintaining frontal velocities well above the freezing threshold ($|u| < 10^{-4}$ m/s). Consequently, although the freezing criterion was active in the simulation, it was practically never triggered. As a result, the melt advanced predominantly by continuous creep, resulting in a relatively uniform thickness profile, in contrast to the pronounced upstream accumulation and slope formation mechanism observed in the LV-F case.

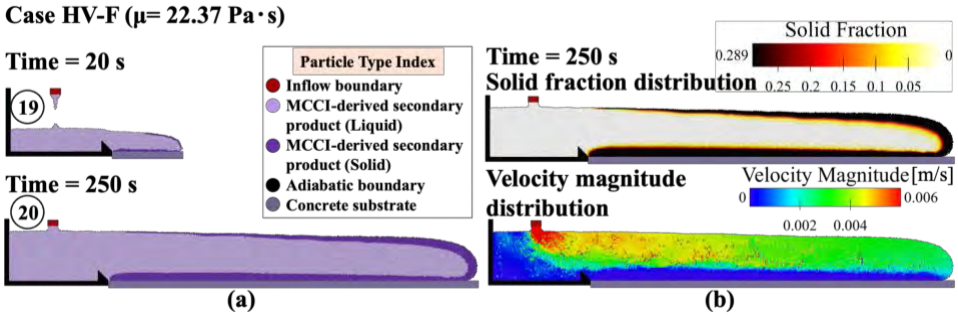

Figure 9 Snapshots of representative moments of MPS simulations for high-viscosity case

4.4 Implications for interpreting Unit-1 PCV deposits

Post-accident investigations of Unit-1 PCV reveal two key requirements for a mechanistic explanation of melt transport in the D/W annulus, i.e., (a) sufficient mobility to spread broadly in the D/W annulus and (b) capability to retain a decreasing-height trend with travel distance (the "slope"). Within the present MPS framework, i.e., treating the melt as a Newtonian fluid with temperature-dependent viscosity and an optional kinematic immobilization rule ("freezing criterion"), the simulations suggest that reproducing these features is facilitated by two rheological attributes:

1. Front crust rigidity to suppress long-term gravitational relaxation. The simulation results show that high viscosity alone is insufficient to maintain a slope over extended timescales. When the frontal region remains a mobile Newtonian layer, thickness gradients progressively relax through creep driven primarily by hydrostatic pressure. A sustained shelf-like morphology therefore requires the frontal region to behave effectively as a mechanically supportive structure, which is represented here by the freezing criterion that allows the front to sustain a hydrostatic head without long-term deformation.

2. Sufficient viscosity contrast between the bulk melt and the crust to enable frontal anchoring. Slope formation is favored when the bulk melt remains sufficiently less viscous relative to the crust. This allows the interior melt to flow without generating enough viscous drag to mobilize the frontal crust, permitting the leading edge to slow down and anchor while the inflow piles up upstream. Conversely, a relatively high-viscosity interior exerts strong drag on the crust, physically pulling the frontal region forward and maintaining a continuous creep regime to disrupt stable slope formation.

These findings imply that one plausible scenario for the observed Unit-1 deposit morphology is that the MCCI-derived secondary product initially possessed high flowability during relocation, but upon cooling developed a locally rigid frontal structure that effectively anchored the deposit geometry against gravitational leveling.

5. CONCLUSIONS

A 2-D model with free-surface radiative / convective cooling and temperature-dependent viscosity was applied to simulate the spreading of a hypothesized MCCI-derived secondary product using the MPS method, to clarify the mechanisms of the sloped deposits in the Fukushima Daiichi Unit-1 D/W annulus. Three sensitivity cases were used to separate the effects of bulk viscosity and frontal crust behavior. The comparative results support the following interpretation.

The simulations indicate that reproducing slope formation requires a kinematic anchoring mechanism (modeled here via a freezing criterion) that acts as an effective rigidity, allowing the frontal crust to sustain a hydrostatic head without long-term deformation. Another key finding is that a large bulk-crust viscosity contrast promotes the conditions for front anchoring, facilitating slope formation.

Although the present modeling employs a simplified representation of crust rigidity through a kinematic immobilization criterion, this interpretation provides a physically consistent basis for relating the observed deposit morphology to melt mobility and frontal anchoring behavior and potentially offers a useful framework for future studies incorporating more detailed descriptions of the rheological properties of debris deposits in the Unit-1 PCV. A potential future step is to identify the in-pedestal processes capable of generating an MCCI-DSP with such rheological attributes, including coupled interactions among concrete, steel / iron oxides, and possible chemical modifiers, supported by dedicated material-property measurements.

ACKNOWLEDGMENTS

This study has been performed by the funds from Japanese Ministry of Economy, Trade, and Industry as The Subsidy Program “Project of Decommissioning, Contaminated Water and Treated Water Management (Development of Analysis and Estimation Technologies for Characterization of Fuel Debris)” starting FY2025.

REFERENCES

1. Tokyo Electric Power Company Holdings, Inc., “Fukushima Daiichi Nuclear Power Station Unit 1 Primary Containment Vessel Internal Investigation Completion of the detailed visual investigation of the perimeter of the pedestal using submersible ROV-A2” (2022).
2. NRA, “Investigation and analysis of TEPCO’s Fukushima Daiichi NPS Accidents (1/9),” presented at OECD/NEA International Conference on Regulator’s Views and Priorities on Nuclear Safety and Radiation Protection 10 Years After TEPCO Fukushima Daiichi NPS Accident, 28 November 2022.

3. Tokyo Electric Power Company Holdings, Inc., "1号機格納容器底部堆積物分析結果 [Analysis Results of Bottom Deposits in the Unit 1 Primary Containment Vessel]," Material 6-4, Nuclear Regulation Authority, Japan, Tokyo, Japan (2025).
4. C. Journeau et al., "Ex-vessel corium spreading: results from the VULCANO spreading tests," Nucl. Eng. Des. **223** 1, 75 (2003).
5. J. J. Foit, "Large-scale ECOKATS experiments: Spreading of oxide melt on ceramic and concrete surfaces," Nucl. Eng. Des. **236** 24, 2567 (2006).
6. M. T. Farmer, "Melt spreading code assessment, modifications, and application to the EPR core catcher design.," Argonne National Lab.(ANL), Argonne, IL (United States) (2009).
7. B. Spindler and J. M. Veteau, "The simulation of melt spreading with THEMA code: Part 1: Model, assessment strategy and assessment against analytical and numerical solutions," Nucl. Eng. Des. **236** 4, 415 (2006).
8. B. Spindler and J. M. Veteau, "The simulation of melt spreading with THEMA code: Part 2: Assessment against spreading experiments," Nucl. Eng. Des. **236** 4, 425 (2006).
9. G. Duan et al., "An accurate and stable multiphase moving particle semi-implicit method based on a corrective matrix for all particle interaction models," Int. J. Numer. Methods Eng. **115** 10 (2018).
10. G. Duan, A. Yamaji, And S. Koshizuka, "A novel multiphase MPS algorithm for modeling crust formation by highly viscous fluid for simulating corium spreading," Nucl. Eng. Des. **343**, 218 (2019).
11. A. Yamaji And X. Li, "Development of MPS Method for Analyzing Melt Spreading Behavior and MCCI in Severe Accidents," in Journal of Physics: Conference Series **739** 1 (2016).
12. Jubaidah et al., "Investigation on corium spreading over ceramic and concrete substrates in VULCANO VE-U7 experiment with moving particle semi-implicit method," Ann. Nucl. Energy **141**, 107266 (2020).
13. Y. Umazume et al., "2D MPS method analysis of ECOKATS-V1 spreading with crust fracture model," Nucl. Eng. Des. **379**, 111251, North-Holland (2021).
14. Z. Sun et al., "Modified MPS method for the 2D fluid structure interaction problem with free surface," Comput. Fluids **122**, 47 (2015).
15. M. Ramacciotti et al., "Viscosity models for corium melts," Nucl. Eng. Des. **204** 1, 377 (2001).
16. M. Pellegrini et al., "Analysis of the Long-Term Interaction Between Molten Core and Dry Concrete at Fukushima Daiichi Unit 1," Nucl. Technol. **211** 10, 2595, Taylor & Francis (2025).
17. M. Farmer, "The CORQUENCH code for modeling of ex-vessel corium coolability under top flooding conditions," Argonne National Lab.(ANL), Argonne, IL (United States) (2018).
18. H. Ida et al., "Fundamental study on melting behavior of aggregate and mortar under high temperature conditions over 1000℃," Cem. Sci. Concr. Technol. **78**, 571 (2024).
19. C. Journeau et al., "The VULCANO VE-U7 Corium spreading benchmark," Prog. Nucl. Energy **48** 3, 215 (2006).
20. M. Dragoni, M. Bonafede, And E. Boschi, "Downslope flow models of a Bingham liquid: Implications for lava flows," J. Volcanol. Geotherm. Res. **30** 3, 305 (1986).

The 12th European Review Meeting on Severe Accident Research
ERMSAR 2026
Madrid | May 18-22, 2026

130

Investigation on the Melt Transport Behavior in the Drywell of Fukushima Daiichi Nuclear Power Station Unit-1 with MPS Method

*Xin Li[1], Akifumi Yamaji[2], Ikken Sato[2], Takuya Yamashita[1]

1. Japan Atomic Energy Agency
2. Waseda University

Background - Distinctive Deposits Observed in Unit-1 D/W

Findings from PCV Internal Investigations of Fukushima Daiichi Unit-1

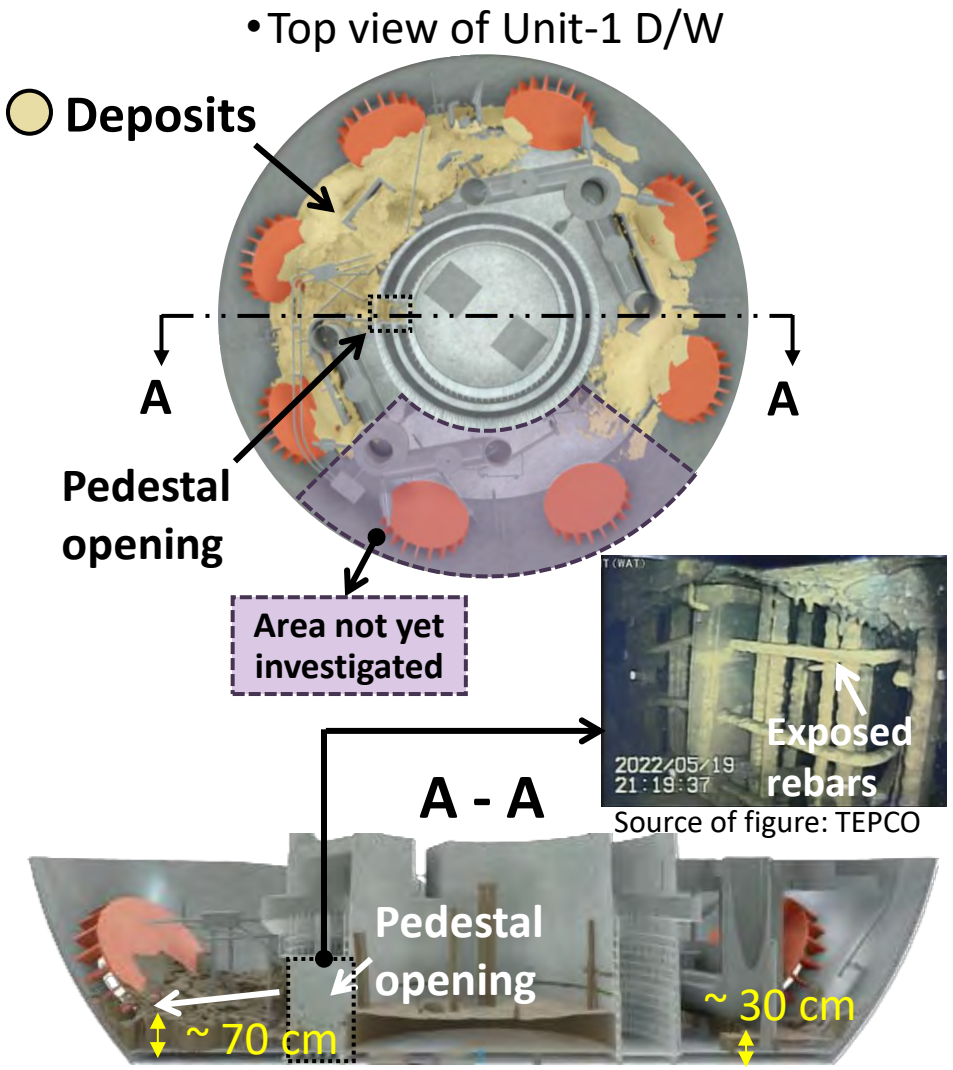

Source of figure: TEPCO

"Slope" - Deposit height decreases with distance from the pedestal opening

Source of figures: debrisEye

1. Widespread deposits in the D/W annulus
Deposits extending far beyond the pedestal opening to cover a large area of the D/W annulus

2. Sloped Deposit Morphology
Deposit height decreases with distance from the pedestal opening — a Unit-1-specific feature.

3. No melt traces on jet deflectors
Difficult to reconcile with direct high-temperature fuel-debris spreading.

4. Exposed & Standing rebars near pedestal opening
Suggests low-to-moderate temperature transport & ablation of concrete, instead of classical MCCI

These features are difficult to explain with simple high-temperature corium spreading.

From Unit-1 Evidence to a Non-Classical MCCI Interpretation

Classical high-temperature spreading

- Thermal damage on metallic structures expected (not observed in Unit-1).
- Spreading often treated as short-duration release (experimental limitation).
- Post test slope not evident, except a few cases (e.g., FARO L-26S), mechanism unclear.

Conflicts with Unit-1 observations.

Unit-1 accident progression

- No effective cooling by water injection.
- Sustained concrete interaction under moderate decay power.
- Corium crust likely suppressed mixing of fuel-rich corium and molten concrete.

MCCI remains the source, BUT relocated material to outside pedestal likely NOT classical corium–concrete mixture.

Moderate-temperature transport
+ Continuous melt generation

Interpretation proposed in this study

MCCI-Derived Secondary Product (MCCI-DSP)

Generated by pedestal MCCI product, then relocated into the D/W annulus at moderate temperature.

Proposed interpretation: MCCI-Derived Secondary Product

Definition adopted in this study

Products originating from MCCI but encompassing a broader **spatial and temporal scope** than conventional experiments. They could differ in macroscopic composition and properties from typical residues from MCCI tests, defined as material that has either:

1) **relocated from the vicinity of the primary MCCI region**, or
2) **formed at a location away from the primary MCCI region through concrete melting**

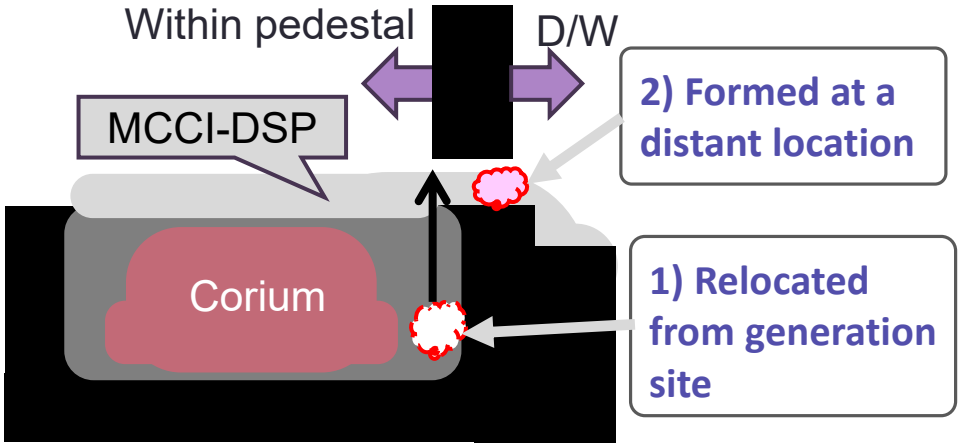

Conceptual schematic

The concept extends the spatial and temporal scope of MCCI:

Not only the initial high-temperature corium, but also materials that evolve, relocate, or re-generate after corium–concrete interaction are considered.

Primary MCCI in pedestal
High-T corium + concrete

→ **Secondary product forms**
composition / properties evolve

→ **Relocation into D/W annulus**
moderate-temperature transport

→ **D/W spreading**
cooling + crust formation

→ **Sloped deposit**

- In the context of 1F Unit-1, this MCCI-DSP is considered to be a concrete-rich melt.

Knowledge Gaps in Past Studies

- Past severe-accident spreading studies have established a strong foundation, **but key features of the Unit-1 deposition scenario remain outside their scope.**

1 Experimental scope is limited

- VULCANO, ECOKATS: **single-release, short-duration** tests
- Focus on **maximum spreading length** — not long-time morphology

2 Existing spreading codes lack vertical resolution

- MELTSPREAD / THEMA rely on the **shallow-water approximation**
- Cannot resolve vertical **velocity, temperature, or phase** profiles

3 Frontal crust dynamics are unresolved

- Crust under **continuous inflow** + **extended timescales** not well addressed

  → ***the regime that governs Unit-1 deposits***

Research focus and objectives

Research focus

What flow and solidification mechanism produces the observed thickness gradient of Unit-1 D/W deposits?

Assumptions from Unit-1 PCV Internal Investigations

- **Origin**

  Deposit interpreted as an **MCCI-DSP** that **originated inside the pedestal** and relocated / solidified in the D/W annulus.

+

- **Material Properties**

  Thermal physical properties close to molten concrete (composition not yet uniquely constrained).

↓ Based on these assumptions, the deposit mechanism is investigated

Research objectives

Clarify the **frontal crust dynamics** under **continuous inflow** + extended timescales

Moving Particle Semi-implicit (MPS) Method

Basics of MPS method : Lagrangian particle method

No mesh; Fluid treated as a set of particles; Each particle carries mass, momentum, and enthalpy.

Discretization by particle interaction

Gradient, divergence, and Laplacian operators approximated using neighbor particles within an influence radius (r_e) , weighted by ***w(r)***.

Fit for free-surface, large-deformation flows

Handles solid–liquid phase change accompanied by flow heat transfer

Multiphase MPS with corrective matrix (Duan et al. 2019) — stable & accurate at high viscosity, suitable for crust formation.

Governing Equations

Mass

$$\frac{D\rho}{Dt} = -\rho\nabla.\mathbf{u} = 0$$

Navier-Stokes

$$\rho\frac{D\mathbf{u}}{Dt} = -\nabla P + \mu\nabla^2\mathbf{u} + \rho\boldsymbol{g} + \boldsymbol{f}$$

Energy

$$\rho\frac{Dh}{Dt} = k\nabla^2 T + Q$$

Weight Function

$$w(r) = \begin{cases} \left(\frac{r_{ij}}{r_e} - 1\right)^2, & 0 \le r_{ij} < r_e \\ 0, & r_e \le r_{ij} \end{cases}$$

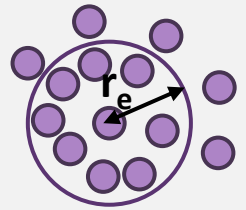

Particle Interaction Models

Gradient:

$$\langle\nabla\phi\rangle_i = \frac{1}{n_0}\sum_{\mathbf{j}\neq i}\left\{w_{ij}\frac{\phi_j - \phi_i}{r_{ij}}\left(\begin{bmatrix}\mathbf{C}_1\\ \mathbf{C}_2\\ \mathbf{C}_3\end{bmatrix}P\right)\right\}$$

Laplacian:

$$\langle\nabla^2\phi\rangle_i = \frac{1}{n_0}\sum_{\mathbf{j}\neq i}\left\{w_{ij}(\phi_j - \phi_i)\frac{[\mathbf{C}_4 + \mathbf{C}_5 + \mathbf{C}_6]P}{l_0 r_{ij}}\right\}$$

[1] G. Duan, A. Yamaji, and S. Koshizuka, "A novel multiphase MPS algorithm for modeling crust formation by highly viscous fluid for simulating corium spreading," *Nucl. Eng. Des.*, vol. 343, pp. 218–231, 2019.

Free surface cooling, Viscosity & Crust models

Free surface cooling: source term Q of Energy equation

Convective cooling (Newton cooling law)

$$q_c = h_c(T_i - T_\infty)$$

q_c, q_r: Heat flux T_i: Temperature of free surface,

h_c : convective heat transfer coefficient (W/m²/K), current study used 10 (W/m²/K)

T_∞, T_b: atmosphere, background Temperature, current study used 573 K.

Radiative heat loss (Stefan-Boltzmann Law)

$$q_r = \sigma\varepsilon(T_i^4 - T_b^4)$$

σ : Stefan-Boltzmann constant, 5.67×10^{-8} W·m^{-2}·K^{-4}

ε: Emissivity, current study used **0.5**

μ_{crust}: Solid viscosity, current study used **10^5 (Pa·s)**

μ_l : Liquid viscosity （Pa·s）

γ : Solid fraction (linearly changes between solidus and liquidus)

γ_{th} : Threshold solid fraction when crust forms / melts

C : Empirical parameter, current study used **6**

Phase change and temperature/solid-fraction-dependent viscosity and crust immobilization model

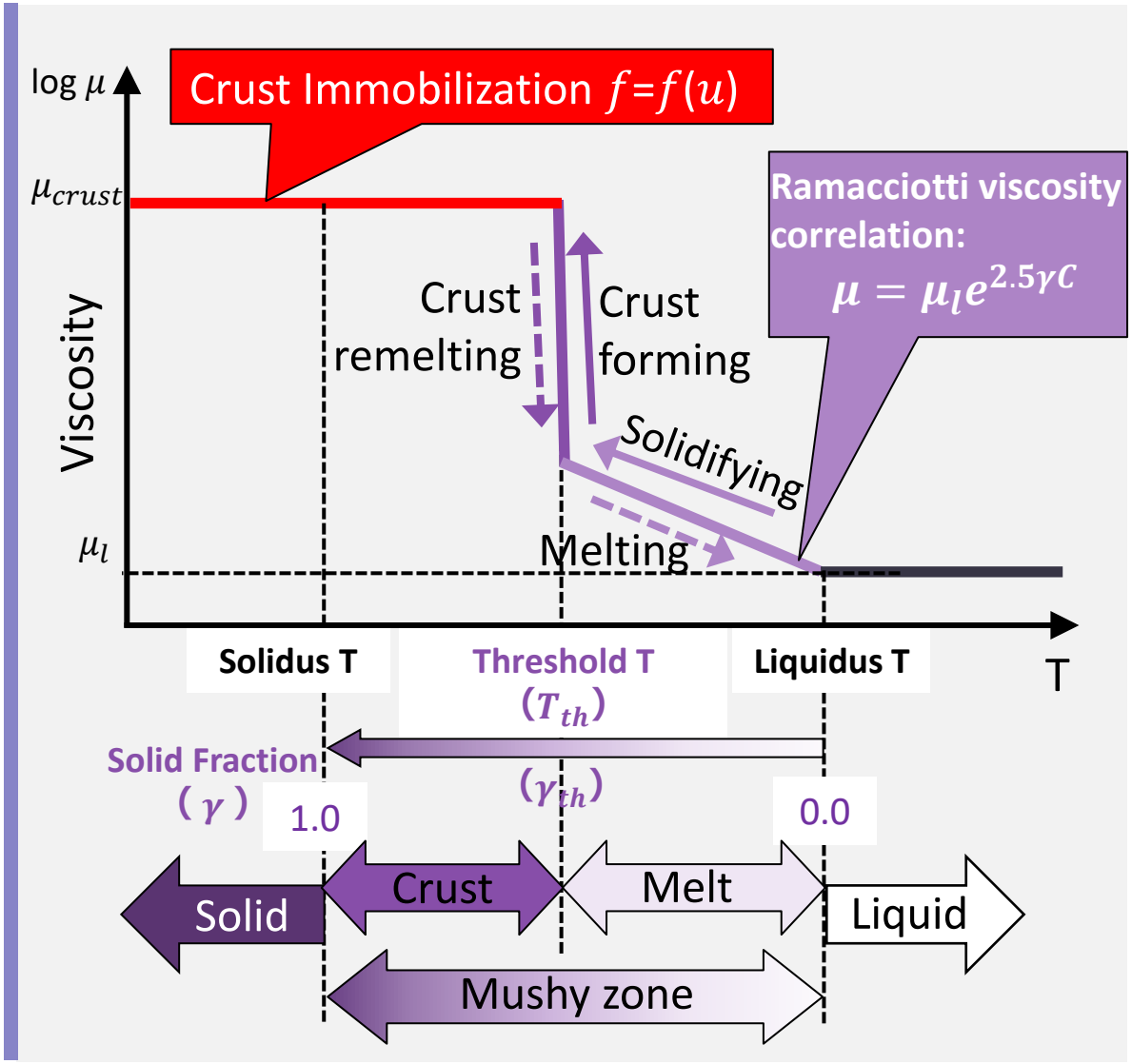

[1] Ramacciotti, M., et al., 2001. Viscosity models for corium melts. Nuclear engineering and design, 204(1-3), pp.377-389.

Simulation Initial Conditions and Boundary Conditions

2D MPS simulation — circumferential slice of Unit-1 D/W annulus

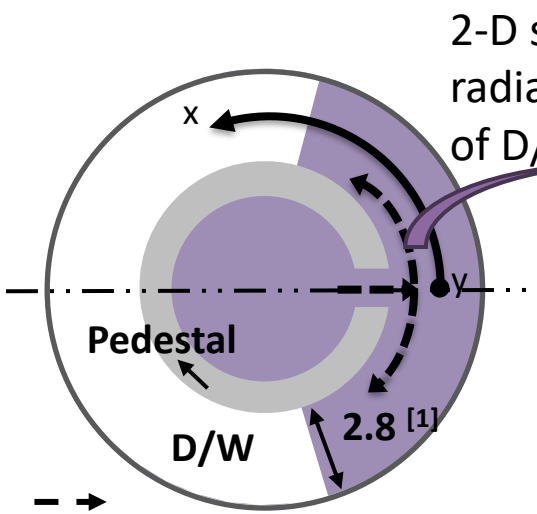

2-D slice of the radial cross-section of D/W annulus

MCCI-DSP relocation path (assumed)

- **Top view of Unit-1 D/W**

2-D MPS geometry

Unit : m

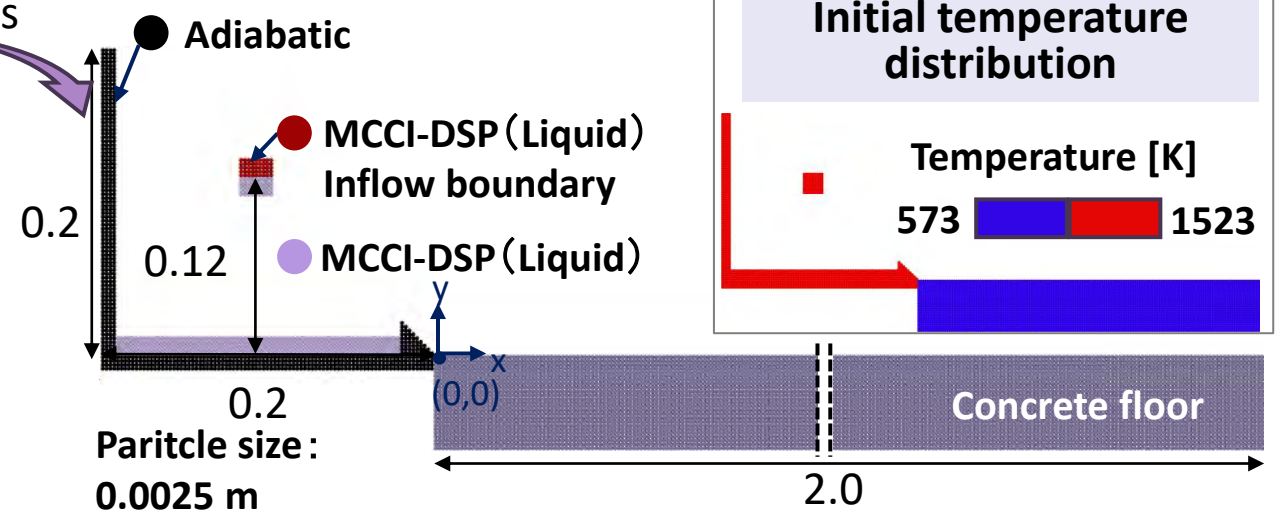

Paritcle size : 0.0025 m

Simulation boundary conditions

Boundary conditions	Value
Convective heat transfer coefficient (W/m²/K)	10
Atmosphere / Background Temperature (K)	573
Inflow velocity (m/s)	0.016*

*Inflow velocity scaling

Total power of debris (Decay power without gaseous and volatile FPs ≈7MW) ÷ **Concrete ablation Enthalpy** (Decomposition enthalpy 1779 kJ/kg)

≈ **Generated melt mass rate** (≈ 4 kg/s)

Equally divided from pedestal opening (half D/W annulus) = 2.0 kg/s.

[1] Robb, Kevin R., et al. ORNL/TM-2014/1 (2014).

Thermal-Physical properties and Simulation cases

Thermal-physical properties	Basaltic Concrete	MCCI-DSP
Density (kg/m³)	2240	〃
Specific heat (J/kg/K)	1250 [2]	
Fusion heat (J/kg)	4.425 x 10^5 [2]	〃
Emissivity	-	0.5
Thermal conductivity (W/m/K)	2.5	〃
Solidus T (K)	1350 [3]	〃
Liquidus T (K)	1650 [3]	1523 (Tentative)
Threshold temperature for flowability T_{th} (K)	-	1473 [4]

Sensitivity cases: Liquid bulk viscosity

Cases	Viscosity range before solidification ($\gamma<\gamma_{th}$) (Pa・s)
Low viscosity	5 x 10^{-3} to ~1.0 (Image : Water to Gum syrup)
High viscosity	22.4 [5] to ~10^3 (Image: Mayonnaise to Dry paste)

Viscosity・Crust Freezing Model

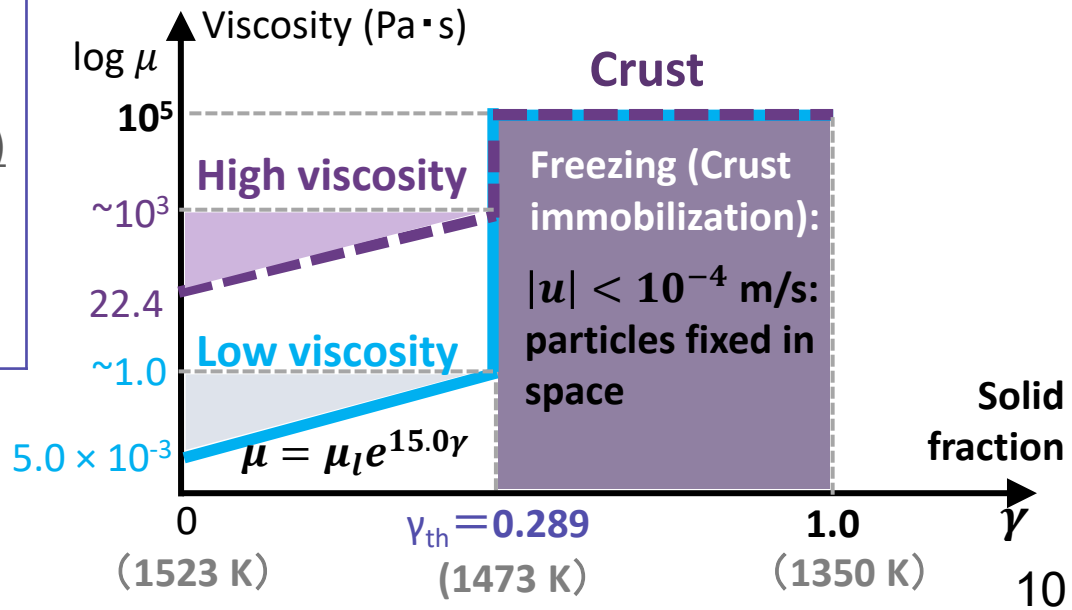

[1] Ramacciotti et al., NED (2001). [2] Sevón, VTT Rep. (2005).
[3] Farmer, ANL-18/22 (2018).
[4] Ida et al., Cement Science and Concrete Technology (2024).
[5] Viscosity of basalt : Ramacciotti et al., NED (2001).

Results – Spreading Length Histories

Cases ID		Liquid bulk viscosity μ_l (Pa·s)	Crust Freezing Criterion
LV-F	Low Viscosity – Freezing	5×10^{-3}	ON
LV-NF	Low Viscosity – No Freezing	5×10^{-3}	OFF
HV-F	High Viscosity –Freezing	22.4	ON

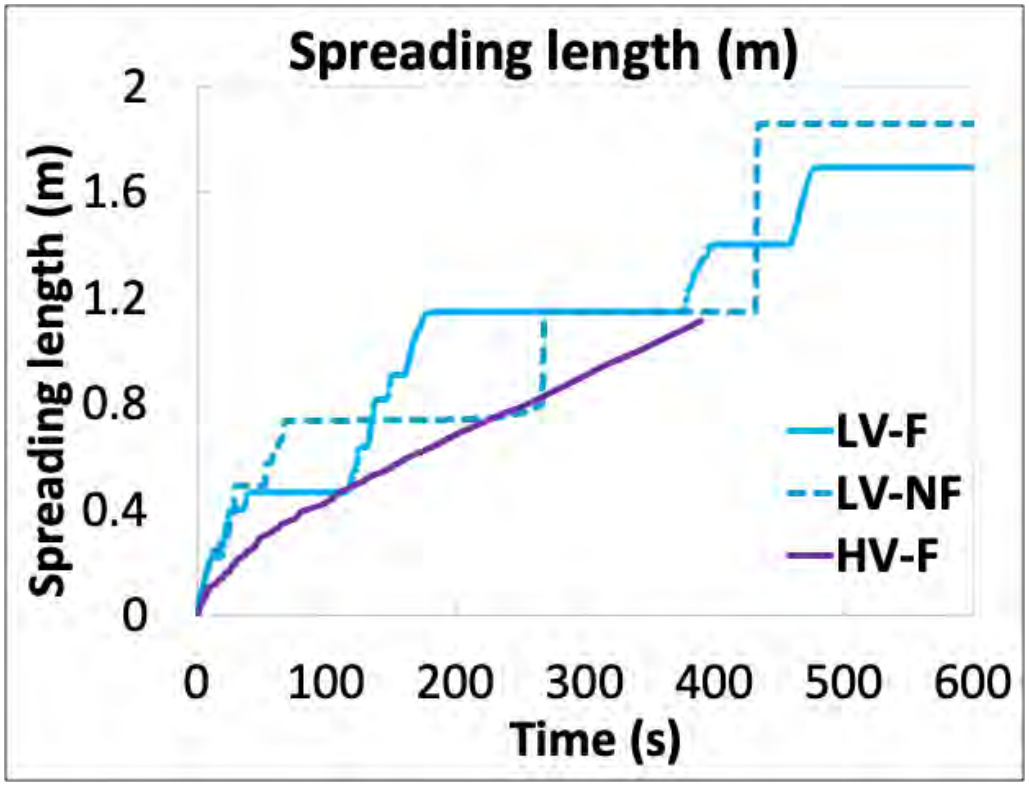

History of the leading-edge position of MCCI-DSP spreading: low and high viscosity cases.

- **Low-Viscosity Cases**
  - **Intermittent Advance ("Stop-and-Go")**
  - Thin melt is temporarily blocked by frontal crust, then resumes via overriding or pushing through.
- **High-Viscosity Case**
  - **Continuous Advance (No stagnation)**
  - The thicker spreading melt is not blocked by the crust.
- **Impact of Time Evolution & Crust Anchoring (LV cases)**
  - **Early Phase (< 50 s)**: **Negligible effect**; crust is underdeveloped.
  - **Later Phase (> 50 s)**: **Significant effect**; developed crust and its anchoring strongly influence the results.

LV-F: Early Stop & Go Cycles (0 – 50 s)

Cases ID		Liquid bulk viscosity μ_l (Pa·s)	Crust Freezing Criterion
LV-F	Low Viscosity – Freezing	5 x 10^{-3}	ON

- **Early phase: Frontal-crust formation (Stop) and Remelting (Go)**

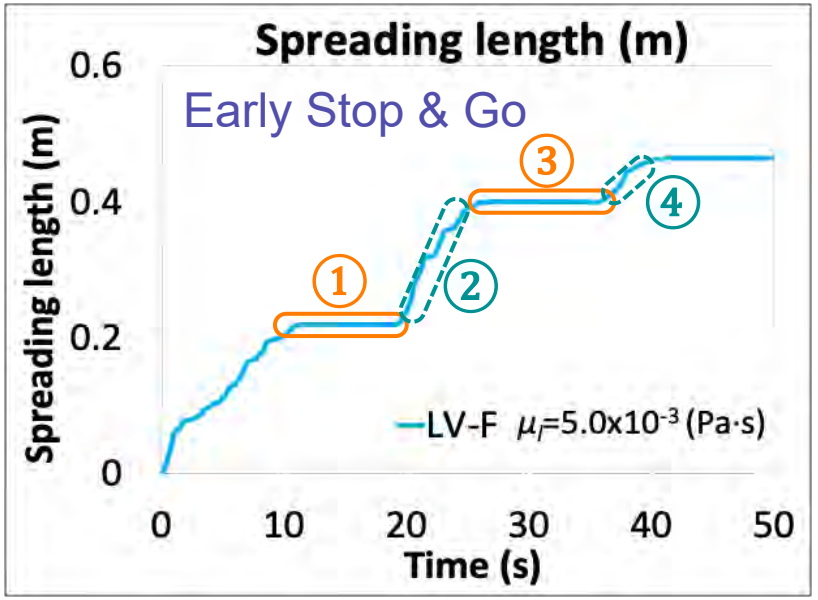

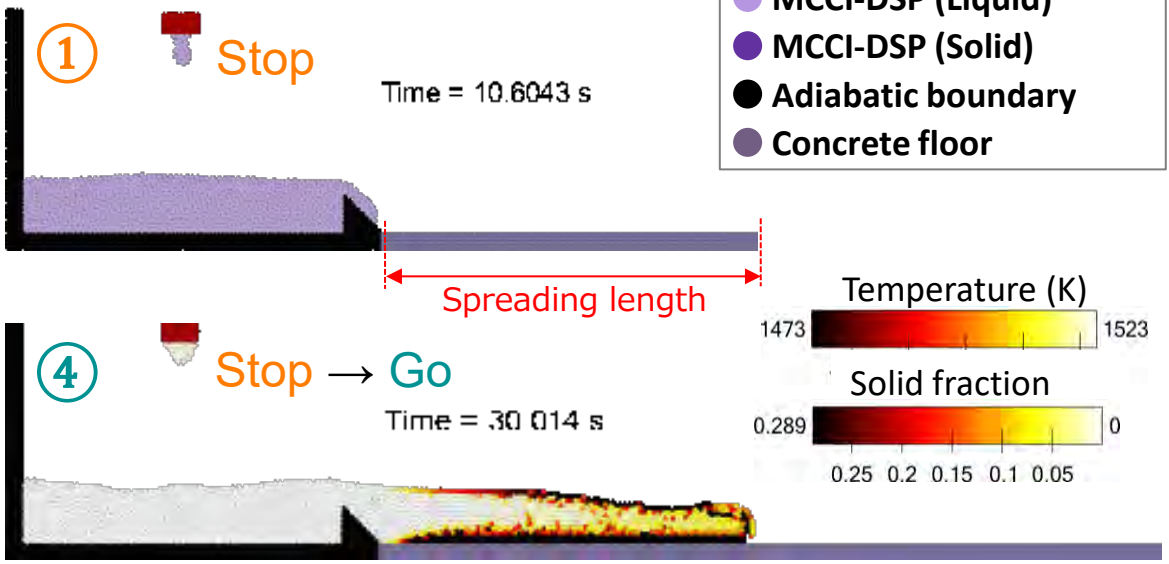

Stop **Temporary halts of melt front advance (①③ in above figure)**

Melt front advance is obstructed by **thin frontal crust formation**.

Go **Resumption of melt front advance (②④ in above figure)**

Melt front advance resumes via **crust remelting** driven by upstream heat.

Mechanism

- Insulating upper crust sustains high-temperature bulk flow.
- Stop-and-go advance of the leading edge driven by crust formation/remelting.

LV-F: Slope Formation & Overriding (> 50 s)

Later phase: Persistent slope forms → Rigid crust supports the hydrostatic head without deformation.

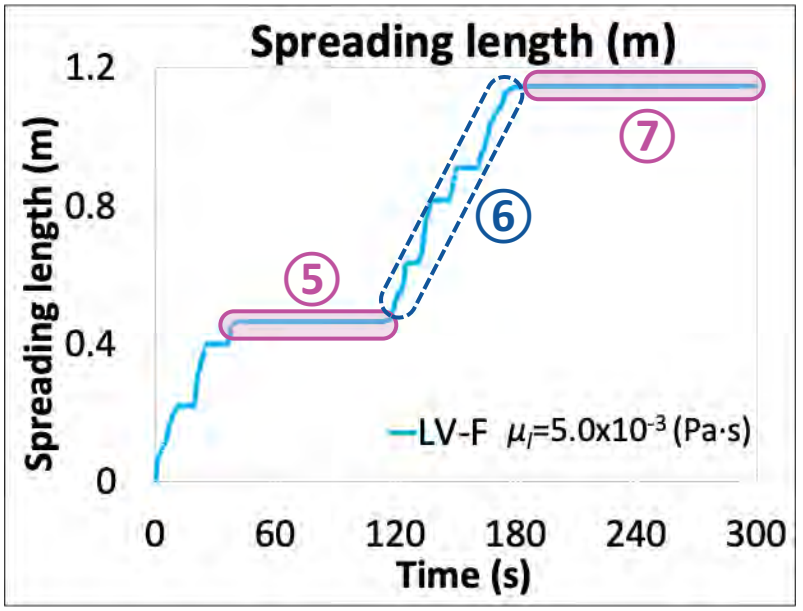

⑤ Stop-2 **Long stagnation & Slope formation**

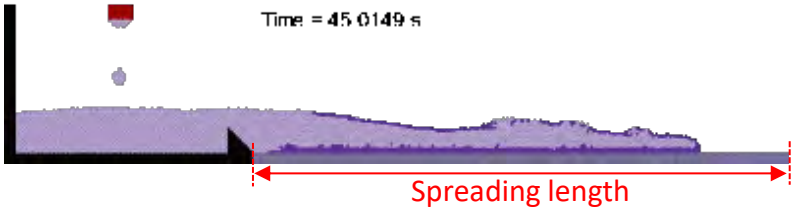

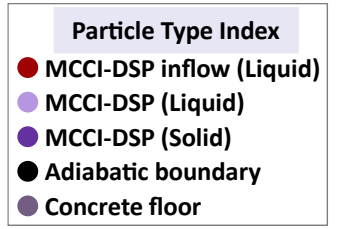

⑥ Go-2 **Flow resumption by overriding**

→ Melt flow path

Slope-formation mechanism

Frontal crust develops & fixed in space → effectively rigid "dam"

↓

Continued inflow piles up behind the dam → thickness gradient grows

↓

Hot interior melt eventually overrides the immobilized front → new advance, new crust

Cycle repeats → leaves a persistent thickness gradient profile (slope)

Stop-2 **Long stagnation & Slope formation (⑤⑦ in above figure)**

Slope grows via continuous inflow during front stagnation.

Go-2 **Resumption of melt front advance by overriding (⑥ in above figure)**

Melt overrides the sloped crust, advancing as a thin layer.

LV-F vs. LV-NF: Crusts Fixed in space vs. Not Fixed

Cases ID		Liquid bulk viscosity μ_l (Pa·s)	Crust Freezing Criterion
LV-F	Low Viscosity – Freezing	5×10^{-3}	ON
LV-NF	Low Viscosity – No Freezing	5×10^{-3}	OFF

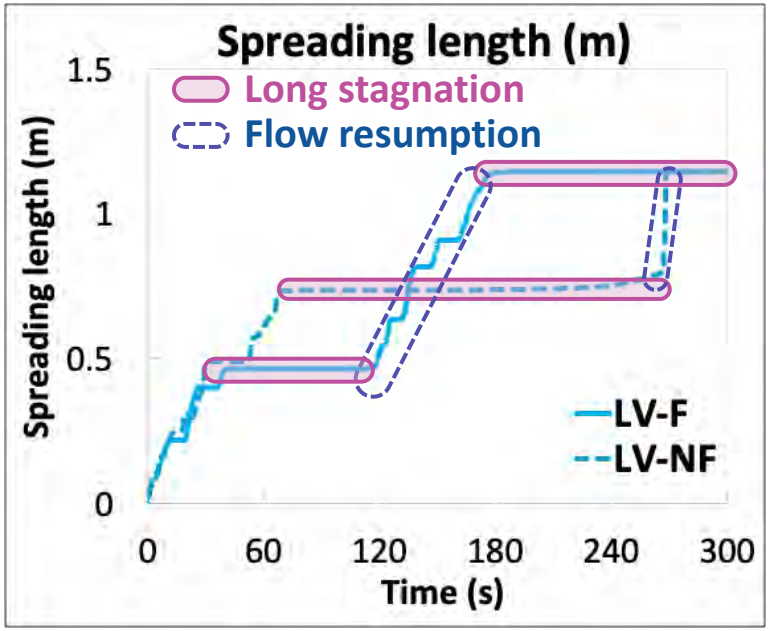

LV-F: Crust fixed in space

Long stagnation → Slope forms

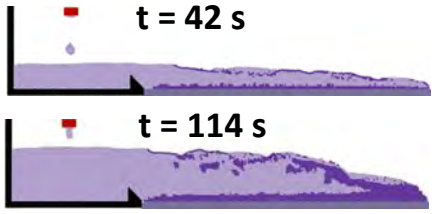

Flow resumes → Persistent slope

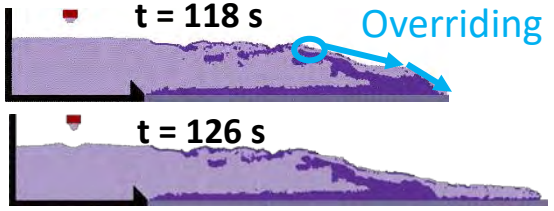

Slope forms & persists

LV-NF: Crust Not Fixed in space

Long stagnation → crust creeps, slope relaxes

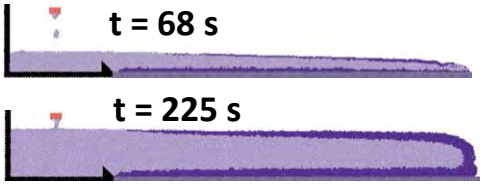

Flow resumes → No slope

Advance resumes by pushing the frontal crust

Slope flattens — not sustained

Particle Type Index
- MCCI-DSP inflow (Liquid)
- MCCI-DSP (Liquid)
- MCCI-DSP (Solid)
- Adiabatic boundary
- Concrete floor

LV-F (Crust fixed in space): Immobilized frontal crust acts as a rigid barrier to the continuous inflow, building and preserving the slope during overriding.

LV-NF (Crust Not Fixed in space): Crust is a highly viscous but mobile Newtonian fluid; Hydrostatic pressure drives slow creep, flattening the slope.

HV-F: High Liquid Bulk Viscosity, Freezing ON

Cases ID		Liquid bulk viscosity μ_l (Pa·s)	Crust Freezing Criterion
LV-F	Low Viscosity – Freezing	5×10^{-3}	ON
HV-F	High Viscosity – Freezing	22.4	ON

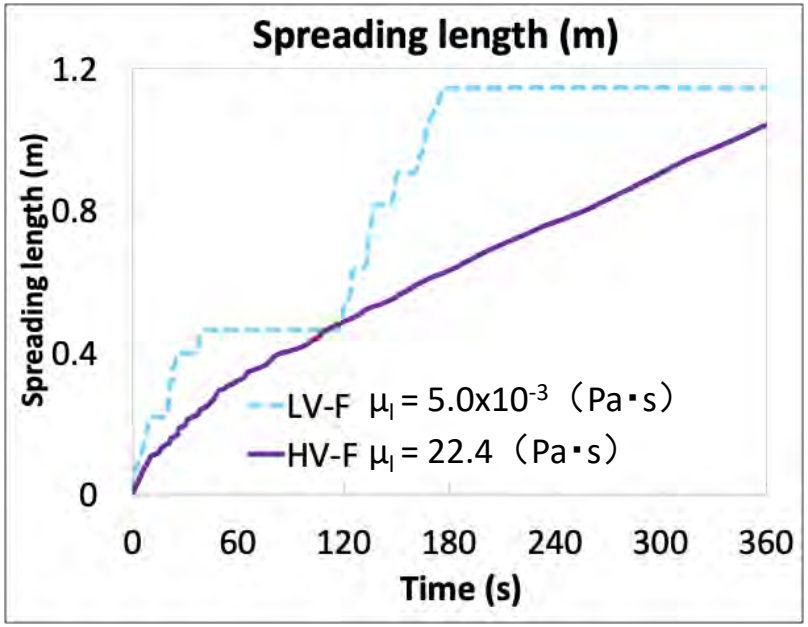

High viscosity : Continuous advance

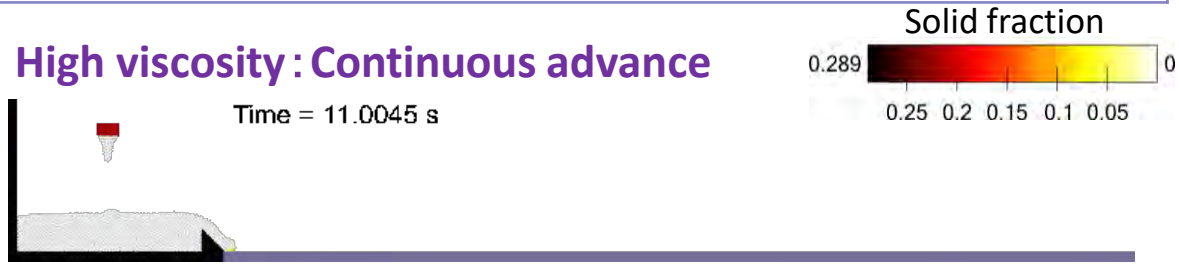

Velocity magnitude distribution (t = 320 s)

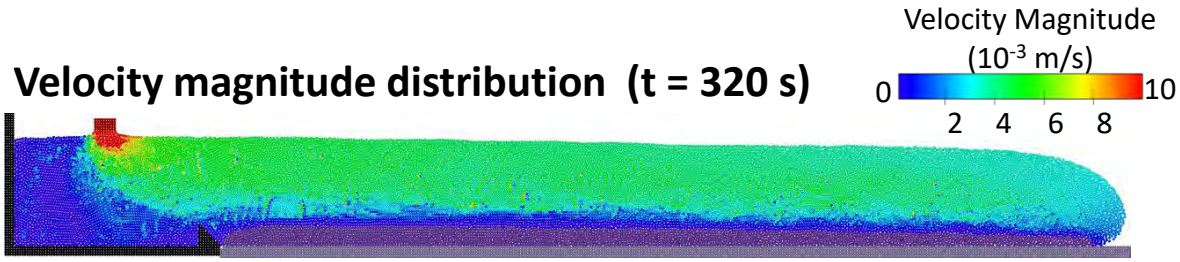

Efficient momentum diffusion with low velocity gradient

→ **Crust moves together with the bulk melt**

→ **Relative uniform thickness**

High viscosity case characteristics

- **High bulk viscosity** (μ_l = 22.4 Pa·s) enables efficient momentum diffusion from interior to front.
- **Viscous interior physically drags the forming crust forward**, keeping its velocity above the freezing threshold $|u| < 10^{-4}$ m/s.
- Although **the crust freezing criterion** is active in the simulation, it is **essentially never triggered**.

Continuous creep, uniform thickness → ✕ No slope formation

Conclusion: MPS Findings & Implication to Unit-1

MPS simulation results — which case reproduces the observed slope?

LV-F *Low μ + crust anchoring* ✓

Sustained slope by Stop & Go

✓ *Matches Unit-1*

LV-NF *Low μ + mobile crust* ✗

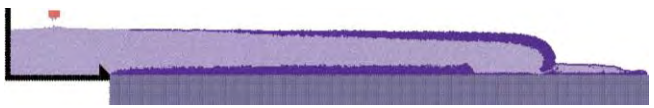

Creep flattens the slope

X Cannot sustain slope

HV-F *High μ → crust drags* ✗

Continuous, uniform spreading

X No slope formation

Three Requirements for Sustained Slope Formation

1 Viscosity contrast

$\mu_{bulk} \ll \mu_{crust}$

Sufficient viscosity contrast prevents the interior melt from dragging the frontal crust, allowing it to anchor.

2 Crust anchoring

non-creeping front

Crust anchors to the floor and sustains a hydrostatic head — no creep relaxation under gravity.

3 Continuous Inflow

1F-specific

Sustained supply during stagnation drives upstream thickness build-up — unlike short spreading tests.

Implication for Unit-1 D/W deposits

- **Possible Unit-1 Deposit Formation Process:**

  Highly fluid MCCI-DSP ➔ Cooling ➔ Rigid frontal crust formation ➔ crust anchoring against gravitational leveling ➔ sustained slope

Thank you for your attention!

Questions & discussion welcomed!

Acknowledgments

This study has been performed by the funds from Japanese Ministry of Economy, Trade, and Industry as The Subsidy Program “Project of Decommissioning, Contaminated Water and Treated Water Management (Development of Analysis and Estimation Technologies for Characterization of Fuel Debris)” starting FY2025.

Xin Li — li.xin@jaea.go.jp · Japan Atomic Energy Agency

An advanced graph neural network application to highly viscous Newtonian fluid flow towards the rapid corium spreading simulation

***Ryo Yokoyama, Hiroki Asatsuma, Shuichiro Miwa, Koji Okamoto**
The University of Tokyo
Corresponding Address
yokoyama@vis.t.u-tokyo.ac.jp;miwa@n.t.u-tokyo.ac.jp ; okamoto@n.t.u-tokyo.ac.jp

ABSTRACT

Ex-vessel corium spreading is one of the most critical phenomena in nuclear safety. Because large-scale experiments are difficult to conduct, numerical simulations—particularly those based on the Lagrangian particle method—are widely employed, as this approach is well suited for phenomena involving large deformations. However, conventional corium spreading simulations remain highly computationally expensive, as they rely on implicit algorithms to stabilize the viscosity term and to solve the pressure Poisson equation (PPE) in the momentum equation. Consequently, even with parallel computation, simulating the entire process requires considerable computational time.
To overcome these limitations and achieve significant acceleration of corium spreading simulations, this study proposes an advanced graph neural network (GNN)-assisted particle method. Instead of explicitly computing mathematical operators such as gradients, divergences, and Laplacians through neighbor particle interactions, the Lagrangian particle coordinates are reorganized into graph structures, enabling efficient learning-based approximations of particle interactions. The GNN is trained to learn and reproduce these graph structures using datasets generated by our in-house moving particle hydrodynamics (MPH) code.
To validate the proposed method, the dam-break problem—one of the representative benchmark cases—was simulated using the GNN-particle method in both 2D and 3D. The results show that the total RMSE was on the order of 1×10^{-4}, demonstrating that the GNN-particle method can accurately reproduce the results of the conventional particle method. Furthermore, in terms of computational performance, the GNN-particle method achieved nearly a 40-fold speed-up compared to OpenMP parallel computation and even outperformed OpenACC GPU computing. These findings indicate that the proposed method provides substantial computational efficiency, paving the way toward real-time simulation in the near future.

KEYWORDS
Deep Learning, Machine Learning, Neural Networks, Corium spreading, CFD

1. INTRODUCTION

Corium spreading is a crucial phenomenon during severe accidents because it governs the initial distribution of molten material and strongly influences subsequent processes such as molten core–concrete interaction (MCCI) [1]. Although several prototype experiments have been conducted [2], numerical simulation remains essential for deepening mechanistic understanding, as it enables visualization of transient flow behavior and quantitative evaluation of key metrics (e.g., run-out distance, thickness evolution, and thermal–hydraulic loads). In particular, Lagrangian particle methods have been widely applied to corium spreading because they naturally capture large deformation and free-surface flows [3]. However, applying Lagrangian methods to highly viscous corium spreading is computationally demanding. Severe time-step restrictions imposed by the Courant–Friedrichs–Lewy (CFL) condition and viscous diffusion constraints often necessitate fully implicit treatments for both the pressure field and the viscous term, resulting in prohibitively high computational cost and limiting applicability to real-scale analyses.

*

In parallel, machine-learning-based surrogate modeling has attracted considerable attention as a promising strategy to reduce the computational cost of conventional CFD. Most existing work has focused on Eulerian, grid-based solvers, where convolutional neural networks (CNNs) and related architectures are used to learn flow-field mappings, predict temporal evolution, or accelerate key sub-solvers such as the pressure Poisson equation (PPE) . For example, Guo et al. applied CNNs to infer velocity fields around vehicle geometries [4]. Tompson et al. proposed a hybrid pipeline that alternates the pressure projection step with a CNN-based surrogate to accelerate incompressible flow simulations [5]. Kim et al. employed generative models to reconstruct high-resolution flow fields from coarse CFD results [6].

More recently, surrogate modeling for Lagrangian particle simulations has progressed rapidly with the emergence of graph-based architectures. Graph neural networks (GNNs) can learn particle interactions from trajectory data by representing particles as nodes, neighbor relations as edges, and updating latent states through message passing [7]. Sanchez-Gonzalez et al. (2020) introduced the Graph Network–based Simulator (GNS), which learns fluid-particle dynamics from SPH trajectories [7]. Nevertheless, most prior learned simulators are largely data-driven, and their internal representations are not readily interpretable in terms of the governing equations, which can limit robustness and generalization. In addition, existing studies have predominantly targeted low-viscosity flows, whereas surrogate modeling for highly viscous Newtonian fluids—central to corium spreading—remains largely unexplored.

In this study, we propose a physics-informed GNS that explicitly incorporates discretized governing equations within the graph network to improve robustness and extrapolation capability. Training datasets are generated using a moving particle hydrodynamics (MPH) solver [8,9] for multiple scenarios, including dam-break, box drop, a static water column, and flows over complex geometries. We first present the baseline GNN architecture and then introduce a momentum-equation-constrained, physics-informed formulation on particle graphs. The proposed model is evaluated by comparing predicted run-out distance, pressure histories, and root mean squared error (RMSE) against the reference MPH simulations. Finally, we assess extrapolative performance by predicting cases beyond the training distribution using the trained model.

2. CFD model

The governing equation of the MPH method is consisting of momentum equation

$$\frac{\mathrm{D}\mathbf{u}}{\mathrm{Dt}} = -\frac{1}{\rho_0}\nabla p + \nu\nabla^2\mathbf{u} + \mathbf{g}, \tag{1}$$

and pressure equation for incompressible control

$$p = -\lambda\nabla\cdot\mathbf{u} + \kappa\frac{\Delta\rho}{\rho_0}, \tag{2}$$

where ρ_0, u, p , ν, g, λ, and κ, correspond to the density, pressure, kinematic viscosity, gravity acceleratio n, bulk viscosity, and bulk modulus, respectively.

The MPH method proposes the following interaction models between particles i and j for the discretizatio n of the gradient, divergence, and Laplacian operators, respectively.

$$\nabla\phi = \sum_j (\phi_j + \phi_i) r_{ij} \frac{w'_{ij}}{|r_{ij}|}, \tag{3}$$

$$\nabla \cdot \mathbf{\Pi} = \sum_j \left(\mathbf{\Pi}_j - \mathbf{\Pi}_i\right) \cdot r_{ij} \frac{w'_{ij}}{|r_{ij}|}, \tag{4}$$

$$\nabla^2 \phi = 2 \sum_j \left(\phi_j - \phi_i\right) \frac{w'_{ij}}{|r_{ij}|}, \tag{5}$$

where the terms ϕ and Π are an arbitrary scalar parameter and an arbitrary vector, respectively. The term w'_{ij} represents the derivative of the normalized weight function w_{ij}, which are defined as:

$$w_{ij} = \frac{W_{ij}}{\sum_j W_{ij}}, \tag{6}$$

$$W_{ij} = \begin{cases} (r_e - r_{ij})^2 \ ; \ (r_{ij} < r_e) \\ 0; (r_{ij} > r_e) \end{cases}, \tag{7}$$

$$w'_{ij} = -\frac{\partial w(r)}{\partial r}, \tag{8}$$

where W_{ij} , r_e, and r_{ij} are weight function, the effective radius and the distance between particles *i* and *j*, r espectively. The governing equations (Eqs. (1)-(2)) are discretized with the particle interaction models (Eq s.(3) - (5)) as

$$\frac{\mathrm{D}\mathbf{u}}{\mathrm{Dt}} = -\frac{1}{\rho_0} \sum_j \left(p_j + p_i\right) \frac{r_{ij}}{|r_{ij}|} w'_{ij} + 2\nu \sum_j \left(\mathbf{u}_j - \mathbf{u}_i\right) \frac{w'_{ij}}{|r_{ij}|} + \mathbf{g}, \tag{9}$$

$$p_i = -\lambda \sum_j \left(\mathbf{u}_j - \mathbf{u}_i\right) \cdot \frac{r_{ij}}{|r_{ij}|} w'_{ij} + \kappa(n_i - n_0). \tag{10}$$

However, the discretized momentum equation (Eq.(9)) does not conserve the angular momentum. In order to conserve the angular momentum, Eq.(9) is modified as

$$\frac{\mathrm{Du}}{\mathrm{Dt}} = -\frac{1}{\rho_0} \sum_j \left(p_j + p_i\right) \frac{r_{ij}}{|r_{ij}|} w'_{ij} + 2\nu(d+2) \sum_j \left(\frac{\mathbf{u}_j - \mathbf{u}_i}{|r_{ij}|} \cdot \frac{r_{ij}}{|r_{ij}|} \right) \frac{r_{ij}}{|r_{ij}|} w'_{ij} + \mathbf{g}. \tag{11}$$

Here, d is the dimension of the calculation geometry.

In this study, the 1st order explicit Euler time integration is applied to estimate the acceleration of the each particle. First, the pressure is estimated as

$$p_i^k = -\lambda \sum_j \left(\mathbf{u}_j^k - \mathbf{u}_i^k\right) \cdot \frac{r_{ij}}{|r_{ij}|} w'_{ij} + \kappa(n_i - n_0). \tag{12}$$

By substituting (12) into Eq.(11), the acceleration $\frac{\mathrm{Du}}{\mathrm{Dt}} \sim \mathbf{a}_{data}$ is obtained.

$$\mathbf{a}_{data} \sim \frac{\mathrm{D}\mathbf{u}_i^k}{\mathrm{Dt}} = -\frac{1}{\rho_0}\sum_j \left(p_j^k + p_i^k\right)\frac{r_{ij}}{|r_{ij}|}w_{ij}' + 2\nu(d+2)\sum_j \left(\frac{\mathbf{u}_j^k - \mathbf{u}_i^k}{|r_{ij}|}\cdot\frac{r_{ij}}{|r_{ij}|}\right)\frac{r_{ij}}{|r_{ij}|}w_{ij}' + \mathbf{g}. \quad (13)$$

3. Deep Learning

3.1. Fundamental Graph Neural Networks based simulation

Figure 1 provides an overview of the fundamental GNN framework. In the encoder, the particle system is mapped to a graph representation. Node features consist of scalar and vector quantities associated with each particle, such as velocity and the material property while edge features characterize the interaction between neighboring particles, including the relative displacement and/or distance between particles i and j. Thus, the graph representation explicitly stores both the physical state of each particle and the strength/geometry of its interactions with neighboring particles.

The node feature of particle i at time step k is defined as

$$\mathbf{h}_i^k \equiv \left[\tilde{\mathbf{u}}_i^k, \tilde{\mathbf{u}}_i^{k-1}, \tilde{\mathbf{u}}_i^{k-2}, \tilde{\mathbf{u}}_i^{k-3}, \tilde{\mathbf{u}}_i^{k-4}, \tilde{\Delta}_{wall}^k\right], \quad (14)$$

where $\tilde{\mathbf{u}}_i^k$ is the normalized velocity vector defined as

$$\tilde{\mathbf{u}}_i^k \equiv \frac{\mathbf{u}_i^k}{U} = \left[\frac{\mathrm{u}_i^k}{U}, \frac{\mathrm{v}_i^k}{U}, \frac{\mathrm{w}_i^k}{U}\right]. \quad (15)$$

Here, U is a representative velocity scale. Following prior work, the current and previous four-time steps are included to provide a short velocity history. To encode wall effects, we additionally use the normalized distances to the nearest wall,

$$\tilde{\Delta}_{wall}^k \equiv \left[clip\left(\frac{\Delta x_{i,wall}^k}{R}, 0,1\right), clip\left(\frac{\Delta y_{i,wall}^k}{R}, 0,1\right), clip\left(\frac{\Delta z_{i,wall}^k}{R}, 0,1\right)\right], \quad (16)$$

$\Delta x_{i,wall}^k$, $\Delta y_{i,wall}^k$, and $\Delta z_{i,wall}^k$ denote the x-directional, y-directional and z-directional distances toward the nearest wall, which are normalized with the connectivity radius R and then clipped within the range [0,1].

The edge feature between nodes i and j at time step k is defined as

$$\boldsymbol{e}_{ij}^k \equiv \left[\frac{x_j^k - x_i^k}{R}, \frac{y_j^k - y_i^k}{R}, \frac{z_j^k - z_i^k}{R}, \frac{r_{ij}}{R}\right], \quad (17)$$

where x_i^k, y_i^k, and z_i^k are the coordinate of the node. r_{ij} is the distance between the nodes i and j defined as

$$r_{ij} = \sqrt{(x_j^k - x_i^k)^2 + (y_j^k - y_i^k)^2 + (z_j^k - z_i^k)^2}. \quad (18)$$

Following the encoding, which is the graph construction, the GNN updates the dynamical states through message passing, in which information is exchanged along edges and aggregated at each node to represent neighbor interactions. Specifically, for each edge $\boldsymbol{e}_{ij}$, an edge message is computed from the sender and receiver node features and the edge features, and the incoming messages to node i are aggregated to obtain a neighborhood representation. The node state is then updated using this aggregated message, yielding an updated latent feature for each.

The message passing consists of three stages. An edge message is computed from the receiver and sender node features and the edge attributes:

$$\mathbf{m}_{i,j}^k = \phi_e\left(\mathbf{h}_i^k, \mathbf{h}_j^k, \mathbf{e}_{ij}^k\right). \quad (19)$$

Incoming messages are aggregated to form a neighborhood representation:

$$\bar{\mathbf{m}}_i^k = \sum_{j \in N(i)} \mathbf{m}_{i,j}^k. \quad (20)$$

The node state is then updated with a residual form:

$$\mathbf{h}_i^{k+1} = \mathbf{h}_i^k + \phi_h\left(\mathbf{h}_i^k, \sum_{j\in N(i)} \phi_e(\mathbf{h}_i^k, \mathbf{h}_j^k, \mathbf{e}_{ij}^k)\right), \tag{21}$$

The edge message function ϕ_e learns how information is exchanged between neighboring particles. It takes as input the receiver-node features $\mathbf{h}_i^k$, the sender-node features $\mathbf{h}_j^k$, and the edge attributes $\mathbf{e}_{ij}^k$, and outputs a latent message $\mathbf{m}_{i,j}^k$ that encodes the influence of particle j on particle i. In practice, ϕ_e is commonly implemented as a shared multilayer perceptron (MLP) applied to every edge, which ensures permutation equivariance with respect to node ordering and enforces a consistent interaction rule across all particle pairs.

The aggregation step in Eq. (20) then combines the incoming messages to node (i) into a single neighborhood representation $\bar{\mathbf{m}}_i^k$. Summation is widely used because it is permutation-invariant to the ordering of neighbors and naturally reflects the additive structure of many particle interactions. Depending on the targeted behavior, other aggregators such as mean or max pooling may also be employed.

Finally, the node update function ϕ_h integrates the aggregated neighborhood information with the previous node state $\mathbf{h}_i^k$ to produce the updated node feature $\mathbf{h}_i^{k+1}$ in Eq. (21). Similar to ϕ_e, ϕ_h is typically parameterized as a shared MLP (often augmented with residual connections and normalization) and applied identically to all nodes. This message-passing procedure is repeated for M steps to progressively refine the latent particle states.

The updated node features $\mathbf{h}_i^{k+1}$ are then passed to a decoder that maps the latent representation back to physical quantities of interest, such as the acceleration $\mathbf{a}$. These predicted quantities are subsequently used to advance the particle system in time through symplectic Euler scheme as

$$\mathbf{u}_i^{k+1} = \mathbf{u}_i^k + \mathbf{a}_i^k * \Delta t, \tag{22}$$

and

$$\mathbf{x}_i^{k+1} = \mathbf{x}_i^k + \mathbf{u}_i^{k+1} * \Delta t. \tag{23}$$

All the process is conducted to minimize the following the loss function as

$$\mathcal{L}^{data} \equiv \frac{1}{N}\sum_i^N \|\mathbf{r}\|^2 = \frac{1}{N}\sum_i^N \left\|\tilde{\mathbf{a}}_{i,predict}^k - \tilde{\mathbf{a}}_{i,data}^k\right\|^2, \tag{24}$$

where N, $\tilde{\mathbf{a}}_{i,data}^k$ and $\tilde{\mathbf{a}}_{i,predict}^k$ denote all the nodes, the ground truth data on the acceleration, and the predicted acceleration data, respectively.

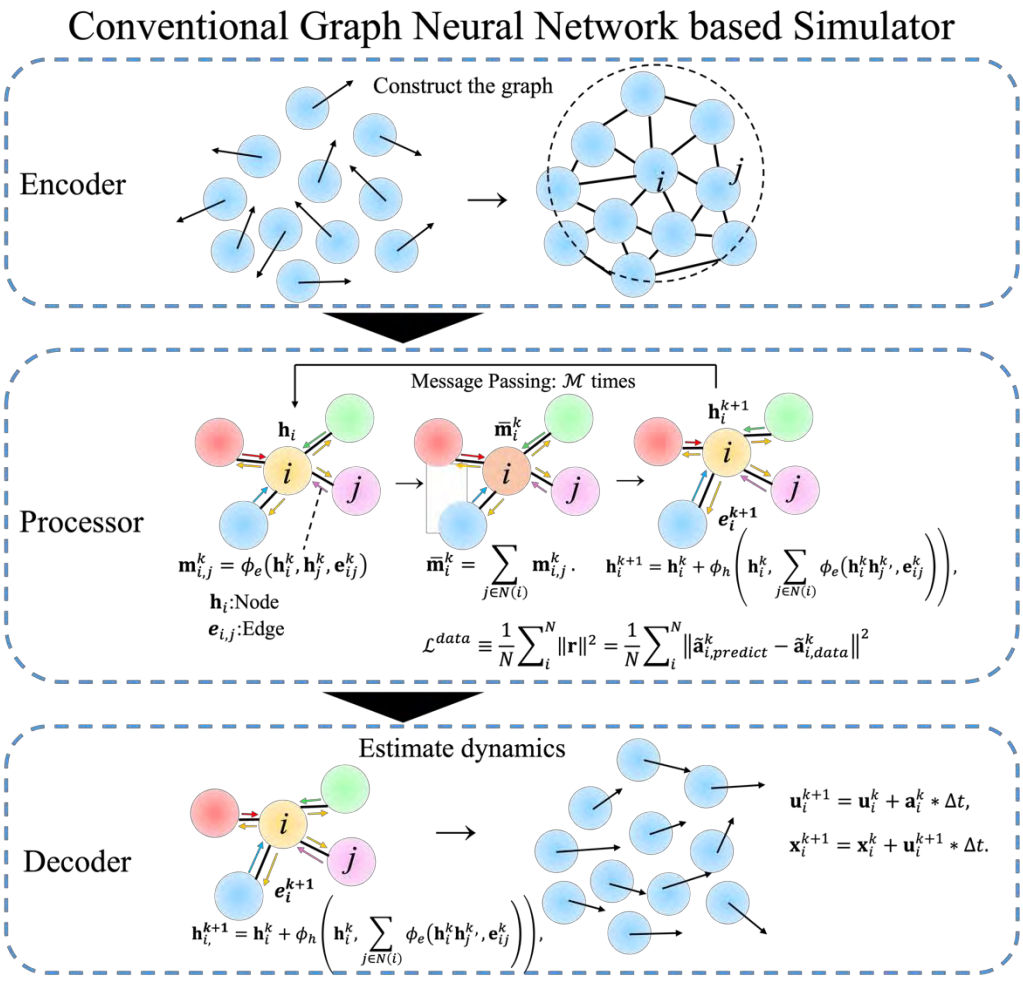

Figure 1 Schematic illustration of the fundamental Graph Neural Networks

3.2. Discretized Momentum-Equation-Constrained Physics-Informed Neural Networks

Since Eq.(1) does not include the pressure as the feature and viscosity which are essential to solve the Navier-Stokes equations, following node features are applied

$$\mathbf{h}_i^k \equiv \left[\tilde{\mathbf{u}}_i^k, \tilde{\mathbf{u}}_i^{k-1}, \tilde{\mathbf{u}}_i^{k-2}, \tilde{\mathbf{u}}_i^{k-3}, \tilde{\mathbf{u}}_i^{k-4}, \tilde{p}_i^k, \tilde{p}_i^{k-1}, \tilde{p}_i^{k-2}, \tilde{p}_i^{k-3}, \tilde{p}_i^{k-4}, \tilde{\Delta}_{wall}^k, \nu_i\right], \tag{25}$$

where $\tilde{p}_i^k$ is the normalized the pressure defined as

$$\tilde{p}_i^k \equiv \frac{p_i^k}{P}, \tag{26}$$

with p_i^k denoting the pressure at node i and time step k, and P a representative pressure scale. The pressure head is trained by minimizing the mean-squared error between the predicted and reference increments:

$$\mathcal{L}^{pressure} \equiv \frac{1}{N}\sum_i^N \|\mathbf{r}\|^2 = \frac{1}{N}\sum_i^N \left\|\Delta\tilde{p}_{i,predict}^{k+1} - \Delta\tilde{p}_{i,data}^{k+1}\right\|^2. \tag{27}$$

In the meantime, we inspire the particle-based discretization models. First, We adopt a smooth radial kernel with connectivity radius R and Eq.(28):

$$n_{ij}^k = exp^{-\left(\frac{(r_{ij}^k)^2}{R^2}\right)}, \tag{28}$$

the normalized graph weight

$$w_{ij}^k = \frac{n_{ij}^k}{\sum_{j\in N(i)} n_{ij}^k}, \tag{29}$$

From the normalized the graph weight, we can compute the graph-based node interaction models. First, we approximate the graph-based gradient operator as:

$$\nabla\phi_i^k = \sum_{j\in N(i)} \left(\phi_j^k - \phi_i^k\right) \frac{\mathbf{r}_{ij}}{(r_{ij})^2} w_{ij}^k . \tag{30}$$

With a similar way, the Laplacian operator is approximated as:

$$\nabla^2\phi_i^k = 2\sum_{j\in N(i)} \left(\phi_j^k - \phi_i^k\right) \frac{w_{ij}}{(r_{ij})^2}. \tag{31}$$

We can define a physics-based estimate of the nodal acceleration as the result of neighbor interactions. For incompressible flow, we write

$$\tilde{\mathbf{a}}_{i,physic}^k = \mathbf{g} + \nu\nabla^2\mathbf{u}_i^k - \frac{1}{\rho_0}\nabla p_i^k. \tag{32}$$

By substituting Eqs. (30) and (31) into Eq.(32),

$$\tilde{\mathbf{a}}_{i,physic}^k = \mathbf{g} + 2\nu\sum_{j\in N(i)} \left(\tilde{\mathbf{u}}_j^k - \tilde{\mathbf{u}}_i^k\right) \frac{w_{ij}}{(r_{ij})^2} - \frac{1}{\rho}\sum_{j\in N(i)} \left(p_j^k - p_i^k\right) \frac{\mathbf{r}_{ij}}{(r_{ij})^2} w_{ij}. \tag{33}$$

Here, $\tilde{\mathbf{u}}^k$ and $\tilde{p}^k$ denote the predicted velocity and pressure used to compute the physics term (i.e., before applying the physics loss). Similar to message passing, the GNN produces predicted states (and thus predicted acceleration) through M processor layers. We impose a physics-consistency loss by minimizing the discrepancy between the model-predicted acceleration and the physics-based acceleration estimate:

$$\mathcal{L}^{Physics} = \frac{1}{N}\sum_i^N \|\mathbf{r}\|^2 = \frac{1}{N}\sum_i^N \left\|\tilde{\mathbf{a}}_{i,predict}^k - \tilde{\mathbf{a}}_{i,physics}^k\right\|^2 . \tag{34}$$

4. Prediction of CFD results with PI-GNN

Figure 2 and Table I. summarize the simulation cases considered in this study: (i) a fundamental dam-break configuration and (ii) a case with a more complex geometry. Training data were generated using our Moving Particle Hydrodynamics (MPH) solver, and the developed GNS was trained on these MPH datasets. Each simulation involved approximately 8,600 particles, with a time step of $\Delta t = 1.0 \times 10^{-5}$ s. Table II is the PI-GNN training conditions.

Figure 3 presents representative snapshots of the dam-break simulation (MPH) and the corresponding PI-GNN predictions. The dynamic viscosity was set to 1.0×10^3 Pa·s and 1.0×10^2 Pa·s, and the color contour indicates the velocity magnitude. For $\mu = 1.0 \times 10^3$ Pa·s, the highly viscous fluid exhibits only limited spreading, as evidenced by both the snapshots and the low velocity levels; the square-shaped fluid body shows little deformation even after $t = 0.6$ s. In contrast, for $\mu = 1.0 \times 10^2$ Pa·s, the spreading behavior is clearly more pronounced than in the $\mu = 1.0 \times 10^3$ Pa·s case. The PI-GNN reproduces the same trend across both viscosities and closely matches the MPH results overall. The RMSE of the acceleration is 1.27×10^{-5} for $\mu = 1.0 \times 10^3$ Pa·s and 6.31×10^{-5} for $\mu = 1.0 \times 10^2$ Pa·s, indicating that the PI-GNN predicts the dam-break dynamics with good accuracy.

Figure 4 shows representative snapshots of the box-drop simulation with a complex geometry and the corresponding PI-GNN predictions. Overall, the PI-GNN captures the main features of the MPH solution. However, for $\mu = 1.0 \times 10^3$ Pa·s, an evident discrepancy appears at $t = 0.6$ s: the MPH simulation shows a relatively low velocity for the small falling object, whereas the PI-GNN predicts a higher velocity. The acceleration RMSE is 6.32×10^{-6} for $\mu = 1.0 \times 10^3$ Pa·s and 1.78×10^{-6} for $\mu = 1.0 \times 10^2$ Pa·s, suggesting that the PI-GNN achieves high predictive accuracy overall despite this localized mismatch.

Figure 5 shows the time histories of the mean displacement, mean velocity, and mean pressure of the dam-breaking fluid body. The PI-GNN reproduces the MPH simulation results well for all three quantities. In th e velocity profile, a small oscillatory behavior appears around $t = 0.6$ s in the PI-GNN prediction, which i s not observed in the simulation.

Figure 6 shows the mean displacement, mean velocity, and mean pressure of the large square box in the co mplicated-geometry case. While the PI-GNN predictions of displacement and velocity remain in good agre ement with the MPH results, the pressure prediction exhibits a noticeable discrepancy compared with the d am-break case.

Table III compares the computational cost of the conventional MPH simulation and the proposed PI-GNN inference, both evaluated on an NVIDIA A100 GPU. A substantial speedup is achieved by the PI-GNN acr oss all tested cases. In particular, the high-viscosity simulations ($\mu = 1.0 \times 10^3$ Pa·s) require very small-ti me steps, leading to long runtimes of 2321.3 s and 1436.8 s on the GPU. In contrast, the PI-GNN performs the full prediction in only 6.54 s and 3.97 s for the corresponding cases, respectively, which corresponds t o an acceleration of nearly 350×. These results highlight the strong potential of the PI-GNN framework for enabling prompt surrogate simulations of highly viscous free-surface flows, and ultimately for acceleratin g practical corium spreading analyses.

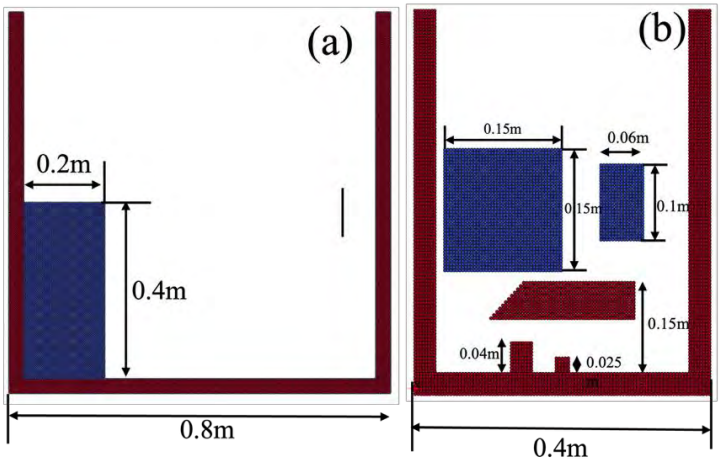

Figure 2 Simulation and PI-GNN prediction geometry

Table I. Simulation conditions

	(a) Dam-break	(b) Box Drop
Particle Size	0.004m	0.004m
Effective Radius	0.010m	0.010m
Bulk Modulus	1.0×10^6 (Pa)	1.0×10^6 (Pa)
Viscosity	1.0×10^3 (Pa.s), 1.0×10^2 (Pa.s)	1.0×10^3 (Pa.s), 1.0×10^2 (Pa.s)
Δt	1.0×10^{-5} (s) for $.0\times10^3$ (Pa.s), 1.0×10^{-4} (s) for 1.0×10^2 (Pa.s)	1.0×10^{-5} (s) for $.0\times10^3$ (Pa.s), 1.0×10^{-4} (s) for 1.0×10^2 (Pa.s)

Table II. PI-GNN parameters

	(a) Dam-break	(b) Box Drop
Batch size	4	4
Noise	6.7×10^{-4}	6.7×10^{-4}
MLP layers	128	128
Graph Radius	0.012m	0.012m

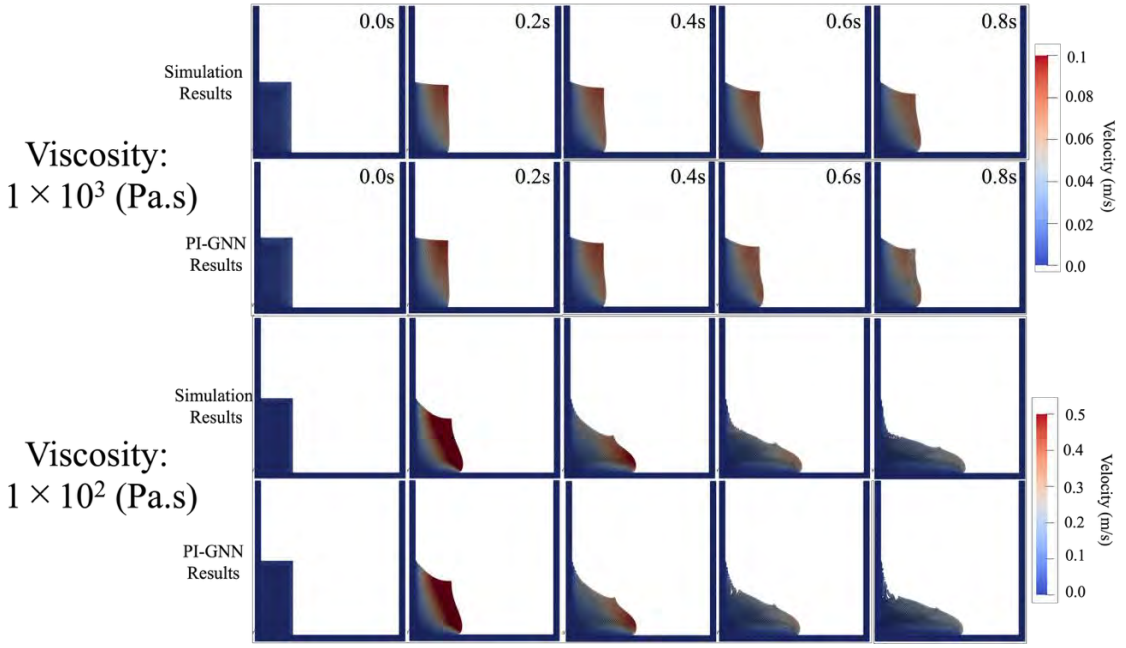

Figure 3 Velocity profile comparison between the CFD and the PI-GNNs prediction during the dam-break

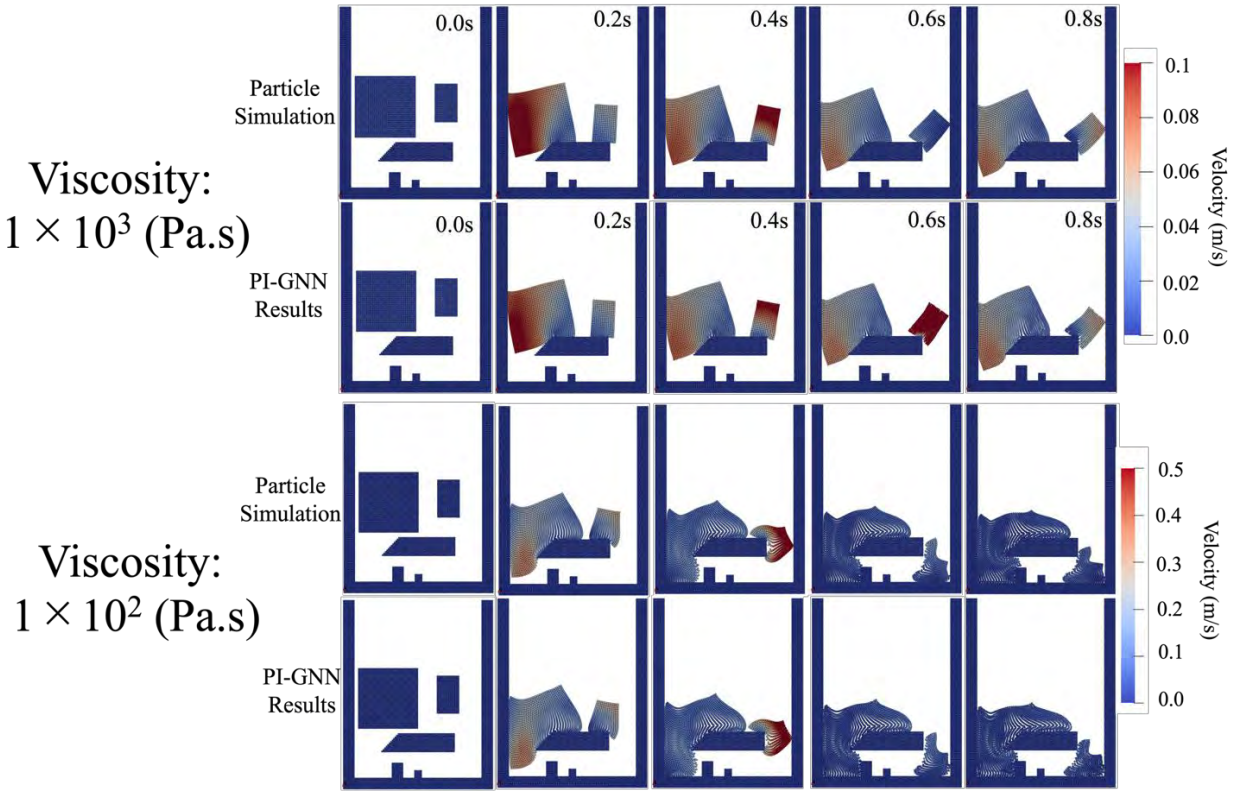

Figure 4 Velocity profile comparison between the CFD and the PI-GNNs prediction on the complicated geometry

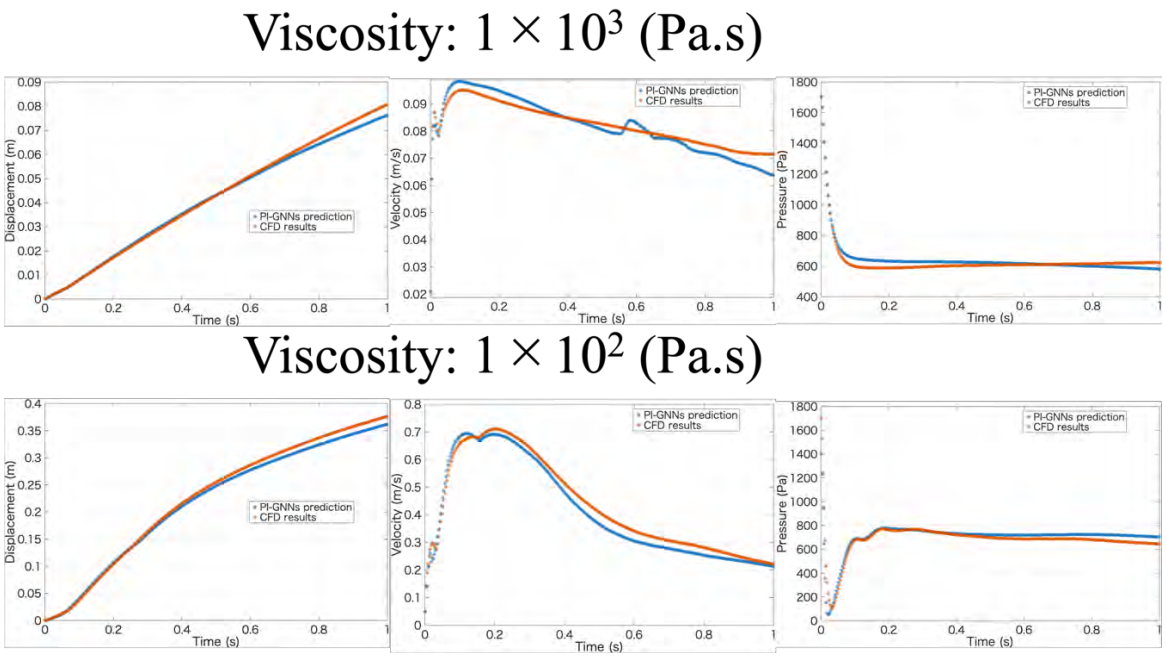

Figure 5 Quantitative comparison with respect to the mean displacement, velocity and pressure of the dam-breaking object

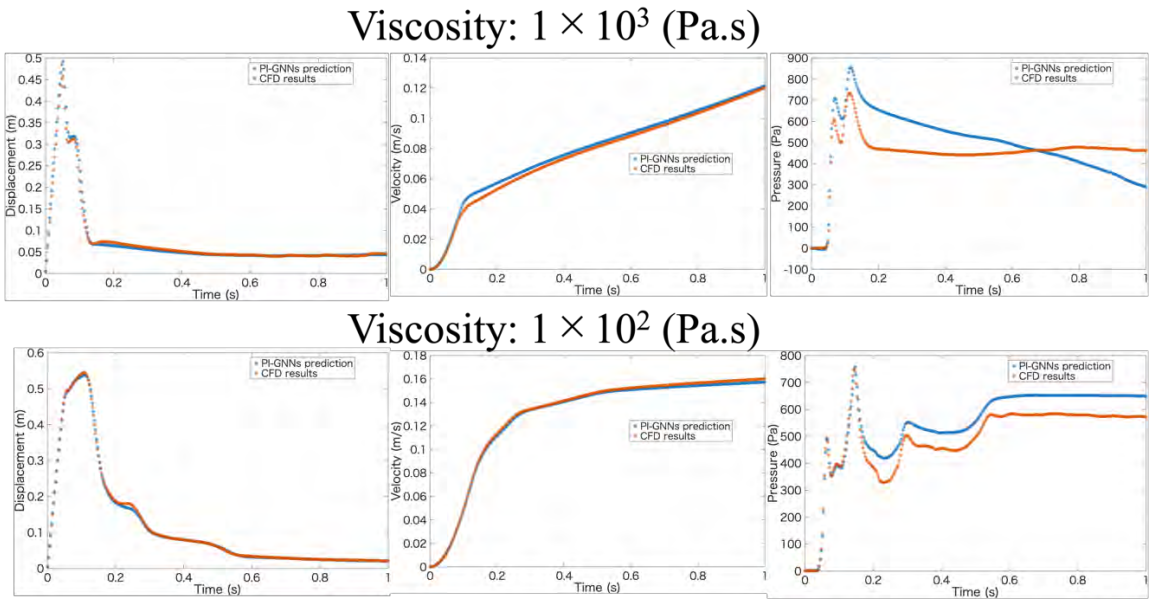

Figure 6 Quantitative comparison with respect to the mean displacement, velocity and pressure of the box drop with complicated geometry

Table III. Calculation time

	CPU	GPU	PI-GNN	Speed-up
Dam-break (1×10^3 Pa.s)	14948.8s	2321.3s	6.543s	354.8 times
Dam-break (1×10^2 Pa.s)	2772.5	469.2s	6.631s	70.8 times
complex geometry (1×10^3 Pa.s)	10149.5s	1436.8s	3.97s	361.9 times
complex geometry (1×10^2 Pa.s)	1078.7s	295.2s	4.046s	73.0 times

5. CONCLUSIONS

This study proposed a physics-informed graph neural network (PI-GNN) surrogate for Lagrangian particle simulations and validated its performance on (i) a fundamental dam-break problem and (ii) a box-drop problem with complicated geometry. By embedding physics-consistent constraints into the message-passing framework, the PI-GNN accurately reproduced the main transient dynamics predicted by the Moving Particle Hydrodynamics (MPH) solver over a wide viscosity range, including highly viscous conditions representative of corium spreading.

For the dam-break case, the PI-GNN captured the viscosity-dependent spreading behavior for $\mu = 1.0 \times 10^3$ Pa·s and $\mu = 1.0 \times 10^2$ Pa·s, showing close agreement with MPH snapshots and low acceleration-based RMSE. In the complicated-geometry case, the PI-GNN similarly reproduced the dominant flow and object motion, although a localized discrepancy was observed around $t = 0.6$ s in the high-viscosity condition, where the velocity of a small falling object was overestimated. Time-history comparisons further indicated that mean displacement and velocity were generally well predicted, while pressure remained more challenging—especially in the complicated-geometry scenario—suggesting that improving pressure robustness is a key remaining issue.

A major outcome is the significant computational acceleration enabled by the PI-GNN. The runtime comparison on an NVIDIA A100 GPU demonstrated that cases requiring extremely small time steps in MPH (e.g., $\mu = 1.0 \times 10^3$ Pa·s) can be predicted in a few seconds by the PI-GNN, achieving nearly $O(10^2$–$10^3)$ speedups (approximately 350× in the present tests). These results demonstrate the strong potential of PI-GNNs to provide prompt, high-fidelity surrogate predictions for highly viscous free-surface flows, and to support practical, large-scale corium spreading assessments.

Future work will focus on improving pressure prediction and rollout stability under complex interactions (e.g., enhanced loss balancing, better boundary/geometry encoding, and multi-step consistency constraints), and extending the framework to more realistic severe-accident conditions, including broader geometries, non-Newtonian behavior, multiphase effects, and phase change.

ACKNOWLEDGMENTS

This work is funded by JSPS KAKENHI grant number JP24K22849. This work was supported by JAEA Nuclear Energy S&T and Human Resource Development Project Grant Number JPJA24H24020026

REFERENCES

1. Dinh, T.-N., Konovalikhin, M. J., & Sehgal, B. R. (2000). Core melt spreading on a reactor containment floor. *Progress in Nuclear Energy*, **36**(4), 405–468. https://doi.org/10.1016/S0149-1970(00)00088-3.
2. Journeau, C., Boccaccio, E., Brayer, C., Cognet, G., Haquet, J.-F., Jégou, C., Piluso, P., & Monerris, J. (2003). Ex-vessel corium spreading: Results from the VULCANO spreading tests. *Nuclear Engineering and Design*, **223**(1), 75–102. https://doi.org/10.1016/S0029-5493(02)00397-7.
3. Koshizuka, S., & Oka, Y. (1996). Moving-particle semi-implicit method for fragmentation of incompressible fluid. *Nuclear Science and Engineering*, **123**(3), 421–434. https://doi.org/10.13182/NSE96-A24205.
4. Guo, X., Li, W., & Iorio, F. (2016). Convolutional Neural Networks for Steady Flow Approximation. In *Proceedings of the 22nd ACM SIGKDD International Conference on Knowledge Discovery and Data Mining (KDD '16)* (pp. 481–490). https://doi.org/10.1145/2939672.2939738.
5. Tompson, J., Schlachter, K., Sprechmann, P., & Perlin, K. (2017). Accelerating Eulerian Fluid Simulation With Convolutional Networks. In *Proceedings of the 34th International Conference on Machine Learning (ICML 2017)*, *Proceedings of Machine Learning Research*, **70**, 3424–3433. https://doi.org/10.48550/arXiv.1607.03597.
6. Kim, B., Azevedo, V. C., Thuerey, N., Kim, T., Gross, M., & Solenthaler, B. (2019). Deep Fluids: A Generative Network for Parameterized Fluid Simulations. *Computer Graphics Forum*, **38**(2), 59–70. https://doi.org/10.1111/cgf.13619.
7. Sanchez-Gonzalez, A., Godwin, J., Pfaff, T., Ying, R., Leskovec, J., & Battaglia, P. W. (2020). Learning to Simulate Complex Physics with Graph Networks. In *Proceedings of the 37th International Conference on Machine Learning (ICML 2020)*, *Proceedings of Machine Learning Research*, **119**, 8459–8468. https://doi.org/10.48550/arXiv.2002.09405.
8. Kondo, M., Fujiwara, T., Masaie, I., & Matsumoto, J. (2022). A physically consistent particle method for high-viscous free-surface flow calculation. *Computational Particle Mechanics*, **9**, 265–276. https://doi.org/10.1007/s40571-021-00408-y.
9. Yokoyama, R., Xu, Y., Miwa, S., & Okamoto, K. (2025). A novel fully explicit GPU-accelerated discrete element method coupled with moving particle hydrodynamics (DEM-MPH) for simulating the underwater particle sedimentation behavior. *Progress in Nuclear Energy*, **180**, 105615. https://doi.org/10.1016/j.pnucene.2025.105615.

ERMSAR 2026

An advanced graph neural network application to highly viscous newtonian fluid flow towards the rapid corium spreading simulation

THE UNIVERSITY OF TOKYO

***Hiroki Asatsuma**, Ryo Yokoyama

Background

Understanding the behavior of highly viscous fluids in severe accidents is critically important.

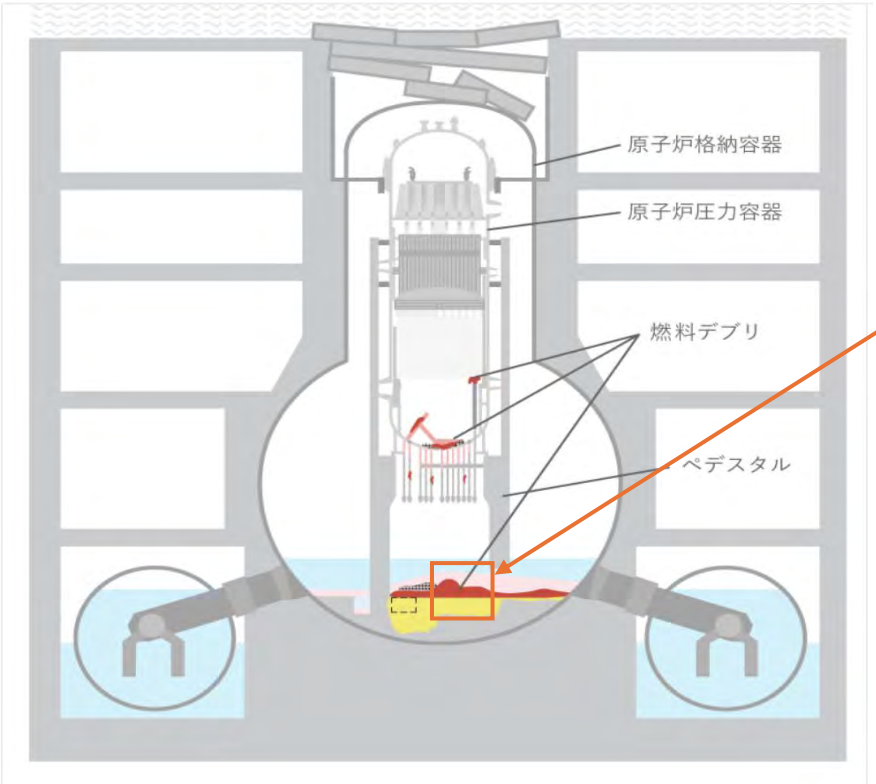

Fukushima Daiichi Unit 1[1]

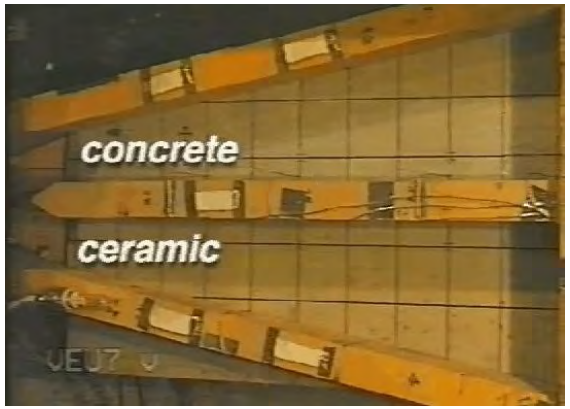

Numerical Simulation is useful

- The problem involves phase change
- Experimental approaches are difficult and limited in scale
- Highly viscous flows involve free surfaces and large deformation

→ **Particle methods** are suitable for this problem

[1] https://www.tepco.co.jp/decommission/progress/retrieval/unit1/index-j.html

Challenges in High-Viscosity CFD

Explicit Euler:

- Constraint imposed by the viscous diffusion condition
- Extremely small Δt for high viscosity

$$\Delta t < \frac{x^2}{8\nu}$$

Implicit Euler:

- Requires solving large sparse matrices
- The iteration count to convergence depends on the problem size.

$$\rho_0 \frac{\mathbf{u}^{k+1}}{\Delta t} = -2\mu(dim+2)\sum_j \left(\frac{\mathbf{u}_j^{k+1} - \mathbf{u}_i^{k+1}}{|\boldsymbol{r}_{ij}|} \cdot \mathbf{e}_{ij}\right)\mathbf{e}_{ij}w'_{ij} -$$

$$\sum_j \left(\lambda \sum_j (\mathbf{u}_{ji}^{k+1} - \mathbf{u}_{ij}^{k+1}) \cdot \mathbf{e}_{ij}w'_{ij} + \lambda \sum_i (\mathbf{u}_{ij}^{k+1} - \mathbf{u}_{ji}^{k+1}) \cdot \mathbf{e}_{ij}w'_{ij}\right)\mathbf{e}_{ij}w'_{ij}$$

$$= \rho_0 \frac{\mathbf{u}^k}{\Delta t} - \kappa \sum_j \left((n_j - n_0) + (n_i - n_0)\right)\mathbf{e}_{ij}w'_{ij} + \rho_0 \mathbf{g}$$

High computational cost is unavoidable, regardless of the method.

→ Acceleration methods are required.

AI-based Surrogate model

Graph Neural Networks (GNNs)

A neural network that constructs a graph structure based on relationships between nodes and edges and learns those relationships.

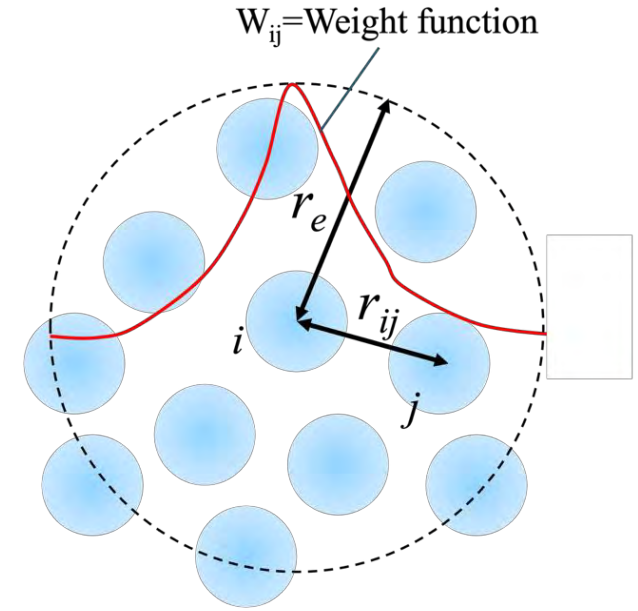

Concept of Particle Simulation (e.g. MPS)

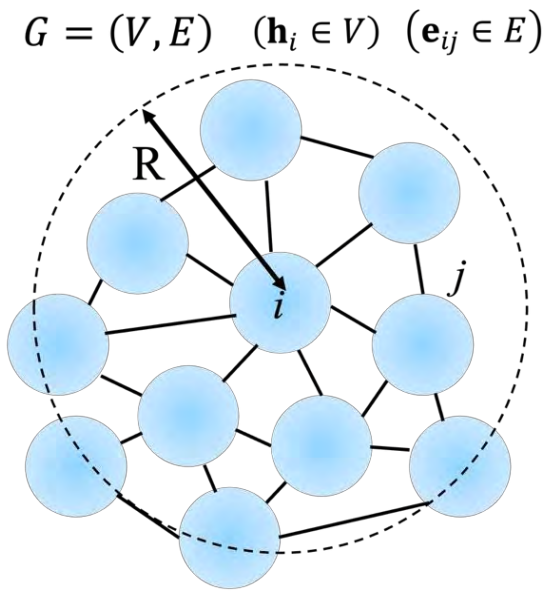

Concept of GNN

GNNs can effectively handle irregular structures such as unstructured meshes.

suitable surrogate models for particle methods

Concept of GNS (Graph Network-based Simulators)

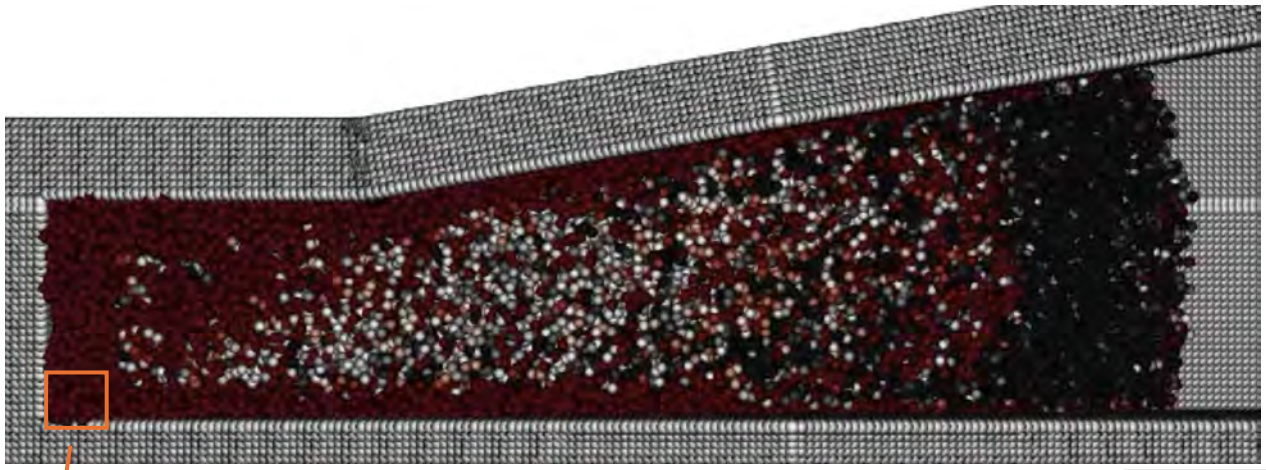

Representing particle relationships as a graph structure

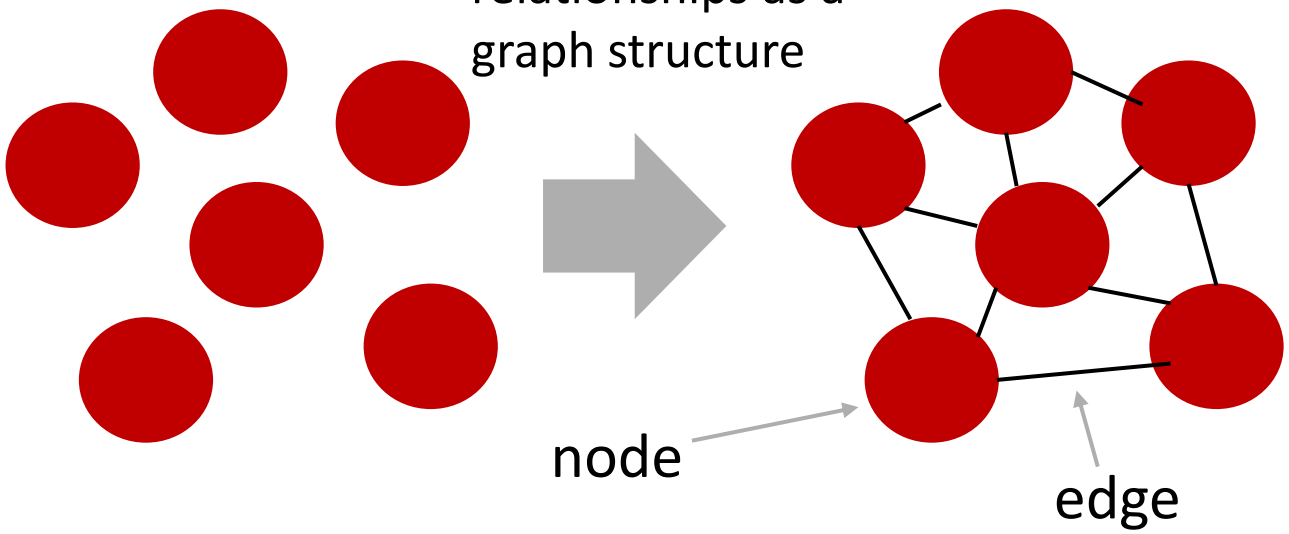

Deep learning of graph structures and temporal relationships

↓

No need to solve matrix equations or discretized equations

↓

Significantly reduces computational cost

Performance of conventional GNS

Viscosity= 1.0×10^{1} (Pa.s)

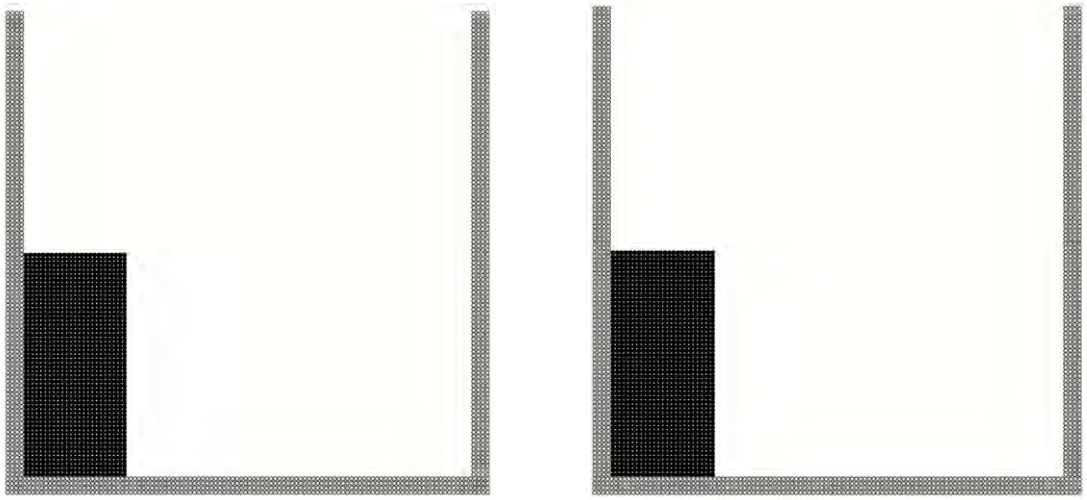

CFD GNS(1200 epochs)

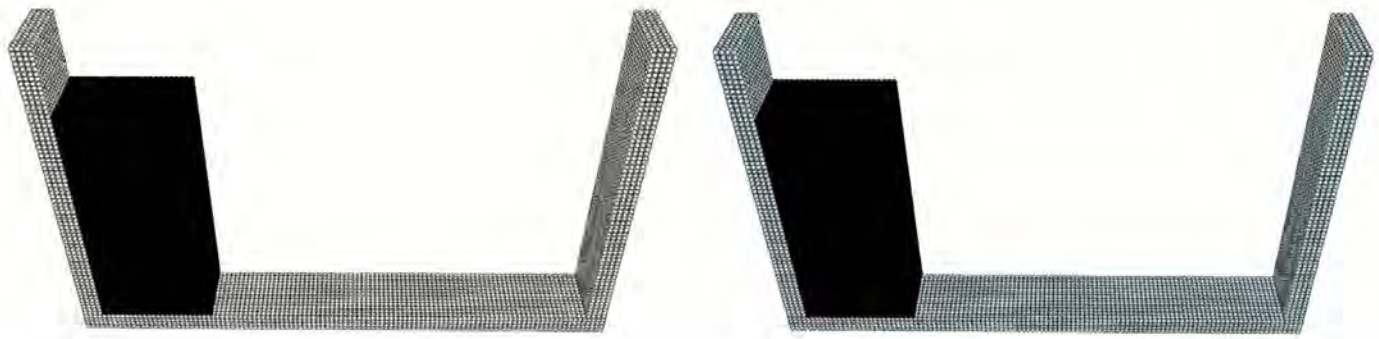

CFD GNS(1000 epochs)

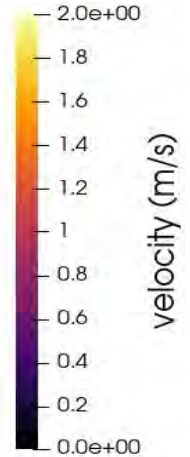

	CFD (CPU)	GNS	Speed-up
2D-Dam-break	99.17s	5.87s	16.9 times
3D-Dam-break	686.90s	38.03s	18.1 times

Conventional GNS achieved more than 15× speed-up in both cases.

Limitations of conventional GNS

- **Only position, velocity, and acceleration can be predicted**

  pressure estimation is also important in fluid simulations.
- **Fully data-driven and limited in scalability**

  Prediction accuracy drops sharply even with slight changes

  in geometry or a small increase in the number of particles.
- **Low interpretability**

  It is difficult to understand how the model learns internally.
- **Long training time**

  Achieving highly accurate results requires many training epochs.
  (More than 1000 epochs)

Objective of this study

Develop a graph neural network with embedded discretized equations to enable rapid severe-accident simulation and improve extrapolation performance

Key Evaluation Points

- the model's extrapolation capability under untrained conditions
- Number of training epoch compared with conventional GNS
- How much the computational time can be reduced compared with CFD

Conventional GNS (Graph Network-based Simulators)

- **Encoder**

  Converts particle data into a graph structure that can be processed by the GNN

  - Nodes: velocity history, distance to boundaries $\mathbf{h}_i^k \equiv \left[\tilde{\mathbf{u}}_i^k, \tilde{\mathbf{u}}_i^{k-1}, \tilde{\mathbf{u}}_i^{k-2}, \tilde{\mathbf{u}}_i^{k-3}, \tilde{\mathbf{u}}_i^{k-4}, \tilde{\Delta}_{wall}^k\right]$
  - Edges: relative distance between particles $\boldsymbol{e}_{ij}^k \equiv \left[\frac{x_j^k - x_i^k}{R}, \frac{y_j^k - y_i^k}{R}, \frac{z_j^k - z_i^k}{R}, \frac{r_{ij}}{R}\right]$

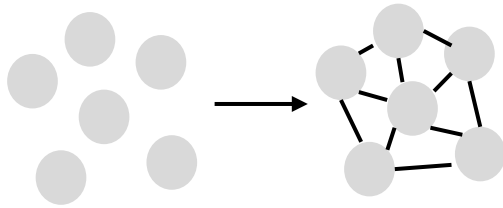

- **Processor**

  Node features are updated through message passing to reflect inter-particle interactions.

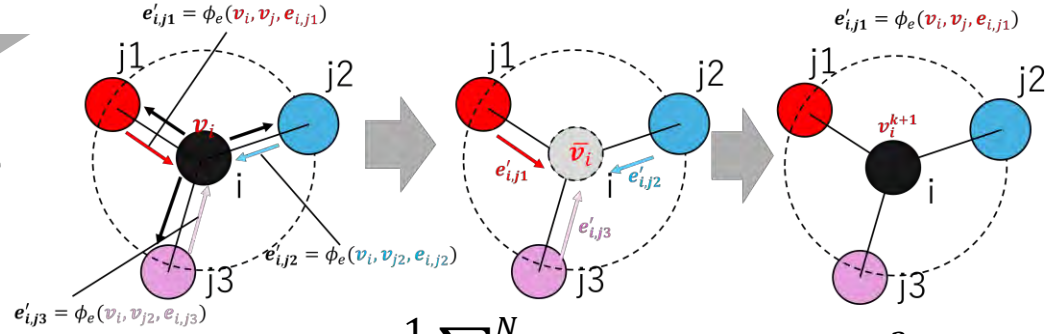

$$\mathcal{L}^{data} = \frac{1}{N}\sum_i^N \left\|\tilde{\mathbf{a}}_{i,predict}^k - \tilde{\mathbf{a}}_{i,data}^k\right\|^2$$

- **Decoder&Rollout**

  Converts learned features into physical quantities and updates velocity and position from the predicted acceleration using Euler integration

$$u_i^{t+1} = u_i^t + y_i^t \Delta t$$

$$x_i^{t+1} = x_i^t + u_i^{t+1} \Delta t$$

Improvement of conventional GNS

(1) Modifications to Feature amount

$$\mathbf{h}_i^k \equiv \left[\tilde{\mathbf{u}}_i^k, \tilde{\mathbf{u}}_i^{k-1}, \tilde{\mathbf{u}}_i^{k-2}, \tilde{\mathbf{u}}_i^{k-3}, \tilde{\mathbf{u}}_i^{k-4}, \tilde{\Delta}_{wall}^k\right]$$

$$\mathbf{h}_i^k \equiv \left[\tilde{\mathbf{u}}_i^k, \ldots, \tilde{\mathbf{u}}_i^{k-4}, \tilde{p}_i^k, \ldots, \tilde{p}_i^{k-4}, \tilde{\Delta}_{wall}^k, \nu_i\right]$$

- Add pressure information from five time steps to the features.
- Include kinematic viscosity to enhance the representation of viscosity–flow behavior.

(2) Training the GNS to learn pressure

$$\Delta\tilde{p}_i^{k+1} = \tilde{p}_i^{k+1} - \tilde{p}_i^k$$

$$\mathcal{L}^{pressure} \equiv \frac{1}{N}\sum_i^N \|\mathbf{r}\|^2 = \frac{1}{N}\sum_i^N \left\|\Delta\tilde{p}_{i,predict}^{k+1} - \Delta\tilde{p}_{i,data}^{k+1}\right\|^2$$

Train the GNS to learn the pressure increment.

- Learning absolute pressure would restrict the range of pressures that can be handled.
- Enable the model to handle larger pressures so it remains applicable when the scale increases.

Discretized Momentum-Equation-Constrained Physics-Informed Graph Neural Networks

Hypothesis: Discretization is possible within the graph connectivity radius, and the acceleration of node can be calculated based on the discretized Navier–Stokes equation.

$$\tilde{\mathbf{a}}_{i,physic}^{k} = \mathbf{g} + \nu\nabla^2\mathbf{u}_i^k - \frac{1}{\rho_0}\nabla p_i^k$$

$$= \mathbf{g} + 2\nu\sum_{j\in N(i)}\left(\tilde{\mathbf{u}}_j^k - \tilde{\mathbf{u}}_i^k\right)\frac{w_{ij}}{(r_{ij})^2} - \frac{1}{\rho_0}\sum_{j\in N(i)}\left(p_j^k - p_i^k\right)\frac{\mathbf{r}_{ij}}{(r_{ij})^2}w_{ij}$$

estimates the "theoretical" acceleration from the momentum equation, which is spatially discretized in the graph.

Based on the discretization model used in SPH

$$\nabla^2\mathbf{u}_i^k = \sum_{j\in N(i)}\left(\tilde{\mathbf{u}}_j^k - \tilde{\mathbf{u}}_i^k\right)\frac{w_{ij}}{(r_{ij})^2}$$

$$\nabla p_i^k = \sum_{j\in N(i)}\left(p_j^k - p_i^k\right)\frac{\mathbf{r}_{ij}}{(r_{ij})^2}w_{ij}^k$$

$$\mathcal{L}^{Physics} = \frac{1}{N}\sum_i^N \|\mathbf{r}\|^2 = \frac{1}{N}\sum_i^N \left\|\tilde{\mathbf{a}}_{i,predict}^k - \tilde{\mathbf{a}}_{i,physics}^k\right\|^2$$

We define a loss function based on the acceleration obtained from the discretized equation and the acceleration estimated by GNS, and correct the GNS-predicted acceleration to be physically consistent.

Discretized Momentum-Equation-Constrained Physics-Informed Graph Neural Networks

Loss function for the entire processor

$$\mathcal{L}^{total} = \mathcal{L}^{data} + w_{phys}\mathcal{L}^{physics} + w_p\mathcal{L}^{pressure}$$

w_p and w_{phys} are weighting coefficients.

$$\mathcal{L}^{data} = \frac{1}{N}\sum_i^N \left\|\tilde{\mathbf{a}}^k_{i,predict} - \tilde{\mathbf{a}}^k_{i,data}\right\|^2$$

In conventional GNS, this was the only loss function used for training.

$$\mathcal{L}^{Physics} = \frac{1}{N}\sum_i^N \left\|\tilde{\mathbf{a}}^k_{i,predict} - \tilde{\mathbf{a}}^k_{i,physics}\right\|^2$$

$$\mathcal{L}^{pressure} = \frac{1}{N}\sum_i^N \left\|\Delta\tilde{p}^{k+1}_{i,predict} - \Delta\tilde{p}^{k+1}_{i,data}\right\|^2$$

The physics-based correction is not reliable in the early stage of training.

The loss weight is automatically adjusted through backpropagation: the data term is emphasized in the early stage, while the physics-informed term is emphasized in the later stage.

Making datasets

Make three datasets with different initial conditions

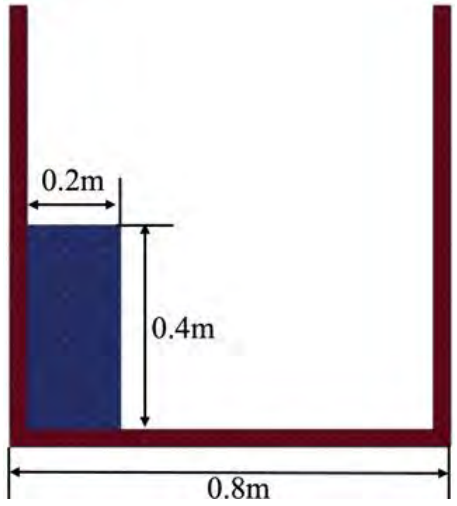

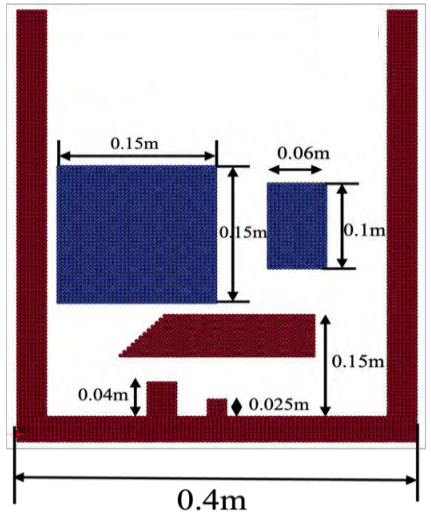

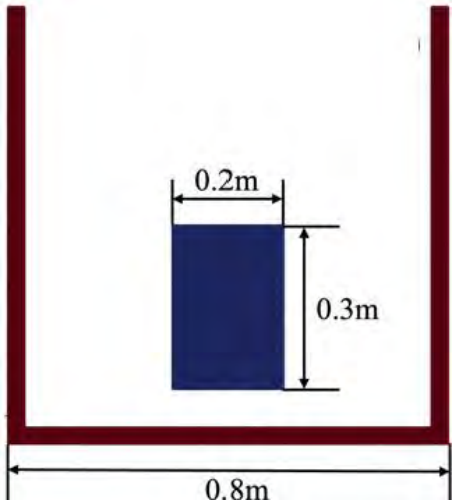

Extract data every 1.0×10^{-3}s from 2.0 s simulations
→ 2000 data samples

Calculation Conditions common to All Cases

	Value
Particle Size	0.004m
Effective Radius	0.010m
Bulk Modulus	1.0×10^{6} (Pa)
Viscosity	1.0×10^{3}(Pa.s), 1.0×10^{2}(Pa.s), 1.0×10^{1}(Pa.s), 1.0×10^{0} (Pa.s)
Δt	1.0×10^{-5} (s) for 1.0×10^{3} (Pa.s), 1.0×10^{-4} (s) for 1.0×10^{2} (Pa.s)

PI-GNS Hyperparameters

	Value
Batch size	2
Noise	6.7×10^{-4}
MLP layers	128
Graph Radius	0.012m

Results(Representative Example)

Pressure Field Prediction $\mu = 1.0 \times 10^3$ Pa · s, Epoch 600

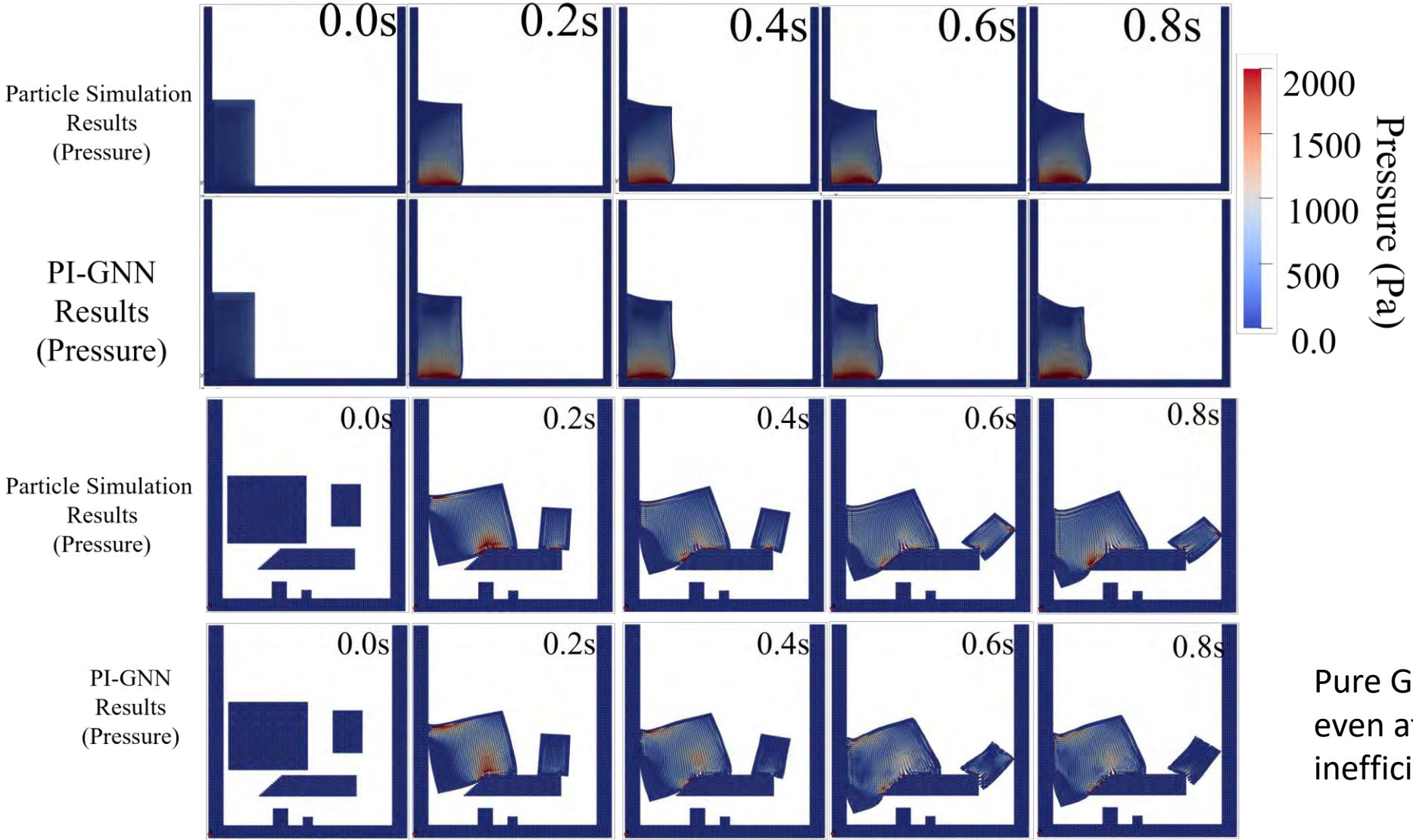

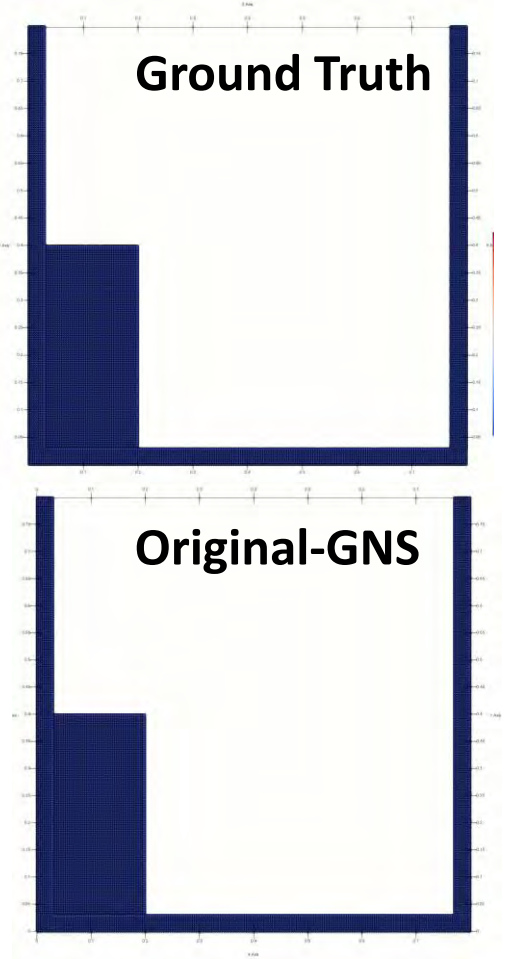

Pure GNN shows poor reproducibility even after 1000 epochs, indicating inefficient training.

Results

Quantitative Comparison of Displacement, Velocity, and Pressure in the Dam-Break Case

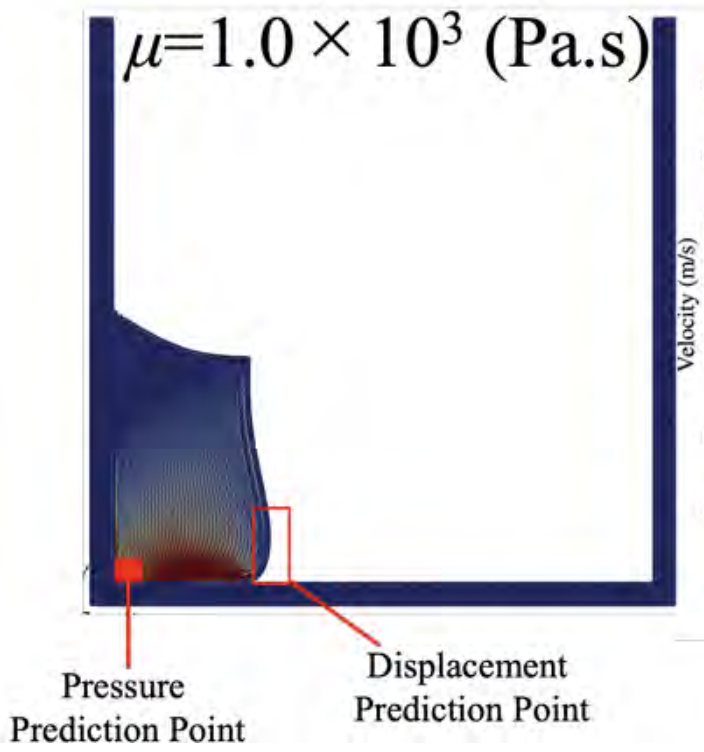

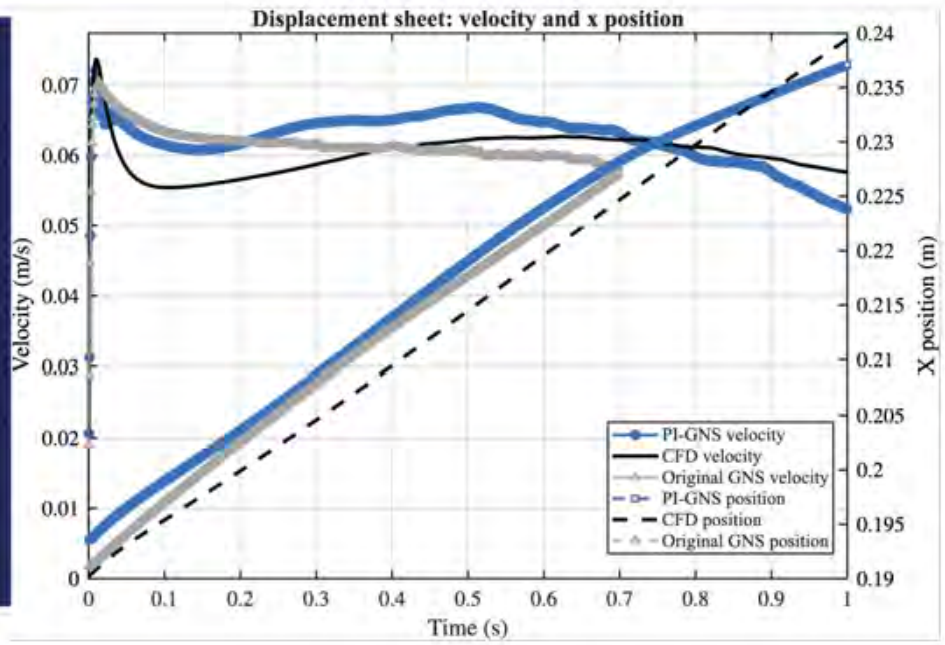

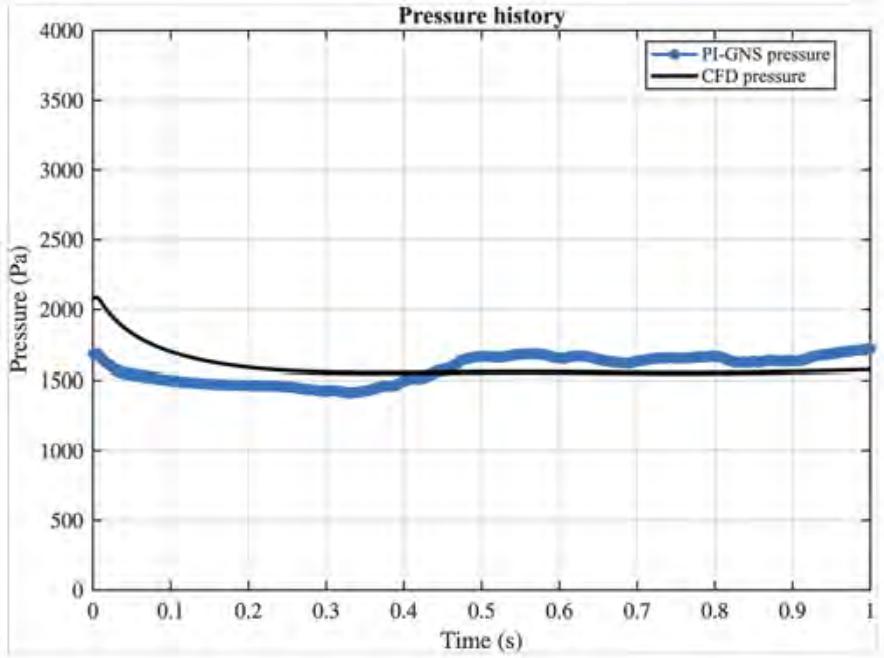

Comparison of Computational Time

	CFD (CPU/ OpenMP)	CFD (GPU)	PI-GNS	Speed-up (CPU)	Speed-up (GPU)
Dam-break (1×10^3 Pa.s)	14948.8s	2321.3s	6.543s	2285 times	354.8 times
Dam-break (1×10^2 Pa.s)	2772.5s	469.2s	6.631s	418.1 times	70.8 times
complex geometry (1×10^3 Pa.s)	10149.5s	1436.8s	3.97s	2556.5 times	361.9 times
complex geometry (1×10^2 Pa.s)	1078.7s	295.2s	4.046s	266.6 times	73.0 times

- PI-GNS achieved a 2285× speed-up compared with CPU-based CFD and a 354× speed-up compared with GPU-based CFD.
- As viscosity increases, CFD becomes more time-consuming, while the computational time of GNS remains almost constant.

→This method is particularly advantageous for highly viscous flows.

Prediction of Geometrically Similar Dam-Break Cases

We made PI-GNS predict a 3× scaled geometrically similar system.

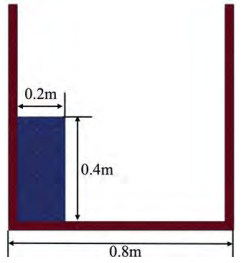

the geometry used for training

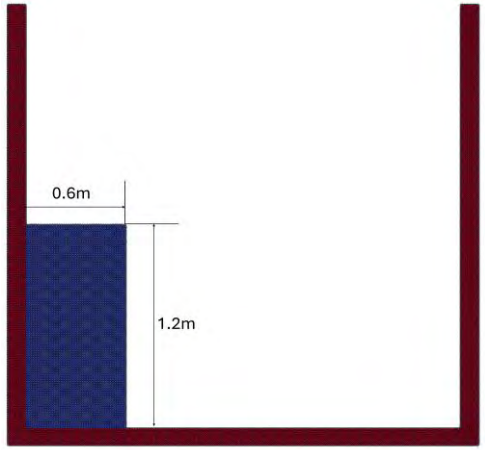

predicted geometry

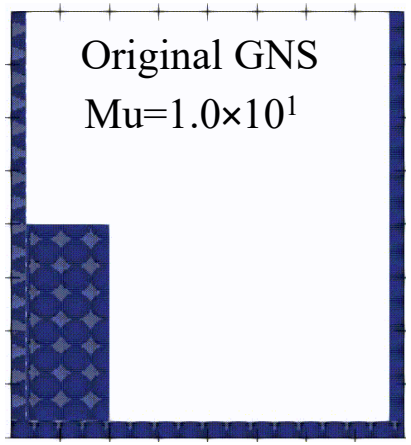

When the pure GNS predicts a 2× scaled geometrically similar system, the prediction becomes highly unstable and crashes.

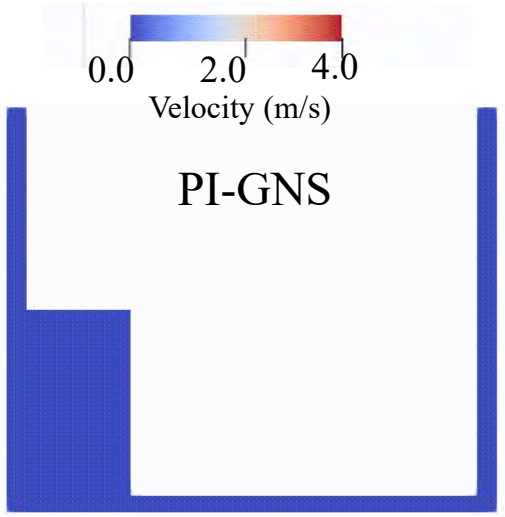

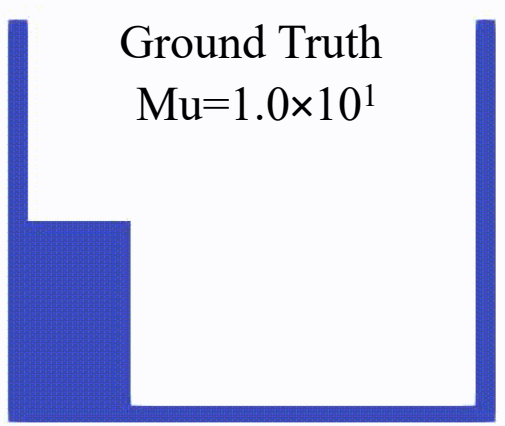

PI-GNS greatly improved prediction accuracy.

This suggests that large-scale behavior may be predicted from small-scale training data, which is difficult with conventional GNS.

Conclusion

- Introduced **pressure** and **kinematic viscosity** as additional features into the conventional GNN framework
- Developed an **inter-node spatial discretization model**, assuming that particle-method-like discretization can be applied within the graph
- PI-GNS reproduced flow behavior more accurately than conventional GNS with fewer training epochs
- PI-GNS significantly improved accuracy for scaled-up particle systems, which was difficult for conventional GNS

THE UNIVERSITY OF TOKYO

科研費 KAKENHI

Thank you for listening!

This work was supported by JSPS KAKENHI Grant Number JP26K17787 and by the JAEA Nuclear Energy S&T and Human Resource Development Project Grant Number JPJA24H12345678.

※ Definition of the Kernel function

$$n_{ij}^k = exp^{-\left(\frac{(r_{ij}^k)^2}{R^2}\right)} \qquad w_{ij}^k = \frac{n_{ij}^k}{\sum_{j \in N(i)} n_{ij}^k}$$

It means nearby particles have larger influence weights.

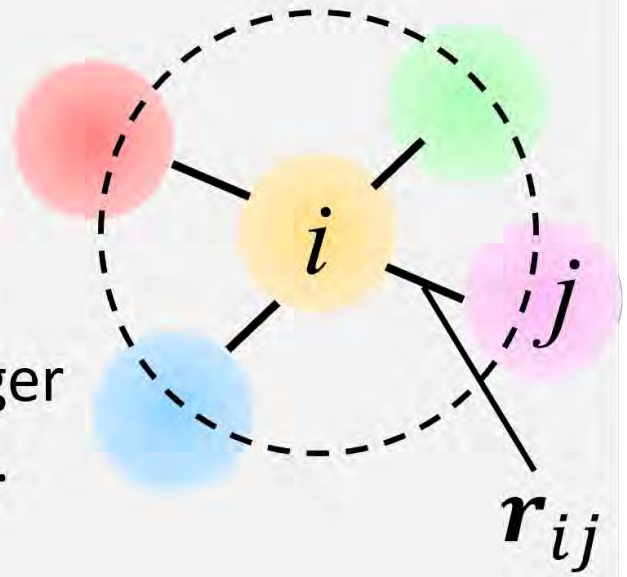

The 12th European Review Meeting on Severe Accidents Research

May 18-22, 2026, Universidad Carlos III de Madrid, Madrid, Spain

TECHNICAL SESSION 1.5: SEVERE ACCIDENT SCENARIOS - INTEGRAL CODES AND RESEARCH FRAMEWORKS

Chairs: J. Fontanet (CIEMAT), L. Lovasz (GRS)

ID196	**A Modernized Architecture for MELCOR** D. Luxat (SNL)	**Presentation**
ID189	**CNL Severe Accident Analysis Research to Support Safe Deployment of Small modular and Advanced Reactors** A. Morreale (CNL)	**Paper** **Presentation**
ID192	**Development of the SAFARI Code for Comprehensive Severe Accident Analysis in Nuclear Reactors: Containment Thermal-Hydraulics Analysis Module** K.H. Han (FNC Technology)	**Presentation**

ADVANCING NUCLEAR SAFETY TECHNOLOGY

A Modernized Architecture for MELCOR

Generalized core damage progression, multi-physics coupling, and the dynamics of an evolving component network

David L. Luxat · Lucas Albright · Brad Beeny · Troy Haskin · Dallin Keesling
Dept. 8852 · Nuclear Energy Safety Technologies · Sandia National Laboratories

SAND2026-XXXXP

Sandia National Laboratories is a multimission laboratory managed and operated by National Technology & Engineering Solutions of Sandia, LLC, a wholly owned subsidiary of Honeywell International Inc., for the U.S. Department of Energy's National Nuclear Security Administration under contract DE-NA0003525.

This is not a new code

MELCOR remains MELCOR. A modernized physics layer runs alongside it through a named, auditable external bridge — no edits to MELCOR source are required to add new physics.

What is new

- The validated MELCOR is preserved, with 30+ years of regulatory pedigree intact; every historical input deck still runs.
- The modernized layer makes it possible to introduce new ways of representing physics more readily — core damage progression is treated as an evolving network of components, with inter-component transport rates carried as state variables and advanced by the same integrator as the components.
- The same component-network describes a fuel rod, a debris bed, a corium pool, core components in an external vessel, or a heat-pipe reactor block — resolution and geometry are deck-level choices, not code-level constraints.

What this talk covers

- The two-layer architecture and the external bridge between original code and modernized layer
- The generalized dynamical form — state and the couplings between state, on one integrator
- Thermal structures with moving-boundary ablation; heat pipes as a sub-network behind a boundary closure
- Coated-particle fuel in a heat-pipe reactor — a non-light-water-reactor application of the same framework
- Lower-head retention and drain into an external vessel under two failure modes

Purpose. Preserve the validation basis; extend the code beyond what the original physics packages can represent.

PART 1

External Bridge and Numerics

The External Bridge — how the original code and the modernized layer compose

By design, the original code and the new physics layer share no internal state directly. They communicate only through the bridge.

- The original code runs its full step first, package by package, using its own numerics.
- The bridge extracts the end-of-step state from the original code and writes it to named exchange variables on the new physics side.
- The new physics layer advances the same time interval with that state held as a fixed boundary condition, then stages its outputs as source terms for the next step in the original code.
- Every exchanged quantity is declared in the input deck — a reviewer can audit the coupling without reading source code.

Consequence. A new submodel is developed, tested, and validated **without running MELCOR at all**. The bridge connection is added only when the submodel is ready to integrate.

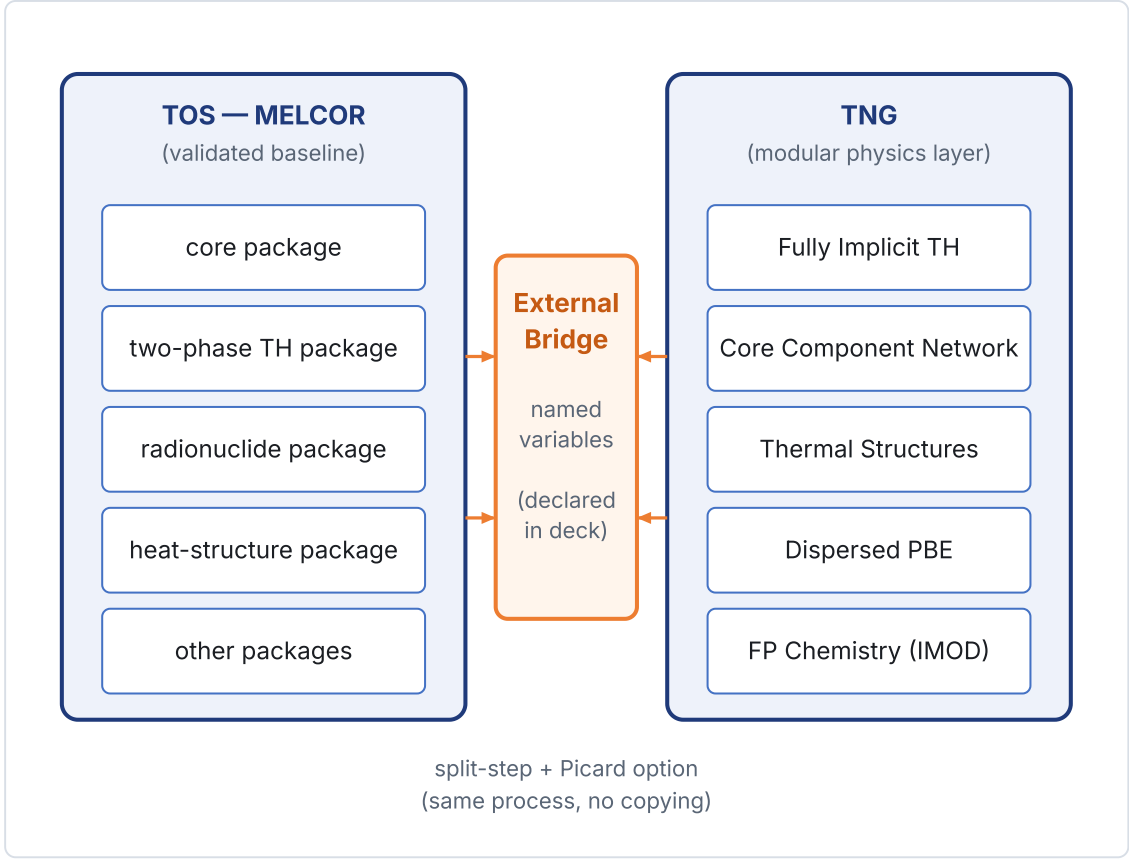

Separating numerics from physics

Physics submodels describe what equations to solve. Numerics describe how to advance them in time. They meet through a defined interface, not through shared internals.

- **Physics submodel** — carries its state variables, its residual equations, and the closures that act on it. Independent of the integrator.
- **Shared exchange variables** — every quantity that crosses between submodels has a name. All inputs and outputs are referenced by name; the references are stable for the whole run.
- **Integration interface** — a common interface between a physics submodel and a time integrator. Lets the same submodel run under fully-implicit Newton, IDA, or Runge–Kutta methods without changes to the physics submodel.
- **Common access pattern** — the integrator reads and writes

Why this matters for core damage

- Adding a new closure (e.g. eutectic dissolution) is a self-contained activity. The closure attaches to a node type, and the integrator does not need to change.
- A stiff transient (oxidation + phase change + reactive heat) can be re-routed onto a fully-implicit Newton solver with one entry in the input deck — same physics submodel.
- The Jacobian is built automatically from the residual — no hand-coded derivatives.

The result. Numerics improvements (better linear solvers, preconditioning, graphics-processor offload) and physics improvements (new closures) evolve on independent schedules. Neither blocks the other.

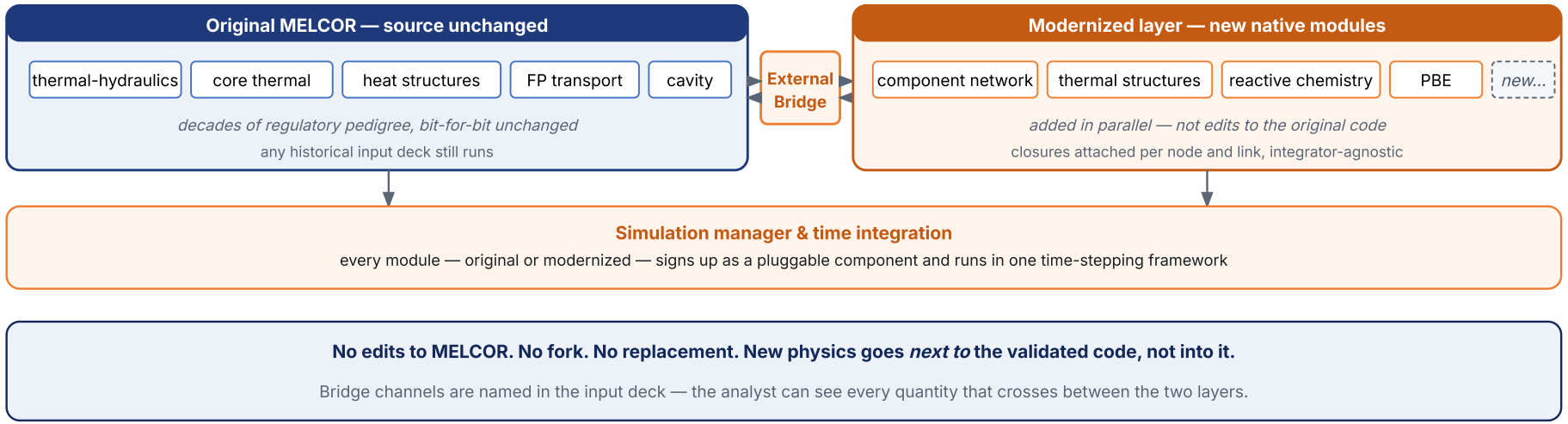

PART 2

Generalized Dynamical Form

State dynamics and coupling dynamics

Classical formulation: state variables on a fixed network topology.

CLASSICAL (STATIC TOPOLOGY)

$d\mathbf{x}/dt = \mathbf{f}(\mathbf{x}; \mathbf{A})$ — adjacency $\mathbf{A}$ is prescribed

Generalized formulation: the network itself is dynamical, with the couplings carried as state variables.

GENERALIZED (EVOLVING TOPOLOGY)

$d\mathbf{x}/dt = \mathbf{f}(\mathbf{x}, \mathbf{c})$ — component state

$d\mathbf{c}/dt = \mathbf{g}(\mathbf{x}, \mathbf{c})$ — couplings between components

What's in c: per-link drainage strength, per-node oxide thickness, per-face boiling-regime weights, eutectic progress fraction, cladding-failure fraction. Each entry evolves continuously through g; no on/off switching.

The same fuel column at three snapshots — the network of contacts evolves with the state:

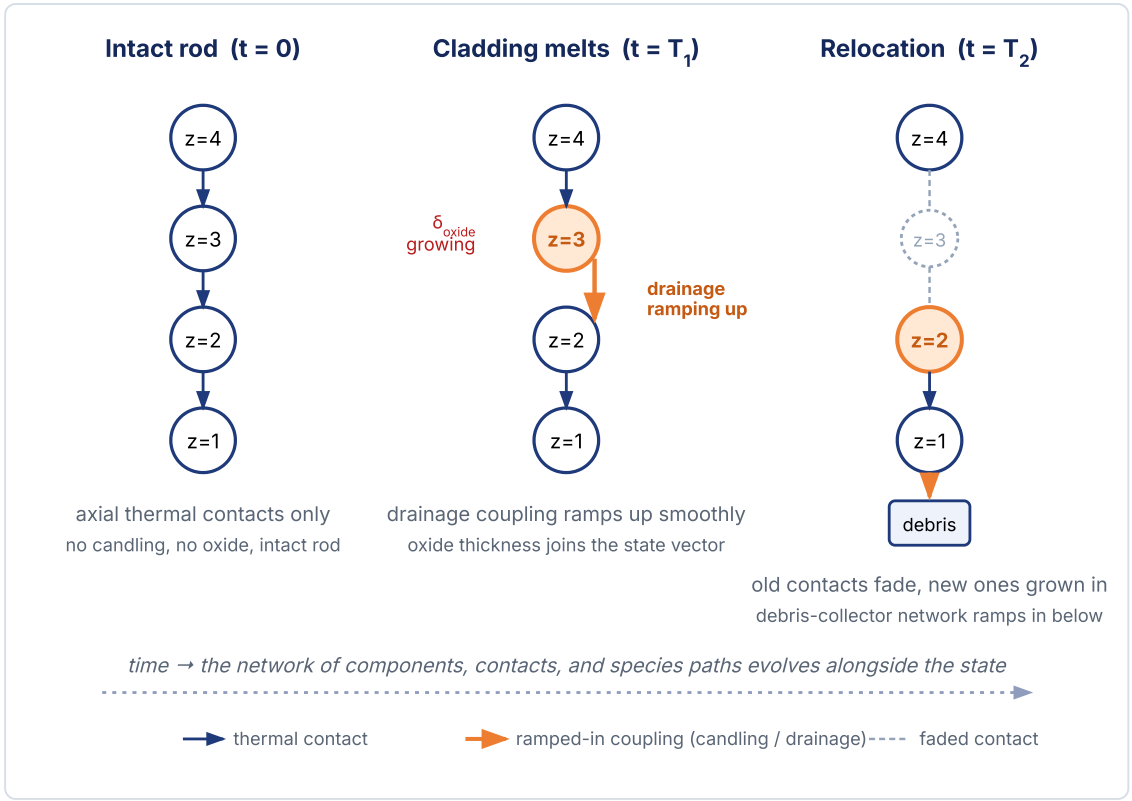

Panel 1
$d\mathbf{x}/dt = \mathbf{f}(\mathbf{x}, \mathbf{c})$; $d\mathbf{c}/dt = 0$

Panel 2
$d\mathbf{c}/dt = \mathbf{g}(\mathbf{x}, \mathbf{c})$ — coupling ramps up smoothly

Panel 3
$\mathbf{c}$ has evolved — $\mathbf{f}$ now lives on a different network

Take-away. In the original code, component types and inter-component transport laws are hard-coded. Here both are input, advanced by the same integrator as the state.

Component network — the flow-network pattern, generalized

A familiar pattern. Classical flow networks placed the state inside control volumes and let flow paths transport between them. The component network reuses that idea for solids and condensed phases.

- **Node** — a spatial location that holds state. An axial slice of a fuel rod, a debris box, a coated-particle compact, one lump of a relocated pool.
- **Node-component pair** — a material at a node. The same node holds many: fuel pellet, cladding, oxide layer, dissolved liquid, gas gap.
- **Link** — a typed exchange between nodes. Thermal contact, melt drainage, fission-product transport, mechanical contact. **Mass and energy transport rates between components are the couplings**.

> **Why the analogy matters.** In a thermal-hydraulic flow network, junctions are static; the topology is fixed by piping. Here the network is **dynamic** — links open as cladding melts and pours; new networks appear when material relocates into a receiving vessel.

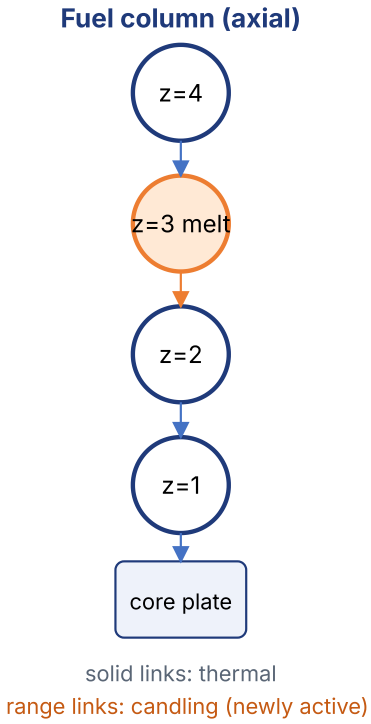

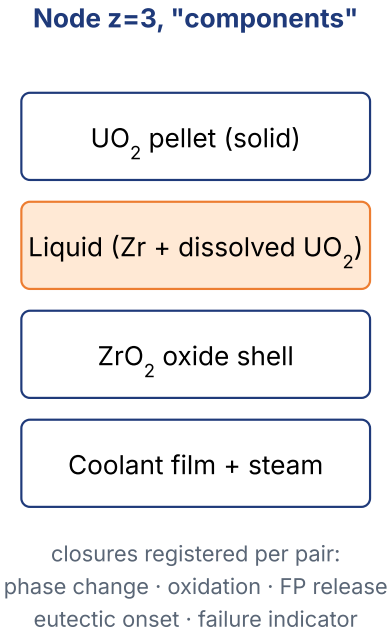

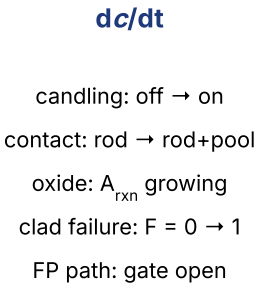

Thermal structures — meshed solids with moving-boundary ablation

A thermal structure is the second building block of the modernized layer. Where the component network resolves components at a node, a thermal structure resolves a meshed solid — cladding, lower head, calandria wall, debris-bed crucible — cell by cell.

- **Multi-region mesh.** A wall can carry stacked regions — crust, oxide, base metal, outer cladding — each with its own material card and its own per-cell state.
- **Named faces.** Inner, outer, top, bottom, side. Each face carries its own boundary closure (radiation, pool convection, external boiling, contact to a neighbouring network).
- **Moving-boundary ablation.** When the surface cell exceeds wall solidus while corium is in contact, a Stefan front advances into the wall. The integrated melt enthalpy comes out of the incoming heat flux; the ablation depth is a continuously evolving state variable per face cell.
- **Boundary topology is dynamic.** As a cell ablates fully, the moving-boundary manager retires it and exposes the next cell behind it as the new surface — the per-face boundary closure picks up the new geometry automatically.
- **Coupling back to the network.** Ablated mass and its enthalpy are sourced into the receiving network node (a debris bed, a relocating pool) — the same cross-network mass and energy balance that holds for every other link.

A lower-head wall slice — multi-region, multi-face

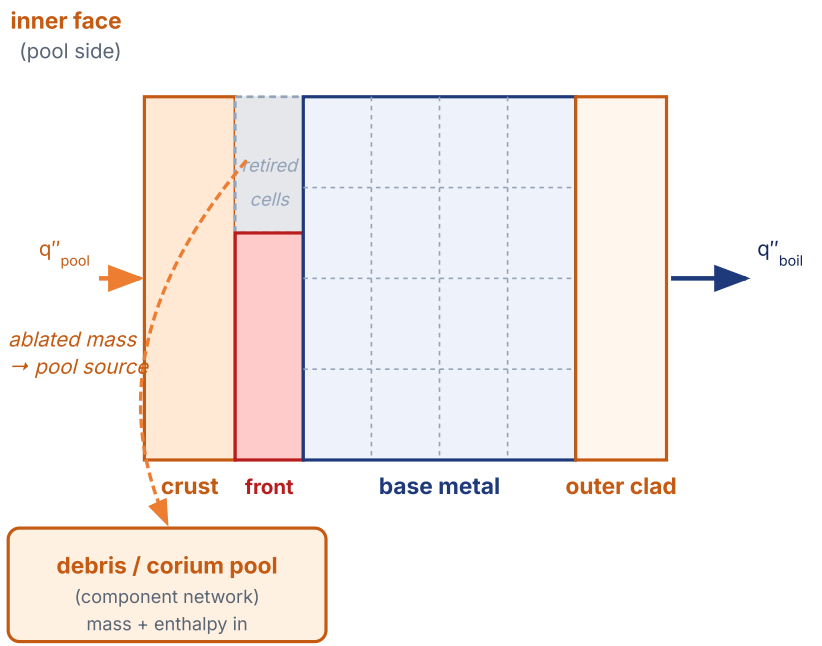

Per-face state: $\delta_{remaining}$, $T_{surface}$, ε_{creep}

Breach event: $\delta_{remaining} < \delta_{min}$ or $\varepsilon_{creep} > \varepsilon_{crit}$ — hands off to the orifice closure.

Heat pipes — a sub-network behind a boundary closure

A heat pipe is a closed two-phase device. Working fluid evaporates at the hot end, vapor flows to the cold end, condensate returns through a wick by capillary force. Effective conductance is tens to hundreds of times higher than a solid bar of the same size — but only inside an operating envelope.

- **Inside the heat pipe**: its own small network — evaporator, wick, vapor space, condenser — each carrying state, exchanging mass and energy through internal couplings.
- **Outside**: a boundary closure on the host node. Heat extraction follows a prescribed axial profile with an effective conductance $G_{HP}(T_{block}, T_{HP})$ attached to the affected cell faces.
- **Operating limits live in c**: capillary, entrainment, sonic, and boiling margins — each a continuously evolving distance-to-dryout, not a binary flag.
- **Failure is a closure swap, not an event**: as a margin crosses zero, the boundary path smoothly degrades from full HP transport to thermal-resistance-only. Integrator sees a continuous transition; the deck names the margin.

> The HPR result later shows this directly — the "central-HP-failed" case is the same model with one pipe's closure swapped.

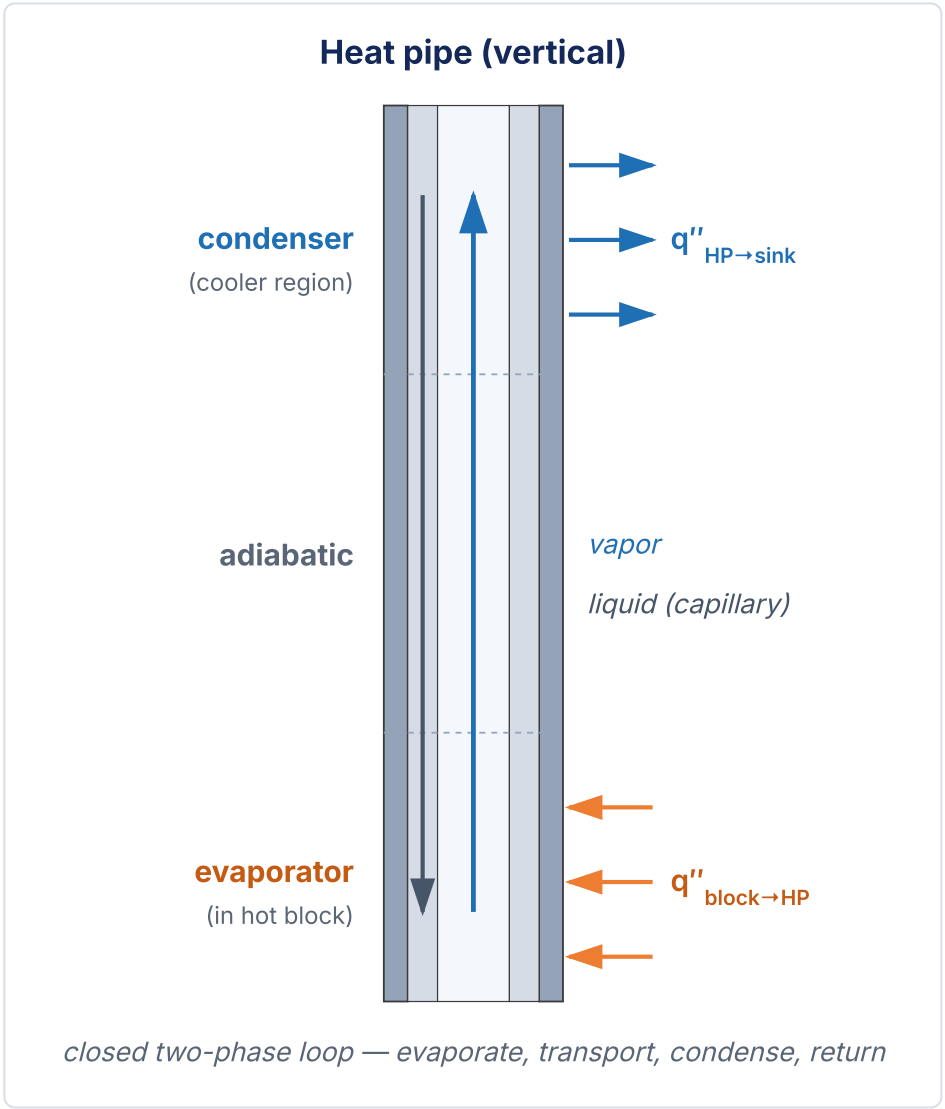

PART 3

Illustrative examples

What the HPR model represents — block, heat pipes, compacts, particles

A coated micro-particle fuel form composes into the same generalized network used throughout the deck. Only the closures attached to the nodes and links change.

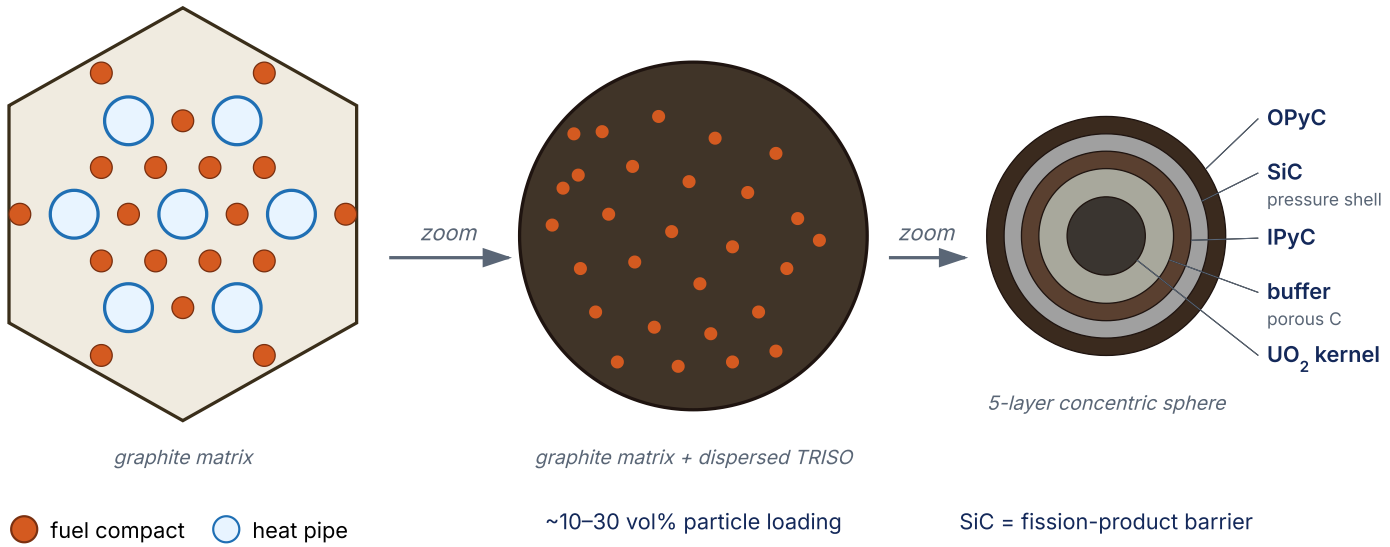

What lives where

- **Block** → meshed node, radial + axial
- **Compacts** → effective **k** closure (ME / ZBS / Bruggeman)
- **Heat pipe** → boundary closure; HP failure = closure swap
- **TRISO particle** → one analytical 5-layer submodel; Weibull SiC failure

The zoom is conceptual. Millions of particles are not tracked individually. The block carries a homogenized k_{eff}; one analytical particle stands in for the population and carries the Weibull failure statistic plus the species transport path.

Matrix is an input, not a hard-coded assumption. The compact matrix shown here is graphite, but the framework treats matrix material as a property of the node — SiC, ZrC, or any other matrix can be selected by changing the material assignment in the input deck. The same homogenization closures and the same analytical-particle submodel apply.

TRISO HPR result — block T under degraded cooling at t = 1 h

Block holds at ~830 K while cooling works. At t = 1 h cooling degrades; block peaks at 2133 K at 2.2 h and cools back to 1611 K by 24 h as Q‴(t) falls.

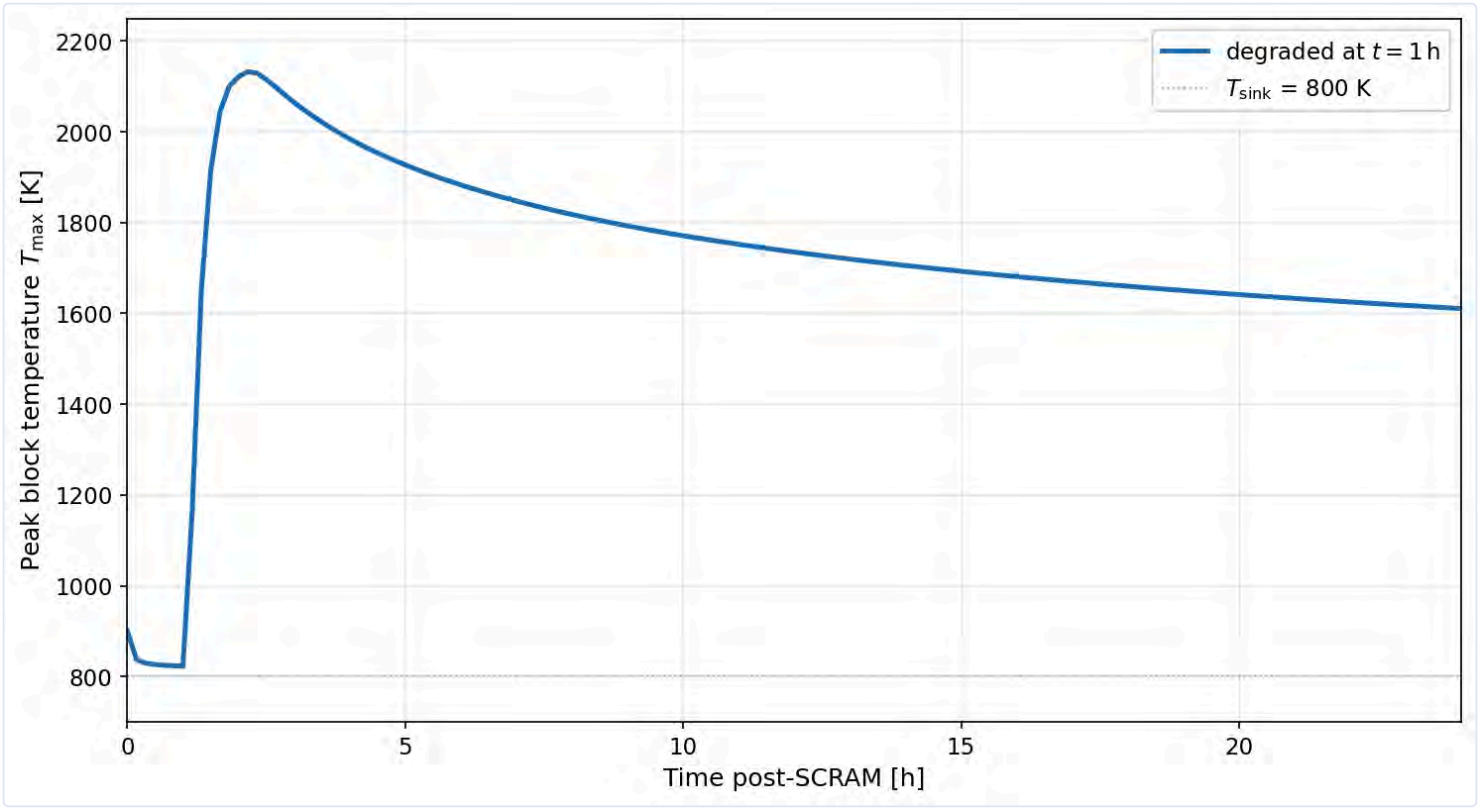

Block temperature, degraded cooling at t = 1 h. T_{sink} (800 K) shown as a reference.

One hour of working cooling lets Q‴(t) fall enough that the system recovers once cooling degrades.

In-vessel retention — five-step coupled solve

A relocated corium pool sits inside the lower head; operator action floods the outer vessel surface. Whether the wall survives depends on five physics steps running together, not in sequence.

1. **Decay heat** deposited in the pool from relocated fuel and metallic inventory
2. **Pool natural convection** redistributes the heat — up to the free surface, down and out to the curved wall, sideways into a metallic layer if one exists
3. **Crust solidification** on the inner wall sets a thermal resistance and protects the steel from direct contact with molten material
4. **Wall conduction** through the lower-head steel mesh, per angular zone
5. **External boiling** on the outer surface removes the heat — subject to a boiling-limit set by geometry and surface coverage

A change in pool convection shifts the angular flux distribution; the changed flux shifts crust thickness; the changed crust shifts wall temperature; the changed wall temperature shifts the boiling regime. All five reach a self-consistent solution in **one** Picard iteration per time step — not lagged across steps.

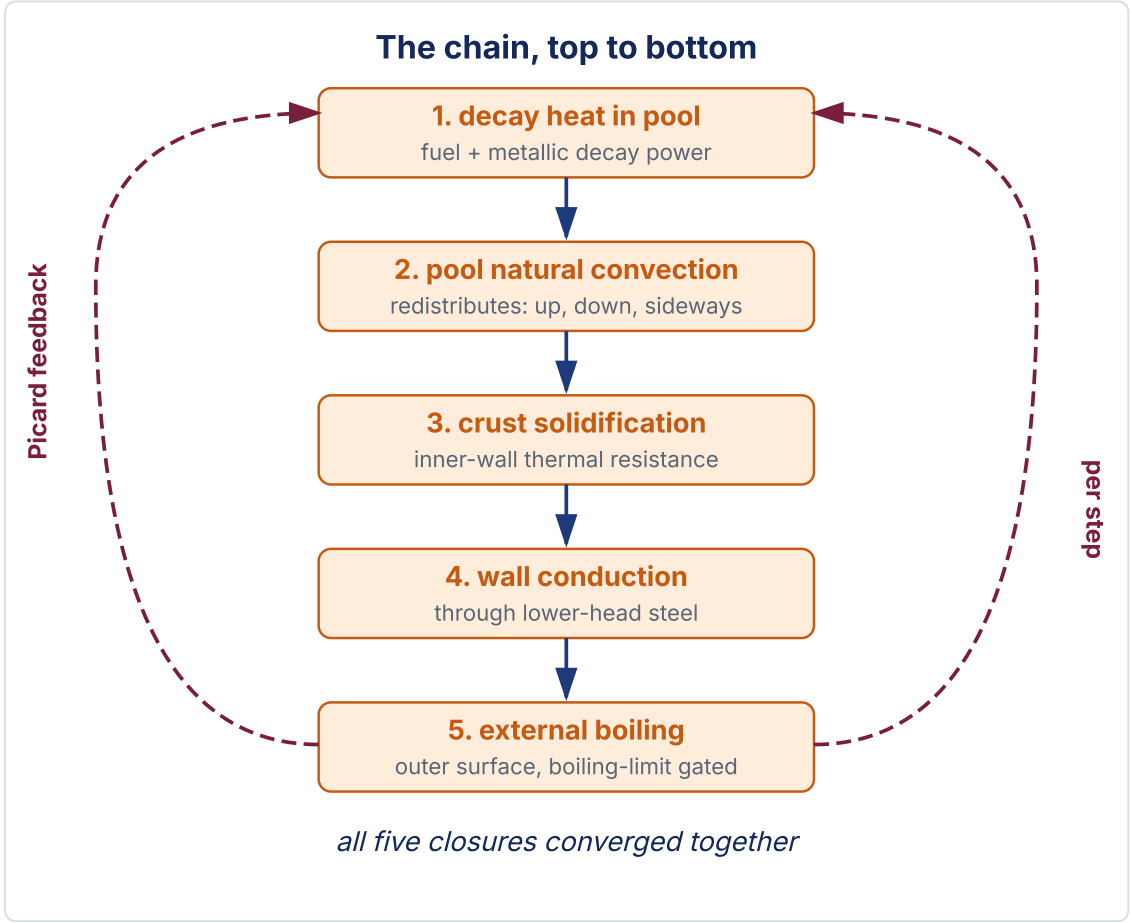

Lower-head ablation and cross-network melt pour

Ablation dynamics are central. When the pool is hotter than wall solidus, a Stefan front advances into the steel face by face. When remaining thickness drops below a threshold, the breach event fires.

- **Per-face Stefan front.** Each angular zone tracks its own remaining wall thickness; partial breaches (a single failed band) are the natural outcome.
- **Two failure paths watched together.** Creep damage accumulates under sustained stress at sub-solidus temperatures; ablation thins the wall at solidus contact. Whichever crosses its threshold first fires the breach.
- **Breach hands off to a gravity-drainage closure.** Drain rate is set by the breach area and the hydrostatic head above the breach — a single-phase orifice law, no flashing, no critical-flow regime relevant for this type of melt drainage.
- **Driving head** is gravity ($\rho\, g\, h_{pool}$) plus any system overpressure between donor and outer vessel.

Mass and energy balance across the boundary

Four named quantities cross every cross-network link, summing to machine zero each step:

- **Mass per species** — donor decremented, outer vessel incremented, by the same per-species amount
- **Enthalpy** — jet specific enthalpy is the donor-side value; no flash losses, no artificial mixing
- **Decay-heat carry-along** — each transferred kilogram brings its decay-power generation rate with it
- **Full composition vector** — every tracked species follows the mass; the outer vessel composition is mass-weighted by the arriving stream

The same balance applies to **every** cross-network link: rod region to lower plenum, lower plenum to ex-vessel cavity, lower plenum to an external vessel.

Result — lower-head wall under nominal ex-vessel cooling

- Large-PWR hemispherical lower head, full-submergence outer cooling
- Same mesh and closures as Part 2
- Equator at **z = 0**, pole at **z = −R**
- Gray cells: retired by the moving-boundary manager

> Ablation self-limits to a one-cell band at the peak-flux polar angle. Wall survives 10 h.

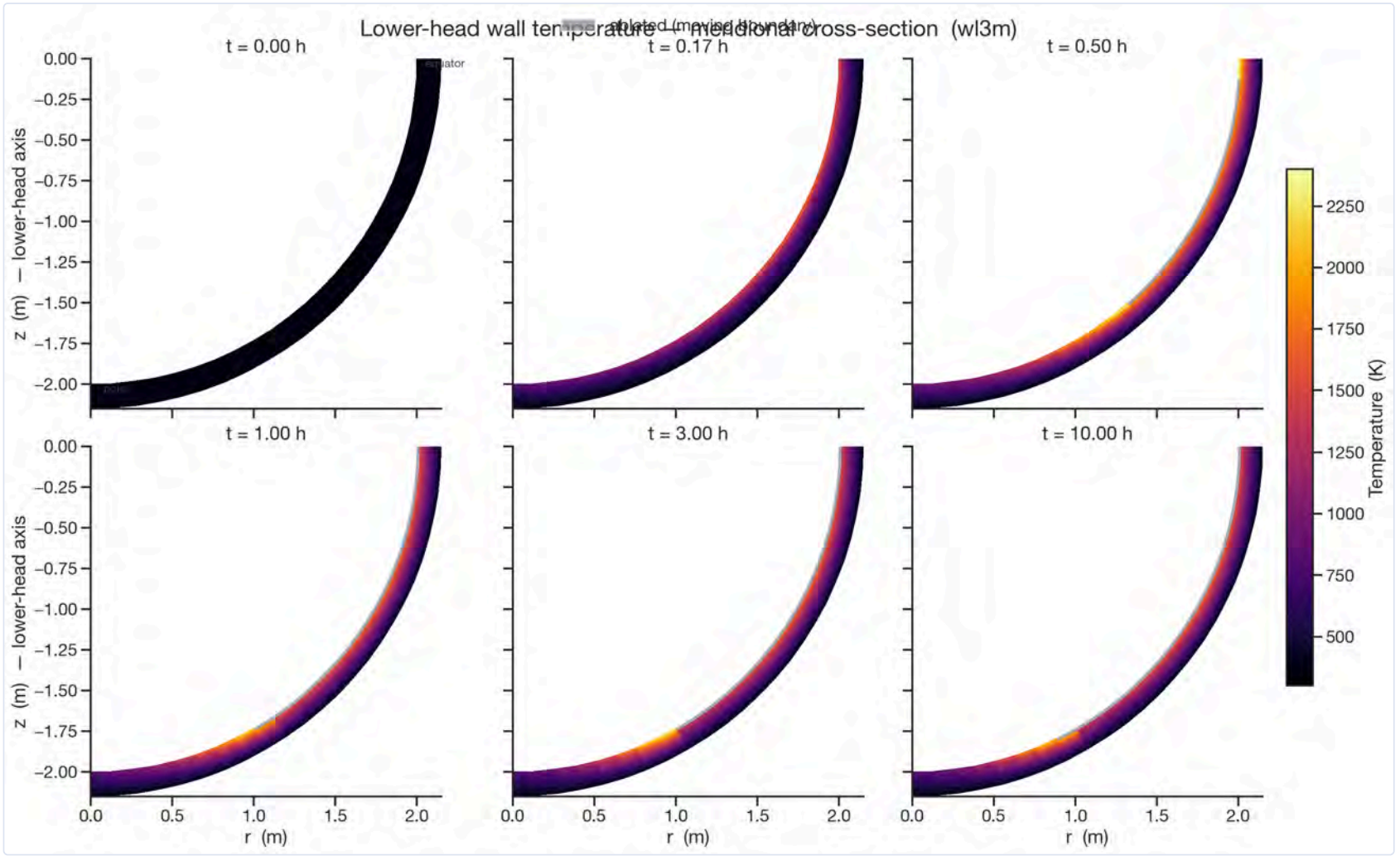

Wall temperature, six snapshots over 10 h.

Result — same model, degraded outer cooling, breach at 77 min

- Same mesh, same closures, same integrator
- Outer water dropped: upper hemisphere on radiation only ($h_{dry} \approx 100$ W/m²·K)
- Per-face breach fires at **t ≈ 77 min** when $\delta_{remaining} < \delta_{min}$

> Only the outer face closure changed. Front cascades; wall breaches.

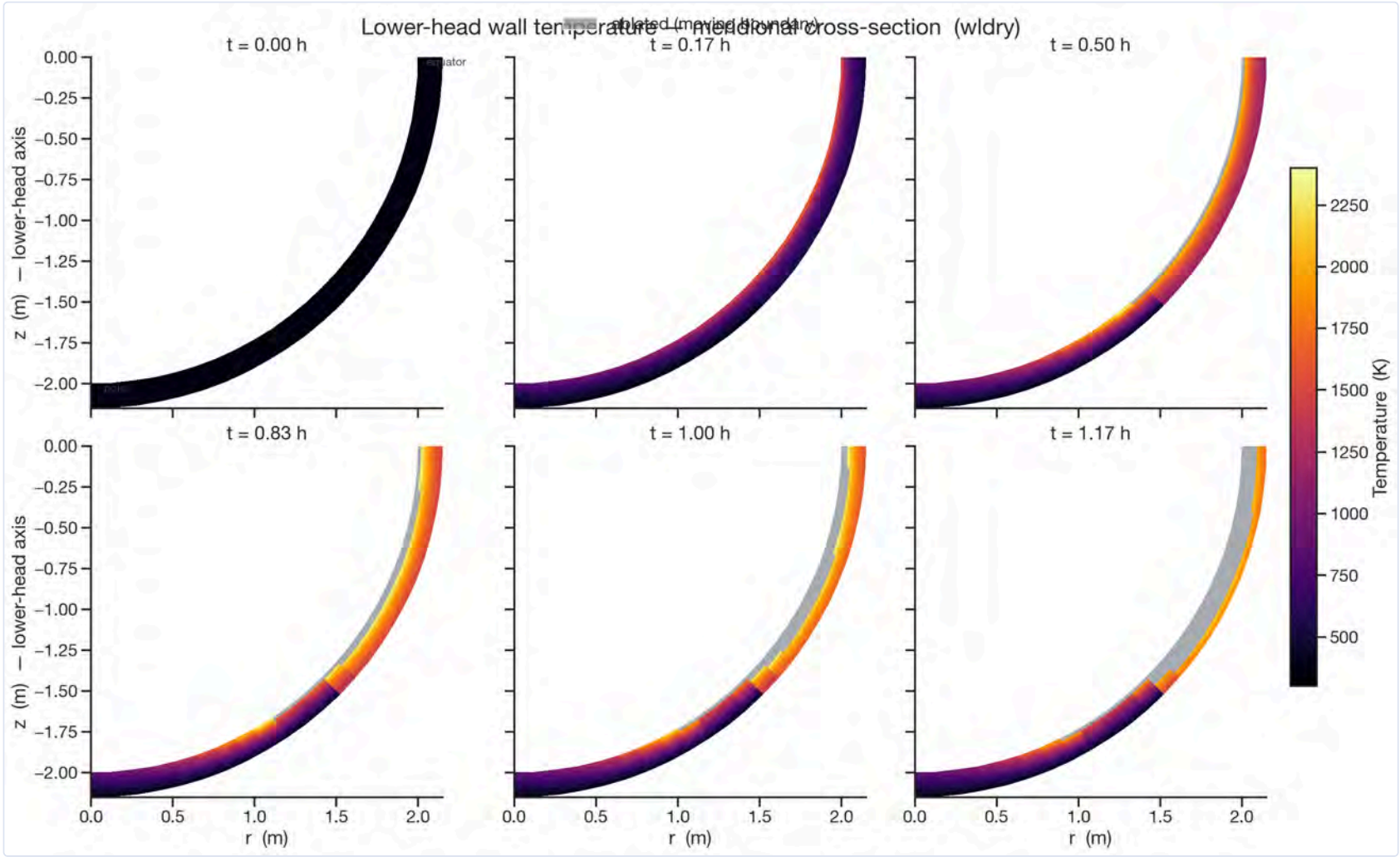

Same six-snapshot format. Run halts at t ≈ 1.28 h on outer-ring breach.

Core components in external vessels

The component-network building block does not care which vessel a component sits in. Each vessel is its own connected component graph; cross-network links transport mass and energy between them under the same audited balance.

- **Integrated small modular reactors.** Designs like NuScale place the reactor pressure vessel inside an outer containment vessel submerged in pool water. If the RPV breaches, relocated material drains into that containment vessel — an external vessel that the framework now represents as a separate network on the receiving end of the cross-network link.
- **Heavy-water designs.** The shield tank in the 900 MWe-class CANDUs built in Ontario (Bruce, Darlington) is a large water-filled vessel surrounding the calandria. In late-phase progression, relocated core material is retained in the shield-tank water inventory — a network of its own, populated by the same kinds of nodes and links.

Why this matters at the engineering level

- No new closures need to be written to extend physics into an external vessel — the same melt drainage, the same heat-transfer correlations, the same failure indicators all apply the same way
- The run log lists each vessel as a named network with its own component inventory — the analyst sees exactly which vessels contain what, when
- The cross-network conservation balance is checked independently for every vessel-to-vessel link — an automatic check on every run, not a tolerance band

The pattern is general. If a new advanced design places core components in a vessel the original code never modelled, those components are represented in the existing framework as another network. No changes to MELCOR itself; the existing validated physics is undisturbed.

Debris accumulation in the external vessel

Global / hole ablates: ~100 t debris by 150 min — the breach widens as the orifice erodes. **Global / no ablation**: ~40 t at fixed orifice. **Progressive cell failure**: ~5 t debris — a much slower per-zone failure mode.

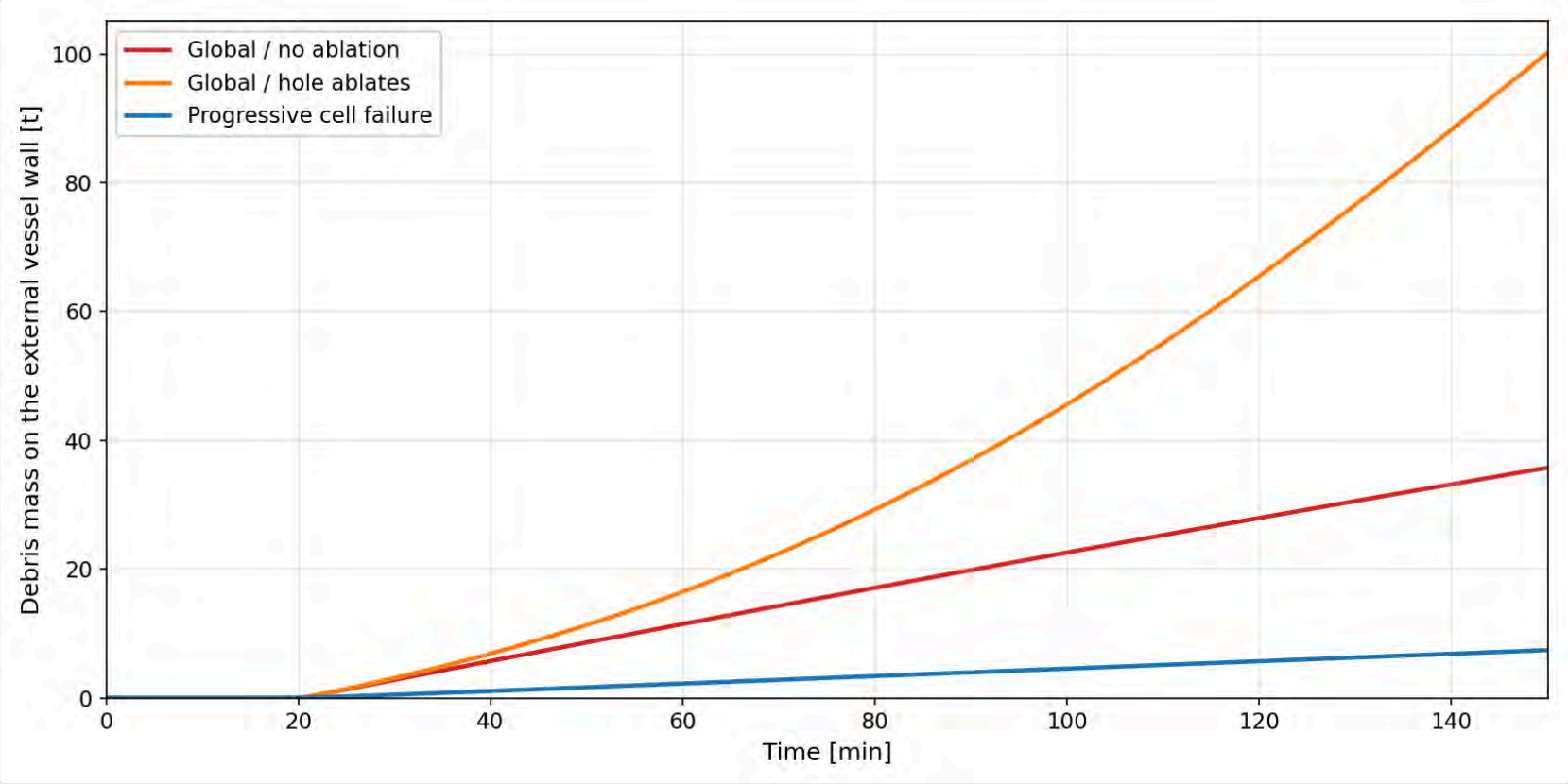

Debris mass on the external-vessel wall, three failure-mode scenarios.

Looking forward — where this can go

The component-network representation does not prescribe geometry or resolution. Heat transfer, mass transfer, and species transport between any set of nodes follow the same form. What the analyst chooses to declare in the input deck is what gets simulated.

Any network, any resolution

- Lumped region, one assembly, every rod — resolution is a modeling choice, not a code constraint
- Heat-transfer, mass-drainage, species-transport links coexist on the same network
- New components are added by declaring new node types and the closures attached to them

3D-resolved core, if the question asks for it

- Every fuel assembly meshed independently in a true 3D arrangement
- Every rod within an assembly resolved separately when intra-bundle behavior matters
- Cross-assembly thermal coupling, in-bundle melt drainage, intra-rod failure all in one framework

Beyond the reactor vessel

- A spent-fuel pool with rod-by-rod inventory under loss-of-cooling scenarios
- Heat-pipe reactors, fluoride-salt designs, micro-reactors, integrated SMRs
- Any external vessel that receives core material — calandria shield tanks, ex-vessel cavities, dedicated catchers

ADVANCING NUCLEAR SAFETY TECHNOLOGY

Thank you

David L. Luxat · Lucas Albright · Brad Beeny · Troy Haskin · Dallin Keesling
dlluxat@sandia.gov
Dept. 8852 · Nuclear Energy Safety Technologies · Sandia National Laboratories

SAND2026-XXXXP

Sandia National Laboratories is a multimission laboratory managed and operated by National Technology & Engineering Solutions of Sandia, LLC, a wholly owned subsidiary of Honeywell International Inc., for the U.S. Department of Energy's National Nuclear Security Administration under contract DE-NA0003525.

The 12th European Review Meeting on Severe Accident Research (ERMSAR2026) Log Number: 189
Madrid, Spain, May 18-22, 2026.

153-126800-CONF-011551 – Rev 0

CNL SEVERE ACCIDENT ANALYSIS RESEARCH TO SUPPORT SAFE DEPLOYMENT OF SMALL MODULAR AND ADVANCED REACTORS

Andrew C. Morreale*, Garik Patterson, Luke S. Lebel, David W. Hummel, Chuk Azih, Eric D. Jia, Abishek Sridhar, Ernesto Geiger
Canadian Nuclear Laboratories, Ltd. (CNL)
286 Plant Road, Chalk River, Ontario, K0J 1J0, Canada
andrew.morreale@cnl.ca; garik.patterson@cnl.ca; luke.lebel@cnl.ca; david.hummel@cnl.ca; chuk.azih@cnl.ca; eric.jia@cnl.ca; abishek.sridhar@cnl.ca; ernesto.geiger@cnl.ca
*corresponding author

ABSTRACT

Small modular reactor (SMR) and advanced reactor (AR) designs see increased interest in new markets for nuclear energy to combat climate change. Canadian Nuclear Laboratories' (CNL) reactor safety research supports safe deployment with a flexible technical program supporting regulatory and industry stakeholder needs. SMR/ARs for remote (off-grid) locations and grid-level applications using various technologies are being explored based on the deployment landscape in Canada. Severe accident research is a key component focused on potential scenarios, progression, and prediction of radionuclide source terms, which informs design, regulation, and emergency response. CNL has developed competencies and is building additional capabilities in reactor safety research of technologies being deployed in Canada and has a base understanding of other designs of interest. Major technologies include water-cooled (primarily small boiling water reactors, BWRs), high temperature gas reactors (HTGR), and micro-reactors (micro-HTGR and heat-pipe designs). Baseline capabilities and early research are being developed for sodium fast reactors and molten salt designs. CNL is constructing experimental apparatus and conducting tests to generate knowledge and data regarding important phenomena where gaps have been identified. Modelling efforts are focused on experimental benchmarks and the development of generic integral analysis models for these different technologies, both in severe accidents and containment. Recent developments in experiments include passive containment cooling experiments for small BWR containments, and the commissioning of early tests/results of an onset of natural circulation experiment for HTGR, as well as a self-heated pebble bed core experiment. Integral accident analysis models and uncertainty and sensitivity investigations have been conducted for small BWR and HTGR models in MELCOR, and CNL is participating in the SASPAM-SA project. In micro-reactor space heat pipe experiments, ongoing and new agreements for custom heat pipe designs will enhance CNL capabilities. There is also an evaluation of historic AECL designs, including the SLOWPOKE and Nuclear Battery, as well as the development of a microreactor framework to support deployment in Canada.

KEYWORDS
Small Modular Reactors, source term, high temperature gas cooled reactors (HTGR), small BWR, heat pipes

1. INTRODUCTION

The resurgence in nuclear energy worldwide continues, and the deployment of new nuclear is growing closer in many markets. Planned deployments include new large builds, small modular reactors (SMR), advanced reactors (AR), and micro-reactor designs. There is interest in the deployment of all these classes of reactors in Canada to contribute to clean energy generation and meet the needs of government and industry.

The most recent developments in Canada have been related to the GE-Hitachi BWRX-300, a small boiling water reactor (BWR), deployment at the Ontario Power Generation (OPG) Darlington site, where the construction license for the first of four units was approved by the Canadian Nuclear Safety Commission (CNSC) in 2025 April. The nuclear construction at the site is now underway, and the licensing process is moving on to the next stage, where the objective will be a license to operate. OPG is targeting the end of 2029 for the commissioning and connection to the grid of the first BWRX-300 unit at Darlington. There are also advancing plans for deployment in Saskatchewan with SaskPower selecting the BWRX-300 as their technology of choice and moving forward with siting plans in the southern part of the province, with deployment timed for the mid-2030's. AR development is continuing with the ARC sodium fast reactor and MOLTEX molten salt reactor designs in New Brunswick, with these companies incrementally pushing forward with the various aspects of their technologies.

In terms of new large builds, major announcements include 4800 MW of new nuclear at Bruce Power's "C" site and up to an additional 10 reactor units planned for OPG's new Wesleyville site east of Toronto. These commitments to large new builds are tied to the recent success of the Darlington refurbishment project, which was delivered ahead of schedule and under budget, with the fourth unit completing its refurbishment and returning to power operations with CNSC approved initial power testing starting in 2026 February [1]. In addition, the major component refurbishment of the Bruce Power plant continues to proceed well, and the refurbishment of OPG's Pickering B plant was recently announced (definition and planning in 2026-2027 and refurbishment beginning in the end of 2028, the end of the current license to operate), which is expected to complete in the mid-2030s [2], solidifying further the long-term supply of nuclear energy for Ontario.

The micro-reactor deployment picture has evolved with Global First Power changing hands (Ultra Safe Nuclear Corporation (USNC) went bankrupt and was bought out by Nano Nuclear) and now realigning its potential siting of the micro-modular high temperature gas cooled reactor (HTGR) design, now known as Kronos, at the AECL (Atomic Energy of Canada Limited) Chalk River Laboratory Site. The Westinghouse e-Vinci effort has also refocused on defense opportunities and paused civil deployment, which puts on hold former agreements with the Saskatchewan Research Council for deployment of an e-Vinci in Saskatchewan. There is also renewed interest in AECL historic intellectual properties, such as the SLOWPOKE district heating reactor and AECL Nuclear Battery, with a request for expression of interest call in early 2025 [3], as well as a developing framework for microreactor deployment undertaken by AECL/CNL and the government of Canada. Additionally, the Canadian Department of National Defence is exploring the potential for integrating nuclear power into its plans for expanded operations in the north of Canada as part of increased efforts to meet North Atlantic Treaty Organization (NATO) commitments. All in, this shows a significant push towards microreactor development and deployment in Canada.

Canadian Nuclear Laboratories (CNL) maintains its role of supporting current nuclear fleet operations and the deployment of the future fleet and is expanding its research efforts in reactor safety to support interest in new nuclear deployment in Canada. The reactor safety research program has significant ongoing efforts, primarily under AECL federal nuclear science and technology funding. Reactor safety encompasses neutronics, fuel safety, thermalhydraulics, containment, and severe accidents and covers both the current fleet of reactors and the expansion to come, regardless of size or technology. This research program includes experiments and modelling and has the robustness and adaptability to support the needs of both industry and government stakeholders. There are key efforts throughout this program to support safe new nuclear deployment based on the current landscape and interests in Canada. The specific focus of this paper is the research efforts related to severe accidents in the context of SMR and advanced reactor deployment. This paper builds on previous overviews of CNL severe accident research related to SMR/ARs [4] [5] to provide an update on the severe accident research efforts at CNL in this area and to showcase new developments in experiments, modelling, and analysis.

Before discussing the severe accident research in detail, it is worth mentioning the evolving research and future strategy at CNL regarding new nuclear deployment. AECL/CNL has more than 80 years of experience in nuclear research and is the pioneering organization in Canada. The design, development, deployment and operation of the fleet of CANDU reactors in Canada and abroad is the major source of CNL experience, but over the last 10 years, CNL has developed capabilities and competencies that expand its knowledge into SMR/AR designs that are moving towards deployment. Over these ten years of focus on SMR/AR research development, the strategic outlook for reactor safety has evolved. Initial approaches focused on a technology agnostic view with a drive to develop tools and methods that could be applied across multiple potential technologies/designs. The development of a good set of tools and capabilities has led to more focused research related to specific technologies and phenomena, led by the deployment landscape in Canada and other countries, as well as the technology readiness level (TRL). The reactor safety program builds a base of knowledge commensurate with the TRL, deployment landscape and ongoing research worldwide to ensure Canada has the tools necessary to support safe deployment and make unique, more in-depth research contributions to technologies of interest that align with CNL skills and capabilities. In this way, CNL can develop and maintain the necessary knowledge and contribute complementary research important to Canada and to the international community. The major technologies of interest for CNL are i) water-cooled SMRs, specifically small BWRs and related passive cooling; ii) high-temperature gas reactors, including both SMR and micro-reactors; iii) microreactor focused phenomena and technologies such as heat pipes; and iv) select areas of interest for other advanced designs, such as SFRs and MSRs, commensurate with the development of capabilities that may be needed in the future when TRLs and deployment of these technologies advance. The primary areas of severe accident research align with these and are discussed in depth in the previous review papers [4] [5] and updated with the most recent developments herein.

The method for selecting important research areas and major goals for the reactor safety, and consequently the severe accident, research program has remained consistent as previously discussed [4] [5]. Phenomena Identification and Ranking Table (PIRT) efforts, conducted by CNL or others, highlight the important gaps in knowledge. CNL's experience in developing and evaluating PIRTs related to SMRs/ARs is key to this step. The PIRT results/evaluations identify gaps that need to be addressed, and CNL sets targeted research priorities based on needs and capabilities. Gaps are addressed with experiments/modelling to investigate important phenomena, generate valuable data, develop models, and conduct benchmarking, qualification, and validation of the analysis codes, leading towards the closure of the research gaps.

The final piece of the CNL reactor safety/severe accident strategy is participation in the international research community, which allows CNL to leverage its own efforts to benefit from the valuable work of others and make its own unique contributions. CNL connects to academia, other research laboratories bilaterally and international organizations such as the Organization for Economic Cooperation and Development Nuclear Energy Agency (OECD-NEA), International Atomic Energy Agency (IAEA), Generation IV International Forum (GIF) and European Commission EURATOM. As mentioned previously [4] [5], CNL has taken on leadership positions in expert groups and working groups in these organizations as well as in joint projects under their purview. This is commensurate with the advanced interest in Canada for SMR/AR deployment. Major SMR/AR severe accident interactions include the US Nuclear Regulatory Commission Cooperative Severe Accident Research Project (CSARP) and MELCOR Code Assessment Project (MCAP), the SNETP (Sustainable Nuclear Energy Technology Partnership)/EURATOM initiatives such as SASPAM-SA, SEAKNOT and the ERMSAR Conference, as well as NEA and IAEA joint projects.

The approach builds knowledge and experimental/modelling capabilities to support development and assessment of SMR/AR regulatory/licensing requirements, and emergency planning and response. Considering the above strategy and international engagement, CNL can ensure its knowledge and capabilities meet the needs of its stakeholders (both industry and government) and can support the safe deployment of SMR/ARs in Canada. This paper updates previous overviews of CNL severe accident research on SMRs/ARs, [4] [5], discussing both experimental efforts, Section 2, and modelling, Section 3.

2. EXPERIMENTAL EFFORTS SUPPORTING SMR SAFETY

The experimental campaigns discussed in the previous overviews, [4] [5], have continued to progress and are focusing on a few major areas as identified in PIRTs. For water-cooled SMRs, it is the containment behaviour in integrated pressurized water reactors (iPWRs) and small BWRs, including passive systems. In the case of HTGRs, the focus continues to be on the potential for air ingress, as well as new investigations into pebble bed core heat transfer in accident conditions. Efforts with microreactors, especially heat pipes, are now progressing towards accident analysis. Finally, there are some minor continued efforts in fission product release and the self-heating behaviour in molten salts.

2.1. Water Cooled Reactor Experiments

Research on water-cooled SMRs focuses increasingly on passive safety features. CNL has examined containment behaviour, passive-system reliability, and the conditions that govern their success or failure. Earlier reviews summarized iPWR work [4] [5], which the latest experiments extend to small-BWR containment behaviour. Passive emergency-cooling loops rely on steam condensation on major heat sinks, with condensate returning by gravity. Condensation is most effective at high temperatures and low non-condensable content. Hydrogen produced during fuel-sheath oxidation, and air ingress both reduce heat-transfer coefficients and degrade passive-system performance.

These effects were studied in the Strong Condensation Containment Apparatus (SCCA) program [4][5]. Phase 1 (2021) investigated steam injection and wall heating in an iPWR-like vented annulus; Phase 2 (2022) added helium to simulate hydrogen-rich severe-accident conditions, with results reported in [6][7][8]. Phase 3 (2025) reconfigured the facility for a small-BWR passive containment cooling system (PCCS), using a heat-exchanger analog instead of a chilled wall. Both forced and natural PCCS modes were tested; passive cooling showed lower performance, but all tests produced the same characteristic stratified structure of a hot upper layer over a cooler under-layer. Data from all phases support the SASPAM-SA (Safety Analysis of SMR with Passive Mitigation Strategies – Severe Accident) collaboration on passive-system behaviour in water-cooled SMRs.

The most important thermalhydraulics observation for all three phases of the SCCA experiments (covering both iPWR and small BWR containment analogies) is the strong thermalhydraulic stratification seen with multi-gas mixtures, resulting in a hot upper layer and cooler under layer. The hot upper layer is strongly condensing, and the transition to the cooler layer is a sharp temperature gradient. The cooling capacity exceeds the energy input from the steam, and the condensation enhances the heat transfer coefficients (HTCs) significantly compared to natural convection. Heat transfer primarily occurs in the hot upper layer, the thickness of which is dictated by the energy balance of the steam injection and condensation. Phase 3 results confirmed this interpretation for the PCCS configuration. HTCs followed Dehbi-type correlations (Figure 1), increasing with steam concentration and decreasing with helium, with values ranging from ~600 W/m²·K in high-steam down to ~100 W/m²·K at high helium fractions. The HTCs for forced and natural PCCS modes are comparable, though natural circulation produced slightly higher gas temperatures.

When a light non-condensable gas like helium (or, in a reactor accident, hydrogen) is introduced, it does not separate from steam in the upper layer because of its buoyancy and instead dilutes the upper layer, reducing its effective heat-transfer coefficient and causing the layer to swell. The light gas also diffuses into the lower layer, where it can reach concentrations of 10–30%, which would have combustibility implications if it were hydrogen. The Phase 3 experiments confirmed these behaviours: helium accumulated strongly in the upper layer, reaching dry concentrations above 90% (nearly pure steam–He). The steam also migrated downward by diffusion and interface mixing, achieving wet concentrations of 10%-60% at the highest injection rates.

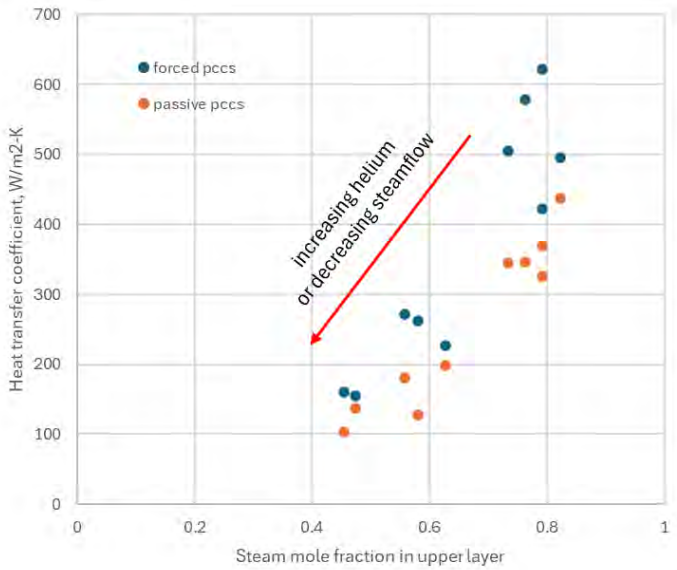

Figure 1. Experimental HTCs as a function of steam concentration in the hot upper layer, under both natural and forced convective flow conditions in PCCS. Results are preliminary

Aerosol transport is primarily diffusiophoresis, driven by steam condensation and turbulent impaction, both concentrated in the hot upper layer. Stratification limits aerosol deposition area and creates an evaporative barrier promoting re-entrainment of aerosols back into the hot upper layer, keeping concentrations in this region high. Phase 3 measurements of turbulence and droplet characteristics supported this picture, where the steam–gas interface remained stable at 2–2.6 m elevation, with suppressed vertical velocity and minimal turbulent kinetic energy (TKE). Above the interface, TKE was much higher, and the droplet size distribution (GSD) was broader, consistent with the vigorous condensation-cloud region observed in all phases.

The next stage, SCCA testing, Phase 4, will continue to explore the PCCS configuration for a small BWR, but will shift perspective upward in containment to look at a bottom injection of steam with a cold heat structure at the top of the volume, along with the PCCS heat exchanger on the side wall. This configuration is commensurate with the top section of a small BWR containment where the containment upper head is cooled by the PCCS pool. In addition, accompanying benchmark modelling of these Phase 3 and 4 PCCS tests will be conducted with CFD, containment (GOTHIC) and severe accident (MELCOR) codes.

With the completion of the four SCCA experimental phases covering both iPWR and small BWR containment configurations, and the accompanying modelling and benchmarking activities, the next stage of the program will shift towards the investigation of the passive Isolation Condenser System (ICS) of a small BWR. This work will extend the experimental foundation established in the SCCA campaigns by examining heat transfer, condensation behaviour, and non-condensable gas effects within a tube-bank configuration directly analogous to the ICS. The SCCA derived experiments may also be paired with other experimental apparatus focused on different aspects of the ICS to provide additional dimensions of investigation and data to better understand the phenomena related to ICS operation.

Regarding late stages of severe accidents, CNL's Cold Crucible Induction Furnace (CCIF) enables high temperature synthesis and rapid quenching of corium materials, supporting studies of phase behaviour, melt miscibility, stratification, and chemical interactions with structural materials [9]. Designed for ~2 kg charges containing depleted or natural uranium, the facility can reach temperatures above 2,300 °C and produces resolidified corium samples suitable for the determination of mechanical properties and developing and validating thermodynamic databases such as TAF-ID. While the CCIF has been extensively applied to

CANDU corium, recent work has produced the first corium representative of Accident Tolerant Fuel (ATF) concepts using FeCrAl cladding—an important development for SMR and advanced reactor safety. Thermodynamic analysis indicates that FeCrAl must be partially oxidized for significant interaction with UO_2 to occur, including dissolution and formation of eutectic phases; therefore, the experiment required a high oxidation ratio, using FeCrAl that was 70% oxidized. This charge was successfully melted, reaching 2,417 °C and yielding high quality in vessel UO_2–FeCrAl corium. Pictures of the charge before and after melting are presented in Figure 2. Currently under characterisation, these pioneering samples will support validation of ATF thermodynamic models and open the door to future experimental programs on melt stratification, vessel material interactions, and even ex-vessel systems such as UO_2–FeCrAl–concrete.

Figure 2: FeCrAl-UO_2 in-vessel corium produced at CNL's CCIF (right), and samples recovered after test (left). Stratification of a metallic phase was observed.

2.2. High Temperature Gas Reactor Experiments

The focus of HTGR experiments at CNL for severe accidents is on the behaviour of the heat transport system under accident conditions and investigations into the heat transfer behaviour of a pebble bed core. Regarding the heat transport system, investigation has been focused on the transition from stagnant flow conditions to bulk natural circulation of air within the core after a break of the helium pressure boundary. It is difficult to reliably predict the timing of this transition, referred to as the onset of natural convection (ONC), and the potential for air interacting with hot graphite (resulting in graphite oxidation) makes this an important event. This ONC phenomenon and its potential impact of air flow on the graphite oxidation rate was studied in the Helium-Air Natural Convection (HANC) experiment. The HANC experimental apparatus geometry resembles an inverted letter "U" that models the coolant flow path within the pressure vessel of a modular HTGR. This shape/configuration is consistent with other apparatus used to study air ingress phenomena found in literature. HANC is set apart from previous studies as it is the full core height of some small modular HTGR concepts (3 m) and was designed to go up to typical operating temperature (700°C).

The structure of the HANC apparatus was primarily 3" Schedule 40 316 stainless steel pipe with welded elbows to create the "U" shape. The principal regions of the HANC apparatus (Figure 3) were: (i) hot leg – the side of the inverted "U" that operated at the highest temperature, (ii) cold leg – the side of the inverted "U" that operated at the lowest temperature, (iii) upper plenum – the section of pipe that connected the hot and cold legs, (iv) lower head – connected the cold leg to the environment through openings with removable seals, and (v) lower plenum – connected the hot leg to the environment also through openings with removable seals. The upper plenum, lower head, and lower plenum were named after the corresponding regions of a modular HTGR that they represented. The pipe forming the inverted "U" was electrically heated with clamp-on band heaters. Custom-formed tubular heaters were also placed inside the lower head and lower plenum. The primary measurements were of surface and gas temperatures.

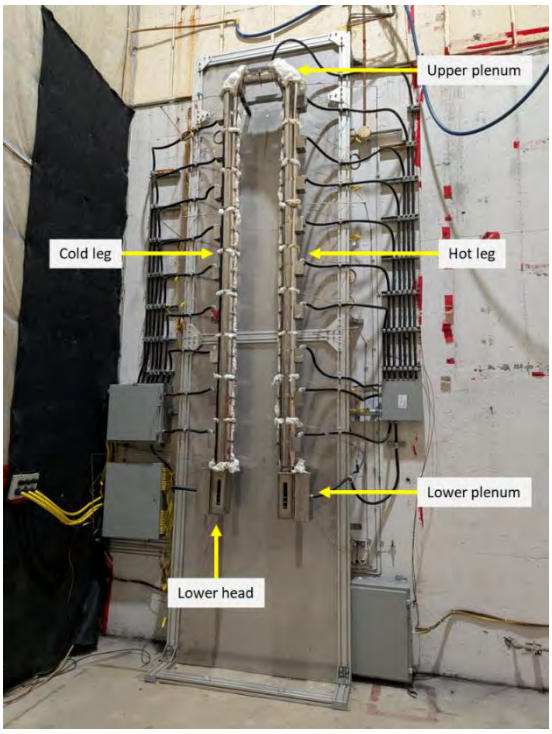

Figure 3. Annotated photograph of the HANC apparatus.

The first HANC test series (HANC-1) was completed in December 2025/January 2026, where ONC was measured in a range of test conditions (200°C to 300°C on the cold leg and 400°C to 700°C on the hot leg). Also studied were variable opening orientations (horizontal and vertical) in the lower head and lower plenum to represent different gas duct and break orientations in modular HTGRs. The measurement data will be used for future model benchmarking with computer codes like RELAP5, GOTHIC, and MELCOR. Refinements to the HANC apparatus are being considered for a second test series (HANC-2) in future years.

The second experimental program at CNL focused on HTGR, which relates to experiments on heat transfer and flow in a Pebble Bed (PB) core, under normal operation and accident conditions (natural convection). The PB-HTGR typically utilizes a discrete bed of fuel elements (pebbles) reactor core, where the pebbles are ~6 cm spheres of pyrolytic graphite matrix comprising thousands of tristructural-isotropic (TRISO) fuel (^{235}U) particles coated with silicon carbide. These pebbles continuously move (flow) through the reactor core, and spent fuel is continuously replenished. The modes of heat transfer in HTGR cores involve convection to the coolant gas (typically helium), radiation between the pebbles and to the gas, and conduction between contacting pebbles. In a molten salt cooled PB reactor, the primary mode of heat transfer is only convection to the salt and conduction between the pebbles. The present work focuses on PB-HTGR cores, while the results are generally extensible to other PB reactor cores.

The current iteration of the Pebble Bed Experiments for Analysis of Core Heat transfer (PebbleBEACH) facility at CNL considers stationary pebbles for the purposes of generating steady state data for model development and code validation. Photographs of the PebbleBEACH facility are shown in Figure 4. These experiments are similar to the SANA [10] experiments performed in Germany in the mid 1990's (which involved stationary graphite pebbles heated by 5 cylindrical graphite heaters placed vertically inside the core), with additional measures to evaluate the individual contributions of surface radiation, convection, contact conductance, and the impact of internal heat generation (as opposed to external heating) in the pebbles, on core heat transfer. Individual contributions of radiation, convection and contact conductance are

correlated using different pebble materials and surface emissivities, while internal heat generation is simulated using pebbles with impregnated heaters. Other experiments, such as those at UC Berkley [11], had considered inductively heated spheres at smaller scales for simulating internal heat generation. The pebbles considered for the first series of experiments performed at CNL in 2025, shown in Figure 4, are polished stainless steel with an emissivity <0.1. These experiments involved external heating, reactor scale pebble sizes, and dimensionless properties for the coolant and flow consistent with normal operations.

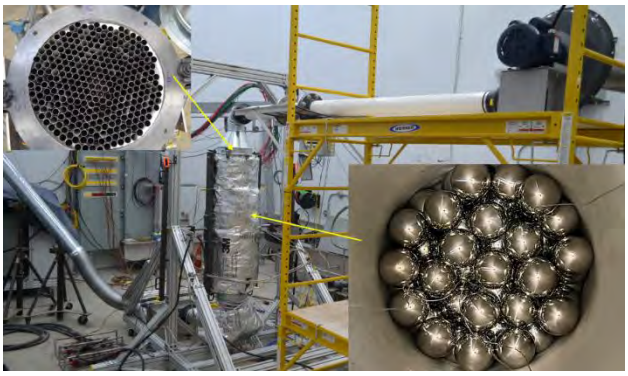

Figure 4: Photograph of the PebbleBEACH facility at CNL

The third component of the HTGR experiments relates to the characterization of dust generation for graphite pebbles in PB-HTGR. Due to the numerous interactions and friction resulting from the continuous movement of pebbles through the core and contact with each other and the reactor internals, PB-HTGRs are expected to produce a significant amount of graphite dust during operation. This is an important source term for safety evaluations as well as a phenomenon critical for evaluating accidents due to the pyrophoric nature of fine graphite under sufficiently small particle sizes. The Pebble bed Aerosol Generation Experiments (PAGE) at CNL will involve accelerated frictional deterioration of the reactor scale pebbles, resulting in dust production and characterization. This facility is currently under the conceptualization stage.

2.3. Heat Pipe Experiments

A newer area of interest based on the deployment landscape is that of microreactors, and in terms of severe accidents, there are interesting research areas being explored. In a general sense, the extent of analysis needs is being evaluated as the size, and potential source terms of these designs are much different from a large reactor or SMR. A microreactor related technology of interest that is being explored for normal operations and accident conditions is a heat pipe cooled reactor design.

Heat pipe reactors (HPR) are commonly configured as a core block with numerous fuel channels interspersed with many coolant channels, not dissimilar to the core block of a HTGR. However, the coolant channels in HPRs comprise heat pipes that passively remove heat from the core block through natural circulation of the sealed alkali metal working fluid within the tube. Thus far, heat pipe reactors are microreactor concepts often targeted for remote deployment with fully- or semiautonomous operating modes. In these scenarios, complete failure of 5% of the heat pipes is a credible failure ratio based on probabilistic safety assessments for a design basis scenario [12]. Heat pipe experiments have been operated at CNL to study alkali-metal heat pipe behaviour under startup, operational transients, and off-normal transients for nuclear reactors. Building upon a series of fundamental studies conducted at CNL using the AHPAT single heat pipe testing apparatus with sodium and potassium as the working fluid [13][14], a multi-heat pipe array AHPAT testing system was developed with five parallel sodium heat pipes operating in vertical orientation and rated at 50 kW, resembling a reactor core block configuration. This apparatus has

been used to look at scenarios beyond the design basis with the potential to progress into severe accidents, where a 20 to 60 % failure rate of heat pipes (simultaneous failure) was investigated with simultaneous delay of activation of shutdown systems (i.e. full power maintained) [14]. The tests were performed with a nominal heat pipe operating temperature of 550°C and an average core-block temperature of 750°C, and the delay in the activation of shutdown systems was 1 hour. For the case with 60% heat pipe failure, the temperature of the failed heat pipes quickly increases to match the core-block temperature within 5 minutes (i.e. 200°C temperature increase). The core temperature remains relatively constant for ~35 minutes and then increases at a rate of up to 250°C/hr over the rest of the transient before activation of shutdown systems is simulated by reducing the power. Future studies with the AHPAT multiple heat pipe scenarios include extension of scenarios identified in MELCOR assessments on accident progression in HPRs [15], such as reactivity insertion during normal operation but with a high failure rate of heat pipes and a 1-hour delay in shutdown rod insertion. CNL is also in the process of scaling up the AHPAT multiple heat pipe apparatus to higher power with more heat pipes to improve the correlation of experimental results to postulated reactor scenarios.

2.4. Molten Salt Reactor Related Experiments

CNL has conducted experimental work focused on molten salt characterization, production capabilities, and on fission product release under severe accident conditions, as discussed in the previous overviews [4] [5], as well as associated molecular dynamics modelling to study fission product behaviour in molten salts. These efforts position CNL well to address MSR related issues that emerge as the deployment of this technology advances. In terms of severe accident research, recent efforts have focused on completing confirmatory experiments on the conversion of UO_2 to a UF-based fluoride/fluoride-chloride molten salt, using depleted uranium, to provide further data to augment the results and conclusions of the previously conducted fission product release experiments [4]. When these confirmatory studies are completed, CNL molten salt severe accident research related to fission product behaviour will reach an appropriate baseline, and further efforts will be paused until emerging research needs are identified by stakeholders.

One other area of MSR related research that is being explored is the volumetric heat generation in core, which includes the development of ‘scalable’ experimental capability for self heating fluids for use in natural circulation loops to simulate MSR cores. Several natural convection loops are available at both CNL and at external laboratories, including Massachusetts Institute of Technology (MIT) and Centrum výzkumu Řež (CVR), for the simulation of molten salt flow and heat transfer in MSR cores. Experimental facilities involving forced circulation of molten salt are not common, due to challenges in identifying pumps and other flow control components that are compatible with molten salts at high temperatures, which are notoriously corrosive. Molten salt loops at CNL and other organizations typically employ heating of the channels through which the salt flows (i.e., indirect heating of the salt). In fuel salt MSR cores, however, heat is generated volumetrically inside the coolant. The molten FLiBe or FLiNaK type salt carries uranium fuel in the form of UF_4, which fissions when it passes through the moderated portion of the core loop. Temperature distributions and associated flow could be distorted due to indirect heating techniques, especially during natural circulation.

Several techniques for introducing volumetric heat generation in molten salts have been considered in the past. These include induction heating with salt simulants with added dopants, microwave heating and Joule heating. While both microwaves and induction can heat volumetrically, the scalability of these techniques beyond just one or a few channels is not practical due to the loss in penetration depth of the induction or microwave fields. Additionally, the introduction of heating in moderator region (usually a graphite block) close to the fuel channel is non-trivial. After critically examining various strategies for a potential scalable apparatus, introduction of volumetric heating of salts using the Joule heating technique was determined to be most practical. However, challenges related to electrolysis (due to application of high voltages), corrosion and the presence of electrically live fluid in the loop, and non-conductive materials suitable for high

temperature operation, will need to be resolved. The test apparatus used for ongoing experiments for joule heating of simulant molten salts is shown in Figure 5. These experiments are intended towards the investigation and mitigation of corrosion and electrolysis (by applying suitable voltage waveforms), material compatibility (high temperature plastics suitable for use with FLiBe and FLiNaK loops) and alternative (to thermocouple) local temperature measurement instrumentation, and their scalability for the development of larger loops.

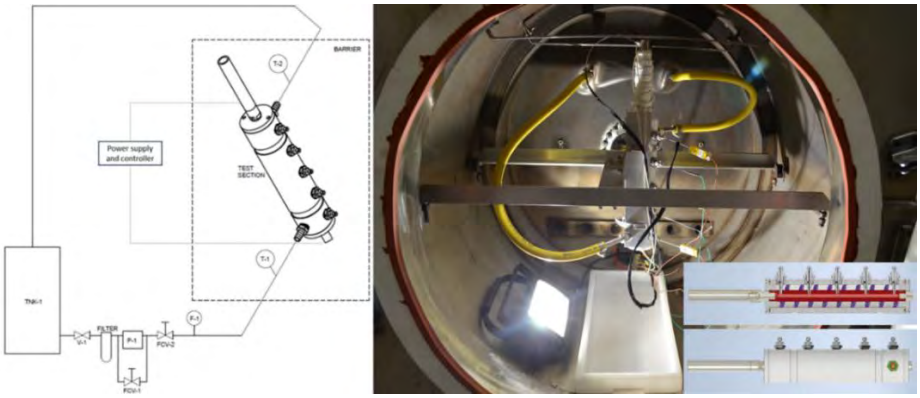

Figure 5: Depiction of the joule heating apparatus for MSR core heat transfer experiments

3. SEVERE ACCIDENT MODELLING AND ANALYSIS EFFORTS FOR SMR

CNL is conducting both full reactor and experimental apparatus benchmarking, modelling and analysis efforts to increase knowledge and expand capabilities for integrated severe accident analysis and source term calculations for a variety of SMR/AR designs. Experimental benchmarking is focused on the SCCA experiments for iPWR containment configurations, but will be extended to new experiments for small BWR PCCS and for HTGR air ingress (HANC) configurations. Integrated reactor analysis is being conducted for several SMR designs using the MELCOR code, including generic iPWR, small BWR, pebble bed HTGR, and SFR. These analyses do not contribute to licensing yet, but focus on building capability and exploring the important phenomena and systems involved in severe accidents in each reactor technology.

3.1. Water Cooled Reactor Analysis

CNL efforts in modelling of water cooled SMRs have focused on iPWR and small BWR, which represent the major designs being deployed. Given the strong reliance of these designs on passive safety systems, the overall focus of these models has been on quantifying the impact that disruptions of passive safety systems have on severe accident progression and source term generation. The primary tool for this has been MELCOR, and as introduced previously [4] [5], CNL has developed reference models for both a generic iPWR design and a generic small BWR design. These efforts are part of CNL's contributions in the EU SASPAM-SA project, including MELCOR analysis of both iPWR (SASPAM-SA design 2) and a generic small BWR (design 3). CNL is contributing a generic small BWR model to SASPAM-SA to support analysis by the other participants and eventual benchmarking to CNL results.

The recent developments of CNL water cooled SMR analysis have been captured in publications in the recent NUTHOS-14 Conference (2024 August) for iPWR [16] [17] and small BWR [18]. The finalized models for iPWR and small BWR are now being used in more detailed studies to assess the performance/impacts of passive systems and understand accident behaviour over a variety of conditions. The iPWR studies were extended across many scenarios to build the understanding needed to support

emergency planning and operation intervention levels [5] [16] [17]. The generic small BWR MELCOR model, introduced in [5], was completed, and analysis of common accident scenarios was conducted, including station blackout accidents (SBO) and loss-of-coolant accidents (LOCA) involving ICS and/or PCCS impairment to varying degrees. The analysis indicated that in the SBO case, significant impairments (e.g., 100% losses in ICS and/or PCCS) were required for any fuel damage to occur [18]. For the SBLOCA cases, the small break was placed 2.5 m below the top of the active fuel to determine the impact of fuel failures on passive safety performance. The results showed that non-condensable gases, such as hydrogen generated through oxidation of hot cladding material, would migrate into the passive ICS, cause a blockage in flow, and diminish the heat removal capability, causing a positive feedback loop of fuel degradation [18].

Another important recent effort was a phenomena identification and ranking table (PIRT) for design extension conditions in the BWRX-300 small modular reactor, which was delivered to the CNSC. With one licensing assessment already underway for the Darlington New Nuclear Project, and the prospect of several more to be initiated in the near future, the CNSC requested expert support and consultation from CNL. Design extension conditions are a subset of beyond-design basis accidents considered in the design of a facility that could include some severe accidents. Using only open-literature information, a panel of CNL subject matter experts from across the Science & Technology organization developed the PIRT to identify knowledge gaps that could be used as the basis for planning a future research & development program supporting BWRX-300 safety and licensing. The generic small BWR MELCOR model was also used to conduct an analysis that supported this PIRT effort.

Continued efforts in severe accident uncertainty and sensitivity (U&S) analysis included using the generic small BWR MELCOR model in a MELCOR-DAKOTA coupled code analysis, implementing the Wilks method [19]. The analysis explored 19 input parameters with 124 simulations and tracked hydrogen generation (Figure 6) and radionuclide releases for the same SBLOCA case performed in the previous best-estimate simulations [18]. The uncertainty analysis modelling framework builds on the foundation for CNL's small BWR severe accident uncertainty analysis knowledge and expertise and will be used to support future severe accident uncertainty and sensitivity analyses.

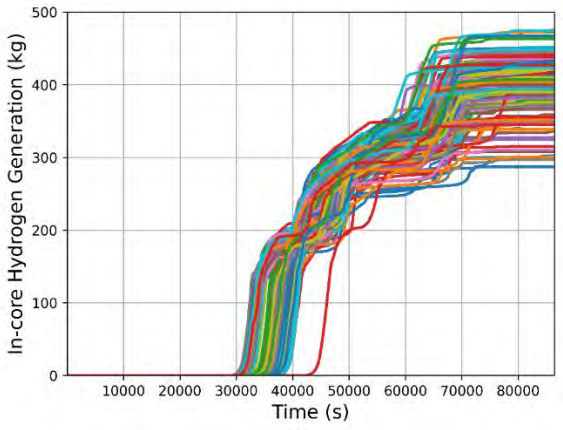

Figure 6: Generic Small BWR Uncertainty Analysis Total H2 Generation over the Transient

In addition to the full reactor modelling and analyses, benchmarking studies of the SCCA experiments, discussed in Section 2.1, for passive safety systems have been performed using MELCOR and the more detailed thermal-hydraulic code GOTHIC to ensure that phenomena are appropriately captured [20]. Benchmarking of the SCCA Phase 1 and 2 iPWR focused experiments with MELCOR and GOTHIC showed that accurately reproducing this stratification was essential. The MELCOR 3×3 model matched the

experimental profiles reasonably well at intermediate injection rates (6–10 g/s) but performed less accurately at low and high flow rates. The finer 6×3 nodalization did not consistently improve results and often underestimated the steam-layer thickness. GOTHIC, using 30 vertical zones, more reliably captured the two-layer structure and demonstrated the importance of sufficiently detailed vertical nodalization; treating the SCCA as a lumped or overly coarse volume could not reproduce the experimental behaviour. This stratification also governed aerosol transport. Buoyancy suppressed vertical mixing, confining droplets to the steam-rich upper layer, an effect captured in both codes. Deposition occurred primarily in this region, making leak-path elevation important for source-term assessment. Diffusiophoresis was identified experimentally as the dominant deposition mechanism, with turbulence providing a secondary contribution. At higher steam injection rates, discrepancies between experiments and GOTHIC predictions grew due to limitations in its turbulence modelling, while MELCOR's restriction of the steam layer to only the top control volumes led to underprediction of its thickness.

Overall, the SCCA Phase 1 and 2 tests and associated modelling provided valuable insight into thermalhydraulic and aerosol behaviour in submerged containments relevant to iPWR. The benchmarking exercises showed that MELCOR and GOTHIC can capture many key behaviours but also highlighted limitations related to nodalization, stratification, turbulence, and particle transport. These findings support the need for complementary CFD analyses incorporating advanced turbulence and droplet-transport models to better reproduce the complex flow patterns observed in the tests. A more detailed CFD analysis of the Phase 1 and 2 tests is upcoming, as well as future benchmarking of MELCOR and GOTHIC against the updated SCCA Phase 3 and 4 tests focused on small BWR PCCS operation.

3.2. HTGR Analysis

The CNL MELCOR model of a 200 MWth pebble bed HTGR, discussed in [5], has been used to simulate a severe air-ingress accident (also referred to as the depressurized loss of forced circulation, DLOFC) by imposing a simultaneous guillotine break of the co-axial inlet/outlet pipe that connects to the RPV [21]. A detailed nodalization was developed to better capture air-ingress into the vessel, and the results indicated a relatively short air-ingress period on the order of 4 hours and elucidated the role of the onset of natural circulation on the graphite oxidation during the accident. These simulations reinforced the importance of the onset of natural circulation phenomena and the need for experimental analysis with the HANC apparatus, as discussed in Section 2.2. The HTGR severe accident model has also been used in uncertainty and sensitivity analysis using the MELCOR-DAKOTA coupling and implementing the Wilks method. The simulations explored the impact of 11 uncertain input parameters on key figures of merit during the DLOFC transient scenario, such as peak fuel temperature (to determine the margin to TRISO fuel failure limits), ONC timing (to determine the onset of significant graphite oxidation), and radionuclide release over 124 simulations. The analysis and results are complete and submitted for publication.

3.3. SFR Analysis

As part of developing baseline capabilities for SFR analysis and considering the planned deployment of the ARC-100 SFR in New Brunswick, CNL is exploring SFR related severe accidents and source terms analysis. A generic SFR model was developed in MELCOR using a literature review of past and present SFR designs to simulate the unprotected loss of flow accident (ULOFA) and unprotected transient overpower accident (UTOPA) for a generic 250 MWth pool-type SFR. The best-estimate analysis was carried out for each scenario (an example output is shown in Figure 7, left), with an uncertainty and sensitivity analysis carried out by simulating 60 input decks for the ULOFA scenario, with the reactivity coefficients used as uncertain input parameters tracking FOMs of coolant boiling margin, clad melting temperature margin, and fuel melting temperature margin (an example output for fuel melting margin under a ULOFA is shown in Figure 7, right). With this baseline model developed and the initial analysis accomplished, further efforts will be considered based on the deployment landscape of this technology in Canada.

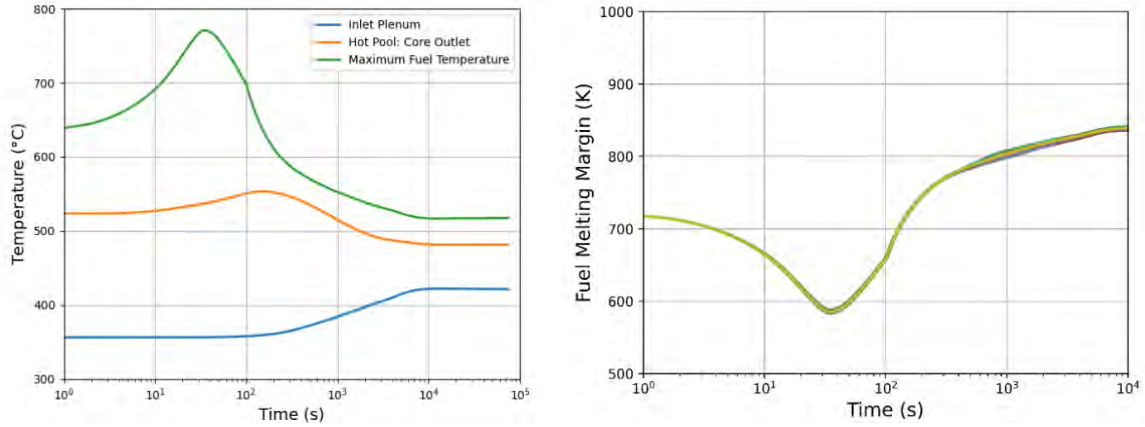

Figure 7: Temperature transient behavior during a best-estimate ULOFA simulation (left) and horsetail plot of fuel melting margin under a ULOFA for 60 simulations.

3.5. Severe Accident Uncertainty and Sensitivity Capabilities

CNL is, and has been, developing capabilities in severe accident uncertainty and sensitivity (U&S) analysis, as discussed in [4] [5]. CNL's participation in the IAEA Coordinated Research Project (CRP) I31033 – "Advancing the State-of-Practice in Uncertainty and Sensitivity Methodologies for Severe Accident Analysis in Water-Cooled Reactors" (2019-2023) [22], went well and focused on MAAP-CANDU severe accident and SUSA uncertainty analysis for CANDU severe accident U&S [23]. This analysis is captured in a paper to the Journal of Nuclear Technology and will be published soon [24]. The analysis methods and knowledge developed during the CRP have been leveraged to perform other uncertainty analyses on other CANDU severe accident variations, as well as non-CANDU type reactors, including SMRs. CNL also seeks to build on the international collaboration under the IAEA CRP through exploring, in more detail, the results from the CANDU portion of the CRP—particularly hydrogen releases—and aims to organize a form of international workshop between the CANDU focused CRP participants (namely CNL, KAERI, and UPB) to identify and potentially improve computer code models for CANDU severe accidents.

Parallel to the MAAP-CANDU and SUSA uncertainty analysis, developments have been made with the MELCOR severe accident code and the DAKOTA uncertainty analysis package. These developments include the development of a Python-based coupling of the two codes and deployment on the CNL ATHENA high-speed computing cluster. This framework has been applied to several small modular reactor severe accident analysis models, including the small BWR, pebble bed HTGR, and the SFR model, as discussed in the previous sections. The MELCOR/DAKOTA coupling is currently the preferred tool for non-CANDU analysis, but the applicability of SUSA will be explored in the future. In previous analysis, the MELCOR-DAKOTA uncertainty analysis framework used the Wilks method, but it has recently been expanded to use other methods, including variable importance measurement through the Morris method, as well as applying correlational structures (as opposed to only simple independent random sampling) using the Iman-Conover method. This has been accomplished through custom Python scripts combined with the DAKOTA uncertainty analysis package. Python analysis scripts have also been developed to better elucidate data patterns and facilitate simpler and more robust data analysis by providing scatterplots of raw data, as well as the residual plots that determine the partial correlation coefficients and simple regression coefficients. The capabilities developed at CNL, and efforts to assess the U&S for severe accident calculations for several reactor technologies, position CNL well to make significant contributions to international efforts and identify improvements for severe accident computer code modelling.

3.6. Emergency Planning Zones

CNL is building on previous work in emergency planning zones (EPZs), discussed in [4] [5], including participation in the IAEA CRP on SMR EPZs and the associated technical document, as well as CNL's own studies on challenges related to SMR EPZs and a framework for EPZ sizing. CNL is at the forefront of using high-fidelity computational fluid dynamics (CFD) simulations to study atmospheric dispersion of radionuclides in complex semi-urban environments [25]. As SMRs are expected to be deployed closer to end users in urban settings, CNL has advocated incorporating CFD into the existing suite of Gaussian and Lagrangian particle dispersion models to reduce excessive conservatism in EPZ sizing [26]. CNL is also supporting the ongoing development of EPZs for iPWR designs in the SASPAM-SA collaboration.

4. CONCLUSIONS

New nuclear deployment in Canada is accelerating to meet clean energy goals, and CNL is supporting safe deployment through robust reactor safety research. CNL capabilities and knowledge are developed to align with the SMR/AR deployment landscape in Canada and support both industry and regulatory stakeholders. Reactor safety and severe accident research, in particular, has and is further developing base capabilities for the range of popular SMR/AR technologies and pursuing deeper expertise for the key technologies nearing deployment. This flexible program allows research gaps to be identified and addressed through experiments and modelling to provide knowledge and data that are needed to support safety analysis reports and licensing reviews.

Severe accident research at CNL is focused primarily on water cooled SMR containment behaviour, especially for small BWRs, passive system reliability and performance in severe accident conditions and integral accident analysis to compute potential radionuclide source terms. HTGRs are another near deployment technology of interest, and CNL has developed experiments in core heat transfer, heat transport system onset of natural circulation, and is working towards confinement phenomena. Integral severe accident analysis, along with uncertainty and sensitivity assessments provide insight on HTGR accident behaviour and helps to refine experiments. An area of active research development moving beyond normal operations into accident conditions is heat pipe reactor cooling systems utilized in microreactors. The baseline capabilities in SFR integral analysis, and understanding molten salt reactor designs, especially focused on fission product behaviour and simulating self heated cores, positions CNL to move deeper with ease should the deployment of these technologies accelerate. CNL's research program is enhanced through international participation in joint projects under NEA, IAEA and EU, as well as with the GIF working groups. It is also enhanced through knowledge sharing in major conferences, especially ERMSAR. The reactor safety and severe accident research program continually evolves to address identified gaps, generate knowledge to address regulatory and industry stakeholder needs and support safe deployment of new nuclear in Canada.

ACKNOWLEDGMENTS

Much of the work discussed herein and CNL participation in various international working groups, projects and initiatives is funded through the Atomic Energy of Canada Limited (AECL) Federal Nuclear Science and Technology Program.

REFERENCES

1. "Ontario Delivers Darlington Refurbishment Project Ahead of Schedule and Under Budget", https://news.ontario.ca/en/release/1006993/ontario-delivers-darlington-refurbishment-project-ahead-of-schedule-and-under-budget (2026).
2. "OPG set to refurbish Pickering Nuclear to secure decades more reliable, low-carbon power for Ontario", https://www.opg.com/story/opg-set-to-refurbish-pickering-nuclear-to-secure-decades-more-reliable-low-carbon-power-for-ontario/ (2025).
3. "AECL and CNL explore market interest in SLOWPOKE and Nuclear Battery reactor technologies", https://www.cnl.ca/aecl-and-cnl-explore-market-interest-in-slowpoke-and-nuclear-battery-reactor-technologies/ (2025).
4. A.C. Morreale, D.W. Hummel, L.S. Lebel, Y-S. Chin, R.S. Dickson, K. Stoll, and C. Maxwell, "Severe Accident Analysis Research at CNL for Small Modular and Advanced Reactor Designs", *Proceedings of the 10th European Review Meeting on Severe Accident Research (ERMSAR-2022)*, Karlsruhe, Germany, May 16-19, 2022.
5. A.C. Morreale, L.S. Lebel, F. Zhou, D.W. Hummel, E. Jia, J. Cui, C. Maxwell, T.P. Kaloni, E. Geiger, and G. Patterson, "Update on Severe Accident Analysis Research at CNL for Small Modular and Advanced Reactor Designs", *Proceedings of the 11th European Review Meeting on Severe Accident Research (ERMSAR-2024)*, Stockholm, Sweden, May 13-16, 2024.
6. L. Lebel, E. Jia, D. Grand-Maitre, T. Clouthier, "Impact of hydrogen on iPWR containment Thermal-Hydraulics in severe accidents", *Nuclear Engineering and Design*, (2025) https://doi.org/10.1016/j.nucengdes.2025.113953.
7. L.S. Lebel, A.C. Morreale, K. Batten and T. Clouthier, "Aerosol retention within submerged Containment-Type iPWRs: Experiments and Modeling," *Nuclear Engineering and Design*, **Vol. 398**, p. 111994, (2022). doi: 10.1016/j.nucengdes.2022.111994
8. Lebel, L., Grand-Maitre, D., Clouthier, T., "Transport characteristics of fission product surrogates in water-cooled small modular reactor containments.", Journal of Aerosol Science, 190, p.106663, (2025) https://www.sciencedirect.com/science/article/pii/S0021850225001405
9. David, R., Mitchell, B., Spencer, J. H., Lair, N., and Petoukhov, S. M. (November 1, 2023). *Cold Crucible Facility for Severe Accident Research at Canadian Nuclear Laboratories.* **ASME Journal of Nuclear Engineering and Radiation Science**, **10**(2), 024501. https://doi.org/10.1115/1.4063673
10. Stoecker, B., Niessen, H. F., & Forschungszentrum Juelich GmbH (Germany). Inst. fuer Sicherheitsforschung und Reaktortechnik. (1997). Data sets of the SANA experiment 1994-1996.
11. https://fhr.nuc.berkeley.edu/fhr-research-areas/pebble-bed-heat-transfer-experiment-pbhtx/
12. P. Li, H. Zhang, Z. Zhang, C. Wang, K. Guo, W. Tian, & S. Qiu. Heat Pipe Failure Accident Analysis of the Multipurpose Dual-Mode Heat Pipe Nuclear Reactor Power System. *Available at SSRN 5230560*.
13. C. Azih, Development of experimental and modelling capabilities and tools at Canadian Nuclear Laboratories for investigations on inherent and passive safety designs of advanced reactor concepts", International Conference on Topical Issues in Nuclear Installation Safety: Strengthening Safety of Evolutionary and Innovative Reactor Designs, No. IAEA-CN—308, Vienna, Austria, (2022).
14. P. Maqueo, R. MacCoy, R. McGrath, and C. Azih, Sodium Heat Pipe Under Pulsed Power Near Operation Limits, 21st International Topical Meetings on Nuclear Reactor Thermal Hydraulics (NURETH-210), Busan, Korea, 2025 Aug. 31 – Sep 5
15. K. Wagner, C. Faucett, R. Schmidt & D. Luxat. (2022). MELCOR Accident Progression and Source Term Demonstration Calculations for a Heat Pipe Reactor (No. SAND2022-2745). Sandia National Lab. (SNL-NM), Albuquerque, NM (United States).
16. J. Cui, L. Lebel, A. Morreale and D. Hummel, "MELCOR Model of iPWR and Application to Emergency Planning Zone Study", 14th International Topical Meeting on Nuclear Reactor Thermal-Hydraulics, Operation and Safety (NUTHOS-14), Vancouver, August 25–28, 2024.
17. J. Cui, L. Lebel, A. Morreale and D. Hummel, "MELCOR Model of iPWR and Application to Emergency Planning Zone Study", Nuclear Engineering and Design, Vol. 442, October 2025.

18. F. Zhou, A. C. Morreale, L. Lebel, J. Cui, G. Patterson, "Severe Accident Analysis of a Generic Small Boiling Water Reactor", 14th International Topical Meeting on Nuclear Reactor Thermal-Hydraulics, Operation and Safety (NUTHOS-14), Vancouver, August 25-28, 2024.
19. S. S. Wilks. Determination of sample sizes for setting tolerance limits. *The Annals of Mathematical Statistics*, 12(1), pp. 91-96, 1941.
20. Jia, D. E., Lebel, L., Morreale, A., & Zhou, F. (2024). GOTHIC and MELCOR benchmarking of the CNL strong condensation containment apparatus experiments. *Nuclear Engineering and Design*, *427*, 113440.
21. F. Zhou, L. Lebel, A. Morreale, D. Wojtaszek, J. Cui, "Simulation of DLOFC Accident in a Generic Pebble Bed High-Temperature Gas-Cooled Reactor using MELCOR", 5th Generation IV and Small Reactors (G4SR) Conference, Ottawa, Canada, October 1-4, 2024.
22. F. Mascari et. al., "Overview of IAEA CRP I31033 "Advancing the State-of-Practice in Uncertainty and Sensitivity Methodologies for Severe Accident Analysis in Water Cooled Reactors", *Proceedings of the 10th European Review Meeting on Severe Accident Research (ERMSAR-2022)*, Karlsruhe, Germany, May 16-19, 2022.
23. S.M. Petoukhov, A.C. Morreale, J-H. Bae, D. Dupleac, R-M. Nistor-Vlad, T. Jevremovic, F. Mascari, A. Bersano, F. Gabrielli, D. Luxat, K.I. Ahn, L.I. Albright, J. Ortiz, J.M. Garcia, H.U. Rheman, "Uncertainty and Sensitivity Analysis of a CANDU 6 Plant by Means of Severe Accident Codes in the Framework of the IAEA CRP I31033: Preliminary Results", *Proceedings of the International Conference on Topical Issues in Nuclear Installation Safety (TIC-2022)*, Vienna, Austria, October 18-21, 2022.
24. Petoukhov, S., Morreale, A., Patterson, G., Bae, J. H., Ahn, K.-I., Dupleac, D., & Nistor-Vlad, R.-M. (2026). *A Summary and Future Work Plans of the Uncertainty and Sensitivity Analysis of a Severe Accident in a Generic CANDU 6 Plant in the Framework of IAEA CRP I31033*. **Nuclear Technology**. https://doi.org/10.1080/00295450.2025.2602406
25. John, A., Lal, S., LeFrancois, N., Copping, A., Bowden, R., & Lebel, L. (2025, November). Recommendations on an Integrated Approach for Modelling Nearfield Atmospheric Dispersion for a Prototypical SMR Site. In Division of Fluid Dynamics Annual Meeting 2025.
26. S. Lal, A. John, L. Lebel, "Benchmarking Nearfield Radionuclide Dispersion with CFD and Gaussian Model", IAEA International Conference on SMRs and their Applications, Oct 2024.

Canadian Nuclear Laboratories | Laboratoires Nucléaires Canadiens

CNL Severe Accident Analysis Research to Support Safe Deployment of Small Modular and Advanced Reactors

Andrew C. Morreale*, Garik Patterson, Luke S. Lebel, David W. Hummel, Chuk Azih, Eric D. Jia, Abishek Sridhar, Ernesto Geiger.

Canadian Nuclear Laboratories (CNL)

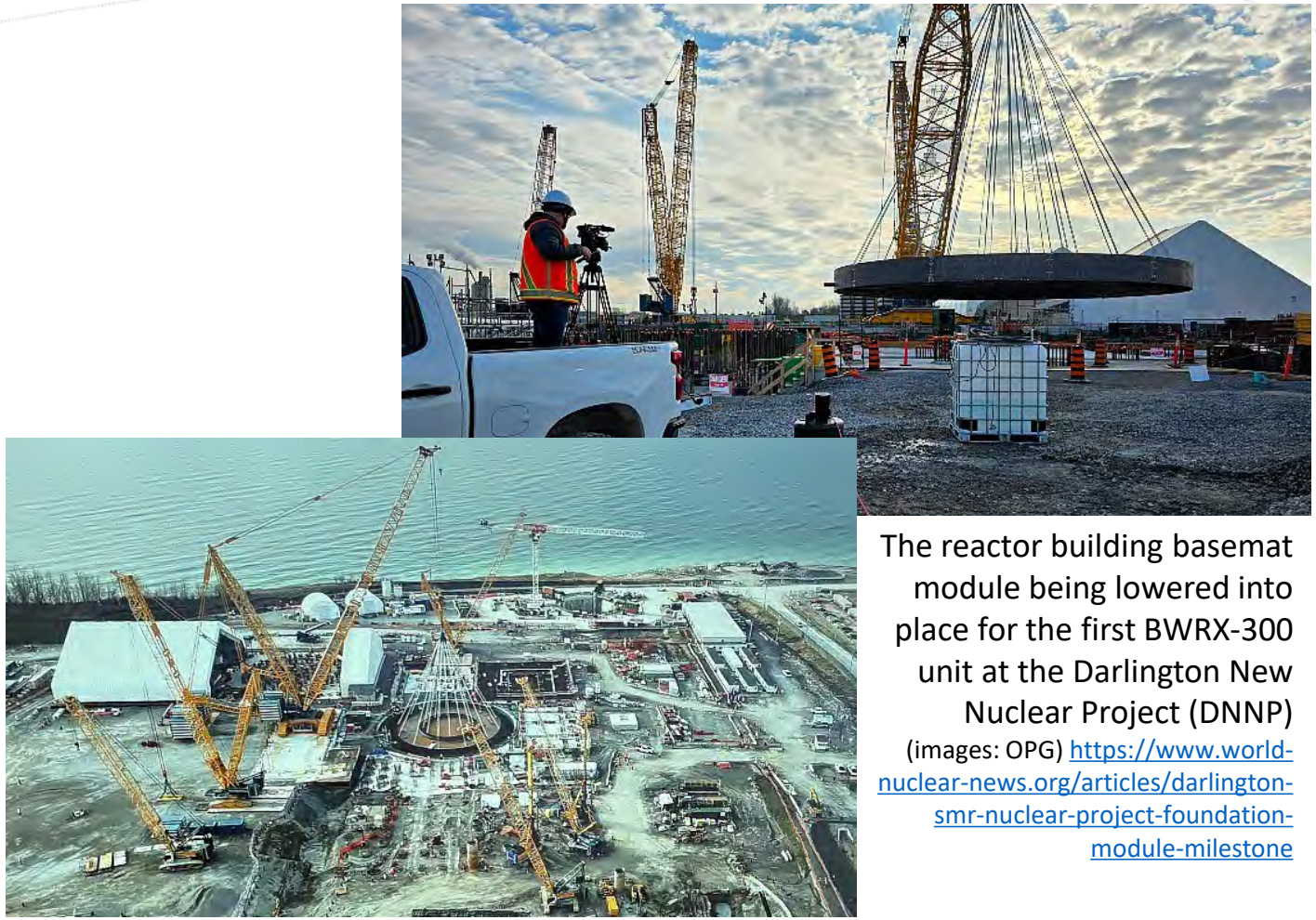

The reactor building basemat module being lowered into place for the first BWRX-300 unit at the Darlington New Nuclear Project (DNNP) (images: OPG) https://www.world-nuclear-news.org/articles/darlington-smr-nuclear-project-foundation-module-milestone

The 12th European Review Meeting on Severe Accident Research (ERMSAR-2026), Madrid, Spain, May 18-22, 2026

Outline

- Introduction
  - Updates on SMR and large reactor deployment in Canada
  - CNL Reactor Safety/Severe Accidents Research Program and Strategy
- Experimental Efforts
  - Small BWR PCCS experiments
  - Corium production in the CCIF
  - HTGR Experiments: Helium-Air Natural Convection, and Pebble Bed Core
  - Heat Pipes
  - Molten salt experiments
- Modelling Analysis
  - Water cooled reactor analysis
  - Advanced reactors (HTGR and SFR)
  - Severe accident Uncertainty and Sensitivity
- Conclusion

New Nuclear Deployment Landscape in Canada

Stream 1: On-Grid, ~300 MW_e

- Ontario Power Generation & SaskPower select GE-Hitachi BWRX-300: 1st CL 2025 April
  - Darlington 4 units (2029 first).
    - U1 containment base (2026 April)
  - SK 4 units (2034-2042)
- Alberta
  - SMART MOU
  - OPG & Capital Power

Large Nuclear

- Refurbishments:
  - Darlington complete;
  - Bruce MCR going well
  - Pickering B (planed 2028)
- Bruce "C" = 4800MWe
- OPG Wesleyville siting (10 units)
- AtkinsRéalis 1,000 MW CANDU® MONARK™

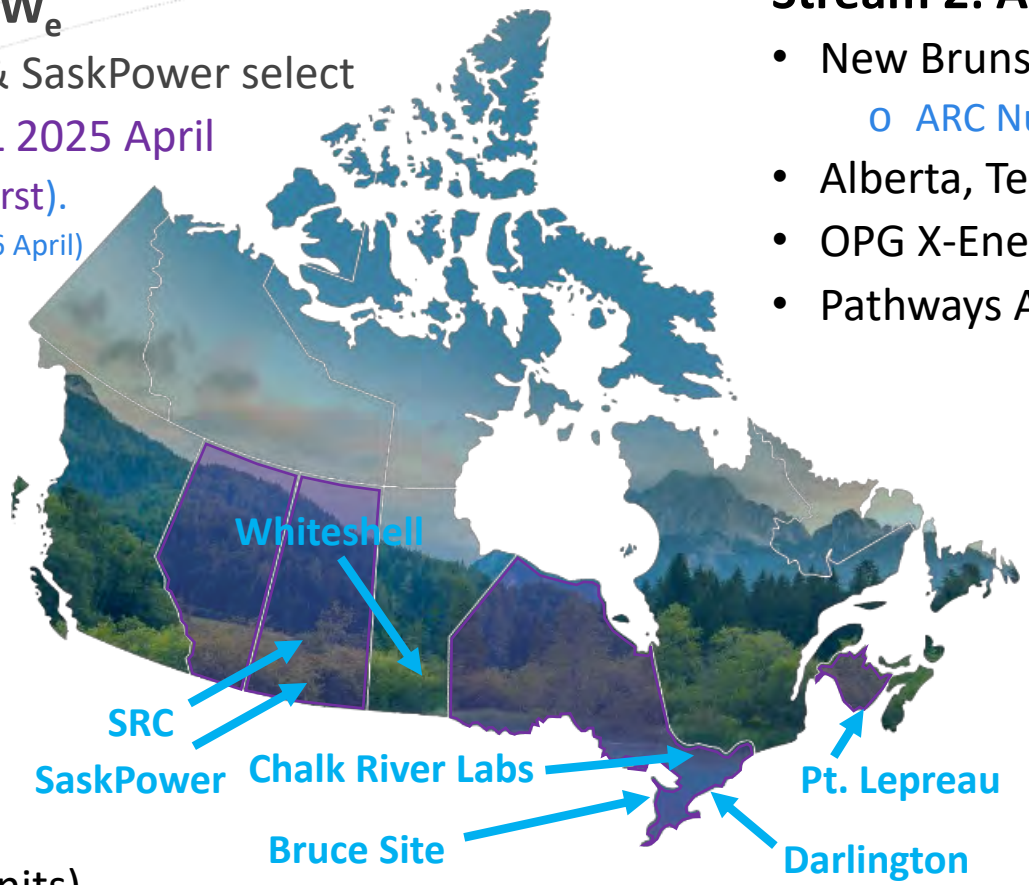

Stream 2: Advanced Reactors

- New Brunswick Power, Point Lepreau
  - ARC Nuclear ARC-100, LTPS submitted; Moltex SSR-W
- Alberta, Terrestrial Energy MOU
- OPG X-Energy framework agreement
- Pathways Alliance

Stream 3: Off-Grid, <15 MW_e

- Canadian Nuclear Laboratories
  - Global First Power (NANO Nuclear)
- McMaster University/GFP MOU
- Saskatchewan Research Council (SRC) searching for options instead of eVinci
- AECL Nuclear Battery/SLOWPOKE RFEOI
- DND/DRDC Microreactor interest for nuclear in the north

Government efforts:

- Federal SMR Roadmap/Action Plan; AECL/CNL microreactor framework (in progress)
- Canadian Nuclear Safety Commission (CNSC) pre-licensing vendor design review
  - 11 SMRs; 3 large reactors

Canadian Nuclear Laboratories | Laboratoires Nucléaires Canadiens

CNL Reactor Safety Overview

- CNL is Canada's premier nuclear science and technology organization
  - Supporting government research priorities, regulatory and industry stakeholders, and representing Canada (with CNSC and NRCan) in the international community.
  - Flexible technical research program supports new reactor deployment and stakeholder needs
- Reactor safety = support current fleet + build capabilities/analysis for future fleet
  - Develop understanding of phenomena/technologies and build/expand modelling and experimental analysis capabilities. *Evolving research guided by Canadian deployment (interest, builds, CNSC VDRs).*
- SMRs and Advanced Reactors
  - Canadian SMR deployment landscape
  - Coolants: water, gas, sodium, molten salts (f/c) + micro-reactors (heat pipes)
  - Continually evolving research program
    - Initial base knowledge is expanded as technologies move towards deployment
- Current Fleet and New Large Builds
  - Large builds in Canada (selecting technologies)
  - R&D to explore emerging issues
  - R&D for current and future fleet
    - Focus on severe accidents to better understand accident progression, source term consequence and impact on emergency response.

CNL research is leveraged by international (NEA, IAEA, GIF) & bilateral cooperation + industry/vendor work

Reactor Safety and Severe Accidents

- Robust technical program supports SMR research, development, and deployment
  - Built upon decades of CANDU experience and recent efforts in SMR and Advanced Reactor analysis driven and refined by the Canadian deployment landscape as well as technology readiness level.
  - Advancing development of tools for multiple designs + focused research on near term deployment
- Severe accidents are a significant part of the reactor safety program
  - Phenomena Identification and Ranking Table (PIRT) activities: highlight knowledge gaps, set research
    - CNL experience in conducting and evaluating PIRTs related to SMR/AR
  - Experiments and modelling investigate gaps and better understand phenomena including special focus on severe accident scenarios, phenomena, progression and source term
    - Containment phenomena, fission product behaviour, passive safety features, integral assessment of generic SMR designs to evaluate systems/design features and impacts on source term and emergency response.
- International collaborations are key to reactor safety/severe accidents
  - IAEA CRPs (IVMR, Ex-Vessel, SA Uncertainty); US NRC's CSARP/MCAP
  - NEA joint projects (FACE, TCOFF-2, ROSAU, COPS, THEMIS, PANDA, WGAMA-CCVM, TAF-ID)
  - EURATOM/SNETP (key projects: SEAKNOT, IPRESCA, AMHYCO, SASPAM-SA, and ERMSAR conference)

Experimental Campaigns

- Progression of tailored experiments to address research gaps, paired with benchmarking
  - PIRTs and previous campaigns have focused research in certain areas.
- **Water cooled SMRs:** pathways disrupting passive safety systems + source term impact
  - Natural circulation + effects of small and/or integrated containment on gas mixing and FPs
  - Benchmarking of the iPWR containment passive cooling experiments (condensation, leakage/air ingress) and the new small-BWR passive containment cooling system (PCCS) experiments
  - Late-stage severe accident investigation of corium materials in the cold crucible induction furnace
- **High temperature gas reactors:**
  - Air ingress and potential for graphite oxidation: **1st experiment on onset of natural circulation**
  - New investigations into pebble bed heat transfer in accident conditions
- **Heat pipes:** Progress in HP microreactor efforts to benchmarks and accident behavior
- **Molten salt designs:** some progression in fission product (FP) behaviour/retention in molten salts and new efforts in self heating experiments

SCCA Experiments: iPWR & small BWR Containment

- Experiments using the **Strong Condensation Containment Apparatus** (SCCA) aim to study detailed containment thermal-hydraulic and aerosol phenomena within a prototypical containment section.
  - Dimensions: 3.6 m high × 0.75 m wide × 0.40 m deep.
  - Operating Conditions (iPWR): 2 kW heated wall, ~10°C chilled wall, steam injection rates 2 to 15 g/s, and helium injection from 0-40%.
  - Aerosol Measurements: NaCl solution droplet aerosols tracked and collected at multiple locations to quantify aerosol transport.
  - Optical Diagnostics: 3D LDA/PDA employed to measure near-wall aerosol size and velocity distributions.
- **iPWR Phase 1** (March 2021): Investigated the influence of steam injection and wall heating in a vented vessel configuration.
- **iPWR Phase 2** (June 2022): Examined effects of He injection, relevant to the core damage phase where H_2 and radionuclides are co-released.
- **Small BWR PCCS Phase 1** (June 2025): New test using a passive containment cooling system (PCCS) heat exchanger (forced or natural circulation flows) similar to BWR containment (instead of chilled wall).
- **Small BWR PCCS Phase 2** (2026 planned): different location in containment (top of containment with cooled dome upper surface)

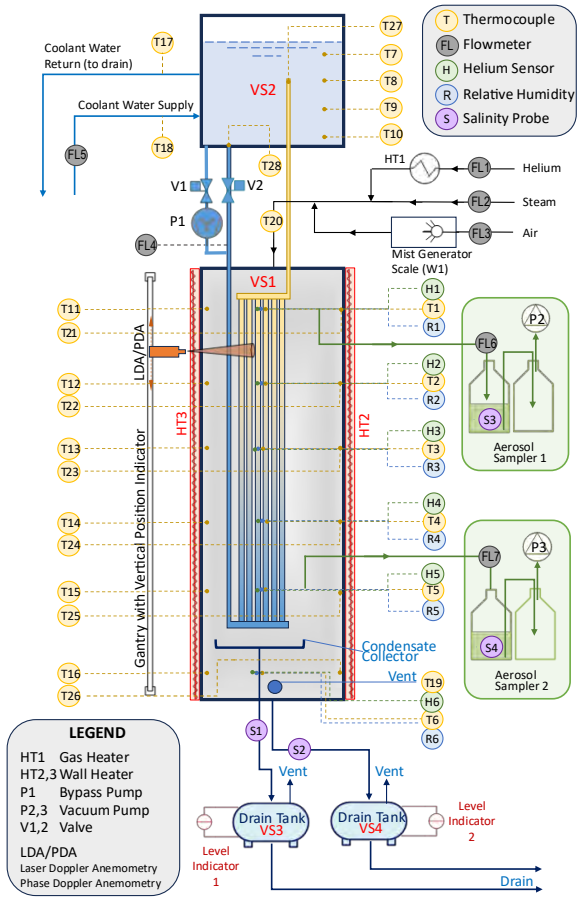

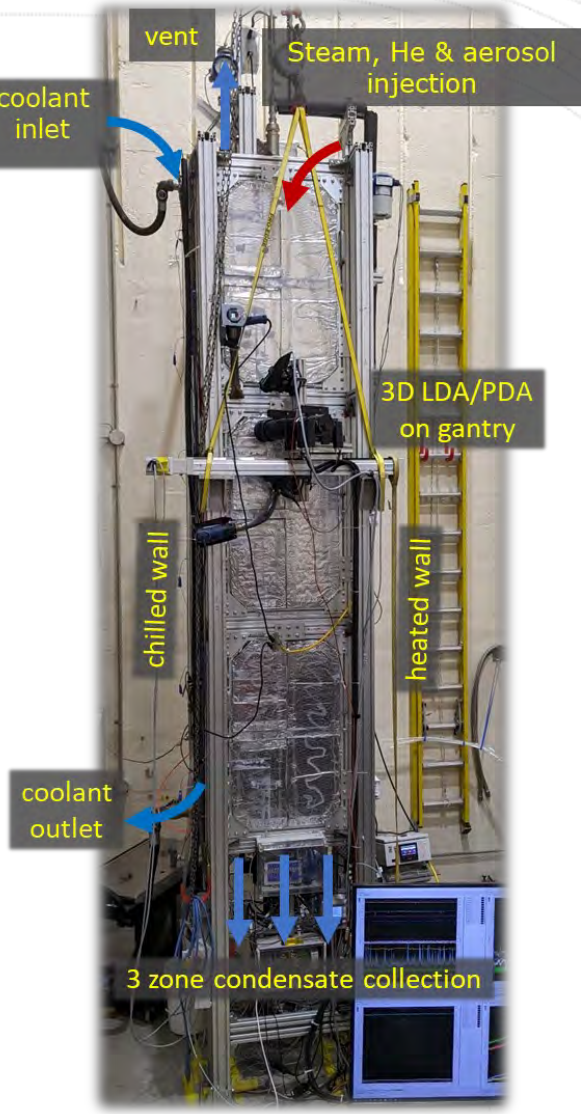

iPWR Experiments in the SCCA (2021 and 2022)

- **SCCA iPWR Experiments:** Combined thermalhydraulics and aerosol transport experiments for an immersed containment iPWR configuration
  - Experiments analogous to loss-of-containment isolation accident; LDA/PDA + salinity
  - Two distinct layers (hot upper layer and cooler under-layer) formed, whose thickness depends on steam injection rate and He, with suppression of HTC
  - Accumulation of hydrogen analog (He) in under-layer, forming flammable mixtures
  - Dense fog formation (deposition dominated by diffusiophoresis & turbulence)
  - 'evaporative barrier' forms between layers (traps aerosols in upper layer; effectively shuts off gravitational settling)
  - Tests run March 2021 (team injection and wall heating) and June 2022 (influence of non-condensables)

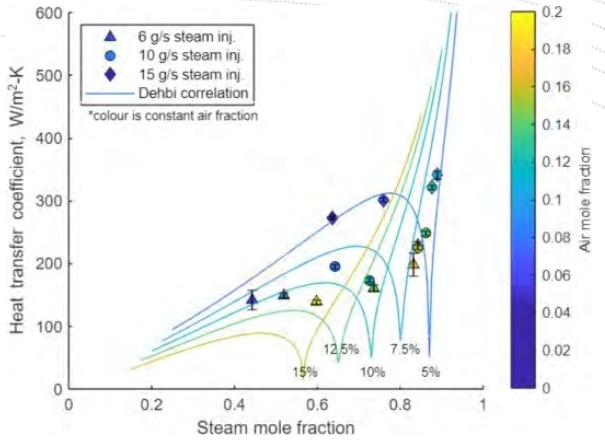

Figure: *Experimental HTC as a function of steam concentration in the hot upper layer, compared to Dehbi [1] correlation (air and helium [3].*

[1] Dehbi, A., A generalized correlation for steam condensation rates in the presence of air under turbulent free convection. Int. J. Heat Mass Transfer, 86, 2015

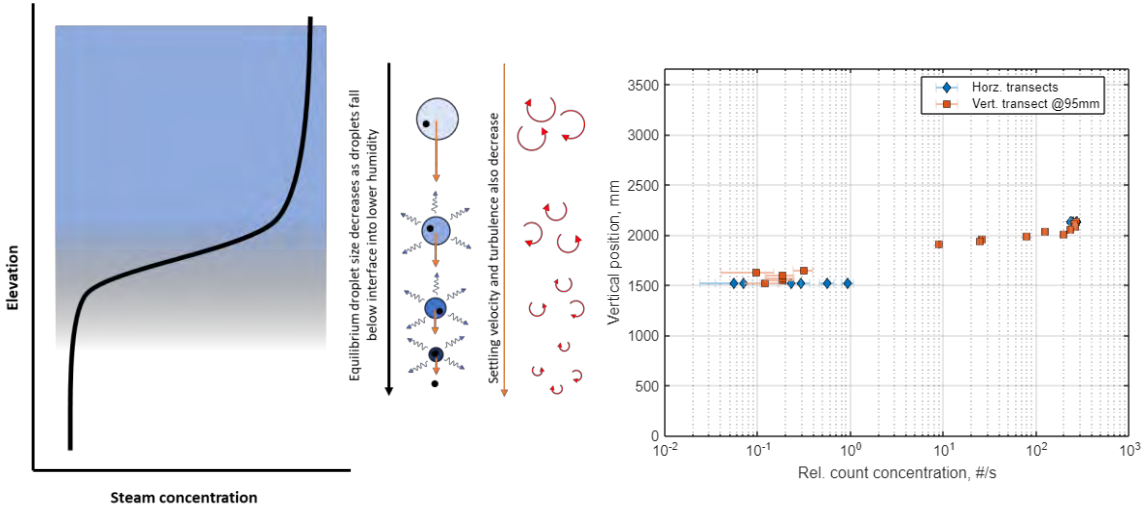

Evidence for "evaporative barrier" that traps fission products in upper layer of volume

[2] Lebel et al. (2022) "Aerosol retention within submerged Containment-Type iPWRs: Experiments and modeling", Nuc.Eng.Des., 398

[3] Lebel et al. (2025) "Impact of hydrogen on iPWR containment Thermal-Hydraulics in severe accidents", Nuc.Eng.Des., 435

[4] Lebel et al., (2025) "Transport Characteristics of Fission Product Surrogates in Water-Cooled Small Modular Reactor Containments", J.Aer.Sci., 190

SCCA Conversion to Study PCCS in Small BWR

- Small BWR utilizes tube bank heat exchangers for passive containment cooling system (PCCS)
  - Natural-circulation driven (or forced) with tube bank suspended in the containment
    - Similar to GDCS (gravity driven cooling system) in Economic Simplified BWR (ESBWR) design
    - Condensate falls directly to bottom of containment
- SCCA modified with a tube bank (PCCS simulant)
  - Investigate impact of non-condensable gases on heat transfer on containment side
    - Study deposition patterns, aerosol properties, and flow dynamics, and stratification phenomena
    - Change “chilled wall” to tube bank + water reservoir
  - Phase 1 tests 2025 July (mid-containment; steam injection from above), Phase 2 summer 2026 (top containment)
  - Benchmarks planned: MELCOR (underway), CFD and GOTHIC (coming soon)

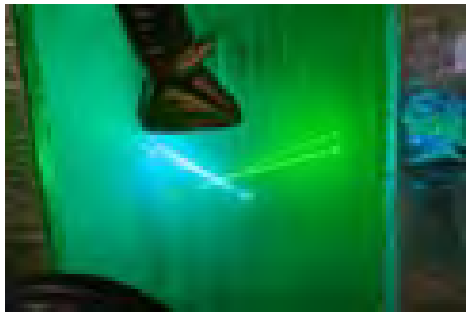

L: New configuration of SCCA for PCCS tests
R: LDA/PDA measurements
B: diagram of small BWR containment

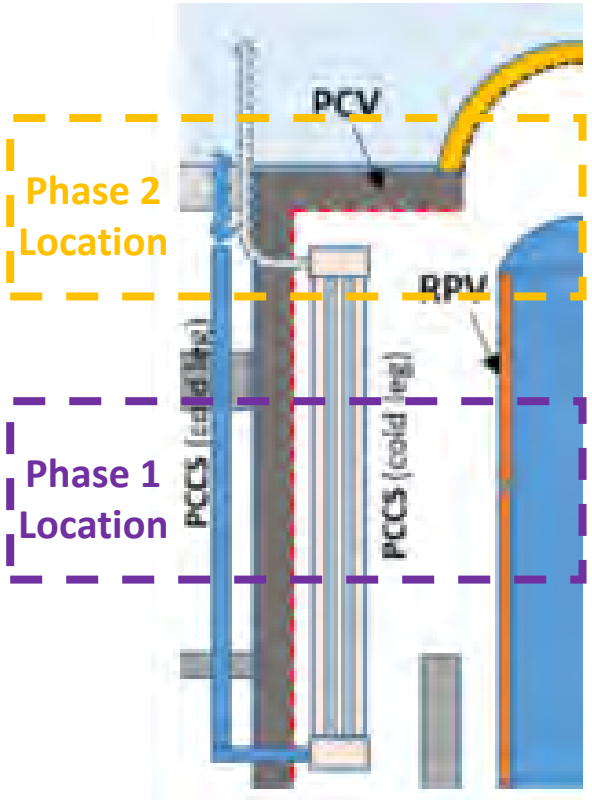

PCCS Experiments – Key Takeaways

1) Gas Stratification and Heat Transfer
   - Active (forced convection) and passive (natural convection) cooling modes tested. NC tests had lower heat transfer rates.
   - Two distinct layers (hot upper layer and cooler under-layer) with thickness dependent on steam injection rate (equilibrium of heat in from steam injection and heat out from condensation).
   - Condensation occurs primarily in hot upper layer due to strong dependence of heat transfer on local steam concentration.
   - He co-injection cools upper layer (according to Antoine's equation), expanding it to increase surface area and maintain equilibrium.
2) He Dilution Impacts on Heat Transfer Coefficient
   - HTCs track Dehbi's correlations: ↑ with steam, ↓ with helium, and trends are consistent with Dehbi except near the unstable density transition zone.
   - Upper-layer HTCs for forced flow vs natural circulation PCCS: Natural mode has slightly higher gas T, but comparable HTC to forced.
   - More He (or less steam) drops HTC from ~600 to ~100 W/m²·K.

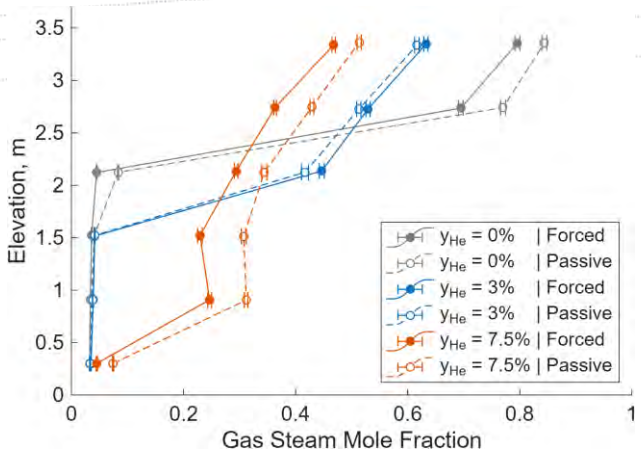

Figure: *Steam stratification and layer separation, under both natural and forced convection conditions, with 10g/s steam.*

Figure: *Inflation (and lower temperature) as a result of helium co-injection with 6g/s steam, under natural and forced convection conditions.*

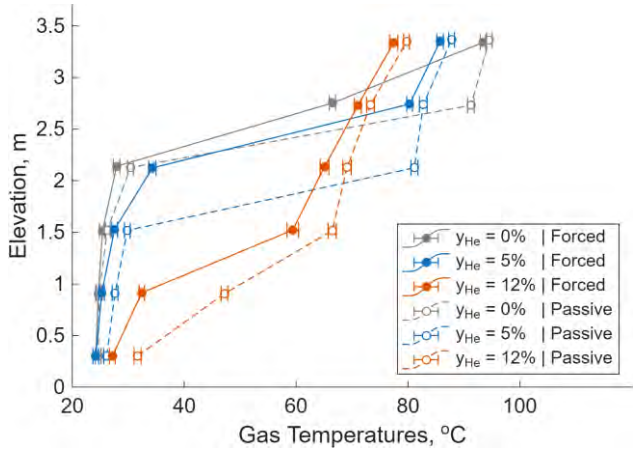

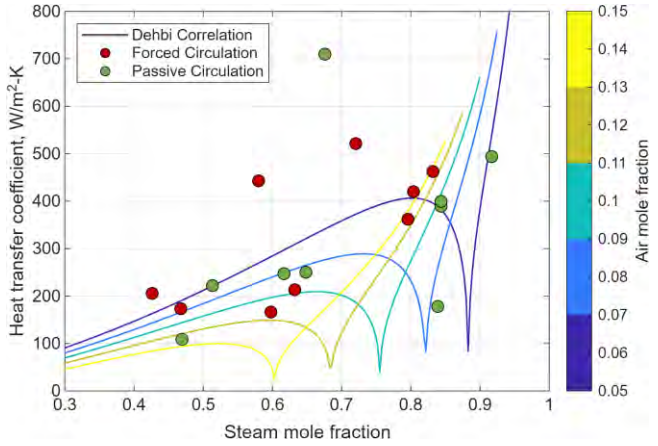

Figure: *Experimental heat transfer coefficients as a function of steam concentration in the hot upper layer, under both natural and forced convective flow conditions in PCCS, compared to Dehbi's correlation [1].*

[1] Dehbi, A., A generalized correlation for steam condensation rates in the presence of air under turbulent free convection. Int. J. Heat Mass Transfer, 86, 2015

Key Takeaways Helium (H_2 analog) and Aerosols

- **He accumulates in upper layer:** localized steam condensation, mass-transfer barrier (He rich; >90% dry) just above interface
- **He downward Migration & Mixing:** He diffuses across interface into under-layer (10-60% wet) and smooths the vessel's vertical temperature gradient.
- Aerosol concentrations drop 1-2 orders of magnitude at interface: evaporative barrier traps the bulk inventory in upper layer.
- Unlike heated iPWR tests, unheated PCCS under-layer droplets can re-condense and form fog after shrinking through barrier.
- LDA/PDA (10-30 um particle sizes) were mostly fog (can't discern NaCl droplets)
- Broader size distribution in steam layer and particles in cool underlayer below detection

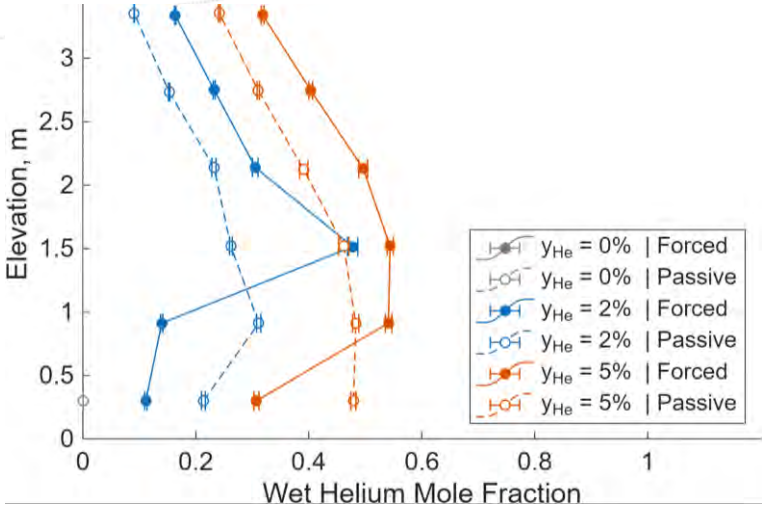

Figure: *Wet helium concentration under both natural and forced convection conditions, with 6 g/s steam.*

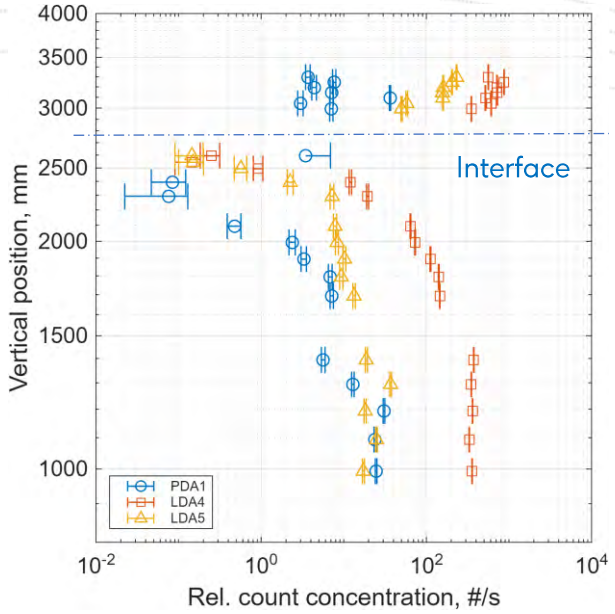

Figure: *Relative droplet count concentrations for 0% He and 10 g/s steam under natural circulation.*

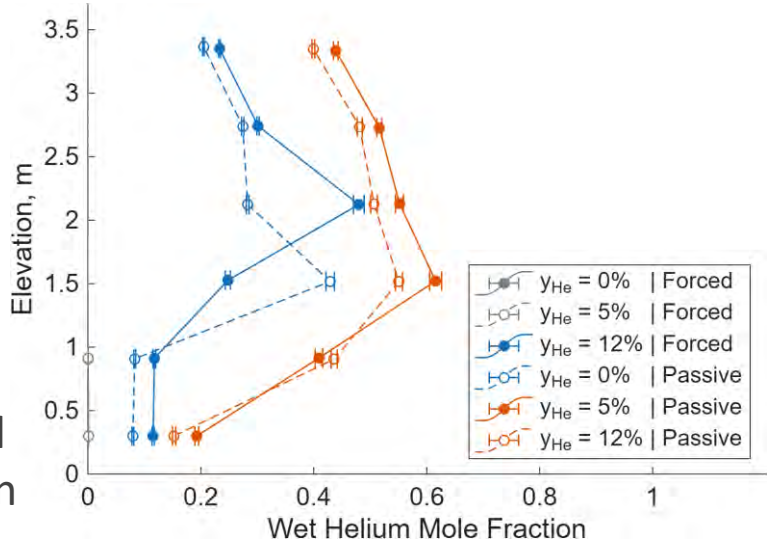

Figure: *Wet helium concentration under both natural and forced convection conditions, with 15 g/s steam.*

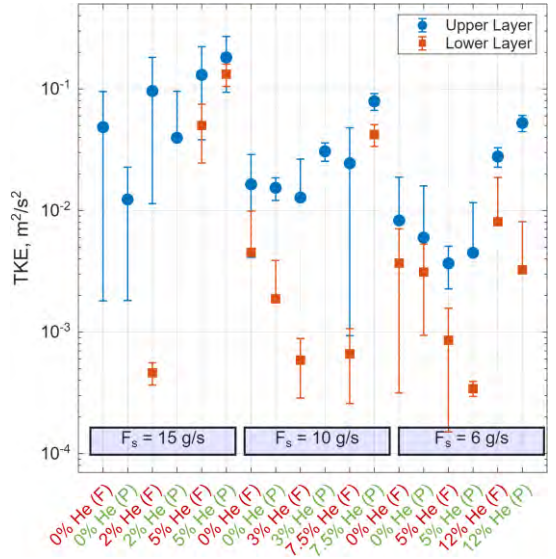

Figure: *TKE at different test conditions.*

Late-stage Severe Accidents:

- CNL's Cold Crucible Induction Furnace (CCIF)
  - High temperature synthesis & rapid quenching of corium
  - Studies phase behaviour, melt miscibility, stratification, and chemical interactions with structural materials
  - Up to 2 kg charges with DU or NU; temperature = ~2300°C
  - Resolidified corium samples suitable for mechanical properties testing and database (TAF-ID) validation.
- Extensive experiments with CANDU corium and recent new tests with Accident Tolerant Fuel (ATF) - FeCrAl
  - Partial oxidation of FeCrAl (~70% in tests) required for UO_2 interaction (dissolution; eutectic phase formation)
  - Charge reached 2417°C = high quality UO_2–FeCrAl corium
  - Characterisation is underway to produce data to support validation of ATF thermodynamic models
  - Future experiments planned for melt stratification, vessel material interactions, & ex-vessel (UO_2–FeCrAl–concrete)

Above: CCIF producing FeCrAl corium
Left: FeCrAl corium samples post-test

Helium-Air Natural Convection (HANC) Experiment Studying Air Ingress

- PIRT exercise for DLOFC accident in HTGR
  - Phenomena of forced-to-natural circulation transition found highly important to accident source, but poorly understood
- HANC is designed to measure the time to the onset of natural convection (ONC)
  - conditions resembling guillotine break of coaxial inlet/outlet duct in an inverted “U” type geometry.
  - Initially filled with He and electrically heated up to 700°C. Each test initiated by opening seals on the lower head / plenum (boxes).
- First test series (HANC-1) completed January 2026. Test reports to be completed by mid 2026.
- Apparatus design improvements and new test series (HANC-2) to start planning in late 2026.

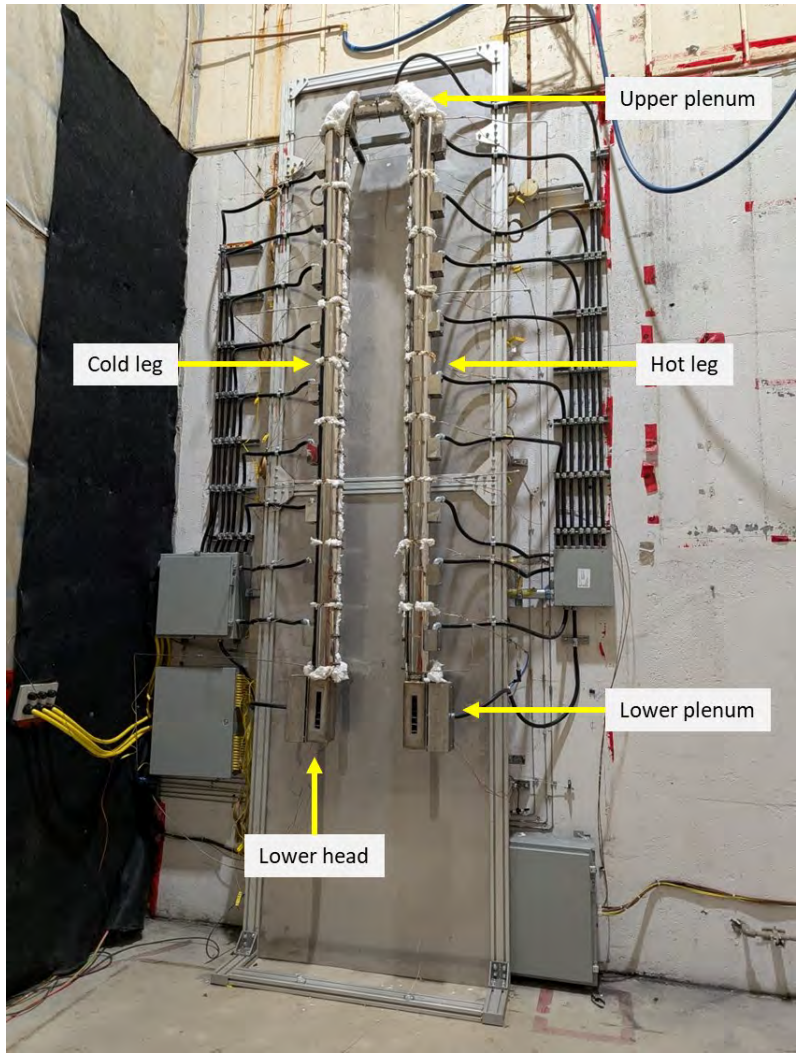

Annotated photograph of the completed HANC apparatus showing the represented regions of a HTGR.

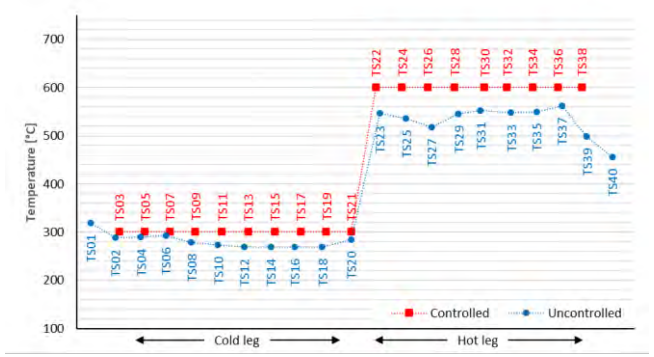

Example steady temperature profile before ONC (300°C / 600°C cold leg / hot leg).

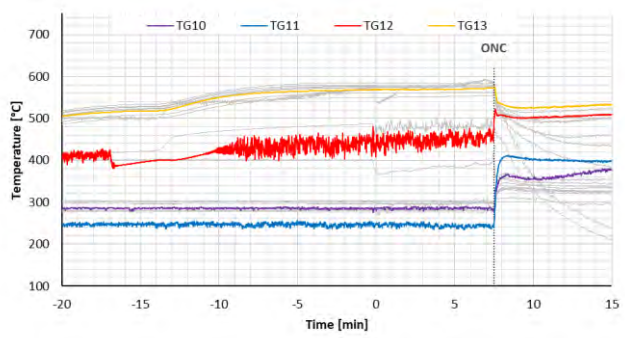

Example measured gas temperature transient including clear evidence of ONC.

Planned benchmarks with RELAP5, GOTHIC, & MELCOR

HTGR Core Heat Transfer Experiments

Pebble Bed Experiments for Analysis of Core Heat transfer (PebbleBEACH):

- Both forced (upward/downward) and natural convection (+radiation), with externally/internally (coming soon) heated pebbles;
- Measuring contributions of surface radiation, contact conductance, & convection to heat transfer (using pebbles with different materials and emissivity)
- In pebble cartridge heaters will be installed to study impact of internal heat generation (as opposed to external heating) in the pebbles, on core heat transfer
- First Pebble Beach tests conducted in 2025 December:
  - Pebbles are polished stainless steel with an emissivity <0.1
  - External heating, reactor scale pebble sizes, and dimensionless properties for the coolant and flow consistent with normal operations.

Pebble Bed Aerosol Generation Experiments (PAGE) – *concept design*

- Focused on characterization of graphite dust generation for PB-HTGR cores
  - An important potential source term in safety evaluations, and due to the pyrophoric nature of the dust may have implications on accident behaviour/progression
  - Experiments will involve accelerated frictional deterioration of the reactor scale pebbles, resulting in dust production and characterization.

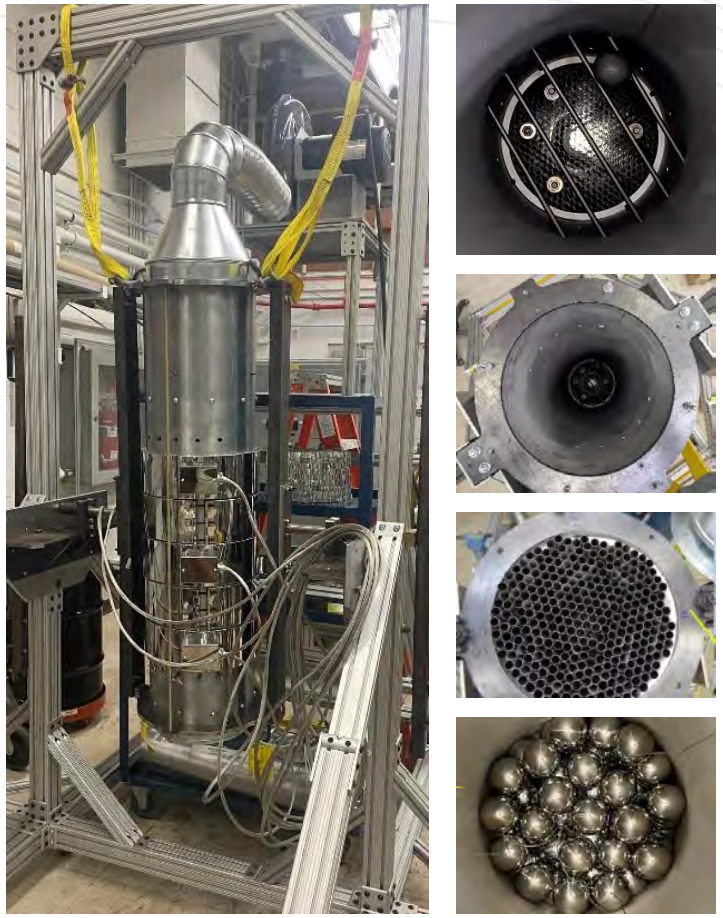

Pebble BEACH apparatus

Measures T and HTCs for normal operation (forced convection) & accident (natural circulation)

Future: aerosols (from pebble movement) and flow reversal and instability investigations.

Heat Pipe (HP) Experiments

- Heat pipe array (Na working fluid) setup.
- 5 parallel HPs at 50kw
- Scaling up array: more HPs and higher power

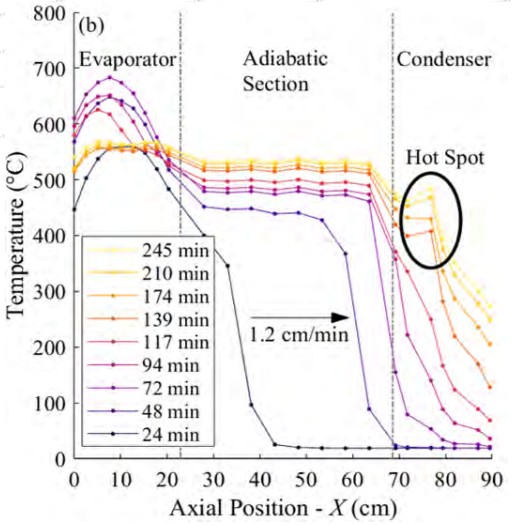

- Example test results of start up transient for a single heat pipe.

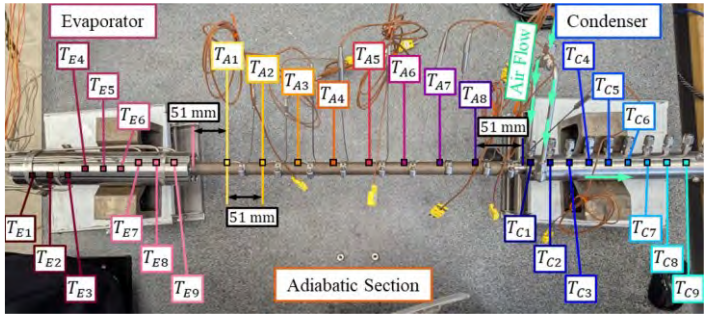

- Set up of a single heat pipe with sodium working fluid.

- Evaluating heat transfer and thermalhydraulics of sodium and potassium HPs for start-up, steady state, cyclical, and shutdown
- Severe accident scenarios using HP array (20-60% HP failure rate) with HP at 550˚ C & block at 750˚C (shutdown system delay 1H)
  - 60% failure case: 1) core increases to block temp in 5 min; constant for 35 mins; then increases by 250˚C/hr until shutdown simulated

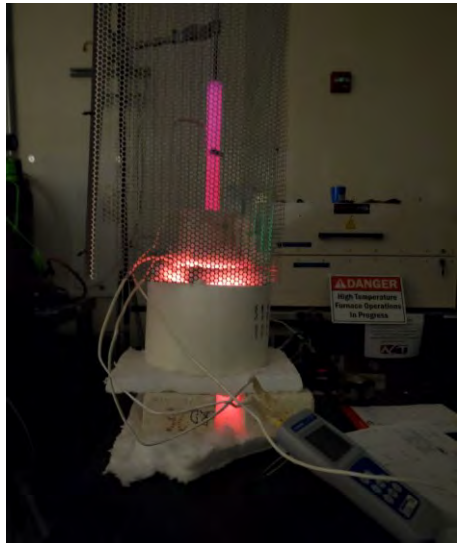

- QA testing of a 0.5m potassium heat pipe
- TH and heat transfer experiments now underway

Experiments + Modelling

- Na HPs (up to 1000˚C) including single and multiple rupture; Single potassium heat pipe tests.
- Working with partners (UW-Madison) on design and building of custom heat pipes.
- Heat pipe modelling using both CFD (STAR-CCM+) and system-TH (ARIANT) codes

Molten Salt Reactor (MSR) Related Experiments

- Molten salt characterization, production, & FP release under accident conditions
- Molecular dynamics modelling of fission product behaviour in molten salts.
- **Recent FP efforts:** confirmatory experiments on conversion of UO_2 to a UF-based fluoride/fluoride-chloride molten salt, using depleted uranium.
  - Data to augment results/conclusions of previous FP release experiments
- **Volumetric heat generation in core:**, development of 'scalable' experimental capability for self heating fluids for natural circulation loops to simulate MSR.
  - Focused on a joule heating technique with simulant molten salts
  - Investigate and mitigate corrosion and electrolysis, material compatibility and local temperature measurements.
- Application of voltage waveforms
- High temperature plastics suitable for use with FLiBe and FLiNaK loops)
- Alternatives to thermocouples for local temperature measurement
- Scalability for developing larger loops.

Molten Salt Volumetric Heating

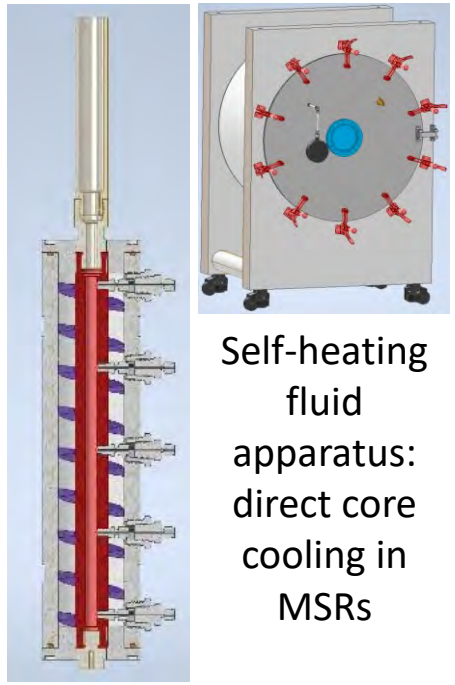

Self-heating fluid apparatus: direct core cooling in MSRs

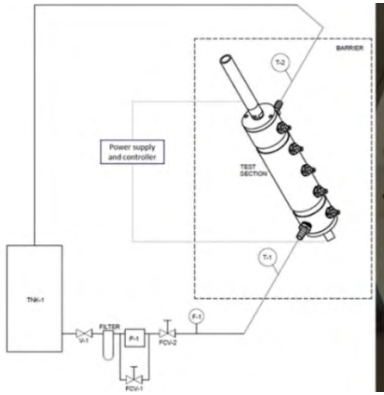

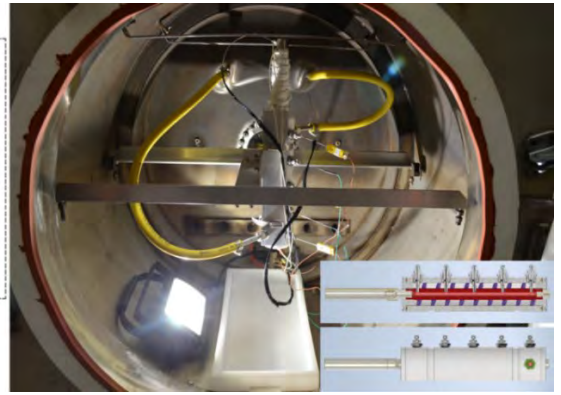

Benchtop Joule Heated Salt Experiment: Dynalene 450 simulant salt (~120 °C MP); steady state water jacket cooling; extendable to fluoride salts

Severe Accident Modelling and Analysis – Water Cooled efforts

- Completion of the benchmarking of SCCA Experiments
  - **Benchmarking:** MELCOR (Phase 1); GOTHIC (Phase 1 & 2); CFD (Phase 1 refining, Phase 2 coming)
  - Jia, D. E., Lebel, L., Morreale, A., & Zhou, F. (2024). GOTHIC and MELCOR benchmarking of the CNL strong condensation containment apparatus experiments. Nuc. Eng. and Des., 427, 113440.
- iPWR Severe Accident Modelling and Emergency Response:
  - J. Cui, L. Lebel, A. Morreale and D. Hummel, "MELCOR Model of iPWR and Application to Emergency Planning Zone Study", Nuclear Engineering and Design, Vol. 442, October 2025.
- Experiments and benchmarking of SCCA small BWR PCCS experiments Phase 1 (2025 June)
  - MELCOR Benchmarking of Phase 1 in progress; planned GOTHIC Benchmarking to start in spring 2026 and CFD Benchmarking of BWR PCCS experiments planned following iPWR benchmarks.
- Integrated severe accident analysis with MELCOR to evaluate passive systems
  - Assessing impacts of passive system failures (including failure modes) for iPWRs and small BWRs.
- Participation in the EU SASPAM-SA Project – Water Cooled SMR Severe Accidents
  - SASPAM-SA (Safety Analysis of SMR with Passive Mitigation Strategies – Severe Accident)
  - CNL contributing data/experience from SCCA iPWR and small-BWR experiments, benchmarking and integral severe accident analysis for iPWR and small BWR + emergency response methodologies.

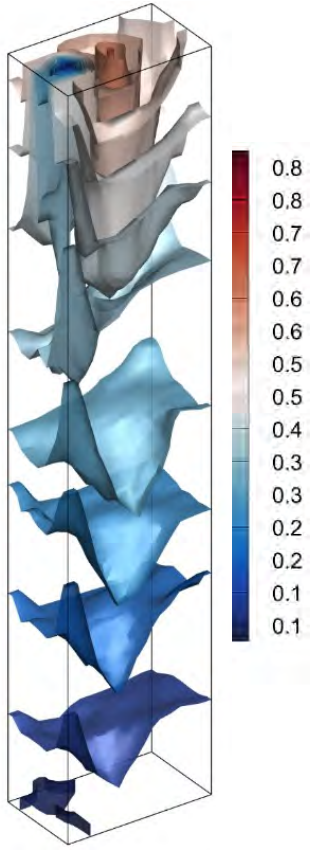

GOTHIC modelling of the SCCA (steam fractions)

MELCOR Benchmarking of small BWR PCCS Tests

- Benchmarking PCCS Phase 1 (2025 June) experiments with MELCOR
  - Using a 6x3 nodalization to track the natural convection with 6x1 PCCS heat exchanger
  - Initial challenges with radiation modelling corrected improving temperature predictions for the bottom layer
  - Steam layer can cross CVH volumes
- Future Benchmarking to include:
  - MELCOR analysis of Phase 1 PCCS tests nearly complete; eventual benchmarking of Phase 2 test (test to be conducted in 2026-2027)
  - GOTHIC & CFD modelling of PCCS Phase 1 & 2 planned to start 26-27.

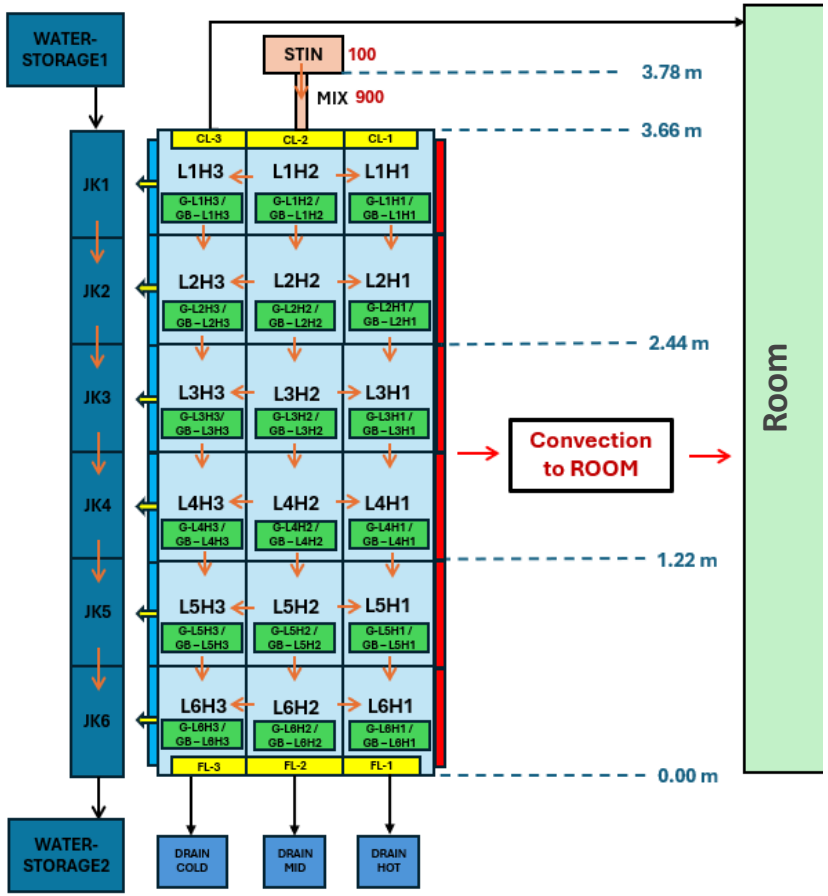

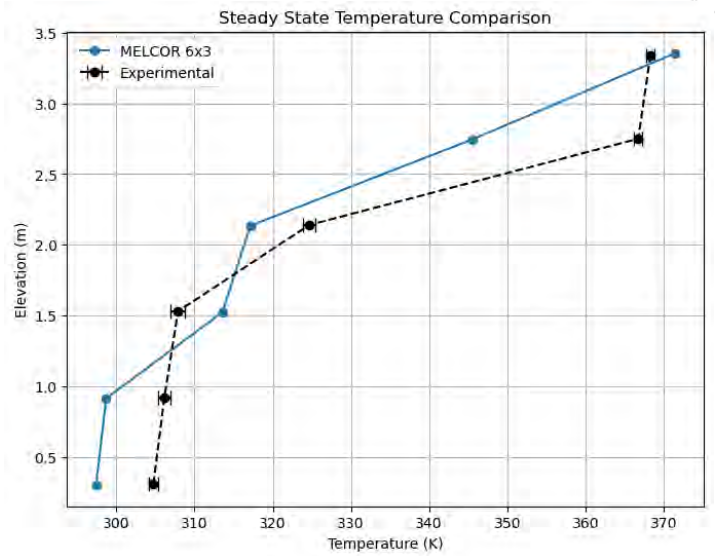

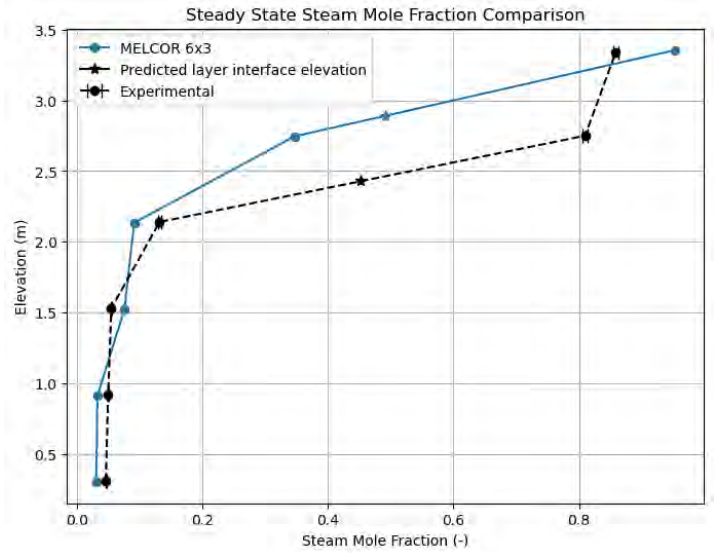

Above: MELCOR nodalization for PCCS tests.

Right Top: Steady State Temperature Comparison

Right Bottom: Steady State Steam Mole Fraction Comparison

Small BWR Severe Accidents

- MELCOR Severe Accident Analysis Code
- Generic small-BWR MELCOR model
  - Natural circulation driven primary coolant and safety systems
- Initial analysis of SBO and SBLOCA cases to explore core degradation
  - SBO w/ varied ICS/PCCS impairment
  - SBLOCA (on 1'' instrument line) – H_2 (NCG) impact on ICS performance
  - ICS condensate return into chimney region (early studies to downcomer)
- Modelling and analysis of small BWR passive system phenomena
- Modelling support for DEC PIRT
- MELCOR + DAKOTA Uncertainty Analysis focused SBLOCA cases to explore core degradation

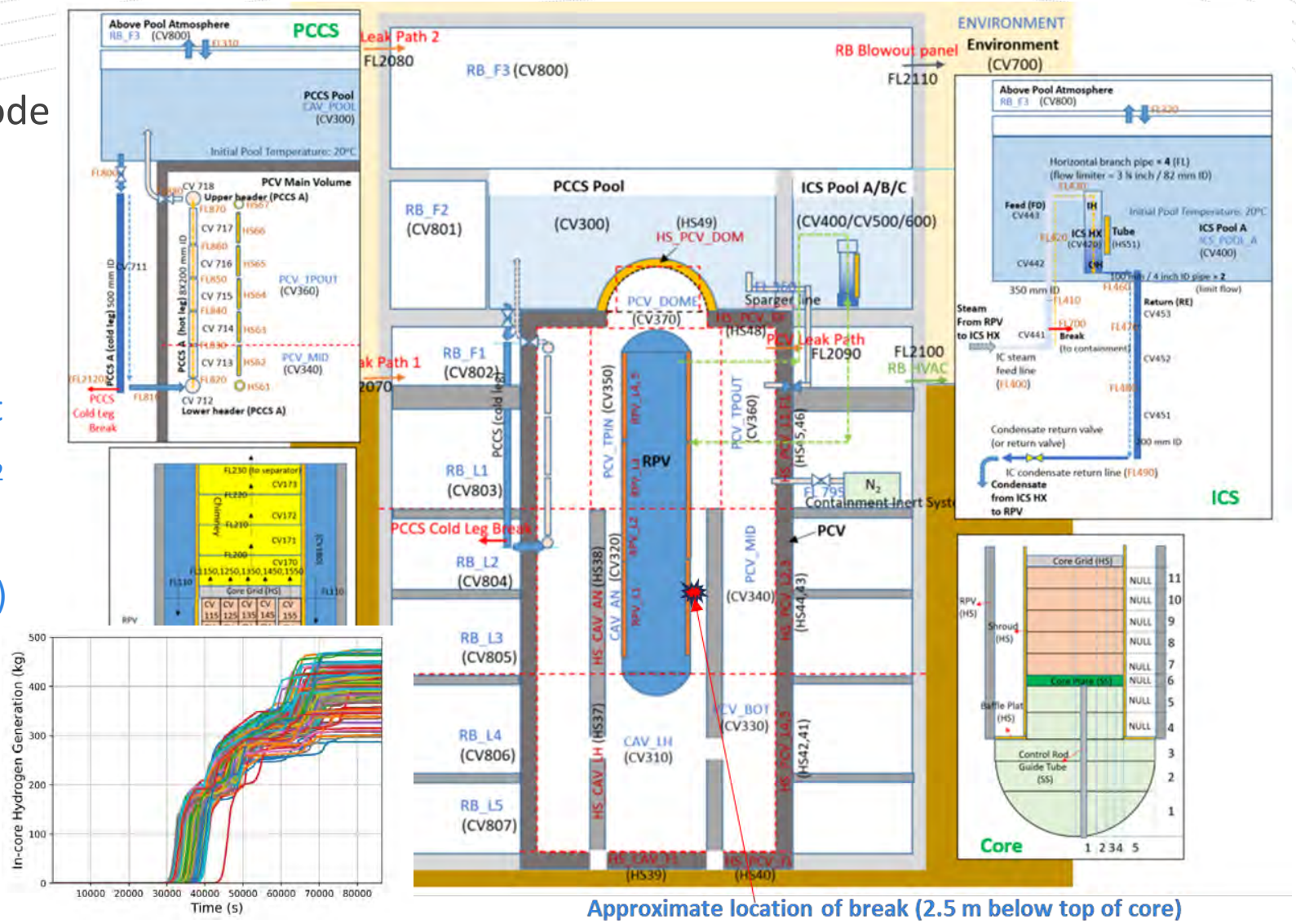

F. Zhou, A. C. Morreale, L. Lebel, J. Cui, and G. Patterson, "Severe accident analysis of a generic small boiling water reactor", submitted to NUTHOS-14, Vancouver, Aug 25-28, 2024

HTGR and SFR Reactor Analysis UPDATE

HTGR (High Temperature Gas Reactor):

- Further analysis of 200 MWth pebble bed HTGR: onset of natural circulation/air ingress and DLOFC, as well as uncertainty/sensitivity using MELCOR-DAKOTA with Wilks method
  - Air ingress period seen to be ~4H; **U/S analysis:** impact of 11 uncertain inputs on key figures of merit during DLOFC (peak fuel temperature, ONC timing, and radionuclide release) over 124 simulations.
- Preparing to benchmark recent HANC tests (MELCOR model dev.)

SFR (Sodium Fast Reactor):

- Generic 250 MWth SFR MELCOR analysis for unprotected loss of flow accident (ULOFA) & unprotected transient overpower accident (UTOPA)
  - Best-estimate analysis (below), and U/S analysis of ULOFA (60 input decks for the ULOFA scenario, with the reactivity coefficients used as uncertain input parameters tracking FOMs of coolant boiling margin, clad melting temperature margin, and fuel melting temperature margin.

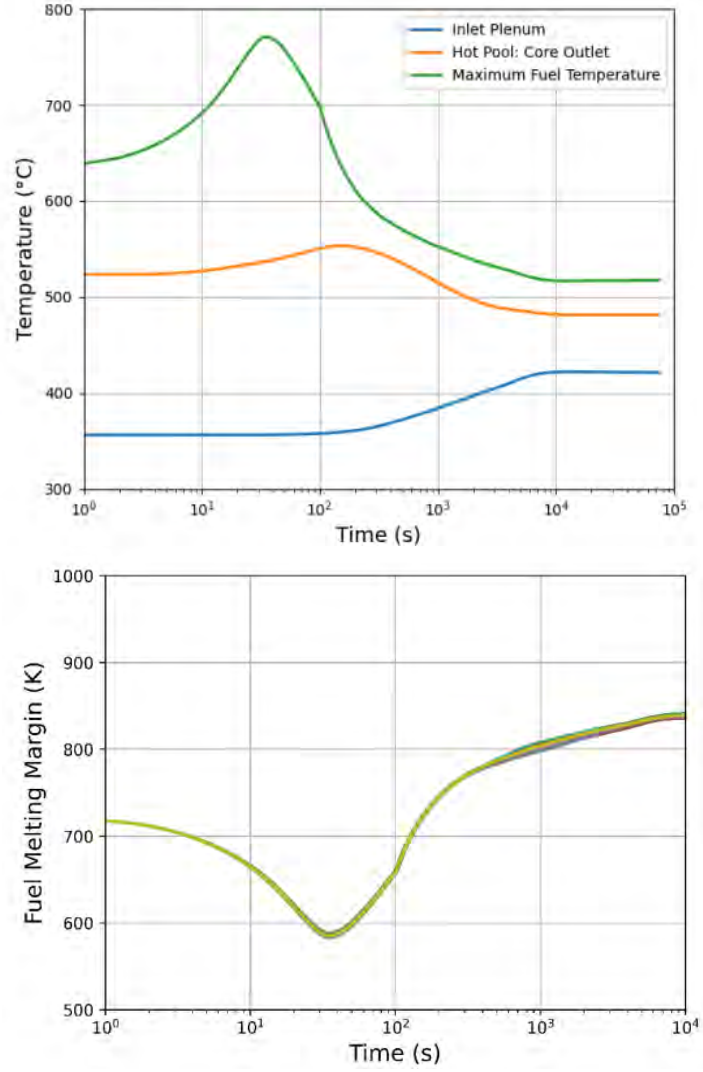

Top: ULOFA Temperature transient
Bottom: horsetail plot of fuel melting margin under a ULOFA for 60 simulations

Sensitivity and Uncertainty Analysis

- Building on previous participation in IAEA CRP
  - Further efforts in CANDU focused on hydrogen releases (international workshop with CRP CANDU partners: CNL, KAERI, and UPB)
  - MAAP-CANDU + SUSA toolset for S/U analysis
- MELCOR + DAKOTA coupling using Python developed and applied to
  - Small BWR model
  - Sodium fast reactor model
  - High temperature gas reactor model
- Initial efforts using Wilks method
- Implementation of Morris method and Iman-Conover method via DAKOTA and Python scripts

MELCOR + DAKOTA Coupled Uncertainty and Sensitivity Analysis

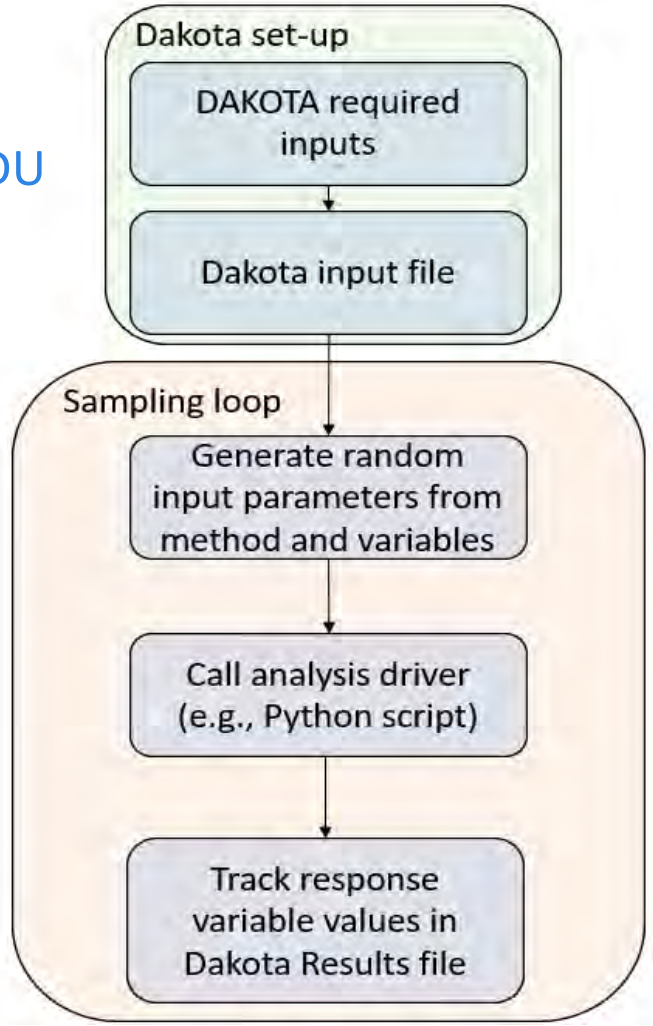

Morris Method

Wilks Method

Iman-Conover Input Correlations

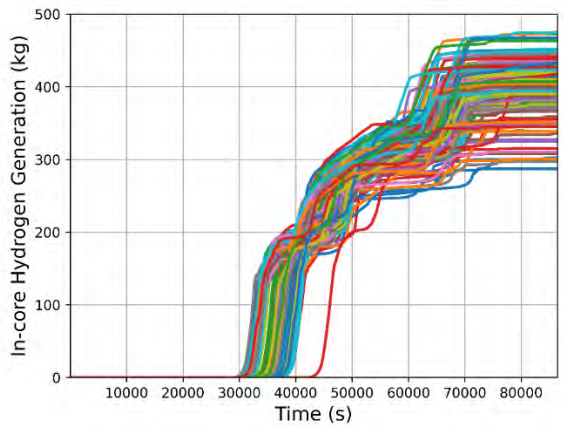

Generic Small BWR Uncertainty Analysis Total H2 Generation over the Transient

Conclusions

- New nuclear deployment, including Small Modular and Advanced Reactor, interest in Canada and abroad to achieve clean energy goals and Canadian government support for nuclear energy
- CNL operates a flexible research program, guided by the SMR/AR deployment landscape in Canada
  - Develops and maintains capabilities and knowledge to support industry and regulatory stakeholders
  - Reactor safety and severe accident research further developing base capabilities for range of SMR/AR technologies and pursuing deeper expertise for key technologies closer to deployment.

- Severe accident research focus on WC designs (especially small BWRs) and HTGRs as near term.
  - Experiments (core heat transfer, heat transport system, natural circulation, and containment)
  - Integral severe accident analysis, along with uncertainty and sensitivity assessments.
- Other focuses include heat pipe cooling systems, SFRs and molten salt FP behaviour
  - Baseline capabilities/understanding positions CNL to move deeper should deployment accelerate
  - Experiments (core heat transfer, heat transport system, natural circulation, and containment)
- CNL research enhanced by international involvement (NEA, IAEA, EU, GIF) + ERMSAR especially

Thank you. Merci.

ACKNOWLEDGMENTS

The work discussed herein and CNL participation in various international working groups, projects and initiatives is primarily funded through the Atomic Energy of Canada Limited (AECL) Federal Nuclear Science and Technology Program.

Canadian Nuclear Laboratories | Laboratoires Nucléaires Canadiens

Andrew Morreale, Ph.D.
Technical Manager – Reactor Safety:
andrew.morreale@cnl.ca

The 12th European Review Meeting on Severe Accident Research (ERMSAR2026)
Madrid, Spain, May 18-22, 2026

Development of the SAFARI Code for Comprehensive Severe Accident Analysis in Nuclear Reactors: Containment Thermal-Hydraulics Analysis Module

Kum Ho Han (FNC Technology)
Jehee Lee, Yeon-Jun Choo
2026. 05. 21

FNC TECHNOLOGY CO., LTD.

CONTENTS

1 Introduction

2 SAFARI Framework

3 SAVANNAH Module

4 Verification & Validation

5 Conclusion & Future Work

Copyright 2022. FNC Technology Co., Ltd. all rights reserved.

Introduction

- **Heavy Dependence on Foreign Codes**: South Korea has depended entirely on international codes like MELCOR for severe accident safety analysis.

- **Source Code Access Restrictions**: Recent US NRC restrictions on source code access make it difficult to modify software for Korea's specific reactor features or to respond quickly to local regulatory needs.

- **Objective of Development**: To achieve technological independence by creating a domestic severe accident analysis code (SAFARI) tailored to Korea’s regulatory and management environment.
  - SAFARI Framework: The main, integrated system for severe accident analysis.
  - SAVANNAH Module: A specialized module dedicated to simulating ex-vessel containment behavior and thermal-hydraulics.

FNC Technology Co., Ltd.

SAFARI (Safety Analysis Code For Severe Accident Risk Identification)

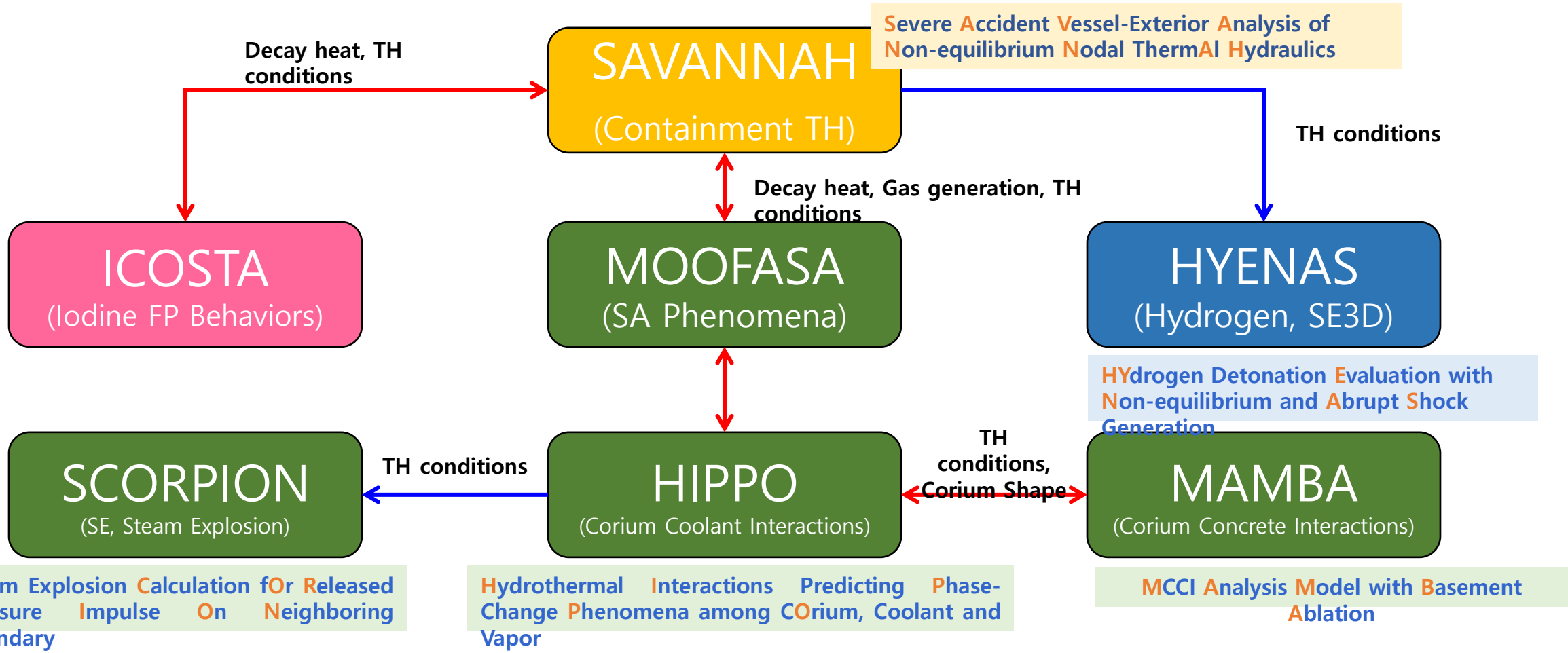

Concept & Nodalization

- Lumped-parameter model
- Compartment-based nodalization
  - CELL: containment Compartment
  - FLOP: inter-compartment flow path
- Non-equilibrium treatment:
  - **Pool** region (Liquid Water + Steam)
  - **Atmosphere** region (Steam, Non-condensable gases)

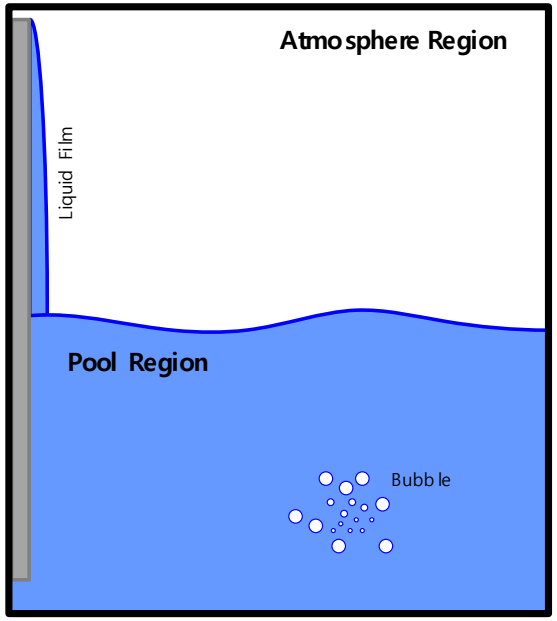

[Concept of Cell]

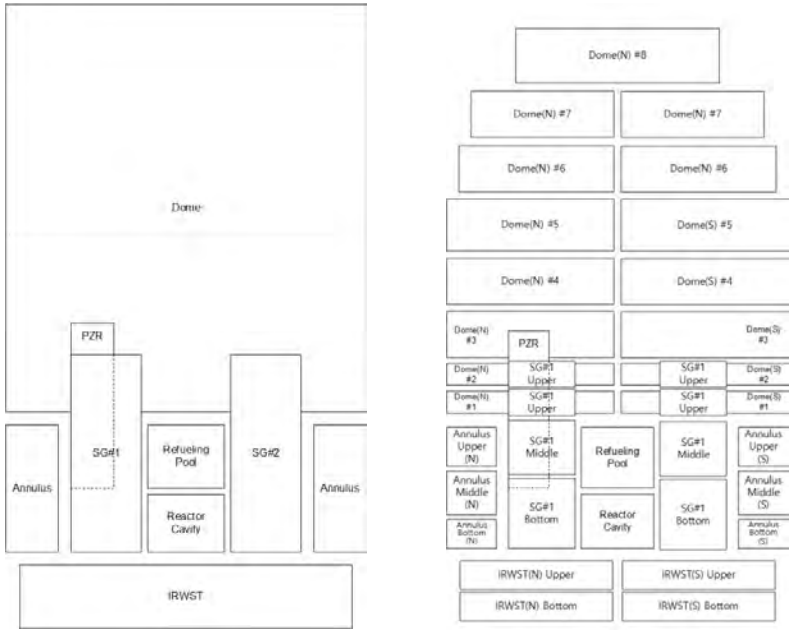

[Containment Nodalization]

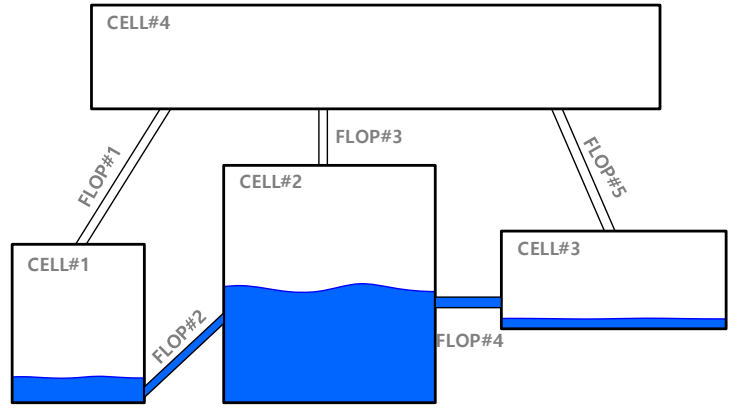

[Example connections between Cell and Flow path]

Governing Equations

Mass Conservation Equation (**Each Material**)

$$M_{i,m}^{n} - M_{i,m}^{n} = \sum_{j} \underbrace{\sigma_{ij}\alpha_{j,\phi}^{n}\rho_{j,m}^{d}v_{j,\phi}^{n}A_{j}\Delta t}_{\text{Convection Term}} + \underbrace{\delta M_{i,m}}_{\text{Source Term}}$$

Energy Conservation Equation (**Each Phase**)

$$E_{i,\phi}^{n} - E_{i,\phi}^{n} = \sum_{j} \underbrace{\sigma_{ij}\alpha_{j,\phi}^{n}(\rho_{j,m}^{d}h_{j,m}^{d})v_{j,\phi}^{n}A_{j}\Delta t}_{\text{Convection Term}} + \underbrace{\delta E_{i,\phi}}_{\text{Source Term}}$$

Momentum Conservation Equation (Each Phase)

$$v_{j,\phi}^{n} = v_{j,\phi}^{o} + \frac{\Delta t}{\rho_{j,\phi}L_{j}}\Bigg[\underbrace{P_{i}^{\tilde{n}} + \Delta P_{pp} - P_{k}^{\tilde{n}}}_{\text{Pressure Difference}} + \underbrace{(\rho g \Delta z)_{j,\phi}^{\tilde{n}}}_{\text{Elevation Change}} \underbrace{- \left(f\frac{L_{j}}{D} + \sum K\right)\frac{\rho_{j,\phi}}{2}\left(|v_{j,\phi}^{n-1} + v_{j,\phi}^{n-2}|v_{j,\phi}^{n} - |v_{j,\phi}^{n-2}|v_{j,\phi}^{n-1}\right)}_{\text{Frictional Term}}\Bigg]$$

Primary Unknown Variables

- Each material mass: $M_{i,m}^{n}$[kg]
- Each phase internal energy: $E_{i,\phi}^{n}$[J]
- Each phase velocity: $v_{j,\phi}^{n}$ [m/s]

[Super script]
n: new variable
o: old variable

[Sub script]
i: cell index
k: cell index 2
j: flowpath index
m: material index
ϕ: phase index
pp: pump

[Variable]
M: material mass [kg]
E: phase internal energy [J]
P: Pressure
σ: connectivity [-]
α: volume fraction [-]
ρ: density [kg/m^3]
h: specific enthalpy [J/kg]
v: velocity
t: time
g: gravitational constant [m/s^2]
f: frictional coefficient
K: form loss coefficient

Numerical Solution Scheme [1/2]

- Step 1. Update Frictional Coefficient (f, K)
- Step 2. Update Pressure Equation: **Pressure-Velocity Coupling**

$$P_i^{\tilde{n}} = P_i^{o+} + \sum_{m=1}^{M}[(\frac{\partial P}{\partial M})\Delta M]_m + (\frac{\partial P}{\partial E})_{pool}\Delta E_{pool} + (\frac{\partial P}{\partial E})_{atm}\Delta E_{atm}$$

- Step 3. Setup Velocity Matrix

$$\begin{vmatrix} a_{P,1}+c_{P,1.1} & c_{P,1.2} & \cdots & c_{P,1.J} & b_{P,1}+d_{P,1.1} & d_{P,1.2} & \cdots & d_{P,1.J} \\ c_{P,2.1} & a_{P,2}+c_{P,2.2} & \cdots & c_{P,2.J} & d_{P,2.1} & b_{P,2}+d_{P,2.2} & \cdots & d_{P,2.J} \\ \vdots & \vdots & \ddots & \vdots & \vdots & \vdots & \ddots & \vdots \\ c_{P,J.1} & c_{P,J.2} & \cdots & a_{P,J}+c_{P,J.J} & d_{P,J.1} & d_{P,J.2} & \cdots & b_{P,J}+d_{P,J.J} \\ a_{A,1}+c_{A,1.1} & c_{A,1.2} & \cdots & c_{A,1.J} & b_{A,1}+d_{A,1.1} & d_{A,1.2} & \cdots & d_{A,1.J} \\ c_{A,2.1} & a_{A,2}+c_{A,2.2} & \cdots & c_{A,2.J} & d_{A,2.1} & b_{A,2}+d_{A,2.2} & \cdots & d_{A,2.J} \\ \vdots & \vdots & \ddots & \vdots & \vdots & \vdots & \ddots & \vdots \\ c_{A,J.1} & c_{A,J.2} & \cdots & a_{A,J}+c_{A,J.J} & d_{A,J.1} & d_{A,J.2} & \cdots & b_{A,J}+d_{A,J.J} \end{vmatrix} \begin{vmatrix} v_{1,P}^n \\ v_{2,P}^n \\ \vdots \\ v_{J,P}^n \\ v_{1,A}^n \\ v_{2,A}^n \\ \vdots \\ v_{J,A}^n \end{vmatrix} = \begin{vmatrix} e_{P,1} \\ e_{P,2} \\ \vdots \\ e_{P,J} \\ e_{A,1} \\ e_{A,2} \\ \vdots \\ e_{A,J} \end{vmatrix}$$

- Step 4. Solve Velocity Matrix
- Step 5. Solve Mass & Energy Equation
  - Determination of cell mass [kg] and energy [J]
  - Once the velocity field is resolved, the final mass and phase energies are determined
- Step 6. Calculate P, T, and Phase Volume

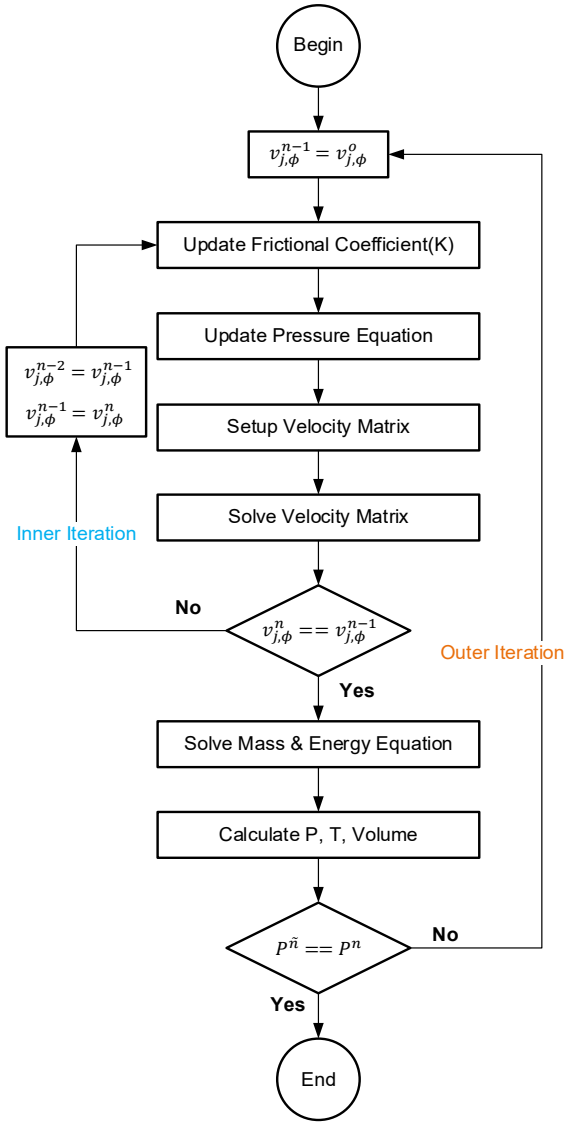

Numerical Solution Scheme [2/2]

- Step 6. Calculate P, T, and Phase Volume: EOS (Equation Of State)
- 1. Find Pool TH State
  - Find properties using **assumed pressure** and **pool energy**
- 2. Calculate Phase Volume
  - After calculating the pool volume, remaining volume is assumed to be the atmosphere volume
- 3. Find Atmosphere TH State
  - Find properties using **each material density** and **phase internal energy**

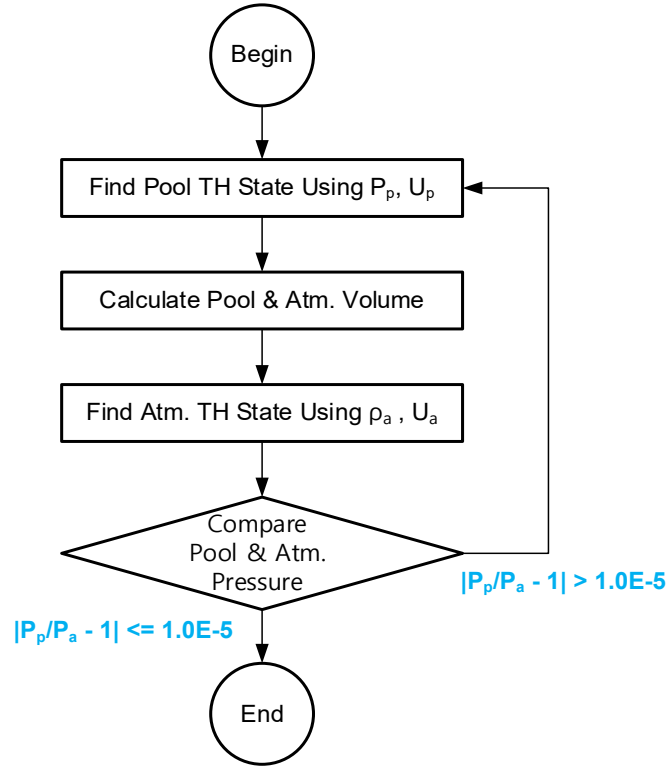

Constitutive Equations

Type		Models	Remarks
1. Wall Heat Transfer			
Natural Convection		$Nu = max\left(0.59Ra^{1/4}, 0.10Ra^{1/3}\right)$	McAdams
Forced Convection	Laminar	$Nu = 0.664Re^{0.5}Pr^{1/3}$	Re < 30,000
	Turbulent	$Nu = 0.037Re^{0.8}Pr^{1/3}$	Re > 60,000
	Transient	Interpolation	
Condensation		$\Gamma'' = \frac{M_s Sh D_{sg} \bar{c}}{D_h} \ln\left(\frac{P_{tot}-P_{s,i}}{P_{tot}-P_{s,b}}\right)$	HMTA, Bird
Boiling		$q'' = F \cdot h_{cv}\left(T_w - T_p\right) + S \cdot h_{npb}\left(T_w - T_{sat}\right)$	Churchill-Chu
2. Friction			
Wall Friction (Darcy)	Laminar	$f_\phi = 64/Re$	
	Turbulent	$\frac{1}{\sqrt{f_\phi}} = -2\log_{10}\left[\frac{1}{3.7}\frac{\epsilon}{d} + \frac{2.51}{Re}\left\{1.14 - 2\log_{10}\left(\frac{\epsilon}{d} + \frac{21.5}{Re^{0.9}}\right)\right\}\right]$	
	Transient	Interpolation	
Interfacial Friction		$f_i = 900[\alpha\sqrt{\rho}_g + (1-\alpha)\sqrt{\rho}_l]$	MELCOR Default
3. Interfical Heat & Mass Transfer			
Poo & Atm Transfer		Sensible Heat Transfer Between Pool & Atm.	

V&V Matrix

Problem	Category	Target Physics	Reference
Adiabatic Expansion of Hydrogen	Verification	EOS (Equation Of State)	MELCOR
Isochoric process of steam in a closed system		EOS (Equation Of State)	CAP*
Two gas mixing		EOS (Equation Of State)	CAP*
Establishment of Flow		Momentum Conservation	MELCOR
Natural circulation		EOS + Momentum Conservation	Conceptual
Transient Heat Flow in a Semi-Infinite Heat Slab		Heat Conduction	MELCOR
Cooling of Heat Structures in a Fluid		Heat Conduction	MELCOR
1-D flow with minor loss (or form loss)		Momentum Conservation	CAP
HDR Test V44	Validation	Blowdown + Condensation	MELCOR/CAP*
ThAI		NC Gas Convection + Condensation	MELCOR/CAP*
Battelle-Frankfurt Test 2/6		NC Gas Convection	MELCOR/CAP*
Battelle-Frankfurt Test D1 / D15		Steam Blowdown	CAP*
Battelle-Frankfurt Test D16		Water Blowdown	CAP*
Battelle-Frankfurt Test C13		Steam/Water Blowdown	CAP*

*CAP (Containment Analysis Package): Containment TH Analysis Code for DBA in South Korea

Verification - Adiabatic Expansion of Hydrogen [1/2]

- Utilized for MELCOR code verification
- Two cells are connected via a flow path (Flop)
- The two cells possess distinct geometries and th conditions
- Hydrogen is transfer through the Flop, with Cell #1 acting as the donor cell

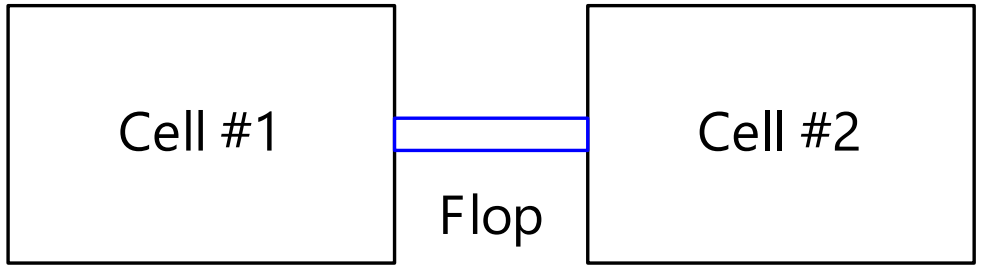

Case	Cell #1			Cell #2			Flop	
	Volume [m^3]	P [bar]	T [K]	Volume [m^3]	P [bar]	T [K]	Area [m^2]	Minor loss [-]
1	1000	2.0	300	1000	1.0	300	0.05	2
2	1000	5.0	300	1000	1.0	300	0.05	2
3	100	2.0	300	1000	1.0	300	0.05	2
4	10000	2.0	300	1000	1.0	300	0.05	2
5	1000	2.0	300	1000	1.0	300	50.0	2
6	1000	2.0	300	1000	1.0	300	0.05	0.1

Verification - Adiabatic Expansion of Hydrogen [2/2]

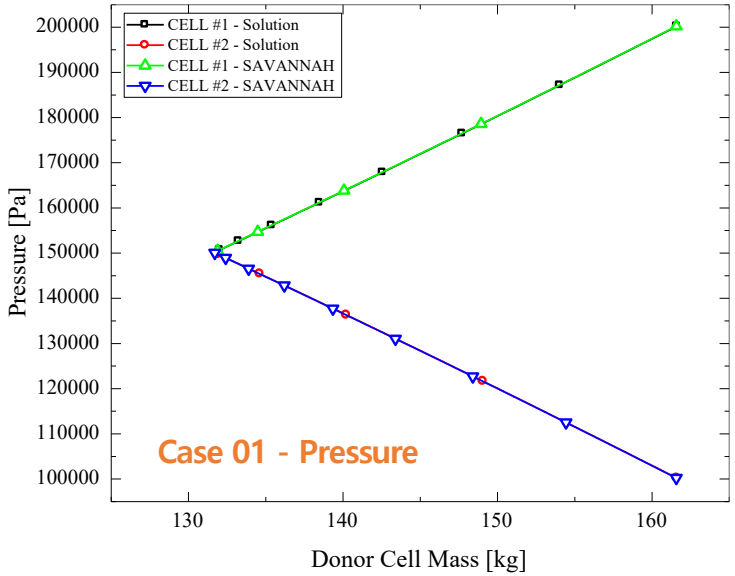

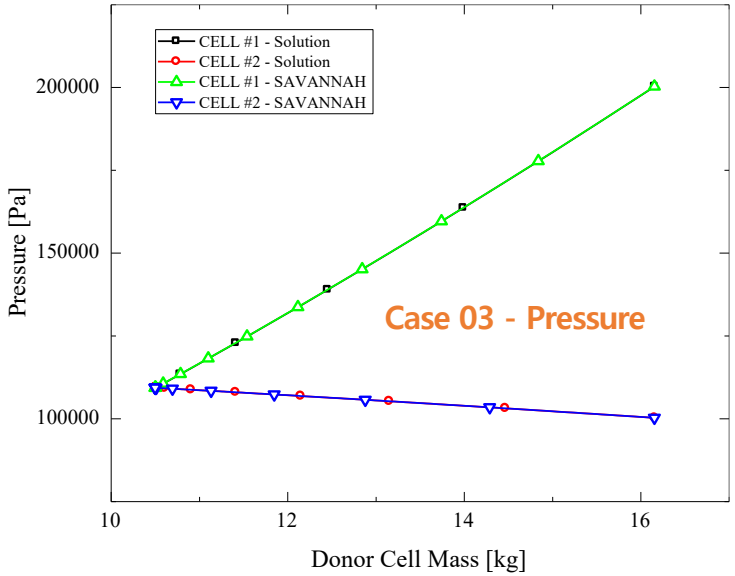

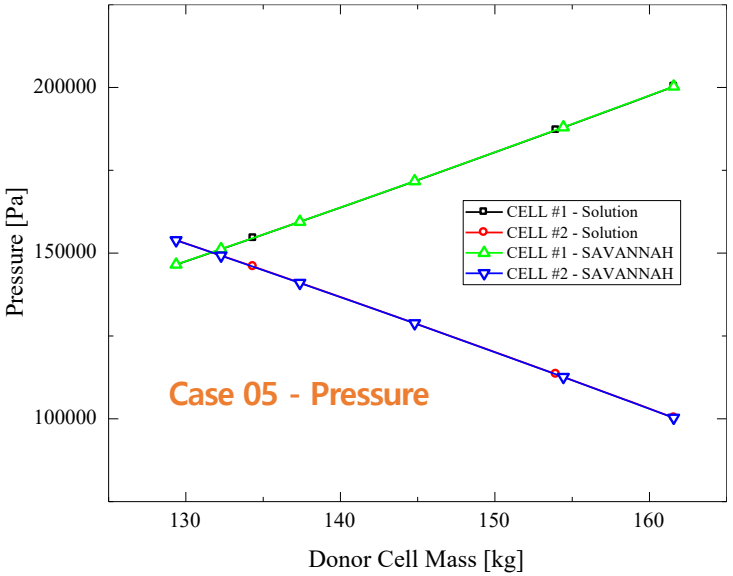

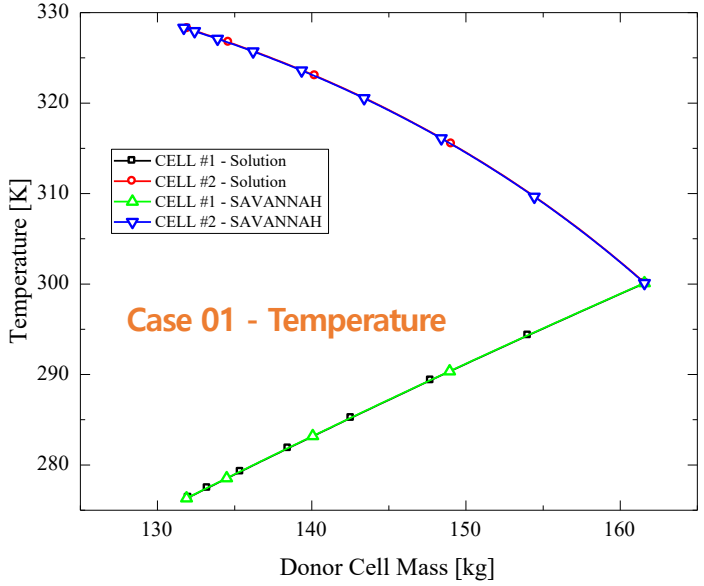

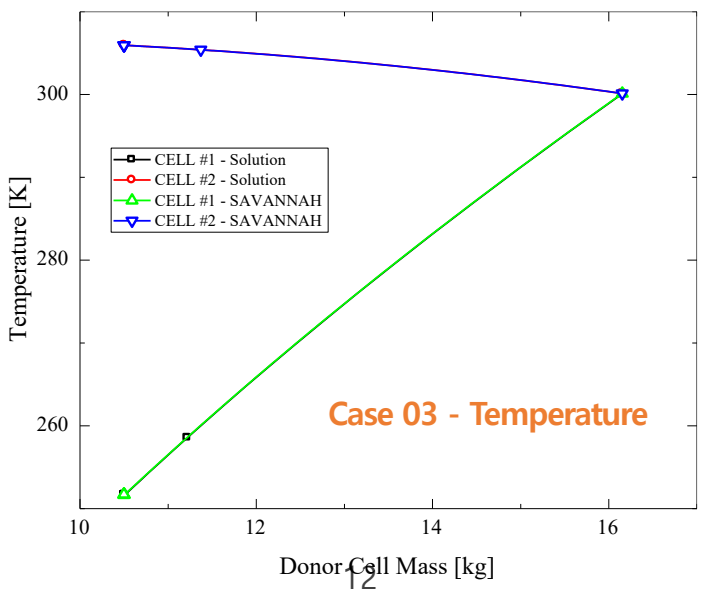

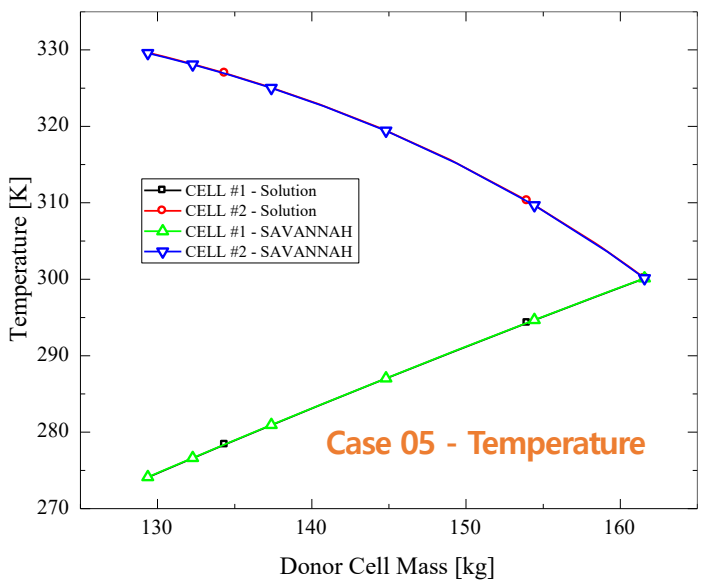

Verification – Semi-Infinite Solid Heat Structure [1/2]

- Utilized for MELCOR code verification
- Heat structure thickness: 10 m
- Boundary Conditions
  - Left side: In contact with fluid
    - Fluid temperature varies by case
    - HTC: Fixed at 10 W/m^2-K
  - RIght side: Adiabatic

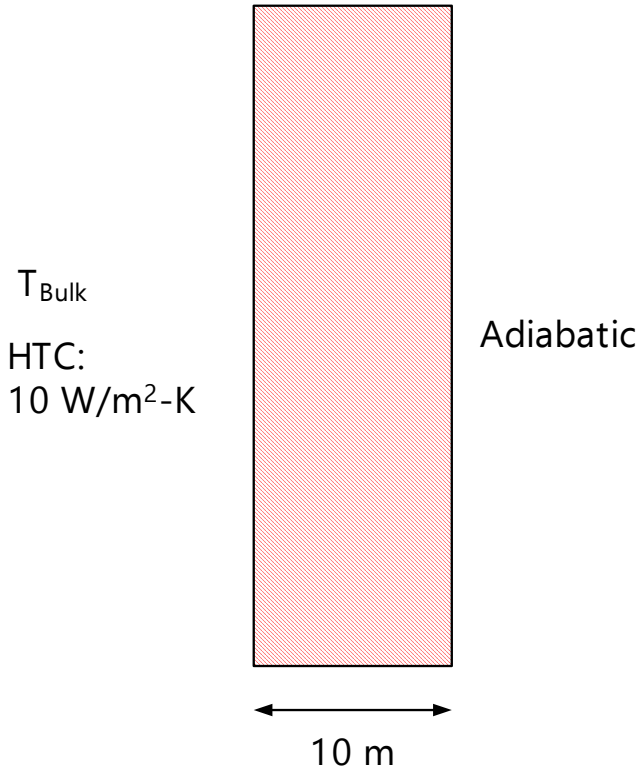

Case	Fluid	Heat Structure				
	Bulk Temp. [K]	Initial Temp. [K]	Material	Density [kg/m^3]	Heat Capacity [J/kg-K]	Conductivity [W/m-K]
1	450.0	300.0	Concrete	2300.0	650.0	1.6
2	450.0	300.0	Steel	7850.0	500.0	47.0
3	600.0	300.0	Concrete	2300.0	650.0	1.6

Verification – Semi-Infinite Solid Heat Structure [2/2]

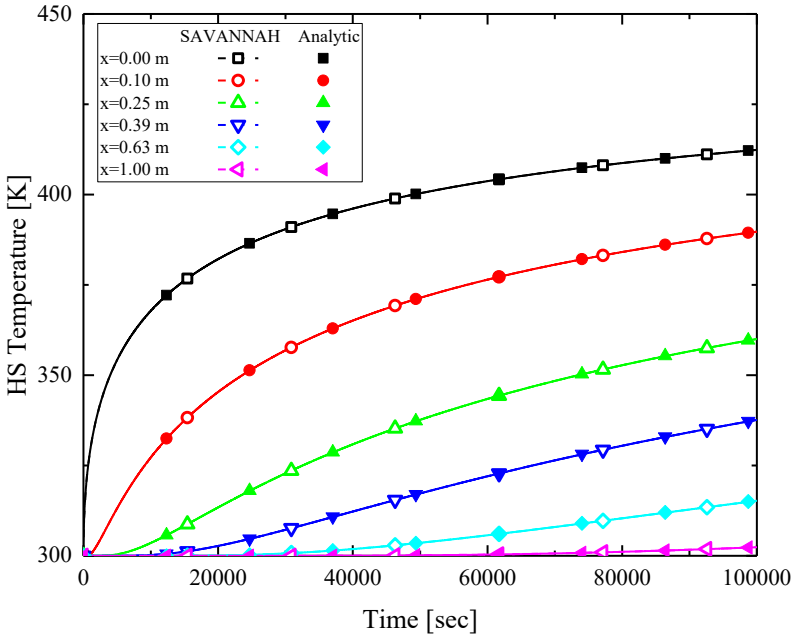

Case 01

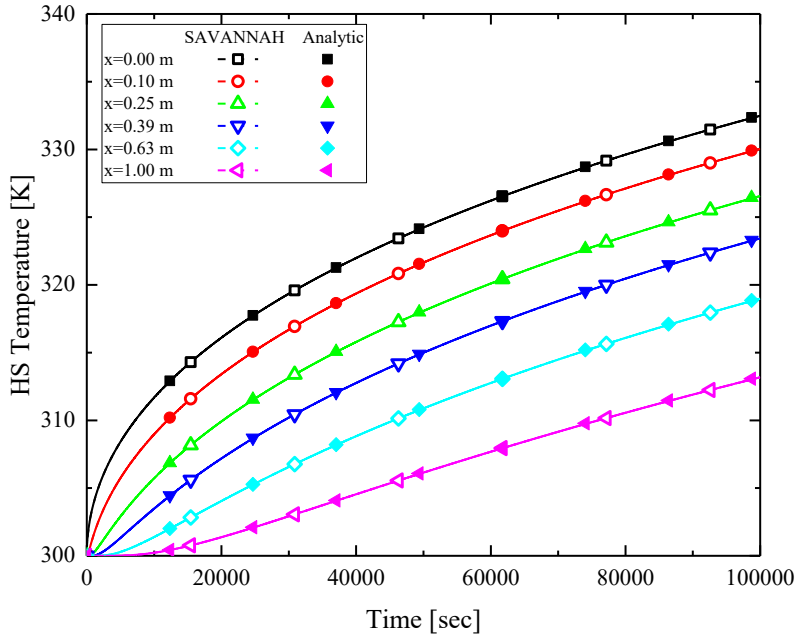

Case 02

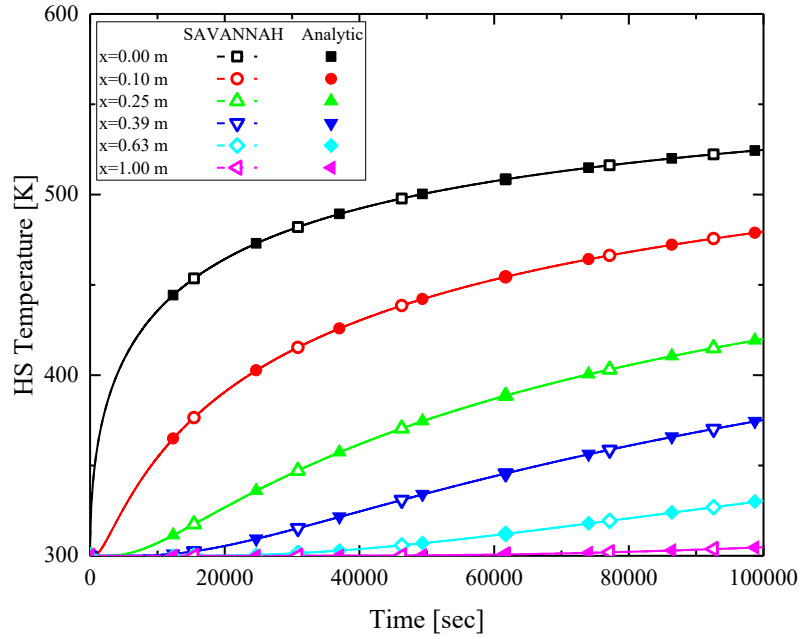

Case 03

Verification – 1D Flow with Minor Loss

- Utilized for CAP code verification
- Configuration: Two sufficiently large volumes connected by a single flow path
- Flowpath Specifications
  - Total Length: 160 m
  - Diameter: 0.2 m
  - Surface Roughness: 0.046 mm
  - Total minor loss coefficient: 12.2

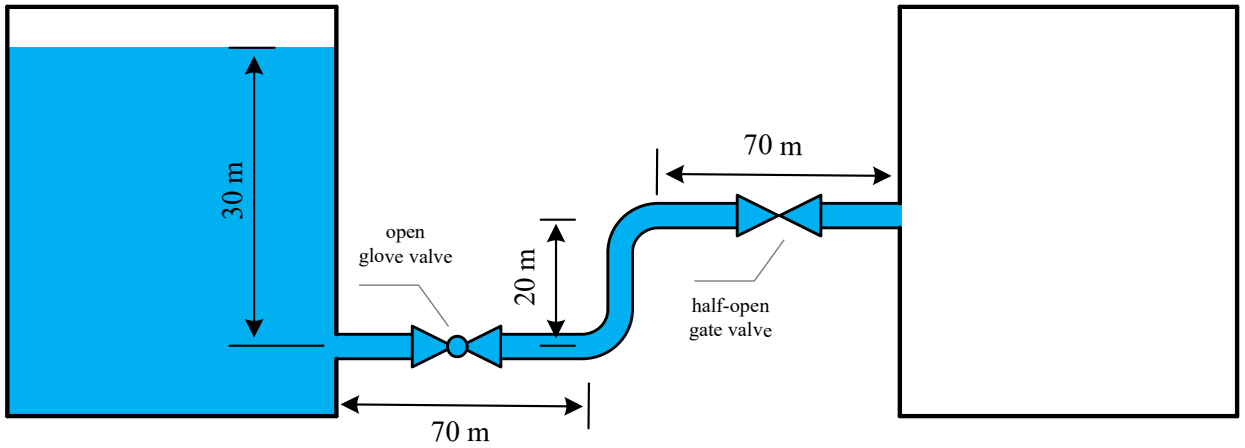

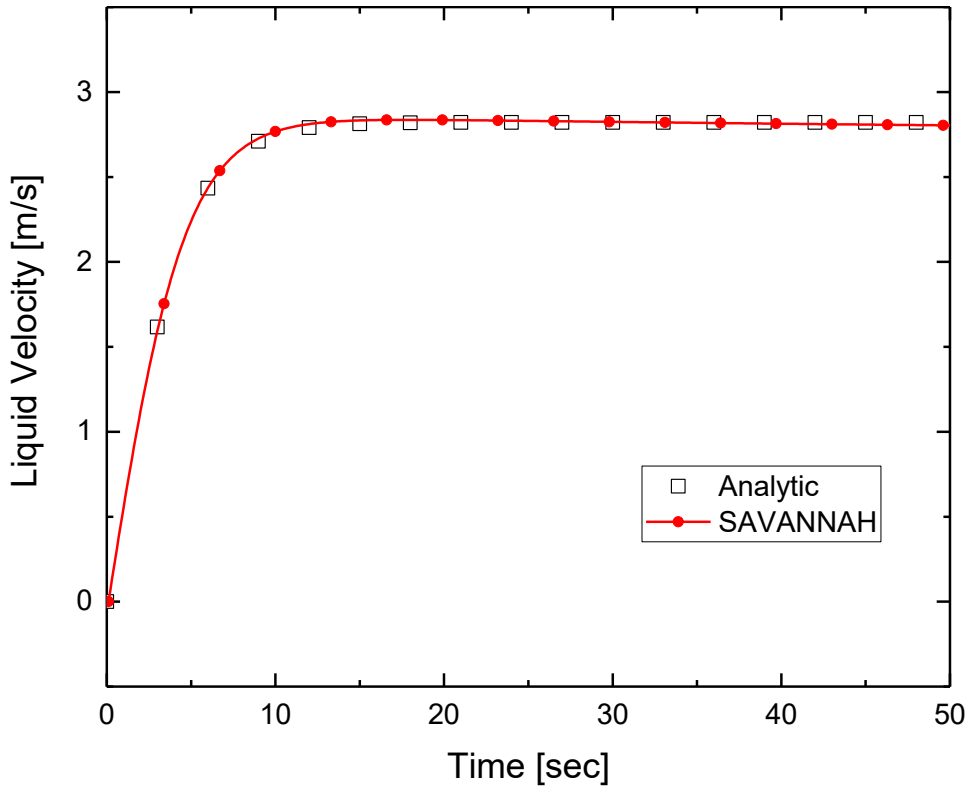

Verification Results

Validation – ThAI [1/2]

- Target Physics
  - Helium Distribution, Condensation
- Geometry
  - Total Height: 9.2 m
  - Diameter: 3.2 m
  - Total Volume: 60.0 m^3
  - Material: Carbon Steel
- Initial Condition
  - 1.0 bar / 295.15 K / 70% Humidity
- Test Condition
  - 0.0 – 2,700 sec: Helium Injection (0.6 g/s)
  - 2,700 – 4,700 sec: Steam Injection (35 g/s)
    - Injection Location: Annulus
  - 4,700 – 5,700 sec: Steam Injection (35 g/s)
    - Injection Location: Lower Plenum

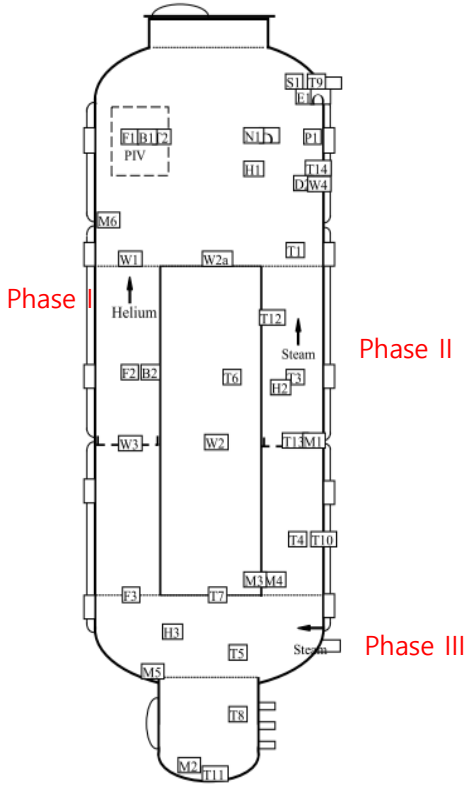

Schematic Diagram

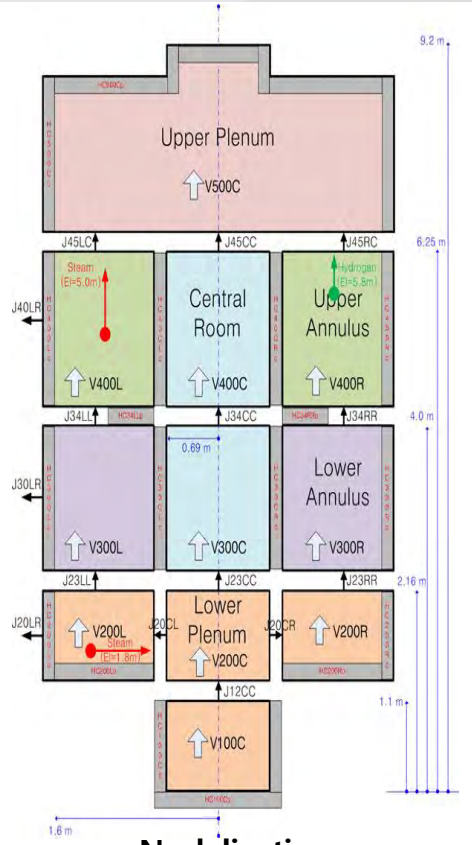

Nodalization

Table 2. **ThAI test sequence**

Phase	Time (s)	Activity
I	0 - 2700	Vertical helium jet injection.
II	2 700 - 4 700	Vertical steam jet injection at the upper injection nozzle.
III	4 700 - 5 700	Horizontal steam plume injection at the lower injection nozzle.
IV	5 700 - 7 700	No injection, passive cool-down of the facility.

Validation – ThAI [2/2]

Key Findings

- SAVANNAH predicts containment pressure reasonably well
- Lumped-parameter approach shows limited spatial stratification prediction
- Helium Distribution
  - SAVANNAH: Predicts a uniform distribution
  - CAP & MELCOR: Predict slight spatial variations depending on the location.

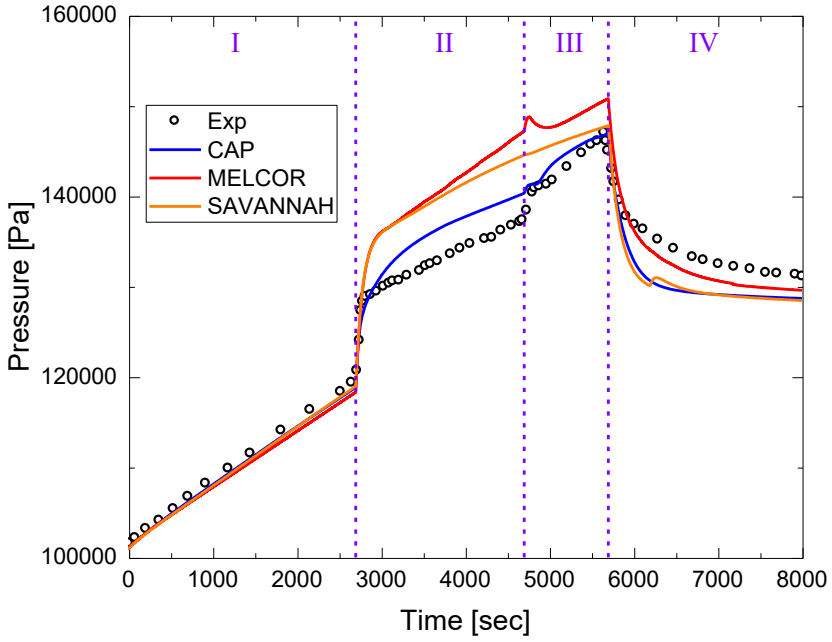

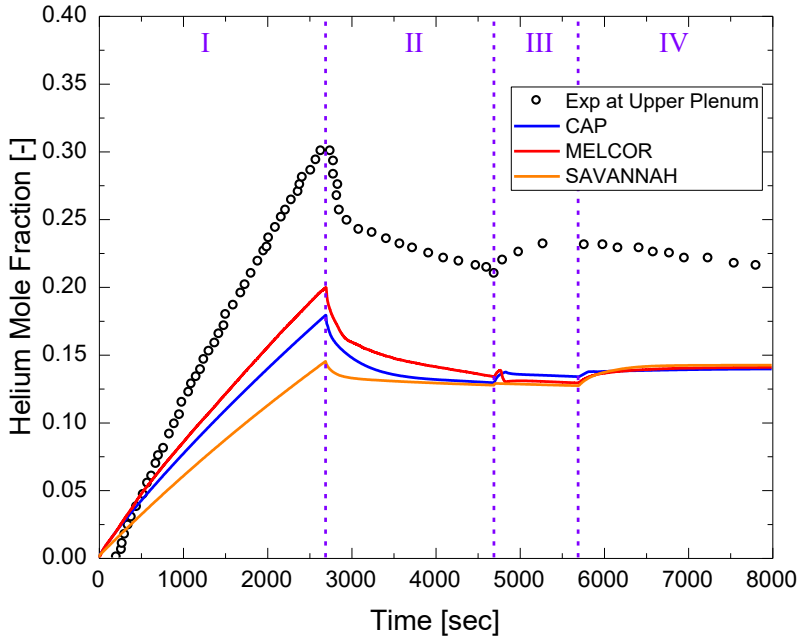

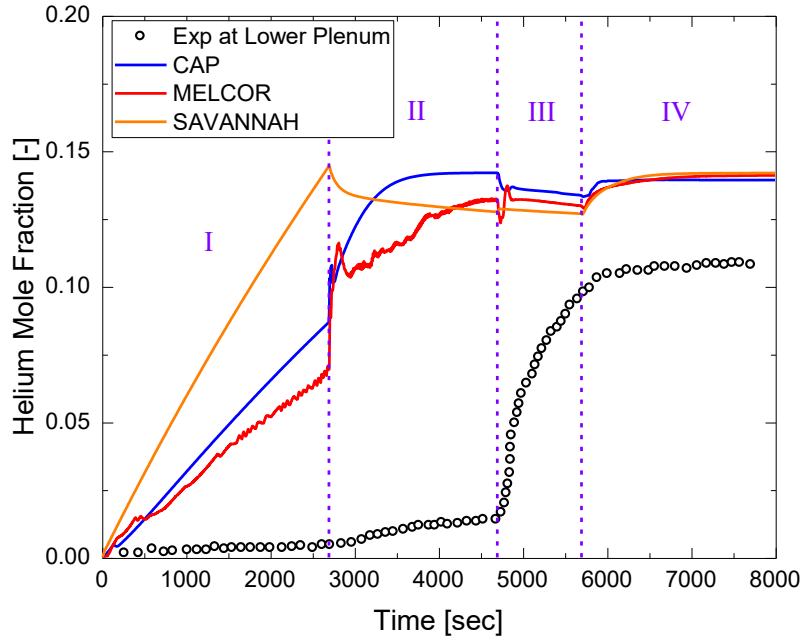

Validation – HDR V44 [1/2]

Target Physics

- Steam/Water Blowdown, Condensation

Geometry

- Total Height: 60 m
- Diameter: 20 m
- Total Volume: 11,300 m^3

Blowdown Condition

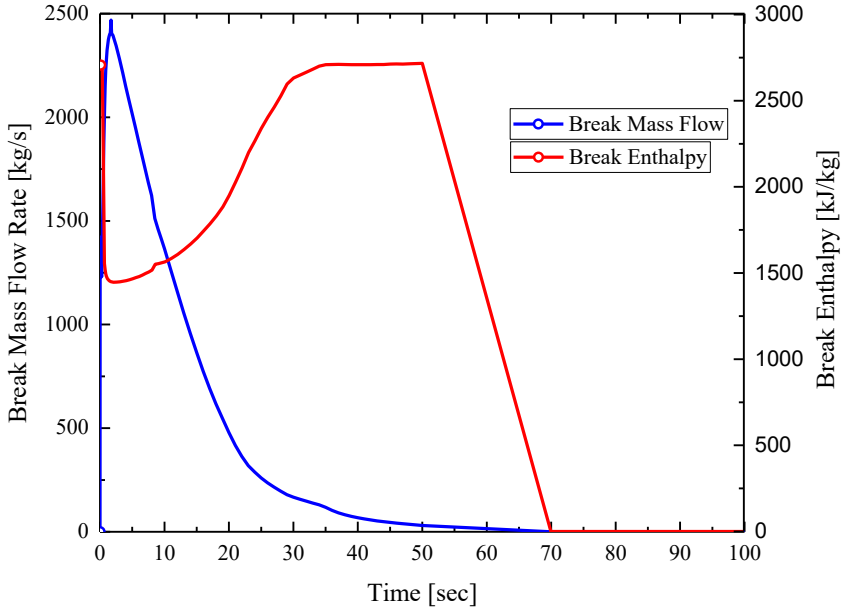

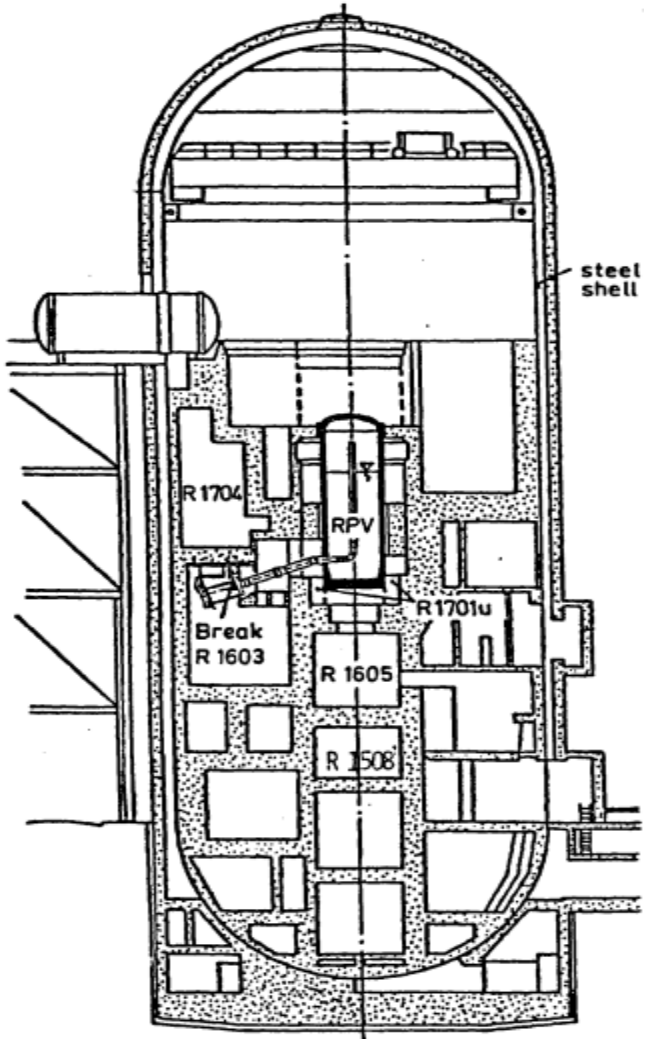

Schematic Diagram

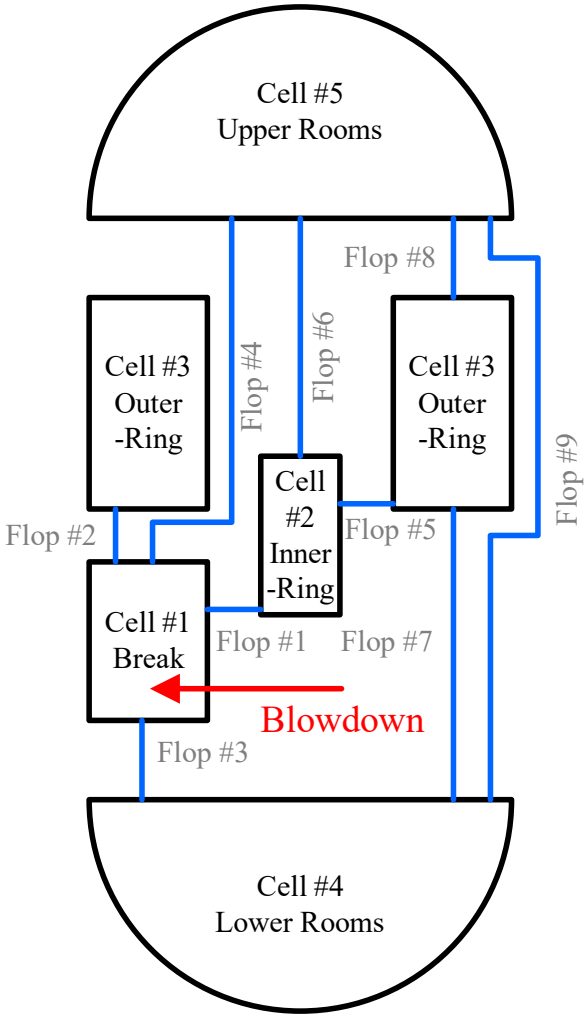

Nodalization

Validation – HDR V44 [2/2]

- Peak pressure slightly over-predicted by all codes
- SAVANNAH shows similar long-term behavior to MELCOR
- CAP predicts pressure and temperature lower than other codes

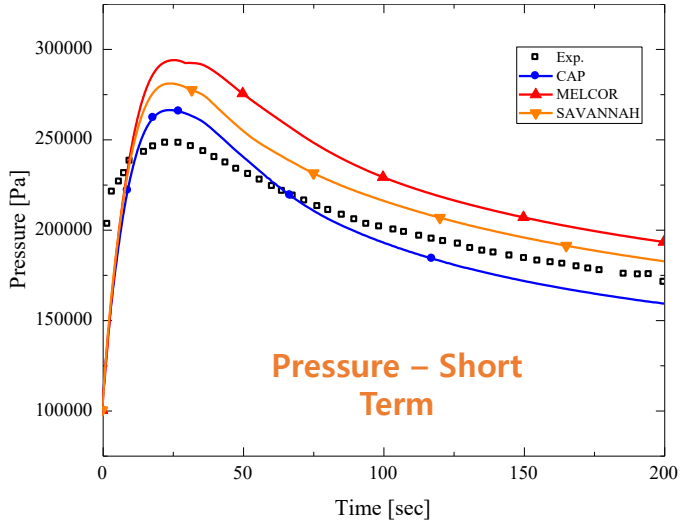

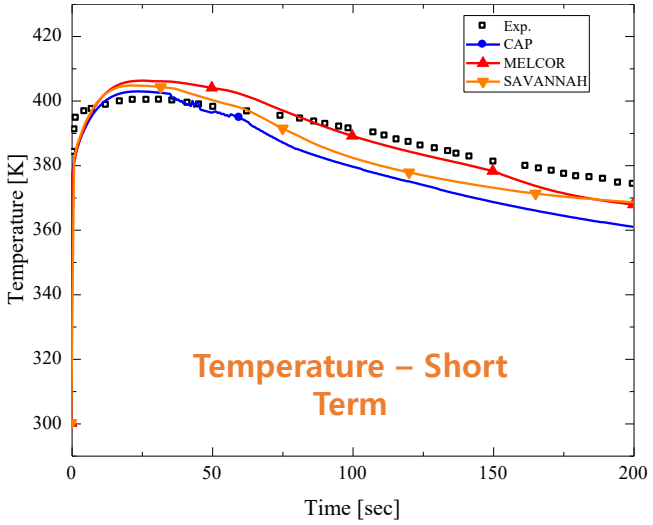

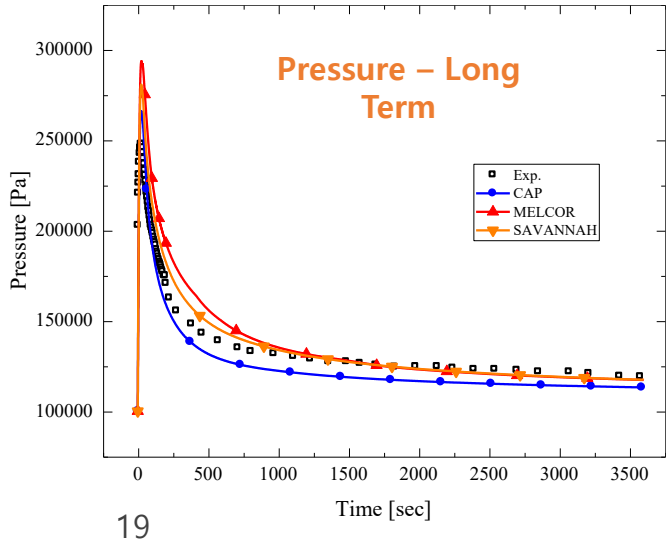

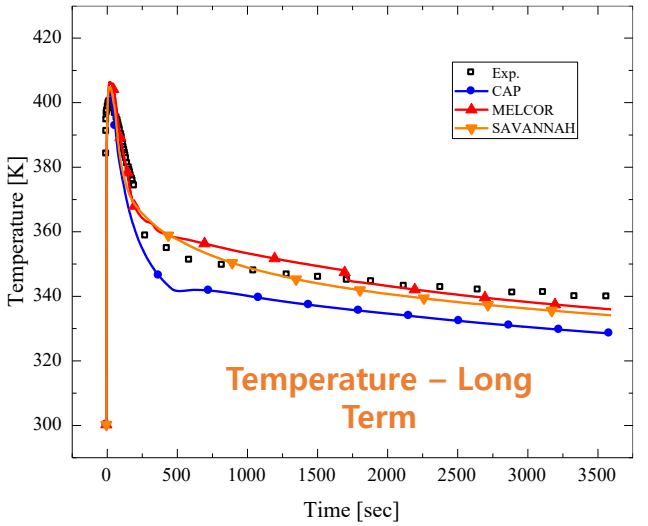

5 Conclusion & Future Work

Conclusions

- SAVANNAH was developed as a containment thermal-hydraulic analysis module within the SAFARI framework
- The governing equations for TH is similar with MELCOR
- Verification results showed good agreement with analytic solutions
- Validation tests demonstrated that SAVANNAH can reasonably predict:
  - Blowdown behavior
  - Pressure response
  - Condensation trends in containment thermal-hydraulic response

Future Work

- Integrate SAVANNAH with other SAFARI modules for coupled analysis.
- Advanced code refinement to improve prediction accuracy under highly transient and multi-dimensional convective conditions

ABOUT

FNC TECHNOLOGY CO., LTD.

Headquarters

Heungdeok IT Valley Bldg. 32F, 13, Heungdeok 1 ro,
Giheung gu , Yongin si , Gyeonggi do, 16954, Korea
+82-31-8065-5114

Daejeon Branch

Daeduk Tech Business Center, 1004-2, 593, Daedukdae-ro,
Yusung-gu, Daejeon-si, 34112, Korea
+82-42-867-5114

Institute of Future Energy Technology

Main | 46, Tapsilro, Giheung-gu, Yongin-si
Gyeonggi-do, 17084, Korea
+82-31-8005-5618

New | 44, Tapsilro, Giheung-gu, Yongin-si
Gyeonggi-do, 17084, Korea
+82-31-8005-8236

UAE Abu Dhabi Branch

#2335, Sky Tower, Al Reem Island PO Box 5101041,
Abu Dhabi, UAE
+971-2-406-9719

US Maryland Branch

11140 Rockville Pike, Suite 380A, Rockville, MD
20852 USA
+1-202-577-5537

Copyright 2022. FNC Technology Co., Ltd. all rights reserved.

THANK YOU

FNC TECHNOLOGY CO., LTD.

Velocity Matrix [1/2]

$$P_i^{\tilde{n}} = P_i^{o+} + \sum_{m=1}^{M} [(\frac{\partial P}{\partial M})\Delta M]_m + (\frac{\partial P}{\partial E})_{pool}\Delta E_{pool} + (\frac{\partial P}{\partial E})_{atm}\Delta E_{atm}$$

- Mass Conservation Equation (**Each Material**)

$$\Delta M = M_{i,m}^n - M_{i,m}^n = \sum_j \sigma_{ij}\alpha_{j,\phi}^n \rho_{j,m}^d v_{j,\phi}^n A_j \Delta t + \delta M_{i,m}$$

- Energy Conservation Equation (**Each Phase**)

$$\Delta E_\phi = E_{i,\phi}^n - E_{i,\phi}^n = \sum_j \sigma_{ij}\alpha_{j,\phi}^n (\rho_{j,m}^d h_{j,m}^d) v_{j,\phi}^n A_j \Delta t + \delta E_{i,\phi}$$

- Predicted cell pressure can be substituted with a function of the connected flowpath velocity
- This allows the momentum equation to be expressed solely as a function of velocity

$$v_{j,\phi}^n = v_{j,\phi}^o + \frac{\Delta t}{\rho_{j,\phi} L_j}\left[P_i^{\tilde{n}} + \Delta P_{pp} - P_k^{\tilde{n}} + (\rho g \Delta z)_{j,\phi}^{\tilde{n}} - \left(f\frac{L_j}{D} + \sum K\right)\frac{\rho_{j,\phi}}{2}\left(|v_{j,\phi}^{n-1} + v_{j,\phi}^{n-2}|v_{j,\phi}^n - |v_{j,\phi}^{n-2}|v_{j,\phi}^{n-1}\right)\right]$$

Velocity Matrix [2/2]

$$\begin{vmatrix} a_{P,1}+c_{P,1.1} & c_{P,1.2} & \cdots & c_{P,1.J} & b_{P,1}+d_{P,1.1} & d_{P,1.2} & \cdots & d_{P,1.J} \\ c_{P,2.1} & a_{P,2}+c_{P,2.2} & \cdots & c_{P,2.J} & d_{P,2.1} & b_{P,2}+d_{P,2.2} & \cdots & d_{P,2.J} \\ \vdots & \vdots & \ddots & \vdots & \vdots & \vdots & \ddots & \vdots \\ c_{P,J.1} & c_{P,J.2} & \cdots & a_{P,J}+c_{P,J.J} & d_{P,J.1} & d_{P,J.2} & \cdots & b_{P,J}+d_{P,J.J} \\ a_{A,1}+c_{A,1.1} & c_{A,1.2} & \cdots & c_{A,1.J} & b_{A,1}+d_{A,1.1} & d_{A,1.2} & \cdots & d_{A,1.J} \\ c_{A,2.1} & a_{A,2}+c_{A,2.2} & \cdots & c_{A,2.J} & d_{A,2.1} & b_{A,2}+d_{A,2.2} & \cdots & d_{A,2.J} \\ \vdots & \vdots & \ddots & \vdots & \vdots & \vdots & \ddots & \vdots \\ c_{A,J.1} & c_{A,J.2} & \cdots & a_{A,J}+c_{A,J.J} & d_{A,J.1} & d_{A,J.2} & \cdots & b_{A,J}+d_{A,J.J} \end{vmatrix} \begin{vmatrix} v_{1,P}^n \\ v_{2,P}^n \\ \vdots \\ v_{J,P}^n \\ v_{1,A}^n \\ v_{2,A}^n \\ \vdots \\ v_{J,A}^n \end{vmatrix} = \begin{vmatrix} e_{P,1} \\ e_{P,2} \\ \vdots \\ e_{P,J} \\ e_{A,1} \\ e_{A,2} \\ \vdots \\ e_{A,J} \end{vmatrix}$$

$$a_{\phi,j} = \left[1 + \left(f\frac{L_j}{D} + \sum K\right)\frac{\Delta t}{2L_j}|v_{j,\phi}^{n-1} + v_{j,\phi}^{n-2}| + \frac{\alpha_{j,-\phi} f_2 L_2 \Delta t}{\rho_{j,\phi} L_j}\right]$$

$$b_{\phi,j} = -\frac{\alpha_{j,-\phi} f_2 L_2 \Delta t}{\rho_{j,\phi} L_j}$$

$$c_{\phi,j} = -\frac{\Delta t}{\rho_{j,\phi} L_j}\left\{\sum_j F_j A_j \Delta t \sum_m \rho_{j,m}^d \alpha_{j,P}^n \left[\sigma_{ij}\left(\frac{\partial P^*}{\partial M_{i,P}} + \frac{\partial P^*}{\partial E_{i,P}} h_{j,m}^d\right) - \sigma_{kj}\left(\frac{\partial P^*}{\partial M_{k,P}} + \frac{\partial P^*}{\partial E_{k,P}} h_{j,m}^d\right)\right]\right\}$$

$$d_{\phi,j} = -\frac{\Delta t}{\rho_{j,\phi} L_j}\left\{\sum_j F_j A_j \Delta t \sum_m \rho_{j,m}^d \alpha_{j,A}^n \left[\sigma_{ij}\left(\frac{\partial P^*}{\partial M_{i,m}} + \frac{\partial P^*}{\partial E_{i,A}} h_{j,m}^d\right) - \sigma_{kj}\left(\frac{\partial P^*}{\partial M_{k,m}} + \frac{\partial P^*}{\partial E_{k,A}} h_{j,m}^d\right)\right]\right\}$$

$$e_{\phi,j} = v_{j,\phi}^{o+} + \frac{\Delta t}{\rho_{j,\phi} L_j}\left\{\widehat{P}_i + \Delta P_j - \widehat{P}_k + (\rho g \Delta z)_{j,\phi}^o + \frac{\partial (\rho g \Delta z)_{j,\phi}}{\partial M_{i,P}}(\widehat{M}_{i,P}^o - M_{i,P}^{o+}) + \frac{\partial (\rho g \Delta z)_{j,\phi}}{\partial M_{k,P}}(\widehat{M}_{k,P}^o - M_{k,P}^{o+}) + v_{j,\phi}^o (\rho \Delta v)_{j,\phi}^o\right\} + \frac{K^* \Delta t}{2L_j}|v_{j,\phi}^{n-2}| v_{j,\phi}^{n-1}$$

Condensation Heat Transfer Model

- While CAP adopts the Uchida model, SAVANNAH and MELCOR employ the Heat and Mass Transfer Analogy(HMTA) model under non-condensable gas conditions;

- Condensation Model
  - CAP: $h = 450(\frac{\rho_{ncg}}{\rho_{steam}})^{-0.8}$
  - MELCOR: $h = Sh\frac{D}{L_c}$

    $Sh = NuSc^{1/3}Pr^{-1/3}$
  - SAVANNAH: $h = \frac{\Gamma_d'' h_{fg}}{T_g - T_w}$

    $\Gamma_d'' = \frac{\rho_{stm} ShD_{sg}}{L_c} ln[\frac{max(P_{tot} - P_w, 0.1)}{P_{ncg}}]$

    $Sh = NuSc^{1/3}Pr^{-1/3}$

The 12th European Review Meeting on Severe Accidents Research

May 18-22, 2026, Universidad Carlos III de Madrid, Madrid, Spain

TECHNICAL SESSION 6.4: SOURCE TERM

Chairs: A. Bentaib (NEA), I. Kljenak (JSI)

ID001	**Assessment of pool scrubbing predictive capabilities: benchmarking SPARC90 against an ad-hoc database** G. Tinfena (University of Pisa)	Paper Presentation
ID005	**Pool Scrubbing in Water Cooled SMRs: Scenarios, Peculiarities and Challenges** L. E. Herranz (CIEMAT)	Paper Presentation
ID075	**MAAP6 Mechanistic Pool Scrubbing Model** P. McMinn (Westinghouse)	Paper Presentation
ID125	**COCOSYS simulation of CsI decomposition under irradiation and the formation of organic iodide in the containment** C. Lu (GRS)	Paper Presentation

ASSESSMENT OF POOL SCRUBBING PREDICTIVE CAPABILITIES: BENCHMARKING SPARC90 AGAINST AN AD-HOC DATABASE

G. Tinfena, M. Angelucci, S. Paci
University of Pisa
Largo Lucio Lazzarino, 56122 Pisa, Italy
giacomo.tinfena@phd.unipi.it; michela.angelucci@unipi.it; sandro.paci@unipi.it

L.E. Herranz
CIEMAT
Avenida Complutense 40, 28040 Madrid, Spain
luisen.herranz@ciemat.es

ABSTRACT

Pool scrubbing is a process for the mitigation of the source term in many Severe Accident (SA) scenarios, regardless of reactor technology. Naturally set and/or *ad-hoc* included in some safety systems, its efficiency depends on thermal-hydraulic and physicochemical variables, whose variability ranges are extremely broad. As a result, estimating accurate and reliable predictions poses a big challenge for SA system and stand-alone codes. This work presents a broad and systematic evaluation of SPARC90, which is the basis of the pool scrubbing module in MELCOR and ASTEC, against a credited database of more than 100 tests, which encompasses prevailing boundary conditions of any scenario in which pool scrubbing might play a role. The results indicate that SPARC90 generally follows, but underestimate data, with a mean signed relative error of -21%. Nonetheless, the code systematically misses data points representing specific scenarios, like Steam Generator Tube Rupture (SGTR) or Filtered Containment Venting System (FCVS) experiments, consistently with its modeling capabilities. Conditions representative of Molten Core Concrete Interaction (MCCI) are also explored through selected surrogate tests, suggesting that a reasonable predictive capability might still be achievable. The discussion of these findings provides a rational basis to orient future developments in pool scrubbing modelling.

KEYWORDS
Pool scrubbing, SPARC90, model validation, source term.

1. INTRODUCTION

Pool scrubbing is an efficient source term mitigation process during Severe Accidents (SA). It refers to the set of mass transfer phenomena responsible for particulates and vapors absorption by a continuous liquid body when a gaseous disperse phase moves across it. Pool scrubbing is not a reactor-specific process, but it might occur in several safety relevant scenarios of water-cooled reactors. Some examples are: Boiling Water Reactors (BWR), such as Fukushima [1], Pressurized Water Reactors, particularly in Steam Generator Tube Rupture (SGTR) accidents [2], Small Modular Reactors [3], Filtered Containment Venting Systems (FCVS) [4], and Molten Core Concrete Interaction (MCCI) [5]. This scenario diversity results in broad ranges of boundary conditions that may even change over time, from sub-cooled to saturated pools, high to low injection velocities, or deep to shallow pools. As a consequence, a large and sound database is of utmost importance to thoroughly characterize pool scrubbing and to benchmark dedicated codes.

The efficiency of pool scrubbing is indeed determined by a wide range of parameters, which are generally categorized according to the physical phase they influence on. Factors related to the carrier gas include its

composition, temperature, and flow velocity; those associated with Fission Products (FP) involve their physical state (aerosol or vapor), particle size distribution, and composition; while the pool parameters encompass its thermal condition, its size, submergence, and the configuration and type of injectors. Over the past several decades, these aspects have been the subject of extensive experimental and analytical research ([6], [7], [8]). Notably, the intensive programs conducted during the 1980s and 1990s produced several standalone computational models, such as BUSCA ([9]), SUPRA ([10]), and SPARC90 [11], that were later integrated into integral system codes like MELCOR ([12], [13]) or ASTEC [14]. However, as other studies have already shown, pool scrubbing models need enhancements and/or extensions [15].

In this direction, the long-term objective of this research is to establish a modelling framework capable of simulating pool scrubbing in a flexible and consistent way across the different reactor types and accident scenarios in which this process may occur. As a necessary first step toward such a framework, SPARC90 has been selected to be systematically assessed to quantify its predictive capabilities, identify its main limitations, and thereby provide a rational basis for any subsequent model development or extension.
To this end, a unique and high-quality experimental database has been built, gathering information from more than 900 tests performed in nearly 50 independent programs [16]. A subset of "Qualified for Validation" (QfV) experiments, selected through an adequacy analysis [17], is then simulated in SPARC90, with the goal of systematically assessing its capabilities in simulating a broad and diverse dataset. While earlier assessments have typically relied on limited subsets of experiments, the availability of a broader and rigorously characterized dataset enables a comprehensive and homogeneous understanding of the SPARC90 predictive performance over a wide spectrum of conditions. The work provides indeed an in-depth understanding of the similarities and discrepancies between numerical predictions and experimental evidence. Beyond a global evaluation of the code accuracy, the analysis further addresses safety-relevant configurations, including SGTR, FCVS, and MCCI scenarios, with the objective of identifying priorities and directions for subsequent model improvement.

The variable adopted as reference metric to assess SPARC90 is the Decontamination Factor (DF), defined as the ratio of the incoming over the outgoing mass of aerosols in the pool. The present study is restricted to aerosol scrubbing, so that FP vapors are beyond scope.

2. METHODS

2.1. SPARC90

SPARC90 is a semi-empirical simulation tool developed at the Pacific Northwest Laboratory to evaluate FP retention in BWRs pressure suppression pools during SA [11]. The code models the complex thermal-hydraulic and physicochemical interactions between gas-aerosol mixtures discharged through submerged vents and the pool, providing estimates of aerosol and iodine scrubbing efficiencies. The code's formulation and validation rely predominantly on experimental programs from the 1980s and 1990s, which were largely conducted under BWR conditions and reflect vent geometries typical of suppression-pool designs.

SPARC90 represents the suppression pool as a system of interacting zones: the vent exit region, the unstable globule breakup region, the rising bubble swarm, and the pool surface. The code, however, explicitly calculates aerosol removal only in two regions: the vent-exit region, where inertial impaction and condensation driven deposition dominate, and the rising bubble swarm region, where centrifugal deposition, gravitational settling, and Brownian diffusion govern particle capture. The unstable globule breakup region is not modeled for scrubbing; instead, the breakup length determines the starting point of the swarm. The pool surface region is assigned a unit decontamination factor (DF = 1), because scoping calculations suggested that any additional retention associated with bubble bursting or surface condensation is negligible under expected BWRs SA conditions [11].

SPARC90 also simulates the effects of bubble coalescence and cooling during rise, incorporating coupled heat and mass transfer between the gas phase and the surrounding liquid. These processes produce supersaturated vapor conditions that promote aerosol hygroscopic growth, treated by both mechanistic (Mason-type) and thermodynamic-limit models. The code also features additional subroutines for volatile iodine species.

SPARC90 can represent different vent or injector geometries, such as downcomers, horizontal vents, and multi-hole "T" or "X" quenchers, through specific correlations for globule formation, breakup length, and vent Weber number. Input parameters define the pool geometry, vent configuration, aerosol size distribution, and gas composition, while output includes DFs for each particle size class and overall system performance. Figure 1 illustrates the SPARC90 flow chart [11].

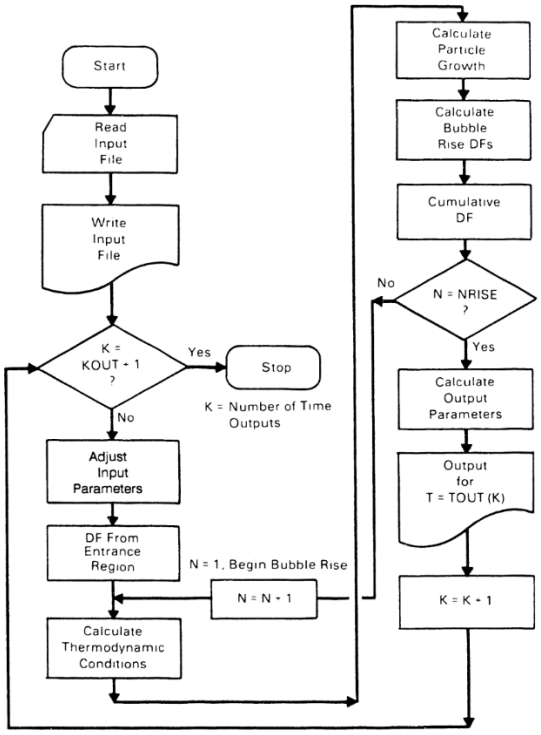

Figure 1. SPARC90 flow chart [11]**.**

2.2. Database

The global pool scrubbing database retrieved from the open literature for this ongoing research consists of more than 908 experiments belonging to 48 experimental programs carried out from the 1960s to 2025. After compiling it with available information, a database adequacy analysis was carried out to achieve the highest quality standard feasible for code validation [17], [18]. This methodology allows a systematic evaluation of representativeness and completeness of a database. The resulting validation matrix collects 106 QfV experiments which address a wide range of conditions of the key variables affecting pool scrubbing, like particle size distribution, gas and aerosol flow rates and compositions, pool depth and thermal state, and injection configurations. Table I collects the most relevant information of this validation matrix, whereas more details are provided in [16].

Table I. Pool scrubbing validation matrix [16].

Boundary Conditions \ Programs		EPRI (8)	ACE (4)	LACE-España (5)	RCA (4)	POSEIDON – II (17)	AASC-PS (4)	SG-Experiments (15)	PASSAM (CIEMAT + RSE) (13)	TYFON (11)	THAI (12)	YOON (10)	SAPOS (7)
Particle Characteristics	Chemical Species	CsI	CsOH, MnO, CsI	CsI	Ni	SnO2	Ni	TiO2, Nanophase TiO2, SiO2	SiO2	CsI	SnO2	SiO2	TiO2
	Aerodynamic Mass Median Diameter (μm)	0.4	1.7 to 2.9	0.6 to 7.2	1.1 to 1.3 (MMD)	0.3 to 0.5	2.4 to 2.8	1.4 to 4.6	0.4 to 1.0	0.8	0.22 to 0.85 (MMD)	0.7	0.5
	GSD	-	1.8 to 2.4	1.4 to 5.4	1.4 to 1.4	1.4 to 1.7	1.5 to 1.8	2.0 to 3.0	1.2 to 1.6	2	2.0 to 3.0	1.46	1.25
Carrier Gas	Composition	Air/air+steam	N2 + steam	N2 + steam	N2	N2/N2 + steam	Air	N2/N2 + steam	Air/air + steam	Air	Air/air+steam	Air	N2 + steam
	Mass Flow Rate (kg/s)	2.05E-03 to 1.251E-02	6.4E-02 to 1.1E-01	1.0E-04 to 7.2E-03	7.3E-03 to 7.8E-03	0.02 to 0.04	1.052E-03 to 1.341E-03	1.3E-02 to 1.8E-01	2.19E-03 to 1.30E-02	1.846E-04 to 2.633E-03	6.3E-04 to 3.15E-02	2.42E-03 to 9.70E-03	1.90E-02
	Steam Mass Fraction (%)	0.0 to 98.0	0.8 to 31.4	6.7 to 85.3	0	0.0 to 75.0	0	0.0 to 77.0	0.0 to 9.8	0	0.0 to 80.0	0	50.0 to 90.0
Thermal Hydraulics	Pool Temperature (K)	373	297.0 to 356.0	382.3 to 385.4	386.9 to 391.5	335.9 to 363.6	392.4 to 399.5	295.0 to 368.2	293.0 to 307.8	298.15	329.95 to 378.15	ambient	323.2
	Pool Pressure (Pa)	1.01E+05	1.00E+05	2.8E+05 to 3.0E+05	2.3E+05 to 2.5E+05	1.00E+05	2.30E+05	1.0E+05 to 1.1E+05	9.2E+04 to 1.0E+05	atmospheric	1.23E+05 to 4.0E+05	atmospheric	-
	Gas Temperature (K)	410-524	411.0 to 423.0	397.1 to 444.3	394.9 to 414.1	485.9 to 583.8	377.9 to 393.4	297.0 to 430.1	273.2 to 383.1	298.15	373.05 to 393.45	ambient	443.15
	Injection Pressure (Pa)	-	1.2E+05 to 1.5E+05	3.3E+05 to 3.5E+05	2.8E+05 to 2.9E+05	1.2E+05 to 1.7E+05	2.7E+05 to 2.8E+05	1.1E+05 to 4.9E+05	9.6E+04 to 1.6E+06	-	1.29E+05 to 4.02E+05	1.20E+05 to 2.31 E+05	1.34E+05
Pool Geometry	Injector Configuration	Single orifice	Quencher (51 holes)	Single orifice/ multi-orifice (9 holes)	Single orifice	Single orifice	Single orifice	Tube break	Single orifice	Single orifice	Single orifice	Single orifice	Multi-orifice injector (6 holes)
	Injector Orientation	Horizontal	Upward	Horizontal	Horizontal	Upward	Horizontal	Horizontal	Upward/Horizontal	Upward	Horizontal	Upward	Downward
	Injector Diameter (m)	1.27E-02	9.5E-03	1.0E-02	1.00E-02	2.0E-02	1.0E-02	1.7E-02	6.5E-03 to 1.0E-02	2.00E-03	1.50E-02	5.00E-03	1.0E-02
	Submergence (m)	1.65	1.4 to 4.6	2.5	0.3 to 2.5	0.3 to 4.0	1.3	0.0 to 3.80	0.3 to 1.0	0.1 to 1.0	0.25 to 2.0	0.5	1.2 to 3.0
Number of Tests QfV		8	4	4	4	17	4	15	13	8	12	10	7

Several researchers, such as ([10], [15], [19]) have discussed the limitations of current pool scrubbing predictions, particularly in relation to SPARC90. However, a broad and comprehensive evaluation of this code is still lacking in the literature, as most previous modeling efforts have relied on relatively small subsets of experiments. Therefore, assessing SPARC90 against a broad and diverse database such as the one shown in Table I is of primary importance for a comprehensive analysis of its capabilities. Most of these experiments consist of injecting gases into a bare pool as it happens in multiple pool scrubbing scenarios, like suppression pools, quench tanks or even auxiliary buildings in V-sequences. Notably, however, few SGTR experiments are available among the QfV ones, which could provide meaningful information as for the SPARC90 specific capabilities in this scenario. Considering instead FCVS, available experiments such as [20], are not considered QfV for different reasons [16], but labeled Useful for Understanding (UfU), and usable to study FCVS pool scrubbing performance. MCCI, on the other hand, does not feature dedicated experiments, yet some QfV tests share relevant boundary conditions with MCCI, making them suitable to assess SPARC90 capabilities in this scenario.
Furthermore, most QfV experiments (82/106) were conducted under jet injection regime. However, SPARC90 hydrodynamics models only consider bubble regime. Assessing the code against these experiments may therefore highlight deficiencies and indicate specific directions for improvement.

Finally, when performing code validation, it is mandatory to assess the validity range of the validation exercise. In this context, Table II summarizes the ranges of the most relevant boundary conditions covered by the pool scrubbing validation matrix (Table I). These ranges describe the experimental conditions included in the database and set the limits of the present benchmark.

Table II. Boundary conditions covered by the pool scrubbing validation matrix.

Boundary Conditions		
Particle Characteristics	Composition	CsOH,MnO,CsI, DOP, Ni, SnO_2, TiO_2, Nanophase TiO_2, SiO_2

	AMMD (μm)	0.2-7.2
Carrier Gas	Composition	Air, Air+Steam, N2+Steam
	Mass Flow Rate (kg/s)	1.04E-04 to 1.09E-01
	Weber number	6.93E+01 to 9.49E+06
	Steam Mass Fraction (%)	0 to 98
Thermal Hydraulics	Pool Temperature (K)	293.0 to 399.5
	Pool Pressure (Pa)	1.23E+05 to 4E+05
	Injection Pressure (Pa)	3.27E+04 to 1.6E+06
Geometry	Injector Orientation	Upward, horizontal, downward
	Injector Diameter (m)	5E-03 to 2E-01
	Submergence (m)	0 to 4.61

3. RESULTS AND DISCUSSION

3.1. Global Behavior

Figure 2 illustrates the simulation results: experimental DF with error bands, and SPARC90 DF values are plotted for QfV experiment. As noted, SPARC90 generally underestimates measurements: a Mean Signed Relative Error (MSRE) of -21% is calculated between predictions and experimental values. The MSRE, defined as $MSRE = \frac{1}{N}\sum\left(\frac{prediction-experiment}{experiment}\right) * 100$, is a performance metric used to evaluate how much a model's predictions differ from the actual values. A MSRE closer to zero indicates a global higher accuracy, while its sign represents the direction of the error.

Despite this reasonable global agreement, SPARC90 shows a markedly different behavior depending on the magnitude of the experimental DF, as highlighted in Figure 2. For this reason, three DF ranges are considered to cluster the experiments: DF lower than 20, DF between 20 and 100, and DF higher than 100.

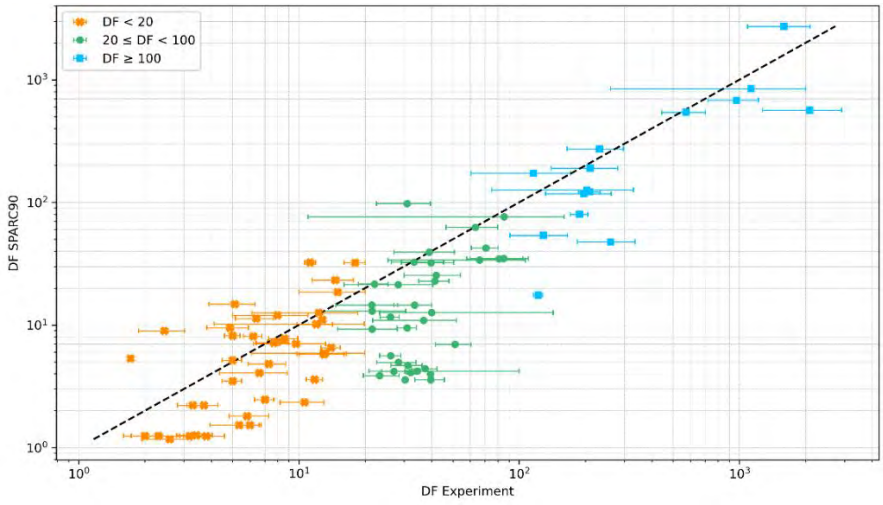

Figure 2. SPARC90 vs experimental DF.

In the low-DF range (DF < 20), which includes 42 experimental points, the MSRE is approximately +2%, indicating a slight overestimation of the experimental values and an overall very good agreement. In the intermediate range (20 < DF < 100), the MSRE decreases significantly to -47%. This range includes 34 experiments, providing sufficient statistical robustness to confirm a systematic underestimation by the code. Finally, in the high-DF range (DF > 100), only 15 experimental points are available, but an MSRE of -27%

is still observed, confirming the general tendency of SPARC90 to underestimate experimental DF values. In this region, a Root Mean Square Error (RMSE) of 509 indicates that the MSRE is dominated by a few experiments characterized by very high DF values.

At this point, it must be stressed that a global MSRE of -21% might be within the expected accuracy for pool scrubbing analytical tools, considering the intrinsic uncertainties of the experimental measurements. The determination of the DF relies on the ratio of two distinct mass measurements: the incoming and the outgoing aerosol mass. While the incoming mass is typically measured in a well-defined injector geometry with controlled isokinetic sampling, measuring the outgoing mass is significantly more challenging.
The aerosol exiting the pool spreads across a broad cross-section, where the hydrodynamic complexity of the bubble swarm, characterized by continuous coalescence, break-ups, and interfacial exchanges, generates radial concentration gradients [21]. Achieving a perfectly representative sample in such conditions is technically demanding, and even minor deviations in sampling representativeness can propagate into the calculated DF. In fact, the impact of these experimental challenges is reflected in the magnitude of the error bars observed in the experimental data points, as visible in Figure 2.
Therefore, the global SPARC90 MSRE seems consistent with the order of magnitude of the inherent experimental uncertainty. This comparison, however, does not intend to overlook the physical deficiencies of SPARC90, but it suggests that the code's predictions are reliable enough to capture the dominant features of the decontamination process within the limits of experimental data.

It is also worth recalling that DF is the parameter most commonly adopted in pool scrubbing analyses. However, from a nuclear safety perspective, the truly relevant quantity is the actual mass of radionuclides leaving the pool, as it directly contributes to the source term. For this reason, Figure 3 compares SPARC90 predictions and experimental data in terms of outgoing aerosol mass.

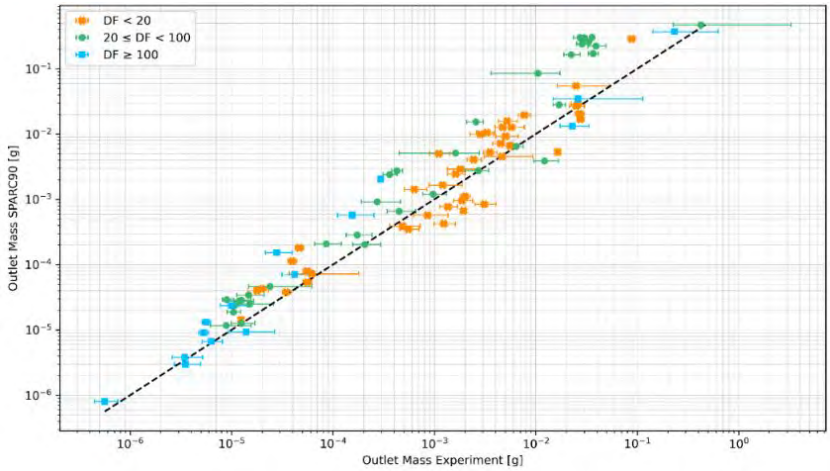

Figure 3. SPARC90 vs experimental outgoing mass from the pool.

Notably, absolute mass values are strongly dependent on the specific facility and experimental protocol, which makes direct comparison between different experiments less straightforward. Therefore, the three DF ranges previously defined are considered again in order to consistently analyze SPARC90 behavior.

Furthermore, pool scrubbing experiments are often conducted in small-scale facilities, where tiny aerosol masses are injected and measured. As a consequence, even a small absolute difference between simulated and experimental outgoing mass can result in a large relative error. Indeed, MSRE values computed in terms of outgoing mass are significantly larger than those obtained for DF: a global MSRE of 155% is obtained, with values of 63% for DF < 20, 284% for the intermediate DF range, and 119% for DF > 100. Although larger in magnitude, these trends are consistent with those observed for DF. In most cases, SPARC90 yields

conservative results by overestimating the outgoing mass, while showing better accuracy at low DF and larger discrepancies at higher DF.

Overall, these results are partially in contrast with previous SPARC assessments, such as ([8], [22]), which showed much larger discrepancies between experiments and calculations, particularly at high DF and under jet injection. The difference between the present assessment and previous ones is likely attributable to the different datasets employed. As stated earlier, in the current work the validation relies on a wider and more rigorously characterized set of experiments, selected through a systematic approach (i.e., adequacy analysis). This ensures that the comparison between model and data relies on measurements with well-understood conditions and quantified experimental errors. This said, specific insights on SPARC90 accuracy will be further discussed below.

3.2. High-velocity injection regime

As said above, a good number of data points in the database fall in what is known as jet-injection regime (i.e., We $\geq 10^5$). As shown in Fig. 4, SPARC90 can predict DF values from jet experiments with reasonable accuracy. Jet experiments exhibit a larger scatter, with both under- and over-predictions, and with calculated DF values up to an order of magnitude lower than measured and other times 3 times higher than measured. Anyway, when expressed in terms of MSRE is -23% (7 points over the globule's one, -16%). Therefore, it is important to bear in mind the limitations of MSRE itself for a full characterization of analytical estimates. The largest deviations span indeed from a -91% to a +267% MSRE.

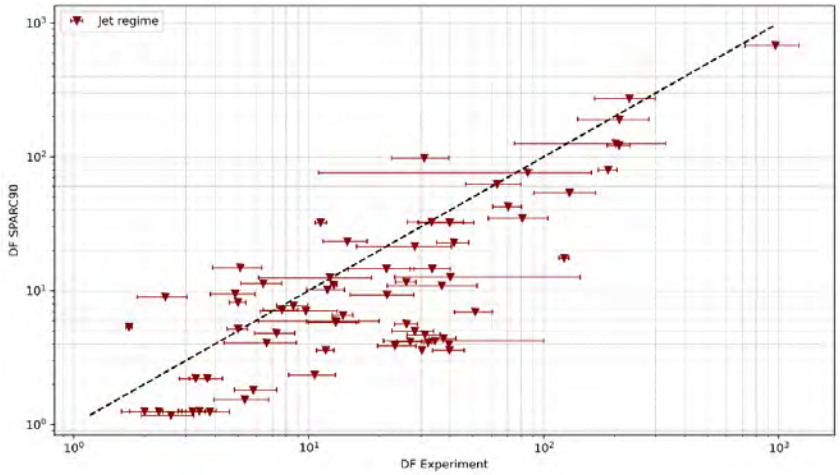

Figure 4. SPARC90 vs experimental DF highlighting jet and bubble experiments.

Beyond what said in the paragraph above, the most interesting observation is the fact that SPARC90 estimates under jet-injection regime do not rely on any analytical model, either empiric or mechanistic, of the jet injection regime. As highlighted by [23], a mathematical algorithm of any kind is missing in the SPARC90 source code. And yet, SPARC90 seems to be able to capture this effect. A deeper look into the estimates allows finding that what is happening is closely related to the integral nature of DF. In jet-injection scenarios, SPARC90 cannot remove particles due to inertial deposition nearby the injection spot. However, other removal mechanisms acting on the way the gas reaches the pool surface makes the job (aerosol removal processes are proportional to in-bubble airborne concentration). Therefore, those accurate SPARC90 estimates happen just due to an error compensation [22].

3.3. SGTR scenario

SGTR experiments are systematically underpredicted, as shown in Figure 5. Slightly smaller deviations are observed when steam is present in the carrier gas, supported by a MSRE of -74% in steam experiments, versus -93% for the others. Condensation is a fast thermal phenomenon that likely occurs nearby injection, so that it is responsible for an early decontamination of the carrier gas. For this reason, whenever present, it fades off the influence of the huge surface exposed to the tight pack of inverted U-tubes, which foster in-pool particle absorption.
Since SPARC90 currently lacks models for submerged structures, this assessment is not intended as a validation of the code for SGTR conditions. Rather, it serves to identify its present limitations and to support future model development. Previous studies ([24] [25]) show that SGTR scenarios exhibit enhanced in-pool retention because the U-tube bundle increases gas fragmentation and turbulence. These mechanisms are not represented in SPARC90, which explains its discrepancy under SGTR conditions.

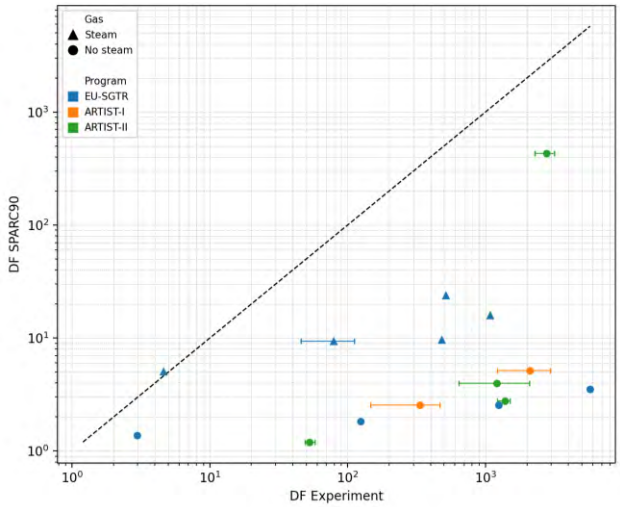

Figure 5. SPARC90 vs experimental DF for SGTR experiments.

3.4. FCVS scenario with Venturi injector

Experiments employing a venturi-scrubber injector represent some wet FCVS designs. As expected, given the lack of an *ad-hoc* venturi model in SPARC90, the results (Figure 6) confirm that SPARC90 is unable to accurately reproduce these data causing a systematic underprediction. Similarly to the SGTR case, this assessment aims at quantifying performance discrepancies arising from missing FCVS physics rather than validating current code capabilities.
It is worth noting, though, that the venturi tests conducted by [20] were not included among the QfV experiments listed in Table I. However, they were classified as UfU with respect to venturi behavior [16].

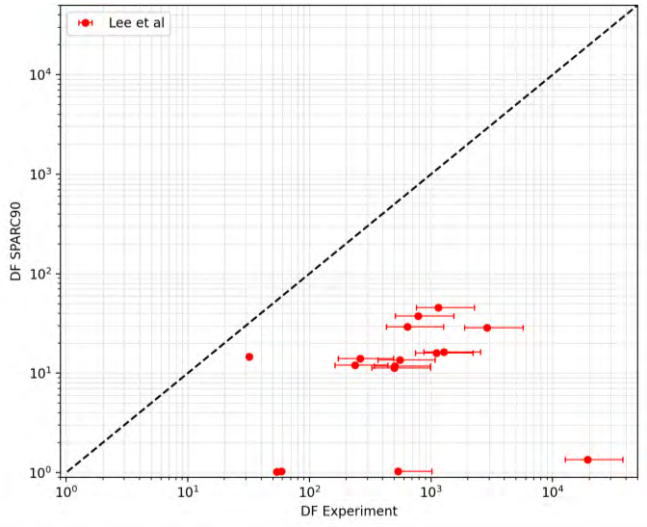

Figure 6. SPARC90 vs experimental DF for VENTURI experiments.

3.5. MCCI scenario

Pool scrubbing during the ex-vessel phase of an accident scenario would occur whenever a water layer covers the corium melt. Concrete thermal decomposition generates H_2O_v and CO_2, which going through the melt oxidize remaining metals and turn into CO and H_2. As a result, those gases contaminated by FPs absorbed when moving across the corium reach the corium interface and bubble in the water phase. Even though few studies have specifically addressed this scenario [26], some of the experiments in the database might be considered partially representative, by comparing the most relevant boundary conditions:

- Water temperature. Given the hot temperatures of corium melt, it is reasonable to assume that water will be near or at saturation soon after the interaction onset.
- Particle size. Several experimental programs investigated the features or aerosols emitted from MCCI processes ([5], [26], [27]), indicating a 0.1-4 μm AMMD range for MCCI aerosols.
- Gas flow rate and composition. At MCCI beginning, metals are still present within the corium and are oxidized by the MCCI gases, resulting in a gas mixture predominantly composed of CO and H_2. Since the molecular weight of CO is close to that of air (28 vs 29 g/mol), and CO would dominate the mixture by mass, it is reasonable to approximate MCCI pool scrubbing using air experiments.
- Multiple-hole injection. Gas and FPs injections would be distributed across multiple openings at the interface between the corium crust and the water.

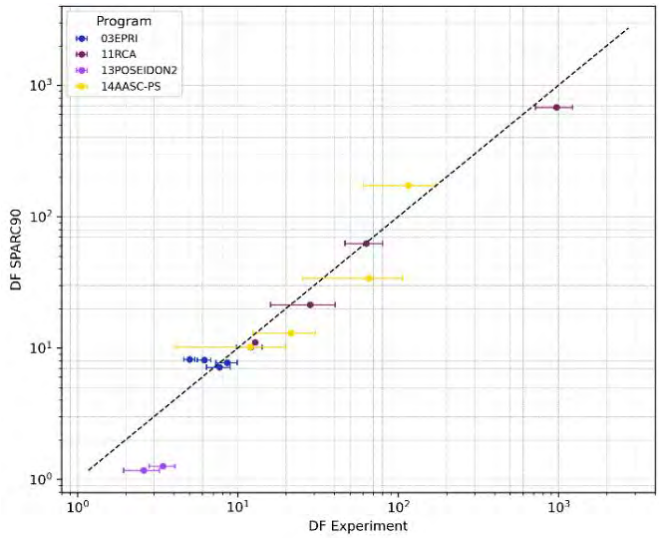

Figure 7. SPARC90 vs experimental DF for MCCI-like experiments.

In sight of these conditions, no condensing tests with air injection meeting the rest of requirements above might be adopted as MCCI-like tests. Among the QfV experiments, 15 of them meet these criteria, although none employ a multi-hole injector, which is a decontamination enhancer.
Data-SPARC90 comparison is displayed in Figure 7. Agreement of estimates and data is visible. In other words, the analysis suggests that SPARC90 is capable of simulating MCCI pool scrubbing. Dedicated experiments under anticipated prevailing conditions, though, would help to further validate this observation.

4. CONCLUSIONS

This paper presents a rigorous and systematic assessment of SPARC90 against a broad and QfV database. Three major takeaways can be highlighted:

- Broadly speaking, SPARC90 demonstrates a good predictive capability when compared against more than 100 data, showing a DF MSRE deviation a bit higher than 20% in absolute terms. A closer look to the SPARC90-data comparisons highlight the fact this deviation falls down to the range of 2% for scenarios with limited retention efficiencies (≤95%). For higher retention efficiencies (i.e., less contamination going out of the pool), MSRE are higher but with a dominant bias to underpredict.
- When compared to MCCI-representative data, SPARC90 displays a remarkable agreement with data, which highlights its ability to address those scenarios, even if not initially considered in the code conception.
- On the contrary, according to the results shown and discussions held in previous sections, SPARC90 use in scenarios with any high injection gas velocities, venturi scrubbers (FCVS) or submerged structures (SGTR) is not credited. Even in cases where estimates might be considered acceptable (high injection regime), SPARC90 does not feature the proper physical models at the pool injection zone; in other words, numerical consistency comes from the wrong reasons. In the other two scenarios, the configuration makes some of SPARC90 hypotheses not to be valid anymore. Addressing those scenarios would entail a substantial extension of SPARC90 formulation.

Further analyses are planned to enhance the understanding of SPARC90 behavior and to support targeted improvements of the model. In the short run, the authors aim to:

- Quantitatively test the assumptions currently adopted in SPARC90 for the inlet region (globule breakup transition) and the pool surface, which were originally validated for BWR conditions, and assess their impact on the overall DF in a wider range of accident scenarios.
- Extend the physics of SPARC90 to explicitly address the jet injection regime by implementing a physically consistent jet model, thereby ensuring that current satisfactory DF predictions are supported by sound physical grounds, thus improving the overall robustness of the code.

5. ACKNOWLEDGEMENT

Partially funded by the European Union. Views and opinions expressed are however those of the authors only and do not necessarily reflect those of the European Union or EURATOM. Neither the European Union nor the EURATOM can be held responsible for them.

6. REFERENCES

[1] L. E. Herranz, "Pool scrubbing in unit 1 of fukushima daiichi," *Ann. Nucl. Energy*, vol. 183, Apr. 2023, doi: 10.1016/j.anucene.2022.109637.
[2] A. Auvinen *et al.*, "Steam generator tube rupture (SGTR) scenarios," *Nuclear Engineering and Design*, vol. 235, no. 2–4, pp. 457–472, Feb. 2005, doi: 10.1016/j.nucengdes.2004.08.060.
[3] M. Garcia, T. Lugo, and L. E. Herranz, "SEVERE ACCIDENTS IN SMALL MODULAR REACTORS: THE ROLE OF POOL SCRUBBING IN A GENERIC iPWR," in *51ª Reunión Anual de la Sociedad Nuclear Española*, 2025.
[4] OECD/NEA, "Status Report on Filtered Containment Venting. NEA/CSNI/R(2014)7," 2014.
[5] OECD/NEA, "State-of-the-Art Report on Molten Corium Concrete Interaction and Ex-Vessel Molten Core Coolability. NEA/CSNI/R(2016)15," 2017.
[6] M. Escudero Berzal, M. J. Marcos Crespo, M. Swiderska-Kowalczyk, M. Martin Espigares, and J. Lopez Jimenez, "State-of-the-art review on fission products' aerosol pool scrubbing under severe accident conditions, Report EUR 16241 EN, ISSN 1018-5593," 1995.
[7] L. E. Herranz, F. Sánchez, and S. Gupta, "Validation Matrix for Pool Scrubbing Models," *Nucl. Technol.*, vol. 209, no. 10, pp. 1523–1536, Oct. 2022, doi: 10.1080/00295450.2022.2122679.
[8] K. Fischer, "Modelling of Retention Processes in Water Pools. BF-R68.411-1.," 1998.
[9] M. Calvo, S. Guntay, and S. A. Ramsdale, "Development and validation of BUSCA code: a modelto assess the aerosol and fission product retention in a water pool," *J. Aerosol Sci.*, vol. 22, pp. S765–S768, 1991, doi: 10.1016/S0021-8502(05)80212-5.
[10] S. A. Ramsdale, G. J. Bamford, S. Fishwick, and H. C. Starkie, "Status of Research and Modelling of Water-Pool Scrubbing, Final Report EUR 14566 EN," 1992.
[11] P. C. Owczarski and K. W. Burk, "SPARC-90: A Code for Calculating Fission Product Capture in Suppression Pools. NUREG/CR-5765," 1991.
[12] L. L. Humphries *et al.*, "MELCOR Computer Code Manuals Vol. 2: Reference Manual Version 2024.0," 2024.
[13] L. L. Humphries *et al.*, "MELCOR Computer Code Manuals Vol. 1: Primer and Users' Guide Version 2024.0," 2024.
[14] P. Chatelard *et al.*, "ASTEC V2 severe accident integral code main features, current V2.0 modelling status, perspectives," *Nuclear Engineering and Design*, vol. 272, pp. 119–135, Jun. 2014, doi: 10.1016/j.nucengdes.2013.06.040.
[15] L. E. Herranz, R. D. Tardáguila, T. Berschart, T. Lind, and S. Morandi, "Remaining Issues in Pool Scrubbing: Major Drivers for Experimentation within the EU-PASSAM Project," in *Proceedings of ICAPP '14*, 2014.
[16] G. Tinfena, M. Angelucci, S. Paci, and L. E. Herranz, "Validation Database for Pool Scrubbing: an Update," *submitted to Annals of Nuclear Energy*.

[17] J. Baccou *et al.*, "A systematic approach for the adequacy analysis of a set of experimental databases: Application in the framework of the ATRIUM activity," *Nuclear Engineering and Design*, vol. 421, May 2024, doi: 10.1016/j.nucengdes.2024.113035.

[18] A. Ghione, L. Sargentini, G. Damblin, and P. Fillion, "Adequacy analysis, validation and input uncertainty quantification for critical flow predictions using the CATHARE 3 code in the framework of the OECD-NEA ATRIUM project," *Nuclear Engineering and Design*, vol. 446, p. 114595, Jan. 2026, doi: 10.1016/j.nucengdes.2025.114595.

[19] C. Berna, A. Escrivá, J. L. Munõz-Cobo, and L. E. Herranz, "Enhancement of the SPARC90 code to pool scrubbing events under jet injection regime," *Nuclear Engineering and Design*, vol. 300, pp. 563–577, Apr. 2016, doi: 10.1016/j.nucengdes.2016.02.027.

[20] J. Lee, W. Y. Jung, H. C. Lee, G. T. Kim, and D. Y. Lee, "Experimental study on aerosol scrubbing efficiency of self-priming venturi scrubber submerged in water pool," *Ann. Nucl. Energy*, vol. 114, pp. 571–585, Apr. 2018, doi: 10.1016/j.anucene.2017.12.052.

[21] T. Albiol *et al.*, "PASSAM Final Synthesis Report," 2017.

[22] L. E. Herranz, R. Iglesias, and J. Fontanet, "Mitigation of source term in suppression pools: Large uncertainties in predictability," *Ann. Nucl. Energy*, vol. 120, pp. 509–515, Oct. 2018, doi: 10.1016/j.anucene.2018.06.010.

[23] L. E. Herranz, C. Lopez, and J. Penalva, "Investigation on jet scrubbing in nuclear reactor accidents: From experimental data to an empirical correlation," *Progress in Nuclear Energy*, vol. 107, pp. 72–82, Aug. 2018, doi: 10.1016/j.pnucene.2018.04.019.

[24] T. Lind, S. Campbell, L. E. Herranz, M. Kissane, and J. H. Song, "A summary of fission-product-transport phenomena during SGTR severe accidents," *Nuclear Engineering and Design*, vol. 363, Jul. 2020, doi: 10.1016/j.nucengdes.2020.110635.

[25] T. Betschart, T. Lind, and H. M. Prasser, "Investigation of two-phase flow hydrodynamics under SGTR severe accident conditions," *Nuclear Engineering and Design*, vol. 366, Sep. 2020, doi: 10.1016/j.nucengdes.2020.110768.

[26] D. A. Powers and J. L. Sprung, "A simplified model of aerosol scrubbing by a water pool overlying core debris interacting with concrete. NUREG/CR-5901.," Albuquerque, NM, and Livermore, CA (United States), Nov. 1993. doi: 10.2172/10108322.

[27] M. T. Farmer, D. J. Kilsdonk, and R. W. Aeschlimann, "CORIUM COOLABILITY UNDER EX-VESSEL ACCIDENT CONDITIONS FOR LWRs," *Nuclear Engineering and Technology*, vol. 41, no. 5, pp. 575–602, Jun. 2009, doi: 10.5516/NET.2009.41.5.575.

ASSESSMENT OF POOL SCRUBBING PREDICTIVE CAPABLITIES: BENCHMARKING SPARC90 AGAINST AN AD-HOC DATABASE

G. Tinfena[1], M. Angelucci[1], S. Paci[1], L.E. Herranz[2]

[1]University of Pisa - Department of Civil and Industrial Engineering
[2]CIEMAT - Unit of Nuclear Safety Research

ERMSAR2026
Madrid (Spain) - May 18-22, 2026

Contents

01 Background

02 Validation Database

03 Results

04 Main Insights

01

Background

POOL SCRUBBING PROCESS

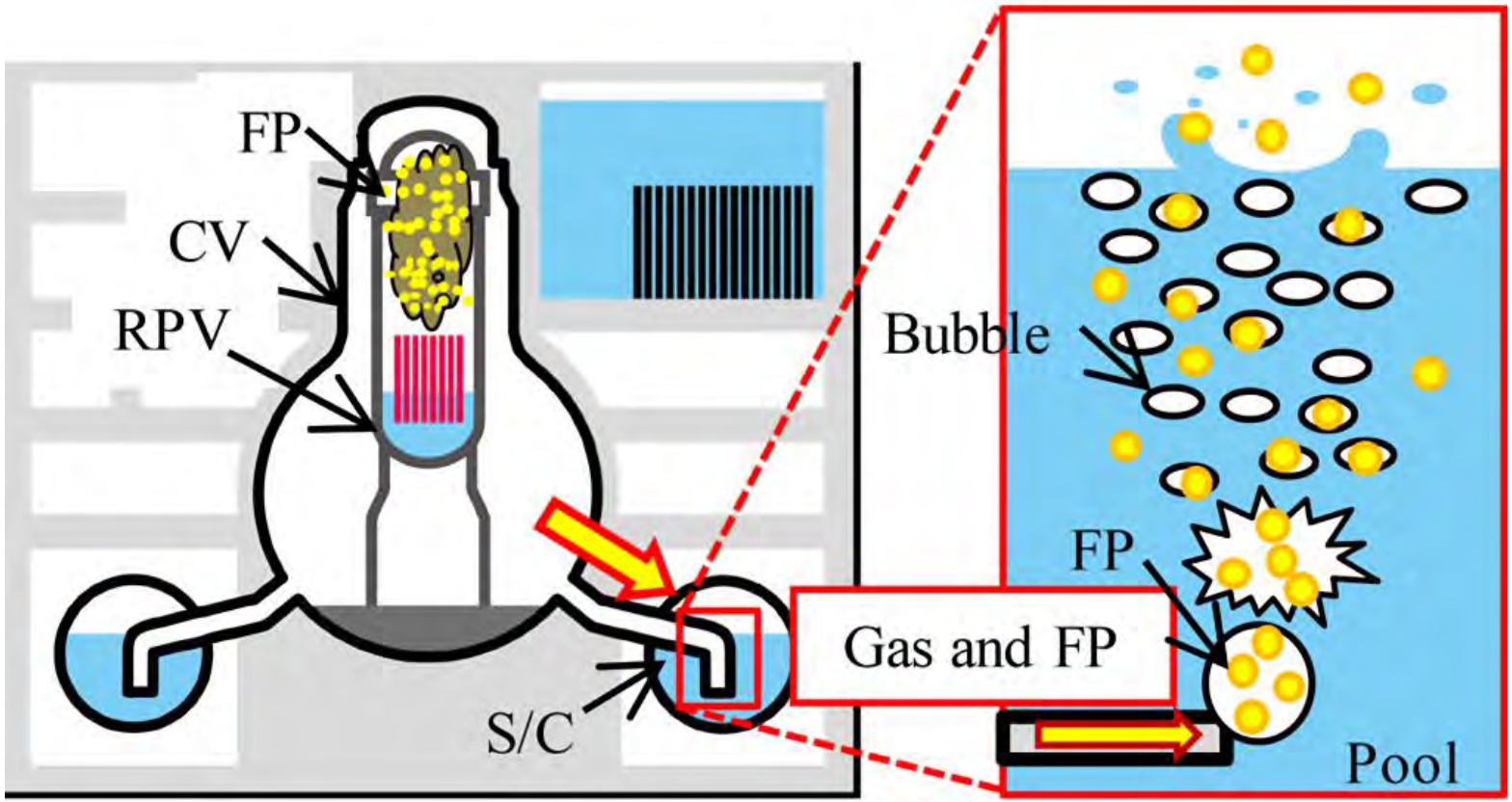

- Passive and effective **FP retention** process.
- Different **scenarios**: BWR, SGTR, FCVS, MCCI.
- **FoM**: decontamination factor or outgoing mass.

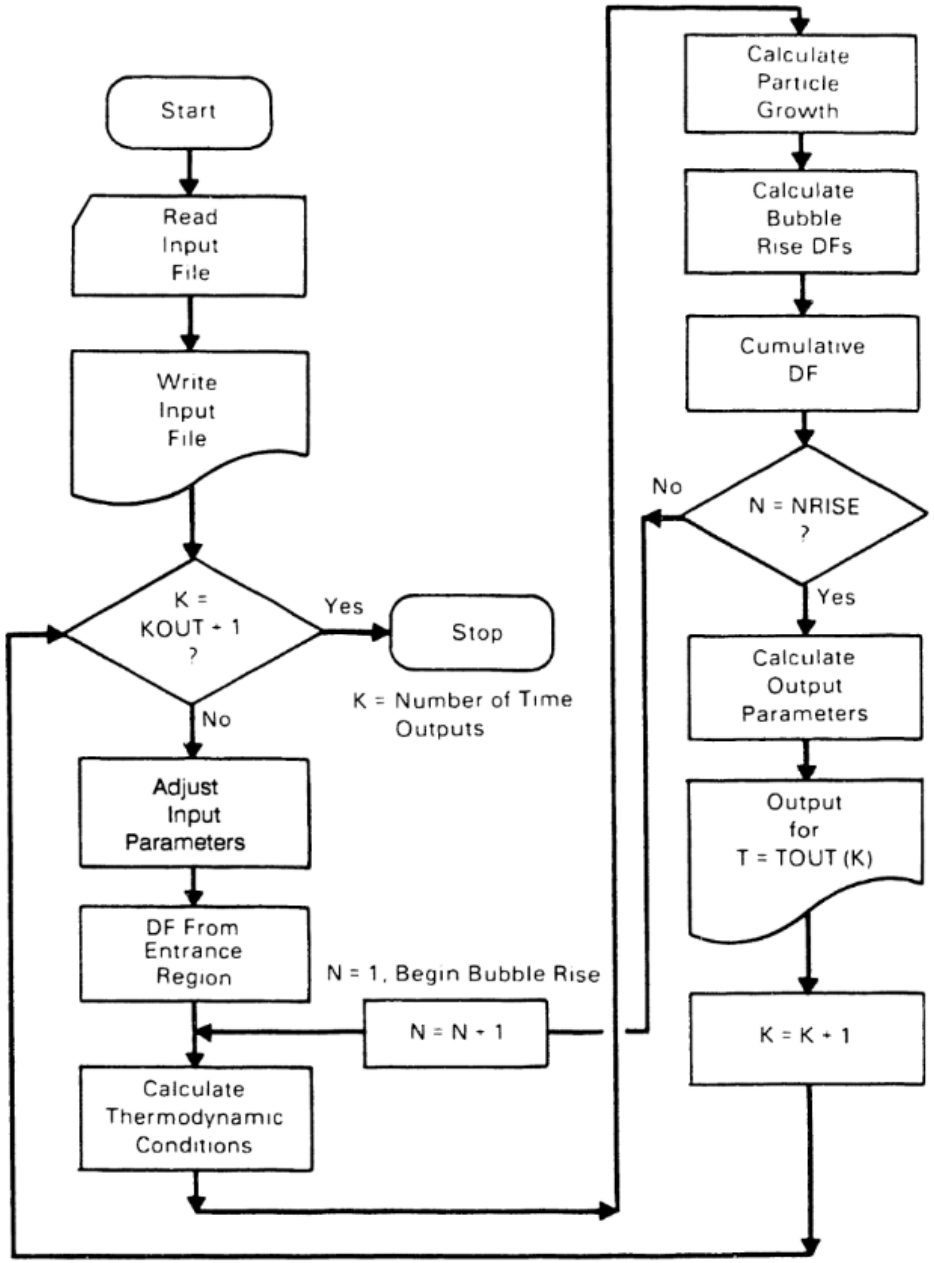

SPARC90

- **Lumped parameter** code for fission product scrubbing in suppression pools.
- Several **retention mechanisms** modeled: diffusion, impaction, gravitational settling, phoretic processes, hygroscopicity, gas-liquid interactions, iodine chemistry.
- Features different **injector types**: quencher, downcomer, horizontal vent.
- Its models are **implemented in severe accident codes** such as MELCOR and ASTEC.

RESEARCH QUESTION

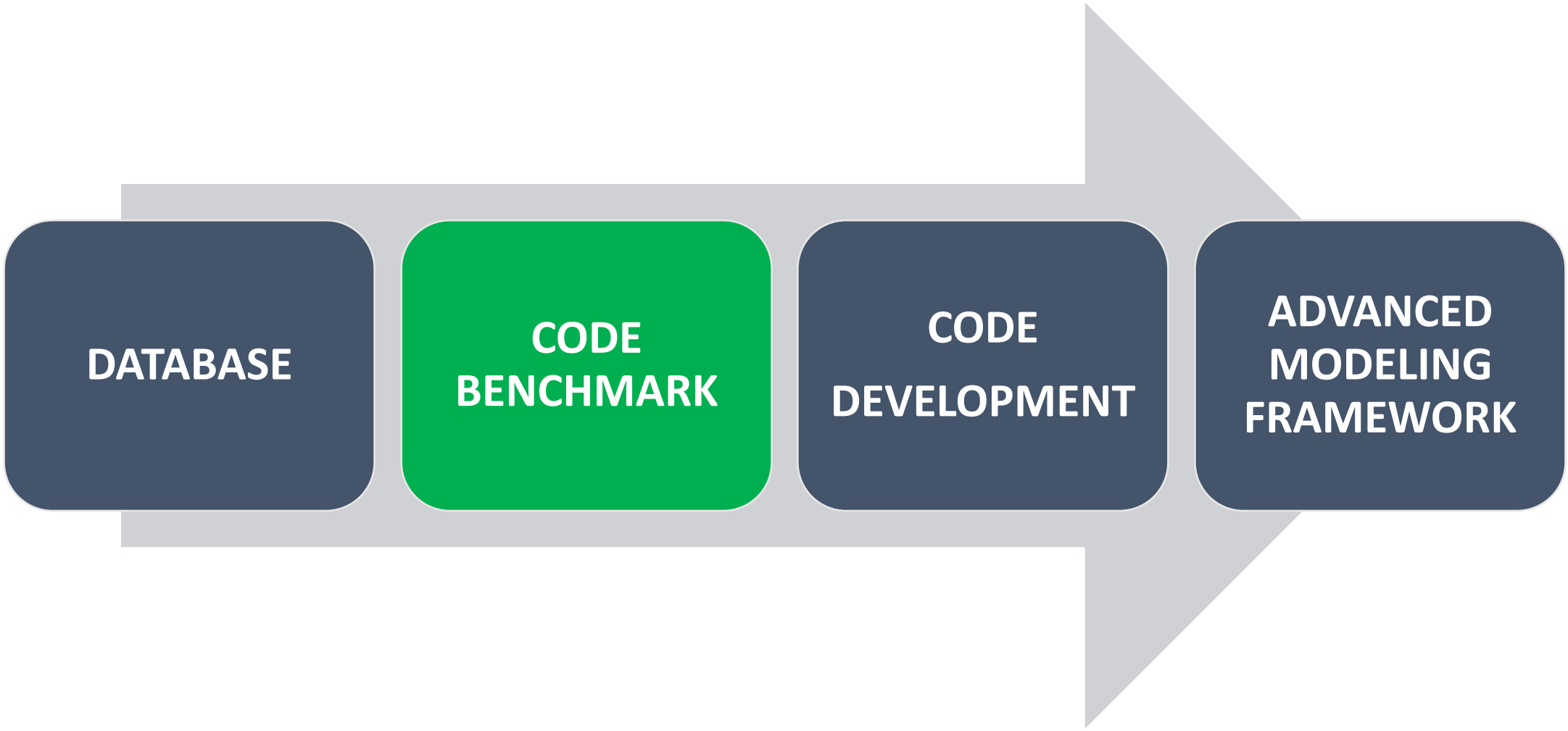

02 Validation Database

ADEQUACY ANALYSIS

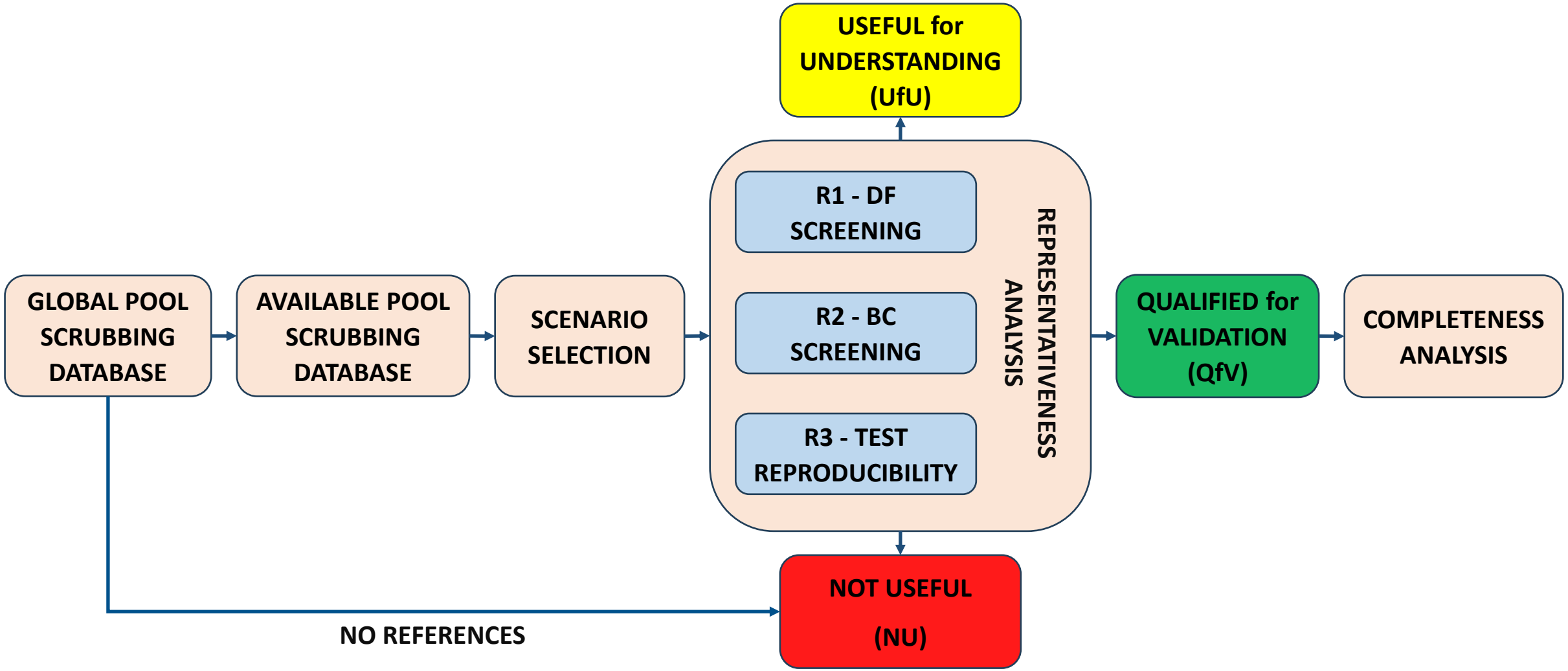

VALIDATION MATRIX

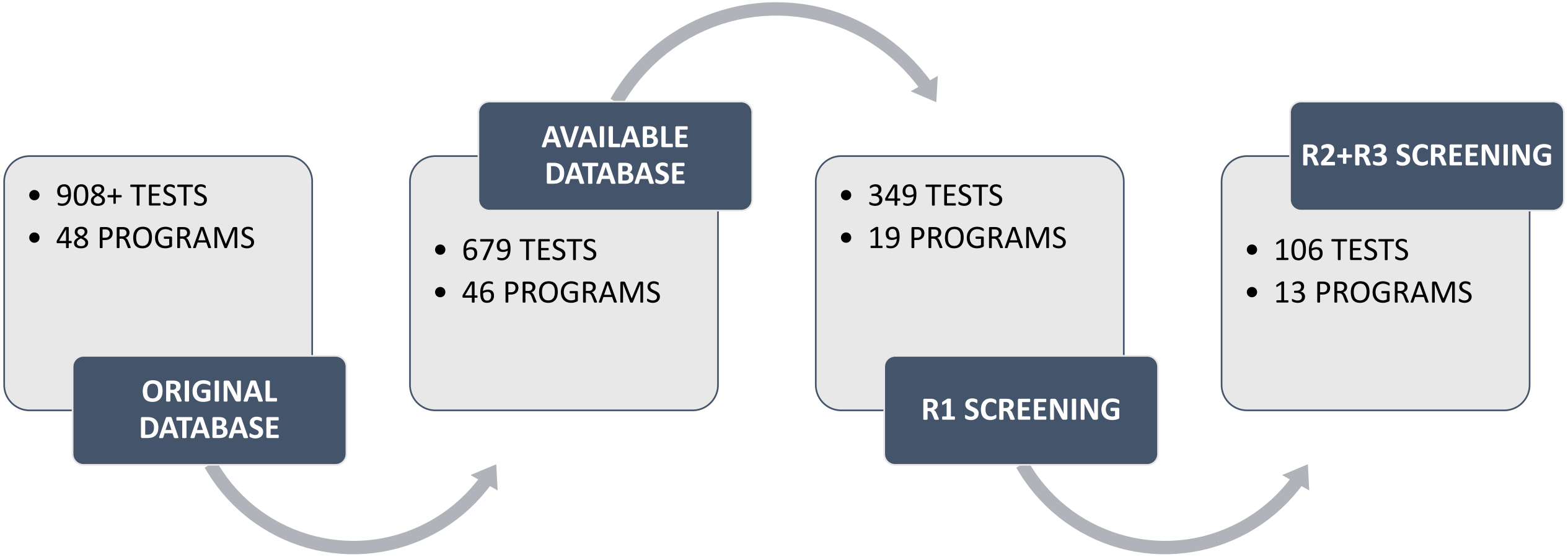

VALIDATION MATRIX

Programs / Boundary Conditions		EPRI (8)	ACE (4)	LACE-España (5)	RCA (4)	POSEIDON – II (17)	AASC-PS (4)	SG-Experiments (15)	PASSAM (CIEMAT + RSE) (13)	TYFON (11)	THAI (12)	YOON (10)	SAPOS (7)
Particle Characteristics	Chemical Species	CsI	CsOH, MnO, CsI	CsI	Ni	SnO2	Ni	TiO2, Nanophase TiO2, SiO2	SiO2	CsI	SnO2	SiO2	TiO2
	Aerodynamic Mass Median Diameter (μm)	0.4	1.7 to 2.9	0.6 to 7.2	1.1 to 1.3 (MMD)	0.3 to 0.5	2.4 to 2.8	1.4 to 4.6	0.4 to 1.0	0.8	0.22 to 0.85 (MMD)	0.7	0.5
	GSD	-	1.8 to 2.4	1.4 to 5.4	1.4 to 1.4	1.4 to 1.7	1.5 to 1.8	2.0 to 3.0	1.2 to 1.6	2	2.0 to 3.0	1.46	1.25
Carrier Gas	Composition	Air/air+steam	N2 + steam	N2 + steam	N2	N2/N2 + steam	Air	N2/N2 + steam	Air/air + steam	Air	Air/air+steam	Air	N2 + steam
	Mass Flow Rate (kg/s)	2.05E-03 to 1.251E-02	6.4E-02 to 1.1E-01	1.0E-04 to 7.2E-03	7.3E-03 to 7.8E-03	0.02 to 0.04	1.052E-03 to 1.341E-03	1.3E-02 to 1.8E-01	2.19E-03 to 1.30E-02	1.846E-04 to 2.633E-03	6.3E-04 to 3.15E-02	2.42E-03 to 9.70E-03	1.90E-02
	Steam Mass Fraction (%)	0.0 to 98.0	0.8 to 31.4	6.7 to 85.3	0	0.0 to 75.0	0	0.0 to 77.0	0.0 to 9.8	0	0.0 to 80.0	0	50.0 to 90.0
Thermal Hydraulics	Pool Temperature (K)	373	297.0 to 356.0	382.3 to 385.4	386.9 to 391.5	335.9 to 363.6	392.4 to 399.5	295.0 to 368.2	293.0 to 307.8	298.15	329.95 to 378.15	ambient	323.2
	Pool Pressure (Pa)	1.01E+05	1.00E+05	2.8E+05 to 3.0E+05	2.3E+05 to 2.5E+05	1.00E+05	2.30E+05	1.0E+05 to 1.1E+05	9.2E+04 to 1.0E+05	atmospheric	1.23E+05 to 4.0E+05	atmospheric	-
	Gas Temperature (K)	410-524	411.0 to 423.0	397.1 to 444.3	394.9 to 414.1	485.9 to 583.8	377.9 to 393.4	297.0 to 430.1	273.2 to 383.1	298.15	373.05 to 393.45	ambient	443.15
	Injection Pressure (Pa)	-	1.2E+05 to 1.5E+05	3.3E+05 to 3.5E+05	2.8E+05 to 2.9E+05	1.2E+05 to 1.7E+05	2.7E+05 to 2.8E+05	1.1E+05 to 4.9E+05	9.6E+04 to 1.6E+06	-	1.29E+05 to 4.02E+05	1.20E+05 to 2.31 E+05	1.34E+05
Pool Geometry	Injector Configuration	Single orifice	Quencher (51 holes)	Single orifice/ multi-orifice (9 holes)	Single orifice	Single orifice	Single orifice	Tube break	Single orifice	Single orifice	Single orifice	Single orifice	Multi-orifice injector (6 holes)
	Injector Orientation	Horizontal	Upward	Horizontal	Horizontal	Upward	Horizontal	Horizontal	Upward/Horizontal	Upward	Horizontal	Upward	Downward
	Injector Diameter (m)	1.27E-02	9.5E-03	1.0E-02	1.00E-02	2.0E-02	1.0E-02	1.7E-02	6.5E-03 to 1.0E-02	2.00E-03	1.50E-02	5.00E-03	1.0E-02
	Submergence (m)	1.65	1.4 to 4.6	2.5	0.3 to 2.5	0.3 to 4.0	1.3	0.0 to 3.80	0.3 to 1.0	0.1 to 1.0	0.25 to 2.0	0.5	1.2 to 3.0

VALIDATION MATRIX

Boundary Conditions		
Particle Characteristics	Composition	CsOH,MnO,CsI, DOP, Ni, SnO_2, TiO_2, Nanophase TiO_2, SiO_2
	AMMD (µm)	0.2-7.2
Carrier Gas	Composition	Air, Air+Steam, N2+Steam
	Mass Flow Rate (kg/s)	1.04E-04 to 1.09E-01
	Weber number	6.93E+01 to 9.49E+06
	Steam Mass Fraction (%)	0 to 98
Thermal Hydraulics	Pool Temperature (K)	293.0 to 399.5
	Pool Pressure (Pa)	1.23E+05 to 4E+05
	Injection Pressure (Pa)	3.27E+04 to 1.6E+06
Geometry	Injector Orientation	Upward, horizontal, downward
	Injector Diameter (m)	5E-03 to 2E-01
	Submergence (m)	0 to 4.61

- **Broad ranges** covering the most relevant boundary conditions.
- Different **configurations and scenarios** represented.
- Mostly **small-scale** experiments.
- Mostly focused on **integral DF**.

03

Results

GLOBAL BEHAVIOR

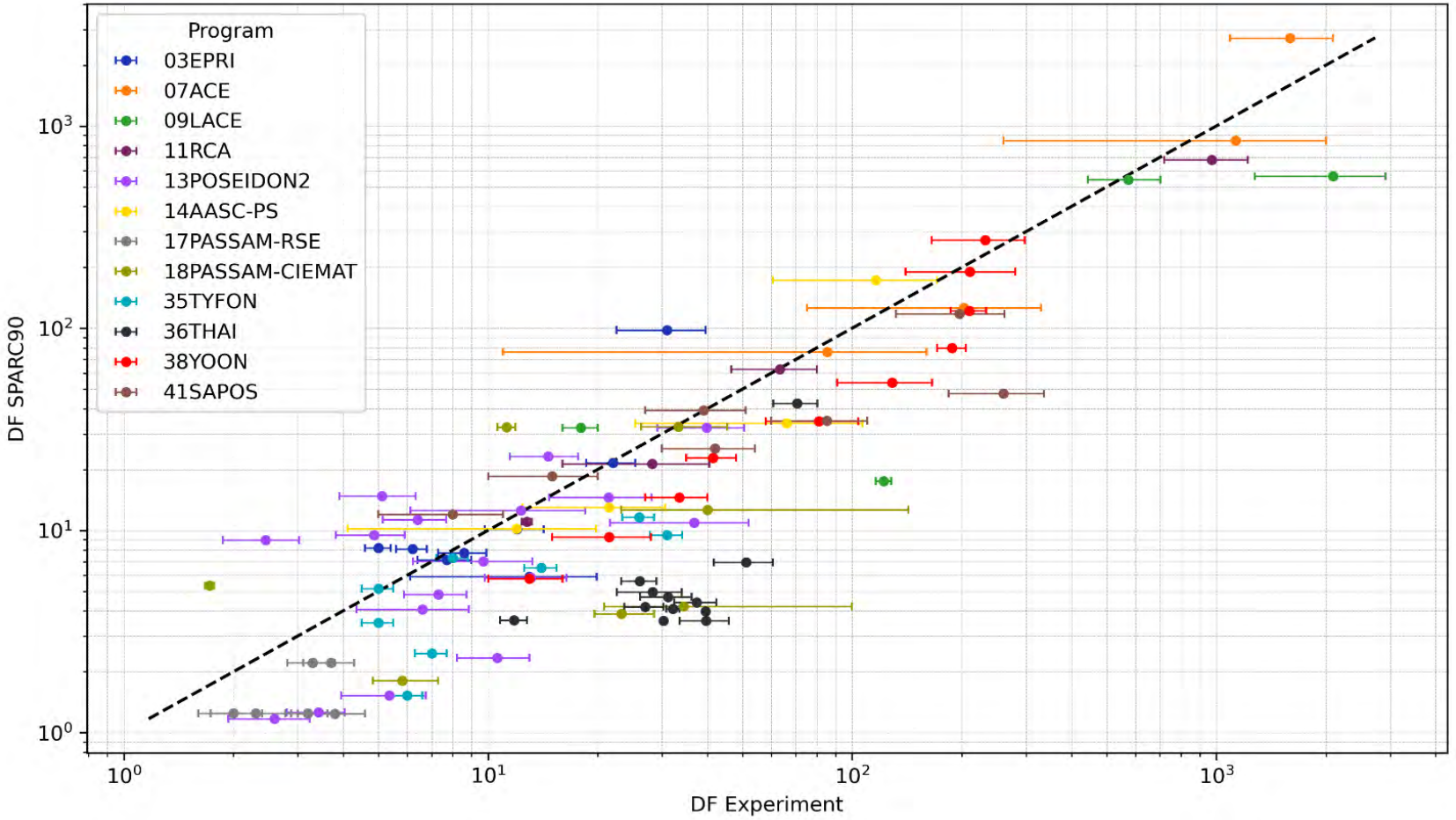

- Global **-21% average relative error** between experiments and predictions.
- Fewer experiments at very high DF.
- c

GLOBAL BEHAVIOR

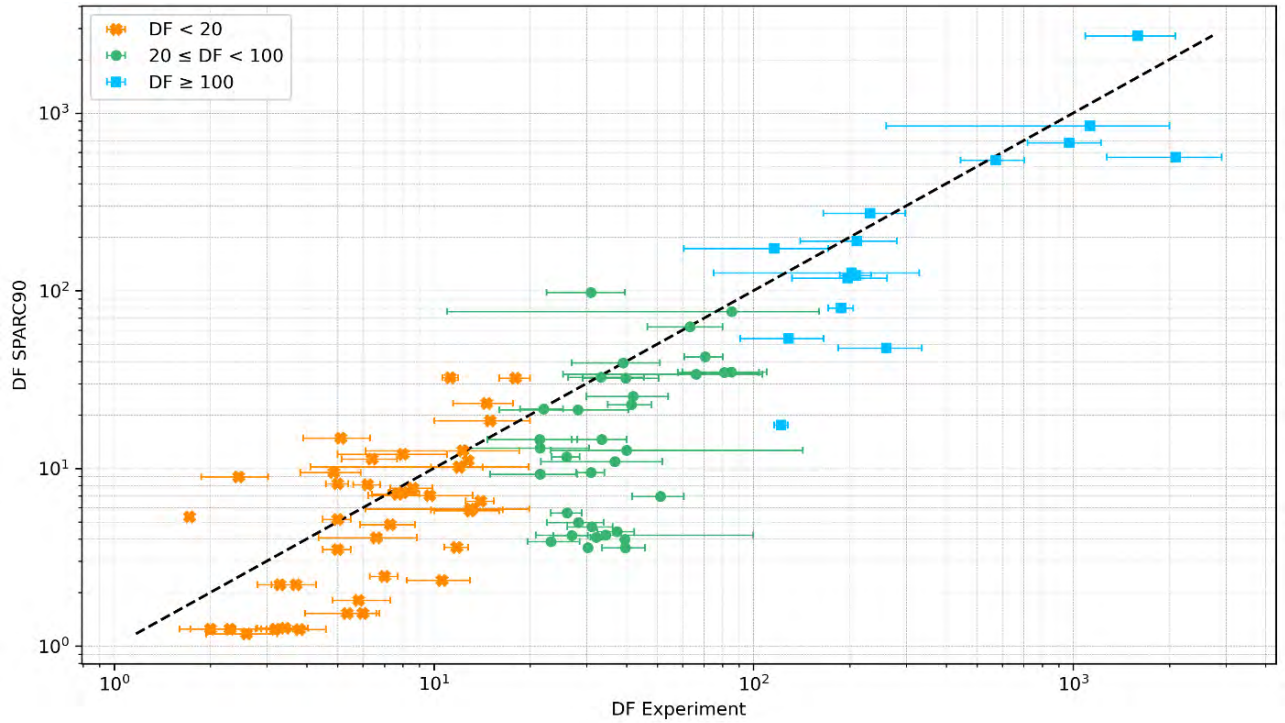

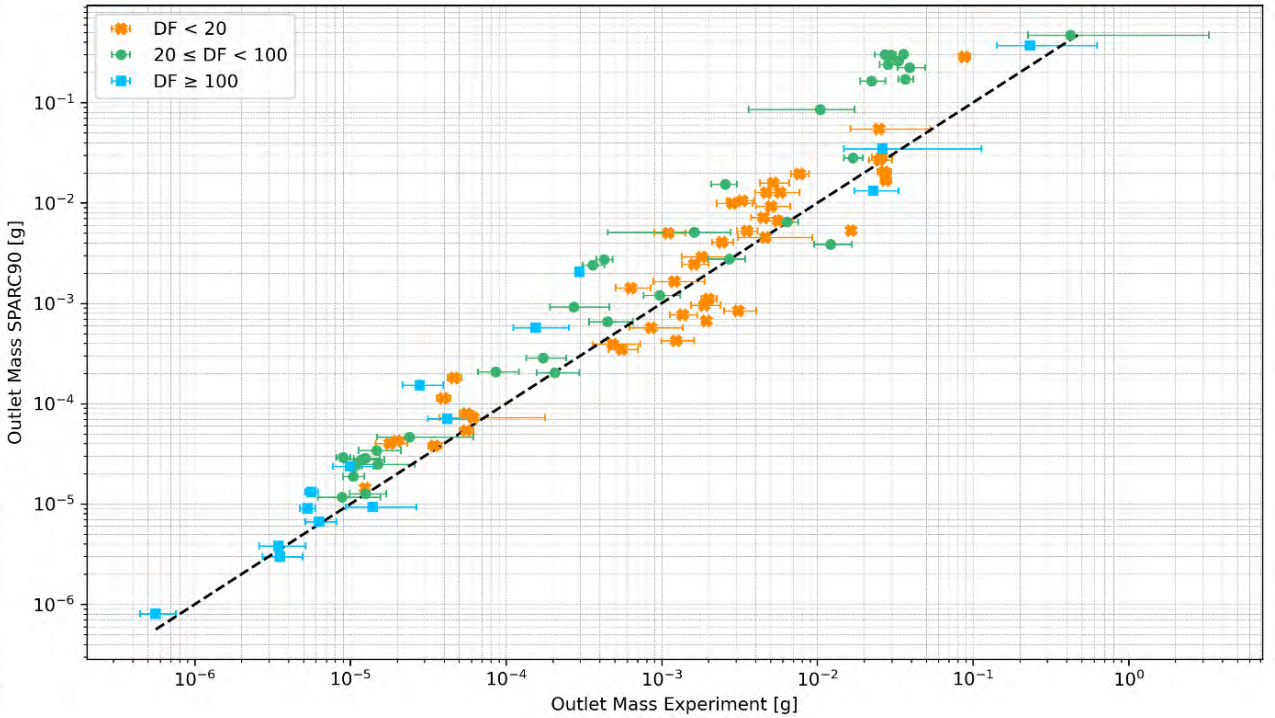

GROUP	N	MSRE (%)	RMSE
Global	91	-21	208
DF < 20	42	2	6
20 ≤ DF < 100	34	-47	27
DF ≥ 100	15	-27	509

GROUP	N	MSRE (%)	RMSE
Global	91	155	7.08e-2
DF < 20	42	63	3.16e-2
20 ≤ DF < 100	34	284	1.08e-1
DF ≥ 100	15	119	3.63e-2

SPECIFIC BEHAVIOR - JET REGIME

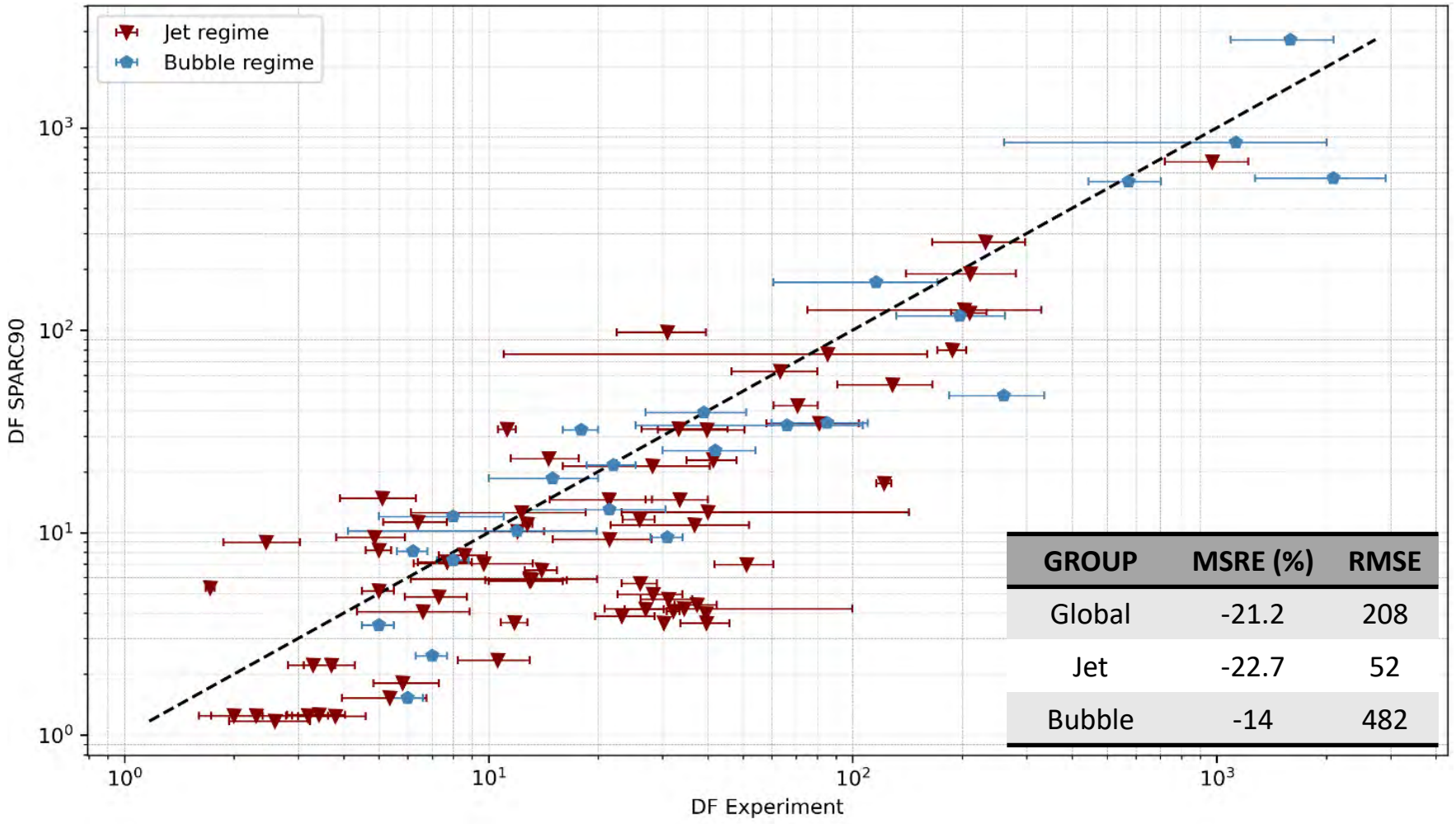

GROUP	MSRE (%)	RMSE
Global	-21.2	208
Jet	-22.7	52
Bubble	-14	482

- **82/106** experiments under jet regime.
- Jet regime **enhance decontamination**.
- **No jet models** in SPARC90.
- **Similar accuracy** in both injection regimes.

SPECIFIC BEHAVIOR - SGTR

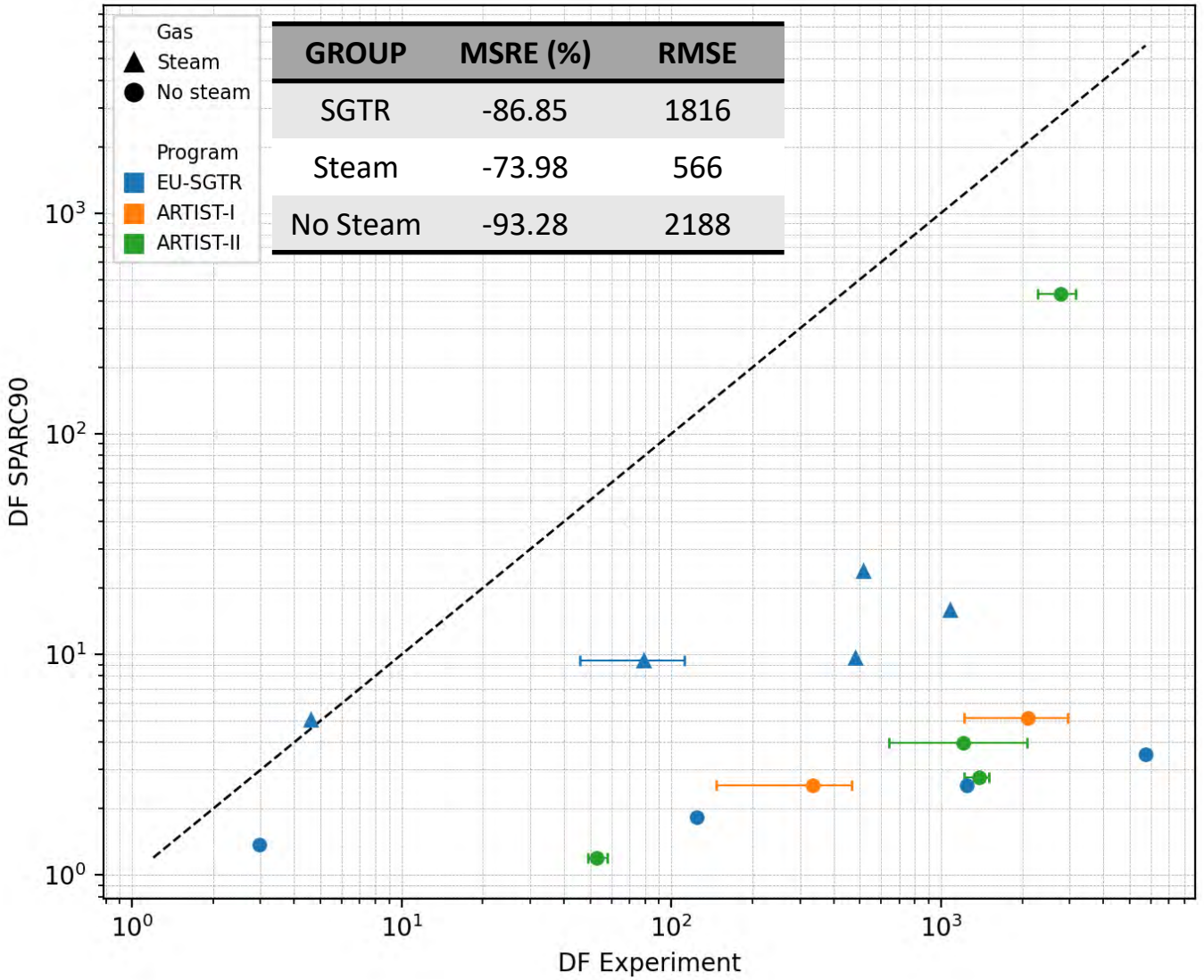

GROUP	MSRE (%)	RMSE
SGTR	-86.85	1816
Steam	-73.98	566
No Steam	-93.28	2188

- **No submerged structures**, typical of SGTR, modeled in SPARC90.
- Submerged structures **increase gas fragmentation and turbulence**, enhancing radionuclide retention.
- **Huge underpredictions** of most experiments.
- **Steam condensation** partially fades submerged structures effect.

SPECIFIC BEHAVIOR - FCVS

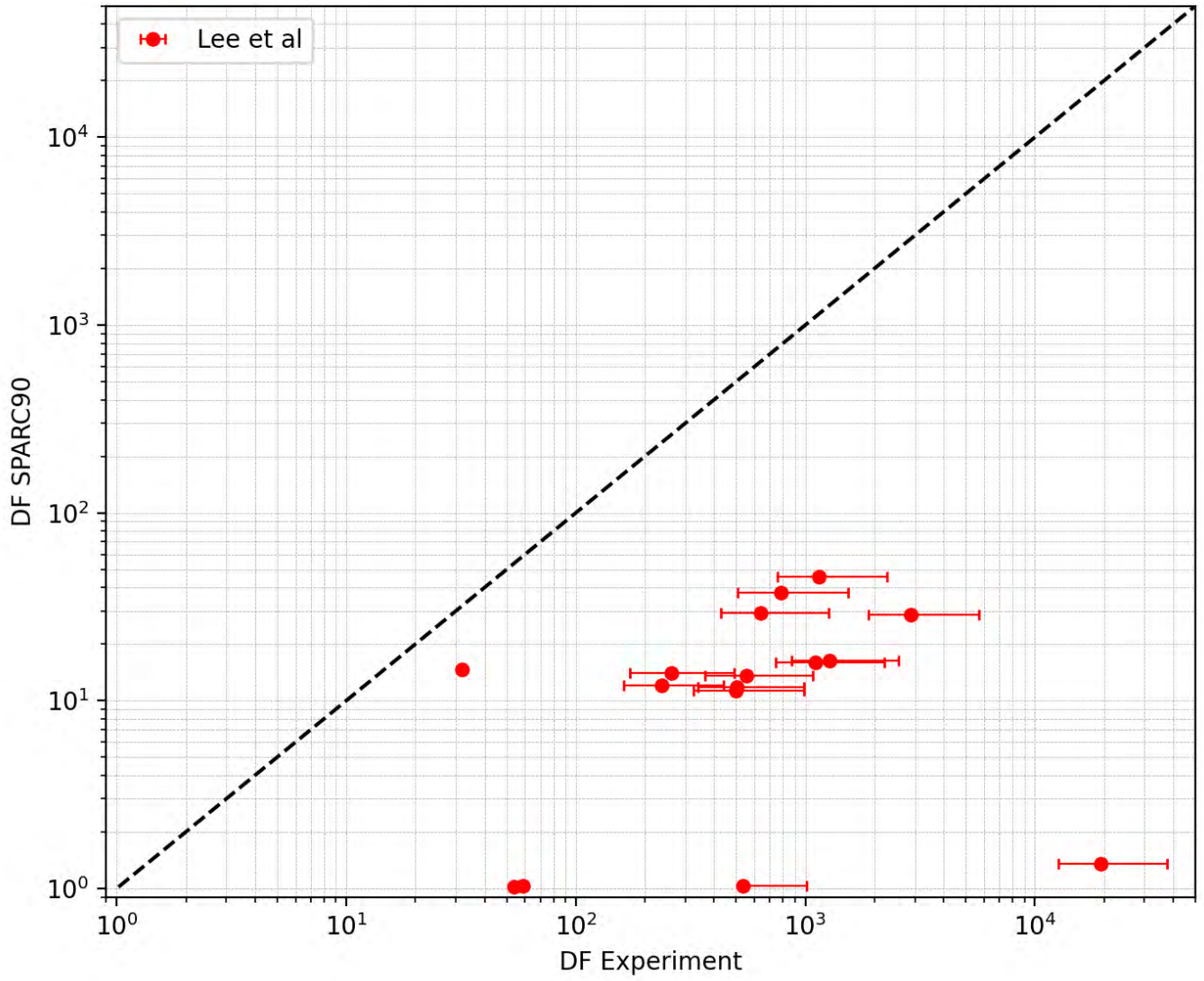

- FCVS often features Venturi nozzle; **partial decontamination** already occurs **within the Venturi**.
- SPARC90 **doesn't model Venturi** and mostly **misses prediction**.

SPECIFIC BEHAVIOR - MCCI

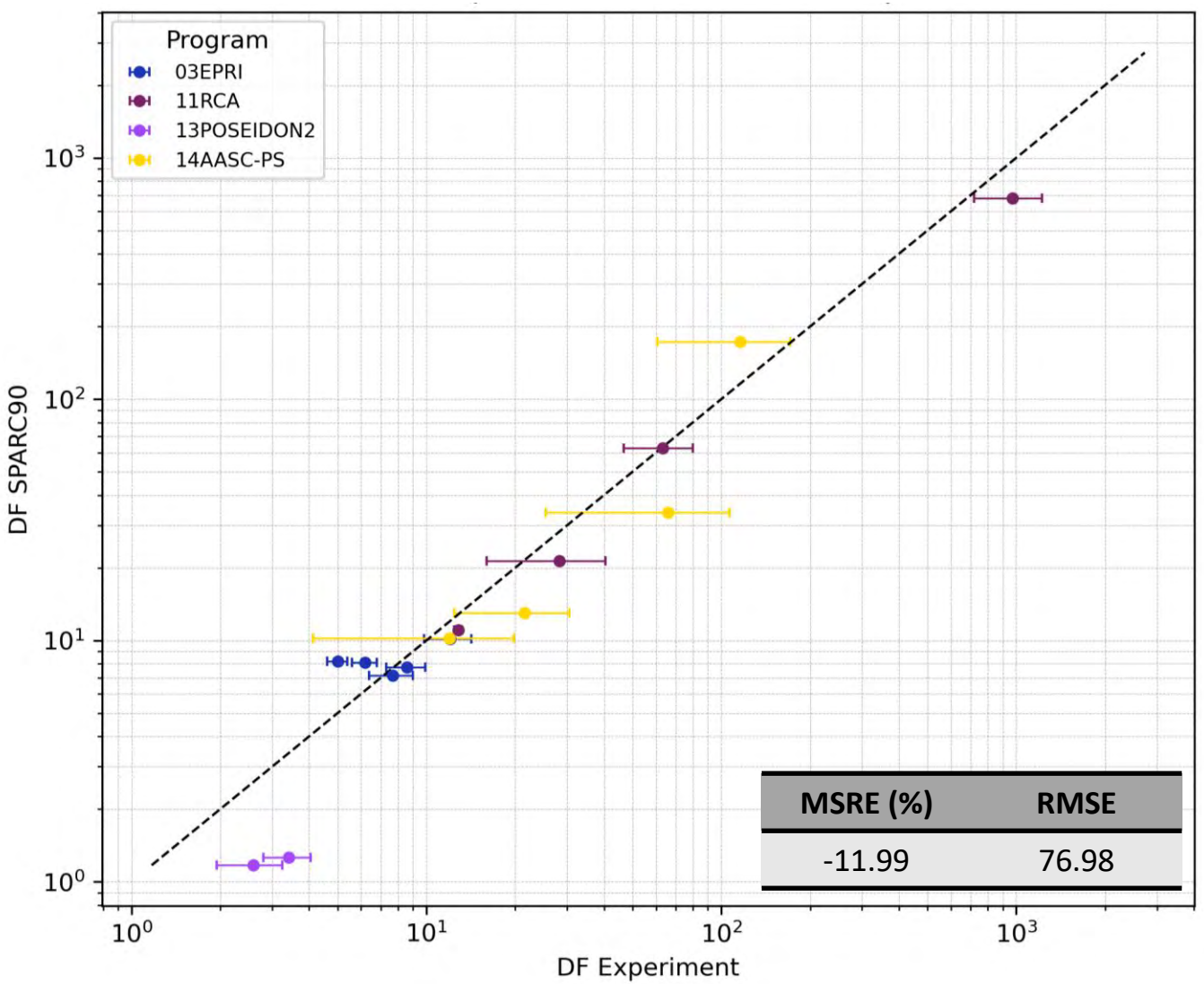

MSRE (%)	RMSE
-11.99	76.98

- **Assumptions:**
  - early MCCI dominated by CO.
  - hot and saturated pool.
  - no condensation.

- **MCCI-like tests:**
  - 15 tests from 4 programs.
  - air injection only.
  - hot pool experiments.

04

Main Insights

WRAP-UP

General Reliability

- SPARC90 demonstrated **reasonable predictive accuracy** across 100+ experiments, with a global MSRE of -21%.
- Remarkable **agreement with MCCI**-representative data, despite being a non-native scenario for SPARC90.

Modeling Gaps

- SPARC90 **misses FCVS and SGTR predictions**, consistently with the models it features.
- SPARC90 predicts with **reasonable accuracy jet-injection** DF despite lacking specific models: **right results for the wrong reasons**.

NEXT STEPS

- The **transition region** during globule breakup is only partially treated in SPARC90.
- The pool **surface region** is not presently simulated in SPARC90 (DF = 1 in this zone).
- **New physics**: jet, FCVS and SGTR physics must be included in SPARC90 to ensure long-term consistency.

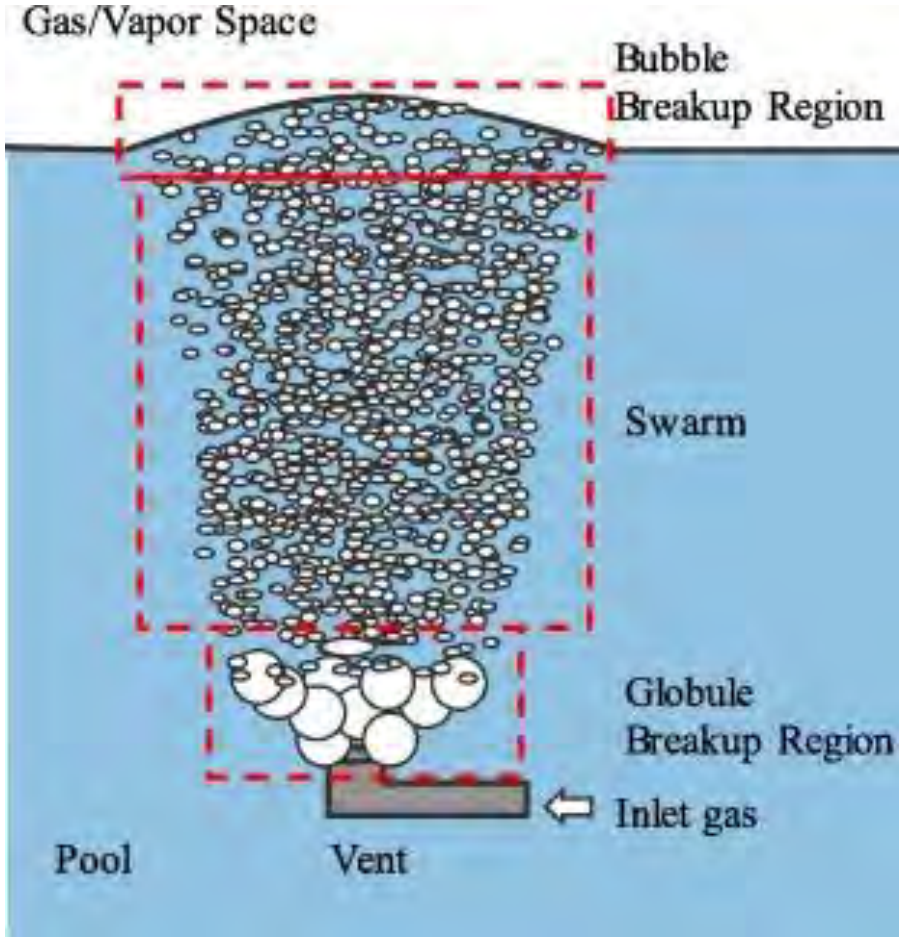

THANK YOU FOR YOUR ATTENTION!

Giacomo Tinfena
giacomo.tinfena@phd.unipi.it

UNIVERSITÀ DI PISA

GOBIERNO DE ESPAÑA
MINISTERIO DE CIENCIA, INNOVACIÓN Y UNIVERSIDADES
Ciemat
Centro de Investigaciones Energéticas, Medioambientales y Tecnológicas

BACK UP SLIDES

Giacomo Tinfena
giacomo.tinfena@phd.unipi.it

Università di Pisa

Gobierno de España
Ministerio de Ciencia, Innovación y Universidades
Ciemat
Centro de Investigaciones Energéticas, Medioambientales y Tecnológicas

SPARC INPUT DATA

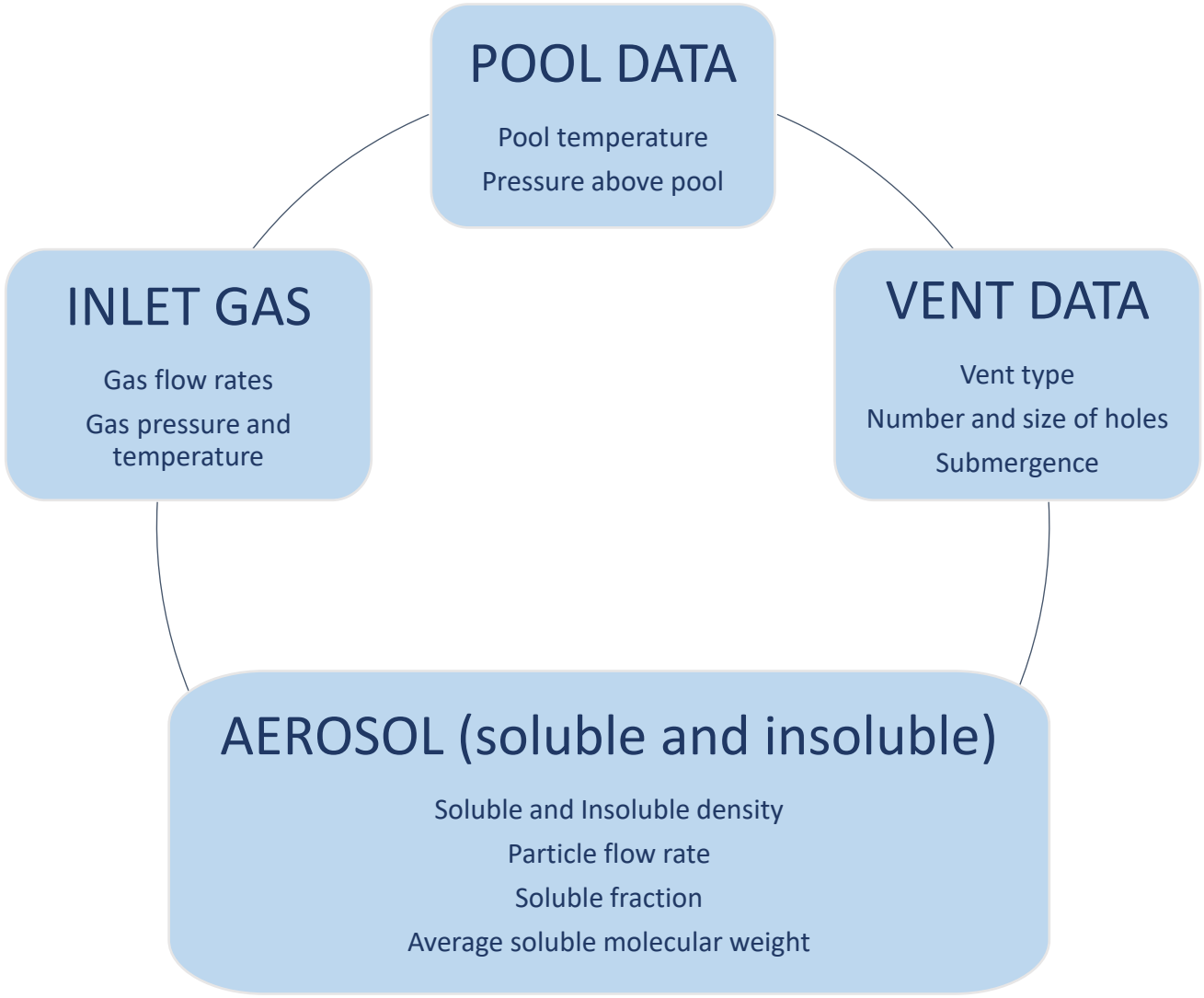

DEPOSITION MECHANISMS

- INTEL REGION
  - Steam condensation
  - Impaction
  - Centrifugal deposition
- SWARM RISE REGION
  - Sedimentation
  - Brownian diffusion
  - Centrifugal deposition
- POOL SURFACE REGION
  - No models for particle retention at the pool surface in SPARC90

GLOBAL BEHAVIOR - DF RATIO

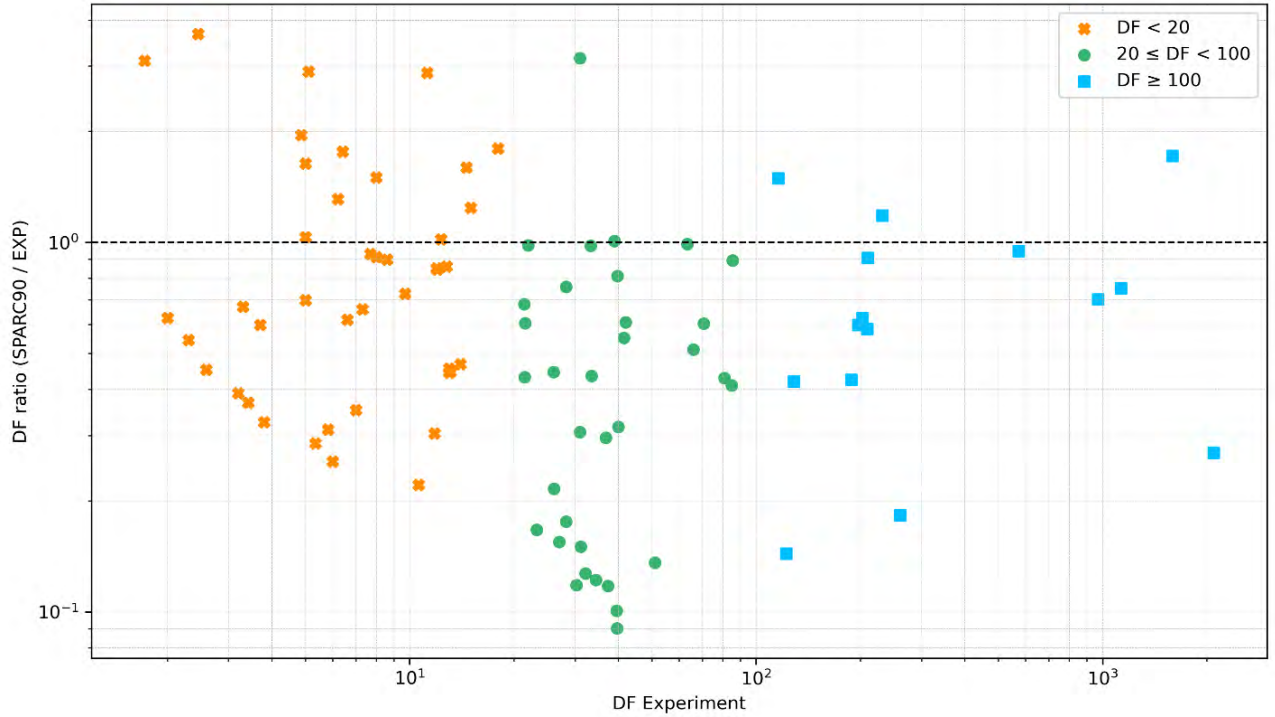

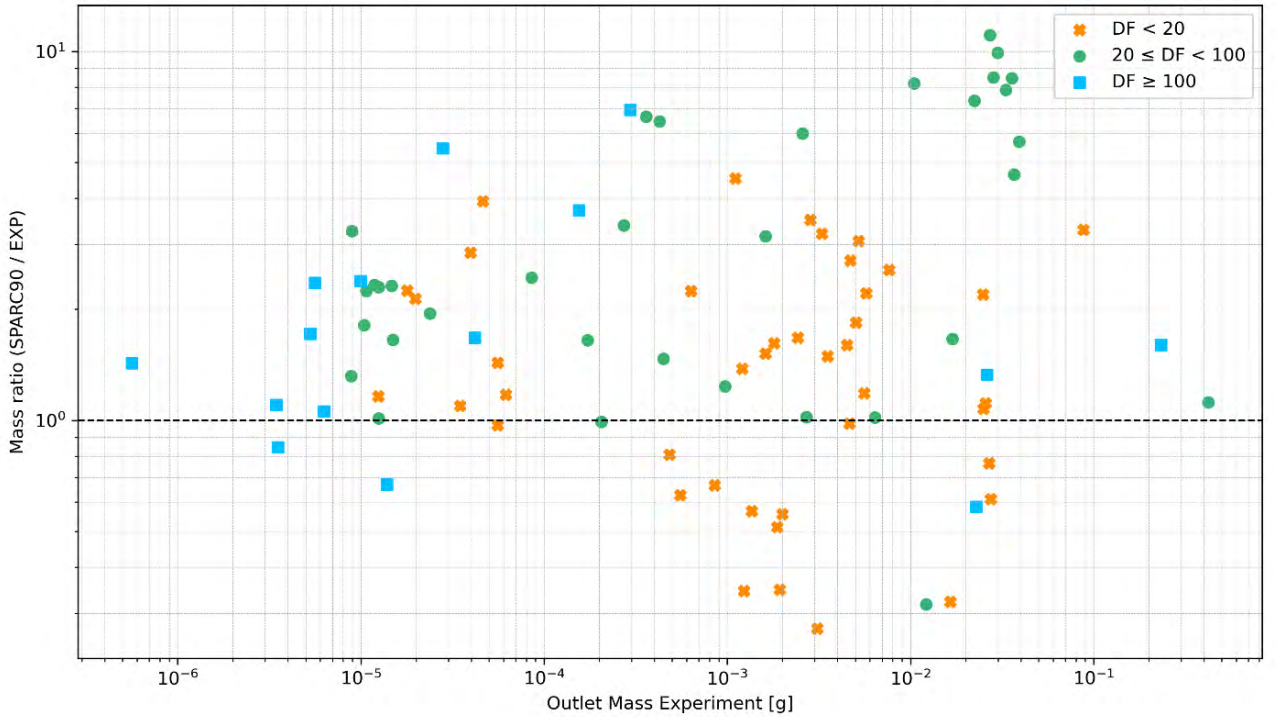

GLOBAL BEHAVIOR - SOLUBILITY

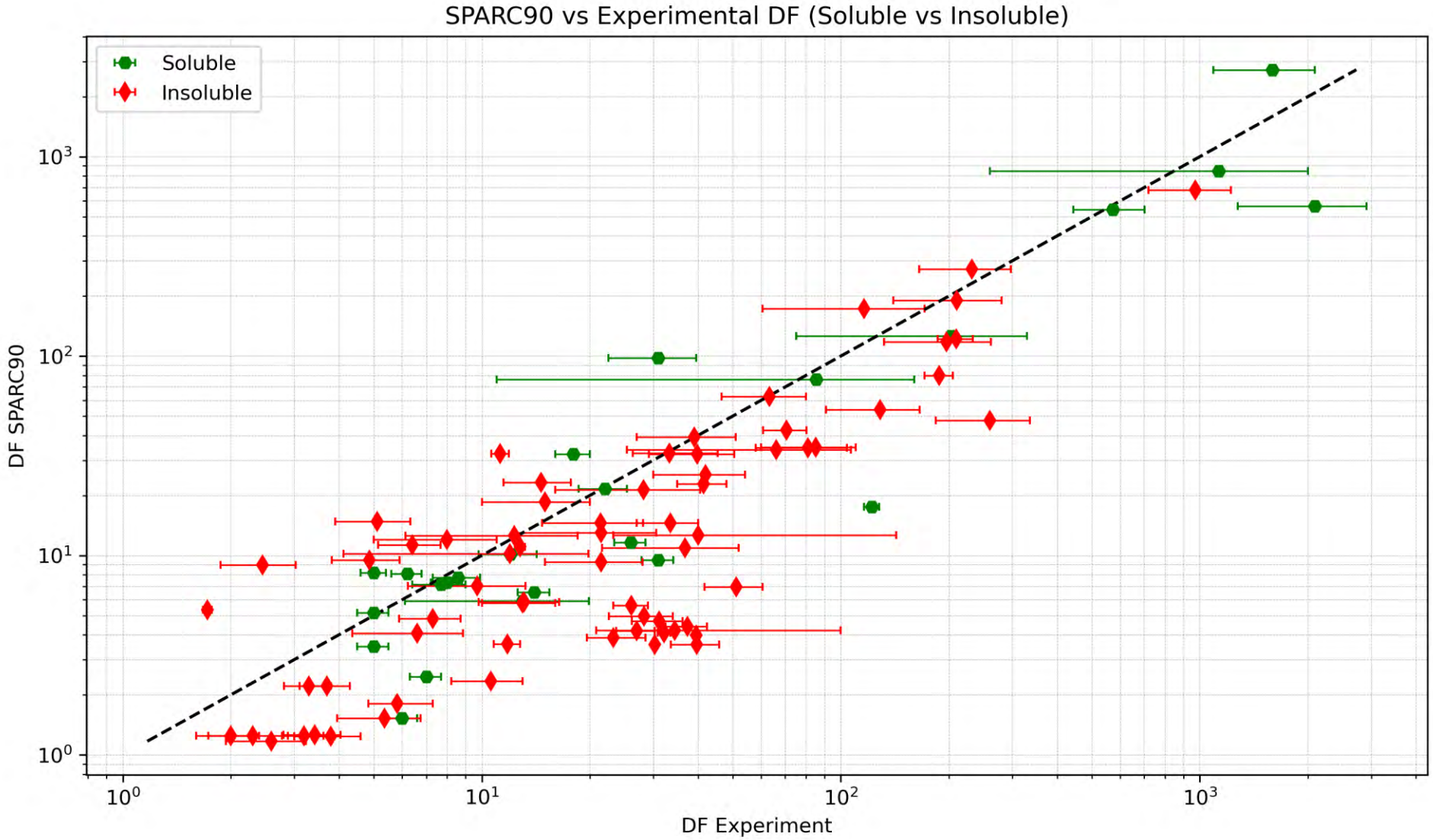

GLOBAL BEHAVIOR - STEAM

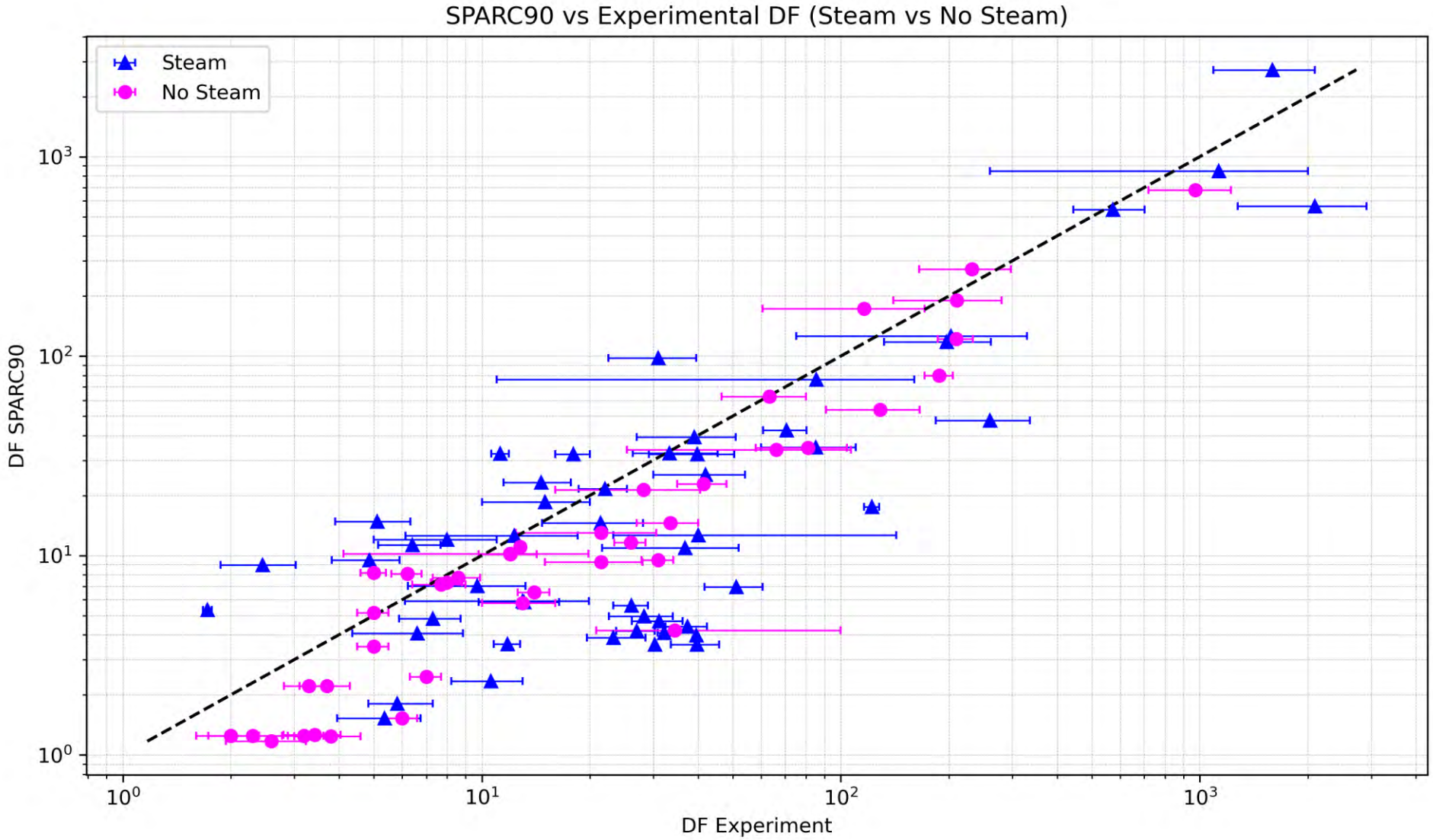

SPARC - FISHER

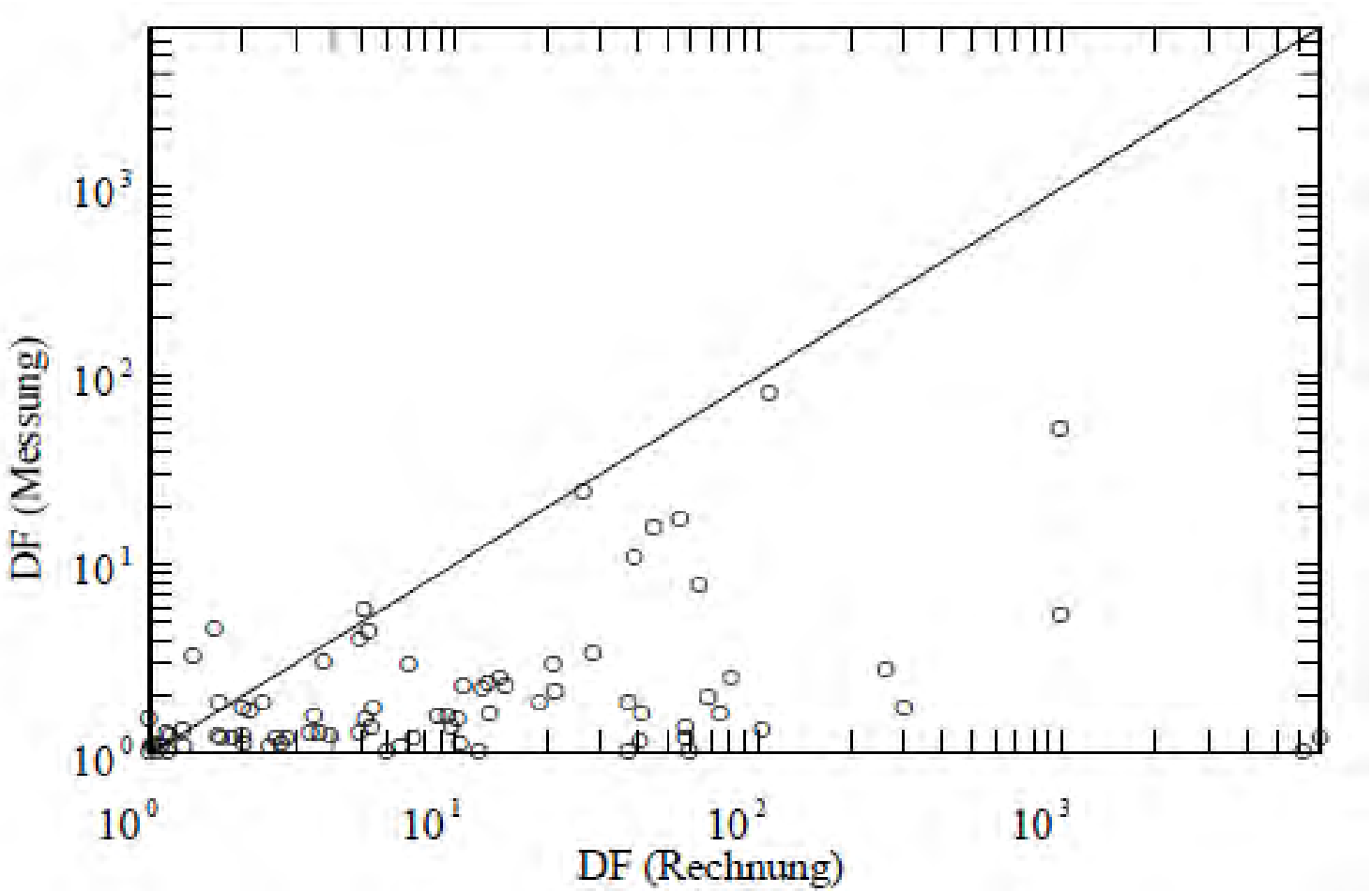

- Most data are EPRI (63 tests)
- Few data from RCA (4 tests) and POSEIDON-II (14 tests)
- Used SPARC-B/98

SPARC - FISHER

Nachrechnung der POSEIDON-Experimente																
Lfd. Nr.		Aerosol	Experiment	Tiefe	Experiment		RS979		Battelle		COCOSYS		COCOSYS		ASTEC	
		Größen-verteilung					SPARC-90		SPARC-B/98		SPARC-B/98mod		Heute		Heute	
				[cm]			0,30/1,37									
					DF	DE	DF	DE	DF	DE	DF	DE	DF	DE	DF	DE
1	55 % Dampf	"kleines" Aerosol AMMD/GSD = 0,30/1,37	PA-07	30	6,61	0,8487	7,18	0,8607	1,06	0,0566	1,19	0,1562	1,32	0,24	1,03	0,27
2			PA-06	100	7,30	0,8630	7,11	0,8594	1,19	0,1597	1,64	0,3894	1,85	0,46	1,03	0,03
3			PA-09	200	9,72	0,8971	8,72	0,8853	1,36	0,2647	2,58	0,6129	2,65	0,62	1,07	0,07
4			PA-08	400	21,40	0,9533	10,30	0,9029	2,12	0,5283	3,38	0,7042	3,78	0,74	3,81	0,74
5	kein Dampf		PA-13	30	2,59	0,6136	2,98	0,6644	1,19	0,1597	1,02	0,0150	1,01	0,01	1,05	0,05
6			PA-12	100	3,42	0,7075	2,51	0,6016	1,55	0,3548	1,04	0,0338	1,04	0,04	1,11	0,10
7			PA-11	200	5,35	0,8132	2,81	0,6441	1,71	0,4152	1,06	0,0600	1,09	0,08	1,24	0,20
8			PA-10	400	10,63	0,9059	2,84	0,6479	2,28	0,5614	1,33	0,2465	1,37	0,27	2,15	0,53
9	> 70 % Dampf		PA-21	30	2,45	0,5917	13,57	0,9263	1,09	0,0826	1,46	0,3162	1,52	0,34	1,05	0,05
10			PA-15	100	4,86	0,7944	15,90	0,9371	1,26	0,2063	2,84	0,6476	2,94	0,66	1,03	0,03
11			PA-20	200	5,11	0,8043	21,11	0,9526	1,53	0,3464	4,21	0,7623	4,40	0,77	4,11	0,76
12			PA-14	400	14,62	0,9316	21,82	0,9542	2,24	0,5536	4,65	0,7849	4,93	0,80	6,36	0,84
13		"großes" Aero-sol	PA-17	100	12,33	0,9189	21,98	0,9545	2,15	0,5349	2,97	0,6635	3,09	0,68	1,18	0,15
14		AMMD/GSD = 0,54/1,69	PA-16	400	38,94	0,9743	43,44	0,9770	10,87	0,9080	6,61	0,8486	7,14	0,86	15,99	0,94

SPARC - FISHER

			Dekontaminationsfaktor (DF)					
			Experi-ment	NRC	GRS	Battelle	GRS	***GRS***
Experi-ment	Dampf anteil	Ein-tauch-tiefe		SPARC-90	SPARC-90	COCOSYS/ SPARC-B/98	COCOSYS/ SPARC-B/98mod	***COCOSYS V2.4dev***
	[%]	[m]	/DEH 96/	/OWC 91/	/ALL 99/	/FIS 98/	/SCH 03b/	
PA-09	55	2	**9,72**	5,12	9,94	1,36	2,58	***2,69***
PA-11	0	2	**5,35**	1,15	2,81	1,71	1,06	***1,09***
PA-15	70	1	**4,86**	8,16	17,61	1,26	2,84	***2,89***
PA-20	70	2	**5,11**	10,58	23,27	1,53	4,21	***4,32***

blau - berechneter DF kleiner als experimenteller Wert
rot - berechneter DF größer als experimenteller Wert

DF vs AMMD

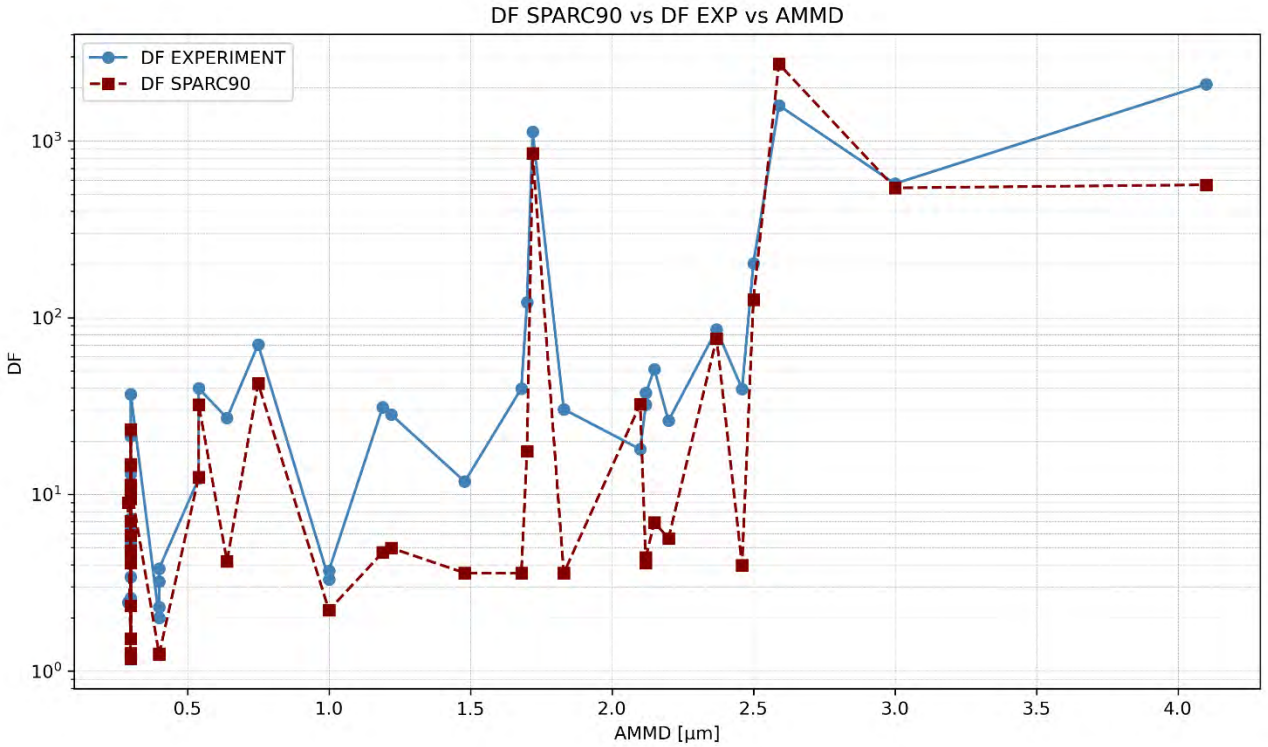
DF SPARC90 vs DF EXP vs AMMD
DF EXPERIMENT
DF SPARC90
DF
AMMD [µm]

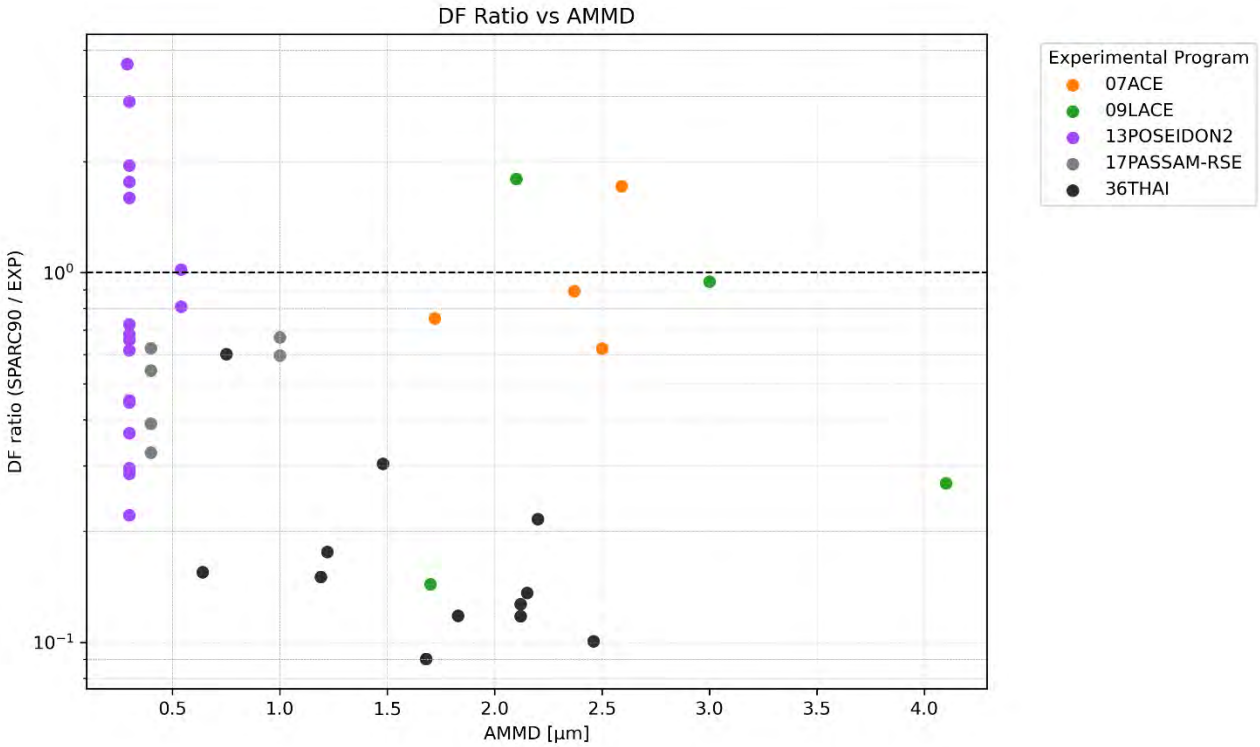
DF Ratio vs AMMD
DF ratio (SPARC90 / EXP)
AMMD [µm]
Experimental Program
07ACE
09LACE
13POSEIDON2
17PASSAM-RSE
36THAI

DF vs FLOW RATE

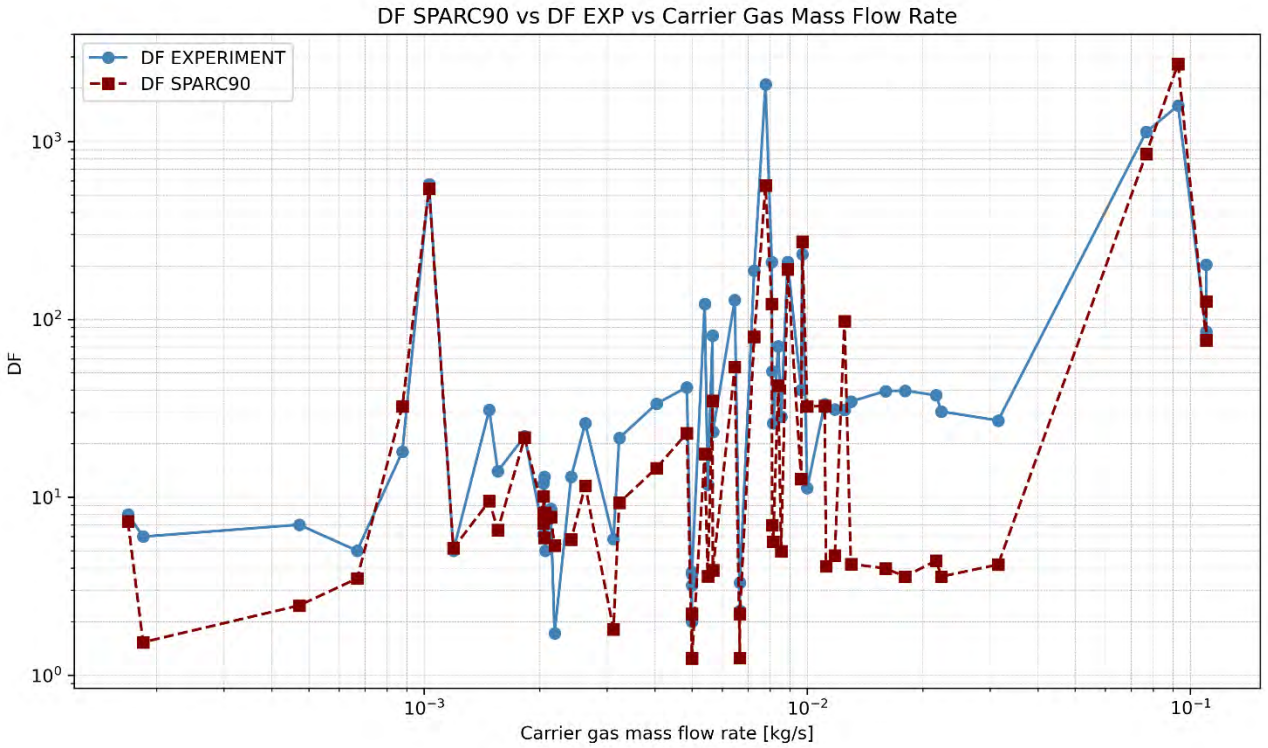

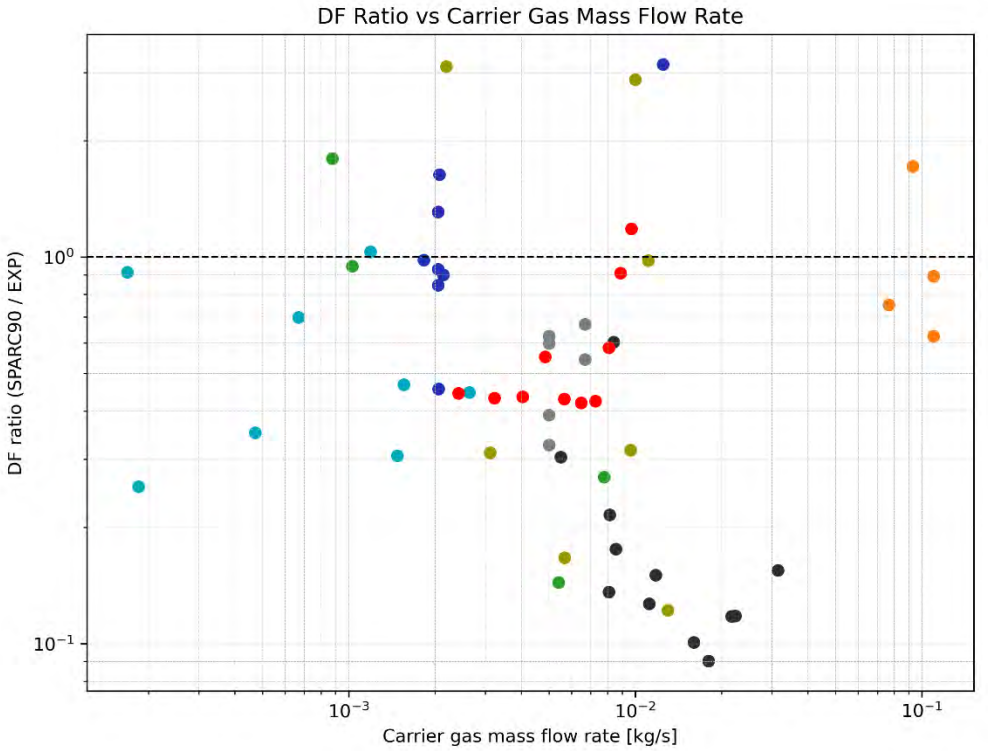

DF vs FLOW RATE

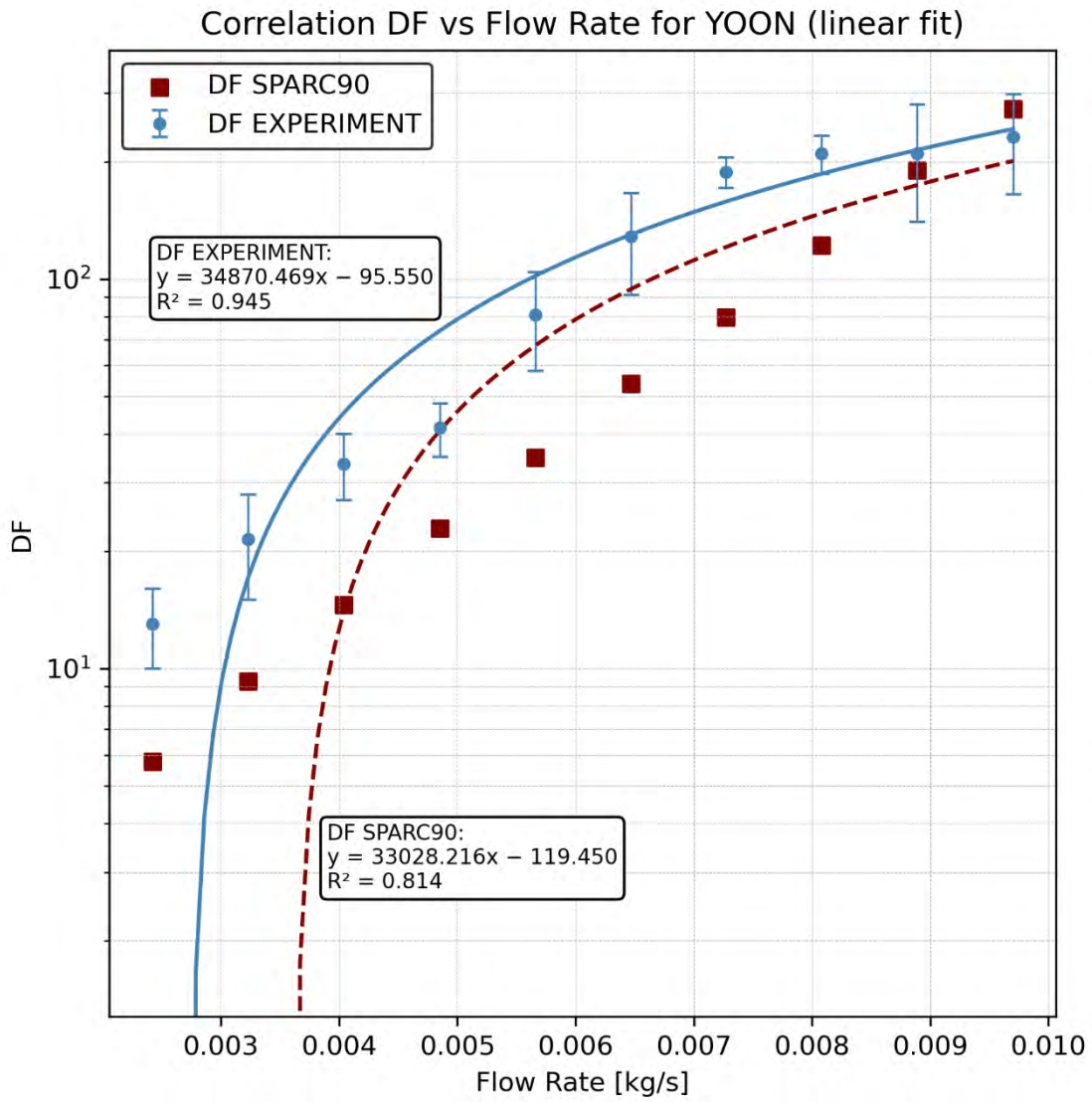

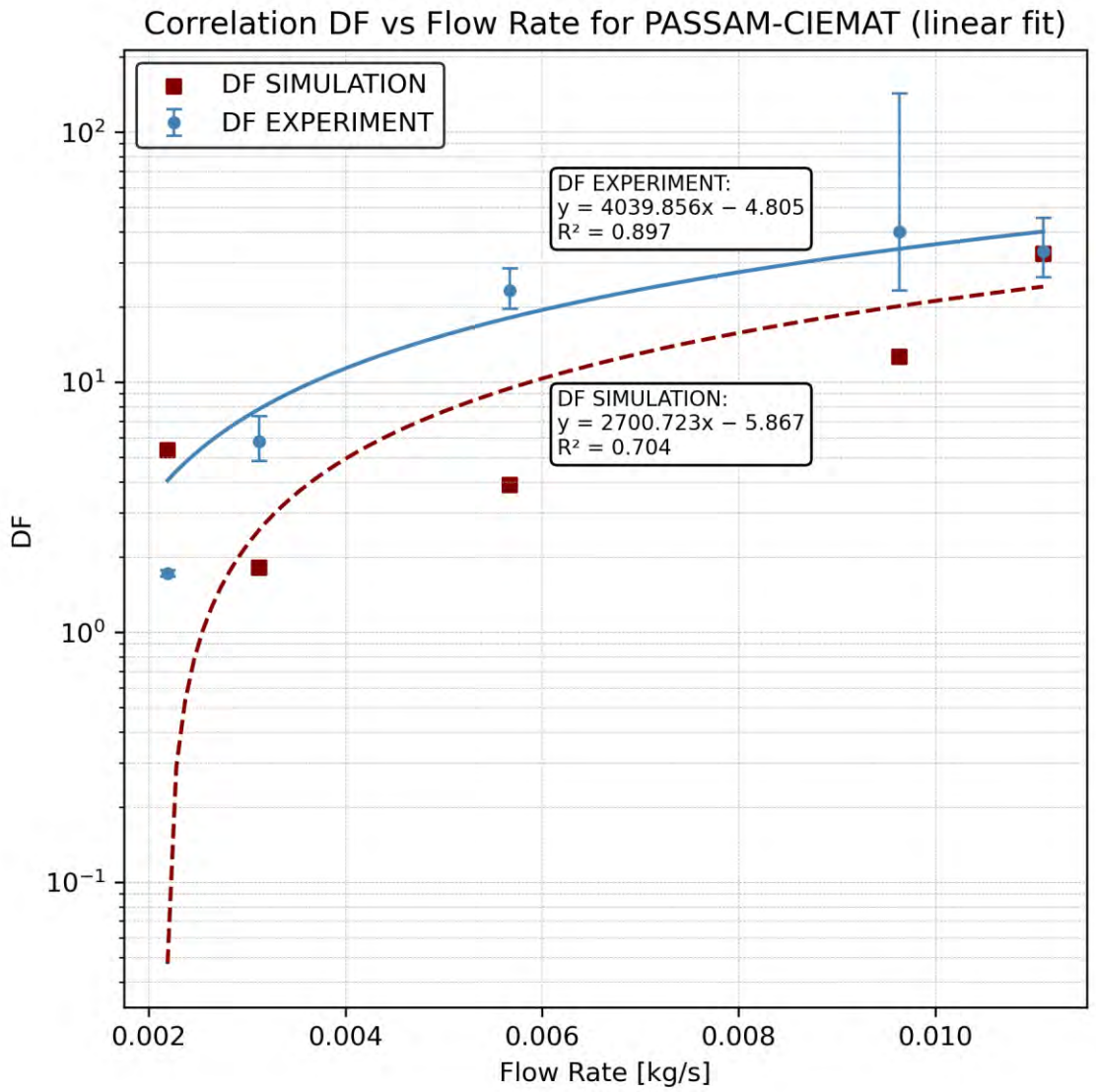

DF vs SATURATION RATIO

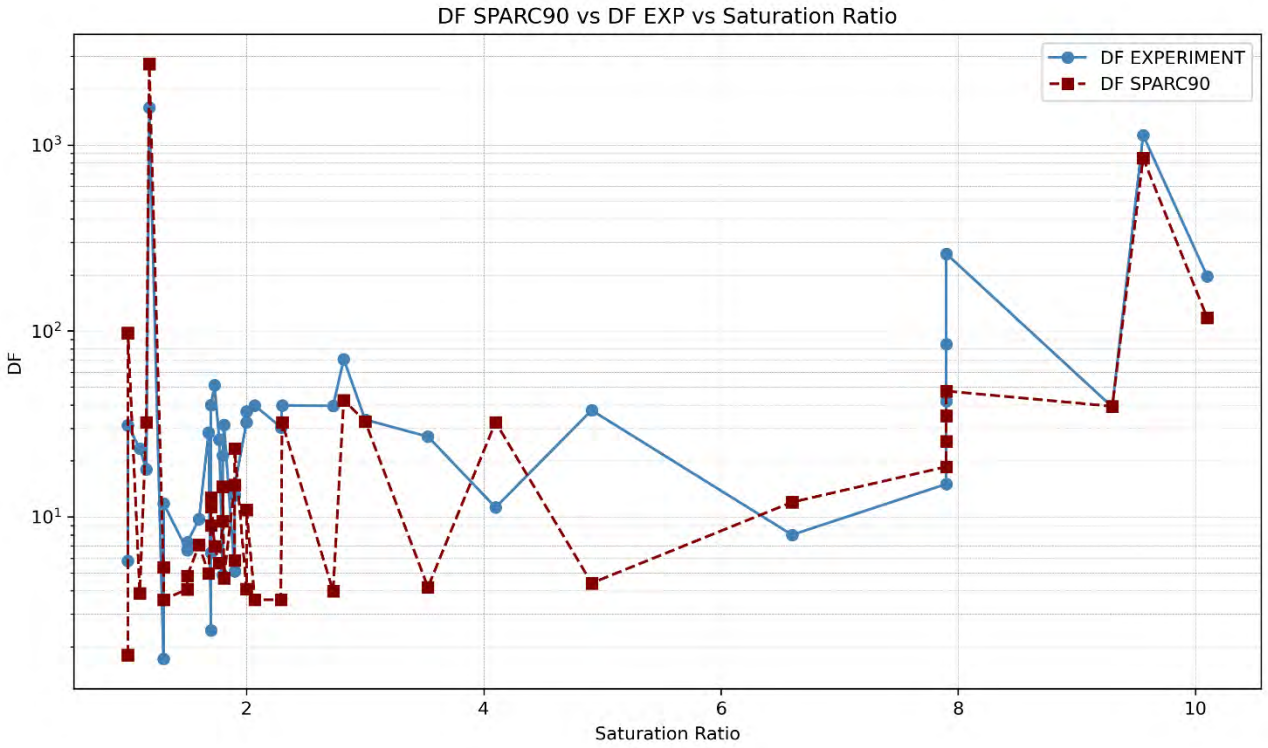

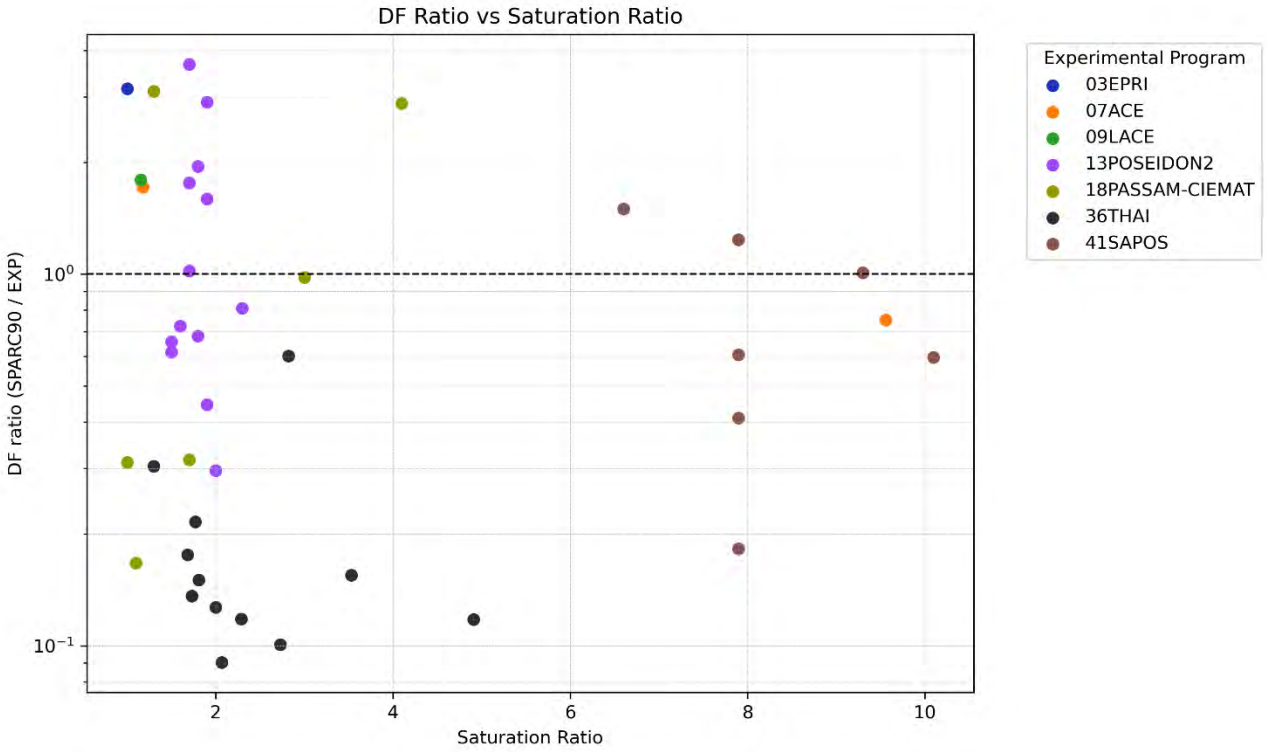

DF vs SATURATION RATIO

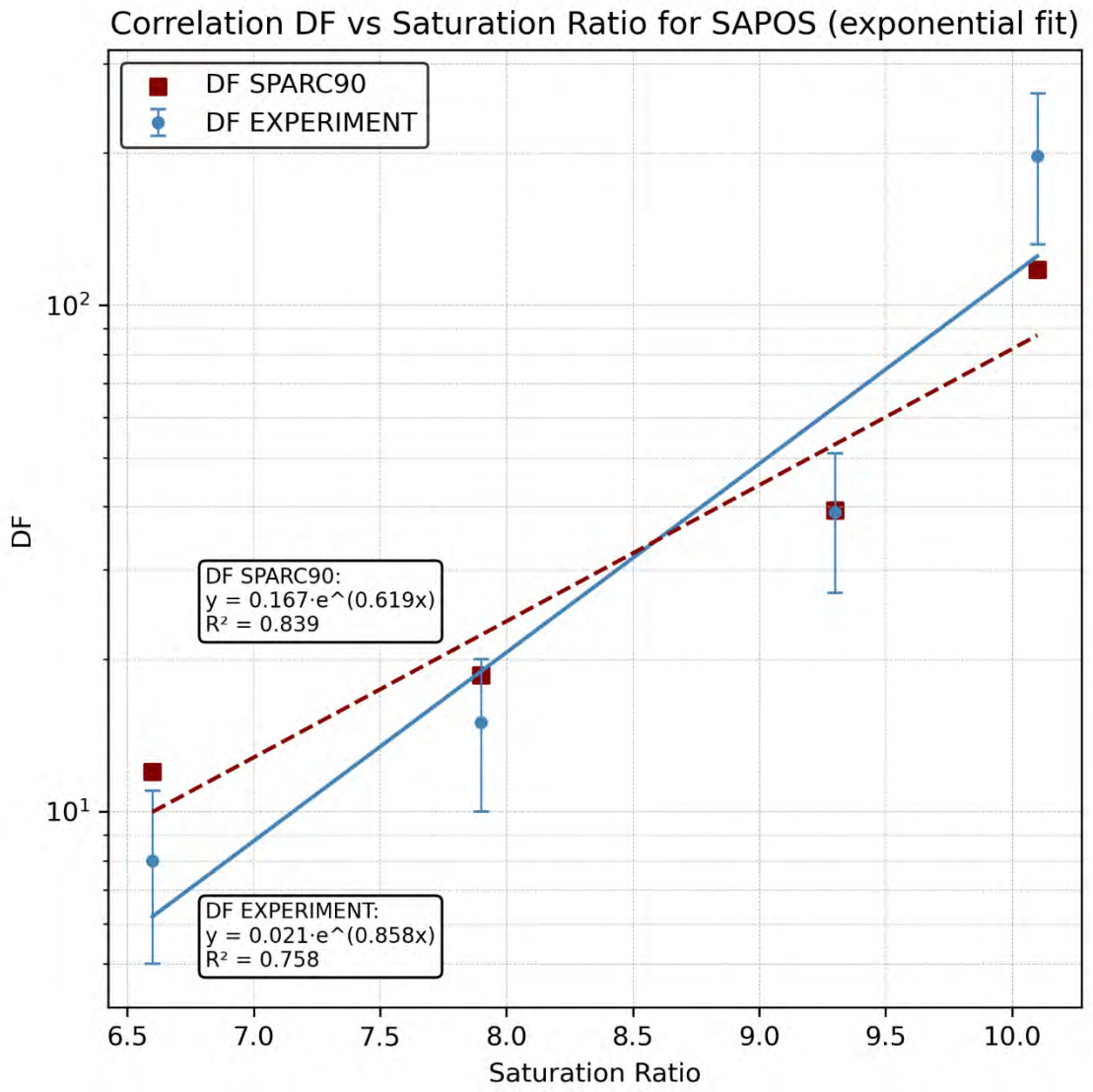

DF vs SUBMERGENCE

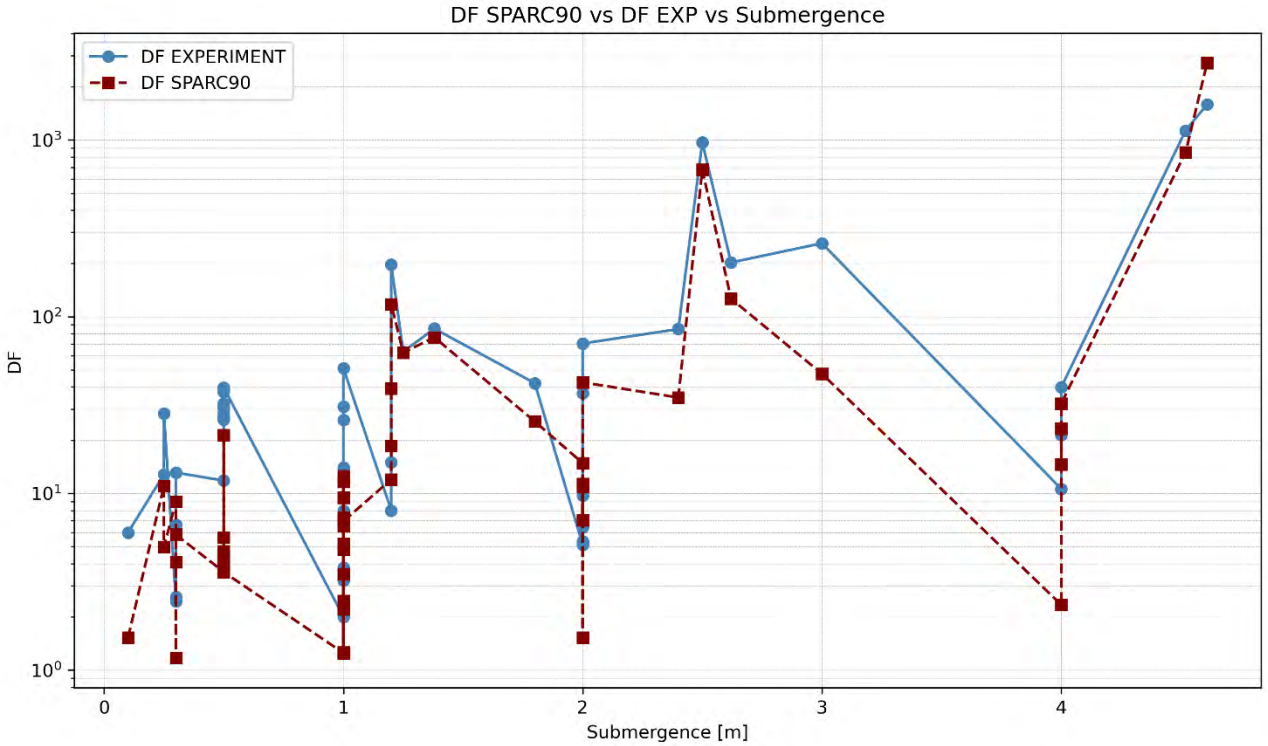

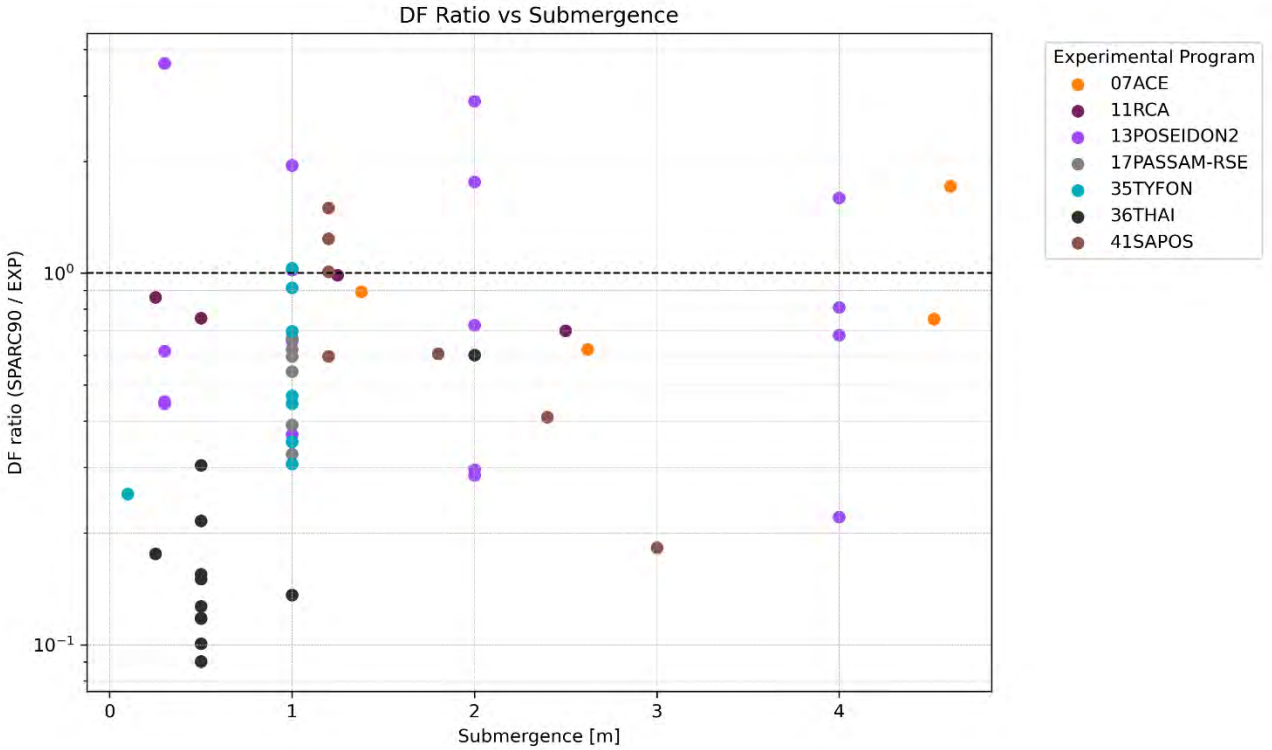

DF vs SUBMERGENCE

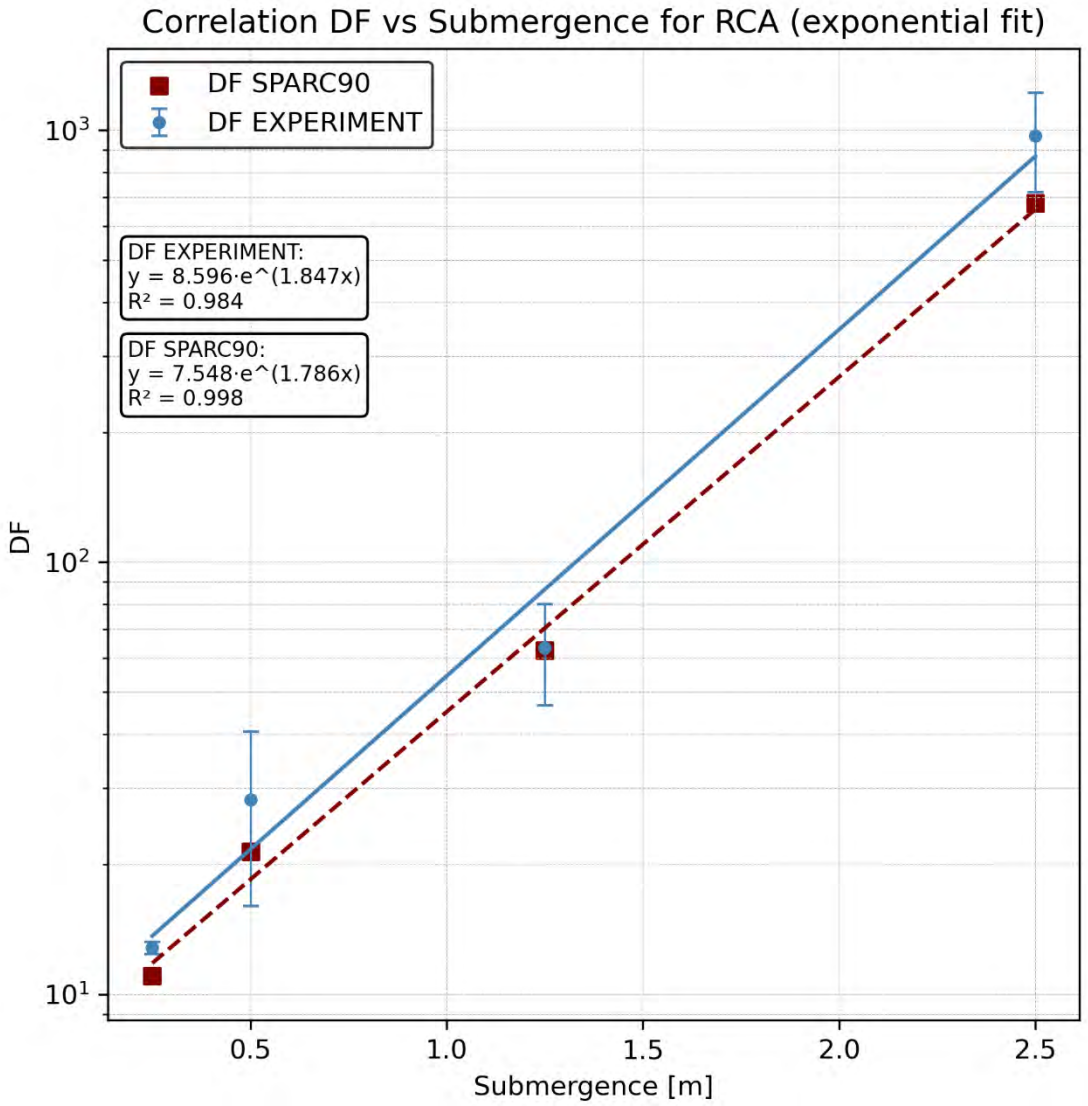

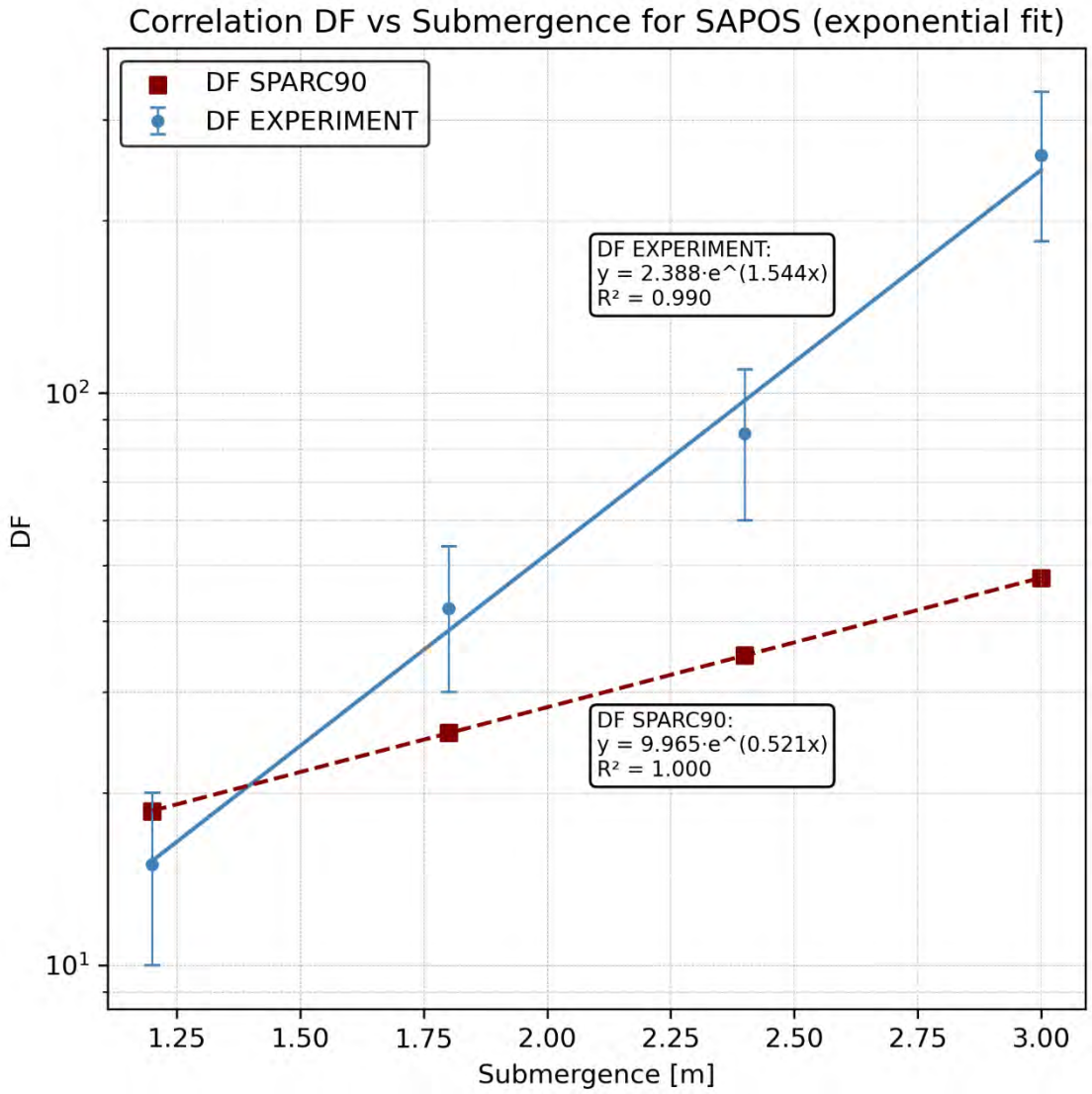

NEXT STEPS - HYDRODYNAMICS

- To better understand pool scrubbing hydrodynamics **in support of DF calculations**.
- SPARC90 decently simulate jet experiments, although **no jet model implemented** into it.
- Set up and **hydrodynamics database** (review paper).
- Possibly, identify some phenomena to be included into SPARC as a **new correlation** (paper).

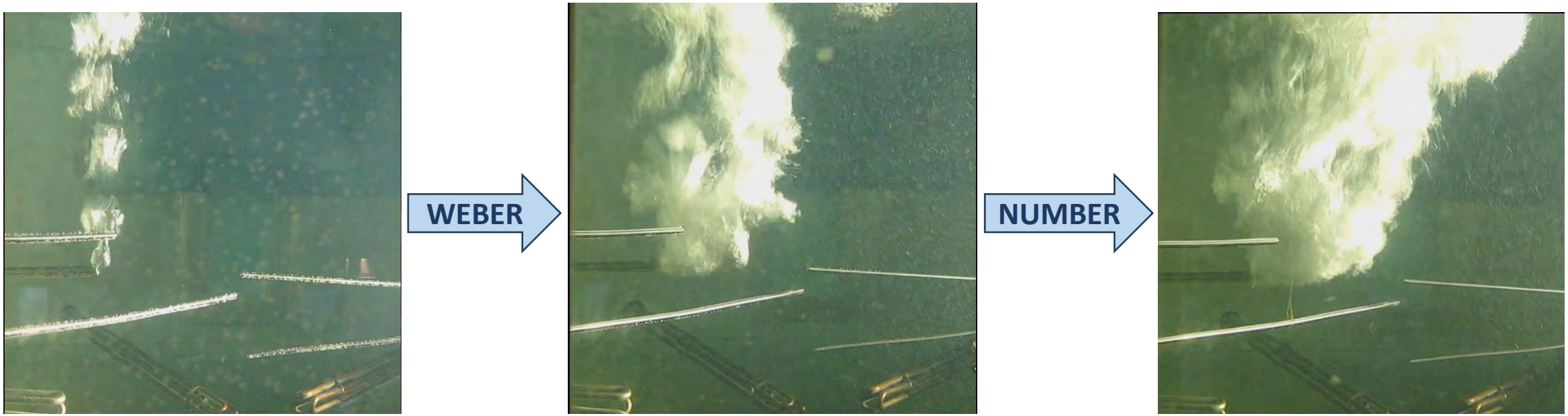

POOL SCRUBBING IN WATER COOLED SMRs: SCENARIOS, PECULIARITIES AND CHALLENGES

L.E. Herranz, M. Garcia, T. Lugo
CIEMAT
Avenida Complutense 40, 28040 Madrid (Spain)
luisen.herranz@ciemat.es; monica.gmartin@ciemat.es; tamara.lugo@ciemat.es

ABSTRACT

Pool scrubbing might be an add-on to the built-in passive systems used in most WC-SMRs, strengthening even further the passive nature of accident management. This work investigates potential pool scrubbing scenarios in a generic 300 MWe integral Pressurized Water Reactor. By using MELCOR 2.2 accident scenarios in which pool scrubbing might play a role in mitigating any potential source term to the environment have been identified and thoroughly analyzed. The results indicate that some water-filled components potentially playing a role in cleaning-up the contaminated gases entering containment are by-passed due to reverse flow caused by an earlier containment failure. In other scenarios, though, components like the pressurizer quench tank provided an effective filtering of the radioactive gas (up to 70% of the mass entering), even under unfavorable conditions for the scrubbing process. The present paper, framed within the Euratom SASPAM project, will thoroughly discuss these finding.

KEYWORDS
Source Term, Severe Accident, Pool Scrubbing, WC-SMRs

1. INTRODUCTION

Fission products retention in water ponds, hereafter pool scrubbing, is known to be an efficient way to mitigate potential source term to the environment in case of a SA in nuclear power plants. When hot, contaminated gas gets into a water pond, thermal and hydraulic interactions between gas and water are the origin of a set of phenomena (including steam condensation, droplet entrainment or internal gas circulation) that foster aerosol and vapour depletion mechanisms (diffusiophoresis, inertial impaction or centrifugal deposition among others) causing the transport of radioactive material to the gas-water interface and, finally, their absorption into the pool. The efficiency of these processes is dependent on prevailing conditions in the carrier gas, radioactive material properties and thermal state of the pool. A vast investigation has been conducted over decades to thoroughly understand the multi-physics that govern these complex processes [1], [2], [3], [4], [5], [6].

Given the huge amount of water bodies in WC-SMRs**,** and particularly in iPWR designs, the potential of pool scrubbing is relevant. Many iPWR concepts incorporate a submerged containment or water pools that could act as a passive scrubbing barrier during a SA, enhancing defense-in-depth by increasing retention of fission products before they could reach the environment. Few studies [7] have specifically addressed pool scrubbing in iPWRs so far, but traditional source term analysis methods are being tested in frameworks like EU SASPAM [8].

Within the framework of the Horizon Euratom SASPAM project [8], CIEMAT has investigated postulated SA scenarios in a generic 300 MWe iPWR design. Beyond identifying those scenarios and thoroughly

characterize them, the focus of such analyses was to assess the role of pool scrubbing in mitigating source term. In this work the analytical tool used is MELCOR 2.2 [9], [10].

2. STUDY APPROACH

A generic 300 MWe iPWR characterized by a dry spherical containment and the use of several passive systems is the focus of the present study. During normal operation, the reactor functions with forced circulation, while in the event of accidental transients, it relies on a passive safety strategy. The design features an integral RPV that houses the core, a compact SG, the CRDM, the primary pumps, and the PRZ located in the upper section, which is separated from the riser by a perforated plate. Heated water exiting the core rises through a circular riser up to the primary pumps suction [11]. The use of passive SSs offers improvements in plant simplification, safety, reliability, and investment protection compared to conventional plant designs [12]. A sketch of the plant and the passive SSs configuration is shown in Fig. 1 and includes:

- The EHRS consists of 4 independent loops operating in natural circulation. Each loop includes a horizontal U-tube heat exchanger connected to a separate SG feed/steam line. The heat exchangers are located in the RWST (two units) outside the containment. Its functions are both core cooling and containment depressurization.
- Two full-system pressure EBTs to provide borated water to the RPV by gravity for reactor shutdown.
- The ADS assists the EHRS in depressurizing the RPV when/if the RPV coolant inventory drops below a specific level by releasing steam in the pool of the QT located in the DW (ADS st-1) and allows the pressure equalization between containment and RPV atmospheres (ADS st-2).
- The containment PSS consists of two tanks connected to the DW through a vent pipe to condense the steam released into the containment following a LOCA or steam/feed line break accident, thereby limiting containment pressurization. Additionally, the PSS provides an elevated water source for gravity injection into the RPV in the event of a LOCA accident.
- The LGMS consists of two large tanks located in the DW and connected to the DVI lines.

The modeling and the analysis of the sequences included in this study were conducted using the MELCOR 2.2 code [9], [10].

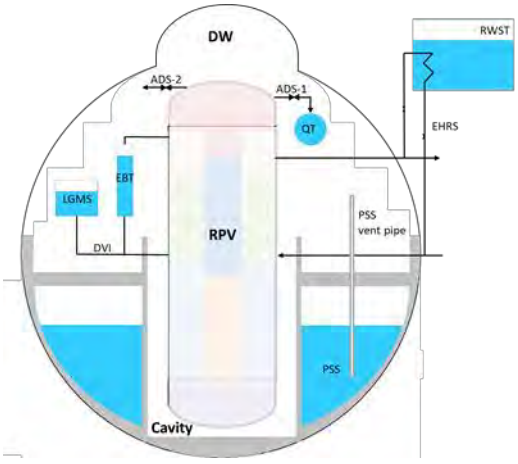

Figure 1. Passive SSs sketch (for simplicity, only one line is reported for redundant systems).

In case of a SA initiated by a small break ($4.28 \cdot 10^{-2}$ m diameter) in the DVI pipe connecting RPV and LGMS and EBT, pool scrubbing might happen in two specific locations: the PSPs, when FPs reaching the DW from the reactor core are carried through the connecting pipe into PSP; the QT, when FPs released from the core find their way through the ADS st-1 system (activated by low RCS pressure) to the aqueous phase in the QT and, from there, to the containment DW atmosphere.

Four scenarios have been considered in this analysis, based on the work conducted under the WP2 frame of the SASPAM project. Table II shows the safety systems assumed operative during the accident unfolding. It is worth noting that triggering a SA requires failure of EHRS.

Table II. Working safety systems along the sequences analyzed.

SSs	SA1	SA2	SA3	SA2*
ADS_st1	-	-	✓	✓
ADS_st2	✓	-	✓	-
EBT	✓	-	✓	-
LGMS	✓	-	✓	-
EHRS	-	-	-	-

2.1. Modeling Overview

MELCOR requires two types of nodalization within RPV: one is specifically devoted to tracking fuel along the accident, i.e., fuel degradation through the COR package; the other is used for THs calculation through the CVH package [9], [10].

The reactor core is located inside the integral RPV and features internal structures and assembly configurations similar to the Westinghouse 17x17 XL fuel assembly design [13]. For modeling fuel degradation through the COR package, the core is segmented into 6 radial zones (rings) and 16 axial levels (Fig. 2a). The 89 FAs are distributed from ring 1 to 4. The FAs are divided into 16 axial core levels being the active part of the reactor core from axial level 7 to 14. Cells belonging to fifth and sixth rings correspond, respectively, to the LP zone under the DC and the core-bypass.

The reactor core is represented by a single CV and is connected to the LP and riser through FLs. Similarly, the core-bypass, also represented by 1 CV, establishes connections with the LP and the riser. The LP consists of one CV divided into 5 segments to represent its geometric form and is connected through FLs to the cavity (for vessel breach simulation), DC, core, and core-bypass. The DC is represented by 1 CV, which is connected through FLs to the DVI line, the first CV of the SG primary side, and the first CV of the SGs-bypass. The riser is represented by 6 CVs, with FLs allowing flow movement among them. Additionally, FLs connect the riser to the core, core-bypass, PRZ, UP, and SGs-bypass. The SGs PCS is defined by 4 CVs with FLs for interconnection among them; besides SGs PCS is connected to the DC, UP, and SGs-bypass through FLs. Likewise, the SGs-bypass consists of 4 CVs connected to each other and to the DC, UP, riser, and SGs PCS. The UP is defined by 1 CV connected to the SGs PCS and SGs-bypass, and it is also connected to the EBTs (A/B) and to the riser. Finally, the PRZ is represented by 1 CV divided into 5 segments. Two FLs from the PRZ represent the ADS st-1 and st-2 lines, and the PRZ is also connected to the riser (see Fig. 2a).

The spherical containment is divided in two parts: one CV that represents the DW in the upper part of the containment with a total volume of 3237 m^3, and 1 CV to define the cavity volume (450 m^3) (Fig. 2b). The

containment is filled with N_2 to reduce the combustion risk and it is thermodynamically coupled with the primary system through FLs connecting it to the RPV and cooling systems. Each PSS tank is connected to the DW atmosphere through vent pipes to control containment pressure and LGMS water supply system into the RPV when its internal pressure approaches containment one via the ADS st-2 line. Besides, the DW is connected to the QT through the ADS st-1 line. A leak due to overpressure to the environment is also modelled as a FL. The cavity, located below the DW, collects liquid break flow and condensates from the containment to ensure cooling of the lower vessel part in case of SA.

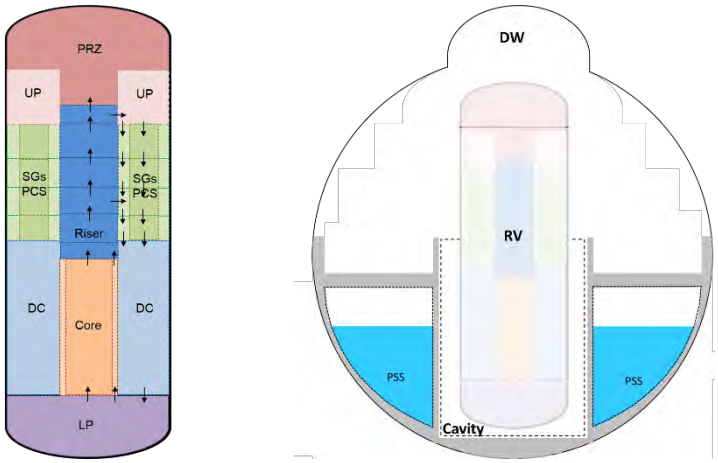

a) RPV b) Containment

Figure 2. TH nodalization.

According to the characteristics of the iPWR analyzed, pool scrubbing might happen during a SA sequence in two specific locations into the containment: the PSPs and the QT.

The PSS was conceived to prevent containment overpressure in case of a LOCA or steam/feed line break accident. It consists of two tanks connected to the DW through a vertical vent pipe. Steam entering the sub-cooled aqueous phase of PSP condenses, thereby limiting containment pressurization. Additionally, the PSP provides an elevated water source for gravity injection into the RPV in the event of a LOCA accident.

Each PSP is modeled through 5 CVs with a total volume of 459 m^3 and interconnected horizontally and vertically by FLs to differentiate specific regions (Fig. 3a). Top and bottom regions and near- and far-field regions, result in a pool split into 4 zones. The gas phase of PSP is the fifth node (see Fig. 3a). By doing so, it is intended to provide MELCOR model the chance to simulate natural circulation, despite the inherent difficulties to do so in a lumped parameter code. In-pool injection is defined as a horizontal vent (0.06283 m^2) with an initial submergence of 3.41 m.

The pressurizer quench system consists of a vent pipe and a QT. The QT is modeled as a single open volume (33.6 m^3), connected to the PRZ through the quench vent pipe. At low PRZ pressure (<11.7 MPa), ADS st-1 is activated and the quench vent discharges steam from PRZ to the QT through a FL defined as a multi-hole sparger (800 holes with a hydraulic diameter of 0.01 m for each hole) with an initial submergence of 1.94 m (Fig. 3b). The quench vent pipe is modeled as 1 CV (10.7 m^3) connected to the PRZ and the QT through FLs.

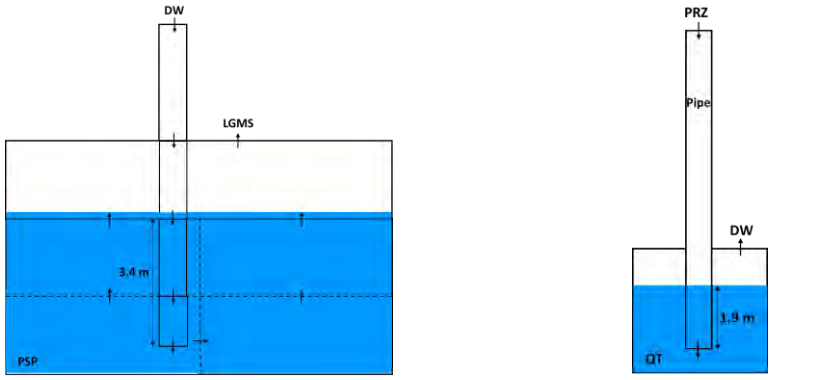

a) PSP-TH nodalization b) QT-TH nodalization

Figure 3. TH nodalization.

3. RESULTS

A steady-state analysis preceded the analysis presented in this section, which extends over 2 days.

3.1. Scenario Analysis

The key events during the sequences analyzed are shown in Table II.

Table II. Summary of the relevant phenomenological events time-table.

Key Event (h)	SA1	SA2	SA3	SA2*
Start of the transient	0	0	0	0
Scram time	0.01	0.01	0.01	0.01
RI-DC valves opening	0.03	0.03	0.03	0.03
EHRS	-	-	-	-
EBT actuation	0.04	-	0.04	-
ADS-st1 activation	-	-	0.05	0.05
LGMS activation	12.42	-	67.50	-
ADS-st2 activation	-	-	68.19	-
Time core uncovers	0.17	0.47	0.06	0.06
Liquid collapsed level at DVI level	0.33	0.60	0.05	0.05
Containment failure	1.29	1.69	0.50	0.48
Reverse flow from the PSP	1.29-1.59	1.69-1.89	0.55-0.84	0.48-0.85
Time of H_2 production onset	3.50	2.61	2.56	1.91
Gap release	3.50	2.60	2.62	1.97
Core completely uncovered	6.66	5.52	6.12	5.56
Time of vessel failure	-	-	-	-

As shown in Fig. 4, all sequences unfolding is similar in broad terms, the availability of SSs impacting the key events timing, but not the major trends of key variables like RPV pressure (a) and peak clad temperature (b). After the scram, due to the DVI break, a rapid RPV depressurization, partially dumped by the secondary system isolation occurs in all the sequences (Fig. 4a). Independently on the availability of SSs this depressurization of RPV is fast and if the ADS-st1 is available (SA3, SA2*), this rapid depressurization allows its activation, which makes the QT an efficient sink of the decay heat. In all the sequences, when the water level at the DC reaches the DVI line breach (7.9 m high with respect to) it can be observed an exponential pressure decay. In all the cases, the slight pressure oscillations correspond to fluctuations experienced during core degradation and the higher-pressure peaks result from pieces of core slumping in the partially water-filled RPV bottom.

The decrease of cooling rate and the eventual exposure of fuel to steam being produced in RPV, leads to core heat up to temperatures over 2000 K causing the onset of in-vessel FP and H_2 release. As expected, cladding temperature sharply rise up from roughly 1500 K due to oxidation enthalpy released from the Zr-steam interaction (Fig. 4b). During the temperature excursion, temperatures at the upper levels of the FAs (ring 1 in all the sequences) reach about 2500 K and triggers the loss of core integrity until its complete relocation into the LP.

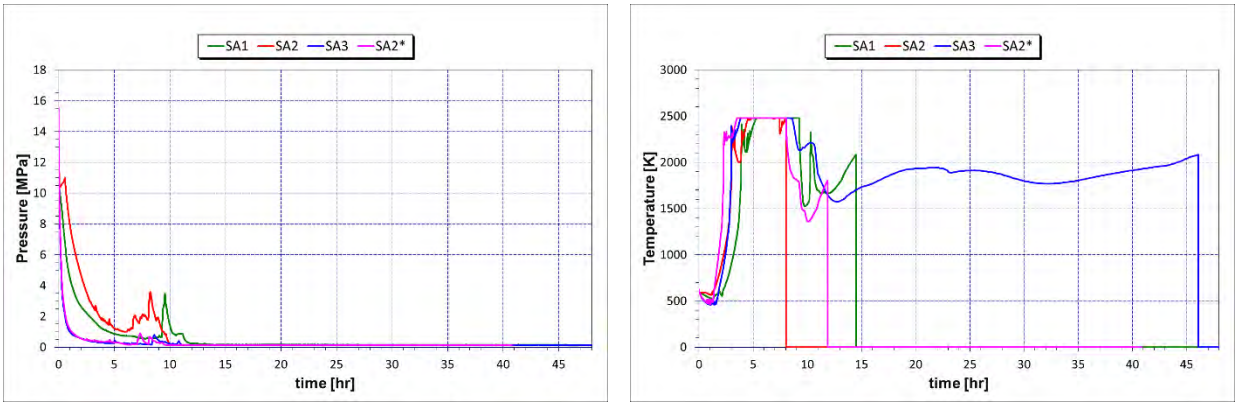

a) RPV pressure b) Max. cladding temperature

Figure 4. Sequences evolution.

In all the analyzed sequences, DW pressure reaches the containment failure threshold (P_{DW} > 1.5 MPa) and the prompt depressurization of DW makes it decreasing faster than in PSP, causing an inverse pressure gradient between DW and PSP ("reverse flow"). Namely, pressure difference sucks water from PSP into the DW atmosphere. In all the cases, such a water injection in the DW from PSP causes its level in the PSP to fall right below the pipe injection spot before FP release onset, as shown in Fig. 5a (dotted line). Therefore, no pool scrubbing is predicted to occur in the PSP. In other words, the filter potential of PSP is lost in the SA sequences analyzed. For the same reason, no significant amount of radioactivity is dragged by the "flow reversal" into the containment atmosphere.

Actuation of the ADS st-1 in SA3 and SA2*, opens an alternative path to the steam produced in RPV. A fraction of steam flows from PRZ to the QT, where it gets condensed and water temperature rises. In both cases, at the time FPs reach the QT, water get close to or at saturation and the continuous water evaporation eventually results in the quencher uncovery (Fig. 5b). Therefore, in both sequences FPs get scrubbed for some time in the QT (2.62 h - 5.18 h, in SA3; 1.96 h - 4.94 h, in SA2*). The vertical dotted lines mark the onset of FP injection in the QT in each sequence.

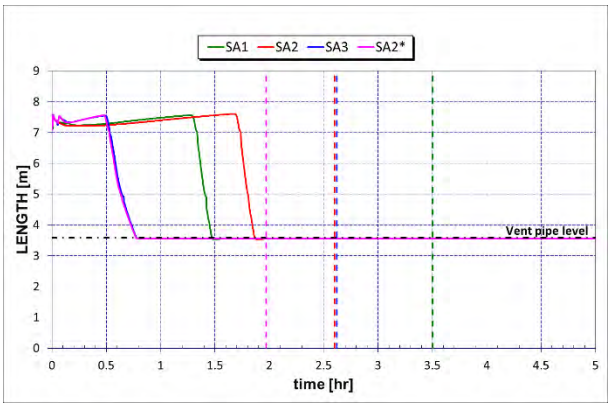

a) PSP water level

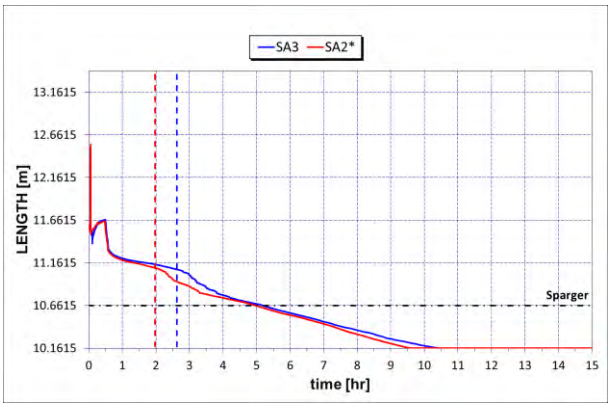

b) QT water level

Figure 5. Water level in PSP&QT.

3.2. Pool Scrubbing Results

Pool scrubbing phenomena can play a role on the source term decontamination in the QT whenever the ADS st-1 system is available. How effective it is in each sequence is the matter for discussion in next sub-sections.

3.2.1. Boundary conditions

The thermal-hydraulic conditions in the QT during the period of interest for pool scrubbing in both sequences (SA3, SA2*) are shown in the next figures (Fig. 6).

The prevailing boundary conditions are very similar in both sequences. After the activation of the ADS st-1 (0.05 h in both cases) steam starts to flow down the QT line from the PRZ, where it gets condensed and water temperature rises (Fig. 6a, 6b): while QT pressure remains above atmospheric pressure (a bit lower in SA3 due to the performance of additional cooling systems), the pool temperature rises. Water is close to or at saturation most time during FP arrival. Consequently, condensation of steam within the aqueous pond is not anticipated to play any major role on FP retention. The carrier gas is composed mainly by steam and, at some time intervals, H_2 concentration shows a peaky structure, but just occasionally, it goes over 30% of the mole fraction (Fig. 6c, 6d). According to the Weber non-dimensional number at the sparger (Fig. 6e, 6f), jet regime dominates gas injection all the time, showing values more than 3 orders of magnitude over the jet threshold ($We \geq 10^6$).

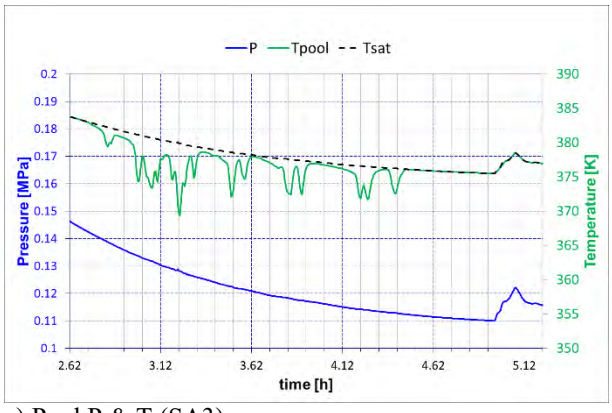

a) Pool P & T (SA3)

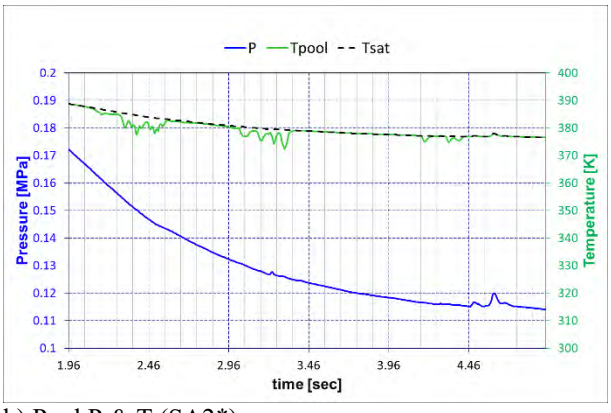

b) Pool P & T (SA2*)

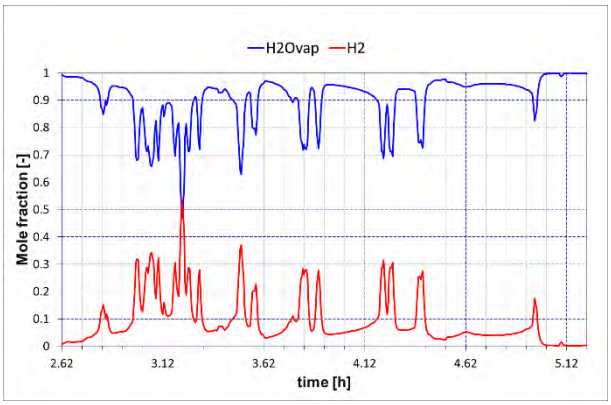

c) Inlet gas composition (mole fraction) (SA3)

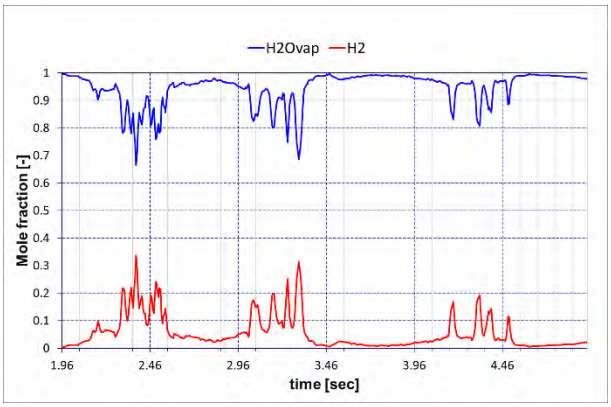

d) Inlet gas composition (mole fraction) (SA2*)

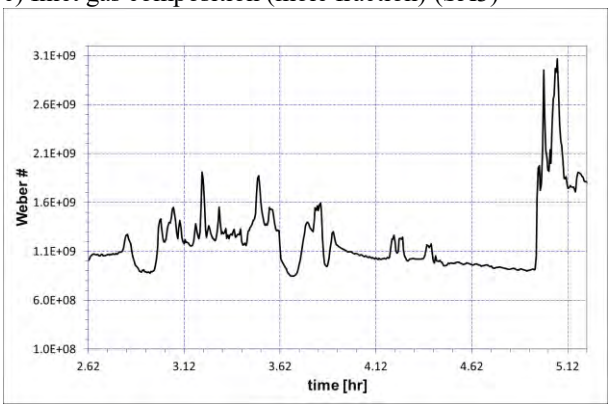

e) Weber number (SA3)

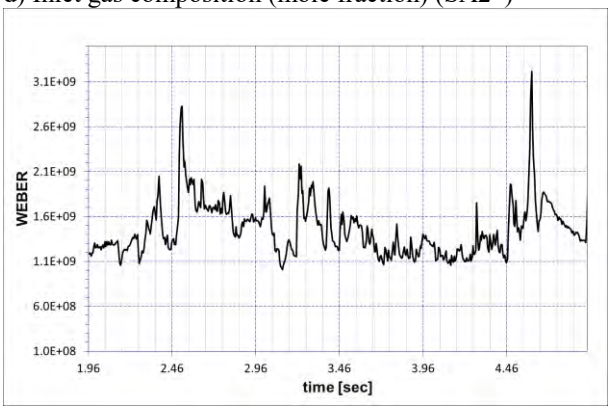

f) Weber number (SA2*)

Figure 6. QT THs conditions.

3.2.2. Source term

The initial fuel inventory, according to WP2, has been estimated with an ORIGEN calculation in MELCOR default model, scaled down properly from a 3410 MWth Westinghouse PWR at the end of the cycle with different burnups per region and a three-year refueling cycle [13]. Most FPs, except NG and a minor fraction of iodine, turns into aerosols and their behavior is modeled through the radionuclide package [9]. As in NUREG-1465 [14], radionuclides are grouped in 14 classes of elements with similar chemical properties; other classes have been introduced "ad-hoc" according to the code developers' recommendations, representing CsI and Cs_2MoO_4. The FPs reported in this section are xenon (Xe), as a representative of NG, and cesium (Cs) and iodine (I) as the most volatile and radiologically significant.

The aerosols (mix of FPs, fuel, structural and control rod material) are assumed to have a density of 4500 kg/m^3 and their size distribution is assumed to be a lognormal function with lower and upper bounds of 0.1 μm and 20 μm, respectively. Particles are assumed to be spherical.

Pool scrubbing is modeled in MELCOR through an adaptation of the SPARC-90 code [15]. The models include the effect of steam condensation at the pool entrance and aerosol deposition by Brownian diffusion, gravitational settling and inertial impaction during bubble rise. The injection in the QT through a multi-hole sparger (800 holes with a hydraulic diameter of 0.01 m each) enhances particle deposition at the injection zone.

MELCOR calculates the accumulated mass of FPs and other materials leaving the core and transported through the NPP systems. The following figures show the FPs fraction (initial inventory, i.i.) entering and

leaving the QT-pool for both sequences (Fig. 7a, 7b) from the time of their arrival. As expected, Xe, as a noble gas, is immediately transported through one volume to another (nearly 100% of the Xe is released to the environment at the end of the calculation). As it can be observed from the figure, the fraction of Cs and I absorbed in the pool reduces more than one order of magnitude the entering fraction of both elements. Regarding aerosol size, Figs. 7c and 7d show the aerosol size reduction (MMD) caused by the QT pool retention. The pool scrubbing effect is noticeable at both the beginning and end of the time interval. At the beginning, high We numbers foster inertial effects at the inlet of the pool (jet impaction) despite the small absolute size of particles; whereas at the end of the interval, the close-to-zero non-condensable fraction extends the bubbles residence time and enlarges the bubble exchange surface, which results in a visible decrease of the concentration leaving the water surface (i.e., a higher decontamination) mostly due to centrifugal deposition. This latter effect makes particles size outgoing the pool visibly smaller (around a factor of 4.0 compare to the incoming ones).

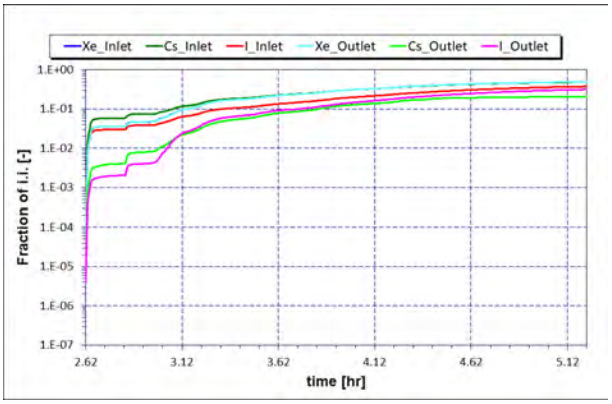

a) FPs fraction entering & leaving the QT-pool (fraction of i.i.) (SA3)

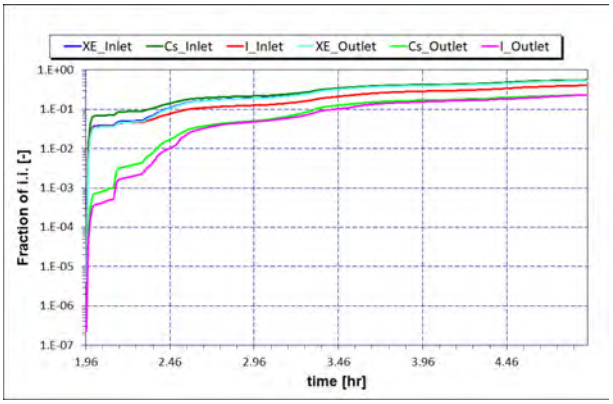

b) FPs fraction entering & leaving the QT-pool (fraction of i.i.) (SA2*)

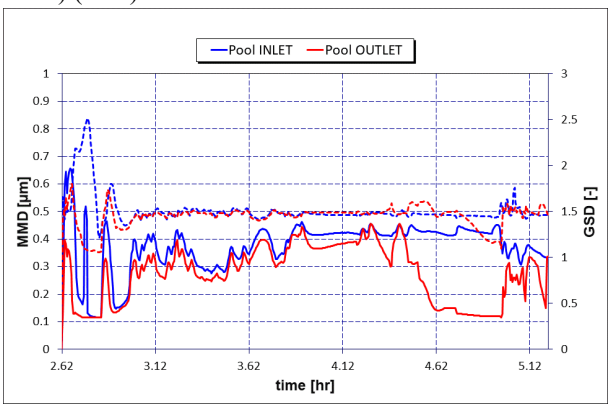

c) Inlet and outlet aerosol MMD in/from the QT (SA3)

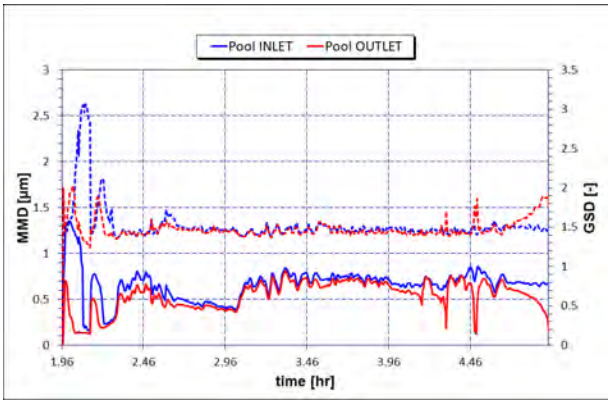

d) Inlet and outlet aerosol MMD in/from the QT (SA2*)

Figure 7. Effect of pool scrubbing on aerosols entering the QT-pool.

As shown in Figs. 8a and 8b, in both sequences the ADS st-1 via for fission products and aerosols to enter the DW is the dominant (98%) when compared to the DVI line one (2%). According to the sequence's evolution, the QT scrubbing effect affects roughly 45% of the total mass potentially entering the DW (almost 70 kg arrived once QT scrubbing was not effective anymore because water level falls below the injection point). As derived from the retention efficiency shown in Figs. 8c and 8d, in-QT pond absorbs around 70% of the incoming mass during the pool scrubbing period (roughly 55/60 kg arriving during that time). In other words, pool scrubbing affects less than half of the mass entering the DW.

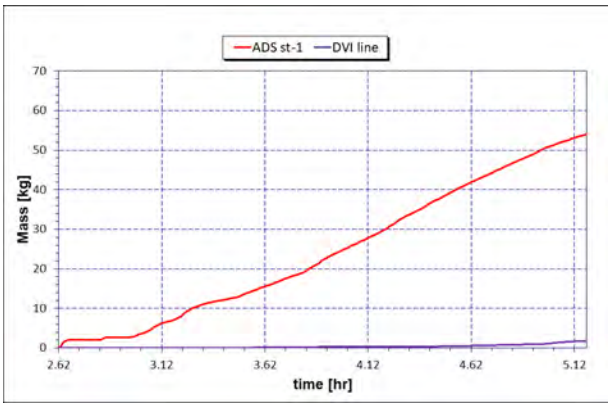

a) Mass of aerosols through the ADS st-1 and DVI lines (SA3)

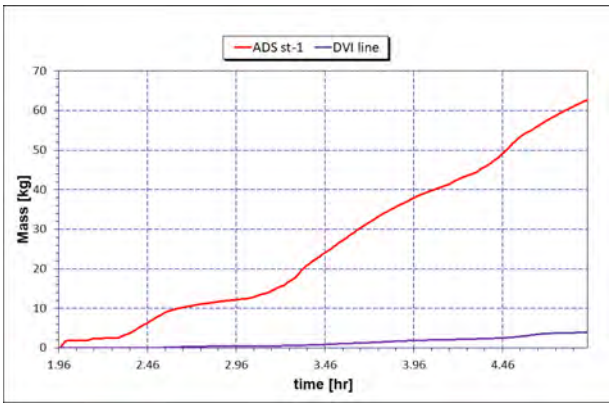

b) Mass of aerosols through the ADS st-1 and DVI lines (SA2*)

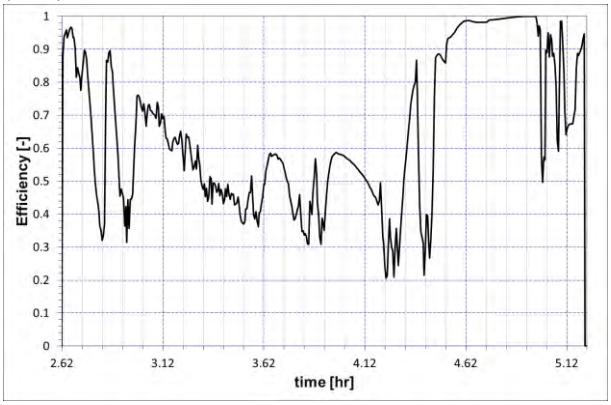

c) QT pool retention efficiency (SA3)

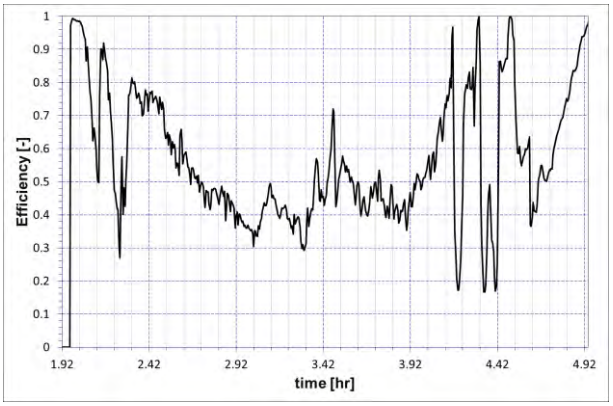

d) QT pool retention efficiency (SA2*)

Figure 8. DW results.

4. CONCLUSIONS

The effect of pool scrubbing on the potential source term to the environment has been investigated with the MELCOR code. The analysis of several postulated scenarios indicates that scrubbing in water ponds might visibly affect the eventual source term coming to the environment, although its quantitative effect is not massive (a reduction factor less than a factor 2.0).

Some specific conclusions might be withdrawn from the study:

- MELCOR 2.2 modelling capability can cope with the conditions addressed in the scenarios studied, although some missing models in the code (i.e., jet injection regime) might exacerbate the code deviations in the scenarios analyzed.
- The FPs bypass of the PSP in SA3 and SA2* is highly dependent on the reactor design (flow reversal). Different pressure settings for containment performance might turn the system in an efficient FP trap; this might be also so if a FCVS was installed.
- A high-pressure scenario, SA3 and SA2*, entails FP scrubbing in the QT of the reactor pressurizer. Despite unfavorable thermal conditions for pool scrubbing in the QT, in-QT pool scrubbing is estimated to substantially reduce the mass entering the DW from the PZR. All in all, in-QT scrubbing results in a mild impact on the source term to the environment (a reduction of about 30%).
- Given the containment early failure, FPs would have the chance to escape into the environment after little more than 2 h.

- In terms of particle sizes, though, the submicron particles predicted to be released to the environment would not show any major change.

NOMENCLATURE

ADS	Automatic Depressurization System	MMD	Mass Median Diameter
CV	Control Volume	NG	Noble Gas
CRDM	Control Rod Drive Mechanism	PSP	Pressure Suppression Pool
DC	Downcomer	PCS	Primary Containment System
DVI	Direct Vessel Injection	PRZ	Pressurizer
DW	Drywell	PSS	Pressure Suppression System
EBT	Emergency Borated Tank	QT	Quench Tank
EHRS	Emergengy Heat Removal System	RCS	Reactor Containment System
FA	Fuel Assembly	RPV	Reactor Pressure Vessel
FCVS	Filtered Containment Venting System	RWST	Refueling Water Storage Tank
FL	Flow Path	SA	Severe Accident
FP	Fission Product	SG	Steam Generator
iPWR	Integral Pressurized Water Reactor	SS	Safety System
LGMS	Long Gravity Make-up System	TH	Thermal-Hydraulic
LOCA	Loss Of Coolant Accident	UP	Upper Plenum
LP	Lower Plenum	WC-SMR	Water Cooled SMR

ACKNOWLEDGMENTS

Funded by the European Union

Funded by the European Union. Views and opinions expressed are however those of the author(s) only and do not necessarily reflect those of the European Union or European Commission-Euratom. Neither the European Union nor the granting authority can be held responsible for them.

REFERENCES

[1] L. E. Herranz, “Pool scrubbing in unit 1 of fukushima daiichi,” *Annals of Nuclear Energy*, vol. 183, p. 109637, Apr. 2023, doi: 10.1016/j.anucene.2022.109637.

[2] L. E. Herranz, F. Sánchez, and S. Gupta, “Validation Matrix for Pool Scrubbing Models,” *Nuclear Technology*, vol. 0, no. 0, pp. 1–14, Nov. 2022, doi: 10.1080/00295450.2022.2122679.

[3] K. Kischer and W. Häfner, “Modellierung von Abscheidungsvorgängen in Wasservorlagen –Modelling of retention processes in water pools,” Battelle Ingenieurtechnik GmbH, Eschborn, Abschlußbericht/Final Report BF-R68.411-1, 1998.

[4] L. E. Herranz, C. Lopez, and J. Penalva, “Investigation on jet scrubbing in nuclear reactor accidents: From experimental data to an empirical correlation,” *Progress in Nuclear Energy*, vol. 107, pp. 72–82, Aug. 2018, doi: 10.1016/j.pnucene.2018.04.019.

[5] M. Swiderska-kowalczyk, M. Escudero-Berzal, M. Marcos-Crespo, M. Martin-Espigares, and J. Lopez-Jimenez, “State-of-the-art review on fission product aerosol pool scrubbing under severe accident conditions,” in *Institute of Nuclear Chemistry and Technology annual report 1995*, 1996, pp. 48–48. Available: https://inis.iaea.org/records/2zkgh-d1y09

[6] M. R. Kuhlman, J. A. Gieseke, M. Merilo, and R. Oehlberg, “Scrubbing of fission product aerosols in LWR water pools under severe accident conditions,” in *Source term evaluation for accident conditions*, 1986, pp. 633–648. Available: https://inis.iaea.org/records/0ck14-1n536

[7] S. Gupta *et al.*, “Integration of pool scrubbing research to enhance Source-Term calculations (IPRESCA) project – Overview and first results,” *Nuclear Engineering and Design*, vol. 404, p. 112189, Apr. 2023, doi: 10.1016/j.nucengdes.2023.112189.

[8] F. Gabrielli *et al.*, “Analysis of postulated severe accidents in generic integral PWR small modular reactors in the frame of the Horizon Euratom SASPAM-SA project,” presented at the The 11th European Review Meeting on Severe Accident Research (ERMSAR2024), KTH, Stockholm,Sweden, May 2024.
[9] L. L. Humphries *et al.*, “MELCOR Computer Code Manuals Vol. 2: Reference Manual Version 2.2.18019,” SAND2021-0241 O, Jan. 2021.
[10] L. L. Humphries *et al.*, “MELCOR Computer Code Manuals Vol. 1: Primer and Users’ Guide Version 2.2.19018,” SAND2021-0252 O, Jan. 2021.
[11] F. Gabrielli *et al.*, “Analysis of postulated severe accidents in generic integral PWR small modular reactors in the frame of the Horizon EURATOM SASPAM-SA project,” presented at the ERMSAR2024, 2024.
[12] M. D. Carelli *et al.*, “The design and safety features of the IRIS reactor,” *Nuclear Engineering and Design*, vol. 230, no. 1, pp. 151–167, May 2004, doi: 10.1016/j.nucengdes.2003.11.022.
[13] M. Imperatori, F. Giannetti, and M. D’Onorio, “DESIGN 2 MELCOR input deck description document - DRAFT,” Nuclear Engineering Research Gropu, SAPIENZA Universitá di Roma, Dec. 2022.
[14] U.S. Nuclear Regulatory Commission, “Accident Source Terms for Light-Water Nuclear Power Plants,” U.S.N.R.C., NUREG-1465, Feb. 1995. Available: https://www.nrc.gov/reading-rm/doc-collections/nuregs/staff/sr1465/index
[15] P. C. Owczarski and K. W. Burk, “SPARC-90: A code for calculating fission product capture in suppression pools,” US Nuclear Regulatory Commission (NRC), Washington, DC (United States). Div. of Regulatory Applications; Pacific Northwest National Lab. (PNNL), Richland, WA (United States), NUREG/CR-5765; PNL-7723, Oct. 1991. doi: 10.2172/6120360.

GOBIERNO DE ESPAÑA
MINISTERIO DE CIENCIA, INNOVACIÓN Y UNIVERSIDADES

Ciemat
Centro de Investigaciones Energéticas, Medioambientales y Tecnológicas

Pool Scrubbing in WC-SMRs: Scenarios, Peculiarities and Challenges

Luis E. Herranz*, M. Garcia, T. Lugo

*luisen.herranz@ciemat.es
Unit of Nuclear Safety Reseach
Departament of Nuclear Fission
CIEMAT

12th European Review Meeting on Severe Accident Research (ERMSAR2026)
May 18-22, 2026, Madrid, Spain

Contents

01 Introduction

02 Study Approach

03 Results

04 Conclusions

GOBIERNO DE ESPAÑA
MINISTERIO DE CIENCIA, INNOVACIÓN Y UNIVERSIDADES

Ciemat
Centro de Investigaciones Energéticas, Medioambientales y Tecnológicas

01

Introduction

Framework

The International Context

- The H-2020 **SASPAM-SA** project

Coordinated by **ENEA**

- **Objective**
  - Investigation of the effect of pool scrubbing on ST in iPWRs.

- **Plant model** (Original deck from UNIROMA/ENEA)
  - Generic iPWR (300 MWe).
  - Dry spherical containment.
  - Passive safety systems.

Study Approach

Plant Overview

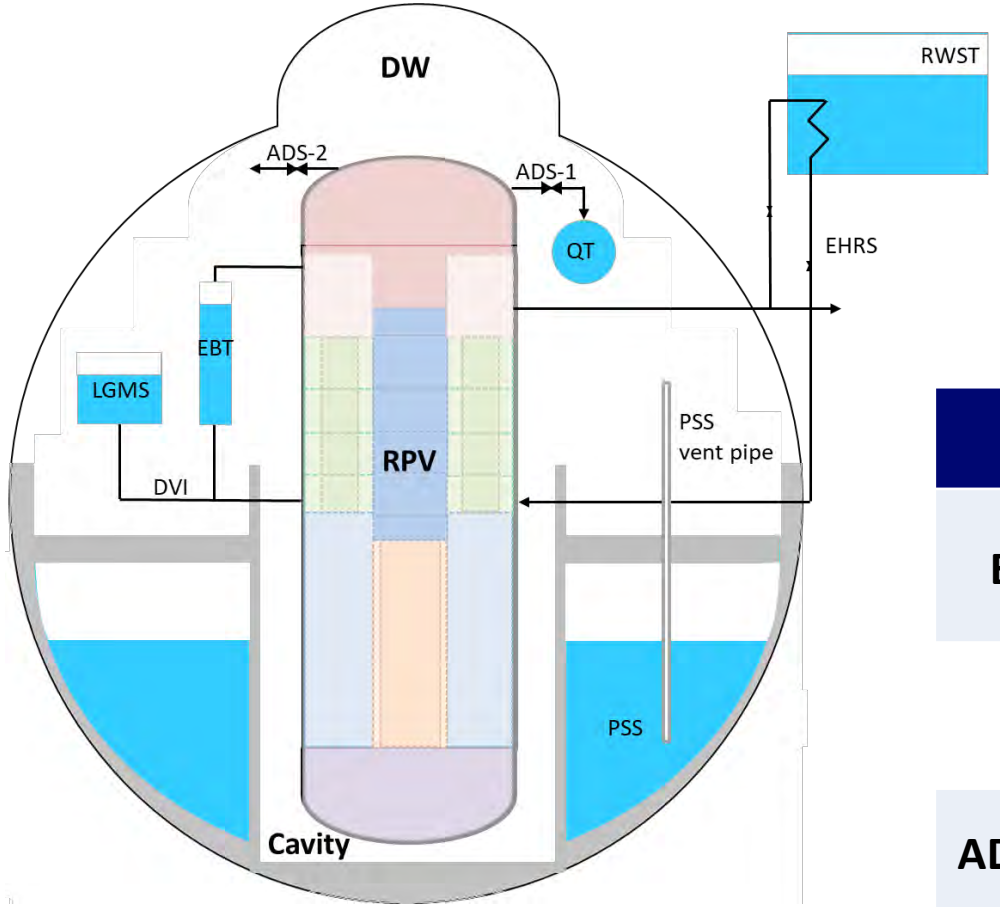

SS	#	Actuation	Function	Connections
EHRS	2	High DW P Low PRZ P Low PRZ level	DCH removal	RPV/RWST
EBT	2	Low PRZ P	HP injection	UP/EBT EBT/DC
ADS st-1	3	Low PRZ P	Automatic DPZ	PRZ/QT
ADS st-2	2	Low LGMS mass	RPV P relief	PRZ/DW
LGMS	2	Small RPV/DW dP	LP injection	LGMS/DC

02

Study Approach

Code Evaluation Model

MELCOR 2.2.18019

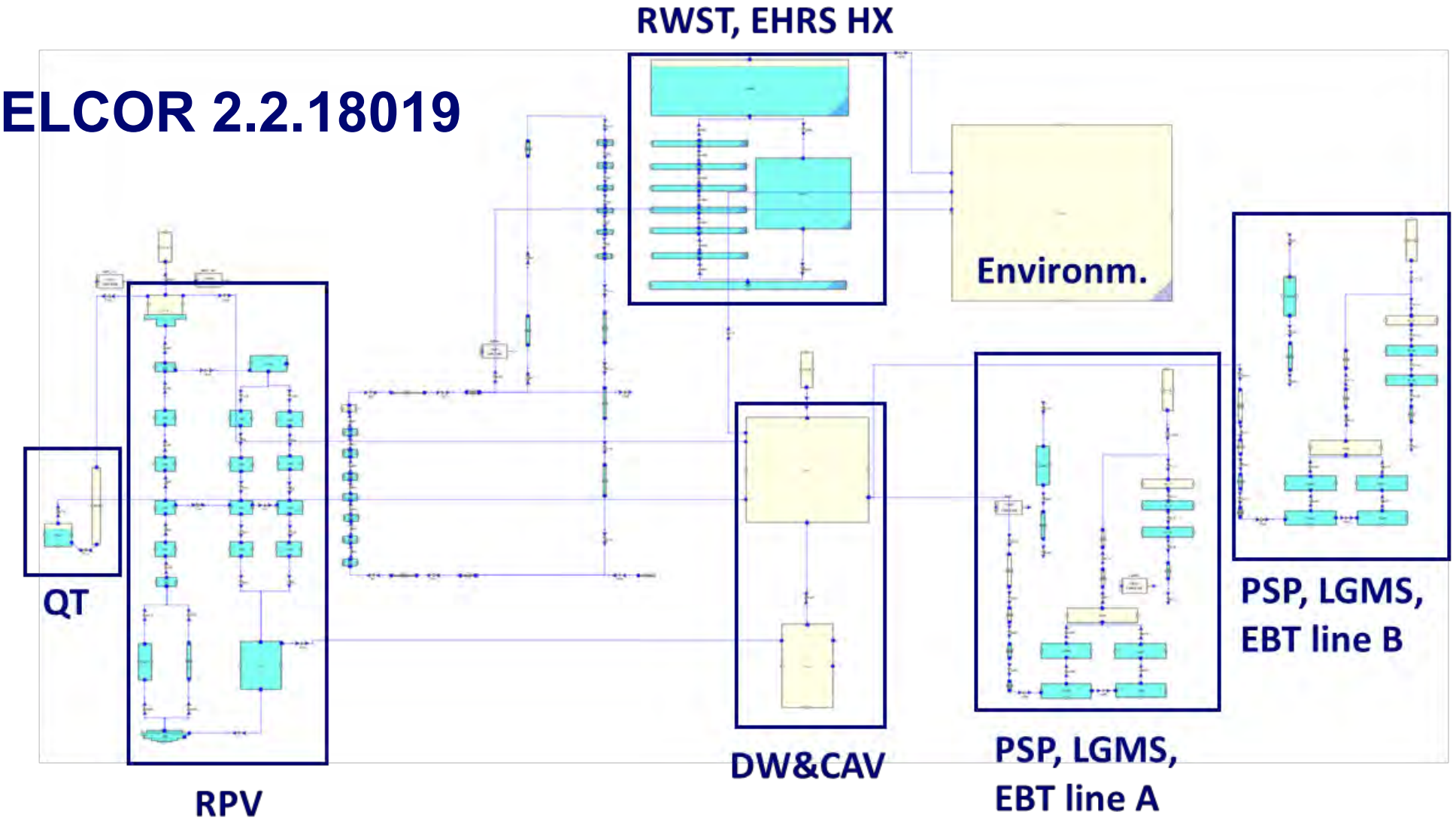

RPV: 20 CVs
Core: 6 radial rings, 16 axial nodes

Containment: 1 CV
NPP: 97 CVs, 112 FLs, 121 HSs, 206 CFs

Scrubbing Models

GOBIERNO DE ESPAÑA
MINISTERIO DE CIENCIA, INNOVACIÓN Y UNIVERSIDADES
Ciemat
Centro de Investigaciones Energéticas, Medioambientales y Tecnológicas

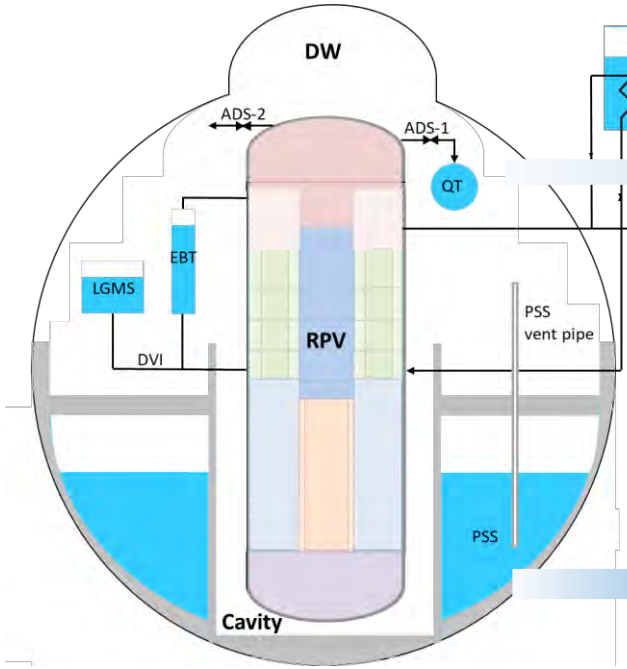

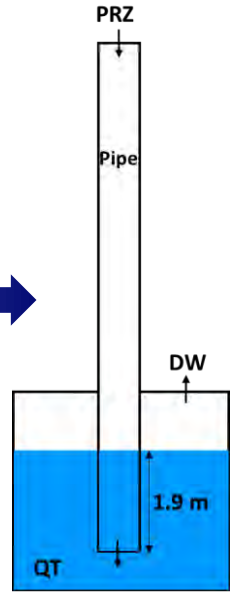

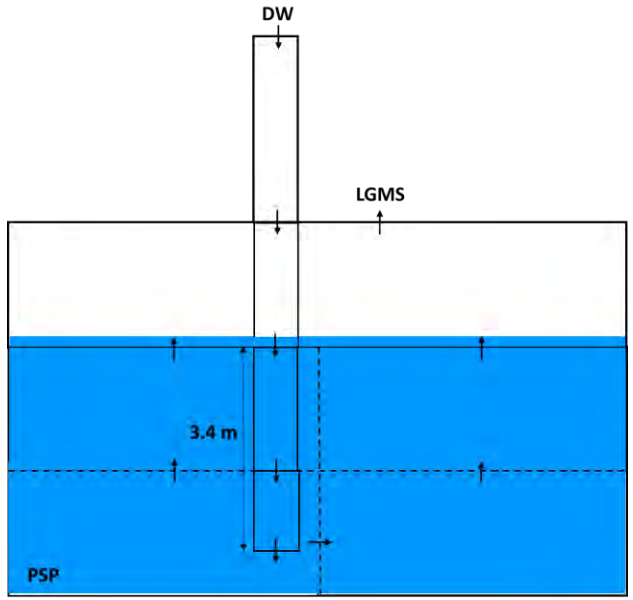

QT-TH nodalization

- 1CV (33.6 m^3)
- Multi-hole quencher
- 800 holes ($7.85 \cdot 10^{-5}$ m^2 each)
- Initial submergence ~ 2.0 m

PSS-TH nodalization

- 5 CVs (459 m^3)
- Quencher
- 1 hole ($6.3 \cdot 10^{-2}$ m^2)
- Initial submergence ~ 3.4 m

03

Results

Pool Scrubbing Scenarios

Initiating event
Small LOCA in a Direct Vessel Injection (DVI) line

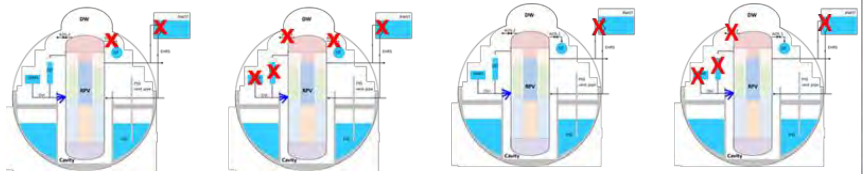

Key Event (h)	SA1	SA2	SA3	SA2*
Start of the transient	0	0	0	0
Scram time	0.01	0.01	0.01	0.01
ADS-st1 activation	-	-	0.05	0.05
LGMS activation	12.42	-	67.50	-
ADS-st2 activation	-	-	68.19	-
Time core uncovers	0.17	0.47	0.06	0.06
Containment failure	1.29	1.69	0.50	0.48
Reverse flow from the PSP	1.29-1.59	1.69-1.89	0.55-0.84	0.48-0.85
H_2 production onset	3.50	2.61	2.56	1.91
Gap release	3.50	2.60	2.62	1.97
Time of vessel failure	-	-	-	-

RPV P

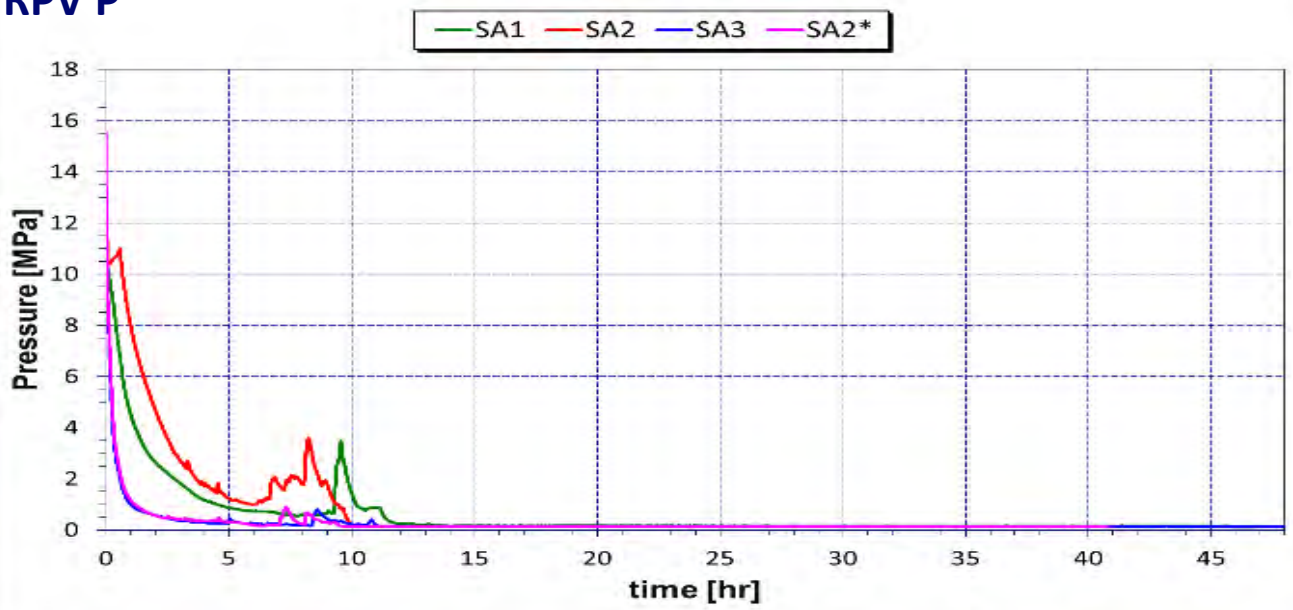

Max. Cladding T

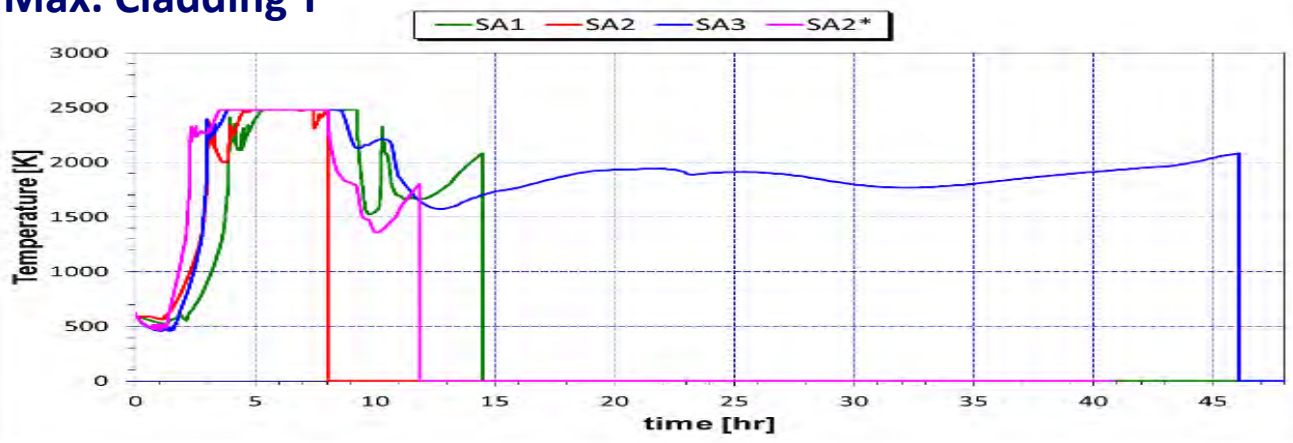

Results

Pool Scrubbing Scenarios

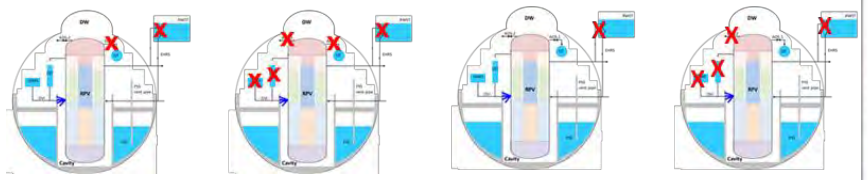

Key Event (h)	SA1	SA2	SA3	SA2*
Start of the transient	0	0	0	0
Scram time	0.01	0.01	0.01	0.01
ADS-st1 activation	-	-	0.05	0.05
LGMS activation	12.42	-	67.50	-
ADS-st2 activation	-	-	68.19	-
Time core uncovers	0.17	0.47	0.06	0.06
Containment failure	1.29	1.69	0.50	0.48
Reverse flow from the PSP	1.29-1.59	1.69-1.89	0.55-0.84	0.48-0.85
H_2 production onset	3.50	2.61	2.56	1.91
Gap release	3.50	2.60	2.62	1.97
Time of vessel failure	-	-	-	-

RPV P

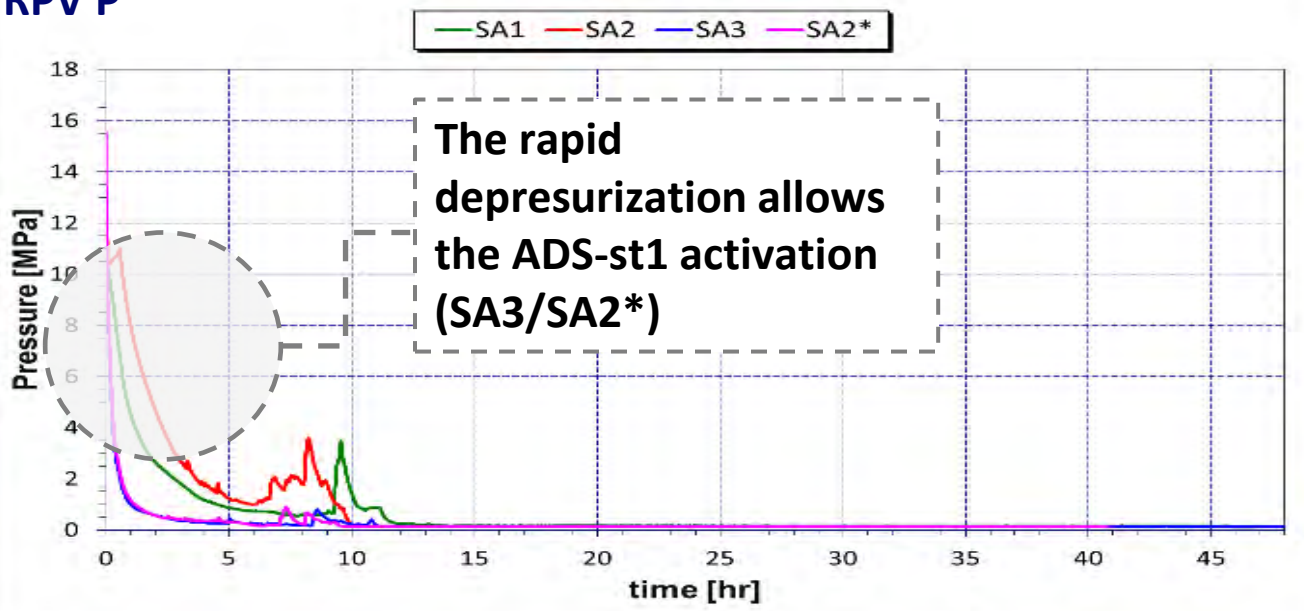

Max. Cladding T

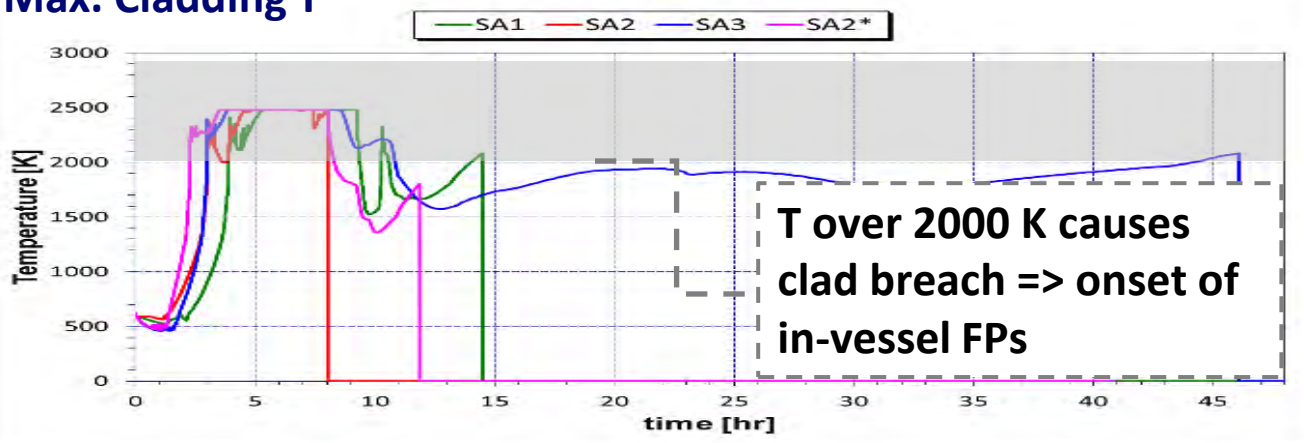

Results

Major Results: Water level

PSP

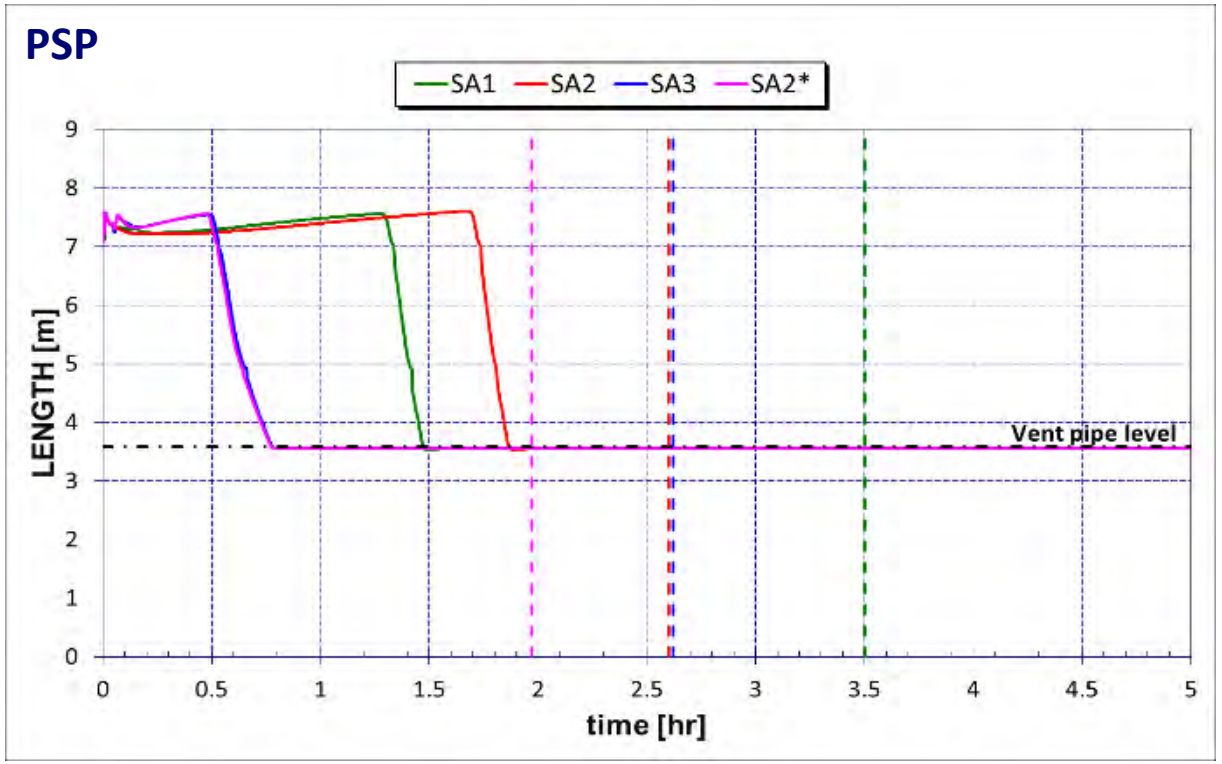

QT

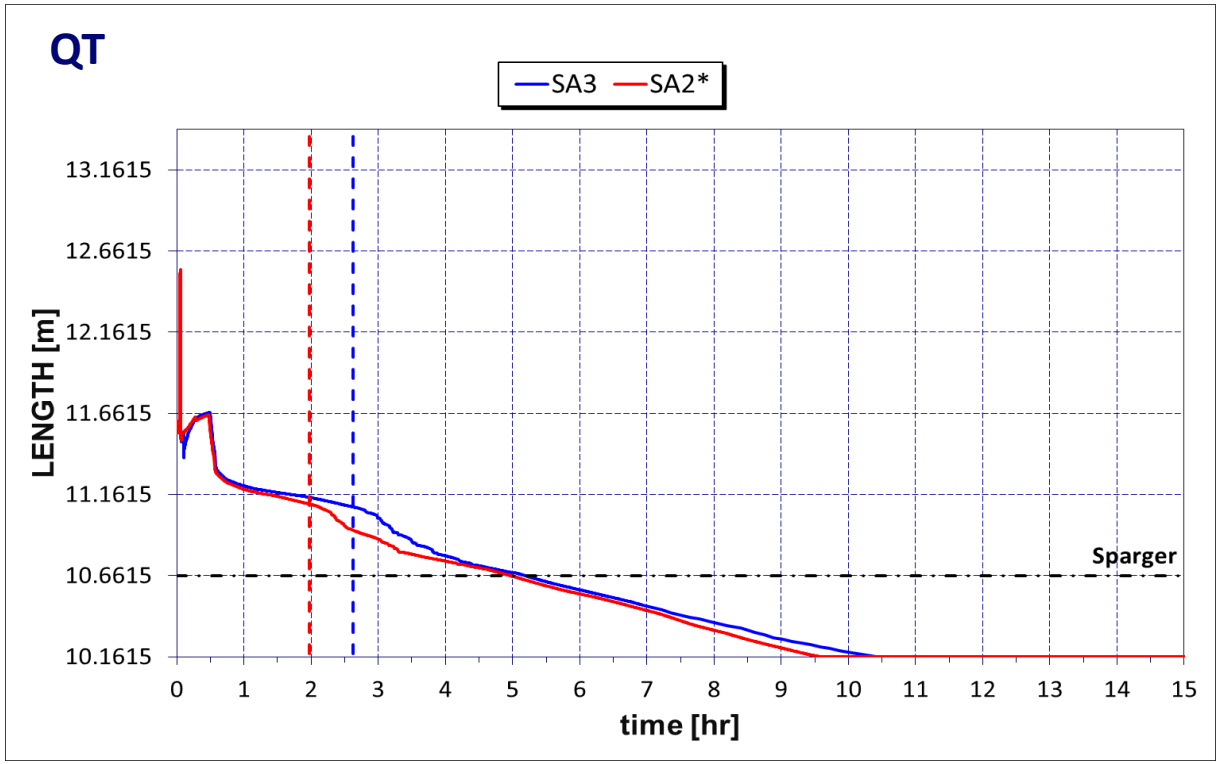

Major Results: Water level

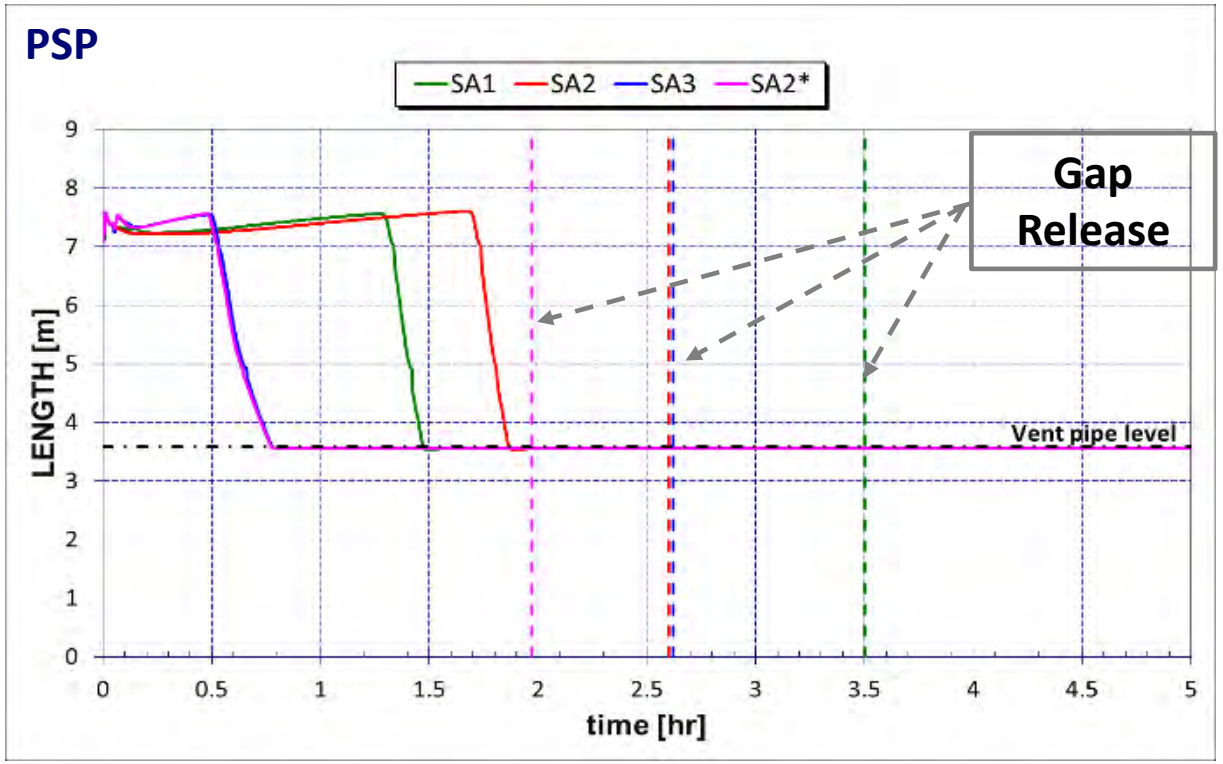

- No scrubbing in the PSP in all the sequences.

Major Results: Water level

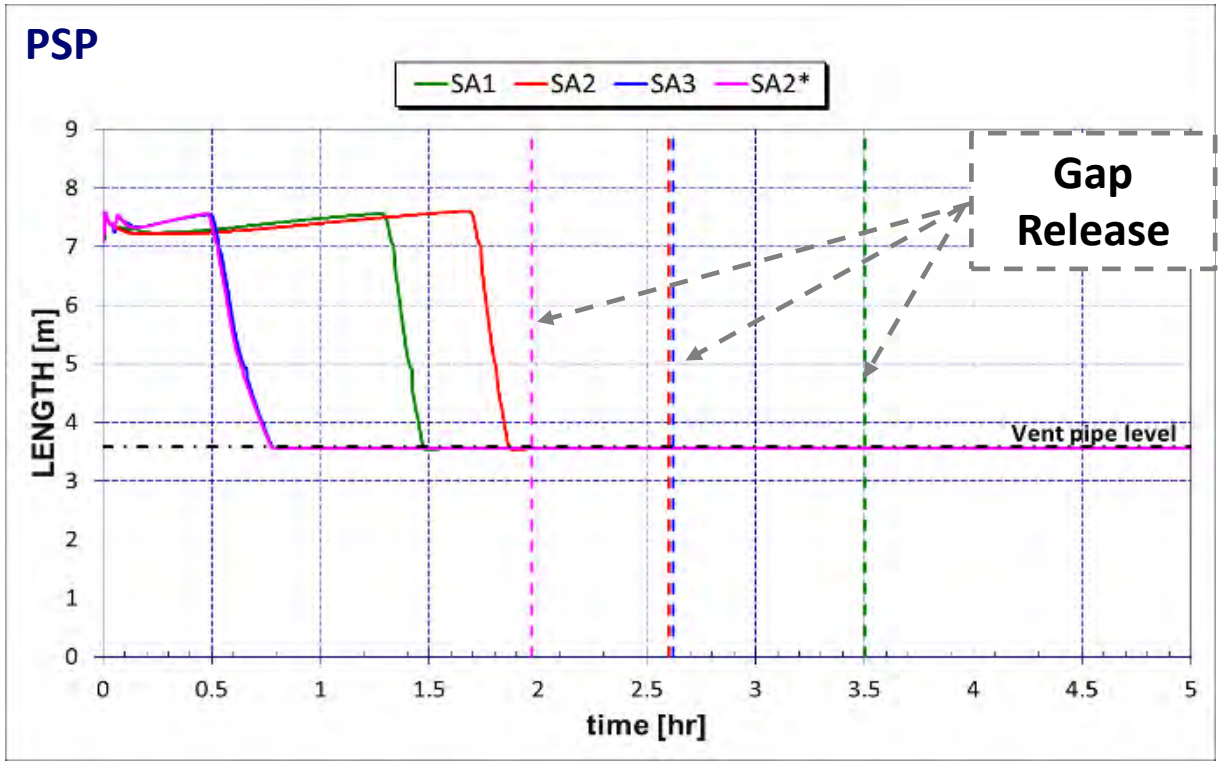

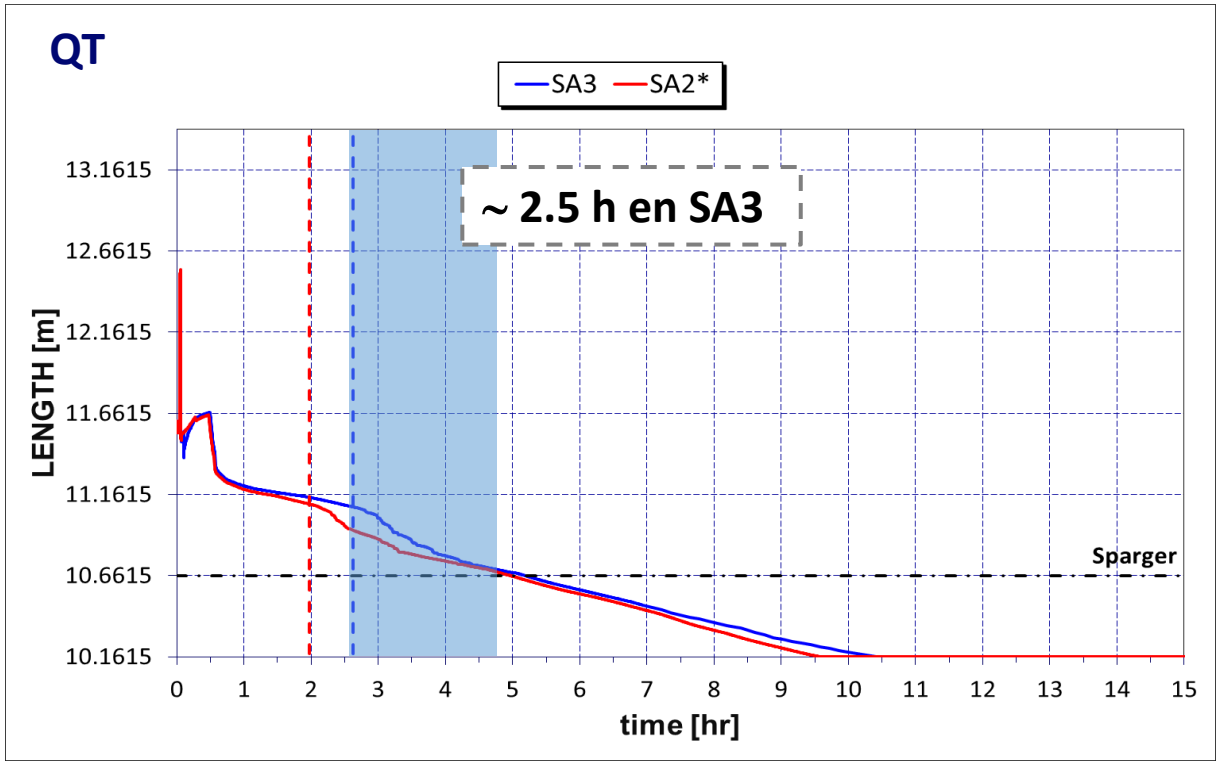

- No scrubbing in the PSP in all the sequences.
- In-QT scrubbing during some temporary window (SA3, SA2*).

Major Results: Water level

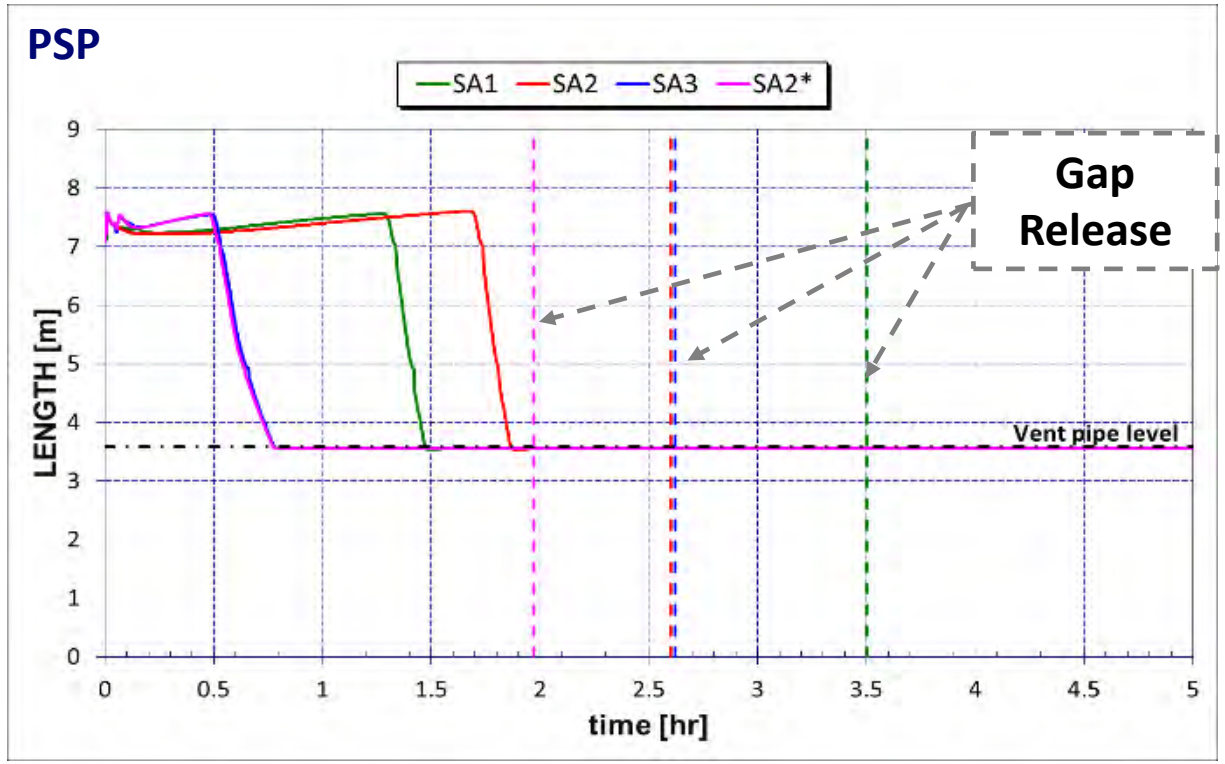

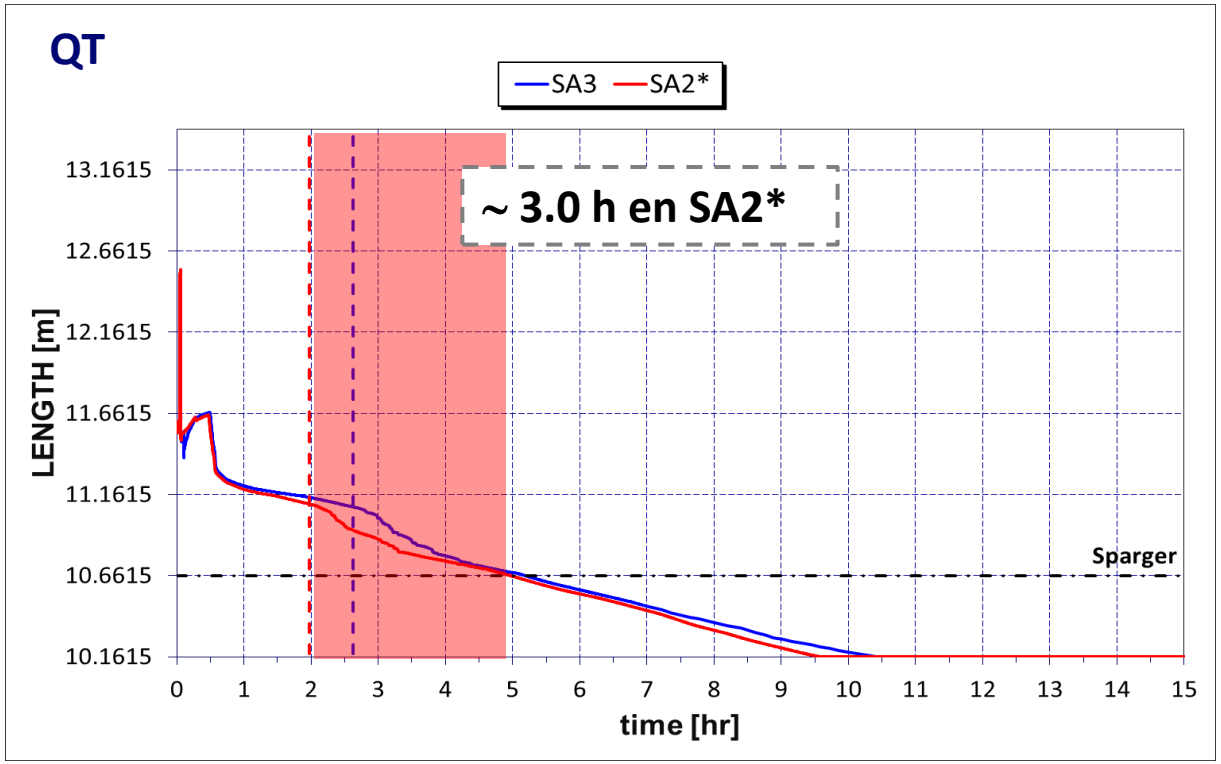

- No scrubbing in the PSP in all the sequences.
- In-QT scrubbing during some temporary window (SA3, SA2*).

Major Results: Scrubbing BCs

Variable	Min value	Max. value
Atmosphere P in the QT (MPa)	0.11	0.17
Pool T (K)	372	389
Inlet gas T (K)	527	1040
Inlet gas H_2O_{vap} content (mole fraction)	0.66	0.99
Inlet gas H_2 content (mole fraction)	0.005	0.336
We number	$1.01 \cdot 10^9$	$3.22 \cdot 10^9$

- Atmospheric P in the QT.
- Water close to T_{sat} most of the time.
- Carrier gas composed mainly by steam.
- H_2 mole fraction up to 30% just at some intervals.
- Jet regime ($We \geq 10^9$).

Major Results: Source Term

Inlet & outlet aerosol MMD in/from the QT

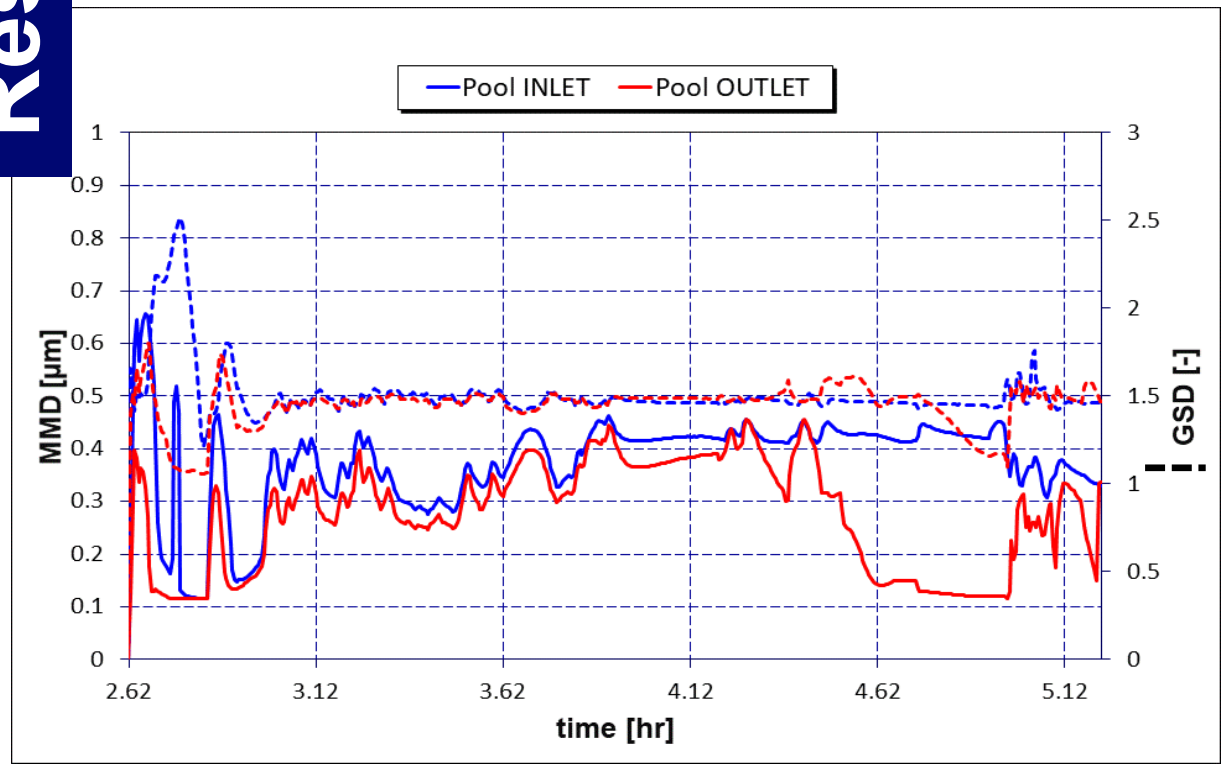

- MMD∈[0.1-1.0] (μm)
- Noticiable size reduction at both the begining and end of time interval.

Major Results: Source Term

Inlet & outlet aerosol MMD in/from the QT

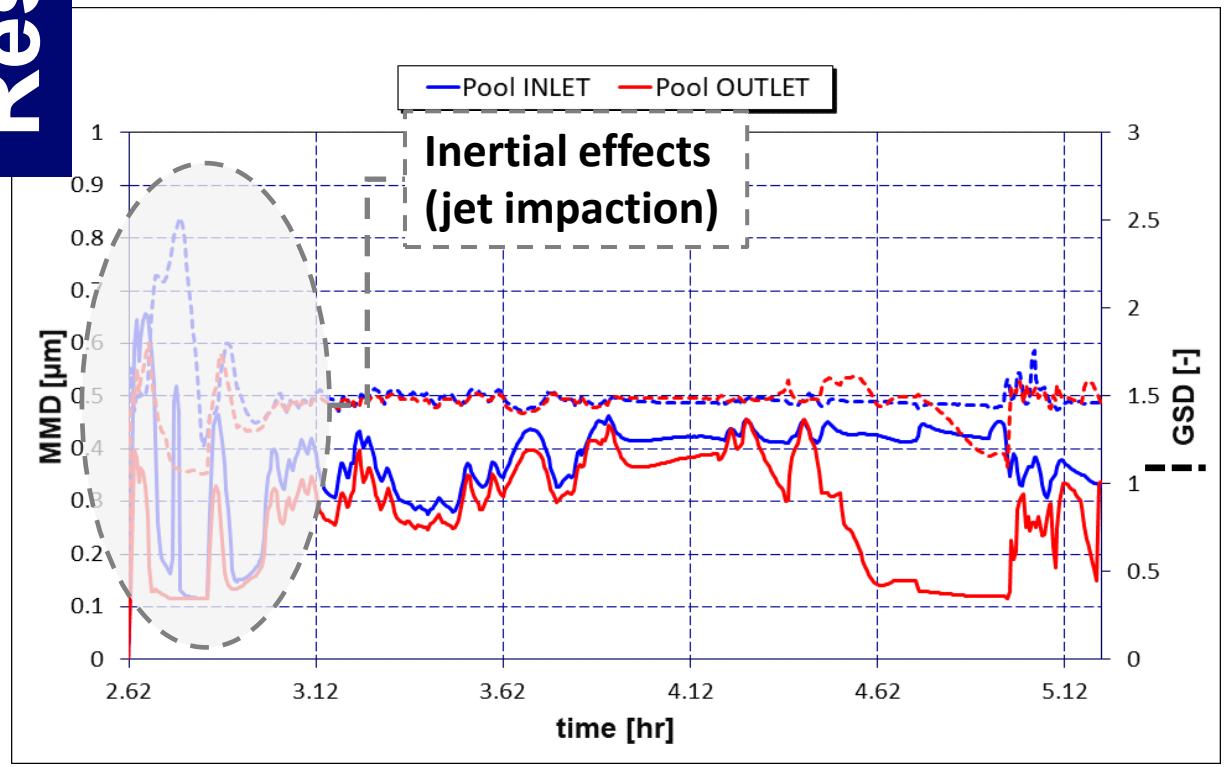

- MMD∈[0.1-1.0] (μm)
- Noticiable size reduction at both the begining and end of time interval.

Major Results: Source Term

Inlet & outlet aerosol MMD in/from the QT

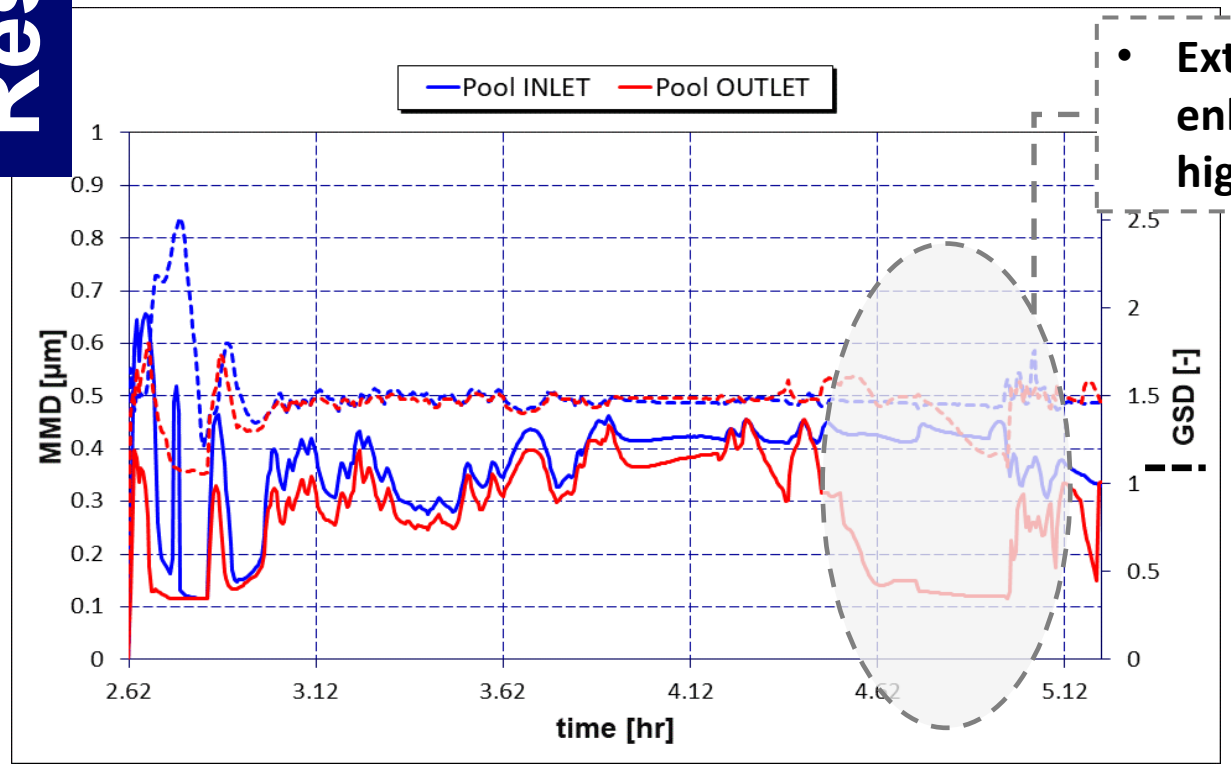

- **Extension of bubbles residence time => enlargement of the bubble exchange surface => higher decontamination (centrifugal deposition)**

- MMD∈[0.1-1.0] (µm)
- Noticiable size reduction at both the begining and end of time Interval by pool scrubbing (up to a factor of 4.0).

Major Results: Source Term

Inlet & outlet aerosol MMD in/from the QT

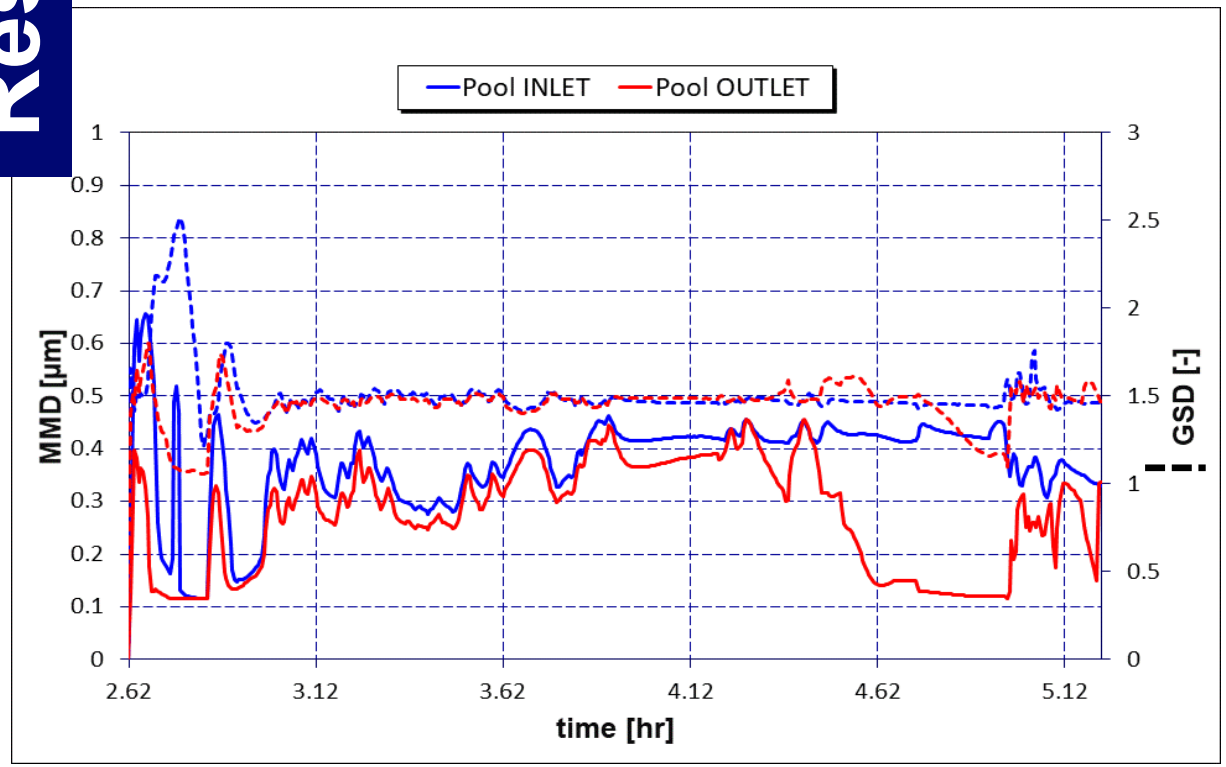

- MMD∈[0.1-1.0] (μm)
- Noticiable size reduction at both the begining and end of time interval.

- QT scrubbing effect affects ~ 45 % of total mass entering the DW.
- In-QT pool absorbs ~ 70% of the incoming mass.

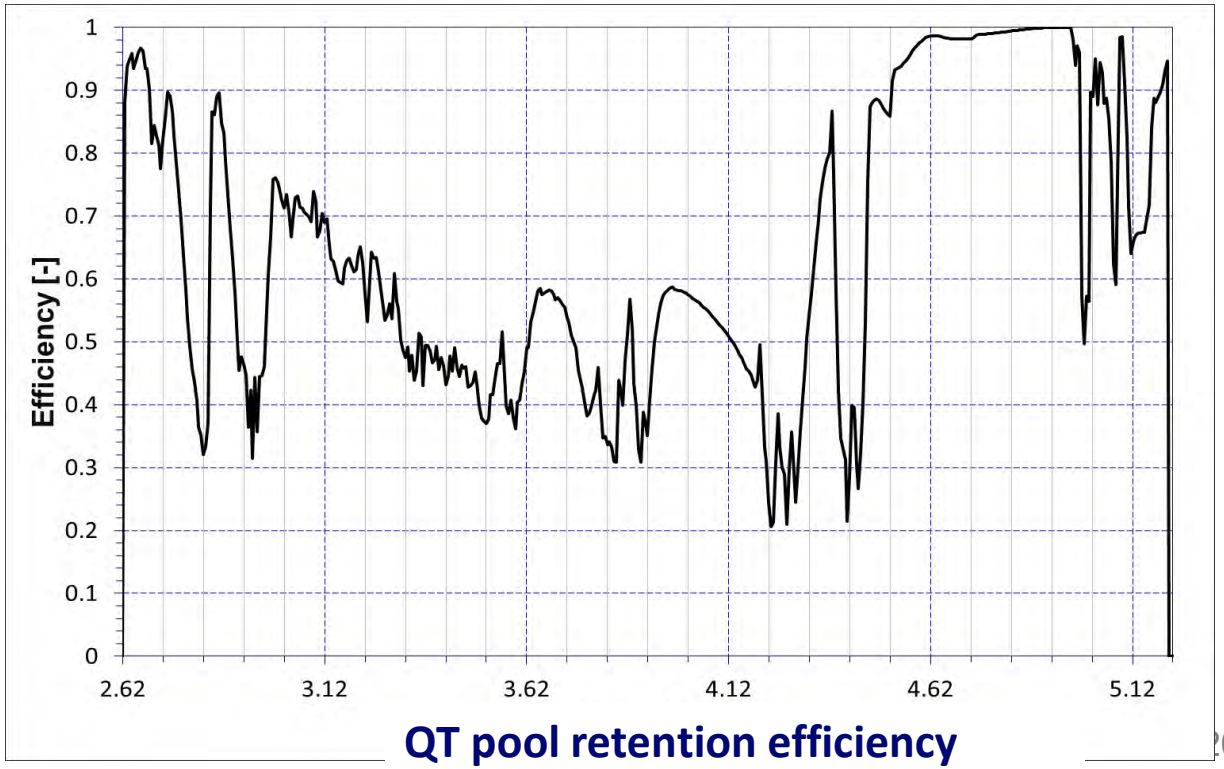

QT pool retention efficiency

04

Conclusions

Main Insights

- MELCOR 2.2 can simulate accident scenarios in iPWRs.
- In the analysed sequences, FPs bypassed the PSP pool due to flow reversal (direct connection to containment design).
- High pressure scenarios with ADS-st1 activated involves significant scrubbing in the quench tank.
- In terms of Source Term to the environment, in-QT scrubbing might mean a reduction of up to 30%.

Thank you for your attention!

Unit of Nuclear Safety Research
Department of Nuclear Fission
CIEMAT
luisen.herranz@ciemat.es

MAAP6 MODEL IMPLEMENTATION OF SUPPRESSION POOL AEROSOL SCRUBBING

Autumn Crisafulli, Paul McMinn, Michael Epstein
Fauske and Associates
16W070 83rd St, Burr Ridge, IL 60527
Crisafulli@fauske.com; McMinn@fauske.com; Epstein@fauske.com

Matthew Nudi
Electric Power Research Institute
1300 West WT Harris Blvd | Charlotte NC 28262-2867
MNudi@epri.com

ABSTRACT

Accurate predictions of aerosol removal via pool scrubbing is critical for evaluating source term behavior during severe accident analysis in light water reactors. Sequences such as BWR suppression pool scrubbing, filtered containment venting systems (FCVS), and PWR steam generator tube rupture (SGTR), inject fission product laden gas into water pools. Aerosol particles are removed in the pool via inertial impaction, condensation driven capture, and bubble rise deposition.

This work presents recent development and benchmarking of the pool scrubbing model implemented in the MAAP6 severe accident code. The model calculates the overall decontamination factor (DF) as the product of three independent contributions: (1) injection zone scrubbing, which includes jet entrainment and orifice driven capture, (2) condensation zone scrubbing, based on diffusiophoresis, and (3) bubble rise zone scrubbing, accounting for Brownian motion, gravitational settling, and bubble breakup dynamics.

The MAAP6 model implementation has been compared and validated against experimental results, from tests spanning jet injection and bubble rise regimes. Results demonstrate the MAAP6 pool scrubbing model captures observed DF trends across multiple flow conditions, providing improvements over previous empirical formulations.

KEYWORDS
Suppression pool scrubbing, aerosol decontamination factor, bubble rise, gas jetting, MAAP6

1.0 INTRODUCTION

The Modular Accident Analysis Program version 6 (MAAP6) is a severe accident systems code being developed by the Electric Power Research Institute (EPRI). This paper describes a new model developed to calculate pool scrubbing of aerosols. The new model replaces simplified aerosol scrubbing calculations in previous versions of the MAAP code which were based on lookup tables based on the results calculated by the SUPRA code.

The decontamination capability of a pool depends mainly on the behavior of the fission-product-containing-gas bubbles as they form at and detach from multihole spargers, downcomer pipes or side vents and rise

through the pool. The expressions derived here for the decontamination factors (DF's) of the gaseous fission products and the fission product aerosols are based on modeling that results in explicit, algebraic forms. The fission products are carried by a mixture of steam and noncondensible gas of known molecular weight. The components of the noncondensible gas may include hydrogen, carbon dioxide, carbon monoxide, and/or nitrogen.

In developing the models for the fission product DF's, it is convenient to divide the pool into three zones. These zones are (including the key modeling assumptions):

1. Injection Zone: At low gas discharge rates single bubbles grow and detach periodically from the discharge orifice. During bubble growth aerosol particles deposit on the bubble surface by centrifugal force and inertia. All other mechanisms of deposition are neglected. At high gas discharge rates, gas jets are formed at the orifice, and the principal mechanism of aerosol depletion is aerosol inertial deposition upon entrained liquid drops.

2. Condensation Zone: Particle removal by steam condensation, diffusiophoresis and thermophoresis is assumed to occur immediately after the bubble detaches from the orifice (or jet) and before it breaks up until a stable bubble size is reached. Therefore, the thickness of the condensation zone is small on the scale of the pool depth. The stable size bubble is assumed to be in thermodynamic equilibrium with the surrounding pool. Heat and mass transfer analogies are used to estimate particle removal by diffusiophoresis and thermophoresis during the bubble's approach to equilibrium. The experimental conditions presented in this paper have low steam content in the carrier gas such that the contributions of the condensation zone are relatively small. Thus, overall aerosol removal tends to be dominated by injection/jetting and bubble rise regimes. However, follow on work is planned to analyze experiments with higher steam content.

3. Bubble Rise Zone: Following injection and initial gas cooling and condensation near the pool surface, gas bubbles detach and rise through the surrounding liquid as a buoyant plume. The plume buoyancy is due only to the noncondensible gas contained in the bubbles. The large detachment bubble is mechanically unstable and undergoes breakup until a stable distribution of many smaller bubbles is reached some distance above the discharge orifice. Fission product scrubbing is assumed to be negligible in the bubble breakup zone and is therefore not treated as a separate suppression pool zone. The small bubbles generated above the discharge orifice continue to rise through the pool. Removal of gaseous fission products from the bubbles occurs by in-series gas-side and liquid-side-controlled convective diffusion, while aerosol particle scrubbing within the rising bubbles occurs by sedimentation, centrifugal force, and Brownian motion. In hot pools there is a significant increase in the size of a rising bubble because of the reduction in the hydrostatic pressure and concomitant water evaporation into the bubble. The bubble grows beyond its largest stable size and breaks up. During breakup a portion of the bubble is converted into many small bubbles, thereby dividing the pool into two bubble rise zones: a lower zone with relatively large bubbles and an upper zone with smaller bubbles. The model to predict the break-up bubble size in the upper zone uses a critical Weber number and a characteristic velocity that is proportional to the turbulent energy dissipation rate generated by the rising bubble plume.

2.0 MODELING APPROACH

MAAP6 implements a regime dependent injection decontamination factor (DF) such that the discharge is treated as either bubble plume formation or jet discharge, based on a critical velocity comparison. The critical discharge of orifice gas velocity for jet formation is computed and compared to the actual orifice velocity obtained from continuity. Zhao and Irons [1] derived the semi-empirical expression for the critical discharge orifice gas velocity $u_{o,cr}$ for the formation of a gas jet, Eq. (1), where σ_f and ρ_f are the water pool surface tension and density, respectively, and d_o is the diameter of the orifice. From here, the model

determines if conditions correspond to a bubble plume path or if conditions correspond to a jet discharge path.

$$u_{o,cr} = 3.24 \left(\frac{\rho_f}{\rho_{g,o}}\right)^{1/4} \left(\frac{\sigma_f}{\rho_{g,o} d_o}\right)^{1/2} \quad (1)$$

If the actual orifice velocity is less than or equal to the critical velocity, the discharge is treated as a bubble plume. If the actual velocity exceeds the critical value, the discharge is treated as a gas jet.

2.1 Injection Zone Decontamination Factor

For a bubble plume path, the model calculates Stokes number from Eq. (2), where C is the aerosol particle slip correction factor, ρ_a density of dry aerosol material, d_a is the diameter of dry aerosol particle, g is gravity, $\dot{Q}_{g,o}$ is volumetric flow of gas mixture at discharge orifice and $\mu_{g,o}$ is the viscosity of gas mixture at discharge orifice.

$$St = 0.685 \frac{C\rho_a d_a^2 (g^2 \dot{Q}_{g,o})^{1/5}}{\mu_{g,o} d_o} \quad (2)$$

Then the efficiency of particle capture is calculated from Eq. (3) and the dimensionless parameter χ_o from Eq. (4). The position of the ε versus St curve for jet Reynolds number above 100 is relatively constant. Therefore, for practical applications just one efficiency curve may be considered to represent all efficiency curves. A typical circular jet impactor efficiency curve is shown in Figure 1 [2].

$$\varepsilon = 1 - \frac{1}{1 + \exp\left[\frac{St^{1/2} - 0.447}{0.0453}\right]} \quad (3)$$

Aerosol mass conservation in the forming bubble states that the rate of change of aerosol mass in the bubble is due to the inlet mass flow rate of aerosol minus the mass rates of aerosol deposition on the bubble surface due to inertial impaction and centrifugal force.

$$\chi_o = \frac{19.67\, C\rho_a d_a^2 (\dot{Q}_{g,o}^3 g)^{1/5}}{d_o^2 \mu_{g,o}} \quad (4)$$

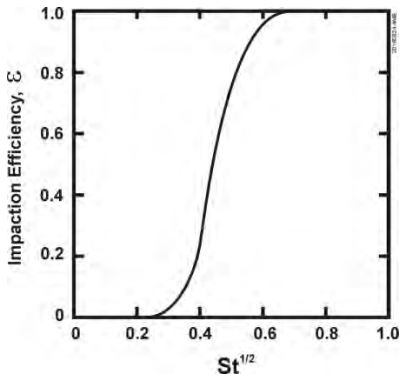

Figure 1 Jet Impactor Efficiency Curve

In MAAP6, this bubble plume injection calculation is implemented directly through the fitted efficiency expression and the closed form DF_{fb} expression using St, ε, and χ_o, with particle slip correction included

through C. The resulting expression for the bubble decontamination factor at detachment is shown in Eq. (5).

$$DF_{fb} = \frac{\chi_o^3}{3(1-\varepsilon)[\chi_o^2 - 2\chi_o + 2(1-e^{-\chi_o})]} \quad (5)$$

As mentioned previously, above a critical injector gas velocity there is a transition from the bubbly flow regime to the gas jetting regime. MAAP6 model implements compressible discharge handling using stagnation pressure logic and critical stagnation pressure check. When choked or under expanded flow conditions occur, the model is solved for expansion region outlet conditions using momentum and mass conservation, which yields an effective jet velocity and an effective jet diameter prior to aerosol removal calculations.

The entrainment and atomization of the liquid within the jet is postulated to be complete when the jet velocity u falls below the gas velocity required for droplet formation from capillary wave growth on the liquid surface. The available experimental data on air flowing over a horizontal liquid surface, [4], shows that a minimum gas velocity is required for atomization of the liquid by the gas flow. A constant drop size is selected based on the pneumatic atomization of the entrained liquid in the immediate vicinity of the injector. Finally, the in-jet aerosol decontamination factor DF_j is calculated using Eq. (6).

$$DF_j = \exp\left[\beta\left(\frac{1}{S} + \frac{1}{S^2}\ln\frac{S+\frac{u_{atm}}{u_o}}{\frac{(1+S)\,u_{atm}}{u_o}} - \frac{1+S}{S\left(S+\frac{u_{atm}}{u_o}\right)}\right)\right] \quad (6)$$

Where S is an inverse Stokes number, β is defined by Eq. (7), u_{atm} is the gas velocity above which liquid (water) atomization occurs, and u_o is the gas mixture velocity at discharge orifice. Though, before Eq. (6) can be used, expressions are needed to estimate the effective droplet velocity lag constant, f, and the effective droplet diameter d_f. In MAAP6, f is either treated as a constant or solved iteratively depending on user input settings.

$$\beta = \frac{3fd_o}{8E_o(1-f)d_f}\left(\frac{\rho_{g,o}}{\rho_f}\right)^{3/2} \quad (7)$$

Where ρ_f is density of pool water and E_o is the empirical entrainment coefficient (0.08 for jet; 0.12 for bubble plume).

2.2 Condensation Zone Decontamination Factor

MAAP6 implemented the condensation zone DF to account for steam condensation and resulting gas composition changes as the plume rises.

Thermophoretic transport coefficient, K_T, is determined including mean free path and slip effects. The model then computes equilibrium inert fraction and two alternate condensation DFs, bubble volume reduction and bubble mass reduction, then conservatively selects the smaller. Though, diffusiophoresis has a modifying effect on the condensation induced particle deposition velocity and DF_{con} must be adjusted to account for this. Therefore, DF_{cz}, total condensation zone DF, is determined with the dimensionless diffusiophoretic particle transport coefficient, K_D, fluid Prandtl number, and temperature ratio effects. In MAAP6 the fluid Prandtl number used for DF_{cz} is evaluated using the gas properties at pool temperature.

$$DF_{cz} = (DF_{con})^{K_D} \left[\frac{1 - (K_T Pr)^{\frac{1.25 T_0}{T_f}}}{1 - (K_T Pr)^{1.25}} \right] \quad (8)$$

2.3 Bubble Rise Zone Decontamination Factor

The MAAP6 model also calculates the decontamination factor in the bubble rise zone with explicit capture mechanisms during rise, including inertial capture, gravitational settling, and Brownian diffusion. The model first determines bubble rise velocities and transition behavior using the terminal velocity and bubble rise absolute velocity that depend on the volumetric inert gas discharge rate.

In this zone, the aerosol deposition mechanisms are centrifugal force v_{cf}, sedimentation v_{sed} and Brownian diffusion v_B. The major assumptions made in quantitatively dealing with these deposition mechanisms are that they are uncoupled from one another and additive, and that all the particles are of the same size and uniformly distributed. For constant average bubble diameter, from $z = z_{br}$ where $c_a = c_{a,br}$ to the top of the pool at $z = H$ where $c_a = c_a(H)$ results in the desired formula for the aerosol removal during bubble ascent is expressed by the bubble rise decontamination factor Eq. (9) [9, 10, 11, 12, 13]

$$DF_{rise} = \frac{c_{a,br}}{c_a(H)} = \exp\left[\frac{6(H - z_{br})}{U_b \bar{D}_b} \left(v_{cf} + \frac{1}{4} v_{sed} + v_B \right) \right] \quad (9)$$

MAAP6 computes z_{br} as a breakup distance based on the broken-up bubble diameter. If the discharge inert gas flow is below the transition value then z_{br} is set to 0. MAAP6 also computes an average bubble diameter for rise capture and uses that average bubble diameter in the rise deposition velocities and DF_{rise} expression.

If the suppression pool is hot enough for secondary bubble breakup to occur in the upper portion of the pool, then, a pool threshold temperature split is evoked and the two segment treatment for superheated conditions is applied, with separate rise DFs for lower and upper regions.

$$DF_{rise,1} = \exp\left[\frac{6(z_{br,2} - z_{br})}{U_b \bar{D}_{b,1}} \left(v_{cf} + \frac{1}{4} v_{sed} + v_B \right) \right] \quad (10)$$

$$DF_{rise,2} = \exp\left[\frac{6(H - z_{br,2})}{U_b \bar{D}_{b,2}} \left(v_{cf} + \frac{1}{4} v_{sed} + v_B \right) \right] \quad (11)$$

Hygroscopic particle growth effects are available in the model formulation. In MAAP6, soluble aerosol behavior is implemented through a soluble particle growth diameter calculation, and the slip correction factor is recalculated using the resulting soluble particle diameter.

2.4 Total Weighted Decontamination Factor

The overall pool scrubbing DF is then formed as a product which ensures stable behavior and prevents nonphysical DF values below 1. In MAAP6, each zone DF is bounded to be at least 1.0 prior to multiplication.

$$DF_{pool} = \begin{cases} (DF_{fb})(DF_{cz})(DF_{rise}); \text{ gas bubbling at injector} \\ (DF_j)(DF_{cz})(DF_{rise}); \text{ gas jetting at injector} \end{cases} \quad (12)$$

3.0 BENCHMARK CONFIGURATIONS
3.1 CRIEPI Experimental Setup

To validate the MAAP6 model, data provided by the Central Research Institute of Electric Power Industry (CRIEPI), Tokyo, Japan, were used to perform benchmark the MAAP6 aerosol scrubbing model. Two sets of experiments were considered: one focusing on aerosol removal dominated by bubble rise mechanisms [5] and the other focusing on the jetting and impaction regime [6].

3.1.1 Bubble Rise Regime

The CRIEPI bubble rise experiments were performed to investigate aerosol removal under conditions dominated by discrete bubble formation and buoyant rise in a water pool. Air was used as the carrier gas and was injected through a multi-hole orifice plate consisting of 100 circular holes, each with an inner diameter of 5 mm. This configuration distributed the gas uniformly and limited the gas exit velocity, thereby suppressing jet formation and inertial impaction near the injection point.

The volumetric air flow rate varied between approximately 1000 and 2500 L/min, corresponding to gas velocities at the orifice exit of approximately 8.5 to 21 m/s. The pool submergence depth varied from 1.5 m to 3.5 m in increments of 0.25 m. All experiments were conducted at ambient pressure and temperature under stagnant air water conditions. Insoluble barium sulfate ($BaSO_4$) particles were used as the aerosol simulant, with geometric mean particle diameters ranging from approximately 0.2 to 1.2 μm.

In the MAAP6 benchmark model, the bubble rise configuration was represented using a fixed submergence depth of 1.5 m. The carrier gas temperature and pool temperature were both set to 293.15 K, and the steam mass fraction was set to zero. Aerosol particle diameters were varied within the experimental range to evaluate particle size effects on removal efficiency.

The model calculated decontamination factors were compared to CRIEPI experimental values and to the empirical correlation proposed by CRIEPI for the bubble rise regime. CRIEPI DF_{BR} empirical formula was expressed by the function of the $BaSO_4$ aerosol diameter ($D_{p,GEO}$) and submergence depth (x). This correlation was used as an additional reference for trend comparison in the results plot and can be seen demonstrated as the red dashed line (DFBR(x, Dp.GEO)) in Figure 2, though, the primary benchmark assessment focused on agreement between MAAP6 predictions and measured decontamination factors.

3.1.2 Jetting Regime

The CRIEPI jetting experiments were conducted to characterize aerosol removal under high velocity gas injection conditions where a submerged jet forms and aerosol removal is dominated by inertial impaction and turbulent mixing. From these experiments, MAAP6 modeled air injected through a single circular orifice with an inner diameter of 13 mm.

The volumetric gas flow rate ranged from 756 to 2789 L/min, corresponding to gas exit velocities of approximately 95 to 350 m/s. Additionally, all experiments were performed at ambient pressure (1.013×10^5 Pa) and room temperature, with stagnant pool conditions. Based on the reported flow conditions, the experiments fall entirely within the jetting regime, as the CRIEPI Weber numbers (Jet regime, We number $>> 10^5$) exceed both the experimental regime transition threshold and the corresponding MAAP6 critical discharge velocity criterion for jet formation.

For the MAAP6 benchmark implementation, cases implemented consist of three particle size sets, each containing 17 flow conditions. The first set used an aerodynamic mass median diameter (AMMD) of 0.2

μm (2.0×10^{-7} m), the second set used an AMMD of 0.3 μm (3.0×10^{-7} m), and the third set used an AMMD of 0.5 μm (5.0×10^{-7} m). For each particle size, the same sequence of volumetric flow rates was applied.

Experimental volumetric flow rates provided by CRIEPI were interpreted as normal volumetric flow rates and converted to gas mass flow rates using the ideal gas relationship consistent with CRIEPI's formulation of Q_{G1} (the volumetric flow rate of the gas). A constant ambient pressure (1.013×10^5 Pa) and temperature (293.15 K) were assumed for all cases, with air properties used to evaluate gas density. The resulting gas mass flow rates ranged from ~ 0.0163 kg/s to 0.0601 kg/s and were supplied directly to the MAAP6 model. The steam mass fraction is set to zero for all cases and the gas and pool surface temperature were assumed to be ambient. The pool submergence depth was set to 2.125 m for all jetting cases, consistent with the experimental configuration provided by CRIEPI for the selected dataset. A single representative Weber number within the jetting regime was applied uniformly across all benchmark cases to isolate the effects of particle size and gas flow rate on decontamination factor predictions.

CRIEPI experimental decontamination factors for the jetting regime were provided directly and were mapped one to one to the corresponding MAAP6 cases. These values were used as the reference data for evaluating MAAP6 predictions of aerosol removal in the jetting and impaction regime.

In addition to comparison with experimental decontamination factors, the empirical jetting correlation developed by CRIEPI was also evaluated and added to the results comparison as seen through the red dashed line (DFJET(vG, Dp.GEO)), in Figure 3, Figure 4, and Figure 5. CRIEPI's empirical correlation captures the exponential increase in DF_{JET} with inlet gas velocity and the increasing sensitivity of DF_{JET} with particle size. This expression was evaluated alongside the MAAP6 predictions and CRIEPI experimental data for the jetting benchmark cases.

3.2 UW Madison Experimental Setup

In addition to the CRIEPI experimental benchmarks, MAAP6 was evaluated against experimental data generated by the University of Wisconsin Madison to examine aerosol removal behavior over a wider particle size range than that available in the CRIEPI dataset. The UW Madison experiments investigated extensive parametric effects, including bubble size, aerosol size, aerosol density, aerosol concentration, pool depth, system temperature, and bubble swarm behavior [7]. Accordingly, the MAAP6 comparison is limited to the UW Madison aluminum aerosol tests that vary particle size and pool depth, with bubble swarm and multi-material datasets excluded from the benchmark dataset.

For comparison with MAAP6, experimental data was taken from tests using powdered aluminum aerosols with particle sizes ranging from approximately 0.01 to 18 μm and pool heights of 1.8 m and 0.9 m. Aluminum particles were selected to hold aerosol material properties constant while varying pool depth. For consistency with the MAAP6 input definition, the UW Madison aerosol sizes reported as aerodynamic diameters were converted to equivalent physical diameters assuming spherical aluminum particles with a density of 2.7 g/cm³, using the standard aerodynamic diameter relationship, with no shape factor or agglomeration correction applied.

Pool height influences both local pressure and bubble residence time during ascent. Specifically, bubble residence time determines the duration of aerosol liquid interaction during bubble rise and directly affects overall decontamination performance. To isolate the effect of pool height, UW Madison experiments were performed using two pool depths (1.8 m and 0.9 m) at a temperature of 200 °C, with a fixed bubble diameter of approximately 3.63 cm. Although the UW Madison experiments were conducted in a liquid sodium pool at elevated temperatures, they are still used here for qualitative trend comparison as the current MAAP6 model evaluates pool scrubbing using water properties rather than liquid metal properties, which may effect bubble hydrodynamics and residence time.

The experimental results show that decontamination performance decreases with increasing aerosol size in the submicron regime and increases again for larger particles as dominant removal mechanisms transition from Brownian diffusion to inertial impaction and gravitational settling. These trends provide a complementary benchmark to the CRIEPI data by extending the evaluation of MAAP6 across multiple aerosol removal regimes.

4.0 MAAP6 RESULTS

4.1 CRIEPI Benchmark Comparison

4.1.1 Bubble Rise Regime

The purpose of these benchmark comparisons was to examine and validate the MAAP6 pool scrubbing model with data provided by the jetting and bubble rise experiments conducted by CRIEPI.

CRIEPI's water scrubber experiments developed an empirical framework describing bubble rise decontamination as a function of aerosol diameter and submergence depth. For direct comparison, submergence depth was held constant in the MAAP6 bubble rise simulations while particle size was varied. Results from the MAAP6 model, CRIEPI experimental data, and the CRIEPI empirical correlation data (shown in the red dashed line in Figure 2) consistently indicate that larger particles are removed more efficiently than smaller particles, and that bubble rise decontamination factors increase strongly with particle size. This behavior is evident in Figure 2, where agreement is strongest at smaller particle sizes and decontamination factors increase rapidly as particle diameter approaches 1 μm.

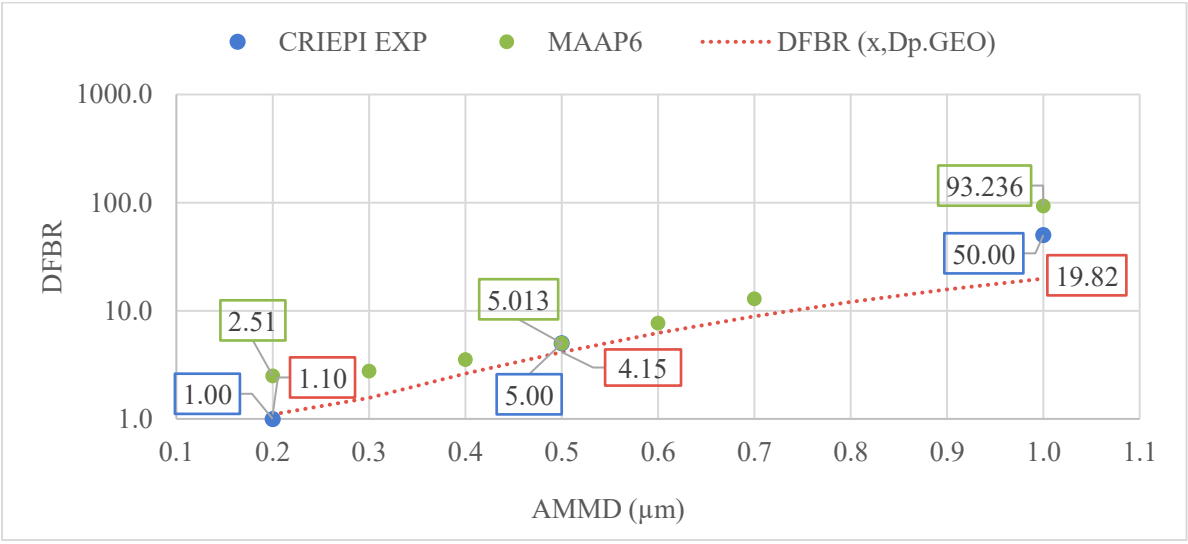

Figure 2 DFBR experimental data, model output and empirical correlation for ranging particle sizes

4.1.2 Jetting Regime

In addition to the bubble rise benchmarks, the MAAP6 model was evaluated against CRIEPI jetting experiments and the CRIEPI empirical jetting correlation, seen as the red dashed line DFJET(vG, Dp.GEO). In these cases, pool submergence depth was held constant while particle size was varied across 0.2μm, 0.3μm, and 0.5μm. For each particle size, comparisons show that decontamination factors generally increase with increasing inlet gas velocity, and that larger particles exhibit greater sensitivity to velocity, consistent with CRIEPI observations. While experimental data exhibits scatter and nonmonotonic behavior at

individual conditions, MAAP6 reproduces the overall scaling trends with velocity and particle size observed in the jetting regime, seen in Figure 3, Figure 4, and Figure 5.

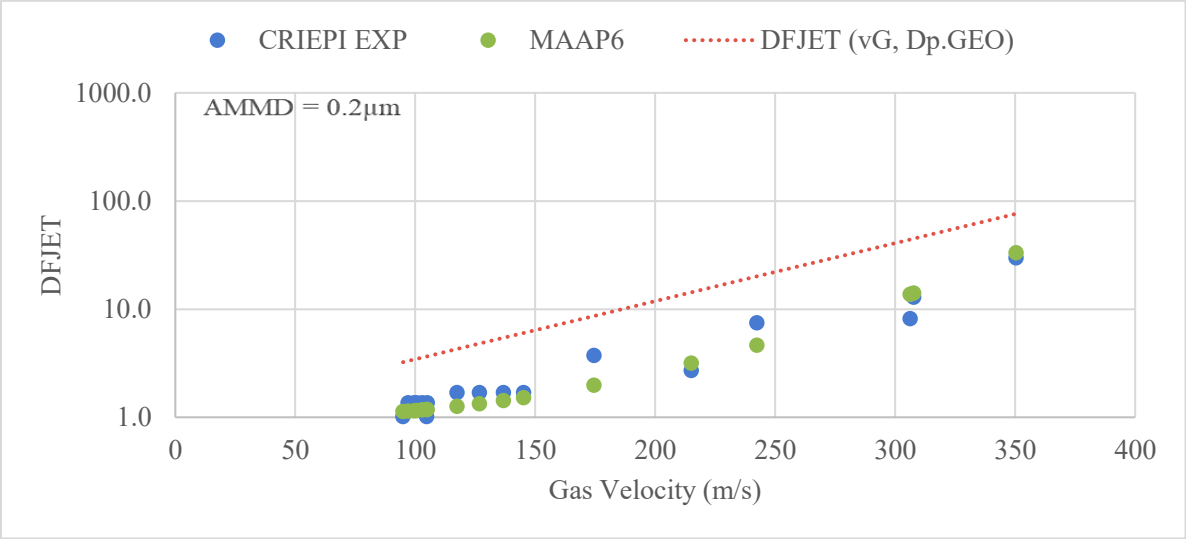

Figure 3 DFJET experimental data, MAAP6 model output and empirical correlation curves for 0.2 µm aerosols as a function of inlet gas velocity(vG)

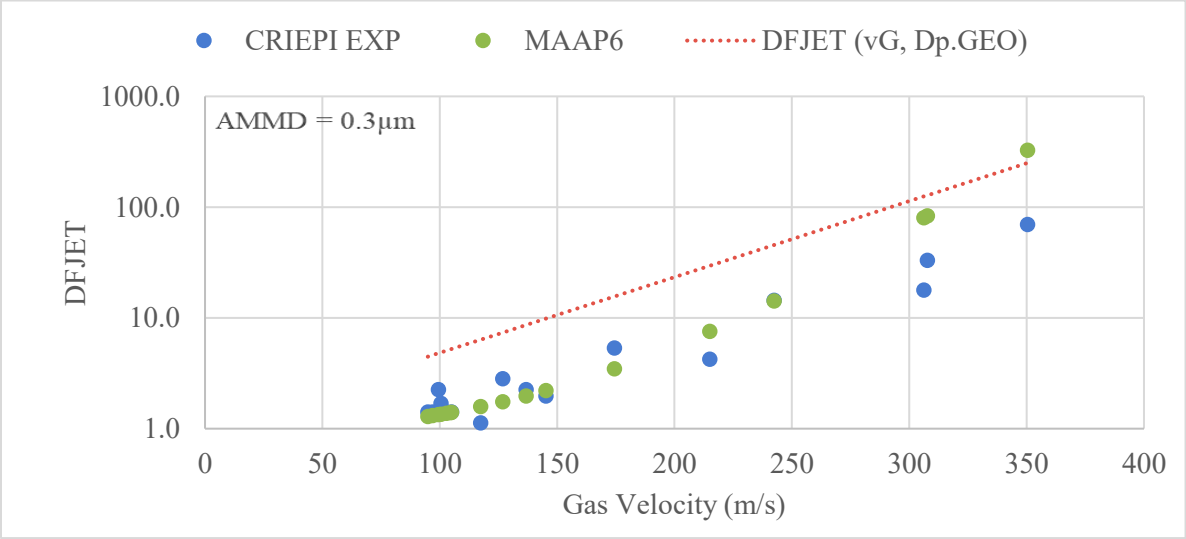

Figure 4 DFJET experimental data, MAAP6 model output and empirical correlation curves for 0.3 µm aerosols as a function of inlet gas velocity(vG)

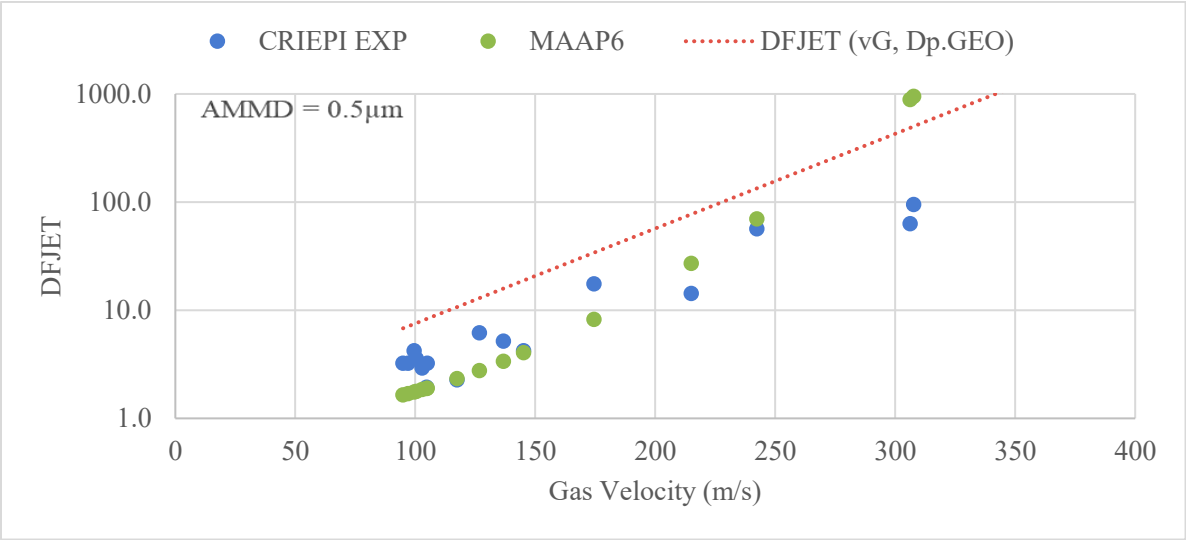

Figure 5 DFJET experimental data, MAAP6 model output and empirical correlation curves for 0.5 µm aerosols as a function of inlet gas velocity(vG)

4.2 UW Madison Benchmark Comparison

University of Wisconsin Madison data was incorporated into the MAAP6 benchmarks to extend model evaluation to a broader aerosol size range and additional dominant removal mechanisms. The UW Madison experiments demonstrate that total decontamination factors are relatively high at very small aerosol diameters, decrease in the intermediate size range, and increase again for larger particles as inertial and gravitational mechanisms become dominant.

These trends are observed across multiple pool depths, with higher decontamination factors reported for the deeper 1.8 m pool compared to the 0.9 m pool, reflecting increased bubble rise time. MAAP6 predictions are consistent with these trends and reproduce the qualitative dependence of decontamination factor on aerosol size and pool depth observed in the UW Madison experiments.

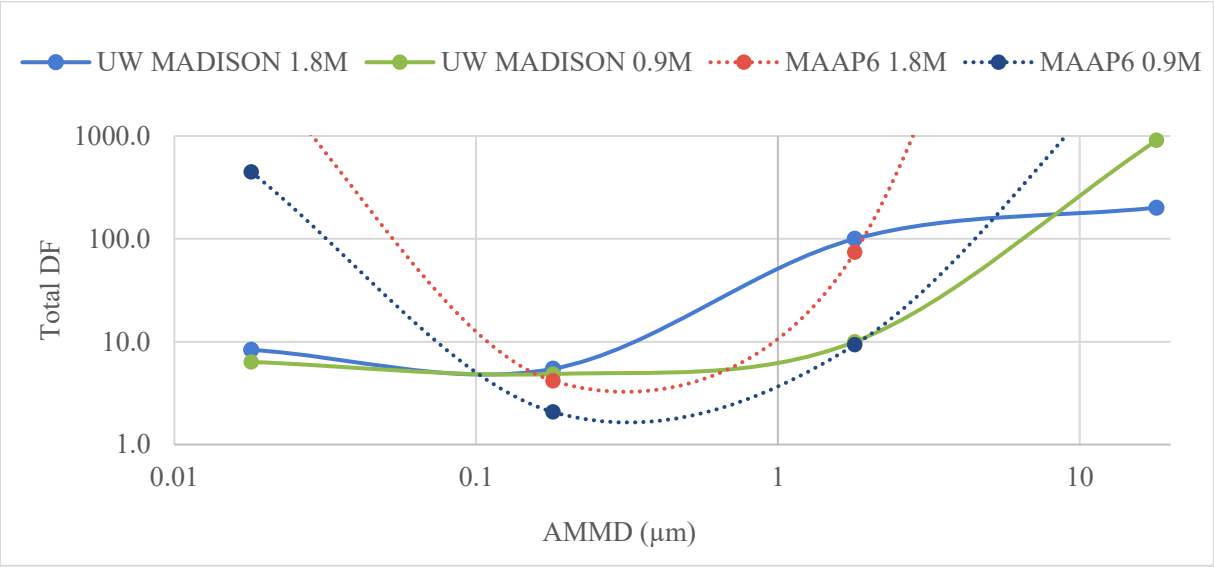

Figure 6 Comparison of DF by pool depth between experimental data and model output

5.0 CONCLUSIONS

This study benchmarked the MAAP6 suppression pool aerosol scrubbing model against experimental data from to examine model behavior across bubble rise and jetting dominated regimes. The benchmark comparisons focused on aerosol size dependence, gas injection conditions, and pool depth effects on decontamination factors.

The MAAP6 model predictions reproduce the primary trends observed in the experimental datasets. In the bubble rise regime, decontamination factors increase with particle size and submergence depth, consistent with CRIEPI benchmark observations. In the jetting regime, MAAP6 captures the dependence of decontamination factor on inlet gas velocity and the increasing sensitivity with particle size. Comparison with UW Madison aluminum aerosol data extends the evaluation to a broader particle size range and shows consistent qualitative dependence on aerosol size and pool depth.

Overall, the benchmark results indicate that the MAAP6 suppression pool scrubbing model provides a reasonable representation of dominant aerosol removal trends across the experimental conditions considered. It is noted that experiments investigated in this paper are limited subset of the available experimental data [8]. Further evaluation is planned to assess model behavior for higher steam fractions, additional aerosol materials, alternative pool conditions, and hygroscopic aerosols.

NOMENCLATURE (IF NEEDED)

c_a aerosol volume concentration (m^3 aerosol per m^3 spatial volume)
$c_{a,br}$ aerosol volume concentration in broken-up bubbles, above condensation zone

C aerosol particle slip correction factor
d_a diameter of dry aerosol particle
d_o discharge orifice diameter or effective diameter of gas mixture jet discharge
d_f effective average diameter of entrained drops (water) in jet
$\overline{D}_b$ average diameter of bubble in bubble rise zone
DF decontamination factor
DF_{con} decontamination factor due to steam condensation in bubble
DF_{cz} total aerosol decontamination factor for the condensation zone
DF_{fb} aerosol decontamination factor for forming bubble at discharge orifice
DF_j aerosol decontamination factor for jet at discharge orifice
DF_{rise} aerosol decontamination factor for bubble rise zone
E_o empirical entrainment coefficient (0.08 for jet; 0.12 for bubble plume)
f drop velocity lag coefficient in jet
g gravitational constant
H depth of submerged discharge orifice
K_T thermophoretic transport coefficient
Pr fluid Prandtl number: kinematic viscosity divided by thermal diffusivity
$\dot{Q}_{g,o}$ volumetric flow of gas mixture at discharge orifice
S inverse Stokes number parameter
T_f temperature of suppression pool
T_o temperature of gas mixture at discharge orifice or effective gas mixture jet discharge temperature
u_{atm} gas velocity above which liquid (water) atomization occurs
$u_{o,cr}$ critical discharge orifice gas mixture velocity above which jetting occurs
U_b absolute bubble rise velocity
u_o gas mixture velocity at discharge orifice or effective gas mixture jet discharge velocity
v_B aerosol particle deposition velocity due to Brownian diffusion
v_{cf} aerosol particle deposition velocity due to centrifugal force
v_{sed} aerosol particle deposition velocity due to sedimentation
z_{br} bubble breakup distance above discharge orifice
$z_{br,2}$ elevation in hot pool above which secondary bubble breakup is possible
β dimensionless parameter
ε efficiency of particle capture by bubble surface or entrained drops
μ_g viscosity of gas mixture
λ mean free path of gas mixture
ρ_a density of dry aerosol material
ρ_f density of pool water
$\rho_{g,o}$ gas mixture density at discharge orifice or effective gas mixture discharge density
σ_f surface tension of pool water
χ_o dimensionless parameter

Subscripts
atm refers to end of atomization zone in jet
o refers to conditions at discharge orifice exit plane when flow is subsonic or effective discharge conditions in jet when discharge is choked
1 refers to lower bubble rise zone in hot pool
2 refers to upper bubble breakup zone in hot pool when secondary bubble breakup occurs

ACKNOWLEDGMENTS

The authors gratefully acknowledge the Central Research Institute of Electric Power Industry (CRIEPI) and the University of Wisconsin Madison for providing experimental data and technical clarification that supported benchmarking and implementation of the MAAP6 suppression pool aerosol scrubbing model.

REFERENCES

1. Y. F. Zhao, and G. A. Irons, "The Breakup of Bubbles into Jets During Submerged Gas Injection," Metallurgical Trans. B 21B, pp. 997-1003, 1990.
2. 15. V. A. Marple, and B. Y. H. Liu, "Characteristics of Laminar Jet Impactors," Envir. Sci. & Technol. 8, pp. 648-654, 1974
3. J. J. van Rossum, "Experimental Investigation of Horizontal Liquid Films," Chem. Engng. Sci. 11, pp. 35-52, 1959.
4. S. S. Kutateladze, "Elements of the Hydrodynamics of Gas-Liquid Systems," J. Fluid Mech. – Soviet Research 1, pp. 29-50, 1972.
5. T. Kanai, M. Furuya, T. Arai, Y. Nishi, “Development of an aerosol decontamination factor evaluation method using an aerosol spectrometer,” Nuclear Engineering and Design, Vol.303, pp.58-67 (2016)
6. T. Kanai, M. Saito,”AEROSOL REMOVAL PROPERTIES UNDER JET INJECTION REGIME”, The 13 th Korea-Japan Symposium on Nuclear Thermal Hydraulics and Safety (NTHAS 13), (2024)
7. K.F. Becker, M.H. Anderson, “Experimental Measurements Of Fission Product Retention Via Bubble Transport In A Sodium Coolant Pool,” Ph.D Dissertation, University of Wisconsin-Madison, 2022.
8. L. E. Herranz, F. Sánchez, and S. Gupta, “Validation Matrix for Pool Scrubbing Models,” Nucl Technol, vol. 209, no. 10, pp. 1523–1536, Oct. 2022, doi: 10.1080/00295450.2022.2122679.
9. G. B. Wallis, One-Dimensional Two-Phase Flow, McGraw-Hill, New York, 1969.
10. F. J. Moody, "Dynamic and Thermal Behavior of Hot Gas Bubbles discharged into Water," Nucl. Engr and Design 95, pp. 47-54, 1986.
11. N. A. Fuchs, The Mechanics of Aerosols, Pergaman Press, Oxford, 1964.
12. F. N. Peebles, and H. J. Garber, "Studies on the Motion of Gas Bubbles in Liquids," Chem. Eng. Prog. 49, pp. 88-97, 1953.
13. I. Liebson, E. C. Holcomb, A. G. Cacoso, and J. J. Jacmic, "Rate of Flow and Mechanics of Bubble Formation from Single Submerged Orifices," AIChE J. 2, pp. 296-306, 1956.

MAAP6 MODEL IMPLEMENTATION OF SUPPRESSION POOL AEROSOL SCRUBBING

Autumn Crisafulli and Paul McMinn
Fauske and Associates (FAI)
Matt Nudi
Electric Power Research Institute (EPRI)

ERMSAR 2026

© 2026 Electric Power Research Institute, Inc. All rights reserved.

MAAP6 Suppression Pool Aerosol Scrubbing Model

- Historical motivation for model development:
  - A concern was raised that the decontamination factor (DF) calculated by MAAP for a sparger injection release geometry was not monotonically increasing with pool depth

Mass fraction of steam	DF calculated by MAAP	
	4 m pool	6 m pool
0.0	2,218	561
0.5	106.7	106.7
0.9	19.5	19.5
0.99	25.6	55.7

- MAAP6 now implements a mechanistic pool scrubbing model that replaces prior simplified empirical lookup table treatment and was benchmarked against bubble rise and jetting data

© 2026 Electric Power Research Institute, Inc. All rights reserved.

Mechanistic Pool Scrubbing Model-Pool Scrubbing Zones

- Overall DF is calculated as the product of injection, condensation, and bubble rise zone contributions.
- Injection Zone:
  - The gas can leave the discharge location as bubbles or by forming a jet, depending on the discharge volume to flow area ratio.
- Condensation Zone
  - After the flow has developed the plume will rise and any steam will condense if conditions allow.
- Bubble Rise Zone
  - The mechanism for decontamination changes once the rising plume is in thermal equilibrium with the surrounding pool

© 2026 Electric Power Research Institute, Inc. All rights reserved.

Mechanistic Pool Scrubbing Model-Bubble Plume Path DF_{bf}

- At low gas discharge rates single bubbles grow and detach periodically from the discharge orifice.
- During bubble growth aerosol particles deposit on the bubble surface by centrifugal force and inertia.
- All other mechanisms of deposition are neglected.

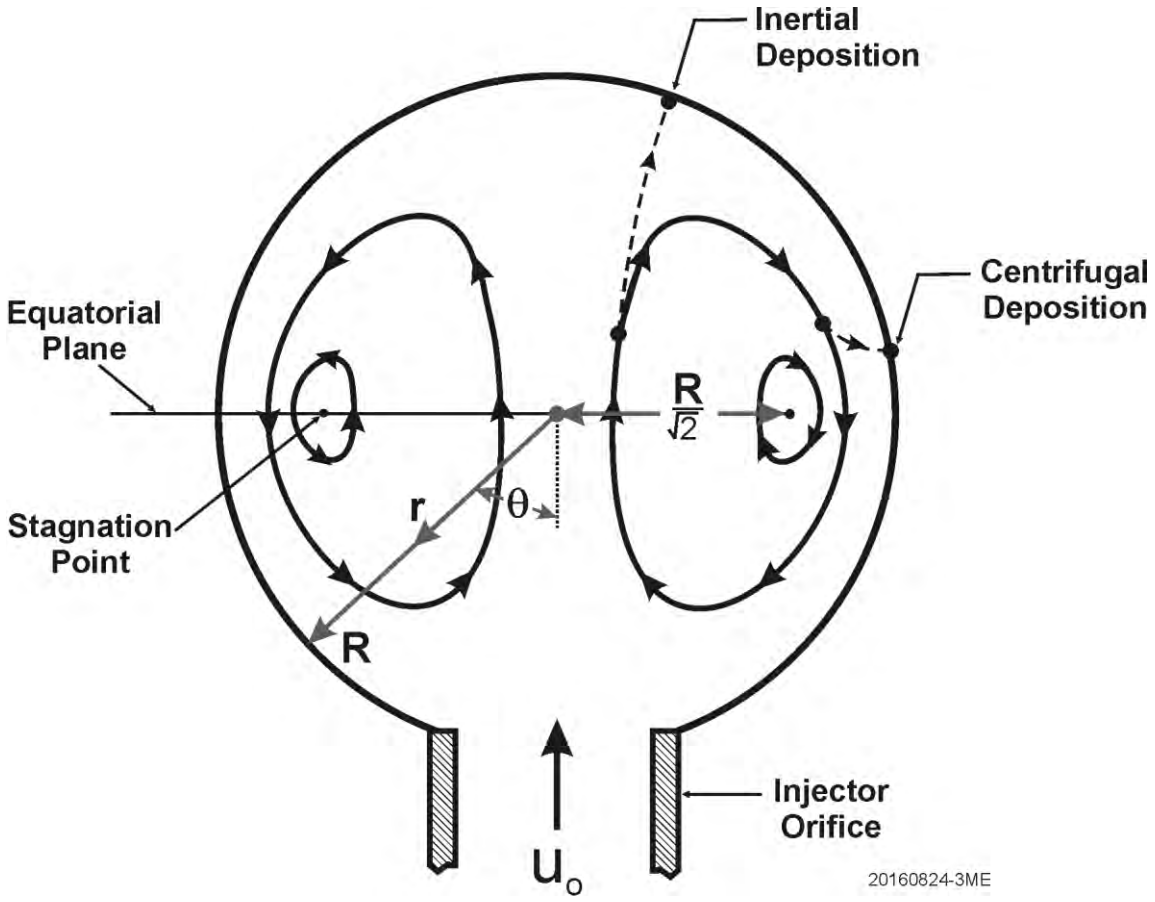

© 2026 Electric Power Research Institute, Inc. All rights reserved.

Mechanistic Pool Scrubbing Model-Gas Jet Region DF_j

- At high gas discharge rates gas jets are formed at the orifice
- The principal mechanism of aerosol depletion is aerosol inertial deposition upon entrained liquid drops.
- MAAP6 applies compressible discharge handling and calculates an effective jet velocity and diameter prior to evaluating in-jet aerosol capture.

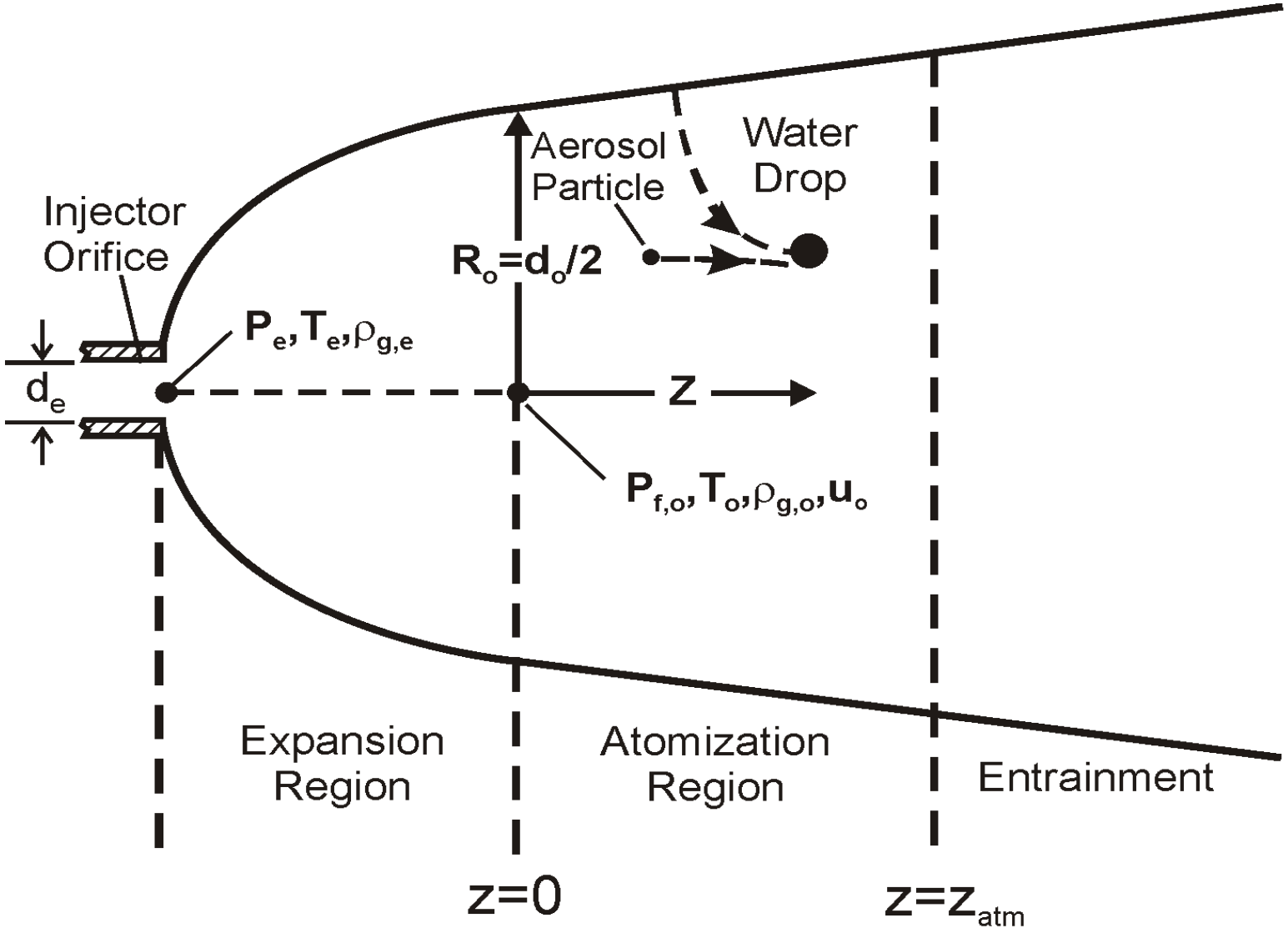

© 2026 Electric Power Research Institute, Inc. All rights reserved.

Mechanistic Pool Scrubbing Model-Condensation Zone DF_{cond}

- Particle removal by steam condensation, diffusiophoresis and thermophoresis is assumed to occur immediately after the bubble detaches from the orifice (or jet) and before it breaks up until a stable bubble size is reached.
- The thickness of the condensation zone is small on the scale of the pool depth.
- The stable size bubble is assumed to be in thermodynamic equilibrium with the surrounding pool.
- Heat and mass transfer analogies are used to estimate particle removal by diffusiophoresis and thermophoresis during the bubble's approach to equilibrium.
- In practice, its contribution is relatively small for the cases studied, with overall DF tending to be dominated by injection/jetting and bubble rise.

© 2026 Electric Power Research Institute, Inc. All rights reserved.

Mechanistic Pool Scrubbing Model-Bubble Rise Zone DF_{rise}

- The removal of the gaseous fission products from the bubbles occurs by in-series gas-side and liquid-side-controlled convective diffusion.
- Aerosol particle scrubbing within the rising bubbles occurs by sedimentation, centrifugal force, and Brownian motion.
- MAAP6 computes breakup distance and average bubble diameter explicitly for rise-zone capture and can apply a two-segment rise treatment for hot pool conditions.

$$DF_{rise} = exp\left[\frac{6(H - z_{br})}{U_b \bar{D}_b}(v_{cf} + 0.25v_{sed} + v_B)\right]$$

  - D_b (the average bubble break-up diameter) is a function of the Weber number.
  - H is the pool height
  - Z_{br} is the top of the break-up zone
  - U_b is the bubble rise velocity
  - v_{cf},v_{sed},v_B are the centrifugal force, sedimentation and Brownian motion deposition velocities, respectively.

© 2026 Electric Power Research Institute, Inc. All rights reserved.

MAAP6 MODEL VALIDATION

Validating MAAP6 Pool Scrubbing Model

- Mechanistic model was implemented to the MAAP6 code framework and benchmarked against experimental data.
  - Data from CRIEPI allowed for comparison on MAAP6 Bubble rise regime and Jetting regime. MAAP6 outputs are examined against experimental data and against CRIEPI's developed empirical model
  - University of Wisconsin Madison (UW Madison) also provided data to benchmark total DF aerosol removal behavior over a wider particle size range and removal mechanisms.

© 2026 Electric Power Research Institute, Inc. All rights reserved.

CRIEPI BENCHMARK

CRIEPI Benchmark Configuration-MAAP6 Model Evaluation

- Objective
  - Evaluate MAAP6 prediction of aerosol removal in the (1) jetting regime and in (2) bubble rise regimes
  - Benchmark MAAP6 DF trends against CRIEPI experimental data and their developed empirical correlations (DFJET, DFBR)

© 2026 Electric Power Research Institute, Inc. All rights reserved.

CRIEPI Benchmark Configuration-MAAP6 Model Evaluation

- Methodology

Bubble Rise Configuration:

- Represent CRIEPI multi-hole injection (100 holes, 5 mm diameter) to suppress jetting
- Fix submergence depth at 1.5 m and vary particle size (0.2 to 1.2 µm)
- Use ambient air conditions with no steam contribution

Jetting Configuration:

- Implement CRIEPI jetting test conditions directly (single 13 mm orifice, ambient air, stagnant pool)
- Apply 17 flow conditions per particle size at constant submergence depth (2.125 m)
- Evaluate three particle sizes: 0.2 µm, 0.3 µm, 0.5 µm

© 2026 Electric Power Research Institute, Inc. All rights reserved.

CRIEPI Benchmark Results ~ Bubble Rise Regime

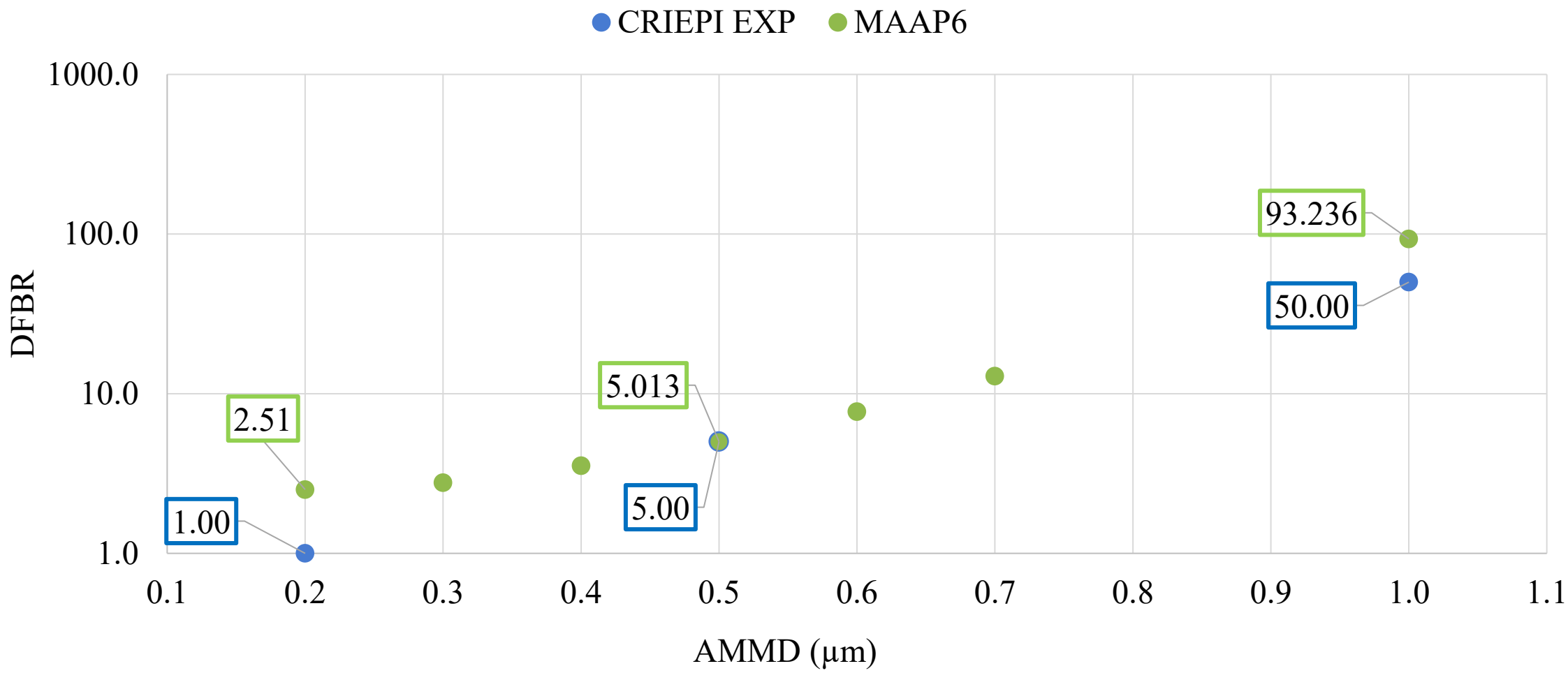

© 2026 Electric Power Research Institute, Inc. All rights reserved.

CRIEPI Benchmark Results ~ Bubble Rise Regime (Key Trends)

- DF increases strongly with particle size
- Larger particles are removed more efficiently than smaller particles
- MAAP6 shows strongest agreement at smaller particle sizes
- Rapid increase in DF observed as particle size approaches ~1 µm

© 2026 Electric Power Research Institute, Inc. All rights reserved.

CRIEPI Benchmark Results ~ Jetting Regime 0.2 µm

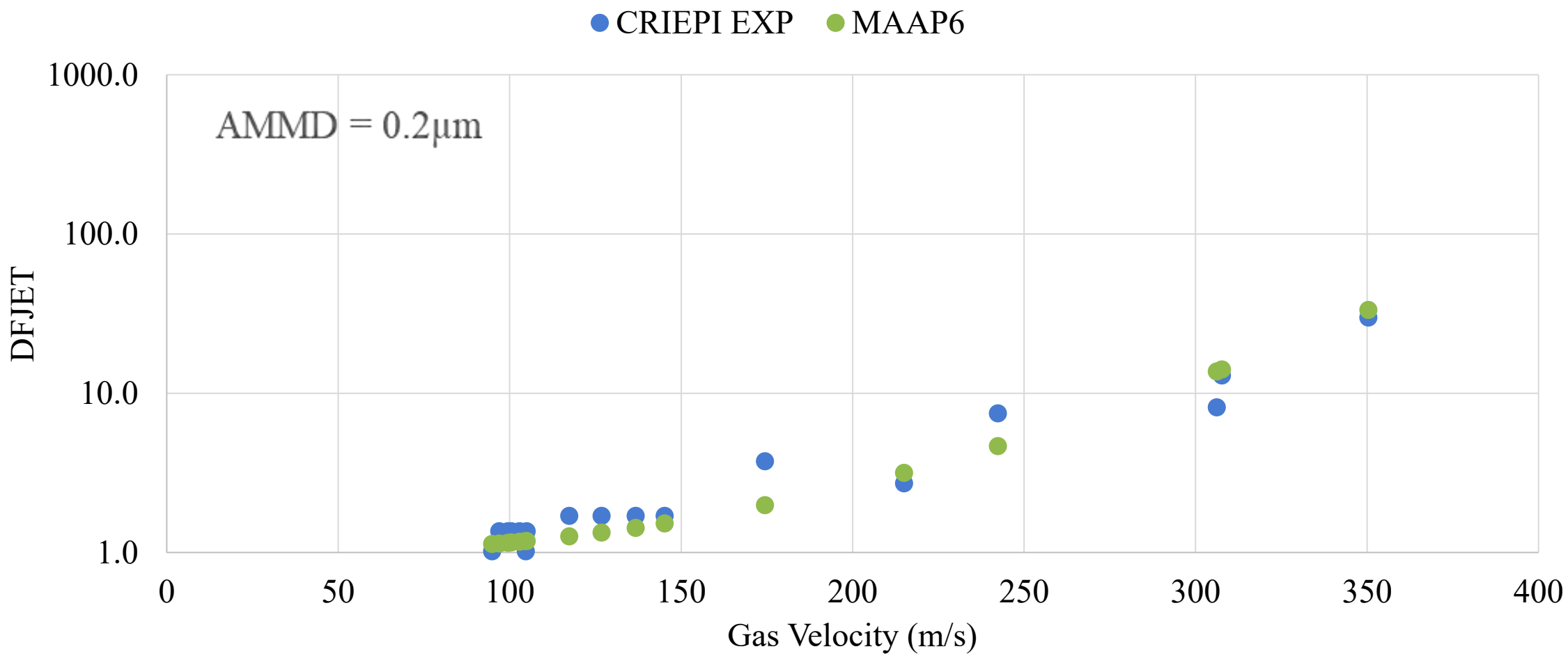

© 2026 Electric Power Research Institute, Inc. All rights reserved.

CRIEPI Benchmark Results ~ Jetting Regime 0.3 µm

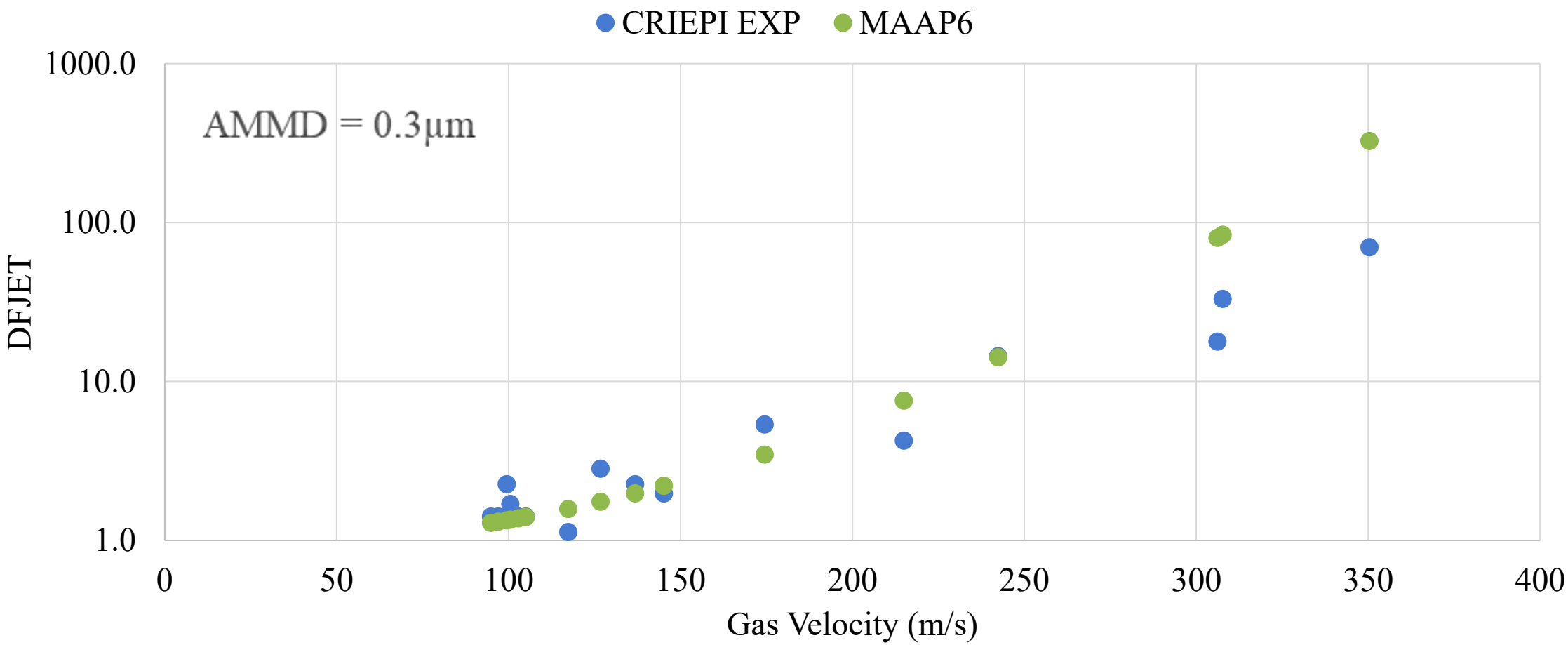

© 2026 Electric Power Research Institute, Inc. All rights reserved.

CRIEPI Benchmark Results ~ Jetting Regime 0.5 µm

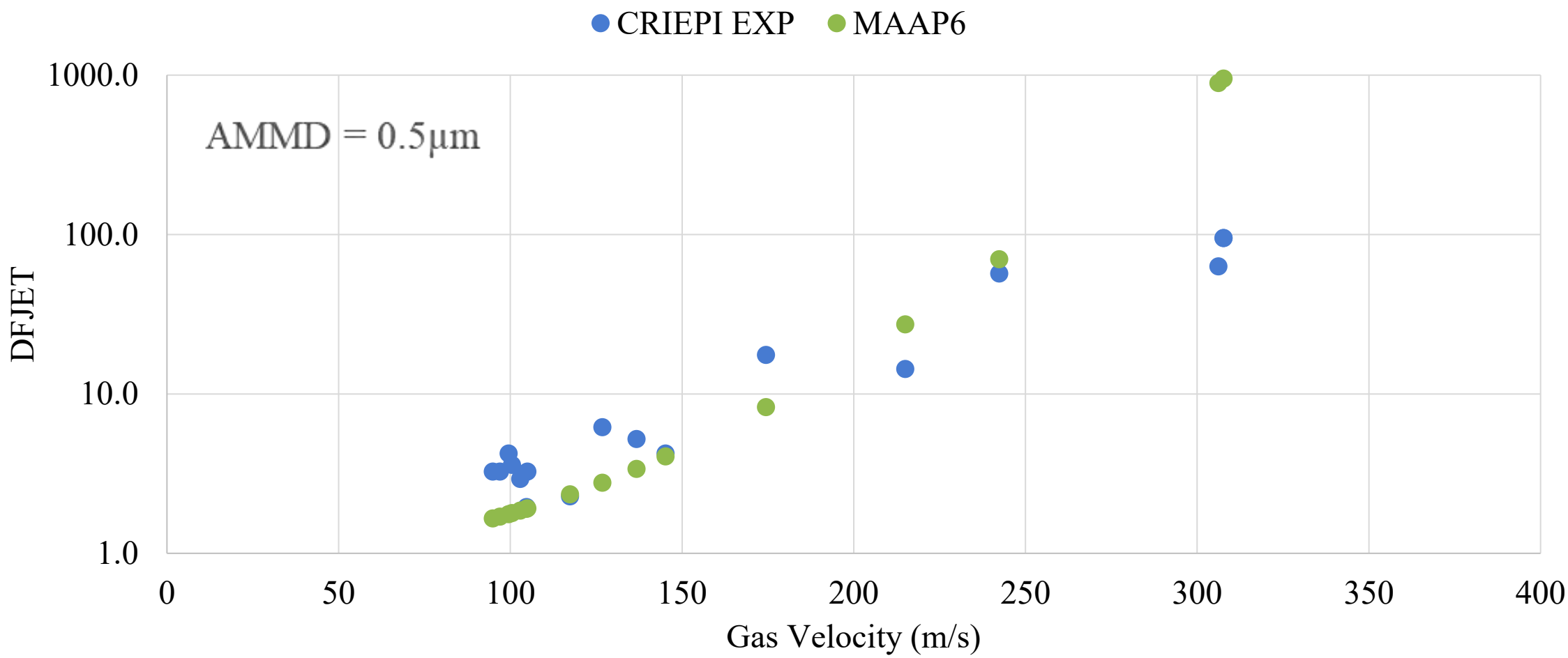

© 2026 Electric Power Research Institute, Inc. All rights reserved.

CRIEPI Benchmark Results ~ Jetting Regime (Key Trends)

- DF increases with increasing gas velocity across all particle sizes
- Larger particles show stronger sensitivity to velocity (inertial effects dominate)
- MAAP6 captures overall scaling with velocity and particle size

© 2026 Electric Power Research Institute, Inc. All rights reserved.

UW MADISON BENCHMARK

UW Madison Benchmark Configuration – MAAP6 Model Evaluation

- Objective
  - Extend MAAP6 validation to a broader aerosol size range and additional removal mechanisms
  - Evaluate model behavior across regimes transitioning from diffusion, impaction, and gravitational settling
- Methodology
  - Use UW Madison aluminum aerosol experiments with particle sizes ~0.01 to 18 µm
  - Convert reported aerodynamic diameters to physical diameters assuming spherical particles ($\rho = 2.7\ g/cm^3$)
  - Evaluate two pool depths: 0.9 m and 1.8 m to assess residence time effects
  - Maintain consistent material properties and isolate effects of particle size and pool depth
  - Results are used for qualitative trend comparison due to water vs sodium pool

© 2026 Electric Power Research Institute, Inc. All rights reserved.

UW Madison Benchmark Results

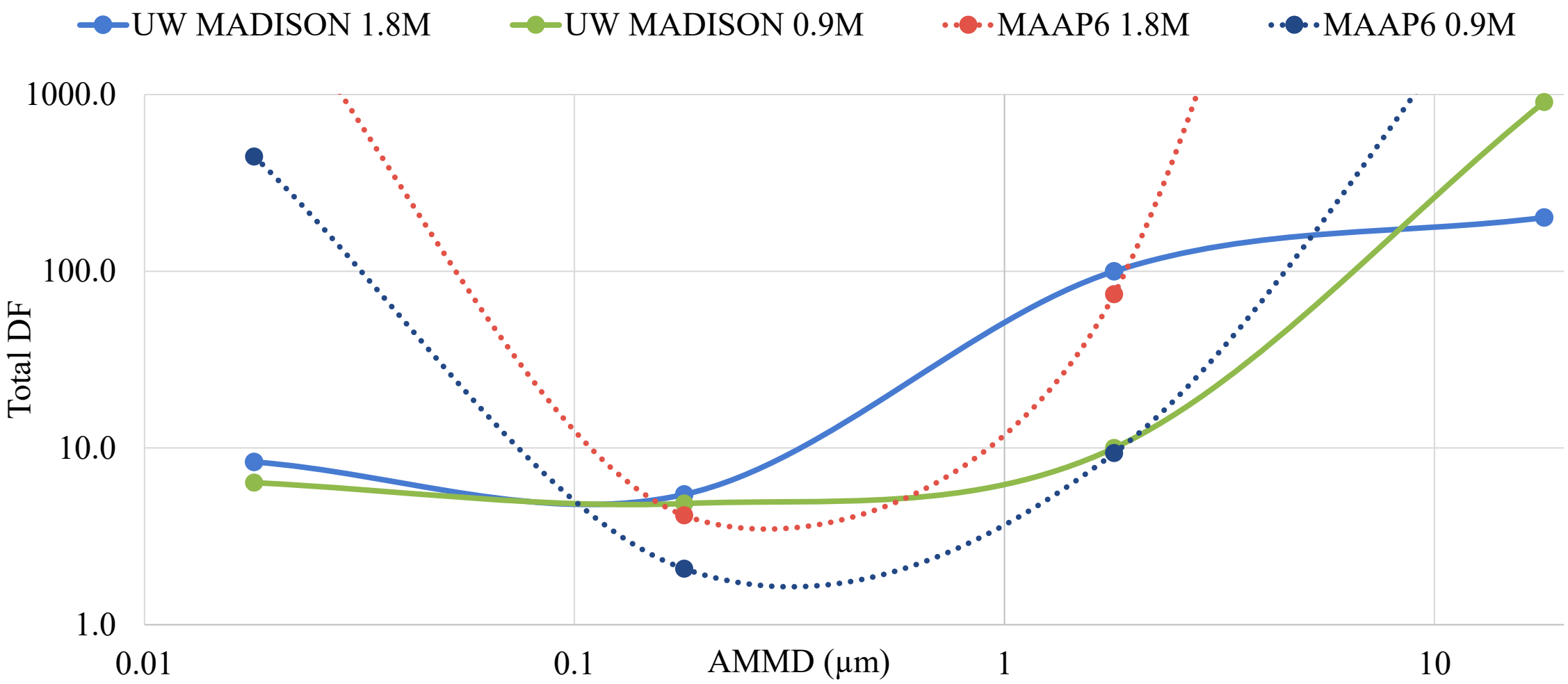

© 2026 Electric Power Research Institute, Inc. All rights reserved.

UW Madison Benchmark Results (Key Trends)

- DF is high at very small particle sizes, decreases in the intermediate range, then increases again for larger particles
- Trend reflects transition from diffusion-dominated to impaction to also gravitational settling mechanisms
- Deeper pool (1.8 m) results in higher DF due to increased bubble residence time
- MAAP6 reproduces the qualitative dependence of DF on particle size and pool depth
- Provides complementary validation beyond CRIEPI by covering multiple removal regimes

© 2026 Electric Power Research Institute, Inc. All rights reserved.

Conclusions and Future Work

- MAAP6 now includes a mechanistic pool scrubbing model with separate injection, condensation, and bubble rise zone contributions
- Benchmarking against CRIEPI data showed the model captures key DF trends in both bubble rise and jetting regimes
- Comparison with UW Madison data extended evaluation across a broader aerosol size range and multiple dominant removal mechanisms
- Overall, MAAP6 reproduced the primary trends observed across experimental datasets

- Looking Forward
  - Continue evaluation against additional aerosol materials and pool conditions
  - Assess model behavior for hot pool and hygroscopic aerosol cases
  - Apply the model in plant-relevant severe accident analyses where pool scrubbing influences source term predictions

© 2026 Electric Power Research Institute, Inc. All rights reserved.

COCOSYS simulation of CsI decomposition under irradiation and the formation of organic iodide in the containment

Chuanhe Lu*, Holger Nowack
Gesellschaft für Anlagen- und Reaktorsicherheit (GRS)
D-50667 Cologne, Germany
chuanhe.lu@grs.de; holger.nowack@grs.de

ABSTRACT

Iodine is one of the most hazardous fission products (FP) released to the containment of a nuclear power plant during a severe accident. The metallic iodide aerosol CsI is one of the main airborne iodine species in the containment and the CsI decomposition with formation of gaseous iodine species is a primary concern in nuclear accident scenarios. The thermal and radiolytic decomposition of CsI generates molecular iodine, which can further react with organic compound and form the organic iodide. In this paper the AC^2/COCOSYS code is applied to simulate and analyze the CsI decomposition and related iodine aerosol transport in the containment of LOCOV tests. The LOCOV experiment in the French EPICUR facility studied the decomposition of deposited CsI aerosol and the reactivity of I_2(g) with methane to quantify the organic iodide formation rate in the presence of volatile organic compounds (VOC) [1]. The COCOSYS simulation investigates the decomposition of CsI aerosol, the organic iodide formation and the distribution of the different iodine species across the coupon, the atmosphere, the vessel walls and the filter. The simulation results of LOCOV model show that the thermal decomposition of CsI is very slow, but a fast decomposition of CsI is observed under irradiation. The injected methane reacts with I_2 and organic iodide is generated, while the oxidation of I_2 with ozone produces iodine oxide aerosol IO_x. The gas phase I_2 in vessel deposits on the surfaces of vessel wall. With the time going on, the deposited I_2 reacts with Fe. Higher dose rates caused higher CsI decomposition and RI generation rates. The comparisons between simulation results and measurements show the modelling capabilities of organic iodide formation with COCOSYS in two LOCOV tests.

KEYWORDS
CsI decomposition, organic iodide, aerosol, irradiation

1. INTRODUCTION

Iodine is one of the most hazardous fission products (FP) released to the containment during a severe nuclear reactor accident. The evolution of volatile iodine concentration is determined by a balance between formation and deposition processes [2-4]. Volatile molecular iodine (I_2) can be produced from the iodine deposited on painted surfaces or from suspended aerosols [2-5]. The organic iodide compounds (RI) can be produced from iodine deposited on painted surfaces or reaction between iodine and organic gas, like methane [1-12]. The low-molecular-weight RI is harder to trap for the filter, making it more likely to be released into the environment. It makes the studies of volatile molecular iodine release and RI formation very important in the severe accident management.

The metallic iodide aerosol CsI is one of the main airborne iodine species in the containment and the CsI decomposition with formation of gaseous iodine species is a primary concern in nuclear accident scenarios [1, 7, 13]. The CsI decomposition process can be affected by many parameters. The AER-CsI test series in

the STEM-EPICUR program studies the behavior of CsI aerosols deposited on different surfaces of the containment and the ability to produce volatile iodine species [1]. The effects of various experimental parameters on the iodine species releases were evaluated: initial CsI concentration on the coupon, relative humidity, temperature, dose rate and nature of the coupon surface (stainless steel, quartz or EPOXY paint). The extensive experiment program STEM-EPICUR has been performed to obtain data concerning iodine volatilizations.

STEM-EPICUR program also investigated the formation of organic iodide from the painted surface in the containment atmosphere under various conditions [4, 6]. The initial concentration of iodine deposited on the painted coupon and the relative humidity were found to have significant impacts on the volatilization of organic iodide [6]. The ESTER-EPICUR tests investigated the iodine chemistry within the containment, focusing on the RI formation pathways not involving paints [14]. Specifically, the LOCOV tests examined reactivity under gamma irradiation on metal surfaces, such as electropolished stainless and galvanized steel, within an oxygen-depleted atmosphere containing organic gases (CH_4). The effects of methane, ethylene, surface, species and dose rate are checked through different tests.

The advanced iodine model (AIM), part of the AFP2 module in the AC^2-COCOSYS containment code, was developed to simulate aerosols, fission products and iodine chemistry [15-17]. Within AFP2, the CsI decomposition rate is calculated based on the dose rate, available CsI mass and a 'damage term' that accumulates proportionally to radioactivity, and a model dependent recovery rate. The recovery rate serves to buffer both the acceleration and deceleration of the decomposition process. In this study, COCOSYS is utilized to simulate CsI decomposition, RI formation, and the resulting distribution of iodine species across the coupons, atmosphere, vessel walls, and filters as investigated in the LOCOV and LOCOV2 tests.

2. Model Setup

The LOCOV and LOCOV2 tests utilized steel coupons as substrates for CsI deposits within a containment vessel. While the LOCOV test employed electropolished stainless steel with an initial iodine concentration of 1.86×10^{-4} mol/m^2, the LOCOV2 test used galvanized steel with a concentration of 1.60×10^{-4} mol/m^2 (see Table 1).

Table I. Experimental setups of LOCOV and LOCOV2

Test	LOCOV	LOCOV2
Coupon	Electropolished stainless steel	Galvanized steel
Aerosol	CsI	CsI
CsI concentration (mol/m^2)	$1.86\text{x}10^{-4}$	$1.60\text{x}10^{-4}$
Temperature (°C)	120	120
Pressure (bars)	3.5	3.5
Pre-irradiation	1 hour with dry air	1 hour with dry air 3 hours with wet air 50% R.H.
Irradiation	43 hours with Air (3% O_2) + 2% CH_4 + 50% R.H.	
Post-irradiation	1 hour with dry air (3% O_2) + 2% CH_4	
Dose rate (kGy/h)	1.2	6.9

Compared with LOCOV test, LOCOV2 test was performed with higher dose rate. The experiment is performed with continuous air flow that is directed through the vessel and released over a filter line in which the released chemical iodine components are trapped and analyzed according to the chemical compositions

that are separated in the different stages of the used May-pack filters. The air temperature in vessel is 25 °C and the pressure is 3.5 bar; both stay constant during the experiments LOCOV and LOCOV2. There is 1-hour pre-irradiation sweeping phase and 1-hour post-irradiation sweeping phase with 8.72×10^{-6} kg/s dry air (3% O_2 + 2% CH_4) for LOCOV test. LOCOV2 has extra 3 hours of pre-irradiation wet air sweeping period after the one-hour dry air sweeping phase. The irradiation phase duration is about 44.3 hours with 50% R.H. air (3% O_2 + 2% CH_4), in which the air gas injection rate is 6.25×10^{-6} kg/s and water injection rate is 1.54×10^{-6} kg/s. The different volatile iodine species (I_2, IO_x, RI) released during the test are transferred to the May-pack device and trapped on the different filters. The conceptual setup of the tests is shown in Fig.1.

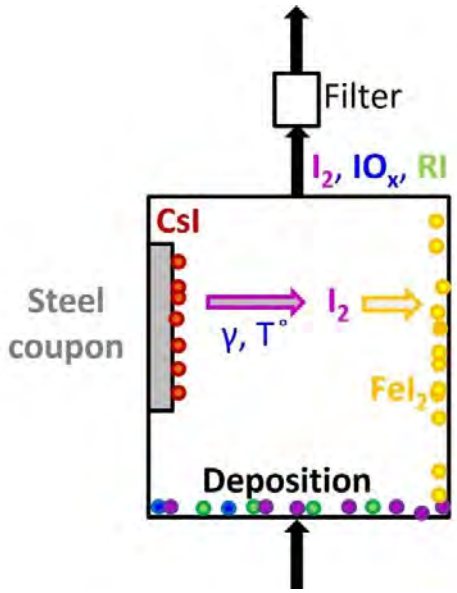

Figure 1. Conceptual model of LOCOV and LOCOV2 tests.

The principal reactions related to the CsI decomposition, RI formation and related iodine chemistry are shown in Fig. 2. In the iodine model AIM the decomposition of deposited CsI(dep) at the surface of coupon is simulated with two reactions that take place under irradiation: a faster reaction under irradiation with the production of I_2 and a slower reaction with the production of IO_x.

$$2\mathrm{CsI(dep)} + 2\mathrm{H_2O(g)} \xrightarrow{\gamma} \mathrm{I_2(g)} + 2\mathrm{CsOH(dep)} + 2\mathrm{H^+} \quad (1)$$

$$\mathrm{CsI(dep)} + \frac{1}{2}\mathrm{H_2O(g)} + \frac{x+0.5}{3}\mathrm{O_3(g)} \xrightarrow{\gamma} \mathrm{CsOH(dep)} + \mathrm{IO_x(g)} \quad (2)$$

A new conceptual model with a damage term is implemented for the CsI reaction under irradiation (Eq. 3). The idea behind the new model is to model the typical time dependent behavior of a delayed decomposition of CsI by introducing a damage term H (H for harm and to distinguish it from the dose D) in the reaction mechanism. The damage term accumulates proportional to the deposited mass, a model dependent recovery rate and the reaction rate of CsI:

$$\frac{dH}{dt} = m_{CsI} D_{gas} - H f_{rec} - \frac{\dot{r}}{m_{CsI}} H \quad (3)$$

The new CsI decomposition rate is then simply described as:

$$\frac{d[\mathrm{CsI}]}{dt} = -k_r^{\gamma} H \quad (4)$$

Where:

H	Damage term [kg·kGy/h]
m_{CsI}	Available CsI mass [kg]
D_{gas}	Dose rate [kGy/h]
f_{rec}	Recovery factor, which is a function of decomposition rate [1/s]
$\dot{r}$	Reaction rate of CsI [kg/s]
[CsI]	CsI concentration at the coupon surface [kg/ m^2]
k_r^{γ}	Radiolytic reaction coefficient [1/(m^2·kGy)]

Generally, the decomposition rate is high when there is more available CsI mass and the dose rate is high. At the beginning, there is more CsI available for reaction, so the decomposition rate will be high. As irradiation consumes more CsI, the amount available for reaction diminishes, leading to a decrease in the decomposition rate. However, the recovery factor f_{rec} also declines alongside the decomposition rate, effectively buffering the overall rate reduction.

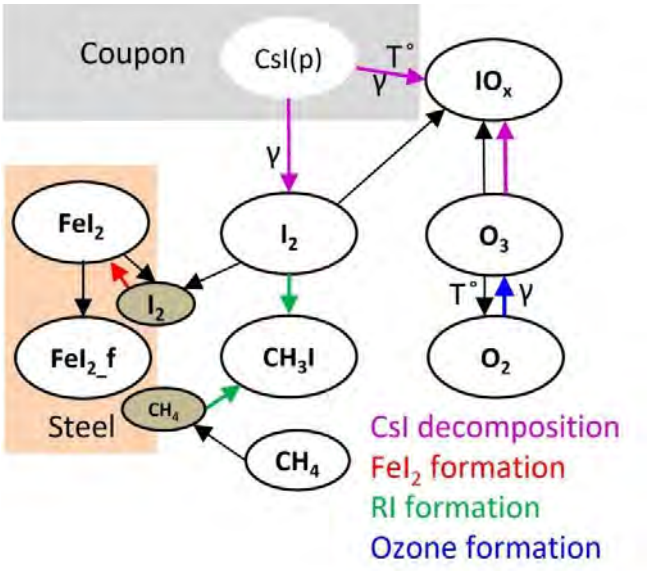

Figure 2. Schematic modelling of CsI destruction and RI formation.

Depending on the dose rate, ozone is formed from the oxygen in the air. Radiolytically produced ozone can react with gaseous I_2 to form IO_x aerosols, which exhibit distinct behavior compared to gaseous I_2. The backward conversion of IO_x to I_2 is also possible under accident typical gas temperatures. Deposition of I_2 onto steel surface and the subsequent chemical reaction with steel is an unwanted removal process for volatile iodine from the gas phase e.g. in iodine tests. The reaction of gaseous iodine (I_2) with dry stainless-steel surfaces can be described as the sequence of two processes: an initial, fast and reversible physisorption process, followed by a slower chemical reaction of the physical sorbed I_2 with the steel producing chemisorbed, non-volatile metal iodides (represented by FeI_2). FeI_2 can be further oxidized forming strongly bound iron-iodide-oxides FeI_2_f, which is a permanent iodine sink, and no iodine can be released from it into the gas phase again. Organic iodine formation occurs through a reaction of deposited methane with gaseous I_2, which was considered as the best model through comparing the different RI generation mechanisms models results with test measurements.

3. Simulation Results

3.1. LOCOV test simulation

The measurement showed that there is 30.7% missing mass balance at the end of LOCOV test [14]. Therefore, the LOCOV model simulated with COCOSYS focuses on the released iodine mass evolution in filter, the mismatch of iodine mass on coupon at the end is ignored.

Methane is injected into the vessel during the whole test process, so in the first 1 hour, the concentration of methane in the vessel increases quickly. When the irradiation starts, the radiolysis of the air/steam atmosphere produces ozone immediately (Fig. 3). The radioactive decomposition of CsI releases I_2. The oxidation of I_2 by ozone produces IO_x; simultaneously, the thermal production of IO_x also consumes ozone. Due to these ozone-consuming reactions, the ozone concentration decreases slightly and then maintains a constant level until the end of irradiation. Due to the extremely slow thermal decomposition of CsI, the IO_x concentration remains negligible and therefore omitted from the figure. Injected methane reacts with I_2 to generate organic iodine; however, the generation rate declines as the I_2 concentration is depleted. Once the irradiation stops, the production of both ozone and I_2 from CsI decomposition also ends. The remaining ozone and I_2 react rapidly, consuming both reactants in a short timeframe. Consequently, the concentration of methane begins to recover, while the concentration of organic iodine decreases sharply.

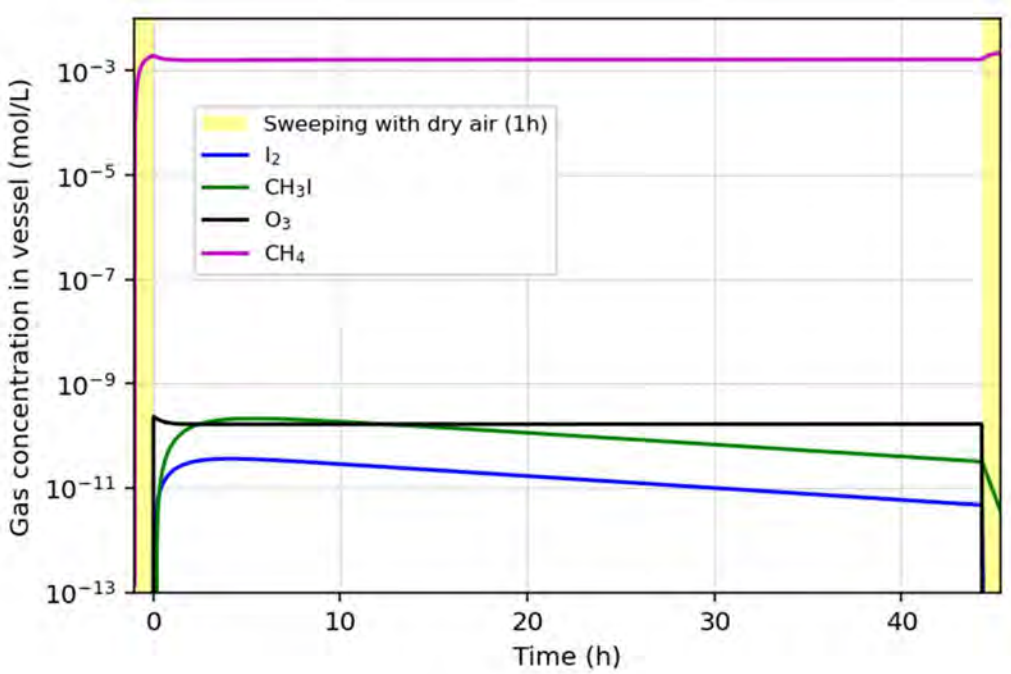

Figure 3. Evolution of gas phase species concentration in the containment for LOCOV model.

Fig. 4 illustrates the overall iodine balance across the hosts coupon, vessel atmosphere, vessel structures, and filter. At the end of simulation, there is totally 74.9% iodine deposited at the steel surface, 14.5% iodine in filter, 10.6% iodine on coupon. Due to the continuous flow design of the experiment, only a small fraction is present in the vessel atmosphere during the whole experimental sequence. The released gas phase I_2 from CsI decomposition in vessel deposits on the surfaces of the vessel walls. With the time going on, the deposited I_2 reacts with Fe and the FeI_2 is produced. FeI_2 can be further oxidized forming strongly bound iron-iodide-oxides, so the deposited iodine mass in form of FeI_2 continues increasing (Fig. 5). On the other hand, the deposited I_2 starts decreasing 10 hours after the irradiation. Because of the low concentration of

airborne IO_x, the deposited iodine in form of IO_x can be ignored. At the end of simulation, 95% of steel surface deposited iodine are FeI_2, only 5% are in form of I_2. Characterizing the spatial and chemical distribution of iodine is essential for understanding the system's behavior. This approach ensures the model can be accurately calibrated as more detailed experimental data becomes available.

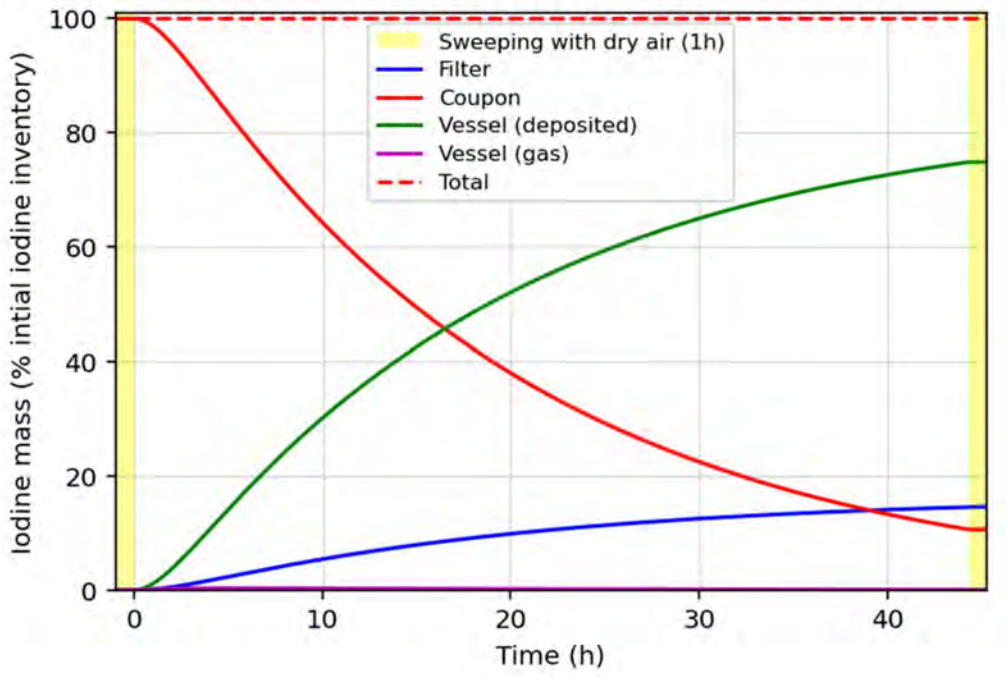

Figure 4. Evolution of iodine mass distribution for LOCOV model.

The simulated iodine mass in the filter is compared with experimental measurements from the LOCOV test in Fig. 6. The simulation indicates that the I_2 generation and subsequent organic iodine production rates are lower during the initial irradiation phase, resulting in a more gradual increase in the filter load. Generally, the simulation accurately captures the observed evolution of organic iodine. For the molecular iodine on the filter, there is 3.5% deposition at the end of simulation, which is a little bit lower than the measured data. The linear gradient trend in the measured data suggests a quasi-constant gas I_2 concentration within the vessel. However, during the final one-hour dry air weeping phase, after irradiation stopped, a sudden release of molecular iodine was detected on the filter. The mechanism behind this release remains unclear and requires more detailed observation. The simulation shows no more molecular iodine released from the system in the last hour. Same as the test observation, the concentration of IO_x is very low and can be ignored. The radioactive decomposition dominates the CsI release.

Within the COCOSYS calculation a large part of iodine is trapped on the steel walls of the vessel. This is a possible explanation for the large balance error observed in the experiment. However, the iodine-steel model of COCOSYS is derived from the specifics of the THAI vessel operated by Becker Technologies in Germany [18]. The steel inside the EPICUR facility is different and assumed to be inert to iodine deposition and reaction to a great extent. Therefore, the actual iodine sink remains unknown, though the piping utilized during the experiment may also account for the large balance error.

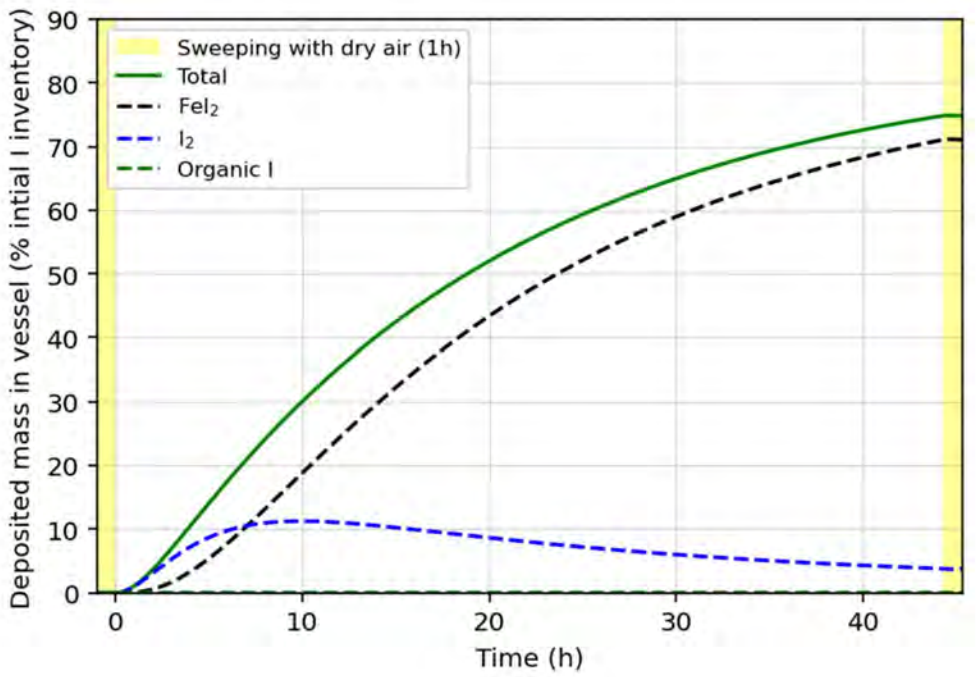

Figure 5. Evolution of deposited iodine at the steel surface for LOCOV model.

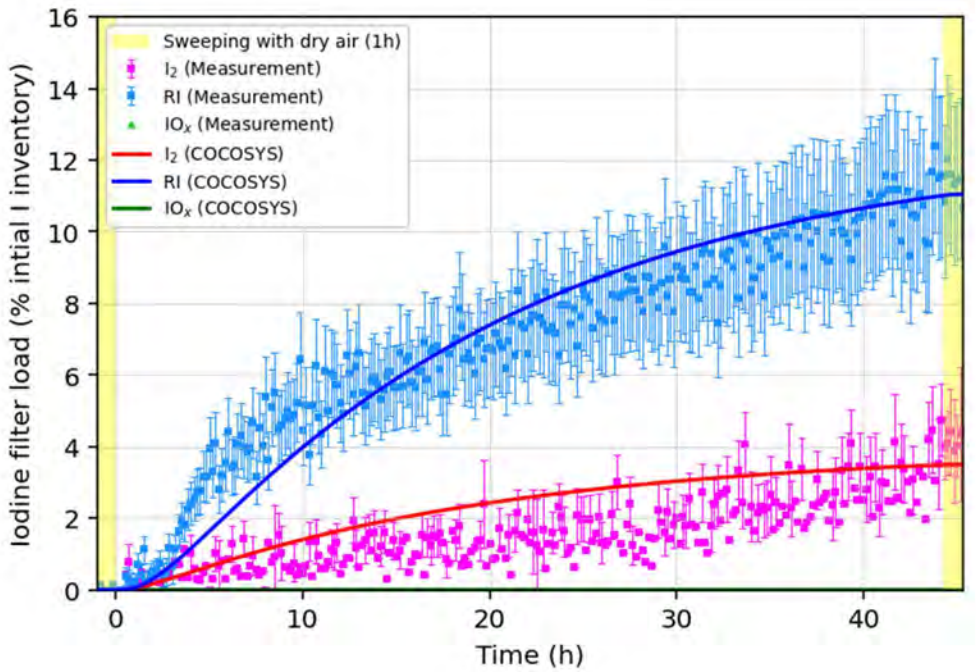

Figure 6. Comparison of measured and simulated iodine activity in filter for LOCOV test.

3.2. LOCOV2 test simulation

The chemical model implemented in COCOSYS as depicted in Fig.2 has been developed on LOCOV results. To estimate the general validity of this model and check the sensitivity of dose rate on CsI

decomposition and RI generation, also the experiment LOCOV2 has been simulated. Different from LOCOV test, LOCOV2 used galvanized steel as the coupon surface material and higher dose rate. Because of the higher dose rate in LOCOV2, which is 6.9 kGy/h compared to only 1.2 kGy/h in LOCOV test, the decomposition rate of CsI on coupon and the ozone generation rate are higher in LOCOV2 simulation. Therefore, the molecular iodine I_2 concentration in the containment increases quickly when the irradiation starts, and the concentration of ozone is much higher compared with LOCOV model (Fig. 7). Consequently, the generation rate of RI is higher, too. These higher concentrations of I_2 and RI cause more iodine mass transport out of the vessel and into the filter (Fig. 8). This fast mass flow-out limits the deposition of iodine on the steel wall surfaces. At the end of simulation, there is almost 54% iodine mass in the filter, and there is still 46% iodine mass on the coupon (Fig. 8). The iodine deposition at the containment wall surface can be ignored.

At the end of experiment LOCOV2 there is 0.3% IO_x, 29.1% I_2 and 23.0% RI deposition on the filters compared to the initial inventory. Compared to the LOCOV test, higher rates of CsI decomposition of RI formation resulted in a greater release of molecular and organic iodine. Generally, the simulated organic iodine on the filter shows good agreement with the measured RI evolution (Fig. 9). Regarding the molecular iodine on the filter, the simulation shows a slower release rate in the first 20 hours compared to experimental results. The damage term implemented in COCOSYS buffers the high CsI decomposition rate when both the dose rate and available CsI mass are elevated. This likely explains why the model underestimates the initial rapid release of molecular iodine; However, the simulation successfully captures the overall release trends.

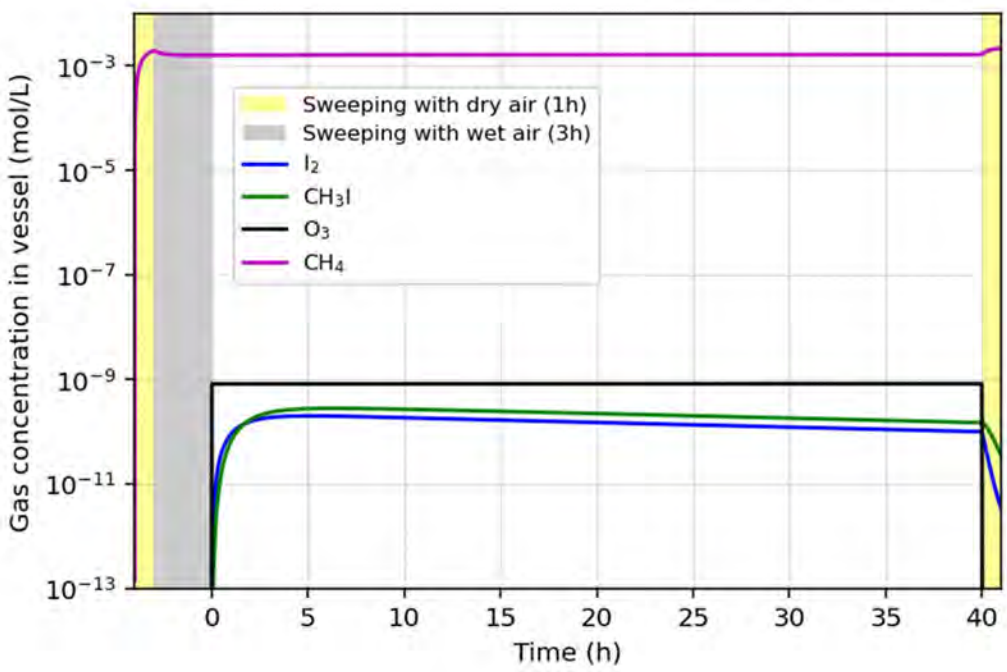

Figure 7. Evolution of gas phase species concentration in the containment for LOCOV2 model.

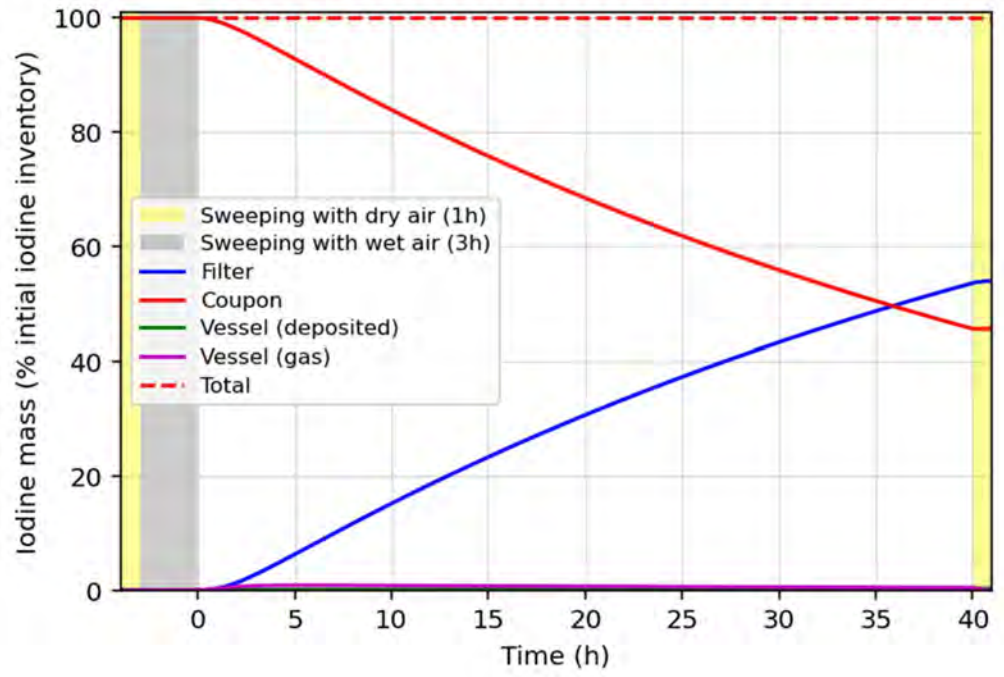

Figure 8. Evolution of iodine mass distribution for LOCOV2 model.

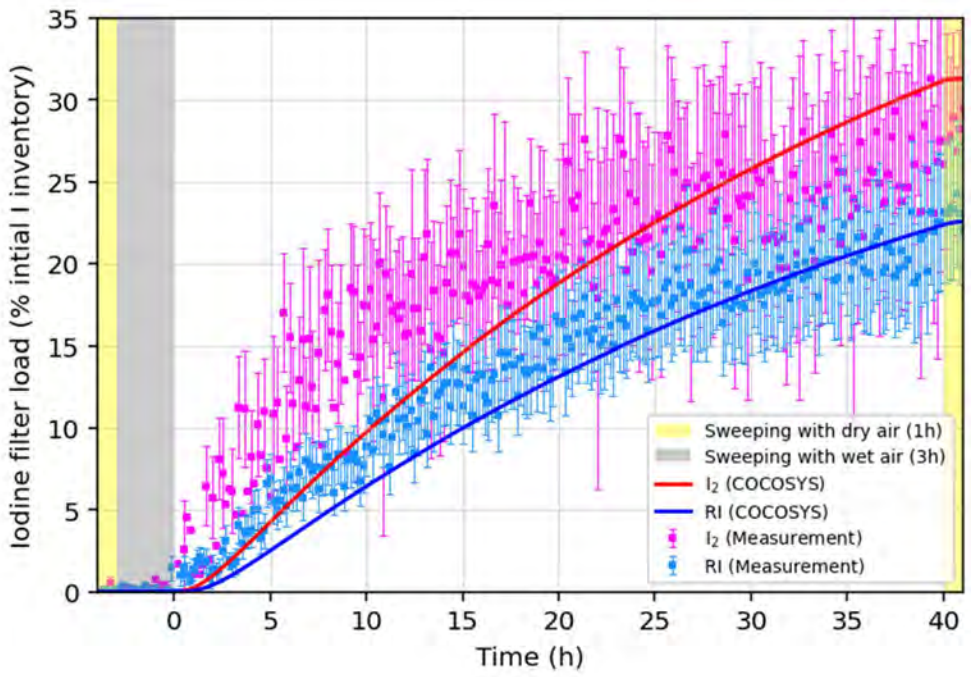

Figure 9. Comparison of measured and simulated iodine activity in filter for LOCOV2 test.

4. CONCLUSIONS

The LOCOV and LOCOV2 tests, which investigate CsI decomposition and RI generation, were simulated using the AFP2 module in COCOSYS. The models show that irradiation significantly accelerates CsI decomposition compared to thermal processes. Injected methane reacts with I_2 to generate organic iodine, while the oxidation of I_2 by ozone produces IO_x aerosols. Additionally, gaseous I_2 deposits onto the steel vessel walls, where the model predicts a subsequent reaction with iron to form FeI_2. While higher dose rates increased CsI decomposition, the lower I_2 deposition rate on the steel wall in LOCOV2 may be attributed to relatively high humidity, a phenomenon warranting further study. Overall, the agreement between simulation and experimental data demonstrates the robust capabilities of COCOSYS in modelling organic iodide formation.

In these experiments, a specific fraction of iodine reacts with volatile organic compounds (VOC). While these species may form directly at the steel surfaces, the underlying mechanisms remain unidentified. Additionally, mass balances are often incomplete across various tests. COCOSYS simulations indicate this may be due to the trapping of iodine species on the EPICUR vessel walls or within the external piping. To further clarify the generation processes of organic and molecular iodine, additional measurement data on the coupon and steel structure surfaces are required.

ACKNOWLEDGMENTS

The authors acknowledge the OECD ESTER project and the IRSN team (now ASNR) with respect to the experiment data and the related synthesis reports.

This paper reflects only the author's view, and the OECD NEA is not responsible for any use that may be made of the information it contains.

The development and the validation of AC^2 is sponsored by the German Federal Ministry for Environment, Climate Action, Nature Conservation and Nuclear Safety (BMUKN) based on decisions by the German Bundestag within several projects.

The authors are grateful to the anonymous reviewers for their thorough evaluation and valuable suggestions, which helped improve the clarity and impact of this paper.

REFERENCES

1. J. Colombani, C. Pascal, L. Martinet, C. Duffieus and O. Leroy, *AER-CsI STEM/EPICUR tests synthesis report: Formation and release of iodine volatile species from CsI aerosols under radiation,* IRSN, France, Rapport n° PLEIADE PSN-RES/SEREX/2015-00292, STEM n° 23 (2015).
2. J.C. WREN, J.M. Ball and G.A. Glowa, "Chemistry of iodine in containment," Nuclear technology, 129(3), pp. 297-325 (2000).
3. R. Zilliacus, P. Koukkar, T., Karjunen, H. Sjövall, *Formation and behaviour of organic iodine*, Nordic nuclear safety research, ISBN 87-7893-095-2, Finland (2002).
4. S. GUILBERT et al, "Radiolytic oxidation of iodine in the containment at high temperature and dose rate," *Proceedings of the Nuclear Energy for New Europe*, Portoroz, Slovenia, Sept 10-13 (2007).
5. L. Bosland, K. Chevalier-Jabet, *Main lessons learnt from 40 years of R&D on iodine source term prediction: Identification of the main parameters governing iodine volatility in PHEBUS FP tests*, Progress in Nuclear Energy 177, 105473, ISSN 0149-1970, https://doi.org/10.1016/j.pnucene.2024.105473 (2024).

6. J. Colombani, L. Bosland, C. Pascal, L. Martinet and C. Gomez, *Experimental study of organic iodide formation from painted surfaces in the containment atmosphere during a severe accident,* ICAPP 2011, Nice & Fréjus, France, May 2011. Irsn-04841918 (2011).
7. L. Bosland, O. Leroy, C. Alvarez, M. Chebbi, C.M. Louvet, S. Bourrous and K.C. Jabet, *Study of CsI and iodine oxides (IOx) aerosols and trapping efficiency of small aerosols on sand bed and metallic filters under irradiation*, Annals of Nuclear Energy, 142, pp.104013, 10.1016/j.anucene.2021.104013, hal-03409665 (2021).
8. L. Bosland, J. Colombani, *Study of iodine releases from epoxy and polyurethane paints under irradiation and development of a new model of iodine-Epoxy paint interactions for PHEBUS and PWR severe accident applications*, J Radioanal Nucl Chem, 314, 1121-1140, https://doi.org/10.1007/s10967-017-5458-9 (2017).
9. L. Bosland, S. Dickinson, G.A. Glowa, L.E. Herranz, H.C. Kim, D.A. Powers, M. Salay, S. Tietze, *Iodine–paint interactions during nuclear reactor severe accidents*, Annals of Nuclear Energy, 74, 184-199, https://doi.org/10.1016/j.anucene.2014.07.016 (2014).
10. S. Guilbert, L. Bosland, S. Fillet, D. Jacquemain, B. Clement, F. Andreo, G. Ducros, S. Dicknson, L. E. Herranz, J. Ball, *Formation of organic iodide in the containment in case of a severe accident,* 2008 Annual Meeting on American Nuclear Society, Anaheim (CA), United States, June 2008, pp.261-292, Irsn-04841909 (2008).
11. X. Gong, D. Qin, M. Zhong, H. Liu, H. Wu, M. Kang, *Kinetic study of diiodine adsorption behavior on the epoxy paint in PWRs*, J Radioanal Nucl Chem 334, 2891-2900, https://doi.org/10.1007/s10967-025-10050-0 (2025).
12. O. Leroy and L. Bosland, *Study of the stability of iodine oxides (IxOy) aerosols in severe accident conditions*, Annals of Nuclear Energy, 181, pp.109526, 10.1016/j.anucene.2022.109526, hal-03969323 (2023).
13. L. Bosland and J. Colombani, *Study of the radiolytic decomposition of CsI and CdI_2 aerosols deposited on stainless steel, quartz and Epoxy painted surfaces*, Annals of Nuclear Energy, 141, pp.107241, https://doi.org/10.1016/j.anucene.2019.107241 (2020).
14. O. Leroy, *ESTER-EPICUR synthesis experimental report*, ISRN, France, Report n° IRSN/2024-00170, ESTER n° 9 (2024).
15. J. Hoffrichter and M. K. Koch, *Simulation of LOCA-typical containment conditions with COCOSYS on the basis of THAI-test TH-29.3*, Kerntechnik, 84 (5), pp.434-440, https://doi.org/10.3139/124.190035 (2019).
16. L. Tiborcz and S. Beck, *Uncertainty and sensitivity analysis of the fission product behaviour in the Phébus FPT1 test with the system code AC2*, Nuclear Engineering and Design, 429, pp.113594, ISSN 0029-5493, https://doi.org/10.1016/j.nucengdes.2024.113594 (2019).
17. S. Arndt, S. Band, S. Beck, D. Eschricht, D. Iliev, H. Nowack, N. Reinke, C. Spengler, W. Klein-Heßling, M. Sonnenkalb, G. Weber, *COCOSYS 3.3.0 User Manual*, Gesellschaft für Anlagen- und Reaktorsicherheit (GRS) gGmbH, GRS-P-3/ Vol. 1 (2025).
18. S. Gupta, T. Kanzleiter, K. Fischer, G. Poss, *Reactor Safety Research Program at THAI Test Facility,* Proceedings of the 17th Pacific Basin Nuclear Conference, Cancun, Mexico, October 2010 (2010).

COCOSYS simulation of CsI decomposition under irradiation and organic iodide formation

ERMSAR 2026, Madrid, **Chuanhe Lu**, Holger Nowack 20.05.2026

Contents

- New CsI decomposition and organic iodide formation model
- Simulation model set-up
- Simulation results
- Summary

Key factors for CsI decomposition

Experimental results (EPICUR AER-CsI, ESTER-EPICUR organic iodides experiments):

- **CsI concentration on the coupon**
- **Dose rate**
- Temperature
- Relative humidity
- Nature of the coupon

Updated AFP2 module in AC²-COCOSYS: aerosols, fission products and iodine chemistry

New CsI decomposition mechanism

- Simplified CsI decomposition process: no sensitive fraction

$$2CsI(dep) + 2H_2O(g) \xrightarrow{\gamma} I_2(g) + 2CsOH(dep) + 2H^+$$

$$CsI(dep) + \frac{1}{2}H_2O(g) + \frac{x+0.5}{3}O_3 \xrightarrow{\gamma,T} CsOH(dep) + IO_x(g)$$

- Delayed CsI decomposition (new terms are introduced into the reaction mechanism)

$$\frac{dH}{dt} = m_{CsI}D_{gas} - Hf_{rec} - \frac{\dot{r}}{m_{CsI}}H$$

$$\frac{d[CsI]}{dt} = -k_r^{\gamma}H$$

- New recovery factor:
  - buffers the decomposition rate decreases process

H	Damage term [kg·kGy/h]
m_{CsI}	Available CsI mass [kg]
D_{gas}	Dose rate [kGy/h]
f_{rec}	Recovery factor, which is a function of decomposition rate [1/s]
$\dot{r}$	Reaction rate of CsI [kg/s]
[CsI]	CsI concentration at the coupon surface [kg/ m^2]
k_r^{γ}	Radiolytic reaction coefficient [1/(m^2·kGy)]

New organic iodide generation model

LOCOV test:

- check if organic iodide also occurs at the surface of steel directly with volatile organic compounds (VOC)

$$I_2(g) + 2R(dep) \rightarrow 2RI(g)$$

- CsI decays under irradiation (γ)
- CsI builds I_2 in the gas phase under γ
- I_2 adsorbs on steel and forms Fe-species
- Methane is also sorbed on the steel surface
- Reaction on the steel surface between CH_4 and **I_2 in the gas phase**
- Production of organic iodine in the gas phase

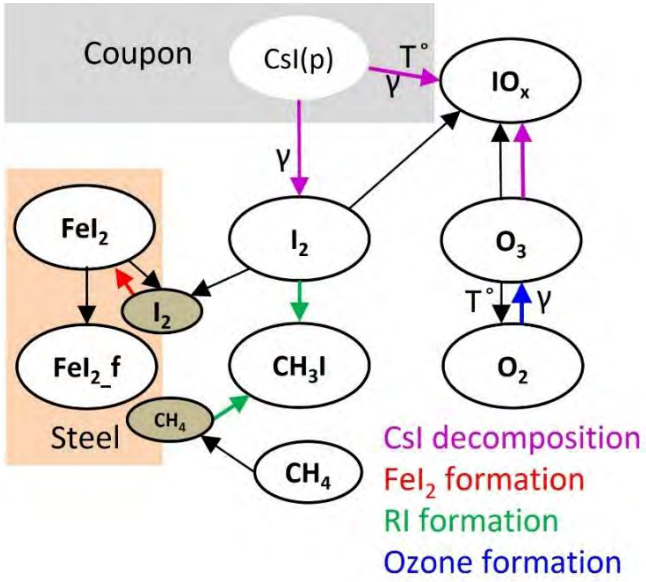

LOCOV tests

Test	LOCOV	LOCOV-2
Objectives	Surface Effect	
Sample	Stainless steel	Galvanized steel
Aerosol	CsI	CsI
Concentration ([I] in mol/m^2)	1.86×10^{-4}	1.60×10^{-4}
Temperature(°C)	120	
Pressure (bar)	3.5	
Gas	Air(3% O_2) + 2%CH_4 + 50% R.H.	
DR(kGy/h)	1.2	6.9
Pre-irradiation	1h with dry air	1h with dry air then 3 h with Air-50% R.H.

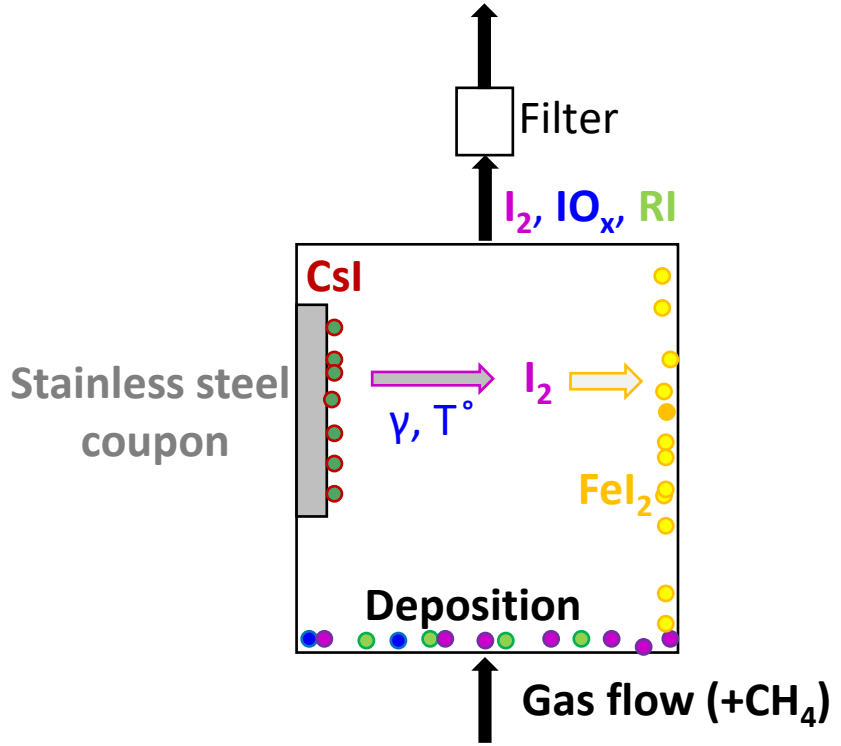

- Calculation with AFP2 module in AC^2-COCOSYS V3.2

LOCOV simulation results

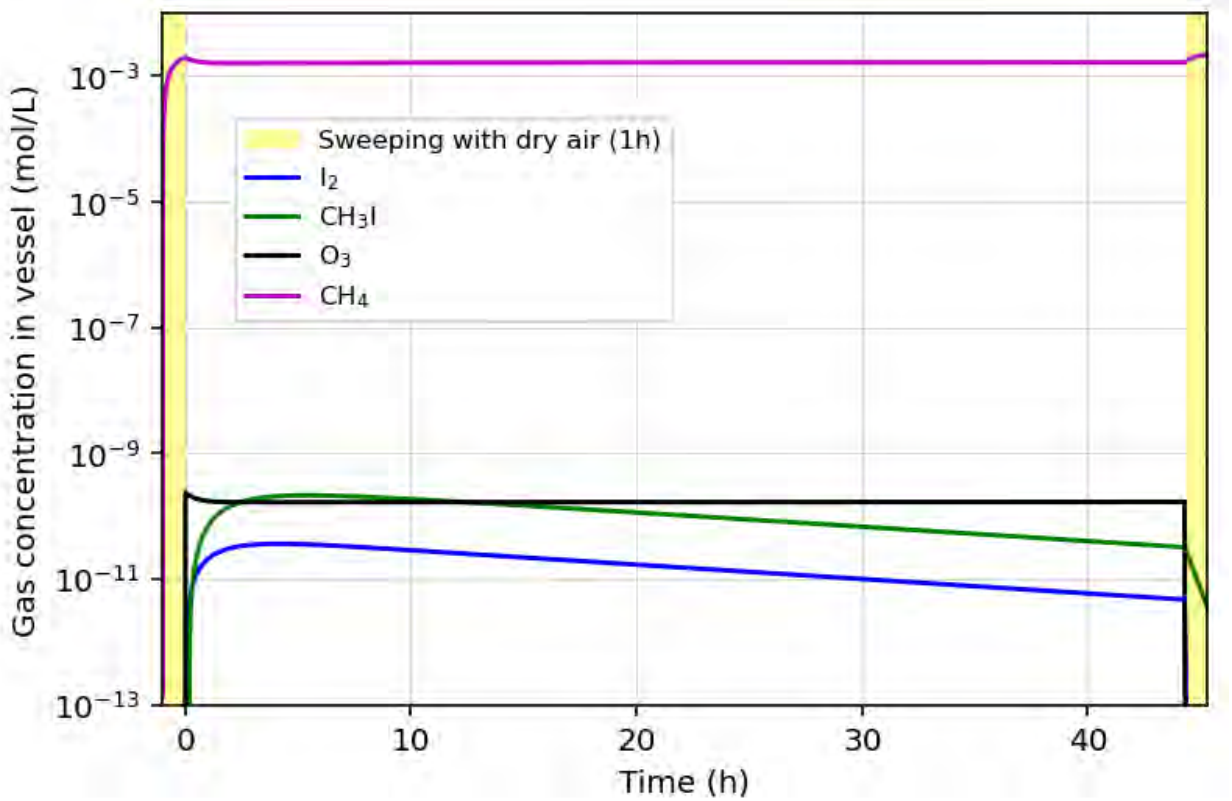

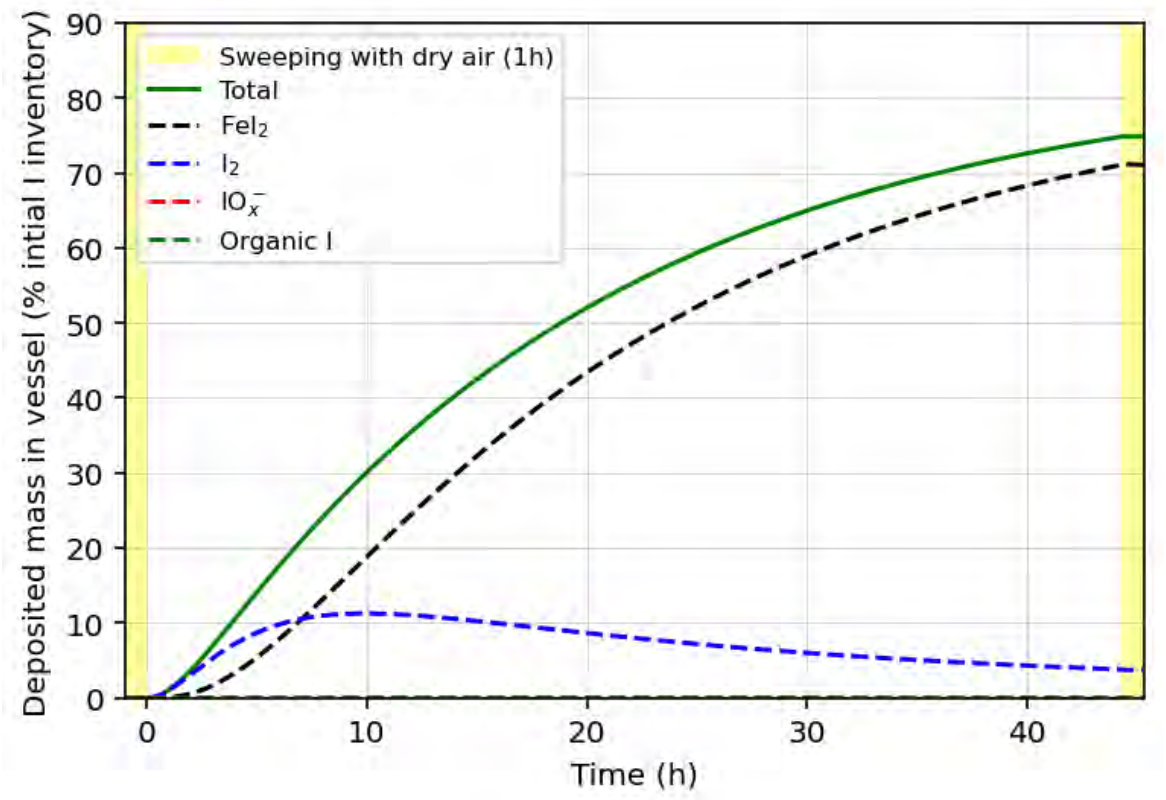

- There is more gas phase organic iodide than gas phase I_2 in the containment
- Most of Iodine mass on the steel surface is in form of FeI_2

LOCOV simulation results

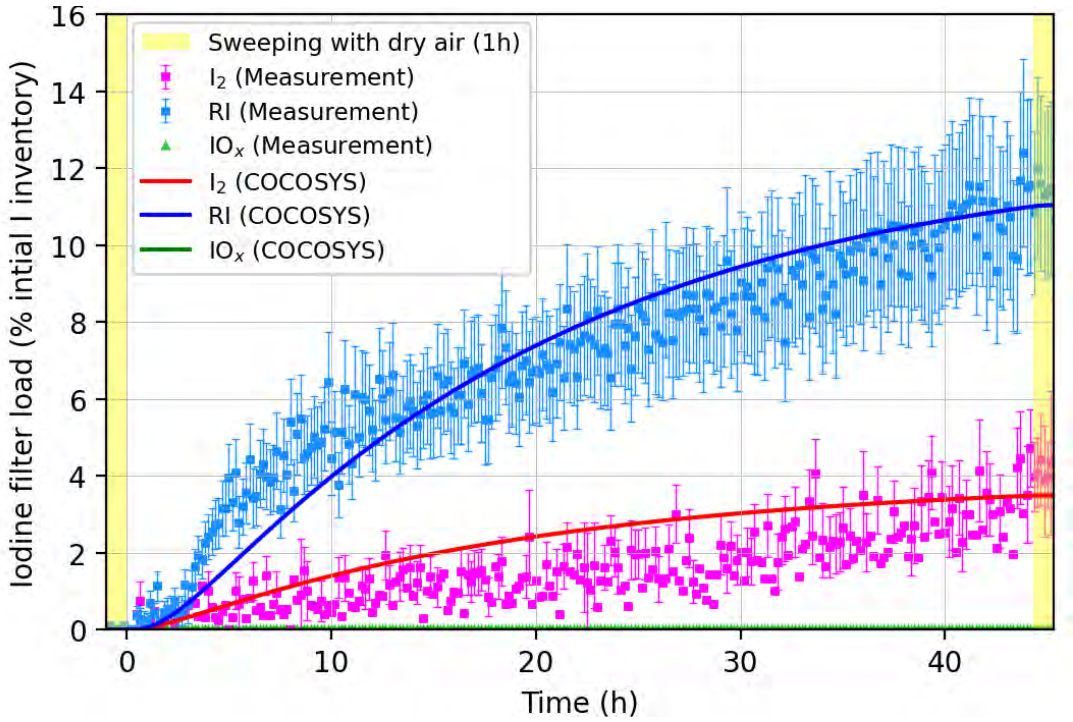

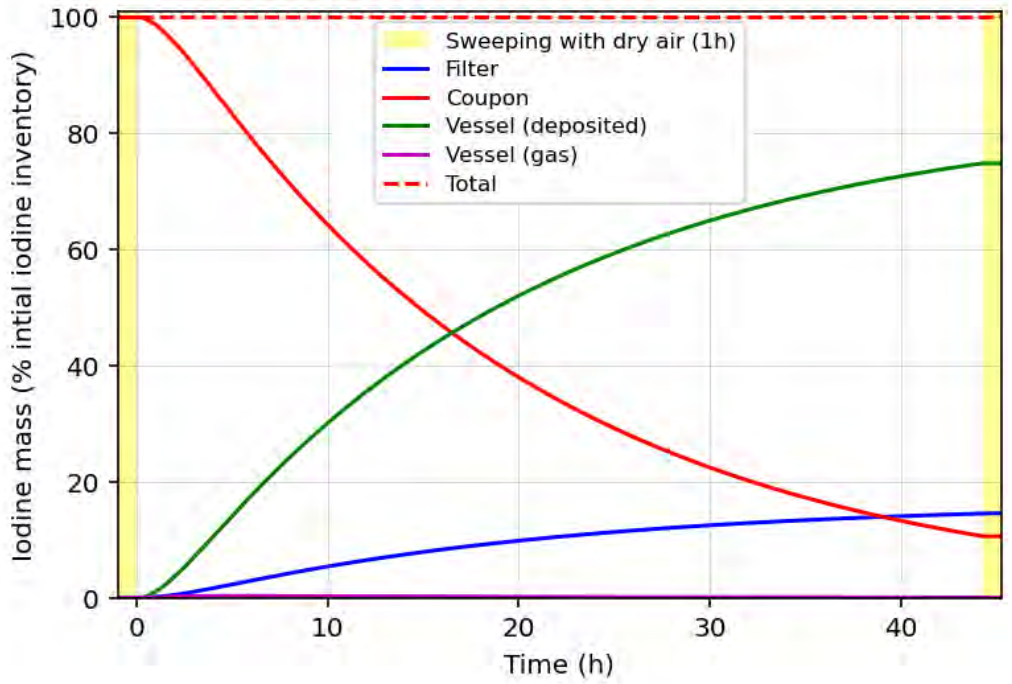

- More organic iodide than molecular iodine in filter
- Most of iodine mass is deposited at the steel surface

LOCOV2 simulation results

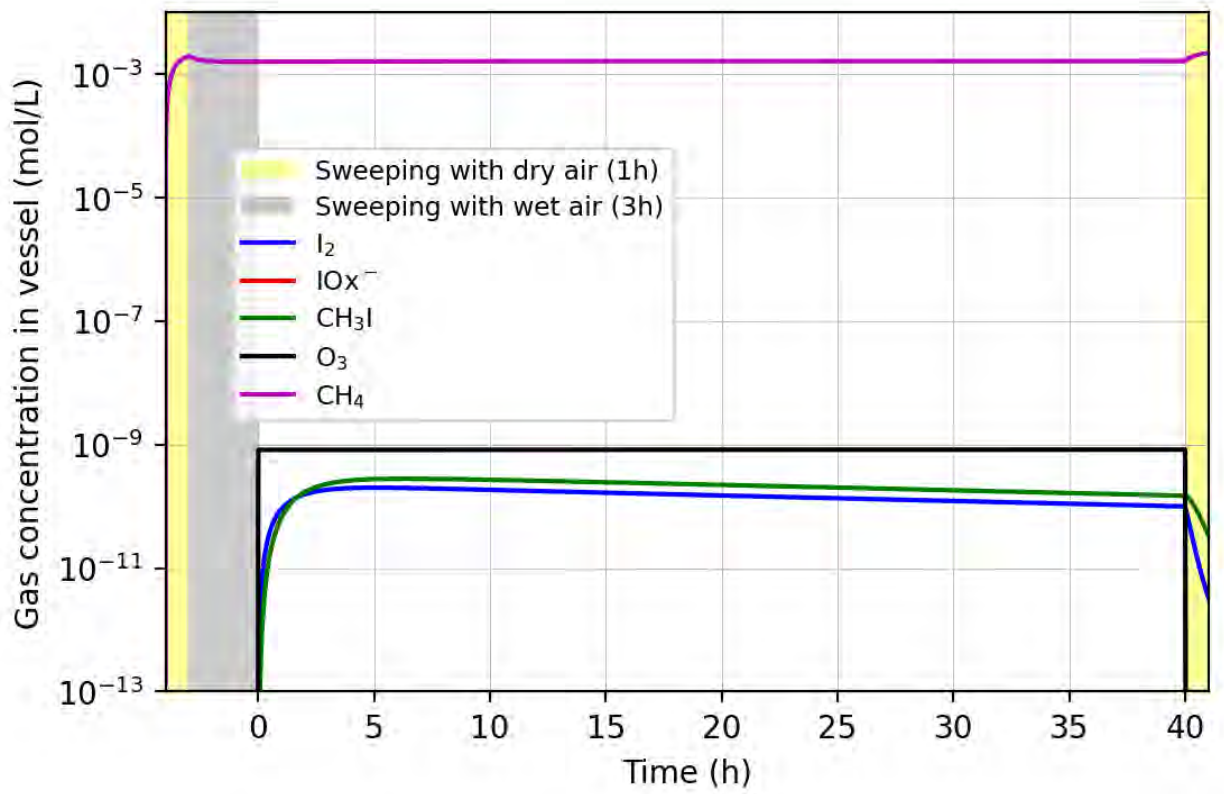

- Higher gas phase I_2 concentration in the containment compared with LOCOV.

LOCOV2 simulation results

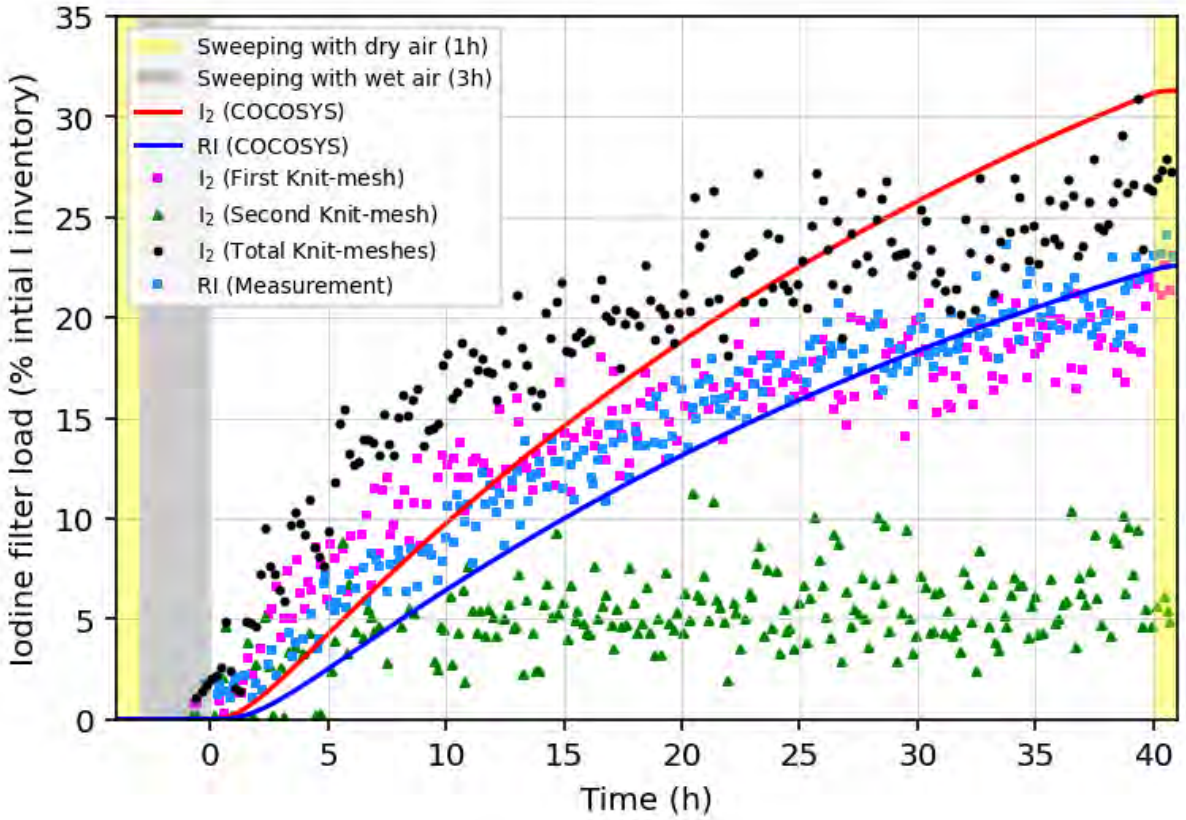

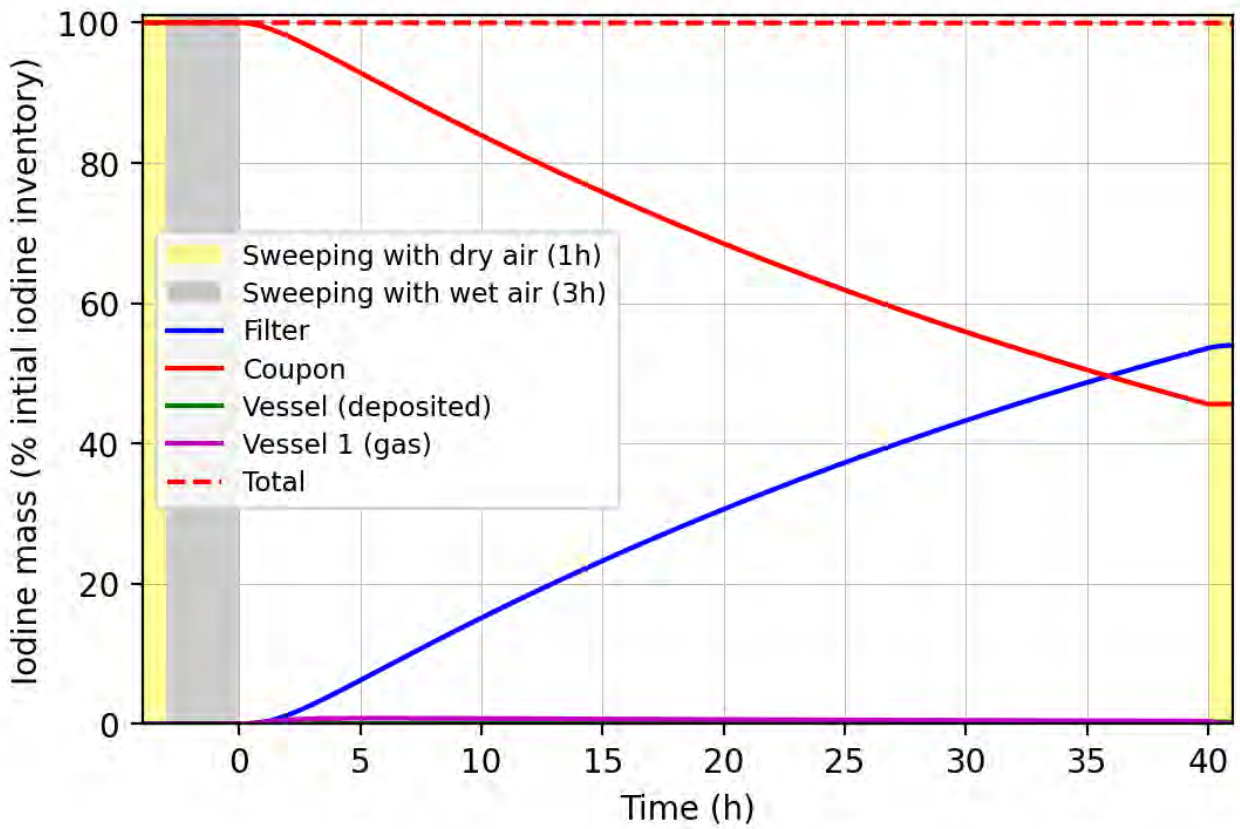

- More molecular iodine in filter
- Most of iodine mass is transported into filter
- There is still many iodine mass on the coupon
- Almost no iodine deposited at the steel surface

Conclusion

- Simulation with new CsI decomposition and RI production has similar results as the findings of experiment.
- The new CsI decomposition function and RI generation are properly implemented.
- Controlling process for fast iodine release at the early period of irradiation needs to be discussed.
- Iodine sorption on steel surface requires more detailed study.

Thank you for your attention!

This work was supported by

On the basis of a decision by the

The 12th European Review Meeting on Severe Accidents Research

May 18-22, 2026, Universidad Carlos III de Madrid, Madrid, Spain

TECHNICAL SESSION 5.4: HYDROGEN RISK AND CONTAINMENT BEHAVIOR

Chairs: S. Gupta (Framatome), K. Dieter (Becker Technologies GmbH)

ID128	**Ex-Vessel Severe Accident 3D Simulation with GOTHIC 8.3(QA): Methodology and Application to a PWR-KWU Containment** G. Jiménez (Universidad Politécnica de Madrid)	Paper Presentation
ID146	**Implementation of a Safety-Related Air-Cooling System in a PWR-W Dry Containment using GOTHIC 3D** A. García-Herranz (Universidad Politécnica de Madrid)	Paper Presentation
ID173	**Passive Autocatalytic Recombination of Hydrogen – An Application in the ITER Fusion Reactor** M. Braun (Framatome GmbH)	Paper Presentation

EX-VESSEL SEVERE ACCIDENT 3D SIMULATION WITH GOTHIC 8.3(QA): METHODOLOGY AND APPLICATION TO A PWR-KWU CONTAINMENT

Serra, L.*, Jiménez, G.
Universidad Politécnica de Madrid, ETSI Industriales
c/ José Abascal, 2, 28006 Madrid
luis.slopez@upm.es ; gonzalo.jimenez@upm.es

Braun, M.
Framatome GmbH, 91052 Erlangen, Germany
matthias.braun@framatome.com

Herranz, L.E.
CIEMAT, 28040 Madrid, Spain
luisen.herranz@ciemat.es

ABSTRACT

The European AMHYCO project (Euratom 2019–2020, GA No 945057) investigated the risk of H_2/CO combustion within nuclear power plant containments during the ex-vessel phase of a severe accident (SA), with the objective of supporting the enhancement of the Severe Accident Management Guidelines (SAMGs). In this framework, a detailed model of a generic PWR-KWU containment was created with the 3D code GOTHIC 8.3(QA). For a selected Total Loss of AC Power (TLAP) scenario, more than ten hours in the ex-vessel progression were simulated.. This represents a novel achievement, as the GOTHIC code was not specifically designed for ex-vessel phenomenology. The results proved the capability of the code to reproduce relevant footprints of the accident at a reasonable computational cost using a desktop PC.
A robust and efficient 3D containment model was established in the GOTHIC code, using the Preventive Methodology (as developed by UPM). For the mass & energy input into the containment model, a procedure was created to adapt selected ex-vessel outputs from integral codes such as MELCOR. This was implemented through a Lumped Parameter (LP) cavity control volume in GOTHIC, configured with thermal structures and injection sources, and embedded in the 3D mesh. This allows GOTHIC to handle the large mass and energy releases coming from the reactor vessel at the time of its failure, including heat and combustible gas inputs.
Comparisons with MELCOR calculations of the same TLAP sequence during AMHYCO´s Work Package 4 showed consistent trends in containment temperature and gas concentration evolution across the main regions driving natural circulation. Furthermore, GOTHIC provided enhanced spatial resolution of H_2 stratification and local ex-vessel effects, visualized through post-processing of cell-averaged values. The results support cross-code benchmarking and contribute to strengthening the methodological basis for containment performance and combustion risk assessment under SA conditions.

KEYWORDS
AMHYCO, combustion risk, ex-vessel phase, SAMG, GOTHIC

1. INTRODUCTION

Severe accidents (SAs) in light water reactors can lead to the in-core generation and subsequent in-containment accumulation of combustible gases, primarily hydrogen (H_2) and — during the ex-vessel phase — also carbon monoxide (CO). If these gases are transported to regions of the containment prone to accumulation, they can form flammable clouds whose combustion could threaten containment integrity and the safety systems availability [1]. Therefore, when analyzing SAs, one of the main concerns is to simulate adequately the spatial distribution of those gases. During long SA sequences, the containment atmosphere is shaped by buoyancy-driven circulation, condensation patterns, and geometry-driven recirculation loops that may sustain stratification and localized accumulation pockets [2]. In highly compartmentalized designs, such as the PWR-KWU containment, non-intuitive concentration gradients can develop across elevations and rooms, challenging the well-mixed conditions assumption and making the assessment of combustion risk strongly dependent on spatial resolution [3]. After the Fukushima Daiichi accident, many European utilities and regulators implemented a broad set of hardware upgrades, including the installation of passive autocatalytic recombiners (PARs) and filtered containment venting systems. These, together with updated insights from experiments and modelling, have driven the revision and strengthening of Severe Accident Management Guidelines (SAMGs). In European pressurized water reactors (PWRs), PARs are a key mitigation measure, but their effectiveness depends on the local availability of combustible gases and oxygen (O_2). In the late accident phase, the situation is further complicated by the presence of additional non-condensable gases (NCGs), potential O_2 depletion, and instrumentation limitations, in particular for CO monitoring [4].

The AMHYCO project (Euratom 2019–2020, GA No 945057) specifically targeted the ex-vessel phase, combining experiments, models, and containment simulations to translate academic advances into SAMG-oriented guidance [5]. From the simulation standpoint, AMHYCO provided a shared geometrical database for lumped parameter (LP), 3D, and computational fluid dynamics (CFD) analyses of representative PWR containments (Western, KWU, VVER). The aim was to enable consistent cross-code comparisons and targeted investigations of phenomena that LP approaches may lack due to inherent spatial averaging. This follows in the footsteps of mature methodologies which recommend a hierarchical and systematic approach towards SA phenomenology and H_2 risk studies [6]. Integral/system codes such as MELCOR can simulate the most relevant phenomenology surrounding core degradation and ex-vessel phenomena over many hours [7]. However, the LP approach of these codes allow only limited spatial resolution of the containment atmosphere. Conversely, 3D containment tools can resolve circulation and stratification patterns from the compartment or room scales down to cell-averaged fields [8]. Yet, some of these codes, e.g. GOTHIC, do not mechanistically compute ex-vessel melt evolution and must rely on externally prescribed source terms for molten corium-concrete interaction (MCCI) related mass and energy (M&E) releases. This creates a key methodological challenge: ensuring that long-term ex-vessel source terms extracted from an integral code are translated into numerically robust, physically coherent, and reproducible boundary conditions (BCs) for 3D containment simulations — while ensuring mass and energy conservation, avoiding artificial discontinuities [9].

This work focuses on the PWR-KWU case and addresses one specific gap: extending a detailed 3D GOTHIC 8.3(QA) containment model beyond the in-vessel phase and into the ex-vessel progression of a SA sequence, at computational costs acceptable when using a desktop PC. The paper is structured as follows. Section 2 summarizes the 3D containment model creation under a common database. Section 3 presents the hybrid cavity concept and a proposed MELCOR-to-GOTHIC BC translation workflow. Section 4 discusses the main results of an unmitigated Total Loss of AC Power with late depressurization (TLAP) sequence simulated with GOTHIC 8.3(QA). Results are compared with MELCOR calculations that used the same containment database and in/ex-vessel BCs. Section 5 closes with conclusions and recommendations for cross-code benchmarking and for extended 3D containment analyses supporting late-phase SAMG assessment.

2. PWR-KWU CONTAINMENT DATABASE, MELCOR AND GOTHIC 3D MODELS

2.1. From the Plant Layouts to a Generic Containment Database

The modelled PWR-KWU containment corresponds to a 1300-MWe KONVOI-type plant. The reactor building consists of a spherical steel containment (UJA) surrounded by a reinforced-concrete airplane-crash shell (UJB). The UJA layout is highly compartmentalized, separating accessible rooms (during power operation) from equipment rooms hosting the reactor coolant system, and with additional internal structures (e.g., shrapnel protection and large steel components such as walking grids and the polar crane). The CAD model was built from containment layouts that were publicly available [10]. The main walls, floors, and internal partitions were reconstructed by a bottom-to-top extrusion process level by level, producing a geometrically traceable 3D "generic containment" representation. As several geometric details were incomplete, the CAD reconstruction followed an iterative refinement process, including internal reviews by partners with prior modelling experience on the PWR-KWU design to confirm key architectural features (e.g., overlaps, missing openings, or unrealistic compartment separations). Once the 3D CAD model captured the relevant compartmentalization and major internal connections, the information needed for containment simulations was extracted into a generic database provided as structured tables [11] (Table I gathers the main structural characteristics of the containment). The main objective was to formalize the containment subdivision and connectivity in a way that can be shared by LP and 3D users, while maximizing code-to-code comparability under a shared geometric basis. In turn, spaces expected to behave similarly under accident conditions were grouped into regions, which are defined by their free volume and total heat transfer surfaces (namely, concrete and steel). For UJA, ten regions were defined, and an additional one for the UJB to capture dominant long-term heat losses.

2.2. PWR-KWU MELCOR Model Overview

The PWR-KWU MELCOR (LP) containment model was developed by FRAMATOME GmbH following the AMHYCO generic containment database. The UJA regions are depicted in Figure 1 (except the spent fuel pool, SFP) along with 19 of the 24 junctions used to connect the spaces. To ensure internal consistency with MELCOR modelling practices while preserving the global inventory of the generic database, minor practical adjustments were introduced (e.g., selected junction loss characterization and limited geometric/elevation refinements affecting the lumped heat structures). Additional flow resistances were applied in some inter-compartment connections to avoid unrealistically weak circulation and over-mixing through nominally "open" pathways. Overall, the objective of this LP model was a transparent mapping between where M&E are released and how they are transported across the main containment regions, later used as a baseline for comparison against the 3D GOTHIC results.

2.3. PWR-KWU 3D GOTHIC Model Overview

GOTHIC is an integrated, coarse-grid CFD, multi-physics code that solves the conservation equations of mass, momentum and energy for multi-component, multi-phase flows and can be applied using lumped-parameter (LP), 3D, or hybrid LP–3D domains [12]. Geometry is represented on a user-defined Cartesian mesh through a porous-media approach, where volumetric and surface porosities are assigned to cells and faces to model blockages and hydraulic separations. Heat transfer to structures is handled through nodalized thermal conductors, which solve 1D heat diffusion in solids and apply user-selected heat-transfer correlations at fluid interfaces; for condensation in the presence of NCGs, the diffusion layer model is typically used. LP and 3D models share the same governing equations but differ in spatial resolution and numerical treatment. LP volumes are fully mixed with average state variables and momentum conservation only across 1D junctions, with closure correlations applied globally. In 3D, the domain is discretized into

structured cells where local balances are solved, enabling gradients, flow directionality and spatially resolved application of closure relations. In this work, 3D turbulence effects are represented using the standard k–ε model. GOTHIC 8.3(QA) [13] was employed, consistent with AMHYCO activities.

The PWR-KWU GOTHIC 3D containment model was developed by translating the AMHYCO generic containment database into a numerically robust 3D representation [14]. The model has ~25200 active cells (from a total of ~60000, adding up the blocked cells) and a mesh size range of 1-8 m^3. The overarching aim was not to reproduce the CAD geometry in a body-fitted sense, but to preserve the compartment free volumes, hydraulic separation paths, and main structure inventories. To achieve this at practical computational cost, the model construction follows the Preventive Methodology, developed at Universidad Politécnica de Madrid (UPM), which aims to avoid mesh-induced solver pathologies and to enable long transient runs with stable timesteps at practical resolution [15]. As sketched in Figure 2, the detailed CAD is simplified with the target homogeneous Cartesian mesh in mind: compartments are shaped to remain hydraulically independent while avoiding cell configurations prone to solver failures (e.g., low-porosity or obstructed cells). The simplified geometry is then transferred to GOTHIC through an automated CAD-to-GOTHIC pipeline, where coordinates are transferred to GOTHIC via dedicated Python scripts, minimizing manual editing and improving reproducibility. Beyond the standard workflow, the PWR-KWU implementation incorporates refinements, facilitating long SA calculations.

Table I. PWR-KWU containment parameters

Structural Parameters	
UJA containment free volume (m^3)	73945
UJB containment free volume (m^3)	49255
Steel shell diameter (m)	56.00
Steel shell thickness (mm)	38.00
Shrapnel cylinder outer diameter (m); thickness	41.20; 0.80
Lower cup average concrete thickness (m)	2.90
Concrete thickness: cavity floor to foundations (m)	7.30
Heat Structures (UJA+UJB)	
Area of concrete surfaces exposed to the fluid (m^2)	66571
Volume of concrete structures (m^3)	54277
Area of steel surfaces exposed to the fluid (m^2)	40030

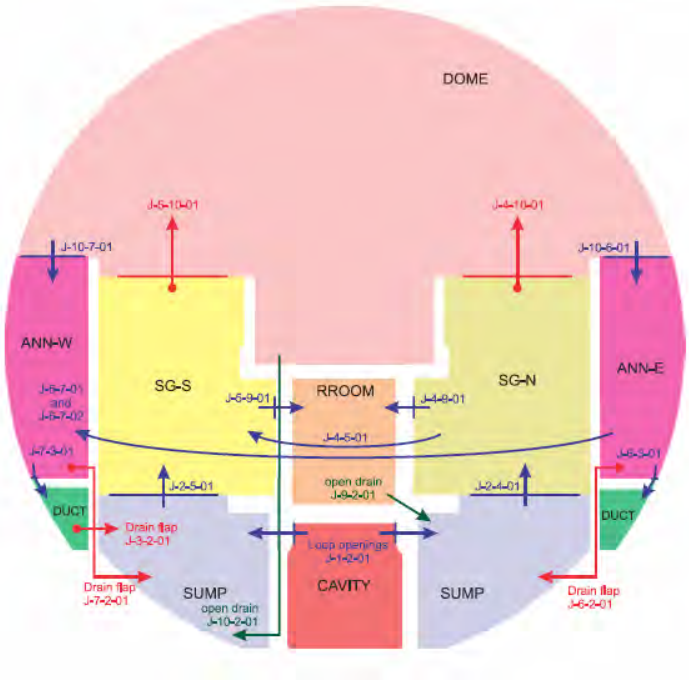

Figure 1. PWR-KWU containment UJA LP regions.

First, the containment is intentionally built as a hybrid LP–3D representation, with UJB, the SFP and the reactor cavity represented as LP CVs, while the open gas spaces governing natural circulation and stratification are resolved in 3D with locally adapted mesh resolutions. Second, the model is pre-configured for localized high M&E releases by performing a study of structures before geometry simplification, so that locations likely subjected to high-velocity jets can be as unblocked as possible. This should improve stability

and reduce solver failures in demanding phases. Third, specific attention is paid to curved, porosity-generating structures characteristic of the PWR-KWU (e.g., dome/liner and missile shield). Early mesh subdivision choices and local geometry adaptations are supported by automated parsing of solver-error outputs to guide iterative CAD corrections. Then, the number of persistent low-porosity cells is reduced, a process that otherwise would require time-consuming cell-by-cell correction. Moreover, heat-transfer realism is maintained by selecting thermal conduction settings consistent with the chosen mesh; in particular, thresholds are defined so that wall-to-fluid heat transfer is properly partitioned between vapor and liquid as pool heights evolve during the transient. Finally, the agreement of integrated free volumes, flow areas and structure surfaces was checked to be acceptable (below maximum 3% relative differences). Thus, subsequent LP–3D differences can be interpreted as code-induced, either from different models, e.g., convective heat transfer, or directly due to the higher spatially resolution of the 3D model.

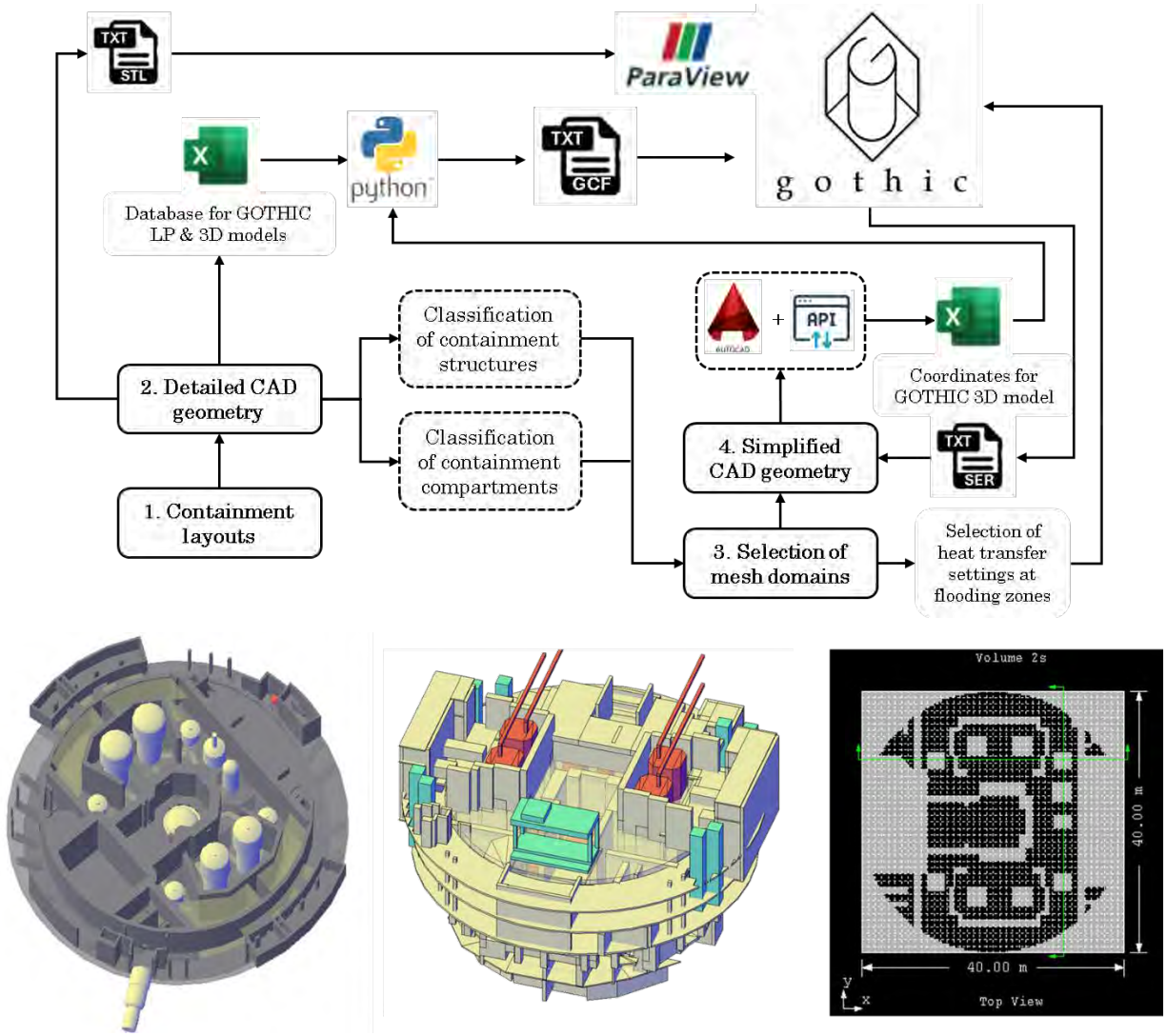

Figure 2. Scheme of the pre-processing steps and tools of the Preventive Methodology (up); detailed CAD, simplified adaptation, and GOTHIC model (bottom, from left to right).

3. METHODOLOGY: EXTENDING GOTHIC TO EX-VESSEL SIMULATIONS

GOTHIC is well-suited to resolve containment thermal-hydraulics and gas transport at LP and 3D scales, but it is not a mechanistic ex-vessel code: it does not explicitly simulate corium thermochemistry, MCCI kinetics, melt pool evolution, fuel-coolant interaction, or the detailed cavity flooding/quenching processes that govern late-phase M&E releases after RPV failure. However, for containment-scale purposes, the key requirement is not resolving the corium physics itself but reproducing the impact onto the containment, i.e., the time-dependent injection of steam, NCGs and the associated thermal loads that drive pressurization, circulation and stratification. To bridge this gap, ex-vessel source terms predicted by MELCOR are imposed in GOTHIC through an embedded LP cavity control volume (CV) coupled to a mesh-optimized 3D containment domain. The cavity CV acts as a numerically robust interface that absorbs demanding ex-vessel M&E releases and transfers their effects to the surrounding in 3D modelled containment through controlled junctions, enabling a single GOTHIC setup to cover the in-vessel phase and several hours of ex-vessel accident progression.

This work formalizes a phenomenon-oriented selection of MELCOR ex-vessel outputs that must be preserved, and a traceable output-to-input translation into GOTHIC. As summarized in Figure 3, the procedure extracts a limited set of time histories from MELCOR cavity/CVH results that define the source term driving containment response: (i) cavity pressure and the thermodynamic state and composition of released gases (steam and NCGs, including H_2/CO), (ii) component mass release rates, and (iii) thermal power terms associated with melt-surface heat transfer to the cavity atmosphere and structures, including heat losses through cavity walls. Dry-cavity and flooded-cavity configurations are represented consistently; in the flooded case, once biological shield breach enables sump-to-cavity water ingress, MCCI gases are cooled, and additional steam generation is reflected in the source histories. These series are then mapped to GOTHIC flow-type BCs (mass flow with composition and temperature/enthalpy) applied to the cavity LP CV. Built-in heater components are used to inject energy into the vapor or liquid phase. Also, heat transfer coefficients are imposed on the corresponding GOTHIC thermal conductors to reproduce evolving convective regimes in the cavity. The geometric and hydraulic descriptors of the connections between cavity and containment (elevation, area, hydraulic diameter, and loss coefficients) are taken from the generic database, ensuring physical consistency of the interfaces rather than treating them as “outputs”. Finally, because integral-code outputs may contain sharp transients and non-uniform sampling that would enforce restrictive timesteps in GOTHIC, time series are pre-processed using conservative smoothing/resampling (e.g., moving averages or piecewise interpolation) under the constraint that time-integrated injected mass (per species) and injected energy/enthalpy are preserved.

Within this framework, the cavity LP CV functions as a composite boundary-condition-generator embedded in the subdivided containment domain: it does not attempt to model the cavity mechanistically, but it imposes their containment-scale consequences at physically consistent temperatures and gas compositions and transfers them to the 3D regions through controlled junctions. The cavity-as-interface concept was verified through MELCOR–GOTHIC test cases that exercise the main ex-vessel loading modes and the associated mapping logic (Figure 4), where GOTHIC reproduces the reference evolution of cavity CVs pressure and gas phase temperature over a 28-hour dry-cavity transient with good agreement.

4. APPLICATION CASE AND BENCHMARK COMPARISON

The TLAP sequence considered in this paper originates from AMHYCO WP2, where bounding accident scenarios in which the combustible gases cause a risk for containment integrity were simulated with integral codes [16]. The reference accident progression was first produced with a detailed MELCOR model to define a consistent timeline and to provide the in-vessel and ex-vessel release histories used by project partners.

Thus, in AMHYCO WP4, the TLAP was simulated using the shared generic containment database. This paper reports on UPM's GOTHIC 8.3(QA) calculations and compares them to the corresponding MELCOR v2.2.15254 calculation performed by FRAMATOME GmbH, under the cross-code benchmark database shared during the project. GOTHIC 3D output was averaged per region, using UPM´s ProTON code, considering an equivalent free volume by extracting coherent coordinates from the mesh and ensuring comparability. The focus of the results is put on temperatures and gas concentrations across the key circulation regions outside the cavity, which is treated as an interface to impose ex-vessel source terms rather than as a target region for benchmarking. The case was simulated in 15 days CPU time, with only 2 core CPUs (i7-9700@3.0 GHz) and a maximum time step of 0.04 s, maintaining solver stability.

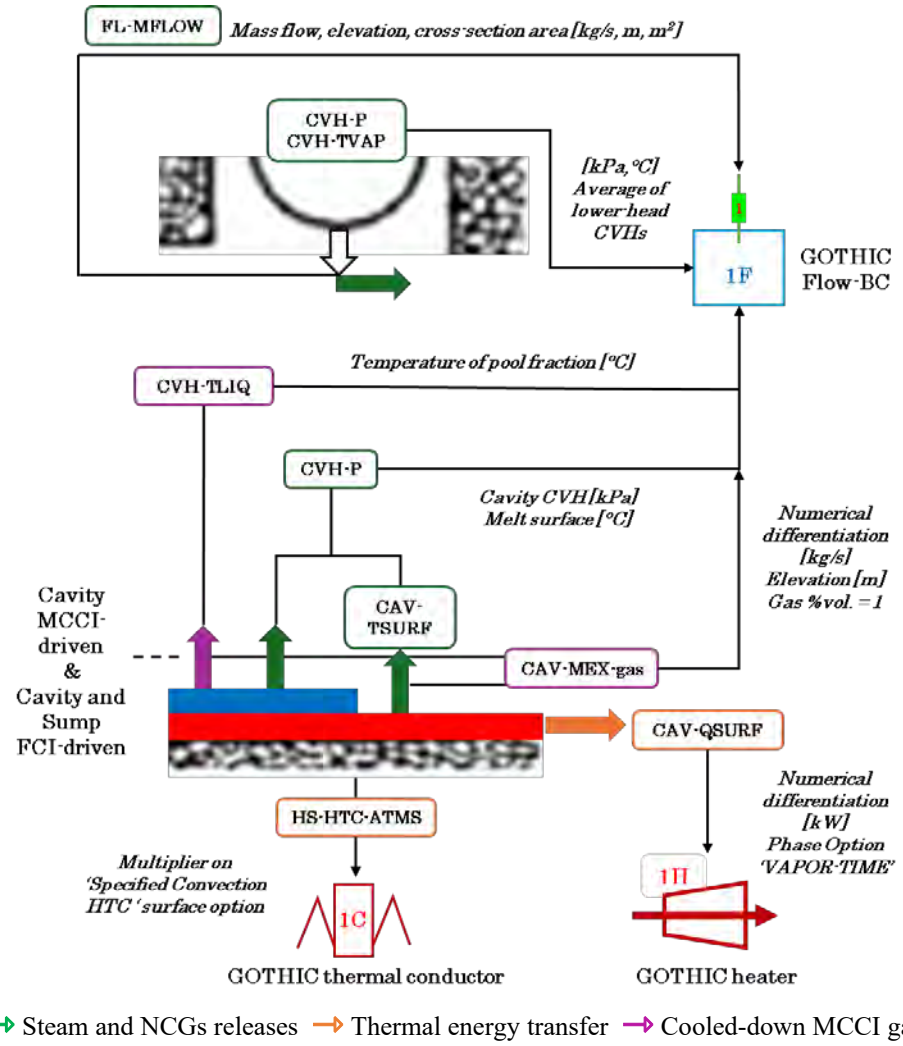

Figure 3. Conceptual mapping of MELCOR ex-vessel outputs into GOTHIC inputs.

Regarding the TLAP scenario, a complete loss of AC power is assumed. Following reactor trip, decay heat is initially removed by the steam generators (SG), which discharge steam to the environment until SG dryout (≈1 h). Thereafter, primary pressure increases and steam is released to containment through pressurizer safety valves, while the remaining primary inventory keeps the core covered for roughly one additional hour. As the core uncovers, temperatures rise and a depressurization action is initiated at 3 h 11 min (650°C signal at 2 h 41 min plus 30 min delay), producing a short, intense release of steam and H_2 to the containment. Accumulators then inject and delay degradation, but core damage progresses and the reactor pressure vessel fails at 9 h 44 min, marking the start of the ex-vessel phase. Corium relocation to the cavity

initiates MCCI and sustained M&E releases, and at 14 h 49 min biological shield penetration leads to sump-to-cavity water ingress, partial melt submergence, and melt relocation towards the sump. The released gases mass flows and temperature histories for twenty hours of the accident can be found in [9], [14].

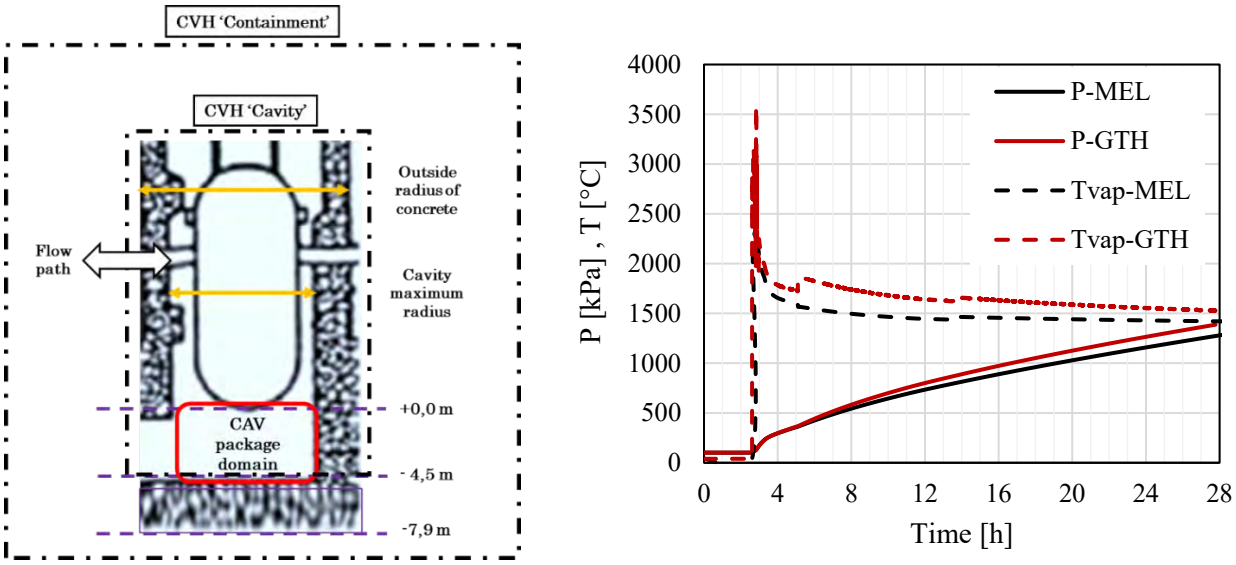

Figure 4. Conceptual representation of MELCOR test case model (left), comparison of cavity CV pressure and temperature during a 28-hour dry cavity scenario (flooded scenario not shown here).

4.1 Comparison of MELCOR vs GOTHIC 3D Global Gas Distribution

The pressure, temperature and volumetric fractions are compared in the generic-database regions that govern containment-scale circulation and accumulation, namely SUMP, SG-N, DUCT and DOME (Figure 5 and Figure 6). For the in-vessel phase (0-9 h), both codes reproduce the expected containment response driven by steam releases and the primary depressurization sequence (detailed differences are discussed in [9]). The main pressure peak occurs at around 4 h, with GOTHIC predicting a systematically higher value (maximum deviation reaches ~+0.61 bar). This offset should not be interpreted as a direct consequence of different gas homogeneity alone. Rather, it is more plausibly linked to differences in the treatment of condensation, wall heat transfer, and effective heat-storage capacity between the MELCOR and GOTHIC models, which control the net steam removal from the containment atmosphere. The use of a shared generic database ensures comparable geometry and source-term basis, but not identical thermal-hydraulic closure behavior or structure-to-fluid heat exchange in both codes. Regional gas temperatures show consistent trends, while differences in steam redistribution are observed across the circulation path: compared to GOTHIC, MELCOR tends to predict stronger steam removal in the SG-N, DUCT and DOME regions, and higher steam retention in the SUMP. In addition, MELCOR predicts a 50% higher H_2 peak in the SG-N region at the time of release from the primary circuit. In the ex-vessel phase (9-20 h), the bulk containment regions remain steam-dominated, and both codes capture the long-term evolution of H_2 and CO across the main circulation pathway. Overall, the benchmark indicates consistent global trends in the key accumulation regions. However, GOTHIC maintains a higher pressurization level during the whole phase. A plausible contributor is the different net steam removal and redistribution driven by condensation/heat-transfer treatment between codes. Regarding gas composition and temperature, differences are most evident in the DUCT, where GOTHIC systematically predicts a warmer and more combustible-gas-enriched corridor than

MELCOR. In contrast, the DOME shows closer agreement and smoother trends, with GOTHIC typically slightly leaner in combustible gases and slightly lower in steam. Finally, UJB temperatures show close agreement between MELCOR and GOTHIC, supporting that the global heat-loss pathway at containment scale is consistently represented.

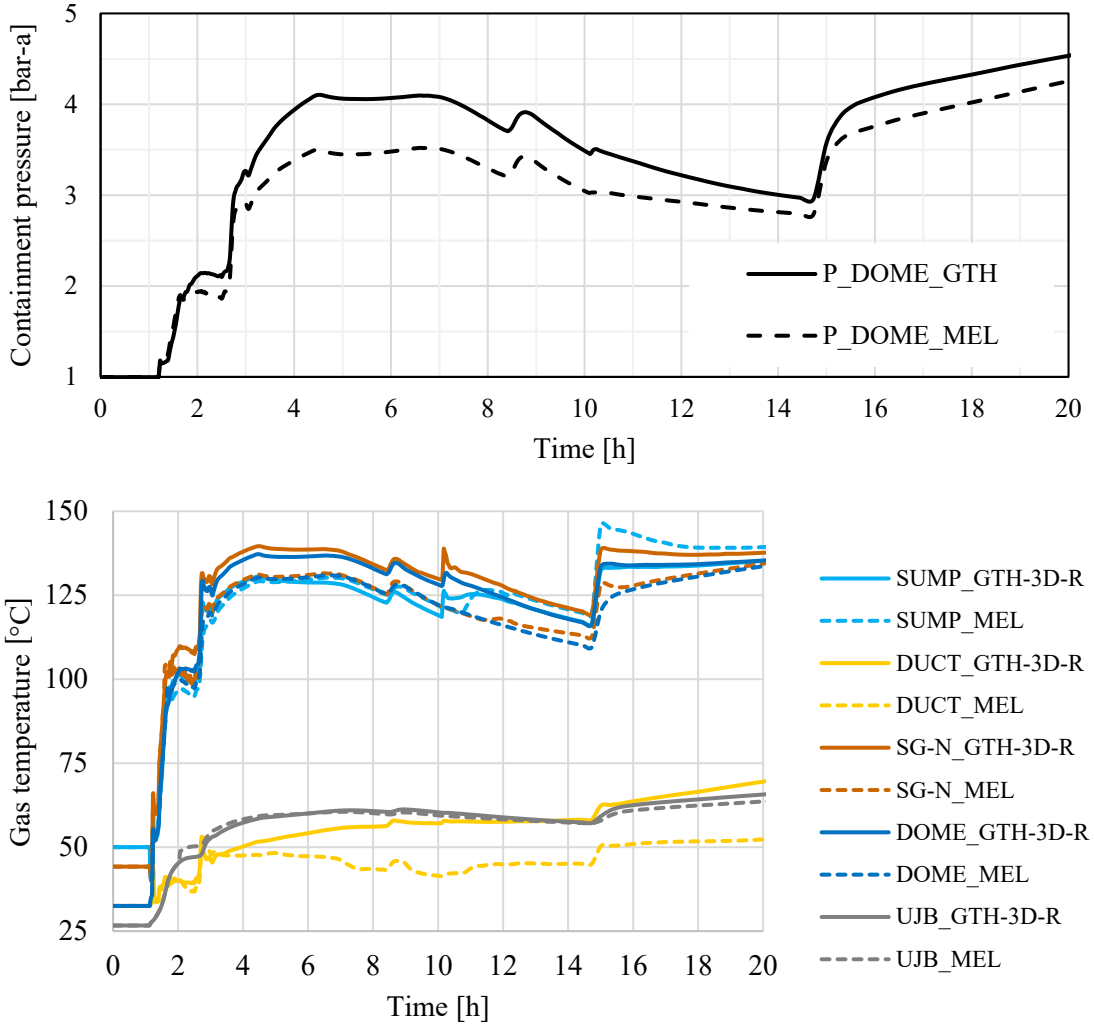

Figure 5. TLAP gas phase pressure (up) and temperature (bottom).

4.2 3D hydrogen stratification footprints along the TLAP progression

The regional differences motivate a closer look at the 3D spatial resolution to interpret circulation and stratification beyond LP trends. Figure 7 illustrates how the GOTHIC 3D model resolves containment-scale H_2 distribution by capturing the imprint of phenomena such as buoyancy-driven transport and enrichment of light gases driven by steam condensation and limited mixing. At 4.5 h, H_2 appears highly non-uniform. Enriched layers develop in the lower sump level, indicating that condensation is substantially higher in that region due to the accumulated water pool. As seen in Figure 6, MELCOR did not capture that accumulation and yielded lower concentration values. Also, GOTHIC predicts H_2 gradients in the operational floor due to perhaps an inverse stratification pattern due to condensation at the DOME liner. This indicates that the early H_2 release has limited immediate homogenization across the full containment height. At 14.5 h, the picture changes qualitatively. The overall H_2 level is higher and the containment exhibits a large-scale stratified

structure, with smoother gradients across wide volumes. This reflects the combined effect of sustained ex-vessel gas generation and thermal driving, which strengthens natural circulation loops and progressively fills larger regions, while still preserving vertical gradients. Also, structures are hotter and condensation is less present. However, for instance MELCOR did not capture the same accumulation in the DUCT region, being slightly higher in GOTHIC. Finally, these 3D fields translate directly into combustion-risk relevance by revealing stratified layers and local pockets where flammability conditions may exist despite possible benign region-averaged values.

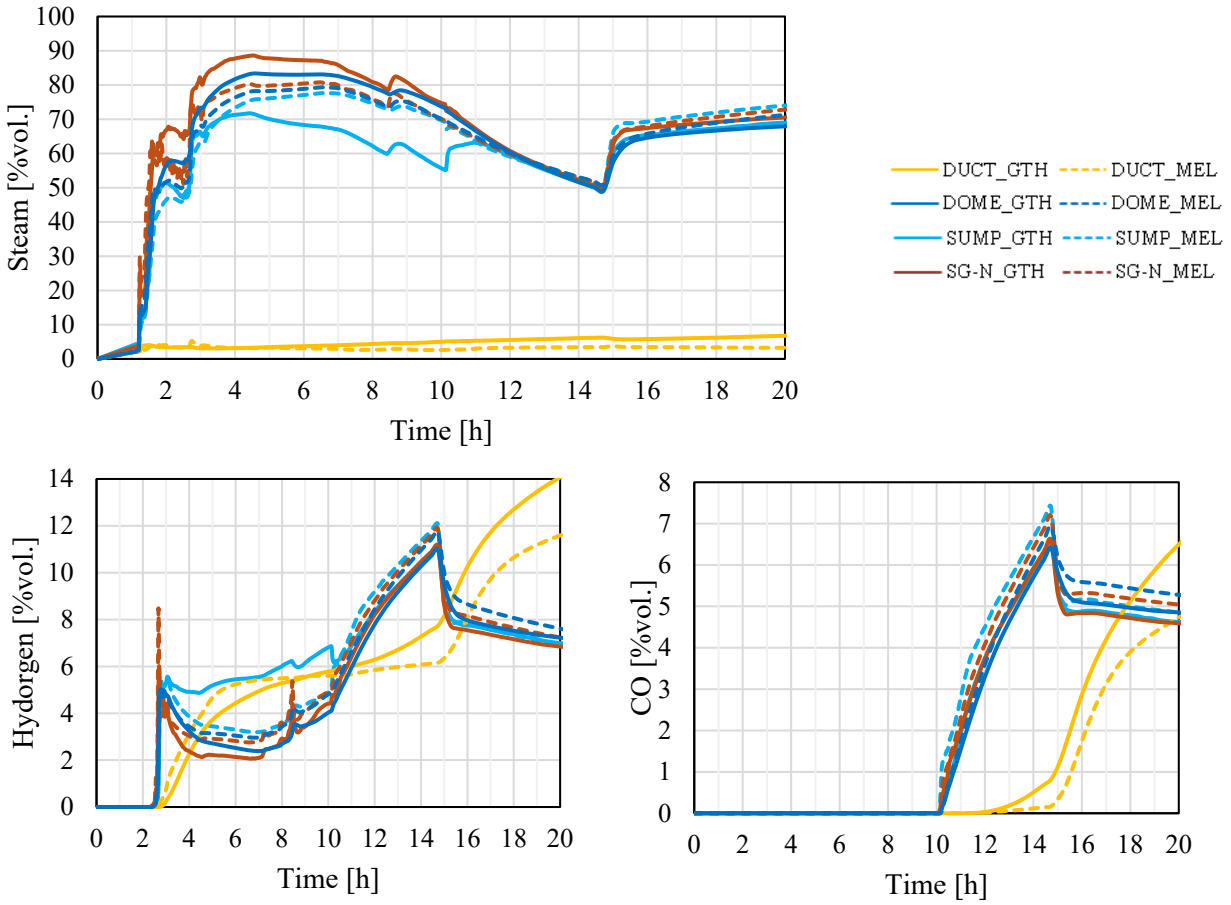

Figure 6. TLAP gas components concentrations: steam (up), H_2 and CO (bottom).

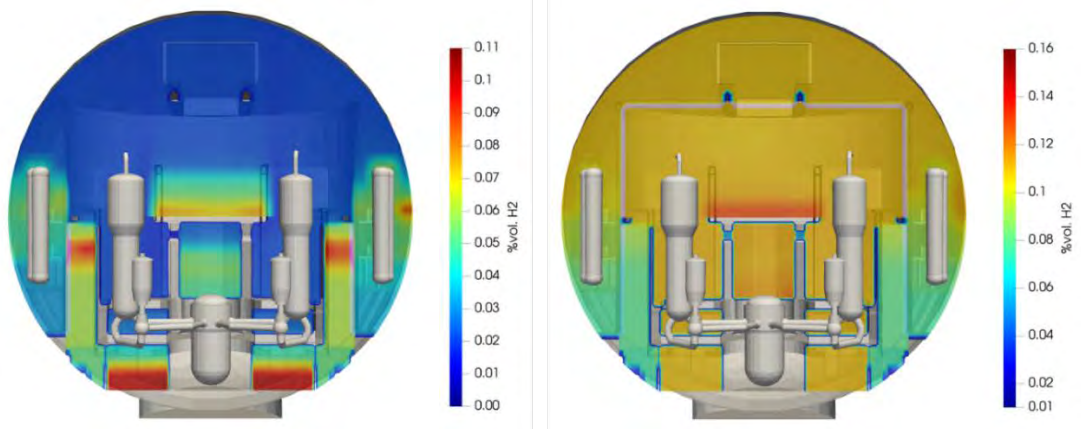

Figure 7. GOTHIC 3D hydrogen concentration at 4.5 h (left) and 14.5 h (right).

5. CONCLUSIONS AND OUTLOOK

This paper shows that GOTHIC 8.3(QA) can be extended to late-phase severe accident containment simulations by introducing relevant ex-vessel releases through a reproducible MELCOR-to-GOTHIC boundary condition translation. This is achieved by using an embedded GOTHIC LP cavity acting as an interface to the GOTHIC 3D domain. Using the AMHYCO database, GOTHIC 3D and MELCOR LP results can display coherent trends, showing consistent global pressure and temperature trends, and the evolution of steam, H_2 and CO compositions in the main circulation regions. This has been achieved with moderate systematic pressure differences that could be explained due to the different heat/mass-transfer and mixing treatments between the codes, which are affected by the inherently different level of spatial resolution.

Beyond trend benchmarking, the 3D calculation provided an added value by resolving stratification and localized accumulation footprints (e.g., the distinct H_2 layering patterns between the in-vessel and ex-vessel phases) that can be masked by the LP well-mixed control volume assumptions. The approach has clear modelling limits. The ex-vessel phase is condensed into an LP cavity, so melt pool hydrodynamics, detailed flooding/quenching and local condensation phenomena are not resolved explicitly, and the 3D containment response depends on the fidelity of the imposed source terms. Also, as the ex-vessel phase is driven by prescribed source terms, the largest modelling sensitivity is expected to be confined to the short interval immediately after RPV failure (order of minutes to tens of minutes), while longer-term containment trends remain robust; an exception would be highly energetic short-time phenomena (e.g., steam explosions and fuel-coolant interactions), which are outside the scope of the present approach.

Nonetheless, the workflow is largely transferable: the database-driven LP/3D consistency, the preventive CAD-to-mesh strategy, the automated geometry import, and the cavity-interface concept can be applied to other containments and sequences provided that the plant-specific subdivision and flow paths are defined coherently. The next steps include sensitivity studies (mesh strategy, junction losses, heat-transfer options and source-term preprocessing), extension to additional scenarios and mitigation configurations, and — where relevant — coupling or upgrading combustible-gas treatment (including consistent H_2/CO mitigation/combustion capabilities) to bridge the gap of SAMG monitoring limitations.

ACKNOWLEDGMENTS

The AMHYCO project has received funding from the Euratom research and training programme 2019-2020 under Grant Agreement nº945057. The content of this paper reflects only the author's view. The European Commission is not responsible for any use that may be made of the information it contains.
GOTHIC™ incorporates technology developed for the electric power industry under the sponsorship of EPRI, the Electric Power Research Institute. This work was completed using a GOTHIC license for educational purposes provided by Numerical Advisory Solutions, LLC. The authors also wish to extend their appreciation to the personnel of EPRI and Numerical Advisory Solutions company for their invaluable technical assistance and support, especially to senior consultant Dr Jeffrey W. Lane.

REFERENCES

[1] OECD/NEA, 'ISP-49 on Hydrogen Combustion', OECD-NEA, NEA/CSNI/R(2011)9, Jan. 2012.
[2] B. R. Sehgal, *Nuclear Safety in Light Water Reactors*. Elsevier, 2012. doi: 10.1016/B978-0-12-388446-6.00001-0.

[3] P. Royl, H. Rochholz, W. Breitung, J. R. Travis, and G. Necker, 'Analysis of steam and hydrogen distributions with PAR mitigation in NPP containments', *Nucl. Eng. Des.*, vol. 202, no. 2–3, Art. no. 2–3, Dec. 2000, doi: 10.1016/S0029-5493(00)00332-0.
[4] M. Braun, E. Reinecke, A. Bentaib, and G. Jiménez, 'AMHYCO D5.1 – Lessons Learned of the AMHYCO Project and Guidelines for SAMG Development, Minimizing the H2/CO Combustion Risk in a Containment', European Commission, Deliverable Report, H2020 AMHYCO Project WP5, Mar. 2025. [Online]. Available: https://cordis.europa.eu/project/id/945057/results
[5] G. Jimenez *et al.*, 'AMHYCO PROJECT - TOWARDS AN ENHANCED ACCIDENT MANAGEMENT OF THE H2/CO COMBUSTION RISK', in *Proc. 19th International Topical Meeting on Nuclear Reactor Thermal Hydraulics (NURETH 19)*, Brussels, Belgium, 6 Mar 2022 - 11 Mar 2022, 2022.
[6] W. Breitung and P. Royl, 'Procedure and tools for deterministic analysis and control of hydrogen behavior in severe accidents', *Nucl. Eng. Des.*, vol. 202, no. 2–3, pp. 249–268, Dec. 2000, doi: 10.1016/S0029-5493(00)00380-0.
[7] L. L. Humphries, B. Beeny, and F. Gelbard, 'MELCOR Computer Code Manuals', Sandia National Laboratories, Albuquerque, NM 87185-0748, SAND2017-0876 O, Jan. 2017.
[8] OECD/NEA, 'State-of-the-Art Report (SOAR) on Containment Thermalhydraulics and Hydrogen Distribution', OECD Publishing, Paris, NEA/CSNI/R(1999)16, 1999.
[9] S. Kelm, M. Braun, A. Bentaib, and A. Iskra, 'AMHYCO D4.3 – Lessons Learned during the Full Containment Analysis of KWU, Western, and VVER PWRs and Quality Assurance Measures', European Commission, Deliverable Report, H2020 AMHYCO Project WP4-Task 4.6, Mar. 2025. [Online]. Available: https://cordis.europa.eu/project/id/945057/results
[10] SIEMENS, 'Dokumentationen SIEMENS / KWU Sicherheitsbericht für die KKW Stendal GmbH 1990'. SIEMENS, 1990. [Online]. Available: http://www.ycdt.de/kkw-stendal/siemens-reaktor-stendal.htm
[11] L. Serra *et al.*, 'AMHYCO D2.1 – Data for the generic containment analysis (PWR-W, PWR-VVER, PWR-KWU)', European Commission, Deliverable Report, H2020 AMHYCO Project WP2-Task 2.1, 2023. [Online]. Available: https://cordis.europa.eu/project/id/945057/results
[12] R. C. Harvill, J. W. Lane, and T. L. George, 'Hybrid System Level and Coarse Grid CFD Tool for Three-Dimensional Natural Circulation, Mixing, and Stratification Modeling', *Nucl. Technol.*, pp. 1–26, May 2021, doi: 10.1080/00295450.2020.1870371.
[13] EPRI, 'GOTHIC Thermal Hydraulic Analysis Package, Version 8.3 (QA).', Palo Alto, CA, 2018.
[14] L. Serra *et al.*, 'From the plant layouts to optimized LP and 3D PWR-KWU containment models for combustion risk assessment with GOTHIC 8.3(QA)', *Nucl. Eng. Des.*, vol. 445, p. 114459, Dec. 2025, doi: 10.1016/j.nucengdes.2025.114459.
[15] C. Vázquez-Rodríguez *et al.*, 'The Preventive Methodology: A priori modification of the containment geometry to boost the computational efficiency of GOTHIC 3D models', *Nucl. Eng. Des.*, vol. 432, Feb. 2025, doi: 10.1016/j.nucengdes.2024.113718.
[16] L. E. Herranz and J. Fontanet, 'AMHYCO D2.2 – Identification and analysis of accident sequences with posing high H2/CO combustion risk', European Commission, Deliverable Report, H2020 AMHYCO Project WP2-Task 2.2-2.4, 2023. https://cordis.europa.eu/project/id/945057/results

ERMSAR 2026

AMHYCO

Enhancing H_2 & CO Combustion Risk Management

EX-VESSEL SEVERE ACCIDENT 3D SIMULATION WITH GOTHIC 8.3(QA): METHODOLOGY AND APPLICATION TO A PWR-KWU CONTAINMENT

Session 5.4 - Hydrogen risk and Containment behavior

luis.slopez@upm.es
gonzalo.jimenez@upm.es

This project has received funding from the Euratom research and training programme 2019-2020 under Grant Agreement n°945057.The content of this document reflects only the author's view. The European Commission is not responsible for any use that may be made of the information it contains.

Luis Serra (UPM)

Gonzalo Jiménez (UPM)

Matthias Braun (FRAMATOME)

Luis Enrique Herranz (CIEMAT)

20/05/2026

Contents

1. Background
   a. Phenomena during ex-vessel phase
   b. The AMHYCO project
2. Objectives
3. Overview of PWR-KWU containment database & models
4. Extending GOTHIC to ex-vessel simulations
5. MELCOR vs GOTHIC application case
6. Conclusions and outlook

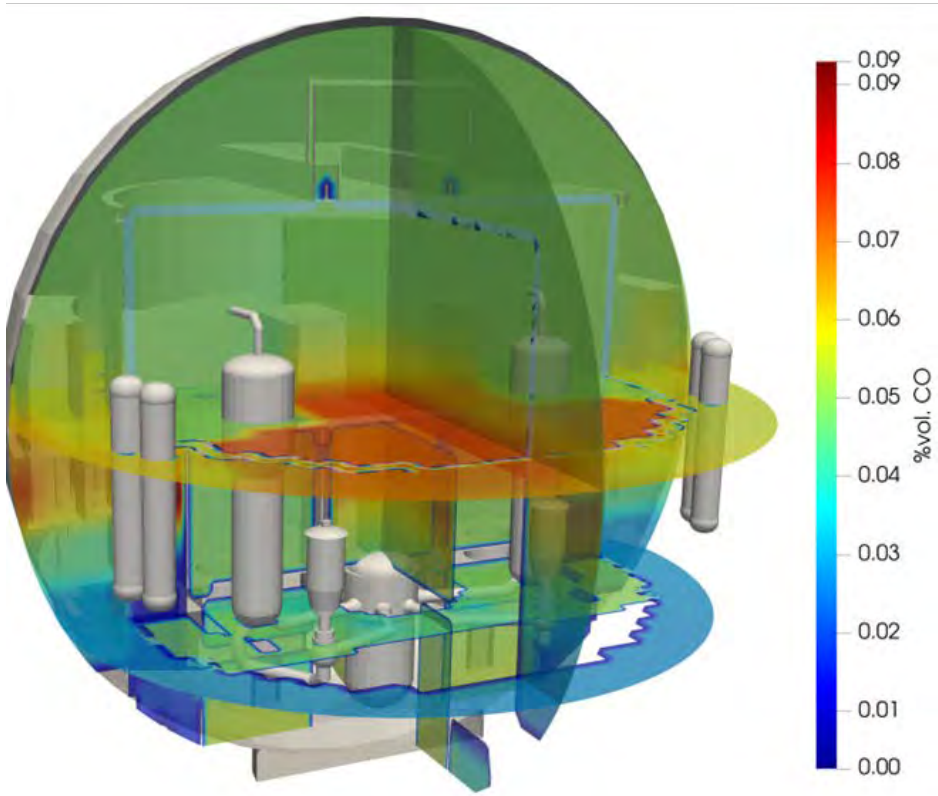

1. Background: Phenomena during ex-vessel phase

- In-containment expected flow patterns after mass & energy releases.
- Combined effect of steam and H_2, CO & CO_2: stratification and flammable conditions.
- Containment-dependent phenomena: e.g., equipment rooms of a PWR-KWU.

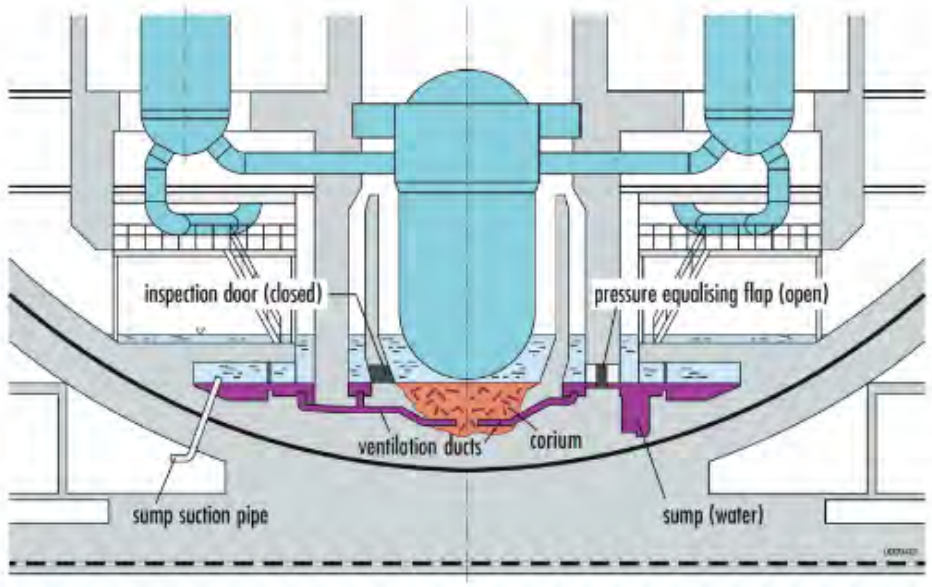

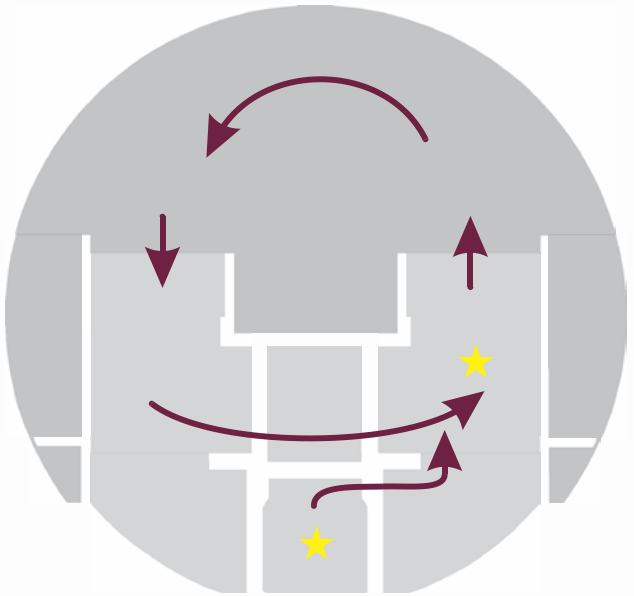

GRS (2002). *"Assessment of the Accidental Risk of Advanced Pressurized Water Reactors in Germany. Methods and Results of a Comprehensive probabilistic Safety Analysis"*. GRS GmbH, Germany.

Kelm, S., et. al, (2025). "*AMHYCO D4.2 – Full Containment Analyses of KWU, Western and VVER PWRs*". Deliverable Report, H2020 AMHYCO Project. European Commission.

1. Background: Phenomena during ex-vessel phase

- LP misses local stratification and heterogeneity.
- Combustion partially covered by integral or containment codes.
- Dedicated tools and post-processing for FA/DDT.
- Ex-vessel physics is a gap in GOTHIC (vs. in-vessel phenomena).
- 3D adds value in local gas distribution + ESF local effects.

Cross-code modelling gaps & methodological needs

Process name	ANSYS-CFX code	GASFLOW code	GOTHIC code	TONUS code	COCOSYS code	CONTAIN code	RELAP/SCDAP code	MELCOR code	MAAP code
Metal oxidation with steam									
Metal corrosion									
MCCI									
Oxidation in molten pool									
Stainless steel, B_4C oxidation									
Hydrogen stratification									
Condensation on surfaces									
Buoyancy induced mixing									
Momentum induced mixing									
Deflagration									
Flame acceleration									
Detonation									
Diffusion flame									
Hydrogen-CO deflagration									
Hydrogen re-combiner									
Igniter									
CO recombination									
Ventilation system									
Air cooler/Fan									
Spray systems									

Gharari, R. (2018). *"A review on hydrogen generation, explosion, and mitigation during severe accidents in light water nuclear reactors"*. Int. J. Hydrog. Energy 43.

1. Background: AMHYCO project (2020-2025)

WP1
- SAMG/EOP
- equipment survivability
- existing approaches

WP2
- GenCont database
- bounding accident sequences

WP3
- H2/CO combustion and recombination characteristics

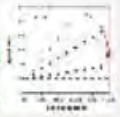

WP4

LP / System codes
(most penalizing scenarios from WP2)

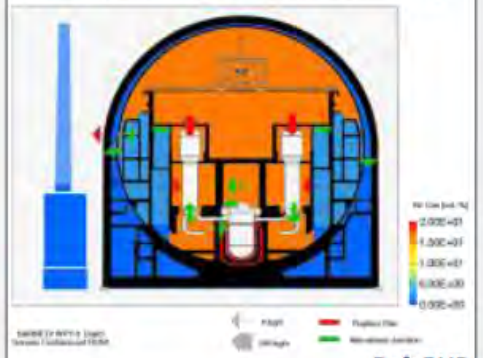

Ref: RUB

GOTHIC-3D
(Selected transients)

Ref: UPM

CFD
(Selected compartments)

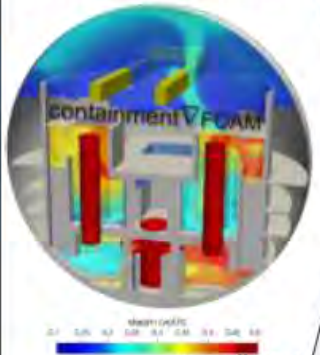

Ref: JÜLICH

- **Task 4.1:** Derive and implement extended correlations/parametric models
- **Task 4.2-3:**
  - 3 Containments: **PWR-KWU**, **PWR-W** and **PWR-VVER**
  - Consecutive analysis chain LP → 3D → CFD
- **Task 4.5:** Summarize Lessons Learned

WP5

- containment response and risk assessment

2. Objectives

- Present a methodology to extend GOTHIC 3D to the ex-vessel phase of a severe accident in a PWR-KWU containment
- Show benchmark consistency between MELCOR & GOTHIC LP/3D for a selected sequence under a shared database and source-term basis
- Highlight added value of GOTHIC 3D in resolving stratification and local combustible-gas accumulation

3. Overview of PWR-KWU containment database & models

AMHYCO WP2 D2.1: Generation of a shared generic database

Public layouts

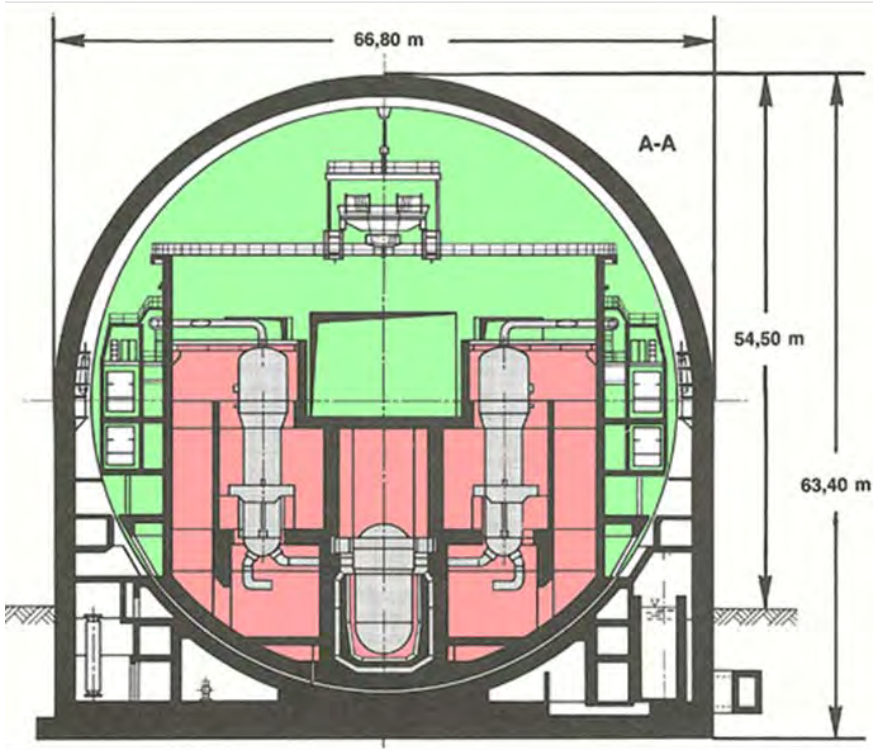

MELCOR nodalization (FRG)

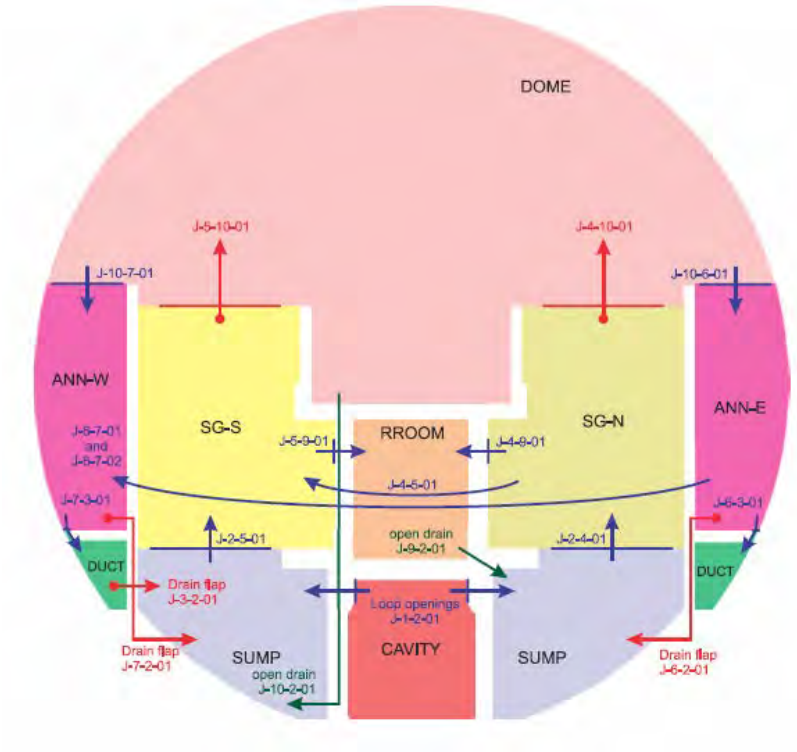

Structural Parameters	
UJA containment free volume (m^3)	73945
UJB containment free volume (m^3)	49255
Steel shell diameter (m)	56.00
Steel shell thickness (mm)	38.00
Shrapnel cylinder outer diameter (m); thickness	41.20; 0.80
Lower cup average concrete thickness (m)	2.90
Concrete thickness: cavity floor to foundations (m)	7.30
Heat Structures (UJA+UJB)	
Area of concrete surfaces exposed to the fluid (m^2)	66571
Volume of concrete structures (m^3)	54277
Area of steel surfaces exposed to the fluid (m^2)	40030

3. Overview of PWR-KWU containment database & models

GOTHIC LP model (UPM) 10 UJA CVs + 1 UJB CV

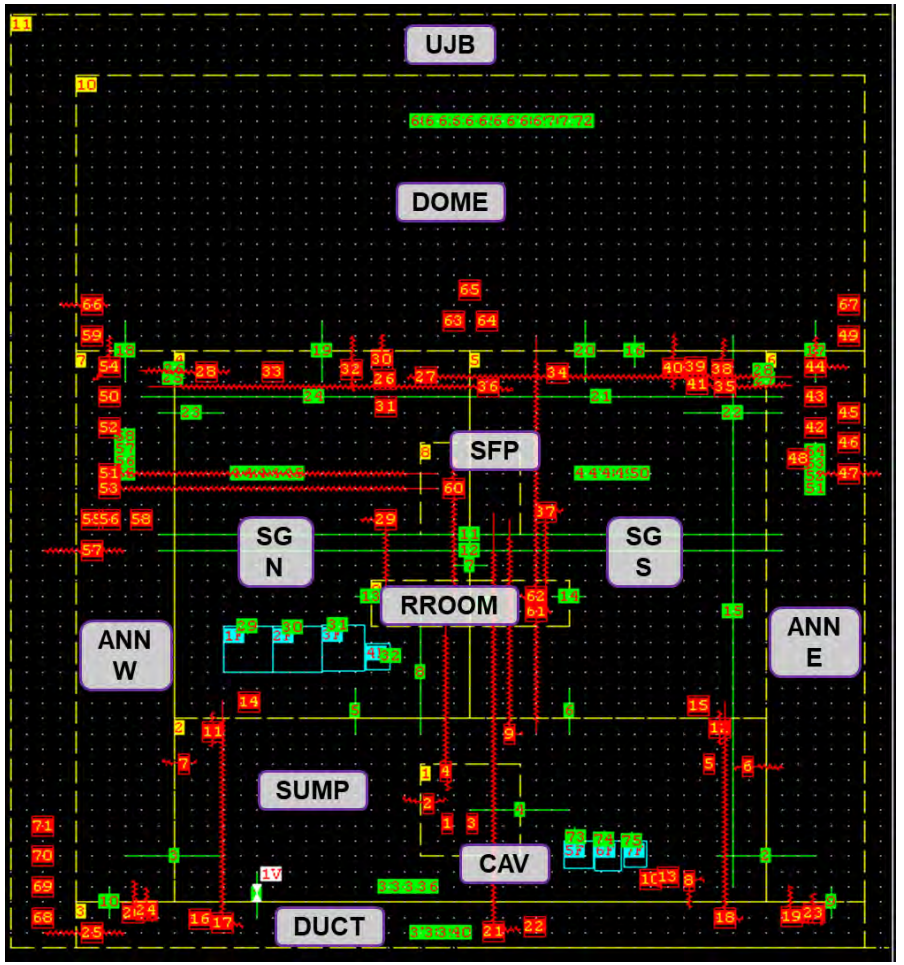

3. Overview of PWR-KWU containment database & models

GOTHIC 3D model (UPM) and *Preventive Methodology* cost-effective workflow

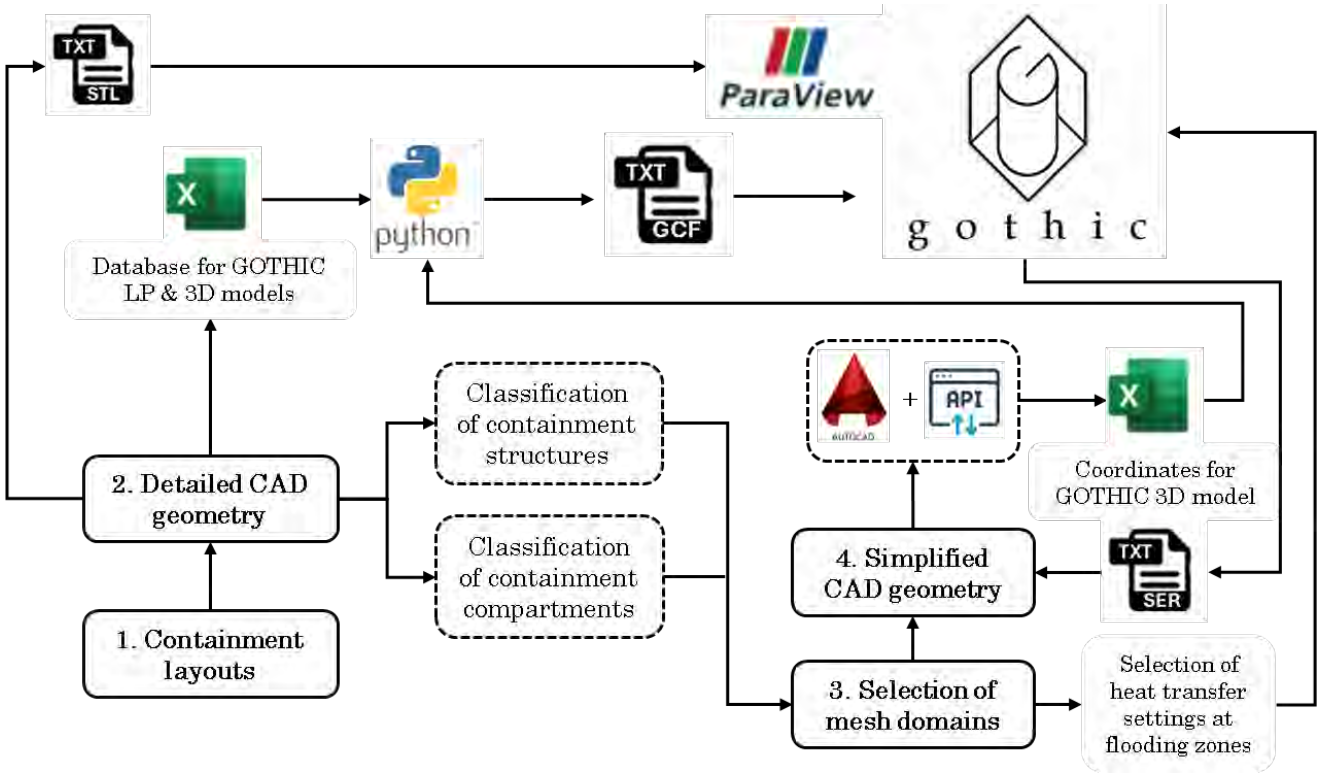

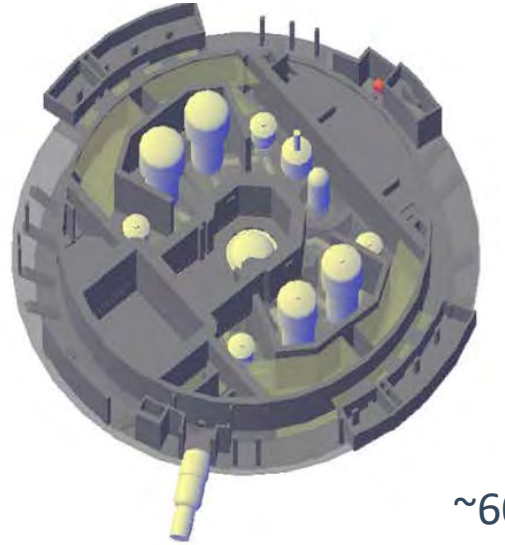

~60,000 cells

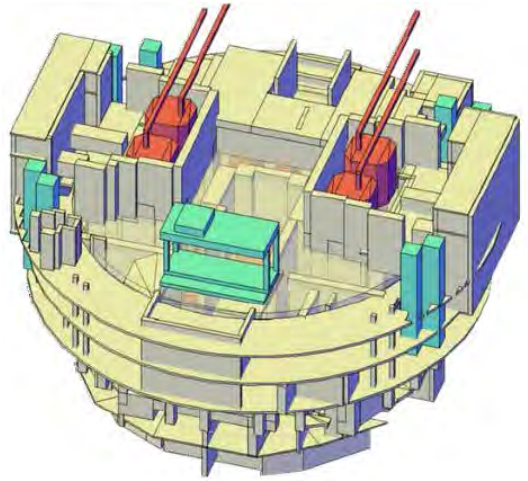

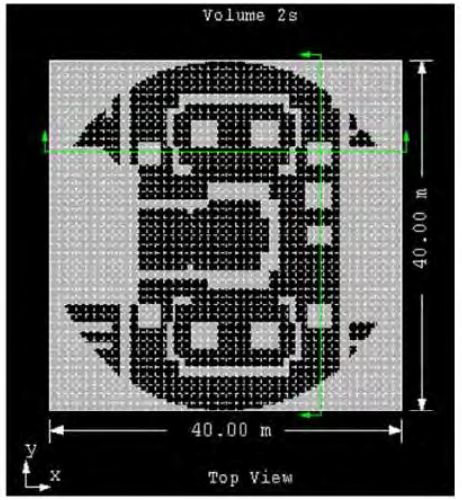

4. Extending GOTHIC to ex-vessel simulations

- GOTHIC doesn´t mechanistically simulate melt phenomena.
- MELCOR provides the ex-vessel mass and energy source terms.
- An embedded LP cavity should be used as a robust interface to the 3D containment.
- Selected MELCOR outputs are translated traceably into GOTHIC inputs (BCs).
- This enables one single GOTHIC model to cover in-vessel and long ex-vessel progression.

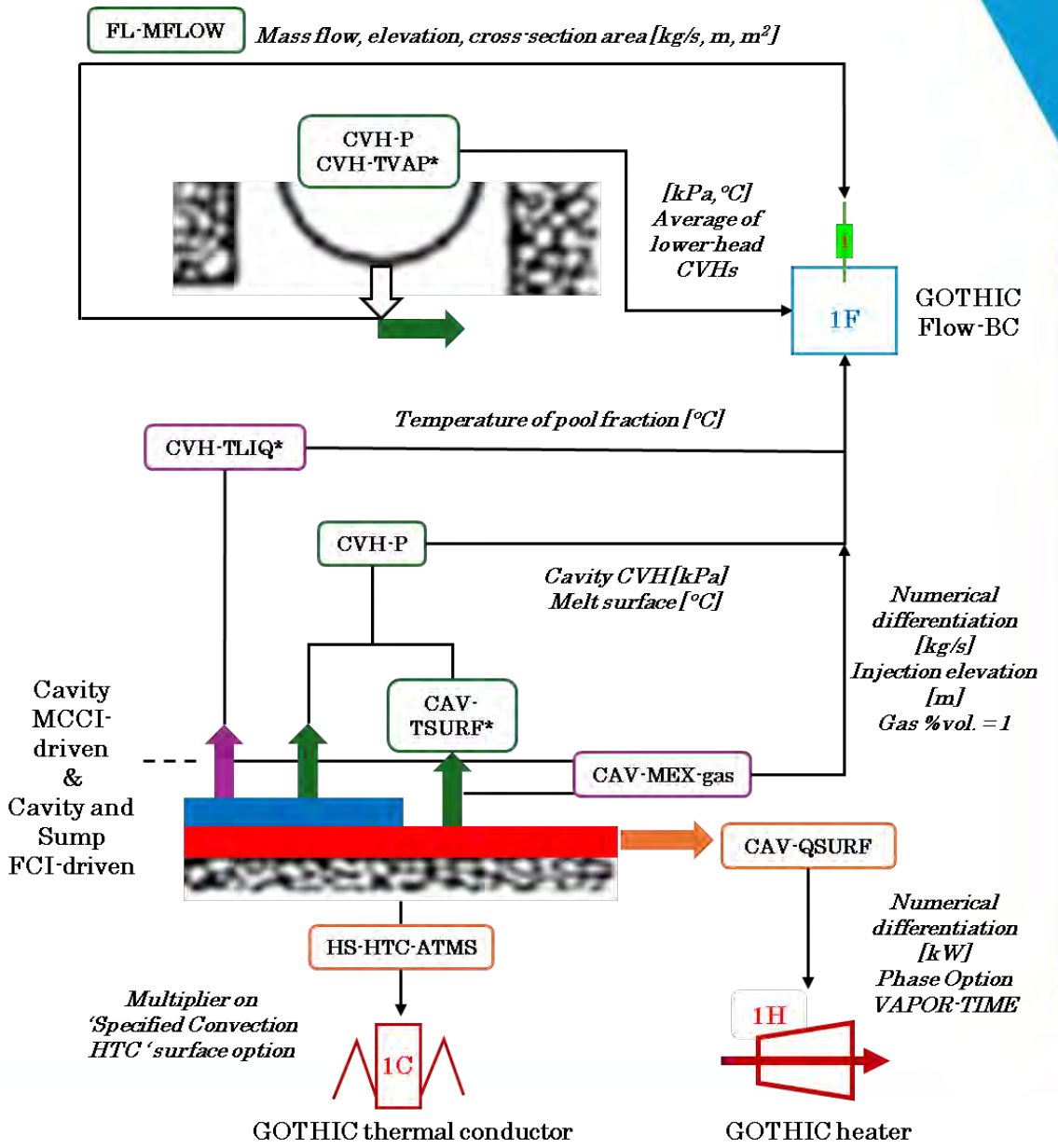

4. Extending GOTHIC to ex-vessel simulations

MELCOR-to-GOTHIC test configuration (dry cavity)

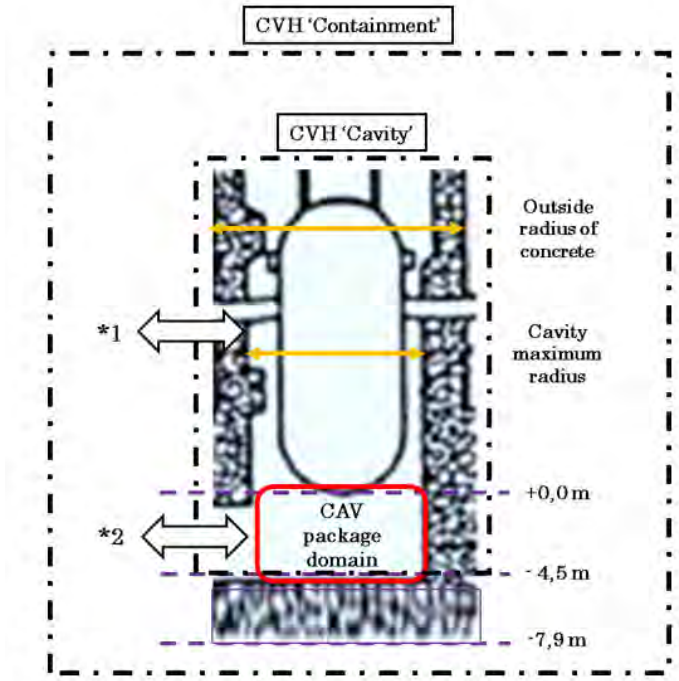

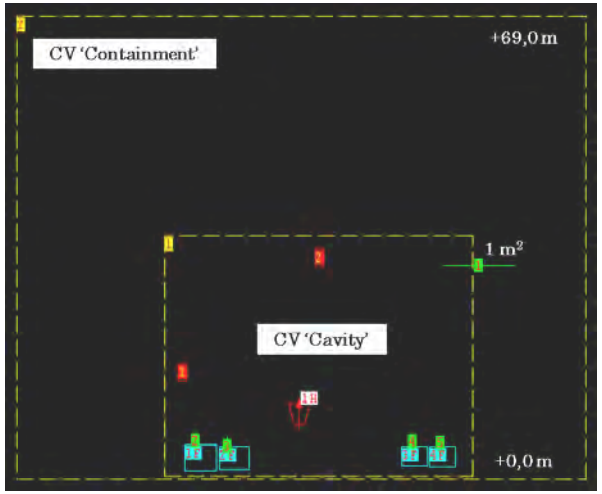

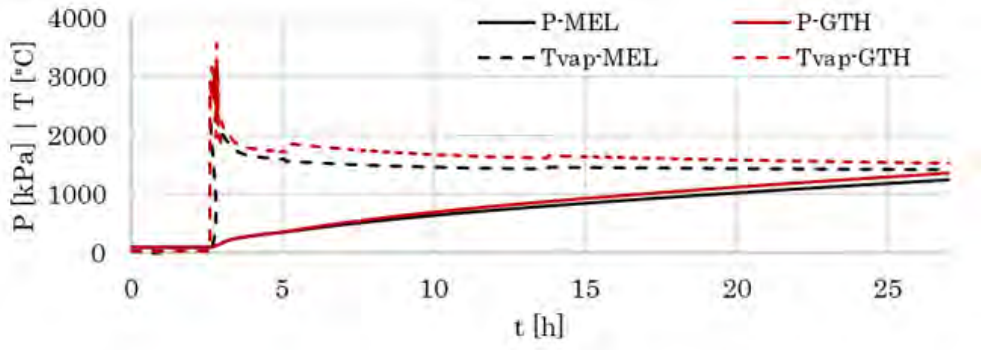

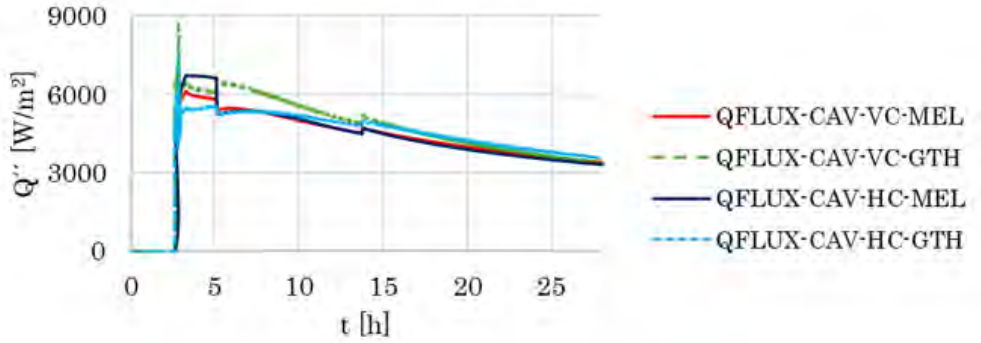

** 1. Flow path connection between cavity and containment control volumes.*
** 2. Flow path connection for water ingress into the cavity control volume.*

** VC stands for Vertical Concrete, HC stands for Horizontal Concrete*

Several test cases verified the MELCOR-to-GOTHIC approach and showed that a sufficiently-complex GOTHIC boundary condition can successfully reproduce the cavity releases to the adjacent volumes without compromising computational effort

5. MELCOR vs GOTHIC application case

TLAP scenario (complete loss of AC power) + late depressurization

AMHYCO D2.2 – Identification and analysis of accident sequences with posing high H_2/CO combustion risk

- Short, intense release of steam and H_2 to the containment (in-vessel, 0.7 ton).
- RPV fails at ~9 h. then, sustained M&E releases from MCCI at the cavity floor (1.62 ton H_2 + 13.9 ton CO).
- Biological shield penetration leads to sump-to-cavity water ingress, partial melt submergence, and melt relocation towards the sump.
- Total simulation window: 9 h (in-vessel) + 11 h (ex-vessel).

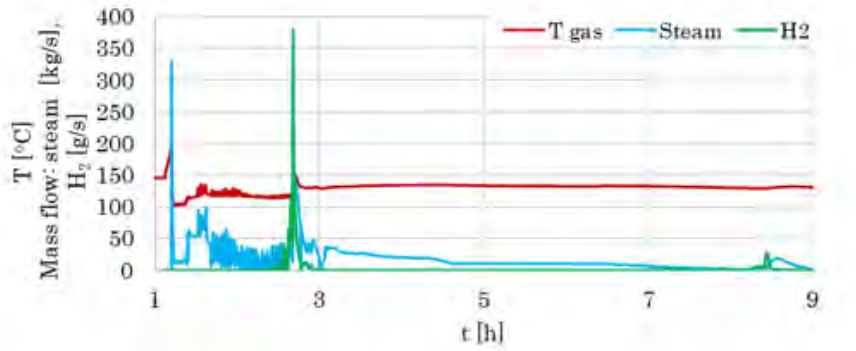

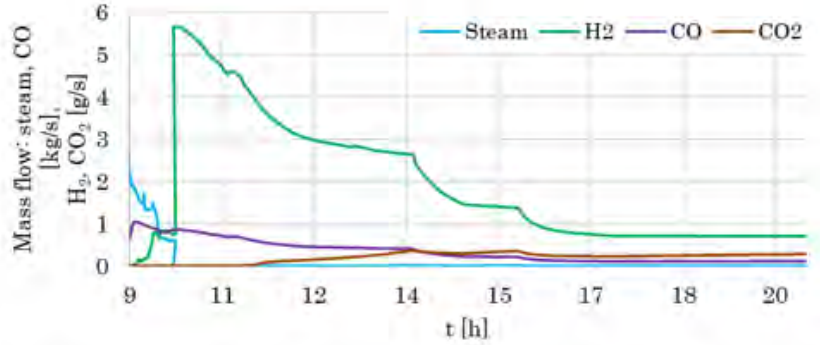

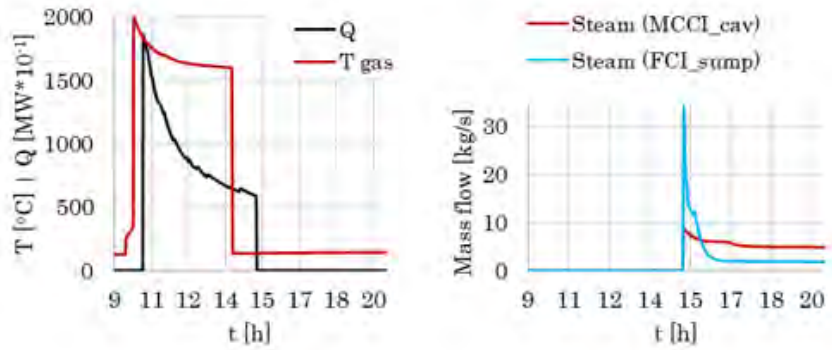

5. MELCOR vs GOTHIC LP/3D application case

- MELCOR vs GOTHIC LP (equivalent CVs) vs GOTHIC 3D (equivalent free volume).
- Unmitigated (U) scenario (wo/ PARs).
- GOTHIC 3D ran on 4 core CPU (i7-9700@3.0 GHz) w/ $t_{step_max} = 0.04$ s
- GOTHIC CPU time: 2,13 h (LP case), ~355 hours (14,8 days) (3D case).

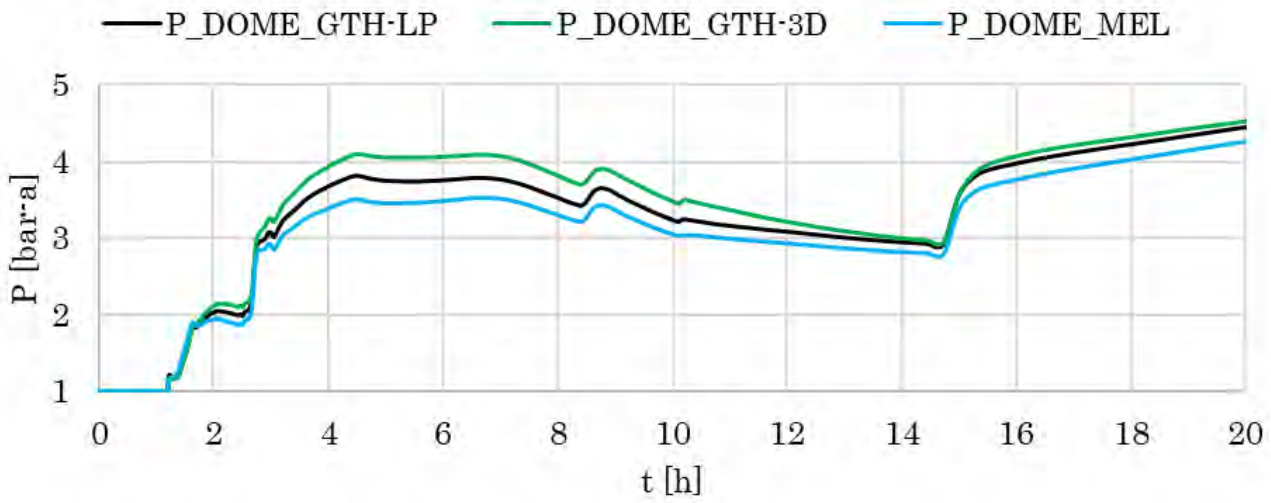

GOTHIC systematically predicts higher pressure

5. MELCOR vs GOTHIC 3D application case

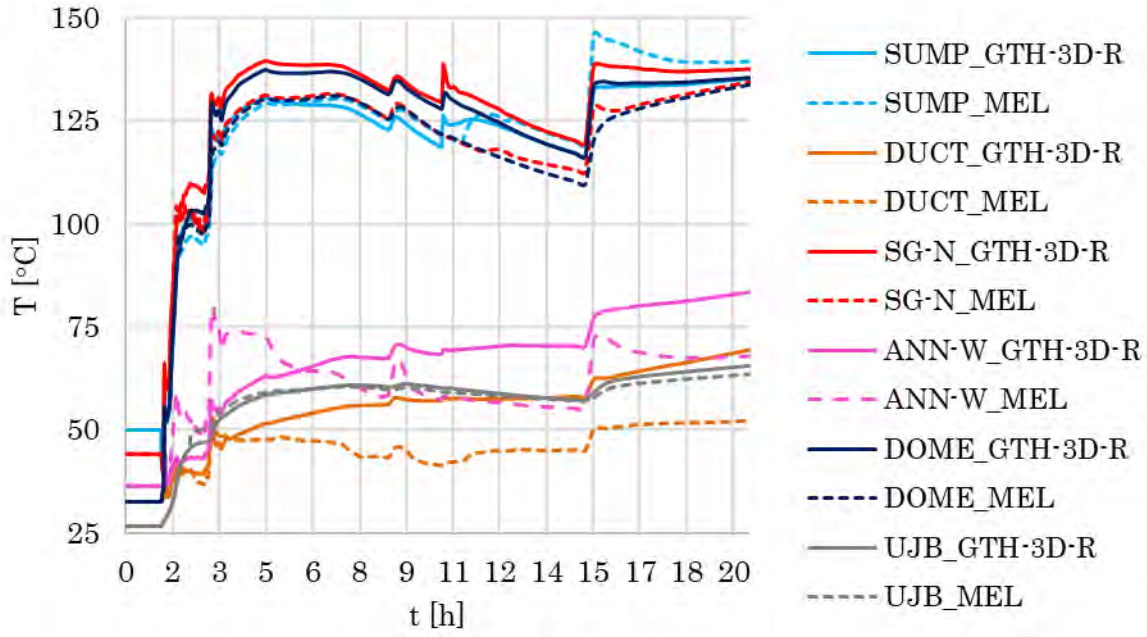

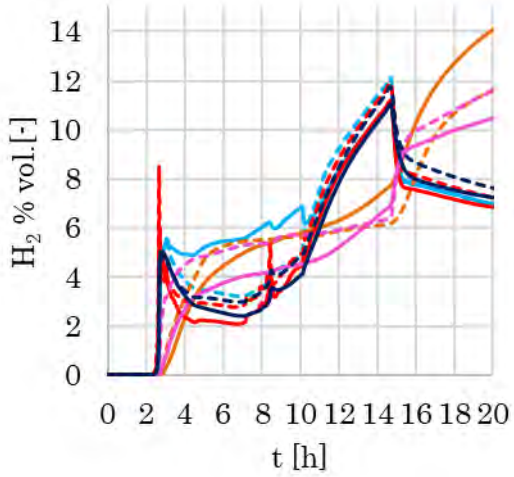

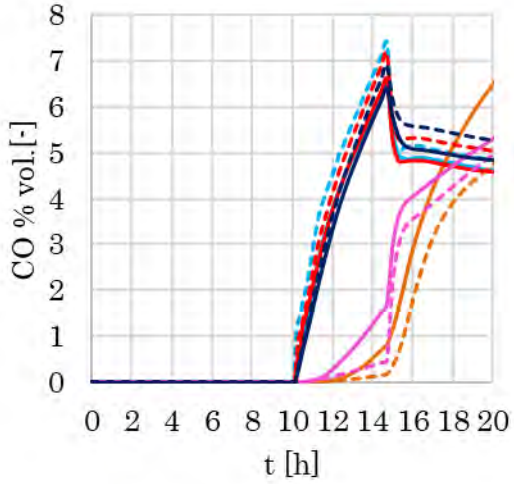

- All approaches reproduce the same global accident progression.
- Reasonable agreement in main circulation and accumulation regions.
- Main discrepancies are linked to condensation, heat transfer and mixing treatment.
- DUCT and ANN-W are the most sensitive regions; DOME: smoother agreement.

5. MELCOR vs GOTHIC LP/3D application case

- Main objective: verify pre-ignition screening figures of merit.

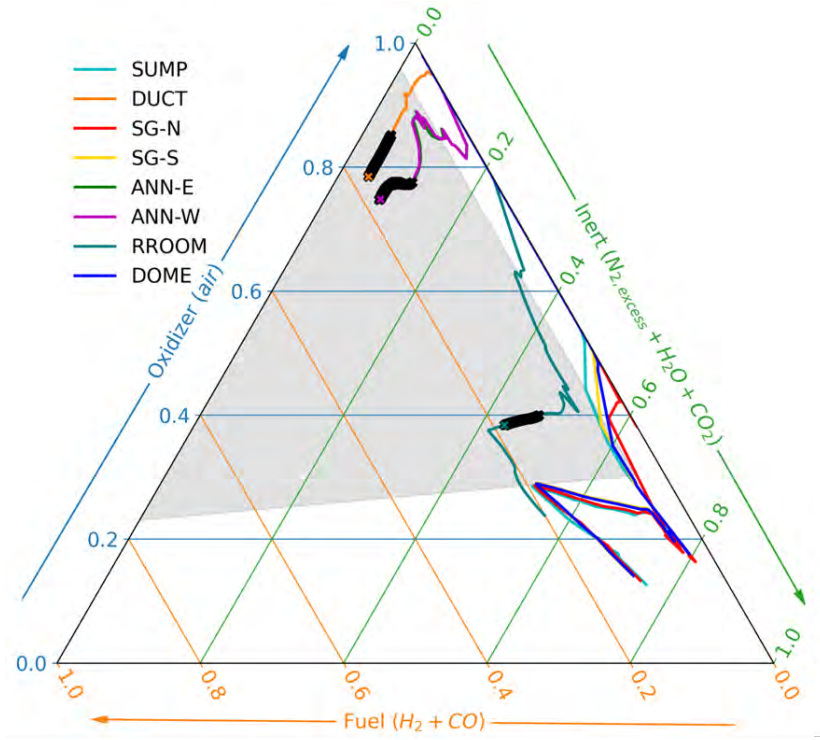

MELCOR

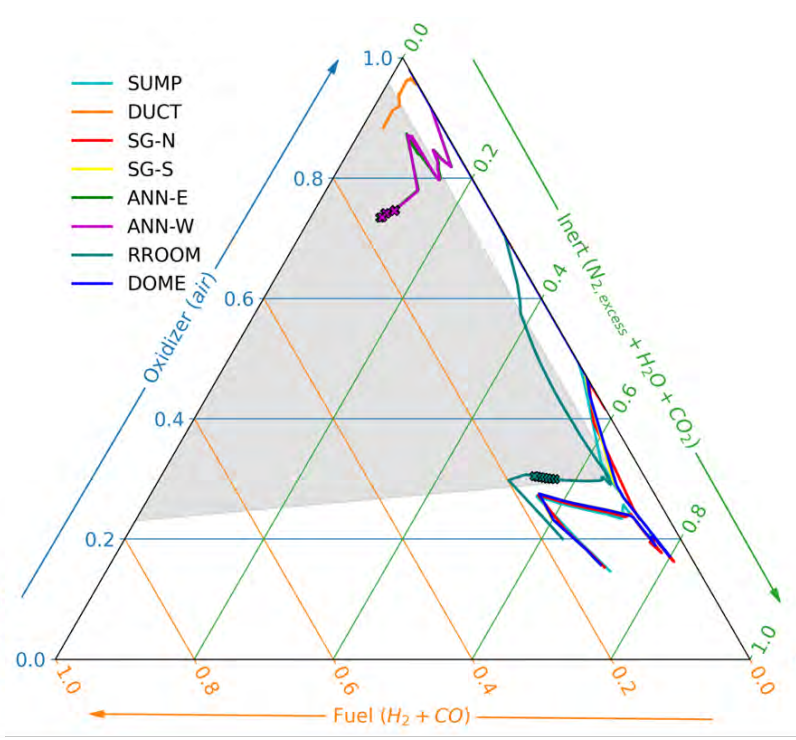

GOTHIC - LP

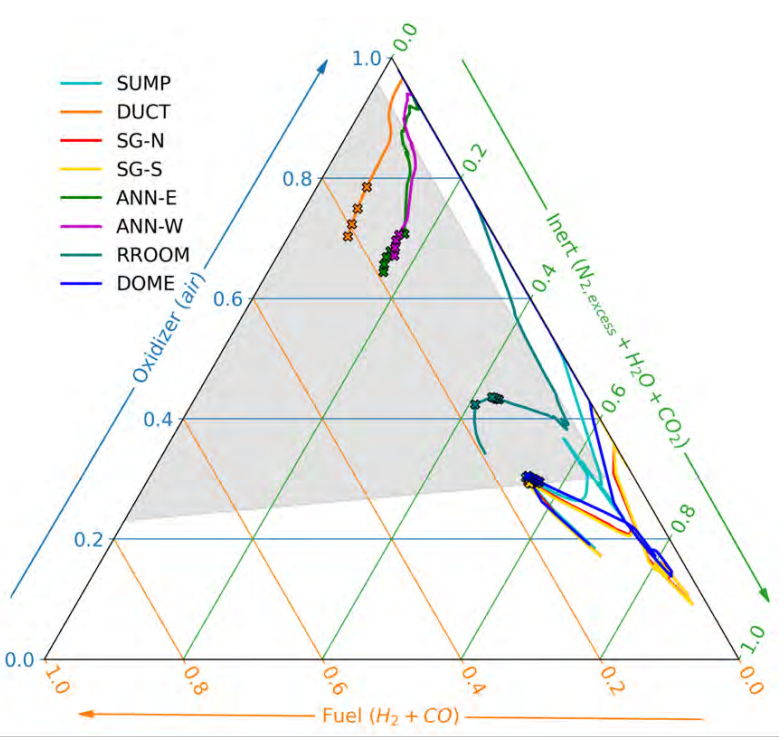

GOTHIC – 3D

5. MELCOR vs GOTHIC LP/3D application case

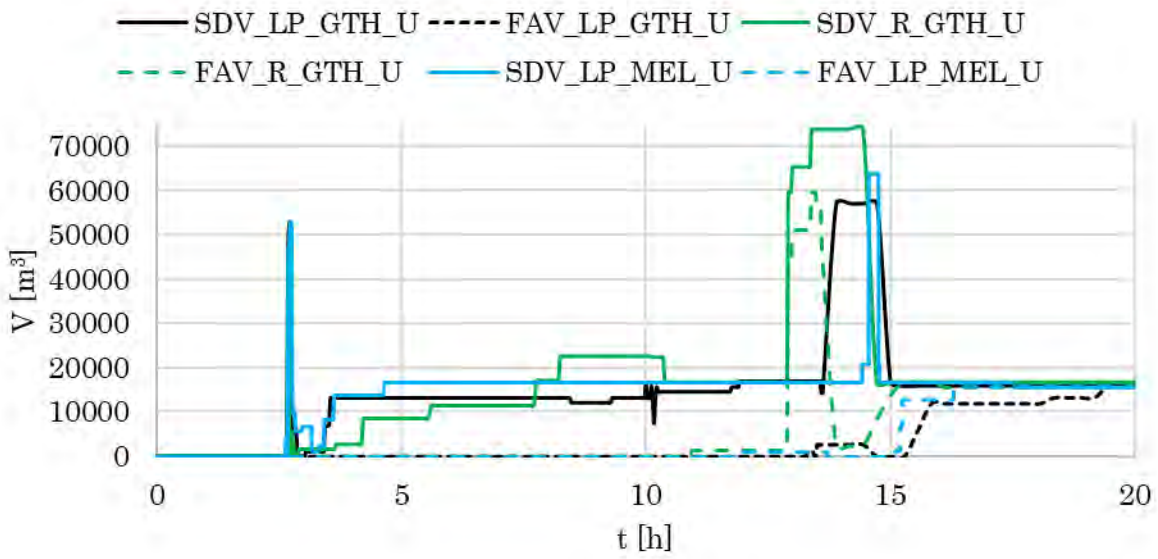

Time evolution of flammable-cloud and FA-prone-cloud free-gas volumes (V) and corresponding fuel masses (M) (H_2+CO), reported as global totals

SD = slow deflagration
FA = flame acceleration
R= 3D equivalent region

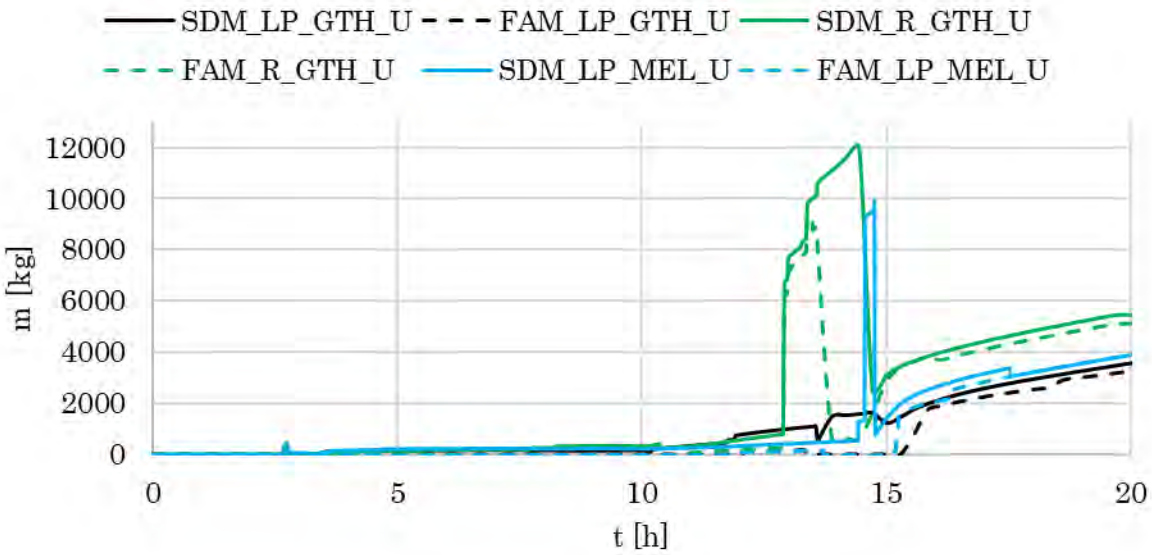

- Both codes can predict a very similar flammable atmosphere.
- Differences propagate to the total free-gas V and fuel M classified as flammable or FA-prone.

5. MELCOR vs GOTHIC 3D application case

- 3D resolved stratification footprints hidden by LP averages.
- Early phase: localized H_2 enrichment and lower-level accumulation.
- Ex-vessel phase: broader stratified structure driven by sustained releases.
- 3D highlighted transport-sensitive regions such as the DUCT.
- Added value: local accumulation and combustion-relevant pockets.

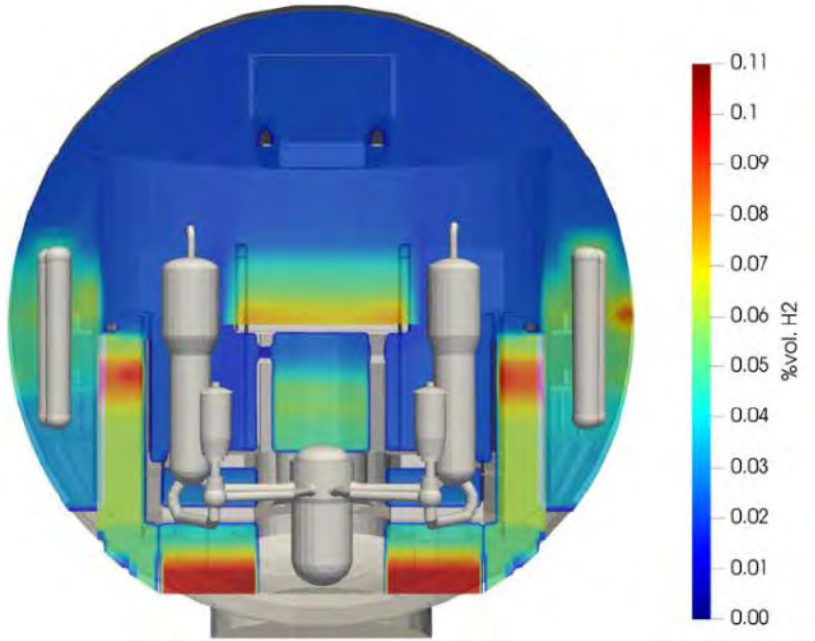

4.5 h

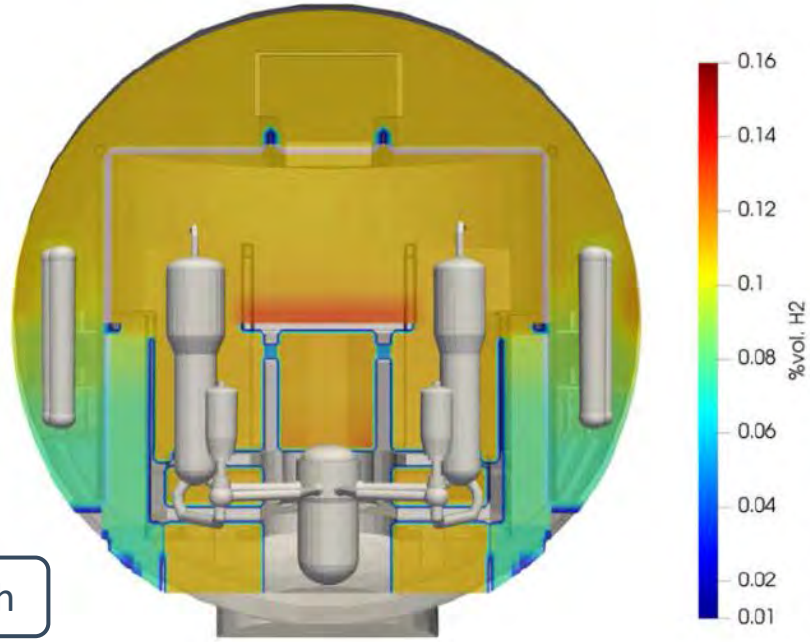

14.5 h

6. Conclusions and outlook

GOTHIC 3D can be extended to the ex-vessel phase in a robust and traceable way, combining an embedded LP cavity with a systematic MELCOR-to-GOTHIC boundary-condition translation.

MELCOR and GOTHIC provided a consistent global accident narrative, which supports the use of GOTHIC for cross-code benchmarking of late-phase containment response.

GOTHIC 3D resolved stratification and local accumulation footprints that remained hidden in LP approaches and were directly relevant for combustion-risk interpretation.

Acknowledgements

AMHYCO
Enhancing H_2 & CO Combustion Risk Management

INDUSTRIALES
ETSII | UPM

GOBIERNO DE ESPAÑA
MINISTERIO DE CIENCIA, INNOVACIÓN Y UNIVERSIDADES

Ciemat
Centro de Investigaciones Energéticas, Medioambientales y Tecnológicas

EPRI
ELECTRIC POWER RESEARCH INSTITUTE

NUMERICAL ADVISORY SOLUTIONS
a Zachry Group company

Thank you

Connect with us for more information:

luis.slopez@upm.es
gonzalo.jimenez@upm.es

https://amhyco.eu/

5. MELCOR vs GOTHIC LP/3D application case

LP / Region (CV)	Total time (h) *First and last entry-exit time* (h)		
	TLAP-U-MELCOR	TLAP-U-GOTHIC-LP	TLAP-U-GOTHIC-3D (R)
SUMP	0.45 *2.72-3.17*	0.15 *2.72-2.87*	4.53 *2.74-2.80* *13.02-14.84*
DUCT	15.34 *4.66-20.00*	9.81 *10.19-20.00*	14.43 *5.57-20.00*
SG-N	0.04 *2.64-2.68*	0.03 *2.66-2.69*	1.38 *13.42-14.80*
SG-S	0.49 *2.70-2.84* *14.41-14.76*	0.07 *2.69-2.77*	1.41 *13.41-14.82*
ANN-W	16.38 *3.62-20.00*	16.54 *3.46-20.00*	11.78 *8.23-20.00*
ANN-E	16.57 *3.43-20.00*	16.47 *3.53-20.00*	15.80 *4.21-20.00*
RROOM	14.54 *2.98-17.52*	10.02 *3.07-8.46* *11.50-15.15*	16.33 *3.67-20.00*
DOME	0.28 *2.69-2.77* *14.55-14.75*	0.05 *2.69-2.75*	1.97 *2.70-2.72* *12.93-14.87*

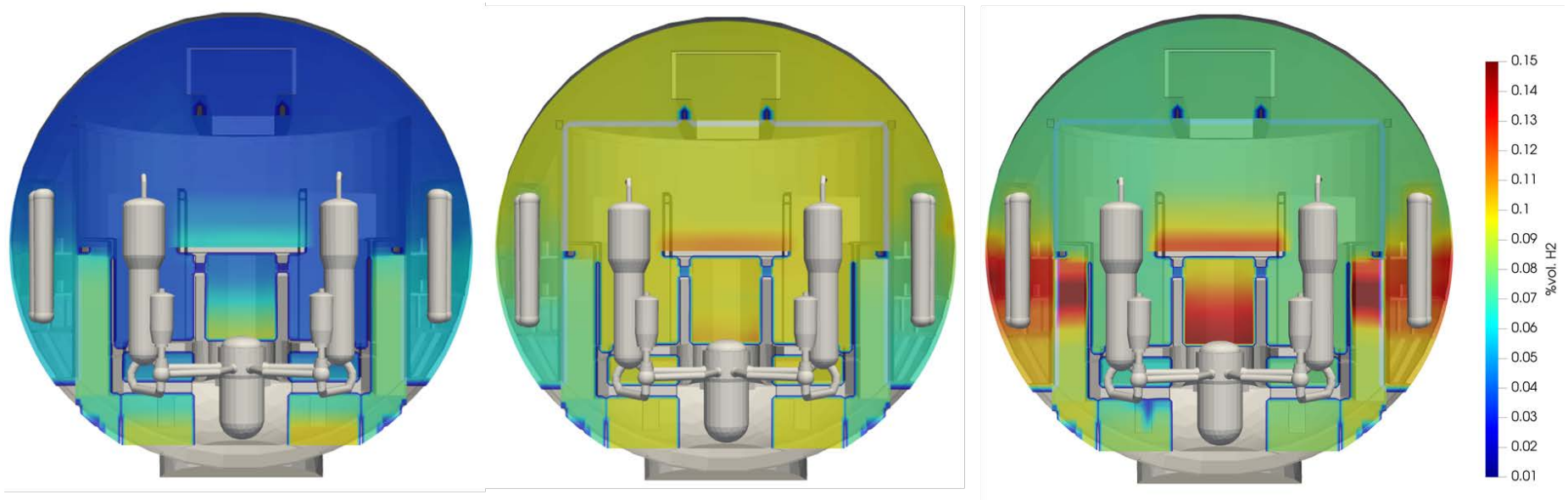
0.15
0.14
0.13
0.12
0.11
0.1
0.09
0.08
0.07
0.06
0.05
0.04
0.03
0.02
0.01
%vol. H2

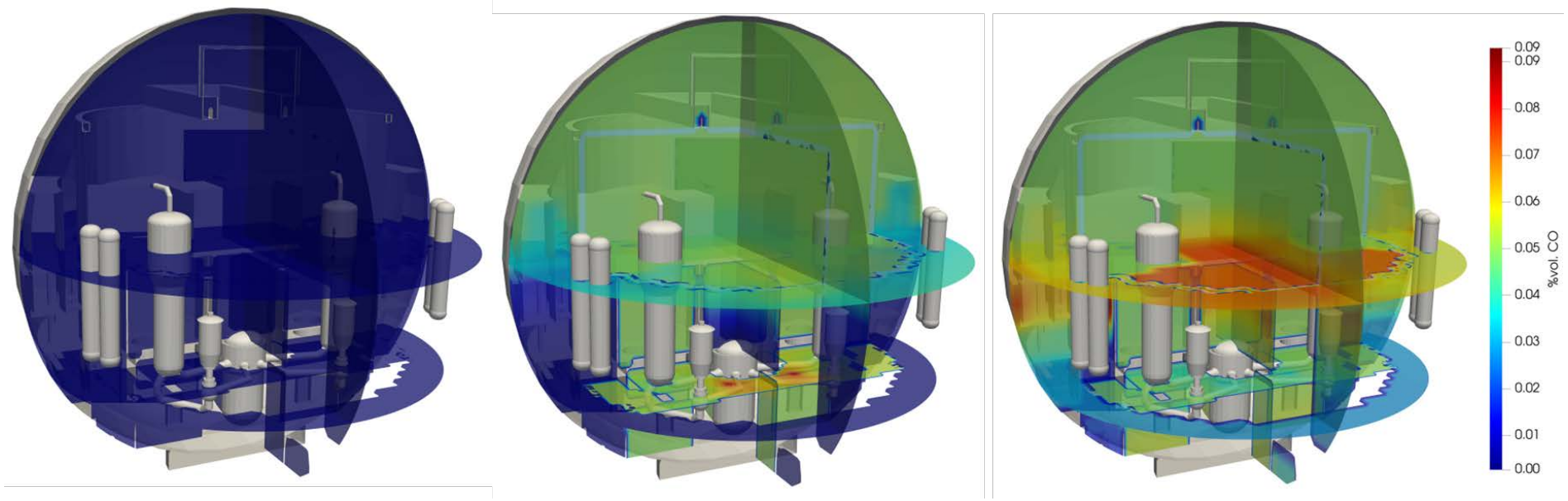
0.09
0.09
0.08
0.07
0.06
0.05
0.04
0.03
0.02
0.01
0.00
%vol. CO

IMPLEMENTATION OF A SAFETY-RELATED AIR-COOLING SYSTEM IN A PWR-W DRY CONTAINMENT USING GOTHIC 3D

Alberto García-Herranz, Gonzalo Jiménez
Department of Energy Engineering
Universidad Politécnica de Madrid (UPM)
José Gutiérrez Abascal, 2, 28006 Madrid, Spain.
a.gherranz@upm.es; gonzalo.jimenez@upm.es;

Carlos Vázquez-Rodríguez
Forschungszentrum Jülich (FZJ)
Wilhelm-Johnen-Straße, 52428 Jülich, Germany
c.vazquez-rodriguez@fz-juelich.de

Ignacio Molina de la Peña
Consejo de Seguridad Nuclear (CSN)
Pedro Justo Dorado Dellmans, 11, 28040 Madrid, Spain.
ignacio.molina@csn.es

ABSTRACT

From the Design Basis Accident (DBA) perspective, the actuation of the containment safety systems has been focused on pressure and temperature control. However, the complex phenomenology inside the containment during severe accidents makes such systems cause unexpected effects, like heterogeneity in the temperature distribution and local flammable gas clouds. This last phenomenon is a cause for serious concern due to the potential risk of a fast hydrogen detonation occurring inside small rooms or ventilation ducts, which could lead to conditions exceeding the containment's design parameters.

This fact has motivated the present study, where the Containment Air-Cooling System (CAS) of a PWR Western-designed (PWR-W) containment has been implemented in a GOTHIC 3D model for the first time in the literature. In detail, this work, conducted within the framework of the CSN's INTERCON3D project, shows how containment safety systems (CAS and sprays) influence global and local thermal-hydraulic and flammable conditions.

The paper presents different large break Loss of Coolant Accident (LOCA) scenarios, performed with GOTHIC 8.3(QA), which consider the temporary interruption of the safety injection to the reactor cooling system. This simulation involves the generation of a relevant amount of hydrogen that challenges the conventional performance of safety and mitigation systems. Simulations show how safety systems promote the cooling of the containment atmosphere, resulting in a fast depressurisation. Nevertheless, the condensation of the steam makes the installation of PARs crucial to address flammable gases in the evaluated scenarios.

KEYWORDS
CONTAINMENT ANALYSIS, GOTHIC, HYDROGEN, SPRAY, FAN COOLERS

1. INTRODUCTION

The containment building is a crucial component for the accident management of PWR reactors, playing the role of the last barrier against a potential radiological release. In addition, this enclosure serves as protection for the reactor against external threats and provides biological protection while operating [1]. During its design and commissioning phases, the containment is tested to comply with the highest safety standards. Those include withstanding postulated internal/external Design Basis Accidents (DBA) and, last designs, Beyond DBA (BDBA); such as Severe Accidents (SA) [2]. To be able to manage these scenarios, the containment includes safety and mitigation systems, which minimise the consequences of accidents to avoid exceeding its design limits. Safety systems of conventional PWRs, such as the spray system, the air-cooling system or ice condensers, have the safety function of depressurising and cooling down the containment after an accident [1]. On the other hand, mitigation systems in conventional PWRs, such as Passive Autocatalytic Recombiners (PARs) and Filtering Containment Venting System (FCVS), were mainly considered after the Fukushima Daiichi accident [3]. These systems are useful for the late phases of BDBA accidents, controlling the concentration of flammable gases and the containment pressure, as well as minimising the source term released in case of venting.

The presence of safety and mitigation systems in the PWR Western-designed (PWR-W) containment should be enough to ensure containment integrity. Nevertheless, the use of these systems may involve drawbacks during the accident progression. One example is the increase in the hydrogen volume fraction due to the sprays' actuation, pointed out by Dimmelmeier et al. in [4] and Paranjape et al in [5]. There are several references in the literature focused on the performance of the containment spray system. However, there are fewer authors who study the impact of safety-related ventilation systems in the presence of flammable gases. The safety function of this system matches the spray function; thus, its operation may also be subject to similar drawbacks. Studies which include this kind of system, such as those carried out by Kapulla et al. in [6] and Soloviev et al. in [7], do not address their performance in a 3D full-containment scale, including flammable gases. These reasons led to the creation of the INTERCON3D project, a national project financed by the Spanish regulator (CSN) to analyse the interaction between safety and mitigation systems of a PWR-W dry containment building under severe accident conditions. In addition, another objective of this project is to identify alternative strategies in system operation which involve a lower risk of flammability.

In line with the objectives of the INTERCON3D project, this paper examines the use of safety and mitigation systems during a BDBA in a PWR-W dry containment, using a 3D computational model with GOTHIC 8.3(QA) [8]. In sections 2-4, the base model and the functioning of the systems are described. Then, section 5 introduces the description of the accident and initial conditions for the simulation. Finally, section 6 addresses the impact of considering safety/mitigation systems on variables related to the conventional safety analysis, such as pressure and temperature, and the risk associated with flammable gases.

2. THE PWR-W DRY CONTAINMENT MODEL

The UPM PWR-W dry containment model has been built with the general-purpose thermal-hydraulic GOTHIC code, which allows for studying the local conditions inside a containment due to its 3D capabilities [8]. This model has been developed and modified throughout the last ten years by the UPM research group [9]. The last version, which is the base for this study, was created following the "Preventive methodology", a specific model-building process for GOTHIC which reduces computational errors and simulation bottlenecks [10]. This model uses a single volume of 40x40x67 m, with a mesh of 1.0 x 1.0 x 1.5 m and 68800 cells.

2.1. CONTAINMENT AIR-COOLING SYSTEM (CAS) IMPLEMENTATION

As was previously mentioned, the Containment air-cooling system (CAS) is a safety system designed to deal with postulated accidental scenarios. Nevertheless, this system has multiple purposes, working during both normal operation and emergency modes. During normal operation, its goal is to keep the inner atmosphere of the containment in adequate environmental conditions for components, equipment and maintenance activities. On the other hand, during emergencies, this system works together with the spray system, depressurising and evacuating the heat load introduced by mass and energy releases into the containment [1]. To address this hybrid purpose, the CAS is composed of different sub-systems, which are:

- **The main Cooling units**. These units are responsible for removing the main heat load of the containment. These are designed with multiple cooling coils and a high-capacity fan to cool down and drive gases to the lower zones of the containment through integrated vertical shafts. Based on current operating plant values, the volumetric output of these units has been estimated at ~45 m^3/s for normal operation and ~20 m^3/s for emergency scenarios. The subsystem has four units, separated into two redundant trains of 100% capacity. These units are interconnected and connected with the containment by means of an extensive duct network. The duct network ensures that cold gases reach most of the lower zones. In an emergency involving Reactor Cooling System (RCS) release, the operation of these units changes, turning on the units on reserve, reducing the velocity of heat-capacity fans and opening a connection between units and the containment dome. This alignment promotes the cooling of gases in the upper zones by the generation of new convection loops. This sub-system is the only one required in most of the emergency scenarios; the following sub-systems are only required in specific accident situations, out of normal operation.

- **The Control Rod Driven Mechanism (CRDM) cooling units.** The CRDM is an energised component that is operated to insert/remove the control rods from the reactor core. According to operating plant values, cooling units must address a heat load of ~600 kW during normal operation to ensure the proper functioning of the CRDM. For this purpose, the present PWR-W design incorporates two redundant, high-capacity fans that evacuate gases surrounding the CRDM. Based on current NPPs, these units deliver ~20 m^3/s. Finally, the main cooling units cool down these gases.

- **The Cavity cooling units**. The cavity is one of the most isolated zones of the containment; thus, its cooling requirements during normal operation are not fulfilled by the main cooling units. In the PWR-W design, the cavity contains relevant elements that require cooling, such as the vessel the nuclear instrumentation. This subsystem introduces two additional Fan-Coolers (FCs) to address the cavity heat load. For similar systems in current NPPs, their output is ~12 m^3/s and ~110 kW.

- **The Filtering units**. These units have the single purpose of removing particles and dust from the containment atmosphere during normal operation, ensuring air quality standards. However, they help with the aerosol retention purpose of the spray system in accidents using a combination of filters and fans. In addition, the unit's fans, which provide ~7 m^3/s (based on operating NPPs) of filtered gas, may be useful due to the mixing effect on the containment atmosphere.

All these subsystems were implemented in the generic PWR-W 3D model in GOTHIC to study the impact of their operation in complex accidental sequences such as severe accidents that may involve the presence of flammable gases. Available data allowed us to create a generic configuration for cooling units and the ducts above the operational floor (see Figure 1). The position of the ducts throughout the containment is not trivial; however, the analysis of the conditions inside them may be relevant for safety analyses. For this reason, the main cooling units and the duct network were geometrically integrated into the 3D model using the Preventive methodology (See Figure 1). The rest of the devices and ducts were implemented with GOTHIC built-in components, such as coolers, fans and junctions.

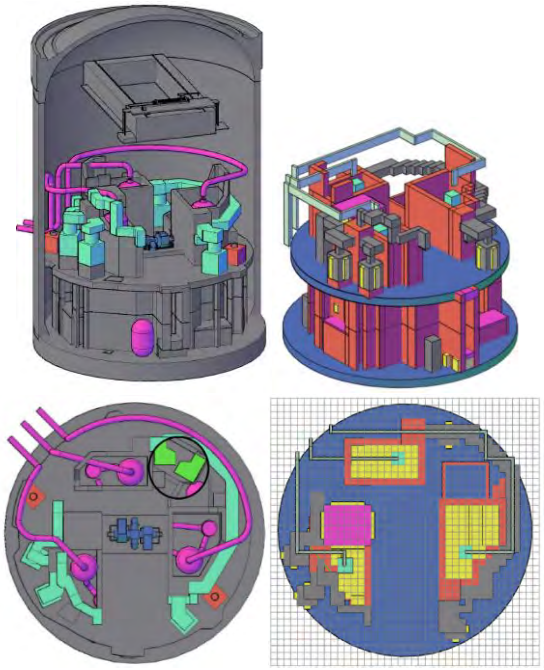

Figure 1:CAS implementation in the detailed 3D CAD model and its geometrical simplification using the preventive methodology.[1]

In detail, the main cooling units and ducts were simplified, adapting their geometry to GOTHIC's Cartesian mesh. In particular, Figure 2 shows how these elements are modified to match the mesh. This process ensures the hydraulic independence of cells that represent the system's inner volume. The mesh was selected previously to the CAS implementation; thus, the design tries to match as much as possible the original duct size, preserving the area throughout the entire duct.

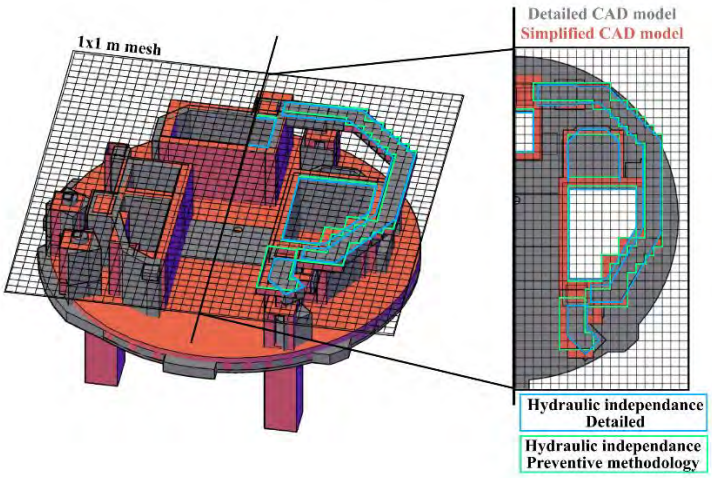

Figure 2: Geometrical simplification of the Main cooling units and ducts.

[1] CAS elements located at the detailed CAD model: Main cooling units (TURQUOISE), cavity cooling units (GREEN), CRDM cooling units (BLUE) and filtering units (RED)

Apart from geometry, the CAS model uses GOTHIC built-in components for Fans and cooling coils. In particular, the FCs cooling coils were introduced as "Coolers". These built-in components are the simplest way of representing a specified heat sink, such as condensers or heat exchangers. These elements do not need much data, because they remove/add a specific amount of heat from the cell where they are placed, promoting the condensation of steam in the cell if its temperature decreases below the saturation temperature. Regarding the performance of these coolers, a heat removal model is included for "coolers" of the main cooling units. This heat removal model uses reference data reserved for the UPM group within the INTERCON3D project. The model calculates the total heat removal by one main cooling unit depending on the temperature of the gases in the cell and the temperature of the water inside the cooling coil tubes. Despite the reference data considering the temperature inside the tubes at ~45 ºC, this model is adapted to match other temperatures. Finally, the reference data include a limitation on the removed heat load from ~135 ºC. This limitation has not been included in this work for: (i) being non-conservative from the hydrogen risk evaluation perspective; and (ii) because of the lack of information on the physical mechanism behind this limitation, probably coming from a conservative threshold for containment cooling.

2.2. OTHER SAFETY/MITIGATION-RELATED CONTAINMENT SYSTEMS

In the present analysis, two additional PWR-W safety-related and mitigation-related components have been considered: the spray system and the Passive Autocatalytic Recombiners (PARs). Their importance for the early stages of an accident and their impact on the late phases, especially in the presence of combustible gases, make them crucial to perform a comprehensive analysis of the CAS. The FCVS is considered out of scope because the accident postulated for the present analysis does not cause the activation set-point of this system to be achieved. Nevertheless, this system may involve drawbacks in a heterogeneous atmosphere in the presence of flammable gases.

- **Spray system**

The spray system is the most used containment safety system on PWR reactors. This system uses several nozzles to inject small cold drops into the containment, which condense steam, mix and cool down the containment atmosphere. This phenomenology causes a fast decrease in pressure and temperature in the case of an accident involving an RCS release. However, the increase of elements, like droplets, which promote steam condensation, may result in issues related to the containment inertisation against combustion reactions. This system actuates during an emergency, after the containment high-pressure signal is generated (P > 250 kPa). This system may operate in two different regimes: injection from external sources and recirculation from the containment sump. The spray system implemented in the PWR-W dry containment 3D model includes two redundant trains of 100 nozzles, each injecting 1 l/s of droplets at ~25 ºC (injection) or ~80 ºC (recirculation). These nozzles are radially distributed in three rings at different elevations to cover 90 % of the containment free volume [1]. Regarding their modelling in GOTHIC, Sprays are created by the built-in component "Spray nozzles", which turn the spray mass through a junction into drops of a specific size.

- **Passive Autocatalytic Recombiners (PARs)**

The PARs are mitigation components included in a large fleet of PWR-W containment, especially after the Fukushima-Daiichi accident. These devices are completely passive, and their operational basis is to promote the removal of flammable gases, such as hydrogen, from the containment by their recombination with oxygen on catalytic surfaces. The design of a PAR configuration must be adapted to the space and capacity requirements of the NPPs [11]. In particular, the present PWR-W 3D model incorporates 40 Framatome-type PARs, distributed throughout the containment following the lessons learnt from the AMHYCO project [12]. Regarding their modelling in GOTHIC, PARs are created by the built-in component "H2 recombiners", which enables the recombination of the hydrogen mass through a junction with a provided efficiency. This efficiency is externally calculated and provided for each time step with a script that includes an engineering correlation provided by Framatome for the AMHYCO project.

2.3. INITIAL CONDITIONS AND OPERATIONAL SPECIFICATIONS

The case selected to analyse the impact of the implementation of the safety/mitigation systems has been a 10.000 s large break LOCA in the cold leg. However, it includes a delay of the Low-Pressure Safety Injection (LPSI) actuation until ~15 min of the simulation. This event, which does not involve core damage, causes a strong oxidation of fuel Zr cladding and the generation of hydrogen (~334 kg) when the core turns partially uncovered and not properly cooled. The recovery of the safety injection causes a quench effect, promoting the fast generation of hydrogen and steam at high temperatures. This input, generated from previous simulations using the PWR-W 3-loop RCS model running in MELCOR, allows us to study the performance of the CAS in the presence of flammable gases. This model was created in the UPM research group in the 80's and updated later by the same group [13]. The communication between MELCOR and GOTHIC is not made by direct coupling; the key variables to simulate the rupture, such as mass, pressure or temperature of streams through the rupture, are introduced as boundary conditions.

On the other hand, initial conditions were generated by a previous steady-state case, which ensures quasi-stationary conditions considering the normal operation of the CAS components. This steady state was validated by the Spanish regulatory body (CSN) within the INTERCON3D project.

3. SAFETY ANALYSIS RESULTS

The present analysis is focused on the impact of the safety/mitigation systems interaction with the containment atmosphere in a post-accidental scenario. In particular, the implementation of the CAS and its operation. For this reason, it is convenient to address how this system impacts the evolution of the transient, independently and in conjunction with other systems or devices, such as the Sprays and PARs. In addition, this section aims to show the differences promoted by two possible operational behaviours of the CAS, the one described in the system's manual and the success criterion required for the containment cooling system during an emergency. Taking this into account, the next cases are proposed:

1. **"W/o SYSTEMS"**. The base case of the comparison. This case considers all safety and mitigation systems not available during the simulation.
2. **"CAS" case**. This case considers only the actuation of the CAS, which follows the description of the system. The system's description considers 3/4 main cooling units before the break takes place and 4/4 main cooling units operating at low load after. In addition, cooling units incorporate discharging gates that open a direct connection between units and the containment dome at high temperature. Regarding other changes, the second filtering unit starts operating, the CRDM is de-energised, and the Cavity cooling starts working on close loop to isolate the zone.
3. **"Sprays +CAS (Syst. description)" case**. This case considers the actuation of Sprays and the CAS, following the description of systems. The CAS actuates as described above, while the Sprays system works by injecting spherical drops (0.1 cm) through 1/2 trains of nozzles located at the top of the containment.
4. **"Sprays +CAS (Succ. criterion)" case**. This case considers the actuation of Sprays and the CAS. However, for this case, a common "success criterion" has been considered. The "success criterion", a concept which sets the minimum sufficient condition on systems or components to progress towards a safety shutdown after a postulated accident. In this specific case, the correct operation of 1/2 redundant trains of both systems (100 nozzles and 2/4 main cooling units).
5. **"Sprays +CAS (Syst. Description) +PARs" case.** This case introduces PARs as the main mitigation action against the flammability potential of hydrogen. This configuration matches case 3, which is the most conservative case in terms of flammability risk, with the greatest number of condensing mechanisms working simultaneously. This case will be considered only for the flammability risk analysis due to the low impact of PARs on pressure and temperature.

First, it is important to describe the containment thermal hydraulics before and after the LOCA-type event. As shown in Figure 3, during normal operation, the main cooling units take gases which surround them and drive them into the ducts and vertical shafts. This operation creates large convection loops in the lower zones of the containment, cooling down the main components and equipment. In Figure 3, it is visible how the configuration of units generates a flow pattern throughout the ducts. This flow pattern helps to understand which units contribute more to cool down all containment zones. This is especially relevant for the selection of the units in operation for case 4. Five seconds after the break, the flow patterns change radically (see Figure 3). The fast release of gases from the RCS produces a chaotic atmosphere inside the containment. However, hot gases tend to flow towards the upper parts of the containment, changing the cooling needs. For that reason, the main cooling units change their operation, driving the cooled gases into the containment dome. This mode generates large convection loops in this zone, which enhance condensation. Nevertheless, after the break, the flow through the ducts and vertical shafts decreases, with the flow reversing in some zones (see Figure 3).

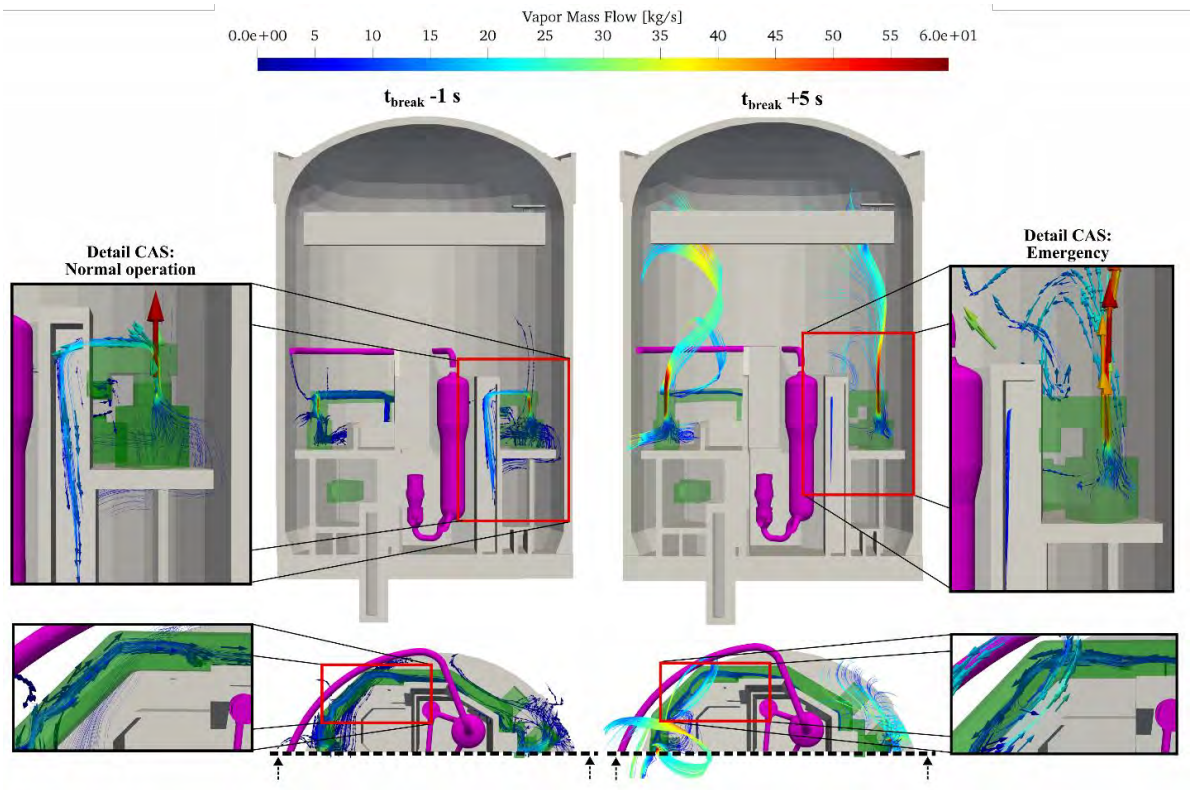

Figure 3: Gas stream paths from the main cooling units for different operational modes.[2]

In Figure 4, the evolution in global pressure and temperature is shown; these variables are the result of an average by volume, considering values cell by cell. Focusing on pressure, systems have a low impact on the first pressure peak because systems need time to absorb the load released in the first seconds of the LOCA. Then, the introduction of safety systems led to a significant depressurisation of the containment minutes after the break. The depressurisation is caused by the increase of elements which promote steam condensation, such as drops and coolers, which condense the steam introduced by the break. Cases involving

[2] CAS components and ducts coloured in green.

safety systems have a similar pressure evolution. The case with the highest depressurisation involves both sprays and the CAS at full capacity, as expected. On the other hand, cases without sprays or systems working to comply with the success criteria show similar results. These results are reasonable, considering the redundant design of both systems.

Regarding temperature, apart from the significant difference between the cases with and without safety systems, some relevant deviations exist between the rest of the cases. In Figure 4, around 1000 s after the break, the highest temperature peak takes place, caused by the recovery of the safety injection, which promotes the release of steam and hydrogen from the core at high temperatures. These gases ascend quickly from the affected cold leg to the containment dome. The cases that include sprays can buffer the impact of the release of those gases because of the influence of the system on the entire containment dome and Steam Generator (SG) compartments. On the other hand, the CAS has a more localised influence; thus, these units need more time to produce an equivalent cooling effect than the spray system. The configuration of the main cooling units after the break causes hot gases to have to reach the containment dome and take part in the convection loops to be cooled down by these devices. The differences in the cooling process provoke an avoidable temperature peak in the case without sprays. After the peak, the evolution of temperature becomes similar to the pressure evolution for cases with safety systems.

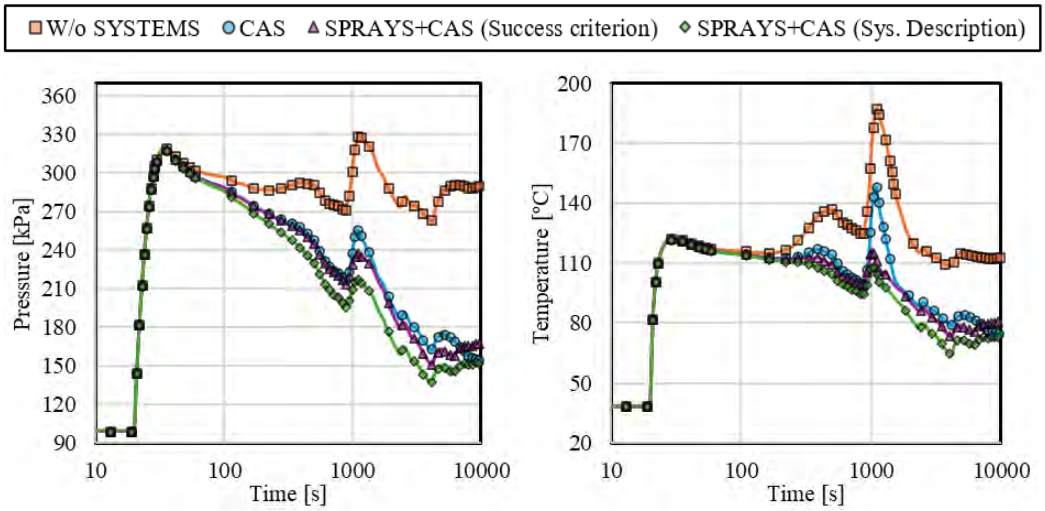

Figure 4: Evolution in global pressure and temperature of analysed cases.

As mentioned before, hydrogen is introduced to the containment when the core is not properly cooled, a situation provoked by a delay in the LPSI actuation. That hydrogen may accumulate in specific locations depending on the containment geometry and flow patterns. Local concentrations of hydrogen may pose a risk to the integrity of the containment. Nevertheless, hydrogen flammability risk is governed by certain chemical, geometrical and thermal conditions. This risk may be quantified by the calculation of flammability limits; these are the lowest (LFL) and highest (UFL) hydrogen concentrations which may combust at a specific temperature. In addition, the amounts of O_2 and steam affect these flammability limits. The Shapiro-Mofette diagram [14] is commonly used, due to its simplicity, to evaluate the risk of hydrogen deflagration or detonation. However, this diagram just represents the flammability limits at specific thermal conditions, being sensitive to temperature variations. For this reason, Martin-Valdepeñas et al. in [15] propose the linearization of those limits, whose expressions depend on molar fractions of gases (x_{H_2}, x_{H_2O}, x_{O_2}) and temperature (T). These expressions are included below (1) – (3). In addition, the fourth expression considers that O_2 must achieve a specific molar fraction to permit the combustion reaction to take place [16].

$$x_{H_2}^{LFL} \geq 0.037 + 0.011x_{H_2O} - 4.16 \times 10^{-5}(T - 373) \quad (1)$$

$$x_{H_2}^{UFL} \leq 0.772 + 1.087x_{H_2O} - 2.71 \times 10^{-4}(T - 373) \quad (2)$$

$$x_{H_2O} \leq 0.63 + 3 \times 10^{-4}(T - 373) \quad (3)$$

$$x_{O_2} \geq 0.05 \quad (4)$$

These equations can be used to identify flammable gases in each cell of the 3D model. This enables us to locate flammable clouds and study their propagation throughout the containment free volume by summing the volume of the cells in a flammable state. This calculation is performed using the UPM post-processing tool, ProTON [17]. As an example of applications, Figure 5, created by this tool, shows how the safety systems impact the flammable cloud volume.

As was mentioned before, the safety systems involve the introduction of new elements which promote steam condensation, contributing to the depressurisation of the containment following a LOCA accident. However, the steam condensation also increases the hydrogen volume fraction. This is clearly noticeable in Figure 5, where, in contrast to the "W/o SYSTEMS" case, the flammable volume occupies the entire containment before 3000 s of the simulation. Among cases that consider safety systems, the one with sprays the CAS at full capacity represents the worst-case scenario. Nevertheless, in the other cases, the simulation predicts how flammable clouds take more time to spread throughout the entire containment's free volume. This window could be crucial to actuate on the system's operation, based on flammable gas or steam pressure measures, to avoid the complete propagation of clouds.

Finally, the case including PARs is shown as well in Figure 5. The introduction of these devices is crucial due to their impact on the control of flammable gases. In this case, the safety systems can operate with a lower risk of local deflagration of flammable clouds. Nevertheless, as shown in Figure 5, even the case with PARs has a time window where 10% of the containment volume is flammable. This is why, even considering mitigation measures, it is important to locate those clouds to take specific actions against their formation, expansion and combustion.

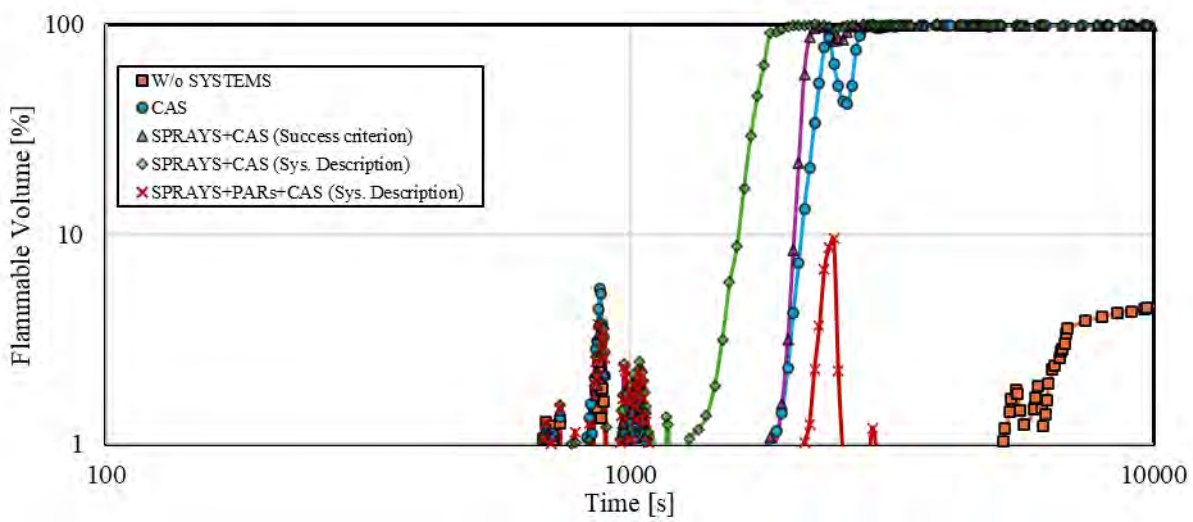

Figure 5: Evolution in containment volume in flammable conditions of analysed cases.

Regarding the location, Figure 6, created using ProTON and visualisation Software Paraview, shows the formation of flammable clouds (in RED) and how safety/mitigation systems impact it. For space limitations, only the most restrictive case is displayed, the "Sprays +CAS (Syst. description)" case. As shown in Figure 6, during the progression of the accident, flammable clouds start appearing. At the beginning, the effect of hydrogen and the sprays govern the formation of clouds. Nevertheless, the main cooling units start to accumulate flammable gases, which are driven to the dome. The effect of both systems, together with the rest of the elements which promote steam condensation, causes the entire containment to achieve flammable conditions. If the PARs were added, they would help to address this severe scenario. However, this would not imply a zero-risk situation, because the FCs continue condensing gases and promoting the presence of flammable clouds. In view of these results, even in the presence of PARs, the conventional operation of safety systems may result in a safety issue for scenarios involving flammable gases.

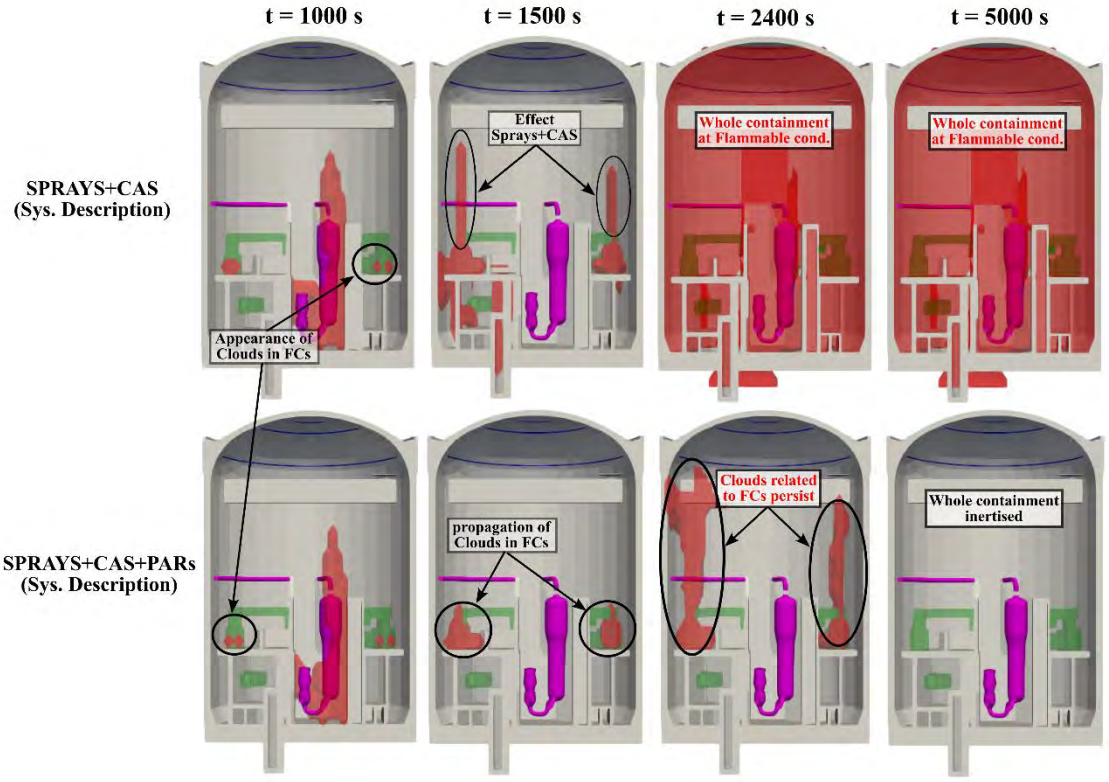

Figure 6: Evolution of flammable clouds inside the containment considering safety/mitigation systems.

4. CONCLUSIONS

The implementation of the main components and ducts of the CAS into a PWR-W 3D model in GOTHIC, using the preventive methodology, has allowed us to locally study the advantages and drawbacks of their operation in scenarios involving flammable gases.

The simulation of an LOCA-type scenario shows the effectiveness of the conventional use of safety systems for managing DBAs, providing a fast depressurisation and temperature decrease. Nevertheless, the continuous use of these systems during the accident and their cooling effect may result in a significant safety issue in the presence of hydrogen.

As the present study shows, PARs are crucial to address sequences involving safety systems, due to their capabilities to effectively remove the hydrogen clouds inside the containment in a few hours for the cases shown. However, their operation, which strongly depends on recombination capacity and location, may not mitigate some flammable clouds, which may persist for a longer time in isolated zones or components, such as FCs and ducts. For this reason, an operation strategy of systems based on the monitoring of containment atmospheric conditions would be a step forward towards safety in conventional PWR NPPs. The new strategies could be based on a method for detecting flammable gases or on a method for maintaining steam pressure above inerting conditions inside the CAS. The choice of method should depend on the utility company and the resources available.

ACKNOWLEDGMENTS

The authors want to acknowledge the technical and financial support granted by the Spanish Nuclear Regulatory Body (CSN) through the INTERCON3D project (ref. SN-080-2022).

This work was completed using a GOTHIC license for educational purposes provided by Numerical Advisory Solutions, LLC. GOTHIC™ incorporates technology developed for the electric power industry under the sponsorship of EPRI, the Electric Power Research Institute. The authors also wish to extend their appreciation to the personnel of EPRI and Numerical Advisory Solutions company, particularly Tom George and Jeff Lane, for their invaluable technical assistance and support.

REFERENCES

1. Westinghouse Electric Company LLC, *WESTINGHOUSE TECHNOLOGY SYSTEMS MANUAL*, chapters 5.3 -5.4, Chattanooga, USA (2016).
2. M. Sonnenkalb, “Beyond design basis accidents and accident management,” *FJOH Summer School*, Aix-en-Provence, France (2010).
3. CSN, *Plan de acción europeo post-Fukushima - España plan de acción nacional*, Madrid, España (2014).
4. H. Dimmelmeier, J. Eyink, and R. P. Martin, “The Impact of Early Spray Activation During a Postulated Severe Accident in the AREVA EPR™ Containment”, Proceedings of *2010 International Congress on Advances in Nuclear Power Plants '(ICAPP'10)*, San Diego, CA, USA, June 13-17, 2010, pp. 1165–1176 (2010).
5. S. Paranjape, G. Mignot, R. Kapulla, and D. Paladino, “Experimental investigation of gas transport induced by containment spray activation during a scaled severe accident scenario,” *Nuclear Engineering and Design*, **342**, pp. 88–98 (2019).
6. R. Kapulla, G. Mignot, and D. Paladino, “Large-Scale Containment Cooler Performance Experiments under Accident Conditions,” *Science and Technology of Nuclear Installations*, **2012**, pp. 1–20 (2012).
7. S. L. Soloviev, A. V. Shishov, V. P. Povarov, and S. V. Yaurov, “Computational simulation of the heat and mass transfer processes occurring in the containment of Novovoronezh NPP II’s units 1 and 2,” *Nuclear Energy and Technology (NUCET)*, **10(1)**, pp. 19–25 (2024).
8. EPRI, *GOTHIC THERMAL HYDRAULIC ANALYSIS PACKAGE. Version 8.3(QA)*, Palo alto, CA, USA (2018).
9. R. Bocanegra, G. Jimenez, and M. K. Fernández-Cosials, “Development of a PWR-W GOTHIC 3D model for containment accident analysis,” *Annals of Nuclear Energy*, **87**, pp. 547–560 (2016).
10. C. Vázquez-Rodríguez *et al.*, “The Preventive Methodology: A priori modification of the containment geometry to boost the computational efficiency of GOTHIC 3D models,” *Nuclear Engineering and Design*, **432**, p. 113718 (2025).
11. M. Sonnenkalb, S. Band, H. Nowack, and S. Schwarz, “Re-Evaluation of PAR Concept in German PWR with Revised PAR Model,” *Proceedings of the 16th International Topical Meeting on Nuclear*

Reactor Thermal Hydraulics (NURETH-16), Chicago, IL, USA, August 30 - September 4, 2015, pp. 1489 - 1501 (2015).

12. G. Jimenez *et al.*, "AMHYCO Project – Towards an Enhanced Accident Management of the H2/CO Combustion Risk," *19th International Topical Meeting on Nuclear Reactor Thermal Hydraulics (NURETH-19)*, Brussels, Belgium, March 6 - 11, 2022 (2022).
13. R. Bocanegra, M. Ruíz-Zapatero, G. Jimenez, and C. Queral, "Enhanced MELCOR models for standard PWR-Westinghouse design," *11th International Topical Meeting on Nuclear Reactor Thermal Hydraulics, Operation and Safety (NUTHOS-11)*, Gyengju, Korea, October 9 -13, 2016 (2016).
14. Z. M. Shapiro and T. R. Moffette, *Hydrogen Flammability Data And Application To PWR Loss-Of-Coolant Accident*, WAPD-SC-545, pp. 11 - 13, Pittsburgh, PA, USA (1957).
15. J. M. Martín-Valdepeñas, M. A. Jiménez, F. Martín-Fuertes, and J. A. Fernández, "Improvements in a CFD code for analysis of hydrogen behaviour within containments," *Nuclear Engineering and Design*, **237**, pp. 627–647 (2007).
16. L. L. Humphries *et al.*, *MELCOR Computer Code Manuals Vol. 2: Reference Manual Version 2.2 r2023.0,* SAND2023-10994 O, pp. 21-23, Albuquerque, NM, USA (2023).
17. C. Vázquez-Rodríguez, *Advanced Implementation of the Spray Safety System into a 3D-GOTHIC PWR-W Containment Model and Its Impact on the Hydrogen Combustion Risk,* PhD Thesis, Universidad Politécnica de Madrid (UPM), pp. 92 - 96, Madrid, Spain (2023).

IMPLEMENTATION OF A SAFETY-RELATED AIR-COOLING SYSTEM IN A PWR-W DRY CONTAINMENT USING GOTHIC 3D

Alberto García Herranz (UPM)*,Gonzalo Jiménez Varas (UPM), Carlos Vázquez Rodríguez (FZJ), Ignacio Molina de la Peña (CSN)

*a.gherranz@upm.es

12th CONFERENCE ON
SEVERE ACCIDENTS RESEARCH
May 18-22, 2026 - Madrid, Spain
ERMSAR 2026

INDUSTRIALES ETSII | UPM

INTER CON3D

Contents

- Context
- PWR-W Dry Containment 3D Model
- Conventional Safety Analysis Results
- Combustión Risk Analysis Results
- Conclusions and future works

Context

POLITÉCNICA

Working on containment analysis since 2013

AMHYCO

- European Project
- Extension 2020 – 2025 (5 years)
- Improve the predictability of LP – CFD codes regarding Hydrogen risk

GO-MERES

CSN CONSEJO DE SEGURIDAD NUCLEAR

- National Collaboration Agreement
- Extension 2019 – 2022 (4 years)
- Simulation of PANDA experiments on 3D GOTHIC for full-containment applications

INTER CON3D

- National project financed by the CSN
- Extension 2023-2025 (3 years)
- 3D analysis of safety/mitigation systems of PWR-W containments
- Identification of improvements on the management of flammable gases

PWR-W Dry Containment 3D model

PWR-W Dry Containment 3D model → GOTHIC Characteristics

Thermal-hydraulic code for **containment-specific** applications

3D Models (Cartesian Mesh): CFD behavior on free volume, ingeniering correlations for mass and energy transfer on surfaces

Porous media approach: presence of solid and fluid in the same cell

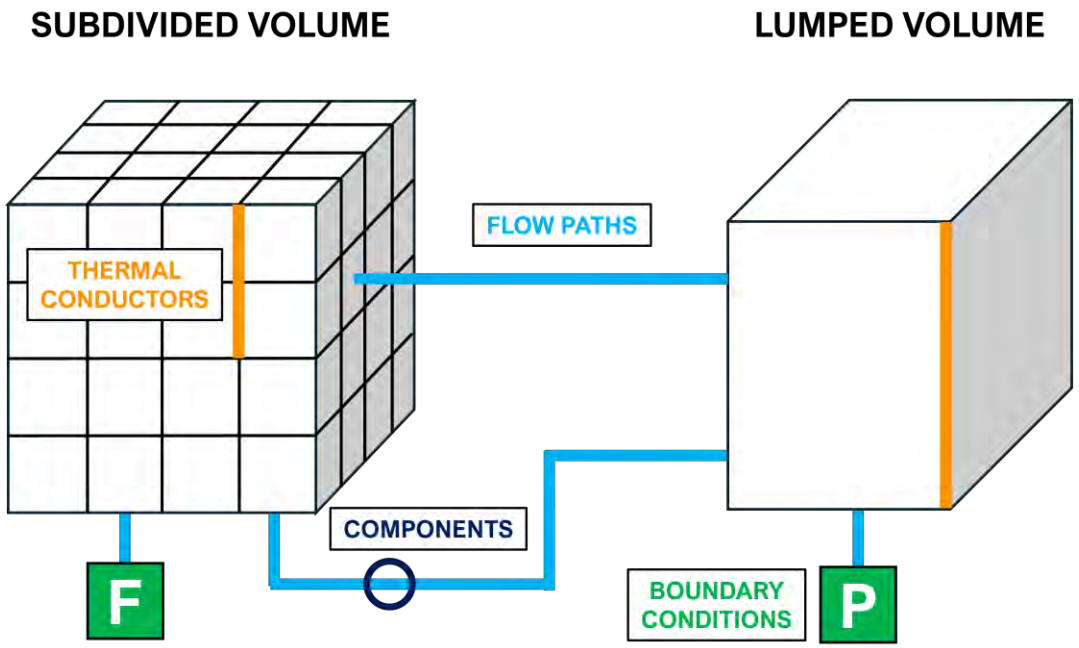

PWR-W Dry Containment 3D model → Modelo Base UPM

Dry containment design for 3-Loop PWR-W reactor

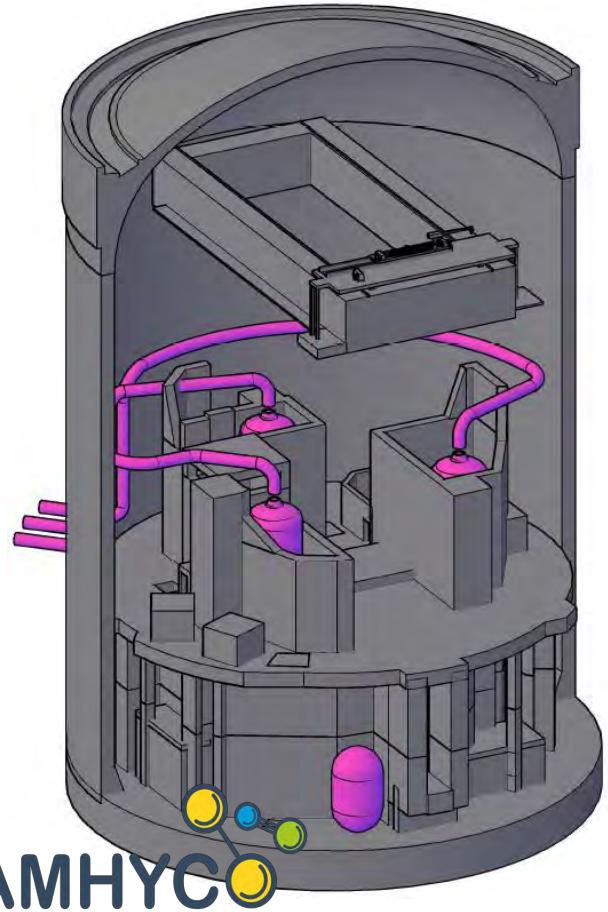

Dry containment design for 3-Loop PWR-W reactor
Including Safety Systems

Sprays

PARs

FCVS

CAS

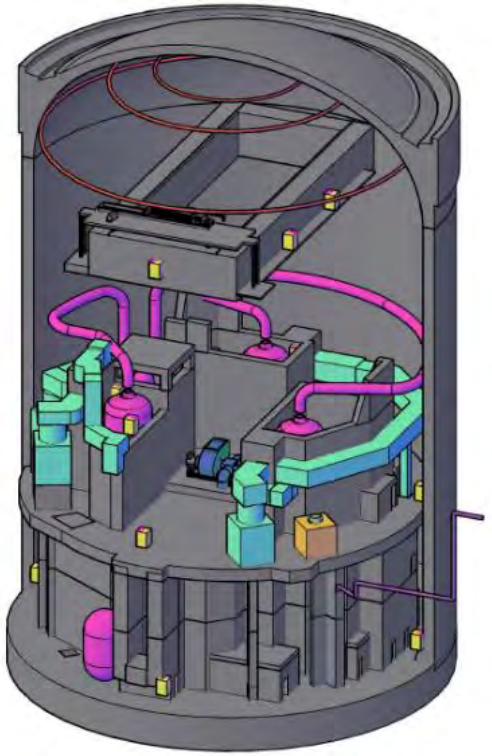

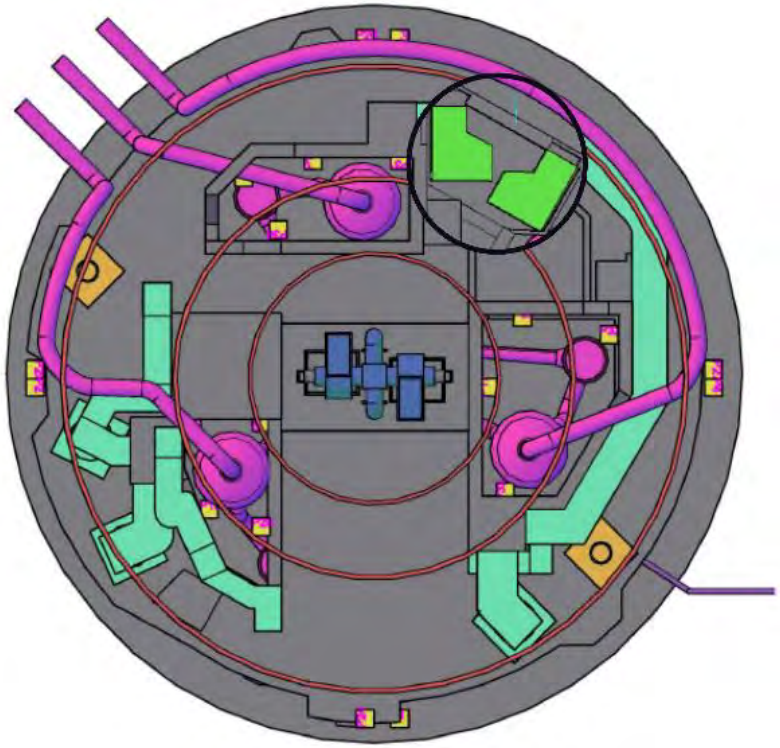

PWR-W Dry Containment 3D model → CAS

Filtering Units

CAS: Containment **A**ir-cooling **S**ystem

Cavity cooling units

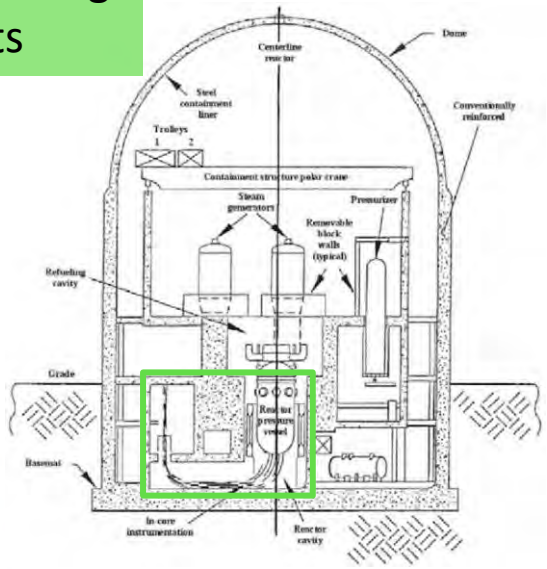

Unidades principales de refrigeración:

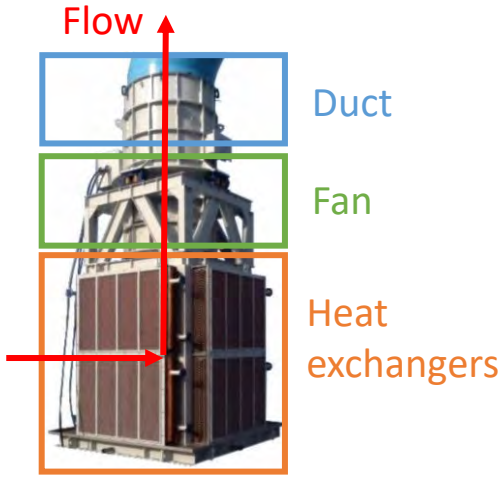

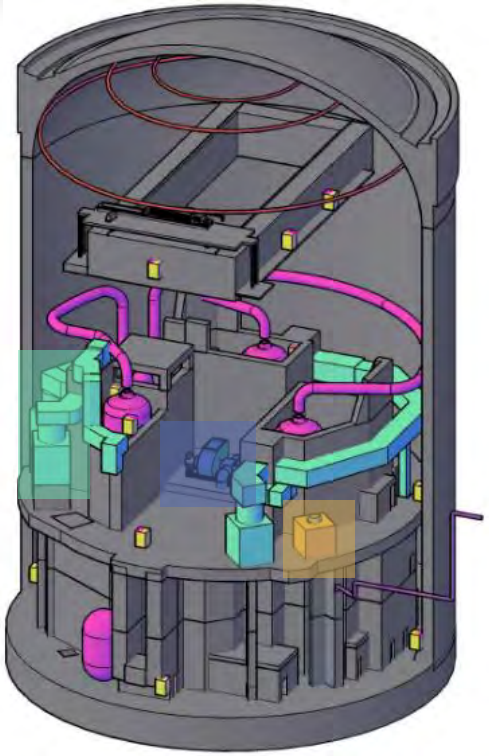

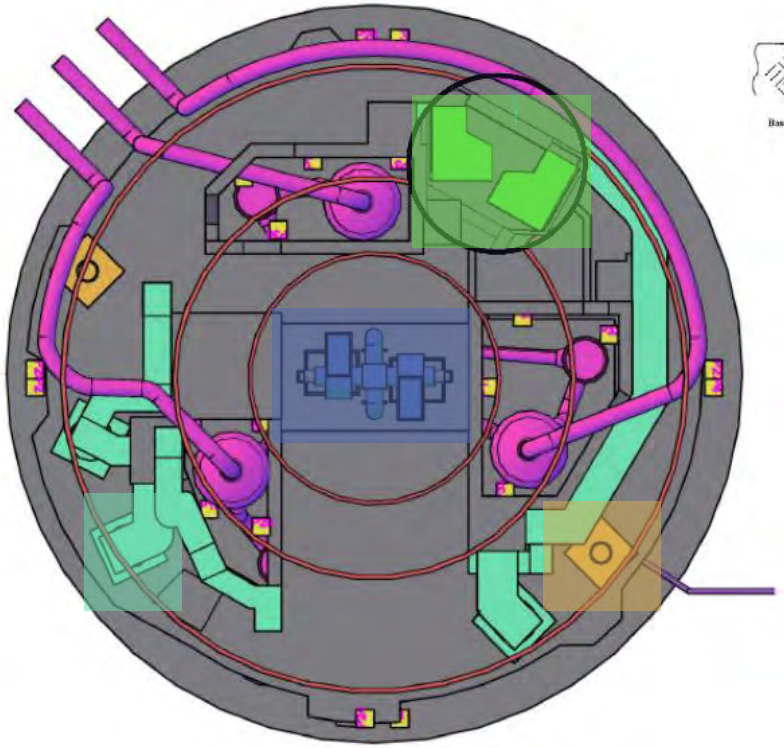

CRDM cooling units

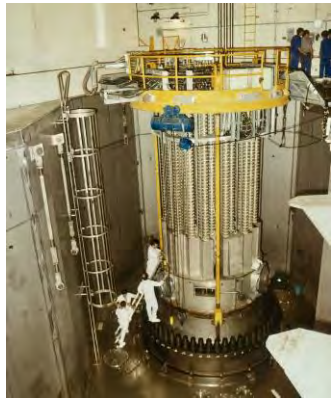

Westinghouse Electric Company LLC, 2016. *WESTINGHOUSE TECHNOLOGY SYSTEMS MANUAL.*

INDUSTRIALES ETSII | UPM
50 REUNIÓN ANUAL SOCIEDAD NUCLEAR ESPAÑOLA
INTER CON3D

PWR-W Dry Containment 3D model → CAS

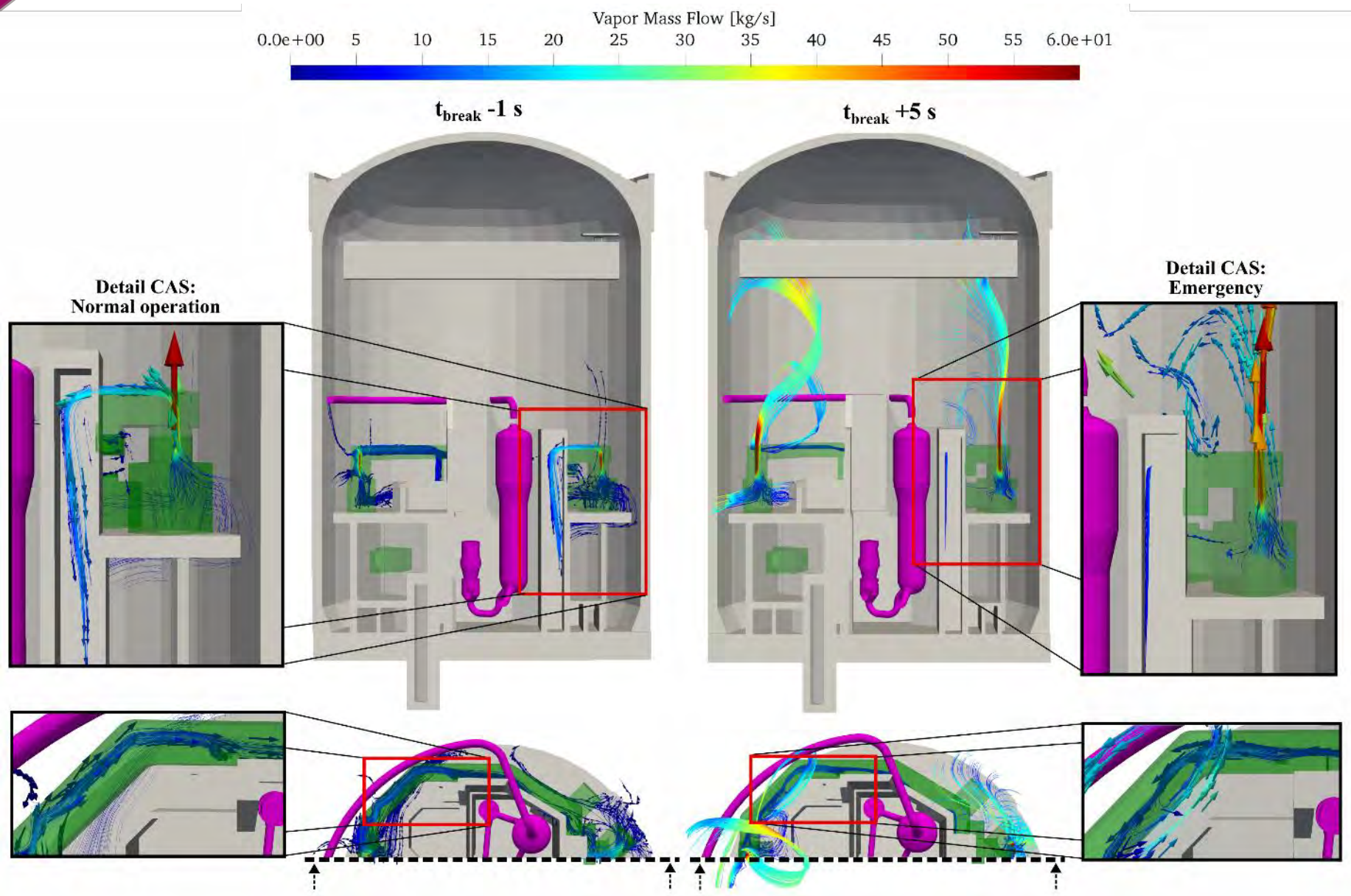

PWR-W Dry Containment 3D model → Additional Systems

PARs:

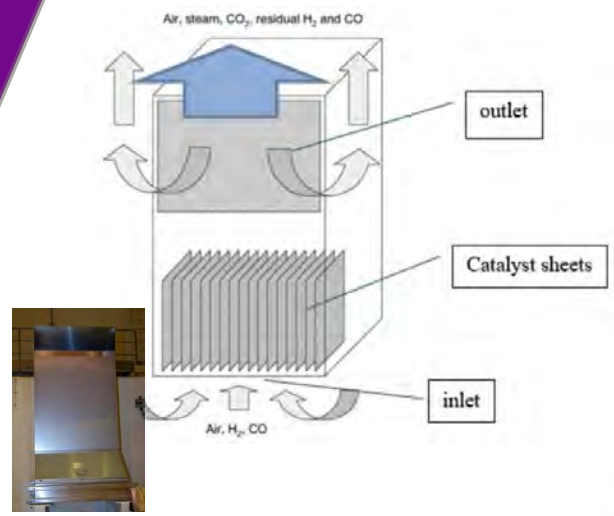

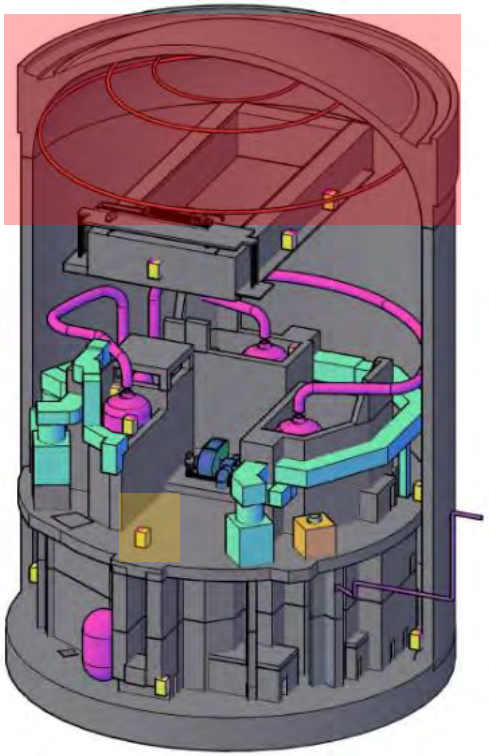

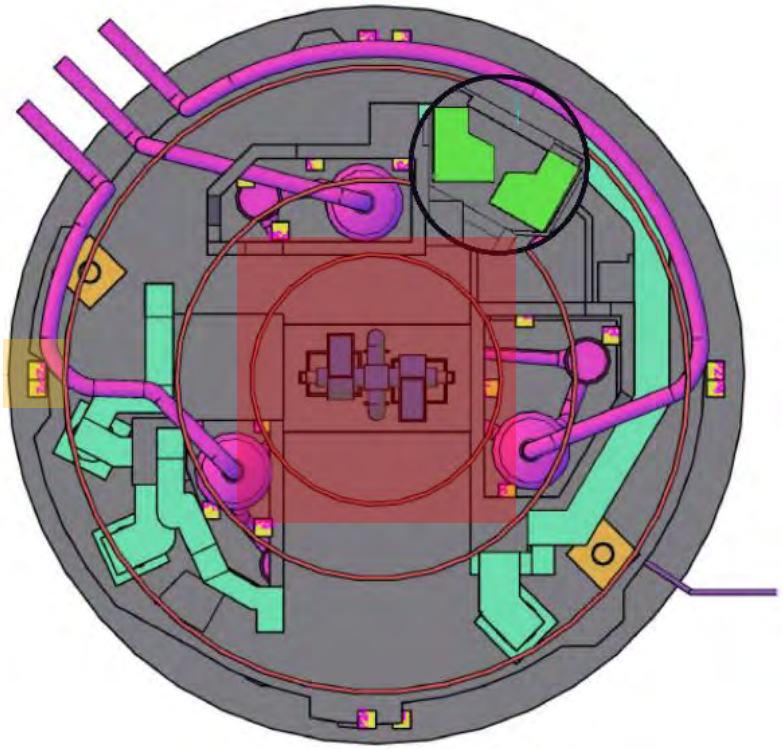

Sprays:

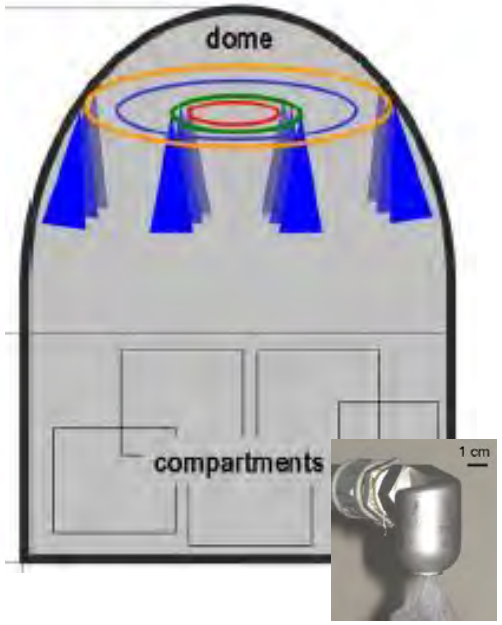

PWR-W Dry Containment 3D model → GOTHIC implementation

C. Vázquez-Rodríguez *et al.*, «The Preventive Methodology: A priori modification of the containment geometry to boost the computational efficiency of GOTHIC 3D models», *Nuclear Engineering and Design*, vol. 432, p. 113718, feb. 2025, doi: 10.1016/j.nucengdes.2024.113718.

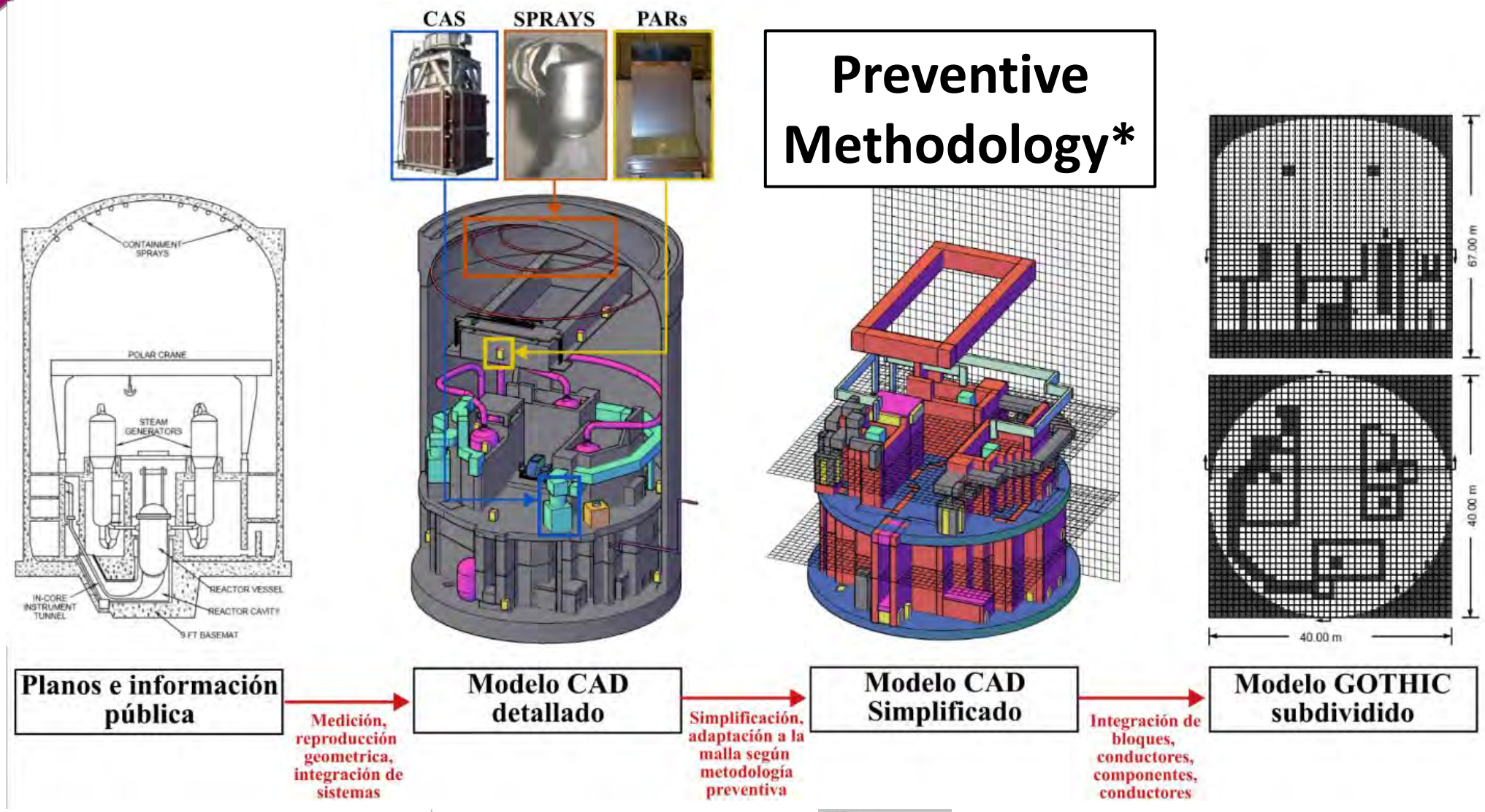

Conventional Safety Analysis Results

Conventional Safety Analysis Results → Initial configuration and cases

- Large break LOCA in cold leg
- Actuation of high-pressure safety injection and accumulators
- Delay on Low-pressure safety injection (15 min) → Maximization of hydrogen output

Casos
Unmitigated without cooling
Unmitigated with sprays
Unmitigated with CAS
Unmitigated with sprays and CAS
Mitigated without cooling
Mitigated with sprays
Mitigated with CAS
Mitigated with sprays and CAS

Los casos parten de una simulación steady-State común

Configuración de sistemas tras la rotura

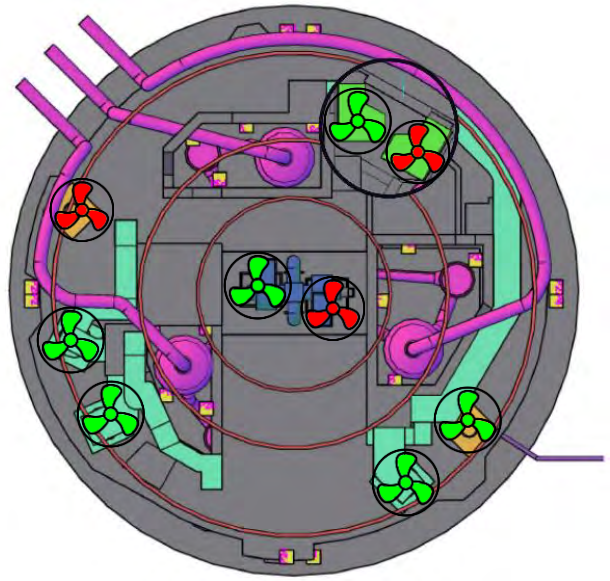

1/2 FCs CAV

1/2 CDRM

4/4 FCs

1/2 Filtros

1/2 Tren Sprays

R. Bocanegra, M. Ruíz-Zapatero, G. Jimenez, y C. Queral, «Enhanced MELCOR models for standard PWR-Westinghouse design», en 11th International Topical Meeting on Nuclear Reactor Thermal Hydraulics, Operation and Safety, Gyengju, Korea: ANS, oct. 2016.

Conventional Safety Analysis Results → Initial configuration and cases

- Large break LOCA in cold leg
- Actuation of high-pressure safety injection and accumulators
- Delay on Low-pressure safety injection (15 min) → Maximization of hydrogen output

Emergency configuration (Syst. Description)

"Initiation of all remaining main FCs units at low velocity"

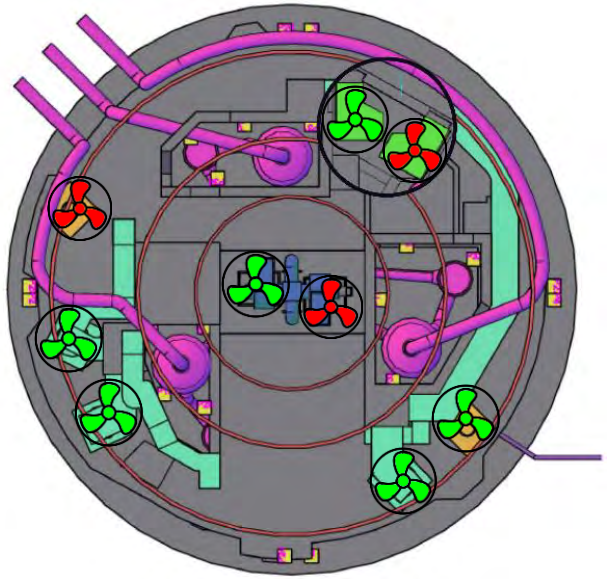

- 1/2 CAV units
- 1/2 CDRM units
- 4/4 main FCs
- 1/2 Filters
- 1/2 Spray trains

Emergency configuration (PRA)

The success criterio considers de operation of 1/2 redundant trains

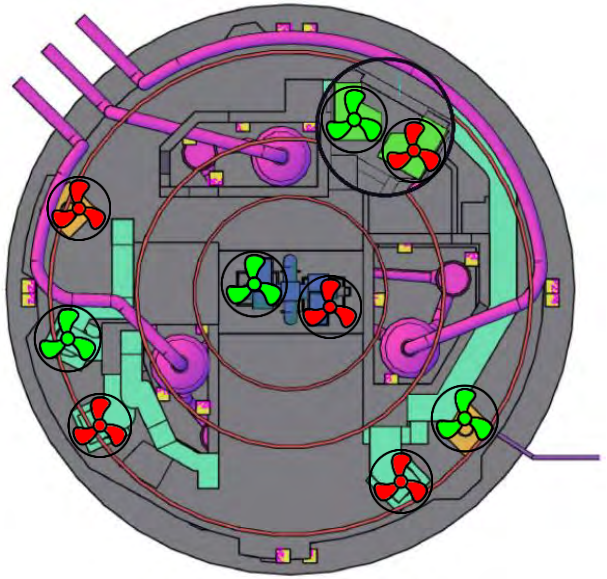

- 1/2 CAV units
- 1/2 CDRM units
- 2/4 main FCs
- 1/2 Filters
- 1/2 Spray trains

Conventional Safety Analysis Results → Initial configuration and cases

Emergency configuration (Syst. Description)

"Initiation of all remaining main FCs units at low velocity"

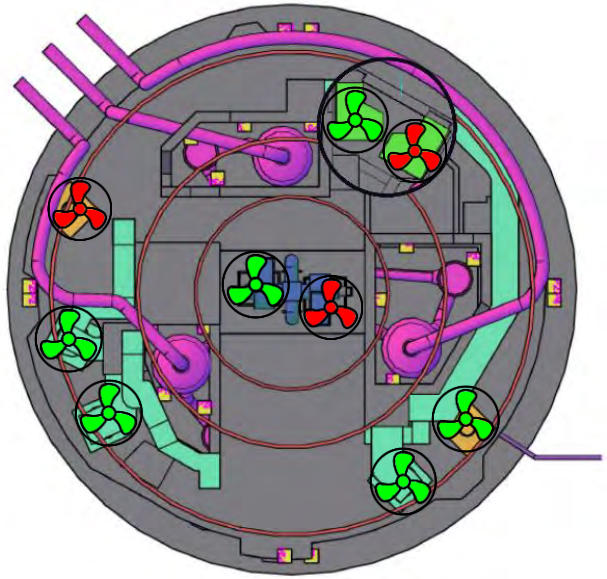

- 1/2 CAV units
- 1/2 CDRM units
- 4/4 main FCs
- 1/2 Filters
- 1/2 Spray trains

Emergency configuration (PRA)

The success criterio considers de operation of 1/2 redundant trains

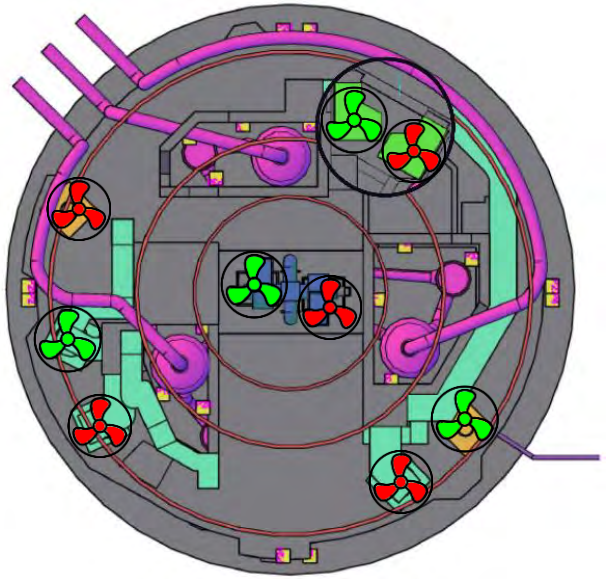

- 1/2 CAV units
- 1/2 CDRM units
- 2/4 main FCs
- 1/2 Filters
- 1/2 Spray trains

Cases
Unmitigated case without cooling
Unmitigated with CAS
Unmitigated case with CAS and Sprays (Syst. description)
Unmitigated case with CAS and Sprays (Succ. Criterion)
Unmitigated case with CAS, Sprays and PARs (Syst. description)

Conventional Safety Analysis Results → Global Pressure Evolution

Unmitigated case without cooling

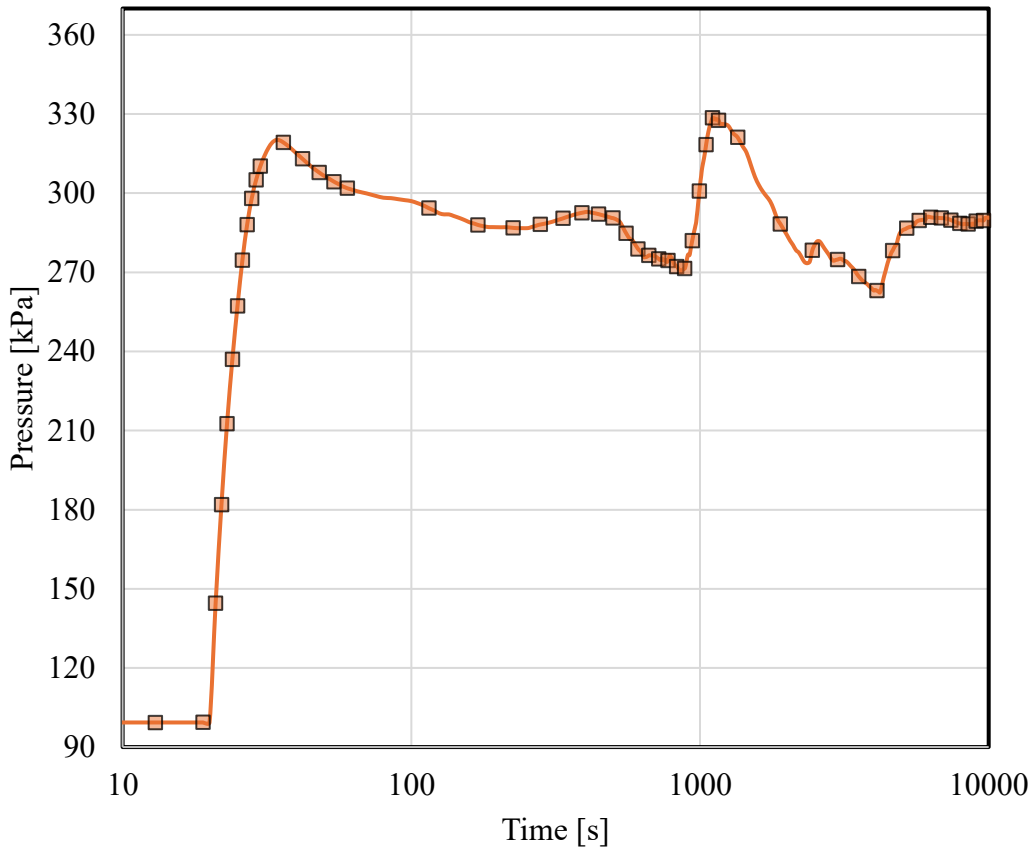

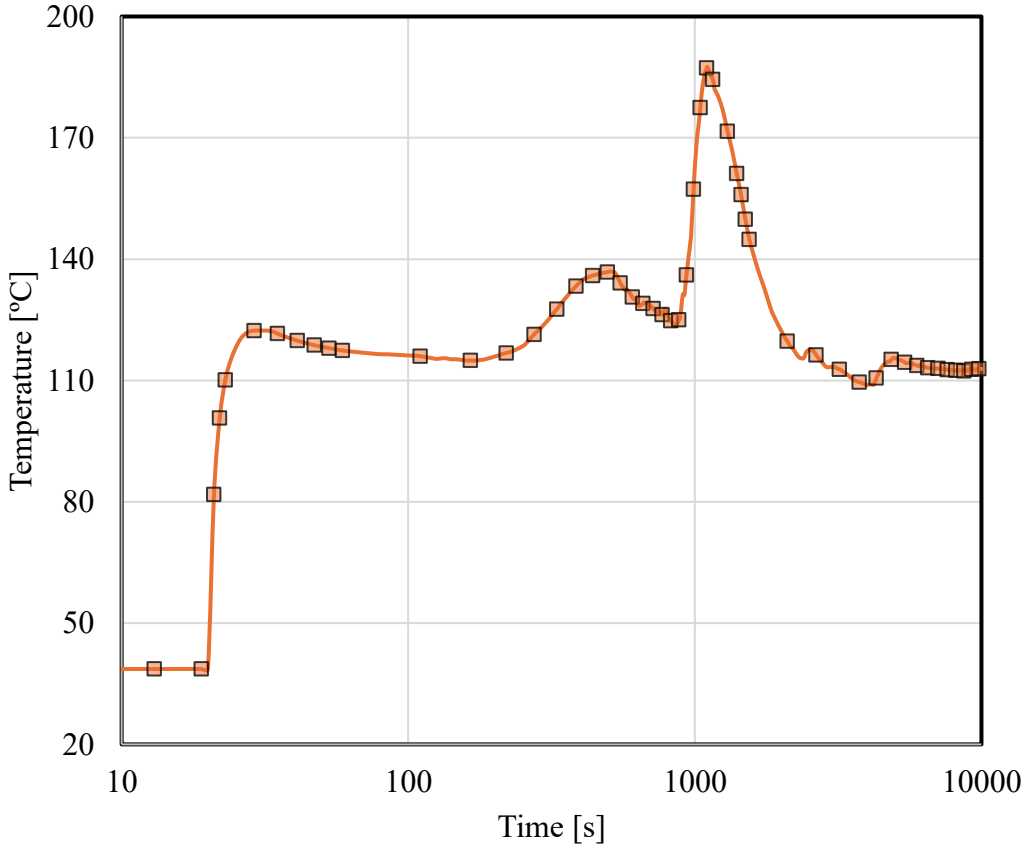

Conventional Safety Analysis Results → Global Pressure Evolution

Unmitigated case with CAS

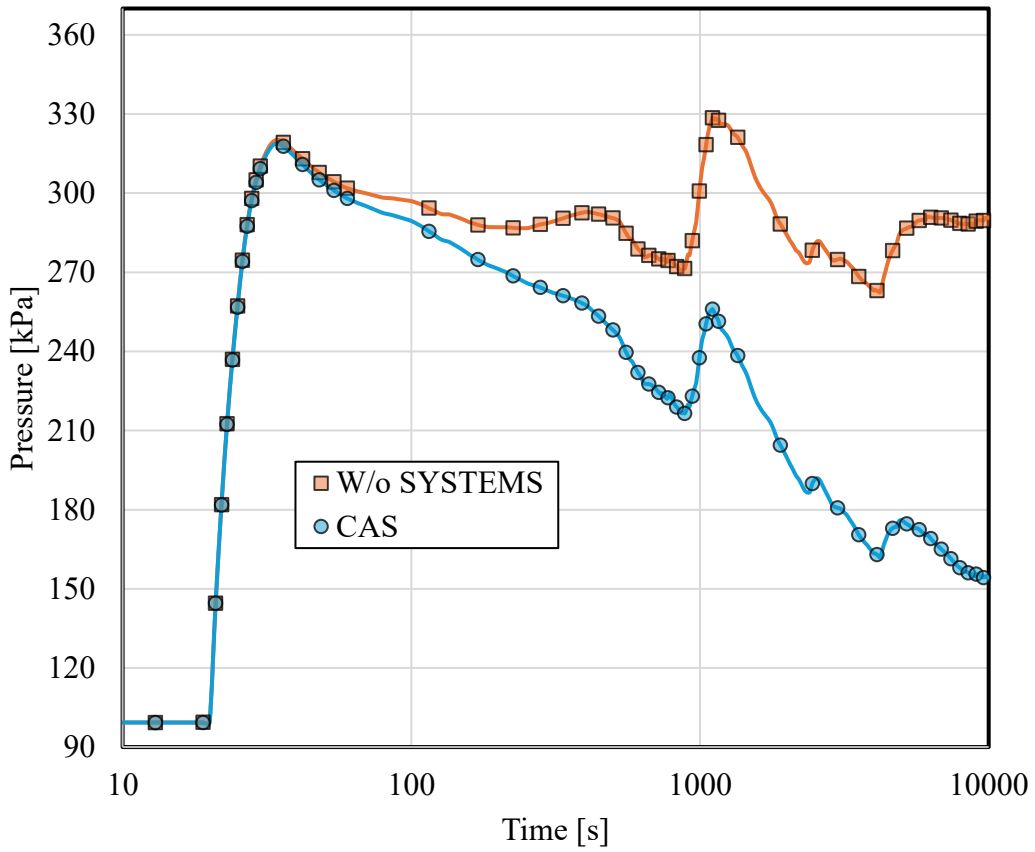

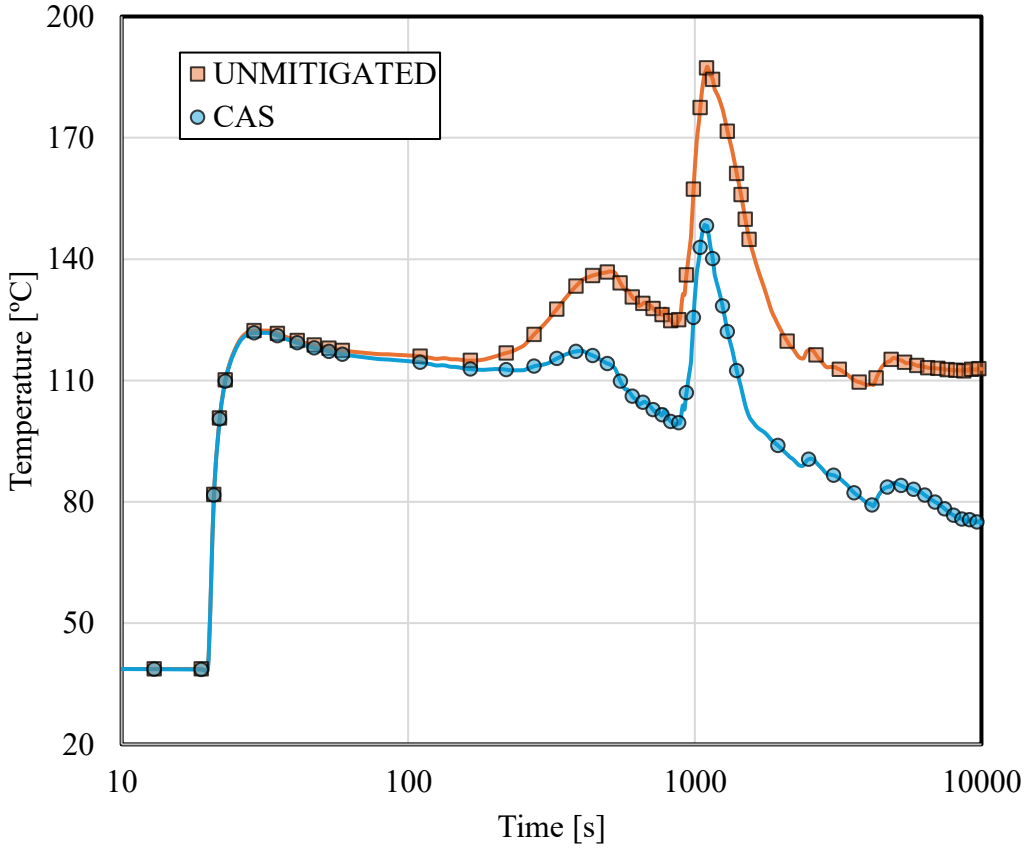

Conventional Safety Analysis Results → Global Pressure Evolution

Unmitigated case with CAS and Sprays (Syst. description)

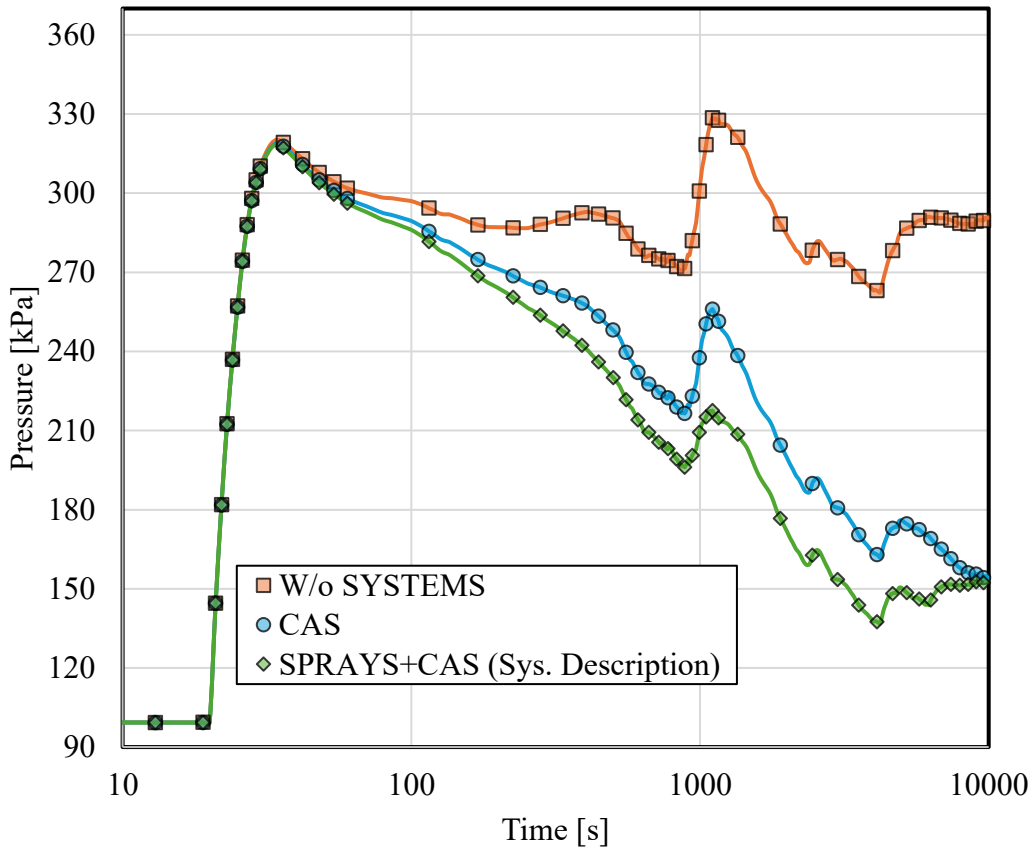

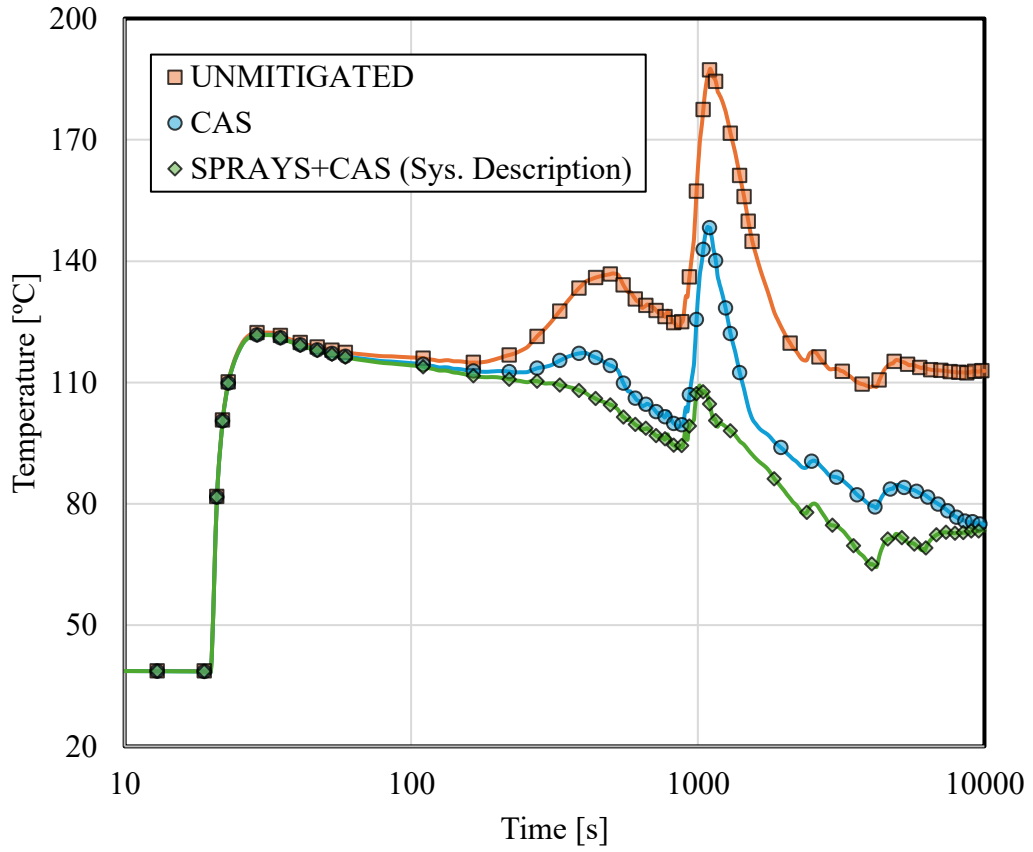

Conventional Safety Analysis Results → Global Pressure Evolution

Unmitigated case with CAS and Sprays (Succ. Criterion)

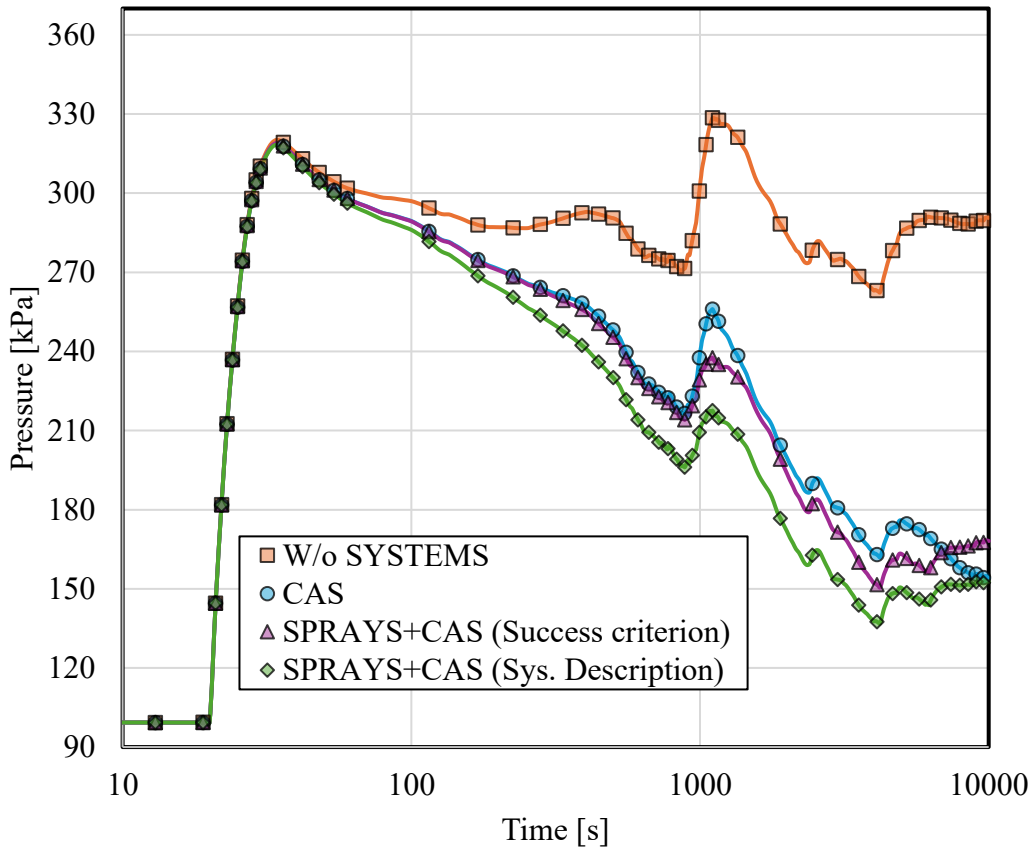

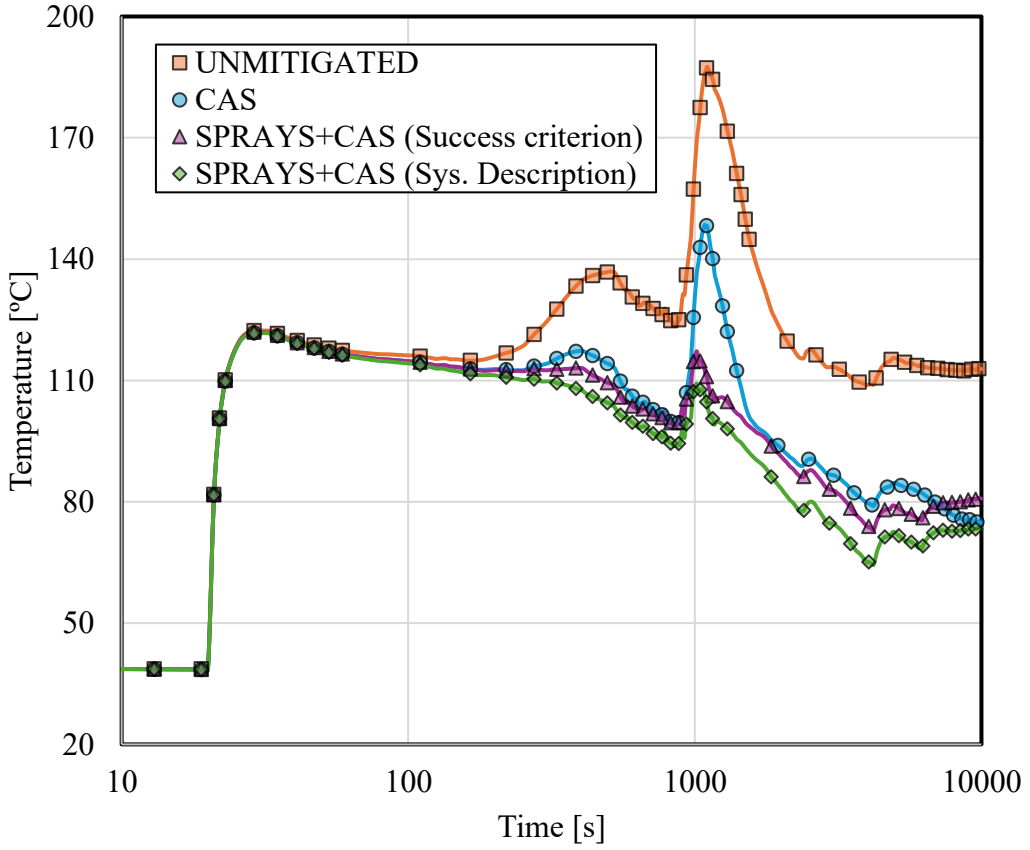

Combustión Risk Analysis Results

Combustión Risk Analysis Results → Cuantification

Hydrogen combustion ($H_2 + \frac{1}{2}O_2 \rightarrow H_2O + \boldsymbol{Energy}\ \left(1.41 * 10^5\ \frac{kJ}{kg}\right)$)

$\rightarrow P_{containment} > P_{design}$

$\rightarrow T_{containment} > EQ_{limit}$

The Sapiro-Moffete Diagram (373 K)

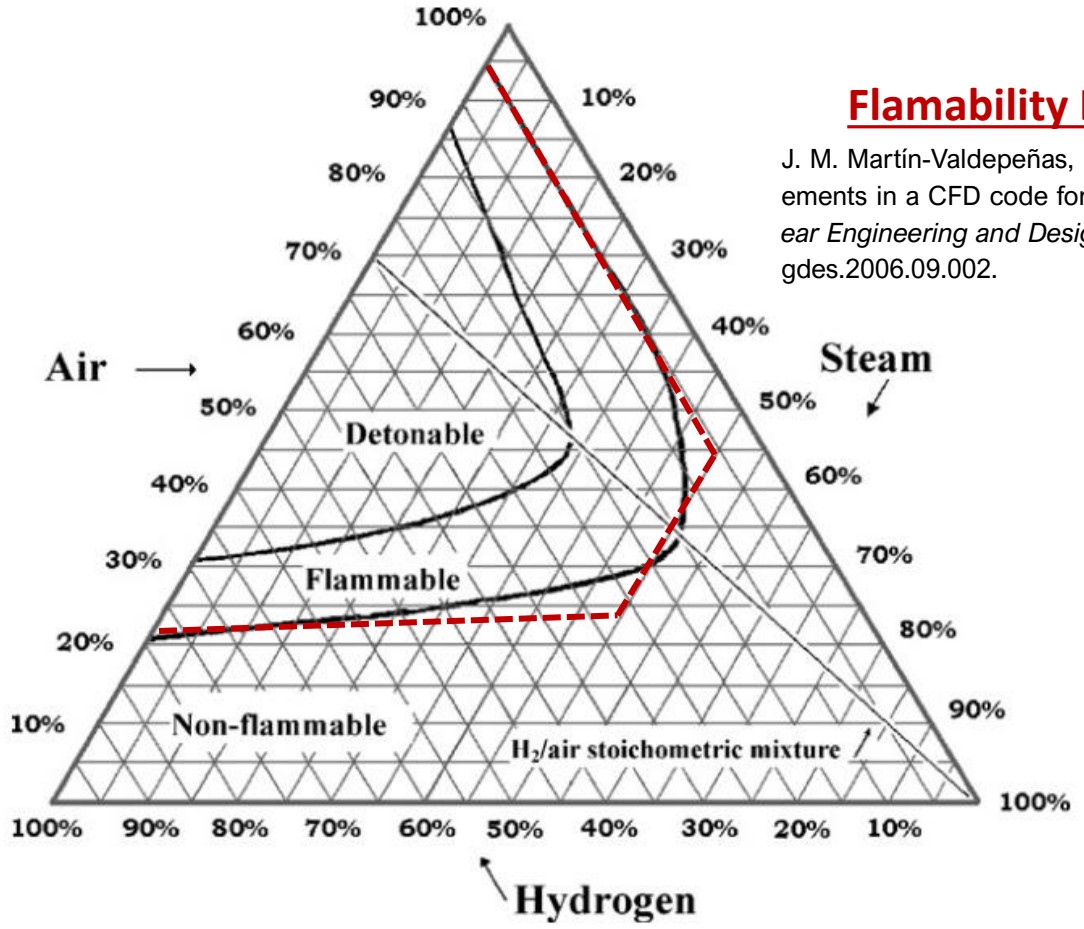

Flamability Limts

J. M. Martín-Valdepeñas, M. a. Jiménez, F. Martín-Fuertes, y J. a. Fernández, «Improv ements in a CFD code for analysis of hydrogen behaviour within containments», *Nucl ear Engineering and Design*, vol. 237, n.º 6, Art. n.º 6, mar. 2007, doi: 10.1016/j.nucen gdes.2006.09.002.

Combustión Risk Analysis Results → Cuantification

Safety systems integration

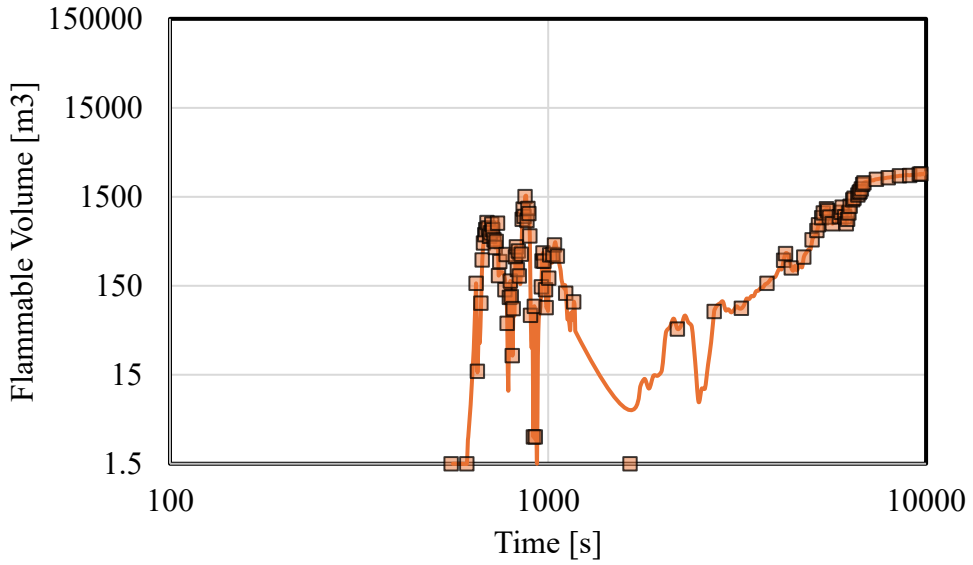

Cases
Unmitigated case without cooling
Unmitigated with CAS
Unmitigated case with CAS and Sprays (Syst. description)
Unmitigated case with CAS and Sprays (Succ. Criterion)
Unmitigated case with CAS, Sprays and PARs (Syst. description)

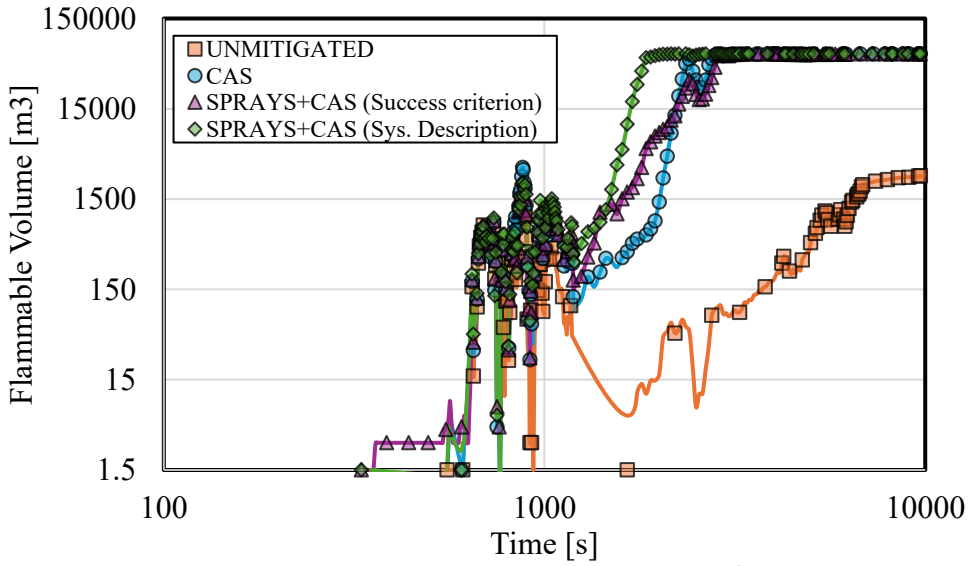

PARs Introduction

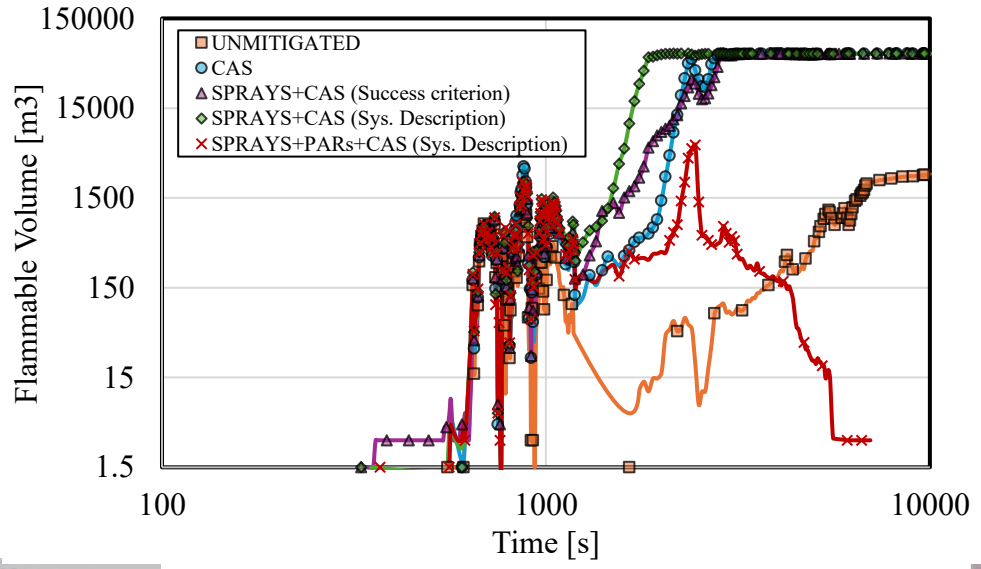

Thanks for yoyur attention!

Acknowledgements

Further questions?
a.gherranz@upm.es

12th CONFERENCE ON
SEVERE ACCIDENTS RESEARCH
May 18-22, 2026 - Madrid, Spain
ERMSAR 2026

Extra → CAS Flow streams (Pointed)

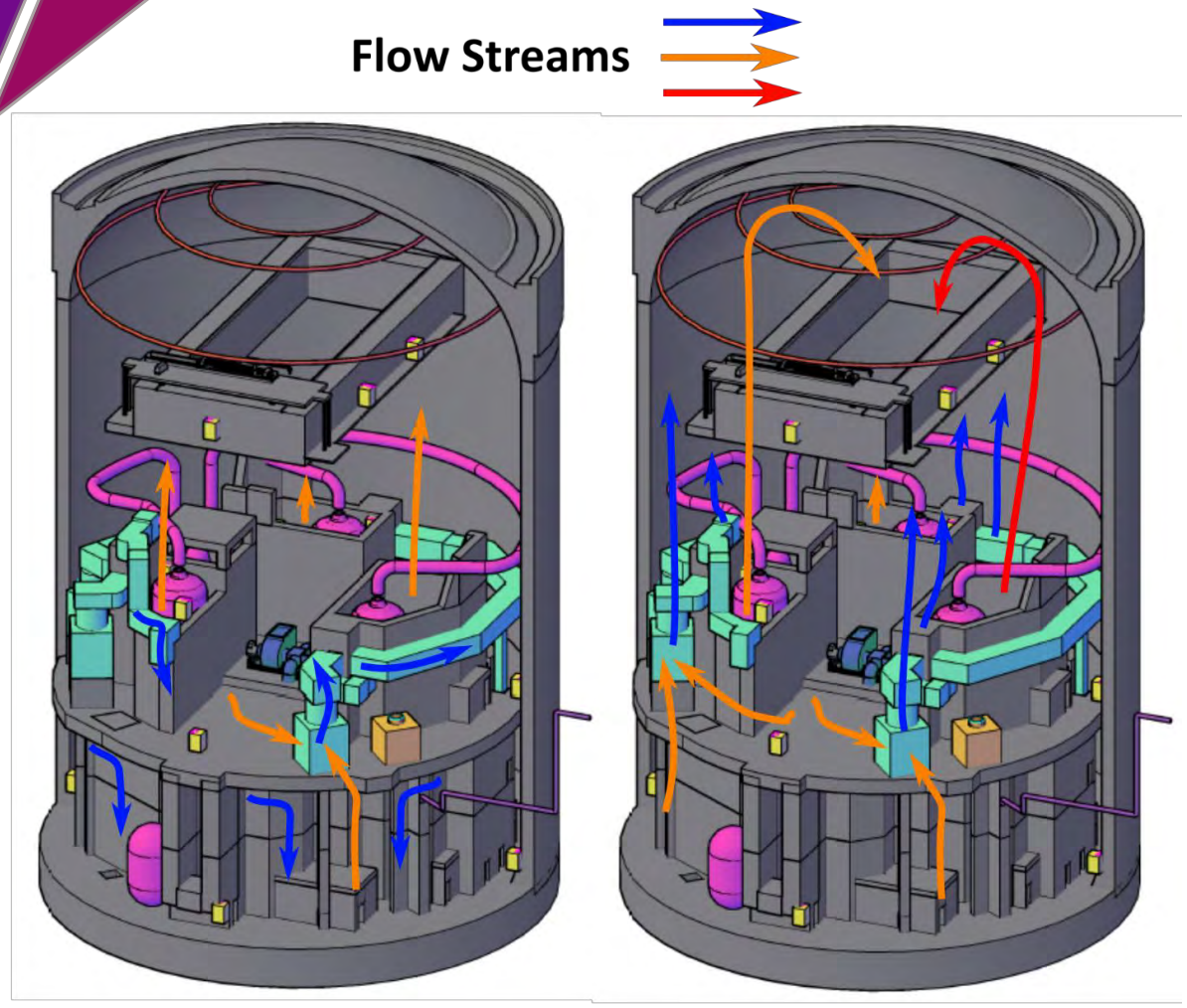

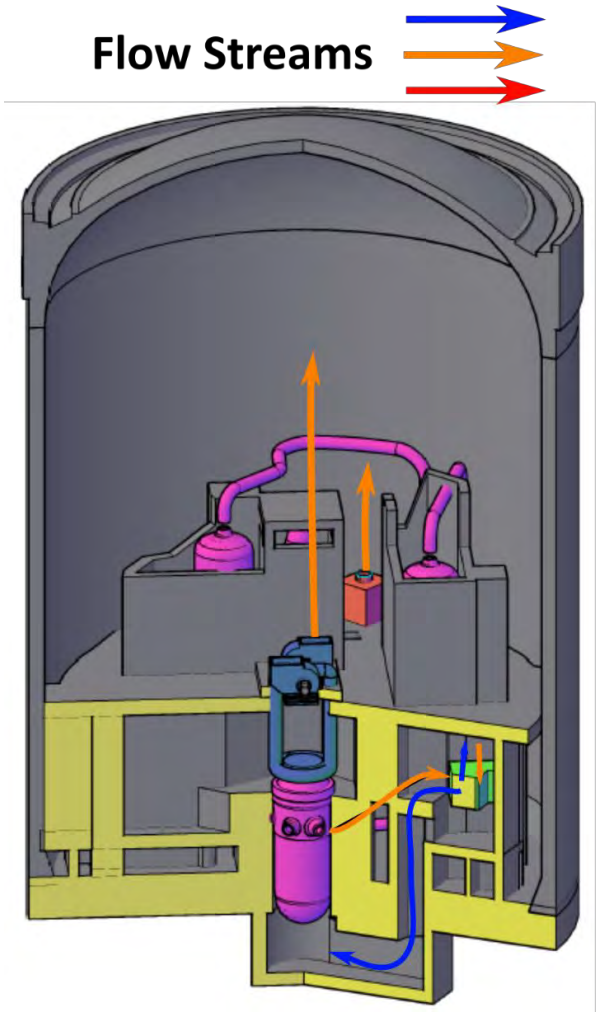

Main Fan-cooler Units

Filtering units

Cavity cooling units

CRDM cooling units

Extra → Preventive methodology basis

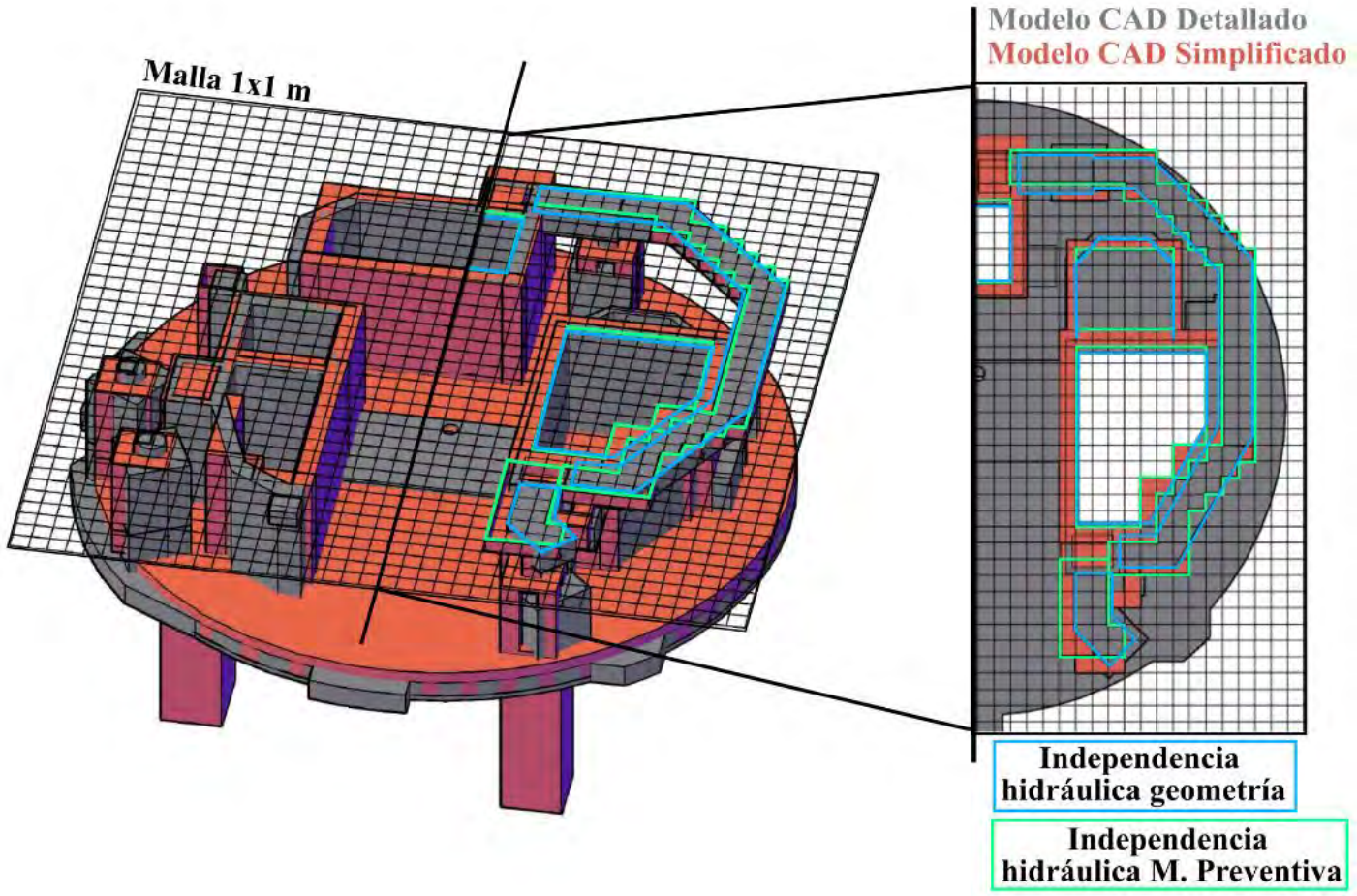

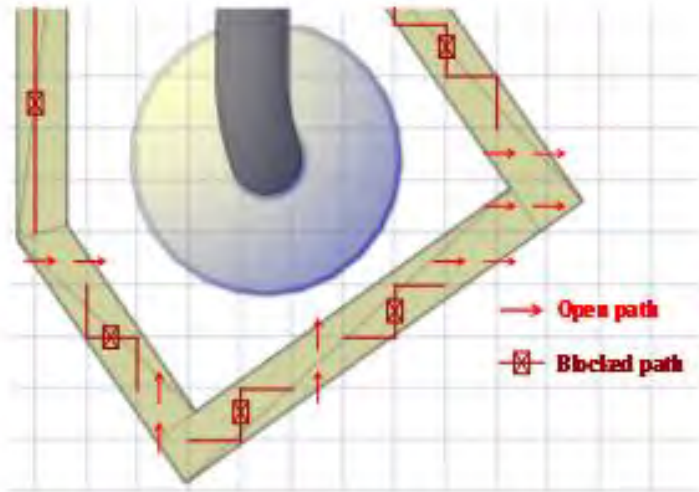

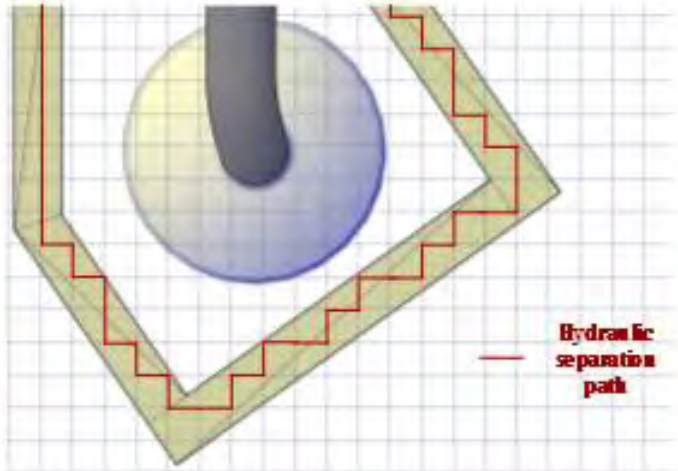

Configuración del Caso estacionario

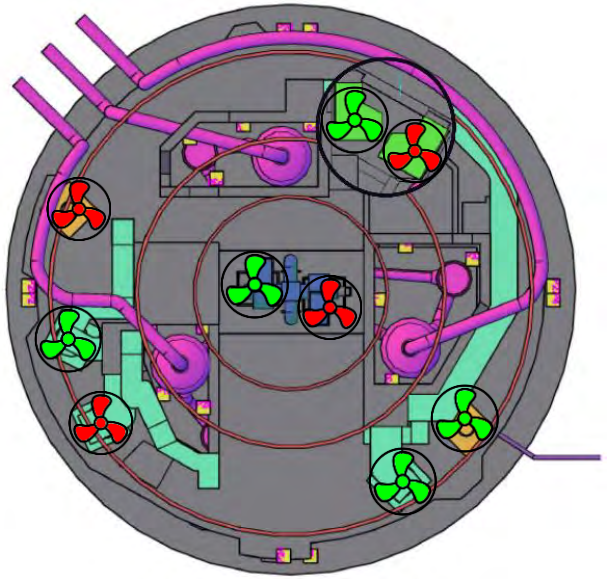

- 1/2 FCs CAV
- 1/2 CDRM
- 3/4 FCs
- 1/2 Filtros

Inner Temperature [ºC]	39
Outer Temperature [ºC]	24
Inner pressure [kPa]	101.325
Relative Humídity [%]	77.5

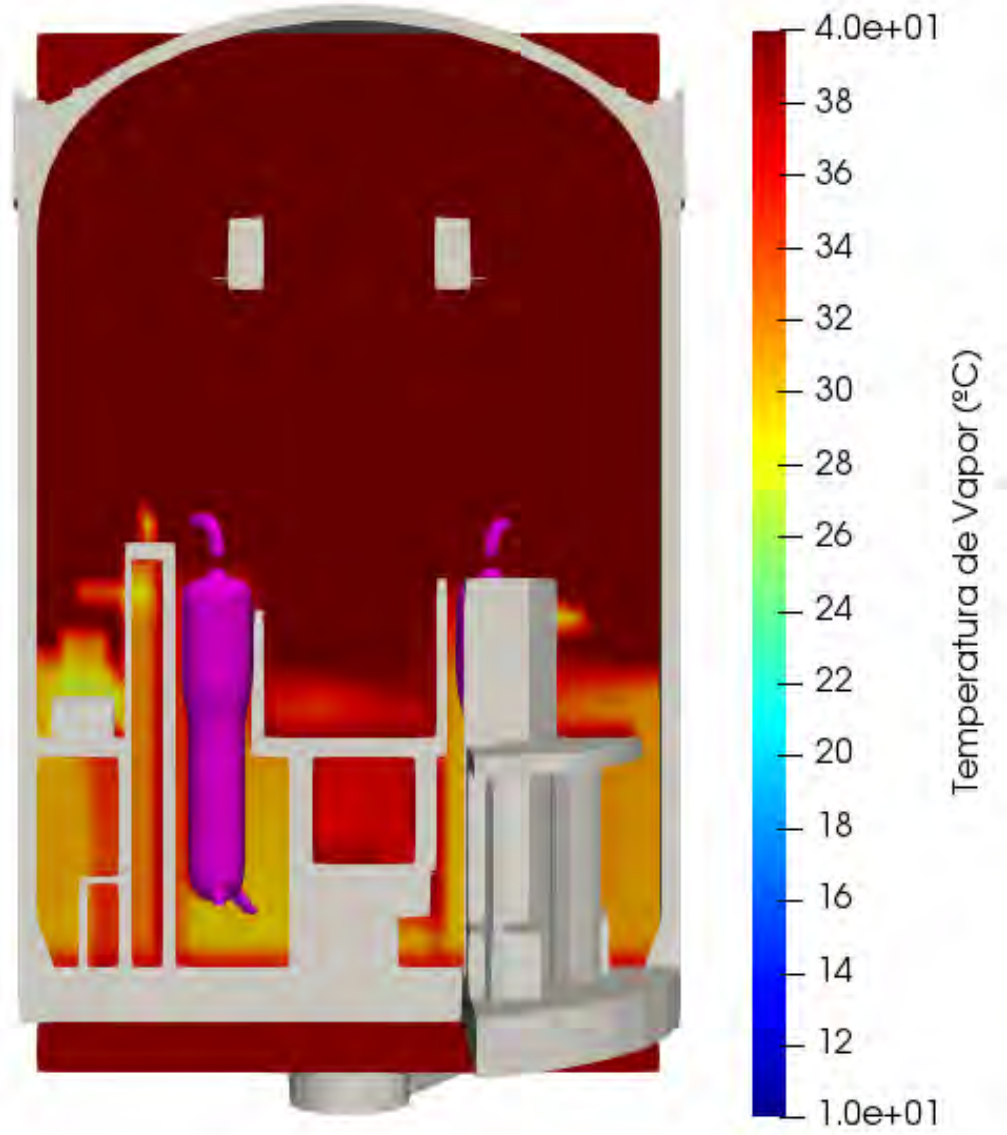

Westinghouse Electric Company LLC, 2016. *WESTINGHOUSE TECHNOLOGY SYSTEMS MANUAL.*

Extra → influence of PARs in P-T evolution

Casos con PARs

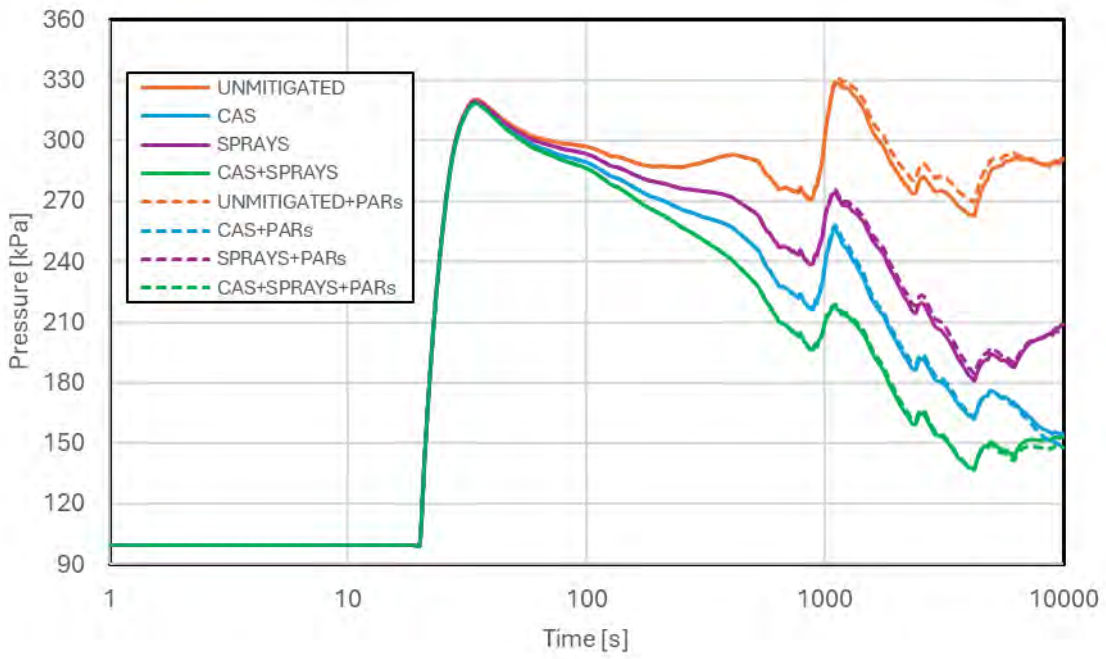

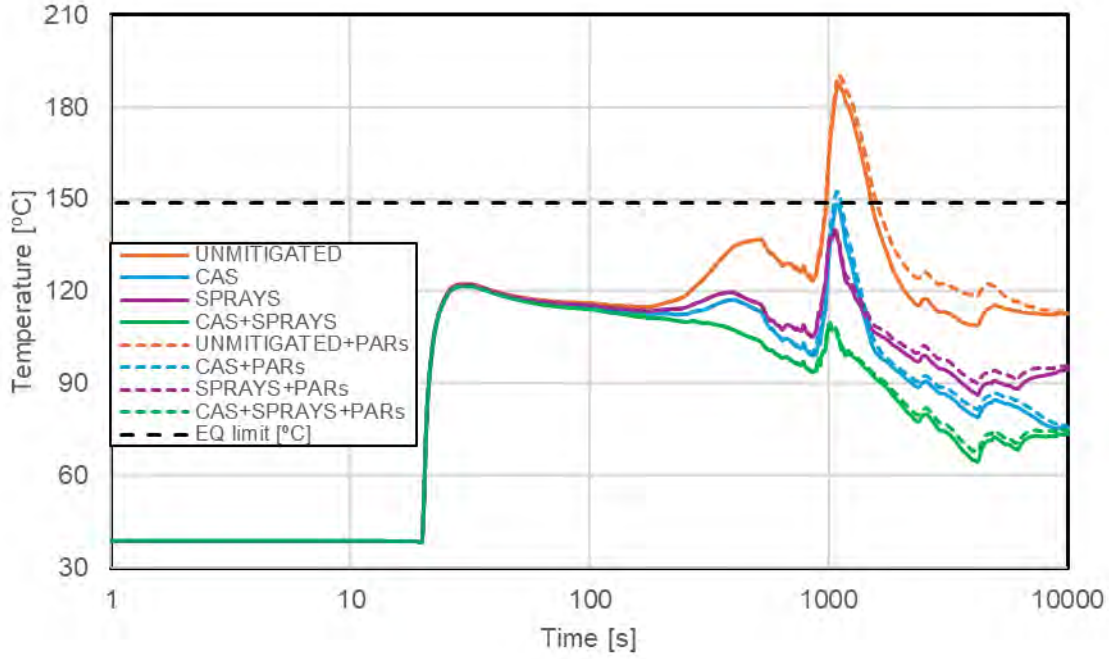

Extra → Equations for flammability limits

Shapiro-Moffete diagram (373 K)

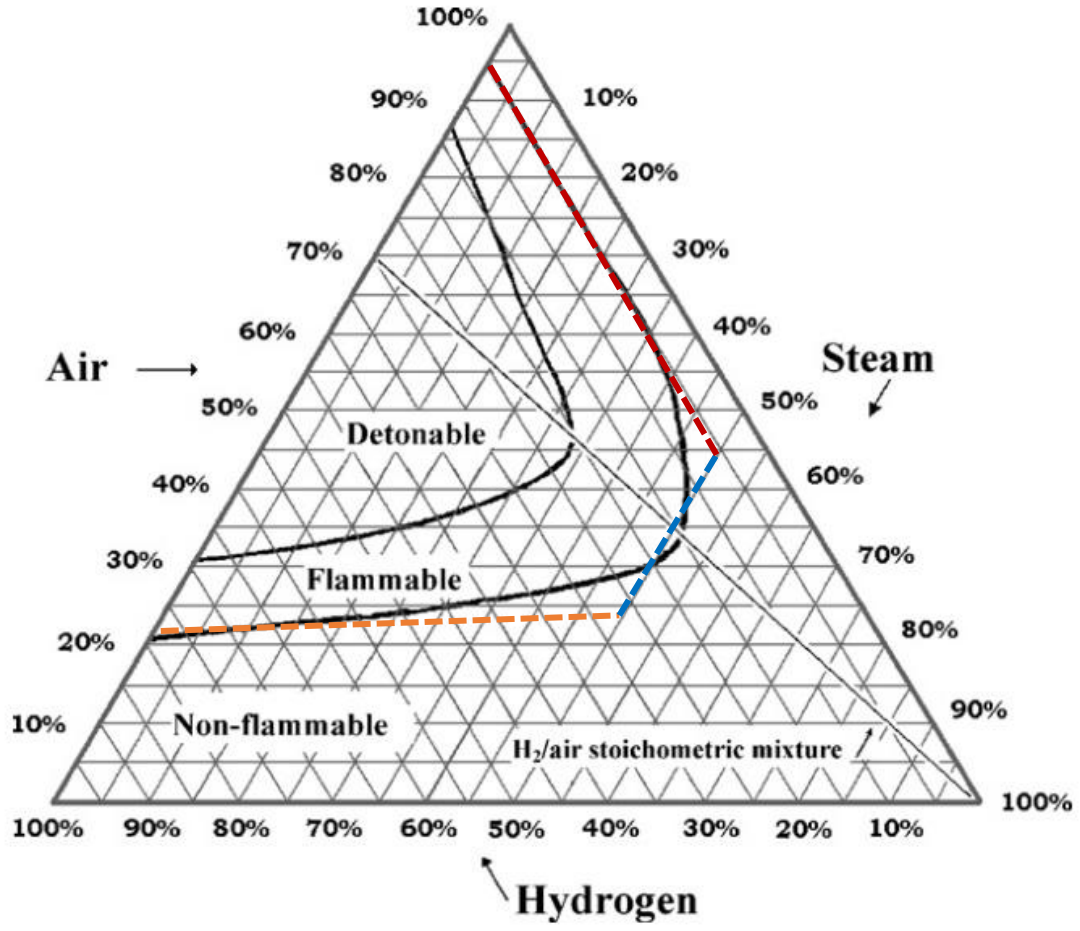

Flammability Limits

$$X_{H_2}^{LFL-UPW} \geq 0.037 + 0.011X_{H_2O} - 4.16 \times 10^{-5}(T$$

$$X_{H_2}^{UFL} \leq 0.772 + 1.087X_{H_2O} - 2.71 \times 10^{-4}(T - 373)$$

$$X_{H_2O} \leq 0.63 + 3 \times 10^{-4}(T - 373)$$

$$X_{O_2} \geq 0.05$$ *From MELCOR

J. M. Martín-Valdepeñas, M. a. Jiménez, F. Martín-Fuertes, y J. a. Fernández, «Impro vements in a CFD code for analysis of hydrogen behaviour within containments», *Nu clear Engineering and Design*, vol. 237, n.º 6, Art. n.º 6, mar. 2007, doi: 10.1016/j.nu cengdes.2006.09.002.

Extra → Equations for flammability limits

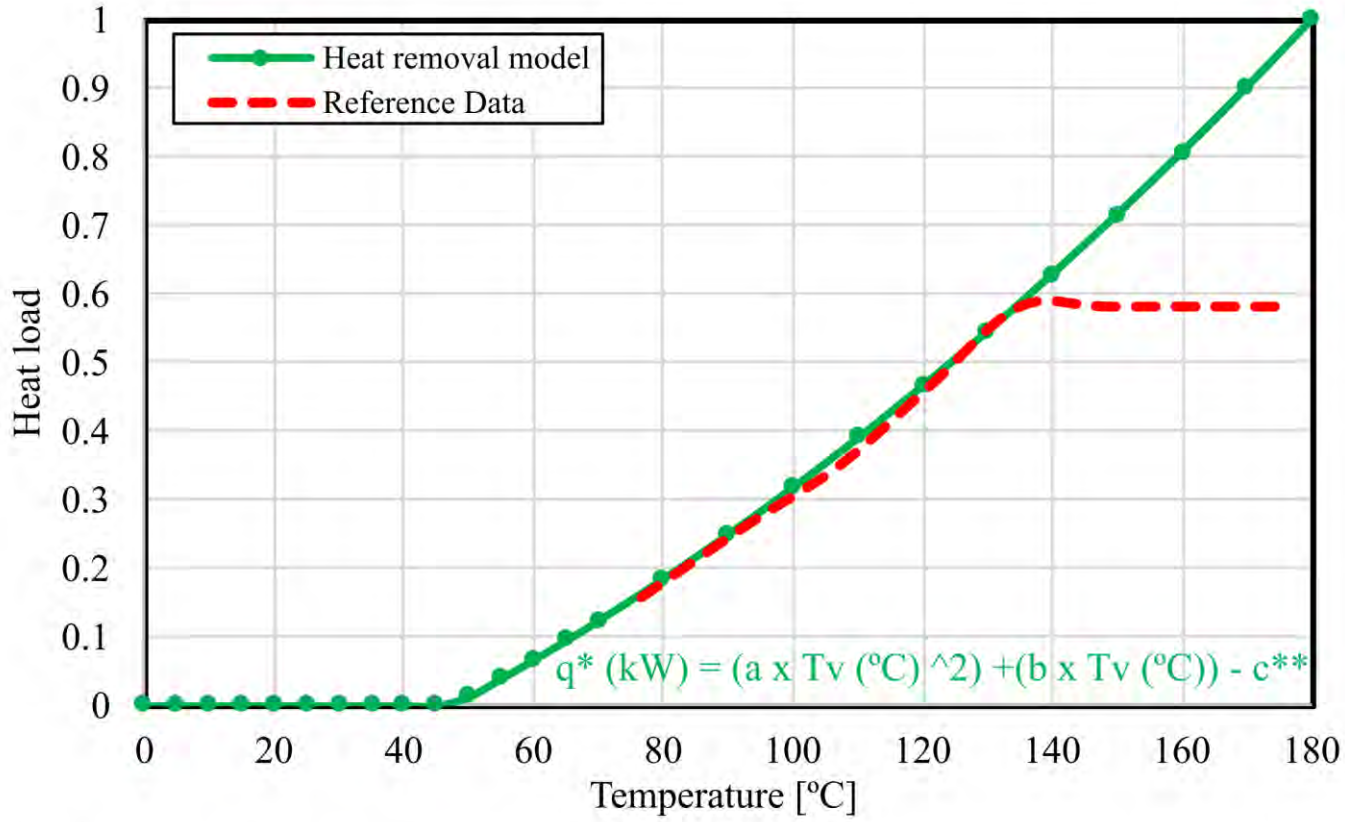

*Reference data considers temperature of water inside the tubes at ~ 45 ºC

**Heat removal model include the temperature of water inside the tubes (Twit) in the third term of the second order equation. This term, which represent the heat when Tv (ºC) = 0 is reached, is adjusted to match the solution with different Twit

PASSIVE AUTOCATALYTIC RECOMBINATION OF HYDROGEN – APPLICATION IN THE ITER FUSION REACTOR

Matthias Braun, Sebastian Buhlmann, Norbert Losch
Framatome GmbH
91052 Erlangen, Germany
matthias.braun@framatome.com

Chandran Nidhin, Hall Christopher,
ITER Organization,
Route de Vinon-sur-Verdon, CS 90 046, 13067 St. Paul-lez-Durance, France
Nidhin.Chandran@iter.org, Christopher.Hall@iter.org

ABSTRACT

In the exhaust ventilation path of the vacuum vessel pressure suppression system in the ITER fusion reactor, the possibly present hydrogen shall be removed by a hydrogen mitigation system utilizing catalytic recombination. For this application, the Framatome passive autocatalytic recombiner (PAR) technology, as used in fission plants, was adapted.

On one side, Framatome has an in-house developed and fully nuclear qualified catalytic material, reducing overall physical uncertainties and supply chain issues. On the other side, the anticipated application of the catalytic recombiner in ITER significantly deviates from the application of PARs in nuclear fission plants, causing new phenomena to dominate the catalyst behavior.

For the application in ITER, a corrugated catalyst carrier was selected and experimentally charactered at lab-scale. Based on the obtained experimental data, an engineering correlation was constructed, allowing a numerical representation of this component in integral simulations. The validation of the correlation on full-scale tests is pending.

KEYWORDS
Hydrogen, Tritium, Passive Autocatalytic Recombiner, PAR, Wet recombiner, WRC

1. INTRODUCTION

In the ITER fusion reactor, certain accident sequences may release hydrogen, especially due a water ingression into the vacuum vessel. There, a redox reaction between water and the hot metallic vacuum vessel walls or present metallic dust may reduce water to hydrogen. To prevent an overpressure damage to the vacuum vessel, the vacuum vessel atmosphere is discharged into a pressure suppression system. To minimize a hydrogen combustion risk within the pressure suppression system, it is ventilated by a heating, ventilation, and air conditioning system (HVAC). At the exhaust of the ventilation system, the hydrogen shall be recombined, and the subsequent steam condensed for the following reasons:

- Safety function: Exclude any gas combustibility in the subsequent HVAC system
- Safety function: Minimize the release of radioactive material (tritium) from the plant
- Operational Function: Recover tritium in the condensate to be reused as fusion fuel

To counteract an accumulation of hydrogen within the containment of a nuclear fission plant during a severe accident with core damage, passive autocatalytic recombiners (PAR) were invented [1], developed, and qualified to nuclear standards [2] [3] by Framatome (as successor of Siemens Kraftwerk Union / AREVA). Due to the highly reliable performance in tests, the proven resistance against poisoning [4] and due to the extensive qualification [5] and test program [6], the availability of Framatome PAR during a nuclear incident or accident is broadly accepted by regulatory institutions.

For PARs in fission plants, the catalytic material is carried by numerous thin stainless-steel plates [5]. The coated steel plates are arranged vertically in a drawer at the bottom end of a larger metal housing, see Figure 1(left). These housings are then installed in the containment of a fission nuclear plant. In case of the presence of hydrogen, the natural convection through these housings draws the gases into the catalytic region. To not impede the natural convection flow, the packing of the catalyst plates is rather loose, resulting in a larger system size, which, however, is not an issue as large space in a nuclear fission plant containment does not impose restrictive size constraints.

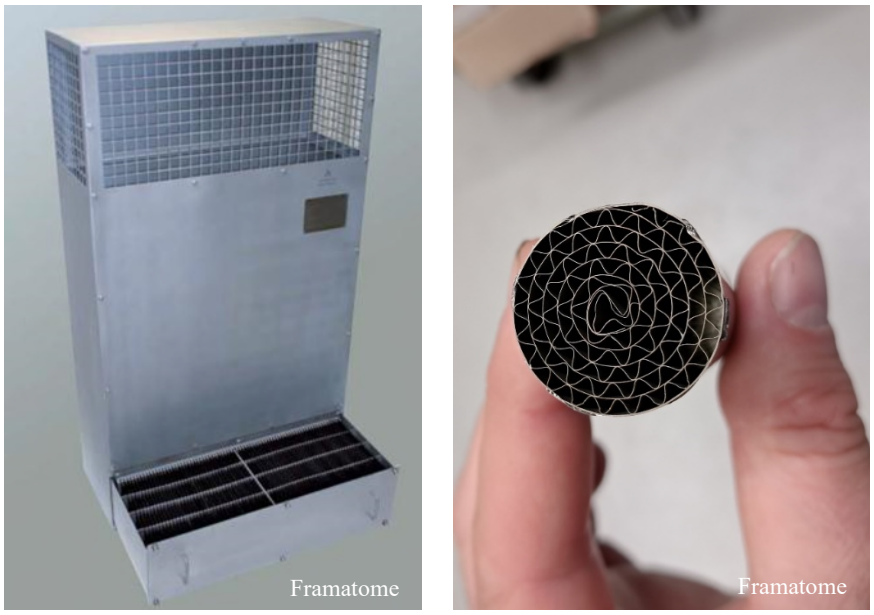

Figure 1. Comparison of plate-type PAR (left) and corrugated WRC (right)

For the application in the fusion plant ITER, Framatome proposed to use the same well-developed, characterized, and validated catalytically active material as used on the plate-type PAR. However, the recombiner shall be installed within a closed HVAC system, which enforces a defined volume gas flow. Therefore, instead of plates, a corrugated cylindrical stainless-steel structure is chosen as carrier structure, see Figure 1(right). This carrier geometry increases the active surface area per volume, shrinking the component size to facilitate the installation in a closed cylindrical pipe or vessel. An unavoidable disadvantage of this design is that it doesn't allow for a visual inspection of the catalytic surface anymore, which was possible in plate-type PARs.

In the following text, the different catalyst applications and designs are labelled as "plate-type PAR" in fission plants and "corrugated wet recombiner (WRC)" in fusion plants respectively.

Plate-type PARs in a nuclear fission reactor containment must operate under a wide range of atmospheric conditions. In contrast, the corrugated WRC in ITER will operate under much more defined conditions. However, these conditions can significantly deviate from the accidental conditions in a fission plant:

- Low concentrations of hydrogen ≤ 8% in normal air
  (i.e. oxygen is always in excess, no transition to oxygen starvation)

- Low inflowing gas temperatures 30°C – 60°C
  (defined by the temperature of the scrubbing liquid in the pressure suppression system and an electric heating register prior WRC entry)
- Humidity of up to 100%
  (due to the scrubbing in the suppression tanks)
- Operation at sub-atmospheric pressures
  (0.75 to 1 bar-abs instead of 1 to 6 bar-abs for plate-type PAR – not expected to make significant impact, see Reference [8])
- Externally defined flow velocity 0.5 m/s to 1.2 m/s
  (forced flow conditions instead of the natural convection through a plate-type PAR, albeit the flow velocities do not differ much)
- Absence of strong catalyst poisons like carbon monoxide
  (also other materials possibly acting as catalyst poisoning must be considered)

To characterize the performance of the corrugated WRC, lab-scale experiments were performed, see Chapter 2. Based on that characterization, a numerical representation of the corrugated WRC was developed (compare Chapter 3) to credit the component in numerical system simulations.

Note that all statements within this work are only valid for the catalytic material of the nuclear vendor Framatome. No claims about catalytic recombination at other materials are made. Experimental evaluation of different catalysts, e.g., in Phebus, showed that catalytic materials of different origin are not interchangeable, neither in performance nor in reliability.

2. LAB-SCALE EXPERIMENTS

The lab scale experiments to characterize the corrugated WRC were performed at the VB265 facility, see Figure 2, located at the Framatome Technical Center Karlstein. The Framatome Technical Center is accredited according to DIN EN ISO/IEC 17020 & 17025.

Figure 2. Photo of the VB265 facility at the Framatome Technical Center Karlstein

In the VB265 vessel facility, a stack of four corrugated WRC cartridges was exposed to specified environmental conditions, and a defined gas volume flow forced through the WRC stack. A test matrix was developed, to exposes the WRC to conditions enveloping the conditions expected in the pressure

suppression system of the ITER, to test for poisoning, ageing, and delayed light-off of the catalyst. A typical test result can be seen in Figure 3.

After a calibration phase, environmental air is forced through the WRC cartridge stack. At t=0s, the atmosphere from the VB265 vessel, having a high humidity and a predefined hydrogen content, gets discharged through the WRC. The catalyst reacts to the incoming hydrogen-containing gas. However, due to its low reactivity at low temperatures, and the cooling effect of the forced flow gas, the catalyst shows a certain startup delay. This will be elaborated in more detail later.

After light-off of the catalyst, the hydrogen concentration in the exhaust drops down to the measurement limit hydrogen (~0.02 vol%). Interestingly, already the first WRC cartridge fully consumes all incoming hydrogen, Thus, in steady-state operation, the first cartridge becomes the hottest. The temperatures of the subsequent WRC cartridges are given by the heating via the hot exhaust gases and the radial heat losses out of the WRC mounting pipe. Note that this is a different behavior of the corrugated WRC in comparison to the plate-type PAR.

In the Framatome plate-type PAR design for fission plants, the limiting factor is the gas transport from the reactor containment onto the catalytic surface [7]. Gas is transported into the PAR housing by a convective gas flow, created by the draught within the PAR housing. Additionally, within the PAR housing, the oxygen and hydrogen molecules must diffuse out of the gas phase onto the catalytic plates. Overall, for hydrogen gas concentrations >1 vol%, this leads to a gas flow velocity of typically 1 m/s through the PAR and a recombination efficiency of ~50% (i.e. half of the hydrogen entering the PAR housing leaves the PAR housing unrecombined). This is consistently observed e.g. in the THAI experiments [9]. The spacing of the catalytic plates in the PAR housing, see Figure 1(left), are a trade-off to keep the hydraulic distances large, not impeding the convective gas flow, and keeping the required gas diffusion length as short as possible.

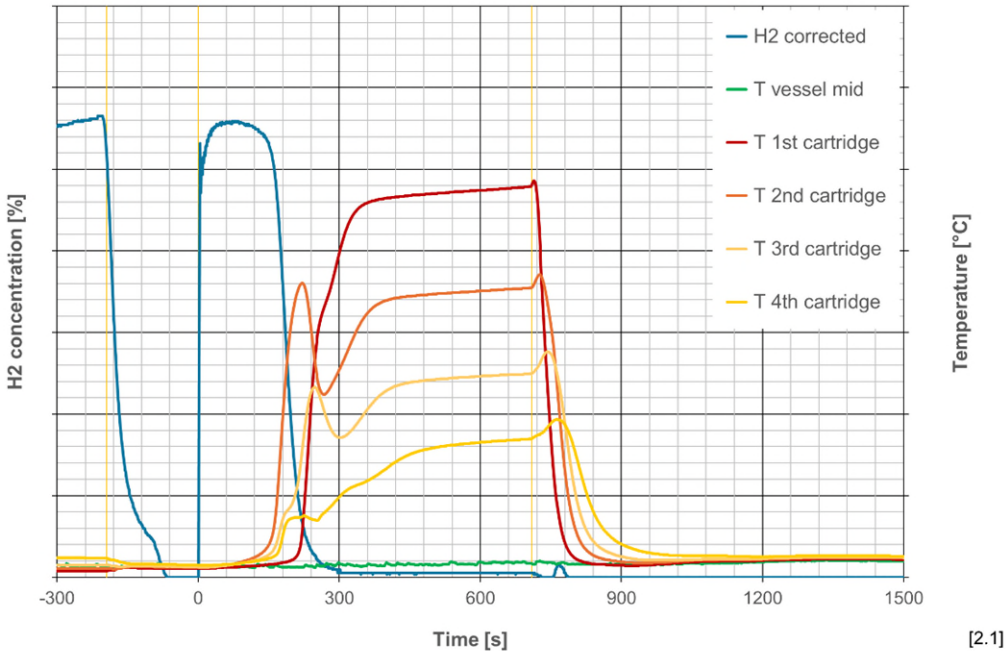

Figure 3. Hydrogen concentration and cartridge temperatures (Experiment 2.1)

In the corrugated WRC, the gas is transported into the cartridges by a forced flow. There is no need to keep the hydraulic distances large. This corrugated carrier design offers a larger catalytic surface/volume ratio, improving the molecular transport onto the surface linearly, but it also reduces the required gas diffusing length, generating an exponential leverage. Thus, after WRC startup, already a single corrugated WRC

cartridge consumes practically all incoming hydrogen. This was later confirmed by using only a single cartridge instead of a stack of four.

3. COMPUTATIONAL MODEL OF THE CORRUGATED WRC

For the deduction of an engineering correlation, the experimental raw data, especially the hydrogen measurement was adapted to correct for measurement artefacts and finite detector responsiveness. Based on the refined data, the following engineering correlation is constructed, relating the hydrogen concentration x_{ex} (in vol%) in the exhaust of the corrugated WRC, to the inlet hydrogen concentration x_{in} as

$$x_{\mathrm{ex}} = x_{\mathrm{in}} \cdot \left(1 - c_{\mathrm{start}} \cdot c_{\mathrm{delay}} \cdot c_{\mathrm{stop}}\right). \quad (1)$$

The unitless factor c_{start} describes the ability of the WRC catalyst to light-off (see Chapter 3.1), the factor c_{delay} describes the WRC startup delay (see Chapter 3.2), and the factor c_{stop} describing the shutdown of the WRC at low hydrogen concentrations (see Chapter 3.3). These factors are binary, i.e. have a numerical value of either zero or one. Mathematically, c_{delay} fully envelopes c_{start}, so that latter factor could be omitted. However, the separate consideration of these factors makes the deduction of this engineering correlation in the following subchapters more transparent.

The fact that the engineering correlation complies with all evaluated experiments, irrespective of their boundary conditions, can be seen as a nuclear-grade Verification and Validation in accordance to IAEA standards [10] [11]. An additional validation step at full system scale remains to be done.

3.1. WRC Startup Criterion

That the WRC can switch from its off-state into its autocatalytic on-state, the catalyst must be able to heat up. The catalyst temperature is given by the competition of chemical energy release due to the hydrogen recombination and heat losses, mostly by the process gas itself, forced with a defined flow rate though the WRC. If the inlet gas is sufficiently cold or the hydrogen concentration in the gas sufficiently low, the cooling capacity of the forced gas flow can overcome the heat generation on the catalytic surface. Thus, the WRC is unable to startup.

To deduce a criterion when the WRC can startup, the parameter space of inlet gas temperature T_{in} and inlet gas hydrogen concentration x_{in} is shown in Figure 4. The green markers represent experiments where the WRC started up, completely consuming all incoming hydrogen. The yellow markers indicate experiments where the WRC operated instable, but still consumed >50% of the incoming hydrogen. The red markers indicate experiments where the WRC did not consume a significant amount of hydrogen. The markers without boarder indicate experiments with a flow velocity of 1 m/s, and the markers with black boarder indicate experiments with 0.5 m/s flow velocity.

As the temperature reached within the WRC should depend linearly on the initial gas temperature and on the hydrogen concentration, a straight line (red-dashed line in Figure 4) should split the parameter space into an active and an inactive zone. Further, the equivalence of 1 vol% hydrogen to 80 K heat-up should define the inclination of the line separating the parameter. Thus, only the lateral positioning of the line is fitted to the available data. Based on the available data in Figure 4, the WRC startup criterion c_{start} is proposed as

$$c_{\mathrm{start}} = \begin{cases} 1 \text{ if } T_{\mathrm{in}} > \left(\boldsymbol{T}_{\mathrm{Start}} - \dfrac{80\ \mathrm{K}}{1\ \mathrm{vol\%}} \cdot x_{\mathrm{in}}\right) \\ 1 \text{ if start criterion was reached before}' \\ 0 \text{ otherwise} \end{cases} \quad (2)$$

with $\boldsymbol{T}_{Start}$ as only free fit parameter.

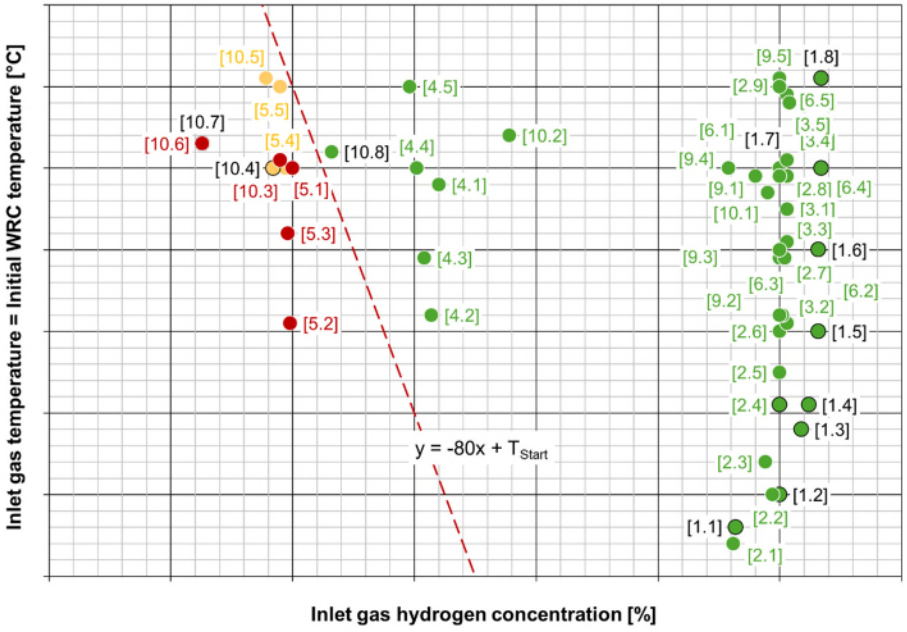

Figure 4. Parameter space for WRC startup

3.2. WRC Startup Delay & Hydrogen

In the lab-scale experiments, when the cartridge inlet valve is opened, hydrogen rushes through the WRC cartridges. Usually, in the initial time after valve opening, hydrogen is recorded in the exhaust gas stream. The WRC first must heat up to be able to consume all the inflowing hydrogen. Thus, even though the boundary conditions would allow for a WRC startup, a WRC may exhibit a certain startup delay during which hydrogen breaks through.

This startup delay is related to the low heating power of the catalyst in its autocatalytic off-state, the heat capacity of the WRC carrier material and mounting pipe, the radial heat loss of the carrier mounting pipe, as well as possible humidity and other contaminants attached to the catalytic surface. Based on the experiences with plate-type PARs, it is expected that especially the experimentally unknown surface contaminations of the catalyst lead to significant uncertainty regarding the startup delay.

In the THAI experiments it can be observed that a plate-type PAR only exhibits a noticeable startup delay if the PAR was not active before in the respective experimental day. This is interpreted that when the PAR was active before, it burned away the surface contaminations. In Reference [7], an energy criterion is proposed for the PAR startup delay.

For the lab-scale experiments, the WRC cartridges were pre-aged for each experimental series. Thus, the 1st test point of each testing day may be more representative for the WRC startup delay than the subsequent experiments. The following observations were made during the experimental campaign:

- The startup delay increases for lower inlet gas temperatures
- There is an inlet gas temperature $\mathbf{T}_D$, where any WRC startup delay vanishes.
- The startup delay increases for lower inlet gas hydrogen concentrations

- For some test series, the pre-ageing of the cartridges has a noticeable impact. However, the inlet gas temperature seems to have a stronger impact than the fact that the cartridges were pre-aged.
- Series 1 shows a constant startup delay of ~70 s for high inlet gas temperatures. This is an artefact of the experimental procedure, which was changed in the subsequent experimental series.
- The data show a significant spreading also for situations where the boundary conditions are equivalent.
- For high hydrogen concentrations (Series 7 and Series 8), practically no hydrogen breakthrough is seen. With sufficient hydrogen available, the WRC starts up faster than the responsiveness of the hydrogen measurement equipment.

For constructing a numerical description of the WRC startup delay, the following assumptions were made.

- The catalyst temperature is the relevant criterion for start of the hydrogen consumption.
- The startup delay should diverge in case the WRC cannot operate at all.
- The WRC startup delay shall decrease with increasing distance in parameter space from the startup criterion.
- The WRC startup delay should depend on the actual temperature of the catalyst (determining the surface chemical reaction speed), and not on the inlet gas temperature. If the inlet gas is warmer than the catalyst, the catalyst will rapidly approach the gas temperature due to surface heat transfer. However, if the catalyst temperature is already elevated, then it will likely require a shorter period to switch into the autocatalytic on-state.

From these considerations, the following phenomenological equation for the WRC startup delay $\Delta t_{\mathrm{delay}}$ (in s) is deduced

$$\Delta t_{\mathrm{delay}} = 500\mathrm{s} \cdot \frac{\boldsymbol{T}_{\mathrm{D}} - \max\left(T_{\mathrm{WRC,initial}}, T_{\mathrm{in}}\right)}{\left(T_{\mathrm{in}} + \frac{80\ \mathrm{K}}{1\ \mathrm{vol\%}} \cdot \mathrm{x}_{\mathrm{in}} - \boldsymbol{T}_{\mathrm{Start}}\right)}, \tag{3}$$

with the initial catalyst temperature $T_{\mathrm{WRC,initial}}$ (in °C) when the hydrogen inflow starts (in the experiments equal to T_{in}). The denominator represents the startup criterion in Equation (2), and the numerator represents the temperature the catalyst needs to heat up until no delay is observed anymore. The temperatures $\boldsymbol{T}_{\mathrm{Start}}$ (see Chapter 3.1), $\boldsymbol{T}_{\mathrm{D}}$ (see discussion above), as well as the leading factor of "500 s" are fit parameters.

In Figure 5 the experimentally observed startup delay is plotted versus the delay predicted in Equation (3) as blue marker. To allow for a logarithmic plot, the experiments with no measurable startup delay are indicated as having 5 s startup delay. The red line represents the x=y condition.

For all data points below the red line, Equation (3) conservatively predicts a longer startup delay. For the markers above the red line, Equation (3) underestimates the startup delay. Note that due to experimental limitations, the Series 1 data points (white-filled marker) show a systematic too long measured startup delay. Thus, these data points shall not be considered when judging the accuracy of the correlation. Based on the available data, it can be stated that the startup delay predicted in Equation (3) is either rather accurate or conservatively enveloping the experimentally observed delays. With the knowledge of the WRC startup delay duration, the criterion for the WRC start delay becomes

$$c_{\mathrm{delay}} = \begin{cases} 1 \text{ if } \mathrm{t} > \Delta t_{\mathrm{delay}} \\ 0 \text{ otherwise} \end{cases}, \tag{4}$$

whereby t is the time since start of a hydrogen exposure of the WRC. Note that Equation (4) is deduced for constant hydrogen concentration. For a generalization to variable hydrogen concentrations in the inflow gas

stream, the mathematical approach of a cumulative damage function as e.g. used to describe creep failure can be used.

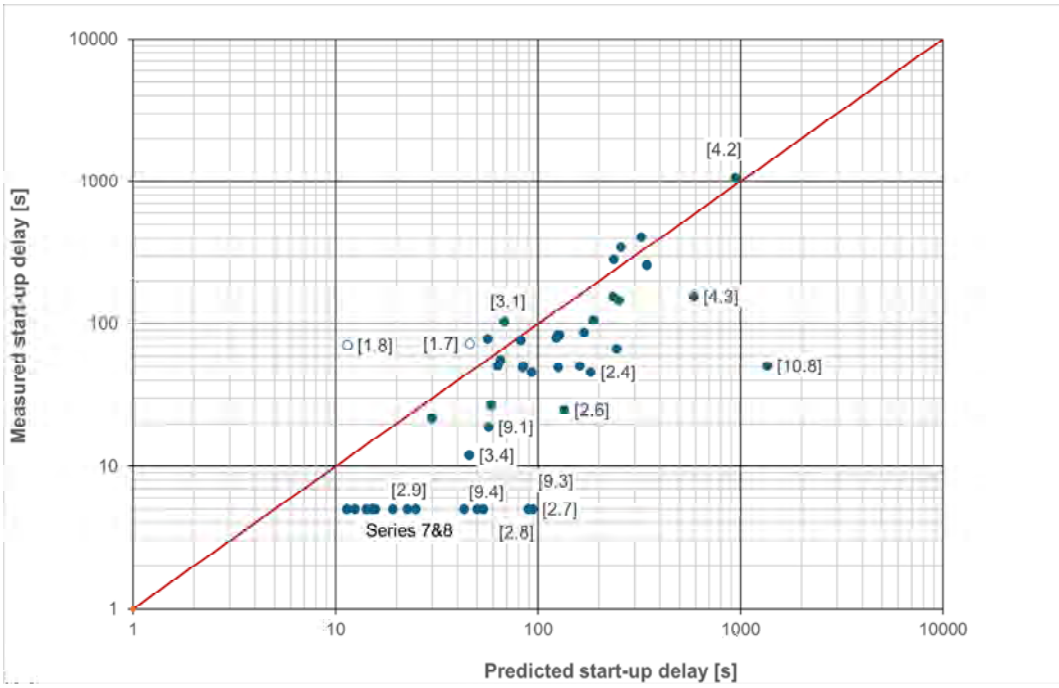

Figure 5. WRC startup delay – comparison observation and prediction

3.3. WRC Shut-down at low Gas Concentrations / Catalyst Temperatures

From the THAI experiments it is known that in case a plate-type PAR is in its autocatalytic on-state, it is hard to bring the PAR in its off-state again as long as even traces of combustible gases are present. As example, in the experiment HR-13, the catalytic foil temperature remained well above ambient temperature even down to ~0.1 vol% hydrogen. The operating characteristics of a plate-type PAR exhibits a certain hysteresis - it remains longer in operation even in circumstances where it would not start up.

To examine the shut-down behavior of a corrugated WRC, the hydrogen concentration was continuously reduced in the inlet gas at the end of Experiment [9.5]. The WRC operated stable down to a hydrogen concentration of ~ 0.4 vol% at an inflowing gas temperature of ~54°C. Thereafter, hydrogen started to leak through the WRC. And at an even lower hydrogen concentration, the WRC started to be come inactive altogether.

For the engineering correlation of the corrugated WRC, it is conservatively assumed that the WRC stops working entirely when the experiment shows a start of incomplete hydrogen recombination. With the equivalence of 80 K temperature increase per vol% hydrogen consumed, the shut-down criterion c_{stop} is deduced in analogy to the start-up criterion as

$$c_{\mathrm{stop}} = \begin{cases} 0 \text{ if } T_{\mathrm{in}} < \left(\mathbf{T}_{\mathrm{Stop}} - \dfrac{80\ \mathrm{K}}{1\ \mathrm{vol\%}} \cdot x_{\mathrm{in}}\right), \\ 1 \text{ otherwise} \end{cases} \tag{5}$$

with the fit parameter $\mathbf{T}_{\mathrm{Stop}}$. As seen at the plate-type PAR, the corrugated WRC exhibit a certain hysteretic operating behavior as $\mathbf{T}_{\mathrm{Stop}} < \mathbf{T}_{\mathrm{Start}}$, i.e. when started, then the WRC consumes hydrogen also in a

parameter space where it would not be able to start. Note that Equation (5), is based on one experiment only. Thus, a limited validity of this criterion must be considered.

3.4. Absence of WRC Poisoning

Catalytic reactions can be sensitive to poisoning, which could endanger the hydrogen-mitigating function of WRC or PARs. In Reference [7], it was shown that Framatome PAR are highly resistant against especially carbon monoxide, the strongest catalytic poison expected to be present during a severe accident in a fission plant [12]. In a fusion plant, other materials and possible reactor poisons could be present. Therefore, the WRC performance was tested under the influence of

- noble gases (He, Ar, Ne),
- tungsten dust (e.g. ablated from the vacuum vessel walls),
- SF_6 as Sulphur-containing compound, and
- hydrazine from water conditioning.

The lab-scale test results show no noticeable impact of these contaminant materials on the WRC operation, within the overall experimental uncertainties. Based on this result, the engineering correlation for the corrugated WRC does not consider poisoning by these materials.

4. CONCLUSIONS

For the ITER fusion plant, the ventilation exhaust of the vacuum vessel pressure suppression system shall be equipped with an autocatalytic wet recombiner (WRC) to convert possible present hydrogen into steam. For this application, a newly designed corrugated carrier structure was coated with the proven and nuclear qualified Framatome catalytic material which is used on the passive autocatalytic recombiner (PAR) for fission plants. The choice for this design is based on the extensive operating experience of Framatome PARs, and the existing nuclear-qualified supply chain.

A lab-scale experimental campaign was conducted to explore the operating characteristics of the WRC, its compliance with bounding environmental conditions in a fusion plant, and its resistance against contaminants possibly present in a fusion plant. Overall, the WRC operated better than initially expected and showed no noticeable impact (within the experimental accuracy) to the tested contaminants.

Based on the experimental results, a phenomenological correlation for the WRC was developed. This correlation describes the impact of temperature and hydrogen concentration of the inflowing gas on the WRC operation, and defines criteria for WRC startup, startup delay, and shutdown.

The fact that the engineering correlation complies with all evaluated experiments, irrespective of their boundary conditions, can be seen as a nuclear-grade Verification and Validation in accordance to IAEA standards [10] [11]. A validation at a full-sized system remains to be done.

Note that all statements within this report are to be considered valid only for catalyst material and catalyst carrier design from the nuclear supplier Framatome. No statements concerning reliability or performance can be made for designs of other nuclear vendors.

ACKNOWLEDGMENTS

This work was supported by the Framatome SAMICO severe accident management community.

REFERENCES

1. Catalyst system and recombination device for recombining hydrogen and oxygen, in particular for a nuclear power station and method for operating a catalyst system, US6054108A, PCT/DE97/01860, [link]
2. International Atomic Energy Agency, B.A. Eckhardt, N. Losch, "Passive Autocatalytic Recombiner Process Features and New Status of International Qualification", Bulgarian Nuclear Energy, Varna, June 9 – 11, 2010, [link]
3. OECD/NEA THAI Project, "Hydrogen and Fission Product Issues, Relevant for Containment Safety Assessment under Severe Accident Conditions", NEA/CSNI/R(2010)3, 22-Jun-2010, [link]
4. M. Freitag, B. von Laufenberg, M. Colombet, M. Klauck, "Measurements of the impact of carbon monoxide on the performance of passive autocatalytic recombiners at containment-typical conditions in the THAI facility", *Annals of Nuclear Energy* **141** (2020) 107356
5. Framatome, "Passive Autocatalytic Recombiner, Severe Accident-Qualified PAR for Combustible Gas Control", [link]
6. Framatome (AREVA), "Qualification and Testing of the U.S. EPR Passive Autocatalytic Recombiner", Technical Report ANP-10322NP, Revision 0, June 2012, [link]
7. M. Braun and E.-A. Reinecke, "AMHYCO engineering correlation to describe the conversion of flammable gases in Framatome passive autocatalytic recombiners", *Nuclear Engineering and Design* **442** (2025) 114206
8. P.-M. Steffen, E.-A. Reinecke, N. Meynet, A. Bentaib, N. Chaumeix, H.-J. Allelein, "Operational Behavior of a Passive Auto-catalytic Recombiner under Low Pressure Conditions", *Fusion Engineering and Design* **124** (2017) 1281–1286
9. OECD/NEA THAI-3 Project, "Final Report on Fission Product Behaviour, Hydrogen Mitigation, and Hydrogen Combustion in Water Cooled Reactors under Severe Accident Conditions", NEA/CSNI/R(2021)8, August 2023-08-02, [link]
10. International Atomic Energy Agency IAEA, "Good Practices with Respect to the Development and Use of Nuclear Power Plant Procedures", TECDOC 1058 (1998), [link]
11. "Guide to Verification and Validation of the SCALE-4 Radiation Shielding Software", NUREG/CR-6484, ORNL/TM-13277, [link]
12. M. Klauck, E.-A. Reinecke, H.-J. Allelein, "Effect of PAR Deactivation by Carbon Monoxide in the Late Phase of a Severe Accident", *Annals of Nuclear Energy* 151 (2021) 107887

Passive Autocatalytic H2 Recombination – Application in the ITER Fusion Reactor

ERMSAR 2026

Braun, Buhlmann, Losch (Framatome)

Chandran, Hall (ITER)

framatome

iter

2026 © Framatome – All rights reserved / C1 - Framatome Restricted / Framatome's know-how / Export Control EU EC: DE–N US EC: N

Confidentiality

☒ **This document contains *Framatome's know-how***
When the box is checked, add the information in the 'Footer'

Export Control COEDM

EU EC	US EC	OTH EC
country code = DE marking code = N	marking code = N	country code = N marking code= N

Goods marked EU EC different to "N" are subject to export authorization of the States members of the European Union (EU) in case of export outside EU, and also for certain sensitive goods (e. g. goods marked "EU EC": "0E001") in case of transfer within UE ; they cannot be reexported nor transferred back without a prior agreement from the State of the first export. Goods marked US EC different to "N" are subject to export, re-export or transfer authorization of the United States of America. Goods marked OTH EC (country code(s)) different to "N" are subject to export, re-export or transfer authorization of the mentioned county(ies). Even for goods marked "EU EC: N" and "US EC: N" and "OTH EC: N", an export authorization may be required depending on their final destination or end-use.

Export Control Other

AL = N	ECCN = N

Goods labeled with "AL not equal to N" are subject to European or German export authorization when being exported within or out of the EU.
Goods labeled with "ECCN not equal to N or EAR99" are subject to U.S. reexport authorization. Even without a label, or with label: "AL: N" or "ECCN: N" or "ECCN: EAR99," authorization may be required due to the final whereabouts and purpose for which the goods are to be used.

Framatome's information protection rules

☐ **C1 :** This document and any and all information contained therein and/or disclosed in discussions supported by this document are **restricted**.

☐ **C2 :** This document and any and all information contained therein and/or disclosed in discussions supported by this document are sensitive and **Framatome confidential,** such as its disclosure, alteration or loss are detrimental with a significant-to-high impact for Framatome.

The document, if disclosed, and any information it contains are intended for the sole attendees. The disclosure or reference to such information or document shall be made only on a proper judgment basis and by mentioning expressly "this information shall not be disclosed / transferred without prior consent".

☐ **C3 :** This document and any and all information contained therein and/or disclosed in discussions supported by this document are classified **Framatome Secret**. **Each one must commit to keep secret any written or oral information disclosed during the meeting. It is forbidden to disclose it to any legal entity and any individual (including within Framatome) without prior consent of the meeting chairman.**

Dissemination scope: specify a perimeter as narrow as possible.

This document and any and all information contained therein and/or disclosed in discussions supported by this document, are confidential, protected by applicable intellectual property regulations and contain data subject to trade secrets regulations. Any reproduction, alteration, disclosure to any third party and/or publication in whole or in part of this document and/or its content is strictly prohibited without prior written express approval of Framatome. This document and any information it contains shall not be used for any other purpose than the one for which they were provided. Legal and disciplinary actions may be taken against any infringer and/or any person breaching the aforementioned obligations.

Issue

Fusion reactor with magnetic plasma confinement

- Large components not designed against internal pressure
- In case of water coolant LOCA → discharge into pressure suppression system
- Water reaction with vacuum vessel wall / Tungsten dust may generate hydrogen

ITER pressure suppression system design

- Scrubber tanks to condense steam
- Air space of tanks is actively ventilated to dilute hydrogen

→ HVAC exhaust contains possibly hydrogen and tritium

Passive autocatalytic hydrogen recombiner in HVAC exhaust path, with subsequent chiller and condensate recovery

- Safety function: Exclude any gas combustibility in the subsequent HVAC system
- Safety function: Minimize the release of radioactive material (tritium) from the plant
- Operational function: Recover tritium from the condensate to be reused as fusion fuel

framatome

iter

2026 © Framatome – All rights reserved / C1 - Framatome Restricted / Framatome's know-how / Export Control EU EC: DE–N US EC: N

Available Solution

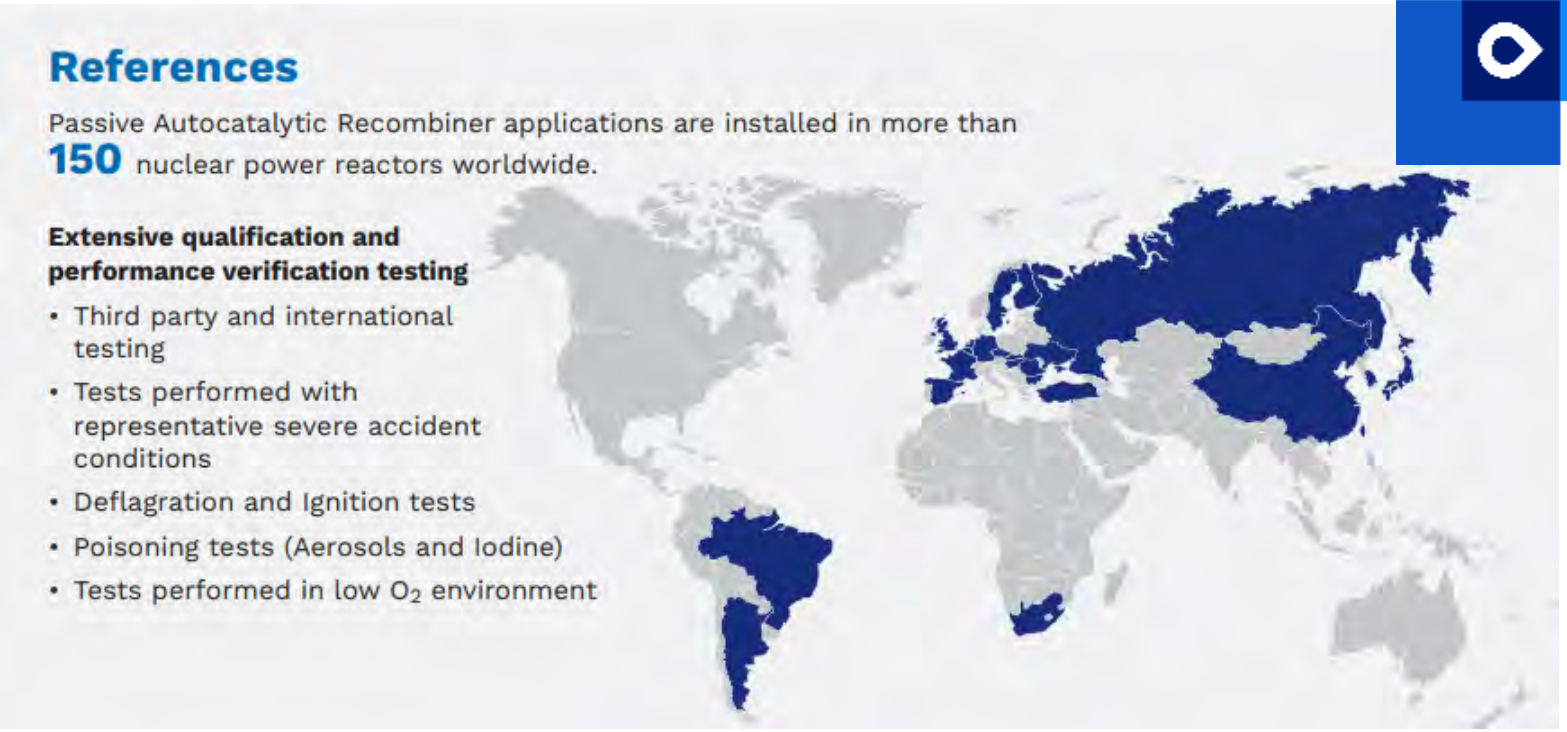

https://www.framatome.com/solutions-portfolio/app/uploads/2025/10/a0642-p-ge-g-en-202405-par.pdf

Framatome PAR Technology

- Nuclear qualified catalytic material - accepted worldwide by nuclear regulators
- Long-term operating experience
- Long history of internal and independent tests (startup, efficiency, ageing, poisoning, ignition)
- Established supply chain

2026 © Framatome – All rights reserved / C1 - Framatome Restricted / Framatome's know-how / Export Control EU EC: DE–N US EC: N

Adaption of Framatome PAR Technology

Changed carrier form-factor – from plates to corrugated geometry

- Forced flow allows for smaller hydraulic diameter
- Size constraint in HVAC system
- No surface inspection possible

Catalyst operating regimes in ITER

- Low concentrations of hydrogen ≤ 8% in normal air
  (flushing of tank air space, no transition to oxygen starvation)
- Humidity of up to 100%
  (due to the scrubbing in the suppression tanks)
- Low gas temperatures 30°C – 60°C
  (cold scrubbing liquid, possible pre-heating)
- Operation at sub-atmospheric pressures
  (0.75 to 1 bar-abs instead of 1 to 6 bar-abs in NPP)
- Externally defined HVAC flow velocity 0.5 m/s to 1.2 m/s
  (forced flow conditions instead of the natural convection)
- Absence of strong catalyst poisons like carbon monoxide
  (other materials possibly acting as catalyst poisoning)

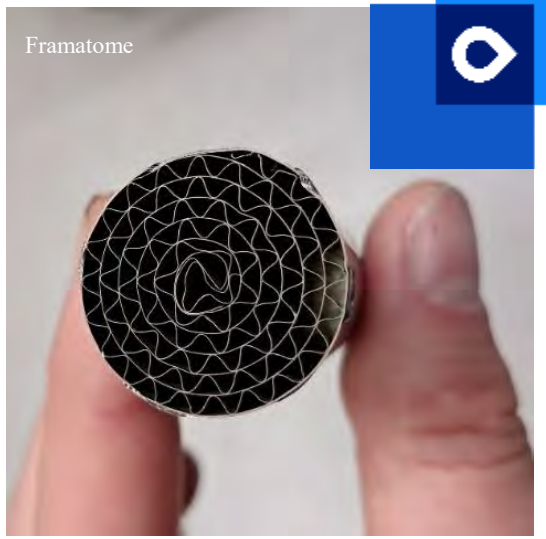

2026 © Framatome – All rights reserved / C1 - Framatome Restricted / Framatome's know-how / Export Control EU EC: DE–N US EC: N

Small-Scale Test Facility

Testing at Framatome Technical Center Karlstein

- Accredited according to DIN EN ISO/IEC 17020 & 17025.
- Stack of four 5 cm diameter scaled catalyst carrier cartridges
- Fixed boundary conditions (H2 concentration, flow velocity, temperature, humidity)

2026 © Framatome – All rights reser

Small-Scale Test Campaign

Typical Test

- Flushed with humid cold air
- At t=0, co-mixing of hydrogen
- After catalyst light-off
  - H2 drops to zero in exhaust
  - Cartridges heat up
- Shut-down of H2, and flushing

Complete consumption of H2

- In NPP-PARs ~ 50%
- Corrugated carrier → smaller diffusion length

Cartridge Temperature

- Not always the first cartridge starts first
- After stabilization, first cartridge is hottest
- Temperature gradient over cartridges
  → First cartridge consumes all H2
  → High lateral heat loss in experiment

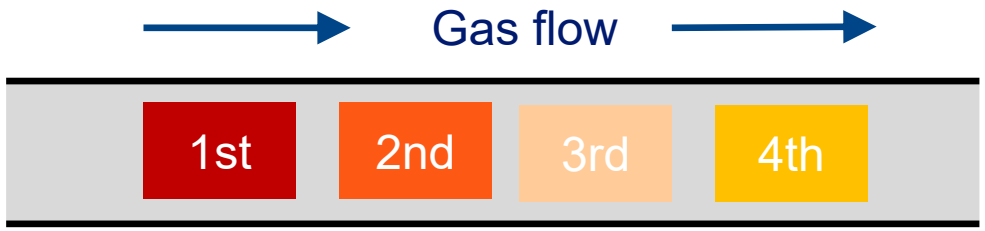

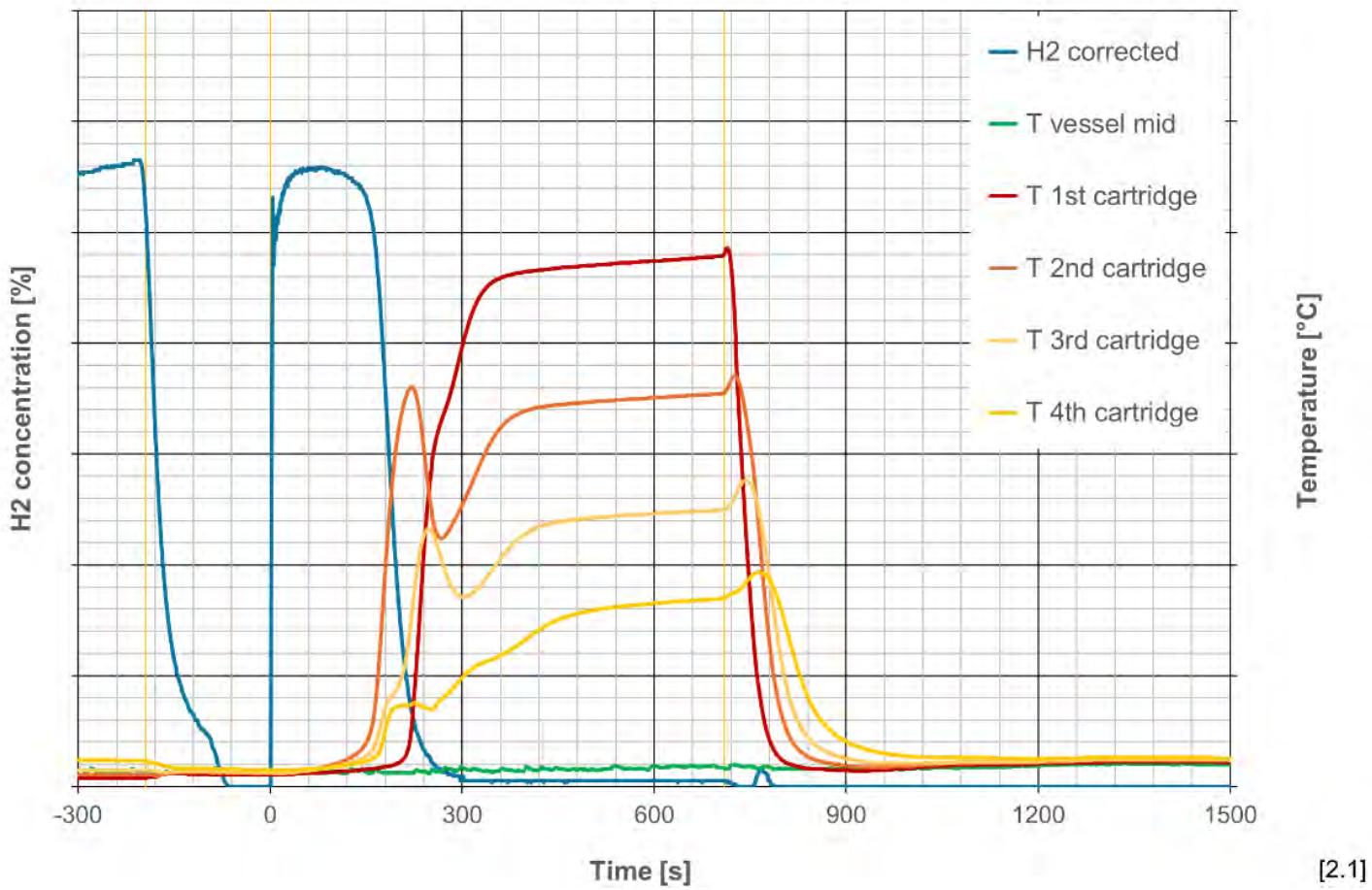

[2.1]

framatome

iter

2026 © Framatome – All rights reser

Numerical Model – Catalyst Startup

Low Gas temperatures are detrimental for catalytic reaction

- low reaction rates
- Cooling of the cartridges by the forced flow
- At sufficiently low hydrogen concentration, the cooling of the cartridges can prevent catalyst light-off

Numerical startup criterion

- Equivalence 1 vol% H2 → 80°K Heatup
- One fit-parameter T_{in}

$$c_{\text{start}} = \begin{cases} 1 \text{ if } T_{\text{in}} > \left(T_{\text{Start}} - \dfrac{80\ \text{K}}{1\ \text{vol\%}} \cdot x_{\text{in}} \right) \\ 1 \text{ if start criterion was reached before} \\ 0 \text{ otherwise} \end{cases}$$

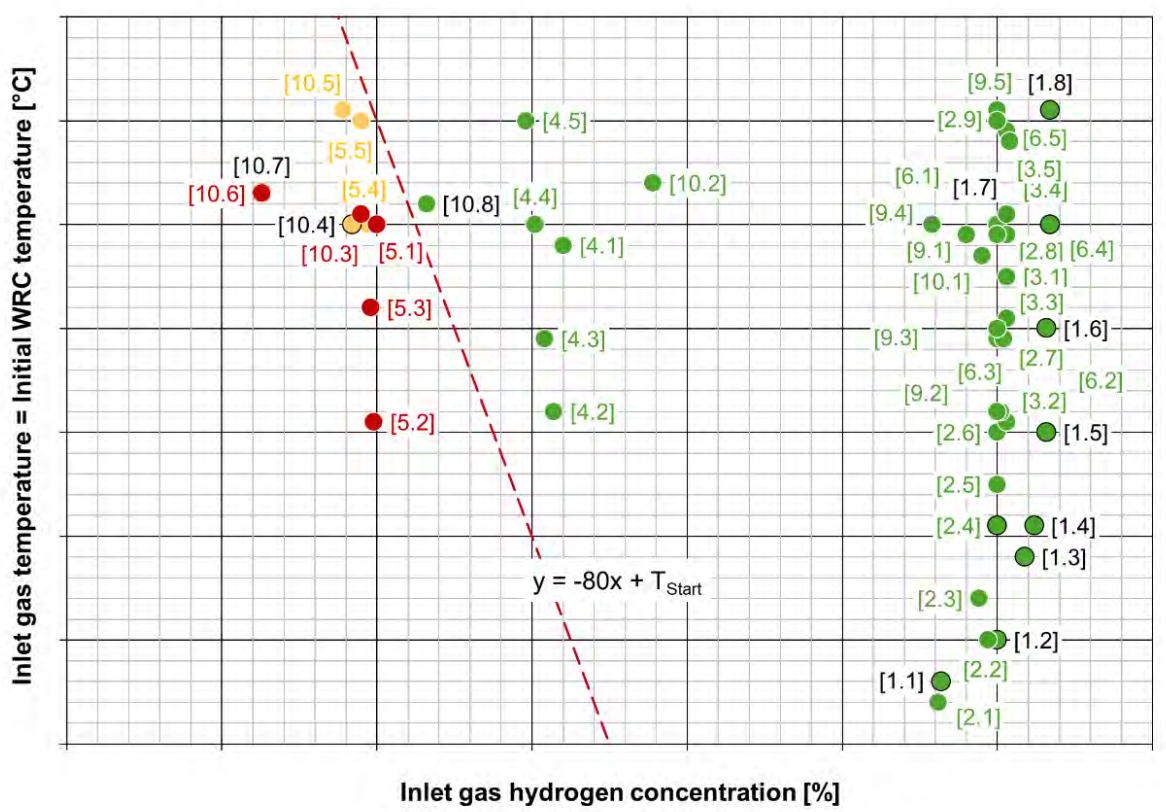

2026 © Framatome – All rights reserved / C1 - Framatome Restricted / Framatome's know-how / Export Control EU EC: DE–N US EC: N

Numerical Model – Catalyst Startup Delay

High uncertainty of the delay of PAR startup

- Oxidation state of the catalyst noble gases
- Humidity adhesion on catalytic surface

Numerical startup delay criterion

- Delay diverges at start-up criterion
- Energy criterion for startup
- One fit-parameter T_D

$$\Delta t_{\mathrm{delay}} = 500\mathrm{s} \cdot \frac{T_{\mathrm{D}} - \max\left(T_{\mathrm{WRC,initial}}, T_{\mathrm{in}}\right)}{\left(T_{\mathrm{in}} + \frac{80\ \mathrm{K}}{1\ \mathrm{vol\%}} \cdot x_{\mathrm{in}} - T_{\mathrm{Start}}\right)},$$

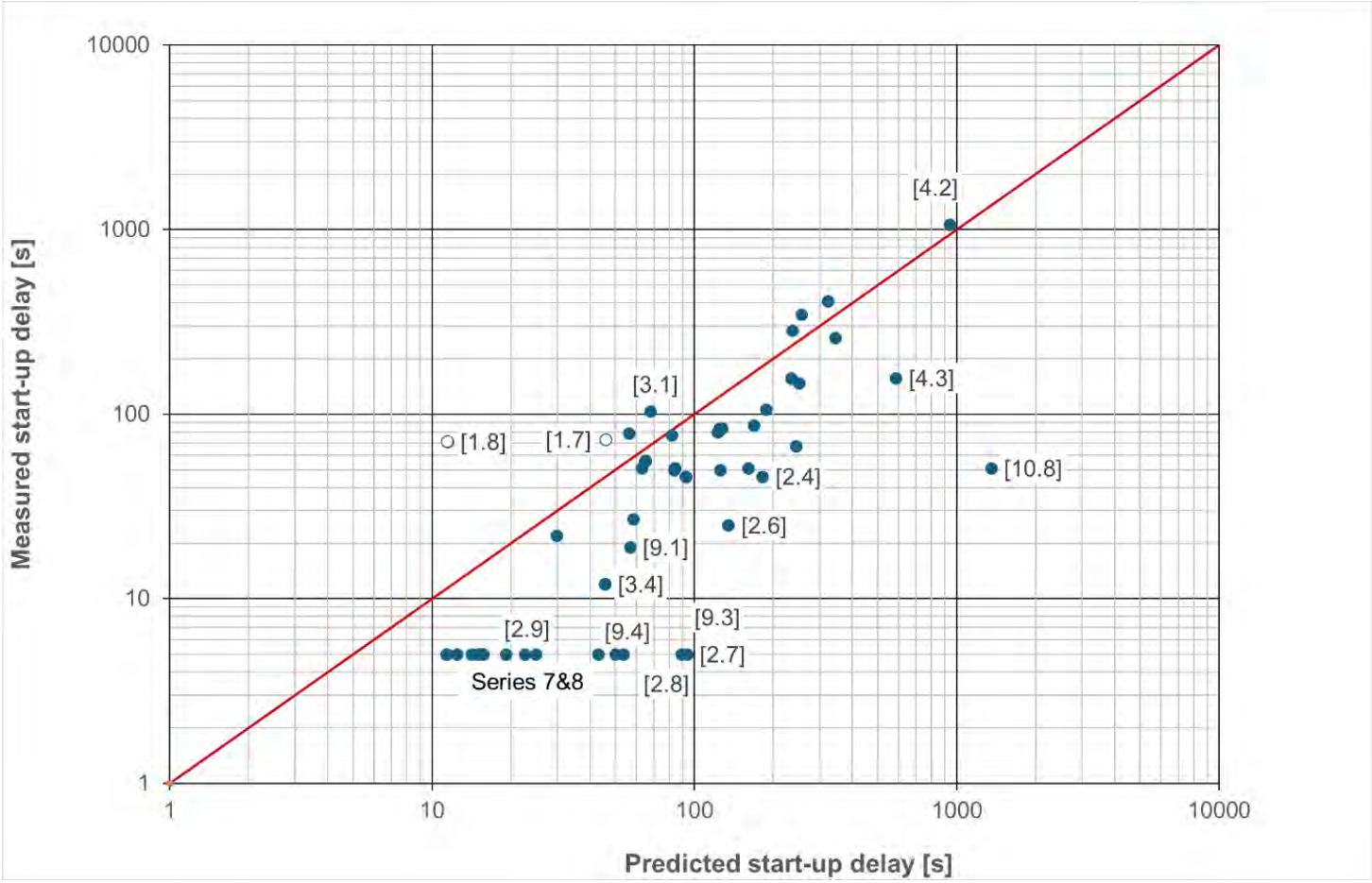

framatome iter

2026 © Framatome – All rights reser tome Restricted / Framatome's know-how / Export Control EU EC: DE–N US EC: N

Poisoning Tests

Tested materials

- Noble gases (He, Ar, Ne),
- Tungsten dust (e.g. ablated from the vacuum vessel walls),
- SF6 as Sulphur-containing compound
- Hydrazine from water conditioning.

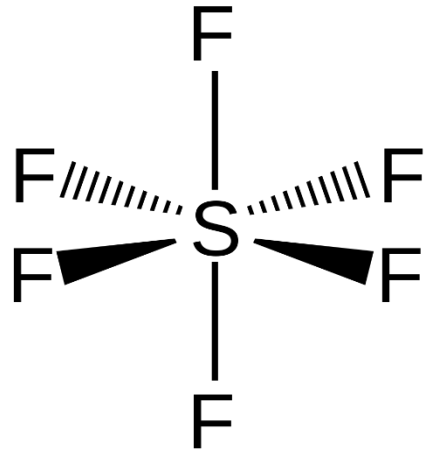

No impact observed
(within the uncertainty of the measurement)

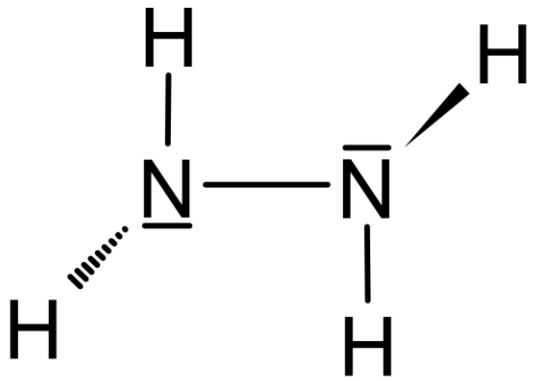

https://www.wikipedia.org/

2026 © Framatome – All rights reserved / C1 - Framatome Restricted / Framatome's know-how / Export Control EU EC: DE–N US EC: N

Summary

- **Framatome PAR technology was adapted to needs in ITER pressure suppression system**
- **Main changes**
  - Change of carrier form plates to corrugated structure
  - Forced flow boundary condition
  - Colder gas
- **Smal-Scale test campaign was executed to numerically characterize the component**
- **No poisoning with fusion-related materials observed**
- **Fusion pressure suppression systems very similar to filtered containment venting system [1]**
  - Industrial base available
  - Nuclear qualified components

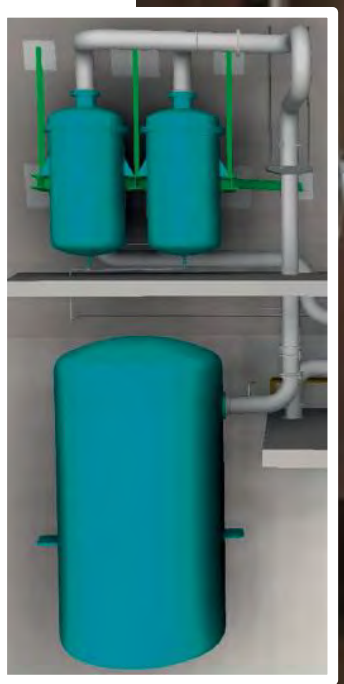

[1] https://www.framatome.com/solutions-portfolio/app/uploads/2025/10/a0653-p-ge-g-en-202403-fcvs-standard.pdf

framatome iter

2026 © Framatome – All rights reserve

Thank you

Contact

Matthias Braun

matthias.braun@framatome.com

IBEP5G

2026 © Framatome – All rights reserved / C1 - Framatome Restricted / Framatome's know-how / Export Control EU EC: DE–N US EC: N

Any reproduction, alteration, transmission to any third party or publication in whole or in part of this document and/or its content is prohibited unless Framatome has provided its prior and written consent.

This document and any information it contains shall not be used for any other purpose than the one for which they were provided.

Legal and disciplinary actions may be taken against any infringer and/or any person breaching the aforementioned obligations.

2026 © Framatome – All rights reserved / C1 - Framatome Restricted / Framatome's know-how / Export Control EU EC: DE–N US EC: N

The 12th European Review Meeting on Severe Accidents Research

May 18-22, 2026, Universidad Carlos III de Madrid, Madrid, Spain

TECHNICAL SESSION 6.5: SOURCE TERM

Chairs: S. Kelm (FZJ), I. Kljenak (JSI)

ID008	**Factors influencing radiation-induced Corium matrix dissolution** H. Aubets (KTH)	Paper Presentation
ID170	**Optimising Electrostatic Precipitators for Severe Accident Scenarios: Impact of Key Operational Parameters** S. Basnet (University of Eastern Finland)	Paper Presentation
ID100	**Overview of Fission Product Behavior Modeling in the SIRIUS Code** J. Ham (KAERI)	Paper Presentation
ID079	**Advanced Modeling of Fission Product Release from Irradiated Fuel during Severe Accident Scenarios** G. Petrosillo (CEA)	Paper Presentation

FACTORS INFLUENCING RADIATION-INDUCED CORIUM MATRIX DISSOLUTION

Helena Aubets and Mats Jonsson

Department of Chemistry, School of Engineering Sciences in Chemistry, Biotechnology and Health
KTH Royal Institute of Technology
SE – 100 44 Stockholm, Sweden
mhao2@kth.se
matsj@kth.se

ABSTRACT

The long-term leaching of the corium formed during a severe nuclear accident will partly depend on the integrity of the corium matrix. One of the major matrix constituents of the corium is UO_2 which in general has relatively low solubility. However, when oxidized to U(VI), the material is more readily dissolved. This will facilitate the release of radiotoxic fission products and heavier actinides. Ionizing radiation emitted from the corium induces water radiolysis and thereby creates oxidizing conditions. The aqueous radiolysis product primarily driving oxidative dissolution of UO_2 is H_2O_2.

The rate of matrix dissolution is also influenced by corium composition as well as by solutes present in the water. A major corium constituent is Zr from the fuel cladding. In this work we have explored the reactivity of a mixture of UO_2 and ZrO_2 towards H_2O_2. The results show that the dissolution of U(VI) from UO_2 decreases with increasing amount of ZrO_2. This is attributed to competing reactions between H_2O_2 and UO_2 on one hand and between H_2O_2 and ZrO_2 on the other hand.

Water in contact with corium may contain borate/boric acid. For this reason, we also explored the impact of boric acid/borate on the H_2O_2-induced oxidative dissolution of UO_2. The results show that borate/boric acid reduces the reactivity of UO_2.

The mechanistic reasons behind these observations will be discussed.

KEYWORDS

Corium · Fission products · Borate/boric acid · Oxidative dissolution · Radiolysis.

1. INTRODUCTION

The global energy demand is increasing constantly and considering the limitations in the fossil fuel reserves and the environmental impact of burning fossil fuels, the need to move towards alternative and more clean energy sources like nuclear power, is strong. Nuclear power offers advantages, like low greenhouse gas emissions and stable long-term energy production among others.

However, there are also significant challenges such as handling of the extremely long-lived radioactive waste and the risk of severe accidents including loss of coolant accidents (LOCA). Although extremely rare, loss of coolant accidents can result in partial or complete melting of the nuclear reactor core and subsequent release of radionuclides into the environment.

A loss of coolant accident occurs when there is a total loss or significant reduction of coolant in the reactor coolant system. This loss may occur for different reasons. Even after reactor shutdown, radioactive decay continues to generate heat, thereby increasing the temperature in the core [1]. If this excess of heat is not removed effectively, it can lead to partial or total core meltdown [1].

If the core melts, the resulting high density and high temperature mass can break the reactor vessel and reach the concrete cavity underneath. The interaction between the concrete and the corium will cause ablation [1].

The composition of the molten core, or corium, can vary depending on different factors such as the reactor and cladding materials and the type of reactor, the progression of the accident and the phyisico-chemical transformations that occur during the accident. Hence, corium is not a well-defined material. For light water reactors (LWR), the main constituents are UO_2 from the fuel and Zr/ZrO_2 from the fuel cladding [1]

Boric acid is used in specific nuclear reactors, like pressurized water reactors (PWR) to control the reactivity of the core. Since boric acid absorbs neutrons, it regulates the fission reaction and thereby the power output [2]. Boron compounds (sodium borate) can also be used as corrosion inhibitors in the secondary circuit of PWRs [3]. In addition, boron plays a key-role in critical emergency situations. In boiling water reactors (BWRs), boron is injected to immediately shut down the reactor [3].

In the case of a severe nuclear accident, the initial phase is normally characterized by the release of volatile radionuclides into the atmosphere and subsequently, the long-term release of radionuclides coming from corium in contact with water [4]. The water in contact with corium can come from different sources, such as groundwater, seawater, or the reactor's cooling systems. The rate of radionuclide release will depend on the composition of both the corium and the contacting water [5] [4]. Most of the radionuclides are incorporated in the UO_2 matrix of the fuel and this applies also in corium. In general, UO_2 has low solubility in water. However, oxidation of UO_2 produces significantly more soluble U(VI) and may therefore drive radionuclide release. After a severe accident, oxidants could be present as a result of intrusion of atmospheric oxygen or simply due to radiolysis of water induced by the inherent radioactivity of corium. Radiolysis of water produces oxidizing species ($HO\bullet$, H_2O_2, and $HO_2\bullet$) and reducing species (e_{aq}^-, $H\bullet$, and H_2) [6].

In research focusing on dissolution of UO_2-based spent nuclear fuel under deep repository conditions it has been shown that H_2O_2 is the primary oxidant. It is therefore reasonable to assume that H_2O_2 plays a major role in the dissolution of corium as well [7] [6]. H_2O_2 reacts with UO_2 through dissociative adsorption producing surface-associated hydroxyl radicals. These reactive species can oxidize UO_2 directly or react with additional H_2O_2 to form $HO_2\bullet$, ultimately producing H_2O_2 and O_2. This sequence of reactions leads to the catalytic decomposition of H_2O_2, like processes observed on other oxide surfaces [7] [8]

In this work we have explored the mechanism and kinetics of H_2O_2-induced dissolution of UO_2 in systems containing ZrO_2 and boric acid/borate

2. EXPERIMENTAL

All aqueous solutions were prepared using ultrapure water obtained from a Millipore Milli-Q system. The UO_2 powder used in the experiments was supplied by Westinghouse AB (specific surface area to be specified). Hydrogen peroxide (30 wt%, Merck KGaA, Lot K52822909 040) was diluted from the stock solution to obtain a working concentration of 0.2 mM. ZrO_2 powder was obtained from Aldrich Chemistry (CAS 1314-23-4; particle size 5 μm; 99% purity, trace-metal basis).

Sodium bicarbonate ($NaHCO_3$; Merck KGaA, Lot K31463629 304; ACS reagent grade) was used to prepare the bicarbonate buffer. Ammonium acetate (CAS 631-61-8, ≥99%), potassium iodide (CAS 7681-11-0, Merck KGaA), and ammonium phosphomolybdate ($(NH_4)_3PMo_2O_7$, ≥99.0%, CAS 12054-85-2) were used as reagents in the analytical measurements.

All experiments were conducted under the same experimental conditions. A known mass of UO_2 powder (40 mg) using an analytical balance (Mettler Toledo AT261; capacity 0–200 g; readability 0.1 mg and 0.01 mg) was accurately weighed and introduced into a 50 mL sealed vial under a nitrogen atmosphere to prevent unwanted oxidation.

Prior to initiating the reaction, the UO_2 powder was washed with a 10 mM sodium bicarbonate solution to remove any pre-oxidized surface layers. Immediately before starting the experiment, the washing solution was discarded and replaced with 15 mL of a 10 mM sodium bicarbonate solution containing borate/boric acid at the desired concentration (0, 20, 80, 120, 160, or 300 mM). In the experiments with ZrO_2, borate/boric acid was not present. The amounts of ZrO_2 powder used in the experiments were 1.0,

1.2, 1.8, and 2.4 g. The ZrO_2 powder was added to the vial after the washing of the UO_2 powder had been completed and before the reaction solution was added. It should be noted that the ZrO_2 and UO_2 powders were used as separate powders and were physically mixed in the vial; no mixed $(Zr,U)O_2$ solid solution was prepared or used in these experiments.

Subsequently, 15 mL of a 0.4 mM H_2O_2 solution—prepared in 10 mM sodium bicarbonate and containing the same borate/boric acid concentration as the reaction medium—was added to the powder suspension to initiate the reaction (total volume 30 ml). All experiments were conducted under continuous nitrogen purging, with continuous stirring at 950 rpm using a magnetic stirrer and temperature control maintained at 25 °C using a thermostated water bath.

Liquid samples were withdrawn at predetermined time intervals for analysis. 1 mL aliquots were withdrawn using a 5 mL medical syringe fitted with a needle. The samples were immediately filtered through 0.22 μm cellulose acetate syringe filters. Aliquots of 100–200 μL of the filtered solution were subsequently used for quantitative analysis of uranyl and hydrogen peroxide.

Hydrogen peroxide concentrations were determined using the Ghormley triiodide method [9], [10]. In this method, iodide ions (I^-) react with H_2O_2 to form triiodide (I_3^-) in the presence of potassium iodide and a catalyst mixture consisting of ammonium phosphomolybdate, acetic acid, and sodium acetate. The absorbance of I_3^- was measured at 360 nm using a Thermo Fisher Scientific, Model 4001/4 UV-vis spectrophotometer. Each measurement was performed by mixing 0.100 mL of filtered sample, 0.100 mL of catalyst solution, 0.100 mL of KI solution and dissolved with water until 2ml [9], [10].

U(V) is known to undergo disproportionation in solution, yielding U(IV) and U(VI). In addition, no interactions between U(V) and HCO_3^-/CO_3^{2-} species, nor direct dissolution of U(V), have previously been reported. Therefore, only U(VI)-Arsenazo complexes were considered in the measurements [11] [12], [13].

Uranyl concentrations were measured using the Arsenazo III spectrophotometric method [14] , [15]. The analysis was performed by adding 1 $mol \cdot L^{-1}$ HCl and 0.16% (w/v) Arsenazo III reagent to the filtered samples. The measurement solution consisted of 0.40 mL Arsenazo III reagent, 0.60 mL HCl, 0.200 mL of filtered sample, and Milli-Q water added to a final volume of 1.6 mL. The resulting colour intensity, measured at 653 nm, is directly proportional to the uranium concentration. Uranyl concentrations were quantified using a calibration curve constructed from standards of known uranyl concentration [14], [15].

3. RESULTS AND DISCUSSION

3.1 Impact of ZrO_2

The concentrations of uranyl and hydrogen peroxide were monitored as a function of reaction time for pure UO_2 powder suspensions and for mixed UO_2/ZrO_2 powder suspensions. At the bicarbonate concentrations used in these experiment (10 mM), U(VI) is rapidly and quantitatively dissolved due to the formation of soluble carbonate complexes. In figure 1, the uranyl and hydrogen peroxide concentrations are given as function of time for the UO_2/ZrO_2 powder suspension containing 1.2 g ZrO_2.

.

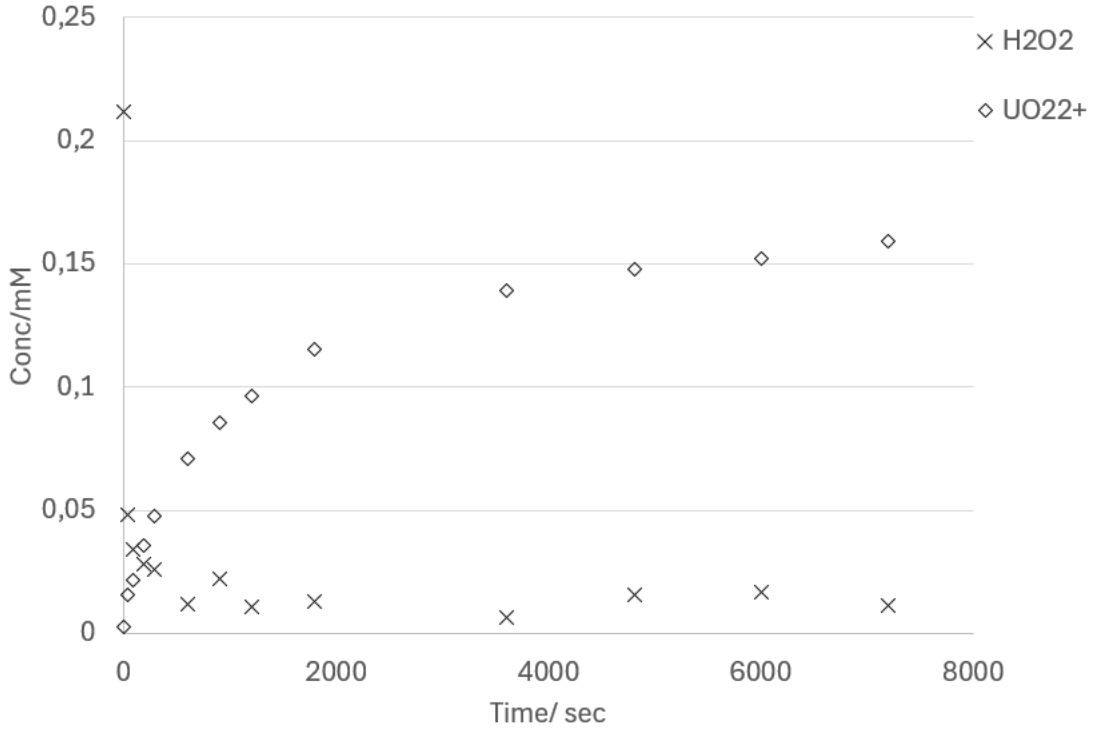

Figure 1: Concentrations of Uranyl dissolution (square) and hydrogen peroxide consumption concentrations (cross) as a function of time for powder suspensions 40 mg of UO_2 and powder suspensions 1.2 grams zirconium dioxide in presence of 10 mM HCO_3^- and 0.2mM H_2O_2.

In a real scenario involving corium–water interactions, radiolysis initially generates H_2O_2, causing its concentration to increase from zero over time. Eventually, the system reaches a steady-state where the rate of H_2O_2 production equals the rate of its consumption through chemical reactions of which one is the reaction with the corium surface.

As can be seen, in the experiments where hydrogen peroxide was added initially, the hydrogen peroxide concentration decreases very rapidly while the release of uranyl is significantly slower. In a system containing only UO_2, two competing reactions involving hydrogen peroxide can occur on the UO_2 surface. The surface-bound hydroxyl radicals formed upon adsorption of H_2O_2 can either oxidize UO_2 resulting in dissolution or react with H_2O_2 resulting in catalytic decomposition of H_2O_2. The latter reaction is favoured by higher H_2O_2-concentration. At 0.2 mM H_2O_2, catalytic decomposition on UO_2 powder is negligible [7], [8]. The mechanism is summarized below:

$$H_2O_2 + 2\ UO_2 \rightarrow 2\ HO\bullet —UO_2 \quad (1)$$

$$H_2O_2 + HO\bullet —UO_2 \rightarrow HO_2\bullet + H_2O + UO_2 \quad (2)$$

$$HO_2\bullet + HO_2\bullet \rightarrow H_2O_2 + O_2 \quad (3)$$

$$HO\bullet —UO_2 \rightarrow OH^- + UO_2^+ \quad (4)$$

ZrO_2 is also known to react with H_2O_2 [16] In this case, the only possible reaction is catalytic decomposition of H_2O_2 (corresponding to reaction 1-3), since Zr cannot be oxidized beyond Zr (IV). The expected effect of mixing UO_2 and ZrO_2 is therefore decreased dissolution of uranyl since part of the H_2O_2 will be consumed by ZrO_2. In

figure 1 we can see that the concentration of dissolved uranyl is lower than the initial H_2O_2 -concentration. This is, at least qualitatively, what would be expected from competition kinetics.

In figure 2, the normalized hydrogen peroxide concentration is plotted as a function of reaction time for a pure UO_2 powder suspension and for UO_2/ZrO_2 powder mixtures containing 1.0, 1.8 and 2.4 g ZrO_2, respectively. All suspensions contain 40mg of UO_2.

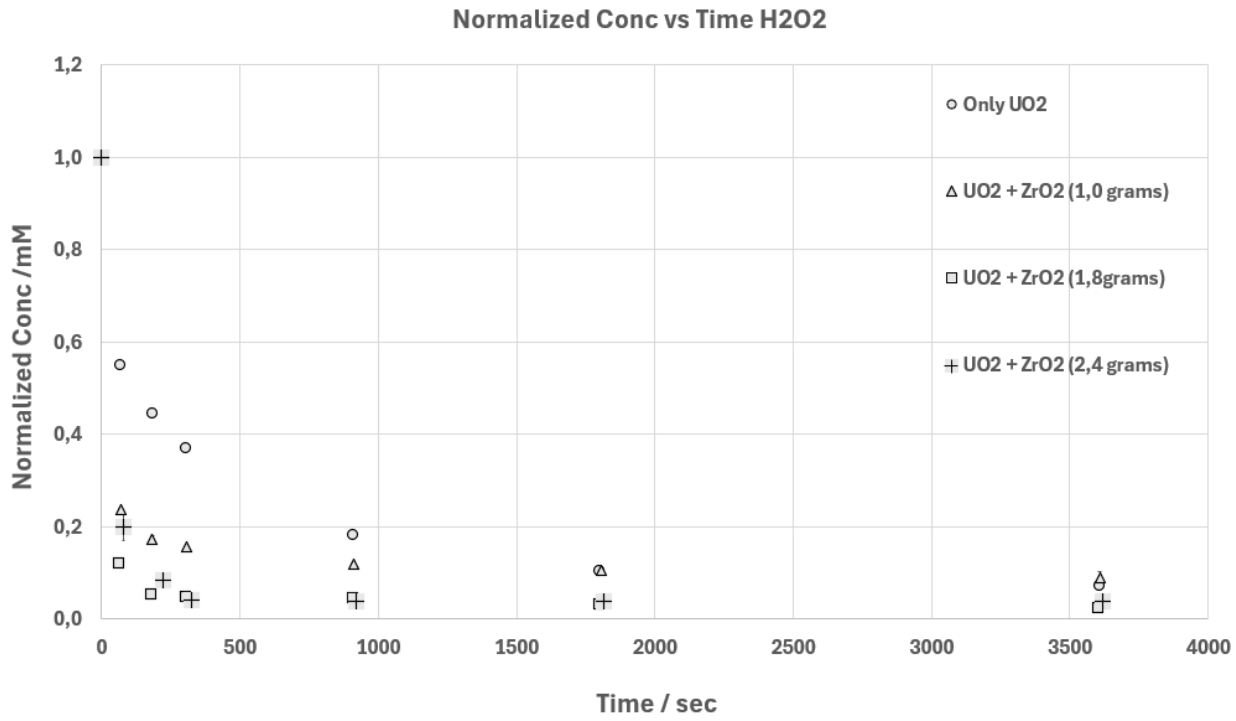

Figure 2: Normalized hydrogen peroxide consumption concentrations as a function of time for systems with powder suspensions of 40 mg UO_2 and with different quantities of zirconium dioxide powder suspensions 1,0grams, 1,8grams and 2,4grams and without, in presence of 10 mM HCO_3^- and 0.2mM H_2O_2.

The graph clearly shows that the rate of H_2O_2-consumption increases in the presence of ZrO_2 powder. Again, this is what would be expected from competition kinetics. Judging from the plot, the rate of H_2O_2 consumption increases with the amount of ZrO_2 although this trend cannot be quantified based on the present data.

The competition between UO_2 oxidation and catalytic decomposition of H_2O_2 in these systems can be quantified using the so-called dissolution yield[17] The dissolution yield is the ratio between the amount of dissolved uranyl and the amount of consumed H_2O_2. In a system with only oxidation the dissolution yield is 100 %. The final dissolution yields for the systems under study here are presented in Table 1.

Table 1: Percentage of dissolution yield of Uranyl in the different systems with different concentrations of ZrO_2.

System	% Dissolution yield
UO_2	95.9
UO_2 + ZrO_2 (1,0gram)	80.2
UO_2 + ZrO_2 (1,8gram)	68.1
UO_2 + ZrO_2 (2.4gram)	47.6

As expected, the dissolution yield decreases with increasing amount of ZrO_2. In a recent study, Kumagai et al., studied H_2O_2-induced oxidation of UO_2 in UO_2/ZrO_2 powder mixtures produced from crushed

pellets that were originally produced from mixtures of UO_2 and ZrO_2 oxide powders pressed and sintered at 2023 ± 10 K for 6 h under an Ar atmosphere [18]. These mixtures are solid solutions. At a UO_2/ZrO_2 powder mass ratio of 1:25 (corresponding to 1 g of ZrO_2 in our system), very little uranyl dissolution was observed, and the dissolution yield was close to 0 %. In the present study, the dissolution yield under the same conditions is around 80 %. A dissolution yield of 80 % for a powder mixture is well in line with what can be expected from competition kinetics. The reduced dissolution yield at higher ZrO_2/UO_2-ratios is also in line with competition kinetics. The discrepancy between the results presented here and the results presented by Kumagai et al., [18], can most probably be attributed to the fact that a solid solution of UO_2/ZrO_2 powder displays a different reactivity towards H_2O_2 as compared to the UO_2/ZrO_2 powder mixture. Previous studies of the reactivity of solid solutions of UO_2 and other oxides have shown that the solid solutions are much less redox active than pure UO_2 [19], [20]. As shown above, catalytic decomposition of H_2O_2 on oxide surfaces produces O_2, which is also capable of oxidizing UO_2. However, the powders suspensions studied in this work are continuously purged with N_2, which will rapidly remove the O_2 from the system. Hence, the reduced dissolution yields at increasing ZrO_2/UO_2-ratios.

3.2 Impact of Borate/Boric acid

Boric acid/borate has long been assumed not to interfere significantly with aqueous radiolysis products. However, recent studies have shown that boric acid/borate displays reactivity towards hydroxyl radicals [21]. It is also known that boric acid/borate forms complexes with hydrogen peroxide [22] and this may also influence oxidative dissolution of corium as well as spent nuclear fuel. In figure 3 the normalized H_2O_2 concentration is plotted as a function of reaction time for UO_2 suspensions containing different concentrations of borate/boric acid.

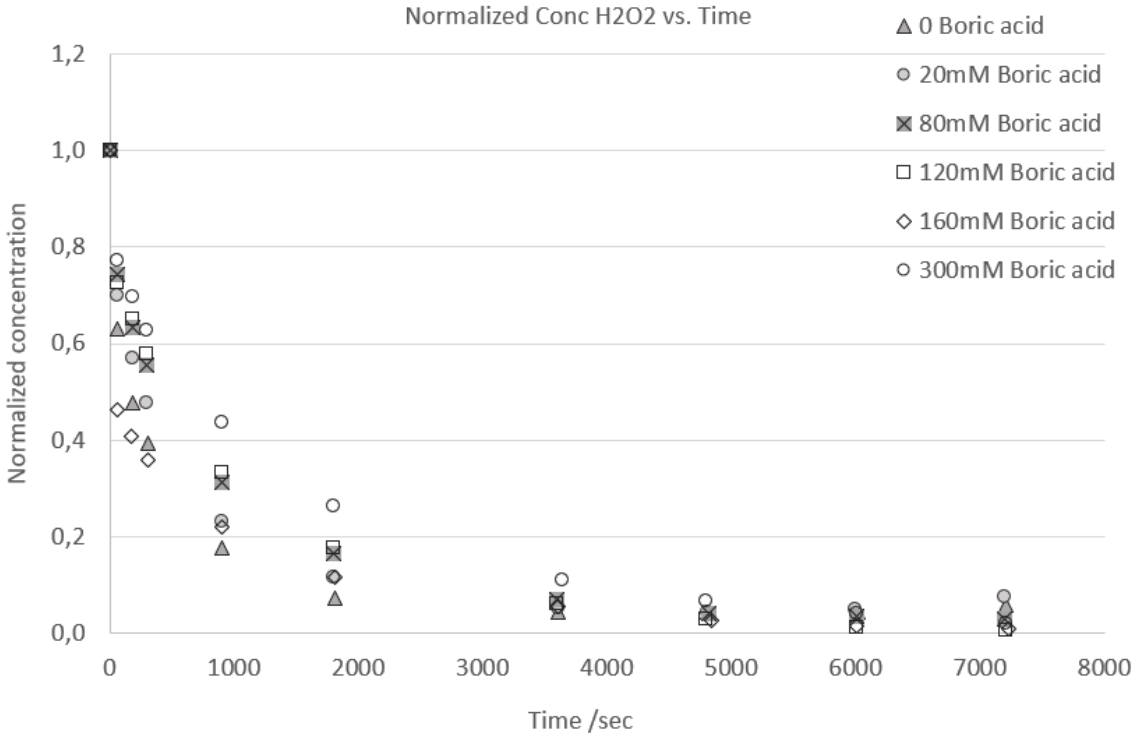

Figure 3: Normalized hydrogen peroxide consumption concentrations as a function of time for systems with powder suspensions of 40 mg UO_2 in presence of 0.2mM H_2O_2, 10 mM HCO_3^- and different concentrations of boric acid in each system (no boric acid, 20mM, 80mM, 120mM, 160mM, 300mM).

The difference in the rate of H_2O_2-consumption between the different borate/boric acid concentrations is very small and no trend can be established with statistical significance. However, it is quite clear that

the H_2O_2-consumption is fastest in the absence of boric acid/borate and slowest at the highest concentration of boric acid/borate. The uranyl concentration was also monitored in these experiments, and the resulting final dissolution yields are plotted as a function of boric acid/borate concentration in figure 4.

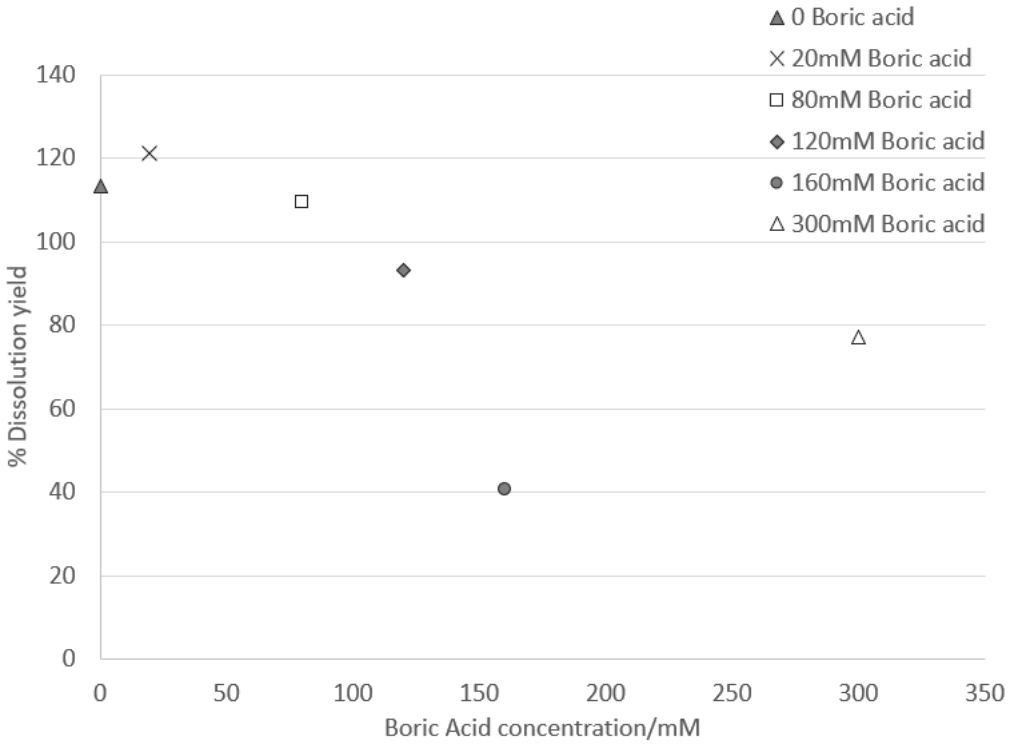

Figure 4: Percentage of Uranyl dissolution yield as a function of boric acid concentrations for systems with powder suspensions of 40 mg UO_2 in presence of 0.2mM H_2O_2, 10 mM HCO_3^- and different concentrations of boric acid in each system (no boric acid, 20mM, 80mM, 120mM, 160mM, 300mM).

Interestingly, the dissolution yield decreases with increasing boric acid/borate concentration with the notable exception of the highest concentration for which the dissolution yield is increasing compared to the second highest concentration. These experiments have been repeated several times, and the observed trend is reproducible. In other systems (other oxides) it has been observed that boric acid/borate decreases the reactivity of H_2O_2. As mentioned above, it is also known that boric acid/borate and hydrogen peroxide can form complexes [21] [22].These complexes are likely less reactive than free hydrogen peroxide as has been observed for other peroxide complexes [21] [22].

4. CONCLUSIONS

The results obtained in this study show that the presence of ZrO_2 and the presence of boric acid/borate, have significant impact on the oxidative dissolution of uranium dioxide. In both cases, the dissolution yield (i.e., the amount of dissolved uranium divided by the amount of consumed hydrogen peroxide) decreases compared to the reference system containing only UO_2 and no boric acid/borate. This implies that the presence of ZrO_2 in corium and the presence of boric acid/borate in water in contact with corium will reduce rate of radiation-induced leaching of radionuclides in case of a severe accident.

The influence of boric acid/borate could possibly be attributed to the formation of complexes with H_2O_2.

ACKNOLEDGMENTS

The Swedish Centre for Nuclear Technology (SKC) is gratefully acknowledged for financial support.

REFERENCES

[1] I. Khurshid, M. A. Amidu, M. Hassan, M. Faizan, I. Afgan, and Y. Addad, "A Thermal Approach for Modeling Concrete Ablation During Molten Corium–Concrete Interaction," *Arab. J. Sci. Eng.*, vol. 50, no. 5, pp. 3317–3335, Mar. 2025, doi: 10.1007/s13369-024-09377-9.
[2] "The benefits of using enriched boric acid in commercial nuclear power plants."
[3] "Borates in nuclear energy: Preventive and emergency nuclear safety | U.S. Borax." Accessed: May 28, 2026. [Online]. Available: https://www.borax.com/products/applications/nuclear-energy
[4] B. Grambow and C. Poinssot, "Interactions between Nuclear Fuel and Water at the Fukushima Daiichi Reactors," *Elements*, vol. 8, no. 3, pp. 213–219, Jun. 2012, doi: 10.2113/gselements.8.3.213.
[5] A. Nakayoshi, C. Jegou, L. De Windt, S. Perrin and T. Washiya. "Leaching behavior of prototypical corium samples: A step to understand the interactions between the fuel debris and water at the Fukushima Daiichi reactors''. Nuclear Engineering and Design. 2020-04, Vol.360, p.110522, Article 110522.
[6] A. Henglein, "J. W. T. Spinks. R. J. Woods: An Introduction to Radiation Chemistry, Third Edition, John-Wiley and Sons, Inc., New York, Toronto 1990. ISBN 0-471-61403-3. 574 Seiten, Preis: DM 91, 45.," *Berichte Bunsenges. Für Phys. Chem.*, vol. 95, no. 3, pp. 451–451, 1991, doi: 10.1002/bbpc.19910950346.
[7] A. Barreiro Fidalgo, Y. Kumagai, and M. Jonsson, "The role of surface-bound hydroxyl radicals in the reaction between H_2 O_2 and UO_2," *J. Coord. Chem.*, vol. 71, no. 11–13, pp. 1799–1807, Jul. 2018, doi: 10.1080/00958972.2018.1466287.
[8] A. Hiroki and J. A. LaVerne, "Decomposition of Hydrogen Peroxide at Water−Ceramic Oxide Interfaces," *J. Phys. Chem. B*, vol. 109, no. 8, pp. 3364–3370, Mar. 2005, doi: 10.1021/jp046405d.
[9] J. A. Ghormley and A. C. Stewart, "Effects of γ-Radiation on Ice[1]," *J. Am. Chem. Soc.*, vol. 78, no. 13, pp. 2934–2939, Jul. 1956, doi: 10.1021/ja01594a004.
[10] A. O. Allen, C. J. Hochanadel, J. A. Ghormley, and T. W. Davis, "Decomposition of Water and Aqueous Solutions under Mixed Fast Neutron and γ-Radiation," *J. Phys. Chem.*, vol. 56, no. 5, pp. 575–586, May 1952, doi: 10.1021/j150497a007.
[11] D. M. H. Kern and E. F. Orlemann, "The Potential of the Uranium (V), Uranium (VI) Couple and the Kinetics of Uranium (V) Disproportionation in Perchlorate Media," *J. Am. Chem. Soc.*, vol. 71, no. 6, pp. 2102–2106, Jun. 1949, doi: 10.1021/ja01174a055.
[12] K. Yuan, D. Renock, R. C. Ewing, and U. Becker, "Uranium reduction on magnetite: Probing for pentavalent uranium using electrochemical methods," *Geochim. Cosmochim. Acta*, vol. 156, pp. 194–206, May 2015, doi: 10.1016/j.gca.2015.02.014.
[13] J. Du *et al.*, "Evidence for ligand- and solvent-induced disproportionation of uranium(IV)," *Nat. Commun.*, vol. 12, no. 1, p. 4832, Aug. 2021, doi: 10.1038/s41467-021-25151-z.
[14] S. Savvin, "Analytical use of arsenazo III Determination of thorium, zirconium, uranium and rare earth elements," *Talanta*, vol. 8, no. 9, pp. 673–685, Sep. 1961, doi: 10.1016/0039-9140(61)80164-1.
[15] I. K. Kressin, "Spectrophotometric method for the determination of uranium in urine," *Anal. Chem.*, vol. 56, no. 12, pp. 2269–2271, Oct. 1984, doi: 10.1021/ac00276a070.
[16] C. M. Lousada and M. Jonsson, "Kinetics, Mechanism, and Activation Energy of H_2 O_2 Decomposition on the Surface of ZrO_2," *J. Phys. Chem. C*, vol. 114, no. 25, pp. 11202–11208, Jul. 2010, doi: 10.1021/jp1028933.
[17] S. Nilsson and M. Jonsson, "H2O2 and radiation induced dissolution of UO2 and SIMFUEL pellets," *J. Nucl. Mater.*, vol. 410, no. 1–3, pp. 89–93, Mar. 2011, doi: 10.1016/j.jnucmat.2011.01.020.

[18] Y. Kumagai, M. Takano, and M. Watanabe, "Reaction of hydrogen peroxide with uranium zirconium oxide solid solution – Zirconium hinders oxidative uranium dissolution," *J. Nucl. Mater.*, vol. 497, pp. 54–59, Dec. 2017, doi: 10.1016/j.jnucmat.2017.10.050.

[19] A. Barreiro Fidalgo and M. Jonsson, "Radiation induced dissolution of (U, Gd)O2 pellets in aqueous solution – A comparison to standard UO2 pellets," *J. Nucl. Mater.*, vol. 514, pp. 216–223, Feb. 2019, doi: 10.1016/j.jnucmat.2018.11.037.

[20] R. Pehrman, M. Trummer, C. M. Lousada, and M. Jonsson, "On the redox reactivity of doped UO2 pellets – Influence of dopants on the H2O2 decomposition mechanism," *J. Nucl. Mater.*, vol. 430, no. 1–3, pp. 6–11, Nov. 2012, doi: 10.1016/j.jnucmat.2012.06.016.

[21] F. Petersson and M. Jonsson, "The Reactivity of Hydroxyl Radicals toward Boric Acid as a Function of pH," *J. Phys. Chem. A*, vol. 128, no. 36, pp. 7593–7600, Sep. 2024, doi: 10.1021/acs.jpca.4c03933.

[22] S. Rey and D. M. Davies, "Photochemistry of Peroxoborates: Borate Inhibition of the Photodecomposition of Hydrogen Peroxide," *Chem. – Eur. J.*, vol. 12, no. 36, pp. 9284–9288, Dec. 2006, doi: 10.1002/chem.200600437.

Dissolution and radionuclide release from corium in contact with water

Helena Aubets and Mats Jonsson
Department of Chemistry
School of Engineering Sciences in Chemistry, Biotechnology and Health
KTH, Royal Insitute of Technology

Table of contents

- Background
- Context of the study
- Objective and methodology overview
- Experimental part
- Results
- Conclusions

Background:

Post-accident scenarios:

After debris cooling, Corium can come in contact with water, which enables dissolution of the matrix and therefore, release of radionuclides.

The radionuclide release depends on:

1. Availability, radionuclides present on the surface will be dissolved first upon contact with water.
2. Rate of corium dissolution. Radionuclides in the corium matrix will be released as the corium matrix is dissolved.

Questions: How does corium matrix dissolution depend on corium composition and water composition?

Chernobyl's Elephant's Foot, HowStuffWorks.

What can we learn from spend nuclear fuel dissolution?

- Spend nuclear fuel is mainly UO_2.
- UO_2 has low solubility in water.
- In the presence of oxidants UO_2 can be oxidized to U(VI) which is much more soluble.
- The radiation emitted from the fuel induces radiolysis of water.

Le Caër, Sophie Water 2011, 3, 235-253

The carbonate radical ion, is produced as a secondary product of the radiolysis of water, by the reaction of carbonate or bicarbonate ions with hydroxyl radicals.

*(The Journal of Physical Chemistry **1970** 74 (10), 2206-2210)*

The radiation from the fuel drives the oxidative dissolution, and the same will happen with Corium.

The mechanism of radiation induced dissolution of spent nuclear fuel (simplified)

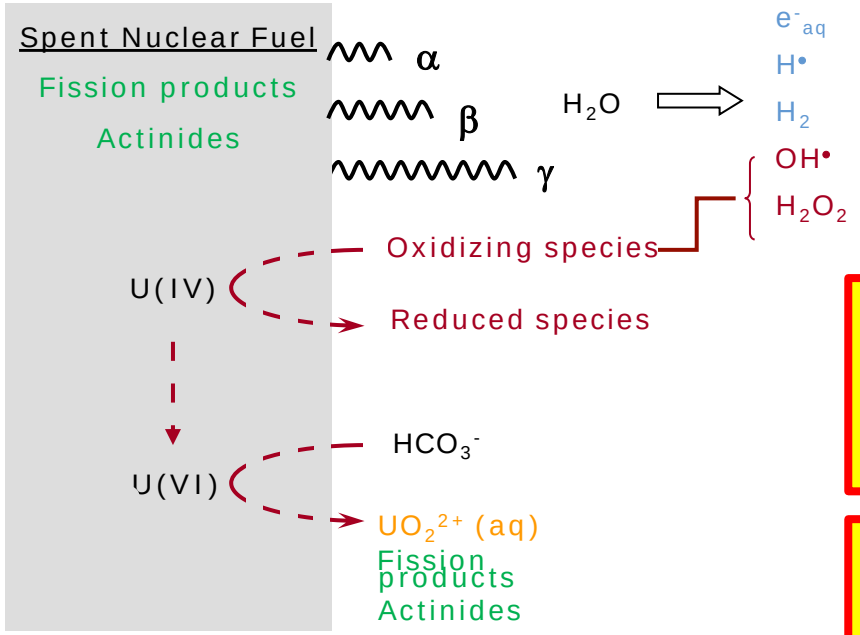

Oxidative radiolysis products of relevance:

H_2O_2, O_2, $HO_2^{\bullet}/O_2^{\bullet-}$, $CO_3^{\bullet-}$, $HO^{\bullet}$, $HOCl^{\bullet-}$

In a system where reactive species are produced at a constant rate, steady-state will eventually be approached (production balanced by consumption)

The maximum rate of fuel matrix oxidation is then given by the rate of production of radiolytic oxidants

How to calculate the rate of radiation-induced dissolution

- The **maximum rate** of oxidative dissolution is given by the rate of production of **radiolytic oxidants**

(Journal of Nuclear Materials2008, 374, 286–289, Journal of Nuclear Materials, 2012, 420, 409–423)

- The rate of production of **radiolytic oxidants** depends on the **dose rate** (and the radiation chemical yields)

(Journal of Nuclear Materials, 2008, 372, 32–35)

- The **dose rate** depends on the **specific activity** of the fuel.

- The **specific activity** of the fuel depends on the burn-up, fuel irradiation history and time after removal from the reactor.

- The specific activity and dose rate profiles can be accurately modelled using existing codes.
(Nuclear Engineering and Technology, 2025, 57, 103814)

Reactivity of H_2O_2 towards UO_2

H_2O_2 is the radiolytic oxidant of highest impact:

- It is more stable than other radiolytic oxidants which allows H2O2 formed further away from the surface to diffuse to the surface making more H2O2 available to the surface.

(*Journal of Nuclear Materials 355 (2006) 38–46*)

Therefore, **hydrogen peroxide** is expected to be the main oxidant for both spent nuclear fuel and corium, while molecular **oxygen** from air may also contribute to the oxidation of corium.

H_2O_2 reacts with UO_2 :

1. **By catalytic decomposition** producing O2 and H2O → $H_2O_2 \rightarrow 2\ H_2O + ½\ O2$
2. **Oxidative dissolution,** oxidizing U(IV) to U(VI). → $H_2O_2 + UO_2 \rightarrow 2OH^- + UO_2^{2+}$

Journal of Nuclear Materials, 410(1-3), 89–93. (2011)

Dissolution yield

- **Dissolution yield**, defined as the ratio between dissolved uranyl with consumed hydrogen peroxide.

  ↑ Dissolution yield → **H_2O_2** reacts by Oxidative dissolution.

(Journal of Nuclear Materials 410 (2011) 89–93)

- Oxides from fission products present in the **UO_2 modify the surface redox chemistry of UO_2.**

  ↓ **Dissolution yield will be reduced**

- **The reactivity of UO_2 towards H_2O_2** depends how the surface has been exposed previously to oxidizing or reducing conditions. Exposures of H_2O_2 changes the **UO_2** surface chemically, over time the surface becomes partially oxidized **As a consequence:**

  ↑ H_2O_2 decomposes catalytically

  ↓ Smaller fraction contributes to uranium oxidation and release ↓ Dissolution yield

(Dalton Trans., 2020, 49, 1241)

Reaction mechanism between oxides and H_2O_2.

1. For metal oxides where metal is in the highets oxidation state **H_2O_2** reacts **by catalytic decomposition** (producing O2 and H_2O).
2. $H_2O_2 \rightarrow 2\ H_2O + ½\ O2$

The mechanism:

$$H_2O_2 \rightarrow 2OH^{\cdot}(ads)$$

$$OH^{\cdot}(ads) + H_2O_2 \rightarrow H_2O + OH^{\cdot}{}_2$$

$$2OH^{\cdot}{}_2 \rightarrow H_2O_2 + O_2$$

(A. Hiroki, J.A. LaVerne. J. Phys. Chem. B, 109, 3364 (2005))

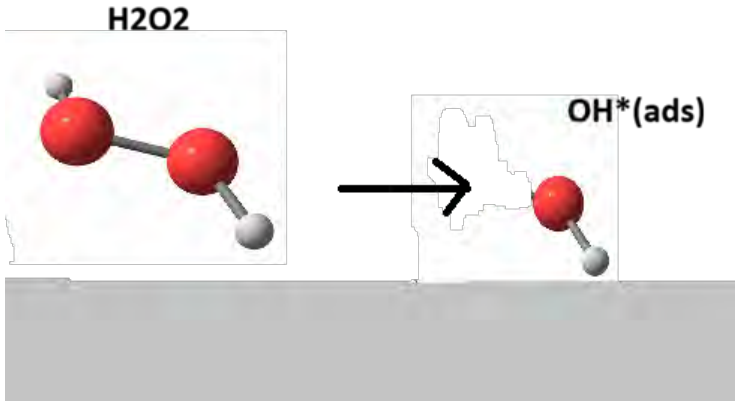

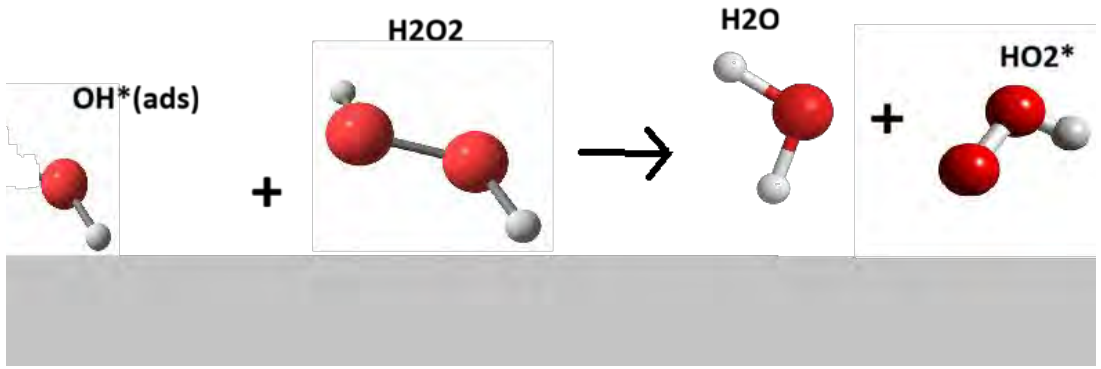

These radicals are largely **surface-bound**:

- They react very close to where they are formed,

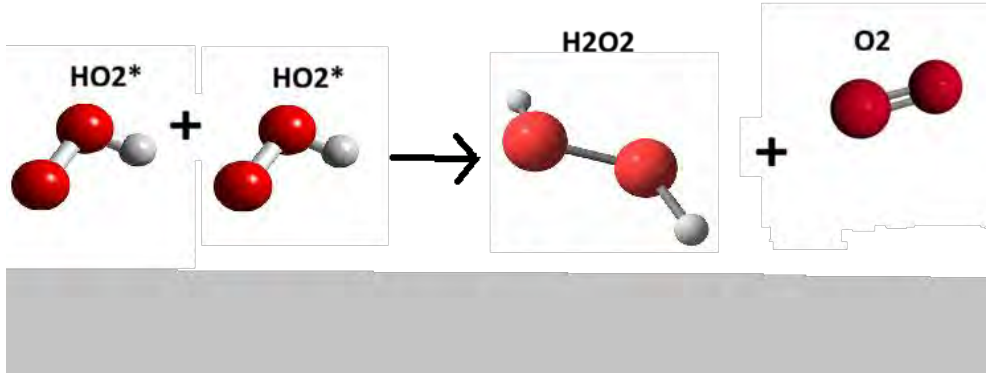

Previous observations

- This is the behaviour of UO_2 with H_2O_2 in the presence of bicarbonate.
- Bicarbonate is present in most types of waters, and it is good complexant of U(VI).

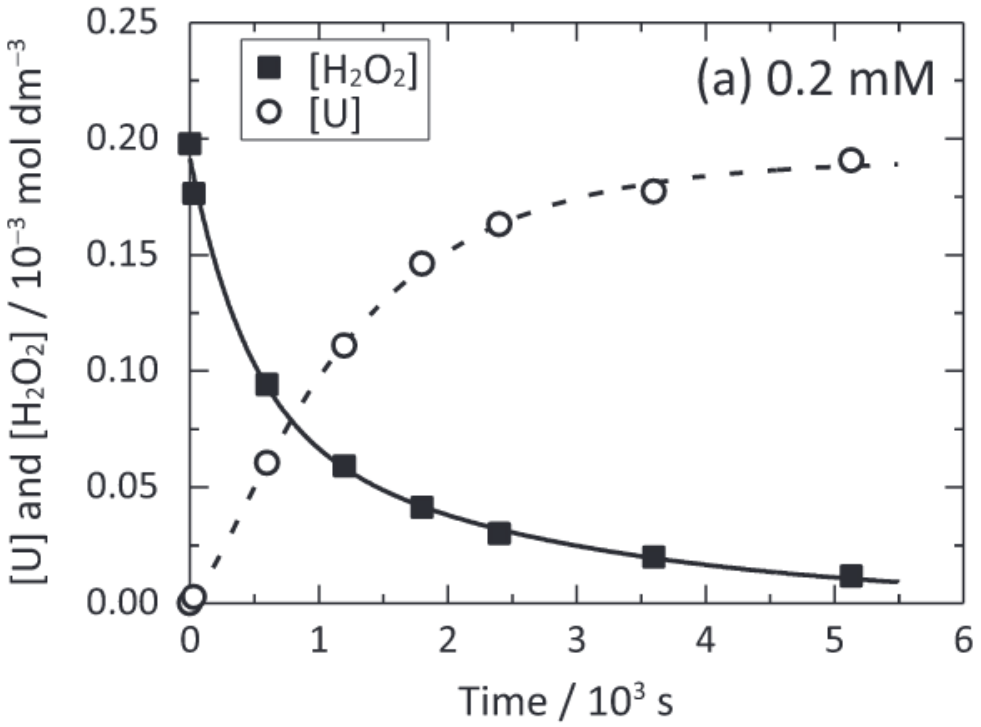

Fig 4: Journal of Coordination Chemistry. (2018), 71:11-13, 1799-1807.

Objective and methodology overview

Objective:
To explore the kinetics and mechanism for H_2O_2 induce dissolution of corium models

Experimental setup:

- **Corium analogue:**
  -UO_2, ZrO_2
- **Aqueous phase conditions:**
  -Boric acid, HCO_3^-/CO_3^{2-}

*Boric acid is used in **PWR** dissolved in the water system as **a neutron moderator**, and in **BWR,** as an **emergency stop**.*

Design of the Leaching experiment

1) Washing:

N2 purging

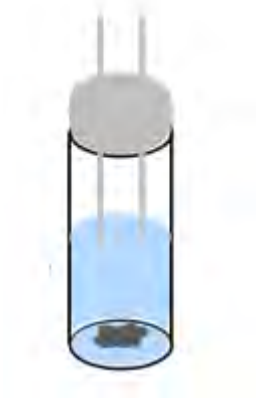

10mM
Sodium bicarbonate
Solution

40mg UO2 powder.

2) Leaching:

N2 purging

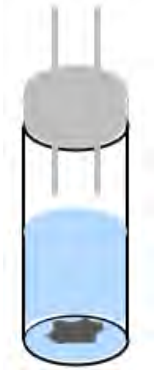

40mg UO2 powder in 15mL
10mM Sodium bicarbonate solution.
RT
constant stirring 850rpm.

ZrO2

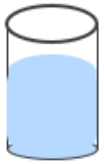

H2O2

0,2mM
15mL

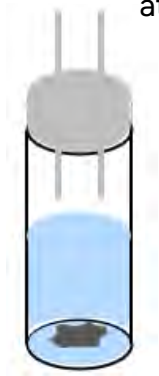

N2 purging
and stirring
constantly

Aliquots
at specific
times

0,22µm
Cellulose
Acetate
Syringe filter

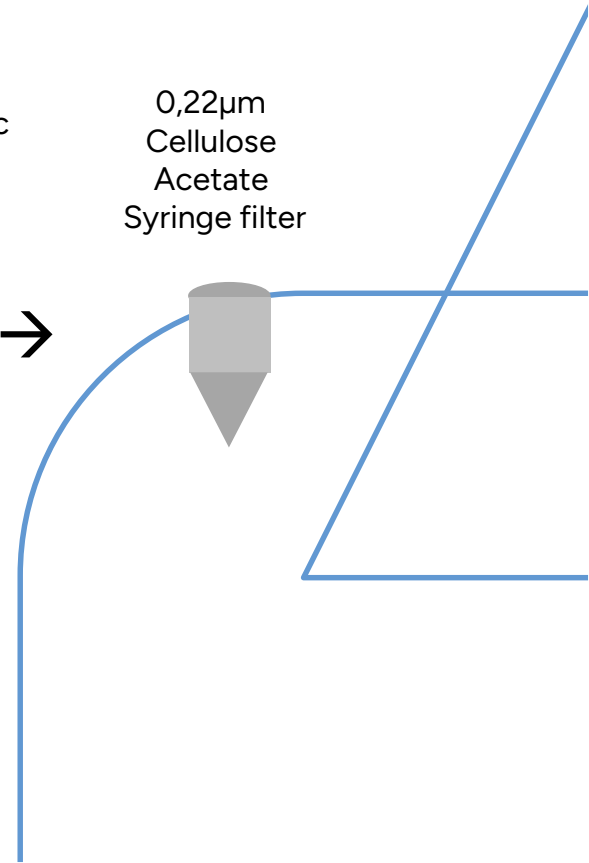

Analysis of the solutions

- Monitoring H_2O_2 and U(VI) concentrations with time using **UV-vis spectrophotometer**.

- H_2O_2 was measured using the **Ghormley triiodide** method, at 360nm wavelength.

- Concentrations of H_2O_2 are measured indirectly

$$2I^- + H_2O_2 \rightarrow I_2 + 2OH^-$$

$$I_2 + I^- \rightarrow I_3^-$$

- Hydrogen peroxide can oxidize potassium iodide (KI) with catalytic $(NH_4)_6Mo_7O_{24}$ to produce triiodide, which absorbs light at 352 nm.

(Journal of the American Chemical Society, 1956, 78 (13), 2934-2939, and Journal of physical chemistry. 1952, 56, 587-594.)

Analysis of the solutions

- UO_2^{2+} was measured using **Arsenazo-III** method, at 653nm wavelength.
- Reagent Arsenazo III form coloured complexes with metal ions, like Uranium.
- Materials containing these elements can be analysed directly in the solutions formed after dissolving the sample.

(Talanta 1961, 8, 673–685. and Analytical chemistry (Washington), 1984,.56 (12) .2269-2271)

Previous investigations

- Previous investigations (Kumagai, 2017) showed high stability of UO_2/ZrO_2 compared to UO_2 against H_2O_2.
- This experiment was done from sintered pellets of UO_2 and ZrO_2 and crashed.
- There is a decrease in dissolution yield of Uranyl when there is ZrO_2
- Rate constant consumption of H_2O_2 increases with the amount of ZrO_2.
- The trend can be attributed to competing consumption of H_2O_2 on ZrO_2 and UO_2, respectively.

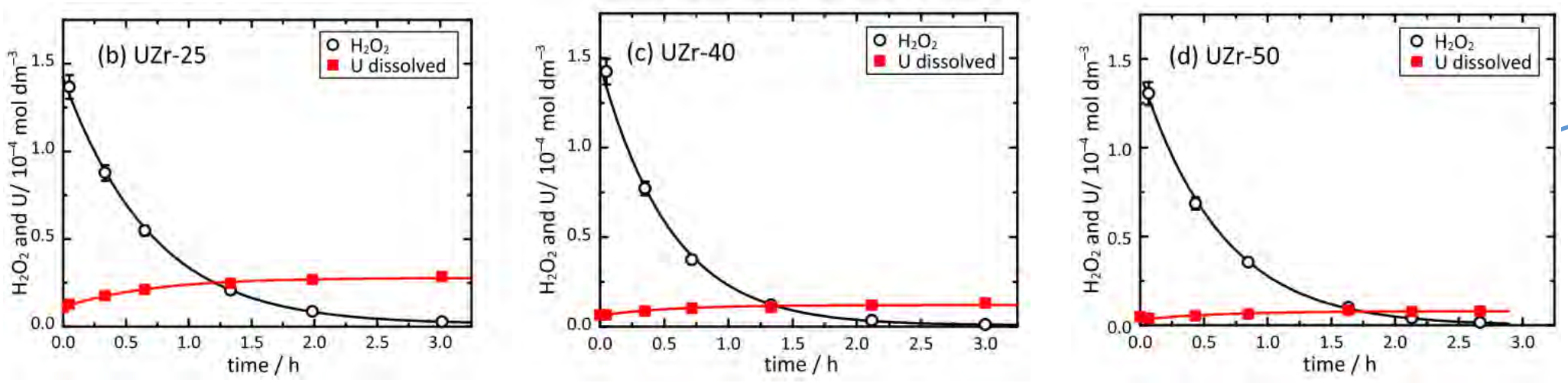

Fig 5, 6, 7: Journal of Nuclear Materials 497 (2017): 54–59..

Expected results in the UO_2/ZrO_2 experiments

1. O_2 form from the catalytic decomposition, is continuously removed from the system by N_2 purging.

2. In our experiments at current **ZrO_2/UO_2 ratios compared with systems with only UO_2** we expect:
   1. **Faster consumption** of **H_2O_2** becasue it is reacting with ZrO_2 and UO_2.
   2. **Less oxidation** of UO_2 (since O_2 is removed from the system).

H_2O_2 consumption and UO_2^{2+} dissolution in UO_2/ZrO_2 systems purged with N2

Consumption of hydrogen peroxide:

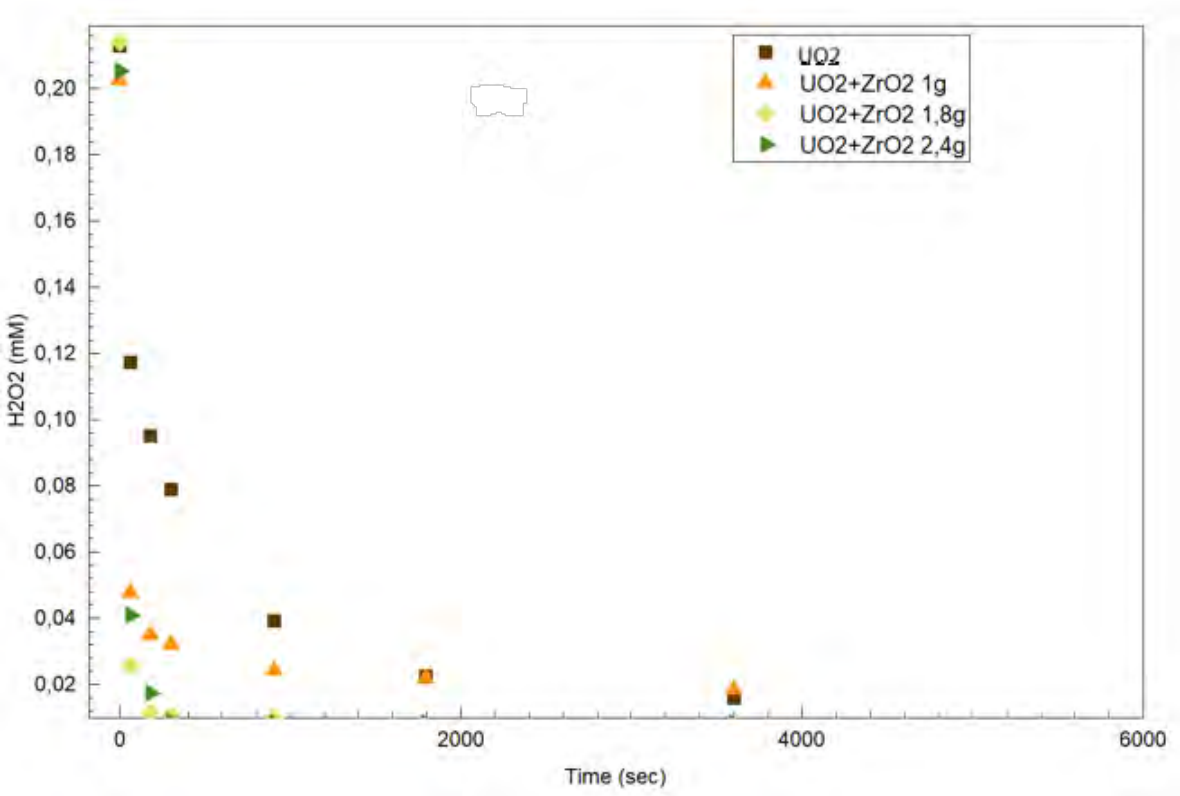

Dissolution of Uranyl:

UO2-ZrO2 (mass ratio 96)
UO2-ZrO2 (97.8)
UO2-ZrO2 (98.3)

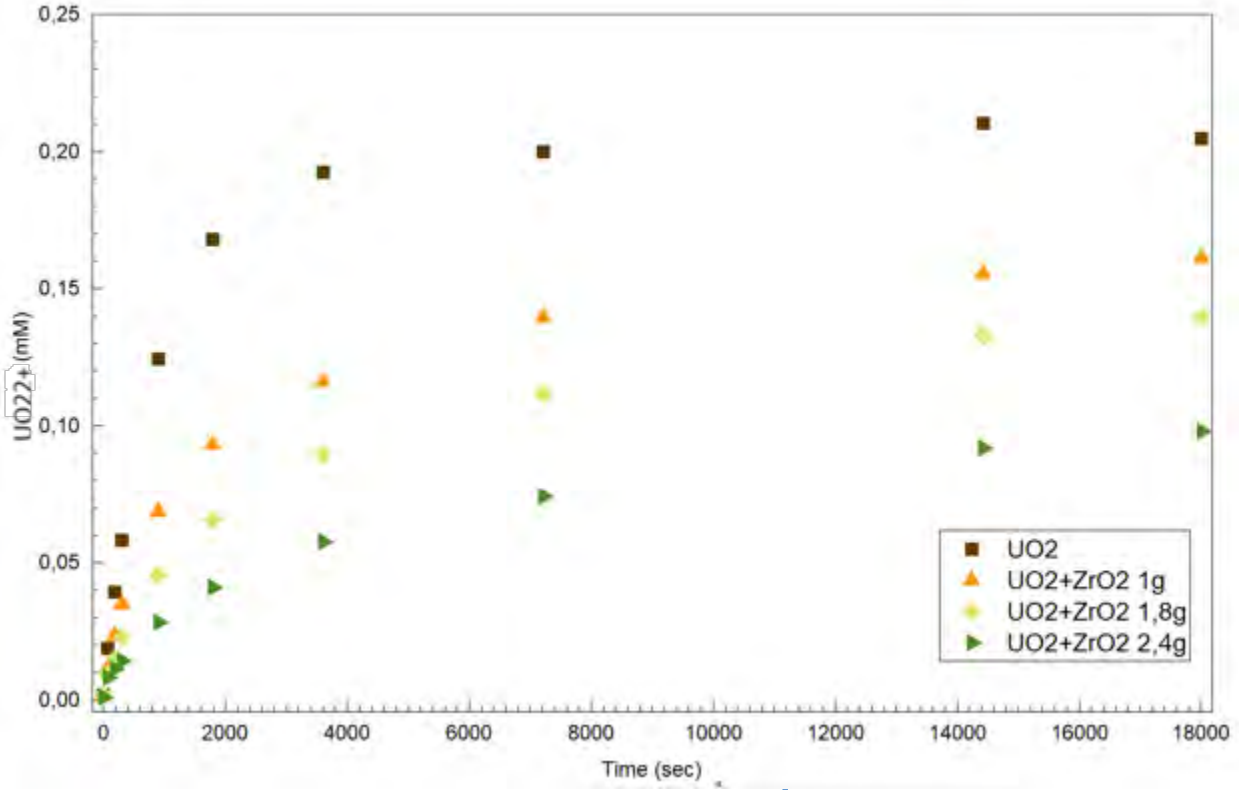

H_2O_2 consumption and UO_2^{2+} dissolution in UO2/ZrO2 systems in sealed reaction vessels

Consumption of hydrogen peroxide:

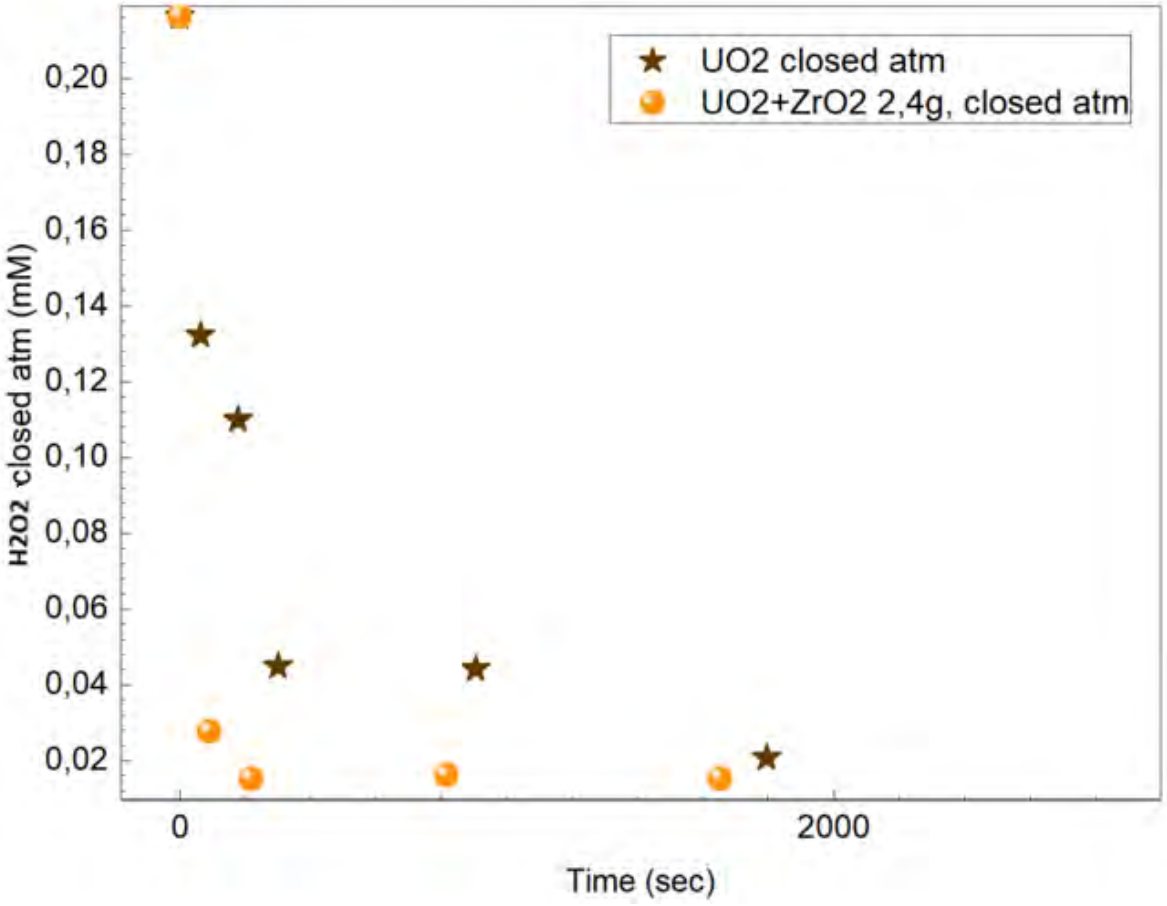

Dissolution of Uranyl:

UO2

UO2-ZrO2 (mass ratio 98.3

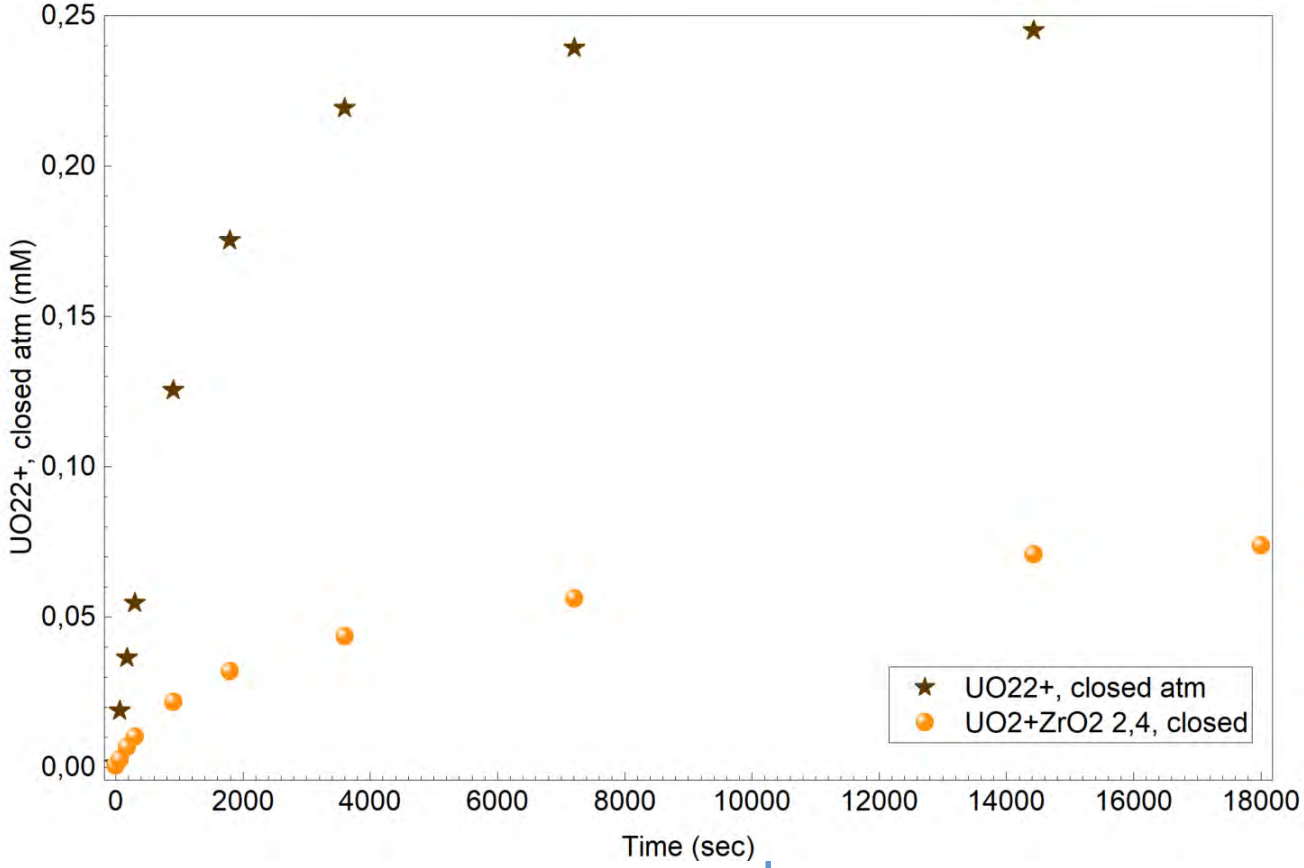

Conclusions

- Presence of ZrO_2 has an impact in the dissolution yield of Uranyl.
- In the closed systems, we observe that the results are the same, what it means that the molecular oxygen does not contribute to the oxidation of UO_2.

Experiments with Boric Acid and expected Impact

- Boric acid is used in some nuclear reactors, for this reason we performed experiments with Boric acid/borate.
- Same experiments were performed with presence of Boric acid/borate with the pH at 9.4. At this pH, the system will expect to have:
  - ✓ The counter-base borate ($B(OH)_4^-$)
  - ✓ And two polyanion species diborate and tetraborate
- We know they can act as a **competitive scavenger of •OH radicals**.

J.Phys.Chem.A2024,128,7593−7600

- Boric acid/borate can be absorbed in oxide surfaces and change the reactivity.

(Under review in ACS Omega)

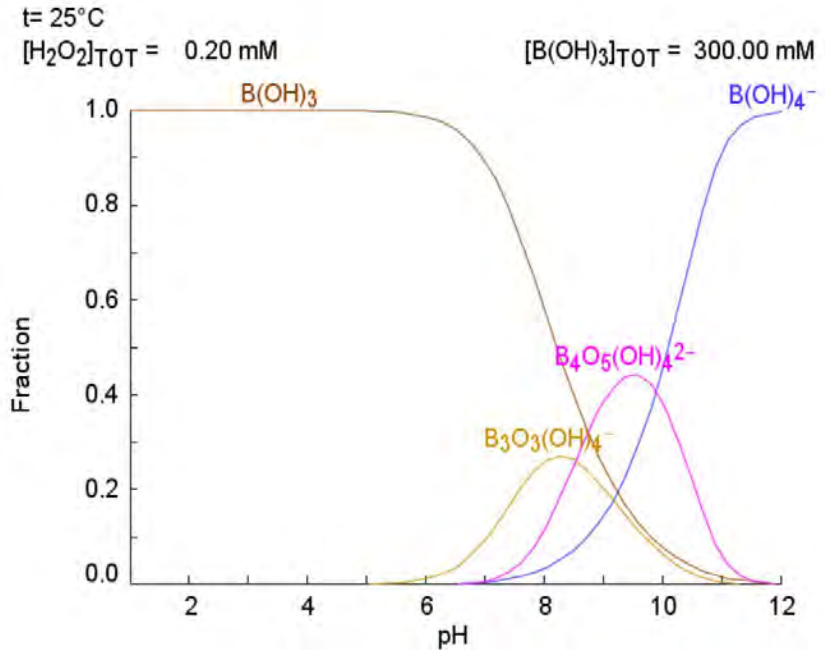

Reaction between UO_2 and H_2O_2 in the presence of bicarbonate and boric acid

Experiments were performed in the same conditions.

We changed the aqueous phase, adding different concentrations of boric acid: 20mM, 80mM, 120mM, 160mM and 300mM.

1) Washing:

N2 purging

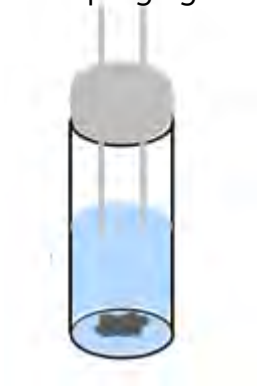

10mM Sodium bicarbonate Solution
40mg UO_2 powder.

2) Leaching:

N2 purging

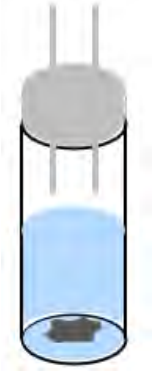

H_2O_2 0,2mM.

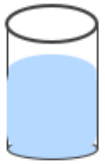

N2 purging and stirring constantly

Aliquots at specific times

0,22µm Cellulose Acetate Syringe filter

Results of experiments of UO_2 against H_2O_2 with boric acid

Consumption of Hydrogen peroxide:

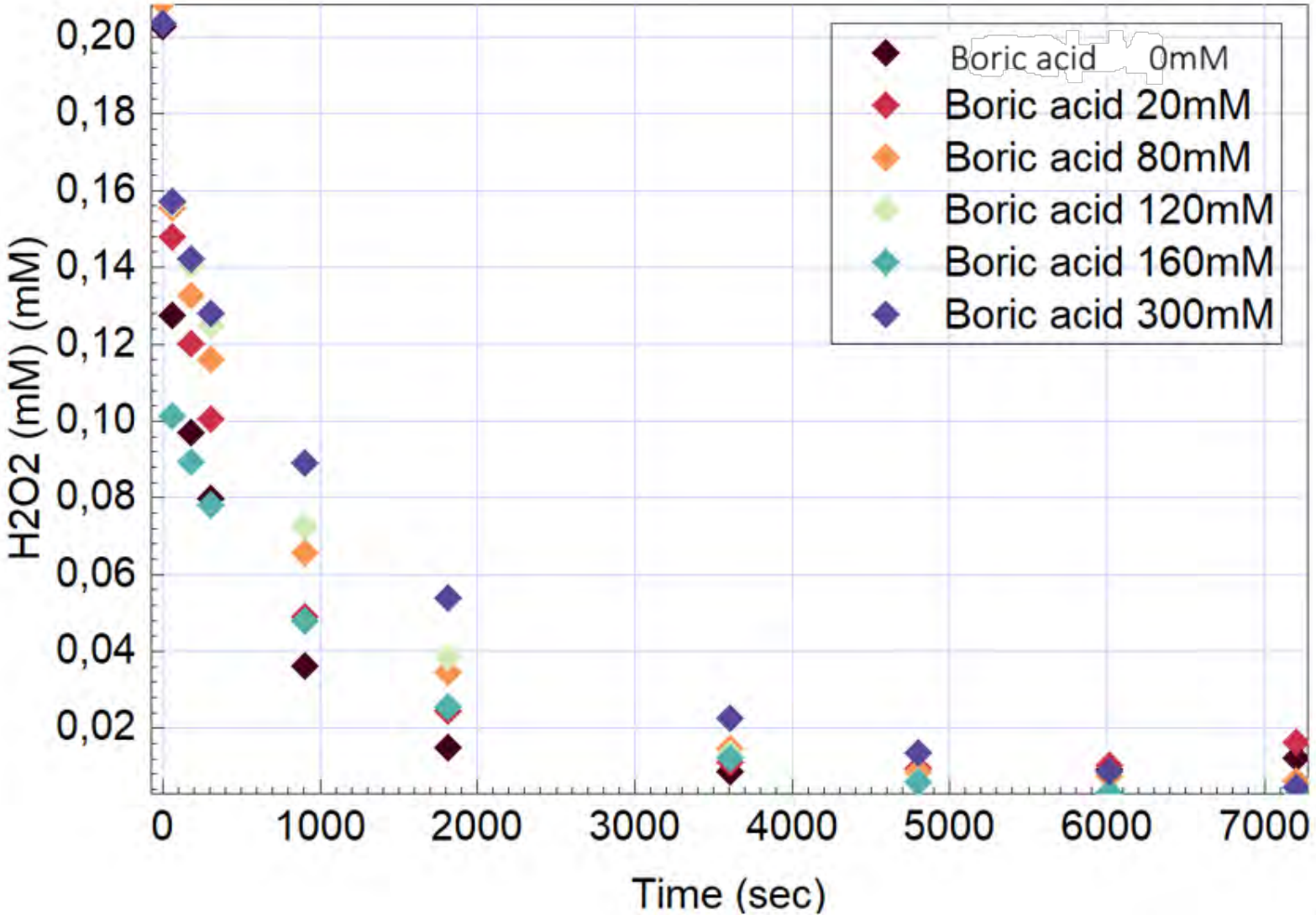

Results of experiments of UO_2 against H_2O_2 with boric acid

Dissolution of Uranyl with time:

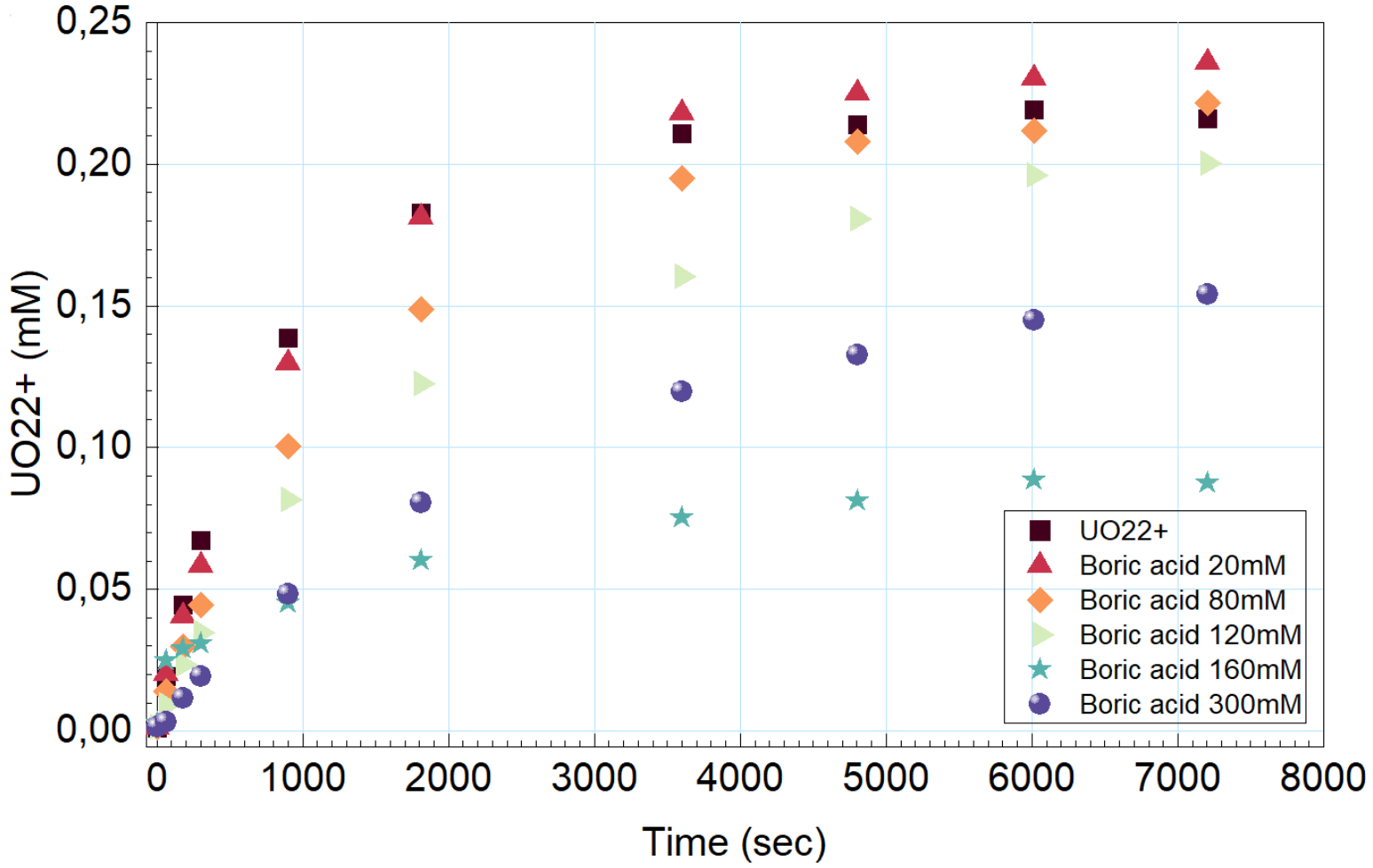

Dissolution yield of Uranyl in boric acid

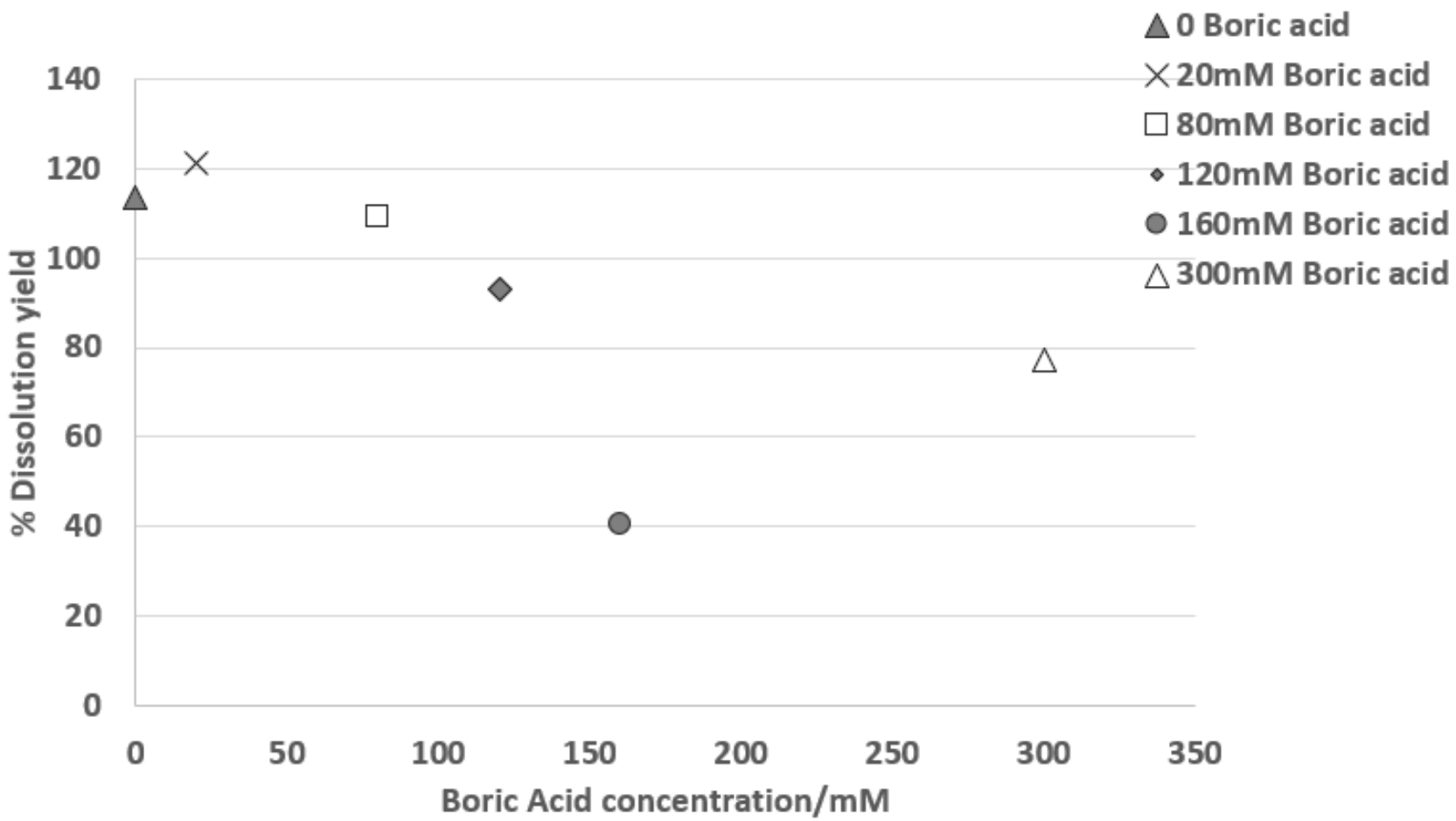

Conclusions

- We can have absorption of boric acid in the surface, blocking the surface.
- Peroxoborates have different reactivity than free Hydrogen peroxide.

Acknowledgments

The Swedish Centre for Nuclear Technology (SKC) is gratefully acknowledged for financial support.

Thank you for your attention

OPTIMISING ELECTROSTATIC PRECIPITATORS FOR SEVERE ACCIDENT SCENARIOS: IMPACT OF KEY OPERATIONAL PARAMETERS

Satish Basnet[1], Olli Sippula[1] and Anna Lähde[1]
University of Eastern Finland
FI-70211, Kuopio, Finland
satish.basnet@uef.fi; olli.sippula@uef.fi; anna.lahde@uef.fi

ABSTRACT

Electrostatic precipitation (ESP) is widely recognized as an efficient method for removing aerosol particles and is frequently employed in industrial applications. In this study, a laboratory-scale tubular ESP was designed and operated in dry and wet configurations to investigate the migration and capture of caesium iodide (CsI) aerosols relevant to nuclear accident scenarios. ESP performance was assessed through measurements of overall particle removal efficiency while key operational parameters were systematically varied. Factors investigated included discharge-electrode geometry, inlet particle concentration, and interactions between suspended particles and water droplets in the wet configuration. Three electrode geometries (fishbone, sawtooth, and wire) were compared. Among these, the electrodes with protrusion (i.e., fishbone and sawtooth) achieved the best collection efficiencies in both dry and wet configurations for particles larger than 0.1 μm. The higher efficiency of the wet ESP was due to aggregation of the particles with water droplets, which improved removal relative to the dry mode. These efficiencies were maintained over a voltage range of 10–18 kV and temperatures from ambient up to 300 °C. These results highlight the importance of electrical, geometric, and physicochemical parameters in determining ESP effectiveness. The findings provide practical guidance for optimizing ESP design and operation for the mitigation of iodine-containing and other radioactive aerosols, with implications for both nuclear safety systems and broader industrial applications where fine-particle control is essential.

KEYWORDS
Electrostatic precipitators, electrode geometry, CsI, aerosol, severe accidents

1. INTRODUCTION

The effective removal of radioactive aerosols plays a crucial role in mitigating radiological risks during nuclear power plant accidents. Following the failure of containment barriers, volatile fission products such as caesium and iodine readily form aerosols that can be transported throughout the containment and potentially released into the environment [1]. These particles dominate airborne release and are particularly difficult to remove using traditional methods such as filtration, natural deposition, or containment sprays due to their relatively small size, which is typically below a micron [2], [3]. The difficulty with iodine is further associated with its frequent phase change from gaseous to solid and vice versa during the accident. As a result, the development of advanced technologies that can efficiently capture such aerosols under accident-relevant conditions remains a crucial objective for enhancing nuclear safety.

Electrostatic precipitation (ESP) represents one of the most promising active techniques for fine particle removal. The principle of ESP operation is based on imparting an electric charge to suspended particles and collecting them on surfaces maintained at an opposite potential [4]. Owing to their high efficiency, scalability, and long operational history, ESPs have been widely adopted in industrial applications such as

power generation, metallurgy, and waste incineration for controlling particulate emissions [5], [6], [7]. Their application to nuclear systems, however, has only recently gained interest as a possible method for reducing the airborne source term during severe accidents and filtered containment venting [3], [8], [9]. Experimental and modeling studies have indicated that properly designed ESPs can achieve over 90–99% removal efficiency for caesium iodide (CsI) and similar aerosols, even under high-temperature, steam-rich, or radiation-intense environments [8], [9], [10].

Despite these advantages, the practical application of ESPs to nuclear containment systems still faces several challenges. The efficiency of collection depends strongly on particle charge distribution, gas composition, and electric field strength, all of which vary under accident conditions. In addition, most previous investigations have focused on industrial dust or soot aerosols, with limited studies addressing fission product analogs such as caesium iodide [10], [11], [12]. The influence of electrode geometry, applied voltage, and temperature on ESP performance for fission product aerosols remains insufficiently understood. Similarly, the comparative performance between dry and wet ESP configurations has not been systematically evaluated under identical test conditions. Wet ESPs, which utilize water films or droplets to wash collection surfaces continuously, can mitigate re-entrainment and fouling [13]; however, their interaction with particle charging and collection processes requires detailed examination [10], [11], [14].

To address these research gaps, the present study investigates the removal of CsI aerosols using both dry and wet tubular electrostatic precipitators developed at the laboratory scale. Three discharge electrode types, wire, sawtooth, and fishbone, were tested across three voltages (10, 15, and 18 kV). The performance was assessed based on corona discharge characteristics, aerosol migration behavior, and total collection efficiency. The results provide insights into the effect of electrode geometry, electric field intensity, and their interactions on ESP operation under nuclear-relevant conditions. The findings from this study will contribute to the ongoing efforts to enhance source term mitigation systems by integrating ESP technology into containment and venting architectures. Understanding how particle charge, collection area, droplet, and water flow interaction influences removal efficiency can guide the design of more robust and efficient filtration systems for severe accident management. Moreover, the results may be applied to broader applications of ESP beyond the traditional nuclear industry and into small modular reactors, along with the high-temperature and droplet-laden environments.

2. EXPERIMENTAL IMPLEMENTATION

2.1. Electrostatic Precipitator Configuration

The study was conducted to evaluate the collection performance of laboratory-scale ESPs for CsI aerosols under controlled flow, temperature, and voltage conditions. Both dry and wet ESP configurations were examined to compare their performance in removing aerosols representative of fission product particles.

Two ESP systems, dry and wet, were designed with identical tubular geometries to enable direct comparison of their operating characteristics. Each ESP consisted of a galvanized steel cylindrical collection tube with an internal diameter of 100 mm and a length of 1000 mm. The discharge electrode was positioned axially at the center of the tube, supported by a plastic insulator. The discharge electrode was interchangeable to allow testing of three different geometries: a wire electrode with a straight metal wire of 1 mm diameter, a sawtooth electrode with a stainless-steel stripe featuring evenly spaced triangular protrusions, and a fishbone electrode with a central spine and lateral, pointed branches.

For the wet ESP, a continuous thin film of water was maintained along the collection surface using a top-mounted nozzle system. The liquid flow rate was regulated at 1.5 l/min to ensure uniform coverage without droplet entrainment.

2.2. Electrical and Flow Conditions

All tests were conducted under direct current (DC) corona discharge using a high-voltage power supply (Genvolt 72030 series, 0–20 kV, 1.5 mA). Three applied voltages, 10, 15, and 18 kV, were selected to evaluate the impact of electric field intensity on charging and collection performance. The volumetric air flow rate was maintained at 15 l/min, corresponding to an average residence time of approximately 31 seconds inside the ESP.

Three temperature levels were selected to simulate varying thermal conditions (room temperature (25 °C), 100 °C, and 300 °C) post-severe accident for the generated aerosols. Desired temperatures were achieved by passing the aerosols through a tube furnace, which was monitored with K-type thermocouples. The aerosols were then cooled in a separate chamber before entering the ESP. This chamber, before the ESP, was further utilized as a mixing chamber for aerosols during experiments with water droplets.

For the wet ESP with water droplets (referred hereafter as droplet-assisted ESP), the influence of droplet interaction with particles was examined by introducing a controlled spray of fine mist of water droplets generated via an ultrasonic atomizer. The average droplet diameter was approximately 5 μm. The interactions between droplets and CsI particles were analyzed through their aggregation and charge-neutralization behavior, which were observed indirectly as changes in the measured particle size spectra downstream.

2.3. Aerosol Generation and Characterization

High-purity CsI powder (99.9%, Sigma-Aldrich) was dissolved in Milli-Q water to prepare a 0.5% CsI solution. CsI aerosol was generated with an RBI Pyrosol and was carried with a controlled carrier nitrogen stream. Aerosol mass and number concentrations were continuously measured upstream and downstream of the ESP using an Electrical Low-Pressure Impactor (ELPI, Dekati). The instrument provided real-time data on particle size distribution and concentration over the 0.01–10 μm range.

The results are presented as a comparison between the inlet and outlet of the ESP from ELPI measurements, according to Eq.1, and defined as the filtration efficiency (η) of the ESP, based on the measured particle number.

$$\eta = \left(1 - \frac{Aerosol_{out}}{Aerosol_{in}}\right) \times 100 \quad (1)$$

3. RESULTS AND DISCUSSION

The measurements showed clear differences in the removal of CsI aerosol with different discharge electrode geometries, the applied voltages, and the ESP operating modes. Table 1 summarizes the removal efficiency of CsI aerosol (based on particle number concentration) under all tested configurations. The initial aerosol size distribution ranged primarily between 0.1 and 5 μm, with a geometric mean diameter of approximately 0.8 μm under baseline conditions. The wet ESP with the fishbone discharge electrode produced the highest mean particle number removal efficiency (≈ 99.6%) and the lowest variability (standard deviation ≈ 0.06%). The wire electrode, especially under dry and droplet-assisted modes, showed the largest variability and the lowest average efficiency among all configurations.

Table I. Summary of CsI aerosol experiments. The table reports ESP filtration efficiency for three ESP modes; each operated with three electrodes and at three different voltages. Geometric mean diameter (GMD) and geometric standard deviation (GSD) are derived from ELPI particle number

size distributions. Efficiency was calculated from upstream and downstream particle number concentrations.

ESP mode	Electrode type	Voltage (kV)	Mean particle number filtration efficiency (%)	GMD (nm)	GSD	Number of tests (n)
Dry	Wire	10	77.72	725.3	3.02	3
	Wire	15	92.92	390.1	2.81	3
	Wire	18	95.20	30.62	1.71	3
	Sawtooth	10	98.18	33.27	1.78	3
	Sawtooth	15	93.37	36.51	1.80	3
	Sawtooth	18	89.60	33.88	1.78	3
	Fishbone	10	95.74	29.19	1.75	3
	Fishbone	15	91.01	30.90	1.76	3
	Fishbone	18	95.70	31.54	1.75	3
Droplet-assisted	Wire	10	64.08	366.9	2.79	3
	Wire	15	90.54	242.5	2.68	3
	Wire	18	97.37	25.11	1.72	3
	Sawtooth	10	97.11	28.49	1.72	3
	Sawtooth	15	85.59	31.49	1.74	3
	Sawtooth	18	82.44	29.97	1.72	3
	Fishbone	10	98.12	27.13	1.71	3
	Fishbone	15	92.91	30.82	2.22	3
	Fishbone	18	95.16	27.81	1.69	3
Wet	Wire	10	73.76	461.4	3.67	3
	Wire	15	98.32	82.26	4.23	3
	Wire	18	99.47	24.61	1.63	3
	Sawtooth	10	99.38	26.60	1.68	3
	Sawtooth	15	97.80	25.96	1.62	3
	Sawtooth	18	96.24	27.21	1.64	3
	Fishbone	10	99.53	25.52	1.65	3
	Fishbone	15	99.64	26.22	1.63	3
	Fishbone	18	99.58	25.12	1.66	3

3.1. Performance of dry ESPs

Under dry conditions, removal efficiency strongly depended on electrode shape and applied voltage (Figure 1). The fishbone electrode provided stable, high removal across all voltages tested, with the smallest standard deviation among the dry ESPs, see Table 1. Downstream size distributions (Figure 2b) show nearly complete removal of particles below 1μm for all applied voltages, suggesting efficient charging and uniform migration of the particles to the collection surface. This indicates a uniform electric field distribution and stable corona conditions along the fishbone electrode, which enhance particle charging and transport across the cross-section. It also agrees with observations from surface-enhanced corona electrodes described by Bendilmi et al. (2022).

The sawtooth electrode showed an interesting variable voltage dependence. At 10 kV, the removal efficiency exceeded that at 18 kV (98.2%) (Figure 1). This suggests that local field enhancement at the sawtooth tips can compensate for lower overall voltage, maintaining sufficient ion production and charging for migration. This result highlights that electrode geometry can counterbalance lower voltage under certain conditions [16].

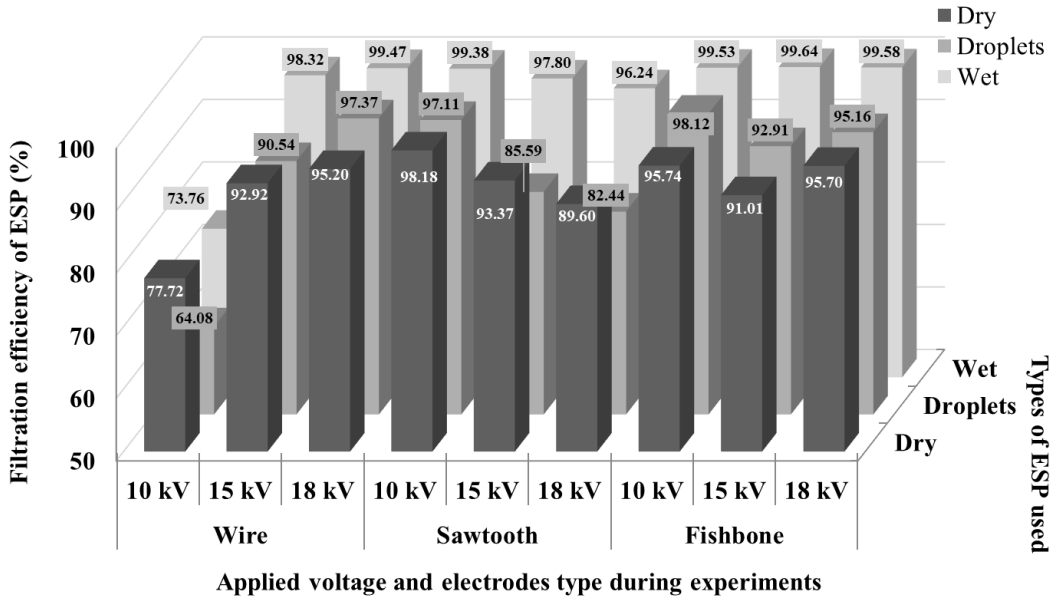

Figure 1. Filtration efficiency of the ESP as a function of applied voltage and electrode geometry. Results are shown for wire, sawtooth, and fishbone electrodes at 10, 15, and 18 kV under dry, droplet-assisted, and wet operating conditions.

In contrast, the wire electrode exhibited the poorest performance under dry conditions. At 15 kV, efficiency dropped to roughly 71.8%. The ELPI spectra (Figure 2b) show that a measurable fraction of mid-size particles remained downstream. This indicates that a simple wire-type electrode lacks sufficient ion dispersion or field uniformity for effective charging and migration, particularly under corona conditions that may be unstable or spatially non-uniform. Under dry ESP, a uniform field or proper geometry is critical to reach high and consistent removal [17], [18]. These results confirm that dry ESP performance can be limited by non-uniform corona discharge and poor ion distribution. Such limitations are well documented in particulate control literature, especially for fine or resistive aerosols.

3.2. Performance of the droplet-assisted ESP

Introducing droplets changed the aerosol removal dynamics (Figures 1). The fishbone electrode maintained high efficiency (> 92.9%) across all voltages in droplet-assisted mode. The outlet ELPI spectra (Figure 2d) show almost complete removal of particles above ~300 nm diameters. This indicates that droplet presence did not prevent charging and migration; instead, the system maintained very good collection efficiency, which was further aided by droplet–particle interactions or aggregation.

Once again, for the sawtooth electrode, the highest performance was recorded at the lowest experimental voltage of 10 kV (≈ 97.1%). The strong electric field at the sawtooth tips and the sharp edges around it may

have offset droplet-induced charge losses, maintaining sufficient ion concentration for charging [19]. By contrast, the wire electrode under droplet conditions exhibited poor performance at 10 kV, with removal dropping to ~64.1%. The outlet spectra show residual particles in the 200–500 nm range, suggesting that droplets may have neutralized some particle charge or scavenged ions before charging could occur, thereby reducing net charge on CsI aerosol. This phenomenon likely impaired the migration effectiveness of particles toward the collection surface.

These observations reveal that droplet injection into the ESP does not guarantee improved performance. The benefit depends strongly on electrode geometry and applied field. Wire electrodes under low voltage appear particularly vulnerable to droplet-induced charge losses. The results align with prior studies on wet ESPs, indicating that droplet–particle interactions and ion scavenging can influence collection efficiency depending on geometry and operating conditions [19], [20], [21], [22].

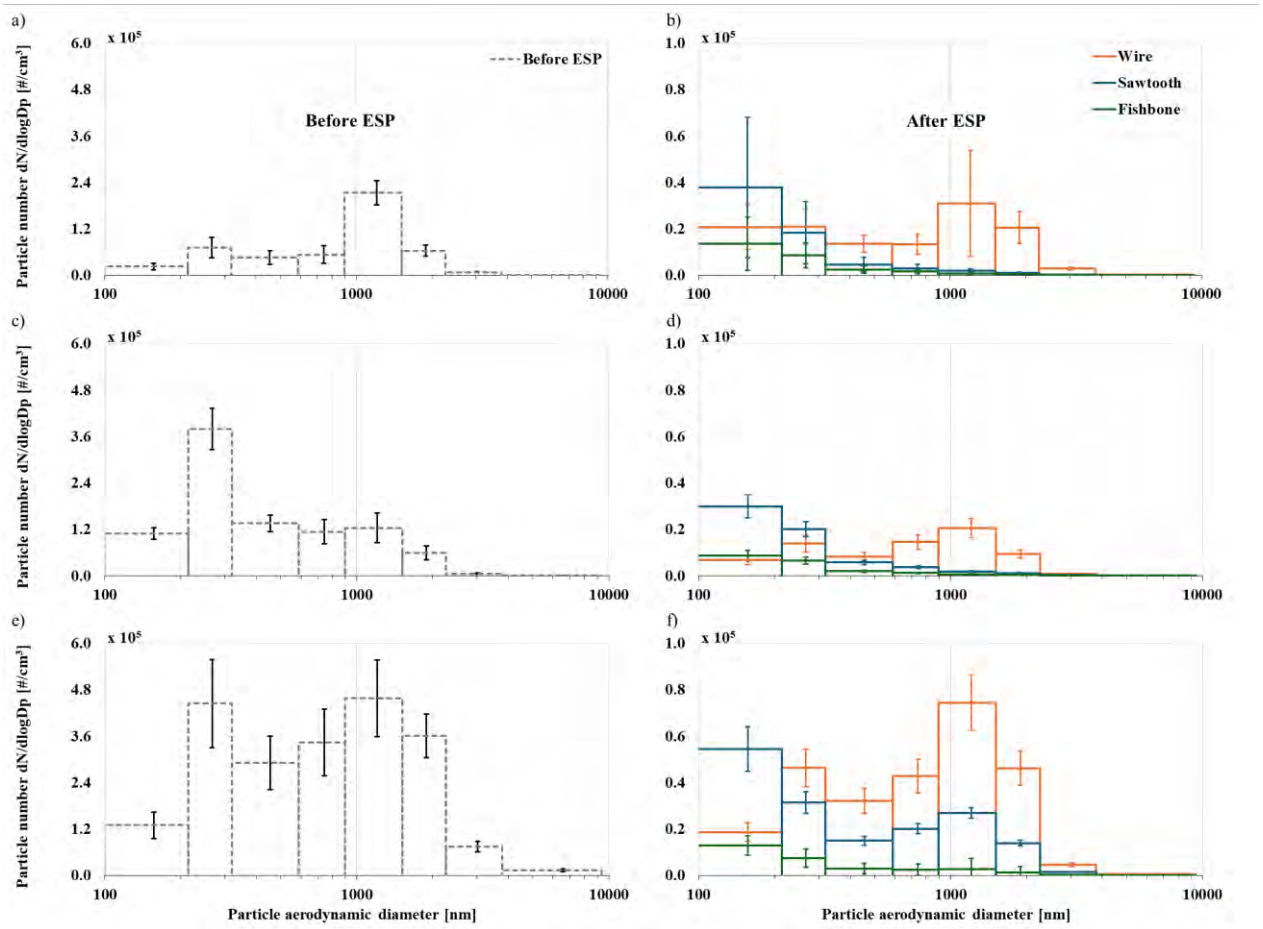

Figure 2. Average particle size distributions measured by the ELPI upstream (left) and downstream (right) of the ESP. Data are averaged over applied voltages (10 - 18 kV) and all temperatures. Panels a and b show the dry ESP. Panels c and d show the droplet-assisted ESP. Panels e and f show the wet ESP. Downstream results (After ESP) compare wire, sawtooth, and fishbone electrodes. Error bars indicate standard deviation.

3.3. Performance of wet ESP

The wet mode produced the most consistent and highest removal efficiencies for CsI aerosol (Figure 1). The wet ESP operation enhanced performance across all geometries, but the degree of improvement strongly depended on geometry and applied field, as shown in the previous studies [11], [23]. The combination of fishbone geometry and wet film proved most effective and stable across all applied voltages. The downstream ELPI spectra (Figure 2f) and the reduction efficiency (Figure 1) show the removal of particles across the full measured size range. The fishbone electrode in wet mode reached nearly 100% removal at all tested voltages (≈ 99.6%). This is due to the combination of a continuous conductive water film and a uniform field geometry, which stabilizes a corona discharge, enhances charge transfer, and suppresses particle re-entrainment or back-corona [11]. The sawtooth electrode in wet mode also performed well, with efficiencies above 96.2% for all voltages. The water film likely helped distribute charge uniformly from the sawtooth tips and improved particle adhesion to the wet surface. The results support conclusions from recent studies that wet ESPs outperform dry ESPs in removing fine or resistive particles and mitigate common issues such as dust cake build-up or re-entrainment [13], [19].

The wire electrode in wet mode was affected by the applied voltage, unlike with other geometries, especially at 10 kV, when efficiency dropped to ~73.8%. The ELPI spectra show residual mid-size particles under these conditions. However, at 15 and 18 kV, the wire-wet ESP reached high efficiency (≥98.3%). These results indicate that the water film alone cannot fully compensate for weak or non-uniform fields in simple wire geometries; sufficient applied voltage remains necessary to ensure efficient charging and migration [24].

3.4. Implication of Particle Size, Voltage, and ESP Design

Size-resolved efficiency data (Figure 2) show that particle aerodynamic diameter influences removal significantly. In dry and droplet-assisted modes with wire electrodes, submicron particles, particularly those around and below ~300 nm, were less efficiently removed. These results align with the known behavior of ESPs' charging behavior, reducing migration velocity, and collection probability [25], [26], [27]. In contrast, wet mode using fishbone or sawtooth electrodes achieved near-complete removal across the entire measured size range (100 nm and above). Similar results have been reported by [9], [11], [23]. This is achieved by combining charging with conductive film deposition, which enhances charge transfer efficiency, reduces re-entrainment, and mitigates back-corona [11], [13].

The dataset shows a clear effect of applied voltage on removal efficiency. Across all conditions (both dry and wet ESPs and all electrode types), the overall efficiency increased from ≈ 86.4% at 10 kV to ≈ 98.6% at 18 kV. The increase reflects stronger ion generation, higher electric field strength, and therefore increased migration velocity of charged particles. In size-resolved data, efficiencies for the removal of particles above a few hundred nanometers improved notably with higher voltage under all tested electrode geometries. However, voltage did not always dominate. In all experiments with sawtooth geometry, the low voltage (10 kV) outperformed the higher voltage. For the fishbone electrode, filtration efficiencies changed with the change in voltage, but the variation was small and depending on the ESP type, the lower voltage could already achieve the maximum efficiency (Figure 1). This indicates that electrode geometry can compensate for lower applied voltage by creating locally enhanced fields, especially in tip-type electrodes [12], [19]. These observations underscore the interplay between applied field, electrode design, and particle dynamics.

Based on the present data, the optimal configuration for a laboratory-scale ESP treating CsI aerosol combines a fishbone discharge electrode, a wet collection surface, and a moderate voltage (≥ 10 kV). This configuration produces high removal efficiency (> 99.5%) with low variability across tested conditions. The results suggest that such an ESP would perform robustly under a wide range of operational conditions, including variations in particle size distribution, aerosol load, and possibly environmental parameters (e.g.,

humidity). These findings support the potential application of wet ESPs for the removal of radioactive aerosol analogs (such as CsI) in nuclear safety systems. The high efficiency, stability, and robustness suggest that wet ESP could be integrated into source-term mitigation or filtered venting architectures, provided that operational conditions (voltage, water supply, corrosion resistance) are properly managed.

4. CONCLUSIONS

The experiments demonstrate that CsI aerosol removal depends strongly on electrode geometry, operating mode, and applied voltage. The wet ESP equipped with a fishbone electrode delivered the highest and most stable performance. Mean removal efficiency remained close to 99 % across all voltages, and the variability across repeated tests stayed low. The sawtooth electrode also performed well in wet mode and maintained high efficiency even at reduced voltage. The wire electrode showed the highest sensitivity to voltage and operating mode. It required a higher voltage to reach efficiencies comparable to the two structured electrodes.

With three different ESP types, where the individual ESP was tested with three different types of electrodes and operated at three different voltages, the wet ESP demonstrated improved performance for all electrode types. Dry operation showed that the charging environment is dependent on the electrode geometry, while droplet-assisted operation altered the charging behavior. The water film in the wet system stabilized the corona, reduced local discharge fluctuations, and enhanced particle adhesion. The fishbone and sawtooth electrodes showed the highest removal across the full-size range. The wire electrode benefited when operated at a higher voltage. The size-resolved data confirm that wet operation controls both submicron and micron-size CsI particles. These findings demonstrate that a wet ESP equipped with a fishbone electrode and operating at voltages above 15 kV yields the most robust configuration for CsI aerosol control. This setup produces high efficiency, low variability, and minimal sensitivity to operating conditions. These characteristics make it suitable for applications that require reliable mitigation of radioactive aerosols.

Future work should quantify the long-term stability of wet ESP operation and examine how film thickness, water conductivity, and flow rate influence particle removal. Additional studies should investigate how mixed aerosols containing CsI and other fission products respond to wet and droplet-assisted charging. Experiments under transient voltage conditions and fluctuating inlet concentrations would support the evaluation of ESP robustness during accident scenarios. Computational modelling of particle charging and migration in structured electrodes would help optimize electrode design for next-generation mitigation systems.

ACKNOWLEDGMENTS

Funding: The Doctoral Education Network supports this work under the SAFER2028 (DENSE) project (VYR REST2028, grant no. 29350001281).

REFERENCES

[1] L. Högberg, “Root Causes and Impacts of Severe Accidents at Large Nuclear Power Plants,” *Ambio*, vol. 42, no. 3, p. 267, Apr. 2013, doi: 10.1007/S13280-013-0382-X.

[2] J. Ahad, M. Ahmad, A. Farooq, K. Waheed, and N. Irfan, “Removal of iodine by dry adsorbents in filtered containment venting system after 10 years of Fukushima accident,” *Environmental Science and Pollution Research*, vol. 30, no. 30, pp. 74628–74670, Jun. 2023, doi: 10.1007/S11356-023-27485-1/TABLES/3.

[3] M. E. Moore, M. E. Keillor, D. M. Kasparek, A. R. Day, and B. D. Glasgow, “Electrostatic precipitator collection efficiency studies using atmospheric radon progeny as aerosol

analogs for nuclear explosion radionuclides," *J Environ Radioact*, vol. 270, p. 107306, Dec. 2023, doi: 10.1016/J.JENVRAD.2023.107306.

[4] J. H. Turner *et al.*, "Electrostatic Precipitators," in *EPA Air Pollution Control Cost Manual, Sixth Edition*, D. C. Mussatti, Ed., North Carolina, 2002, ch. 6/3, pp. 690–758.

[5] E. Sokolovskij, A. Kilikevičius, A. Chlebnikovas, J. Matijošius, and D. Vainorius, "Innovative Electrostatic Precipitator Solutions for Efficient Removal of Fine Particulate Matter: Enhancing Performance and Energy Efficiency," *Machines 2024, Vol. 12, Page 761*, vol. 12, no. 11, p. 761, Oct. 2024, doi: 10.3390/MACHINES12110761.

[6] V. Arrondel, G. Bacchiega, and M. Hamlil, "The Electrostatic Precipitator External Parameters at the Heart of Dust Collection Efficiency Performance: Coal Characteristics, Combustion Quality and SCR Chemical Process," *Int. J. Plasma Environ. Sci. Technol.*, vol. 6, no. 1, pp. 25–32, Mar. 2012.

[7] S. H. Kim and K. W. Lee, "Experimental study of electrostatic precipitator performance and comparison with existing theoretical prediction models," *J Electrostat*, vol. 48, no. 1, pp. 3–25, Nov. 1999, doi: 10.1016/S0304-3886(99)00044-3.

[8] S. Basnet, A. Jäntti, P. Yli-Pirilä, M. Kortelainen, O. Sippula, and A. Lähde, "Performance of dry electrostatic precipitator for the removal of CsI aerosol particles under simulated severe nuclear accident conditions," *Nuclear Engineering and Design*, vol. 445, p. 114440, Dec. 2025, doi: 10.1016/j.nucengdes.2025.114440.

[9] M. Gouëllo, J. Hokkinen, T. Kärkelä, P. Rantanen, and A. Auvinen, "Development and qualification of an innovative wet electrostatic precipitator in view of gaseous iodine filtration on laboratory-scale," *Nuclear Engineering and Design*, vol. 327, no. August 2017, pp. 7–21, 2018, doi: 10.1016/j.nucengdes.2017.12.002.

[10] C. Teng, X. Fan, and J. Li, "Effect of charged water drop atomization on particle removal performance in plate type wet electrostatic precipitator," *J Electrostat*, vol. 104, p. 103426, Mar. 2020, doi: 10.1016/J.ELSTAT.2020.103426.

[11] Z. Yang *et al.*, "Fine particle migration and collection in a wet electrostatic precipitator," *J Air Waste Manage Assoc*, vol. 67, no. 4, pp. 498–506, 2017, doi: 10.1080/10962247.2016.1260074.

[12] M. Badran and A. M. Mansour, "Evaluating Performance Indices of Electrostatic Precipitators," *Energies 2022, Vol. 15, Page 6647*, vol. 15, no. 18, p. 6647, Sep. 2022, doi: 10.3390/EN15186647.

[13] J. Y. Syu *et al.*, "The Applications and Distinctions of Three Different Material Collection Plates in Wet Electrostatic Precipitator," *Aerosol Air Qual Res*, vol. 22, no. 10, pp. 220133-, Oct. 2022, doi: 10.4209/AAQR.220133/METRICS.

[14] M. Molaei Najafabadi, H. Basirat Tabrizi, A. Aramesh, and M. A. Ehteram, "Effects of geometric parameters and electric indexes on performance of a vertical wet electrostatic precipitator," *J Electrostat*, vol. 72, no. 5, pp. 402–411, Oct. 2014, doi: 10.1016/J.ELSTAT.2014.06.005.

[15] M. S. Bendilmi, T. Zeghloul, Z. Ziari, K. Medles, and L. Dascalescu, "Experimental characterization of electric potential uniformity at the surface of polymer plates corona charged by multiple-row needle-type electrodes," *J Electrostat*, vol. 115, p. 103656, Jan. 2022, doi: 10.1016/J.ELSTAT.2021.103656.

[16] C. Zheng *et al.*, "Experiments on Enhancing the Particle Charging Performance of an Electrostatic Precipitator," *Aerosol Air Qual Res*, vol. 19, no. 6, pp. 1411–1420, Jun. 2019, doi: 10.4209/AAQR.2018.11.0400.

[17] Z. Ning *et al.*, "Electrode geometry optimization in wire-plate electrostatic precipitator and its impact on collection efficiency," *J Electrostat*, vol. 80, pp. 76–84, Apr. 2016, doi: 10.1016/J.ELSTAT.2016.02.001.

[18] D. Brocilo, J. Podlinski, J. S. Chang, J. Mizeraczyk, and R. D. Findlay, "Electrode geometry effects on the collection efficiency of submicron and ultra-fine dust particles in spike-plate electrostatic precipitators," *J Phys Conf Ser*, vol. 142, p. 012032, Dec. 2008, doi: 10.1088/1742-6596/142/1/012032.

[19] C. Zheng *et al.*, "Current density distribution and optimization of the collection electrodes of a honeycomb wet electrostatic precipitator," *RSC Adv*, vol. 8, no. 54, pp. 30701–30711, Aug. 2018, doi: 10.1039/C8RA04765K.

[20] R. C. Xu, A. K. Sharma, E. Ozdemir, S. Miwa, and S. Suzuki, "Experimental investigation on effective aerosol scavenging using different spray configurations with pre-injection of water mist for Fukushima Daiichi decommissioning," *Nuclear Science and Techniques 2024 35:5*, vol. 35, no. 5, pp. 42-, Apr. 2024, doi: 10.1007/S41365-024-01401-9.

[21] L. Su, Q. Du, M. Tang, Q. Ou, and D. Y. H. Pui, "Effects of Particle Hydrophilicity and Morphology on Aerosol Scavenging in a Wet Electrostatic Scrubber," *Aerosol Air Qual Res*, vol. 19, no. 10, pp. 2331–2340, Oct. 2019, doi: 10.4209/AAQR.2019.04.0207.

[22] Z. Yang *et al.*, "Developing a Compact Particle Collector by Integrating a Wet Electrostatic Precipitator and an Inertia Mist Eliminator," *Aerosol Air Qual Res*, vol. 21, no. 12, pp. 210209-, Dec. 2021, doi: 10.4209/AAQR.210209/METRICS.

[23] M. M. Badami, R. Tohidi, M. Aldekheel, V. J. Farahani, V. Verma, and C. Sioutas, "Design, optimization, and evaluation of a wet electrostatic precipitator (ESP) for aerosol collection," *Atmos Environ*, vol. 308, p. 119858, Sep. 2023, doi: 10.1016/J.ATMOSENV.2023.119858.

[24] M. S. Kim *et al.*, "Performance Evaluation of a Novel Pilot-Scale Wet Electrostatic Precipitator in a Bio-Drying-Assisted Solid Recovered Fuel (SRF) Generation Plant: Particulate Matter (PM) Collection Efficiency," *Sustainability 2022, Vol. 14, Page 8702*, vol. 14, no. 14, p. 8702, Jul. 2022, doi: 10.3390/SU14148702.

[25] W. C. Hinds, *Aerosol Technology, Properties, Behaviour, and Measurement of Airborne Particles*, 2nd edition. New York: John Wiley & Sons Inc., 1999.

[26] A. Hernandez-Sierra, F. J. Alguacil, and M. Alonso, "Unipolar charging of nanometer aerosol particles in a corona ionizer," *J Aerosol Sci*, vol. 34, no. 6, pp. 733–745, Jun. 2003, doi: 10.1016/S0021-8502(03)00033-8.

[27] A. Jaworek, A. Krupa, and T. Czech, "Modern electrostatic devices and methods for exhaust gas cleaning: A brief review," *J Electrostat*, vol. 65, no. 3, pp. 133–155, Mar. 2007, doi: 10.1016/J.ELSTAT.2006.07.012.

Optimizing Electrostatic Precipitators for Severe Accident Scenarios:

Impact of Key Operational Parameters

Satish Basnet[1], Olli Sippula[1,2], Anna Lähde[1]

[1] Department of Environmental and Biological Sciences, University of Eastern Finland, Kuopio
[2] Department of Chemistry and Sustainable Technology, University of Eastern Finland, Joensuu

Severe Accidents | CsI Aerosols | Electrostatic Precipitation | FCVS

Motivation: Severe Nuclear Accidents & Radioactive Releases

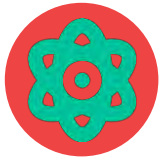

Fission Product Release

Degraded fuel releases Cs and I into containment — as gases and aerosols. Both can be discharged to the environment through containment venting.

Current FCVS Limitations

Filtered Containment Venting Systems (FCVS) are effective for large particles but struggle with submicron iodine oxide aerosols in the most-penetrating size range.

Enhancement Needed

Post-Fukushima reinforcement of FCVS required. Fine-particle control remains a critical gap. ESP offers a promising complementary technology due to:

- High efficiency for fine and ultrafine particles.
- Low pressure drop, crucial for venting systems.
- Can operate at high temperatures and in humid/corrosive environments.
- A promising complementary technology to enhance FCVS.

Why CsI? Iodine & Cesium Chemistry in Containment

Iodine Speciation

- CsI (particulate) — non-volatile, dissolves in water
- Gaseous I_2 — from radiolytic oxidation of dissolved I^-
- Organic iodine (CH_3I) — surface & organic reactions
- Iodine oxides — radiolysis → submicron aerosols
- Continuous interconversion creates dynamic aerosol population

Radiological Impact

Iodine (I)

Short-term health impact — thyroid uptake. Requires rapid intervention.

Cesium (Cs)

Long-term environmental contamination. Persists for decades in soil.

Submicron aerosols

Most hazardous — evade conventional filters, deep lung penetration.

CsI (focus)

Major particulate form. Stable, non-volatile, water-soluble — ideal ESP target.

Research Objectives

This study systematically investigates how ESP design parameters govern CsI aerosol removal efficiency under accident-relevant conditions.

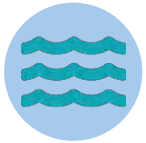

Operating Mode

- Dry
- Droplet-assisted (~5 µm diameter water mist)
- Wet ESP operation for re-entrainment prevention and back-corona suppression

Electrode Geometry

- Fishbone (multiple sharp points)
- Sawtooth (strip with trapezoidal protrusions)
- Wire (1 mm diameter) discharge electrodes for corona uniformity and particle charging efficacy

Applied Voltage

- 10 kV
- 15 kV
- 18 kV DC on corona stability, space charge, and size-resolved collection efficiency

Temperature Effects

- Room temperature
- 100 °C
- 300°C to cover accident-relevant thermal evolution in containment

Experimental Setup & Aerosol Generation

Tubular ESP Specifications

Collection tube:	Galvanized steel, Ø 100 mm, L = 1000 mm
Flow rate:	15 lpm (residence time ~31 s)
Voltage supply:	10, 15, 18 kV DC (Genvolt 72030)
Temperature:	Room temp / 100°C / 300°C
Water film (wet):	1.5 lpm – continuous wall flushing
Aerosol:	CsI 0.5 wt% solution (Pyrosol 7901)
Carrier gas:	Nitrogen
Measurements:	ELPI + SMPS (0.01–10 µm)

Flow Path

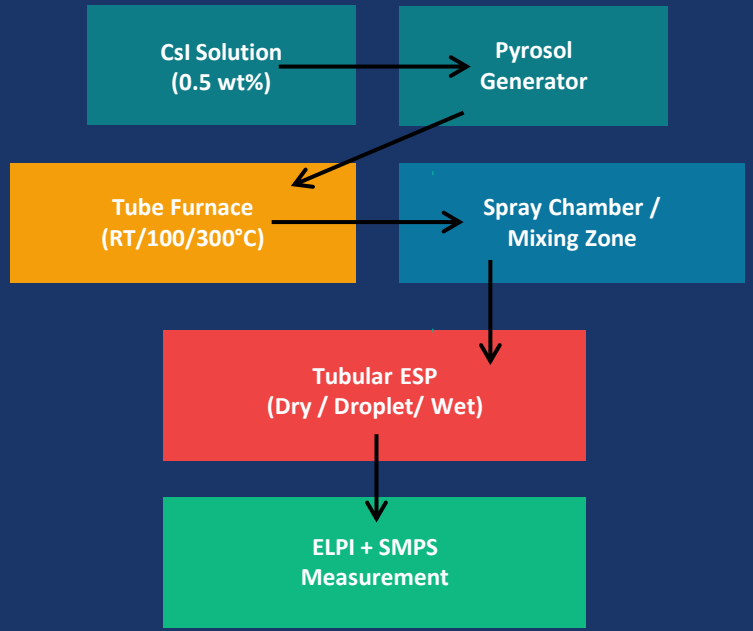

Discharge Electrode Geometries

Wire Electrode

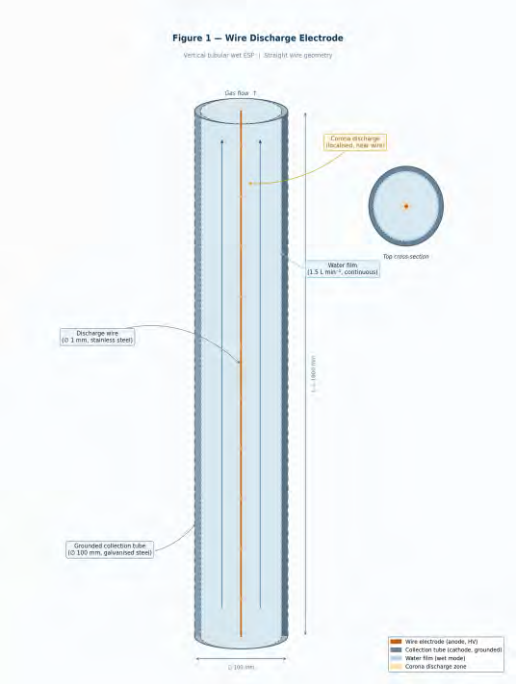

Sawtooth Electrode

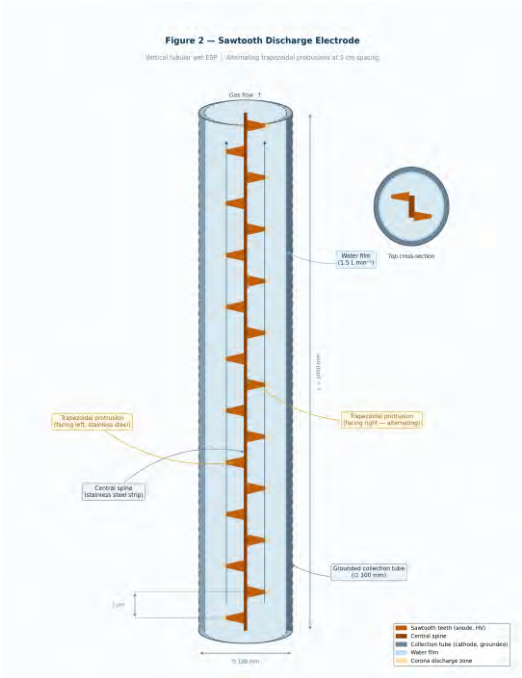

Fishbone Electrode

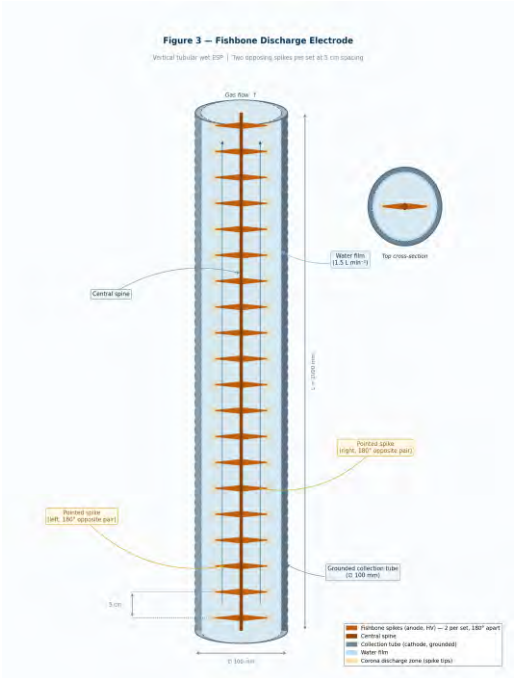

Result 1: Electrode Geometry Dominates Performance

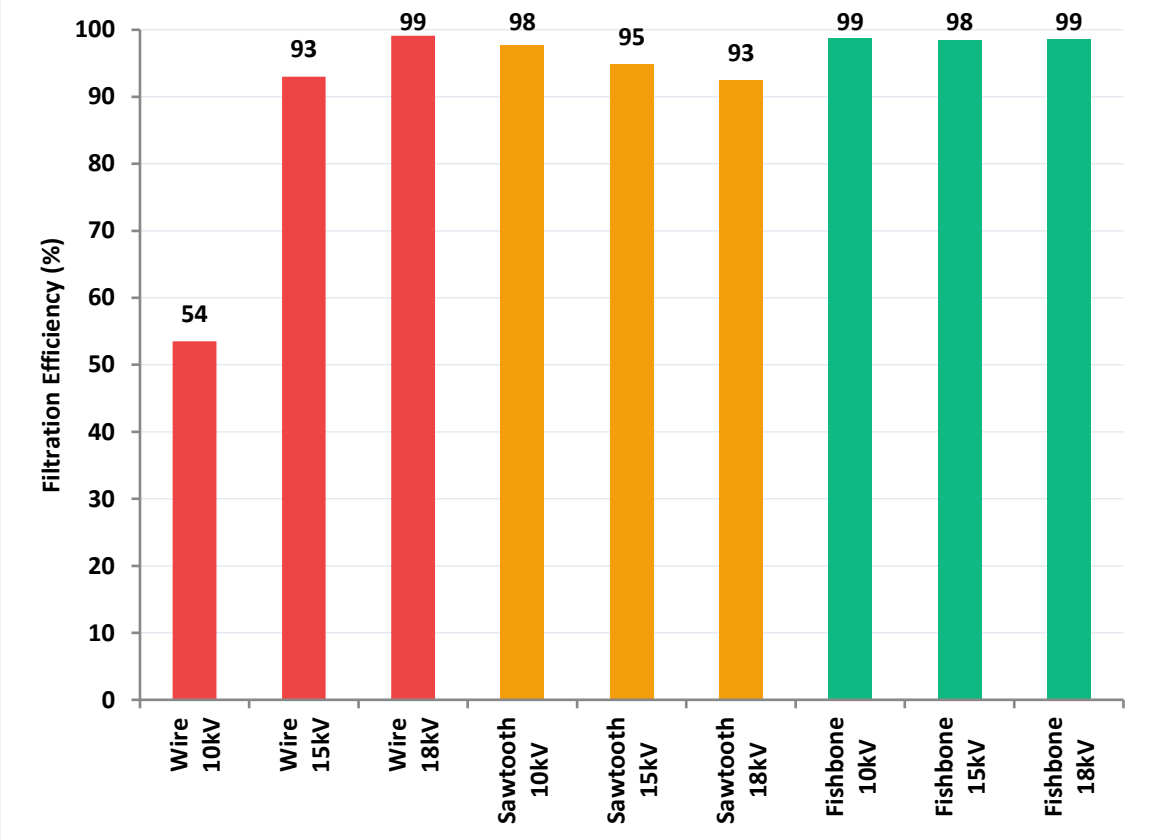

Wet Mode — Filtration Efficiency (%) by Electrode & Voltage

Performance Hierarchy:

Fishbone

Consistently >97%
All voltages robust

Sawtooth

88–99.7%
Voltage-dependent

Wire

44–99%
Highly variable

Fishbone > Sawtooth >> Wire
Consistent across all modes & temperatures

Result 2: Wet Operation — Why It Outperforms Dry & Droplet-Assisted

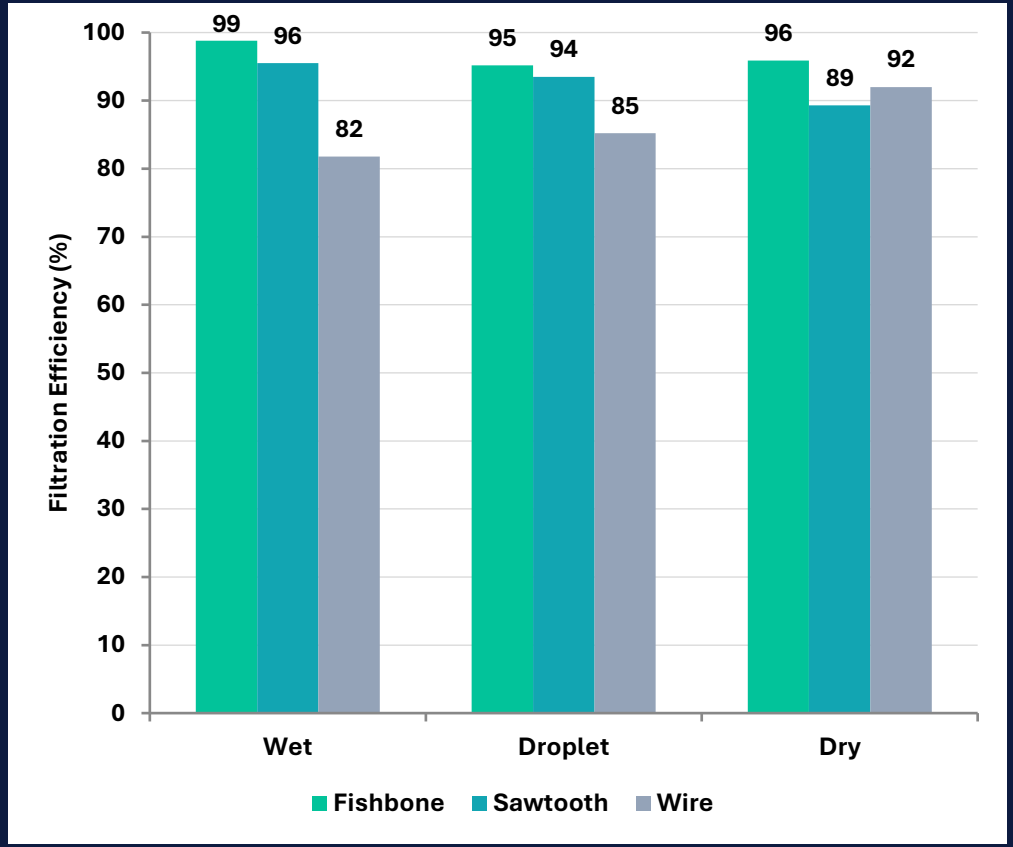

Mean Filtration Efficiency (%) by Operating Mode & Electrode (all voltages & temperatures)

Why Wet Mode Wins:

- Prevents back-corona — conductive water film maintains consistent collection surface
- Eliminates re-entrainment — collected particles continuously washed away
- Stabilizes corona discharge — suppresses space charge buildup on plates
- Critical for CsI — water solubility ensures permanent capture and retention

Water film quality is as critical as corona strength!

Result 3: Voltage & Temperature as Conditional Drivers

Voltage Effects

Fishbone (wet):

Plateaus >99% across 10–18 kV. Optimal charging achieved even at 10 kV — low voltage sufficient with structured electrode.

Wire electrode:

Acutely voltage-dependent. Efficiency jumps from 10→15 kV but may decline at 18 kV (corona saturation / space charge opposition).

Key insight:

Higher voltage is NOT always better. Space charge buildup at 18 kV can hinder particle migration, especially for wire electrodes.

Temperature Effects

300°C enhances structured electrodes:

Reduced gas density → longer electron mean free path → stable corona, higher ion mobility → better diffusion charging.

Wire electrode at high T:

May worsen performance. Thermal effects disrupt already marginal corona stability; ionic agitation increases turbulent mixing.

Practical implication:

Temperature benefit is conditional — only realized when a stable, uniform corona exists. Electrode design determines the thermal response.

Top-Performing Configurations (>99% Efficiency)

ESP Mode	Electrode	Voltage (kV)	Temperature	Efficiency (%)	GMD Out (nm)
Wet	Fishbone	10	300°C	**99.90 ★**	24.2
Wet	Fishbone	15	300°C	**99.28**	26.5
Wet	Fishbone	18	Room temp	**99.29**	26.0
Wet	Sawtooth	15	300°C	**99.66**	24.1
Wet	Sawtooth	10	300°C	**99.78**	30.6

★ Best configuration: Wet + Fishbone + 10 kV + 300°C → 99.90% efficiency, outlet GMD = 24 nm

Result 4: Size-Selective Collection & Outlet Size Distributions

Inlet aerosol GMD: 400–800 nm (accumulation mode) → Best-case outlet GMD: 20–40 nm (nucleation/Aitken mode)

Charging Physics

> 300 nm

Field charging dominates — charge ∝ dp^2. Strong electrophoretic force → efficient collection.

< 100 nm

Diffusion charging — low charge levels, low migration velocity, drag dominates → nanoparticle escape.

100–300 nm

Transition zone — efficiency minimum. Most challenging size range for any ESP.

Practical Implications

- GMD shift from ~600 nm to 20–30 nm means mass concentration is reduced far more than number concentration alone suggests
- Wire electrode in dry mode: outlet GMD can exceed inlet GMD — re-entrainment of agglomerates or selective small-particle removal
- Even with near-100% number efficiency, some nanoparticle penetration remains — multi-stage filtration may be required for maximum DF
- Fission product aerosols span 0.1–10 µm; ESP alone may not capture all freshly nucleated particles without condensational pretreatment

Result 5: Particle Charge Analysis — Mechanistic Evidence

Measuring charge on penetrating particles reveals WHETHER failure is charging or migration — a key diagnostic beyond efficiency alone.

High Charge on Penetrators

(Fishbone — Wet)

Penetrating nanoparticles carry measurable positive charge — charging was successful. Escape is due to boundary layer slippage or micro-scale re-entrainment, **NOT** charging failure. Performance limited by hydrodynamics.

Intermediate Charge

(Sawtooth — Droplet/Dry)

Mixed charging efficacy. Some particles escape uncharged, others with partial charge. Suggests non-uniform field zones between sawtooth protrusions. Design is functional but not optimal.

Near-Zero Charge

(Wire — Dry/Droplet)

Primary failure mode is **INCOMPLETE CHARGING**. Particles pass through the corona zone acquiring insufficient charge to respond to the electric field. Ion density too low in dead zones. Geometry is the root cause.

Temperature effect on charge: Fishbone shows increasing charge at 300°C (improved corona); Wire may show decreasing charge (corona disruption)

Mechanistic Summary: How Electrode Design Controls Performance

	Corona Discharge	Particle Charging	Space Charge	Migration & Collection
Fishbone	Dense, uniform multi-point ion cloud	Uniform across entire duct cross-section	Distributed → lower local density	Strong, uniform → near 100%
Wire	Narrow, localized sheath	Only particles near wire zone	Concentrated → opposing field	Weak, localized → dead zones

Key principle: Electrode design must prioritize a WIDE, STABLE ionization zone over peak field intensity at the discharge tip.

Optimal Configuration: Synergistic Parameter Combination

Fishbone Electrode

Dense, uniform multi-point corona ensures every particle is exposed to charging field regardless of trajectory

Wet Operation

Conductive water film prevents back-corona and re-entrainment; permanent particle capture via dissolution

WET ESP
Fishbone
10 kV
300°C
→ 99.90%

10–15 kV Moderate Voltage

Sufficient ion production without space charge suppression; reduced energy use and insulation stress

300°C Temperature

Reduced gas density stabilizes corona; enhanced ion mobility boosts diffusion charging of submicron particles

This optimal combination is not parameter maximization — it is SYNERGISTIC BALANCE of complementary mechanisms.

Design Implications for FCVS in Severe Accident Management

1. Use Structured Electrodes

Fishbone or multi-point designs are essential for nuclear safety applications. Wire electrodes are unsuitable where high reliability is required — their dead zones are unacceptable in safety-critical filtration.

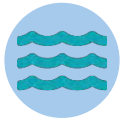

2. Prioritize Wet Operation

Water film quality is a primary performance parameter. Back-corona suppression and re-entrainment elimination are decisive, especially for sticky or reactive CsI and iodine oxide aerosols.

3. Operate at Moderate Voltage (10–15 kV)

Higher voltage does not guarantee higher efficiency. 10 kV with fishbone achieves near-100%; maximizing voltage increases energy use and failure risk without benefit.

4. Consider Multi-Stage Filtration

Even the best ESP allows some nanoparticle penetration (<50 nm). Multi-stage or complementary mechanisms (condensation growth, pool scrubbing + ESP) are recommended for maximum decontamination factor.

5. Charge Diagnostics for Validation

Measure electrical charge on penetrating particles — not just efficiency. This identifies whether failure is in charging or migration and enables targeted design improvements.

Comparison with Prior Dry ESP Studies & Broader Applicability

vs. Prior Dry ESP Study (Basnet et al. 2025)

	Dry	Wet
Configuration	Dry ESP — no water	Wet ESP — water film
Re-entrainment	Significant risk	Eliminated
Back-corona	Occurs at high load	Suppressed
Best efficiency	Moderate (design-dependent)	99.90% (fishbone, 10kV)
Key limitation	Resistive particle layer	Water supply management

Broader Applicability

Small Modular Reactors (SMR)

Compact tubular ESP geometry is ideal for space-constrained SMR containment venting designs

High-Temperature Environments

300°C performance demonstrated — applicable to industrial hot-gas filtration beyond nuclear sector

Iodine Oxide Filtration

Mechanism-based design provides pathway for targeting hard-to-capture iodine oxide aerosols in future FCVS

Industrial Fine-Particle Control

Fishbone electrode and wet mode principles transfer directly to power plant stack emission control

Conclusions

1

Electrode geometry is the decisive hardware parameter

Fishbone > Sawtooth >> Wire across virtually all conditions. Multi-point designs providing wide, stable ionization zones outperform localized discharge.

2

Wet operation provides superior and stable performance

Back-corona suppression, re-entrainment elimination, and stable corona discharge make wet mode the preferred configuration for nuclear safety applications.

3

Voltage optimization beats voltage maximization

10–15 kV with fishbone achieves near-100% efficiency. Pushing to 18 kV risks space charge suppression with no additional gain — especially for wire electrodes.

4

Charge diagnostics identify the root cause of failure

High charge on penetrators → hydrodynamic limit. Near-zero charge → charging failure. This diagnostic framework enables targeted design improvements.

5

Clear design roadmap for FCVS integration

Wet ESP + structured electrode at 10–15 kV delivers the decontamination factors needed for severe accident source term mitigation with minimal power consumption.

UNIVERSITY OF EASTERN FINLAND

We are FINE
FINE PARTICLE & AEROSOL TECHNOLOGY LABORATORY

Thank You

Questions & Discussion

satish.basnet@uef.fi | University of Eastern Finland

Funded by SAFER2028 (DENSE REST project)

SAFER 2028

Overview of Fission Product Behavior Modeling in the SIRIUS Code

Jaehyun Ham*, Kwang-Soon Ha
Korea Atomic Energy Research Institute (KAERI)
111, Daedeok-daero 989 beon-gil, Yuseong-gu, Daejeon, Republic of Korea 34057
jhham@kaeri.re.kr, tomo@kaeri.re.kr

ABSTRACT

SIRIUS has been developed at KAERI since 2015 as a C++ language-based code for analyzing fission product (FP) behavior under severe accident conditions. It models FP release from molten corium, gas-to-aerosol conversion, and transport in steam–gas mixtures, including deposition on structures or water surfaces.
Instead of solving thermal-hydraulic equations, SIRIUS receives input from lumped-parameter thermal-hydraulics analysis codes. It can be coupled in real time via MS-MPI or run stand-alone using text input, enabling analyses of systems such as Pressurized Water Reactors (PWRs) and Molten Salt Reactors (MSRs). Initial FP inventories and decay heat are provided by core analysis codes such as ORIGEN.
For PWRs, SIRIUS calculates gap release axially connected fuel rods, Arrhenius-based release from the core, and release from structural components such as shrouds. Chemical combinations (e.g., CsI, Cs_2MoO_4) are modeled with user-defined combination ratios. For MSRs, FP gas release follows evaporation–condensation. FPs moving into cooler regions may form aerosols based on saturation vapor pressure, while hygroscopic Cs compounds absorb water vapor depending on humidity. Aerosols are subject to spray removal and several deposition mechanisms, with resuspension from pools modeled by evaporation–condensation.
Mass conservation of gaseous and aerosol FPs can be solved using implicit or explicit schemes, with removal processes represented by λ-coefficients. The time step can be optimized for large-scale analyses such as uncertainty analysis and AI-based surrogate model development. Recently, SIRIUS has been validated against various separate-effect tests (AHMED, etc.) and integral experiments (PHEBUS, etc.) to support the licensing of PWR-based i-SMRs. In addition, comparative studies against the MAAP code have been conducted for large-scale containment cases. Future work includes a multi-component sectional method and coupling with chemical codes such as GEMS to incorporate Gibbs free energy minimization based saturation pressure models.

KEYWORDS
SIRIUS Code, Severe Accident, Fission Product Behavior Analysis, Lumped Parameter Approach

1. Introduction

CINEMA code, which has recently been utilized in the licensing of integral Small Modular Reactor (i-SMR), is an integral code developed in Korea since 2011 for Pressurized Water Reactor (PWR) applications, based on a lumped-parameter approach. Figure 1 shows CINEMA code structure. CSPACE and SACAP codes each analyze in-vessel and ex-vessel phenomena based on separate thermal-hydraulic analyses. These two codes interlink their thermal-hydraulic data at each time step through MASTER, which collects and shares the data to facilitate integrated analysis [1]. Within this framework, SIRIUS performs fission product

* Footnote, if necessary, in Times New Roman font and font size 10

(FP) behavior analysis based on mass conservation equations using external thermal-hydraulic analysis results. The scope of SIRIUS covers the release, transport, and removal behavior of FPs within reactor pressure vessel (RPV), reactor coolant system (RCS), and containment.

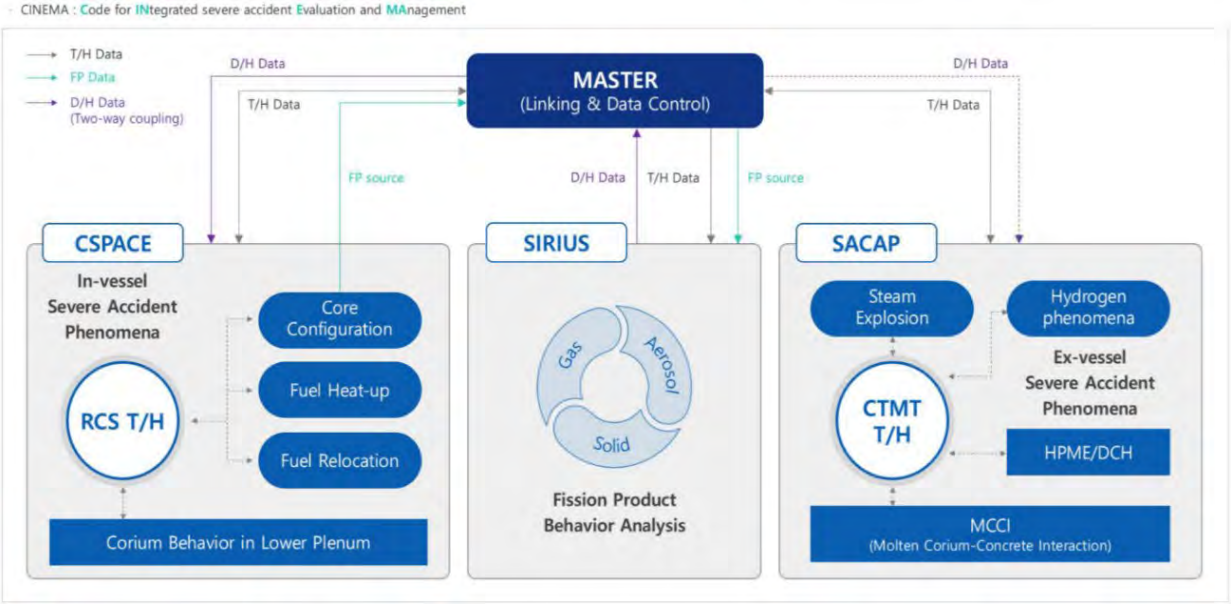

Figure 1. CINEMA code structure

Specifically, it models FP release mechanisms such as gap release from fuel rods and release due to fuel melting, as well as inter-node transport of released FPs. The code simulates condensation, evaporation, impaction, gravitational settling, diffusion, thermophoresis, and removal processes due to containment spray systems. In addition, SIRIUS tracks and calculates the FP decay heat associated with the release, transport, and wall deposition.

As the necessity for FP behavior analysis has expanded to advanced reactors such as Molten Salt Reactor (MSR), SIRIUS has been enhanced to evaluate FP release through the evaporation and condensation of compounds within liquid fuel. This improved framework utilizes a saturation vapor pressure database to simulate release mechanisms at the salt-gas interface, accounting for the unique absence of traditional fuel cladding.

This paper is organized as follows. Chapters 2 and 3 establish the core framework and physical models of SIRIUS for FP behavior in Pressurized Water Reactors (PWRs). Chapter 4 presents technical extensions and modifications for advanced reactor applications.

2. Modeling of Fission Product Behavior for PWR

Figure 2 illustrates the calculation flow of SIRIUS. It is initialized using node and link information provided by user input or coupled thermal–hydraulic modules (CSPACE and/or SACAP), and the initial inventories of FPs are evaluated. FPs are treated in three phases at each node: solid (retained), gaseous, and aerosol. Based on fuel rod temperature, solid-phase FPs are released as gaseous species and transported between nodes. Aerosol FPs are likewise transported with the carrier gas flow, while undergoing removal processes. Phase transitions between gaseous and aerosol states are determined by local node temperatures, and the final inventories of each phase are calculated at every time step. Released gaseous and aerosol FPs are assumed to instantaneously reach thermal equilibrium with the local fluid, and therefore energy equations are not solved. For efficient computation, SIRIUS time step can be set larger than the time steps of the thermal–hydraulic modules. The user can determine whether the decay heat of FPs is considered as a heat source in the thermal–hydraulic modules through the two-way coupling option.

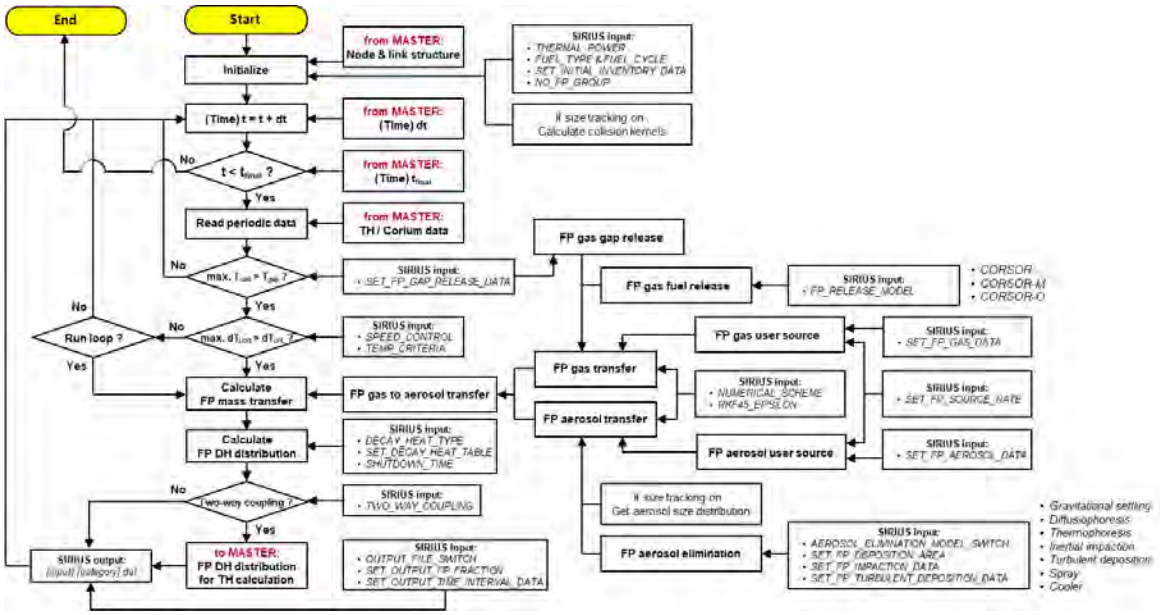

Figure 2. SIRIUS calculation flowchart

2.1. Initial Inventory and Transport of Solid-Phase Fission Products

For best-estimate calculations, SIRIUS provides optional generalized initial inventories of major FP nuclides for representative nuclear power plants, expressed as mass per thermal power (g/MW_{th}) as a function of core burnup. In addition to the built-in options, users may directly specify nuclide-specific initial inventories based on fuel cycle characteristics by utilizing core calculation results obtained from codes such as ORIGEN or OpenMC.

Using user-provided information on reactor thermal power and burnup, SIRIUS evaluates the total initial inventories of individual FP nuclides present in the entire core. The total mass of solid-phase (retained) FP is then distributed to each core node according to the fraction of UO_2 mass contained in that node. The UO_2 initial mass assigned to each node is provided by the thermal–hydraulic module.

Solid-phase (retained) FP elements contained within the fuel and structures in the core region are released as gas as the temperature increases. In addition, when the temperature rise compromises the structural integrity of the fuel or structures, relocation toward lower nodes occurs. In this process, the solid-phase FP initially contained in the fuel and structures is transported downward along with phenomena such as candling and slumping.

SIRIUS receives inter-node transfer rates from the CSPACE and directly calculates the time-dependent change in FP mass from the initial mass of each core node. The transfer rate between core nodes is defined as the mass of fuel or structure relocated from the sending node divided by the total fuel or structure mass in that node. The reason for transferring the rates rather than directly coupling the time-dependent node masses is that, when temperature distributions vary among nodes, the FP mass can change independently of the fuel mass. Therefore, accurate calculation of solid-phase FP release requires that inter-node transport be calculated precisely first.

To simulate transport between non-directly connected nodes, such as the relocation of fuel to the lower hemisphere due to core support plate failure, in the same manner as the CSPACE, SIRIUS applies a vertical-node-specific model: when the fuel mass in an upper core node falls below 2% of its initial value (in CSPACE, transfer is terminated when the fuel mass falls below 1% of the initial value to avoid numerical issues, effectively setting the node's fuel mass to zero), the remaining mass is transferred entirely to the lower node.

$$m_{s,i}^{n}(t+\Delta t) = \sum_{k=1}^{N} m_{s,i}^{n}(t)\frac{\Delta m_{cspace}^{k-n}(t+\Delta t)}{m_{cspace}^{k}(t)} \quad (1)$$

Equation (1) describes the update of the mass of solid-phase FP *i* in node *n* at time $t+\Delta t$, denoted $m_{s,i}^{n}(t+\Delta t)$. The mass is updated based on its value at the previous time step, $m_{s,i}^{n}(t)$, scaled by the fraction of the carrier mass (fuel and structural materials) transferred from each node *k* to node *n*, given by $\frac{\Delta m_{cspace}^{k-n}(t+\Delta t)}{m_{cspace}^{k}(t)}$.

2.2. Release Modeling of Gaseous Fission Products

In SIRIUS, when the temperatures of the fuel rods and other structures rise, various FPs contained in the fuel rods are released in gaseous form as illustrated in Figure 3. Gas release is categorized into two types: gap release and meltdown release. The activated core is divided into *m x n* grid in the axial and radial directions, and the temperature and mass of the cladding and fuel in each node are calculated. Gap release is calculated for each node with a UO_2 mass greater than zero at the initial condition when the cladding temperature exceeds the gap release setpoint temperature (the default value assumed in SIRIUS is 1173 K).

Since the fuel and cladding are a single structure in the axial direction, gap release actually occurs for each individual structure (i.e., the gaps are connected along the axial direction). To simulate this more realistic behavior, users can manually specify the axial connections between core nodes, allowing gap release to occur simultaneously across axially connected nodes. In other words, for core nodes connected in the axial direction, gap release can be simulated to occur simultaneously regardless of the cladding temperature.

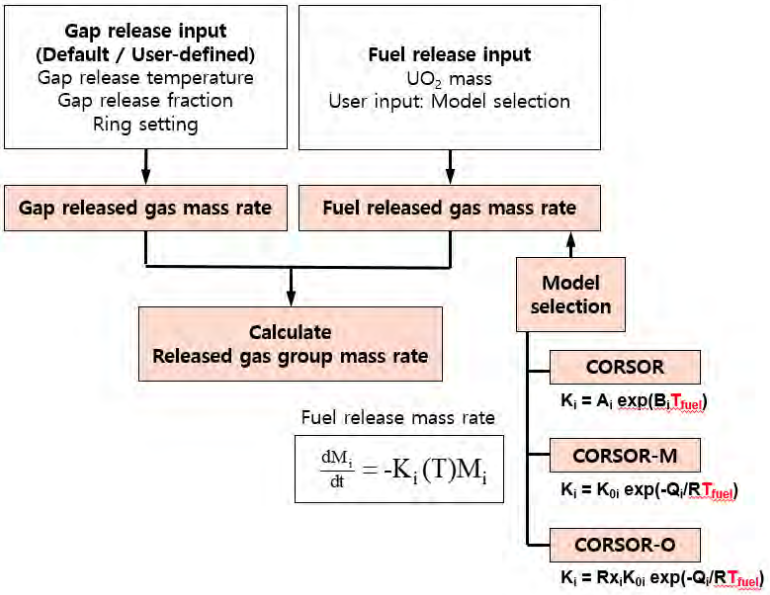

Figure 3. Calculation procedure for gaseous fission product release in SIRIUS

Gaseous release from fuel and structural materials can be simulated using three models in SIRIUS: CORSOR, CORSOR-M, and CORSOR-O. In CSPACE, energy exchange between core nodes and surrounding structures, such as the shroud, upper head, and core support plate, is calculated. These structures are discretized into *m x n* grid for temperature evaluation, and, similar to nuclear fuel, they can undergo melting, relocation. Based on this information, SIRIUS evaluates temperature-dependent gas generation not only from structures within the core nodes, such as cladding and spacer grids, but also from ex-core structures including the core support plate and upper head. These structures are assumed to be composed of

stainless steel, and the releasable species considered are iron (Fe), chromium (Cr), nickel (Ni), and copper (Cu). These species are known to be released more slowly at high temperatures compared to other FPs. However, because their initial masses are significantly larger than those of typical volatile FPs, their release can substantially increase the aerosol concentration in the atmosphere when gas generation is taken into account.

2.3. Fission Product Groups and Inter-Group Combination Model

SIRIUS allows the analysis of major volatile FPs by grouping them based on the NUREG-1465 report [3] and has recently been improved to enable grouping based on the SAND2011-0128 report [4] as well. FP grouping based on the SAND2011-0128 report, as shown in Table I, classifies 41 FPs into 15 groups. The bolded nuclides are used as the representative molecular weights for each group.

Table II. Fission product group based on the SAND2011-0128 report [4]

No.	Group name	Components	Molar weight (g/mole)
1	Noble gases	**Xe**, Kr	131.3
2	Alkali metals	**CsOH**, RbOH	149.913
3	Cesium iodide	**CsI**	259.8054
4	Cesium molybdate	**Cs_2MoO_4**	425.75
5	Halogens	**I_2**, Br_2	253.8008
6	More volatile main group	**Cd**, Sb, As	112.4
7	Less volatile main group	**Sn**, Ag, In	118.69
8	Alkaline earths	**BaO**, SrO	153.34
9	Chalcogens	**Te**, Se	127.6
10	Early transition elements	**Mo**, Nb, Tc	95.94
11	Platinoids	**Ru**, Rh, Pd	101.07
12	Trivalents	**La**, Y, Pr, Nd, Pm, Sm, Eu, Gd, Am, Cm	138.91
13	Uranium	**UO_2**	270.03
14	Tetravalent	**Ce**, Zr, Np, Pu	140.12
15	Structural materials	**Fe**, Cr, Ni, Mn	55.845

When using the group classification based on the SAND2011-0128 report, the combination ratio for Group 3 (CsI) and Group 4 (Cs_2MoO_4) in Table II can be specified. The combination ratio set by the user represents the maximum fraction achievable under “possible conditions.” The combination ratio is a real value between 0 and 1. For example, if the “I→CsI” value is 1, all released iodine can combine with the released cesium to form CsI under possible conditions. Here, “possible conditions” refer to situations in which the mass of released cesium is greater than the mass of released iodine. If the released cesium mass is less than that of iodine, the effective combination ratio becomes less than 1. Combination between nuclide groups is first calculated during the release from the fuel, and then recalculated after the transport and deposition of gaseous and aerosol species to each node (i.e., after solving the mass conservation equations). This approach is used to ensure that the combination between species with significantly different release rates, such as Cs and Mo, can approach the user-defined combination ratio, as illustrated in Figure 4. The reactivity of the combination is assumed to be higher for CsI than for Cs_2MoO_4, allowing sequential combination to be modeled. That is, iodine first combines with cesium according to the specified combination ratio, and any remaining cesium then combines with molybdenum according to its defined combination ratio.

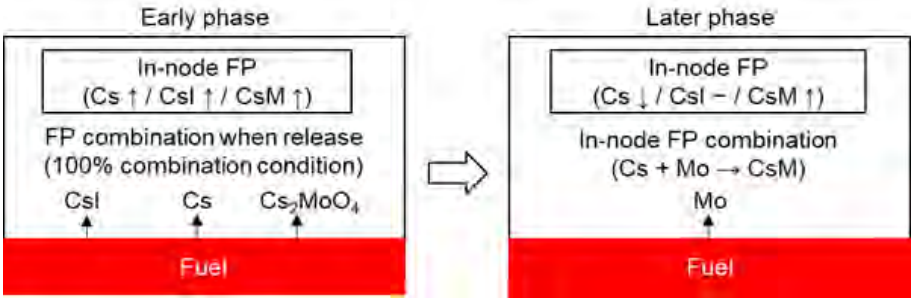

Figure 4. Inter-group combination modeling in SIRIUS

2.4. Transformation, Condensation, and Evaporation of Gaseous and Aerosol Fission Products

FP groups can exist in both gaseous and aerosol phases. The masses of the gaseous and aerosol phases are calculated based on the temperature-dependent vapor pressure. If the pressure of the gaseous FP group exceeds the vapor pressure, the excess gaseous FP is assumed to condense into aerosols. In other words, for each node, the number of moles that can exist in the gas phase is limited by the saturation vapor pressure, and any moles exceeding this limit are converted to aerosols.

For a node n with temperature T^n and volume V^n, let the number of moles of group i gaseous FP be $n_{v,i}^n$. The mass of group i aerosol FP formed, $\Delta m_{a,i}^n$, can then be expressed as Equation (2). In Equation (2), M_i represents the molecular weight of the group i FP, and the saturation mole number of the group i, $n_{v,sat,i}^n$, can be calculated using the saturation vapor pressure $P_{i,sat}^n$ as shown in Equation (3).

$$\Delta m_{a,i}^n = \left(n_{v,i}^n - n_{v,sat,i}^n\right) M_i \tag{2}$$

$$n_{v,sat,i}^n = \frac{P_{i,sat}^n V^n}{R\,T^n} \tag{3}$$

The saturation vapor pressure of group i FP in Equation (3) can be calculated using the equation form shown in Equation (4), with coefficients A, B, and C for each group taken from references [5, 6]. The coefficients for the structural material group are assumed to be the same as those for the Mo group, following the methodology of references [5, 6].

$$log_{10}\left[P_{i,sat}(mmHg)\right] = -\frac{A_i}{T} + B_i + C_i\, log_{10}(T) \tag{4}$$

If group i aerosol FP exists in a given node and the vapor pressure of group i gaseous FP is below the saturation vapor pressure, the aerosol is assumed to evaporate into the gas phase. In other words, whenever aerosol FP is present, the gaseous FP is always maintained at its saturation vapor pressure. Inert gases always exist in the gaseous phase, so no conversion between gas and aerosol is calculated.

SIRIUS includes a model to calculate evaporation and condensation based on the saturation vapor pressure, as shown in Equation (5), in order to simulate the interactions between gas and liquid phases that can occur in actual conditions. Equation (5) calculates the amount of evaporation for each type of fission product in the liquid based on the saturation vapor pressure and the concentration difference in air. In a closed system, as fission products evaporate from the liquid, the saturation vapor pressure decreases and the concentration in the air increases, gradually reducing the evaporation rate while increasing condensation, until an equilibrium between the two phases is reached.

$$\frac{dm_i}{dt} = \mathrm{A}k_i(C_i^a - C_i^s) \tag{5}$$

m_i represents the condensed mass of group i, C_i^a is the airborne concentration of group i, C_i^s is the saturated concentration of group i, A is the surface area, and k_i is the mass transfer coefficient for group i.

Gaseous fission products can undergo evaporation and condensation reactions with liquids, as illustrated in Figure 5, and can also be converted into aerosols.

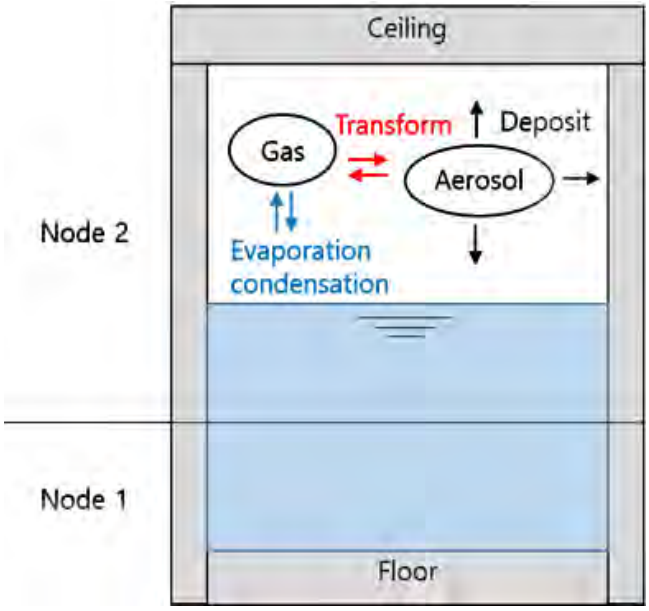

Figure 5. Modeling of aerosol deposition on liquid surfaces and gas phase evaporation/condensation in SIRIUS

2.5. Modeling of Aerosol Fission Products

The aerosol deposition and removal model simulate the reduction of aerosol mass as aerosols are transported within the RCS and containment due to various physical phenomena. Six mechanisms of aerosol deposition and removal are considered in SIRIUS.

1. Sedimentation or Gravitational Settling: Aerosols collide and agglomerate, increasing in size and mass, and settle to the RCS floor under the influence of gravity.
2. Inertial Impaction: Aerosols carried by the vapor–non-condensable gas mixture flow collide with surfaces, such as bends in RCS piping, and attach to the walls.
3. Thermophoresis: Aerosols move toward cooler surfaces due to temperature gradients in the vapor–non-condensable gas mixture and deposit on these surfaces.
4. Diffusiophoresis: As vapor condenses on cold surfaces, non-uniform aerosol distributions are created. Aerosols migrate radially due to concentration gradients and attach to walls upon collision.
5. Turbulent Deposition: In high-velocity pipe flows, aerosols deviate from the streamlines and deposit on the pipe walls or other surfaces.
6. Spray: Aerosols are removed from the air and deposited onto floors or walls by water droplets sprayed from containment spray systems.

To simulate such aerosol removal phenomena, a total removal rate, λ_t, was introduced as shown in Equation (6), which is a correlation developed based on experimental results.

$$\lambda_t = \lambda_{sed} + \lambda_{imp} + \lambda_{diff} + \lambda_{th} + \lambda_{turb} + \lambda_{spray} \quad (6)$$

The total removal rate (λ_t) has units of "1/s" and is multiplied by the aerosol mass on the right-hand side of the mass conservation equation to simulate the rate of aerosol mass reduction. When both inertial

impaction and gravitational settling are considered simultaneously, the deposition removal rates for each mechanism are corrected according to reference [7], as expressed in Equations (7) and (8).

$$\lambda_{sed} = \lambda_{sed} * e^{-\frac{1}{3}\left(\frac{\lambda_{imp}}{\lambda_{sed}}\right)^2} \quad (7)$$

$$\lambda_{imp} = \lambda_{imp} * e^{-\frac{1}{3}\left(\frac{\lambda_{sed}}{\lambda_{imp}}\right)^2} \quad (8)$$

SIRIUS tracks the amount of aerosol deposited on surfaces using six different models. Figure 6 illustrates the definition of aerosol deposition surfaces. In SIRIUS, each node is treated as having a cylindrical shape, with the upward-facing surface defined as the floor, the vertically oriented surfaces as walls, and the downward-facing surface as the ceiling. Considering the porosity of the node, gaseous and aerosol FPs are assumed to be uniformly distributed within the gas volume, and deposition is assumed to occur only within this gas volume (shown as the green area in Figure 6).

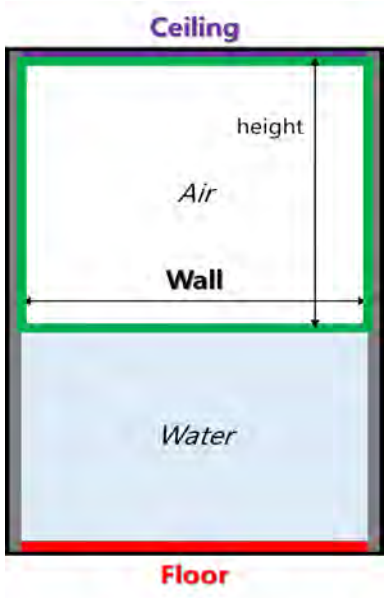

Figure 6. Definition of aerosol deposition surfaces in SIRIUS

When nodes are connected vertically, for example as shown in Figure 5, if *Node 1* is completely filled with liquid (void fraction = 0) and *Node 2* contains liquid only partially (0 < void fraction < 1, liquid height ≥ 1 cm), the amount of aerosol deposition is calculated based on the liquid surface area. The liquid surface area is assumed to be equal to the node's floor area, so the floor area value is used regardless of whether liquid is present. Thus, the regions available for aerosol deposition include the floor, walls, ceiling, and the liquid surface on the floor, for a total of four regions. Aerosols deposited on the liquid surface are resuspended into the gas phase if the liquid completely evaporates (i.e., void fraction = 1), allowing the resuspension of aerosols previously dissolved in the liquid to be calculated.

When a liquid layer exists on wall or ceiling surfaces, deposited aerosols can be transported downward along with the liquid. A fraction of the aerosol mass deposited on walls and ceilings, as defined by user input, is reclassified as floor-deposited aerosol mass due to mechanisms such as diffusiophoresis and thermophoresis. For example, if this fraction is set to 1, the aerosol mass on walls and ceilings is calculated as zero, and the corresponding mass is added entirely to the floor deposition.

SIRIUS utilizes wall temperatures by linking to the temperatures of heat structures connected to each node in the thermal-hydraulic modules. A thermal–hydraulic node may be connected to multiple heat structures, but in actual physical phenomena, aerosol deposition predominantly occurs on the coldest

surfaces, such as heat exchangers, regardless of their area. Therefore, by default, the lowest surface temperature among all heat structures connected to a single node is used in the calculations. If needed, the highest surface temperature can also be used, which can be specified through user input.

The growth of hygroscopic aerosols is not calculated incrementally over time steps in SIRIUS; instead, it is assumed that particles immediately reach the maximum diameter allowed under the prevailing thermal–hydraulic conditions. The saturation vapor pressure used for relative humidity calculations is based on the water temperature if liquid is present, or on the vapor temperature if no liquid exists. A node is considered to contain water if the liquid height is 1 cm or greater. The particle diameter ratio reflecting hygroscopic growth is calculated using an equation based on Mason formula. The density and surface tension of water are assumed to remain constant. When the particle diameter ratio is much greater than 1, the properties of water dominate, making this assumption reasonable. The base diameter of aerosols is set to 1 μm. By default, CsOH, CsI, and Cs_2MoO_4 are treated as hygroscopic aerosols, and their solubility is calculated by linear interpolation based on the gas temperature. When the gas temperature exceeds 600 K, the solubility begins to decrease, and it becomes zero at temperatures of 647 K or higher.

2.6. Numerical Methods

Gaseous FPs are assumed to be generated and released from the fuel and to move together with the carrier gas. Aerosol FPs are assumed to form from the gaseous FPs and, like the gaseous phase, move together with the carrier gas. Therefore, only mass conservation is considered, and separate momentum conservation equations are not solved. Figure 7 illustrates the concept of FP transport between nodes as considered in SIRIUS.

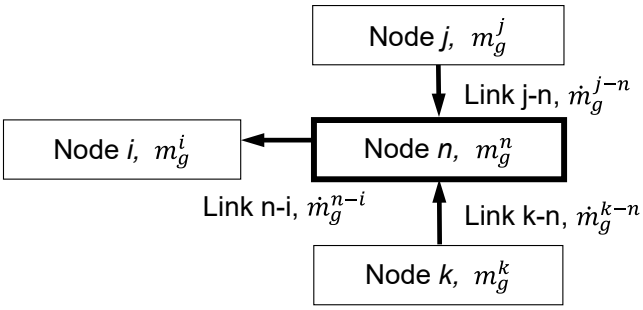

Figure 7. Fission product transport calculation in SIRIUS

The transport of gaseous and aerosol FPs can be expressed using the mass conservation equations shown in Equations (9) and (10). SIRIUS allows the use of either explicit or implicit methods to numerically solve the FP transport equations in the RCS and containment.

$$\frac{dm_{v,i}^n}{dt} = \dot{m}_{v,i,in}^n - \dot{m}_{v,i,out}^n + \dot{G}_{v,i}^n \tag{9}$$

$$\frac{dm_{a,i}^n}{dt} = \dot{m}_{a,i,in}^n - \dot{m}_{a,i,out}^n - \lambda_{t,i}^n m_{a,i}^n + \dot{G}_{a,i}^n \tag{10}$$

$m_{v,i}^n$ represents the mass of gaseous group *i* FP in node n. $\dot{m}_{v,i,in}^n$ is the mass flow rate of gaseous group *i* FP entering node *n*. $\dot{m}_{v,i,out}^n$ is the mass flow rate of gaseous group *i* FP leaving node *n*. $\dot{G}_{v,i}^n$ represents the mass generation rate of gaseous group *i* FP in node *n*. $m_{a,i}^n$ is the mass of aerosol group *i* FP in node *n*. $\dot{m}_{a,i,in}^n$ represents the mass flow rate of aerosol group *i* FP entering node *n*. $\dot{m}_{a,i,out}^n$ is the mass flow rate of aerosol group *i* FP leaving node *n*. $\dot{G}_{a,i}^n$ represents the mass generation rate of aerosol group *i* FP in node *n*. Finally, $\lambda_{t,i}^n$ is the total removal rate of aerosol group *i* FP in node *n*.

By default, SIRIUS performs calculations using the same time step as the coupled thermal–hydraulic modules. However, since SIRIUS simulates FP generation based on core fuel temperatures and transport between thermal–hydraulic nodes according to gas flow rates, the results do not change significantly if there are no substantial variations in thermal–hydraulic conditions. This characteristic allows the user to set SIRIUS time step larger than that of the thermal–hydraulic module to increase computational speed.

However, this approach does not utilize the thermal–hydraulic module data at every time step, which may lead to distorted results. That is, important changes in thermal–hydraulic conditions, such as variations in gas flow rates between thermal–hydraulic nodes, may not be reflected in the FP behavior calculations. To prevent such issues when setting SIRIUS time step, the thermal–hydraulic data at all time steps are compared with the values used at the previous SIRIUS calculation. If the change in any variable exceeds a predefined threshold, SIRIUS is forced to perform a calculation at that time step. The threshold for forced calculation can be set individually for the following four variables.

- Core fuel temperature
- Gas temperature in the thermal–hydraulic node
- Pressure in the thermal–hydraulic node
- Gas flow rate between thermal–hydraulic nodes

If the rate of change exceeds the threshold due to gradual variations, it does not pose a problem; however, if it results from numerical noise or a sudden fluctuation, the integration may produce distorted results. To prevent this, when the rate of change of a key thermal–hydraulic variable exceeds the threshold (i.e., at a time step satisfying the forced calculation condition), the previous time step is first recalculated using the same time step as CINEMA code, and then the current time step is computed consecutively, eliminating the possibility of result distortion.

When the time step of SIRIUS is not the same as that of the CSPACE, differences in the core fuel mass may occur. Therefore, the calculation of gaseous FP release from the core fuel uses CINEMA code time step. The gaseous FPs released from the core continue to accumulate in the core nodes during the periods when SIRIUS is not performing calculations, and are then transported and converted to aerosols at the next calculation time step.

The purpose of SIRIUS time step model is to optimize the computational speed of CINEMA code while maintaining “calculation accuracy.” Here, “calculation accuracy” refers to the difference between the results obtained using SIRIUS time step and those obtained when CINEMA code is run without SIRIUS time step model, i.e., using the original CINEMA code time step. As shown in Figure 8, using SIRIUS time step model can significantly reduce the calculation frequency while maintaining “calculation accuracy”. This capability may also be useful for large-scale SIRIUS calculations related to uncertainty analysis and AI-based surrogate model training.

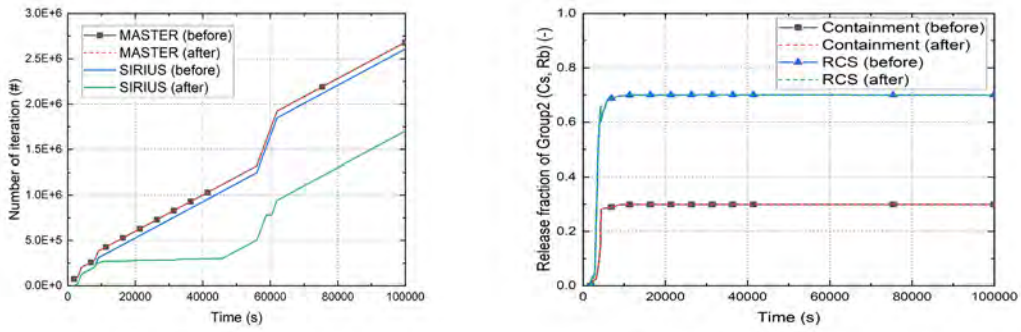

Figure 8. Effect of increasing time step on SIRIUS calculation frequency and comparison of key results using CINEMA time step and SIRIUS time step

3. Extensions for Advanced Reactor Applications

Unlike pressurized water reactors, MSRs do not have fuel cladding; therefore, under normal operating conditions, FPs exist while circulating together with the liquid fuel salt. As a result, FPs can chemically react and combine with the molten salt during normal operation, and condensation and evaporation can be calculated based on the concentration differences between the liquid fuel interface and the surrounding atmosphere. Information on releasable compounds can be obtained through calculations of inter-nuclide molecular binding based on Gibbs free energy, and thermochemical analysis codes such as FactSage and GEMS can be used for these calculations. Based on the approaches presented in references [8] and [9], a FP release calculation model for accident conditions in an MSR was developed. The time-dependent evaporation amount of compound *i* in the molten salt can be calculated as shown in Equation (5).

The molten salt can consist of multiple compounds, and Equation (5) represents the formulation used to calculate the evaporation or condensation rate from the molten salt based on the difference between the saturated mole fraction of compound *i* in the molten salt and the mole fraction of compound *i* in the atmosphere. Equation (11) is used to calculate the saturated mole fraction from the saturation vapor pressure based on the ideal gas law.

$$C_i^S = \frac{P_i^S(T) M_i}{RT} \tag{11}$$

The time-dependent values of the Lennard–Jones parameters can be obtained through thermodynamic behavior analyses and should be provided as input for fission product release calculations. After release, fission product behaviors such as phase change, transport, and deposition are evaluated using the same models as those described above for the PWR-oriented SIRIUS code.

4. Conclusions

This study introduced the C++ based SIRIUS code, a computational tool for analyzing the release, transport, and removal of FPs under severe accident conditions in RPV, RCS, and containment, using results from an external lumped-parameter thermal–hydraulic analysis. For PWR applications, the modeling framework includes node-wise initialization of solid-, gaseous-, and aerosol-phase FP inventories; temperature-dependent solid-to-gas release from fuel and structural materials; inter-node redistribution associated with fuel and structural material behavior; volatile FP grouping with user-defined inter-group chemical combination; gas–aerosol phase transformation governed by saturation vapor pressure; and multiple aerosol deposition mechanisms represented by λ-type removal coefficients. Numerical solution schemes based on mass conservation equations for gaseous and aerosol phases were presented, together with a dedicated time-step control approach that enables efficient coupling with CINEMA code while maintaining consistency with the underlying thermal–hydraulic behavior. In addition, an extended SIRIUS modeling approach for MSRs was described, incorporating evaporation–condensation at the salt–gas interface, evaluation of releasable chemical compounds through thermochemical analysis, and application of the same phase-change, transport, and deposition models as those used for pressurized water reactor analyses to simulate FP behavior.

Future work will first focus on introducing a multicomponent sectional aerosol model into SIRIUS code to enable more detailed analysis of particle size distribution and compositional changes during transport and deposition processes in the reactor coolant system and the containment. In addition, the coupling with external thermochemical equilibrium codes such as GEMS will be extended to establish a database of saturation vapor pressures and chemical species distributions based on Gibbs free energy minimization, and to develop a computational framework that consistently incorporates these data into evaporation–condensation and chemical combination models under both pressurized water reactor and MSR conditions.

ACKNOWLEDGMENTS

This work was supported by the Korea Institute of Energy Technology Evaluation and Planning (KETEP) and the Ministry of Climate, Energy & Environment (MCEE) of the Republic of Korea (No. KETEP-20224B10300050).
Also, this work was supported by the Nuclear and Development of the National Foundation of Korea (NRF) grant funded by the Korea government (Ministry of Science and ICT) (No. RS-2022-00144202).
Also, this work was supported by the Innovative Small Modular Reactor Development Agency grant funded by the Korea government (MSIT) (No. RS-2023-00259516).
Also, this work was supported by the National Research Foundation of Korea (NRF) grant funded by the Korea government (MSIT) (No. RS-2023-00261295).

REFERENCES

1. Jaehyun Ham and Kwang-Soon Ha, “Current status of SIRIUS code development,” Transactions of the Korean Nuclear Society Spring Meeting, Jeju, Korea, May 22-23 (2025).
2. KHNP, KAERI, and FNC Technology, “Theory Manual for CINEMA Version 2.3,” December (2025).
3. U.S. Nuclear Regulatory Commission, “Accident Source Terms for Light-Water Nuclear Power Plants,” NUREG-1465, February (1995).
4. Sandia National Laboratories, “Accident Source Terms for Light-Water Nuclear Power Plants Using High-Burnup or MOX Fuel,” SAND2011-0128, January (2011).
5. Sandia National Laboratories, “MELCOR Computer Code Manuals Vol. 1: Primer and Users’ Guide Version 2.2.9541 2017,” SAND2017-0455 O, January (2017).
6. Sandia National Laboratories, “MELCOR Computer Code Manuals Vol. 2: Reference Manual Version 2.2.9541 2017,” SAND2017-0876 O, January (2017).
7. M. Epstein and P. G. Ellison, “Correlations of the Rate of Removal of Coagulation and Depositing Aerosols for Application to Nuclear Reactor Safety Problems,” Nuclear Engineering and Design, 107, pp. 327-344 (1988).
8. J. Kalilainenm, S. Nichenko, and J. Krepel, “Evaporation of materials from the molten salt reactor fuel under elevated temperatures,” Journal of Nuclear Materials, 533, p. 152134 (2020).
9. R. B. Bird, W. E. Stewart, and E. N. Lightfoot, “Transport Phenomena, 2nd ed.,” John Wiley & Sons, New York, NY, USA (2002).

The 12th European Review Meeting on Severe Accident Research (ERMSAR2026)
Madrid, Spain, May 18-22, 2026

Overview of Fission Product Behavior Modeling in the SIRIUS Code

2026. 05. 21.

Jaehyun Ham, Kwang-Soon Ha

Korea Atomic Energy Research Institute (KAERI)
111, Daedeok-daero 989 beon-gil, Yuseong-gu, Daejeon, Republic of Korea 34057

Contact : jhham@kaeri.re.kr

CONTENTS

01 Introduction

02 SIRIUS modeling

03 Application examples

04 Conclusion

❖ SIRIUS within CINEMA framework

- CINEMA is a lumped-parameter integral code for PWR SA analysis, recently utilized in Korean i-SMR licensing.
- CSPACE, SACAP, and SIRIUS are C++ based modules, coupled via MASTER using MS-MPI.
- SIRIUS analyzes FP behavior using T/H data, with optional decay heat feedback to coupled modules.

· CINEMA : Code for INtegrated severe accident Evaluation and MAnagement

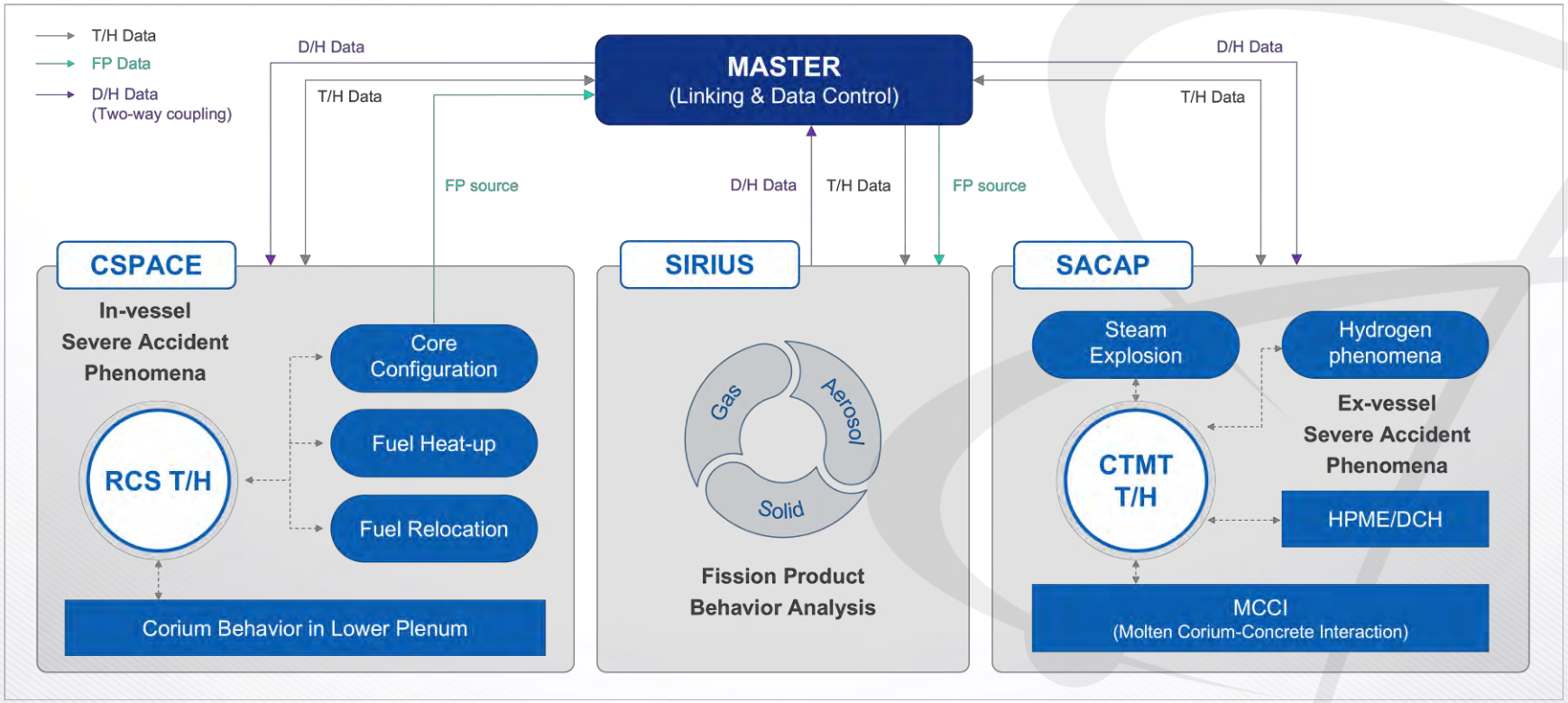

❖ Calculation flow

- SIRIUS activation (when $T_{clad} > T_{gap}$) → Time step control → Solid FP relocation & Gas release → Aerosol removal rate (λ) → Transport (mass conservation) → FP phase/state update → Decay heat & T/H feedback

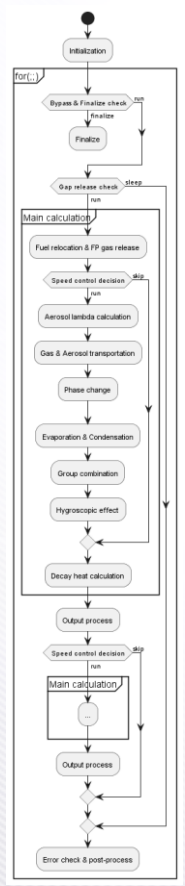

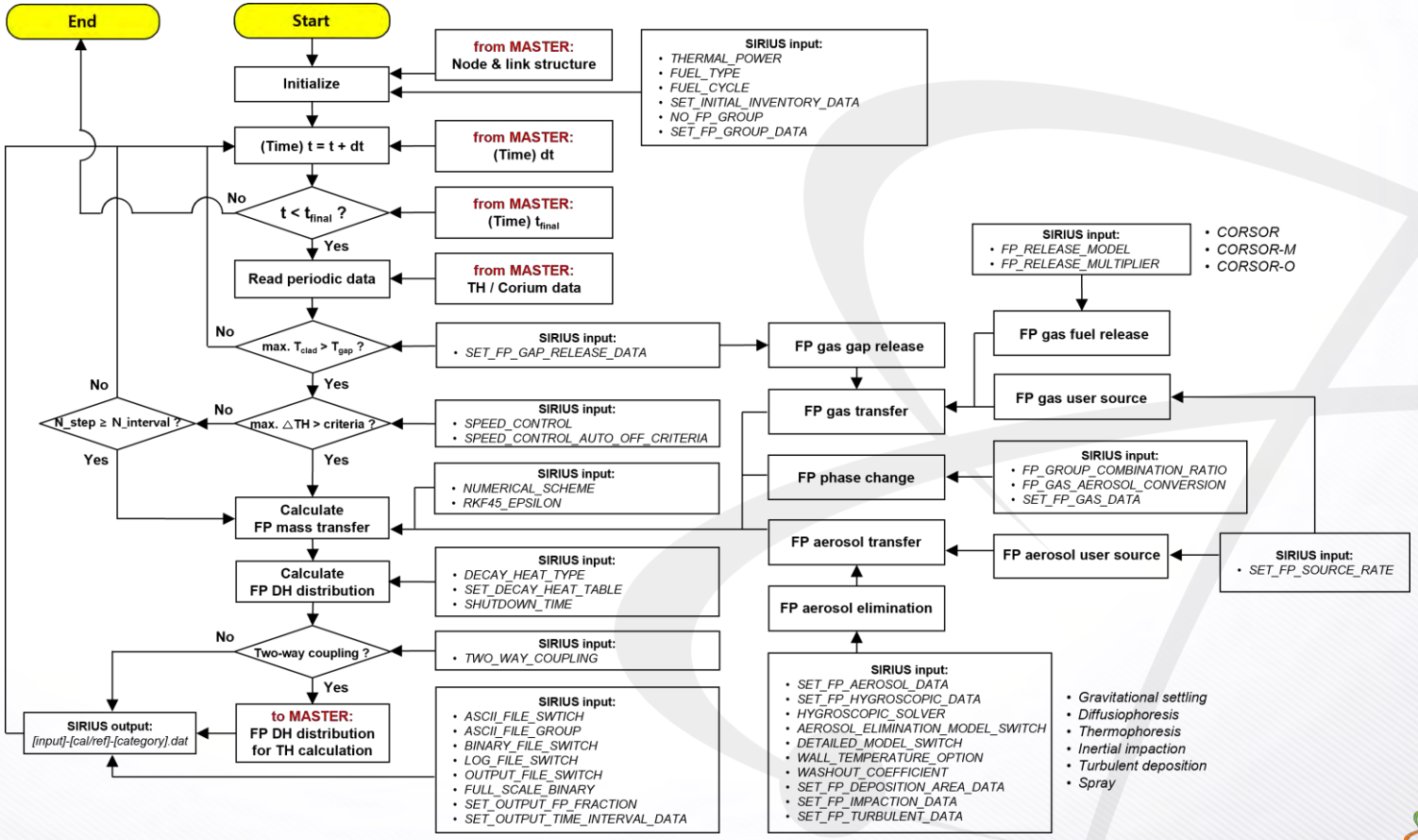

❖ Initial inventory & Transport of solid FP

- Initial FP inventories are evaluated from reactor power, burnup, and fuel-cycle data.
- Solid FP are distributed to core nodes according to the local UO_2 mass.
- CSPACE transfer rates are used to track retained FP relocation during core degradation.

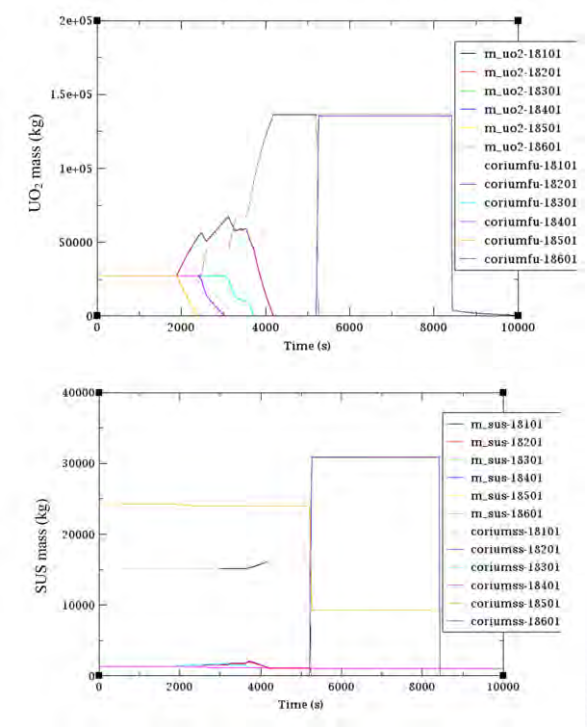

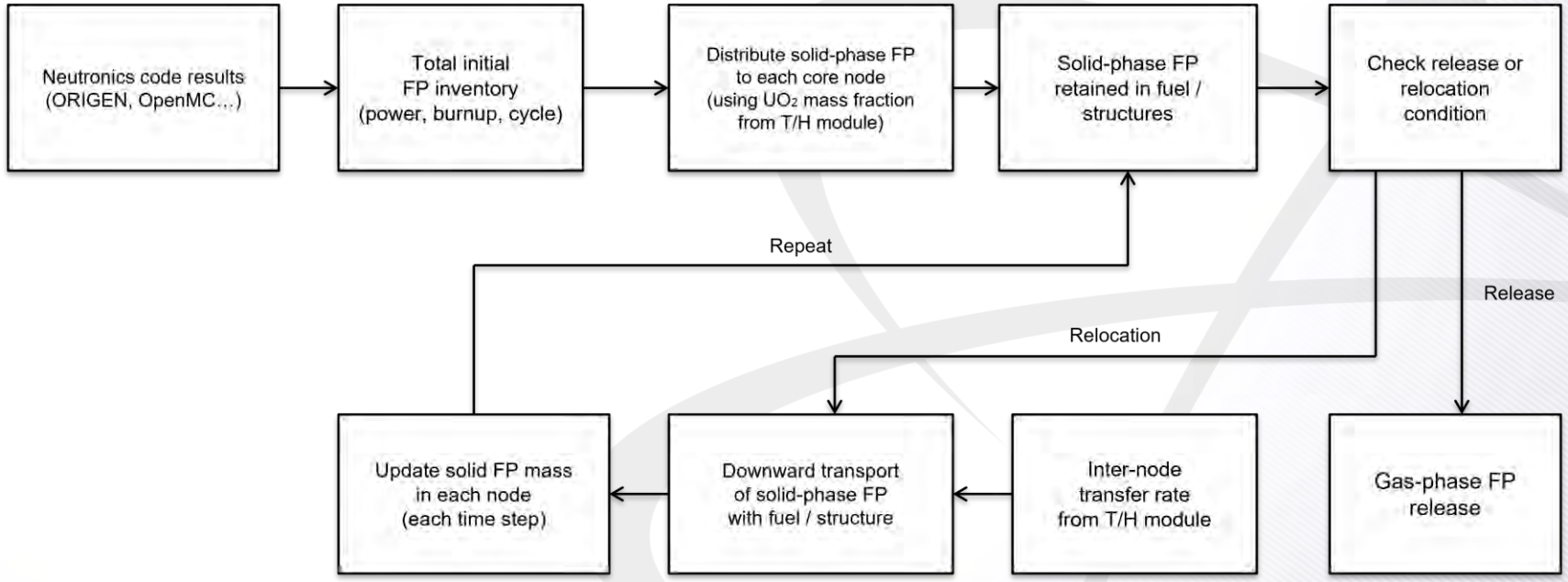

$$m_{s,i}^{n}(t+\Delta t) = \sum_{k=1}^{N} m_{s,i}^{n}(t)\frac{\Delta m_{cspace}^{k-n}(t+\Delta t)}{m_{cspace}^{k}(t)}$$

❖ FP gas release

- Gap release is calculated per node; axially connected nodes release simultaneously via ‘ring’ setting.
- Gas generation from ex-core structures (Shroud,CSP, …) is also evaluated based on temperature.

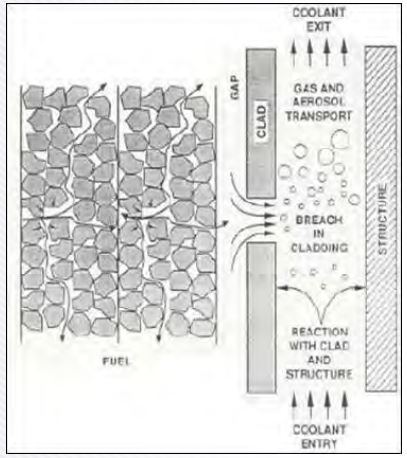

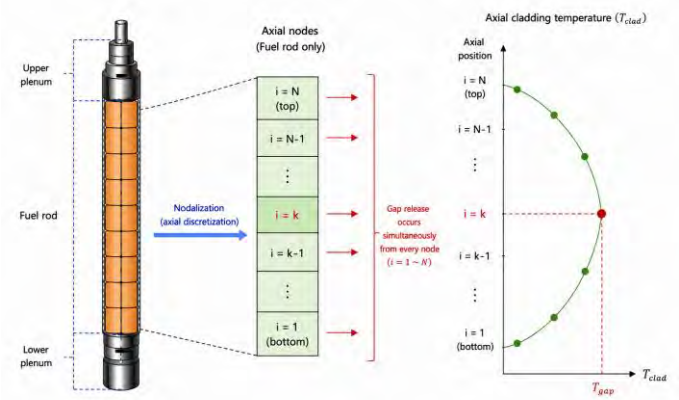

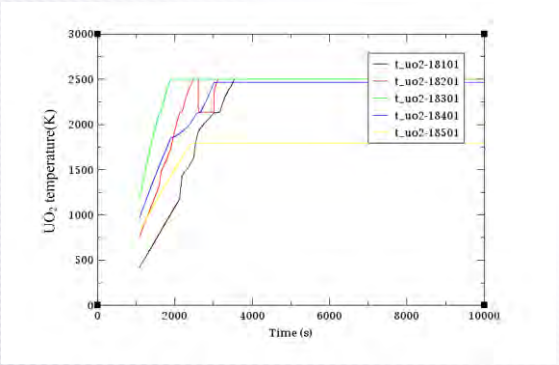

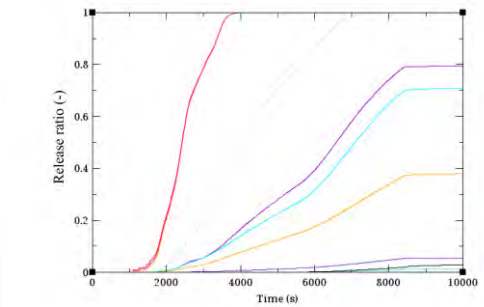

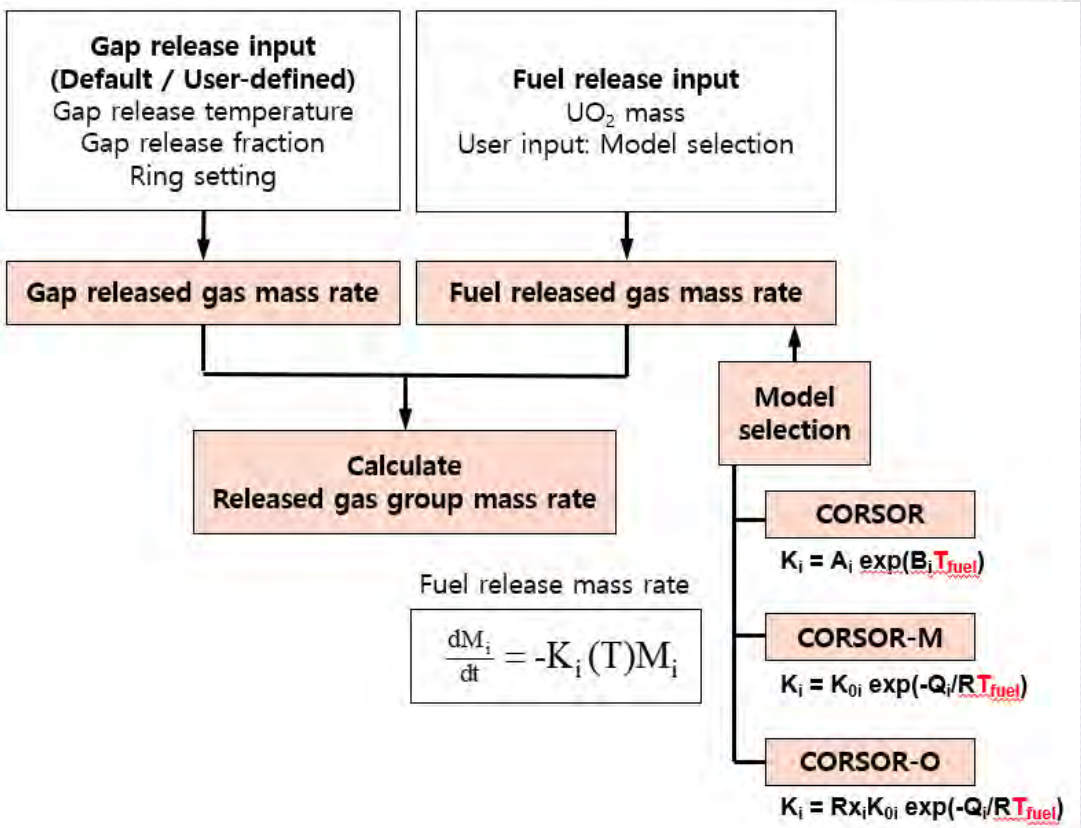

❖ FP grouping & Inter-group combination

- FPs are grouped into 8 groups (NUREG-1465) or 15 groups (SAND2011-0128) based on chemical properties.
- User-defined combination ratios for CsI and Cs_2MoO_4 represent the maximum fraction achievable.
- Combination is first calculated at release from fuel, then recalculated after transport and deposition at each node.

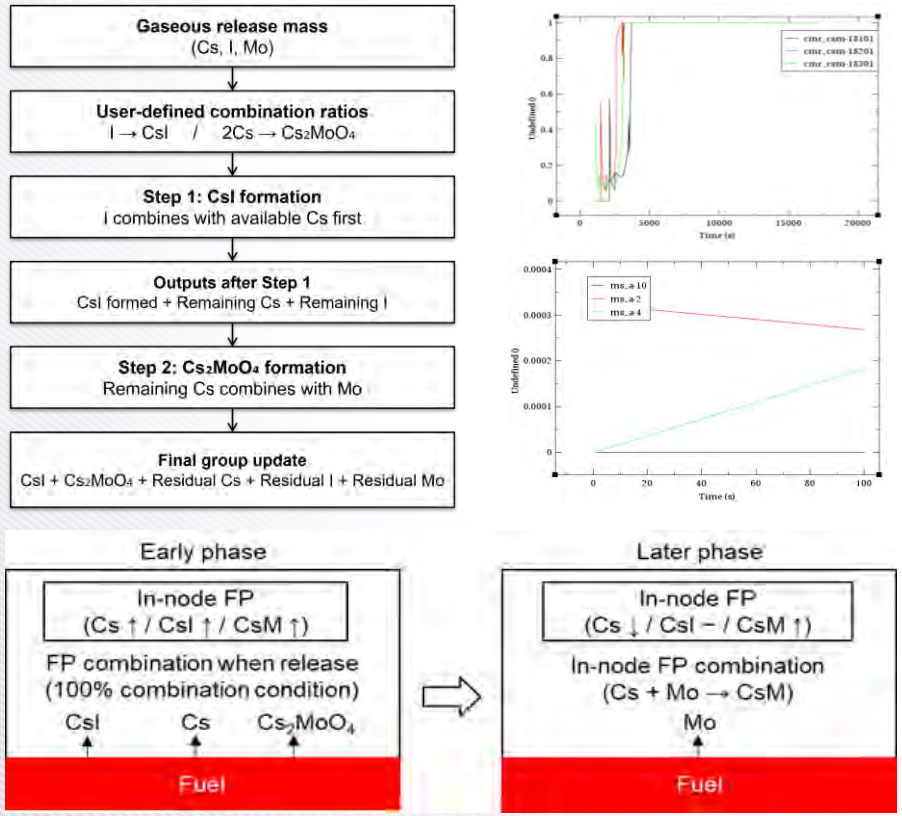

No.	Group name	Components
1	Noble gases	**Xe**, Kr
2	Alkali metals	**CsOH**, RbOH
3	Cesium iodide	**CsI**
4	Cesium molybdate	**Cs_2MoO_4**
5	Halogens	**I_2**, Br_2
6	More volatile main group	**Cd**, Sb, As
7	Less volatile main group	**Sn**, Ag, In
8	Alkaline earths	**BaO**, SrO
9	Chalcogens	**Te**, Se
10	Early transition elements	**Mo**, Nb, Tc
11	Platinoids	**Ru**, Rh, Pd
12	Trivalents	**La**, Y, Pr, Nd, Pm, Sm, Eu, Gd, Am, Cm
13	Uranium	**UO_2**
14	Tetravalent	**Ce**, Zr, Np, Pu
15	Structural materials	**Fe**, Cr, Ni, Mn

❖ Transformation & Evaporation/Condensation

- Gaseous FP converts to aerosol when its partial pressure exceeds sat. vapor pressure at local node temperature.
- Evaporation/condensation between gas and liquid phase calculated based on concentration difference.
- Gas–liquid interfacial transport is represented by a lumped mass-transfer coefficient.

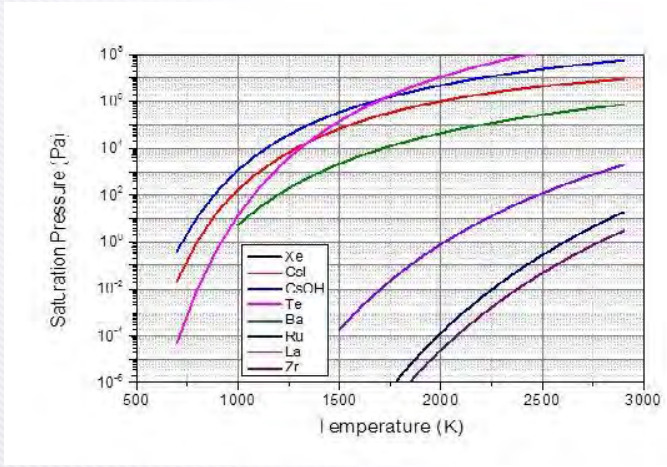

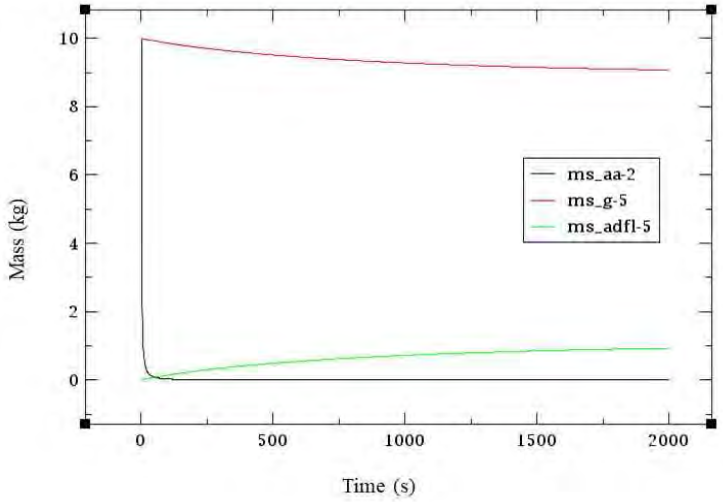

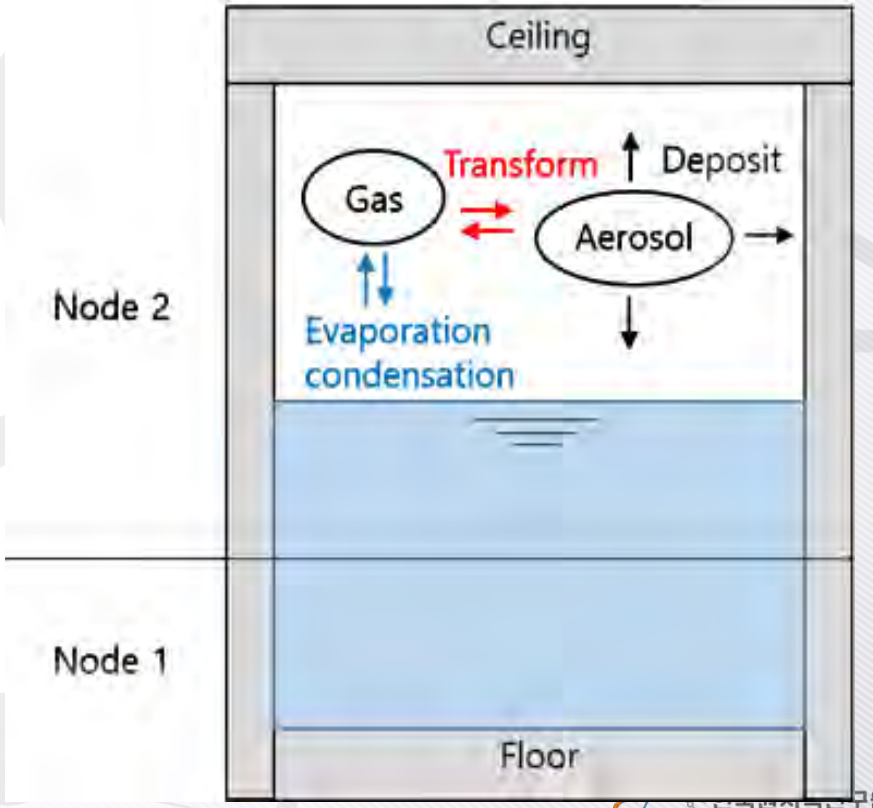

$$\Delta m_{a,i}^{n} = \left(n_{v,i}^{n} - n_{v,sat,i}^{n}\right) M_i$$

$$n_{v,sat,i}^{n} = \frac{P_{i,sat}^{n}\, V^{n}}{R\, T^{n}}$$

$$log_{10}\left[P_{i,sat}(mmHg)\right] = -\frac{A_i}{T} + B_i + C_i\, log_{10}(T)$$

$$\frac{dm_i}{dt} = \mathrm{A} k_i (C_i^{a} - C_i^{s})$$

$$C_i^{s} = \frac{P_i^{s}(T) M_i}{RT}$$

❖ Aerosol deposition, removal & Hygroscopic growth

- The total removal rate, λ_t [1/s], is multiplied to the airborne aerosol mass in the conservation equation.
- Deposited aerosols on liquid can be resuspended by evaporation or when the liquid completely evaporates.
- Hygroscopic growth is not time-resolved; aerosols are simply assumed to be in equilibrium for each time step.

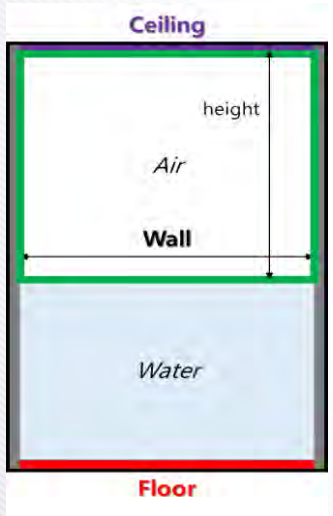

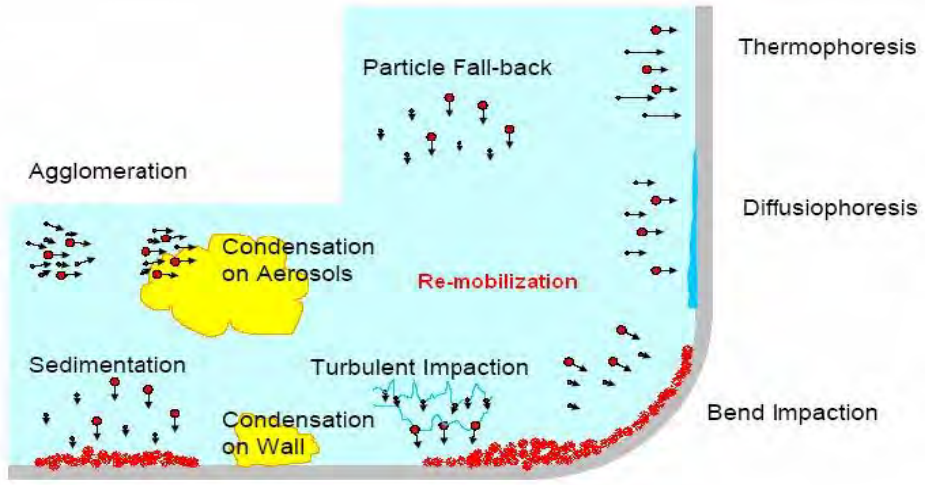

$$\lambda_t = \lambda_{sed} + \lambda_{imp} + \lambda_{diff} + \lambda_{th} + \lambda_{turb} + \lambda_{spray}$$

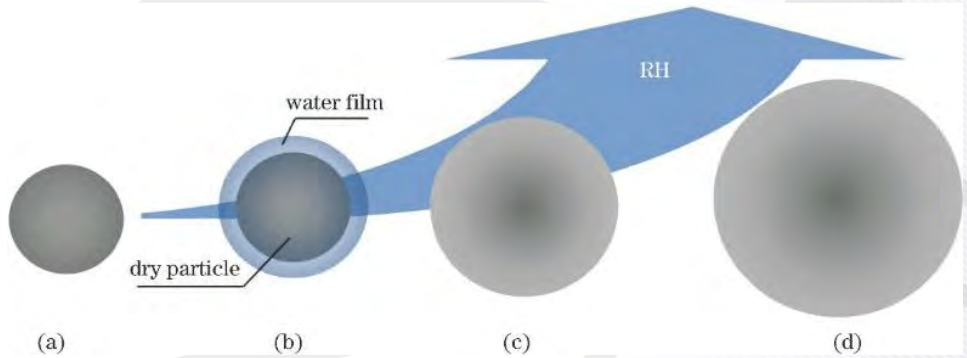

$$M_{aw} = (V_{wet}\,\rho_W)(r^3 - 1)$$

$$M_{aw} \leq \emptyset^n * S * M_a \;\; (S = \textit{hygroscopic solubility})$$

❖ Numerical methods

- Gas and aerosol FP transport is calculated using node-wise mass conservation equations.
  - ➢ Implicit or Explicit (RKF45) schemes can be selected.
- SIRIUS time step can be increased to reduce calculation frequency.
  - ➢ Forced calculations are triggered by significant changes in key T/H variables.

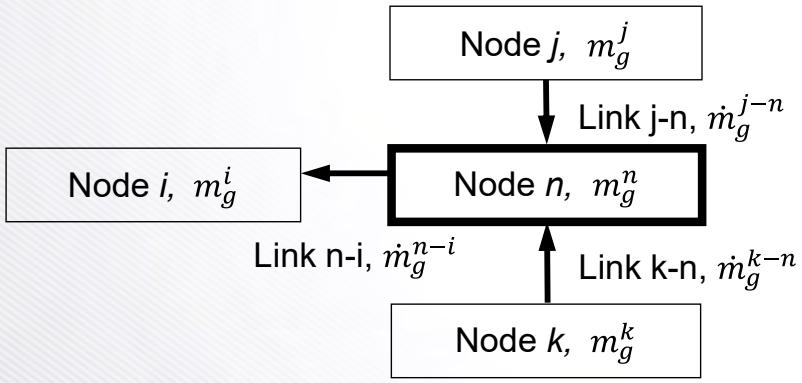

$$\frac{dm_{v,i}^n}{dt} = \dot{m}_{v,i,in}^n - \dot{m}_{v,i,out}^n + \dot{G}_{v,i}^n$$

$$\frac{dm_{a,i}^n}{dt} = \dot{m}_{a,i,in}^n - \dot{m}_{a,i,out}^n - \lambda_{t,i}^n m_{a,i}^n + \dot{G}_{a,i}^n$$

1. Core fuel temperature
2. T/H node gas temperature
3. T/H node pressure
4. Gas flow rate between T/H nodes

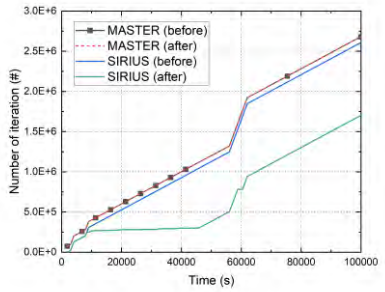

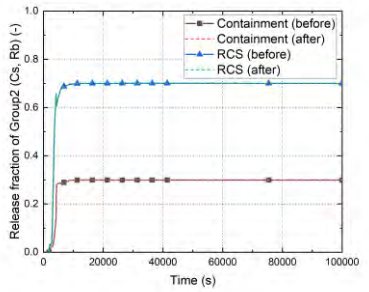

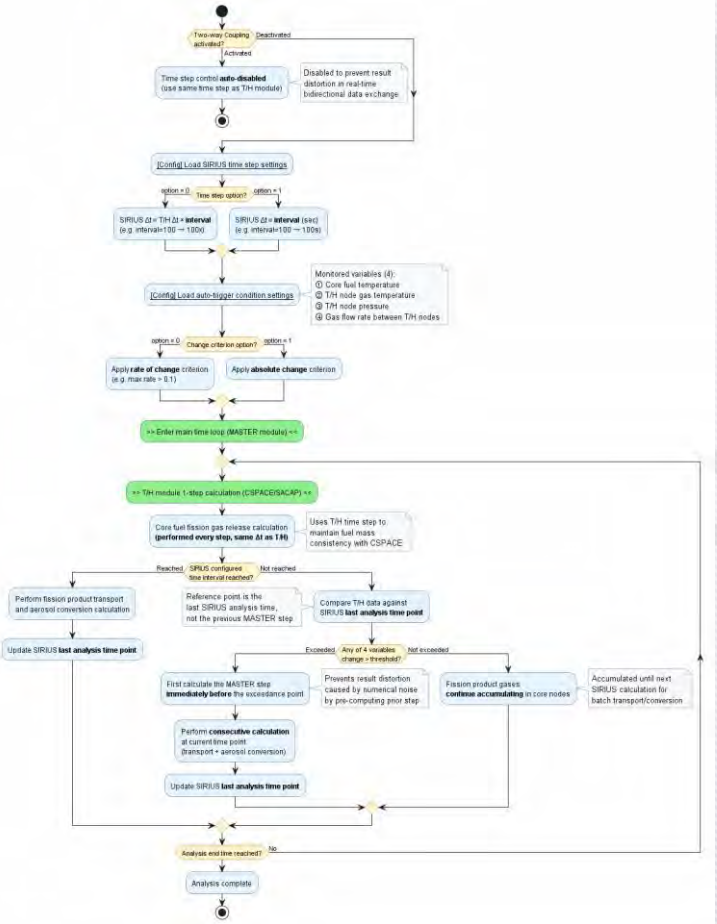

❖ Validation status

Title	Type
PHEBUS-FPT1	Integral
PHEBUS-FPT3	Integral
AHMED: RH22, 82, 96	Hygroscopic
Marviken ATT-2b	Integral
ABCOVE Series: 5, 6, 7	Aerosol deposition
LACE LA-2	Aerosol deposition
STORM SR-11	Aerosol deposition
VANAM M3*	Integral
TOSQAN spray	Aerosol deposition

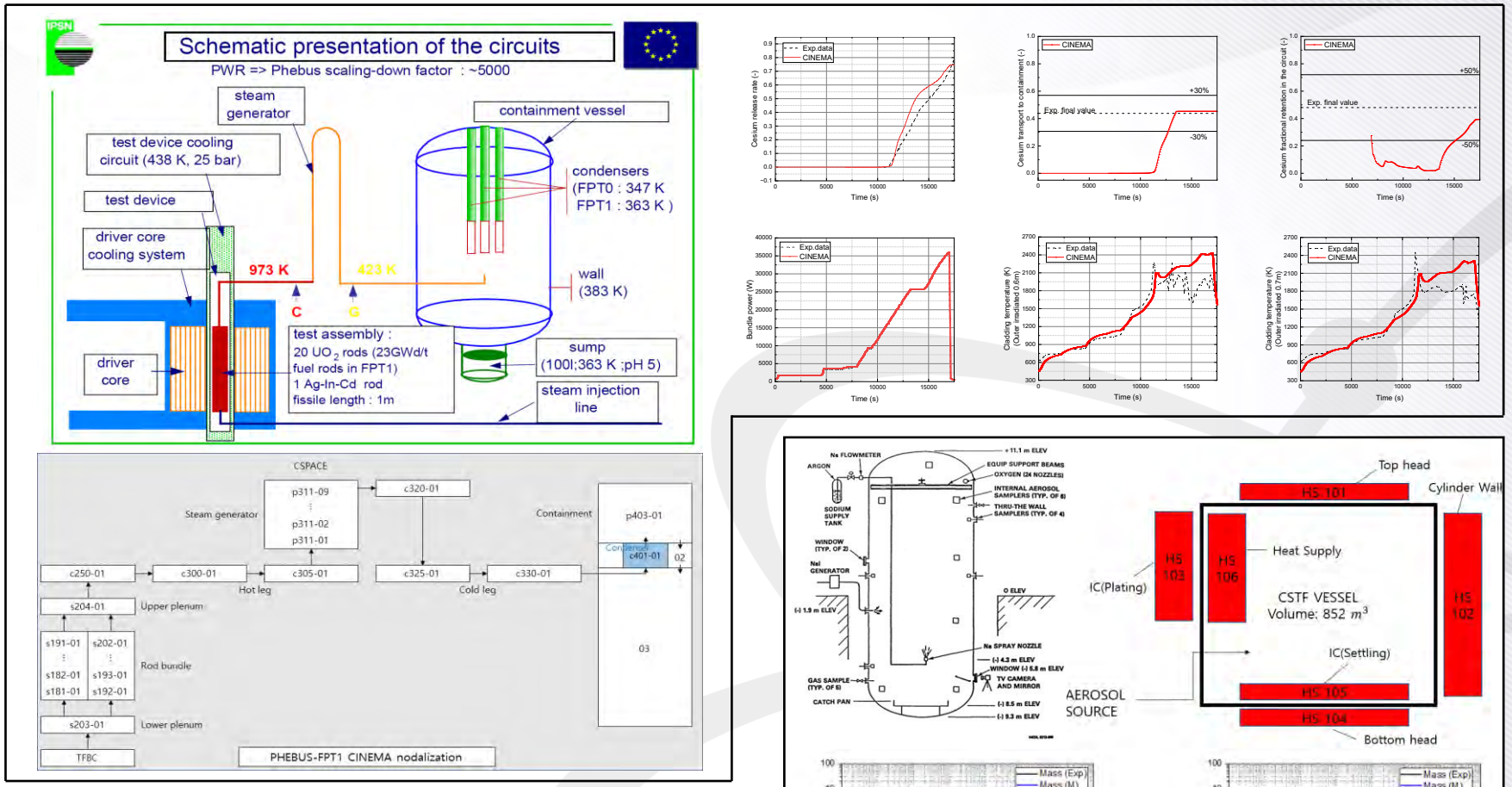

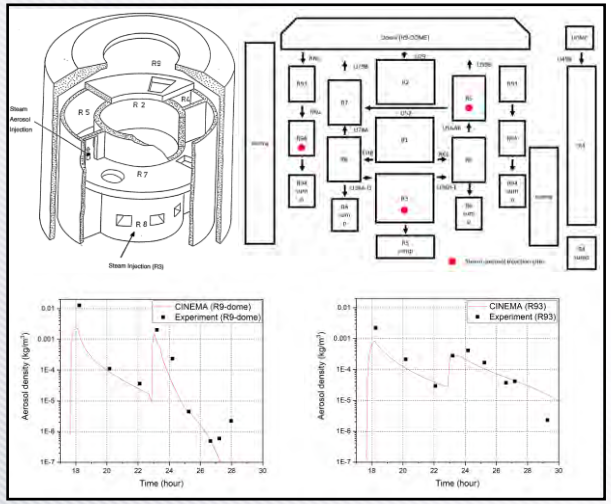

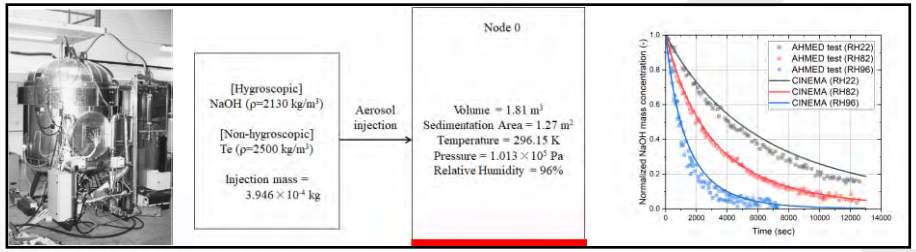

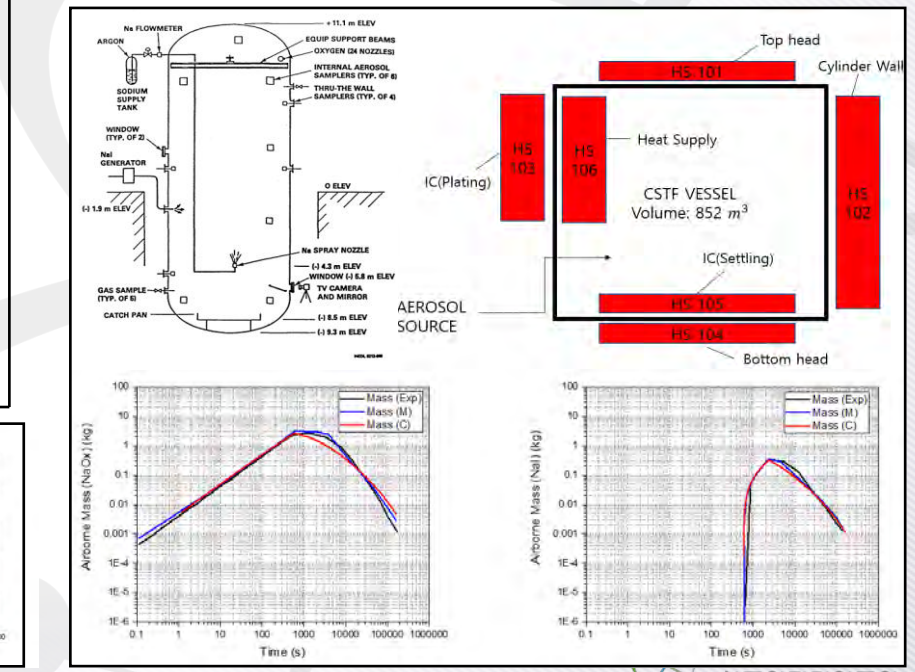

*D.H. Shin, J. Ham, S. H. Kim, C. H. Kim, Y. H. Kim, and Y. H. Jeong, "Analysis of thermal-hydraulic and aerosol behavior in the VANAM-M3 experiment using the CINEMA code," Annals of Nuclear Energy, Vol. 236, Article 112454, October 2026.

❖ PWR case (i-SMR)*

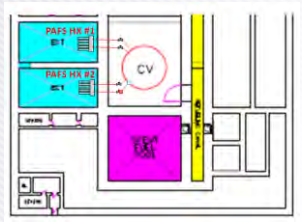

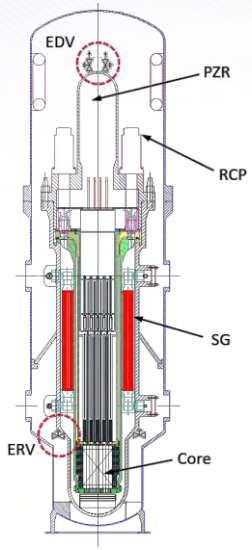

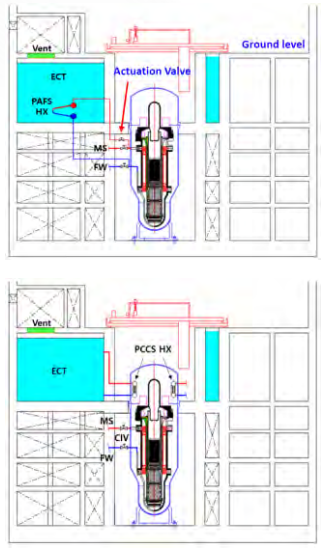

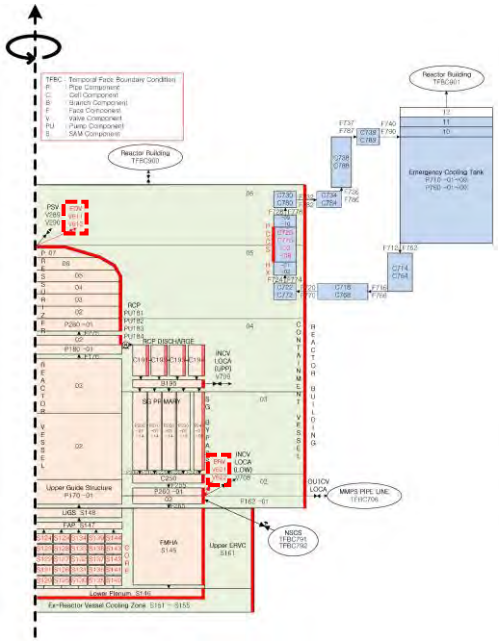

Event	Time
Spurious opening of 2 EDVs (EDV-LOCA occur)	0 s
Reactor shut down	7 s
Active core top uncovering	6.2 hours
Gap release (Cladding temp. > 1173 K)	7.9 hours
Cladding oxidation	8.3 hours
Corium relocation to lower plenum	15.9 hours
RV failure	-

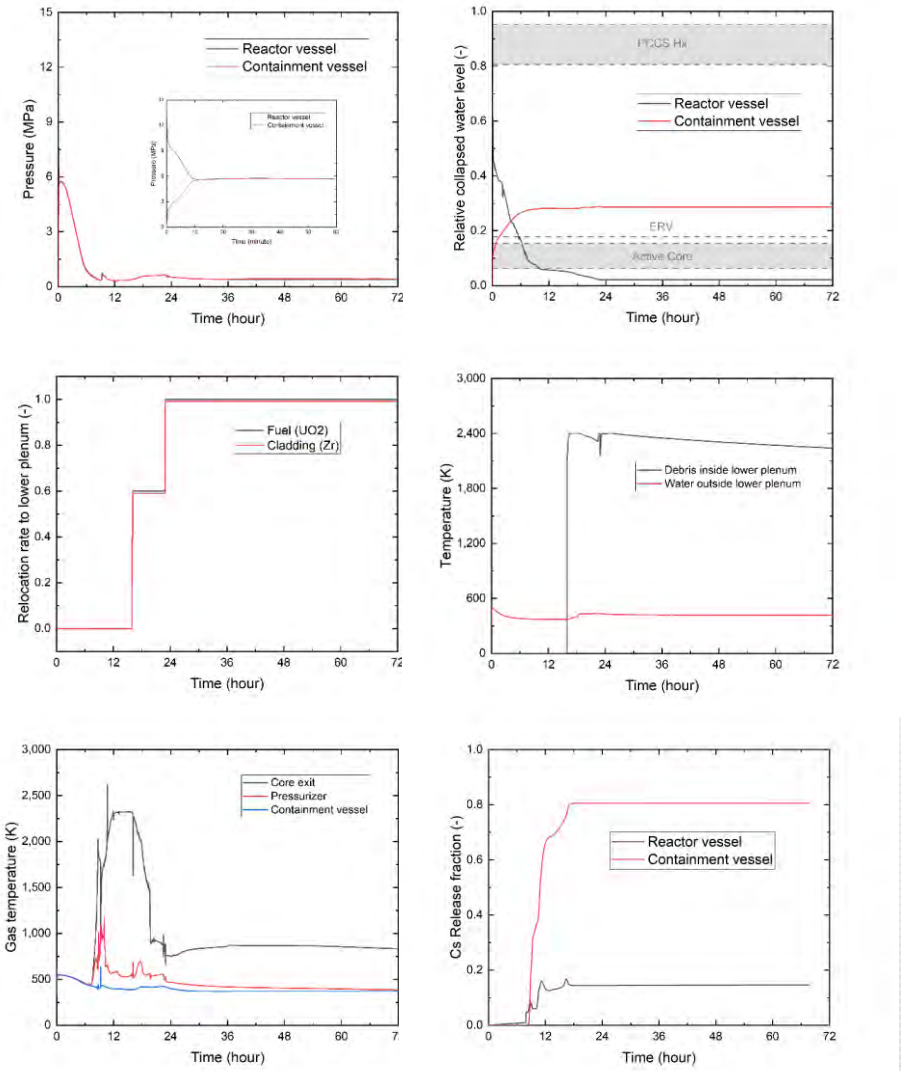

*Jaehyun HAM, Sang Ho KIM, Seokgyu JEONG, "Overview of i-SMR design and severe accident analysis using CINEMA code," International Workshop on SMR Safety for a Sustainable Short-term Deployment, 17-18, October, 2024, Fontenay-aux-Roses, France.

03 Application examples

❖ MSR case

1. Accident scenarios
2. Molten salt spreading
3. Molten salt coolability
4. State & Mass of FP compounds
5. Release of FP compounds
6. Transport & Behavior

External work
1 - 4

SIRIUS
5 - 6

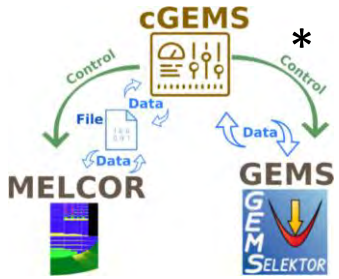

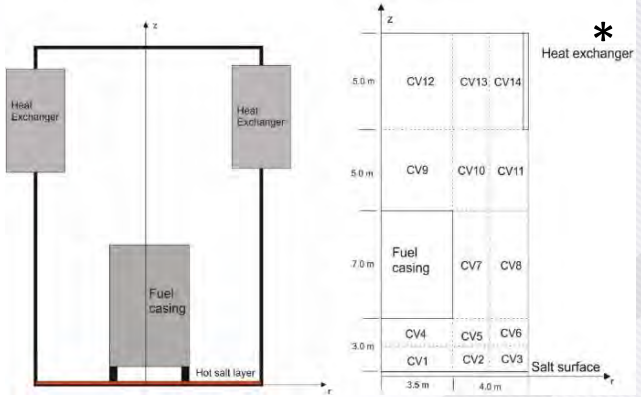

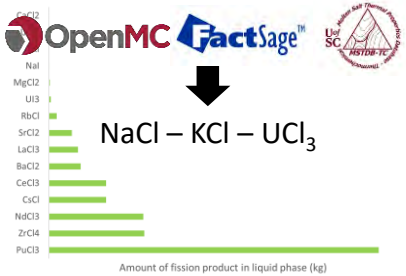

NaCl – KCl – UCl_3

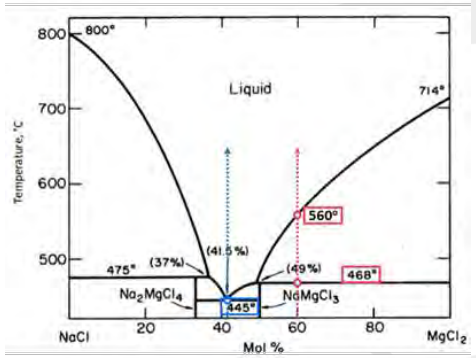

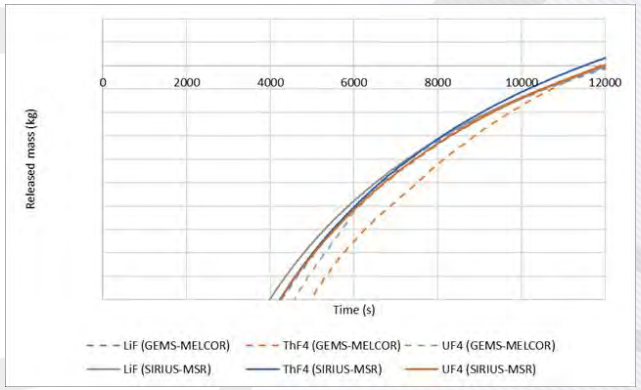

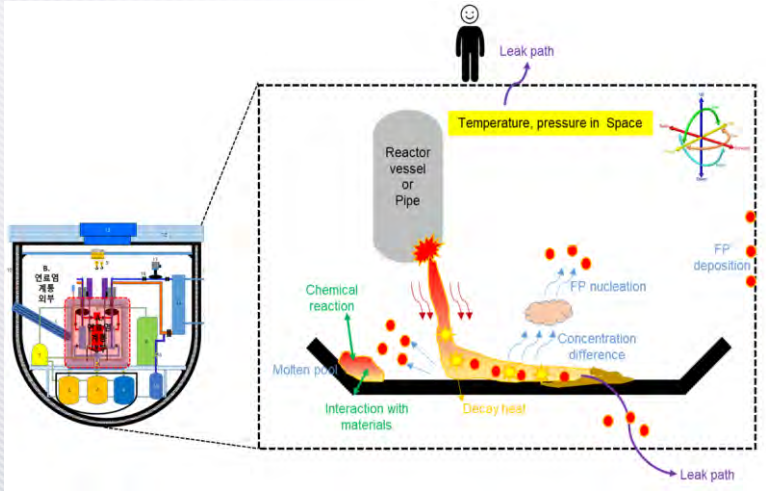

$$\frac{dm_i}{dt} = Ak_i(C_i^s - C_i^a)$$

$$C_i^s = \frac{P_i^s(T)M_i}{RT}$$

$$\frac{k_i}{k_{st}} = \frac{D_{i,N_2}}{D_{st,a}}$$

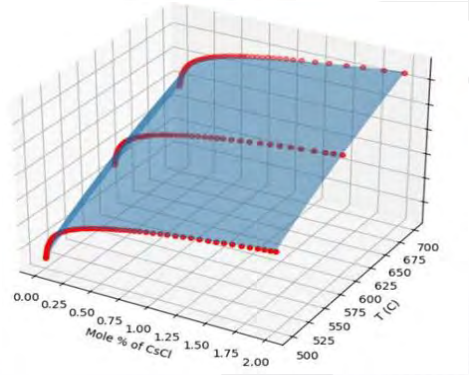

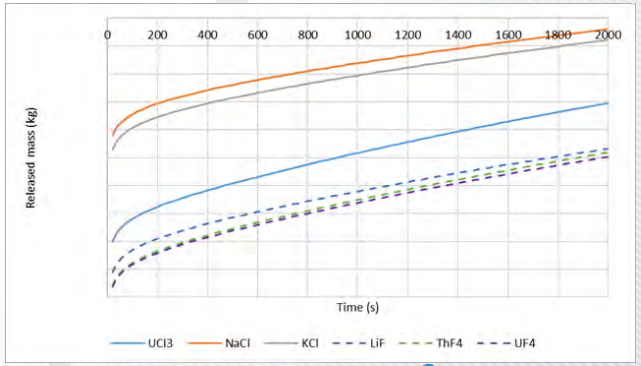

*J. Kalilainen, S. Nichenko, and J. Krepel, "Evaporation of materials from the molten salt reactor fuel under elevated temperatures," Journal of Nuclear Materials, Vol. 533, Article 152134, 2020.

04 Conclusion

- This work presents the current status of SIRIUS development for FP behavior analysis.

❖ Future work

- Incorporate mechanistic FP release models.
- Implement time-dependent aerosol size tracking model as an option.
- Include more detailed FP behavior options to support best-estimate analyses.
- Supplement the validation database with additional experimental benchmarks.
- Extend coupling with thermochemical equilibrium codes.

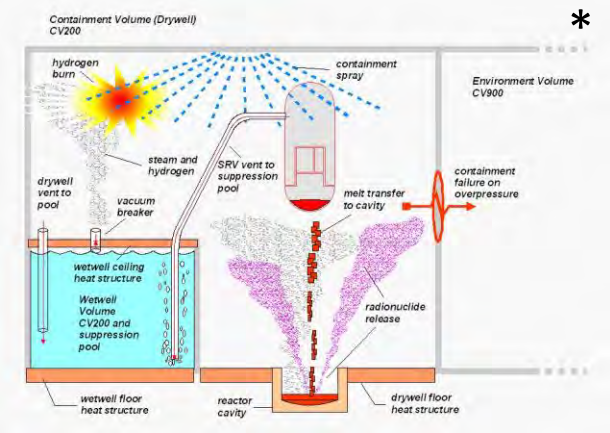

*

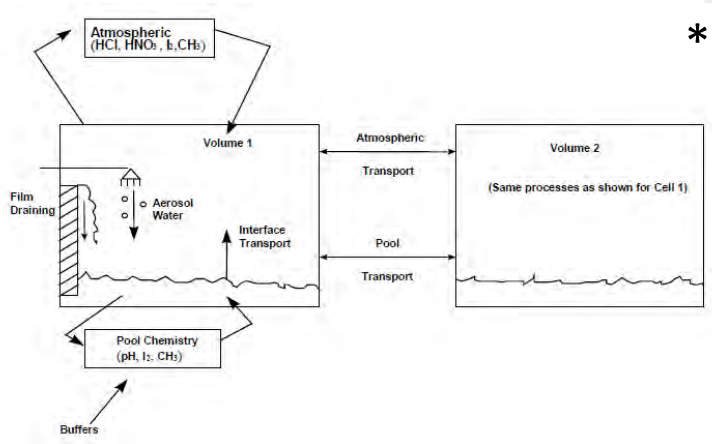

*

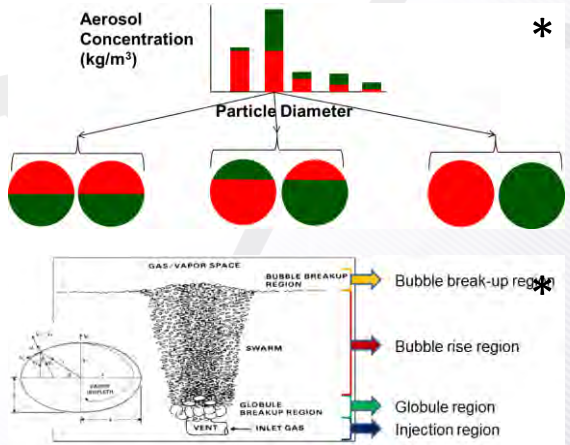

*

*L.L. Humphries, B.A. Beeny, F. Gelbard, D.L. Louie, J. Phillips, "MELCOR Computer Code Manuals Vol. 2: Reference Manual Version 2.2.9541 2017", SAND2017-0876 O, January 2017.

THANK YOU

Contact : jhham@kaeri.re.kr

ACKNOWLEDGEMENT

This work was supported by the Korea Institute of Energy Technology Evaluation and Planning (KETEP) and the Ministry of Climate, Energy & Environment (MCEE) of the Republic of Korea (No. KETEP-20224B10300050).
Also, this work was supported by the Nuclear and Development of the National Foundation of Korea (NRF) grant funded by the Korea government (Ministry of Science and ICT) (No. RS-2022-00144202).
Also, this work was supported by the Innovative Small Modular Reactor Development Agency grant funded by the Korea government (MSIT) (No. RS-2023-00259516).
Also, this work was supported by the National Research Foundation of Korea (NRF) grant funded by the Korea government (MSIT) (No. RS-2023-00261295).

ADVANCED MODELING OF FISSION PRODUCT RELEASE FROM IRRADIATED FUEL DURING SEVERE ACCIDENT SCENARIOS

G. Petrosillo, J. Sercombe, L. Noirot, C. Introini, Y. Pontillon
CEA, DES, IRESNE, DEC
Cadarache, F-13108 Saint-Paul-lez-Durance – France
giacomo.petrosillo@cea.fr

L. Luzzi
Politecnico di Milano, Department of Energy, Nuclear Engineering Division
Via La Masa 34, 20156 Milano – Italy

ABSTRACT

This paper presents simulations of two VERCORS annealing tests (VC5 and HT2), performed on fuels irradiated to average burnups of 38 and 48 GWd/t_U, respectively, and conducted under oxidizing conditions, using the MARGARET–Active FP model coupled with the OpenCalphad thermochemical solver and the TAF-ID database. Initially developed to simulate the production, decay, and transport of over 70 fission products during standard PWR irradiation, MARGARET Active FP provides key microstructural parameters—such as bubble distribution, high burnup structure, and fuel swelling—to describe irradiated fuel. In this work, a new model has been introduced to describe the intragranular transport of bubbles under annealing conditions, representative of scenarios without a thermal gradient, as in VERCORS tests. MARGARET is coupled with a thermochemical module within the ALCYONE fuel performance code to provide a more mechanistic description of non-inert fission product behavior during severe accidents, taking into account their chemical state prior to transient conditions. Model predictions are compared with experimental data, focusing on the release of fission products. The results demonstrate that the coupled mechanistic–thermochemical approach provides a consistent and detailed description of fission-product release under annealing conditions.

KEYWORDS
Fission Product Release, Modeling, Severe Accident, MARGARET, Thermochemistry

1. INTRODUCTION

Different tests at various scales, including both integral and separate-effect tests (such as the VERCORS program [1–4]), are reported in the literature and have provided fundamental insights into the behavior of Fission Products (FPs) during severe accident. It has been highlighted that temperature, oxygen potential, fuel burnup, and cladding–pellet interactions play a crucial role in this context.
These experimental programs enabled the classification of FPs into four main categories: volatile, semi-volatile, low-volatile, and non-volatile. Volatile FPs—such as Xe, Kr, I, Cs, Te, Sb, Cd, Rb, and Ag—are almost completely released by the end of the tests, and their final release is largely insensitive to external conditions (e.g., thermochemical environment), whether oxidizing or reducing [1–4].
Semi-volatile FPs, including Mo, Ba, Rh, Tc, and Pd, exhibit release fractions ranging from 50% to 100%, with both the extent and kinetics of release being strongly influenced by the surrounding atmosphere and by interactions with the cladding [1–4].
Low-volatile FPs—such as Ru, Ce, Sr, Y, Eu, and Nb—generally exhibit release fractions below 10% of their initial inventory, although variations may occur depending on atmospheric conditions or fuel sample

characteristics. Finally, non-volatile species, including most actinides as well as U and Zr, remain essentially unreleased (i.e., final release below 1%) regardless of experimental conditions [1–4].
In the context of FP-release modelling, several computational codes have been developed, depending on the load sequence considered and on the external factors that may influence the release [5–7]. For the simulation of severe accident scenarios in particular, the level of model complexity varies according to the scale and scope of the analysis. Integrated system codes typically rely on simplified models to represent FP behavior [8,9]. At smaller scales—down to the fuel-grain scale—and when focusing on specific aspects of severe accident phenomena, models originally developed for normal operation and incidental conditions have been extended to address severe accident sequences. In this framework, the inclusion of detailed thermochemical calculations is essential to accurately represent FP chemical speciation and its impact on release kinetics [6,10].
Germain et al. enhanced the PLEIADES/ALCYONE fuel performance code by incorporating a gas diffusion model coupled with thermodynamic equilibrium calculations to evaluate the release of non-inert FPs. Their approach considers only the stable elements, not their isotopes, and employs a simplified model for fission gas transport [10].
The main limitation of mechanistic modeling using the typical fission gas model [5] for the considered scenario (annealing sequence) lies in the description of intra-granular FP transport to the grain surface. Experimental results for inert FPs, where thermochemistry has no significant effect, show that nearly complete Xe release is achieved. However, intra-granular fission gas release during annealing tests cannot be accurately predicted without accounting for bubble migration. Indeed, in the absence of irradiation, the equilibrium between gas trapping and re-solution is strongly shifted toward trapping, as the dynamic resolution caused by fission spikes is no longer present. Gas trapped in apparently immobile bubbles would not escape, which contradicts experimental observations.
By analyzing high-temperature release of volatile fission products, Germain et al., showed that assuming gaseous species to be transported to the grain boundary with the same kinetics as xenon yields accurate predictions, suggesting that these species and xenon migrate via the same moving bubbles [10].
Verma et al. showed that neither bubble motion driven by vacancy gradients, nor Brownian motion, nor a combination of the two, is sufficient to account for the large fission gas release observed during post-irradiation annealing [11]. In a subsequent study, Noirot et al. proposed a mechanism involving the coupled transport of bubbles pinned to edge dislocations and the climb of these dislocations. They demonstrated that this mechanism can lead to significant intra-granular fission gas release and provides a consistent explanation for the migration of intragranular bubbles toward the grain boundary [12].
In this paper, we advance FP-release modelling within the PLEIADES/ALCYONE fuel performance code by employing a mechanistic transport model capable of computing the release of radioactive fission products and explicitly incorporating thermochemistry. Specifically, we use the MARGARET Active FP model coupled with the OpenCalphad thermochemical solver and the TAF-ID database [13]. The dislocation-climb mechanism proposed by Noirot et al. has been implemented in MARGARET to address transport limitations under annealing conditions (i.e., in the absence of thermal gradients). Two post-irradiation severe-accident annealing scenarios—VERCORS 5 (VC5), with a fuel average burnup of 38 GWd/t_U and VERCORS HT2 (HT2), with fuel average burnup of 48 GWd/t_U—have been simulated [1]. After a brief presentation of the modelling framework—comprising the ALCYONE fuel performance code, the MARGARET Active FP module, and the thermochemical model—the simulations of the two tests are presented. A comparison between measured and calculated releases of volatile, semi-volatile, low-volatile, and non-volatile FPs is performed to assess the predictive capabilities of the model.

2. ALCYONE Fuel Performance Code

ALCYONE is a fuel performance code co-developed by CEA, EDF, and FRAMATOME within the PLEIADES computational platform [14]. It provides multi-dimensional (1.5D, 2D, 3D) modelling capabilities for fuel rods under normal operation, incidental conditions and, severe accidents. In the present

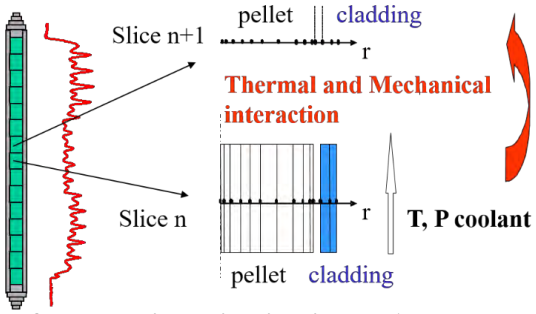

Figure 1. Typical fuel rod discretization in the 1.5D scheme of ALCYONE.

work, only the 1.5D calculation scheme is employed. As shown in Figure 1, the fuel rod is discretized axially into slices and radially into concentric annular rings.

In normal operation conditions, ALCYONE simulation relies on three main solvers: (i) a thermo-mechanical solver that computes temperature and stress fields in the fuel and cladding, (ii) a neutronic solver that evaluates local power deposition and FP inventories, (iii) a mechanistic fission-gas solver predicting FGR and fuel swelling due to Xe and Kr.

The thermo-mechanical module is based on the CAST3M finite-element code and solves the heat balance and mechanical equilibrium equations, accounting for potential fuel–clad contact; iterations are performed until convergence in temperature, stress, fuel–clad gap, and swelling. More details can be found in reference [15]. The neutronic solver, PRODHEL, tracks 199 FP isotopes and 23 actinide isotopes, modelling their production, depletion, and decay using the JEFF-3.1.1 library [16]. The mechanistic fission-gas module, MARGARET, provides a detailed description of Xe and Kr behavior in each radial ring, including dissolution in grains, bubble and pore evolution, grain-boundary accumulation, release to the rod free volume, and HBS formation [5].

The advanced version of the ALCYONE fuel performance code is developed and used in this work to evaluate FP release under severe-accident conditions. Specifically, a dedicated sub-model of MARGARET, referred to as MARGARET–Active FP, is employed to simulate the transport of radioactive fission products. This module is coupled with a thermochemical solver—OpenCalphad solver using the TAF-ID database—which determines through equilibrium calculations the composition of compounds formed through reactions among FPs, actinides, and oxygen within the fuel [13].

As shown in Figure 2, multiple interactions occur during the simulation. In this work, it is important to note that the input parameters for the thermochemical calculations rely on information provided both by MARGARET–Active FP (FP composition, pressure, and temperature) and by PRODHEL (actinide inventories). Details on the coupling strategy are presented in the following sections.

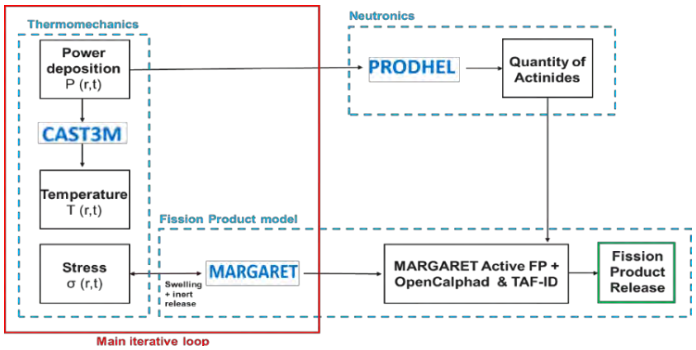

Figure 2. Schematics of the interactions in the updated version of ALCYONE between the thermomechanical, neutronic, fission-gas, and thermochemical solvers. (r, t) denote the radial position of a ring and the time within the simulated irradiation sequence.

3. MARGARET

MARGARET is a mechanistic fission-gas model that describes Xe and Kr migration at the grain scale under normal, transient, and incidental conditions. It operates as a point model, providing—for each radial position—the released gas fraction, the swelling induced by fission gases, and the formation of the high-burnup structure (HBS).
Figure 3 illustrates the main intra-granular and inter-granular phenomena described by MARGARET. The HBS description is not shown, as it is not the focus of this work; the analyzed cases do not reach sufficiently high burnup for this phenomenon to be relevant. On the left, intra-granular processes include gas production, atomic diffusion, bubble nucleation and growth, trapping and re-solution due to fission spike interaction, and bubble or pore motion toward the grain boundary.
Gas escaping the grain becomes the source term for inter-granular behavior. On the right, inter-granular processes involve gas accumulation at the grain boundary, the formation and growth of inter-granular bubbles, swelling, and eventual bubble coalescence that creates interconnected pathways enabling fission-gas release by percolation, as well as direct release when parts of the grain surface are directly exposed to the fuel rod free volume. Details on MARGARET model can be found in [5].

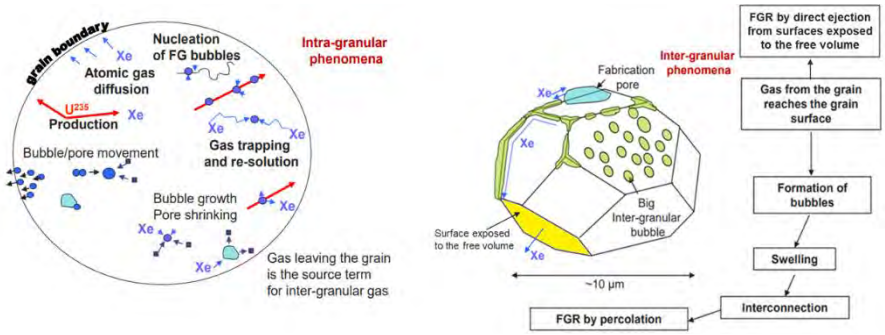

Figure 3. Intra- and inter- granular phenomena described by MARGARET. Scheme reproduced with the permission from Noirot et al., J. Nuclear Science and Technology, 2006.

As stated in Section 1, the original MARGARET model is not able to reproduce the massive intra-granular gas release under annealing conditions, because—without irradiation—insoluble gas remains trapped in intra-granular bubbles, dynamic re-solution is absent, and random bubble motion is not sufficient (absence of thermal gradient). To address this limitation, the dislocation-climb mechanism proposed by Noirot et al. [12] has been implemented in MARGARET.
Figure 4 (left) shows an over-pressurized intragranular bubble pinned at the core of an edge dislocation, which provides the driving force for dislocation motion. The schematic on the right of the Figure 4 illustrates

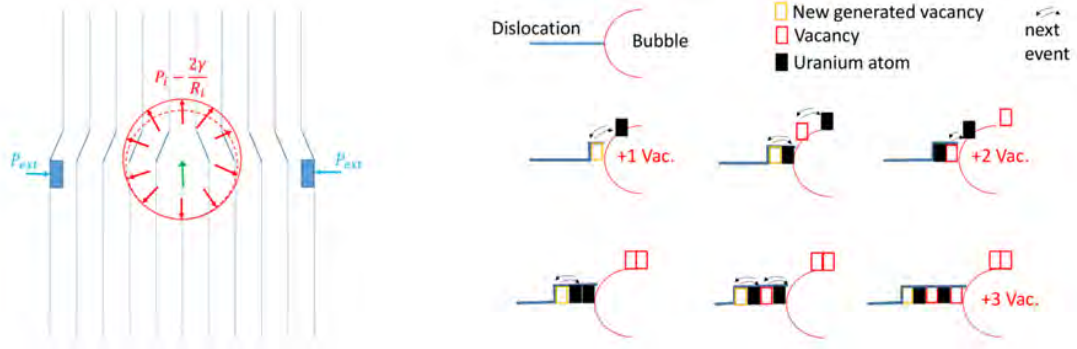

Figure 4. (left) Overpressurised intra-granular bubbles pinned at the core of an edge dislocation. (Right) Vacancy generation, diffusion along the dislocation core, and trapping by the bubble. Scheme reproduced with the permission from Noirot et al., J. Nuclear Materials, 2023.

the coupled bubble–dislocation mechanism: the high internal pressure of the pinned bubble generates vacancies along the dislocation, which diffuse toward the bubble, while uranium atoms accumulate along the dislocation line. This enables dislocation climb, leading to bubble growth, pressure relaxation, and ultimately bubble motion, leading to intra-granular gas transport. Further details on the model are provided in the cited references [12].

To model the dislocation-climb mechanism, new state variables and bubble populations have been introduced in MARGARET. In particular, a dislocation density ρ_d^{climb} associated with climb (edge dislocation) and a population of bubbles pinned on climbing dislocations (referred to as *bprec*) are defined. These bubbles are characterized by their concentration C_{bprec}, xenon content $C_{Xebprec}$, and volume V_{bprec}. Their evolution is governed by several coupled processes: gas exchange between the dissolved phase and *bprec*, swelling of pinned bubbles, pinning of free intra-granular bubbles onto dislocations, bubble coalescence, and the release *bprec* when they reach the grain boundaries. The velocity of climbing dislocations v_d, which controls the transport of gas toward the grain boundary, as well as the associated swelling, depends on the characteristics of *bprec* and is expressed by the relations reported below:

$$v_d = \frac{12D^*}{kT} \frac{P_{bprec} - {2\gamma}/{R_{bprec}} - P_{hydr}}{\frac{C_{bprec}}{\rho_d^{climb}} \left(\frac{\rho_d^{climb}}{C_{bprec}} - 2R_{bprec} \right)^3} \times \Omega^{4/3} \qquad \frac{dV_{bprec}}{dt}\Big|_{climb} = v_d \times w \times \rho_d^{climb}$$

where D^* is the coefficient of vacancy creation and diffusion on the dislocation, P_{bprec} and R_{bprec} are respectively the internal pressure and radius of *bprec* bubbles, P_{hydr} is the hydrostatic pressure, T is the temperature, k is the Boltzmann constant, Ω is the volume of the UO_2 pattern, and w is the width of the dislocation core. The dislocation density ρ_d^{climb} is estimated using the correlation proposed by Nogita et al. [17], under the assumption that the density of dislocations capable of climb is of the same order of magnitude as the experimentally measurable total dislocation density. At present, experimental techniques do not allow this specific dislocation population to be identified and quantified separately. The input parameters of the model— D^*, described by an Arrhenius-type expression with a pre-exponential factor and an activation energy—were fitted using three isothermal annealing experiments reported in the PhD thesis of Valin [18]. In these experiments, UO_2 fuel pellets from a PWR, irradiated for one cycle to a burnup of 14.2 GWd/t_U, were used. Three pellet were annealed for 3 h at temperatures of 1600, 1500, and 1400 °C, respectively, while krypton release was continuously monitored using a gamma spectrometry [18]. The results of the fitting procedure are shown in Figure 5, yielding an activation energy of 4 eV and a pre-exponential factor of 2×10^{-7} m^2s^{-1}.

It is important to emphasize that this represents a first implementation of the model within MARGARET, and its parameters require deeper investigation.

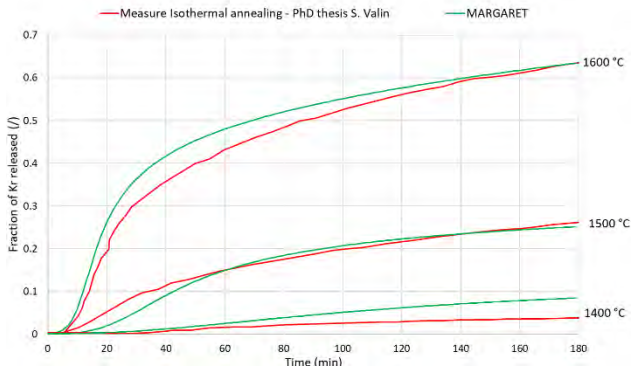

Figure 5. Comparison between measured and calculated krypton release fractions during isothermal annealing experiments at 1400, 1500, and 1600 °C. Experimental data from the PhD thesis of S. Valin are shown in red, while MARGARET simulations are shown in green.

4. MARGARET Active FP

MARGARET–Active FP is a dedicated sub-model within MARGARET to account for chemically reactive and radioactive fission products. Initially, MARGARET Active FP was developed to investigate potential contamination of the primary circuit by radioactive fission products, during base irradiation. It handles 75 isotopes, ranging from short-lived to long-lived isotopes. The transport of each isotope follows the same procedural framework as the original MARGARET model and is governed by equations derived analogously, accounting also for production by fission as well as by radioactive decay and neutron capture of precursor nuclides [13].
MARGARET Active FP does not provide feedback to the MARGARET model, under the assumption that radioactive fission products are present in quantities sufficiently small compared to stable gases that their influence on microstructural evolution is negligible. Consequently, all microstructural parameters—such as the evolution of bubble populations—are taken directly from MARGARET. The model enables the specification of isotope-dependent intrinsic diffusion coefficients and re-solution frequencies (via fission spikes), typically using inert gases from MARGARET as reference values [13].
MARGARET–Active FP includes the capability to account for the impact of thermochemistry on the transport of fission products, which is crucial during high-temperature sequences as it strongly affects release behavior, as demonstrated by severe-accident experiments and corresponding modelling [10]. A coupling strategy between MARGARET-Active FP and a thermochemical module, composed of the OpenCalphad solver and the TAF-ID database, was proposed, successfully tested, and applied in previous work to simulate fission-product release during incidental sequences, such as power-ramp experiments [13]. This coupling was subsequently implemented in ALCYONE.

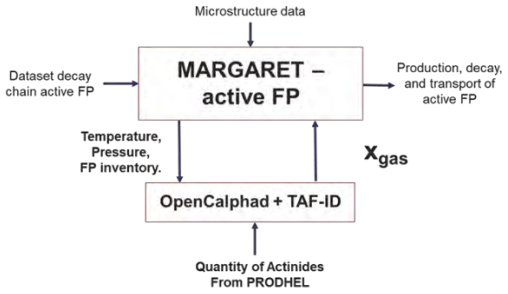

Figure 6. Coupling scheme between MARGARET Active FP and the thermochemical model.

The coupling scheme is shown in Figure 6. The thermochemical behavior is incorporated through the variable x_{gas}, calculated by the thermochemical module, which represents the fraction of each fission product present in the gas phase: $x_{gas} = mol_{FP}\ in\ gas\ phase / mol_{FP}\ in\ all\ phases$.
This fraction is used in the mechanisms that govern release from grain boundaries, namely percolation through intergranular cavities and direct ejection when portions of the grain surface are exposed to the free volume. A key assumption of the model is that only the gaseous fraction of fission products is releasable, while condensed phases remain confined within the fuel [13].

5. Fuel Thermochemistry

The thermochemical module is used to compute x_{gas} using as input the temperature and pressure from MARGARET–Active FP and the actinide inventories provided by PRODHEL. The chemical system considered in the calculation includes the elements: He, Kr, Xe, U, O, Pu, Ba, Sr, Zr, Cs, Rb, I, Br, Te, Se, Mo, Ru, Rh, Tc, Pd, Ce, Pr, La, Y, Gd, Eu, Sm, and Nd. Details on the assumptions adopted for the thermochemical system are provided in reference [13].
Fuel thermochemistry modelling in this work relies on the OpenCalphad Gibbs energy minimizer [19,20], which computes the equilibrium state of the multicomponent nuclear-fuel system and determines phase

compositions (gas, solid solution, liquid) and the stoichiometric compounds formed through chemical interactions between actinides, fission products, and oxygen. In this work, the thermodynamic descriptions are taken from the OECD Thermodynamics of Advanced Fuels – International Database (TAF-ID) [21], developed to support calculations under both normal and accidental conditions. TAF-ID includes an extensive set of fission products, structural materials, and absorbers, enabling detailed modelling of irradiated-fuel thermochemistry and chemical interactions with surrounding materials. The version used here (v20) contains thermodynamic assessments for 257 binary systems, 145 ternary systems, and 3 quaternary systems.

6. Modeling of the VERCORS 5 & HT2 tests

This section describes the two simulated tests, VC5 and HT2. The experiments consist of thermal annealing of fuel-rod segments in a furnace. Both tests were performed on three-pellet samples extracted from two different fuel rods, previously irradiated to an average burnup of 38 GWd/t_U for VC5 and 48 GWd/t_U for HT2 [1].

The experimental sequences were similar, as illustrated in Figure 7. An initial temperature plateau was applied at approximately 350–400 °C under a helium flow. The temperature was then increased to 1300 °C for VC5 and 1500 °C for HT2 under an oxidizing atmosphere (steam) and maintained for 60–75 minutes, depending on the test, in order to fully oxidize the cladding. After this oxidizing plateau, one temperature ramp was applied in the VC5 test, whereas several ramps with intermediate plateaus were performed in the HT2 test. In both experiments, the carrier gas consisted of steam (H_2O) with a small fraction of hydrogen (H_2) to ensure oxidizing conditions within the furnace [1].

Before simulating the two tests, preliminary calculations were carried out with ALCYONE to reproduce the base irradiation, the cooling and storage period, and the pre-test re-irradiation. This step was required to rebuild the fission-product inventory, including short-, medium-, and long-lived isotopes.

In the simulations of the two experimental sequences, the fuel rod was represented using a single axial slice, while the fuel pellet was discretized radially using 41 nodes, with increased refinement near the pellet periphery. Also in the simulation, the impact of the carrier-gas composition on fission-product behaviour is explicitly taken into account in the thermochemical calculations.

Regarding the experimental measurements, all isotopes, FG excepted, discussed in the following were measured by gamma spectrometry sighting on the fuel samples located inside the fournace. Inert fission gases (Xe, Kr) were monitored on-line by gamma spectrometry using a dedicated gas capacity. For the HT2 test, gamma spectrometry on the fuel was not performed until the end of the experiment due to specimen movement within the furnace chamber; nevertheless, sufficient data were collected to allow a comprehensive analysis of volatile (Xe, Kr, Cs, I) and semi-volatile (Mo, Ba, Ru) fission-product release. Further details on the experimental setup are provided in references [1,2].

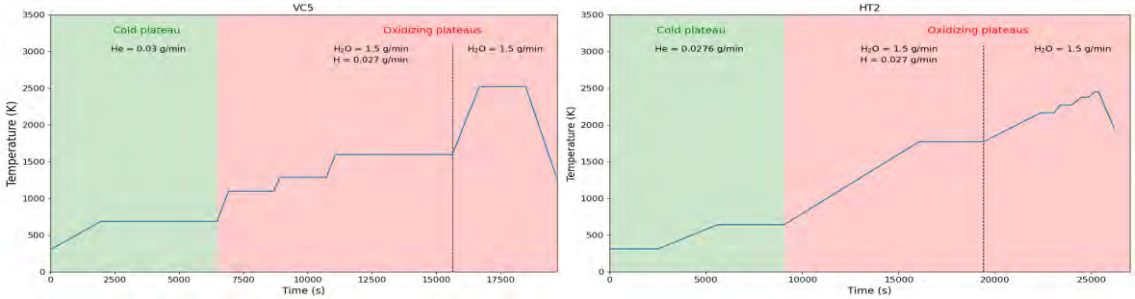

Figure 7. Temperature evolution during the VC5 (left) and HT2 (right) annealing tests.

The analysis starts with the release of fission gases and volatile fission products. For the VC5 test, the fission gas analysed is ^{133}Xe, whereas for the HT2 test the fission gas considered is ^{85}Kr. Concerning volatile fission products, the elements examined in both tests are ^{137}Cs and ^{131}I.

In the VC5 case, both fission gases and volatile fission products reach final release fractions between 90% and 100%, as shown in Figure 8. Experimental data show a difference in release kinetics between these two groups. Release starts for both during the plateau at 1570 K; however, volatile fission products are released more rapidly than fission gases. The release kinetics of volatile species exhibit larger experimental uncertainties at this temperature and at lower temperatures, as indicated by increased data scatter. In addition, since fission-gas measurements are performed in a downstream gas-capacity system rather than directly on the fuel, the thermo-hydraulic behaviour of the experimental setup may influence the observed release kinetics.

Simulations provide a good representation of the final release fractions for both fission gases and volatile fission products during VC5 (Figure 8, left). For ^{133}Xe, the model predicts only limited release during the 1570 K plateau, due to the negligible presence of this short-lived isotope at the grain boundaries. The main release occurs between 1600 and 1800 K, with a release rate higher than that observed experimentally. In this temperature range, intra-granular release is driven by the dislocation-climb transport mechanism implemented in the model. The release kinetics are strongly dependent on the assumed dislocation density, which is estimated using the correlation proposed by Nogita et al. as a function of burnup. However, in both experiments a low-temperature re-irradiation phase was applied prior to annealing, potentially leading to the formation of additional defects. This introduces increased uncertainty in the effective dislocation density and, consequently, in the predicted release kinetics. This uncertainty also propagates to the release of other fission products, as the same transport parameters as those used for inert gases are applied, with differences arising only from their thermochemical behaviour.

For volatile fission products (Figure 8, right), the model predicts their complete final release, consistent with the high chemical volatility predicted by the thermochemical calculations. In particular, a fraction of ^{137}Cs is released during the 1570 K plateau, reflecting its longer half-life and presence at the grain boundaries. In contrast, ^{131}I follows a release pattern similar to that of ^{133}Xe, owing to its short half-life.

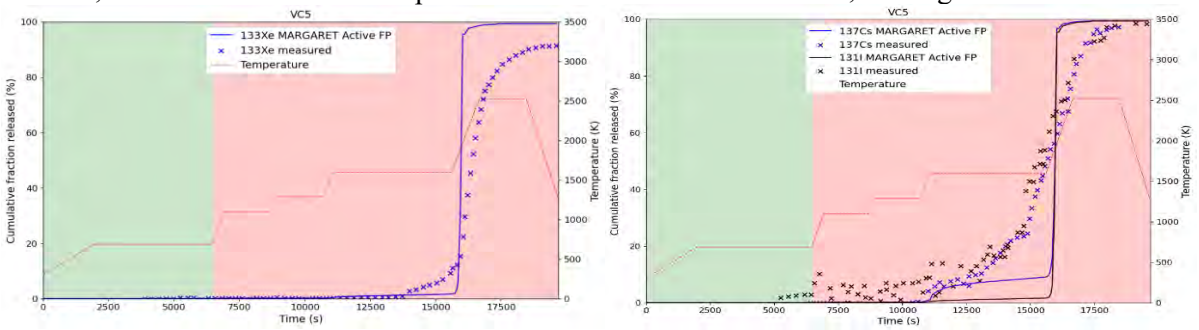

Figure 8. Measured and calculated cumulative release of ^{133}Xe (left), ^{137}Cs and ^{131}I (right) during the Vercors 5 test.

The analysis is extended to the HT2 test. Experimentally, complete release is observed for both FP categories, as illustrated in Figure 9. As in the VC5 case, similar differences are observed between fission gases and volatile species. Release starts at temperatures around 1500 K, and at lower temperatures volatile fission products exhibit higher release rates than fission gases, a trend that generally persists throughout the test. Simulations also predict complete release for ^{85}Kr, ^{137}Cs, and ^{131}I. In this case, the model provides a better representation of the release rate of ^{85}Kr compared to ^{133}Xe in the VC5 test. For volatile fission products, the trends are consistent with those observed in the VC5 test, with differences at lower temperatures arising from the short half-life of iodine, which limits its presence at the grain boundaries. Thermochemical calculations indicate that, also in this case, iodine and cesium are entirely present in the gas phase when released.

The analysis is now extended to semi-volatile and low-volatile fission products. For the VC5 test, the isotopes considered are ^{99}Mo, ^{140}Ba, and ^{103}Ru. For the HT2 test, the analysis is limited to ^{99}Mo, as the data collected for ^{140}Ba, and ^{103}Ru were not sufficiently significant for the analysis due to specimen movement

within the furnace chamber. The experimental results and the corresponding calculations are shown in Figure 10.

For molybdenum, both tests exhibit trends similar to those observed for volatile fission products. This behaviour is attributed to the oxidizing environment, which enhances the volatility of Mo and leads to comparable release kinetics. For the VC5 test, the model predicts a nearly complete final release, in agreement with the experimental data. In this case, the release kinetics resemble those observed for volatile short-lived species: no significant release is predicted during the 1570 K plateau, and most of the release occurs during the final temperature transient leading to the last plateau. At that stage, molybdenum is predicted to be entirely present in the gas phase.

For the HT2 test, the model tends to underestimate the final release, predicting 82% compared to the complete release observed experimentally. This discrepancy arises because, according to the thermochemical calculations, part of the molybdenum inventory remains trapped in the liquid phase. Nevertheless, the model provides a good representation of the release kinetics, closely reproducing the experimental trends.

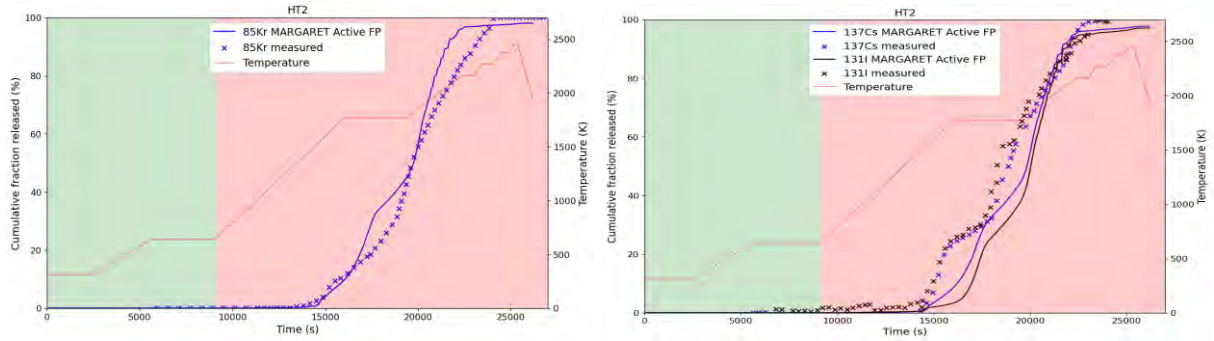

Figure 9. Measured and calculated cumulative release of ^{85}Kr (left), ^{137}Cs and ^{131}I (right) during the HT2 test.

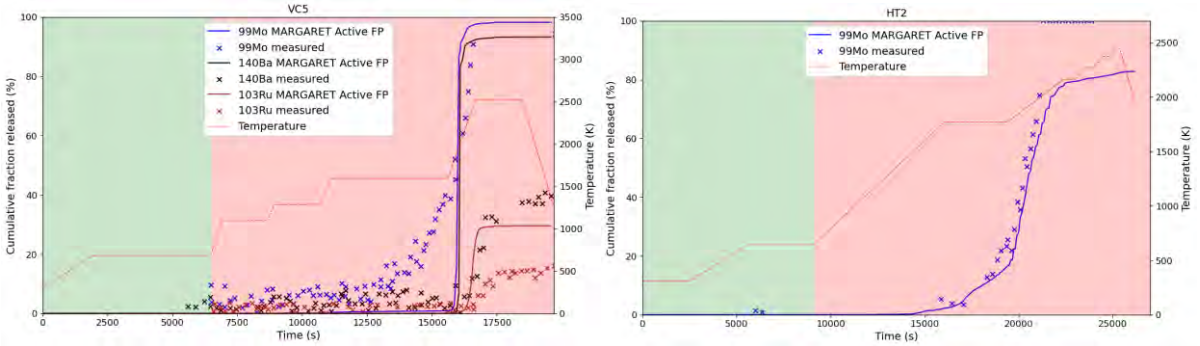

Figure 10. Measured and calculated cumulative release of semi-volatile and low-volatile fission products during the VC5 test (^{99}Mo, ^{140}Ba, and ^{103}Ru) (left), and of the semi-volatile fission product ^{99}Mo during the HT2 test (right).

Considering the experimental release of ^{140}Ba in VC5 case, the final release fraction is approximately 40%, with the release occurring at higher temperatures and later in the test compared to molybdenum. This is attributed to the thermochemical behaviour of barium. Post-annealing analyses of the specimens, including gamma tomography, show that barium reacts with the cladding—which is oxidized at the time of Ba release—and remains trapped as a result [3].

In the simulation, barium exhibits a release behaviour similar to that of molybdenum, with a predicted final release close to 90%, resulting in a significant overestimation compared to the experimental data. Indeed, according to the thermochemical calculation results, barium is fully present in the gas phase during the final temperature plateau, whereas during the preceding temperature transient it is distributed between the gas

and liquid phases (see Figure 11, left). This discrepancy arises because the interaction between barium and the cladding is not considered in the current modelling framework. As a consequence, when only fuel-side processes are taken into account, Ba release is overestimated. Moreover, on-line gamma spectrometry does not allow potential interactions of fission products with the cladding to be distinguished, and therefore does not permit isolation of the release originating solely from the fuel. As a result, a dedicated modelling approach that explicitly includes fission-product interactions with the cladding is required to achieve a more realistic representation of barium release.

In the case of ^{103}Ru (low-volatile) in the VC5 test, the experimental data indicate a final release of about 18%, with a release rate lower than that observed for Ba or Mo. Model calculations also overestimate the final release in this case, predicting a value approximately twice the experimental one. This discrepancy originates from the thermochemical calculations. Analysis of the phase distribution of Ru predicted by the model shows that it is mainly found into an hexagonal close-packed (HCP) metallic phase, with small fractions in the gas phase and in a face center cubic (FCC) metallic phase (see Figure 11, right). The tendency of Ru to form metallic phases suggests that additional metallic phases potentially formed through interactions between fission products and the cladding may react with ruthenium, thereby affecting its release.

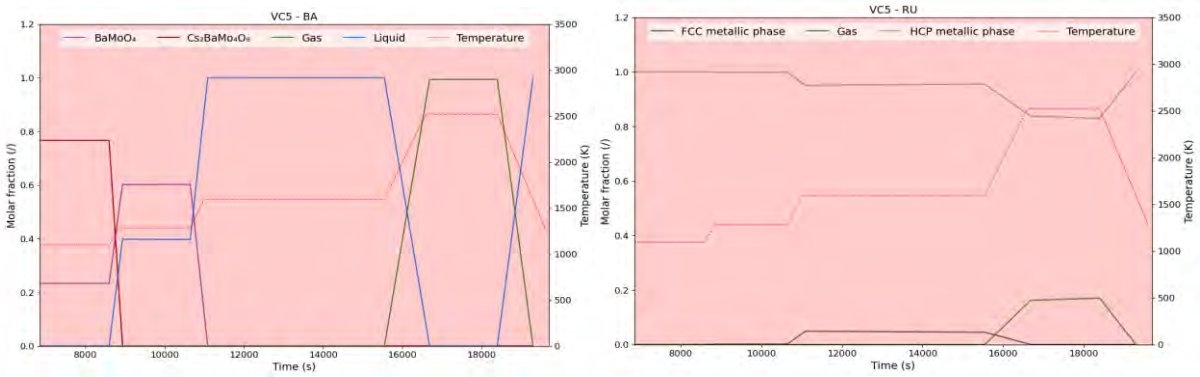

Figure 11. Distribution of Ba (left) and Ru (right) among all phases and stoichiometric solid compounds during the VC5 test.

For non-volatile fission products, such as ^{95}Zr, no release is observed experimentally. This result is consistent for both the VC5 and HT2 tests and is fully reproduced by the model calculations, which also predict no release for these species.

To further investigate the discrepancies observed between experimental results and model predictions, particularly for Ba and Ru fission products, an additional post-processing analysis was performed to assess potential chemical interactions between the cladding and fission products. Specifically, a thermochemical equilibrium calculation was carried out between the cladding material and the fission products released from the fuel, using the temperature and pressure conditions of the VC5 test.

The calculation was performed considering the entire cladding. In this case, the cladding was assumed to be fully oxidized (ZrO_2), consistent with the highly oxidizing environment of the test. The calculation includes the total inventory of fission products released from the fuel, as well as a fraction of uranium. The latter accounts for fuel–cladding interaction under oxidizing conditions. Indeed, Veshchunov et al. investigated this interaction and reported the formation of a ceramic $(U,Zr)O_x$ phase. Their results indicate that between 3% and 6% of the total fuel can interact with ZrO_2 [22]; in the present calculation, the upper bound of 6% was conservatively assumed.

It is important to emphasize that this represents a first-order approach, in which it is assumed that the entire released fission-product inventory can potentially interact with the cladding. In addition, spatial effects and kinetic limitations of these interactions are not considered.

The results of this post-processing calculation indicate that only Ba and Ru are retained by the cladding, while all other fission products remain in the gas phase; consequently, no chemical interaction with the cladding is predicted for these FP other than Ba and Ru.

As shown in Figure 12, the released quantities of ^{140}Ba and ^{103}Ru are drastically reduced, bringing the predicted final release into much closer agreement with the experimental data. In addition, the release kinetics are also improved in this case, highlighting the importance of explicitly accounting for interactions with the cladding. These results further emphasize the level of detail provided by the thermochemical modelling and by the database employed. The calculations show that barium preferentially reacts with and is retained by zirconium oxide, but also forms a hexagonal close-packed (HCP) metallic phase with zirconium. This metallic phase, in turn, traps part of the ruthenium inventory, thereby limiting its release.

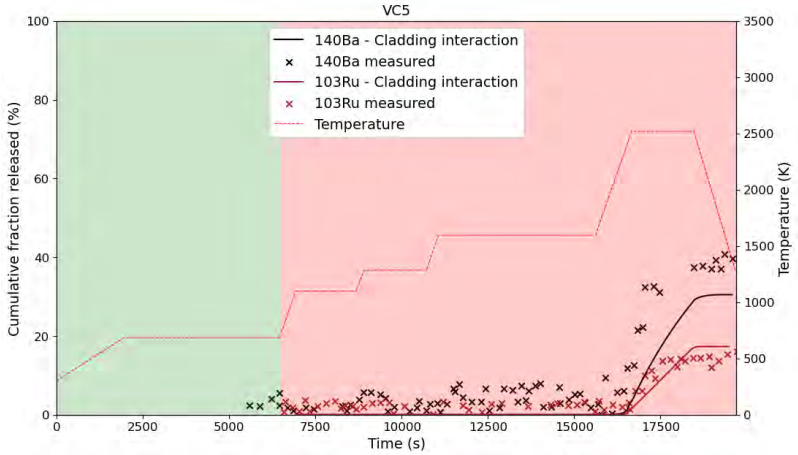

Figure 12. Measured and calculated cumulative release of semi-volatile and low-volatile fission products during the VC5 test (^{140}Ba, and ^{103}Ru), after accounting for thermochemical equilibrium with the cladding.

7. Conclusions

In this paper, simulations of two accidental scenario sequences were performed using an advanced modelling approach that couples a mechanistic fission-gas transport model with a thermochemical model within the ALCYONE fuel performance code.

The mechanistic fission-product model MARGARET was extended through the implementation of a transport approach based on a dislocation-climb mechanism. This development overcomes a key limitation of the original model in annealing scenarios, where—in the absence of irradiation and thermal gradients—gas would otherwise remain trapped within intra-granular bubbles. The dislocation density was estimated using the correlation proposed by Nogita et al. [17], while the vacancy creation and diffusion coefficients were fitted using three isothermal annealing experiments reported in the PhD thesis of Valin [18].

The coupling between the MARGARET–Active FP transport model and the thermochemical module was also introduced, enabling the explicit treatment of chemical interaction on fission-product transport and release, which is particularly important for high-temperature accidental conditions.

The analysed cases correspond to two annealing experiments, VC5 and HT2, performed on fuels irradiated to burnups of 38 GWd/tU and 48 GWd/tU, respectively. Although the two tests involve slightly different temperature ramp sequences, they are conducted under similar chemical environments. Model predictions were compared with experimental gamma-spectrometry measurements.

For fission gases and volatile fission products, the model reproduces well the final release fractions in both tests, with an improved representation of release kinetics for the HT2 case. In both scenarios, the predicted release is directly driven by the dislocation-climb transport mechanism, yielding encouraging results in terms of released quantities. Nevertheless, uncertainties remain, mainly related to the assumed dislocation density. In particular, the low-temperature re-irradiation applied prior to annealing may promote additional defect formation, while the parameter fitting was performed using fuel samples irradiated for a single cycle and characterized by significantly lower burnup than that of the VC5 and HT2 tests. Both aspects may affect the predicted release kinetics and warrant further investigation.

From a thermochemical perspective, volatile fission products behave as expected, exhibiting high volatility and release patterns similar to those of fission gases. For semi-volatile and low-volatile fission products, the model predicts high volatility in both tests. For molybdenum, good agreement with experimental final release is obtained in the VC5 test, whereas release is underestimated in HT2, partly due to the presence of Mo in the liquid phase during the temperature transient. Under these conditions, additional Mo release via aerosol formation transported by the carrier gas may occur, a mechanism not currently included in the modelling framework.
For Ba and Ru, the model initially overestimates their release. However, post-processing calculations accounting for cladding–fission product interactions demonstrate that these interactions effectively limit their release, bringing model predictions into agreement with experimental observations, particularly for Ba retention in the cladding. This highlights the fundamental role of the cladding, which cannot be neglected in this type of analysis.
Finally, non-volatile fission products behave as expected, with no release observed experimentally or predicted by the model for species such as Zr.
Overall, this work demonstrates the high level of detail achieved by the modelling approach, from both mechanistic and thermochemical perspectives. The influence of key model parameters has been clearly identified and will be the focus of future, more detailed investigations.

8. Bibliography

1. Pontillon, Y., Ducros, G. & Malgouyres, P. P. *Nucl. Eng. Des.* **240**, 1843–1852 (2010).
2. Pontillon, Y. & Ducros, G. *Nucl. Eng. Des.* **240**, 1853–1866 (2010).
3. Pontillon, Y. & Ducros, G. *Nucl. Eng. Des.* **240**, 1867–1881 (2010).
4. Pontillon, Y. *et al. J. Nucl. Mater.* **495**, 363–384 (2017).
5. Noirot, L. *Nucl. Eng. Des.* **241**, 2099–2118 (2011).
6. Veshchunov, M. S. *et al. Nucl. Eng. Des.* **236**, 179–200 (2006).
7. Pizzocri, D., Barani, T. & Luzzi, L. *J. Nucl. Mater.* **532**, 152042 (2020).
8. Chatelard, P. *et al. Nucl. Eng. Des.* **272**, 119–135 (2014).
9. Gauntt, R. O. *Report Sandia National Laboratories* (2010).
10. Germain, A. *et al. J. Nucl. Mater.* **560**, 153429 (2022).
11. Verma, L., Noirot, L. & Maugis, P. *J. Nucl. Mater.* **528**, 151874 (2020).
12. Noirot, L., Verma, L. & Maugis, P. *J. Nucl. Mater.* **577**, 154311 (2023).
13. Petrosillo, G. *et al. J. Nucl. Mater.* **622**, 156400 (2026).
14. Introïni, C. *et al. Ann. Nucl. Energy* **207**, 110711 (2024).
15. Sercombe, J., Michel, B., Riglet-Martial, C. & Fandeur, Olivier. *Comprehensive Nuclear Materials* 417–465 (2020).
16. Lemoine, F., Bernard, D. & Federici, E. *Conference: Water Reactor Fuel Performance Meeting* (2011).
17. Nogita, K. & Une, K. *J. Nucl. Mater.* **226**, 302–310 (1995).
18. Valin, S. *PhD Thesis* (1999).
19. Sundman, B., Lu, X. G. & Ohtani, H. *Comput. Mater. Sci.* **101**, 127–137 (2015).
20. Introini, C., Sercombe, J. & Sundman, B. *Nucl. Eng. Des.* **369**, (2024).
21. Guéneau, C. *et al. Calphad* **72**, 102212 (2021).
22. Veshchunov, M. S. & Berdyshev, A. V. *J. Nucl. Mater.* **252**, 98–109 (1998).

ADVANCED MODELING OF FISSION PRODUCT RELEASE FROM IRRADIATED FUEL DURING SEVERE ACCIDENT SCENARIOS

G. PETROSILLO, J. SERCOMBE, L. NOIROT, C. INTROINI, L. LUZZI*, Y. PONTILLON

CEA, DES, IRESNE, DEC, Cadarache, F-13108 Saint-Paul-lez-Durance – France

*Politecnico di Milano, Department of Energy, Nuclear Engineering Division, Via La Masa 34, 20156

Milano – Italy

1. Introduction

Fission Products Behavior in Oxide Fuel during Severe Accident

Focus:

- Modeling the **source term** during a **severe accident** in a PWR is essential for developing effective mitigation strategies.
- Experimental programs like **VERCORS**, **VERDON** (CEA) :
  - **Classification of Fission Products (FP) behavior**

VOLATILE

Fission gases, iodine, caesium, antimony, tellurium, cadmium, rubidium, silver

SEMI-VOLATILE

Molybdenum, rhodium, barium, palladium, technetium

LOW-VOLATILE

Ruthenium, cerium, strontium, yttrium, europium, niobium, lanthanum

NON-VOLATILE

Zirconium, neodymium, praseodymium

Fission Products Behavior in Oxide Fuel during Severe Accident

Focus:

- Modeling the **source term** during a **severe accident** in a PWR is essential for developing effective mitigation strategies.

- Experimental programs like **VERCORS**, **VERDON** (CEA) :

  - Classification of Fission Products (FP) behavior

  - **Main parameters** influencing release kinetics/rates:
    - **Temperature**
    - **Chemical conditions**
    - **Fuel burn-up**
    - **Interaction with structural materials**
    - **Fuel state**

Implication for Modeling:
Accurate mechanistic model for the description of FP release
+
Accurate thermochemistry for predicting the release of FP

Research Aim

The focus of this work is the coupling between a mechanistic model for the description of FP release and a model for the thermochemistry of irradiated fuel in the **fuel performance code PLEIADES/ALCYONE**:

- Fission product release: **MARGARET (stable + active FP*);**
- Thermochemistry: **OpenCalphad (Gibbs Energy Minimizer) + TAF-ID (thermodynamic database).**

This work also presents **the simulations of two annealing experiments reproducing severe accident conditions (VERCORS 5 & HT2)**, with FP release results compared to experimental data.

**active FP* refer collectively to chemically reactive and radioactive fission products.*

*(C. Introini et al. , doi.org/10.1016/j.anucene.2024.110711
L. Noirot ,doi.org/10.1016/j.nucengdes.2011.03.044
B. Sundman et al., doi.org/10.1016/j.commatsci.2016.08.045,
C. Guéneau et al., doi.org/10.1016/j.calphad.2020.102212)*

2. Model presentation

2. Model presentation

Fuel Performance Code

ALCYONE FUEL PERFORMANCE CODE (standard version)

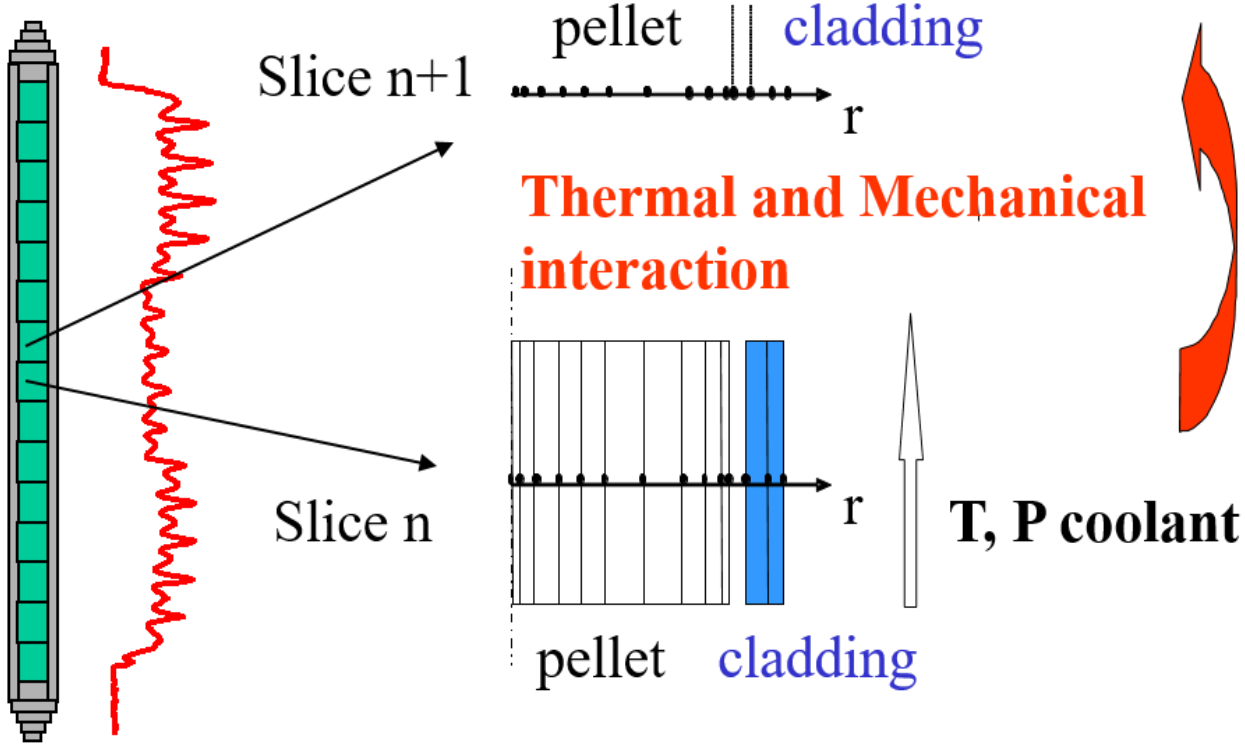

ALCYONE 1.5D scheme is used to model the fuel rod behavior during:

- Nominal irradiation in PWR,
- Incidental condition (Power ramps)
- Accidental condition (RIA, LOCA)
- Annealing
- pool and dry interim storage.

Typical fuel rod discretization in the 1.5D scheme of ALCYONE

(C. Introini et al. , doi.org/10.1016/j.anucene.2024.110711)

ALCYONE FUEL PERFORMANCE CODE (advanced version)

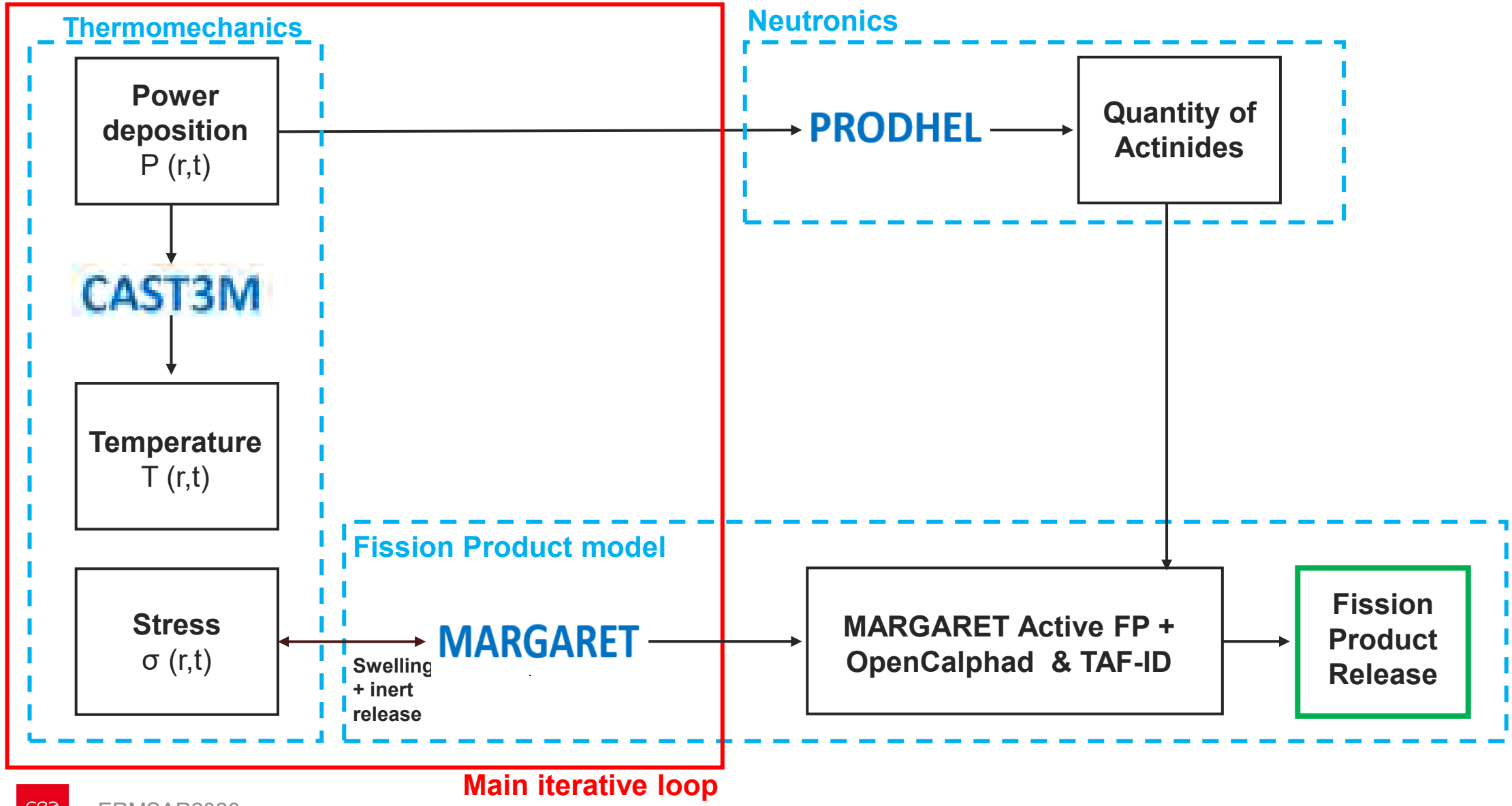

2. Model presentation

Fuel Performance Code

Margaret Stable

MARGARET Stable

MARGARET Stable is a mechanistic model to describe the behaviour of the inert and stable gases (xenon and krypton) generated by fission of uranium in the fuel at the grain scale.

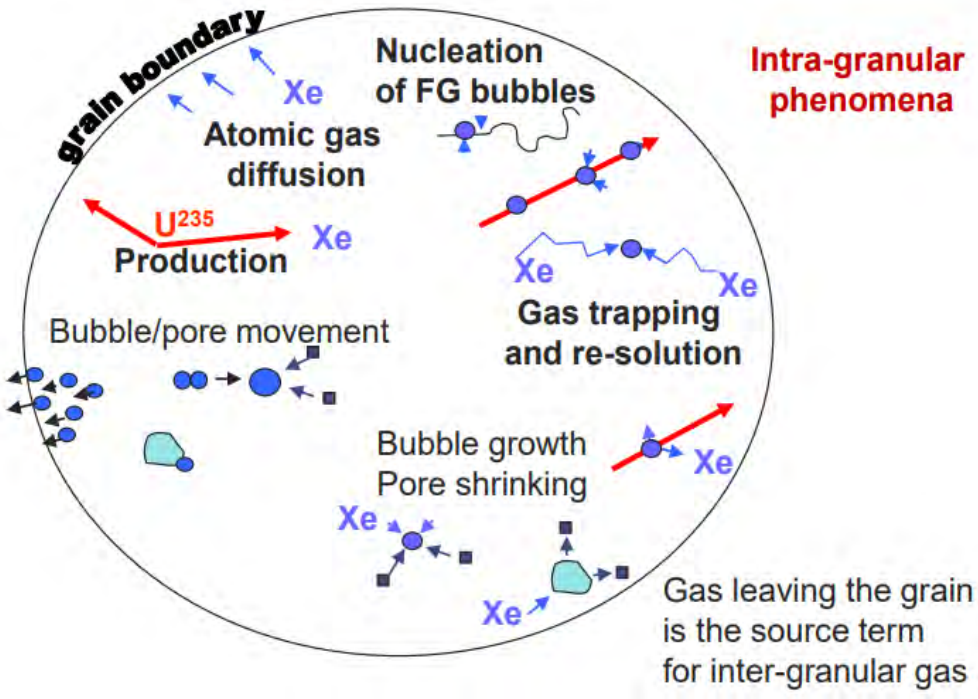

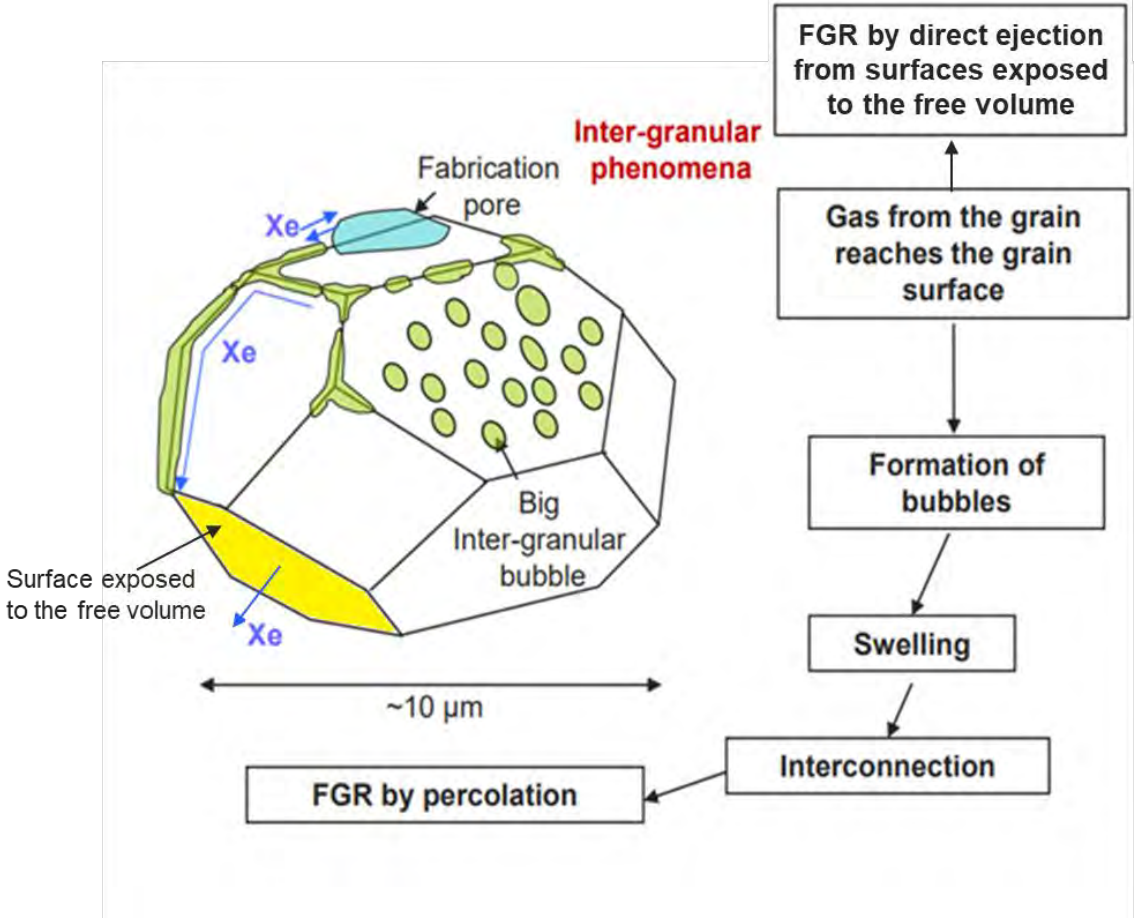

(L. Noirot ,doi.org/10.1016/j.nucengdes.2011.03.044)

Fission Gas Behavior During Irradiation & Annealing

❖ **Base Irradiation and Power Ramp Irradiation:**

- Dynamic re-solution from **bubble/fission fragment interactions**
- **Part of Xenon is retained** in UO_2 matrix, able to diffuse within grains

❖ **Annealing:**

- **No fissions → no dynamic re-solution**
- **Fission gas rapidly trapped** in bubbles

❖ **Key Issue with annealing:**

- **Intragranular → intergranular migration** depends on bubble movement
- **Random motion insufficient** to explain high release rates

Coupled bubble/dislocation mechanism in MARGARET Stable

Driving Forces & Vacancy Creation:

- Work of **gas pressure inside bubbles** (driving)
- Opposed by **external pressure**
- Provides **energy for vacancy creation** along the dislocation

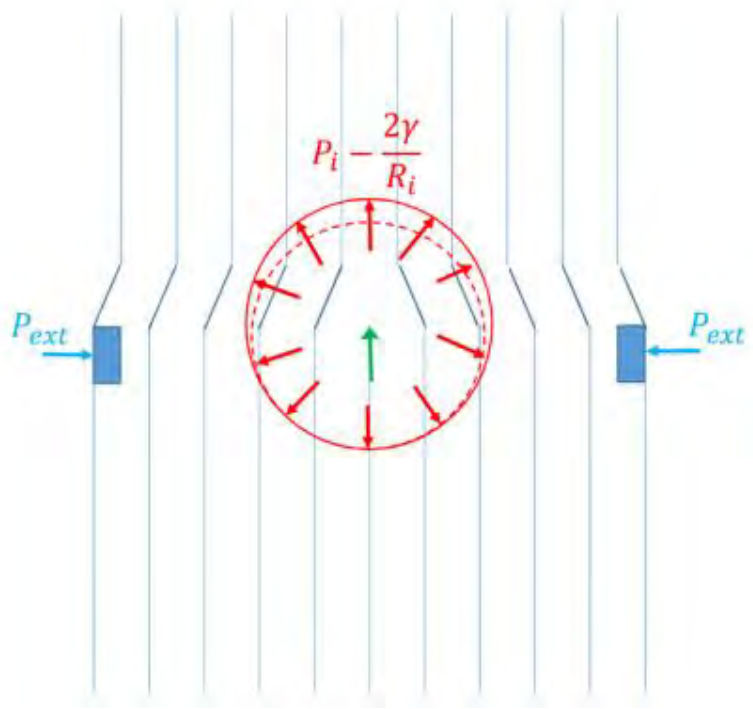

(L. Noirot et al. , doi.org/10.1016/j.jnucmat.2023.154311)

Coupled bubble/dislocation mechanism in MARGARET Stable

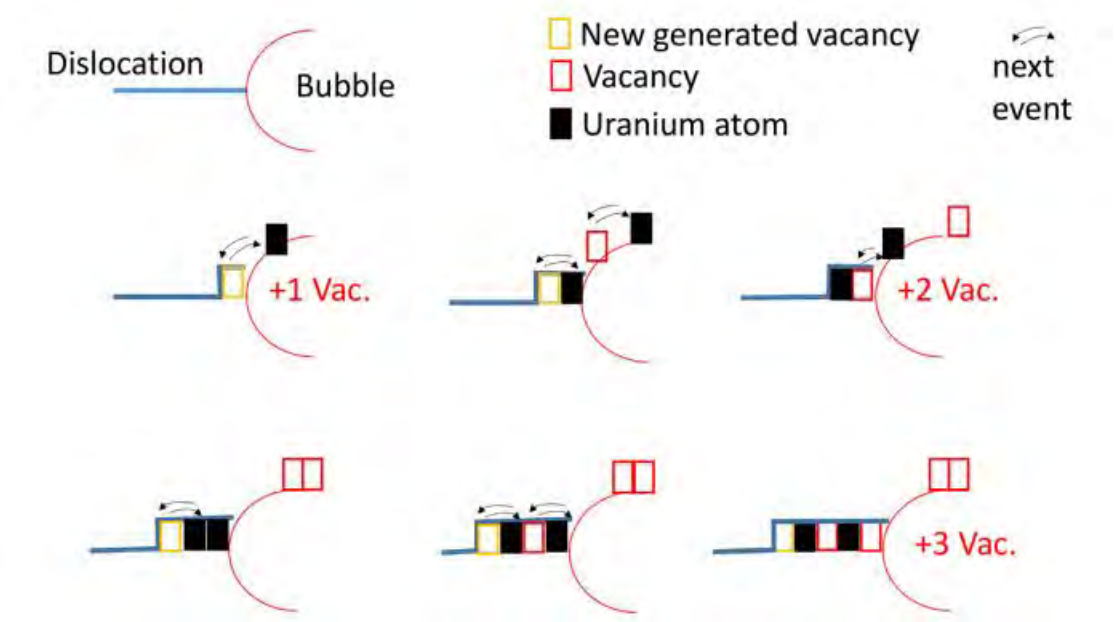

Vacancy Diffusion & Dislocation Climb

- **Vacancies diffuse** toward the bubble
- **U atoms accumulate** along the dislocation
- Leads to:
  - **Dislocation climb**
  - **Bubble growth**
  - **Relaxation of internal pressure**

(L. Noirot et al. , doi.org/10.1016/j.jnucmat.2023.154311)

2. Model presentation

Fuel Performance Code

Margaret Stable

Margaret Active FP

Overview of MARGARET-active FP

Element	Atomic Number
Xe	130, 131, 132, 133, 134, 135, 136
Kr	82, 83, 84, 85, 86
Ba	134, 135, 136, 137, 138
Sr	86, 88, 89, 90
Zr	95, 96
Cs	133, 134, 135, 136, 137
Rb	85, 86, 87
I	127, 129, 130, 131, 132
Br	81, 81m
Te	125, 126, 127, 127m, 128, 129m, 130,132
Se	77, 78, 79, 80, 82
Mo	95, 96, 97, 98, 99, 100
Ru	100, 101, 102, 103, 104, 106
Rh	103, 104, 105, 106
Tc	99, 100
Pd	104, 105, 106, 107, 108,109

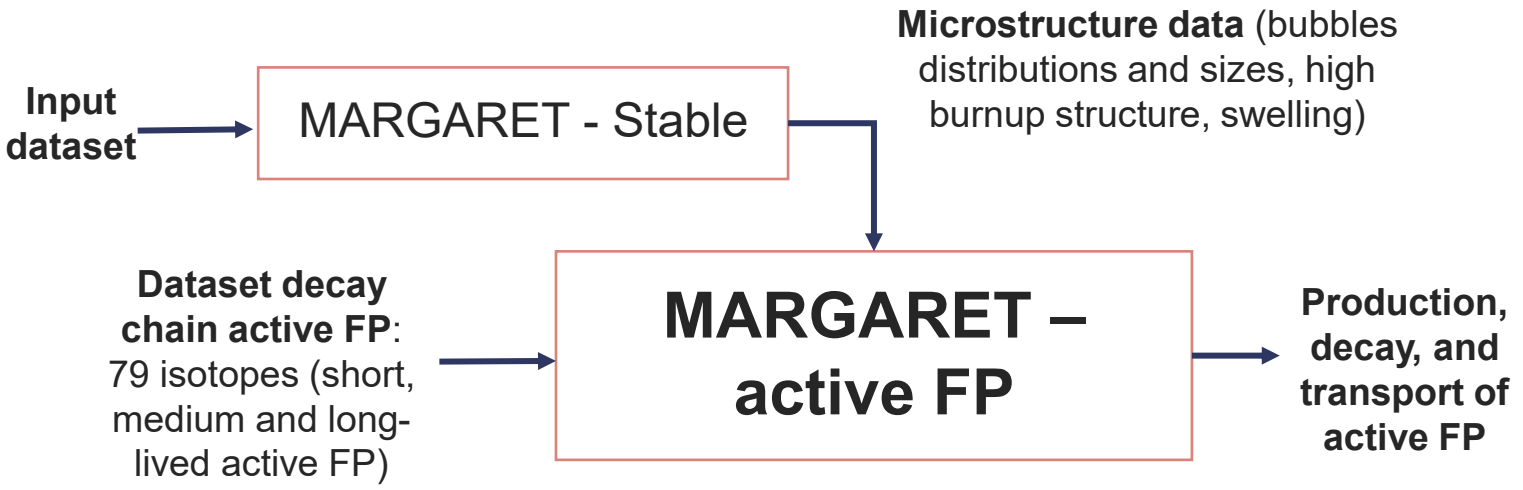

MARGARET-active FP Modeling Assumptions:

- **No feedback from active FP** on stable gases.
- **Isotope-Specific Parameters**: the stable (Xe) transport parameters are taken as default.

2. Model presentation

Fuel Performance Code

Margaret Stable

Margaret Active FP

Margaret Active FP + thermochemistry

MARGARET-active FP & Thermochemistry

During a high temperature transient, active FP behavior varies based on chemical reactivity, unlike inert gases like Xenon.

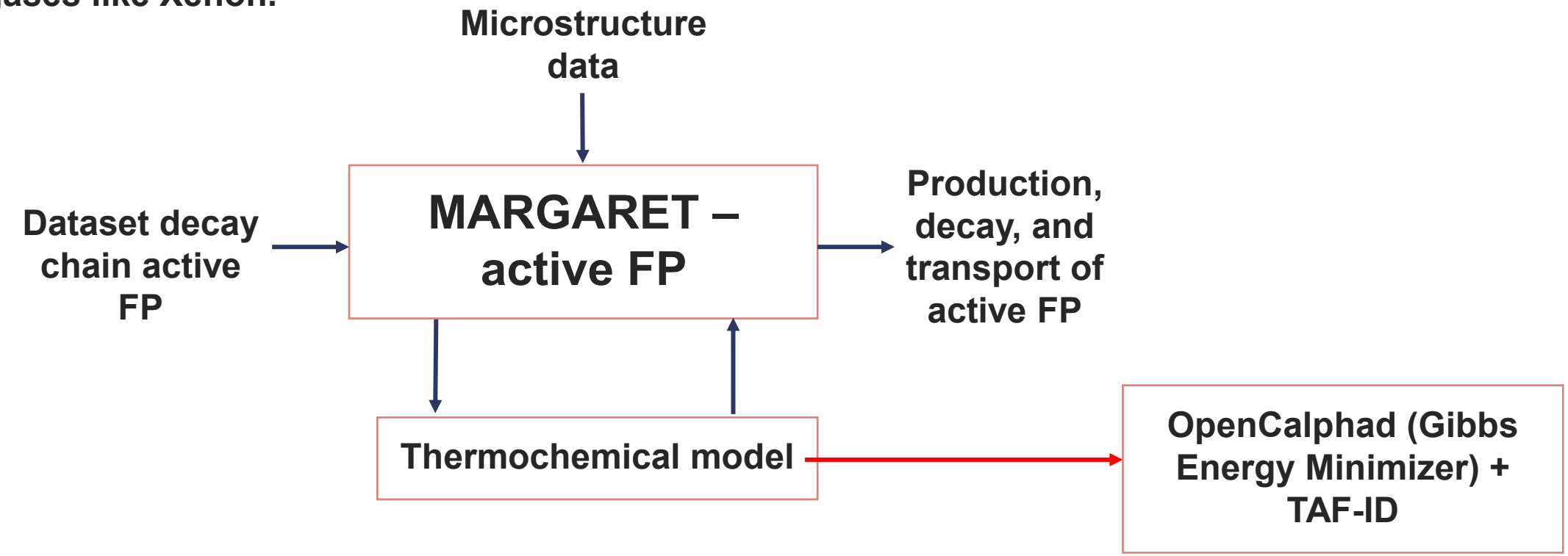

(B. Sundman et al., doi.org/10.1016/j.commatsci.2016.08.045,
C. Guéneau et al., doi.org/10.1016/j.calphad.2020.102212)

He	Kr	Xe	U	O	Ba	Sr	Zr
Cs	Rb	I	Br	Te	Se	Mo	Ru
Rh	Tc	Pd	Ce	Pr	La	Y	Gd
Eu	Sm	Nd					

Composition of the system used for the thermochemical calculations.

MARGARET-active FP & Thermochemistry

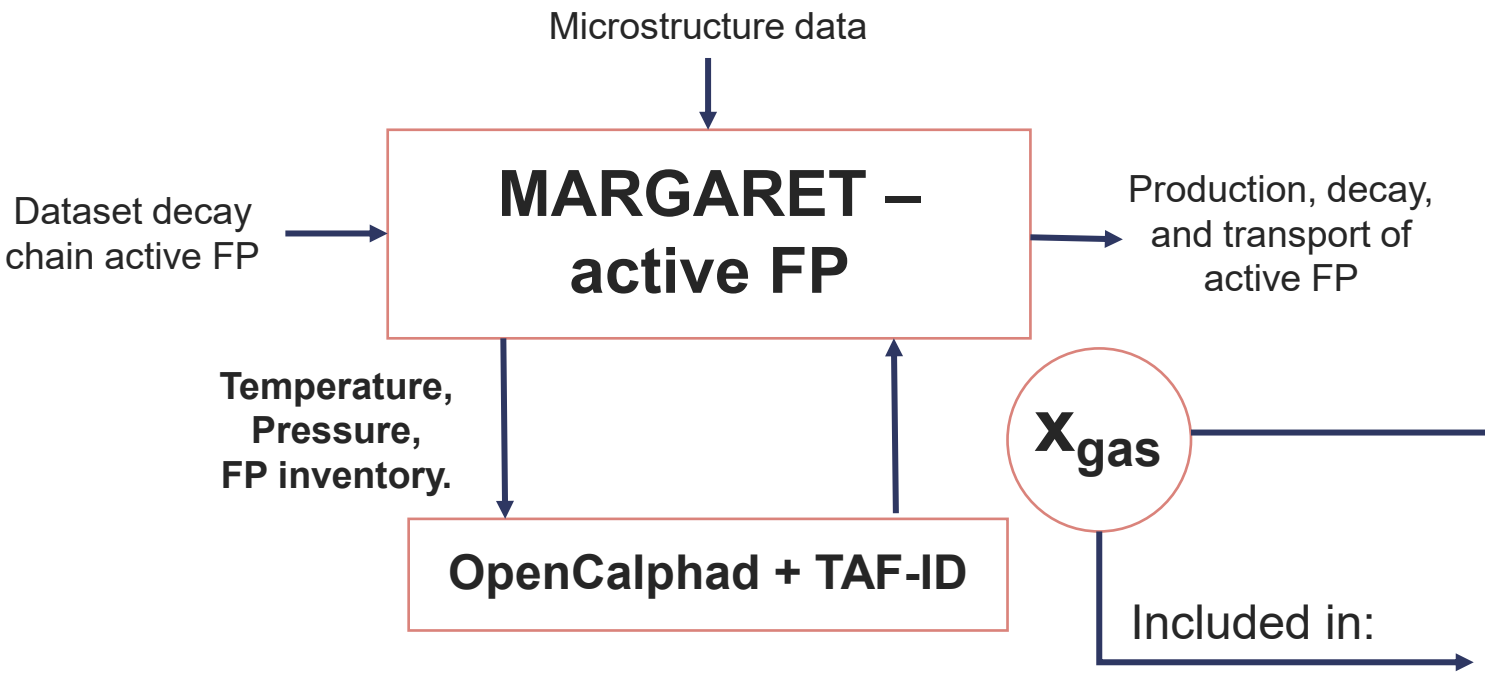

Fraction of FP in the gas phase

$$x_{gas} = \frac{mol_{FP}\ in\ the\ gas\ phase}{mol_{FP}\ in\ all\ phases}$$

Assumption:

Only the gas phase can be release; other phases remain confined.

Fission product release from grain boundaries

- **Percolation via intergranular cavities → free volume**

$$-K_{tunj}\frac{k_{perm}}{\mu T_k} f_p x_{gas}(P^2_{int(bjv)} - P^2_{ext})$$

- **Grain boundary fracture**

3. Annealing simulations & comparison with Experimental Data

Case under analysis

VERCORS 5 (38 GWd/tU)

Main characteristics of the case:

- **Thermal annealing** of a fuel rod segment (UO_2-Zy_4) in a furnace (crucible model geometry)
- Specimen exposed to **oxidizing conditions** (carrier gas) during annealing.

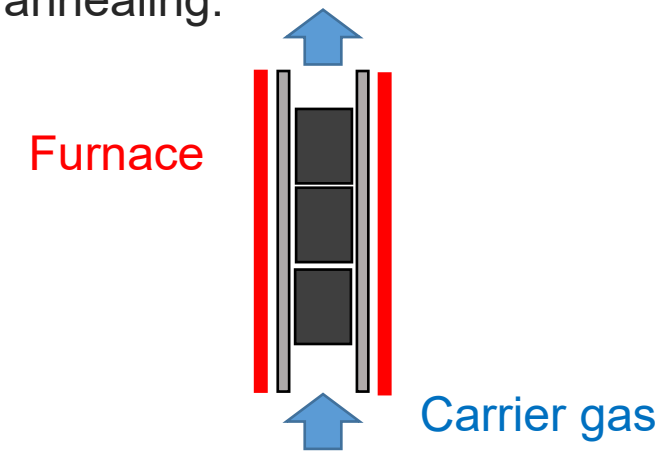

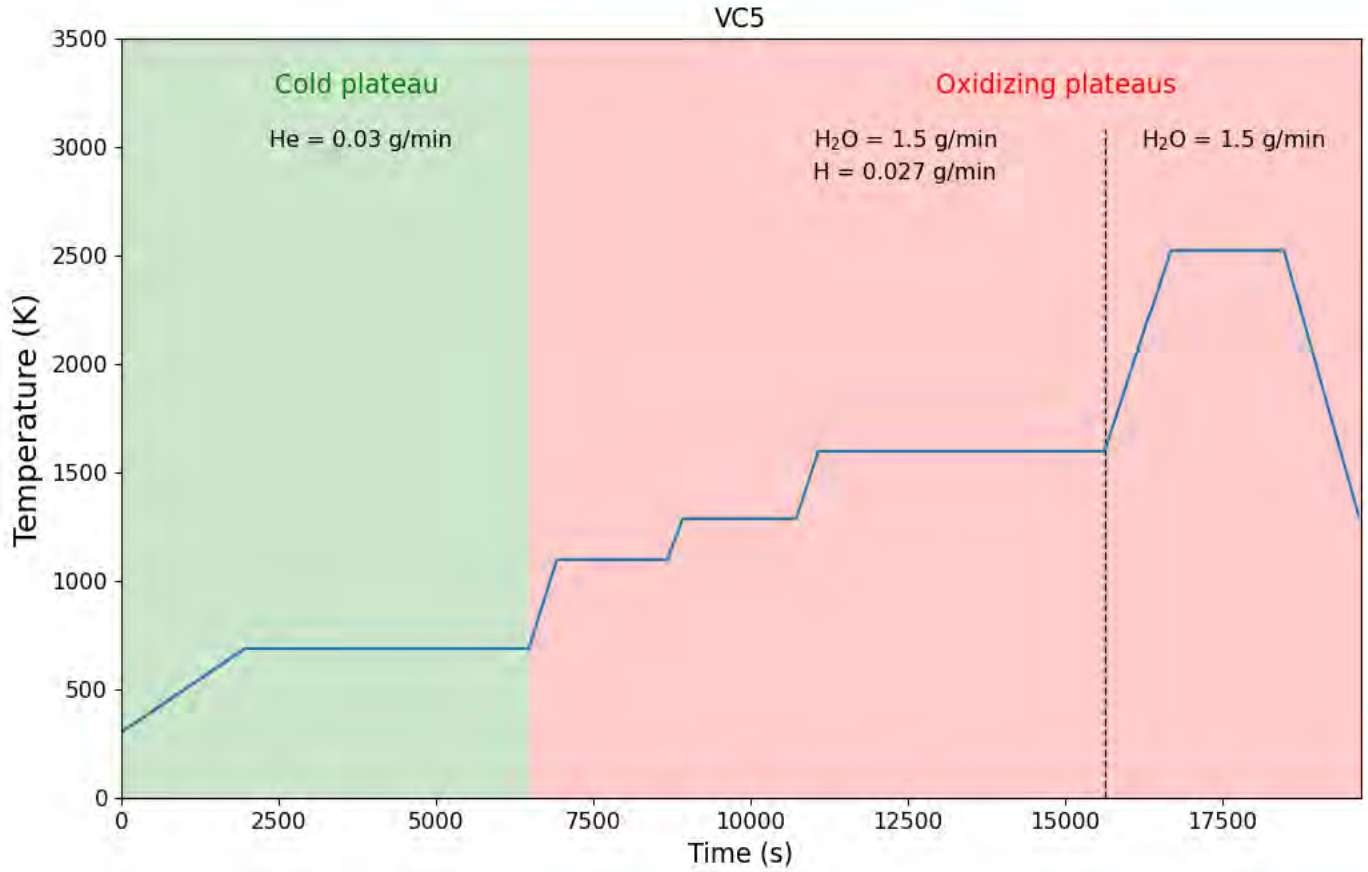

(Y. Pontillon et al. , doi.org/10.1016/j.nucengdes.2009.06.028)

Case under analysis

VERCORS HT2 (48 GWd/tU)

Main characteristics of the case:

- **Thermal annealing** of a fuel rod segment (UO_2-Zy_4) in a furnace (crucible model geometry)
- Specimen exposed to **oxidizing conditions** (carrier gas) during annealing.

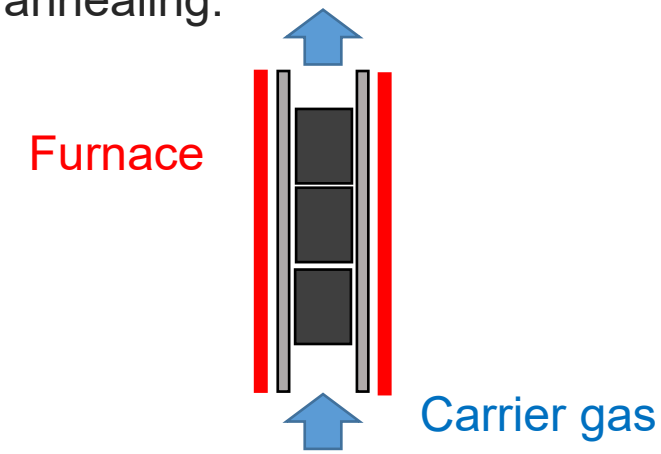

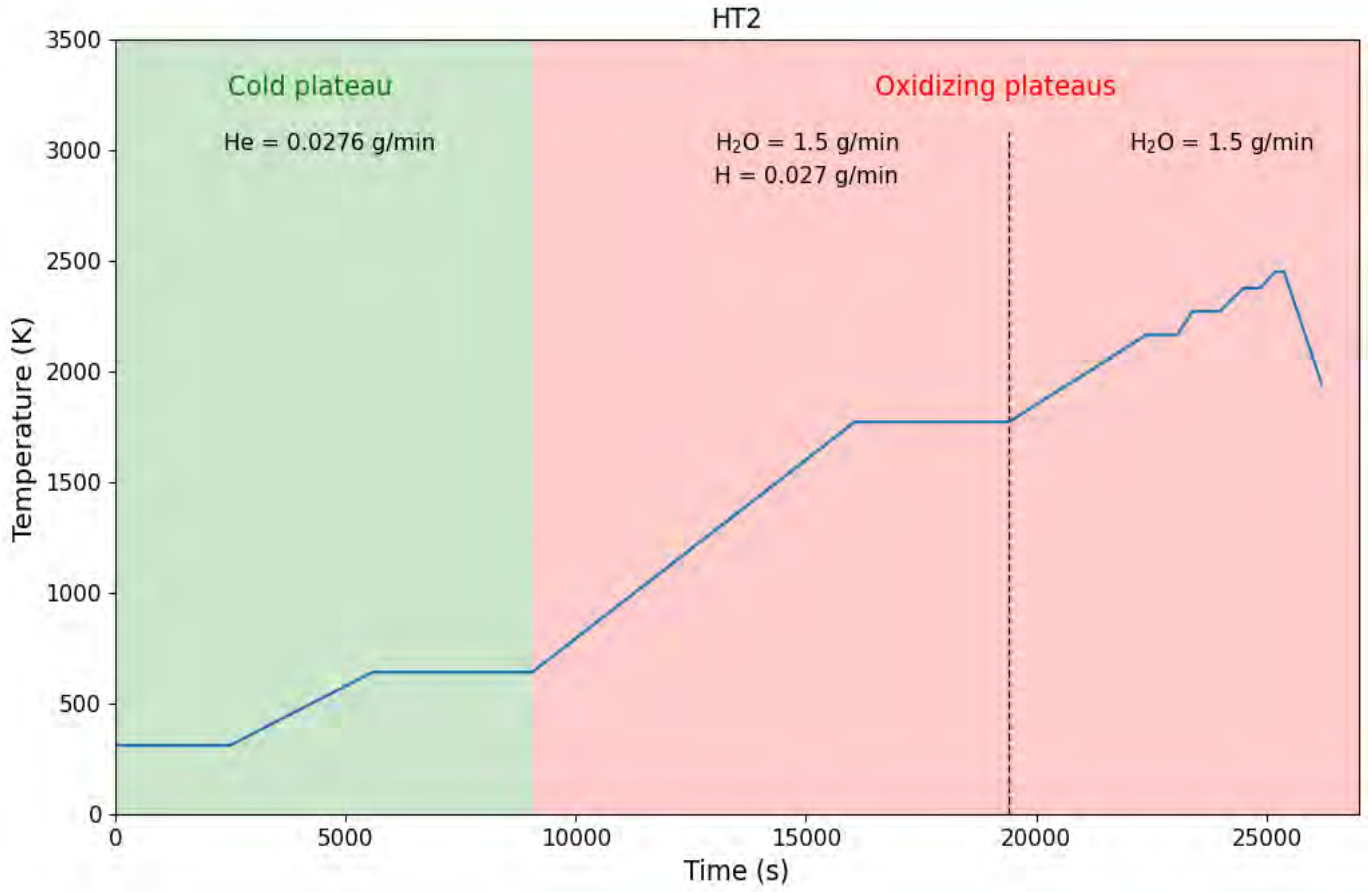

In the thermochemical calculation the impact of the carrier gas is considered.

(Y. Pontillon et al. , doi.org/10.1016/j.nucengdes.2009.06.028)

Calculated FP release from the whole pellet

VERCORS 5
Inert: 133Xe

Final release well captured (~95%)

- Driven by dislocation-climb mechanism above 1600 K
- Limited release during 1570 K plateau (short half-life)

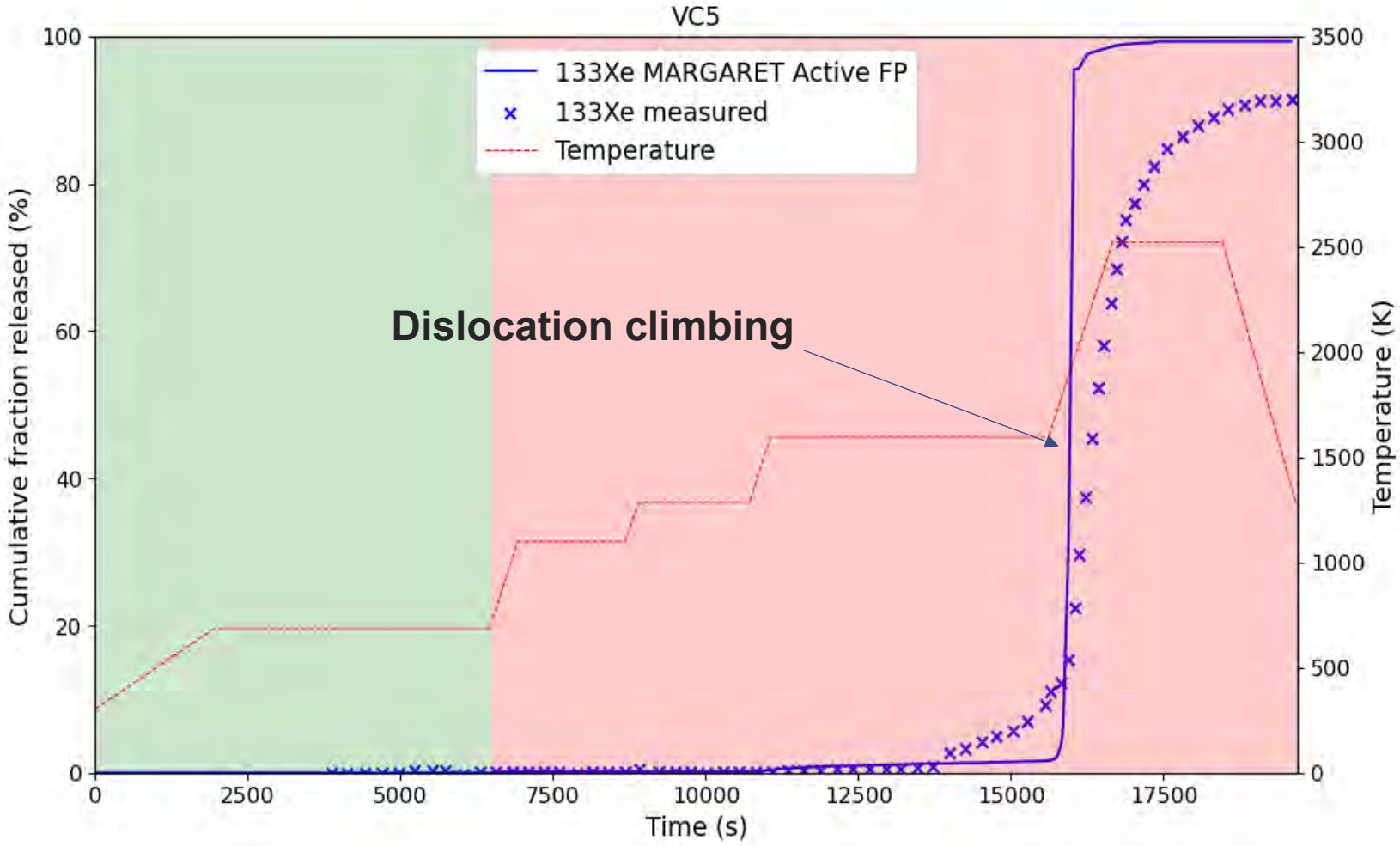

Calculated FP release from the whole pellet

VERCORS HT2
Inert: 85Kr

Kinetics better reproduced than VC5

- Long half-life → grain-boundary inventory available
- Release onset ~1500 K well captured

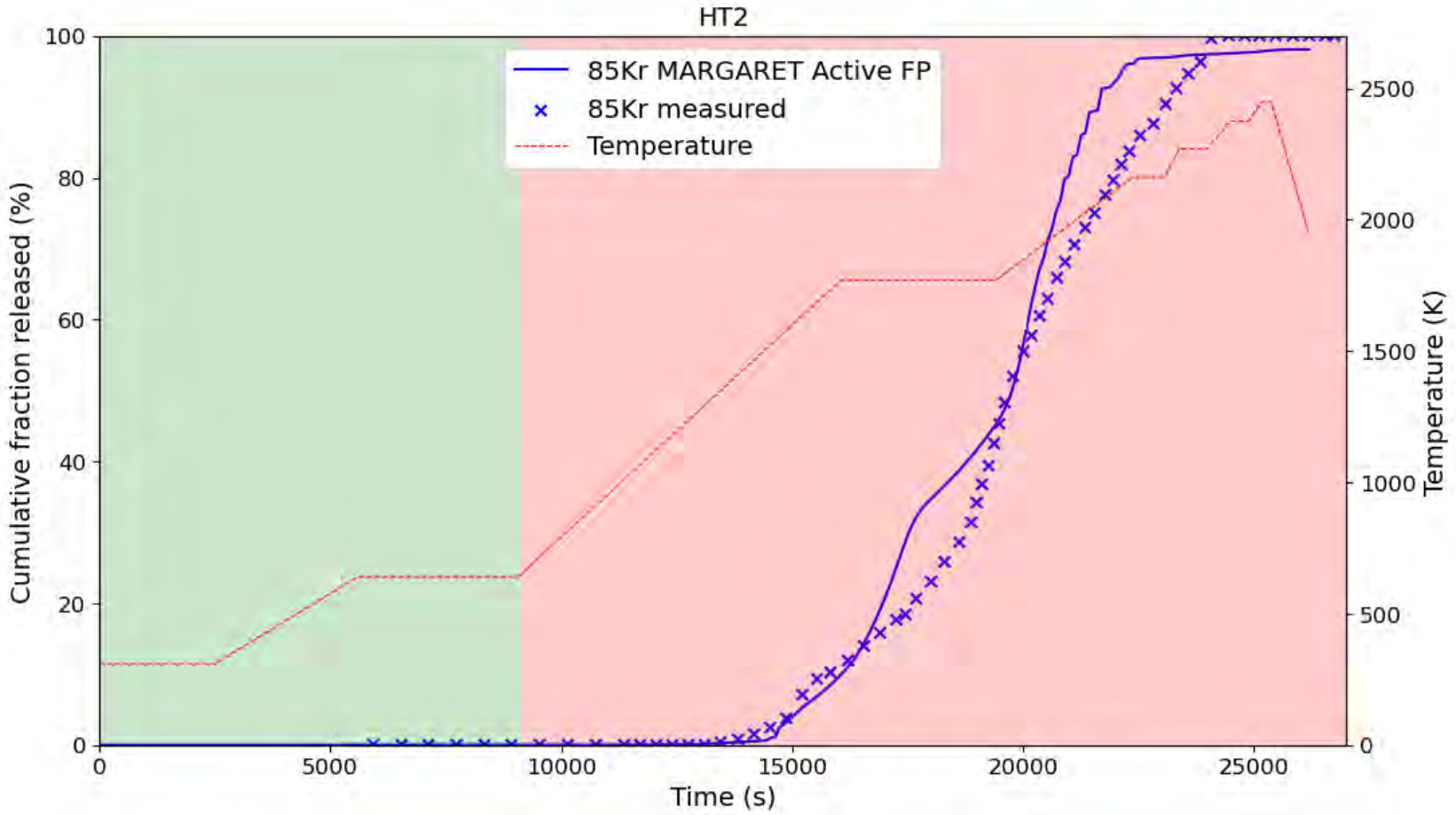

Calculated FP release from the whole pellet

VERCORS 5
Volatile: 137Cs and 131I

Complete release, consistent with experimental data

- 137Cs released already at 1570 K plateau (longer half-life)
- 131I follows 133Xe kinetics (short half-life)

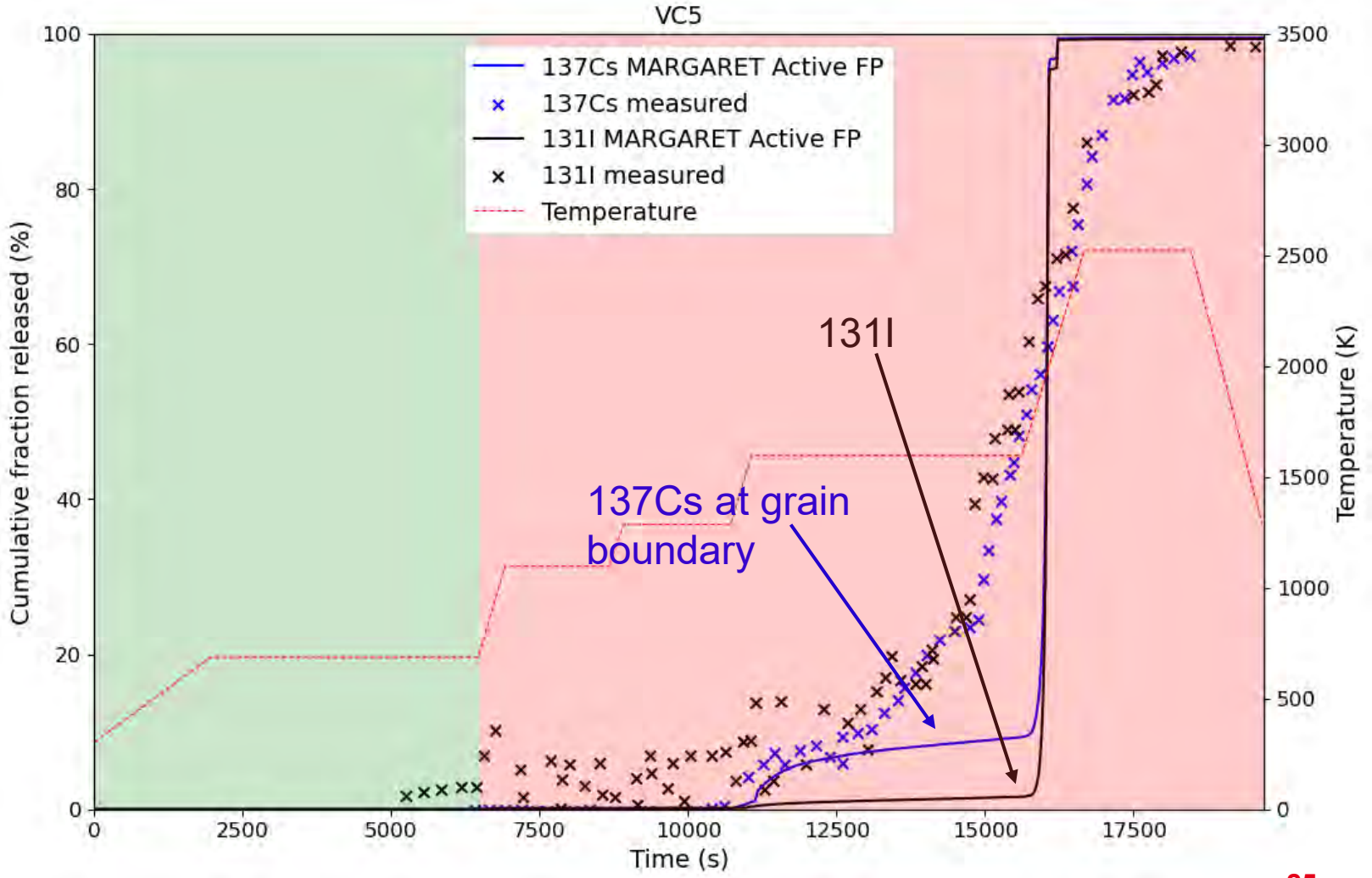

Calculated FP release from the whole pellet

VERCORS HT2
Volatile: 137Cs and 131I

Complete release reproduced

- Trends consistent with VC5

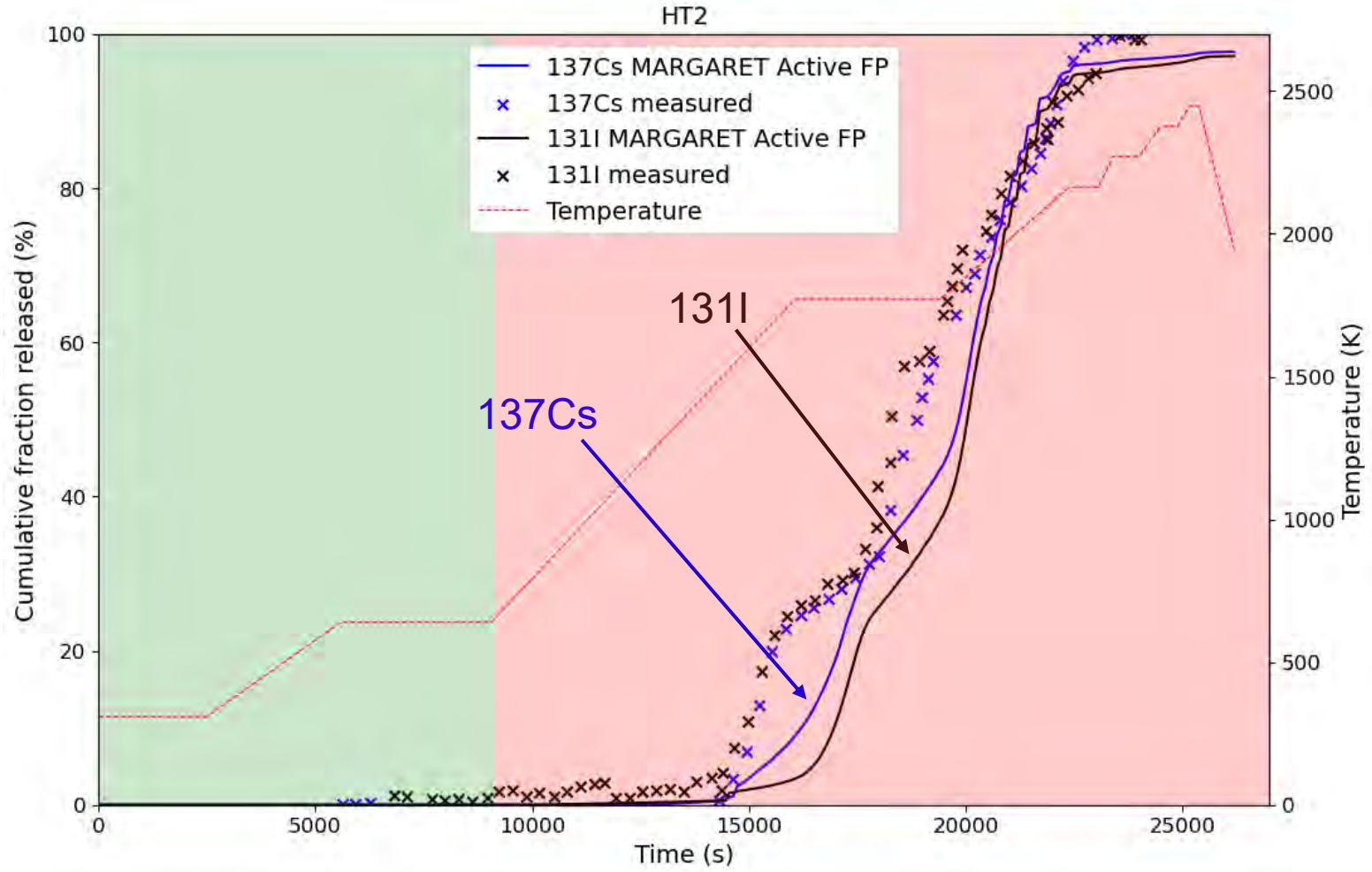

Calculated FP release from the whole pellet

VERCORS 5

Semi – volatile and low - volatile: 99Mo, 140Ba and 103Ru

Mo well captured;
Ba and Ru overestimated

- 99Mo ~100%: oxidizing atmosphere enhances volatility
- 140Ba and 103Ru: cladding interaction missing in fuel-side model

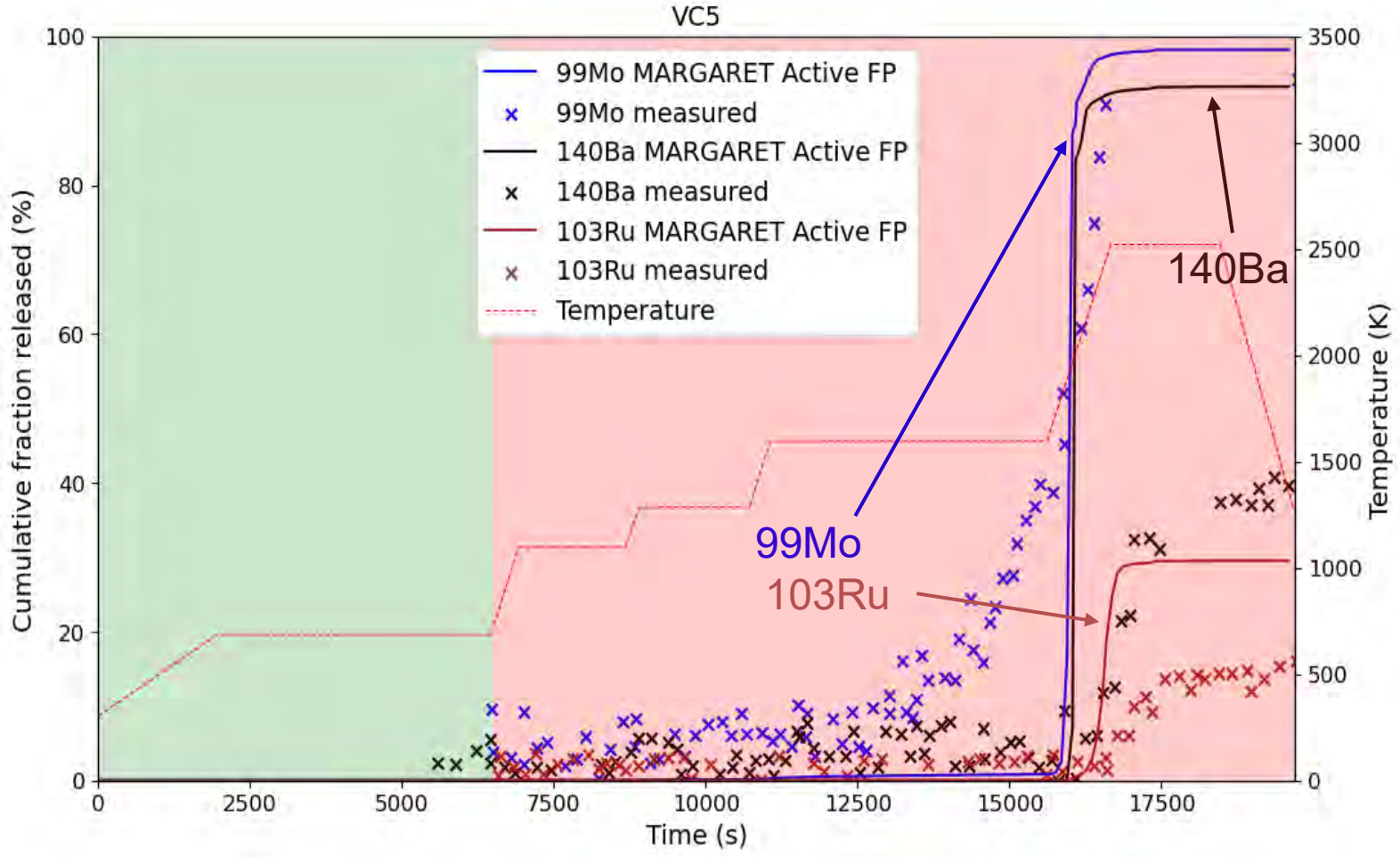

Calculated FP release from the whole pellet

VERCORS 5

Semi – volatile and low - volatile: 99Mo, 140Ba and 103Ru

Mo well captured;
Ba and Ru overestimated

- 99Mo ~100%: oxidizing atmosphere enhances volatility
- 140Ba and 103Ru: cladding interaction missing in fuel-side model

Post-annealing analyses of the specimens, including gamma tomography, show that barium reacts with the cladding.

(Y. Pontillon et al. , doi.org/10.1016/j.nucengdes.2009.06.028)

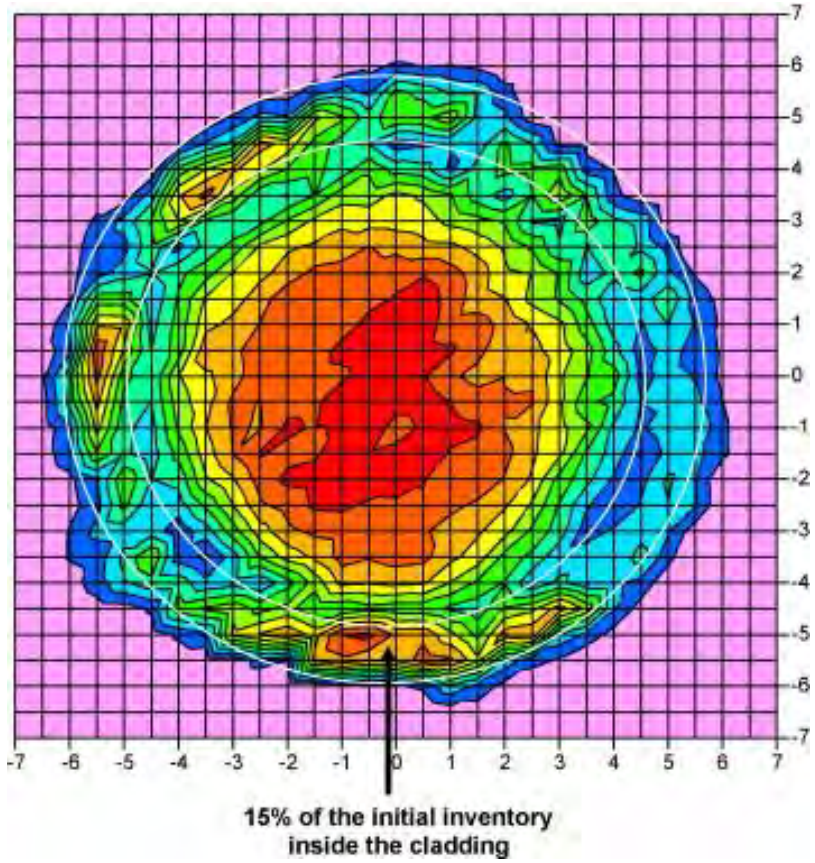

Gamma emission tomography of ^{140}Ba after VERCORS 5.

Semi-volatile and low-volatile cladding interaction

- Discrepancies observed for Ba and Ru → **thermochemical equilibrium calculation on cladding performed**
- **Cladding assumed fully oxidized (ZrO_2)**, consistent with test conditions
- Inputs: **Released fission product inventory + uranium fraction** (fuel–cladding interaction)
- Veshchunov et al. 1990**: formation of ceramic ($(U,Zr)O_x$ phase** → 3%–6% of fuel interacts with ZrO_2
- **Conservative assumption**: 6% upper bound adopted

(Veshchunov et al., doi.org/10.1016/0022-3115(90)90422-J)

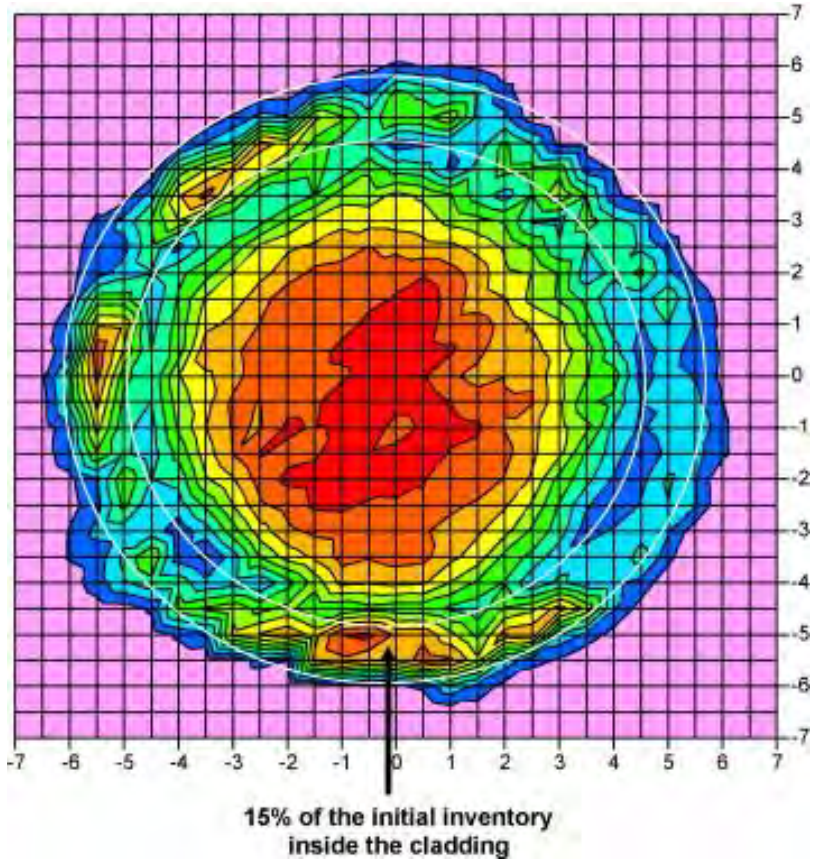

Gamma emission tomography of ^{140}Ba after VERCORS 5.

Semi-volatile and low-volatile cladding interaction

- **Only Ba and Ru retained by cladding**
- Released quantities of 140Ba and 103Ru **drastically reduced**
- **Release kinetics also improved**
- **Ba preferentially reacts with ZrO_2 and it forms also an HCP metallic phase with Zr**
- **This metallic phase traps part of the Ru inventory, limiting its release**

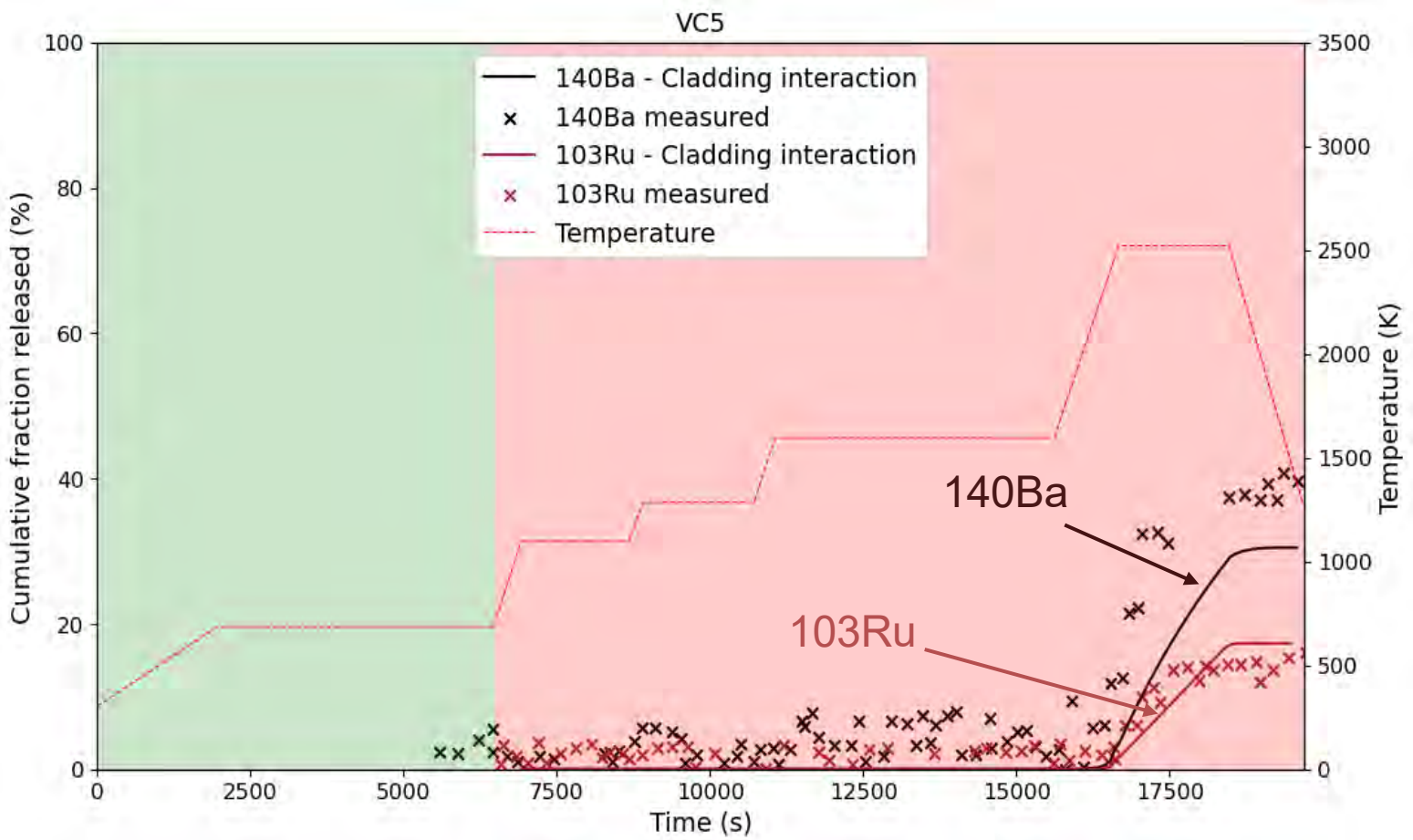

Calculated FP release from the whole pellet

VERCORS HT2
Semi – volatile: 99Mo

Kinetics well reproduced;
final release underestimated (82%)

- Part of Mo inventory predicted in liquid phase
- Possible aerosol release not modeled

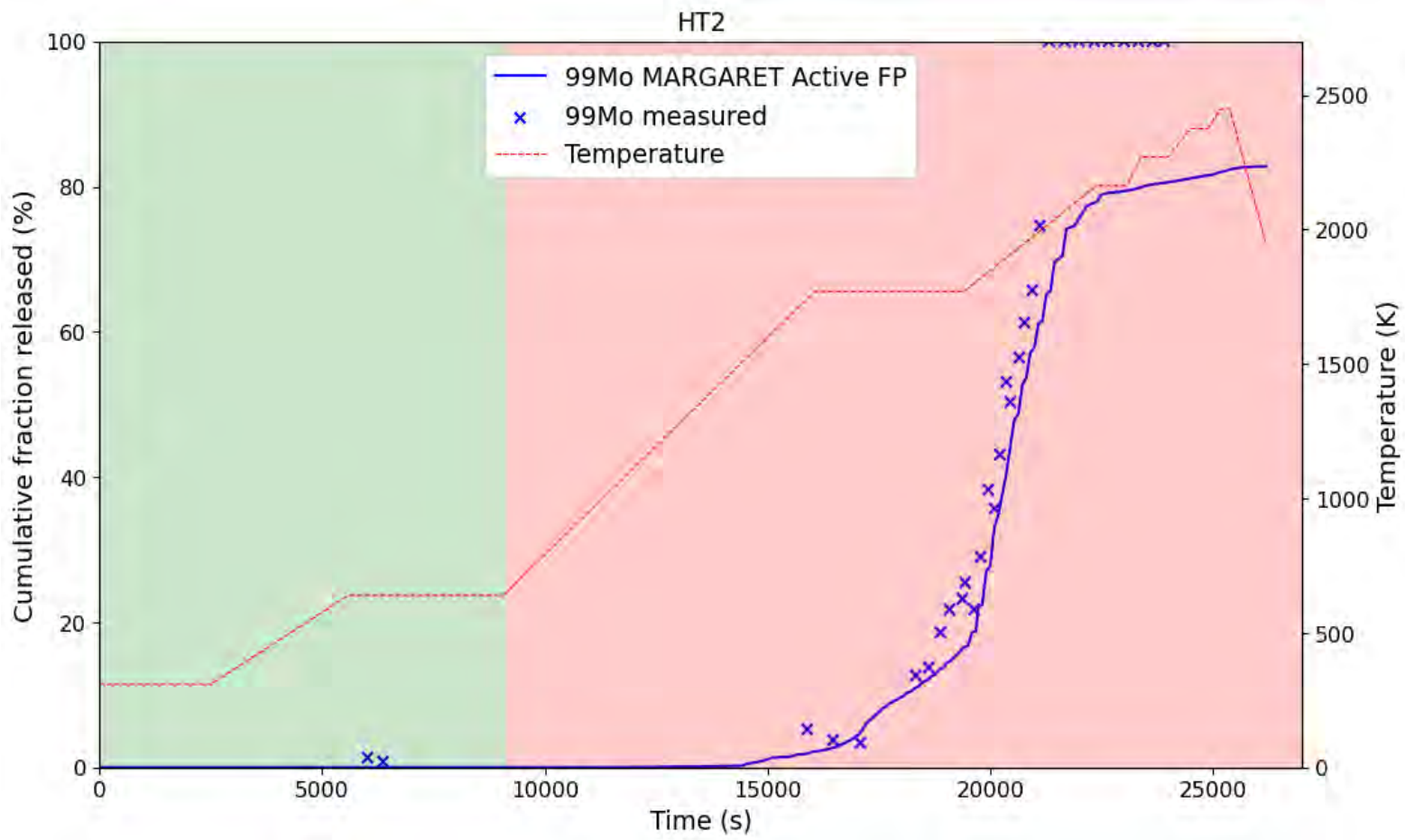

4. Conclusions

Conclusions

A model is proposed to specifically address the **behavior of active fission products (active FP) during severe accident:**

- Capable of modeling a **large number of isotopes**

- Considers **multiple phenomena**, including:
  - Grain boundary fracturing and percolation
  - Dislocation climb and bubble migration

- **Impact of thermochemistry of FP** is included in the calculation

- **Results:**

  - good agreement for fission gases and volatile FPs

  - Thermochemistry essential for semi-volatile and low-volatile species (Mo, Ba and Ru) → sensitive to chemical environment and cladding–FP interaction

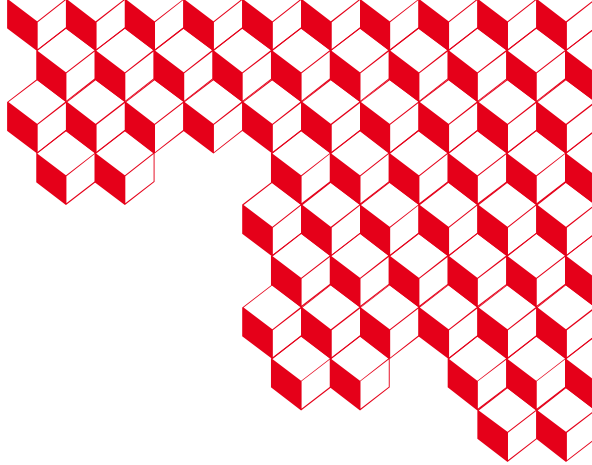

Thank you for your attention.

Giacomo Petrosillo
CEA CADARACHE
13115 Saint Paul Lez Durance Cedex
France
giacomo.petrosillo@cea.fr

Coupled bubble/dislocation mechanism in MARGARET Stable

New variable introduced:

- **Dislocation Density** ρ_d^{climb} : correlation proposed by Nogita et al.
- New Bubble Populations:
  - **BPREC:** Pinned bubbles on climbing dislocations characterized by:
    - C_{bprec} : pinned bubble concentration
    - $C_{xebprec}$: Xe concentration in pinned bubble
    - V_{bprec} : volume of the pinned bubbble

Dynamics:

- **Gas exchange** between dissolved phase ↔ BPREC
- BPREC **Swelling**
- **Pinning of free bubbles** (B) on climbing dislocations
- **Coalescences**: B/BPREC and BPREC/BPREC
- **Exit of climbing dislocations and BPREC at grain boundaries**

The velocity of the climbing dislocations v_d and the associated swelling of BPREC are related to the characteristics of BPREC, through

$$v_d = \frac{12D^*}{kT} \frac{P_{bprec} - \frac{2\gamma}{R_{bprec}} - P_{hydr}}{\frac{C_{bprec}}{\rho_d^{climb}} \left(\frac{\rho_d^{climb}}{C_{bprec}} - 2R_{bprec} \right)^3} \times \Omega^{\frac{4}{3}}$$

$$\frac{dV_{bprec}}{dt}|_{climb} = v_d \times w \times \rho_d^{climb}$$

(L. Noirot et al. , doi.org/10.1016/j.jnucmat.2023.154311)

Coupled bubble/dislocation mechanism in MARGARET Stable

D^* evaluation from experimental data

$$v_d = \frac{12D^*}{kT} \frac{P_{bprec} - \frac{2\gamma}{R_{bprec}} - P_{hydr}}{\frac{C_{bprec}}{\rho_d^{climb}} \left(\frac{\rho_d^{climb}}{C_{bprec}} - 2R_{bprec} \right)^3} \times \Omega^{\frac{4}{3}}$$

Isothermal annealing

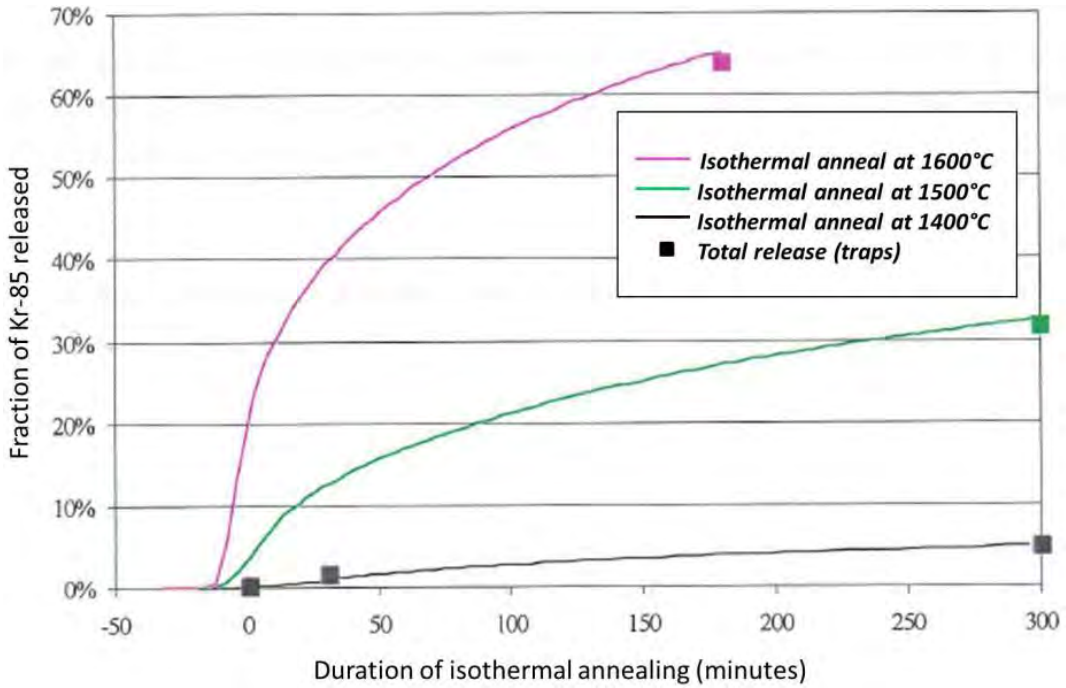

MARGARET

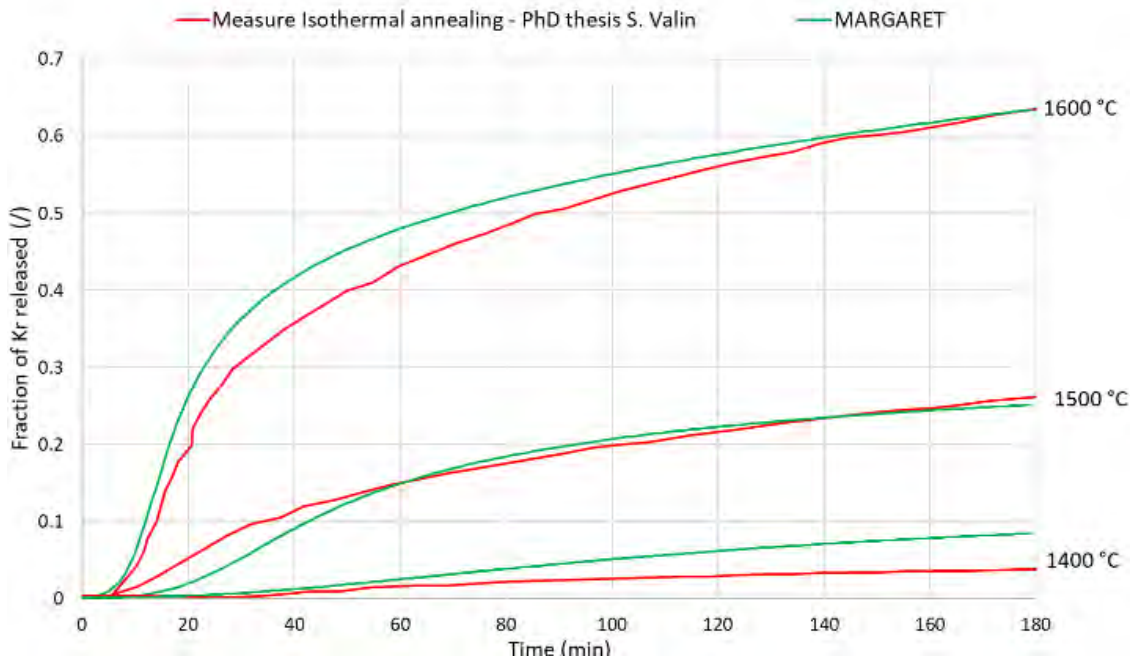

Thermochemical model

TAF-ID Database

The main active fission products are gathered into several categories according to their physical and chemical states inside the fuel pellet:

- **UO_2 solid solution**;
- **Metallic precipitates**;
- **Oxide precipitates**;
- **Gases and volatile FP**.

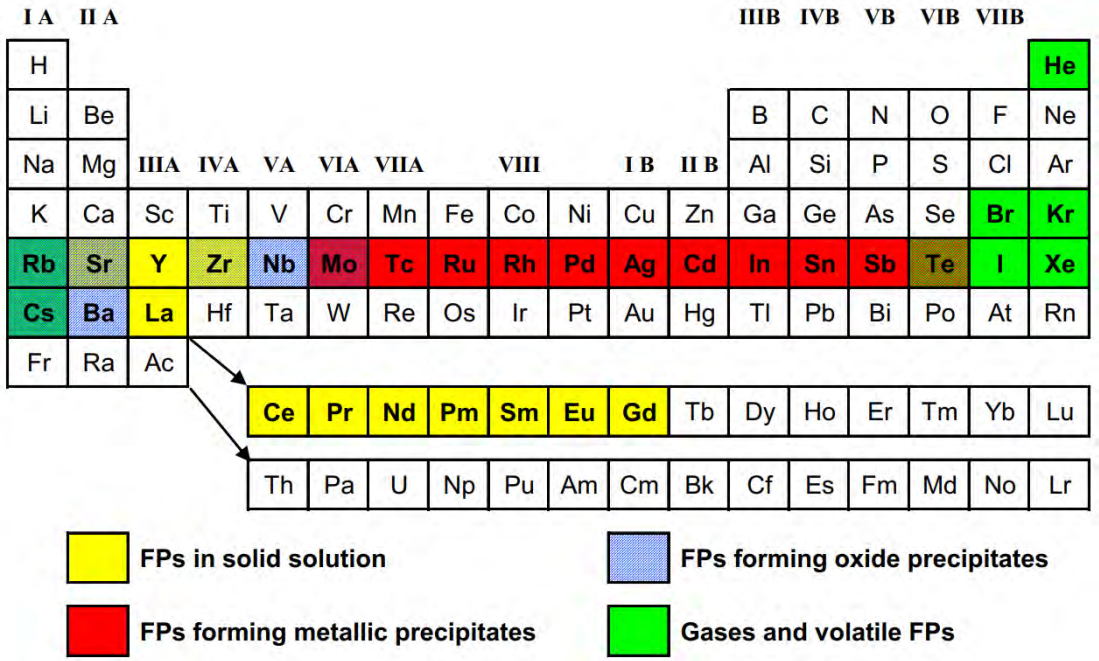

Thermochemical model

TAF-ID Database

Numerous possible phases that can be calculated using the TAF-ID database

Gas phase	(GAS) (Ba, Ba_2, BaH, BaI, BaI_2, BaO, Ba_2O, Ba_2O_2, $BaMoO_4$, BaOH, BaO_2H_2, Ce, CeO, Cs, Cs_2, CsH, CsI, Cs_2I_2, Cs_2MoO_4, CsO, Cs_2O, Cs_2O_2, CsTe, Cs_2Te, Cs_2Te_2, Cs_2Te_3, Gd, GdO, H, H_2, HI, HO, HO_2, H_2O, H_2O_2, HTe, H_2Te, HIO, He, I, I_2, La, LaI_3, LaO, LaO_2, La_2O, La_2O_2, LaTe, Mo, Mo_2, MoI, MoI_2, MoI_3, MoI_4, MoO, MoO_2, MoO_3, Mo_2O_6, Mo_3O_9, Mo_4O_{12}, Mo_5O_{15}, MoO_2I_2 Nd, NdO, Np, NpO, NpO_2, O, O_2, O_3, Pd, Pu, PuO, PuO_2, Rh, RhO, RhO_2, Ru, RuO, RuO_2, RuO_3, RuO_4, RuO_2H_2, Sr, Sr_2, SrH, SrI, SrI_2, SrO, SrOH, SrO_2H_2, Te, Te_2, Te_3, Te_4, Te_5, Te_6, Te_7, TeI_2, TeI_4, TeO, TeO_2, Te_2O_2, U, UI, UI_2, UI_3, UI_4, UO, UO_2, UO_3, Zr, Zr_2, ZrH, ZrI, ZrI_2, ZrI_3, ZrI_4, ZrO, ZrO_2)
$(U,Zr)O_2$	Fluorite phase (C1_MO2) $(Ce^{3+}, Ce^{4+}, Gd^{3+}, La^{3+}, Nd^{3+}, Np^{3+}, Np^{4+}, Pu^{3+}, Pu^{4+}, U^{3+}, U^{4+}, U^{5+}, Zr^{2+}, Zr^{4+}, Sr^{2+})_1 (O^{2-}, Va)_2 (O^{2-}, Va)_1$
$BaZrO_3$	Perovskite phase (PEROVSKITE) $(Ba^{2+}, Sr^{2+})_1 (Ba^{2+}, U^{4+}, Mo^{4+}, U^{6+}, Zr^{4+})_1 (O^{2-})_3$
ZrO_2-M	Monoclinic zirconia phase (ZRO2_MONO) $(Zr^{4+})_1 (O^{2-}, Va)_2$
ZrO_2-T	Tetragonal zirconia phase (ZRO2_TETR) $(Ba^{2+}, U^{4+}, Zr^{4+})_1 (O^{2-}, Va)_2$
Liquid	Liquid phase (LIQUID) $(Ba^{2+}, Ce^{3+}, Cs^{+}, Gd^{3+}, La^{3+}, Mo^{4+}, Nd^{3+}, Np^{4+}, Pd^{2+}, Pu^{3+}, Rh^{3+}, Ru^{4+}, Sr^{2+}, Tc^{4+}, U^{4+}, Zr^{4+})_P (I^{-}, MoO_4^{2-}, O^{2-}, Va^{Q-}, CeO_2, CsO_2, Cs_2Te, I_2, MoO_3, O, Te, PuO_2, TeO_2)_Q$
FCC	Face Centered Cubic metallic phase (FCC) (Ba, Ce, Cs, Gd, La, Mo, Pd, Pu, Rh, Ru, Tc, Te, U, Zr)$_1$ (O, Te, Va)$_1$
HCP	Hexagonal Close Packed metallic phase (HCP) (Ba, Ce, Cs, Gd, Mo, Pd, Pu, Rh, Ru, Tc, U, Zr)$_1$ (O, Va)$_{0.5}$
	Stoichiometric phases
$BaMoO_4$	$BaMoO_4$
CsI	CsI
Cs_2MoO_4-O	Cs_2MoO_4
Cs_2MoO_4-H	Cs_2MoO_4
MoO_2	MoO_2
MoO_3	MoO_3
MoRh	MoRh
$MoRh_3$	$MoRh_3$

The TAF-ID database has a crucial role in the description of the active FP release.

VOLATILE

Fission gases, iodine, caesium, antimony, tellurium, cadmium, rubidium and silver

SEMI-VOLATILE

Molybdenum, rhodium, barium, palladium and technetium

LOW-VOLATILE

Ruthenium, cerium, strontium, yttrium, europium, niobium and lanthanum

NON-VOLATILE

Zirconium, neodymium and praseodymium

Thermochemical calculation and grouping elements

Concentration Data for the thermochemical equilibrium calculation:

- Volatile and semi-volatile fission product concentrations are obtained via MARGARET-active FP (green).
- Concentrations of uranium, oxygen, and low/non-volatile elements are obtained from ALCYONE's PRODHEL module (yellow).

Grouping of Elements:

- **TAF-ID Database Limitations:** Includes a limited number of fission products. Elements are grouped based on similar chemical properties and release behavior.

Thermochemical Equilibrium Calculations:

- **Representative Elements:** For each group, a representative element from the TAF-ID database is selected. The representative element's concentration is the sum of all group elements' concentrations.

Representative element	HE	U	O	BA	SR	ZR	CS	I	TE	MO	RU	TC	PD	CE	LA	GD
Elements	He	U	O	Ba	Sr	Zr	Cs	I	Te	Mo	Ru	Tc	Pd	Ce	La	Gd
	Kr						Rb	Br	Se		Rh			Pr	Y	Eu
	Xe															Sm
																Nd

The 12th European Review Meeting on Severe Accidents Research

May 18-22, 2026, Universidad Carlos III de Madrid, Madrid, Spain

TECHNICAL SESSION 7.2: GENERATION IV SYSTEMS - SODIUM FAST REACTORS

Chairs: N. Seiler (CEA), A. Miassoedov (IAEA)

ID197	**Validation of Species Transport Modeling in Liquid Sodium Systems: Extension of SPARC-90/University of Wisconsin-Madison Benchmarks to Modernized MELCOR** D. Luxat (SNL)	Presentation
ID140	**Experimental validation of the core catcher safety measures in Gen IV ESFR conceptual design against long-term ablation** Gaus-Liu Xiaoyang (KIT)	Paper Presentation
ID010	**Investigation of film boiling in liquid sodium: qualification of the SERUA experimental program** R. Clavier (CEA)	Paper Presentation
ID034	**Benchmarking of Advanced GPU-Accelerated Discrete Element Method and Elastoplastic Constitutive Granular Flow Models for Large-Scale Debris Bed Formation in Severe Accidents of Sodium Fast Reactors** R. Yokoyama (University of Tokyo)	Paper Presentation

ADVANCING NUCLEAR SAFETY TECHNOLOGY

Validation of MELCOR Pool Scrubbing Model on UW Bubble Transport Experiments

Water and sodium pool scrubbing · single bubble and swarm rise · benchmark to ANL SRT

Bradley Beeny · Brandon De Luna
Sandia National Laboratories

SAND2026-XXXXP

Sandia National Laboratories is a multimission laboratory managed and operated by National Technology & Engineering Solutions of Sandia, LLC, a wholly owned subsidiary of Honeywell International Inc., for the U.S. Department of Energy's National Nuclear Security Administration under contract DE-NA0003525.

Why pool scrubbing matters for SFR source term

- A liquid pool standing over a gas-injection source acts as a passive filter: rising bubbles carry FP aerosols and vapors, which transfer to the pool and are retained there.
- This mechanism is well established for LWRs and is the dominant source-term reduction credited in BWR suppression pools.
- For pool-type metal-fueled SFRs the geometry is similar — molten sodium sits over the core — so a comparable scrubbing role is expected, but had not been quantified.
- ANL identified sodium pool scrubbing as a **high-importance, high-uncertainty** knowledge gap for SFR source-term work.
- ANL developed the SRT code as a stand-alone scrubbing benchmark; NEUP funded the UW experiments that anchor it.
- SNL was tasked under the FY25 DOE Fast Reactor Program to use the UW data to validate MELCOR's pool-scrubbing model.

MELCOR's relevant features

- A **generalized EOS** lets the same pool model handle either LWR (water) or non-LWR (sodium) pools without code branches.
- Bubble composition is unrestricted — condensable vapor, NCG, or any mixture — so the same closures cover vapor-rich LWR conditions and dry-argon SFR injection.
- Arbitrarily many FP species can be carried in aerosol form, each with its own size distribution and density.
- The pool-scrubbing kinetics derive from **SPARC-90**, extended in MELCOR to handle bubble swarms in addition to single isolated bubbles.

PART 1

Pool Scrubbing Theory in MELCOR

Vent-exit and swarm-rise regions

- FP-aerosol-laden gas is injected at depth, and the rising flow splits into two distinct hydrodynamic regions.
- **Vent-exit region** — large globules form just above the nozzle and break up into the rising swarm; deposition here is driven by jet inertia and orifice geometry.
- **Swarm-rise region** — many oblate-spheroid bubbles coalesce and redisperse as they rise; centrifugal, Brownian, and gravitational mechanisms remove aerosol from the bubble interior.
- **DF** = (aerosol mass entering the pool) / (aerosol mass leaving the surface), reported per particle-size bin so the kernel can be probed across the diameter spectrum.

Why only swarm rise is exercised by the UW conditions

- The UW pools are deep and subcooled, with pure NCG bubbling — no boiling, no condensable vapor in the carrier gas.
- Injection velocity is low, so inertial deposition at the vent is negligible.
- The injector is a single low-velocity inverted nozzle, not a high-velocity multi-hole quencher — there is no jet-driven impaction, no shear-driven small-bubble formation, and no vent-region condensation, so the SPARC-90 vent-exit term is essentially inert.
- No Stefan flow and no FP vapor in the carrier gas — phase-change perturbations are absent by design.

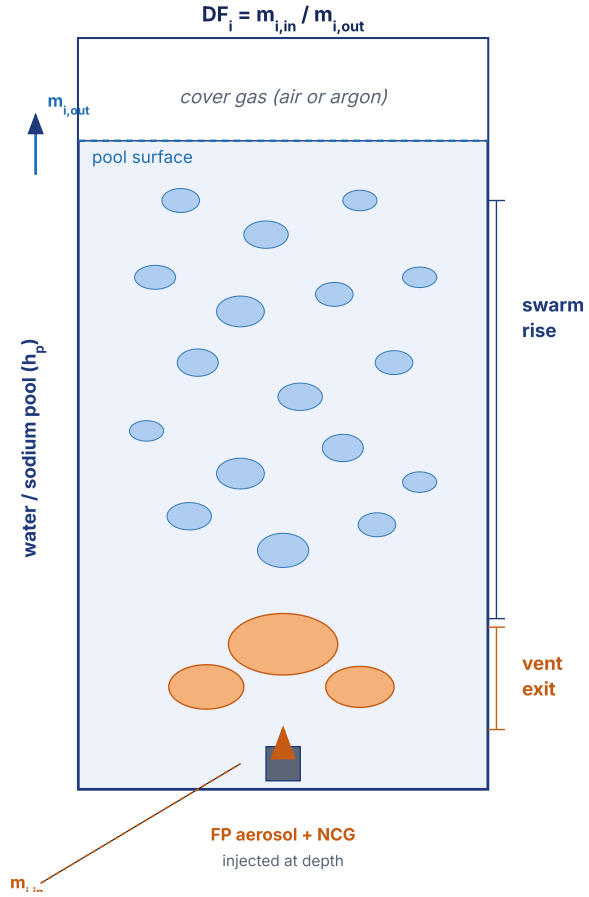

Swarm scrubbing mechanisms

- **Centrifugal capture** — particles drift toward the bubble wall as the rising bubble oscillates; dominates for larger aerosol.
- **Brownian diffusion** — random thermal motion deposits sub-micron particles onto the interface.
- **Gravitational sedimentation** — settling onto the upward-facing lower surface of the oblate bubble; matters most for dense/coarse particles.
- Each mechanism contributes an aerosol flux normal to the interior interface; their sum gives the **net deposition velocity** that sets the first-order scrubbing rate inside every bubble.
- **Phase change perturbs the kernel.** When the bubble is supersaturated, the condensable vapor (water vapor over a water pool, sodium vapor over a sodium pool) condenses on the cooler interface and drives **Stefan flow inward**, sweeping particles to the wall and boosting DF; evaporation reverses the flow and degrades it. SPARC-90 absorbs this into the deposition velocity.

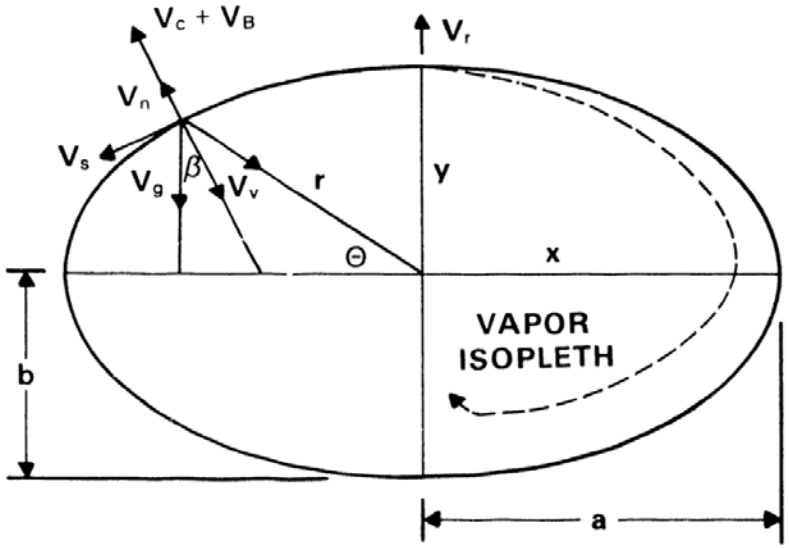

Swarm-rise bubble geometry and deposition-velocity components.

Bubble geometry in the swarm

EQUIVALENT DIAMETER

$$d_{vm}[cm] = 0.7 \times 10^{(-0.2265 + (0.0203 + 0.0313 \cdot x_{ncg})^{1/2})}$$

ASPECT RATIO

$$a/b = 0.84107 + 1.13466 \cdot d_{vm} - 0.3795 \cdot d_{vm}^{2}$$

- The UW injection is essentially pure NCG ($x_{ncg} \approx 1$), so the default correlation predicts $d_{vm} \approx 0.7$ cm regardless of test conditions.
- Every numerical constant in these correlations is exposed as an RN-package sensitivity coefficient, so the same equations can be re-anchored to a specific experiment without code edits.

Default vs. user geometry

- **Default** — the correlation form is retained and the RN coefficients are scaled proportionally; closest to the SPARC-90 baseline.
- **User** — the same coefficients are set directly to match a measured bubble size and aspect ratio, overriding the correlation.

The water experiments show the **default** geometry actually agrees with data better than heavy-handed user overrides — the correlation captures the swarm-averaged effective bubble better than a single measured value.

Bubble and swarm rise velocities

BUBBLE RISE VELOCITY

$$V_r[\mathrm{cm/s}] = 7.875\cdot(\sigma/\rho_l)^{1/4},\ d_{vm} \le 0.5\ \mathrm{cm}$$

$$V_r[\mathrm{cm/s}] = 1.40713\cdot d_{vm}^{\,0.49275}\cdot V_r(d_{vm}=0.5),\ \text{else}$$

SWARM RISE VELOCITY

$$V_s(y)[\mathrm{cm/s}] = [(Q_s+5.33)/0.003011]^{1/2}\cdot[1 - y\cdot 3.975\times 10^{-4}]$$

AVERAGE SWARM VELOCITY (USED BY MELCOR)

$$\bar{V}_s = \tfrac{1}{2}[V_s(0) + V_s(h_p)]$$

- **V_r** — single-bubble rise velocity, set by pool surface tension σ, liquid density ρ_l, and the equivalent diameter d_{vm}; piecewise to handle the small-bubble Stokes-like and large-bubble cap-bubble regimes.
- **$V_s(y)$** — swarm rise velocity at depth **y**, driven by the total gas volumetric flux Q_s; MELCOR averages it head-to-base to get the height-averaged swarm velocity used in the kinetics.
- Every numerical constant is exposed as an RN-package sensitivity coefficient, so the correlations can be re-anchored without code edits.
- Scrubbing along the column is then computed by spatially marching the first-order absorption equation up the rise height.

Aerosol scrubbing kinetics

SECTIONAL SCRUBBING RATE

$$dc_i/dt = -[(1/v_b)\int(A_b \cdot V_{n,i})\,dA]\,c_i$$

NET NORMAL DEPOSITION VELOCITY

$$V_{n,i} = V_{c,i} + V_{B,i} - V_{g,i}\cdot\cos(\beta) - V_v$$

- Scrubbing is treated as **first-order absorption** at the bubble surface — the depletion rate is linear in the bubble's aerosol concentration c_i.
- Any particle that reaches the interface is assumed to be captured with unit efficiency; the kernel is therefore a flux-to-surface, not a sticking, problem.

STOKES SEDIMENTATION

$$V_{g,i} = \rho_i \cdot g \cdot S_i \cdot d_i^2 \,/\, (18 \cdot \mu)$$

CENTRIFUGAL CAPTURE (SCALED FROM V_G)

$$V_{c,i} = V_{g,i} \cdot (V_s^2/r_c) \,/\, g$$

BROWNIAN (PENETRATION THEORY)

$$V_{B,i} = (D_i/\pi\cdot\tau_e)^{1/2}, \quad D_i = k_B T_{pool} S_i/(3\pi\cdot\mu\cdot d_i)$$

PART 2

MELCOR Input Deck for the UW Facility

Nodalization and RN inputs — common across all experiments

- **SOURCE** CV (1 m^3) — inlet boundary representing the aerosol generator that delivers FP-laden NCG to the nozzle.
- **COLUMN** CV — the active scrubbing volume; holds the liquid pool plus the cover-gas headspace and is where the SPARC-90 kinetics fire.
- **SINK** CV (1 m^3) — outlet boundary held at constant thermodynamic state to mimic the laboratory exhaust train.
- **INJECTOR** FL — nozzle geometry connecting SOURCE to COLUMN; one bubble per second; this is the flow path that activates pool scrubbing.
- **OUTLET** FL — passive flow path that vents COLUMN to SINK so the model can run to steady-state DF.
- Same nodalization in every run; only the pool fluid (water / sodium) and cover gas (air / argon) change.

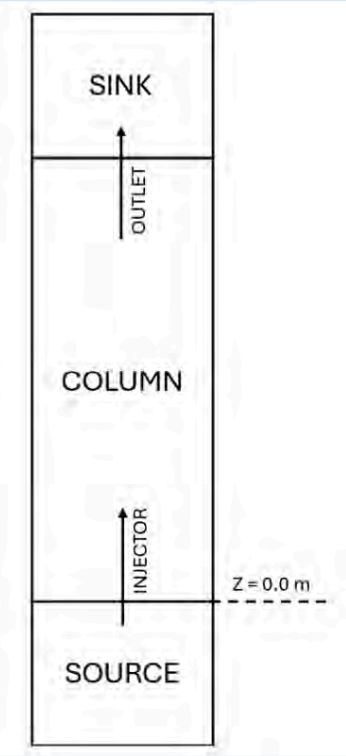

UW pool-scrubbing MELCOR CV/FL nodalization.

RN aerosol inputs — defaults exercised, only the size grid refined

- **20 size bins over 0.001 – 18 µm** (vs. default 10 bins over 0.1 – 50 µm) to resolve the DF U-shape across the UW measurement window.
- **Aerosol density** set per material via RN1_ASP (Al 2.7 / Ni 8.9 / W 19.3 g/cm^3); initial mass and source size-distribution set via RN1_AG / RN1_AS.
- **Single-class FP with vapor pressure forced to zero** — the species stays in aerosol form so the test exercises scrubbing kinetics, not condensation onto droplets.
- **Vent associated to COLUMN** via RN2_PLS as a single hole with area = INJECTOR; class-level sensitivity coefficients (RN1_CSC) left at defaults.

PART 3

UW Experimental Setup

UW pool-scrubbing facility — CAD model and as-built rig

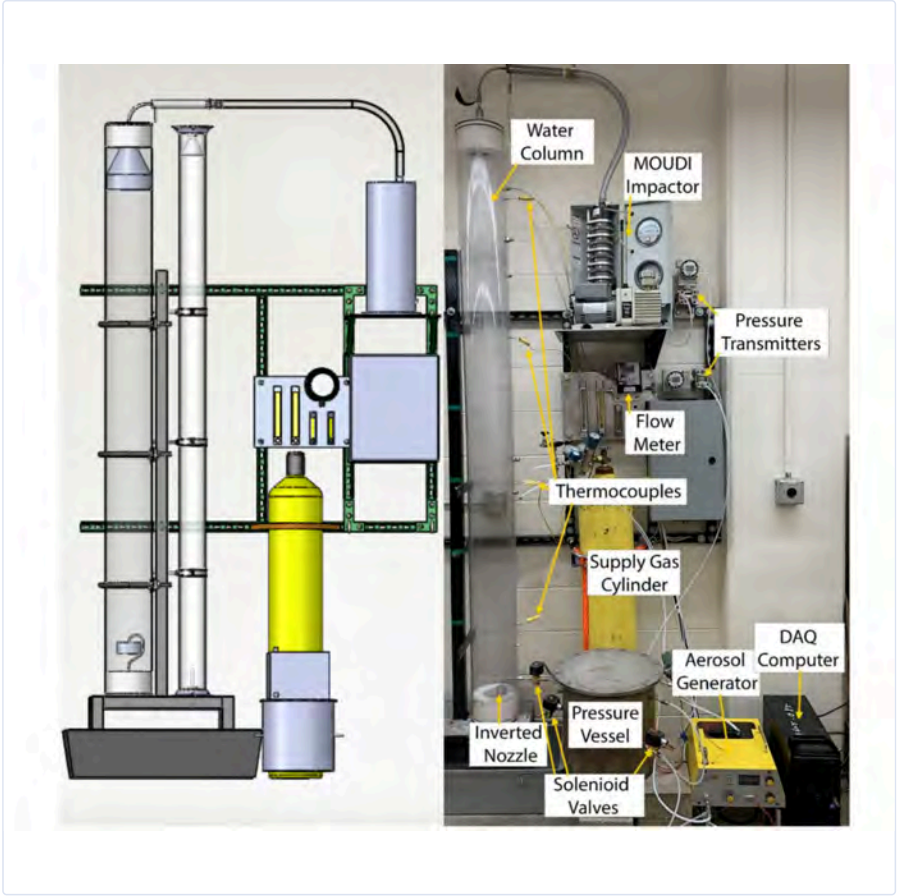

UW bubble-transport facility (Becker, K. PhD dissertation, U. Wisconsin–Madison, 2022).

Two experimental classes

- **Single isolated bubble rise** — one bubble at a time, with tightly controlled size and shape, isolating the per-bubble scrubbing kernel.
- **Bubble swarm rise** — a continuous bubble swarm with a realistic size distribution, exercising the collective behavior MELCOR's swarm-rise extension is meant to capture.

Key components on the rig

- **Aerosol generator + supply-gas cylinder** — deliver the aerosol-laden NCG (air for water tests, argon for sodium) at controlled flow.
- **Inverted nozzle / pressure vessel** — carefully designed injection geometry that sets bubble size and detaches them cleanly into the pool.
- **Water (or sodium) column** — the scrubbing volume itself; depth selected per test; instrumented for thermocouples and pressure transmitters.
- **MOUDI impactor + flow meter + DAQ** — size-resolved aerosol sampling above the pool surface to compute DF(d_p).

Parametric matrix: aerosol size, material density, and gas-phase concentration; bubble equivalent diameter; pool depth; pool temperature (sodium only) — each varied while holding the rest fixed.

Test conditions — water and sodium pools

Water pool

- Pool and atmosphere held at room conditions (297 K) with an air cover gas; no thermal sweep.
- Aerosol diameter spans three decades: **0.018 – 18 µm**, straddling the DF U-shape.
- Two aerosol materials chosen for density contrast: **Al** 2.7 g/cm^3 vs. **Ni** 8.9 g/cm^3.
- Four gas-bubble sizes (1.81 / 2.19 / 2.87 / 3.27 cm) tracking the single-bubble correlation regime.
- Two carrier-gas aerosol concentrations — 13.2 (low) and 26.5 (high) g/m^3 — to probe first-order scrubbing.
- Two pool depths — 0.9 m (low) and 1.8 m (high) — doubling the rise residence time.

Sodium pool

- Argon cover gas throughout; pool and atmosphere temperatures swept to probe the sodium kinetics.
- Four pool temperatures (423.15 / 473.15 / 523.15 / 573.15 K) covering the SFR primary-pool range.
- Same aerosol diameter window as the water tests: **0.018 – 18 µm**.
- Three aerosol materials for a wider density spread: **Al** 2.7 / **Ni** 8.9 / **W** 19.3 g/cm^3.
- Four bubble sizes (2.36 / 2.86 / 3.63 / 4.11 cm) — the larger sodium-pool bubbles reflect surface-tension scaling.
- Two concentrations (5.4 / 15.3 g/m^3) and two depths (0.9 / 1.8 m), so the same parametric handles are exercised as for water.

PART 4

Water Pool Validation

Water — variation across particle diameter and bubble size

- Conditions: water single-bubble experiment #1 with Al aerosol, swept across four bubble sizes (1.81 – 3.27 cm).
- The characteristic **U-shape** of DF(d_p) — high DF at both small (diffusion-dominated) and large (inertial) ends — is reproduced at every bubble size.
- Quantitative agreement is excellent in the 1 µm neighborhood where centrifugal and Brownian kernels are both modest.
- In the 0.1 – 1 µm valley — where Brownian, gravitational, and centrifugal kernels all weaken — MELCOR **under**-predicts DF by a factor of 2 – 3.
- Below 0.1 µm the trend is still matched; the 2 – 3× under-prediction persists but does not diverge with diameter.
- MELCOR and SRT track each other tightly across every bubble size, suggesting the under-prediction is a kernel-level issue shared by both codes.

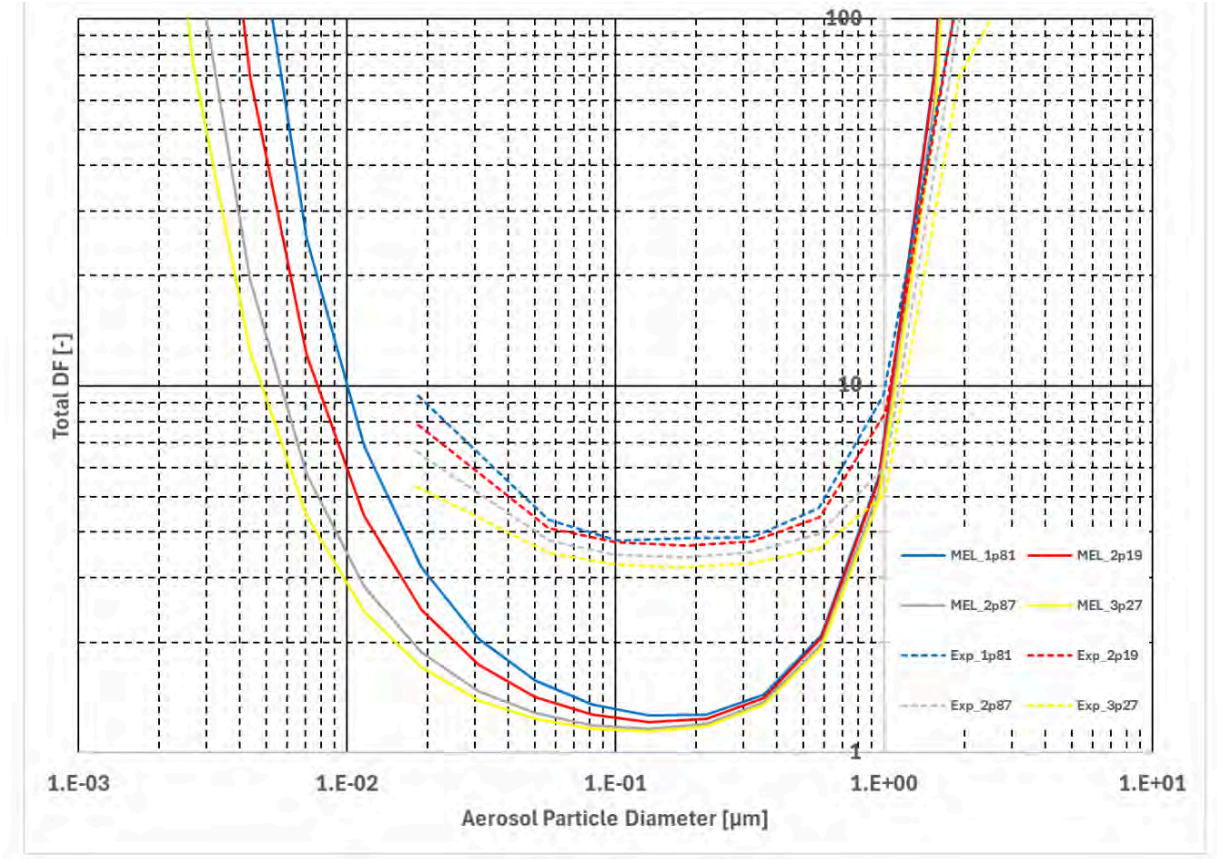

Water single-bubble #1 — MELCOR (default geometry) vs. UW data.

Water — parametric sensitivities for single-bubble rise

- **Material density** — heavier aerosol (Ni vs. Al) pulls the large-d_p side of the curve apart through the V_g, V_c dependence on ρ_i; MELCOR captures the separation.
- **Pool depth** — doubling the depth doubles the residence time and the data show the expected DF increase, which MELCOR matches.
- **Aerosol concentration** — high vs. low loadings collapse onto the same curve, confirming the first-order absorption regime in both data and model.
- **Default vs. user bubble geometry** — defaults consistently agree with the data better than user-specified geometry, even when the user inputs come from direct bubble measurements.

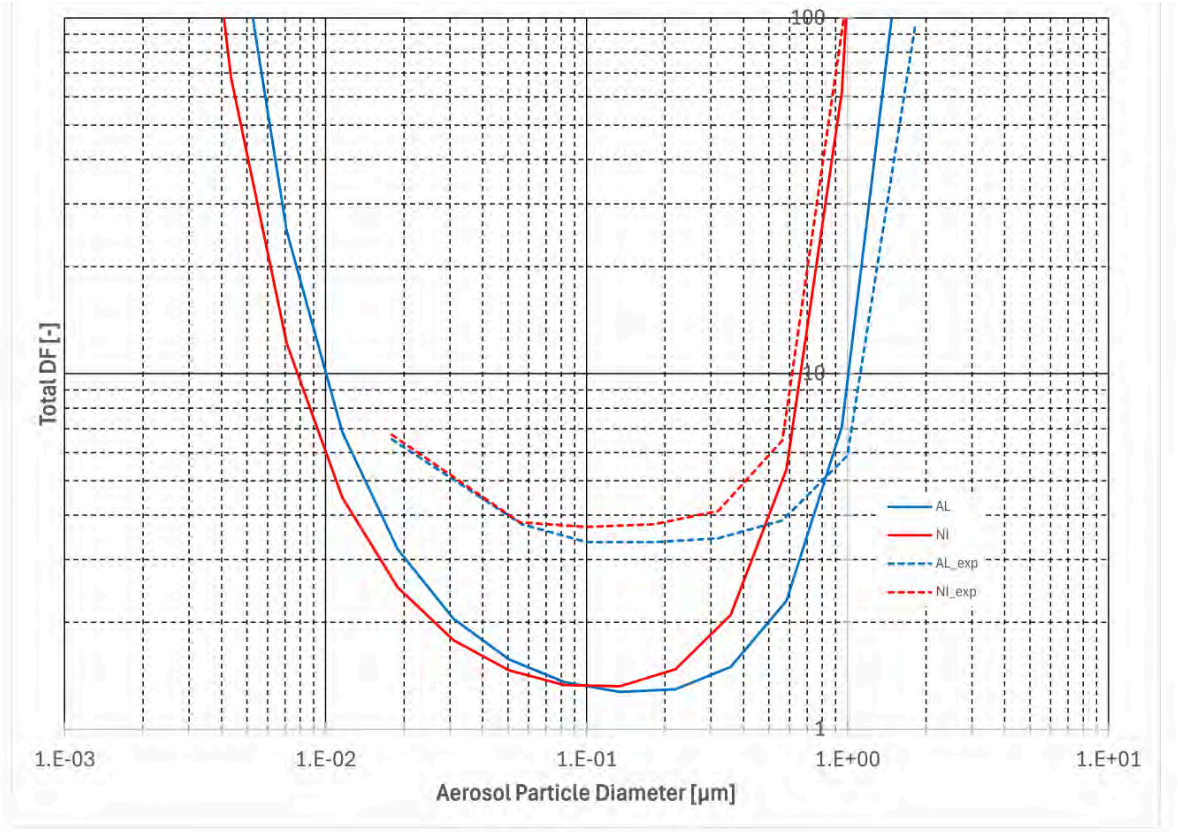

Density effect — Al vs. Ni aerosol, water single-bubble rise.

Water — bubble-swarm rise validation

- The single-bubble correlation is replaced by the swarm-rise extension: the same kernels, but with a swarm-averaged equivalent diameter d_{vm} and a height-averaged rise velocity.
- **Sensitivity to d_{vm}** — smaller swarm-averaged bubbles raise DF, just as the single-bubble correlation predicts; the trend direction is correct at every diameter tested.
- At **d_{vm} = 0.25 cm** MELCOR is within 2× of the swarm DF data across the entire 0.05 – 0.5 µm range — the same band where the single-bubble runs show their largest under-prediction.

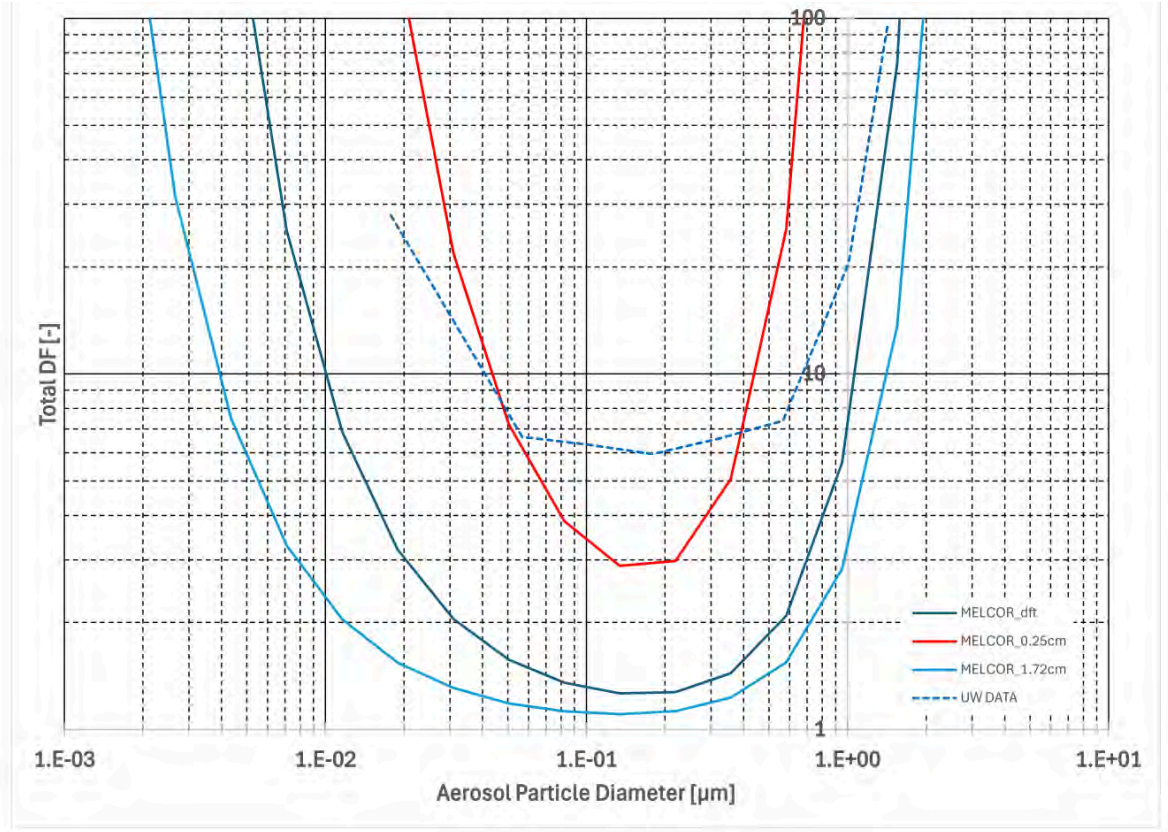

Swarm rise — equivalent-diameter sensitivity vs. UW swarm data.

PART 5

Sodium Pool Validation

Sodium scrubbing — experiment matrix

Six experiments, dry aerosol-laden argon

- **#1 Bubble size** — four argon bubble sizes (2.36 / 2.86 / 3.63 / 4.11 cm), all other inputs fixed; isolates the bubble-diameter dependence of the scrubbing kernel.
- **#2 Material** — Al / Ni / W to span an order of magnitude in aerosol density.
- **#3 Concentration** — high vs. low loading to verify the first-order absorption regime in sodium.
- **#4 Pool depth** — 0.9 m vs. 1.8 m, doubling residence time at fixed bubble dynamics.
- **#5 Pool temperature** — four temperatures (423 / 473 / 523 / 573 K) probing sodium-property and Stokes–Einstein effects.
- **#6 Swarm** — full bubble-swarm rise at one nominal condition for direct comparison to MELCOR's swarm extension.

Conditions held in common

- Aerosol diameter range matches the water tests: 0.018 — 18 µm, sectionalized into 20 MELCOR bins.
- Aerosol materials span density: Al 2.7 / Ni 8.9 / W 19.3 g/cm^3.
- Pool and atmosphere temperatures co-vary per run; cover gas is argon throughout to suppress sodium combustion.

Sodium Exp #1 — bubble size variation

- Conditions: four argon bubble sizes; Al aerosol; high concentration; deep pool; 473.15 K. Bubble size is the only thing swept.
- Across 0.02 — 0.4 µm MELCOR predictions sit inside the data error bars for all four bubble sizes.
- The lone soft spot is the smallest (2.36 cm) bubble at the small-d_p end of the curve.
- Above ~0.4 µm MELCOR consistently **over**-predicts DF — the centrifugal kernel pulls aerosol out too aggressively in this regime, a pattern that recurs in the next experiments.

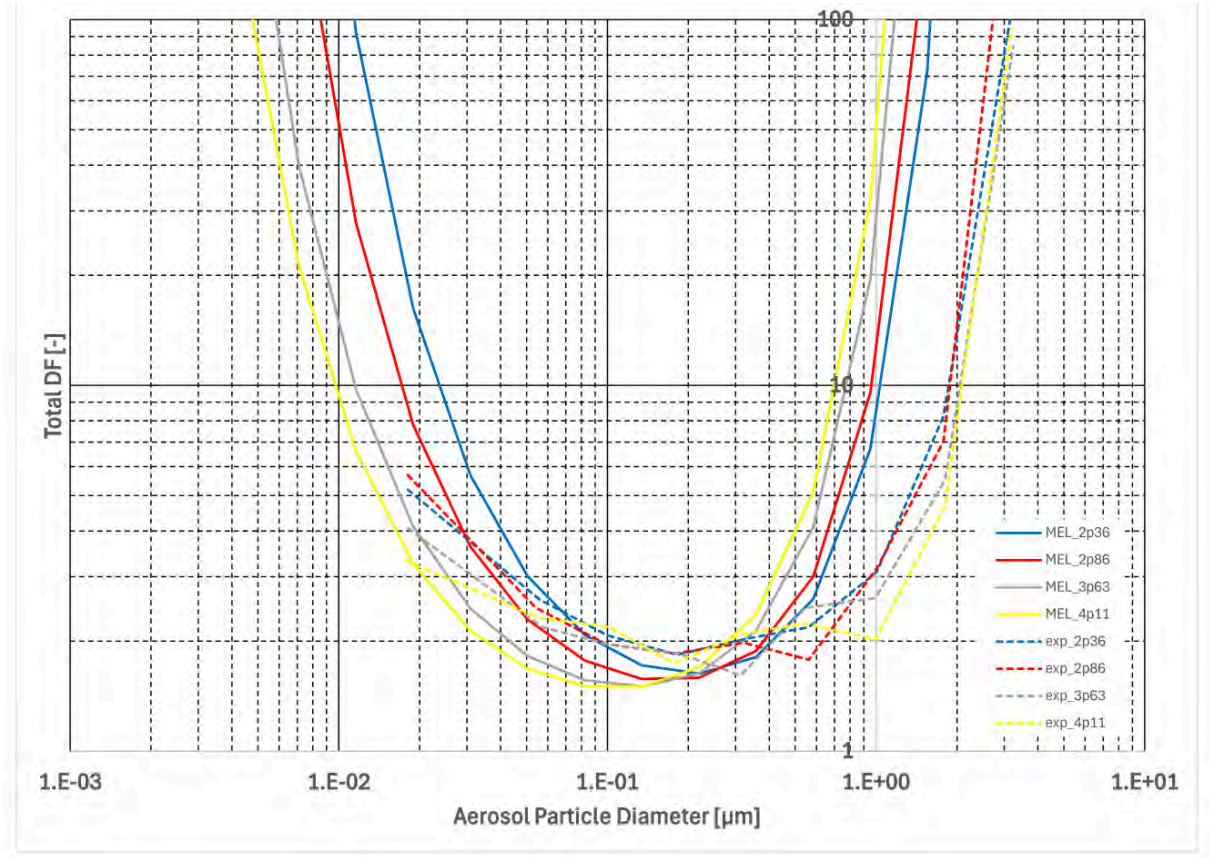

Sodium #1 — bubble size.

Sodium — MELCOR benchmark to ANL SRT

- The two codes are qualitatively in step across the entire d_p spectrum and all four bubble sizes.
- Where they diverge quantitatively it is in distinct diameter ranges, not in the overall U-shape — the disagreements are diagnosable rather than chaotic.
- At small d_p MELCOR sits closer to the data than SRT, suggesting its Brownian/diffusion kernel is the better-tuned of the two.
- At large d_p MELCOR **over**-predicts both SRT and the data — the centrifugal capture is the kernel most worth revisiting.

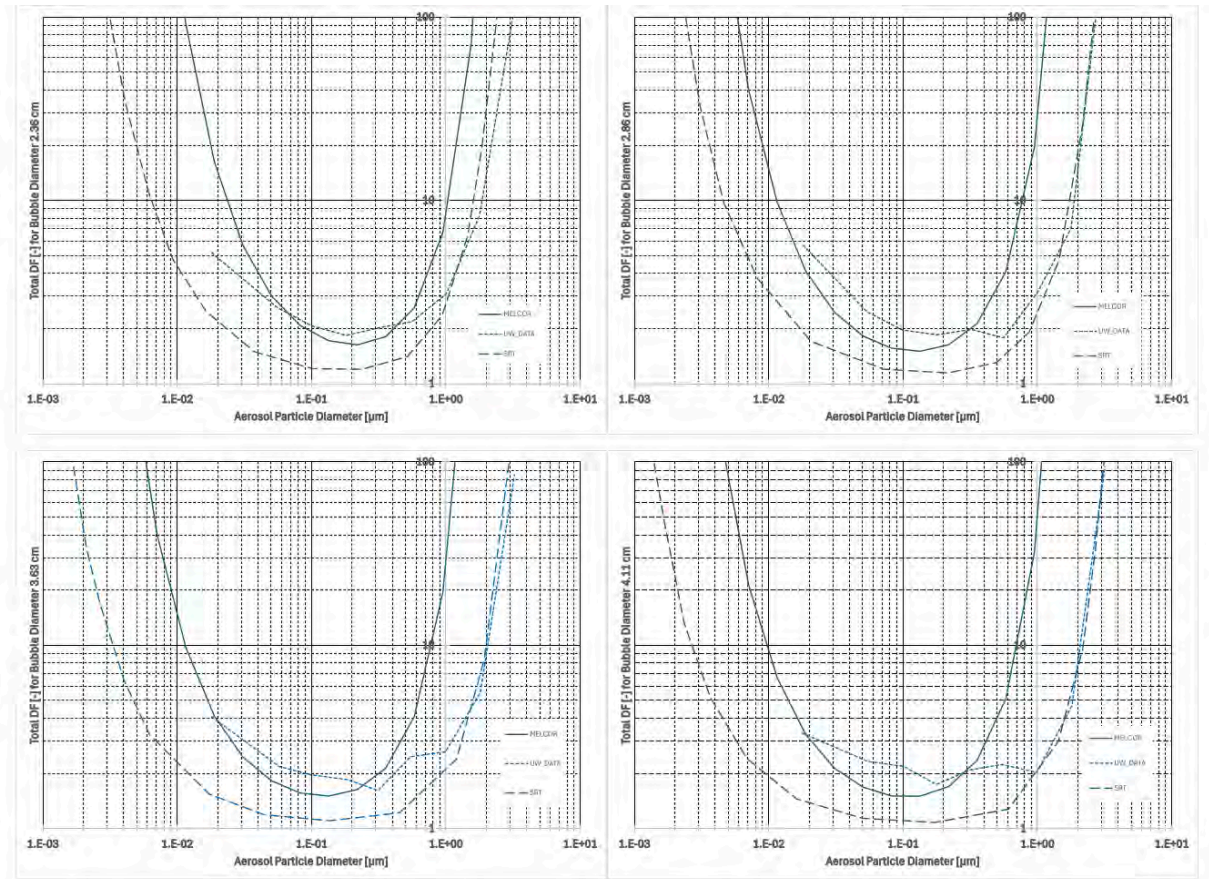

Sodium #1 — MELCOR vs SRT vs UW data.

Sodium Exp #2 — aerosol material / density

- Conditions: Al / Ni / W aerosols at fixed 3.63 cm bubbles, high concentration, 473.15 K. Aerosol density is the only sweep.
- The same large-d_p over-prediction seen in Exp #1 reappears here, confirming it is not an artifact of a single material.
- The onset of the over-prediction shifts to **smaller** d_p as material density rises from Al → Ni → W — heavier particles cross the centrifugal-dominated threshold sooner.
- This is the expected fingerprint of the V_g and V_c dependence on ρ_i, pointing the discrepancy at the inertial side of the deposition velocity rather than a material-specific error.

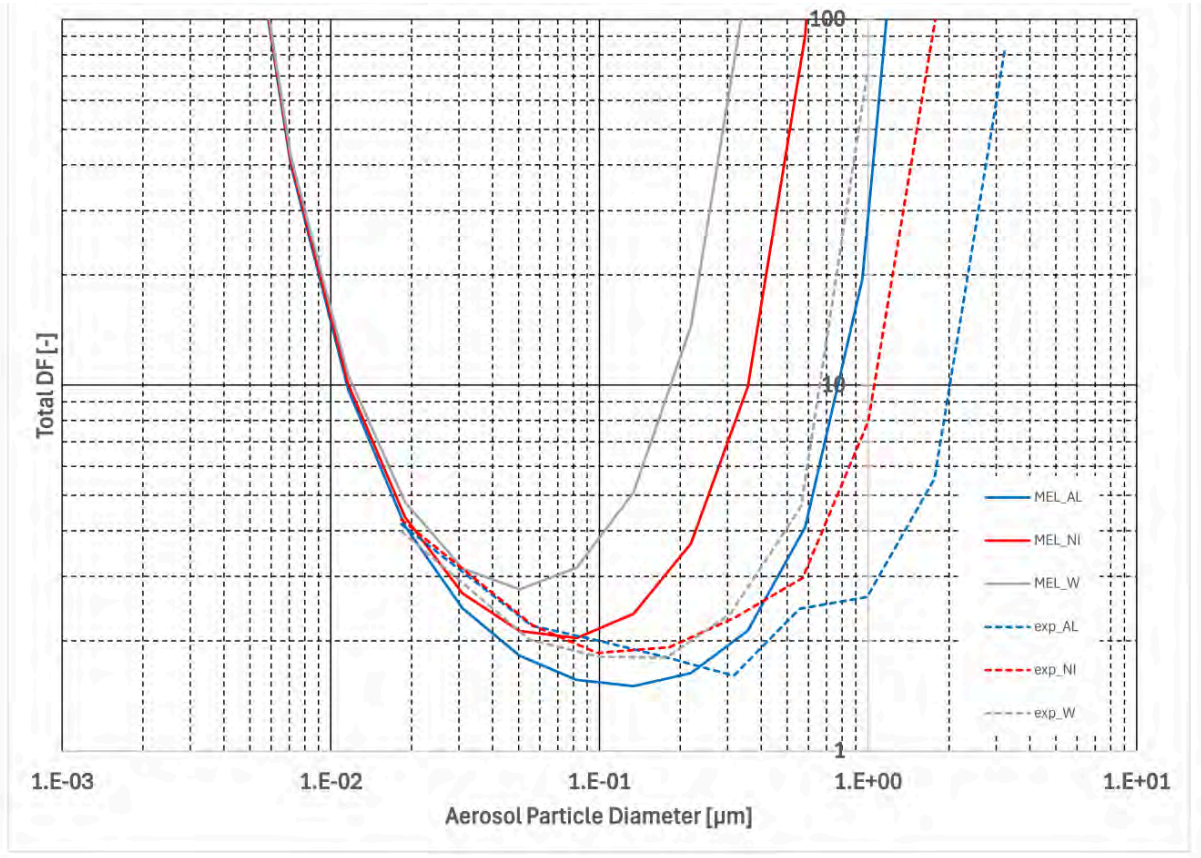

Sodium #2 — aerosol material.

Sodium Exp #3 — aerosol concentration in bubbles

- Conditions: Al aerosol; deep pool; 473.15 K; 3.63 cm bubbles. Loading varied between low and high.
- Doubling the aerosol concentration leaves DF essentially unchanged in the measurements, just as the model predicts.
- MELCOR reproduces this insensitivity exactly — the predicted high- and low-concentration curves overlay.
- This is the cleanest direct confirmation that pool scrubbing in this regime is genuinely first-order: the depletion rate is linear in c_i, so loading cancels out of DF.

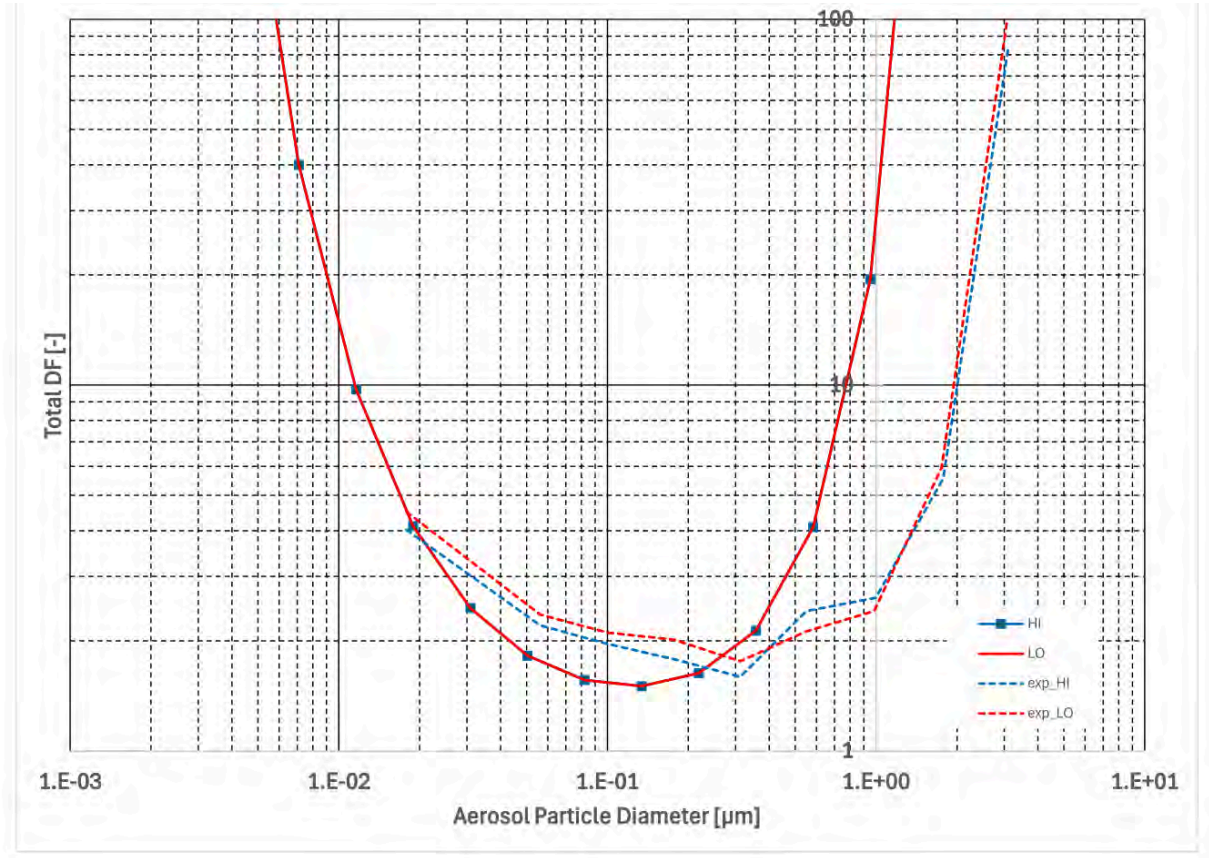

Sodium #3 — aerosol concentration.

Sodium Exp #4 — pool depth

- Conditions: 0.9 m vs. 1.8 m pool depths; Al aerosol; high concentration; 473.15 K; 2.87 cm bubbles. Pool depth is the only sweep.
- MELCOR predicts increased DF in the deeper sodium pool, consistent with longer bubble residence time and a longer integration of the first-order absorption.
- The data show the same qualitative trend, so the direction of the depth effect is correct.
- At the small- and large-d_p ends, however, MELCOR appears to **over**-state how much extra DF the deeper pool buys, suggesting the column-march kernel is too aggressive in those wings.
- For intermediate d_p the depth scaling matches the measurements quantitatively, indicating the issue is band-localized, not global.

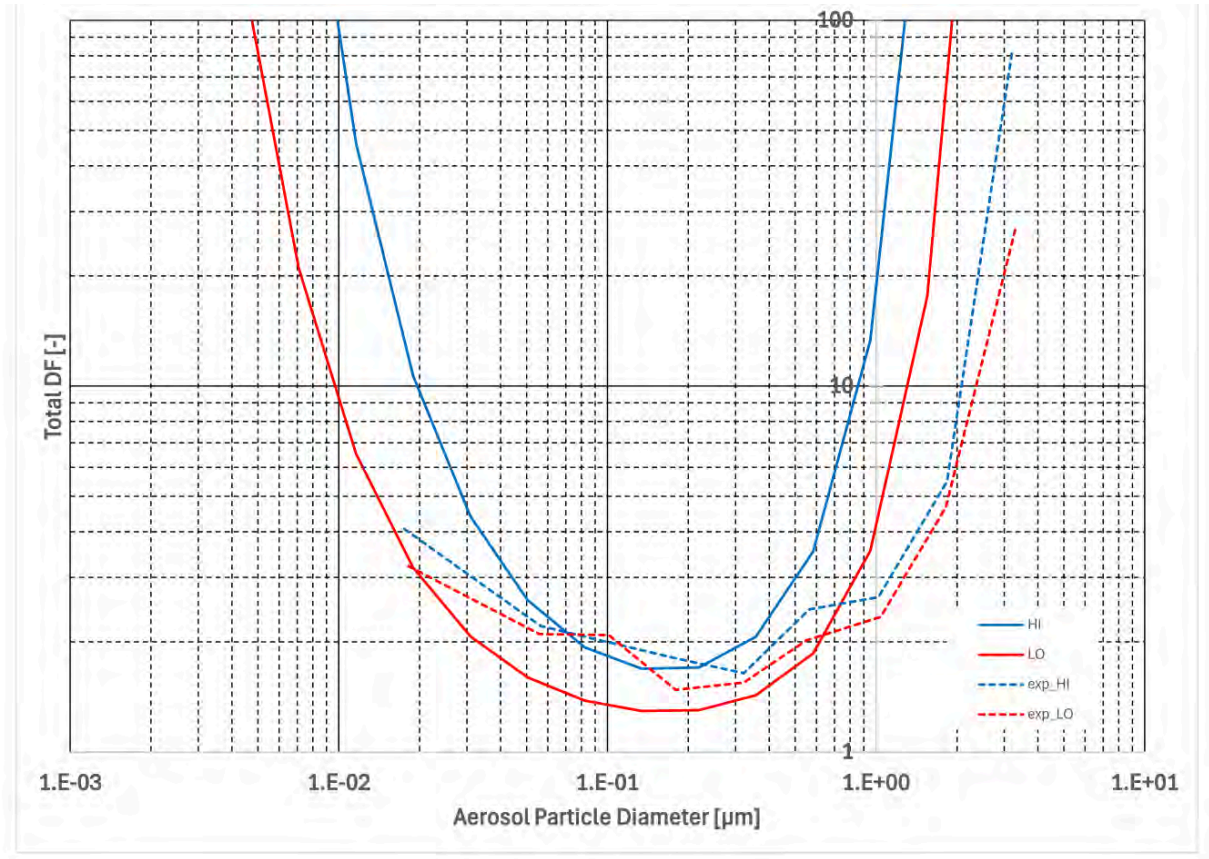

Sodium #4 — pool depth.

Sodium Exp #5 — pool temperature

- Conditions: four pool temperatures spanning 150 — 300 °C; Al aerosol; high concentration. The full SFR primary-pool temperature range.
- Both measurements and MELCOR show a **small** temperature effect on DF — the curves shift slightly but do not change shape.
- The temperature-driven variation is well below the bubble-size variation seen in Exp #1, so geometry (not thermophysics) dominates the kernel.
- Temperature enters the kernel through the Brownian diffusivity D_i (Stokes–Einstein) and through sodium fluid properties (μ, ρ_l, σ); their net effect is muted in this regime.

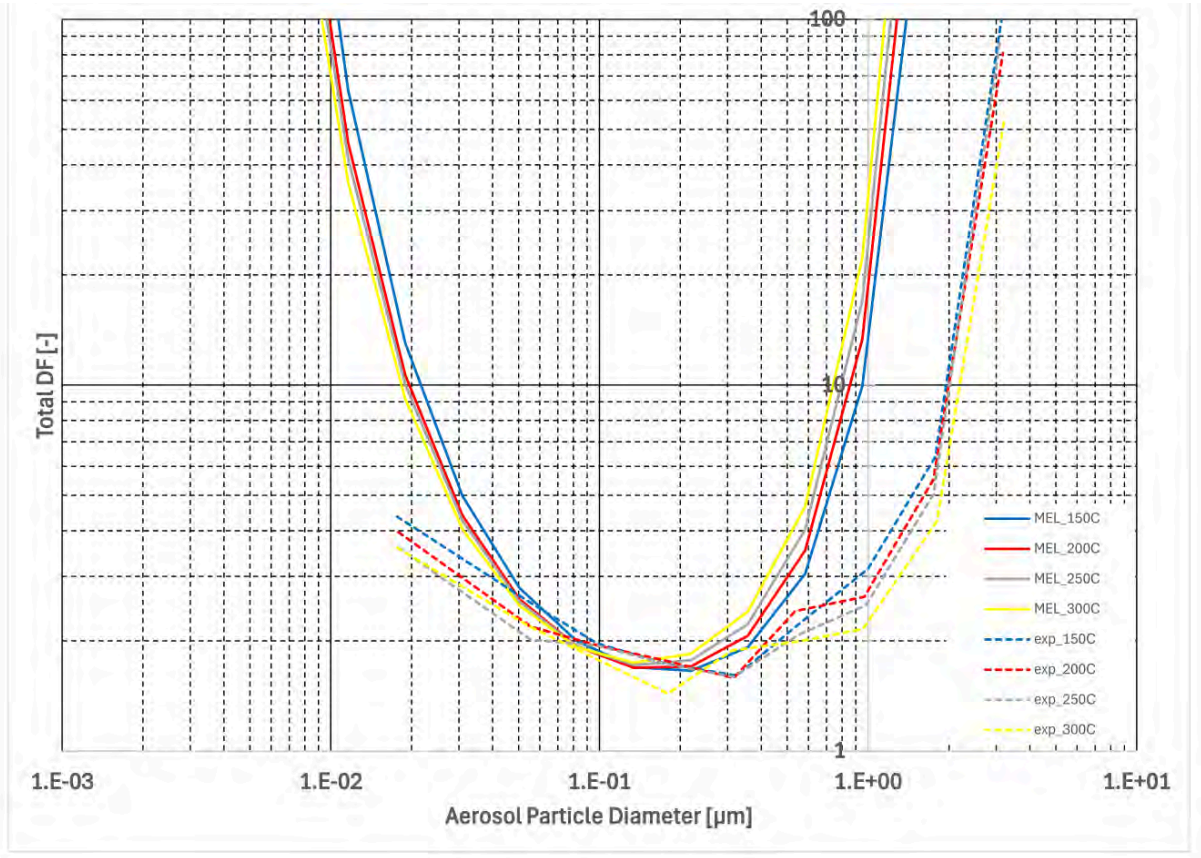

Sodium #5 — pool temperature.

Sodium Exp #6 — bubble swarm

- Conditions: Al aerosol; high concentration; deep pool; 473.15 K; default swarm geometry. The first direct test of MELCOR's swarm-rise extension on sodium.
- MELCOR is qualitatively consistent with both the single-bubble and swarm data sets, so the swarm extension does not break the kernel.
- At the small- and large-d_p tails the predicted DF approaches the swarm data quantitatively.
- MELCOR **over**-predicts for d_p < 0.035 µm and > 0.6 µm — the same large-d_p centrifugal pattern as the single-bubble sodium runs, now extended to the small-d_p wing as well.
- In between, MELCOR under-predicts the swarm DF and instead tracks the single-bubble curve — the swarm coupling is too weak in this intermediate band.

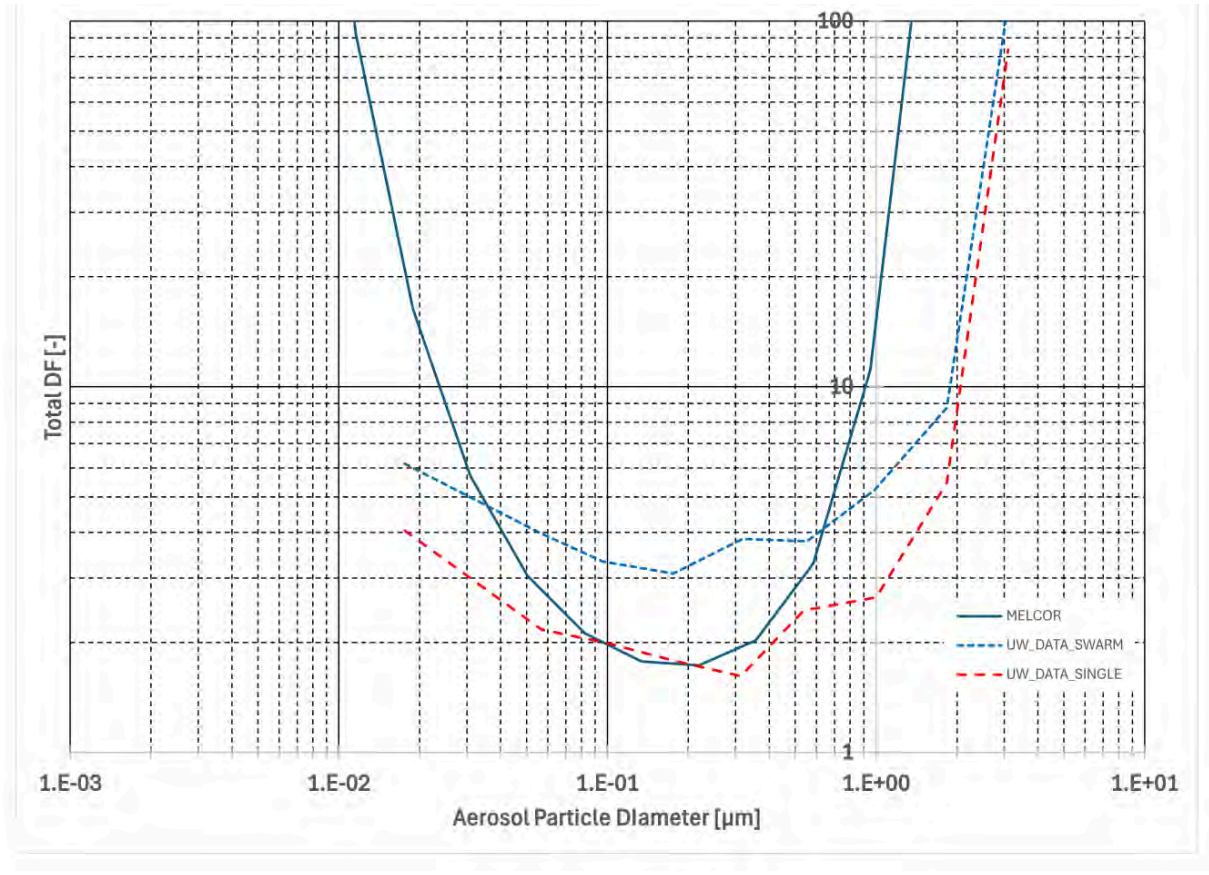

Sodium #6 — bubble swarm.

Conclusions

Validation outcome

- Across both fluids and every parametric sweep, MELCOR qualitatively reproduces the UW DF(d_p) trends — no surprises and no missed regimes.
- Quantitative agreement is good over wide diameter ranges; where MELCOR misses, it misses in identifiable, kernel-localized ways.
- The MELCOR ↔ SRT benchmark closes well in both qualitative and quantitative terms, so the two independent code bases corroborate one another.
- None of this required physics development or heavy-handed user tuning — the shipped defaults did the work.

Implication for SFR source term

- MELCOR is suitable for SFR sodium pool-scrubbing best-estimate and uncertainty analysis at the level of fidelity these experiments resolve.
- The model plugs directly into integral SFR source-term workflows — from in-vessel release through cover-gas leakage to environment — without a stand-alone scrubbing code.
- That out-of-the-box defaults are this credible is encouraging for the broader non-LWR source-term effort — the modeling framework generalizes.

ADVANCING NUCLEAR SAFETY TECHNOLOGY

Thank you

Bradley Beeny · Brandon De Luna
Sandia National Laboratories

SAND2026-XXXXP
Supported by the U.S. Department of Energy Office of Nuclear Energy's Fast Reactor Program.

The 12h European Review Meeting on Severe Accident Research (ERMSAR2026) Log Number: 140
Madrid, Spain, May 18-22, 2026

Experimental benchmark of the core catcher safety measures in Gen IV ESFR conceptual design during long-term thermal attack

X. Gaus-Liu[1], B. Fluhrer[1],

[1]: Karlsruhe Institute of Technology (KIT)
Hermann-von-Helmholz-Platz 1, Eggenstein-Leopoldshafen, 76344 Germany
xiaoyang.gaus-liu@kit.edu; Beatrix.fluhrer@kit.edu; Heiko.neuerberger@kit.edu

ABSTRACT

In the frame of Horizon-Euratom ESFR-SIMPLE project, the safety design of the European SFR is being developed further, building on previous designs developed during earlier European projects (CP-ESFR, ESFR-SMART). Of the many safety issues, special concern is given to the implementation of safety measures for an ESFR-type in-vessel core catcher. Based on the knowledge gained from the ESFR-SMART project, that the ablation of the core catcher by a melt jet originated from a core-melt accident scenario could be a very fast process under jet impingement, the current ESFR-SIMPLE project suggests local enhancement measures inside the core catcher to mitigate the localized ablation, such as pods at the impingement locations. To validate the effect of the local enhancements during a long-term ablation period after the molten material has been collected in the core catcher, which poses a threat to the core catcher integrity, three tests were performed in the LIVE-Core Catcher facility at Karlsruhe Institute of Technology. These tests provided experimental benchmark including the ablation dynamics, heat transfer inside and around the enhancements as well as the thermos-hydraulics of pre-ablated core-catcher in a molten pool with all-boundary cooling conditions. The numerical simulation is the other part of the task in the project is not the context in this study. The three experiments were successfully conducted using a eutectic binary K-Na-NO_3 salt as liquid melt under simulated internal heating condition. Salt pods were used as meltable enhancements and metal pods as non-meltable enhancements. Many beneficial impacts have been observed of such enhancement in a molten pool configuration. Many insights concerning the melting dynamics and heat transfer to the local enhancement are achieved.

KEYWORDS
Gen-IV ESFR, ESFR-SIMPLE, core catcher, LIVE-CC experiment

1. INTRODUCTION

The core catcher in the lower plenum of a SFR reactor vessel is an important safety implementation of a future European type SFR [1]. In the event of hypothetical severe accident, it must minimize the neutron positive criticality inside the core by collecting the discharged liquid core material, also named as corium. At the same time, it must protect the reactor vessel from corium jet thermal attack during the downward melt relocation and long-term exposure in the decay-heat-generating corium. In this context, the safety of the European SFR core-catcher was initially assessed the ESFR-SMART project [2, 3] [4] in which the vulnerability of the core catcher have been demonstrated in certain critical circumstances, e.g. under a high-temperature jet of metallic corium during the corium relocation period, or insufficient cooling of the upper surface during long-term exposure to corium [5]. The safety measures for the core-catcher are continually investigated in the follow-up ESFR-SIMPLE project, which

assesses protective measures against the core-catcher ablation. Local objects placed under the jet shall protect against the jet impingent and under the thermal attack of a melt pool in the long term. The long-term behavior of the core catcher was experimentally evaluated in the LIVE-CC experimental facility at KIT. In the following, the experimental set up and the test condition is described in Section 2, Section 3 depicts the dynamics of the melting or solidification and heat transfer of the local protective objects, Section 4 arises the discussion of the similarity issue and the overall effect of the objects, which is followed by Section 5 Conclusion.

2. DESCRIPTION OF EXPERIMENTAL CONDITIONS

LIVE-CC mockup is tailer-designed for ESFR-Core catcher research. Several tests regarding the general character of core catcher safety have been investigated in ESFR-SMART project. The activities in the current project are focused on local protective measures against short-term jet ablation and their long-term resilience exposed in a molten pool enclosed in the core-catcher.

2.1 The LIVE-CC Test Facility

The test vessel of LIVE-CC is located at a 3m-platform**,** see Figure 1**.** It mimics the typical tray geometry of an in-vessel ESFR core catcher: with a truncated cone-form lower part ad cylindrical upper part, as shown in Figure 2**.** The height of the truncated cone is 0.08 m**,** and the inner diameter of the upper cylinder is 1 m. The upper part corresponds to 1:6 scale of the prototype. The whole height of the test vessel inner cavity is 0.38 m.

An external cooling vessel with a cooling channel width of 6 cm embraces the test vessel. The cooling fluid liquid Na is simulated by water cooling. The cooling water inflow locates at the central bottom and the four outflows at the vessel upper flange. The flow rate is controlled to enable a temperature difference between the inlet and outlet of about 10 °C. This difference is large enough for a precisive determination of the water-side heat removal rate. The top surface cooling of the vessel is realized by a floating water-cooled lid (Figure 1). The cooling lid can be placed at all the vertical position of the cylindrical part.

Besides the test vessel, the platform includes apparatus for the melt preparation, pouring and extraction. A heating furnace melts and store the simulant melt material and serves also as discharge device of the melt to be poured into the test vessel. In addition, the heating furnace is equipped with a vacuum pump for the extraction of the residual liquid melt from the test vessel back into the heating furnace once the test is ended.

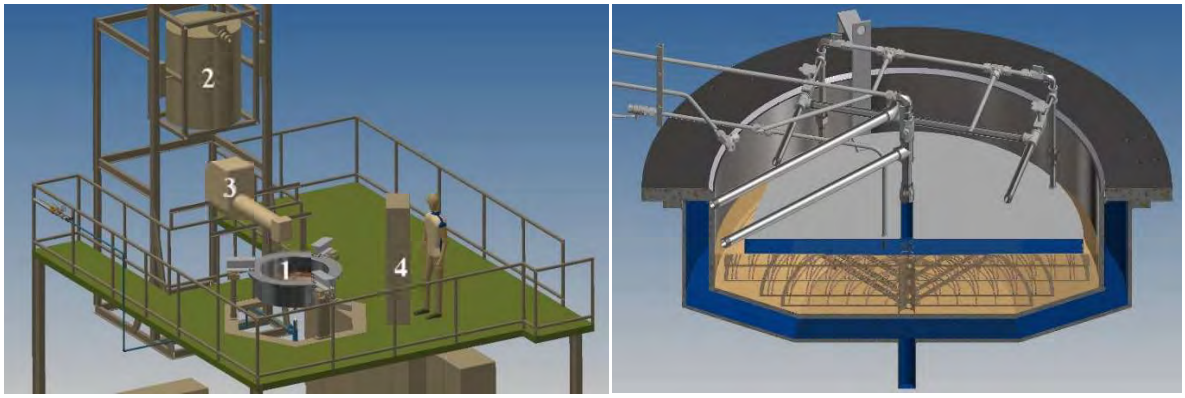

Figure 1. Left: LIVE experimental platform with LIVE-CC facility. 1- ESFR test vessel, 2 - heating furnace for melt preparation, 3 - pouring spout, 4 - instrumentation board. Right: Cooling and heating system.

Four planes of 4 mm resistance heating cable in the form of spiral winding are designed to simulate the volumetrically dissipated decay heat of the corium, which are named HE1 to HE4 from the bottom upwards, as

shown in Figure 2. Two planes are in the truncated cone (HE1 and HE2) and the other two are in the cylindrical part (HE3 and HE4). The heating cables were adapted in the current experiments to make space for the local objects.

The measurements are mainly temperatures with Type K thermocouples (TCs). This includes 44 pairs TCs on the inner and outside of test vessels, distributed at 225-45 °C axis, 49 TCs inside the vessel. Beneath the top cooling lid, the boundary temperatures were measured with three arrays of TCs. Besides, cooling water temperature and flow rates were recorded.

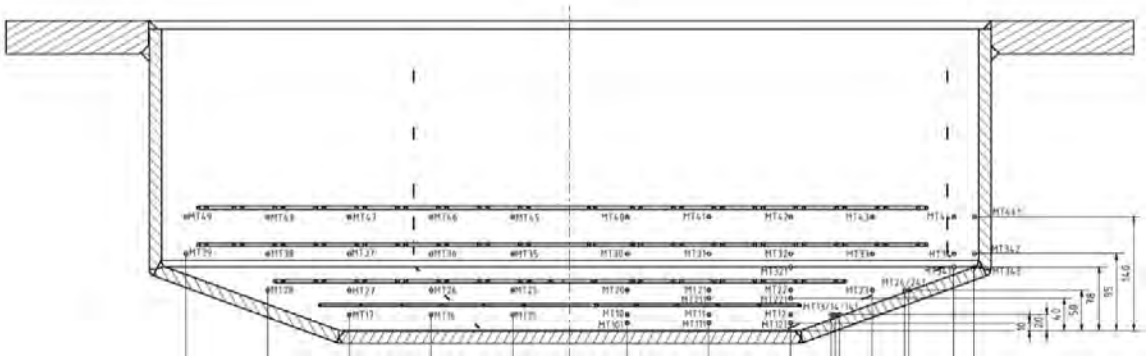

Figure 2. Instrumentation of test vessel.

2.2 The Realization of Local Protective Measures

For each of these LIVE-CC tests, local objects were implemented at two positions in the test vessel, see Figure 3. The geometry of the objects, either pods or holes is cylindrical in 80 mm diameter. The heating wires, which has a distance of 45mm between each winding, were bent at these positions to enable the space of these local objects.

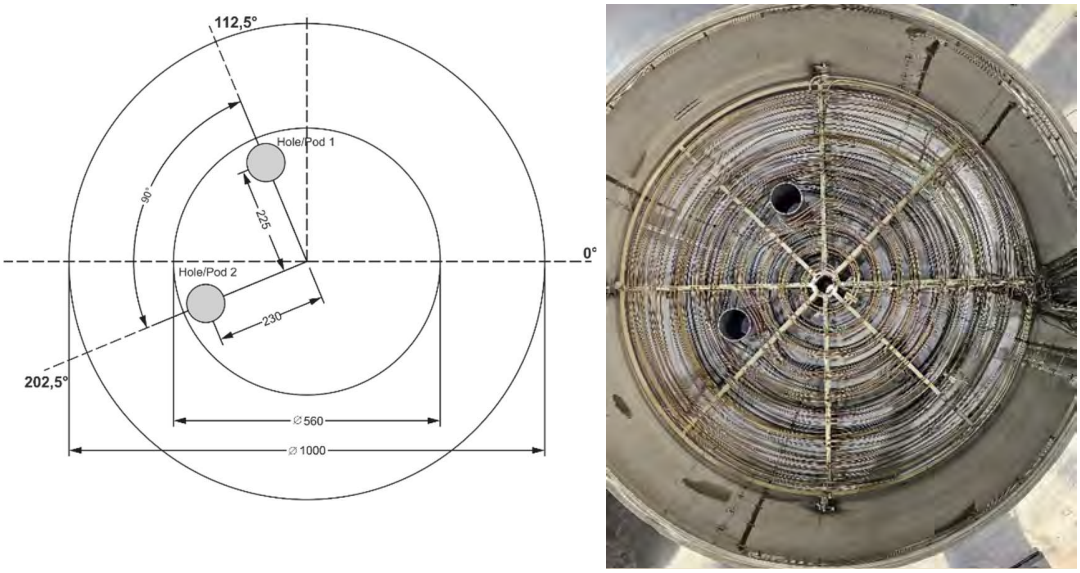

Figure 3. Position of pods in the LIVE-CC test vessel.

2.3 Test Condition

Three test series have been performed: LIVE-CCH (**C**ore-**C**atcher with **H**oles), LIVE-CCS (**C**ore-**C**atcher with **S**alt pods) and LIVE-CCM (**C**ore-**C**atcher with **M**etal pods). LIVE-CCH test investigates whether and how an ablated cavity in core-catcher bottom plate can be filled if the cooling of sodium around the core catcher is available. LIVE-CCS test assesses the ablation dynamic of meltable pods. LIVE-CCM evaluates the heat transfer around and inside pods. A eutectic mixture of $NaNO_3$ and KNO_3 with the melting point 220 °C was used as the liquid melt and as the bottom plate material in the LIVE-CCH test, as well as the solid pods in the LIVE-CCM test. The pods in LIVE-CCM were made of stainless steel und are not meltable during the experiment. For all the experiments, the test vessel was cooled externally and at the melt top surface. External cooling was already activated before the melt pour. There is a slight delay of ~ 10 minutes of top cooling after the melt pour, since this period was needed to place the cooling lid on the melt pool.

Table I. LIVE-CCH test conditions

tests	Local objects	Material of object	Geometry	Heaters in operation	Vessel initial condition
CCH	Hole in the bottom crust	Solid salt crust plate with holes	Depth of hole: 40mm Thickness of plate: 80 mm	No heating in the 80 mm bottom plate	With bottom plate
CCS	Salt pods	Solid salt	Height of pods: 80 mm	All heaters	Only with two pods
CCM	Metal pods	Stainless steel	Height of pods: 80 mm	All heaters	Only with two pods

For each test, additional 90 pieces of TCs were installed inside and near the two objects to capture the melting front or the local heat transfer features. One TC shows the solidification temperature as the solidification front passes through its position. In this way, the position and the time point of the changing contour of the hole /pod can be detected. In Figure 4, the instrumentation schema and its realization are shown for one hole in CCH test. The TCs were arranged in the middle between the two heating windings and are assigned to 0° and 180 ° for the same radius. This arrangement allows a low influence of the heating cable at the measured position.

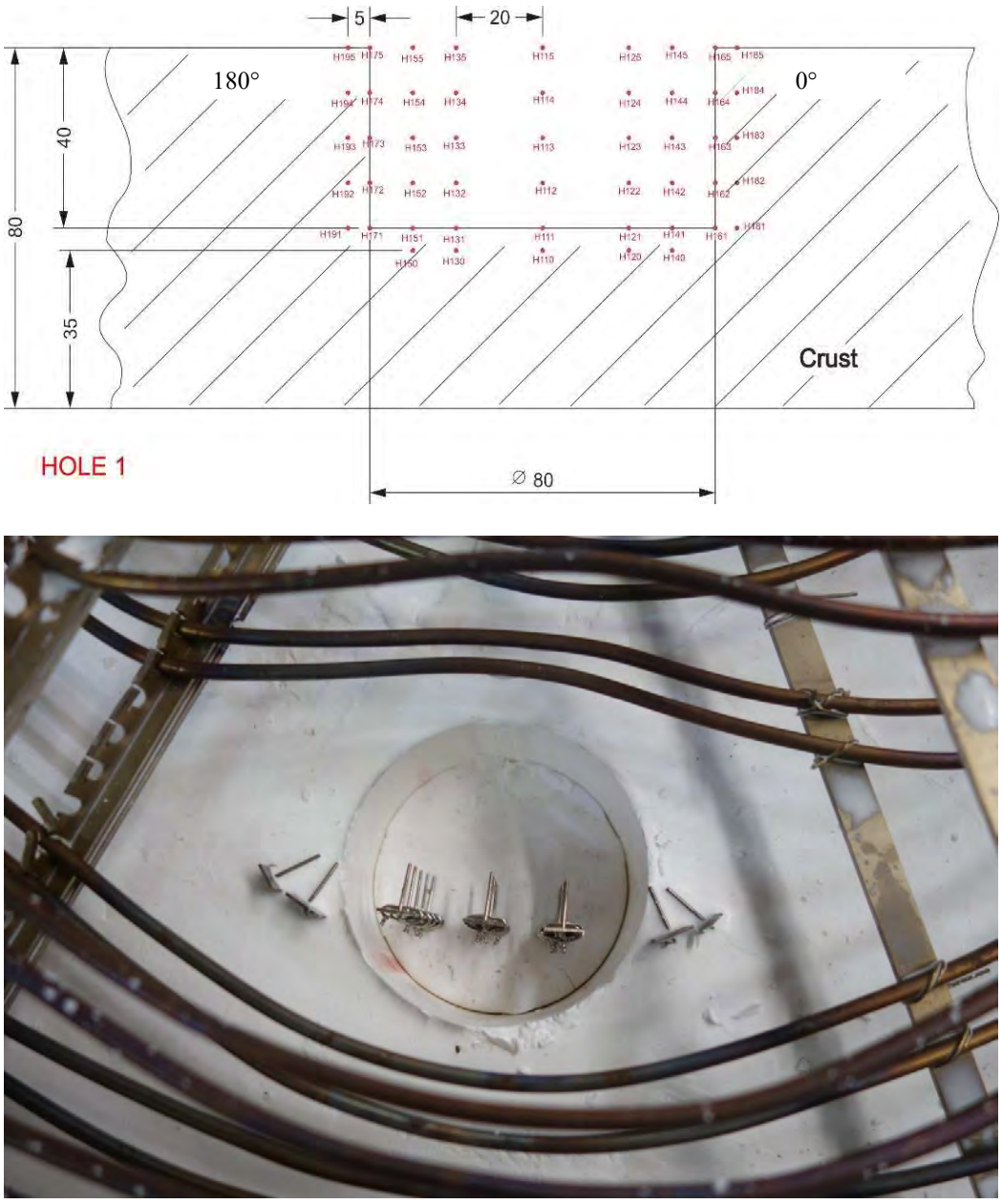

Figure 4. Positions of TCs for one hole in LIVE-CCH test. Bottom image: TCs installed inside and adjacent of the hole at the bottom plate before the melt pour.

3. EXPERIMENTAL RESULTS

3.1 LIVE-CCH Results

Inside the ablated hole at the bottom plate, solidification took place due to the external cooling around the test vessel. In Figure 5, the shrinkage process of the contour of the hole 1 is depicted. The solidification progressed upwards and inwards simultaneously, and the holes were totally filled with solidified salt at about 3000 sec. The results prove the beneficial effect of the sodium cooling in general to heal a previously ablated cavity.

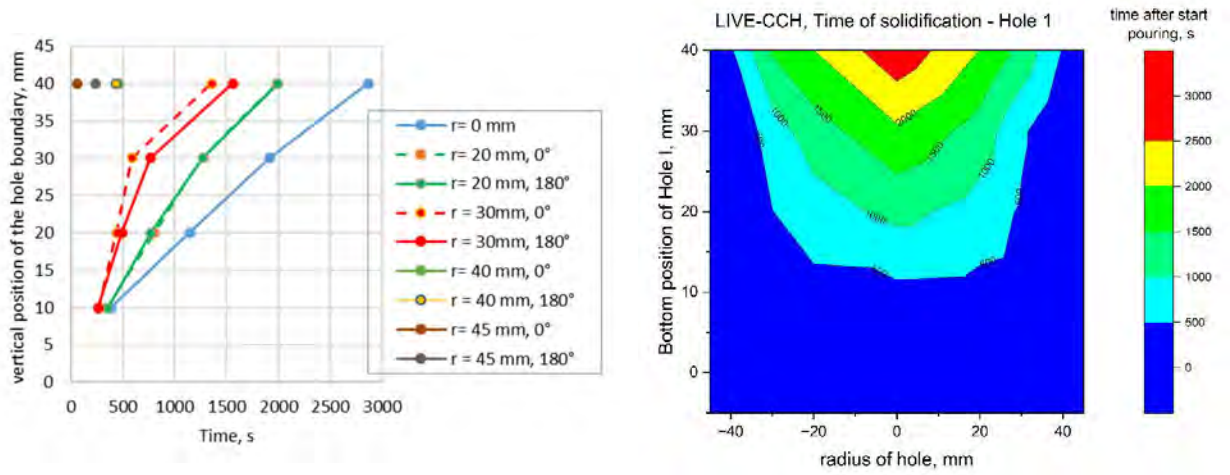

Figure 5. Left: boundary position of the hole 1 measured by TCs. Right: Illustration of the changing contour of hole 1 with time.

3.2 LIVE-CCS Results

The test started with the melt pour, marked as 0 sec. 236 kg liquid salt at 260 °C was poured into the vessel to form a 186 mm height pool. The power was provided by the upper two heaters which was totally 9.5 kW before the cooling lid was placed on the melt at the 707 sec. Thereafter the power was increased to 19 kW. The adjust of power input before and after the top cooling bears the purpose to maintain the melt temperature stable.

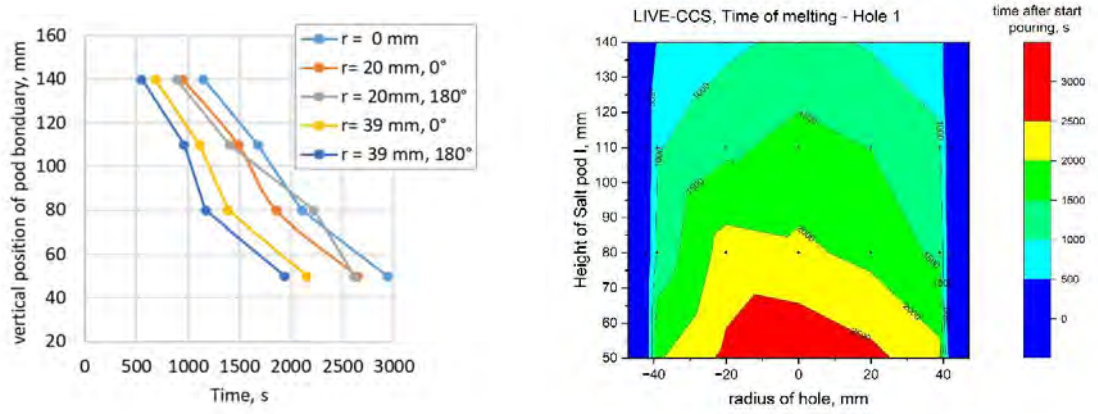

Figure 6. Progression of melting process of the Salt pod I. left: boundary position of the pod measured by TCs. Left: Illustration of the melting process of the pods I based on the measurement.

The progression of melting the two salt pods is illustrated in Figure 6. The melting progressed straight inwards and downwards which was completed at ~3000 sec. The pods molten to the level of the bottom crust. Their lower parts were merged into the newly formed bottom crust. The temperature responses inside the Pod 1 during the initial transient period are shown in Figure **7**.

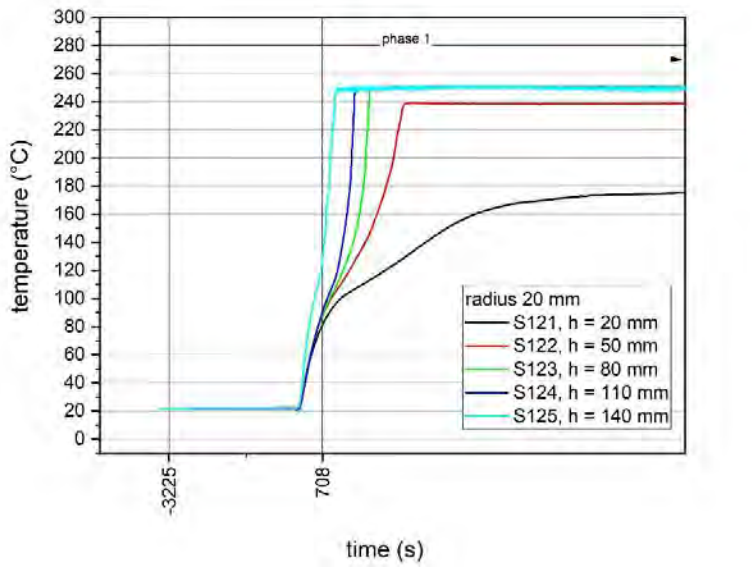

Figure 7. Temperature inside the Pod 1 after the melt pour (0 sec). The TC positions are 20 mm radially to the central axis. The time point at 708 marked the start of top cooling.

3.3 LIVE-CCM Results

An array of TCs was installed at a cross section inside the pods and adjacent to the pods. In the left image of Figure 8, the positions of the local TCs are shown. 234 kg of liquid salt with initially 310 °C was poured into the test vessel containing the two previously installed metal pods. All the four heaters were switched on and provided totally 33,5 kW during the time from melt pour till the cooling lid was placed on the melt surface at 917s. As soon as the top cooling was activated, the melt temperature dropped due to the very strong cooling by the top lid. The temperature decline was stopped at 1240 s because the total heat input was increased from 33,5 kW to 67 kW.

The responses of the local TCs during the initial period after melt pour are shown in the right image of Figure 8. It is noted that a delay of the temperature inside the pods to the bulk temperature, e.g. by comparing M155 (in the pod) to M195 /MT40 (out of the pod). It indicates the existence of a temperature boundary layer around the pods. The fact that the upper part of the metal pod was colder than its surrounding melt was not only induced by a heat transfer delay radially from the surface to the core of the pod, but also the result of an effective top-down heat removal inside the pod due to the high thermal conductivity of the metallic pod. This temperature discrepancy, which was the driving force of the local heat transfer, was declined with time. Its thermal inertia can also be observed between 917 s and 1240 s in decreasing temperature. During this time that the cooling down of the bulk melt took place, the metallic pod remains slightly hotter than its surrounding melt.

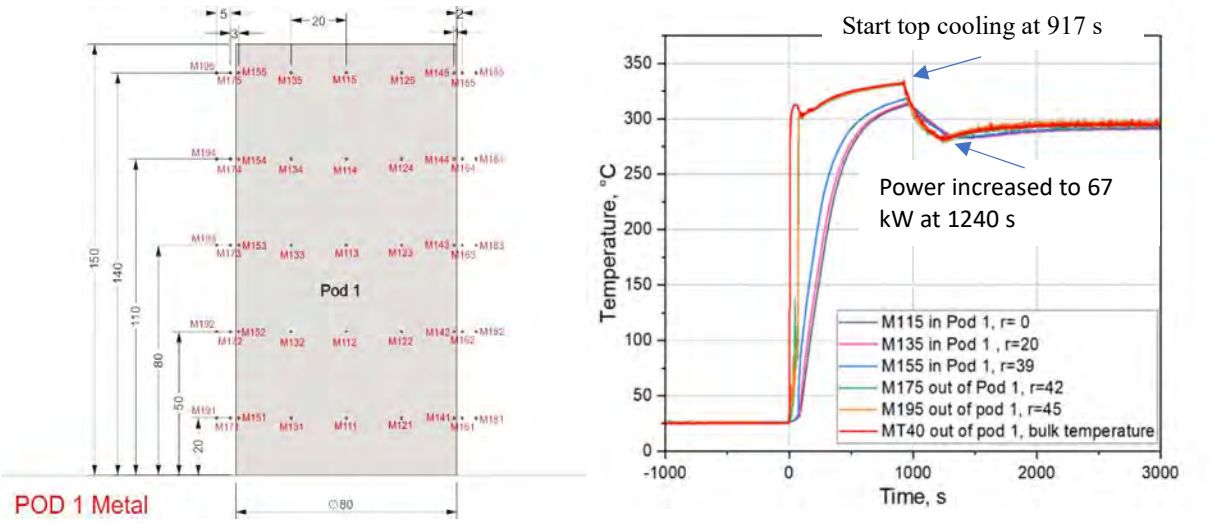

Figure 8. Left: TC positions inside and near the metallic metal pod 1. Right: Response of temperature after the melt pour.

3.4 Overall Heat Transfer

The heat balance of the molten pool is firstly to examine the credibility of the measurement and to secondly to allocate the heat transfer rate upwards and sidewards. The heat balance shown in the Figure 9 proves the balance between the power input on one side and the heat removal rate from the external cooling and from the top cooling on the other side.

The overall heat transfer from the liquid pool through the vessel wall to the external coolant are characterized with isotherm boundary defined by the solid solidification temperature. Similar results are obtained as the LIVE- test in the LIVE-SMART project with following heat transfer features with a heating density of 454 kW/m³ corresponding a heating power of 37 kW LIVE-CCM test:

- Bulk temperature: 300 °C, boundary temperature 220 °C
- Ra upwards: $5 \cdot 10^{8,}$ Ra sidewards: $11 \cdot 10^{9}$
- HF_{up} = 33 kW, HF_{side} = 18 kW, HF_{bottom} = 2 kW
- $Q_{up} / Q_{sidewards}$ = 2

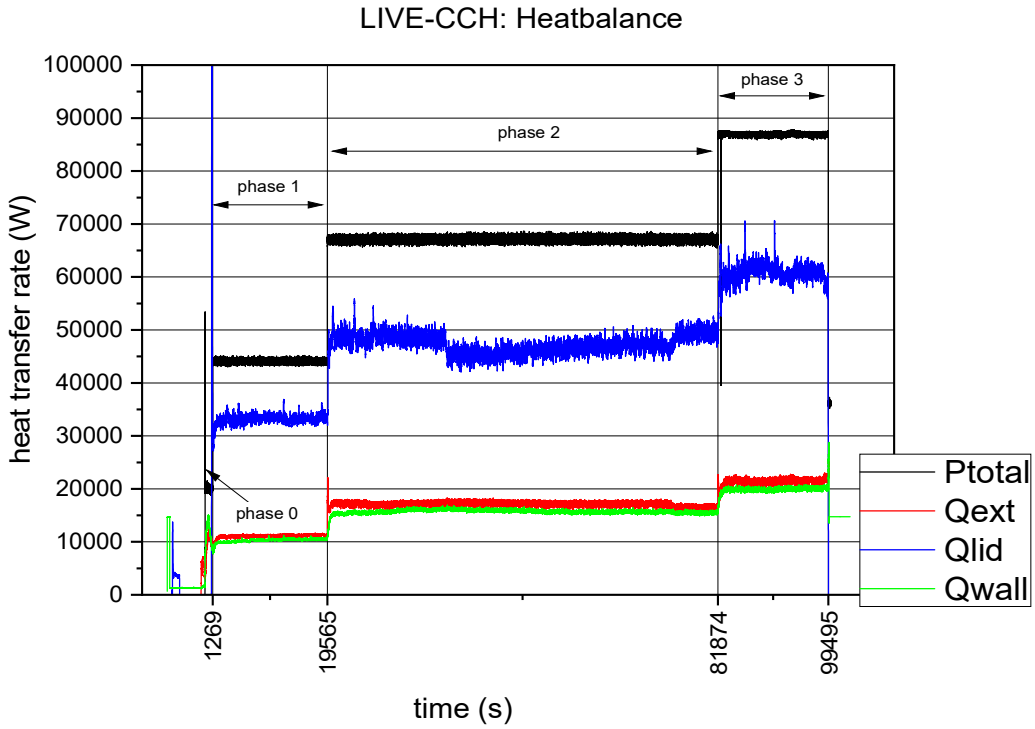

Figure 9. Heat rate of power input (P_{total}), removed heat via top cooling lid (Q_{lid}), and the heat through the sidewall (Q_{wall}), the heat removed by external cooling water ($_{Qext}$).

4. DISCUSSION

4.1 Treatment of experimental data and similarity issues

The data acquisition frequency was one measurement pre second. The TCs used for temperature measurement were calibrated to minimize their own measurement uncertainties prior to installation. By evaluation of parameters based on the temperature difference from two TCs, the offset-difference of the TCs at same temperature were balanced to zero during the post-test data analysis. The average data during a steady state were 120-second mean values at the end of this steady state with a standard error of 1%. The reliability of the whole measurement is further confirmed by the heat balance shown in Figure 9 for example. The time-dependent values, such as the contour of a hole or a pod during the solidification or ablation process is based on the TC measurements which act as detectors of the boundary in way that they react very sensibly and mark the change point in the temperature course as soon as they are involved in the solidification or melting process.

As the case of any experiment employs many simulate conditions to investigate prototypical scenario, the similarity of the experiment results to the prototypical ones shall be discussed. Concerning this test series, three similarity issues are focused on: cavity geometry, heating method and the simulant material.

- Cavity geometry: The most important parameter in the geometry in the sense of heat transfer is the characteristic length, which influence the scale of natural heat convection. In this study the height of the pool is the characteristic length, given that the vessel wall boundary does not limit the turbulent flow. In all the three test series, the strong top cooling owns the character of Rayleigh-Bernard convection [6]. Since the up and down swirl cells repeatedly appears in the whole region, the vessel wall boundary doesn´t constitute the restriction of the convection. The pool height in LIVE CC test vessel is 185 mm, which

constituted the same scale of the characteristic length of a prototypical pool, which has the internal Ra-$9{\cdot}10^{11}$ at a maximal power of 67 kW.

- Influence of the heating wire in the whole pool and near the local objects. Due to the strong turbulent flow inside the melt pool, the heating wire doesn´t constitute overall disturbance in the bulk melt pool region. However, the lower heater constraint the lower bottom crust thickness, since the crust cannot grow beyond the lowest heating plane. The influence of this aspect is comparable low since the downward heat rate was very low, only driven by thermal conduction. The heat wires near the local pods or holes could build temperature hot spot. However, the instrumentation scheme was arranged in the middle between the wings, where there was almost not influenced by the heating wires.

- Similarity of simulant material: The crust formed at the vessel wall build isothermal boundary condition at all boundaries, which is a very important feature in prototypical case. LIVE-CC tests do consider and enable this feature.

4.2 The General Effects of Local Objects on the Overall Heat Transfer

The local objects as protective measure against the ablation of the melt jet coming from the core regio exert beneficial influences in long term in the point of view of thermal inertia and material addition. The own thermal initial of the initially cold objects acts as heat sink inside the hot melt. The addition of no-decay heat-spending objects in the melt, either meltable or not, enlarges the volume and the mass of the whole pool without increasing the total decay dissipation, leading correspondingly to lower heat density, larger heat transfer area at the boundary.

5. CONCLUSION

Three test series have been performed to validate local protective measures in a long-term inside a melt pool in an ESFR-core catcher. The results brought the insights of the solidification process of an ablated cavity in the core catcher, the melting process of the pods and the heat transfer through the pods during the initial period of the formation of melt pool. LIVE-CCH test verifies that the ablated cavity can be restrengthen by the solidification of the melt inside the hole. The local objects positioned under the corium transfer tube can not only prevent direct thermal attack of the jet the core catcher, but also act as heat sink und sacrificing material in the pool to retard and to mitigate the overall thermal attack at the core catcher in the long term.

ACKNOWLEDGMENT

The experimental study is financially supported by the EU- Project ESFR-SIMPLE and the Germen Helmholtz Society.

REFERENCE

1. David, D.K., et al., *Numerical simulation of passive heat removal under severe core meltdown scenario in a sodium cooled fast reactor.* Nuclear Engineering and Design, 2015. **291**: p. 188-203.
2. Bigot, B., et al., *EXPERIMENT AND NUMERICAL SIMULATIONS ON SFR CORECATCHER SAFETY ANALYSIS AFTER RELOCATION OF CORIUM*, in *The 10th European Review Meeting on Severe Accident Research (ERMSAR2022)*. 2022: Karlsruhe. p. 355.
3. Payot, F., et al. *A new experimental R&D program associated with the corium jet impingement on the astrid core catcher sacrificial material*. in *Proceedings of the 2018 International Congress on Advances in Nuclear Power Plants, ICAPP 2018*. 2018.
4. Lecoanet, A., et al., *Study of the ablation consecutive to jet impingement on a meltable solid – Application to SFR core-catcher.* Nuclear Engineering and Design, 2021. **377**: p. 111147.

5. Tromm, W. and X. Gaus-Liu, *KIT-JIMEC Experiments to Investigate Jet Impingement on the Ablation of Core Catcher Bottom*, in *NENE2021*. 2021: Bled, Slovenia.
6. Gaus-Liu, X., *Impact of vessel geometry and boundary condition on the heat transfer of liquid corium in LWR lower head*, in *27th International Conference on Nuclear Engineering: Nuclear Power Saves the World!, ICONE 2019; Tsukuba International Congress CenterTsukuba, Ibaraki; Japan; 19 May 2019 through 24 May 201*. 2019, American Society of Mechanical Engineers (ASME), New York (NY).

Karlsruhe Institute of Technology

Experimental validation of the ESFR core catcher safety measures during long-term thermal attack

Dr. Xiaoyang Gaus-Liu, KIT

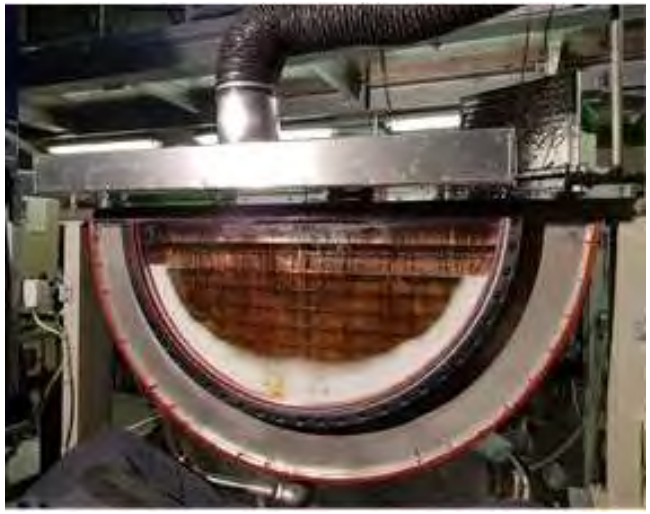

Outline

Background and Objektives

Test facility and realization of test requirement

Performance and results

- LIVE-CCH test
- LIVE-CCS test
- LIVE-CCM test

Conclusion

Core-Catcher integrity is one of the main concern of European SFR safety issues

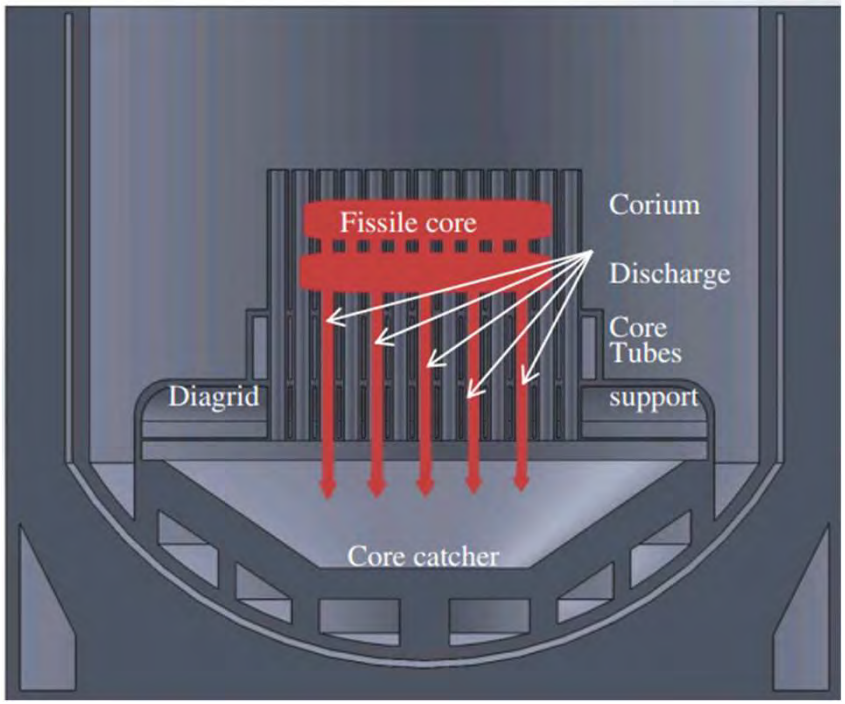

Primary design of Astrid core catcher

https://doi.org/10.1080/00295450.2018.1479580

- A further development of Astrid core-catcher
- An internal core-catcher inside the reactor vessel
- Function of the core-catcher:
  - Collect the whole corium
  - Prevent uncontrolled scattering of corium
  - Maintain the sub-criticality of fissile material

Descruptive scenario to the core-catcher integrity

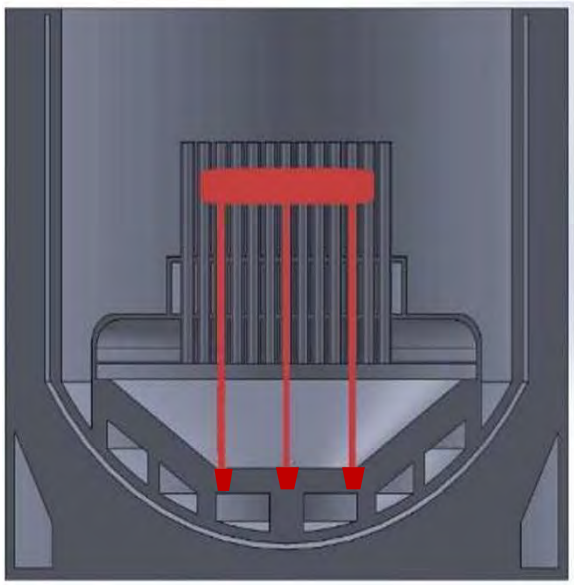

Corium jet impingement

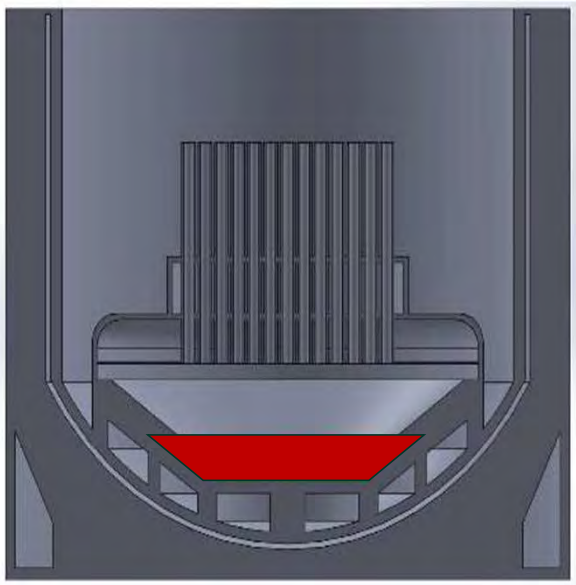

Long-term ablation by a molten pool

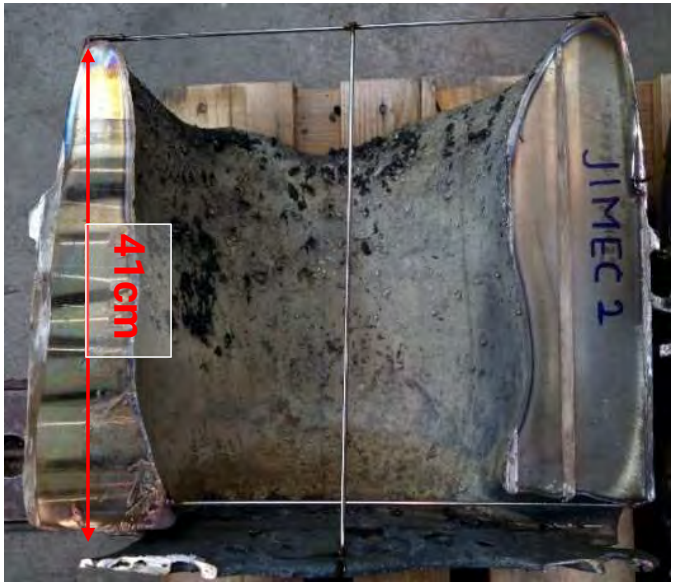

Jet impingement test at KIT: Metallic jet at 2000 °C melted through a steel substrate in 30 sec.

Objectives of the LIVE-CC experiment: Long-term behavior of an ablated core-catcher and additive prevention objects

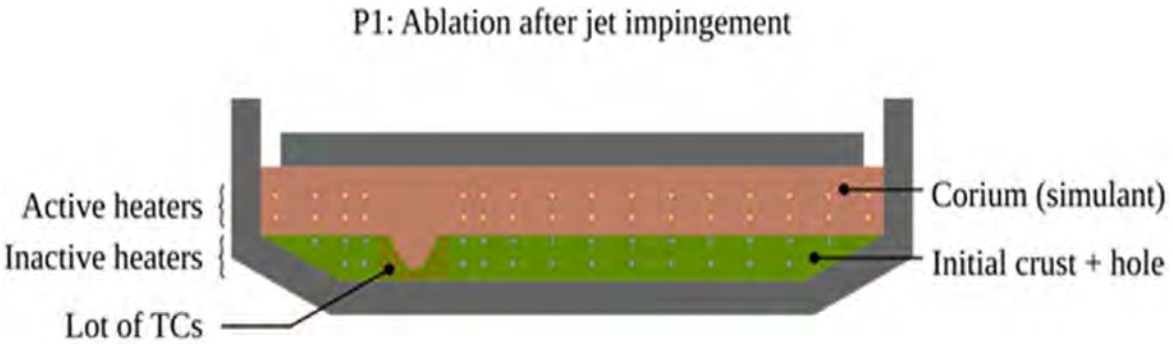

Ablation on the bottom plate of the core catcher

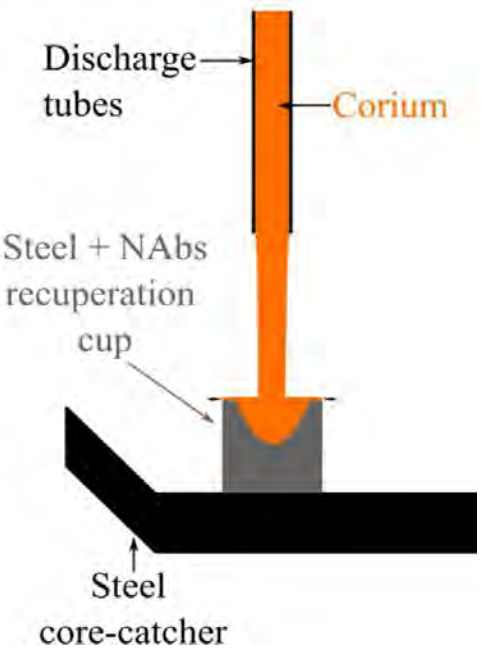

Additive measures beneath the corium transfer tube

LIVE-CC facility

LIVE-CC factility

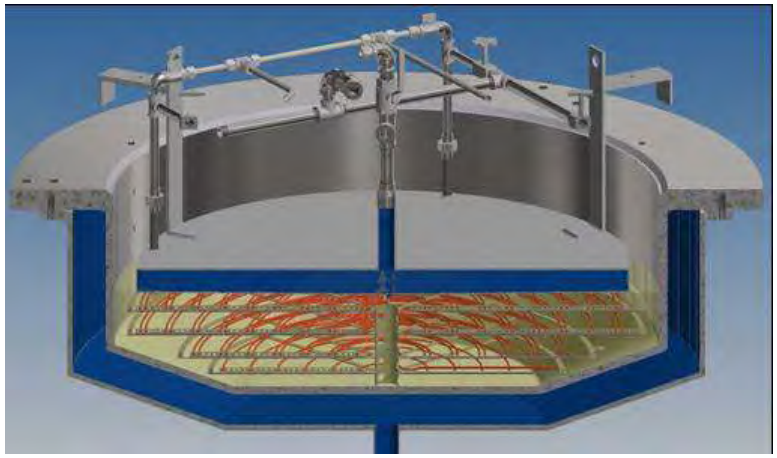

- Top cooling and external cooling with water
- Four Heating planes for volumetric heating, with maximum 90 kW
- Ra: 10^{11}

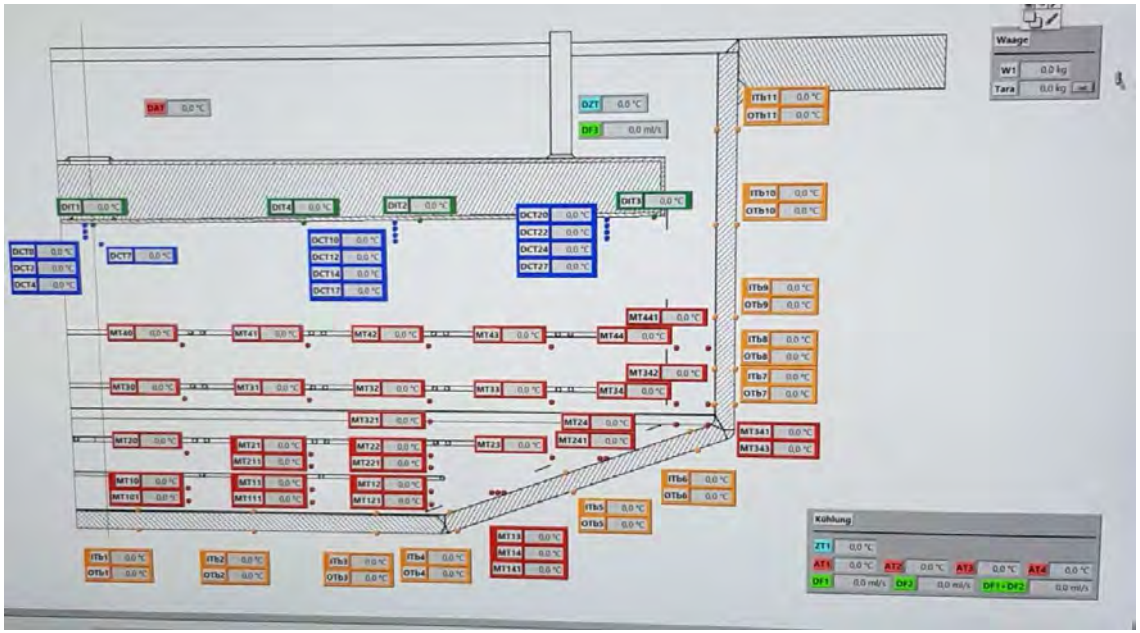

- Extensive temperature measurement inside and on the vessel wall
- Available parameter: Heat flux, heat balance and 2D - temperature mapping

Three test series in the LIVE-CC facility

Three tests on long-term ablation of Core-Catcher:

- **LIVE-CCH**: **H**ole test
- **LIVE-CCS**: **S**alt pod test
- **LIVE-CCM**: **M**etal pod test

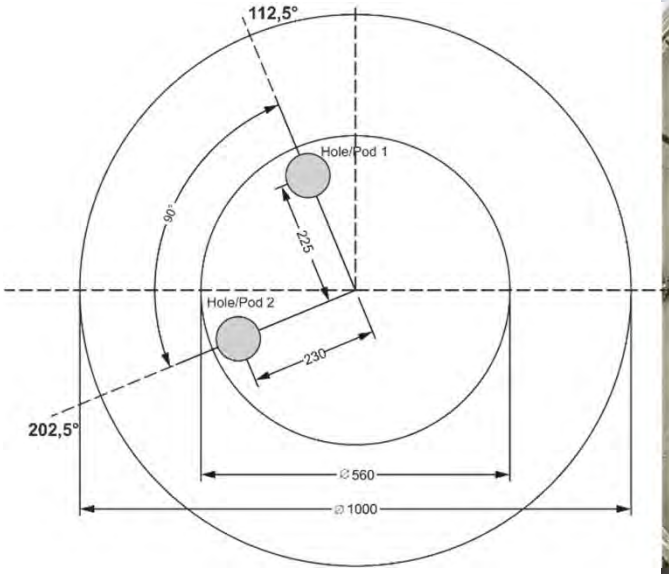

- Two local objects in each test
- Located in the enlarged spaces between heating wires

Test conditions

Tests	Local objects	Material of object	Geometry	Heaters in operation	Power level and chronology, kW	Vessel initial condition
CCH	Hole in the bottom crust	Solid salt crust plate with holes	Depth of hole: 40mm Thickness of plate: 80 mm	No heating in the 80 mm bottom plate	44, 67 , 90	With bottom plate
CCS	Salt pods	Solid salt	Height of pods: 150 mm	All heaters	19	Only with two pods
CCM	Metal pods	Stainless steel	Height of pods: 150 mm	All heaters	67, 35, 50, 20	Only with two pods

Geometry of local objects

Hole geometries: Diameter: 80 mm, depth: 40 mm.
Pod geometries: Diameter: 80mm, height: 150 mm.

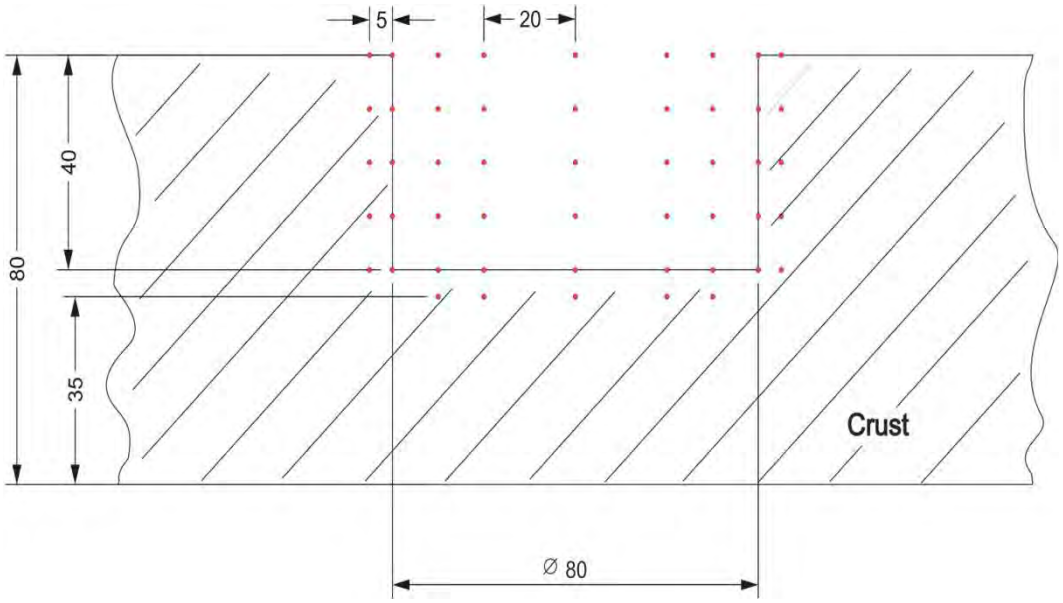

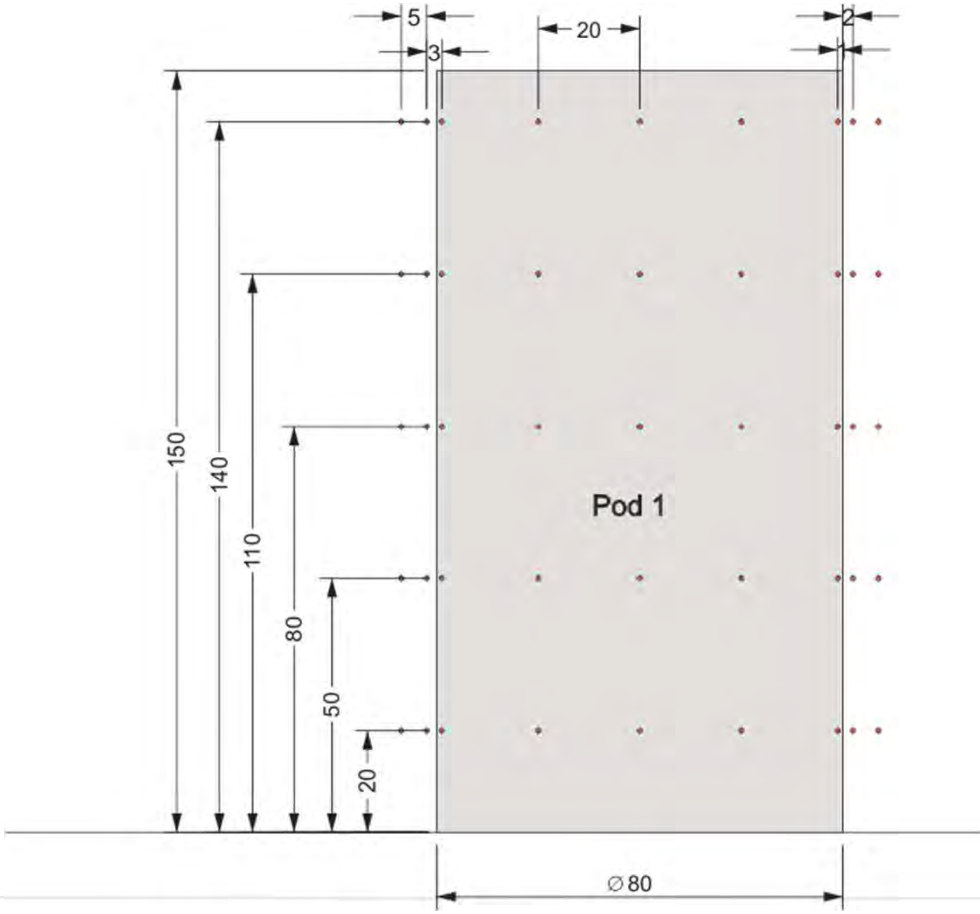

Additional TC Instrumentation

Totally 90 additional thermocouples for one test

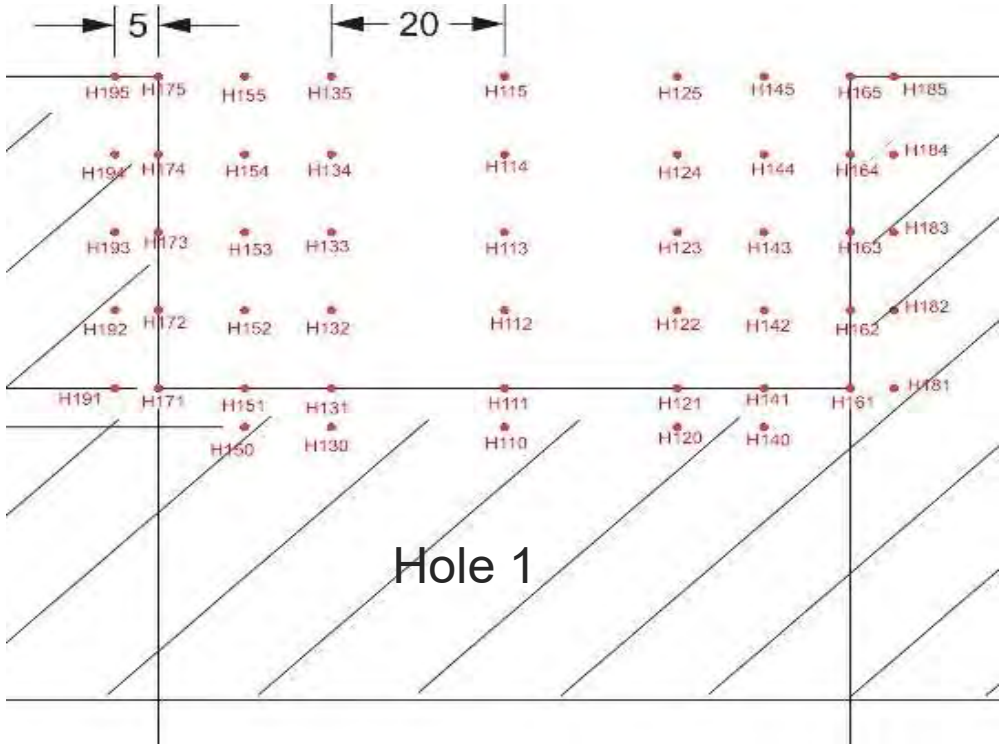

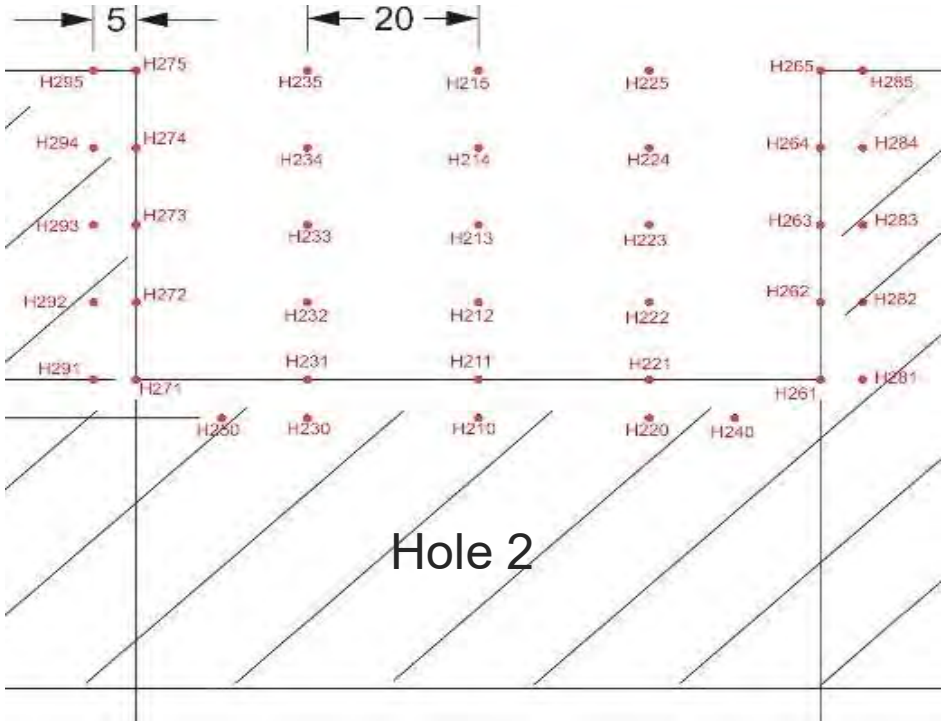

Preperation and Installation of thermocouples

- Calibration of thermocouples before the installation
- Installation of new thermocouples inside the vessel
- General calibration of heaters

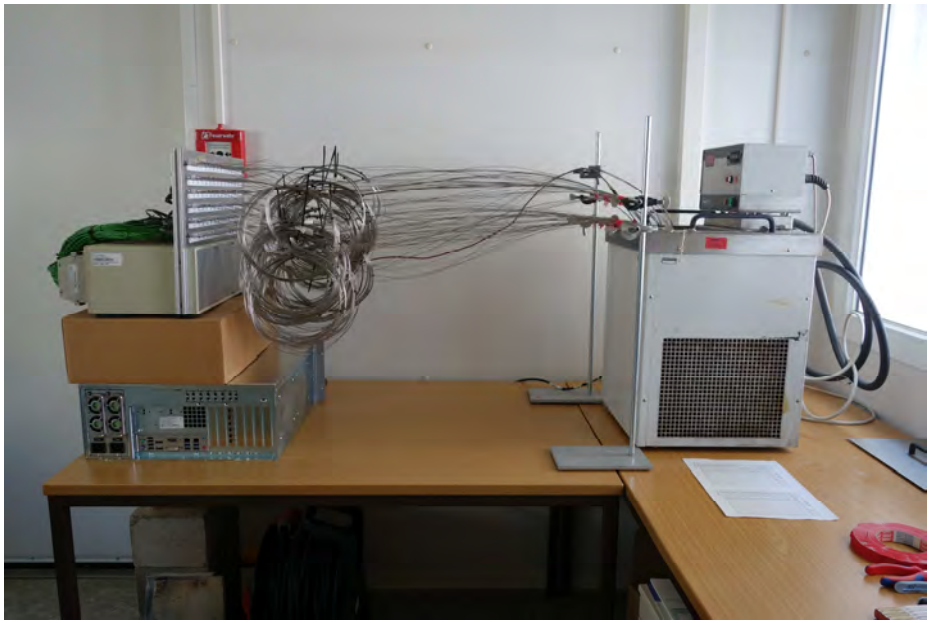

Generation of the two holes in the crust in 3 steps

- Step 1: Place holder for two holes

- Step 2: 80 mm crust with two holes

- Step 3: fill in the hole bottom till 40 mm

Heat balance in LIVE-CCH test

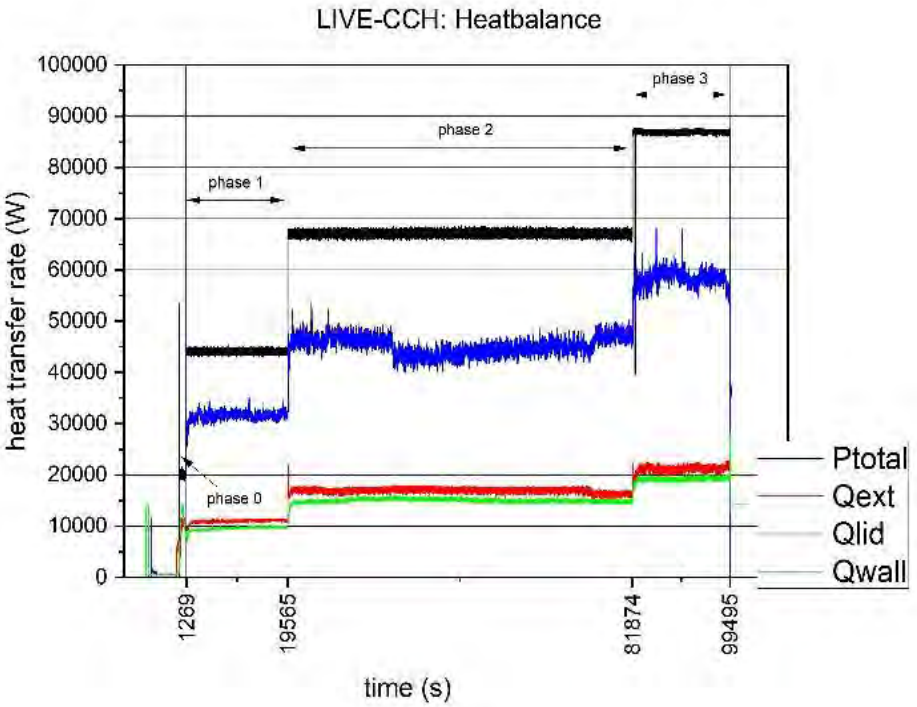

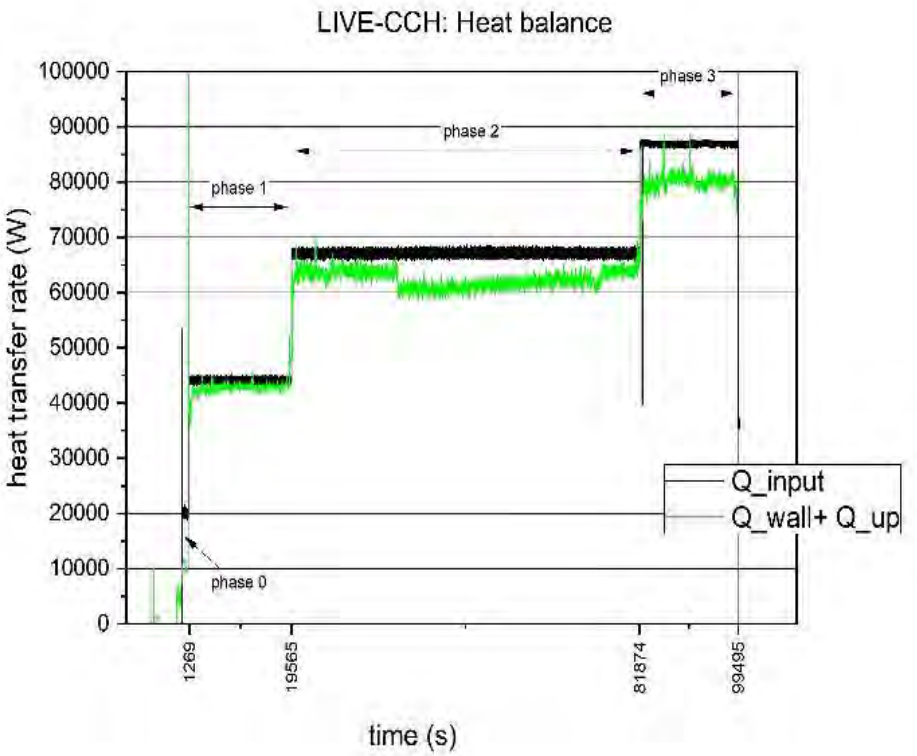

Heat balance in LIVE-CCM test

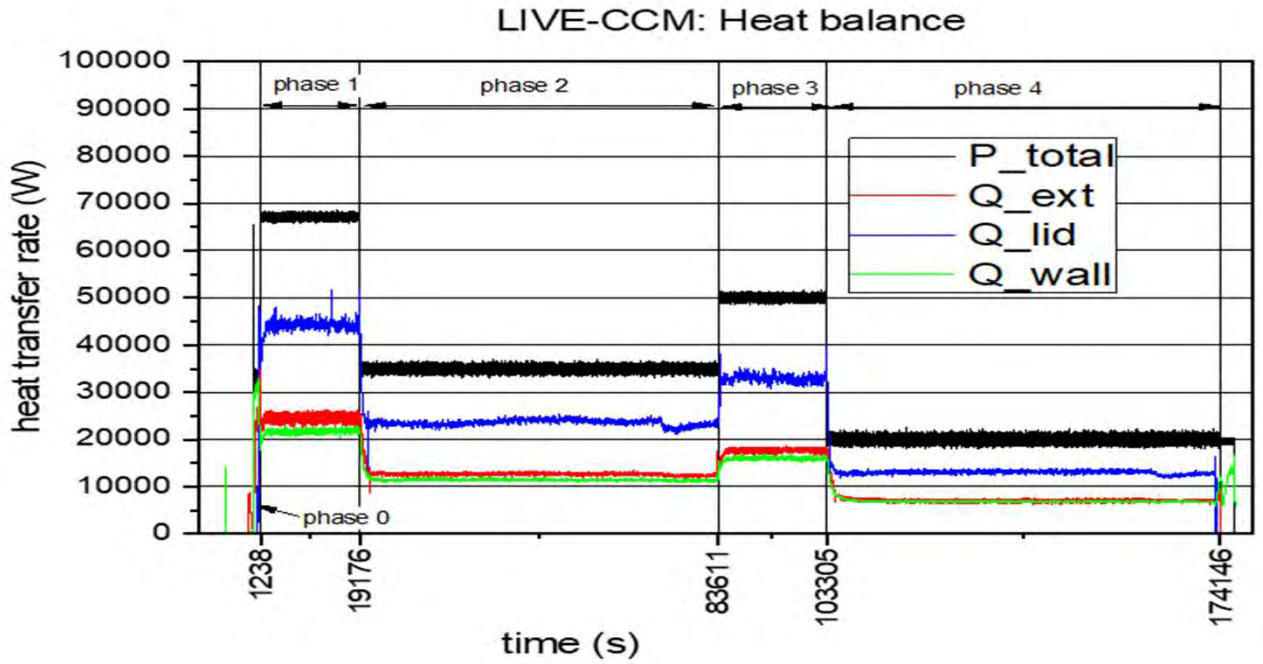

	20kW	35kW	50kW	67kW
%Q_w/Q_in	34.1%	32.6%	32.1%	32.9%
%Qlid/Qin	64.0%	63.8%	66.9%	66.3%
%Q_wall+Q_lid	98.1%	96.4%	99.0%	99.2%

Performance of LIVE-CCH test

Top view after the pouring of liquid salt inside the vessel

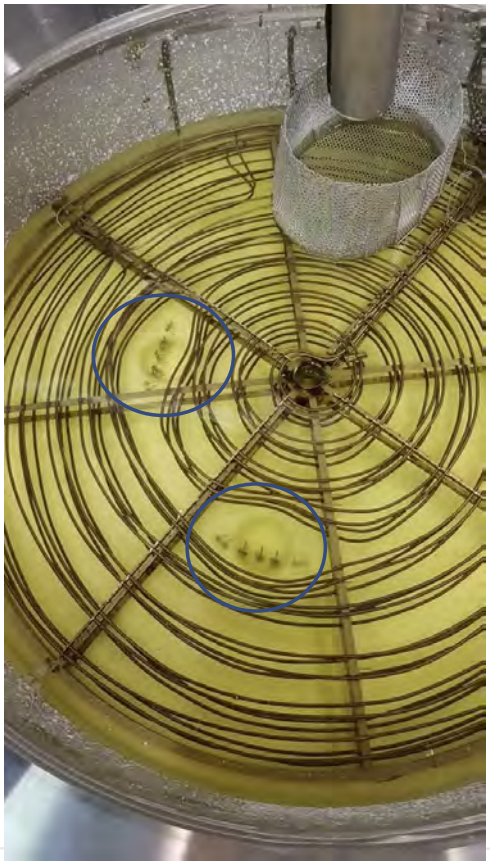

Top view after of the test

LIVE-CCH: Dynamics of the solidification inside the Hole 1

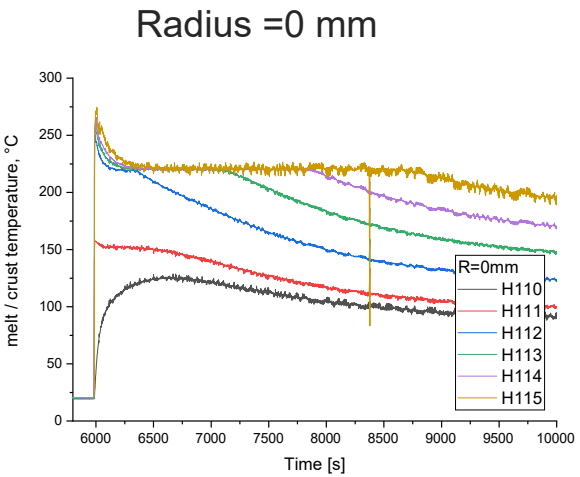

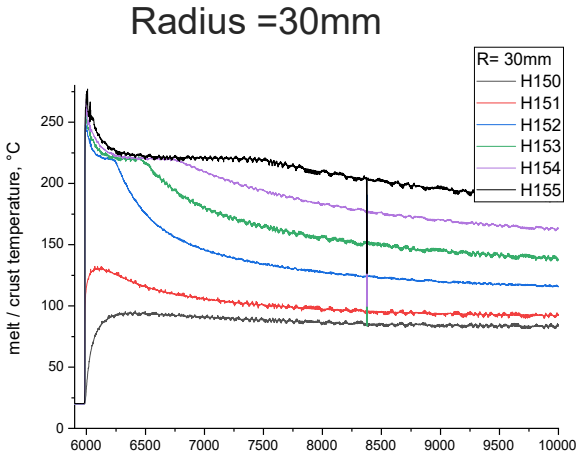

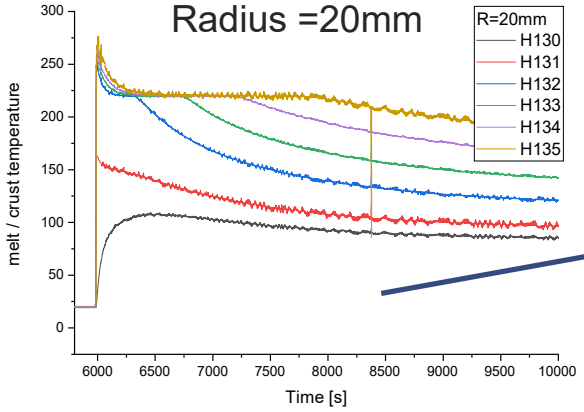

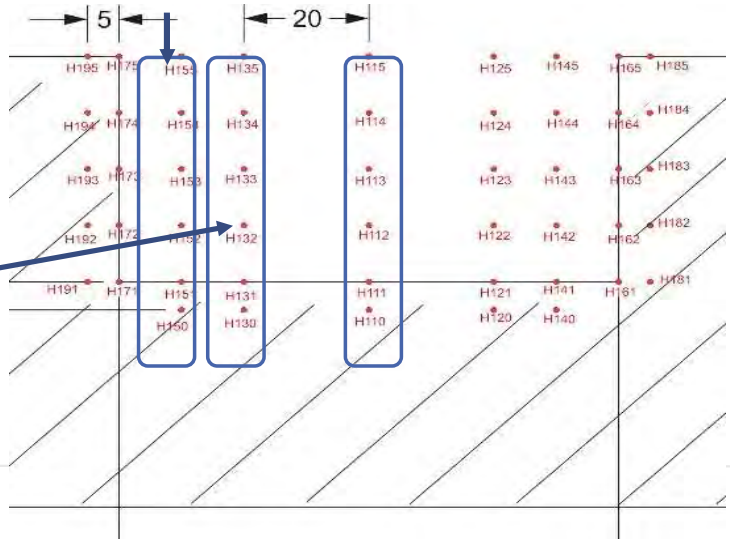

Temperature curves in Hole 1

- Indication of time of solidification (at 220 °C)

LIVE-CCH: Solidification dynamics in ablated holes

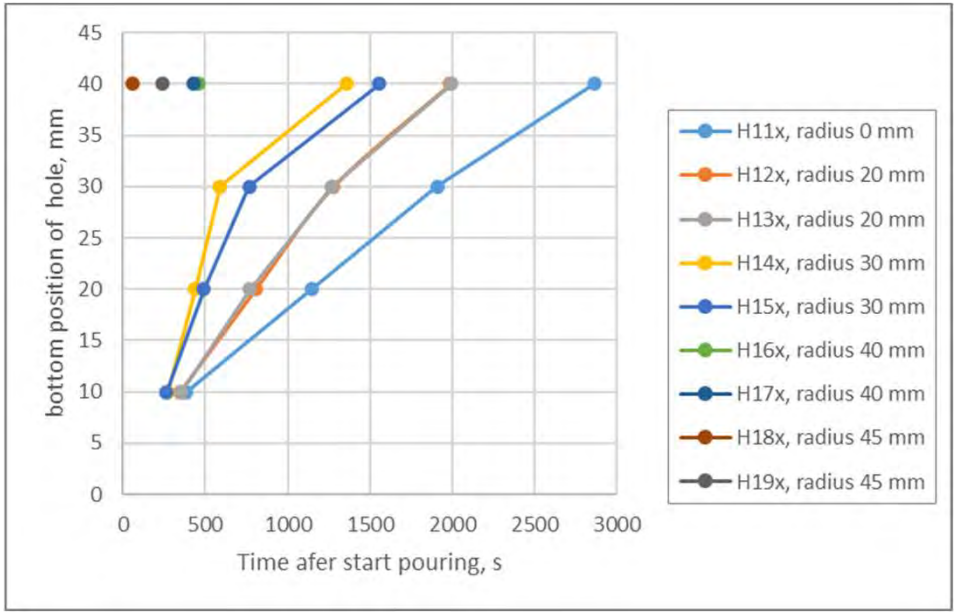

Hole 1

- Simultaneous solidification inwards and upwards
- Completion in 2800 sec

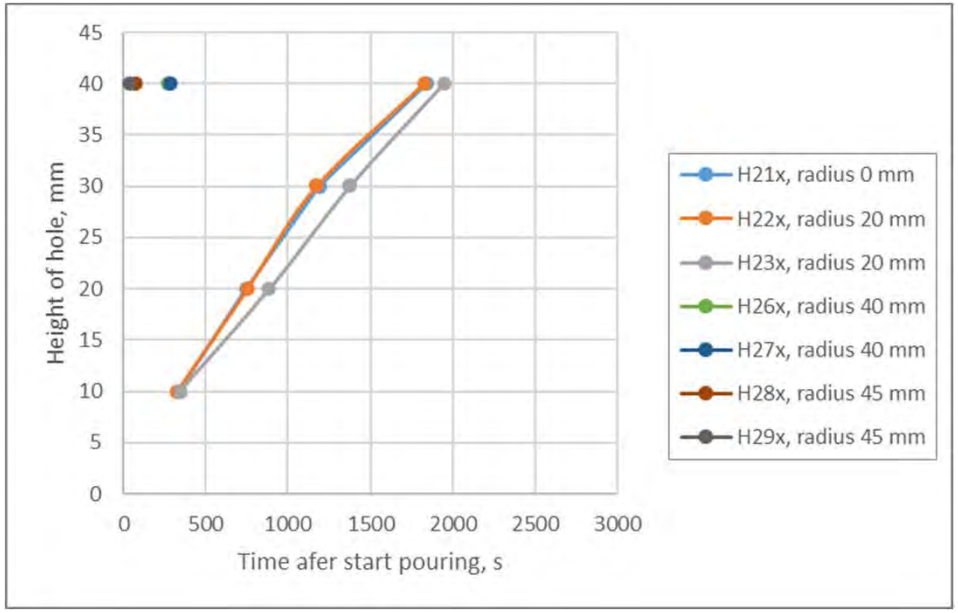

Hole 2

- Upwards ablation for all radial positions
- Almost constant ablation rate
- Completion in 2000 sec.

LIVE-CCH: Progression of the contours of holes

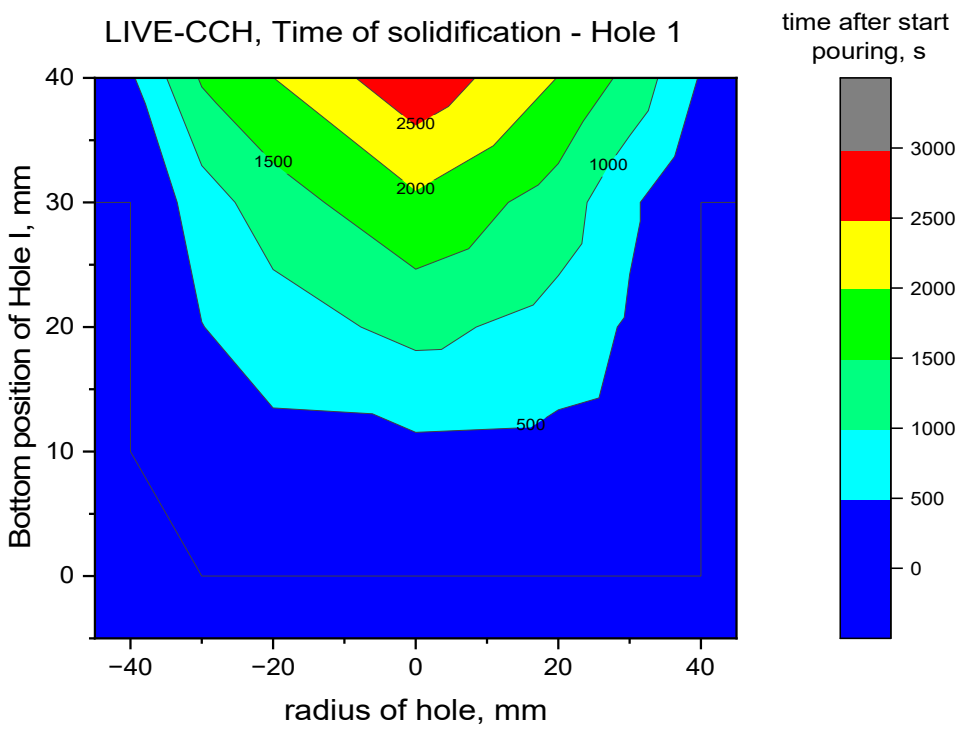

Hole 1

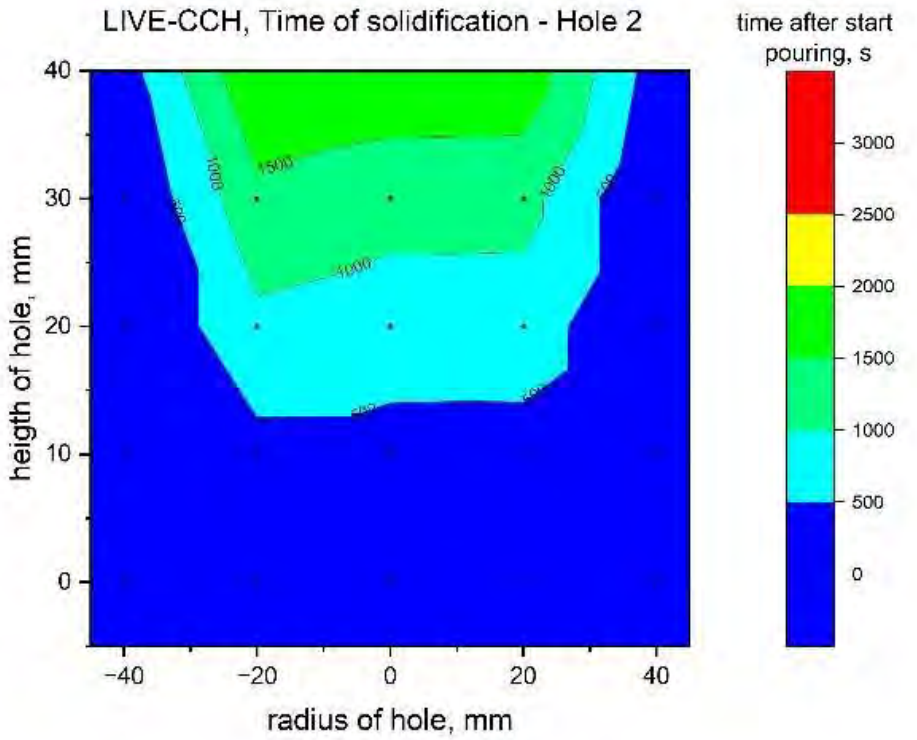

Hole 2

LIVE-CCS: Ablation of meltable pods in a melt pool

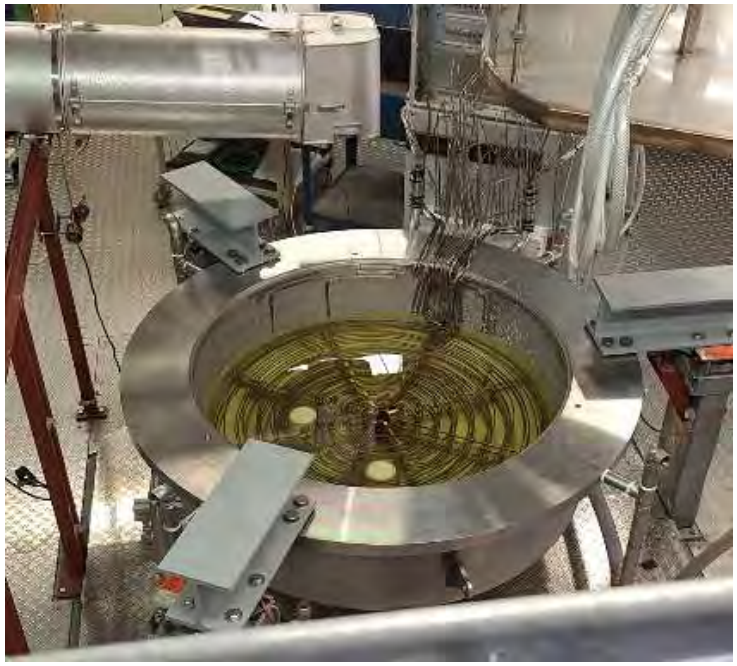

Phase	Time [s]	Top cooling	External cooling	Heating power
0	0 - 707	no	yes	9.5 kW
1	708 - 83759	yes	yes	19 kW

LIVE-CCS: Melting of local objects

Synchronic melting of pods and pool temperature stratification

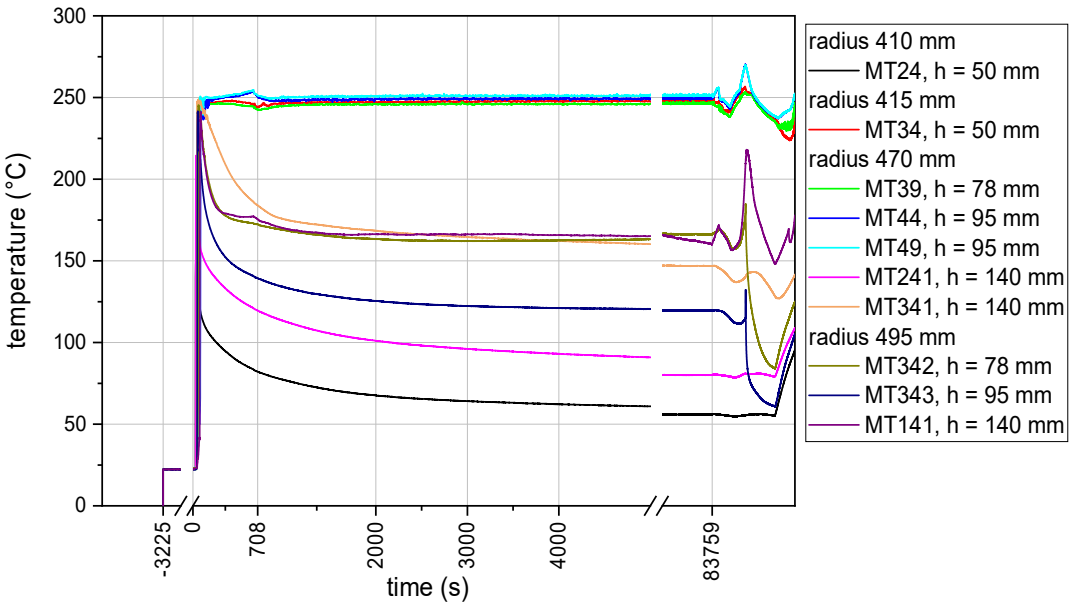

Melt pool under temperature stratification

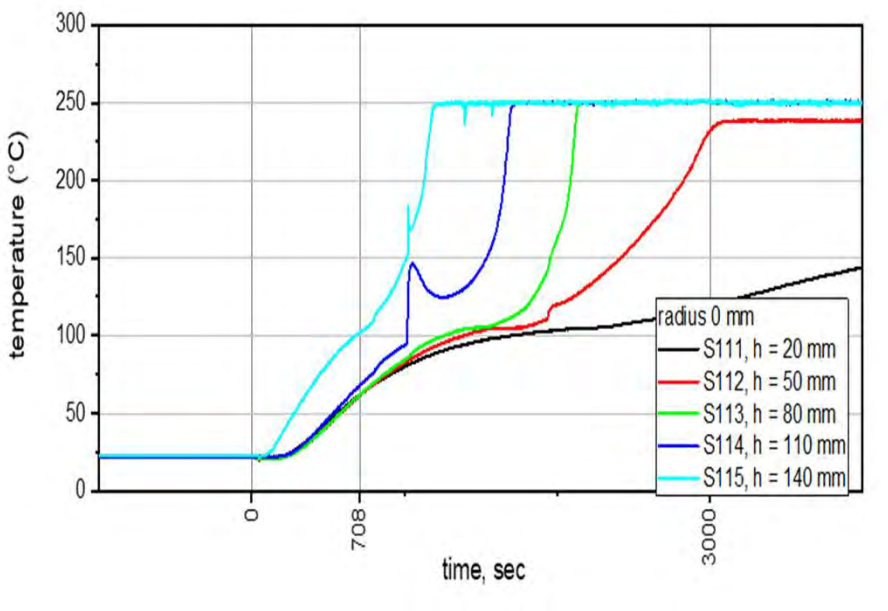

Ablation of melt pod, at the vertical axis.

LIVE-CCS: Ablation dynamics of meltable pods

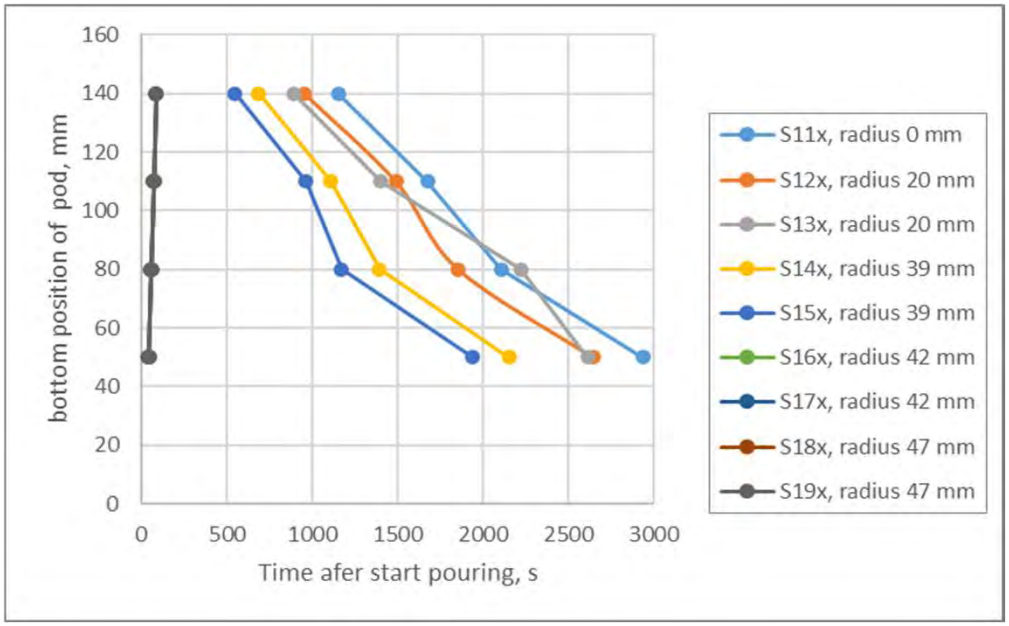

Pod 1

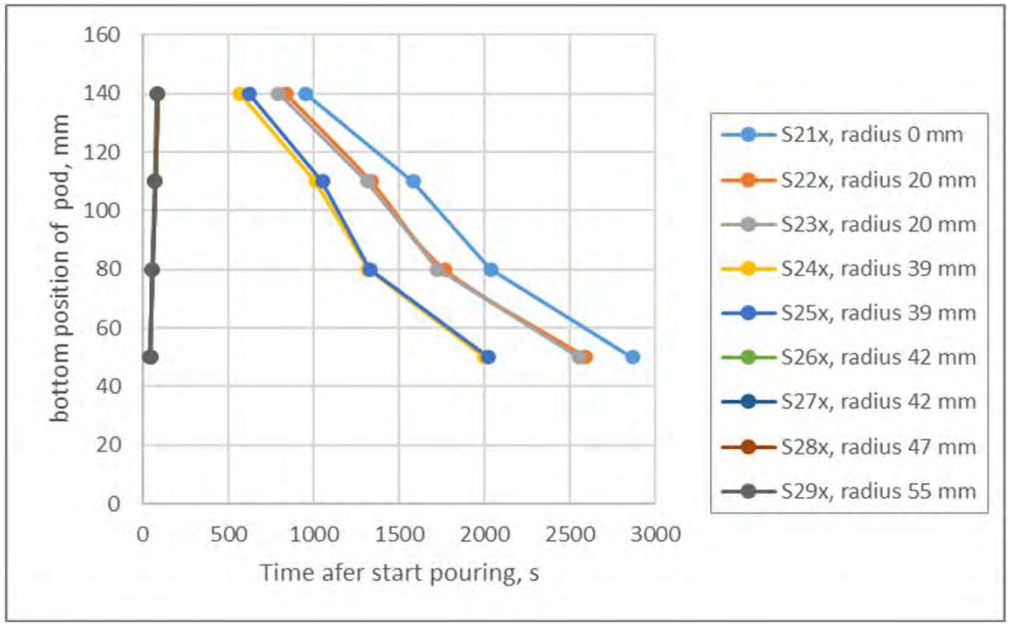

Pod 2

- Simultaneous inwards and downwards ablation of both pods.
- The total ablation period were about 3000 sec.

LIVE-CCS: Ablation dynamics

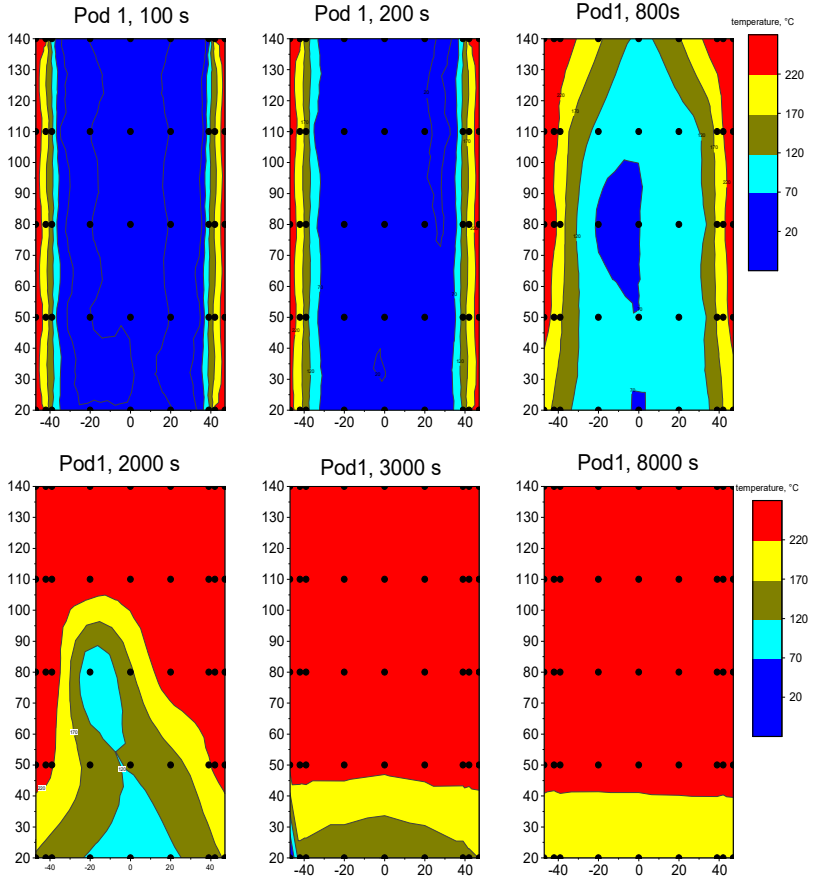

Pod 1

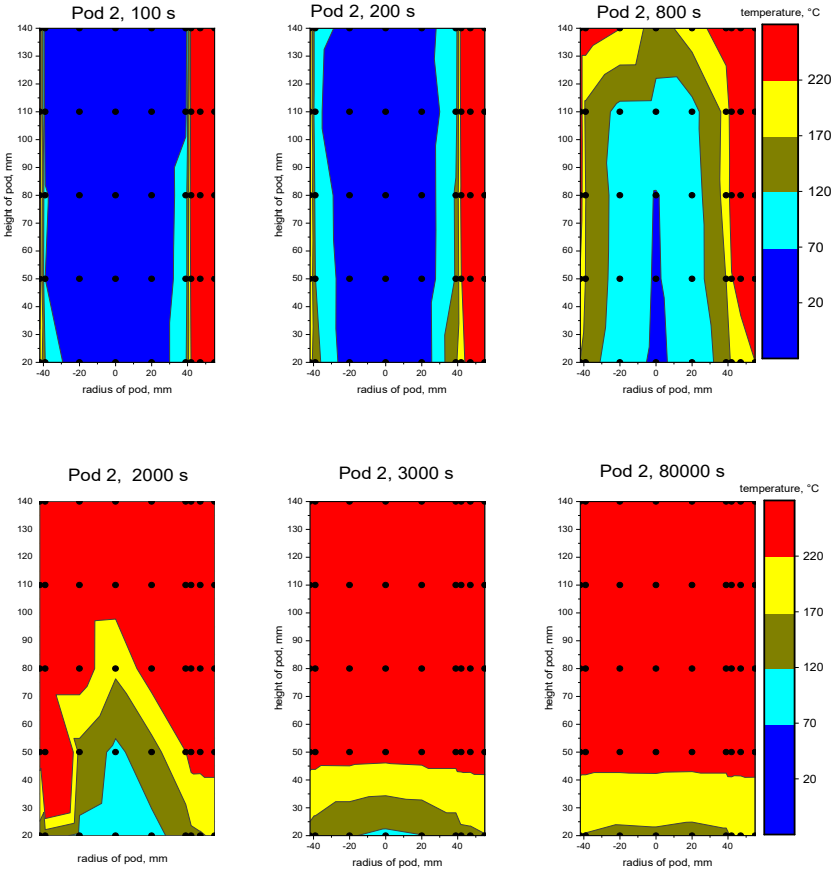

Pod 2

LIVE-CCM test: Instrumentation of metal pods

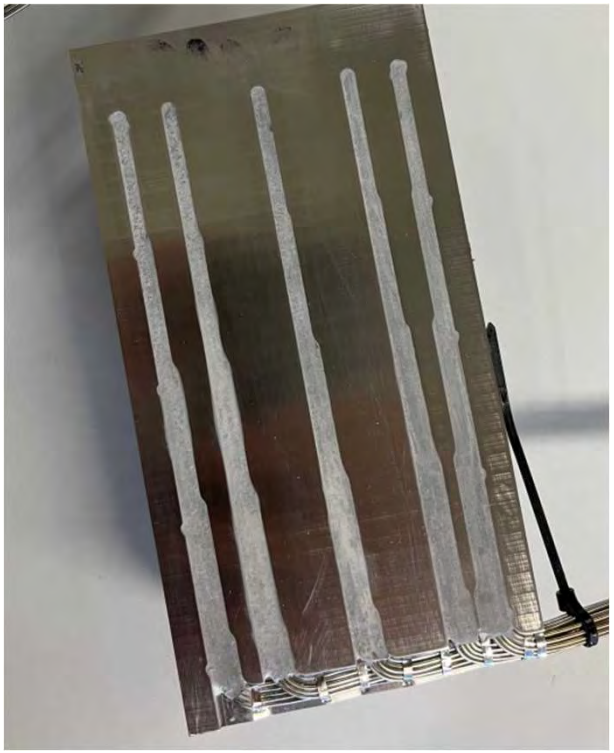

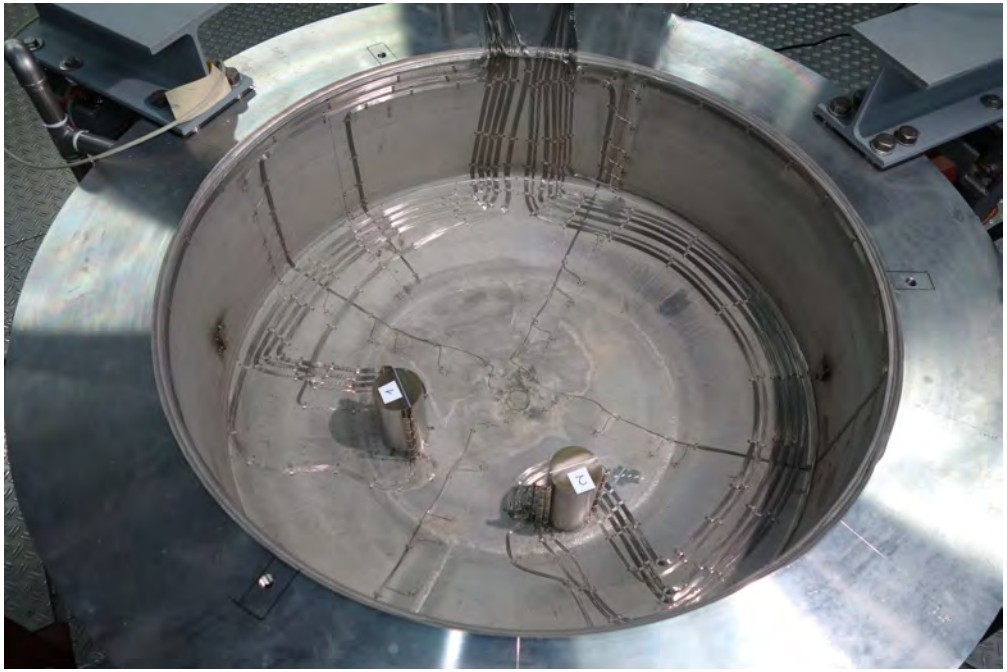

LIVE-CCM: Temperature inside and around metallic pods

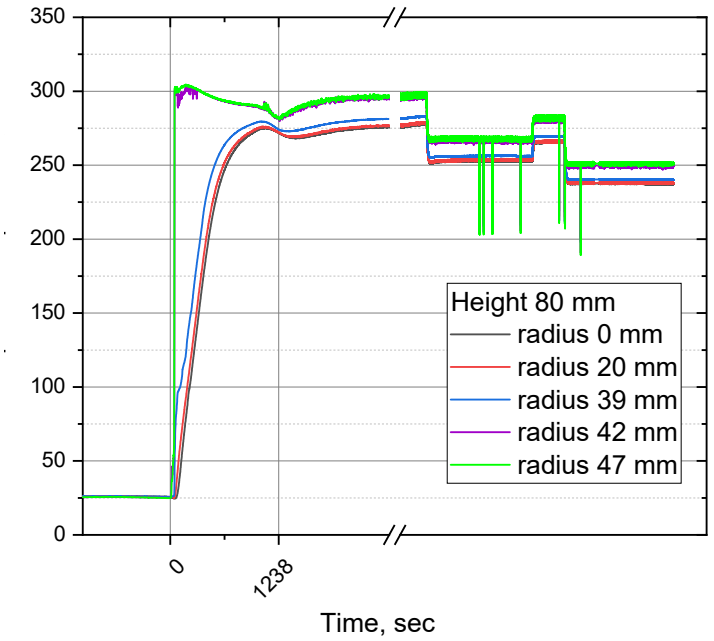

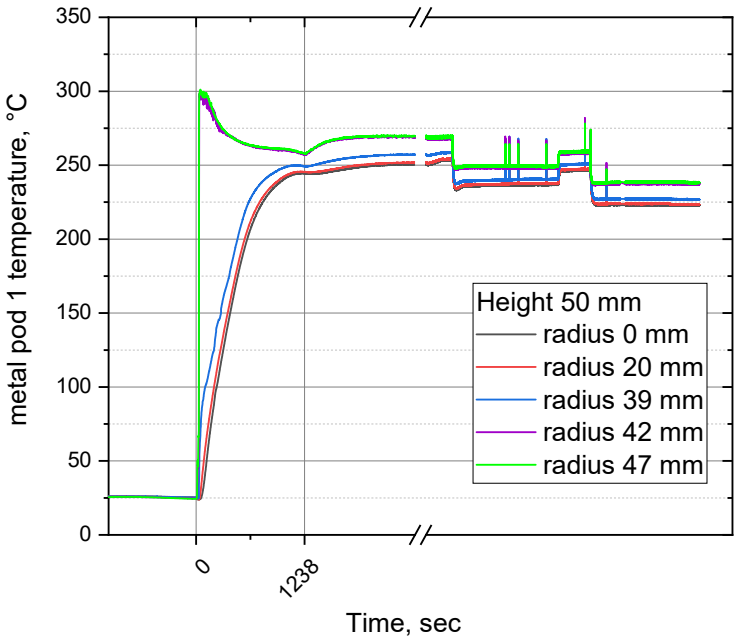

- Pods are high thermal conductive;
- Almost no temperature difference inside the pods;
- Temperature difference between pod and the surrounding salt existed over the entire period, demonstrating a good heat sink effect of the pods.

Conclusions

General heat transfer characteristics

Overall heat transfer	Upward heat transfer of a cooling surface amounts of ~ 66% of total heat inside the molten pool

Long-term behaviour of local objects

Ablated holes	▪ The holes can be completely filled by solidified melt despite of the overlaid hot liquid melt ▪ The experiment has demonstrated the effectiveness of the thermal conductive cooling from the bottom plate
Ablation of additive objects	▪ Synchronic process of pod melting and melt pool stratification; ▪ Bottom part of pods was integrated in the bottom crust
Heat transfer of the local objects	▪ Heat sink effect of metallic objects observed ▪ Acting as an extension of the cold bottom plate inside the pool

This work is funded by the EU ESFR-SIMPLE project and the German government.

Thank you for your attention!

Contact: Xiaoyang Gaus-Liu
Xiaoyang.gaus-liu@kit.edu

INVESTIGATION OF FILM BOILING IN LIQUID SODIUM: QUALIFICATION OF THE SERUA EXPERIMENTAL PROGRAM

Rémi CLAVIER*, Kévin PONS, Jérôme FRANCESCATTO, Claude BRAYER
CEA, DES, IRESNE, DTN, SMTA, Severe Accident Modelling Laboratory
Cadarache, 13108 Saint-Paul-lez-Durance, France
remi.clavier@cea.fr ; kevin.pons@cea.fr ; jerome.francescatto@cea.fr ; claude.brayer@cea.fr

Gwendal BLEVIN
CEA, DES, IRESNE, DTN, STCP, Sodium Technology Laboratory
Cadarache, 13108 Saint-Paul-lez-Durance, France
gwendal.blevin@cea.fr

Jules DELACROIX, Diego MOLINA, Christophe JOURNEAU
CEA, DES, IRESNE, DTN, SMTA, Severe Accident Experimentation Laboratory
Cadarache, 13108 Saint-Paul-lez-Durance, France
jules.delacroix@cea.fr ; diego.molina@cea.fr ; christophe.journeau@cea.fr

ABSTRACT

Fuel Coolant Interaction (FCI), during a Severe Accident in a Sodium-cooled Fast neutron Reactor, strongly depends on the film boiling regime around liquid corium droplets at ~3000 °C under quenching in liquid sodium between ~400 °C (reactor nominal temperature) and ~880 °C (sodium saturation temperature). The intrinsic complexity of film boiling at very high temperature makes experiments with simulant fluids irrelevant to derive predictive models. Yet, most of current knowledge concerning film boiling regimes in sodium relies on the only experimental study involving sodium, performed by M. Farahat in the 1970's, which basically consisted in quenching a high temperature tantalum sphere heated by induction into a liquid sodium pool at regulated temperature close to saturation. The detailed re-analysis of Farahat results and limitations of the experimental device showed that they are not sufficient to validate our theoretical approach. The objective of the SERUA experimental program is to fill this gap of knowledge by producing more precise experimental data on film boiling regimes in liquid sodium. Before the SERUA facility construction and commissioning, a qualification program involving both experimental tests and associated numerical simulations has been conducted to validate our technological choices and ensure our control on the physical conditions concerning the inductive heating of the sphere (up to ~2300 °C), its instrumentation and the heating of the sodium close to the saturation point (at ~860 °C). The positive results of this qualification program now support commissioning of the SERUA facility, expected by the end of 2026.

KEYWORDS
SFR, FCI, Sodium, Film boiling

1 INTRODUCTION

Fuel-Coolant Interaction (FCI) is anticipated during the relocation phase of a hypothetical Core Disruptive Accident (CDA) in a Sodium-cooled Fast neutron Reactor (SFR) [1]. More precisely, it might occur when

* Corresponding author

molten core materials (commonly designated as "corium") penetrate as a more-or-less-coherent jet in the lower plenum *via* Control Rod Guide Tube (CRGT), ingression through the core diagrid, or specifically-designed corium discharge tubes (DCS-M-TT / FAIDUS concept), as represented on the Figure 1.

FCI has received considerable attention from the scientific community since the 1970's, with a large number of experiments involving interaction of sodium and oxide or metallic fuel at different scales from a few kg to ~100 kg. The most significant of which, used for the safety demonstration of previous SFRs, were:

- The CORECT II program in France [3], where subcooled sodium was poured onto a pool of 5 kg of molten UO_2, resulting in significant pressure peaks, up to 70 bar for the most energetic one.
- The FARO-TERMOS experiments at the European Joint Research Centre, in Italy [4], where up to 140 kg of molten UO_2 were released into sodium, bringing the sodium to saturation over a depth of 1 m along which a coherent jet could penetrate before fragmenting under hydrodynamic and thermal effects. Pressure peaks up to 60 bar have been observed into the sodium pool.

The physical interpretation of the above "large"-scale experiments, using computing tools such as the SCONE (Software for COrium-Na interaction Evaluation) simulation code under development at CEA, requires a better understanding of smaller-scale phenomena. In particular, heat transfers between corium droplets and boiling sodium must be more precisely characterized in the different boiling regimes, especially in film boiling and transition boiling [5,6]. This is the purpose of the SERUA facility (Sodium boiling Experimental Rig for Understanding of fuel-coolant interAction), proposed by the CEA, and inspired by the Farahat experiments [7], whereby a tantalum sphere heated by induction at high temperature is quenched in a liquid sodium pool close to saturation. This experimental program will provide crucial data for the development of SCONE, and more generally for severe accident codes in SFR like SIMMER.

2 SCIENTIFIC INTEREST OF THE SERUA PROGRAM

This section presents with more details how the study of film boiling in sodium contributes to the global efforts for FCI modelling. FCI is very complex and involves many physical phenomena which are still not fully understood at this time. Several initial configurations can be considered depending on technical details of the reactor. The scope of this paper focuses on the SFR technology so the following presentation is oriented for sodium-related experiments but most of the presented phenomena may be encountered in severe accidents in other kinds of reactors (PWR, BWR, etc.).

2.1 Fuel-Coolant Interaction

FCI starts when a large corium mass, typically a liquid jet with T~3000 °C, comes into contact with the sodium coolant with T~400-880 °C, depending on the accident history. The time sequence of FCI is basically divided into the "premixing" phase and the "expansion" phase. In the case of strongly sub-cooled sodium, the premixing phase is very short, and FCI may be better described by a succession of weak expansion phases. When the sodium is close to its saturation point (T~880 °C), however, the premixing phase itself includes the so-called "primary" and "secondary" fragmentations, and lasts as long as the fragmentation of corium and the subsequent sodium vaporization are sufficiently slow to allow the system to relax smoothly. The expansion phase corresponds to quasi-simultaneous droplet fragmentations that rapidly increase the vapor generation. This induces pressure waves in the medium, whose coalescence leads to the steam explosion. The reader interested in a more detailed description of FCI may refer, for instance, to Jiang *et al.* [8] for a recent review on the state-of-knowledge concerning FCI physical phenomena.

Film boiling may occur or not around the corium during the premixing phase, depending on the sodium sub-cooling. In the case where the sodium is close to saturation, for example because it has been locally heated up by previous corium relocations, film boiling initiates around the corium jet because of the conductive thermal transfers that provoke the vaporization of the sodium immediately after the contact. At the same

time, destabilization phenomena such as Rayleigh instabilities (due to surface tension) or Kelvin-Helmholtz instabilities (due to shear stress between the gravity-driven corium and the liquid sodium carrier phase) develop in the jet, leading to the so-called "primary fragmentation" of the jet (Figure 1). The corium droplets generated by the primary fragmentation also induce film boiling of the surrounding sodium. Then the "secondary fragmentation" occurs, resulting in various sizes of corium droplets. Mainly three physical phenomena are considered in the literature as the source of the secondary fragmentation: hydrodynamic instabilities may develop at the surface of the biggest droplets, as for the jet; some liquid sodium may be trapped within a corium droplet, vaporize and fragment the droplet; and, in case of film-boiling, the destabilization of liquid-vapor interface leads to direct contacts between the corium and the liquid sodium, inducing thermomechanical constraints within the droplet.

Film boiling is then involved at various stages of the premixing phase, and is thus of major interest to better understand FCI. In particular, film boiling around corium droplets appears as a potential "trigger" for vapor explosion.

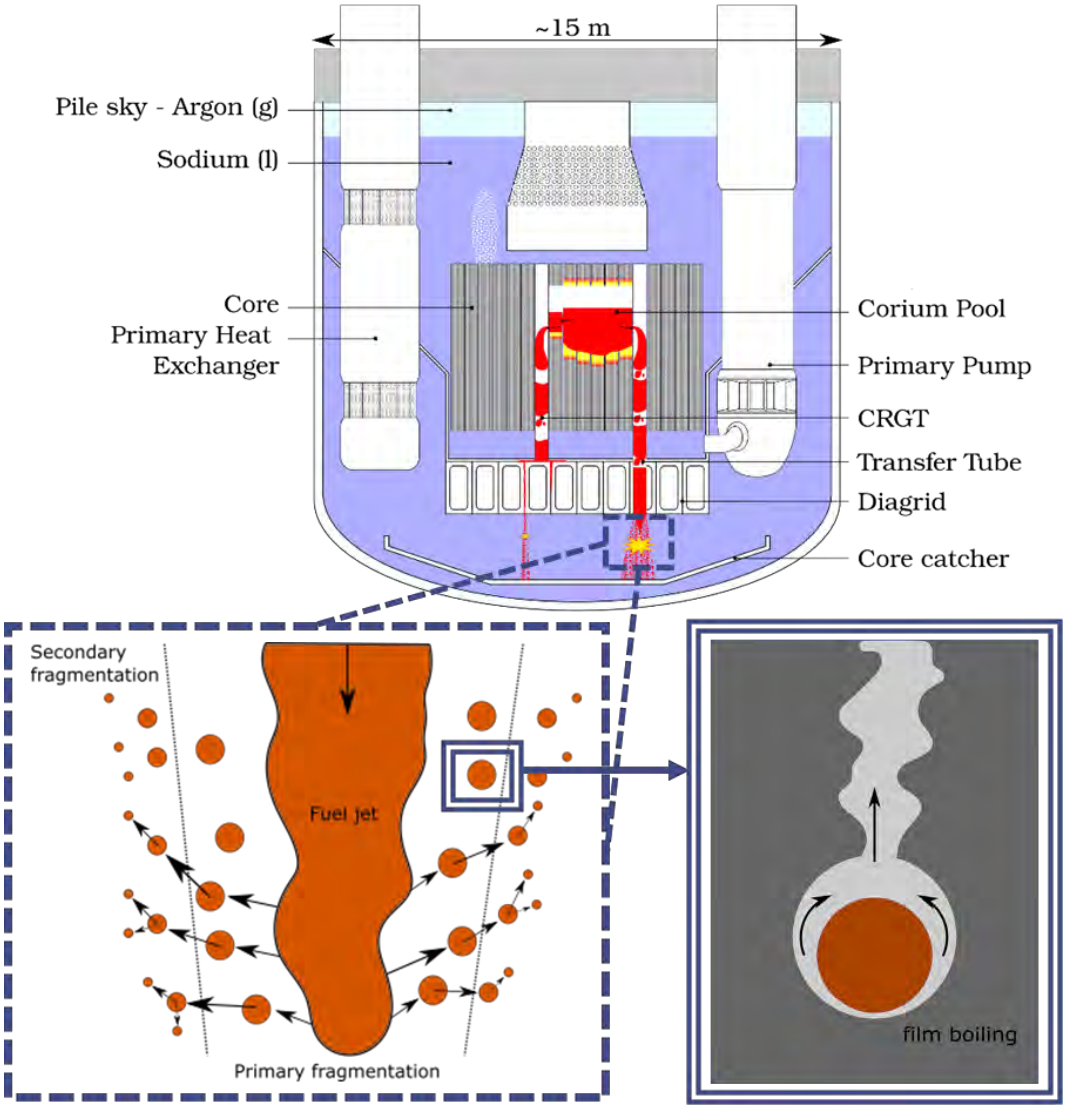

Figure 1. From corium jet to film boiling around a fragmented droplet in FCI event

2.2 Film-boiling around spheres in sodium

The classical Nukiyama curve [9], for a quasi-static system with imposed wall temperature, exhibits 3 boiling regimes (see Figure 2a): nucleate boiling is observed for relatively low wall temperature, while film boiling regime occurs above the so-called "Temperature Minimum Film Boiling" T_{MFB}. In fast-transient systems like quenching, a 4th regime may be observed between the classical film boiling and the transition regime, where unstable vapor films still exist but regularly collapse and reform. This regime has been experimentally observed in water, for example by Honda *et al.* [10].

Experimental characterization of film boiling in sodium are very scarce in the literature: only one experimental work has been reported, carried out by M. Farahat [7] in the 1970's, where a sphere of Tantalum was heated by induction then quenched it in a pool of resting liquid sodium close to saturation. Heat transfer were monitored by a single thermocouple placed inside the sphere. Wall temperature and heat flux were determined from the measured temperature thanks to a postprocessing method based on a simplified inverse problem, in order to produce boiling curves at imposed wall temperature from the film boiling to the nucleate boiling regime. A possible unstable film boiling regime has been highlighted as shown in Figure 2b [5].

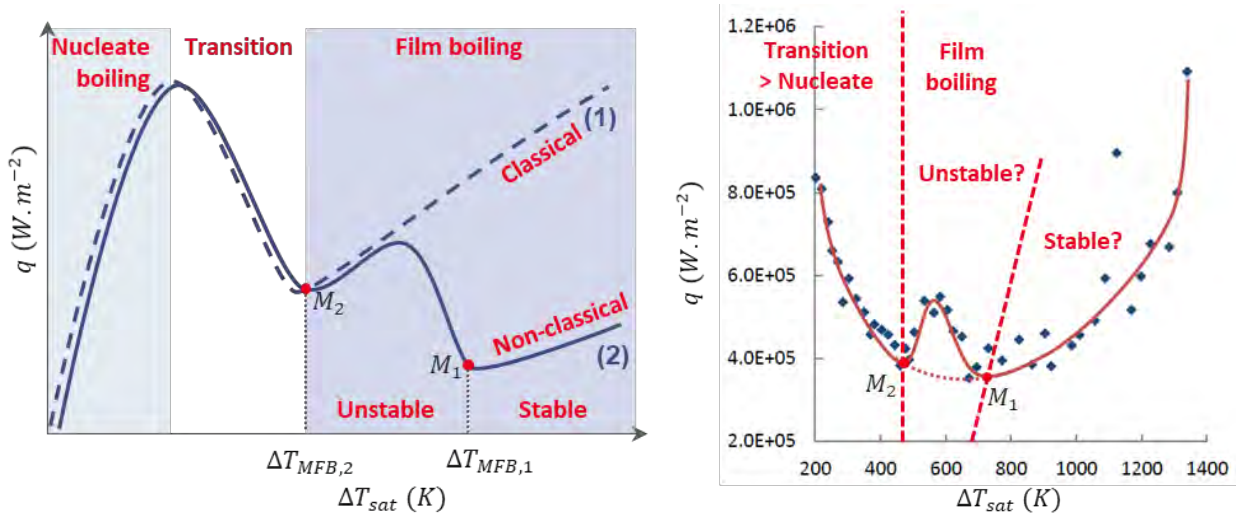

(a) **(b)**

Figure 2: (a) The Nukiyama boiling curve at imposed surface temperature; and (b) experiment in sodium by M. Farahat [7], analyzed by Le Belguet [5]

The modelling of film boiling in sodium have been studied by Le Belguet and Berthoud et al. [5,6] on the basis of a previous modeling for water by Dhir and Purohit [11] and considering experimental data of Farahat for validation. The analyzed parameters included the sphere superheat, the emissivity, the sodium temperature and the sodium velocity. The experimental parameters and the postprocessing methods proposed by Farahat induced significant uncertainties on the results. New experiments with film boiling around superheated spheres in sodium therefore appear necessary for the development of future numerical tools for FCI like SCONE. Indeed, sub-cell models are required to account for the heat exchange between a large number of particles and the sodium carrier phase:

$$\phi_{droplet \to Na} = h\left(T_{droplet} - T_{Na}\right) \quad (1)$$

The heat transfer coefficient (h) in the equation above must be provided by experimental correlations. The correlation proposed by Epstein and Hauser [12] is currently considered as the most precise one, but its reliability remains questionable in sodium. The data obtained thanks to the SERUA facility should reduce these uncertainties.

3 SERUA DESIGN AND PRINCIPLE

This section presents the principle of the SERUA facility, a typical test conduct and the instrumentation.

3.1 Experimental Layout

The SERUA facility basically includes 3 main parts (Figure 3):

- The induction furnace (Figure 3a) ensures the tantalum sphere heating. The atmosphere of the sphere is separated from the one of the inductor by a quartz tube. A glass window allows the visualization of the sphere during the heating, which allows to ensure the initial temperature of the sphere by pyrometry, and eventually to determine the emissivity of the sphere (see section 4.1);
- The thermostatic sodium pot (Figure 3b) is placed under the induction furnace and is isolated from it by a dedicated insulation valve during the heating phase. It contains the sodium pool, suspended to the cap, inside the isolation vessel filled with Argon gas and protected from the hot sodium pool by insulation blankets. The sodium pool is heated by 3 heating canes and the temperature of the sodium is measured all around the sphere thanks to an instrumented grid (see section 3.3);
- The sphere transfer device (Figure 3c) ensures the correct transfer of the heated sphere from the induction furnace to the sodium pool. It contains the support rod of the sphere, which must be long enough to cover the distance between the furnace and the sodium pool. The transfer velocity must be high enough for the sphere to reach the sodium with sufficient temperature to generate film boiling and low enough to avoid too much sodium projection when the sphere penetrates through the surface [13].

3.2 Typical test conduct

The principle SERUA test conduct is very similar to Farahat's [7]:

- The instrumented sphere in tantalum suspended to a tantalum rod mimics the corium droplet. The sphere is heated by an induction furnace up to ~2300 °C;
- At the same time, a pool of liquid sodium is heated up to the desired temperature close to saturation;
- The inductive heating is suddenly cut-off and the sphere is quenched into the sodium volume;
- The evolution of the heat flux and wall temperature of the sphere is monitored during quenching until the complete thermalization of the sphere with the sodium.

3.3 Instrumentation

The central element of the experiment is the instrumented sphere (Figure 4a). The reference results, stemming from Farahat's experiment, were obtained with a single hot junction. This will be improved in the SERUA experiment, as a so-called duplex type-C thermocouple sensor will be used, with two separated hot junctions of tungsten-rhenium wires. This duplex thermocouple is used to measure and monitor the heat fluxes and wall temperatures of the sphere, following the method described briefly in the following section.

The sodium transition boiling regime is expected to occur for $\Delta T_{\mathrm{sat}} \in [450; 650]$ °C, *i.e.* for a sphere surface temperature between ~1350 °C and ~1550 °C. The tantalum sphere will be quenched very rapidly from 2300 °C to the sodium temperature, leaving a measurement window of a few dozens of seconds to observe

the film boiling regime and a few seconds to capture the transition regime. This requires a dedicated instrumentation with a suitable response time and data acquisition frequency (around 100 Hz).

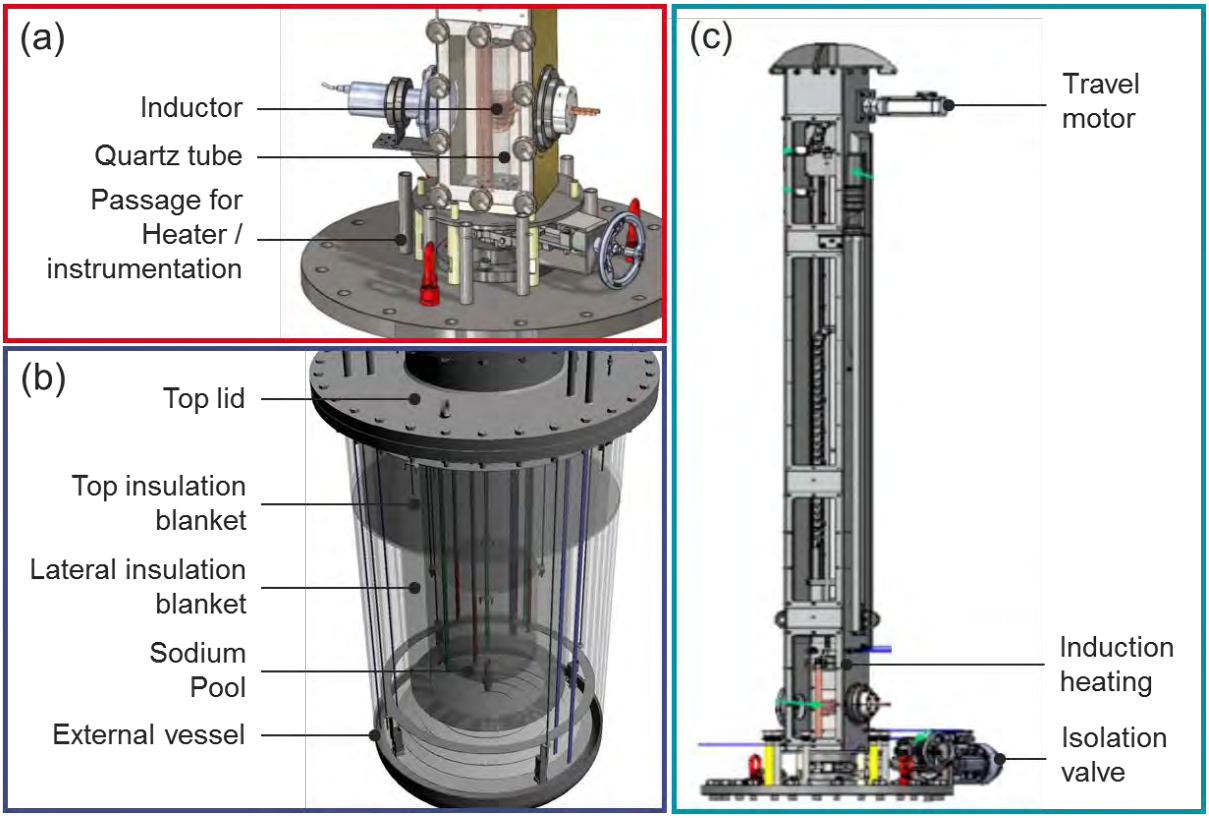

Figure 3: The SERUA experimental layout

(a) **(b)**

Figure 4: (a) Instrumentation inside the sphere; (b) Instrumented grid immersed into the sodium pool to measure the temperature field around the sphere

It is equally important to access the temperature of the liquid sodium, to determine a heat transfer coefficient in equation (1). To this end, an instrumented grid is immersed as close as possible to the vicinity of the sphere (Figure 4b), with 24 type-K thermocouples homogeneously distributed on 4 axes for thermal mapping of the sodium volume surrounding the sphere. This instrumented grid will also include piezoelectric sensors to detect the pressure waves due to the direct contacts between the liquid sodium and

the sphere in the unstable film boiling regime, as well as the generation of bubbles in the nucleate boiling regime, giving some hints at the occurrence of different boiling regimes. Before immersion, it can also help to detect a possible nucleate boiling around heating rods, for the sake of test conduct.

Besides, at such high temperatures, radiative heat transfer plays a significant role in the thermal balance of the tantalum sphere. Its contribution in the heat transfer coefficient must be assessed, through the tantalum emissivity. The latter is not well-known at high temperatures, and presents several sources of uncertainties (impurities, roughness, etc.). A set of pyrometers with different working wavelengths shall be implemented in the upper part of the facility, focusing on the tantalum sphere during the induction heating process. The pyrometers measurements will be used not only to monitor the induction heating and verify the sphere temperature, but also to estimate its emissivity, following the approach described in the section 4.1.

3.4 Determination of wall temperature and heat flux

The determination of wall temperature and heat flux in the sphere is the central element of SERUA data analysis. The used method relies on the resolution of non-linear inverse heat conduction problem at sphere scale, whose methodology is well-documented in the literature, following the reference work of Monde *et al*. [14]. This methodology relies on an analytical solution of the heat equation in the Laplace space. The wall temperature and heat transfer may then be expressed as convolution products between the measured temperatures and the inverse Laplace transform of transfer functions, estimated using the Stehfest algorithm. Input data of the method are the thermocouples measurements and their positions (1st and 2nd hot junctions in the sphere, fluid temperature in liquid sodium), and the thermal diffusivity of the sphere. The results may then be used to determine the time evolution of the heat transfer coefficient h (including both convective and radiative effects) between the sphere and the surrounding sodium.

The quantification of the performance of the method in terms of applicability and uncertainty is still under investigation.

4 QUALIFICATION OF SERUA CONCEPT

The main elements for the SERUA qualification program are shown in Figure 5, and can be distinguished between the upper and lower part of the experiment: the sphere design and characterization during the induction heating process has been qualified on the VITI facility, and the control of the high-temperature sodium pool, qualified during the ESCOBAR test series. The experience acquired after the VITI qualification program has been used to adapt a new induction device, PELE, to the SERUA requirements.

4.1 Sphere design and characterization: VITI qualification program

A key aspect of the characterization of boiling heat transfer at the surface of the tantalum sphere concerns the precision to which the wall temperature, heat flux and heat transfer coefficient can be determined from measurements and understanding of the thermal behavior of the sphere, including the contribution of radiative heat transfer through emissivity. Another important issue regarding the preparation of the SERUA experiments is the prediction of the cooling rate of the sphere between the end of the heating phase and its entry into the liquid sodium, so that the conditions of transition boiling regime characterization are ensured. To address both issues, dedicated experiments have been conducted in the VITI facility, coupled to magneto-thermal simulations.

The VITI facility consists of an induction furnace, contained inside a water-cooled confinement vessel, whose configuration inspired the design of the SERUA furnace. The temperature distribution across the surface of the tantalum sphere was investigated through multi-wavelength pyrometry and infrared thermal imaging during heat treatment representative from the SERUA experiments.

Classical pyrometry without emissivity correction gives access to blackbody surface temperature distribution, assuming that emissivity is constant and equal to unity. However, Allen *et al.* [15] determined emissivity values of 0.288-0.324 for polished tantalum surfaces in the 2300-3300 K range, increasing with temperature. More precise characterization of the emissivity of the spheres under investigation is therefore required to determine the real temperature, because their level of impurities, roughness, and other surface features can significantly differ from the one used in reference [15]. Preliminary calculations have shown that 20 % uncertainty in the emissivity values may lead to more than 100 °C error in surface temperature estimation. This is why a specific methodology is under development to get a better estimation of the tantalum sphere emissivity and to improve the predictability of the calculations. This methodology is summarized in the Figure 6 and may be divided into two main steps: i) experimental data treatment to determine the accurate surface temperature; and ii) adjustment of the total emissivity in a numerical model based on COMSOL Multiphysics© to match the previous surface temperature.

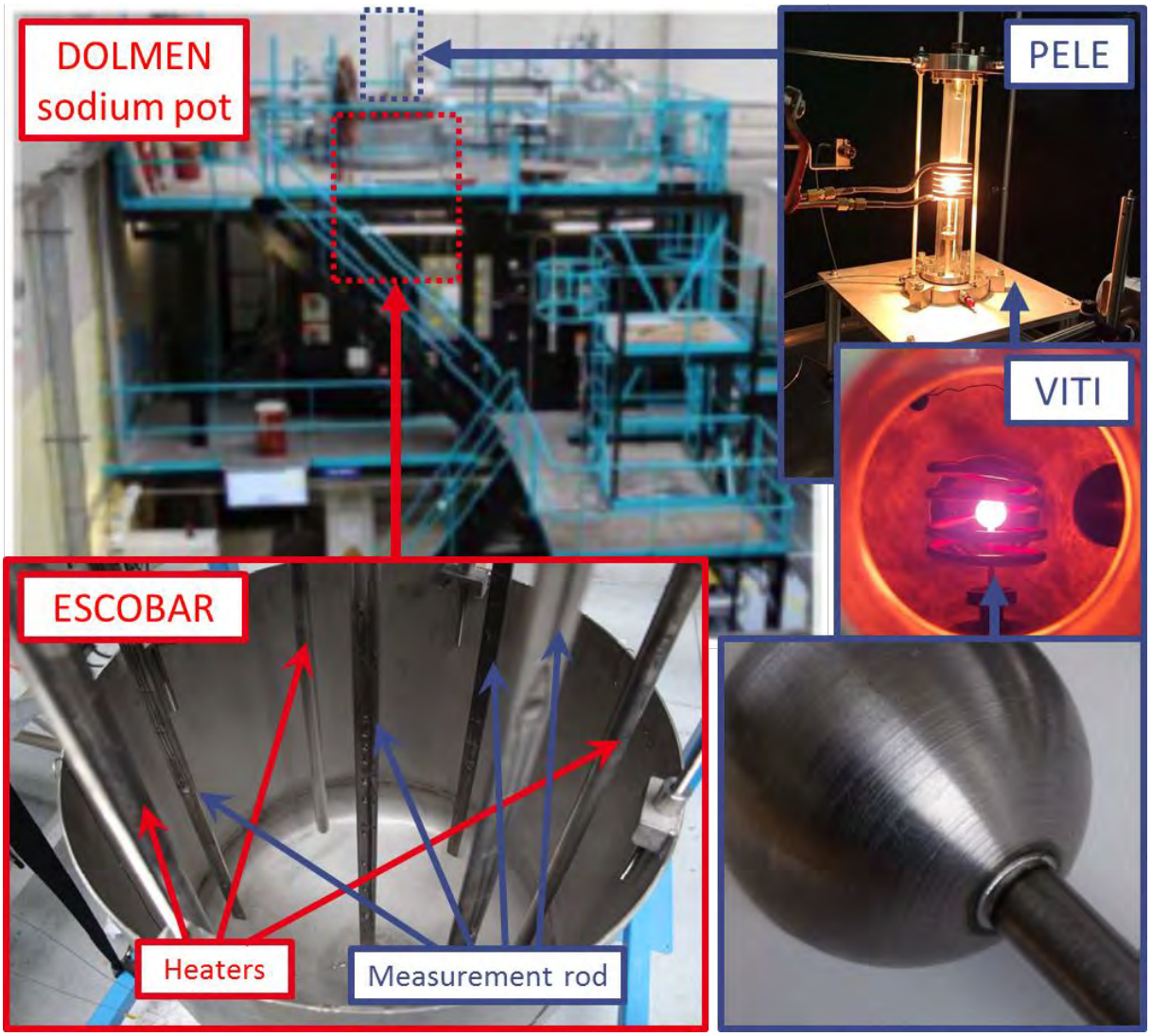

Figure 5: Main elements for the qualification of the SERUA concept. (Top left) the DOLMEN loop who will host the SERUA experiment; (Top right) the PELE induction furnace to qualify the sphere heating process; (Bottom left) the sodium pot used in ESCOBAR experiments to qualify the sodium heating process; (Bottom right) the Tantalum sphere welded on its support tube.

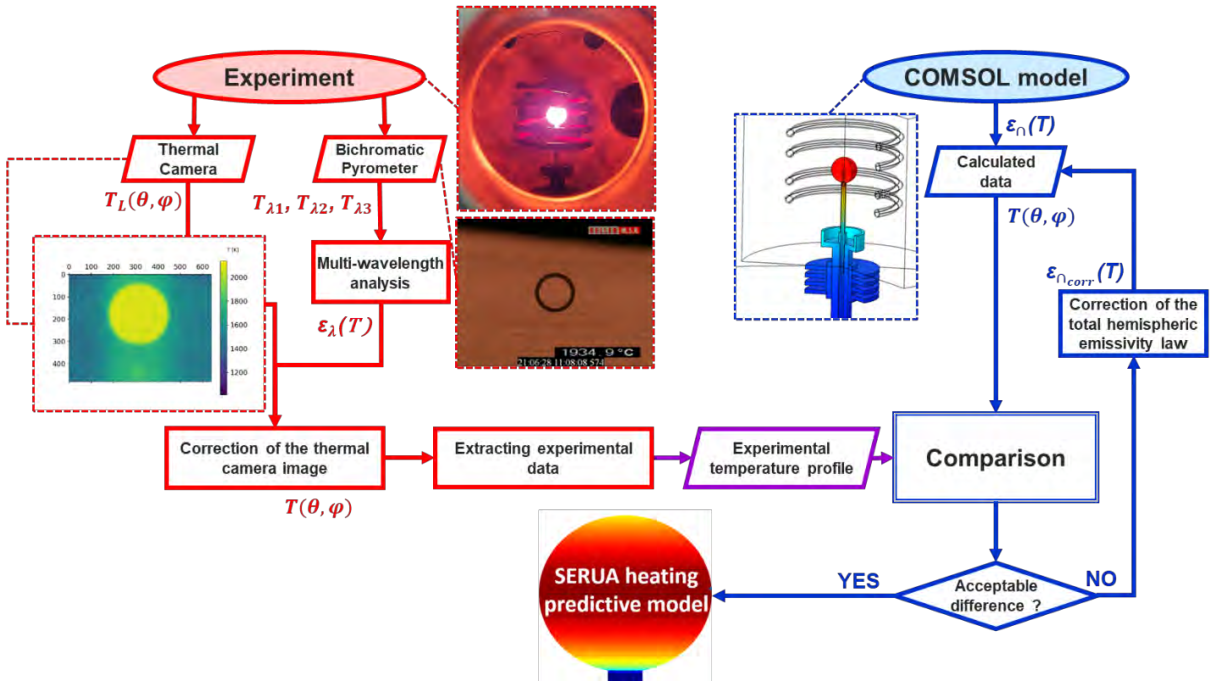

Figure 6: Coupled experimental and numerical approach for the estimation of emissivity and temperature fields at tantalum sphere scale for SERUA experiments.

4.2 Sodium pool control: ESCOBAR qualification program

The production and characterization of a stable liquid sodium pool at ~860 °C is another key aspect for the feasibility of the SERUA program. The ESCOBAR experimental program has been conducted in the future host facility for SERUA to demonstrate the validity and robustness of the selected technology for the heating of the sodium pool, as well as for the characterization of the sodium temperature field in representative conditions of the SERUA experiments. In parallel, numerical simulations are carried out with OpenFoam in order to get a deeper insight of the sodium pool configuration, notably to characterize the velocity field (Figure 7).

The Figure 8 shows the temperature measurements inside the sodium pool during the maximal power plateau of the ESCOBAR experiments. The capability of the selected sodium heating technology to maintain a stable temperature of 860 °C during ~30 min has been demonstrated, which is the objective for the first SERUA experiments.

Taking advantage of the many temperature measurements inside the sodium pool, the OpenFoam numerical model has been used to extend our knowledge of the state of the sodium pool to the velocity field, which will be an important parameter for the SERUA experiments. The model performs 3D simulations of the natural convection with turbulence modelling (k-ε and k-ω have been tested) on 1/6th of the test section. Simple boundary conditions are used (Figure 7, left): symmetry on the sodium edges, to reflect the symmetry of the problem, no-slip condition on the lateral wall and the heater, heat convection on the lateral wall with a user-adjusted heat transfer coefficient, imposed heat flux in the heating part of the heater. Finally, a slipping-wall condition with heat convection, including another user-adjusted heat transfer coefficient, is imposed at the top, and is considered as a satisfactory approximation of the sodium pool free-surface conditions. By adjusting the external heat exchange coefficients, the model is able to match the measured temperature profiles with a satisfactory agreement (Figure 9).

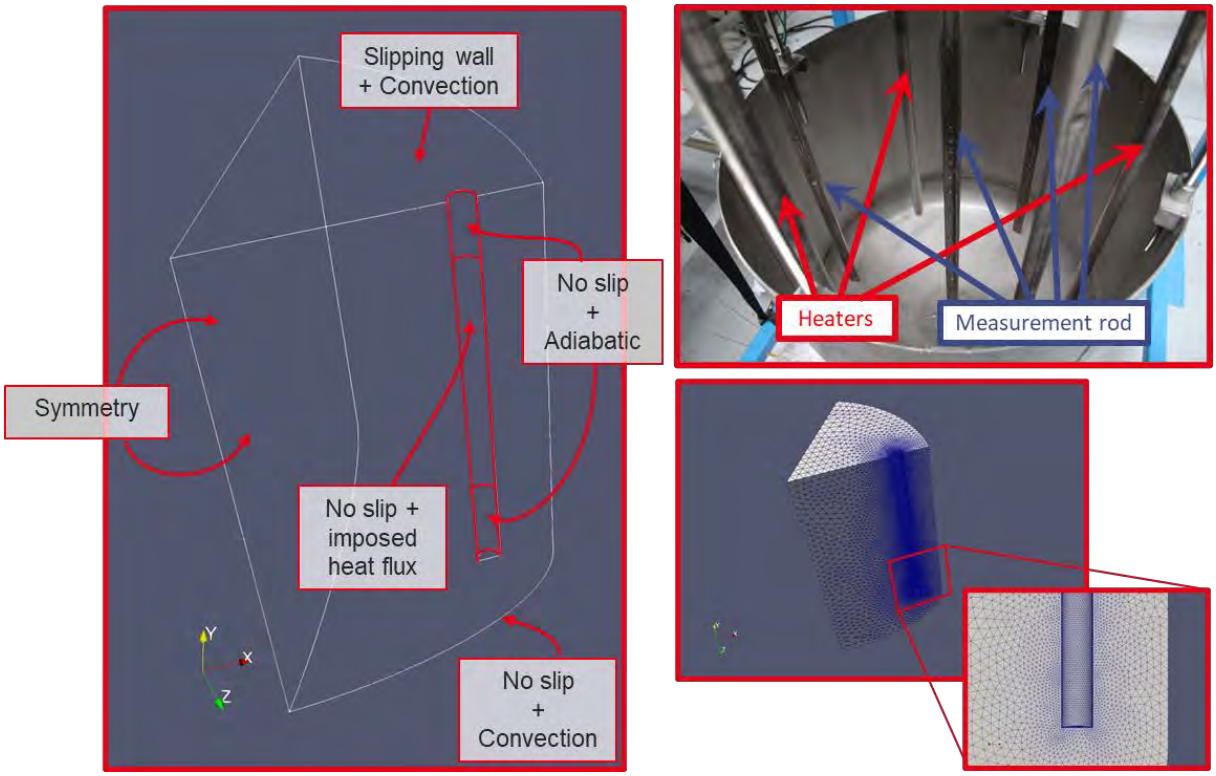

Figure 7: (Top right) Experimental pot for ESCOBAR experiments and (Left and Bottom right) corresponding OpenFoam modelling

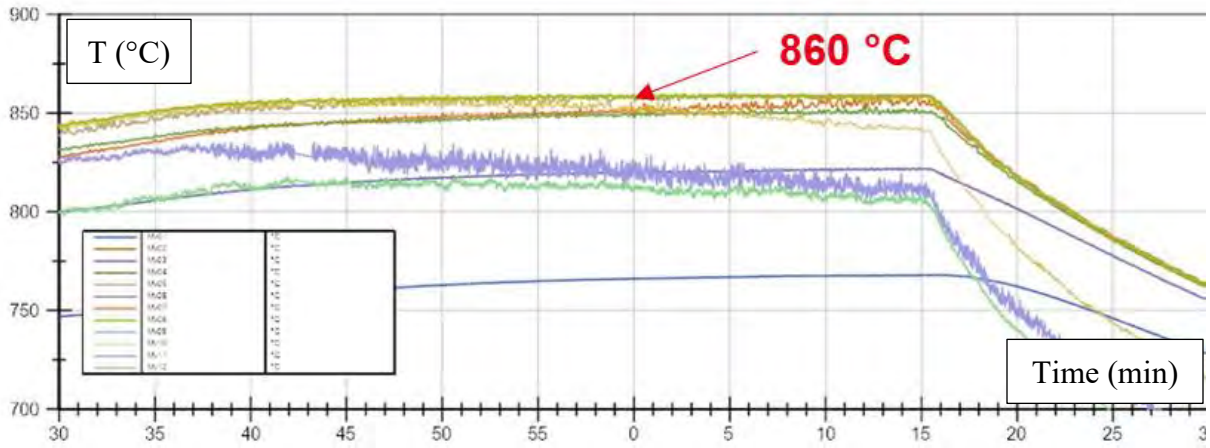

Figure 8: Sodium temperature measurements at the end of ESCOBAR experiments

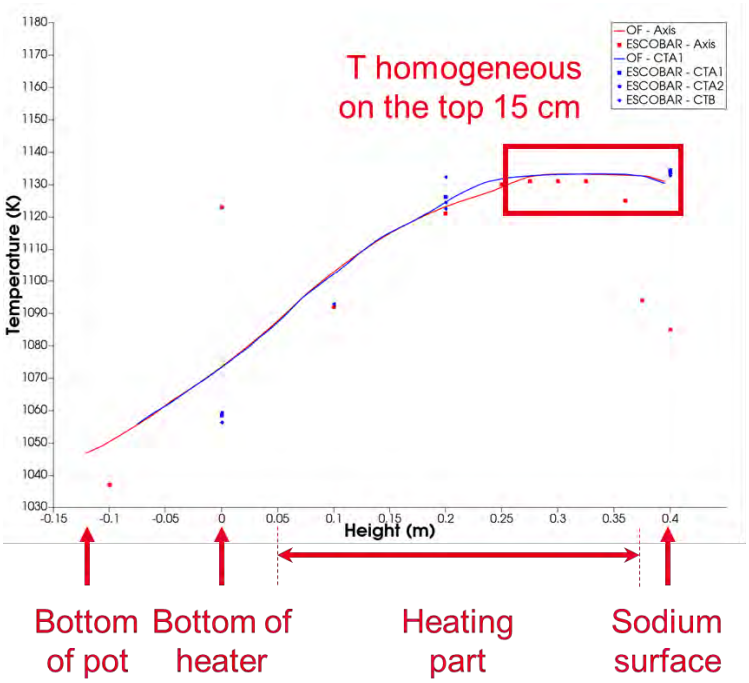

Figure 9: Comparison of simulation results with ESCOBAR experimental data on the central axis

The temperature (Figure 10a) and velocity (Figure 10b) fields in the adjusted model reveal that before the arrival of the heated sphere in the SERUA experiments, the sodium temperature should be almost homogeneous in a ~Ø15 x 15 cm cylinder near the top center of the pool, which is where the sphere and instrumented grid will be placed (white dashed lines on the figure). Furthermore, a moderate velocity of ~3 cm/s is calculated in this homogeneous temperature zone. Considering the adopted boundary conditions for the simulations (symmetry planes at the lateral boundaries), this value constitutes a maximum rather than a real estimate of the sodium velocity in the future SERUA experiments, but it remains an interesting order of magnitude for their interpretation.

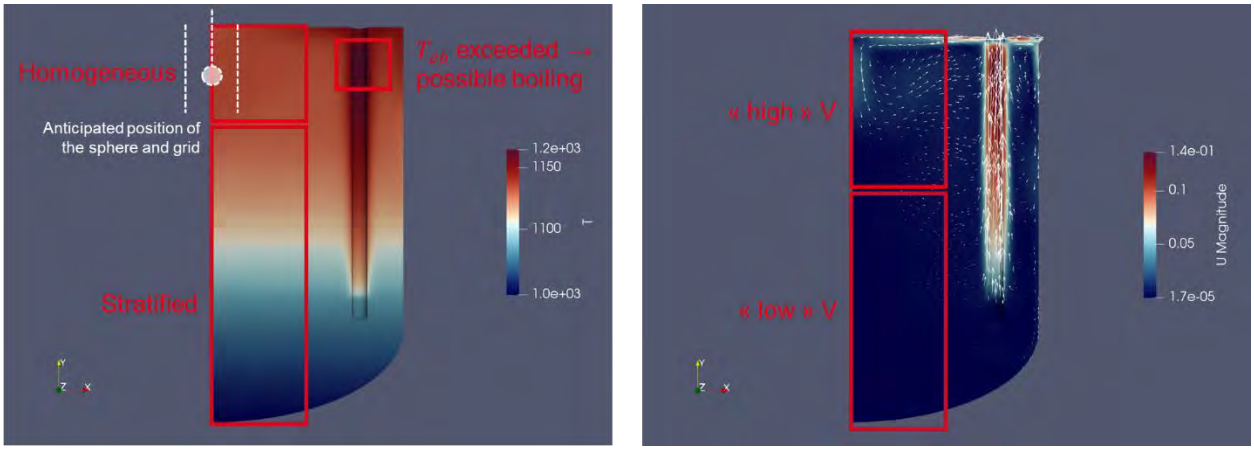

(a) **(b)**

Figure 10: (a) Temperature and (b) velocity fields calculated in the sodium at the end of ESCOBAR experiments

4.3 Further qualification and commissioning activities

The SERUA experimental device is currently under construction at the CEA Cadarache center. After completion of its assembly, a qualification test program in air is planned, which will consist in validating the operability and safety of the facility in the various configurable configurations such as (the list is not exhaustive): the argon inerting of the induction furnace; the heating of the sphere; the high-velocity transfer of the sphere in argon; the slow-velocity movement at the moment of the immersion of the sphere in the sodium; the holding time in the sodium bath. The commissioning of the facility is planned at the end of 2026.

5 CONCLUSIONS

The objective of the SERUA experiments is the characterization of film boiling regimes in liquid sodium close to saturation, which is a key-aspect for the modelling of Fuel-Coolant Interaction (FCI) during a severe accident in a Sodium-cooled Fast neutron Reactor. More particularly, it should provide validated heat transfer correlations for the heat transfer coefficient between corium droplets and sodium, and transition temperatures for the boiling regime, to be implemented into FCI simulation codes like SCONE as a sub-mesh model.

The experimental device is inspired by experiments conducted by Farahat in 1972, which remain the only experiments of this kind performed with sodium, and is intended to improve those results in terms of precision and reliability. The principle of the experiment consists in i) heating a tantalum sphere up to ~2300 °C with induction; ii) stabilize the temperature of a sodium pool close to the saturation point of the sodium; iii) quench the heated sphere into the sodium.

The facility is currently under construction at the CEA Cadarache center. A dedicated qualification program has been conducted in order to demonstrate that the desired experimental conditions are achievable with accurate precision and stability. The induction heating of the sphere at 2300 °C is feasible, and it will be measured in two points in the sphere using a duplex thermocouple during the quenching. The sodium temperature can be regulated at 860 °C during ~30 min with sufficient stability and homogeneity and it will be monitored during the quench by a specific instrumented grid immersed into the sodium. The sphere characteristics (initial temperature, emissivity) can be characterized by use of a dedicated pyrometry instrumentation. This will allow to measure the wall temperature, heat flux and heat exchange coefficients in all boiling regimes.

After completion of the experimental device assembly, the end of the qualification program and commissioning is anticipated by the end of 2026.

ACKNOWLEDGEMENTS

The authors express their warmest acknowledgements to Dr. Magali ZABIEGO, Dr. Alix LE BELGUET and Dr. Georges BERTHOUD who originally proposed the SERUA experiment and demonstrated its scientific interest.

REFERENCES

1. Bertrand, F., Bachrata, A., Seiler, N., Journeau, C. (Eds.). *Severe Accidents in Sodium Fast Reactors: Safety Study Approach, Prevention and Mitigation by Design*. Academic Press, Elsevier (2024).
2. Kubo, S. et al. “France-Japan collaboration on the SFR severe accident studies, outcomes and future work program”, *Proceedings of the International Conference on Fast Reactors and Related Fuel Cycles: Sustainable Clean Energy for the Future (FR22)*, Vienna, Austria, 19-22 April, 2022 (2022).

3. Berthoud, G., Amblard, M. "Presentation of significant results from the CORECT-II facility", *Proceedings of the CSNI Group of Experts on the Science of Fuel-Coolant Interactions and Vapour Explosion*, Grenoble, France, 27-29 September, 1978 (1978).
4. Magallon, D., Hohmann, H., Schins, H. "Pouring of 100-kg-scale molten UO2 into sodium", *Nuclear Technology* **98**, 1992.
5. Le Belguet, A. *Etude de l'ébullition en film du sodium autour d'une sphère à haute température*, Ph.D. thesis, Université de Grenoble (2013).
6. Berthoud, G., Le Belguet, A., Zabiégo, M. "The Farahat sodium natural convection film boiling experiment revisited", *Experimental Thermal and Fluid Science* **91**, pp. 117-125 (2018).
7. Farahat, M.-M.-X. *Transient boiling heat transfer from spheres to sodium*, Ph.D. thesis, University of Alexandria, Argonne National Laboratory (1971).
8. Jiang, W., Zhou, S., Wang, S., Hao, R., Lu, T. "A review of research on melt and coolant interaction under different injection modes", *Annals of Nuclear Energy* **220**, 111495 (2025).
9. Nukiyama, S. "The maximum and minimum values of the heat Q transmitted from metal to boiling water under atmospheric pressure", *International Journal of Heat and Mass Transfer* **9**, pp. 1419-1433 (1966).
10. Honda, H., Takamatsu, H., Yamashiro, H. "Minimum heat-flux point and liquid-solid contact during rapid quenching of thin wires", *Heat Transfer - Japanese Research* **24**, pp. 517-537 (1995).
11. Dhir, V. K., Purohit, G. P. "Subcooled film boiling heat transfer from spheres", *Nuclear Engineering and Design* **47**, pp. 49-66 (1978)
12. Epstein M., Hauser G. "Subooled forced-convection film boiling in the forward stagnation region of a sphere or cylinder", *International Journal of Heat and Mass Transfer* **23**, pp. 179-189 (1980).
13. Payot, F., Braillard, O., Clavier, R., Delacroix, J., Pluyette, E., Sauvecane, P. "Avancement des actions du programme SERUA : conception et qualification", Technical report CEA/DES/IRSENE/DER/NT 2021/08 Indice A (2021).
14. Monde, M. "Estimation of surface temperature and heat flux using inverse solution for one-dimensional heat conduction", *Journal of Heat Transfer* **125**, pp. 213-223 (2003).
15. Allen, R. D., Glasier, L. F., Jordan, P. L. "Spectral emissivity, total emissivity, and thermal conductivity of molybdenum, tantalum, and tungsten above 2300 K", *J. Appl. Phys.* **31**, pp. 1382–1387 (1960).

Investigation of film boiling in liquid sodium: qualification of the SERUA experimental program

CLAVIER Rémi[1], BLEVIN Gwendal[2], DELACROIX Jules[3], MOLINA Diégo[3], PONS Kévin[1], FRANCESCATTO Jerome[1], BRAYER Claude[1], JOURNEAU Christophe[3]

[1] CEA, DES, IRESNE, DTN, SMTA, LMAG, Cadarache, France

[2] CEA, DES, IRESNE, DTN, STCP, LESC, Cadarache, France

[3] CEA, DES, IRESNE, DTN, SMTA, LEAG, Cadarache, France

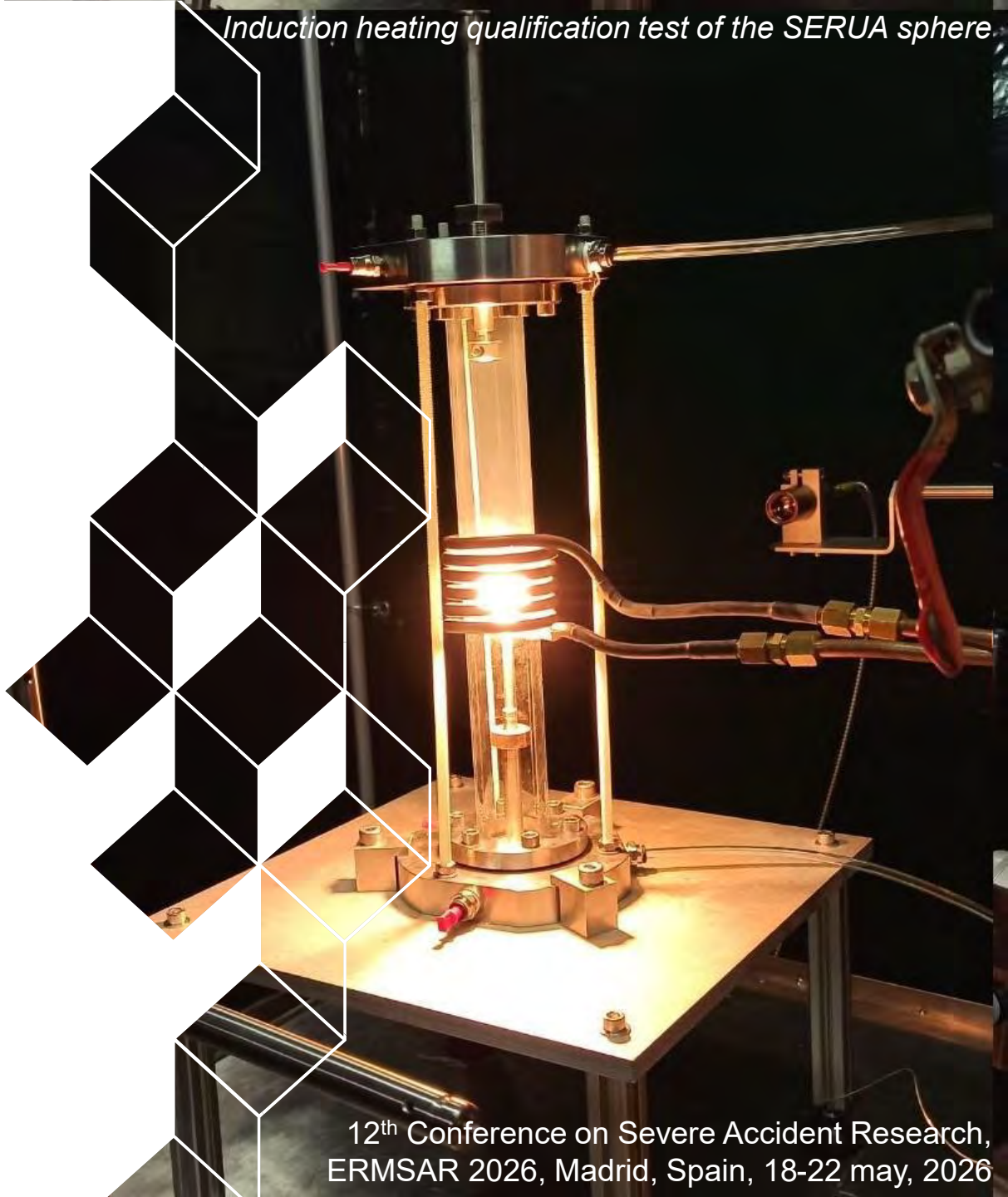

Induction heating qualification test of the SERUA sphere

12th Conference on Severe Accident Research, ERMSAR 2026, Madrid, Spain, 18-22 may, 2026

Why studying film boiling in liquid sodium?

Modelling of **Fuel-Coolant Interaction** in Severe Accident Situation in a **Sodium** Fast-neutron Reactor

- Contact between high T corium (~3000 K) and “low” T liquid coolant (~1000 K) > **Na film boiling around corium**
- Risk: **“steam” explosion**, resulting from:
  - High **Na vaporisation** rate, due to
  - An increasing **heat exchange surface**, due to
  - The **fragmentation** of the corium:
    - Primary fragmentation > hydrodynamic constraint
    - Secondary fragmentation
      - Mechanical > Na droplet entrainment into corium
      - Thermal > Liquid-liquid contact > shock wave / **vapor film destabilisation**
- Vapor film destabilisation > **“trigger” for steam explosion**
  - Necessary to predict the occurrence and energy of the steam explosion
  - Need to rely on validated correlation(s) for film boiling heat transfer (vapor production) and boiling regime transitions

Objective: Calibration of FCI numerical simulation software like **SCONE**

(Software for COrium Na interaction Evaluation)

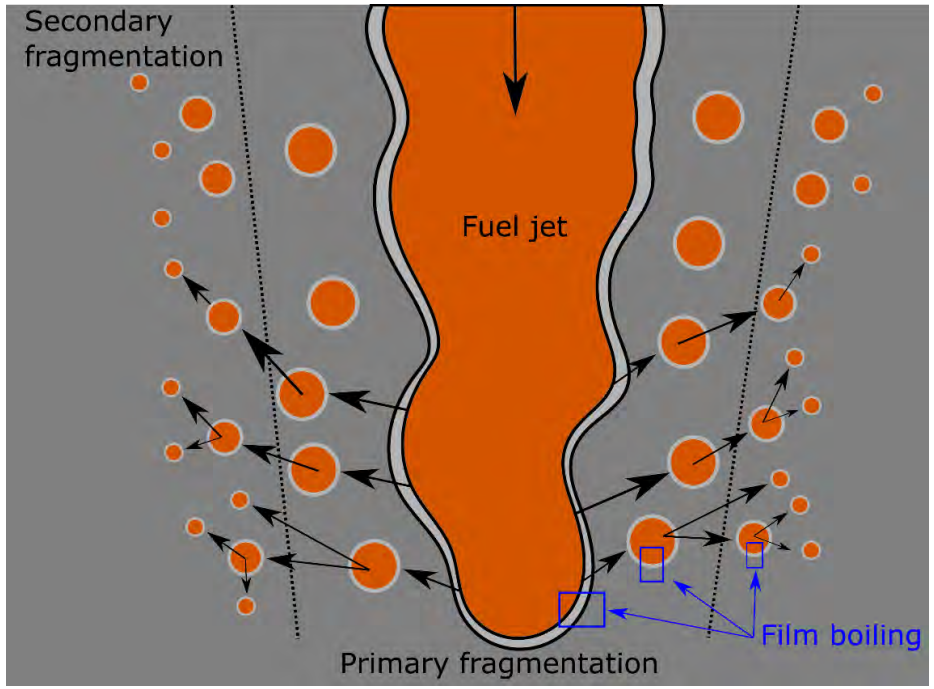

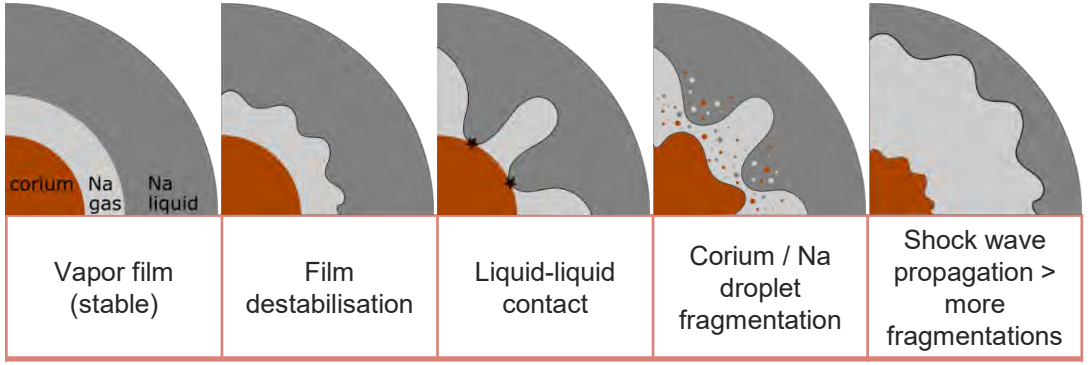

Current state of knowledge on film boiling in liquid sodium

Theory: Nukiyama curve around a sphere with imposed wall temperature

- Non-classical form (2): 2 film boiling sub-regimes:
  - Stable: high contact T (above M1), low flux
  - Unstable: lower contact T (between M1 – M2), liquid Na/sphere contacts, higher flux

Experimental observations:

- Complex physical phenomena > experiments with simulant fluid irrelevant for quantitative predictions
- **Only one experimental program in sodium: Farahat, 1972** > Confirmation of general phenomenology but uncertainties are too important for the needs of the simulation tools

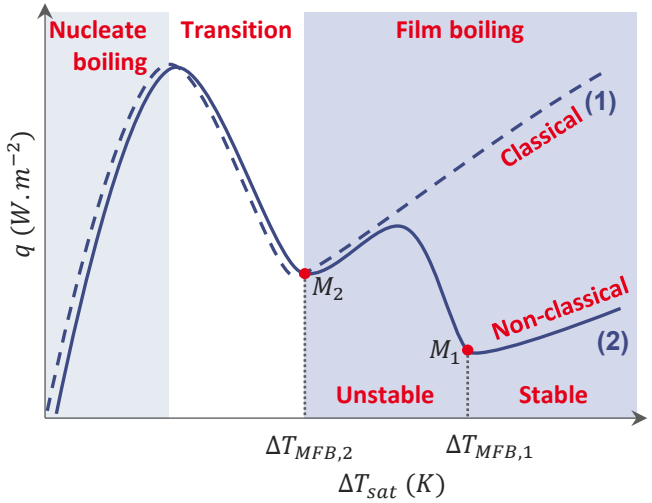

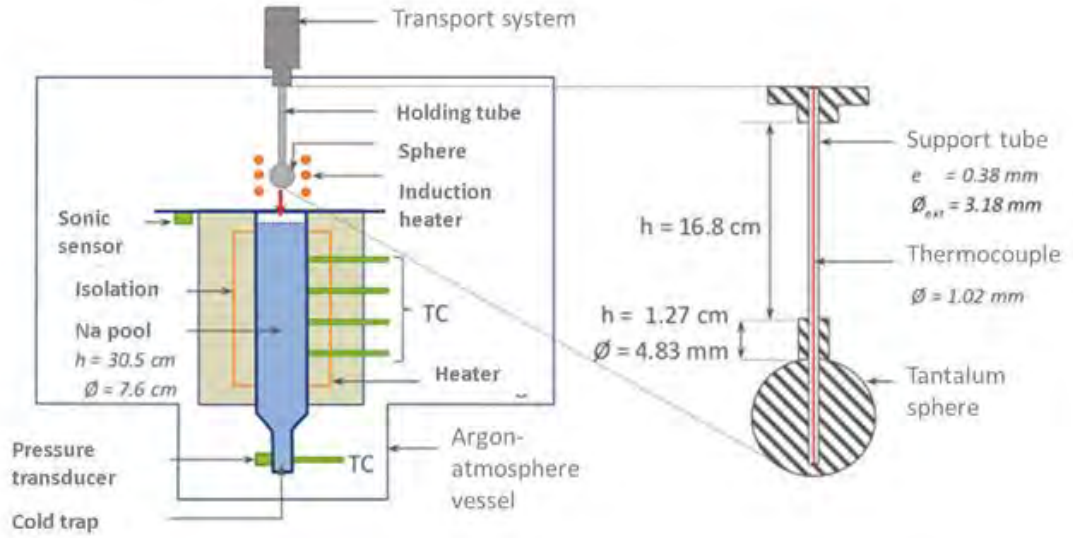

Farahat (1972) experimental setup

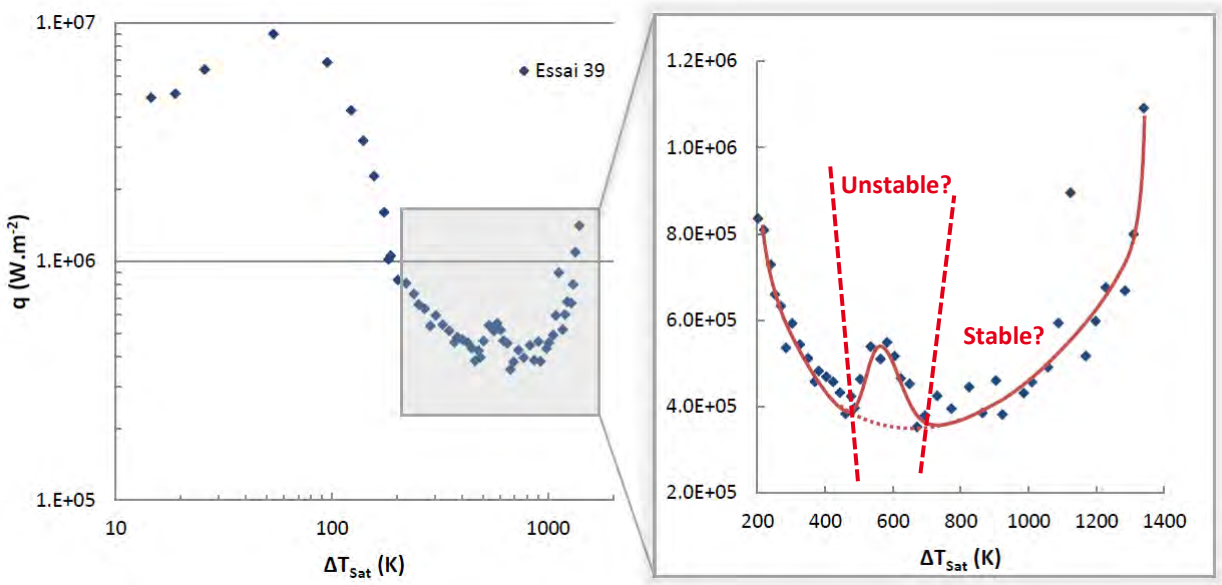

Shape of the heat flux density at the wall with respect to the wall overheat (Le Belguet, 2013)

SERUA experimental program at CEA

Sodium boiling Experimental Rig for Understanding of fuel-coolant interAction

Objective: fill the knowledge gaps left after Farahat experiments:

- Describe the Na boiling curve
  - Measure the heat exchanges in the different boiling regimes
  - Characterize the transitions between boiling regimes

- Experimental parameters
  - Sphere initial temperature ~2000 – 2500 °C
  - Na temperature ~800 – 870 °C
  - Sphere diameter ~12 – 25 mm

- Measurements: 2-points TC sensors to measure:
  - Transient heat flux in all the boiling regimes (Stable film, unstable film, transition, nucleate)
  - Wall temperature evolution

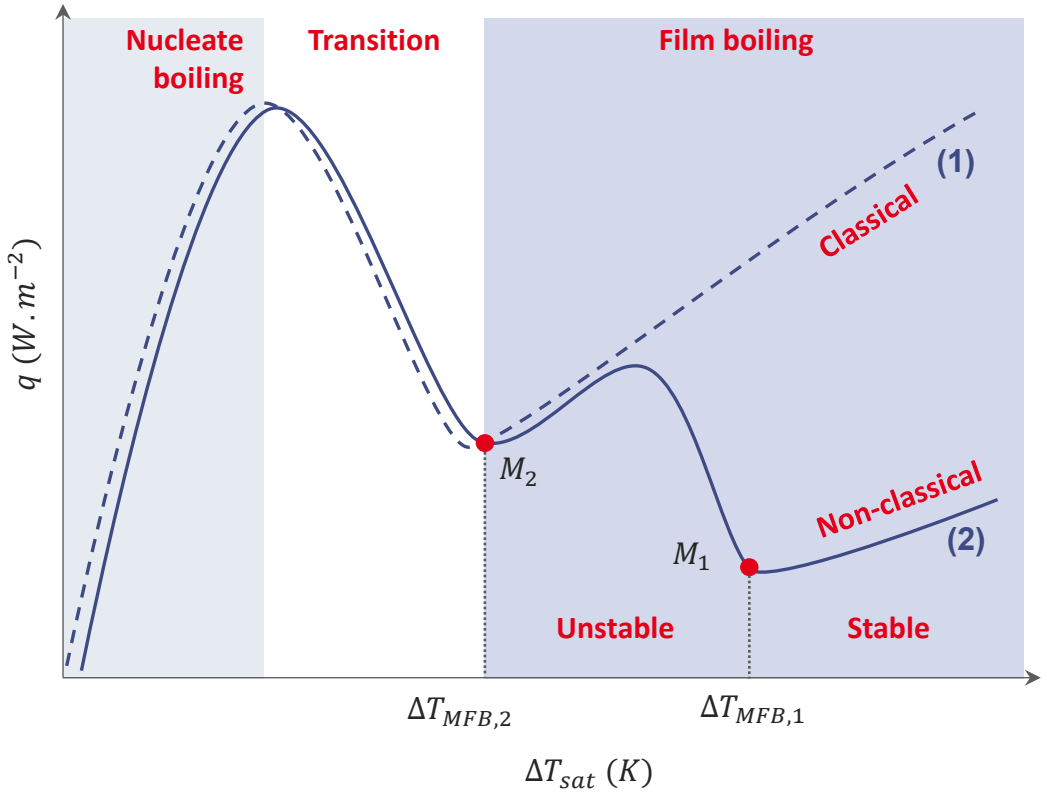

Conceptual design of SERUA experiments

1 – Inductive heating of the Tantalum sphere ~2500 °C

2 – Sphere quenching in sodium (~870 °C)

3 – Study of film boiling around the sphere

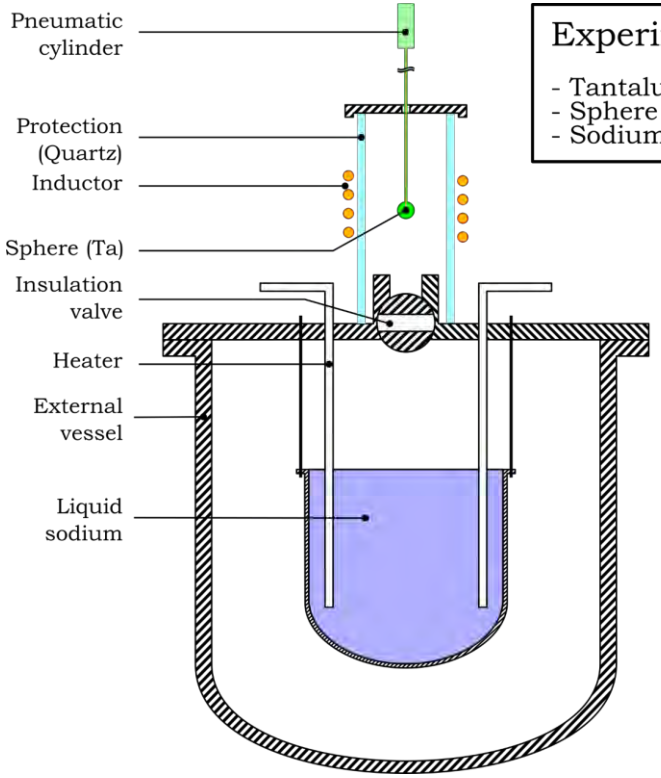

Experimental conditions:

- Tantalum sphere size: 25.4 mm
- Sphere temperature: 1500 - 2300 °C
- Sodium temperature: 400 - 880 °C

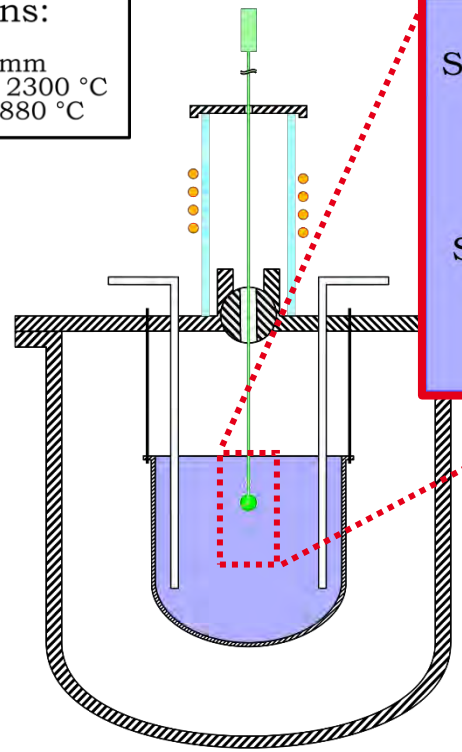

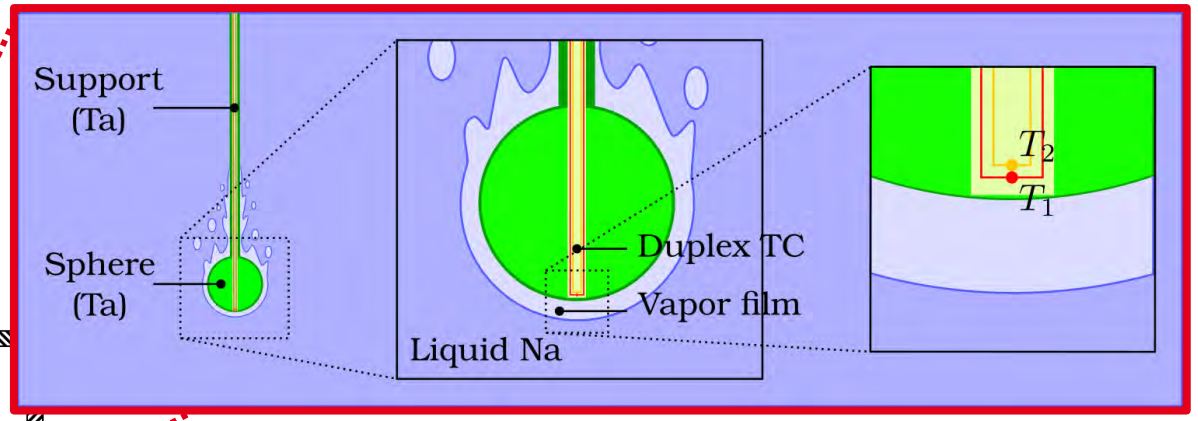

Study of boiling regimes at imposed temperature ($\varphi - \Delta T$):

- Film boiling (beyond Leidenfrost point)
- Transition (below Leidenfrost point)
- Nucleate boiling (end of experiment)

From the conceptual design to actual experiments

3 technological challenges:

- **Sphere heating system** (~2500 °C)
  - Induction generator
  - Insulation from environment
- **Na pool control**
  - Heating (~870 °C)
  - T / v characterization
- **Sphere design and characterization**
  - Initial surface temperature measurement and emissivity
  - Surface temperature and heat flux during quench

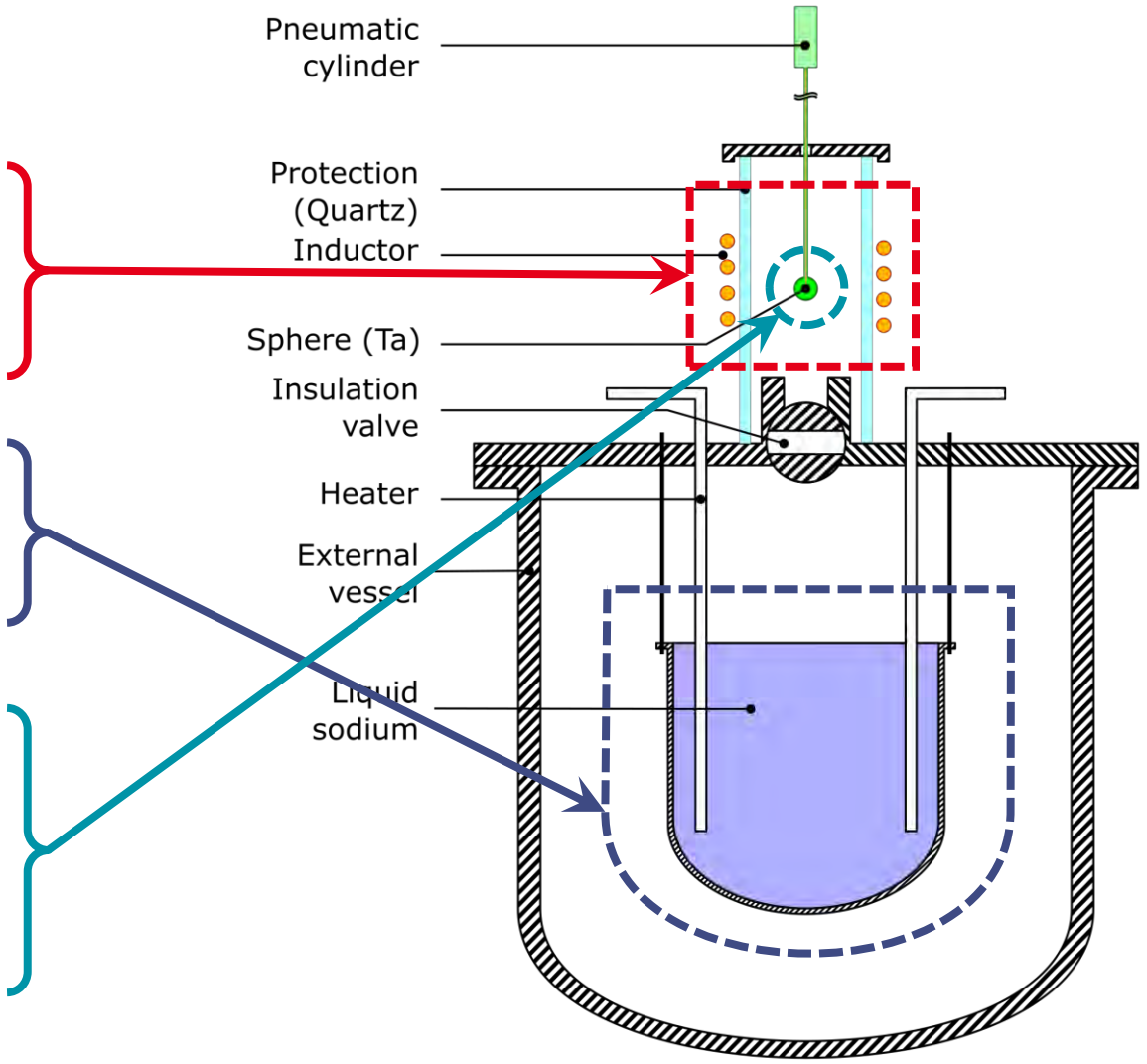

Sphere heating system: Induction generator

VITI

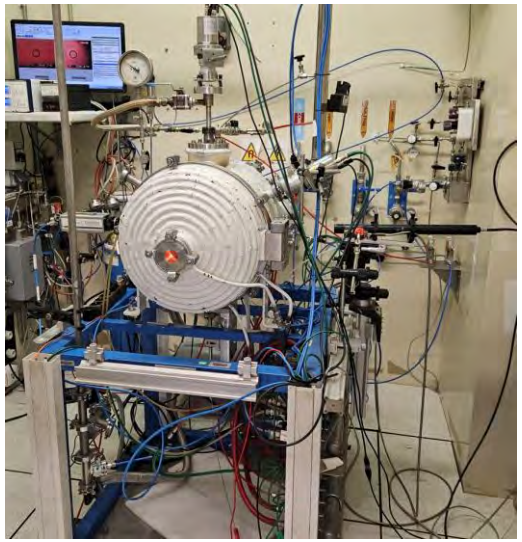

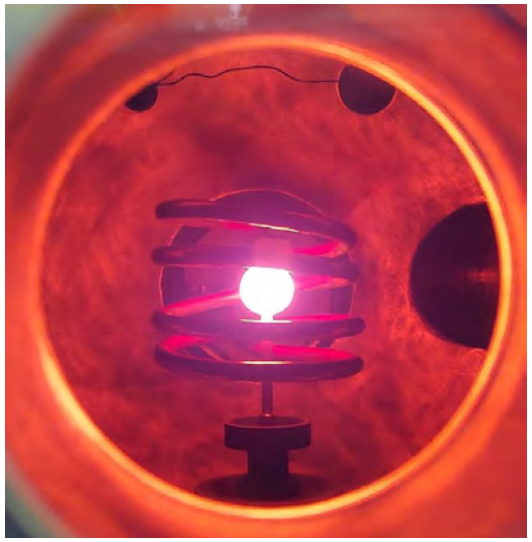

Technological qualification

- Inductive heating up to 2300 °C → OK

Sphere characterization and instrumentation

- Emissivity of the sphere
- Pyrometry and thermal camera

PELE

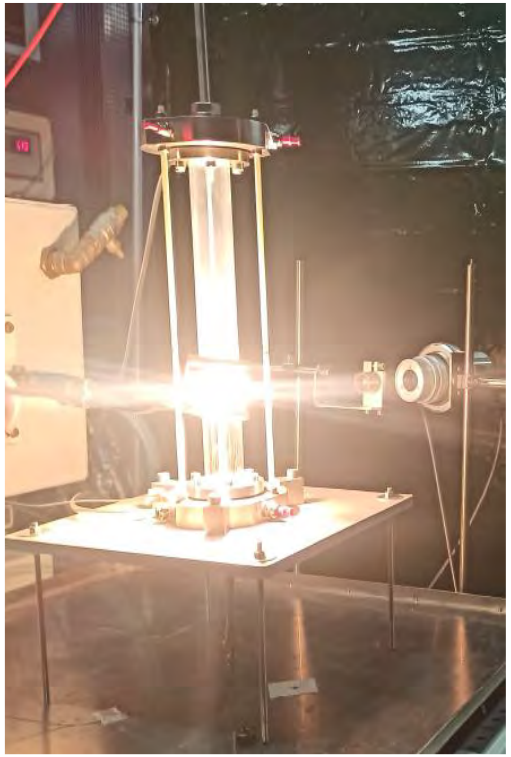

Transposition to the sodium platform

- Adapted induction generator
- Quartz tube for isolation
- Laser welding of the sphere and its support

Na pool control: ESCOBAR experiments

Goal : achieve stable liquid sodium heating at ~860 °C

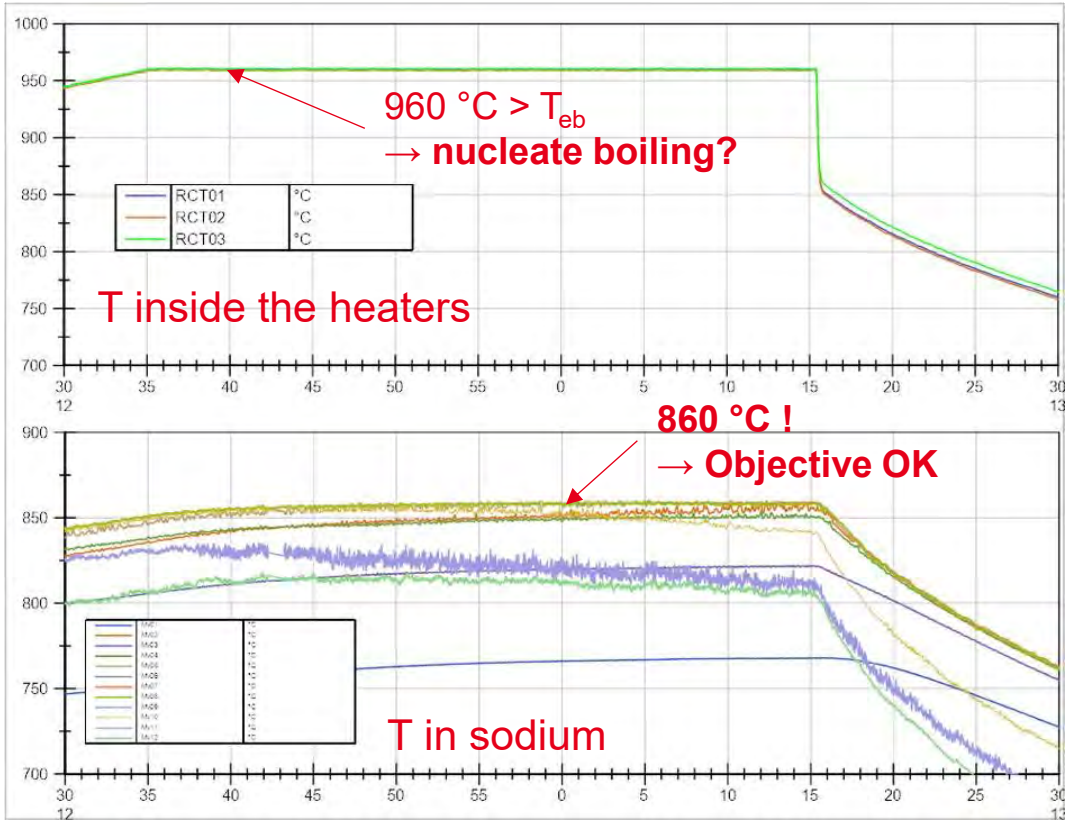

DOLMEN sodium pot

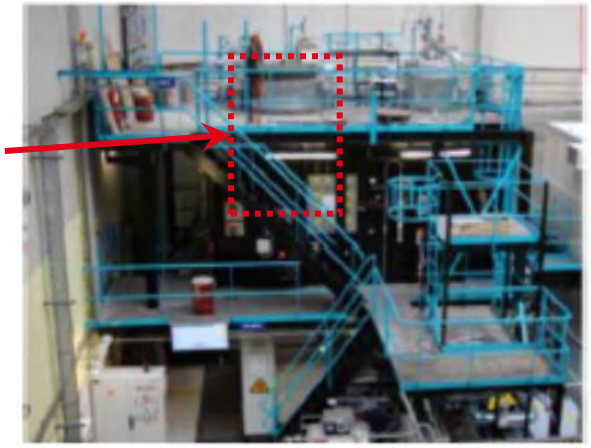

Experimental pot and instrumentation (before insertion inside the vessel and filling with sodium)

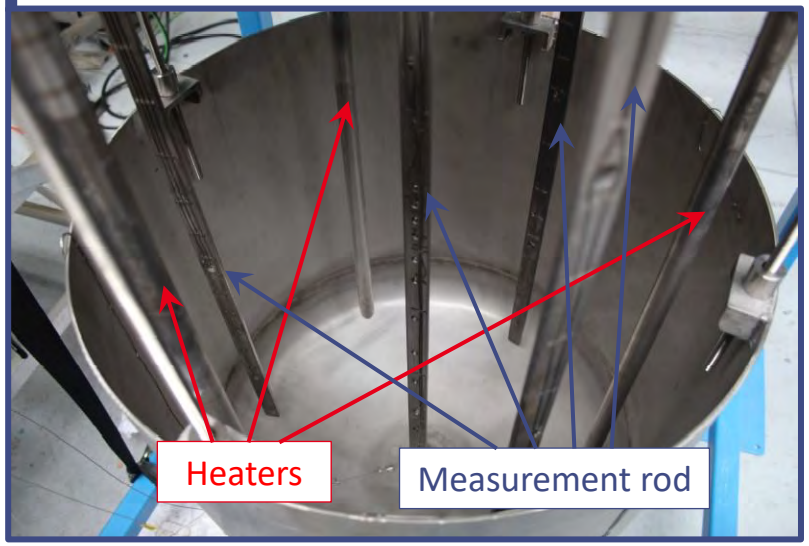

Fully assembled experimental pot during its transfer towards the DOLMEN facility

Na pool control: CFD study (OpenFoam)

3D calculation

- 1/3 test section
- Satisfactory agreement with experiment

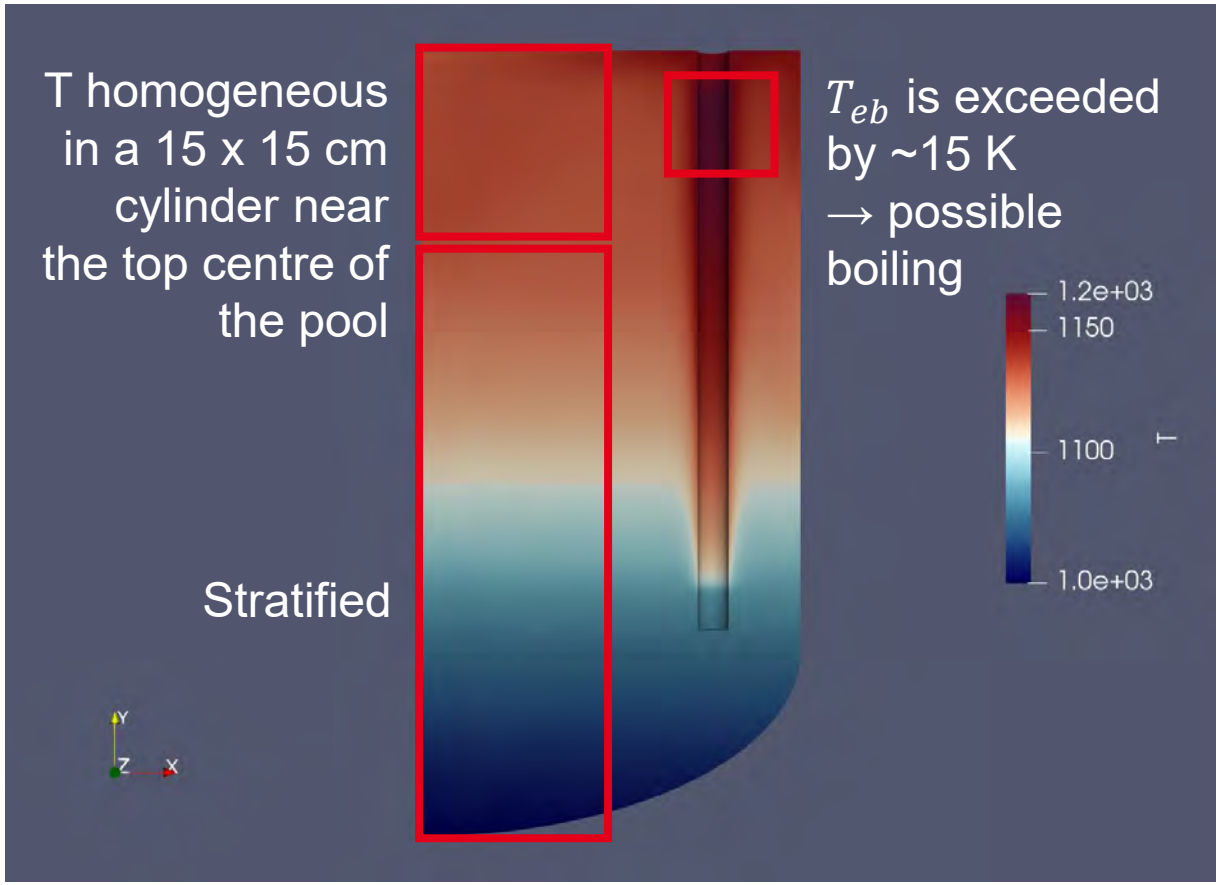

Open Foam model

- buoyantBoussinesqSimpleFoam solver (steady-state)
- Natural convection with turbulence model

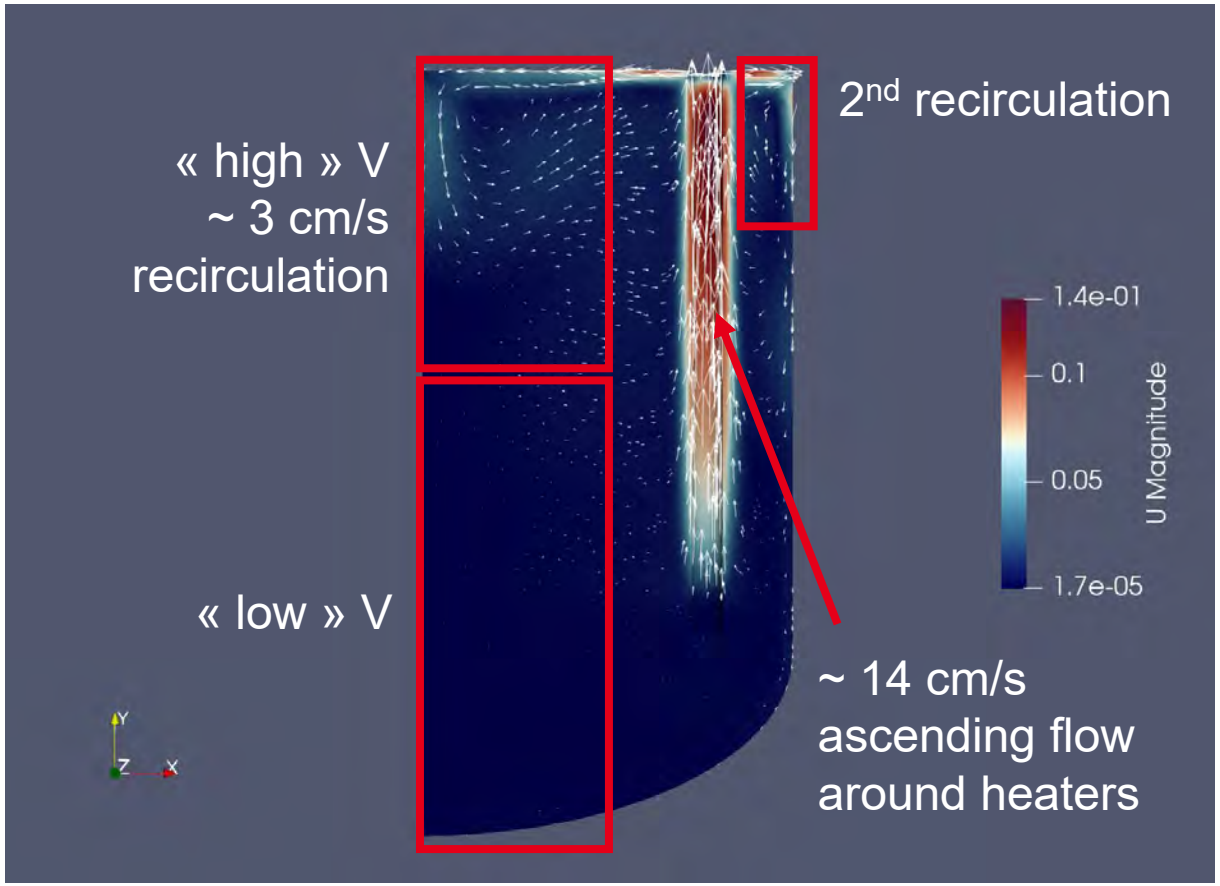

Sphere design and caracterisation: Initial surface temperature measurement and emissivity

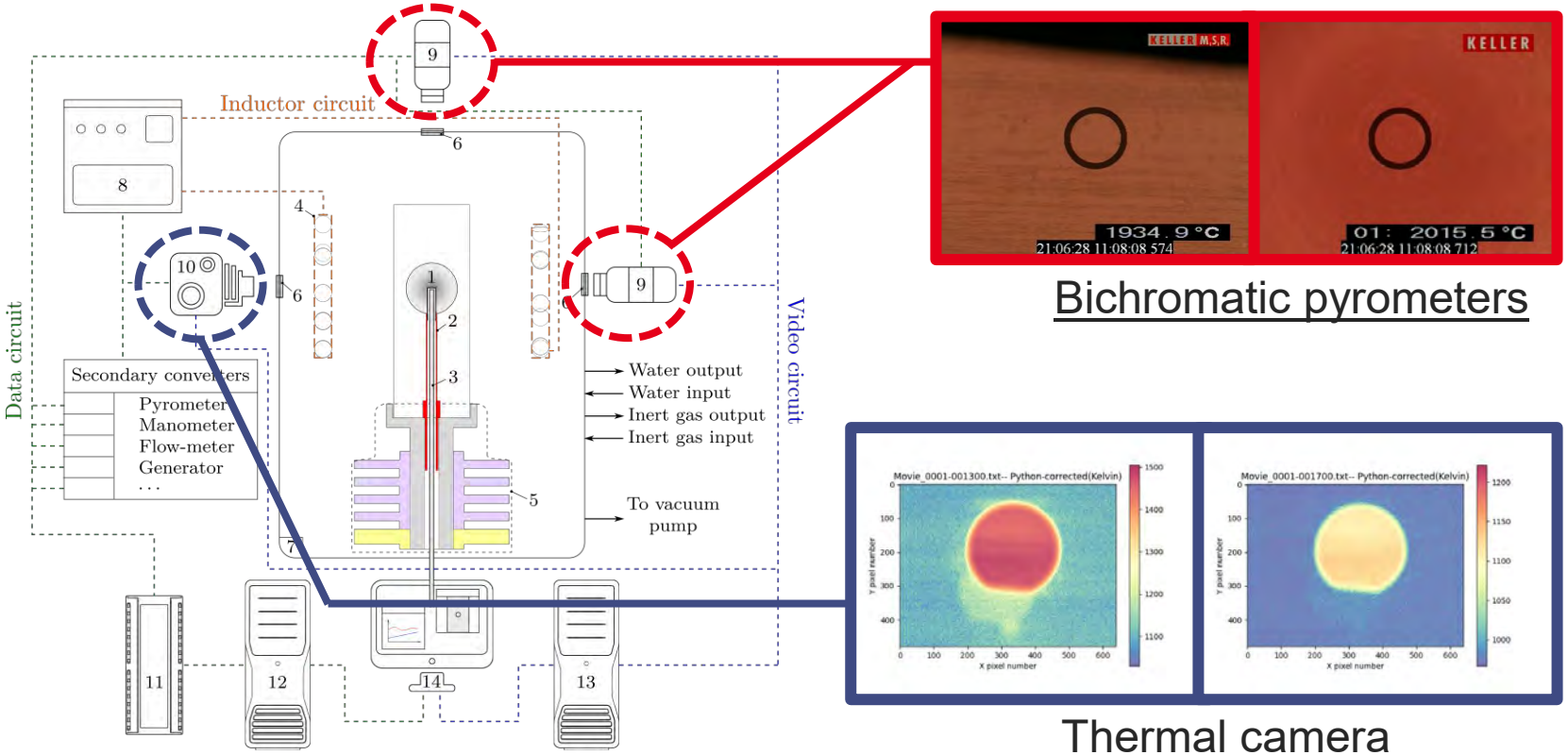

Bichromatic pyrometers

Thermal camera

Instrumentation used in VITI qualification tests

To be used in SERUA

The sphere emissivity is required:

- Pyrometers and thermal camera provide black-body temperatures → The sphere **spectral emissivity is needed** to correct black-body temperatures
- The sphere **total emissivity is needed** to interpret the SERUA experiments

Sphere design and caracterisation: Initial surface temperature measurement and emissivity

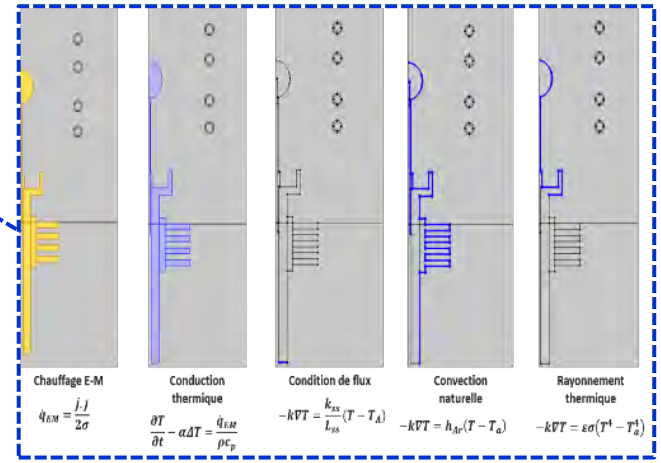

Experiment

Bichromatic Pyrometer → $T_{\lambda 1}, T_{\lambda 2}, T_c$

Emissivity leading to $T_{\lambda_1}^{cor} = T_{\lambda_2}^{cor} = T_c^{cor}$ → $\varepsilon_\lambda(T), T$

Experimental temperature at $\theta = 90°$

COMSOL model

(initial guess) $\varepsilon_\cap(T)$

$T(\theta)$ ← Solve T field

Calculated temperature at $\theta = 90°$

Comparison

Acceptable difference ?

YES → SERUA heating predictive model

NO → Correction of the total hemispheric emissivity law → $\varepsilon_\cap^{cor}(T)$

Sphere design and caracterisation: T measurement

Required output data

- Wall temperature T_W
- Wall heat flux density φ_W

Measurements → **Duplex TC**

- Temperature T_1 at $r = r_1$
- Temperature T_2 at $r = r_2$

→ Resolution of an **inverse problem**

Methodology (work in progress)

- Resolution of Fourier Equation in the Laplace space using temperature measurements T_1 and T_2
- Laplace inversion → T_W and φ_W

Schematic view of a Duplex TC

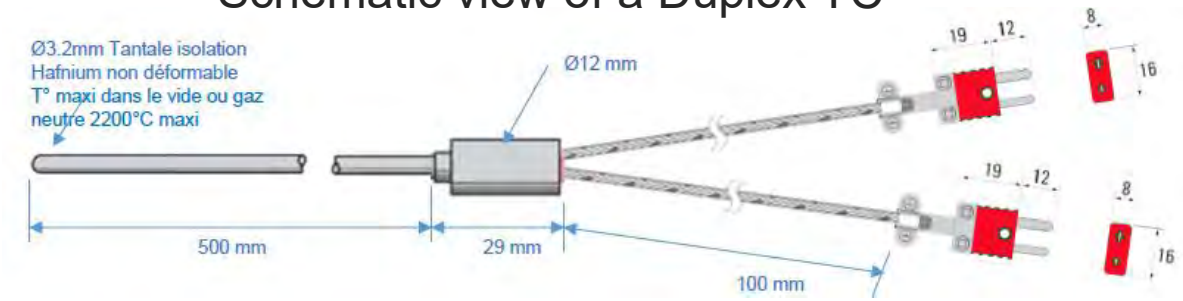

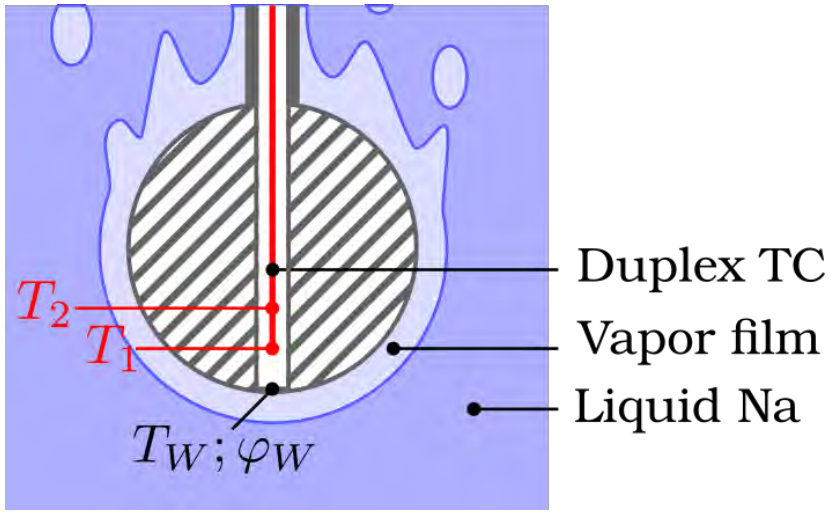

Conclusions

Objectives of the SERUA experiments:

- Characterisation of film boiling regimes in liquid sodium close to saturation
- Get a more precise insight compared to the reference experiments by Farahat in 1972
- Necessary input for Fuel-Coolant Interaction simulation codes (SCONE)

Perspectives

- Completion of the instrumentation of the sphere
- Device assembly and commissioning by the end of 2026
- First test in 2027

Technical issues and current status

- Sphere heating system (~2300 °C) → OK
- Na pool heating (~870 °C) and control
  - Stable heating at 860 °C → OK
  - Temperature homogeneity and velocity field investigated by CFD simulation
- Sphere design and characterization
  - Determination of the initial temperature by pyrometry → OK
  - Methodology for emissivity characterisation
  - Measurement interpretation for the determination of wall temperature and heat flux → On-progress

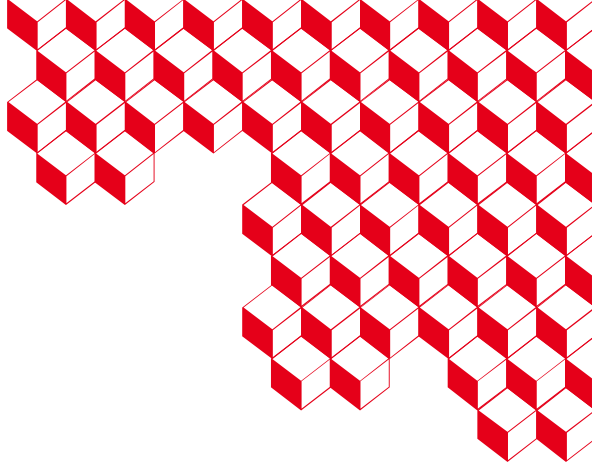

Thank you!

Rémi Clavier

Ingénieur-Chercheur

Laboratoire de Modélisation de Accidents Graves

CEA CADARACHE

13115 Saint Paul Lez Durance Cedex

France

remi.clavier@cea.fr

Tel. + 33 4 42 25 43 74

Appendix

Sphere design and caracterisation: Emissivity

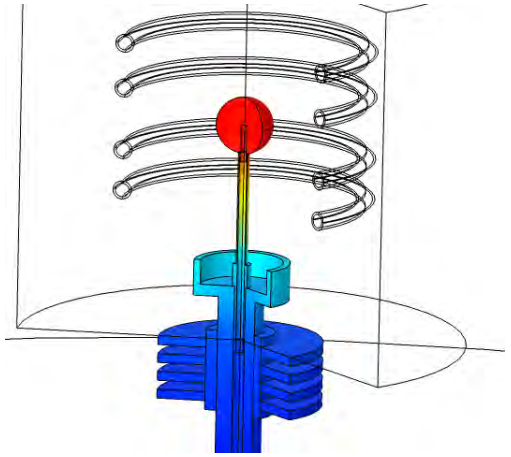

COMSOL model for the VITI configuration

- Tantalum sphere – central hole
- Tantalum tube
- Graphite support

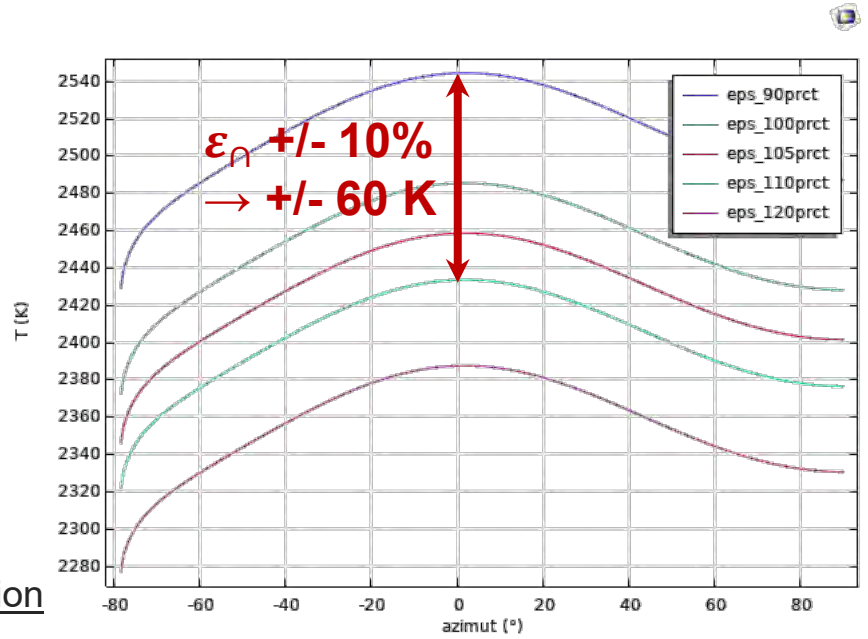

Sensitivity of the surface temperature to emissivity

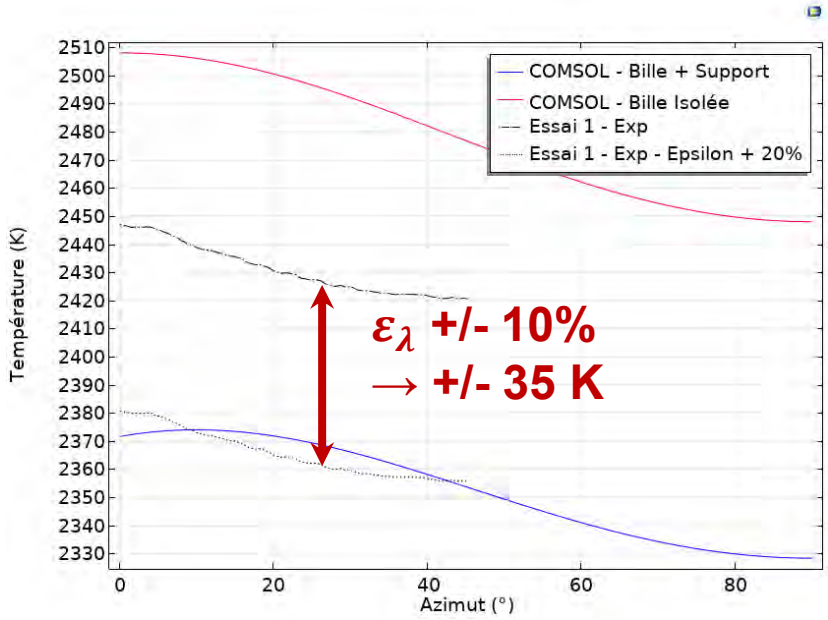

Sensitivity of the corrected black-body temperature to emissivity

On the importance of the spectral emissivity ε for pyrometry measurement interpretation

- **Significant sensitivity on ε** of both calculated and measured temperatures regarding the desired precision for SERUA
- **Significant uncertainty** on this parameter: at least 30%
- *In situ* characterisation is necessary → A **specific methodology** has been developed

Instrumentation and physical conditions

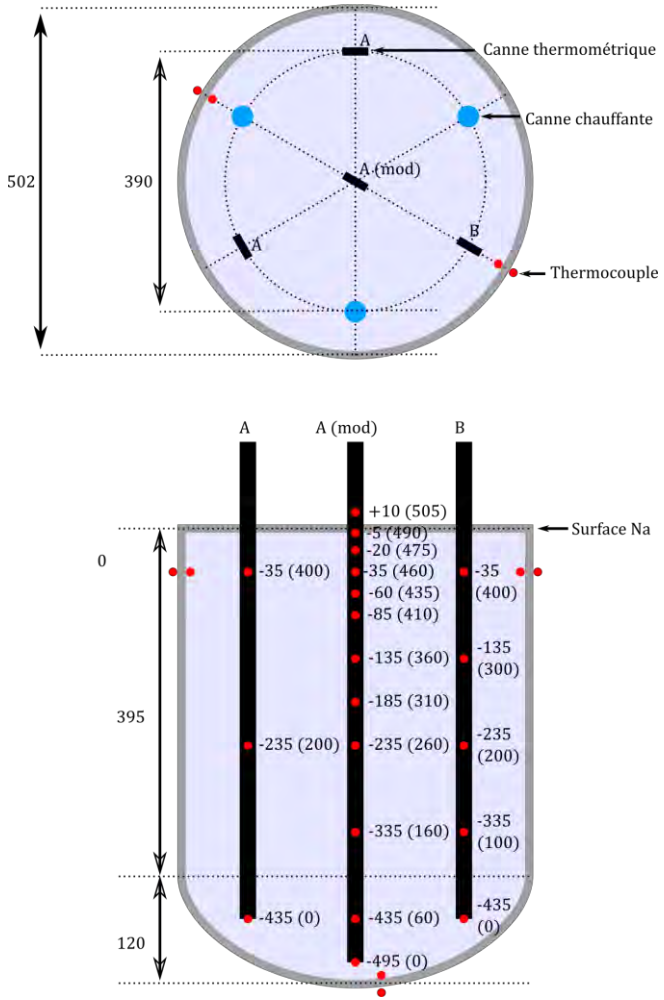

Heating:

- 3 heaters (4,9 kW each) regularly located in the pool

Instrumentation (thermocouples)

- 4 measurement rods (measure the temperature profile along the rod)
- Thermocouples on the experiment pot (internal / external)

Na physical properties	
ρ	744 kg.m^{-3}
β	3,40×10^{-4} K^{-1}
k	49,4 W.m^{-1}.K^{-1}
c_p	1280 J.kg^{-1}.K^{-1}
α	5,19×10^{-5} m^2.s^{-1}
μ	1,59×10^{-4} Pa.s
ν	2,14×10^{-7} m^2.s^{-1}

Turbulent natural convection in the liquid pool.

Turbulence around the heaters is characterized by the Grashof number:

$$Gr = \frac{g\beta\Delta T L^3}{\nu^2} = 5 \times 10^{10} > 10^9 \Rightarrow \text{Turbulent}$$

Prandtl number for sodium

$$Pr = \frac{\nu}{\alpha} = 4 \times 10^{-3} \ll 1$$

$$\Rightarrow \text{heat diffusion} \gg \text{momentum diffusion}$$

- **Need to check that the used turbulence model is adapted to low Pr numbers**

Physical conditions	
g	9,81 m.s^{-2}
β	3,40×10^{-4} K^{-1}
ΔT	~20 K
L	0,325 m

Boundary conditions and uncertainties

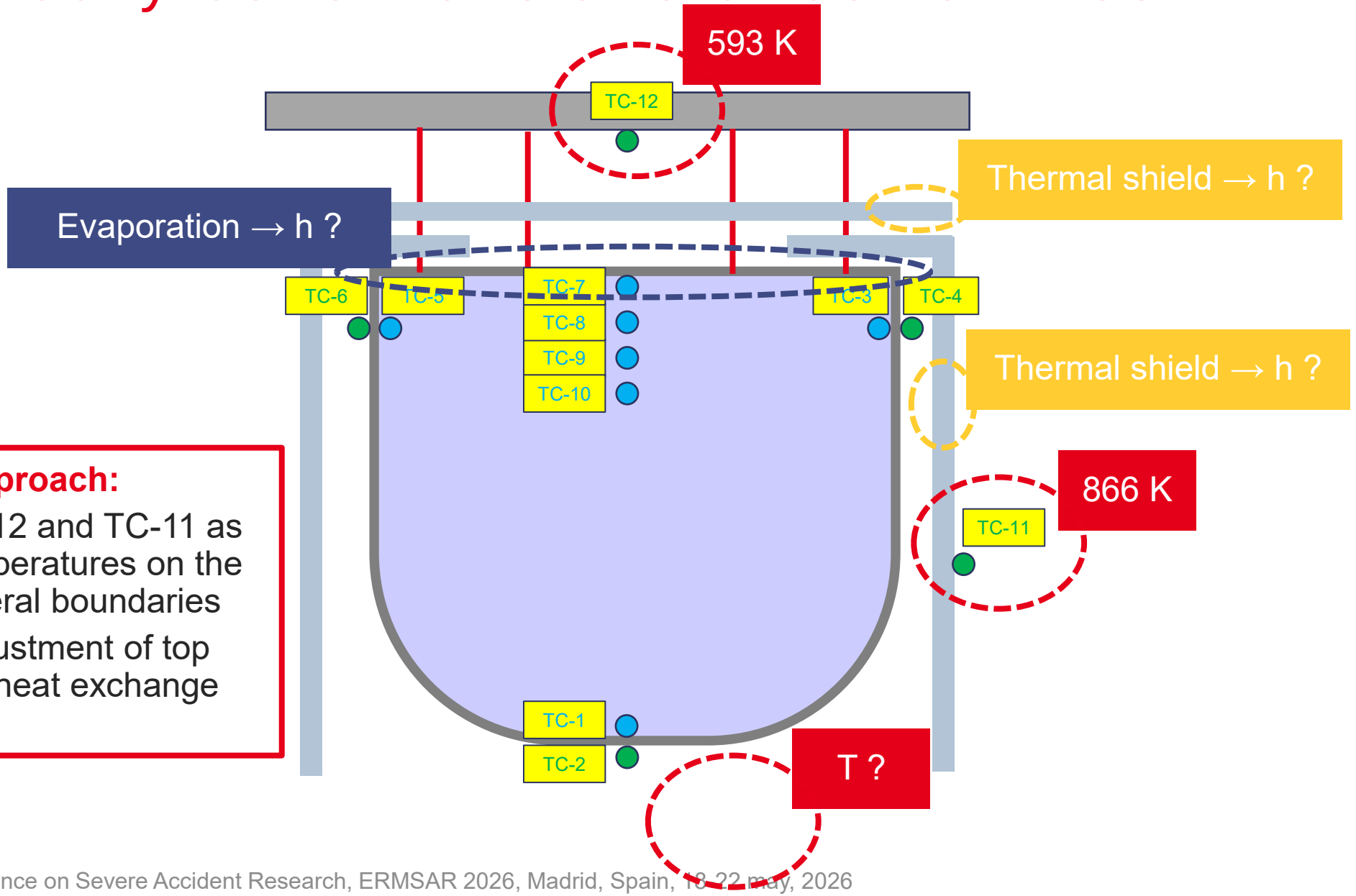

Modelling approach:

- Use of TC-12 and TC-11 as “room” temperatures on the top and lateral boundaries
- Manual adjustment of top and lateral heat exchange coefficients

Validation of turbulence models

Experiment by Betts et and Bokhari

- Imposed temperatures at both walls
- $Gr = 8.5 \times 10^5$
- $Pr = 0.704$

Geometry of the benchmark case:

- L = 76 mm
- H = 2.18 m
- D = 260 mm

Available data:

- Mean Temperature profiles
- Mean Vertical Velocity profiles

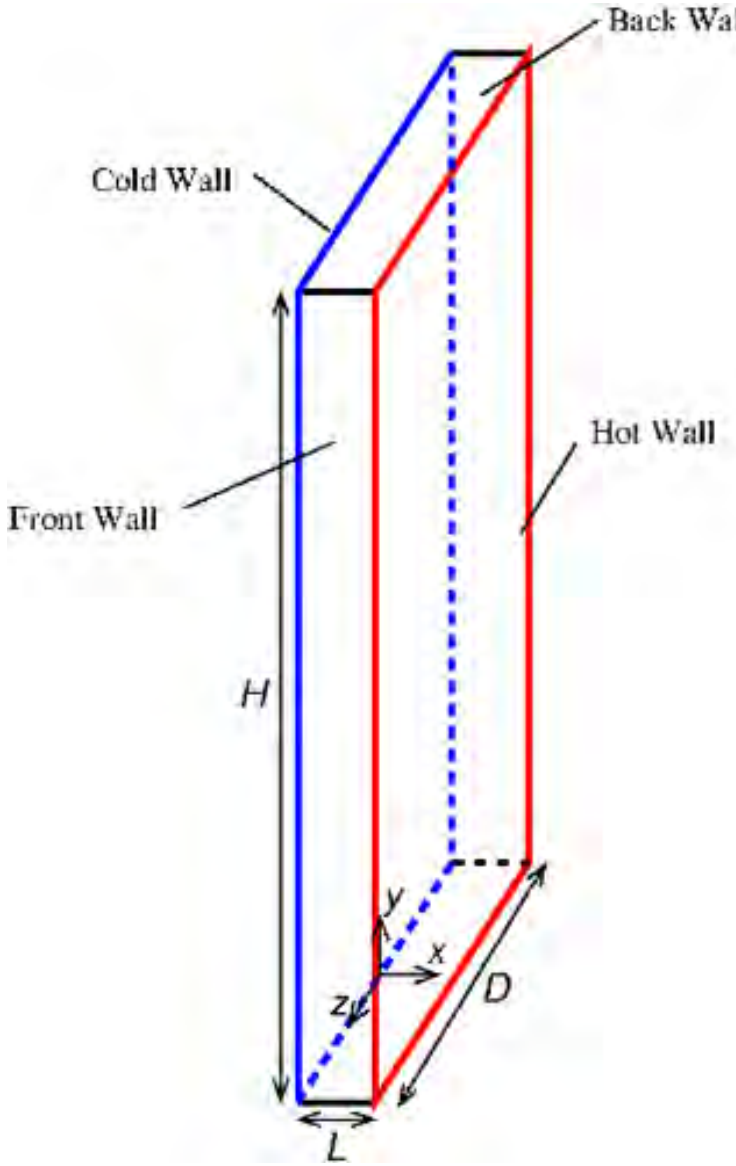

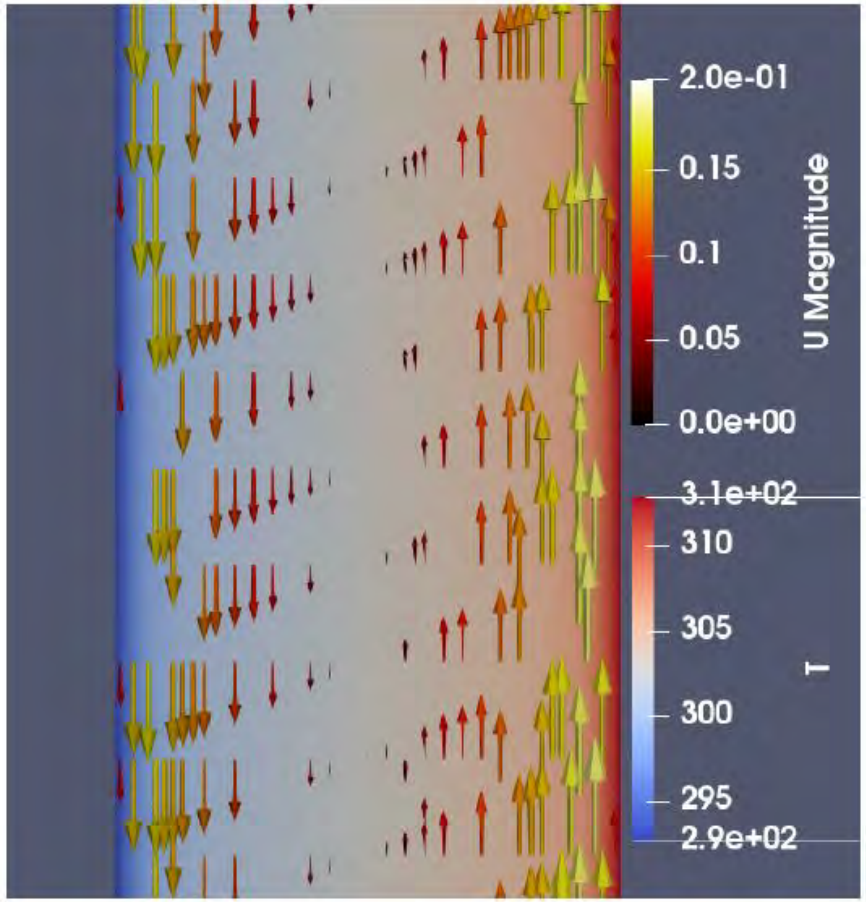

Validation of turbulence models

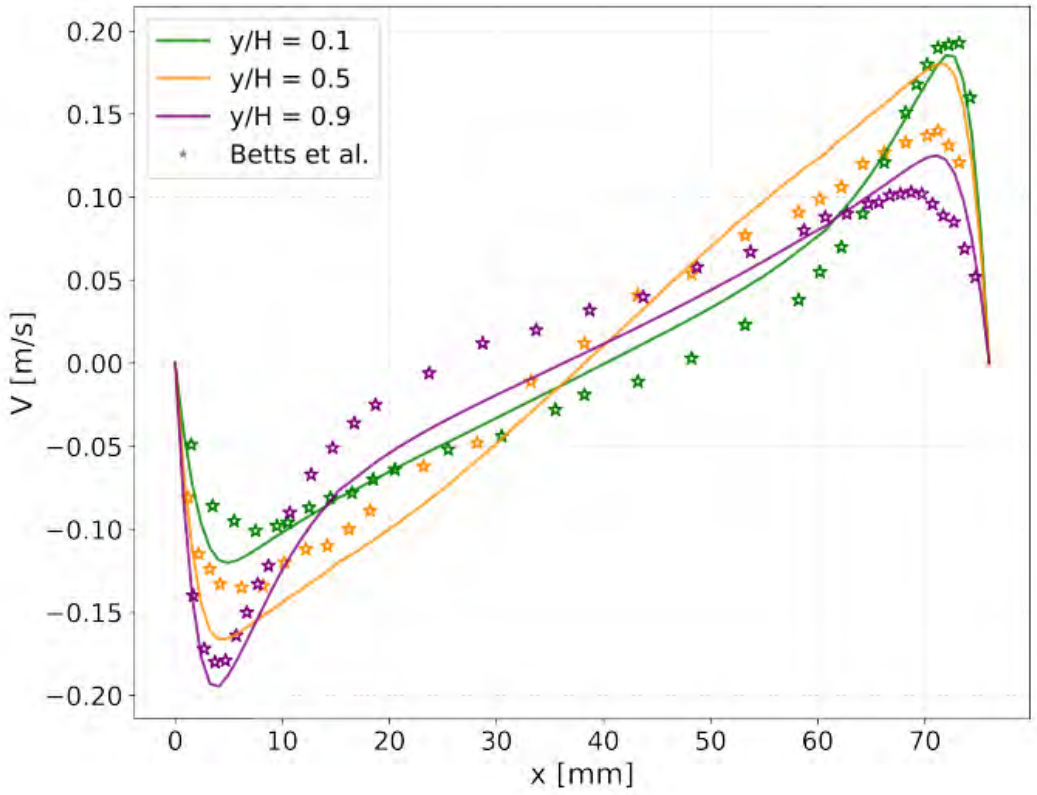

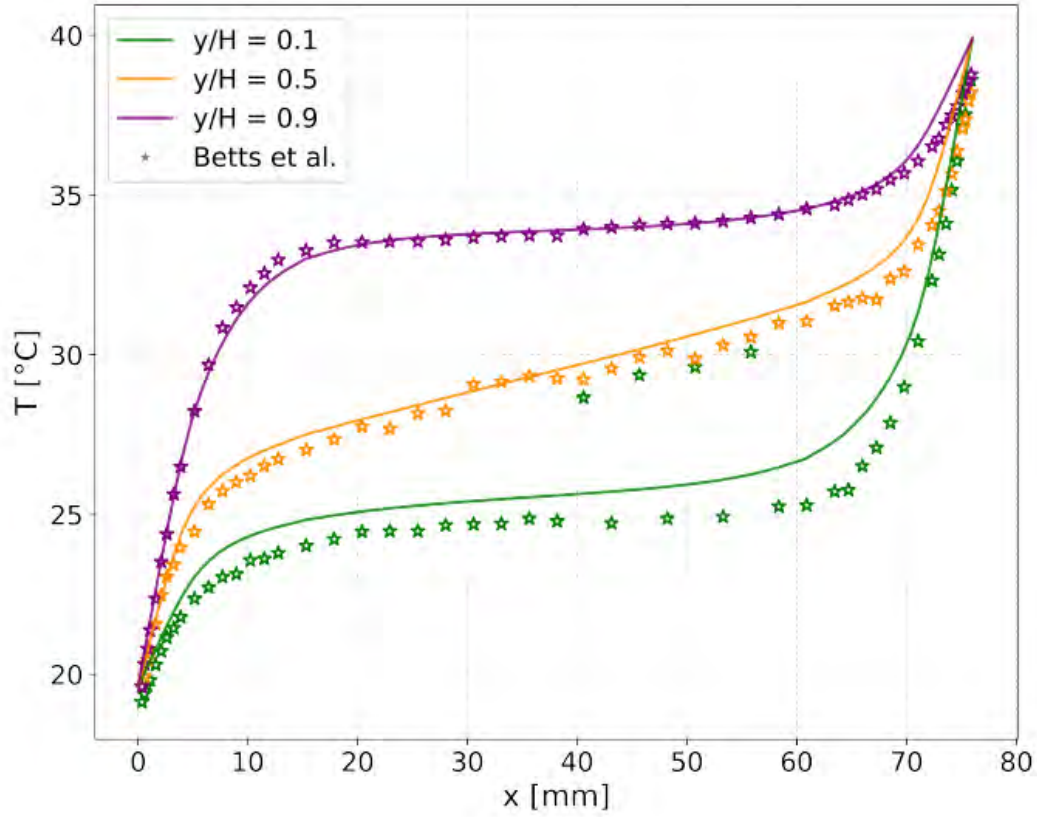

Good agreement between simulation and experimental data

Modelling approach

1/3 test section

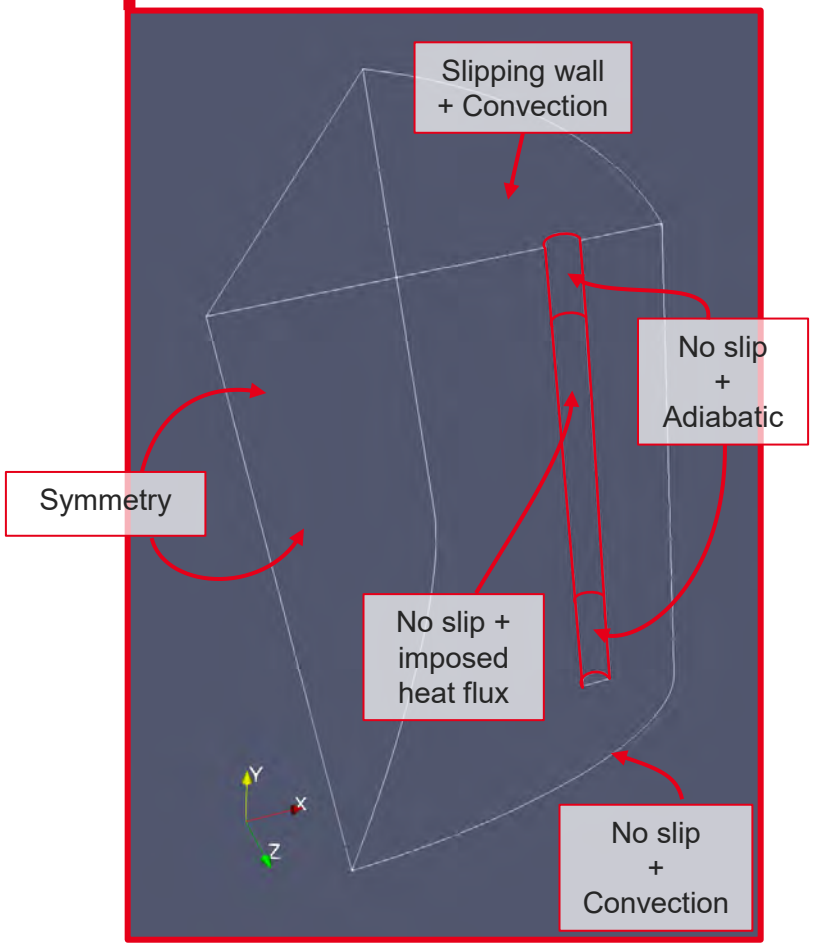

Open Foam model

- buoyantBoussinesqSimpleFoam solver
- Natural convection
- Steady-state
- Turbulence

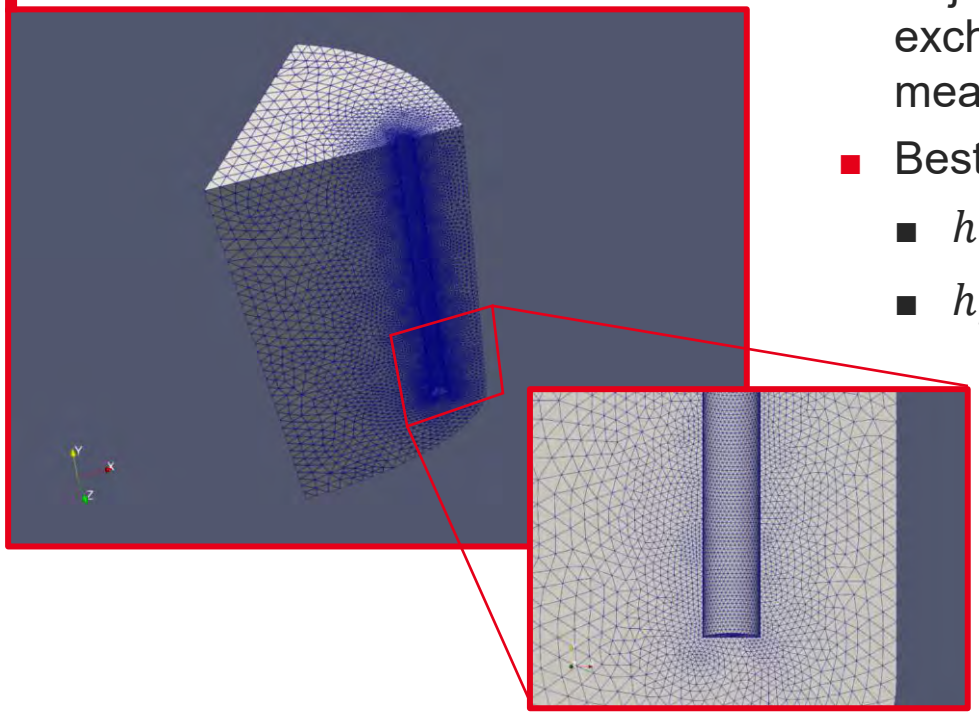

Method:

- Validation of turbulence models on similar experiments
- Modelling of the test section with adapted boundary conditions
- Adjustment of external heat exchange coefficients to match the measured temperature profiles
- Best-match values:
  - $h_{top} = 60\ W.m^{-2}.K^{-1}$
  - $h_{bottom} = 30\ W.m^{-2}.K^{-1}$

Results: Temperature profiles along the measurement rods (axis + outer region)

Results obtained for:

- $k - \omega$ turbulence model
- $h_{top} = 60\ W.m^{-2}.K^{-1}$
- $h_{bottom} = 30\ W.m^{-2}.K^{-1}$

Satisfactory agreeement between simulation and experiments

Observations:

- Heat exchange at the surface is not correctly reproduced → not surprising since the physics is not integrally reproduced (evaporation)
- Temperature underestimated by 10-15 K in the stratified zone → probably due to uncertainties in the boundary conditions

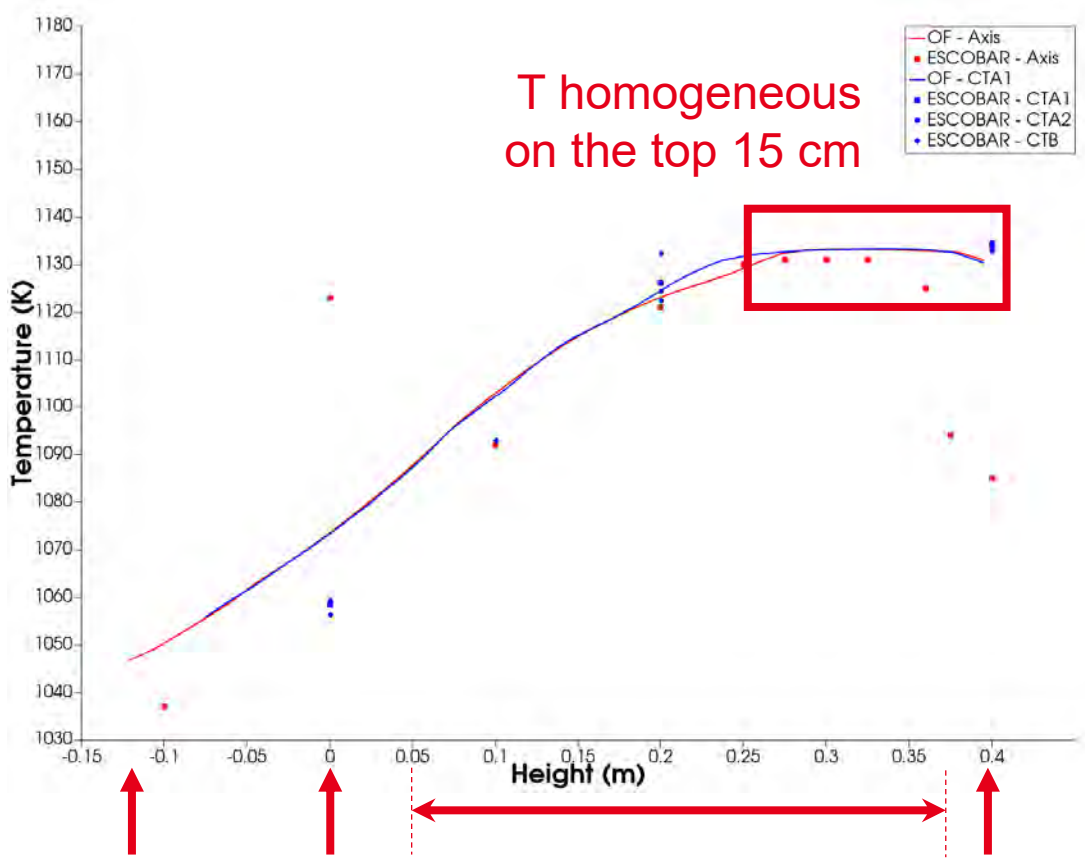

Results: Temperature radial profiles in the homogeneous region (top ~15 cm)

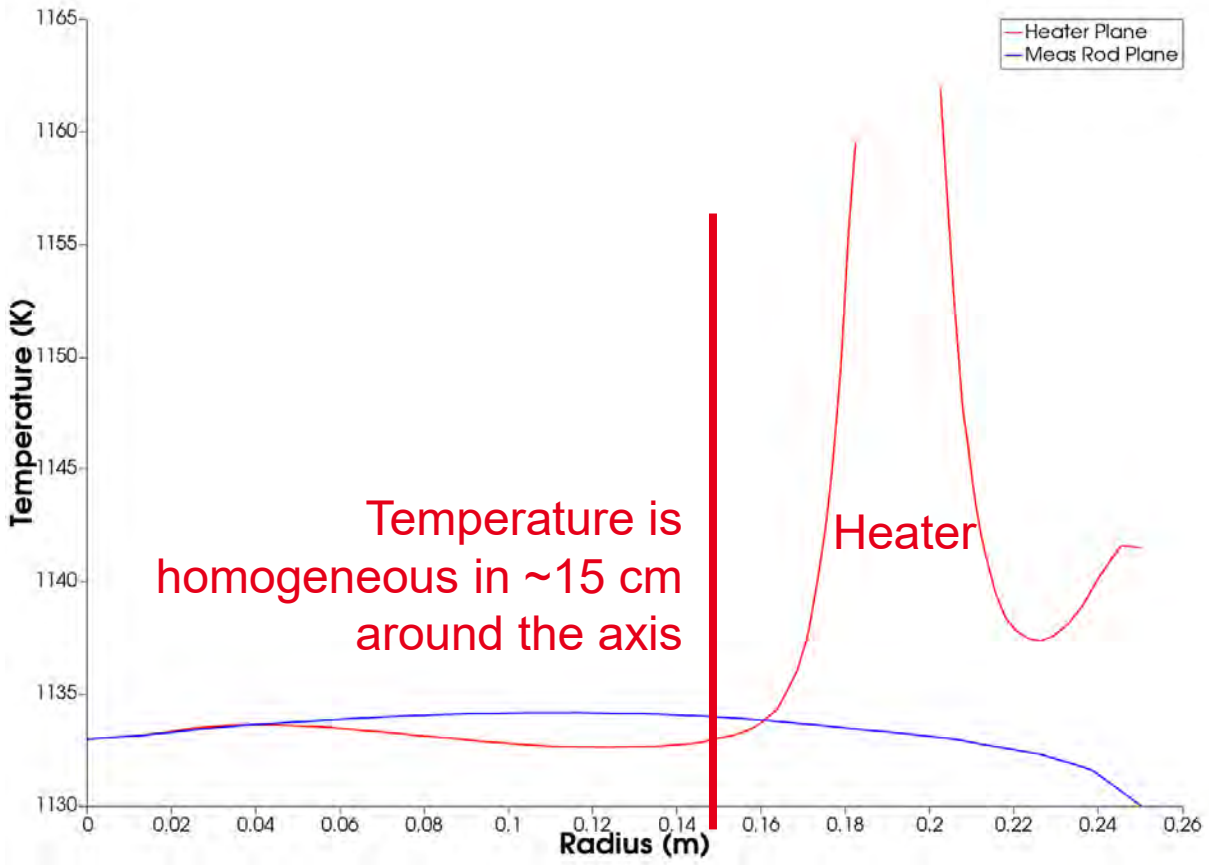

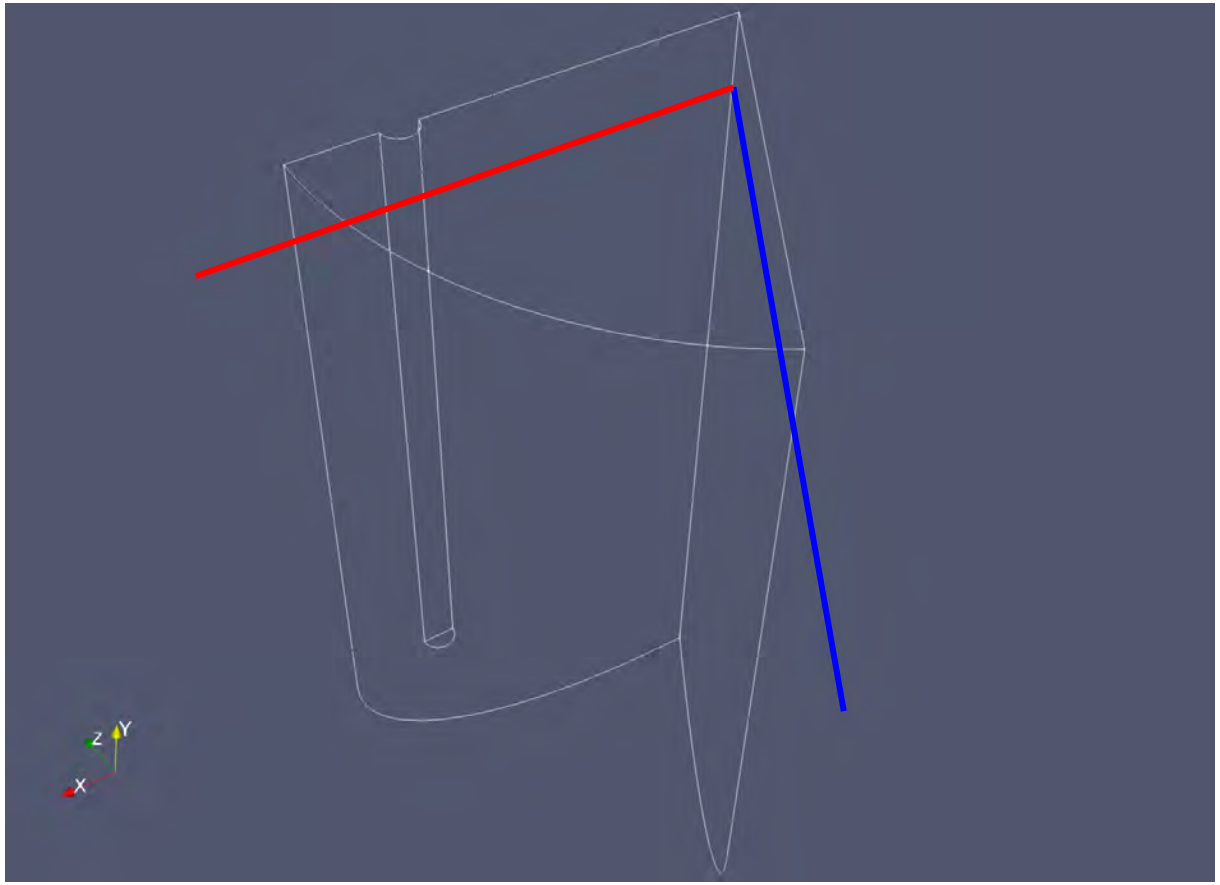

Results: Velocity profile along the axis

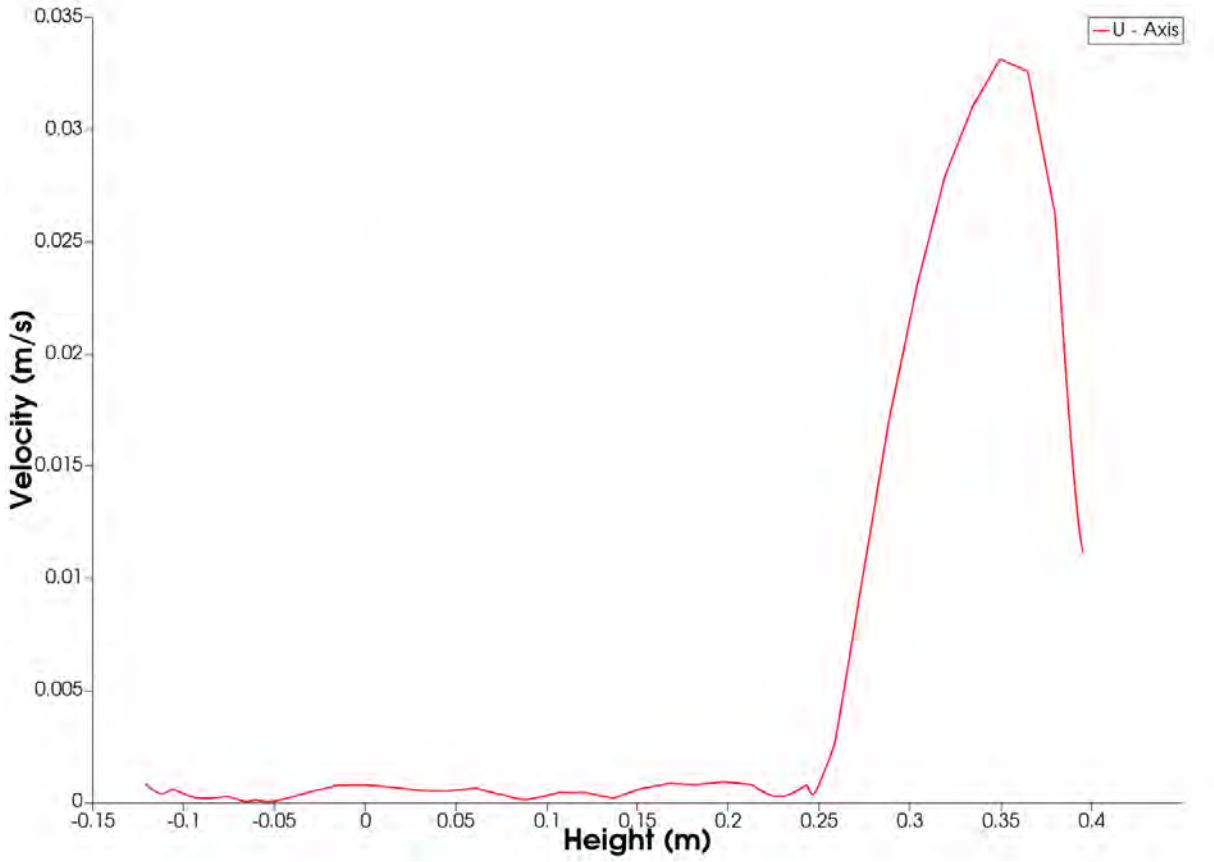

Significant velocity in the top ~15 cm under the sodium surface

Maximum velocity in this zone: ~3 cm/s

This order of magnitude represents a maximum estimate of the real velocity:

- Velocity is forced to be vertical by the symmetry boundary conditions
- In reality, the downards recirculation at the centre of the pool should move around the axis so the velocity on the axis should be more homogeneous around the axis (lower on the axis and higher near the axis)

It is pointless to try characterizing the effect of the flow velocity below ~50 cm/s with SERUA

Results: Temperature and velocity fields in the axis-heaters plane

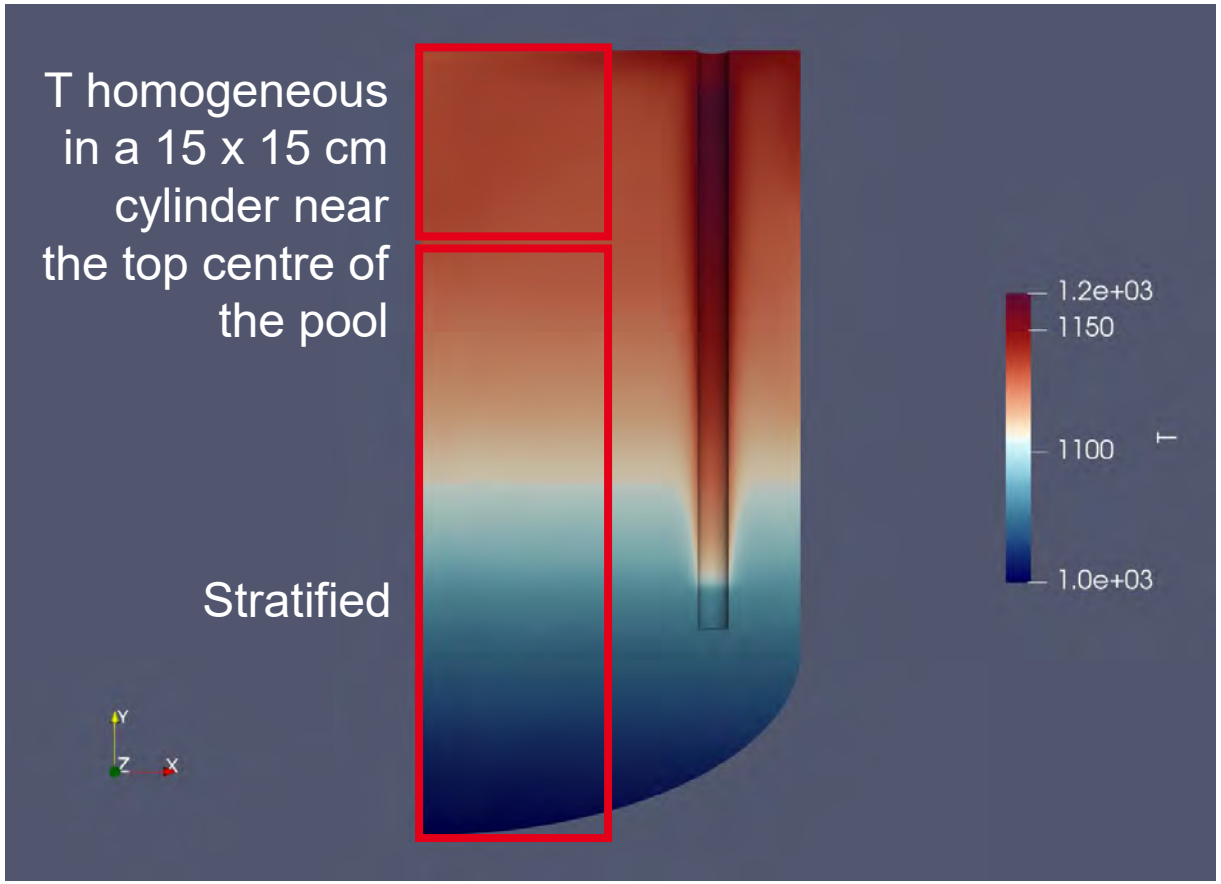

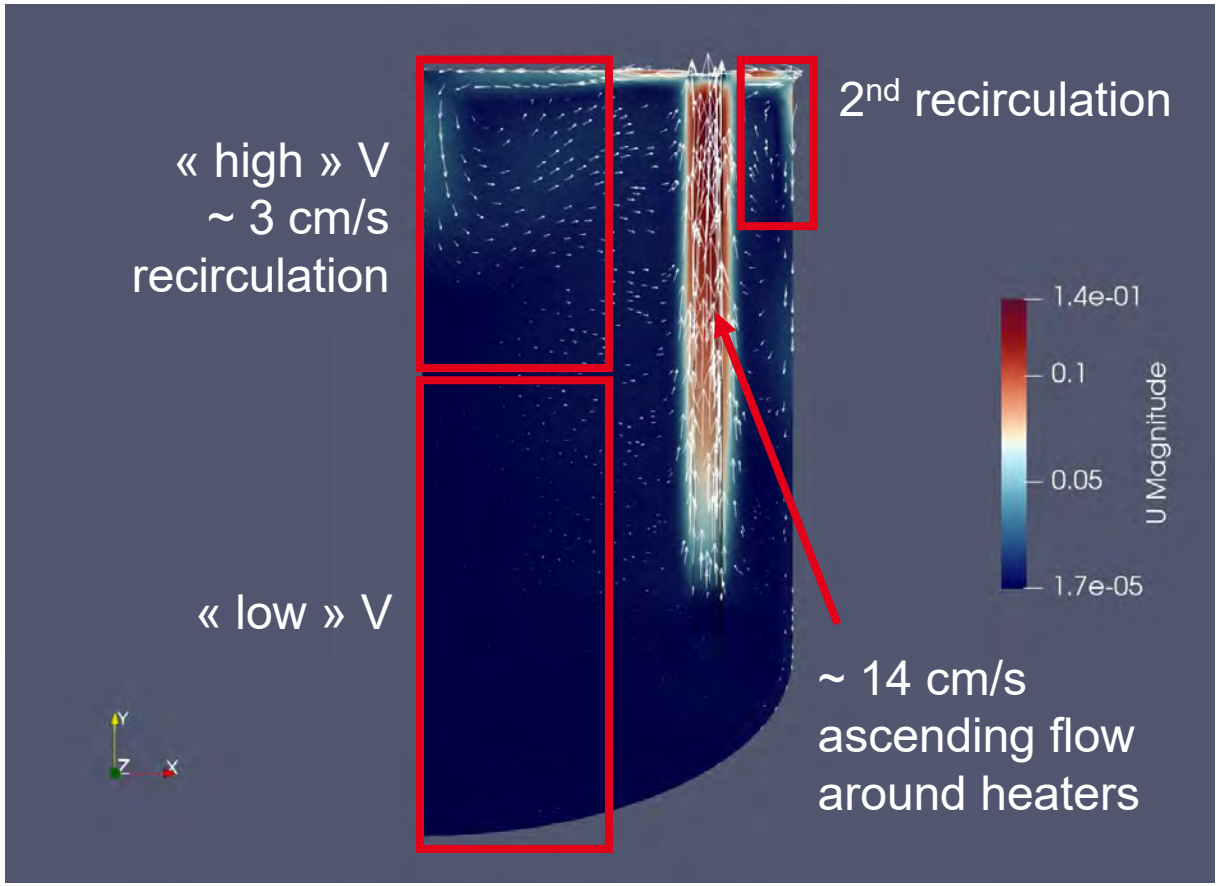

Results: Temperature and velocity fields at the top and lateral walls

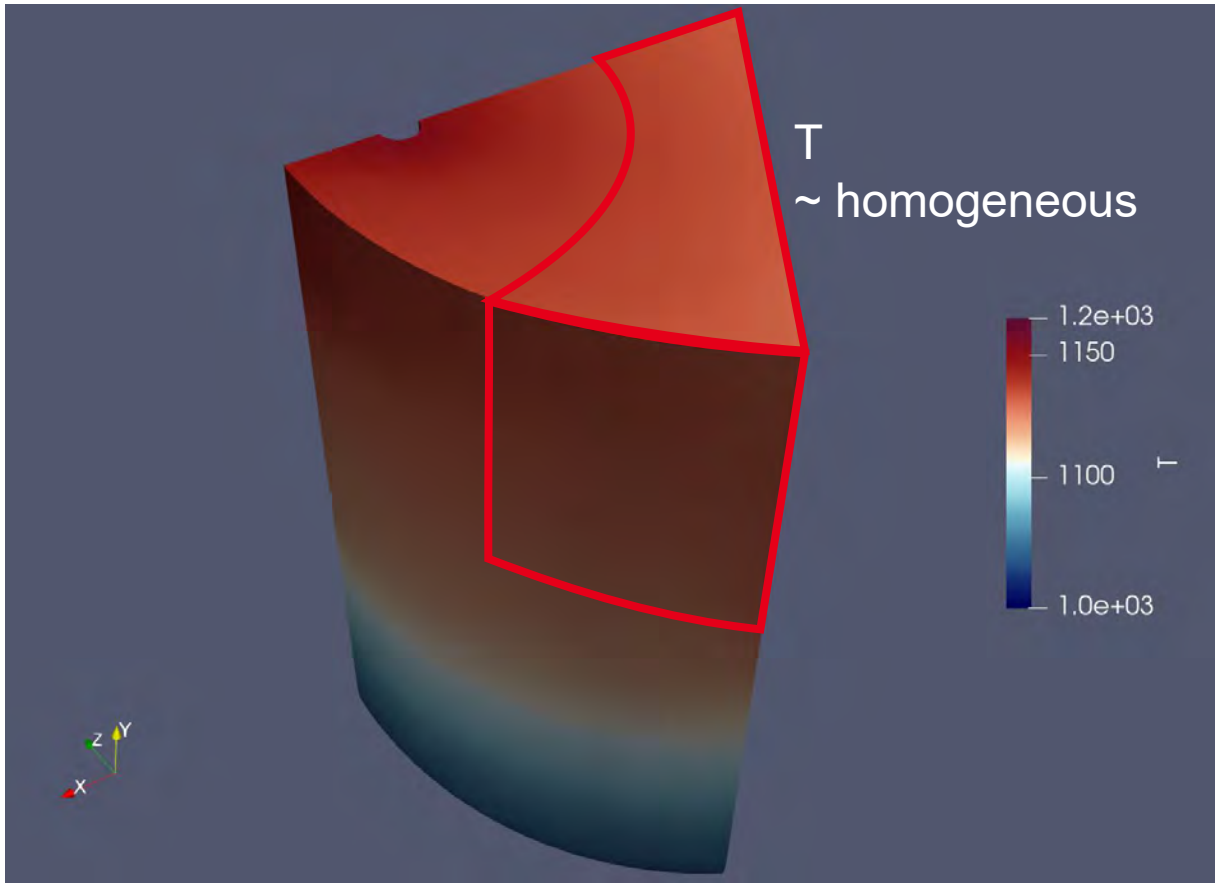

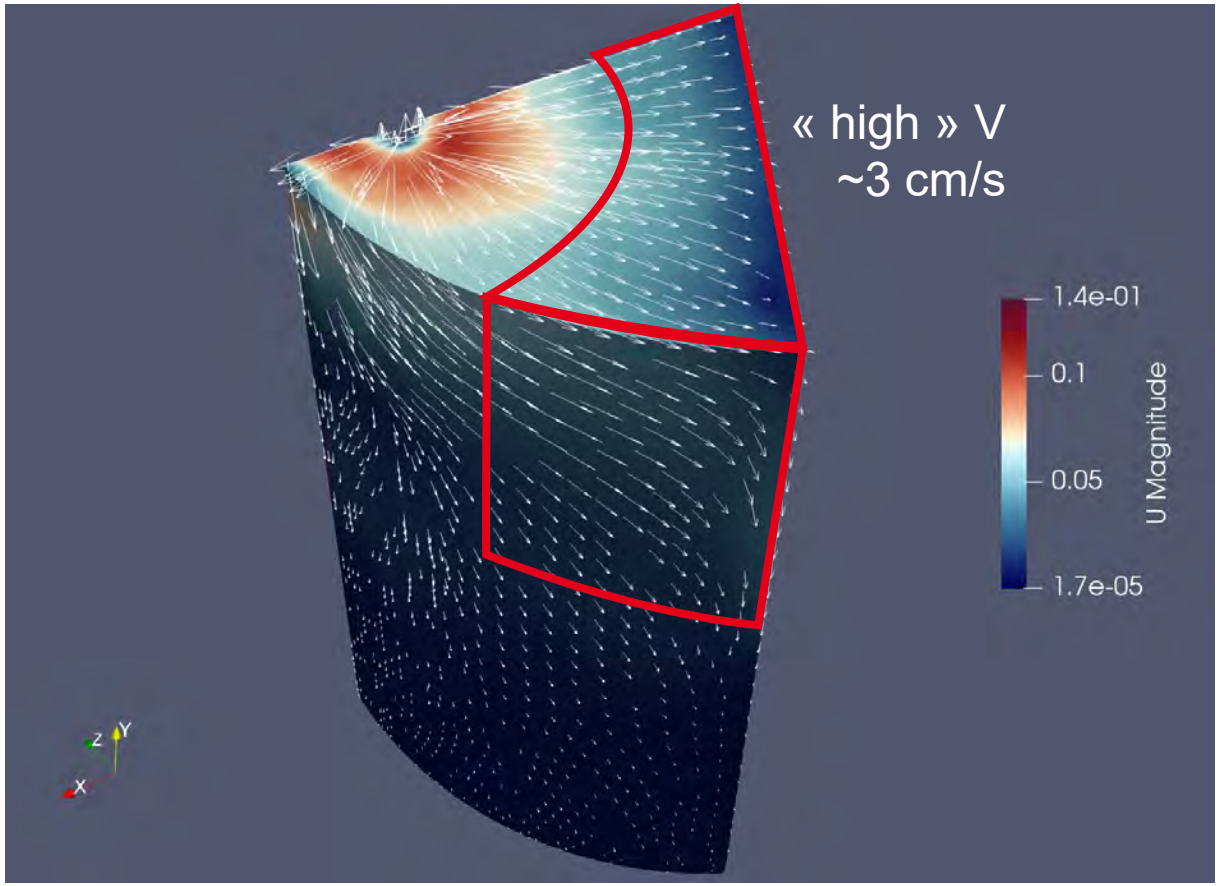

Results: Turbulence intensity in the axis-heaters plane

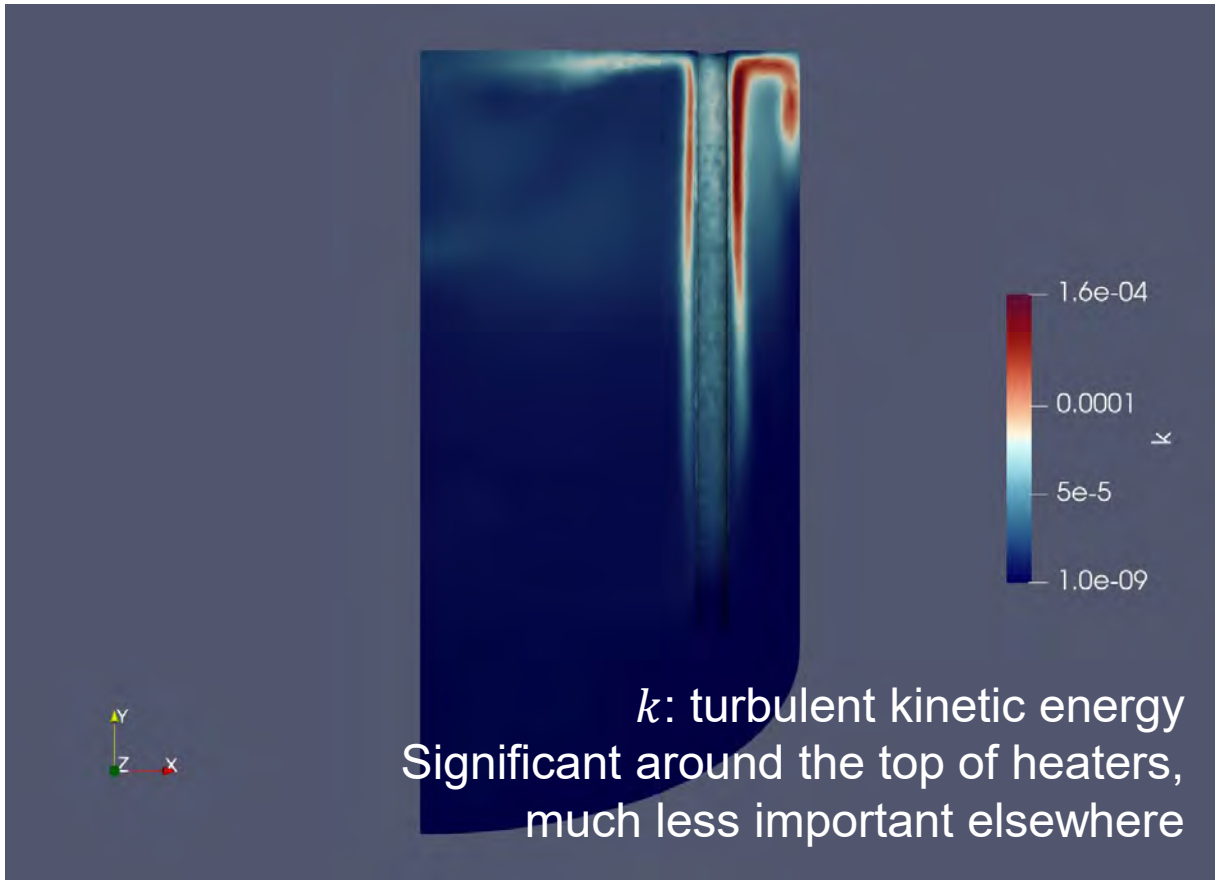

k: turbulent kinetic energy
Significant around the top of heaters, much less important elsewhere

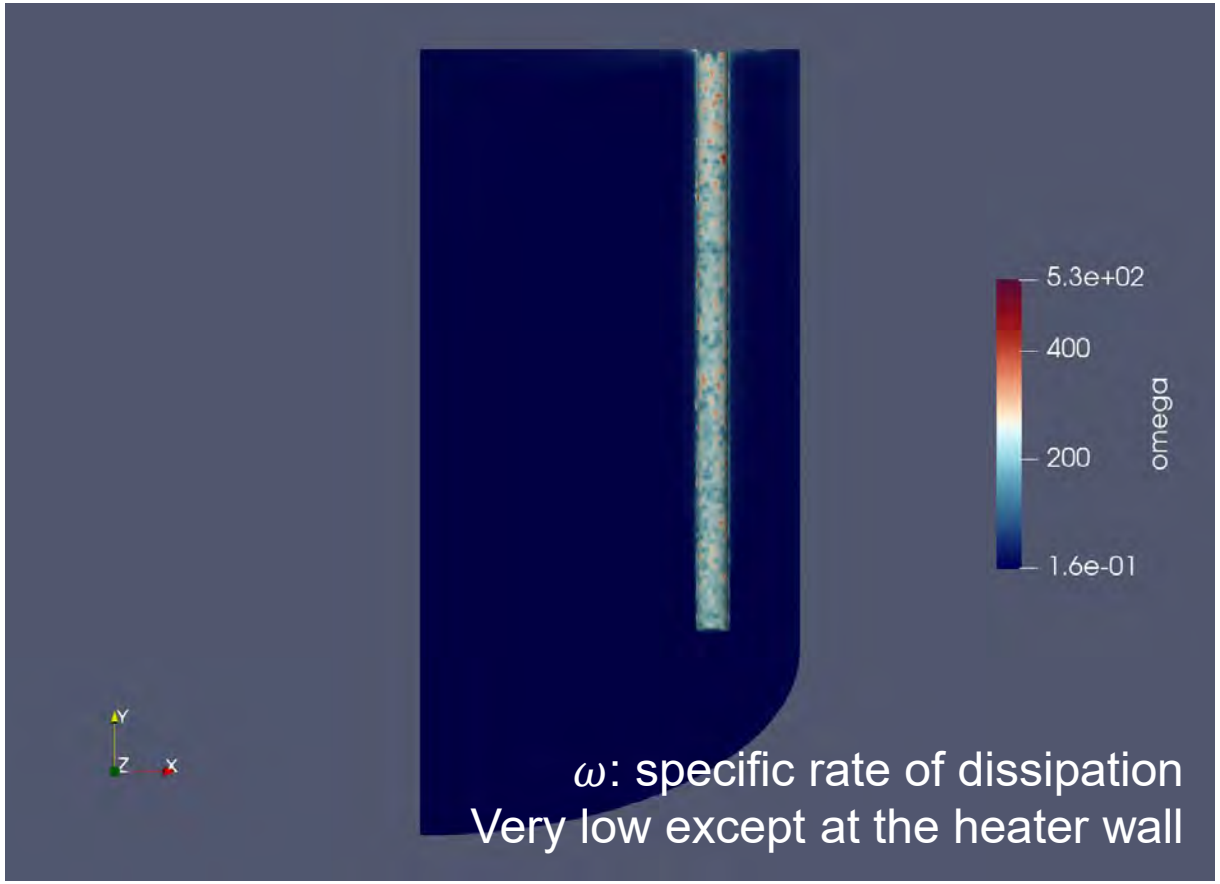

ω: specific rate of dissipation
Very low except at the heater wall

Results: Wall temperature along the heaters

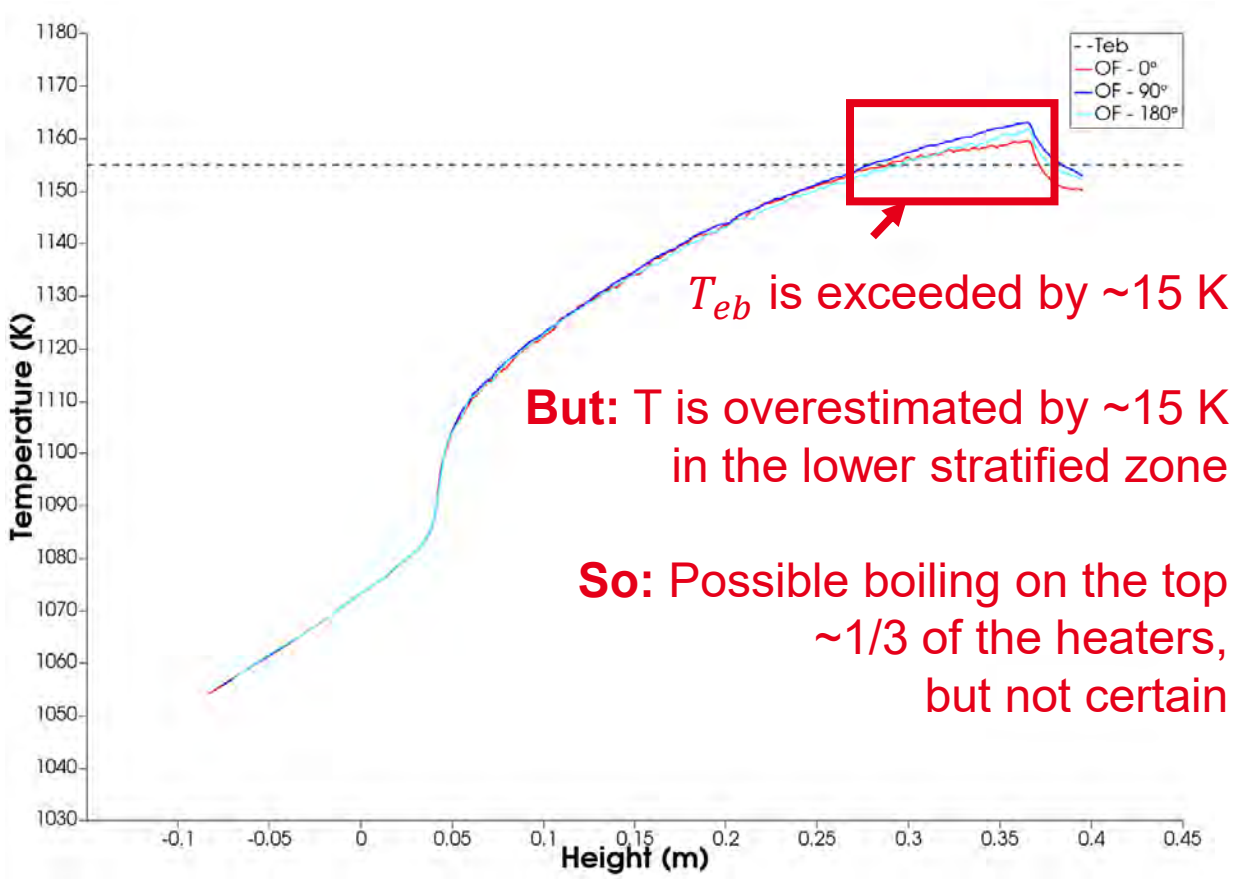

T_{eb} is exceeded by ~15 K

But: T is overestimated by ~15 K in the lower stratified zone

So: Possible boiling on the top ~1/3 of the heaters, but not certain

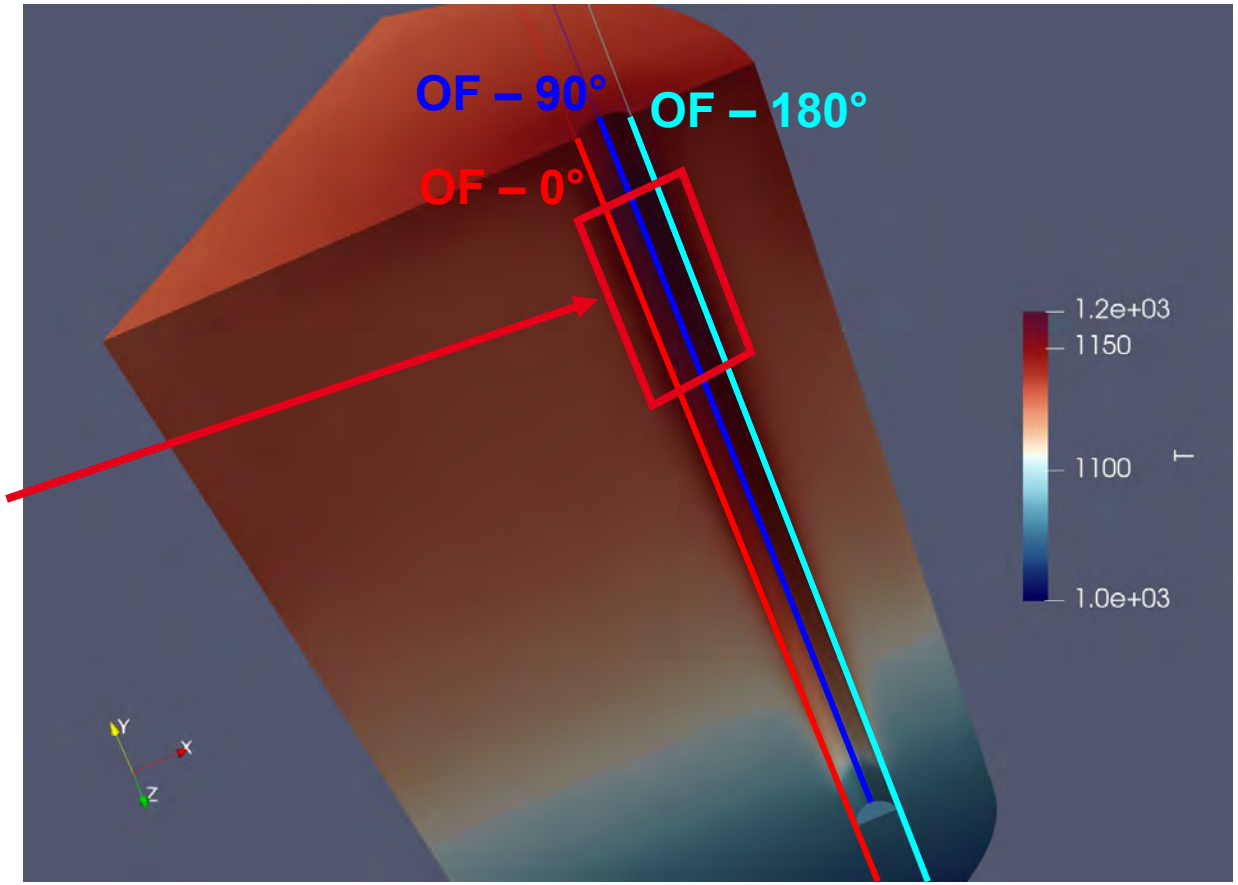

Experimental device assembly

Integration of all elements on DOLMEN:

- Induction furnace
  - Included into a protection vessel
  - Heating / sodium part separation valve
- Sphere suspension and transfer system
  - Velocity adaptation during transfer
    - Fast transfer from the furnace to the gas cover above the sodium pool
    - Slow velocity during the immersion of the sphere into the sodium
  - Adjustable immersion time

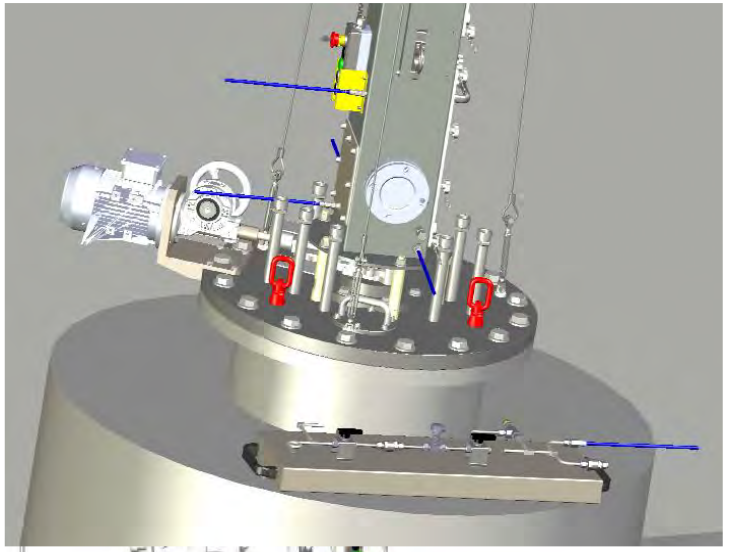

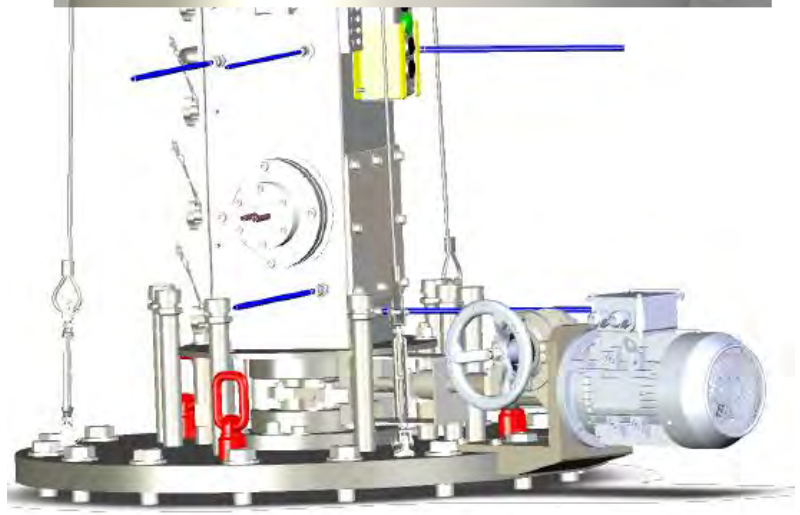

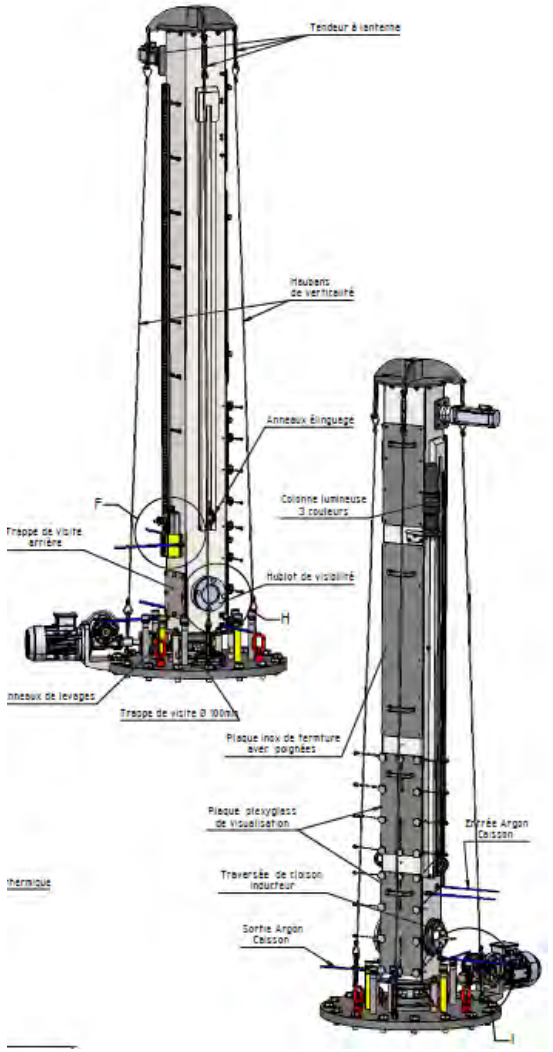

Benchmarking of Advanced GPU-Accelerated Discrete Element Method and Elastoplastic Constitutive Granular Flow Models for Large-Scale Debris Bed Formation in Severe Accidents of Sodium Fast Reactors

***Ryo Yokoyama, Yihua Xu, Tomonari Mashiko, Shuichiro Miwa, Koji Okamoto**
The University of Tokyo
Corresponding Address
yokoyama@vis.t.u-tokyo.ac.jp;

Maria Saussol
École Centrale de Marseille
Address
maria.saussol@centrale-marseille.fr

ABSTRACT

Ensuring the safety integrity of the core catcher system during a hypothetical core disruptive accident (CDA) in a sodium fast reactor (SFR) is essential, particularly with respect to debris bed formation. Because the expected debris size is less than 1.0 mm—owing to the rapid quenching of corium caused by the high thermal conductivity and high melting temperature of sodium—the number of particles accumulating on the core catcher is extremely large. This makes direct numerical simulation of debris bed formation computationally very demanding.

To address this challenge, we developed and compared two advanced simulation approaches for SFR applications: a GPU-accelerated fully explicit discrete element method coupled with moving particle hydrodynamics (DEM–MPH), and elastoplastic constitutive model based granular flow simulation method (MPH-Granular). The DEM–MPH method is a fully meshless approach in which the debris phase is modeled using a spring–dashpot interaction, while the fluid phase is solved by MPH with a weakly compressible formulation. In contrast, elastoplastic constitutive granular flow model solves the bulk behavior of the granular materials without solving individual discrete particle to avoid computing massive particle numbers.

Validation was carried out against debris bed formation experiments performed in China. Both methods successfully reproduced sedimentation and dispersion trends depending on particle size. DEM–MPH offered more robust predictions of solid behavior; however, its application to full 3D simulations was constrained by the high computational cost. Conversely, MPH-based granular flow model efficiently handled larger-scale problems owing to its continuum formulation, although it exhibited reduced accuracy in describing the compression of sedimented particles. Overall, DEM–MPH provides higher fidelity at smaller scales, while MPH-Granular would ensure scalability, highlighting a complementary relationship between the two approaches.

KEYWORDS
Severe accident, debris bed, SFR, DEM, SPH

* **Ryo Yokoyama, The University of Tokyo (yokoyama@vis.t.u-tokyo.ac.jp)**

1. INTRODUCTION

Lessons learned from the Fukushima Daiichi Nuclear Power Plant (1F NPP) accident highlighted the critical importance of retaining corium—consisting of molten fuel and in-core structural materials—inside the reactor vessel. Preventing its relocation beyond the vessel and maintaining it in a controllable state is essential to substantially reduce the risk associated with the loss of core inventory. For Generation IV reactors, particularly sodium-cooled fast reactors (SFRs), core catcher systems are therefore being considered to efficiently cool the relocated core debris and mitigate the risk of re-criticality. During a postulated core disruptive accident, corium may be released into the surrounding sodium. Owing to the high boiling point and high thermal conductivity of sodium, the contact interface between corium and sodium can remain a liquid–liquid interface without the formation of a stable vapor film, which has a much lower heat transfer coefficient of the film boiling. As a result of the rapid quenching, fragmentation of the corium is expected due to the generation of the mechanical energy, and the characteristic debris particle size is estimated to be on the order of 0.1–1.0 mm [1]. these fragmented debris would pile up over the core-catcher. In order to ensure the integrity of the core-catcher system, understanding the debris bed formation over the core-catcher system is crucial. Although many experiments have been performed by the various organizations to clarify the effect of the particle size [2,3], particle characteristics, and the dimension, the numerical simulation is one of the promising approaches to deepen our knowledge as the simulation offers the insight that we cannot measure or visualize.

For the debris bed formation analysis, the most well-known approach is the discrete element method (DEM) in which Newton's second law is applied and each collision and damping are modeled with the spring-dashpot model together with the friction slider [4]. As the DEM approach is quite straightforward and can reproduce the complicated granular flow behavior, DEM can be also applied to the nuclear engineering [5]. However, the DEM has several difficulties to apply to the practical nuclear scale analysis. First, DEM typically resolves particles at or near their actual size, so modeling very small particles across meter-scale domains becomes computationally prohibitive. Second, neighbor searching—essential for contact detection—scales as $O(N^2)$ in its basic form, making large-scale simulations costly. Third, strong polydispersity in particle size and shape introduces additional difficulties. Size variation complicates neighbor-search algorithms which is initially designed for uniform radii, while non-spherical particles require orientation-dependent contact detection and specialized force models to correctly simulate its impulse.

In order to address these issues, we propose two numerical simulation methods. The first is a discrete element method (DEM) coupled with Moving Particle Hydrodynamics (MPH) [6], which is a fully explicit algorithm parallelized on graphics processing units (GPUs) to handle an enormous number of particles that would be almost impossible to treat with conventional Central Processing Units (CPUs)-based simulations. The second is a bulk granular-flow simulation method incorporating an elastic–perfectly plastic Drucker–Prager constitutive law (namely MPH-Granular) [7], which reduces the computational burden by avoiding the need to resolve individual particle–particle collisions. Moreover, this method does not need to consider the heterogeneity of the debris shape and the size distribution. In this paper, we present benchmark simulations to demonstrate and validate these two approaches.

2. Mathematical Formulation of all approaches [6,7]

In this sentence, the mathematical formulation of DEM, MPH, and MPH-Granular flow simulation and their discretization are presented.

2.1. Discrete Element Method (DEM)

The governing equation of DEM is Newton's second law which consists of translation motion equation

$$m\frac{\mathrm{D}\mathbf{u}}{\mathrm{Dt}} = \overrightarrow{\mathrm{F_g}} + \overrightarrow{\mathrm{F_{nc}}} + \overrightarrow{\mathrm{F_{tc}}}, \tag{1}$$

and the rotational motion equation

$$\frac{\mathrm{D}\boldsymbol{\omega}}{\mathrm{D}t} = \mathrm{I}^{-1}\mathrm{T}, \tag{2}$$

respectively. Here, m, $\mathbf{u}$, I, T, $\overrightarrow{F_g}$, $\overrightarrow{F_{nc}}$, $\overrightarrow{F_{dc}}$, and $\boldsymbol{\omega}$ denote the mass of particle, velocity vector, inertial tensor, torque, gravitational force, normal direction force, tangential direction force, and angular velocity vector, respectively. For the contacting force, spring-dashpot model is applied. Fig.1 illustrates the schematic of the spring-dashpot model. The normal direction force is calculated as

$$\overrightarrow{\mathrm{F_{nc}}} = -K_{n,ij}X_n\boldsymbol{n_{ij}} - \eta_{n,ij}\mathbf{u}_{\boldsymbol{n,ij}}, \tag{3}$$

where K, X, $\boldsymbol{n}$, $\boldsymbol{u}$, and η render the spring constant, displacement, unit vector, relative velocity vector, and damping constant, respectively. Subscript n, i and j represent the normal direction, particle i and particle j. For the translational motion force, we need to take the frictional effect into consideration. If the tangential force is greater than the maximum friction coefficient, the following formula is given as:

$$\overrightarrow{F_{tc}} = \begin{cases} -K_{t,ij}\mathrm{X}_t - \eta_{t,ij}\mathbf{u}_{\boldsymbol{t,ij}} & \left(\overrightarrow{F_{tc}} \le \mu\left|\overrightarrow{F_{nc}}\right|\right) \\ \varphi\left|\overrightarrow{F_{nc}}\right|\dfrac{\mathbf{u}_{\boldsymbol{t,ij}}}{\left|\mathbf{u}_{\boldsymbol{t,ij}}\right|} & \left(\overrightarrow{F_{tc}} > \mu\left|\overrightarrow{F_{nc}}\right|\right) \end{cases}, \tag{4}$$

where φ is the viscous friction coefficient. The subscript t denotes the tangential direction. The spring constant and viscous damping constant for each direction are calculated with Herltz theorem and Mindlin contact theorem [8,9].

The spring constant and the damping constant for the normal direction are calculated as

$$K_{ij}^n = \frac{4}{3}\frac{E_iE_j}{\left(1-\nu_i^2\right)E_j + (1-\nu^2)E_i}\sqrt{\frac{R_iR_j}{R_i+R_j}\sqrt{\delta}}, \tag{5}$$

and

$$\eta_{ij}^n = -\frac{2\ln e}{\sqrt{\pi^2 + (\ln e)^2}}\sqrt{\frac{m_im_j}{m_i+m_j}K_{ij}^n}, \tag{6}$$

where E, ν, e, and δ are Young modulus, Poisson ratio, attenuation coefficient, and effective overlap distance. Similarly, the spring constant and the damping constant for the tangential direction are computed as

$$K_{ij}^t = \frac{8E_iE_j}{(1+\nu_i)(2-\nu_i)E_j + \left(1+\nu_j\right)\left(2-\nu_j\right)E_i}\sqrt{\frac{R_iR_j}{R_i+R_j}\sqrt{\delta}}, \tag{7}$$

$$\eta_{ij}^t = -\frac{2\ln e}{\sqrt{\pi^2 + (\ln e)^2}}\sqrt{\frac{m_im_j}{\mathrm{m}_i+m_j}K_{ij}^t}. \tag{8}$$

2.2. Moving Particle Hydrodynamics for weakly compressible flow and elastic–perfectly plastic Drucker–Prager constitutive law

2.2.1. Particle Interaction models for the discretization

In the present study, the governing equations are discretized using particle interaction models—namely, the gradient, divergence, and Laplacian operators—evaluated with a particle-based weight (kernel) function. The particle interaction models are given as follows:

$$\nabla\phi = \sum_{i\neq j}\left(\phi_j - \phi_i\right)\mathbf{e}_{ij}w'_{ij}\,, \tag{9}$$

$$\nabla\cdot\mathbf{A} = \sum_{i\neq j}\left(\mathbf{A}_j + \mathbf{A}_i\right)\cdot\mathbf{e}_{ij}w'_{ij}\,, \tag{10}$$

$$\nabla^2\phi = 2\sum_{i\neq j}\frac{\left(\phi_j - \phi_i\right)}{\left|r_{ij}\right|}w'_{ij}\,, \tag{11}$$

where the terms ϕ, $\boldsymbol{A}$, and $\mathbf{e}_{ij}$ are an arbitrary scalar parameter, an arbitrary vector and the unit vector from particle *i* to *j*, which is defined as

$$\mathbf{e}_{ij} = \frac{r_{ij}}{\left|r_{ij}\right|}, \tag{12}$$

where $\boldsymbol{r}_{ij}$ is the relative velocity between particle *i* and *j*.

The term w'_{ij} represents the derivative of the normalized weight function w_{ij}, which are defined as:

$$w_{ij} = w\left(\left|r_{ij}\right|\right), \tag{13}$$

$$w(r) = \begin{cases}\dfrac{1}{S_f}\dfrac{1}{r_e^{dim}}\left(1-\dfrac{r}{r_e}\right)^2 & (r\le r_e)\\ 0 & (r > r_e)\end{cases}, \tag{14}$$

$$S_f = \frac{1}{l^{dim}}\int_{r<r_e}\frac{1}{r_e^{dim}}\left(1-\frac{r}{r_e}\right)^2 dv\,, \tag{15}$$

and

$$w'_{ij} = -\frac{\partial w(r)}{\partial r}, \tag{16}$$

where w, r_e, and *l* denote that the weight function, the effective radius of the particle *i*, and the particle diameter, respectively

2.2.2 Weakly compressible flow model and its discretization

The governing equation of the weakly compressible fluid is consisting of momentum equation

$$\rho_0\frac{\mathrm{D}\mathbf{u}}{\mathrm{Dt}} = -\nabla\mathrm{P} + \mu\nabla^2\mathbf{u} + \rho_0\mathbf{g}, \tag{17}$$

and pressure equation for incompressible control

$$\mathrm{P} = -\lambda\nabla\cdot\mathbf{u} + \kappa\frac{\Delta\rho}{\rho_0}, \tag{18}$$

where ρ_0, $\mathbf{u}$, P , μ, $\mathbf{g}$, λ, and κ, correspond to the density, pressure, dynamic viscosity, gravity acceleratio n, bulk viscosity, and bulk modulus, respectively. The governing equations (Eqs. (18)-(20)) are discretized with the particle interaction models (Eqs.(21) and (23)) as

$$\rho_0\frac{\mathrm{D}\mathbf{u}}{\mathrm{Dt}} = -\sum_j\left(\mathrm{P}_j + \mathrm{P}_i\right)\frac{\boldsymbol{r}_{ij}}{\left|\boldsymbol{r}_{ij}\right|}w'_{ij} + 2\mu\sum_j\left(\mathbf{u}_j - \mathbf{u}_i\right)\frac{w'_{ij}}{\left|\boldsymbol{r}_{ij}\right|} + \rho_0\mathbf{g}, \tag{19}$$

$$\mathrm{P} = -\lambda\sum_j\left(\mathbf{u}_j - \mathbf{u}_i\right)\cdot\frac{\boldsymbol{r}_{ij}}{\left|\boldsymbol{r}_{ij}\right|}w'_{ij} + \kappa(n_i - n_0). \tag{20}$$

Finally, the position of the fluid is updated as

$$\mathbf{x}^{(k+1)} = \mathbf{x}^k + \mathbf{u}^{(k+1)}Dt. \tag{21}$$

2.2.3 MPH-Granular: Hyper elastoplastic constitutive law for the granular material

The governing equation of the hyper elastoplastic constitutive law is mass conservation

$$\frac{D\rho}{Dt} + \rho\nabla\cdot\mathbf{u} = 0, \tag{22}$$

and momentum conservation

$$\frac{D\mathbf{u}}{D\mathrm{t}} = \frac{1}{\rho}\nabla\cdot\boldsymbol{\sigma} + \mathbf{g}. \tag{23}$$

Here $\boldsymbol{\sigma}$ is the stress tensor. In order to handle the large deformation of the granular flow, time derivative of $\boldsymbol{\sigma}$ with the Jaumann stress tensor can be expressed as:

$$\dot{\boldsymbol{\sigma}} = \dot{\boldsymbol{\omega}}\boldsymbol{\sigma} - \boldsymbol{\sigma}\dot{\boldsymbol{\omega}} + \lambda_e tr(\dot{\boldsymbol{\varepsilon}}_e)\boldsymbol{I} + 2\mu_e\dot{\boldsymbol{\varepsilon}}_e, \tag{24}$$

$$\dot{\boldsymbol{\varepsilon}}_e = \dot{\boldsymbol{\varepsilon}} - \dot{\boldsymbol{\varepsilon}}_p, \tag{25}$$

$$\dot{\boldsymbol{\varepsilon}} = \frac{1}{2}(\nabla\mathbf{u} + (\nabla\mathbf{u})^T), \tag{26}$$

$$\dot{\boldsymbol{\omega}} = \frac{1}{2}(\nabla\mathbf{u} - (\nabla\mathbf{u})^T), \tag{27}$$

Lames constants λ_e and μ_e are defined as

$$\lambda_e = \frac{E\nu}{(1+\nu)(1-2\nu)}, \tag{28}$$

$$\mu_e = \frac{E}{2(1+\nu)}, \tag{29}$$

where E and ν stand for the Young's modulus and Poisson's ratio, respectively. The plastic strain rate is estimated from the following plastic flow rule:

$$\dot{\boldsymbol{\varepsilon}}_p = \dot{\lambda}\frac{\partial \mathrm{g}_p}{\partial\boldsymbol{\sigma}}, \tag{30}$$

where g_p is the plastic potential function. $\dot{\lambda}$ is the rate of change of the plastic multiplier, which are defined as

$$\mathrm{g}_p = \sqrt{3J_2} - \alpha_\psi p, \tag{31}$$

$$\dot{\lambda} = \frac{\lambda_e tr(\dot{\boldsymbol{\varepsilon}})tr\left(\frac{\partial f_p}{\partial\boldsymbol{\sigma}}\right) + 2\mu_e\frac{\partial f_p}{\partial\boldsymbol{\sigma}}:\dot{\boldsymbol{\varepsilon}}}{\lambda_e tr\left(\frac{\partial f_p}{\partial\boldsymbol{\sigma}}\right)tr\left(\frac{\partial \mathrm{g}_p}{\partial\boldsymbol{\sigma}}\right)2\mu_e\frac{\partial f_p}{\partial\boldsymbol{\sigma}}:\frac{\partial \mathrm{g}_p}{\partial\boldsymbol{\sigma}}}. \tag{32}$$

Here we install the yield function f_p which is a pressure-dependent Drucker-Prager function. If $f_p < 0$, the elastic deformation occurs whereas the plastic deformation occurs if $f_p \geq 0$. f_p can be described as

$$f_p = \sqrt{3J_2} + \frac{\alpha_\phi}{dim}tr(\boldsymbol{\sigma}) - \kappa, \tag{33}$$

where J_2 is the second invariant of the deviatoric stress tensor. In this yield function, constitutive parameters α_ϕ and κ should be determined with the physics based parameters. Following equations relevant to the material dependent internal friction angle and cohesion are introduced.

$$\alpha_\phi = \frac{3\,tan\phi}{\sqrt{9+12tan^2\phi}}, \tag{34}$$

$$\kappa = \frac{3c}{\sqrt{9+12tan^2\phi}}. \tag{35}$$

where ϕ and c are internal friction angle and the cohesion of the granular material. Generally, the c=0 under the dry condition.

More detailed information is available in our published papers and on my GitHub repository [6,7,13].

2.2.4 Solid-Liquid Interaction models

The solid–liquid interaction model is essential for reproducing jet fragmentation. To simulate the interaction force between the fluid and particles, we introduce a drag-force model. The drag force arises from the relative motion between the particle and the surrounding fluid and is given by

$$F_d = \frac{1}{2} C_d \rho_0 A |V_s| V_s, \tag{36}$$

where C_D, A_p, and $\mathbf{V}_s$ denote the particle drag coefficient, the projected area of a particle, and the relative velocity between the solid and fluid phases, respectively. We employ the Wen–Yu and Ergun correlations [10,11] to evaluate the drag force acting on spherical solid particles. Although these correlations were originally developed for gas–solid flows, their applicability to liquid–solid systems has also been confirmed [12].

$$C_d = \frac{4}{3}(150\frac{1-\alpha}{\alpha Re} + 1.75), \qquad (\alpha < 0.8) \tag{37}$$

otherwise

$$C_d = \frac{24(1 + 0.15Re^{0.687})}{\alpha Re}\alpha^{-2.65}, \qquad (Re \le 1000) \tag{38}$$

$$C_d = 0.44, \qquad (Re > 1000) \tag{39}$$

where α is volume fraction in the local area and Re is Reynolds number given by

$$Re = \frac{\alpha \rho_0 |V_s| l}{\mu}. \tag{40}$$

3. Validation of the granular simulation model

The validation of the granular simulation models is presented in this section. Figure 1 shows the experimental setup used for validation. The experiments were conducted in an acrylic tank, in which stainless-steel (SS) balls with a diameter of 5.0×10^{-4} m were initially packed in a narrow compartment with a width of 2.0 cm. The initial bed height H and the opening size O were selected as the primary control parameters. The x-coordinate of the advancing granular front along the substrate was extracted via image processing, and the runout distance was evaluated by aggregating the front position over all video frames.

In addition, the angle of repose—defined as the slope angle at the advancing front—was quantified during post-processing. In the numerical simulations, the free surface was identified as the region with low particle number density. The coordinates of the free-surface particles were exported to ImageJ, and the angle of repose was determined by applying a linear fit to the extracted free-surface profile. The initial conditions, boundary conditions, and material properties employed in the experiments and simulations are summarized in Table I (DEM) and Table II (MPH-Granular).

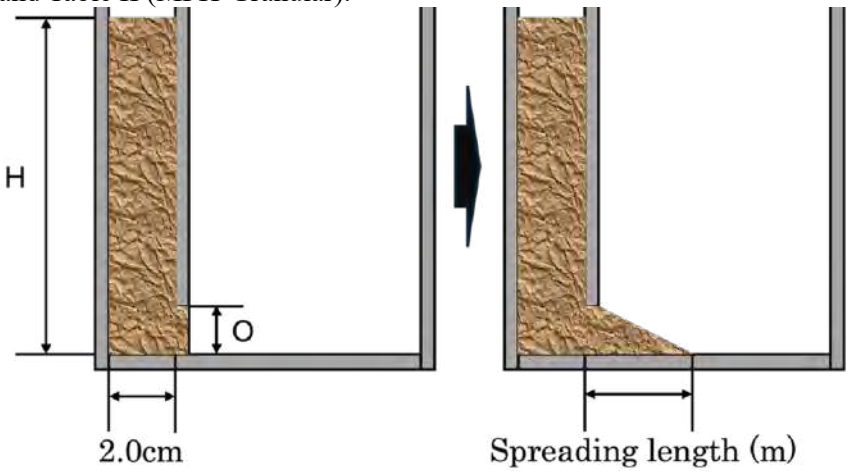

Figure 1 benchmark target experiments: granular dam breaking experiment with 0.5mm spherical SS balls

Table I. DEM calculation parameters

Parameters	SS	Wall
Density (kg m^{-3})	7900	4000
Young's Modulus (GPa)	20	10
Poisson's Ratio (-)	0.3	0.3
Viscous Friction Constant (-)	0.18	0.1
Time Step (s)	1.0×10^{-6}	

Table II. MPH-Granular calculation parameters

	Case 1	Case 2	Case 3
Height H (cm)	5.0	10	15
Outlet O (cm)	1.0	1.0	3.0
Particle size l (m)	5.0×10^{-4}	5.0×10^{-4}	5.0×10^{-4}
Effective radius r_e(m)	$2.5\times l$	$2.5\times l$	$2.5\times l$
Young's modulus (Pa)	3.0×10^{5}	3.0×10^{5}	3.0×10^{5}
Poisson's ratio (-)	0.3	0.3	0.3
Internal Friction Angle (°)	30	30	30
Dilatancy Angle (°)	0.2	0.2	0.2
Cohesion (Pa)	0.0	0.0	0.0

Figure 3 illustrates the final resting configuration of the granular mass after motion ceases. The color scale indicates the magnitude of the vertical stress within the deposit. Overall, the stopping position of the granular front is primarily controlled by the outlet width O and is largely insensitive to the initial filling height H. Accordingly, the runout distances in cases 1 and 2 differ only slightly. Moreover, the steep angle of repose observed in the experiments is successfully reproduced under all test conditions.

The MPH-Granular simulations exhibit a similar trend. For case 1, the experimental runout length is 0.052 m, whereas the simulation predicts 0.049 m. For case 2, the experiment yields 0.051 m and the simulation gives 0.052 m. The characteristic sharp slope at the leading edge of the deposit is also captured. For case 3, the experiment shows a distinct sharp front, whereas the MPH-Granular simulation produces a slightly smoother front. This discrepancy is likely attributable to particles near the outlet being pushed forward by subsequent discharge through the larger opening, which tends to round the front edge.

A notable advantage of the proposed MPH-Granular is that it enables direct evaluation of internal stress fields. The simulations indicate elevated stresses near the corner regions in all cases. In cases 2 and 3, pronounced stress concentrations are also observed along the vertical wall adjacent to the outlet. These results suggest that spreading is arrested when particles near the wall experience high shear stresses, become effectively immobilized, and thereby impede further motion of the granular mass.

Figure 4 summarizes the runout lengths obtained from the experiments, the DEM reference calculations, and the MPH-Granular simulations. Overall, smaller particles tend to spread farther, irrespective of the configuration. In case 1 (Figure 4(a)), the coarse-particle simulation departs noticeably from the experimental data, whereas the fine-particle simulation reproduces the experimental trend well. A comparable behavior is found in case 3 (Figure 4(c)), for which the smallest particle size of 1.0×10^{-4} m provides the best agreement with the experiment. By contrast, in case 2 (Figure 4(b)), simulations with relatively coarse particle sizes (5.0×10^{-4} m and 3.0×10^{-4} m) still yield reasonable agreement with the measurements.

Finally, it should be emphasized that Young's modulus and Poisson's ratio are treated as effective (calibrat ed) parameters in the present formulation, similar to how spring stiffness and friction coefficients are tune d in DEM. Consequently, minor deviations from the experimental measurements are inevitable.

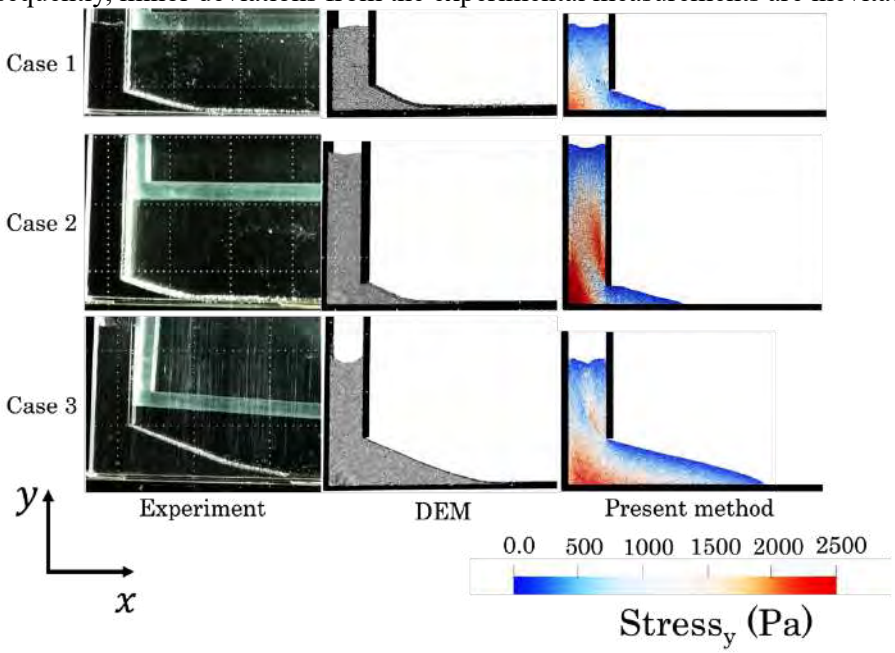

Figure 2 Granular Dambreak simulation results with different approaches: (a) experiment, (b) DEM simulation results, and (c) MPH-based granular flow model [7]

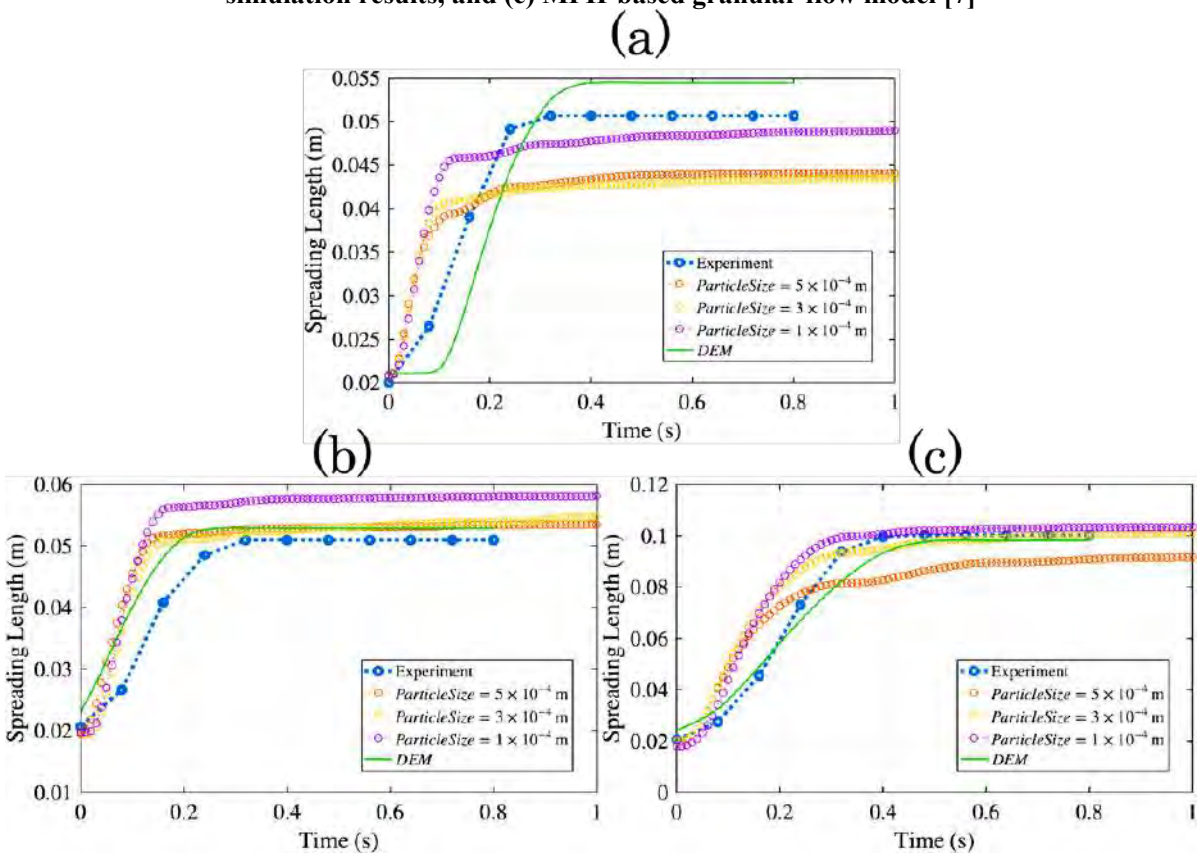

Figure 3 Time evolution of the advancing front position during the run-out granular flow for (a) Case 1, (b) Case 2, and (c) Case 3. [7]

4. Validation on debris bed formation under water

Validation results of the DEM–MPH and MPH-Granular methods, benchmarked against experimental measurements reported by the SYSU group, are presented in this section. The results demonstrate that particle size plays a critical role in debris-bed characterization because it alters the flow regime and, consequently, the deposition behavior [3].

Figure 4 shows the computational geometry, which was designed to replicate the experimental facility described in Cheng et al.[3]. In the simulations, particles are discharged from an outlet nozzle with an inner diameter of 3.0 cm. According to the experimental observations, the falling height has a negligible influence on debris-bed formation because the particle terminal velocity is primarily governed by the water level (Cheng et al., 2017a; Cheng et al., 2017b). Therefore, the falling height is fixed at 120 cm throughout this study.

Table III summarizes the physical properties used in the DEM–MPH simulations, whereas Table IV lists those adopted in the MPH-Granular simulations. Unless otherwise noted, the particle diameter is set to 5.0 mm in the present validation cases.

Figure 5 presents snapshots of the debris-bed formation process. The top row shows the DEM–MPH results, and the bottom row shows the MPH-Granular results. At $t = 5.0\,\mathrm{s}$, no clear difference is observed between the two approaches. At $t = 12.0\,\mathrm{s}$, however, noticeable discrepancies emerge: in the DEM–MPH simulation, the debris does not spread toward the side walls, whereas the MPH-granular simulation shows apparent lateral spreading. This behavior is attributed to the fact that granular–wall friction is not explicitly modeled in the current MPH-Granular formulation, which leads to less resistance to lateral motion and therefore larger spreading compared with DEM–MPH. After $t = 12.0\,\mathrm{s}$, both simulations exhibit substantial piling-up and the formation of a steep deposit profile. Differences are also observed in the velocity field of the surrounding water. In the DEM–MPH simulation, forced convection in the pool is not pronounced, while in the MPH-Granular simulation a clear circulation pattern is already visible at $t = 5.0\,\mathrm{s}$. In the MPH-Granular model, a representative particle diameter is introduced to evaluate buoyancy and drag forces. As a result, the interphase momentum exchange acting on the MPH-Granular "particles" may differ from that acting on the discrete DEM particles, potentially leading to an overestimation of drag and/or buoyancy and, consequently, a stronger induced flow.

Figure 6 compares the debris-bed height obtained in the simulations with the experimental measurements: panel (a) shows the DEM–MPH results and panel (b) shows the MPH-granular results. The DEM–MPH prediction at $t = 73\,\mathrm{s}$ agrees well with the experimentally observed sedimentation height. In contrast, the MPH-Granular simulation exhibits a notable discrepancy in the final bed height. One reason for the improved agreement of DEM–MPH is that its input parameters (e.g., particle density, diameter, and contact model parameters) can be set close to the physical properties of the materials used in the experiments; consequently, the experimental trend is reproduced without dedicated parameter calibration. By comparison, the MPH-Granular approach relies on a continuum constitutive description, and its effective material parameters—such as Young's modulus and internal friction coefficients—must be calibrated to represent the bulk response of the granular assembly. Therefore, a more systematic and sensitive calibration with respect to these parameters is required to reduce the discrepancy in the sedimentation height.

Overall, DEM–MPH is well suited for high-resolution, small-scale analyses and for producing reference data. For realistic core-catcher–scale simulations, however, the MPH-Granular solver is more practical because it can represent the bulk debris behavior efficiently without explicitly resolving an enormous number of individual particles or accounting for particle-size and shape heterogeneity in detail.

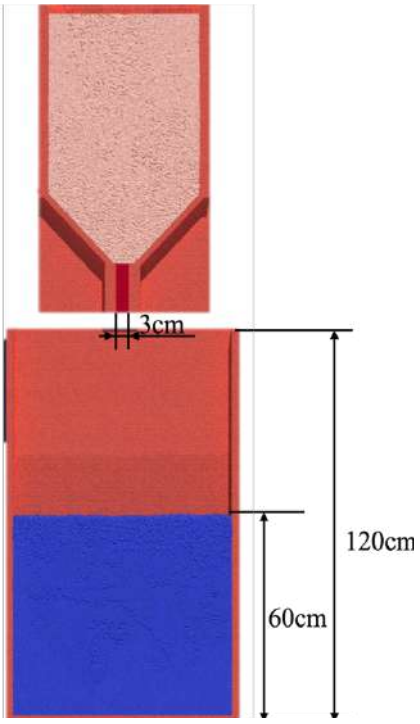

Figure 4 debris bed simulation geometry [6]

Table III. DEM-MPH calculation parameters

Parameters	Debris	Water
Density (kg m^{-3})	2300	1000
Young's Modulus (GPa)	10	
Poisson's Ratio (-)	0.37	
Viscous Friction Constant (-)	0.1	
Bulk Modulus (Pa)		1×10^{6}
Bulk Viscosity (Pa.s)		1×10^{3}
Surface tension (N/m)		0.072
Time Step (s)	1.0×10^{-6}	

Table IV. MPH-MPH Granular calculation parameters

Parameters	Debris	Water
Density (kg m^{-3})	2300	1000
Young's Modulus (MPa)	30	
Poisson's Ratio (-)	0.20	
Bulk Modulus (Pa)		1×10^{6}
Bulk Viscosity (Pa.s)		1×10^{3}
Internal Friction Angle (°)	32	
Dilatancy Angle (°)	0.2	
Cohesion (Pa)	0.0	
Time Step (s)	1.0×10^{-7}	

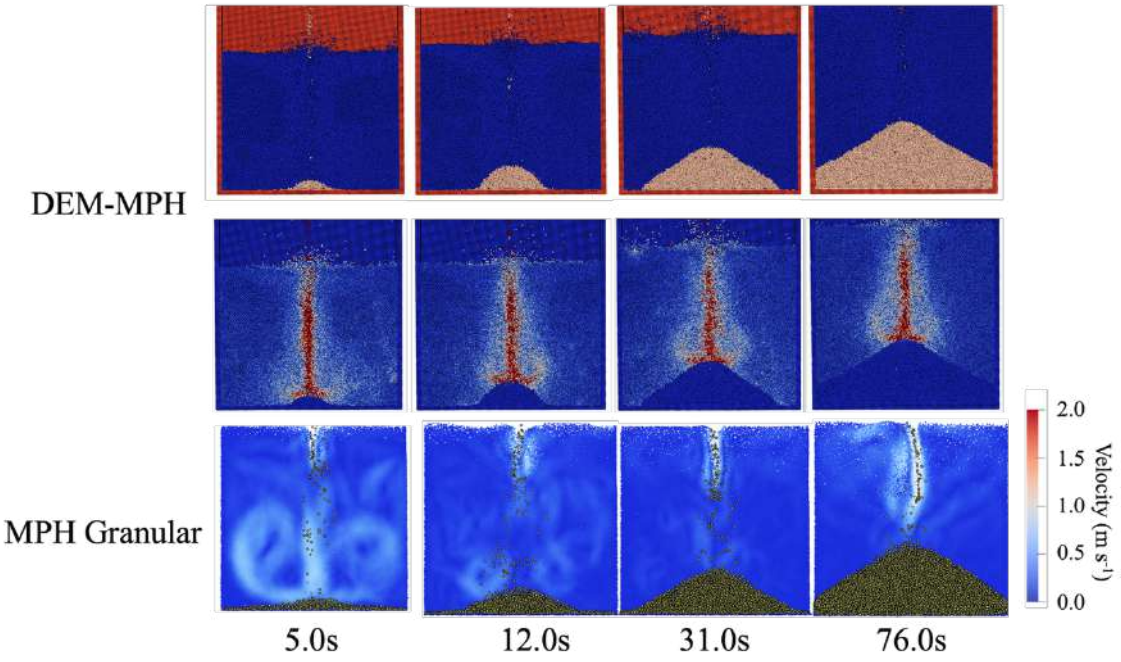

Figure 5 Snapshots of the debris bed formation calculated with DEM-MPH and MPH-Granular method [6]

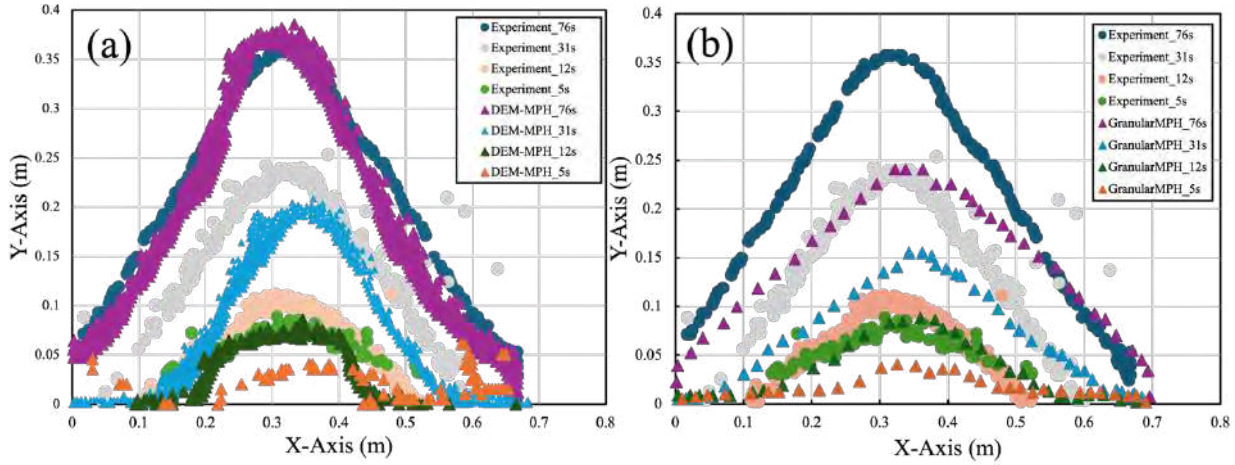

Figure 6 Debris height comparison with the experimental results of 5.0mm spherical particles (a) DEM-MPH cases, (b) MPH-granular simulator cases

5. CONCLUSIONS

Ensuring the safety integrity of the core catcher system during a hypothetical core disruptive accident (CDA) in a sodium-cooled fast reactor (SFR) requires reliable prediction of debris-bed formation. Because the expected debris size is typically below 1.0 mm due to rapid quenching in liquid sodium, an enormous number of fragments can accumulate on the core catcher, making direct high-fidelity simulation computationally impractical. To address this challenge, this study developed and evaluated two complementary numerical approaches for SFR applications: a GPU-accelerated, fully explicit discrete element method coupled with moving particle hydrodynamics (DEM–MPH), and an MPH-Granular flow model incorporating an elastoplastic constitutive law.

Validation was conducted against debris-bed formation experiments performed by the SYSU group and at the University of Tokyo. Both approaches successfully reproduced the key macroscopic trends of sedimentation and dispersion, including the pronounced dependence of debris-bed characteristics on particle size. DEM–MPH provided a more detailed representation of solid-phase dynamics through explicit spring–dashpot interactions, resulting in higher fidelity in capturing local kinematics and deposit morphology. However, its applicability to full three-dimensional, reactor-relevant scales is limited by the high computational cost associated with resolving a vast number of discrete particles.
In contrast, the MPH-Granular model enables efficient large-scale simulations without explicitly tracking individual fragments, offering practical scalability for reactor-scale assessments. Although it captures the overall spreading and settling behavior, it underestimates the compression and packing of the sedimented debris, indicating that improved constitutive descriptions and/or more systematic calibration strategies are needed for dense deposition regimes.

Overall, the results show that DEM–MPH is well suited for high-resolution, small-scale analyses and for generating reference data, whereas the MPH-Granular provides a promising path toward scalable evaluations of debris-bed formation on core-catcher geometries. The two approaches are therefore complementary, motivating a multi-fidelity strategy for future SFR safety assessments: using DEM–MPH to support calibration and uncertainty quantification, and employing the continuum formulation for practical three-dimensional, plant-scale simulations.

Source codes are available freely from my GitHub repository [13].

ACKNOWLEDGMENTS

This work is funded by JSPS KAKENHI grant number JP24K22849. This work was supported by JAEA Nuclear Energy S&T and Human Resource Development Project Grant Number JPJA24H24020026

REFERENCES

1. Suzuki, T., *et al.*, Fragmentation behavior of molten core materials in sodium. *Nucl. Eng. Des.* **272** (2014) 245–257.
2. Shamsuzzaman, M., *et al.*, Experimental study on debris bed characteristics for sedimentation behavior of solid particles. *Ann. Nucl. Energy* **111** (2018) 474–486.
3. Cheng, X., *et al.*, Large-scale experiments on debris bed formation and flow regimes. *Nucl. Eng. Des.* **312** (2017) 233–245.
4. Cundall, P.A., *et al.*, A discrete numerical model for granular assemblies. *Géotechnique* **29**(**1**) (1979) 47–65. https://doi.org/10.1680/geot.1979.29.1.47.
5. Shamsuzzaman, M., *et al.*, Numerical simulation on sedimentation of solid particles used as simulant fuel debris. *J. Nucl. Sci. Technol.* **51** (2014) 681–699. https://doi.org/10.1080/00223131.2014.885957.
6. Yokoyama, R., *et al.*, A novel fully explicit GPU-accelerated discrete element method coupled with moving particle hydrodynamics (DEM–MPH) for simulating underwater particle sedimentation behavior. *Prog. Nucl. Energy* **180** (2025) 105615.
7. Yokoyama, R., *et al.*, A particle-based method for fine granular flow and degradation analysis with an elastic–perfectly plastic Drucker–Prager law. *Powder Technol.* **469**(**3**) (2026) 121927. https://doi.org/10.1016/j.powtec.2025.121927.
8. Hertz, H., Über die Berührung fester elastischer Körper. *J. Reine Angew. Math.* 92 (1881) 156–171.
9. Mindlin, R.D., *et al.*, Elastic spheres in contact under varying oblique forces. *J. Appl. Mech.* **20** (1953) 327–344. https://doi.org/10.1115/1.4010702.
10. Wen, C.Y., *et al.*, Mechanics of fluidization. *Chem. Eng. Prog. Symp. Ser.* **62** (1966) 100.
11. Ergun, S., Fluid flow through packed columns. *Chem. Eng. Prog.* **48**(**2**) (1952) 89–94.
12. Sakai, M., *et al.*, Verification and validation of a coarse grain model of the DEM in a bubbling fluidize d bed. *Chem. Eng. J.* **244** (2014) 33–43. https://doi.org/10.1016/j.cej.2014.01.029.
13. https://github.com/Ryo1011gd

Benchmarking of Advanced GPU-Accelerated Discrete Element Method and Elastoplastic Constitutive Granular Flow Models for Large-Scale Debris Bed Formation in Severe Accident of Sodium Fast Reactors

The University of Tokyo
Ryo Yokoyama, Ph.D.
(yokoyamaryo395@g.ecc.u-tokyo.ac.jp)

NPS 東京大学原子力専攻
Nuclear Professional School, The University of Tokyo

❖ This work was supported by JSPS KAKENHI Grant Number JP26K17787
❖ And by JAEA Nuclear Energy S&T and Human Resource Development Project Grant Number JPJA24H12345678.

First, all my works are stored on my Github account. Please check it.

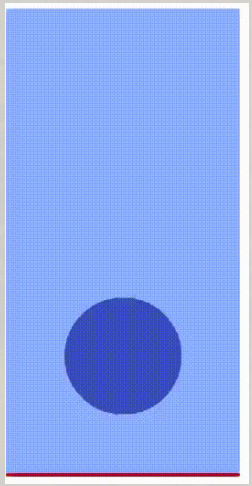

Bubbly Flow

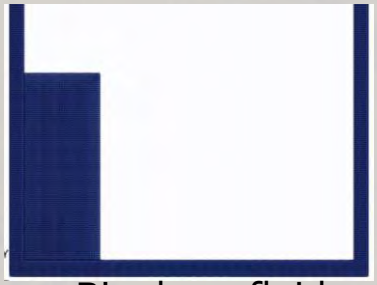

Bingham fluid

Hyper-elastic

ALE elastoplastic, crack propagation

Melting/Solidification

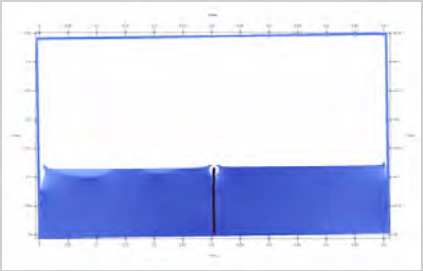

Fluid-Structure Interaction

Structure damage

Motivation (1)

Sodium Fast Reactor (SFR) R&D in Japan

- Medium-size tank-type SFR is the candidate for the demonstration reactor
- Both Monju and Joyo are loop type (high earthquake resistance)
- Fundamental R&D for Japan's advanced SFR beyond Monju should be completed by FY2028

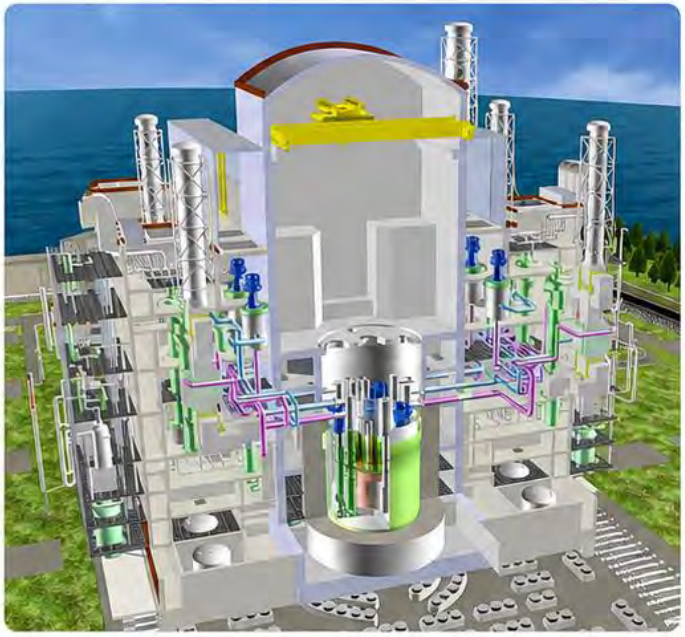

Conceptual image of demonstration SFR in Japan [1]

Major Concern: Core Disruptive Accident (CDA) [2]

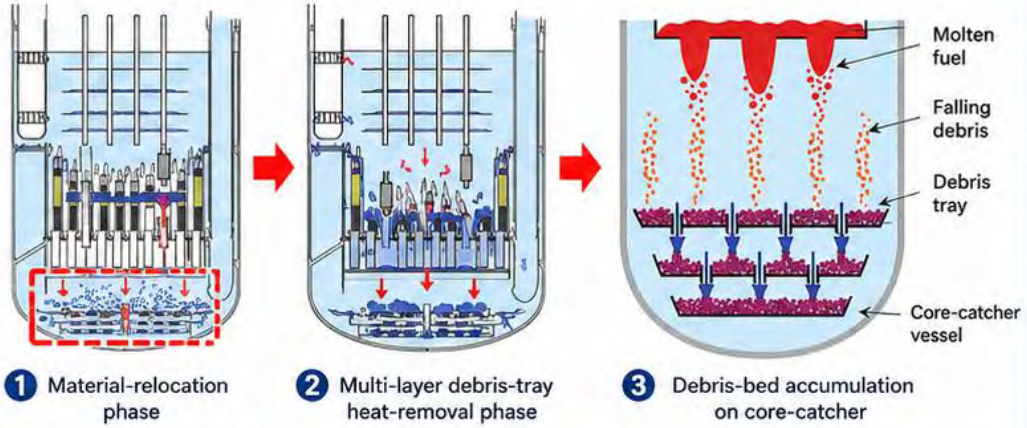

- Fragmented debris piles up on the core-catcher
- Integrity of the core-catcher is of significant importance

[1] https://www.mhi.com/jp/group/mfbr/company/technology/project
[2] Suzuki, T et al., 2014. A scenario of core disruptive accident for Japan sodium-cooled fast reactor to achieve in-vessel retention. J. Nucl. Sci. Technol. 51, 493–513.

Motivation (2)

Numerical Simulation of the Debris Bed Formation

- **DEM** based simulation is the most popular in solving the debris phase
- CFD either **Eulerian** or **Lagrangian** is employed for fluid phase

Target phenomena

Solid-Solid Collision

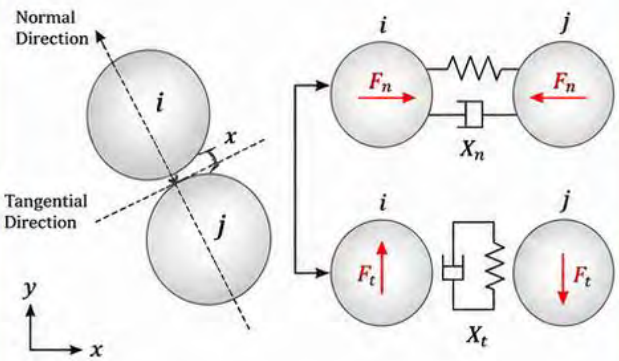

$$m\frac{\mathrm{D}\mathbf{u}}{\mathrm{D}t} = \overrightarrow{F_{\mathrm{g}}} + \overrightarrow{F_{\mathrm{nc}}} + \overrightarrow{F_{\mathrm{tc}}} + \overrightarrow{F_{\mathrm{b}}}$$

$$\frac{\mathrm{D}\omega}{\mathrm{D}t} = I^{-1}\mathbf{T}$$

Solid-Fluid Coupling Scheme

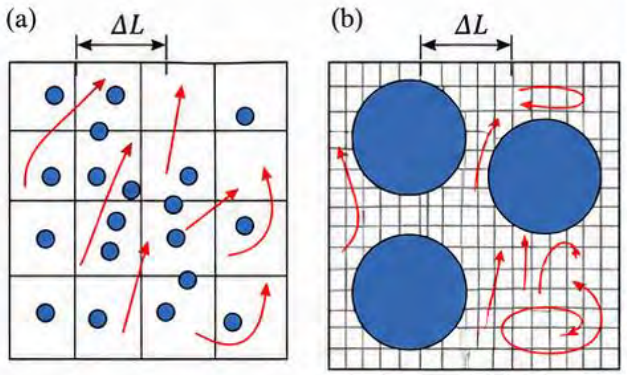

$$\nabla \cdot \mathbf{u} = 0$$

$$\frac{\partial \mathbf{u}}{\partial t} + (\mathbf{u}\cdot\nabla)\mathbf{u} = -\frac{1}{\rho}\nabla p + \nu\nabla^2\mathbf{u} + \mathbf{g}$$

Issues of Discrete Element Method for CDA

DEM is

- A robust approach for granular flow
- But NOT a practical approach for CDA

1. Computational cost

The DEM resolution must be comparable to the actual resolution of the target phenomenon, which makes it unsuitable for very large-scale systems such as NPPs (potentially involving nearly a billion particles). Moreover, the DEM time step, Δt, is generally extremely small.

2. Polydispersity

DEM is primarily designed for monodisperse or simplified particle systems, whereas debris generated during CDA is highly polydisperse.

3. Shape inhomogeneity

Standard DEM contact models are mainly based on spherical particles and are not orientation dependent. Therefore, when particle shapes differ significantly, the applicability of DEM becomes limited.

Research Objective

Previous method

- ~~DEM: Discrete model~~
- CFD: Continuum model

Present method

- MK-SPH: Continuum model
- CFD: Continuum model

✓ Good for large scale
✓ No need to consider the monodisperse
✓ Easily handle shape inhomogeneity

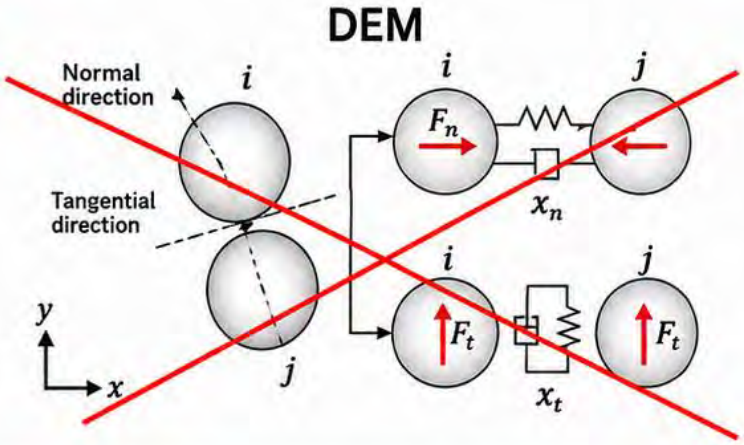

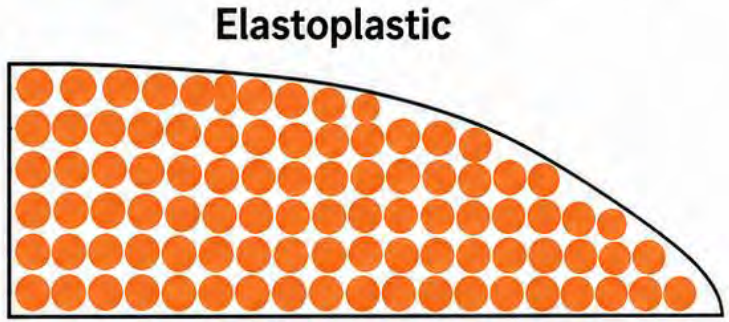

Research Objective

For assessing debris-bed formation on the core catcher, a fully continuum-based solid–liquid two-phase simulation method was developed and compared with a DEM–CFD approach.

Multi-Kernel Moving Particle Hydrodynamics For Solid-Liquid Two Phase Flow

Governing Equations and Explicit Time Integration

1. Governing equation

$$\rho \frac{D\mathbf{u}}{Dt} = \mathbf{F}^{internal} + \mathbf{F}^{external}$$

$$\mathbf{F}^{internal} = \nabla \cdot \boldsymbol{\sigma}$$

$$\mathbf{F}^{external} = \rho \mathbf{g}$$

2. Quantities needed for stress update

$$\boldsymbol{\sigma} = \boldsymbol{\sigma}^k + \frac{\partial \sigma}{\partial t} \Delta t$$

$$\frac{\partial \sigma}{\partial t} = \dot{\boldsymbol{\omega}}\, \boldsymbol{\sigma}^k - \boldsymbol{\sigma}^k\, \dot{\boldsymbol{\omega}} + \lambda_e\, tr(\dot{\boldsymbol{\varepsilon}}) I + 2\mu_e \dot{\boldsymbol{\varepsilon}}$$

$$\dot{\boldsymbol{\varepsilon}} = \frac{1}{2}\left(\nabla \mathbf{u} + (\nabla \mathbf{u})^T\right)$$

$$\dot{\boldsymbol{\omega}} = \frac{1}{2}\left(\nabla \mathbf{u} - (\nabla \mathbf{u})^T\right)$$

$$\lambda_e = \frac{E\nu}{(1+\nu)(1-2\nu)}$$

$$\mu_e = \frac{E}{2(1+\nu)}$$

3. Time update by Forward Euler

$$\mathbf{u}^{(k+1)} = \mathbf{u}^k + \frac{\mathbf{F}^{internal} + \mathbf{F}^{external}}{m} \Delta t$$

$$\boldsymbol{x}^{(k+1)} = \boldsymbol{x}^k + \mathbf{u}^{(k+1)} \Delta t$$

$\nabla \mathbf{u}$ ➡ $\dot{\boldsymbol{\varepsilon}}, \dot{\boldsymbol{\omega}}$ ➡ $\frac{\partial \sigma}{\partial t}$ ➡ $\boldsymbol{\sigma}$ ➡ $\mathbf{F}^{internal}$ ➡ $\mathbf{u}^{(k+1)}$ ➡ $\boldsymbol{x}^{(k+1)}$

✓ Update the stress from the strain rate and spin, compute the internal force from the stress, and then update velocity and position using the Forward Euler method.

○**Ryo Yokoyama et al.,** , A particle-based method for fine granular flow and degradation analysis with an elastic–perfectly plastic Drucker–Prager law, Powder Technology, 469, (2026), 121927

Elastoplastic Stress Update by Return Mapping

Assume the total strain is elastic at first, and apply plastic correction only when yielding occurs.

1. Elastic trial stress

$$\boldsymbol{\sigma}^{trial} = \boldsymbol{\sigma}^{k} + \frac{\partial \boldsymbol{\sigma}}{\partial t}\Delta t$$

2. Yield check

$$f^{trial} = q^{trial} - \alpha_\phi p^{trial} - \kappa$$

$$q = \sqrt{3J_2}$$

$$p = \frac{1}{3}tr(\boldsymbol{\sigma})$$

$$J_2 = \frac{1}{2}\boldsymbol{s} : \boldsymbol{s}$$

$$\boldsymbol{s} = \boldsymbol{\sigma} - p\boldsymbol{I}$$

3. Plastic multiplier

$$K = \lambda_e + \frac{2}{3}\mu_e$$

$$\Delta\gamma = \frac{f^{trial}}{3\mu + K\alpha_\phi\alpha_\psi}$$

4. Stress correction

$$q^{(k+1)} = q^{trial} - 3\mu\Delta\gamma$$

$$p^{(k+1)} = p^{trial} - K\alpha_\psi\Delta\gamma$$

5. Stress reconstruction

$$\boldsymbol{\sigma}^{(k+1)} = \boldsymbol{s}^{(k+1)} + p^{(k+1)}\boldsymbol{I}$$

If no yielding occurs:

$$\boldsymbol{\sigma}^{(k+1)} = \boldsymbol{\sigma}^{trial}$$

Elastic predictor → **Yield check** → **Compute $\Delta\gamma$** → **Stress projection** → **Stress update**

In return mapping, the elastic trial stress is computed first. Only when the yield condition is satisfied is the stress returned to the Drucker–Prager yield surface. This allows the stress to be updated without directly computing the plastic strain.

Fluid Formulation from Lagrangian-Rayleigh Dissipation

1. Lagrangian with Rayleigh dissipation

$$\frac{d}{dt}\left(\frac{\partial \mathcal{L}}{\partial \mathbf{u}_i}\right) - \left(\frac{\partial \mathcal{L}}{\partial x_i}\right) + \left(\frac{\partial \mathcal{D}}{\partial \mathbf{u}_i}\right) = 0$$

$$\mathcal{L} = \mathcal{T} - \mathcal{V}$$

$\mathcal{L}$: Lagrangian
$\mathcal{D}$: Dissipation energy
$\mathcal{T}$: Kinetic energy
$\mathcal{V}$: Potential energy

2. MPH assumptions

$$\mathcal{L} = \sum_i \left(\frac{1}{2}\rho^f \left|\mathbf{u}_i^f\right|^2 + \rho^f \mathbf{g}\cdot\mathbf{x}_i^f\right) V$$

$$\mathcal{D} = \sum_{j'} \left(\frac{\lambda^f}{2}(G_{ij})^2 + \nu^f \sum_{j'} \left(\mathbf{u}_j^f - \mathbf{u}_i^f\right)^2 \frac{w'_{ij}}{|r_{ij}|}\right) V$$

$$G_i = \sum_{j'} \left(\left(\mathbf{u}_j^f\right)^k - \left(\mathbf{u}_i^f\right)^k\right) \cdot \mathbf{e}_{ij}\, w'_{ij}$$

3. Discrete terms

$$\frac{d}{dt}\left(\frac{\partial \mathcal{L}}{\partial \mathbf{u}_i}\right) = \rho^f \frac{D\mathbf{u}_i^f}{Dt} V \qquad \frac{\partial \mathcal{L}}{\partial x_i} = \rho^f \mathbf{g}\, V$$

$$\frac{\partial D_1}{\partial \mathbf{u}_i} = \sum_j (p_j + p_i)\, \mathbf{e}_{ij}\, w'_{ij}\, V$$

$$\frac{\partial D_2}{\partial \mathbf{u}_i} = -2\mu^f \sum_j \left(\mathbf{u}_j^f - \mathbf{u}_i^f\right) \frac{w'_{ij}}{|r_{ij}|} V$$

$$p_i = -\lambda^f G_i + \kappa^f (n_i - n_0)$$

4. Resulting fluid momentum equation & explicit update

$$\frac{D\mathbf{u}_i^f}{Dt} = -\frac{1}{\rho_0^f}\sum_j (p_j + p_i)\, \mathbf{e}_{ij}\, w'_{ij} + 2\nu^f \sum_j \left(\mathbf{u}_j^f - \mathbf{u}_i^f\right) \frac{w'_{ij}}{|r_{ij}|} + \mathbf{g}$$

Explicit time integration (fluid solver only)

$$p_i^k = -\lambda^f \sum_j \left(\left(\mathbf{u}_j^f\right)^k - \left(\mathbf{u}_i^f\right)^k\right) \cdot \mathbf{e}_{ij}\, w'_{ij} + \kappa^f (n_i - n_0)$$

$$\left(\mathbf{u}_i^f\right)^{k+1} = \left(\mathbf{u}_i^f\right)^k + \left[-\frac{1}{\rho_0^f}\sum_j (p_j^k + p_i^k)\mathbf{e}_{ij}\, w'_{ij} + 2\nu^f \sum_j \left(\left(\mathbf{u}_j^f\right)^k - \left(\mathbf{u}_i^f\right)^k\right) \frac{w'_{ij}}{|r_{ij}|} + \mathbf{g} + \frac{1}{\rho_0^f}\mathbf{F}_{ext}\right] \Delta t$$

$$\left(\mathbf{x}_i^f\right)^{k+1} = \left(\mathbf{x}_i^f\right)^k + \left(\mathbf{u}_i^f\right)^{k+1} \Delta t$$

The Lagrangian–Rayleigh formulation yields a mathematically and physically consistent discretized fluid momentum equation, and the explicit fluid scheme remains stable without artificial force.

Fluid-Granular 2 Way Coupling

1. DEM-CFD: Granular size = DEM size, thus modeling is straightforward
2. Present method: Granular size ≠ particle size, thus a control-volume-based scaling is introduced

1 DEM-based simulation

DEM size = Debris size

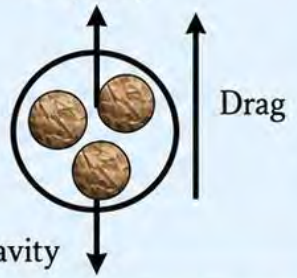

2 MK-MPH based simulation

MK-SPH size ≠ Debris size

1 DEM-CFD formulation

$$F_{Buoyancy} = \rho_f V_d g$$

$$F_{Drag} = \frac{1}{2} C_d \rho_s A_d |V_d| V_d$$

Drag coefficient C_d

$$C_d = \frac{4}{3}\left(150\frac{1-\varepsilon_f}{\varepsilon_f Re} + 1.75\right), \quad (\varepsilon_f < 0.8)$$

$$C_d = \frac{24(1+0.15Re^{0.687})}{\varepsilon_f Re}\varepsilon_f^{-2.65}, \quad (Re \le 1000)$$

$$C_d = 0.44, \quad (Re > 1000)$$

2 MK-MPH based formulation (control-volume scaling)

$$V_{control} = \Delta x^3$$

$$V_d = \frac{\pi {d_d}^3}{6}$$

$$\alpha_s = \frac{N_d V_d}{V_{control}}$$

$$\varepsilon_f = 1 - \alpha_s$$

$$F_{Buoyancy} = \rho_f \alpha_s V_{control} g$$

$$F_{Drag} = \beta V_{control}(\mathbf{u}_f - \mathbf{u}_d)$$

$$\beta = \frac{3}{4} C_d \rho_f \alpha_s \frac{|\mathbf{u}_f - \mathbf{u}_d|}{d_d}$$

- α_s: solid volume fraction of actual debris in one control volume
- ε_f: fluid volume fraction / porosity
- β: interphase momentum exchange coefficient

Thus, buoyancy and drag are scaled by the **actual debris fraction** and **actual debris size**, not by the numerical particle size.

Calculation Results

Dam Break Simulation

Granular Flow Dam Break:

1. Angle of Repose
2. Spreading Length depends on outlet

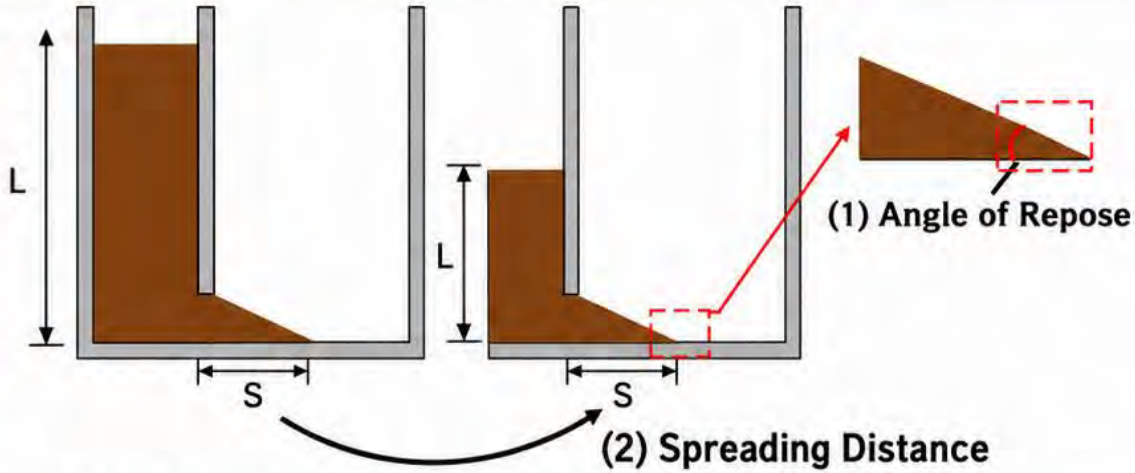

Table 1. Calculation conditions on DEM

Parameters	SS	Wall
Density (kg m^{-3})	7900	4000
Young Modulus (GPa)	20	10
Poisson Ratio (-)	0.3	0.3
Viscous Friction Constant (-)	0.18	0.10
Time Step (s)	1.0×10^{-6}	

Table 2. Calculation conditions on MK-SPH

	Case 1	Case 2	Case 3
Height H (cm)	5.0	10	15
Outlet O (cm)	1.0	1.0	3.0
Particle size l (m)	5.0×10^{-4}, 1.0×10^{-4}	3.0×10^{-4}, 1.0×10^{-4}	5.0×10^{-4}, , 3.0×10^{-4}, 1.0×10^{-4} 1.0×10^{-4}
Effective radius r_e (m)	$2.5\times l$	$2.5\times l$	$2.5\times l$
Young's modulus (Pa)	3.0×10^{5}	3.0×10^{5}	3.0×10^{5}
Poisson Ratio (-)	0.3	0.3	0.3
Internal Friction Angle (°)	30	30	30
Dilatancy Angle (°)	0.2	0.2	0.2
Cohesion (Pa)	0.0	0.0	0.0

DEM vs Developed MK-SPH method

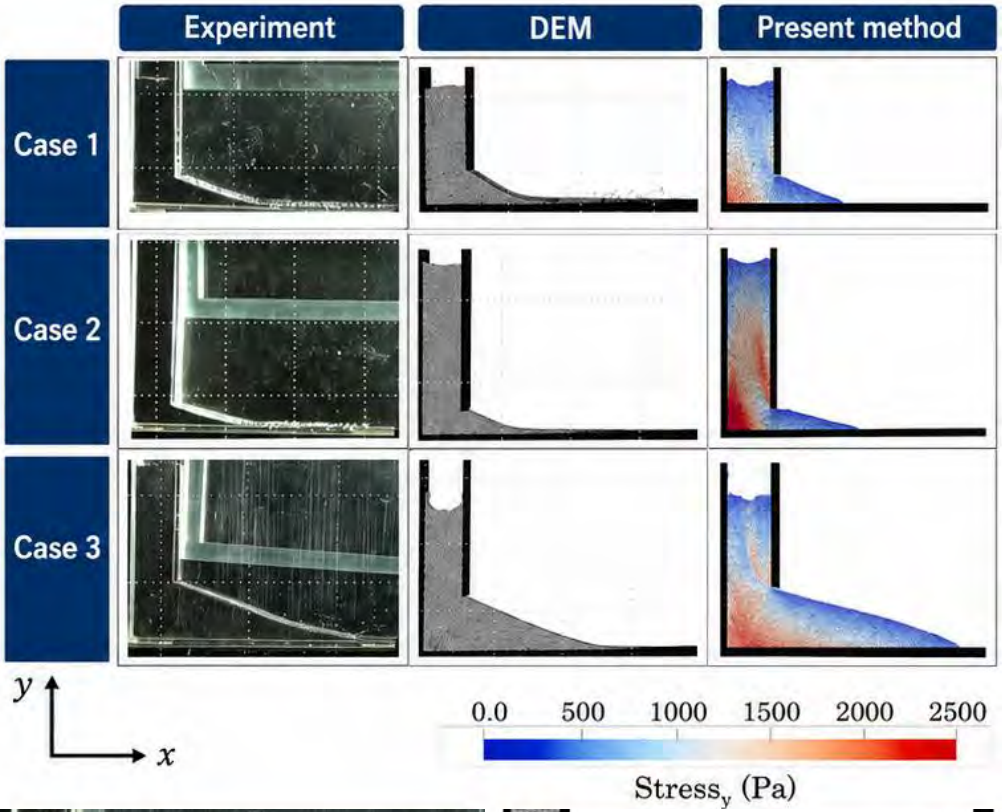

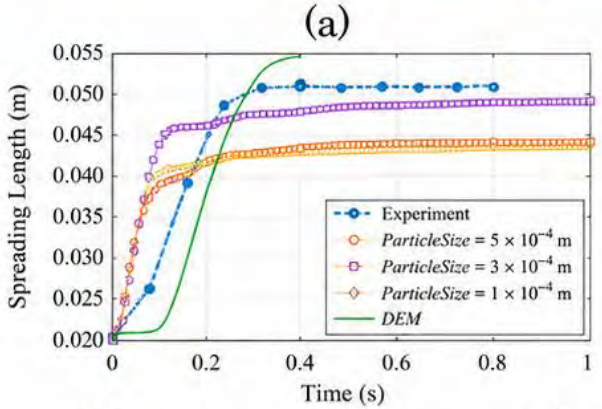

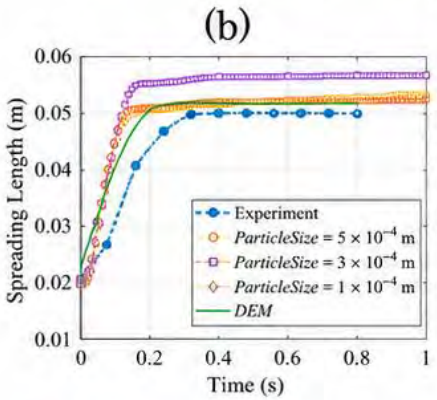

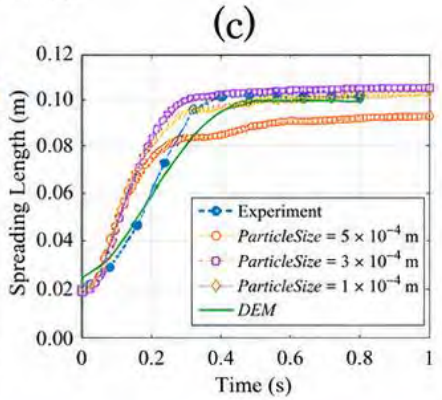

Fig. Experiment

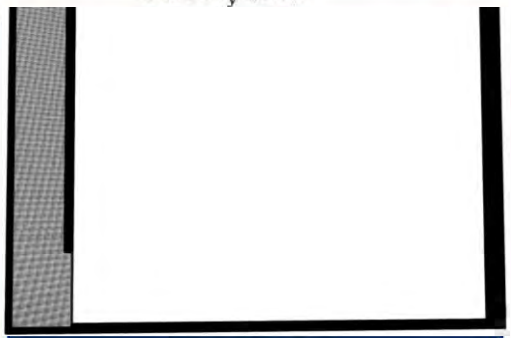

Fig. DEM

Remarks

- Developed MK-SPH simulation method has almost same results as DEM
- N of particles in MK-SPH is almost 1/3 of DEM employed, significantly reducing the computational time

Investigation of Debris Size on Sedimentation

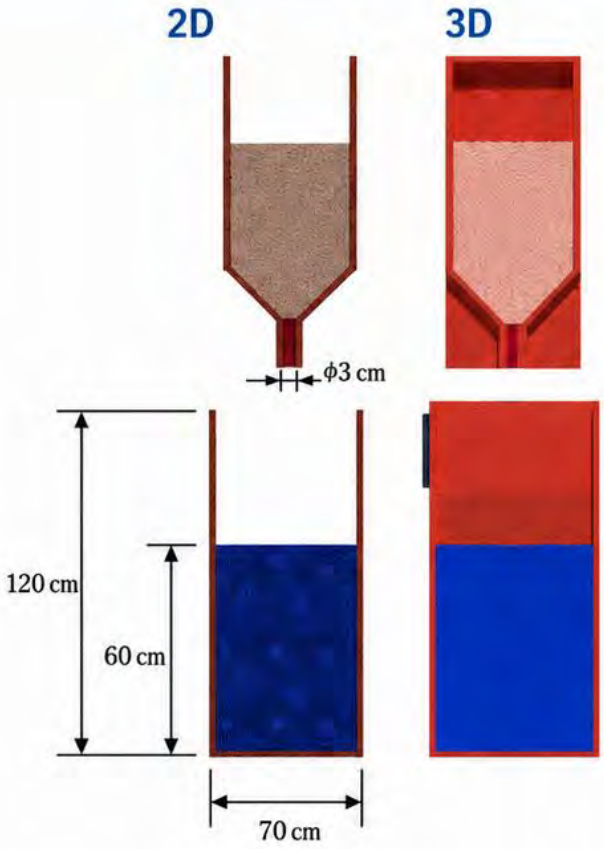

Granular Phase

Parameter	Value
Particle size l (m)	0.003
Effective radius r_e(m)	2.5×l
Density (kg/m^3)	4200
Young's modulus (Pa)	1.0×10^7
Poisson Ratio (-)	0.3
Internal Friction Angle (°)	42
Dilatancy Angle (°)	0.0
Cohesion (Pa)	0.0

Fluid Phase

Parameter	Value
Particle size l (m)	0.003
Effective radius r_e(m)	2.5×l
Density (kg/m^3)	1000
Viscosity (Pa.s)	1.0×10^{-3}
Surface Tension (N/m)	0.072
Bulk Modulus (Pa)	1.0×10^5

Summary of GPU-DEM simulation results

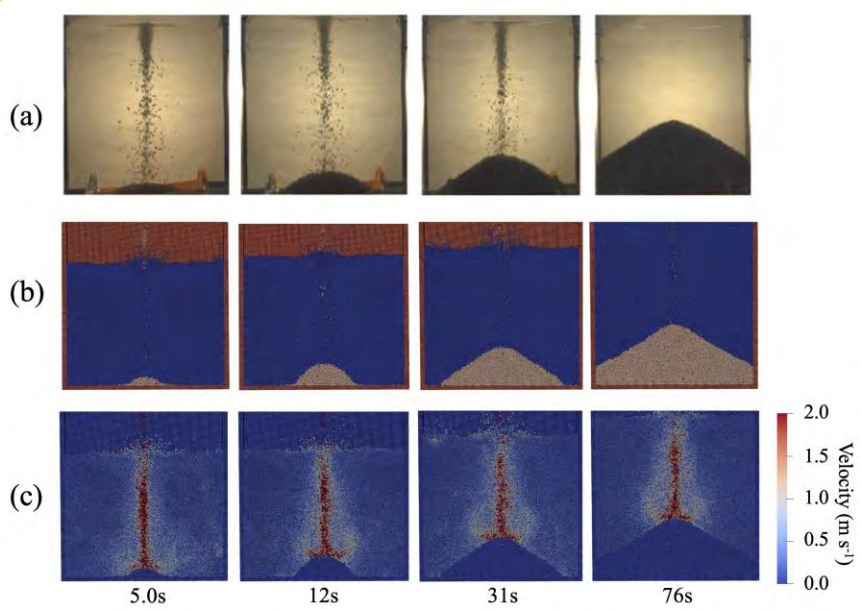

Fig. 5.0mm debris sedimentation with DEM-MPH

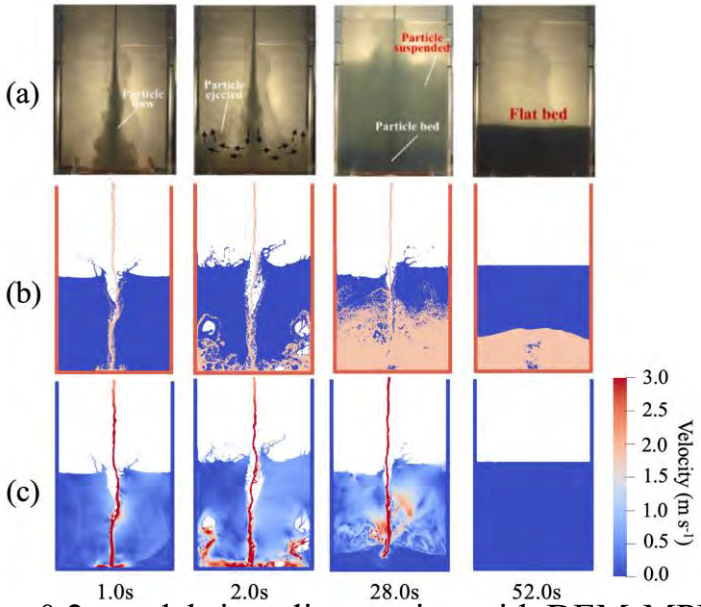

Fig. 0.2mm debris sedimentation with DEM-MPH

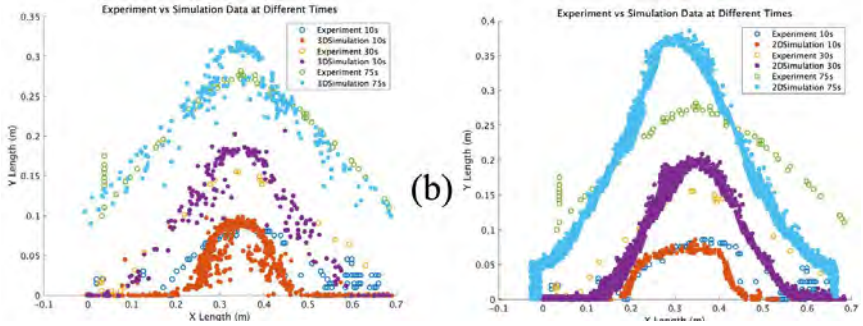

Fig. Sedimentation height of the debris with 5.0mm DEM size

- DEM-MPH simulates the debris sedimentation and dispersion qualitatively.
- 5.0mm case: **5.0 million** particles in 3D and 0.2mm case: **8.6 million** particles in 2D

Extremely high computational cost

[1] Cheng, S.et al.,. Ann. Nucl. Energy 109, 658–666. https://doi.org/10.1016/j.anucene.2017.06.014.
[2] R.Yokoyama et al., Prog. Enregy, 2024

Debris Bed Formation with 5.0mm Debris Size

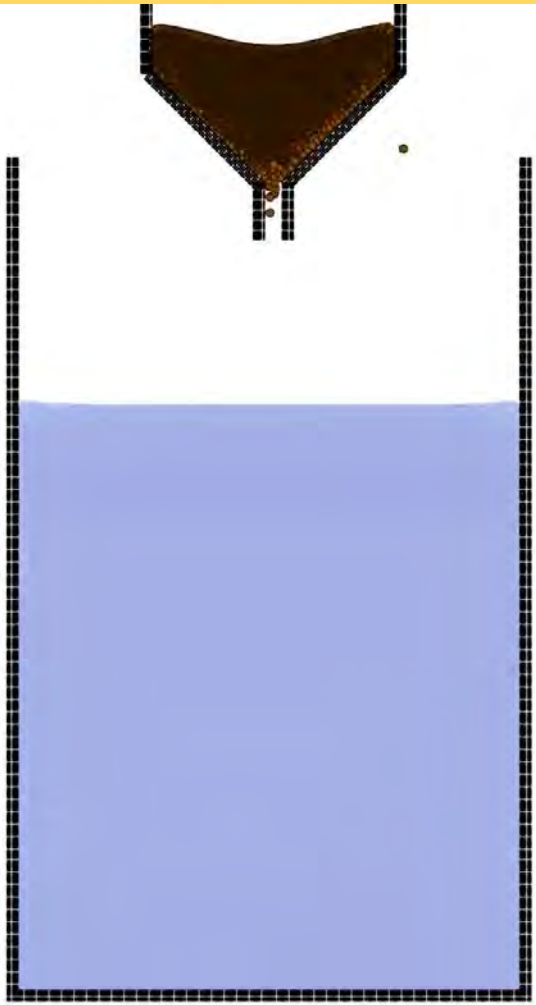

Fig. MK-SPH simulation with 5.0mm particle scaling

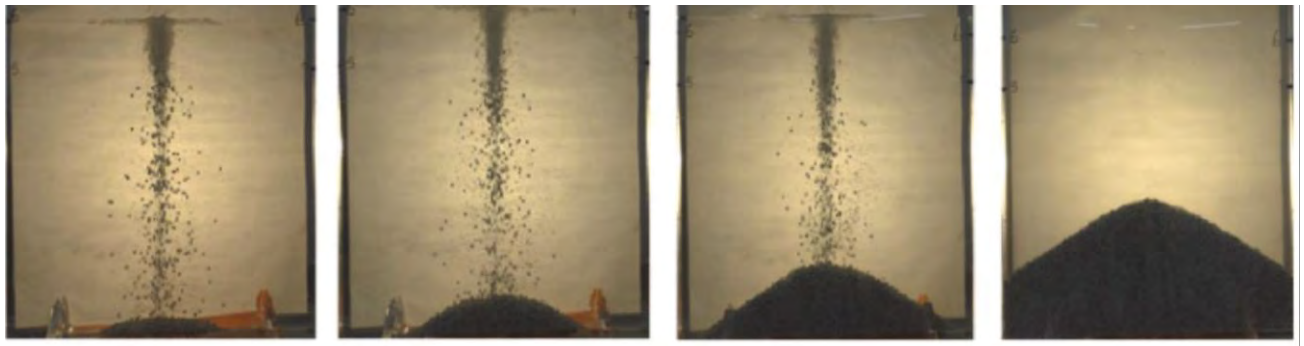

Fig. Experimental observation of 6.0mm particles sedimentation

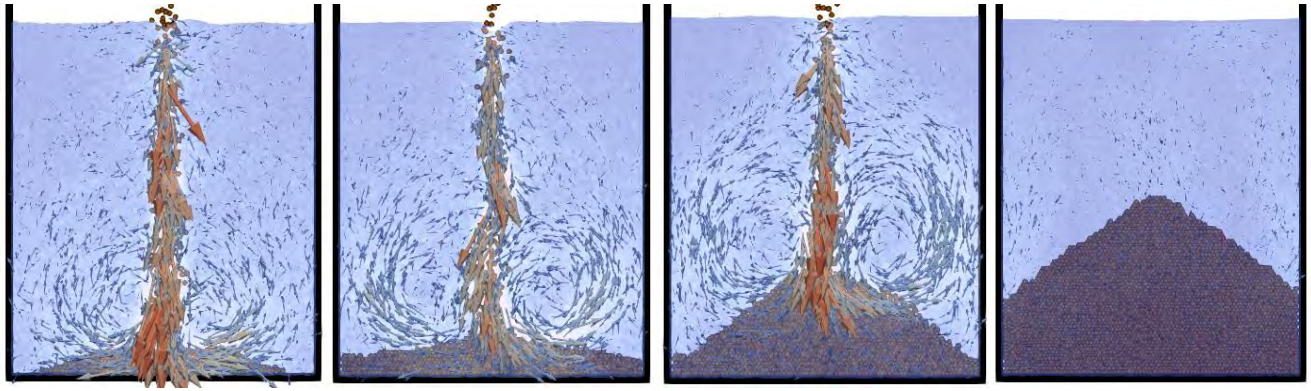

Fig. Simulation results of MK-SPH with 5.0mm scaling particle

- Jet velocity is obvious while the convection is limited
- Debris is piled up, forming Mt.Fuji Shape.
- Just 55,000 particles and 40 min GPU calculation. (DEM took 3days)

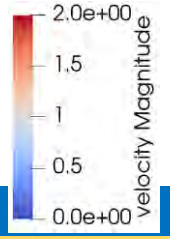

[1] Cheng, S.et al.,. Ann. Nucl. Energy 109, 658–666. https://doi.org/10.1016/j.anucene.2017.06.014.

Debris Bed Formation with 2.0mm Debris Size

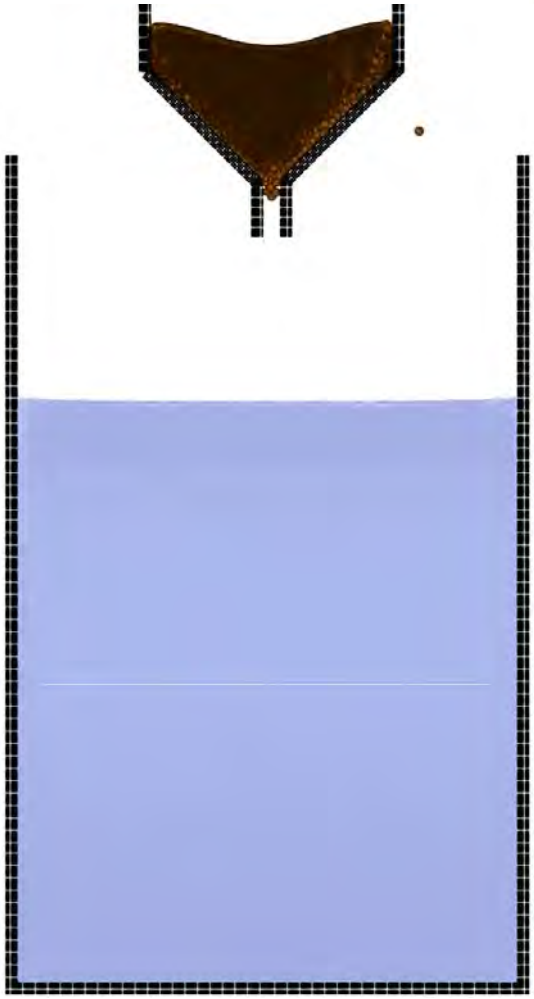

Fig. MK-SPH simulation with 2mm particle scaling

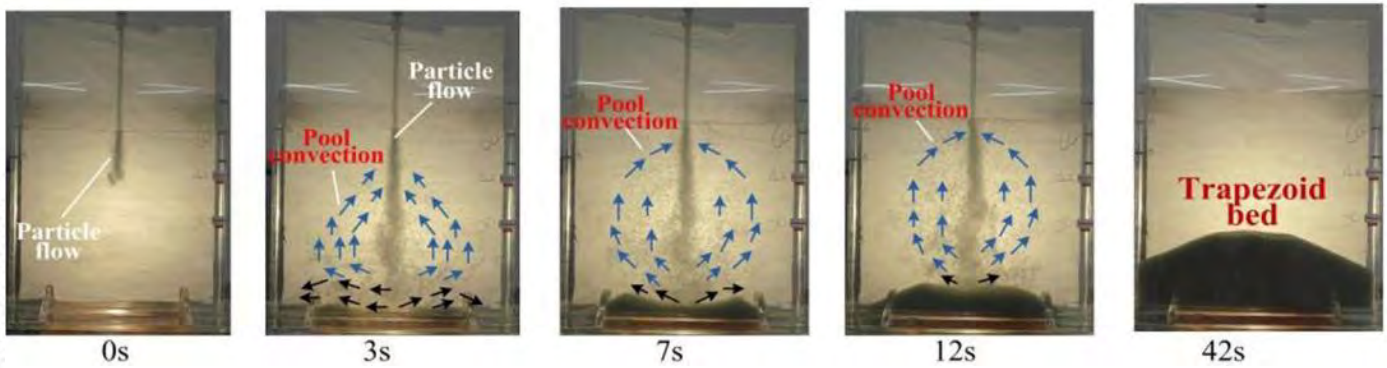

Fig. Experimental observation of 2.0mm particles sedimentation

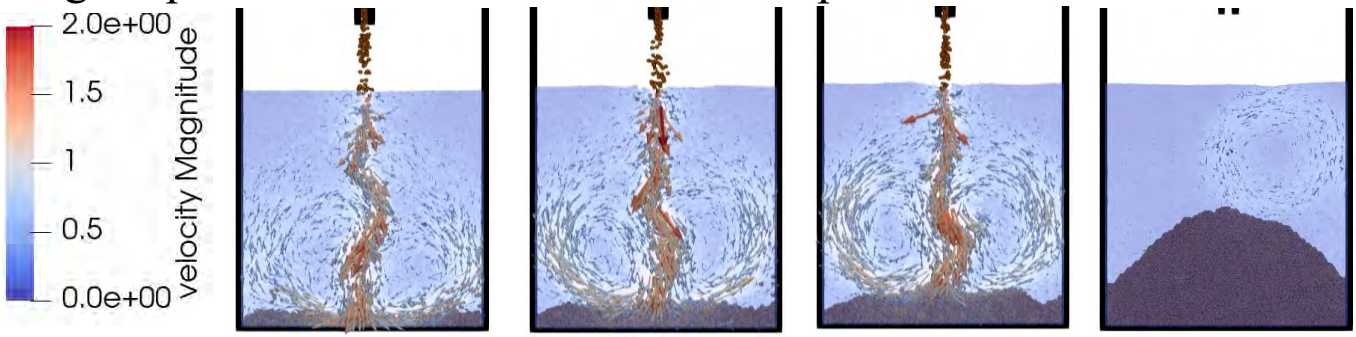

Fig. Simulation results of MK-SPH with 2.0mm scaling particle

- Jet velocity is reduced due to the drag force
- Obvious pool convection can be seen together with piling up
- Just 55,000 particles and 40 min GPU calculation.

[1] Cheng, S.et al.,. Ann. Nucl. Energy 109, 658–666. https://doi.org/10.1016/j.anucene.2017.06.014.

Debris Bed Formation with 0.3mm Debris Size

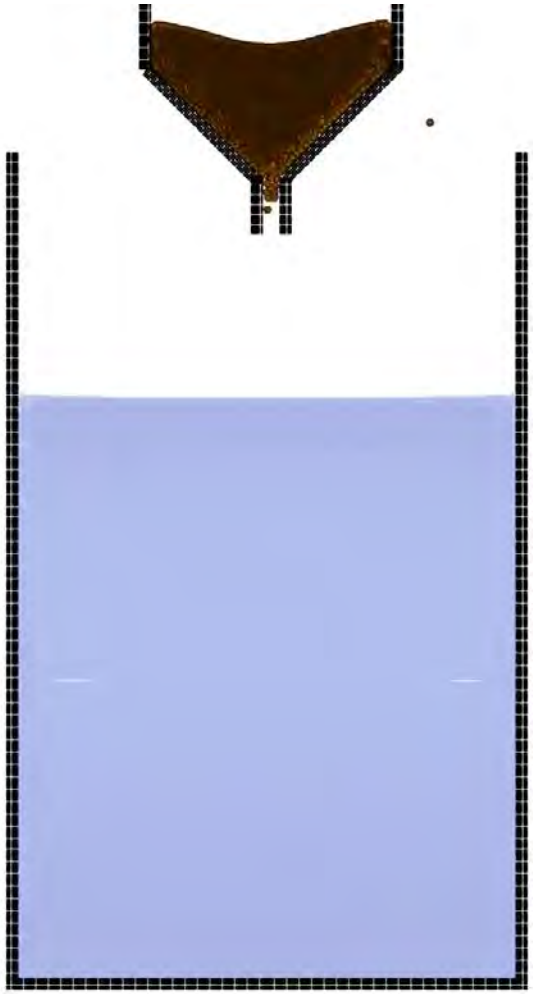

Fig. MK-SPH simulation with 0.3mm particle scaling

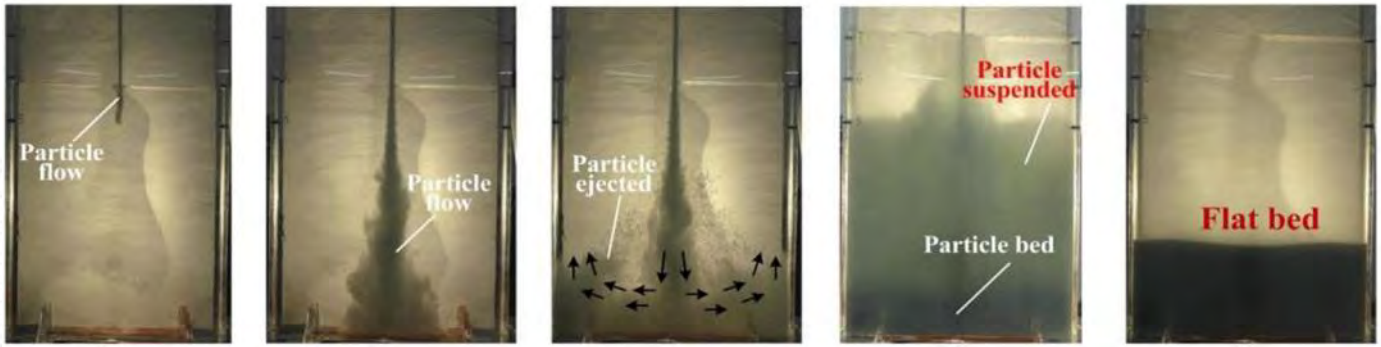

Fig. Experimental observation of 0.25 mm particles sedimentation

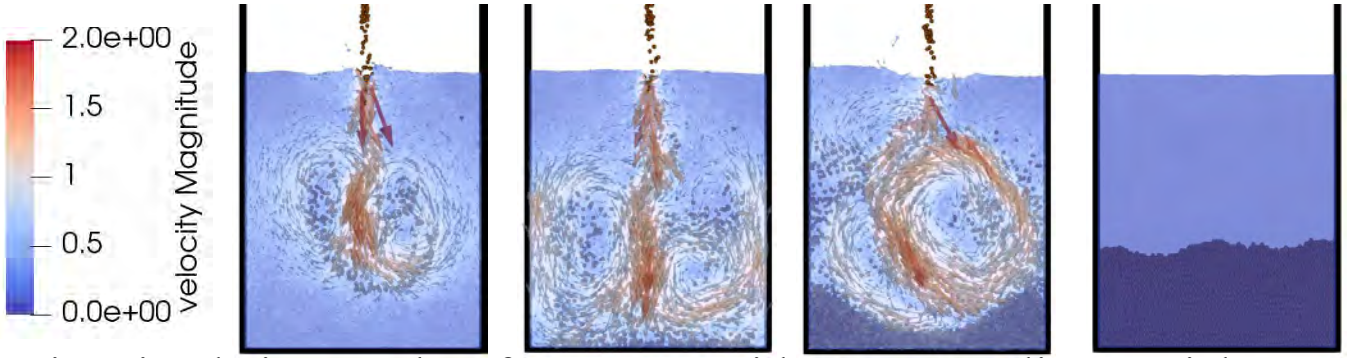

Fig. Simulation results of MK-SPH with 0.3mm scaling particle

- Substantial convection generates the significant dispersion of the particles
- No Mt.Fuji like sedimentation mimicking the experiment.
- Just 55,000 particles and 40 min GPU calculation.

[1] Cheng, S.et al.,. Ann. Nucl. Energy 109, 658–666. https://doi.org/10.1016/j.anucene.2017.06.014.

Supercomputing for Large Scale Phenomena

Computing

CUDA-MPI hybrid parallel computing

×

Visualization

Generative Adversarial Network (GAN) for prompt high resolution rendering

Real-Time High-Resolution Simulation with High-Performance Computing

Conclusion

<Objective> Establish a novel MK-SPH/MPH-based solid–liquid flow simulation framework to enable practical and accurate analysis of debris bed formation in SFRs.

- To overcome the practical limitations of DEM, including high computational cost and complex polydisperse/inhomogeneous behavior, a fully continuum fluid–granular model based on the elastoplastic Drucker–Prager framework is developed.
- The return-mapping stress update enables fast and stable computation through an implicit update of the plastic strain.
- Scaled solid–liquid coupling models are employed to account for the difference between the computational particle size and the actual debris size.
- Benchmarking against in-house GPU DEM shows accurate granular-flow reproduction with reduced computational cost.
- The MK-SPH/MPH method successfully reproduces large-scale debris-bed formation experiments, regardless of particle size.
- High computational speed and scalability enable real-scale debris-bed formation simulations in SFRs.

Pleas follow my github

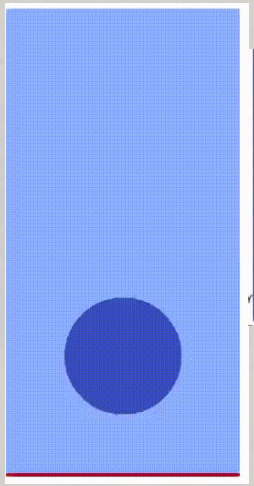

Bubbly Flow

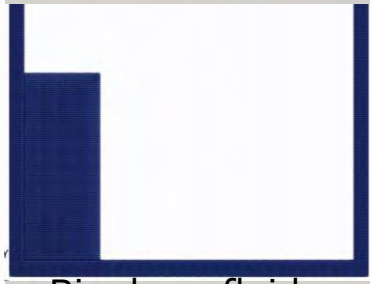

Bingham fluid

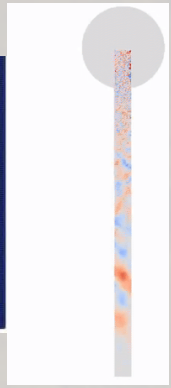

Hyper-elastic

ALE elastoplastic, crack propagation

Melting/Solidification

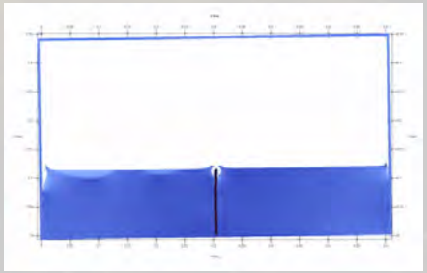

Fluid-Structure Interaction

Structure damage

The 12th European Review Meeting on Severe Accidents Research

May 18-22, 2026, Universidad Carlos III de Madrid, Madrid, Spain

TECHNICAL SESSION 7.3: ADVANCED TECHNOLOGICAL FUELS AND MATERIALS

Chairs: M. E. Cazado (KIT), L. Tiborcz (GRS)

ID040	**Cr-coated claddings modelling in the severe accident code ASTEC** L. Carénini (ASNR)	Paper Presentation
ID064	**Development and Validation of the FeCrAl oxidation model of the ASTEC integral code based on the QUENCH Experimental Results** Z. I. Jiménez Balbuena (KIT)	Paper Presentation
ID052	**The integral air ingress CODEX-ATF-AIT experiment** R. Farkas (HUN-REN Centre for Energy Research)	Paper
ID071	**Comparative Analyses of Creep Models for Predicting Behavior of RPV Steel under Extreme High Temperatures** X. Li (KTH)	Paper Presentation

CR-COATED CLADDINGS MODELLING IN THE SEVERE ACCIDENT CODE ASTEC

Carénini L, Fichot F
Autorité de Sûreté Nucléaire et de Radioprotection (ASNR)
F–13115 Saint-Paul-lez-Durance, France
laure.carenini@asnr.fr; florian.fichot@asnr.fr

ABSTRACT

The Accident Source Term Evaluation Code (ASTEC) developed by ASNR is dedicated to simulating Severe Accidents (SA) in nuclear facilities. It has been continuously improved since its first developments in 1996, following the two objectives of being at the state of the art of scientific knowledge and increasing the scope of code application with consideration of new reactor designs. In the last decade, significant work was done worldwide to propose new materials for the reactor core, with the objective of improving efficiency and safety. Those Advanced Technology Fuels (ATF) are numerous and cover both fuel and claddings materials. Among them, the Cr-coated Zr-based claddings have attracted a lot of interest and are considered today as a mature concept for application in light water nuclear reactors. Dedicated models for Cr-coated claddings have thus been recently developed in ASTEC code based on available knowledge from R&D. They will be part of V3.2 ASTEC version.
Based on experimental data published in literature, it is shown that the protective effect of the Cr-coating against oxidation at low temperature is well reproduced by ASTEC code. It is also the case for the Cr diffusion into Zr substrate leading to possible loss of protective effect even below the Cr-Zr eutectic temperature. Lack of experimental data at high temperatures (above 1300°C) prevents further model development and validation. The simplified model proposed for the oxidation runaway at the Zr-Cr eutectic temperature may underestimate this effect, particularly for the high heating rates expected. With regard to the simulation of the cladding failure and material relocation phenomena, in the absence of quantitative data, no modifications taking into account the impact of the Cr coating have been implemented in the code at this stage. Applications at reactor scale were performed and allow quantification of impact of Cr-coated claddings for two different Station Black Out (SBO) SA scenarios in a typical Pressurized Water Reactor (PWR) of 900MWe. Results showed that the Cr-coated claddings have a noticeable impact on the behaviour of the core heating and the H_2 production. However, this effect is dependent on the SA scenario considered. No generic conclusions on the H_2 mass and production rate can be drawn due to combination of several effects. In particular, the main impacts of the residual power and of the possible water injections in the vessel are illustrated.
In the future, modelling improvements should continue for the behaviour at higher temperatures and up to the mechanical failure or melting of Cr-coated claddings.

KEYWORDS
ASTEC code, Cr-coated Zr-based cladding, modelling, severe accident

1. INTRODUCTION

The Accident Source Term Evaluation Code (ASTEC) developed by ASNR is dedicated to simulating severe accidents in nuclear facilities [1]. This mechanistic computer code models the ongoing accident sequence from initiating events to release of the source term outside the containment, covering core degradation,

fission product chemistry and transport up to environment and containment behaviour. ASTEC has been continuously improved since its first developments in 1996, following the two objectives of being at the state of the art of scientific knowledge and increasing the scope of code application with consideration of new reactor designs [2][3][4]. In addition, code versatility and flexibility allow performing exploratory evaluations. Such evaluations were done in particular to estimate impact of new fuel material properties [5][6]. Indeed, in the last decade, significant work was done worldwide to propose new materials for the reactor core, with the objective of improving efficiency and safety. Those Advanced Technology Fuels (ATF) are numerous and cover both fuel and claddings materials. Among them, the Cr-coated Zr-based claddings have attracted a lot of interest and are considered today as a mature concept for application in light water nuclear reactors. In this context, ASNR decided to implement dedicated models in ASTEC code to properly deal with such cladding material. Even if these new materials cannot significantly affect the evolution of a severe accident and core degradation kinetics in a scenario without effective cooling system, it is necessary to adapt the modelling in the SA codes to be able to predict their behaviour at least with the same level of uncertainties as for existing fuels.

Most of the experimental and modelling works performed up to now have been done for Design Basis Accident (DBA). The phenomenology of Cr-coatings under steam oxidizing atmosphere until Zr-Cr eutectic temperature has been well characterized and understood. However, for higher temperatures, the experimental data remain limited. Recently, the first bundle test in SA conditions was performed in the scope of the OECD QUENCH-ATF project [7]. In the late phase of the SA, the impact of the Cr-coating is expected to be negligible due to the limited mass of Cr added. Nevertheless, existing models in SA codes already consider the presence of Cr in the corium pool due to its incorporation after the melting of steel structures in the reactor.

In this paper, models implemented in ASTEC V3.2 code for the simulation of Cr-coated Zr-based claddings in early phase of SA are presented and validated based on available experimental results published in literature. The transition phase around the Zr-Cr eutectic temperature after which oxidation acceleration is observed is also modelled with a simplified approach and results are compared with experimental data. Further needs for better understanding of the phenomena involved and model improvements are identified. Finally, applications at reactor scale in a generic PWR900 reactor for two SBO scenarios with different levels of residual power in the core when degradation occurs, are presented. These evaluations highlight the impact of Cr-coated claddings on the core degradation as predictable based on existing knowledge.

2. ASTEC MODELLING

The Cr-coating is simulated in ASTEC code with a dedicated layer modelled at the surface of the cladding component. The concept of 'LAYER' in ASTEC code has been used for many years, in particular to model the Zr oxidation and associated formation of α-Zr and ZrO_2 layers at the surface of the claddings. Each 'LAYER' has its own composition and material properties but the different 'LAYER' which belong to the same cladding component have the same temperature. The main phenomena associated with this Cr-coating during the early phase of a SA have been modelled in ASTEC code and are listed below:

- Cr oxidation to form Cr_2O_3 layer at the external surface of the cladding
- Cr diffusion into β-Zr substrate
- Progressive loss of Cr protection below Cr-Zr eutectic temperature
- Cr-Zr eutectic leading to loss of Cr layer integrity
- Once burst opening is reached, the internal surface of the cladding, made of Zr is oxidized in parallel with the oxidation of the Cr-coated external surface

The modelling developed in ASTEC for the first four points are described in the paragraphs below. The last point uses ASTEC capacities already developed in the past. Associated description of these phenomena (burst opening, oxidation of claddings internal surface and Zr oxidation models) is available in the code documentation [8][9]. It should be noted that, at this stage, the Cr volatilization is neglected. Indeed, it was shown experimentally [10] that the volatilization rate remains limited for temperatures under which the Cr layer remains protective (i.e. typically below the one of the Cr-Zr eutectic temperature). In accordance, both

experimental results analyses proposed by Brachet et al. 2020 [11] and modelling work of Wu et al. 2023 [12] show negligible impact of the consideration of the Cr_2O_3 volatilization in the evolution of the Cr consumption kinetics up to 1300°C.

2.1. Cr oxidation

Cr oxidation reaction is modelled as a parabolic law for oxygen mass gain, as classically used for metals oxidation when the kinetics are driven by diffusion process through the oxide layer. By default in ASTEC code, the kinetics proposed is derived from experimental data of Brachet [11] and associated correlation for Cr_2O_3 thickness evolution, as illustrated Figure 1. Compared with other available experimental data, this kinetics is valid for dense Cr layer providing an efficient protection regarding oxygen diffusion and thus Zr-substrate oxidation. As described by Kashkarov [13], higher oxidation kinetics have been measured especially for columnar Cr-coating. This effect was also studied in [11], with experimental study of the effect of annealing on the coating layer microstructure and consequently on oxidation kinetics. Thanks to user parameters which allow modification of the Cr oxidation law in ASTEC code, different kinds of coating can be simulated. The kinetic of Cr oxidation modelled in ASTEC code is calculated with following mass evolution equation:

$$\frac{m_O(t+dt)}{S} = \left(\left(\frac{m_O(t)}{S}\right)^2 + A\, e^{-\frac{B}{RT}} dt\right)^{0.5} \quad (1)$$

With m_o the Oxygen mass (kg), S the surface (m²), R=8.314 J/mole.K, T the temperature (K), t the time (s) and dt the time step (s). Default value derived from Brachet's data [11] for constants A and B are respectively A=16.75 kg²/m⁴/s and B=238.7 kJ/mole.

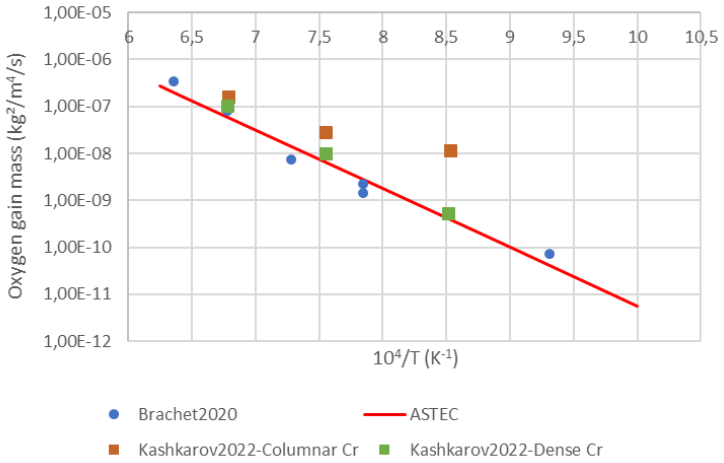

Figure 1. Oxidation law for Cr-coated claddings in ASTEC code and comparison with experimental data [11][13][1].

2.2. Cr diffusion and loss of Cr protectiveness

Cr diffusion into β-Zr has been observed experimentally and reported in many studies, for examples Brachet [11], Yang [15], Kim [16] and Li [17]. At the Cr/Zr interface, a $ZrCr_2$-intermetallic layer is formed, consistently with the Zr-Cr phase diagram [18], even at low temperatures. During high temperature

[1] Note that correlations are usually derived based on experimental measurements of Cr_2O_3 thickness. In ASTEC code, oxidation law is based on Oxygen mass gain and conversion has been done for all experimental data presented in Figure 1 based on the same reference for the Cr_2O_3 density law depending on temperature [14].

oxidation, Cr-Zr inter-diffusion takes place and may, after a certain time, lead to loss of the Cr layer integrity. This transition from protective to non-protective Cr-coating was phenomenologically described by Brachet in 2020 [11] and further by Wu [12] for example. It involves several complex physical phenomena induced by Cr oxidation at the external surface, diffusion through $ZrCr_2$ layer into the β-Zr phase, formation of porosities and deformation at the interfaces of the Cr layer and intergranular diffusion of Zr through the residual metallic Cr layer with finally formation of a zirconia intergranular network leading to loss of Cr protectiveness. Models have been developed to simulate the Cr diffusion into the β-Zr phase as well as the $ZrCr_2$ thickness evolution [12][16][19]. However, due to the complexity of the phenomena involved, there is no model available to simulate the porosities and intergranular network formations. In the scope of Design Basis Accident (DBA) studies, Brachet proposed a macroscopic criterion able to represent the fragilization of the Cr-coating called Equivalent Chromium Reacted (ECrR) in reference to the Equivalent Cladding reacted (ECR) parameter used for Loss Of Coolant Accident (LOCA) [20]. This parameter takes into account the Cr-coating "consumption kinetics" under high temperature oxidizing environment and the influence of the initial Cr-coating thickness. It corresponds to the fraction of the Cr-coating that has been consumed either due to the oxidation or to the diffusion. Experimental tests reveal that post quenching Ductile-to-Brittle Transition (DBT) is reached for a ECrR of nearly 70%. This fragilization of the cladding can be related to the loss of Cr layer integrity. This approach is used in ASTEC code to model the loss of Cr protectiveness below the Zr-Cr eutectic temperature.

In this model, the thickness of the $ZrCr_2$ layer is neglected and a parabolic law is used for the reduction of the Cr layer thickness due to Cr diffusion into β-Zr based on the kinetics given by Brachet [20]. It should be noted that implicitly the $ZrCr_2$ phase formation is considered in this modelling since its presence limits the diffusion of Cr in β-Zr and impacts the kinetic. The default values implemented in the ASTEC model for the Cr diffusion kinetics based on Brachet's work and recalled below are applicable to dense Cr coating. As shown by Yang [15] and Kashkarov [13], different types of Cr coating may lead to faster Cr diffusion and Cr oxidation kinetics. For such coating, it is possible for the ASTEC user to adapt, similarly to the oxidation kinetic, the diffusion kinetics in order to represent coating specificities.

$$\Delta Cr_{Cr\ diffusion\ into\ \beta-Zr}(t+dt) = \left(\left(\Delta Cr_{Cr\ diffusion\ into\ \beta-Zr}(t)\right)^2 + \left(ADIF\ e^{-\frac{BDIF}{RT}}\right)^2 dt\right)^{0.5} \quad (2)$$

With $\Delta \mathrm{Cr}_{Cr\ diffusion\ into\ \beta-Zr}$ the thickness of Cr layer consumed due to Cr diffusion into β-Zr. Default value from Brachet's work [20] for constants ADIF and BDIF are respectively ADIF=8610 μm/$s^{0.5}$ and BDIFF=142.7 kJ/mole.

The progressive loss of the coating protectiveness is evaluated based on the evolution of the ECrR parameter (XREA parameter in ASTEC code) considering the following law for the surface fraction of Zr in contact with Oxygen:

$$Xzr = (1 - XPRO_MIN).\left(\frac{XREA - XREA_MIN}{XREA_MAX - XREA_MIN}\right)^2 \quad (3)$$

With XPRO_MIN, XREA_MIN and XREA_MAX three parameters of the model which are by default chosen to represent the loss of Cr protectiveness for dense Cr layer respectively to 0.3, 0.6 and 0.9. The determination of these values will be presented and discussed in § 3.1.2 dedicated to validation works.

When XREA variable (fraction of initial Cr thickness which has reacted due to oxidation or diffusion) is below XREA_MIN, the Cr layer is fully protective. Then, the oxidation of the Zr begins progressively until XREA reaches the value of XREA_MAX at which the surface of Zr available for oxidation is considered equal to (1-XPRO_MIN) i.e. 70% of the available surface for XPRO_MIN default value of 0.3. Indeed, it is assumed that not all the Zr surface is available for oxidation even after disappearance of the Cr layer due to the presence of the chromia layer. This parameter can be changed by the user for sensitivity study.

It is worth noting that the loss of protection remains limited after reaching the XREA_MIN threshold and becomes significant when the XREA variable approaches the XREA_MAX parameter, due to the parabolic function used in equation (3). This modelling is used to represent in a simplified way the physical transition

from intergranular diffusion of Zr through the residual metallic Cr layer to formation of a zirconia intergranular network observed experimentally [11]. For less dense coating, the criteria used for loss of coating integrity may be adapted by the users. Indeed, the coating deposition method significantly affects the coating properties involved in the loss of integrity due to differences in microstructures of the layer.

2.3. Zr-Cr eutectic

Formation of Zr-Cr eutectic in the cladding is not simulated in ASTEC code for now. Its effect on the evolution of the cladding oxidation being predominant with strong increase of H_2 production once Cr protection is lost at this temperature, it is modelled by the melting of the Cr layer leading to expose of the Zr surface to steam. Eutectic temperature is specified in the input deck thanks to the modification of the Cr solidus and liquidus temperatures (respectively to 1332°C and 1333°C). Once molten, the Cr layer below the oxidized Cr layer is no longer protective and Zr oxidation begins in the code. The liquid Cr layer is however maintained at the periphery of the cladding until mechanical failure (user defined failure criteria for claddings) or melting of the Cr_2O_3 external layer.

3. VALIDATION BASED ON AVAILABLE EXPERIMENTAL RESULTS

3.1. Isothermal tests

3.1.1. Inert atmosphere

Isothermal tests performed in inert atmosphere are designed to study the Cr-Zr interaction. They allow validation of the Cr diffusion model implemented in ASTEC code. Since the kinetics used in ASTEC has been proposed by Brachet based on CEA and Framatome experimental results, it is proposed to validate ASTEC based on independent data obtained by Kim [16] and Yang [17]. In Figure 2, the evolution of the residual Cr thickness with time, at different temperatures ranging from 1000°C to 1300°C, evaluated by ASTEC code is compared with experimental data. These validations show satisfactory results and thus confirm validity of the simplifying assumptions considered in the model as neglecting the $ZrCr_2$ thickness. In particular, it should be noted that more complex models, as presented in [16], show comparable deviation with experimental results.

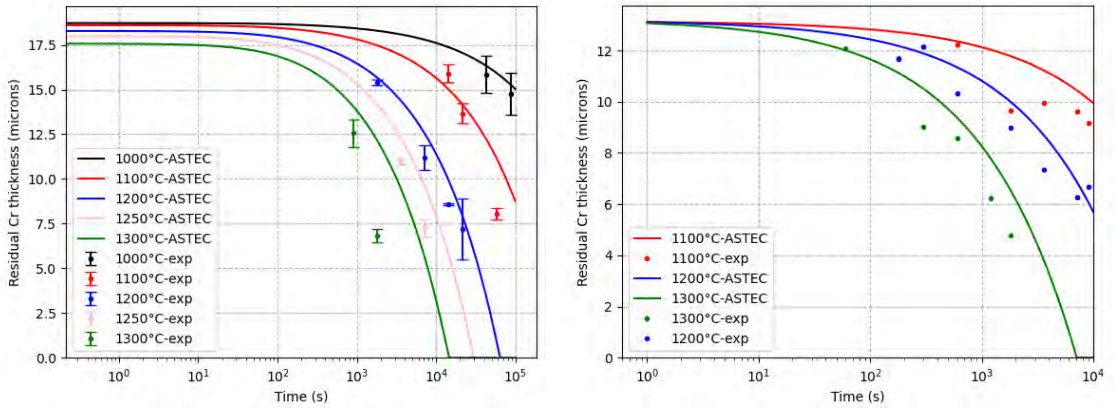

Figure 2. Validation of Cr diffusion model in ASTEC code against experimental results of Kim et al. [16] (left) and Yang et al. [17] (right).

3.1.2. Oxidizing atmosphere

Experimental results obtained in oxidizing atmosphere are used to validate first the kinetics of Cr oxidation (equation (1)) and then the progressive loss of Cr protectiveness (equation (3)).

Figure 3 shows ASTEC results for isothermal oxidation of a 15µm protective Cr coating and comparison with non-coated case and experimental results at 1100°C and 1200°C. Bischoff and Brachet data are obtained for cylindrical geometry and a 10-15µm Cr coating on M5 substrate. A good agreement with experimental data is obtained and the strong reduction of oxidation due to the Cr coating is well captured.

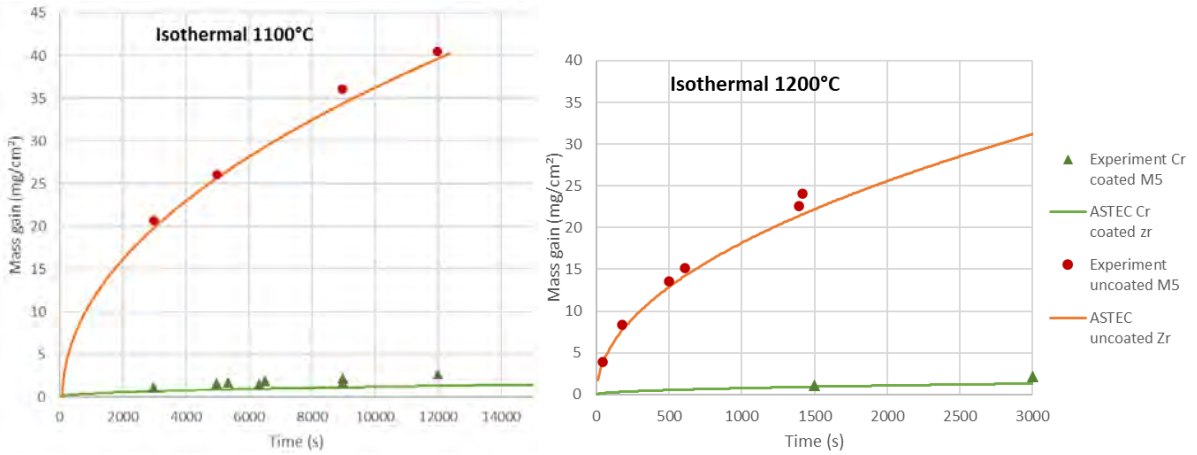

Figure 3. Comparison of ASTEC code oxidation results at 1100°C (left) and 1200°C (right) against experimental data from Bischoff [21] and Brachet [22] when Cr layer is protective.

Then, oxidation law for protective Cr coating and its transition to unprotective coating below Cr-Zr eutectic temperature as implemented in ASTEC code are compared to the same experimental data available also for longer durations. As illustrated in Figure 4, ASTEC code well predicts experimental results. The loss of Cr layer integrity and subsequent start of Zr oxidation is clearly visible with changes in the oxidation rates. As expected, the transition occurs earlier for higher temperatures. The experimental results obtained at 1200°C have been used to select the default parameters of the transition model as illustrated in Figure 5.

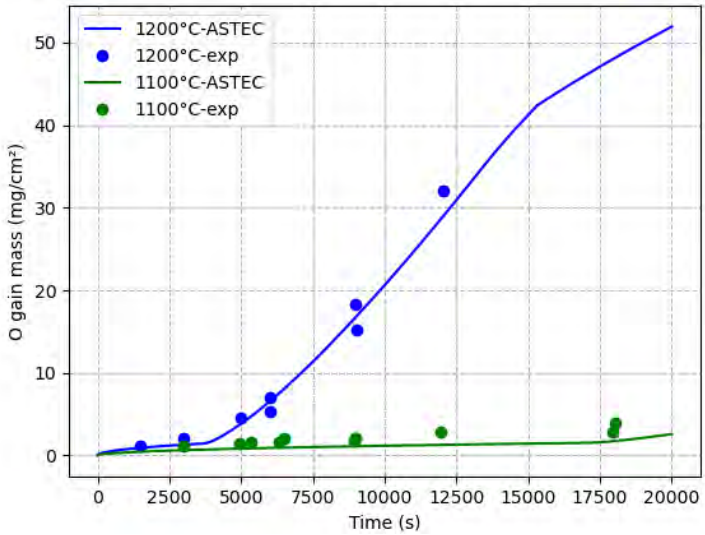

Figure 4. Comparison of ASTEC code oxidation results at 1100°C and 1200°C against experimental data from Bischoff [21] and Brachet [22] up to loss of protective Cr layer.

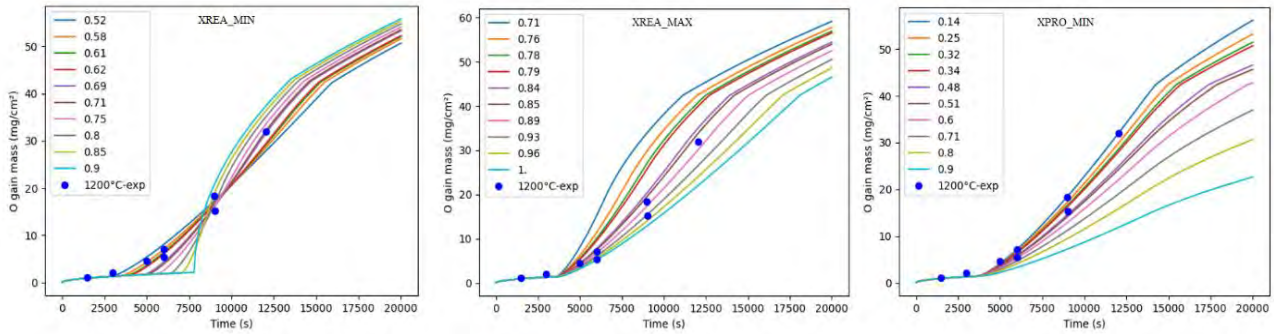

Figure 5. Influence of ASTEC code modelling parameters for the simulation of the transition phase.

3.2. Transient tests up to temperature above the Zr-Cr eutectic

In this part, it is proposed to check ASTEC predictions at higher temperatures above Zr-Cr eutectic temperature, even if simplified modelling is considered in the code for now. For this purpose, experimental results published by Kim et al. [23] are used. In these tests, Zircaloy 4 plates coated with 17µm Cr layer are oxidized and heated up to 1380°C with different heating rates. Results of ASTEC simulations presented in the left side of Figure 6 show that acceleration of oxidation reaction above eutectic temperature, compared to uncoated claddings is well reproduced by the code. A reduction of the maximum mass gain rate for the case of 2K/min heating rate, is visible and can be explained by the loss of the protectiveness of the Cr layer before reaching the Zr-Cr eutectic temperature. This reduction for low heat rate is also obtained experimentally (see Figure 6, right). For the other cases, a maximum mass gain rate of about 70mg/min is evaluated by ASTEC. In the experiment, this maximum value reaches 100mg/min for the highest heating rate of 50K/min but is about 35mg/min for 30K/min. A rapid decrease of the mass gain rate is observed in the ASTEC simulation after the runaways which is not observed experimentally, at least in this small range above eutectic temperature (only 50 K). This analysis shows that, as expected, the simplified approach proposed currently in ASTEC code is not sufficient to reproduce the physical phenomena occurring in the Cr-coated claddings when Zr-Cr eutectic temperature is reached. However, it is also interesting to see that for high heating rate (typically 50K/min) the proposed modelling is not conservative, despite the instantaneous switch to the Zr oxidation model considered. This can be interpreted as an indication of the primary role of the liquid eutectic phase in this runaway of the oxidation kinetics which requires further studies before drawing any conclusion.

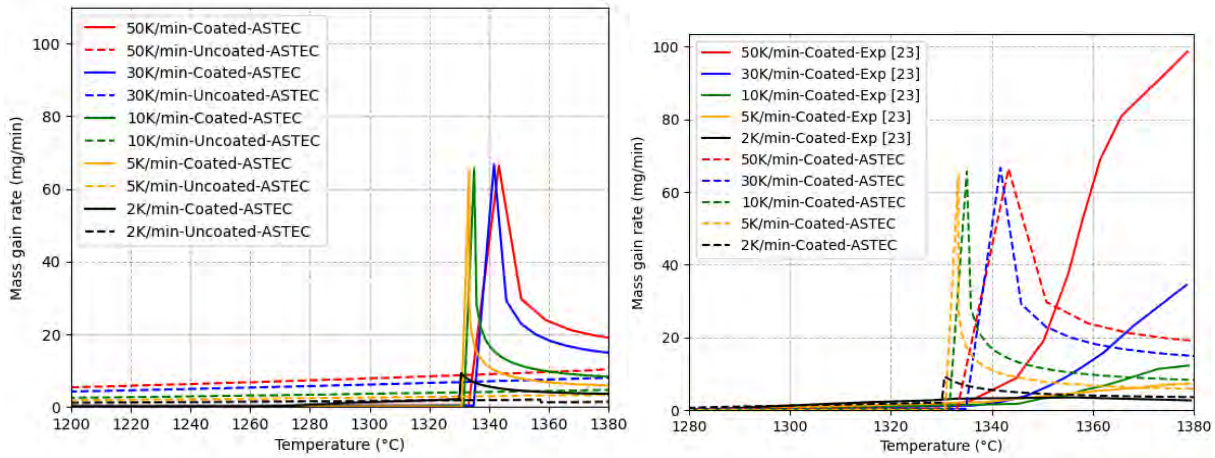

Figure 6. ASTEC code results for transient heating tests with coated and uncoated claddings (left) and comparison for coated claddings with Kim experimental data [23] (right).

Further experiments, in particular in cylindrical geometry, are thus necessary to better understand the main physical processes occurring and to propose adapted models for severe accident codes. Indeed, the plane geometry may have an impact on the kinetics of the loss of Cr layer protectiveness compared to cylindrical geometry.

4. REACTOR APPLICATIONS

Knowing the validation status of the models developed in ASTEC code for Cr-coated claddings, it is proposed in this part to present exploratory calculations at reactor scale to evaluate potential impact of these new claddings. Since too few experimental data (one QUENCH test [7]) are available at temperatures corresponding to the mechanical failure and melting of the Cr-coated claddings, the integrity criteria used for uncoated claddings are used also for the Cr-coated claddings, in these exploratory simulations of SA at reactor scale. This means that it is assumed that the Zr-Cr eutectic has no impact on the cladding mechanical strength. The failure is achieved considering the two following steps:

- Cracking of the oxide layer allows relocation of molten materials (including Cr) when temperature and zirconia thickness criteria are met (melting temperature of Zr if no zirconia layer and linear function up to 2500K for 500µm of ZrO_2).
- Collapse of the claddings and solid debris formation between 2550K and 2600K depending on the zirconia thickness.

It should be kept in mind that for Cr-coated claddings, it would be necessary to justify the validity of these criteria. In particular, it can be expected that loss of cladding integrity will be reached at lower temperature due to Zr interaction with Cr but no quantitative data is available at this time.

A Station Black Out (SBO) scenario is selected. The main events occurring in this scenario for the reference ASTEC simulation (i.e. with uncoated claddings) are summarized below:

- Start of core dewatering ~2h20 after the reactor scram
- Degradation begins at high pressure
- Break opening in the hot leg at about 3h, leading to vessel depressurization
- Start of accumulators discharge, leading to reflood partially the core
- 3h45 restart of core degradation

In order to study the impact of the residual power, a second scenario has also been considered based on the first one but considering the availability of safety injection systems during 24h after the start of the accident. In this case, the water inventory in the vessel is maintained thanks to the high-pressure injection system, as long as it is operational. Then, the main events occurring are similar to the first SBO scenario: The core dewatering occurs 28h after the reactor scram and the second core degradation after accumulators discharge (due to breach opening in the primary circuit and depressurization) at about 30h. For simulations with Cr-coated cladding, a coating of 10µm is considered for all fuel claddings. Control rods guide tubes and instrumentation guide tubes in Zr are also coated but not the grids. The creep law used to evaluate the ballooning and the burst opening of the claddings is considered not modified by the coating. In any case, differences can be considered as negligeable for SA progression. Once burst opening is achieved, internal oxidation of the cladding starts but is limited at the corresponding elevation. Associated impact at reactor scale remains thus limited.

Comparison of hydrogen production with or without Cr coating and for the two SBO scenarios is presented in Figure 7. After the start of the H_2 production, a plateau is visible in the curves associated with the accumulators discharge as discussed above. Then, degradation restarts and further H_2 is produced until reactor vessel failure and corium transfer to the reactor pit. In the first scenario, a delay in the H_2 production is visible of about 15min. The total hydrogen produced is reduced by about 100kg in the simulation with the Cr-coated claddings. The origin of the H_2 masses is also described in the Figure 7. It is worth noting that here, H_2 production from corium includes molten or resolidified materials either in form of corium films or corium pool. It allows identifying that this reduction is mainly due to the reduced oxidation of the claddings surface before melting of material and relocation outside of the claddings. Oxidation of corium is not

impacted by the Cr-coating in this scenario with current modelling assumptions of claddings failures. In the second scenario, with core dewatering delayed of about 24h, a strong reduction of the H_2 production before accumulator's discharge is visible (Figure 7, right). The Cr-coated claddings prevent significant core heating before accumulators discharge. Then, the total H_2 masses produced during core degradation are comparable. This is explained by a larger oxidation of the corium in case of Cr-coated claddings compensating partly for the reduction of the cladding oxidation (reducing the Zr oxidation of the claddings leads to the formation of a corium with a lower degree of oxidation, which will then potentially be more oxidized). At the end the total mass of H_2 produced is lower for Cr-coated claddings mainly due to the reduced production during the first degradation phase. Thanks to the accumulators discharge, the massive hydrogen production (100kg) is delayed by about 2h. However, considering the time when the cumulated H_2 mass reaches 200kg, this delay is reduced to 30min. These results highlight the combined effect of the water injection and the residual power on the capacity of Cr-coated claddings to delay accident progression.

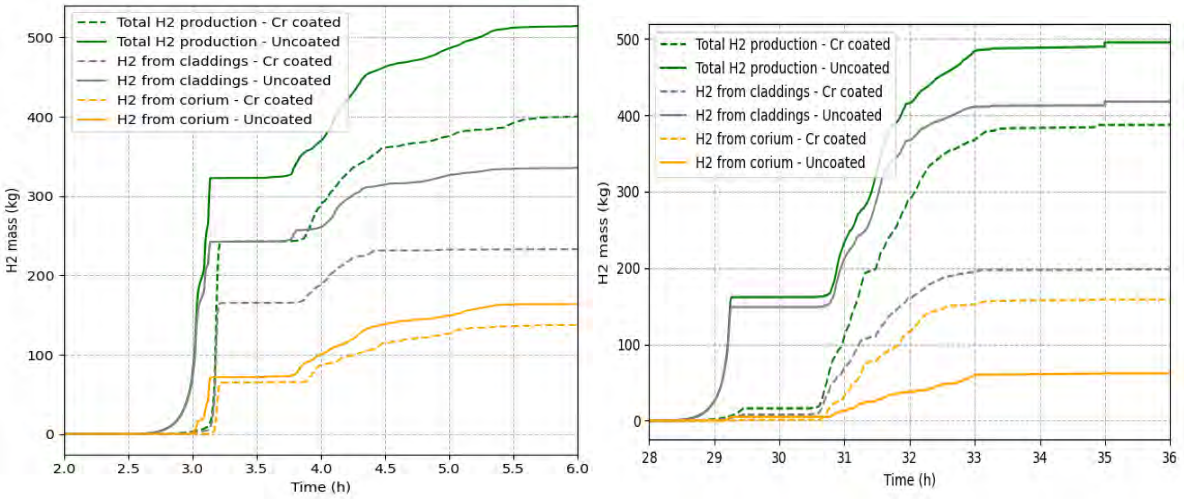

Figure 7. H_2 production during core degradation: impact of Cr-coating on claddings and corium oxidation for SBO scenario with loss of all safety system (left) and SBO scenario with loss of high- and low-pressure injection systems 24h after the reactor shutdown (right).

Comparison of temperature evolutions in case of uncoated and Cr-coated claddings is presented on the left of Figure 8 for the SBO reference scenario. It exhibits the start of exothermic Zr oxidation reaction in the case of uncoated claddings with a progressive increase of the slope of the curves until about 1800K, where oxidation runaway is predicted by Zr oxidation law. On the contrary, the temperatures evolution for Cr-coated claddings remains mainly affected only by the residual power until reaching the Zr-Cr-eutectic temperature at 1600K. At this point, Zr oxidation begins with strong impact and stiff temperature escalation. Due to this sudden loss of Cr protection, the maximum instantaneous heating rates calculated in the case of Cr-coated claddings are even higher than those observed for uncoated claddings at oxidation runaway (cf. right side of Figure 8). This behaviour is also observed at reactor scale for the total H_2 mass produced, as illustrated on the left of Figure 9: the kinetics of cumulated H_2 production rate is higher for Cr-coated claddings compared to uncoated.

On the contrary, in the SBO scenario with 24h delay, the first degradation phase is stronger for uncoated materials leading to higher H_2 production rates. Then, during the second degradation phase, the Cr-coated simulation does not exhibit high H_2 production rate at reactor scale. This may be explained by two factors associated with the reduced residual power in this scenario (15MW at start of core dewatering versus 30MW for the reference scenario) leading to a lower heating rate of the core before oxidation runs away. Firstly, due to a more progressive heating of the core (in the case of the reference SBO scenario, a large part of the core heats up at the same time), the Zr-Cr eutectic temperature is reached only locally and, as a consequence, the local increase of H_2 production rate is not visible at reactor scale. Secondly, in this scenario, part of the

claddings loses the Cr protectiveness before reaching the Zr-Cr eutectic temperature. As observed in § 3.2 for the validation based on Kim experiments, this phenomenon prevents the strong oxidation above Zr-Cr eutectic temperature due to the preliminary formation of protective ZrO_2 layer.

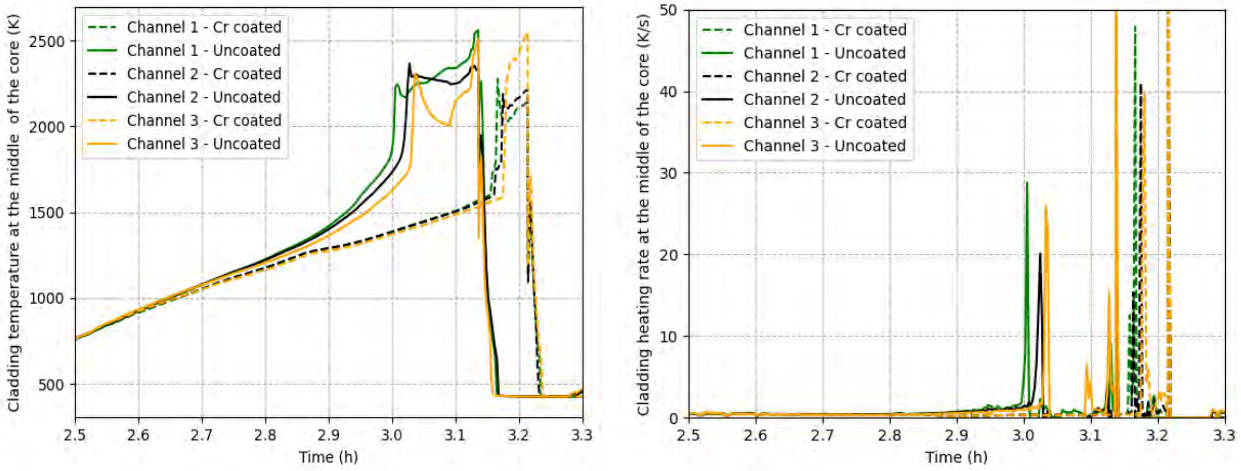

Figure 8. Evolution of claddings temperatures (left) and heating rates (right) at the middle of the core (axially and for the 3 channels in the center of the core[2])

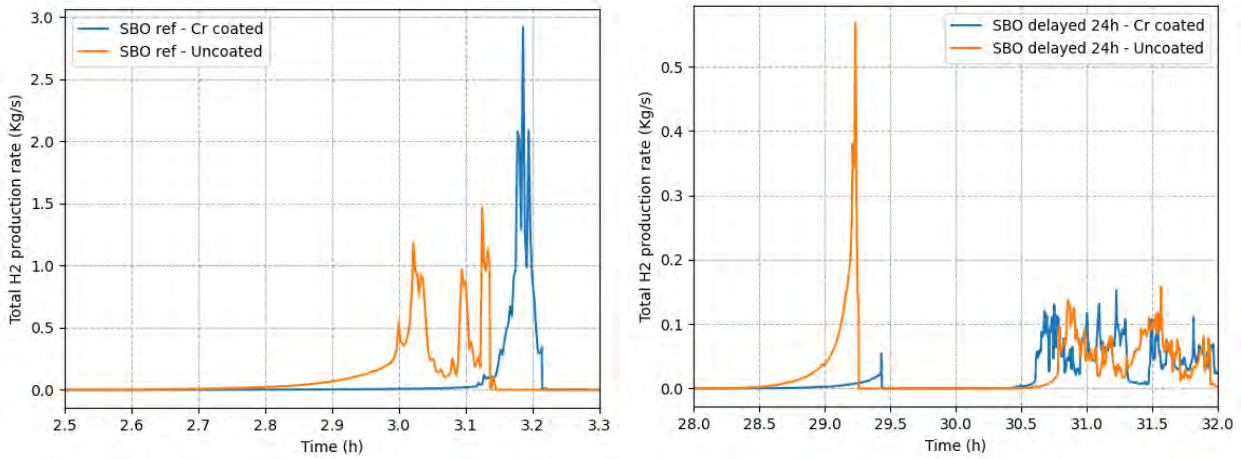

Figure 9. Evolution of H_2 production rate for uncoated and Cr-coated claddings during core degradation for the two SBO scenarios studied

The evolution of the maximum value of Cr reaction rate (XREA parameter) in all the claddings in the core during the degradation is presented for both SBO scenarios on the left side of Figure 10. It is shown that in the case of the reference SBO scenario, the Cr coating integrity is not lost before reaching the eutectic temperature of Zr-Cr. A maximum value of 0.57 is obtained which is close to the minimum value of 0.6 considered in the model (XREA_MIN parameter, cf. § 2.2). For the SBO scenario with the delay of 24h, as mentioned above, the lower residual power in the core leads to slower heating rate of the claddings and the maximum cladding's reaction rate in the core reaches 0.7. Locally loss of Cr protection has thus been reached below Zr-Cr eutectic temperature in this scenario.

[2]A total of 5 channels is used for the radial discretization of the core. The temperatures evolutions in the two channels at the periphery of the core are not presented because they are influenced by the relocation of molten material from the central part of the core which prevents identification of claddings oxidation at high temperature.

In the right side of Figure 10, a detailed study of the loss of cladding integrity at one selected location in the reactor among places, where it is observed, is proposed. The evolution of the Cr cladding reaction rate is presented in relation with the cladding temperature, the fraction of Zr surface available for oxidation and the associated H_2 production. At 30h, the accumulators' discharge is finished, and the cladding temperature is rising again. During the first degradation phase before reflooding, the Zr-Cr eutectic temperature has not been reached at this location, but the Cr reaction rate has already reached the threshold value of 60%. However, it has been for a short time, and the associated hydrogen production is negligible. When the temperature is above 1100K, the impact of Zr oxidation begins to be visible in both temperature evolution and H_2 production. The Cr reaction rate and the surface fraction of Zr available for oxidation increases in accordance with the temperature increase until Zr-Cr eutectic temperature is reached and melting of Cr layer. It is observed that even a limited fraction of Zr surface (about 3%) has a measurable impact on both temperature and H_2 evolutions at a given location in the reactor core. On the opposite of isothermal tests, high Cr reaction rate cannot be reached because small loss of Cr protectiveness induces temperature increase and the time interval before reaching Zr-Cr eutectic temperature is thus reduced.

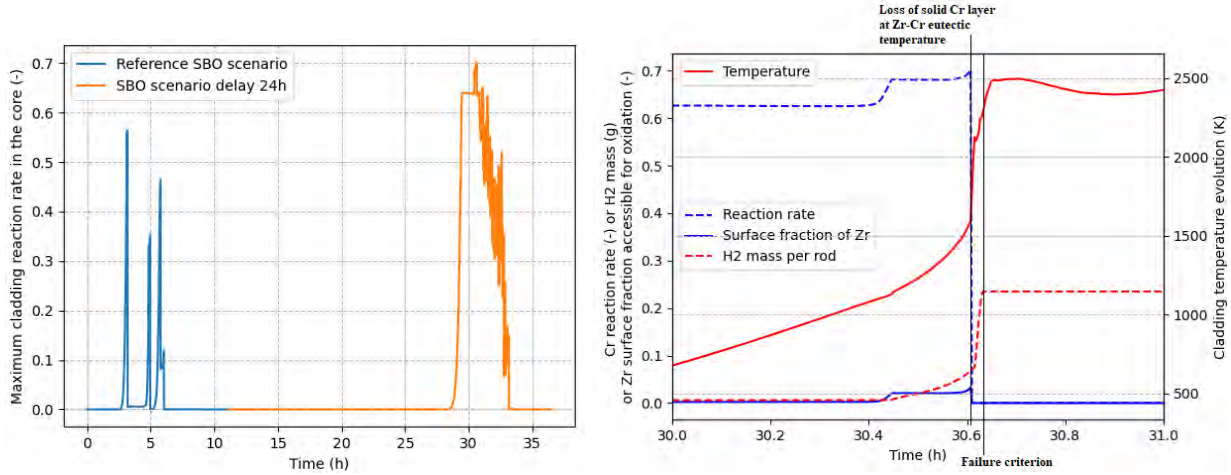

Figure 10 – Evolution of maximum Cr reaction rate in all the claddings during core degradation for the two SBO scenarios studied (left) and evolution of main parameters during loss of Cr protectiveness before Zr-Cr eutectic (analysis at the top of the core in channel 2 during SBO scenario with 24h delay) (right).

5. CONCLUSIONS

In this paper, ASTEC models developed to simulate Cr-coated Zr based claddings during SA have been presented. Based on available experimental data, these models mainly focus on early phase of the core degradation and low temperatures (typically below 1600K). The validation works performed illustrate the good capacities of ASTEC code to capture the protective effect of the Cr coating against oxidation and the Cr diffusion in the Zr substrate. Based on the ECrR approach developed by Brachet [20], a simplified model suitable for SA codes has been proposed and implemented in ASTEC code for the prediction of the loss of the Cr protectiveness at temperature below the Zr-Cr eutectic. Kinetics of oxidation, Cr diffusion and Cr layer progressive loss of integrity have been considered for dense Cr coating. However, the possibility is given to the user to adapt those kinetics in order to simulate different coating microstructures such as columnar Cr-coating.

Simplified modelling for the transition at the Zr-Cr eutectic temperature has also been proposed but its validation remains partial due to lack of experimental data. It was shown that, depending on the heating rate, the proposed approach may be conservative or not. There is thus a clear need to further study the behaviour of Cr-coated claddings when reaching Zr-Cr eutectic temperature and above. In addition, the study of the possible impact of the Cr coating on the loss of cladding integrity at high temperatures remains to be done. For such issue, both separate effect tests and bundle tests are necessary.

Exploratory simulations at reactor scale have been performed with these new models to assess the potential impact of Cr-coated claddings for two SBO scenarios. In the SBO reference scenario with loss of all safety injection systems at the beginning of the accident, the core degradation occurs in 3h. The presence of Cr-coated claddings delays the H_2 production of about 15min. The total hydrogen mass at the vessel failure is reduced by 20% (400kg compared to 500kg) due to less H_2 produced by the Cr-coated claddings. For the SBO scenario with a 24h delay before failure of safety injection systems, the core degradation occurs 28h after the reactor scram. The residual power is divided by two compared to the first scenario and this has a significant effect on the Cr-coated claddings behaviour, even if the total H_2 mass reduction due to Cr-coated claddings is comparable. In the transient core dewatering before accumulators discharge, due to the reduced residual power (15MW), Cr-coated claddings prevent significant H_2 production and core heating. Consequently, the production of 100kg of H_2 is delayed by about 2h but this delay is reduced to 30min when considering the times at which 200kg of H_2 have been produced. A compensating effect is also identified with a higher corium oxidation due to the reduced Zr oxidation in the rod geometry.
The loss of Cr protectiveness below the Cr-Zr temperature due to Cr consumption by diffusion and oxidation reactions is observed in the SBO scenario with delayed loss of high- and low-pressure safety injection systems. It is shown that when Cr reaction rate reached criterion for start of progressive Zr surface oxidation, even limited access of Oxygen to the Zr substrate has a significant impact on both H_2 production and temperature increase. Due to the exothermic reaction of the Zr oxidation, the Zr-Cr eutectic temperature is then reached rapidly and before significant increase of the Zr surface fraction accessible to Oxygen below the Cr layer.
Finally, in the fast kinetics scenario, it is observed that the maximum H_2 production rate is higher for Cr-coated claddings due to the fact that Zr oxidation occurs at higher temperature after Zr-Cr eutectic without protective oxide layer. On the contrary, for the SBO scenario with 24h delay, this effect is not visible at reactor scale. Only local increase of H_2 production is observed when Zr-Cr eutectic temperature is reached. In addition, the beginning of Zr oxidation before Zr-Cr eutectic temperature at some locations in the core also contributes to the reduction of this bifurcating effect.
In conclusion, based on these first integral calculations, interesting specificities of Cr-coated claddings and respective influences of the different assumptions considered for the modelling have been highlighted. In general, it can be said that the Cr-coated claddings have a noticeable impact on the behaviour of the core heating and the H_2 production. However, this effect is dependent on the SA scenario considered. No generic conclusions on the H_2 mass and production rate can be drawn due to combination of several effects. In particular, the main impacts of the residual power and of the possible water injections in the vessel were illustrated. Dedicated models for such coating in SA codes appear then as necessary before performing any safety studies. Modelling improvements should continue for the behaviour at higher temperatures and up to the mechanical failure or melting of Cr-coated claddings.

REFERENCES

1. P. Drai et al., “ASTEC V3: A comprehensive Integral Code for Nuclear Safety Analysis and Research”, *Proceedings of NURETH conference*, Busan, Korea (2025).
2. J.P. Van Dorsselaere et al., “The ASTEC integral code for severe accident simulation”, *Nucl. Tech.* **165** (3) pp. 293-307 (2009). https://doi.org/10.13182/NT09-A4102
3. P. Chatelard et al., “ASTEC V2 severe accident integral code main features, current V2.0 modelling status, perspectives”, *Nucl. Eng. Design* **272**, pp.119-135 (2014). https://doi.org/10.1016/j.nucengdes.2013.06.040
4. P. Chatelard et al., “Main modelling features of ASTEC V2.1 major version”, *Ann. Nucl. Energy* **93**, pp.83-93 (2016). https://doi.org/10.1016/j.anucene.2015.12.026
5. J. Stuckert, Z. Hozer, A. Khaperskia, K. Sim, “IAEA ATF-TS Benchmark for Simulation of Bundle Tests”, *Proceedings of Top Fuel Conference*, Grenoble, France (2024).

6. J. Zhang, M. Ševecek, K. Sim, A. Khaperskia, "ATF-TS: IAEA Coordinated Research Project on Testing and Simulations for Accident Tolerant and Advanced Technology Fuels", *Proceedings of Top Fuel Conference*, Grenoble, France (2024).
7. NEA, "QUENCH-ATF project", Nuclear Energy Agency, Organisation for Economic Co-Operation and Development, https://www.oecd-nea.org/jcms/pl_36597/quench-atf-project
8. V. Topin et al. *ASTEC V3 Physical modelling of the ICARE module*, IRSN report, France (2022)
9. V. Topin et al. *ASTEC V3: ICARE module - User manual*, IRSN report, France (2022)
10. L. Royer et al., "On the Oxidation and Nitridation of Chromium at 1300 °C", *Oxid. Met.* **74**, pp. 79-92 (2010). https://doi.org/10.1007/s11085-010-9198-2
11. J.C. Brachet et al., "High temperature steam oxidation of chromium-coated zirconium-based alloys: kinetics and process", *Corros. Sci.* **167** (2020). https://doi.org/10.1016/j.corsci.2020.108537
12. S. Wu et al., "Model development for oxidation and degradation behavior of accident tolerant Cr coating on Zr alloy cladding under high temperature steam atmosphere", *J. Nucl. Mater.* **589** (2024). https://doi.org/10.1016/j.jnucmat.2023.154836
13. E.B. Kashkarov et al. "Influence of coating parameters on oxidation behavior of Cr-coated zirconium alloy for accident tolerant fuel claddings" *Corros. Sci* **203** (2022). https://doi.org/10.1016/j.corsci.2022.110359
14. Y. Fei, *Mineral Physics and Crystallography: A Handbook of Physical Constants*, vol 1 American Geophysical Union (1995).
15. J. Yang et al., "High temperature Cr-Zr interaction of two types of Cr-coated zirconium alloy in inert gas environment", *J. Nucl. Mater.* **547** (2021). https://doi.org/10.1016/j.jnucmat.2021.152806.
16. D. Kim, Y. Lee, "Diffusion of chromium coating on Zircaloy accident tolerant fuel cladding: model development and experimental validation", *Surface & Coatings Technology* **468** (2023). https://doi.org/10.1016/j.surfcoat.2023.129698
17. B. Li et al., "Experimental kinetic study of interdiffusion behavior and intermetallic compound $Zr(Fe,Cr)_2$ formation at the Cr/Zry4 interface under elevated temperatures", *J. Nucl. Mater.* **585** (2023). https://doi.org/10.1016/j.jnucmat.2023.154595
18. P. Lafaye, C. Toffolon-Masclet, J.-C. Crivello, and J.-M. Joubert, "Experimental investigations and thermodynamic modelling of the Cr–Nb–Sn–Zr system", *Calphad*, **64**, pp. 43–54 (2019). https://doi.org/10.1016/j.calphad.2018.11.002
19. J.C. Brachet et al. "Early studies on Cr-coated Zircaloy-4 as Enhanced Accident Tolerant Nuclear Fuel Claddings for Light Water Reactors", *J. Nucl. Mater.* **517,** pp. 268-285 (2019). https://doi.org/10.1016/j.jnucmat.2019.02.018
20. J.C. Brachet et al. "A new "ECR" parameter to support high temperature (one-sided) steam oxidation behavior of Cr-coated Zr-based E-ATF claddings, in relation with their post-quenching mechanical strength and ductility" *Proceedings of TOPFUEL conference*, Grenoble, France (2024).
21. J. Bischoff et al. "Cr-coated cladding development at Framatome". *Proceedings of TOPFUEL conference*, Prague, Czech Republic (2018).
22. J. C. Brachet et al. "Behavior of Cr-coated M5 claddings during and after high temperature steam oxidation from 800°C up to 1500°C (Loss-Of-Coolant Accident & Design Extension Conditions)". *Proceedings of TOPFUEL conference*, Prague, Czech Republic (2018).
23. D. Kim et al., "Eutectic reaction and oxidation behavior of Cr-coated Zircaloy-4 accident-tolerant fuel cladding under various heating rates", *J. Nucl. Mater.* **583** (2023). https://doi.org/10.1016/j.jnucmat.2023.154538

ASNR Autorité de sûreté nucléaire et de radioprotection

21st MAI 2026

Cr-COATED CLADDINGS MODELLING IN THE SEVERE ACCIDENT CODE ASTEC

L. CARÉNINI

ERMSAR Conference, Madrid (Spain)

MODELLING OF THE REACTOR CORE IN ASTEC CODE

ASTEC
ACCIDENT SOURCE TERM EVALUATION CODE

- 2D axisymmetric
- Radial (~25cm) and axial (~15cm) meshing
- Sub-meshing of the structures

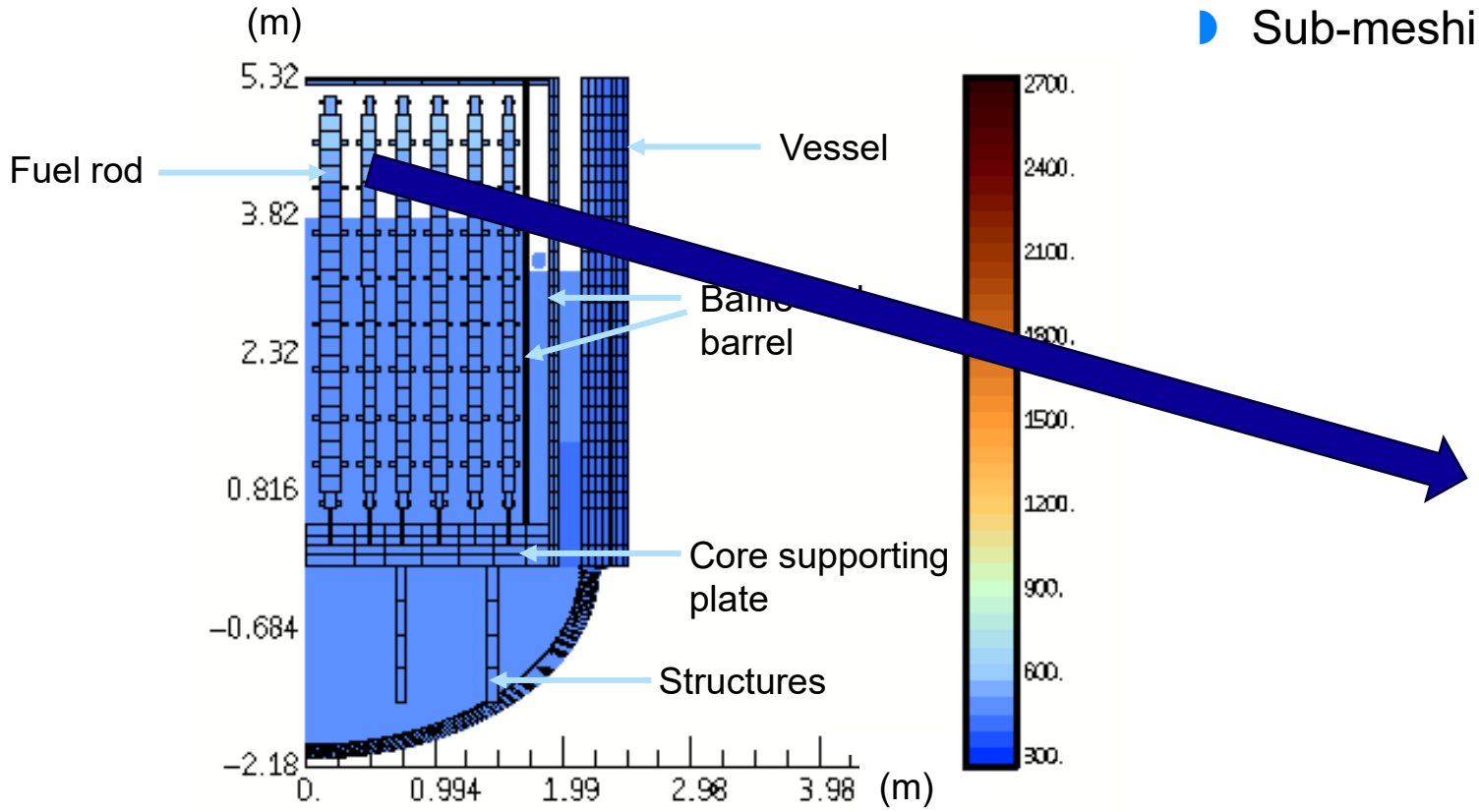

Temperature field (K)

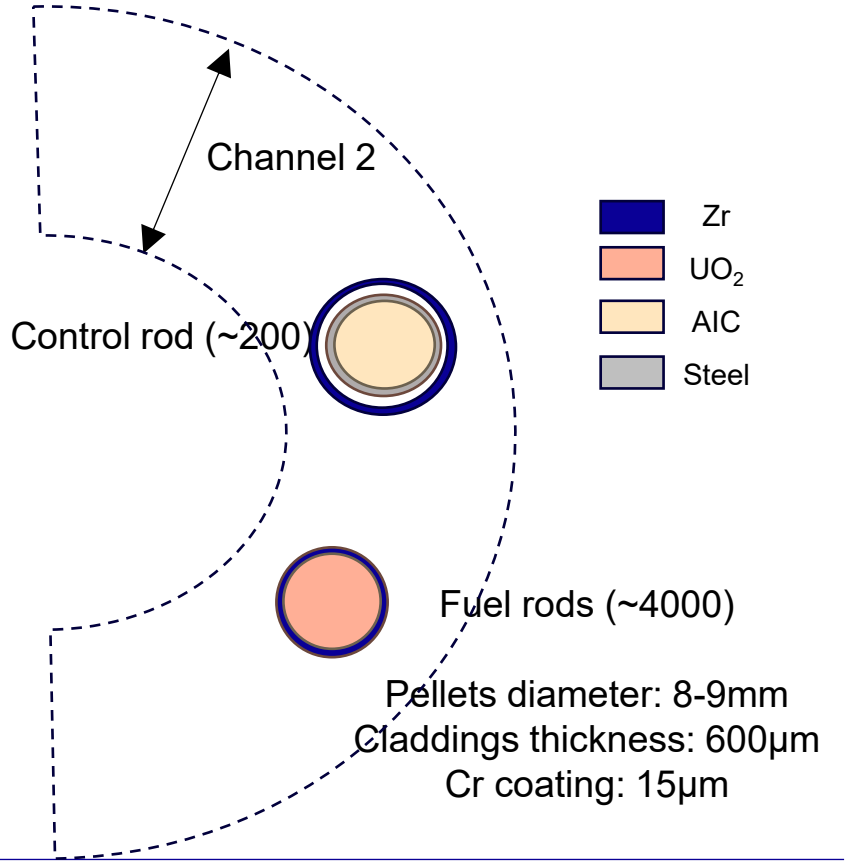

Pellets diameter: 8-9mm
Claddings thickness: 600µm
Cr coating: 15µm

Cr COATED Zr CLADDING MODELLING IN ASTEC V3.2

- Main phenomena observed experimentally and modelled in ASTEC code:
  - Cr oxidation by steam to form Cr_2O_3 layer at the external surface of the cladding
  - Cr diffusion into β-Zr substrate
  - Once burst opening is reached, the internal surface of the cladding, made of Zr is oxidized
  - Cr-Zr eutectic (1332°C) leading to loss of Cr layer integrity
  - Progressive loss of Cr protection below Cr-Zr eutectic temperature

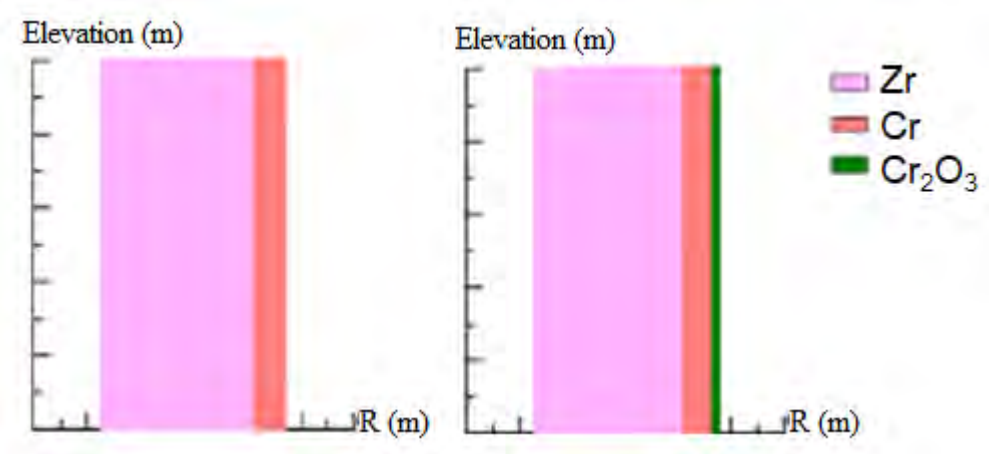

PROGRESSIVE LOSS OF Cr PROTECTION BELOW Cr-Zr EUTECTIC TEMPERATURE

- Several phenomena identified:
  - Oxidation of Cr at the external surface
  - Diffusion of Cr in the Zr substrate
  - Formation of porosities and deformation at interfaces
  - Intergranular diffusion of Zr in the remaining Cr layer
  - Formation of Zirconia channels at the grain boundaries

→ Complex phenomena but well studied experimentally

- Summary of the proposed oxidation and degradation mechanisms for Cr-coated Zr alloy in steam atmosphere (below Zr-Cr eutectic temperature)

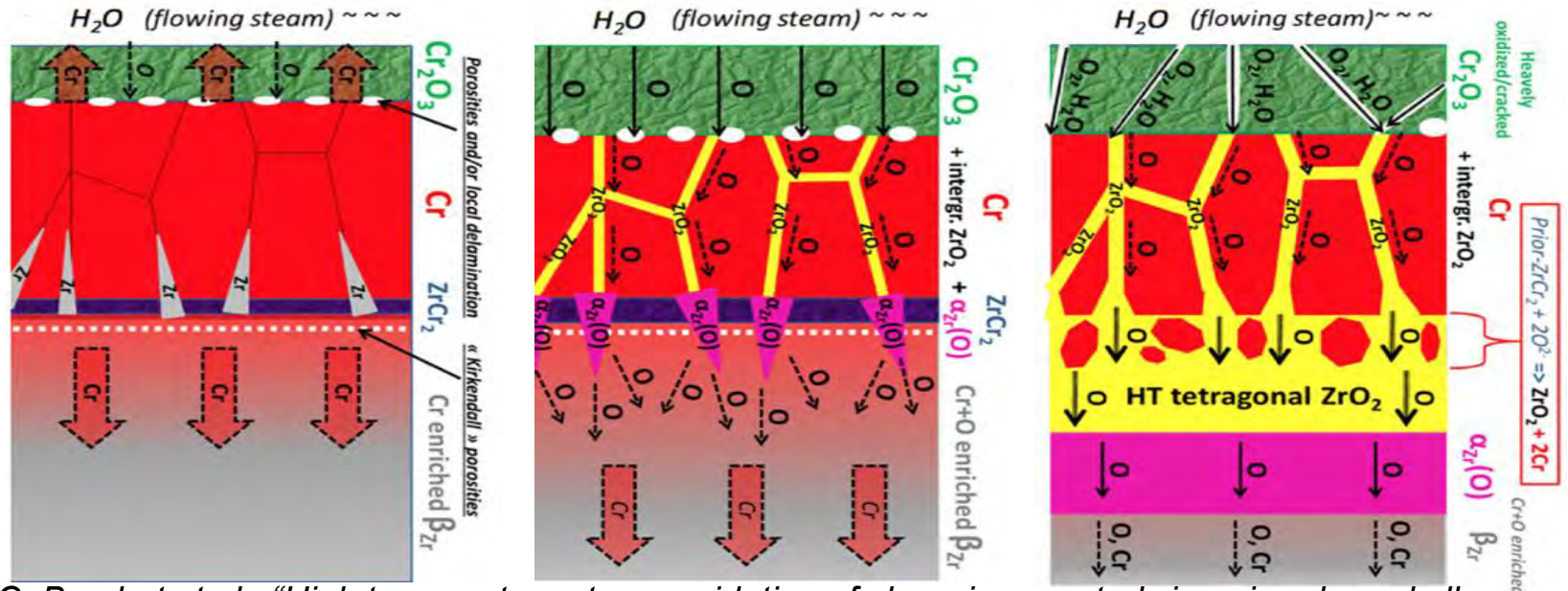

J.C. Brachet et al., "High temperature steam oxidation of chromium-coated zirconium-based alloys: kinetics and process", Corros. Sci. 167 (2020)

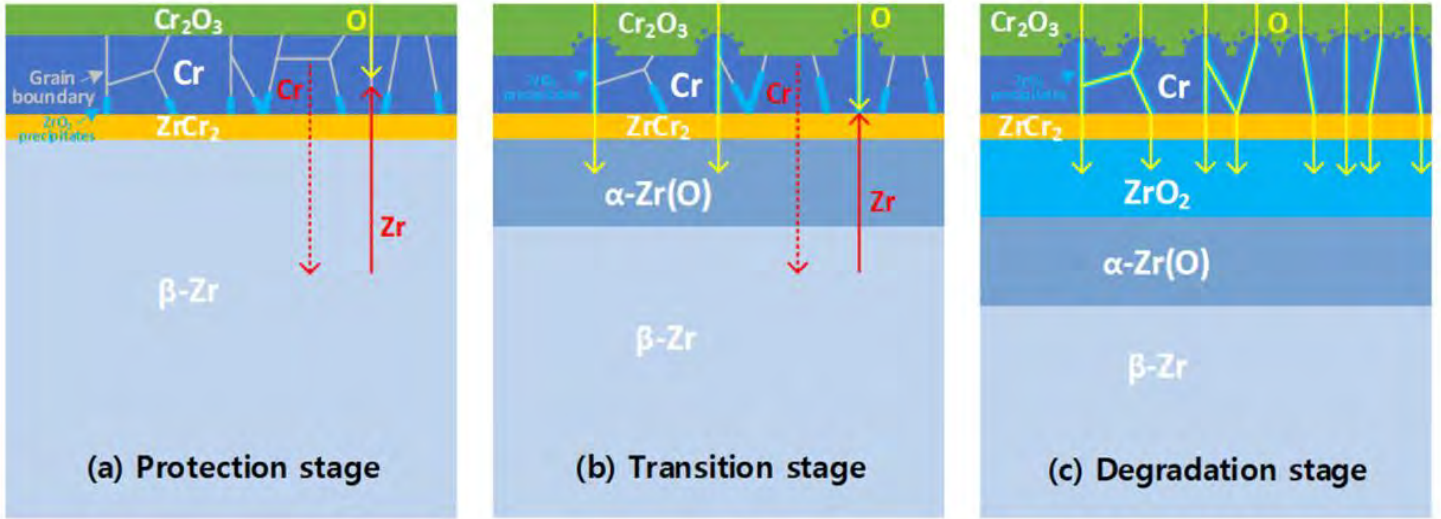

S. Wu et al., "Model development for oxidation and degradation behavior of accident tolerant Cr coating on Zr alloy cladding under high temperature steam atmosphere", J. Nucl. Mater. 589 (2024)

PROGRESSIVE LOSS OF Cr PROTECTION BELOW Cr-Zr EUTECTIC TEMPERATURE

- Work from J.C. Brachet (2025) dedicated to the DBA: *J.C. Brachet et al., J. Nucl. Nat. 606 (2025)*
  - Definition of a new criterion ECrR (Equivalent Chromium Reacted) for the identification of the mechanical failure of the cladding

$$\text{ECrR} = \frac{\text{Thickness of consummed Cr due to diffusion and oxidation}}{\text{Initial Cr thickness}}$$

  - Threshold identified experimentally at 70% for mechanical properties
  - Interpretation: **loss of mechanical resistance due the creation of the channels in the Cr layer leading to Zr oxidation**

PROGRESSIVE LOSS OF Cr PROTECTION BELOW Cr-Zr EUTECTIC TEMPERATURE

- Steps followed:
  - Diffusion of Cr in the Zr substrate → validation in inert atmosphere
  - Oxidation of Cr at the external surface → validation based on the kinetics of H_2 production when Cr remains protective
  - Transition between protective to non protective after a certain threshold of ECrR → choice of model parameters based on experimental results

TRANSITION LAW BASED ON ECrR

- The law proposed is dedicated to the surface fraction of Zr in contact with oxygen
- A parabolic function is used: transition from intergranular diffusion of Zr through the metallic Cr layer to formation of a zirconia intergranular network observed experimentally
- A maximum fraction of the Zr surface is available for oxidation below Zr-Cr eutectic.

$$Xzr = (1 - XPRO_MIN).\left(\frac{ECrR - XREA_MIN}{XREA_MAX - XREA_MIN}\right)^2$$

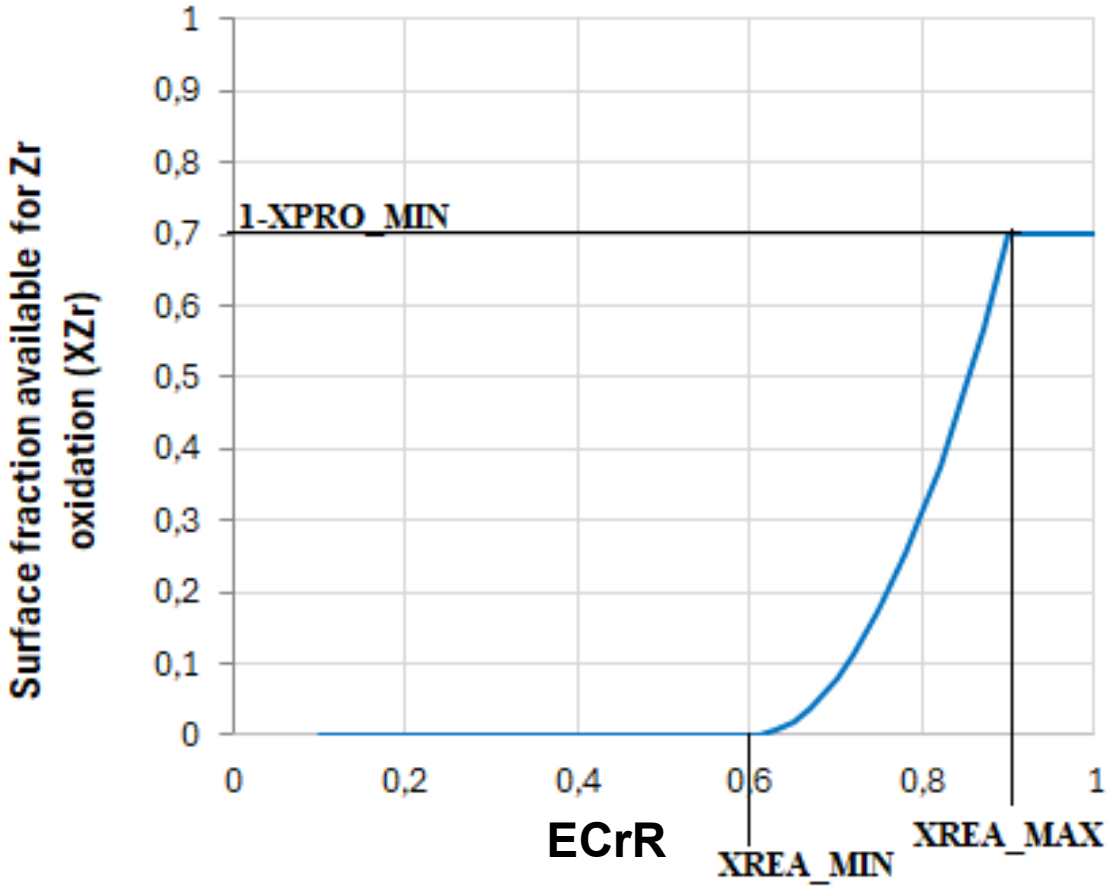

PROGRESSIVE LOSS OF Cr PROTECTION BELOW Cr-Zr EUTECTIC TEMPERATURE

Inert atmosphere

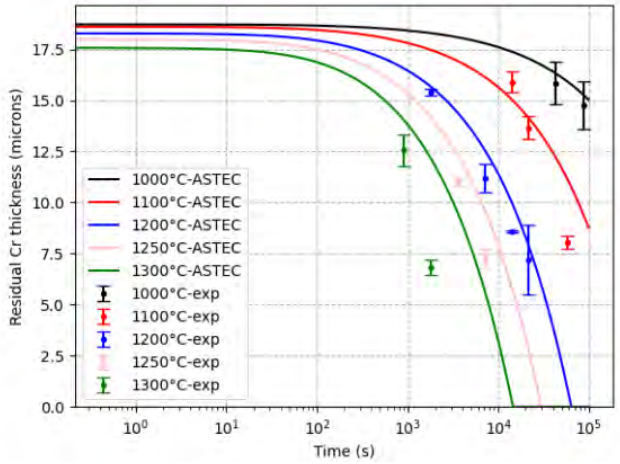

Kim and Lee 2023

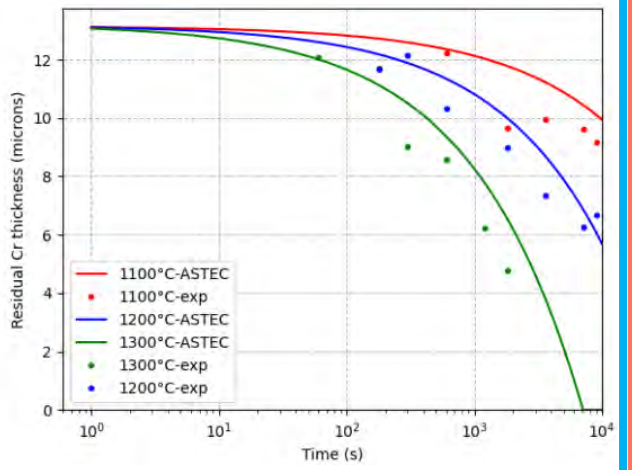

Yang 2021

Steam atmosphere

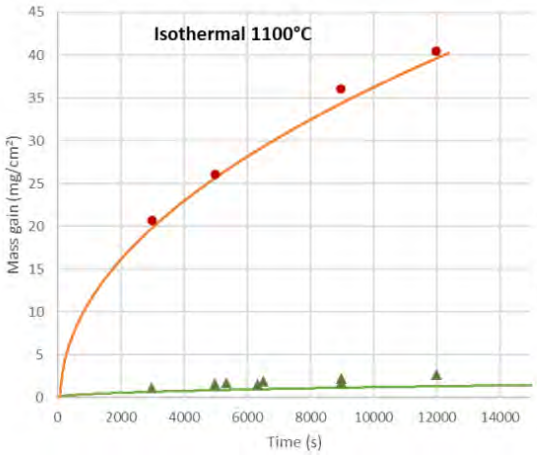

Bischoff 2018

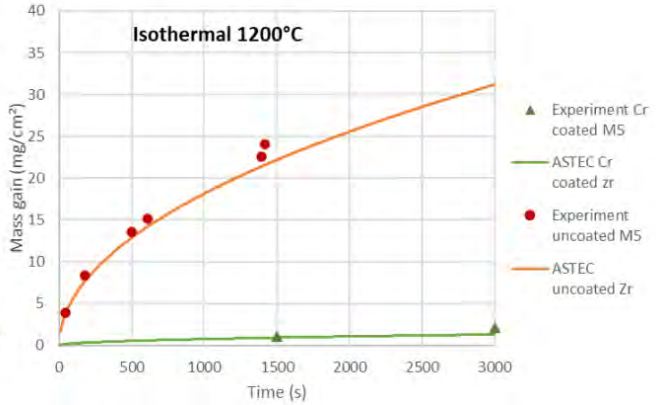

Brachet 2017

Brachet 2017

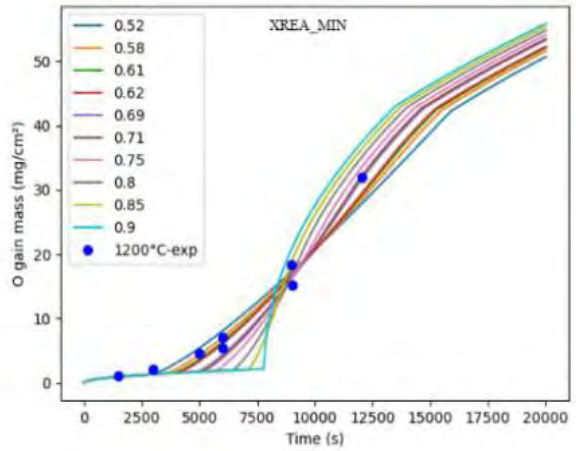

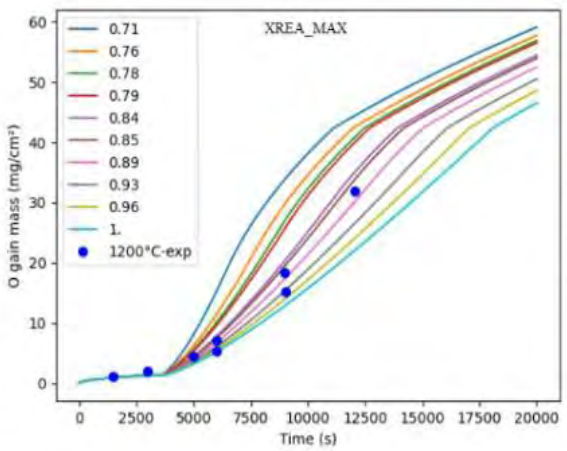

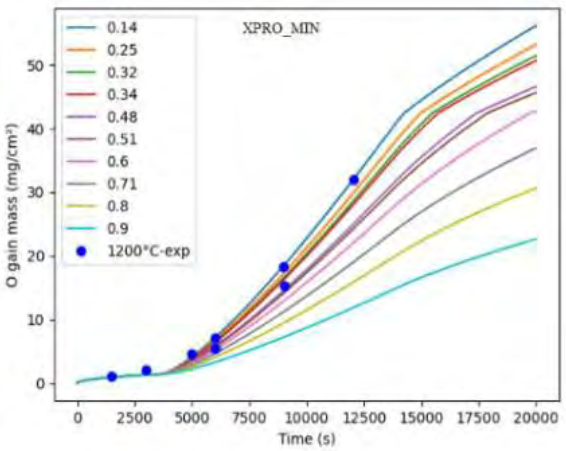

PROGRESSIVE LOSS OF Cr PROTECTION BELOW Cr-Zr EUTECTIC TEMPERATURE

- Satisfying results obtained on published experimental data

→ Validity of the approach proposed

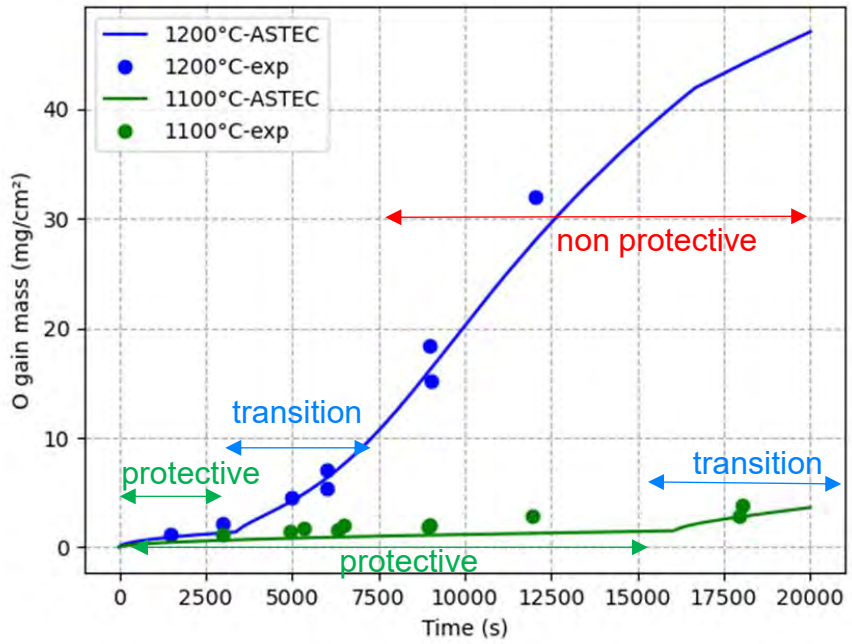

Brachet 2017, Bischoff 2018

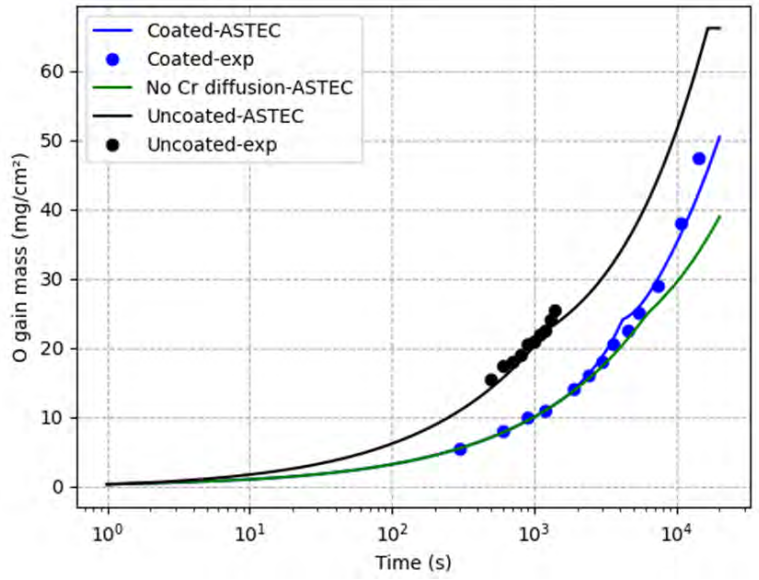

Wang 2022, Isotherm 1200°C, External coating and double-sided oxidation

PRELIMINARY REACTOR APPLICATIONS

- Generic PWR900 reactor and SBO scenario
- Failure criteria of uncoated claddings are kept
- Cr layer impacts the cladding temperature evolution
- After Zr-Cr eutectic, strong temperature escalation

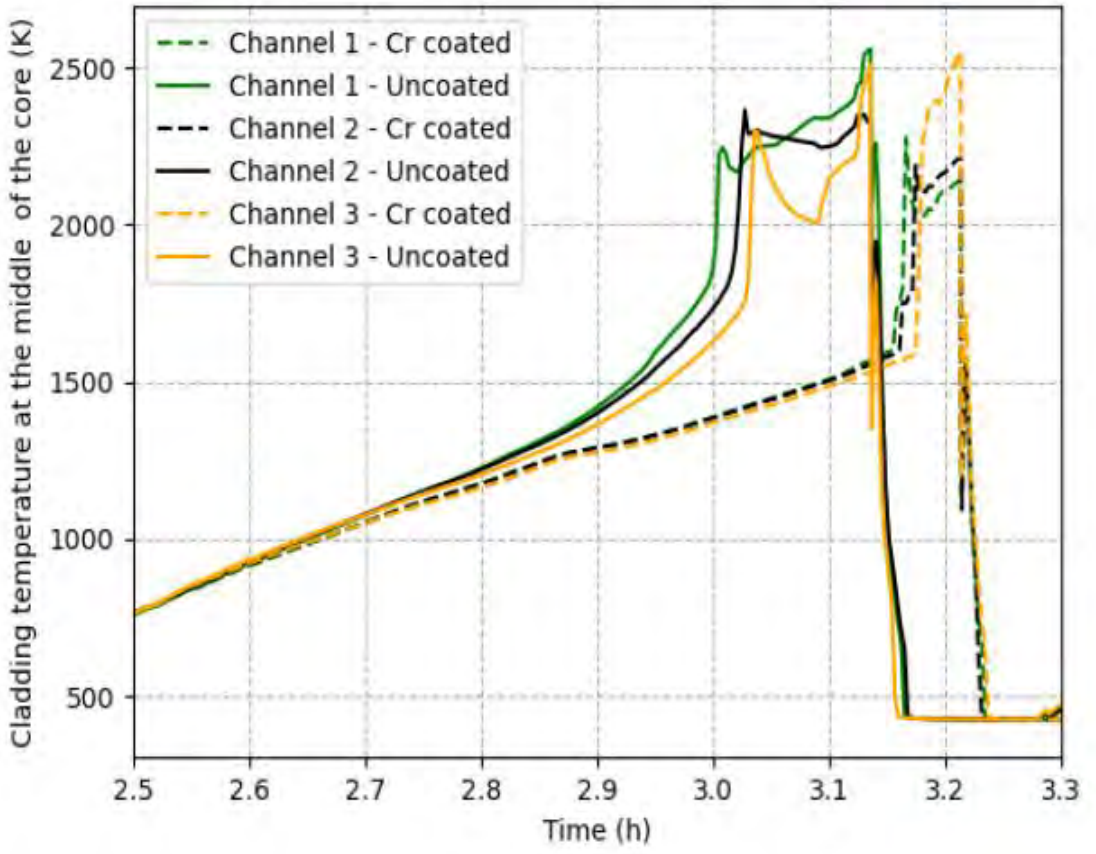

PRELIMINARY REACTOR APPLICATIONS

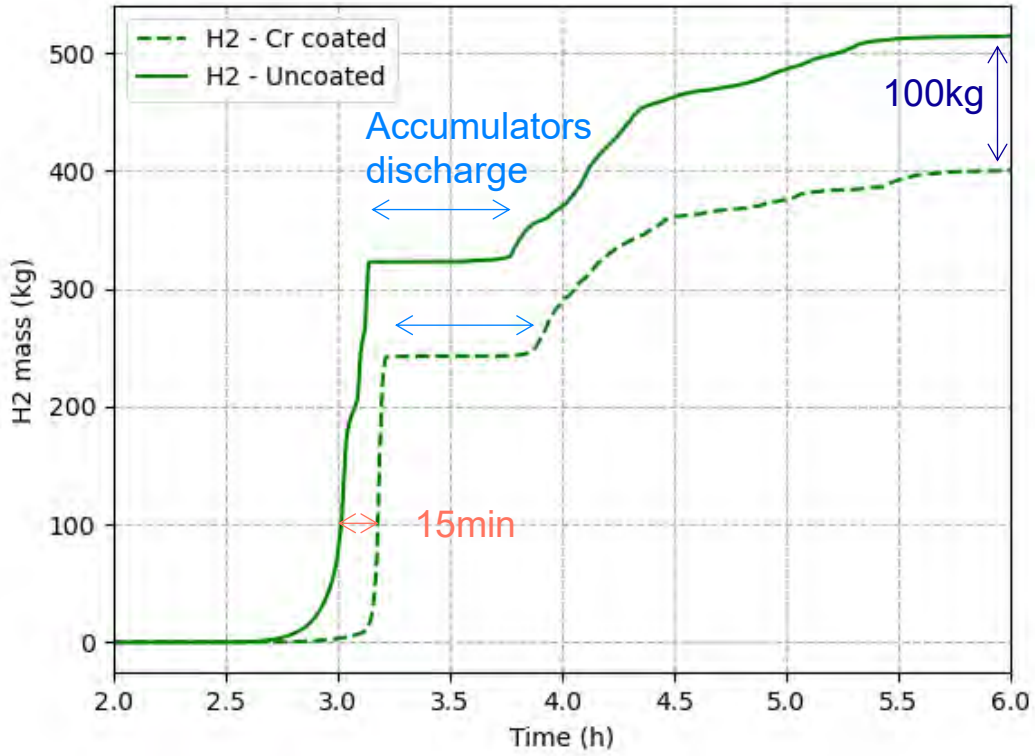

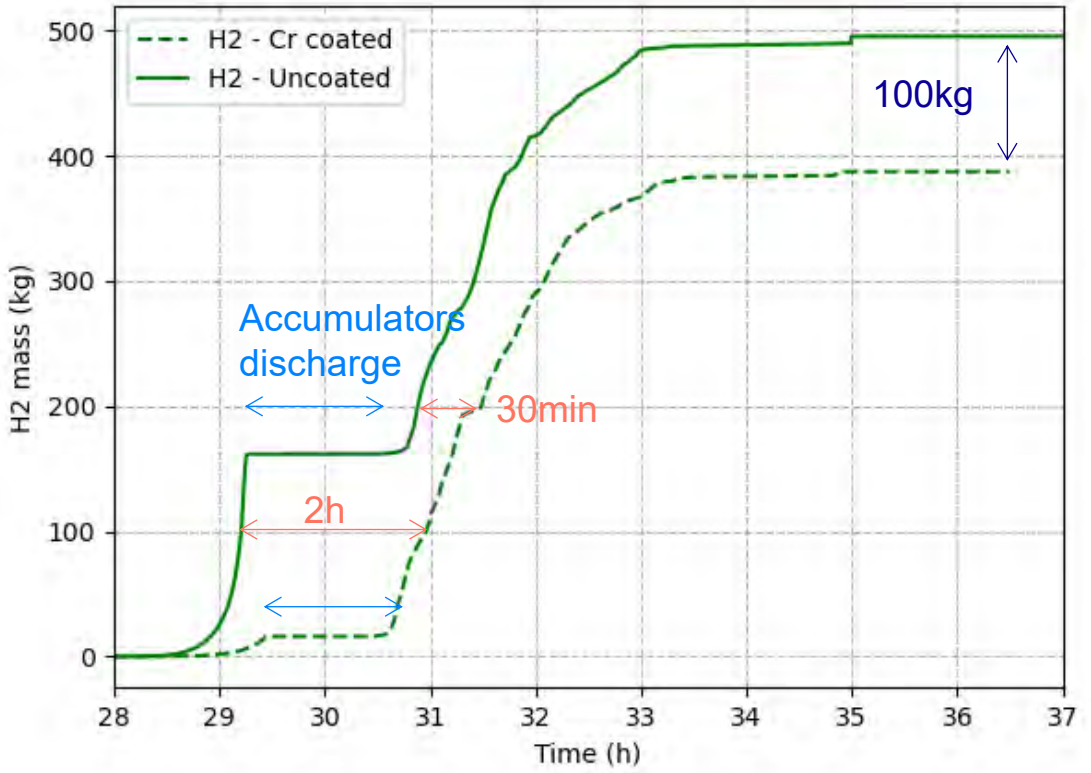

- Impact of residual power in the core when degradation occurs

→ Start of core dewatering ~2h20 or 28h after the reactor scram

PRELIMINARY REACTOR APPLICATIONS

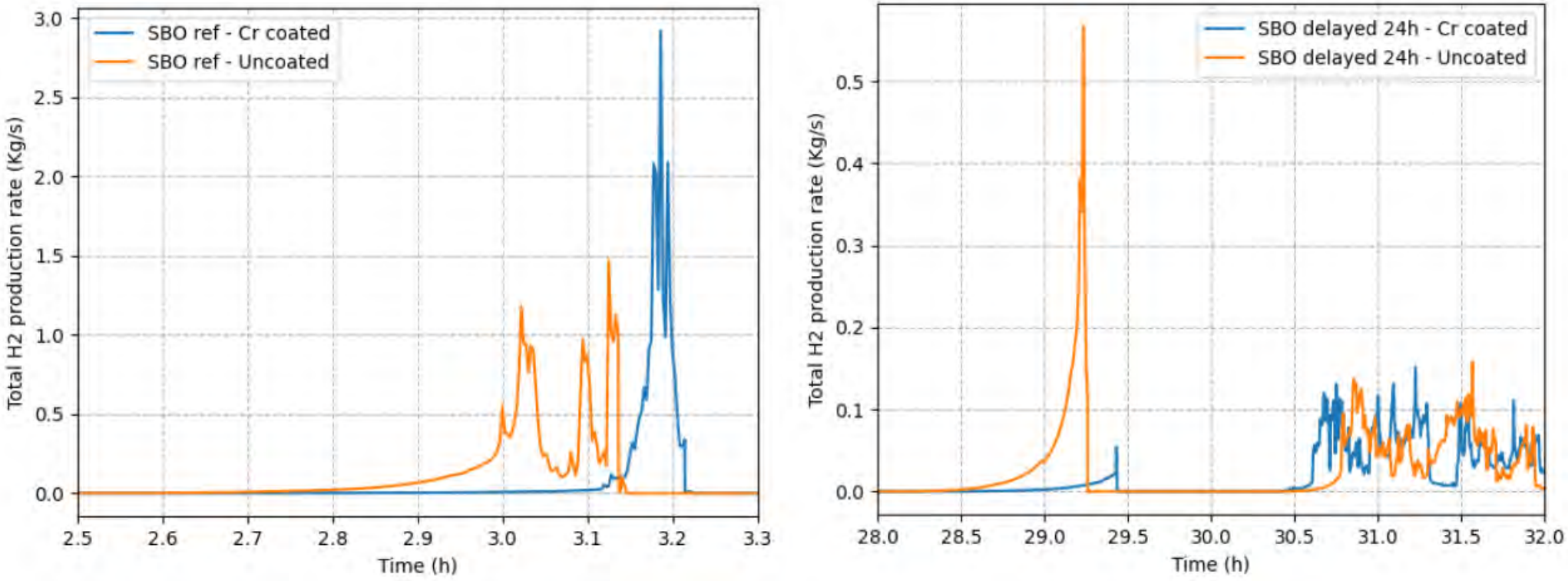

- Possible higher H_2 rate production for Cr coated claddings due to strong oxidation when Cr protection is lost.
- Impact of core heat up kinetics (temperature gradients in the core): H2 rate increase may remain local

PRELIMINARY REACTOR APPLICATIONS

- Loss of Cr protection before Zr-Cr eutectic

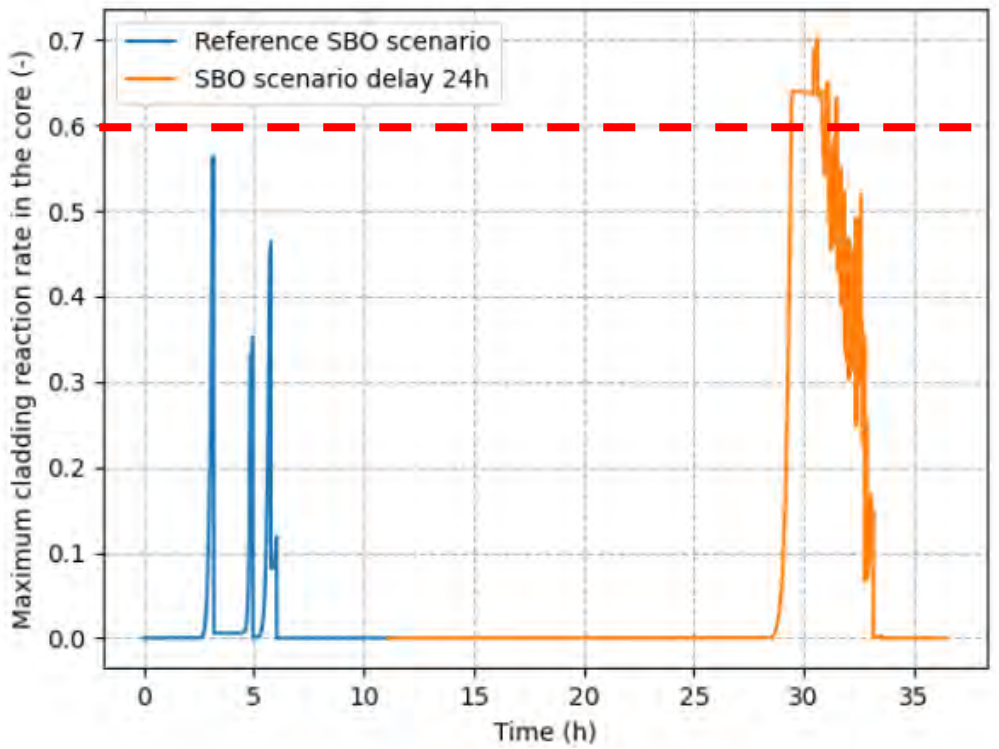

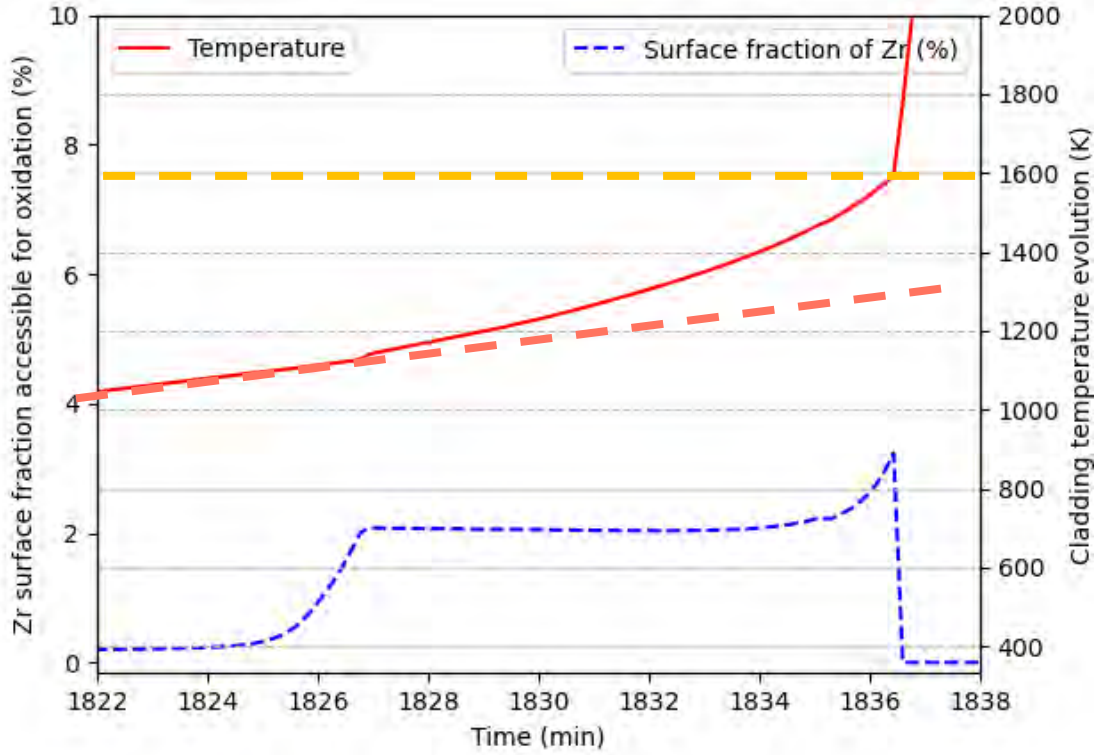

- Impact of exothermic reactor of Zr oxidation on the heating rate → the Zr fraction oxidized before Zr-Cr eutectic temperature is limited

CONCLUSION AND PERSPECTIVES

- Models for Cr-coated claddings have been implemented in ASTEC code based on available experimental data
- In particular, a **new model for loss of Cr protectiveness against oxidation** adapted for SA codes has been proposed based on the work of J. C. Brachet (ECrR concept)
- **Need for more experimental data (single rod and bundle tests) for modelling at Zr-Cr eutectic temperature and above** (oxidation runaway and failure criteria) → OECD projects QUENCH-ATF Phase I and II
- Impact at reactor scale (based on simplified assumptions for high temperature behaviour):
  - **Limited but noticeable impact on the kinetics of core heating and H_2 production** → need to be modelled in SA codes
  - Dependent on the SA scenario considered (combination of mainly the residual power and of the possible water injections in the vessel) the **impact of Cr-coated cladding on the degradation evolution or H_2 production will be different**

THANK YOU FOR YOUR ATTENTION

LAURE.CARENINI@ASNR.FR

ECrR FOR IDENTIFICATION OF CLADDING FRAGILIZATION

J.C. Brachet et al., J. Nucl. Nat. 606 (2025)

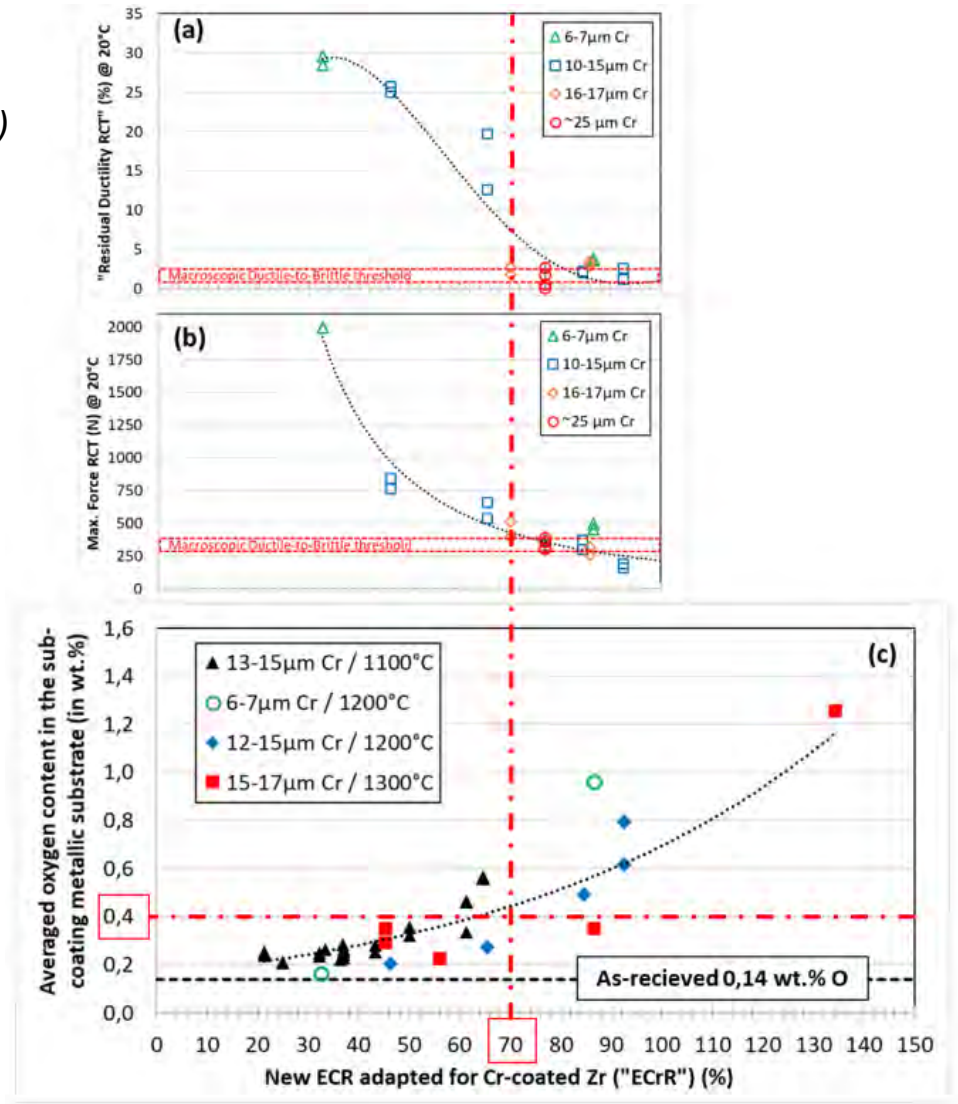

VALIDATION ABOVE Zr-Cr EUTECTIC TEMPERATURE

- Simplfy assumption of Zr oxidation after Zr-Cr eutectic
- Kim experiments (*Kim et al. J. Nucl. Mat., Vol 583, 2023*)

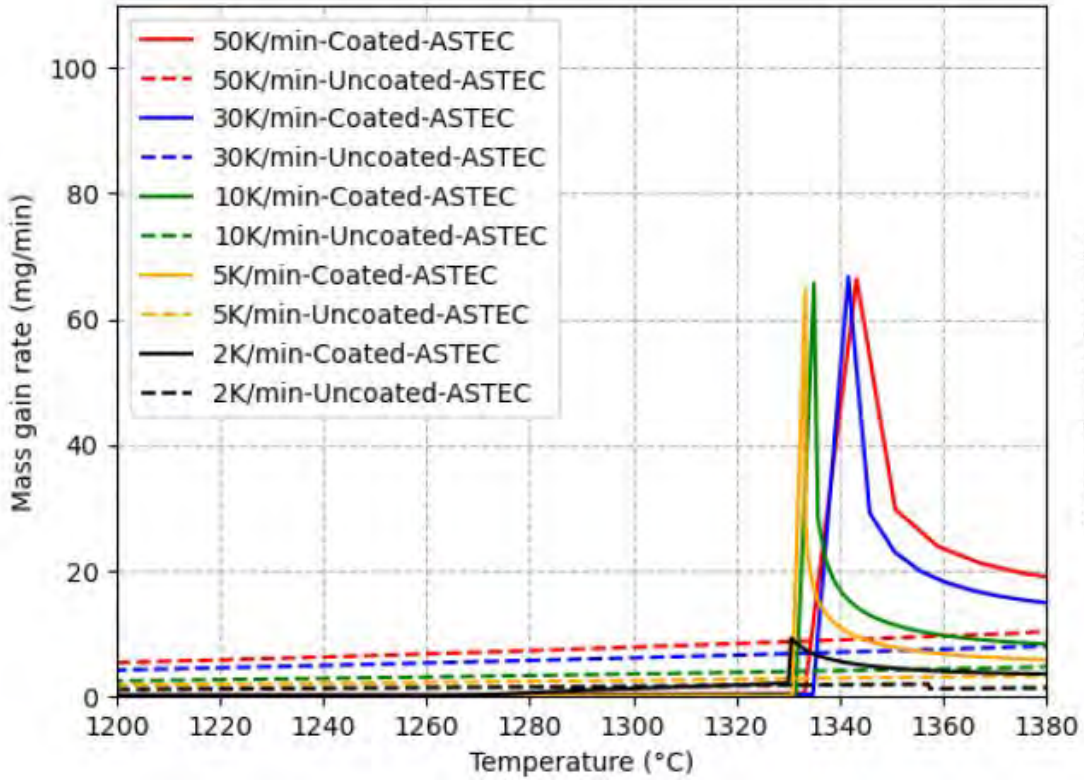

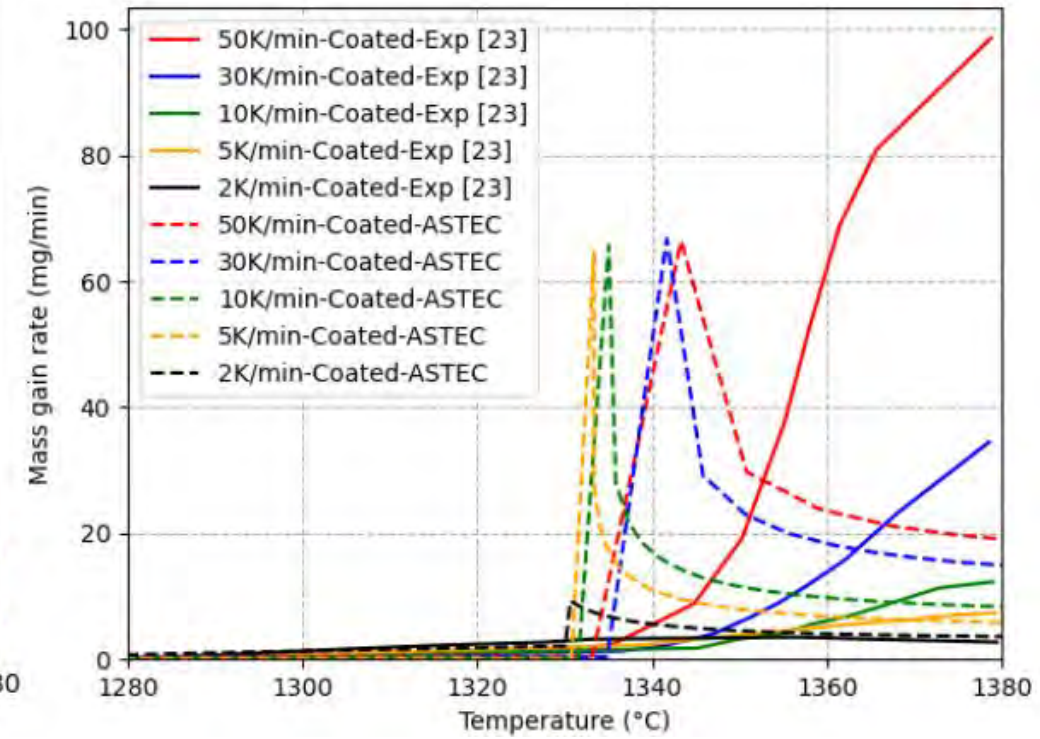

DEVELOPMENT AND VALIDATION OF THE FeCrAl OXIDATION MODEL OF THE ASTEC INTEGRAL CODE BASED ON THE QUENCH EXPERIMENTAL RESULTS

Zaira I. Jiménez-Balbuena, Fabrizio Gabrielli, Mauricio Exequiel Cazado, and Victor Sánchez-Espinoza
Karlsruhe Institute of Technology
Hermann-von-Helmholtz-Platz 1, 76344 Eggenstein-Leopoldshafen, Germany
zaira.balbuena@kit.edu; fabrizio.gabrielli@kit.com; mauricio.cazado@kit.edu;
victor.sanchez@kit.edu

ABSTRACT

Nuclear-grade FeCrAl alloys, a type of Advanced-Technology Fuels (ATFs), show outstanding resistance to oxidation at high temperatures, and represent a promising alternative to Zircaloy (Zry-4) cladding, which could enhance the safety of Nuclear Power Plants (NPPs). Understanding and modelling their oxidation behavior is therefore essential to reliably assess their performance under normal and off-normal conditions. The Karlsruhe Institute of Technology (KIT) actively contributes by providing reference data through the experimental test at the KIT QUENCH facility and by extending the range of application of integral codes to such innovative materials. This paper presents an analytical model to describe the oxidation behavior of FeCrAl alloys under a steam environment. The model was developed through a joint KIT/ASNR effort to improve the ATF-related modelling capabilities of the Accident Source Term Evaluation Code (ASTEC, developed by ASNR), using the Separate-Effect Tests (SETs) performed by KIT as the experimental basis. The oxidation model consists of implementing a parabolic rate law to predict the oxygen mass gain due to Al oxidation at low temperatures. Then, at higher temperatures (above ~1600K), the Fe and Cr oxidation model already available in ASTEC is used. The model has been integrated into the ASTEC code, and validation was performed against the QUENCH-19 bundle test conducted at KIT, which provides integral data on FeCrAl behavior under Beyond Design Basis Accident (BDBA) conditions. The simulation results with their experimental comparison demonstrate that the model is capable of estimating key parameters, including oxygen mass gain, oxide layer thickness, and hydrogen (H_2) production.

KEYWORDS
ATFs, FeCrAl, ASTEC, BDBA, Steam Oxidation

1. INTRODUCTION

Following major nuclear SA such as Three Mile Island accident, Chernobyl disaster, and Fukushima Daiichi nuclear disaster, substantial efforts have been undertaken worldwide to enhance NPPs safety. In this framework, ATFs classified as near- or long-term concepts depending on technological maturity, have attracted significant attention due to their potential to improve fuel and cladding performance and mitigate SA consequences [1]. Among the proposed cladding candidates, nuclear-grade FeCrAl alloys are considered strong alternatives to conventional Zry-4 claddings, owing to their high mechanical strength, resistance to hydride formation under H_2 exposure, and superior oxidation resistance in high-temperature steam environments [2].
The application of FeCrAl alloys as cladding materials in nuclear reactors has the potential to significantly reduce H_2 generation and to extend the time to cladding failure during SA scenarios. These characteristics

are particularly relevant for Beyond Design Basis Accidents (BDBAs), whose progression and consequences are typically assessed using integral severe accident codes [3]. Despite the growing experimental database on ATFs, most integral codes currently lack validated models capable of accurately describing the behavior of FeCrAl claddings. This limitation hinders the consistent assessment of ATF concepts within SA analyses and highlights the need for dedicated modelling approaches that capture the underlying physicochemical phenomena [4].

In response to this need, the Karlsruhe Institute of Technology (KIT), in collaboration with the French Authority for Nuclear Safety and Radiation Protection (ASNR), has extended the capabilities of the Accident Source Term Evaluation Code (ASTEC), developed by ASNR [5], [10], through the development and validation of a new model for FeCrAl alloys. The model development is based on Single Effect Tests (SETs), while its validation relies on the QUENCH19 bundle test, both conducted at KIT. This paper presents the modelling methodology and discusses the corresponding simulation results in comparison with experimental data.

2. FeCrAl ALLOYS

Iron–chromium–aluminum (FeCrAl) alloys are structural materials widely used in high-temperature applications requiring enhanced oxidation resistance. Due to their favorable performance, they have attracted increasing interest for NPP applications and are considered promising from a safety perspective because of their potential to significantly reduce H_2 generation during high-temperature oxidation.

Nuclear-grade FeCrAl alloys are primarily composed of iron (Fe), chromium (Cr), and aluminum (Al), with typical weight fractions of approximately 80%, 13%, and 6%, respectively. In addition to these major constituents, minor alloying elements such as carbon (C), yttrium (Y), and silicon (Si) are included in small amounts to tailor the material properties [6]. Depending on their specific composition, a wide range of FeCrAl alloys exists, among which B136Y3 and C26M2 are representative examples studied in reference experiments [7]. Alloys from the C series are further characterized by the presence of molybdenum (Mo) and niobium (Nb) as additional alloying elements [8]. Both alloys were developed by Oak Ridge National Laboratory and supplied to the KIT for experimental investigations at the large-scale QUENCH facility; in this study, B136Y3 is used as the reference alloy.

The presence of Al promotes the formation of a stable and protective alumina (Al_2O_3) oxide layer, which is responsible for the high oxidation resistance of FeCrAl alloys at elevated temperatures. Cr contributes to corrosion resistance and phase stability, while minor additions of yttrium and silicon enhance the adherence and integrity of the oxide scale, limiting spallation and reducing oxygen diffusion through the oxide layer. These beneficial effects, however, may be accompanied by a moderate reduction in thermal conductivity and, at very high temperatures, by the potential breakdown of the protective alumina layer followed by rapid iron oxidation, which must be considered in reactor design and BDBA safety analyses [9]. Overall, the combination of high-temperature mechanical strength, oxidation resistance, and corrosion resistance makes FeCrAl alloys suitable candidates for demanding NPP applications.

2.1. Steam Environment Oxidation Kinetics

After extensive experimental analyses aimed at characterizing the B136Y3 and C26M2 alloys were performed at KIT QUENCH facility, the oxidation behavior of nuclear-grade FeCrAl alloys in steam environments was identified as being governed by distinct kinetic regimes, depending on the nature of the oxide scale formed on the material surface. Based on results obtained from isothermal SETs, the oxidation kinetics of the B136Y3 alloy can be classified according to temperature as follows.
At lower temperatures, the oxidation process is controlled by θ-alumina–dominated kinetics, associated with the formation of a metastable oxide layer. With increasing temperature, a transition to stable, protective α-

alumina–controlled kinetics is observed, providing enhanced oxidation resistance. At higher temperatures, this protective behavior deteriorates, and iron oxide–dominated kinetics become prevalent, leading to the loss of oxide scale integrity, material deformation, and rapid degradation characteristic of catastrophic oxidation [7]. Based on the description above, the oxidation kinetic regimes are distributed as a function of temperature as follows:

- **873 K < T < 1173 K:** θ-alumina–controlled oxidation
- **1173 K ≤ T ≤ 1273 K:** constant oxidation rate regime
- **1273 K < T < 1600 K:** α-alumina–controlled oxidation
- **T ≥ 1600 K:** iron oxide–dominated oxidation

This classification enables the identification of the kinetic coefficients associated with each oxidation regime, which are presented and discussed in the following section.

3. ASTEC CODE IMPLEMENTATION

ASTEC is an integral severe accident code developed by ASNR [5], [10] to simulate the complete progression of an accident sequence, from its initiation to the release of radioactive source terms into the environment. Prior to the present work, ASTEC was capable of modelling conventional cladding materials such as Zircaloy-4. To extend its capabilities to ATFs concepts, KIT, developed and implemented in collaboration with ASNR a dedicated oxidation model for FeCrAl alloy claddings.

The implementation of the new model was carried out following a three-stage methodology. The first stage consisted of the definition of the oxidation model based on experimental observations. Results from SETs indicated that FeCrAl alloys predominantly form aluminum-based oxides at lower temperatures, while iron-based oxides become dominant at higher temperatures. This experimental evidence enabled the development of an oxidation model in which the FeCrAl alloy behavior is represented through the contribution of two material systems—aluminum and stainless steel—and their corresponding oxides. While ASTEC already includes a validated model to simulate stainless steel oxidation in steam environments, no equivalent model was available for Al when considered as a cladding material.

The second stage involved formulating and developing the aluminum oxidation model, in accordance with the underlying physical phenomena. The approach is based on a two-layer oxidation model, in which oxidation initiates upon contact with steam at temperatures above 800 K and leads to the formation of a protective Al oxide layer within the temperature range corresponding to stable alumina-controlled kinetics.

The final stage comprised two main steps. First, the model performance was assessed against the QUENCH SETs by calculating and comparing experimental measurements of key model parameters, including oxygen mass gain, oxide layer thickness, and cumulative H_2 production, which characterize the oxidation behavior of FeCrAl alloys in steam environments. Second, the model validation against the QUENCH-19 bundle test by comparing cladding temperatures at different axial elevations and the total cumulative H_2 production, thereby providing a comprehensive assessment of the model under severe accident conditions.

4. MODEL DEVELOPMENT AND VALIDATION

Isothermal and transient single-effect tests (SETs) were performed at KIT on two different FeCrAl alloys, namely B136Y3 and C26M2. The temperature dependence of the parabolic oxidation rate constants for both alloys provided the basis for the development of the oxidation model. Selected results from the isothermal experiments conducted on the B136Y3 alloy were used as reference data for assess the model.

The isothermal tests consisted of exposing small cylindrical FeCrAl specimens to a steam environment for a duration of 20 hours. The experiments were conducted over two distinct temperature ranges, depending on the experimental facility employed. The low-temperature tests covered the range from 873 K to 1373 K,

while the high-temperature tests were performed between 1573 K and 1773 K [7]. Prior to steam exposure, the samples were preheated under an argon atmosphere to reach the target temperature. Experimental parameters such as specimen diameter and length, preheating time, argon flow rate, and steam flow rate differed between the low- and high-temperature tests. The geometric characteristics of the specimens and the main experimental conditions are summarized in Table 1.

Table I. Experiment Description: geometric characteristics and conditions of the experiment.

Parameter / Temperature	Length [mm]	Outer Diameter [mm]	Preheating time [min]	Argon flow rate [l/h]	Steam rate [g/h]
Low	10	9.6	10	20	2
High	20	9.6	30	20	20

The experimental test enabled the measurement of oxygen mass gain and the determination of oxidation parabolic rate constants at each investigated temperature. In addition, the oxide layer thickness was measured, and for the high-temperature tests, cumulative hydrogen production was also quantified.

Based on the oxidation behavior observed during the isothermal tests, the parabolic rate constant k_p was categorized into three distinct temperature ranges corresponding to the oxidation kinetic regimes identified for the B136Y3 alloy. These regimes were determined from post-test X-ray diffraction (XRD) analyses and are associated with θ-alumina–controlled kinetics, α-alumina–controlled kinetics, and iron oxide–dominated kinetics [7]. From the resulting k_p values, the oxidation kinetic coefficients were derived assuming a parabolic oxidation law with Arrhenius-type temperature dependence for each identified oxidation regime. The corresponding kinetic parameters were obtained through linear regression according to the following equation [11]:

$$k_p = Ae^{\left(\frac{-E_a}{RT}\right)} \quad \ldots(1)$$

Where, **A** represents the pre-exponential and $\mathbf{E_a}$ the activation energy. The coefficients were calculated and integrated into ASTEC as part of the oxidation model for Aluminum, and are shown in Table II. For T ≥ 1648 K, where iron-controlled kinetics becomes dominant, the coefficients of the SSTEEL model available in ASTEC were retained without modification.

Table II. Experiment Description: Oxidation kinetic coefficients as a function of temperature range

Temperature [K] / Coefficient	873<T<1173	1173 ≤ T ≤1273	1273<T<1600	T ≥ 1600
A $\left[\frac{kg^2}{m^4 s}\right]$	$5.376\text{x}10^{-03}$	$4.692\text{x}10^{-12}$	5.018	$2.399\text{x}10^{+08}$
$\mathbf{E_a}$ $\left[\frac{kJ}{mol}\right]$	184.730	0.000	287.748	352.514

4.1. ASTEC Performance Assessment against QUENCH SETs

The ASTEC representations of the SETs performed at KIT were assessed using the previously described dedicated ASTEC model developed for FeCrAl alloys. In this representation, the geometry consists of a cylindrical specimen surrounded by a steam flow. The outer surface of the cylinder is modeled as a composite material, accounting for the FeCrAl alloy composition through two distinct constituents: aluminum (6%) and an iron–chromium–based material (94%), corresponding to the typical composition of the B136Y3 alloy. According to this configuration, the outermost surface is assumed to be enriched in Al, and the initial oxidation process upon exposure to steam is governed by the formation of an Al oxide layer. As the temperature increases and reaches 1648 K, the oxidation of the iron–chromium–based material is activated in the model, leading to the formation of iron oxides and reflecting the transition toward non-protective oxidation regimes.

The implementation of the SET configuration in ASTEC allows the calculation of the same parameters measured during the experiments and provides a direct means to assess the performance of the newly developed Al oxide model. This comparison enables the evaluation of the code capability to reproduce the experimental results and, consequently, to represent the underlying physical oxidation phenomena.

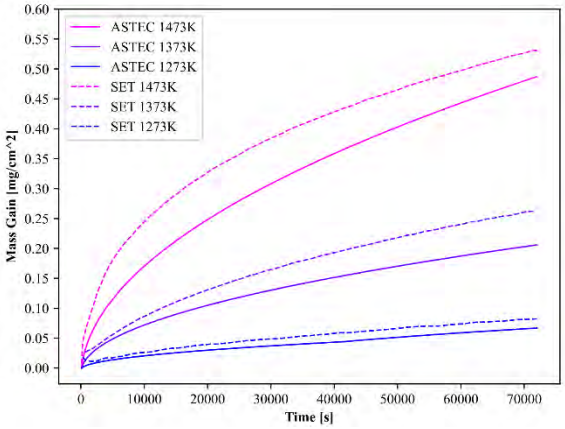

Figure 2. Weight gains comparison SETs vs. ASTEC code

Figure 2 presents a comparison between calculated and experimental oxygen mass gain at three different temperatures—1273, 1373, and 1473 K—within the temperature range where α-alumina–controlled oxidation is dominant. The continuous lines represent the results calculated using the ASTEC code, while the dotted lines correspond to the experimental data. The maximum relative error observed in this dataset does not exceed 25% and occurs at 1473 K at 20,000 s, which corresponds to the largest deviation between the experimental measurements and the simulation results.

Table III. Model Development: Comparison of oxide layer thickness SETs vs. ASTEC

Temperature [K]	Thickness SETs (µm)	ASTEC (µm)
1373	~1.500	1.110
1473	~3.000	2.616
1573	~6.500	5.538

On the other hand, Table III reports the calculated and measured oxide layer thicknesses at selected temperatures. For this parameter, the maximum relative error is observed at 1273 K and amounts to 26%.

Overall, the results show reasonable agreement between simulations and experimental data, supporting the validity of the implemented oxidation model.

4.2. Bundle Test QUENCH-19 Description

The KIT QUENCH facility is an integral experimental installation that provides a scaled representation of a reactor fuel assembly with a reduced number of fuel rods, designed to reproduce the dominant thermal–hydraulic and chemical conditions in a nuclear reactor core. It is widely used for testing material and the validation of SA models implemented in integral codes. The QUENCH-19 bundle test represents the first integral BDBA experiment conducted with FeCrAl alloy cladding [12]. The experiment was performed at KIT on 29th August 2018 using the B136Y3 FeCrAl alloy as cladding material, with the objective of assessing its behavior under SA conditions and comparing it with that of conventional ZIRLO cladding tubes [12].

The configuration consisted of a Pressurized Water Reactor (PWR)–type fuel bundle comprising 24 rods, with tungsten heater rods located at the center to simulate the electrical power input. The cladding material was B136Y3 FeCrAl alloy, and the heaters were surrounded by annular ZrO_2 pellets to represent the fuel. The bundle also included seven corner rods and five grid spacers; the shroud and shroud insulation were made of Kanthal and ZrO_2 fiber, respectively, while the cooling jacket was composed of Inconel. The experiment lasted 10,281 s and was conducted in four main phases: first, the bundle was heated to approximately 873 K, corresponding to the onset of FeCrAl oxidation; subsequently, the electrical power was increased to 11.5 kW to establish pre-oxidation conditions; in the third phase, the power was further raised to 18.12 kW, leading to a maximum temperature of about 1730 K; finally, following the quenching phase, the power was reduced to 4.1 kW.

The experiment was instrumented with thermocouples installed at different axial elevations to monitor the temperature evolution along the bundle, while hydrogen production was measured using a quadrupole mass spectrometer (GAM300). These measurements provide key experimental data for validating the FeCrAl oxidation model implemented in ASTEC. The results indicate that the cumulative hydrogen generation during the QUENCH-19 test was significantly lower for FeCrAl cladding (9.2 g H_2) than for ZIRLO (47.6 g H_2) [12], the latter having been previously investigated in the QUENCH-15 bundle experiment as a reference for conventional cladding materials. This marked reduction in hydrogen release confirms the superior oxidation resistance of FeCrAl alloys under severe accident conditions.

4.3. Bundle Test QUENCH-19 Implementation

The ASTEC model of the QUENCH-19 test was assessed through a nodalized representation of the experimental configuration. The total number of fuel rods was distributed among three separate thermal–hydraulic channels, comprising four, twelve, and eight rods, respectively, as illustrated in Figure 3.

This radial discretization allows for an efficient representation of the bundle while preserving the main thermal and oxidation phenomena observed experimentally. The rod cladding was modeled using the B136Y3 FeCrAl alloy for the fuel rods, corner rods, shroud, and four of the five grid spacers. The remaining grid spacer and the cooling jacket were represented using the SSTEEL material. Although SSTEEL corresponds to a Fe–Cr–Ni alloy with compositional differences compared to Inconel, it was employed as a surrogate material consistent with the experimental configuration.

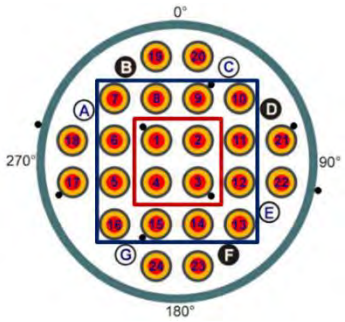

Figure 3. Channel distribution for implementation (adapted from Stuckert et al., 2017).

Several key events observed during the QUENCH-19 experiment were reproduced in the simulation. These include the continuous increase in hydrogen release starting at approximately 6570 s, followed by a sharp rise at around 8260 s, the attainment of a maximum temperature of about 1773 K at 9110 s, and the onset of probable massive cladding failures at approximately 9119 s, shortly after the quenching phase. The experiment was instrumented to monitor relevant physical parameters, including cladding temperature at different elevations and cumulative hydrogen production, which were also calculated by the ASTEC simulation for model validation purposes.

Figure 4 presents a comparison between calculated and measured cladding temperatures at two axial elevations, 850 mm and 950 mm, where post-test examinations identified the largest number of damaged claddings. The continuous lines represent the temperatures obtained from ASTEC simulations, while the dotted lines correspond to experimental measurements acquired using thermocouples. The plots include at least one experimental reference value for each channel and, in some cases, two values corresponding to different fuel rods located at different positions within the bundle.

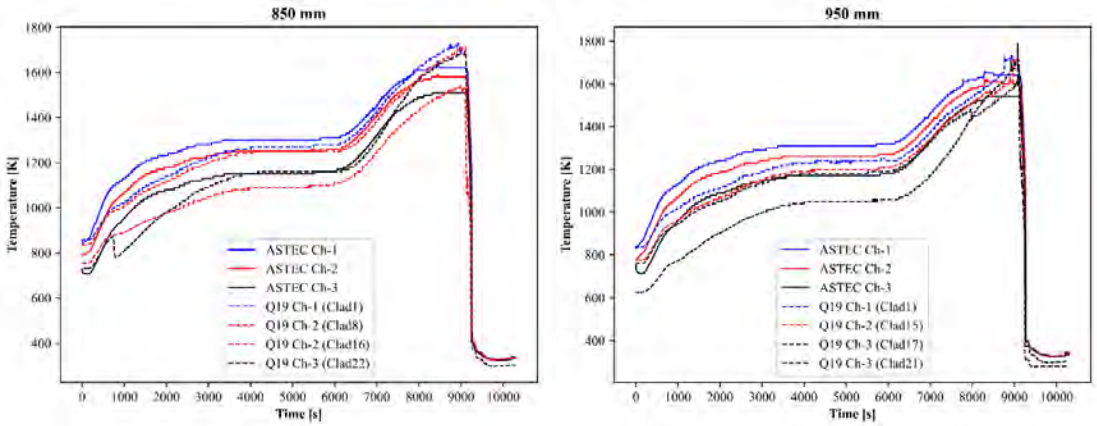

Figure 4. Axial cladding temperature profiles at 850 mm and 950 mm: Simulation–Experiment comparison

The maximum temperature difference between experimental measurements and ASTEC predictions does not exceed 50 K in most cases, which is considered an acceptable criterion for model validation from a thermal–hydraulic perspective. In the cases where this criterion is not met, the discrepancy can be attributed to the specific position of the fuel rod within the bundle, likely closer to the periphery of the channel. This positioning results in lower measured temperatures and, consequently, larger deviations when compared with the simulated values.

Figure 5 shows the evolution of cumulative hydrogen production as a function of time. Compared with the experimental data, the ASTEC simulation underestimates hydrogen generation up to approximately 7800 s and slightly overestimates the total hydrogen release thereafter, resulting in a final cumulative hydrogen production that is about 6.6% higher than the experimental value. The above-mentioned underestimation of hydrogen generation is attributed to the non-consideration of thermocouples' oxidation in the model [12]. Overall, ASTEC provides a reasonable estimate of the total hydrogen production, reaffirming the applicability of the implemented model [12].

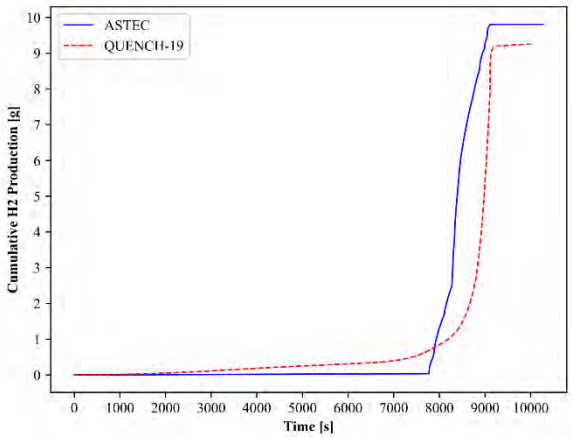

Figure 5. Total hydrogen release ASTEC vs. Bundle Test Q19

5. LIMITATIONS AND OUTLOOK

The next step will involve evaluating the functionality of the Al oxidation model, recently integrated into the ASTEC code, by simulating a hypothetical BDBA scenario in an SMR. This analysis will serve as a case study to evaluate ASTEC's capability to simulate the progression of an SA involving FeCrAl cladding oxidation and to predict the associated physical and chemical phenomena.

The simulation of this scenario will pose significant challenges, mainly due to current limitations in the code regarding the modelling of specific phenomena once core degradation initiates, which involves the interaction between FeCrAl alloys and other materials present in the reactor core. Several modelling criteria will require adjustment to ensure a consistent and physically meaningful simulation. Therefore, the simulation should be considered a preliminary investigation of the capabilities of the FeCrAl oxidation model when applied to plant-level analyses.

Models describing UO_2 and ZrO_2 dissolution by liquid Zircaloy, as well as cladding dissolution by Inconel, liquid Ag–In–Cd alloy, and solid stainless steel, should not be activated in either simulation (FeCrAl and Zircaloy). This approach will be adopted to ensure methodological consistency, as equivalent dissolution models are not yet available for FeCrAl claddings, as well as for FeCrAl oxidation in debris or magma components, thereby limiting the analysis to the stage of core degradation.

Furthermore, the material integrity criteria and the conditions governing the decanting phenomenon must be adapted for FeCrAl alloys. The first criterion involves the change in material state and the activation of the steel oxidation process, which are defined by the component temperature and the oxide layer thickness, and represent the loss of integrity of the Al_2O_3 layer above a specific temperature. The second criterion refers to the liquid fraction of the material, from which material decantation may occur.

We expect that applying this to the plant will allow us to analyze the material's behavior up to the loss of cladding geometry, through the core state, assess the impact of FeCrAl alloys as cladding materials, and their potential for mitigating the progression of SA in comparison with traditional cladding.

In this context, the sequence of events during the severe accident scenario will play an important role, as will the generation of hydrogen at the end of the simulation.

6. CONCLUSIONS

The single-effect tests performed at KIT provided a robust foundation for the development of a model capable of reproducing the physical phenomena governing the oxidation behavior of FeCrAl alloys. This foundation enabled significant improvements to the ASTEC code, which is now capable of modelling the behavior of FeCrAl alloys as a cladding material in steam environments up to the loss of the cladding geometry. To achieve this, the implementation of dedicated modelling extensions was successfully validated by accurately reproducing the SET and the QUENCH-19 (bundle test) experimental results.

The appropriate configuration for predicting the behavior of FeCrAl alloys within the ASTEC framework requires the representation of two distinct oxidation mechanisms and, consequently, the implementation of two complementary models. The first one, Al oxidation model, addresses aluminum oxidation at temperatures up to 1600 K and was recently integrated into the code. In this regime, the formation of a stable Al_2O_3 layer provides a protective effect against further oxidation. The second model, FEOX, is applied at higher temperatures and accounts for the oxidation behavior of an iron–chromium mixture, including the formation of the corresponding oxide layers.

Future work includes the application of the model to the plant level in order to make a preliminary assessment of the analysis of a postulated BDBA scenario in an SMR with FeCrAl claddings. The goal of that proposed activity is to evaluate the potential benefits of FeCrAl to mitigate hydrogen generation and extend the coping time. Nevertheless, further modelling efforts will be required to properly quantify material behavior after cladding rupture, and fully capture the phenomenology under BDBA conditions.

REFERENCES

1. Li, Y., You, E., Wang, T., Xing, D., Xu, J., & Zhang, H. (2024). Developments, challenges and prospects in thermal-hydraulic research on accident tolerant fuel. *Heliyon*, ***10***(19).
2. Rebak, R. B., Terrani, K. A., & Fawcett, R. M. (2016, July). FeCrAl alloys for accident tolerant fuel cladding in light water reactors. In *Pressure Vessels and Piping Conference* **Vol. 50435**, p. V06BT06A009. American Society of Mechanical Engineers.
3. Gamble, K. A., Barani, T., Pizzocri, D., Hales, J. D., Terrani, K. A., & Pastore, G. (2017). An investigation of FeCrAl cladding behavior under normal operating and loss of coolant conditions. *Journal of nuclear materials*, ***491***, 55-66.
4. Zinkle, S. J., Terrani, K. A., Gehin, J. C., Ott, L. J., & Snead, L. L. (2014). Accident tolerant fuels for LWRs: A perspective. *Journal of Nuclear Materials*, ***448***(1-3), 374-379.
5. Chatelard, P., Belon, S., Bosland, L., Carénini, L., Coindreau, O., Cousin, F., ... & Chailan, L. (2016). Main modelling features of the ASTEC V2. 1 major version. *Annals of Nuclear Energy*, *93*, 83-93.
6. Yamamoto, Y., Snead, M. A., Field, K. G., & Terrani, K. A. (2017). *Handbook of the materials properties of FeCrAl alloys for nuclear power production applications* (No. ORNL/TM-2017/186). Oak Ridge National Laboratory (ORNL), Oak Ridge, TN (United States).
7. Kim, C., Tang, C., Grosse, M., Maeng, Y., Jang, C., & Steinbrueck, M. (2022). Oxidation mechanism and kinetics of nuclear-grade FeCrAl alloys in the temperature range of 500–1500 C in steam. *Journal of Nuclear Materials*, ***564***, 153696.

8. Yamamoto, Y., Sun, Z., Pint, B. A., & Terrani, K. A. (2016). *Optimized Gen-II FeCrAl cladding production in large quantity for campaign testing* (No. ORNL/TM-2016/227). Oak Ridge National Lab.(ORNL), Oak Ridge, TN (United States).
9. Jiang, G., Xu, D., Feng, P., Guo, S., Yang, J., & Li, Y. (2021). Corrosion of FeCrAl alloys used as fuel cladding in nuclear reactors. *Journal of Alloys and Compounds*, ***869***, 159235.
10. Van Dorsselaere, J. P., Seropian, C., Chatelard, P., Jacq, F., Fleurot, J., Giordano, P., ... & Luther, W. (2009). The ASTEC integral code for severe accident simulation. *Nuclear Technology*, ***165***(3), 293-307.
11. Field, K. G., Snead, M. A., Yamamoto, Y., & Terrani, K. A. (2017). Handbook on the material properties of FeCrAl alloys for nuclear power production applications. *Nuclear Technology Research and Development*.
12. Stuckert, J., Grosse, M., & Steinbrück, M. (2017). *Results of the bundle test QUENCH-19 with FeCrAl claddings* (Technical report). Karlsruhe Institute of Technology (KIT), IAM-AWP, Karlsruhe, Germany.

“Development and Validation of the FeCrAl oxidation model of the ASTEC Integral Code Based on the QUENCH Experimental Results”

Zaira I. Jiménez-Balbuena, F. Gabrielli, M. Cazado
Institute for Neutron Physics and Reactor Technology
21 May 2026

Content

1. Motivation
2. FeCrAl alloys
   - Separate-Effect Test
   - Steam Oxidation Kinetics
3. Oxidation Model
   - Model Development
   - Model Implementation
   - Assessment and Model Validation
4. SMR Application
   - Postulated BDBA Scenario
   - Core Degradation and H_2 Production
5. Conclusion
   - Outlook

Motivation

Advanced-Technology Fuels

- Resist oxidation
- Reduce H_2 generation
- Reduce fire/explosion risk from cladding
- Slow down fuel degradation and melting

Reactor Safety

- Mitigate the consequences of hypothetical severe accident scenarios
- Evaluate the behavior of FeCrAl in a SA scenario (H_2 release)
- Evaluate the impact of the use of ATF in reactor's application
- KIT strategy for severe accident (SA) analyses → continuous improvement of the codes

Meltdown after power loss, H_2 explosions

Fukushima Daiichi 2011

Steam explosion
Core fire

Chernobyl 1986

Three Mile Island 1979

Partial meltdown due to coolant loss

GOAL:
Capabilities Extension of the Accident Source Term Evaluation Code (ASTEC)

- ✓ Model Development based on Separate-Effect Test
- ✓ Model Implementation in ASTEC code
- ✓ Model Validation against QUENCH-19
- ✓ Small Modular Reactor Application.

The Accident Source Term Evaluation Code (ASTEC)

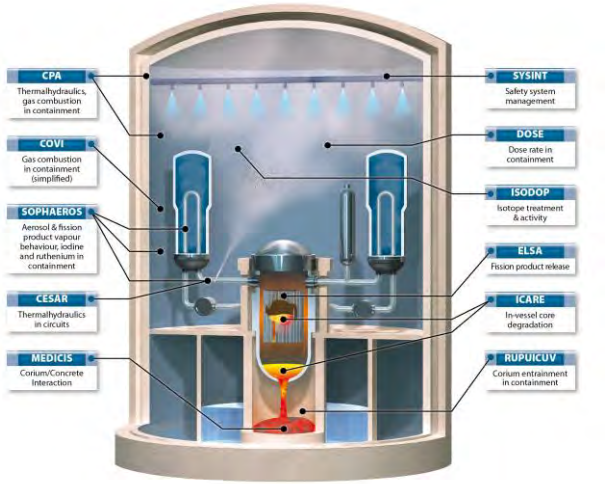

Fig. 1 ASTEC code distribution by modules

Developed by ASNR (ASNR all rights reserved, [2025])

Capable of simulating an entire severe accident (SA)

ASTEC models all the physical phenomena involved in SA

ICARE module describes the in-vessel degradation phenomena

Advanced Technology Fuels (ATFs)

Advanced technologies to enhance safety at NPP

- Near-Term
  - Coated claddings
  - Dopped pellets
  - **FeCrAl cladding**
- Long-Term
  - Uranium Nitride pellets
  - Silicone carbide cladding
  - Extruded metallic fuel

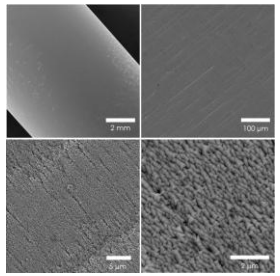

Fig. 2 Innovative claddings

Fig. 3 Doped pellets

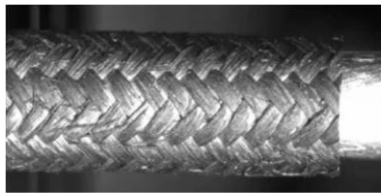

Fig. 4 Silicone carbide cladding

Separate effect test (SETs)

B136Y3: $^{80.81\%}Fe^{12.97\%}Cr^{6.19\%}Al^{0.03\%}Y$

C26M2: $^{79.88\%}Fe^{11.87\%}Cr^{6.22\%}Al^{1.98\%}Mo^{0.03\%}Y^{0.02\%}Si$

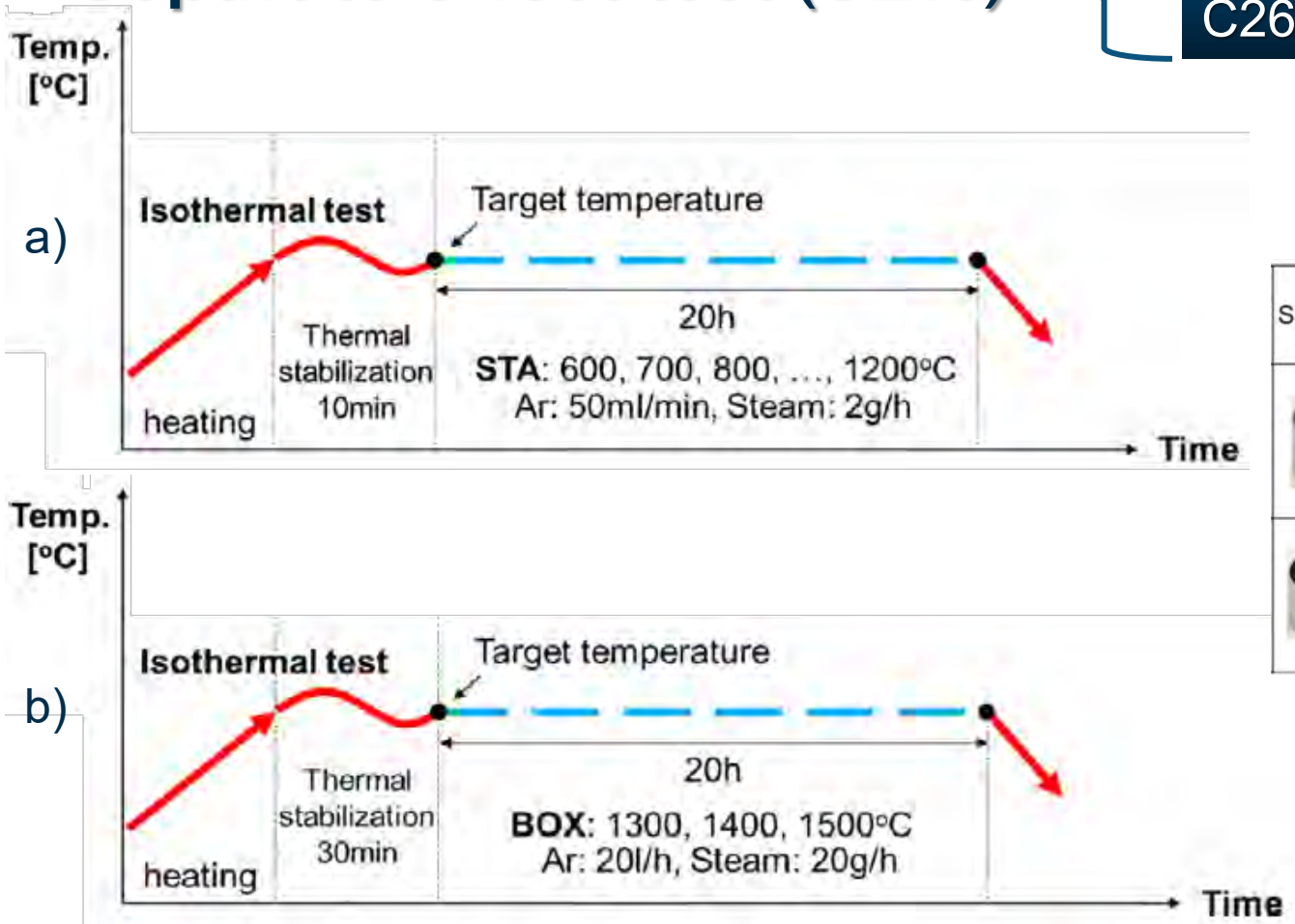

Fig. 6. The test schedules for the isothermal steam oxidation in (a) STA and (b) BOX facilities edited from*

Post-test observation

- Protective oxide layer up to 1573 K
- Catastrophic oxidation at T>1673 K

Fig. 5 Nuclear-grade FeCrAl alloys before and after the isothermal steam oxidation at 873K to 1773K for 20 h. from*

- Weight gain $\left(\frac{mg}{cm^2}\right)$
- Thickness oxide layer (m)
- Hydrogen production (mg)

*Kim, C., Tang, C., Grosse, M., Maeng, Y., Jang, C., & Steinbrueck, M. (2022). Oxidation mechanism and kinetics of nuclear-grade FeCrAl alloys in the temperature range of 500–1500 C in steam. *Journal of Nuclear Materials*, *564*, 153696.

Steam Oxidation Kinetics

Al-Oxides | Cr-Oxides | Fe-Oxides

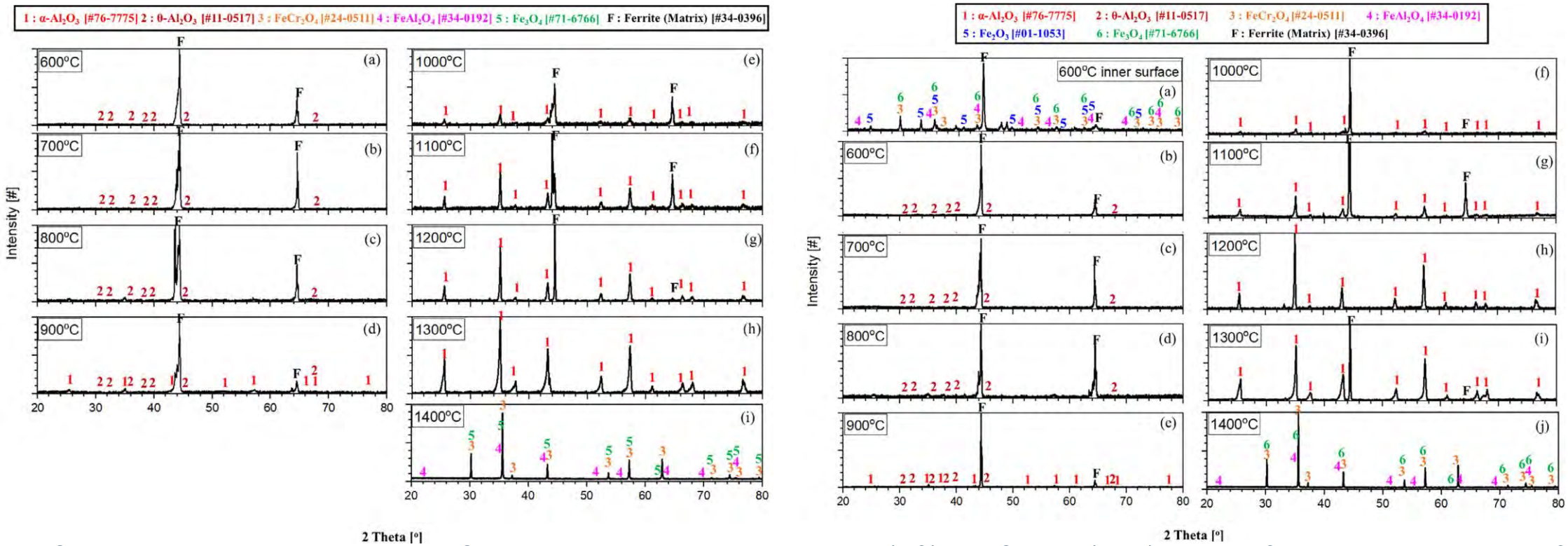

Fig. 7 Oxidation kinetics present in the FeCrAl alloy oxidation process B136Y3 (left) and C26M2 (right) adapted from Kim et al., Journal of Nuclear Materials, 2022.

Aluminum Oxidation Model

$$2\,Al_{(s)} + 3\,H_2O_{(g)} \rightarrow Al_2O_{3(s)} + 3\,H_{2(g)}$$

Oxidation Model

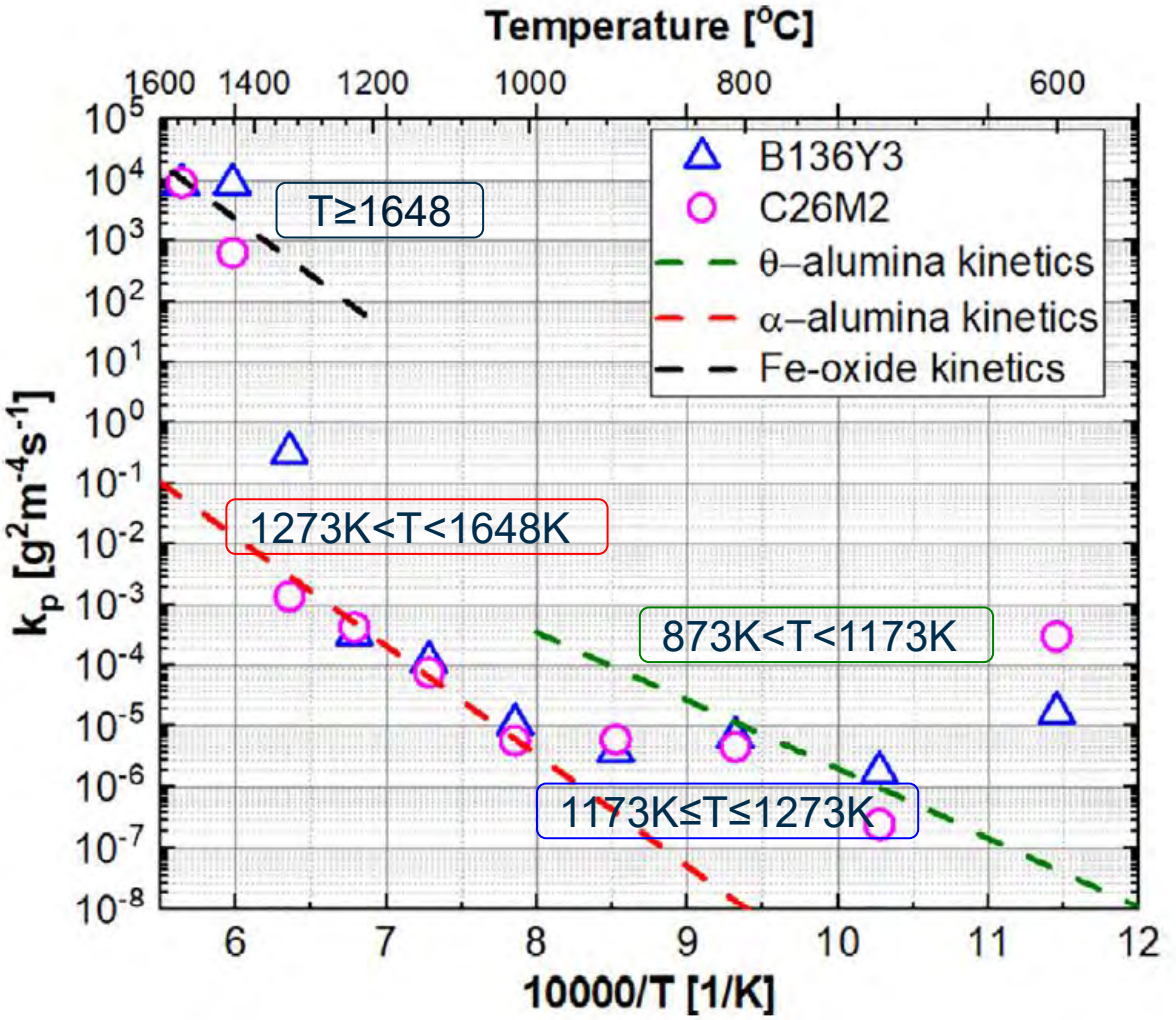

Fig. 8 Parabolic rate constants of B136Y3 and C26M2 as a function of temperature*

➢Oxygen Mass Gain

❖Parabolic correlation

❖Different coefficients according oxidation kinetics

$$\frac{dm_{O_2}^2}{dt} = K_p \qquad (1)$$

$$k_p \left[\frac{kg^2}{m^4 \cdot s}\right] = A_{gain} e^{\left(-\frac{B_{gain}}{RT}\right)} \qquad (2)$$

➢ K_p: rate constant for mass gain

➢Coefficients

❖ Linear regression

$$\ln k_p = \ln A_{gain} - B_{gain}/RT$$

ln k_p = Dependent variable

1/T = Independent variable

- B_{gain} /R = Slope

ln A_{gain} = origin ordinate

B_{gain} = -slope*R

A_{gain} = $e^{intersection}$

Oxidation Model Implementation

Stainless Steel
'SSTEEL'

Aluminum Oxide
ALOX

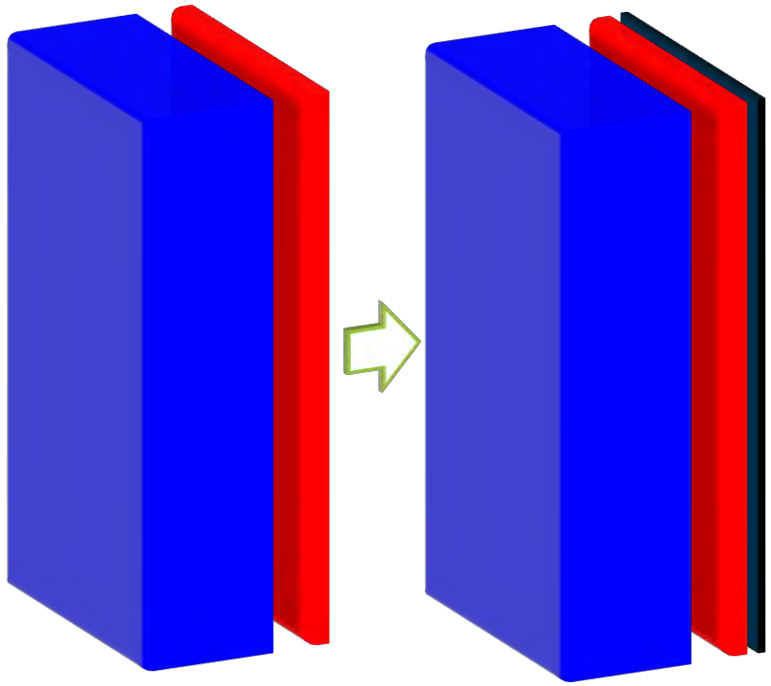

Aluminum
'Al'

Iron Oxides
FEOX

'SSTEEL' (with modified composition) :Fe–Cr

Oxidation Onset
T= 800K
Aluminum oxidation

ALOX Model
θ-alumina kinetics
873K<T<1173K

ALOX Model
alumina-transition
1173K≤T≤1273K

ALOX Model
α-alumina kinetics
1273K<T<1600K

Al_2O_3 layer no longer a barrier for Fe Oxidation
T=1600K

Fe Oxidation Onset
T>1600K

Model Assessment SETs

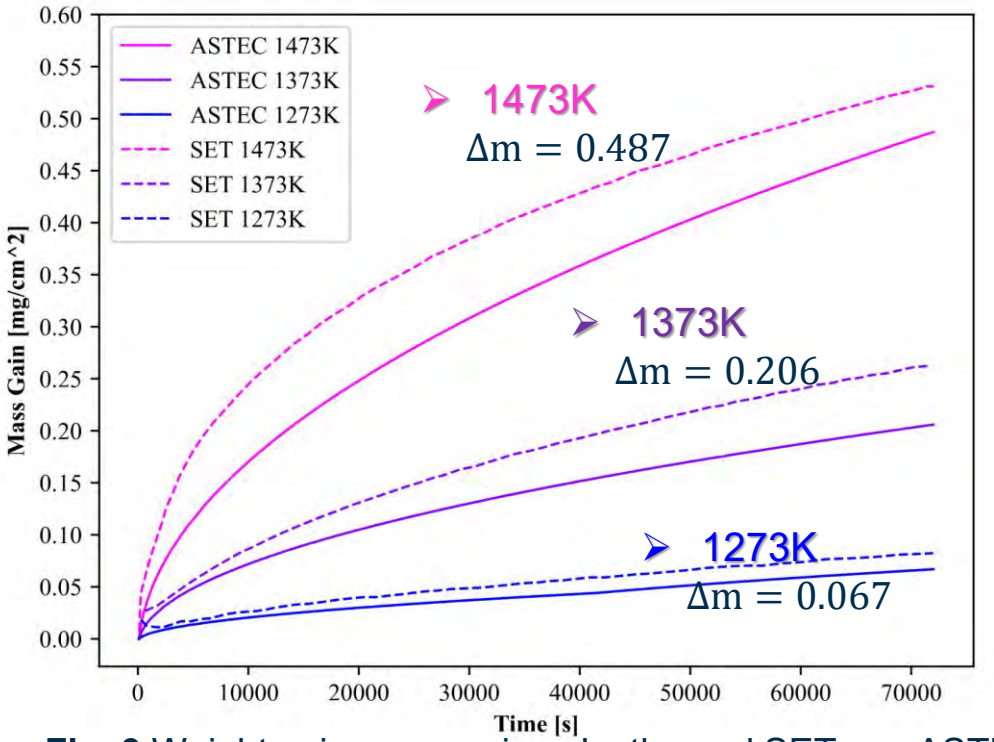

Fig. 9 Weight gains comparison Isothermal SETs vs. ASTEC

T (K)	Experiment Outer Surface (μm)	ASTEC Outer Surface (μm)
873	Too thin	0.031
973	Thin	0.117
1073	Thin	0.341
1173	Thin	0.317

Θ-alumina

alumina-transition

T (K)	Experiment Outer Surface (μm)	ASTEC Outer Surface (μm)
1273	Thin	0.360
1373	~1.500	1.110
1473	~3.000	2.616
1573	~6.500	5.538

E_a=0

α-alumina

$$2\,Al + \tfrac{3}{2}\,O_2 \rightarrow Al_2O_3$$

$$\delta_{Al_2O_3} = m_o \frac{MM_{Al_2O_3}}{f_s MM_{O_2}} \frac{1}{\rho_{Al_2O_3}}$$

$$2\,Al_{(s)} + 3\,H_2O_{(g)} \rightarrow Al_2O_{3(s)} + 3H_{2(g)}$$

$$mH_2 = \frac{3m_{Al_2O_3} MMH_2}{PM_{Al_2O_3}}$$

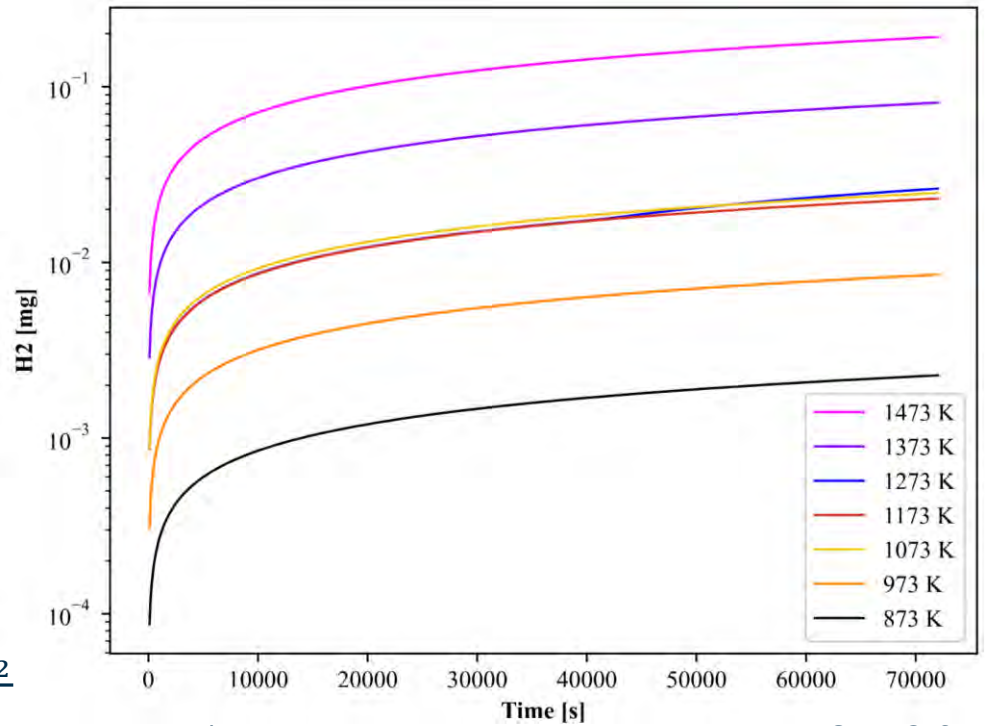

Fig. 10 a) Hydrogen production calculated in ASTEC for the isothermal steam oxidation test at 873 K to 1473 K

Bundle test QUENCH-19

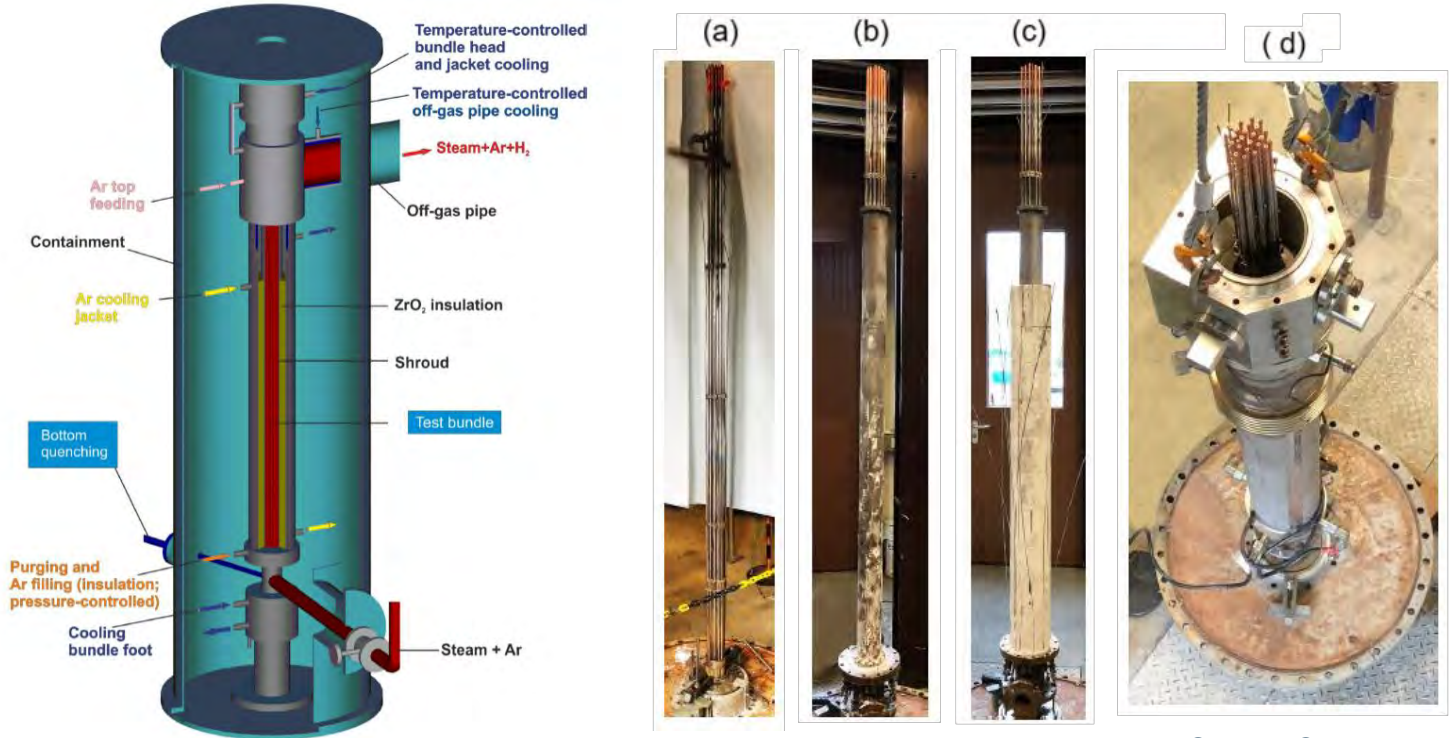

Fig. 11 Preparation bundle test QUENCH-19

Phase 1	Heating up to ~600 °C (4 kW).
Phase 2	Power increase up to 11.5 kW (pre-oxidation).
Phase 3	Power increased up to 18.12 kW (T_{pct}~1500 °C).
Phase 4	Power reduced to 4.1 kW.

0 (11:29:36)	• Start data recording.
6570… 8260	• Continuous increase of hydrogen release rate
8260	• Sharp increase of hydrogen release rate
9110	• Maximum temperature reached
9116	• Start of quench water flow
9119	• Probable massive failures of claddings
10281 (14:20:57)	• End of data recording.

ASTEC model of QUENCH 19

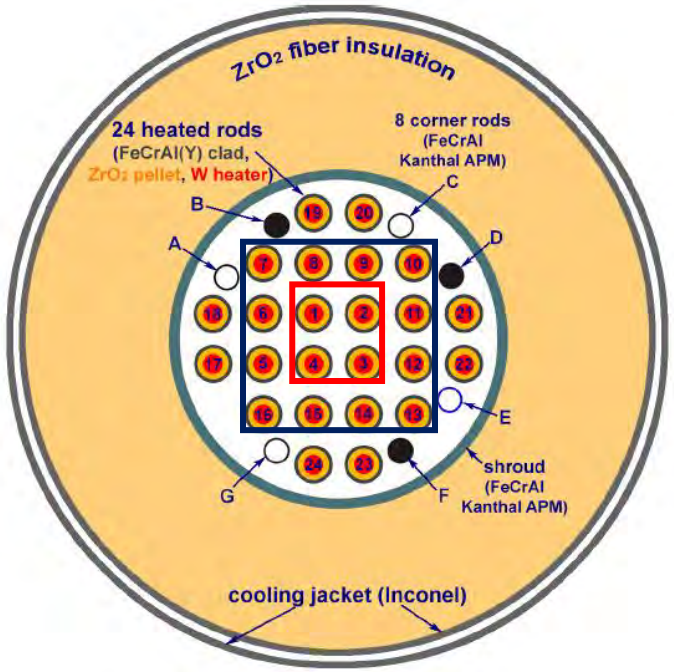

Fig. 12 Channels distribution QUENCH-19

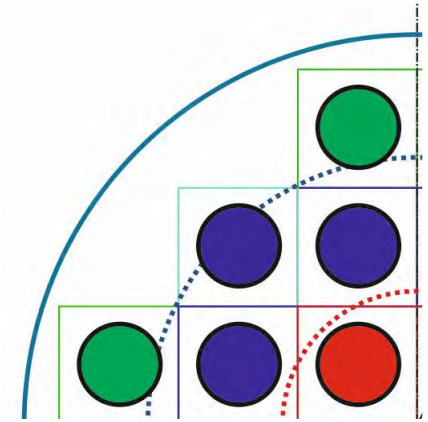

Ch. 3, 8 rods, r_{ext}= 41.5 cm

Ch. 2, 12 rods, r_{ext}= 28.4 cm

Ch. 1, 4 rods, r_{ext}=14.2 cm

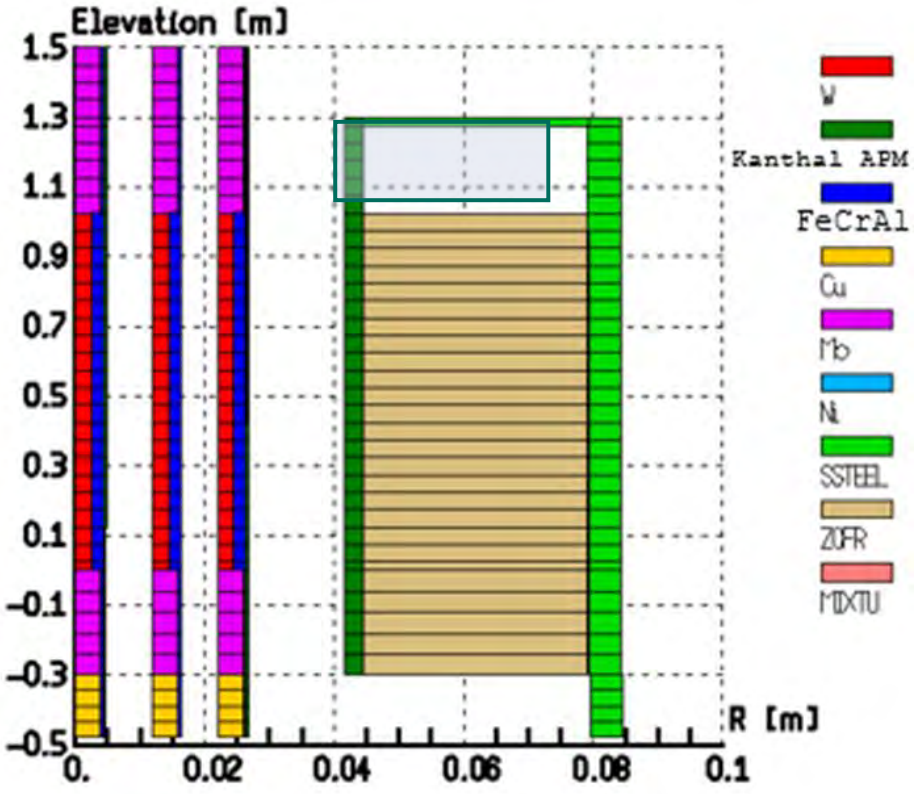

Fig. 13 ASTEC representation of QUENCH-19

Cladding temperature

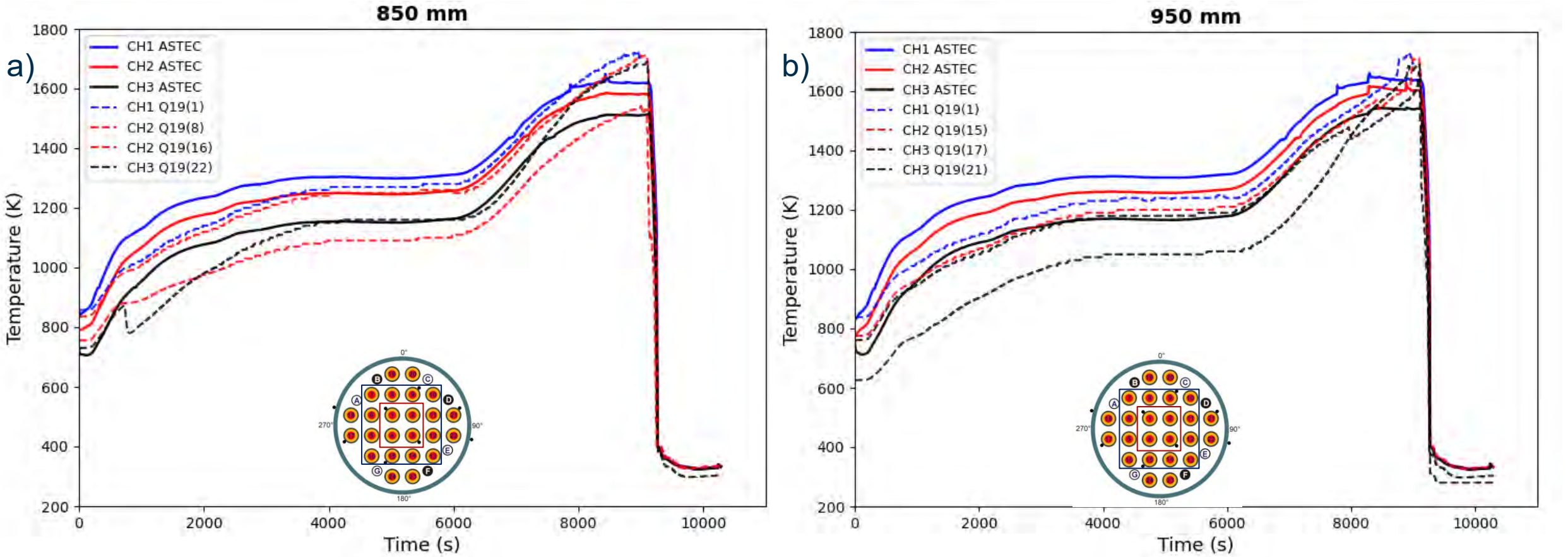

Fig. 14 Axial Cladding Temperature Profiles at 850 mm and 950 mm: Simulation–Experiment Comparison

The maximum ΔT between experimental measurements and ASTEC predictions does not exceed 50 K

Validation Q19 - H_2 Production

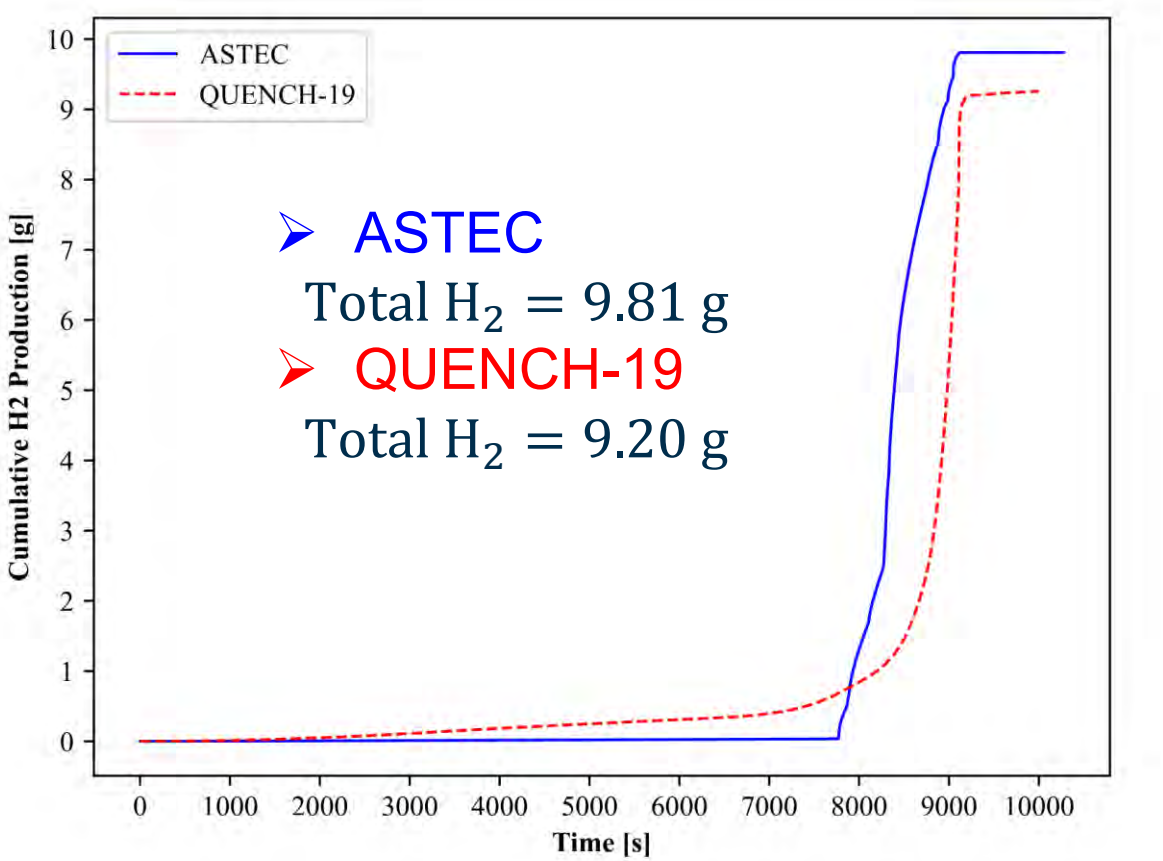

- ASTEC
  Total $H_2 = 9.81$ g
- QUENCH-19
  Total $H_2 = 9.20$ g

Fig. 15 Total hydrogen release ASTEC vs. Experiment

ASTEC simulation underestimates hydrogen (H_2) generation.

The underestimation of hydrogen generation is attributed to the non-consideration of thermocouples' oxidation in the model

The cumulative hydrogen production is about 6.6% higher than the experimental value

ASTEC provides a reasonable estimate of the total hydrogen production

Small Modular Reactor Application

Initiating Event:

- Break Location: Discharge line (Downcomer to containment)
- Break Elevation: 5.3 m above TAF
- Break Diameter: 4.3 cm
- Break initiation time: t = 0 s

Electrical Conditions:

- Offsite AC power: Total loss at t = 0 s

Steam System:

- Main steam line isolation: 5 s after break initiation

Safety System:

- ECCS actuation criterion:
  ΔP (RPV-Containment) < 6.9 MPa
- Containment water level > 5.8 m
- Reactor venting valves: Available
- Reactor recirculation valves: Unavailable

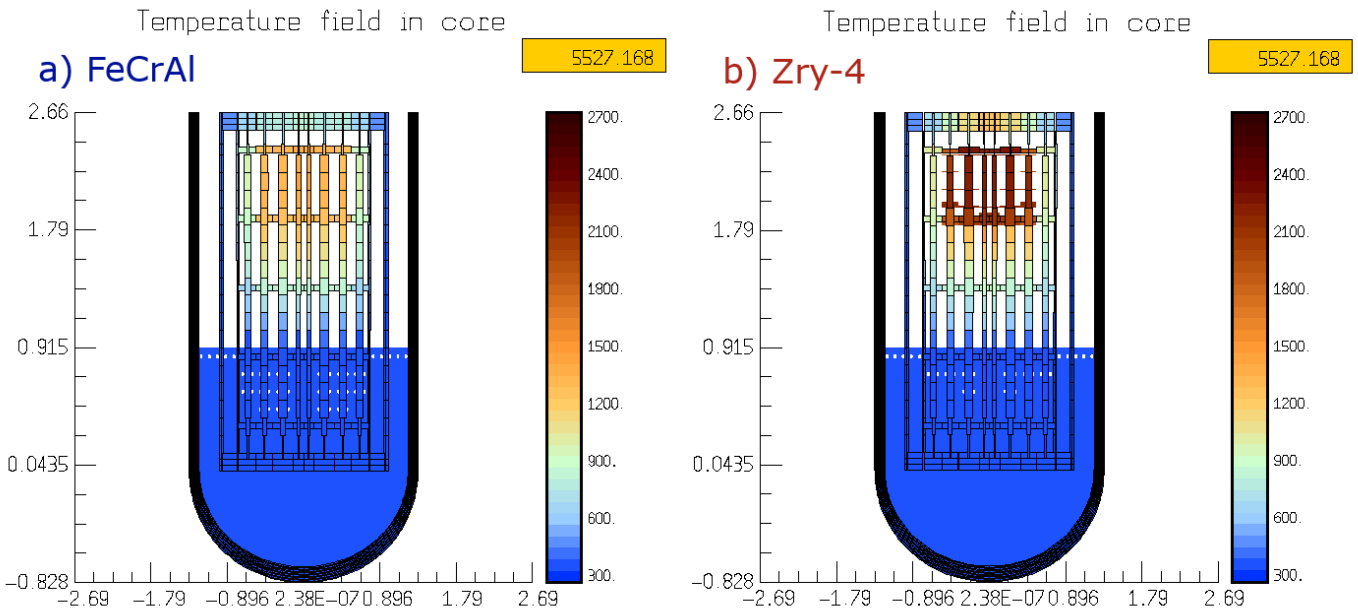

Fig. 16 Core Damage for a BDBA: FeCrAl versus Zry-4

Cladding Material Event (s)	Zry-4	FeCrAl
H_2-onset	3147	3639
First cladding rupture	4415	5492

Impact on H_2 Production

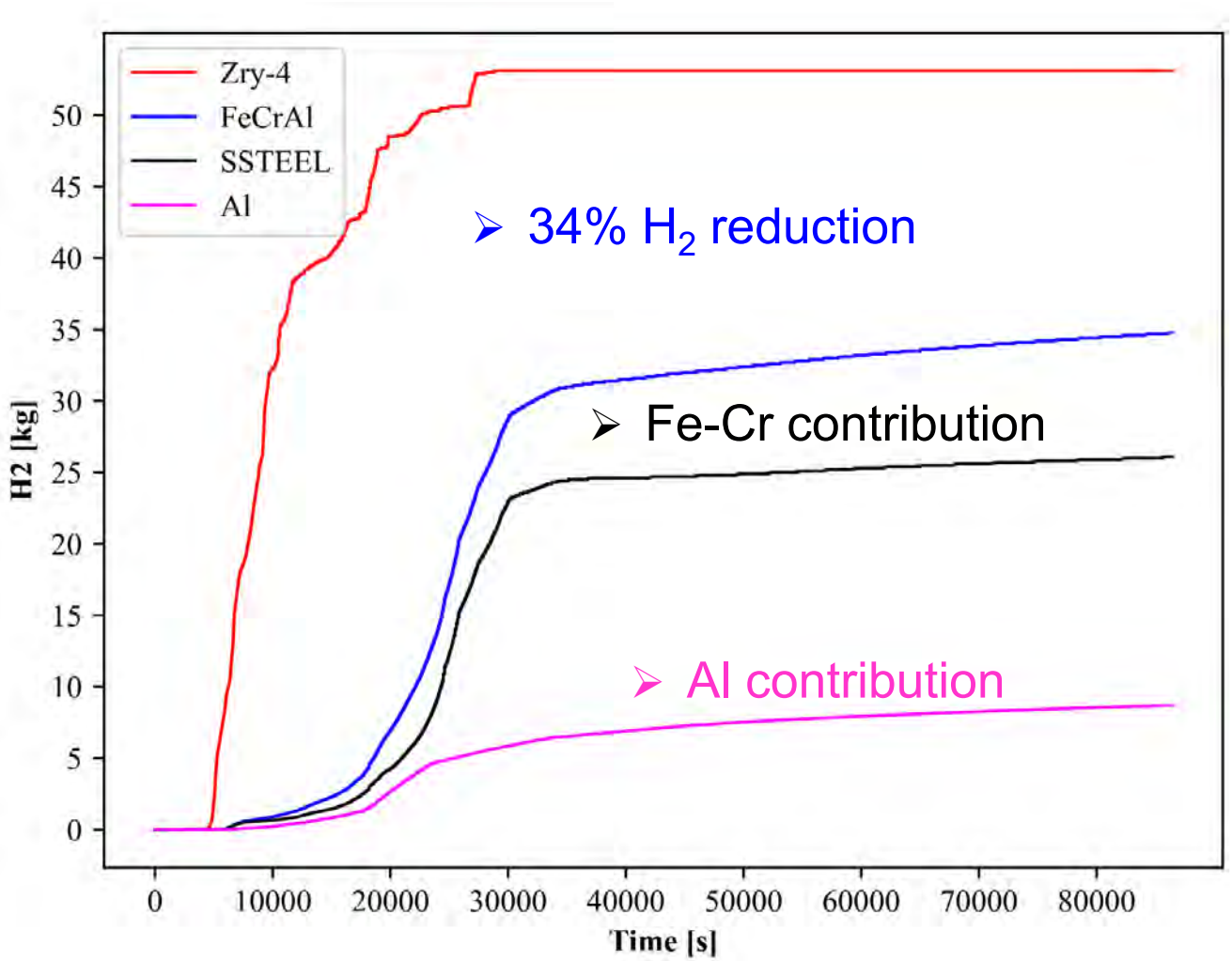

Fig. 17 Impact of Cladding Material on Hydrogen Production during BDBA

Delay in hydrogen onset.

- Approximately 492 s

No lower head failure is predicted

- Simulated time: 1 day scenario

Fe-Cr oxidation:

- Contributes approximately 75% to the total H_2 production

Aluminum oxidation:

- Contributes the remaining 25%

Cumulative hydrogen release amounts:

- Zircaloy 6.34 kg → 53 kg
- FeCrAl 0.01 kg → 35 kg

Conclusion

- Modelling extensions have been implemented in ASTEC for FeCrAl alloys also based on the QUENCH Experiments results
  - Validation of the ASTEC FeCrAl modeling has been performed
  - ALOX model for temperatures T<1500K
    - The Al_2O_3 layer leads to a strong, stable protective role
  - SSTEEL model at very high T
    - Real Fe oxidation is included in the modelling, with corresponding oxide layers
- QUENCH SETs:
  - Modeling strategy for FeCrAl alloys (multilayer material) reproduce reasonable the experimental data with respect to Weight gain and Thickness oxide layer.
- QUENCH-19
  - ASTEC was used to performed the QUENCH-19 bundle test simulations.
    - The code is able to reproduces with good agreement the experimental temperatures and H_2 production, considering two different oxidation processes.
- SMR Application
  - Preliminary assessment of the analysis of a postulated BDBA scenario with FeCrAl cladding was performed
    - Some results must be interpreted qualitatively due to the previously mentioned limitations of the FeCrAl oxidation model once core degradation initiates.
    - Further modelling efforts are required to validate the assumptions adopted for the FeCrAl failure criteria and properly quantify material behavior after cladding rupture.

Thank you for your attention

Questions?

Zaira I. Jiménez Balbuena
Institute for Neutron Physics and Reactor Technology
Karlsruhe Institute of Technology
zaira.balbuena@kit.edu

THE INTEGRAL AIR INGRESS CODEX-ATF-AIT EXPERIMENT

Róbert Farkas, Nóra Vér, Berta Bürger, Zoltán Hózer
HUN-REN Centre for Energy Research (HUN-REN EK)
29-33 Konkoly-Thege Miklós rd., 1121, Budapest, Hungary
robert.farkas@ek.hun-ren.hu

ABSTRACT

The experimental scenario was designed to investigate key phenomena of chromium coated zirconium cladding behavior during air ingress accident conditions, including cladding burst, oxidation, nitriding, and eutectic formation. During the preparatory phase, the facility was heated to 600 °C under a steam-argon atmosphere. In the subsequent pre-oxidation phase, the rod heating power was increased stepwise, leading to pressurization and cladding burst between 750–800 °C in most rods. The burst openings allowed coolant ingress, initiating chemical reactions on both sides of the cladding.
In the air ingress phase, the temperature rise was significantly slower and smoother compared to the reference experiment CODEX-AIT-3 [1] conducted with traditional Zr materials, demonstrating the protective effect of the Cr coating. The duration of the air ingress phase was extended to 1.5 hours (compared to 1 hour in the reference test), with a maximum cladding temperature of 1545 °C (compared to 1600 °C). The temperature profile shifted during this phase, with the peak moving from the upper bundle section to lower elevations due to intense chemical interactions in the less oxidized regions.
Gas analysis confirmed steam and oxygen starvation conditions during air ingress. The partial consumption of nitrogen indicated nitride formation. A total of 1.4 g of hydrogen was generated during the pre-oxidation phase, followed by 3.3 g during the air ingress phase. A controlled cool-down in argon flow was performed to avoid further reactions.

KEYWORDS
Bundle test, ATF cladding, air ingress, Cr-Zr eutectic reaction, burst

1. INTRODUCTION

The main objective of the CODEX-ATF-AIT test was to determine whether accident-tolerant fuel (ATF) cladding with a chromium (Cr) coating would provide protection in the event of severe accidents at nuclear power plants (NPPs) involving air ingress. An integral bundle test involving electrically heated chromium-coated fuel rod simulators was conducted at the CODEX facility [2] at the HUN-REN Centre for Energy Research. The proposed scenario involved a reactor accident in which corium melted through the bottom head of the pressure vessel, resulting in an air and steam mixture penetrating from the reactor cavity into the reactor vessel. The experiment focused on several phenomena of fuel behaviour during accidents, such as bursting, oxidation, nitriding and eutectic formation. Slow cooling was selected to provide information on the bundle's state before quenching.

2. THE TEST FACILITY

A Hexagonal bundle was built in VVER geometry using VVER type Cr coated spacer grids. In the bundle Cr coated optZIRLO^{TM} cladding tubes were used. The height of test section was 1000 mm, but the active part with the rods was only 890 mm, so the upper part of the shroud was used for thermocouples, without fuel rods. The fuel rods were filled with zirconia pellets. The rods were pressurised by krypton. Electrical

heating with two tungsten heaters in each rod was used. External heating was also applied to the test section. The bottom of the test section was connected to the steam generator unit. The condenser cooled down the hot steam+gas flowing out from the top of the test section. The bundle was covered by Cr coated Zr shroud. The shroud had no perforations and it was surrounded by several thermal insulation layers, electrical heaters and a steel tube (Fig. 1). SiO_2+Al_2O_3+ZrO_2 fibre was used between the Zr shroud and the steel tube.

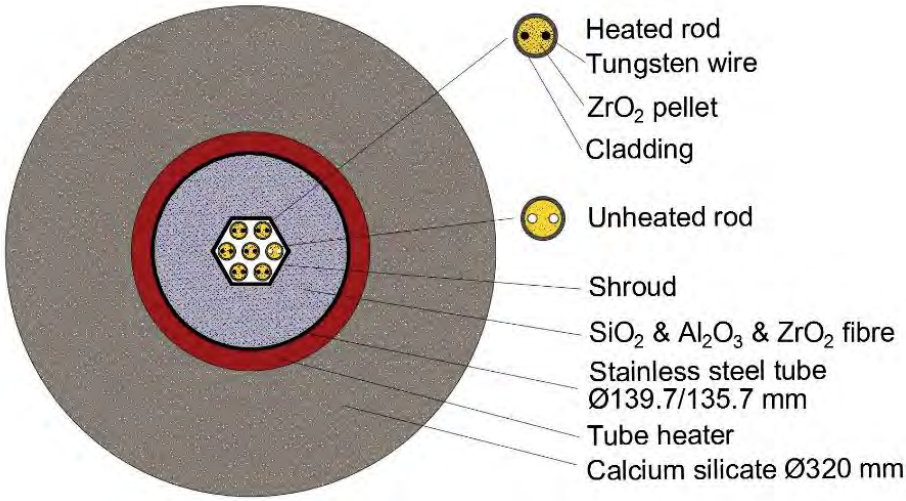

Figure 1. Horizontal cross section of the test section with thermal insulations

Steel vessel (diameter 139.7/135.7 mm) with external electrical heating housed the test section with fibre insulation. External heaters were applied on the surface of the stainless steel tube. Calcium silicate covered the steel tube as external layer of thermal insulation with external diameter of 320 mm.

The instrumentation included a large number of thermocouples in and around the heated bundle and a mass spectrometer for analysing the composition of the outlet gas.

3. SELECTED SCENARIO

The scenario consisted of the following phases (Fig. 2):

- Preparation phase: technological heat-up of the facility, initiation of steam supply, moderate power and target temperature of 500 °C.
- Pre-oxidation phase: further heat-up with increased power, pressurisation of fuel rods to reach burst, target temperature of 1100 °C.
  In case of Cr coated zirconium materials, no significant oxidation of cladding external surface is expected during the pre-oxidation phase. However, if the Cr coated zirconium cladding tubes suffer significant ballooning, the Cr-layer may become cracked and the oxidation of zirconium could start locally through the cracks of the Cr-layer. On the other hand, oxidation of inner (non-coated) cladding surface and secondary hydriding may take place after cladding burst and penetration of steam into the fuel rods.
- Intermediate cool-down phase: slow cooling down the bundle to 900 °C at reduced power.
- Steam-air phase: steam and oxygen-starvation condition, heat-up with moderated power, target temperature of 1400 °C.
- In the steam-air phase, a steam- and oxygen-starvation condition was aimed at, in order to investigate the effect of nitriding. Because one of the main failure mechanisms of Cr coated zirconium claddings is the Cr-Zr eutectic formation, it was intended to reach about 1400 °C in this

phase in order to observe the oxidation behaviour of ATF cladding in air above the Cr-Zr eutectic formation temperature.

- Slow cool-down: slow cool-down was selected to provide information on the state of the bundle before quench.

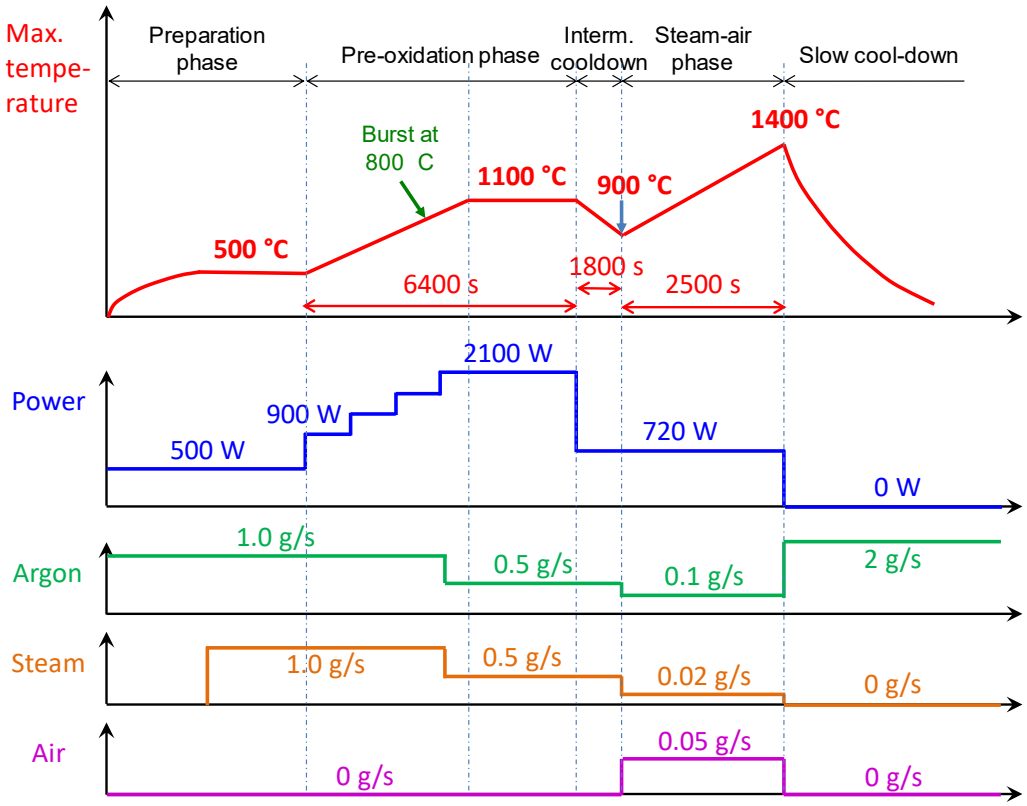

Figure 2. Main parameters of proposed CODEX-ATF-AIT scenario

4. THE CODEX-ATF-AIT EXPERIMENT

I. Preparation phase

The preparation phase started with switching on the external heaters with 750 W power (Fig. 3). The argon and steam flows through the bundle were set to 1.0 g/s. The water cooling system was put into operation, the bundle power was set to 500 W and later were varied up to 1000 W. The fuel rod internal pressure was set individually for each rod between 20-30 bars after 5112 s.

II. Pre-oxidation phase

The pre-oxidation phase was initiated after 6883 s. From this phase the same power history was applied than in the CODEX-AIT-3 experiment, but with reduced power (90% of the CODEX-AIT-3, Fig. 3). The reduction in performance compared to the reference experiment was due to the fact that the rods were 10% shorter. The bundle power was increased in a stepwise manner up to 1728 W, the flow rate of both steam and argon was 1.0 g/s. The power increase resulted in significant heat-up of the bundle. The argon and the steam flow rate was reduced from 1.0 g/s to 0.5 g/s after 10181 s in order to reach higher temperature increment for the bundle. The maximum temperature at 750 mm elevation was 1170 °C and it was reached at 12344 s (Fig.4). In order to avoid too high degree of oxidation in this phase, the high temperature plateau was maintained for 15 min by

manipulating the bundle power. The maximum electric power of the bundle was 2129 W. At the end of the pre-oxidation phase the rod maximum temperature was 1084 °C, while the shroud heated up to 1013 °C and the stainless steel tube temperature was above 725 °C.

The cladding bursts took place in the pre-oxidation phase, mainly between 8850-9250 s (Fig. 5). Rod No. 5. failed at 37.0 bar (≈760 °C at 750 mm), rod No. 4. at 36.4 bar (≈770 °C at 750 mm), rod No. 1. at 29.7 bar (≈780 °C at 750 mm) and rod No. 2. at 35.3 bar (≈810 °C at 750 mm). The delay between the measured pressure drops inside the rods and the Kr signals at the mass spectrometer was about 10 s. Because of leakage, rod No. 6. was not pressurized and rod No. 3. and rod No. 7. were pressurized but did not burst.

The total hydrogen release measured in the pre-oxidation phase was around 1.4 g.

III. Intermediate cool-down

The bundle power was reduced in three steps after 13195 s (Fig. 3). The maximum rod temperature decreased to 728 °C (Fig. 4).

IV. Steam-air phase

The steam-air phase started after 15082 s. The steam generator was switched off. The argon flow rate was reduced from 0.5 g/s to 0.1 g/s and the air flow was initiated with 0.05 g/s flow rate. The operation of small HPLC pump was started resulting in 0.02 g/s water injection to the bottom of the bundle. The bundle power was increased to 720 W (Fig. 3). The maximum cladding temperature was ≈1030 °C and it was measured at 750 mm elevation (Fig. 4).

Unlike in the CODEX-AIT-3 experiment, no temperature escalation occurred during the steam-air phase with the Cr coated cladding and shroud material. In order to observe the air oxidation behaviour of ATF cladding above the Cr-Zr eutectic formation temperature, the test was continued with a slight power increase to 1000 W (Fig. 3). The maximum temperatures were initially recorded at the top of the bundle (≈1350 °C at 650-750 mm). However, over time, the hottest section of the bundle moved gradually downwards and in succession levels of 500, 400, 200 and 150 mm reached the highest (≈1500 °C) temperature (Fig. 4). A possible explanation could be that eutectic melt formation occurred, and the melted zirconium reacted strongly with the limited steam and air available in the coolant. The maximum measured cladding temperature was 1544 °C and it was recorded at 400 mm elevation. The maximum shroud temperature was 1480 °C and it was measured at 750 mm elevation.

In the extended air ingress phase oxygen was completely consumed from the gas stream though the bundle at about 18700 s (Fig. 6). Shortly afterwards, from about 19000 s considerable nitrogen consumption started, which indicates an overall oxygen and steam starvation. This coincides with the temperature escalation of the middle-lower part of the bundle (at 500-150 mm). Parallel with oxygen, steam was also consumed from the beginning of the air-ingress phase. Interestingly, not complete steam consumption was experienced in the outlet gas. Despite the detected steam consumption from the start of the air-ingress phase, hydrogen produced by the zirconium (chromium) – steam reaction became detectable in the outlet gas only after the complete consumption of oxygen. As long as oxygen was available, the produced hydrogen could recombine with oxygen and produce water.

From about 19200 s the quantity of nitrogen started to increase in the outlet gas due to the re-oxidation of the formed nitrides. The total hydrogen release measured in the extended air-ingress phase was about 3.3 g, while the total uptakes of oxygen and nitrogen also calculated only for the extended air-ingress phase were about 17 and 9 g, respectively.

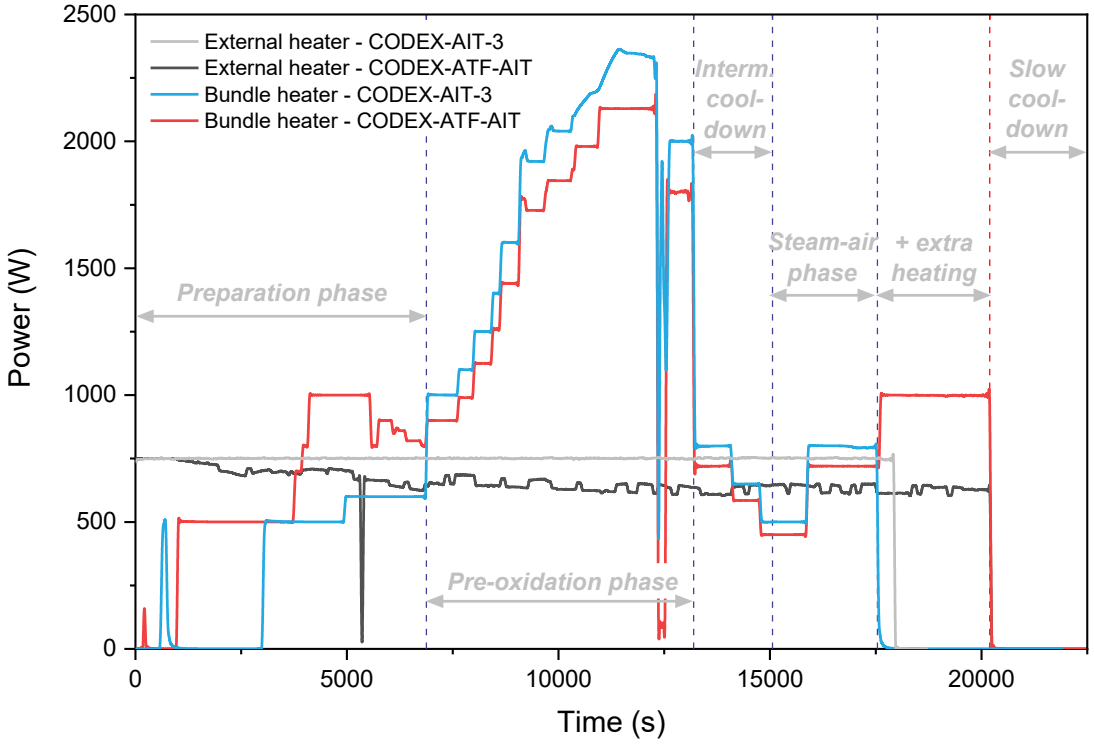

Figure 3. Comparison of power histories of the CODEX-AIT-3 and CODEX-ATF-AIT tests

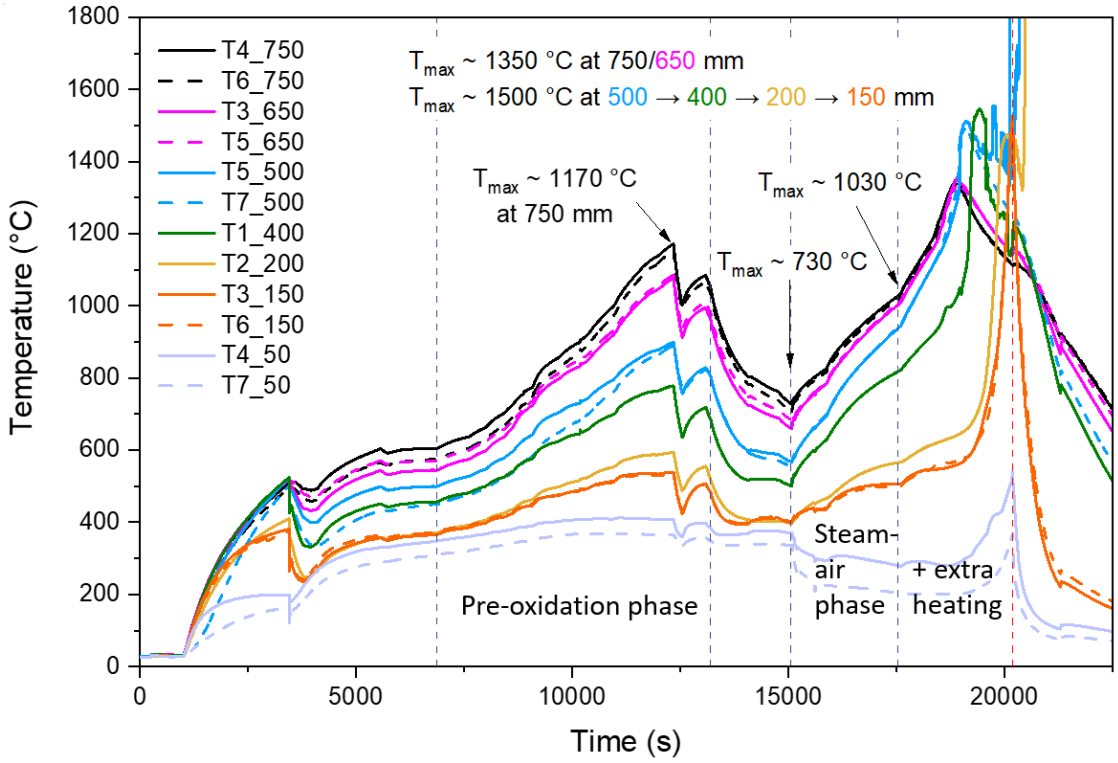

Figure 4. Cladding temperatures in the CODEX-ATF-AIT test

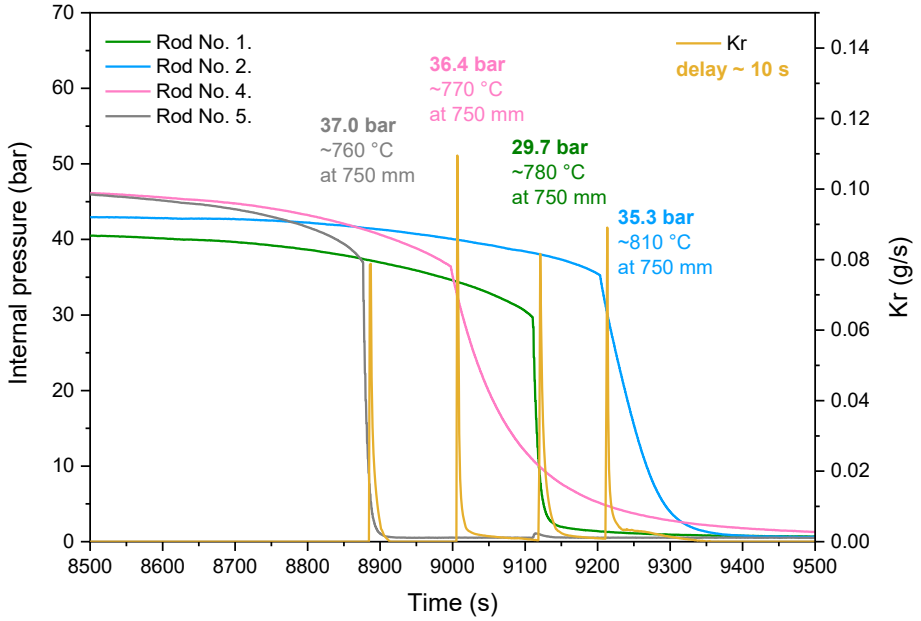

Figure 5. Comparison of measured fuel rod pressure drops and Kr signals at MS in the CODEX-ATF-AIT test

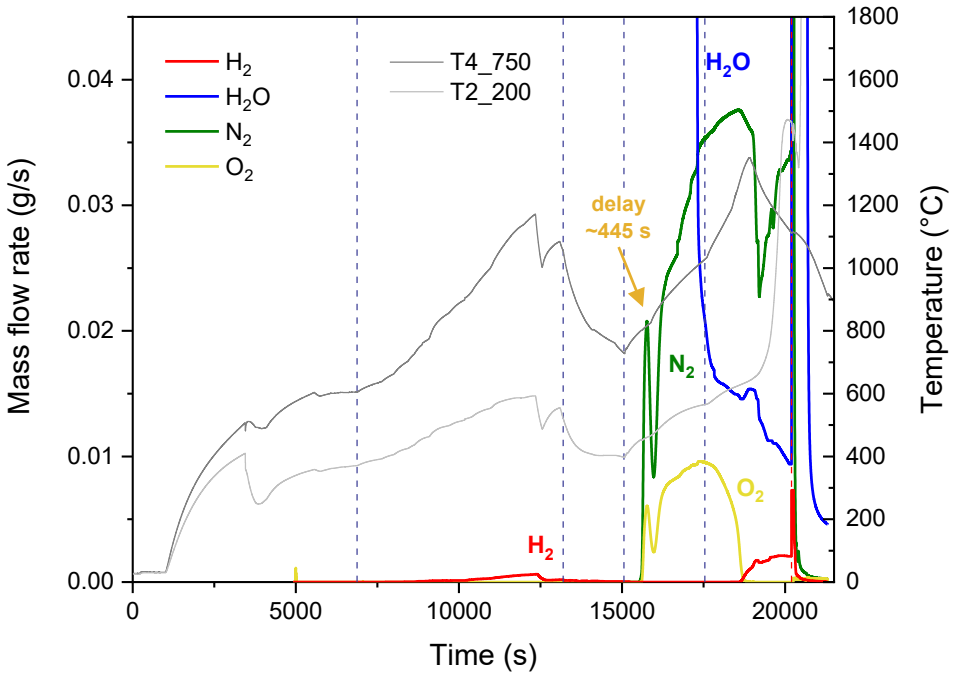

Figure 6. Outlet gas flow rates in the CODEX-ATF-AIT test

V. Slow cool-down

The slow cool-down was initiated at 20212 s with switching off the bundle and the external heater power (Fig. 3). The steam and air flow rates were set to zero, while the argon flow rate was increased to 2.0 g/s. It took two and a half hours to cool down the facility and after that the argon flow rate was set to zero.

5. SUMMARY

The CODEX-ATF-AIT test was successfully performed on 29 October 2024 at the HUN-REN Centre for Energy Research (EK) in Budapest. The test section included a seven-rod bundle that was electrically heated and composed of zirconium (Zr) cladding tubes coated with chromium (Cr) and provided by the Czech Technical University in Prague (CTU).
During the preparatory phase, the facility was heated to 600 °C using a steam-argon flow, with heat supplied by both external and fuel rod heaters. The pre-oxidation phase continued with the same flow rates and stepwise increased heating power on the rods. During the heating phase, the rods were pressurised, resulting in a cladding burst between 750 and 800 °C on most of the rods. This allowed the coolant to enter the rods and initiate chemical reactions on both sides of the cladding. During the intermediate cooling phase, the temperatures were reduced below 750 °C. During the steam-air phase, the temperature increased more smoothly than in the reference experiment, CODEX-AIT-3. The slower temperature increase was due to the protective effect of the Cr coating. The air ingress phase in the reference experiment lasted 1 hour, with a maximum cladding temperature of 1600 °C, whereas in the CODEX-ATF-AIT it lasted 1.5 hours, with a maximum cladding temperature of 1545 °C. Similar to the reference experiment, the temperature profile changed significantly during the air ingress phase: the maximum temperature (≈1500 °C) moved from the upper section of the bundle to lower elevations due to intense chemical interactions in the less oxidised and/or melted lower part. The maximum shroud temperature was around 1470 °C at elevations of 300, 500, and 700 mm.

Analysis of the outlet gas composition showed that steam and oxygen starvation conditions were established during the air ingress phase. The partial consumption of nitrogen also indicated the formation of nitrides. A total of 1.4 g of hydrogen was produced during the pre-oxidation phase, compared to 3.3 g during the air ingress phase. The bundle was slowly cooled in an argon flow to avoid interactions that might occur during water quenching.

ACKNOWLEDGMENTS

The CODEX-ATF-AIT experiment was conducted with the support of EURATOM OFFERR project and the Paks Nuclear Power Plant.

REFERENCES

1. R. Farkas, Z. Hózer, I. Nagy, N. Vér, M. Horváth, M. Steinbrück, J. Stuckert, M. Grosse, “Effect of steam and oxygen starvation on severe accident progression with air ingress,” *Nuclear Engineering and Design*, pp. 396 (2022) 111884
2. R. Farkas, Z. Hózer, I. Nagy, N. Vér, P. Szabó, M. Horváth, P. Kostka, G. Lajtha, “Experimental simulation of selected design extension condition scenarios without core meltdown in the CODEX facility,” *Progress in Nuclear Energy*, pp. 161 (2023) 104720.

Development of a Continuous-Parameter Creep Model for Predicting Behavior of RPV Steel under Severe Accident Conditions

Xiangyu Li, Weimin Ma, Sevostian Bechta

Royal Institute of Technology
Roslagstullbacken 21, 10691 Stockholm
Xiangyl@kth.se; Weimin@kth.se; Sevostian@kth.se

ABSTRACT

During severe accidents of a light water reactor, the relocation of the molten core to the lower head of the reactor pressure vessel (RPV) may exert challenging thermal loads to the RPV wall due to extreme high temperatures, potentially leading to creep failure or melt-through of the lower head. Consequently, modeling the creep behavior of the RPV wall plays an important role in severe accident analysis. A key limitation of widely used creep models in reactor safety analysis is their inability to simulate the tertiary stage, which is crucial for material failure prediction. The present study is motivated to calibrate a continuum damage mechanics (CDM) creep model (Liu-Murakami model) for reactor pressure vessel (RPV) steel SA533B1. The calibration is performed using experimental data across a wide temperature range from 900 to 1623 K, ensuring wide thermo-mechanical applicability of the model. Furthermore, to facilitate scenarios involving significant temperature variations, temperature-dependent relationships for the model constants are established to reduce the interpolation errors. Comparative evaluation demonstrates that the Liu-Murakami model offers superior predictive performance over the full temperature range. These findings provide a more reliable creep model for thermo-mechanical analysis of RPV deformation during severe accidents.

KEYWORDS
Severe accident, Reactor pressure vessel, Thermos-mechanical analysis, Creep

1. INTRODUCTION

Creep refers to the time-dependent, permanent deformation of a solid structural material when subjected to sustained mechanical stress, and it becomes particularly pronounced at elevated temperatures [1, 2]. High-temperature conditions may be encountered during severe accidents of light water reactors, where molten core (corium) relocates to the lower head of the reactor pressure vessel (RPV) and consequently heats up the vessel wall [3,4]. Under the thermal and mechanical loads, the RPV lower head undergoes considerable creep deformation, and fails ultimately [5-7]. Consequently, creep analysis is essential for predicting severe accident progression, where the fidelity and accuracy of creep models for RPV steels play an important role, especially under the very high temperatures occurring in severe accidents.

Mant creep models have been developed and applied in thermo-mechanical analysis (i.e. finite element analysis – FEA). The most widely used creep model is the power law model, commonly referred to as the Norton model [8]. Through mathematical transformations, the Norton model has yielded several variants, including the time hardening model [9]. Another example is the MPC omega model proposed by Prager [10]. While these models are effective in describing the primary and/or secondary creep stages, they generally lack predictive capability for the tertiary stage of the creep curve. In response, researchers have tried to explore alternative formulations which can be divided into two principal approaches. One is the theta-projection model introduced by Evans et al. [11]. Another principal approach is based on continuum damage mechanics (CDM), such as the Kachanov-Rabotnov (K-R) model [12]. To address notable limitations in the K-R model, such as convergence difficulties and mesh dependency, Liu & Murakami proposed an enhanced CDM creep damage model [13].

The present study is conducted to advance the Liu & Murakami (L-M) creep model by using the

available experimental data for the creep behavior of RPV steel SA533B1 specimens. The datasets are from the series of creep tests [5,6] performed by Idaho National Engineering Laboratory (INEL) for SA533B1 material temperature range of 900~1373 K, and the tests carried out by Japan Atomic Energy Agency (JAEA) for temperature ranging from 1250 K to 1623 K which is near the melting point of S533B1 [14,15]. The chemical composition of SA533B1 steel is detailed in Table **I**. The test matrix of both INEL and JAEA creep tests are shown in Table **II**.

Table I**. Chemical composition of SA533B1 steel (wt.%) [5]**

	C	Si	Mn	P	S	Ni	Cr	Mo	V	Cu
INEL	0.17	0.20	1.22	0.006	0.010	0.67	0.10	0.55	0.003	0.009
JAEA	0.17	0.23	1.47	0.014	0.017	0.57	0.10	0.51		0.15

Table II**. Adopted Creep Test Matrix from INEL and JAEA [14]**

	INEL					**JAEA**			
Temp (K)	900	1050	1150	1250	1373	1250	1473	1573	1623
Stress (MPa)	69.70	13.90	12.50	8.00	3.50	12.6	4.50	2.27	2.07
		26.30	26.50			17.0	4.99	2.61	2.37

The structure of this paper is organized as follows: Section 2 introduces the L-M creep model [13] and its modification based on the INEL and JAEA creep tests [5-6, 14-15]; Section 3 illustrates the predictive capabilities of the new model, in terms of agreement with experimental creep curves and key parameters (e.g., minimum creep strain rate), as well as the interpolation accuracy; Finally, Section 4 presents the conclusions.

2. CREEP MODEL

The Liu & Murakami creep model is a creep damage model based on continuum damage mechanics [13]. Its multiaxial form of creep damage and creep strain equation is as follows:

$$\dot{\varepsilon}_c = \frac{3}{2} C \sigma_{eq}^{n} \frac{S_{ij}}{\sigma_{eq}} \exp\left(\frac{2(n+1)}{\pi\sqrt{1+3/n}}\left(\frac{\sigma_1}{\sigma_{eq}}\right) \cdot \omega^{3/2}\right) \tag{1}$$

where C and n are material constants. $\dot{\varepsilon}_c$ is the creep strain rate, σ_{eq} is the equivalent stress, $\sigma_1$is the maximum principal stress, ω is the damage factor, S_{ij} is deviatoric stress.

If we neglect the multiaxial influence in the present study, the multiaxial Liu-Murakami (L-M) creep model can be simplified to a uniaxial form:

$$\dot{\varepsilon}_c = C \sigma_{eq}^{n} \, exp\left(\frac{2(n+1)}{\pi\sqrt{1+3/n}} \cdot \omega^{3/2}\right) \tag{2}$$

$$\dot{\omega} = D \frac{(1-e^{-q})}{q} \sigma_{eq}^{p} e^{q\omega} \tag{3}$$

where p and q are model constants. All parameters (constants: C, n, D and p) except q (q=1.5) are obtained from regression analyses of the experimental data. The regression analyses yield:

$$C(T) = \begin{cases} \exp\left(-0.0372T + 12.449\right) & T \leq 1050 \text{ K} \\ \exp\left(0.0263T - 54.1\right) & T > 1050 \text{ K} \end{cases} \tag{4}$$

$$n(T) = \begin{cases} 0.0216T - 18.312 & T \leq 1050 \text{ K} \\ -0.0046T + 9.2 & T > 1050 \text{ K} \end{cases} \tag{5}$$

$$D(T) = \begin{cases} \exp(-0.0299T + 6.862) & T \leq 1050\ \text{K} \\ \exp(0.00235T - 49) & T > 1050\ \text{K} \end{cases} \quad (6)$$

$$p(T) = \begin{cases} 0.0173T - 14 & T \leq 1050\ \text{K} \\ -0.0045T + 8.64 & T > 1050\ \text{K} \end{cases} \quad (7)$$

Table **III** shows the values of the constants in the modified L-M creep model for the temperature points employed in the INEL and JAEA tests. Figures 1(a) through 1(d) illustrate the variation of the modified L-M model constant with temperature.

Table III**. L & M creep mode material constants for SA533B1 steel (σ_{eq} in MPa and t in s)**

Temp (K)	C	n	D	p	q
900	7.12E-10	1.19	1.87E-09	1.64	1.5
1050	2.58E-12	4.35	1.96E-11	4.14	1.5
1150	2.80E-11	3.96	2.65E-10	3.80	1.5
1250	5.15E-10	3.63	3E-09	3.45	1.5
1373	2.44E-08	3.03	1.47E-07	2.95	1.5
1473	1.20E-07	2.38	6.03E-07	2.48	1.5
1573	1.16E-06	1.94	3.57E-06	2.01	1.5
1623	6.27E-06	1.72	1.67E-05	1.78	1.5

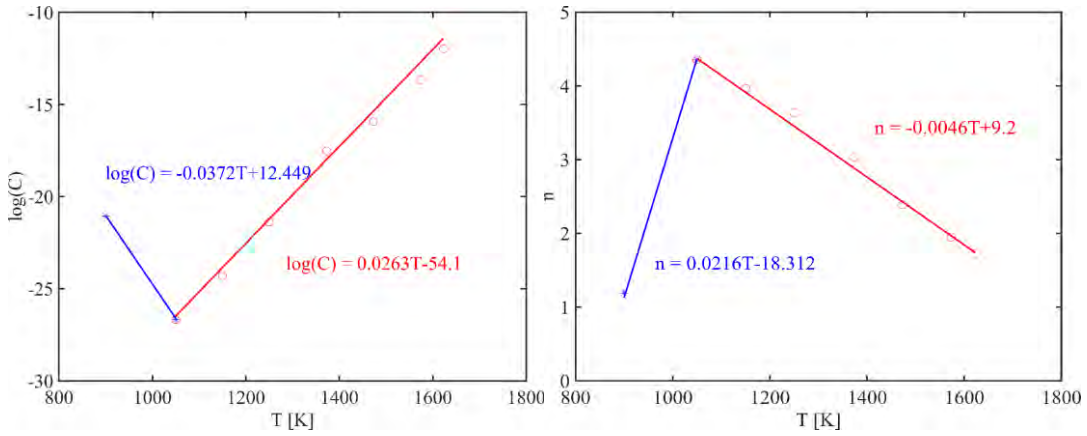

(a) $C(T)$ (b) $n(T)$

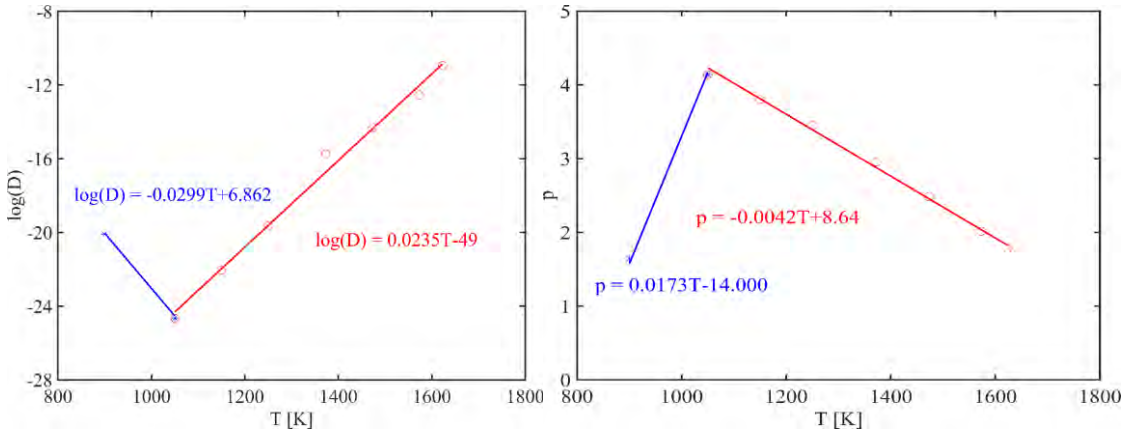

(c) $D(T)$ (d) $p(T)$

Figure 1. Parameters of the modified L-M model.

3. RRSULTS AND DISCUSSION

3.1 Simulation of INEL Tensile Tests

Finite element analyses (FEA) of the INEL creep tensile tests were conducted to assess the predictive capability of the modified L-M creep model. The schematic diagram and axisymmetric FE model of the test specimen are shown in Figure 2. Specimen dimensions follow the ASTM standards. In the simulation, stress was applied uniformly to the cross-section of the reduced section to maintain a steady stress state throughout the analysis.

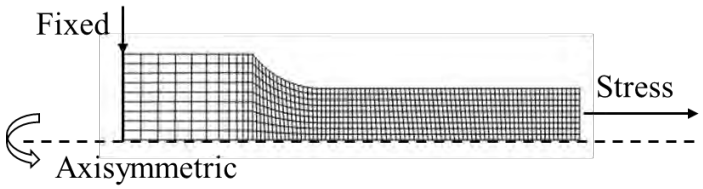

Figure 2. Schematic of Axis-symmetric FE model for creep test simulation.

The remaining material properties of SA533B1 steel, including Young's modulus, density, thermal conductivity, thermal expansion coefficient, heat capacity, were taken from previous studies [5].

All numerical simulations were performed using the Ansys code. The modified L-M creep model was implemented via User Programmable Features (UPF) of Ansys. Two other well-known creep models, Norton creep model [16] and Modified Time Hardening (MTH) creep model [17] were also employed to compare their predictive capability with the modified L-M creep model.

Figures 3 through 7 present comparisons between the INEL experimental data and simulation results of different creep models. As shown in Figure 3, when temperature is 900 K and stress is 69.7 MPa, the modified L-M model exhibits excellent agreement with the experimental data across the entire creep curve. In contrast, both the MTH and Norton models tend to overestimate creep strain during the primary and secondary stages. As these two models primarily describe secondary creep behavior, they fail to accurately capture the accelerated creep deformation characteristic of the tertiary stage, resulting in underpredictions of creep strain near failure.

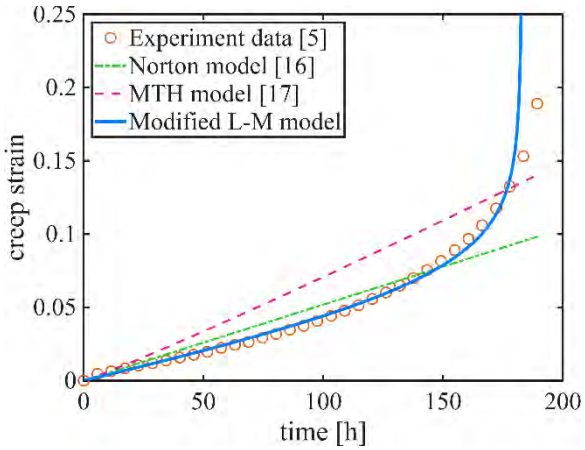

Figure 3. Comparison of the experimental creep strain with the simulation results: T= 900 K, Stress=69.7 MPa

Figure 4(a) and 4(b) present a comparison between the model predictions and experimental data at a temperature of 1150 K under the stress levels of 12.5 MPa and 26.5 MPa, respectively. In Figure 4(a),

the modified L-M model shows superior agreement with the experiment data compared to other models. The Norton model consistently underestimates creep strain throughout the test duration, whereas the MTH model significantly overestimates it. In Figure 4(b), both the modified L-M and MTH models demonstrate good agreement with the experimental data, while the Norton model prediction remains lower than observed.

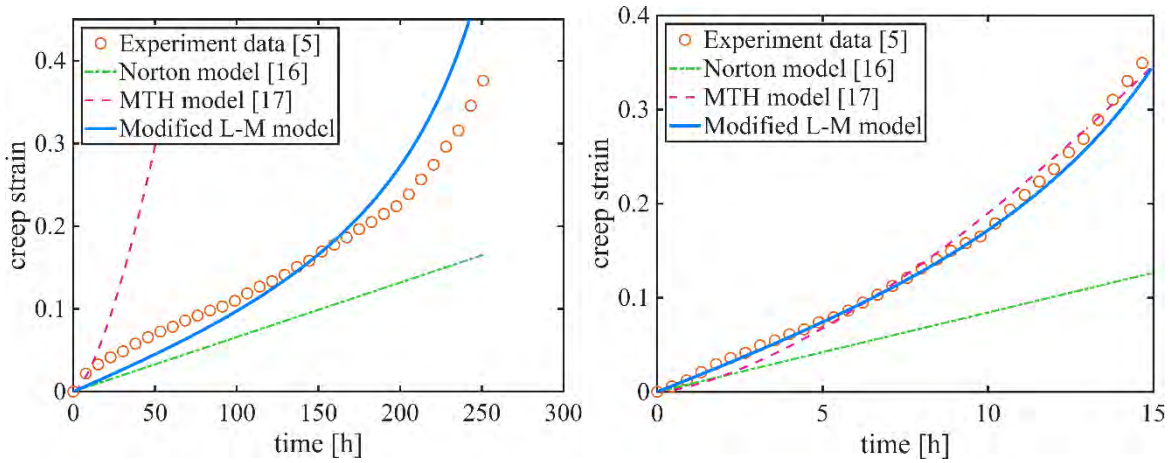

(a) Stress=13.9 MPa (b) Stress=26.3 MPa

Figure 4. Comparison of the experimental creep strain with the simulation results: T= 1050 K.

Figure 5(a) and 5(b) compare the model predictions with experimental data at 1150 K under stress level of 12.5 MPa and 26.5 MPa. As shown in Figure 5(a), the modified L-M model successfully captures non-linear behavior during the tertiary stage, while the Norton and MTH model exhibit linear trends. The Norton model prediction matches the experimental data during the initial half stage; however, the difference increases significantly as creep progresses into the tertiary stage. While the modified L-M model slightly underestimates creep strain, its overall performance surpasses the other models in critical phase. In Figure 5(b), the modified L-M model overpredicts creep strain during the tertiary stage, whereas the MTH model demonstrates improved agreement with experimental results. The Norton model continues to slightly underestimate creep strain.

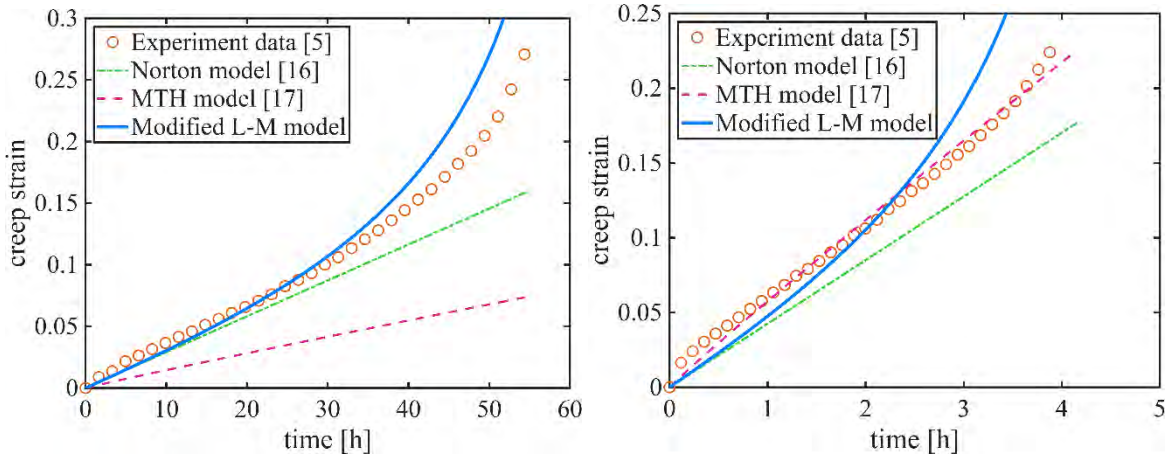

(a) Stress=12.5 MPa (b) Stress=26.5 MPa

Figure 5. Comparison of the experimental creep strain with the simulation results: T= 1150 K

Figure 6 presents a comparison between the predicted creep behavior from various models and the experimental data at 1250 K and stress of 8 MPa. Both the L- M and MTH models demonstrate good agreement with the experimental results. However, the modified L-M model exhibits a superior ability

to capture the nonlinear deformation trend throughout the entire creep stage. This improved performance is further pronounced in **Figure 7**.

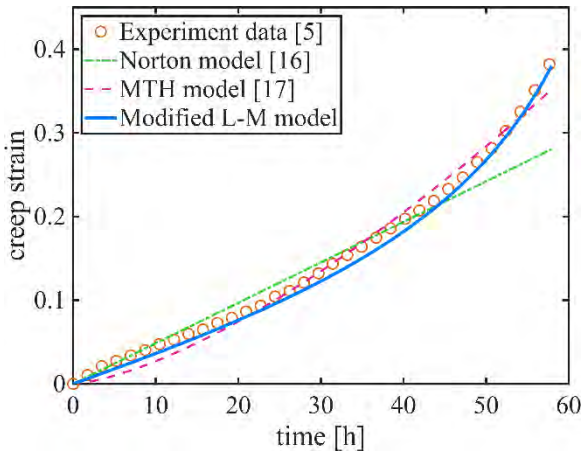

Figure 6. T=1250 K, stress=8 MPa.

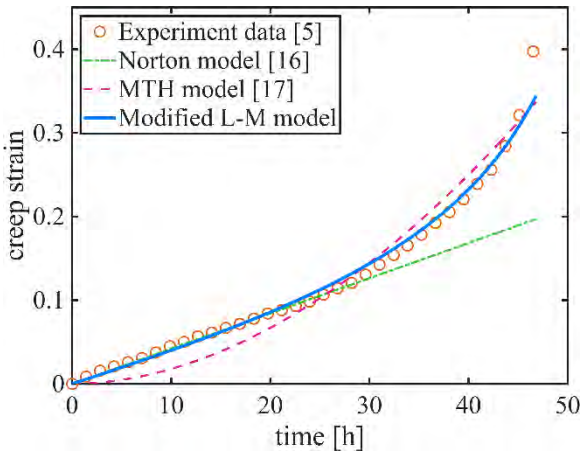

Figure 7. T=1373 K, stress=3.5 MPa.

In summary, the comparison clearly demonstrates that the modified L-M model offers substantially improved prediction accuracy over both the Norton and MTH models in capturing the full-range creep deformation behavior of SA533B1 steel under diverse conditions.

3.2. Simulation of JAEA Tensile Tests

Complete creep strain versus time curves were not provided in the relevant JAEA tensile test literature. However, key creep parameters, specifically the minimum creep strain rate and rupture time, have been reported and are summarized in Table IV [14,15].

Table IV. Experimental conditions and results of JAEA creep test for SA533B1.

Temp (K)	Stress (MPa)	Time to failure (h)	Minimum creep strain rate (/h)
1250	12.60	18.40	0.022
	17.00	6.91	0.056
1473	4.50	10.40	0.018
	4.99	8.52	0.02
1573	2.27	17.70	0.01
	2.61	11.30	0.027
1623	2.07	5.80	0.055
	2.37	3.40	0.10

A Kachanov-Rabotnov (K-R) model has been recommended in the JAEA literature for describing the creep behavior of SA533B1 steel at very high temperature (1250 K-1623 K). To evaluate the predictive accuracy of various models, a comparative analysis was conducted among experimental data from INEL and JAEA, and simulation results obtained using the Norton model, the K-R model, and the modified L-M model.

Figure 8 illustrates the predictive capability of different models for the minimum creep strain rate at elevated temperatures. The height of each bar represents the absolute value of the minimum creep strain rate, with the corresponding error between experimental and simulated values indicated above each bar. As shown in Figure 8 (a), at 1250 K and 8 MPa, the modified L-M model exhibits superior accuracy compared to the K-R model and Norton model. When the stress increases to 12.6 MPa, the K-R model achieves the lowest error of 0.5%, while the error in the modified L-M model rises to 16%. However,

at 17 MPa, the modified L-M model's performance matches that of the K-R model. At a higher temperature of 1473 K, as shown in Figure 8(b), both the K-R and Norton models overpredict the minimum creep strain rate, whereas the modified L-M model maintains good agreement, underestimating the experimental value by 13.3% at 4.5 MPa and matching it closely at 4.99 MPa. Figure 8 (c) and 8(d) further demonstrate that the Norton model significantly overestimates minimum creep strain rates at very high temperatures, while the modified L-M model remains consistent with experimental data at relatively higher stress levels. Overall, both the modified L-M and K-R models demonstrate strong capability in predicting minimum creep strain rates under high-temperature conditions, though their relative effectiveness depends on the specific stress level.

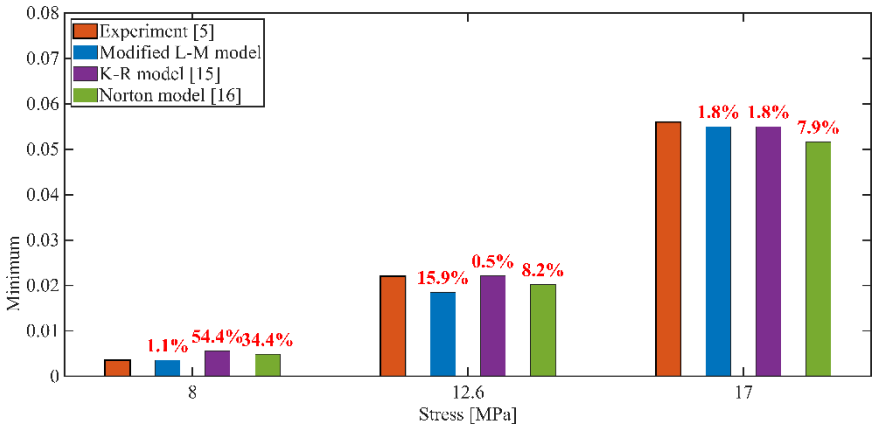

(a) T=1250 K

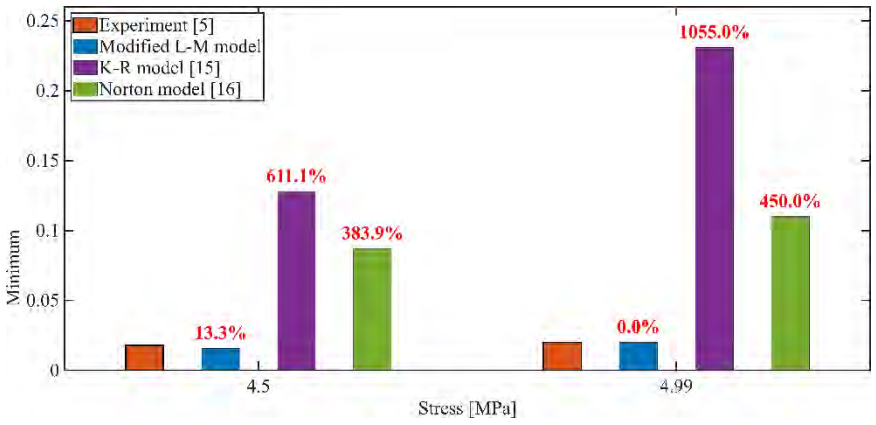

(b) T=1473 K

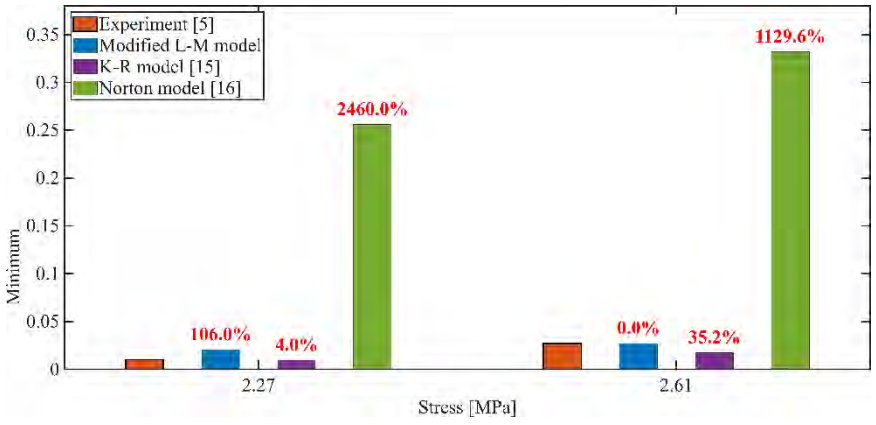

(c) T=1573 K

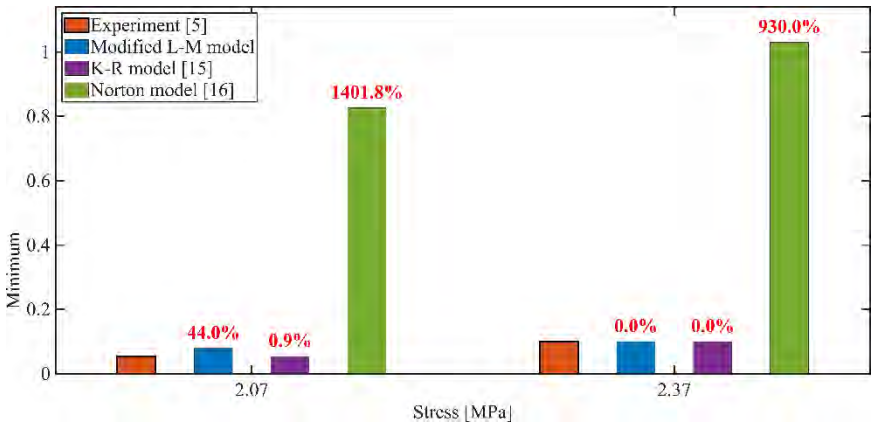

(d) T=1623 K

Figure 8. Comparison of the experimental minimum creep strain rate with simulation results.

3.3 The Interpolation of Creep Model

The OECD lower head failure (OLHF) program conducted creep tests at 1000 K on SA533B1 steel supplied by INEL [7]. Figure 9 compares the simulation results with the corresponding experimental creep curves. Regardless of whether the applied stress is 40.2 MPa or 73.6 MPa, the modified L-M model shows good agreement with the experimental data. This demonstrates that at intermediate temperatures, using regression equations to derive model constants does not introduce significant interpolation errors.

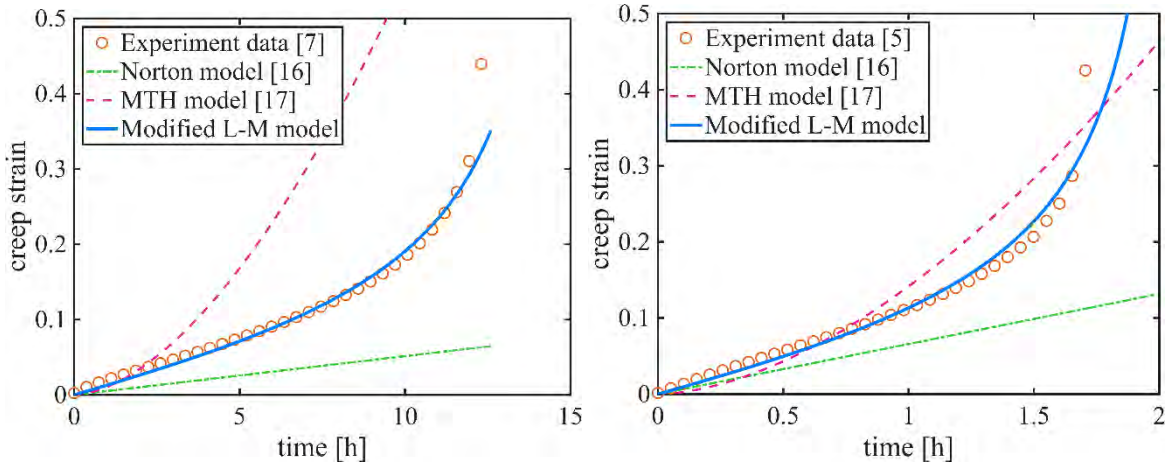

(a) Stress=40.2 MPa (b) Stress=73.6 MPa

Figure 9 Comparison of the experimental creep strain with the simulation results: T= 1000 K.

4. CONCLUSIONS

Creep deformation is a critical factor in lower head failure research during severe accidents. A reliable creep model is essential for accurate thermo-mechanical simulation of deformation and failure behavior. In this research, a continuous-parameter Liu-Murakami creep model for reactor pressure vessel steel SA533B1 is proposed based on the analysis of creep tensile tests conducted by INEL and JAEA. This model effectively describes the tertiary creep stage by incorporating a damage factor and establishes functional relationships between material constants and temperature. The main findings and contributions of this work are summarized as follows:

(1) Compared to existing creep models for SA533B1, such as Norton and MTH models, the modified L-M model successfully captures the tertiary creep behavior and accurately predicts key parameters including the minimum creep strain rate. Simulation results closely align with experimental creep strain curves.

(2) The new model significantly extends the applicable temperature range from 900 K, where creep behavior becomes clearly observable, up to 1623 K, near the melting point of the steel.

(3) By expressing the material constants of the modified L-M model as continuous functions of temperature, interpolation errors during simulations involving temperature changes are greatly reduced, thereby improving stability and accuracy.

REFERENES

1. M. Sattar, A.R. Othman, S. Kamaruddin, et al., "Limitations on the computational analysis of creep failure models: A review," *Engineering Failure Analysis*, **134**, pp. 105968 (2022).
2. M. McLean, "Creep deformation of metal—matrix composites," *Composites Science and Technology*, **23**(1), pp. 37-52 (1985).
3. B.R. Sehgal (ed.), Nuclear safety in light water reactors: severe accident phenomenology, Academic Press (2011).
4. D. Zhan, F. Liu, X. Zhang, et al., "Ablation and thermal stress analysis of RPV vessel under heating by core melt," *Nuclear Engineering and Design*, **330**, pp. 550-558 (2018).
5. J.L. Rempe, S.A. Chavez, and G.L. Thinnes, "Light water reactor lower head failure analysis," Nuclear Regulatory Commission, Washington, DC, USA (1993).
6. M.M. Pilch, J.S. Ludwigsen, T.Y. Chu, et al., "Creep failure of a reactor pressure vessel lower head under severe accident conditions," Sandia National Lab. (SNL-NM), Albuquerque, NM, USA (1998).
7. L.L. Humphries, T.Y. Chu, J. Bentz, et al., "OECD lower head failure project final report," *Sandia National Laboratories*, pp. 1139 (2002).
8. F. Norton, *The Creep of Steels at High Temperatures*, pp. 90, Mc Graw Hill, New York, USA (1929).
9. R. W. Bailey, "The Utilization of Creep Test Data in Engineering Design," *Proceedings of the Institution of Mechanical Engineers*, **131**(1), pp. 131-349 (1935).
10. M. Prager, "Development of the MPC Omega Method for Life Assessment in the Creep Range," *Journal of Pressure Vessel Technology*, **117**(2), pp. 95–103 (1995).
11. R.W. Evans, J.D. Parker, and B. Wilshire, "The θ projection concept—A model-based approach to design and life extension of engineering plant," *International Journal of Pressure Vessels and Piping*, **50**, pp. 147–160 (1992).
12. L.M. Kachanov, "Rupture Time Under Creep Conditions," *International Journal of Fracture*, **97**, pp. 11–18 (1999).
13. S. Murakami, Y. Liu, and M. Mizuno, "Computational methods for creep fracture analysis by damage mechanics," *Computer methods in applied mechanics and engineering*, **183**(1-2), pp. 15-33 (2000).
14. G.L. Thinnes, G.E. Korth, S.A. Chavez, et al., "High-temperature creep and tensile data for pressure vessel steels SA533B1 and SA508-CL2," *Nuclear engineering and design*, **148**(2-3), pp. 343-350 (1994).
15. Y. Yamaguchi, J. Katsuyama, Y. Nemoto, et al., "Development of failure evaluation method for BWR Lower head in severe accident; high temperature creep test and creep damage model," *Mechanical Engineering Journal*, **4**(6), pp. 15-00694-15-00694 (2017).
16. E.K. Park, J.S. Kim, J.W. Park, et al., "Failure simulation of nuclear pressure vessel under severe accident conditions: Part I-Material constitutive modeling," *Nuclear Engineering and Technology*, **55**(11), pp. 4146-4158 (2023).
17. H. Wang, *Thermo-mechanical Assessment of Reactor Pressure Vessels of Light Water Reactors During Severe Accidents*, KTH Royal Institute of Technology (2023).

Comparative Analyses of Creep Models for Predicting Behavior of RPV Steel under Extreme High Temperatures

Xiangyu Li, Weimin Ma, Sevostian Bechta

2026/5/21

KTH Royal Institute of Technology

Contents

01
Introduction
Background & Motivation

02
Methodology
Modeling and Parameter Calibration

03
Evolution
Comparative Results and model accuracy

04
Conclusion
Key Finding and Future Applications

01

PART ONE

Introduction

Background & Research Motivation

1.1 Background

Background

- **Severe Accidents:** Molten core relocation poses extreme thermal-mechanical loads on RPV lower head;
- **Failure Prediction:** Finite Element Analysis (FEA) is a critical tool to predict '**when, where, and why**' RPV fails for accident management.
- **Crucial Mechanism: creep** is one of the primary mechanism leading to lower head failure.
- **The Key:** Accurate **creep models** are essential for reliable FEA predictions.

Challenges:

- **Existing creep models (SA533B1) are limited in:**
  - Applicable temperature ranges.
  - Tertiary stage prediction: the critical stage for failure.
  - Interpolation errors in transient thermal analysis.

Objectives:

- **Calibrate a creep model for SA533B1 covering:**
  - Wide temperature scopes.
  - Tertiary stage prediction.
  - Less interpolation errors in transient thermal analysis.

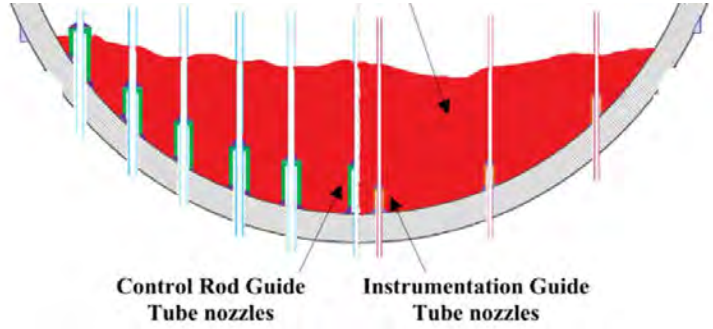

RPV lower head with penetrations & molten pool

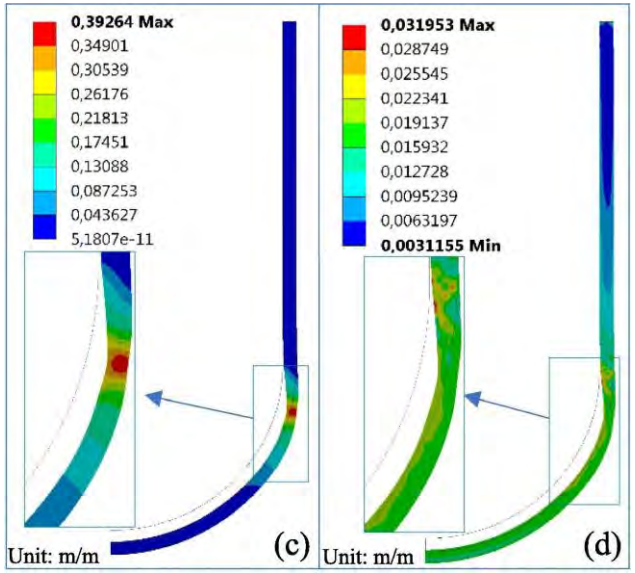

Field of creep strain and plastic strain closed to failure [1]

1.2 Model Development and Evaluation Process

Problem Definition → Input & Selection → Model Calibration → Comparative Evaluation

Core limitations:

- Restricted thermal range;
- Failure to simulate the tertiary creep stage;
- Interpolation errors in transient thermo-mechanical analysis.

Experimental Data (900 – 1623 K):

- INEL lower head failure program (900-1373 K);
- JAEA high-temperature data (1250-1623 K).

Model selection:

- Liu-Murakami (L-M) creep model

Key enhancement:

- Establishing temperature-dependent relationships for model constants;

Evaluation:

- Comparison against traditional models across the full temperature range;

02

PART TWO

Methodology

CDM Modeling & Parameter Calibration

2.1 Introduction of Creep

Creep refers to the **time-dependent, permanent deformation** of a solid material when subjected to **sustained mechanical stress**, especially at **high temperature**. Typical creep curves can be characterized by three stages: primary, secondary, and tertiary stage.

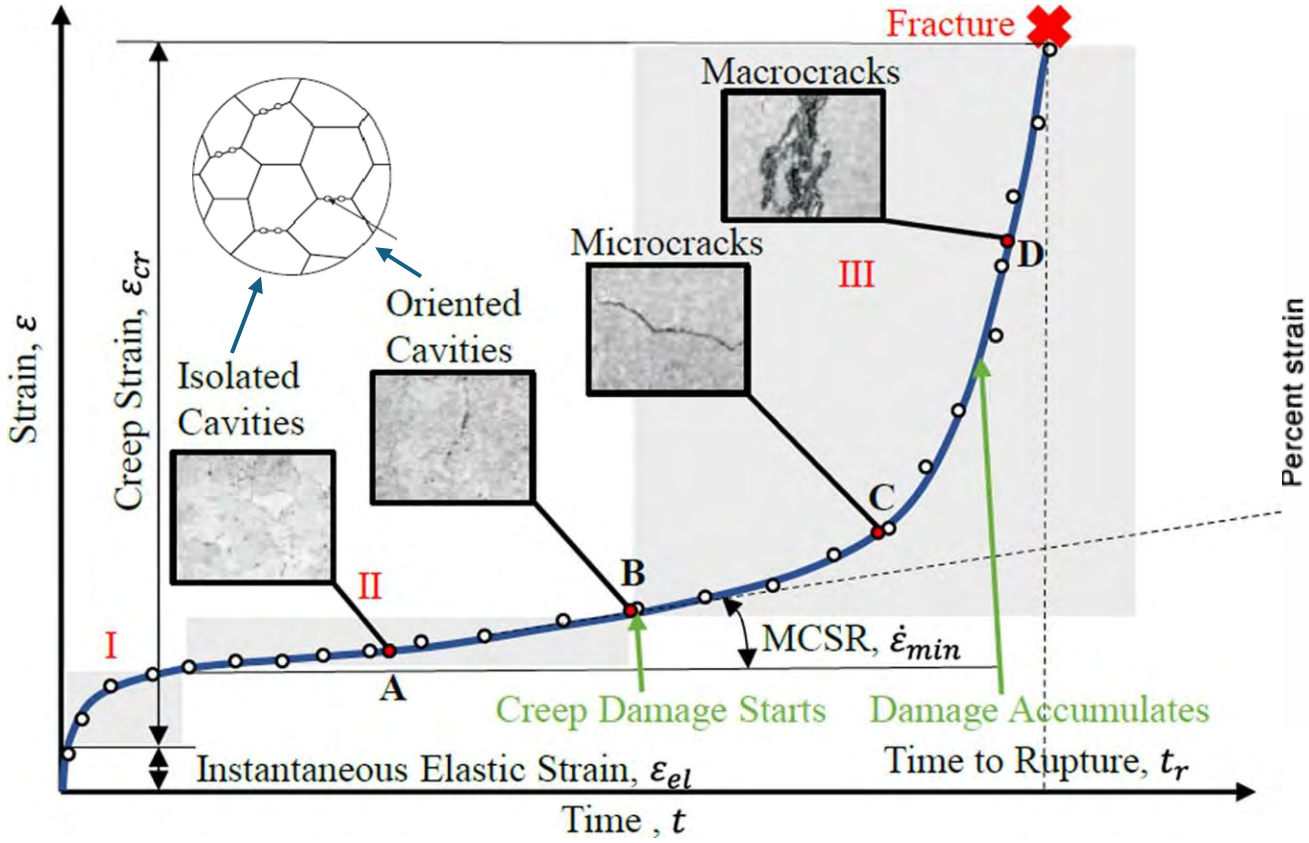

Formation of cavities and cracks at different stages of creep deformation [2]

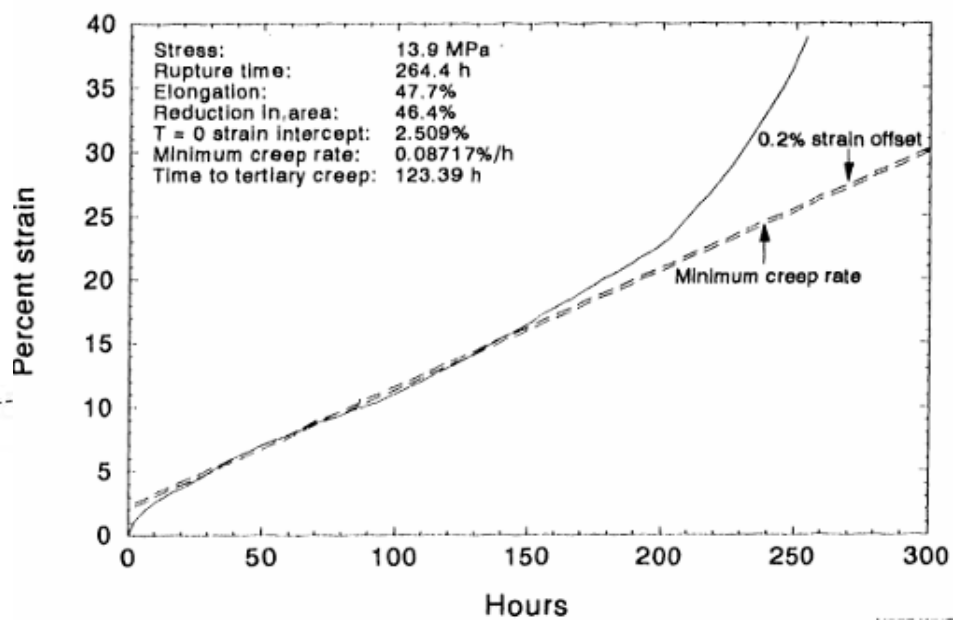

Experimental creep strain with time[3].

2.2 Creep Models

Liu-Murakami (L-M) creep model[4]:

$$\dot{\varepsilon}_c = C\sigma_{eq}^n \cdot exp\left(\frac{2(n+1)}{\pi\sqrt{1+3/n}} \cdot \omega^{3/2}\right) \quad (1)$$

$$\dot{\omega} = D\frac{(1-e^{-q})}{q}\sigma_{eq}^p e^{q\omega} \quad (2)$$

Where $\dot{\boldsymbol{\varepsilon}}$ is the steady state creep rate; $\boldsymbol{C, n, D, p, q}$ are the model constants, $\boldsymbol{\sigma_{eq}}$ is the equivalent stress, and $\boldsymbol{\omega}$ is the damage factor.

The L-M model can be divided into two parts: $\dot{\varepsilon}_c = C\sigma_{eq}^n$ & $exp\left(\frac{2(n+1)}{\pi\sqrt{1+3/n}} \cdot \omega^{3/2}\right)$

The first part is the Norton's power law (Norton model) [5], which is the most widely used creep model. It describes the **secondary creep stage** by building the relationship between the minimum creep strain rate and equivalent stress at a given temperature. The second part is the damage term for describing the **tertiary creep stage**.

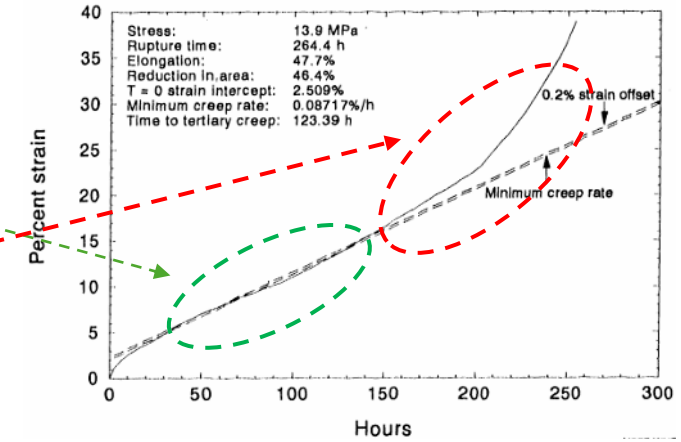

2.3 Experiments

The creep tests for SA533B1 steel conducted by the Idaho National Engineering Laboratory (INEL) [3] and the Japan Atomic Energy Agency (JAEA) [6]. The INEL experiment covered a temperature range from 900 K to 1373 K. The JAEA experiment covered a temperature range from 1250 K to 1623 K.

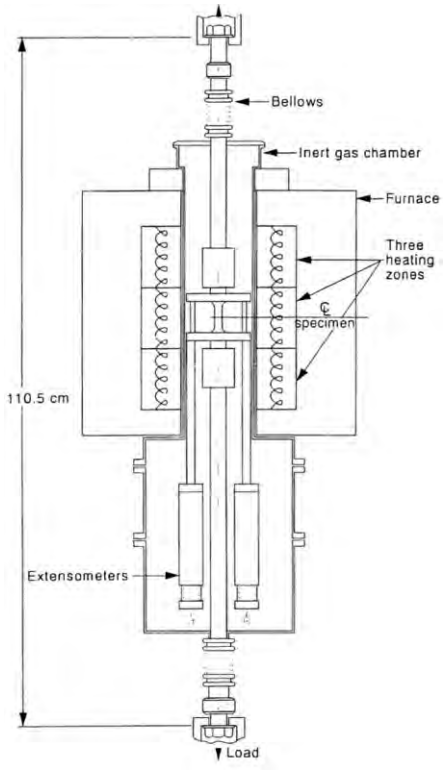

Schematic of the INEL creep test setup [3]

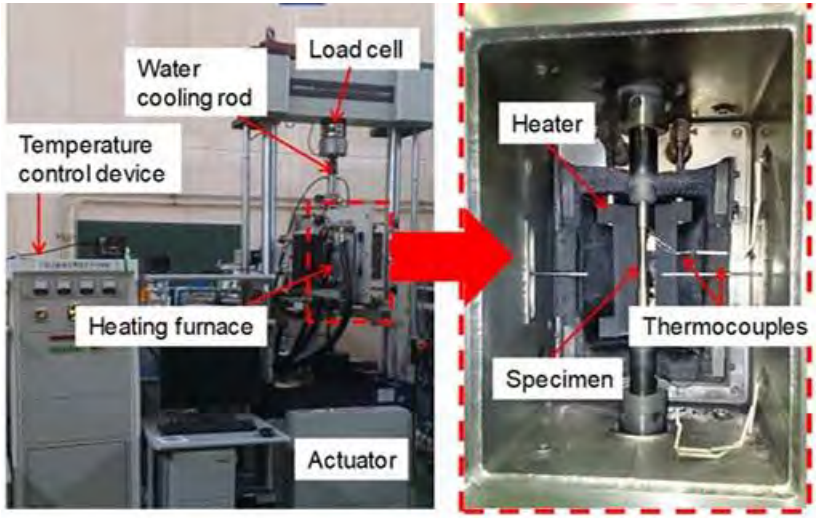

Schematic of the JAEA creep test setup [6]

Adopted Creep Test Matrix from INEL and JAEA

	INEL					JAEA			
Temp (K)	900	1050	1150	1250	1373	1250	1473	1573	1623
Stress (MPa)	69.70	13.90	12.50	8.00	3.50	12.60	4.50	2.27	2.07
		26.30	26.50			17.00	4.99	2.61	2.37

2.4 Parameter Calibration

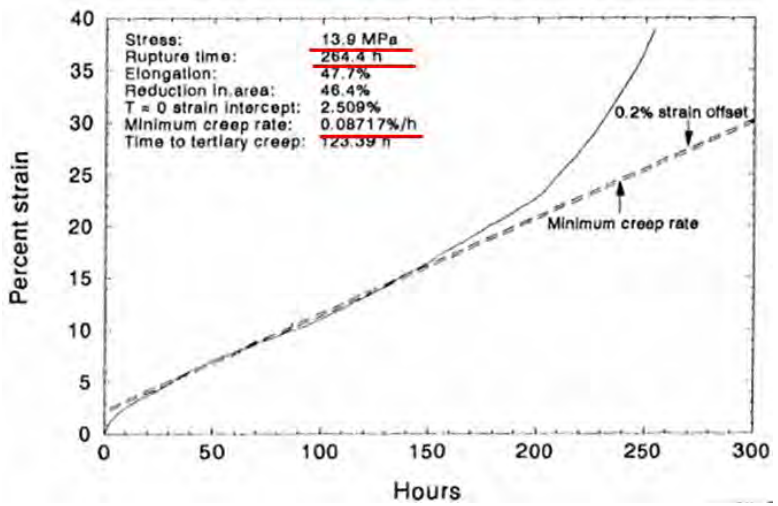

Primary experimental inputs for parameter fitting:

- **Equivalent stress (σ_{eq})**
- **Minimum creep strain rate ($\dot{\varepsilon}_c$)**
- **Rupture time (t_r)**

Step A: Creep strain rate calibration

$$\dot{\varepsilon}_c = C\sigma_{eq}^{n}\, exp\left(\frac{2(n+1)}{\pi\sqrt{1+3/n}}\cdot\omega^{3/2}\right)$$

$$\boldsymbol{ln(\dot{\varepsilon}_c) = nln(\sigma_{eq}) + ln(C)}$$

Step B: Damage/Failure time calibration

$$\dot{\omega} = D\frac{(1-e^{-q})}{q}\sigma_{eq}^{p}e^{q\omega}$$

$$\boldsymbol{ln(t_r) = -pln(\sigma_{eq}) - ln(D)}$$

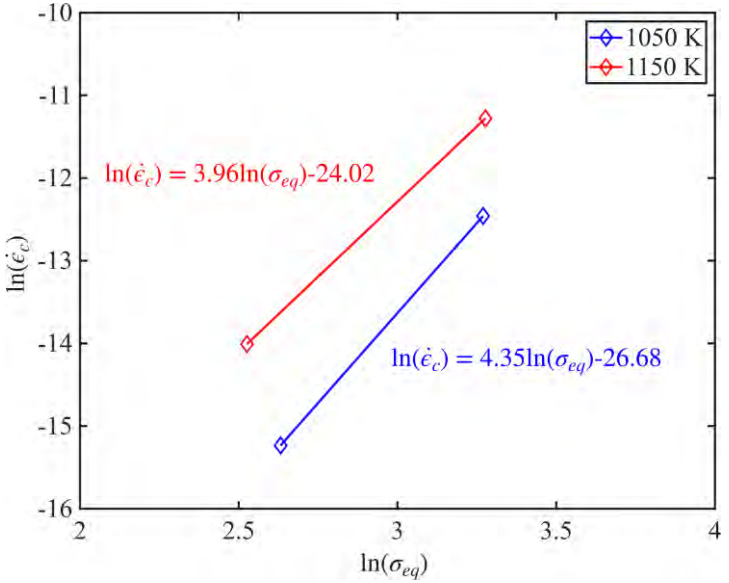

Fitting of $ln(\dot{\varepsilon}_c)$ to $ln(\sigma_{eq})$ for material constants C and n

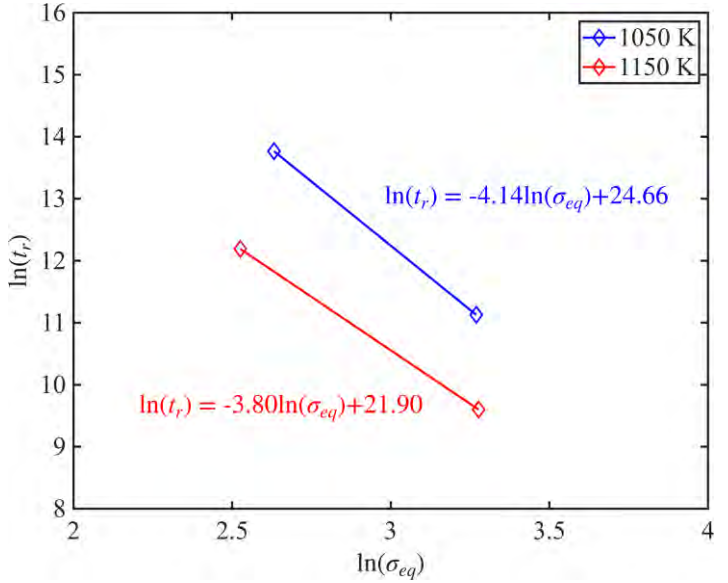

Fitting of $ln(t_r)$ to $ln(\sigma_{eq})$ for material constants D and p

2.5 Model Constants

Functional relationships between model constants and temperature are obtained to reduce the interpolation errors during temperature-change conditions.

Temp (K)	C	n	D	p	q
900	7.12×10^{-10}	1.19	1.87×10^{-9}	1.64	1.31
1050	2.58×10^{-12}	4.35	1.96×10^{-11}	4.14	2.57
1150	3.68×10^{-11}	3.96	3.08×10^{-10}	3.80	1.89
1250	5.29×10^{-10}	3.65	3.40×10^{-9}	3.39	1.2
1373	2.44×10^{-8}	3.03	1.47×10^{-7}	2.95	0.3
1473	1.20×10^{-7}	2.38	6.03×10^{-7}	2.48	0.3
1573	1.16×10^{-6}	1.94	3.57×10^{-6}	2.01	0.3
1623	6.27×10^{-6}	1.72	1.76×10^{-5}	1.78	0.3

$$C(T) = \begin{cases} \exp(-0.037T + 12.45) & T \le 1050\ K \\ \exp(0.026T - 53.70) & T > 1050\ K \end{cases}$$

$$n(T) = \begin{cases} 0.022T - 18.7 & T \le 1050\ K \\ -0.0046T + 9.2 & T > 1050\ K \end{cases}$$

$$D(T) = \begin{cases} \exp(-0.030T + 6.86) & T \le 1050\ K \\ \exp(0.0023T - 48.25) & T > 1050\ K \end{cases}$$

$$p(T) = \begin{cases} 0.017T - 13.70 & T \le 1050\ K \\ -0.0042T + 8.64 & T > 1050\ K \end{cases}$$

Phase transformation from ferrite to austenite alters the creep mechanism at 1000~1050 K [9].

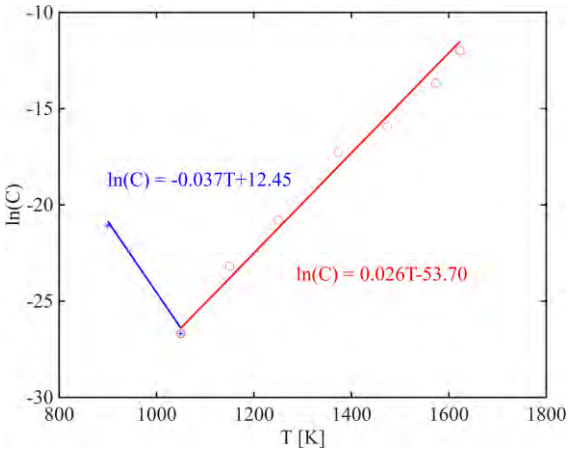

$C(T)$

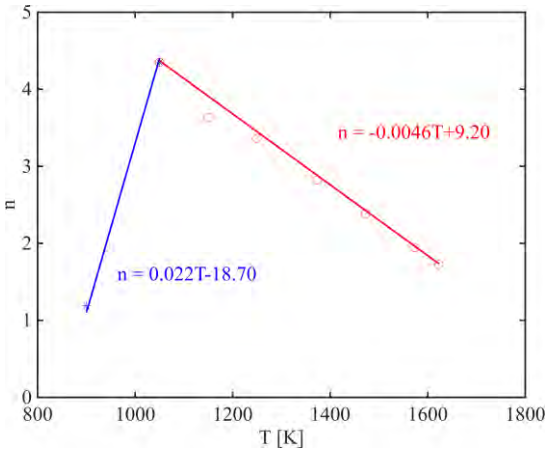

$n(T)$

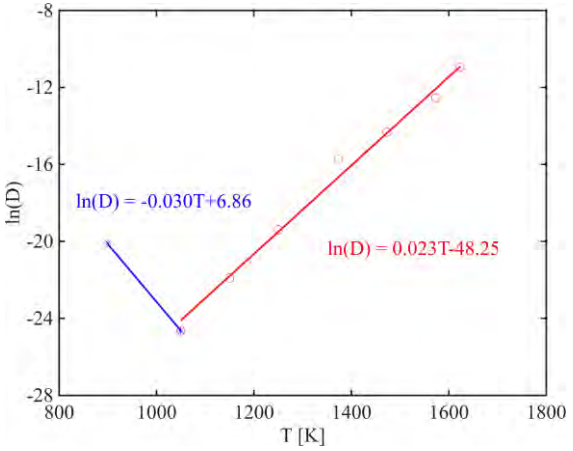

$D(T)$

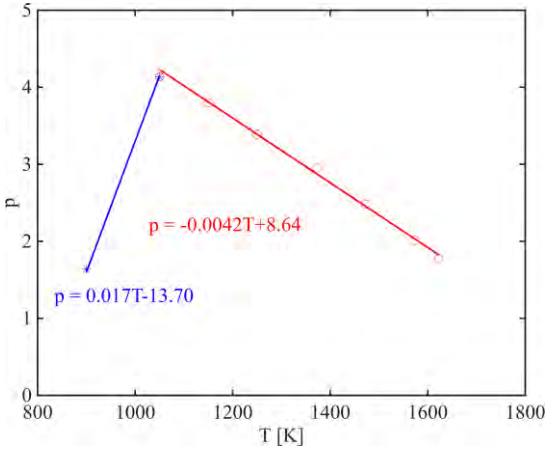

$p(T)$

Regression equation of the L-M model constants

PART THREE

Performance Evaluation

Comparative Results & model accuracy

3.1 Comparative Models

Established creep models for SA533B1.

Models	Equation	Constant Form	Temperature Range of Constants (K)
Norton model [7]	$\dot{\varepsilon}_c = C\sigma_{eq}^n$	function	**900-1373***
Modified time hardening model (MTH) [8]:	$\varepsilon_c = \frac{C\sigma_{eq}^n t^{k+1}}{k+1}$	point	900-1373
Kachanov-Rabotnov model [6]	$\dot{\varepsilon}_c = C\left(\frac{\sigma}{1-\omega}\right)^n \quad \dot{\omega} = B\frac{\sigma^\chi}{(1-\omega)^\varphi}$	point	1250-1623
New fitted L-M model	$\dot{\varepsilon}_c = C\sigma_{eq}^n \, exp\left(\frac{2(n+1)}{\pi\sqrt{1+3/n}} \cdot \omega^{3/2}\right)$ $\dot{\omega} = D\frac{(1-e^{-q})}{q}\sigma_{eq}^p e^{q\omega}$	function	900-1623

*Model constants at 1373-1623 K are extrapolated.

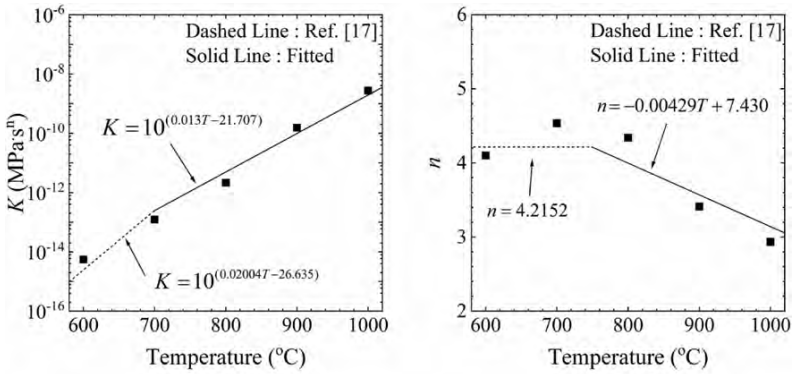

Norton creep constants [7]

MTH creep constants [8]

T	643K	900K	1000K	1050K	1150K	1250K	1373K
c_1	0	6.35E-31	4.58E-41	9.07E-31	9.14E-41	4.54E-51	2.52E-48
c_2	0	2.947	4.2749	3.0602	4.7656	6.1262	5.7264
c_3	0	0.0733	0.7135	0.4897	-0.0427	0.4596	0.9001

K-R creep constants [6]

	Temperature [°C]	Parameter of K–R model			
		A	*B*	*k*	*n*
SA533B	1000	1.00×10^{-5}	3.59×10^{-6}	3.23	3.04
	1200	***2.46×10^{-5}***	***9.55×10^{-6}***	***5.50***	***5.69***
	1300	2.78×10^{-4}	4.35×10^{-4}	4.02	4.32
	1350	***2.05×10^{-3}***	***1.97×10^{-3}***	***3.95***	***4.51***

3.2 Simulation vs. INEL Tensile Test Results (900 - 1373 K):

Finite element analysis (FEA) of creep tensile test was conducted in ANSYS to assess the predictive capability of the L-M creep model.

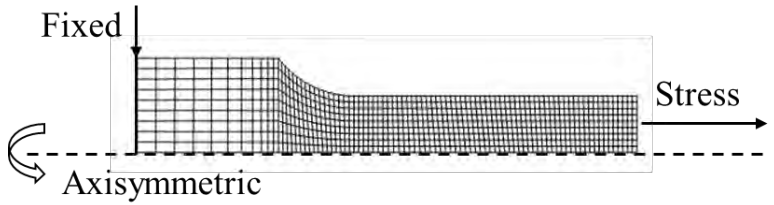

Schematic of Axis-symmetric FE model for simulation

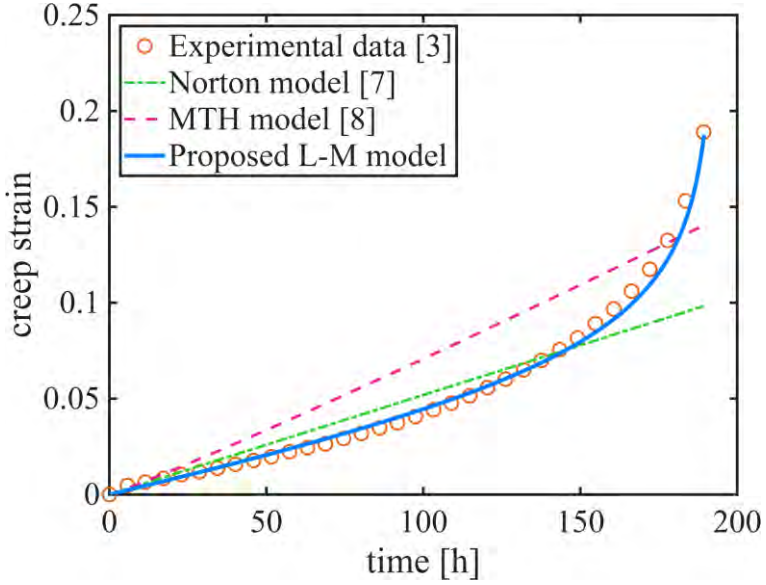

T= 900 K, Stress=69.7 MPa

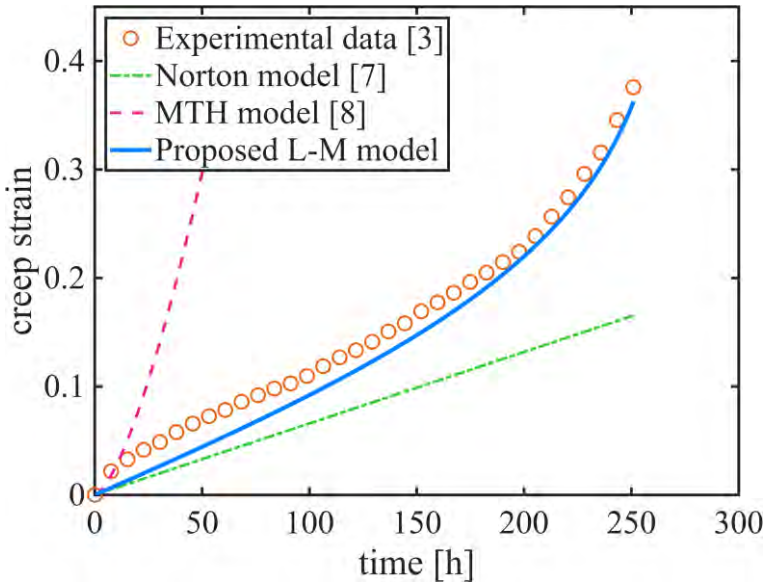

T= 1050 K, Stress=13.9 MPa

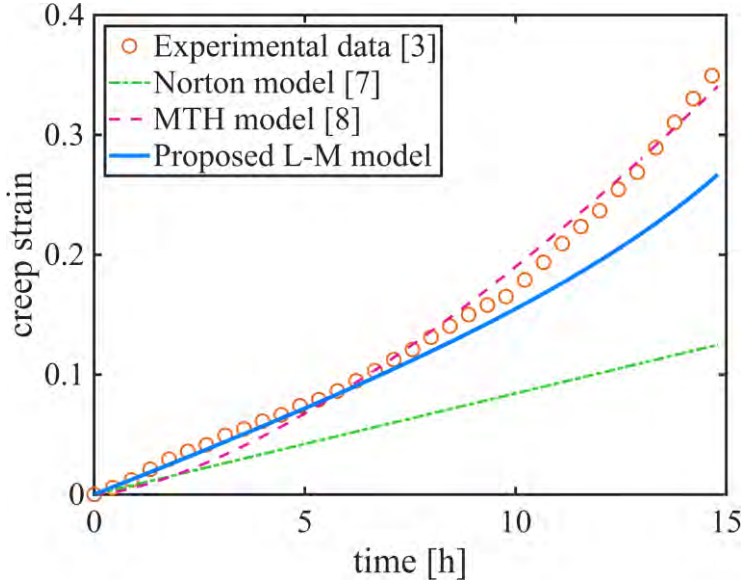

T= 1050 K, Stress=26.3 MPa

3.2 Simulation vs. INEL Tensile Test Results (900 - 1373 K):

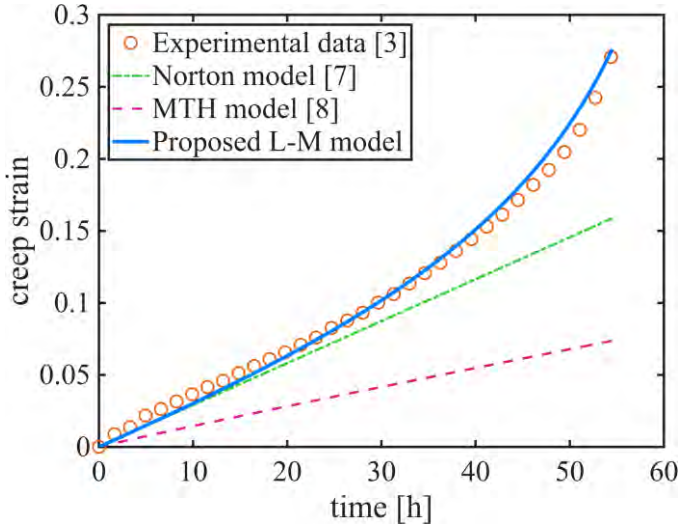

T= 1150 K, Stress=12.5 MPa

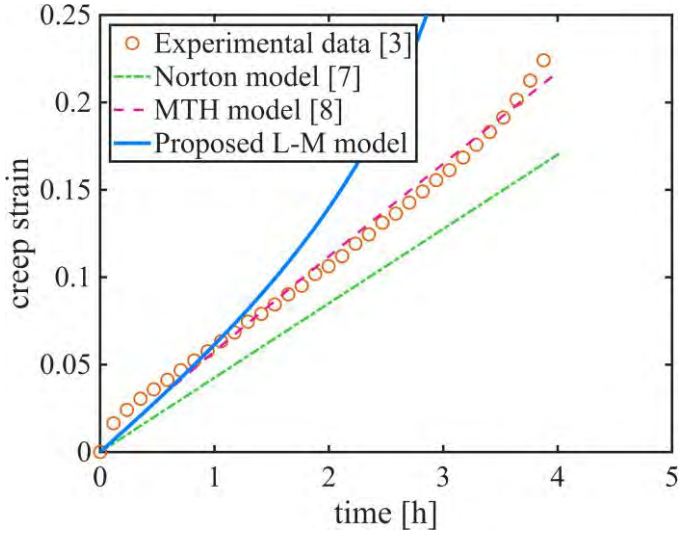

T= 1150 K, Stress=26.5 MPa

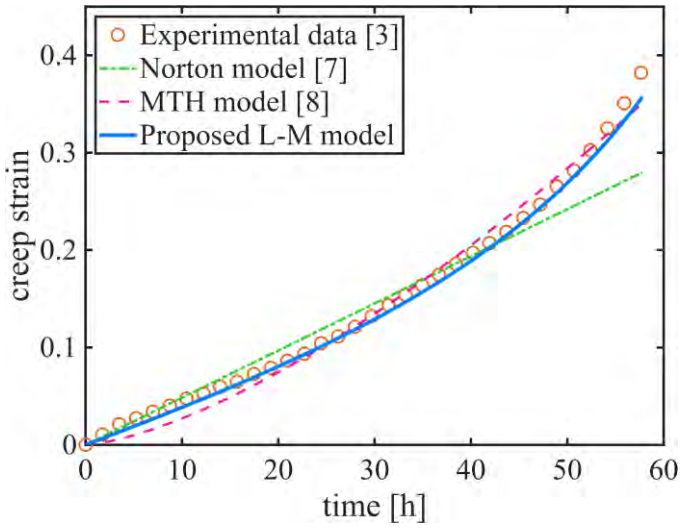

T= 1250 K, Stress=8 MPa

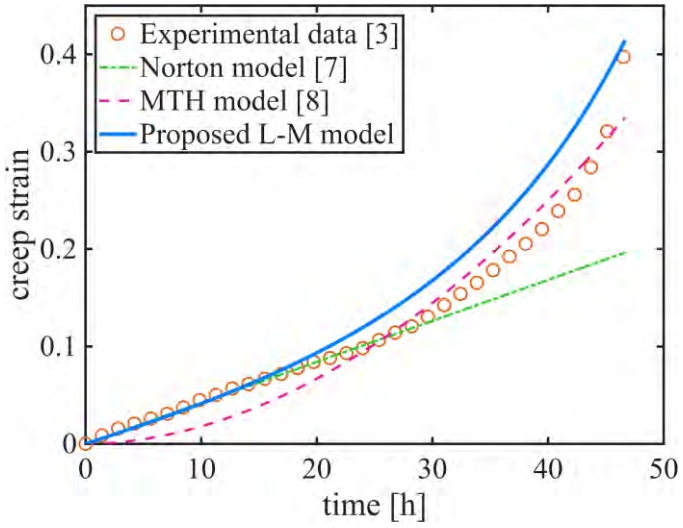

T= 1373 K, Stress=3.5 MPa

The L-M model demonstrates **higher accuracy** and better performance in **capturing the overall trend** of creep behavior throughout the entire stage.

3.3 Simulation vs. JAEA Tensile Test Results (1250 - 1623 K):

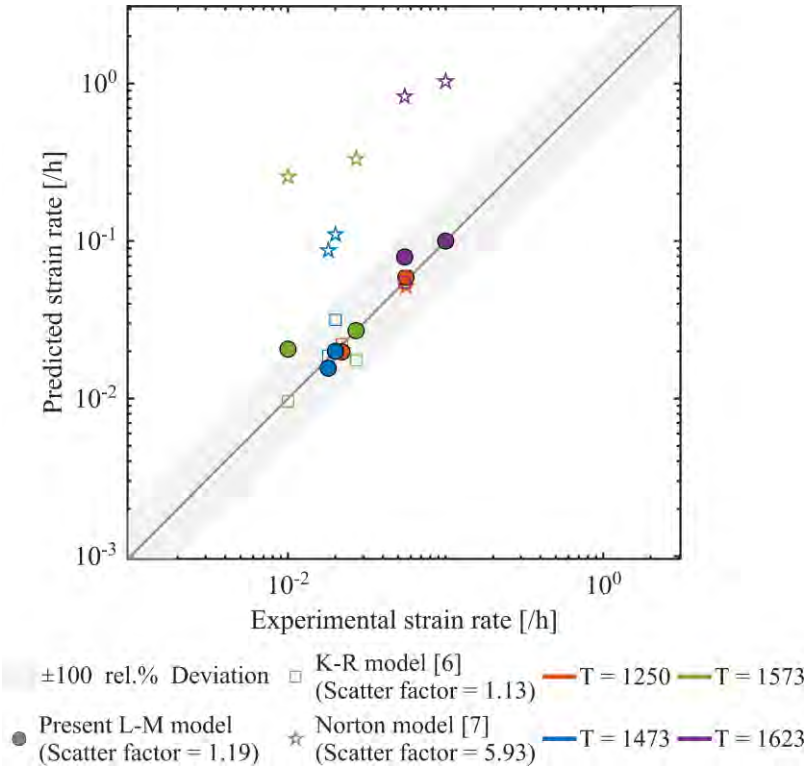

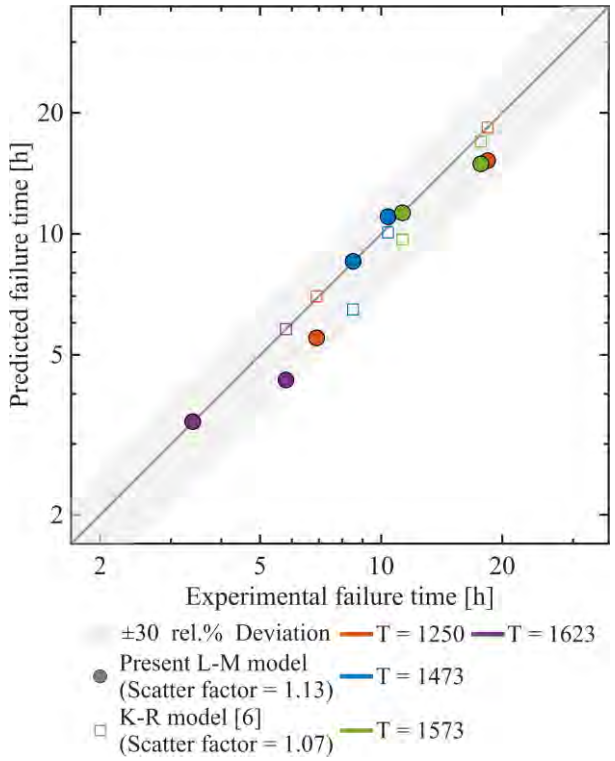

	LM model (Proposed)	K-R model
Scatter factor (strain rate)	1.19	1.13
Scatter factor (failure time)	1.13	1.07
Temp. range	900-1623 K	1250-1623 K
Temp. consistency	Superior	Bad

While maintaining high accuracy (comparable to K-R model), the proposed LM model offers **superior temperature consistency** and a significantly **broader thermal application range** (900–1623 K).

3.4 Model Generalizability and Interpolation Capability

Simulation vs. OECD Tensile Test Results (1000 & 1250 K):

The OECD lower head failure (OLHF) program [9] conducted creep tests at 1000 K & 1250 K on SA533B1 steel supplied by INEL. The interpolation accuracy and generalizability of **L-M model** are validated with this experiment.

$$C(T) = \begin{cases} exp(-0.037T + 12.45) & T \le 1050\ K \\ exp(0.026T - 53.70) & T > 1050\ K \end{cases}$$

$$n(T) = \begin{cases} 0.022T - 18.7 & T \le 1050\ K \\ -0.0046T + 9.2 & T > 1050\ K \end{cases}$$

$$D(T) = \begin{cases} exp(-0.030T + 6.86) & T \le 1050\ K \\ exp(0.0023T - 48.25) & T > 1050\ K \end{cases}$$

$$p(T) = \begin{cases} 0.017T - 13.70 & T \le 1050\ K \\ -0.0042T + 8.64 & T > 1050\ K \end{cases}$$

The model constants are calculated by fitted equations!

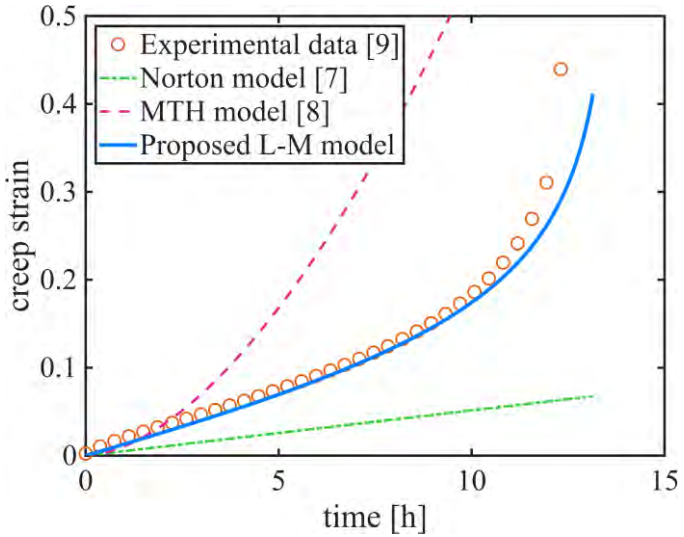

T= 1000 K, Stress=40.2 MPa

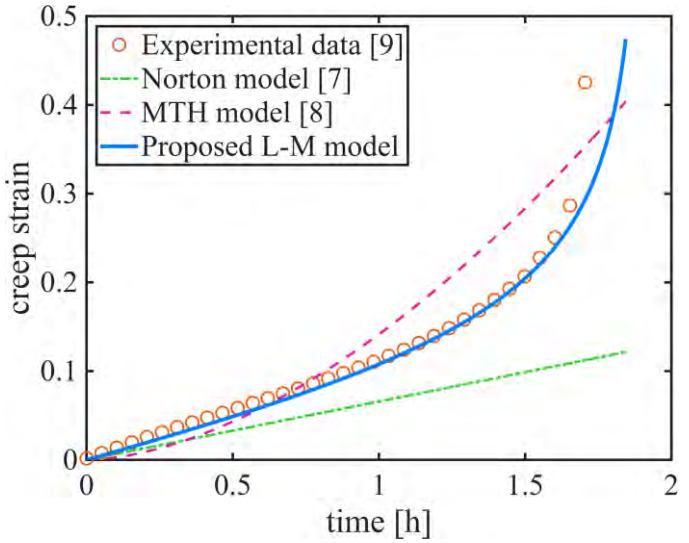

T= 1000 K, Stress=73.6 MPa

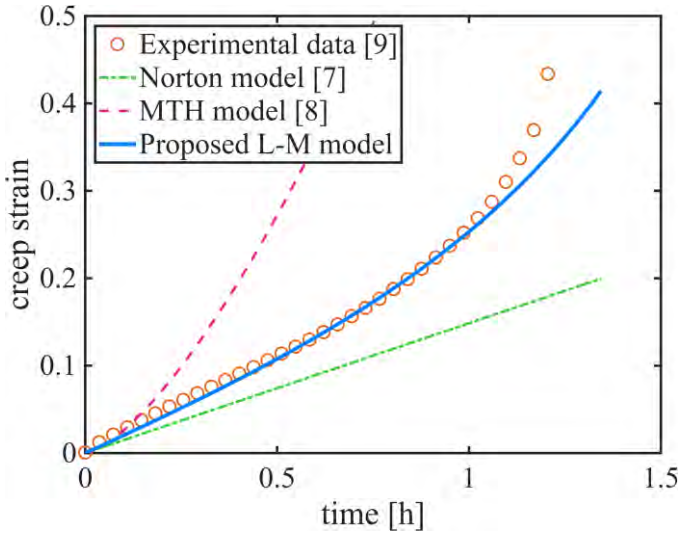

T= 1250 K, Stress=23.8 MPa

04 PART FOUR

Conclusion & Outlook

4 Conclusion

Conclusion:

Our research calibrated and validated the Liu-Murakami creep model for SA533B1, the results show that:

- The proposed model successfully captures the critical tertiary creep stage, demonstrating superior accuracy over traditional models.
- The newly developed model successfully extends the applicable temperature range continuously from 900 K to 1623 K.
- The model exhibits exceptional generalizability when applied to independent test data, alongside interpolation capability.

Outlook:

- High-quality experimental data at near-melting regimes (above 1623 K) is highly desirable.
- A multiaxial L-M creep model are needed to better replicate the multi-dimensional stress state of an actual RPV lower head.

REFERENCES

1. Yu, P., & Ma, W. (2020). A modified theta projection model for creep behavior of RPV steel 16MND5. Journal of Materials Science & Technology, 47, 231-242.
2. M. Sattar, A.R. Othman, S. Kamaruddin, M. Akhtar, R. Khan, Limitations on the computational analysis of creep failure models: A review, Engineering Failure Analysis 134 (2022) 105968.
3. Rempe J L, Chavez S A, Thinnes G L. Light water reactor lower head failure analysis[R]. Nuclear Regulatory Commission, Washington, DC (United States). Div. of Systems Research; EG and G Idaho, Inc., Idaho Falls, ID (United States), 1993.
4. Y. Liu, S. Murakami, Damage Localization of Conventional Creep Damage Models and Proposition of a New Model for Creep Damage Analysis., JSME Int. J., Ser. A 41 (1998) 57–65.
5. Norton, F. (1929). The Creep of Steels at High Temperatures (Vol. 1, No. 1). McGraw Hill, New York, p. 90.
6. Yamaguchi, Y., Katsuyama, J., Kaji, Y., et al. (2020). Expansion of high temperature creep test data for failure evaluation of BWR lower head in severe accident. Mechanical Engineering Journal, 7(3), 19-00560.
7. E.-K. Park, J.-W. Park, Y.-J. Kim, Y. Takahashi, K. Lim, E.S. Kim, Failure simulation of nuclear pressure vessel under severe accident conditions: Part II – Failure modeling and comparison with OLHF experiment, Nuclear Engineering and Technology 55 (2023) 4134–4145.
8. Wang, H. (2023). Thermo-mechanical Assessment of Reactor Pressure Vessels of Light Water Reactors During Severe Accidents, KTH Royal Institute of Technology.
9. L.L. Humphries, T.Y. Chu, J. Bentz, R. Simpson, OECD Lower Head Failure Project Final Report, Sandia National Laboratories, Albuquerque, NM, 2002.

Thanks for your listening!

The 12th European Review Meeting on Severe Accidents Research

May 18-22, 2026, Universidad Carlos III de Madrid, Madrid, Spain

TECHNICAL SESSION 4.5: EX-VESSEL CORIUM AND DEBRIS COOLABILITY

Chairs: P. Piluso (CEA), T. Hollands (GRS)

ID161	**Development of the SAFARI Code for Comprehensive Severe Accident Analysis in Nuclear Reactors: Corium–Coolant Interaction Analysis Module** M. Kwon (Seoul National University)	Paper Presentation
ID200	**Evaluation of concrete ablation by a hot heat-generating solid** A. Villarreal-Larrauri (EDF)	Paper Presentation

DEVELOPMENT OF THE SAFARI CODE FOR COMPREHENSIVE SEVERE ACCIDENT ANALYSIS IN NUCLEAR REACTORS: CORIUM-COOLANT INTERACTION ANALYSIS MODULE

Minchan Kwon, Eung Soo Kim, Hyun Sun Park*
Department of Nuclear Engineering
Seoul National University
1 Gwanak-ro, Gwanak-gu, Seoul, 08826, South Korea
ksn5014@snu.ac.kr; kes7741@snu.ac.kr; hejsunny@snu.ac.kr

Seokwon Whang
FNC Technology Co., Ltd.
13 Heungdeok 1-ro, Giheung-gu, Yongin-si, Gyeonggi-do, 16954, South Korea
s.whang@fnctech.com

ABSTRACT

This study introduces the development of a Corium–Coolant Interaction module within the SAFARI (Safety Analysis Code for Severe Accident Risk Identification) code, which is currently under development in Korea as an analysis tool to support regulating evaluation for Nuclear Power Plants. The module is of particular importance because it represents the initial phase of ex-vessel accidents following reactor pressure vessel failure, and it directly governs the boundary conditions for subsequent phenomena such as molten core–concrete interaction (MCCI) and steam explosions, both of which critically affect containment integrity.

The module has been designed with the primary objective of evaluating the redistribution and coolability of ex-vessel corium during the accident progression with designed Severe Accident Management (SAM). The module has been developed as a C++-based lumped-parameter code, incorporating mechanistic models for melt jet breakup, particle size distribution, and particle/corium lump heat transfer and sedimentation dynamics, as well as a debris-bed/corium formation model. In addition, the module is coupled with the containment thermal-hydraulic model, SAVANAH to account for system-level interactions.

Validation has been carried out against representative experimental programs, such as DAVINCI test [1], DEFOR experiment [2]. The module reproduced key experimental trends across these benchmarks, including jet breakup length, particle size distribution, and debris-bed morphology.

Overall, the module is under active development to establish a comprehensive and predictive framework for mechanistic analysis of Corium–Coolant Interaction during severe accidents. In this work, we present our development status of the module.

KEYWORDS
Corium-Coolant Interaction, Corium Coolability, Debris Bed Formation, Module Development, Severe Accident

1. INTRODUCTION

1.1. Background and Motivation

In the current regulatory environment, severe accident analysis has become a core element of nuclear power plant safety evaluation, with increasing emphasis on quantitative assessment of accident progression beyond reactor vessel failure. In particular, corium relocation into the containment and subsequent ex-vessel phenomena, such as corium–coolant interaction and molten core–concrete interaction, play a critical role in determining containment thermal-hydraulic conditions and associated safety margins under beyond-design-basis scenarios.

Integrated severe accident analysis codes, including MELCOR, MAAP, and ASTEC, have been widely applied for safety and regulatory evaluations. However, these tools are developed and maintained by foreign organizations, and their modeling assumptions and update pathways are not always fully transparent or readily adaptable to domestic regulatory requirements and reactor-specific features.

To address the need for an independent and mechanistic analysis capability for ex-vessel severe accident phenomena, the SAFARI (Safety Analysis code for Severe Accident Risk Identification) program has been initiated in Korea. SAFARI is conceived as a modular integration framework for ex-vessel severe accident analysis, emphasizing physical consistency, traceable model development, and regulatory-oriented application.

1.2. Scope of the Present Work

The SAFARI framework integrates dedicated mechanistic modules for key ex-vessel severe accident phenomena with a simplified containment thermal-hydraulic model, enabling consistent evaluation of corium behavior and containment response following reactor vessel failure. Within this framework, the HIPPO module addresses early-phase ex-vessel corium–coolant interaction.

The present study describes the development and validation of HIPPO, which models melt jet breakup, particle generation and sedimentation, debris bed formation, and thermal interaction with continuous melt. The module provides time-dependent heat and mass source terms to the containment model through a structured coupling strategy. Validation against representative experiments is performed to demonstrate the applicability of HIPPO as a mechanistic, regulatory-oriented tool for evaluating ex-vessel corium redistribution and coolability within the SAFARI framework.

2. OVERVIEW OF THE HIPPO COMPUTATIONAL FRAMEWORK

HIPPO is a mechanistic, lumped-parameter framework developed to represent corium–coolant interaction during the early ex-vessel phase of severe accidents, with emphasis on computational efficiency and consistent coupling with containment thermal-hydraulic behavior.

2.1. Modeling Philosophy and Assumptions

HIPPO is designed to predict ex-vessel corium redistribution and coolability following reactor pressure vessel failure and to provide consistent thermal and mass boundary conditions for debris bed cooling, melt lump evolution, and containment response.

Fragmented corium produced by melt jet breakup is modeled using a particle-based approach based on empirical correlations. Particles are characterized by statistical size distributions and treated as discrete elements during sedimentation to evaluate transport and heat transfer to the coolant.

Sedimented particles either form a debris bed or merge into a continuous melt lump according to temperature-based criteria. Both are represented as lumped control volumes conserving mass and energy, with debris bed geometry governed by slope-angle-controlled redistribution. Thermodynamic equilibrium is assumed between vapor and saturated liquid phases, while subcooled liquid is treated separately. HIPPO is sequentially coupled with a simplified containment thermal-hydraulic model through exchange of boundary conditions and buffered heat and mass source terms to ensure conservation and numerical stability.

2.2. Modular Structure and Coupling Strategy

The framework consists of a corium–coolant interaction block, which evaluates melt fragmentation, particle transport, debris bed formation, and melt lump evolution, and a containment block that determines global thermodynamic conditions using lumped control volumes.

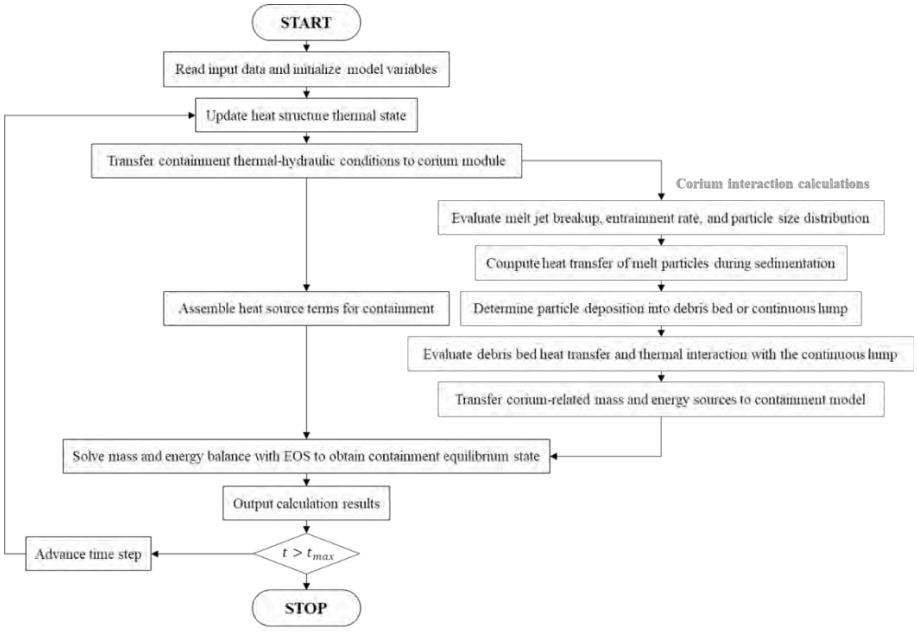

Figure 1. Overall computational flow of the HIPPO Corium–Coolant Interaction module coupled with the simplified containment thermal-hydraulic model(HOTCB)

Coupling between the two blocks is implemented sequentially through exchange of boundary conditions and time-dependent heat and mass source terms. At each global time step, coolant conditions provided by the containment model are supplied to the corium block, which computes local corium phenomena and returns the resulting source terms.

3. CORIUM-COOLANT INTERACTION MODELING (HIPPO MODULE)

This section describes the HIPPO module for mechanistic modeling of melt jet breakup, particle generation and sedimentation, debris bed formation, and thermal interaction with a continuous melt lump during ex-vessel corium–coolant interaction.

3.1. Melt Jet Breakup and Particle Generation

Melt jet breakup defines the initial mass, size, and velocity distributions of dispersed corium particles and thus establishes the primary conditions for downstream transport, deposition, and coolability evaluation.

3.1.1. Jet breakup correlations and entrainment modeling

Melt jet breakup is treated as the primary mechanism governing the redistribution of corium mass between a coherent jet and dispersed particulate phases. To represent the effective extent of jet fragmentation under different hydrodynamic and thermodynamic conditions, selectable empirical correlations are adopted.

The Taylor-type [3] and Saito-type [4] correlations are expressed as

$$\frac{L_{br}}{D_{jet}}\left(\frac{\rho_m}{\rho_l}\right)^{-0.5} = 10\mathrm{C_{br}} \tag{1}$$

$$\frac{L_{br}}{D_{jet}}\left(\frac{\rho_m}{\rho_l}\right)^{-0.5} = 2.1\mathrm{C_{br}}\left(\frac{V_j^2}{gD_{jet}}\right)^{0.5} \tag{2}$$

To explicitly account for the influence of vapor generation and condensation on jet fragmentation behavior, the Jung-type [5] correlation is employed:

$$\frac{L_{br}}{D_{jet}}\left(\frac{\rho_m}{\rho_l}\right)^{-0.5} = 3.3C_{br}\mathrm{Fr}^{0.5\left[1-\frac{1}{2154Q+1}\right]} \tag{3}$$

This formulation introduces thermodynamic coupling between jet breakup behavior and coolant subcooling conditions through the vapor generation intensity parameter.

3.1.2. Particle size distribution formulation

The size distribution of generated particles is represented using a Rosin–Rammler formulation to provide a statistically consistent description of fragmented melt:

$$F = 1 - exp\left[-\left(\frac{D_p}{D_e}\right)^n\right] \tag{4}$$

where F is the cumulative mass fraction of particles with diameter smaller than D_p, D_e is the characteristic distribution diameter, and n is the distribution constant, taken as $n = 1.5$.

The characteristic diameter D_e is related to the mass median diameter (MMD) through

$$D_e = \frac{MMD}{(log2)^{(1/n)}} \tag{5}$$

The mass median diameter is evaluated using an empirical correlation expressed in terms of the Bond number based on the particle diameter,

$$\mathrm{Bo}_p = \frac{g\rho_m D_{MM}^2}{\sigma_m} \tag{6}$$

which is related to coolant subcooling and density ratio by

$$Bo_p^{1/2} = C_{dmm} F_{sb} \left(\frac{\rho_v}{\rho_l}\right)^{1/3} \left(\frac{\rho_l}{\rho_m}\right)^{2/3} \tag{7}$$

with

$$F_{sb} = 25\{2.2 - \exp(-13N_{sb})\}, \qquad N_{sb} = \frac{c_{pl}\Delta T_{sub}}{\Delta h_{fg}} \tag{8}$$

For particles deposited into the debris bed, a truncated Rosin–Rammler distribution [6] is applied to exclude unrealistically small particles while preserving the statistical characteristics of the original distribution:

$$F = \begin{cases} 0, & D_P < D_{min} \\ 1 - exp\left[-\left(\frac{D_p}{D_e}\right)^n + -\left(\frac{D_{min}}{D_e}\right)^n\right], & D_p \geq D_{min} \end{cases} \tag{9}$$

Particle diameters are sampled under an ergodicity assumption and grouped into representative particle elements with identical thermomechanical properties. Initial particle velocities are derived from the jet velocity with stochastic perturbations to represent turbulence-induced dispersion.

3.2. Particle Sedimentation and Heat Transfer

Heat transfer from sedimenting melt particles to the surrounding coolant is evaluated by coupling implicit particle energy conservation with regime-dependent surface heat flux correlations. This formulation ensures stable evaluation of particle cooling across boiling regimes while avoiding numerical stiffness associated with explicit heat transfer treatment.

The internal energy change of a representative particle over a time step is expressed as

$$\Delta Q = -m_p c_{pm}(T_{av}^n - T_{av}^{n-1}) \tag{10}$$

The corresponding heat transferred to the coolant during the same time step is given by

$$\Delta Q = \Delta t\, A_p h_{eff}(T_{av}^n - T_l) \tag{11}$$

Combining the two relations yields the coupled implicit energy balance

$$-m_p c_{pm}(T_{av}^n - T_{av}^{n-1}) = \Delta t\, A_p h_{eff}(T_{av}^n - T_l) \tag{12}$$

The effective heat transfer coefficient is defined in terms of the regime-dependent surface heat flux as

$$h_{eff} = C_{htc} \left|\frac{q''}{T_{av} - T_l}\right| \tag{13}$$

To account for internal temperature gradients within particles, a simplified thermal boundary layer model is adopted. The evolution of the thermal boundary layer thickness is evaluated from

$$\delta\left(1-\frac{3\delta}{4R}+\frac{1}{5}\left(\frac{\delta}{R}\right)^2\right)\frac{d\delta}{dt}=3k \tag{14}$$

with the initial value approximated by

$$\delta_0=\sqrt{6k\Delta t} \tag{15}$$

The surface temperature is related to the average particle temperature through

$$T_{av}-T_{sf}=\frac{q^{''}\delta}{2\lambda} \tag{16}$$

For a computational node containing identical particles, the total heat released to the coolant is evaluated as

$$\Delta Q_{node}=N_{node}\Delta Q \tag{17}$$

After heat transfer is evaluated, the particle internal energy is updated including decay heat generation:

$$e_{int}^{n}=e_{int}^{n-1}-\frac{\Delta Q}{m_p}+q_{decay}\Delta t \tag{18}$$

Through this formulation, particle cooling during sedimentation is evaluated by consistently coupling implicit energy conservation, regime-dependent surface heat transfer, and internal temperature correction. The resulting heat release histories are subsequently supplied as source terms to debris bed formation and containment thermal-hydraulic coupling calculations.

3.3. Debris Bed and Melt Lump Evolution

This section describes the formation and thermal evolution of the debris bed and its interaction with the underlying continuous melt lump. The modeling objective is to provide a conservative and physically consistent evaluation of long-term corium coolability while preserving mass and energy during phase transition between particulate debris and coherent melt.

The debris bed and continuous melt lump are treated as coupled but distinct control volumes. This separation enables explicit representation of porous-bed cooling limitations governed by two-phase flow interactions, as well as enhanced vapor generation driven by heat input from the continuous melt.

3.3.1. Deposition criteria and debris bed formation

Sedimented particles are deposited into debris bed nodes or merged into a continuous melt lump according to temperature-based criteria:

$$\begin{aligned} &T_{av}>T_{mel}+0.5f_{tcr}\left(T_{liq}-T_{sol}\right), \qquad or\\ &T_{sf}>T_{sol}+f_{tcr}\left(T_{liq}-T_{sol}\right) \end{aligned} \tag{19}$$

This criterion is applied consistently to newly deposited particles and to debris bed particles reheated by decay heat, allowing reversible transition between particulate and coherent melt phases while preserving energy conservation.

The macroscopic geometry of the debris bed is governed by vapor-induced lateral particle transport. Under strong vapor generation, lateral dispersion becomes significant, resulting in a conical debris bed characterized by a side slope angle. Based on an energy flux interaction model, the slope angle is evaluated as

$$\tan(\theta_s) = 4.127\left(\frac{\rho_g h_{lg}}{(\rho_l-\rho_g)^2}\right)\left(\frac{\dot{m}^2}{q_d''' H_s^2}\right)\left(\frac{u_p^4}{\alpha u_b D_{pc}^4}\right) \tag{20}$$

A critical slope angle is imposed to represent the limiting repose angle of wet granular materials. When the calculated slope exceeds this limit, lateral redistribution of upper debris bed nodes is applied to maintain geometric stability.

3.3.2. Debris bed heat transfer and thermal interaction with continuous melt lump

Heat removal from the debris bed is governed by two competing mechanisms: (i) local particle-scale heat transfer evaluated from microscopic heat transfer correlations, and (ii) global limitation imposed by counter-current flow limitation due to vapor generation within the porous debris bed.

For each debris bed node, local heat transfer is evaluated using the same particle heat transfer models applied during sedimentation, with attenuation to account for particle crowding effects. Assuming a fully developed internal thermal boundary layer, the relation between average and surface temperatures is expressed as

$$T_{av} - T_{sf} = \frac{q''R}{5\lambda} \tag{21}$$

In parallel, the maximum allowable heat removal rate is constrained by the dryout heat flux, which originates from counter-current flow limitation between upward vapor flow and downward liquid penetration. The actual debris bed heat removal rate is determined as

$$Q_{dbr} = \min(Q_{htr}, Q_{lim}) \tag{22}$$

where the limitation term is defined as

$$Q_{lim} = F_{dhf} Q_{dhf} - Q_{btm} \tag{23}$$

The influence of the continuous melt lump beneath the debris bed is explicitly accounted for through the heat input term

$$Q_{btm} = \min\left(A_b F_{htmp} \lambda_m \frac{T_{lmp} - T_{sat}}{H_{lmp}/2}, F_{qbdhf} F_{dhf} Q_{dhf}\right) \tag{24}$$

The debris bed energy balance per unit mass is expressed as

$$(-\dot{q} + \dot{q}_{dc})\Delta t = e(T_{av}^{(n)}) - e(T_{av}) \tag{25}$$

which can be rewritten in terms of temperature difference as

$$\dot{q} = R_{eff}(T_{av}^{(n)} - T_{sat}) \tag{26}$$

When the debris bed temperature reaches the melting criterion, partial re-melting is allowed. The re-melted mass is evaluated from

$$m[(-\dot{q} + \dot{q}_{dc})\Delta t - e(T_{cr}) + e(T_{av})] = m_{rm}\left[e(T_{liq}) - e(T_{cr})\right] \tag{27}$$

Through this coupled formulation, debris bed heat transfer is constrained by both microscopic particle-scale heat transfer and macroscopic counter-current flow limitation. Interaction with the underlying continuous melt lump further reduces the effective cooling capacity, providing a physically consistent and conservative evaluation of debris bed coolability during ex-vessel corium–coolant interaction.

4. SIMPLIFIED CONTAINMENT THERMAL-HYDRAULIC MODEL

This section briefly describes the simplified containment thermal-hydraulic model used to couple with the HIPPO corium–coolant interaction module. The model provides the thermodynamic boundary conditions for HIPPO and receives time-dependent heat and mass source terms generated by corium cooling processes.

The containment is represented using a lumped control-volume formulation under vapor–liquid thermodynamic equilibrium. Corium components, including melt particles, debris beds, and continuous melt lumps, are treated as internal heat and mass sources. Mass and energy balance equations are solved using an implicit equilibrium scheme to ensure numerical stability under strong thermal coupling.

4.1. Containment Modeling Approach

The containment atmosphere is modeled as a well-mixed control volume composed of vapor, liquid, and non-condensable gas components. Vapor and saturated liquid are assumed to be in thermodynamic equilibrium, while subcooled liquid is treated separately. Heat structures are represented as lumped heat-capacity bodies exchanging energy with the fluid.

This simplified formulation provides a computationally efficient and physically consistent basis for coupling with the HIPPO module without resolving detailed spatial thermal-hydraulic fields.

4.2. Governing mass and energy balance equations

The containment control volume conserves total mass and internal energy while accounting for inflow/outflow, phase change, and volumetric heat sources. The governing equations are expressed as

$$\frac{dM_k}{dt} = \sum(\dot{m}_{k,in}) - \sum(\dot{m}_{k,out}) + \dot{m}_{k,ph} \tag{28}$$

$$\frac{dE}{dt} = \sum(\dot{m}_{in}h_{in}) - \sum(\dot{m}_{out}h_{out}) + Q_{src} - P\frac{dV}{dt} \tag{29}$$

where Q_{src} includes decay heat and thermal energy transferred from corium components evaluated by HIPPO. The total pressure is evaluated as the sum of vapor and non-condensable gas partial pressures.

4.3. Coupling with the HIPPO Module

The containment model is sequentially coupled with HIPPO through the exchange of boundary conditions and source terms at each global time step. The containment model provides the thermodynamic state of the coolant to HIPPO, while HIPPO returns the heat and mass sources generated by melt particles, debris beds, and the continuous melt lump.

From the containment model to HIPPO, the transferred state variables are defined as

$$\mathbf{X}_{cav} = \{p_{tot}, T_l, T_s, \rho_l, c_{p,l}, \beta_l, h_l, V_l, \dot{m}_{dil}, e_l, e_v, p_v, \rho_v, m_v\} \tag{30}$$

The total heat source transferred from HIPPO is expressed as

$$\dot{Q}_{cor}(t) = \dot{Q}_{par}(t) + \dot{Q}_{dbr}(t) + \dot{Q}_{lmp}(t) \tag{31}$$

To account for residence-time effects associated with particle tracking and sedimentation, HIPPO employs a time-dependent heat buffer. The buffered heat source is supplied to the containment model as an external volumetric heat source. Mass exchange due to evaporation and condensation induced by corium cooling is also transferred as a source term.

The coupled HIPPO–containment system is advanced in time using an explicit sequential procedure combined with an implicit equilibrium solver in the containment model, ensuring numerical stability and global mass and energy conservation.

5. VERIFICATION AND VALIDATION OVERVIEW

To evaluate the predictive capability of the HIPPO module for corium–coolant interaction phenomena, validation was performed against representative melt jet breakup and debris bed formation experiments. The validation focuses on key integral quantities governing ex-vessel accident progression, including jet breakup length, particle size distribution, and debris bed geometry.

Two experimental programs were selected: the DAVINCI experiment, providing quantitative data on debris bed formation under flooded conditions, and the DEFOR experiment, offering detailed measurements of melt jet breakup and fragmentation behavior in a water pool. Validation is conducted by comparing numerical predictions with experimental results, emphasizing dominant trends and integral characteristics rather than local small-scale fluctuations.

5.1. Validation against DAVINCI Experiment

The DAVINCI experiment was used to validate the debris bed formation model implemented in HIPPO. The experiment provides axisymmetric debris bed profiles formed by particle sedimentation in a quiescent water pool, allowing direct comparison of deposited layer geometry.

Figure 2 compares the experimentally measured debris bed profiles with the corresponding numerical predictions. Both results show similar overall growth behavior, with a maximum height near the center and a gradual decrease toward the outer radius, indicating that HIPPO reproduces the conical debris bed geometry and its temporal evolution.

The numerical results exhibit a slightly wider radial spread at later times, leading to a modest overprediction of the bed radius. This difference is attributed to particle representation, as cylindrical particles were used in the experiment whereas spherical particles with a representative mean diameter are assumed in HIPPO. Despite this discrepancy, the validation demonstrates that HIPPO captures the principal features of debris bed formation under quiescent pool conditions.

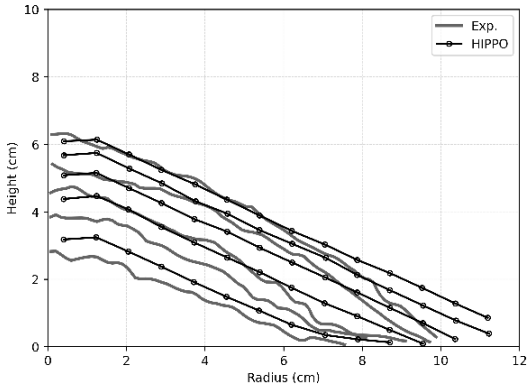

Figure 2. Time evolution of debris bed height profiles: DAVINCI experiment vs. HIPPO predictions.

5.2. Validation against DEFOR Experiment

The HIPPO module was further validated against the DEFOR experiment, which provides detailed measurements of melt jet breakup behavior and resulting particle characteristics in a water pool. The validation addresses three key aspects: jet breakup length, particle size distribution, and debris bed formation.

5.2.1. Jet breakup length

Figure 3 compares the experimentally measured melt jet breakup length with the numerical prediction obtained by the HIPPO module. In the DEFOR experiment, the breakup length is evaluated from the axial variation of the melt jet front-edge velocity, showing a distinct transition from coherent jet behavior in air to rapid fragmentation after entering the water pool.

In the numerical analysis, the breakup length is extracted from the time evolution of the under-water melt jet length predicted by HIPPO. A representative breakup length is defined from the quasi-steady phase prior to the onset of rapid jet collapse. The predicted breakup length of 0.36951m shows close agreement with the experimental value of 0.37104 m, with a relative difference of approximately 0.4%.

The numerical results reproduce the experimentally observed breakup behavior, including the abrupt loss of jet coherence upon water entry. The close agreement in the breakup length indicates that the implemented jet breakup correlations and entrainment modeling in HIPPO provide a physically consistent representation of melt jet fragmentation under DEFOR experimental conditions.

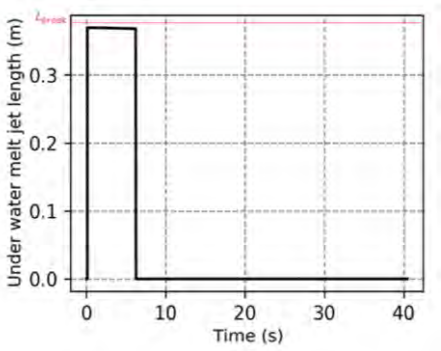

Figure 3. Time evolution of under-water melt jet length and the resulting breakup length in the DEFOR M-12 case (HIPPO prediction).

5.2.2. Particle size distribution

The particle size distribution obtained from the DEFOR experiment was compared with numerical predictions. The numerical model reproduces the overall shape of the particle size distribution, including the dominant particle size range and the monotonic increase of cumulative mass fraction with particle diameter.

Both experimental and numerical results indicate that most of the fragmented mass is concentrated in the millimeter-scale particle range. The agreement in cumulative mass fraction demonstrates that the implemented breakup and particle generation models provide a realistic representation of fragmentation behavior. Discrepancies observed in the distribution tails, particularly for the smallest particle classes, are attributed to experimental resolution limits and the use of representative particle sizes in the numerical model.

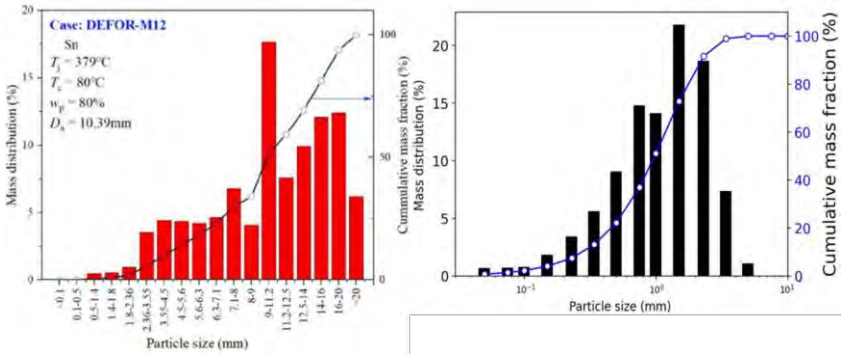

Figure 4. Comparison of particle size distributions between the DEFOR M-12 experiment and HIPPO prediction.

5.2.3. Debris bed formation

The final debris bed configuration in the DEFOR experiment was examined qualitatively. Figure 5 compares the experimentally observed debris bed with the numerical prediction. The experimental debris bed exhibits a mound-shaped structure with a maximum height near the jet impingement region and a gradual decrease toward the outer radius.

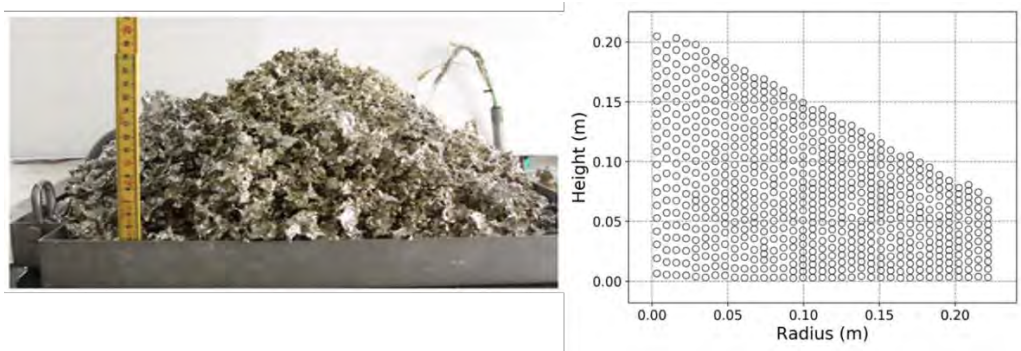

Figure 5. Comparison of debris bed configuration in the DEFOR M-12 experiment and HIPPO prediction

The numerical result reproduces the overall debris bed morphology, including the inclined surface and radial spreading of deposited particles. Although local irregularities observed in the experiment are not

fully resolved due to model discretization, the predicted debris bed geometry is consistent with the global experimental pattern.

6. CONCLUSIONS

This paper presented the development of the HIPPO corium–coolant interaction module coupled with a simplified containment thermal-hydraulic model. The HIPPO framework provides a mechanistic representation of melt jet breakup, particle generation and sedimentation, debris bed formation, and thermal interaction with a continuous melt lump within a unified computational structure.

The coupling strategy employs a sequential exchange of boundary conditions and time-dependent heat and mass source terms, enabling consistent integration of local corium cooling processes with global containment thermal-hydraulic behavior. A time-dependent heat buffering scheme was adopted to ensure numerical stability and conservation of mass and energy.

Validation was conducted against the DAVINCI and DEFOR experiments, focusing on debris bed formation, jet breakup length, and particle size distribution. The results showed that the HIPPO module reproduces the dominant experimental trends and integral characteristics of melt fragmentation and deposition under flooded conditions.

Overall, the developed HIPPO framework offers a physically consistent and computationally efficient tool for analyzing early ex-vessel corium–coolant interaction and its coupling with containment thermal-hydraulic response. Further work will extend the validation database and improve model fidelity for broader severe accident applications.

ACKNOWLEDGMENTS

This work was supported by the Nuclear Safety Research Program through the Korea Foundation of Nuclear Safety (KoFONS) using the financial resource granted by the Nuclear Safety and Security Commission (NSSC) of the Republic of Korea. (RS-2021-KN057910).

REFERENCES

1. Kim, E., Jung, W. H., Park, J. H., Park, H. S., & Moriyama, K. (2016). Experiments on sedimentation of particles in a water pool with gas inflow. *Nuclear Engineering and Technology, 48*(2), 457-469.
2. Xiang, Y., Deng, Y., Fang, D., Liang, D., & Ma, W. (2023). Experimental investigation on debris bed formation from metallic melt coolant interactions. *International Journal of Thermal Sciences, 192*, 108398.
3. G.I. Taylor. The dispersion of jets of metals of low melting point in water. In G.K. Batchelor, editor, *The scientific papers of Sir Geoffrey Ingram Taylor, vol.3 Aerodynamics and the mechanics of projectiles and explosions*, pages 304–305. Cambridge University Press, Cambridge, 1963.
4. M. Saito, K. Sato, and S. Imahori. Experimental study on penetration behaviors of water jet into freon-11 and liquid nitrogen. In *ANS Proc. National Heat Transfer Conference, Houston*, U.S., volume 3, pages 173–183, 1988.
5. Jung, W. H., Park, H. S., Moriyama, K., & Kim, M. H. (2019). Analysis of experimental uncertainties in jet breakup length and jet diameter during molten fuel-coolant interaction. *Nuclear Engineering and Design, 344*, 183-194.
6. Jung, W. H., Park, H. S., Oh, J. H., Hwang, B., Lee, M., & Kim, M. H. (2020). Minimum diameter limit of particle size distribution and its effect on coolability of debris bed. *Nuclear Engineering and Design, 363*, 110606.

ERMSAR 2026 | Madrid, Spain

Development of the SAFARI Code for Comprehensive Severe Accident Analysis

Korea's Regulatory-Oriented Ex-vessel Severe Accident Analysis Framework
SAFARI and the HIPPO CCI Module

Minchan Kwon, Eung Soo Kim, Hyun Sun Park*

Seoul National University

PRESENTATION OUTLINE

Roadmap for a 20-minute talk

1. Why SAFARI?
Domestic, traceable severe accident analysis capability for regulatory-oriented evaluation

2. SAFARI Modules
HIPPO within a broader module ecosystem: MAMBA, SCORPION, containment T-H

3. HIPPO Framework
Jet breakup → particles → debris bed/lump → containment source terms

4. Brief V&V Status
Only a compact status snapshot; detailed model-by-model V&V is not the focus today

5. Publication Roadmap
Correlation-level V&V will be expanded as a continuing conference and journal series

6. SAFARI Coupling
Detailed MAMBA–HIPPO and HIPPO–SCORPION pathways, with future SAVANNAH linkage

AUDIENCE-DRIVEN FRAMING

What is strengthened in this presentation

Overview first

Position HIPPO as the CCI/FCI entry module inside SAFARI, rather than as a standalone validation talk.

V&V scoped

Use DAVINCI, DEFOR, and FARO L33 only as compact status anchors in this overview presentation.

Series plan

Keep detailed V&V for each modeling correlation as a continuing conference and journal publication track.

Ecosystem answer

Answer the expected question: how HIPPO connects to SCORPION, MAMBA, and SAVANNAH within SAFARI.

Response strategy

Use HIPPO to explain SAFARI's modular severe-accident ecosystem, while reserving detailed V&V for follow-up papers.

Ex-vessel severe accident progression

Core melt
Relocation to lower plenum

→

RPV failure
Melt discharge into cavity

→

Ex-vessel CCI
Jet breakup and fragmentation

→

Debris / lump
Deposition, cooling, remelting

→

Containment response
Heat and mass source terms

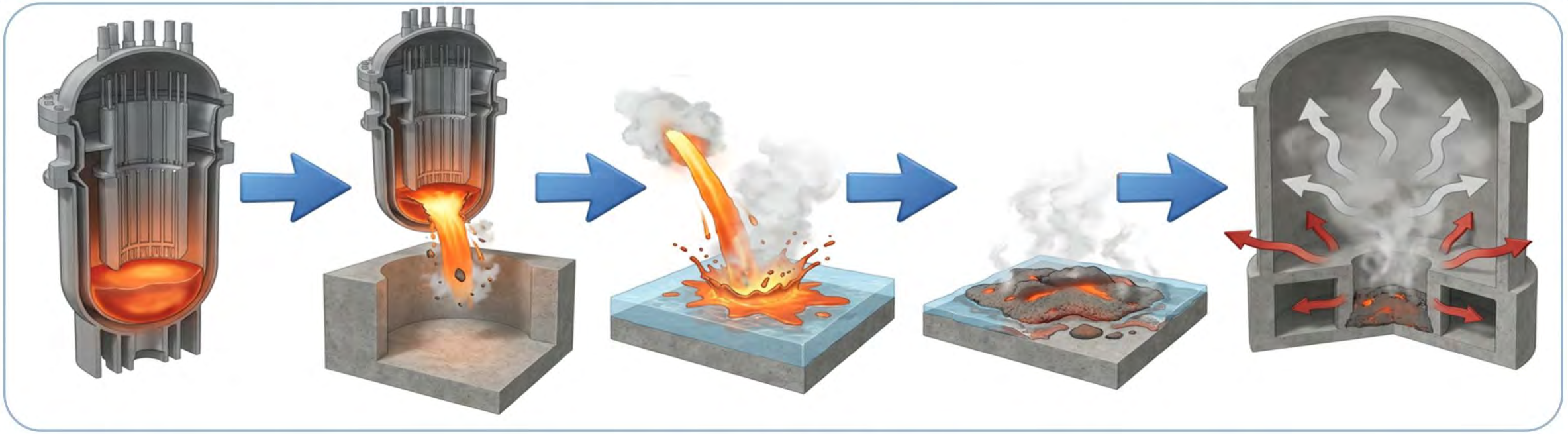

Analysis focus
Early ex-vessel phase immediately after reactor pressure vessel failure

Modeling need
Traceable domestic severe accident analysis for regulatory-oriented evaluation

Why corium–coolant interaction matters

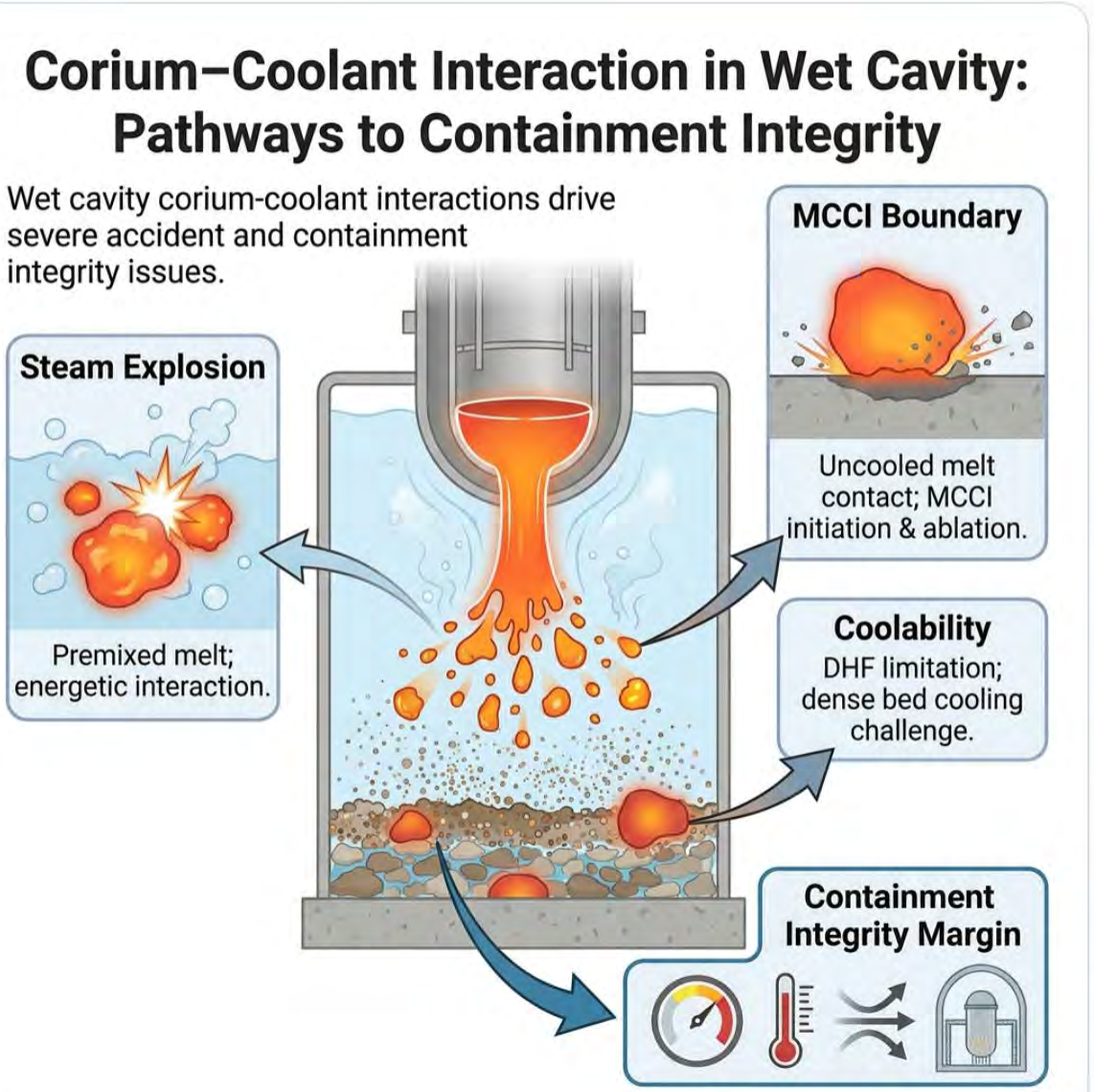

CCI
Melt jet breakup
particle generation
debris/lump formation

↓

Steam explosion
Premixed melt mass and energetic interaction potential

MCCI boundary
Amount and morphology of corium reaching concrete

Coolability
Debris bed DHF limitation and residual melt lump

↓

Containment integrity margin

Pressure, temperature, heat/mass source terms, and long-term cooling state

Reliable CCI analysis is required to quantify ex-vessel accident progression and preserve containment integrity margin.

Objective: introduce SAFARI through the HIPPO module

Introduce SAFARI
Korea's regulatory-oriented framework for integrated ex-vessel severe accident analysis

Demonstrate HIPPO
Representative CCI module producing corium redistribution and heat/mass source terms

Show integration path
Coupled analysis with MAMBA and SCORPION for downstream severe-accident phenomena

Not only
A detailed model-by-model explanation of HIPPO

→

Main message
HIPPO is the entry point for presenting SAFARI's integrated ex-vessel analysis capability.

HIPPO is presented not as an isolated code, but as a gateway module for SAFARI's integrated ex-vessel severe accident analysis capability.

SAFARI: beyond a single CCI module

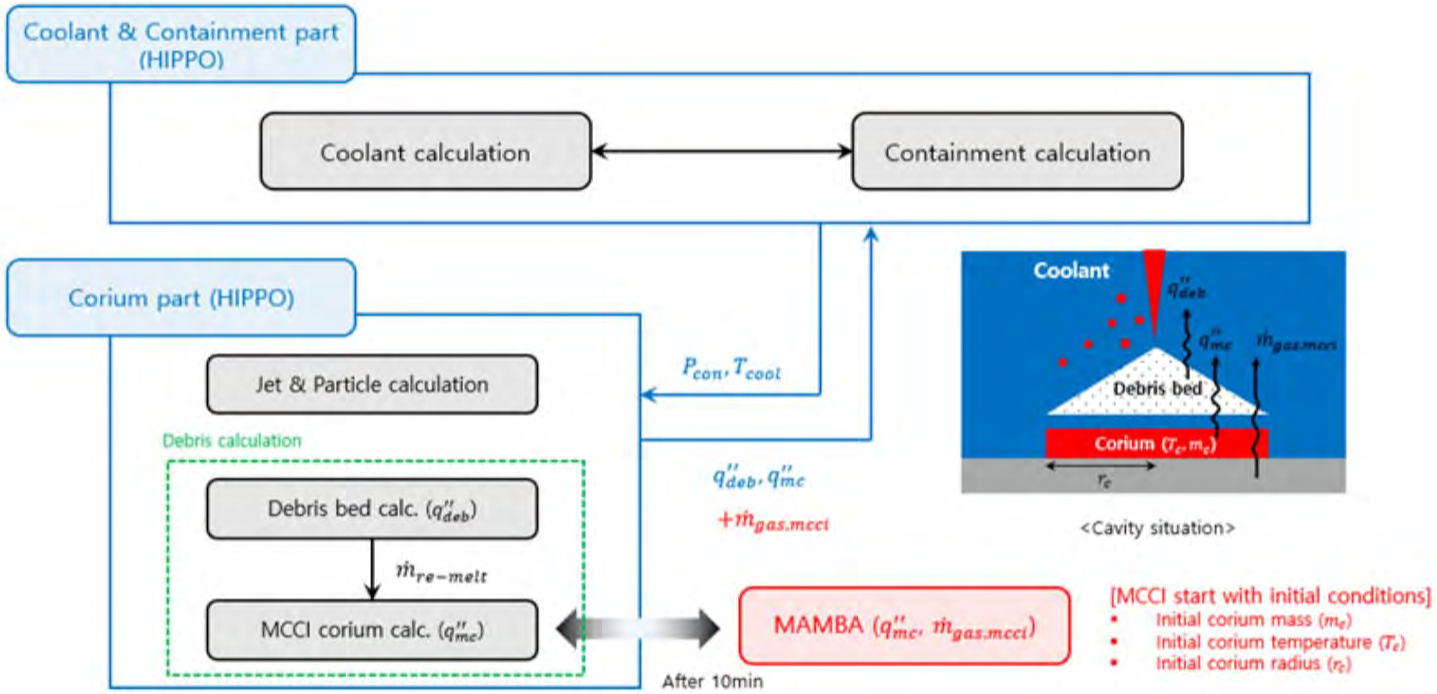

SAFARI should be introduced as a Korean integrated ex-vessel severe accident framework — not as a single HIPPO presentation.

Integration message

HIPPO provides the early ex-vessel CCI state that can feed downstream phenomenon modules in SAFARI.

CCI / FCI

HIPPO

Jet breakup, particles, debris bed, melt lump, and containment source terms

MCCI

MAMBA

Melt–concrete interaction and concrete ablation after corium relocation

STEAM EXPLOSION

SCORPION

Steam-explosion evaluation using premixing-related information

Coupled analysis pathways enabled by HIPPO

MAMBA–HIPPO two-way pathway

HIPPO supplies the FCI-informed cavity state, while MAMBA returns MCCI source terms through containment/coolant coupling.

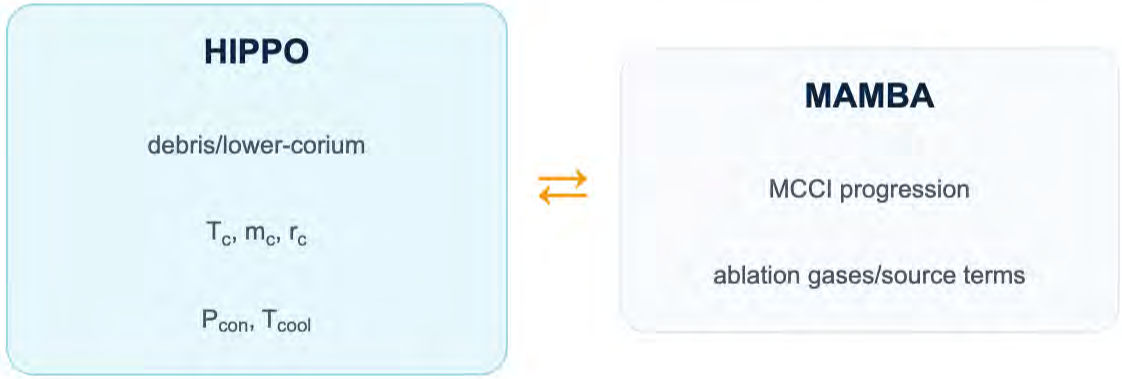

HIPPO–SCORPION pathway

HIPPO premixing time series is transferred through a standardized CSV interface to steam-explosion analysis.

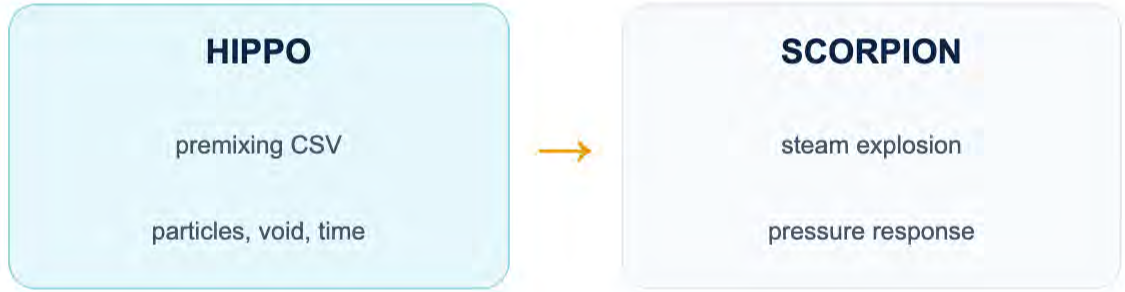

Strategic role of HIPPO

HIPPO couples early ex-vessel CCI with MCCI in two directions, and transfers premixing state to SCORPION for steam-explosion load.

Development lineage: COOLAP-II to HIPPO

COOLAP-II heritage

Simplified melt jet breakup, particle tracking, debris bed/lump cooling, DHF limitation, and HOTCB coupling.

melt jet | particles | DHF | HOTCB

HIPPO present module

SAFARI-oriented CCI module extended with additional breakup, particle distribution, and bed morphology models.

Jung-type breakup | Truncated R-R PSD | Conical bed

Inherited
Jet profile, sedimentation, heat transfer

Extended
Jung breakup, truncated PSD, conical bed

Separated
Heritage review ≠ HIPPO validation

Containment coupling: HOTCB now, SAVANNAH next

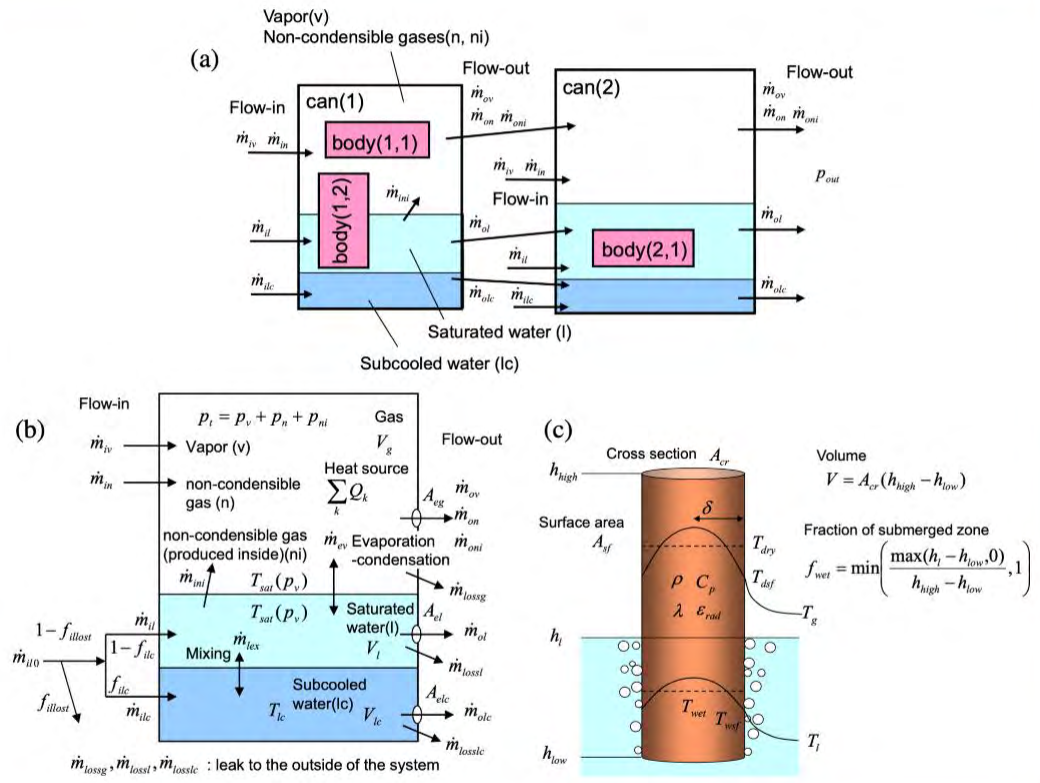

Current simplified coupling

HIPPO contains a simplified containment/coolant part based on HOTCB to exchange boundary conditions and heat/mass sources.

Can model

Water / steam / non-condensable gas equilibrium

Body model

Solid heat-capacity structures

Future SAFARI integration

SAVANNAH is expected to replace or extend HOTCB for more detailed containment thermal-hydraulic response.

Overall HIPPO computational flow

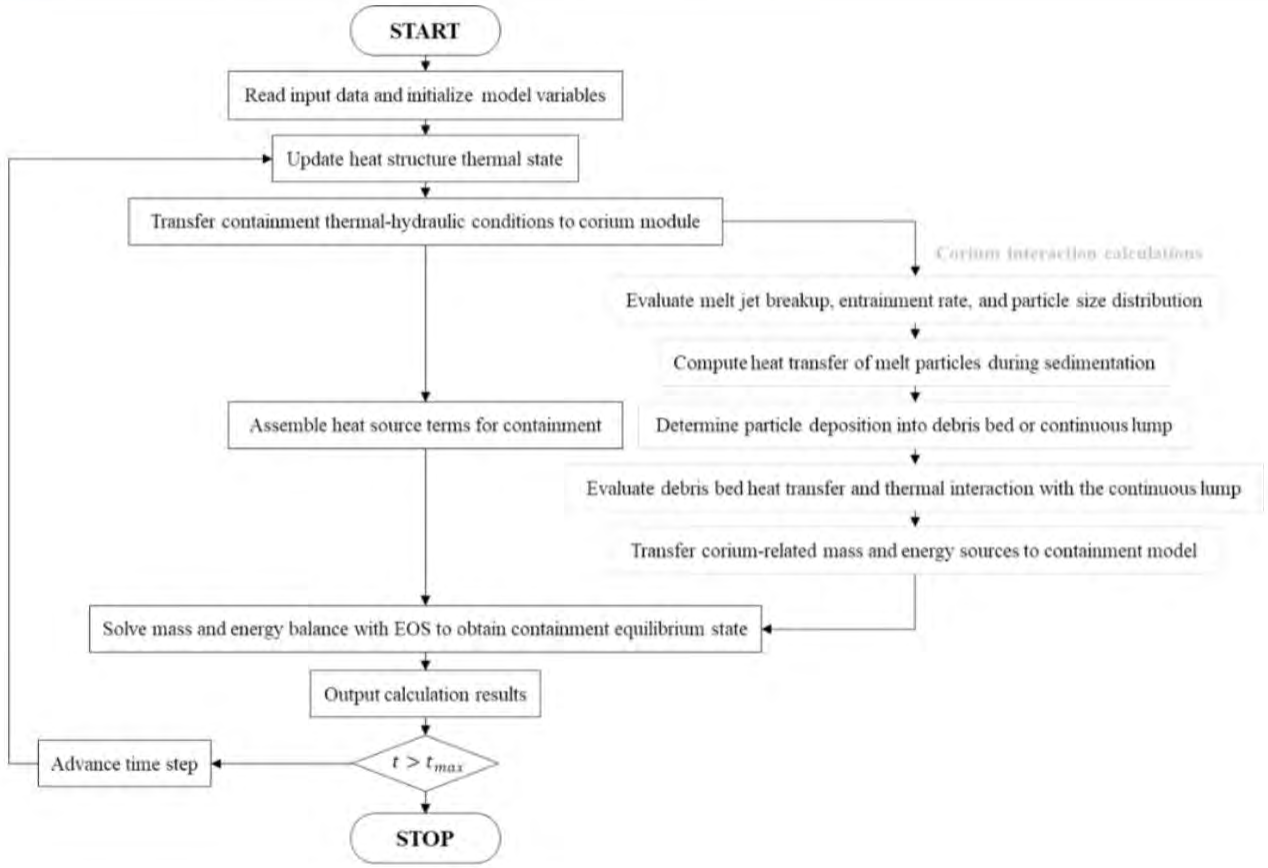

1. Containment state

Coolant pressure, temperature, liquid/vapor properties

2. Corium module

Jet breakup, particles, debris bed, melt lump

3. Mass and energy feedback

Mass and energy returned to the containment model

Closure map for reproducibility

Model element	Closure / correlation used	Constants or criteria to state	Status / V&V use
Jet breakup	Taylor, Saito, and Jung-type breakup models with vapor-generation intensity term	C_{br}; Fr; ρ_m/ρ_l; q''_{gen}/q''_{cond}	Brief DEFOR status anchor; detailed breakup V&V reserved for follow-up paper
Particle PSD	Rosin-Rammler distribution; MMD from Bond-number basis; truncated R-R for deposited debris	n = 1.5; D_{MM}; D_{min}; truncation/stretching rule	PSD publication thread: $D_{10}/D_{50}/D_{90}$ and fit-error metrics
Particle heat flux	Forced convection, nucleate boiling, transition boiling, film boiling, CHF, MFB, radiation	Regime transition temperatures; q" map; implicit particle energy balance	Model-basis transparency; detailed heat-transfer validation deferred
Debris bed	Particle-scale heat transfer with crowding attenuation; 1D top-flooding DHF / CCFL limit	$C_{htc,bed} \approx 0.1$; $F_{dhf} = 1.0$ default; Q_{dhf}	Brief DAVINCI morphology anchor; detailed profile metrics in later V&V work
Bed-lump interaction	Bottom heat input from continuous melt lump reduces allowable debris-bed heat removal	$Q_{lim} = F_{dhf}Q_{dhf} - Q_{btm}$; $F_{qbdhf} = 0.5$ default	Coolability publication thread: DHF margin, remelting, and heat removal
Containment coupling	HOTCB-style can/body mass-energy balance with source-term heat buffer	Sequential coupling; vapor-saturated liquid equilibrium; source conservation check	Source-term accounting check and future SAVANNAH/M1 coupling path

Core equations inherited from COOLAP-II

Taylor type breakup

$L_{br}/D'_j = C_{br} \cdot 10 \cdot (\rho_m/\rho_l)^{1/2}$

Saito type breakup

$L_{br}/D'_j = C_{br} \cdot 2.1 \cdot (\rho_m/\rho_l)^{1/2} \cdot (V'^2_j/gD'_j)^{1/2}$

Jet entrainment source

$m''_e = \rho_m D'_j V'_j/(2L_{br})$, then $m'_e(\zeta)$ is distributed along the shrinking jet profile.

Rosin-Rammler PSD

$F(D_p) = 1 - \exp[-\ln 2(D_p/D_{MM})^n]$, with $n = 1.5$

MMD correlation basis

$Bo_p^{1/2} = C_{dmm}F_{sb}(\rho_v/\rho_l)^{1/3}(\rho_l/\rho_m)^{2/3}$

Particle heat balance

$-Q_{ex} = -m_p c_{pm}(T_{av}^{n+1}-T_{av}^{n}) = \Delta t A_p h_{eff}(T_{av}^{n+1}-T_l)$

HIPPO extensions: equations to state explicitly

Jung-type breakup extension

$L_{br}/D'_j = f(Fr, \rho_m/\rho_l, Q)$, where $Q = q''_{gen}/q''_{cond}$.

Truncated Rosin-Rammler PSD

$F_{tr}(D) = [F(D)-F(D_{min})]/[1-F(D_{min})]$ for $D \geq D_{min}$

Surface-temperature correction in bed

$T_{av}-T_{sf} = q''R/(5\lambda_m)$, or $T_{sf} = (T_{av} + CT_{sat})/(1+C)$

Conical debris-bed morphology

$R_{75\%} = 0.414\Phi^{1/3}$, $\Phi = [(\rho_l-\rho_g)^2(q'''_d H_s^2 \tau)(u_b D_{pc}^4)]/[\rho_p \rho_g h_{lg} \dot{m}(1-\varepsilon)u_p^4]$

DHF-limited bed cooling

$Q_{lim} = F_{dhf}Q_{dhf} - Q_{btm}$, and $Q_{dbr} = \min(Q_{htr}, Q_{lim})$

Deposit / remelt threshold

$T_{sf} > T_{sol} + f_{tcr}(T_{liq}-T_{sol})$, with $f_{tcr} = 0$ as the documented default.

Melt jet breakup and particle generation

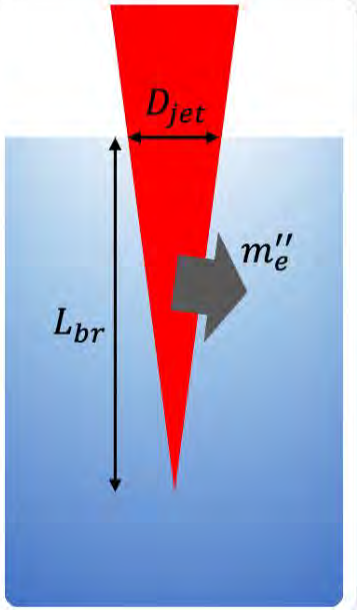

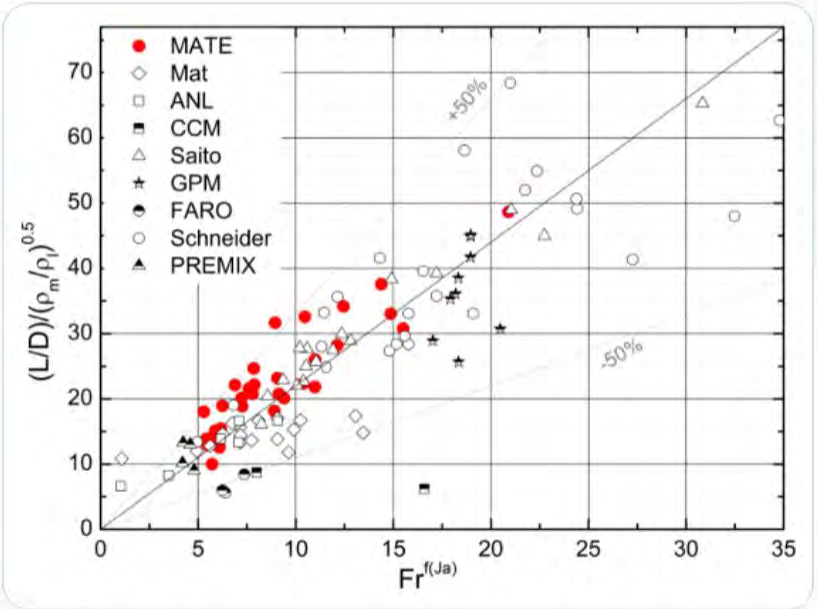

<Mass Flux on the jet surface>

$$m_e'' = \frac{\rho_m D_{jet} V_{jet}}{2\sqrt{L_{br}^2 + \frac{1}{4}D_{jet}^2}}$$

Breakup length determines

coherent jet fraction | particle source location | debris/lump split

Selectable correlations

Taylor-type and Saito-type correlations are inherited basis; Jung-type correlation adds thermodynamic coupling through vapor generation and subcooling effects.

<Jet Breakup Length Correlation>

- Taylor type

$$\frac{L_{br}}{D_{jet}}\left(\frac{\rho_m}{\rho_l}\right)^{-0.5} = 10C_{br}$$

- Saito type

$$\frac{L_{br}}{D_{jet}}\left(\frac{\rho_m}{\rho_l}\right)^{-0.5} = 2.1C_{br}Fr$$

- Vapor generation intensity parameter

$$Q = \frac{Heat\ flux\ for\ vapor\ generation}{Heat\ flux\ for\ vapor\ condensation} = \frac{Ja_v}{Ja_l}$$

$$Ja_l = \frac{\rho_l c_p (T_w - T_{sat})}{\rho_v h_{fg}} \qquad Ja_v = \frac{c_p (T_l - T_{sat})}{h_{fg}}$$

$$\frac{L_{br}}{D_{jet}}\left(\frac{\rho_m}{\rho_l}\right)^{-0.5} = 3.3C_{br}Fr^{0.5\left[1-\frac{1}{2154Q+1}\right]}$$

Particle size distribution model

Rosin–Rammler distribution

Represents cumulative mass fraction of fragmented melt particles.

↓ lower cutoff

Truncated distribution

Excludes unrealistically small deposited particles while preserving statistical characteristics of the original distribution.

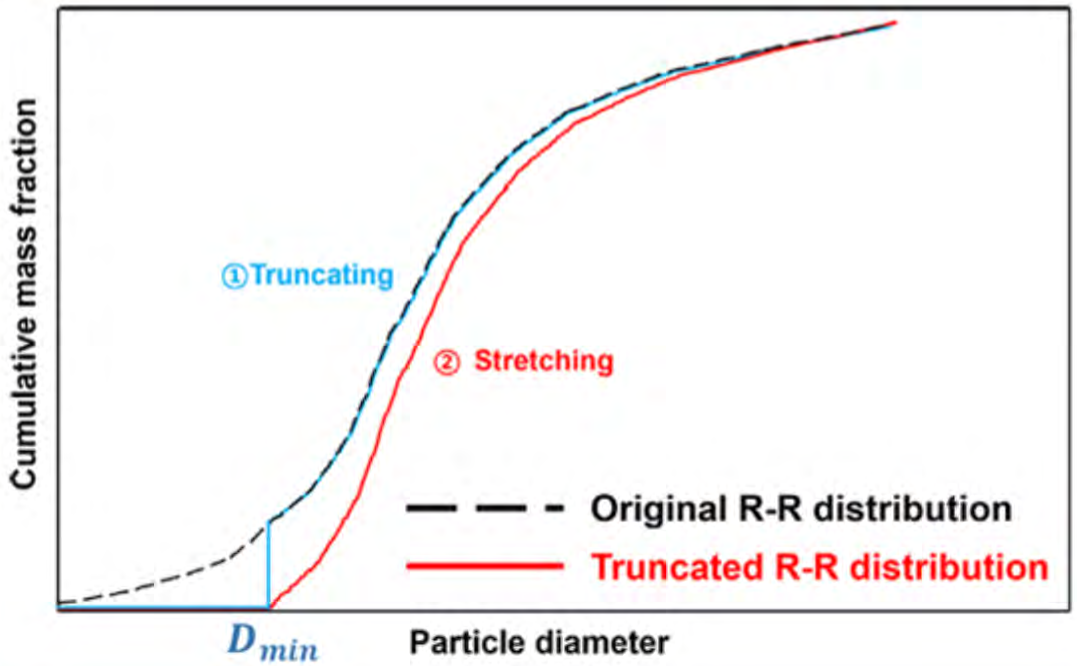

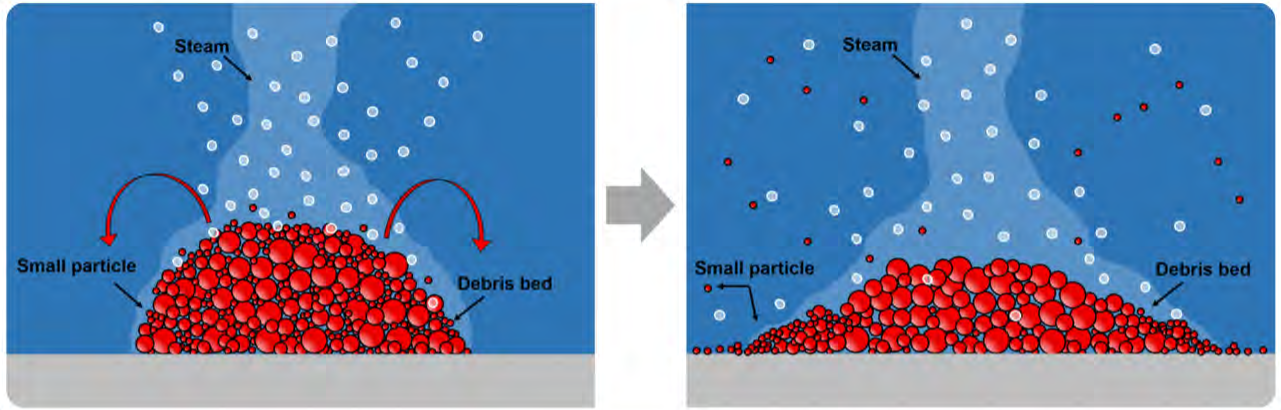

<Original Distribution>

$$F = 1 - \exp\left[-\left(\frac{D_p}{D_e}\right)^n\right]$$

<Truncated Distribution>

$$F = \begin{cases} 0, & D_P < D_{min} \\ 1 - \exp\left[-\left(\frac{D_p}{D_e}\right)^n + -\left(\frac{D_{min}}{D_e}\right)^n\right], & D_p \geq D_{min} \end{cases}$$

$$d = F^{-1}(U) = D_e[-\ln(1-U)]^{\frac{1}{n}} = D_{mm}\left(-\frac{\ln(1-U)}{\ln 2}\right)^{\frac{1}{n}}$$

$$Bo_p \equiv \frac{g\rho_m D_{mm}^2}{\sigma_m}$$

$$Bo_p^{1/2} = C_{dmm} F_{sb} \left(\frac{\rho_v}{\rho_l}\right)^{\frac{1}{3}} \left(\frac{\rho_l}{\rho_m}\right)^{\frac{2}{3}}$$

$$F_{sb} = 25[2.2 - \exp(-13N_{sb})]$$

$$N_{sb} = \frac{c_l \Delta T_{sub}}{\Delta h_{fg}}$$

$$D_{min} = \frac{q''^2 + \sqrt{q''^4 + 8ab\rho_g(\rho_p - \rho_l)gh_{latent}^3\mu_g q''}}{2b\rho_g(\rho_p - \rho_l)gh_{latent}^2}, \quad a = 33.7, b = 0.0408$$

Particle sedimentation and heat transfer

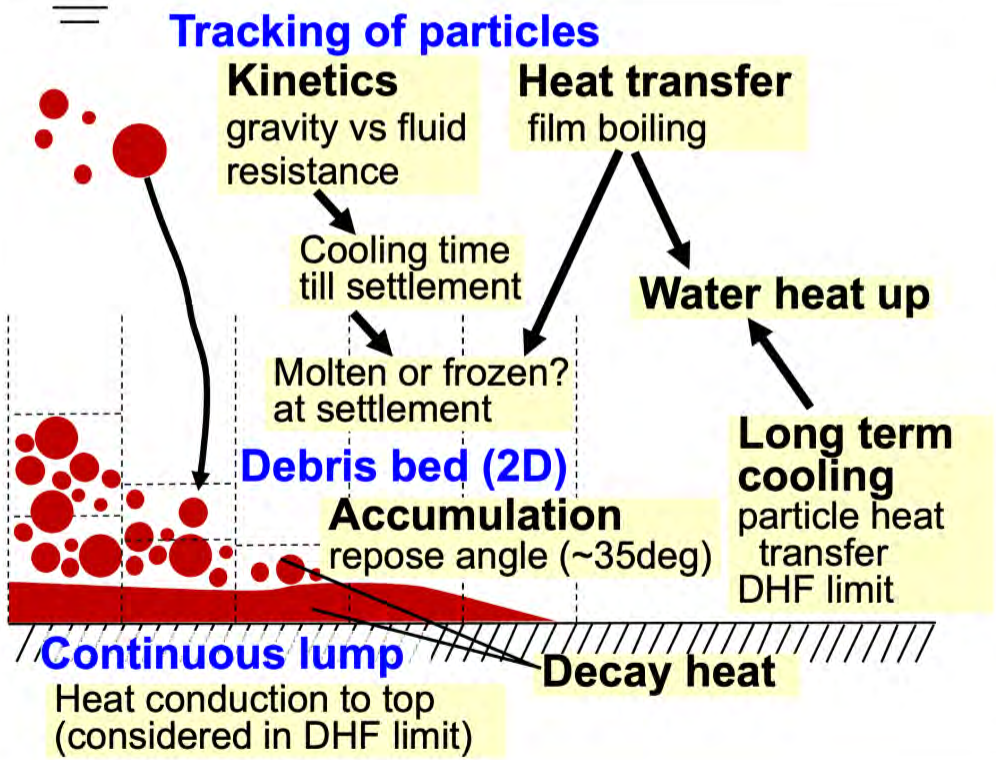

- Internal energy loss

$$\Delta Q = -m_p c_{pm}(T_{av}^n - T_{av}^{n-1})$$

- Heat transfer to coolant during a time step

$$\Delta Q = \Delta t A_p h_{eff}(T_{sf} - T_l) \approx \Delta t A_p h_{eff}(T_{av}^n - T_l)$$

$$\Delta Q = -m_p c_{pm}(T_{av}^n - T_{av}^{n-1}) = \Delta t A_p h_{eff}(T_{av}^n - T_l)$$

During sedimentation

drag-controlled motion | boiling-regime heat flux | implicit energy balance

Surface temperature correction

A thermal boundary layer model accounts for lower particle surface temperature caused by low oxide thermal conductivity.

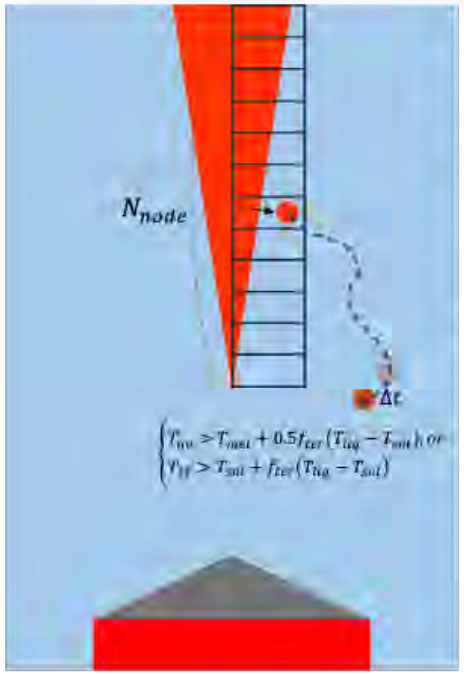

1. Calculate heat transfer from a particle

$$\Delta Q = m_p c_{pm}\Delta T\left(1 - \frac{m_p c_{pm}\Delta T}{\Delta t A_p C_{htc}|q''| + m_p c_{pm}\Delta T}\right) = \frac{x_1}{1+x_2}(T_{av}^{n-1} - T_l)$$

2. Update e_{int}

$$e = e - \frac{\Delta Q}{m_p} + q_{decay}\Delta t$$

3. Update T_m from e_{int}
4. Update particle properties

5. Update T_{sf} considered δ

$$\delta_0 = \sqrt{6\kappa\Delta t} \longrightarrow \delta\left\{1 - 0.75\frac{\delta}{R} + 0.2\left(\frac{\delta}{R}\right)^2\right\}d\delta = 3\kappa dt$$

$$\delta = \delta + d\delta$$

$$T_{sf} = T_{av} - \frac{q''\delta}{2\lambda}\left\{1 - \frac{\delta}{R}\left\{1 - 0.5\frac{\delta}{R} + 0.1\left(\frac{\delta}{R}\right)^2\right\}\right\}$$

Particle heat-flux regime map

Regime / quantity	Correlation used in COOLAP-II/HIPPO heritage	How it enters HIPPO
Forced convection	Sphere convection Nusselt correlation	Fallback or pre-boiling convective heat transfer around sedimenting particles
Nucleate boiling	Kutateladze correlation	Boiling heat flux below CHF
Critical heat flux	Zuber CHF	Upper point for boiling curve and transition to film/transition boiling
Film boiling	Liu-Theofanous film-boiling model plus radiation correction	Dominant high-temperature particle cooling mode
Minimum film boiling	Kondo et al. MFB temperature	Lower point for film-boiling stability
Transition boiling	Linear interpolation between CHF and MFB points	Provides continuous heat-flux evaluation across regime transition
Surface-temperature correction	Thermal boundary-layer model	κ is thermal diffusivity [m^2/s]; λ is thermal conductivity [W/m-K]
Numerical treatment	Implicit particle energy balance	q'' is evaluated through the regime-dependent boiling curve

Deposition pathway: debris bed or continuous melt lump

Arriving particle state

Average temperature and surface temperature are evaluated after sedimentation cooling.

Temperature-based decision

If the particle remains sufficiently molten, it merges into the continuous melt lump; otherwise, it is deposited into the debris bed.

↓

Solidified / cooled

Deposited into 2D debris bed nodes

Molten / reheated

Merged into continuous melt lump
or re-melted from debris bed

Threshold parameter

f_{tcr} shifts the merge/remelt threshold within the solidus-liquidus interval. COOLAP-II documents $f_{tcr} = 0$ as the default, with surface-temperature and average-temperature criteria treated as sensitivity options.

Debris bed formation and conical shape model

Vapor-induced lateral transport

Upward vapor flow promotes radial spreading of sedimented particles.

↓

Slope-angle control

If the calculated slope exceeds a critical value, upper debris nodes are laterally redistributed.

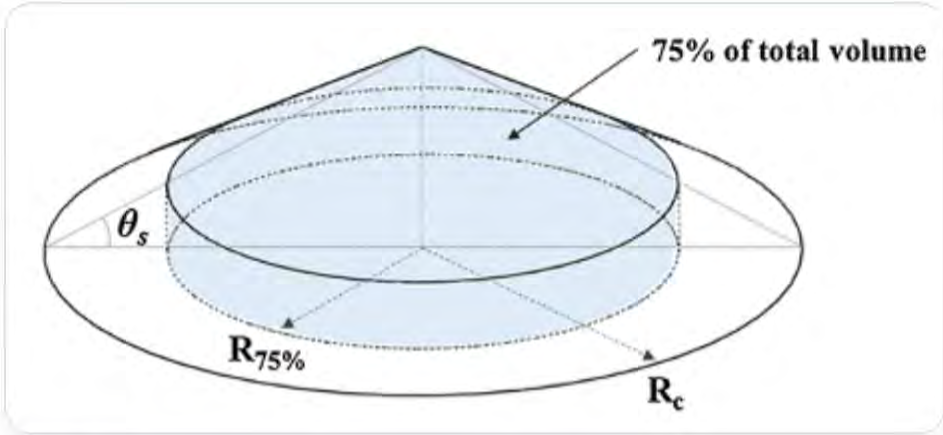

$$R_{75\%} = 0.414\left[\left(\frac{(\rho_l-\rho_g)^2}{\rho_p\rho_g\Delta h_{lg}}\left(\frac{q_d'''H_s^2\tau}{\dot{m}}\right)\left(\frac{\alpha u_b D_{pc}^4}{(1-\varepsilon)u_p^4}\right)\right)\right]^{\frac{1}{3}}$$

$$\theta_s = \operatorname{atan}\left(4.127\left(\frac{\rho_g\Delta h_{lg}}{(\rho_l-\rho_g)^2}\right)\left(\frac{\dot{m}^2}{q_d'''H_s^2}\right)\left(\frac{u_p^4}{\alpha u_b D_{pc}^4}\right)\right)$$

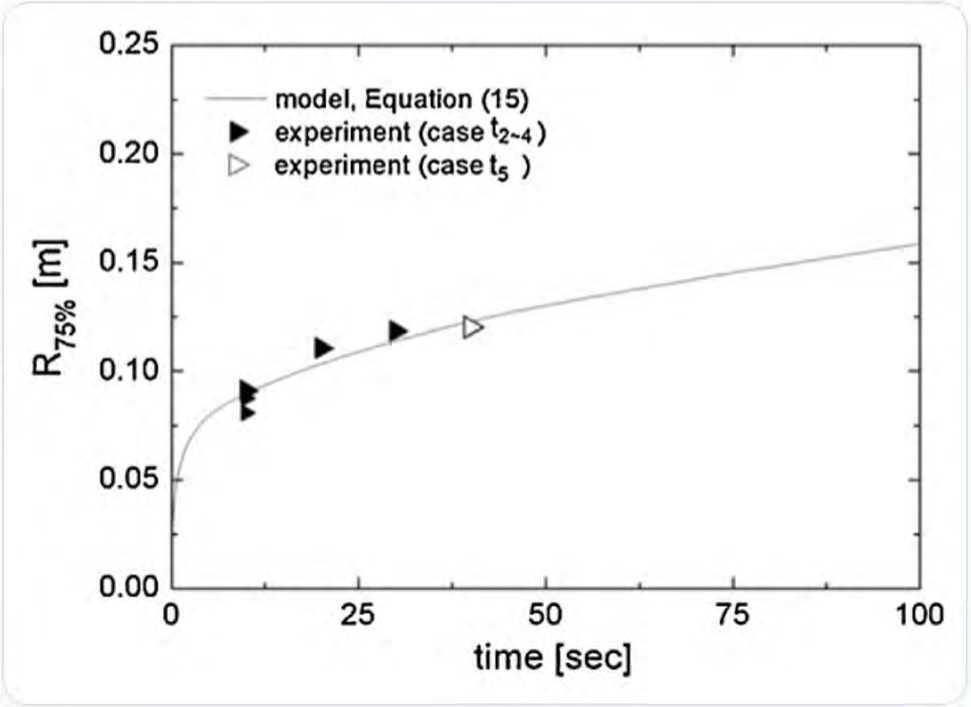

Debris bed and melt lump cooling

Top-flooded debris bed
Particle-scale heat transfer

limited by

DHF / CCFL limit
Vapor outflow vs liquid ingression

reduced by

Bottom heat input
Continuous melt lump beneath the bed

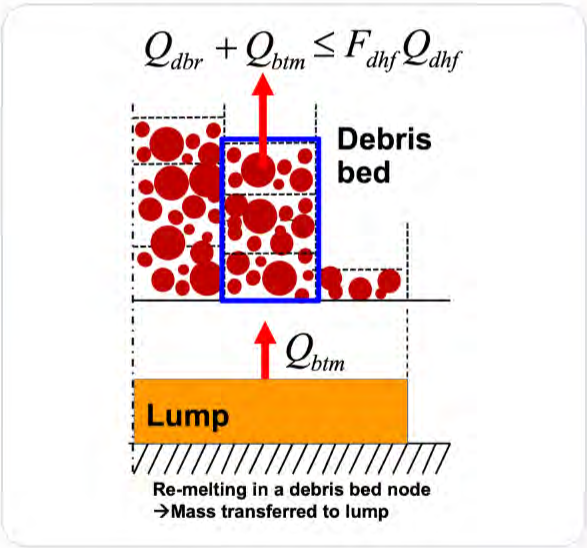

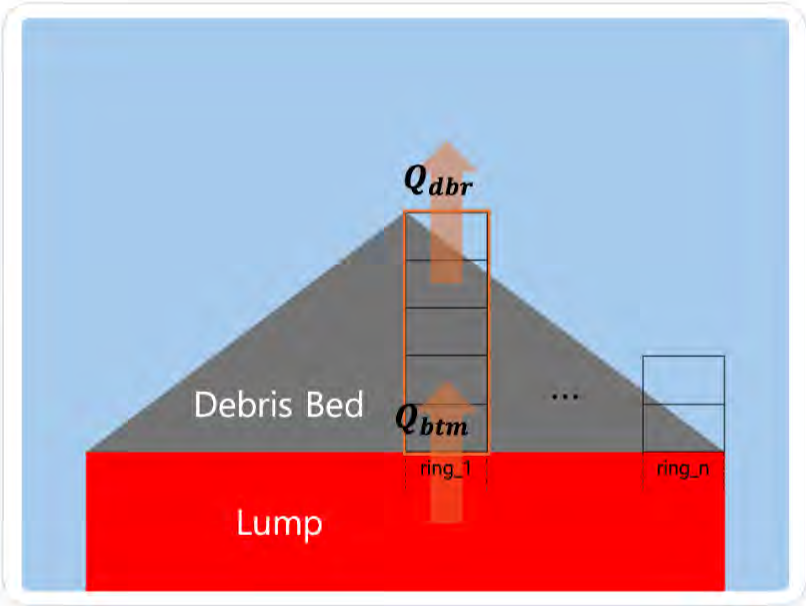

- Q_{dbr} in the ring

$$Q_{htr} = \sum_{Node_{vertical}} q'' A_p \qquad q'' = q''_{boil} + q''_{cond} + \frac{7}{8} q''_{rad}$$

$$Q_{lim} = F_{dhf} Q_{dhf} - Q_{btm} \qquad Q_{btm} = \min\left(A_b F_{htlmp} \lambda_m \frac{T_{lmp} - T_{sat}}{H_{lmp}/2}, F_{qbdhf} F_{dhf} Q_{dhf} \right)$$

  - $\therefore Q_{dbr} = \min(Q_{htr}, Q_{lim})$

- Update T_{av} of D.B by Energy Balance Equation

$$(-\dot{q} + \dot{q_{dec}})\Delta t = e(T_{av}^n) - e(T_{av}^{n-1}) \approx \frac{de}{dT}(T_{av}^n - T_{av}^{n-1})$$

$$\rightarrow T_{av}^n = \frac{(R_{eff} T_{sat} + \dot{q}_{dc})\Delta t + \frac{de}{dT} T_{av}^{n-1}}{\frac{de}{dT} + R_{eff}\Delta t} \qquad R_{eff} = \frac{q''_{dbr}}{T_{av}^{n-1} - T_{sat}}$$

- Update T_{sf} of D.B by δ

$$T_{av} - T_{sf} = \frac{q'' R}{5\lambda} = \frac{h_{eff}(T_{sf} - T_{sat})R}{5\lambda}$$

$$\rightarrow T_{sf}^n = \frac{T_{av}^n + C T_{sat}}{1 + C}, \qquad C = \frac{h_{eff} R}{5\lambda}$$

Debris-bed cooling closures made explicit

Closure item	Model treatment	Equation / setting	Default or note
Crowding attenuation	Debris-node heat transfer reuses the particle heat-transfer model with a crowding multiplier	$C_{htc,bed} \cdot q''_{particle}$	$C_{htc,bed} \approx 0.1$
DHF model	One-dimensional top-flooding dryout heat flux with Lipinski-type CCFL framework	Q_{dhf} from porous-media option	Rahman / Reed / Lee options
Actual heat removal	Node/ring heat removal is limited by local heat transfer or dryout capacity	$Q_{dbr} = \min(Q_{htr}, Q_{lim})$	Prevents overcooling above DHF
DHF limit	Bottom heat input reduces the allowable top-flooded debris-bed cooling capacity	$Q_{lim} = F_{dhf}Q_{dhf} - Q_{btm}$	$F_{dhf} = 1.0$ default
Bottom heat cap	Heat input from the continuous melt lump is bounded relative to DHF	$F_{qbdhf}F_{dhf}Q_{dhf}$	$F_{qbdhf} = 0.5$ default
Porosity	Debris-bed hydraulic resistance and DHF calculation use a porosity input	ε in porous-bed correlations	Reference cases commonly use 0.5

Source-term coupling with containment model

1. Containment state
Pressure, coolant temperature, liquid/vapor properties

↓

2. HIPPO CCI
Particles, debris bed, melt lump

↓

3. Time buffer
Residence-time effect during particle tracking

↓

4. Containment update
Heat and mass source terms

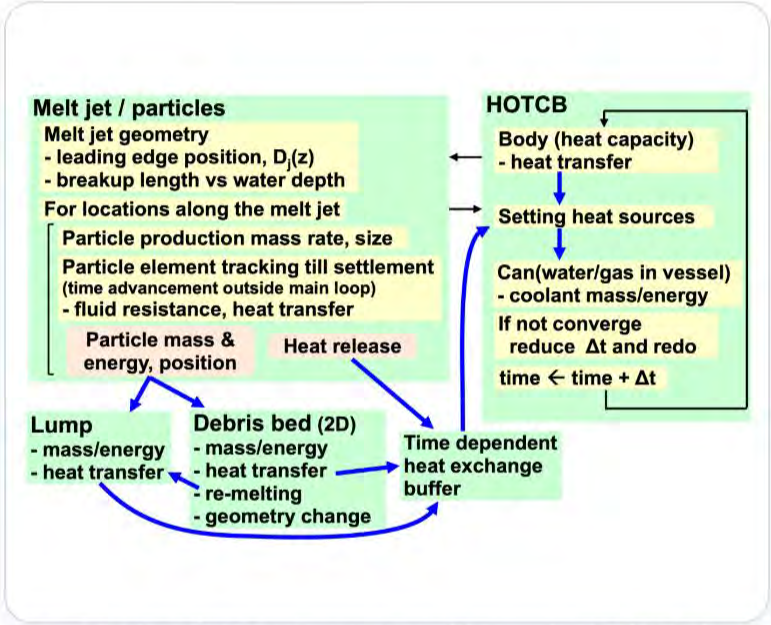

Computation flow of HIPPO code: a coupling of the present melt/debris bed model and HOTCB

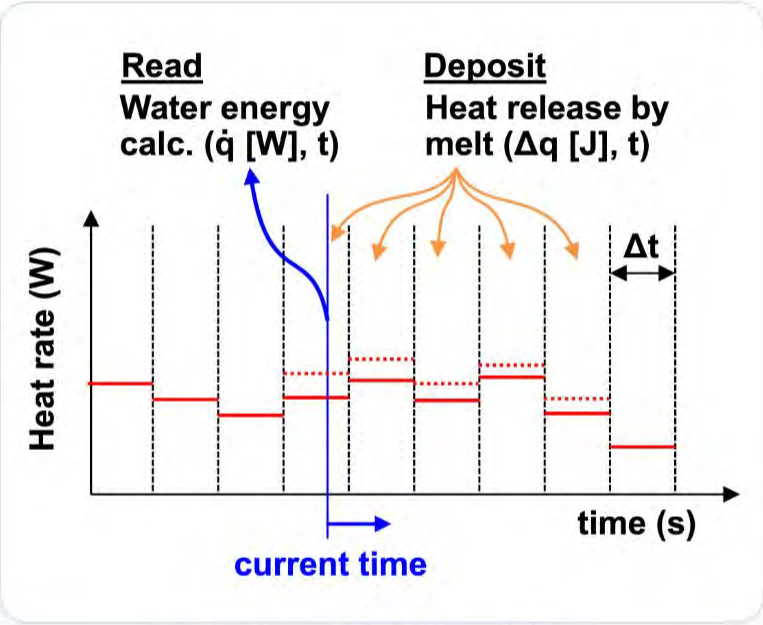

Time dependent heat exchange buffer

Particle
transient sedimentation heat release

Debris bed
DHF-limited heat removal

Lump
bottom heat input

Coupled containment accounting check

Accounting item	Balance or tracked state	Expected behavior	Use in this talk
Mass accounting	HOTCB can track vapor, saturated water, subcooled water, and non-condensable gas masses	Mass changes follow inflow/outflow, evaporation, and condensation	Shows how CCI-generated vapor enters the containment-side balance
Energy accounting	Particle, debris-bed, and lump source terms enter the containment energy balance	Σ heat removed from corium matches supplied containment heat source over the same window	Connects local CCI cooling to containment pressure/temperature response
Buffer accounting	Particle heat-release histories are accumulated in time bins	Residence-time effects are preserved instead of collapsed into one instant	Explains why particle sedimentation heat release is time-dependent
Corium inventory	Jet, particles, debris bed, and lump are treated as redistribution reservoirs	Total corium mass is conserved across deposition and remelting	Supports the later MAMBA-HIPPO and HIPPO-SCORPION coupling discussion

V&V scope for this overview talk

Purpose today
Introduce the overall SAFARI code direction and HIPPO's role as the CCI/FCI entry module.

V&V today
Show only compact status anchors: DAVINCI/DEFOR for HIPPO and FARO L33 for the HIPPO–SCORPION chain.

V&V later
Publish detailed model-by-model validation as a continuing conference and journal paper series.

How to present it	What is included in this talk	What is intentionally deferred
V&V depth	Representative evidence and current status	Full uncertainty bands, complete test matrices, and case-by-case sensitivity studies
Validation claim	Dominant trends and integral quantities are reproduced for selected anchors	Regulatory-grade correlation validation for every model closure
Presentation focus	Why HIPPO matters inside SAFARI and how the modules exchange information	Detailed derivation and justification of every empirical correlation

Model-by-model V&V publication roadmap

Publication thread	Modeling target	Validation anchor	Primary metrics
Jet breakup	Breakup length and jet penetration	DEFOR / FARO-type tests	Breakup length, penetration time, sensitivity to inlet velocity
Fragmentation / PSD	Particle-size distribution and sampling model	DEFOR, TROI/KROTOS follow-up	D_{10}, D_{50}, D_{90}, fit error, dominant particle range
Debris morphology	Conical bed formation and spreading	DAVINCI and debris-bed experiments	Top height, $R_{75\%}$, $H/R_{75\%}$, bed volume uncertainty
Coolability	DHF limitation, debris/lump cooling, remelting	Dedicated cooling benchmarks	Heat removal, dryout margin, remelting mass flux
FCI–SE chain	HIPPO–SCORPION premixing-to-load interface	FARO L33, later KROTOS/TROI	Peak pressure, impulse, trigger-time sensitivity, C_{fr} range
FCI–MCCI chain	MAMBA–HIPPO pre-flooded cavity analysis	PWR-scale cavity scenarios	Corium geometry, ablation depth, gas generation, containment source terms

MAMBA–HIPPO: FCI-informed MCCI analysis

Why the coupling matters

- Pre-flooded cavity cases require FCI-informed MCCI initial conditions.
- HIPPO estimates debris-bed and lower-corium geometry after jet breakup and sedimentation.
- MAMBA can start from cavity-dependent corium distribution, not a uniform floor-spreading assumption.

Current staged workflow

- External in-vessel discharge input defines the melt release into the cavity.
- HIPPO runs the early FCI period until debris-bed stabilization, assumed about 10 min in the report example.
- MAMBA then performs long-term MCCI calculation, e.g., 72 h scale.

Information path	Transferred information	Physical meaning
HIPPO → MAMBA	Debris/lower-corium shape, corium temperature T_c, mass m_c, radius r_c	Initial MCCI state after FCI, including non-uniform cavity loading
HIPPO containment → MAMBA	Containment pressure P_{con} and cavity coolant temperature T_{cool}	Boundary conditions controlling heat transfer and cooling
MAMBA → HIPPO containment	Concrete-ablation gases and source terms, including H_2O, CO_2, H_2, CO	Noncondensable/steam source terms affecting containment pressure

HIPPO–SCORPION: premixing to explosion load

Coupling interface

HIPPO

premixing time series

particles, void, coolant state

CSV

SCORPION

steam explosion

pressure / impulse

A standardized CSV interface preserves the premixing time axis and reduces manual input conversion.

Direct HIPPO variables

Fuel/coolant temperature, pool depth, upper slug area, jet diameter, fuel/coolant mass, slug mass, interacting fuel mass, average mixing diameter, void fraction, and mixing time.

FARO L33 is used as a coupled-analysis anchor because both premixing and explosion response are measured at large scale.

Validation anchor

HIPPO premixing output is used directly as SCORPION input for FARO L33 coupled analysis.

Key sensitivity

Fragmentation constant C_{fr} controls fine fragmentation, steam generation, peak pressure, and timing.

Numerical robustness

SCORPION_BETA 2.0 uses a ResNet-supported property path near the critical region for stable pressure response.

4. V&V SCOPE AND SAFARI COUPLING

Why the SAFARI ecosystem is different

Conventional integrated-code expectation

- One code package gives a broad accident sequence solution.
- Phenomenon-specific assumptions may be hidden inside a large integrated workflow.
- Changing one phenomenon model can be difficult to validate independently.

SAFARI module ecosystem

- HIPPO, MAMBA, SCORPION, and SAVANNAH retain phenomenon-focused physics roles.
- Interfaces preserve physically meaningful variables and time histories.
- Each module and each coupling path can be validated and published transparently.

Role clarity

HIPPO handles early CCI/FCI; MAMBA handles long-term MCCI; SCORPION handles steam-explosion load.

Traceable coupling

Data exchanged through explicit variables such as debris geometry, P_{con}, T_{cool}, void fraction, and premixing mass.

Regulatory path

Focused V&V papers can build evidence module by module before full SAFARI integration.

Answer to the expected audience question

HIPPO is the early ex-vessel state generator that lets SAFARI connect CCI to MCCI, steam explosion, and containment thermal hydraulics in a traceable modular ecosystem.

Conclusions and future work

Message / work item	Content	Purpose for the presentation
SAFARI introduced	Korean regulatory-oriented framework for integrated ex-vessel severe accident analysis	Positions the talk beyond a single HIPPO module result
HIPPO positioned	CCI/FCI entry module producing debris/lump state, premixing state, and heat/mass source terms	Answers what HIPPO does inside SAFARI
V&V scoped	Representative anchors are shown briefly; detailed correlation-level V&V is deferred to a paper series	Keeps this talk aligned with the code-overview objective
MAMBA link explained	HIPPO-derived debris/lower-corium geometry and T_c, m_c, r_c initialize FCI-informed MCCI	Shows why pre-flooded cavity analysis needs the HIPPO–MAMBA path
SCORPION link explained	HIPPO premixing time series is passed by CSV to steam-explosion load calculation	Shows how SAFARI connects premixing to pressure/impulse evaluation
Next integration	Strengthen MAMBA–HIPPO, HIPPO–SCORPION, and SAVANNAH/M1 containment T-H coupling	Builds the modular evidence base for full SAFARI applications

Q&A

Thank you for your attention.

Questions and comments are welcome.

BACKUP

COOLAP-II model basis and review history

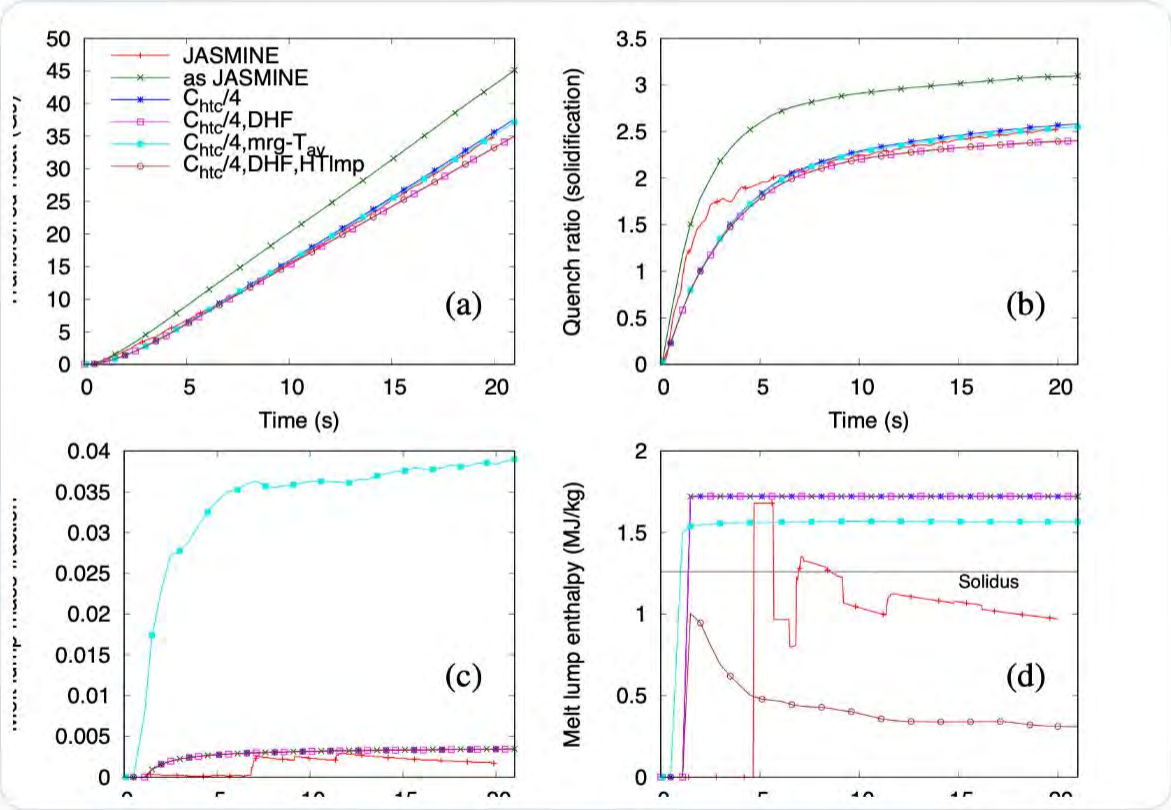

Purpose of COOLAP-II

Simplified assessment of ex-vessel melt jet breakup, sedimentation, heat transfer, debris bed formation, and cooling.

How to use in this talk

Heritage review only. COOLAP-II/JASMINE/FARO comparisons should not be presented as HIPPO validation results.

BACKUP

HOTCB reference and assumptions

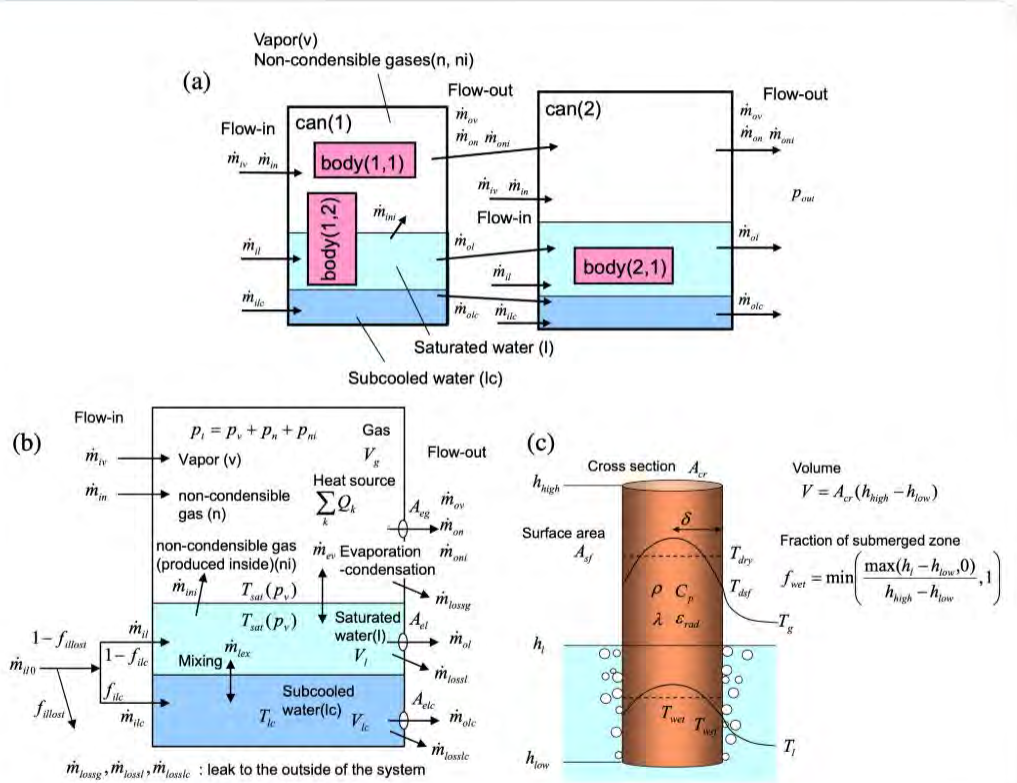

HOTCB

Hot Cans and Bodies: a JAEA code for simplified mass and energy balance of water/steam/non-condensable gas systems.

Key assumptions

- Lumped control-volume representation
- Vapor–liquid thermal equilibrium for saturated phases
- Heat-capacity bodies coupled to fluid regions

BACKUP

Selected model correlations and parameters

Model component	Representative treatment	Constants / settings to state in Q&A
Jet breakup length	Taylor / Saito / Jung-type correlations	C_{br} default 1.0 in COOLAP-II; Jung term uses vapor-generation intensity from heat-flux ratio
Particle size distribution	Rosin-Rammler; truncated distribution for debris bed particles	n = 1.5; MMD from Bond-number/subcooling correlation; minimum diameter from fluidization concept
Particle heat transfer	Convection, Kutateladze nucleate boiling, Zuber CHF, Liu-Theofanous film boiling, Kondo MFB, transition interpolation, radiation	C_{htc} is a model multiplier; COOLAP-II sensitivity used particle C_{htc} = 0.5 after comparison with JASMINE
Debris bed cooling	Local particle heat transfer limited by DHF / CCFL	$C_{htc,bed} \approx 0.1$ for crowding; porosity commonly 0.5 in reference cases; F_{dhf} default 1.0
Melt lump interaction	Bottom heat input to debris bed reduces Q_{lim}	$Q_{lim} = F_{dhf}Q_{dhf} - Q_{btm}$; F_{qbdhf} default 0.5
Deposit / remelt criterion	Surface-temperature or average-temperature threshold	f_{tcr} shifts threshold; default 0; criterion should be treated as sensitivity parameter

BACKUP

Nomenclature clarifications for reviewer questions

Symbol	Definition / unit	How computed or selected in HIPPO context
κ	Thermal diffusivity [m^2/s]	Used for transient thermal boundary-layer growth in particle surface-temperature correction
λ	Thermal conductivity [W/m-K]	Used in average-to-surface temperature drop; λ_m for melt/lump conduction
q''	Surface heat flux [W/m^2]	Selected from regime-dependent boiling curve and radiation correction
q'''_d	Volumetric decay heat rate [W/m^3]	Input/accident-condition parameter in DAVINCI conical-bed model
ρ_g, ρ_l, ρ_p	Vapor, liquid, particle densities [kg/m^3]	Fluid properties from containment/coolant state; particle density from material input
h_{lg}	Latent heat of vaporization [J/kg]	Water/steam property used in vapor-generation and energy-flux terms
θ_s, $R_{75\%}$	Side slope angle [deg], radius containing 75% of bed volume [m]	DAVINCI morphology metrics for conical bed spreading
f_{tcr}	Threshold modifier [-]	User/sensitivity parameter; COOLAP-II default 0

BACKUP

Current limitations and uncertainty considerations

Current limitations

- Limited validation database and mostly M-12 HIPPO comparison for DEFOR
- Lumped/discretized treatment of local morphology and non-axisymmetric cavities
- Ergodic particle sampling and representative debris-node diameter
- Vapor/saturated-liquid equilibrium in simplified containment model

Breakdown conditions to state

- Highly transient venting or pressure relief with strong spatial gradients
- Strong non-condensable stratification affecting condensation and breakup enhancement
- Subcooling/condensation regimes outside Jung-type correlation database
- Long-term remelting where bed permeability and morphology evolve beyond current closure

BACKUP

Integrated SAFARI coupling roadmap

HIPPO
CCI / FCI
premixing, debris, lump

→

MAMBA
MCCI
concrete erosion

+

SCORPION
Steam explosion
pressure response

⇄

SAVANNAH
Containment T-H
future integration

Current pre-integration role

HIPPO provides a simplified containment/coolant part to test M2-module coupling before full SAFARI integration.

Target role

SAVANNAH can provide detailed containment thermal-hydraulic states for system-level SAFARI applications.

BACKUP

Source separation used in this presentation

Source	Used for	Not used for
ERMSAR2026 HIPPO paper	Current HIPPO model and DAVINCI/DEFOR validation	Full SAFARI module portfolio details
Annual project report	SAFARI module ecosystem, MAMBA–HIPPO and HIPPO–SCORPION coupling context	Replacing HIPPO paper validation results
COOLAP-II manual	Development basis and HOTCB-coupled heritage model	Presenting heritage cases as new HIPPO validation
Jung thesis / DAVINCI / DEFOR papers	Physical background and experimental context	Overstating validation scope

References

- ERMSAR2026 full paper: *Development of the SAFARI Code for Comprehensive Severe Accident Analysis in Nuclear Reactors: Corium–Coolant Interaction Analysis Module*.
- Moriyama, K., Lee, M., Park, J.H., Park, H.S. *COOLAP-II: A simplified model for ex-vessel melt jet breakup, debris bed formation and cooling*, 2018.
- Sibamoto, Y. et al. *A simple mass and heat balance model for estimating plant state in severe accident management*, Journal of Nuclear Science and Technology, 2012.
- Kim et al. 2016; Xiang et al. 2023; Jung et al. 2019, 2020 — experimental and model references cited in the ERMSAR2026 paper.

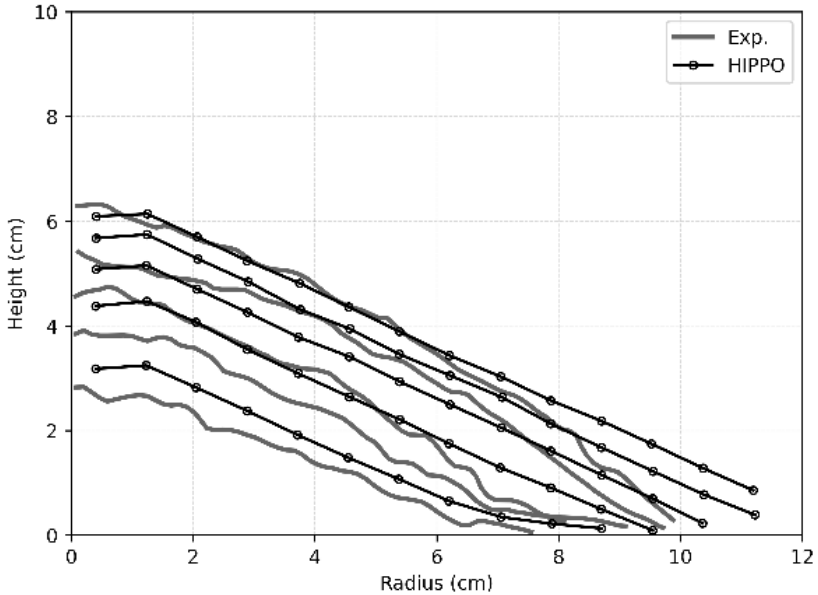
Exp.
HIPPO
Height (cm)
Radius (cm)

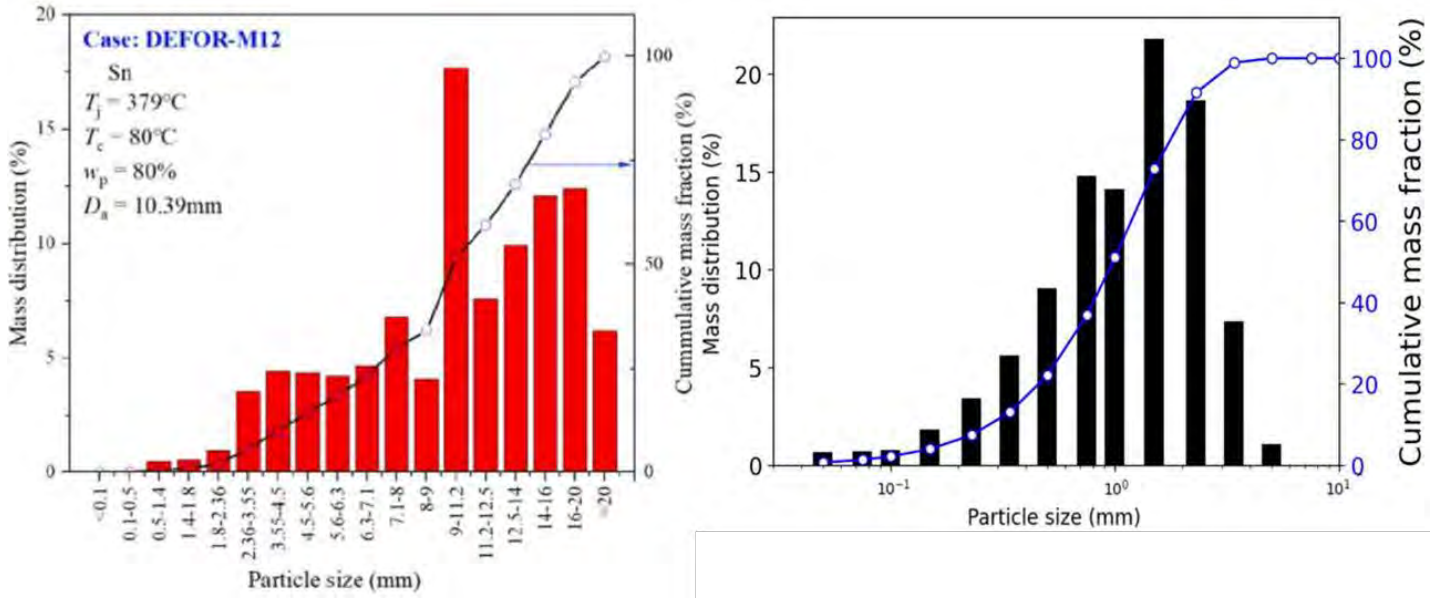
Case: DEFOR-M12
Sn
T_j = 379°C
T_c = 80°C
w_p = 80%
D_a = 10.39mm
Mass distribution (%)
Cummulative mass fraction (%)
Particle size (mm)
Mass distribution (%)
Cumulative mass fraction (%)
Particle size (mm)

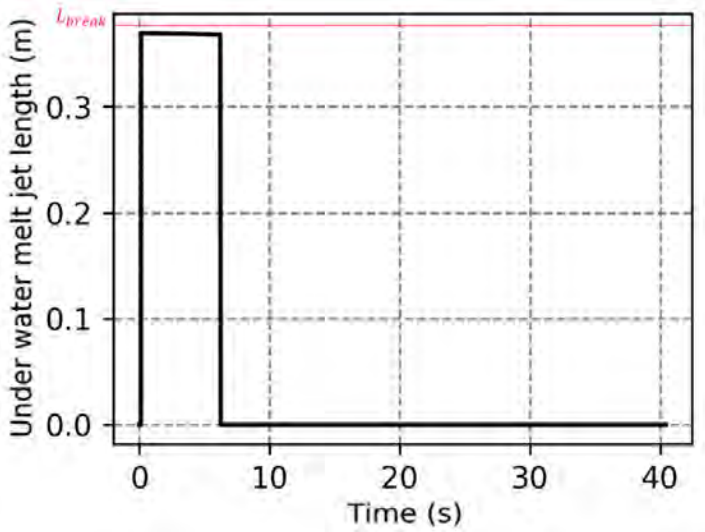
L_{break}
Under water melt jet length (m)
Time (s)

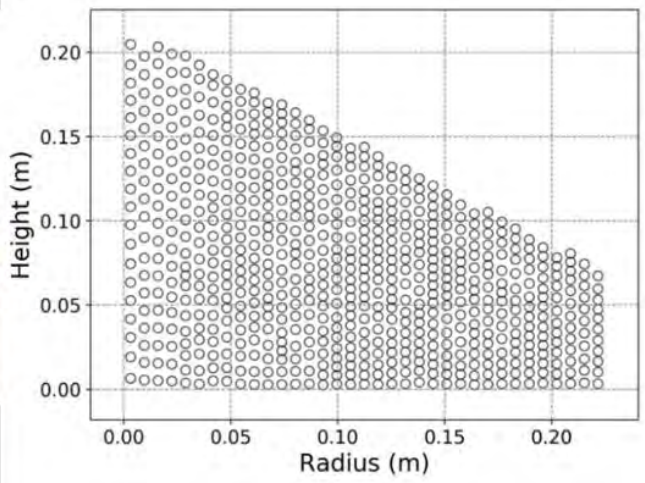
Height (m)
Radius (m)

EVALUATION OF CONCRETE ABLATION BY A HOT HEAT-GENERATING SOLID

Villarreal Larrauri A*, Tourniaire B
Electricité de France (EDF)
EDF – DirIN – Direction Technique, 19 Rue Bourdeix,69007 Lyon
alejandro.villarreal-larrauri@edf.fr; bruno.tourniaire@edf.fr

ABSTRACT

Accurate evaluation of concrete ablation during a Molten Corium-Concrete Interaction (MCCI) is a key element of Severe Accident (SA) management in scenarios in which vessel failure cannot be avoided. In cases for which water can be injected on top of the corium, it is considered that corium can be stabilized due to the formation of a debris bed by corium ejection, a fractured crust by water ingression, and a dense crust. Nevertheless, in that configuration, once the corium is completely solidified, a part of the decay heat can still be transferred to the concrete by heat conduction through the crust in contact with the concrete. If that part of the decay heat cannot be evacuated by conduction in the concrete, then MCCI goes on until heat transfer by conduction in the concrete balances the decay heat transferred to the concrete. Thus, the evaluation of the final concrete erosion by MCCI should take into account the ablation that could result from the interaction between a solidified corium with decay heat and concrete.
To enable evaluation of post corium-solidification concrete ablation following an MCCI, a one-dimensional transient heat conduction model has been developed. Validation against experimental results using a heated metallic solid ingot in contact with concrete demonstrates that the model can successfully reproduce the kinetics of concrete ablation driven by a hot, internally heat-generating solid. The purpose of this paper is to present the model that has been developed to calculate the interaction between a solidified corium and concrete and the validation that has been performed.

KEYWORDS
Molten Corium-Concrete Interaction, heat conduction, concrete ablation

1. INTRODUCTION

Accurate evaluation of concrete ablation during a Molten Corium-Concrete Interaction (MCCI) is a key element of Severe Accident (SA) management in scenario in which vessel failure cannot be avoided [1]. In cases for which water can be injected on top of the corium, it is considered that corium may be stabilized due to the formation of a debris bed by corium ejection, a fractured crust by water ingression in contact with water, and a dense crust in contact with concrete [2].
The stabilization of corium during a severe accident depends on the kinetics of the MCCI. The progression of MCCI, in turn, is conditioned by the thermophysical properties of the corium, the accidental scenario, the chemical composition of the concrete basemat, amongst others. The phenomena governing the phases of MCCI (dry and flooded) are highly non-linear and can lead to a vastly large array of stabilization conditions. If the concrete releases a large percentage of decomposition gases, melt-ejection will be predominant leading to a stabilized corium in the form of, mainly, a large debris bed. Conversely, in case of concrete with a low

* Corresponding author

gas content, corium stabilization is controlled by crust formation and fracturing, i.e. water-ingression. In some cases, the analysis of the final configuration show that heat flux towards the concrete and the erosion rate remains non-zero [1]. Since the concrete has a relatively low thermal conductivity and this heat flux is not negligible in some conditions (i.e., it cannot be entirely transferred by conduction within the concrete), a one-dimensional model enabling the calculation of the erosion of the concrete basemat by a solidified heat-generating corium is here established.

2. POST-SOLIDIFICATION ONE-DIMENSIONAL HEAT-CONDUCION MODEL FOR CORIUM-INDUCED CONCRETE ABLATION

The model presented in this paper was proposed by Rhodes and Quintiere [3] to calculate the mass loss rate of a solid during combustion. As explained in [4], the mass loss rate measured in the experiments in [3] can be related to the erosion velocity of a solid. For this reason, the model proposed in [3] has been adapted to calculate long-term phase of molten-core concrete interaction when transient conduction heat transfer could lead to concrete ablation despite complete solidification of corium in [4]. This model has recently been modified to improve its behavior during the transition between the solid heating phase (i.e. without ablation) and the ablation phase. A similar model is also presented as an option in CORQUENCH [5] to calculate ablation during MCCI .

2.2. Transient Conduction Heat Transfer Modeling in Concrete for the Simulation of Long-Term Phase of Molten Core-Concrete Interaction

2.1.1. Governing Equations and Boundary Conditions

Fig. 1 here below shows the post corium-solidification configuration which serves as boundary conditions for the model presented hereafter. Inside the concrete basemat, the one-dimensional transient heat conduction equation can be written as:

$$\frac{\partial T}{\partial t} = \alpha \frac{\partial^2 T}{\partial z^2} \tag{1}$$

with the following boundary conditions:

$$\begin{aligned} \mathrm{T}(z) = \begin{cases} T_{fus}, & z = z_{cr} = e_{sup} + e_{inf} \\ T_0 \ , & z = z_{cr} + \delta \end{cases} \\ \frac{\partial T}{\partial z} = 0, \qquad z = z_{cr} + \delta \\ \frac{dz}{dt} = v_{ablation} = \frac{m''}{\rho_{con}} \\ m'' \, \Delta \mathrm{H} = \mathrm{q}_{\mathrm{net}} + \lambda_{con} \frac{\partial T}{\partial z}, \quad z = z_{cr} \end{aligned} \tag{2}$$

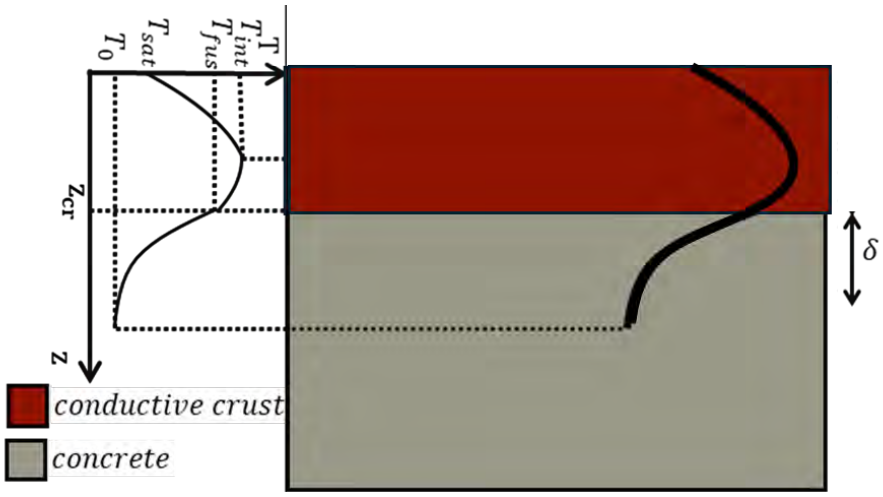

Figure 1. Final corium configuration upon its solidification following MCCI.

Contrary to the quadratic temperature profile assumed in [2] inside the concrete, the present approach employs a fourth-order polynomial representation of the temperature field inside the concrete which can be written as:

$$\frac{T-T_0}{T_{fus}-T_0} = \left(1-\frac{z-z_{cr}}{\delta}\right)^4 \tag{3}$$

From (3):

$$\left.\frac{\partial T}{\partial z}\right|_{z=z_{cr}} = -\frac{4}{\delta}\left(T_{fus}-T_0\right) \tag{4}$$

hence (2) becomes

$$m'' \, \Delta H = q_{net} - \frac{4\lambda_{con}}{\delta}\left(T_{fus}-T_0\right) \tag{5}$$

with q_{net} the heat flux between the corium and the concrete. Eq. (5) expresses the evolution of the surface mass flow rate of concrete degradation induced by the heat flux emanating from the solidified corium at the interface limited by heat conduction through the concrete.

The partial derivative of the temperature of the moving boundary with respect to time $\frac{\partial T}{\partial t}$ can be expressed as:

$$\frac{\partial T}{\partial t} = \frac{\partial T}{\partial z_{cr}} \cdot \frac{dz_{cr}}{d_t} + \frac{\partial T}{\partial \delta} \cdot \frac{d\delta}{d_t} \tag{6}$$

hence (1) becomes:

$$\frac{\partial T}{\partial z_{cr}} \cdot \frac{dz_{cr}}{d_t} + \frac{\partial T}{\partial \delta} \cdot \frac{d\delta}{d_t} = \alpha \frac{\partial^2 T}{\partial z^2} \tag{7}$$

To solve the system of equations, the thermal boundary layer needs to be evaluated. This can be done by solving for $\frac{d\delta}{d_t}$. To achieve this eq. (7) can be integrated between z_{cr} and $z_{cr}+\delta$, as:

$$\underbrace{\int_{z_{cr}}^{z_{cr}+\delta}\left(\frac{\partial T}{\partial z_{cr}}\cdot\frac{dz_{cr}}{d_t}\right)d_z}_{A}+\underbrace{\int_{z_{cr}}^{z_{cr}+\delta}\left(\frac{\partial T}{\partial \delta}\cdot\frac{d\delta}{d_t}\right)d_z}_{B}=\underbrace{\int_{z_{cr}}^{z_{cr}+\delta}\left(\alpha\frac{\partial^2 T}{\partial z^2}\right)d_z}_{C} \tag{7a}$$

where it can be found that terms A, B, and C are:

$$A\rightarrow\int_{z_{cr}}^{z_{cr}+\delta}\left(\frac{\partial T}{\partial z_{cr}}\cdot\frac{dz_{cr}}{d_t}\right)d_z=v_{ablation}(T_{fus}-T_0) \tag{8}$$

$$B\rightarrow\int_{z_{cr}}^{z_{cr}+\delta}\left(\frac{\partial T}{\partial \delta}\cdot\frac{d\delta}{d_t}\right)d_z=\frac{d\delta}{dt}\left[\frac{1}{5}\left(T_{fus}-T_0\right)\right] \tag{9}$$

$$C\rightarrow\int_{z_{cr}}^{z_{cr}+\delta}\left(\alpha\frac{\partial^2 T}{\partial z^2}\right)d_z=\frac{4\alpha}{\delta}\left(T_{fus}-T_0\right) \tag{10}$$

Substituting (8), (9), and (10) into (7a) gives:

$$\frac{d\delta}{d_t}=\frac{20\alpha}{\delta}-\frac{5m''}{\rho} \tag{11}$$

The temperature difference that drives the heat conduction from the corium's crust to the concrete $\left(T_p(t)-T_{fus}\right)$ can be calculated by solving the heat transfer equation, with internal heat generation, within the crust:

$$\rho_{cr}c_{p_{cr}}\frac{\partial T}{\partial t}=\lambda_{cr}\frac{\partial^2 T}{\partial z^2}+q_v \tag{12}$$

Eq. (5) depends not only on the thermal boundary layers' thickness, but also on the heat flux transferred to the concrete by the corium's crust. This last can be calculated as:

$$q_{net}(t)=\frac{\lambda_{cr}}{\Delta z^2}\cdot\left(T_p(t)-T_{fus}\right) \tag{13}$$

To calculate $T_p(t)$ in eq. (13), eq. (12) can be discretized (as shown in Fig. 2) and solved explicitly as follows:

$$T_i^{n+1}=T_i^n+\frac{\lambda_{cr}\,\Delta t}{\rho_{cr}c_{p_{cr}}\Delta z^2}\left(T_{i+1}^n-2T_i^n+T_{i-1}^n\right)+\frac{q_v\,\Delta t}{\rho_{cr}c_{p_{cr}}} \tag{14a}$$

$$T_1^{n+1}=T_i^n+\frac{\lambda_{cr}\,\Delta t}{\rho_{cr}c_{p_{cr}}\Delta z^2}\left(T_2^n-3T_i^n+2T_{sat}\right)+\frac{q_v\,\Delta t}{\rho_{cr}c_{p_{cr}}} \tag{14b}$$

$$T_p^{n+1}=T_p^n+\frac{\lambda_{cr}\,\Delta t}{\rho_{cr}c_{p_{cr}}\Delta z^2}\left(2T_{fus}-3T_p^n+T_{p-1}\right)+\frac{q_v\,\Delta t}{\rho_{cr}c_{p_{cr}}} \tag{14c}$$

where eq. (14b) and eq. (14c) are slightly adapted to take into account that the boundary condition temperatures (T_{sat} in the case of the first mesh following the fractured crust, and T_{fus} in the case of the mesh just next to the corium-concrete interface) are located at a distance $\frac{\Delta z}{2}$ from the center of the mesh. Eq. (14a) then gives the temperature at the center of all other meshes. This scheme is nevertheless limited by the choice of time step Δt which must satisfy the following condition for numerical stability:

$$\lambda_{cr}\cdot\Delta t<\frac{1}{2}\rho_{cr}c_{p_{cr}}\Delta z^2 \tag{15}$$

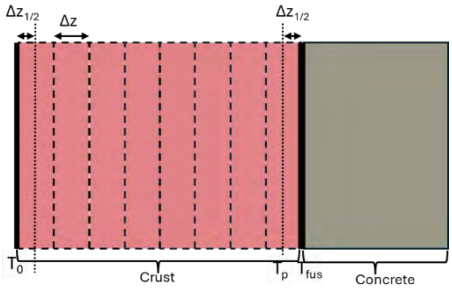

Figure 2. Spatial discretization of the corium's crust.

2.2. Validation with Hot Solid Block - Concrete Interaction Experiment

In the context of the Hot Solid program [6] two tests were performed to assess, amongst others, the concrete ablation induced by a hot heat-generating solid block. In this work, only HSS-1 will be analyzed. The experimental set-up, show in Fig. 3, included thermocouples in the concrete block, as well as X-ray imaging to follow the concrete erosion rates, and a coil to inductively heat the solid block. The experimental measurement uncertainties are not discussed in the paper (except the thermocouple location uncertainty of 2 mm in both directions). The tests occurred in two phases: a pre-heating phase that aimed to heat the solid block up to a target temperature that allows concrete ablation but does not result in solid block melting, followed by a heating phase that aimed to keep the solid block at the target temperature and continue the concrete ablation. The test parameters are summarized in Table I.

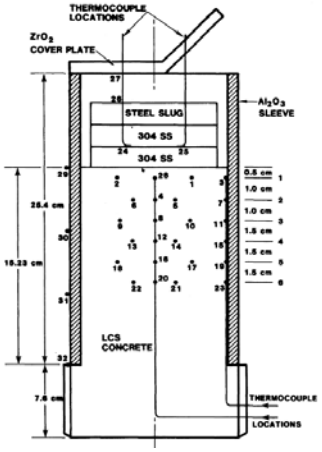

Figure 3. HSS-1 geometry, from [6].

Table I. HSS-1 input parameters, from [6].

Test	Block's composition	Dimensions [cm]	Block's Mass [kg]	Initial Temperature [K]	Avg. Power [kW] (q_{in})	Avg. Losses [W/cm²]	Concrete type
HSS-1	Stainless Steel 304	14 x 8	9	491	3.2	4.9	Limestone Common Sand (LCS)

As can be seen in Table I, the thermal power loss is given as an average without explicitly stating how it was evaluated. In this work, the heat losses will be considered to occur only through the surfaces not in contact with the concrete. Furthermore, as can be seen in Fig. 4, the inductive heating does not appear to affect the temperature of the steel block before the 25-minute mark. Here the power losses are calculated only during the heating period, where they increase linearly interval between the 25th minute and the ablation start (~85th minute), and then kept constant until the end of the heating period, around the 300th minute (see Fig. 5).

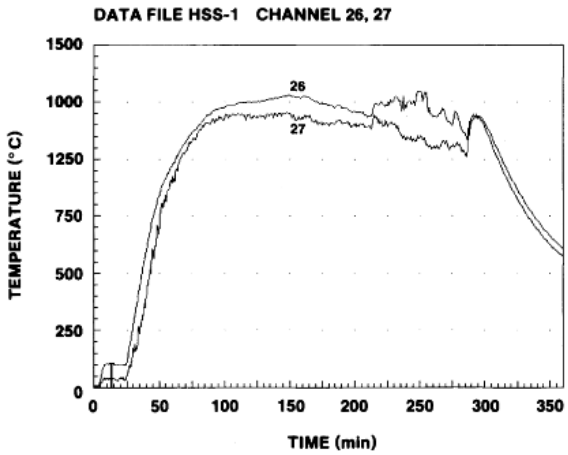

Figure 4. Steel's surface temperature (channel 26), from [6].

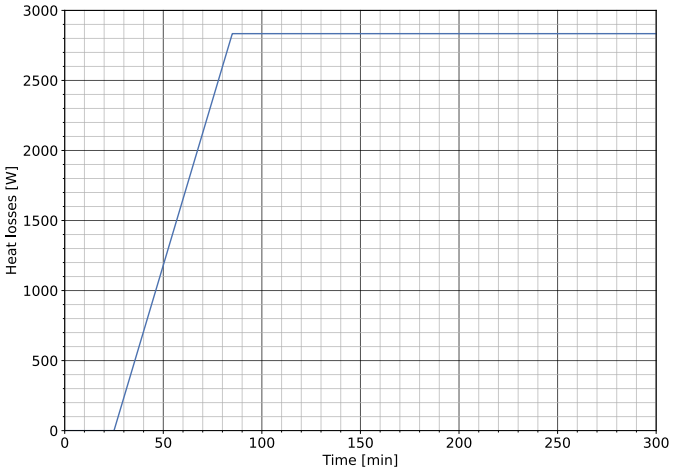

Figure 5. Estimated heat losses, where the total heat loss by cm² approximates the one reported Table I.

To properly evaluate the thickness of the thermal boundary layer when the ablation starts, the experimental preheating phase is simulated using a similar discretization scheme as the one presented above (see Fig. 2) where the corium crust represents the steel ingot (initialized at a temperature of 491K at 25 minutes) and the concrete is also discretized (with an initial temperature of 283 K). Eq. (14) would stay the same, but eq. (13) becomes for the solid block and the concrete domain respectively:

$$\rho_{cr} c_{p_{cr}} \frac{\partial T}{\partial t} = \lambda_{cr} \frac{\partial^2 T}{\partial z^2} + q_v - q_{th} \quad (16a)$$

$$\rho_{con} c_{p_{con}} \frac{\partial T}{\partial t} = \lambda_{con} \frac{\partial^2 T}{\partial z^2} \quad (16b)$$

where q_{th} is the estimated heat loss presented in Fig. 5. The results of the heat conduction calculations for the pre-heating phase are here shown in Fig. 6 where the concrete temperature at different depths is shown as a function of time and is compared to the experimental measures. Furthermore, the temperature of the whole domain (solid steel ingot and concrete) is shown in Fig. 7 at the moment when the temperature at the steel-concrete interface is estimated to reach the concrete ablation temperature. Finally, the steel ingot surface temperature is plotted in Fig. 8 as a function of time for the pre-heating phase.

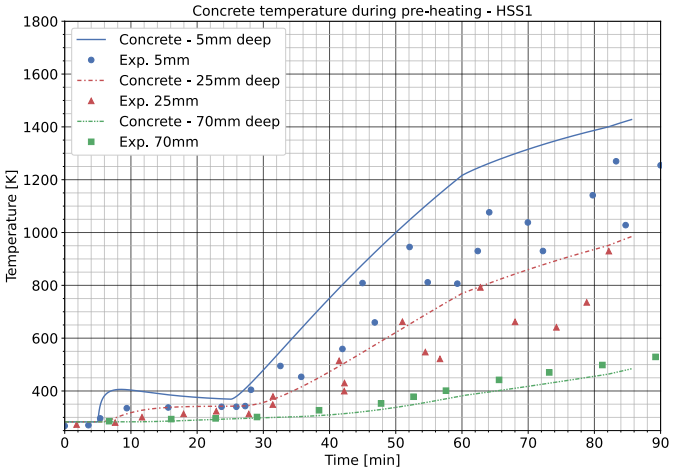

Figure 6. Concrete temperature for different depths as a function of time during the pre-heat phase.

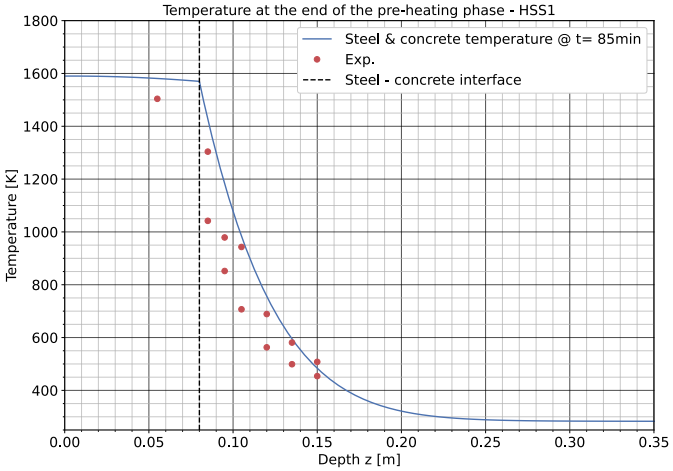

Figure 7. Temperature profile at the end of the pre-heating phase as a function of depth at ~85 min.

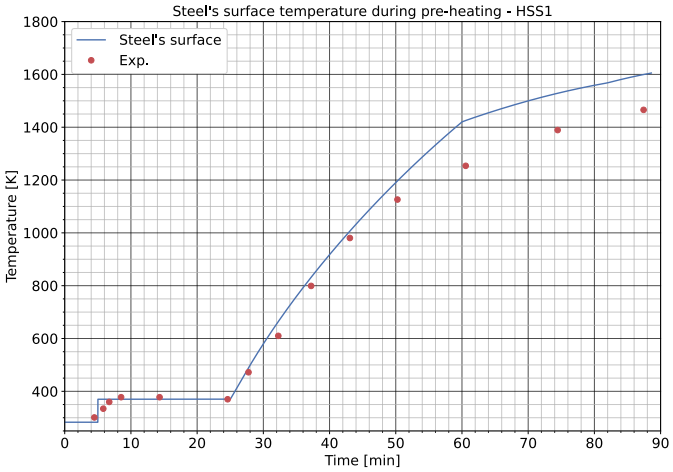

Figure 8. Steel ingots' temperature as a function of time during the pre-heat phase.

The temperature differences shown in Fig. 6 can be attributed to the limitations of the 1D modeling approach, to the simplified treatment of heat losses, the absence of consideration of possible thermal contact resistance, and uncertainties of sensor positioning. Nevertheless, the figure shows an overall good agreement with the experimental measurements. Improving the pre-heating phase agreement can be expected if volumetric heat loss is imposed individually to each cell depending on its temperature or if the discretization scheme is improved, but this is out of the scope of this work.

The initial conditions for the ablation phase are shown in Fig. 7 where good accordance is shown with respect to the temperatures of the domain. As expected, the steel ingot temperature is rather homogeneous ($z < 0.08$ m) given the good thermal conductivity of the material. In order to calculate the erosion using eq. (12) to eq. (14), the initial thermal boundary layer thickness, δ, is determined by finding the value for which the temperature profile given by eq. (3) matches the right-hand portion of the computed temperature as shown in Fig. 9. The value here retained is $\delta = 18$ cm since it is in better agreement with the results of the one-dimensional discretization. Indeed, a small variation of this parameter shows a limited impact on the final temperature profile, which serves as an indication of the pertinence of using a degree-4 polynomial to describe the temperature of the corium crust.

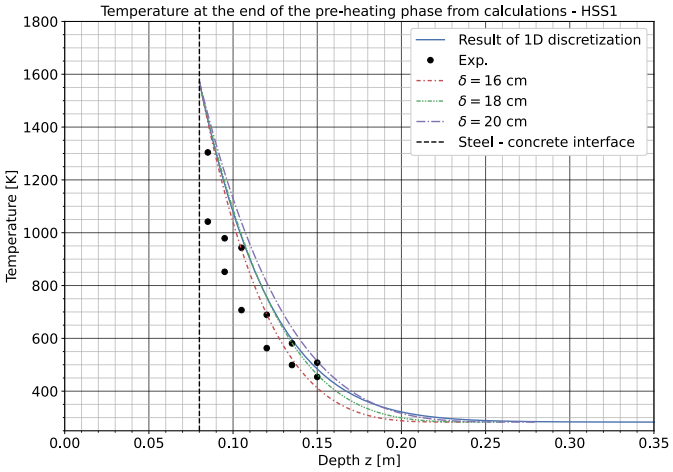

Figure 9 Temperature profile at the end of the pre-heating phase (~85 min) calculated by spatial discretization and solving eq. (3) with different values of δ.

Fig. 10 shows the evolution of the concrete ablation during the ablation phase (t>~85 min) obtained from the experimental results, and the results obtained by solving eq. (12) to eq. (14) with different values of q_v in order to evaluate the effect of the heat losses. As can be seen, even though the results of the experiment can be reproduced by introducing $q_v = 0.42 \cdot q_{in}$ into the model, the results are quite sensitive to the power. Indeed, some small changes to this factor can either double or halve the ablation depth. This can be explained by comparing the total estimated heat losses (~2.8 kW, see Fig. 5) to the power input (~3.2 kW). During the ablation phase, the heat losses are quite elevated and are close to the average power input, hence the power introduced to the steel ingot is somewhat difficult to properly estimate.

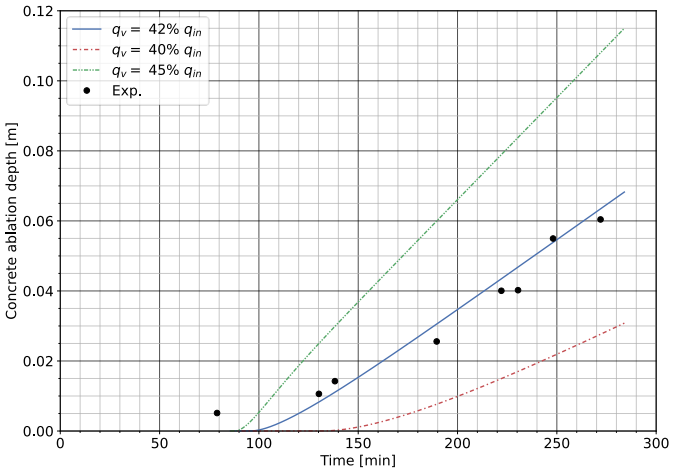

Figure 10 Concrete ablation calculated by solving eq. (12) – eq. (14) with different values of q_v.to analyze the effects of heat losses

Finally, having calculated both the concrete ablation depth and the thickness of the thermal layer using the values that fit the experimental result the most ($q_v = 0.42 \cdot q_{in}$) it is possible to confirm the validity of this assumption by calculating the temperature profile during the ablation phase at different concrete depths. The concrete temperatures during the pre-heating phase are the same as the ones shown in Fig. 6, whilst those of the ablation phase are calculated using eq. (3)[1]. The slight discontinuities of the curves between the pre-heating phase and the ablation phase are due to the limitations of the discretization scheme used to calculate the former. These results show a notable rise in the concrete temperature before the arrival of the ablation front. In other words, this indicates that the ablation speed is not fast enough to impede the propagation of a conduction-limited temperature front within the concrete. The curves show a general agreement with the tendencies of the experimental results, without matching exactly the time at which a certain concrete depth reaches the ablation temperature. Nevertheless, in view of the uncertainties induced by the heat losses, the agreement is rather acceptable.

[1] For these evaluations both z and δ are set to the results of the ablation calculations using $q_v = 0.42 q_{in}$ at each depth

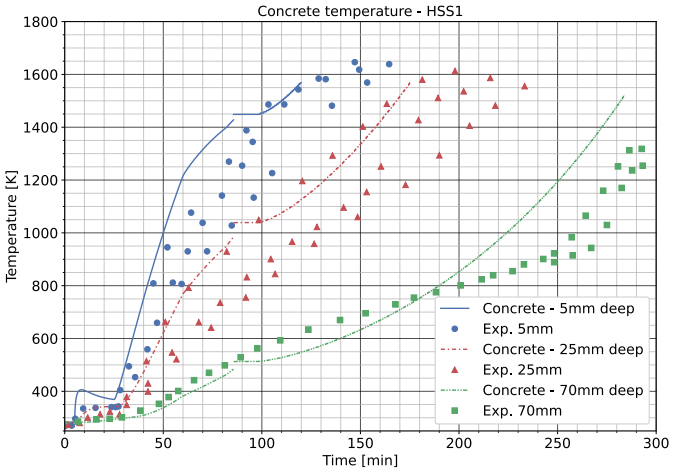

Figure 11 Concrete temperature for different depths as a function of time during both the pre-heat phase and the ablation phase

3. CONCLUSIONS

The objective of this work was to validate the model developed to evaluate whether specific configurations of post-solidification corium–concrete heat flux may still induce concrete ablation. This work was based on a comparison between the results of the model and the results of the HSS experiment, which aimed to study the interaction between a solid block heated volumetrically and concrete. From this work the following can be concluded:

- The HSS-1 main results are successfully reproduced, namely the concrete ablation rates and the temperature profiles as a function of concrete depth, within the limits of the simple model here developed. The results serve also to validates a key assumption of the model, which consists in considering that the evolution of temperature in the concrete can be described by a fourth-degree polynomial.
- The calculations are very sensitive to the assumptions made regarding the thermal losses. The analysis carried out in this work makes it possible to explain this behavior by the fact that, in these experiments, most of the injected power is dissipated through thermal losses.

The model developed can be thus used to evaluate the impact of the conduction-induced concrete ablation post corium solidification for reactor-scale MCCI calculations. Indeed, the surfaces of the final corium-concrete interfaces in reactor calculations are rather large, meaning that the applicability of the hypothesis of a one-dimensional configuration, such as the one described in the model, is sufficiently validated here.

NOMENCLATURE

$T_i[K]$	Temperature of the layer "i" where i = int for interface temperature between the upper and lower conductive corium crusts, fus for concrete fusion temperature, sat for saturation temperature of water, and 0 for initial concrete temperature respectively.
$\alpha\left[\frac{m^2}{s}\right]$	Thermal diffusivity calculated as $\frac{\lambda}{\rho \cdot c_p}$.
$t[s]$	Time.
$z\,[m]$	Position within the corium crust.

$e_i\ [m]$	Thickness of the layer "i" where i = "ME" for debris bed from Melt Ejection, "WI" for Water Ingression induced fractured corium crust, "sup" for upper conductive corium crust, and "inf" for total lower conductive corium crust.
$\delta\ [m]$	Thermal boundary layer.
$m''\left[\frac{kg}{m^2 s}\right]$	Concrete mass flux at ablation front.
$\Delta H\left[\frac{J}{kg}\right]$	Concrete ablation enthalpy (latent heat + sensible heat).
$\rho_i\left[\frac{kg}{m^3}\right]$	Density of the layer "i" where i = con for the concrete, and i = cr for the corium's crust.
$\lambda_i\left[\frac{W}{m \cdot k}\right]$	Thermal conductivity of the layer "i" where i = con for the concrete, and i = cr for the corium's crust.
$c_{p_i}\left[\frac{J}{\mathrm{kg\ K}}\right]$	Heat capacity of the layer "i" where i = con for the concrete, and i = cr for the corium's crust.
$q_{net}\left[\frac{kW}{m^2}\right]$	Heat flux from the corium to the concrete.
$q_v\left[\frac{MW}{m^3}\right]$	Volumetric decay heat.
$q_{in}\left[\frac{kW}{m^3}\right]$	Average induction power.

REFERENCES

1. Pellegini M. Journeau C. Seiler N., Herranz L.E., Spengler C., Bouillet C., Barrachin M., Luxat D., Albright L., " Analysis of the Long-Term Interaction Between Molten Core and Dry Concrete at Fukushima Daiichi Unit 1 ", *Nuclear Technology* **211**(10), pp. 2595-2608 (2025). https://doi.org/10.1080/00295450.2024.2371267
2. Farmer M.T., Kilsdonk D.J., and Aeschlimann R.W., "Corium coolability under ex-vessel accident conditions for LWRs", *Nuclear Engineering and Technology*, **41**(5) (2009) https://doi.org/10.5516/NET.2009.41.5.575
3. Rhodes B.T. and Quintiere J.G., "Burning rate and flame heat flux for PMMA in a cone calorimeter", *Fire Safety Journal*, **26**(3), pp. 221-240 (1996). https://doi.org/10.1016/S0379-7112(96)00025-2
4. Tourniaire B., Spindler B., and Guillaumé M. "Transient Conduction Heat Transfer Modeling in Concrete for the Simulation of Long-Term Phase of Molten Core-Concrete Interaction", *Nuclear Technology*, **170**(1), pp. 201–209, (2010). https://doi.org/10.13182/NT10-A9458
5. Farmer M. T., « The CORQUENCH Code for Modeling of Ex-Vessel Corium Coolability under Top Flooding Conditions », Argonne National Lab. (ANL), Argonne, IL (United States), ANL--18/22 (2018). https://www.osti.gov/biblio/1483840
6. Copus E. R., and Bradley D. R. "Interaction of Hot Solid Core Debris with Concrete". NUREG/CR-4558; SAND-85-1739. Sandia National Labs., Albuquerque, NM (USA) (1986). https://doi.org/10.2172/5203250

Evaluation of concrete ablation by a hot heat-generating solid

A. VILLARREAL LARRAURI
B. TOURNIAIRE

Electricité de France (EDF)
EDF/DirIN/DT – 19 Rue Bourdeix, 69007 Lyon, France

alejandro.villarreal-larrauri@edf.fr
bruno.tourniaire@edf.fr

Summary

1. Introduction
2. 1D Transient Conduction Heat Transfer Modeling in Concrete
3. Validation with Hot Solid Block - Concrete Interaction Experiment
4. Conclusion

1.

Introduction

Long-term MCCI configuration

Introduction

Frame of the study = severe accident with vessel failure

- Corium spread over the basemat of the reactor cavity.
- The residual power released by low-volatily fission products keeps the corium at a high temperature → concrete ablation by the corium
- Basemat melt-through should be avoided to limit fission product release outside the containment.
- Concrete ablation during molten core concrete interaction must be evaluated accurately to assess the risk of basemate melt-through.
- In case MCCI can be stopped before basemat melt-through, complex configuration with solidified corium in contact with concrete can be obtained.

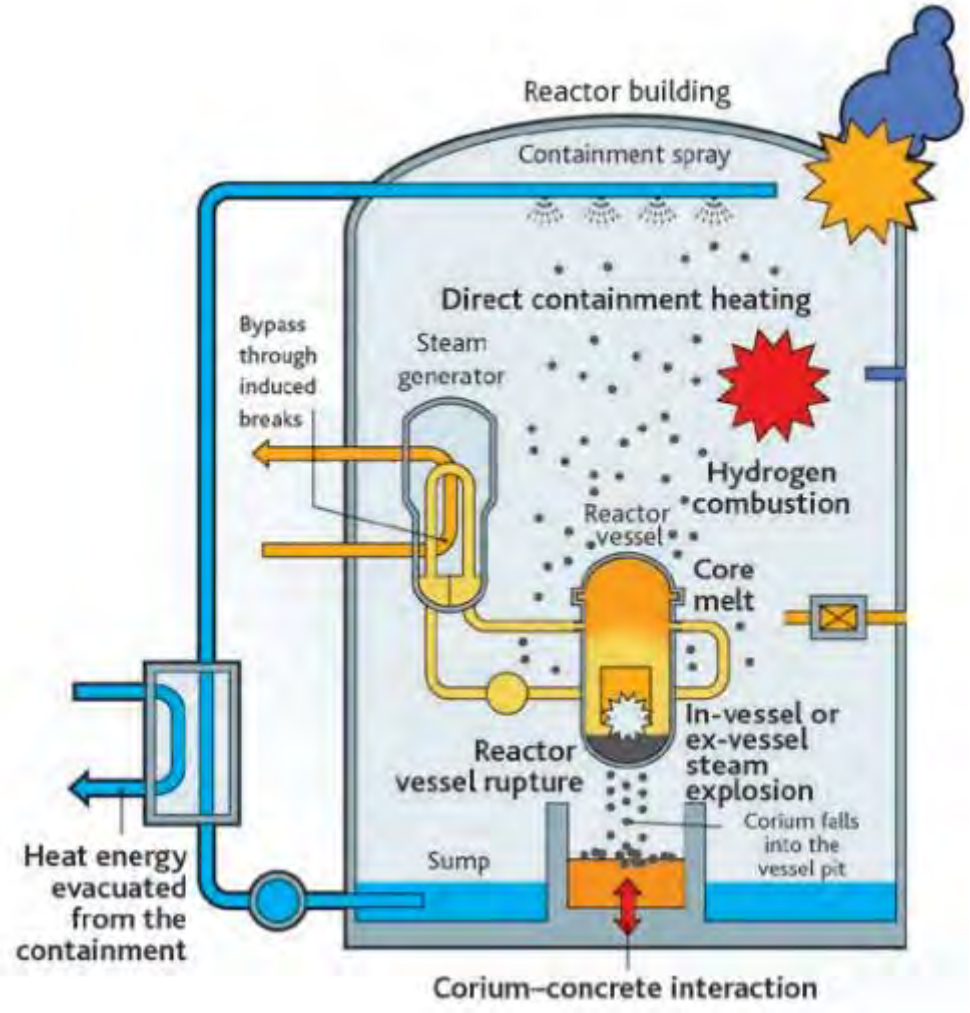

Introduction

Corium post-solidification configuration

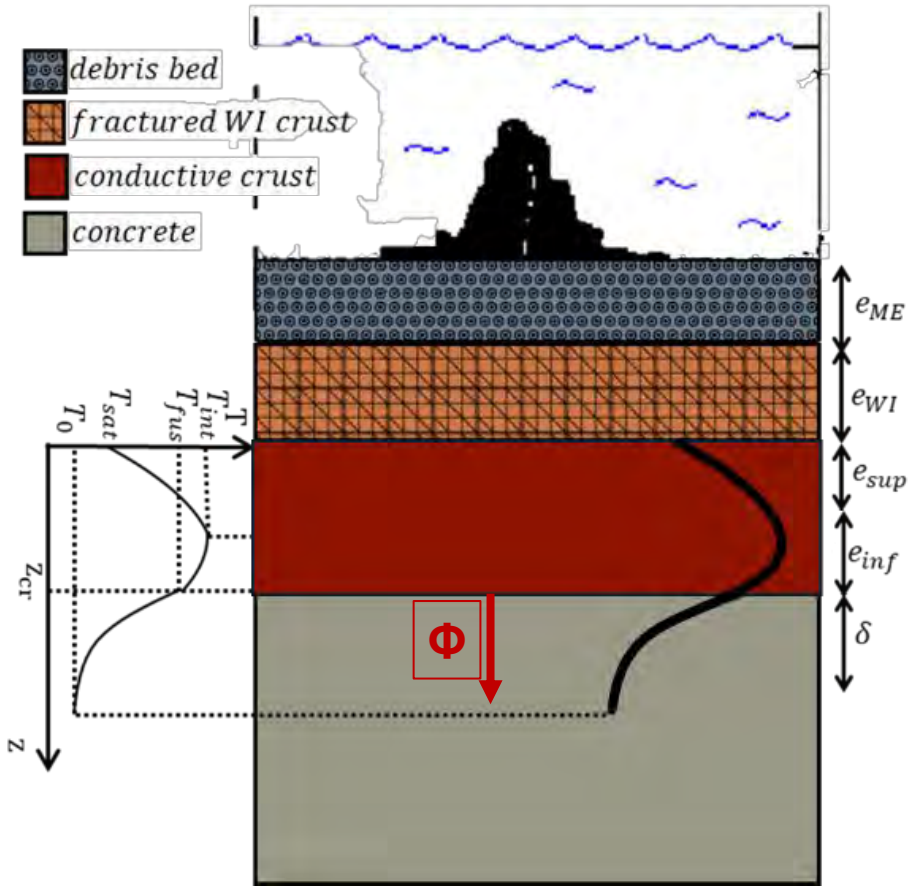

- Corium stabilization after long term MCCI is conditioned by the thermophysical properties of the corium, the accidental scenario, the chemical composition of the concrete basemat...
- Phenomena governing the phases of MCCI (dry and flooded) are highly non-linear and can lead to a vastly large array of stabilization conditions.
- In some cases, the analysis of the final configuration (i.e. once the corium is solidified) show that heat flux towards the concrete and the erosion rate remains non-zero.

Can the concrete accommodate the heat flux (Φ) coming from the corium crust? If not, how can post-solidification ablation be evaluated?

A model dealing with concrete ablation by a hot heat generating solid has been studied, modified and validated.

2.

1D Transient Conduction Heat Transfer Modeling in Concrete

1D Transient Conduction Heat Transfer Modeling in Concrete

Main assumptions of the model

- Ablation of a solid by heating (q_{net}) with heat conduction in the solid.
- Quadratic temperature profile in the concrete due to heat conduction.
- Thickness of the thermal gradient (δ).
- End of ablation when m”=0 i.e. when the heat flux transferred to the solid is equal to the heat flux that can be transferred by conduction inside the concrete.

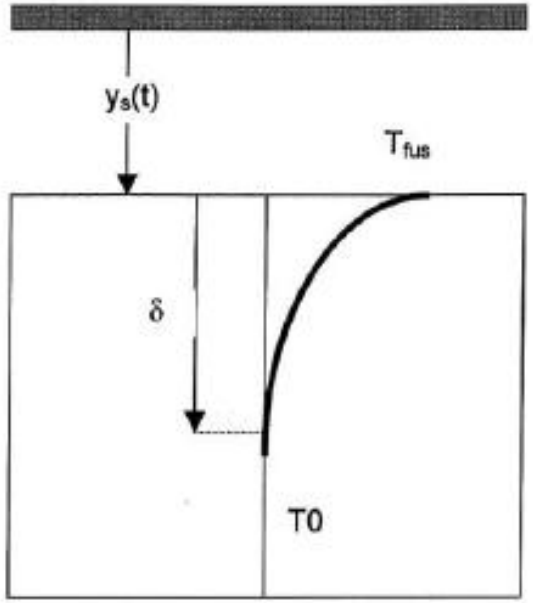

Fig. 1. Modeling of the temperature profile.

$$\frac{T - T_0}{T_{fus} - T_0} = \left(1 - \frac{y - y_s}{\delta}\right)^2$$

$$\frac{d\delta}{dt} = \frac{6 \cdot \alpha}{\delta} - \frac{3 \cdot m''}{\rho} \qquad m'' \cdot \Delta H = q_{net} - \frac{2 \cdot \lambda}{\delta}(T_{fus} - T_0)$$

[1]

1D Transient Conduction Heat Transfer Modeling in Concrete

- Model adapted to MCCI to address concrete ablation by a solid corium (crust) generating heat.
- Evolution of the model → the degree of the polynomial has been increased (2 → 4) to improve the accuracy of the model (a new equation for δ has been derived).

concrete

$$\frac{T - T_0}{T_{fus} - T_0} = \left(1 - \frac{z - z_{cr}}{\delta}\right)^4$$

$$\frac{d\delta}{d_t} = \frac{20\alpha}{\delta} - \frac{5m''}{\rho}$$

$$m'' \, \Delta H = q_{net} - \frac{4\lambda_{con}}{\delta}\left(T_{fus} - T_0\right)$$

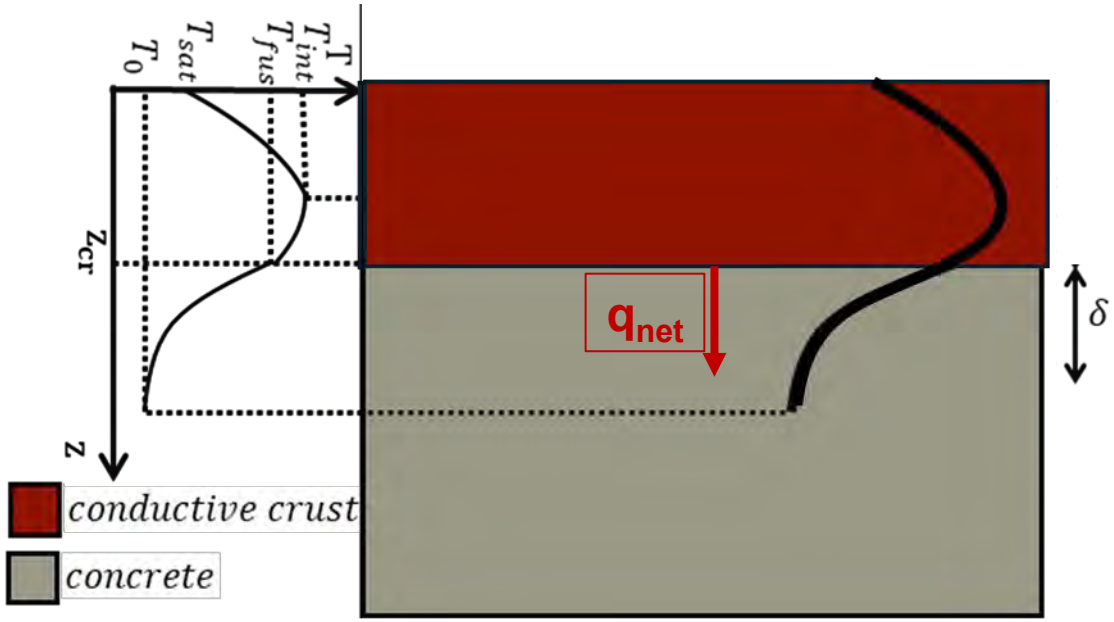

crust

$$\rho_{cr} c_{p_{cr}} \frac{\partial T}{\partial t} = \lambda_{cr} \frac{\partial^2 T}{\partial z^2} + q_v$$ + Temperature profile in the crust to calculate q_{net}

1D Transient Conduction Heat Transfer Modeling in Concrete

- The temperature profile in the crust with residual power is calculated to estimate the heat flux between the crust and the concrete.
- A classical spatial discretization is used + explicit approach for the transient term

Spatial discretization of the corium's crust

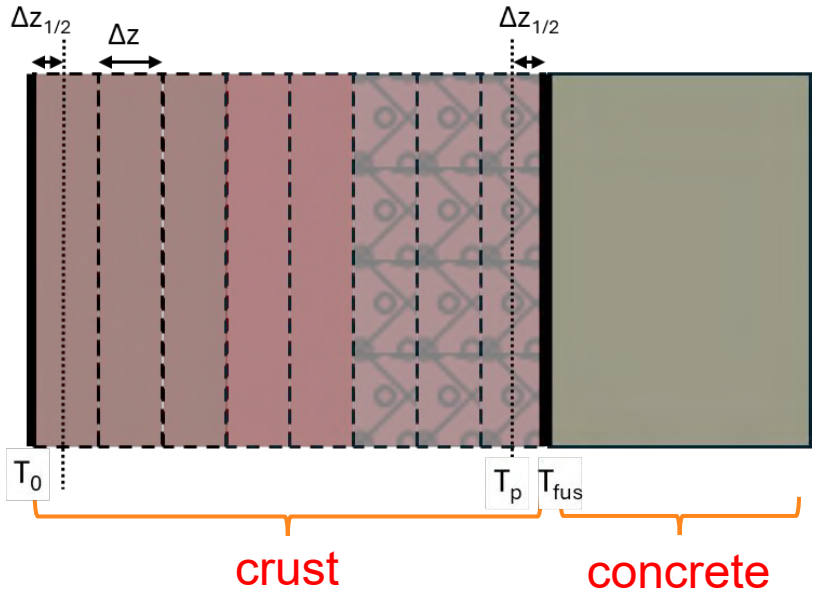

Discretization

$$\rho_{cr} c_{p_{cr}} \frac{\partial T}{\partial t} = \lambda_{cr} \frac{\partial^2 T}{\partial z^2} + q_v$$

$$T_i^{n+1} = T_i^n + \frac{\lambda_{cr}\,\Delta t}{\rho_{cr} c_{p_{cr}} \Delta z^2}\left(T_{i+1}^n - 2T_i^n + T_{i-1}^n\right) + \frac{q_v\,\Delta t}{\rho_{cr} c_{p_{cr}}}$$

$$T_1^{n+1} = T_i^n + \frac{\lambda_{cr}\,\Delta t}{\rho_{cr} c_{p_{cr}} \Delta z^2}\left(T_2^n - 3T_i^n + 2T_0\right) + \frac{q_v\,\Delta t}{\rho_{cr} c_{p_{cr}}}$$

$$T_p^{n+1} = T_p^n + \frac{\lambda_{cr}\,\Delta t}{\rho_{cr} c_{p_{cr}} \Delta z^2}\left(2T_{fus} - 3T_p^n + T_{p-1}\right) + \frac{q_v\,\Delta t}{\rho_{cr} c_{p_{cr}}}$$

3.

Validation with Hot Solid Block - Concrete Interaction Experiment (HSS tests)

Validation with Hot Solid Block - Concrete Interaction Experiment

DESIGN & TECHNOLOGY BRANCH

HSS-1

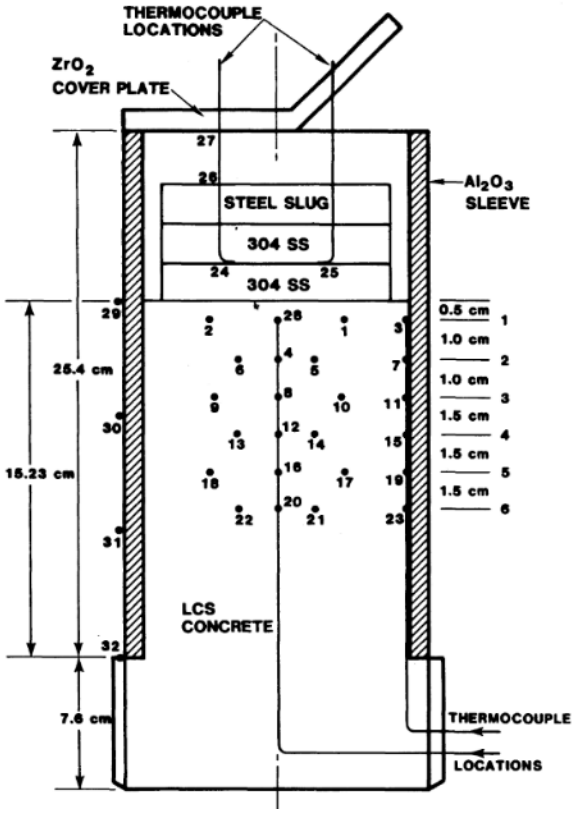

[2]

Tests	HSS-1
Block's composition	Stainless Steel 304
Dimensions [cm]	14 x 8
Block's Mass [kg]	9
Initial Temperature [K]	491
Avg. Power [kW] (q_{in})	3.2
Avg. Losses [W/cm²]	4.9
Concrete type	Limestone Common Sand (LCS)

Pre-heating phase

- Inductive heating used to pre-heat the steel slug to reach 1400°C.
- The pre-heating phase ends around 80 minutes once the temperature of the steel ingot is high enough to start concrete ablation. Power is then slightly reduced to maintain ablation without melting the steel ingot.
- Power losses from the induction coils are considered minor before the 25th minute and are calculated linearly between the 25th and 85th minute and then continues until the 300th minute (end of the heating period) so that the integral matches the reported data (4.9 W/cm²).

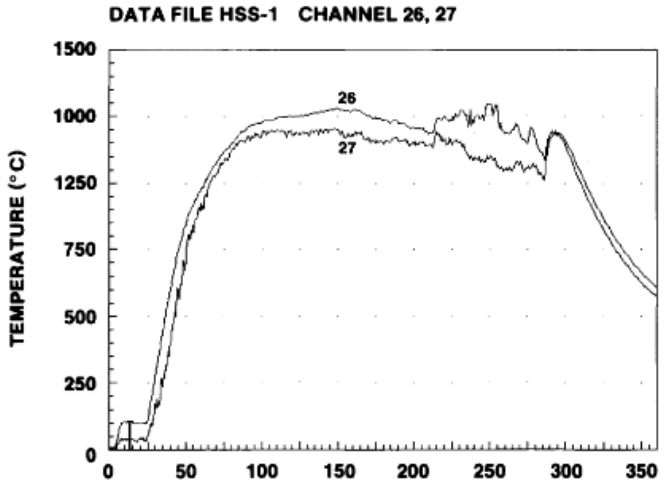

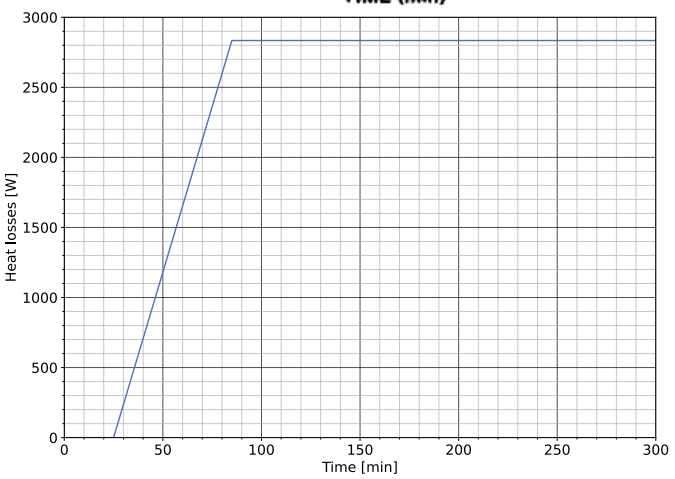

Validation with Hot Solid Block - Concrete Interaction Experiment

Pre-heating phase

- To initialize the ablation phase, the pre-heating phase must be modeled to obtain the initial conditions and an initial thermal boundary layer thickness in the concrete.

- Similar discretization scheme is used to model the crust and the concrete layer:

$$\rho_{cr} c_{p_{cr}} \frac{\partial T}{\partial t} = \lambda_{cr} \frac{\partial^2 T}{\partial z^2} + q_v - q_{th}$$

$$\rho_{con} c_{p_{con}} \frac{\partial T}{\partial t} = \lambda_{con} \frac{\partial^2 T}{\partial z^2}$$

- Results of the heat conduction calculations for the pre-heating phase match with sufficient degree of satisfaction the experimental results. Overestimation of the temperature close to the steel surface can be attributed to limitations of 1D modeling.

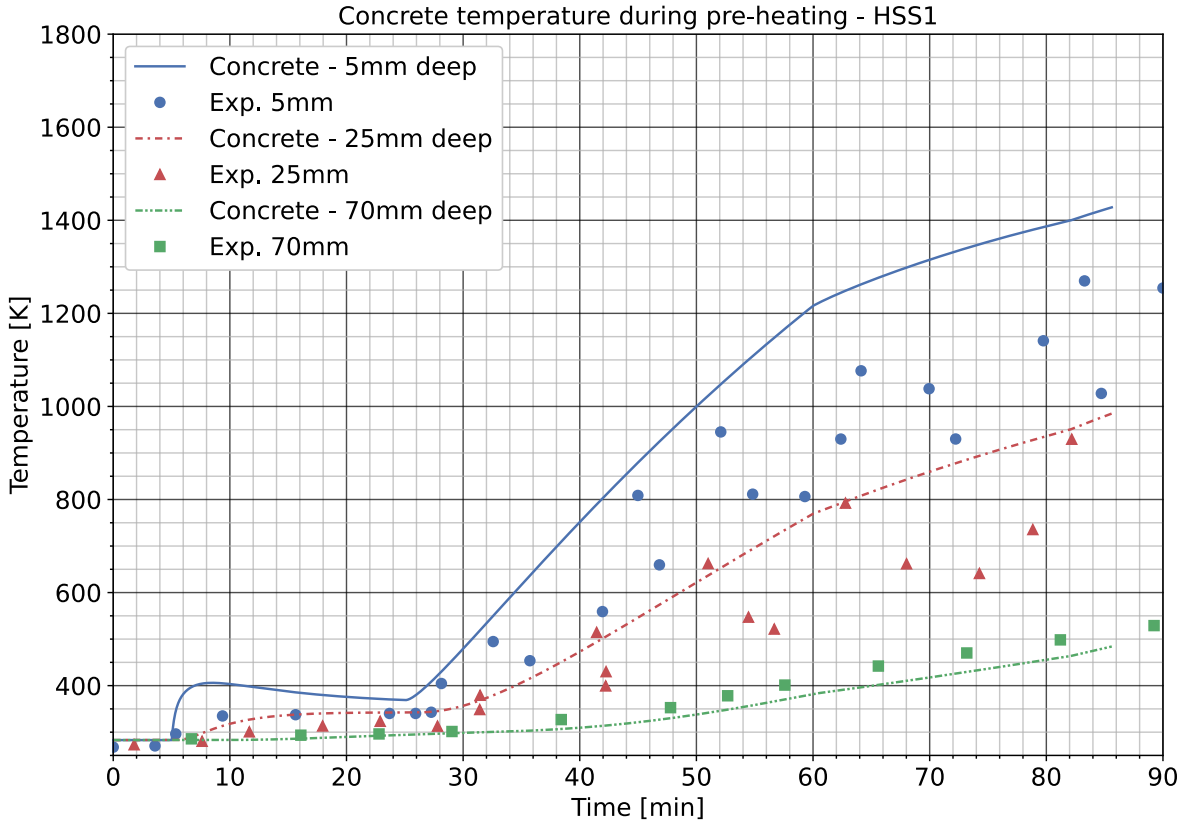

Validation with Hot Solid Block - Concrete Interaction Experiment

Pre-heating phase

- Pre-heating phase heat conduction calculations show good agreement with concrete temperature measurements at the time when the temperature at the steel-concrete interface is estimated to reach the concrete ablation temperature (~85 min).

- To model the ablation phase, the initial thermal boundary layer's thickness is determined by identifying the value for which the temperature best matches the results of pre-heating calculations:

  δ= 18 cm

- A small variation of this parameter shows a limited impact on the final temperature profile : degree-4 polynomial is a good fit to describe the temperature of the corium crust.

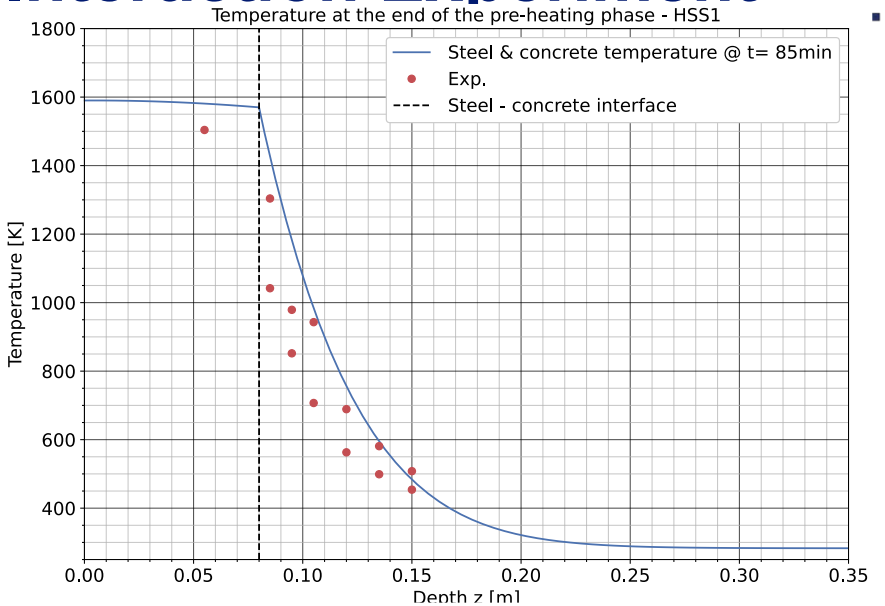

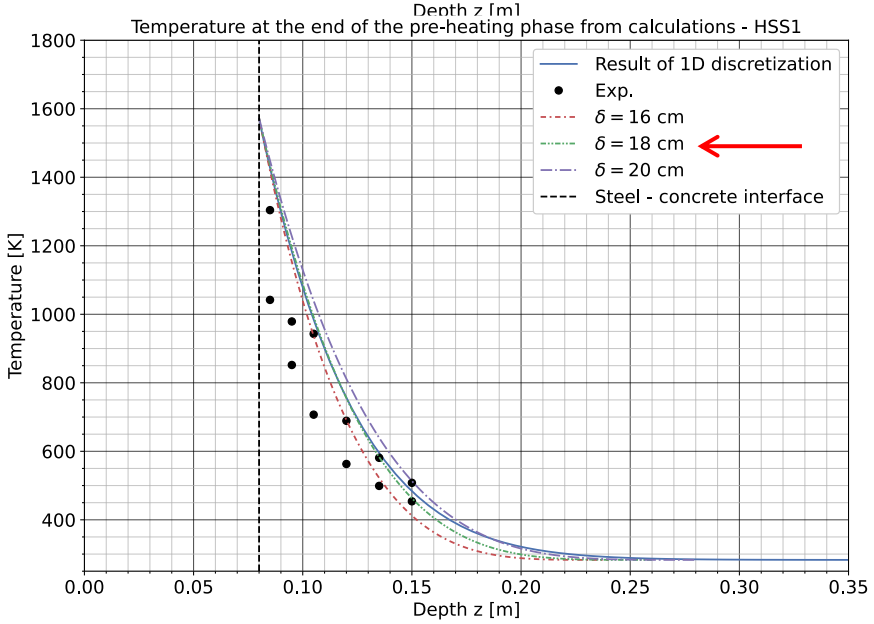

Validation with Hot Solid Block - Concrete Interaction Experiment

DESIGN & TECHNOLOGY BRANCH

Concrete ablation during heating phase

- Power losses during the ablation phase (~2.8 kW) are comparable to the power input (~3.2 kW) → sensitivity study shows a significant impact of the power input with respect to the concrete ablation compared to the experimental measurements. A value of $\mathbf{q_v = 42\%\ q_{in}}$ is retained.

- The validity of the retained power introduced to the steel ingot is verified by calculating the temperature profile during the ablation phase at different concrete depths.

- The concrete temperatures during the ablation phase reproduce properly the tendencies measured during the experiments (the discontinuities of the curves between the pre-heating phase and the ablation phase are due to the limitations of the discretization scheme used to calculate the former).

- These results show a notable rise in the concrete temperature before the arrival of the ablation front, i.e. the ablation speed is not fast enough to impede the propagation of a conduction-limited temperature front within the concrete.

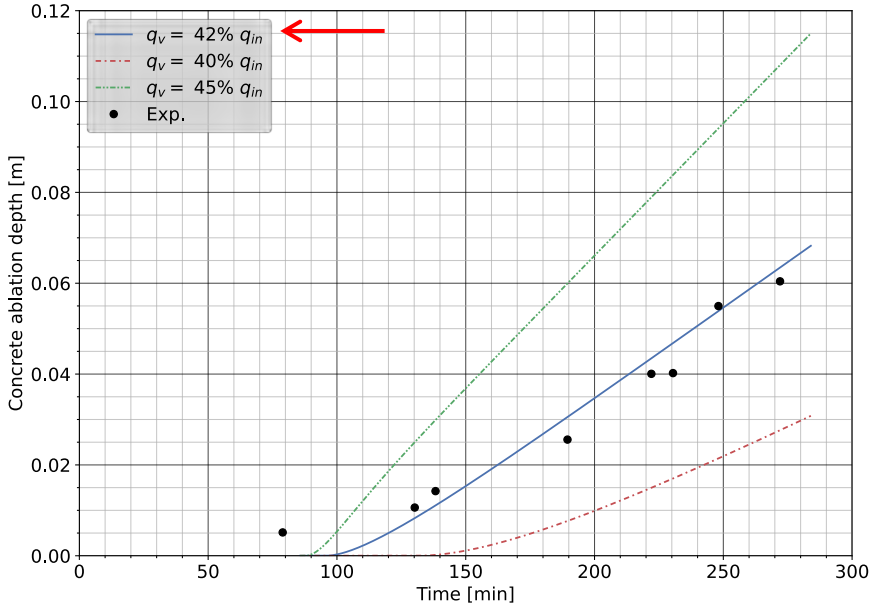

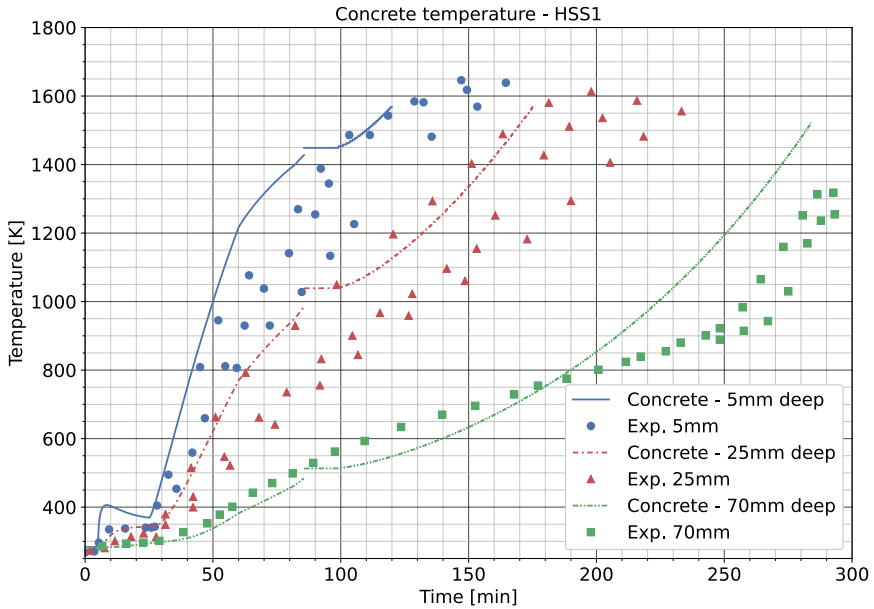

4.

Conclusion

Conclusion

- A 1D model was developed to evaluate whether specific configurations of post-solidification corium–concrete heat flux may still induce concrete ablation

- The HSS-1 main results are successfully reproduced, namely the concrete ablation rates and the temperature profiles as a function of concrete depth, within the limits of the simple model here developed.

The model developed can be thus used to evaluate the impact of the conduction-induced concrete ablation post corium solidification for reactor-scale MCCI calculations (the surfaces of the final corium-concrete interfaces in reactor calculations are rather large, hence the applicability of a one-dimensional configuration is sufficiently validated).

Thank you

DESIGN & TECHNOLOGY BRANCH

References

[1] B. Tourniaire, B. Spindler, et M. Guillaumé, « Transient Conduction Heat Transfer Modeling in Concrete for the Simulation of Long-Term Phase of Molten Core-Concrete Interaction », Nuclear Technology, vol. 170, nº 1, p. 201-209, Avr. 2010.

[2] Copus E. R., and Bradley D. R. “Interaction of Hot Solid Core Debris with Concrete”. NUREG/CR-4558; SAND-85-1739. Sandia National Labs., Albuquerque, NM (USA) (1986). https://doi.org/10.2172/5203250Corium post-solidification configuration

The 12th European Review Meeting on Severe Accidents Research

May 18-22, 2026, Universidad Carlos III de Madrid, Madrid, Spain

TECHNICAL SESSION 7.4: GENERATION IV SYSTEMS

Chairs: A. Stakhanova (KIT), S. Gupta (Framatome)

ID154	**High temperature oxidation behavior of silicon carbide fuel matrix during Beyond Design Basis Accident in Gen IV reactors** Y. Nishimura (University of Tokyo)	Paper Presentation
ID199	**MSR Modeling Capabilities and Development with the MELCOR Reactor Simulation** D. Luxat (SNL)	Presentation
ID149	**Computational verification of the functionality of the cooling system of the ALLEGRO reactor core catcher** J. Komrska (UJV)	Paper Presentation

High temperature oxidation behavior of silicon carbide fuel matrix during Beyond Design Basis Accident in Gen IV reactors

Yosuke Nishimura*, Ruicong Xu, Zongda Yang, Chao Yang, Bo Li, and Hiroaki Abe
The University of Tokyo
2-22, Shirakata Shirane, Tokai, Naka-Gun, Ibaraki 319-1188, Japan
nishimura-y@g.ecc.u-tokyo.ac.jp

ABSTRACT

Having an anti-oxidation property is one of the pivotal roles of the silicon carbide (SiC) fuel matrix for safety during air ingress accident which is the worst scenario among Beyond Design Basis Accidents (BDBAs) in Generation-IV reactors such as high-temperature gas-cooled reactors (HTGRs). At high temperature oxidation, SiC has two different modes: passive or active oxidation mode. Passivated SiC contributes to nuclear fuel safety, preventing unpreferable chemical reaction between the fuel matrix and oxidation gas, reducing risks of fuel damage and radioactive release from the embedded TRISO fuel particles. Depending on oxygen partial pressures, however, active mode may be dominant that causes a huge degradation of mass while accelerating volatile SiO and CO gases release from the surface. Given the importance of oxidation resistance in the fuel matrix, investigating oxidation behavior, phase changes, morphology characterization, and microstructure observation at high temperatures are valuable for predicting the fuel behavior during the accidents and evaluating the reactor safety. We report that passive mode is dominant up to 1400 ℃ in air, which is the accidental scenario; at the same temperature with 1 ppm oxygen/argon mixed gases, however, active mode occurs. The result indicates that with very few amounts of oxygen existing in the highly purified helium coolant may cause corrosion of the fuel matrix at higher temperatures as burn-up progresses. The study suggests the corrosion during normal service operation has potential concerns rather than high-temperature oxidation during the accidents. This knowledge is valuable for determining the operational range of the reactor cores and improving the system design as feedback for future demonstration of innovative nuclear reactors.

KEYWORDS
Silicon carbide, BDBA, HTGR, Oxidation

1. INTRODUCTION

Having an anti-corrosion property is one of the pivotal roles of the nuclear fuel matrices for safety during normal operation service and even accidental phenomena; preventing unpreferable chemical reaction between the fuel matrix and primary coolant ensures material integrity, reducing risks of fuel damage and radioactive release. Given the importance of anti-corrosion property in the fuel matrix, investigating potential interaction between the fuel matrix and coolant, phase changes, morphology characterization and microstructure observation at high temperatures offer insightful knowledges that would allow us to predict the fuel behavior in the core and estimate the lifetime of fuel assembly for the following maintenance or replacement.

In the case of sleeveless fuel design of high-temperature gas-cooled reactors (HTGRs) [1], each fuel compact directly contacts with helium coolant gas at high temperatures, thus heat transfer from the fuel

compact to helium gas would be significantly improved which results in higher power density operation compared with the current fuel assembly with graphite sleeve in entire axial direction. This innovative fuel design benefits economic and reactor safety such as simplified fuel structure and higher power outputs with lower fuel temperatures. Many attractive features, however, the solid-gas interaction between the fuel compact and helium gas may pose a potential concern of the fuel matrix degradation in the worst scenario [2]. SiC fuel matrix exhibits an excellent oxidation resistance to air ingress accident at high temperatures [3]; on the contrary very few amounts of oxygen existing in the highly purified helium coolant may cause corrosion with a huge degradation of mass (active oxidation) [4]. Which means that the active oxidation mode may jeopardize the fuel matrix in a long term during the normal operation period, reducing lifetime of the fuel assembly. This corrosion may be a crucial issue for the fuel safety, which requires any prevention technology or limitations on the reactor operational conditions.

In an effort to mitigate or partially control the corrosion, this work investigates the oxidation behavior of well-passivated SiC substrate in an active oxidation condition at 1400 C with 1 ppm argon/oxygen mixed gas flow. We assume that silica oxide layer may inhibit the following corrosion in the active condition. The measurement aims to evaluate how the pre-passivation works on the passive/active transition that suggests a boundary of limit for nuclear engineering use. The present study, however, reports that this very simple surface modification of SiC cannot fully prevent the active oxidation mode. Through morphology observation and characterization of the test specimens, we find intricate silica microstructures and nanowires products near the active oxidation spot. In this paper, we report their characterization and propose a dynamic model that offers potential mechanisms how these silica structures are formed. Also, we discuss the application of this technology for the nuclear fuel matrix.

The outline of this paper is provided as follows; in the Experimental details section, the experimental procedures, materials and methods are shown; Results and discussion section briefly summarize all the findings and discuss the model with measured data; finally, the conclusive remarks are presented.

2. EXPERIMENTAL DETAILS

The SiC oxidation tests were conducted within a vertically oriented alumina tube furnace (Thermogravimetry Differential Thermal Analysis (TG-DTA), Bruker, model TG-DTA2020SA). The substrates employed for pre-passivation consisted of SiC spheres with an approximate diameter of 4 mm (Sato Tekko Co. Ltd.). Prior to oxidation, the substrates underwent ultrasonic cleaning in acetone for 10 minutes, followed by air drying, and were subsequently arranged in alumina dishes inside the tube furnace. The mass variation during the oxidation process was continuously monitored at a sampling interval of 1.0 second with a precision of 0.1 μg, utilizing an electronic balance integrated into the furnace.

The SiC substrates were subjected to high-temperature oxidation to ensure effective passivation. The substrates were gradually heated to 1000 ℃ at a controlled rate of 20 ℃/min and maintained at this temperature for either 1 or 2 hours in static air. This process induced passive oxidation, resulting in the formation of a silica layer on the substrate surface. The duration of oxidation determined the oxide layer thickness, reaching approximately 0.8 μm after 1 hour and 1.5 μm after 2 hours. Following confirmation of complete oxide coverage, the substrates were reintroduced into the tube furnace.

Subsequently, the furnace chamber was evacuated to a pressure below 1.0 Pa over a duration of 1 hour using a mechanical rotary pump. To minimize residual oxygen levels, ultra-high-purity argon gas (purity: 99.9995%) was introduced at a controlled flow rate of 50 mL/min. The furnace was then heated to 1400 ℃ at a ramp rate of 20 ℃/min under continuous argon flow. Upon reaching 1400 ℃, the argon supply was discontinued, and a gas mixture comprising 1 ppm oxygen in argon (JAPAN FINE PRODUCTS) was introduced at the same flow rate for 30 minutes. Based on our previous research, exposure to 1400 ℃ in a 1 ppm oxygen environment induces active oxidation and SiO gas evaporation [2], which provides the targeted corrosion environment. Finally, the furnace was gradually cooled to ambient temperature while maintaining an argon atmosphere.

Following the oxidation tests, the morphology and microstructure observation of the SiC substrates were examined using a field emission scanning electron microscope (FE-SEM; S-4800, Hitachi High-Tech Corporation, Japan) and transmission electron microscopy (TEM; FE-TEM, JEM-2010F, JEOL, Japan). The TEM system was further equipped with an energy-dispersive spectrometer (EDS, Genesis APEX2, EDAX, USA) for compositional analysis.

3. RESULTS AND DISCUSSION

3.1. Localized active oxidation after one-hour passivation: silica nanowires formation

SiC substrates exposed to 1 ppm O_2/argon at 1400 ℃ developed distinct circular patterns. A scanning electron microscopy (SEM) image (Figure 1(a)) of the SiC top surface verifies the formation of these patterns. Zone 1 (Figure 1(b)) corresponds to exposed SiC, where the SiO_2 layer formed during passivation is nearly absent. In contrast, Zone 2 (Figure 1(c)) exhibits a substantial presence of elongated fiber-like structures (nanowires). The occurrence of exposed SiC in Zone 1 indicates active oxidation, which resulted in the degradation of the oxide film and subsequent corrosion of the SiC. This oxidation process follows Eq. 1, leading to the generation of SiO gas. Further confirmation of active oxidation and material degradation was obtained through thermogravimetric analysis.

$$\mathrm{SiC} + \mathrm{O_2} \rightarrow \mathrm{SiO\,(g)} + \mathrm{CO\,(g)} \qquad (Eq.1)$$

Localized eruptions resulting from interfacial reactions between the SiO_2 film and the underlying SiC substrate [5] can significantly enhance SiO gas production (Equation 2). As the oxygen partial pressure declines, a critical threshold is reached at which SiO and CO gases readily form at the interface, governing the transition from passive to active oxidation [6]. This transition is characterized by the degradation of the protective SiO_2 layer, leading to the formation of pits at the boundary between exposed SiC and the remaining oxide film [7]. These localized corrosion sites play a crucial role in supplying SiO gas for nanowire synthesis.

$$\mathrm{SiC} + \mathrm{2SiO_2} \rightarrow \mathrm{3SiO\,(g)} + \mathrm{CO\,(g)} \qquad (Eq.2)$$

Under specific conditions, the volatile SiO gas can migrate to other regions, particularly those with slightly lower temperatures or higher oxygen partial pressures. We propose that SiO gas released from the corrosion sites diffuses outward to Zones 2, facilitating nanowire growth.

A substantial quantity of nanowires was observed on the substrate within Zone 2. SEM images of the synthesized nanowires are presented in Figure 1 (d), illustrating a uniform diameter distribution. The nanowires exhibit a relatively straight morphology, with an average diameter of 63±18 nm and lengths

extending to tens of micrometers, featuring exceptionally clean surfaces. Most of the nanowires appear extremely long and randomly oriented. The nanowires exhibit uniform diameters and smooth surfaces, with a distinct nanoparticle encapsulated within a shell at the nanowire tip. The pronounced contrast difference between the shell and the nanoparticle suggests a variation in elemental composition. The nanoparticle is generally spherical and enclosed by a relatively thick amorphous layer, resulting in a total diameter of 130–170 nm. The relationship between the nanowire diameter and the nanoparticle diameter aligns well with an empirical equation describing silicon nanowires synthesized via SiO evaporation combined with the vapor-liquid-solid (VLS) mechanism [8].

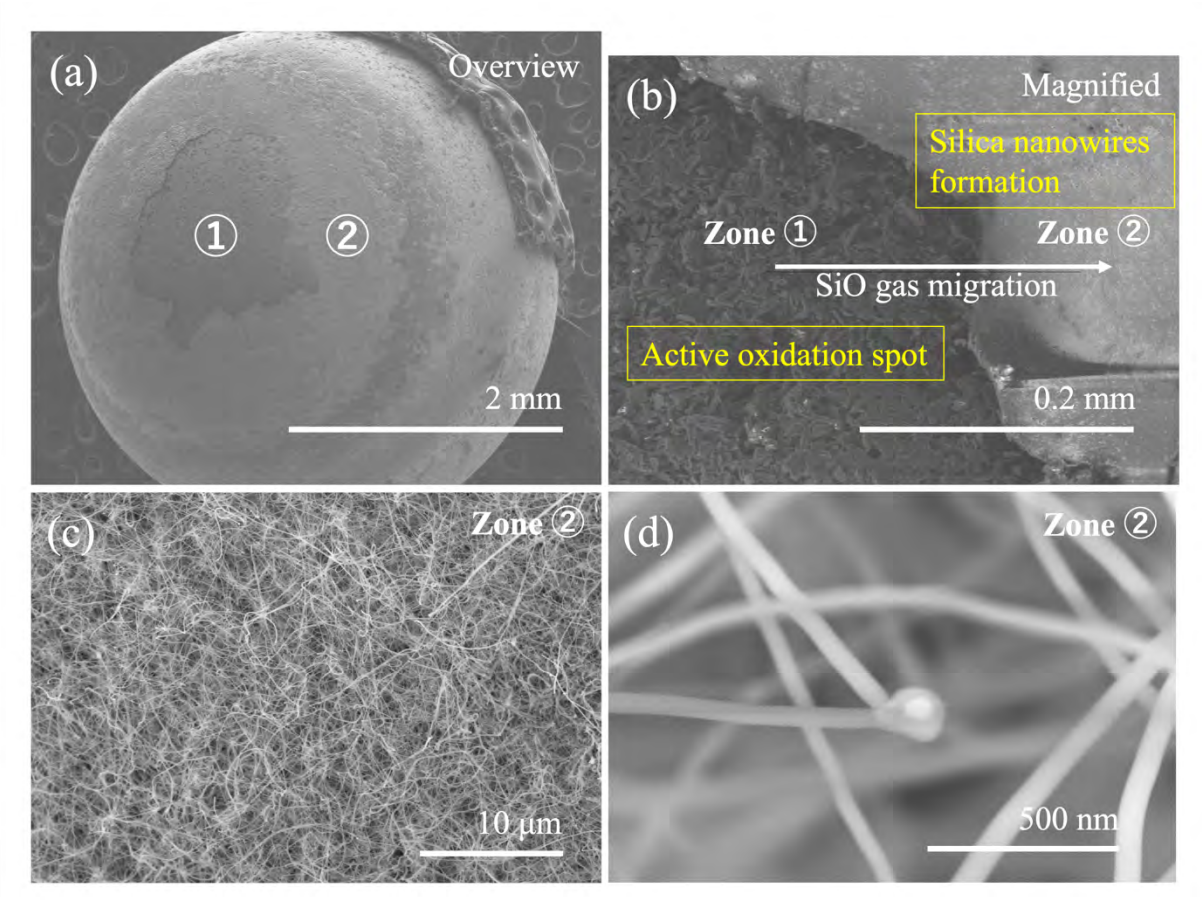

Figure 1. FE-SEM images of SiC substrate (pre-passivated for 1 hour) after oxidation at 1400 ℃ for 30 min. (a) Low-magnification top-view image showing three distinct zones. (b) Boundary between the exposed SiC area without a SiO_2 film (Zone 1) and the silica nanowires area (Zone 2). (c) Typical nanowires synthesized in Zone 2. (d) Nanowires view in higher magnification.

A typical nanowire morphology, including its associated nanoparticle, is further illustrated in the TEM image (Figure 2(a) and (b)), with corresponding EDS spectra provided onset. The EDS analysis reveals that the nanowire consists exclusively of Si and O, while the nanoparticle comprises Si, Mo, Rh, W, and Pt, with Mo and Si being the predominant elements. The detected Cu signal originates from the TEM sample mesh, while the presence of Rh, W, and Pt is attributed to evaporation from the heater inside the furnace. Notably, Mo is detected exclusively within the nanoparticles and is absent in the nanowires.

The presence of nanoparticles at the tips of the nanowires strongly suggests that the silica nanowires formed via a vapor-liquid-solid (VLS) growth mechanism [9]. This process involves the formation of a liquid

catalyst, the nucleation and growth of eutectic alloy droplets containing nanowire components, and subsequent nanowire growth driven by supersaturation within the liquid droplets. Given that the synthesis temperature in this study is significantly lower than the melting point of Mo (2900 K), the formation of a liquid catalyst containing Mo requires further explanation. Based on the EDS results, the small amount of Si detected in the nanoparticle likely plays a key role in lowering the melting point of Mo [10], thereby facilitating the formation of a liquid catalyst. Additionally, nanoparticles generally exhibit lower melting points compared to their bulk counterparts [11], further supporting the possibility of liquid-phase catalyst formation under the given experimental conditions.

In this study the Si-Mo alloy is likely the primary catalyst, given that $MoSi_2$ is commonly used as a sintering additive for bulk SiC fabrication [12]. To the best of our knowledge, based on an extensive literature review, Mo has not been previously reported as a catalyst for nanowire growth. The findings of this study demonstrate that Si-Mo alloy nanoparticles can serve as a viable catalyst for nanowire growth via the VLS mechanism.

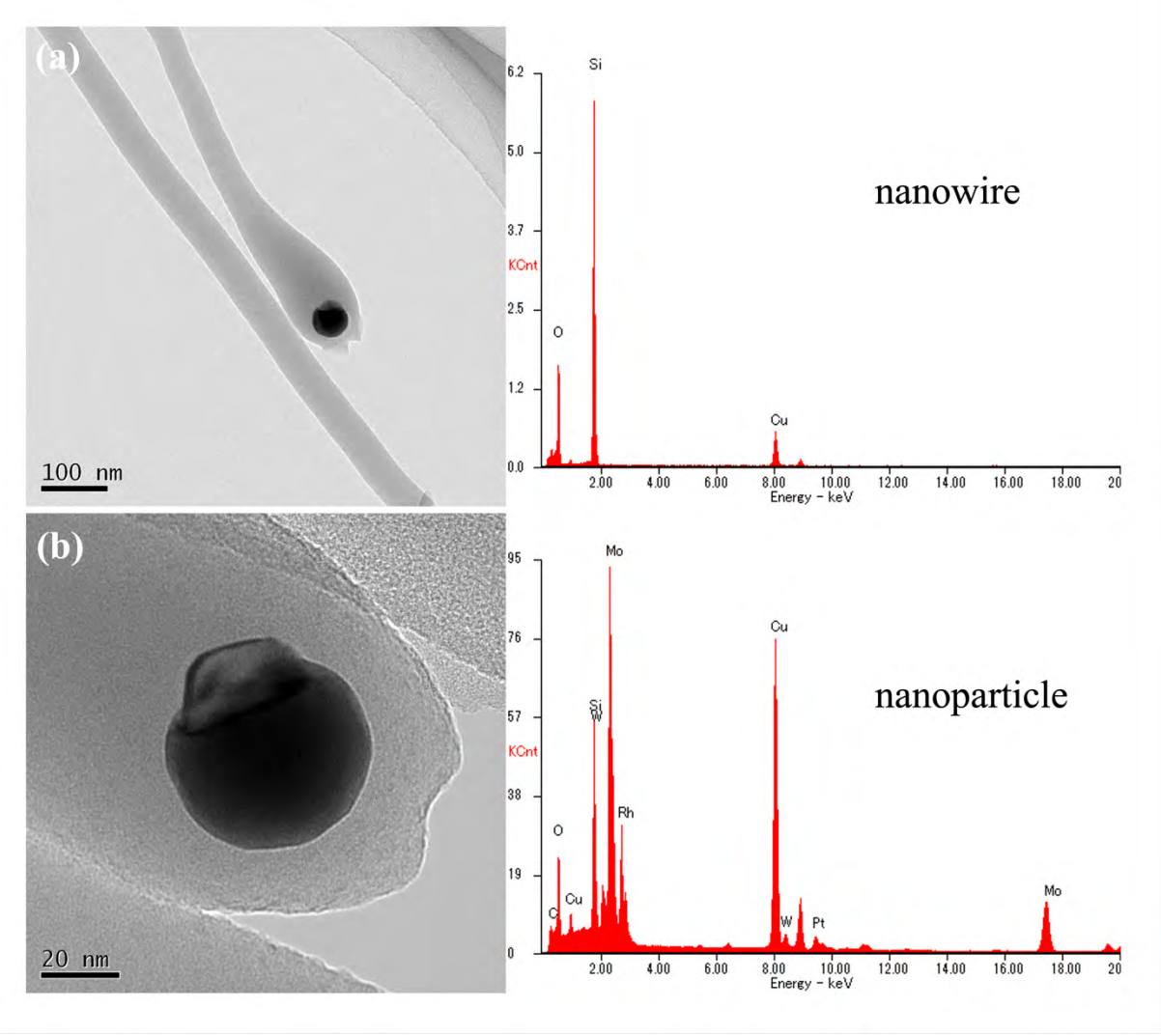

Figure 2. (a) (b) TEM image of a typical nanowire with a nanoparticle encapsulated (dark region) at the nanowire with EDS spectra of the nanowire and nanoparticle (inset), indicating that the nanowire is

composed of Si and O (the Cu signal comes from the TEM grids). The Si-rich stoichiometry also implies the presence of Si in the nanoparticle.

The presence of the SiO_2 film is a critical factor in significantly enhancing nucleation and promoting the development of one-dimensional nanostructures. The nucleation of nanoparticles is governed by the decomposition of oxide vapor species at specific temperatures. Concurrently, the system reaches equilibrium through the reaction described in Equation 3, further supporting the growth of nanowires.

$$2SiO \rightarrow Si + SiO_2 \qquad (Eq.3)$$

This decomposition process led to the precipitation of silicon nanoparticles, which serve as the nuclei for Si-Mo alloy nanoparticles, encapsulated by a silicon oxide shell, as observed. The influence of the oxide boat on nanowire synthesis has been previously confirmed [13]. Initially, dense SiO vapor condenses near the Si-Mo nuclei, forming deposits. Subsequently, these nuclei clusters act as reservoirs, effectively absorbing additional SiO vapor. As more SiO vapor is absorbed, nanowires grow preferentially along a specific orientation, facilitating rapid elongation.
Finally, the formation of an outer SiO_2 layer may result from the oxidation of residual SiO vapor and/or the introduction of 1 ppm O_2/argon gas. The supersaturation of Si and O induces phase separation [14] between Si and SiO_2, a process driven by the cooling effect of the gas flow within the furnace.

3.2. Localized active oxidation after two-hour passivation: silica whiskers formation

To highlight the critical role of oxide control during pre-passivation, a detailed microstructural characterization of a sample subjected to a 2-hour passivation process is presented as a reference. At the top region (Zone 1, Figure 3 (a)) of the spherical sample, a similar circular pattern on the test sample's surface after 2 hours of passivation, followed by exposure to an active oxidation environment of 1 ppm O_2/argon at 1400 °C. That corresponds to the region where active oxidation of SiC occurs, leading to the release of SiO gas.

Zone 1 serves as the primary source of SiO gas, which is subsequently transported to Zone 2, where more intricate silica structures develop. In Zone 2, a substantial accumulation of silica microstructures is observed, including worm-like (Figure 3 (b)), needle-like (Figure 3 (c) and (d)), and flower-like whiskers (Figure 3 (e)) as shown with SEM-EDS images onset. These whiskers exhibit diameters ranging from 1.0 to 1.4 μm and lengths extending up to 10 μm. The anisotropic growth of these structures is likely attributed to variations in surface energy along different crystallographic planes of SiO_2. The needle-like whiskers in Zone 2 possess a high aspect ratio, characterized by relatively small diameters and elongated lengths.

Although the synthesis mechanisms for silica micro- and nanostructures share similarities, both being driven by the chemical pump effect of SiC vapor supply during the active oxidation of pre-passivated SiC, the final products exhibit notable differences.

The worm-like structures, on the other hand, appear more irregular in shape but share similar growth mechanisms with the needle-like whiskers. The flower-like structures likely represent agglomerations of whiskers that have grown from a single nucleation point and spread out radially.

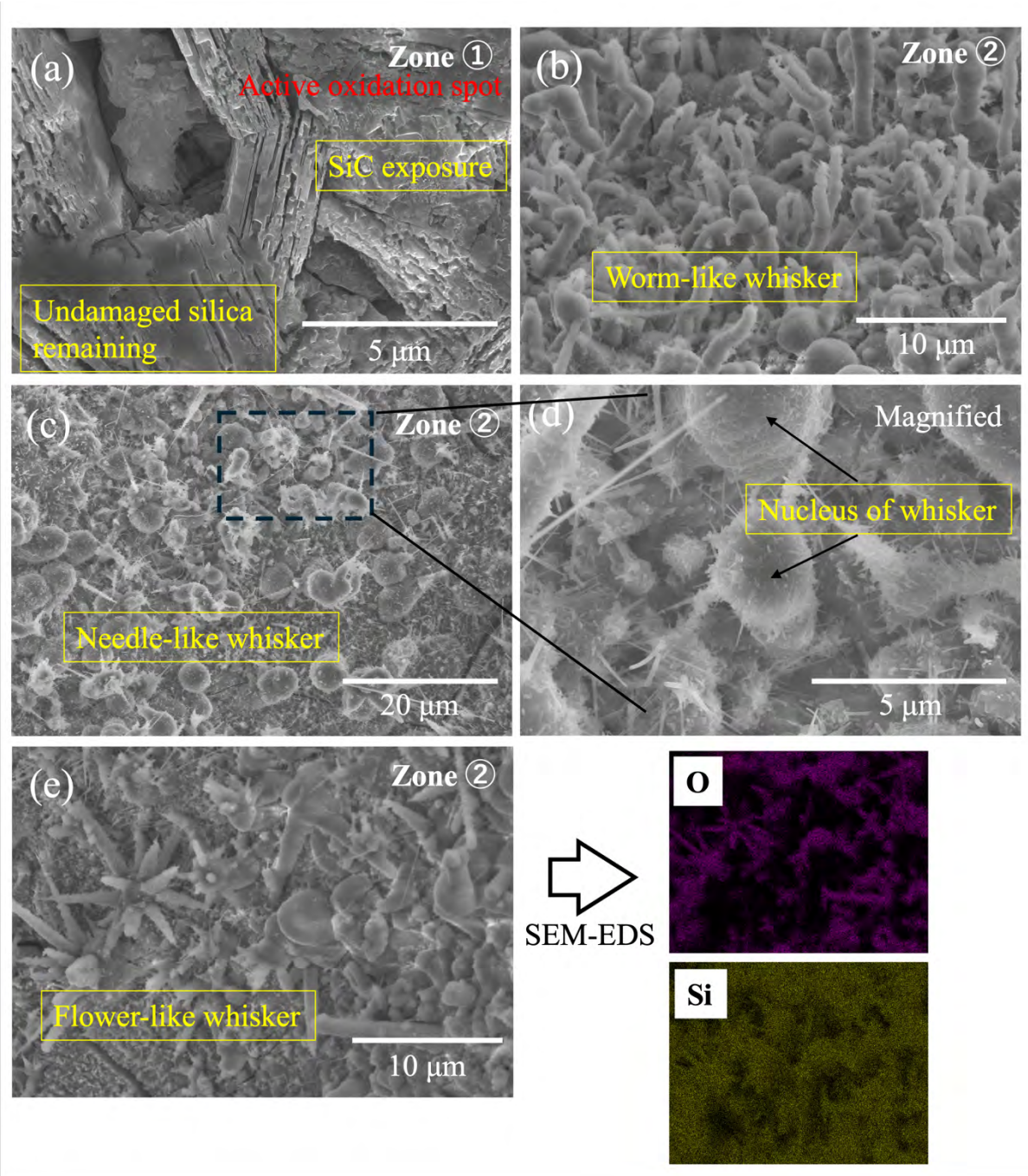

Figure 3. FE-SEM images of SiC sample (pre-passivated for 2 hours) after oxidation at 1400 °C. (a) Active oxidation spot in Zone 1. (b) Worm-like silica whisker in Zone 2. (c) Needle-like silica whisker in Zone 2 with magnified (d). (e) Flower-like silica whisker in Zone 2 with SEM-EDS results (inset).

The growth of silica whiskers and other structures observed in these zones can be explained by the vapor-liquid-solid (VLS) mechanism or, more specifically in this case, the vapor-solid (VS) mechanism, since no liquid phase is involved in the oxidation of SiC. The VS mechanism involves the following steps: SiO gas produced in Zone 1 migrates to Zone 2, where it encounters a slightly different environment, such as higher local oxygen concentrations or lower temperatures. This creates the conditions necessary for SiO_2 to nucleate on the surface of the SiC substrate (Nucleation). Once nucleation occurs, the whiskers grow via

anisotropic deposition of SiO_2. The growth is primarily governed by the diffusion of SiO gas to the growth front. The needle-like shape of the whiskers suggests that the diffusion process is anisotropic, with growth favoring one crystallographic direction more than others (Growth). In some areas, multiple whiskers nucleate close to each other and grow in different directions. These agglomerations can result in flower-like structures, as observed in Zone 2 (Coalescence).

The formation of these silica whiskers has significant implications for high-temperature applications, such as nuclear reactors, where SiC is used as a structural material or as a fuel cladding material. The oxidation behavior of SiC in environments containing small amounts of oxygen, such as in accident scenarios in gas-cooled reactors, is a critical concern for material integrity and safety. The formation of silica whiskers could contribute to the formation of a protective SiO_2 layer that prevents further oxidation of the SiC substrate. The whiskers could act as a diffusion barrier, slowing the transport of oxygen to the underlying SiC and reducing the rate of oxidation. The growth of whiskers, especially in the form of needle-like structures, however, could lead to a reduction in mechanical integrity, particularly if the whiskers act as stress concentrators or if they grow in such a way that they weaken the material. Further studies would be needed to assess the mechanical properties of SiC after whisker formation.

As previously discussed, excessive pre-passivation hinders the formation of silica nanowires, favoring the development of more complex whisker-like microstructures instead. We propose that, in the case of the 2-hour pre-passivation, the resultant oxide layer became too thick to effectively support the vapor-liquid-solid (VLS) mechanism essential for nanowire synthesis.

In summary, the growth mechanism of silica nanowires is proposed to be governed by several phenomena and enhanced by three key factors (active oxidation, VLS growth and passivated oxide), all influenced by the chemical pump effect. First, a SiOx cluster is anchored on the SiC substrate through active oxidation, consistent with the nucleation dynamics observed on metal silicides. The transport of SiO gas from the active oxidation region to the outer circular patterns can be described by the chemical pump effect, where localized SiO gas production creates a concentration gradient that drives its migration to other regions. This gas-phase transport of SiO is essential for the formation of complex nanostructures. Additionally, the catalytic activity of SiOx clusters likely aids in the oxide-assisted growth of silica nanowires. For the formation of these silica micro-nano structures, however, oxide thickness plays most important role. Depending on the pre-passivation thickness, either silica nanowires or whiskers are formed. As seen from Figure 4, at the initial stage of the reaction, severe mass loss occurs (active mode); then total mass gain reaction follows, resulting in SiO gas transportation to silica production areas. Apparently, the mass change is positive during their synthesis but both local active mode and passive mode occur simultaneously. Although the present pre-passivation treatment cannot completely prevent active mode, these silica microstructures synthesis largely contribute to enhance passive mode.

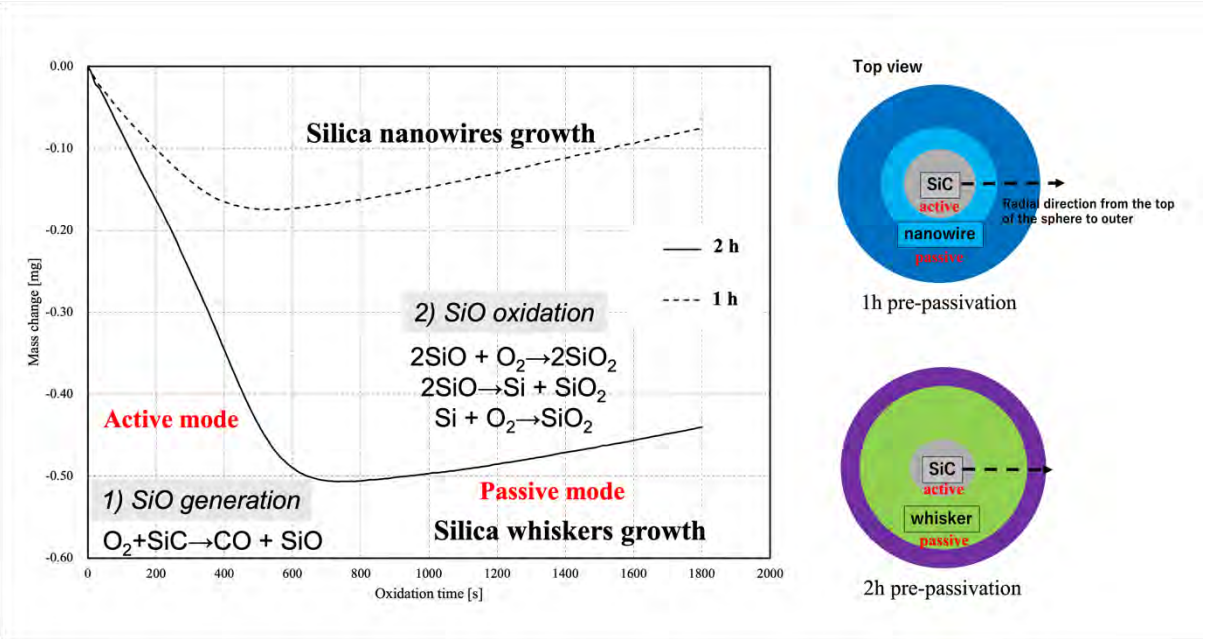

Figure 4. Measurement of mass changes of the samples (1-hour/2-hour pre-passivation) during the silica nanowire/whisker synthesis with simplified illustration of each sample.

As highlighted in this study, the pre-passivation time significantly impacts microstructure development. An optimal oxide thickness promotes nanowire growth, while excessive oxide thickness hinders the participation of nanoparticles within the SiC in the VLS mechanism, thereby impeding nanowire formation (Figure 5). Nanowire growth can also proceed in strongly oxidative conditions, contributing to silica nanowire synthesis. Concurrently, the oxidation of the nanowire walls (from SiOx to SiO_2) serves to passivate their surfaces [15]. At steady-state, equilibrium is reached between further SiOx deposition and its oxidation, resulting in a constant nanowire diameter, as observed in both SEM and TEM images. The uniformity of the nanowires indicates a stable growth environment, with minimal fluctuations in local gas concentrations or temperature gradients.

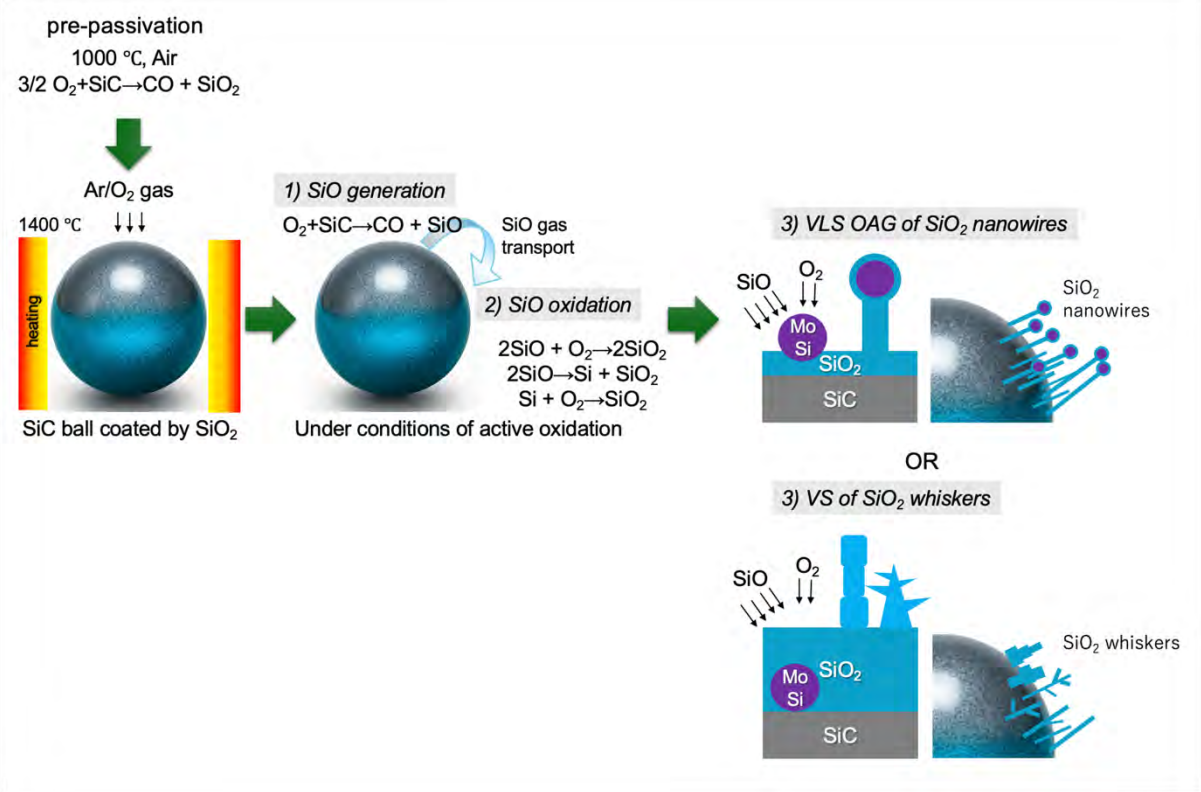

Figure 5. The proposed mechanisms on silica nanowires/whiskers growth associated with OAG.

3. CONCLUSIONS

To minimize the risk of nuclear fuel damage and prevent unacceptable corrosion during use, we investigate the effects of pre-passivation on the active oxidation of SiC at high temperatures in an extremely low-oxygen gas flow. While active oxidation still occurs locally, pre-passivation significantly mitigates long-term mass degradation. This treatment has a proven effect on active oxidation and simultaneously induces the formation of various intricate silica microstructures on SiC due to the chemical pump effect. During this process, the thickness of the passivated oxide layer plays a crucial role in determining the synthesis, growth, and morphology of silica nanowires or whiskers. In particular, the growth of nanowires is initiated by metal nanoparticles such as Mo, making the selection of sintering additives in SiC manufacturing a critical consideration. We propose synthesis mechanisms for these silica microstructures, which provide a useful model for evaluating nuclear fuel behavior.

ACKNOWLEDGMENTS

This work is supported by MEXT Innovative Nuclear Research and Development Program Grant Number JPMXD21457197.
The authors would like to thank the Materials Analysis Division, Open Facility Center, Institute of Science Tokyo for TEM-EDX observation.

REFERENCES

1. Y. Nishimura, A. Gubarevich, K. Yoshida, and K. Okamoto, Comparison of SiC and graphite oxidation behavior under conditions of HTGR air ingress accident, *Mech. Eng. Lett.*, **2022**, 8, 22-00315.
2. Y. Nishimura, A. Gubarevich, K. Yoshida, A. K. Sharma, and K. Okamoto, Modeling passive/active transition in high-temperature dry oxidation of reaction-sintered SiC for innovative fuel matrix in high-temperature gas-cooled reactors, *Journal of the European Ceramic Society*, **2024**, 44, 3031-3038.
3. Y. Nishimura, A. Gubarevich, K. Yoshida and K. Okamoto, An Innovative Fuel Design for HTGRs: Evaluating a 10-Hour High-Temperature Oxidation of the SiC Fuel Matrix During Air Ingress Accident Conditions, *Energies*, **2024**, 17, 5366.
4. Y. Nishimura, A. Gubarevich, K. Yoshida and K. Okamoto, Oxide growth and corrosion resistance of Si-containing SiC fuel matrices fabricated by reaction sintering for high-power nuclear reactors, *Open Ceramics*, **2025**, 21, 100740.
5. N. S. Jacobson and D. L. Myers, Active Oxidation of SiC, *Oxidat. Met.* **1** 25 (2010).
6. N. S. Jacobson, D. L. Myers, and B. J. Harder, Active oxidation of silicon carbide, *Materials at high temperatures* **29** 3 (2012).
7. S.-H. Li, X.-F. Zhu, and Y.-P. Zhao, Carbon-Assisted Growth of SiO_x Nanowires, *J. Phys. Chem. B* **108** 17032-17041 (2004).
8. F. M. Kolb, H. Hofmeister, R. Scholz, M. Zacharias, U. Gosele, D. D. Ma, and S.-T. Lee, Analysis of Silicon Nanowires Grown by Combining SiO Evaporation with the VLS Mechanism, *J. Electrochem. Soc.* **151** G472 (2004).
9. N. Wang, Y. H. Tang, Y. F. Zhang, C. S. Lee, and S. T. Lee, Nucleation and growth of Si nanowires from silicon oxide, *Phys. Rev. B* **58** 24 (1998).
10. C. C. Tang, S. S. Fan, Marc Lamy de la Chapelle, and P. Li, Silica-assisted catalytic growth of oxide and nitride nanowires, *Chem. Phys. Lett.* **333** 12-15 (2001).
11. A. N. Goldstein, C. M. Echer, and A. P. Alivisatos, Melting in Semiconductor Nanocrystals, *Science* **256** 1425 (1992).
12. A. Kaledin, S. Shikunov, K. Komarov, B. Straumal, and V. Kurlov, SiC-Based Composite Material Reinforced with Molybdenum Wire, *Metals* **13** (2) 313 (2023).
13. B. T. Park and K. Yong, *Nanotechnol.* **15** 365-370 (2004).
14. W. N. Zhou, Z. X. Yang, F. Zhu, and Y. F. Zhang, *Physica E* **31** 9-12 (2006).
15. A. Tricoli, M. Righettoni, F. Krumeich, W. J. Stark, and S. E. Pratsinis, Scalable flame synthesis of SiO_2 nanowires: dynamics of growth, *Nanotechnol*. **21** 465604 (2010).

High temperature oxidation behavior of silicon carbide fuel matrix during Beyond Design Basis Accident (BDBA) in Gen IV reactors

Yosuke NISHIMURA
PhD, Assistant Professor
Nuclear Professional School
The University of Tokyo

Ruicong Xu, Zongda Yang, Chao Yang, Bo Li, and Hiroaki Abe

Background

High temperature gas-cooled reactor (HTGR) project

Sleeveless fuel design→higher heat transfer→high-power density core

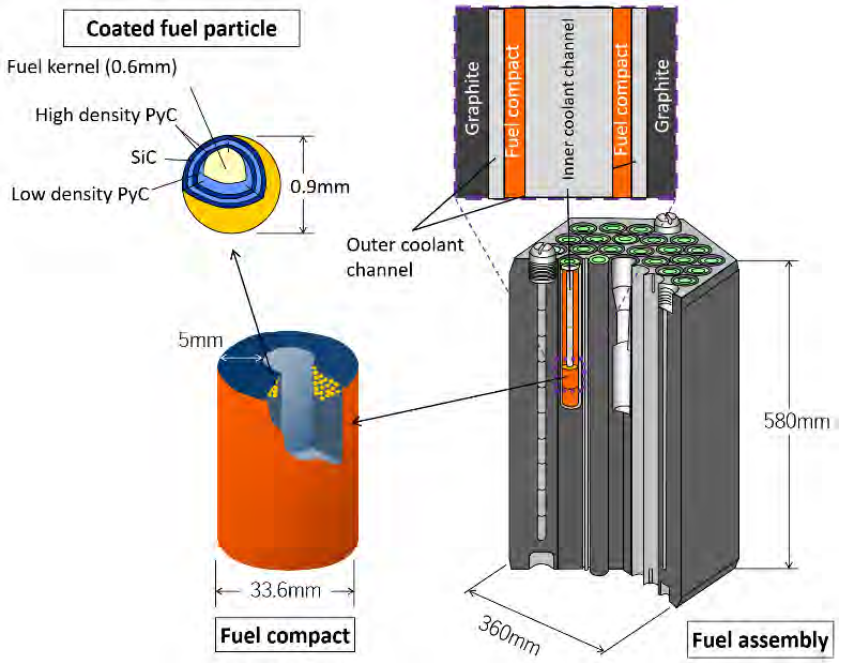

Fig. Fuel assembly of the core

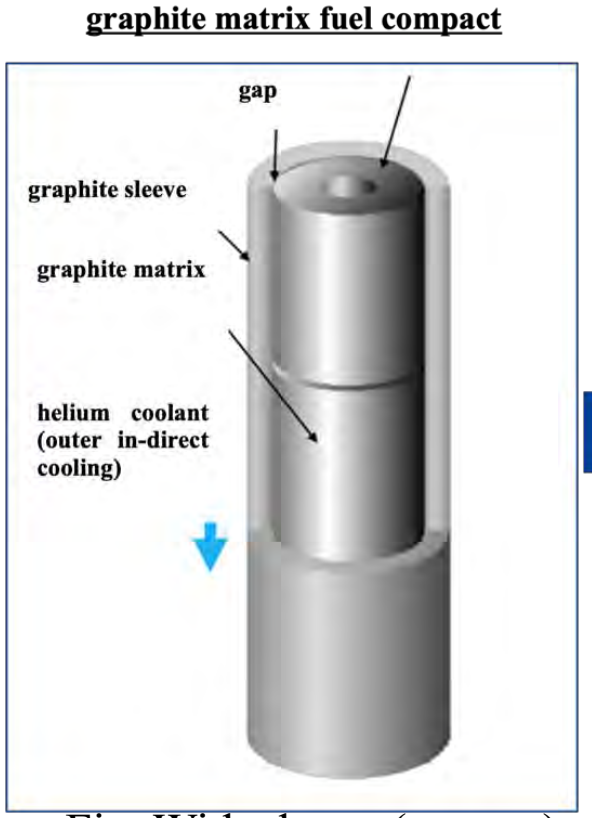

Fig. With sleeve (current)

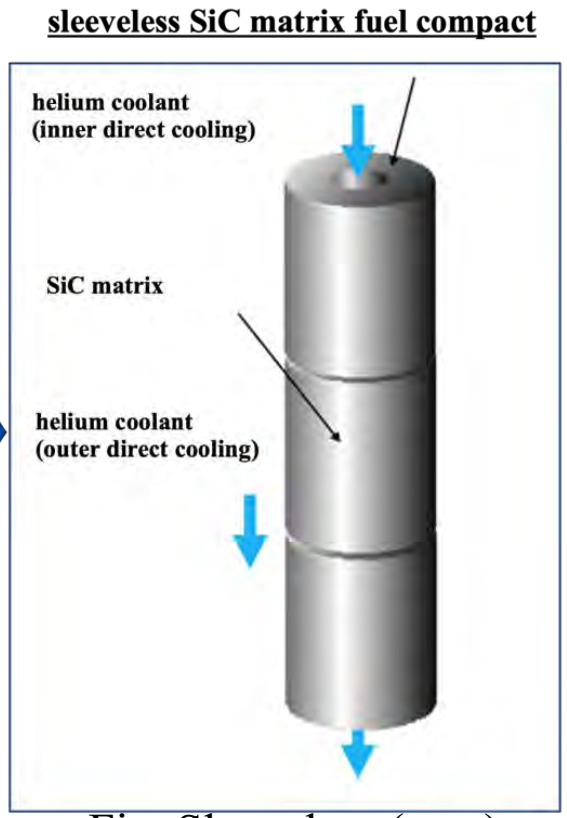

Fig. Sleeveless (new)

Dual-separate direct cooling

UTokyo

Oxidation behaviors of RS-SiC during accidents

Guillotine type break of primary coolant pipe

↓

Loss-Of-Coolant-Accident (LOCA)

↓

Depressurization

↓

Air-ingress (Beyond Design Basis Accident)

Fuel matrix needs **anti-oxidation** properties
Ex. Silicon carbide ceramics

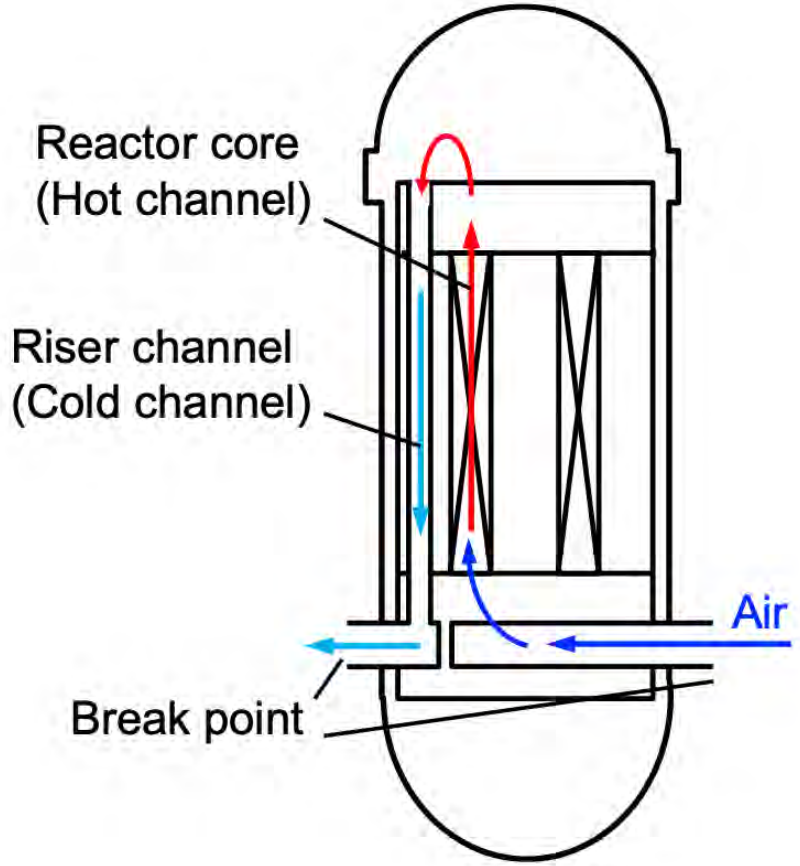

Fig. Schematic of air ingress phenomena in case of complete cross duct failure

Passive/active transition diagram for HTGR operational ranges

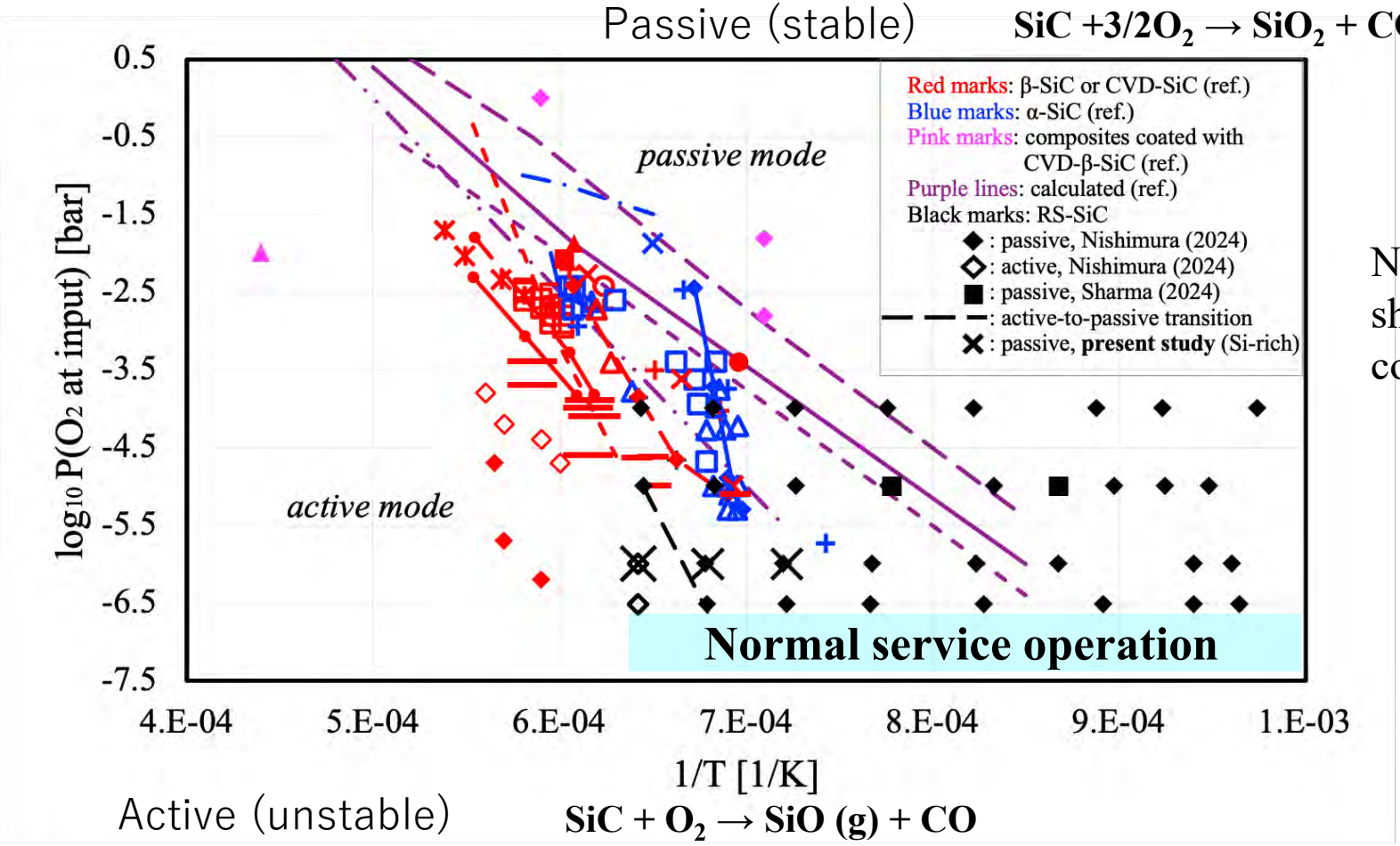

Normal service operation range should be under 1300 ℃ to prevent corrosion of the fuel matrix

FIG. passive/active transition diagram of the RS-SiC at high-temperature oxidation

UTokyo

Research target

Fuel safety assessment of HTGRs

Predicting the oxidation behavior of the SiC fuel matrix

Obtained SiC oxidation data in wide range of parameters
Proposed oxidation model that is useful for fuel safety

FINAL GOAL

Obtained feasibility of the SiC fuel matrix design

Application for real-scale fuel compacts

Today's main topic

A method to control active oxidation mode

UTokyo

How to prevent unacceptable corrosion of the SiC fuel matrix…

Either operate the HTGR core within passive environment

or

Control active oxidation mode of the SiC

*The easiest, simple way is "**pre-passivation** treatment"*

1. Pre-passivation at lower temperature
2. Test in active environment at higher temperature

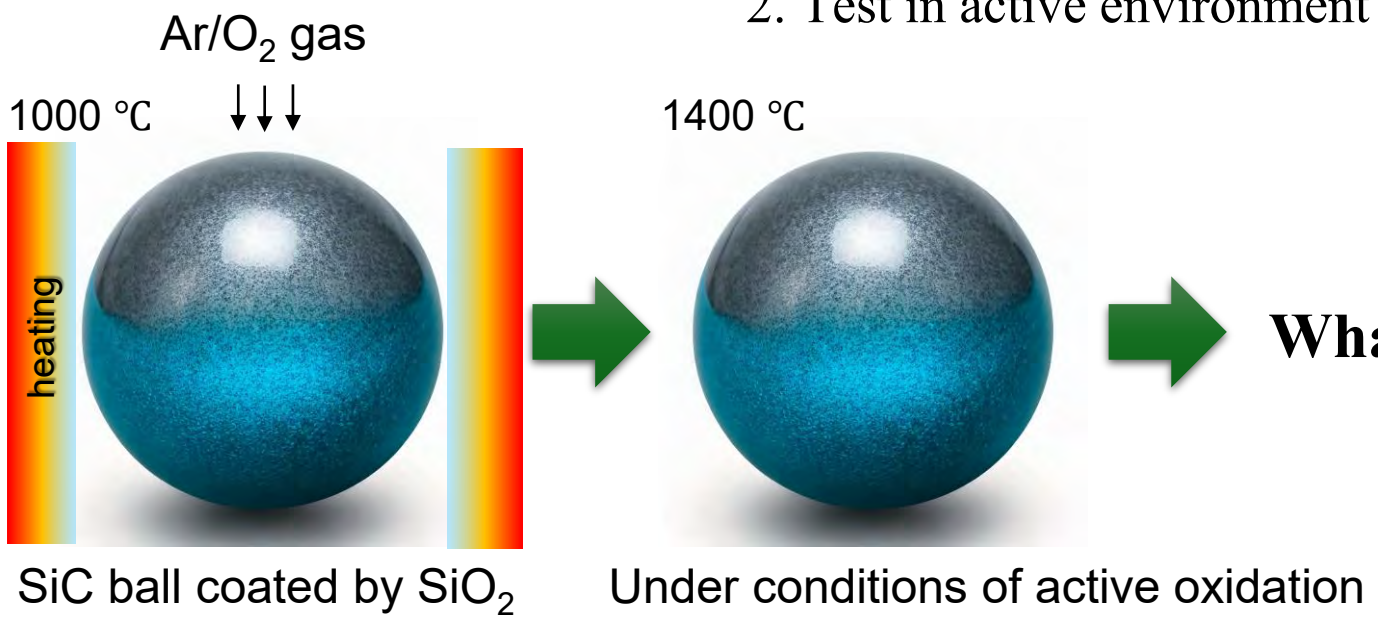

UTokyo

Experimental setup

- sample: commercially available RS-SiC (Sato Tekkou Co., Ltd.)
- heating rate 20 ℃/min
- sampling time 1.0 sec
- measurement accuracy 0.1 μg

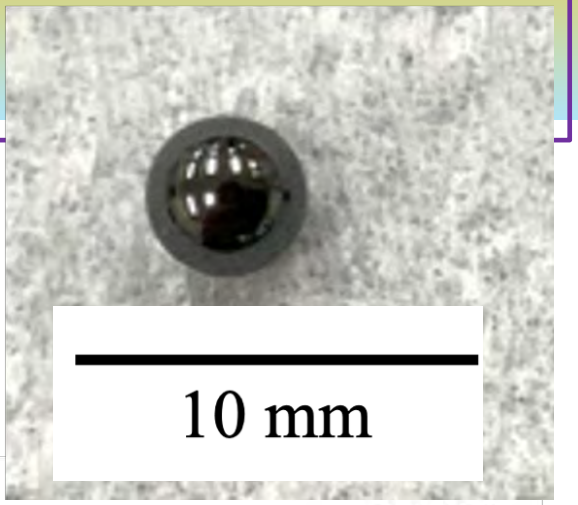

2 patterns of pre-passivation

	pre-passivation	active environment
targeted temperature	1000℃	1400 ℃
duration	60 min or 120 min	30 min
Oxygen concentration	open air	1 ppm in Ar/O_2 gas flow

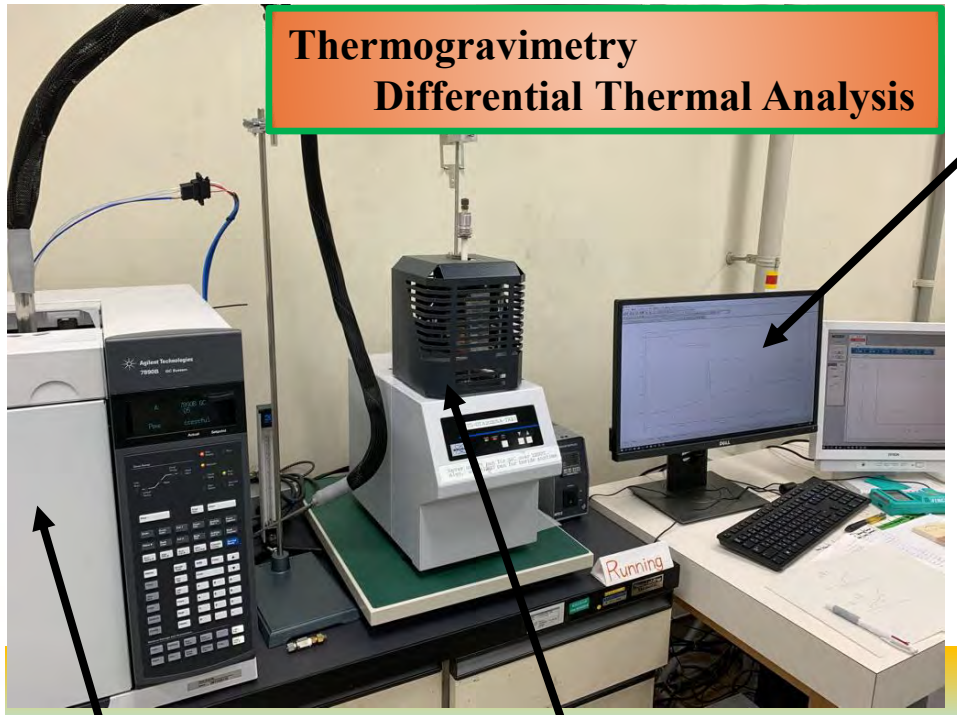

Fig. TG-DTA setup

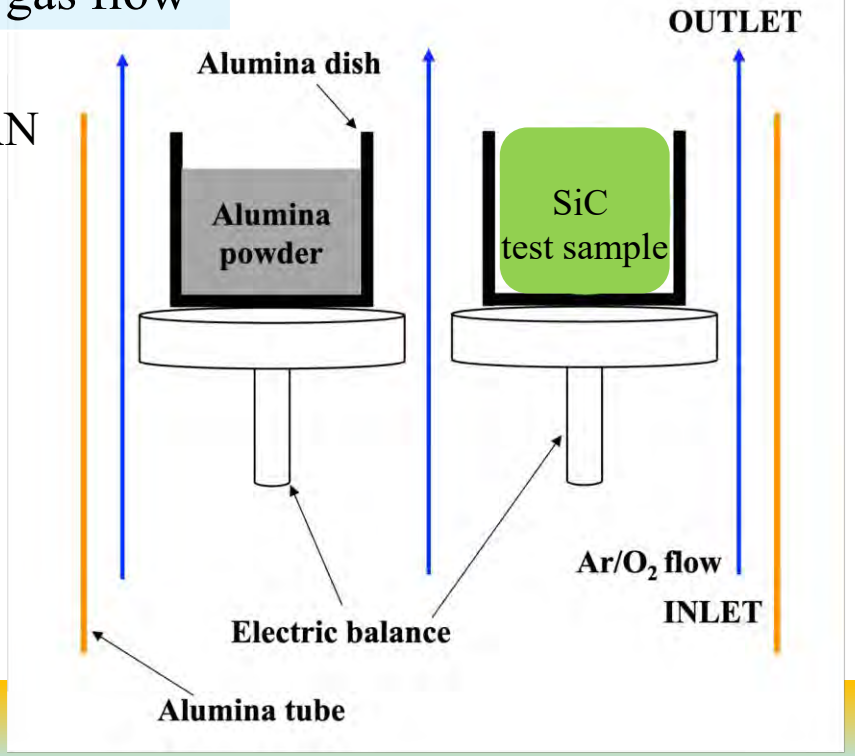

Fig. electric balance in the furnace

UTokyo

Results & discussion

60 min pre-passivation case (0.8 µm oxide thickness)

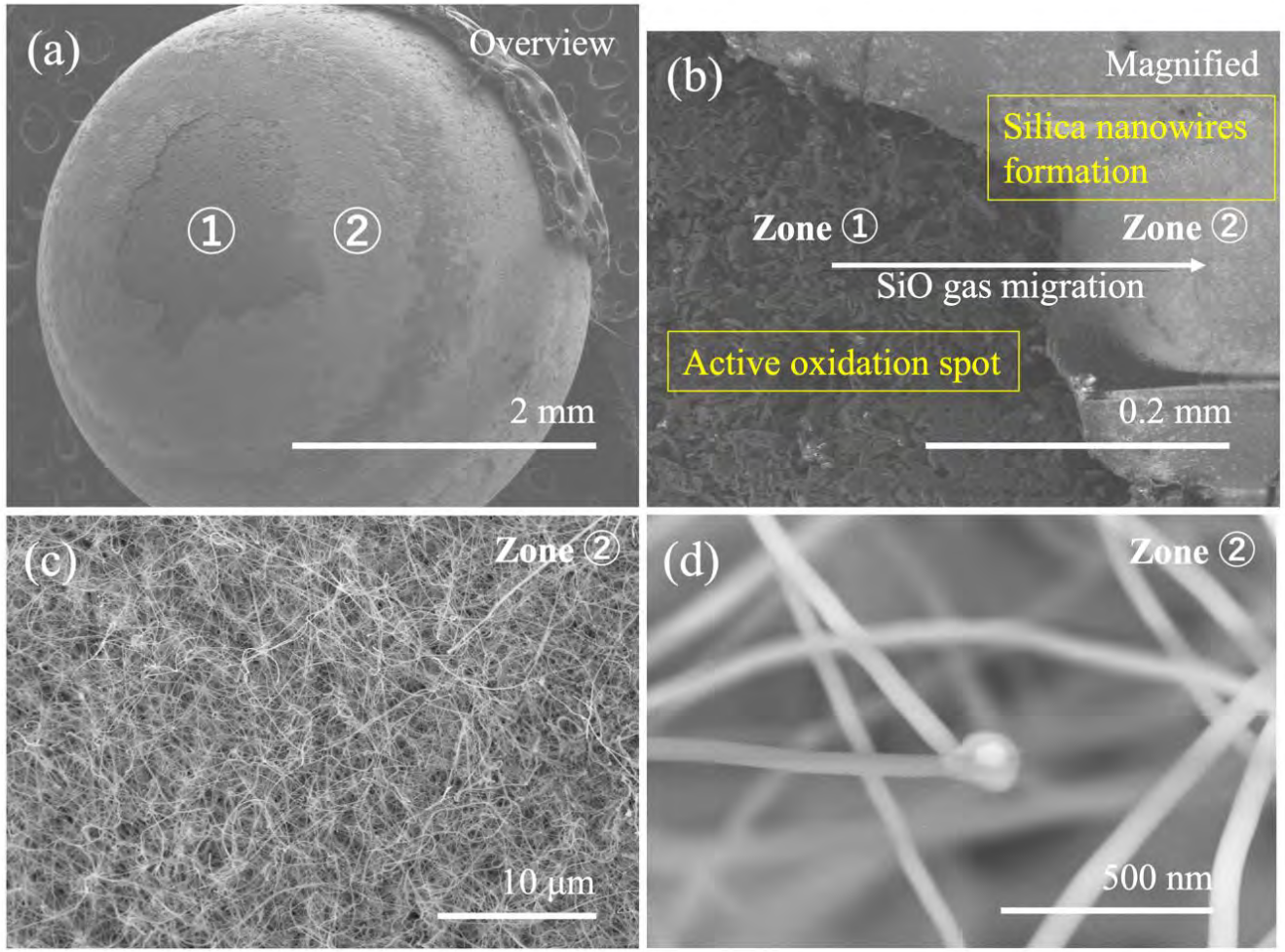

- Circular pattern with zone 1 and 2
- SiC was exposed (active mode in zone 1)
- Nanowires formation in zone 2

FIG. FE-SEM images of SiC substrate (pre-passivated for 1 hour) after oxidation at 1400 ℃ for 30 min.
(a) Low-magnification top-view image showing three distinct zones.
(b) Boundary between the exposed SiC area without a SiO_2 film (Zone 1) and the silica nanowires area (Zone 2).
(c) Typical nanowires synthesized in Zone 2.
(d) Nanowires view in higher magnification.

UTokyo

Results & discussion

60 min pre-passivation case (0.8 μm oxide thickness)

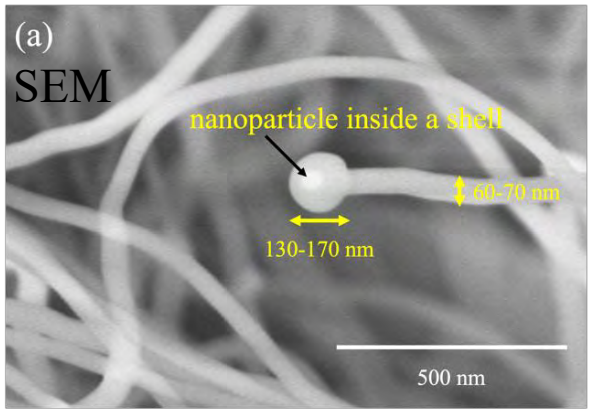

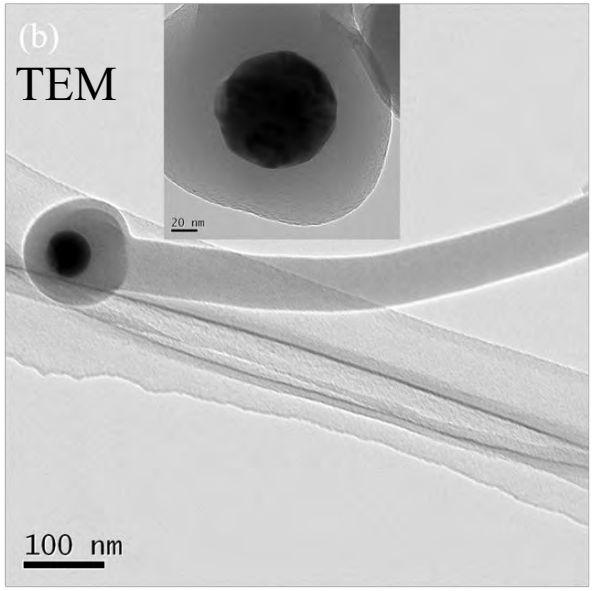

Silica nanowire synthesis

(a) FE-SEM image of the typical nanowires at higher magnification and
(b) TEM images of a typical nanowire with a nanoparticle encapsulated (dark region) at the nanowire (inset).

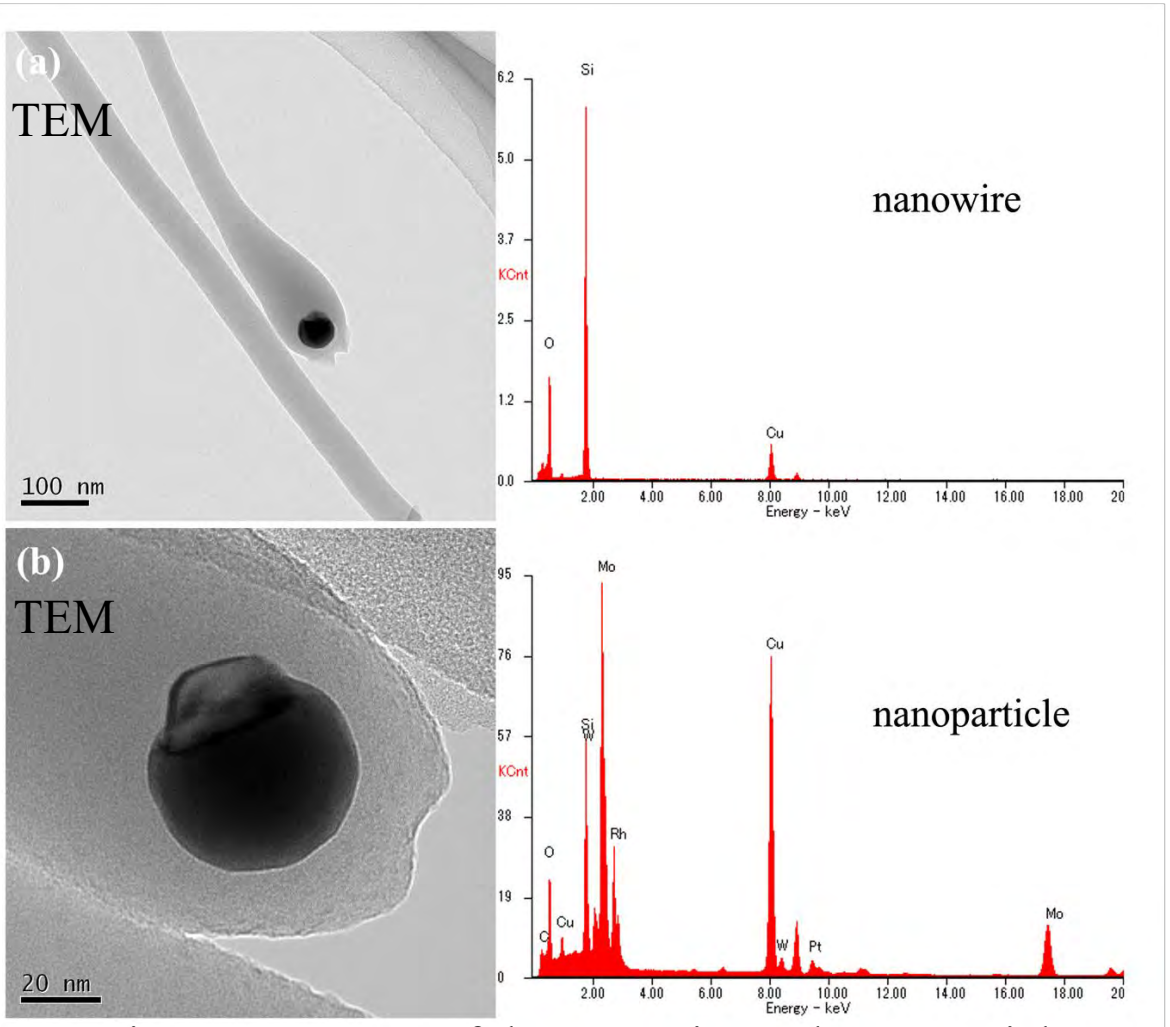

Fig. EDS spectra of the nanowire and nanoparticle

Si-Mo alloy in the nanoparticle

Cu peak comes from sample mesh
Rh, W, Pt comes from heating components
Mo comes from additive of $MoSi_2$

UTokyo

Element analysis of clean SiC sample by Laser-Induced Breakdown Spectroscopy (25 points)

- Mo comes from $MoSi_2$ additives in the SiC
- Pt peaks come from surface coating before LIBS measurement

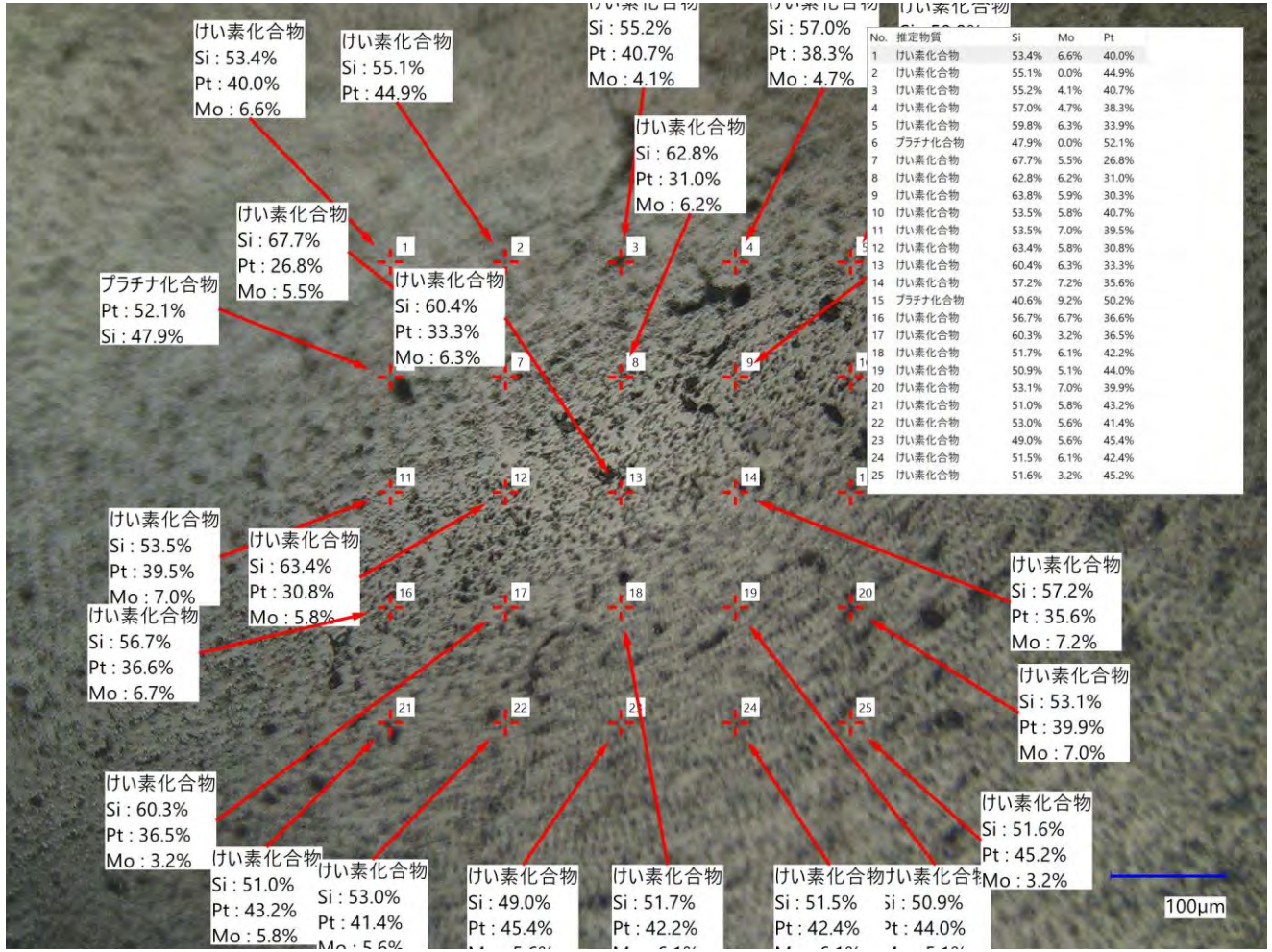

FIG. Composition analysis by LIBS

UTokyo

Mechanism of the silica nanowires synthesis

Pre-passivated oxide promotes
"*Oxide Assisted Growth* (OAG [1])"

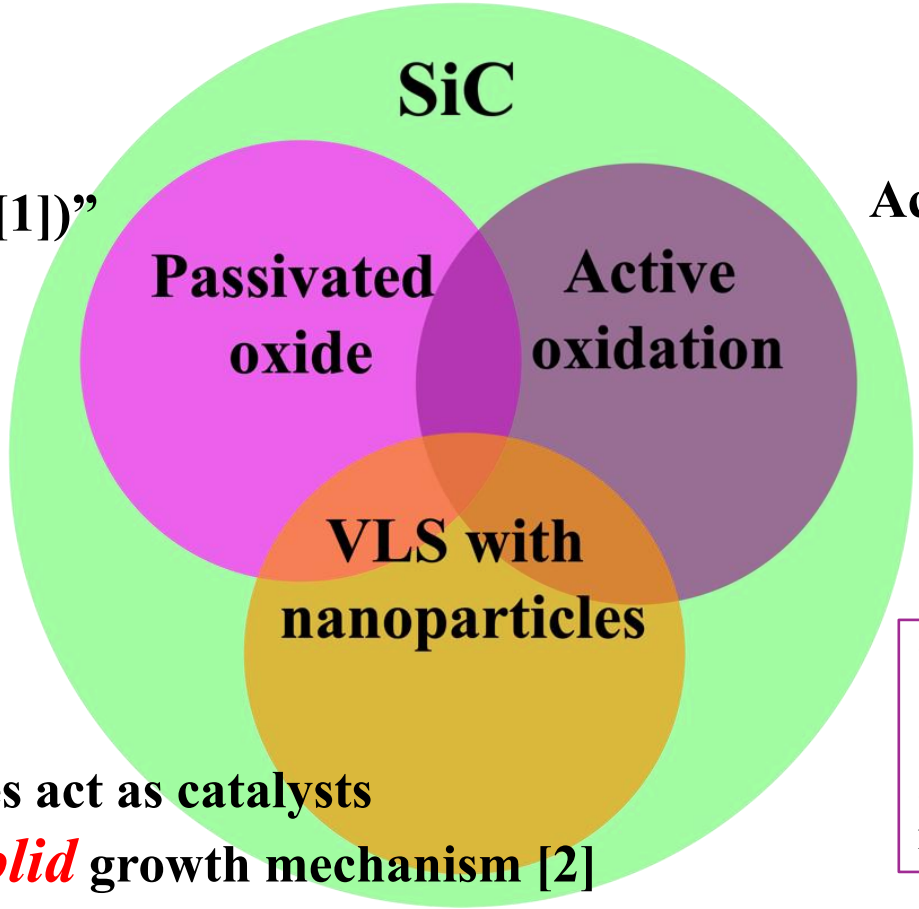

Active oxidation in zone 1 generates SiO gas as a growth precursor

Si-Mo alloy nanoparticles act as catalysts to facilitate the *Vapor-Liquid-Solid* growth mechanism [2]

This three-key factors coupling is found very coincidentally, but each growth mechanism has been already reported respectively.

FIG. Key factors enhancing silica nanowire growth in this study

[1] W. N. Zhou *et al.*, *Physica E* 31 9-12 (2006).

[2] F. M. Kolb *et al.*, *J. Electrochem. Soc.* 151 G472 (2004).

UTokyo

Results & discussion

120 min pre-passivation case (2 μm oxide thickness)

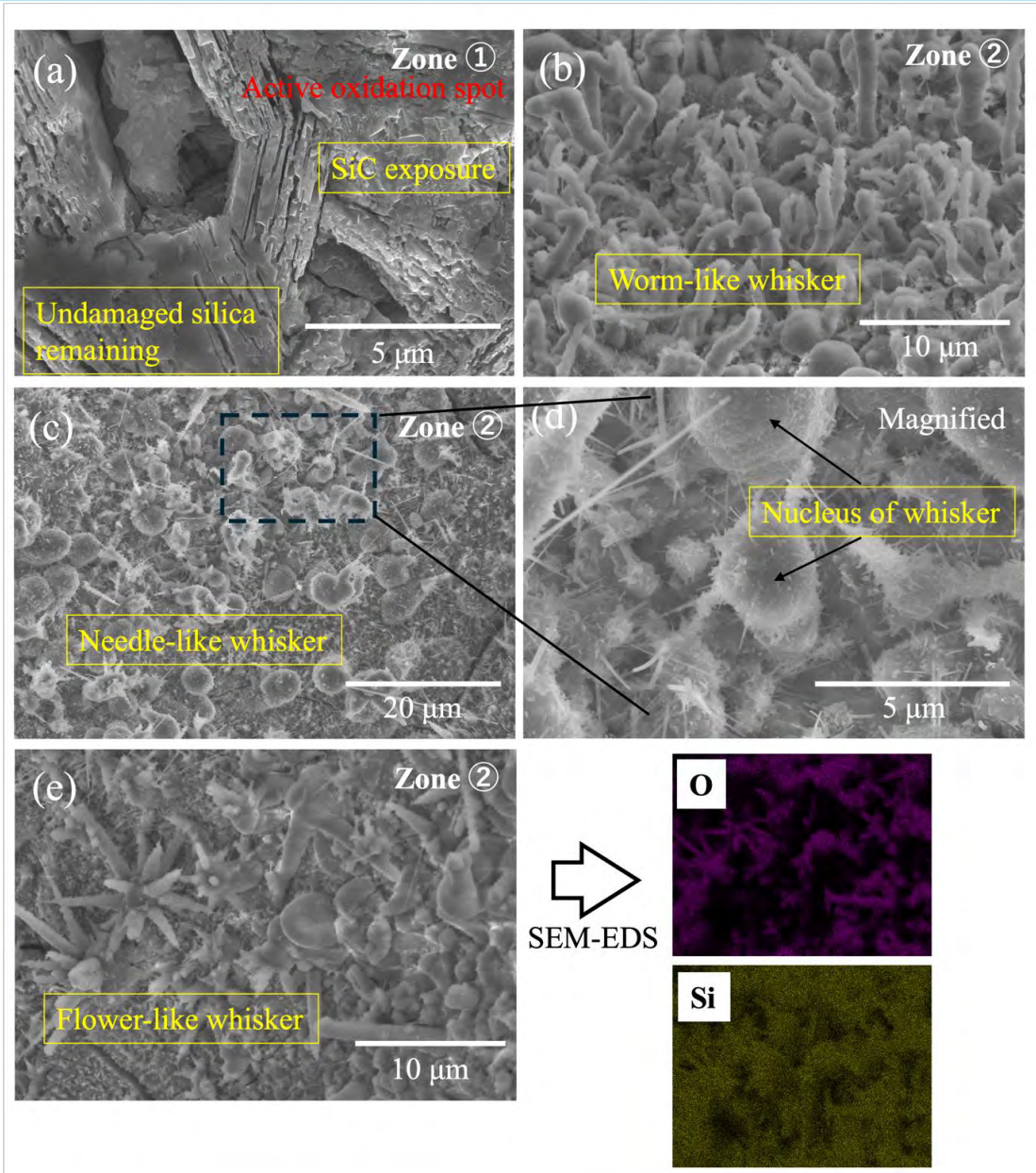

- Similar circular patterns as zone 1 and 2
- Many intricate silica micro-whiskers formation
- No silica nanowires formation

Unlike silica nanowires, silica whiskers formation associates with Vapor-Solid (VS) mechanism [1, 2]

[1] W. Haller *et al.*, *Nature* 191 662 (1961)
[2] R. J. Jaccodine *et al.*, *Nature* 189 298 (1962)

UTokyo

Results & discussion

60 min (0.8 µm) pre-passivation vs 120 min (2 µm)

Localized active mode and ***passive*** mode with silica nanostructures formation

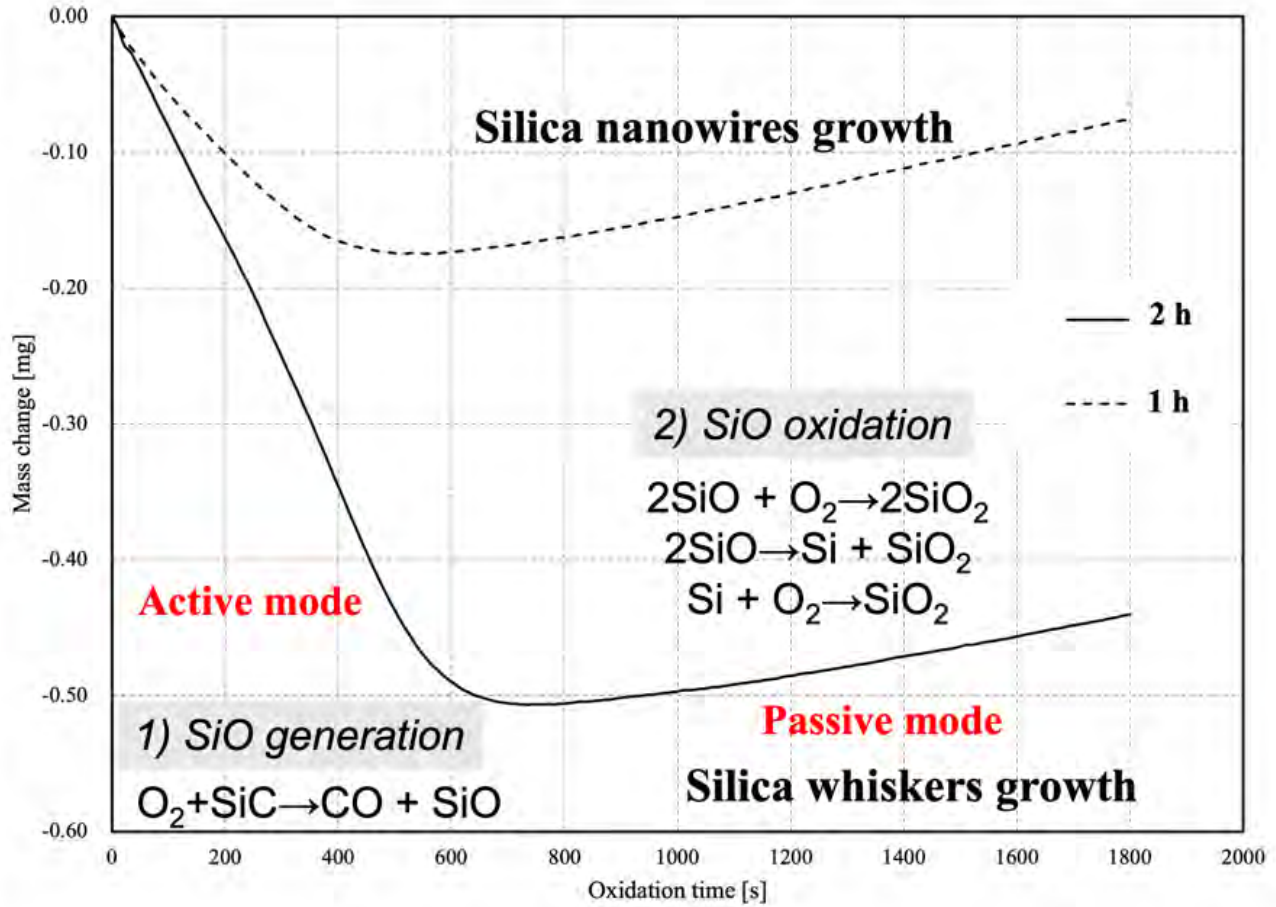

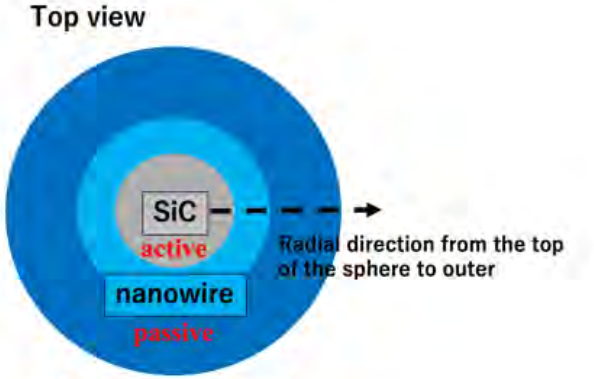

1h pre-passivation

2h pre-passivation

Thickness of pre-passivated oxide determines the silica formation either nanowires or micro-whiskers

Oxide Assisted Growth (OAG) has an appropriate range for silica nanowires synthesis

UTokyo

Model: Chemical pump effect on silica nanowires synthesis during active oxidation

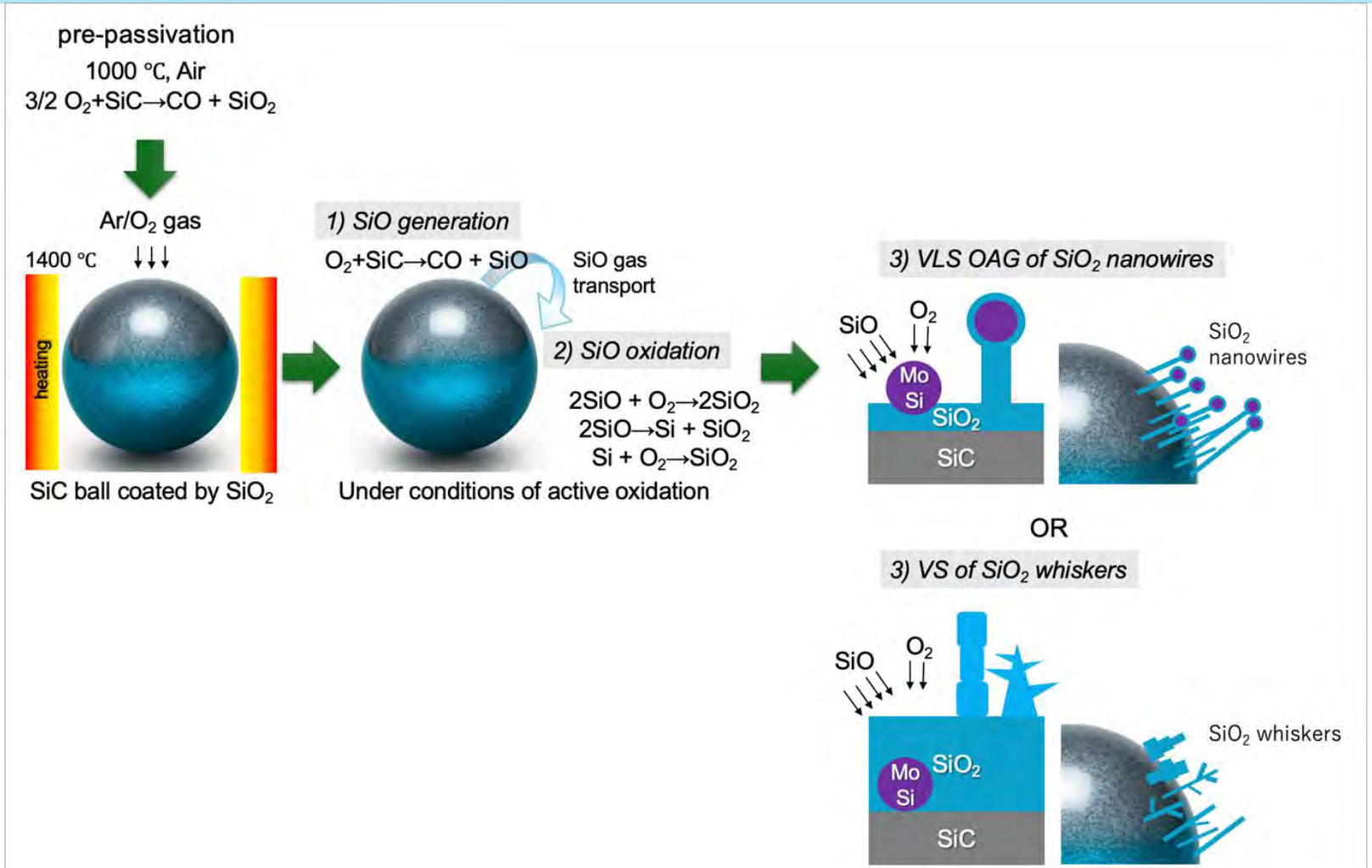

FIG. The proposed mechanisms on silica nanowires/whiskers growth associated with OAG.

UTokyo

CONCLUSION

◆ While active oxidation still occurs locally, pre-passivation significantly mitigates long-term mass degradation.

◆ simultaneously induces the formation of various intricate silica microstructures on SiC

◆ the growth of nanowires is initiated by metal nanoparticles such as Mo,
making the selection of sintering additives in SiC manufacturing a critical consideration

these microstructures themselves are tough materials and are helpful for mechanical strength (pros),
however, they may change fuel dimension and block the coolant channel (cons)

propose synthesis mechanisms for these silica microstructures,
which provide a useful model for evaluating nuclear fuel behavior

UTokyo

Thank you for attention!

ACKNOWLEDGMENTS

This work is supported by MEXT Innovative Nuclear Research and Development Program Grant Number JPMXD21457197.

UTokyo

Materials

Fabrication of SiC fuel compacts by reaction sintering process

FIG. SiC-matrix fuel compact

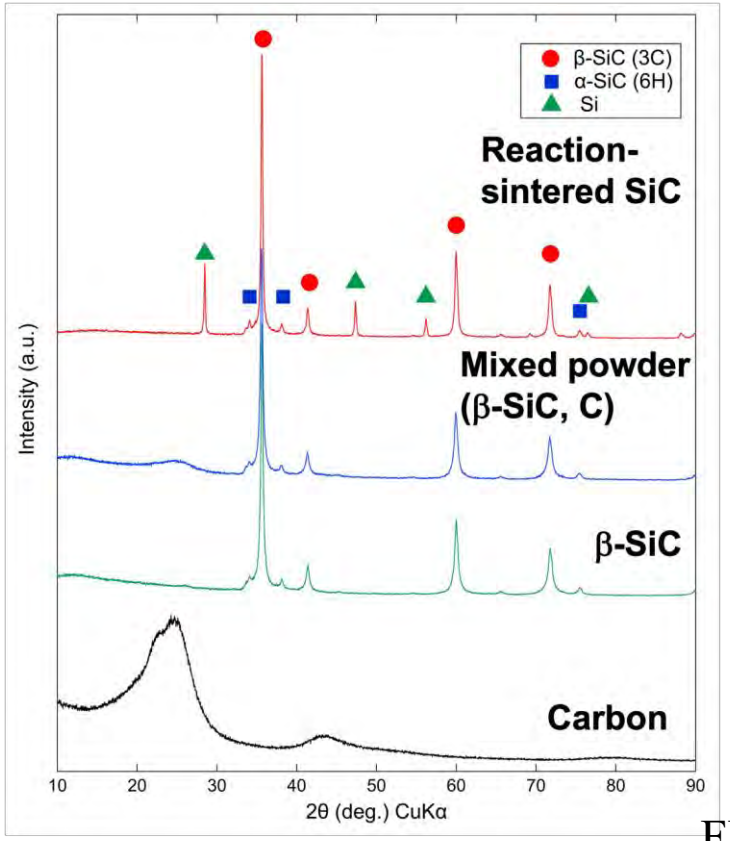

FIG. XRD patterns of the fabricated RS-SiC

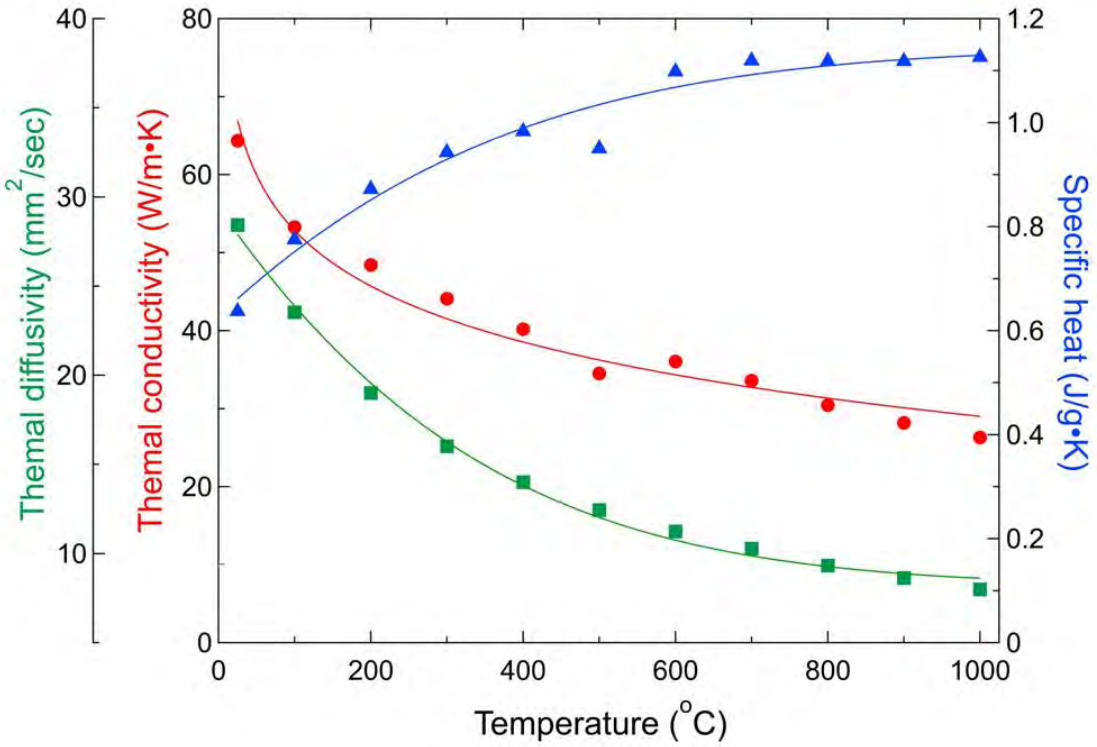

FIG. Measurement of thermal conductivity by laser flash method

94% theoretical density and adequate thermal conductivity for nuclear applications

UTokyo

ADVANCING NUCLEAR SAFETY TECHNOLOGY

Fission Product Transport in Molten Salt Systems

Particulate PBE in liquid and vapor · differential vaporization · freeze entrapment · tritium transport across fluids and structures

David L. Luxat · Matthew Christian · Ed Duchnowski · Lucas Albright · Brad Beeny · Troy Haskin · Dallin Keesling

Dept. 8852 · Nuclear Energy Safety Technologies · Sandia National Laboratories

SAND2026-XXXXP

Sandia National Laboratories is a multimission laboratory managed and operated by National Technology & Engineering Solutions of Sandia, LLC, a wholly owned subsidiary of Honeywell International Inc., for the U.S. Department of Energy's National Nuclear Security Administration under contract DE-NA0003525.

Why molten-salt source-term physics is different

Molten salt reactors change the source-term picture in five qualitative ways. Each motivates an element of the framework presented in this deck.

- **Fuel is the coolant.** Soluble FPs (Cs, I, Sr) stay in the salt; noble metals (Mo, Ru, Pd) precipitate; noble gases (Xe, Kr) sparge out continuously.
- **The carrier salt is itself multi-component.** BeF_2 is more volatile than LiF; the liquid composition drifts; partial pressures must be computed per constituent. In MSBR fuel salt at 1000 °C, $P_{sat,BeF_2} \approx 1100$ Pa while $P_{sat,UF_4} \approx 39$ Pa.
- **Particulate nucleation happens in the liquid.** Classical aerosol PBE only carries vapor-phase particulates — here we need a sectional PBE in both phases.
- **Freezing is normal operation.** Freeze plugs and drain-tank crusts trap dissolved FPs; melt-back releases them.
- **Tritium dominates the dose path?** It is generated in the salt, transports through structures by diffusion + trapping, and needs Soret thermophoresis in the liquid.

PART 1 — CURRENT CAPABILITY

MELCOR for the MSBR fuel cycle

Scenario — emergency drain to a cooled drain tank

Pump trip with failure to insert shutdown rods initiates an emergency salt drain from the primary loop to the drain tank, completing in approximately 7 minutes.

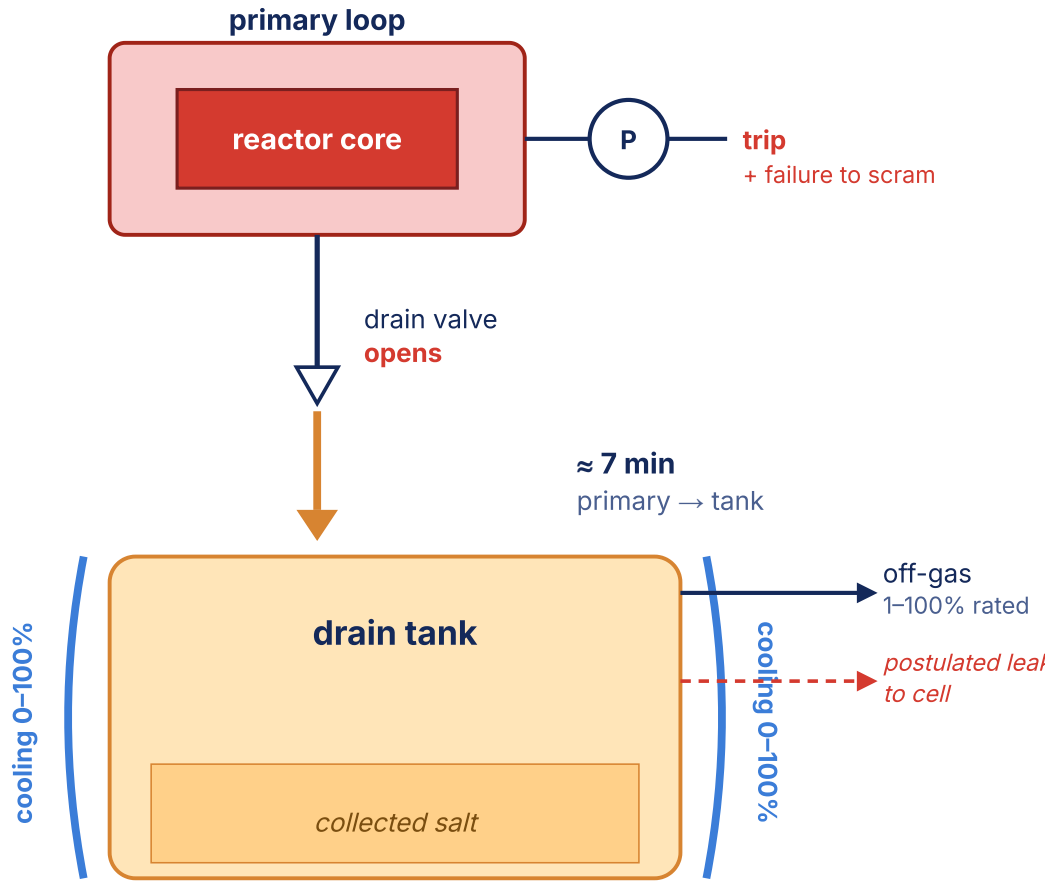

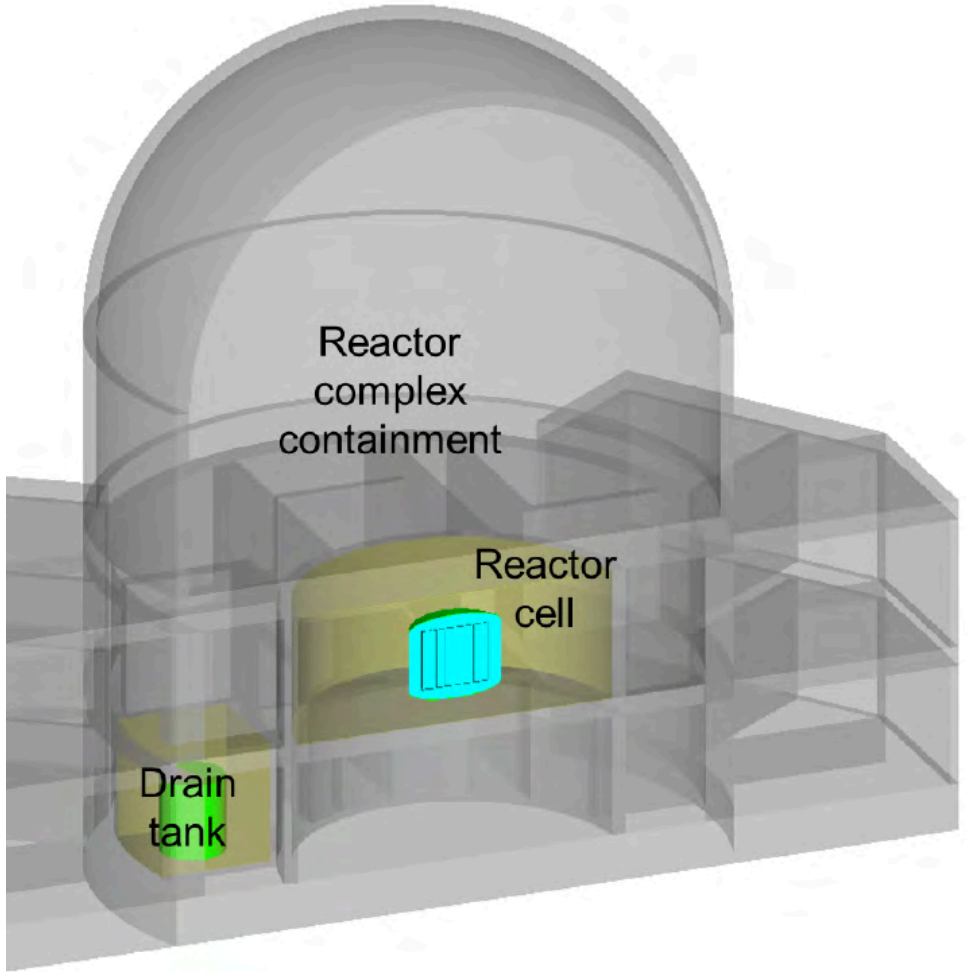

Reactor complex containment, reactor cell, drain tank. After Robertson et al. ORNL-4541 (1971); model build per Duchnowski et al., SAND2024-07835PE.

Species partial pressures decide release

The vapor-pressure curve determines the volatility hierarchy at the salt-cover-gas interface. Decay heat by class sets the thermal driver for that hierarchy as the transient evolves.

- **BeF_2** — volatile carrier; P_{sat} ≈ 1100 Pa at 1000 °C; dominates airborne mass once released.
- **UF_4** — fuel; P_{sat} ≈ 39 Pa at 1000 °C; non-negligible at drain-tank temperatures.
- **$CsBeF_3$, LiI** — dominant Cs and I compounds; sub-pascal in the MSBR operating window. Direct vaporization is not the release pathway for these species.

> BeF_2 and UF_4 are assigned dedicated radionuclide classes. Aggregation into generic carrier or fuel classes would obscure the per-constituent partial pressure that governs release.

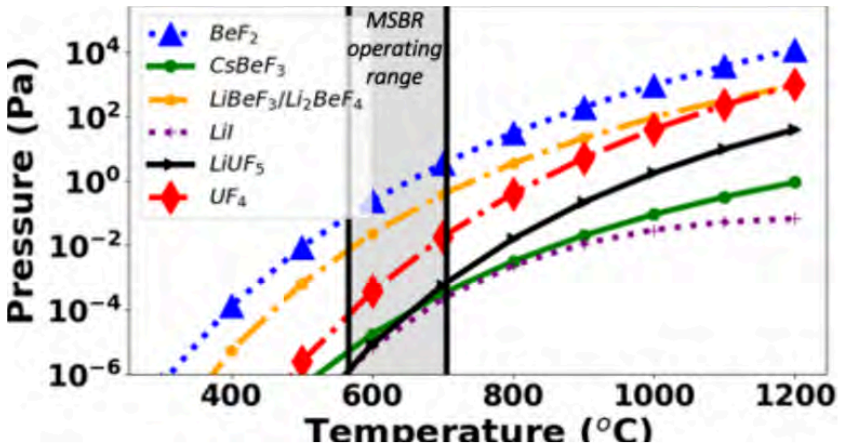

P_{sat}(T) for the species classes tracked; MSBR operating range shaded.

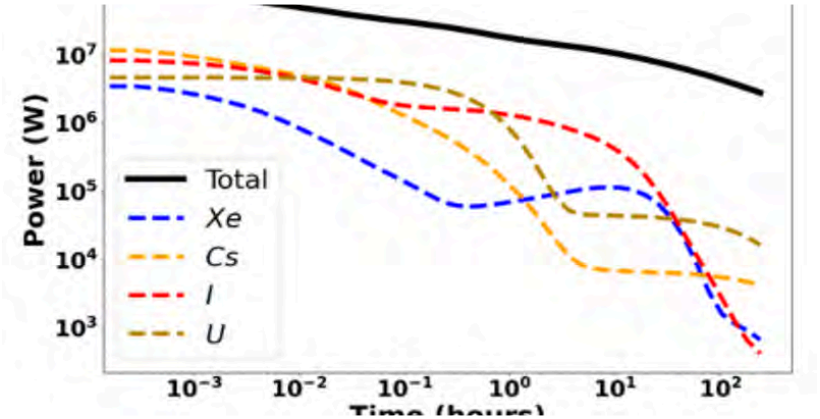

Decay heat by class (Xe, Cs, I, U) and total — Xe dominates early; Cs takes over after ~hours.

MELCOR nodalization — primary loop

- Four identical loops — one shown. CV-212, CV-213, CV-312, CV-313 are a single loop; all loops recombine at CV-301.
- Each hot leg carries a pump with a pump bowl — the bowls are the off-gas source.
- Primary heat exchangers are shell-and-tube; the secondary side is a **boundary condition**, not a coupled secondary CV network.
- Core (left) is the same node grid that receives the SCALE-averaged power map — seven axial levels, eight radial channels per level, plus inlet/upper plenum.

> Boundary-condition coupling on the secondary side isolates the primary-side response; secondary-loop thermal hydraulics are not resolved in this scenario.

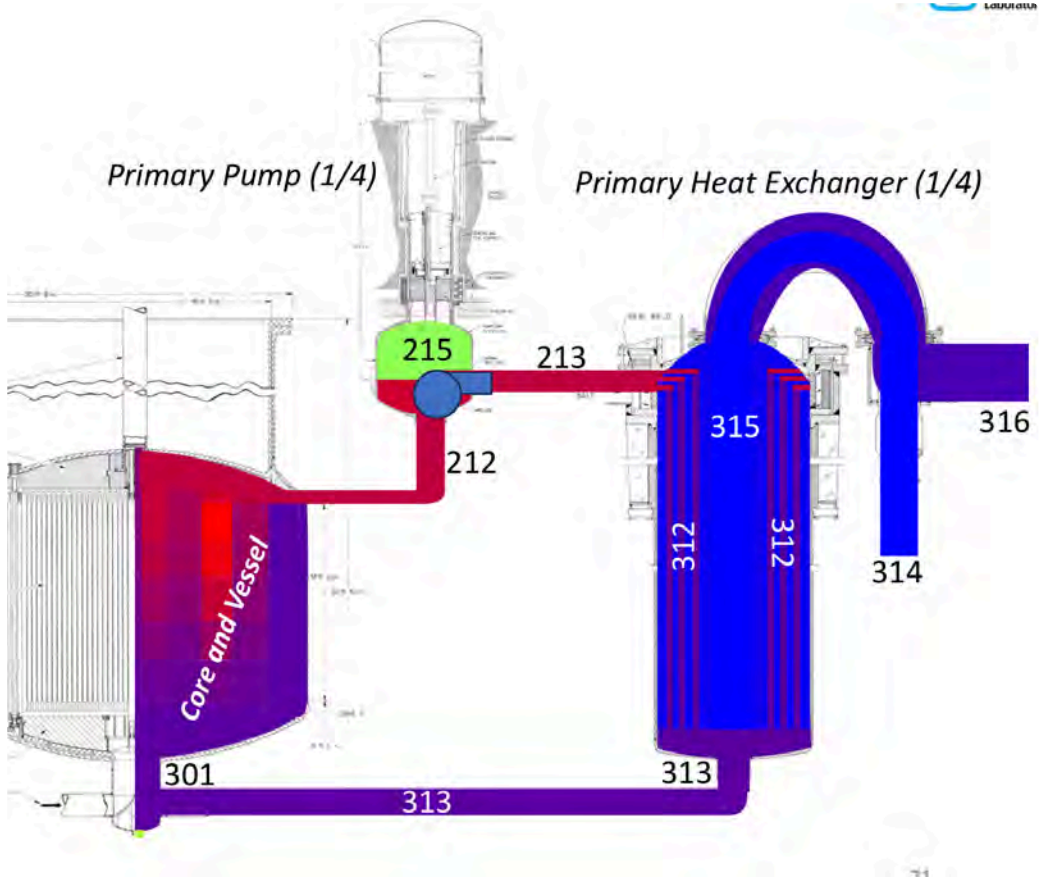

Core/vessel → pump bowl (215) → hot leg (213) → PHX (312) → return (313) → CV-301. After Duchnowski et al., SAND2024-07835PE.

Drain tank and off-gas system

Off-gas loop

- **47-hour holdup tank** — sized for Xe decay.
- **90-day holdup / gas clean-up** — long-lived isotopes.

Drain tank (CV-604)

- 2-hour holdup of off-gases from the pump bowls.
- Filled from pump-bowl overflow, returned to the primary loop — closed circuit by design.
- Active cooling system handles decay heat from the drained salt.

The drain tank must dissipate approximately 30 MW of residual decay heat over an extended period while limiting carrier vaporization to the off-gas path.

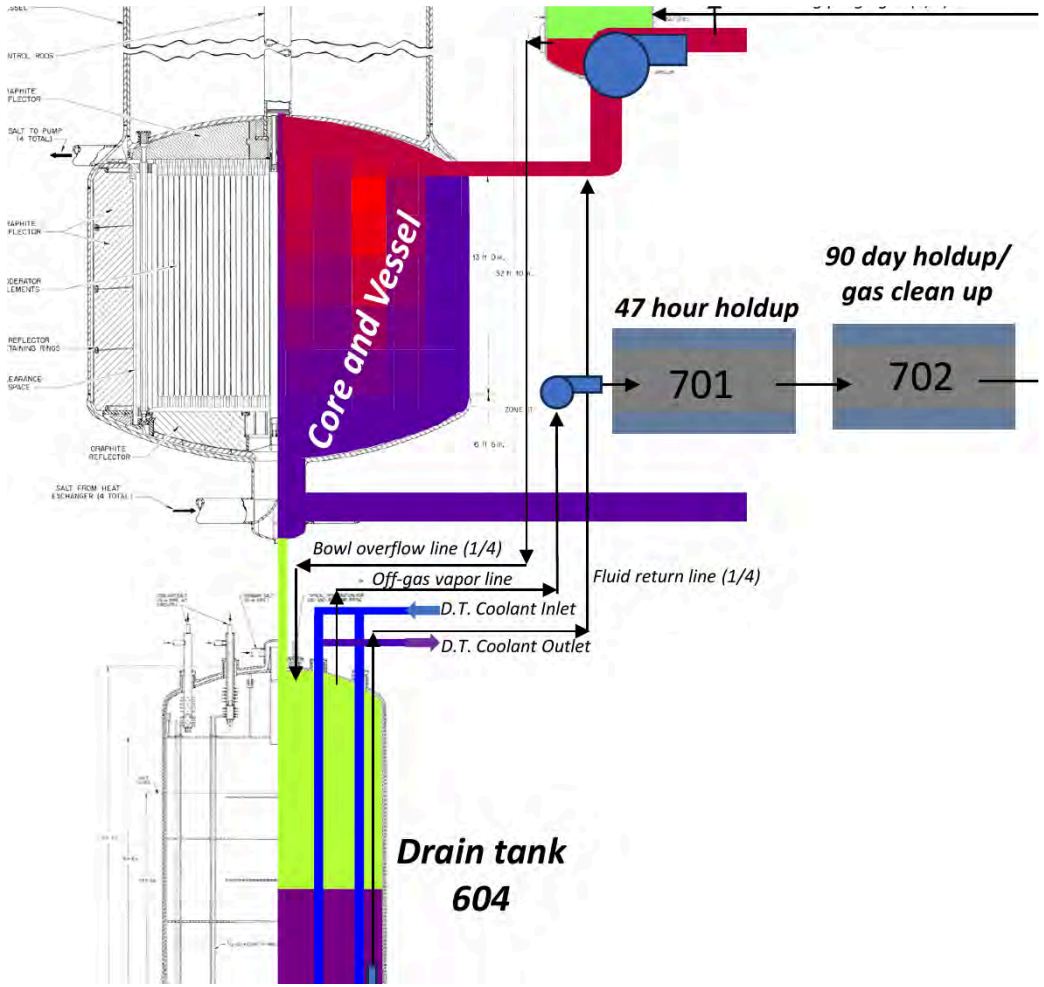

Pump bowl → off-gas vapor line → drain tank (604) → 47-h holdup (701) → 90-d clean-up (702).

Drain-tank thermal response — cooling-effectiveness sweep

- Active cooling capacity is swept from 0% (passive only) to 100% (18 MW nominal).
- At the 50% baseline, peak liquid temperature is below 1000 °C, well under the Hastelloy N solidus (1370 °C).
- At 0% active cooling, passive radiation and conduction from the tank walls bound the temperature response.
- The FLiBe freezing temperature (459 °C) bounds the 100% case from below; over-cooling can produce wall solidification.

> The sweep operates entirely within the FLiBe freezing temperature and the Hastelloy N solidus. The two-population solidification closures apply throughout.

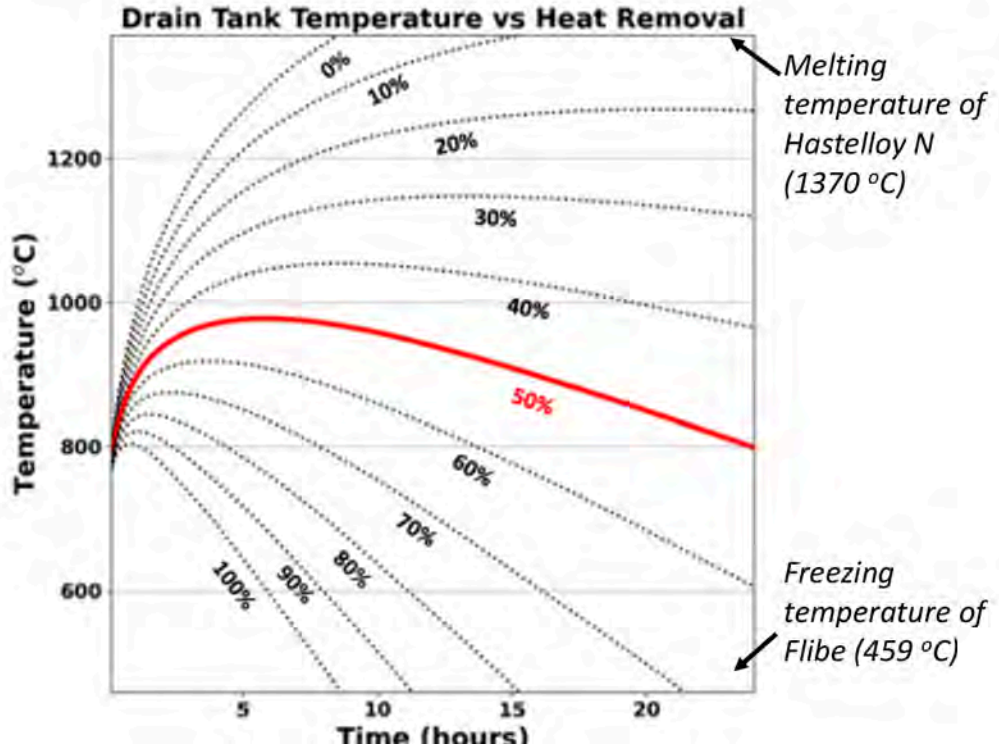

Drain-tank temperature family for active-cooling capacity 0–100%; 50% baseline highlighted (red). Hastelloy N melting and FLiBe freezing bracket the window.

Carrier release — airborne BeF_2 and UF_4

- BeF_2 and UF_4 are continuously released from the drained inventory at rates determined by their partial pressure at the instantaneous liquid temperature.
- Airborne species condense onto the pool surface and deposit on the cooled drain-tank walls via the standard evaporation/deposition closures.
- The majority of airborne inventory remains within the drain tank; off-gas inventory is approximately an order of magnitude lower.

Under baseline cooling, airborne BeF_2 peaks at approximately 10^{-4} of initial inventory; airborne UF_4 peaks at approximately 10^{-7}. The three-decade separation reflects the ratio of partial pressures.

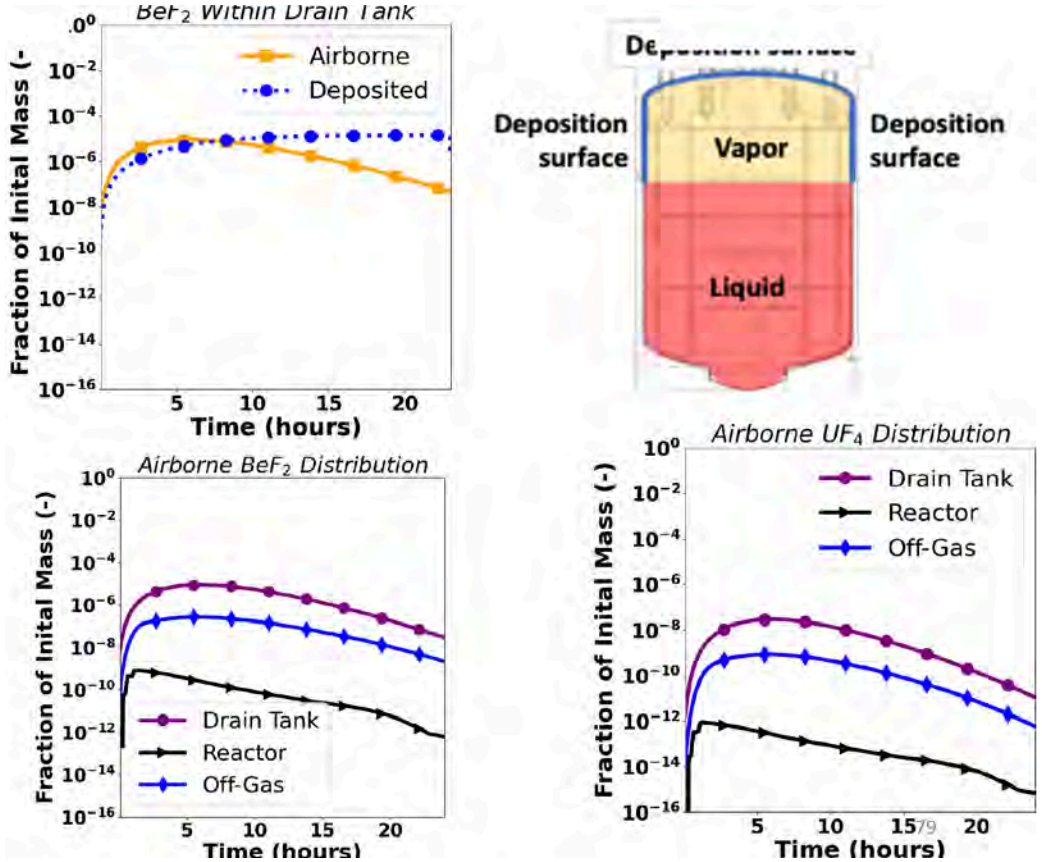

BeF_2 within the drain tank — airborne vs deposited (top-left); deposition surfaces on the drain-tank dome and walls (top-right); airborne BeF_2 and UF_4 distribution by region (bottom).

ORIGEN coupling on vs off — release pathways change

The same drain transient is run with and without ORIGEN-driven transmutation between radionuclide classes.

Without ORIGEN coupling

- Elements grouped into classes (solubility, isolating non-soluble corrosion products).
- MELCOR transports the classes — advection and evaporation only.
- $CsBeF_3$ partial pressure is sub-pascal → **essentially no Cs release**.

With ORIGEN coupling

- Transmutation transfers mass between classes during the transient.
- $^{135}I \rightarrow {}^{135}Xe \rightarrow {}^{135}Cs$ — the iodine decay chain produces Cs in regions that initially contained no Cs.
- Cs reaches the off-gas via the Xe transport route, not via salt vaporization.

The closures are identical in both runs. The Cs source-term result derives from inter-class transmutation operating on a registered channel, not from MSR-specific source-term logic.

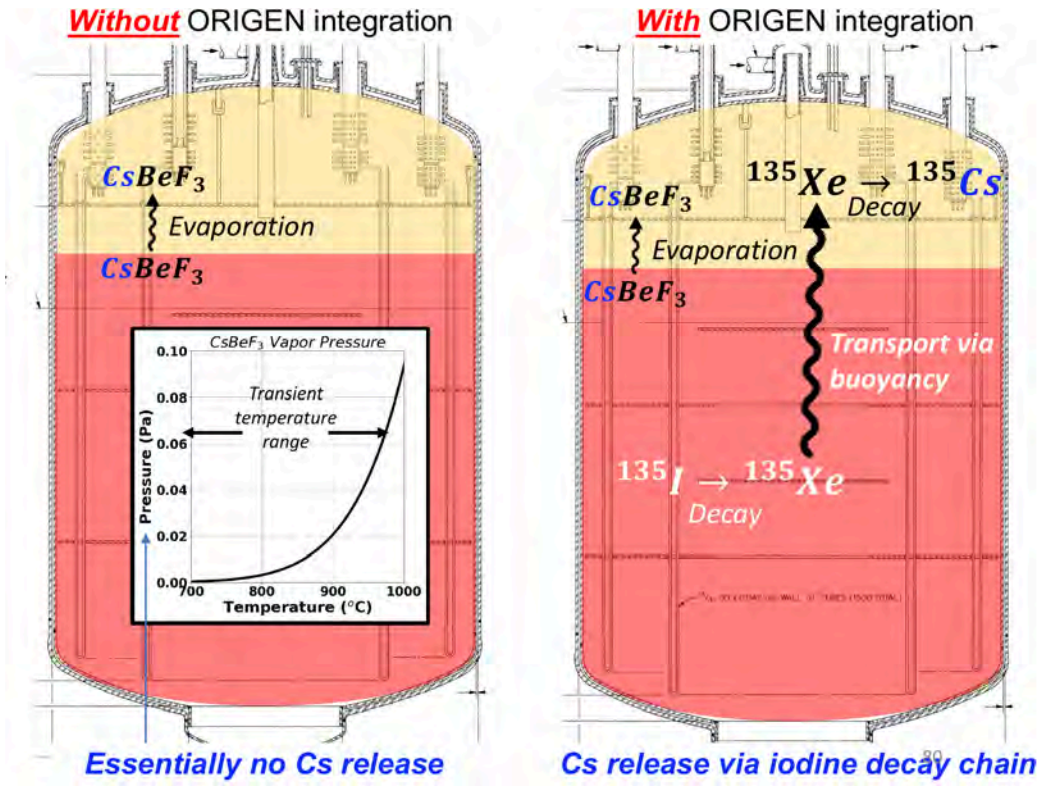

Left: $CsBeF_3$ evaporation only — essentially no Cs release. Right: I → Xe → Cs decay chain produces Cs that the Xe-class transport then carries.

PART 2 — NEW CAPABILITIES

Capabilities we are adding for MSR (and other) systems

CAPABILITY 1

Particulates in Liquid and Vapor Phases

Sectional PBE on two carrier phases

The sectional PBE state is (bin × species × carrier × volume). The same closure registry serves the liquid-borne distribution and the vapor-borne distribution.

SECTIONAL BALANCE PER (BIN **K**, SPECIES **S**, CARRIER **C**)

$$\partial n_{k,s,c}/\partial t = J^{nuc}_{k,s,c} + G^{cond}_{k,s,c} + A^{agg}_{k,s,c} - B^{brk}_{k,s,c} - D^{dep}_{k,s,c} + T^{L\leftrightarrow V}_{k,s}$$

- **Carrier-aware closures.** In molten salt, electrostatic double-layer stabilization collapses (Debye length is atomic-scale) so liquid-phase agglomeration is governed by Brownian collision plus interfacial-energy-driven attraction; vapor-phase agglomeration uses Brownian plus turbulent shear. Same closure interface; different kernels selected per carrier.
- **Phase transfer $T^{L\leftrightarrow V}$** is what couples the two distributions when the salt vaporizes or condenses.

Terms in the sectional balance

- $n_{k,s,c}$ — number density of particles in size bin **k**, species **s**, carrier **c**.
- J^{nuc} — nucleation source: new particles formed from supersaturated dissolved solute (liquid) or vapor (gas).
- G^{cond} — condensational growth: monomers / dissolved species deposit onto existing particles, moving mass across bins.
- A^{agg} — agglomeration source: particles collide and merge into bin **k** (Brownian + interfacial-energy attraction in salt; Brownian + turbulent shear in vapor).
- B^{brk} — breakup sink: fragmentation of larger particles by shear or thermal stress.
- D^{dep} — deposition sink: particle loss to wetted surfaces, gravitational settling, or pump-bowl trapping.
- $T^{L\leftrightarrow V}$ — inter-phase transfer: particles cross between the liquid-borne and vapor-borne distributions as the salt vaporizes or condenses.

In MSR the gas plenum, the cover-gas system, and the salt itself all carry particulate FPs. One PBE engine populates all three with different carrier closures plugged in.

Nucleation — in salt and on solid seeds

Classical Nucleation Theory provides homogeneous rates driven by supersaturation. For vapor-phase nucleation (CsI, CsOH, NaI condensing from the cover gas) $S = p / p_{sat}(T)$ where p is the species partial pressure. For liquid-phase nucleation in molten salt (noble metals, oxide impurities) $S = c / c_{sat}(T)$ where c is the dissolved concentration and $c_{sat}(T)$ is the salt-phase solubility limit at temperature T. The CNT functional form is unchanged; only the driving force is redefined per carrier.

HOMOGENEOUS CNT

$$J^{hom} = K(T) \cdot \exp[\, -16\pi\sigma^3 v_m^2 / (3\, k_B^3 T^3 (\ln S)^2) \,]$$

HETEROGENEOUS ON SOLID PARTICLES

$$J^{het} = J^{hom} \cdot (1 + \gamma \cdot \alpha_{sp})$$

When the bulk salt produces solid seeds (precipitating noble metals, crust fragments), J^{het} dominates and the PBE picks up the enhancement automatically.

Material data ship with the model

- CsI: ρ=4510 kg/m^3, σ=0.07 N/m, $P_{sat}(T)$ from JANAF
- CsOH: ρ=3680 kg/m^3, σ=0.10 N/m
- NaI: ρ=3670 kg/m^3, σ=0.09 N/m

Liquid-phase precipitation of noble metals (Mo, Ru, Pd) applies the same homogeneous and heterogeneous CNT closures with molten salt as the carrier phase. The closure form is unchanged; the supersaturation S is defined relative to the salt-phase solubility limit.

CAPABILITY 2

Differential Vaporization

Two-component vaporization from a FLiBe pool

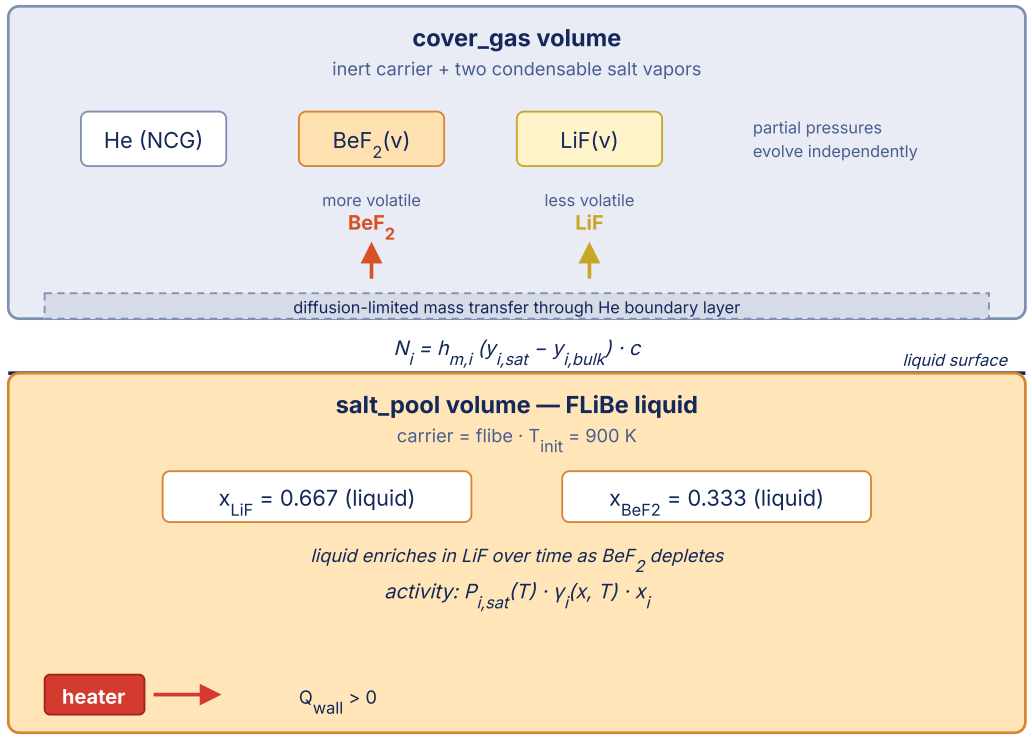

A hot FLiBe pool sits below a cover-gas plenum. FLiBe is two components — LiF and BeF_2 — with different saturation pressures. The cover gas receives both as separate vapor species.

Why a single-species condensable model is insufficient

- The condensable phase is a mixture — one saturation curve does not define it.
- BeF_2 vaporizes faster than LiF; pool composition drifts as the transient evolves.
- Cover-gas partial pressures of LiF and BeF_2 evolve independently.
- Source-term predictions depend on **which** salt enters the gas phase, not on the total vapor mass.

Link to the MSBR drain-tank scenario. After the emergency drain, hot salt sits in the cooled drain tank for hours. BeF_2 — a beryllium-bearing chemical hazard — vaporizes preferentially and is the dominant carrier of airborne mass into the cover gas (Part 1 result: peak airborne $BeF_2 \approx 10^{-4}$ of initial inventory). LiF vaporizes more slowly but carries activation and tritium inventory on a longer timescale. A postulated leak from the drain tank into the surrounding cell transports both vapor species; the chemical-hazard and radiological source terms scale with the composition that vaporizes, not with the total vapor

Concrete example — hazardous BeF_2 release from a heated FLiBe pool

Be is the most toxicologically significant constituent in MSR fuel salt; occupational exposure limits are in the µg/m^3 range. The multi-component vaporization closure produces a quantitative release rate.

MASS-TRANSFER-LIMITED RELEASE FROM THE SALT SURFACE

$$F_{BeF_2} = A_{surf} \cdot k_m \cdot (P_{sat,BeF_2}(T) \cdot M / RT),$$

$$k_m = Sh\, D_{vap}/L$$

- Drain tank: ~30 m^2 free surface; Sh ~ 10^2 on natural convection; $D_{vap} \sim 10^{-5}$ m^2/s.
- $P_{sat,BeF_2}(T)$: 1100 Pa at 1000 °C, approximately 10 Pa at 700 °C — two decades over a 300 K range.

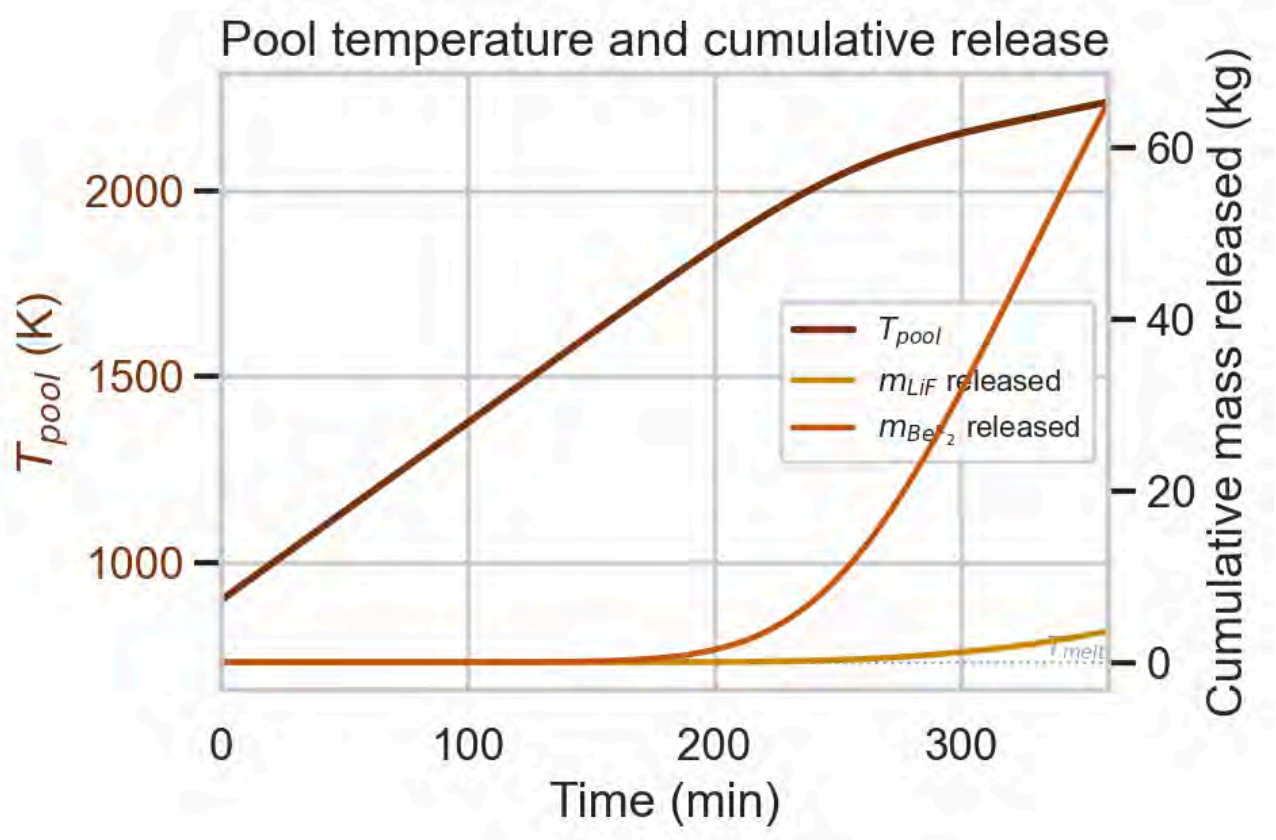

Closure output — pool temperature (left axis) and cumulative LiF and BeF_2 release (right axis) for a generic FLiBe pool heated from ~700 K through ~2200 K. BeF_2 release dominates and rises sharply above ~1700 K. At 1000 °C the corresponding release rate is of order 1 g·s^{-1}; at 700 °C it is approximately two decades lower.

CAPABILITY 3

Freezing and the Frozen Carrier

Solidification model — what it tracks

Volume cross-section at the cold wall

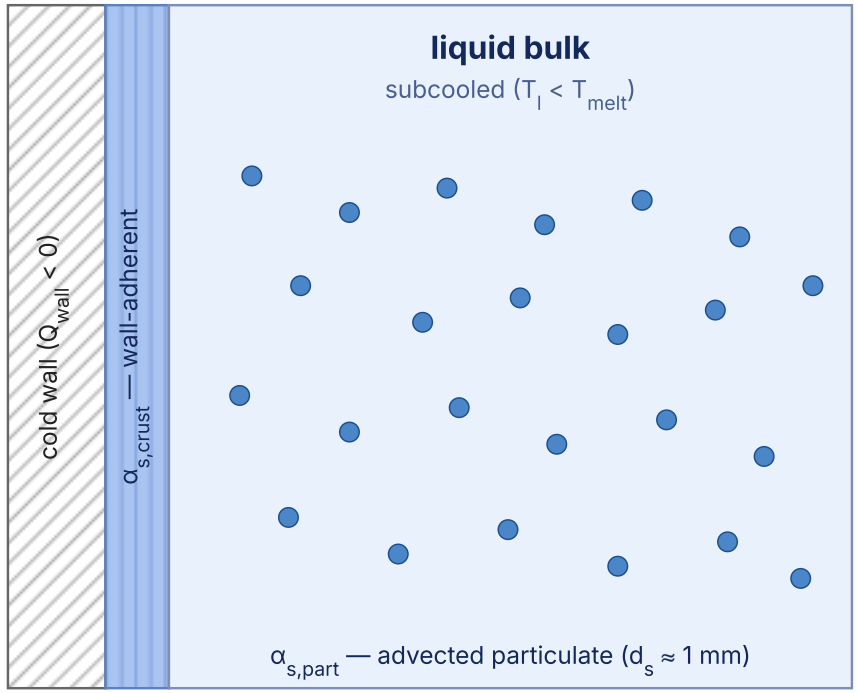

TWO SOLID POPULATIONS — WALL CRUST AND ADVECTED PARTICULATE

Mushy viscosity & junction blockage

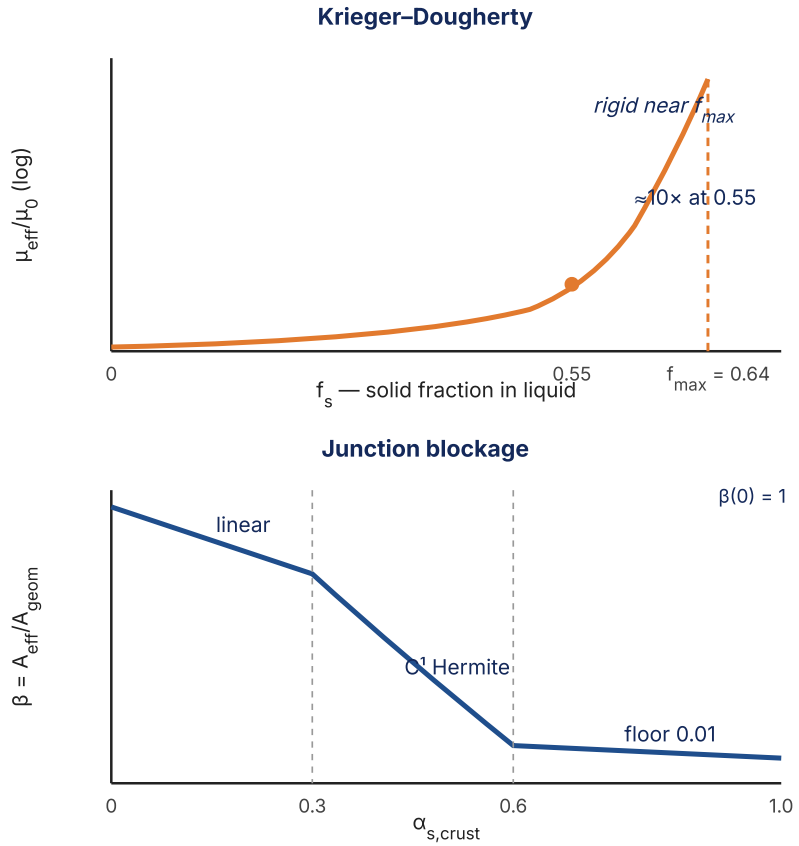

TWO NONLINEARITIES THE SOLVER HAS TO SEE TOGETHER

C^1 continuity across regime transitions. Every activation, the K–D viscosity curve, and the Hermite blending region have continuous values **and** continuous slopes. Newton sees one smooth residual and does not stall at regime transitions. $A_{eff} = A_{geom} \cdot \beta$; $D_{h,eff} = D_h \cdot \sqrt{\beta}$; donor-cell advection of β keeps crust transport consistent with the flow.

Freeze trapping — species into the frozen carrier

When the salt freezes, dissolved fission products partition into the advancing front in proportion to their liquid mass fraction. The species ledger is closed across liquid, frozen, and decayed inventories.

PER SPECIES IN THE LIQUID

$$d\mathbf{m}_{diss}/d\mathbf{t} \mathrel{-}= \Gamma_{freeze} \cdot \mathbf{Y}_{species}$$

PER SPECIES IN THE FROZEN LAYER

$$d\mathbf{m}_{frozen}/d\mathbf{t} \mathrel{+}= \Gamma_{freeze} \cdot \mathbf{Y}_{species} - \Gamma_{melt} \cdot \mathbf{Y}_{frozen}$$

Frozen species continue to decay; the radioactive chain solver runs on the frozen inventory. Frozen species do not advect, so convective transport sees only the liquid inventory.

Three coupled processes during freezing

- **Solute trapping.** Dissolved Cs, I, Sr, and soluble fluorides are captured at the freezing front (above).
- **PBE crust deposition.** `pbe_solidification_coupling`: existing PBE particulates deposit onto the growing crust face at an efficiency η_{dep}.
- **Heterogeneous nucleation seed.** The newly-formed solid particles α_{sp} seed further homogeneous-supersaturated species via J^{het}.

Melt-back resuspension is the symmetric inverse: $R_{resusp} \propto \Gamma_{melt}$. A freeze plug that thaws releases its trapped inventory with a decay-shifted isotopic composition.

Concrete example — freeze trapping of dissolved FPs in a drain-tank crust

During an emergency drain, salt at the cooled tank wall freezes inward at $v_f \approx 1$ mm/min. Dissolved Cs, I, and soluble fluorides are entrained by the advancing front. The closure quantifies the resulting trap inventory.

The initial closure assumes a species partition coefficient of approximately unity for the tracked FPs in their FLiBe carrier. Each parcel of salt that freezes into the crust carries its dissolved FP inventory with it, so the trapped FP fraction matches the frozen-mass fraction. More accurate species-specific partition coefficients can be substituted as phase-equilibrium data become available without changing the closure interface.

- **Cs example.** Trapped Cs fraction equals $\alpha_{s,crust}(t)$; at the cooler outlet this reaches ≈ 5% of the local dissolved inventory by 1000 s of solidification.
- The freeze-trapping ledger is run per species. Radioactive decay continues on the trapped inventory while convective transport treats it as removed from the liquid.

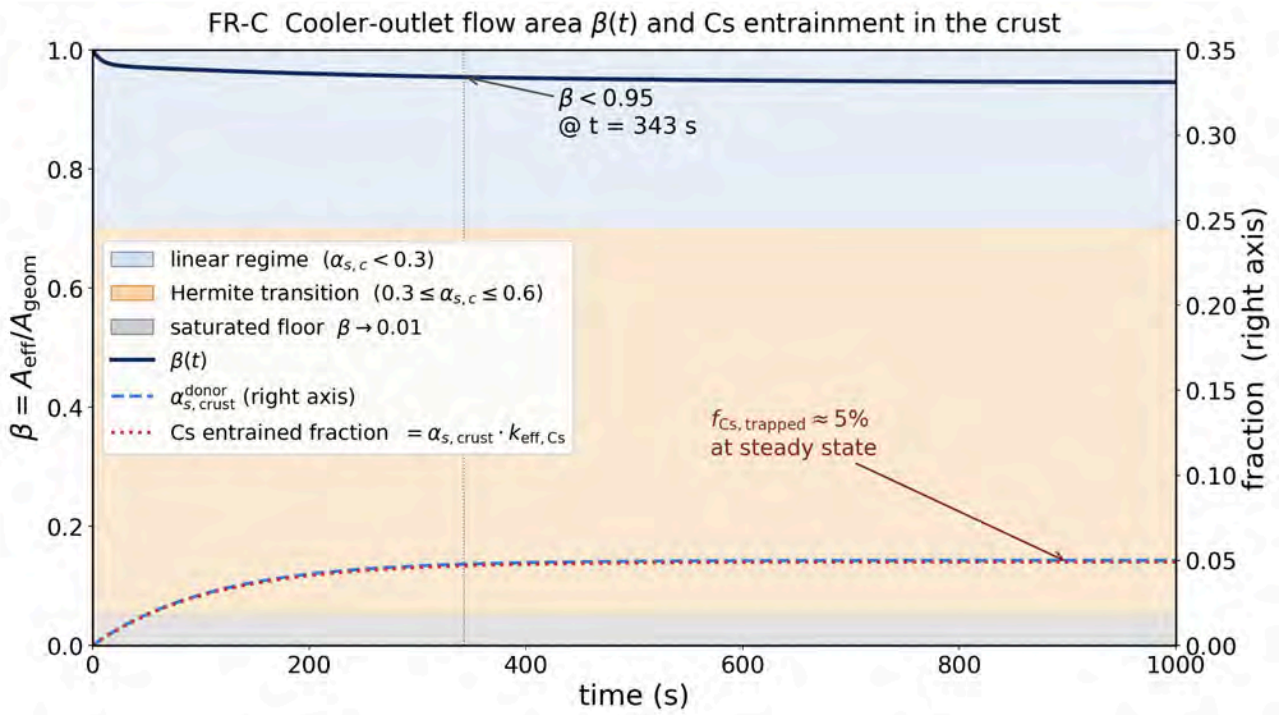

Closure output — flow-area ratio β(t) at a cooled outlet (left axis) with the donor-cell solid fraction and the Cs-entrained fraction $f_{Cs,trapped} = \alpha_{s,crust} \cdot k_{eff,Cs}$ on the right axis. For CsF in FLiBe, $k_{eff,Cs} \approx 1$, so the trapped Cs fraction matches the crust fraction and reaches ≈ 5% by 1000 s.

CAPABILITY 4

Interfaces and Tritium Through Structures

Mass transfer across interfaces — Sherwood correlations

The species flux across a fluid-fluid or fluid-solid interface uses the heat-mass transfer analogy. A catalog of Sh(Re, Sc) and Sh(Gr, Sc) correlations is available for the relevant flow regimes.

INTERFACE FLUX

$$J_i = k_m \cdot (C_{i,bulk} - C_{i,interface}) \,, \quad k_m = Sh\, D_i / L$$

Flat plate laminar: $Sh = 0.664\, Re^{1/2}\, Sc^{1/3}$

Flat plate turbulent: $Sh = 0.037\, Re^{0.8}\, Sc^{1/3}$

Tube turbulent (Dittus–Boelter): $Sh = 0.023\, Re^{0.8}\, Sc^{0.4}$

Natural convection (vertical): $Sh = 0.59\, (Gr\, Sc)^{1/4}$

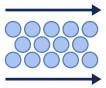

Packed bed (Wakao–Funazkri): $Sh = 2 + 1.1\, Re^{0.6}\, Sc^{1/3}$

Where each one shows up in MSR

- **Liquid ↔ cover gas free surface** — natural convection on the vapor side, sets the volatile-species partition rate
- **Liquid ↔ pipe wall** — Dittus–Boelter for both sensible heat and species deposition
- **Liquid ↔ crust face** — flat plate laminar; couples to `pbe_solidification_coupling`
- **Off-gas ↔ charcoal bed** — Wakao–Funazkri
- **Cell-to-cell transport through a leak path** — natural convection on both sides; the same closure describes airborne BeF_2 transport from a leaking drain tank into the drain-tank cell and on to the reactor cell.

Equilibrium at the interface is set by Raoult / Henry / partition coefficient; the Sherwood closure controls how fast the bulk approaches that equilibrium.

Tritium in structures — trap kinetics and barrier coatings

Inside metal walls, mobile tritium C_L and trapped tritium $C_{T,i}$ at each trap class i evolve together. The structure closure provides both an equilibrium and a kinetic trapping model with optional permeation-barrier coatings on either face.

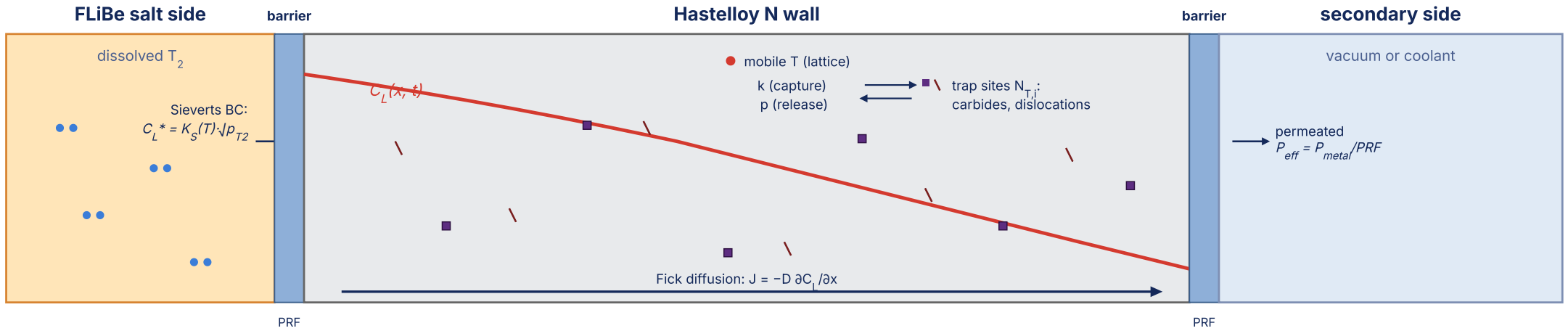

ORIANI LOCAL EQUILIBRIUM

$$K_i = \exp(E_{b,i} / RT)\,,\quad C_{T,i} = N_{T,i} \cdot K_i\,\theta_L / (1 + K_i\,\theta_L)$$

MCNABB–FOSTER KINETIC

$$dC_{T,i}/dt = k \cdot C_L \cdot (N_{T,i} - C_{T,i}) - p \cdot C_{T,i}$$

Permeation barrier coatings

- Barrier specification: **PRF** (permeation reduction factor) and coating type
- Built-in entries: Al_2O_3, Er_2O_3, Cr_2O_3
- Applied at the structure boundary; effective permeability becomes $P_{eff} = P_{metal}/PRF$

Demonstration — tritium permeation through a 5 mm wall

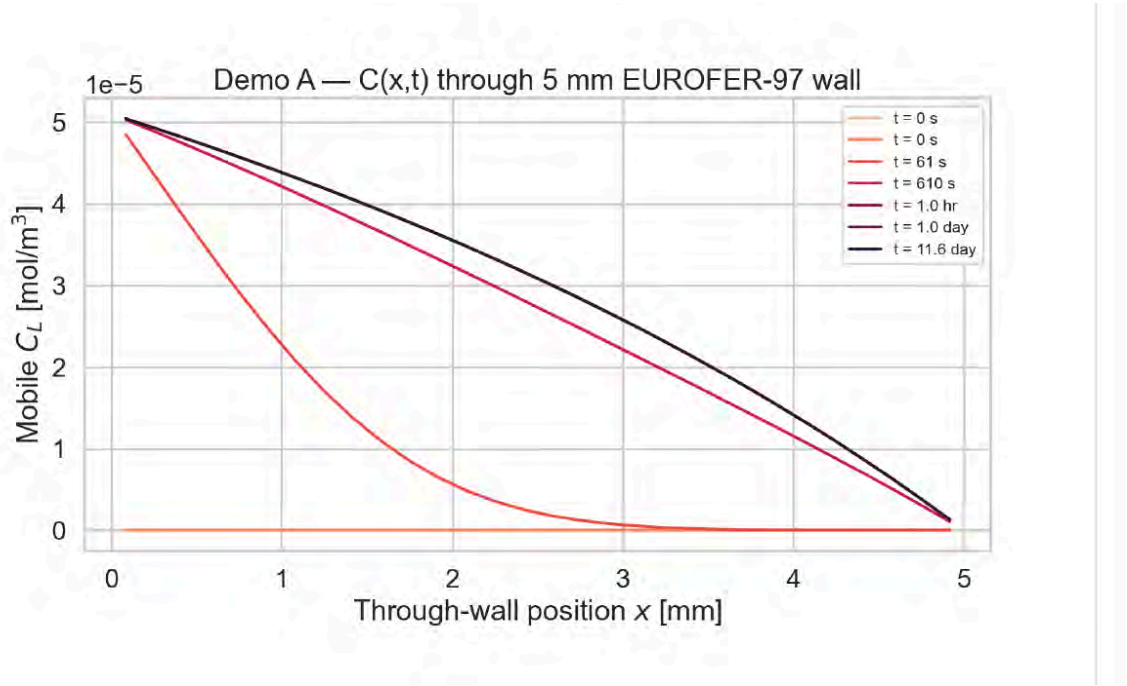

$C_L(x, t)$ at t = 0 s, 61 s, 610 s, 1 hr, 1 day, 11.6 day. Classic permeation-front shape; trapping retards breakthrough toward the He-side.

The structure-transport closure is exercised on a 5 mm wall with a Sieverts boundary condition on the upstream face and a vacuum sink on the downstream face. Fick diffusion is coupled to McNabb–Foster trapping on dislocations and carbides.

What the demo verifies

- The front shape evolves from a sharp profile near the upstream face through a transient permeation regime to the linear steady state.
- Trapping retards breakthrough — the t = 1 hr and t = 1 day curves remain well below the steady profile near the He-side.
- Three-ledger mass balance: |source − storage − permeated| / total < 3×10^{-5} over the 12-day transient.

Demo uses EUROFER-97 properties from the fusion-blanket literature. The same closure operates on Hastelloy N with FLiBe-relevant $K_S(T)$, $D(T)$, and trap-density inputs; permeation barriers are layered as $P_{eff} = P_{metal}/PRF$.

Recap

Particulate transport

- Sectional PBE in liquid **and** vapor carriers
- Multi-species, multi-component particles
- CNT homogeneous + heterogeneous nucleation
- Brownian collision with interfacial-energy attraction (no DLVO stabilization in molten salt); deposition coupling

Salt thermodynamics

- Multi-component liquid provider with per-constituent $P_{sat}(T)$
- FLiBe and FLiNaK constituents (LiF, BeF_2, NaF, KF)
- Incongruent vaporization producing a quantitative BeF_2 release from a heated pool
- Two-population solidification with freeze trapping of dissolved FPs

Interface and structure transport

- Sherwood catalog (laminar, turbulent, natural convection, packed bed)
- Oriani equilibrium and McNabb–Foster kinetic trap models in metals
- Permeation barriers via PRF (Al_2O_3, Er_2O_3, Cr_2O_3)

Each capability is a registered closure against a named channel. The PBE engine that tracks LWR aerosols runs unchanged in molten salt; the freeze closures developed for sodium pool solidification handle FLiBe crusts; the trap-kinetic closures developed for fusion blanket structures apply to MSR tritium permeation.

ADVANCING NUCLEAR SAFETY TECHNOLOGY

Thank you

David L. Luxat · Matthew Christian · Ed Duchnowski · Lucas Albright · Brad Beeny · Troy Haskin · Dallin Keesling
dlluxat@sandia.gov
Dept. 8852 · Nuclear Energy Safety Technologies · Sandia National Laboratories

SAND2026-XXXXP

Sandia National Laboratories is a multimission laboratory managed and operated by National Technology & Engineering Solutions of Sandia, LLC, a wholly owned subsidiary of Honeywell International Inc., for the U.S. Department of Energy's National Nuclear Security Administration under contract DE-NA0003525.

COMPUTATIONAL VERIFICATION OF THE FUNCTIONALITY OF THE COOLING SYSTEM OF THE ALLEGRO REACTOR CORE CATCHER

Jan Komrska and Pavel Zácha
Czech Technical University
Technicka 4, 166 07 Praha 6, Czech Republic
jan.komrska@fs.cvut.cz, pavel.zacha@fs.cvut.cz,

Petr Vácha
ÚJV Řež, a.s.
Hlavní 130, Řež, 250 68, Husinec, Czech Republic
petr.vacha@ujv.cz

ABSTRACT

This paper addresses the description of the computational verification process for the design of the core catcher of the ALLEGRO demonstration reactor. The aim is to present the methodology and results of the analysis that ensure the safety and effectiveness of the core catcher during long-term cooling of the corium melt. For the calculations, various simulation tools were used, specifically the CORQUENCH, Thermo-Calc codes, and the CFD code Ansys Fluent. By combining these codes and methodologies, a comprehensive analysis of the long-term cooling of the core melt in the core catcher was developed, providing important insights for the verification of the safety characteristics of the ALLEGRO reactor.

KEYWORDS
Core Catcher, Ex-Vessel Retention, Severe Accident, Numerical Simulations, ALLEGRO

1. INTRODUCTION

The objective of this study is to employ the CFD code Ansys Fluent [1] to simulate the cooling of reactor core melt within a core catcher, with heat being transferred through the individual structural layers of the core catcher to cooling water circulating by natural convection beneath the structure.

Preparatory analyses were performed using the CORQUENCH code [2], as well as Thermo-Calc with the NUCLEA database [3], to obtain the necessary material properties of the reactor core melt. Using these codes we were able to ascertain necessary corium properties for subsequent CFD simulation of long-term cooling of the corium using Ansys Fluent 2025R1.

The CFD simulation represents a bounding scenario corresponding to an unfavorable progression of the late phase of an ex-vessel severe accident and the subsequent long-term cooling of the resulting corium. In this scenario, the sacrificial material is assumed to underperform and to be fully consumed without reducing the corium temperature to the required solidus level.

2. ALLEGRO CORE CATCHER

ALLEGRO is a gas-cooled fast reactor (GFR) demonstrator unit currently under development by the V4G4 CoE (Visegrad 4 for Generation IV Centre of Excellence) [4]. The primary objective of the ALLEGRO demonstrator is to provide an experimental platform that supports the research and development activities required for the future deployment and operation of commercial nuclear reactors based on GFR technology.

Among the systems specifically designed for ALLEGRO is the core catcher. This dedicated safety system is intended for the stabilization and localization of corium in the event of a severe accident involving reactor core melt. Its principal function is to retain and cool the corium, thereby preventing melt-through of the containment concrete basemat and reducing the risk of significant radionuclide release. The device is conceived as a dry, spreading, ex-vessel core catcher incorporating extensive use of sacrificial materials.

Presented work is of a late ex-vessel phase of severe accident in the ALLEGRO reactor and is a part of a broader scope of core catcher design and follows directly after long term simulation of corium ablation of sacrificial materials atop with focus of long-term cooling capabilities of the core catcher. Following figures 1 and 2. describe the core catcher system and individual layers of the core catcher floor.

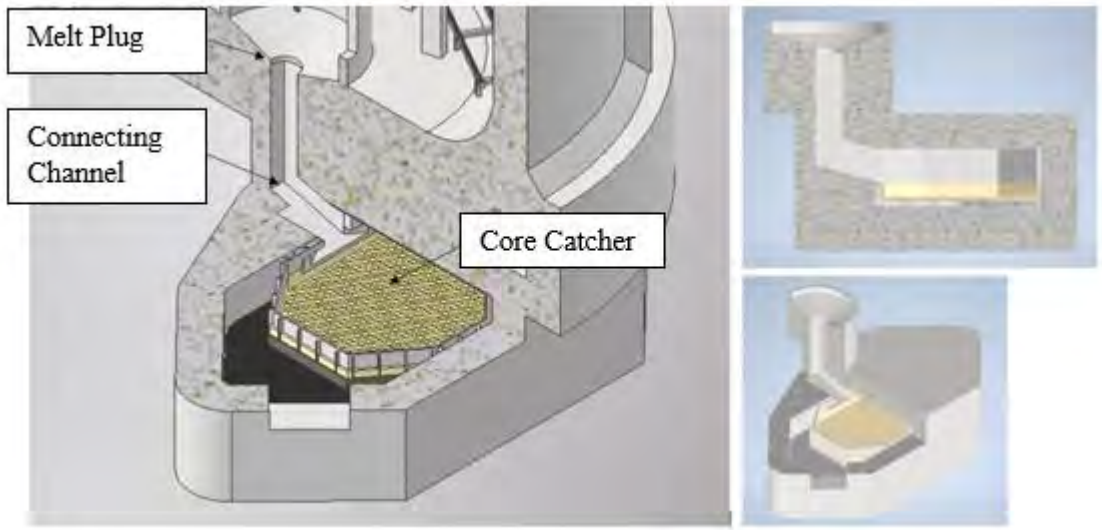

Figure 1. ALLEGRO Core Catcher

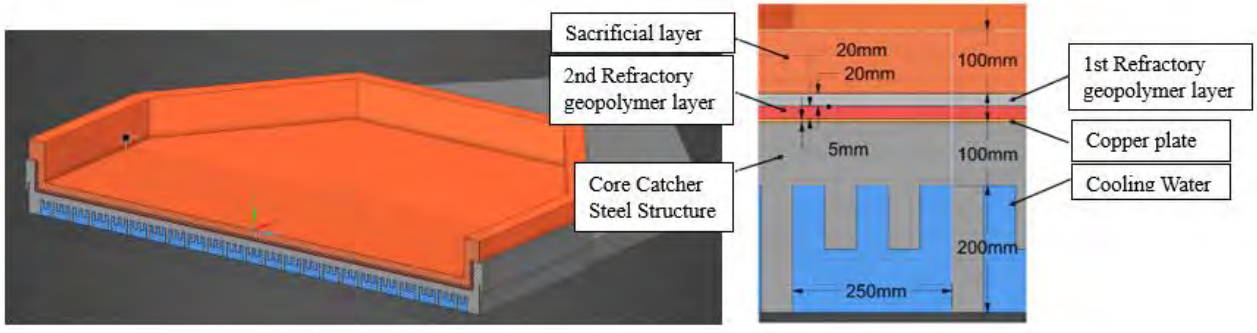

Figure 2. Core Catcher cross-section with layer descriptions

2.1 Core Catcher Cooling System

The cooling system outside the core catcher itself is designed on natural circulation principle and is connected to the same cooling loop as the DHR system [5]. It makes use of a significant height difference between the heated section (the core catcher) and the heat exchanger (see Fig, 3), which is realized by a tubular heat exchanger submerged in a water pool at the top of the containment guard vessel.

During normal reactor operation, residual decay heat from the containment is removed by the cooling system in an amount that is 20 times lower than the maximum design capacity of the cooling system. During a hypothetical severe accident, heat losses from the primary circuit decrease to approximately 5% of nominal, which should theoretically be sufficient to keep the core catcher cooling loop in a standby state, while at the same time there is no risk of its damage.

If corium melts through the bottom of the reactor vessel and is released into the core catcher space, there is no longer any significant heat source inside the primary reactor circuit. Consequently, the core catcher cooling system is then loaded only by the heat produced by the decay heat of the corium, for which it has been designed.

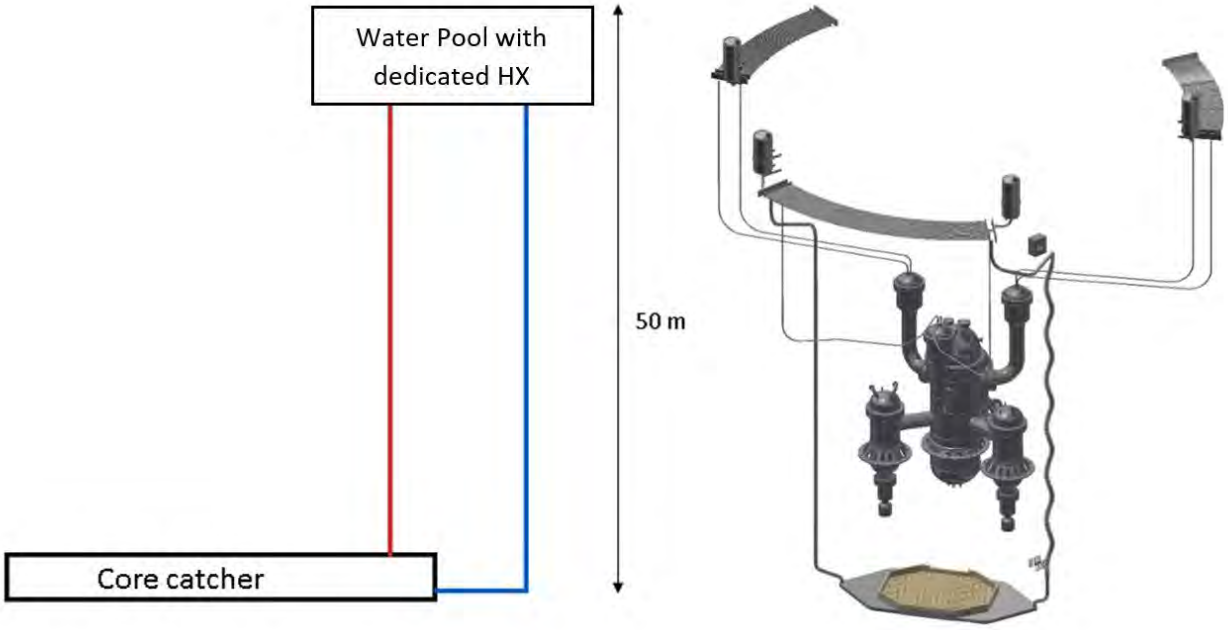

Figure 3. Core Catcher Cooling System

3. SUMMARY OF PREPARATORY ANALYSES USING THERMO-CALC (NUCLEA) AND CORQUENCH 4.1

NUCLEA is a database used to obtain corium properties based on the composition and initial conditions specified in the Thermo-Calc program. This database can be applied to both the IVR and EVR phases of a severe accident. Using this database, it is possible to calculate thermochemical equilibrium states of individual compounds (O–U–Zr–Ag–In–B–C–Fe–Cr–Ni–Ba–La–Sr–Ru–Al–Ca–Mg–Si + Ar–H) during a severe accident.

The input conditions for the equilibrium model calculation were the initial corium temperature, the pressure of the defined system, the system size (mass), and the elemental composition of the considered system.

The initial conditions of this model assumed a temperature of 1900 K and atmospheric pressure of 0.1 MPa. The total mass was taken as the corium mass after melt plug failure, 10,653.08 kg, and the mass of ablated sacrificial materials (geopolymers with high Fe_2O_3 content [6,7]), 14,109.73 kg. The total mass of the considered system was therefore 24,762.81 kg.

It was further necessary to decompose the entire system—i.e., the corium and the ablated materials—into elements using the atomic ratios of the individual materials. The corium + ablated materials system was decomposed into the following elemental composition (Table 1.):

Table I. Initial boundary Corium composition

Element	Molar concentration of element [-]
Oxygen	0.5212
Hydrogen	0.0578
Silicon	0.08
Calcium	0.03
Magnesium	0.01
Aluminium	0.0425
Iron	0.2445
Uranium	0.014

The calculation of corium material properties was performed as a function of temperature in the range from 1500 to 1930 K with a step of 10 K. This temperature interval was selected based on analyses in the CORQUENCH code, which indicate that at about 1500 K the corium begins to cool progressively, and significant crust formation occurs at the corium boundaries.

The result of this analysis is the temperature-dependent material composition of the corium (see Fig.4). The composition plot shows the gradual cooling of LIQUID and LIQUID#2, which represent the metallic phase and the oxidic phase of the corium:

- Metallic corium phase: represented by LIQUID, which at approximately 1800 K cools into the BCC_A2_2 phase and at approximately 1660 K transitions into the solid FCC_A1_1 phase.
- Oxidic corium phase: denoted as LIQUID#2, which begins to cool at about 1810 K into the FCC_C1 phase. At around 1550 K, the solid SPINEL phase forms from the oxidic corium.

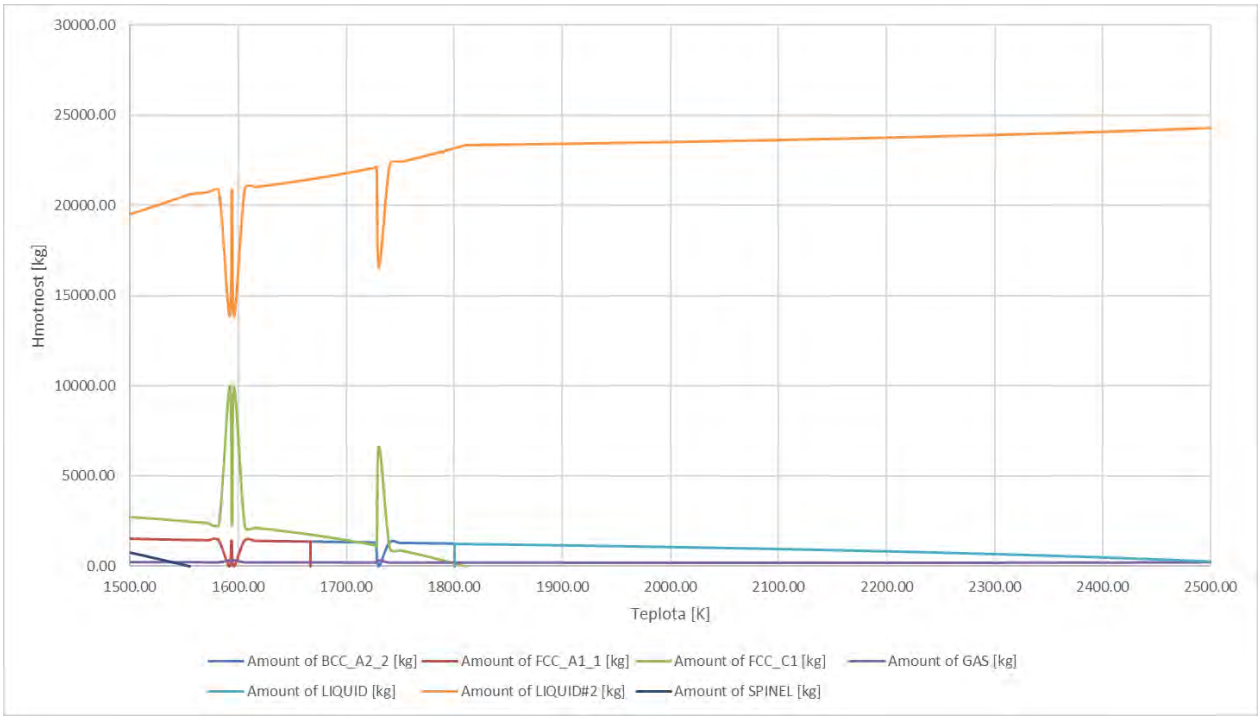

Figure 4. Thermo-Calc results of various corium compositions

From the perspective of using these properties, we are mainly interested in the situation at 1700 K, which was selected as the initial temperature for the CFD simulation of long-term cooling of the reactor core melt. Using NUCLEA, we can determine how thick the layers of stratified corium will be, which then allows us to prepare the geometry and the CFD model.

According to source [8], steel at very high temperatures has a density of about 7000 kg/m³. At 1700 K, the mass of this steel is 1330 kg. Converting using the density, the phase volume, and the core-catcher area—assuming a uniform distribution of the metallic corium layer—yields a metallic corium layer height of approximately 3.5 mm.

Using the same approach, and the calculated density of oxidic corium 3741.7 kg/m³ (from the CORQUENCH code analysis), we obtain a resulting oxidic corium layer height of approximately 115 mm.

Unfortunately, in used version of the program (Thermo-Calc 2024 A), it is not possible to obtain the thermophysical properties of corium from NUCLEA database. It was therefore necessary to use the CORQUENCH code, where additional analyses of the material properties of the oxidic corium layer were performed for the use in final CFD calculations.

The CORQUENCH code was used to obtain the thermophysical properties of the oxidic phase of corium, since this was not possible using only Thermo-Calc with the NUCLEA database. A parametric study of thermophysical properties as a function of temperature was carried out in CORQUENCH. The resulting properties of the oxidic phase are presented in the Table 3.:

Table II. Initial boundary Corium composition for CORQUENCH simulation

Core Catcher layer material	Solidus Temperature [K]	Liquidus Temperature [K]	Ablation Temperature [K]	Initial layer Temperature[K]	Layer Height [mm]
Sacrificial layer – Geopolymer with higher Fe_2O_3 cont.	1120	1750	1370	323.15	100
Refractory layer- Geopolymer with higher Al_2O_3 cont.	1120	2250	1400	323.15	20
Refractory layer – Geopolymer with higher MgO cont.	1120	2250	1470	323.15	20
Copper Plate	1357	1358	1357.5	323.15	5
Steel Structure	1699	1700	1699.5	323.15	100

Table III. Material properties of Oxidic Corium using CORQUENCH

Temperature [K]	Conductivity [W/m·K]	Density[kg/m^3]	Heat Capacity[J/kg·K]	Viscosity[kg/m·s]	Surface Tension [N/m]	Emissivity [-]
1450	1.67	3741.7	920.3	$8.08 \cdot 10^{14}$	0.52	0.83
1500	3.93	3741.7	976.51	2.591	0.52	0.83
1600	3.94	3741.7	992.08	1.2974	0.52	0.83
1700	3.94	3741.7	1004.2	0.73848	0.52	0.83
1800	3.94	3741.7	1013.9	0.46108	0.52	0.83
1900	3.94	3741.7	1022.5	0.30231	0.52	0.83
1930	3.94	3741.7	1024.9	0.26878	0.52	0.83
2000	3.94	3741.7	1030.4	0.20625	0.52	0.83

4. CFD SIMULATION OF LONG-TERM COOLING OF CORIUM

The primary requirement for verifying the functionality of the core-catcher cooling system is the reduction of the corium temperature to 1450 K (1176.85 °C), which - according to CORQUENCH results - corresponds to the solidus temperature and thus to the condition where the corium is fully solidified. In addition, it is required that the maximum temperature of the cooling water does not exceed its saturation temperature. At the design pressure of 2 MPa in the core catcher, the corresponding boiling temperature is 485.55 K (212.4 °C).

With respect to the initial conditions of the simulation, a scenario representing an unfavourable progression of the late phase of a severe accident was selected. In this case, the sacrificial material may fail to perform as intended and could become completely consumed without cooling the corium to the required solidus temperature. Accordingly, the initial corium temperature was set to 1700 K, and the

corium composition was defined assuming complete ablation of the 100 mm sacrificial material layer on the floor of the core catcher.

As noted above, the considered scenario corresponds to the state after complete ablation of all sacrificial materials with which the core catcher was equipped. In this late phase of a severe accident, the corium is assumed to be stratified into two layers: an oxidic layer and a metallic layer.

This represents a computationally demanding problem, both in terms of mesh size and the necessary modelling simplifications. It was necessary to adjust the composition and thicknesses of the individual layers of the core catcher to generate a computational mesh suitable for performing the simulation.

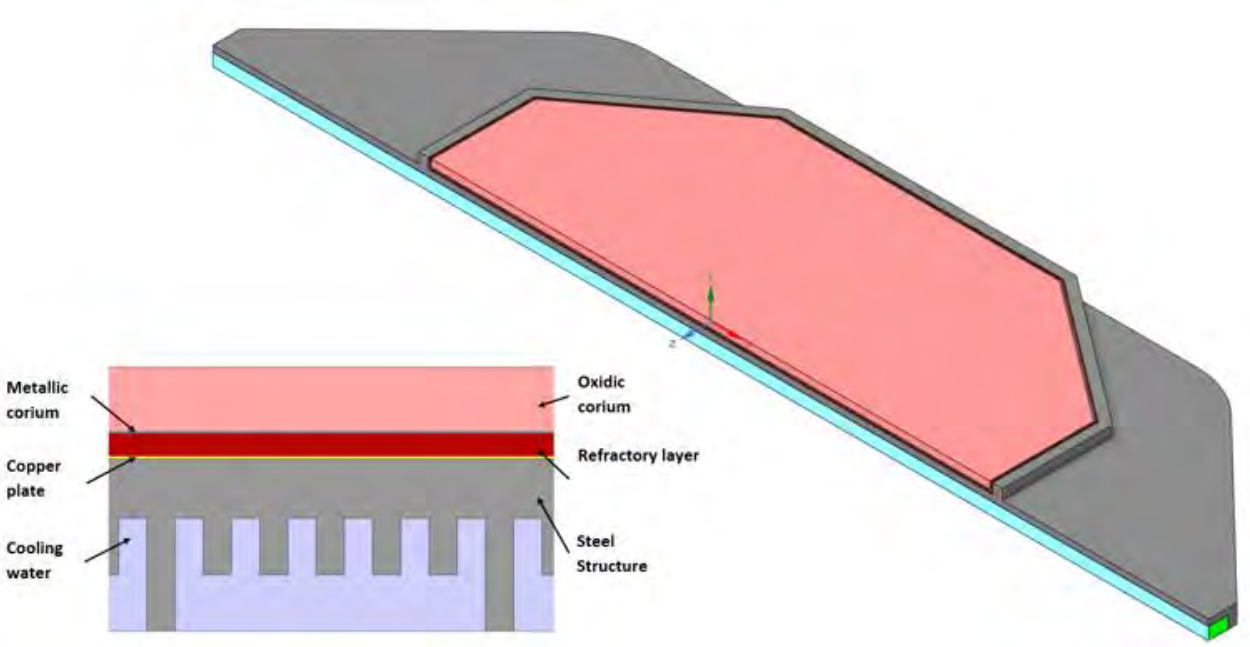

Figure 5. ½ Symmetry of CFD calculation domain

4.1 Used Simplifications

From the computational standpoint, several simplifications were introduced that significantly affect the calculation time and simulation convergence. A minor geometric modification of the so-called core-catcher rim was implemented by shortening it to a height equal to the maximum melt level. This reduced the computational domain by excluding a region that is not relevant for the melt cooling analysis and can instead be represented by an appropriate boundary condition.

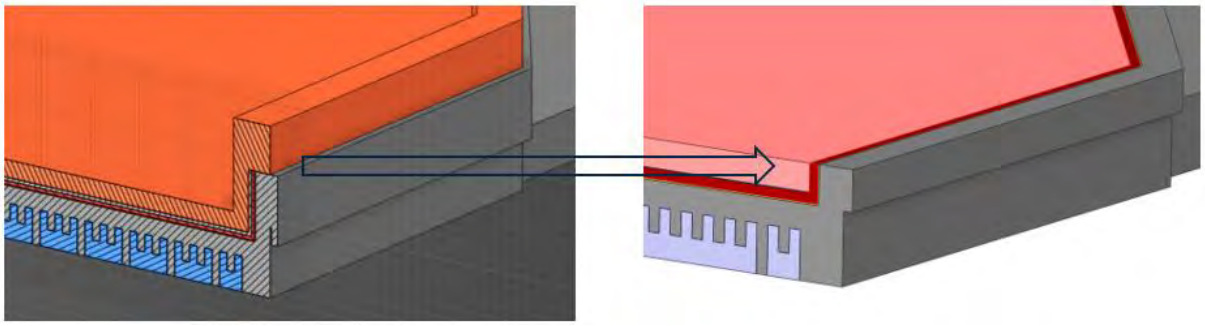

Figure 6. Core Catcher rim simplification

Furthermore, it was necessary to implement one major modification in the layer arrangement of the core catcher. This simplification was adopted due to the inability to generate a sufficiently high-quality computational mesh for the original layer configuration of the core catcher, as shown in Figure 7. The primary cause was the extremely small thickness of the metallic corium layer (3.5 mm) and the similarly thin copper layer (5 mm).

These dimensions, being significantly smaller than the other characteristic dimensions of the core catcher, resulted in extreme disparities in adjacent cell sizes and consequently very unfavourable aspect ratio values. Several test calculations were performed; however, the mesh quality issues repeatedly led to divergence of the numerical solution.

Therefore, a simplification of the core catcher layer arrangement was introduced as follows:

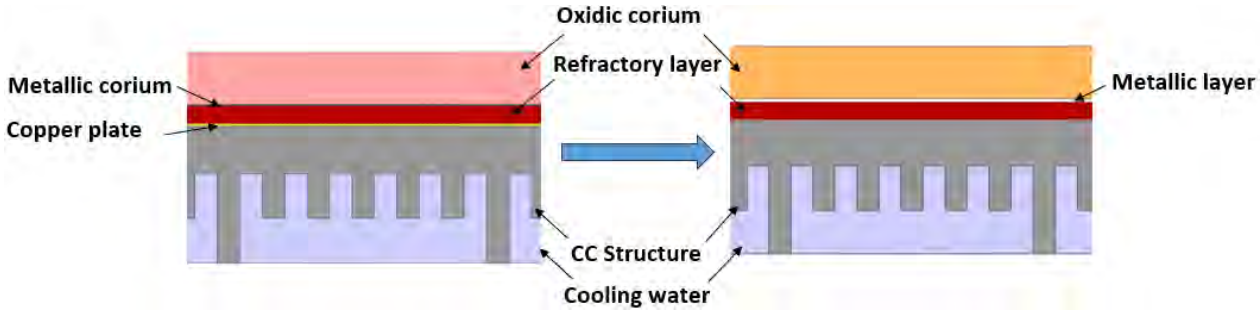

Figure 7. Core Catcher layer rearrangement simplification

Since the metallic corium layer is already considered solid at the initial simulation temperature of 1700 K, only heat conduction to the cooling water takes place within this layer. Moreover, because the material is metallic, it can be reasonably assumed to exhibit conductive behaviour like that of the copper plate. Therefore, to obtain a convergent solution and improve mesh quality, an approximation was introduced in which the two metallic layers were merged into a single equivalent layer with properties averaged according to the original thicknesses of the individual layers.

4.2 CFD Computational Mesh

The computational mesh was generated using polyhedral cells. Initially, tetrahedral cells of the specified sizes were created throughout the entire volume, after which they were converted into polyhedral cells.
In total, 38,442,704 volume cells were generated. The minimum orthogonal quality reached 0.15, and the maximum aspect ratio was 92.65. The relatively high aspect ratio is a consequence of the very fine mesh in the boundary layer combined with the effort to maintain the largest possible cell size in the bulk fluid region.

Given the large fluid volume and the presence of multiple regions requiring local refinement, the mesh was constructed to ensure at least 15 computational cells across the fluid regions (reactor core melt and cooling water) between adjacent solid surfaces. In the solid regions, where only heat conduction occurs (metals, refractory layer, and steel structure), a minimum of 4 cells across the wall thickness was prescribed.

The minimum cell size was set to 4 mm and the maximum to 40 mm. In the metallic layer region, a BOI (Body of Influence) function was applied to locally refine the mesh to a maximum cell size of 2 mm. Near the core catcher walls (in the fluid regions—the reactor core melt and the cooling water), a uniform boundary layer mesh was generated with a first cell height of 0.75 mm, 5 boundary-layer layers, and a growth rate of 1.2.

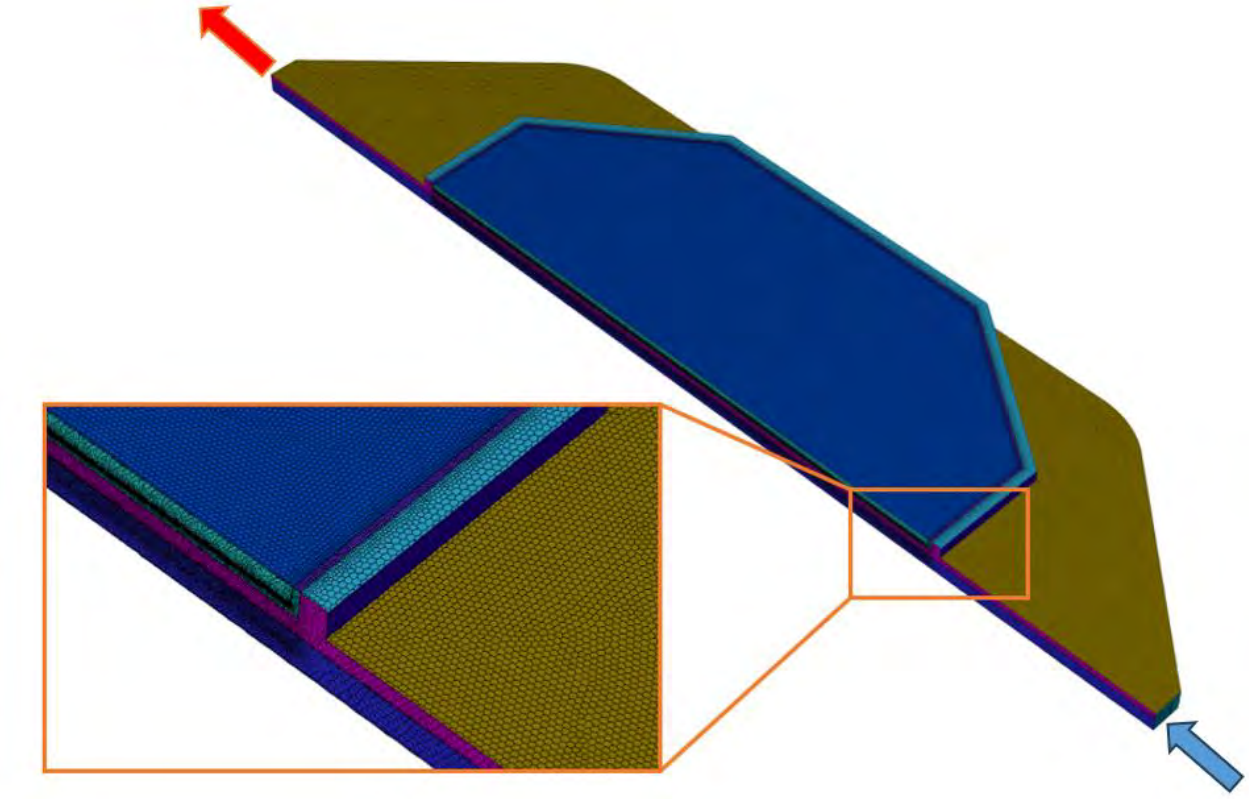

Figure 8. Computational CFD Mesh with designated water inlet (blue) and outlet (red)

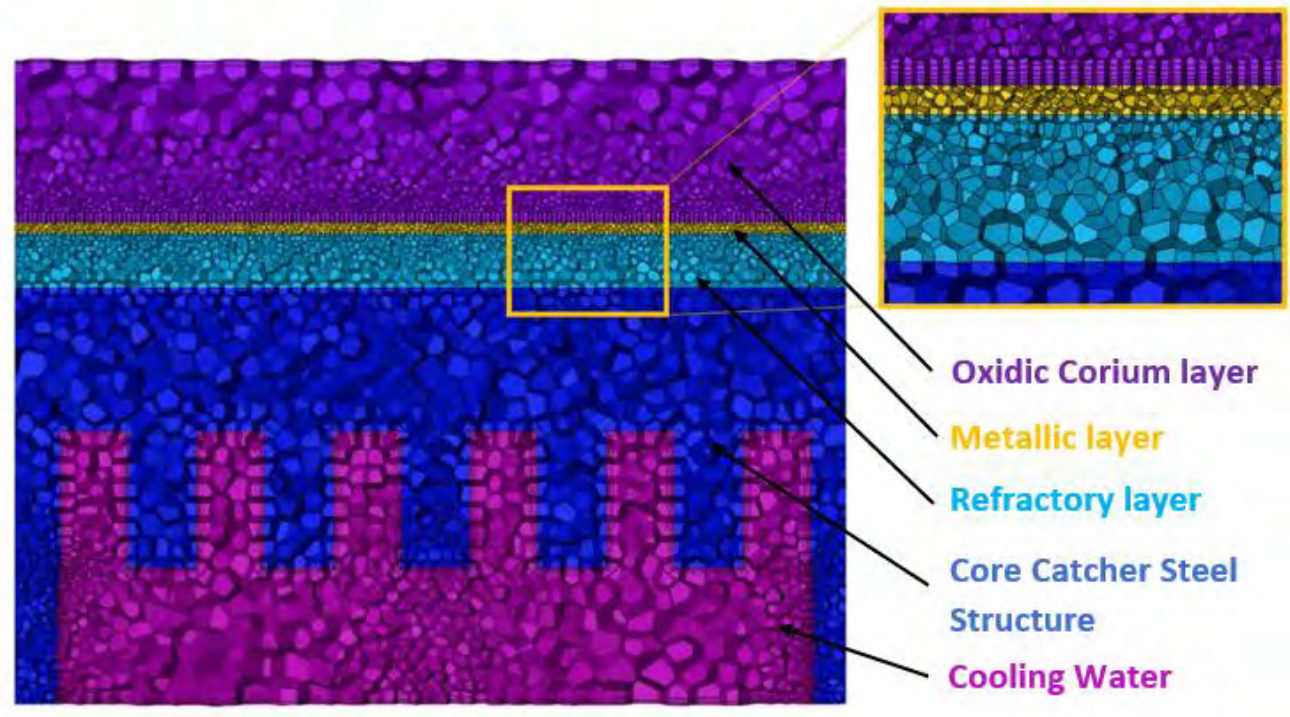

Figure 9. Cross-Section of CFD Mesh

4.3 CFD Simulation Setup and Boundary Conditions

A bounding scenario representing an unfavourable late phase of a severe accident was considered, in which the sacrificial material is fully ablated without cooling the corium below the solidus. The initial corium temperature was set to 1700 K, assuming complete depletion of the 100 mm sacrificial layer.

The key acceptance criterion is cooling the corium to 1450 K (1176.85 °C), corresponding to the solidus temperature from CORQUENCH results. Additionally, the cooling-water temperature must remain below the saturation temperature of 485.55 K (212.4 °C) at 2 MPa. Corium decay heat is removed through the core-catcher walls to the water below and from the top by radiation and natural convection (modelled via boundary conditions).

A cooling-water mass flow rate of 17.531 kg/s was prescribed at the inlet. Convergence was monitored via equation residuals and by tracking velocity and pressure to exclude nonphysical behaviour. The simulation was terminated once the flow field stabilized and the average corium temperature fell below 1450 K.

Crust formation during cooling was modelled by imposing step changes in corium thermal conductivity and viscosity at 1450 K, effectively suppressing corium motion and representing solidification. The coolant flow behaviour had been pre-validated in earlier optimization studies, which supported the stable coupling of two-fluid flow with conductive heat transfer in the present model.

5. CFD CALCULATION RESULTS

The results are primarily presented through graphical outputs of the core catcher temperature field and temperatures of both fluid regions (corium and cooling water) in the CFD simulation. The simulation time step was initially set to 0.001 s and was gradually increased up to 0.1 s, while maintaining convergence within 20 inner iterations at each time step. The maximum water pressure drop stabilized and oscillated around 1511 Pa ± 2 Pa. The maximum cooling-water velocity reached 1.76 m/s, and the average cooling-water velocity in the computational domain was 0.045 m/s.

The following figures show the resulting temperature field after the average temperature of the reactor core melt dropped below the solidus temperature (1450 K). This value is taken as the criterion for successful completion of the calculation. The plots (Figures 11 and 12) present the evolution of the maximum and average corium temperatures, as well as the maximum cooling-water temperature.

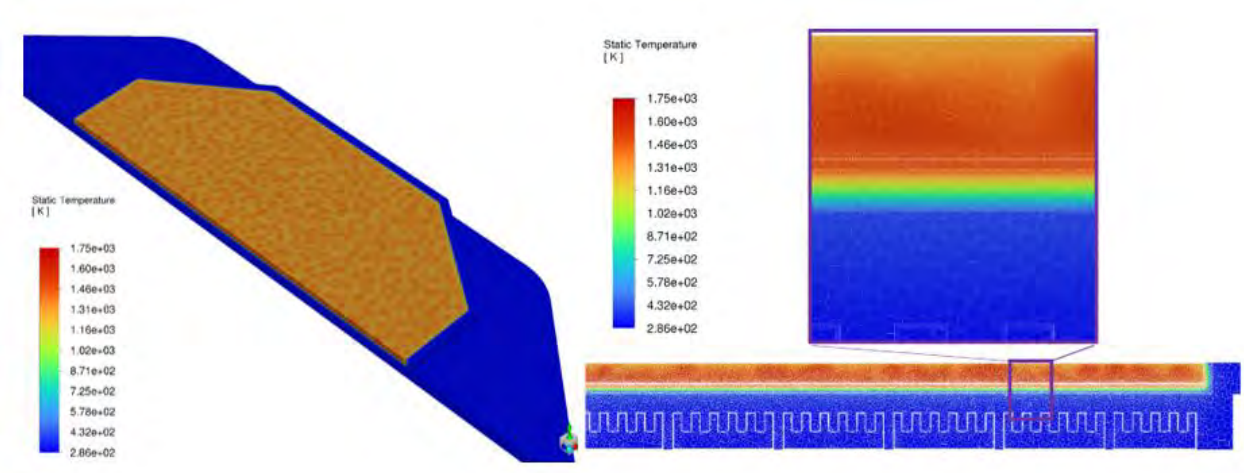

Figure 10. ½ Symmetry and Cross-Section of Temperature Field within the Core Catcher

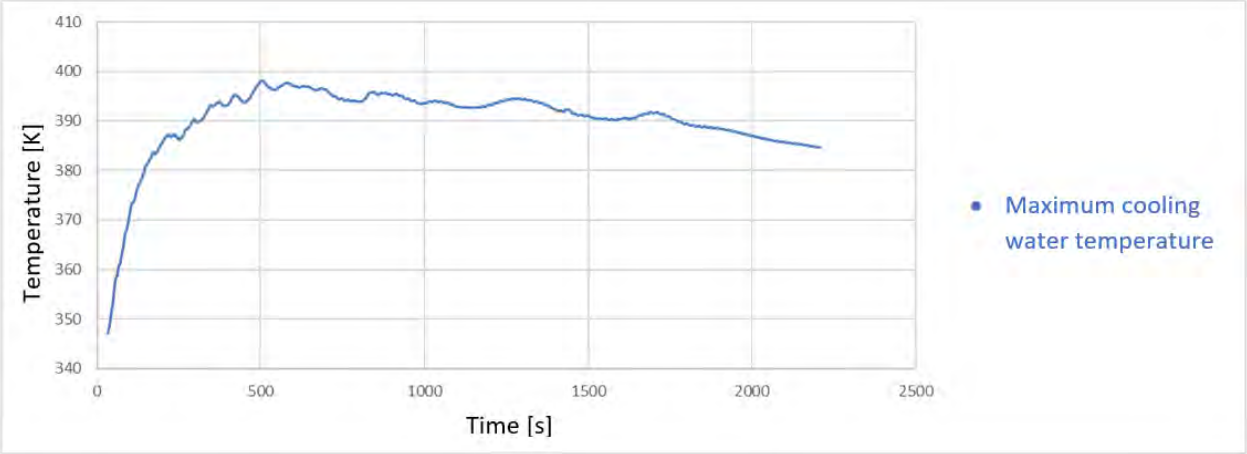

Figure 11. Graph of Maximum Water Temperature in the CFD Simulation

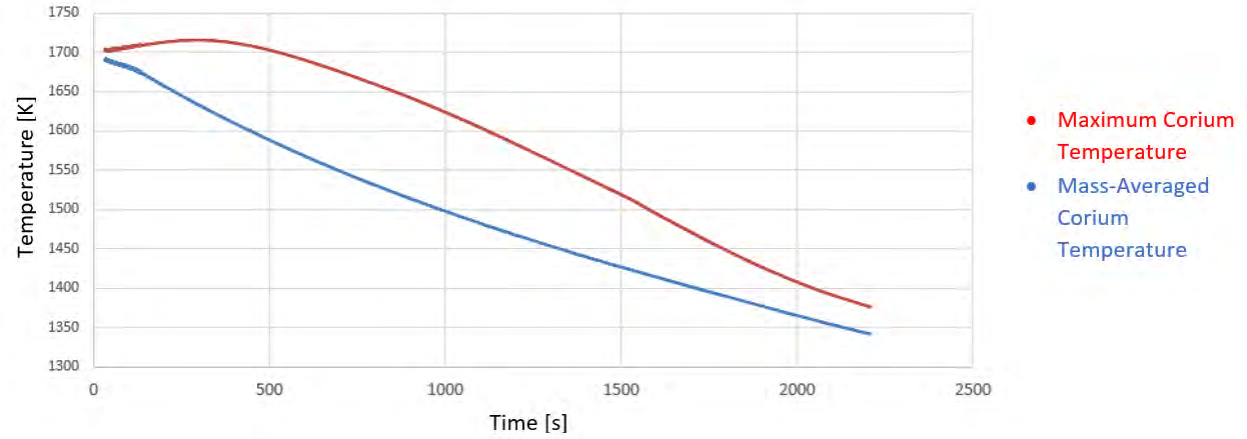

Figure 12. Graph of Maximum and Mass-Averaged Oxidic Corium Temperature

The maximum water temperature of 398.4 K did not exceed the boiling threshold of 485.55 K at any time during the simulation. The margin to the onset of boiling in the transient case was approximately 90 K, and after reaching its peak the water temperature gradually decreased. It can therefore be concluded that no boiling of the cooling water occurs anywhere within the computational domain.

The temperature of the steel structures does not exceed 480 K, which is safely below the melting temperature. The transient simulation was continued to temperatures even lower than 1450 K, and it was further confirmed that all monitored temperatures continued to exhibit a decreasing trend.

6. CONCLUSIONS

This CFD model represents the culmination of the preceding analyses and describes a scenario in which the sacrificial materials have been fully ablated while the corium has not yet cooled below the solidus temperature. The simulation considers a stratified corium pool consisting of metallic and oxidic phases, with a defined residual decay heat source in the oxidic layer, cooled by water flowing via natural circulation beneath the core catcher. The objective was to verify effective corium cooling and to confirm that boiling of the cooling water does not occur. The simulation was considered successfully completed when the average corium temperature decreased below the solidus temperature of 1450 K.

The results indicate progressive cooling of the melt down to the solidus temperature, with the temperature trend suggesting continued decrease beyond this point. The maximum cooling-water temperature reached 398.4 K in the transient simulation, well below the saturation temperature of 485.55 K at 2 MPa.

Based on the performed analysis, it can be concluded that the functionality of the conceptual design of the core melt localization and stabilization system—the core catcher—has been successfully verified through detailed CFD simulations using Ansys Fluent.

ACKNOWLEDGEMENTS

This work was carried out under the auspices of the Project: 101164616 — TREASURE — HORIZON-EURATOM-2023-NRT-01.

REFERENCES

1. Ansys Fluent Users Guide, Release 2025R1. Ansys Inc., Southpointe, 2600 Canonsburg, PA 15317, USA, (2025)
2. M. T. Farmer, “The CORQUENCH Code for Modeling of Ex-Vessel Corium Coolability under Top Flooding Conditions” Code Manual, Argonne National Laboratory, USA, (2023)
3. IRSN NUCLEA-20 Nuclear Alloys-Oxides Database (NUCL20). Thermo-Calc Software, Råsundavägen 18, SE-169 67 Solna, SWEDEN, (2022)
4. B. Kvizda, P Vácha, et al., “ALLEGRO Gas-cooled Fast Reactor (GFR) demonstrator thermal hydraulic benchmark,” *Nuclear Engineering and Design*, **345**, 47–61. (2019)
5. Z. Bali, G. Mayer, “Investigation of decay heat removal systems in the ALLEGRO helium-cooled fast reactor”, *Nuclear Engineering and Design*, **435**,113952. (2019)
6. B. Meszaros, et. al, “Refractory geopolymers: Thermal shock resistant material for nuclear safety”, *Nuclear Engineering and Design*, **418**, 112918. (2024)
7. Z. Černý, et. al, “Development of geopolymer based sacrificial materials for GEN IV severe accident mitigation”
8. G. Wang: “Flow Mechanism of Molten Steel in a Single-Strand Slab Caster Tundish Based on the Residence Time Distribution Curve and Data”, *ISIJ International*, 55(5): 984-992, (2015)

COMPUTATIONAL VERIFICATION OF THE FUNCTIONALITY OF THE COOLING SYSTEM OF THE ALLEGRO REACTOR CORE CATCHER

ERMSAR 2026

Madrid, 18-22 May 2026

Jan Komrska, Pavel Zácha, Petr Vácha

Faculty of Mechanical Engineering, Department of Energy Engineering

Czech Technical University in Prague

Introduction

CFD simulation of corium cooling in a conceptual core catcher using Ansys Fluent

Heat transfer through core catcher layers to naturally circulating cooling water

Corium properties obtained using:

- CORQUENCH
- Thermo-Calc + NUCLEA database

Long-term cooling analyzed in Ansys Fluent 2025 R1

Bounding severe accident scenario considered:

- Late-phase ex-vessel accident
- Sacrificial material fully consumed (poor performance leading to consumption of entire layer)
- Corium remains above solidus temperature

ALLEGRO Core Catcher Design

ALLEGRO is a gas-cooled fast reactor (GFR) demonstrator developed by V4G4 CoE and includes a dedicated core catcher system for severe accidents

Core catcher functions:

- Stabilize and retain corium
- Provide long-term cooling
- Prevent containment basemat melt-through
- Reduce radionuclide release risk

Design concept:

- Dry, spreading, ex-vessel core catcher
- Extensive use of sacrificial materials

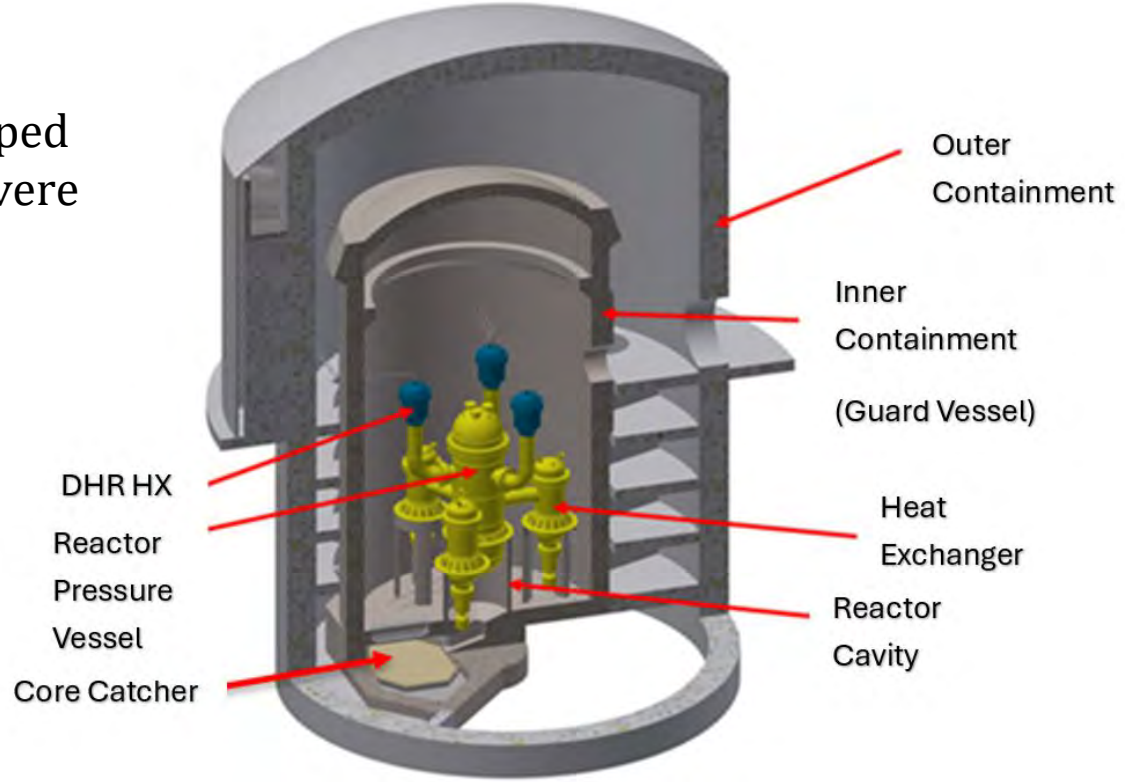

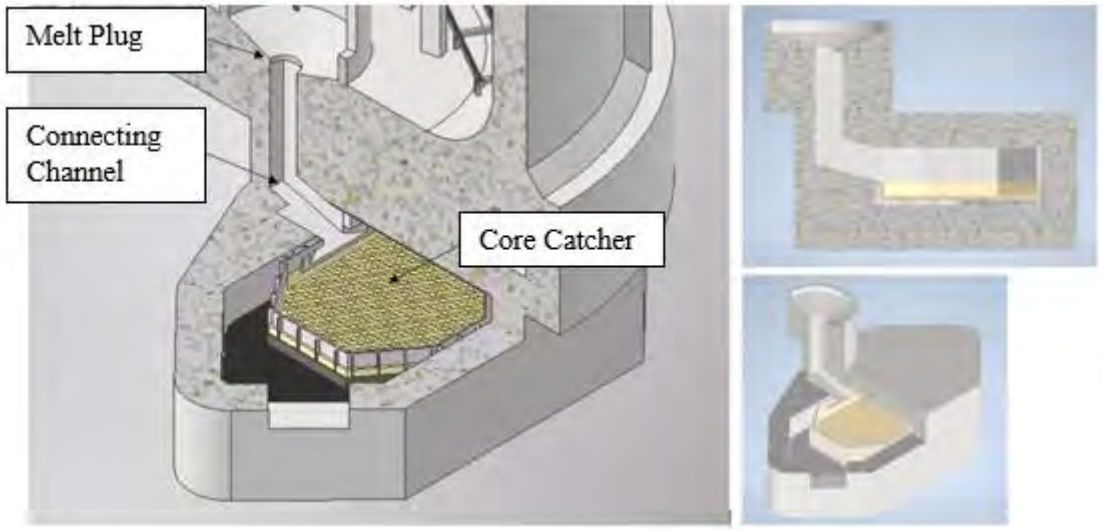

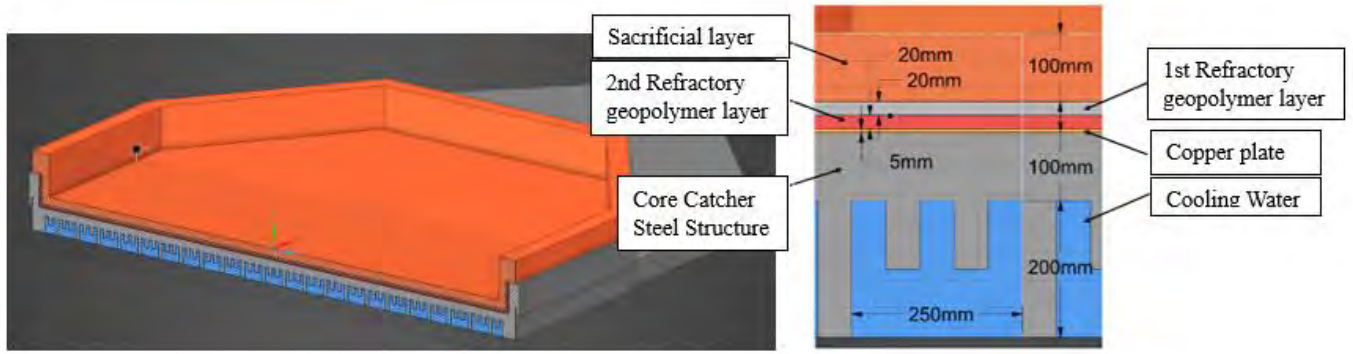

ALLEGRO Core Catcher Cooling System

Core catcher cooling system operates via natural circulation

Connected to the same loop as the Decay Heat Removal system

Design principle:

- Relies on height difference between core catcher (heat source) and heat exchanger
- Heat exchanger is a tubular design submerged in a water pool at the top of the containment guard vessel

Normal operation:

- Removes residual decay heat
- Operates at ~20× lower load than maximum capacity

Severe accident conditions:

- Heat losses from primary circuit drop to ~5% of nominal
- Cooling system remains in standby without risk of damage

Core melt scenario:

- Reactor vessel failure leads to corium release into core catcher
- Primary circuit heat source becomes negligible
- Cooling system removes only corium decay heat, as designed

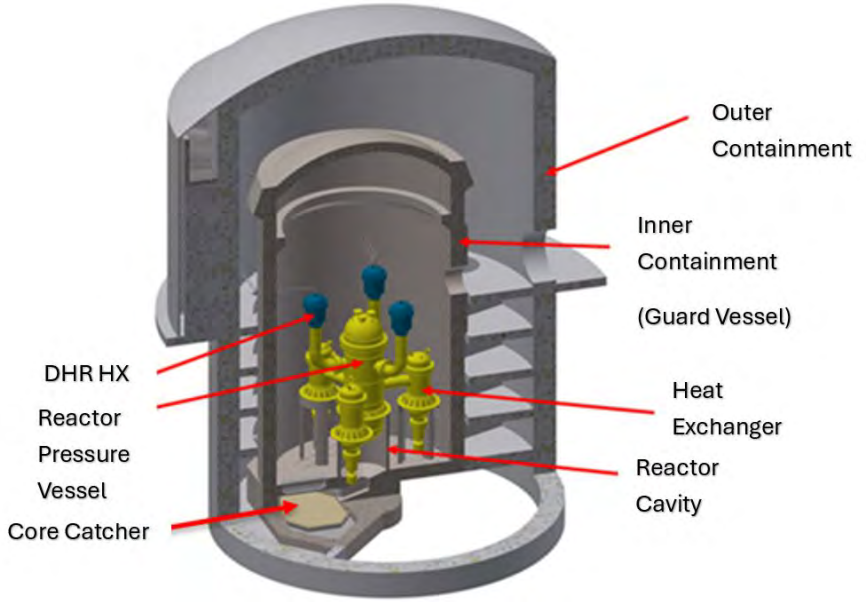

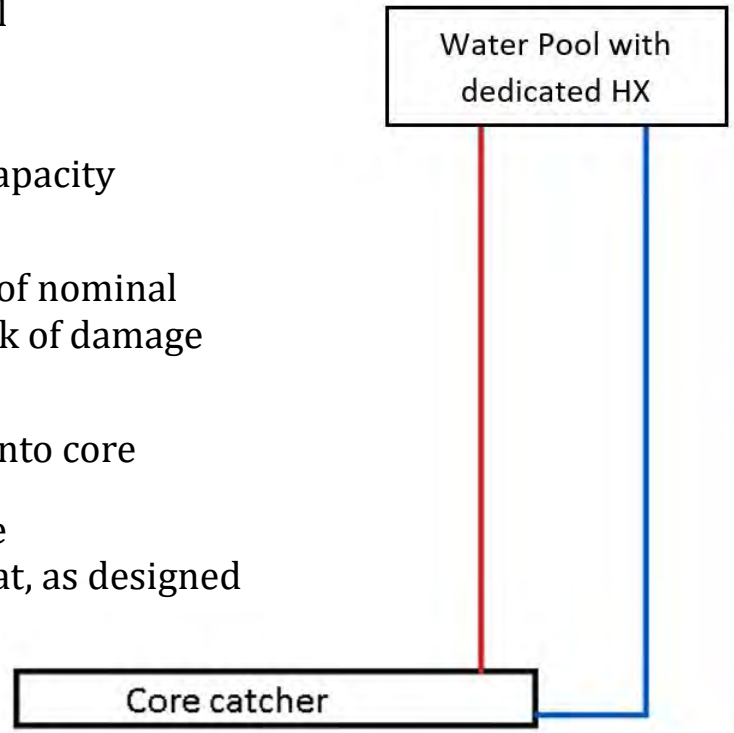

ALLEGRO Core Catcher Design Process

- MCCI of reactor pit and Melt plug
- Corium properties

MELCOR 2.2

CORQUENCH 4.1 + Thermo-Calc NUCLEA

- Additional Corium properties

- Mesh sensitivity analysis
- Corium spreading simulation
- Validated with VULCANO VE-U7 and VALVERDE project

Ansys Fluent

CORQUENCH 4.1 + Thermo-Calc Nuclea

- MCCI of Core Catcher Floor
- Corium properties after spreading and MCCI

- Core Catcher Cooling via heat convection/radiation from corium and conduction into underlying water

Ansys Fluent

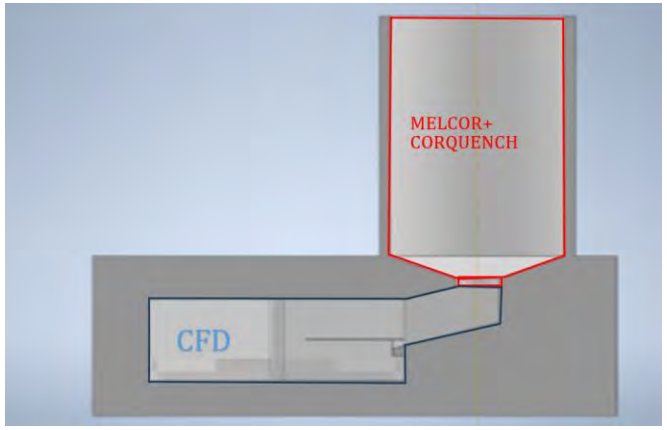

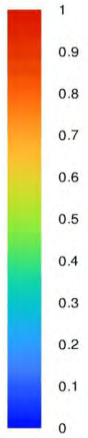

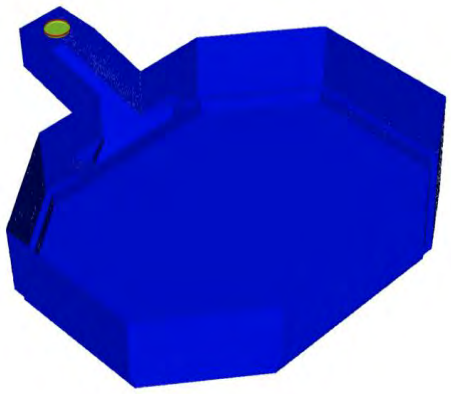

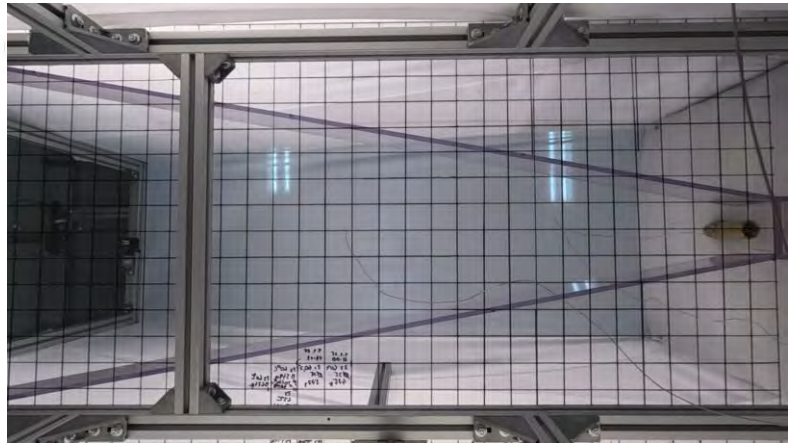

Summary of Preparatory Analyses – Thermocalc + NUCLEA

NUCLEA used to determine corium properties via Thermo-Calc

Application:

- Supports both IVR (in-vessel retention) and EVR (ex-vessel retention) severe accident phases
- Calculates thermochemical equilibrium of multi-component systems
- Modeled chemical system includes:
  - O–U–Zr–Ag–In–B–C–Fe–Cr–Ni–Ba–La–Sr–Ru–Al–Ca–Mg–Si + Ar–H

Input parameters for equilibrium calculation:

- Initial temperature: 1900 K
- Pressure: 0.1 MPa (atmospheric)
- Total system mass: 24,762 kg
  - Corium: 10,653 kg
  - Ablated sacrificial materials: 14,109 kg

Element	Molar concentration of element [-]
Oxygen	0.5212
Hydrogen	0.0578
Silicon	0.08
Calcium	0.03
Magnesium	0.01
Aluminium	0.0425
Iron	0.2445
Uranium	0.014

Summary of Preparatory Analyses – Thermocalc + NUCLEA - Results

Late Ex-Vessel scenario after all sacrificial materials were consumed

Corium properties calculated in the 1500–1930 K range (10 K steps)

Temperature-dependent corium composition obtained using Thermo-Calc + NUCLEA database

Metallic phase behavior (LIQUID):

- Transitions to BCC_A2_2 at ~1800 K
- Solidifies into FCC_A1_1 at ~1660 K

Oxidic phase behavior (LIQUID#2):

- Begins cooling into FCC_C1 at ~1810 K
- Forms solid SPINEL phase at ~1550 K

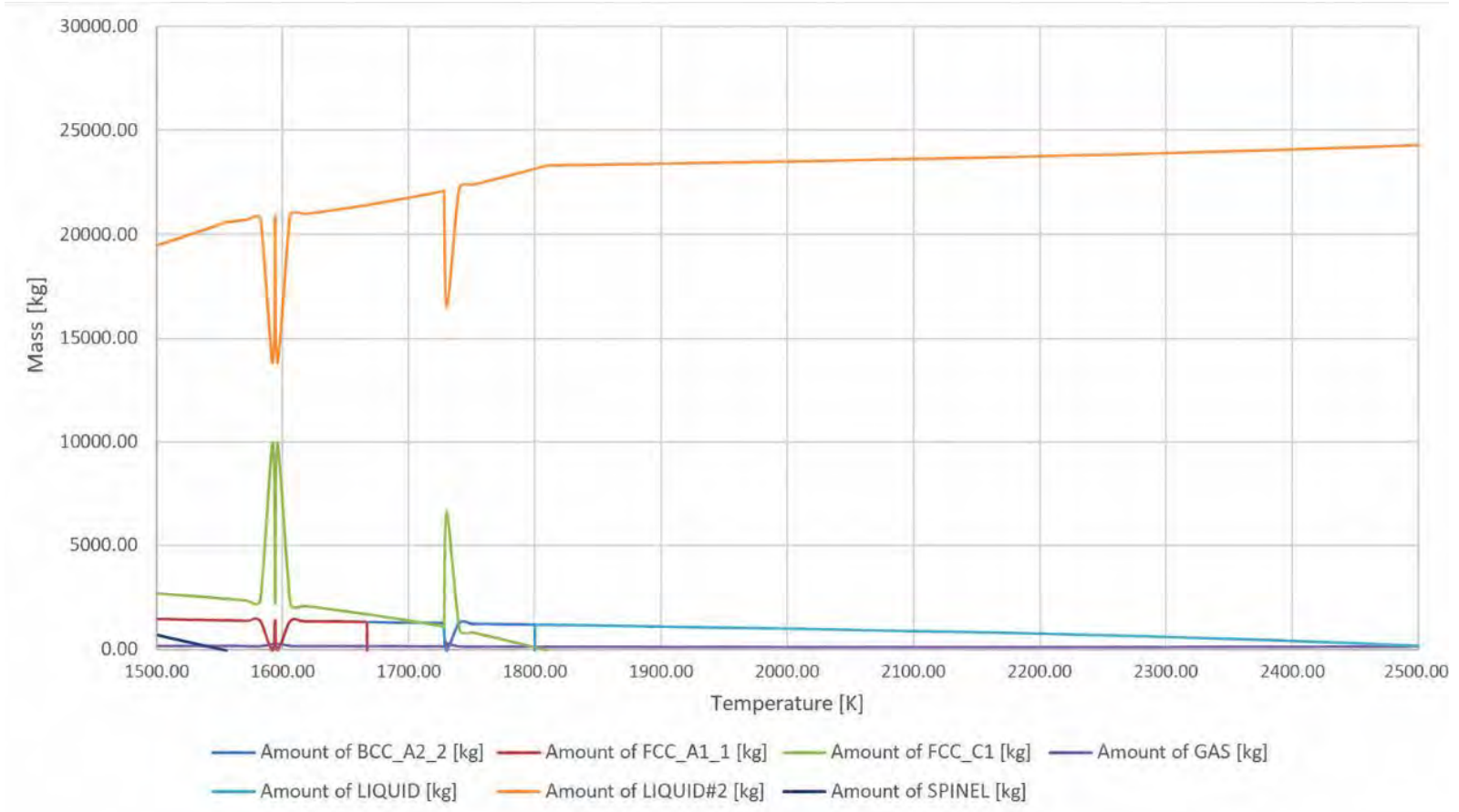

Summary of Preparatory Analyses – CORQUENCH

Thermo-Calc 2024A + NUCLEA database could not provide corium thermophysical properties directly for use in CFD calculations

Additional analyses performed using CORQUENCH Which was used to determine thermophysical properties of the oxidic corium phase

Core Catcher layer material	Solidus Temperature [K]	Liquidus Temperature [K]	Ablation Temperature [K]	Initial layer Temperature[K]	Layer Height [mm]
Sacrificial layer – Geopolymer with higher Fe_2O_3 cont.	1120	1750	1370	323.15	100
Refractory layer- Geopolymer with higher Al_2O_3 cont.	1120	2250	1400	323.15	20
Refractory layer – Geopolymer with higher MgO cont.	1120	2250	1470	323.15	20
Copper Plate	1357	1358	1357.5	323.15	5
Steel Structure	1699	1700	1699.5	323.15	100

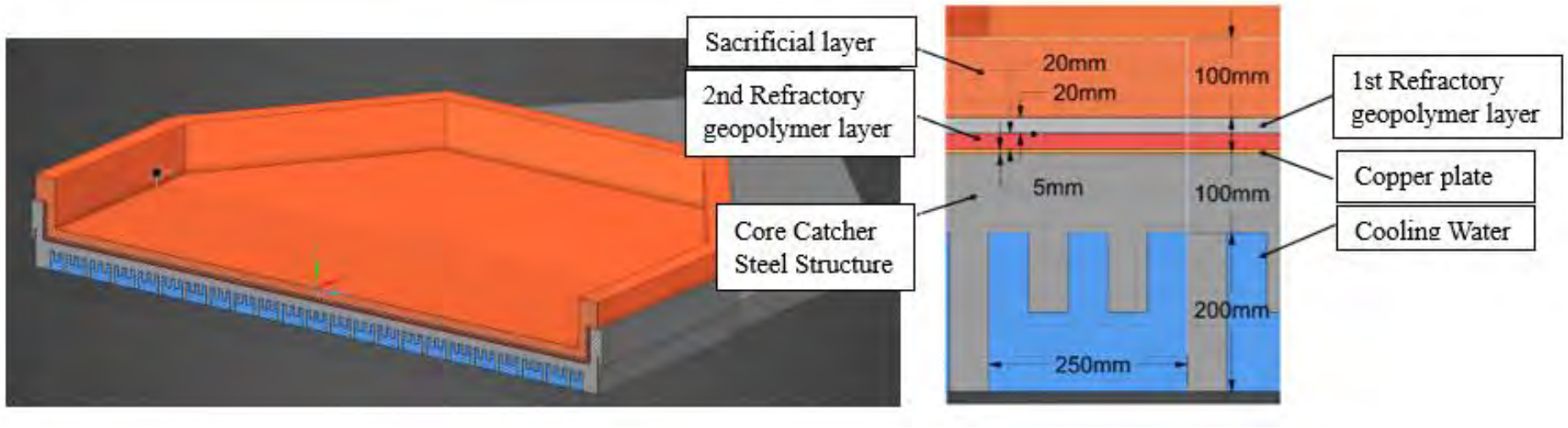

Summary of Preparatory Analyses – CORQUENCH - Results

Temperature [K]	Conductivity [W/m·K]	Density[kg/m³]	Heat Capacity[J/kg·K]	Viscosity[kg/m·s]	Surface Tension [N/m]	Emissivity [-]
1450	1.67	3741.7	920.3	$8.08 \cdot 10^{14}$	0.52	0.83
1500	3.93	3741.7	976.51	2.591	0.52	0.83
1600	3.94	3741.7	992.08	1.2974	0.52	0.83
1700	3.94	3741.7	1004.2	0.73848	0.52	0.83
1800	3.94	3741.7	1013.9	0.46108	0.52	0.83
1900	3.94	3741.7	1022.5	0.30231	0.52	0.83
1930	3.94	3741.7	1024.9	0.26878	0.52	0.83
2000	3.94	3741.7	1030.4	0.20625	0.52	0.83

We were able to obtain temperature-dependent oxidic corium properties for final CFD simulations

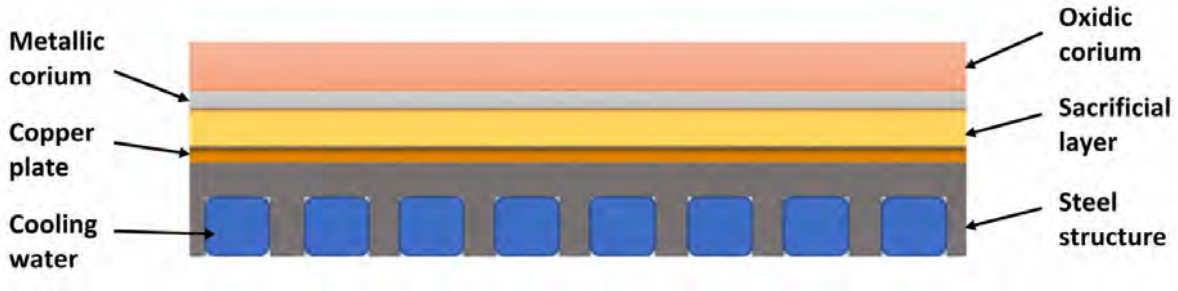

CFD Simulation of Long-Term Cooling of Corium

Core Catcher functionality criterion:

- Corium cooled below solidus temperature of 1450 K
- Cooling water temperature must remain below saturation temperature of 485.55 K at 2 MPa

Bounding severe accident scenario assumed:

- Full ablation of 100 mm sacrificial layer

Initial simulation conditions:

- Corium initial temperature of 1700 K
- Corium composition includes fully ablated sacrificial material

Late accident phase modeled with two stratified corium layers:

- Oxidic layer
- Metallic layer

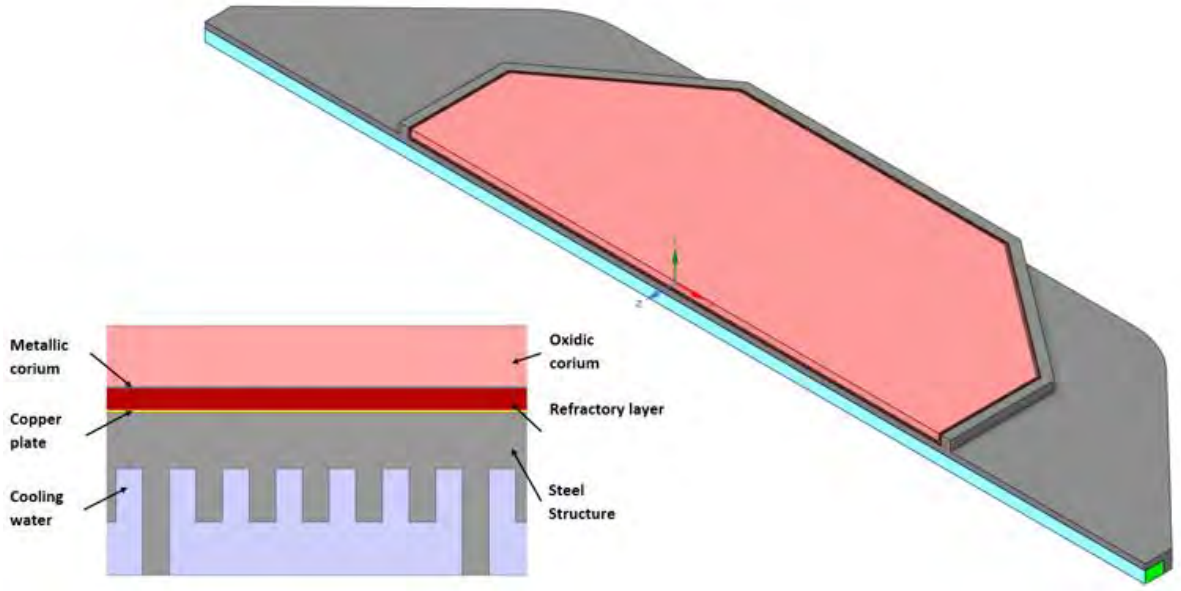

CFD Simulation of Long-Term Cooling of Corium – Used Simplifications

Several computational simplifications introduced to improve convergence and reduce calculation time

Geometric simplification:

- Core-catcher rim shortened to maximum melt level
  - Reduced computational domain using boundary conditions
- Simplification in core catcher layer arrangement required for mesh generation
  - Original thin layers caused poor mesh quality:
    - Metallic corium layer: 3.5 mm
    - Copper layer: 5 mm
  - Resulting mesh issues:
    - Large disparities in cell sizes
    - High aspect ratio cells
    - Repeated divergence in test simulations
  - Metallic layers merged into one layer with mass-averaged properties
- ½ Symmetry

Metallic corium layer assumed solid at initial temperature of 1700 K

Heat transfer in metallic layers dominated by conduction

Final approximation:

- Metallic corium and copper layers merged into one equivalent layer
- Effective properties averaged according to original layer thicknesses

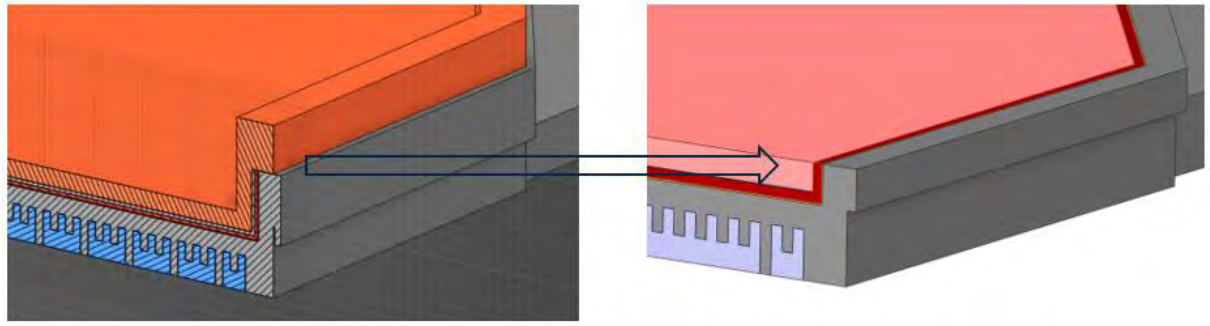

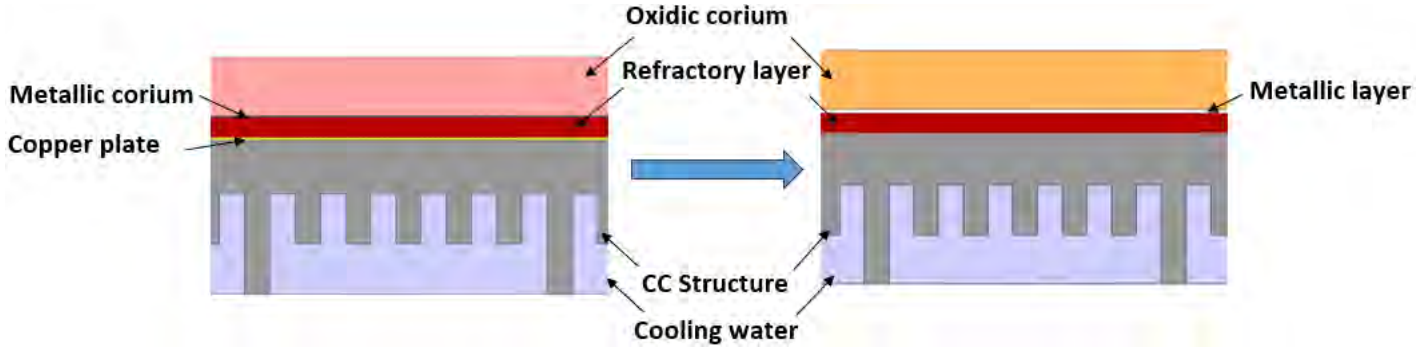

CFD Simulation of Long-Term Cooling of Corium – CFD Mesh

Mesh size and quality:

- 38,442,704 total volume cells
- Minimum orthogonal quality: 0.15
- Maximum aspect ratio: 92.65 (due to boundary layer refinement + large bulk cells)

Mesh Resolution strategy:

- ≥15 cells across fluid regions (corium + cooling water)
- ≥4 cells across solid thicknesses (conduction-dominated regions)

Mesh sizing:

- Minimum cell size: 4 mm
- Maximum cell size: 40 mm

Local refinement:

- BOI (Body of Influence) applied in metallic layer region
- Local max cell size reduced to 2 mm

Boundary layer mesh (fluid–wall regions):

- First layer height: 0.75 mm
- 5 layers total
- Growth rate: 1.2

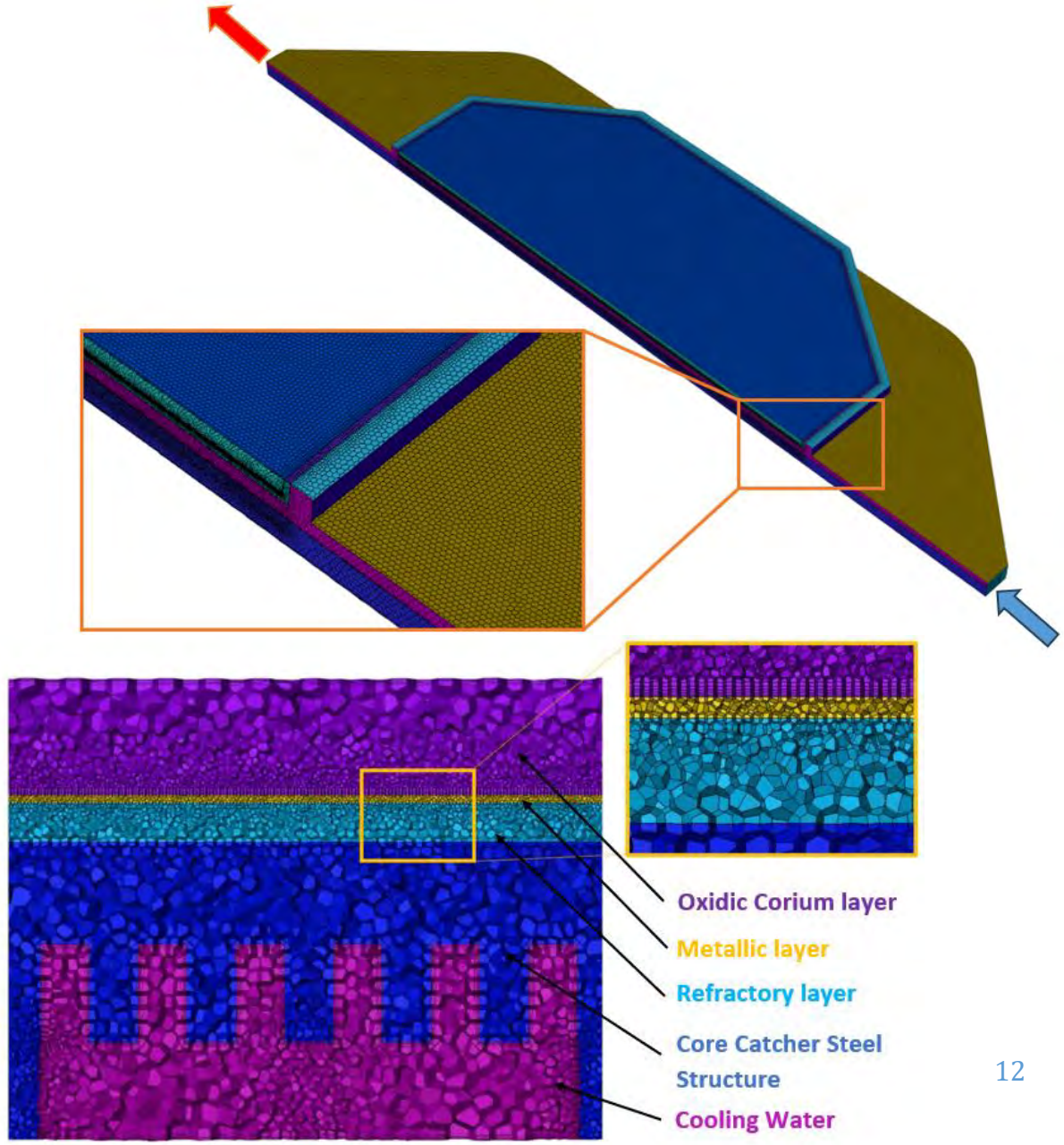

CFD Simulation of Long-Term Cooling of Corium – Boundary Conditions

Bounding severe accident scenario:

- Late-phase ex-vessel accident
- Full ablation of 100 mm sacrificial material
- Initial corium temperature: 1700 K
- Radiation and natural convection from top surface (boundary conditions – Atmosphere = 1048 K, Emissivity = 0.83)
- Cooling-water inlet mass flow rate: 17.531 kg/s

Numerical setup:

- Convergence monitored via residuals, velocity, and pressure fields
- Simulation stopped after flow stabilization and corium temperature < 1450 K

Solidification modelling:

- Crust formation enforced via step change in thermal conductivity and viscosity at 1450 K
- Corium motion effectively suppressed after solidification

Acceptance criteria:

- Corium cooled to 1450 K (solidus, from CORQUENCH results)
- Cooling water temperature < 485.55 K at 2 MPa (saturation limit)

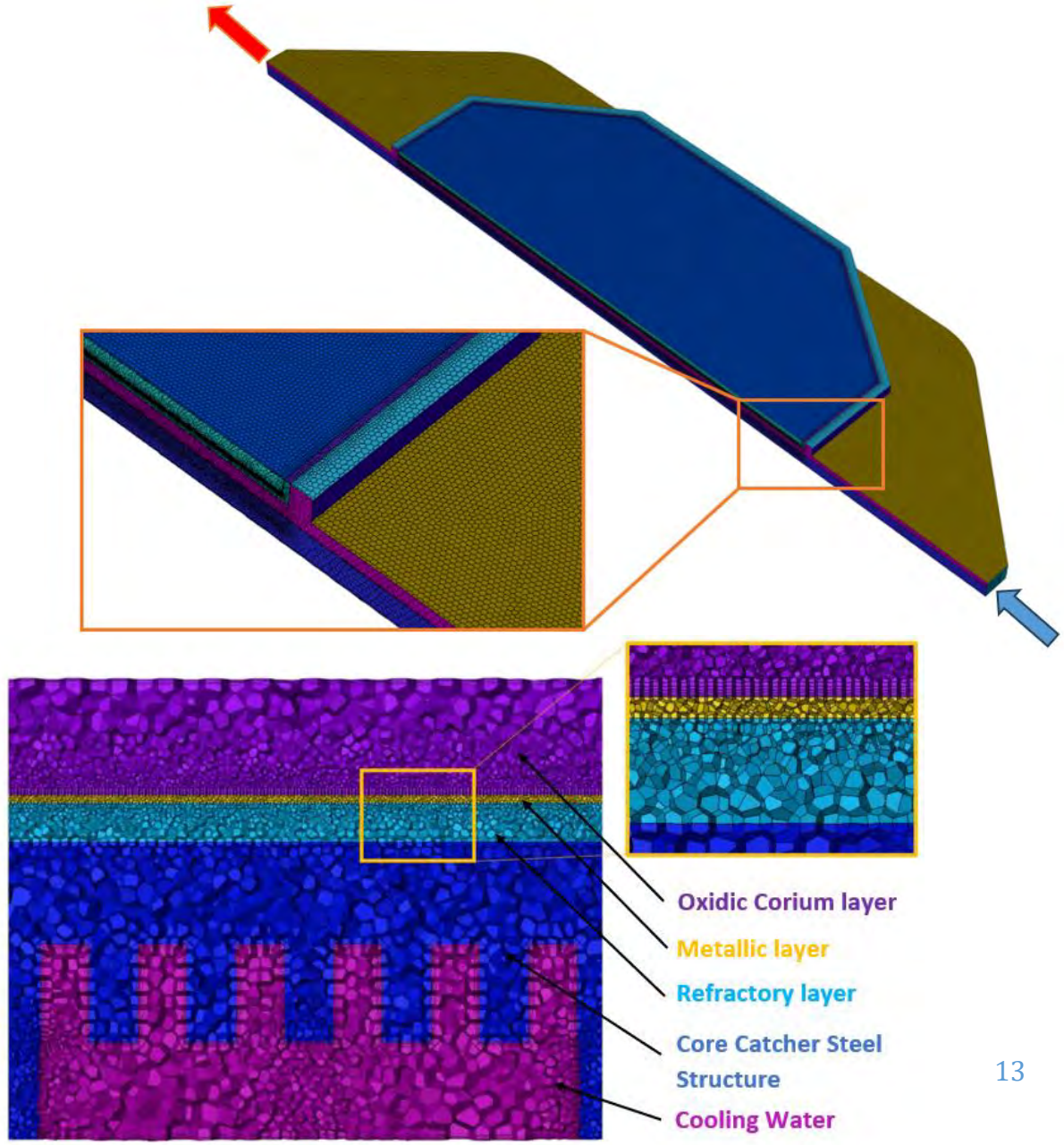

CFD Simulation of Long-Term Cooling of Corium – Results

Numerical setup:
- Time step: 0.001 s → gradually increased to 0.1 s
- 20 inner iterations per time step

Water Flow stability:
- Pressure drop stabilized at 1511 Pa ± 2 Pa
- Max cooling-water velocity: 1.76 m/s
- Average cooling-water velocity: 0.045 m/s

Core Catcher Thermal performance:
- Corium cooled below solidus criterion (1450 K) → **simulation success condition achieved**
- Max cooling-water temperature: 398.4 K
- Boiling threshold: 485.55 K (2 MPa) → **not exceeded**
- **Safety margin to boiling: ~90 K**

Structural integrity:
- Steel structures remain below 480 K (safe vs melting limit)

Overall outcome:
- No boiling occurs in the domain
- All temperatures show continuous decreasing trend beyond 1450 K
- Stable and successful long-term cooling of corium demonstrated

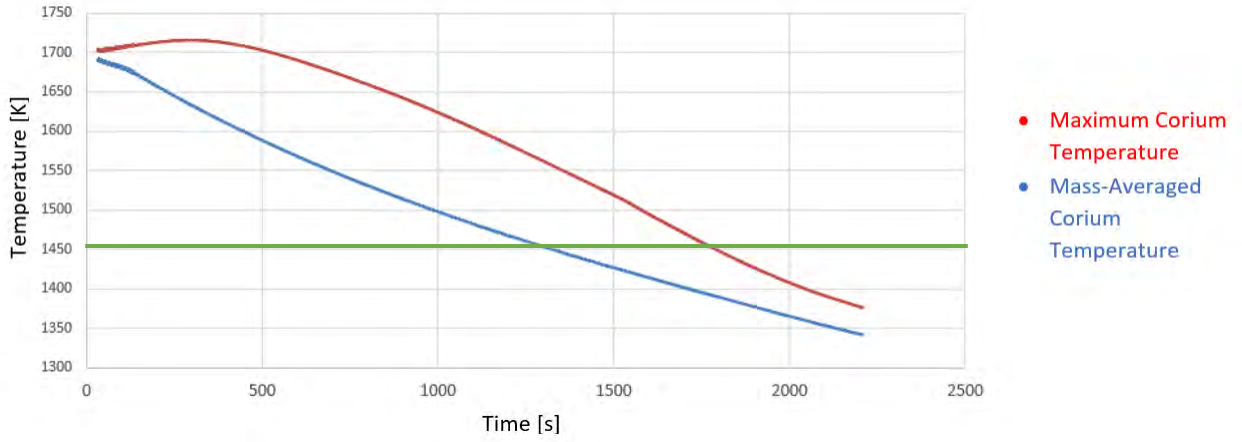

Conclusions & Outlooks

CFD model represents final integration of preceding analyses for core catcher performance assessment

The objective was to verify effective corium cooling and to confirm that boiling of the cooling water does not occur

The simulation was considered successfully completed when the average corium temperature decreased below the solidus temperature of 1450 K

- The results indicate progressive cooling of the melt down to the solidus temperature, with the temperature trend suggesting continued to decrease beyond this point

Further work to be performed includes:

- CC Room ceiling heat effects
- More initial scenarios (with more realistic oxidic/metallic corium distribution)
- Reduce number of simplifications

Thank you for your attention!

The work carried out on the ALLEGRO core catcher was done under the auspices of the 101164616 — TREASURE — HORIZON-EURATOM-2023-NRT-01.

Jan.Komrska@fs.cvut.cz

CFD Simulation of Long-Term Cooling of Corium – Results

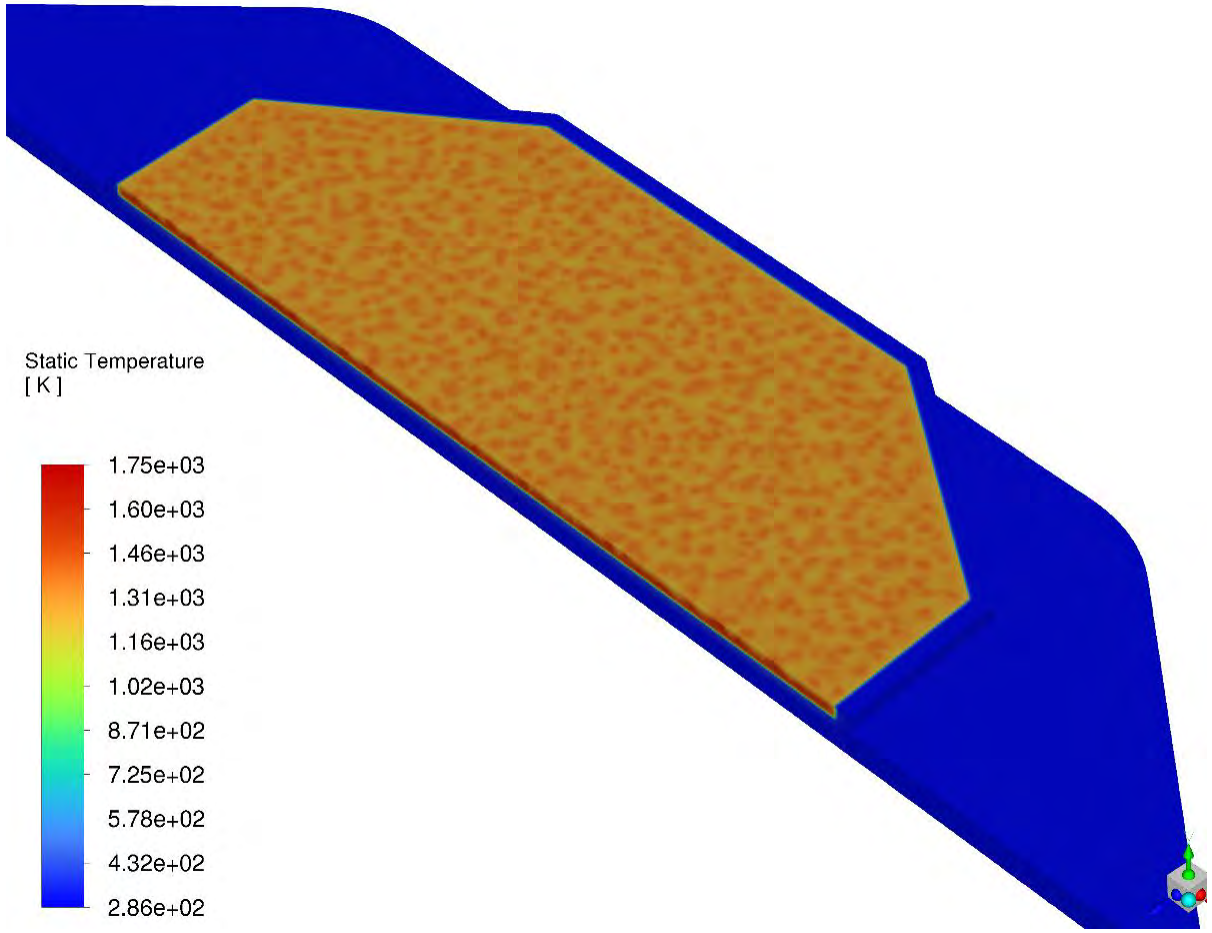

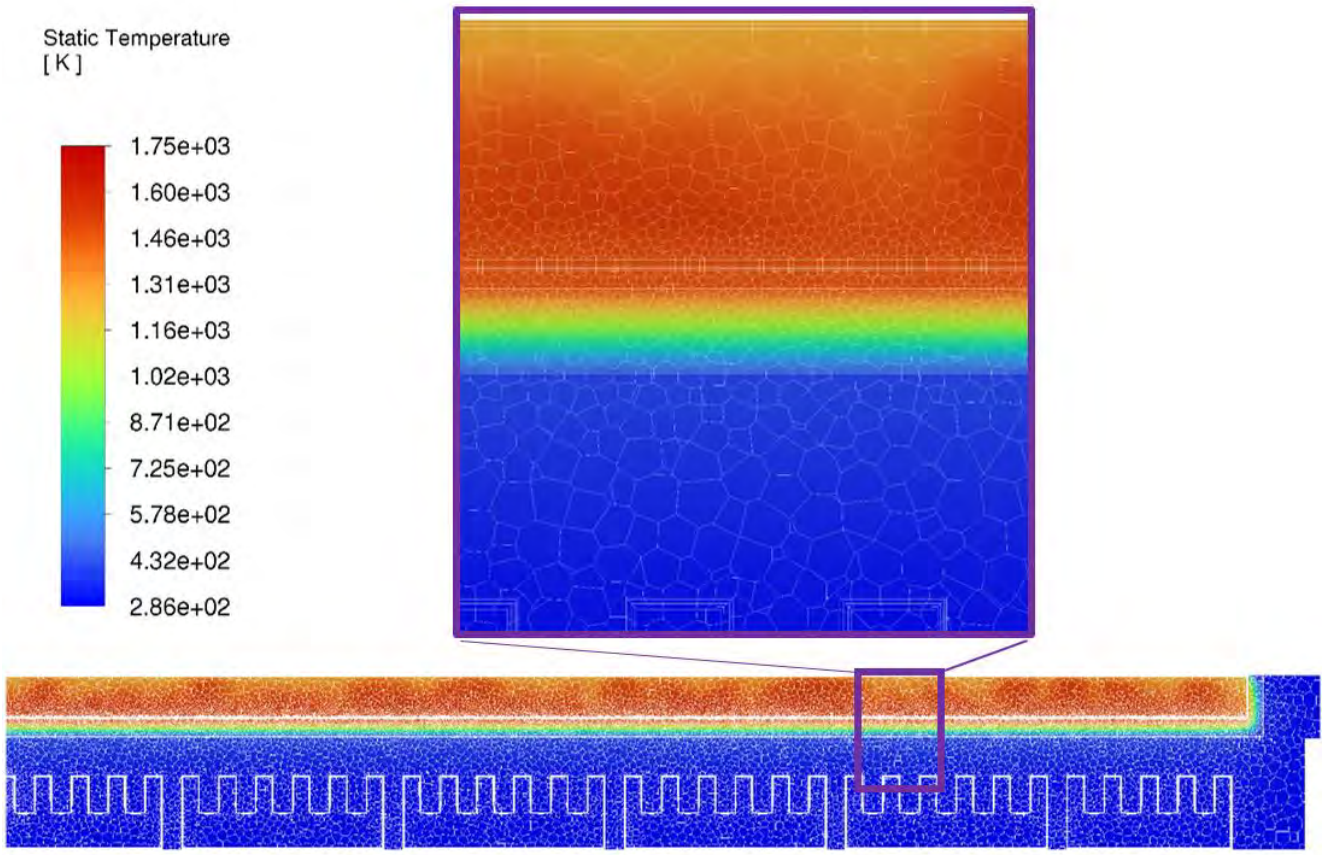

The 12th European Review Meeting on Severe Accidents Research

May 18-22, 2026, Universidad Carlos III de Madrid, Madrid, Spain

CLOSING PLENARY SESSION

Chairs: S. Paci (University of Pisa), F. Gabrielli (KIT)

ERMSAR2026 An Overview in Numbers

F. Gabrielli (KIT)

Concluding and Final Remarks

L.E. Herranz (CIEMAT), Coordinator of the SEAKNOT project

Introduction to ERMSAR2028

I. Kljenak (JSI)

In cooperation with

ERMSAR 2026

An Overview in numbers

F. Gabrielli, L. E. Herranz, S. Paci

In cooperation with

Many thanks to CIEMAT (and Madrid) for the hosting

L. E. Herranz

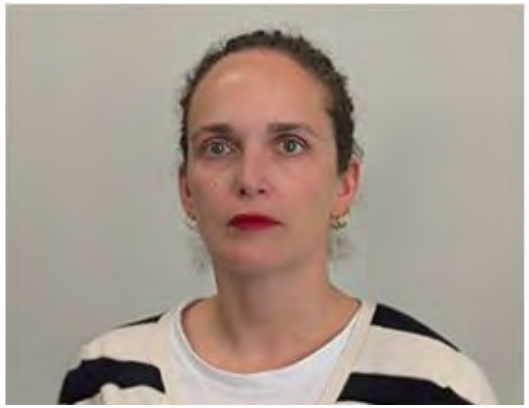

M. Garcia Martin

J. Fontanet Saez

C. Aguado Basabe

and the whole CIEMAT team

SEAKNOT

NUGENIA TA2
Nuclear Generation II&III Alliance

SNETP
Sustainable Nuclear Energy Technology Platform

In cooperation with

NEA
Nuclear Energy Agency

IAEA
International Atomic Energy Agency
Atoms for Peace and Development

The Technical Scientific Committee

L. E. Herranz (CIEMAT, Spain)
S. Paci (University of Pisa, Italy)
F. Gabrielli (KIT, Germany)
P. Piluso (CEA, France)
I. Kljenak (IJS, Slovenia)
F. Rocchi (ENEA, Italy)
S. Gupta (Framatome GmbH, Germany)
S. Bechta (KTH, Sweden)
L. Carénini (ASNR)
C. Journeau (CEA, France)
T. Kärkela (VTT, Finland)
S. Kelm (FZJ, Germany)
T. Lind (PSI, Switzerland)
M. Freitag (Becker Technologies, Germany)
G. Urzua Torres (Framatome GmbH, Germany)
T. Hollands (GRS, Germany)
P. Groudev (INRNE, Bulgaria)
M. Braun (Framatome GmbH, Germany)
A. Miassoedov (IAEA, Austria)
S. Brumm (JRC, Netherlands)
D. Jacquemain (OECD/NEA, France)
M. Adorni (OECD/NEA, France)
A. Bentaib (OECD/NEA, France)
V. H. Sanchez Espinoza (KIT, Germany)
W. Tromm (KIT, Germany)

Università di Pisa

KIT Karlsruher Institut für Technologie

SEAKNOT

NUGENIA TA2
Nuclear Generation II&III Alliance

SNETP
Sustainable Nuclear Energy Technology Platform

NEA
Nuclear Energy Agency

In cooperation with

IAEA
International Atomic Energy Agency
Atoms for Peace and Development

The Chairpersons (3 parallel technical sessions)

M. Angelucci (University of Pisa, Italy)
S. Bechta (KTH, Sweden)
A. Bentaib (OECD/NEA, France)
M. Braun (Framatome GmbH, Germany)
S. Brumm (JRC, Netherlands)
L. Carénini (ASNR, France)
M. E. Cazado (KIT, Germany)
K. Dieter (Becker Technologies GmbH, Germany)
F. Fichot (ASNR, France)
J. Fontanet (CIEMAT, Spain)
M. Garcia Martin (CIEMAT, Spain)
F. Giannetti (University of Rome 'La Sapienza')
A. C. Grégoire (ASNR, France)
S. Buhlmann (Framatome GmbH, Germany)
L. E. Herranz (CIEMAT, Spain)
T. Hollands (GRS, Germany)
G. Jiménez (UPM, Spain)
C. Journeau (CEA, France)
T. Kärkela (VTT, Finland)
S. Kelm (FZJ, Germany)
I. Kljenak (JSI, Slovenia)
T. Lind (PSI, Switzerland)
L. Lovasz (GRS, Germany)
D. Luxat (SNL, USA)
M. Malicki (PSI, Switzerland)
F. Mascari (ENEA, Italy)
A. Miassoedov (IAEA)
S. Paci (University of Pisa)
P. Piluso (CEA, France)
E.-A. Reinecke (FZJ, Germany)
F. Rocchi (ENEA, Italy)
N. Seiler (CEA, France)
A. Stakhanova (KIT, Germany)
L. Tiborcz (GRS, Germany)
X. Gaus-Liu (KIT, Germany)

Università di Pisa

KIT Karlsruher Institut für Technologie

SEAKNOT

NUGENIA TA2
Nuclear Generation II&III Alliance

SNETP
Sustainable Nuclear Energy Technology Platform

In cooperation with

NEA
Nuclear Energy Agency

IAEA
International Atomic Energy Agency
Atoms for Peace and Development

The invited speakers

M. Steinbruck (KIT, Germany)

M. Farmer (ANL, USA)

M. Sánchez (CSN, Spain)

T. Fuketa (NDF and NRA, Japan)

L. Borondo Arribas (Iberdrola, Spain)

A. Giner (Westinghouse, Spain)

A. Iorizzo (European Commission)

A. Miassoedov (International Atomic Energy Agency)

M. Adorni (OECD Nuclear Energy Agency)

Università di Pisa

KIT Karlsruher Institut für Technologie

SEAKNOT

NUGENIA TA2
Nuclear Generation II&III Alliance

SNETP
Sustainable Nuclear Energy Technology Platform

In cooperation with

NEA
Nuclear Energy Agency

IAEA
International Atomic Energy Agency
Atoms for Peace and Development

The Sponsors & Supporting Organizations

enusa

Westinghouse

GOBIERNO DE ESPAÑA
MINISTERIO DE CIENCIA, INNOVACIÓN Y UNIVERSIDADES

Ciemat
Centro de Investigaciones Energéticas, Medioambientales y Tecnológicas

KIT
Karlsruhe Institute of Technology

SNETP
Sustainable Nuclear Energy Technology Platform

Funded by the European Union

This event has been partially supported by the **ENEN2plus project** (HORIZON-EURATOM-2021-NRT-01-13 101061677) founded by the European Union.

Università di Pisa

KIT
Karlsruher Institut für Technologie

SEAKNOT

NUGENIA TA2
Nuclear Generation II&III Alliance

SNETP
Sustainable Nuclear Energy Technology Platform

NEA
Nuclear Energy Agency

In cooperation with

IAEA
International Atomic Energy Agency
Atoms for Peace and Development

ERMSAR 2026: Main Numbers

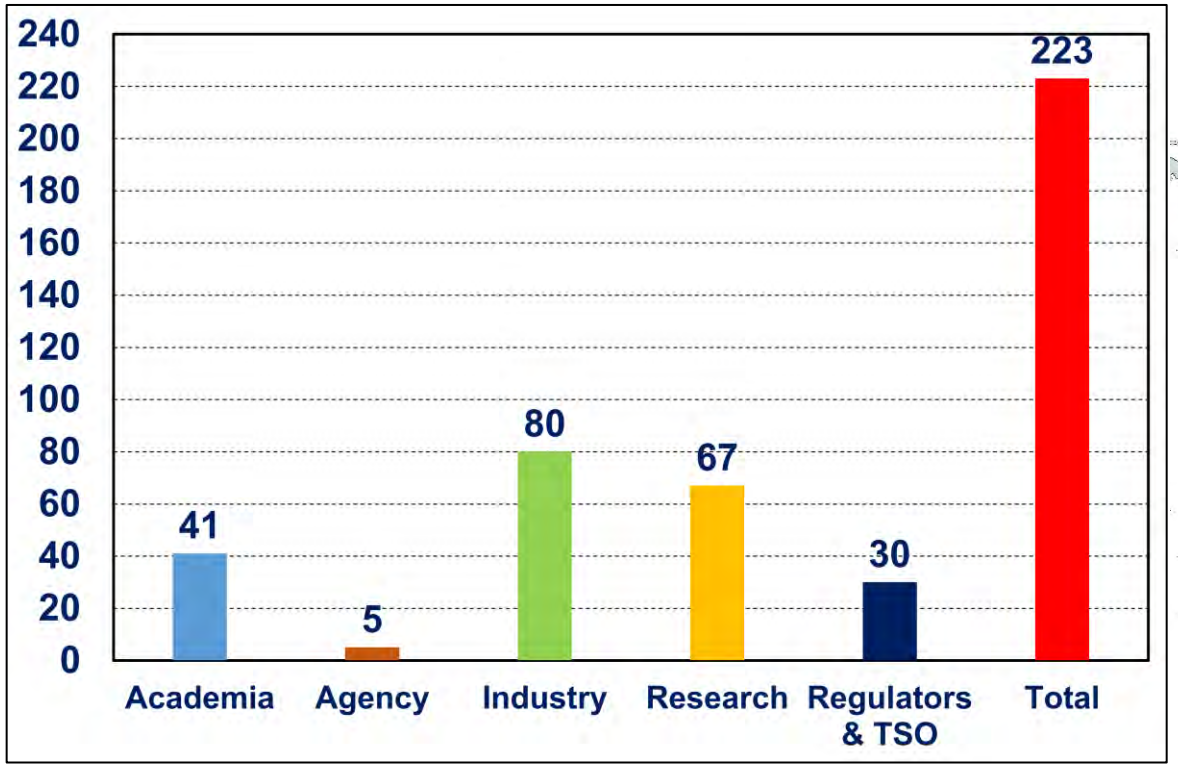

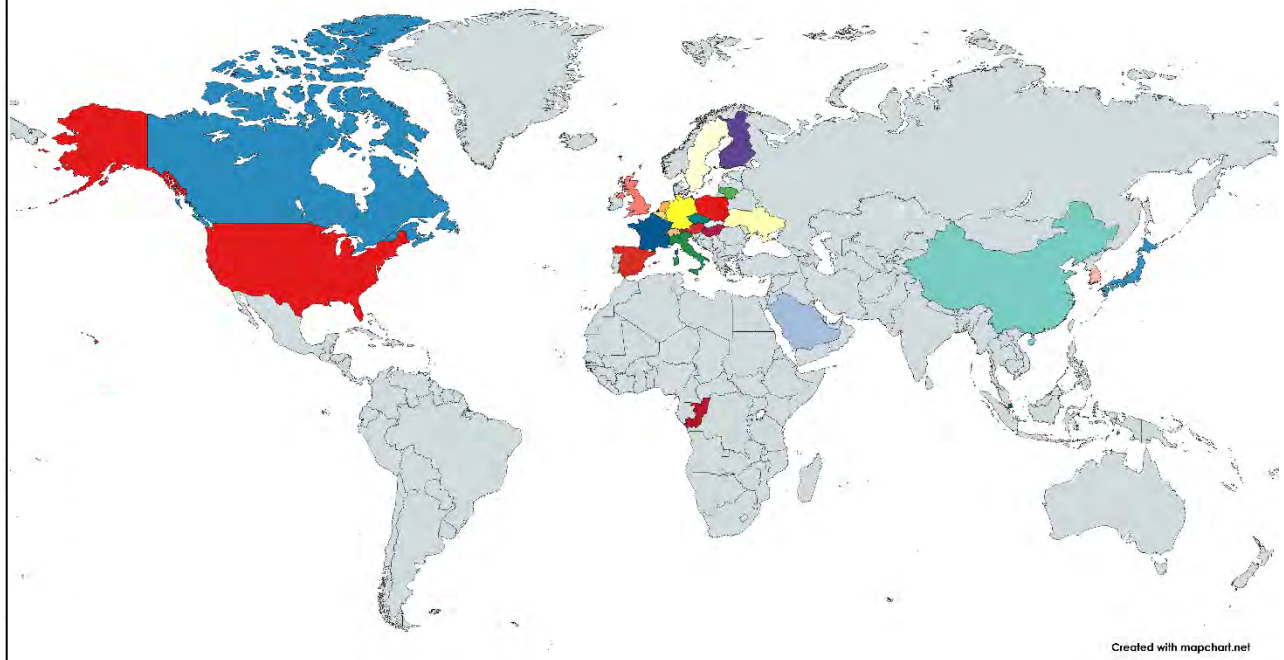

223 participants (35 students) from 27 countries
Contributions from 84 institutions from 26 countries
23% of the participants from no-EU institutions

KIT
Karlsruher Institut für Technologie

SEAKNOT

NUGENIA TA2
Nuclear Generation II&III Alliance

SNETP
Sustainable Nuclear Energy Technology Platform

NEA
Nuclear Energy Agency

In cooperation with

IAEA
International Atomic Energy Agency
Atoms for Peace and Development

Our ERMSAR Serie

Year	Location	Host	Framework	Notes	Dissemination
2005	Aix		SARNET	FP6 internal forum	
2007	Karlsuhe	FZK	SARNET	FP6 internal forum	
2008	Nesseber		SARNET	FP6 internal forum	Special Issue PNE
2010	Bologna	ENEA	SARNET2	FP7 internal forum	
2012	Colonia	GRS	SARNET2		
2013	Avignone	IRSN	SARNET2	open	
2015	Marseille	CEA	NUGENIA		Special Issue ANE
2017	Warsaw	NCBJ	NUGENIA		Special Issue ANE
2019	Praga	UJV Rez	NUGENIA		Special Issue ANE
2022	Karlsuhe	KIT	NUGENIA	OECD/NEA and IAEA as co-organizers	Special Issue ANE + Proc. with DOI (KIT repository)
2024	Stockholm	KTH	SEAKNOT	OECD/NEA and IAEA as co-organizers	Special Issue ANE + Proc. with DOI (KIT repository)
2026	Madrid	CIEMAT	SEAKNOT	OECD/NEA and IAEA as co-organizers	Special Issue ANE + Proc. with DOI (KIT repository)

SEAKNOT

NUGENIA TA2
Nuclear Generation II&III Alliance

SNETP
Sustainable Nuclear Energy Technology Platform

NEA
Nuclear Energy Agency

In cooperation with

IAEA
International Atomic Energy Agency
Atoms for Peace and Development

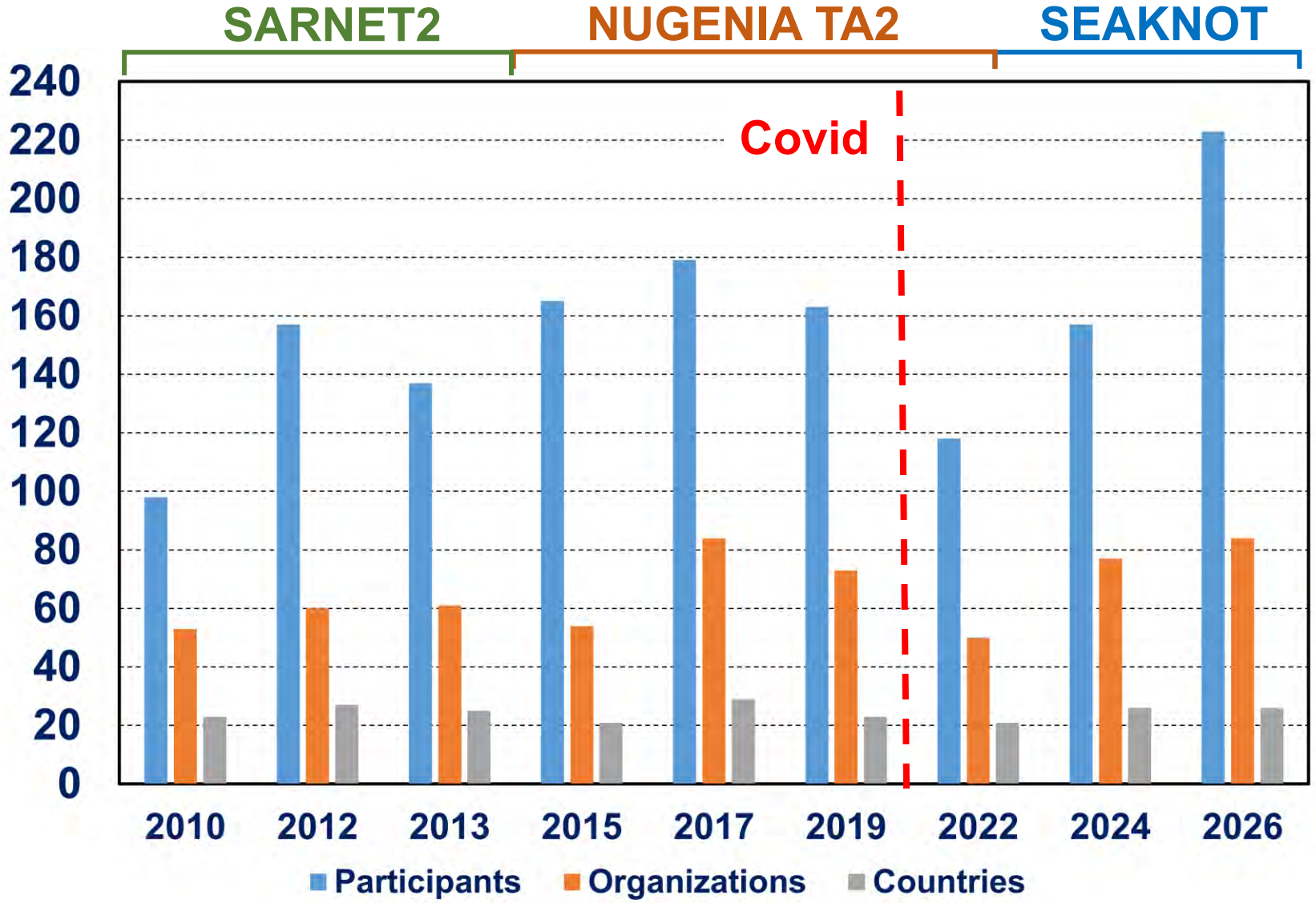

ERMSAR 2026	
Participants	223
Organizations	27
Countries	84

Università di Pisa

KIT
Karlsruher Institut für Technologie

SEAKNOT

NUGENIA TA2
Nuclear Generation II&III Alliance

SNETP
Sustainable Nuclear Energy Technology Platform

NEA
Nuclear Energy Agency

In cooperation with

IAEA
International Atomic Energy Agency
Atoms for Peace and Development

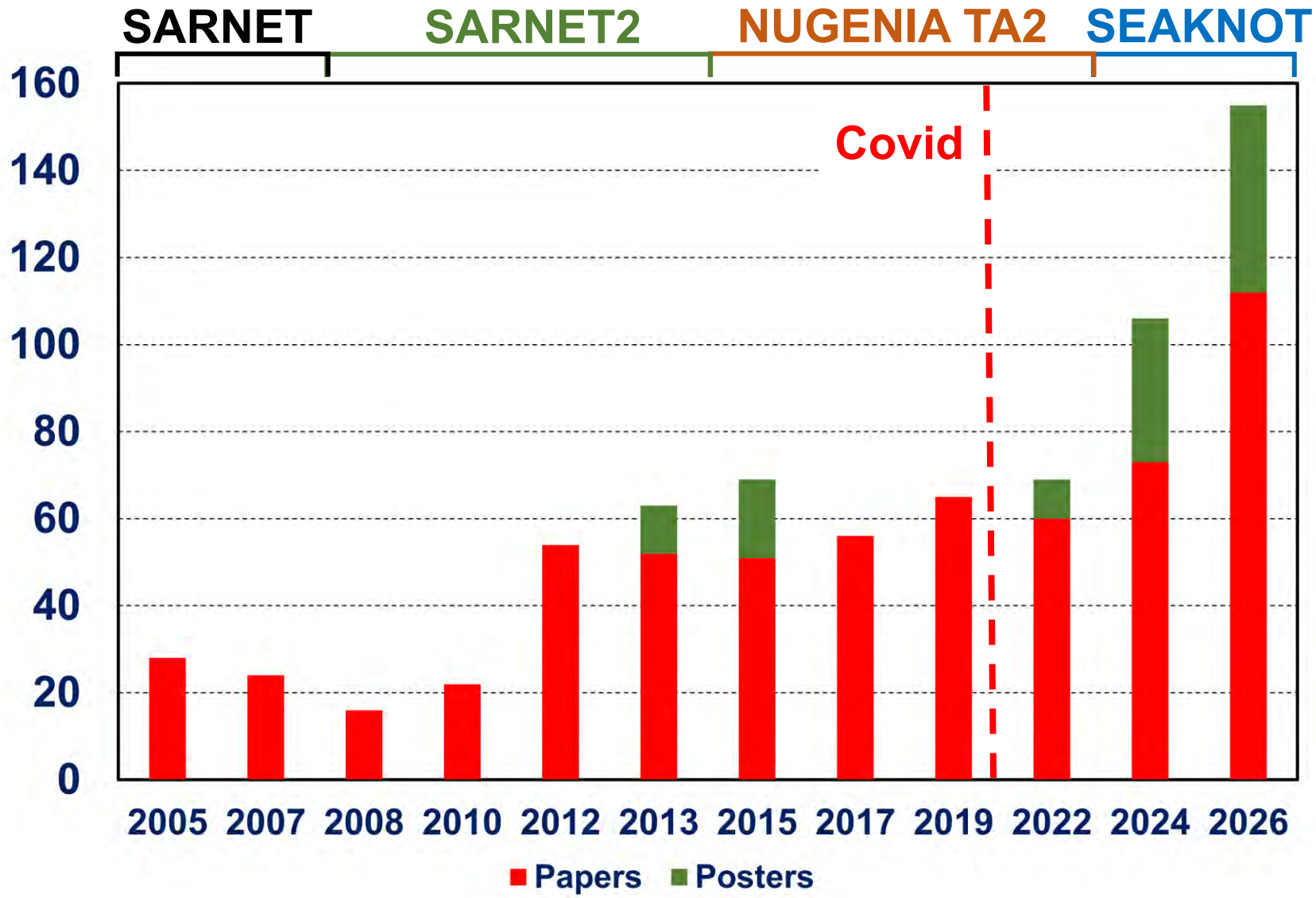

ERMSAR 2026	
Papers	112
Posters	43

Università di Pisa

KIT Karlsruher Institut für Technologie

SEAKNOT

NUGENIA TA2
Nuclear Generation II&III Alliance

SNETP
Sustainable Nuclear Energy Technology Platform

NEA
Nuclear Energy Agency

In cooperation with

IAEA
International Atomic Energy Agency
Atoms for Peace and Development

ERMSAR 2026: Papers per Topic

Topic	Papers	Posters
Analysis, Management, and Consequences of Severe Accidents for Gen I/III reactors	16	12
Containment behaviour incl. H2 explosion risk	15	5
Ex-vessel corium interactions and coolability	17	6
In-vessel corium and debris coolability	15	5
Source term issues	20	4
Severe accidents in Small Modular Reactors (SMRs)	16	4
Severe accidents in Gen IV concepts	7	5
Other applications (fusion reactors, interim SNF storage, Accident Tolerant Fuels (ATFs), etc	6	4
ERMSAR 2026	**112**	**43**

Università di Pisa

KIT
Karlsruher Institut für Technologie

SEAKNOT

NUGENIA TA2
Nuclear Generation II&III Alliance

SNETP
Sustainable Nuclear Energy Technology Platform

NEA
Nuclear Energy Agency

In cooperation with

IAEA
International Atomic Energy Agency
Atoms for Peace and Development

Why joining again ERMSAR?

The unique nuclear conference worldwide fully focused on severe accidents

Continuous focus on the latest progress of international knowledge on severe accidents in NPPs

Università di Pisa

KIT
Karlsruher Institut für Technologie

SEAKNOT

NUGENIA TA2
Nuclear Generation II&III Alliance

SNETP
Sustainable Nuclear Energy Technology Platform

NEA
Nuclear Energy Agency

In cooperation with

IAEA
International Atomic Energy Agency
Atoms for Peace and Development

Why joining again ERMSAR?

"Before I came here I was confused about this subject. Having listened to your lecture I am still confused. But on a higher level." (Enrico Fermi)

- Preserving, Promoting, and Disseminating the knowledge by promoting the exchange among the participants
  - **Cheaper registration fees compared with other nuclear conferences**
  - **25' per lectures!**
  - Round tables on key topics
  - Insightful plenary sessions
  - **Open access proceedings**

Università di Pisa

KIT
Karlsruher Institut für Technologie

In cooperation with

Next Steps from the TC

1. **Book of the Proceedings**
   - edited and published in June as a book in the KITOpen library repository (with DOI number)
   - will be uploaded on Zenodo
   - **Deadline of the final paper submission June 5th!**
2. Preparation of a summary report for CSNI (Dec. 2026)
3. **Selection of the papers for the Virtual Special Issue (VSI) in Annals of Nuclear Energy**

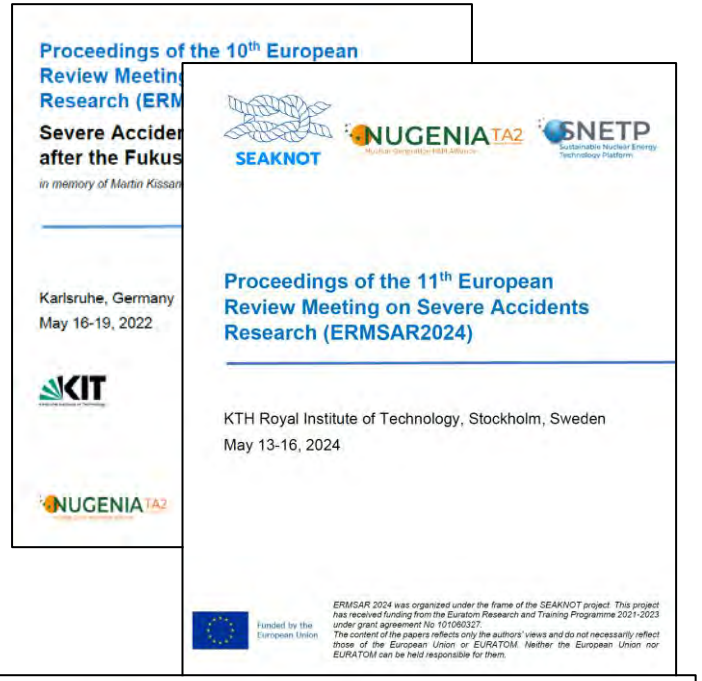

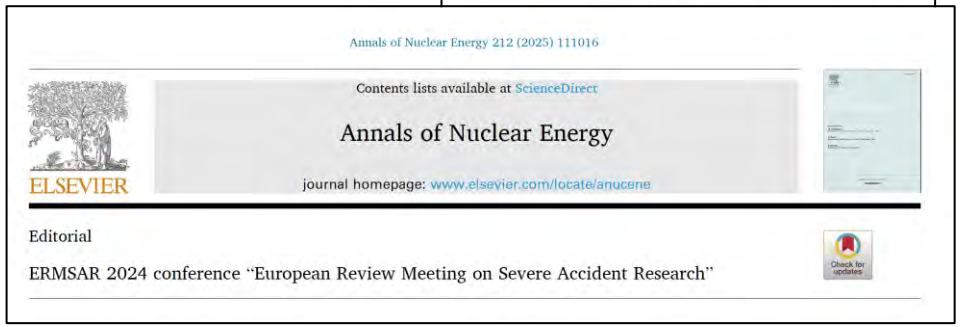

SEAKNOT

NUGENIA TA2
Nuclear Generation II&III Alliance

SNETP
Sustainable Nuclear Energy Technology Platform

NEA
Nuclear Energy Agency

In cooperation with

IAEA
International Atomic Energy Agency
Atoms for Peace and Development

'Knowledge is the antidote to fear.' (cit. Ralph Waldo Emerson)

Looking forward we meet again in 2028

Università di Pisa

KIT
Karlsruher Institut für Technologie

SEAKNOT

NUGENIA TA2
Nuclear Generation II&III Alliance

SNETP
Sustainable Nuclear Energy Technology Platform

NEA
Nuclear Energy Agency

In cooperation with

IAEA
International Atomic Energy Agency
Atoms for Peace and Development

Acknowledgement

Funded by the European Union

The work presented in this communication was done under the frame of the SEAKNOT project. This project has received funding from the Euratom Research and Training Programme 2021-2023 under grant agreement No 101060327. The content of this paper reflects only the authors' view. The European Commission is not responsible for any use that may be made of the information it contains.

Università di Pisa

KIT
Karlsruher Institut für Technologie

SEAKNOT

12th CONFERENCE ON

SEVERE ACCIDENTS RESEARCH

May 18-22, 2026 - Madrid, Spain

ERMSAR 2026

ERMSAR 2026 – TECHNICAL PROGRAMME

May 18–22, 2026 • Universidad Carlos III de Madrid, Puerta de Toledo Campus

MONDAY, 18 MAY 2026

TIME	AUDITORIO	ROOM 1.A.04	ROOM 1.A.01
08:20 – 09:00	REGISTRATION		
09:00 – 09:45	WELCOME & OPENING		
09:45 – 10:45	PLENARY SESSION Singular Careers in Severe Accident Research		
10:45 – 11:10	COFFEE BREAK		
11:10 – 13:00	3.1 Severe Accident Scenarios: SMRs	2.1 In-vessel Corium and Debris Coolability	1.1 SA Scenarios
13:00 – 14:00	LUNCH BREAK		
14:00 – 15:40	6.1 Source Term	5.1 Hydrogen & Containment Behaviour	4.1 Ex-vessel Corium and Debris Coolability
15:40 – 16:00	COFFEE BREAK		
16:00 – 17:05	3.2 Severe Accident Scenarios: SMRs	7.1 Gen IV Systems: Spent Fuel Pools	

TUESDAY, 19 MAY 2026

TIME	AUDITORIO	ROOM 1.A.04	ROOM 1.A.01
09:00 – 10:40	1.2 SA Scenarios: U&S Analyses	2.2 In-vessel Corium and Debris Coolability	3.3 Sevese Accident Scenarios: SMRs
10:40 – 11:10	COFFEE BREAK		
11:10 – 13:00	3.4 Severe Accident Scenarios: SMRs	5.2 Hydrogen & Containment Behaviour	6.2 Source Term
13:00 – 14:00	LUNCH BREAK		
14:00 – 15:30	PLENARY ROUND TABLE Expectations from SA R&D		
15:30 – 16:30	POSTER SESSION & COFFEE BREAK		
16:30 – 17:45	1.3 SA Scenarios: U&S Analyses	2.3 In-vessel Corium and Debris Coolability	4.2 Ex-vessel Corium and Debris Coolability
19:30 – 21:00	FLAMENCO SHOW		

WEDNESDAY, 20 MAY 2026

TIME	AUDITORIO	ROOM 1.A.04	ROOM 1.A.01
09:00 – 10:50	PLENARY SESSION R&D International Frameworks		
10:50 – 11:10	COFFEE BREAK		
11:10 – 13:00	2.4 In-vessel Corium and Debris Coolability	1.4 SA Scenarios	4.3 Ex-vessel Corium and Debris Coolability
13:00 – 14:00	LUNCH BREAK		
14:00 – 15:40	5.3 Hydrogen & Containment Behaviour	6.3 Source Term	4.4 Ex-vessel Corium and Debris Coolability
15:40 – 16:00	COFFEE BREAK		
16:00 – 17:45	1.5 SA Scenarios: Codes & Research Frameworks (Integral Codes)	6.4 Source Term	5.4 Hydrogen & Containment Behaviour
20:00 – 22:30	COCKTAIL (20:00) • CONFERENCE DINNER (20:30)		

THURSDAY, 21 MAY 2026

TIME	AUDITORIO	ROOM 1.A.04	ROOM 1.A.01
09:00 – 10:40	6.5 Source Term	7.1 Gen IV Systems	7.2 Gen IV Systems: Advanced Fuels & Materials
10:40 – 10:55	COFFEE BREAK		
10:55 – 12:20	4.5 Ex-vessel Corium and Debris Coolability	7.3 Gen IV Systems	
12:20 – 12:35	GROUP PHOTO		
12:35 – 13:10	CLOSING PLENARY SESSION		
15:00 – 17:00	NUGENIA TA2 MEETING (RESTRICTED)		

LUNCH BREAK

FRIDAY, 22 MAY 2026

MORNING	TECHNICAL VISITS (OPTIONAL) • Westinghouse Simulators • CIEMAT Facilities

BIG THANKS TO …

- **All of you …** for trusting the LOC. Enjoy ERMSAR & enjoy Madrid!
- **F. Gabrielli (KIT) & S. Paci (UNIPI)** for their wise guidance.
- **TPC** for your expertise & dedication in ERMSAR 2026 preparation.
- **Chairs & Co-chairs** for orchestrating the “synphony” in your sessions.

If things go smoothly, as expected, … The ones to thank for …

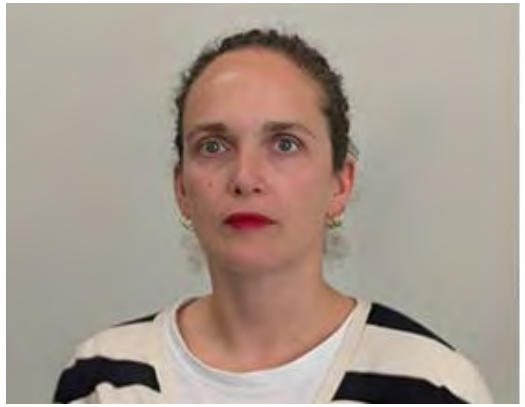

M. Garcia Martin

J. Fontanet Saez

C. Aguado Basabe

+ Alexander Roy
+ Ethan Descamps
Daniel Pozo

+ Amaya Rey

But if things go unexpectedly South …The one to blame for …

SEAKNOT

12th CONFERENCE ON
SEVERE ACCIDENTS RESEARCH
May 18-22, 2026 - Madrid, Spain
ERMSAR 2026

CONCLUDING REMARKS

- Beyond numbers … the “Community” spirit
- Technical rigor embedded in a friendly atmosphere.
- The 25’ recipee – The importance of Exchange!
- The joy of networking! … An essential element!

- **Learning …** from small to … less small.
  from mistakes … to make “wrongs”, rights.
  from bringing other views onboard.

- **SA research TRULY feed NUCLEAR SAFETY!**

- **“International” … fundamental!** Awareness of challenges
  Willing to listen
  Getting ready to “serve”

Thank you for trusting Madrid!!!

12th CONFERENCE ON

SEVERE ACCIDENTS RESEARCH

May 18-22, 2026 - Madrid, Spain

ERMSAR 2026

Thank you for trusting CIEMAT!

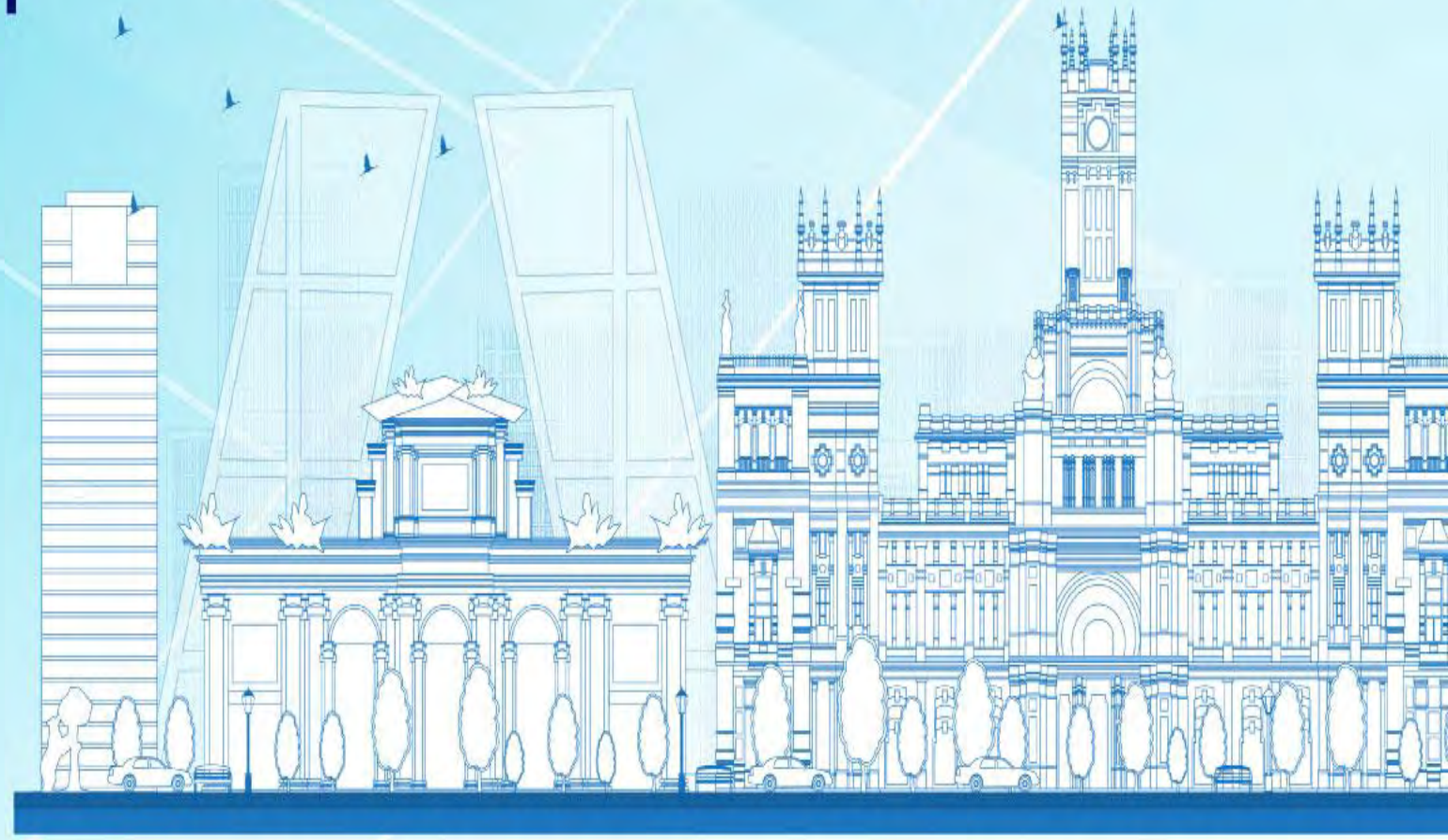

Jožef Stefan
Institute

R4

Reactor
Engineering
Division

ERMSAR 2028

Bled, Slovenia

27 – 30 March 2028

Ivo Kljenak , Janez Kokalj

Bled

Canadianhockey91

Bled – Nuclear meetings

NUCLEAR SOCIETY OF SLOVENIA ANNUAL INTERNATIONAL CONFERENCE

- Nuclear Energy in Central Europe: 1997, 2000.
- Nuclear Energy for New Europe: 2005, 2009, 2013, 2017, 2021, 2025.

SEVERE ACCIDENTS RESEARCH NETWORK (SARNET)

- Annual Review Meeting (1 week): February 2008
- WP3.2 Containment Atmosphere Mixing: March 2008
- Governing Board Meeting: April 2008
- WP7 Containment Meeting: February 2012

Conference hotel

Conference organizer

Nuclear Society of Slovenia

www.nss.si

“Conferences”

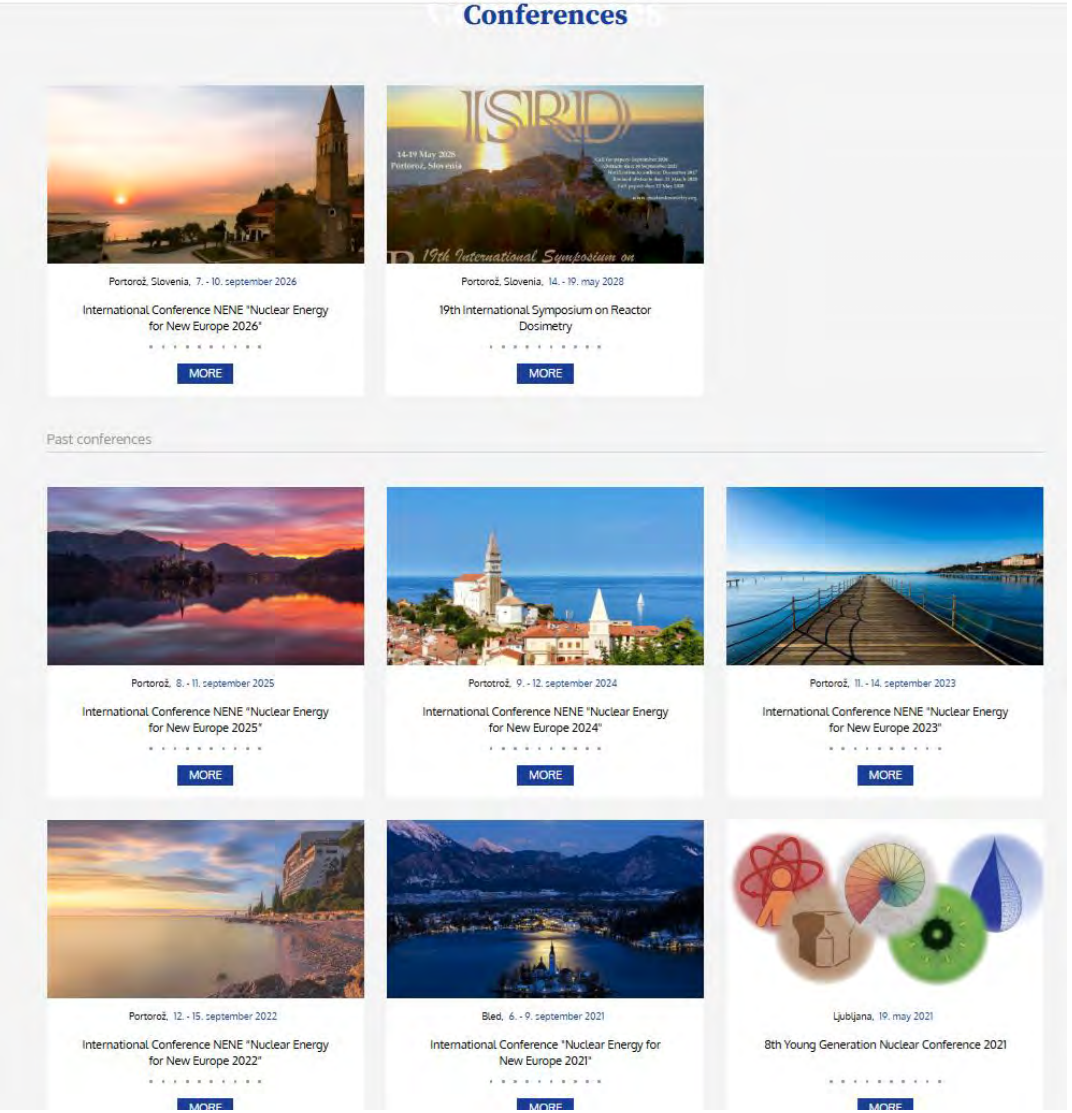

Basic information (1/2)

- **Schedule**
  - Monday 27 March 2028: full day
  - Tuesday 28 March 2028: full day, conference dinner
  - Wednesday 29 March 2028: full day
  - Thursday 30 March 2028: half day

Basic information (2/2)

- **Pleasant beginning of spring** (due to climate change)
  - Walking / running around the lake: ~ 6 km
  - However, too cold for swimming
- **Pre-pre-summer season period**
  - lower room rates
  - more flexibility with room reservations
  - more availability of budget accomodation

Accessibility

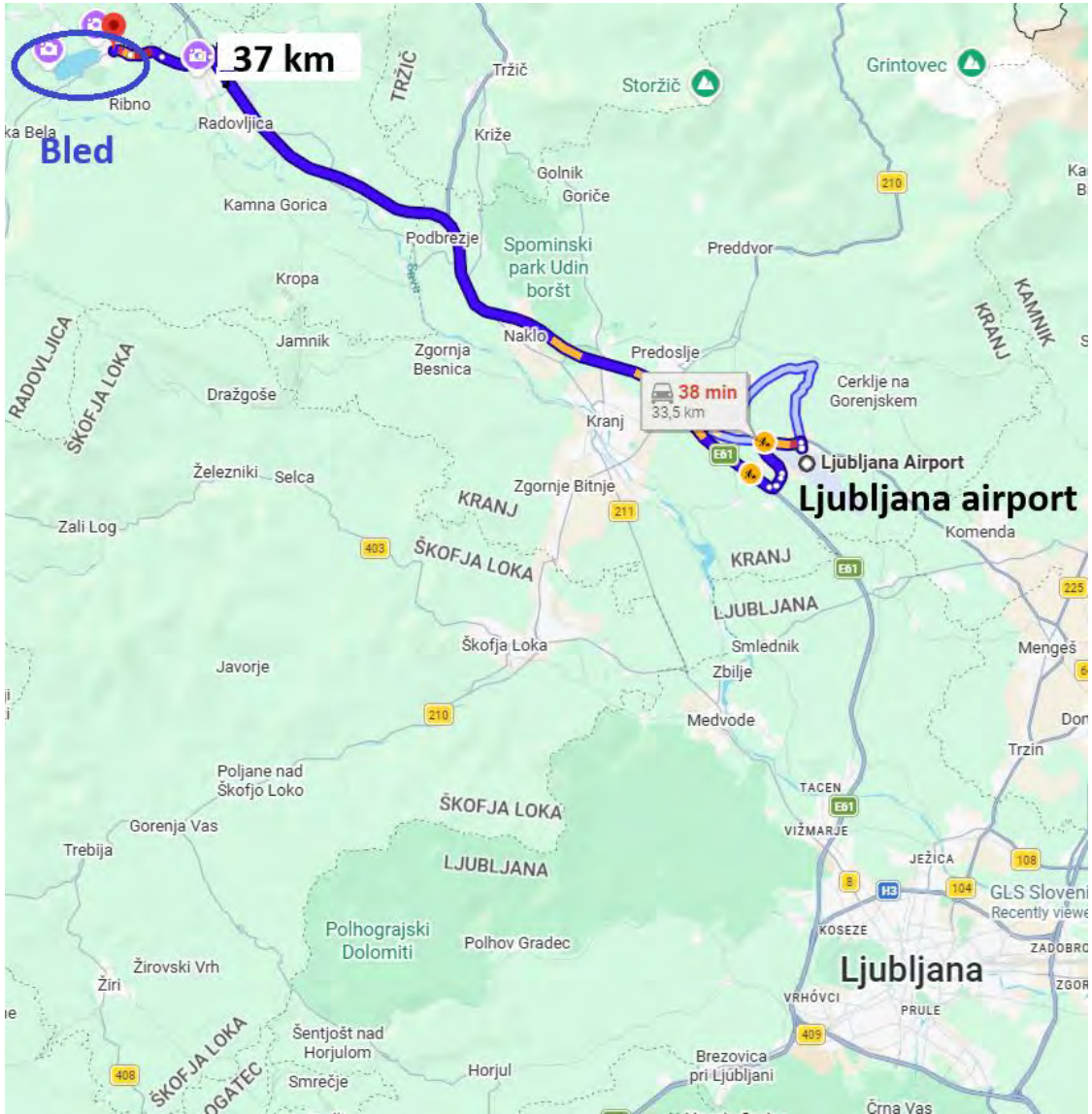

See you two years from now!

Canadianhockey91